JOURNAL OF THE ELECTROCHEMICAL SOCIETY

ELECTROCHEMICAL SCIENCE AND TECHNOLOGY

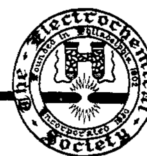

JANUARY 1978

The Anodic Behavior of Lithium in Aqueous Lithium Hydroxide Solutions

John F. Cooper,* Pamela K. Hosmer, and Robert V. Homsy

Lawrence Livermore Laboratory, University of California, Livermore, California 94550

ABSTRACT

The anodic behavior of lithium in 3-5M LiOH was investigated at ambient temperatures under well-defined hydrodynamic conditions using a flow channel. The electrode showed a linear polarization behavior up to a mass-transfer limited anodic current density. The rate of the parallel chemical corrosion of lithium was determined over a range of current densities, flow rates, and concentrations using a gas coulometer to measure the total rate of hydrogen evolution. The corrosion rate approaches zero linearly as the current density approaches the diffusion-limited level. On the basis of electrode resistance and efficiency, the plane-parallel electrode configuration was judged suitable for batteries of the lithium-water type.

It is remarkable that the most reducing of the alkali metals, lithium, has been utilized in practical aqueous electrolyte batteries (1-3). In the lithium-water battery, lithium and water react to form lithium hydroxide and hydrogen gas. The hydrogen is evolved at an iron-screen cathode. The lithium-water cell is the prototype of a family of galvanic cells employing lithium anodes, aqueous electrolytes, and inert cathodes in combination with dissolved oxidizing agents. Analogous cells have been demonstrated using as oxidizing agents: oxygen (4), hydrogen peroxide (5), nitrite (6, 7), sulfite, hypochlorite, bromate, and iodate (7), and aqueous complexes of bromine or iodine (8).

The relative stability of lithium in the presence of water (compared to that of, *e.g.*, sodium) is the consequence of the properties of an adherent surface film which develops under certain conditions of polarization and electrolyte composition. In a manner which is not yet fully understood, the layer impedes the electron transport necessary for the reduction of water (and of other dissolved oxidizing agents), thereby preventing the catastrophic corrosion of the metal. The layer allows for the unusual cell configuration adopted for lithium-water batteries in which the anode and iron-mesh cathode are pressed together without the use of separator. Internal *IR* losses are thereby minimized while the layer prevents internal shorting of the electrodes.

The aqueous electrochemistry of lithium has been studied by Littauer and Tsai using experimental cells with internal anode-cathode contact, and both a transient and permanent passivation phenomena have been reported (3). Bennion and Littauer developed a mathematical model to describe battery discharge voltage, efficiency, and rate (9). The model, based on the assumption that the diffusion of water through the surface layer to the metal substrate is rate-determining, shows qualitative agreement with experiment. Egorov *et al.* have studied the dissolution of rotating-disk lithium electrodes in KOH solutions and have found the self-discharge of lithium to be proportional to the square root of rotation rate, suggesting that lithium dissolution is controlled by the solution-side mass transport (10). To date, no complete set of data has been reported for the rates of lithium dissolution and hydrogen evolution at the Li/LiOH(aq) electrode under well-defined conditions of hydrodynamics and current distribution.

The primary purpose of this study is to determine the effect of solution-side mass transport on the dissolution of lithium and on the reduction of water at the lithium electrode. For this we have used systems of simple geometry and well-defined hydrodynamics. Lithium polarization and coulombic efficiency of lithium dissolution at ambient temperatures have been measured as functions of flow rate, electrolyte concentration, and current density. A secondary purpose of this study is to evaluate the suitability of the closely spaced, plane-parallel electrode configuration, which has not been previously used in batteries of the lithium-water type.

Apparatus and Materials

The influence of electrolyte flow rate on the polarization of the lithium electrode was investigated using the flow channel shown schematically in Fig. 1. Electrodes of lithium and platinum, 9.8 mm square, were placed opposite each other, flush with the horizontal walls of a rectangular duct. The electrode separation was 3.2 mm, while the width of the channel (10.3 mm) just exceeded the electrode width. The channel entrance length, 650 mm, was chosen to assure fully developed laminar flow profiles in the vicinity of the electrodes. Electrolyte was forced through the channel at a steady rate with the use of a single stroke piston pump of 2.3 liter capacity. Pump and channel were constructed of Lucite; interconnecting tubes were of reinforced polyvinyl chloride. No metal or glass parts were allowed to come into contact with the electrolyte.

In the experiments with the flow channel, current was either held constant or programmed as a linear ramp, using a commercial programmable power supply

* Electrochemical Society Active Member.

Key words: lithium, hydroxide, corrosion, dissolution.

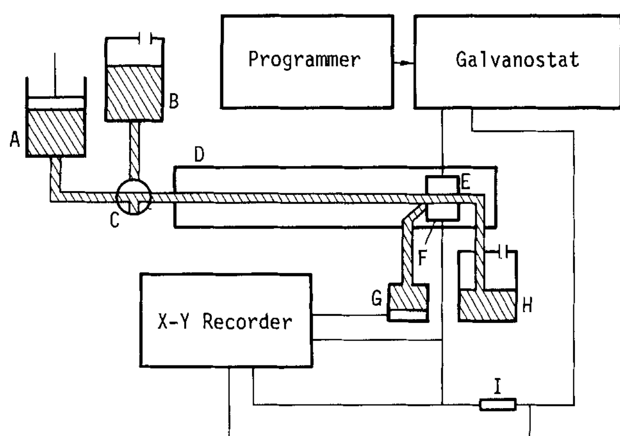

Fig. 1. Flow channel apparatus (schematic). A, piston pump; B, fresh electrolyte reservoir; C, valve; D, flow channel; E, platinum cathode; F, lithium anode; G, Hg/HgO, 1M LiOH reference electrode; H, used electrolyte reservoir; I, current-measuring resistor.

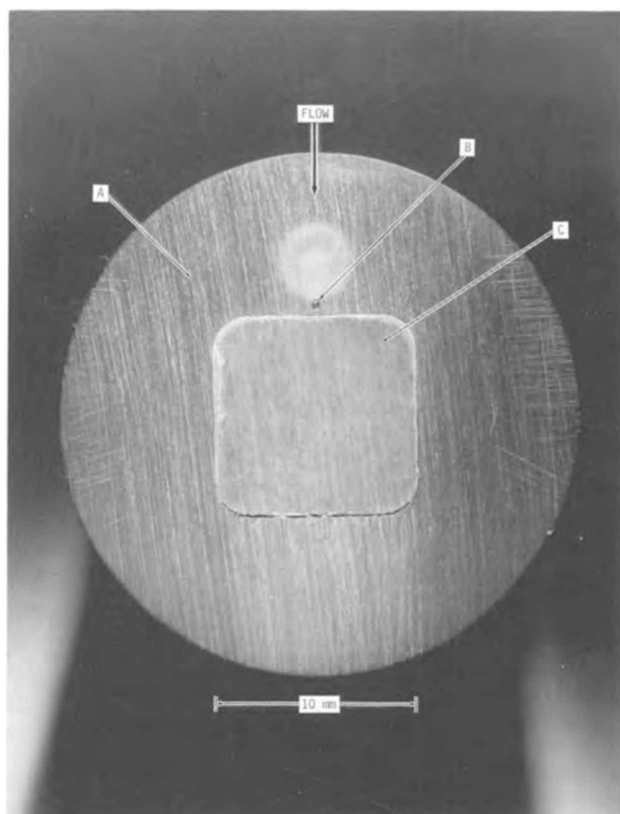

Fig. 2. Removable section of flow channel floor containing lithium electrode. A, epoxy holder; B, capillary opening for reference electrode; C, lithium anode. Arrow indicates direction of electrolyte flow.

(Princeton Applied Research, Princeton, New Jersey, Models 173, 175, and 176). Electrode potential was measured relative to the reference electrode, Hg/HgO, 1M LiOH. Current and potential were recorded on a 1 MΩ X-Y recorder (Mosely, Pasadena, California, Model 2D2).

Shown in Fig. 2 is a removable section of the flow channel floor which contains both the lithium electrode and a reference electrode capillary opening. The 0.3 mm diam hole, drilled into this epoxy plug just 0.5 mm upstream of the lithium electrode, was connected by means of flexible tubing to a vessel containing the reference electrode. The lithium electrodes were prepared by extruding the metal into a rectangular cavity

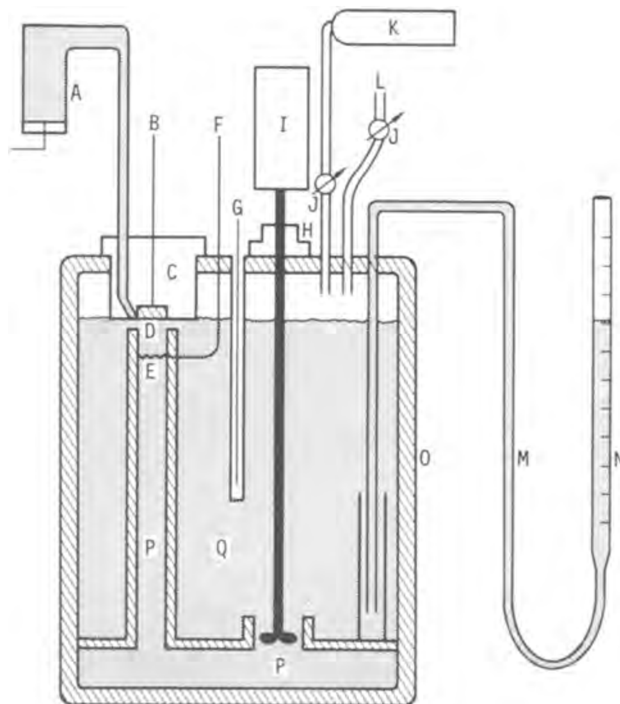

Fig. 3. Hydrogen gas coulometer (schematic). A, reference electrode; B, lithium electrode lead; C, lithium electrode holder; D, lithium anode; E, platinum counterelectrode; F, counterelectrode lead; G, thermometer; H, magnetic feed-through; I, variable speed motor; J, valve; K, hydrogen gas bottle; L, exhaust port; M, flexible tubing; N, pipette; O, Lucite vessel; P, flow channel; Q, electrolyte.

in the plug. The surfaces were then gently ground flat against emery paper wetted with a methanol-water mixture.

Coulombic efficiency was determined from the total rate of evolution of hydrogen from anode and cathode, using the apparatus shown schematically in Fig. 3. The electrodes were contained in a closed Lucite vessel. Electrolyte was internally circulated by means of an impeller and allowed to impinge vertically onto the 100 mm^2 lithium disk imbedded in a removable plug. Electrode potential was measured as in the flow channel. The steady-state hydrogen gas evolution rate was determined from the rate at which the electrolyte was displaced into the pipette. The vertical position of the pipette was continually adjusted to maintain zero head and a constant (atmospheric) pressure within the vessel. Prior to experiments, the electrolyte was purged with hydrogen. In the gas coulometer, no metal or glass parts came in contact with the electrolyte.

Reagent grade lithium hydroxide was used in all experiments (G. Frederick Smith Chemical Company, Columbus, Ohio). The lithium was supplied by D. S. Goldsmith Chemical and Metal, Incorporated (Evanston, Illinois); it was analyzed in our laboratory and found to have the impurities listed in Table I.

Experimental Results

Current-voltage curves.—Typical polarization curves obtained with the flow channel are shown in Fig. 4.

Table I. Analysis of lithium electrodes

Impurities were detected by spectrochemical analysis and are given as ppm by weight.

Element	ppm
Si	35
Ca	14
Cu	14
Ag	10
Be	10
Al	3
Mg	3
Na	<100

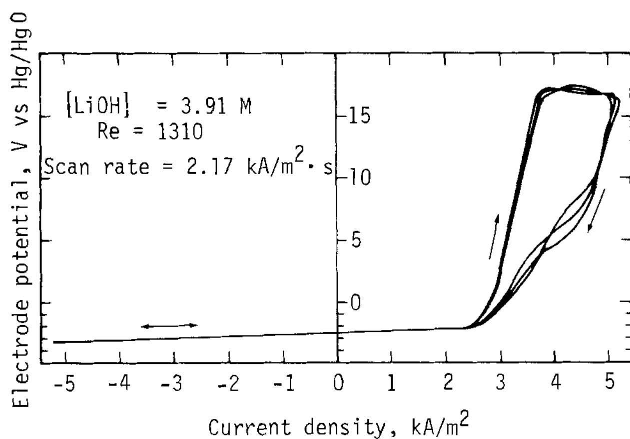

Fig. 4. Voltammetry of the Li/LiOH(aq) electrode. $T = 22°C$; galvanodynamic technique (triangular current wave applied to the electrode); begin anodic scan at zero current.

The applied current was cycled as a triangular waveform. The curves show a low potential, linear polarization behavior, and a high potential region occurring above a critical anodic current density. The resistance in the high potential region generally decreases with time. Consequently, the voltage for scans in the anodic direction may exceed those for the cathodic direction. This phenomenon probably indicates changes in the surface layer's microscopic structure or electronic properties rather than simple changes in electrode area. No gross changes in surface topography or area were observed for the duration of an experiment, the surface remaining smooth and flat.

A different behavior was noted for solutions close to the saturation concentration of 5.3M (see Fig. 5). Once passivated, the electrode would maintain its high resistance state for a time following current reversal. In saturated electrolytes, the passivation was permanent and not destroyed by cathodic polarization and the accompanying vigorous hydrogen evolution. The cathodic behavior was not further investigated.

Electrode resistance (*i.e.*, the differential of polarization with respect to current density in the linear polarization region) is reported in Table II. The range, $(0.5\text{-}1.8) \times 10^{-4}\ \Omega\text{-m}^2$, is comparable to that reported

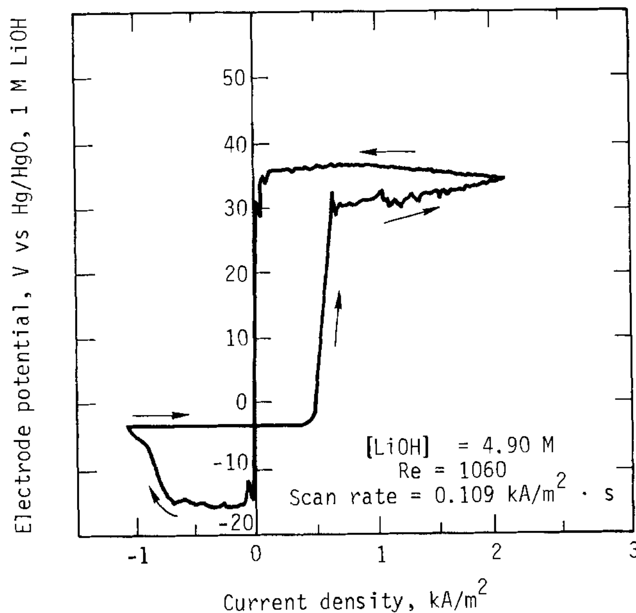

Fig. 5. Voltammetry of the Li/LiOH(aq) electrode near saturation concentrations. $T = 22°C$; galvanodynamic technique; begin anodic scan at zero current. The high voltages reflect high electrode resistances under passive conditions.

Table II. Electrical characteristics of the lithium anode

Experimental conditions: flow channel; $A = 92$ mm^2; $h = 3.16$ mm; $L = 9.8$ mm; channel width = 10.3 mm; $dI/dt = 0.010$ A/sec: $T = 21° \pm 1°C$

Concentration c_b (mole/liter)	Flow rate* $\langle v \rangle$ (m/sec)	Resistance** $\sigma \times 10^5$ (V-m^2/A)	Critical current density i_k (kA/m^2)	Limiting current density $\langle i_l \rangle$ (kA/m^2)
2.94	0.092	5.8	2.88	4.0
	0.135	6.4	3.12	4.5
	0.240	6.3	3.55	5.4
	0.375	6.4	4.06	6.3
	0.568	5.9	4.54	7.2
	0.906 ± 0.03	6.7	4.79	8.5
3.91	0.092	8.9	1.29	1.9
	0.135	7.9	1.47	2.2
	0.240	7.4	1.76	2.7
	0.375	6.4	2.08	3.1
	0.906 ± 0.03	5.5	2.69	4.1
4.25	0.092	12.4	0.71	1.4
	0.369	9.6	1.21	2.2
	0.553	11.0	1.47	2.5
	0.922 ± 0.03	18.3	1.61	3.0
4.44	0.135	9.8	0.35	1.2
	0.240	9.2	0.39	1.5
	0.375	8.5/9.7	0.45/0.95	1.7
	0.568	11.7	1.16	2.0
	0.906 ± 0.03	9.0	1.36	2.3
	1.22 ± 0.03	8.5	1.49	2.5
4.70	0.092	13.0	0.31	0.7
	0.369	10.0	0.31	1.1
	0.553	16.0	0.31	1.3
	0.922 ± 0.03	17.0	0.33	1.5
4.90	0.374	8.9	0.27	0.7
	0.568	11.0	0.30	0.8
	0.906 ± 0.03	12.0	0.28	1.0
	1.22 ± 0.03	16.0	0.30	1.1
5.10	0.568	6.8	0.33	0.4

* Precision ±0.015 m/sec unless otherwise noted.
** Precision ±5%; "resistance" is defined as the differential of electrode polarization with respect to the current density, and applies to the linear polarization region.

by Littauer and Tsai for cells with direct anode-cathode contact (3). In our work, no correction was made for *IR* drop between anode and capillary (an *IR* error of at most $0.2 \times 10^{-4}\ \Omega\text{-m}^2$), or for the enhanced current density near to the anode's leading edge. The values reported in Table II represent the average of three or more separate experiments. In all cases studied, the open-circuit potential, $E(O)$, was within 10 mV of -2.86V *vs.* Hg/HgO, 1M LiOH.

The critical anodic current density.—The critical anodic current density, i_k, which separates low and high potential regions of the current voltage curve, was determined for concentrations from 2.9M to saturation and for flow rates in the laminar flow regime. Typical scans are shown in Fig. 6. The scan rate, 100

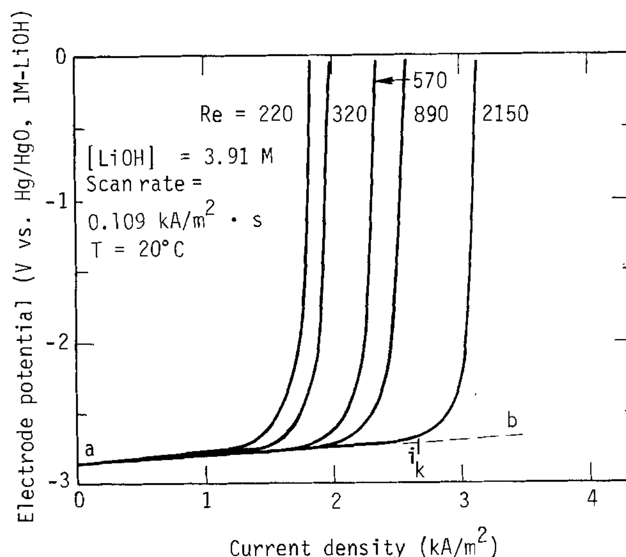

Fig. 6. Typical polarization curves for lithium dissolution at various flow rates. Critical current density, i_k, determined from extrapolation of the linear polarization region, a-b.

A/m²-sec, was sufficiently slow to assure a steady-state concentration profile in the diffusion layer and yielded values of i_k which were indistinguishable from those obtained from discrete galvanostatic experiments. For purposes of analysis, we have adopted a consistent, though somewhat arbitrary definition of i_k: at the critical current density, the electrode polarization $(E(i_k) - (E(O))$ exceeds that extrapolated from the linear region by 30%

$$i_k \equiv \frac{E(i_k) - E(O)}{1.3\, dE/di} \quad [1]$$

Thus, i_k corresponds to a 30% increase in electrode polarization.

In Fig. 7, i_k is plotted against linear flow rate for various electrolyte concentrations. Two distinct groupings are evident in the plot. In one, i_k increases with flow rate and with dilution of the electrolyte. In the other, which is found at low flow rates or high concentrations, i_k does not vary with concentration or flow rate. Near the boundary of the two regions (*e.g.*, at [LiOH] = 4.44M, $<v>$ = 0.38 m/sec) a quasidiscontinuous change between the two kinds of behavior was observed.

Plots of i_k against flow rate to the one-third power are linear (Fig. 8). The relation between i_k and concentration is also approximately linear (Fig. 9). This behavior suggests that the critical current density corresponds to the mass-transfer limited flux of dissolved lithium hydroxide away from the anode surface. Proof of this concept requires knowledge of the rate of dissolution of lithium which, in general, exceeds that expected on the basis of the current applied to the cell because of the ongoing chemical corrosion of lithium.

Coulombic efficiency.—For the cell, Li/LiOH(aq)/Pt, electrode reactions and their rates expressed as currents may be written as follows

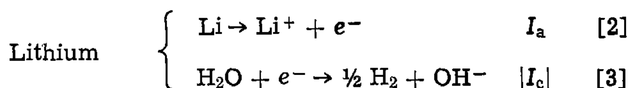

Lithium
$$Li \rightarrow Li^+ + e^- \quad I_a \quad [2]$$
$$H_2O + e^- \rightarrow \tfrac{1}{2} H_2 + OH^- \quad |I_c| \quad [3]$$

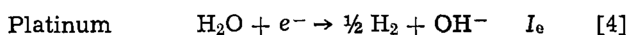

Platinum
$$H_2O + e^- \rightarrow \tfrac{1}{2} H_2 + OH^- \quad I_e \quad [4]$$

(By convention, I_a and I_e are positive quantities; I_c is negative.) Only I_e, the current in the external circuit, is directly measurable. Equating the rates of oxidation and reduction in the cell, we have

$$I_a = I_e + |I_c| \quad [5]$$

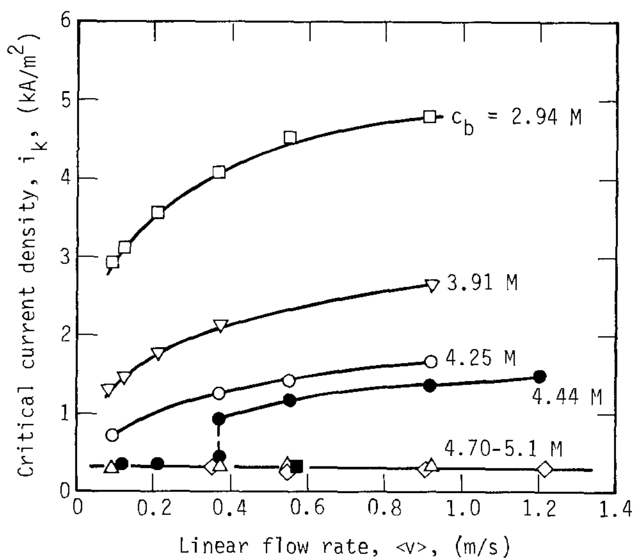

Fig. 7. Dependence of critical current density on flow rate (flow channel).

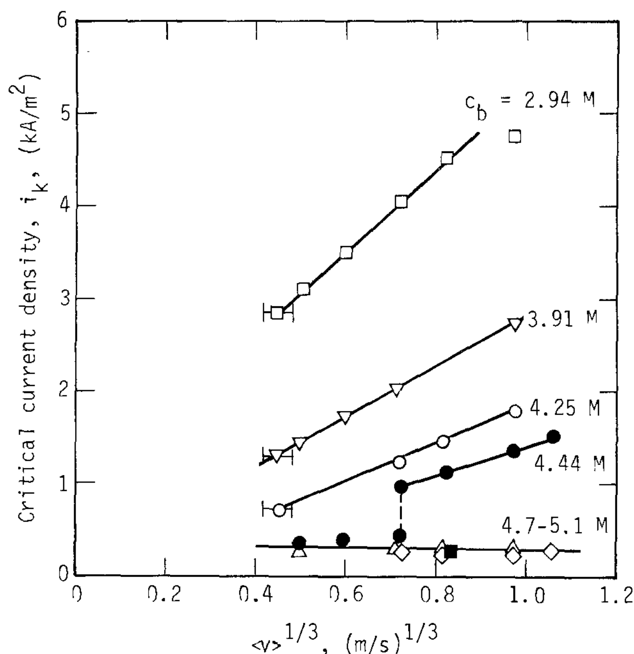

Fig. 8. Critical current density is proportional to $v^{1/3}$

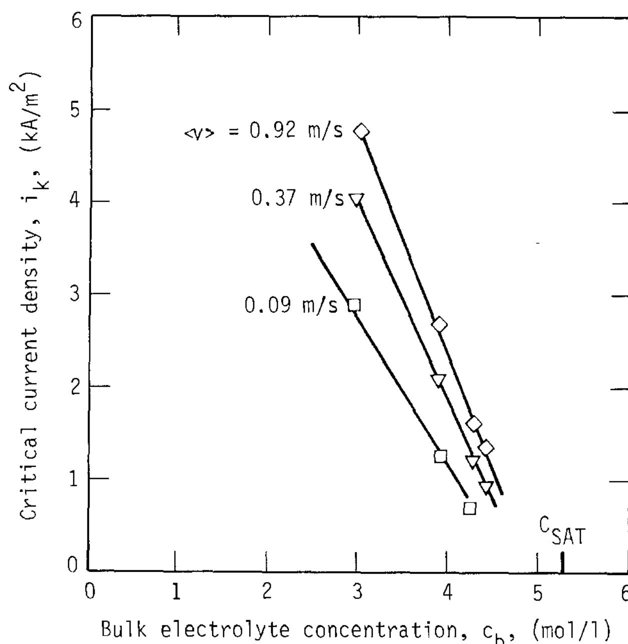

Fig. 9. Critical current density is proportional to electrolyte concentration. Saturation concentration of LiOH at ambient temperature is indicated.

We may define the coulombic efficiency of reaction [2] as

$$\epsilon \equiv I_e/I_a \quad [6]$$

Finally, we may calculate the coulombic efficiency from the total rate of hydrogen gas production using Eq. [5] and [6], Faraday's law, and the ideal gas law. Coulombic efficiency may then be expressed

$$\epsilon = \frac{I_e/2\mathbf{F}}{p_{H_2}\Delta V/RT\,\Delta t} \quad [7]$$

Here, p_{H_2} is the partial pressure of hydrogen gas above the lithium hydroxide solution, ΔV is the volume of gas evolved in the time interval, Δt, and T is the absolute temperature.

Experimentally determined coulombic efficiencies are plotted in Fig. 10 and 11. Typically, efficiency in-

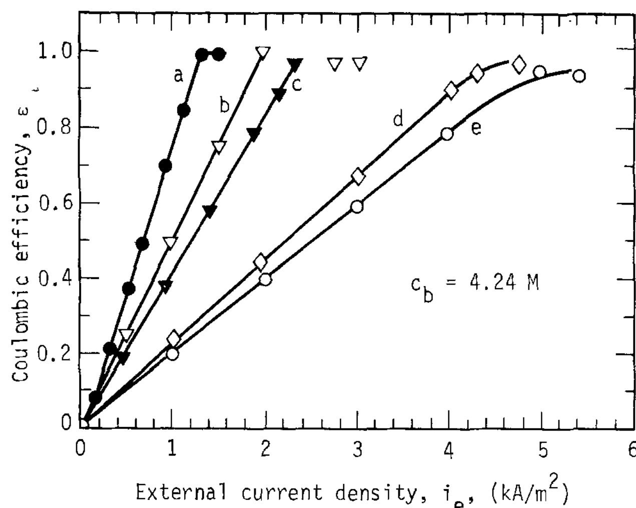

Fig. 10. Coulombic efficiency increases linearly with current density. Critical current density (kA/m²) = (a) 1.3; (b) 2.0; (c) 2.3 ± 0.1; (d) 4.2 ± 0.2; (e) 4.6 ± 0.3. Flow rate increases in the order, a-e.

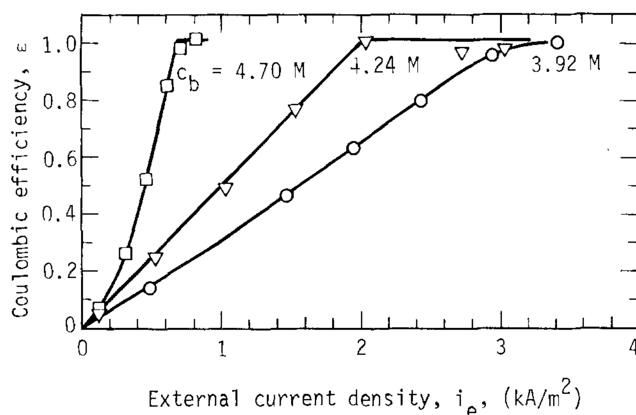

Fig. 11. Dependence of coulombic efficiency on current density at various concentrations.

creases linearly with current and approaches unity near the critical current density. The effects of increased mass transport rate (*i.e.*, increased flow rate) are shown in Fig. 10. As solution flow rate could not be easily measured in this apparatus, the experimentally determined critical current density was treated as an experimental parameter. Efficiencies were determined for flow conditions producing critical current densities up to five times the maximum obtained with the flow channel in the laminar regime.

Discussion of Results

The coulombic efficiencies of less than one indicate that the lithium is partially consumed in a corrosion reaction which contributes no net current to the external circuit. Consequently, the rate of dissolution of lithium will generally exceed the external current. In Fig. 12, the anodic current (I_a) and the corrosion current (I_c) are plotted against the current in the external circuit (I_e). These quantities are expressed as fractions of the external current at which $\epsilon = 1$. In general, the rate of dissolution of lithium is independent of the external current in the region of linear polarization, except at the lowest mass transport rates. Correspondingly, the corrosion current falls to zero as the external current is increased from zero to the critical level. At low flow rates, the corrosion current generally exceeds the critical current. This is most likely the result of enhanced mass transport resulting from the local stirring of the electrolyte during hydrogen gas evolution and from the local heating of the electrolyte caused by the corrosion reaction.

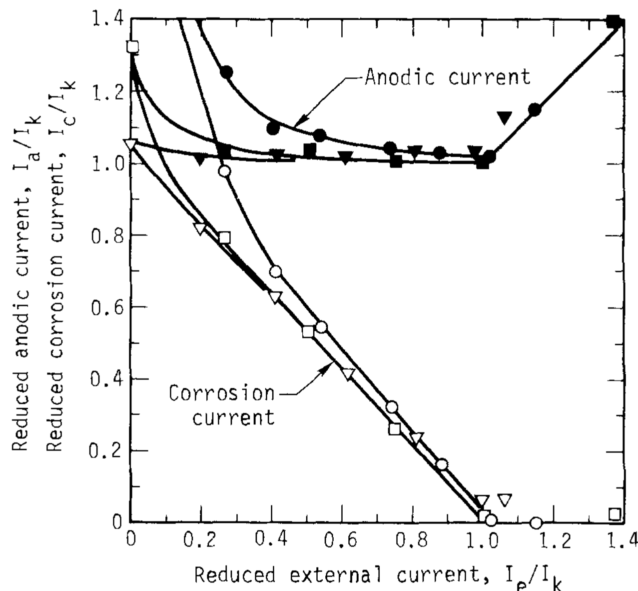

Fig. 12. Dependence of corrosion and anodic currents on external circuit current for various flow rates. $T = 21° \pm 1°C$; i_k (kA/m²) = (○) 1.3; (□) 2.0; (▽) 4.2 ± 0.2. Open symbols, corrosion current; closed symbols, lithium dissolution current.

As mentioned above, the dependences of i_k on flow rate and concentration suggest that the critical current density is determined by the rate of mass transfer of dissolved lithium hydroxide away from the lithium/electrolyte interface. When dissolution is forced to occur above this rate, by the use of an external power supply or by coupling the lithium with a cathode more oxidizing than water, a continuous accumulation of solid lithium hydroxide at the electrode will occur. The surface will be blocked and the electrode resistance will rise dramatically.

We may predict the limiting current density using the mass transfer equation for the region between two flat plates (11)

$$\langle Nu \rangle = 1.848 \, (Re \, Sc \, 2h/L)^{1/3} \qquad [8]$$

Evaluating this equation for the lithium hydroxide solution, the limiting current density may be expressed (see the Appendix)

$$\langle i_1 \rangle = \frac{1.467\mathbf{F}(c_{sat} - c_b) D^{2/3}}{(1 - t_+)(hL)^{1/3}} \langle v \rangle^{1/3} \qquad [9]$$

Here, the limiting concentration at the anode/electrolyte interface, c_{sat}, is taken as the saturation concentration of lithium hydroxide, 5.3M. Diffusion coefficient and transference number are evaluated at bulk electrolyte concentrations c_b. Calculated limiting current densities are shown in Table II.

In Fig. 13, experimental values of i_k are plotted against $\langle i_1 \rangle$ calculated using Eq. [9]. The calculated values exceed the experimental by a factor of about 1.6. The quantitative agreement is quite satisfactory considering the approximations involved in the application of Eq. [9] to our experimental system. In this analysis we have neglected the variation of transport properties within the diffusion boundary layer. (A closer agreement was obtained by evaluating [9] at an average concentration, $(c_b + c_{sat})/2$.) In addition, we have not considered "edge effects" caused by the restriction of electrolyte flow near the corners of the flow channel. While refinements of Eq. [9] are possible, they were judged unnecessary to support the conclusion that the critical current density is the mass-transport limited dissolution rate of solid lithium hydroxide.

Electrode polarizations obtained with the flow channel were as low or lower than those reported for cell

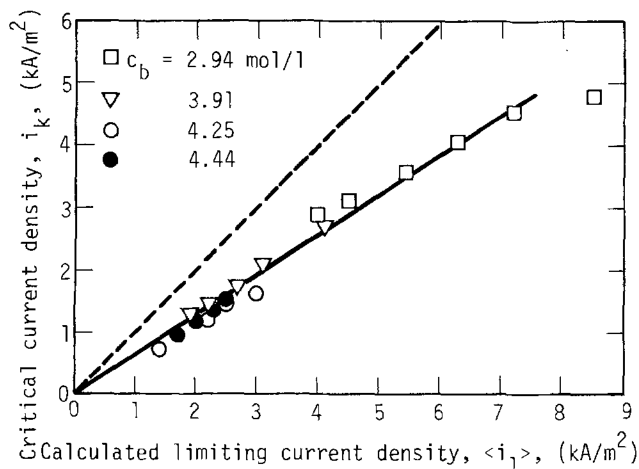

Fig. 13. Comparison of experimental critical current density with calculated diffusion-limited current density. Perfect agreement would be indicated by dashed line.

configurations with direct anode-to-cathode contact (3). More precise measurements of the complex impedance of the lithium electrode are planned. Nevertheless, it is evident that the low electrode polarizations and the high coulombic efficiencies obtained near to the limiting current density make the plane-parallel electrode configuration suitable for batteries of this type.

Conclusions

The lithium electrode sustains two electrochemical reactions: the anodic dissolution of lithium and the reduction of water (Eq. [3]). The rate of anodic dissolution appears to be controlled by the solution-side mass transport of dissolved lithium hydroxide. The rate of water reduction is controlled by the current flowing through the external circuit and is equal to the difference between dissolution and external currents. Consequently, the coulombic efficiency of lithium dissolution increases from 0 to 100% as the external current increases from zero to the mass-transport limited level. When the rate of dissolution is forced to occur above the mass-transport limited level, a net accumulation of solid lithium hydroxide occurs at the anode surface, rapidly blocking the electrode surface and causing the resistance to rise.

With the plane-parallel electrode configuration, the anode shows both a low polarization and a coulombic efficiency approaching 100% within the linear polarization region. Electrode polarizations are at least as low as those obtained with direct anode-cathode contact. The plane-parallel configuration therefore seems suitable for batteries of this type.

The model presented is consistent with experimental data reported here and elsewhere in the literature, but it is not necessarily a unique interpretation. A precise measurement of the electrode's complex impedance would help elucidate the nature of the anode surface film and its role in dissolution kinetics.

Acknowledgment

This work was performed under the auspices of the Energy Research and Development Administration under Contract No. W-7405-Eng-48.

Manuscript submitted Jan. 17, 1977; revised manuscript received Sept. 8, 1977. This was Paper 61 presented at the Las Vegas, Nevada, Meeting of the Society, Oct. 17-22, 1976.

Any discussion of this paper will appear in a Discussion Section to be published in the December 1978 JOURNAL. All discussions for the December 1978 Discussion Section should be submitted by Aug. 1, 1978.

Publication costs of this article were assisted by the University of California.

APPENDIX

To interpret the limiting current densities obtained with the flow channel, we will use the theory of mass transport of a binary electrolyte between two plane-parallel electrodes. The average diffusion-limited current density is given by the equation (11)

$$\langle i_l \rangle = \frac{1.467 n\mathbf{F} D^{2/3} (c_s - c_b)}{(1 - t_+)(hL)^{1/3}} \langle v \rangle^{1/3} \quad \text{[A-1]}$$

Here, D is the diffusion coefficient of the electrolyte, c_s and c_b are surface and bulk concentrations, t_+ is the cation transference number, and h and L are electrode separation and length in the direction of flow. We make the assumption that lithium hydroxide precipitates at the anode surface when the concentration reaches the saturation level, *i.e.*, $c_s = c_{sat}$.

The coefficient of $\langle v \rangle^{1/3}$ in Eq. [A-1]

$$F(c) = \frac{1.467 n\mathbf{F} D^{2/3} (c_{sat} - c_b)}{(1 - t_+)(hL)^{1/3}} \quad \text{[A-2]}$$

is given at the bulk electrolyte concentrations in Table III. Values of D and t_+ have been computed elsewhere (12) and are listed here along with reported values of specific viscosity (13). Specific viscosity and the diffusion coefficient show strong dependences on concentration, and the concentration of the electrolyte varies across the diffusion layer. This fact is neglected in the derivation of Eq. [A-1].

LIST OF SYMBOLS

A	projected anode area, mm²
c_b, c_s, c_{sat}	bulk electrolyte concentration, surface concentration, saturation concentration, mole/liter
D	diffusion coefficient of LiOH(aq), m²/sec
$E(i)$	electrode potential at current density i, V
$\mathbf{F}$	Faraday constant, C/equiv.
$F(c)$	coefficient of $\langle v \rangle^{1/3}$ (Eq. [9], [A-3]) A-sec$^{1/3}$/m$^{7/3}$
h	anode-cathode separation distance, mm
i	current density, A/m²
i_c	corrosion current density, A/m²
i_e	external circuit current divided by anode area, A; Amperes
i_k	critical current density, A/m²
i_l	limiting current density, A/m²
I, I_k, I_e, etc.	current, critical current, external current, etc.; A/m²
L	electrode length in direction of flow, mm
n	number of electrons transferred per unit reaction
N	flux of dissolved LiOH, mole/m²-sec
Nu	Nusselt number, $N\ 2h/D\Delta c$
p_{H_2}	partial pressure of hydrogen gas, Pa
R	gas constant, J/°K-mole
Re	Reynolds number, $2h \langle v \rangle/\nu$
Sc	Schmidt number, ν/D
t	time, sec
T	temperature, °K
t_+	transference number of Li$^+$
v	linear flow velocity, m/sec
ΔV	volume of gas evolved, m³
ϵ	coulombic efficiency
μ, μ_0	viscosity, solvent viscosity; Pa-sec
ν	kinematic viscosity, m²/sec
σ	electrode resistance, Ω-m²
$\langle\ \rangle$	spatial average

Table III. Data used in the calculation of limiting current density

T = 21°C; h = 3.16 mm; L = 9.8 mm; c_s = 5.29 mole/liter

c (mole/liter)	D × 10¹⁰ (m²/sec)	t_+*	F(c) (kA sec$^{1/3}$/m$^{7/3}$)	μ/μ_0
2.94	6.4	0.101	8.7(5)	2.1(6)
3.91	4.9	0.096	4.2(7)	2.8(6)
4.25	4.5	0.096	3.0(4)	3.1(3)
4.44	4.2	0.095	2.3(7)	3.3(0)
4.70	4.0	0.095	1.5(9)	3.5(4)
4.90	3.8	0.094	1.0(2)	3.7(2)
5.10	3.7	0.094	0.4(9)	3.9(1)

* Values estimated at T = 18°C.

REFERENCES

1. H. J. Halberstact, E. L. Littauer, and E. S. Schaller, in Proceedings of the Tenth Intersociety Energy Conversion Engineering Conference, Institute of Electrical and Electronics Engineers, p. 1120, (1975).
2. D. D. Kemp, E. L. Littauer, W. R. Momyer, and J. J. Redlien, in Proceedings of the Eleventh Intersociety Energy Conversion Engineering Conference, American Institute of Chemical Engineers, p. 462, (1976).
3. E. L. Littauer and K. C. Tsai, *This Journal*, **123**, 771 964 (1976); see also articles to be published by these authors.
4. "Proposal for the Development of the Lithium-Water-Air Battery for Automotive Propulsion," Lockheed Missiles and Space Company, Palo Alto, Calif., LMSC-D: 83765 (1975).
5. W. Momyer, U.S. Pat. 4,001,043 (1977).
6. E. L. Littauer and K. C. Tsai, Paper 73 presented at The Electrochemical Society Meeting, Las Vegas, Nevada, Oct. 17-22, 1976.
7. Private communication, Lockheed Missiles and Space Co. (1976).
8. J. F. Cooper and P. K. Hosmer, Work in progress at Lawrence Livermore Laboratory, University of California, Livermore, Calif.
9. D. N. Bennion and E. L. Littauer, *This Journal*, **123**, 1462 (1976).
10. I. M. Egorov *et al.*, "Tezisy Dokladow—Vsesoyoznoe Soveschchanie po Electrokhimii," Vol. 2, pp 456-488 (1974).
11. J. S. Newman, "Electrochemical Systems," pp. 316-319; p. 223, Prentice-Hall, Englewood Cliffs, N.J. (1973).
12. R. V. Homsy, "Aqueous LiOH: Physical, Thermodynamic, and Transport Properties," Lawrence Livermore Laboratory, University of California, UCID-17159 (1976).
13. "International Critical Tables of Numerical Data, Physics, Chemistry, and Technology," Vol. 5, E. W. Washburn, Editor, McGraw-Hill, New York (1926).

Thermodynamic Properties of the Intermetallic Systems Lithium-Antimony and Lithium-Bismuth

W. Weppner and R. A. Huggins*

Department of Materials Science and Engineering, Stanford University, Stanford, California 94305

ABSTRACT

Galvanic cells of the type "LiAl," Al|LiCl-KCl(*e*), l|Li-X (X = Sb, Bi) were employed to determine the Gibbs free energy of formation ($\Delta G_f°$), and the corresponding enthalpies ($\Delta H_f°$), and entropies ($\Delta S_f°$) for the systems Li-Sb and Li-Bi as a function of composition from pure X to the Li-rich side of the Li_3X phases. The Li/X ratio was changed systematically by use of the coulometric titration technique. $\Delta G_f°$ values were obtained by integration of the coulometric titration curve from pure X to the composition of interest. Thermodynamic data have been determined for the trilithium compounds as a function of the stoichiometry. $\Delta S_f°$ and $\Delta H_f°$ were calculated from the temperature dependence of $\Delta G_f°$. Data were obtained over the temperature range 355°-600°C. At 400°C the following values were found for the standard Gibbs free energy of formation: -176.0 kJ mole^{-1} (Li_2Sb), -260.1 kJ mole^{-1} (Li_3Sb), -76.0 kJ mole^{-1} (LiBi), and -215.3 kJ mole^{-1} (Li_3Bi), all ± 0.1 kJ mole^{-1}. The standard enthalpies of formation are: -220.4 kJ mole^{-1} (Li_2Sb), -325.2 kJ mole^{-1} (Li_3Sb), -108.9 kJ mole^{-1} (LiBi), -293.5 kJ mole^{-1} (Li_3Bi), all ± 0.7 kJ mole^{-1}. The standard entropies of formation are: -66 J mole^{-1}K^{-1} (Li_2Sb), -97 J mole^{-1}K^{-1} (Li_3Sb), -49 J mole^{-1}K^{-1} (LiBi), and -116 J mole^{-1}K^{-1} (Li_3Bi), all ± 1 J mole^{-1}K^{-1}. The experimental results were also used to examine the phase diagrams for Li-Sb and Li-Bi. The range of stoichiometry of $Li_{3+\delta}Sb$ is very narrow ($\Delta\delta = 7 \times 10^{-3}$), whereas $Li_{3+\delta}Bi$ exhibits a large deviation from the ideal stoichiometry ($\Delta\delta = 0.22$), predominantly on the lithium-deficit side. Li_2Sb and LiBi have been found to be the only intermediate phases existing beside the trilithium phases in the temperature range investigated.

The voltage E of galvanic cells is a measure of the change of the Gibbs free energy ΔG due to the reaction which occurs upon a virtual current flux, $E = -\Delta G/nq$, where n is the number of elementary charges q necessary for one formula reaction. ΔG is the corresponding Gibbs free energy change at constant pressure and temperature. From the temperature dependence of E the changes of the enthalpy, ΔH, and the entropy, ΔS, may also be determined. Therefore, the application of electrochemical cells has become one of the standard techniques for the measurement of thermodynamic data with high accuracy (1).

Although the coulometric titration technique was introduced more than two decades ago (2) for systematically changing the composition of phases which are employed as electrodes in galvanic cells, this method has been used in only a small number of cases for the determination of thermodynamic properties as a function of the stoichiometry within individual phases [*e.g.*, (3, 4)]. Use of this technique can be especially valuable, however, in the case of phases with narrow composition ranges, as it can be employed to quantitatively produce very small, and reversible, compositional changes. By making measurements as a function of composition on a single sample, one can avoid errors which often occur in the preparation of a series of individual samples with different compositions.

Since the equilibrium potentials of galvanic cells with electrodes consisting of two adjacent phases of a binary system are independent of the over-all composition (according to Gibbs' phase rule) it is also possible to determine phase boundaries from measurements of the galvanic cell voltage as a function of the over-all composition in a binary system. Measurements at various temperatures can be used in this way to construct phase diagrams.

* Electrochemical Society Active Member.
Key words: Gibbs free energy of formation, enthalpy of formation, entropy of formation, coulometric titration, galvanic cell method.

Experiments are reported here involving electrochemical measurements of the thermodynamic properties of the systems Li-Sb and Li-Bi in the temperature range between 355° and 600°C. The composition ranges investigated extended from the pure Va metals to the lithium-rich compositions within the phases "Li_3Sb" and "Li_3Bi" which coexist with lithium. Emphasis was given to the measurement of the thermodynamic properties of the phases "Li_3Sb" and "Li_3Bi" as a function of their stoichiometry.

Some fragmentary calorimetric measurements have been reported in these systems, both at room temperature and at high temperatures (5-11). Electrochemical methods have also been used at temperatures above 500°C over a limited range of concentration of Li in liquid Bi (11, 12).

The phase diagram of the system Li-Bi has been investigated by several authors, primarily by the use of nonelectrochemical techniques (13-16) Little is known, however, about the phases existing between Li and Sb; there have been some speculations about the existence of a phase Li_3Sb_2 (17-19) in addition to "Li_3Sb", and recently the phase Li_2Sb has been reported (20). This latter is a stoichiometry which has not been observed in other alkali metal-Va systems.

Aside from the considerable scientific interest in I-Va compounds related to their partially ionic and partially metallic character, the systems Li-Sb and Li-Bi are of special interest as potential electrodes in lithium batteries (21, 22) and also as photocathodes (23-25). It has been shown in previous investigations (26, 27) that "Li_3Sb" and "Li_3Bi" have quite different chemical diffusion coefficients, in spite of the similarity in the chemical properties of the Va constituents and the fact that they have the same crystal structure (15).

Basic Considerations

Galvanic cells have been used to determine thermodynamic data related to the formation of a number of compounds. One of the standard methods involves the use of polyphase electrodes selected to fix the activities of all the relevant species, according to the Gibbs phase rule (1, 28). The difference in the activity of the electroactive species in the two electrodes is determined from the cell voltage, using a suitable solid or liquid electrolyte. This voltage is then used to calculate the free energy change accompanying the cell reaction. Upon assuming simple stoichiometric relationships, this leads to the Gibbs free energy of formation of one phase from prior data on the others. In general, this technique is only precise if the solubilities of the components in each other and the compositional ranges of intermediate phases can be assumed to be negligible. In many cases, this implicit assumption of narrow intermediate phases has not been sufficiently recognized.

On the other hand, the method typically used to obtain integral molar properties, such as the Gibbs free energy, of terminal binary phases which exist over ranges of composition from experimentally determined partial molar data relating to one component is to use the Gibbs-Duhem relation to calculate the partial molar values of the second component as a function of the composition. This involves an integration, which is typically performed by fitting an empirical algebraic relation between the activity (or activity coefficient) of the first component and its concentration to the experimental data (11, 12, 29, 30). This procedure becomes quite messy when dealing with intermediate phases, in which, as illustrated in this work, the compositional dependence of the chemical potentials can be quite complex.

An alternative and more direct approach to the determination of the Gibbs free energy of formation that may be used if precise data relating the activity of the electroactive species and the composition are available, *e.g.*, from the use of a galvanic cell and the coulometric titration technique, is derived below. This method, which does not involve any assumptions about the partial molar quantity-composition relationship, is especially useful when dealing with intermediate phases with wide ranges of concentration. It does not require the commonly used assumption when dealing with one intermediate phase that the other phases are line compounds.

The following general galvanic cell is considered

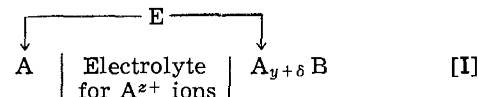

$$A \;|\; \text{Electrolyte for } A^{z+} \text{ ions} \;|\; A_{y+\delta}B \qquad [I]$$

The left-hand side is assumed to be both a reservoir and a reference system for the component A, but may, of course, have a fixed activity different from unity. In such a case, this difference must be taken into account by an additional voltage term. The general formula $A_{y+\delta}B$ is used to denote a binary sample whose composition can be varied all the way from pure B to that which is in equilibrium with the activity $a_A = 1$ by charge transport through the galvanic cell.

Upon virtually passing $d\delta$ A^{z+} ions through the electrolyte (from the left-hand to the right-hand side), the stoichiometry of the electrode phase on the right-hand side is altered. The cell reaction is

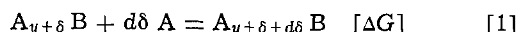

$$A_{y+\delta}B + d\delta\, A = A_{y+\delta+d\delta}B \quad [\Delta G] \qquad [1]$$

In general, adding $d\delta$ A atoms to the sample can cause either a change in the stoichiometry of the existing phase or the nucleation and partial growth of a new phase. At constant pressure and temperature, the Gibbs free energy change ΔG accompanying reaction [1] corresponds to the electrical energy $z\, d\delta\, q\, E$ which is necessary to transport $d\delta$ A^{z+} ions from one side of the electrolyte to the other

$$\Delta G = -z\, d\delta\, q\, E \qquad [2]$$

where E is the emf of the galvanic cell [I].

For a more informative thermodynamic interpretation of the cell voltage, reaction [1] may be separated into a pair of successive partial reactions for the decomposition of $A_{y+\delta}B$, and the formation of $A_{y+\delta+d\delta}B$

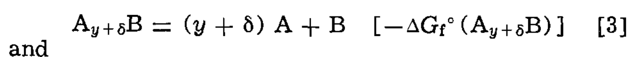

$$A_{y+\delta}B = (y+\delta)\,A + B \quad [-\Delta G_f^\circ(A_{y+\delta}B)] \qquad [3]$$

and

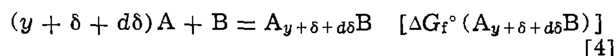

$$(y+\delta+d\delta)A + B = A_{y+\delta+d\delta}B \quad [\Delta G_f^\circ(A_{y+\delta+d\delta}B)] \qquad [4]$$

Then, because of the additivity of the Gibbs free energies

$$\Delta G = \Delta G_f^\circ(A_{y+\delta+d\delta}B) - \Delta G_f^\circ(A_{y+\delta}B) \qquad [5]$$

and by combining Eq. [5] with Eq. [2], we have

$$E = -\frac{1}{zq}\,\frac{d[\Delta G_f^\circ(A_{y+\delta}B)]}{d\delta} \qquad [6]$$

The integration of this equation yields

$$\Delta G_f^\circ(A_{y+\delta}B) = -zq\int_{\delta_0}^{\delta} E\, d\delta + \Delta G_f^\circ(A_{y+\delta_0}B) \qquad [7]$$

The resultant Gibbs free energy of formation may, therefore, be determined for any stoichiometry $(y+\delta)$ from the area under the coulometric titration curve. Under the special circumstance of line phases being present, and negligible solubility of A in B, the integral may be replaced by the sum of the two-phase voltages times the respective changes of the stoichiometry.

If the integration is started when only the pure component B is present $(y+\delta=0)$, the integration constant $\Delta G_f^\circ(A_{y+\delta_0}B)$ is zero. By variation of the upper integration limit, ΔG_f° may be obtained as a function of the composition within any given phase, regardless of the composition ranges of the other phases present.

From the temperature and compositional dependences of the voltage of the galvanic cell [I] the entropy $\Delta S_f°$ and enthalpy $\Delta H_f°$ of formation of the composition $A_{y+\delta}B$ can be obtained with the help of the following equations

$$\Delta S_f°(A_{y+\delta}B) = -\frac{\partial \Delta G_f°(A_{y+\delta}B)}{\partial T} = zq \int_0^\delta \frac{\partial}{\partial T} E(\delta, T)\, d\delta \quad [8]$$

$$\Delta H_f°(A_{y+\delta}B) = \Delta G_f°(A_{y+\delta}B) + T\,\Delta S_f°(A_{y+\delta}B) = -zq \left\{ \int_0^\delta E\, d\delta - T \int_0^\delta \frac{\partial}{\partial T} E(\delta, T)\, d\delta \right\} \quad [9]$$

While the activity a_A of the species A is directly obtained as a function of the composition from the cell voltage E according to

$$\ln a_A(\delta) = -\frac{zq\, E(\delta)}{kT} \quad [10]$$

the activity of the second component, a_B, may be readily calculated as a function of composition from the data on the Gibbs free energy of formation of $A_{y+\delta}B$, rather than integrating the Gibbs-Duhem equation. Since $\Delta G_f°(A_{y+\delta}B)$ is given by the sum of $kT\,(y+\delta)\ln a_A$ and $kT \ln a_B$, we have from Eq. [10]

$$\ln a_B(\delta) = [(y+\delta)\, zq\, E(\delta) + \Delta G_f°(A_{y+\delta}B)]/kT \quad [11]$$

$$= \frac{zq}{kT}\left[(y+\delta)E(\delta) - \int_0^\delta E\, d\delta \right] \quad [12]$$

$$= \frac{zq}{kT}\left[(y+\delta)E(\delta) - \int_{\delta_0}^\delta E\, d\delta + \Delta G_f°(A_{y+\delta_0}B) \right] \quad [13]$$

Experimental Considerations

Pure antimony (> 99.99%), bismuth (> 99.999%), and lithium (> 99.9%) were used as the starting materials for the binary systems to be investigated. The antimony samples were machined into the form of dense polycrystalline pellets of about 1 mm thickness, with initial surface areas of 1-2 cm^2 ,whereas the bismuth was placed in a small molybdenum bucket, because it is molten (at low lithium contents) at the experimental temperatures. In this case, the surface area was 0.6 cm^2.

Both electrochemical titration and potential difference measurements were performed by use of a galvanic cell which can be represented as

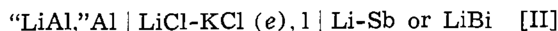

"LiAl,"Al | LiCl-KCl (e), l | Li-Sb or LiBi [II]

The electrolyte was a spectrographically pure LiCl-KCl solution in the eutectic ratio, purchased from Anderson Physics Laboratories, Urbana, Illinois, which was carefully dried and pre-electrolyzed to assure the removal of any relevant impurities. By use of this molten salt excellent contact is provided between the electrolyte and the sample. The operating temperature was between the melting point of the salt at 352°C and ~600°C. Separate reference and (large) counterelectrodes were used, both being two-phase mixtures of Al and "LiAl." They were prepared previously by electrochemically titrating lithium into a high purity (> 99.9999%) aluminum wire, which was wound into a spiral, using molten lithium as the anode. The process of electrochemically introducing the lithium into the "LiAl" phase, which occurs by a highly selective solid-state diffusion process, serves to increase the effective purity of the lithium in the later experimental steps, in which this phase serves as the source of lithium. This same type of lithium purification mechanism also occurs again subsequently when the lithium is selectively diffused into the Li-Sb and Li-Bi phases. Thus, any metallic impurities brought in with the original lithium are of no consequence in the experimental results. For the same reasons, minor amounts of H_2O, N_2, O_2, or other gases present in the glove box are not important.

For the calculation of thermodynamic data the measured cell voltages were corrected for the voltage between the "LiAl," Al electrode, and pure lithium, which is about 300 mV at 400°C (26, 27, 31). The two-phase electrode is advantageous for this purpose, as it is solid, and has a lower lithium activity, thus avoiding problems with the thermodynamic stability of the LiCl-KCl(e) melt (32) in equilibrium with pure lithium, and considerably reducing the electronic leakage of the electrolyte (33). A similar experimental arrangement was used in a recently reported study of the Li-Si system (29).

The electronic leads for the galvanic cell were made from molybdenum wire, which proved to have excellent compatibility at all lithium activities. Alumina crucibles were used as containers for the molten salt, which was heated in a resistance furnace inside a recycling helium dry box. Temperatures were measured by means of Chromel-Alumel thermocouples, which were submerged in the melt inside closed stainless steel tubes. Additional checking thermocouples were also present immediately outside the crucible. Potentials, currents, and charge values were controlled and measured by use of a PAR Model 173 potentiostat/galvanostat and Model 179 digital coulometer.

The coulometric titration was performed by applying constant currents through the cell, typically 10-100 mA/cm^2 in the two-phase regions, and a factor of 10^{-2}-10^{-1} lower in the single phase regions. These relatively high current densities were possible because of the large values of the chemical diffusion coefficients in these systems (26, 27).

The thermodynamic data were calculated from values of the cell voltage that were observed to remain constant within ±1 mV over periods of several hours. In all cases, titrations were carried out in both the forward and backward directions. In addition to the time independence of the cell voltage, the presence of equilibrium was indicated by the attainment of the same voltage value (±1 mV) at any given composition after both adding and deleting lithium from the sample.

Because of the use of the "LiAl," Al electrode, a small voltage drift with time was only found at high lithium activities in the sample, corresponding to voltages less than about 150 mV *vs.* lithium. The reason for this is probably either an instability of LiCl-KCl(e) melts at high lithium activities (32), increased electronic partial conductivity of the electrolyte (33), which results in internal ion transport that is not measured by the current meter in the external circuit and a slight loss of lithium from the sample into the melt with corresponding evaporation of potassium (32), or a combination of these effects. At lower lithium activities the influence of these factors may be neglected.

Only a small number of other errors may limit the use of this general technique, and their presence would be easily detectable. One possibility might be solubility of lithium in the melt, the crucible, or the molybdenum leads, which could add to the current used to change the stoichiometry of the sample. Blind experiments without the sample in place were carried out, and the charge transport involved in going from essentially no initial lithium activity in the molybdenum electrode, to within 100 mV of pure Li (−200 mV *vs.* "LiAl," Al) was found to be negligible compared to the amount of lithium that was electrochemically titrated into the antimony and bismuth samples.

Results

In Fig. 1 and 2, the steady-state open-circuit cell voltages are plotted as a function of the composition, which was electrochemically changed *in situ* from pure Sb (or Bi) to a Li/Va metal ratio of more than 3, corresponding to the composition within the trilithium

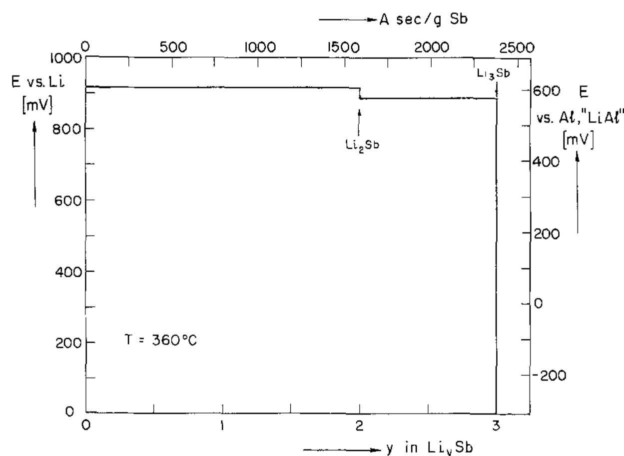

Fig. 1. The steady-state voltage of the galvanic cell with reference to pure lithium as a function of the amount of lithium electrochemically titrated into antimony (coulometric titration curve) at 360°C. The first horizontal part indicates the coexistence of Sb with Li_2Sb, the second one the two-phase region of Li_2Sb and "Li_3Sb."

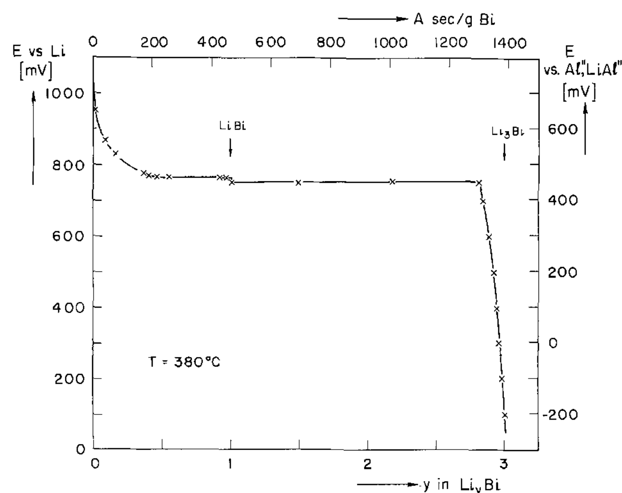

Fig. 2. The coulometric titration curve for the system Li-Bi at 380°C. A large range of solubility of lithium in bismuth is followed by the two-phase region of Bi in equilibrium with LiBi. The second plateau indicates the coexistence of LiBi with "Li_3Bi." The trilithium phase shows a large range of existence.

compounds in equilibrium with lithium. Though both systems are closely related chemically, the curves show significant differences. Antimony is solid in the experimental temperature range, whereas pure bismuth is a liquid. While the solubility of lithium in solid antimony is negligibly small, liquid bismuth dissolves approximately 30 atomic percent (a/o) lithium at 380°C. The extent of solubility and the activity of lithium in liquid bismuth may be determined from the coulometric titration curves, as shown in Fig. 3 for various temperatures. In that figure the voltage of the terminal bismuth-rich liquid solution *vs.* pure lithium is plotted as a function of composition, which was changed by current flux through the galvanic cell. The horizontal straight lines correspond to the coexistence of Bi (+ dissolved Li) with the adjacent binary phase.

The main voltage drops in Fig. 1 and 2, *i.e.,* changes of the activities of the components with composition, appear over the existence regions of the phases "Li_3Sb" and "Li_3Bi." As can be seen from Fig. 4 and 5, which show the coulometric titration curves in these phases in detail, the range of stability of "Li_3Sb" is very small ($\Delta\delta \approx 7 \times 10^{-3}$), whereas "$Li_3Bi$" exists over a much wider range of stoichiometry ($\Delta\delta \approx 0.22$). The composition values for the narrow "Li_3Sb" phase in Fig. 4 were shifted by a factor of about 10^{-4} in order to make

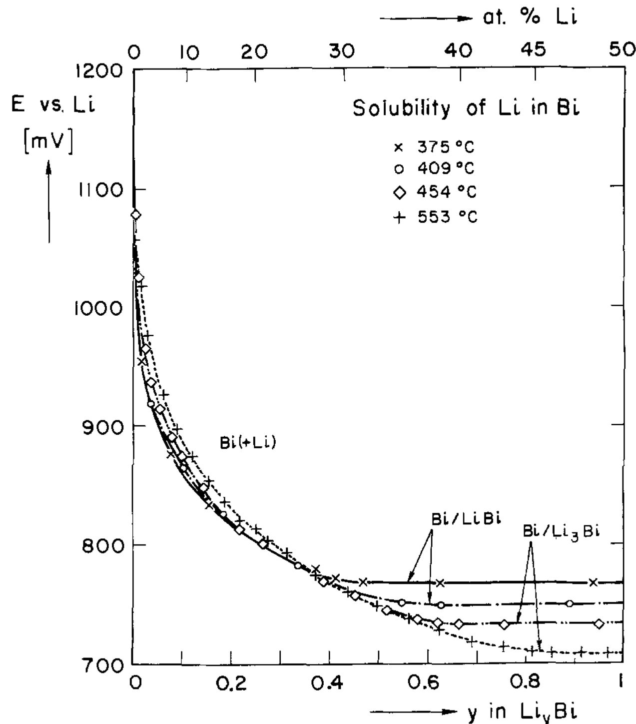

Fig. 3. The solubility of lithium in bismuth at different temperatures. The steady-state galvanic cell voltage *vs.* lithium is plotted as a function of the amount of lithium electrochemically titrated into liquid bismuth.

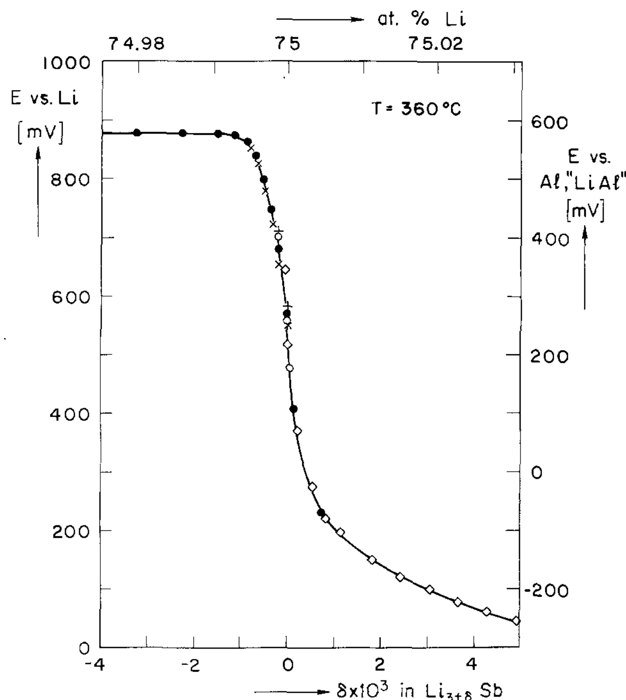

Fig. 4. The coulometric titration curve over the composition range of the single phase "Li_3Sb" at 360°C. The horizontal portion on the left side indicates coexistence with Li_2Sb. Five different symbols indicate data points taken from different experimental sequences, *i.e.,* Li pumped in or out. Their consistency indicates the extremely high resolution of this technique.

the inflection point occur at the ideal 3:1 stoichiometric composition, as that is what is expected from theoretical considerations (34). The results of several forward and backward titration runs are indicated by the use of different symbols. The precision of this technique is shown by their coincidence.

In both cases, only one intermediate phase of lower lithium content has been found. At 360°C neither LiSb

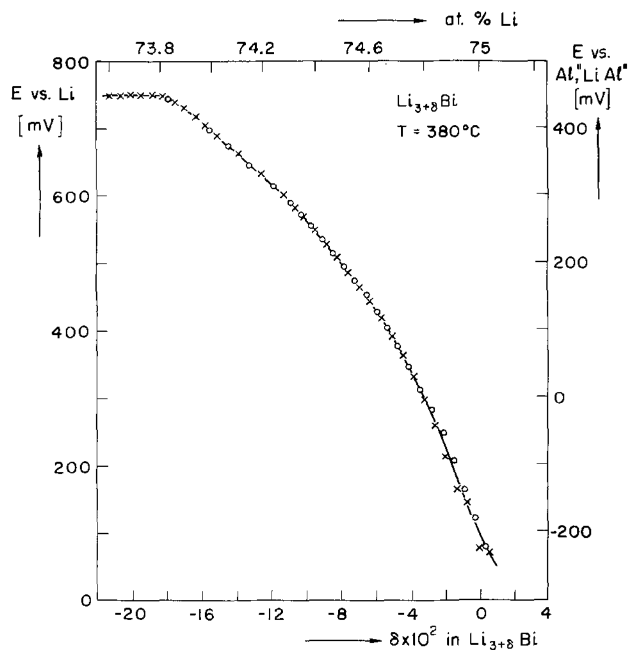

Fig. 5. The coulometric titration curve of the single phase "Li_3Bi" at 380°C. The different symbols indicate the results of two different titration experiments.

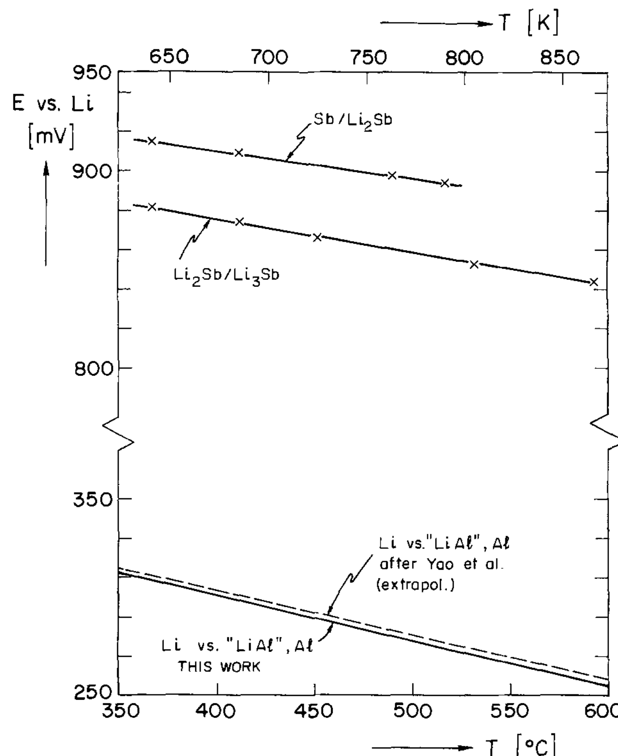

Fig. 6. The steady-state plateau voltages of the galvanic cell for the two-phase mixtures of the system Li-Sb as a function of the temperature with reference to pure lithium. The voltage of pure lithium vs. the actually applied "LiAl," Al electrode is also shown. For comparison, extrapolated literature data (31) are plotted.

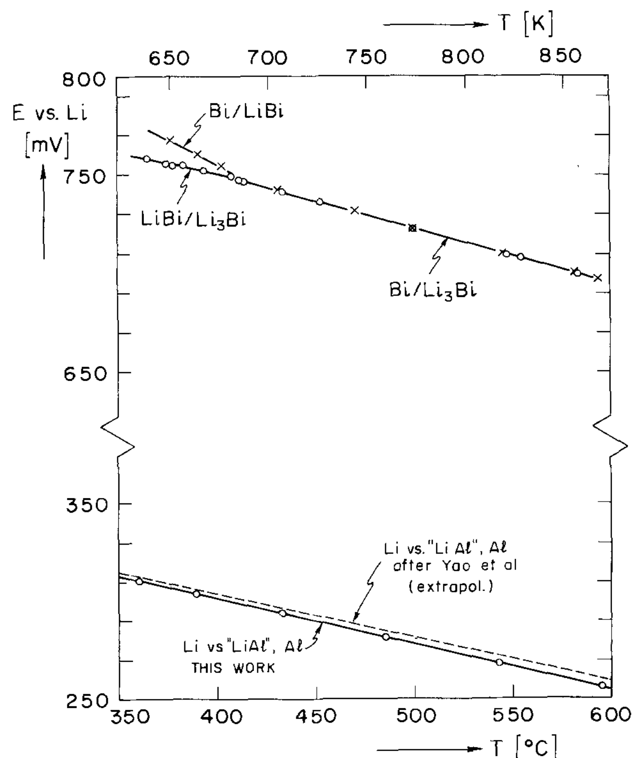

Fig. 7. The steady-state plateau voltages of the galvanic cell for the two-phase regions of the system Li-Bi as a function of the temperature with reference to pure lithium. At temperatures above 420°C only the trilithium phase exists. Below that temperature LiBi exists and the curve separates into two distinct plateau values. A small change of the slope is observed at the transition from the high temperature to the low temperature form of LiBi. The voltage of pure lithium vs. the actually applied "LiAl," Al electrode is also shown. Literature data (31) are plotted for comparison.

nor Li_3Sb_2, as supposed earlier, exists; only the compound Li_2Sb was observed. Extended anneals over periods of several days and repeated forward and backward titrations failed to produce any measurable voltage difference between that of Li-saturated Sb and Li_2Sb. In the system Li-Bi the existence of the phase LiBi was confirmed. Both of these intermediate phases have comparatively narrow ranges of stoichiometry and have very sluggish kinetics. The voltage drops over these phases are also very small, indicating only small changes of the lithium activity within their existence ranges.

Figures 6 and 7 present the composition-independent plateau voltages of the galvanic cell for the two-phase regions of the systems Li-Sb and Li-Bi, respectively, as a function of the temperature. The data were determined by using "LiAl," Al reference electrodes, but are plotted with reference to pure lithium, using the potentials between Li and "LiAl," Al, as also shown in the figures. The latter were determined in separate experiments. For comparison, extrapolated data from the literature (31) are also shown. From Fig. 7, it is seen that the formation of the intermediate phase LiBi can be easily detected below about 420°C. Also, a small change of the slopes of the voltages of "Li_3Bi" in equilibrium with the low temperature and the high temperature phase of LiBi is visible. By comparing Fig. 6 and 7 it is seen that lithium has an activity about one order of magnitude higher in the Li-Bi than in the Li-Sb system.

The phase diagram for the system Li-Bi can be deduced from data on the composition ranges of one and two phase regions determined from the shape of the coulometric titration curves at different temperatures. The general features agree well with those reported in the literature (13, 14, 16). However, they are different in detail, primarily with regard to the stoichiometric ranges of the single phases involved. The phase diagram of the system Li-Sb is relatively simple in the temperature range investigated, because the solubility of lithium in antimony and the stoichiometric ranges of Li_2Sb and Li_3Sb are very small. Therefore, this diagram contains vertical lines at the appropriate ideal compositions.

A special advantage of the use of galvanic cell coulometric titration techniques for the determination of thermodynamic values is the possibility of observing the influence of very small variations in composition

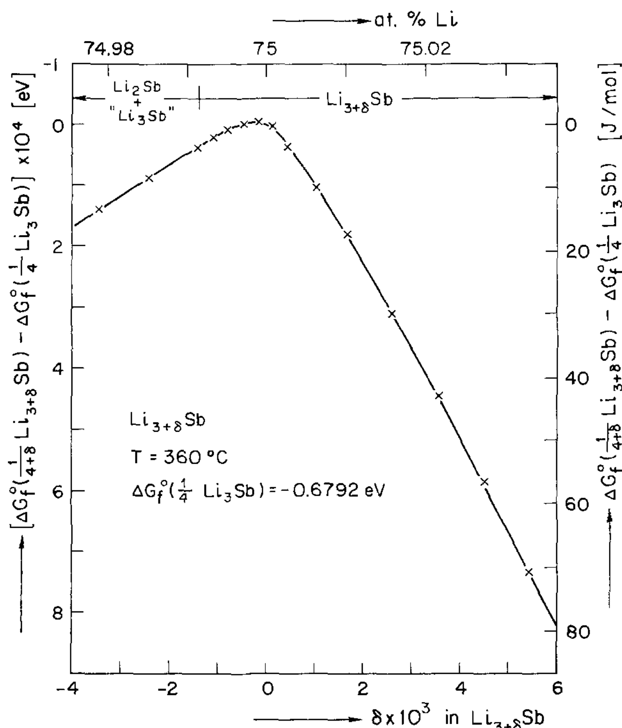

Fig. 8. The Gibbs formation energy of $Li_{3+\delta}Sb$ (per constituent) as a function of the stoichiometry of the single phase at 360°C. The data are plotted relative to the Gibbs formation energy of the compound with ideal stoichiometry, Li_3Sb.

within single phases. The precision obtainable in this way is much greater than that which can be achieved with conventional methods. In Fig. 8, the Gibbs free energy of formation of $Li_{3+\delta}Sb$ is shown as a function of the stoichiometry within the single phase region from $Li_{2.9985}Sb$ to $Li_{3.006}Sb$. The value of $\Delta G_f°$ of stoichiometric Li_3Sb is used for reference. It is seen that the resolution is better than 1 J/mole for these relative values. Their absolute magnitudes, however, are only correct to $\pm$ 100 J/mole. Further comments relating to the precision of this technique are included in the next section.

The corresponding curve for the $Li_{3+\delta}Bi$ phase, which exhibits a much larger range of stoichiometry, is shown in Fig. 9. These data are also given with reference to stoichiometric Li_3Bi. The lowest Gibbs formation energy per particle is observed for the composition having a lithium deficit of about 3%.

The variations of the molar Gibbs free energy of formation and the activities of both components as functions of the mole fraction Li within the phases "Li_3Sb" and "Li_3Bi" are presented in Tables I and II. Since this technique provides greater precision in the relative free energy values within the "Li_3Sb" and "Li_3Bi" phases than in their absolute values, due to the necessity for titration and integration over a wide composition range in the latter case, the values are indexed to those of the respective stoichiometric compositions.

Table I. Gibbs free energy of formation and activities of both components as a function of composition in the phase "Li_3Sb" at 360°C

X_{Li} (mole fraction)	$\Delta G_f°(Li_{3+\delta}Sb)$ $+2.622 \times 10^5$ (J/mole)	a_{Li}	a_{Sb}
0.74990	124.2	1.04×10^{-7}	0.207
0.74995	56.3	1.71×10^{-7}	4.69×10^{-2}
0.75000	0	6.62×10^{-5}	8.14×10^{-10}
0.75005	−23.5	1.48×10^{-2}	7.34×10^{-17}
0.75010	−74.2	5.13×10^{-2}	1.74×10^{-18}
0.75015	−84.2	0.113	1.64×10^{-19}
0.75020	−90.3	0.192	3.31×10^{-20}
0.75025	−94.5	0.304	8.37×10^{-21}
0.75030	−96.8	0.438	2.78×10^{-22}

Table II. Gibbs free energy of formation and activities of both components as a function of composition in the phase "Li_3Bi" at 380°C

X_{Li} (mole fraction)	$\Delta G_f°(Li_{3+\delta}Bi)$ $+2.170 \times 10^5$ (J/mole)	a_{Li}	a_{Bi}
0.738	8.850×10^3	1.63×10^{-6}	0.461
0.740	6.749×10^3	4.25×10^{-6}	3.01×10^{-2}
0.742	4.895×10^3	1.42×10^{-5}	9.58×10^{-4}
0.744	3.193×10^3	6.12×10^{-5}	1.42×10^{-5}
0.746	1.707×10^3	3.88×10^{-4}	6.40×10^{-8}
0.748	5.73×10^2	4.84×10^{-3}	3.71×10^{-11}
0.750	0	3.13×10^{-2}	1.47×10^{-13}
0.752	-1.93×10^3	0.641	1.66×10^{-17}

Figure 10 shows the temperature dependence of the Gibbs free energy of formation of the phases existing in the Li-Sb and Li-Bi systems. In the latter case, the large range of solubility of lithium in bismuth had to be taken into consideration according to Eq. [7]. The data are related to the reaction of one lithium atom with the corresponding formula amount of the Va metal, and are compared with those previously calculated for the formation of "Li_3Bi" by Foster *et al.* (11). However, those authors did not take into consideration the large range of stoichiometry on the lithium-deficient side of that phase.

Entropy changes, $\Delta S_f°$, were calculated from the slopes of the straight lines. With $\Delta G_f°$ and $\Delta S_f°$ being known, values of the enthalpy of formation, $\Delta H_f°$, were also calculated using Eq. [9]. The results are presented in Table III.

Discussion

From the results presented here it is seen that the galvanic cell technique, combined with coulometric titration, can be used to obtain a large amount of thermodynamic information with very high precision. The cell voltage is a direct measure of the activity of the electroactive species, which is directly related to several thermodynamic quantities, and the composition can be reproducibly varied over a wide range.

It has been shown that one can utilize results obtained in this manner to directly calculate integral Gibbs free energy, enthalpy, and entropy data rather than using the common Gibbs-Duhem integration. This

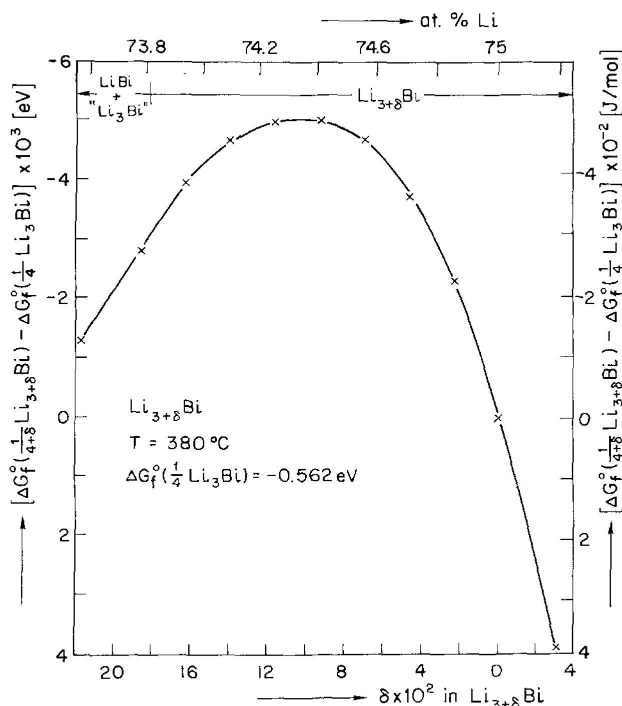

Fig. 9. The Gibbs formation energy of $Li_{3+\delta}Bi$ (per constituent) as a function of the stoichiometry of the single phase at 380°C. The data are plotted relative to the Gibbs formation energy of the compound with ideal stoichiometry, Li_3Bi.

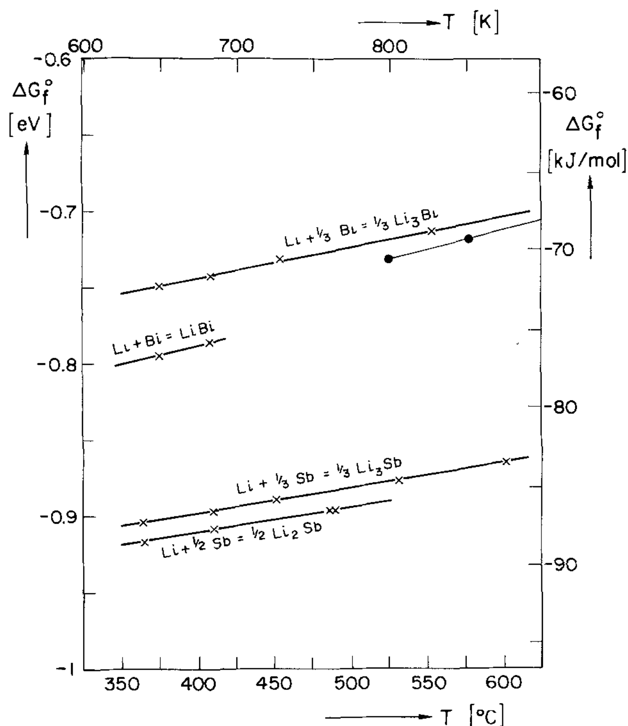

Fig. 10. The Gibbs formation energies of the compounds existing in the systems Li-Sb and Li-Bi as a function of the temperature. The negative slopes are the formation entropies of the compounds. Earlier data from Foster *et. al.* (11), which did not take into account the stoichiometric range of "Li_3Bi," are indicated by solid circles.

new method readily allows one to explicitly take into account the actual shape of the activity-composition relationship and finite composition ranges of other phases when calculating data for a given phase. As a result, greater precision can be obtained than by the use of traditional approaches, *e.g.*, the work of Foster *et al.* (11), who reported measurements on the liquid terminal solution of Li in Bi, and who calculated data on "Li_3Bi" on the assumption that this phase can be treated as a line compound. However, this work has shown that "Li_3Bi" has an appreciable range of composition on the lithium deficit side of the assumed stoichiometric value. As a result of their assumption of a 3/1 atomic ratio, their calculated values for the Gibbs free energy of formation have too great a magnitude.

The precision of the results reported here is unusually high for thermodynamic data, since electrical measurements can be made with high accuracy and the Li-Sb and Li-Bi systems reach equilibrium rapidly. There is negligible drift in the LiCl-KCl molten salt system if the purity is sufficiently high and the lithium activity is kept low enough.

The accuracy of the Gibbs free energy of formation data is due primarily to the good reproducibility of the cell voltages within the two-phase regions, which dominate the ranges of integration. The mean standard deviation was found to be less than ± 0.5 mV in these

Table III. Thermodynamic data for Li-Sb and Li-Bi Systems

Reaction	Temperature range (°C)	$\Delta G_f°$ (kJ mole^{-1}) (± 0.1)	$\Delta H_f°$ (kJ mole^{-1}) (± 0.7)	$\Delta S_f°$ (J mole^{-1} K^{-1}) (± 1)
2Li + Sb = Li_2Sb	355-500	$0.0319T - 197.3$	-197.3	-31.9
3Li + Sb = Li_3Sb	355-600	$0.0492T - 293.3$	-293.3	-49.2
Li + Bi = LiBi	355-420	$0.0245T - 92.6$	-92.6	-24.5
3Li + Bi = Li_3Bi	355-600	$0.0589T - 255.4$	-255.4	-58.9

T = absolute temperature (°K).

composition-independent regimes. This results in a precision of ± 100 J/mole in the free energy values.

The coulometric titration technique allows much greater compositional resolution than can be expected in cases in which one must prepare and analyze a series of separate samples. This is especially advantageous when one wishes to examine the compositional variation of properties within rather narrow phases. In cases such as these, with rapid equilibration and negligible drift, the compositional precision is only limited by the accuracy with which one can measure and control the current-time product. For example, a compositional change from $Li_{2.9985}Sb$ to $Li_{2.9990}Sb$ corresponds to a charge transfer of 1 A sec (*e.g.*, a current of 10 mA for 100 sec) per gram of sample. This is easy to both measure and control.

As a result of this high degree of compositional control, the variation in the relative values of thermodynamic parameters with composition within intermediate phases can be obtained with great accuracy. For example, the data in Fig. 4 show that a change in the stoichiometry of 1×10^{-4} corresponds to a change in cell voltage of about 100 mV. If we assume an error of 1 mV in the voltage, the corresponding error in the relative value of the Gibbs free energy of formation is only 4.8×10^{-3} J/mole.

Composition changes and phase transitions take place in both the Li-Sb and Li-Bi systems by insertion reactions with very high values of chemical diffusion coefficient (26, 27). This occurs by changes in the concentration and distribution of lithium atoms upon interstitial sites within the static Sb or Bi lattices, and thus produces only very minor changes in lattice parameter and sample shape.

In addition to the thermodynamic data already reported in this paper, other quantities may also be evaluated from these results. However, they may be dependent upon additional assumptions or information. For example, one may determine the intrinsic disorder concentration from the slope of the coulometric titration curve (34), if a specific disorder model can be assumed. Under the assumption of prevailing lithium vacancies in "Li_3Sb" at negative deviations from the ideal stoichiometry ($\delta < 0$), and either lithium interstitials or lithium atoms on antimony sites at lithium excess ($\delta > 0$) the mole fraction of intrinsic lithium vacancies at ideal stoichiometry was calculated from the slope at the inflection point to be $X_{V_{Li}} = 2 \times 10^{-5}$. For other disorder models different results would be obtained, but they will vary only slightly for most reasonable assumptions. The shape of the coulometric titration curve that is experimentally observed is very similar to that which is theoretically calculated (34) if one assumes lithium atoms on antimony sites at $\delta > 0$ and lithium vacancies at $\delta < 0$.

In addition to their fast kinetic behavior (26, 27)), it has been shown that the systems Li-Sb and Li-Bi exhibit thermodynamic properties which may make them of interest for possible use as cathodes in high energy- and power-density batteries. The maximum theoretical specific energies are 500 W-hr/kg for Li-Sb and 290 W-hr/kg for Li-Bi, respectively.

Acknowledgments

This work was funded by a grant from the Institute for Energy Studies at Stanford University, which has supported one of the authors (W.W.) on a Standard Oil of California Visiting Professorship. The earlier grant of a NATO Scholarship through the German Academic Exchange Service (DAAD) is also gratefully acknowledged.

Manuscript submitted March 18, 1977; revised manuscript received Sept. 16, 1977.

Any discussion of this paper will appear in a Discussion Section to be published in the December 1978 JOURNAL. All Discussions for the December 1978 Discussion Section should be submitted by Aug. 1, 1978.

Publication costs of this article were assisted by Stanford University.

REFERENCES

1. K. Kiukkola and C. Wagner, *This Journal*, **104**, 308 (1957).
2. C. Wagner, *J. Chem. Phys.*, **21**, 1819 (1953).
3. H. Rickert, V. Sattler, and C. Wedde, *Z. Phys. Chem.*, *NF*, **98**, 339 (1975).
4. B. C. H. Steele, in "Critical Materials Problems in Energy Production," C. Stein, Editor, p. 711, Academic Press, New York (1976).
5. S. A. Shchukarev, E. Vol'f, and M. P. Morozova, *J. Gen. Chem. USSR (Engl. Transl.)*, **24**, 1887 (1954).
6. O. Kubaschewski and E. LL. Evans, "Metallurgical Thermochemistry," p. 254, Pergamon Press, Oxford (1958).
7. G. F. Voronin, *Zh. Fiz. Khim.*, **44**, 1538 (1970).
8. C. E. Messer, in Proceedings of the International Symposium of The Chemical Society, Spec. Publ. No. 22, Burlington House, London (1967).
9. W. Seith and O. Kubaschewski, *Z. Elektrochem.*, **43**, 743 (1937).
10. S. A. Shchukarev, M. P. Morozova, K.-Y. Kan. and V. T. Sharov, *J. Gen. Chem. USSR (Engl. Transl.)*, **27**, 321 (1957).
11. M. S. Foster, S. E. Wood, and C. E. Crouthamel, *Inorg. Chem.*, **3**, 1428 (1964).
12. A. I. Demidov and A. G. Morachevskii, *Sov. Electrochem. (Engl. Transl.)*, **9**, 1321 (1973).
13. G. Grube, H. Vosskühler, and H. Schlecht, *Z. Elektrochem.*, **40**, 270 (1934).
14. E. Zintl and G. Brauer, *ibid.*, **41**, 297 (1935).
15. G. Brauer and E. Zintl, *Z. Phys. Chem.*, **B37**, 323 (1937).
16. R. Hultgren, R. L. Orr, P. D. Anderson, and K. K. Kelly, "Selected Values of Thermodynamic Properties of Metals and Alloys," J. Wiley, New York (1963).
17. P. Lebeau, *C. R. Acad. Sci. (Paris)*, **134**, 231, 284 (1902).
18. O. Kubaschewski and W. Seith, *Z. Metallk.*, **30**, 7 (1938).
19. P. G. Maslov and Yu. P. Maslov, *Zh. Fiz. Khim.*, **33**, 1687 (1959).
20. R. Gérardin and J. Aubry, *C. R. Acad. Sci. Ser. C*, **278**, 1097 (1974).
21. Rheinisch-Westfälisches Elektrizitätswerk AG, Fr. Demande 2,206,593 (1974); Ger. Appl. P. 2254870.5 (1972).
22. J. O. Besenhard and H. P. Fritz, *Electrochim. Acta*, **20**, 513 (1975).
23. E. Mooser and W. B. Pearson, *Phys. Rev.*, **101**, 492, 1608 (1956).
24. Yu. A. Nemilov and V. E. Privalova, *Sov. Phys. Tech. Phys.*, **1**, 56 (1956).
25. R. Gobrecht, *Phys. Status Solidi*, **13**, 429 (1966).
26. W. Weppner and R. A. Huggins, *This Journal*, **124**, 1569 (1977).
27. W. Weppner and R. A. Huggins, To be published in *J. Solid State Chem.*
28. H. Rickert, "Einführung in die Elektrochemie fester Stoffe," Springer-Verlag, Berlin (1973).
29. R. A. Sharma and R. N. Seefurth, *This Journal*, **123**, 1763 (1976).
30. L. S. Darken and R. W. Gurry, "Physical Chemistry of Metals," p. 260ff, McGraw-Hill, New York (1953).
31. N. P. Yao, L. A. Herédy, and R. C. Saunders, *This Journal*, **118**, 1039 (1971).
32. R. N. Seefurth and R. A. Sharma, *ibid.*, **122**, 1049 (1975).
33. R. J. Heus and J. J. Egan, *J. Phys. Chem.*, **77**, 1989 (1973).
34. C. Wagner, in "Progress in Solid State Chemistry," Vol. 6, H. Reiss and J. O. McCaldin, Editors, p. 1, Pergamon Press, Oxford (1971).

Behavior of Bi_2O_3 as a Cathode for Lithium Cells

P. Fiordiponti, G. Pistoia, and C. Temperoni

Centro di Studio sulla Elettrochimica e la Chimica Fisica delle Interfasi del C.N.R., Istituto di Chimica della Facoltà di Ingegneria, Università di Roma, Rome, Italy

ABSTRACT

The performances of lithium cells based on Bi_2O_3 as a cathode have been evaluated. Because of the very high specific capacity of this compound, interesting values of energy densities were obtained at low discharge rates. A 12-electron discharge process is supposed to occur leading to the formation of Li_3Bi. Two steps were noticed, the first one giving rise to metallic Bi through a 6-electron reduction. Comparison is made of the performance of these cells with several lithium cells. In principle, Bi_2O_3 seems to be a very attractive material for cells of this type, encouraging further research on its practical utilization.

In the last few years lithium batteries with both solid and liquid electrolytes have come out of the stage of laboratory prototypes and their commercial development has started. In general, lithium cells seem to be particularly suitable in the field of microelectronics, where high values of specific energies and capacities (especially on a volume basis) are required at low current densities (a few $\mu A/cm^2$). Also in high rate applications nonaqueous cells are now emerging, especially with the Li/SO_2 (1) and the $Li/SOCl_2$ (2) systems.

A class of potentially useful cathode materials for organic electrolyte cells is a set of metal oxides, which seem to assure simultaneously, although to various extents, the characteristics of safety, economy, high energy density, and long life. Among others, CuO (3), MoO_3 (4), Mo_8O_{23} (5), and V_2O_5 (6) have proved to be suitable in this sense.

Key words: lithium batteries, Bi_2O_3, nonaqueous solvents, button organic cells.

During the search for other cathode materials, we observed that Bi_2O_3 has a surprisingly high specific capacity (*ca.* 0.7 A-hr/g) which could compensate for the relatively low cell voltage on load (1.5V at 0.5 mA/cm^2). Furthermore, the high density of this oxide (8.9 g/cm^3) can produce high values of volumetric capacities and energies.

In the open literature no report is given on the performance of cells (either aqueous or nonaqueous) based on Bi_2O_3; only the discharge characteristics in alkaline solutions of cathodes based on Bi_2O_3, Sb_2O_3, and As_2O_3 have been examined (7). In an American patent (8) the possibility of using Bi_2O_3 in lithium cells containing $LiPF_6$ or $LiBF_4$ in methyl acetate is mentioned, but no details on the electrochemical behavior of this oxide are given.

In the present paper the feasibility of Bi_2O_3 as a cathode for primary lithium cells is discussed and particular emphasis is given to the discharge process.

Experimental Aspects

Materials.—Bi_2O_3 was a reagent grade product used without any further treatment. The purification of the solvents [butyrolactone (BL), propylene carbonate (PC), tetrahydrofuran (THF), and methyl formate (MF)] and the preparation of the organic solutions have been described elsewhere (9). $BiPO_4$, Bi_2S_3, and $Bi(IO_3)_3$, which were also tested as cathodes, were prepared in this laboratory by metathetic reactions.

Apparatus and procedure.—Bi_2O_3 was usually mixed with 10% graphite in order to ensure electronic conductivity. This oxide is indeed a semiconductor (10) and a resistance of 1.4×10^6 Ω was measured for a pellet having a thickness of 0.12 cm. In spite of this value, cathodes not containing graphite can work at the current densities (around 0.5 mA/cm^2) used for these cells. A similar pattern was found with silver salts (9, 11) of high resistance. This effect is still obscure and worth a specific investigation. Of course, the use of graphite-free cathodes is welcomed in that higher specific energies may be obtained; furthermore, decomposition phenomena of the solutions were less probable in the absence of graphite (12).

The dry cathode material was pressed at 1600 kg/cm^2 onto a support of silver powder pressed at 550 kg/cm^2. Lower and higher pressures on Bi_2O_3 resulted in a less satisfactory performance. The cathode pellet was then put in a Teflon container having an internal diameter of 1.26 cm. The organic solutions were supported on a triple layer of glass fiber filter paper (Whatman 934 AH); the use of a higher or of a lower number of separators was not profitable. Both lithium and Bi_2O_3 on Ag were in contact with stainless steel terminals. The button-type cells had an internal volume of *ca.* 0.2 cm^3 (referred to the active components) and were maintained in a dry box under argon atmosphere during the constant current discharges obtained with ordinary galvanostats.

Polarization measurements for Bi_2O_3 cathodes in three solutions were made on fresh cells similar to those submitted to discharge. At each current value, the voltage was observed for 5 sec.

The x-ray diffraction pattern was obtained on cathodes discharged at a low rate in $LiAsF_6$-THF and $LiClO_4$-PC. The samples were analyzed under vacuum for 10 hr with the Debye-Scherrer method, using Cr-K_α radiation filtered by V.

The solubility of Bi_2O_3 in 1.5M $LiAsF_6$-THF was checked by polarographic analysis of the Bi^{+3} ion, after leaving Bi_2O_3 in contact with the above solution for 10 days. Blank experiments with a $LiAsF_6$-THF solution containing known amounts of $BiCl_3$ (which is fairly soluble in this solution) were also made.

Visual observations of $LiAsF_6$-THF and $LiAsF_6$-BL solutions containing Bi_2O_3 did not give evidence of unwelcomed reactions, because neither discoloration nor gassing were noticed.

Experimental Results

The OCV of cells of the type Li/organic electrolyte/Bi_2O_3 (with or without C at the cathode) exceeded 3V. However, even at low rates of discharge the potential dropped well below 2V, thus indicating that the observed OCV is not the thermodynamic value of the Li/Bi_2O_3 couple. Graphite could, in principle, be responsible for the high OCV through the formation of intercalation compounds, but even Ag pellets give the same OCV although the formation of lithium-silver compounds should give rise to potentials lower than 200 mV in these solutions (13). Also the presence of O_2 in the system cannot explain the OCV, since the emf of the Li/O_2 couple is equal to 2.9V. On the other hand, we observed that the OCV varied with the electrolyte used. The averages of several cells give values for $LiClO_4$-PC, $LiAsF_6$-BL, and $LiAsF_6$-THF of 3.0, 3.1, and 3.4V, respectively. Therefore, the initial OCV has to be related to the presence of electroactive impurities, mainly due to the solvents, incompletely eliminated by purification. For instance, THF contains peroxides (14) which can form a couple of high voltage with Li.

Table I. Performances of Li/Bi_2O_3 cells containing various electrolytes. 1.0V cutoff, 0.5 mA/cm^2

Electrolyte	$\chi \cdot 10^{-3}$ (Ω^{-1} cm^{-1})	Specific capacity A-hr/g	Specific capacity A-hr/cm^3	Mean discharge voltage (V)	Utilization (% based on 12*e*)
$LiAsF_6$-THF	16	0.380	3.38	1.49	55
$LiAsF_6$-BL	9.2	0.300	2.67	1.49	43
$LiClO_4$-BL	13	0.155	1.38	1.34	23
$LiClO_4$-PC	5.6	0.224	1.99	1.36	32
$LiAlCl_4$-BL	10	0.184	1.63	1.43	27
$LiClO_4$-MF/BL	27	0.100	0.89	1.39	10

Polarization curves for Bi_2O_3 in different solutions were measured. The rapid increase of the voltage drop with current indicates that this material can be useful only at low rate applications. In the range 0-3 mA/cm^2, the polarization decreases in the order $LiAsF_6$-THF, $LiAsF_6$-BL, and $LiClO_4$-PC. The same order has been found for the discharge behavior at 0.5 mA/cm^2, as shown in Table I where the results in three more solutions are also reported (the specific capacity is referred to Bi_2O_3 only). It can be seen that the performance of Bi_2O_3 cannot be connected to the specific conductivity of the solutions (values in the 2nd column), *i.e.*, mass transport phenomena have a minor effect on the electrode polarization. Gabano (12) has proposed a reaction scheme for cathodes not conducting and unable to form intercalation compounds, in which the locus of reduction is in the solution layers immediately near the cathodic surface. Obviously, the structure of these layers would be differently influenced by the various electrolytes through adsorption and solvation/dissolution phenomena.

In Fig. 1 the discharge curves in $LiAsF_6$-THF at different current densities are reported. An initial voltage delay is shown which was also present in all the other solutions. On the other hand, cathode materials such as Ag_2CrO_4 and Ag_3PO_4 do not exhibit such behavior in the same solutions (9), thus indicating that it may be connected with the low solubility of the cathode, *i.e.*, with its low concentration in the solution layers near the electrode (12).

The low solubility of Bi_2O_3 in $LiAsF_6$-THF was ascertained polarographically. A reduction wave of Bi^{+3} was not found with this material, whereas blank experiments with $BiCl_3$ revealed a well-defined reduction wave even at a concentration of 1×10^{-4}M. Obviously, a low solubility is desired in that it can give rise to a long service life. However, no data were obtained in this work on the storage capability of cells based on Bi_2O_3.

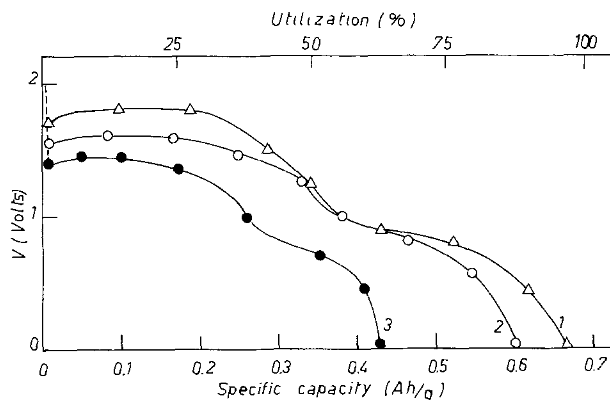

Fig. 1. Discharge curves of Li/Bi_2O_3 cells in $LiAsF_6$-THF at different rates. Curve 1, 0.25 mA/cm^2; curve 2, 0.50 mA/cm^2; curve 3, 1.00 mA/cm^2.

Table II. Influence of the temperature on the performances of $Li/LiAsF_6$-BL/Bi_2O_3 cells. 1.0V cutoff, 0.5 mA/cm^2

Temperature (°C)	Specific capacity A-hr/g	Specific capacity A-hr/cm^3	Mean discharge voltage (V)	Utilization (% based on 12e)
24	0.300	2.67	1.49	43
40	0.331	2.94	1.55	48
60	0.350	3.11	1.57	55

In Table II the influence of the temperature on $Li/LiAsF_6$-BL/Bi_2O_3, C cells is reported. BL was used as a solvent instead of THF, because of the difficulties that may be encountered with the latter at 60°C, since its boiling point is 64.5°C. Evidently, the positive effect of the temperature on solution conductivity and cathode polarization is not counterbalanced by an increase in cathode solubility, which would result in capacity losses. In particular, the result obtained at 40°C can be of some interest if these cells were to be used in cardiac pacemakers.

$BiPO_4$, Bi_2S_3, and $Bi(IO_3)_3$ were also tested. The first salt has a specific energy of 0.29 W-hr/g (which does not compare well with 0.57 W-hr/g obtained for Bi_2O_3), whereas the last two salts show poor discharge behaviors.

The performance of Bi_2O_3 (a two-step reduction process which corresponds to a high experimental capacity) was confirmed by the analogous Sb_2O_3. Also with this oxide good values of specific capacity and energy have been obtained (0.39 A-hr/g and 0.51 W-hr/g at 0.5 mA/cm^2 to 1.0V cutoff, respectively).

Discussion

The specific capacities to zero volt cutoff in $LiAsF_6$-THF (0.60 A-hr/g) and in $LiAsF_6$-BL (0.53 A-hr/g) are higher than the maximum calculated on the basis of the simple reduction of Bi_2O_3 to Bi (0.345 A-hr/g). These high capacities were rationalized through coulometric analysis at low rate, from which it was calculated that 12 electrons are involved in the discharge of each molecule of Bi_2O_3. The discharge has two steps (Fig. 1). The first one, ending a little below 1.0V, is calculated to involve 6 electrons to give the observed specific capacity (0.34 A-hr/g). A 12-electron process implies the formation of compounds in which Bi is in a negative oxidation state.

Indeed, As, Sb, and Bi are known to form with Li compounds of the Li_3Me type both chemically (10, 15) and electrochemically (16). On the basis of these observations and of the coulometric analysis, the discharge process may be written as follows

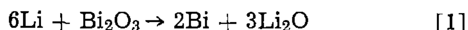

$$6Li + Bi_2O_3 \rightarrow 2Bi + 3Li_2O \qquad [1]$$

$$2Bi + 6Li \rightarrow 2Li_3Bi \qquad [2]$$

The net reaction is

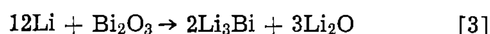

$$12Li + Bi_2O_3 \rightarrow 2Li_3Bi + 3Li_2O \qquad [3]$$

The x-ray diffraction data (Table III) confirm the formation of Bi (especially with the lines having dÅ 2.38 and 2.27), whereas the presence of Li_2O is made uncertain by the coincidence of its principal lines with those of α-Bi_2O_3.

The possibility that the second step (occurring below 1V) could be connected with electrolyte decomposition (12) was greatly reduced by the fact that graphite-free cathodes were frequently used. Anyway, Li/Bi cells with or without graphite, when discharged in $LiAsF_6$-THF, showed very similar values of experimental specific capacity, which resulted near to the theoretical value for the formation of Li_3Bi (0.385 A-hr/g).

Reaction [1] has a ΔG of −283 kcal/mole and a theoretical E_o of 2.05V. This value is in agreement with the 2.0V OCV observed during the initial part of the first discharge plateau.

Table III. X-ray diffraction data for Bi_2O_3 discharged in $LiAsF_6$-THF

Experimental (dÅ)	Literature values (dÅ) α-Bi_2O_3	Bi	Li_2O
3.25 (VS)	3.23 (VS)	3.28 (VS)	2.66 (VS)
2.65 (S)	2.75 (W)	2.38 (M)	2.30 (W)
2.36 (S)	2.68 (S)	2.27 (M)	1.63 (M)
2.26 (S)	2.25 (W)	1.97 (W)	1.39 (W)
2.03 (MW)	1.95 (S)	1.87 (MW)	1.15 (W)
1.96 (W)	1.91 (MW)	1.49 (W)	1.06 (W)
1.86 (M)	1.87 (MW)	1.44 (W)	0.96 (W)
1.64 (MS)	1.74 (MS)	1.33 (W)	
1.55 (W)	1.72 (M)		
1.49 (MW)	1.67 (S)		
1.44 (MS)	1.64 (S)		
1.38 (W)	1.56 (M)		
1.33 (M)	1.48 (MW)		
1.31 (M)	1.46 (MW)		
1.28 (W)	1.34 (M)		
1.18 (W)	1.32 (M)		
1.04 (W)	1.27 (MW)		
0.94 (W)	1.17 (MS)		

VS, very strong; S, strong; MS, medium strong; M, medium; MW, medium weak; W, weak.

No data for the free energy of formation are reported for Li_3Bi at room temperature. Extrapolation to 25°C of ΔG values obtained at high temperatures (17) gives $\Delta G = -56$ kcal/mole. Therefore, reaction [2] has a theoretical $E_o = 0.81V$. This potential is in agreement with an OCV of 0.8V experimentally found by us and by Eichinger (16) for Li/Bi cells.

With reaction [3] a theoretical energy density of 835 W-hr/kg was calculated. From a cell $Li/LiAsF_6$-THF/Bi_2O_3, having a capacity of 50 mA-hr and discharged at 0.5 mA/cm^2, an over-all energy density of 200 W-hr/kg was achieved on the basis of the weight of anode, cathode, solution, and separators. This figure is expected to be increased by working at lower rates and by optimizing the cell structure. Also the volumetric energy is expected to be quite high in view of the density of Bi_2O_3. In Table IV, the performance of several cathode materials tested in this laboratory are compared. The comparison is especially important with respect to MoO_3, Ag_2CrO_4, and Ag_3PO_4 which have been extensively studied also in other laboratories (11, 18) due to their practical interest. Parameters such as cell life and volume variations during discharge have to be carefully evaluated. The low solubility of Bi_2O_3 in organic solutions and the results of preliminary compatibility tests suggest a satisfactory cell life. The performance of Bi_2O_3 reported in the present paper is sufficiently promising that it calls for further research to ascertain the feasibility of practical cells.

Acknowledgment

The authors wish to thank Dr. P. L. Cignini for the x-ray analysis. This work was carried out with financial support of the Consiglio Nazionale delle Ricerche (C.N.R.).

Manuscript submitted Nov. 29, 1976; revised manuscript received Aug. 8, 1977.

Any discussion of this paper will appear in a Discussion Section to be published in the December 1978

Table IV. Performances of various cathode materials tested in this laboratory for lithium cells. 1.0V cutoff, 0.5 mA/cm^2

Cathode	Solution	Specific capacity A-hr/g	Specific capacity A-hr/cm^3	Mean discharge voltage (V)	Utilization (%)
MoO_3	$LiAlCl_4$-BL	0.24	1.13	2.17	66 (2e)
Mo_8O_{23}	$LiAlCl_4$-BL	0.38	—	2.00	100 (2e)
$W_{18}O_{49}$	$LiAlCl_4$-BL	0.23	—	1.30	98 (2e)
Ag_2CrO_4	$LiClO_4$-PC	0.33	1.86	2.34	82 (5e)
$AgIO_3$	$LiAsF_6$-BL	0.27	1.49	1.90	47 (6e)
Ag_3PO_4	$LiClO_4$-PC	0.15	0.98	2.30	80 (3e)
PbF_2	$LiAsF_6$-BL	0.22	1.81	1.82	67 (3e)
$PbCrO_4$	$LiAsF_6$-THF	0.21	1.28	1.28	50 (6e)
PbO_2	$LiAsF_6$-THF	0.41	3.84	1.38	73 (5e)
Bi_2O_3	$LiAsF_6$-THF	0.38	3.38	1.49	55 (12e)

JOURNAL. All discussions for the December 1978 Discussion Section should be submitted by Aug. 1, 1978.

Publication costs of this article were assisted by the University of Rome.

REFERENCES

1. H. Taylor and B. McDonald, Proceedings of the 27th Power Sources Conference, Atlantic City (1976).
2. N. Marincic, J. Epstein, F. Goebel, and A. Lombardi, Paper 39 presented at the Electrochemical Society Meeting, Dallas, Texas, Oct. 5-9, 1975.
3. G. Lehmann, G. Gerbier, A. Brych, and J. P. Gabano, 9th International Power Sources Symposium, Brighton (1974).
4. L. Campanella and G. Pistoia, *This Journal*, **118**, 1905 (1971).
5. B. Di Pietro, V. Filippeschi, M. Lazzari, G. Pistoia, and B. Scrosati, 11th International Power Sources Symposium, Brighton (1976).
6. R. Hornig, Proceedings of the 10th I.E.C.E.C., Newark, p. 424 (1975).
7. R. Glicksman and C. Morehouse, *This Journal*, **104**, 589 (1957).
8. G. Methlie, U.S. Pat. 3,415,687 (1968).
9. S. Conte, V. Filippeschi, and G. Pistoia, *J. Power Sources*, **1**, 193 (1976).
10. R. Gobrecht, *Ann. Phys. (Leipzig)*, **20**, 262 (1967).
11. J. Doe, F. Dampier, K. Jeffries, P. Krouse, N. Margalit, E. Merrick, and L. Thompson, Technical Report AFAPL-TR-74-63 (December 1974).
12. J. Quobex and J. P. Gabano, *Rev. Gen. Electr.*, **84**, 491 (1975).
13. A. Dey, *This Journal*, **118**, 1547 (1971).
14. J. Butler, R. Jasinski, D. Cogley, H. Jones, J. Synnot, and S. Carrol, Technical Report AFCRL-70-0605 (September 1970).
15. Kirk-Othmer, "Encyclopedia of Chemical Technology," Vol. 3, p. 557 (1974).
16. J. Besenhard and H. Fritz, *Electrochim. Acta*, **20**, 513 (1975).
17. M. Foster, S. Wood, and C. Crouthamel, *Inorg. Chem.*, **3**, 1428 (1964).
18. G. Lehmann, T. Rassinoux, G. Gerbier, and J. P. Gabano, "Power Sources 4," p. 493, Oriel Press, London (1973).

The Effect of Noble Metal Additions upon the Corrosion of Copper: An Auger-Spectroscopic Study

J. Gniewek,[1] J. Pezy, B. G. Baker, and J. O'M. Bockris*

School of Physical Sciences, Flinders University of South Australia, Adelaide, Australia

ABSTRACT

Dissolution rates as a function of potential and the corrosion potentials for Cu and five Cu-Pd alloys with varying compositions in the range of (0-30%) Pd were measured. The Auger spectra of the alloy surface and fresh surfaces obtained by argon ion bombardment to a depth up to 30 nm were obtained. Cu dissolves from the alloy and the rate of dissolution of Pd is negligible. The Cu dissolution follows the same laws as from pure Cu. Below a certain critical potential, the initially observed dissolution current decayed towards zero. The electrode potential at zero current follows the surface composition. At zero current the bulk alloy composition was found to have been modified to a depth of about 20 nm. An approximate calculation of i_0 for Cu dissolution of the alloy as a function of composition showed that value is reduced by some ten orders of magnitude compared with that of pure Cu. Corrosion is reduced in a manner consistent with these i_0 reductions when the cathodic O_2 reaction is not rate controlling.

Knowledge of the theory of corrosion in electrode kinetic terms is now widespread (1). However, alloying elements can give rise to commercially interesting reductions in corrosion rate, often more marked than one would have expected according to simple theory. The influence of noble metal alloying upon corrosion protection has not hitherto received studies which contained information sufficient for the evaluation of the mechanism of this effect.

Auger electron spectroscopy (AES) provides information about the composition of alloy surfaces and the relative composition changes in the first few nanometers from the surface. Several earlier studies on AgAu (3) and CuAu (4-6) have established that, as the gold content of the alloy increases, the electrode potentials shift in the positive direction. However, in these studies physical analysis of changes occurring within the alloy has been limited to those corresponding to a high rate of dissolution under external anodic potential control, rather than under corrosion control. The copper-palladium alloy system was chosen for AES study of the corrosion region for the following reasons:

(*i*) Similarly to the AgAu and CuAu systems, there is a significant difference in the standard electrode potentials of the two elements, thereby favoring preferential dissolution of copper.

(*ii*) Copper and palladium form a complete solid solution series (although at low temperatures the β equilibrium phase forms at ~40 atomic percent (a/o) Pd) permitting study of corrosion behavior of the alloy over a wide composition range.

(*iii*) Cu and Pd provide favorable noninterfering Auger spectra.

(*iv*) The ion sputtering yields of Cu and Pd are nearly equal (7), simplifying interpretation of the composition-depth profile measurements obtained by AES studies combined with argon ion bombardment of surfaces arising from corrosion.

Experimental

Alloys were prepared from 99.999% Cu and 99.99% Pd by induction heating melting in boron nitride crucibles under pure argon. The material was held for 15 min at ~100°C above the melting point, solidified, and upon inverting the ingot, remelted for another 15 min. Weight change before and after melting was <0.01%, indicating negligible reaction with the crucible material. The ingots were then cold rolled to strips approximately 0.3 mm thick by 27 mm wide. After cutting into specimens for electrochemical and AES measurements the specimens were cleaned and vacuum annealed for

* Electrochemical Society Active Member.
[1] Present address: IBM Corporation, Systems Products Divisions, East Fishkill, New York.
Key words: palladium, passivity, composition depth profile, dissolution rate.

16 hr at 920°C followed by rapid cooling to room temperature. In addition to alloys of 5, 10, 15, 20, 30 a/o Pd[2] pure Cu and alloys of 80/20 CuAu and 80/10/10 CuPdAu were also prepared.

Two types of specimens were used. Type A, which was used to establish the initial log *i-V* relationships, was circular with 14 mm diam. Prior to electrochemical measurements, the specimen surface was prepared by grinding with 600 grit paper and rinsing with distilled water and alcohol. To obtain meaningful composition depth-profiles, it was found necessary to polish the specimen to a mirror finish. Type B specimens (23 × 9 mm rectangular) which were used for subsequent electrochemical treatments and all AES measurements, were therefore further polished with diamond polishing paste prior to ultrasonic cleaning in distilled water and an alcohol rinse.

Electrochemical apparatus.—All investigations were conducted at room temperature in 0.5M Na_2SO_4-0.005M H_2SO_4 electrolyte. A calomel electrode was used as the reference cell. The potentials reported here are given on the standard hydrogen electrode (SHE) scale. Except where stated, the solution was deoxygenated by bubbling N_2 for several hours.

Initial log *i-V* measurements were obtained using Type A specimens in a standard electrochemical cell (8). Subsequent electrochemical measurements were performed on Type B specimens in an electrolyte flow system cell of similar design to that used by Damjanovic, Setty, and Bockris (9). The Teflon cell was machined with a thin Teflon perimeter ridge so that when held in compression against the specimen a liquid-tight seal was effected with the alloy specimen forming one wall of the cell. With the cell assembled, the volume between the specimen and the Pt counterelectrode was 0.3 cm^3. Electrolyte flow rates in the range of 0.01-0.1 ml/sec were used during electrochemical treatment. A valving arrangement permitted rapid electrolyte removal under N_2 gas followed by rinsing with distilled H_2O and drying in N_2 gas flow. The specimens were held in the N_2 ambient until ready for transfer to the vacuum system for AES measurements. Transfer between the electrochemical apparatus and the vacuum for the AES required exposure to the air ambient of less than 5 min.

Auger apparatus.—The AES equipment was constructed in this laboratory. A retarding grid electron energy analyzer with a post-monochromator after the design of Huchital and Rigden (10) was mounted in a Pyrex tube. A bakeable straight-through high vacuum valve connected the Auger analysis vacuum chamber to an auxiliary liquid nitrogen-trapped oil diffusion pumped vacuum chamber. Following removal from the electrochemical cell the sample was mounted on a stainless steel specimen holder which could be raised and lowered through a feed-through mounted on the auxiliary chamber. After evacuation of the auxiliary chamber to approximately 2×10^{-4} Torr, the sample was transferred to the Auger chamber via a straight-through valve, the transfer rod was withdrawn, and the high vacuum valve closed. AES analysis was begun when the vacuum reached the 10^{-8} Torr range. The auxiliary vacuum chamber and the electrochemical cell were designed so that the latter could be operated in the chamber with the sample being transferred to the Auger vacuum chamber without exposure to the air ambient. However this feature was not utilized in these experiments.

The axis of the energy analyzer was along a line normal to the sample. The axes of the energy analyzer, primary electron beam, and ion gun all lay in the same plane. A 2.4 kV primary electron beam was incident at an angle of ~25° (65° off normal) while the 1 kV argon ion beam was incident at an angle of 25° from the opposite direction. The primary electron beam of ~1.5 mm diam was operated in the center of the ion beam which was defocused to a diameter of 10 mm.

[2] All alloy compositions are reported as atomic percent.

The argon pressure during bombardment was kept between 2×10^{-5} and 5×10^{-5} Torr. The ion-beam current monitored at the specimen was used as a measure of the sputter removal rate. Ion bombardment and AES were performed sequentially, the ion beam being turned off during each AES measurement. The calibration of the sputter removal rate was made by measuring the time required to remove a 90 nm Cu film, which had been vacuum deposited over an evaporated film of Cr. The distance axis of the concentration profile graphs are labeled in angstroms utilizing this calibration result.

Auger analysis.—The dN/dE spectra were recorded utilizing a 7.5V p·p modulation voltage for the 330 eV Pd peak and an 18V p·p modulation voltage for the Cu 918 eV peak. The composition, reported as atomic fraction of palladium, X_{Pd}, was calculated from the measured peak-to-peak heights of the Pd and Cu peaks, by the formula (11)

$$X_{Pd} = \frac{A_{Pd}}{A_{Pd} + \alpha A_{Cu}} \quad [1]$$

While in principle the value of α can be obtained by direct comparison of spectra from the alloy and from pure copper, this method was found to be reliable only when very lightly sputtered samples are compared. Sputtering caused an increase in the copper peak from both alloy and pure copper, presumably due to the effect of surface roughening. Instead, taking the initial surface composition to be that of the bulk, the value of α was determined from Cu and Pd peak height. Measurements were made on 10, 20, and 30 a/o Pd alloys which were mechanically polished and very lightly ion bombarded to remove C contamination. Calculations made from the Cu and Pd peak heights before ion bombardment and correcting for the intensity absorption due to the contaminant overlay film support the assumption that little (*i.e.*, < 3 a/o Pd) surface composition change is caused by the ion bombardment. Measurements on the various alloy samples are reproducible within ±1 a/o Pd. Samples pretreated electrochemically had a lower surface contaminant level than those not so treated and representative surface composition measurements could be made prior to any ion bombardment without the need for intensity correction.

Surface composition determination with concentration gradient.—In cases where the composition changes significantly within distances comparable to the Auger electron mean free path (as found for electrochemically treated specimens), it is necessary to apply a correction factor to determine the true surface composition. For conditions where the concentration gradient can be approximated by an exponential function with characteristic length d, it can be shown that the true surface composition is given by (see Appendix)

$$X_{Pd,surf} = X_{Pd,bulk} + \left\{ \frac{X_{PM} - X_{Pd,bulk}}{d\left[\frac{1}{d + \lambda_{Pd}} - X_{PM}\left(\frac{1}{d + \lambda_{Pd}} - \frac{1}{d + \lambda_{Cu}}\right)\right]} \right\} \quad [2]$$

where λ_{Cu} and λ_{Pd} are the Auger electron mean free paths for copper (1.1 nm) and palladium (0.75 nm). $X_{Pd,bulk}$ = bulk concentration, X_{PM} = measured surface composition calculated from Eq. [1], and $X_{Pd,surf}$ = actual surface composition. Results obtained in this manner indicate that the actual surface compositions could be as much as 5-10 a/o Pd higher than the measured uncorrected determinations, depending upon the concentration gradient.

Results

Electrochemical results.—Steady-state rate potential relations.—The so-called steady-state log *i-V* curves

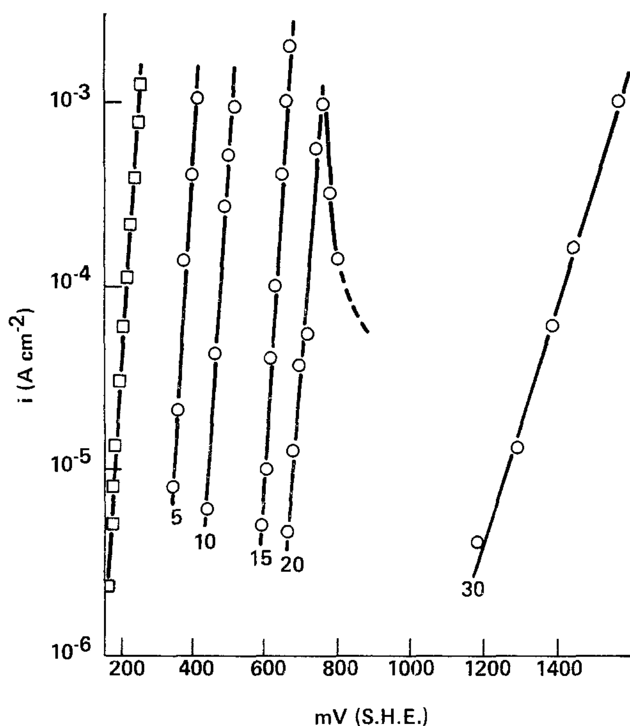

Fig. 1a. Log *i-V* relationship for Cu, Cu-5% Pd, Cu-10% Pd, Cu-15% Pd, Cu-20% Pd, Cu-30% Pd alloys.

for various alloy compositions are shown in Fig. 1a. The potential intercept where the current rises rapidly above 10^{-6} A/cm² can be termed the critical potential, E_c (5). These results were obtained on Type A specimens under potentiostatic control with the current read at 15 min intervals. In the potential range shown, below E_c, where there was no steady-state current, it was necessary to wait 1-2 hr before increasing the electrode potential, in 50 mV increments, to obtain well-defined values of E_c. For each alloy composition within the potential range shown, the results do not differ significantly from those obtained on Type B specimens in the flow cell. There were, however, appreciable differences between the two specimens in the current-time dependence at potentials, $E < E_c$; as discussed in the next section. In the higher current region ($\sim 10^{-4}$ A/cm²) the current on both specimens increased with time after an interval of less than 1 sec.

In Fig. 1a is shown the introduction of passivity at a potential of + 760 mV SHE for the 20% alloy. The result obtained for the 30% Pd alloy differs from the others with respect to the slope of the log *i*-potential relation. Oxygen was evolved under some conditions from this electrode. The results in the first five curves (Fig. 1a) represent the dissolution of copper (characteristic Tafel slope, $2RT/3\mathbf{F}$), while the result for the 30% alloy corresponds to oxygen evolution. For samples held at $\sim 2 \times 10^{-4}$ A/cm² dissolution current for 1 hr, significant grain boundary attack was observed for the 15 and 20% samples.

In Fig. 1b, a comparison of the log *i*-potential results obtained for 80/20 CuPd, 80/20 CuAu, and 80/10/10 CuPdAu is shown. The passivation which sets in for the 20% PdCu alloy is not seen for the gold-containing alloys.

Constant potential current-time relations.—Some initial work was done on log *i-V* curves on pure Cu, thus introducing some Cu^{++} into solution. Subsequent work with alloys was done at lower currents and shorter times than was the initial work with pure Cu. Such measurements lie at the basis of Fig. 1. This same electrolyte was used in all the flow cell measurements and so provides a constant reference for all potentials. In the flow cell, almost all of our work was done at or below the "critical potential," *i.e.*, the final resting current before the electrolyte was blown out

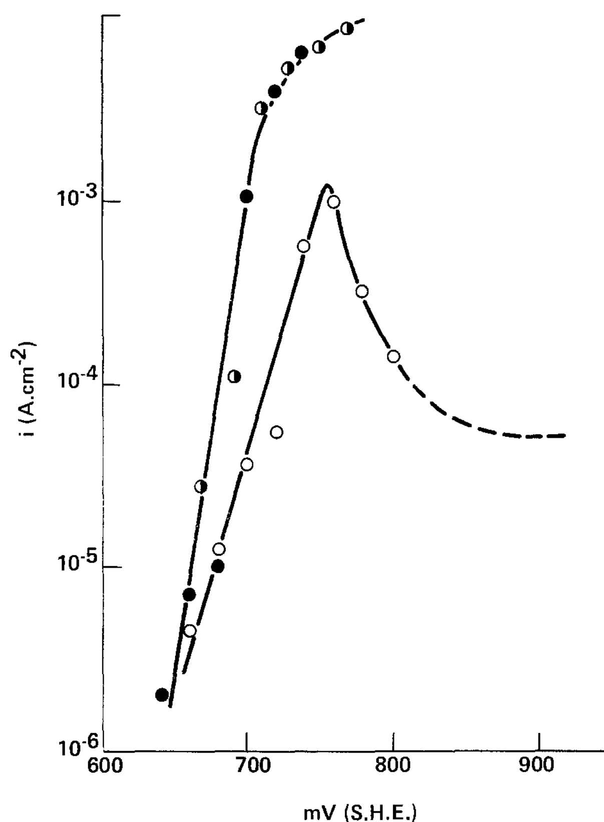

Fig. 1b. Log *i-V* relationship for ○—Cu-20% Pd, ●—Cu-20% Au, ◑—Cu-10% Au-10% Pd.

and the sample submitted for Auger analysis was very low, and, therefore, did not affect the Cu^{++} level of the solution flowing by.

In the potential region less positive than E_c, following a potential step increase, the current showed a step-like increase and subsequent decay. The current decay period was longer for Type A specimens, with current densities of a few microamp/cm² persisting after 2 hr. Except for potentials close to E_c, the current decreased to zero for Type B specimens. The total charge passed for a given potential jump increase could be as much as 5-10 times greater for Type A samples compared to Type B. The Auger data discussed apply to Type B (mechanically polished) samples.

The effect of applying successive 50 mV potential increases is shown in Fig. 2 for the alloy. Following a

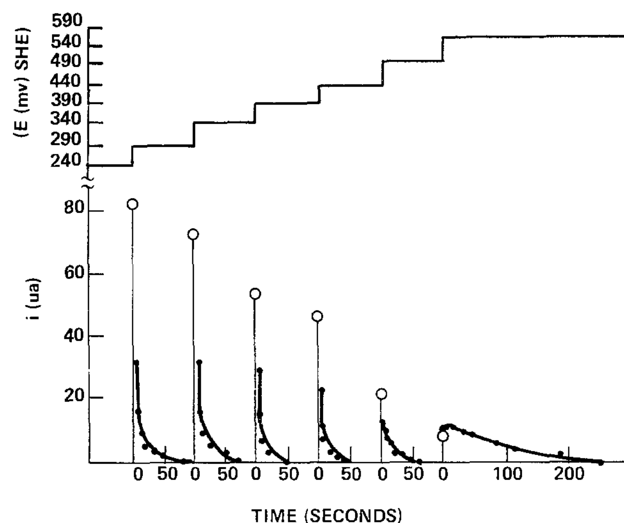

Fig. 2. Current-time behavior for successive 50 mV potentiostatic step increases for Cu-15% Pd alloy. ○ maximum current 15% Pd. Electrode potential shown in upper portion of diagram.

potential increase, the current was allowed to decrease to zero whereupon a second 50 mV potential increase was applied, the process being repeated until the critical potential was reached. As the electrode potential increases, there is a decrease in the maximum current attained for the same potential step increase. As the potential approaches E_c, the decay time increases.

Corrosion.—When the alloy was exposed to the electrolyte without being driven potentiostatically, the electrode potential changed to E_c in a time dependent upon the oxygen content of the electrolyte. The condition of holding the alloy potentiostatically and allowing the current to decay to zero corresponds to a corrosion situation near to the natural one. For set potentials at times when the net current falls to zero, the alloy was removed from the electrolyte and the surface composition measured by AES. The relationship between the corrosion potential and surface composition obtained is shown in Fig. 3 Figure 3 also contains points for the free corrosion situation and for the initial electrode potential measured when the alloy first contacts the electrolyte and before appreciable electrode potential drift has occurred.

AES results.—The Auger spectra from a 70/30 CuPd alloy are shown in Fig. 4. Palladium compositions were calculated utilizing the Pd(330 eV) and Cu(918 eV) peaks and Eq. [1]. The composition depth-profile results for different conditions of potentiostatic control are shown in Fig. 5-7. Surface enrichment by Pd is noted. Figure 5 demonstrates the results of potentiostatically controlling the potential of a 10% Pd alloy at +341 mV SHE for various times. In curve (a) the sample was removed after 480 sec when the current decreased to zero. In curve (b) the alloy was removed after 12 sec when the current had decreased to 4×10^{-5} A/cm^2. The latter case corresponds to ½ the total charge passed at this potential.

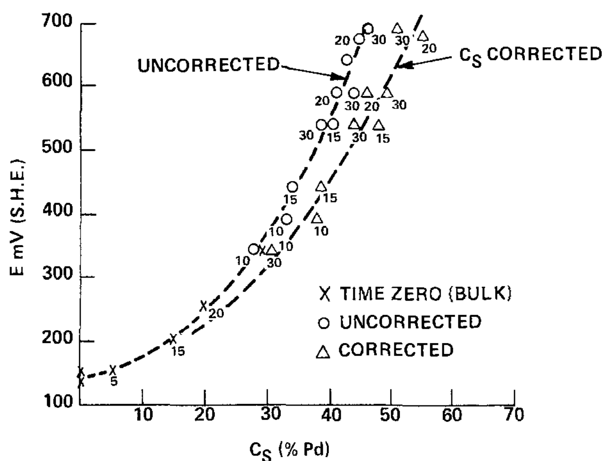

Fig. 3. Surface composition (%Pd) vs. electrode potential. Surface composition determined when net current decreased to zero. All potentials $E < E_c$ for all alloys. ○—C_s as measured; ΔC_s corrected for concentration gradient as described in text; X = initial electrode potential reading for different bulk alloys. Subscripts refer to Pd bulk alloy composition.

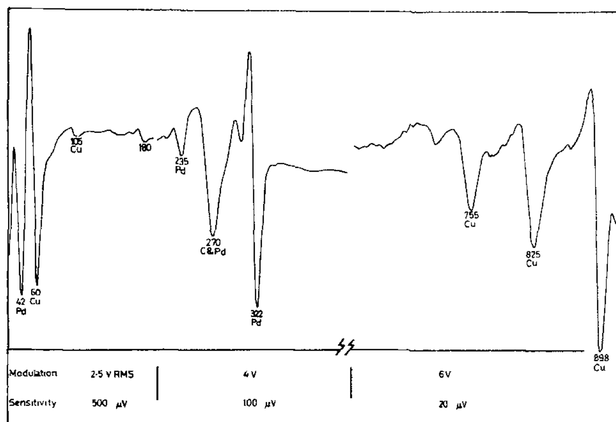

Fig. 4. Auger electron spectra for 70/30 CuPd alloy

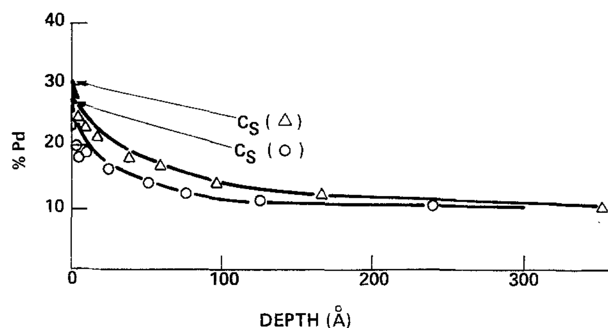

Fig. 5. Composition-depth profile; Cu-10% Pd alloy potentiostated to + 341 mV (SHE). △, t = 480 sec (i = 0); ○, t = 12 sec (i = 40 µa). ○, △; measured data points/full line; corrected composition as described in text.

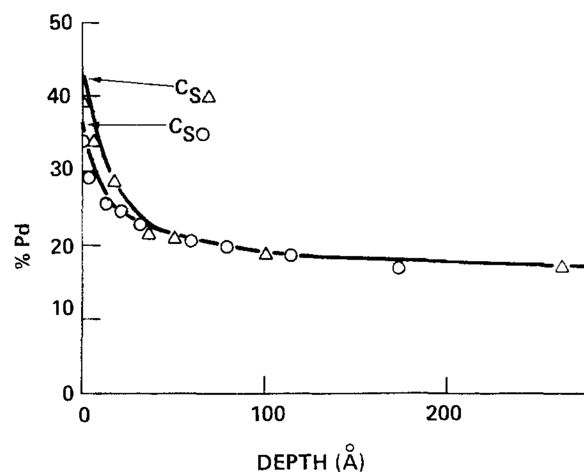

Fig. 6. Composition-depth profile; Cu-15% Pd alloy potentiostated to 441 mV (SHE)○ and 541 mV (SHE)△. ○, △; measured data points/full line; corrected composition as described in text.

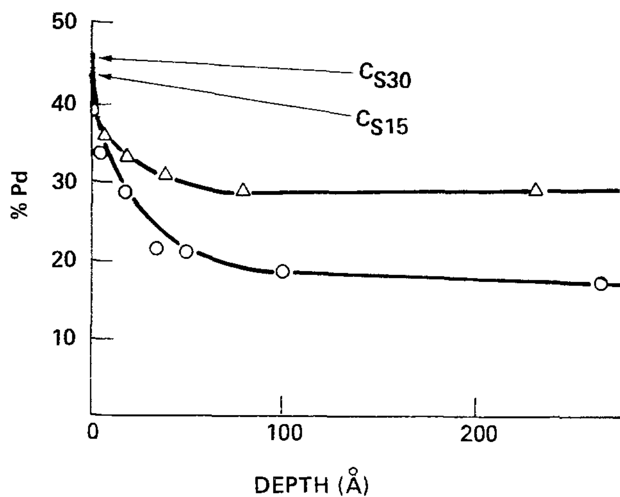

Fig. 7. Composition-depth profile for alloys potentiostated to 541 mV (SHE) △—30% Pd alloy. ○—15% Pd alloy. △, ○ measured points/full line; corrected composition as described in text.

Figure 6 illustrates the concentration profiles obtained after potentiostatic control of a 15% alloy to 441 and 541 mV. In both instances the alloy was removed when the net current decreased to zero, *i.e.*, when corrosion conditions pertain. Figure 7 illustrates the dif-

ference obtained in potentiostatically controlling a 20 and 30% alloy to 541 mV. The alloys were removed from the electrolyte when the current decreased to zero. A key factor to note is that the surface composition is nearly the same for a given set potential independent of the bulk alloy composition and that the concentration gradient is correspondingly steeper for the lower concentration alloy.

Discussion

Exchange current density: An order of magnitude estimate.—The positive shift in electrode potential required for the anodic dissolution of copper from copper-palladium alloys is similar to that observed for CuAu alloys (4-6). This potential shift is greater than that which can be attributed to changes in the reversible potential of Cu in the alloy due to the reduced activity of copper compared with that of pure Cu. The change in the reversible electrode potential, compared to pure copper, as a function of palladium content can be estimated from the thermodynamic data given by Hultgren *et al.* (12). With ΔG_{Cu} values calculated at 278°K from the tabulated values of ΔH_{Cu} and ΔS_{Cu}, the change in the reversible potential $2F(E_{rev}^{alloy} - E_{rev}^{Cu}) = -\Delta G_{Cu}$, is calculated as a function of alloy content with the results tabulated in Table I. As a result of the formation of ordered phases at lower temperatures, these values could be slightly underestimated, but it is improbable that the alteration compared with the calculated values of Table I would exceed 10 mV.

The fact that the measured electrode potential at zero current is nearly 500 mV more positive than E_{rev}^{Cu} for an alloy with a 50% Cu surface composition (Fig. 3) suggests that the electrode potential is a mixed potential arising from an anodic copper dissolution current and a cathodic oxygen reduction current. The positive shift in electrode potential compared with the reversible potential of Cu in the alloy (Table I) is consistent with a decrease in the exchange current density, i_o, for copper dissolution as the palladium content is increased. An estimate of i_o as a function of alloy composition can be obtained from the data in Fig. 1a and the estimated values of the alloy reversible potential. The Tafel slope for the 5-20% Pd alloys is the same as for pure copper. Extrapolation of the log i-V plot back to the reversible potential corresponding to the estimated surface composition allows an estimation of i_o for that composition. The surface composition is taken from Fig. 3 and corresponds to that at the critical potential for each particular value of bulk composition. The pertinent values are given in Table II.

These extremely low values of the exchange current density for the dissolution of Cu from the alloy are to be compared with the measured value of $i_o = 4 \times 10^{-6}$ A/cm^2 for pure copper for this Cu^{++} concentration. The latter value compares not unreasonably with a value of 0.9×10^{-6} A/cm^2 calculated from the data of Mattson and Bockris (13) by using the relationship, $i_o^{(1)}/i_o^{(2)} = (C_{Cu^{++}}^{(1)}/C_{Cu^{++}}^{(2)})^{3/2}$, where $C_{Cu^{++}}$ equals 0.15 M/l in the work of Mattson and Bockris and is 1.7×10^{-6} M/l in the present work. The interpretation of such low values of i_o and their implications for corrosion are discussed in a later section.

The critical potential, E_c.—As the electrode potential becomes more positive, the palladium concentration at the surface during dissolution increases. This occurs both for potentiostatic control and under freely corroding conditions. Potential drift experiments conducted at different oxygen partial pressures show that oxygen reduction ($O_2 + 4H^+ + 4e^- \rightarrow 2H_2O$) is the cathodic reaction. Thus, the quicker rise of the electrode potential for the oxygen-saturated solution compared to a N_2 bubbled solution is shown in Fig. 8. The stable corrosion potential obtained under freely corroding conditions corresponds almost to the critical potential. If the alloy is potentiostatically controlled at potentials more positive than this, the current voltage relationship follows the Tafel line shown in Fig. 1a. Thus, for a given bulk alloy composition, there is an upper limit to the amount of the palladium enrichment which may be attained before copper is anodically dissolved from the alloy with the characteristic copper dissolution Tafel slope.

Gerischer and Rickert (4) proposed that the surface mobility of Au increases with potential, thereby permitting nucleation of Au-rich areas and leaving access to anodic dissolution of the underlying copper. Pickering and Wagner (5) and Pickering and Byrne (6) proposed that copper is supplied to the surface via a divacancy diffusion process (*cf.* Bockris *et al.*). The vacancy concentration is assumed to be potential dependent, and E_c corresponds to conditions where surface roughening commences.

The composition depth profile changes with time during dissolution and this is shown for a 10% Pd alloy potentiostated at +341 mV in Fig. 5. The curve obtained after 12 sec corresponds to 50% of the total charge passed before the current drops to 0 at 480 sec. The surface composition attains its final value when the current drops to zero. As the potential is increased for a given composition of bulk alloy the surface composition is further enriched with palladium (Fig. 6). For a given electrode potential, the surface composition is approximately the same, independent of the bulk concentration, and evidence for this interesting result is given in Fig. 7. Here the 15% alloy has been held at

Table I. The calculated potential of Cu in the Cu-Pd alloys, compared with that of pure Cu

% Cu	$(E_{rev}^{alloy} - E_{rev}^{Cu})$ (mV)
90	+4
80	+13
70	+32
60	+56
50	+72

Table II. Exchange current densities of Cu dissolution from the alloys from Tafel line

C_b(Pd)	E_c(V)	C_s at E_c(Pd)	E_{rev} at C_s*	i_o (A cm^{-2})
0.00		0.00	0.166	4×10^{-6}
0.05	0.320	0.29	0.196	5×10^{-10}
0.10	0.415	0.37	0.215	5×10^{-12}
0.15	0.575	0.47	0.236	1×10^{-15}
0.20	0.645	0.51	0.240	2×10^{-17}

* Corresponding to $Cu^{++} = 10^{-5}$ M/l.

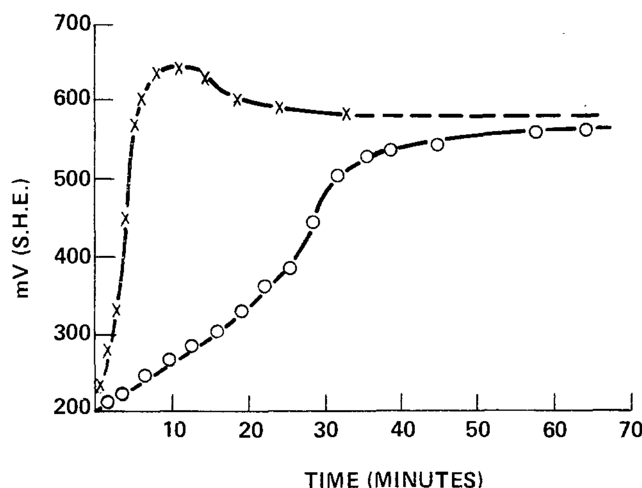

Fig. 8. Electrode potential-time behavior under free corrosion (not potentiostated) conditions for 15% Pd alloy. X = O_2 saturated solution; ○ = deoxygenated by bubbling N_2 for several hours.

~ 30 mV more negative than its critical potential. It is noted that the concentration gradient is steeper than that existing for the 30% alloy which is at a potential well below its critical potential. Thus, at this condition both alloys have the same surface composition and show zero net currents at this potential. Yet, if the electrode potential is raised another 50 mV, the 15% sample will experience anodic dissolution of copper while the 30% alloy remains stable. The difference in the two alloys a few tens of millivolts below the critical potential of the 15% alloy is the magnitude of the concentration gradient.

Corrosion.—The degree to which palladium additions reduce the corrosion rate of copper depends upon the corrosion environment. Although the effective exchange current density decreases by several orders of magnitude for as little as 5 or 10 a/o Pd, the corrosion rate will not necessarily be reduced by the same factor. When the cathodic process is diffusion limited, there will not be a reduction in the alloy corrosion rate compared to pure copper until the alloy i_o for copper dissolution is reduced sufficiently so that the anodic and cathodic currents intersect in the activation-controlled region of the cathodic process. This is illustrated in Fig. 9. Here, the cathodic curve (oxygen dissolution) has been obtained in an O_2 saturated solution for a 30% Pd alloy which was first allowed to corrode freely to a stable corrosion potential. The anodic curves for the various composition alloys are obtained in an N_2 bubbled solution from the data of Fig. 1a. Thus, in spite of the considerable diminution in i_o, the 5% Pd alloy corrodes at the same rate as pure copper, and it is not until the alloy composition reaches 15 a/o Pd that significant reductions in corrosion rate are obtained. The corrosion rate data for this condition are summarized in Table III. These values will change as the value of the cathodic limiting current is changed. The limiting current will be affected by O_2 pressure, stirring, and introduction of impurities which allow alternative cathodic processes, respectively.

Conclusions

Significant findings of this study are summarized below.

1. Passivity of CuPd alloys sets in at 20 a/o of Pd.
2. Composition-depth studies show enrichment of Pd by up to 30%.

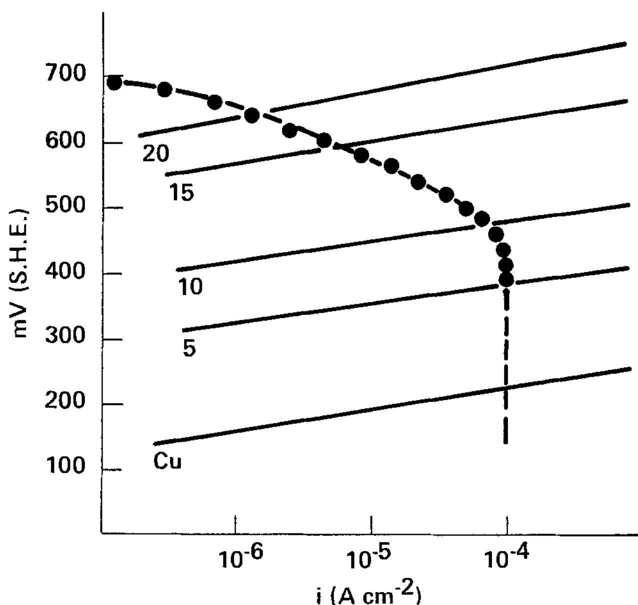

Fig. 9. Log *i-V* plot. Anodic curves for Cu, 5%, 10%, 15%, 20% Pd alloys obtained in N_2 bubbled solution. Oxygen reduction: ● cathodic curve obtained in oxygen-saturated solution for 30% Pd alloy.

Table III. Corrosion rate data for oxygen-saturated solution

C_b(Pd)	i_{corr} (μA/cm^2)	i_{Cu}/i_{alloy}	$V_{corrosion}$
0	100	1.0	215
0.05	100	1.0	380
0.10	72	1.4	475
0.15	5.4	18.5	595
0.20	1.15	87.0	642
0.30	0.3	333.0	680

3. The surface composition is the same under steady-state conditions, for a given potential and is independent of bulk composition.
4. Composition depth profiles are hence steeper for lower Pd concentrations.
5. Addition of Pd to Cu reduces the i_o for Cu dissolution by up to 10^{10} times for Pd concentrations of 20 a/o.

Acknowledgments

We wish to acknowledge R. Parrott for glassblowing expertise in construction of the Auger tube, G. Sage, South Australian Institute of Technology, for use of metallurgical strip rolling facilities, J. K. Howard, IBM Corporation, for supplying the thin film samples used for the ion sputtering calibration, B. Cosh for assistance with electrochemical apparatus, and D. B. Matthews for several helpful discussions. We acknowledge the support of the Australian Research Grants Committee. One of us (J.G.) acknowledges the support of the IBM Corporation in this study.

Manuscript submitted July 18, 1977; revised manuscript received Sept. 7, 1977.

Any discussion of this paper will appear in a Discussion Section to be published in the December 1978 JOURNAL. All discussions for the December 1978 Discussion Section should be submitted by Aug. 1, 1978.

Publication costs of this article were assisted by the Flinders University of South Australia.

APPENDIX

Correction to Measured Composition Depth Profile for High Concentration Gradients

An expression is derived for the corrected surface composition assuming that the initial part of the concentration-depth profile can be approximated by an exponential function. For a homogeneous binary alloy, the Auger signal for component p is given by

$$I_p = K_p X_p \int_0^\infty \exp^{-Z/\lambda_p} dZ = K_p X_p \lambda_p \qquad [A-1]$$

where K_p is a constant incorporating ionization cross section, primary beam current, etc., z is distance into alloy measured from the surface, X_p = atom fraction of component P, and λ_p = Auger electron mean free path for component P.

Similarly $I_c = K_c(1 - X_p)\lambda_c$ for component C of a binary alloy. If X_p is calculated from

$$\frac{I_p}{I_p + \alpha I_c} \qquad [A-2]$$

then

$$\alpha = \frac{K_p \lambda_p}{K_c \lambda_c} \qquad [A-3]$$

Consider a composition gradient which can be approximated by an exponential function, $X_p = (X_{PS} - X_{PB}) \exp^{-z/d} + X_{PB}$, where X_{PB} and X_{PS} equal the bulk and surface compositions of component P, and d equals the exponential decay constant.

Then under this condition

$$I_p = K_p \int_0^\infty [X_{PB} + (X_{PS} - X_{PB}) \exp^{-z/d}] \exp^{-z/\lambda_p} dz$$

$$= K_p X_{PB} \lambda_p + K_p (X_{PS} - X_{PB}) \left(\frac{d\lambda_p}{d + \lambda_p} \right) \qquad [A-4]$$

Similarly

$$I_c = K_c(1 - X_{PB})\lambda_c + K_c(X_{PB} - X_{PS})\left(\frac{d\lambda_c}{d + \lambda_c}\right) \quad \text{[A-5]}$$

Then the measured composition, X_{PM}, calculated from Eq. [A-2] is given by

$$X_{PM} + \frac{\left[X_{PB} + (X_{PS} - X_{PB})\left(\frac{d}{d+\lambda_p}\right)\right]}{\left[X_{PB} + (X_{PS} - X_{PB})\left(\frac{d}{d+\lambda_p}\right)\right] + \left[(1 - X_{PB}) + (X_{PB} - X_{PS})\left(\frac{d}{d+\lambda_c}\right)\right]} \quad \text{[A-6]}$$

After rearranging and solving for X_{PS}, we obtain the surface composition, X_{PS}, in terms of the measured composition X_{PM}, the Auger electron mean free paths, λ_p and λ_c, and the composition-depth exponential decay constant d, which is obtained from the measured, uncorrected composition-depth profile

$$X_{PS} = X_{PB} + \frac{X_{PM} - X_{PB}}{d\left[\frac{1}{d+\lambda_p} - X_{PM}\left(\frac{1}{d+\lambda_p} - \frac{1}{d+\lambda_c}\right)\right]} \quad \text{[A-7]}$$

If d is $>>$ λ_p and λ_c the correction becomes negligibly small.

REFERENCES

1. J. O'M. Bockris, B. Bonciocat, and F. Gutmann, "A Primer in Electrochemistry," Wyckam Press, London (1975).
2. K. Watanabe, M. Hashiba, and T. Yamashina, *Surf. Sci.*, **61**, 483 (1976).
3. R. P. Tischer and H. Gerischer, *Z. Elektrochem.*, **62**, 50 (1962).
4. H. Gerischer and H. Rickert, *Z. Metallkd.*, **76**, 681 (1955).
5. H. W. Pickering and C. Wagner, *This Journal*, **114**, 698 (1967).
6. H. W. Pickering and P. J. Byrne, *ibid.*, **118**, 209 (1972).
7. L. Maissel, "Handbook of Thin Film Technology," pp. 4-40, McGraw-Hill, New York (1970).
8. N. Greene, "Experimental Electrode Kinetics," G.P.I., Troy, N.Y. (1965).
9. A. Damjanovic, T. H. V. Setty, and J. O'M. Bockris, *This Journal*, **113**, 429 (1966).
10. D. A. Huchital and J. D. Rigden, *J. Appl. Phys.*, **43**, 2291 (1972).
11. F. Pons, J. Le Hericy, and J. P. Langeron. *Surf. Sci.*, **51**, 336 (1975).
12. R. Hultgren, R. L. Orr, P. D. Anderson, and K. K. Kelly, "Selected Values of Thermodynamic Properties of Metals and Alloys," John Wiley & Sons, Inc., New York (1963).
13. E. Mattson and J. O'M. Bockris, *Trans. Faraday Soc.*, **55**, 1586 (1959).
14. B. Rubin, A. R. Despic, B. Lovrecek, and J. O'M. Bockris, *Electrochim. Acta*, **17**, 913 (1972).

Reversible Optical Changes Within Anodic Oxide Films on Titanium and Niobium

C. K. Dyer[1] and J. S. L. Leach

Department of Metallurgy and Materials Science, University of Nottingham, University Park, Nottingham NG7 2RD, United Kingdom

ABSTRACT

During passage of cathodic current, large and reversible changes in ellipsometric parameters are interpreted in terms of changes in absorption and/or refractive index of surface anodic oxide films on Nb and Ti without significant change in thickness. A model based on dissolution and ionization of deposited hydrogen satisfactorily accounts for the slow reversible change in the optical absorption of films on Nb and for the impedance changes previously reported. More rapidly reversible changes in both absorption and refractive index occur in films on Ti. The decrease in refractive index is consistent with the reversible formation of TiOOH at negative potentials.

Decreases in electrode impedance of filmed Ti and Nb electrodes occur during cathodic polarization. On raising the electrode potential changes are largely reversible with only a small hysteresis in parallel resistance (R_p) and capacitance (C_p). A bulk mechanism was thought to be involved in which valency changes in the surface oxide films occurred (1). However, the size of the capacitance maximum in both cases was too small to confirm that a bulk faradaic reaction was occurring.

That hydrogen enters the anodic oxide films on Ti and Nb electrodes at low potentials has been demonstrated by measurement of coulombic capacities during potentiodynamic cycling (2). In the case of Nb electrodes the very low impedance at low potential was explained in terms of hydrogen doping of the surface oxide film (3) rather than as a result of a valency change (1). A similar mechanism was proposed to explain the impedance changes of anodic oxide films on Zr (4), and electrolytic rectification can also be explained in this way assuming a bulk oxide effect (2, 5).

Impedance measurements alone cannot justify a model based on bulk changes in the oxide films on Ti and Nb. Coulometric experiments are helpful (2) but the *in situ* optical changes presently reported confirm the bulk nature of the effects at low potentials on filmed Ti and Nb electrodes and support the proposed mechanisms.

Experimental

Specimens.—Spectroscopically pure Ti and Nb rod (Johnson Matthey Chemicals Limited, London) (Table I) was cut, milled, and abraded to reveal

[1] Present address: United Chemi-Con, Incorporated, West Springfield, Massachusetts 01089.

Key words: electrochromism, hydrogen, ellipsometry, impedance, electronic polarizability.

Table I. Spectrographic analysis of materials (impurity element in ppm)

Impurity element	Titanium	Niobium
Cu	40	—
Fe	20	40
Sn	20	—
Al	10	5
Ni	8	—
Si	5	30
Mn	4	—
Mg	<1	<1

a 0.33 cm^2 (Ti) or ~ 1 cm^2 (Nb) flat surface parallel to the rod axis. A Ti wire was permanently attached to the reverse surface and the specimen was anodized to ~200V in 3 weight percent (w/o) ammonium hydrogen tetraborate (99.99% pure) at 50 mA/cm^2 after degreasing in acetone.

After drying, the specimen and contact wire were coated with epoxy resin and hot-cured to give a leak-proof hard seal (6). Several coatings were applied and cured. To reduce the risk of surface beveling during subsequent polishing operations the specimen was mounted, flat surface downward, in thermosetting plastic in a standard metallurgical mounting press. The mounted specimen was abraded in a fixed position on a wheel until the metal surface emerged, which was finally polished also in a fixed position using alumina powder (5-30 nm particle diameter). Polished surfaces obtained in this way were satisfactorily flat. Surfaces were repolished before each anodic film growth.

Cell.—A cylinder, closed at one end, was machined from a block of clear Perspex to 6.3 cm (ID) × 7.6 cm (OD) × 6.5 cm (height). Holes were drilled in the sides to <2.5 cm diam so that their axes intersected at the center of the cylinder at an included angle of 140°. These holes were partly threaded to allow >2.5 cm diam annealed glass windows (F. Wiggins & Son, Sydenham) to be mounted against a PTFE washer, on an internal ledge, applying light pressure by turning a threaded pressure ring. In position, these windows were found to be almost free from strain birefringence and the resulting error was less than that of the ellipsometer itself (<0.015°).

The polished specimen surface was mounted vertically with a rigid clamping system having adjustments for rotation, tilt, and central positioning in the cell.

Ellipsometer.—An automatic ellipsometer with a maximum discrimination of 0.001° was used to follow optical changes during cathodic polarization of anodically filmed Ti and Nb electrodes. The instrument, designed and built by Matheson *et al.* (7), utilized a photoelectric detection system with faraday effect modulation. The light source was a water-cooled compact arc mercury lamp (Wotan HBO 100 W/2 Osram, West Germany). The collimated beam had a diameter of 2 mm and divergence of 0.2° at the specimen surface after passing through a modified Glan-Thompson polarizing prism and a modulator core (of dense SF 57 glass). After reflection from a test surface, the beam then passed through a second modulator core and analyzing prism before reaching the photodetection system. The azimuthal positions of the polarizing (P) and analyzing (A) prisms were measured by Moiré fringe counters to 0.001° and recorded digitally.

The retardation element was a three-reflection Fresnel rhomb (8) which allowed close to 90° retardation over the wavelength range available (from ~390 to ~610 nm). For operation at a single wavelength a quarter-wave mica retardation plate was used in conjunction with a narrow bandpass filter. The quarter-wave plate constants were then determined by four quadrant measurements.

The modulated signal arriving at the photomultiplier tube was electronically decoded and the error signals arising from the out-of-balance position of the polarizing and analyzing prisms were separated by two digital filters. The prisms were then automatically driven to balance positions at 1°/sec by servo motors in response to signals from the electronic decoding system.

The alignment procedure was to set the ellipsometer in the straight-through position and move the specimen surface to bisect the beam. The angle of tilt of the specimen surface was adjusted until, on reflection, there was no movement of the light beam image at the photomultiplier position at all angles of incidence (80°-40°). The sample position during this procedure was not altered since both arms of the ellipsometer were moved simultaneously. Using a dielectric mirror, the system was set so that the positions of the polarizer and analyzer were 0° and 90° ± 0.005° by the method of Forgacs (9). A full description and assessment of the system is published elsewhere (7).

Procedure.—Anodic films on polished Ti or Nb electrodes were grown galvanostatically at 1 mA/cm^2 in 3 w/o ammonium hydrogen tetraborate (99.99%) or 0.1M Na_2CO_3 + 0.1M $NaHCO_3$ buffer solution (AnalaR) both made up with doubly distilled water. From the automatically recorded P and A values tan ψ and Δ values (where tan ψ is the ratio of the resultant reflected amplitude in the plane of incidence and normal to this plane and Δ is the change in phase on reflection) were calculated (10) for a wide range of film thicknesses on each substrate. Polar plots (11) of the vector

$$\overline{Z} = \tan \psi \exp(i\Delta)$$

were compared with polar plots derived from hypothetical values of the film thickness, d, and constant complex refractive indexes of the metal substrate and surface film [$\overline{n}_s = n_s(1 - ik_s)$ and $\overline{n}_f = n_f(1 - ik_f)$, respectively] together with the refractive index of the electrolyte n_m (determined to 3 decimal places by Abbe refractometer). Experimental substrate constants n_s and k_s were determined by comparison of the experimental data with these theoretical polar plots and the assumption of a constant film refractive index (n_f variation <3%) and a zero absorption coefficient, k_f in the experimental data for different thicknesses (6). This is a more reasonable assumption than using "as polished" P and A values which led to calculated refractive indexes which increased with film thickness (6). Using these n_s and k_s values, film thickness, n_f and k_f were calculated using a standard computer program (11a).

During cathodic polarization a constant current was passed and P and A values were recorded together with the electrode potential. The cell was then open-circuited and the recovery of these parameters was followed as a function of time.

Impedance measurements.—Using a square-wave bridge technique described elsewhere (1), the parallel resistance (R_p) and capacitance (C_p) of the electrodes at 300 Hz were measured after the cell was open-circuited following cathodic polarization.

Results

Ti electrodes.—Application of a constant cathodic current density of 0.5 mA/cm^2 to anodically filmed electrodes resulted in rapid and large changes in P and A or Δ and ψ (Fig. 1). The cell was open-circuited at an electrode potential of ~ −1.15V (NHE)[2] which is the potential of the impedance minimum (1, 12) in the carbonate buffer solution (pH 9.7). P and A then returned rapidly to recover ~90% of the change in ~100 sec with complete recovery after 2 hr or on application of an anodic charge ~3 mC/cm^2. The electrode potential and impedance also recovered

[2] All potentials are referred to the normal hydrogen scale.

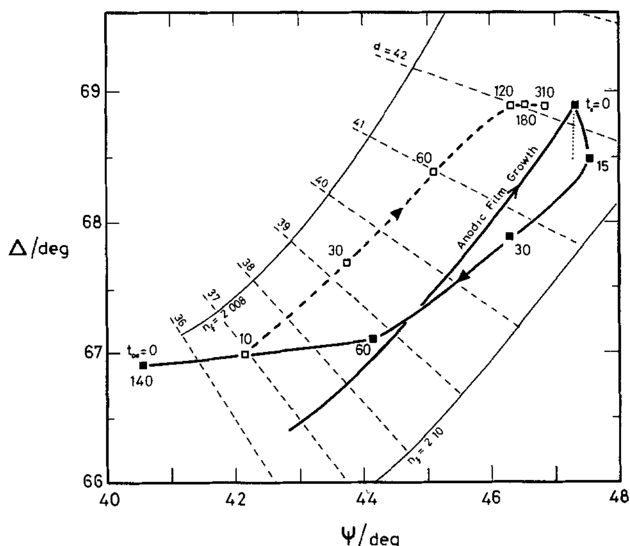

Fig. 1. Effect of a cathodic current (0.5 mA/cm^2) with time, t, on Δ and ψ of a filmed Ti electrode in carbonate buffer before and after open-circuiting at $E = -1.15V$ (NHE). λ = 546.1 nm, angle of incidence = 70°, n_m = 1.335. ■—■ with cathodic current, □- - -□ on open circuit (time in seconds is indicated during each stage). Also shown are calculated Δ/ψ relationships for constant n_f and k_f = 0 (——, variable d), constant d and k_f = 0 (– – – –, variable n_f), and constant d and n_f (. . . . . . ., increasing k_f) for n_s = 2.0, k_s = 2.7.

$\mu F \cdot cm^{-2}$, $\Delta R_p^{-1} = 7 \times 10^{-3} \Omega^{-1} \cdot cm^{-2}$, $\Delta n_f = 0.0115$, $\Delta k_f = 0.001$).

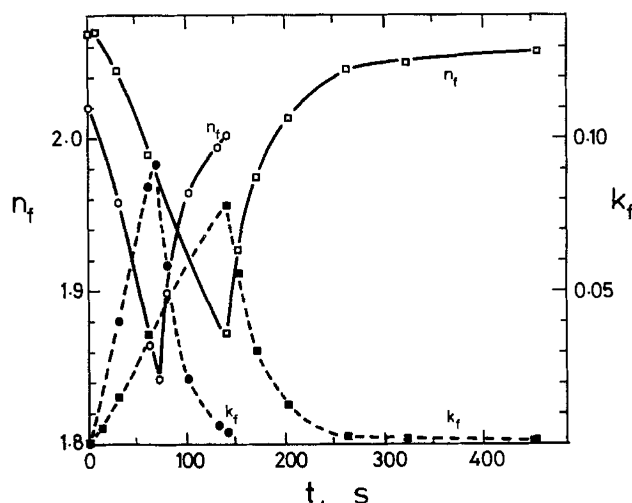

Fig. 2. Effect of a cathodic current (0.5 mA/cm^2) with time on optical parameters of anodic films on Ti before and after open-circuiting at $E = -1.15V$ (NHE): n_f (○), k_f (●) of 34.7 nm film (open circuit after 80 sec), and n_f (□), k_f (■) of 42.2 nm film (from Fig. 1 data) (open circuit after 140 sec) for n_s = 2.0, k_s = 2.7. λ = 546.1 nm, angle of incidence = 70°, n_m = 1.335.

rapidly on open circuit. If the change in ellipsometer readings was influenced wholly or partly by the formation of metallic hydride at the substrate, P and A readings would be irrecoverable on the observed time scale on open circuit because of the irreversibility of hydride formation (6, 12). The substrate was thus considered unaffected by this cathodic polarization.

To determine the effect of cathodic polarization on the thickness and optical properties of the surface film, a range of possible combinations of film thickness, d, refractive index, n_f, and absorption coefficient, k_f, were computed to fit the measured P and A combinations. Since there are only two measured parameters an assumption has to be made about one of the film parameters to determine uniquely the other two. The experimental Δ *vs.* ψ data (Fig. 1) show that the cathodic current does not simply cause film thinning, there is a movement, with time, of the data across lines of constant n_f and k_f. A constant film thickness during cathodic polarization was assumed because with the alternative assumptions that either n_f or k_f were constant, the measured P and A values could arise if the film underwent a large reversible change in thickness, *e.g.*, from 34.7 to 25.4 nm in the present case. It is unlikely that any significant amount of TiO_2 could be reduced to metallic Ti and then reoxidized reversibly and rapidly on open circuit to the original thickness even at the metal/oxide interface under the present conditions. Also reduction then oxidation of the substrate would change the optical constants significantly and irreversibly and thence the P and A readings, which was not the case.

Figure 2 shows that both n_f and k_f change with time during the passage of 0.5 mA/cm^2 cathodic current and on open-circuiting the cell. A constant film thickness is assumed throughout these experiments. For the thicker of the two surface films (42.2 nm) the changes were slower at the same current density.

n_f and k_f together with the electrode capacitance (C_p) and conductance (R_p^{-1}) are all related to time on open circuit, t, initially in a $t^{0.5}$ manner over the same period of time (Fig. 3 and 4). Recovery of C_p, R_p^{-1}, n_f, and k_f is not quite complete after 300 sec where there is a small net change ($\Delta C_p \simeq 19$

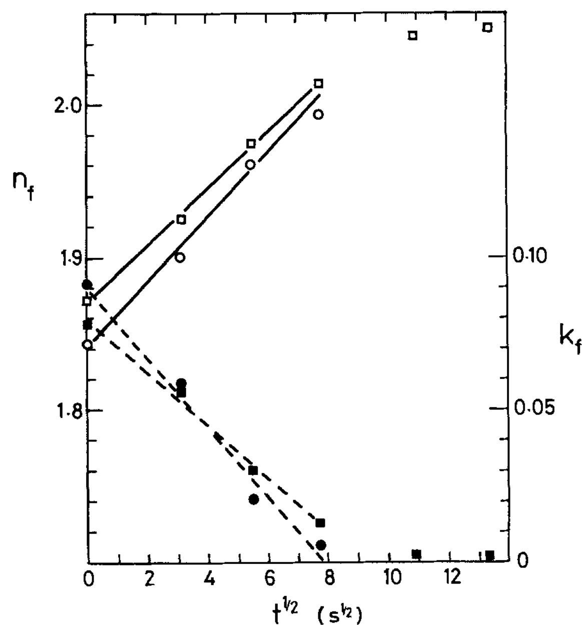

Fig. 3. Data from Fig. 2 plotted against (time on open circuit)$^{1/2}$

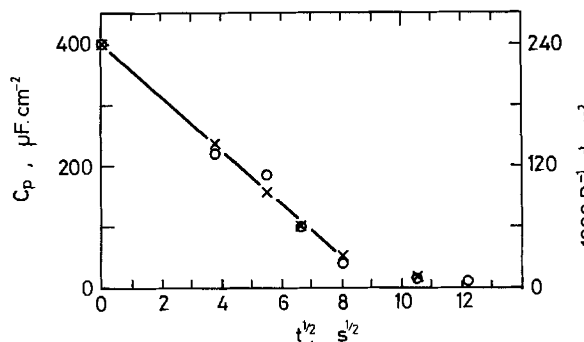

Fig. 4. Open-circuit decay from $E = -1.15V$ (NHE) of parallel electrode capacitance (X) and conductance (○) of Ti electrode filmed to 34.7 nm, in carbonate buffer solution.

Table II. Refractive indexes and derived polarizabilities at (i) −1.15V (NHE), (ii) the maximum change in n_f in carbonate buffer solution, for films (thickness, d) on Ti electrodes

	(i)		(ii)	
d (nm)	34.7	42.2	34.7	42.2
n_f (EXPTL)	1.8442	1.8678	1.7488	1.7577
$\alpha_{EXPTL} \div 10^{-23}$ cm³	0.451	0.447	0.413	0.405
TiOOH (%)	50.8	54.0	80.9	87.3

A more rapid change in n_f and k_f was found to accompany higher cathodic current densities on the same electrodes. After ~30 sec at 2.5 mA/cm², n_f and k_f became constant at values which were lower and higher, respectively, (Fig. 5, Table II) than at −1.15V (NHE) (Fig. 2). Increase in cathodic current density produced no further change. Recovery on open circuit was complete but slower (Fig. 5) than after less severe cathodic polarization (Fig. 3).

Nb electrodes.—The effect of cathodic current on Δ and ψ after anodic oxide growth on a Nb electrode is shown in Fig. 6. The data do not indicate simply film thinning. Recovery occurred on open-circuiting and was complete after long times or on passage of an anodic current [at fields too low for oxide film growth by ionic transport (2, 3)] (Fig. 6). It was thus considered unlikely that any significant film thinning occurred during passage of cathodic current since the observed reversibility of the phenomenon would require substantial film thickening under open-circuit conditions. The film thickness on Nb electrodes was assumed to be constant during cathodic polarization. Alteration of substrate optical constants by hydride formation in this case was again considered unlikely since the electrode showed complete recovery of *P* and *A* values on open circuit and the films had a low capacity for hydrogen (2). Surface hydride forms at very much higher cathodic current densities ~0.5 A/cm² (3) and its formation would be effectively irreversible during the time on open circuit.

Changes in n_f and k_f on passage of cathodic current were computed for films grown to 12.6, 28.7, and 51.9 nm on Nb electrodes. Changes in k_f comparable in magnitude and rate to those of the films on the Ti electrodes required much higher cathodic current densities (~10 mA/cm²) or thinner films (Fig. 7, 8, and 9). Recovery of k_f on open circuit was comparatively slow (Fig. 10) but faster following <10 mA/cm²

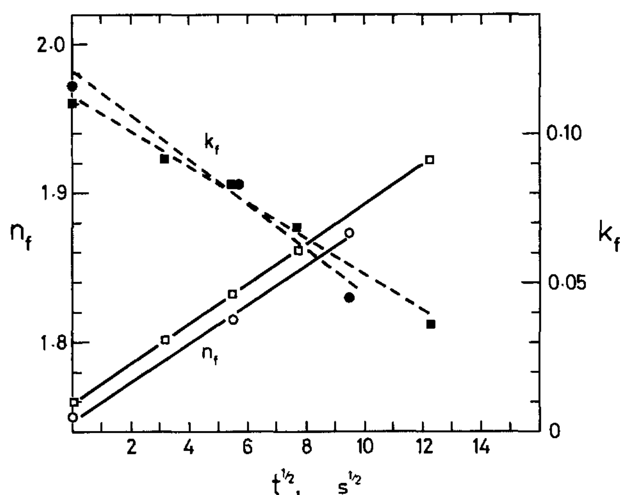

Fig. 5. Recovery of optical parameters of anodic films on Ti with (time on open circuit)$^{1/2}$ after 2.5 mA/cm² cathodic current for 45 sec (34.7 nm film; ○, ●) and 60 sec (42.2 nm film; □, ■).

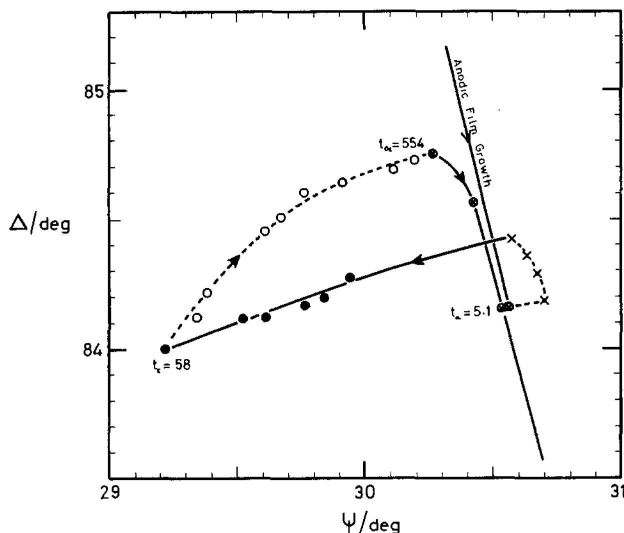

Fig. 6. Effect of cathodic current (10 mA/cm²) with time on Δ and ψ of a filmed Nb electrode. X---X open circuit after film growth, ●——● cathodic current, ○---○ open circuit, ⊗——⊗ anodic current (0.14 mA/cm²) (time in seconds indicated for each of these stages). λ = 546.1 nm, angle of incidence = 70°, n_m = 1.335.

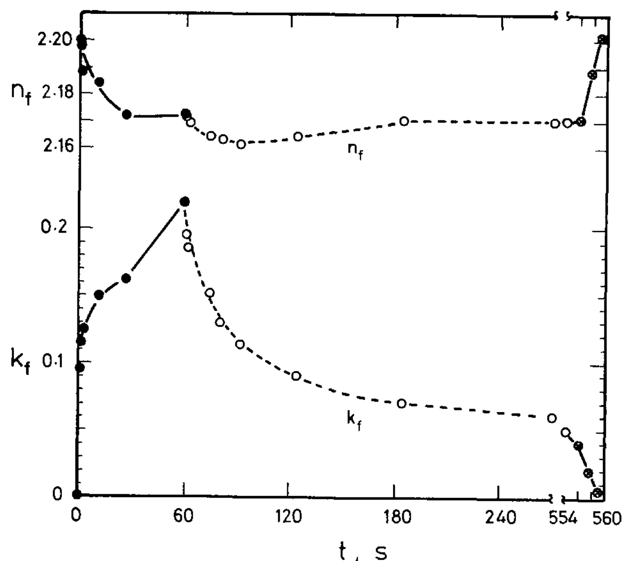

Fig. 7. Effect of cathodic current (10 mA/cm²) with time on optical parameters of 12.6 nm anodic oxide film on Nb electrode. Analysis of data from Fig. 6 with n_s = 2.85, k_s = 3.15.

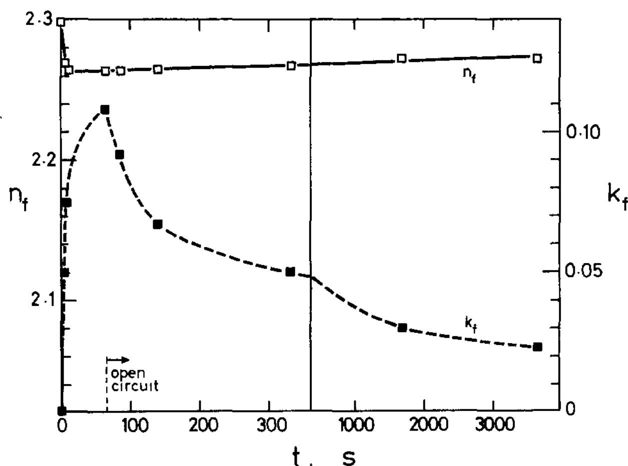

Fig. 8. Effect of cathodic current (10 mA/cm²) with time on optical parameters of 28.7 nm anodic oxide film on Nb electrode. λ = 405.0 nm, n_s = 2.7, n_m = 1.335, angle of incidence = 70°, k_s = 2.5.

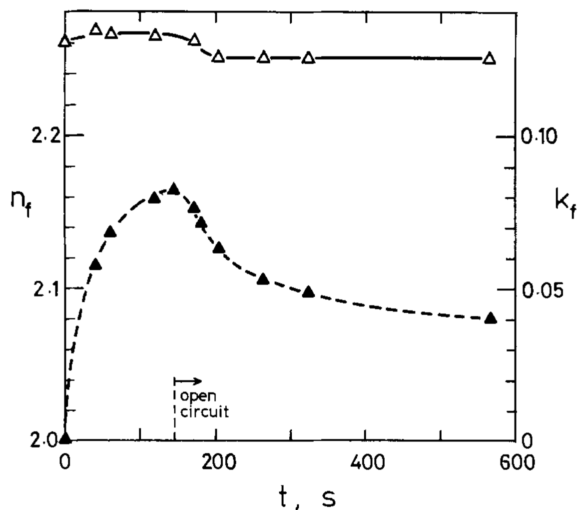

Fig. 9. Effect of cathodic current (10 mA/cm²) with time on optical properties of a 51.9 nm anodic oxide film on a Nb electrode. λ = 470 nm, n_s = 3.0, k_s = 2.9, n_m = 1.335, angle of incidence = 70°.

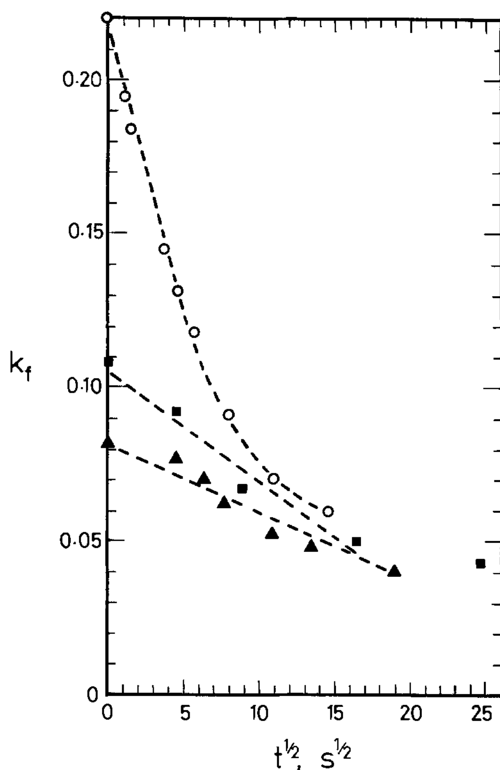

Fig. 10. Optical absorption data from Fig. 7-9 plotted against (time on open circuit)$^{1/2}$.

cathodic current density and was complete after $\geq$10 hr or on passage of a small anodic charge. Changes in n_f were small and slowly reversible in contrast to the behavior of the oxide films on Ti electrodes.

Discussion

The optical properties of oxide films on Ti and on Nb change reversibly during cathodic polarization and the results indicate that: (*i*) There is a significant difference between the optical behavior of the surface films on the two metals; (*ii*) the large changes in the optical parameters suggest that cathodic current flow modifies the bulk properties of the surface oxide films on both metals; and (*iii*) the speed of the decrease in n_f and/or increase in k_f is dependent on oxide thickness, cathodic current density, and the substrate metal. There is a difference in the rates of these changes between films on Ti and Nb electrodes.

Changes in k_f.—The impedance data for Ti electrodes show the same time dependence as n_f and k_f and have been shown previously to be characteristic of an effect in the bulk oxide rather than at the interfaces (metal/oxide or oxide/electrolyte) (12).

The recovery of k_f and of impedance for films on Nb electrodes on open circuit after cathodic polarization were at similar rates taking several hours (3).

Examined with variable wavelength (before cathodic polarization) absorption by anodic Ti oxide does not have a sharp "edge" but in common with other amorphous materials absorption was found to increase steeply (13) at $\lambda \sim 430$ nm corresponding to a bandgap of $\sim$2.88 eV. This value compares with that for the crystalline forms of TiO_2: anatase (3.04 eV) (14) and rutile (3.05 eV) (15). After cathodic polarization the absorption increase had moved to $\lambda \sim 415$ nm, *i.e.*, the bandgap increased to $\sim$2.99 eV but the absorption at longer wavelengths was still significant. Similar observations were reported on reduction of rutile or anatase which also showed an increase in bandgap of the same order of magnitude (14). This was interpreted in terms of donor sites (singly or doubly ionizable oxygen vacancies) in the oxide which, with increasing concentration, produce a "blurring" of the absorption "edge" effectively broadening the bandgap. The donor species in the present case would be hydrogen dissolved in the oxide films on Ti. The bandgap of anodic oxide film on Nb electrodes was $\sim$3.18 eV and the increase, after passage of cathodic current, was to energies corresponding to wavelengths below those available with the ellipsometer.

The proposed interpretation of the recovery in R_p and C_p of filmed Ti and Nb electrodes after cathodic polarization was in terms of the effects of the presence of hydrogen within the surface oxide films (3, 12). At negative potentials hydrogen was considered to act as a donor impurity in raising the conductivity of the surface oxide films [in addition to acting as a faradaic reactant in films on Ti electrodes (12)].

The ionization energy of hydrogen (=13.62 eV) is dependent on the dielectric constant, ϵ, of the medium. Assuming the electron can be considered to move in a coulombic field

$$E_D = E_H \cdot \frac{m_{ef}}{m} \cdot \frac{1}{\epsilon^2} \qquad [1]$$

where E_D is the least energy required to promote an electron from the donor hydrogen to the lowest level of the conduction band, E_H is the ionization energy for hydrogen, m_{ef} is the effective mass and, assuming this is approximately equal to m (electronic mass), $E_D \simeq 1.7 \times 10^{-2}$ eV for the surface films on Ti using $\epsilon \simeq 20$ (6) and $E_D \simeq 6.3 \times 10^{-5}$ eV in anodic films on Nb [$\epsilon \simeq 60$ (3)]. The value of ϵ for TiO_2 is significantly different from that for crystalline rutile but is not unexpected for "glassy" oxides as is the case for low voltage anodic TiO_2 (6). A significant proportion of electrons will be donated at room temperature ($kT \simeq 2.5 \times 10^{-2}$ eV) giving rise to the observed conductivity in addition to optical absorption at low photon energies ($h\nu < E_{bandgap}$).

The nearly complete recovery of k_f, R_p^{-1}, and C_p occur with the same time dependence during the same time interval (Fig. 3 and 4). Previously (3, 12), the frequency dependence of R_p and C_p at low frequencies (*e.g.* < 10 kHz) which are characteristic of the surface of the highly conducting film, was evidence for a reversible surface reaction (the hydrogen deposition reaction) dependent on diffusion in the oxide. The electrode potential, E, under these conditions is expected to be related to the diffusion of hydrogen to the oxide surface since E depends on surface concentration. The change in potential with hydrogen coverage θ_H, is $\partial \ln \theta_H / \partial E = -K$, where K is a constant. In the present case assuming that the change in surface coverage of hydrogen depends on diffusion in the bulk oxide and is proportional to $(Dt)^{-1/2}$

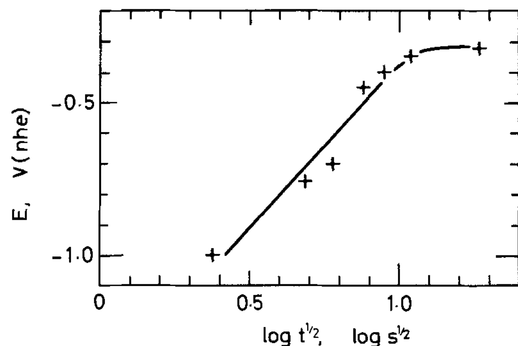

Fig. 11. Electrode potential, E, of a Ti electrode filmed to 34.7 nm as a function of time on open circuit after polarizing to $E = -1.15$V (NHE) at 0.5 mA/cm².

then $E \propto 1/2 \log t$. Figure 11 shows that this relationship is approximately followed on open-circuiting at $E = -1.15$V (NHE) over the same time interval as the (bulk) optical changes, verifying the dependence of the surface reaction on diffusion in the oxide.

The larger cathodic current requirement for significant k_f changes and the slower reversibility in films on Nb electrodes is consistent with the potentiodynamic behavior (2) which showed a lower susceptibility to hydrogen uptake and slower kinetics.

Changes in n_f.—The most remarkable effect of cathodic polarization is the influence on the real part of the refractive index, n_f, of films on Ti electrodes. The change in n_f is large and rapidly reversible with the same time dependence as k_f (Fig. 2, 3, and 5) and indicates an additional effect of the presence of hydrogen in the oxide film.

At negative potentials, coincident capacitance and conductance maxima appear. This is characteristic of a reversible electrochemical reaction (16). The capacitance maxima increased with increasing film thickness and there was no significant change in the surface area at different thicknesses. This indicated (12) that not only reaction at the surface was involved, but that a reaction such as

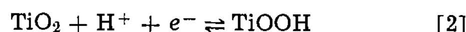

$$TiO_2 + H^+ + e^- \rightleftharpoons TiOOH \qquad [2]$$

was occurring in the bulk of the oxide film. The low magnitude of the capacitance maxima, however, was considered to be a result of the low reversibility of reaction on a time scale ~1 msec or less (12), as indicated by the broadness of the capacitance peak (16).

The observed n_f changes in TiO_2 could possibly be explained in terms of a very large reversible change in film density. However, at low fields (associated with the cathodic current) the electrostrictive effect is vanishingly small and a reversible and major change in the number of molecules in the oxide film at constant thickness is not likely. The reversible changes in n_f on a time scale of tens of seconds imply a reversible change in the electronic polarizability of the film molecules (α_m). The formation of TiOOH, as in Eq. [2] would be accompanied by a decrease in n_f since electronic polarizabilities of ions (α_i) are approximately additive (17) to give α_m, and $\alpha_{O^{2-}} > \alpha_{OH^-}$. Departures from simple additivity arise from a nonideal crystal state and overlapping of wave functions. To test for additivity in the case of TiO_2 the refractive indexes of the different crystalline forms will be considered using the Lorentz-Lorenz equation

$$\frac{n^2 - 1}{n^2 + 2} = \frac{4\pi}{3} \Sigma N_i \alpha_i \qquad [3]$$

where N_i is the number, per unit volume, of ions of polarizability α_i. Thus

$$\alpha_{TiO_2} = \frac{3}{4\pi} \frac{M}{N\rho} \frac{(n^2 - 1)}{(n^2 + 2)} \qquad [4]$$

where M = molecular weight of TiO_2, ρ = density, and N = Avogadro number. For comparison with the anodic film, each of the crystalline forms (anatase, brookite, and rutile) will be considered as randomly oriented microcrystals of single crystal density so that the average refractive indexes (at wavelength, λ = 588.9 nm) are: 2.5246, 2.6226, and 2.7545, respectively, with densities of 3.9, 4.13, and 4.23 g/cm³, respectively (18). Using these data in Eq. [4] the molecular polarizability of TiO_2 is remarkably similar for the widely different crystal forms, *viz.*, 0.522, 0.508, and 0.515×10^{-23} cm³, respectively, for anatase, brookite, and rutile. It is reasonable then to suppose that α_{TiO_2} for the anodic oxide is not dissimilar from an averaged value between the three crystal forms, which is 0.515×10^{-23} cm³. At the wavelength λ = 546.1 nm (Fig. 2, 3, and 5) the correction for optical dispersion is $\sim 0.001 \times 10^{-23}$ cm³ (6). This correction is smaller than the difference between the calculated α_{TiO_2} values of the different crystal structures and will be ignored.

Using $\alpha_{TiO_2} = 0.515 \times 10^{-23}$ cm³ in Eq. [4], the density of the 34.7 nm anodic film is 3.1214 g/cm³. This value of ρ together with M = 80 can be used at negative potentials where a change in the number of molecules or Ti ions is unlikely (Eq. [3]) for a constant film thickness (as already discussed). The amount of water in the film is not expected to change significantly and may contribute $< 0.01 \times 10^{-23}$ cm³ to the derived electronic polarizability.

Using Pauling's value (20) for $\alpha_{Ti^{4+}} \simeq 0.019 \times 10^{-23}$ cm³, the additivity relationship for α_{TiO_2} yields $\alpha_{O^{2-}} = 0.248 \times 10^{-23}$ cm³. With $\alpha_{OH^-} = 0.122 \times 10^{-23}$ cm³ (17) in Eq. [2] and assuming x is the fraction of molecules of TiO_2 converted to TiOOH, the average polarizability per molecule is then

$$\alpha_{Ti^{4+}} + \alpha_{O^{2-}} + (1 - x)\alpha_{O^{2-}} + x\alpha_{OH^-} = \alpha_{EXPTL}$$

so that

$$x = \frac{0.515 - \alpha_{EXPTL}}{0.126} \qquad [5]$$

In deriving Eq. [5] we have assumed that $\alpha_{Ti^{3+}} \simeq \alpha_{Ti^{4+}}$. We can find no published data for the electronic polarizability of Ti^{3+} but do not expect it to significantly alter calculated values of x.

At $E = -1.15$V (NHE), which is the potential of minimum electrode impedance [a phenomenon associated with a reversible or equilibrium potential (16)] the values of α_{EXPTL} derived from the measured n_f correspond to $x \simeq 0.5$ in Eq. [5] (Table II). (If $\alpha_{Ti^{3+}}$ were 50% higher than $\alpha_{Ti^{4+}}$, then values of x would be only ~8% higher.)

At the equilibrium potential of reaction [2] the effective concentrations of TiO_2 and TiOOH would be equal from thermodynamic considerations. The derived molecular composition of the anodic oxide films (Table II) at the reversible potential of the equilibrium reaction [2] (12) supports the concept of changes occurring in the bulk of the oxide film on Ti and the use of this equation to describe them. Below $E = -1.15$ (NHE) (at higher cathodic currents or after a longer time), the lowest refractive indexes found correspond with nearly complete conversion of TiO_2 to TiOOH.

Such large optical changes cannot readily be interpreted by models in which the changes in valency of the oxide occur only at surfaces of the oxide films.

There was more than sufficient cathodic charge passed to account for both n_f and k_f changes. ~35 mC of charge was passed by the 34.7 nm filmed Ti electrode before open-circuiting; this was ~5 times more than required to convert half of the TiO_2 molecules to TiOOH. Most of the hydrogen produced by this charge was released as gas in the hydrogen evolution reaction.

There is a small change in n_f with the passage of cathodic charge by filmed Nb electrodes and it de-

creases with increase in film thickness (Fig. 7-9). Using $\alpha_{Nb_2O_5} = 1.292 \times 10^{-23}$ cm^3 [from $\alpha_{O^{2-}} = 0.248 \times 10^{-23}$ cm^3 and $\alpha_{Nb^{5+}} = 0.026$ (19)] and arguments similar to those for films on Ti, the derived decreases in average polarizability per molecule ($\Delta\alpha_m$) on cathodic polarization are: 0.026, 0.020, and 0.009×10^{-23} cm^3 for the 12.6, 28.7, and 51.9 nm films, respectively. Assuming the formation of OH^- from O^{2-} ions in a reaction such as

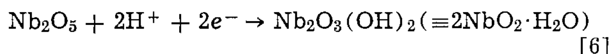

$$Nb_2O_5 + 2H^+ + 2e^- \rightarrow Nb_2O_3(OH)_2 (\equiv 2NbO_2 \cdot H_2O) \quad [6]$$

the change in n_f corresponds to ~10% conversion of the 12.6 film. The decreasing change in n_f and α_m with increase in film thickness is characteristic of a surface effect, which, from the present figures, extends only to a few (3 to 5) (20) molecular layers of oxide.

Impedance measurements over a wide frequency range (3, 12) have also indicated a difference in the behavior of anodic oxide films on Ti and Nb at negative potentials. That the change in n_f on Nb electrodes is not characteristic of a reversible faradaic bulk reaction and is only slowly reversible is consistent with the absence of a distinct impedance minimum (3) at negative potentials. This model implies that the low impedance cathodic behavior of oxide covered Nb electrodes (3) arises mainly from conductivity changes in the bulk of the film and not from a reversible reaction in the bulk oxide. In this respect Nb differs from Ti where impedance changes (12) involve changes in conductivity and a reversible faradaic reaction in the bulk oxide film.

Rates of change of optical parameters.—Changes in the films during cathodic treatment and/or on open circuit are nonhomogeneous since the Δ/ψ data follow a different path during recovery of the electrodes on open circuit. Since hydrogen, deposited at the oxide/electrolyte interface, dissolves in the oxide films, the change in optical properties proceeds from this interface toward the metal/oxide interface. The films may approach homogeneity just after the open-circuit condition or during cathodic treatment to where there is no further change in the ellipsometric parameters at low potentials (Table II). At other conditions, where the parameters are rapidly changing, unambiguous analysis for regions of different optical properties within the oxide films cannot be done since the oxide must be considered multiphase, and two measured optical parameters are insufficient for a complete interpretation; under these conditions our calculated n_f and k_f values are approximations.

For both electrodes, rates of change of the calculated n_f and k_f on cathodic polarization were faster in thinner films (Fig. 2, 7, 8, and 9) as implied by the proposed model of hydrogen diffusion. Similarly on open-circuiting, initial changes were faster for the thinner films.

Calculation of the exact diffusion coefficient is, of course, complicated by the absence of data on the concentration gradient of hydrogen in the oxide, even though at −1.15V (NHE) films on Ti electrodes comprise ~50% TiOOH and TiO_2. Assuming a constant concentration of hydrogen at the surface and bulk concentrations similar for the two oxides, the relative diffusion coefficients for hydrogen in the films on Ti and Nb are $\sim 10^{-13}$ and $\sim 10^{-14}$ cm^2/sec, respectively. The assumption of a higher bulk concentration, which is more likely but unknown, would yield significantly faster rates of diffusion.

Summary

Cathodic polarization of filmed Nb electrodes involves large and reversible changes in the optical absorption due to solution and ionization of deposited hydrogen in the surface films. Only small changes in the refractive index occur.

Cathodic treatment of filmed Ti electrodes produces large and more rapidly reversible changes in both absorption and refractive index of the surface film. The change in electronic polarizability at the reversible potential of reaction [2] corresponds with the formation of ~50% TiOOH and the maximum change in refractive index corresponds with ~85% conversion of TiO_2 which occurs at more negative potentials where reaction [2] would go nearly to completion.

Acknowledgments

The authors wish to thank the Science Research Council for financial support, the Department of Mathematics and Physics, University of East Anglia for the use of the automatic ellipsometer, and Dr. J. G. Wright for valuable discussions on ellipsometry.

Manuscript submitted May 11, 1977; revised manuscript received Aug. 16, 1977.

Any discussion of this paper will appear in a Discussion Section to be published in the December 1978 JOURNAL. All discussions for the December 1978 Discussion Section should be submitted by Aug. 1, 1978.

REFERENCES

1. H. S. Isaacs and J. S. L. Leach, *This Journal,* **110**, 680 (1963).
2. C. K. Dyer, *Electrocomponent Sci. Technol.,* **1**, 121 (1974).
3. C. K. Dyer and J. S. L. Leach, *Electrochim. Acta,* **20**, 151 (1975).
4. A. J. Breen, G. D. Fawkes, H. S. Isaacs, J. S. L. Leach, and A. Y. Nehru, Third International Congress on Metallic Corrosion 1966, MIR, Moscow (1969).
5. P. F. Schmidt, *J. Appl. Phys.,* **28**, 278 (1957).
6. C. K. Dyer and J. S. L. Leach, To be published.
7. C. C. Matheson, J. G. Wright, R. Gundermann, and H. Norris, *Surf. Sci.,* **56**, 196 (1976).
8. P. B. Clapham, M. J. Downs, and R. J. King, *Appl. Opt.,* **8**, 1965 (1969).
9. G. Forgacs, *J. Phys. C.,* **3**, 1573 (1970).
10. R. J. Archer, "Manual on Ellipsometry," Gaertner Scientific Corporation, Chicago.
11. P. Hayfield, in "Advances in Corrosion Science and Technology," Vol. 2, M. G. Fontana and R. W. Staehle, Editors, p. 42, Plenum Press, New York (1972).
11a. F. L. McCrackin, National Bureau of Standards Technical Note 479, U.S. Government Printing Office, Washington, D.C. (1969).
12. C. K. Dyer and J. S. L. Leach, To be published.
13. N. F. Mott and E. A. Davis, "Electronic Processes in Non-Crystalline Materials," Clarendon Press, Oxford (1971).
14. F. Vratny and F. Micale, *Trans. Faraday Soc.,* **59**, 2739 (1963).
15. D. C. Cronemayer, *Phys. Rev.,* **93**, 632 (1954).
16. D. C. Grahame, *This Journal,* **99**, 370C (1952).
17. J. R. Tessman, A. H. Kahn, and W. Shockley, *Phys. Rev.,* **92**, 890 (1953).
18. Handbook of Chemistry and Physics, 52nd ed., Chemical Rubber Co., Cleveland (1971).
19. L. Pauling, *Proc. R. Soc. London, Ser. A,* **114**, 181 (1927).
20. F. P. Emmenegger and M. L. A. Robinson, *J. Phys. Chem. Solids,* **29**, 1673 (1968).

Examination of Aluminum Copper Films during Anodic Oxidation

I. Corrosion Studies

H.-H. Strehblow[1] and C. J. Doherty

Bell Laboratories, Murray Hill, New Jersey 07974

ABSTRACT

Aluminum copper films in the range of 1-70 atom percent (a/o) Cu prepared by vapor deposition were examined in buffer solutions of pH 5.0, 6.0, and 9.2. Films with a low copper content ($\leq$10 a/o) show similar corrosion properties as pure aluminum in weakly acid solutions. The formation of a layer of nonporous aluminum oxide leads to anodization up to a maximum potential of some 10V at which point the film is destroyed locally. For higher copper contents ($\geq$40 a/o) the oxygen evolution cannot be prevented and only brittle noncontinuous oxide films are formed. These metal films have similar corrosion properties to those of pure copper. At pH = 9.2 the polarization curves obtained are closely related to those of pure copper.

Aluminum films with additions of 1-5 weight percent (w/o) copper are widely used in integrated circuits. The copper alloying is used to reduce electromigration and thermal hillock formation and to facilitate chemical etching. However, the addition of copper is also known to accelerate aluminum corrosion in the presence of ionic contamination (1, 2) due to galvanic corrosion between the precipitated Al_2Cu θ phase and the pure aluminum matrix. To investigate the implications of this fact to the use of aluminum/copper metallizations for silicon-integrated circuits, the anodization conditions of evaporated alloy films have been investigated. Besides electrochemical examinations, transmission and scanning electron microscopy and ion backscattering were used to obtain information about the metal films and the anodic oxides.

Experimental

The films were deposited by electron gun evaporation from copper-aluminum melts. The films were deposited on sapphire, quartz, or oxidized silicon substrates. Prior to metal deposition the substrates were degreased with trichlorethylene and acetone followed by cleaning in a mixture of 1 part ammonium hydroxide, 1 part H_2O_2, and 4 parts of water at 80°C and were carefully rinsed with deionized water. Finally they were baked for 30 min at 500°C in air. After metal deposition, the specimens, which were about 1.5 cm^2 in surface area, were contacted electrically by a u-bent copper wire and conducting carbon paste. The whole contact area was covered by epoxy resin and the specimens were mounted to a glass tube.

Three different buffer solutions are used: phthalate buffer pH = 5.0, 0.023M KHPhth + 0.027M K_2Phth; citrate buffer pH = 6.0, 0.1M citric acid + 0.27M KOH; borax buffer pH = 9.2, 0.1M. All solutions were prepared from reagent grade chemical and triply distilled water.

The following reference electrodes were used: Hg|Hg_2SO_4|1N H_2SO_4 E_h = 0.68V; Hg|HgO|0.1M KOH E_h = 0.18V. All potential values are referred to the standard hydrogen electrode and are corrected for liquid junction potentials.

Results

Potentiodynamic examinations.—Aluminum copper films were examined under potentiodynamic conditions. Films of low copper content ($\leq$10 a/o) show, in weakly acid solutions and other metals forming non-behavior similar to pure aluminum with no apparent metal dissolution when passivation is achieved and no appreciable removal of the passive film within a few minutes at negative potentials (E_h = −0.8V) well below the potential of the hydrogen electrode in the same solution. In alkaline solutions like 0.1M borax (pH 9.2), however, the films showed a similar corrosion behavior to that of copper during subsequent potentiodynamic polarization. Apparently there is copper present on the film surface and as copper oxides and hydroxide show very low solubility at pH = 9.2, this metal is oxidized and reduced during subsequent runs. Figure 1 shows typical scans in borax buffer for 1.9 and 71.4 a/o copper films using scan rates of 0.1 V/sec and 0.1 V/min, respectively. The faster scan rate was required for the low copper sample, because the copper peak, corresponding to the surface concentration of this alloy addition, was very small and could not be detected at slower scan speeds. The same peaks are found for copper in the same buffer, as shown in Fig. 2, although with greater current density indicating that the surfaces of the alloy films are only partially covered by copper. The first peak is attributed to the formation of copper (I) oxide and the second to copper (II) oxide or hydroxide (3-5). Cathodic reduction peaks are found when the potential is changed in the negative direction,

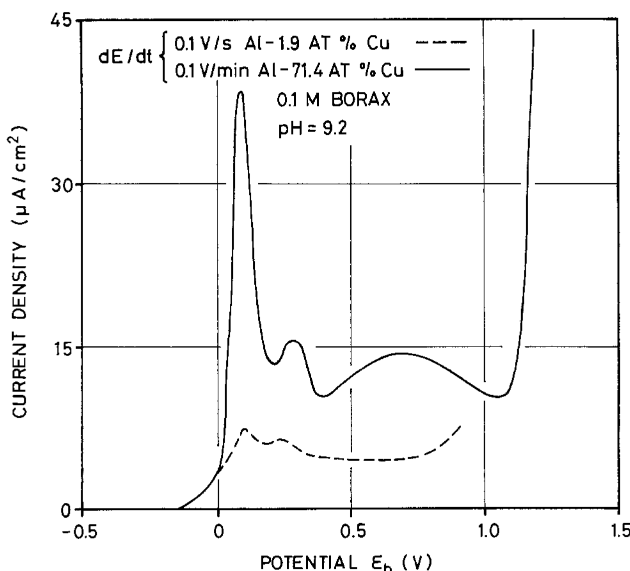

Fig. 1. Potentiodynamic polarization curves for an Al-1.9 a/o and 71 a/o Cu film in 0.1M borax pH = 9.2, *dE/dt* = 100 mV/sec or 100 mV/min, respectively.

[1] Permanent address: Free University Berlin Institute of Physical Chemistry, 1 Berlin 33, Thielallee 63-67, Germany.

Key words: Al-Cu corrosion, metallization, integrated circuits, anodic oxides, metal films.

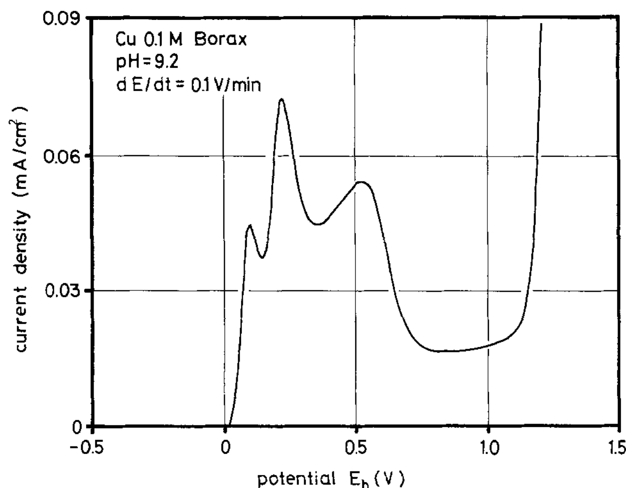

Fig. 2. Potentiodynamic polarization curves for pure copper in 0.1M borax pH = 9.2, dE/dt = 100 mV/min.

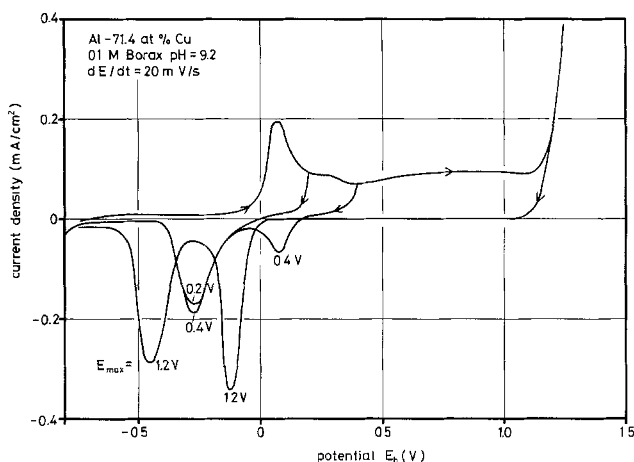

Fig. 3. Potentiodynamic polarization curves for an Al-71 a/o Cu film in 0.1M borax pH = 9.2, dE/dt = 20 mV/sec.

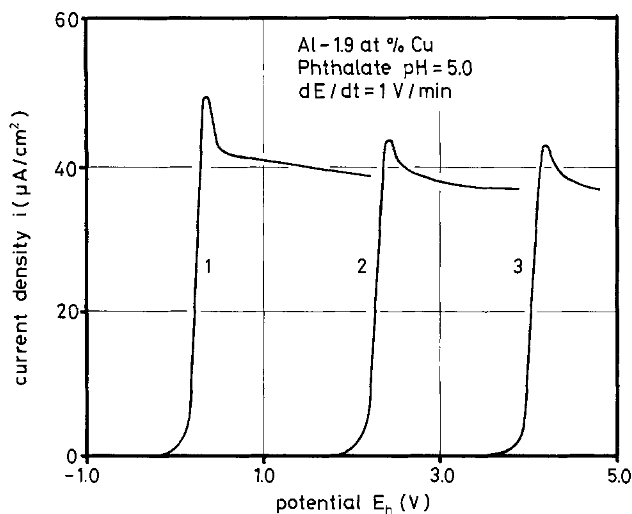

Fig. 4. Subsequent potentiodynamic polarization curves of an Al-1.9 a/o Cu film in phthalate pH = 5.0 showing current increase after exceeding the potential of the previous scan, dE/dt = 1V/min.

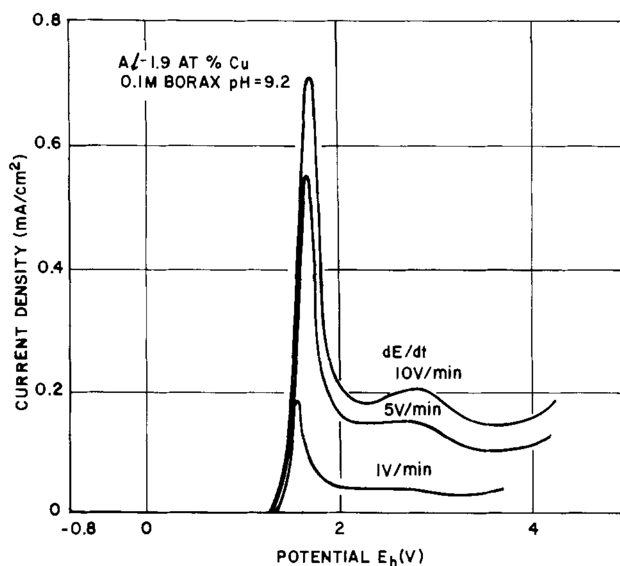

Fig. 5. Potentiodynamic polarization curve for Al-1.9 a/o Cu film in 0.1M borax pH = 9.2 up to some volts.

correspond to the results for pure copper, and are related to the reduction of the surface compounds which are formed during the anodic scan (Fig. 3).

Passivated specimens with a low copper content can be polarized in acid solutions to potentials several volts more positive than the standard hydrogen electrode without an appreciable increase in the current density. For subsequent potentiodynamic scans a current increase is observed only when the potential gets more positive than the run before resulting in a thickening of the anodic oxide (Fig. 4). This corresponds to the behavior of passive aluminum in weakly acid solutions and other metals forming non-electron-conducting poreless passive films (6-8). During repeated potentiodynamic examinations in 0.1M borax, however, a current peak at E_h = 1.6V appears which is attributed to oxygen evolution (Fig. 5). The reversible oxygen potential at a pH 9.2 is somewhat lower, the difference being presumably due to the overpotential typical for oxide-covered metals. The subsequent decrease in current density with increasing potential occurs because the surface becomes increasingly passivated by aluminum oxide and the local enrichment of copper or copper oxide is removed from the surface by dissolution or is covered by the aluminum oxide. In acid solutions (phthalate buffer or citrate buffer), this current peak is not observed for films with low copper content because copper cannot accumulate due to the solubility of its oxides in these solutions. Citrate solutions are especially effective in removing copper from the surface because of its complexing property. In consequence these solutions show higher corrosion current densities for copper and better passivating properties for low copper films.

12 a/o copper films behave similarly to the 1.9 a/o films described above, but 41 and 71 a/o Cu-films, however, show heavy oxygen evolution at potentials more positive than 1.2V and the gas evolution does not decrease at high potentials. The copper content is apparently too high for the formation of a continuous aluminum oxide film over the surface.

The potentiodynamic polarization curves show that the films with a copper content of less than 10 a/o are similar to pure aluminum. In weakly acid solutions passivity is observed and oxygen evolution is prevented up to E_h = 10V and more. These solutions are therefore the most suitable for the anodization of the metal films to high electrode potentials. Greater difficulty would be expected in 0.1M borax, mainly caused by the accumulated copper at the surface resulting in oxygen evolution. This would prevent the galvanostatic formation of thick films at high potentials especially at small current densities and copper concentrations of more than 2 a/o. In these cases, no continuous aluminum oxide film can cover the surface and oxygen evolution consumes a great part of the applied current density at the surface sites containing copper and the semiconducting copper oxide.

Galvanostatic examinations.—The citrate buffer (pH = 6.0) solution proved the most effective for film

anodization. In phthalate buffer (pH = 5.0), localized destruction of the metal film is observed at lower potentials than for the citrate solution; for example, the 1.9 a/o Cu film could be anodized to only 50V in phthalate but to 100V in citrate solution under equivalent conditions ($i = 1$ mA/cm²). In borax buffer galvanostatic experiments with current densities of $i < 500$ μA/cm² failed to reach high potentials. Characteristic corrosion structures appeared on the metal surface. These small stained areas are also found after potentiodynamic experiments in the borax buffer as mentioned above.

In 0.1M citrate solution galvanostatic anodization of the films with different copper content results in a nearly linear increase of the electrode potential with time (Fig. 6). This potential increase stops at a maximum value, potential oscillations and drops are observed, and characteristic local corrosion structures can be detected on the specimen surface (Fig. 7). Immediately before the maximum potential is reached the potential increase grows steeper; the exact potential at which it occurs is dependent on the composition of the film (Fig. 8).

Microscopic examination.—The maximum potential which can be applied to the films is limited by local breakdown. Figure 7 represents a part of the film which has lifted off the substrate forming a bubble. At the center of each bubble is a small area (1-5 μm diam) where the metal film is clearly corroded and appears to be perforated. Electron microprobe analysis of the corrosion product does not show a significantly increased copper concentration in this area. It is postulated that once local film corrosion and perforation have occurred, the electrolyte penetrates to the film/substrate interface and continued gas evolution causes the film to lose adhesion.

Figure 9 shows an Al-11.7 a/o Cu film which could be anodized to only 18 V_H. Continuing anodization at this potential results in the formation of a brittle surface film due to continuous passivation breakdown.

The grain structure of an Al 1.9 a/o Cu film was displayed using transmission electron microscopy. Sample preparation involved dissolving the silicon substrate, followed by ion milling the metal film. Figure 10a and 10b show the grain structure of the metallic and anodized portions of the film, respectively. A cross section of the film is shown in Fig. 10c which clearly shows the anodic oxide on top of the metal film.

Conclusion and Discussion

The following main results are obtained for the corrosion behavior of vapor-deposited aluminum copper films of various compositions.

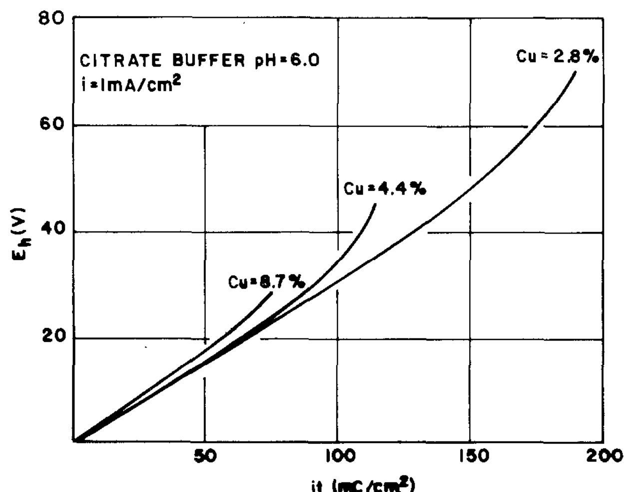

Fig. 6. Galvanostatic oxidation of aluminum-copper films of different composition up to film damage with $i = 1$ mA/cm² in 0.1M citrate pH = 6.0.

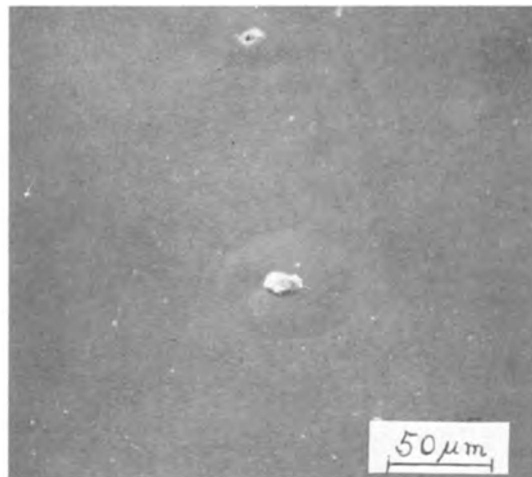

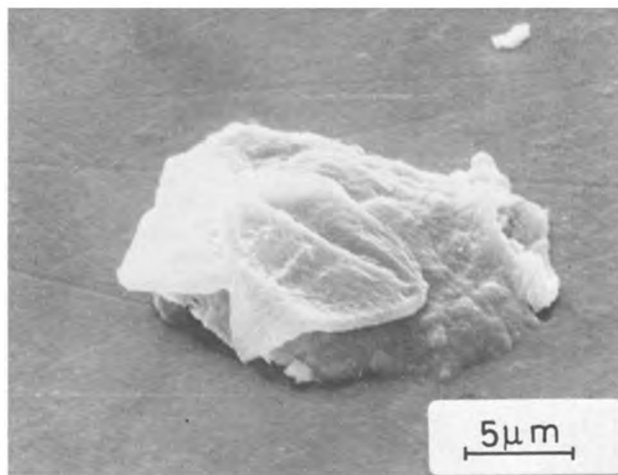

Fig. 7. Damage of an Al-4.3 a/o Cu film on a sapphire slide after oxidation to 70V_H in 0.1M citrate buffer pH = 6.0, with $i = 1$ mA/cm² for 5 min.

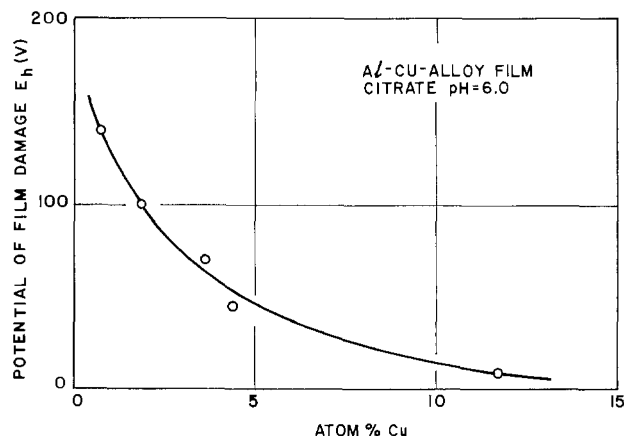

Fig. 8. Potential for film damage as a function of the copper content.

1. Passive behavior is observed in solutions in the range $pH = 5$-9.2. Films with a copper concentration up to about 10 a/o are protected by an anodic film to potentials of at least 10V. For high copper concentration (40 a/o, 70 a/o) oxygen evolution cannot be prevented as these films do not form a continuous film of the nonelectron-conducting aluminum oxide.

2. In 0.1M borax, which has a low solubility for copper oxides and hydroxide, copper is accumulated at the surface of the specimen during potentiodynamic examinations. The anodic and cathodic polarization curves

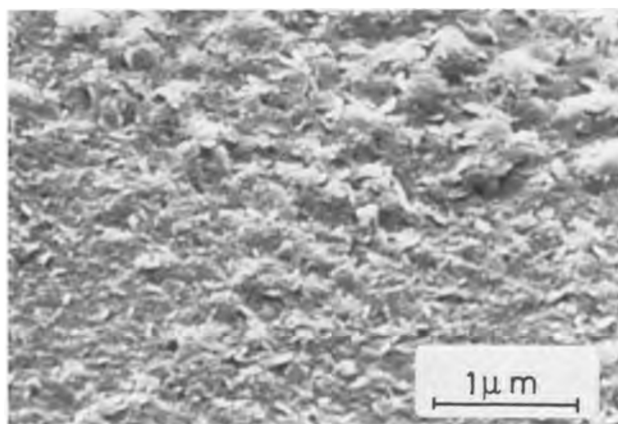

Fig. 9. Formation of noncontinuous brittle oxide on an Al-11.7 a/o Cu film on sapphire under galvanostatic conditions for 120 sec, $i = 3$ mA/cm^2, reached maximum potential $E_h = 18.6$V.

show a peak structure very similar to pure copper. The current densities decrease with the copper content of the film as the passivated aluminum-rich parts do not contribute to the electrochemical current. In acid solutions (pH = 5 or 6) only the copper-rich films (40 a/o, 70 a/o) show the peak structure of copper due to the greater solubility of the copper oxides and hydroxides at these pH values.

3. Optimum galvanostatic anodization is achieved in the citrate buffer. The maximum anodic potential and film thickness which can be obtained is controlled by film perforation and adhesion loss. This maximum potential decreases with increasing copper concentration of the film. Films of high copper content form only brittle discontinuous thick oxide films. Anodization in borax buffer, especially for high copper concentrations and small current densities, is not possible to high potentials as oxygen evolution cannot be prevented.

4. The metal phase consists of crystals of $\leq$1000Å diam. It will be shown elsewhere (9) that the oxide film does not contain any copper. Its failure during galvanostatic anodization at high potentials is closely related to an enrichment of copper at the metal-oxide interface.

5. Vapor-deposited aluminum films containing only a few atom percent of copper are protected against corrosion by the formation of an oxide film in a manner similar to films of pure aluminum. Care should be taken to avoid acid or alkaline environments to prevent the dissolution of the protective film. Anions with complexing properties for copper ions resulting in an increased solubility for copper oxide or hydroxide help to form a copper-free surface.

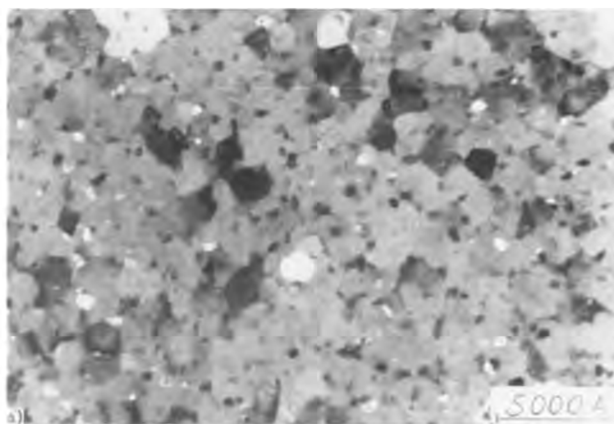

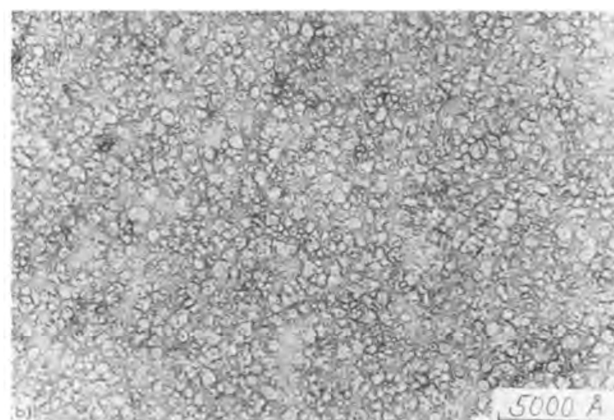

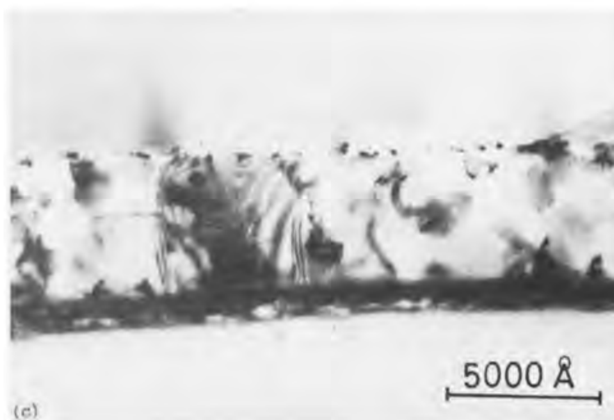

Fig. 10. TEM display of (a) metal phase; (b) anodic oxide; (c) cross section of an Al-1.9 a/o Cu film, anodized with $i = 1.4$ mA/cm^2 to $E_h = 100$V in 0.1M citrate $pH = 6.0$

Acknowledgments

The authors are indebted to C. M. Melliar-Smith and P. A. Turner for their helpful advice and encouragement for this work; T. T. Sheng for the TEM studies; K. L. Tai for the help in operation of the SEM; and L. D. Blitzer for the atomic absorption spectroscopic analysis.

Manuscript submitted May 11, 1977; revised manuscript received Aug. 7, 1977.

Any discussion of this paper will appear in a Discussion Section to be published in the December 1978 JOURNAL. All discussions for the December 1978 Discussion Section should be submitted by Aug. 1, 1978.

Publication costs of this article were assisted by Bell Laboratories.

REFERENCES

1. R. M. Valletta and H. S. Lehman, Abstract 193, p. 474, Electrochemical Society Extended Abstracts, Fall Meeting, Atlantic City, N.J. (1970).
2. P. Totta, Paper presented at the meeting of the American Vacuum Society, Philadelphia (1975).
3. B. Miller, *This Journal*, **116**, 1675 (1969).
4. D. D. McDonald, *ibid.*, **121**, 651 (1974).
5. D. W. Shoesmith, T. E. Rummery, D. Owen, and W. Lee, *ibid.*, **121**, 790 (1974).
6. L. Young, "Anodic Oxide Films," p. 193, Academic Press, New York (1961).
7. D. A. Vermilyea, *Acta Metall.*, **1**, 282 (1953); **2**, 476 (1954).
8. H. Kaeschi, "Dikorrosion der Metalle," p. 210, Springer, Berlin Heidelberg, New York (1966).
9. H.-H. Strehblow, C. M. Melliar-Smith, and V. M. Augustyniak, Submitted to *This Journal*.

The State of Tin in Tin-Anodized Aluminum

R. L. Cohen

Bell Laboratories, Murray Hill, New Jersey 07974

and Ch. J. Raub and T. Muramaki

Edelmetalle Forschungsinstitut, Schwäbisch Gmünd, Germany

ABSTRACT

We have used Mössbauer spectroscopy of Sn^{119} to determine the state of the tin in anodized aluminum surfaces which are colored brown by anodization in acidic stannous sulfate solutions. We conclude that the tin is present predominantly in the form of tin metal.

Aluminum alloys used for architectural and appearance applications are frequently dyed gold, bronze, or dark brown. One way to achieve these brown anodized surfaces is by a-c treatment of anodized aluminum in an electrolyte containing metal salts (1-3). By varying the electrolysis conditions various shades of color can be obtained. Some of the most widely used metal salts in electrolytes for generating bronze to brown colors are those of divalent tin, the effects of which were already well known in the 1930's (4). At that time it was speculated that the coloring might be caused by reduction products of the tin salt, *e.g.*, metallic tin. In the last years more work has been done to establish coloring mechanism. Läser (5) came to the conclusion that the coloring particles consist of metallic tin. A similar result was published in Ref. (6) and (7). This information was obtained by x-ray diffraction. Sheasby and Cooke (2) and Sandera (6) suggest that tin oxides are present in these layers too. Therefore some confusion exists on the nature of the tin compounds responsible for the coloring effect. This is primarily due to the small quantity and fine particle size of the tin-containing phase, and the difficulty of isolating it.

We have used the technique of Mössbauer spectroscopy (8) on Sn^{119} to study these layers, and the results of this work are presented here. Mössbauer spectroscopy is ideally suited for this study—it works well with thin layers of material, is sensitive only to the tin atoms in the layer, and is completely unaffected by the aluminum backing or aluminum oxide matrix. The identification of the tin phase in these experiments is by a "fingerprint" technique, in which the Mössbauer spectrum of the unknown (tin anodized) sample is compared with the spectra of known compounds. In general, the parameters determining the Mössbauer spectrum are insensitive to particle size or crystallinity. Particularly relevant to the problem we consider here, Akselrod *et al.* (9) have recently shown that for SnO with a grain size of ~20Å, the Mössbauer spectrum was indistinguishable from that of bulk SnO.

Experimental Details

Samples were prepared by anodizing both sides of the 0.2 mm thick aluminum sheets in 10% H_2SO_4 at a current of 1 A/dm^2 for the times shown in Table I. These sheets were then colored in a second electrolyte consisting of 20 g/liter $SnSO_4$ dissolved in 5% H_2SO_4, 4 min, at room temperature, 9V, 50 Hz a.c., using Pt as a second electrode. The samples were rinsed in water and allowed to dry in air at room temperature. Four pieces of sheet were stacked, making an absorber composed of 8 anodized layers for the measurements. All of the samples were dark bronze in color.

The Mössbauer spectra were taken with the samples at 78°K, using a source of $BaSnO_3$ at room temperature and a silicon detector for the gamma rays. A Pd critical absorber was used to filter out the Sn K x-rays.

Key words: Mossbauer, anodizing, tin, aluminum.

Data were taken using a multichannel analyzer in the up-down multiscaling mode (8). Spectra of the tin-anodized samples are shown in Fig. 1, along with spectra of stannic hydroxide (10) and tin metal.

The dominant line in the spectrum of the tin-anodized samples clearly corresponds to that of tin metal. Other obvious possible compounds can be conclusively excluded: Both SnO and hydrated SnO have well-resolved symmetric doublets for their Mössbauer spectra (11, 12), as indicated in Fig. 1. Stannic oxide has a broad line similar to that of stannic hydroxide. Stannous sulfate yields a barely resolved doublet centered at 4 mm/sec, while SnS yields a barely resolved doublet centered at 3.5 mm/sec (11). Thus, not only does the primary observed line correspond exactly to that of tin metal, but all of the other simple compounds containing tin, sulfur, oxygen, and hydrogen have obviously different spectra.

There is additional intensity in the spectra near zero velocity, and we attribute this to a small fraction of the tin being combined in the form of stannic oxide or hydroxide (Mössbauer spectra of these materials are almost indistinguishable).

The spectra of the tin-anodized layers have been least squares fitted to establish the relative quantities of the oxide/hydroxide and tin metal. This was accomplished using a constrained least squares fitting routine, which was given the shape, width, and position of lines for stannic hydroxide and for tin metal, and allowed only the intensities of the two lines (and the baseline) as degrees of freedom. The fine line running through the data points in Fig. 1 is the result of this least squares fitting procedure; it is obviously an excellent description of the experimental spectra. From the line intensities, the amount of tin metal present can be determined by comparison with spectra of tin samples of known thickness. For thin samples, the resonance intensity is proportional to the sample thickness. These results are shown in Table I. From the Mössbauer data, there is no way to determine if the oxide/hydroxide

Table I

Sample preparation and tin concentrations determined in these experiments. The relative accuracies of the tin metal determinations are ±5%, of the hydroxide phase, ±25%. The absolute accuracies are ±20% for the metal phase, and ±40% for the hydroxide phase, being limited by the complete line shapes and poorly established recoil-free fractions, f. In determining tin in the hydroxide phase, the value f_{hyd}/f_{metal} = 1.25 at 78°K was used, following results of Ref. (13).

Sample	Anodizing time (min)	Anodized layer thickness (μ)*	Sn (metal phase) (μg/cm²)	Sn (in hydroxide phase) (μg/cm²)
A	5	<1	35	4
B	15	5	40	4
C	30	10	35	4

* Determined by "Lichtschnittmikroskop" (light-section microscope).

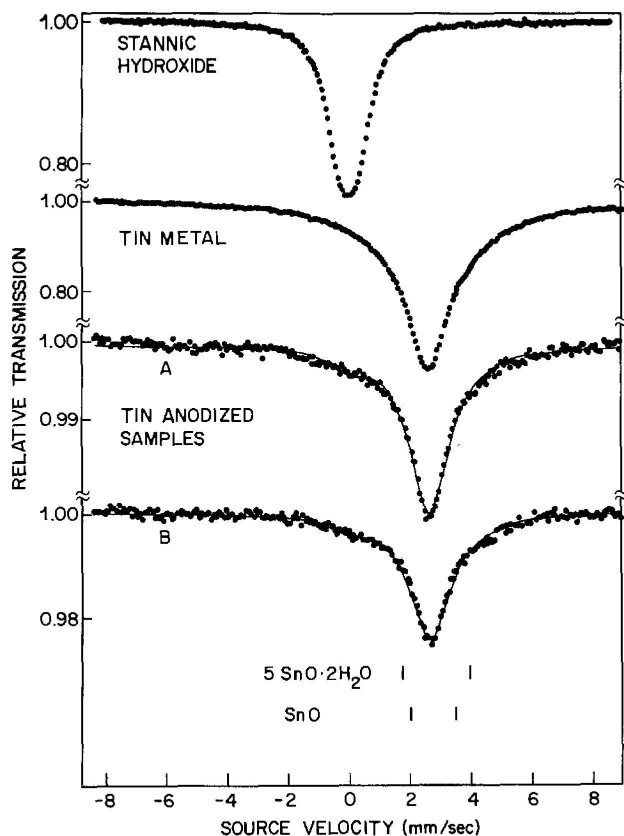

Fig. 1. Mössbauer spectra of the tin-anodized samples A and B along with spectra of stannic hydroxide and tin metal for comparison. The spectra are taken in transmission, so that the absorption lines are downward pointing "peaks." The energy scanning in Mössbauer spectroscopy is normally done by doppler shifting the gamma ray energy by moving the source, so the "source velocity" scale is effectively an energy scale. The spectra of SnO and hydrated SnO are doublets, with the line positions shown at the bottom of the figure. The least squares fit to the data (assuming the layer is composed only of tin metal and stannic hydroxide) is shown by the thin line.

phase is associated with the tin metal phase (*i.e.*, as a surface layer on tin particles) or is entirely independent. The most obvious source for the formation of a stannic hydroxide phase would be hydrolysis of Sn^{4+} ions as the surface *p*H is raised during the wash process (10). The high surface area of the anodized layer would serve as an ideal nucleation site for precipitation of the insoluble stannic hydroxide ions.

It is interesting to note that the amount of metallic tin does not depend on the thickness of the oxide layer, and even at rather small thicknesses (sample A) the same amount of tin is deposited under the conditions used. The quantities of tin shown in Table I are slightly smaller than those determined by Sautter *et al.* (6) for tin-dyed layers produced under slightly different conditions.

In the spectra of the tin-anodized samples shown in Fig. 1, there is a very weak absorption near 4 mm/sec, visible only by the minor departure of the data points from the least squares fit line. This presumably arises from traces of $SnSO_4$ (12) remaining in the porous anodized layer.

In conclusion, studies of the composition of anodized layers dyed by tin have shown that the tin is present primarily in the form of tin metal. The brown coloration of the layers presumably reflects the color of finely divided tin metal particles, dispersed in the aluminum oxide surface layer.

Acknowledgment

We thank K. W. West for assistance with the data taking and data reduction.

Manuscript submitted June 22, 1977; revised manuscript received Aug. 22, 1977.

Any discussion of this paper will appear in a Discussion Section to be published in the December 1978 JOURNAL. All discussions for the December 1978 Discussion Section should be submitted by Aug. 1, 1978.

Publication costs of this article were assisted by Bell Laboratories.

REFERENCES

1. E. Herrmann, *Galvanotechnik*, **63**, 110 (1972).
2. P. G. Sheasby and W. E. Cooke, *Trans. Inst. Met. Finish.*, **52**, 103 (1974).
3. W. Sautter, and J. Meier, *Aluminium (Duesseldorf)*, **51**, 507 (1975).
4. A. Jenny, "Die elektrolytische Oxidation des Aluminiums und seiner Legierungen," p. 215, Th. Steinkopff, Dresden und Leipzig, (1938).
5. L. Laser, *Aluminium (Duesseldorf)*, **48**, 169 (1972).
6. L. Sandera, *ibid.*, **49**, 533 (1973).
7. W. Sautter, G. Ibe, and J. Meier, *ibid.*, **50**, 143 (1974).
8. "Mössbauer Spectroscopy," G. M. Bancroft, Editor, Wiley, New York (1973); "Applications of Mössbauer Spectroscopy," Vol. I, R. L. Cohen, Editor, Academic Press, New York (1976).
9. S. Akselrod, M. Pasternack, and S. Bukshpan, *Phys. Rev.*, **B11**, 1040 (1975).
10. R. L. Cohen and R. L. Meek, *J. Colloid Interface Sci.*, **55**, 156 (1976).
11. R. L. Cohen and K. W. West, *This Journal*, **119**, 433 (1972).
12. J. D. Donaldson, in "Progress in Inorganic Chemistry," Vol. 8, F. A. Cotton, Editor, p. 287, Interscience, New York (1973).
13. C. L. Kordyuk *et al.*, *Ukr. Fiz. Zh. (Russ. Ed.)*, **15**, 505 (1970).

Investigation of Agitation Effects on Electroplated Copper in Multilayer Board Plated-Through Holes in a Forced-Flow Plating Cell

Werner Engelmaier* and Thomas Kessler[1]

Bell Laboratories, Whippany, New Jersey 07981

ABSTRACT

The effect of electrolyte agitation in plated-through holes (PTH's) of multilayer boards (MLB's) is investigated for high conductivity $CuSO_4/H_2SO_4$ electrolytes with and without brightener additives. The experiments were carried out in an 80 liter forced-flow plating system capable of agitation by air sparging also. PTH quality is assessed in terms of the PTH electrical resistance, the PTH deposit uniformity, and the deposit morphology. Correlations are made with plating current density, electrolyte velocity in the PTH's, and two dimensionless plating parameters, $\xi_{T\kappa}$ and $\bar{j}/\bar{j}_{lim}$. The results show that for additive-free plating, the agitation requirements to prevent mass transport-limited plating conditions increase rapidly with increasing current densities and decreasing cupric ion concentrations. At the current densities common in MLB production, the low levels of agitation produced by air sparging alone provide only for marginal plating conditions particularly at the board edges where the test coupons are located. The plating criteria for good PTH deposits, $\xi_{T\kappa} < 1$ and $\bar{j}/\bar{j}_{lim} < 0.25$ are confirmed by the experimental results. Plating with Cubath®M additives is shown to be considerably less sensitive to variations in the plating parameters which are likely to occur in production. The criteria for good PTH quality can be extended to $\xi_{T\kappa} < 2$ and $\bar{j}/\bar{j}_{lim} < 0.25$, which allows for more latitude for plating current density variations.

Among the many critical process steps that a multilayer printed wiring board (MLB) undergoes during its production, the electroplating of copper is one of the most important. MLB's contain plated-through holes (PTH's) which provide electrical connections between the various circuit layers of the MLB (see Fig. 1). During the electroplating step, copper is deposited in the drilled PTH's as well as on the outer MLB surfaces. Since the plating of PTH's in MLB's places much more complex demands on the plating process as compared to standard electroplated product, a better understanding of the plating process and its controlling parameters is necessary (1-3). Efforts have been reported which were designed to gain understanding either through analysis of the existing plating phenomenology (1, 5-12) or through analytical modeling (2-4, 13). Parameters were defined which provide a gauge for the relative importance of the three mechanisms (electrical characteristics of the plating solution, electrochemical kinetics of the plating reaction, and fluid dynamic conditions at the cathode) whose interaction determines the performance of an electroplating process. Different mechanisms become dominant for the copper distribution at the different scales important in the plating of MLB's: macroscale, miniscale, and microscale (3).

The macroscale is characteristic of plating of complete panels. Plating at this scale is dominated by the primary current distribution as long as sufficient electrolyte agitation at the cathode surface prevents the formation of significant gradients in the cupric ion concentration.

For the miniscale, characteristic of the region within and close to a PTH, current distribution, and thus the plating thickness distribution, is determined by the interaction of ohmic conduction, charge transfer kinetics, and mass transfer conditions. Criteria, involving dimensionless plating parameters $\xi_{T\kappa}$ and $\bar{j}/\bar{j}_{lim}$, developed by Kessler and Alkire (3) indicate which of the mechanisms dominates.

On the microscale, which encompasses effects on the scale of surface roughness, deposit thickness, and grain size, additives play a major role. Additives affect the microleveling capability of the plating solution and determine the deposit morphology. Thus, additives have a major effect on the properties of the plated copper.

Sufficient agitation is a common requirement to all three scales. The consequence of insufficient agitation is inadequate mass transport which in turn results in large ion concentration gradients at the cathodic surfaces. Mass transport limited plating results in poor quality deposits and the conditions at which the de-

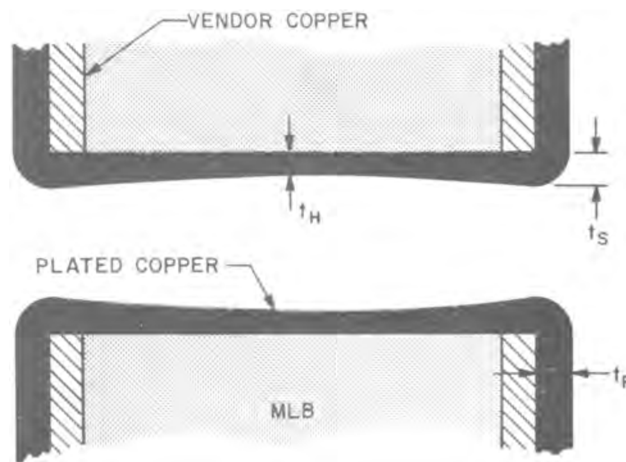

Fig. 1. Sketch of plated-through hole cross section defining throwing power.

* Electrochemical Society Active Member.
[1] Present address: Xerox Corporation, Webster, New York 14580.
Key words: morphology, throwing power, electrolyte brighteners, printed wiring, solution agitation.

posits occur at the cathode do not reflect the condition in the bulk of the plating solution.

For these reasons, agitation has always been an important aspect in the electroplating of copper. Most commonly, agitation is achieved by the discharging of air from sparging pipes located beneath the cathodic work pieces near the bottom of the plating tank. The most obvious effect of air sparging is a stirring of the electrolyte. The rising air bubbles impart velocity to the electrolyte close to the cathodic surfaces. Thus, the surface boundary layer is reduced and plating conditions are less likely to be mass transport limited. For the plating of planar vertical surfaces, the agitation provided by air sparging generally is sufficient for good quality plating.

However, for MLB's air sparging does not provide sufficient agitation in the PTH's in many instances. Therefore agitation by air sparging is sometimes supplemented by mechanical agitation. However, the level of agitation in PTH's resulting from these modes of agitation is exceedingly difficult to predict. The only practical method for the parametric evaluation of the effects of agitation on the electroplated deposit and of what agitation levels constitute sufficient mixing to prevent mass transport limited plating conditions appears to be a phenomenological study of PTH's plated at varying plating conditions. The results of such a study with parametric variations of current densities and forced-flow PTH electrolyte velocities are reported. Some experiments using only air agitation were performed also. The experiments were carried out using a high conductivity acid-copper sulfate plating solution with and without Cubatn®M proprietary organic additives (14).

Analysis

Plating parameters.—Since this study is primarily concerned with the plating inside of PTH's, miniscale considerations are the most important. For the miniscale, two-dimensionless criteria for good plating quality have been analytically determined (2)

$$\xi_{T\kappa} < 1 \quad [1]$$

is necessary for sufficient uniformity of plated copper thickness within PTH's, since it indicates that charge-transfer resistance rather than solution ohmic resistance predominates.

$$\bar{j}/\bar{j}_{\lim} < 0.25 \quad [2]$$

indicates sufficient electrolyte agitation, the absence of mass transport limitations, and smooth copper deposits with acceptable grain structure. From Ref. (2)

$$\xi_{T\kappa} = \frac{\alpha_c \mathbf{F} t_B^2}{2\kappa R_g T r_o} \bar{j} \quad [3]$$

and

$$\frac{\bar{j}}{\bar{j}_{\lim}} = \frac{2 s_i \Gamma(4/3)}{3n\mathbf{F} D_i c_\infty} \left(\frac{9 D_i r_o t_B}{4\bar{v}} \right)^{1/3} \bar{j} \quad [4]$$

For the conditions in this study ($c_\infty = 0.34 \rightarrow \kappa = 0.52\ \Omega^{-1}\ \text{cm}^{-1}$, $D_i = 0.55 \times 10^{-5}\ \text{cm}^2/\text{sec}$) (2)

$$\xi_{T\kappa} = 4.77 \times 10^{-5} \frac{t_B^2}{r_o} \bar{j} \quad [5]$$

and

$$\frac{\bar{j}}{\bar{j}_{\lim}} = 7.10 \times 10^{-4} \left(\frac{r_o t_B}{\bar{v}} \right)^{1/3} \bar{j} \quad [6]$$

From Eq. [5] and [6] and the sample dimensions (t_B = 123 mil, r_o = 23 mil), the plating criteria can be reduced to

$$\bar{j} < 32\ \text{mA/cm}^2 \quad [7]$$

and

$$\bar{v} > \frac{(\bar{j})^3}{15{,}500} \quad [8]$$

From the Eq. [4] and the second criterion minimum mean electrolyte velocities in the PTH's can be calculated and are presented in Table I. This electrolyte velocity is in the direction of the long axis of the PTH's and thus perpendicular to the MLB's (see Fig. 1 and 2). Minimum velocities are given for the cupric ion concentrations used in this study and the preliminary work discussed in Ref. (1).

Table I. Minimum mean PTH electrolyte velocities for electrolytes with different cupric ion concentrations

c_∞ (M/liter)	100	40	32	25	15	10	5	$\bar{j}$(mA/cm²)
0.27	129	8	4	2	0.44	0.13	0.016	$\bar{v}$(cm//sec)
0.34	65	4	2	1	0.22	0.065	0.008	$\bar{v}$(cm//sec)
0.375	48	3	1.6	0.75	0.16	0.05	0.006	$\bar{v}$(cm//sec)

The minimum mean electrolyte convection requirement of 4 cm/sec in PTH's determined in Ref. (2) is correct only for average plating current densities up to 32 mA/cm² at the cupric ion concentration of 0.27 M/liter used in Ref. (2). The level of minimum agitation required for good plating changes dramatically for different current densities and cupric ion concentrations.

Agitation levels.—With forced-flow agitation of the electrolyte, the mean electrolyte velocity in a PTH is easily determined. However, in practical production plating electrolyte agitation by air sparging and/or side-to-side MLB motion are the means employed to achieve electrolyte mixing. The flow fields generated by air sparging cannot be sufficiently described to determine the equivalent PTH electrolyte velocities. Clearly, the mass transfer in PTH's is enhanced by air sparging resulting from the random short duration pressure field variations creating localized pressure differences from one side of the MLB to the other as well as from mixing currents created by the bubble-wake eddies, however, the equivalent PTH velocities are obviously small as compared to either MLB motion or forced flow.

A simple model of the flow in a PTH resulting from the side-to-side MLB motion gives for a typical MLB (r_o = 23 mils, t_B = 123 mils) at a velocity of v_B = 10 cm/sec a mean PTH electrolyte velocity of $\bar{v}$ = 3.4 cm/sec. Decreasing MLB velocitites results in rapidly increasing the $v_B/\bar{v}$ ratios; thus, v_B = 1 cm/sec results in $\bar{v}$ = 0.075 cm/sec.

The level of agitation achievable by transverse motion of the MLB's has practical limitations. The maximum practical velocity in side-to-side agitation is about 10 cm/sec. This would mean that about 3.4 cm/sec is the maximum mean velocity of a near-sinusoidal velocity distribution and that during a considerable portion of the motion cycle the mean velocity falls below the minimum mean electrolyte convection established in Table I. However, these minimum agitation levels are established for steady-state fully developed laminar flow conditions (2, 3). There are a

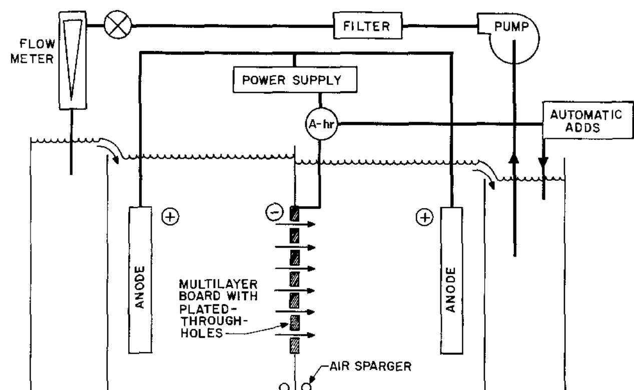

Fig. 2. 80 liter forced-flow electroplating system.

number of considerations, which indicate that fully developed laminar flow constitutes the conservative bound for the mixing in the mass diffusion layer at the PTH surface. Some of these considerations are:

1. The downstream distance from the mouth of the PTH, L_e, to establish fully developed laminar flow is a significant fraction of the total length of the PTH ($L_e = 116$ mils for $\bar{v} = 5$ cm/sec and a 46 mil PTH diam).
2. The oscillating flow field generates a phase shift between the flow in the PTH's and the MLB motion.
3. The sharp-edged PTH entrance and exit result in a *vena contracta* at the entrance and eddies at the exit.

The theoretical prediction of the electrolyte agitation at the PTH surface and the species concentration gradients is exceedingly difficult under these circumstances.

The results from forced-flow experiments, for which the electrolyte agitation is clearly defined, can establish the effects of varying levels of agitation on the quality of the electrodeposited copper. It also can serve as a standard from which effective agitation levels in PTH's resulting from air sparging and/or side-to-side MLB motion may be estimated.

In the determination of the level of agitation, an additional factor can play a significant role. The density of the electrolyte decreases as the cupric ion concentration decreases. Thus, the large ion concentration gradients generated under transport-limited plating conditions result in natural convection flow into and from PTH's.

Mirarefi and Alkire (15-17) have shown that at low flow velocities natural convection effects cause a deviation from the Lévêque equation flow. From the data in Ref. (15-17) and our data, which confirm this deviation, the level of agitation provided by natural convection is estimated to be equivalent to $\bar{v} = 1.7$ cm/sec. This result would indicate that agitation levels much below $\bar{v} = 1.7$ cm/sec cannot meaningfully be investigated and that plating at current densities below minimum values that can be estimated from Table I will be independent of additional external agitation provided. Natural convection appears to explain why air sparging produces good quality PTH's under plating conditions where air sparging alone provides insufficient agitation. Air sparging however is clearly desirable because it provides the bulk stirring necessary to provide at each PTH the bulk concentration of cupric ion.

Experiment

Plating apparatus.—The 80 liter forced-flow plating system, shown in Fig. 2, consists of four discrete chambers separated from each other by impermeable weirs. Suction and discharge chambers separate the spaces for solution pumping and discharge from the plating cells to eliminate spurious flow currents at the cathodic MLB samples. The electrolyte is pumped from the suction chamber by two Sethco Model ZDX-50A pumps, filtered through a 5 μm polypropylene filter, flows through a flow metering valve and a flow meter, and is discharged in the discharge chamber. The electrolyte flows over a weir from the discharge chamber into the upstream plating cell, from there through the PTH's in the MLB cathode into the downstream plating cell, and over a weir into the suction chamber. Each plating cell contained an anode 11 cm from the cathode and an air sparging pipe at the cathode weir close to the tank bottom. The air spargers were supplied with air from a Cyclonair Blower Model VFC201P-IT through a metering valve and a flow meter.

A Nova Tran Model 1221 Digi-Plate Pulse Plater with Model 6001 Ampere Time Controller served as the power supply. The MLB samples were connected to the power supply via an insulated wire and the anodes hung from standard titanium anode hooks. During plating with electrolyte containing brightener additives, a Rapid Electric Precision Solution Metering System Model MPAT-P-SMS in conjunction with a Fisher Volustat metering pump provided for the automatic maintenance of the additive balance. Additives were replenished at the rate of 1 ml every 120 A-min.

Electrolyte.—For the experiments a high conductivity acid-copper sulfate electrolyte containing 0.34M $CuSO_4$, 1.76M H_2SO_4, and 40 ppm Cl^- was used. Experiments were carried out with an additive-free plating bath and with the electrolyte containing the standard levels of Cubath®M proprietary organic additives (14).

MLB samples.—The MLB samples used are 9 × 9 cm in size, have a thickness of 123 mils, and have 46 mil diam PTH's on 125 mil centers. The samples contain 812 PTH's, except for the samples used for the high velocity experiments ($\bar{v} = 87$ cm/sec) where half the PTH's, and thus half the sample area, were masked with plating tape to make the high electrolyte velocities possible. The samples were electroless copper plated with a thin (~0.05 mil) conducting film.

Plating procedure.—To make electrical connection to the plating power supply 18 gauge bare copper wire was threaded through two PTH's on the top edge of the samples and crimped into place. The wire was then insulated with plating tape for its remaining length submerged in the plating solution. The following cleaning procedure was carried out for all samples: (*i*) Neutra-Clean soak of 30 sec at 50°C, (*ii*) DI water rinse for 2 min, (*iii*) etch in 10% sulfuric acid for 3 min, and (*iv*) DI water rinse for 2 min.

After the cleaning procedure, the samples were placed in the opening cut into the cathode weir (see Fig. 2) for this purpose and held in place by a holding frame. To prevent leakage flow of electrolyte from the upstream to the downstream plating cell all seams were sealed with plating tape.

Electrolyte velocities in the PTH's ranging from 0.17 to 87 cm/sec were obtained by varying the solution flow, the number of PTH's in the sample, and by permitting some known bypass flow. During the experiments with forced electrolyte flow, air sparging was not employed. No forced solution flow took place during the air sparging experiments. Experiments were carried out for two sparging rates: 0.25 and 1.0 liter/min-cm sparger length. These rates prevailed per unit length of the air spargers and were identical for the upstream and the downstream cell spargers. The lower sparging rate results in slight agitation of the electrolyte in the vicinity of the MLB samples, whereas the higher rate gives a very vigorous stirring and agitation of the electrolyte throughout the plating cells.

Experiments were carried out for plating current densities ranging from 5 to 100 mA/cm^2. The plating times for the experiments at different current densities were adjusted to plate every sample with the same number of coulombs and thus to yield identical average plating rates per unit total sample area. An automatic shutoff terminated each experiment when the predetermined number of ampere-minutes was attained. At the conclusion of the plating, the samples were removed from the plating tank, thoroughly rinsed with DI water, and dried in a forced air flow.

Sample preparation for analysis.—The MLB samples were visually inspected after the plating procedure and the quality of the deposit "read." A 0.5 × 0.75 in. coupon was cut from the center of each sample. The land areas surrounding each of the 15 PTH's on these coupons were electrically isolated from each other by cutting through the planar surface deposits between the PTH's on both sides of the MLB's. PTH electrical resistance measurements were made using a 4-point probe technique (18). After the resistance measurements, these coupons were cut in half, encapsulated, and the cross sections polished for metallographic examination.

Results and Discussion

Additive-free plating.—The results of the experiments employing additive-free electrolyte are illustrated in Fig. 3-8. In Fig. 3 the PTH resistance is cor-

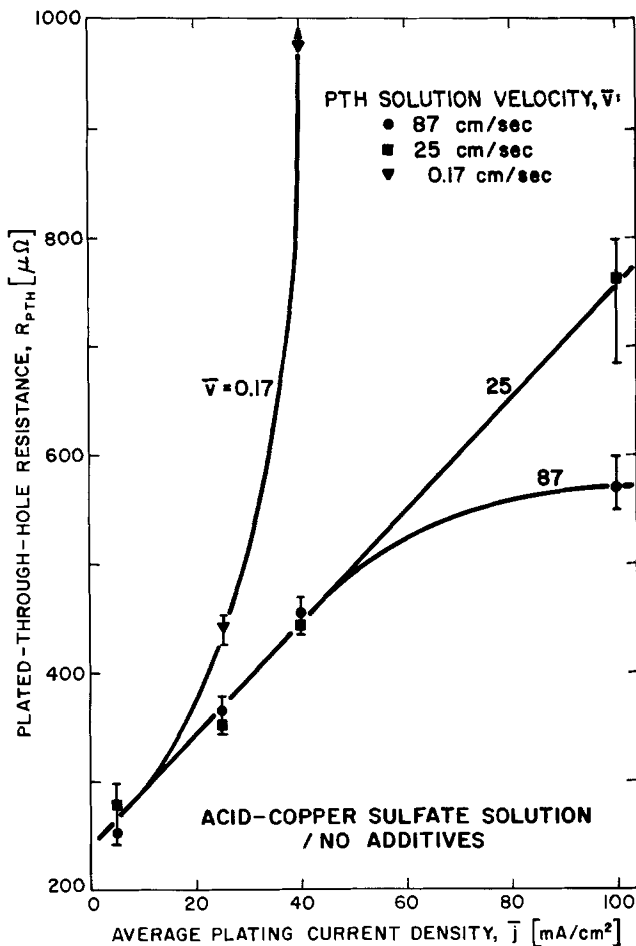

Fig. 3. Plated-through hole resistance as a function of plating current density and agitation velocity for additive-free plating.

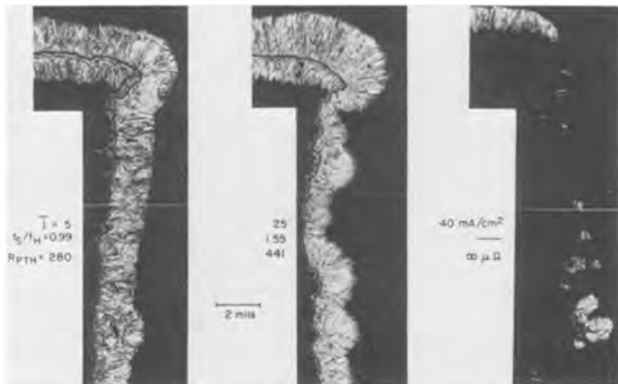

Fig. 4. Metallographic cross sections of plated-through holes plated at an electrolyte velocity $\bar{v}$ = 0.17 cm/sec and various current densities for additive-free plating.

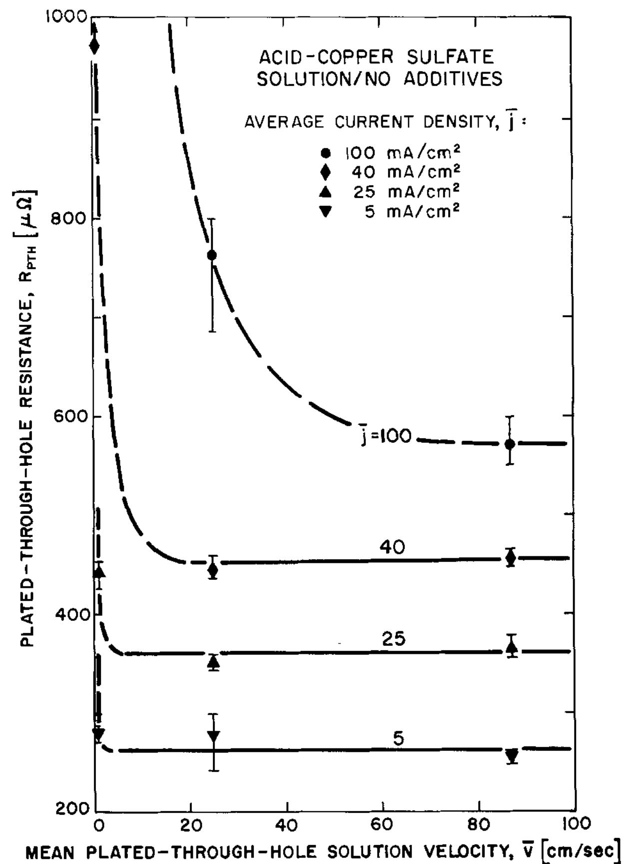

Fig. 5. Plated-through hole resistance as a function of agitation velocity and current density for additive-free plating.

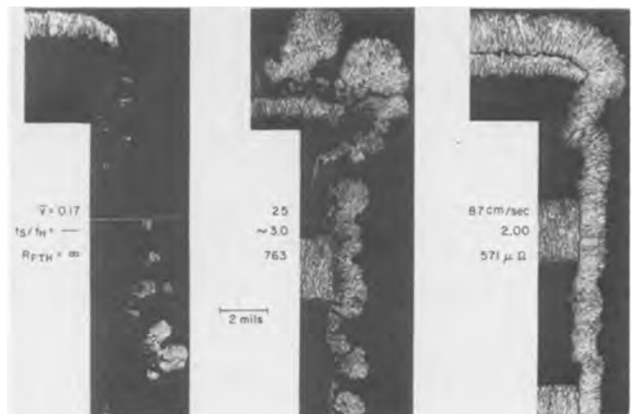

Fig. 6. Metallographic cross sections of plated-through holes plated at a current density of $\bar{j}$ = 100 mA/cm² and various agitation velocities for additive-free plating.

related with the average current density for three solution velocities in the PTH's. In all cases an increase in the plating current density results in a higher PTH resistance because of the deteriorating throwing power and changes in the macrocurrent distribution. The resulting PTH resistances at low current densities are the same for all agitation velocities; however, as the current density increases, the onset of mass transport-limited plating is clearly reflected in a more rapidly increasing PTH resistance for the lower agitation level conditions. These deviations, signaling the onset of mass transport-limited plating condition, are in good agreement with the calculated minimum mean PTH electrolyte velocities given in Table I.

Figure 4 illustrates the results shown in Fig. 3 with metallographic cross sections showing the changes in the copper deposit with increasing current density at a constant electrolyte velocity of 0.17 cm/sec. The deposit quality for 5 mA/cm² is very good. At 25 mA/cm² the deposit is rather rough and at 40 mA/cm² it is very rough and discontinuous.

In Fig. 5 the PTH resistance is plotted as a function of the mean PTH electrolyte velocity for current densities ranging from 5 to 100 mA/cm². It clearly shows that an increase in agitation beyond the level required to prevent mass transport-limited plating conditions does not improve the quality of the copper deposit in the PTH's. PTH resistances will decrease with increasing levels of agitation until mass transport-limited conditions no longer prevail and then will remain at a constant plateau. This also shows that even under optimum plating conditions, a minimum PTH resistance exists for each plating current density. These minimum resistances increase rapidly with increasing

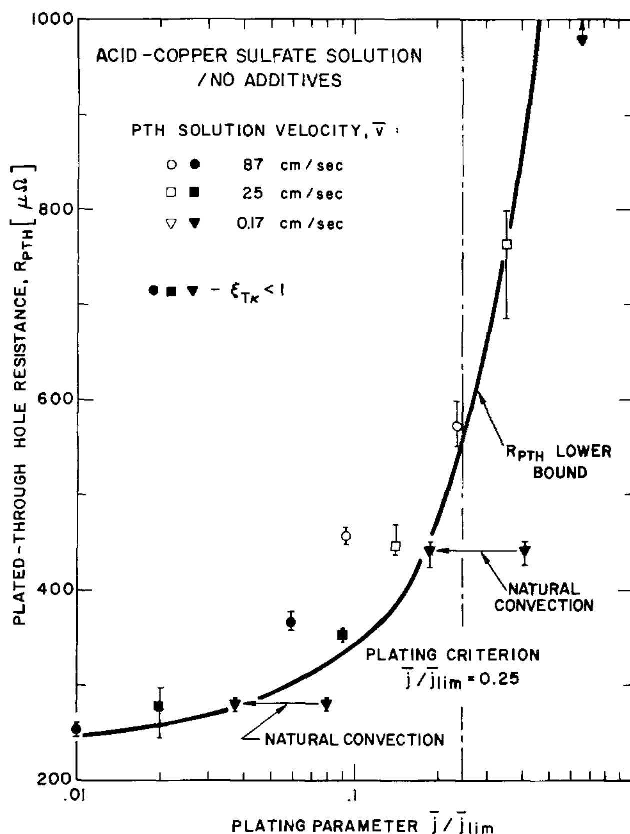

Fig. 7. Plated-through hole resistance as a function of $\bar{j}/\bar{j}_{lim}$ for additive-free plating. Natural convection corrections for low velocity data are indicated.

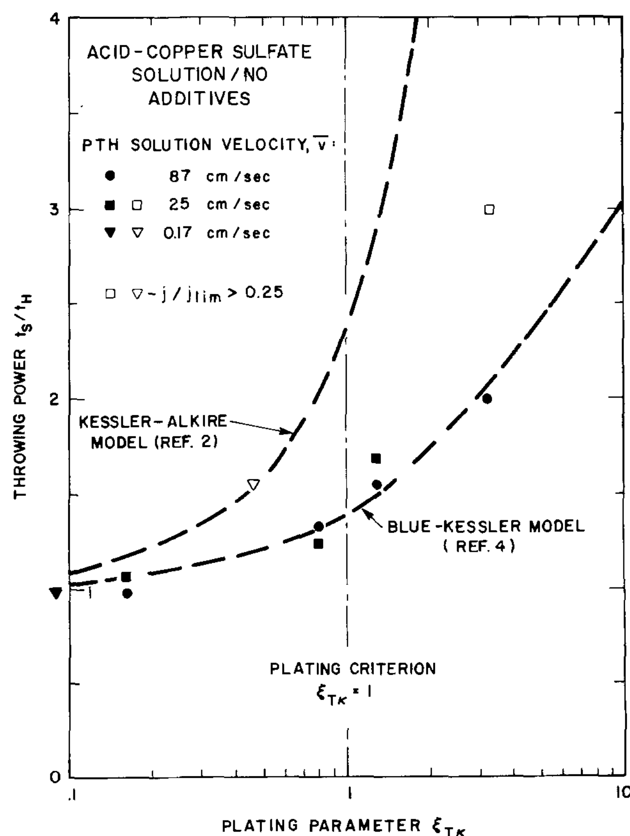

Fig. 8. Throwing power as a function of ξ_{TK} for additive-free plating with superimposed analytical model predictions.

current densities due to the throwing power characteristic for each current density.

Figure 6 exemplifies the results in Fig. 5. The photomicrographs show the PTH deposits for increasing electrolyte velocities at constant current densities of 100 mA/cm^2. The totally discontinuous deposit resulting from the low level of agitation provided by $\bar{v}$ = 0.17 cm/sec improves at $\bar{v}$ = 25 cm/sec to a still extremely rough deposit and changes to a good smooth deposit at a velocity of 87 cm/sec.

In Fig. 7 the PTH resistance is plotted as a function of the plating parameter $\bar{j}/\bar{j}_{lim}$. Since it is shown in Fig. 5 that increases in agitation beyond the minimum level required to prevent mass transport-limited plating conditions have no effect on R_{PTH}, correlation is expected only for results obtained with insufficient agitation. This correlation represents a lower bound for PTH resistances. The results for 25 and 87 cm/sec correlate rather well, but the PTH resistances for the samples plated at $\bar{v}$ = 0.17 cm/sec are much better than would be expected from the corresponding values of $\bar{j}/\bar{j}_{lim}$ and indicate a higher level of agitation. When the natural convection agitation effects are taken into consideration in the calculation of $\bar{j}/\bar{j}_{lim}$, the low velocity data correlate well with the high velocity results. The data plotted in Fig. 7 indicate that if both plating criteria Eq. [1] and [2] are met, PTH resistances of less than 450 $\mu\Omega$ result. Dendritic deposits form at values of $\bar{j}/\bar{j}_{lim} \geqq 0.3$ for the 0.34M $CuSO_4$ solution used.

In Fig. 8 the throwing power is correlated with the plating parameter ξ_{TK} and the results from two plating models (2, 4) are superimposed. The data show that the results from samples plated under conditions that meet the plating criterion Eq. [2] follow the Blue-Kessler (4) model prediction closely. This confirms the findings from a preliminary study (1), which concluded that the Kessler-Alkire model (2, 3) establishes a bound for limiting case behavior and that the Blue-Kessler model would give better predictions for well-controlled nominal conditions. The throwing power obtained under mass transport-limited plating conditions is significantly worse than the predicted optimum. From this plot it can be concluded that values of better than 1.5 for the PTH throwing power result from plating conditions meeting both plating criteria, Eq. [1] and [2].

Plating with Cubath®M additives.—The results of the experiments employing electrolyte with Cubath®M additives are illustrated in Fig. 9 through 13. In Fig. 9 the PTH resistance is shown as a function of the average plating current density for six solution velocities and two levels of air sparging. In contrast to the results for additive-free plating in Fig. 3, the PTH resistance is a much weaker function of the plating current density. Except for results from plating conditions with clearly inadequate agitation ($\bar{v}$ = 0.17 cm/sec and air sparging), the PTH resistance shows an increase with increasing current density only at values in excess of 40 mA/cm^2. In addition, the results for $\bar{v}$ = 25 and 43 cm/sec at $\bar{j}$ = 100 mA/cm^2 indicate a greater tolerance for agitation levels below the minimum electrolyte velocities established analytically (see Table I). On the other hand, at the low agitation levels provided by either forced flow at $\bar{v}$ = 0.17 cm/sec or by any level of air agitation, the rapid increase of the PTH resistance with increasing current density is indistinguishable from the results for additive-free plating. From these results it appears that the agitation provided by air sparging in the PTH's is roughly at the same level as the agitation provided by forced flow at $\bar{v}$ = 0.17 cm/sec.

In Fig. 10 the PTH resistance is correlated with the mean solution velocity in the PTH's. The results show even more vividly than the results for additive-free plating (Fig. 5) that an increase in agitation beyond the level necessary to prevent mass transport-limited plating does not further improve the PTH deposit quality. Compared to the results from additive-free plating the "band width" of possible PTH resistances

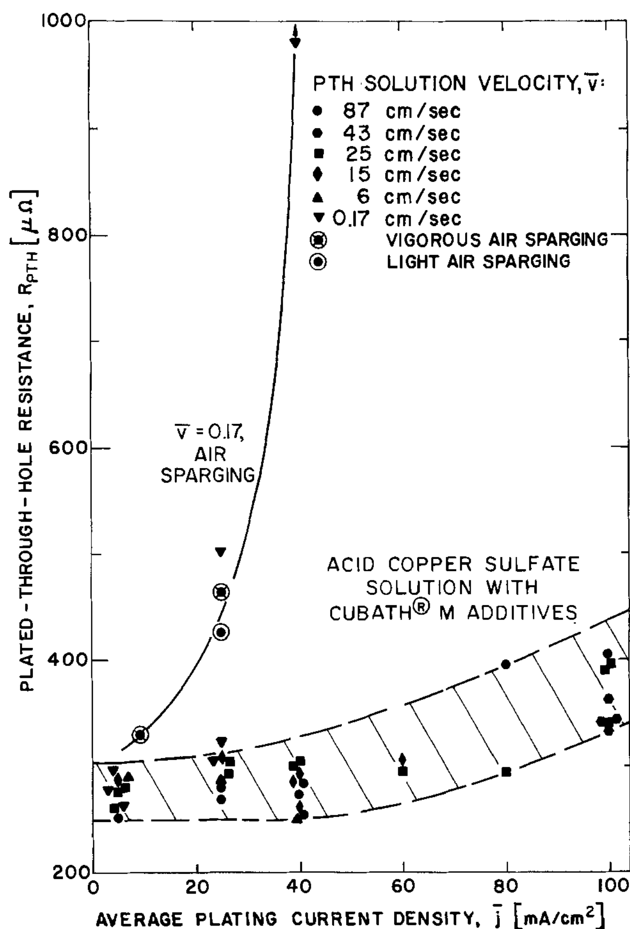

Fig. 9. Plated-through hole resistance as a function of plating current density and agitation velocity for plating with Cubath®M.

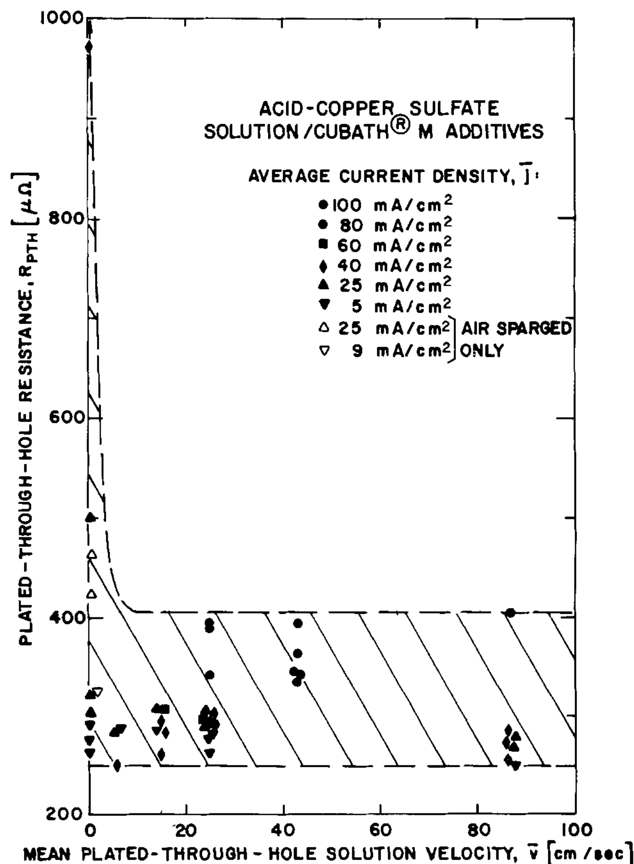

Fig. 10. Plated-through hole resistance as a function of agitation velocity and current density for plating with Cubath®M.

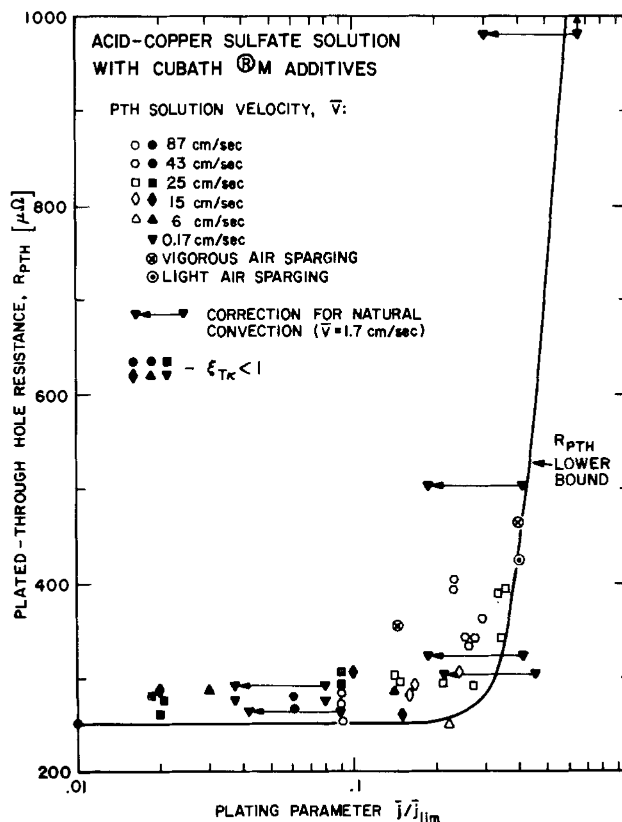

Fig. 11. Plated-through hole resistance as a function of $\bar{j}/\bar{j}_{lim}$ for plating with Cubath®M. Natural convection corrections for low velocity data are indicated.

for plating current densities ranging from 5 to 100 mA/cm² is much narrower for plating at adequate agitation. However, as for additive-free plating, but less pronounced, plating at higher current densities yields PTH's with higher resistances.

In Fig. 11 the PTH resistance is shown as a function of the plating parameter $\bar{j}/\bar{j}_{lim}$. As in Fig. 7, the lower bound for PTH resistances is indicated. Unlike the results for additive-free plating (see Fig. 7), the PTH resistance is virtually independent of $\bar{j}/\bar{j}_{lim}$ for values below the plating criterion $\bar{j}/\bar{j}_{lim} = 0.25$. For higher values of $\bar{j}/\bar{j}_{lim}$ however, the PTH resistance increases very rapidly. The results for very low agitation plating ($\bar{v} = 0.17$ cm/sec) show, as was the case for additive-free plating, improved correlation with the other results when the natural convection agitation effects are taken into consideration. However, for the very rough samples with $R_{PTH} > 300$ $\mu\Omega$, the natural convection is apparently impeded by the surface roughness in the PTH and thus a natural convection correction of $\bar{v} = 1.7$ cm/sec is too large.

An equivalent agitation velocity for both light and vigorous air sparging of $\bar{v} = 0.25$ cm/sec was estimated by fitting the PTH resistances for the air sparged MLB samples onto the lower bound curve in Fig. 11. The results from air sparging are plotted accordingly in Fig. 11. It also appears that natural convection may play a much less significant role in air sparging than for low level forced flow. It can be speculated that air sparging could disrupt natural convection sufficiently to prevent the resulting beneficial agitation effect.

The independence of the PTH deposit from variations in $\bar{j}/\bar{j}_{lim}$ for values of $\bar{j}/\bar{j}_{lim} < 0.25$ is further illustrated in Fig. 12a and 12b. In these figures photomicrographs of PTH's plated at consecutively larger values of $\bar{j}/\bar{j}_{lim}$ are shown. Samples (a)-(d), plated at $\bar{j}/\bar{j}_{lim}$ values ranging from 0.02 to 0.14 all show good, almost indistinguishable deposits with good leveling characteristics. However sample (e) plated at $\bar{j}/\bar{j}_{lim} = 0.41$ shows a

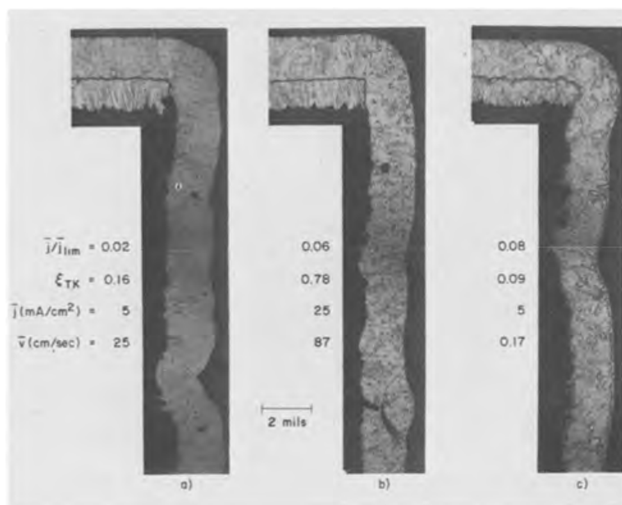

Fig. 12a. Metallographic cross sections of plated-through holes plated with Cubath®M at consecutively increasing values of $\bar{j}/\bar{j}_{lim}$.

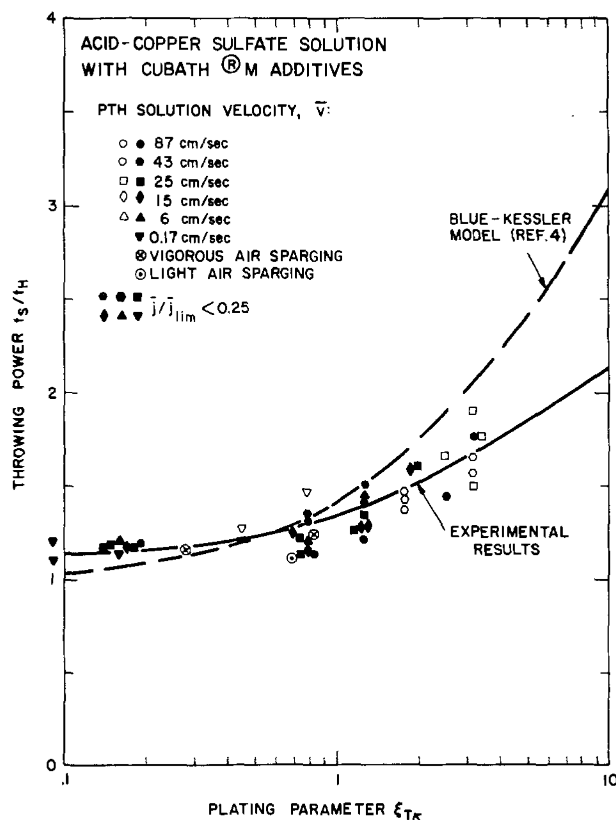

Fig. 13. Throwing power as a function of ξ_{TK} for plating with Cubath®M with superimposed analytical model predictions.

very rough, nonleveling deposit and for sample (f) plated at $\bar{j}/\bar{j}_{lim} = 0.66$ no copper has been deposited onto the electroless copper film and the electrodeposited copper formed isolated dendritic globules. The grain structure from deposits at very low current densities was columnar rather than fine as observed for deposits from higher current densities. Examination of samples (a) and (c), both plated at 5 mA/cm², show a much more pronounced grain structure than the other samples. Interestingly, sample (a) plated at a high level of agitation shows a columnar structure, whereas sample (c) plated at a very low level of agitation shows a large grained structure.

In Fig. 13 the throwing power is correlated with the plating parameter ξ_{TK} and the curve from the Blue-Kessler model (4) is superimposed. A curve is also fitted to the experimental data. Generally, the throwing power worsens as ξ_{TK} increases; however, this in-

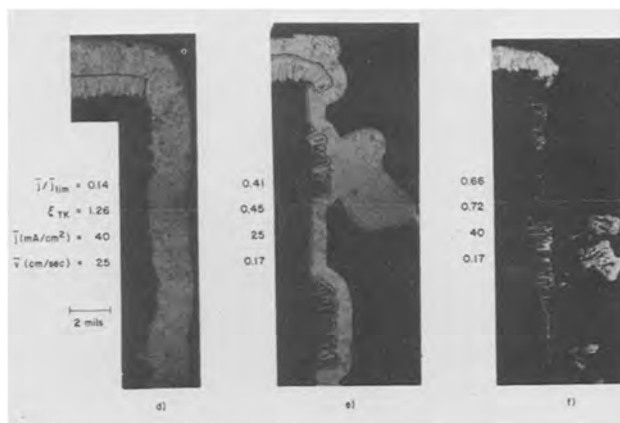

Fig. 12b. Metallographic cross sections of plated-through holes plated with Cubath®M at consecutively increasing values of $\bar{j}/\bar{j}_{lim}$.

crease is less than predicted by the Blue-Kessler model which correlated very well with the results from additive-free plating. This would indicate that Cubath®M additives make the plating quality less sensitive to changes in the plating parameters.

Summary and Conclusions

Additive-free acid-copper sulfate electrolyte.—The plating parameters developed in Ref. (2) correlate very well with the quality of the copper deposit in the PTH. The plating criteria established in Ref. (2) assure good quality PTH's with a throwing power t_S/t_H of better than 1.5. Plating for a given number of amperes-minute, lower plating current densities give lower PTH resistances and better throwing power. Increased levels of agitation improve the deposit quality dramatically up to the point of eliminating ion concentration gradients causing mass transport-limited plating conditions; further increases in the level of agitation, however, provide no further improvement in the PTH copper deposit. To prevent mass transport-limited plating conditions, agitation requirements increase rapidly with increasing current density and decreasing cupric ion concentration. For plating conditions meeting the plating criteria from Ref. (2), the Blue-Kessler model (4) predicts the throwing power into PTH's very well. The Kessler-Alkire model (2, 3), on the other hand, establishes limiting case behavior. Electrolyte agitation provided by natural convection has to be considered when only low levels of electrolyte agitation are provided by other means; an equivalent agitation velocity for natural convection of $\bar{v} = 1.7$ cm/sec has been determined from deviations from the Lévêque flow (15-17) and provides for excellent correlation of the low agitation results.

Acid-copper sulfate electrolyte with Cubath®M additives.—The findings for additive-free plating generally hold for plating with Cubath®M. However, Cubath®M plating is considerably less sensitive to changes in plating parameters such as current density and level of agitation. The dimensionless criteria for good plating (throwing power $t_S/t_H \leq 1.5$) of the miniscale can be relaxed to

$$\xi_{TK} < 2$$

and

$$\bar{j}/\bar{j}_{lim} < 0.25$$

The experimental results show a better deposit quality for higher values of ξ_{TK} than is predicted by the Blue-Kessler model (4). The assumption of negligible effects of additives on the miniscale plating (2, 3) used in the development of the Blue-Kessler model (4) cannot be maintained. This is indicated by the decreased sensitivity to plating parameter variations as well as the higher deposit quality (R_{PTH}, t_S/t_H) of PTH's plated in Cubath®M when compared to PTH's plated under the same conditions but in an additive-

free solution. From a comparison of the plated deposit, assuming no interaction between the sparging air and the brightener additives, it is estimated that air sparging provides electrolyte agitation in PTH's equivalent to $\bar{v} = 0.25$ cm/sec. It also appears that natural convection agitation effects benefiting low level forced flow agitation are impeded by air sparging. It is expected that this estimate is valid for additive-free plating also.

Acknowledgment

The authors would like to acknowledge the helpful discussions with R. C. Alkire and D. A. Rudy and are grateful to A. J. Colucci and G. J. Gass for the experimental measurements.

Manuscript submitted June 17, 1977; revised manuscript received Sept. 9, 1977.

Any discussion of this paper will appear in a Discussion Section to be published in the December 1978 JOURNAL. All discussions for the December 1978 Discussion Section should be submitted by Aug. 1, 1978.

Publication costs of this article were assisted by Bell Laboratories.

LIST OF SYMBOLS

c_∞ cupric ion concentration in bulk region, gmole/cm^3
D_i diffusion coefficient of species i, cm^2/sec
$\mathbf{F}$ Faraday's constant, 96,494 C/g-equivalent
$\bar{j}$ average current density, mA/cm^2
$\bar{j}_{lim}$ average limiting current density, mA/cm^2
L_e entrance length of undeveloped PTH flow, cm
M molecular weight, g/gmole
n number of electrons taking part in electrode reaction
R_g gas constant, 8.21 J/gmole-°K
R_{PTH} PTH electrical resistance, $\mu\Omega$
r_o PTH radius, cm
s_i stoichiometric coefficient of species i, dimensionless
T temperature, °K
t_B MLB thickness, PTH length, cm
t_H plated copper thickness in PTH center, mils
t_P plated copper thickness on planar MLB surface, mils
t_S plated copper thickness at PTH entrance or exit, mils
t_S/t_H throwing power
$\bar{v}$ mean electrolyte velocity in PTH, cm/sec
v_B MLB velocity in direction of PTH axis, cm/sec
α_c cathodic transfer coefficient, dimensionless $\approx$ 0.5
$\Gamma(4/3)$ Gamma function, dimensionless
κ electrolyte conductivity, Ω^{-1}cm^{-1}
$\xi_{T\kappa}$ ratio of ohmic resistance to Tafel charge transfer resistance, dimensionless (see E. [3])

REFERENCES

1. W. Engelmaier, T. J. Kessler, and A. J. Colucci, Paper 150 presented at The Electrochemical Society Meeting, Dallas, Texas, Oct. 5-9, 1975.
2. T. Kessler and R. Alkire, *This Journal*, **123**, 990 (1976).
3. T. Kessler and R. Alkire, *Plating Surf. Finish*, **63**, 22 (1976).
4. J. L. Blue and T. J. Kessler, Submitted to *This Journal*.
5. J. W. Dini, *Plating (East Orange, N.J.)*, **51**, 119 (1964).
6. R. F. Rothschild, *ibid.*, **53**, 437 (1966).
7. E. B. Saubestre and R. P. Khera, in "3rd Symposium on Plating in the Electronics Industry," American Electroplaters Society, pp. 230-242 (1971).
8. J. W. Dini, H. R. Johnson, and D. E. Brown, *Photo Chem. Mach. Photo Chem. Etching*, **7**, (March-April 1972).
9. D. A. Rudy, in "Symposium on the Design and Finishing of Printed Wiring and Hybrid Circuits," America Electroplaters Society, Ft. Worth, Texas, Jan. 21-22, 1976.
10. D. R. Turner, *Plating Surf. Finish*, **63**, 41 (1976).
11. D. A. Rudy, Paper 264 presented at The Electrochemical Society Meeting, Washington, D.C., May 2-7, 1976.
12. D. A. Rudy, Paper 266 presented at The Electrochemical Society Meeting, Las Vegas, Nevada, Oct. 17-22, 1976.
13. T. H. Irvine, *Met. Finish.*, **65**, 85 (1967).
14. Operating Instructions MC-OI 127, "Sel-Rex Cubath®M Process," Sel-Rex Co., Nutley, N.J. (1974).
15. A. A. Mirarefi and R. C. Alkire, Paper 267 presented at the Electrochemical Society Meeting, Washington, D.C., May 2-7, 1976.
16. R. C. Alkire and A. A. Mirarefi, *This Journal*, **124**, 1043 (1977).
17. R. C. Alkire and A. A. Mirarefi, *ibid.*, **124**, (1977).
18. D. A. Rudy, Paper 257 presented at The Electrochemical Society Meeting, Washington, D.C., May 2-7, 1976.

Auger Spectroscopic Evidence That Plasma Anodization Involves Mass Transfer from the Cathode to the Anode

J. D. Leslie and V. Keith[1]
Department of Physics, University of Waterloo, Waterloo, Ontario, Canada

and K. Knorr
Institut für Physik, Johannes Gutenberg-Universitat, Mainz, Germany

ABSTRACT

Auger spectroscopic evidence is presented that cathode material is transported to the anode during plasma anodization, even when the anode is facing away from the cathode and is located on the back of a shield. In the preparation of the plasma oxide samples, anodes of Ta, Nb, and Cu and cathodes of Ta, Nb, Al, and C have been used in various combinations. The Auger spectroscopic results indicate that cathode material does not deposit on the anode unless the anode is passing a current and that the oxide on the anode formed by plasma anodization generally has two layers, with the outer layer consisting of oxide of the cathode material and the inner layer consisting of oxide of the anode material. Evidence is presented which suggests that the transfer of cathode material to the anode is an integral part of plasma anodization.

In this paper we would like to report on an Auger spectroscopic study of metal oxide films produced by plasma anodization. Auger spectroscopy (1) is a technique for identifying atomic elements and determining their percentage concentration on the surface of a sample. When combined with *in situ* ion etching, it allows one to determine the depth profile of the percentage concentrations of the atomic constituents of the sample (2).

In 1963, Miles and Smith (3) introduced a method of forming an oxide layer on a metal surface which they called plasma anodization. They utilized a d-c oxygen gas at a pressure of 0.05 Torr. The surface ring cathode held at -1000V in a bell jar filled with oxygen gas at a pressure of 0.05 Torr. The surface of the metal sample to be anodized was mounted so that it would not see the cathode directly, supposedly to eliminate direct sputtering of cathode material onto the metal sample surface. If a thin oxide layer was desired, the glow discharge was maintained for a short period of time: a few seconds to some tens of minutes. If a thicker oxide layer was desired, the metal sample was made positive with respect to the system ground by means of an external positive voltage applied to the sample by a direct electrical connection, thus making the sample the anode. They found that the oxide thickness increased linearly with the anode voltage applied and that for a fixed anode voltage the anode current decreased to zero as the limiting thickness associated with that voltage was reached. By comparing this behavior with the similar behavior of anodization in an aqueous electrolyte, they called their process plasma anodization and suggested that the oxygen plasma was playing the role of an electrolyte that supplies negative oxygen ions to the surface of the metal anode where the oxide growth occurs.

Since the pioneering work of Miles and Smith, there have been a number of investigations of the phenomenon of plasma anodization. [See the article by Dell'Oca, Pulfrey, and Young (4) for a review of the work up to 1971.] While many of these investigators have questioned the role of negative oxygen ions assumed by Miles and Smith, there have been only a few indirect tests of the effect of negative oxygen ions on plasma anodization. O'Hanlon and Pennebaker (5) by applying a combination of d-c and rf voltages to the anode claimed to have shown that anodization would not occur under conditions where the negative oxygen ion component of the anodizing current was zero. Olive *et al.* (6) questioned the conclusion of O'Hanlon and Pennebaker, in that they pointed out that the bias conditions employed would have prevented oxide growth whether or not negative oxygen ions from the plasma were needed for growth. Olive *et al.* repeated this d-c and rf biasing experiment, but utilized a constant d-c current, and claimed from the result of their experiment that negative oxygen ions in the plasma were not utilized in plasma anodization. However, this test is a very indirect one and, as Olive *et al.* pointed out, it depended on the validity of some of the theoretical equations assumed.

The role of the cathode in plasma anodization, apart from that of being the source of the oxygen plasma, has always been assumed to be that of a source of contamination via reactively sputtered cathode material (7, 8). It is for this reason that in the literature it is always advocated that the sample should face away from the cathode and be suitably shielded, so that the surface being anodized cannot see the cathode directly. However, Leslie and Knorr (9), in an earlier ellipsometric study of the plasma anodization of tantalum, showed that under certain conditions, even if the sample was facing the cathode, there was no direct sputtering contamination of the sample, in that the sample was not being coated with sputtered material independently of the growth of the oxide layer. However, as Knorr and Leslie (10) showed in this earlier work on the plasma anodization of niobium and tantalum, it is necessary to assume a model, *i.e.*, one layer or two, values of refractive indexes, to interpret the ellipsometric data. For this reason, it was decided that only a more direct technique such as Auger spectroscopy would be useful in the present study.

Experimental Procedures

The vacuum system and experimental arrangements for producing the plasma anodized samples were the same, in general, as those used in the earlier ellipsometric studies (9, 10). However, one significant difference was that the samples were mounted facing away from the cathode. An aluminum shield that was 5 cm wide by 10 cm high was positioned parallel to the cathode and 8 cm away and was isolated electrically from the rest of the vacuum chamber. The samples were 0.1 mm foil and were mounted between mica sheets on the side of the shield away from the

[1] Present address: Department of Physics, Queen's University, Kingston, Ontario, Canada.

cathode. The top mica sheet had a hole 0.5 × 1.0 cm that defined the active area of the sample. The samples had a wire spotwelded to them, so that the anodization current could be supplied, and the wire was insulated over its entire length in the vacuum space to prevent leakage current.

Because of the location of the sample facing away from the cathode, it was not possible to make ellipsometric measurements during the growth of the oxide. The thickness of the oxide layer was estimated during growth from the change in the sample voltage at fixed anode current, which was compared to similar plots that had been calibrated in earlier ellipsometric studies.

Before mounting the samples, we had cleaned them by heating the foils to a red heat in a pressure of 10^{-8} Torr for a few minutes. The samples were all polycrystalline foil, and the material was Marz grade Ta and Nb foil purchased from Materials Research Corporation. After the cleaned sample was mounted in the vacuum chamber where the plasma anodization would take place, the system was pumped down to less than 10^{-7} Torr. Then research grade oxygen gas was admitted to the vacuum chamber through a leak valve while a mechanical pump connected to the chamber through a sorption trap kept the pressure in the vacuum chamber at 0.05-0.07 Torr under flow conditions. Once the pressure was stable, the glow discharge was initiated by applying −800V to the cathode. The anodizing current applied to the sample was typically 2 mA, and the samples were anodized for periods of 2-6 hr. A number of different cathode and anode material combinations were used. We used cathodes of Ta, Al, and C, which all measured 4 × 10 cm and a Nb cathode which measured 2.5 × 8 cm.

The Auger spectrometer used in this study was manufactured by Physical Electronics Industries and consisted of a stainless steel vacuum system (Model 12-100) with ion pumps and titanium sublimation pump, a cylindrical mirror analyzer (Model 10-150) with an integral 5 keV electron gun, a 2 keV sputter ion gun (Model 04-161), a carousel specimen manipulator (Model 10-502), and associated electronics. The plasma anodized samples were mounted on the carousel specimen manipulator, which could accommodate 12 samples at one time. After the vacuum system had been pumped down to 10^{-9} Torr, the ion pumps were turned off and the system was backfilled to a pressure of 5×10^{-5} Torr of krypton so that the ion etching could take place. Although the sputter ion gun had a maximum ion voltage of 2 keV, the normal conditions used in these experiments were a 1 keV etching voltage and a constant etching current. Auger spectra were obtained in two ways: First, complete Auger spectra (Auger signal *vs.* electron energy) were taken after different amounts of etching. In this way it was possible to examine the surface of the sample after a specified thickness of the sample had been removed. In particular, this was useful for determining all the elements of particular interest in a plasma oxide associated with a particular combination of cathode and anode materials. Second, through the use of a multiplexer, it was possible to scan the Auger signal occurring within up to eight separate electron voltage ranges. In this way it was possible to pick a voltage range for each multiplexer channel associated with a particular Auger peak identifying a particular element. By scanning cyclically through these voltage ranges and displaying the Auger signal *vs.* ion etching time, it was possible to see directly the variation of the concentration of the different elements as we etched through the sample. Thus we could arrive at an Auger depth profile of the atomic element concentrations throughout the thickness of the plasma oxide layer. The "depths" in these depth profiles are initially in terms of etching time, but by performing subsidiary ion etching experiments, it is possible to find the appropriate factors for converting etching times into thicknesses in angstroms.

These subsidiary experiments consisted of the following: A fairly thick (approximately 2000Å) layer of the plasma oxide, whose etch rate was to be determined, was formed on the anode sample in the standard way, but a cathode of the same metal was used. Then a stainless steel mask with a 2 mm hole in it was placed over the anode sample, which was then mounted in the Auger system. The anodic oxide layer was etched away using the constant current beam of krypton ions of specified voltage, until the oxygen Auger signal had dropped to half its initial constant value. The total etching time for this was noted and the etch was discontinued. The sample was removed from the Auger system and the depth of the resulting circular hole in the plasma oxide layer was measured using a Talysurf 4 depth profile measurer and/or a Gaertner interference microscope. By dividing the measured depth in angstroms by the measured etching time in seconds, one can arrive at the etching rate in angstroms per second for that plasma oxide for the constant current of Kr ions of the specified voltage. This procedure was checked by growing a known thickness of anodic oxide on Ta or Nb in an electrolyte. The thickness was determined from the anode voltage used and the known anodization constant. The resulting anodic oxide layer was then masked, ion etched, and the thickness measured in the same way as for the plasma oxide samples. The thickness measurements so found were within 5% of those given by the anodization constants and the anode voltages, and so we estimate that the thicknesses of the plasma oxide layers were determined within 5%.

Experimental Results

Ta anode and Nb cathode.—The first system that we studied was the plasma anodization of Ta using a Nb cathode. Figure 1 shows the complete Auger spectrum for the surface "as is" of a Ta sample, which we estimated to have a plasma oxide of approximately 1750Å on its surface. The largest peak at 510 eV is associated with oxygen, as are the smaller peaks between 460 and 510 eV. The low energy peaks between 150 and 200 eV are associated with Nb, except for the one peak at 180 eV which is associated with Cl. All the peaks between 1600 and 2000 eV are also associated with Nb. The peaks at 260, 380, and 660 eV are associated with C, N, and F, respectively. The most interesting thing about this spectrum is that there is absolutely no indication of Ta on the surface of the

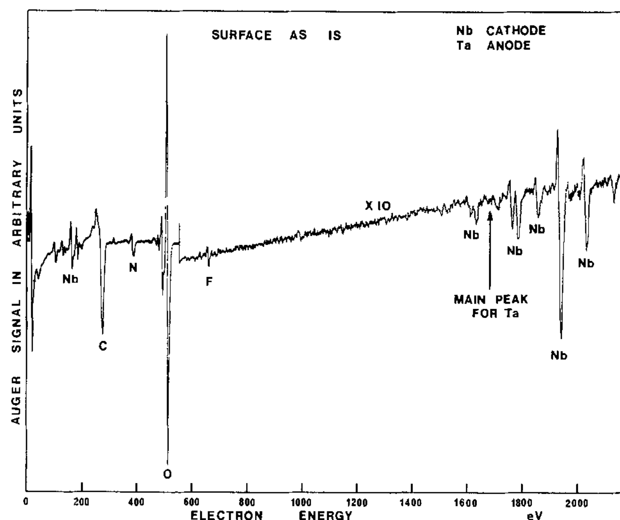

Fig. 1. Complete Auger spectrum of the surface of a plasma anodized Ta foil. Experimental conditions of the anodization: Nb cathode, cathode voltage −800V, oxygen pressure 0.06 Torr, sample area 50 mm², anode current 2 mA for 2 hr.

sample. The arrow in Fig. 1 at 1680 eV indicates the position of the main line for Ta which is at least as strong as the main line for Nb at 1944 eV. In Fig. 1, there is an increase of signal sensitivity of a factor of 10 for the region with electron energy greater than 550 eV. By using the multiplexer, and establishing appropriate channels, *e.g.*, 250-300 eV for C, 490-520 eV for O, 1650-1710 eV for Ta, 1920-1960 eV for Nb, etc., it was possible to monitor the Auger depth profile of the atomic constituents of the plasma oxide layer. We chose to observe the higher energy peaks of Ta (1680) and Nb (1944) rather than the stronger low energy peaks, because the Ta and Nb peaks overlap at low energy.

Figure 2 shows the plot of the Auger signals for Nb, Ta, and O *vs.* etching time in seconds. The Auger signals are plotted in arbitrary units, although it would be possible to process the data to give surface percentages. The Auger peaks associated with Cl, C, N, and F disappeared within 100 sec of etching, so they are associated just with surface contamination of the plasma oxide sample from the laboratory environment during the transfer to the Auger system. The etching was performed with a beam of 1 keV krypton ions. In separate etching experiments, the etching rate of such a beam was established to be 1 Å/sec for Ta oxide and 0.8 Å/sec for Nb oxide.

Figure 2 shows that there is no indication of Ta for at least 1000 sec of etching. The Auger signals for Nb and O are large and constant for the first 1000 sec (apart from the initial 100 sec of surface contamination). Although Auger spectroscopy cannot establish the chemical state that the atomic constituents are in, the constant Nb and O Auger signals and the known reactivity of Nb indicates that the Nb is present as an oxide. We can estimate the thickness of the Nb oxide layer in the following way. If we take the time at which the Nb Auger signal falls to half its initial constant value as an indication of the thickness of the Nb oxide, we see that this is 1520 sec. If we take the half-height of the O Auger signal as a measure of the total oxide thickness, we see that this is 1850 sec. We see that over the time between 1520 and 1850 sec the Ta signal is rising sharply, so we can attribute 1520 sec of etch time to Nb oxide and 330 sec, *i.e.*, 1850 − 1520, to Ta oxide. Using the etch rates of 0.8 Å/sec for Nb oxide and 1 Å/sec for Ta oxide, we find that the plasma oxide consists of a top layer of 1220Å of Nb oxide and a bottom layer of 330Å of Ta oxide. These thickness estimates may be in error from two sources. First, we are neglecting the mixing effect of the Ta and Nb, in that we are using the etching rate for Nb oxide to convert the etching time into a thickness, even though the last few hundred seconds involve an increasing component of Ta oxide. Second, the Ta oxide layer actually produced during the plasma oxidation process will certainly be less than our estimate here, because as soon as the clean Ta surface is exposed to oxygen, a surface layer of oxide will form immediately, even without a plasma.

The interface between Nb oxide and Ta oxide is quite thick, in that the Nb Auger signal drops from 90 to 10% of its initial value over 420 sec of etching time, which corresponds to a thickness of 336Å. The corresponding 10-90% of the final value for the Ta Auger signal yields a width of 640 sec, which would translate into 640Å, if we use the Ta oxide etching rate. However this figure is not as meaningful as that for Nb, since, if there is a 330Å layer of Ta oxide, we would expect the Auger Ta signal to increase to a plateau through the oxide region and then increase again as we reach pure Ta. There is a suggestion in Fig. 2 that this is occurring, so we should really take 90% of this plateau value, which appears to be 130, and 90% yields 117. Therefore the appropriate Ta oxide interface thickness is 320Å; *i.e.*, (1660 − 1340) sec × 1 Å/sec. Thus this simple analysis suggests that there is a cross-over or transition region of Nb oxide to Ta oxide of approximately 320-340Å. The mean escape depth of the Auger electrons in this energy range is 20Å, so this cannot account for such a broad transition region. It may be a real effect of the oxide formation or it may be caused by the polycrystalline foils that we are using, which have very small grain size. The resulting grain boundaries might affect the results in two ways. First, diffusion along grain boundaries is known to occur much faster than through the bulk, and this may be producing a greater mixing distance of the species during the oxidation process. Second, it is possible that the ion etching rate may be greater at the grain boundaries than through the bulk, and thus the etching would expose material farther into the sample along the grain boundaries. This would cause an apparent broadening of the transition region. The magnitude of both of these effects is unknown. Obviously, repeating these experiments on single crystal anodes would eliminate these possible problems and show whether the large transition regions that we obtain in these experiments are intrinsic to the plasma oxidation process. It is for this same experimental reason that we have adopted a rather simple approach to analyzing the plasma oxide into two layers, and we have not worried about the details of what is occurring in the interface region between the layers.

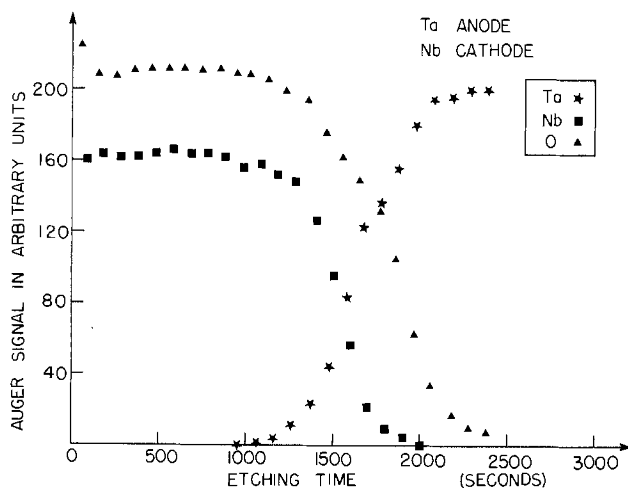

Fig. 2. Auger depth profile of the atomic constituents of the plasma oxide on the Ta anode of Fig. 1. Etching time is a measure of the thickness of the oxide layer that has been etched away, and the Auger signal gives the relative concentration of the atomic constituents on the surface of the layer remaining.

Figure 3 shows the Auger depth profile of the atomic constituents of another plasma oxide layer produced on a Ta anode using a Nb cathode. The experimental conditions of cathode voltage, anode current, and oxygen pressure were similar to those for the sample of Fig. 2, the only major difference between the two being that the plasma oxide in Fig. 3 was grown for a longer time. The most striking feature of Fig. 3 is that once again, as in Fig. 2, there is no indication of any Ta until the sample has been etched for 1500 sec. Let us use the half-heights of the Auger signals for Nb and O to indicate the thickness of the Nb oxide and the total oxide thickness, respectively, *i.e.*, the same procedure as in Fig. 2. We find that the Nb oxide has an etching time of 2220 sec which corresponds to a thickness of 1780Å. The total etching time for the oxide is 2500 sec. Therefore the Ta oxide thickness is 280Å, *i.e.*, (2500 − 2220) sec × 1 Å/sec. The main point to note is that the Nb oxide in Fig. 3 is 560Å thicker than in Fig. 2, whereas the Ta oxide layer is almost the same thickness for the two samples. The other striking feature of Fig. 3 is that there is no indication of a shoulder associated with a plateau in the Ta Auger signal. The thickness of the transition region is hard to establish

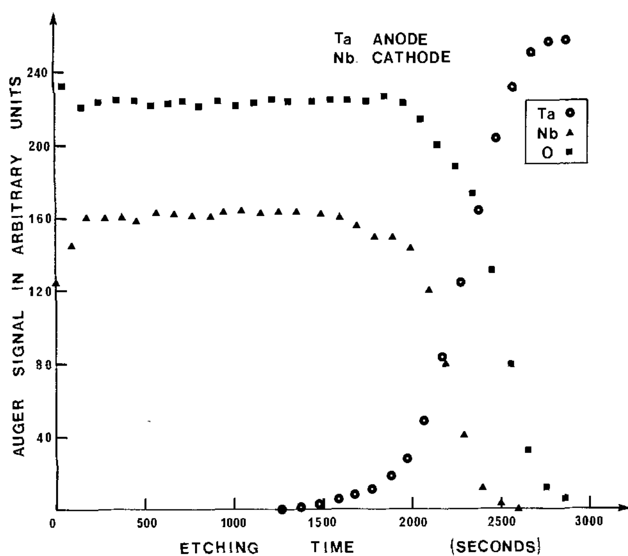

Fig. 3. Auger depth profile of the atomic constituents of the plasma oxide on a Ta anode. Experimental conditions of the anodization: Nb cathode, cathode voltage −800V, oxygen pressure 0.05 Torr, sample area 50 mm^2, anode current 2 mA for 3 hr.

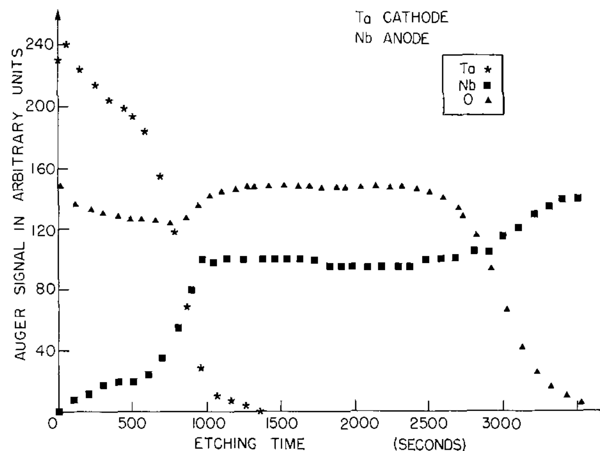

Fig. 4. Auger depth profile of the atomic constituents of the plasma oxide on a Nb anode. Experimental condition of the anodization: Ta cathode, cathode voltage −800V, oxygen pressure 0.06 Torr, sample area 50 mm^2, anode current 2 mA for 4 hr.

because of this fact and also the fact that the Nb Auger signal starts to fall slowly for 500 sec, between 1500 and 2000 sec before descending sharply. If we take the sharp descent as the indication of the interface, then the 90-10% Nb Auger transition region occurs over 400 sec of etching time between 2060 and 2460 sec. This translates into a 320Å Nb oxide transition width which is almost identical to what was found for Fig. 2. However, there is some indication of a slightly longer tail in the Ta distribution into the Nb oxide. The total sample thickness is 1780Å Nb oxide + 320Å Ta oxide for a total thickness of 2100Å.

Now, from the results of Fig. 2 and 3, one might suspect that all that is happening is that cathode material is being sputtered onto the anode sample and contaminating it. However, we must point out, most emphatically, that if no voltage is applied to the anode sample then less than 100Å of cathode oxide is formed on the sample regardless of the length of time that the sample is left in the glow discharge. Ta samples were processed in exactly the same way as those of Fig. 2 and 3 and were exposed to the plasma for the same times as those samples, with the exception that no anode current was supplied. The samples were analyzed in the Auger system, and the Nb oxide on the surface etched away in less than 100 sec. This initial buildup of less than 80Å of Nb oxide can be understood in terms of an effective voltage on the sample due to a difference in potential between the plasma and the sample.

Nb anode and Ta cathode.—Next we studied the growth of a plasma oxide on a Nb anode using a Ta cathode. The experimental conditions of cathode voltage, anode current, and oxygen pressure were similar to the earlier samples. Figure 4 shows the Auger depth profile of the atomic constituents of a plasma oxide layer produced on a Nb anode with a Ta cathode. The most striking feature of Fig. 4 is that a Nb oxide layer has been formed under the Ta oxide layer on the surface. Using the half-heights of the Ta and O Auger signals to determine the etching time through the Ta oxide and the total oxide thickness, we arrive at etching times of 820 sec for the Ta oxide and 2980 − 820 = 2160 sec for the Nb oxide. Using the etching rates of 1 Å/sec for Ta oxide and 0.8 Å/sec for Nb oxide, we arrive at 820Å of Ta oxide as the outer layer and 1730Å of Nb oxide as the inner layer for a total thickness of 2550Å. Other interesting things to note about Fig. 4 are that a low concentration of Nb penetrates through the Ta oxide layer almost to the surface of the sample and the Ta concentration drops throughout the outer oxide layer. So we probably have some mixing going on in this outer layer, with the outer surface being entirely Ta oxide and the concentration of Nb oxide increasing throughout this layer. Using the 90-10% drop in Auger signal for Ta to define the thickness of the Ta oxide interface region, and using the value of the Auger signal at 600 sec, *i.e.*, 186, we find that the interface thickness of the Ta oxide is 320 sec, which translates into 320Å, which is exactly the same as what was found for the samples of Fig. 2 and 3. Since there is this large penetration of Nb oxide into the Ta oxide, it is a little harder to define an interface thickness for the Nb oxide, but if we take 10-90% of the jump between the plateau at 20 and the final value of 100, we find an etching thickness of 310 sec, which is very close to the time for Ta oxide, but using a conversion of 0.8 Å/sec this translates into a thickness of 248Å. The O peak drops off more slowly as we approach the end of the oxide, and the interface region is 640 sec thick, which corresponds to 512Å.

Nb anode and Al cathode.—Many studies of plasma oxidation have used aluminum as the cathode material, consequently, we thought that we should see what effect this would have on the growth of the plasma oxide on Nb and Ta anodes. The experimental conditions of cathode voltage, anode current, and oxygen pressure were similar to the earlier samples. Figure 5 shows the Auger depth profile of the atomic constituents of the plasma oxide obtained for a Nb sample plasma oxidized using an Al cathode. Once again, the most striking feature of Fig. 5 is that the plasma oxide consists of an outer layer of Al oxide and an inner layer of Nb oxide. Using the half-heights of the Al and O Auger signals to determine the etching time through the Al oxide and Nb oxide, we arrive at etching times of 590 sec for the Al oxide and 1820 − 590 = 1230 sec for the Nb oxide. The etching rate for Nb oxide is 0.8 Å/sec and the etching rate for Al oxide is also 0.8 Å/sec, thus, the Al oxide outer layer is 470Å thick and the Nb oxide inner layer is 980Å thick. The 10-90% thickness of the Al oxide interface is 360 sec which corresponds to 290Å. Quite a pronounced dip in the O Auger signal is seen at the interface of the Al oxide and Nb oxide in Fig. 5. It can also be seen to a lesser extent in Fig. 4 at the interface between the Ta oxide and the Nb oxide.

Ta anode and Al cathode.—Figure 6 shows the Auger depth profile of the atomic constituents of the plasma oxide obtained with a Ta anode and an Al cathode. The experimental conditions of cathode voltage, anode

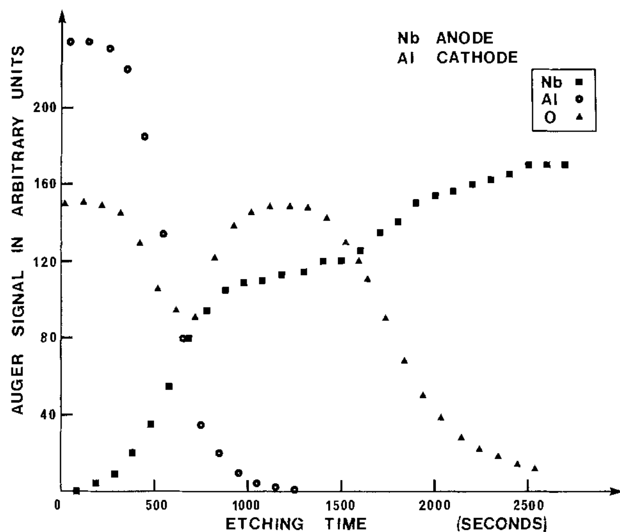

Fig. 5. Auger depth profile of the atomic constituents of the plasma oxide on a Nb anode. Experimental conditions of the anodization: Al cathode, cathode voltage —800V, oxygen pressure 0.06 Torr, sample area 50 mm^2, anode current 2 mA for 4 hr.

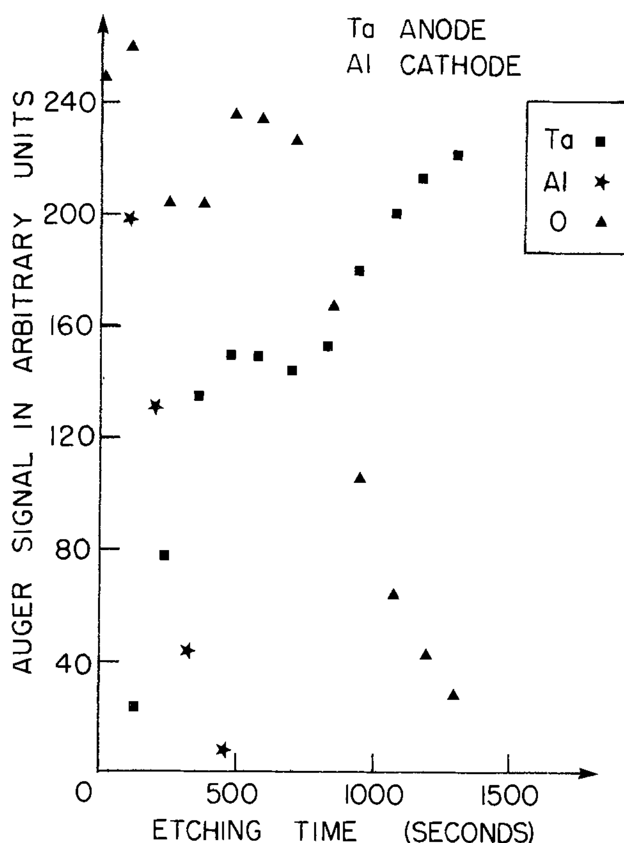

Fig. 6. Auger depth profile of the atomic constituents of the plasma oxide on a Ta anode. Experimental conditions of the anodization: Al cathode, cathode voltage —800V, oxygen pressure 0.07 Torr, sample area 50 mm^2, anode current 2 mA for 3 hr.

current, and oxygen pressure were similar to those for the other samples. Although Fig. 6 shows a much thinner plasma oxide layer than some of the other samples, the general feature of an outer oxide of cathode material and an inner oxide of the anode material can be clearly seen. Using the half-height Auger signals for Al and O to denote the thicknesses of the outer layer and of the outer plus inner layers, respectively, we find that the etching time for the Al oxide layer is 240 sec and for the Ta oxide layer is 930 − 240 ≃ 690 sec. Using the etching rates of 0.8 Å/sec for Al oxide and 1 Å/sec for Ta oxide, the Al oxide has a thickness of 190Å and the Ta oxide has a thickness of 690Å. The transition width (defined as the etching time to go from 10 to 90% of the Auger peak) is 280 sec for both the Al peak and the Ta peak and 590 sec for the O peak.

Cu anode and Ta cathode.—Since all the anode materials that we had tried up to this point were substances that oxidized reasonably well, *i.e.*, Ta and Nb, we thought that it might be interesting to try as an anode material a substance that did not oxidize as readily. We therefore decided to try an anode of Cu foil. We thought that this might give some information on the importance of the oxidation ability of the anode in this plasma anodization process. Figure 7 shows the depth profile of the atomic constituents of the resulting plasma oxide on a Cu anode due to a Ta cathode. Figure 7 shows that a layer of Ta oxide was formed on the surface of the Cu during the plasma anodization process, but there is no evidence of oxidation of the Cu. This can be seen from the fact that the O and Ta Auger signals drop to zero together, and there is no appreciable shift as is evident in the earlier samples (see Fig. 2-6). Using the half-height of the Ta Auger signal, we find that the etching time for the Ta oxide layer is 730 sec which corresponds to a Ta oxide thickness of 730Å. A very small Cu Auger signal was discernible throughout most of the Ta oxide layer, but it only started to increase appreciably at a depth of 700Å into the Ta oxide layer. One other feature that is notable in Fig. 7 is the presence of a sizable C Auger signal throughout the Ta oxide layer. In all the other systems studied, the C Auger signal dropped quickly to zero after the etching commenced, indicating that the C was present just as surface contamination. Whether the presence of this C is important to the formation of the Ta oxide layer is unknown at this time, but the C was present in all samples of this type.

Cu anode and Al cathode.—Having succeeded in forming a Ta oxide layer on the surface of a copper anode using plasma anodization, we thought that it might be interesting to repeat this experiment with an Al cathode. Figure 8 shows the depth profile of the atomic constituents of the resulting oxide. The experimental conditions of cathode voltage, anode current, and oxygen pressure were similar to those for all other samples. While growing this oxide, we noted that the anode voltage was not changing with time as occurred with all the other samples. We con-

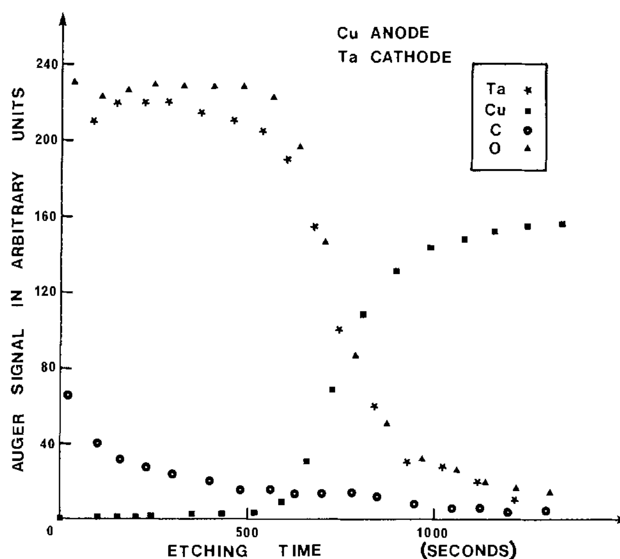

Fig. 7. Auger depth profile of the atomic constituents of the plasma oxide on a Cu anode. Experimental conditions of the anodization: Ta cathode, cathode voltage —800V, oxygen pressure 0.07 Torr, sample area 50 mm^2, anode current 2 mA for 4 hr.

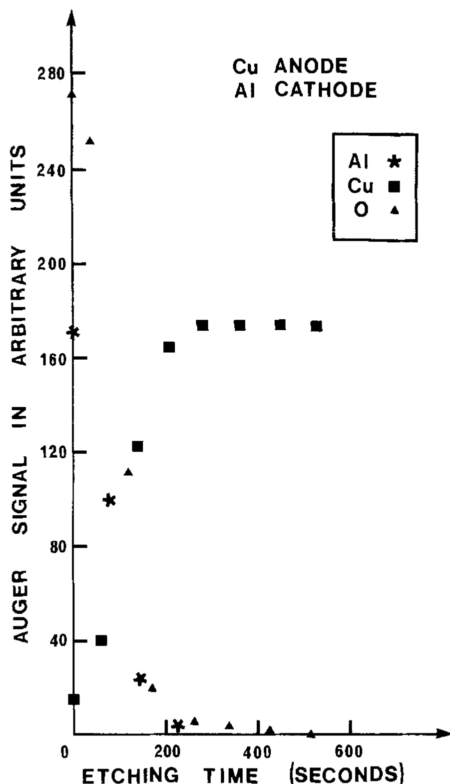

Fig. 8. Auger depth profile of the atomic constituents of the plasma oxide on a Cu anode. Experimental conditions of the anodization: Al cathode, cathode voltage —800V, oxygen pressure 0.06 Torr, sample area 50 mm^2, anode current 2 mA for 6 hr.

tinued the experimental run for 6 hr, whereas all other runs took between 2 and 4 hr. Figure 8 shows that there is at most 100 sec of Al oxide on the surface of the copper and that there is no appreciable indication of oxidation of the Cu. The Cu Auger signal is observable at the surface of the sample and starts to increase as soon as the ion etching commences. The C Auger signal quickly drops to zero within 50 sec of etching, unlike the situation with the Ta cathode, and indicates that C is present only as a surface layer.

C cathode.—All the data that has been presented in Fig. 1-8 involved the use of cathodes such as Nb, Ta, and Al which form stable oxides. If the only thing that is important about the cathode is that it should have a low sputtering rate, then it should be possible to do plasma anodization using a carbon cathode. Carbon has as low a sputtering rate as Ta and Nb and lower than Al. We tried using a graphite cathode and successively anodes of Nb, Ta, and Cu. The experimental conditions of cathode voltage, anode current, and oxygen pressure were similar to those for the other systems. In each case we observed the following two things. First, the anode voltage did not increase with time, although some of the experimental runs lasted for several hours. Second, the plasma was a different color, *i.e.*, a deep blue rather than the greenish white that occurred with the other metallic cathodes. When we observed the anode samples with the Auger system after several hours of trying to form a plasma oxide, we found that there was no evidence of oxidation of the anode metals, apart from the approximately 100Å surface layer of anode oxide that resulted from exposure of the clean anode surfaces to oxygen.

Discussion of Results

Let us commence by enumerating the facts that have been established by this Auger spectroscopic study of plasma anodization:

1. There is clear evidence of transport of cathode material to the anode during plasma anodization, even when the anode is facing away from the cathode and is located on the back of a shield.
2. Deposition of cathode material on the anode does not occur unless a current is passing through the anode.
3. Cathode material is present in the form of an oxide on the anode.
4. The oxide on the anode formed by plasma oxidation is generally composed of two layers, with the outer layer being composed of oxide of the cathode material and the inner layer being composed of oxide of the anode material. The point to note is that the cathode oxide is always found as an outer layer.
5. The cathode oxide thickness can be a significant fraction of the total oxide thickness, but the fraction depends on what materials were used for the anode and cathode.
6. In certain cases, it appears to be impossible to form substantial amounts of cathode oxide on the anode. For example, it appears to be impossible to grow more than 100Å of Al oxide on Cu, but it is possible to form 730Å of Ta oxide on Cu in a comparable amount of time.
7. It is impossible to plasma oxidize Ta, Nb, or Cu using a C cathode.

With the information that is available from these Auger spectroscopy experiments, we cannot arrive at a complete theory of what is occurring in plasma anodization. But we can take the first step toward a theory by considering different possible models that are consistent with the facts revealed in these Auger experiments. In arriving at such models, the best that we can do at this stage is to ask questions and give the most plausible answers consistent with the facts.

The Auger results show that cathode material reaches the anode and is present there as an oxide. Is this cathode material reaching the anode in elemental form or as an oxide molecule? Is the cathode material charged or neutral as it reaches the anode? We feel that it is most likely that the cathode material is reaching the anode in the form of a negatively charged oxide molecule of the cathode material. We feel that the cathode material has to be oxidized, because what is taking place is reactive sputtering of the cathode. We feel that the cathode material has to be charged, because, if it were neutral, what would cause it to reach the anode only when the anode is passing a current? The charging of the cathode oxide molecules could occur during the sputtering, *i.e.*, a certain percentage of the molecules sputtered off the cathode would be charged, or within the plasma by electron attachment.

Is the cathode oxide formed on the anode just a "dirt" effect or is it an integral part of the plasma oxidation process? The usual approach in the literature is to assume that sputtering from the cathode is just a dirt effect that can cause contamination of the growing oxide. The proposed solution is to turn the anode away from the cathode so that the anode sample cannot see the cathode directly. However, the assumption in this approach is that any material sputtered from the cathode will travel in a straight line of sight and stick to the first thing that it hits. At the pressures of 0.05-0.07 Torr used in these studies, the mean free path is so short that any sputtered material is going to make many collisions with gas molecules while traveling from the cathode to the anode, and thus be scattered throughout the volume of the gas. This sputtered cathode material is not sticking to the first surface that it hits, as is assumed, because substantial amounts of cathode material, *i.e.*, more than 100Å, are not found on the anode surface unless the anode is passing a current. Finally, if the cathode oxide is just a dirt effect and the oxide growth is by some other means, *e.g.*, negative oxygen ions, why is not the cathode oxide incorporated into the anode oxide in a uniform manner throughout the whole thickness of the oxide layer on the anode? Instead, we always find that the cathode oxide

occurs as a well-defined layer on the outside of any oxide of the anode material.

Can we suggest a model to explain the observed two-layer structure of the oxides produced by plasma anodization? One possible model is the following: The outer oxide layer is formed by absorption of charged cathode oxide molecules, which have been attracted to the anode surface by the electric field at the surface of the outer oxide. The oxygen for the growth of the inner oxide layer, *i.e.*, the anode oxide layer, comes from the oxygen in the outer oxide layer. Thus the relative reactivity of the anode and cathode materials would be important in determining the relative thicknesses of the inner and outer oxide layers. In this way, one could explain why little Ta oxide forms under the Nb oxide in the Ta anode and Nb cathode situation, whereas lots of Nb oxide forms under the Ta oxide in the Nb anode and Ta cathode situation, if the Nb is more reactive than the Ta and the Nb oxide has a much larger binding energy than the Ta oxide. In this model, no oxygen would have to come directly from the plasma in the form of negative oxygen ions. The absence of oxide growth observed when a carbon cathode is used in the plasma anodization experiment supports this model. The carbon sputtered off the cathode is probably in the form of CO or CO_2 molecules. The binding energies of these molecules are large and it is not possible to form a layer of CO or CO_2 on the surface of the anode. Therefore, we get no layer of cathode oxide which can be a source of oxygen for the growth of the underlying layer of anode oxide.

The only other model that we could have to explain the two-layer nature of the oxides produced in the plasma anodization process is the following: The outer oxide is formed by deposition of the cathode oxide material on the anode surface or by reaction of cathode material and oxygen ions on the anode surface. However, as soon as this outer cathode oxide is formed on the anode surface it is then inactive, and the growth of the underlying anode oxide is due to oxygen ions moving through the outer layer to reach the anode metal underneath. This might be called the cathode dirt model, in that the sputtering of cathode material is given the role of just producing a layer of cathode oxide dirt on the surface of the anode and another mechanism has to be invoked for the growth of the underlying anode oxide. However, such a model has a number of problems. How can it explain the fact that Ta oxide does not grow appreciably under the Nb oxide layer whereas Nb oxide does grow appreciably under a Ta oxide layer? How can it explain the fact that anode materials do not oxidize when a carbon cathode is used? Since C has as low a sputtering rate as Ta and Nb, if we invoke the presence of oxygen ions as the oxidizing agent in the case of Ta or Nb cathodes, it is difficult to see why there would not be oxygen ions present also in the case of a C cathode and we would, consequently, expect some oxidation of the anode materials in contrast to what is observed.

It must be emphasized that the results of the ellipsometric studies (9, 10) mentioned earlier are consistent with the present Auger spectroscopic studies. For example, the ellipsometric study of the plasma oxidation of tantalum (9) showed that there was no direct sputtering contamination of the sample, in that the sample was not being coated with sputtered material independent of the growth of the film. Exactly the same result is observed in this Auger spectroscopic study, in that no appreciable, *i.e.*, more than 100Å, deposition of cathode oxide occurred regardless of the length of time that the sample was exposed to the plasma as long as no anodizing current was supplied to the sample. Of course we can even understand this initial buildup of 100Å of cathode oxide in terms of an effective voltage on the sample due to a difference in potential between the plasma and the sample. The fact that the ellipsometric results for the plasma anodization of Ta could be fitted with a single Ta oxide layer model with a refractive index of 2.21 is not at variance with the general behavior revealed by these Auger spectroscopic studies of a two-layer model, consisting of an outer layer of cathode oxide and an inner layer of anode oxide. In those ellipsometric studies of plasma anodization of Ta and Nb (9, 10), the cathode material used was Ta. Thus in the plasma anodization of Ta, the cathode oxide and the anode oxide would both be Ta oxide and a single layer model could be expected to be an excellent fit. Even in the case of the plasma anodization of Nb, the ellipsometric results could be fitted with a single Nb oxide layer model with a refractive index of 2.30. The Auger spectroscopic results of Fig. 4 for the Nb anode and Ta cathode case suggest that the plasma oxide consisted of an outer layer of Ta oxide comprising 32% of the total thickness of the film and an inner layer of Nb oxide comprising 68% of the total thickness of the film. If the true index of refraction of the Nb oxide layer were slightly higher than 2.30, *e.g.*, 2.37 (4), it is not surprising that a single layer model with an index of refraction of 2.30 might fit quite well to an actual situation consisting of two layers with indexes of refraction of 2.21 and 2.37 with the lower index for 32% of the film thickness and the higher index for 68% of the film thickness.

These Auger spectroscopic results also help us to understand the earlier ellipsometric studies of plasma anodization of Ta and Nb by Lee *et al.* (11). They found that they could fit their ellipsometric results only with a two-layer model for the plasma oxide on Ta or Nb, although Knorr and Leslie (10) showed later that this two-layer fit was not unique since the ellipsometry data could be fitted equally well by a single oxide layer possessing some absorption. However, apart from the problems of interpretation, there are definite differences between the ellipsometry data of Lee *et al.* and that of Knorr and Leslie on the plasma anodization of Nb and Ta. The present Auger spectroscopic study suggests the reason for these differences. In the case of Knorr and Leslie, a Ta cathode was used, while in the case of Lee *et al.*, an Al cathode was used in the plasma anodization process. Figure 5 suggests that their plasma oxide layer on Nb might have consisted of an outer layer of Al oxide forming 32% of the total film thickness and an inner layer of Nb oxide forming 68% of the total film thickness. Figure 6 suggests that their plasma oxide layer on Ta might have consisted of an outer layer of Al oxide forming 22% of the total film thickness and an inner layer of Ta oxide forming 78% of the total film thickness. The index of refraction of Al oxide is 1.62 (12) and is thus very different from the index of refraction of Ta oxide or Nb oxide, which are 2.21 and 2.37, respectively. Thus it is not surprising that Lee *et al.* could not fit their ellipsometry data with a single layer model with a real index of refraction.

Conclusion

These Auger spectroscopic studies of plasma oxides indicate clearly that mass transfer from a cathode to the anode is occurring in the plasma anodization procedure. They show that in general the plasma oxide consists of two layers, with an outer layer consisting of oxide of cathode material and an inner layer consisting of oxide of the anode material. Evidence is presented which suggests that the transfer of cathode material to the anode may be an integral part of the plasma anodization procedure, in that the oxygen for the oxidation of the anode material may come from the outer layer of cathode oxide rather than directly from oxygen ions in the plasma. Obviously, such a suggestion needs further experimental testing before one can conclude that this is the dominant mechanism in plasma anodization. Work is continuing on this aspect of the problem, but perhaps the results so far will focus more attention

on the exact role of the cathode in the plasma anodization process, rather than the current assumption in the literature that the cathode is needed just to produce the oxygen plasma and that any sputtering of cathode material is an unwanted side effect.

Acknowledgments

The authors would like to thank Mr. Dennis Leahy and Mr. William Sinclair who, as physics undergraduates on a fourth year project, designed and constructed the digital timer and multiplexer, respectively, used in the Auger depth profiling experiments. The authors would also like to thank Mr. Dave Sawyer for his assistance in establishing the etching rate calibrations.

Manuscript submitted June 6, 1977; revised manuscript received Sept. 6, 1977.

Any discussion of this paper will appear in a Discussion Section to be published in the December 1978 JOURNAL. All discussions for the December 1978 Discussion Section should be submitted by Aug. 1, 1978.

Publication costs of this article were assisted by the National Research Council of Canada.

REFERENCES

1. J. C. Rivière, *Contemp. Phys.*, **14**, 513 (1973).
2. P. W. Palmberg, *J. Vac. Sci. Technol.*, **9**, 160 (1973); *ibid.*, **10**, 274 (1973).
3. J. L. Miles and P. H. Smith, *This Journal*, **110**, 1240 (1963).
4. C. J. Dell'Oca, D. L. Pulfrey, and L. Young, in "Physics of Thin Films," Vol. 6, M. H. Francombe and R. W. Hoffman, Editors, pp. 1-79, Academic Press, New York (1971).
5. J. F. O'Hanlon and W. B. Pennebaker, *Appl. Phys. Lett.*, **18**, 554 (1971).
6. G. Olive, D. L. Pulfrey, and L. Young, *Thin Solid Films*, **12**, 427 (1972).
7. J. F. O'Hanlon, *This Journal*, **118**, 270 (1971).
8. M. A. Copeland and R. Pappu, *Appl. Phys. Lett.*, **19**, 199 (1971).
9. J. D. Leslie and K. Knorr, *This Journal*, **121**, 263 (1974).
10. K. Knorr and J. D. Leslie, *ibid.*, **121**, 805 (1974).
11. W. G. Lee, G. Olive, D. L. Pulfrey, and L. Young, *ibid.*, **117**, 1172 (1970).
12. C. J. Dell'Oca and P. J. Fleming, *ibid.*, **123**, 1487 (1976).

On the Influence of Sensitization of the Electron Transfer Through the Interface Zinc Oxide/Electrolyte by Salt Additions

U. Bode and K. Hauffe*

Institut für Physikalische Chemie der Universität Göttingen, Göttingen, Germany

ABSTRACT

To study the mechanism of the spectral sensitization with the electrochemical cell

$$+ \text{ In/ZnO-single crystal/dye} + \text{electrolyte/Pt} -$$

measurements of the photocurrent influenced by salt additions to the electrolyte were performed. The ZnO-semiconductor-anode operates as a probe for excited states of dyes acting as sensitizer for the charge transfer through the interface zinc oxide/electrolyte. By addition of Br^-, J^-, SCN^-, and $SeCN^-$ ions to the dye-containing electrolyte a significant increase of the sensitized photocurrent was generated. This enhancement can either be attributed to a change of the dye adsorption on zinc oxide or be explained by the fluorescence quenching of the adsorbed sensitizer in the presence of halide ions. With this quenching, radical anions $\overline{F^{\cdot}}$ or excited triplet states $^3F^*$ of the dyes are produced which are responsible for the increase of the photocurrent. The possible single steps of this reaction are discussed.

The electrochemical photosensitization of the electron transfer through semiconductor interfaces has been studied extensively because of its importance for photographic and electrophotographic processes (1-4). Recently, it has also gained interest with regard to possible application to direct solar energy conversion into electrical energy (5). Proposals for such solar cells have been made (6), however their technical usability must be tested critically for every system. One of the main difficulties of photoconductor-electrolyte cells is the insufficient photochemical stability of the semiconductor electrode, as well as of the electrolyte at continuous operation, a problem which still has to be cleared, although attempts have been made in this field (7).

The first experiments with zinc oxide single crystals as the electrode in an electrochemical cell were carried out by Dewald (8). This technique permits the investigation in more detail of the sensitized charge transfer caused by dyes and dye mixtures which are dissolved in the electrolyte. Zinc oxide belongs to the group of n-type semiconductors because of the presence of an excess of zinc existing as zinc ions in interstitial positions accompanied by an equivalent number of free electrons. With anodic polarization an exhaustion boundary layer is generated owing to a decrease of the concentration of free electrons in zinc oxide near the ZnO/electrolyte interface which results in a bending up of the bandedges. Consequently, by this formation of a blocking barrier layer the inhibited anodic current amounts only to 10^{-11}-10^{-10} A/cm² (V = 1-3V *vs.* Ag/AgCl/0.1*N* KCl) compared to 10^{-6}-10^{-5} A/cm² with cathodic polarization ($V = -1$ to -2V *vs.* Ag/AgCl/0.1*N* KCl) of the zinc oxide crystal.

Illumination with a wavelength of $\lambda = 385$ nm, corresponding to the distance of the bandedges of $E_G = 3.2$ eV (9), causes a photoconductivity. A photocurrent can also be produced if dye molecules adsorbed at the surface are illuminated and inject electrons into the conduction band of zinc oxide. Generally, such a process occurs by electronically excited molecules, generated either by a chemical reaction (10) or by optical excitation. The charge carriers increase the

* Electrochemical Society Active Member.
Key words: dye sensitization, photosensitization, ZnO/electrolyte interface, electrochemical cell, reducing fluorescence quenching, dye adsorption.

anodic current by several orders of magnitude attaining values of $i_{photo} = 10^{-8}$-10^{-7} A/cm^2. The electronic transfer reaction by means of a dye D can proceed in the following way

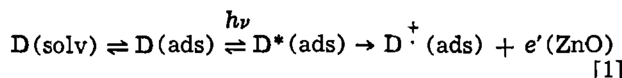

$$D(solv) \rightleftharpoons D(ads) \overset{h\nu}{\rightleftharpoons} D^*(ads) \rightarrow D^{\overset{+}{\cdot}}(ads) + e'(ZnO) \quad [1]$$

In previous investigations (11), it was demonstrated that an enhancement of the sensitized photocurrent appears if halides are added to the dye-containing electrolyte. This process was explained by the fluorescence quenching of the excited dye, particularly rhodamine B, giving rise to the tentative assumption that the halides react by an electron exchange with the dye. Therefore, the yield of fluorescence and thus the corresponding yield of the photocurrent should depend on the redox potential of the added halides as discussed by Baur (12) as well as by Weiss and Fischgold (13). This reducing fluorescence quenching described by Förster (14) effects a permanent regeneration of the injecting sensitizer. In the absence of the quenching anions, the oxidized dye radicals which are formed according to Eq. [1] can bleach photochemically much more easily and are no longer available for a repeated sensitizing reaction. Under this aspect, it was of interest to study the correlation between the decrease in the fluorescence of the sensitizer and the observed increase in the quantum yield of the sensitized photocurrent. These measurements were performed with the following electrochemical cell

$$+ \text{In} \mid \text{ZnO} \mid \text{dye} + \text{electrolyte} \mid \text{Pt} -$$

The anodically polarized ZnO electrode is a probe for the detection of excited states of the adsorbed dye molecules. In contrast to a metal electrode an electron transfer to the semiconductor anode is only possible via energetically high dye levels which can be occupied by optical excitation. In the following experiments, rhodamine B (RHB) was used as sensitizer because of its good sensitizing efficiency. In order to clarify the adsorption of RHB, zinc oxide powder was employed since the amounts of the dye adsorbed on a ZnO single crystal are too small. By these experiments, particularly the question had to be clarified to what extent an increase of the photocurrent is related to an enhanced dye adsorption by addition of salts. Necessarily, a current flowing through the electrochemical cell requires a charge exchange through the interface ZnO/electrolyte. Furthermore, an increase of the anodic photocurrent under constant potentiostatic conditions corresponds to a larger electron injection into the conduction band of ZnO. By means of anodic polarization experiments, the discharge kinetics of the space-charge layer was measured after switching off the external voltage source. The capacity of the space-charge layer will be discharged owing to an uptake of electrons by the positively polarized ZnO crystal which are released due to an oxidation of the adsorbed sensitizer molecules.

As is demonstrated in this paper, under certain conditions measurements in the electrochemical cell represent model experiments for the discharge of electrophotographic layers.

Experimental

Photocurrent measurements.—The experimental setup including the circuit with the electrochemical cell is schematically represented in Fig. 1. An extensive description was published earlier (1). The undoped ZnO single crystal was with its (0001) face (= Zn^{2+} face) in contact with the electrolyte. It was polarized potentiostatically with a voltage of +1.5V *vs.* a Ag/AgCl/0.1*N* KCl reference electrode. The cathode consisted of a platinized platinum net with a sufficiently large area. The illumination was carried out with a xenon high pressure lamp XBO 75W/2 of Osram and a Farrand grating monochromator through the rear of the crystal. The used light was irradiated

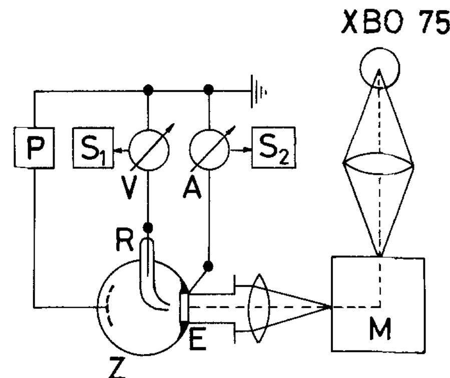

Fig. 1. Electrical circuit and optical arrangement of the experimental setup. P, potentiostat; Z, electrochemical cell; S_1, S_2, recorder; M, monochromator; V, electrometer; E, ZnO-single crystal; A, picoammeter; R, reference electrode.

in the optical absorption maximum of the dye (= RHB) amounting to $\lambda = 555$ nm. The density of the photon flux had a value of 3×10^{14} photons/cm^2 sec at 550 nm and was measured by means of a RCA photodiode SD 100. The action spectra of the photocurrents have been corrected to this photon flux.

The current and the voltage were recorded with a Keithley picoammeter 417 and a Keithley electrometer 610 R, respectively. The aqueous electrolyte with a volume of 15 ml consisted of an acetic acid-sodium acetate buffer of 0.1 mole/liter yielding a *p*H of 4.6. An addition of a conducting salt was not necessary. For the removal of oxygen in the electrolyte, the cell was flushed with purified nitrogen 15 min before every measurement.

Polarization measurements.—In addition to photocurrent measurements discharge experiments were carried out in the electrochemical cell at the ZnO single crystal polarized anodically with 4V. After switching off the external voltage source, the time slope of the discharge of the space-charge layer in the crystal and the electric double layer at the interface ZnO/electrolyte was recorded by potential measurements. These experiments were performed in the presence of various salts in the electrolyte at an open external circuit both in the dark and under illumination.

Discharge experiments with ZnO-resin layers.—In order to study the influence of salt additions to a ZnO-resin layer on the speed of the sensitized discharge under illumination, suitable ZnO-resin layers were charged up under a corona operating at about 12,000V. Then they were exposed to light of a defined photon flux and wavelength in a closed chamber with a revolving plate and a translucent probe for potential measurements. The exact experimental details have been published (15).

For this purpose a dispersion consisting of a RHB[1] doped zinc oxide powder[2] in a toluene-resin solution[3] with and without a salt admixture was coated on an aluminum foil as conductive support. Subsequently, the layer which had generally a thickness of 20μ, was dried at 80°C for 60 min. To obtain constant and reproducible conditions, the preparation of the dispersion and the technique for coating remained unchanged. Finally, the sample was mounted on the revolving plate in the measuring chamber and charged up with a corona. The change of the voltage with time was measured by a probe in connection with a Keithley electrometer and a recorder for the graphs. By this technique we were able to determine the value of the charge of the electrophotographic layer and its charge decay. For a good quality of an electrophotographic copy, this charge decay should proceed slowly in the dark and fast under illumination.

[1] 0.05 mg RHB/g ZnO.
[2] "Fotosiegel KI" of the Zinkweiss-Forschungsgesellschaft, D-4200 Oberhausen.
[3] Sinolac 602 S.

Optical measurements.—The photocurrent measurements of the respective dye solution were compared with its optical spectrum. These two spectra often are identical, in some cases, however, a significant shift of the absorption maximum was detected. The extinction spectra were recorded by a spectral photometer DMR 21 of Zeiss. Complementarily, emission spectra were measured by means of a fluorescence equipment ZFM 4. It is then when the apparatus operates as a one-single beam spectral photometer. The yield of fluorescence was converted into a relative intensity. As an excitation irradiation was emitted, light of a wavelength of 436 nm separated from the line spectrum of a mercury lamp by a monochromatic filter. In order to prevent a reabsorption of the fluorescence light, the cuvette of 1 cm thickness was brought into a sloping position. In combination with the spectral photometer and its remission equipment, remission spectra of the dye adsorbed on zinc oxide were determined. By means of this technique, the scattered remission of a dull surface could be analyzed. For these experiments, zinc oxide powder was mixed with a dye solution and filtered after 30 min stirring. Afterward, the dyed zinc oxide was washed with small amounts of distilled water and finally dried in air at 50°C for 1 hr in a drying chamber. As a white standard a pressed tablet of undyed ZnO "Fotosiegel K1" was used. The relative remission compared to this white standard was measured.

Adsorption measurements.—Furthermore, adsorption measurements on zinc oxide powder were performed. For these experiments 1g ZnO powder was added to a 20 ml dye solution of a defined concentration. The slurry was stirred as long as the adsorption equilibrium was adjusted (about 30-60 min). After centrifuging the dispersion, the concentration of the dye remaining in the solution was determined photometrically. To prevent a bleaching of the adsorbed dye, all adsorption experiments were carried out under red light or in the dark. For the interpretation of the photocurrent measurements it was important to study the influence of salt additions on the extent of the dye adsorption.

Experimental Results and Discussion

In previous experiments it was observed that additions of suitable salts to the electrolyte of the electrochemical cell influence considerably the sensitizing ability of RHB concerning the anodic photocurrent (11). While several ions decrease the sensitized photocurrent (*e.g.*, JO_3^-, JO_4^-) and other ones have no influence (*e.g.*, NO_3^-, SO_4^{2-}), the photocurrent is significantly increased in the presence of halide ions in the sequence Cl^-, Br^-, and J^-. Particularly, high photocurrent yields have also been obtained in the presence of SCN^- and $SeCN^-$ ions while NO_2^- and $S_2O_3^{2-}$ ions exhibit only a poor action. The dependence of the RHB sensitized photocurrents on the salt concentration are represented in Fig. 2. As can be seen, the enhancement of the current is elevated in the sequence $Cl^- < Br^- < J^-$. The rise of the photocurrent with an addition of thiocyanate can be detected at low concentrations and nearly attains the maximum value at 0.1 mole/liter. Selenium cyanate ions cause an extraordinarily strong increase. At a concentration of 0.05 mole/liter the photocurrent will be enlarged to a factor of about 20 of its initial value. Due to a precipitation of selenium at higher *p*H values and higher salt concentrations the current decreases at $c >$ 0.05 mole/liter. In a similar way with thiosulfate a decomposition occurs accompanied by a precipitation of sulfur, the current attaining again its initial value. According to the time slope of the currents in Fig. 3, a slow exponential decay occurs after a steep initial rise. Depending on the salt concentration, the photocurrent can fall back again to the half and only then remain constant.

An entirely different course of the photocurrent can be obtained with thiocyanate and selenium cyanate ions. With SCN^- ions the photocurrent mounts continuously and attains a plateau with an insignificant decay during a long time period. A conspicuous bathochromic shift of 15-20 nm, depending on the salt concentration, has been found in the action spectrum of the photocurrent in the presence of SCN^- and $SeCN^-$ ions. This shift can be gathered from Fig. 4. The photocurrent is plotted *vs.* the wavelength using electrolytes containing RHB and NaSCN of various concentrations, represented by curves 1 and 2. Corresponding curves are plotted with electrolytes satu-

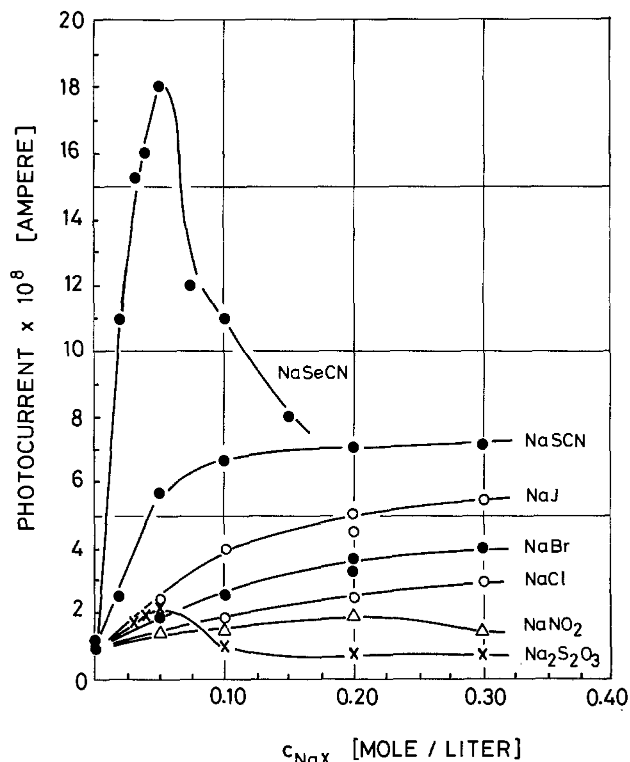

Fig. 2. Sensitized photocurrents of rhodamine B (= RHB) as a function of salt additions: $C_{RHB} = 10^{-4}$ mole/liter, *p*H = 4.6 (sodium acetate buffer), $\lambda = 555$ nm.

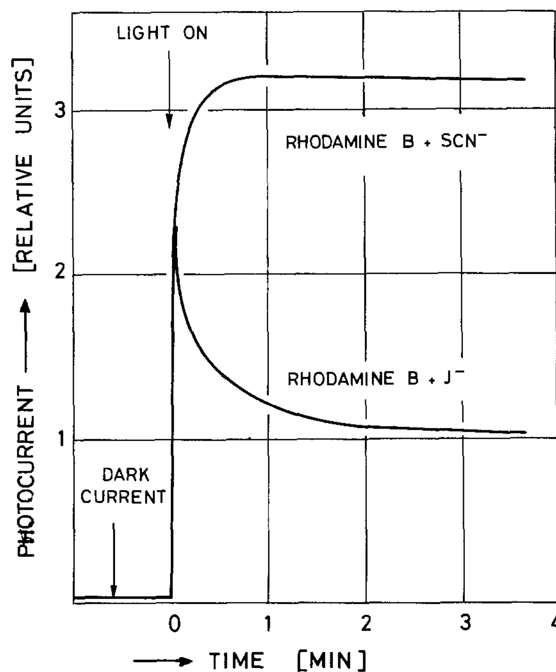

Fig. 3. Time slope of the photocurrent with RHB and NaSCN ($\lambda = 575$ nm) and NaJ ($\lambda = 555$ nm) additions, respectively, during illumination.

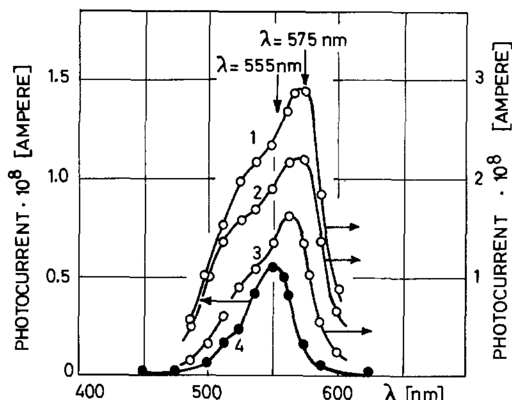

Fig. 4. Photocurrent spectra of RHB with NaSCN addition. RHB + 0.2M NaSCN, curve 1; RHB + 0.01M NaSCN, curve 2; RHB (saturated solution), curve 3; RHB (only), curve 4. $C_{RHB} = 2 \times 10^{-4}$ mole/liter, except curve 3.

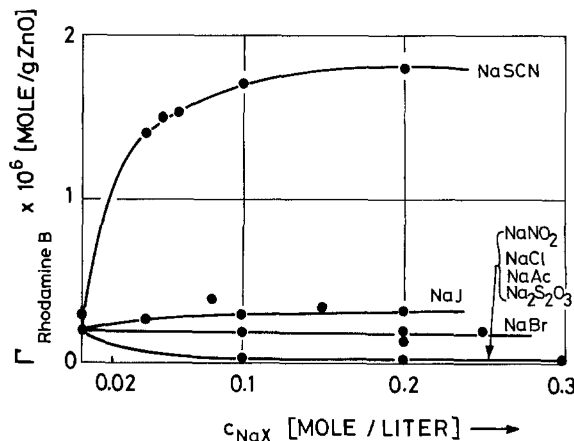

Fig. 6. Change of the RHB adsorption on zinc oxide by addition of various salts, $T = 23°C$.

rated with RHB (curve 3) and with a RHB concentration of 2×10^{-4} mole/liter (curve 4). The band of the spectrum of curve 4 at 555 nm does agree with the optical absorption of a dye solution of the same concentration. The maximum of the photocurrent of curve 1, however, is shifted at larger wavelengths to 575 nm. Since a saturated RHB solution without NaSCN addition exhibits the same shift, we may assume a salt-out effect. Obviously, the adsorption of the dye on the ZnO anode is intensified by the salt addition detectable by the large increase of the photocurrent and by its kinetic (Fig. 3). We may assume an aggregation of the dye which seems also to be responsible for an increased dimer formation. A term scheme for the dimer formation of RHB has been described by Krüger and Memming (16). The S_1 term of the dye is split up into two levels which correspond to the dimer bands. For the longer wavelength main band, an energetic shift of 0.06 eV is outlined. This value corresponds rather well to the experimentally observed shift of 15-20 nm found in the maximum of the action spectrum of the photocurrent with sensitization using the system RHB/SCN^- as well as highly concentrated or saturated RHB solutions.

Further information is obtained from the remission spectra represented in Fig. 5. Because of the increase of adsorption of RHB in the presence of SCN^- ions the remission at $\lambda = 555$ nm is decreased. However, the adsorption of the dye is not so high that the maximum of the remission spectrum is shifted. Therefore an aggregation of the dye does not occur. If the sample tablets are exposed to the daylight, then the dye is bleached. Compared to curve 1, which represents the spectrum of a new sample, both the intensity of remission and on a lower scale the position of the band maximum are changed. Due to the increased dye adsorption by the salt-out effect of NaSCN, a bleaching of the sample, curve 2a, cannot be detected. The extent of the influence of the adsorption of RHB on zinc oxide by anions which influence the photocurrent in

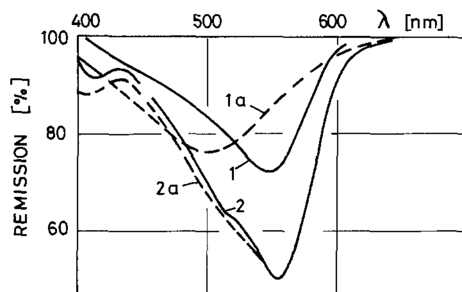

Fig. 5. Remission spectra of RHB with NaSCN addition adsorbed on zinc oxide. RHB, just after the preparation, curve 1; RHB, bleached, curve 1a; RHB + NaSCN, just after the preparation, curve 2; RHB + NaSCN, bleached, curve 2a.

the electrochemical cell was measured on ZnO powder. In Fig. 6, the adsorbed amount of the dye is plotted *vs.* the salt concentration. While NO_2^-, CH_3COO^-, $S_2O_3^{2-}$, and Cl^- ions decrease the adsorption of the dye, Br^- ions have no influence on it and J^- ions cause an insignificant increase. The measurements demonstrate undoubtedly that the rise of the sensitization by the halide ions as well as $S_2O_3^{2-}$ and NO_2^- ions cannot be attributed to adsorption effects. A salt-in effect by halides intensifies the solubility of an organic compound according to the sequence $Cl^- < Br^- < J^-$ (17) and consequently lowers the sensitization because of the decreasing adsorption. Then especially, the well-known salt-out by the sulfate ions should increase the sensitized photocurrent, but no influence is observed. An addition of NaSCN to the electrolyte results in a remarkable enhancement of the adsorption of RHB. With a salt concentration of 0.2 mole/liter the amount of the adsorbed dye is increased about one order of magnitude. As can be seen from the change with time of the photocurrent, the remission spectra and the band shift in the sensitization spectrum in accordance with the adsorption measurements with ZnO powder; the considerable rise of the sensitization with the system RHB/SCN^- is the consequence of an increase of the dye adsorption. A similar mechanism can be assumed with the $SeCN^-$ ions. Adsorption measurements could not be performed because in the presence of the dye selenium is precipitated at low concentration of $SeCN^-$

As may be concluded, the anions in the electrolyte may react electronically with the adsorbed dye molecules whose redox potential is changed during illumination favoring the reaction and, therefore, increasing the speed of electron injection into the conduction band of zinc oxide. The electron injected from the dye molecule into ZnO cannot return to the ground state because it has already been filled up by an electron of the anion. This mechanism has been discussed earlier by other authors (2, 3) assuming a mere redox process. During these redox steps a short-lived intermediate dye radical appears, for example, as a semireduced sensitizer. Allylthiourea (ATU) and hydroquinone (H_2Q) were often employed in these experiments as effective reducing agents.

Recently, it has been demonstrated with an oxazine dye (oxonine) that ATU not only operated as a mere redox species but also took part in a bimolecular quenching reaction with the excited singlet state of the dye (28). This singlet quenching process involves a rise of the intersystem crossing rate and hence leads to an increase of the triplet yield. In a consecutive step via the triplet state a semireduced dye radical and an oxidized ATU radical, $ATU^{\overset{+}{\cdot}}$, are formed. Preliminary experiments carried out by these authors show that with this dye the halides Br^- and J^- cause in a similar way an enhanced triplet formation. In the

same manner as ATU, H_2Q also increases the photocurrent spectrally sensitized by RHB at an n-CdS single crystal operating as anode in an electrochemical cell (27). Here, also, the correlation between cosensitization and fluorescence quenching was discussed. This relation has been stated in a previous paper (11) in which the influence of the viscosity of the electrolyte on the cosensitized current was presented. With increasing viscosity of the solvent the singlet quenching decreases (14). Since the rise of the photocurrent can be traced back to this reaction, consequently the current too should be reduced with growing viscosity. This expectation was confirmed by experiments. In Fig. 7 the results showing the influence of halides on the fluorescence yield of RHB were plotted in a Stern-Volmer relationship. The dependence on the fluorescence efficiency on the salt concentration is described by the following expression.

$$\phi_0/\phi = 1 + k_q\tau[Q^-] \qquad [2]$$

In this equation ϕ denotes the intensity of the fluorescence in the presence and ϕ_0 in the absence of the quenching anion, $[Q^-]$ the concentration of the quencher, and τ the singlet-state lifetime. The experimentally obtained slope $k_q\tau$ of the Stern-Volmer plot is in the case of J^- in approximate agreement with the data published by Wawilow (29). The values with SCN^-, Br^-, and Cl^- are a little larger than those quoted by Majumdar (20). The fluorescence quenching grows in the same sequence $NO_2^- < Cl^- < Br^- < SCN^- < J^- < SeCN^-$ as the sensitized photocurrent in the electrochemical cell except for SCN^- ions. This series of the (pseudo)halide ions has been found by other authors by quenching experiments with hydrocarbons (19) and with dyes belonging to the group of acridine and xanthene compounds (20). Förster (14) has discussed redox reactions for the mechanism of the fluorescence quenching assuming an intensive electronic interaction between excited dye molecule and quencher.

McKay and Hillson (21) have found from photometric investigations with rhodamine 6 G and other dyes that, depending on the concentration and the type of the solvent, the dye ions and their counterions are not separated by solvent molecules. The counterion is incorporated particularly at higher concentrations in the solvating envelope of the dye resulting in corresponding ion pairs. Furthermore, since the action spectrum of the sensitized photocurrent agrees with the optical spectrum of the dye solution except for the systems RHB/SCN^- and $RHB/SeCN^-$, we may assume that the solvating envelope of the dye ion will survive during the adsorption and the sensitization steps. In the case of the pseudo halides, an increase of the dye adsorption has been found which presumably causes a simultaneous formation of aggregates and, therefore, a bathochromic change in the spectrum of the photocurrent.[4] The particularly strong rise of the measured photocurrent could be attributed to a static quenching which appears at an associate formation of two or more molecules according to Förster (14) besides an increased adsorption and a reducing quenching of the fluorescence.

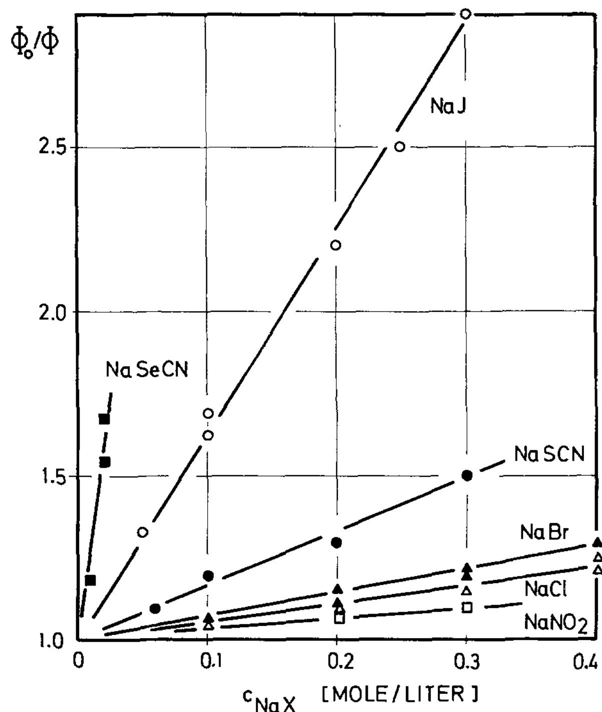

Fig. 7. Stern-Volmer plot of the fluorescence quenching of an aqueous RHB solution depending on the salt concentration, $\lambda_{ex} = 436$ nm, $T = 28°C$, $C_{RHB} = 10^{-4}$ mole/liter, pH 4.6 (sodium acetate buffer), N_2 flushing.

For the halide ions it is obvious to assume a dynamic quenching mechanism which occurs in the transition state via a complex formation of the dye cation and the halide. This very short-lived charge-transfer state and its reaction have often been discussed (19, 23, 24). This reaction is characterized by the fact that only after the formation of the encounter complex with the excited singlet state the specific activated quenching step occurs according to

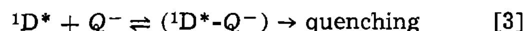

$${}^1D^* + Q^- \rightleftharpoons ({}^1D^*\text{-}Q^-) \rightarrow \text{quenching} \qquad [3]$$

Leonhardt and Weller (24) were the first to supply proofs by spectroscopic methods for a charge transfer during the fluorescence quenching of aromatic hydrocarbons, for example, perylene, etc. It results in a reduction of the excited singlet state under formation of a radical anion at simultaneous oxidation of the quenching molecule. The effectiveness of the quenching anion occurs parallel to the change of the redox potential of $Q\cdot/Q^-$

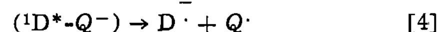

$$({}^1D^*\text{-}Q^-) \rightarrow \bar{D\cdot} + Q\cdot \qquad [4]$$

These results, found particularly at aromatic hydrocarbons with amines as quenchers, cannot be transferred arbitrarily to other systems.

Further experiments of the fluorescence quenching with the strongly effective halides demonstrated that besides the radical anion generated according to step [3] also excited triplet molecules are observed whose formation in some cases is mainly responsible for the quenching process (25, 28)

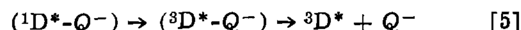

$$({}^1D^*\text{-}Q^-) \rightarrow ({}^3D^*\text{-}Q^-) \rightarrow {}^3D^* + Q^- \qquad [5]$$

Here, the singlet quenching does not occur by an electron transfer but by an intersystem crossing reaction of the singlet to the triplet state during the lifetime of the encounter complex. It depends primarily on the type of the quenching molecule whether radical ions or triplet states are formed predominantly.

The mechanisms of the fluorescence quenching admit an interpretation of the spectral sensitization reaction and its modulation by anionic quenchers. If radical anions are formed by reduction of the dye then the probability of the electron injection from these species is significantly increased because the deactivation generally occurring as competition reaction is no longer possible. The ground state of the dye molecules is already filled up and a regeneration can occur only by delivery of an electron. During the total reaction, the dye will not be changed and is available for repeated sensitization steps. This, however, is not the case if the electronic interaction with the quencher delivers a larger yield of triplet states. Under these circumstances, the increase of the sensitized photocurrent in the electrochemical cell can be attributed also to the longer lifetime of the triplet states. After the electron

[4] Similar results have been obtained by Killesreiter (22) who was able to demonstrate that with RHB a solvate chromic shift in the optical absorption spectrum also occurs in the sensitization spectrum.

injection, the dye is present as a radical cation so that a regeneration cannot occur in a primary step. The sequence of the single steps can be stated as follows

$$\mathrm{D(solv)} \rightleftharpoons \mathrm{D(ads)} \qquad K\mathrm{(ads)} \qquad [6]$$

$$\mathrm{D(ads)} + h\nu \rightarrow {}^1\mathrm{D^*(ads)} \qquad k_1 I \qquad [7]$$

where I = light intensity. The adsorption equilibrium is given in Eq. [6]. Furthermore, it may be assumed that with steady-state conditions the dye diffusion toward the electrode from the solution occurs rapidly enough and thus despite consecutive reactions the concentration of the adsorbed sensitizer D(ads) can be considered constant. Especially, the desorption of products being formed by photochemical bleaching should proceed quickly. This condition is better fulfilled the lower the pH value of the electrolyte, and in an acid environment a constant dissolution of the zinc oxide takes place. The surface of the single crystal will then be etched and therefore renewed continuously. Besides the electrochemical step, the anodic oxidation of the excited and adsorbed dye molecules, the singlet and triplet states, too, are deactivated. In the absence of a quencher the equations can be specified as below

$${}^1\mathrm{D^*} \rightarrow \mathrm{D}^{\dot{+}} + e'(\mathrm{ZnO}) \qquad k_{21} \qquad [8a]$$

$${}^1\mathrm{D^*} \rightsquigarrow \mathrm{D} \qquad k_{22} \qquad [8b]$$

$${}^1\mathrm{D^*} \rightarrow {}^3\mathrm{D^*} \qquad k_{\mathrm{isc}} \qquad [8c]$$

$${}^3\mathrm{D^*} \rightarrow \mathrm{D}^{\dot{+}} + e'(\mathrm{ZnO}) \qquad k_{31} \qquad [9a]$$

$${}^3\mathrm{D^*} \rightsquigarrow \mathrm{D} \qquad k_{32} \qquad [9b]$$

$$k_2 = k_{21} + k_{22} + k_{\mathrm{isc}}$$

$$k_2' = k_{22} + k_{\mathrm{isc}}$$

To simplify the above and following equations the adsorbed state of RHB was not marked. It results from the fluorescence lifetime of τ = 4.3 nsec (in aethanol) (30) for k_2' a value of 2.3×10^8 sec^{-1}. That means for an effective electron injection via S_1 according to Eq. [8a] k_{21} must be greater or at least comparable to k_2'. With optical excitation an intersystem crossing process populates the triplet state T_1 [8c]. The rate constant k_{32} amounts to $k_{32} \sim 2.5 \times 10^3$ sec^{-1} given by the triplet lifetime of $\tau \sim 0.4$ msec thus being higher by several orders of magnitude compared to the singlet lifetime. This suggests a considerable share of the electron injection via T_1 according to Eq. [9a]. Here, too, the deactivation in Eq. [8b] and [8c] is found as a competitive step. Further consideration shall demonstrate the influence of a quenching anion on the fluorescence and on the cosensitized photocurrent. Given the excited singlet state S_1 the quenching is described as below

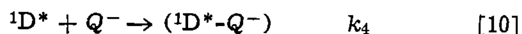

$${}^1\mathrm{D^*} + Q^- \rightarrow ({}^1\mathrm{D^*}\text{-}Q^-) \qquad k_4 \qquad [10]$$

$$({}^1\mathrm{D^*}\text{-}Q^-) \rightarrow \mathrm{D}^{\dot{-}} + Q \qquad k_{51} \qquad [11a]$$

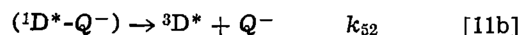

$$({}^1\mathrm{D^*}\text{-}Q^-) \rightarrow {}^3\mathrm{D^*} + Q^- \qquad k_{52} \qquad [11b]$$

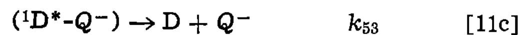

$$({}^1\mathrm{D^*}\text{-}Q^-) \rightarrow \mathrm{D} + Q^- \qquad k_{53} \qquad [11c]$$

$$({}^1\mathrm{D^*}\text{-}Q^-) = \mathrm{D}Q$$

$$k_5 = k_{51} + k_{52} + k_{53}$$

$$k_5' = k_{51} + k_{52}$$

First, according to Eq. [10] an encounter complex DQ is formed by collision with a high rate of formation. During the short lifetime of the complex the electronic interactions between the singlet RHB cation and the added anion take place. The subsequent dissociation leads to a dye radical [11a], to a dye triplet [11b], and to a molecule in the ground state [11c]. In principle, the rate constants of the above single steps are to be accessible by photoflash experiments carried out with dye solutions. The results available at present regarding certain dye-quencher systems (28) show that the intersystem crossing is mainly responsible for the singlet quenching. So, the electron injection in Eq. [12a] and [12b] can occur as the consecutive process of Eq. [11a] and [11b], these leading to an increased photocurrent with participation of the added halides

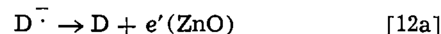

$$\mathrm{D}^{\dot{-}} \rightarrow \mathrm{D} + e'(\mathrm{ZnO}) \qquad [12a]$$

$${}^3\mathrm{D^*} \rightarrow \mathrm{D}^{\dot{+}} + e'(\mathrm{ZnO}) \qquad [12b]$$

One should notice that even the excited triplet can be quenched by anions, either the quencher being oxidized or only the $T_1 \rightarrow S_0$ transition being promoted.

Since, under continuous illumination, the cosensitized current remains roughly constant the relation between current and quencher concentration is given by a steady-state treatment. The kinetics of the formation and the decay of the encounter complex DQ, as well as of the excited singlet, read

$$d[\mathrm{D}Q]/dt = k_1 I[\mathrm{D(ads)}] - (k_2 + k_4[Q^-])[{}^1\mathrm{D^*}] \qquad [13]$$

$$d[{}^1\mathrm{D^*}]/dt = k_4[{}^1\mathrm{D^*}]\,[Q^-] - k_5[\mathrm{D}Q] \qquad [14]$$

According to Eq. [12a] and [12b] and taking [11a] and [11b], respectively, into consideration, the cosensitized current I_{cos} can be stated as

$$I_{\mathrm{cos}} = k_5'[\mathrm{D}Q] \qquad [15]$$

Substituting and rearranging Eq. [13], [14], and [15]

$$I_{\mathrm{cos}} = k_5'\,k_4[Q^-] \times k_1 I[\mathrm{D(ads)}]/k_5(k_2 + k_4[Q^-]) \qquad [16]$$

$$A = k_5 k_2/k_5' k_4 k_1 I[\mathrm{D(ads)}] = \text{constant} \qquad [17]$$

$$B = k_5/k_5' k_1 I[\mathrm{D(ads)}] = \text{constant} \qquad [18]$$

$$1/I_{\mathrm{cos}} = \mathrm{A} + \mathrm{B}/[Q^-] \qquad [19]$$

A linear function should be obtained if the reciprocal cosensitized photocurrent $1/I_{\mathrm{cos}}$ will be plotted $vs.$ the reciprocal value of the quencher concentration $1/[Q^-] = 1/C_{\mathrm{NaX}}$. This correlation is represented in Fig. 8 and is indeed realized for $\mathrm{Cl^-}$, $\mathrm{Br^-}$, and $\mathrm{J^-}$ additions.

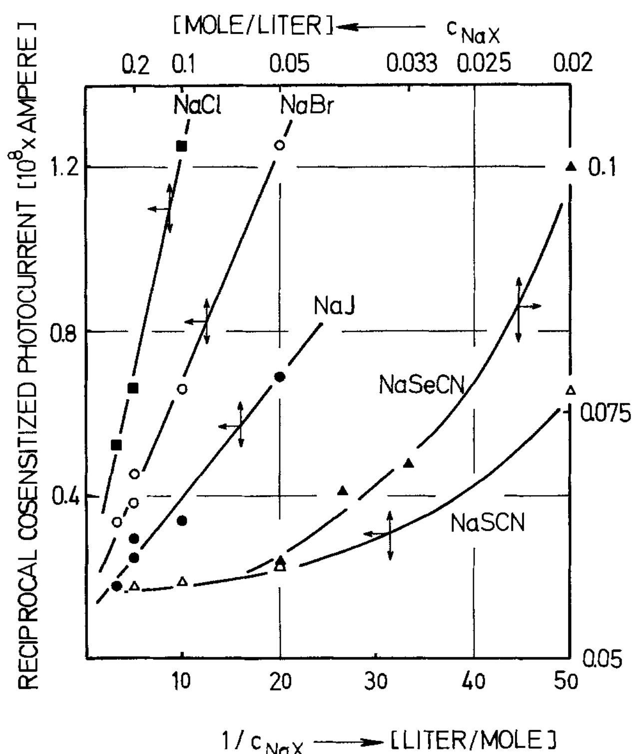

Fig. 8. Reciprocal cosensitized photocurrent as a function of $1/C_{\mathrm{NaX}}$. Data calculated from Fig. 2.

However, it must be noted that the actual concentration of the quenching anion at the electrode surface is higher by specific adsorption at zinc oxide than the bulk concentration in the electrolyte (31). Therefore, the relation between the fluorescence quenching (Fig. 7) and the change of the photocurrent (Fig. 8) can be given only qualitatively at present. Using the halides as quenchers the kinetic model is confirmed but deviations have been found with SCN^- and $SeCN^-$ ions. This result is not surprising since the SCN^- ions influence the adsorption equilibrium of the dye before the sensitization step, so that the increase of sensitization is mainly determined by the enhancement of the dye concentration on the surface. A similar behavior may be assumed for the $SeCN^-$ ions.

In order to demonstrate the effectiveness of salt additions on the sensitization of electrophotographic layers we performed the following model experiments in the electrochemical cell by a 4V anodic polarization of the ZnO crystal. This previously used technique (26) can be compared with charging and discharging experiments with ZnO-resin layers. In Fig. 9 the course of the dark and photodecay after the external voltage is switched off is represented. One can recognize clearly that the sensitized voltage decay is accelerated by the various salts, if the illumination takes place in the optical absorption maximum of the dye causing an electron injection into the ZnO crystal responsible for the avoidance of the barrier effect. The sequence of the effectiveness of the cosensitizing ability of the salts in these experiments is identical to that in the sensitized photoconductivity. The same results have been obtained with discharging experiments employing ZnO-resin layers charged up to about —300V. As can be seen from Fig. 10, where the photodischarge is recorded, a salt addition to the electrophotographic layer accelerates the voltage decay in the same sequence of the salts as was found for the polarization experiments with the ZnO crystal in the electrochemical cell. With too large salt additions, however, the conductivity of the electrophotographic layer becomes too high, so that the charge acceptance becomes too small. Therefore, the optimum concentration of salt and dye must be elaborated for practical purposes. The resin employed for the preparation of the layer undertakes the role of the electrolyte since it acts as

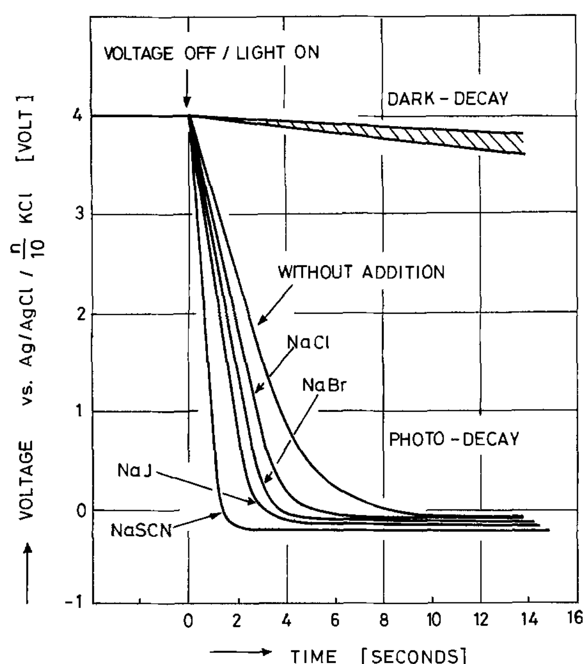

Fig. 9. Time slope of the photo- and dark decay at the anodically polarized ZnO-electrode (u = 4V vs. Ag/AgCl/0.1N KCl) with different salt additions. C_{RHB} = 10^{-4} mole/liter, C_{SALT} = 0.1 mole/liter, λ = 555 nm.

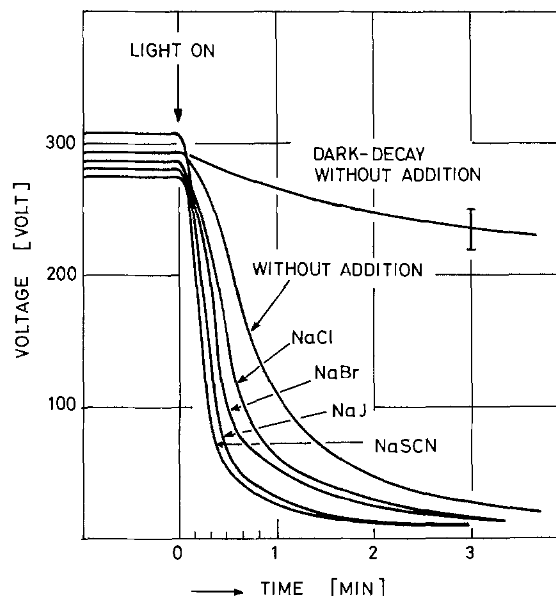

Fig. 10. Time slope of the photo- and dark decay of a ZnO-resin layer with addition of various salts (respectively, 10^{-3} mole NaX per 20g ZnO).

solvent for the dye and the salts. It is well known that the type of the used resin determines also the quality of the electrophotographic layer, presumedly due to the different influence on the solubility and the adsorption of the sensitizer on zinc oxide.

Unfortunately, the results obtained with the electrochemical cell technique based on aqueous electrolytes cannot be transferred for the evaluation of electrophotographic discharging experiments in any case. Therefore, it is desirable to carry out investigations on the sensitization with dyes dissolved in nonpolar solvents, *e.g.*, toluene. Such experiments, which also allow the study of the influence of the resin on the sensitization, are planned.

Acknowledgment

We are grateful to the Deutsche Forschungsgemeinschaft for the financial support and the salary of one of us (U.B). Furthermore we are also indebted to the Fonds der Chemischen Industrie for experimental equipment.

Manuscript submitted April 18, 1977; revised manuscript received Aug. 20, 1977.

Any discussion of this paper will appear in a Discussion Section to be published in the December 1978 JOURNAL. All discussions for the December 1978 Discussion Section should be submitted by Aug. 1, 1978.

REFERENCES

1. K. Hauffe and J. Range, *Z. Naturforsch.*, **23b**, 736 (1968); K. Hauffe, H. Pusch, and J. Range, *Z. Phys. Chem., NF.*, **64**, 122 (1969); K. Hauffe, H. J. Danzmann, H. Pusch, J. Range, and H. Volz, *This Journal*, **117**, 993 (1970).
2. H. Gerischer and H. Tributsch, *Ber. Bunsenges. Phys. Chem.*, **72**, 437 (1968); H. Tributsch and H. Gerischer, *ibid.*, **73**, 251 (1969).
3. R. Memming, *Photochem. Photobiol.*, **16**, 325 (1972).
4. W. P. Gomes and F. Cardon, *Ber. Bunsenges. Phys. Chem.*, **75**, 914 (1971).
5. H. Gerischer, *J. Electroanal. Interfacial Electrochem.*, **58**, 263 (1975); M. D. Archer, *J. Appl. Electrochem.*, **5**, 17 (1975).
6. H. Tributsch and M. Calvin, *Photochem. Photobiol.*, **14**, 95 (1971); M. Calvin, *Science*, **184**, 375 (1974); H. Tributsch, *Photochem. Photobiol.*, **16**, 261 (1972).
7. H. Minoura, T. Oki, and M. Tsuiki, *Chem. Lett.*, 1279 (1976); A. B. Ellis, S. W. Kaiser, and M. S. Wrighton, *J. Am. Chem. Soc.*, **98**, 1635 (1976).
8. J. F. Dewald, *Bell. Syst. Tech. J.*, **39**, 615 (1960).
9. G. Heiland, E. Mollwo, and F. Stöckmann, *Solid State Phys.*, **8**, 191 (1959).

10. H. Kokado, T. Nakayama, and E. Inoue, *J. Phys. Chem. Solids*, **31**, 2785 (1971); M. R. De Riepen, J. Range, and K. Hauffe, *Z. Phys. Chem. N.F.*, **99**, 257 (1976).
11. U. Bode, K. Hauffe, Y. Ishikawa, and H. Pusch, *Z. Phys. Chem. N.F.*, **85**, 144 (1973).
12. E. Baur, *ibid.*, **B16**, 465 (1932).
13. J. Weiss and H. Fischgold, *ibid.*, **B32**, 135 (1936).
14. Th. Förster, "Fluoreszenz Organischer Verbindungen," Vandenhoek & Ruprecht, Göttingen (1951).
15. K. Hauffe and R. Stechemesser, *J. Phot. Sci. Eng.*, **11**, 145 (1967).
16. U. Krüger and R. Memming, *Ber. Bunsenges. Phys. Chem.*, **78**, 670 (1974); *ibid.*, **78**, 679 (1974); *ibid.*, **78** 685 (1974).
17. W. L. Masterton and Tei Pei Lee, *J. Phys. Chem.*, **74**, 1776 (1970).
18. J. Bouchard, *J. Chim. Phys.*, **33**, 325 (1936).
19. R. Beer, K. M. C. Davis, and R. Hodgson, *J. Chem. Soc. D*, 840 (1970).
20. D. K. Majumdar, *Z. Phys. Chem.*, **217**, 200 (1961).
21. R. B. McKay and P. J. Hillson, *Trans. Faraday Soc.*, **61**, 1800 (1965).
22. H. Killesreiter, *Ber. Bunsenges. Phys. Chem.*, **78**, 1252 (1974).
23. A. R. Watkins, *J. Phys. Chem.*, **77**, 1207 (1973); *ibid.*, **78**, 2555 (1974).
24. H. Leonhardt and A. Weller, *Z. Phys. Chem. N.F.*, **29**, 277 (1961); H. Leonhardt and A. Weller, *Ber. Bunsenges. Phys. Chem.*, **67**, 791 (1963).
25. A. Harriman and B. W. Rockett, *J. Chem. Soc., Perkin Trans. 2*, 1624 (1973); K. H. Grellmann, A. R. Watkins, and A. Weller, *J. Lumin.*, **1, 2**, 678 (1970).
26. J. Range, H. Pusch, and K. Hauffe, *Z. Phys. Chem. N.F.*, **7**, 105 (1972).
27. T. Watanabe, A. Fujishima, and K. Honda, *Ber. Bunsenges. Phys. Chem.*, **79**, 1213 (1975).
28. E. Vogelmann and H. E. A. Kramer, *Photochem. Photobiol.*, **24**, 595 (1976); R. Bonneau, *ibid.*, **25**, 129 (1977).
29. S. I. Wawilow, *Z. Phys.*, **53**, 665 (1929); J. M. Frank and S. I. Wawilow, *ibid.*, **69**, 100 (1931).
30. J. B. Berlman, "Handbook of Fluorescence Spectra of Aromatic Molecules," Academic Press, New York (1971).
31. F. Lohmann, *Kolloid Z. Z. Polym.*, **250**, 748 (1972); L. Blok, Doctor Thesis, Utrecht (1968); L. Blok and P. L. De Bruyn, *J. Colloid Interface Sci.*, **32**, 533 (1970).

The Effect of Electrode Placement and Finite Matrix Conductivity on the Performance of Flow-Through Porous Electrodes

James A. Trainham*[1] and John Newman*

Materials and Molecular Research Division, Lawrence Berkeley Laboratory, and Department of Chemical Engineering, University of California, Berkeley, California 94720

ABSTRACT

A one-dimensional model for flow-through porous electrodes is used to predict the effluent concentration as a function of matrix conductivity and electrode length for upstream and downstream placement of the counterelectrode and current collector relative to the fluid inlet to the working electrode. Two chemical systems are considered: (*i*) the removal of copper from sulfate solutions, and (*ii*) the removal of silver from thiosulfate solutions. For an infinite matrix conductivity, the lowest effluent concentration is achieved when the counterelectrode is placed upstream to the fluid inlet of the working electrode. When the matrix conductivity is small, the lowest effluent concentration is still achieved for upstream placement of the counterelectrode; however, the optimum placement of the current collector depends on the chemical system and the value of the matrix conductivity that can be achieved in practice. Calculations show that for downstream placement of the counterelectrode a limiting current distribution cannot be achieved (for electrode lengths of interest here). The most undesirable configuration for achieving a low effluent concentration when the matrix conductivity is low is when both the counterelectrode and current collector are placed downstream of the fluid inlet. Distribution of potential, reaction rate, and electric driving force are presented for four different configurations: (*i*) upstream counterelectrode, downstream current collector, (*ii*) downstream counterelectrode, upstream current collector, (*iii*) upstream counterelectrode, upstream current collector, and (*iv*) downstream counterelectrode, downstream current collector.

The model used in calculating the effects of counterelectrode placement and current collector placement (when the matrix conductivity is moderate) on the performance of flow-through porous electrodes was developed in a previous paper by the authors (1); however, results were presented only for the effective matrix conductivity σ much greater than the effective solution conductivity κ. To date, previous models for flow-through porous electrodes (2-6) have considered only an infinite matrix conductivity, and no comparisons have been made on the performance of these electrochemical reactors as a function of counterelectrode placement.

The purpose of this paper is to suggest the optimum electrode configuration for two cases: (*i*) when $\sigma >> \kappa$ we are concerned only with the upstream and downstream placement of the counterelectrode and (*ii*) when $\sigma \approx \kappa$, placement of not only the counterelectrode is important but also the current collector placement must be considered. At least four geometric configurations are possible: (*i*) upstream counterelectrode, downstream current collector (UD); (*ii*) downstream counterelectrode, upstream current collector

* Electrochemical Society Active Member.
[1] Present address: College of Engineering, The University of South Carolina, Columbia, South Carolina 29208.

Key words: current distribution, potential distribution, mass transfer, axial dispersion, side reaction, copper deposition, silver deposition.

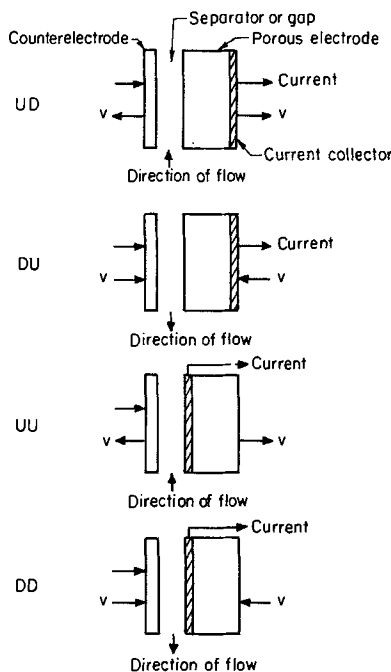

Fig. 1. Various configurations of counterelectrode placement and current collector placement relative to the direction of the fluid flow.

(DU); (*iii*) upstream counterelectrode, upstream current collector (UU); and (*iv*) downstream counterelectrode, downstream current collector (DD); and are shown schematically in Fig. 1. It should be noted that the direction of fluid flow through the counterelectrode is unimportant to the analysis to be considered as long as the products do not enter the electrode of interest.

Analysis

As mentioned earlier, calculations presented here are a direct application of a model for flow-through porous electrodes developed by the authors in a previous paper (1), and, therefore, detailed derivation of the governing equations are not presented here.

For the removal of metal ions from dilute streams, the behavior of a flow-through porous electrode with parallel current and fluid flow as shown in Fig. 1 can be described by two ordinary differential equations: one equation which describes the conservation of the metal-ion reactant

$$\frac{d\theta}{dy} = D' \frac{d^2\theta}{dy^2} - \frac{\theta - P_1 \exp\left[(\alpha_{aR}/\alpha_{cR} + 1)\eta'\right]}{1 + \exp(\eta')} \quad [1]$$

and one charge balance equation

$$\frac{d^2\eta'}{dy^2} = P_2 \left\{ P_3 \exp(-\alpha_{cS}\eta'/\alpha_{cR}) \left[1 - P_4 \exp\left(\frac{\alpha_{aS} + \alpha_{cS}}{\alpha_{cR}}\eta'\right)\right] + \frac{\theta - P_1 \exp\left[(\alpha_{aR}/\alpha_{cR} + 1)\eta'\right]}{1 + \exp(\eta')} \right\} \quad [2]$$

where θ is the reactant concentration divided by its value upstream in the feed, η' is the dimensionless local overpotential defined by

$$\exp(\eta') = -\frac{n\mathbf{F}k_m c_{Rf}}{s_R i_{oR,ref}} \exp(\alpha_{cR}\mathbf{F}\eta/RT) \quad [3]$$

and the reactor coordinate x was made dimensionless by

$$y = xak_m/v = x\alpha \quad [4]$$

Equation [1] describes the conservation of the metal-ion reactant and states that convection is balanced by axial diffusion and dispersion and by the rate of disappearance of the metal ions due to electrochemical reaction at the matrix-solution interface. Mass transfer limitations are included by introducing an average mass-transfer coefficient k_m (see dimensionless parameter defined below) and eliminating the wall concentration of the metal-ion reactant.

The charge balance equation utilizes Ohm's law in both the matrix and solution phases and states that a change in the total current at any point within the electrode ($d^2\eta'/dy^2$) is due to the rates of the side reaction and the main reaction. The term for the rate of the main reaction is the same in Eq. [1] and [2]. The side reaction is characterized by its rate at the half-wave potential of the main reaction.

The dimensionless parameters in Eq. [1] and [2] are defined as follows (1)

$$D' = (D_R + D_a)ak_m/v^2$$

$$P_1 = \left(-\frac{s_R i_{oR,ref}}{n\mathbf{F}k_m c_{Rf}}\right)^{1+\alpha_{aR}/\alpha_{cR}}$$

$$P_2 = \frac{\alpha_{cR} n\mathbf{F}^2 v^2 c_{Rf}}{s_R a k_m RT}\left(\frac{1}{\kappa} + \frac{1}{\sigma}\right)$$

$$P_3 = -\frac{s_R i_{oS,ref}}{n\mathbf{F}k_m c_{Rf}} e^{\alpha_{cS}\mathbf{F}\Delta U/RT}\left(-\frac{n\mathbf{F}k_m c_{Rf}}{s_R i_{oR,ref}}\right)^{\alpha_{cS}/\alpha_{cR}}$$

$$P_4 = \left(-\frac{s_R i_{oR,ref}}{n\mathbf{F}k_m c_{Rf}}\right)^{\frac{\alpha_{aS} + \alpha_{cS}}{\alpha_{cR}}} \exp\left[-(\alpha_{aS} + \alpha_{cS})\Delta U\mathbf{F}/RT\right] \quad [5]$$

Boundary conditions.—Before Eq. [1] and [2] can be solved simultaneously for θ and η', four boundary conditions are required for each electrode configuration shown in Fig. 1. For θ the following conditions were used

$$\theta - D'\frac{d\theta}{dy} = 1 \text{ at } y = 0$$

and

$$\frac{d\theta}{dy} = 0 \text{ at } y = \alpha L \quad [6]$$

which are the Danckwerts (7), Wehner-Wilhelm (8) conditions when axial diffusion and dispersion are included. The conditions on η' depend on electrode configuration and may be determined from Ohm's law

$$\frac{d\eta}{dx} = \frac{d(\Phi_1 - \Phi_2)}{dx} = -\frac{i_1}{\sigma} + \frac{i_2}{\kappa} \quad [7]$$

and are tabulated in Table I. The dimensionless parameters P_5 and P_6 which arise in the analysis are related to P_2

$$P_5 = -\frac{\sigma P_2}{\sigma + \kappa}$$

and

$$P_6 = -\frac{\kappa P_2}{\sigma + \kappa} \quad [8]$$

so that

$$-P_2 = P_5 + P_6 \quad [9]$$

The total current density i to the reactor was made dimensionless with the limiting current density that would exist if all the reactant in the feed were completely reacted

$$I^* = \frac{s_R i}{n\mathbf{F}vc_{Rf}} \quad [10]$$

Now that all the boundary conditions for each electrode configuration have been specified, Eq. [1] and [2]

Table I. Current and potential boundary conditions for various electrode configurations

Electrode configuration	$i_1(0)$	$i_1(L)$	$i_2(0)$	$i_2(L)$	$d\eta/dx\|_{x=0}$	$d\eta/dx\|_{x=L}$	$d\eta'/dy\|_{y=0}$	$d\eta'//dy\|_{y=\epsilon L}$
UD	0	$-i$	$-i$	0	$-i/\kappa$	i/σ	$P_5 I^*$	$-P_6 I^*$
DU	i	0	0	i	$-i/\sigma$	i/κ	$P_6 I^*$	$-P_5 I^*$
UU	i	0	$-i$	0	$-i\left(\frac{1}{\sigma}+\frac{1}{\kappa}\right)$	0	$-P_2 I^*$	0
DD	0	$-i$	0	i	0	$i\left(\frac{1}{\sigma}+\frac{1}{\kappa}\right)$	0	$P_2 I^*$

can be solved simultaneously for θ and η' using Newman's method (9).

The potential distribution in each phase $\Theta_1(x)$ and $\Phi_2(x)$ can then be obtained by solving Eq. [3] for η using the known distribution for η', along with the conservation of charge condition

$$\frac{di_1}{dx} = -\frac{di_2}{dx} \quad [11]$$

and substituting this condition into the derivative of Eq. [7]

$$\frac{d^2\eta}{dx^2} = -\left(\frac{\kappa+\sigma}{\kappa\sigma}\right)\frac{di_1}{dx} \quad [12]$$

then finally substituting the derivative of Ohm's law for the matrix phase into Eq. [12] to yield

$$\frac{d^2\eta}{dx^2} = \frac{\kappa+\sigma}{\kappa}\frac{d^2\Phi_1}{dx^2} \quad [13]$$

Equation [13] may be integrated twice to yield an expression for Φ_1

$$\Phi_1 = \frac{\kappa}{\kappa+\sigma}(\eta + C_1 x + C_2) \quad [14]$$

The value of C_1 for the various configurations is obtained from the derivative of Eq. [14] using the values of i_1 and $d\eta/dx$ at the boundaries found in Table I. The value of C_2 is then obtained by specifying $\Phi_1 = 0$ at the current collector and using a known value of η at the appropriate boundary. Table II summarizes the results for $\Phi_1(x)$ for the various configuration; $\Phi_2(x)$ is simply obtained by subtracting $\eta(x)$ from $\Phi_1(x)$.

Chemical systems.—For the calculations to be presented, two different chemical systems [copper removal from sulfate solutions (11) and silver removal from thiosulfate solutions (10)] are used to illustrate the effects of counterelectrode placement and current collector placement (when the matrix conductivity is finite) on electrode performance. The purpose of presenting results for two different chemical systems is to obtain reasonable values for the model parameters so that a valid comparison of electrode performance can be made when the side reaction is substantial [as for silver removal from thiosulfate solutions (10)] and when it is small [as for the copper recovery process (11)].

Figure 2 compares model calculations to the data of Van Zee and Newman (10) for silver removal from thiosulfate solutions using a porous carbon electrode. The quantities I and VOP are the total current to the reactor and the potential of the cathode current collector relative to a saturated calomel reference electrode placed in the effluent stream, respectively. The experimental effluent silver concentration (in milligrams per liter) are shown as the numbers below each curve corresponding to the open circles 0. The numbers above each curve correspond to the solid dots ● and are the calculated values of the effluent silver concentration (in milligrams per liter).

A similar model fit to the data of Bennion and Newman (11) for copper removal can be found in Ref. (1). Values of the parameters used to fit the data in Ref. (1) and in Fig. 2 are given in Table III.

Four parameters were adjusted to obtain agreement between calculated and experimental values in Fig. 2: one value of the exchange current density for the main reaction (silver deposition from thiosulfate solutions), assumed to be the electrode reaction (12)

$$Ag(S_2O_3)_2^{3-} + e^- \rightarrow Ag + 2S_2O_3^{2-} \quad [15]$$

and has a standard electrode potential (12) $U^0_{Ag/Ag(S_2O_3)_2^{3-}} = 0.0164V$; one value of the exchange current density for the side reaction (the reduction of thiosulfate), which was assumed to be the following reaction (10)

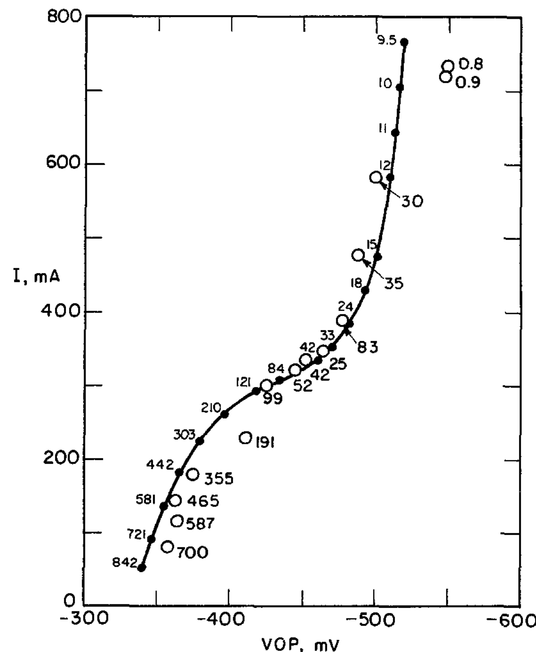

Fig. 2. Current-potential curve for an electrode 5.5 cm deep and superficial electrode area of 61 cm², packed with carbon flakes and chips. Flow rate = 22 cm³/min and the feed concentration = 1000 mg Ag/liter. Numbers below curve corresponding to the open circles 0 are experimental effluent concentrations (in milligrams per liter). The small numbers above the curve corresponding to the solid dots ● are calculated effluent concentrations (in milligrams/liter). *VOP* is the potential of the current collector with respect to a saturated calomel reference electrode placed in the dilute product stream.

Table II. Matrix potential distribution for various electrode configurations

Electrode configuration	Matrix potential distribution $\Phi_1(x)\left(\frac{\kappa}{\kappa+\sigma}\right)$
UD	$\eta(x) - \eta(L) + \frac{i}{\kappa}L(x/L - 1)$
DU	$\eta(x) - \eta(0) - \frac{i}{\kappa}x$
UU	$\eta(x) - \eta(0)$
DD	$\eta(x) - \eta(L)$

Table III. Values of the parameters used in fitting the data in Fig. 2 and in generating Fig. 3 through 17

Copper deposition with simultaneous generation of dissolved hydrogen

$a = 25\ cm^{-1}$	$\epsilon = 0.3$	$D_o = 6 \times 10^{-6}\ cm^2/sec$	$\kappa_o = 0.17$ mho/cm	$s_R = -1$
$n = 2$	$T = 298.15°K$	$\alpha_{aR} = 1.5$	$\alpha_{cR} = 0.5$	$\alpha_{aS} = 0.5$
$\alpha_{cS} = 0.5$	$U_S - U_R = 0.281V$	$L = 6$ cm	$k_m = 0.1922 \times 10^{-3}$ cm/sec	$v = 3.328 \times 10^{-3}$ cm/sec
$i_{oR,ref} = 7.009 \times 10^{-6}\ A/cm^2$		$i_{oS,ref} = 3.717 \times 10^{-13}\ A/cm^2$	$c_{Rf} = 1.05 \times 10^{-5}\ mole/cm^3$	
$c_{Sf} = 10^{-3}\ mole/cm^3$				

Silver reduction with simultaneous reduction of thiosulfate

$a = 25\ cm^{-1}$	$\epsilon = 0.3$	$D_o = 1 \times 10^{-5}$ cm/sec	$\kappa_o = 0.123$ mho/cm	$s_R = -1$
$n = 1$	$T = 298.15°K$	$\alpha_{aR} = 0.5$	$\alpha_{cR} = 0.5$	$\alpha_{aS} = 2.75$
$\alpha_{cS} = 1.25$	$U_S - U_R = 0.489V$	$L = 5.5$ cm	$k_m = 3.330 \times 10^{-3}$ cm/sec	$v = 6.011 \times 10^{-3}$ cm/sec
$i_{oR,ref} = 9.134 \times 10^{-5}\ A/cm^2$		$i_{oS,ref} = 1.20 \times 10^{-22}\ A/cm^2$	$c_{Rf} = 9.27 \times 10^{-6}\ mole/cm^3$	
$c_{Sf} = 0.951 \times 10^{-3}\ mole/cm^3$				

Dimensionless parameters

	Copper	Silver
P_1	1.050×10^{-7}	9.404×10^{-4}
P_2	-3.254 to -6.508	-3.738 to -7.476
P_3	1.247×10^{-4}	5.364×10^{-4}
P_4	5.863×10^{-8}	6.341×10^{-46}
P_5	3.254	3.738
P_6	9.089×10^{-11} to 3.254	3.777×10^{-15} to 3.738
D'	0.1217	0.1168

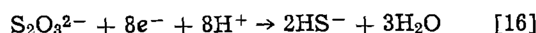

$$S_2O_3^{2-} + 8e^- + 8H^+ \rightarrow 2HS^- + 3H_2O \qquad [16]$$

where the standard electrode potential can be calculated (13, 14) to be $U^\theta_{HS^-/S_2O_3^{2-}} = 0.221V$; one value each for the transfer coefficients for the side reaction α_{aS} and α_{cS}, which were assumed to sum to four. The freedom to assign arbitrary values to α_{aS} and α_{cS} is allowed in the model since the composition dependence of the polarization equation for the side reaction is neglected.

The value of the mass transfer coefficient k_m used in fitting the data was that obtained in fitting the data of Bennion and Newman (11), which was correlated to be (1)

$$\frac{\epsilon k_m}{aD_o} = 0.07054 \left(\frac{v}{aD_o}\right)^{0.5454} \qquad [17]$$

In obtaining the fit to the silver removal data in Fig. 2, it should not be interpreted that there is anything fundamental about the values of the fitted dimensional parameters found in Table III, because not only are the data insufficient, but also the electrode is operating with a highly nonuniform current density and mass-transport limitations dominate in certain regions.

The model predictions of the current-potential behavior in Fig. 2 are in satisfactory agreement with experimental data between 50 and 500 mA total current. However, at higher currents (above 500 mA), the data indicate the beginning of an additional limiting-current plateau, and agreement of the model calculations cannot be expected for the following reasons: (*i*) The postulated side reaction (10) (Eq. [16]) for the reduction of thiosulfate could be incorrect and there appears to be no fundamental kinetic information on this reaction, and (*ii*) if the limiting reactant species for the higher plateau were known, the model used here would not be sufficient since the concentration dependence for the side reaction was neglected and a more general model such as the one proposed by Alkire and Gould (4) would be more appropriate.

Agreement between model predictions for the silver effluent concentration and the experimental values shown in Fig. 2 are satisfactory near the limiting current. This is because the model parameters were chosen so as to fit the data in this region. However, agreement should not be expected over the entire current-potential range because the data exhibit unexplained anomalies (10): (*i*) current efficiencies above 100%, and (*ii*) a minimum in the silver effluent concentration with increasing values of *VOP*.

A comparison of the dimensionless parameters in Table III between the two chemical systems suggests that the parameters P_1 and P_3 account primarily for the difference in behavior of these systems. The parameters P_1 and P_3 represent the relative importance of the backward rate of the main reaction and the forward rate of the side reaction and are 10^4 and 4.3 times greater, respectively, for the silver system than for the copper system. As is observed later a low effluent concentration cannot be achieved for the silver system and this is due to the combined effect of the parameters P_1 and P_3.

The magnitude of the side reaction is substantial for the silver system and this shields the back of the electrode (in the case of an upstream counterelectrode) from having a large electric driving force which results in a very small rate for the deposition of silver in this region. This is accentuated by the fact that P_1 is large, which causes the backward rate of the deposition reaction to be of the same order on the forward rate and the reactor can become thermodynamically limited.

Results and Discussion

As a unifying concept here, let us consider how we can achieve a very high conversion or, equivalently, a very low effluent concentration of the limiting reactant while, at the same time, operating the reactor at as high a flow rate as possible. Toward these ends, we can consider variations of electrode current density and length, flow rate, configuration, and matrix conductivity. By means of the computer program, we have the means to investigate in detail how the presence of a side reaction places limitations on the attainment of these goals.

Effect of electrode length.—For the case of a very high matrix conductivity, Fig. 3 shows the effect of electrode length and current density on the effluent concentration for the copper system. We see, first of all, that we must operate at or above the limiting current in order to reach a really low effluent concentration. If we operate at $I^* = 0.9501$, we cannot expect to remove more than 95% of the copper even if we have very high current efficiencies and substantial electrode lengths.

The curve on Fig. 3 for an upstream counterelectrode and $I^* = 1.038$ shows essentially a limiting-current condition, the effluent concentration decreases almost exponentially with electrode length. [See, for example, the analysis of Bennion and Newman (11) and that of Newman and Tiedemann (15) when axial diffusion and dispersion are included.] However, for downstream placement of the counterelectrode, a limiting-current distribution cannot be maintained except for electrode lengths less than 2 cm, and a truly low effluent concentration cannot be attained at all with this electrode configuration (at this flow rate). The current efficiency must necessarily be somewhat lower, and the extent of the side reaction somewhat higher, with the downstream counterelectrode.

Figures 4 and 5 introduce the effect of a finite matrix conductivity σ. Now, according to Fig. 1, four different

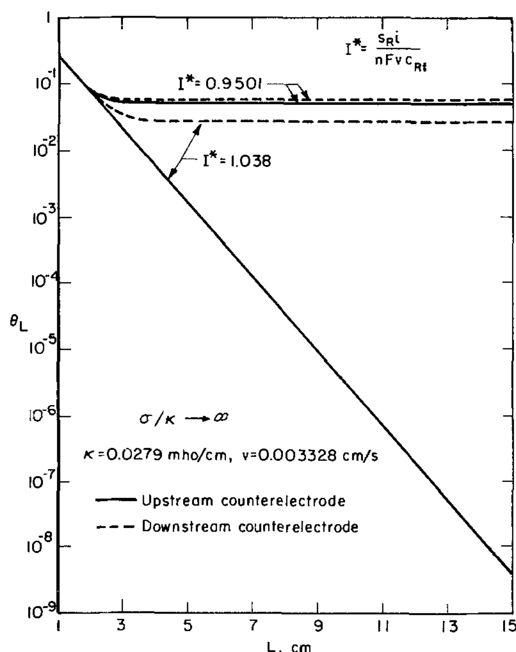

Fig. 3. Effluent copper concentration as a function of electrode length for $c_{Rf} = 0.0105M$.

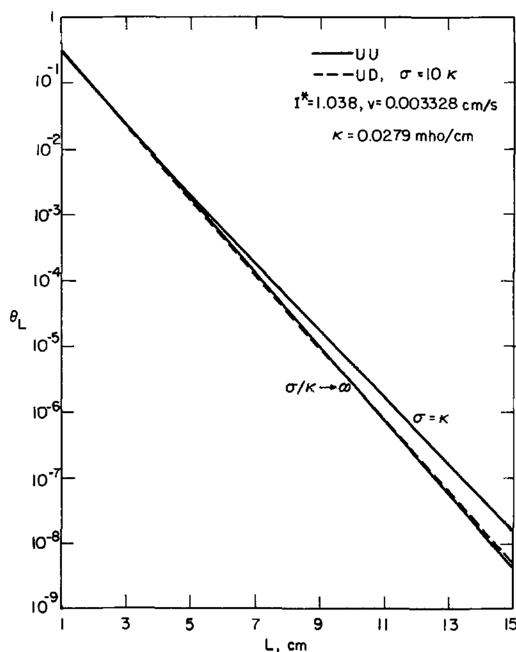

Fig. 4. Effluent copper concentration as a function of electrode length.

configurations are relevant since the placement of the current collector must also be considered. Figure 4 shows that the UU configuration retains the exponential decrease of θ_L with L, although performance is slightly degraded by the additional ohmic potential drop compared to the case of the infinite matrix conductivity. (The curve for $\sigma = 10\kappa$ is discussed later in connection with the optimum matrix conductivity.) Figure 5 shows the relatively poor performance achievable with the other configurations. In these cases, the ohmic potential drop in the matrix and solution phases prevents the entire reactor from being operated at a limiting-current condition, as is discussed in more detail later.

Figure 6 displays the silver effluent concentration as a function of electrode length for the various electrode configurations for cases where $\sigma >> \kappa$ and $\sigma = \kappa$. The results show that none of the electrode configurations yields an exponental decrease in θ_L with electrode

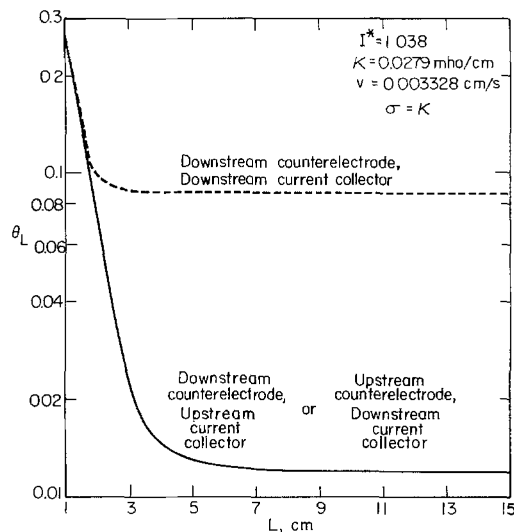

Fig. 5. Effluent copper concentration as a function of electrode length.

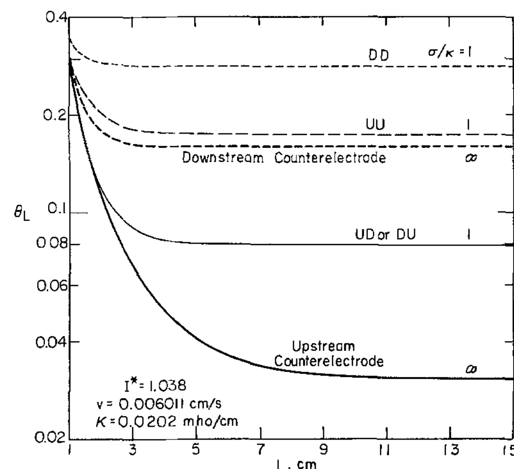

Fig. 6. Effluent silver concentration as a function of electrode length for $c_{Rf} = 0.00927M$.

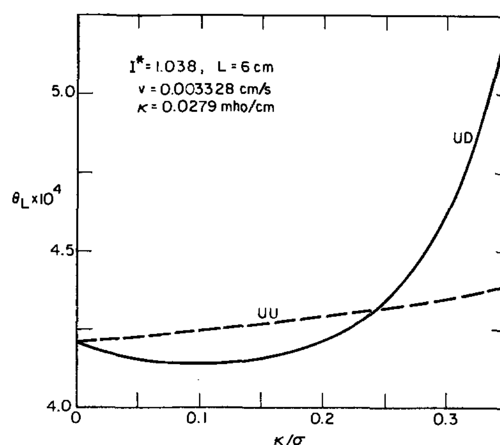

Fig. 7. Dependence of the copper effluent concentration on the matrix resistivity.

length; thus a limiting-current distribution cannot be achieved in any of the geometries due to extensive interference by the side reaction.

Effect of matrix conductivity.—Figures 7 and 8 show the dependence of the effluent copper concentration on the matrix resistivity ($1/\sigma$). Figure 9 shows similar results for the silver system. Calculations for a DD placement are not presented here since this configuration does not allow a low effluent concentration, in

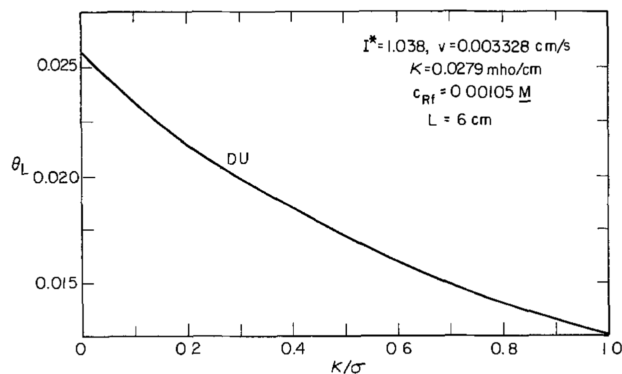

Fig. 8. Dependence of the copper effluent concentration on the matrix resistivity.

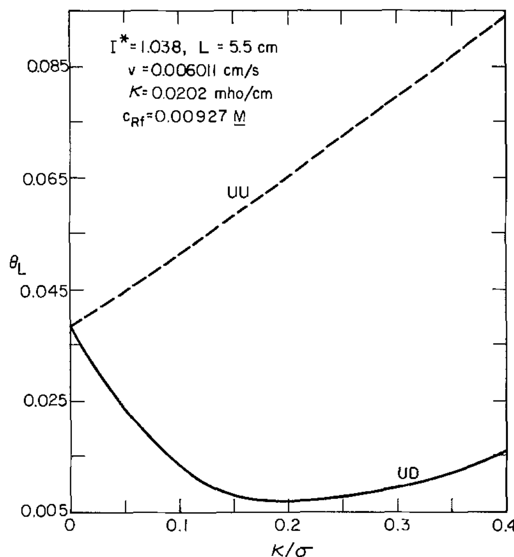

Fig. 9. Dependence of the silver effluent concentration on the matrix resistivity.

comparison to the other configurations when the matrix conductivity is small.

In Fig. 7 and 9, we observe that the UD configuration exhibits a minimum with matrix resistivity and, therefore, has an optimum value for σ (about equal to 0.1κ for the copper system). On the other hand, for the UU configuration, θ_L increases monotonically with increasing matrix resistivity. The DU configuration on Fig. 8 would also show a minimum at values of κ/σ substantially greater than unity. This is of less interest than the minima for the UD configuration because matrix resistivities are usually much less than solution-phase resistivities and because the effluent concentrations are inherently large with the DU configuration. For example, the DU and UD configurations give the same effluent concentration when $\sigma = \kappa$ (see Fig. 5) but at this point, the value of θ_L has risen to 0.0125 from a minimum of 4.14×10^{-4} on Fig. 7. At $\sigma = \kappa$, the UU configuration is still able to attain a value of θ_L of 6.08×10^{-4} (see Fig. 4). (Note, however, that the DU configuration performs better than the UU configuration for $\sigma = \kappa$ in the silver system, as displayed on Fig. 6.)

Return for a moment to the dashed curve on Fig. 4. For this curve, $\sigma = 10\kappa$, which corresponds to the minimum for the UD configuration shown in Fig. 7, and an exponential dependence of θ_L on L can evidently be maintained. The performance is superior to the high matrix-conductivity case for L less than about 10 cm, after which it becomes somewhat inferior. The optimum ratio of κ/σ depends on electrode length, for example, for an electrode 4 cm in length the optimum ratio is approximately 0.17, for an electrode 8 cm long the optimum ratio is approximately 0.07. Note that we get a markedly different view of the effect of configuration and matrix resistivity if we confine our attention to the cases $\sigma >> \kappa$ and $\sigma = \kappa$ on Fig. 3, 4, and 5 from what we get if we include the variation of σ and the optimum value of σ. The UD configuration is totally unsatisfactory at $\sigma = \kappa$ but excellent at $\sigma = 10\kappa$.

For the silver system, other calculations show that, even at the optimum ratio of $\kappa/\sigma = 0.2$ shown on Fig. 9 for the UD configuration, a limiting-current distribution and an exponential dependence of θ_L on L cannot be achieved. Similar results for the copper system can be obtained by increasing the flow rate to somewhat less than three times the value used in calculating Fig. 3, 4, and 5.

Bennion and Newman (11) and more recently Wenger and Bennion (16) have formulated design considerations for achieving a low effluent concentration while operating at as high a flow rate as possible. First, the electric driving force within the electrode must be maintained high enough to attain a limiting-current condition throughout the reactor. The electric driving force must also be maintained low enough to avoid excessive side reactions. These two conditions thus define a limited range of potentials allowable within the reactor. Since the electrode must be of substantial length in order to achieve a given effluent concentration, there is an upper limit on the flow rate above which these constraints cannot be satisfied simultaneously.

The effect of the side reaction is not one which can be compensated for by using a longer electrode or a higher current, even if one is willing to pay the price of a lower current efficiency and a higher cell potential. It is a characteristic of porous electrodes, leading to their inherently nonuniform reaction rate distributions, that substantial current densities flowing over substantial distances in either the matrix or solution phases make it impossible to maintain a uniform electric driving force (for the reactions) throughout the electrode.

On the basis of these considerations, an important quantity is the difference between the minimum electric driving force η_{min} and the maximum electric driving force η_{max} that prevail within the reactor. Figure 10 displays this quantity as a function of the conduc-

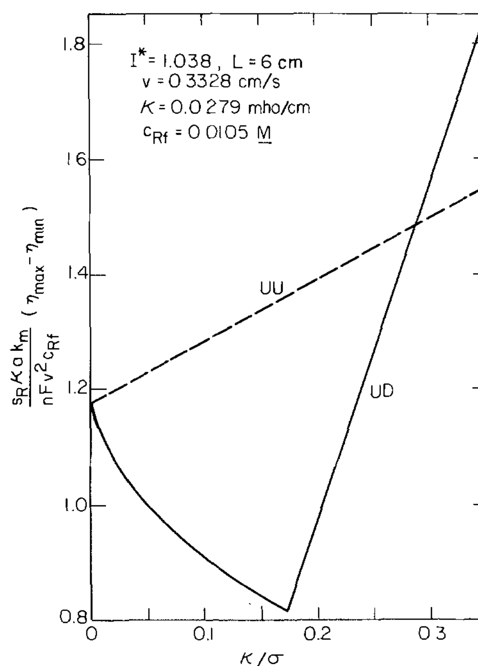

Fig. 10. Variation in the difference between the maximum and minimum driving force for copper deposition with the matrix resistivity.

tivity ratio for the copper system and corresponds directly with the conditions of Fig. 7. The ordinate, made dimensionless with $nFv^2c_{Rf}/s_R\kappa ak_m$, will have a magnitude on the order of unity if the current density is distributed like that for the limiting current for the main reaction (11, 15). A graph similar to Fig. 10 is given by Newman and Tiedemann (15) for the case where the current densities are calculated according to the limiting-current distribution for the main reaction. The computer program used here permits analysis above and below the limiting current and in the presence of a side reaction.

The fact that the ordinate values on Fig. 10 are of order unity illustrates how the constraints on the flow-through porous electrode can better be satisfied by operation at lower flow rates.

There is a correspondence between the shapes of the curves on Fig. 7 and 10. Conditions which lead to an inherently smaller value of $|\eta_{max} - \eta_{min}|$ make it possible to achieve a limiting-current condition through a larger portion of the reactor, without extensive side reaction. For the UD configuration, the maximum electric driving force occurs at the fluid inlet for $\kappa/\sigma < 0.175$. The position of the maximum electric driving force then shifts to the fluid outlet for $\kappa/\sigma > 0.175$. This leads to the sharp minimum for the UD configuration in Fig. 10.

Detailed distributions.—The behavior of these systems can be understood better by consideration of the calculated current, potential, and electric driving force distributions within the electrode. These are illustrated for the copper system with an electrode 6 cm long and by a 5.5 cm electrode for the silver system.

For the copper system with an infinite matrix conductivity, Fig. 11 shows the relative rates of reaction for both the main and side reactions for both upstream and downstream placement of the counterelectrode. Figure 12 shows the corresponding distributions of potential in the matrix and pore solution. The total current density to the electrode was chosen close to the limiting current ($I^* = 1.038$) for the deposition of copper. For upstream placement of the counterelectrode, the main reaction rate decreases almost exponentially

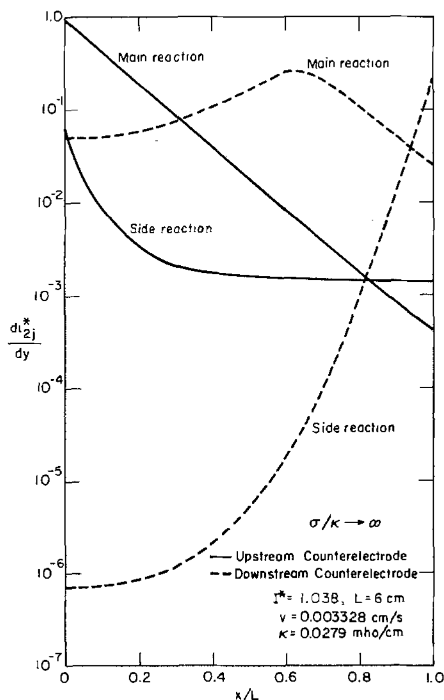

Fig. 11. Current distributions for deposition of copper and generation of dissolved hydrogen within a porous electrode. Calculated for $c_{Rf} = 0.0105M$.

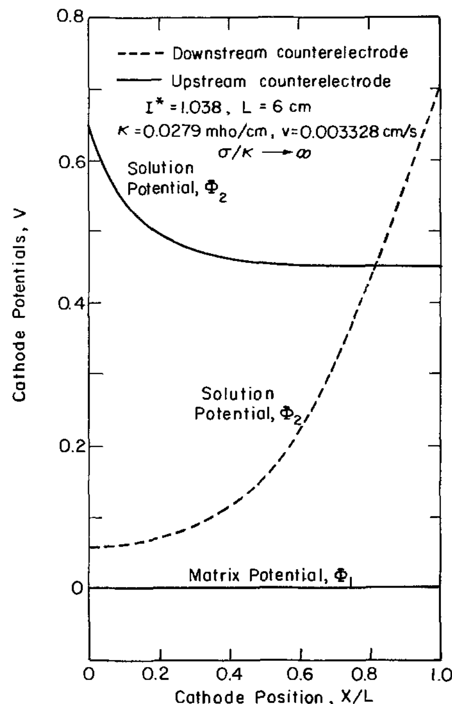

Fig. 12. Calculated solution phase and solid matrix phase potential distributions for the deposition of copper and simultaneous formation of dissolved hydrogen.

with distance through the electrode [as predicted by the limiting-current analyses in Ref. (11) and (15)]. At the same time, the side reaction follows the electric driving force (see Fig. 12), which is high at the fluid inlet and decreases toward a uniform value near the fluid outlet.

On the other hand, for the downstream placement of the counterelectrode, the main reaction rate does not show an exponential dependence on distance. Figure 12 shows that the electric driving force is very large at the outlet but too low at the inlet. Consequently, a limiting-current condition is not maintained near the front. At about 65% of the distance through the electrode, the electric driving force has become large enough to assure a limiting-current condition, and subsequently an exponential dependence on distance is exhibited. However, failure to utilize effectively the front part of the electrode makes it impossible to achieve a truly low effluent concentration, and increasing the electrode length would not help (see Fig. 3). The resulting reaction-rate distribution now has a maximum; as the electric driving force increases toward the back of the electrode, the reaction rate goes up, and copper is depleted from the solution to the extent that the mass-transfer driving force becomes small. The reaction rate exhibits a maximum and then decreases with distance. [Similar reaction-rate distributions have been reported by Alkire and Gould (4). These are examples of a general phenomenon (17-20) resulting from the competition of electric and mass-transfer driving forces.] The side reaction has a distribution in Fig. 11 that again follows that of the electric driving force in Fig. 12. Because of the somewhat lower rate of the main reaction, in comparison to the upstream placement of the counterelectrode, the side reaction now occurs at a somewhat higher rate on the average. For these comparisons at a constant total current ($I^* = 1.038$), an increase in the effluent concentration from one electrode to another is accompanied by a corresponding decrease in the current efficiency.

As in porous electrodes in general, the reaction rate distributions and ohmic potential drop shield the more remote parts of the reactor from having an adequate

electric driving force. In this particular situation, the contrast between the cases of upstream and downstream placement of the counterelectrode arises in the following way. In order for there to be a high conversion, there must be a high reaction rate (generating high current densities in the solution) near the fluid inlet. Since the solution-phase conductivity κ is not high, potential variations in the solution phase can be minimized if the current flows out of the electrode at the nearest possible point, namely, to a counterelectrode placed upstream. If the counterelectrode is placed downstream, the large currents which should be generated near the fluid inlet must flow in the solution through most of the thickness of the electrode, and this necessarily leads to large variations of potential. A similar explanation applies in the more complex cases to follow, where the matrix conductivity is also finite.

Figure 13 shows the reaction-rate distributions for the main and side reactions for the copper system where $\sigma = \kappa$. The corresponding potential distributions are shown in Fig. 14. Because of the complexity of Fig. 14, the distributions of electric driving force are also shown in Fig. 15.

The reaction-rate and electric driving force distributions for the UD and DU configurations happen to be identical when $\sigma = \kappa$ since the boundary conditions given in Table III are then identical. However, the potential distributions in each phase will be different, as seen in Fig. 14. In these configurations, the counterelectrode and the current collector are not at the same end of the reactor. Consequently, the current flows in the same direction in the matrix as in the solution, and to a certain extent the potential drop in the matrix can match in the solution (see Fig. 14). This makes it possible, in some cases, to reduce the variation of the electric driving force within the reactor (see Fig. 10). It also means that the extreme values of the electric driving force occur at the ends of the reactor, with the minimum value occurring somewhere between (see Fig. 15), and the side reaction follows this distribution (see Fig. 13).

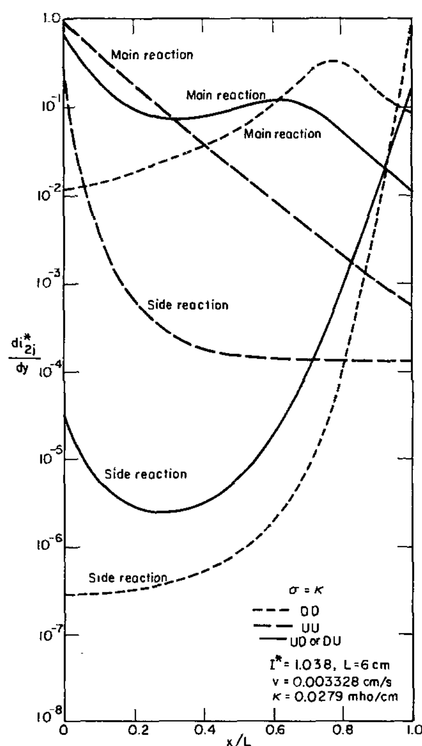

Fig. 13. Current distributions for deposition of copper and generation of dissolved hydrogen within a porous electrode. Calculated for $c_{Rf} = 0.0105M$.

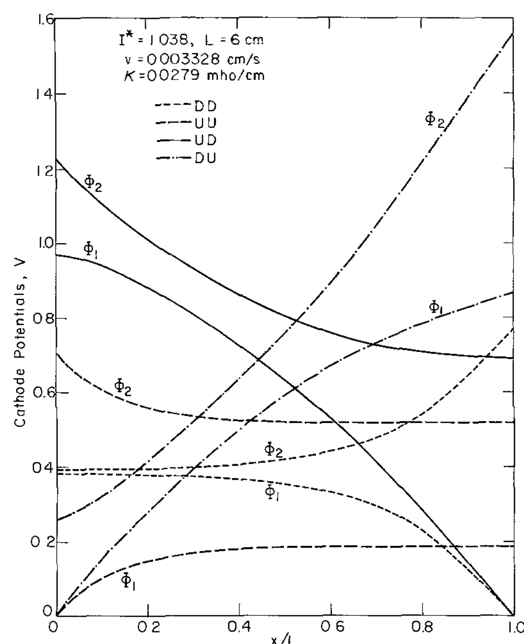

Fig. 14. Calculated solution phase and solid matrix phase potential distributions when $\sigma = \kappa$ for the depositions of copper and simultaneous formation of dissolved hydrogen.

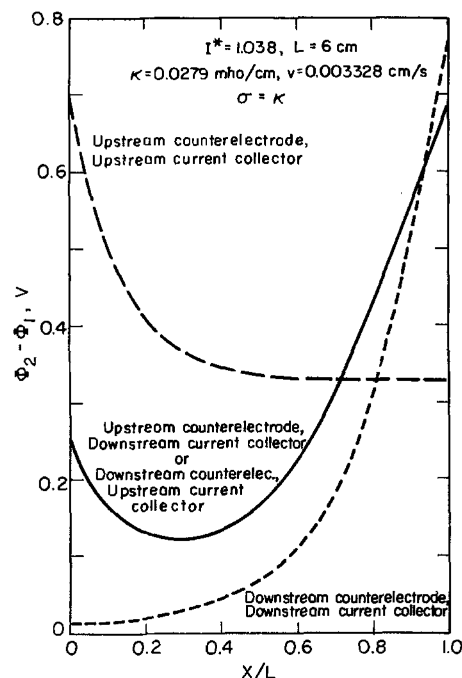

Fig. 15. Electrical driving force distributions for the potential distributions shown in Fig. 14.

For the UU configuration, the maximum electric driving force occurs at the inlet, and the minimum at the outlet, and conversely for the DD configuration. For the main reaction, only the UU configuration shows an exponential dependence of rate on distance (see Fig. 13). For the other configurations, the main reaction is below the limiting current for a substantial (DD) or moderate (UD or DU) region near the inlet, and consequently the effluent concentration cannot be reduced to a truly low value. Only in the UU configuration are the current densities in both the solution and matrix phases small near the back of the electrode. In this region the electric driving force varies little (as is the case also for the upstream counterelectrode case in Fig. 12, where $\sigma >> \kappa$), and measurement of $\Phi_1 - \Phi_2$ at $x = L$ can lead to a lower

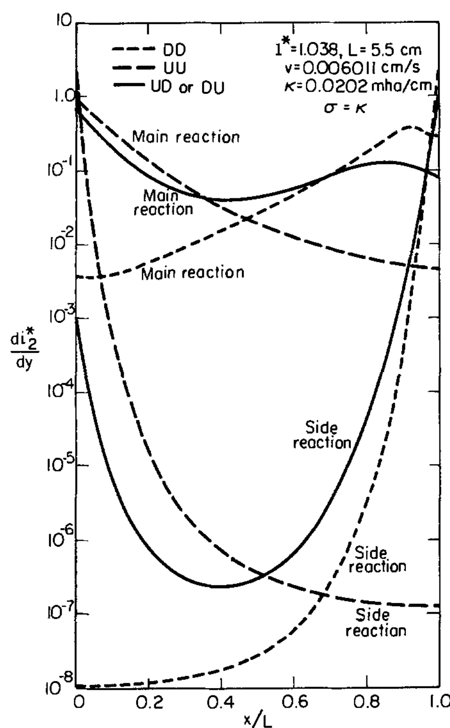

Fig. 16. Current distributions for silver deposition and reduction of thiosulfate within a porous electrode. Calculated for $c_{Rf} = 0.00927M$ and $L = 5.5$ cm.

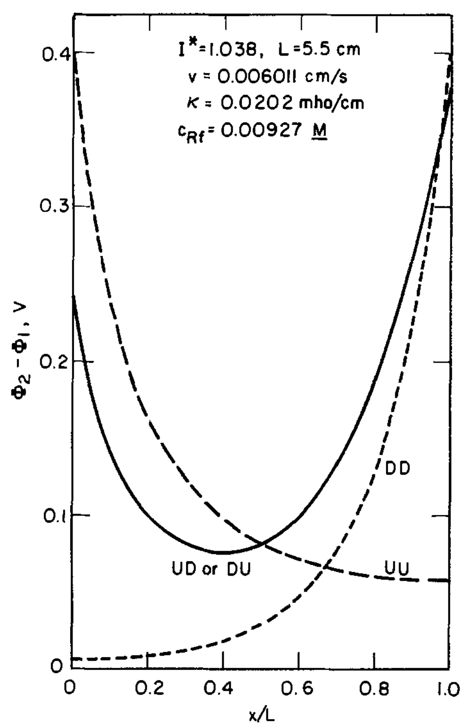

Fig. 17. Electrical driving force distributions for the deposition of silver from thiosulfate solutions.

bound thermodynamic estimate of the minimum attainable concentration in a flow-through porous electrode (12).

Figures 16 and 17 show the reaction-rate and electric driving force distributions for the silver system. A limiting-current distribution is not achieved for any electrode configuration, due to extensive interference by the side reaction, as indeed, it is not, even for an infinite matrix conductivity (see Fig. 6). As for the copper system, the electric driving force for the DD configuration is small at the front of the electrode and, for the UD and DU configurations it is small in the middle and only moderately large at the front. Under these conditions, the front and middle regions of the reactor are not effectively utilized, and a low effluent concentration cannot be achieved even though a limiting-current condition is maintained near the rear. However, for the UU configuration, the lowest electric driving force occurs at the rear of the reactor, and the rate of the main reaction does not decrease exponentially with distance. In fact, with the higher value of P_1 for the silver system, the effluent concentration is very close to the thermodynamic limit determined by the electric driving force prevailing at the fluid outlet (12).

Effect of configuration.—The preceding discussion has permitted a comparison of several configurations under a variety of operating conditions. It is important to recognize that the lowest effluent concentration is achieved for upstream placement of the counterelectrode (see Fig. 3 through 6). For downstream placement of the counterelectrode, a limiting-current distribution cannot be obtained (see Fig. 11 and 13), principally because the current in the solution must flow through most of the length of the electrode, and this leads to a large ohmic potential drop.

For the DU configuration shown in Fig. 8. θ_L decreases with increasing values of matrix resistivity. For a downstream counterelectrode, a situation is created where the ohmic potential drop in the solution is working against the favorable mass-transfer condition near the fluid inlet. Increasing the matrix resistivity increases the electric driving force near the fluid inlet because the matrix current must leave through the current collector placed there. This causes the rate of the main reaction at the front of the electrode to increase from about 0.05 when $1/\sigma \to 0$ (in Fig. 11) to 0.67 when $\sigma = \kappa$ (in Fig. 13).

As mentioned earlier, the DD configuration is the least efficient of the configurations shown in Fig. 1. If the matrix resistivity is increased from zero, the electric driving force is further reduced near the fluid inlet, while it increases somewhat near the fluid outlet (compare Fig. 14 and 15 with Fig. 12). This causes the rate of the main reaction near the front to decrease from about 0.05 when $1/\sigma \to 0$ to 0.012 when $\sigma = \kappa$ (see Fig. 11 and 13). Since the rear of the electrode was already at a limiting current, the increase in the electric driving force in this region is of little benefit; the rate of the main reaction is higher than with $1/\sigma \to 0$ because the flowing stream was not depleted as much in the upstream region, not because the electric driving force is larger. The integrated reaction rate is 6.3% lower when $\sigma = \kappa$, and the rest of the current goes into the side reaction, driven by the higher electric driving force near the rear.

For upstream placement of the counterelectrode, conditions are already more favorable when the matrix resistivity is small. For the UU configuration, increase of $1/\sigma$ decreases the electric driving force in the rear region and causes the current locally to drop below the limiting value. Consequently, σ_L increases, as shown in Fig. 7 and 9. For the UD configuration, the electric driving force decreases near the inlet and increases near the outlet as $1/\sigma$ increases. This is favorable until the reaction rate drops below the limiting value near the inlet, and this leads to the minimum in the curve of θ_L *vs.* κ/σ. The choice between the UD and UU configurations is dependent on the chemical system and the matrix conductivity. However, the UD configuration will display a minimum in the effluent concentration as a function of κ/σ and is therefore the best configuration if this electrode could be built in practice.

Conclusions and Summary

A theoretical model for flow-through porous electrodes (1) has been used to evaluate the effects of

electrode placement relative to the fluid inlet and finite matrix conductivity on the performance of flow-through porous electrodes. If a low effluent concentration is desired, the electrode must be operated at a superficial current density sufficiently high so that the main reaction may achieve a limiting-current distribution. Calculations show that a limiting-current distribution can only be achieved for upstream placement of the counterelectrode and not for a downstream counterelectrode. However, if interference by the side reaction is substantial, as is the case for silver removal from thiosulfate solutions or for the copper system if the superficial velocity is too high, a limiting-current distribution cannot be achieved for any electrode configuration at any matrix conductivity.

For an upstream counterelectrode when the matrix conductivity is not large, the choice between upstream or downstream placement of the current collector depends on the chemical system and what matrix conductivity can be achieved in practice.

Below the limiting current, the performance is only slightly better for an upstream counterelectrode than for downstream placement of the counterelectrode.

Calculations for a small matrix conductivity show that the DD configuration should probably never be built.

It is evident from the results that simple limiting-current calculations are inadequate for describing the behavior of flow-through porous electrodes. Thus, the ability to calculate distributions of current, potential, and concentration in the presence of side reaction above and below the limiting current makes it possible to choose the optimum electrode configuration so as to design and optimize an electrode system for the most economical removal of metal ions.

Acknowledgment

This work was supported by the U. S. Energy Research and Development Administration.

Manuscript submitted May 23, 1977; revised manuscript received July 25, 1977.

Any discussion of this paper will appear in a Discussion Section to be published in the December 1978 JOURNAL. All discussions for the December 1978 Discussion Section should be submitted by Aug. 1, 1978.

Publication costs of this article were assisted by the University of California.

LIST OF SYMBOLS

- a specific interfacial area, cm^{-1}
- c_{Rf} upstream feed concentration of metal-ion reactant, $mole/cm^3$
- DD downstream counterelectrode, downstream current collector
- DU downstream counterelectrode, upstream current collector
- c_S hydrogen ion or thiosulfate ion concentration, $mole/cm^3$
- D_a axial dispersion coefficient of metal-ion reactant, cm^2/sec
- D_o molecular diffusion coefficient of metal-ion reactant, cm^2/sec
- D_R effective diffusion coefficient of metal ion reactant, cm^2/sec
- D' dimensionless parameter describing the relative importance of axial diffusion and dispersion
- $\mathbf{F}$ Faraday's constant, 96,487 C/equiv.
- i superficial current density to an electrode, A/cm^2
- $i_{oj,ref}$ exchange current density for reaction j at a reference composition $c_{i,ref}$, A/cm^2
- i_1 superficial current density in the matrix, A/cm^2
- i_2 superficial current density in pore-solution phase, A/cm^2
- I^* dimensionless superficial current density to an electrode, see Eq. [10]
- i_2^* $= s_R i_2/n\mathbf{F}vc_{Rf}$ dimensionless current density in pore-solution phase
- I total current to an electrode, A
- k_m average mass-transfer coefficient between flowing solution and electrode surface, cm/sec
- L thickness of porous electrode, cm
- n number of electrons transferred in metal deposition reaction
- P_1 dimensionless parameter describing the relative importance of the backward term in the metal deposition reaction
- P_2 dimensionless parameter describing the relative importance of the ohmic potential drop
- P_3 dimensionless parameter describing the relative importance of the forward term in the side reaction
- P_4 dimensionless parameter describing the relative rate of the backward term in the side reaction
- P_5 dimensionless parameter which characterizes the ohmic potential drop in the pore-solution phase
- P_6 dimensionless parameter which characterizes the ohmic potential drop in the matrix phase
- R universal gas constant, 8.3143 J/mole-°K
- s_R stoichiometric coefficient of metal-ion reactant
- T absolute temperature, °K
- UD upstream counterelectrode, downstream current collector
- UU upstream counterelectrode, upstream current collector
- U_j^0 standard electrode potential for reaction j, V
- ΔU $= U_S - U_R$ difference in open-circuit cell potentials of the side reaction and primary reaction at the reference composition, V
- v superficial fluid velocity, cm/sec
- VOP potential of the cathode current collector relative to a saturated calomel reference electrode placed in the dilute product stream, V
- x distance through porous electrode, cm
- y xak_m/v dimensionless distance through porous electrode
- z_i valance or charge number of species i

Greek letters

- α $= ak_m/v$, reciprocal of penetration depth at the limiting current, cm^{-1}
- α_{aj} anodic transfer coefficient for reaction j
- α_{cj} cathodic transfer coefficient for reaction j
- ϵ porosity or void volume
- η $= \Phi_1 - \Phi_2$ local overpotential, V
- η' dimensionless local overpotential
- κ effective conductivity of solution, mho/cm
- σ effective conductivity of solid matrix, mho/cm
- Φ_1 electrostatic potential in matrix phase, V
- Φ_2 quasi-electrostatic potential in the pore solution phase, V
- θ $= c_R/c_{Rf}$, dimensionless concentration of metal-ion reactant

Subscripts

- R metal-ion reactant or primary reaction
- ref reference composition
- S side reactant or side reaction

REFERENCES

1. J. A. Trainham and J. Newman, *This Journal*, **124**, 1528 (1977).
2. R. E. Sioda, *J. Electroanal. Chem. Interfacial Electrochem.*, **34**, 399 (1972).
3. R. Alkire and B. Gracon, *This Journal*, **122**, 1594 (1975).
4. R. Alkire and R. Gould, *ibid.*, **123**, 1842 (1976).
5. B. G. Ateya and L. G. Austin, *ibid.*, **124**, 83 (1977).
6. M. Paulin, D. Hutin, and F. Coeuret, *ibid.*, **124**, 180 (1977).
7. P. V. Danckwerts, *Chem. Eng. Sci.*, **2**, 1 (1953).
8. J. F. Wehner and R. H. Wilhelm, *ibid.*, **6**, 89 (1956).
9. J. Newman, "Electrochemical Systems," Appendix C, Prentice-Hall, Englewood Cliffs, N.J. (1973).
10. J. Van Zee and J. Newman, *This Journal*, **124**, 706 (1977).
11. D. N. Bennion and J. Newman, *J. Appl. Electrochem.*, **2**, 113 (1972).
12. J. A. Trainham and J. Newman, *ibid.*, **7**, 287 (1977).
13. D. D. Wagman, W. H. Evans, V. B. Parker, I. Halow, J. M. Bailey, and R. H. Schumm, Nat. Bur. Stand. Note 270-3, p. 47, Washington, D.C. (1968).
14. J. A. Dean, Editor, "Lange's Handbook of Chemistry," 11th ed., p. 6-14, McGraw-Hill Book Co., New York (1973).
15. J. Newman and W. Tiedemann, "Advances in Electrochemistry and Electrochemical Engineering," Vol. 11, H. Gerischer and C. W. Tobias, Editors,

Wiley-Interscience, (1977).
16. R. S. Wenger and D. N. Bennion, *J. Appl. Electrochem.*, **6**, 385 (1976).
17. J. Newman, *This Journal*, **113**, 1235 (1966).
18. W. R. Parrish and J. Newman, *ibid.*, **116**, 169 (1969).
19. W. R. Parrish and J. Newman, *ibid.*, **117**, 43 (1970).
20. L. Hsueh and J. Newman, *ibid.*, **117**, 1242 (1970).

Extension of Spectral Response of p-Type Gallium Phosphide Electrodes by Metal Adatoms

Hiroshi Yoneyama, Shuichi Mayumi, and Hideo Tamura

Department of Applied Chemistry, Faculty of Engineering, Osaka University, Yamadakami, Suita, Osaka, Japan

ABSTRACT

The spectral response of p-type GaP electrodes was successfully extended to longer wavelengths by depositing a monolayer of any of several kinds of metal such as gold, silver, palladium, or copper onto the electrode surface and then cathodically polarizing the electrode under illumination. The shape, but not the magnitude, of the developed photocurrent spectra, which covered wavelengths between 600 and 1400 nm, were independent of the kind of metal chosen. Impregnated hydrogen seemed to be responsible for the enhanced photocurrent spectra.

p-type GaP is useful as a photocathode of a water photolysis cell (1, 2). Although it dissolves anodically, no appreciable cathodic decomposition has been found (3, 4). It is found that the quantum yield of the hydrogen evolution reaction (HER) on p-type GaP electrodes exceeded unity if the electrode had an appropriate carrier concentration (5). Although no definite mechanism for this phenomenon has been proposed, we have speculated that surface states are responsible for it. A recent report on cathodic polarization characteristics of p-type GaP covered with a small amount of metal also suggested with more clarity the contribution of surface states to the HER (6).

It was first proposed by Memming *et al.* that surface states played an important role in the cathodic reduction of several oxydizing agents such as hexacyanoferrate and persulfate (3, 4). However, rather ambiguous results were presented by them for the role of the surface states in the HER. Therefore, clear evidence for the contribution of the surface states to the HER seems to be required now.

For that purpose, we have investigated the spectral response of the electrode with and without metal adatoms as a function of the cathodic polarization time and have discovered that the photoresponse of the electrode is extended to wavelengths longer than the threshold of the intrinsic absorption of GaP by cathodically polarizing the electrode at potentials to cause hydrogen evolution. In this paper, several results on this subject are presented.

Experimental

p-type GaP wafers having the acceptor concentration of $4 \times 10^{17}/cm^3$, supplied by Sanyo Electric Company Limited, were used as the electrode. The (111) face was chosen as the electrode surface. The wafer was etched with hot aqua regia to give a shiny surface before being mounted in a glass tube with epoxy resin. Just before the electrodeposition, the electrode was dipped in aqua regia at room temperature, followed by washing with deionized water. The electrodeposition of several kinds of metal was made potentiostatically onto the illuminated electrode in the conditions given in Table I. The deposition potential was selected in such a manner that at that potential not the hydrogen evolution but the metal deposition preferentially proceeded under a fixed band bending of the electrode in all the electrolytes chosen; *i.e.*, the deposition potential was shifted cathodically by 60 mV with an increase in unit *p*H of the electrolyte. Thermodynamically, copper cannot be deposited at the potential selected. However, the deposition was possible at the illuminated electrode, since the deposition reaction proceeded as a photosensitized reaction.

Key words: photoelectrochemistry, semiconductor electrode, gallium phosphide, metal adatoms, surface states.

The number of surface sites equivalent to the monolayer coverage was assumed to be $2.4 \times 10^{15}/cm^2$ of apparent surface area by taking the roughness factor into consideration. The assumption of the number of surface sites is not critical to this study, as is shown in a later section. The deposition was made by employing an electronic coulometer (Nichia Keiki, Model N-CR 404). The current for deposition was automatically interrupted by an action of an electronic relay of the coulometer when the charge amounted to the set value. The deposition was usually completed within several seconds at the longest when the monolayer was deposited. If the metal deposition was made with the charge equivalent to the monolayer coverage, the prepared electrode is represented in this paper as $M(\theta = 1)/$p-GaP. After the metal deposition, the electrode was washed in a stream of deionized water for over 1 hr.

When it was necessary to use the wasted electrodes again, the metal-deposited electrodes were usually dipped in aqua regia at room temperature for 5 min before use with the objectives of both removal of the deposited metal and surface pretreatment, if they still retained the shiny surface. The removal proceeded very rapidly, judging from the fact that metals deposited so much as to show their characteristic color completely lost the color within several seconds after immersion in the aqua regia. On the other hand, no appreciable etching of GaP seemed to proceed in a comparable time. Therefore, we believe that the etching proceeded fairly homogeneously throughout the entire surface by the 5 min dipping even when the deposited metal was distributed in patches on the surface.

Table I. Conditions for metal deposition

Metal	Potential (*vs.* SCE)	Composition of electrolyte (g/liter)	*p*H
Pd	−0.27	$PdCl_2 \cdot 2H_2O$ 16, NH_4Cl 30, NH_4OH 30	10.36
Ag	−0.40	$KAg(CN)_2$ 100, K_2CO_3 45	12.51
Au	−0.23	$KAu(CN)_2$ 170, Na_2HPC_4 5	9.60
Cu	0.29	$CuSO_4$ 200, H_2SO_4 50	0.90
Pb	−0.05	$Pb(BF_4)_2$ 200, HBF_4 20, H_3BO_3 20	1.5

The techniques of ion microprobe mass analysis were employed to obtain information on the distribution profiles of the deposited metal on the surface. A focused Ar^+ beam of 1×10^{-7}A with a 4 μm diameter was scanned on the sample surface with a suitable choice of energy selection of the mass spectrometer of an ion microanalyzer (Hitachi, Model IMA-2). The surface distribution pattern of the deposited metal was obtained as a specific ion image by observing the objective metal ions produced only when the Ar^+ beam struck the deposited metal. This technique has been used by other investigators (7, 8). The in-depth analysis of the surface composition was made in a manner similar to that reported by Evans *et al.* (9) by bombarding an Ar^+ beam of 0.5 μA with a 0.47 mm diameter onto a fixed position of the sample surface, and the signal intensity of the objective element was measured as a function of the sputtering time.

The monochromatic light of various wavelengths was obtained by a prism monochrometer. A 500W xenon lamp was used as a light source. A rather large slit width of 2 mm or more was used in order to obtain high illumination intensity of the monochromatic light. The purity of the monochromatic light was, therefore, not high especially in long wavelengths. The number of incident photons at 450 nm, determined by ferrioxalate actinometry, was usually around 2×10^{14}/cm^2sec for the monochromatic light obtained in this manner. Owing to poor purity of the monochromatic light, a photocurrent spectrum obtained is thought to contain undefined errors. As far as discussion in this paper is concerned, however, the purity of light does not cause a serious problem, because we do not discuss fine structure of the spectrum. A sequence of measurements was done with the same experimental setup, so that the irradiation intensity is believed to have been kept constant during the measurements.

In order to develop photoresponse to light of wavelengths longer than that corresponding to the bandgap energy, the electrode was polarized for a fixed period of time usually in 0.5M Na_2SO_4 at -2.0V under illumination with a focused light from the 500W xenon lamp. The light intensity was around 1.2 W/cm^2, as determined by a laser power meter (Coherent Radiation, Model 201). Then, the electrode was set in an electrolytic cell for measurements of photoresponse. After being set in the cell, the electrode was repeatedly subjected to potential sweep polarization at 1 V/min in the dark in a potential range between -1.0 and the potential at which the cathodic current commenced, until stable current-potential curves were obtained.

The polarization curves were measured by using a potentiostat having high input resistance of $10^{11}\Omega$ (Hokuto Denko, Model HA 104). The electrode potentials cited in this paper are referred to SCE. The differential capacitances of electrodes were measured by means of a Wheatstone bridge assembly (1).

Results and Discussion

Appearance and disappearance of response to monochromatic light of 1000 nm.—When an Au ($\theta = 1$)/p-GaP electrode was cathodically polarized in 0.5M Na_2SO_4 at -2.0V under illumination, a noticeable response to monochromatic light of 1000 nm gradually developed with polarization time; when the electrode was not intentionally subjected to the cathodic polarization, it was insensitive to this wavelength. Figure 1 shows typical results. The measurements of current-potential curves were made not in 0.5M Na_2SO_4 but in 0.5M H_2SO_4, because a higher response was observed in the latter electrolyte than in the former (see Fig. 3). The electrode having no adatoms also showed response to 1000 nm light, although very weak, when it was subjected to the same cathodic polarization treatment as stated above. Trials to characterize the deposited metal layers are presented in a later section.

The initial surface etching with hot aqua regia to give a shiny surface seemed to be essential for the electrode to develop the response to 1000 nm light. The initial etching with HCl, for example, brought about quite different electrode behavior. In this case, the development of photoresponse to 1000 nm light was usually negligible, and a relatively high anodic current was observed at potentials anodic to around -0.5V, even after the electrode was cathodically prepolarized in the above-mentioned manner. The instability of p-type GaP as a photocathode, which was reported previously (1) and drew a contradiction from Bockris and Uosaki (10), was also improved by the pretreatment of the electrode with hot aqua regia.

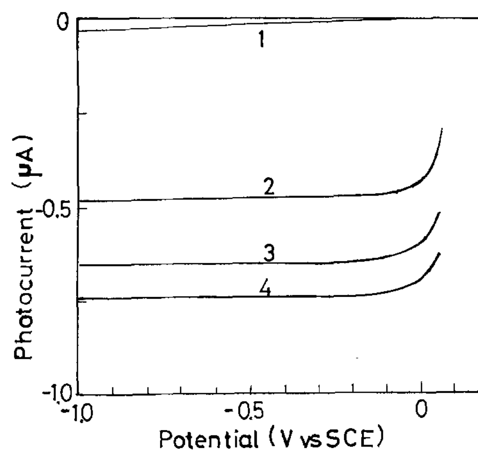

Fig. 1. Increase in photocurrent at 1000 nm with polarization time for an Au($\theta = 1$)/p-GaP electrode polarized at -2.0V in 0.5M H_2SO_4 while under illumination with a 500W xenon lamp. Measuring solution = 0.5M H_2SO_4 and sweep rate = 1 V/min. The cathodic polarization was successively conducted in the order: Curve 1, before the polarization; curve 2, 10 min; curve 3, 20 min; and curve 4, 30 min.

The developed response became weak and finally disappeared if the electrode showing the response was left to stand in the solution under the open-circuit condition or taken out from the solution. Typical examples are given in Fig. 2.

Considering that the minimum bandgap of GaP is 2.38 eV (11), one should recognize that the response to 1000 nm light is caused not by the band-band transitions of electrons but by band-surface state transitions. Then, it seems reasonable to assume that these surface states must have been formed during the 1 hr cathodic polarization and that they disappear after interruption of the cathodic polarization. The cathodic treatment to create the surface states is, therefore, termed here "the activation treatment," and the electrode showing the developed response, "the activated electrode."

The developed response of the activated Au($\theta = 1$)/p-GaP was higher when measurements were made in an acid solution such as 0.5M H_2SO_4 than in a neutral or in an alkaline solution, as Fig. 3 shows. Therefore, measurements of the developed response were usually

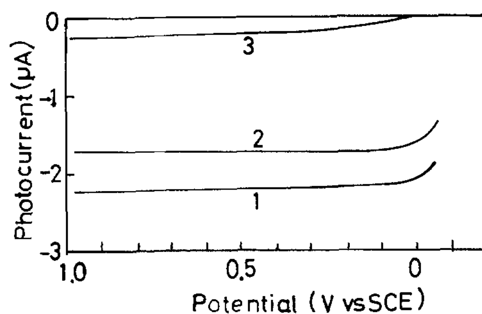

Fig. 2. Decrease in photocurrent at 1000 nm for an activated Au($\theta = 1$)/p-GaP electrode. Measuring solution = 0.5M H_2SO_4 and sweep rate = 1 V/min. Curve 1, immediately after the cathodic polarization for 1 hr under the same condition as given in Fig. 1; curve 2, subsequent to drying for 10 min; and curve 3, subsequent to standing in 0.5M H_2SO_4 for 2 days.

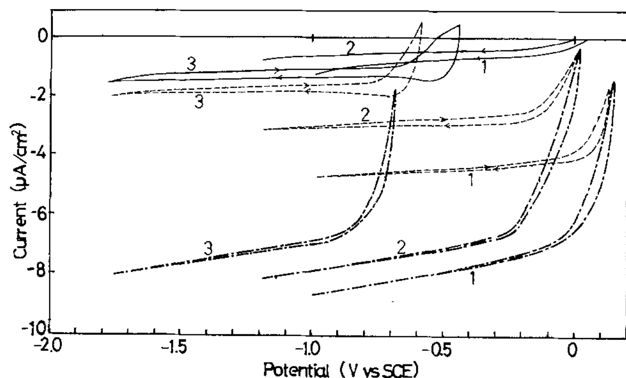

Fig. 3. Current-potential curves for an activated Au(θ = 1)/p-GaP electrode in: Curve 1, 0.5M H_2SO_4; curve 2, 0.5M Na_2SO_4; and curve 3, 0.5M NaOH. (—) In darkness, (- - -) λ = 1000 nm, (· — ·) λ = 440 nm.

made in 0.5M H_2SO_4. On the other hand, the response due to the band-band transition of electrons was not influenced by the nature of the electrolyte used in the measurements.

Activation treatment.—The photocurrent spectra given in Fig. 4 show how the response of an Au(θ = 1)/p-GaP electrode changed with the time of the activation treatment. Notice that in this case in contrast to the conditions of Fig. 1 and 3, the activation treatment was conducted in 0.5M H_2SO_4 at −0.35V. Nevertheless, response appeared at wavelengths longer than 550 nm. This fact, together with a result obtained in 1M NaOH at −2.0V, indicates that the nature of the electrolyte used in the activation treatment is not critical for developing the photoresponse. Also noticeable is the fact that no rigid condition seemed to be required for the polarization potential in the activation treatment. By comparing the potential chosen in the activation treatment of Fig. 4 with that of Fig. 1 and 3, it is recognized that any potential seems to be sufficient to develop the response, providing it is in such a potential region as to give saturated photocurrent under illumination with focused light from the xenon lamp. It follows from these results that there are a variety of activation treatment conditions. However, we usually performed the treatment in 0.5M Na_2SO_4 at −2.0V for 1 hr. The results presented below are for electrodes subjected to this treatment unless otherwise noted.

Figure 4 indicates that the development of response was accompanied with a decrease in the photocurrent owing to the band-band transition of electrons. However, the rate of decrease was quite low compared with the rate of increase in photocurrent in the developed spectrum. The spectral response of p-type GaP could be extended by the activation treatment even when the electrode had no adatoms on it, although the effect was very small.

Effects of the amount of deposited metal on the development of response.—The results given in Fig. 5 show that deposition of one or two monolayers of gold was sufficient to improve the response of p-type GaP. One-half a monolayer was too little and three layers were too much. A similar relation between the amount of deposited metal and the magnitude of photocurrent was also found in the cases of silver and copper deposition. The results on Ag/p-GaP are given in Fig. 6.

These results suggest that the degree of coverage may have a critical role in the improvement of re-

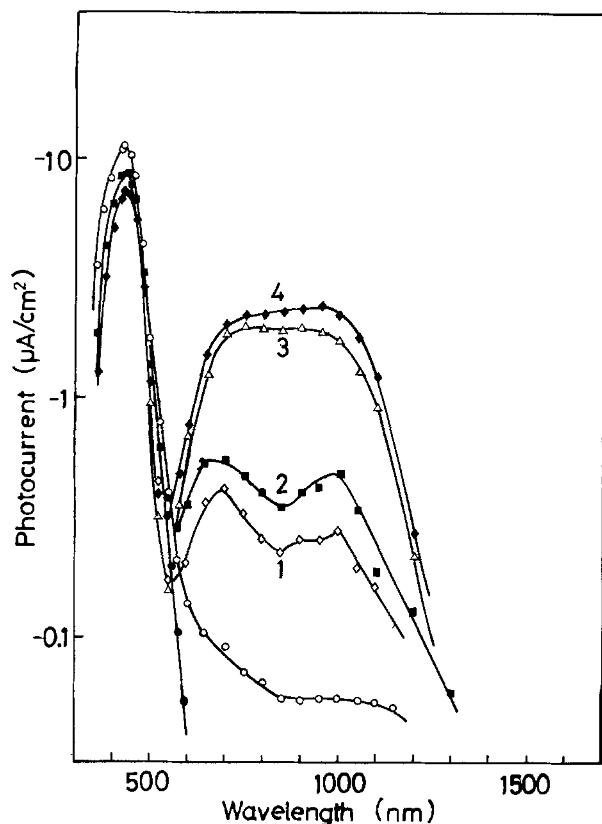

Fig. 4. Development of photoresponse at Au(θ = 1)/p-GaP by the activation treatment in 0.5M H_2SO_4 at −0.35V. Measurements were made with the same condition as in the activation treatment which was successively conducted in the order: Curve 1, 20 min and curve 2, 20 min, both in the dark, and curve 3, 20 min and curve 4, 10 min, both under illumination with a 500W xenon lamp. (—○—) For p-type GaP having no adatom after the activation treatment under illumination for 1 hr, (—●—) for "as chemically pretreated" p-type GaP.

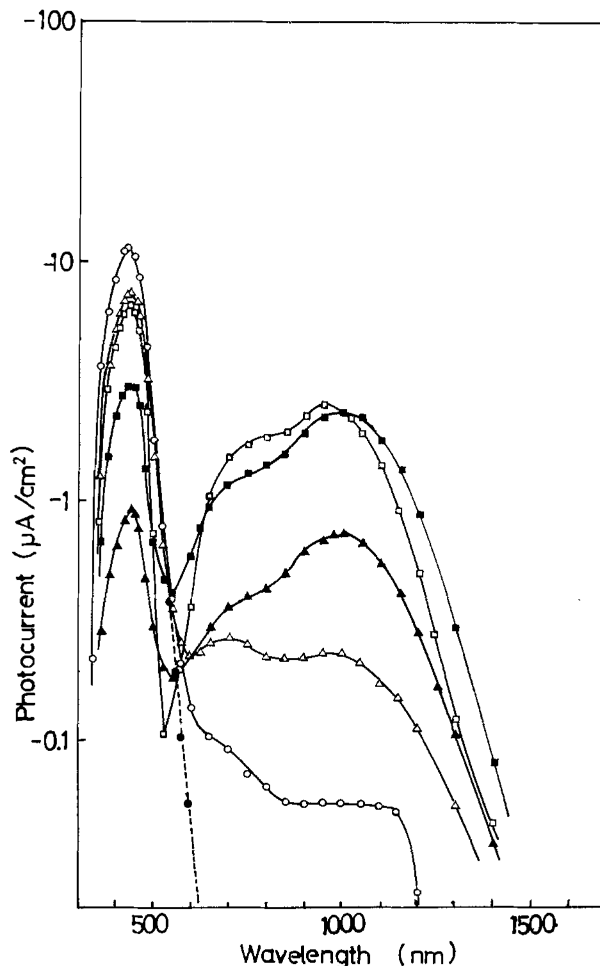

Fig. 5. Effects of the amount of deposited gold on the development of photoresponse of p-type GaP. (—○—) θ = 0, none; (—△—) θ = 0.5; (—□—) θ = 1; (—■—) θ = 2; (—▲—) θ = 3. θ is given in monolayers. (—●—) nonactivated for θ = 0. Solution = 0.5M H_2SO_4, E = −0.35V.

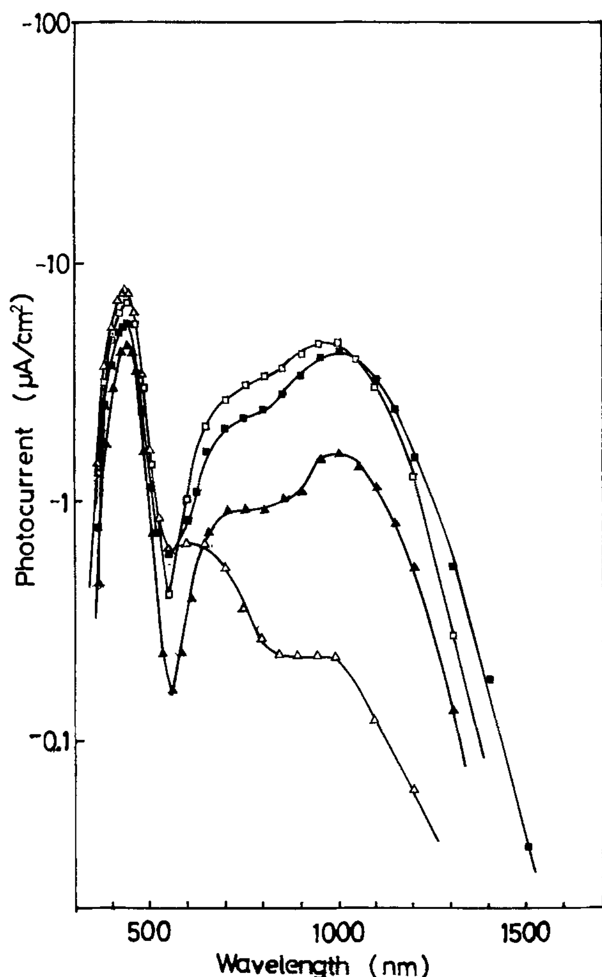

Fig. 6. As in Fig. 5, but for Ag deposition. (—△—) $\theta = 0.5$, (—□—) $\theta = 1$, (—■—) $\theta = 2$, and (—▲—) $\theta = 3$.

sponse. Specific ion image patterns of gold obtained for Au/p-GaP showed, however, that the deposited gold did not cover the entire surface even when the amount corresponding to twenty monolayers was deposited. Therefore, no definite conclusion can be drawn on whether or not the most favorable coverage was attained at the optimum amount of deposition observed and what the optimum coverage is, if any. Figures 4-6 show that the photocurrent spectra of the activated electrodes covered a wide spectral region ranging from 600 to 1400 nm.

Nature of the developed photocurrent.—In order to get information on the nature of the developed spectra, a constant potential electrolysis was conducted in 0.5M H_2SO_4 by using the activated Au($\theta = 1$)/p-GaP electrode. The polarization potential was set at −0.35V, and the electrode was illuminated with a focused light having longer wavelengths than 600 nm which was obtained by setting a colored glass filter (Toshiba, Vr-60) between the xenon lamp and the electrolytic cell. The cathodic current flow of 300 $\mu A/cm^2$ was caused by light irradiation of 0.5 W/cm^2, and gas bubbles were observed to stick to the electrode surface. After the electrolysis for 2.5 hr, the evolved gas was analyzed by a gas chromatograph using a molecular sieve 5A column and was identified to be hydrogen. After the electrolysis no appreciable change was noticed in the electrode surface condition.

Deposited metals as shallow surface states of the electrode.—The monolayer amount of metal deposition did not cover the entire surface of the electrode, but was restricted to areas distributed in patches, as stated above. The activation treatment did not make any change in the ion image pattern obtained. The in-depth analysis of gold, however, showed that the time required for the deposited gold to be sputtered out was

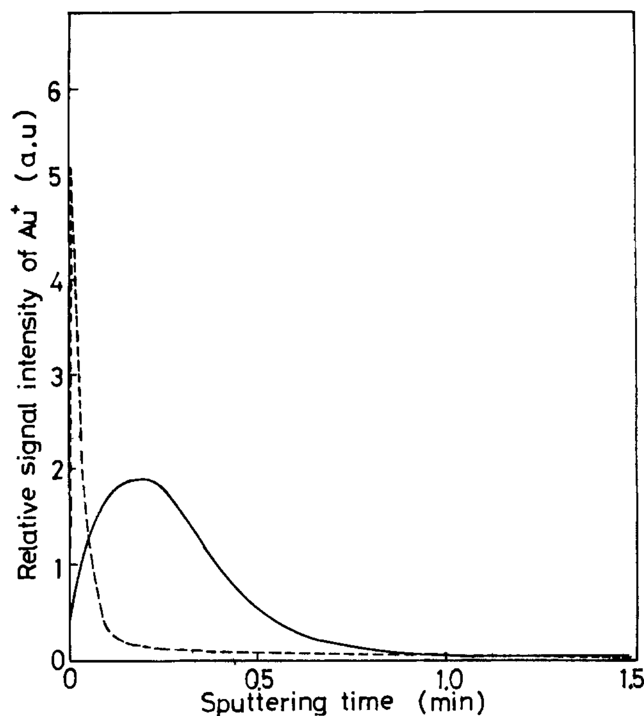

Fig. 7. In-depth distribution profiles for Au($\theta = 1$)/p-GaP before (- - -) and after(—) the activation treatment.

changed and prolonged by the activation treatment (Fig. 7). A simple interpretation may be made that the deposited metal was forced into the electrode surface by the activation treatment. However, this interpretation may draw criticism, since the secondary ion yield for Au will be affected by a change in the bond strength between the adatoms and GaP (12). If the prolongation of sputtering time observed is ascribable to an increase in the bond strength, then one may be able to conclude that the deposited layers became dense by the activation treatment. Any discussion on coarseness of the deposited layers as was done on n-type GaP coated with metal films (6), however, will not be so effective since the deposited layers were distributed in patches. In any case, the deposited gold seems to have no direct relation with the appearance of response at wavelengths longer than 550 nm, because the activated electrode, as mounted in the sample chamber of the ion microanalyzer, had already lost its developed response by the time the ion microprobe mass analysis was made.

The results obtained on CdS and ZnO having metal adatoms also eliminate the possibility for direct participation of deposited metals in the development of photoresponse. According to the results obtained by Gerischer *et al.* (13, 14), the direct optical electron transfer from the adatoms to the conduction band, observed in the anode process, takes place with a very low probability because an electron is required to move in position from the energetic level in the metal adatoms to a place inside the electrode during the course of the optical excitation. A quite analogous situation will be met in the cathode process at p-type GaP having metal adatoms. The optical electron transfer from the valence band to the energetic levels in the metal adatoms, which may lead to the hydrogen evolution, must also proceed with a very low probability even if it would occur.

Formation of deep surface states by the activation treatment.—The above discussion indicates that we have to seek another origin for the development of photoresponse. The results shown in Fig. 1 and 4 suggest that the formation of surface states is a slow process. This is important information for evaluating the origin of surface states. Another important finding is that the shapes of the photocurrent spectra of M(θ=1)/p-GaP are independent of the kind of metal M (Fig. 8). This result suggests that the surface states

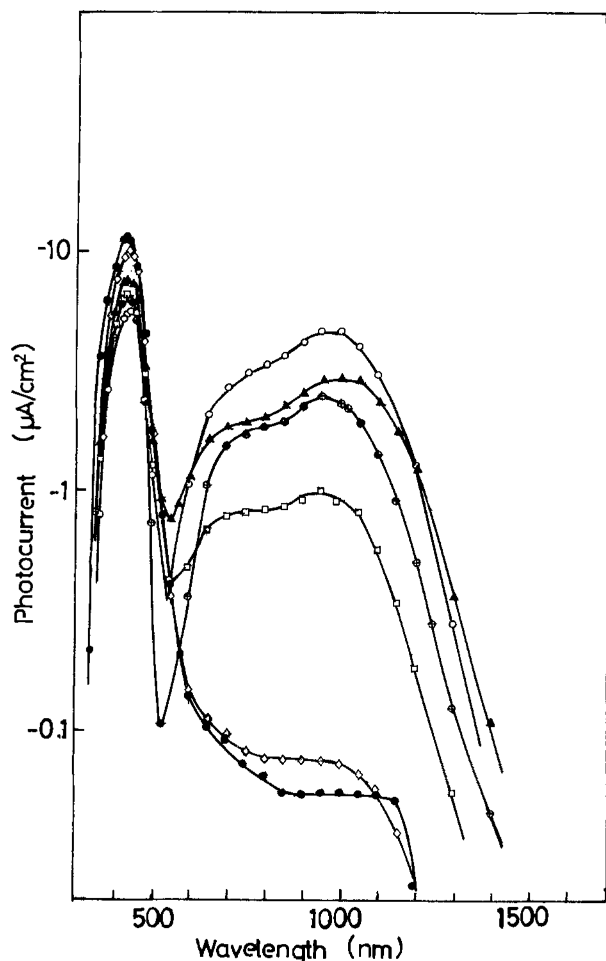

Fig. 8. Photocurrent spectra of activated GaP having the monolayer amount of various metals. (○) Ag, (—▲—) Pd, (—⊕—) Au, (—□—) Cu, (—◇—) Pb, and (—●—) none. Solution = 0.5M H_2SO_4, E = −0.35V.

formed have the same origin. Then, hydrogen impregnation evolves as the most probable cause for the formation of surface states, although we have no definite knowledge of the impregnated condition.

It is well known that the cathodic evolution of hydrogen causes hydride formation for Ge (15) and leads to its decomposition. In the case of compound semiconductors, such as GaAs (16) and InP (17), the nonmetallic elements are removed from the semiconductor surface as hydrides during the course of hydrogen evolution. Compared with these semiconductors, GaP seems to be suitable for the hydrogen evolution, so that it can accommodate the impregnated hydrogen in the electrode surface region.

It was noticed that the activation treatment for 1 hr was enough to develop photoresponse at wavelengths longer than 550 nm and that further activation treatment brought about no appreciable effect. This finding also supports the premise that hydrogen impregnation is closely related to the formation of surface states. The impregnation proceeds toward the interior of the electrode during the course of the activation treatment, and the formed surface states can trap photoexcited electrons with energies smaller than the bandgap energy. If the assumption is made that photoexcited electrons from the valence band to levels of the formed surface states are responsible for the developed cathodic photocurrent, then the magnitude of the developed photocurrent must depend on the trapping probability of photoexcited electrons as well as on irradiation intensity. The dependence of the developed photocurrent on illumination intensity is given in Fig. 9. The trapping probability will become saturated if the formation of surface states extends into the interior for a distance

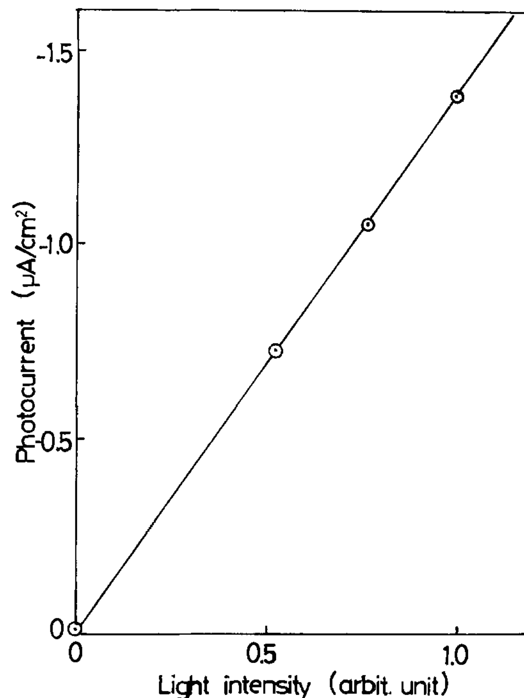

Fig. 9. Photocurrent via the formed surface states as a function of illumination intensity. λ = 1000 nm, solution = 0.5M H_2SO_4, electrode = activated Au(θ = 1)/p-GaP.

comparable to the penetration depth of the illuminated light. The experimental results show that such a condition was almost realized by the activation treatment for 1 hr.

As shown in photocurrent spectra of M(θ=1)/p-GaP, growth of the developed spectrum was usually accompanied by depression in the photocurrent at wavelengths of the intrinsic absorption of GaP. This phenomenon possibly reflects that some of the electrons photoexcited into the conduction band were trapped by the formed surface states.

Energy levels of surface states.—It is possible to determine the energy levels of the surface states from the photocurrent spectra obtained. In the case of Au(θ = 1)/p-GaP, they are distributed from about 0.9 to 2.3 eV above the upper edge of the valence band with a high density between 1.4 and 1.8 eV, although no rigid determination was possible in the present study owing to poor resolving power of the monochrometer as used. It is evident that almost the same distribution profile holds for electrodes having other kinds of deposited metals. From a knowledge of the flatband potential of the electrode, which is given below, relative positions of the energy levels of the surface states to that of the hydrogen electrode can be pictured as shown in Fig. 10. This figure is given for the case when the electrode was polarized at −0.35V in 0.5M H_2SO_4. If one takes into consideration the distribution function of unoccupied electron states in the hydrogen electrode (18, 19), hydronium ions must find a distribution probability in the energies equal to or higher than the lowest level of the surface states. Therefore, the electron transfer from the surface states to hydronium ions in the electrolyte must occur in the energy region covering the entire surface state. Furthermore, this transfer seems to be more feasible than that via the conduction band since the energy levels of the surface states, rather than those of the conduction band, are closer to the energy of the hydrogen electrode.

Memming *et al.* found participation of surface states in the reduction of several oxidizing agents at p-type GaP electrodes (3, 4). It is noteworthy that the energy region covered by the surface states discovered by them is in good agreement with that found in the present study, although their results showed negligible par-

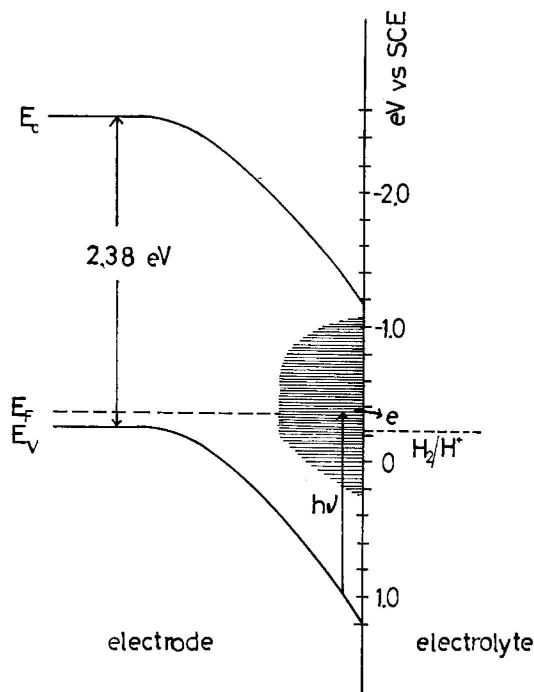

Fig. 10. Schematic energy level diagram at the electrode/electrolyte interface for an activated Au(θ = 1)/p-GaP electrode polarized at −0.35V in 0.5M H_2SO_4.

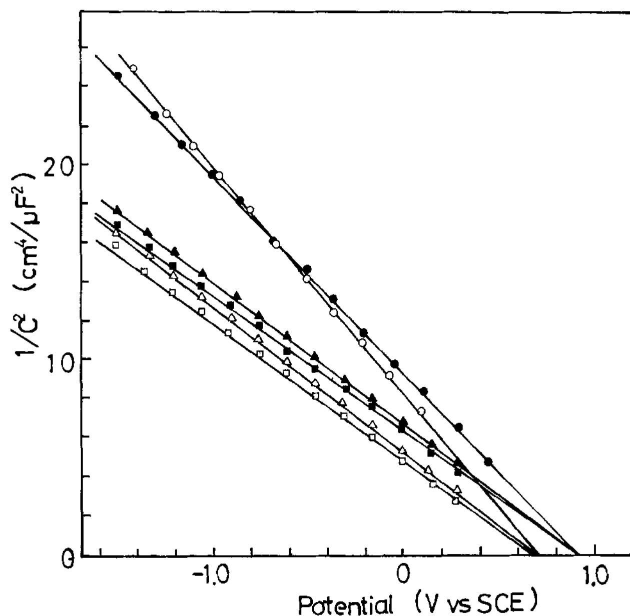

Fig. 11. Schottky-Mott plots of differential capacitances of a p-type GaP electrode before and after the activation treatment. Open symbol, after the treatment; closed symbol, before the treatment. (□, ■) 10 kHz, (△, ▲) 5 kHz, and (○, ●) 1 kHz.

ticipation of the surface states in the hydrogen evolution reaction.

Flatband potentials.—Figures 11 and 12 show Schottky-Mott plots of differential capacitance of p-type GaP and Au(θ = 1)/p-GaP electrodes, respectively, before and after the activation treatment. As the figures show, the potentials obtained by extrapolation of the plots to $1/C^2 = 0$ were independent of the measured frequency. It is then possible to determine the flatband potential in a straightforward manner (20). The flatband potentials of M(θ=1)/p-GaP electrodes determined in this manner are presented in Table II. It will be noticed that the flatband potential of the electrode was shifted negatively by the activation treatment regardless of whether or not the electrode had metal adatoms.

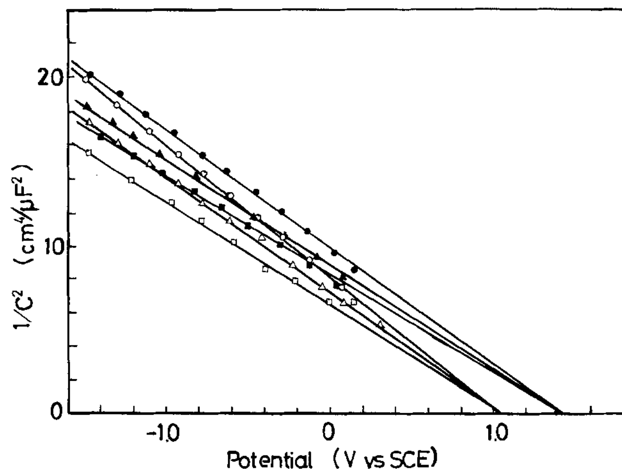

Fig. 12. As in Fig. 11, but for Au(θ = 1)/p-GaP

In the case of Ge electrodes, the cathodic polarization brings about a change in the surface condition from a hydroxyl to a hydride nature, so that the flatband potential is shifted in a negative direction. This phenomenon could successfully be elucidated only when a rapid measurement technique was employed (21, 22). A quite analogous situation is expected on GaP electrodes.

The surface Ga sites of GaP are believed to be responsible for formation of hydroxide and hydride, according to the following equations

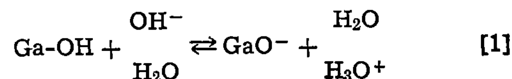

$$\text{Ga-OH} + \underset{H_2O}{\overset{OH^-}{\rightleftarrows}} \text{GaO}^- + \underset{H_3O^+}{\overset{H_2O}{}} \quad [1]$$

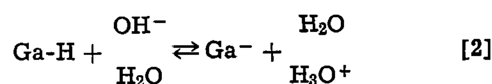

$$\text{Ga-H} + \underset{H_2O}{\overset{OH^-}{\rightleftarrows}} \text{Ga}^- + \underset{H_3O^+}{\overset{H_2O}{}} \quad [2]$$

The surface Ga-H will be too unstable to be detected by a slow measurement technique of differential capacitance such as by employing a Wheatstone bridge assembly, because gallium is an sp metal and cannot retain adsorbed hydrogen (23). In the case when hydrogen is impregnated, however, a different situation may hold, and surface gallium may behave as if it retains adsorbed hydrogen. This is a plausible explanation for the negative shift of the flatband potential of the electrode by the activation treatment.

The values of the flatband potentials were affected by the kind of metals chosen, as Table II shows. An argument similar to that made for CdS electrodes having various kind of metal adatoms (13) would hold here also. Unfortunately, however, a linear relation has not yet been established between the flatband potential of M(θ=1)/p-GaP and the work function of the deposited metals, possibly because of scarcity of experimental results.

It is shown in Fig. 3 that the photocurrent caused by illumination with monochromatic light of 1000 nm was affected by the nature of the electrolyte. A plausible explanation for this is as follows. By changing *p*H values of the electrolyte, the number of the surface hydride sites will be changed according to Eq. [2]. The continuity of the surface-state energy levels from the surface into the interior is then affected, and there will

Table II. Flatband potentials of M(θ = 1)/p-GaP electrodes measured in 0.5M H_2SO_4

	Flatband potential (V *vs.*SCE)	
M	Nonactivated	Activated
Au	1.20	1.02
Ag	1.0	0.9
Cu	0.90	0.86
Pb	0.94	0.80
None	0.95	0.73

be a large tendency in a high pH solution for the continuity to be broken down and thus for the photocurrent to be suppressed.

Conclusion

Extension to longer wavelengths of the photocurrent response of p-type GaP electrodes for the hydrogen evolution reaction was successfully achieved by depositing a monolayer of any of several kinds of metals onto the electrode surface and then cathodically polarizing the resulting electrode under illumination. The cathodic polarization must be related to surface-state formation, and the impregnated hydrogen seems to be the most probable cause for this. The developed response was high enough to have practical significance for solar energy utilization at least in the following two points: First, the activated electrode responds in a wide wavelength region below 1400 nm, so that a large part of the solar spectrum can be utilized. Second, while the activated electrode is being used as a photocathode, there seems to be no problem in the stability of the metal adatoms; thus a long life duration of the activated electrode is to be expected. From a scientific point of view, however, some questions remain on the development of the response to be elucidated, especially on the mechanism of the appearance of the developed response, and on the role of the deposited metals. On the latter point, the catalytic activity of the metals for the hydrogen evolution may have some relation to the development of the response, since deposition of Pb did not give any apprciable effect.

Manuscript submitted July 7, 1977; revised manuscript received Aug. 30, 1977.

Any discussion of this paper will appear in a Discussion Section to be published in the December 1978 JOURNAL. All discussions for the December 1978 Discussion Section should be submitted by Aug. 1, 1978.

REFERENCES

1. H. Yoneyama, H. Sakamoto, and H. Tamura, *Electrochim. Acta*, **20**, 341 (1975).
2. A. J. Nozik, *Appl. Phys. Lett.*, **29**, 150 (1976).
3. R. Memming and G. Schwandt, *Electrochim. Acta*, **13**, 1299 (1968).
4. K. H. Beckmann and R. Memming, *This Journal*, **116**, 368 (1977).
5. H. Tamura, H. Yoneyama, C. Iwakura, H. Sakamoto, and S. Murakami, *J. Electroanal. Chem.*, **80**, 357 (1977).
6. Y. Nakato, S. Tonomura, and H. Tsubomura, *Ber. Bunsenges. Phys. Chem.*, **80**, 1289 (1976).
7. J. M. Morabito and R. K. Rewis, *Anal. Chem.*, **45**, 869 (1973).
8. C. A. Evans, Jr., *ibid.*, **44**, 67A (1973).
9. R. E. Powel, J. P. Pemsler, and C. A. Evans, Jr., *This Journal*, **119**, 24 (1972).
10. J. O'M. Bockris and K. Uosaki, *ibid.*, **124**, 98 (1977).
11. J. C. Philips, "Bonds and Band in Semiconductors," p. 169, Academic Press, New York (1973).
12. A. Benninghoven and A. Muller, *Phys. Lett. A*, **40**, 169 (1972).
13. D. M. Kolb, M. Przasnyski, and H. Gerischer, *Z. Phys. Chem. N.F.*, **93**, 1 (1974).
14. H. Gerischer, B. Pettinger, and M. Lubke, in "Electrocatalysis," M. W. Breiter, Editor, p. 162, The Electrochemical Society Softbound Symposium Series, Princeton, N.J. (1974).
15. J. Berdeleben, *Z. Phys. Chem. N.F.*, **17**, 39 (1958).
16. H. Gerischer and I. Mattes, *ibid.*, **49**, 112 (1966).
17. S. Mayumi, C. Iwakura, H. Yoneyama, and H. Tamura, *Denki Kagaku*, **44**, 339 (1976).
18. H. Gerischer, *Z. Phys. Chem. N.F.*, **26**, 223 (1960); *ibid.*, **27**, 48 (1961).
19. R. Memming and F. Möllers, *Ber. Bunsenges. Phys. Chem.*, **76**, 475 (1972).
20. E. C. Dutoit, R. L. Van Meirhaeghe, F. Cardon, and W. P. Gomes, *ibid.*, **9**, 1206 (1975).
21. H. Gerischer, M. Hoffmann-Perez, and W. Mindt, *ibid.*, **69**, 130 (1965).
22. R. Memming and G. Newmann, *J. Electroanal. Chem.*, **21**, 295 (1969).
23. S. Trasatti, *ibid.*, **39**, 163 (1972).

Homomolecular Oxygen Exchange and the Electrochemical Reduction of Oxygen on Semiconducting Oxides

D. B. Hibbert* and A. C. C. Tseung*

Department of Chemistry, The City University, London EC1V 4PB, United Kingdom

ABSTRACT

The activation energies of the reversible electrochemical reduction of oxygen on $La_{0.5}Sr_{0.5}CoO_3$ and lithiated nickel oxide were shown to correlate with those of the gas phase exchange reaction between $^{16}O_2$ and $^{18}O_2$ on these catalysts. This result suggests that the rate-determining step of the reversible oxygen reduction is the dissociative chemisorption of an oxygen molecule, in agreement with the "joint pseudosplitting/dissociative chemisorption" mechanism. The electrochemical reduction and isotopic exchange reaction on high and low surface area lithiated nickel oxide showed that only above the Neel temperature could oxygen be chemisorbed as $2\,O^-$. The effect of particle size distribution, leading to a mixed potential, may account for the fact that high surface area lithiated nickel oxide is reversible only above 150°C.

Research into the mechanism of the electrochemical reduction of oxygen has stemmed from the quest for a reversible oxygen electrode. Work by Tseung, Hobbs, and Tantram (1) and Bevan and Tseung (2, 3) has shown the importance of the magnetic properties of semiconducting oxide electrocatalysts.

In this paper, the concepts developed in the earlier work are discussed and further evidence from isotopic exchange experiments is reported which clarifies the nature of the rate-determining step of the reaction.

The Theory of Electrochemical Oxygen Reduction

The reduction at an oxygen cathode in alkaline solution may take two paths

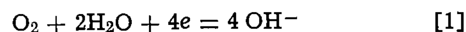

$$O_2 + 2H_2O + 4e = 4\,OH^- \quad [1]$$

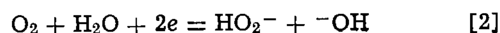

$$O_2 + H_2O + 2e = HO_2^- + {}^-OH \quad [2]$$

* Electrochemical Society Active Member.

Key words: electrocatalysis, lanthanum cobalt oxide, magnetic properties, lithiated NiO, isotopic exchange.

A possible scheme for the four-electron process (Eq. [1]) involves the so-called "joint pseudosplitting/dissociative adsorption" mechanism (2, 4). "Side-on" adsorption of an oxygen molecule followed by partial electron transfer at the catalyst surface and hydrogen bonding to adjacent adsorbed hydroxyl ions leads to a low energy pathway for the cleavage of the oxygen molecular bond. The scheme is depicted in Fig. 1(a)-(d). The initial adsorption is seen as an interaction between the π^* electrons of O_2 and partially filled d orbitals of two adjacent transition metal ions of the semiconducting oxide electrode. This is essentially the "bridge model" discussed by Yeager (5).

If the conditions for side-on adsorption are not favorable bonding may occur through just one oxygen atom leading to "end-on" adsorption and the pathway of Eq. [2] (6). The participation of both reactions at the cathode leads to a mixed potential and irreversible behavior.

By this theory, therefore, an efficient material for a reversible oxygen electrode should be able to chemisorb oxygen in the side-on position. Tseung and Bevan have argued that side-on adsorption of oxygen (a paramagnetic molecule) will be facilitated by the presence of parallel electron spins in the surface of the electrocatalyst. Thus the requirement for the catalyst is that it, too, should be paramagnetic at the temperature of operation of the electrode.

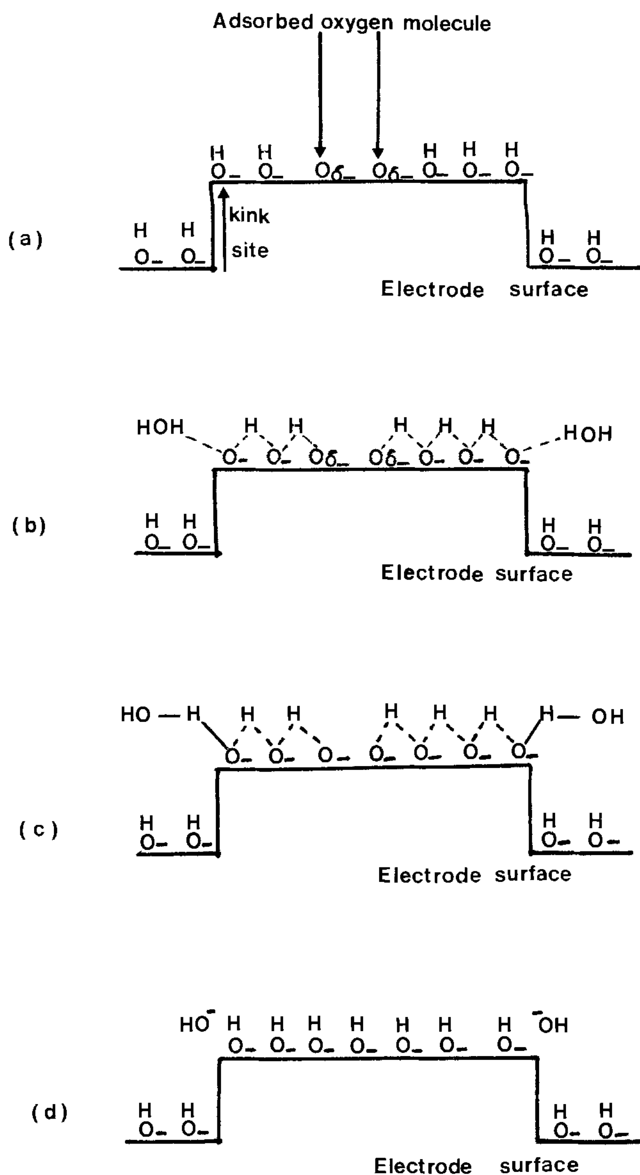

Fig. 1. Stages in pseudosplitting. (a) Partial electron transfer, (b) hydrogen bonding, (c) completion of electron transfer, (d) reorientation. Over-all reaction: $O_2 + 2H_2O + 4e \rightarrow 4\ OH^-$.

Yeager (5), in a recent review, distinguishes two modes of side-on adsorption involving one, or two catalyst sites. A one-site adsorption, the Griffiths model (7), although leading to a weakening of the oxygen molecular bond, does not require a particular magnetic state, in contrast to the two-site (bridge) model discussed above.

In addition, correct spacing of the metal ions is a prerequisite of the bridge model.

Two classes of oxides have been shown to reduce oxygen in alkaline solution via the four-electron path of Eq. [1]; perovskite oxides based on $LaCoO_3$ (3) and lithiated nickel oxide (2). $La_{0.5}Sr_{0.5}CoO_3$ is ferromagnetic at room temperature. Nickel oxide is antiferromagnetic with a Neel temperature (for massive nickel oxide) of 247°C. The apparent Neel point is extremely sensitive to particle size and is reduced to room temperature for nickel oxide of mean particle size diameter of 130Å (8).

Experimental

Preparation of oxide catalyst.—Low surface area lithiated nickel oxide [5 atom percent (a/o) Li^+] was prepared by the freeze drying technique (9) with a reduced volume of nickel acetate and lithium acetate (200 ml for 5g catalyst). $La_{0.5}Sr_{0.5}CoO_3$ was prepared using the same method from a solution of mixed nitrates following the procedure of Tseung and Bevan (3).

High surface area lithiated nickel oxide was prepared by the method given by Teichner (10) in which nickel hydroxide, precipitated by ammonium hydroxide from a solution of nickel nitrate, was wetted with a saturated solution of lithium hydroxide. After agitation for 1 hr in an ultrasonic bath, the resulting slurry was dried and decomposed under vacuum (10^{-3} Torr) at 200°C. High surface area nickel oxide was prepared by the same method.

Catalyst characterization.—The surface area of each catalyst was measured by the BET method from the adsorption of nitrogen at 77°K. The conductivity of the catalyst was measured in a specially designed steel die containing a fixed amount of catalyst powder compressed at a fixed pressure by a Wayne-Kerr a-c bridge (1592 Hz).

The composition of the catalysts was checked by atomic absorption of a solution produced by dissolving a known weight of the catalyst in nitric acid. For the samples of high surface area lithiated nickel oxide, a leach with water was performed to determine the amount of lithium oxide which had remained unreacted on the surface of the nickel oxide.

X-ray powder photographs of $La_{0.5}Sr_{0.5}CoO_3$ (a Phillips machine with molybdenum targets and zirconium filter to select $K\alpha$ radiation) revealed the correct perovskite structure. Table I gives details of the physical properties of the catalysts used.

All the powders used for the isotopic exchange experiments were examined by transmission electron microscopy (by a JEOL, JEM 100B microscope, accelerating voltage 100 kV). Samples were sprayed onto a grid from a dispersion in water. Maximum magnification available was 50,000× which allowed the resolution of particles of 40Å diameter. From this it was possible to obtain a particle size distribution of the powders.

Electrode preparation.—Teflon bonded (1) porous electrodes were fabricated to test the electrocatalyst powders. A slurry of 10 mg catalyst and 3 mg 60% PTFE dispersion in water was ultrasonically dispersed for 10 min, then painted onto a preweighed, degreased, and etched 100 mesh Ni grid. The electrode was cured at 300°C for 1 hr, then spot welded onto a gold strip attached to a gold wire.

Table I. Physical characteristics of the electrocatalysts

Catalyst	Preparation technique*	Surface area (m^2/g)	Conductance** (Ω^{-1} cm^{-1})	X-ray analysis	Experimental investigations
$La_{0.5}Sr_{0.5}CoO_3$	f.d.	30	n.d.	Perovskite	$^{16}O_2/^{18}O_2$ exchange
$La_{0.5}Sr_{0.5}CoO_3$	f.d.	38	>0.1	Perovskite	Electrochemical
$Li_{0.05}Ni_{0.95}O_{0.975}$	h.p.	150	n.d.	n.d.	$^{18}O_2/^{16}O_2$ exchange OCV determined
$Li_{0.1}Ni_{0.9}O_{0.95}$	h.p.	180	>0.1	n.d.	Electrochemical
$Li_{0.85}Ni_{0.95}O_{0.975}$	f.d.	2.5	n.d.	n.d.	$^{18}O_2/^{16}O_2$ exchange
$Li_{0.05}Ni_{0.95}O_{0.975}$	f.d.	10	>0.1	n.d.	Electrochemical
NiO	f.d.	38	n.d.	n.d.	OCV determined
NiO	h.p.	135	n.d.	n.d.	$^{16}O_2/^{18}O_2$ exchange

* f.d. = freeze drying, h.p. = hydroxide precipitation.
** n.d. = not determined.

Electrochemical testing.—The cell used was a modification of the floating electrode cell of Giner and Parry (11). Electrodes of 1 cm^2 area were used in an electrolyte of 45 weight percent (w/o) KOH up to 140°C and 75 w/o KOH between 140° and 230°C. A Witton Model EC108L transistorized 1A potentiostat was used. A platinized platinum electrode was used as a dynamic hydrogen reference electrode (DHE), which was periodically standardized against a reversible hydrogen electrode (RHE). The *i-R* drop between Luggin and electrode surface was determined by the interruptor technique. A 20 cm^2 platinum gauze was used as the counterelectrode.

Isotopic oxygen exchange experiments.—The apparatus used to follow the equilibration of an $^{16}O_2/^{18}O_2$ mixture is essentially similar to that used by Winter (12) and is depicted in Fig. 2. The capillary leak joining mass spectrometer to reaction vessel was such as to allow a pressure of 10^{-5} Torr in the spectrometer for a pressure of 100 Torr in the reaction vessel. The volume of the reactor was 200 cm^3 and for a total pressure of gases of 100 Torr the leak rate to the mass spectrometer caused less than a 2% change in this pressure during the course of an experiment.

The mass spectrometer, an AEI MS10, scanned m/e (mass: electron ratio) 36, 34, and 32 with a sensitivity of 28 μA $Torr^{-1}$ allowing the detection of about 0.1% of any isotope in 10 Torr oxygen in the reaction vessel. "White spot" nitrogen was dried over silica gel. Oxygen containing 63.6% ^{18}O was supplied by British Oxygen Company, Special Gases Division.

In order to observe homomolecular exchange, the catalyst (~1g) was preequilibrated overnight at the temperature of the experiment with the $^{16}O_2/^{18}O_2$ mixture. The system was then evacuated to 10^{-3} Torr and filled with nitrogen to 100 Torr. To start the experiment 5 ml of labeled oxygen mixture was introduced into the reactor (giving a pressure of about 10 Torr). The ion currents of m/e 32, 34, and 36 were recorded at intervals for 400-600 min.

The accuracy of this method is limited by the rate of change of the m/e 36:34 ratio. The results were not considered if this ratio changed by less than 1% in 300 min. Practically, the lowest temperature which could give this rate for the catalysts investigated was between 100° and 150°C.

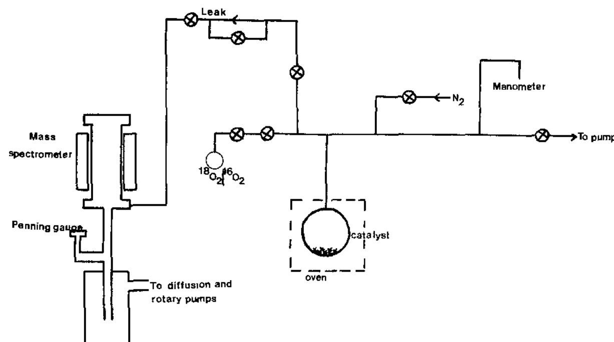

Fig. 2. Apparatus to measure the rate of oxygen exchange on a catalyst surface.

Results

Electrochemical testing.—Current-voltage relations for $La_{0.5}Sr_{0.5}CoO_3$ and lithiated nickel oxide have been published by Tseung and Bevan (2, 3), and Bevan (13).

Low surface area (12 m^2g^{-1}) lithiated nickel oxide electrodes showed reversible behavior (correct OCV, $i \propto p_{O_2}^{1/2}$, no change in slope of *i/V* curves through OCV) above 240°C, but below 220°C the reduction of oxygen was irreversible. For a high area sample (180 m^2g^{-1}) reversibility was shown above 150°C. In the case of $La_{0.5}Sr_{0.5}CoO_3$ the electrodes were reversible at room temperature.

To express the electrochemical rate of oxygen reduction in terms of the number of oxygen molecules reacting per second per square centimeter of true catalyst surface (Ƶ), the value of i_o was calculated from the *i-V* data. For all reversible electrodes the *i-V* curves were linear within 50 mV of the OCV. i_o was therefore calculated from the linear approximation to the Butler-Volmer equation given by Bockris and Reddy (14)

$$i_o = \frac{\Delta i}{\Delta \eta} \frac{\nu RT}{n\mathbf{F}} \quad [3]$$

($\Delta i/\Delta\eta$) is the slope of current density-overpotential line; ν is the stoichiometric number (taken as 2 for reaction [2]); n is the number of electrons associated with the reaction (here 4); and R, T, and $\mathbf{F}$ have their usual meanings. From i_o the rate of reaction, corrected for an atmosphere of 10 Torr oxygen ($i_o p_{O_2}^{0.5}$) may be calculated

$$Ƶ = (Ni_o/4A\mathbf{F})\,(1.32/p_{O_2})^{1/2}$$

where N is Avogadro's number, A is the true surface of the catalyst per square centimeter of electrode, and p_{O_2} is the partial pressure of oxygen used in the experiment expressed as a percentage (10 Torr is 1.32% of 760 Torr).

Figure 3 shows an Arrhenius plot of the results of $La_{0.5}Sr_{0.5}CoO_3$ and 10 a/o Li^+/NiO (ssa 180 m^2/g). These lines give: $La_{0.5}Sr_{0.5}CoO_3$ $Z = 10^{17.56}$ exp ($-13.0/RT$ kcal/mole); lithiated nickel oxide $Z = 10^{12.26}$ exp ($-4.3/RT$ kcal/mole).

The open-circuit voltage (OCV) of nickel oxide electrodes made from both high and low surface area oxide were measured at room temperature. At 25°C hydrophobic nickel oxide electrodes (ssa 135 m^2/g) gave more than 1.063V *vs.* DHE (in 100% oxygen). Attempts to purify the KOH solution by electrolysis (15) resulted in no significant change. Increasing the temperature to 70°C gave the expected decrease in OCV. Low surface area nickel oxide (ssa 38 m^2/g) had an OCV of 1.053V *vs.* DHE in air.

No attempt to measure current voltage curves was made due to the high resistivity of nickel oxide [$10^6\Omega$ cm (1)].

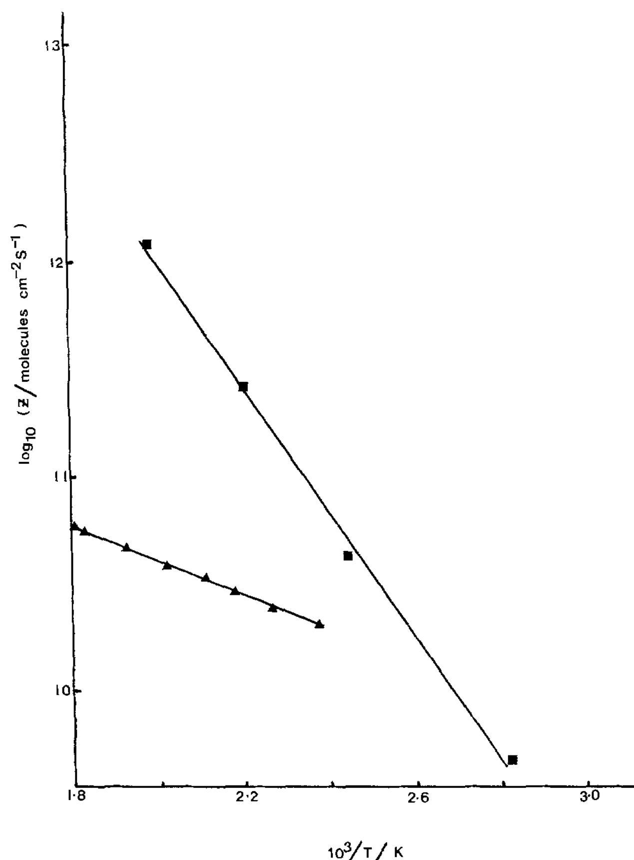

Fig. 3. The rate of the electrochemical reduction of oxygen calculated from i_0 measurements, as a function of temperature. ■ $La_{0.5}Sr_{0.5}CoO_3$, ssa 38 m^2/g; ▲ 10 a/o Li/NiO, ssa 180 m^2/g.

Isotopic exchange studies.—According to Boreskov (16) the rate of exchange of oxygen on a catalyst which has been equilibrated with an isotopic gas mixture is given by

$$\ln \frac{C^{\infty} - C^{0}}{C^{\infty} - C^{t}} = kt \qquad [4]$$

where C^t is the fraction of $^{16}O^{18}O$ molecules at time t, and k is the rate constant for the homomolecular exchange reaction

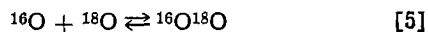

$$^{16}O + {}^{18}O \rightleftarrows {}^{16}O^{18}O \qquad [5]$$

Values of the rate constant k, were determined from Eq. [4] at temperatures between 150° and 300°C for $La_{0.5}Sr_{0.5}CoO_3$, 5 a/o Li^+/NiO (ssa 150 m^2/g and 2.5 m^2/g) and for NiO (ssa 135 m^2/g) at 160°C. k is related to the number of molecules reacting per second per unit surface area (Z) by

$$Z = \frac{N_A k}{A} \qquad [6]$$

where N_A is the total number of oxygen molecules in the reactor and A is the surface area of the catalyst.

Figure 4 is an Arrhenius plot of $\log_{10} Z$ *vs.* $1/T$ for the different catalysts. The rates for $La_{0.5}Sr_{0.5}CoO_3$ and high ssa lithiated NiO are described by

$$Z = 10^{17.2} \exp(-15.8/RT \text{ kcal/mole})$$

$$Z = 10^{10.3} \exp(-4.7/RT \text{ kcal/mole})$$

respectively.

It is noted that the single determination of Z for NiO (ssa 135 m^2/g) at 160° also falls on the lithiated nickel oxide curve.

The line for the low surface area 5 a/o Li^+/NiO shows a distinct change in shape between 220° and 240°C which encompasses the Neel temperature for this oxide.

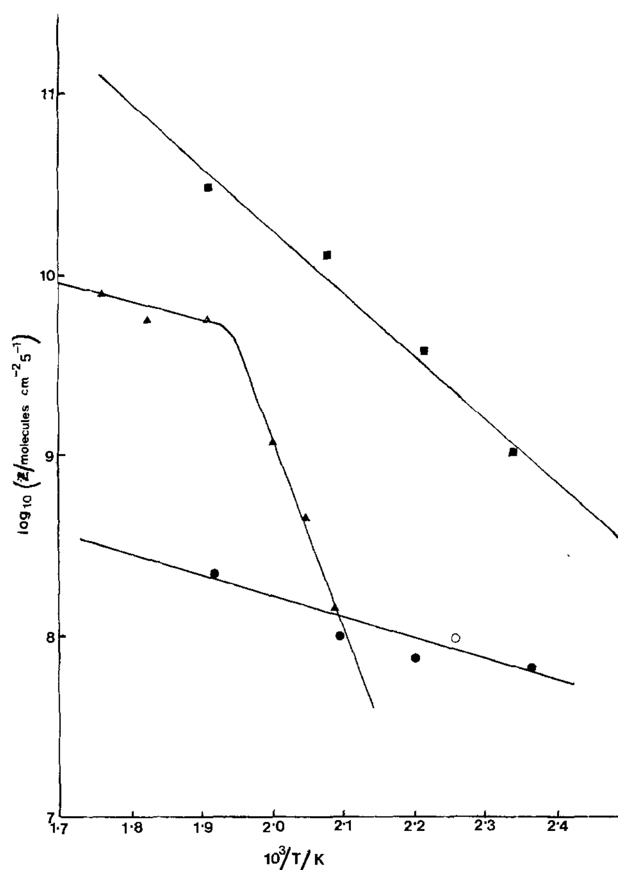

Fig. 4. The rate of homomolecular exchange of oxygen as a function of temperature. ■ $La_{0.5}Sr_{0.5}CoO_3$, ssa 30 m^2/g; ● 5 a/o Li/NiO, ssa 150 m^2/g; ▲ 5 a/o Li/NiO, ssa 2.5 m^2/g; ○ NiO, ssa 135 m^2/g.

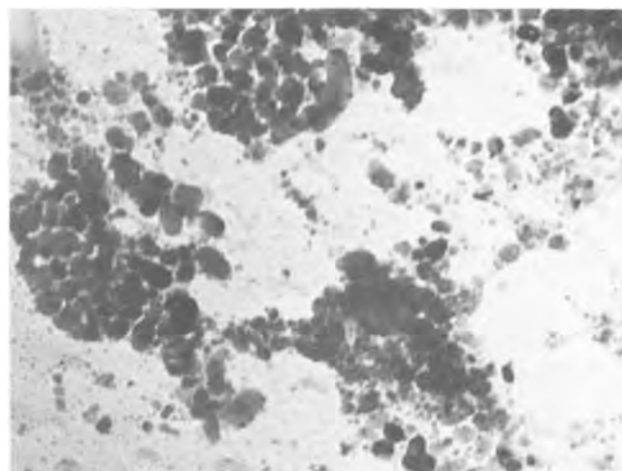

Fig. 5. Electron micrograph of 5 a/o Li/NiO ssa 150 m^2/g, showing crystallite size distribution. Original magnification 50,000X.

Particle size distribution.—Figure 5 gives a transmission electron micrograph of a lithiated nickel oxide sample of ssa 135 m^2/g. A count of the distribution of particle sizes leads to a mean particle size diameter (PSD) of approximately 100Å. That this is larger than is predicted from the BET measurement (67Å) indicates the presence of particles smaller than were resolved by the microscope (40Å). Of interest is that about 5% of the particles counted were of diameter greater than 200Å and particles greater than 600Å diameter were observed.

It is also of interest to note that low surface area lithiated nickel oxide powders showed a much smaller distribution of diameters.

Discussion

The comparison of chemical and electrochemical rates.—In comparing chemical and electrochemical rates of reaction it must be noted that the electrochemical rate determined from i_o will contain not only an element due to the chemical step (here the chemisorption of oxygen), but also to the added effect of potential. However if the rate-determining step is essentially a chemical adsorption of oxygen it would be expected that the slopes of the Arrhenius plots would be a measure of the activation energy of the process for both chemical and electrochemical reactions. It is seen immediately from a comparison of Fig. 3 and 4 that the activation energies for gas phase oxygen exchange and reversible elecrochemical reduction of oxygen on $La_{0.5}Sr_{0.5}CoO_3$ and high ssa lithiated nickel oxide have similar values ($La_{0.5}Sr_{0.5}CoO_3$: 15.8 kcal mole^{-1} and 13.0 kcal mole^{-1}; lithiated NiO: 4.7 kcal mole^{-1} and 4.3 kcal mole^{-1}, respectively). These results support the theory that the rate-determining step in each reaction is the dissociative adsorption of oxygen, which, in the case of electrochemical reduction of oxygen, is the first step in the joint pseudosplitting/dissociative adsorption mechanism.

The effect of particle size on the reversibility of lithiated nickel oxide electrodes.—In accord with their theory that semiconducting oxide electrodes should be reversible above the Neel temperature, Tseung and Bevan (3) found that $La_{0.5}Sr_{0.5}CoO_3$ [$LaCoO_3$ shows antiferro magnetic behavior below 100°K (17)] was reversible at room temperature, and that lithiated nickel oxide of ssa 12 m^2g^{-1} was reversible above 220°C. However, when high surface area (ssa 180 m^2g^{-1}) lithiated nickel oxide was tested, reversibility was shown only at 150°C although the apparent Neel point of nickel oxide of ssa 180 m^2g^{-1} is, according to Richardson and Milligan (8), less than 120°K. The predominance of peroxide production from massive lithiated nickel oxide cathodes at room temperature has also been noted by Yeager's group (18).

There is some dispute concerning the effect of particle size on the Neel temperature of nickel oxide. Richardson and Milligan (8), while finding that the position of the maximum in the susceptibility *vs.* temperature curve moved to lower temperatures with decreasing average particle size, concluded from neutron diffraction studies that the true Neel point of NiO was not changed and that the data could be explained by a change in magnetic environment for small crystallites. Later work by Cohen *et al.* (19) and Kawada and Kawai (20) agreed with the experimental results but attributed these to a shifting Neel point. Neel himself (21) explained the magnetic behavior of small particles of nickel oxide in terms of "superparamagnetism" and "superantiferromagnetism."

Of significance to the present work is that small particles ($<$100Å) of nickel oxide will show paramagnetism at room temperature. The average particle size diameter (PSD) of nickel oxide of ssa 180 m^2g^{-1} is 60Å and so it is necessary to explain why reversibility was not shown at room temperature in our experiments.

On examination of the distribution of particle sizes of the 180 m^2g^{-1} sample (Fig. 5) approximately 5% of the particles were of diameter greater than 200Å. A crystallite of this size will show the normal antiferromagnetic behavior of massive nickel oxide and would not be expected to facilitate side-on adsorption of oxygen at room temperature. Gross magnetic determinations and the isotopic exchange reactions will be relatively unaffected by these particles. In the electrochemical environment, however, the presence of particles which may only allow oxygen reduction to the peroxide via end-on [Pauling (22)] adsorption given by Eq. [2], will give rise to a mixed potential which will be less than a truly reversible potential from the four-electron reaction.

Isotopic exchange on low ssa lithiated nickel oxide.—The break in the Arrhenius plot for low surface area lithiated nickel oxide is explained by the antiferromagnetic-paramagnetic transition at the Neel temperature. Below 240°C the isotopic exchange rate falls and soon becomes unmeasurable. These findings agree with Winter (12) who suggested that adsorption on nickel oxide occurred as 2 O^- above the Neel point but O_2^- below this temperature. That the rate does not fall immediately to zero below the Neel point, but shows an exponential decline (Fig. 4), may again be related to the particle size distribution (see previous section). As crystallite diameter will be distributed normally about the mean particle size, the number of paramagnetic particles will exponentially decrease below the Neel point.

Conclusion

Gas phase and electrochemical data support the conclusion that the rate-determining step in the electrochemical reduction of oxygen in alkaline medium via reaction [2] is the dissociative adsorption of an oxygen molecule. This is in agreement with the joint pseudosplitting/dissociative adsorption theory of Goldstein and Tseung (6).

The effects of particle size on the Neel temperature and the reversibility of an electrode suggest that the electrochemical reduction of oxygen is more sensitive to the presence of large crystallites which will lead to a mixed potential and over-all irreversibility.

Acknowledgment

This work was supported by the Science Research Council.

Manuscript submitted April 5, 1977; revised manuscript received July 6, 1977. This was Paper 296 presented at the Philadelphia, Pennsylvania, Meeting of the Society, May 8-13, 1977.

Any discussion of this paper will appear in a Discussion Section to be published in the December 1978 JOURNAL. All discussions for the December 1978 Discussion Section should be submitted by Aug. 1, 1978.

REFERENCES

1. A. C. C. Tseung, B. S. Hobbs, and A. D. S. Tantram, *Electrochim. Acta* **15**, 473 (1970).
2. H. L. Bevan and A. C. C. Tseung, *ibid.*, **19**, 201 (1974).
3. A. C. C. Tseung and H. L. Bevan, *Electroanal. Chem. Interfacial Electrochem.*, **45**, 429 (1973).
4. U. R. Evans, *Nature (London)*, **218**, 602 (1968).
5. E. Yeager, Nat. Bur. Stand. Special Publ. 455, p. 203 (1976).
6. J. R. Goldstein and A. C. C. Tseung, *Nature (London)*, **222**, 869 (1969).
7. J. S. Griffiths, *Proc. R. Soc. London, Ser. A*, **235**, 23 (1956).
8. J. T. Richardson and W. O. Milligan, *Phys. Rev.*, **102**, 1289 (1956).
9. A. C. C. Tseung and H. L. Bevan, *J. Mater. Sci.*, **5**, 604 (1970).
10. S. J. Teichner, *Adv. Catal.*, **20**, 167 (1969).
11. J. Giner, J. M. Parry, S. Smith, and M. Turchan, *This Journal*, **116**, 1692 (1969).
12. E. R. S. Winter, *J. Catal.*, **6**, 35 (1966).
13. H. L. Bevan, PhD Thesis, The City University, London (1970).
14. J. O'M. Bockris and A. K. N. Reddy, "Modern Electrochemistry," Vol. 2, MacDonald, London (1970).
15. J. Giner, G. Holleck, and P. A. Malachesky, NASA Report CR-72999, chap. 3 (June 1971).
16. G. K. Boreskov, *Adv. Catal.*, **15**, 285 (1965).
17. R. R. Heikes, R. C. Miller, and R. Muzelsky, *Physica*, **30**, 1600 (1964).
18. D. Yore, A. Riga, R. Greef, and E. Yeager, *Electrochim. Acta*, **13**, 1351 (1968).
19. J. Cohen, K. M. Creer, R. Panthenet, and K. G. Srivastava, *J. Phys. Soc. Jpn.*, **17**, (suppl. B-1), 685 (1962).
20. T. Kawada and N. Kawai, *ibid.*, **17**, (Suppl. B-1), 691 (1962).
21. L. Neel, *ibid.*, **17**, (suppl. B-1), 676 (1962).
22. L. Pauling, *Nature (London)*, **203**, 182 (1964).

Ring Electrodes

Peter Pierini*[,1] **and John Newman***

Materials and Molecular Research Division, Lawrence Berkeley Laboratory, and Department of Chemical Engineering, University of California, Berkeley, California 94720

ABSTRACT

The primary and secondary current distributions and the primary resistance for ring electrodes are presented. Current distributions, including mass transfer effects, for various potential dependent heterogeneous kinetics are computed for a representative set of rotating-ring electrode geometries.

Rotating-ring electrodes are a common and useful device for the study of electrochemical systems. They have appeared individually and in conjunction with disks, spheres, and other rings. Ring electrodes have very thin concentration boundary layers at the inner or upstream edge of the electrode, so the limiting current densities are high in that region and infinite at the edge. The primary and secondary current distributions have large densities close to both the inner and outer edges; the primary distribution has infinite values at both edges. The ring electrode thus behaves very much like a short plane electrode in the wall of a wide flow channel, and in the limit of zero ring thickness becomes exactly such a plane electrode. Very thick rings demonstrate characteristics of disk electrodes, and in the limit of zero inner radius are exactly disk electrodes.

A rotating-ring electrode can simulate two of the classic tools used by electrochemical experimenters. A ring electrode can be fitted to practically any rotator used for disks, thus enabling an experimental investigation of processes that were previously studied in flow channels, which are more expensive and specialized pieces of equipment. The problems associated with end effects at the walls of the flow channel do not occur with the ring electrode. The current distributions on rings used as collectors in ring-disk, ring-sphere, and ring-ring systems are not radically different from that on solitary rings, so a detailed study of ring electrodes yields basic information which can be applied qualitatively to all the systems involving ring electrodes.

The asymptotic behavior of thick ring electrodes was experimentally investigated by Gregory and Riddiford (1,2) when they reported the effects of blocking off the center of a disk. Levich (3) provided an expression for the limiting current density distribution on ring electrodes, which was extended to show the average limiting current in a discussion of Gregory and Riddiford's work by Ibl (4). Dagunet (5) first and then Kornienko and Kishinevskii (6) used ring electrodes to study the effect of turbulence on the limiting current. Deslouis and Keddam (7) also measured limiting currents on rings in laminar, transitional, and turbulent flows, and compared their results favorably to the Levich equation for rings. The effect of adding a drag-reducing agent, Polyox, was examined by Deslouis *et al.* (8) with rotating-ring electrodes by the change in limiting current. Shabrang and Bruckenstein (9) experimentally determined the resistance of several ring electrodes by applying alternating current modulation techniques, and they also computed primary resistances by finite differences. Several theoretical studies on ring electrodes have been made of highly reversible heterogeneous reactions possessing potential independent kinetics. Rosner (10) presented calculations for kinetics which included the effect of the reactant concentration only, and he considered ring electrodes as partially blocked disks. Redox kinetics, which included both product and reactant, were analyzed by Albery and Bruckenstein (11) for the case of very thin rings. Matsuda (12) showed a method to compute current distributions for redox reactions on rings of any thickness. Similar work (13,14) can be found in the literature on ring-ring electrodes for rapid heterogeneous reactions where the inner ring is decoupled from the outer ring since the kinetics are not considered to be potential dependent.

Primary Current and Potential Distribution

The primary current distribution for a ring electrode can be easily computed following the method outlined by Miksis and Newman (15) for ring-disk electrodes. The technique involves the solution of Laplace's equation which Newman (16) reduced to an extremely useful (17) integral equation

$$\Phi_0(r) = \frac{2}{\pi\kappa_\infty}\int_{r_0}^{r_1} i(r')K\left(\frac{4rr'}{(r+r')^2}\right)\frac{r'dr'}{r+r'} \quad [1]$$

where Φ_0 is the ohmic potential drop between the surface of the ring electrode and a large counterelectrode which is far enough away from the working electrode so that it does not influence the current distribution, i is the normal component of the current density, K is an elliptic integral of the first kind (18). The use of Eq. [1] implies that the electric conductivity κ_∞ is constant and there are no concentration gradients in the region. The primary current distribution assumes Φ_0 to be constant and allows no kinetic effects. Figure 1 shows the primary current distributions for several values of the geometric parameter r_0/r_1. As r_0/r_1 approaches unity, the current distribution begins to look like the primary current on a plane electrode which was given by Wagner (19) and displayed in Fig. 3 of Parrish and Newman (20)

$$\frac{i}{i_{avg}} = \frac{1}{\pi}\left[\frac{x}{L} - \left(\frac{x}{L}\right)^2\right]^{-1/2} \quad [2]$$

where x is the distance along the plane electrode and L is the length of the electrode. When the geometric parameter tends to zero, the ring assumes essentially the same primary distribution as a disk (21) with the exception of an infinite current density at the inner edge of the ring. The primary resistance of the ring electrode R_r is given in Fig. 2. The solid curve is the result of our calculations. The dashed curve and the bracketed data points are from Shabrang and Bruckenstein (9). The ordinate of Fig. 2 was chosen by applying the criteria used in reporting thermodynamic data such as activity coefficients which have large changes in value with relatively small changes in concentration (22). This allows the ring resistance to be interpolated from the plot for thin rings easily. The abscissa was chosen to show the asymptotic behavior of a ring resistance as it approaches a disk. The rela-

* Electrochemical Society Active Member.

[1] Present address: Department of Chemical and Biological Engineering, Arizona State University, Tempe, Arizona 85281.

Key words: primary current, secondary current, primary resistance, current distribution, mass transfer.

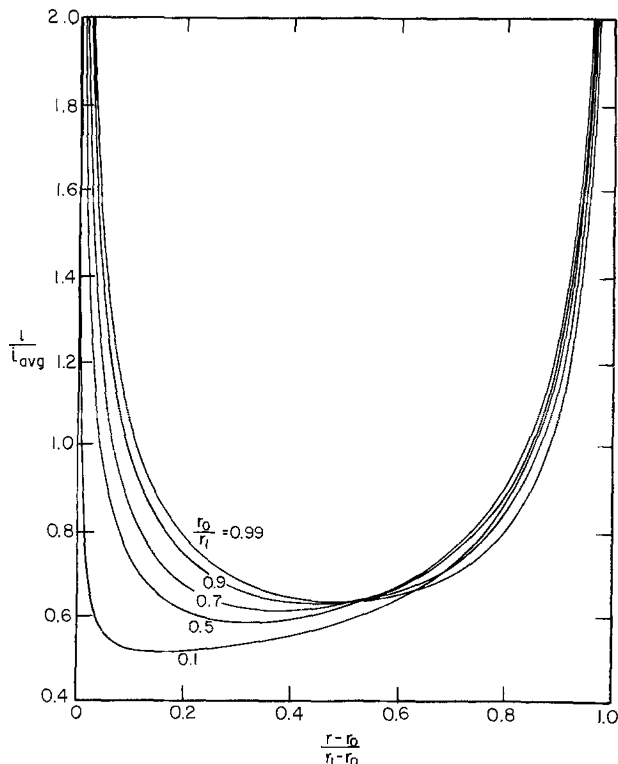

Fig. 1. The primary current distribution on ring electrodes

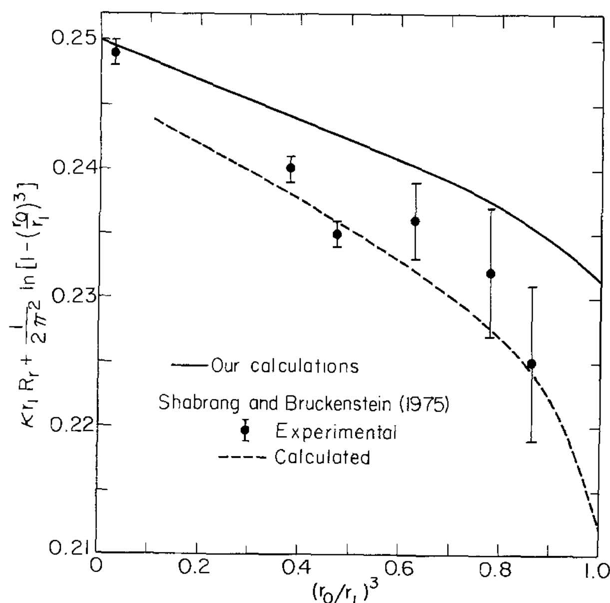

Fig. 2. Resistance of current flow to a ring electrode with a primary current distribution.

tive difference between the data points and the finite difference calculations (9) and our calculations are exaggerated by the ordinate. However it is difficult to approach a primary distribution using alternating current techniques unless frequencies can be extrapolated to infinity. The small effect of a large laboratory-size cell rather than the infinitely dimensioned cell used in computing the resistance could also resolve some of the difference between the data and our calculations. The same sort of difficulty in getting good agreement between the Levich limiting current and measured limiting currents for thin rings was encountered by Deslouis and Keddam (7). We feel that the method of embedding essential singularities as employed in the method of Miksis and Newman (15) is superior to a finite difference approximation. The resistance varies from that of a disk electrode to large values for very thin rings, which is given by (15)

$$\kappa_\infty r_1 R_r + \frac{1}{2\pi^2} \ln\left(1 - \left(\frac{r_o}{r_1}\right)^3\right) = \frac{\ln 96}{2\pi^2} = 0.2312 \quad [3]$$

Equation [3] is the asymptotic value of the ring resistance as the ring width goes to zero, and is the value of the ordinate variable of the solid curve at the right-hand side of Fig. 2 (See Appendix I for the analytical development of Eq. [3].) Equation [1] is also used to compute the variation in the ohmic drop extrapolated to the surface of the ring for nonuniform potential distributions, in the same manner as for ring disks (17).

The Concentration Boundary Layer

A high Schmidt-number formulation of the convective diffusion equation appropriate for binary electrolytes and minor reacting components in a solution with an excess of supporting electrolyte, where migration effects can be safely ignored, has been used in most of the previous studies involving potential independent heterogeneous kinetics (10, 12-14). An integral equation has proven useful for computing analytic and numerical results. The same equations and approach for the concentration boundary layers which were recently applied by Pierini and Newman (17) to ring-disk electrodes are used here for computing the surface concentration when ohmic effects and potential dependent kinetics are included. The results of Levich (3) are easily reproduced with the integral equation to yield

$$\left.\frac{\partial c_R}{\partial y}\right|_{y=0} = \frac{r}{\Gamma(4/3)}\left(\frac{a\nu}{3D_R}\right)^{1/3}\left(\frac{\Omega}{\nu}\right)^{1/2}\frac{c_{R,\infty} - c_{R,0}}{(r^3 - r_o^3)^{1/3}} \quad [4]$$

Figure 3 shows limiting current distributions for rings of various thicknesses computed with Eq. [4]. The thin rings are similar to the limiting current for plane electrodes shown in Fig. 3 of Parrish and Newman (20) while the thick rings have fairly uniform distributions except in the central regions.

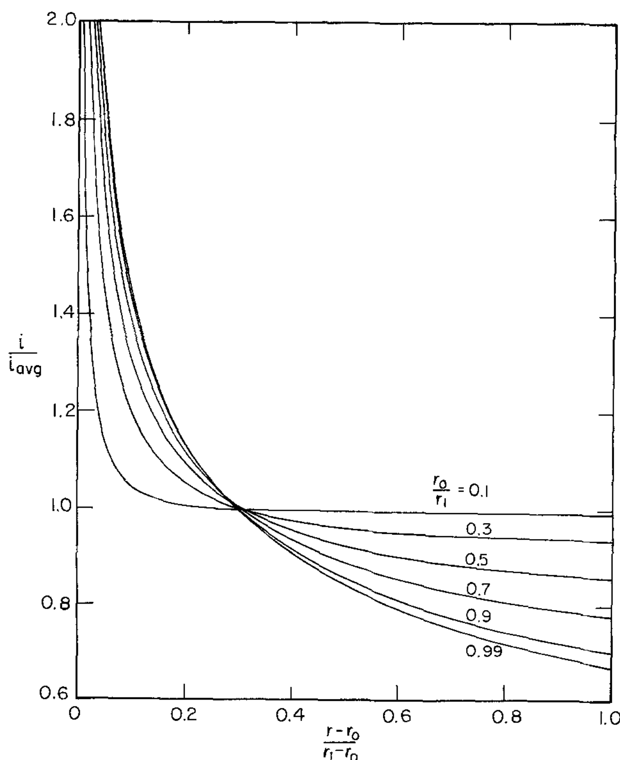

Fig. 3. The limiting current distribution on ring electrodes

Kinetics

A single electrode reaction

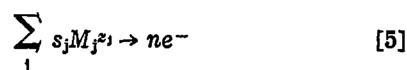

$$\sum_j s_j M_j^{z_j} \rightarrow ne^- \qquad [5]$$

is chosen as the basis for the potential dependent heterogeneous kinetics to demonstrate the manner in which the current distribution varies between the ohmically limited (Fig. 1) and the mass transfer-controlled (Fig. 3) distributions. The applied voltage V can be decomposed (23) as follows

$$V = \Phi_o + U + \eta_s + \eta_c \qquad [6]$$

where Φ_o is the local ohmic potential drop extrapolated to the ring surface and U is the open-circuit potential calculated with the bulk concentrations. The surface overpotential η_s is given implicitly by the kinetic expression

$$i = i_{o,\infty} \prod_j \left(\frac{c_{j,0}}{c_{j,\infty}}\right)^{\gamma_j} \left[\exp\left(\frac{\alpha Z F}{RT}\eta_s\right) - \exp\left(\frac{-\beta Z F}{RT}\eta_s\right)\right] \qquad [7]$$

and the concentration overpotential takes the form (24)

$$\eta_c = \frac{-RT}{ZF}\left[\sum_j \ln\left(\frac{c_{j,\infty}}{c_{j,0}}\right) - t\left(1 - \frac{c_{R,0}}{c_{R,\infty}}\right)\right] \qquad [8]$$

This basic equation covers a variety of situations, such as deposition from a binary electrolyte and redox and deposition reactions with supporting electrolyte.

Results

The problem as stated can be solved numerically (17, 20, 21) with the basic parameters r_o/r_1, α, β, λ_i, t, Z, D_i/D_R

$$J = \frac{i_{o,\infty} r_1 Z F}{RT \kappa_\infty} \qquad [9]$$

$$N = -\left(\frac{r_1^2 \Omega}{\nu}\right)^{1/2}\left(\frac{a\nu}{3D_R}\right)^{1/3} \frac{nZF^2 D_R c_{R,\infty}}{s_R R T (1-t)} \qquad [10]$$

$$\delta = |i_{avg}| \frac{r_1 Z F}{RT} \qquad [11]$$

where the limiting reactant has been subscripted as R. J can be thought of as a dimensionless exchange current density, and N is the dimensionless stirring rate. The concentration boundary layer grows thinner as N gets larger; when N is infinite the boundary layer has zero thickness and the concentrations at the surface of the electrode are uniform and equal to the bulk concentrations.

For examples, three ring geometries are chosen. The cases in which r_o/r_1 is respectively 0.5 and 0.7 represent situations that characteristically behave like rings, that is, they do not tend to simulate either a disk or a plane electrode. The case of r_o/r_1 equal to 0.9 can be easily compared to plane electrodes.

Secondary current distribution.—When N is infinite and the concentration effects may be ignored, the secondary current distribution is achieved. For small surface overpotentials Eq. [7] is linearized to read

$$i = (\alpha + \beta) J \frac{\kappa_\infty}{r_1} \eta_s \qquad [12]$$

The average current density is much smaller than the characteristic exchange current density in this case. Figure 4 shows how a ring with r_o/r_1 equal to 0.5 behaves over a range of kinetic parameters. The distribution varies from a basically uniform current when kinetics control, to the primary distribution when ohmic effects dominate.

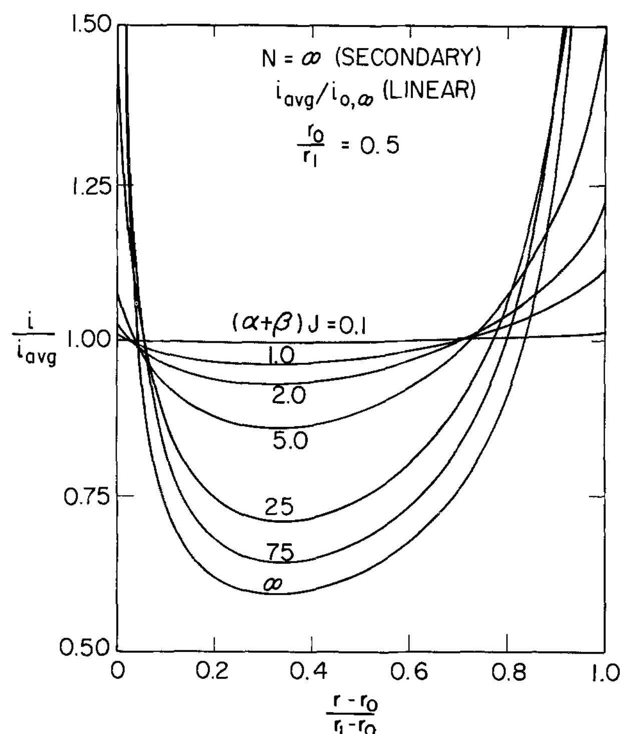

Fig. 4. Secondary current distribution on a ring electrode for linear kinetics. $|i_{avg}|i_o$ is equal to zero.

Tafel polarization occurs when one of the exponential terms in Eq. [4] is small enough to be dropped. Then for a cathodic process the polarization equation may be written

$$\eta_s = -\frac{RT}{\beta ZF}[\ln(-i) - \ln(i_{o,\infty})] \qquad [13]$$

and the characteristic parameter is

$$\beta\delta = \frac{\beta ZF}{RT}\frac{r_1|i_{avg}|}{\kappa_\infty} \qquad [14]$$

The current distribution now depends only on the magnitude of the average current density, and the exchange current density has no effect. Figure 5 for Tafel kinetics is similar to Fig. 4. The change in the shape of the curves is principally due to the difference in the geometric ratio r_o/r_1. Both cases go to a primary distribution as the kinetic parameter goes to infinity, and the effect of the radii ratio can be clearly seen in Fig. 1 for the primary distributions.

Concentration and kinetic effects.—Mass transfer effects must be taken into account for finite values of the dimensionless stirring rate N. Again the situation in which the average current density is much greater than the exchange current density is examined in Fig. 6, where one of the exponential terms in Eq. [7] may be neglected. The reaction is very slow as characterized by the zero value of J, and is considered to have Tafel kinetics but with concentration dependence in contrast to the Tafel kinetics described by Eq. [13] and shown in Fig. 5. The effect of the concentration boundary layer begins to dominate as the controlling factor as the fraction of the limiting current is increased. The behavior of the current distribution at the outer edge of the ring is very similar to that of both disk electrodes (23) and plane electrodes (20) in exhibiting a maximum.

Curves for deposition kinetics in which both terms of Eq. [7] make a contribution but where there is no back-reaction are shown in Fig. 7. This particular reaction, with $J = 1$, would still be considered slow, but

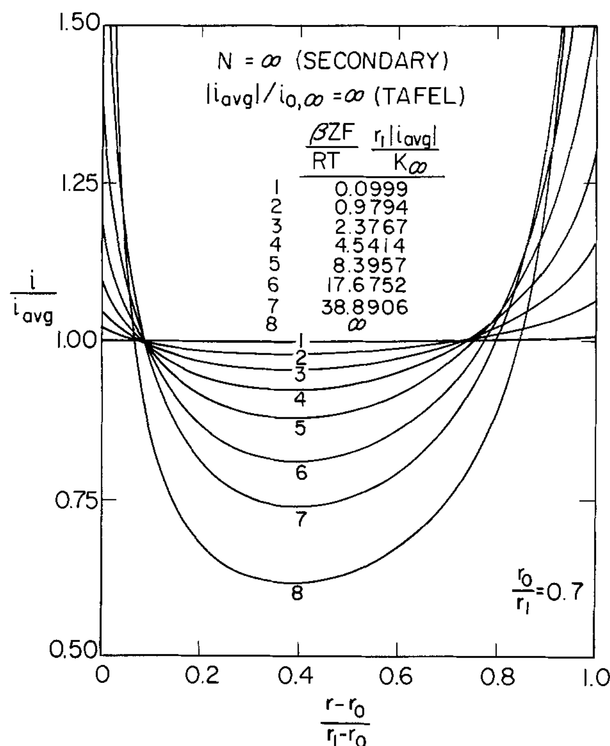

Fig. 5. Secondary current distribution on a ring electrode for Tafel kinetics.

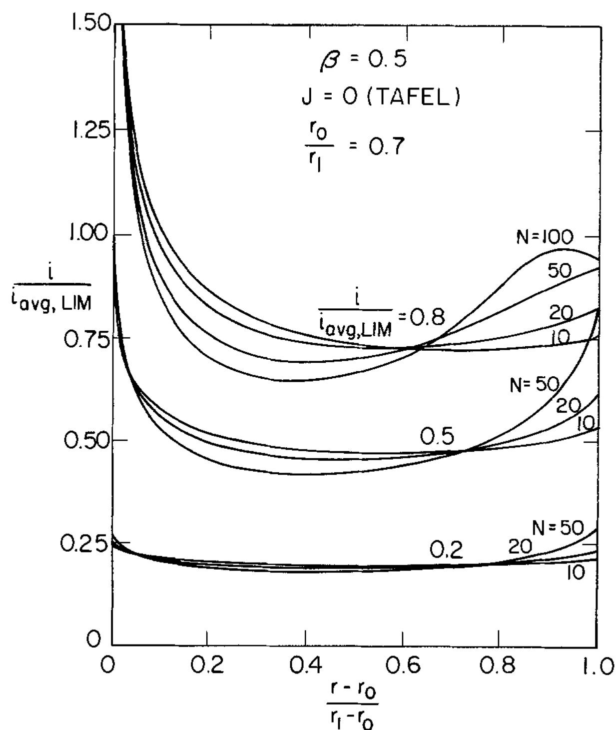

Fig. 6. Current distribution on a ring electrode for Tafel kinetics where $|i_{avg}| >> i_{o,\infty}$ but N is finite and mass transfer effects must be taken into account.

it is more reversible than the previous example as indicated by a larger value of J. The distributions appear to be more disk-like, primarily due to the smaller r_o/r_1, while the differences between the maxima and minimum in the distribution are enhanced by the kinetics.

As a final example, a very fast redox reaction was chosen in conjunction with a very thin ring. The interesting feature of Fig. 8 is the comparison to the limiting current curve (dashed line). The mass transfer is dominant over a wide range of currents influencing the shape of the curves. Also the local cur-

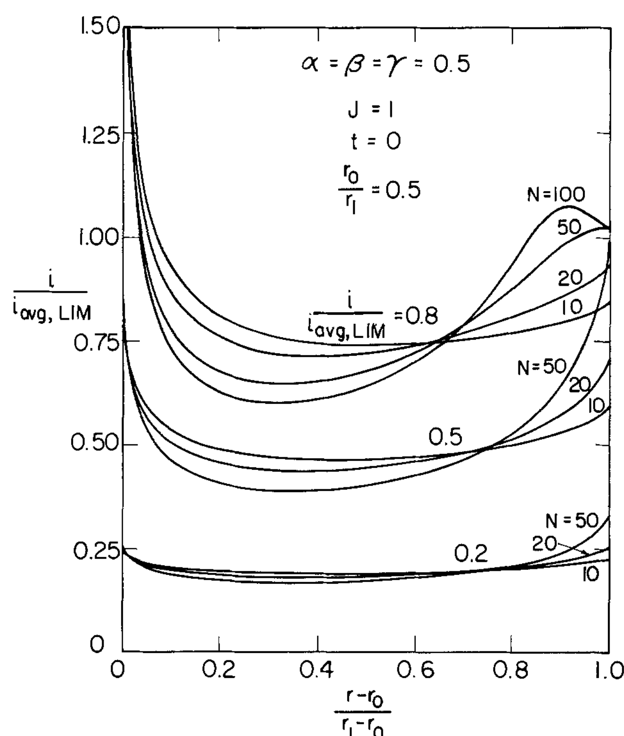

Fig. 7. Current distribution on a ring electrode for product-independent or deposition kinetics with an excess of supporting electrolyte and with mass transfer effects.

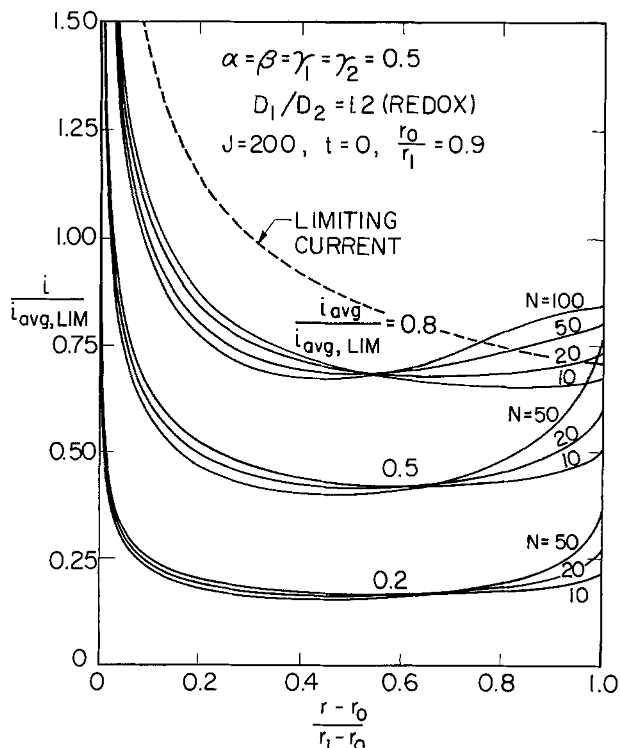

Fig. 8. Current distribution on a ring electrode for product-dependent or redox-type kinetics with an excess of supporting electrolyte with mass transfer effects. Dashed line is the limiting current.

rent densities near the trailing edge of the ring are driven above the local limiting current densities, a situation which is similar to disks (23) and planes (20). Since the ring is very thin, the distributions can be compared to those of Fig. 4 of Parrish and Newman (20), which is a plane electrode with Tafel kinetics.

Landolt, Mueller, and Tobias (25) assessed the design considerations for a cell to study electrochemical

machining processes. The rotating disk electrode and concentric rotating cylinders were deemed unfeasible due to the difficulty in maintaining reasonable cell voltages and because of the radial dependence of resistance and characteristic length. A flow channel was shown to have a primary voltage drop of 50V with a 100 A/cm^2 current for a solution with a specific conductance of 0.1 Ω/cm and an interelectrode gap of 0.5 mm. An equivalent primary voltage with the same solution and operating conditions can be obtained with a ring electrode having an inner radius of 0.2480 cm and a width of 0.0275 cm, dimensions well within practical machining considerations. This particular design required r_o/r_1 to be 0.9, which is the geometric ratio used for the redox reaction shown in Fig. 4. Alternatively the resistance and one length could be specified; Fig. 2 would then provide the remaining length, thus enabing the characteristic length to be varied and the resistance to be fixed. Turbulent flow can be maintained with most commercially available rotators by keeping the inner ring radius greater than 1 cm for common electrochemical machining solutions. Ring electrodes seem feasible to study high current density processes with a smaller capital investment than a thin gap flow channel.

Acknowledgments

This work was supported by the Division of Physical Research of the United States Energy Research and Development Administration.

Manuscript submitted May 2, 1977; revised manuscript received Aug. 15, 1977.

Any discussion of this paper will appear in a Discussion Section to be published in the December 1978 JOURNAL. All discussions for the December 1978 Discussion Section should be submitted by Aug. 1, 1978.

Publication costs of this article were assisted by the University of California.

APPENDIX

The Asymptotic Value of the Primary Resistance of Thin Ring Electrodes

The asymptotic value of the primary resistance of ring electrodes as the geometric parameter r_o/r_1 goes to unity can be determined analytically. An order of magnitude analysis of Laplaces' equation shows that the terms associated with the effect of curvature in the radial direction are small. This means that the physical situation to be analyzed is an analog of the finite width plane electrode embedded in an insulator treated by Wagner (19). Therefore the detailed variation of the current density can be expressed as

$$i(r) = \frac{r_1 - r_o}{2\sqrt{(r_1 - r)(r - r_o)}} \quad \text{[A-1]}$$

where the total current to the ring is

$$I_r = 2\pi \int_{r_o}^{r_1} i(r) r dr = \frac{2\pi}{2}(r_1 - r_o)(r_1 + r_o) \quad \text{[A-2]}$$

The potential drop for the current I_r to the ring is then computed by integrating Eq. [A-1] with Eq. [1] making use of the property of the complete elliptic integral of the first kind that

$$K\left(\frac{4rr'}{(r+r')^2}\right) \rightarrow -\frac{1}{2}\ln\left(\frac{r-r'}{r+r'}\right)^2 \Big/ 16 \quad \text{[A-3]}$$

as

$$\frac{4rr'}{(r+r')^2} \rightarrow 1 \quad \text{[A-4]}$$

This yields after manipulation

$$\Phi_o(r) = -\frac{r_2 - r_1}{4\pi\kappa} \int_{-1}^{1} \ln\left[\frac{(z-z')^2}{64}\left(\frac{r_1 - r_o}{r_1 + r_o}\right)^2\right]\frac{dz'}{\sqrt{1-z'^2}} + \frac{r_2 - r_1}{\pi\kappa}\int_{-1}^{1}\left[\frac{r'}{r+r'}K\left(\frac{4rr'}{r+r'}\right) + \frac{1}{4}\ln\left(\frac{z-z'}{8}\frac{r_1 - r_o}{r_1 + r_o}\right)^2\right]\frac{dz'}{\sqrt{1-z'^2}} \quad \text{[A-5]}$$

where the variables r and y are related by

$$z = \frac{2r - r_1 - r_o}{r_2 - r_1} \quad \text{[A-6]}$$

Because this is the primary distribution, this potential must actually be constant across the ring, and evaluation gives

$$\Phi_o(r) \approx \frac{r_1 - r_o}{2\kappa}\ln\frac{16(r_1 + r_o)}{r_1 - r_o} \quad \text{[A-7]}$$

and the resistance of thin rings is then given by

$$\kappa r_1 R_r + \frac{1}{2\pi^2}\ln\frac{r_1 - r_o}{r_1} = \frac{\ln 32}{2\pi^2} \quad \text{[A-8]}$$

This equation shows explicitly the manner in which the value of R_r increases to infinity as the ring width goes to zero. After transformation to the variable plotted in Fig. 2 is made, the right side of Eq. [A-8] yields the ordinate value of the solid curve at the right side of Fig. 2.

LIST OF SYMBOLS

English Characters

a	0.51023
$c_{R,\infty}$	concentration of limiting reactant in the bulk solution, mole/cm^3
$c_{R,0}$	concentration of limiting reactant at the electrode surface, mole/cm^3
D_j	diffusion coefficient of the jth species, cm^2/sec
e^-	symbol for an electron
F	Faraday s constant, 96,487 C/equiv.
I_r	total ring current, A
i	normal current density at the electrode surface, A/cm^2
i_{avg}	average current density on the ring electrode, A/cm^2
$i_{avg,LIM}$	average limiting current density on the ring electrode, A/cm^2
$i_{o,\infty}$	characteristic exchange current density, A/cm^2
J	dimensionless exchange current density
j	subscript variable
K	complete elliptic integral of the first kind
L	length of planar electrode, cm
M_j	chemical symbol of the jth species
N	dimensionless stirring rate
n	number of electrons in reaction
R	universal gas constant, 8.3143 J/mole-°K
R_r	effective primary resistance of a ring electrode, Ω
r	radial coordinate, cm
r_o	inner ring radius, cm
r_1	outer ring radius, cm
s_j	stoichiometric coefficient of the jth species
T	absolute temperature, °K
t	transference number of reactant
U	open-circuit potential, V
V	potential applied between the ring and a distant counter electrode, V
x	position from leading edge of plane electrode, cm
y	normal distance from surface of ring, cm
Z	$-n$ or $-z + z_-/(z_+ - z_-)$
z	$(2r - r_o - r_1)/(r_1 - r_o)$
z_j	charge number of j the species

Greek Characters

α, β, γ_j	kinetic parameters in Eq. [7]
δ	dimensionless average current density
η_c	concentration overpotential, V

η_s surface overpotential, V
κ_∞ electrical conductivity of the bulk solution, Ω^{-1}-cm^{-1}
ν kinematic viscosity, cm^2/sec
Φ_0 ohmic potential extrapolated to the electrode surface, V
Ω rotation speed, rad/sec

REFERENCES

1. D. P. Gregory and A. C. Riddiford, *J. Chem. Soc.*, **731**, 3756 (1956).
2. D. P. Gregory and A. C. Riddiford, *This Journal*, **107**, 950 (1960).
3. V. G. Levich, "Physiochemical Hydrodynamics," p. 107, Prentice-Hall Inc., New York (1962).
4. N. Ibl, *This Journal*, **108**, 610 (1961).
5. M. Dagunet, *Int. J. Heat Mass Transfer*, **11**, 1581 (1968).
6. T. L. Kornienko and M. Kh. Kishinevskii, *Electrokhimiya*, **8**, 1759 (1971).
7. C. Deslouis and M. Keddam, *Int. J. Heat Mass Transfer*, **16**, 1763 (1973).
8. C. Deslouis, I. Epelboin, B. Tribollet, and L. Viet, *Electrochim. Acta*, **20**, 909 (1975).
9. M. Shabrang and S. Bruckenstein, *J. Electroanal. Chem.*, **65**, 155 (1975).
10. D. E. Rosner, *This Journal*, **113**, 624 (1966).
11. W. J. Albery and S. Bruckenstein, *Trans. Faraday Soc.*, **62**, 2596 (1966).
12. H. Matsuda, *J. Electroanal. Chem.*, **35**, 77 (1972).
13. V. Y. Filinovsky, I. V. Kadija, B. Z. Nikolić, and M. B. Nadić, *J. Appl. Electrochem.*, **1**, 1 (1974).
14. V. Y. Filinovsky and Y. V. Pleskov, *Prog. Surf. Membr. Sci.*, **10**, 27 (1976).
15. J. J. Miksis, Jr., and J. Newman, *This Journal*, **123**, 1030 (1976).
16. J. Newman, *Electroanal. Chem.*, **6**, 326 (1973).
17. P. Pierini and J. Newman, *This Journal*, **124**, 701 (1977).
18. "Handbook of Mathematical Functions," M. Abramowitz and I. A. Stegun, Editors, p. 608, National Bureau of Standards, Washington, D.C. (1964).
19. C. Wagner, *This Journal*, **98**, 116 (1951).
20. W. R. Parrish and J. Newman, *ibid.*, **116**, 169 (1969).
21. J. Newman, *ibid.*, **113**, 501 (1966).
22. G. N. Lewis and M. Randall, revised by K. S. Pitzer and L. Brewer, "Thermodynamics," p. 326, McGraw-Hill Book Co., New York (1961).
23. J. Newman, *This Journal*, **113**, 1235 (1966).
24. J. Newman, *Intern. J. Heat Mass Transfer*, **10**, 983 (1967).
25. D. Landolt, R. H. Muller and C. W. Tobias, *This Journal*, **116**, 1384 (1969).

Variational Approximations to Current Distribution Problems

II. Rectilinear Electrodes and Baffles

S. H. Glarum

Bell Laboratories, Murray Hill, New Jersey 07974

ABSTRACT

Current distribution problems for the flat-strip electrode and the rectangular electrolytic cell with an arbitrary distribution of cathodic elements in a plane are analyzed using a previously formulated variational integral. High impedance baffles permitting the control of macrocurrent distributions are described, equations for their design derived, and several elementary examples analyzed.

In a preceding paper we discussed the use of variational approximations for the analysis of current distribution problems at the rotating-disk electrode (1). The present discussion focuses upon the application of the variational function previously derived to rectilinear geometries, more closely akin to practical electroplating configurations. We treat first the case of an isolated flat-strip electrode, and find a solution for the current density distribution in terms of a superposition of orthogonal polynomials. Next we consider the more general problem of a rectangular electrolytic cell with an arbitrary electrode distribution in a cathodic plane and insulating sidewalls or periodic boundary conditions. Finally, we address the very practical problem of controlling current distributions on a macroscopic scale. High impedance baffles appear to be attractive structures for achieving this objective. General design equations are derived, and several low order baffle designs are analyzed.

The Flat-Strip Electrode

The problem to be solved is depicted in Fig. 1. A flat-strip electrode with width 2a is flushly embedded in an infinite insulating plane. The strip is either sufficiently long or boundary conditions in the y direction are such that the potential is independent of y. A surface $s(x, z)$ to be defined, in the half-space containing electrolyte lies at zero potential, while the electrode is at a potential ϕ_0. This problem has been previously analyzed by Wagner, using a different approach (2).

We begin, as in our treatment of the rotating-disk electrode, with the coordinate transformation

$$z = a\xi\eta$$
$$x^2 = a^2(1 + \xi^2)(1 - \eta^2) \quad [1]$$

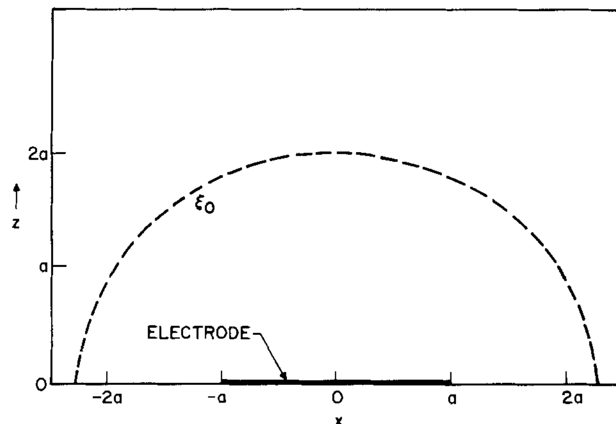

Fig. 1. The flat-strip electrode

Key words: current distribution, high impedance baffles, variational analysis.

Within the electrolyte $\nabla^2\phi = 0$, and Laplace's equation becomes

$$\left[(1-\eta^2)\frac{\partial^2\phi}{\partial\eta^2} - \eta\frac{\partial\phi}{\partial\eta} \right] + \left[(1+\xi^2)\frac{\partial^2\phi}{\partial\xi^2} + \xi\frac{\partial\phi}{\partial\xi} \right] = 0 \quad [2]$$

Letting

$$\phi = F(\eta)G(\xi) \quad [3]$$

a separation of variables gives

$$(1-\eta^2)\frac{\partial^2 F}{\partial\eta^2} - \eta\frac{\partial F}{\partial\eta} + n^2F = 0$$

$$(1+\xi^2)\frac{\partial^2 G}{\partial\xi^2} + \xi\frac{\partial G}{\partial\xi} - n^2G = 0 \quad [4]$$

where n^2 is the constant of separation. The further substitutions

$$\eta = \cos\alpha$$

$$\xi = \sinh\beta \quad [5]$$

reduce these equations to

$$\frac{\partial^2 F}{\partial\alpha^2} + n^2F = 0$$

$$\frac{\partial^2 G}{\partial\beta^2} - n^2G = 0 \quad [6]$$

The boundary condition at the insulating surface

$$\left(\frac{\partial F}{\partial\eta}\right)_{\eta=0} = 0 \quad [7]$$

requires that n be an even integer. At the surface defined by $\xi = \xi_o$ we shall assume ϕ vanishes (Fig. 1). The resulting solution for ϕ is therefore

$$\phi^{(n)} = c_nT_n(\eta)\frac{\sinh[n(\sinh^{-1}\xi_o - \sinh^{-1}\xi)]}{\sinh[n\sinh^{-1}\xi_o]} \quad [8]$$

where

$$T_n(\eta) = \cos[n\cos^{-1}\eta] \quad [9]$$

is a Chebyshev polynomial of even order and c_n is a constant. The general solution for the strip electrode is thus

$$\phi = \sum_{n=0,2,4\ldots} c_nT_n(\eta)\frac{\sinh[n(\sinh^{-1}\xi_o - \sinh\xi)]}{\sinh[n\sinh^{-1}\xi_o]} \quad [10]$$

This function satisfies Laplace's equation in the bulk, and meets all boundary conditions except those at the electrode surface, which remain to be specified.

The linear coefficients may be evaluated by variational analysis. Our general variational function is (1)

$$W = \kappa_o\int d\tau\nabla\phi\cdot\nabla\phi + 2\int dsf(s)\int_o^{\phi_o-\phi} d\theta F(\theta) \quad [11]$$

where κ_o is the bulk electrolyte conductivity, $F(\theta)$ is an overpotential function, the first integral is over the electrolyte volume, and the second is over its bounding surface. The function $f(s)$ vanishes on insulating surfaces, and may be set equal to unity when the overpotential depends only upon local current density. If bulk concentration gradients are significant, $f(s)$ must be found from the simultaneous solution of hydrodynamic and electrical expressions.

For the particular case of linear polarization

$$F(\theta) = \theta/z \quad [12]$$

z being the surface impedance of the electrode in units Ω-cm². Because $\nabla^2\phi = 0$ and the normal derivative $\partial\phi/\partial n$ vanishes on the insulating boundary, the variational function reduces to an integral over the electrode surface

$$W = 2a\int_o^1 \frac{\eta d\eta}{(1-\eta^2)^{1/2}}\left[\kappa_o\phi\frac{\partial\phi}{\partial n} + \frac{1}{z}(\phi_o-\phi)^2\right] \quad [13]$$

The coefficients c_n are found by setting

$$\partial W/\partial c_n = 0 \quad [14]$$

This results in the set of linear equations

$$\Gamma g_nc_n + \sum_{n'} K_{nn'}c_{n'} = K_{On}\phi_o \quad [15]$$

where

$$\Gamma = \pi\kappa_o z/4a$$

$$g_n = n(1+\delta_{n,O})\coth[n\,\text{sech}^{-1}\xi_o]$$

$$K_{nn'} = \int_O^1 d\eta\,\eta(1-n^2)^{-1/2}T_n(\eta)T_{n'}(\eta) \quad [16]$$

Finally, the current density distribution over the strip is given by

$$\vartheta(\eta) = (1/z)[\phi_o - \Sigma c_nT_n(\eta)] \quad [17]$$

Equations [15]-[17] are equivalent to those previously derived for the rotating-disk electrode. The dimensionless parameter Γ is again the ratio of the characteristic throwing distance of the electrolyte-electrode combination, $\kappa_o z$, to the electrode's dimension. When Γ is large the current distribution becomes uniform, and when small it approaches the primary distribution. The matrix $K_{nn'}$, which couples the basis functions, also involves integrals of a set of orthogonal basis functions. In this instance, however, they are Chebyshev instead of Legendre polynomials.

The expressions for the flat-strip and rotating-disk electrodes are sufficiently similar to make further detailed discussion repetitious. By analogy with disk calculations, a low order polynomial accurately describes the current distribution when current variations are small (<10%). Wagner has derived a logarithmic expression also accurate in this regime (2). If larger variations are encountered, both the procedure described by Wagner and that presented here require more extensive numerical computations. Newman's disk results indicate that 10 or more polynomial terms are needed to approximate a primary distribution (3), while Wagner's approach requires the solution of a like number of simultaneous linear equations.

The Rectangular Electrolytic Cell

We shall next examine the rectangular electrolytic cell (Fig. 2). Bounding planes at $x = \pm a$ and $y = \pm b$ are insulating, and plane $z = l_o$ is taken to be an equipotential surface of zero potential. An arbitrary cathodic surface distribution, $f(x,y)$, is assumed for the plane $z = 0$. The insulating planes may represent either real surfaces or planes partitioning a large

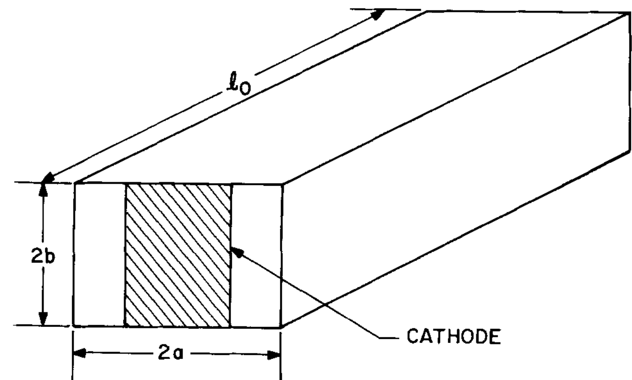

Fig. 2. The rectangular electrolytic cell

assembly of parallel cells. We shall, for convenience only, assume $f(x,y)$ to be symmetric in x and y.

A particular solution for ϕ satisfying all requirements except those at the cathodic plane is

$$\phi^{(m,n)} = \cos\left(\frac{m\pi x}{a}\right)\cos\left(\frac{n\pi y}{b}\right)\frac{\sinh[\lambda(l_o - z)]}{\sinh(\lambda l_o)} \quad [18]$$

where

$$\lambda = \left[\left(\frac{m\pi}{a}\right)^2 + \left(\frac{n\pi}{b}\right)^2\right]^{1/2} \quad [19]$$

and m and n are integers. A general solution is given by a linear combination of these solutions with coefficients c_{mn}. Since ϕ satisfies Laplace's equation in the bulk and all boundary conditions except those at the cathodic plane, the variational function reduces to an integral over this plane. The coefficients c_{mn} correspond to the Fourier components of the current density distribution function. If $f(x,y) = f(x)$ only $(n = 0)$, and a linear polarization function is assumed (Eq. [12]), use of the variational integral yields the set of linear equations

$$\Gamma g_m c_m + \sum_{m'} K_{mm'} c_{m'} = K_{0m}\phi_o \quad [20]$$

with

$$\Gamma = \pi\kappa_0 z/2a$$

$$g_m = (1 + \delta_{m,0})\, m \coth(m\pi l_o/a)$$

$$K_{mm'} = \frac{1}{2a}\int_{-a}^{a} dx\, f(x)\cos\left(\frac{m\pi x}{a}\right)\cos\left(\frac{m'\pi x}{a}\right) \quad [21]$$

The similarity of these equations with the rotating-disk and flat-strip expressions reveals how certain obvious limiting cases follow. Thus, if $f(x) = 1$, the matrix $K_{mm'}$ is diagonal and $c_m = 0$ for $m \neq 0$, giving a uniform current distribution. A uniform distribution is also achieved by making the diagonal elements large, *i.e.*, by increasing the throwing distance of the bath, $\kappa_0 z$, or decreasing the anode-cathode separation, l_o.

The Baffled Rectangular Cell

The control of current distributions, either to obtain more uniform electrodeposits or to plate selectively upon cathodic surfaces, is a high priority technological problem. One approach is through the use of baffles composed of chemically inert, insulating material to direct current flow. An important class of baffling problems can be treated by compounding two rectangular electrolytic cells (Fig. 3). The geometry and boundary conditions are those of the previous problem except that at a distance l from the cathodic plane a baffle with a spatially varying conductance function is interposed. A perforated panel, immersed in electrolyte, with holes of varying density and/or radii would be one realization of such a baffle.

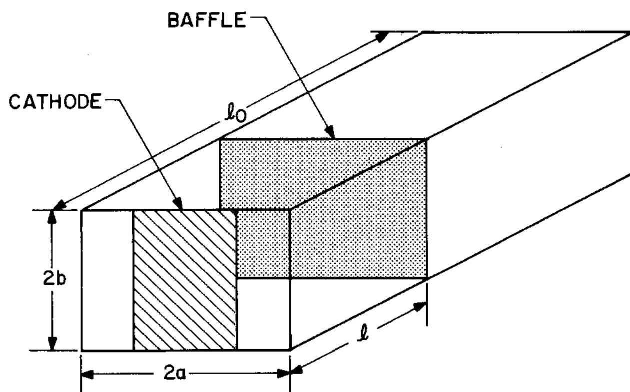

Fig. 3. The baffled rectangular cell

For convenience we shall again neglect variations in the y direction. The potential in the anodic compartment may be expressed as

$$\phi_A = \sum a_m \cos\left(\frac{m\pi x}{a}\right)\frac{\sinh\frac{m\pi}{a}(l_o - z)}{\sinh\frac{m\pi}{a}(l_o - l)} \quad [22]$$

while in the cathodic compartment

$$\phi_C = \sum b_m \cos\left(\frac{m\pi x}{a}\right)\frac{\sinh(m\pi z/a)}{\sinh(m\pi l/a)} + \sum c_m \cos\left(\frac{m\pi x}{a}\right)\frac{\sinh\frac{m\pi}{a}(l - z)}{\sinh(m\pi l/a)} \quad [23]$$

The coefficients have been chosen so that

$$\phi_A(z = l_o) = 0$$

$$\phi_A(z = l) = \sum a_m \cos(m\pi x/a)$$

$$\phi_C(z = l) = \sum b_m \cos(m\pi x/a)$$

$$\phi_C(z = 0) = \sum c_m \cos(m\pi x/a) \quad [24]$$

Implicitly the baffle is of zero thickness, but mathematically we require only that the normal current distributions on each baffle face be identical.

Let us first construct the variational function for the anodic compartment

$$W_A = \int_{-a}^{a} dx \left\{ \kappa_0\phi_A\frac{\partial\phi_A}{\partial n} + \kappa(x)[\phi_A - \phi_C]^2 \right\}_{z=l} \quad [25]$$

where κ_0 is the electrolyte conductivity and $\kappa(x)$ is the baffle conductance function. This expression is to be minimized with respect to variations of ϕ_A only, that is the coefficients a_m. The required conditions are

$$f_m a_m + \sum B_{mm'}(a_{m'} - b_{m'}) = 0 \quad [26]$$

where

$$f_m = (1 + \delta_{m,0})\left(\frac{m\pi}{2a}\right)\coth\left[\frac{m\pi}{a}(l_o - l)\right]$$

$$B_{mm'} = \frac{1}{2a}\int_{-a}^{a} dx\frac{\kappa(x)}{\kappa_0}\cos(m\pi x/a)\cos(m'\pi x/a) \quad [27]$$

For the cathodic compartment

$$W_C = \int_{-a}^{a} dx\left\{\kappa_0\phi_C\frac{\partial\phi_C}{\partial n} + \kappa(x)[\phi_A - \phi_C]^2\right\}_{z=l} + \int_{-a}^{a} dx\left\{\kappa_0\phi_C\frac{\partial\phi_C}{\partial n} + (1/z)f(x)[\phi_o - \phi_C]^2\right\}_{z=0} \quad [28]$$

A linear overpotential function has been assumed and $f(x)$ is again a distribution function for cathodic elements. Setting the variations of W_C with respect to b_m and c_m equal to zero yields

$$g_m b_m - h_m c_m - \sum B_{mm'}(a_{m'} - b_{m'}) = 0$$

$$-\gamma h_m b_m + \gamma g_m c_m + \sum K_{mm'} c_{m'} = K_{0m}\phi_o \quad [29]$$

with

$$\gamma = \kappa_0 z$$
$$g_m = (1 + \delta_{m,0}) \left(\frac{m\pi}{2a} \right) \coth(m\pi l/a)$$
$$h_m = (1 + \delta_{m,0}) \left(\frac{m\pi}{2a} \right) \operatorname{csch}(m\pi l/a)$$
$$K_{mm'} = \frac{1}{2a} \int_{-a}^{a} dx\, f(x) \cos(m\pi x/a) \cos(m'\pi x/a) \quad [30]$$

In matrix notation the equations when solved for c_m give

$$\left(\gamma g + \underline{\underline{K}} - \gamma \left(\frac{hf}{f+g} \right) \left(\frac{fg}{f+g} + \underline{\underline{B}} \right)^{-1} (f + \underline{\underline{B}}) \left(\frac{h}{f} \right) \right) \underset{\sim}{c} = \underline{\underline{K}} \underset{\sim}{\phi_0} \quad [31]$$

where f, g, and h are diagonal, $\underline{\underline{B}}$ and $\underline{\underline{K}}$ are symmetric matrices, and $\underset{\sim}{c}$ and ϕ_0 are column vectors, *i.e.*

$$\underset{\sim}{c} = \begin{pmatrix} c_0 \\ c_1 \\ c_2 \\ \cdot \\ \cdot \\ \cdot \end{pmatrix} \quad \underset{\sim}{\phi_0} = \begin{pmatrix} \phi_0 \\ 0 \\ 0 \\ \cdot \\ \cdot \\ \cdot \end{pmatrix} \quad [32]$$

In the limit $\underline{\underline{B}} \to \infty$, it may be verified that Eq. [20] and [21] are recovered. Given $\underline{\underline{B}}$ and $\underline{\underline{K}}$, numerical solution for $\underset{\sim}{c}$ is straightforward using standard computer routines.

For many practical problems high impedance baffles are an important consideration, and in this limit

$$\left(\frac{fg}{f+g} + \underline{\underline{B}} \right)^{-1} = \left(\frac{f+g}{fg} \right) - \left(\frac{f+g}{fg} \right) \underline{\underline{B}} \left(\frac{f+g}{fg} \right) + \ldots \quad [33]$$

where the expansion has been carried to linear terms in the baffling matrix. This approximation then gives

$$\left(\gamma g \left(1 - \frac{h^2}{g^2} \right) + \underline{\underline{K}} + \gamma (h/g) \underline{\underline{B}} (h/g) \right) \underset{\sim}{c} = \underline{\underline{K}} \underset{\sim}{\phi_0} \quad [34]$$

or equivalently

$$\gamma(1 + \delta_{m,0}) \left(\frac{m\pi}{2a} \right) \tanh \left(\frac{m\pi l}{a} \right) c_m + \sum \left[K_{mm'} + \gamma \operatorname{sech} \left(\frac{m\pi l}{a} \right) \operatorname{sech} \left(\frac{m'\pi l}{a} \right) B_{mm'} \right] c_{m'} = K_{0m} \phi_0 \quad [35]$$

It may be seen by examining the appropriate determinants that when

$$B_{0m}/B_{00} = \cosh \left(\frac{m\pi l}{a} \right) \frac{K_{0m}}{K_{00}}, \quad m = 1, 2, \ldots, n \quad [36]$$

the coefficients $c_1, c_2, \ldots, c_n$ vanish in an nth order calculation, yielding a uniform current density. For a zero-order baffle with $\kappa(x) \propto f(x)$ the current distribution is uniform when $l = 0$. This configuration is, of course, not realizable in practice. More generally we shall define the order of a baffle as the order of the calculation giving a uniform distribution. Thus for a first-order baffle $m = 1$, for a second-order baffle $m = 1, 2$, etc.

To conclude, it may be observed that

$$\kappa(x) \propto \operatorname{Re} f(x + il) \quad [37]$$

is an analytical solution for the baffle distribution giving a uniform current distribution. For passive baffles $\kappa(x)$ is necessarily positive, and for all but the most trivial examples no physical solution exists when $l \neq 0$.

Baffle Designs

The preceding discussion has been somewhat abstract, and it is appropriate to pause and offer a brief explanation of the operation of a high impedance baffle. It is a well-known proposition that the throwing power of a bath is proportional to the electrode surface impedance. This impedance is set by the cathodic current-voltage curve and is fixed within practical limits by the chemical nature of the electrode reaction. Placing a high impedance baffle near the electrode artificially increases the surface impedance seen by the bath to a level where the bath has sufficient throwing power to give a controlled current distribution.

Implementation of the baffle design equations is best illustrated working through several elementary examples. We shall assume for a sample problem

$$\begin{aligned} a &= 20 \text{ cm} \\ f(x) &= 1, |x| < 10 \text{ cm} \\ &= 0, |x| > 10 \text{ cm} \\ \gamma &= 1.0 \text{ cm} \\ B_{00} &= 0.1\, K_{00} \text{ cm}^{-1} \end{aligned} \quad [38]$$

Thus we are dealing with a 20 cm wide panel in a 40 cm wide cell. The value chosen for γ is typical for commercial plating baths.

We shall calculate current distributions to second-order using the high impedance approximation, and the $\underline{\underline{K}}$ matrix in (Eq. [30])

$$\underline{\underline{K}} = \begin{bmatrix} 1/2 & 1/\pi & 0 \\ 1/\pi & 1/4 & 1/3\pi \\ 0 & 1/3\pi & 1/4 \end{bmatrix} \quad [39]$$

For a zero-order baffle

$$\underline{\underline{B}} = 0.1 \underline{\underline{K}} \text{ cm}^{-1} \quad [40]$$

All parameters in Eq. [35] are given, and the three simultaneous equations may be solved for c_0, c_1, and c_2. Normalized current distributions are plotted in Fig. 4 for several baffle-cathode distances. As $l \to \infty$, the current distribution approaches a primary distribution, except near the edge where the current density must remain finite. For $l = 0$ the distribution is necessarily uniform, and for separations less than 3 cm it remains adequately uniform for most applications.

Next let us design a first-order baffle. A variety of baffle distribution functions can be tried. The simplest is given by adjusting the width of the zero-order baffle to compensate for a finite baffle-cathode separation. If the total width of the baffle is $2w$, Eq. [36] indicates

$$\left(\frac{a}{\pi w} \right) \sin \left(\frac{\pi w}{a} \right) = \frac{2}{\pi} \cosh \left(\frac{\pi l}{a} \right) \quad [41]$$

The maximum value of the left-hand term of Eq. [41] is unity ($w \to 0$), corresponding to $l = 6.5$ cm. A first-order baffle solution exists only for separations less than this distance. Current density distributions are shown in Fig. 5. Limiting slit baffle functions have been used for separations greater than 6.5 cm. The distributions in the matched region show a maximum directly beneath the baffle opening and a slight rise at the electrode edge. Within this region current density distributions are uniform to ±20%.

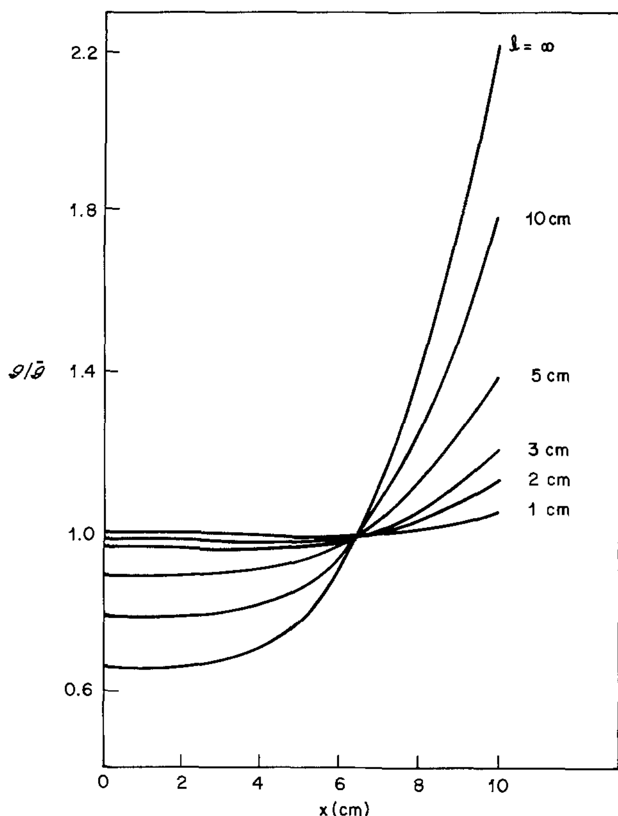

Fig. 4. Normalized current distributions using a zero-order baffle at various baffle-cathode distances.

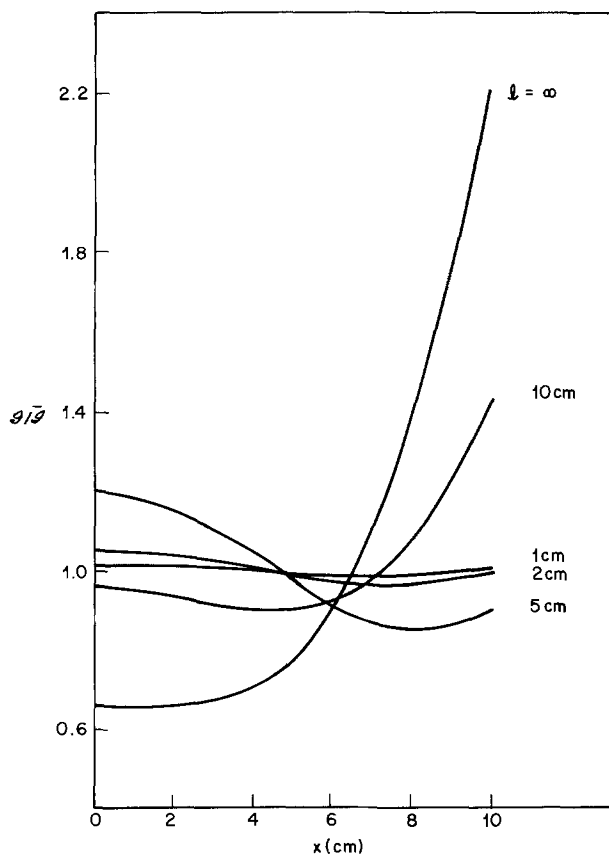

Fig. 5. Normalized current distributions using a first-order baffle at various baffle-cathode separations.

Design of a second-order baffle requires $B_{O2} = 0$. This condition is satisfied when the baffle impedance function is symmetric about $|x| = 5$ cm. The simplest design consists of a pair of variable width slits centered at these positions. Then (Eq. [30])

$$\left(\frac{a}{\pi w}\right) \sin\left(\frac{\pi w}{a}\right) = \frac{\sqrt{8}}{\pi} \cosh\left(\frac{\pi l}{a}\right) \quad [42]$$

Physical solutions exist for $l < 2.97$ cm. Results are given in Fig. 6. Over the matched region the distribution is necessarily uniform, for we are using a second-order calculation of current density. Higher order computations are required to evaluate the residual structure which should reveal maxima beneath the baffle openings.

There are obviously more sophisticated baffle functions to be tried. Smoothing the step functions used should help suppress residual wiggles. More detailed calculations are best reserved for specific design applications. In the final design stages one should solve Eq. [31] using a sufficiently large basis to insure that all approximations made are in fact valid.

Discussion

High impedance baffles have both advantages and disadvantages. The latter include problems of energy loss and mass transport. The baffle impedance should be sufficiently large to spread the current distribution over the baffle's surface. Control over a distance of 100 cm in an electrolyte with $\kappa_0 = 0.5\ \Omega^{-1}\ \text{cm}^{-1}$ requires a nominal surface impedance of 200 Ω cm^2. At a plating current density of 25 mA/cm^2, a 5.0V potential drop across the baffle follows. This is perhaps an extreme case, and proportionately smaller drops are needed to exercise control over smaller distances.

To function properly the baffle must lie within several centimeters of the cathode and will hinder the transfer of fresh electrolyte to the surface. Ideally the baffle should span the entire bath, but it is essential that it extend sufficiently far beyond the cathode to minimize leakage currents.

The primary advantage of high impedance baffles is their ability to control macrocurrent distributions in plating large panels or arrays of smaller compo-

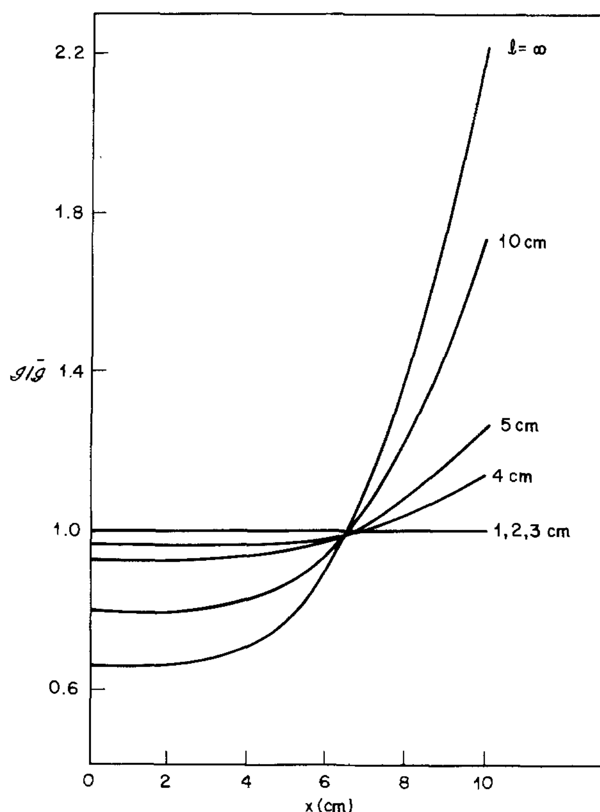

Fig. 6. Normalized current distributions using a second-order baffle at various baffle-cathode separations.

nents. "Burned" edges can be avoided, material savings effected, and, mass transfer permitting, higher plating rates can be maintained without exceeding a maximum current density. In certain applications optimum designs could require higher plating current densities in certain regions, for example where higher local densities of plated-through holes exist, or lower densities in regions serving no useful function. Tailored baffles may accommodate both situations. Further, the baffle effectively isolates the anodic and cathodic compartments, and the current distribution is insensitive to the anodic configuration. Failures due to faulty anode connections or contamination by anodic chemical products can be minimized.

An additional advantage is that baffle design is a straightforward proposition and need not require extensive trial-and-error testing. For a uniform deposit the baffle attempts to construct a uniform potential over the cathode surface. Design is independent of the explicit overpotential function and the operating point of the bath. The design conditions (Eq. [36]) are independent of material properties and involve only geometric parameters.

In summary, high impedance baffles can provide a useful addition to electroplating technology when macroscopic current distribution problems are encountered. The present analysis furnishes a format through which designs can be tested and optimized prior to physical construction.

Manuscript submitted June 3, 1977; revised manuscript received Sept. 9, 1977.

Any discussion of this paper will appear in a Discussion Section to be published in the December 1978 JOURNAL. All discussions for the December 1978 Discussion Section should be submitted by Aug. 1, 1978.

Publication costs of this article were assisted by Bell Laboratories.

REFERENCES

1. S. H. Glarum, *This Journal*, **124**, 518 (1977).
2. C. Wagner, *ibid.*, **8**, 116 (1951).
3. J. Newman, *ibid.*, **113**, 1235 (1966).

Mass Transfer of Dissolved Chlorine to a Rotating-Zinc Hemisphere in $ZnCl_2$ Solution

Jung Taek Kim* and Jacob Jorné**

Department of Chemical Engineering, Wayne State University, Detroit, Michigan 48202

ABSTRACT

The chemical reaction of a rotating-zinc hemisphere with dissolved Cl_2 is mass transfer limited. The diffusion coefficients of dissolved Cl_2 in various $ZnCl_2$ aqueous solutions at 25°C were calculated from the weight loss of the rotating Zn hemisphere at various rotational speeds. The Stokes-Einstein equation was confirmed, $(D\mu/T) = 4.42 \times 10^{-10}$ g cm/sec^2 °K and can be used to estimate diffusion coefficients of total dissolved Cl_2 in various $ZnCl_2$ solutions. The average Cl_2 Stokes radius in $ZnCl_2$ solution is calculated to be 1.64Å. The dissolution rate follows the Levich equation for convection diffusion. Surface roughness is of major importance, and the dissolution rate of Zn increases rapidly at moderate Reynolds number. Spiral markings can be observed on the corroding Zn hemisphere due to instability of the three-dimensional boundary layer, as a result of the increasing surface roughness.

The zinc-chlorine battery is a secondary battery which incorporates zinc and chlorine electrodes and a flowing aqueous $ZnCl_2$ electrolyte (1). The battery is currently being developed for load-leveling and electric car applications.

The chemical reaction which occurs in the battery is straightforward

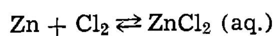

$$Zn + Cl_2 \rightleftarrows ZnCl_2\ (aq.)$$

During charge zinc is deposited at the cathode and chlorine gas is evolved at the anode. The flowing $ZnCl_2$ electrolyte replenishes $ZnCl_2$ and removes the evolving chlorine. On discharge, the flowing electrolyte removes the electrode reaction products, aqueous $ZnCl_2$, and supplies chlorine to the chlorine electrode. The chlorine storage system is cold water, which forms a clathrate compound with chlorine.

One of the main problems facing the use of Zn-Cl_2 battery as a load-leveling device is that of achieving a high coulombic efficiency while maintaining a high voltaic efficiency. The main reason for the coulombic inefficiency in the Zn-Cl_2 battery is the spontaneous reaction between dissolved chlorine and the zinc electrode upon charging. It is expected that the limiting step for this chemical reaction is the mass transfer of dissolved chlorine to the zinc surface. If this is the case, then hydrodynamic conditions and convective effects might be the dominant factors in the design to reduce the coulombic inefficiency during charging.

The effect of hydrodynamic conditions on the mass transfer and consequent reaction of dissolved chlorine with the zinc electrode can be investigated using a rotating-Zn hemisphere is a $ZnCl_2$ solution partially saturated with Cl_2. The rate of the reaction is followed from the weight loss of the rotating Zn hemisphere, and if the rate of weight loss is proportional to the square root of the angular velocity, according to the Levich equations (2), then the process is mass transfer limited and the diffusion coefficient of dissolved chlorine in $ZnCl_2$ solution can be calculated from the slope.

According to Levich (2) the diffusion layer thickness for the laminar flow on a disk electrode is given by

$$\delta = \alpha D^{1/3} \nu^{1/6} \omega^{-1/2} \qquad [1]$$

where D is the diffusion coefficient of dissolved Cl_2, ν is the kinematic viscosity, ω is the rotational velocity, and α is a constant which is equal to 1.62 for a disk and 2.109 for a hemisphere (3). Hemispherical electrode is preferred in the present case because the

* Electrochemical Society Student Member.
** Electrochemical Society Active Member.

Key words: zinc, chlorine, battery, rotating hemisphere, diffusion coefficient.

system's geometry remains unchanged. The hemisphere's limiting current, controlled by diffusion, has been corrected by Newman (4)

$$I_l = n\mathbf{F}DC_bA/\delta = 0.451\, n\mathbf{F}C_bD^{2/3}\nu^{-1/6}\omega^{1/2}A \quad [2]$$

$n\mathbf{F}$ is the number of coulombs per mole, C_b is the bulk concentration, and A is the electrode's area.

The dissolution of Zn is controlled by the diffusion of dissolved chlorine, therefore, the limiting current can be expressed by the weight loss

$$I_l = \frac{\Delta W n\mathbf{F}}{Mt} \quad [3]$$

where ΔW is the weight loss of the Zn hemispherical electrode, t is the time of the experiment, and M is the molecular weight of Zn. The mass transfer coefficient, k_c, is given by

$$k_c = \frac{\Delta W}{MAC_bt} = 0.451\nu^{-1/6}D^{2/3}\omega^{1/2} \quad [4]$$

From the plot of $\Delta W/MAC_bt$ *vs.* $\omega^{1/2}$, the diffusion coefficient of dissolved Cl_2 can be calculated.

At very high rotational speed, the flow becomes turbulent, and the Levich equation for convective diffusion does not hold; however, it is expected that earlier transition to turbulence is initiated due to surface roughness and secondary flow patterns.

The dissolution of Cl_2 in chloride aqueous solution is accompanied by the formation of dissolved molecular Cl_2, hypochlorous acid HOCl, and trichloride ion Cl_3^-. The reaction of dissolved Cl_2 with Zn is governed by the mass transfer of these three species and therefore the diffusion coefficients in the present investigation have an average meaning. The concentrations of the various species are estimated in the discussion section, and the Stokes-Einstein products $D\mu/T$ are interpreted as a function of the chloride concentration and the pH.

Experimental

The rotating-zinc hemisphere consists of a Teflon support rod and a replaceable Zn hemispherical head (Fig. 1). The Teflon support was 1.9 cm diam rod. A zinc hemisphere (99.999% New Jersey Zinc) was embedded in the Teflon rod. The diameter of the Zn hemispheres varied from 0.700 to 0.872 cm. At the center of the support there was a 0.396 cm hole in the central stainless steel shaft. The stainless steel shaft contained a 6-32 female thread to accommodate the Zn hemisphere. The other end of the Teflon support rod was attached to a stainless steel collet which was machined to fit a high speed rotator. The rotator was a Pine Instrument ASR rotator with a range of 0-10,000 rpm.

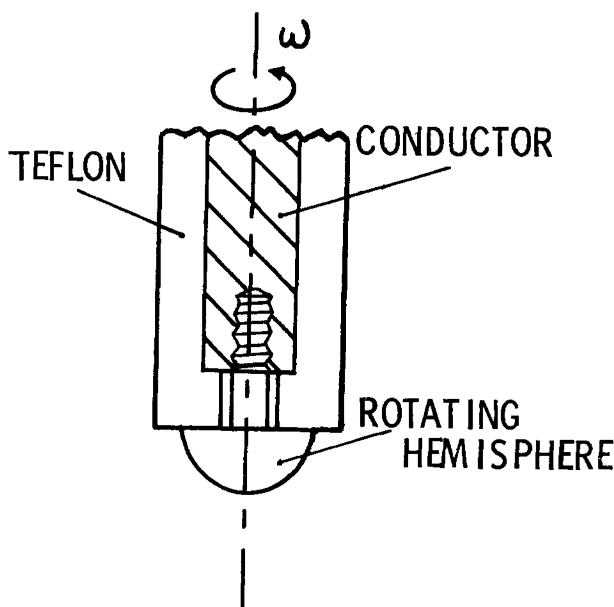

Fig. 1. Rotating Zn hemisphere

A 6-32 Zn screw having a hemispherically shaped head was used as the replaceable hemisphere. The surface of the electrode was polished with waterproof Al_2O_3 paper (grid number 600) and degreased with spectroscopic grade pentane. The Zn hemisphere was weighed on a Mettler Balance and transferred into the cell. After the experiment, the Cl_2-etched Zn hemisphere was rinsed with double distilled water, washed with pentane, and weighed.

A 1000 ml Pyrex vessel fitted with Teflon cover was used as the cell container. It was equipped with Cl_2 gas expenser. The $ZnCl_2$ 37% wt solution was obtained from EDA, Incorporated where the solution was prepared by direct recombination of pure Zn rods with dissolved Cl_2 gas. The $ZnCl_2$ concentrations were measured by hydrometer following the specific gravity data of $ZnCl_2$ (5). Viscosity data was obtained from (6) and the pH of the solution was recorded with Beckman pH meter.

The dissolved Cl_2 concentration was measured by standard titration method using 1/100 normal $Na_2S_2O_3 \cdot 5H_2O$. The solution was deaerated by bubbling nitrogen gas over a 30 min period. Cl_2-N_2 gas mixture was then bubbled for additional 30 min, and continuously bubbled throughout the experiment. Various Cl_2 concentrations were obtained by varying the composition of the Cl_2-N_2 mixture. The flow rates of Cl_2 and N_2 were controlled by needle valves and measured by calibrated rotameters.

Results and Discussion

Chlorinated $ZnCl_2$ solutions.—Table I summarizes the experimental data of the weight losses of Zn hemispheres in chlorinated 37, 22, and 17% wt $ZnCl_2$ solutions and in acidified 26% $ZnCl_2$ solution (pH = 1.0). Figure 2 shows the mass transfer coefficient of chlorine to the Zn hemisphere in chlorinated $ZnCl_2$ solutions *vs.* the square root of the rotational speed. The lines were obtained by a least square method not including the origin. The Levich equation for convective diffusion (2) is satisfied and the diffusion coefficients of dissolved Cl_2 can be determined, using Eq. [4], from the slope of the plot of $\Delta W/MtA(C_b)_{Cl_2}$ *vs.* $\omega^{1/2}$. The obtained diffusion coefficients of dissolved chlorine are shown in Table II. The corrosion of Zn due to H_2 evolution was measured by conducting weight loss measurements without Cl_2 at the same pH range. The weight loss due to H_2 evolution was negligible (<1%).

The value $D_{Cl_2} = 0.633 \times 10^{-5}$ cm^2/sec for 37% $ZnCl_2$ solution is in agreement with the value obtained from limiting current measurements of Cl_2 on a rotating nonporous graphite-disk electrode ($D = 0.664 \times 10^{-5}$ cm^2/sec) (7).

Table II also shows the calculated Stokes-Einstein product $D\mu/T$ for dissolved Cl_2 in the four $ZnCl_2$ solutions. The Stokes-Einstein product was found to be constant and the average value, $(D\mu/T)_{avg} = 4.42 \times 10^{-10}$ g cm/sec^2 °K, can be used to estimate the diffusion coefficients of dissolved Cl_2 at various $ZnCl_2$ solutions. This value is in general agreement with the chronopotentiometry data of Chao (16). The calculated Stokes radii for dissolved Cl_2 are shown in Table II and the average value is $(r_{Cl_2})_{avg} = 1.64$Å.

The present diffusion coefficient data are in good agreement with a value $D_{Cl_2} = 1.22 \times 10^{-5}$ cm^2/sec in H_2O at 20°C (8). The viscosity of pure water at 20°C is 1.0050×10^{-2} poise, and the Stokes-Einstein product is 4.185×10^{-10} g cm/sec^2 °K, in agreement with the present data.

The dissolution of Cl_2 in $ZnCl_2$ solution is governed by the formation of molecular Cl_2, HOCl, and Cl_3^-. The corrosion of Zn is therefore the result of the mass transfer and equilibria of the three species and

Table I. Summary of weight loss of Zn hemisphere in chlorinated $ZnCl_2$ solutions

$ZnCl_2$ % wt	Running time (min)	ω (rpm)	Radius HS (cm)	Cl_2 (mole/cm³) (×10⁵)	pH	Re (×10⁻³)	ΔW (mg)
37% (3.74M) pH = 3.37	60.0	1,000	0.381	1.90	3.20	0.874	11.94
	60.0	2,000	0.381	1.58	3.27	1.75	12.63
	60.0	3,500	0.381	1.61	3.27	3.06	20.43
	60.0	4,390	0.406	0.35	3.35	4.37	6.01
	60.0	4,620	0.406	0.45	3.33	4.59	6.49
	30.0	5,000	0.436	2.78	3.05	5.75	26.70
	10.0	6,000	0.406	2.85	3.04	5.96	9.50
	60.0	7,000	0.406	2.05	3.18	6.96	71.09*
	75.0	8,000	0.436	1.27	3.29	9.20	41.69
	31.0	8,000	0.436	1.96	3.20	9.20	50.54*
	120.0	8,000	0.436	1.90	3.20	9.20	247.05*
22% (1.95M) pH = 3.74	60.0	1,000	0.356	2.82	2.35	0.977	18.93
	60.0	2,000	0.381	2.40	2.55	2.24	28.44
	60.0	3,000	0.381	2.36	2.60	3.36	32.14
	60.0	4,000	0.406	2.75	2.47	5.08	49.71
	60.0	5,000	0.406	2.65	2.50	6.35	64.14*
	60.0	6,000	0.406	2.31	2.62	7.62	58.37*
17% (1.44M) pH = 4.02	60.0	1,000	0.354	2.26	2.35	1.12	17.00
	60.0	2,000	0.381	2.85	2.26	2.59	39.71
	60.0	3,000	0.401	2.13	2.36	4.30	36.03
	60.0	4,000	0.386	1.76	2.40	5.32	34.87
	60.0	5,000	0.352	2.17	2.36	5.53	39.74
	60.0	6,000	0.427	1.97	2.37	9.76	72.50*
26% (2.38M) pH = 1.0	60.0	1,500	0.395	1.20	1.0	1.76	11.06
	60.0	3,000	0.397	1.21	1.0	3.54	17.09
	30.0	4,000	0.350	1.34	1.0	3.67	8.19
	30.0	4,500	0.340	1.20	1.0	3.88	7.69
	30.0	6,000	0.397	1.27	1.0	7.07	12.96

* Denotes spiral markings observed on Zn hemisphere.

the measured diffusion coefficients have an average meaning. In the following section the hydrolysis and equilibria of Cl_2 solution are analyzed. The true diffusion coefficient and the Stokes-Einstein product of dissolved molecular Cl_2 are measured in $HClO_4$ + HCl solution and in acidified $ZnSO_4$ solution, and compared to the average values in the $ZnCl_2$ solutions.

The hydrolysis and equilibria of dissolved chlorine.—The dissolved chlorine exists in chloride aqueous solution partly in the form of free molecular chlorine Cl_2, partly in its hydrolized form hypochlorous acid HOCl, and the remainder in the form of the complex trichloride ion Cl_3^-.

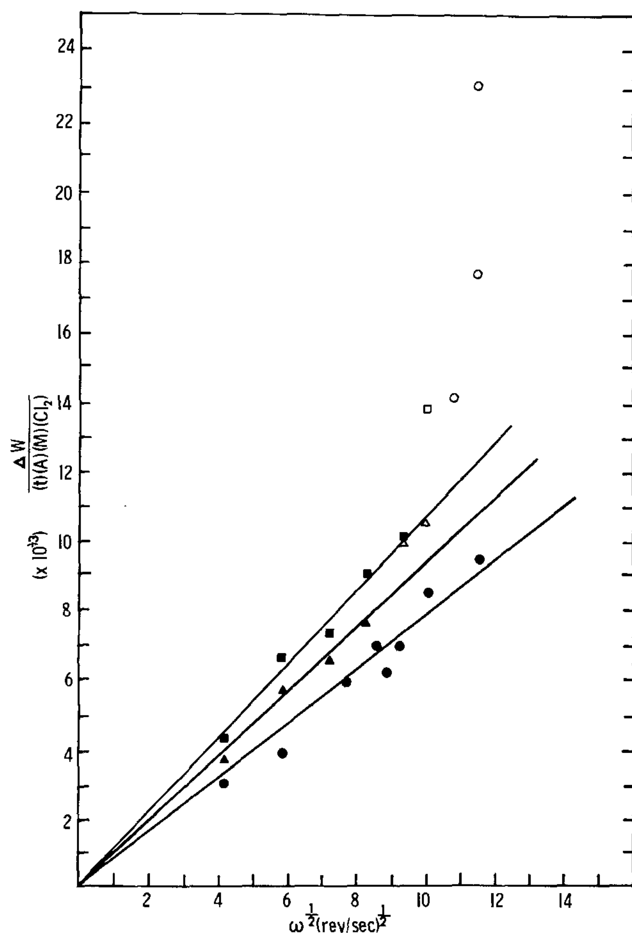

Fig. 2. Zn weight loss vs. the square root of the rotational velocity. ● 37%; ▲ 22%; ■ 17%; $ZnCl_2$ solution. Empty points, spiral markings were observed.

Table II. Diffusion coefficients, Stokes-Einstein products and Stokes radii of dissolved Cl_2 in various $ZnCl_2$ solutions

$ZnCl_2$ M	pH	T, °C	D (cm²/sec) ×10⁵	$D\mu/T$ (g cm/sec² °K) ×10¹⁰	$r_{\Sigma Cl_2}$ A
1.44	2.3	21.3	0.969	4.46	1.64
1.95	2.5	22.0	0.808	4.49	1.63
3.74	3.2	25.0	0.633	4.46	1.64
2.38	1.0	25.0	0.718	4.28	1.70

$(D\mu/T)_{avg} = 4.42 \times 10^{-10}$ g cm/sec² °K
$(r_{Cl_2})_{avg} = 1.64$A

The hydrolysis of chlorine is governed by the following two equilibria with K's at 25°C (14-16)

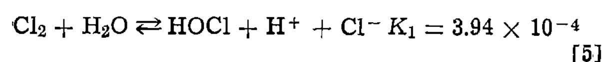

$$Cl_2 + H_2O \rightleftarrows HOCl + H^+ + Cl^- \quad K_1 = 3.94 \times 10^{-4} \qquad [5]$$

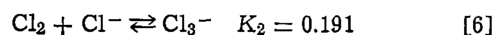

$$Cl_2 + Cl^- \rightleftarrows Cl_3^- \quad K_2 = 0.191 \qquad [6]$$

The hydrolysis of dissolved Cl_2 depends strongly on the pH.

The dissociation constant of hypochlorous acid to hypochlorite (15)

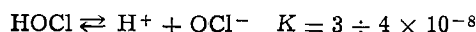

$$HOCl \rightleftarrows H^+ + OCl^- \quad K = 3 \div 4 \times 10^{-8}$$

is very small and in the present acidic solution hypochlorite is not present.

Although the $ZnCl_2$ solutions in the present work are acidic and the dissolved Cl_2 is the predominant species, the concentrations of HOCl and Cl_3^- can be estimated from the equilibrium constants

$$(HOCl)^2 = K_1 \frac{(\Sigma Cl_2) - (HOCl) - (Cl_3^-)}{(Cl^-)\gamma_{HCl}} \qquad [7]$$

$$(Cl_3^-) = K_2[(\Sigma Cl_2) - (HOCl) - (Cl_3^-)](Cl^-) \qquad [8]$$

where ΣCl_2 is the total dissolved Cl_2.

In the following calculations it was assumed that $\gamma_{Cl_2}\gamma_{H_2O}$ cancelled γ_{HOCl} to a good approximation (14), and that $\gamma_{Cl_3^-} \approx \gamma_{Cl^-}$ (15). The initial H^+ concentration can be neglected in comparison to the final H^+ concentration. The activity coefficient of HCl, γ_{HCl}, in $ZnCl_2$ solution was approximated from the available activity coefficient data of HCl in $BaCl_2$ (17).

Table III. Estimated concentration of Cl_2, HOCl, and Cl_3^- in chlorinated $ZnCl_2$, $ZnSO_4$, and $HClO_4$ + HCl solutions

Electrolyte (M)		Initial pH	Final pH	ΣCl_2 10^2 (M)	Cl_2 10^2 (M)	HOCl 10^2 (M)	Cl_3^- 10^2 (M)
$ZnCl_2$	1.44	4.02	2.36	2.0	1.20	0.14	0.66
	1.95	3.74	2.50	2.0	1.09	0.10	0.81
	3.74	3.37	3.20	2.0	0.80	0.06	1.14
	2.38	1.0	1.0	2.0	1.05	0.0004	0.95
$ZnSO_4$	8.74×10^{-3}	1.0	1.0	2.0	1.29	0.71	—
	8.74×10^{-3}	2.5	2.5	2.0	0.25	1.75	—
$HClO_4$+ HCl	0.975M 0.025M	0.02	0.02	2.0	2.0	—	—

Table III presents the calculated concentrations of the various species Cl_2, HOCl, and Cl_3^- in typical 2×10^{-2}M total-dissolved Cl_2 solutions. It appears that for a typical $ZnCl_2$ solution 50 ± 10% of the dissolved chlorine remains as molecular Cl_2, while 50 ± 10% and 5 ± 5% are converted to Cl_3^- and HOCl, respectively. The decrease in the pH upon chlorination is due to the partial hydrolysis of dissolved Cl_2 to HOCl and HCl, according to the first equilibrium (Eq. [5]). The obtained diffusion coefficients of dissolved Cl_2, the calculated Stokes-Einstein product, and the Stokes radius represent an average of the three diffusing species Cl_2, HOCl, and Cl_3^-.

Figure 3 shows the mass transfer coefficient as a function of the square root of the rotational speed in chlorinated acidified 8.74×10^{-3}M $ZnSO_4$ (pH = 1.0), acidified 26% wt $ZnCl_2$ solution (pH = 1.0), and in 0.975M $HClO_4$ + 0.025M HCl chlorinated solution.

In H_2SO_4-acidified $ZnSO_4$ solution (pH = 2.5), most of the dissolved Cl_2, 87.5%, is hydrolyzed to HOCl and therefore, the diffusion coefficient which was calculated from the slope $D = 1.451 \times 10^{-5}$ cm²/sec is the approximate value for HOCl. In the 26% weight $ZnCl_2$ solution (pH = 1.0), HOCl is not present and about 47.5% of the total dissolved Cl_2 is converted to Cl_3^-. The obtained diffusion coefficient $D = 0.718 \times 10^{-5}$ cm²/sec represents an average value for Cl_2 and Cl_3^-.

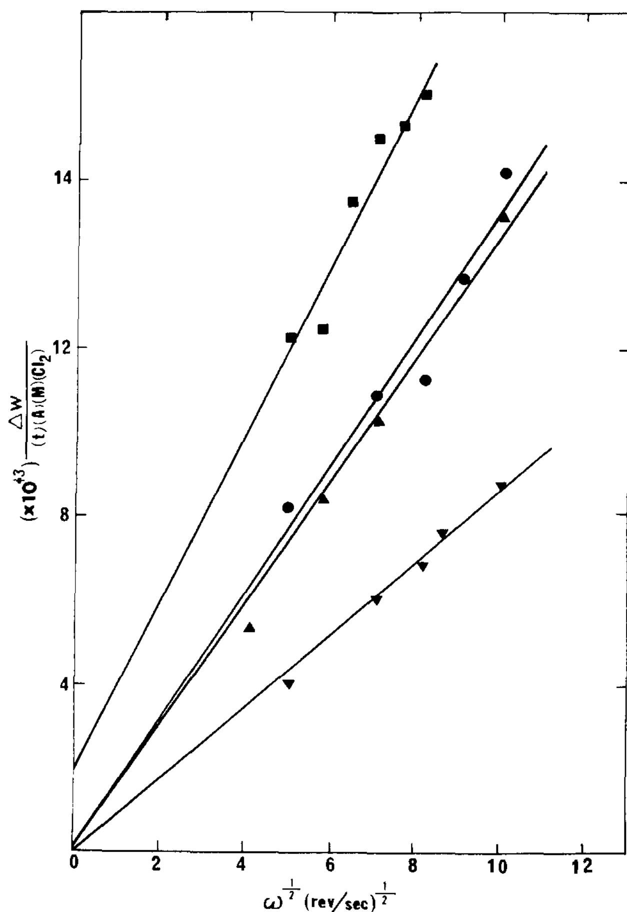

Fig. 3. Zn weight loss vs. the square root of the rotational velocity. 8.74×10^{-3}M $ZnSO_4$; ● pH = 1.0; ▲ pH = 2.5; ■ 0.975M $HClO_4$ + 0.025M HCl; ▼ 26% (pH = 1) $ZnCl_2$.

Similar weight-loss experiments were performed in chlorinated 0.975M $HClO_4$ + 0.025M HCl solution. In this solution all the dissolved Cl_2 remains as molecular Cl_2 and therefore the diffusion coefficient $D_{Cl_2} = 2.14 \times 10^{-5}$ cm²/sec is the true value for Cl_2. In this experiment the weight loss due to H_2 evolution was estimated from a weight loss experiment in the absence of Cl_2 and from the intercept at $\omega = 0$ in Fig. 3. The viscosity of the $HClO_4$ + HCl solution was measured at 28° in our laboratory, $\mu = 8.23 \times 10^{-3}$ g/cm sec, using an Ostwald viscometer.

The Stokes-Einstein products and the Stokes radii of dissolved Cl_2 in acidified $ZnSO_4$ solutions and $HClO_4$ + HCl solution are shown in Table IV. The $ZnSO_4$ pH = 2.5 values can be regarded as an approximation for HOCl

$$(D\mu/T)_{HOCl} \cong 4.45 \times 10^{-10} \text{ g cm/sec}^2\ {}^\circ\text{K}$$

$$r_{HOCl} \cong 1.67\text{Å}$$

The HOCl concentration was quite low in all the experiments, except in the $ZnSO_4$ solutions. The diffusion coefficient of Cl_3^- is expected to be the lowest, followed by HOCl and Cl_2. In $ZnSO_4$ solution at low pH, the diffusion coefficient is higher (Table IV) due to the higher concentration of molecular Cl_2, in agreement with Chao (16).

In the $HClO_4$ + HCl solution, the Stokes-Einstein product is the highest because of the expected high diffusion coefficient of dissolved molecular Cl_2, which is the predominant species. The data from the $HClO_4$ + HCl solution can be regarded as the true values for Cl_2

$$(D\mu/T)_{Cl_2} = 5.85 \times 10^{-10} \text{ g cm/sec}^2\ {}^\circ\text{K}$$

$$r_{Cl_2} = 1.25\text{Å}$$

A Cl_2 bond length of 1.98Å is given by Pauling (13).

Hydrodynamic effects.—Above a rotational speed of about 100 rps, the Levich equation is not satisfied (see Fig. 2), and the weight loss is much higher than expected for laminar flow. The empty data points in Fig. 2 represent experiments where spiral vortex shape markings were observed on the Zn hemisphere at the end of the experiment. The higher weight losses of the Zn hemisphere under these conditions can be explained by an earlier transition to turbulent flow and the appearance of secondary flow pattern near the surface which enhances the mass transfer of dissolved Cl_2 to the Zn surface.

During the Zn dissolution the Zn surface becomes rough. This surface roughness changes the nature of the flow, and transition to turbulence appears earlier than expected for a smooth surface. Levich (2) discusses convective diffusion to a rough surface and relates the size of the protrusions to the thickness of the hydrodynamic boundary layer. If the size of the protrusion is larger than the hydrodynamic boundary layer, then transition occurs earlier. The thickness of the hydrodynamic boundary layer depends on

Table IV. Diffusion coefficients, Stokes-Einstein products and Stokes radii for dissolved Cl_2 in $ZnSO_4$ solution and $HClO_4$ + HCl solution

Electrolyte (M)		pH	T, °C	D (cm²/sec) × 10^5	$D\mu/T$ (g cm/sec² °K) × 10^{10}	r, A
$ZnSO_4$	8.74×10^{-3}	1.0	25	1.517	4.57	1.60
$ZnSO_4$	8.74×10^{-3}	2.5	25	1.451	4.38	1.67
$HClO_4$ HCl	0.975 0.025	0.02	28	2.14	5.85	1.25

$r_{Cl_2} = 1.25$A $r_{HOCl} \cong 1.67$A

the rotational speed through the Reynolds number ($Re = \omega r^2/\nu$). As the rotational speed increases (6000-8000 rpm) the thickness of the boundary layer decreases and reaches the same order of magnitude of the rough surfaces. Secondary flow of small vortexes is initiated, which enhances the mass transfer of dissolved Cl_2 to the surface.

In all the electrodes which exhibited higher weight loss than expected, the corroded surface showed spiral shape patterns of dissolution. Typical spiral markings are shown in Fig. 4 where the rotational speed is high (8000 rpm). The formation of spiral markings on a rotating-disk electrode has been shown (9, 10) to be caused by the formation of wakes behind small protrusions and the formation of secondary flow is due to instability of the three-dimensional boundary layer on the rotating disk or hemisphere. Figure 5 shows the surface of Zn hemisphere after Cl_2 corrosion at lower rotational speed ($Re = 4.37 \times 10^3$). Spiral markings are absent and the grain boundaries can be observed clearly. Ibl (18) explains the formation of the spirals during metal deposition on a rotating-disk electrode by the relative size of the surface protrusions and the mass transfer boundary layer thickness.

Fig. 4. Zn hemisphere after reaction with dissolved Cl_2. $\omega = 8000$ rpm; radius $= 0.436$ cm; $[Cl_2] = 1.96 \times 10^{-2}M$; time $= 31$ min; $Re = 9.2 \times 10^3$; 37% $ZnCl_2$.

Fig. 5. Zn hemisphere after reaction with dissolved Cl_2. $\omega = 4390$ rpm; radius $= 0.406$ cm; $[Cl_2] = 0.35 \times 10^{-2}M$; time $= 60$ min; $Re = 4.37 \times 10^3$; 37% $ZnCl_2$.

The transition flow appears at a Reynolds number of about

$$Re = \frac{\omega r^2}{\nu} = \frac{2\pi(121)(0.4)^2}{1.72 \times 10^{-2}} = 7 \times 10^3$$

which is below the transition Reynolds number of 1.5×10^4 obtained experimentally for a smooth rotating hemisphere (12). The flow near a hemisphere is less stable than near a rotating disk, and the present value for a hemisphere is lower than 10^5, as predicted from linear stability analysis of a flow near a rotating disk (10, 11). The earlier transition in the present case is due to the surface roughness during the corrosion of the zinc surface by the dissolved Cl_2.

In conclusion, it has been shown that the chemical reaction of dissolved chlorine with zinc in $ZnCl_2$ aqueous solution is mass transfer limited. The Zn surface roughness initiates a secondary flow and increases the mass transfer of dissolved Cl_2 to the surface. At low pH the dissolved Cl_2 is in the form of dissolved molecular Cl_2 and trichloride ion, Cl_3^-. At higher pH, the presence of hypochlorous acid, HOCl, is significant.

Acknowledgments

This work was supported by Energy Development Associates, Madison Heights, Michigan, and Electric Power Research Institute, Palo Alto, California. The stimulating discussions with Drs. Philip Symons and Charles Warde are gratefully acknowledged.

Manuscript submitted March 4, 1977; revised manuscript received Aug. 25, 1977.

Any discussion of this paper will appear in a Discussion Section to be published in the December 1978 JOURNAL. All discussions for the December 1978 Discussion Section should be submitted by Aug. 1, 1978.

Publication costs of this article were assisted by Wayne State University.

LIST OF SYMBOLS

- A hemisphere's surface area, cm²
- C_b bulk concentration, g-mole/cm³
- D diffusion coefficient, cm²/sec
- $\mathbf{F}$ Faraday's constant, 96,487 C/g-equiv.
- I_l limiting current, A
- k_c mass transfer coefficient, cm/sec
- M molecular weight of Zn
- n number of electrons transferred in the electrode reaction
- r radius of hemispherical electrode, cm
- r Stokes radius, Å
- Re Reynold's number
- T temperature, °K
- t time, sec
- W electrode weight, g
- α rotating electrode constant, dimensionless
- δ diffusion layer thickness, cm
- μ viscosity, g/cm sec
- ν kinematic viscosity, cm²/sec
- ω angular velocity, rad/sec
- ΣCl_2 total dissolved Cl_2

REFERENCES

1. P. C. Symons and P. Carr, in Proceedings of the 8th Inter-Society Energy Conversion Engineering Conference, Paper No. 739010, pp. 72-77 (1973).
2. V. G. Levich, "Physicochemical Hydrodynamics," pp. 60-72, Prentice Hall, Englewood Cliffs, N.J (1962).
3. D. T. Chin, *This Journal*, **118**, 1434 (1971).
4. J. Newman *ibid.*, **119**, 69 (1972).
5. "Specific Gravity of Aqueous $ZnCl_2$ Solutions," Handbook of Chemistry and Physics, 35th ed., Chemical Rubber Publishing Co. (1953-1955).
6. J. Mellor, "Comprehensive Treatise on Inorganic

and Theoretical Chemistry," Vol. 2, suppl. (1974).
7. J. T. Kim and J. Jorné, *This Journal*, **124**, 1473 (1977).
8. J. H. Arnold, *J. Am. Chem. Soc.*, **52**, 3937 (1930).
9. G. T. Rogers and K. J. Taylor, *Nature (London)*, **200**, 1062 (1963).
10. A. C. Riddiford, in "Advances in Electrochemistry and Electrochemical Engineering," Vol. 4, P. Delahay, Editor, Interscience, New York (1966).
11. F. Opekar and P. Beran, *J. Electroanal. Chem. Interfacial Electrochem.*, **69**, 115 (1976).
12. D. T. Chin, *This Journal*, **118**, 1764 (1971).
13. L. Pauling, "The Nature of the Chemical Bond," 3rd ed., Cornell University Press, Ithaca, N.Y. (1960).
14. R. E. Connick and Y-S. Chia, *J. Am. Chem. Soc.*, **81**, 1280 (1959).
15. M. S. Sherril and E. F. Izard, *ibid.*, **53**, 1667 (1931).
16. M. S. Chao, *This Journal*, **115**, 1172 (1968).
17. H. S. Harned and B. B. Owen, "The Physical Chemistry of Electrolytic Solutions," 3rd ed., pp. 748-751, Reinhold Publishing Co., New York (1958).
18. N. Ibl, Zeitschrift Erzmetall Bd. 22, pp. 87-98, Beiheft Symposium Hydrometallurgie (1969).

Technical Notes

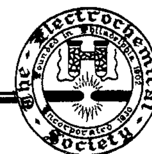

Dynamic-Foamed Electrolyte Hydrogen Electrode

Jacob Jorné*

Department of Chemical and Metallurgical Engineering, Wayne State University, Detroit, Michigan 48202

The potentially advantageous use of foamed electrolyte in fuel cell has been suggested by Nanis and McLarnon (1). They suspended a Pt electrode just above H_2SO_4 or NaOH solution which contained a small amount of surfactant and bubbled the fuel gas (H_2 or O_2) through the solution creating a foam which rose and covered the electrode. The foam contained the fuel gas (H_2) and the bubble walls acted as a thin film when in contact with the electrode's surface. The most significant finding of Nanis and McLarnon's work was that when using a flat platinum electrode the anodic limiting current in the foamed electrolyte was an order of magnitude larger than the limiting current when the electrode was completely immersed in the liquid electrolyte. From the limiting currents they were able to estimate the apparent diffusion boundary layer thickness, using the following equation

$$\delta_D = n\mathbf{F}DC_b/I_l \qquad [1]$$

Where C_b is the bulk concentration of dissolved H_2, D its diffusion coefficient, and I_l is the anodic limiting current. The obtained diffusion boundary layer thickness was on the order of 3-4μ, and Nanis and McLarnon (1) explained it in terms of a thin film of electrolyte covering the electrode when it is in the foam. However, no attempt was made to compare quantitatively the calculated apparent diffusion boundary layer thickness with the average thickness of the foam's wall.

In the present work limiting currents were measured for the anodic reaction

$$H_2 \rightarrow 2H^+ + 2e^-$$

using a dynamic foamed electrolyte where the foam flowed continuously over a platinum electrode. The apparent diffusion boundary layer thickness was calculated using Eq. [1]. The average thickness of the foam's wall δ_F was calculated from the measured average bubble diameter $\bar{d}$ and f, the foam wetness (7, 8)

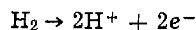

$$\delta_F = f\bar{d}/6 \qquad [2]$$

The two values are in general agreement which substantiates quantitatively the assumption that the thin walls of foam present the major resistance to mass transfer of the dissolved gaseous fuel to the electrode surface.

The importance of thin films in gas electrodes have been noticed by several researchers (2-6). When a gas electrode is partially withdrawn from liquid electrolyte into the gas atmosphere the current increases and the local current density is higher at the thin film covering the electrode surface.

Experimental

The apparatus consisted of a circulatory foam column; the working anode and the countercathode were located at the middle section of the foam column (see Fig. 1). The foam column is similar to the one used in foam separation technique by Rubin and Jorné (7). Hydrogen gas was passed through a rotameter and prehumidifier and bubbled through a glass frit dispersion tube located in the bottom of a 4 liter flask where the electrolyte was initially placed. The column consisted of a 36 cm long 2.8 cm ID Pyrex tube. The upper part of the column was bent to form an angle of about 45° to direct the foam into the rotating foam breaker (7). Near the midpoint of the column the two platinum electrodes were located. The working electrode was a Fisher Scientific Company electrode (Cat. No. 13-639-102) located in a Pyrex cylinder, and the active area of the circular electrode was 0.785 cm^2. The counterelectrode was a 1 cm^2 bright platinum foil attached to a platinum wire. The Luggin capillary tip was introduced below the working electrode and the capillary was connected to the reference electrode container where a standard calomel electrode was placed.

The constant current was maintained by a power supply (Electronic Measurements Model C-613) and the potential between the anode and the reference electrode was measured with a Keithley 600A electrometer. A flat glass window (1 cm diam) was located below the electrode where close-up pictures of the flowing foam were taken in order to measure the average bubble diameter (7, 8)

$$\bar{d} = \frac{\sum_i n_i d_i^3}{\sum_i n_i d_i^2} \qquad [3]$$

* Electrochemical Society Active Member.

Key words: foam, hydrogen, fuel cell, bubbles, mass transfer, limiting current.

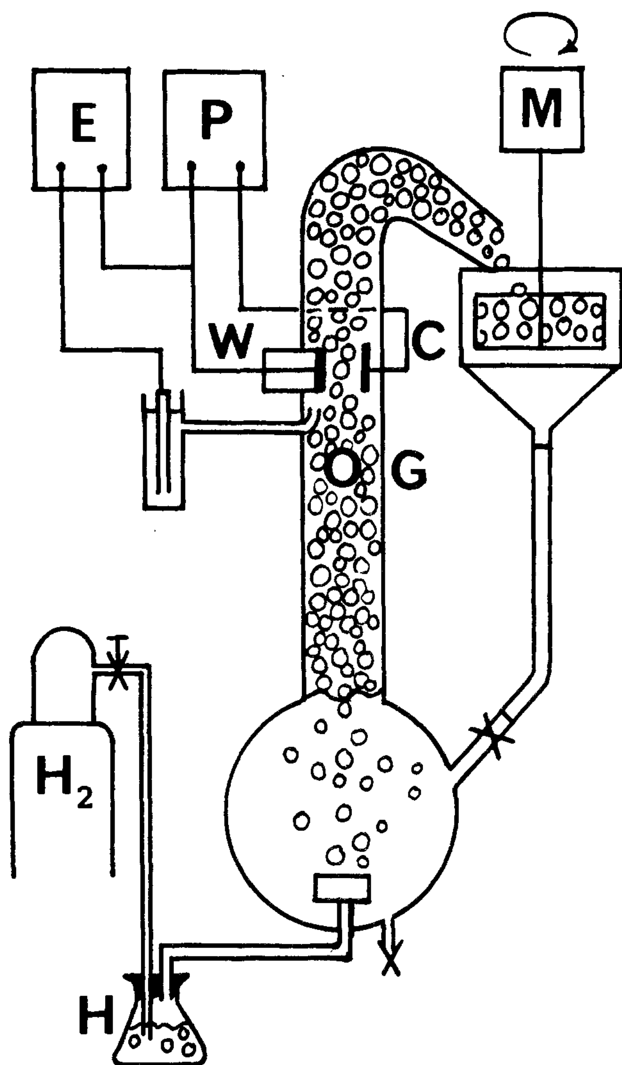

Fig. 1. Circulatory foam column and electrodes arrangement. W, C, R—working, counter, and reference electrode, respectively. P, power supply; E, electrometer; M, motor; G, flat window; H, prehumidifier.

The electrolyte consisted of 4*N* sulfuric acid containing 0.1% wt carboxane TW-100, Textilana Corporation, Hawthorne, California. This surfactant was found to be inert in the potential range (1).

The experiment began by filling the lower flask with 4 liters of the electrolyte. Hydrogen gas was bubbled into the electrolyte-surfactant solution through a fritted glass dispersion tube. The hydrogen bubbles, as they emerged from the electrolyte solution, formed the foamed electrolyte. The foam flowed up the column past the electrodes and was circulated back into the flask after being broken by the rotating foam breaker. The foam wetness f was calculated by measuring the flow rate of the foamate (the broken foam) and the flow rate of the foam in the column. The foamate flow rate was measured by accumulating it over a period of 90 sec. The foam flow rate was measured from the upward velocity of the foam's plug-flow in the 2.8 cm. ID column. The foam wetness f is calculated from

$$f = \frac{\text{foamate flow rate}}{\text{foam flow rate}} \quad [4]$$

and represents the liquid fraction in the foam.

Limiting current data were obtained by increasing galvanostatically the current between the two Pt electrodes and recording simultaneously the overpotential between the working and reference electrode. The limiting currents were measured for various foam velocities. The foam remained stable in all the experiments and the room temperature was around 25°C.

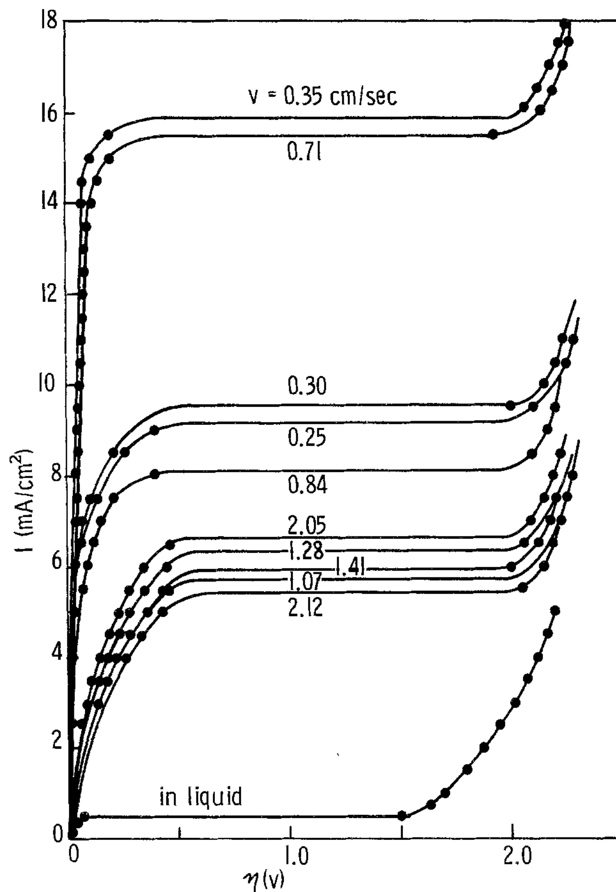

Fig. 2. Current density vs. anode overpotential for H_2 electrode at various foam's upward velocities. 4*N* H_2SO_4, 0.1 w/o carboxane TW-100; $P = 1$ atm; $T \sim 25°C$.

Results and Discussion

Anodic polarization curves for H_2 oxidation in the foamed 4*N* H_2SO_4 electrolyte are shown in Fig. 2. The limiting currents correspond to various foam upward velocities, and can be compared to the lower polarization curve which was measured in the liquid solution where the hydrogen electrode was totally submerged. Table I presents the data for the limiting currents as well as the foam's physical properties: average bubble diameter, foam velocity, and foam wetness. The bias potential between the anode and the calomel reference electrode was about 260 mV, in excellent agreement with the Nernst equation. The missing data in Table I and consequently in Table II are due to the failure of the camera in one case, and the lack of foamate flow rate data in the other.

A comparison between the effective diffusion boundary layer thickness and the average wall thickness of the foam is shown in Table II. The diffusion bound-

Table I. Foam properties and H_2 anodic limiting currents
Electrolyte: 4*N* H_2SO_4, 0.1% carboxane TW-100

Foam upward velocity (cm/sec)	Average bubble diameter $\bar{d}$ (cm)	Foam wetness $10^2 f$	Limiting current density i_l (mA/cm²)
0.25	0.12	—	9.17
0.30	0.12	0.86	9.55
0.35	1.00	2.78	15.90
0.71	0.087	3.66	15.50
0.84	0.079	4.44	8.10
1.07	0.070	5.76	5.73
1.28	0.072	5.20	6.31
1.41	0.070	5.30	5.88
2.05	0.052	4.72	6.57
2.12	—	4.67	5.41

Table II. Comparison between the foam average wall thickness and effective mass transfer boundary layer

Foam upward velocity (cm/sec)	Foam average wall thickness δ_F (μ)	Effective mass transfer boundary layer thickness δ_D (μ)
0.25	—	4.52
0.30	1.72	4.34
0.35	4.62	2.60
0.71	5.31	2.67
0.84	5.84	5.11
1.07	6.72	7.23
1.28	6.24	6.56
1.41	6.17	7.07
2.05	4.08	6.30
2.12	—	7.65

ary layer thickness δ_D and the average wall thickness δ_F were calculated from Eq. [1] and [2], respectively. Hydrogen diffusion coefficient and solubility data were obtained from Ruetschi (9). $D_{H_2} = 3.7 \times 10^{-5}$ cm²/sec, $C_{H_2} = 0.58 \times 10^{-3}M$ (uncorrected from 30°C).

A general agreement can be found between δ_D and δ_F as can be seen from Fig. 3, indicating that the thin walls of the foam bubble represent the diffusion path for the diffusion of H_2 from the bubbles to the electrode's surface. The deviations of δ_D from δ_F, especially at small δ_F, can be attributed to the error in determining the average bubble diameter $\bar{d}$ (Eq. [3]). The error in determining the average bubble diameter is quite large and can reach 100% for a dry foam where the bubbles are not spherical and δ_F should be larger than estimated from Eq. [2]. This explains that the deviation of δ_D from δ_F in Fig. 3 is largest for small δ_F and generally positive for small δ_F. The obtained limiting currents and effective boundary layer thicknesses are in agreement with Nanis and McLarnon's results (1), where the foam was accumulated above the solution. Figure 4 shows the behavior of the limiting current *vs.* the upward foam velocity. The maximum occurs at about 0.5 cm/sec. The foam velocity determines the foam wetness. At very slow upward velocities the foam drainage is complete and the foam is very dry. However the gas flow rate also determines the average bubble diameter; at low flow rate the average bubble diameter is high. Thus as the gas flow rate increases, the two effects, the foam wetness and average bubble diameter, compete in determining the trend of the

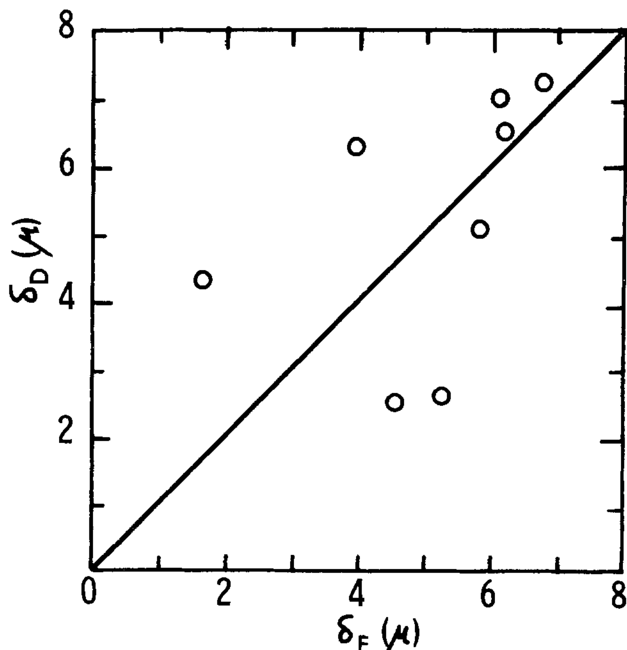

Fig. 3. Comparison between effective diffusion boundary layer and foam's average wall thickness.

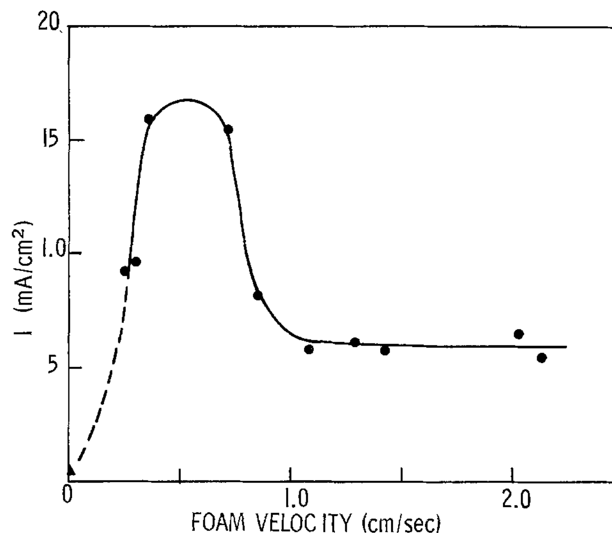

Fig. 4. The anodic limiting current *vs.* the foam's upward velocity. Δ, in liquid.

average wall thickness (according to Eq. [2]) and the optimal upward velocity of the foam corresponds to the formation of a thin film.

Summary

The hydrogen electrode was investigated in a flowing foamed electrolyte. The improved mass transfer effect reported previously by Nanis and McLarnon has been confirmed. A correlation was established between the anodic limiting current and the dynamic properties of the foam. A general agreement was found between the calculated effective mass transfer boundary layer and the measured foam's average wall thickness. These results confirm that the thin walls of the foam represent the resistive path for the diffusion of hydrogen from the bubbles to the surface of the electrode.

Acknowledgments

This work was partially supported by an unrestricted grant from BASF Wyandotte Corporation, Wyandotte, Michigan. The support of BASF Wyandotte Corporation is gratefully acknowledged.

The author is thankful to Mr. Michael Platzke for carrying out the experimental work as partial fulfillment of his senior thesis, Department of Chemical Engineering, Wayne State University.

Manuscript submitted May 11, 1977; revised manuscript received July 25, 1977.

Any discussion of this paper will appear in a Discussion Section to be published in the December 1978 JOURNAL. All discussions for the December 1978 Discussion Section should be submitted by Aug. 1, 1978.

Publication costs of this article were assisted by Wayne State University.

LIST OF SYMBOLS

- C_b bulk concentration, moles/cm³
- D diffusion coefficient, cm²/sec
- d_i bubble diameter, cm
- $\bar{d}$ average bubble diameter, cm
- $\mathbf{F}$ Faraday constant, 96.4 C/equiv.
- f foam wetness, dimensionless
- I current density, A/cm²
- I_l limiting current density, A/cm²
- n number of electrons transferred in electrochemical reaction
- n_i number of bubbles of diameter d_i
- v foam velocity, cm/sec
- δ_D apparent diffusion boundary layer thickness, cm
- δ_F foam's average wall thickness, cm
- η overpotential, V

REFERENCES

1. L. Nanis and F. McLarnon, *This Journal*, **117**, 1527 (1970).

2. D. Bennion and C. Tobias, *ibid.*, **113**, 589 (1966).
3. F. Will, *ibid.*, **110**, 145 (1963).
4. F. Will, *ibid.*, **114**, 138 (1967).
5. R. Müller, *ibid.*, **113**, 943 (1966).
6. R. Burshtein, M. Tarasevich, S. Chernyshov, and Y. Chirkov, *Sov. Electrochem.*, **4**, 1154 (1968).
7. E. Rubin and J. Jorné, *Ind. Eng. Chem. Fundam.*, **9**, 474 (1969).
8. E. Rubin and E. L. Gaden, in "New Chemical Engineering Separation Techniques," H. M. Schoen, Editor, Interscience, New York (1962).
9. P. Ruetschi, *This Journal*, **114**, 301 (1967).

The Reactivity of Metals with Mixtures of Carbon Tetrachloride and Alcohols

James R. Kuppers

Chemistry Department, The University of North Carolina at Charlotte, Charlotte, North Carolina 28223

Al reacts directly with the lower aliphatic alcohols only under anhydrous conditions at elevated temperatures or when amalgamated (1), or when highly stressed surfaces are freshly exposed (2). The reaction of Mg metal with moist ethanol at reflux is accelerated with the addition of small amounts of iodine or an aliphatic halogen compound such as chloroform or CCl_4. Al and its alloys, brasses, bronzes, and iron alloys are subject to corrosion under some stringent conditions such as mechanical stress, high temperatures, or amalgamation (5-9). Some Al alloys undergo a rapid, autocatalytic reaction with CCl_4-methanol mixtures, initiated at room temperature and leading to complete dissolution of the metal (10). The corrosion of metals in halogenated hydrocarbons is currently under intensive study by Heitz and Kyriazis (11).

My interest in this subject stems from reports of corrosion problems encountered in a brass thermal diffusion cell containing CCl_4-alcohol mixtures (12, 13). I report some novel features of this class of reactions.

Experimental

Reactions in sealed tubes.—Separate 125 mg samples of Cu, Zn, Ag, Pt, and Au (each at least 99% pure) were sealed in NMR tubes with 500 mg of CCl_4-methanol mixture (40% CCl_4, air not excluded) and held at 25°C. Zn metal was decomposed overnight leaving a white solid and a colorless solution. Cu metal was consumed after two weeks leaving a yellow-brown solution and no solid residue. Ag metal was faintly discolored after two weeks but otherwise unaffected.

Pt and Au remained bright with no visible indication of reaction. The course of the reaction with Zn and Cu was monitored with proton magnetic resonance spectra. Although the methyl and hydroxy proton signals were progressively shifted downfield (approximately 0.3 ppm in all) no new proton signal developed.

In particular, nothing was seen which would indicate the formation of halohydrocarbons, aldehydes, or compounds containing methylene protons. The methyl and the hydroxy proton signals in the Cu tube were significantly broadened at the end of the reaction. When ethanol, 2-propanol, or 1-butanol were substituted for methanol, the reaction with Zn in sealed tubes was progressively more sluggish in order of increasing molecular weight of the alcohol and NMR spectra revealed no new proton signals which were not present at the beginning of the reaction.

The induction period.—The time required for the initiation of a vigorous, autocatalytic reaction of Zn with CCl_4-methanol mixtures in open containers was sensitive to the composition of the mixture as well as to the presence of certain chemical initiators. This reaction was self-initiated at 25°C over a range of concentrations from 0.60 to 0.98 mole fraction of methanol. The minimum induction period, 2 hr, corresponded to a methanol concentration of approximately 0.90 mole fraction when used with 30 mesh Fisher Reagent Grade Zn powder. The induction period was completely eliminated by adding traces of soluble salts of some less active metals, *e.g.*, $CuCl_2$, $HgCl_2$, and $CrBr_3$. Al and Mg, unlike Zn, required no induction period under any circumstances. Nevertheless, reactions proceeded more vigorously in the presence of the previously mentioned salts.

Key words: corrosion, organic solvents, water.

Reactivity of various metals.—Mg, Al, Si, Ti, Cr, Mn, Fe, Co, Ni, Cu, Zn, Ga, Ag, Cd, Sn, Pt, Au, and Hg were immersed for two weeks at 25°C in CCl_4-methanol mixtures containing 0.90 mole fraction of methanol. Rapid, autocatalytic dissolution of Mg, Al, and Zn occurred. The reaction of Cu and Cr was slow but eventually resulted in complete dissolution of the metals. All the other metals were nonreactive in the sense that whatever reaction occurred was halted by the immediate formation of passive coatings.

Water as a quenching agent.—Reactions of Mg, Al, and Zn with CCl_4-methanol mixtures were quenched with small additions of water. Since there was no induction period for Mg and Al and since Mg reacts with anhydrous methanol at 25°C, even in the absence of CCl_4, these two metals were convenient for a quantitative study of the water-quenched reactions. To the metals immersed in anhydrous methanol, small successive additions of CCl_4 and water were made. The amount of CCl_4 needed to reinitiate the rapid reaction at specified water concentrations were recorded (Fig. 1). Mg did not react with ethanol containing 5.0% water in the presence of CCl_4 at 25°C, but the reaction pro-

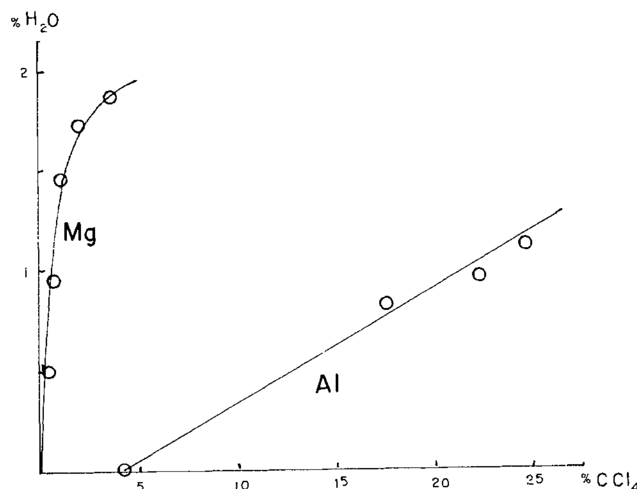

Fig. 1. The concentration of water needed to quench the reaction of Al and Mg and CCl_4-methanol mixtures and its dependence upon the CCl_4 concentration. Concentraotions are expressed in weight percentages in the liquid mixture.

ceeded vigorously with mixtures of CCl_4 and ethanol containing 0.1% water.

Products of the reaction.—The gaseous products of the Zn reactions were swept, in sequence, through a 0° trap and a liquid N_2 trap. Infrared spectral comparisons showed the gas frozen out in the second trap contained methane. The liquid N_2 trap permits the passage of H_2 gas which, of course, is a possible product of the reaction. However, gas density measurements on the gas passing the 0° trap suggested that it was predominantly methane. This conclusion was confirmed by a chromatographic separation on Molecular Sieve "5A" which achieved a good separation of H_2, O_2, N_2, and CH_4 at a column temperature of 80°. Moreover, it was demonstrated that CH_4 was the dominant gaseous product of the reaction of Zn with CCl_4-acetic acid, $CHCl_3$-acetic acid, CH_2Cl_2-acetic acid, and CF_3CCl_3-acetic acid mixtures (the latter three reactions were initiated by adding a trace of CCl_4). It was shown, on the other hand, that H_2 gas was dominant in the Mg and Al reactions with CCl_4-methanol mixtures. The largest yield of gas from any of these reactions was 0.25 mole of gas per mole of metal.

I recovered 1.5g of C_2Cl_6 from a reaction mixture containing 3g Zn, 40g methanol, and 16g CCl_4 which represents 0.15 moles of C_2Cl_6 per mole of metal. The recovery of C_2Cl_6 was performed by distilling away about half of the excess liquid, adding water to precipitate the C_2Cl_6, then subliming the residue at 187°C. Vacuum drying of the residue at 110° left a solid which, on the basis of weight relations and chloride content, was predominantly the oxychloride of Zn with a small amount of waxy material, probably chlorocarbon polymers. The mole ratio of chloride to Zn was 1.03. A mole ratio of CCl_4 to Zn of at least one was required for the complete dissolution of Zn.

Much less C_2Cl_6 was formed with Mg and the mole ratio of chloride to Mg was 0.57. Vacuum drying of reaction products from Al and Cr produced vitreous solids which were very hygroscopic and otherwise were not examined in detail.

Discussion

The reaction of several metals with CCl_4-alcohol mixtures at room temperature occurs in the absence of any electrochemical process. If these oxidation-reduction reactions are coupled with electrochemical reactions, such as those to be expected with alloys, the range of complexity of the reaction may be far more complex.

No aldehydes, acetals, or chloroform were detected in my experiments. I propose that such products, reported previously but not observed in these experiments, appear only with secondary reactions which may occur in the presence of alloys. Proposed mechanisms for this class of reactions (7, 8, 10) may need revision.

The most striking result of this preliminary study was the observation of CH_4 rather than H_2 gas in the Zn reaction and the potential violence of this and related reactions. Such autocatalytic processes could create previously unsuspected hazards in the laboratory and in industrial operations. The results also suggest that CH_4 is formed from the halocarbon compounds, in which case the stoichiometry corresponds to 1/4 mole of CH_4 per mole of Zn when CCl_4 is the halocarbon.

Story and Turner (13) suggested that the yellow color which developed in a thermal diffusion cell containing CCl_4-alcohol mixtures resulted from the reaction with Hg. It is more likely that this color was associated with brass corrosion products in solution. Their experience, along with that of Beyerlein (12), should stress the importance of taking into account the reactivity of CCl_4-alcohol mixtures when designing enclosures for such systems.

Manuscript submitted June 24, 1977; revised manuscript received Aug. 8, 1977.

Any discussion of this paper will appear in a Discussion Section to be published in the December 1978 JOURNAL. All discussions for the December 1978 Discussion Section should be submitted by Aug. 1, 1978.

Publication costs of this article were assisted by The University of North Carolina at Charlotte.

REFERENCES

1. R. Seligman and P. Williams, *J. Soc. Chem. Ind.*, **37**, 159T (1918).
2. M. C. Shaw, *J. Appl. Mech.*, **15**, 37 (1948).
3. H. Lund, *J. Am. Chem. Soc.*, **74**, 3188 (1952).
4. E. V. Zappi, *Annales Soc. Quim. Argentina*, **2**, 217 (1914).
5. K. A. Hoffman and E. Z. Sieler, *Ber.*, **38**, 3058 (1905).
6. F. H. Rhodes and J. T. Carty, *Ind. Eng. Chem.*, **17**, 909 (1925).
7. M. Stern and H. H. Uhlig, *This Journal*, **100**, 543 (1953).
8. R. H. Brown *et al.*, *ibid.*, **106**, 192 (1959).
9. R. P. M. Proctor and H. W. Paxton, *J. Mater.*, **4**, 729 (1969).
10. S. W. Vorster, *Corros. Sci.*, **9**, 801 (1969).
11. R. Heitz and C. Kyriazis, 173rd ACS National Meeting, New Orleans, Louisiana, March 21-25, 1977.
12. A. L. Beyerlein, Private communication.
13. M. J. Story and J. C. R. Turner, *Trans. Faraday Soc.*, **65**, 1523 (1969).

JOURNAL OF THE ELECTROCHEMICAL SOCIETY

SOLID-STATE SCIENCE
AND TECHNOLOGY

JANUARY
1978

SSST

Optical Absorption as a Control Test for Plasma Silicon Nitride Deposition

Myron J. Rand* and David R. Wonsidler

Bell Laboratories, Allentown, Pennsylvania 18103

ABSTRACT

The composition (Si/N) and properties of glow discharge-deposited silicon nitride films are sensitive to variations in many apparatus parameters. A rapid and simple test for film composition is needed to monitor and control production equipment. The position of a defined optical absorption edge in the near ultraviolet and visible ranges serves this purpose over a Si/N atomic ratio range of 0.8-1.5. Film thickness is determined at the same time. The procedure and a typical calibration curve are given; computation is simple. The existence of relatively low energy optical absorption is considered evidence for a highly distorted and irregular structure compared with that of pyrolytic Si_3N_4.

Plasma-deposited silicon nitride has been gaining popularity as a final encapsulation film for integrated circuit chips. This hard, adherent dielectric provides scratch and particle protection during mounting and bonding operations; it also helps to protect the metallization from corrosion and provides some measure of resistance to sodium ion penetration. This nitride is usually deposited with the substrate at 250°-350°C, a temperature which is well tolerated by aluminum metallization.

Plasma nitride deposition is actually a low pressure chemical vapor deposition reaction aided by a radio frequency glow discharge. The mechanism of the reaction is unquestionably complex. The film contains substantial residual bonded hydrogen from the silane and ammonia reactants, and it would be best described as a polysilazane, $Si_xH_yN_z$. Unlike 1 atm pyrolytic silicon nitride, it has no fixed stoichiometry. We have analyzed films with Si/N atomic ratios ranging from 0.7 to 1.5.

As with most plasma reactions, experience has shown that the course of the polymerization and the properties of the resulting film are sensitive to many deposition parameters. Plasma power and pressure, electrode separation, wafer temperature, total flow rate, reactant concentrations, the carrier gas used: these are only some of the variables we have found to be important. Furthermore, interactions among these are common, so that it may be impossible to generalize on the influence of an individual variable. Close control of the deposition machine is required to produce a film with good properties, and control wafers should be included along with device wafers in every run.

For thin film insulators, common control tests include thickness (usually by some optical method), fluoride etch rate, refractive index, flaw density, and film stress. Unfortunately we have not found any of these to be reliable indicators of reproducibility of nitride film composition, and it is composition which largely determines film properties and which responds sensitively to many deposition variables.

* Electrochemical Society Active Member.
Key words: plasma polymerization, thin films.

We believe the best criteria for plasma nitride control are the Si/N ratio of the film (oxygen being absent) and the uniformity of thickness over the batch of wafers. For the latter there are conventional methods. For composition, however, the most unequivocal determination is electron microprobe analysis, which is far too complex for a routine control test. Refractive index, as measured by ellipsometer, was found to correlate only roughly with composition, and furthermore the correlation seems to be somewhat different for different reactors. The films are probably too thick and too nonuniform for ellipsometric work; in addition, there is significant absorption at the measuring wavelength (546 nm), especially for the higher Si/N films. Nomographs or computer programs for refractive index which assume a transparent film give too high a result under this condition, and the error is increasingly serious the thicker the film and the more the absorption.

The presence of optical absorption in the visible range is a clue to another possibility for composition monitoring. Stoichiometric (pyrolytic) Si_3N_4 films have an absorption edge near 225 nm (1), whereas plasma silicon nitride films can have absorption edges well into the visible range and vary in appearance from colorless to deep amber. The latter are silicon-rich, by analysis. The extra absorption could be due to structural disorder, causing band broadening and "tailing" at the edges, or, alternatively, some bonding which is not present in Si_3N_4. Since neither SiH_4 nor NH_3 absorbs strongly in the 200-400 nm range, the absorption is unlikely to be caused by Si-H or N-H bonds, leaving only Si-Si as a reasonable possibility. If excess silicon were present in units as large as two or three bond lengths, the film would begin to show some of the optical properties of pure Si (2), including strong absorption in the near ultraviolet.

Either explanation, disorder or Si-Si bonding, suggests a correlation between composition and absorption or absorption edge. We report here an investigation of this correlation and show that a simple spectrophotometer scan can contain information on both thickness and chemical composition of plasma nitride films. Only an approximate refractive index is required. The answers

are easy to extract, and the method is therefore suitable for controlling deposition machine operation.

Experimental

Plasma nitride films 0.5-1.5 μm thick were deposited from SiH_4 and NH_3 in three different radial-flow reactors of the type first described by Reinberg (3). A 13.6 MHz glow discharge was maintained between two horizontal plates in a capacitor configuration, with substrate wafers resting on the lower (heated) electrode. Reactants entered the discharge around the periphery of the wafer table and were exhausted at the center. By varying plasma power, pressure, and reactant ratios the gamut of plasma nitride compositions could be produced.

For the purposes of this study the films were deposited on 22 mm square Corning microscope cover glasses. These are transparent down to 300 nm, so the more costly vitreous fused silica or sapphire is not really necessary. A 1/4 in. square in the center was defined by a cardboard mask and transmission measured with a Perkin-Elmer Model 202 ultraviolet-visible spectrophotometer. It is an advantage to have a readout directly in absorbance ($\log I_0/I$) units. Either an uncoated glass or an attenuator may be used in the reference beam.

The transmission level fluctuates with wavelength even in the absence of absorption because of interference effects. With a transparent film on a transparent substrate of lower index, maximum transmission is the same as that for the substrate alone. Consequently, for comparability of spectra the maximum transmission in the minimally absorbing 600-750 nm range was set at 100% using the instrument adjustment for this purpose.

After absorbance measurement, the same area of the sample was analyzed with the MAC 400 electron probe microanalyzer (4). CVD pyrolytic Si_3N_4 about 8000Å thick was used as the standard for both Si and N. To minimize surface charging, a 500Å film of carbon was evaporated onto the samples and standard. A new standard specimen was coated along with each group of samples to assure uniform carbon thickness. Some analyses were performed after evaporation of ~300Å of aluminum, with equally satisfactory results.

The microprobe uses wavelength-dispersive Johanson-type spectrometers with flow-proportional x-ray detectors. A Tousimis Research Corporation universal x-ray detector with a Nitrolucid® window was used for nitrogen. The accelerating potential was usually 5.5 keV with an effective penetration depth of ~0.37 μm in plasma SiN if a density of 2.3 is assumed and ~0.27 μm in the Si_3N_4 standard ($d = 3.1$). The analyses on Al-coated films were performed at 7.0 keV with essentially identical results and with standard deviation halved.

Si-Kα and N-Kα x-ray intensities were measured for 20 sec counting periods on samples and standards, taking at least 12 locations at random on each. Averaged background intensities above and below characteristic wavelength positions were subtracted from peak intensities. Intensities were converted to weight percentages utilizing MAGIC IV (5).

In ten of the first eleven samples analyzed, the sum of Si and N weight percentages was 100 ± 2%. The Si data were more reproducible, had smaller 2σ limits, and were less subject to noise than the N counts. Thereafter it was decided to analyze only for Si and calculate N by difference; all the Si:N atomic ratios reported here were obtained this way. In all samples oxygen was at or below the detection limit of ~0.2%.

Before a film may be characterized by its absorbance, variations in thickness among films must be taken into account. According to the Beer-Lambert law, absorbance is directly proportional to absorption path. Thus, readings may be normalized by dividing the absorbance by the film thickness. To make this more convenient for the operator, we have arbitrarily defined the absorption edge as the wavelength λ_a at which this ratio is unity when thickness is in micrometers. In other

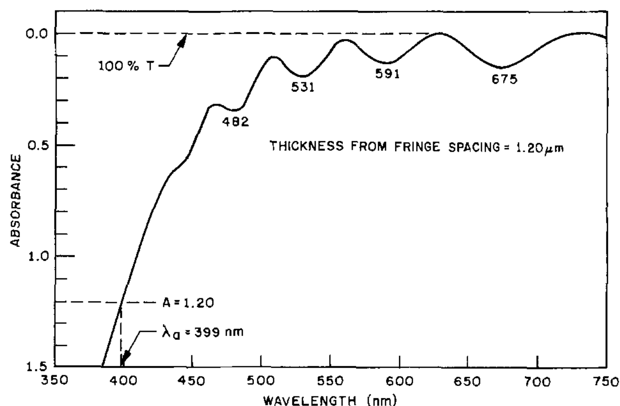

Fig. 1. Typical transmission curve for plasma nitride film on glass, illustrating the method for locating λ_a.

words, λ_a is the wavelength at which the absorption coefficient is $10^4/e$ cm^{-1}. For example, for a 1.25 μm thick film λ_a is where $A = \log I_0/I = 1.25$, or the transmission is down to about 5%. For a film of the same optical properties but only 0.8 μm thick, an absorbance of 0.8 should be found at the same λ_a.

Figure 1 shows a typical spectrophotometer scan and the method for determining λ_a.

The advantage of this procedure lies in the fact that the transmission curve yields thickness as well as absorbance. There is enough difference in index of refraction between plasma SiN, $n > 1.9$, and the glass substrate, $n = 1.51$, to produce interference fringes in the transmission spectrum. A satisfactory approximation for film thickness d in this normal incidence case is

$$d = \frac{N\lambda_2\lambda_1}{2n(\lambda_2 - \lambda_1)}$$

where λ_2 and λ_1 are wavelengths of transmission minima ($\lambda_2 > \lambda_1$), N the order difference, *i.e.*, the number of complete cycles between λ_1 and λ_2, and n the refractive index. The ellipsometer result may be used for the index; Fig. 1 shows that the absorption edge is so sharp that λ_a is not very sensitive to thickness. A 10% error in thickness results in ~3% error in Si/N ratio.

Results and Discussion

In Fig. 2 the results for composition are plotted *vs.* λ_a. Error bars shown are for 2σ limits. It is evident that the wavelength of the absorption edge, as defined here, is indeed a good index of plasma nitride film Si/N ratio, at least in the range of deposition conditions which we used.

Because of the variety of deposition parameters which can influence film composition, we would caution

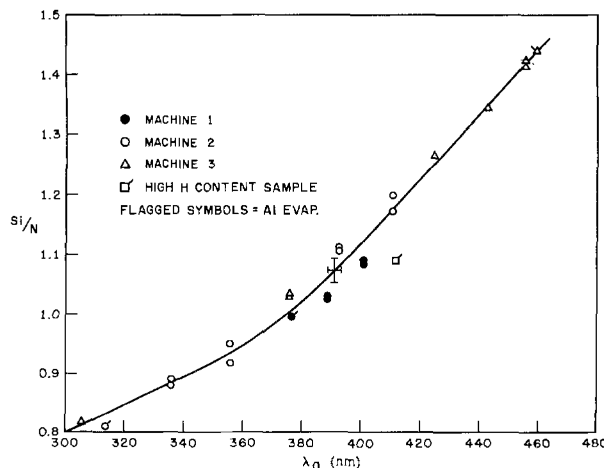

Fig. 2. Correlation of electron microprobe analyses and optical absorption edge. 2σ error bars are shown.

against accepting Fig. 2 as a calibration curve until it is confirmed that it is valid for the particular equipment. Figure 2 covers a wide range of compositions made with some variations in power as well, but there can be no guarantee that it is perfectly general. We believe, however, that for any mode of operation one can establish a Si/N *vs.* λ_a curve as we describe. Note that the one point departing considerably from the Fig. 2 curve represents a sample made under conditions quite different from the normal ones, *i.e.*, five times the SiH_4 concentration, 1/4 the pressure, and twice the deposition rate. Infrared spectra have established that this film contained roughly 50% more hydrogen than usual. Since neither Si-H nor N-H bonding is expected to absorb at >250 nm, the result of having less excess elemental Si, *i.e.*, fewer Si-Si bonds, than usual for a film of given Si/N should be less absorption. This reasoning is evidently naive, since the sample clearly has greater absorption than would be expected for Si/N = 1.1.

The point is emphasized by Fig. 3. Here we show absorption curves for amorphous silicon (6), pyrolytic Si_3N_4 (1), and four typical intermediate plasma nitride compositions. The calculated curve for Si/N = 1.25 [H. R. Philipp, (1)] is based on the statistical probability of each of the allowable types of Si tetrahedral bonding for that composition. The assumption is made that there are no N-N bonds and that all absorption at <5 eV is due to Si-Si bonding. Since the absorption curve for amorphous 100% Si is known, this "bond-counting" approach provides a prediction for the absorption of any composition between the two extremes of Si and stoichiometric Si_3N_4. Any success of such a model, *e.g.*, for SiO_x (2, 6), is evidence that intermediate compounds are not simple mixtures of the extremes of the range but rather an atomic-scale blending or polymer. The absorption curves for plasma nitrides do indeed occupy a position intermediate between those of Si and Si_3N_4; however, agreement with the random bonding model is not very good. In all cases, the plasma

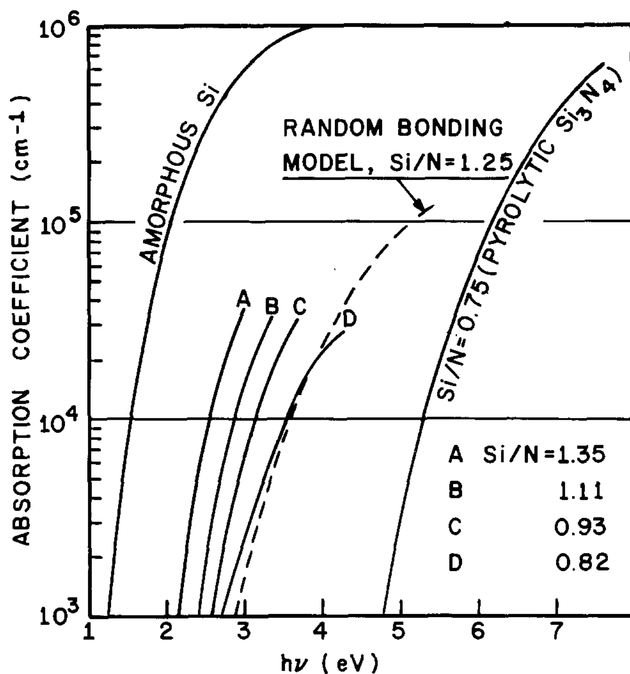

Fig. 3. Optical absorption of various compositions in the range between amorphous Si and stoichiometric Si_3N_4. A, B, C, and D are curves for plasma SiN films from this work.

nitrides have too much absorption for their Si/N ratios. Curve D (Si/N = 0.82) is rather far removed from the curve for Si/N = 0.75, and obviously pyrolytic Si_3N_4 would never fit on the curve of Fig. 2. The calculated curve for Si/N = 1.25 actually fits a plasma nitride curve for Si/N = 0.8.

It is beyond the scope of this report to investigate the optical properties of plasma nitride films in any fundamental or systematic fashion. It seems certain that something more than excess silicon is responsible for absorption in the near ultraviolet region. The most likely cause is severe distortion of the structure, in terms of bond distances and angles. This would shift the edges of the absorption band markedly. A 20% energy difference is not excessive for changing from rings of tetrahedra (Si_3N_4) to the random three-dimensional atomic network which might very well represent this plasma polymer. Furthermore, the presence of hydrogen as a major component (7) can only serve to increase the extent of dislocation and strain the structure even further. Our results support what has been amply demonstrated by now: that plasma-polymerized "silicon nitride" bears little resemblance in structure and properties to pyrolytically deposited Si_3N_4 and should, therefore, be evaluated as a unique material.

Summary

The composition and properties of plasma silicon nitride are sensitive to variations in many deposition parameters. A rapid and simple control test to measure or infer film composition is needed. The position of a defined optical absorption edge in the near ultraviolet and visible meets this requirement over a quite broad Si/N ratio range. A typical calibration curve and the procedure are given; film thickness is determined at the same time. With a rough refractive index available, a commercial spectrophotometer is the only instrument required, and computations are simple. The existence of relatively low energy optical absorption is considered evidence for a highly distorted and irregular structure compared with that of pyrolytic Si_3N_4.

Manuscript submitted July 19, 1977; revised manuscript received Aug. 17, 1977. This was Paper 153 presented at the Atlanta, Georgia, Meeting of the Society, Oct. 9-14, 1977.

Any discussion of this paper will appear in a Discussion Section to be published in the December 1978 JOURNAL. All discussions for the December 1978 Discussion Section should be submitted by Aug. 1, 1978.

Publication costs of this article were assisted by Bell Laboratories.

REFERENCES

1. E. A. Taft, *This Journal*, **118**, 1341 (1971); H. R. Philipp, *ibid.*, **120**, 295 (1973); H. J. Stein, *J. Appl. Phys.*, **47**, 3421 (1976); J. Bauer, *Phys. Status Solidi A*, **39**, 411 (1977).
2. H. R. Philipp and E. A. Taft, *Phys. Rev.*, **120**, 37 (1960); H. R. Philipp, *J. Non-Cryst. Solids*, **8-10**, 627 (1972).
3. A. R. Reinberg, Abstract 6, Extended Abstracts, The Electrochemical Society Meeting, San Francisco, May 12-17, 1974; U.S. Pat. 3, 757,733.
4. Materials Analysis Company, now Etec Corporation.
5. J. W. Colby, Proceedings of the 6th National Conference on Electron Probe Analysis, Pittsburgh, Pa., 1971, Paper 17.
6. H. R. Philipp, *J. Phys. Chem. Solids*, **32**, 1935 (1971); D. E. Carlson *et al.*, *Thin Solid Films*, **45**, 43 (1977).
7. M. J. Rand and W. A. Lanford, Submitted to *J. Appl. Phys.*

The Preparation and Low Energy Electron (LEE) Excitation of SnO_2:Eu Powder Phosphor

T. Matsuoka, Y. Kasahara, M. Tsuchiya, T. Nitta,* and S. Hayakawa

Matsushita Electric Industrial Company Limited, Materials Research Laboratories, 1006 Kadoma, Osaka, Japan

ABSTRACT

We carried out an investigation on preparation and low energy electron (LEE) luminescence of SnO_2:Eu powder phosphors. Solid powder mixing, hydroxide coprecipitation, and oxalate coprecipitation methods were examined for preparation. The oxalate method was found to give best results. SnO_2:Eu powder phosphors made with 0.5 atomic percent (a/o) and more Eu contained $Eu_2Sn_2O_7$ as separate phase. No change of the lattice parameters could be observed up to 8 a/o of added Eu. The amount of Eu actually dissolved in the SnO_2 lattice is estimated to be between 0.05 and 0.5 a/o of Eu/Sn. Cathodoluminescence of SnO_2:Eu phosphors was examined at high and at low excitation voltage. Measured emission spectra did not show green and blue emission lines due to transitions from $^5D_1$ and higher states, in contrast to observations on single crystals by Crabtree. SnO_2:Eu phosphors show orange-red emission without any charge-up effect when excited by electrons as low as 10V. The luminous efficiency was about 0.2-1 lumens/W for various excitation voltages and pulse duties.

Stannic oxide, SnO_2, is widely used as a metal oxide resistor in electronic applications, for transparent electrically conducting coatings on glass, and as u.v. sensor utilizing its photoconducting properties. However, studies of SnO_2 as a phosphor host material are comparatively rare.

Hall *et al.* (1) observed cathodoluminescent emission bands due to Ti and W at ~565 and 440 nm, respectively, in zoned cassiterites of hydrothermal origin. The cathodoluminescence of SnO_2 single crystals doped with Eu and Tb was studied in detail by Crabtree (2, 3). He used crystals grown by vapor phase transport and then doped with Eu or Tb. The emission spectrum contained a broad band of the host material, and lines due to the presence of Eu^{3+} and Tb^{3+} ions. He also studied photo-, cathodo-, and thermoluminescence of Tb-doped SnO_2 crystals containing Li, H, or P as charge compensation and of SnO_2 crystals doped with various amounts of Eu without or with interstitial Li^+ as charge compensation (4-6). Although there are several other reports on SnO_2 phosphors more or less similar to the ones above, we are not aware of studies on low energy electron excitation of these materials.

ZnO phosphors are known for LEE excitation (7-9) and have recently been studied as display tube phosphors excited by LEE from a gas plasma (10, 11). In fact, ZnO is widely used for α-numeric display devices (pocket calculators, etc.) because of its low dead voltage and high efficiency under LEE excitation. However, the emission color of ZnO is restricted to bluish-green. A search for phosphors emitting in other colors with reasonably high efficiencies under LEE excitation had been fruitless (12).

A phosphor suitable for LEE excitation must have low dead voltage and either low electrical dark resistivity or some photoconduction. Most common phosphors do not meet these requirements. Even if they have low dead voltage, they are highly electrically insulating and charge up very rapidly under LEE excitation because of a secondary-electron emission coefficient below unity at low voltage. The resistivity of a phosphor for LEE application must be low to prevent the phosphor screen from charging up negatively.

The present study was done to work out the preparation conditions of SnO_2:Eu powder phosphors and to study their cathodoluminescence. The emission under LEE excitation is affected by the semi- and photoconductive properties of the SnO_2. We have established that SnO_2:Eu phosphors emit a steady reddish-orange emission under excitation by LEE as low as 10V.

Experimental Procedures

Preparation of powder phosphors.—A representative experimental procedure is as follows. 1/5 mole of $SnCl_2 \cdot 2H_2O$ and europium chloride in the concentrations of 0, 0.05, 0.5, 1, 3, and 8 a/o were dissolved in 400 cm^3 ethyl alcohol. 35g of $(NH_4)_2C_2O_4 \cdot H_2O$ were dissolved in 750 cm^3 water at 60°C. The chloride solution was then added to the oxalate solution while vigorously stirring. The suspension was kept at 60°C for about 5 min after which the precipitate was filtered, washed, and dried. The dry powders were fired in vitreous quartz boats in oxygen for 2 hr at 1000°-1300°C.

Two other methods of oxalate precipitation were tested. One of them is to use 0.1*N* HCl in water as a solvent of $SnCl_2 \cdot 2H_2O$ and europium chloride, and a solution of $H_2C_2O_4 \cdot 2H_2O$ in water. The precipitation was carried out at room temperature in this case. Another method used a solution of CH_3COOH in water as solvent for the $SnCl_2 \cdot 2H_2O$ and the europium chloride, and $(NH_4)_2C_2O_4 \cdot H_2O$ dissolved in water. The precipitate in this case was held at 80°C for 30 min while stirring. The *p*H of this mixed solution was kept at about 3-4 by the buffer action of the CH_3COONH_4-CH_3COOH system. Both methods were found to give the same final phosphors as the alcohol method. The latter is preferred nevertheless because of the low solubility of the oxalate.

Two different preparation methods of solid powder mixing and hydroxide coprecipitation were also examined. The solid powder mixing method was found to be poorly reproducible and the resulting phosphors were not bright. The oxalate methods were found to give better precipitates of larger particle sizes, better stability at drying, higher activity during subsequent firing, and generally easier preparation and handling than the hydroxide method.

Measurements.—DTA and TGA measurements, electron microscope, and x-ray powder diffraction were carried out to examine the properties of the powders at various stages of preparation.

The cathodoluminescence of the completed phosphors was tested at 10 kV excitation voltage. Dry phosphor layers in a copper tray were bombarded

* Electrochemical Society Active Member.

Key words: SnO_2:Eu powder phosphor, LEE excitation, oxalate coprecipitation methods.

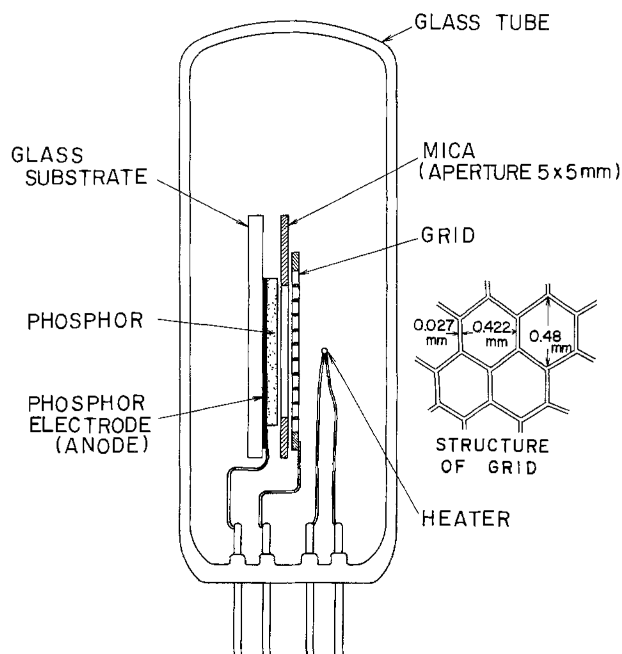

Fig. 1. Schematic of the device used to measure LEE cathodoluminescence.

with d-c electrons from a modified TV-gun at room temperature with a current density of 2.8 $\mu A/cm^2$. A grating spectrometer with 0.1 mm slits and a S-10 photomultiplier were used for emission spectrum measurements.

A schematic diagram of the device to study LEE excitation is shown in Fig. 1. The phosphor was coated at a density of 3 mg/cm^2 on a glass plate coated with a conducting SnO_2 electrode using a centrifugal settling method (3000 rpm) with pure water as dispersing agent. No binder was used. The region actually bombarded with electrons is an aperture area of 5 $\times$ 5 mm size. The grid in front of the phosphor layer is made of stainless steel 60 μm thick and has a honeycomb-like structure as shown in Fig. 1.

The glass substrate coated with the phosphor, the mica aperture, and the grid were annealed at 350°C for 30 min in an atmosphere of 10% H_2 + 90% N_2 at 1 atm pressure. This structure and the heater were then mounted to the electrodes in a glass stem of a TV cathode ray tube. The stem was covered with a glass cap and fused together. The tube was exhausted to below 10^{-6} Torr while heating to 200°C, then the heater coated with $BaCO_3$, $SrCO_3$, and $MgCO_3$ was activated by heating, causing decomposition of the carbonates to the oxides. The tube finally was sealed and the getter operated.

Results and Discussion

Preparational characteristics.—DTA and TGA of thermal decomposition of 36.8 mg of pure SnC_2O_4 in air at a heating rate of 600°C/hr were examined to establish the lowest permissible firing temperature. A decomposition starts gradually at about 245°C accompanied by a broad endothermic peak. More rapid decomposition between 322° and 360°C is indicated by two large exothermic peaks and a strong reduction in weight. The latter is complete already at 345°C and is only 10.8 mg which is smaller than the theoretical decrease of 12.8 mg of a reaction $SnC_2O_4 \rightarrow SnO + CO_2 + CO$ probably because of an oxidation reaction $SnO + \frac{1}{2} O_2 \rightarrow SnO_2$ taking place simultaneously. The two large exothermic peaks are believed to be the result of a superposition of the endothermic reaction of the decomposition of the oxalate and the exothermic reaction of the combustion of CO produced by the oxalate. Also the exothermic reaction of the oxidation of SnO to SnO_2 probably is involved because of the small rapid increase in weight just after 345°C. The latter reaction apparently is still incomplete and is completed only at increasingly higher temperature because of a broad exothermic peak around 500°C and the slow increase in weight above 360°C. The over-all weight decrease up to 655°C is 10.3 mg, coinciding with the theoretical weight loss in the reaction $SnC_2O_4 \rightarrow SnO_2$.

Also an oxalate precipitate containing 8 a/o of Eu in a sample weight of 20 mg was examined by DTA and TGA. A new small endothermic peak was observed at about 210°C and the starting and completion temperatures of the decomposition and oxidation reaction were 311° and 331°C, respectively, both lower than those in case of pure SnC_2O_4. No other difference was observed.

These oxalate precipitations showed a uniform reddish-orange luminescence under u.v. and under electron excitation after firing at 1000°C for 2 hr in oxygen. The actual phosphors were fired at 1300°C, however. When an alumina boat was used for the firing, the boat was destroyed by the thermal shock of the vigorous exothermal reaction. Therefore these samples were fired in quartz boats.

Particles of an oxalate precipitate containing 1 a/o Eu are shown in Fig. 2(a). Each particle has leaf-like shape approximately 60 μm long, 30 μm wide, and 7-8 μm thick. Generally, increasing Eu concentra-

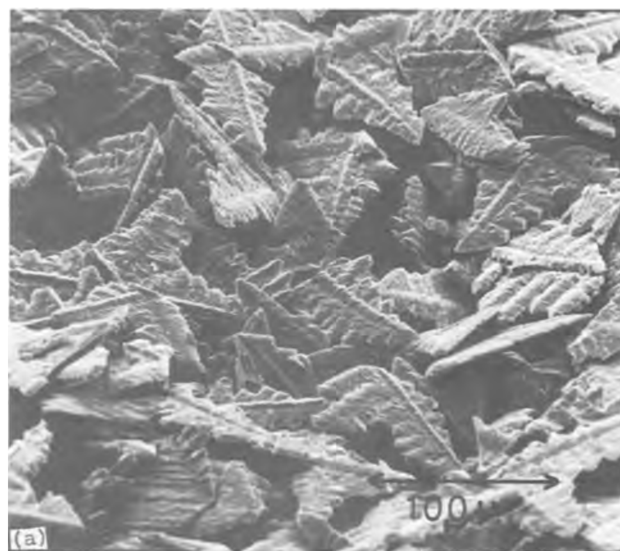

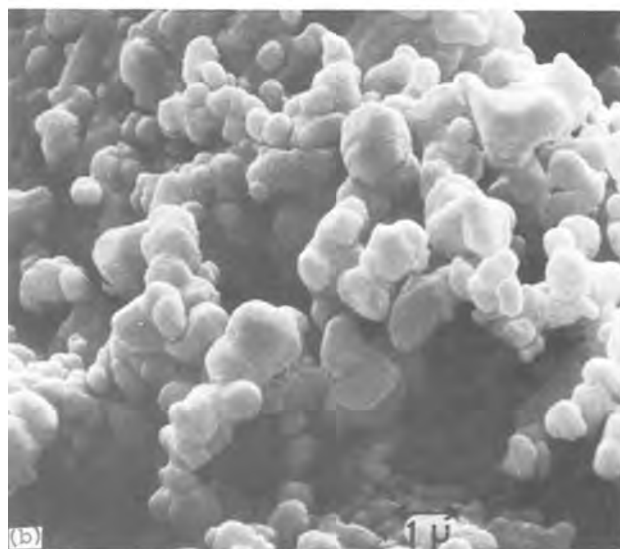

Fig. 2. Particles of precipitated SnC_2O_4:Eu(1%), (a) and particles after firing in oxygen for 2 hr at 1300°C(b).

tion caused smaller particles of more irregular shapes. Particles of the same material, containing 1 a/o Eu after firing for 2 hr at 1300° in oxygen are shown in Fig. 2(b). The particle size from 0.5 to 1.5 μm of this phosphor is smaller than that of the oxalate before firing.

X-ray powder diffraction spectra were taken of all precipitates. The weak diffraction peaks of pure SnC_2O_4 become still weaker with increasing Eu concentration but no change of the d value could be observed up to 8 a/o Eu. However, a new peak at $d = 6.06Å$ was observed at 8 a/o Eu. We believe that Eu is incorporated up to about 3 a/o in the SnC_2O_4 but cannot explain the absence of any shift of the d value with increasing Eu concentration in the diffraction patterns.

Results of similar x-ray powder diffraction measurements of completed phosphors are summarized in Table I. All samples containing 0.5 a/o and more Eu show pyrochlore-type $Eu_2Sn_2O_7$ as minor phase. No change of the lattice parameters with increasing Eu was observed. We conclude that Eu is soluble in SnO_2 to a concentration between 0.05 and 0.5 a/o.

High energy electron excitation.—Studies of cathodoluminescence were restricted to phosphors prepared by the oxalate method. All these phosphors were fired for 2 hr at 1300°C in oxygen.

Figure 3 shows an emission spectrum of pure SnO_2. It extends from about 350 nm in the ultraviolet to about 750 nm in the infrared with a maximum at about 500-520 nm. Its whitish-blue color agrees with that reported by Crabtree on single crystals (2) although Crabtree mentions an intensity maximum at about 600 nm.

An emission spectrum of SnO_2:0.05% Eu is shown in Fig. 4. The emission of pure SnO_2 is completely suppressed now in agreement with Crabtree's observation on single crystals. The most intense emission corresponds to $^5D_0$-$^7F_1$ transitions. Emission contributions due to $^5D_0$-$^7F_0$, $^5D_0$-$^7F_2$, and $^5D_1$-$^7F_4$ transitions are much weaker. No appreciable emission was observed at shorter wavelengths below 580 nm.

The emission spectrum does not appreciably change with increase of the added Eu concentration up to 8 a/o. Only the emission due to $^5D_0$-$^7F_0$ transition increases somewhat relative to the others. For instance, the intensity ratio of $^5D_0$-$^7F_0$ compared to $^5D_0$-$^7F_1$ emission was about doubled at 8% Eu compared to 0.05% Eu. No shorter wavelength emission from $^5D_1$ or higher energy states was observed, in contrast to Crabtree's observations on single crystals. The second phase, $Eu_2Sn_2O_7$ of pyrochlore structure, observed at higher Eu concentrations did not contribute to any visible emission.

Figure 5 shows the voltage dependence of the brightness of cathodoluminescence. This characteristic is different for different Eu additions. The phosphor containing 0.05 a/o Eu increases linearly in brightness up to about 15 kV and saturates above this voltage. The highest brightness was observed on a phosphor containing 1 a/o of added Eu; still higher Eu concentrations cause lower brightnesses. The saturation voltage decreases with increasing Eu concentration. Since the phosphors containing 0.5% and more Eu contain $Eu_2Sn_2O_7$ as separate phase (Table I), some influence of this phase on brightness and saturation voltage can certainly be expected. The decrease of saturation voltage with increase of Eu is considered to be due to lowering of second unity intercept (second crossover voltage) of the secondary-emission ratio *vs.* voltage curves by the coexistence of $Eu_2Sn_2O_7$ where phosphors normally saturate because of negative charge-up in still higher voltage. It is difficult to consider the dead core in each phosphor particle since the saturation voltage rather decreases with increasing of Eu. It is hard to explain all details.

The linear portions of all brightness-voltage curves extrapolate to finite brightnesses. This follows to

Table I. Results of x-ray powder diffraction analysis of SnO_2:Eu phosphors prepared by firing oxalate precipitates in oxygen for 2 hr at 1300°C

No.	Amount of Eu (a/o)	Phases observed	Lattice constant a (A)	c (A)
1	0	SnO_2	4.737	3.187
2	0.05	SnO_2	4.737	3.186
3	0.5	$SnO_2 + Eu_2Sn_2O_7$	4.737	3.186
4	1		4.738	3.187
5	3		4.737	3.187
6	8		4.737	3.187

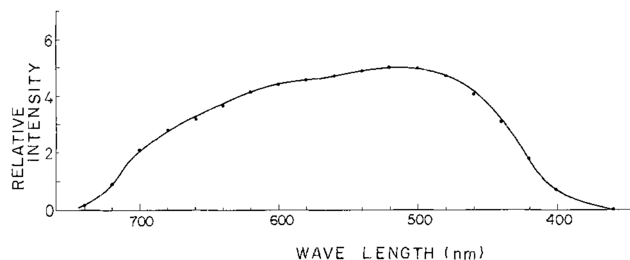

Fig. 3. Emission spectrum of cathodoluminescence of pure SnO_2

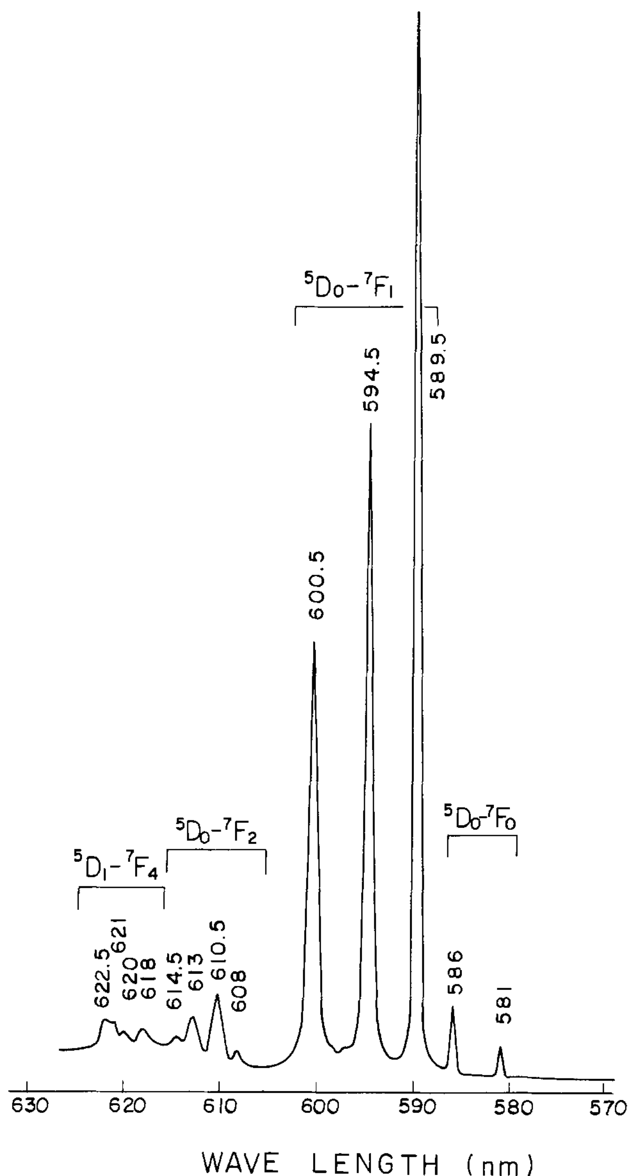

Fig. 4. Emission spectrum of cathodoluminescence of SnO_2: Eu(0.05%).

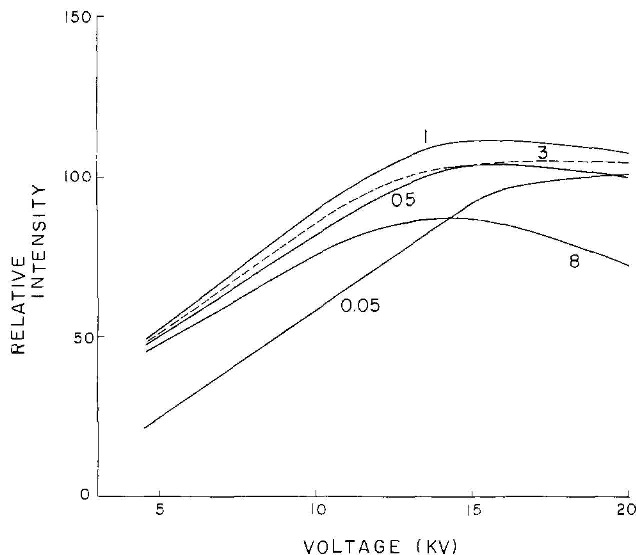

Fig. 5. Brightness-voltage dependence of cathodoluminescence of SnO_2:Eu phosphors. Numbers denote a/o Eu/Sn.

the surface-sensitive particles of the phosphors corresponding to the nonuniform structure particularly at shallow surface region (<0.09 μm from Terrill's equation) as expected from voltage less than 5 kV, but we have no reliable proof supporting this assumption.

The visible brightness of SnO_2:Eu containing 1 a/o of added Eu was compared to that of a commercial Y_2O_2S:5% Eu phosphor and found to be about 20% of the latter at 2.5 kV and 16% at 5 kV. The energy efficiency is somewhat lower, about 10% of that of Y_2O_2S:Eu, because of the different emission spectra.

Low energy electron excitation.—This study was limited to an SnO_2:0.05% Eu phosphor containing no $Eu_2Sn_2O_7$ as separate phase. Its luminescence characteristics under LEE excitation are shown in Fig. 6 as function of V_A (anode voltage) or V_G (grid voltage). Anode and grid were connected so that $V_A = V_G$. The three different duty cycles are excitation by 16.7 μsec pulses repeated every 267 μsec; (duty 1/16, left-hand curves), every 16.7 msec; (duty 1/1000, center curves), and every 167 msec; (duty 1/10,000, right-hand curves). Anode current, I_A, and grid current, I_G, are the currents during the 16.7 μsec pulses, B is the brightness, and η is the luminous efficiency in lumens/W. A heater voltage of 0.9 to 1.0V was used.

The phosphor showed a brightness of 7.5 f-L and an efficiency of 0.3 lumens/W at $V_A = V_G = 50V$, $I_A = 2$ mA, and the duty 1/16. A commercial ZnO:Zn phosphor familiar for LEE excitation applications gave 45 f-L and 2 lumens/W under the same conditions of excitation. When the exciting voltage was raised to 100V and the duty decreased to 1/1000, the SnO_2:Eu phosphor gave $B = 1.8$ f-L, $I_A = 5$ mA, and $\eta = 0.97$ lumens/W. For comparison again the ZnO:Zn phosphor excited under these same conditions gave $B = 4.2$ f-L, $I_A = 5$ mA, and $\eta = 2$ lumens/W. The efficiency of the SnO_2:Eu phosphor became about half of that of the ZnO:Zn phosphor. D.c. excitation of the SnO_2:Eu phosphor gave 60 f-L brightness and 0.18 lumens/W efficiency at $V_A = V_G = 75V$ and $I_A = 1.2$ mA.

The decay time (to 10%) of the luminescence following excitation by 16.7 μsec pulses depends on the excitation voltage (Fig. 7). It is fairly long, about 10 msec, at low voltage but decreases rapidly with increasing voltage above about 300V. The reason for this unexpected long afterglow is not clear. ZnO:Zn does not show a similar dependence of its afterglow on the excitation voltage. However, we believe the long decay of the SnO_2:Eu phosphor to be involved in the increase of the efficiency at 100V when going from duty 1/16 to duty 1/1000 (Fig. 6). Details are not understood.

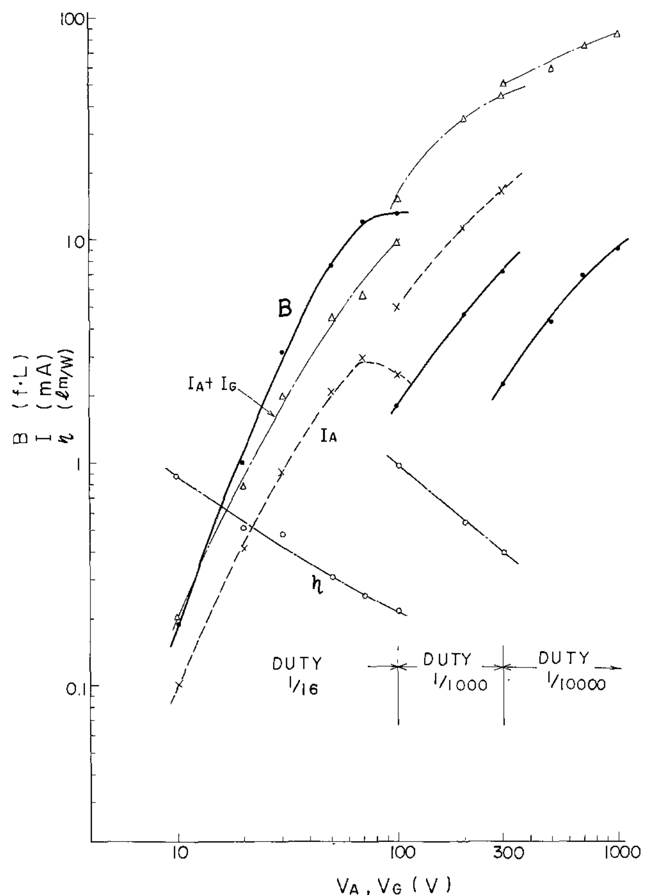

Fig. 6. Cathodoluminescent properties of SnO_2:Eu(0.05%) excited by low energy electrons.

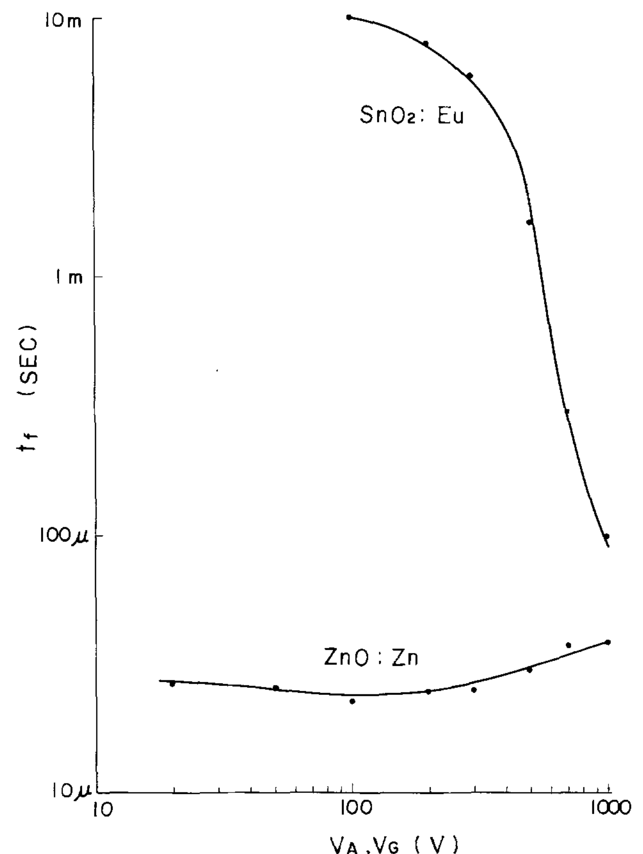

Fig. 7. Afterglow times of SnO_2:Eu(0.05%) and of ZnO:Zn

Summary and Conclusions

The most useful preparation technique of SnO_2:Eu phosphor is by coprecipitation as the oxalate followed by firing at high temperature. The higher the firing temperature, the longer the firing time, and the slower the cooling rate after firing, the more efficient is the final phosphor. In practice, firing for 2 hr at 1300°C in oxygen is sufficient. The maximum Eu concentration under these conditions incorporated in the SnO_2 lattice is between 0.05 and 0.5 a/o.

Cathodoluminescence of pure SnO_2 shows bluish-white emission of a very broad band extending from about 350 to 750 nm. SnO_2:Eu shows only the europium emission, most of it occurring in lines corresponding to $^5D_0$-$^7F_1$ transitions. This implies centrosymmetrical site symmetry such as D_{2h} or C_{2h}. Emission at shorter wavelengths corresponding to transitions from $^5D_1$ or other levels were not observed. The brightness of cathodoluminescence appears to saturate with increasingly high excitation voltage above about 15 kV, depending somewhat on the added europium amount. The energy efficiency of the SnO_2:Eu phosphor performing best under high energy excitation, a material containing 1% of Eu, is estimated to be about 1/10 of that of a commercial Y_2O_2S:Eu phosphor.

SnO_2:Eu phosphors can be excited to steady luminescence by LEE as low as 10V without any charge-up phenomenon. Its luminous efficiency so far is roughly 15-50% of that of ZnO:Zn, the only other phosphor known before suitable for LEE excitation. An SnO_2:Eu phosphor containing 0.05 a/o Eu/Sn shows long afterglow, about 10 msec to 10%, after excitation by electron pulses of 100V; this afterglow shortens considerably with increasingly higher voltage.

SnO_2:Eu phosphors appear to be useful for various applications where excitation by LEE is required as in a He-gas plasma described by Kazan, for instance (9). We provide an additional color, reddish-orange, besides the blue-green of ZnO:Zn. Some improvements can still be expected with further developments. Points under investigation are the optimization of the Eu-concentration, selection of a flux for better particle growth up to 6 ~ 7 μm, addition of sensitizers and charge compensators, and other refinements.

Manuscript submitted Dec. 15, 1976; revised manuscript received Aug. 29, 1977.

Any discussion of this paper will appear in a Discussion Section to be published in the December 1978 JOURNAL. All discussions for the December 1978 Discussion Section should be submitted by Aug. 1, 1978.

Publication costs of this article were assisted by Matsushita Electric Industrial Company, Limited.

REFERENCES

1. M. R. Hall and P. H. Ribbe, *Am. Mineral.*, **56**, 31 (1971).
2. D. F. Crabtree, *J. Phys. D*, **7**, L17 (1974).
3. D. F. Crabtree, *ibid.*, **7**, L22 (1974).
4. D. F. Crabtree, *ibid.*, **8**, 2097 (1975).
5. D. F. Crabtree, *ibid.*, **8**, 107 (1975).
6. D. F. Crabtree, *Phys. Status Solidi*, **A38**, 217 (1976).
7. G. Heiland, E. Mollwo, and F. Stöckmann, "Solid State Physics," Vol. 8, p. 223, Academic Press (1959).
8. C. B. Clark, *J. Opt. Soc. Am.*, **44**, 134 (1954).
9. P. Wachter, *Z. Phys.*, **161**, 62 (1964).
10. B. Kazan and W. B. Pennebaker, *Proc. IEEE*, **59**, 1130 (1971).
11. W. B. Pennebaker and J. F. O'Hanlon, *J. Appl. Phys.*, **45**, 1315 (1974).
12. M. Hiraki, A. Kagami, T. Hase, K. Norita, and Y. Nimura, Paper presented at the International Conference on Luminescence, Tokyo, Japan (1975).

Thermodynamic Considerations in the Use of Polysilicon Oxidation Tubes for Clean SiO_2 Film Preparation

Santos Mayo*

National Bureau of Standards, Electronic Technology Division, Institute for Applied Technology, Washington, D.C. 20234

and William H. Evans

National Bureau of Standards, Physical Chemistry Division, Institute for Materials Research, Washington, D.C. 20234

ABSTRACT

The thermodynamic equilibria established in oxidation atmospheres in polycrystalline silicon tubes operated at 1000°C are analyzed. Silicon oxidation tubes made by chemical vapor deposition through hydrogen reduction of pure trichlorosilane have very low sodium content (about 10 ppb or 1000 times less sodium than in transparent fused silica oxidation tubes). Due to the low sodium content in new oxidation tubes, clean (low alkali content) thermal oxide films can be grown on silicon wafers. However, tube contamination developed during semiconductor processing operations imposes the need for appropriate periodic tube cleaning to maintain sodium contamination in the oxidation atmosphere within acceptable levels. Tube cleaning reactions taking place at oxidation temperature are discussed showing that the quality of thermal oxide films is influenced by tube cleaning efficiency.

Preparation of thermally grown clean oxide films on silicon wafers has great technological impact on successful microelectronic device fabrication. Although the understanding of the role played by alkali ions in such films is not complete, especially concerning the behavior of electrically "active" and "inactive" contamination (1), the presence of alkali species in thermally grown silicon dioxide films has been ex-

* Electrochemical Society Active Member.

Key words: alkali contamination, clean SiO_2 film, microelectronic device preparation, MOS structures.

perimentally demonstrated to cause ionic conductivity and consequently instabilities in metal-oxide semiconductor (MOS) devices (2-5). The presence of sodium and other alkali species in thermally grown oxide films used for semiconductor device preparation has been extensively investigated (6-8). Sources of alkali contamination have also been investigated in processing materials (9-13), in oxidation furnace refractories (14), and in evaporated gate metal films (15). Addition of about 5% chlorine or hydrogen-chloride to the oxidation atmosphere has been reported to enhance the electrical stability of Si-SiO_2 structures, both through cleaning and passivating effects (16-22). HCl diluted in an inert gas carrier (concentration up to 10%) is used for periods of several hours immediately before oxidations to produce low mobile-ion content thermal oxide films for MOS device fabrication.

In a recent paper (23) the development of sodium contamination in oxidation atmospheres contained in transparent fused silica tubes operated at 1000°C was analyzed thermodynamically in terms of the impurity content primarily included in fused silica bulk resulting from the tube manufacturing process. Transparent fused silica tubes currently used in most semiconductor processing furnaces contain about 10 ppm sodium (24-25). *In situ* cleaning of fused silica tubes at 1300°K results in removal of material from the inner tube wall surface creating a sodium-depleted layer. This in turn reduces the sodium content in the oxidation ambient, allowing the thermal growth of cleaner oxide films on silicon wafers. However, due to its high diffusivity in SiO_2 [$D = 2 \times 10^{-6}$ cm²/sec at 1000°C (26)] sodium from furnace refractories or from the room atmosphere around the oxidation tube may be incorporated into the fused silica wall contributing to the maintenance of its contamination level. When fused silica oxidation tubes are replaced by silicon tubes, the conditions established in the oxidation ambient are expected to be more favorable for growing clean thermal oxide films on silicon wafers. This is caused by the low sodium content in silicon tubes fabricated by chemical vapor deposition through hydrogen reduction of trichlorosilane. This process produces high purity polysilicon with only 10 ppb sodium contamination, 1000 times less sodium content than in fused silica tubes (28). However, due to external contamination sources (*i.e.*, sodium from refractories and room ambient), periodic *in situ* cleaning of the tube is necessary to maintain appropriate conditions in the oxidation atmosphere. The cleaning interval for both fused silica or silicon tubes is determined by the boundary conditions at the tube wall outer surface and the diffusion of sodium in the tube wall. The diffusion coefficient of sodium in polycrystalline silicon is higher than in single crystal silicon due to grain boundary effects. At 1000°C the latter is $D = 3 \times 10^{-6}$ cm²/sec (26). Similar effects were reported on the diffusion of boron in silicon at 1050°C (27).

The work presented here is an extension of the previous analysis on the behavior of fused silica oxidation tubes at 1000°C (23).[1] Silicon oxidation tube behavior resembles the fused silica tube behavior except for the initial low sodium content when the tube is new. The effects of HCl cleaning on these tubes are also analyzed.

Oxidation of Silicon Wafers in Silicon Oxidation Tubes

The kinetics of silicon oxidation have been extensively studied by different authors for a number of temperatures in the range of 800°-1200°C and for several oxidation atmosphere compositions contained in fused silica tubes [most early work on this subject is listed in bibliographic compilations on MOS technology (9, 30)]. It was shown that the addition of trace amounts of water to the oxidation ambient causes a significant increase of silicon oxidation rate for all silicon orientations (31). It has also been shown that the equilibrium sodium density in oxidation atmospheres at 1300°K significantly increases when a few ppm water are added to the oxidation atmosphere (23). From these results it can be stated that the preparation of clean, low mobile ion content oxide films on silicon wafers is controlled primarily by four parameters: the oxidation temperature, the amount of sodium (in general, alkali) contamination in the tube wall bulk, the amount of water content in the oxidation atmosphere, and the furnace environment. The use of strictly controlled hydrocarbon-free dry oxygen in addition to alkali-free oxidation tubes operated at high temperatures (above 1000°C) may result in clean thermal oxide preparations if appropriate care is taken concerning clean room environments around oxidation facilities. For high temperature (close to 1200°C) processes where devitrification of fused silica may produce serious problems, silicon tubes are preferred due to their better mechanical behavior and low sodium contamination level.

In the present work, the equilibrium atmosphere established at 1300°K in a silicon oxidation tube was studied theoretically for a number of cases of practical interest.[2] Table I shows the equilibrium atmo-

[1] For these thermodynamic calculations data at 1300°K are used.
[2] The scheme for these calculations is outlined in the appendix of Ref. 23. Because of errors and approximations involved in thermodynamic data used to evaluate the equilibrium results, an absolute error of ±50% could be expected in these calculations. The relative error is much smaller.

Table I. Equilibrium atmosphere in silicon wet oxidation tube at 1300°K

Sodium content in silicon bulk: 10 ppb, oxygen at 1 atm, water at 10^{-4} atm

Reaction	K	Product	P (atm)	Na(cm^{-3})
$Si(c) + O_2(g) + H_2O(g) \rightarrow SiO_2(c) + \frac{1}{2}H_2(g) + OH(g)$	2.54×10^{19}	O_2	1.0	
$2H_2(g) + O_2(g) \rightarrow 2H_2O(g)$	1.35×10^{14}	$H_2(g)$	8.61×10^{-12}	
$Si(c) + O_2(g) \rightarrow SiO_2(c)$	1.8×10^{27}*	OH	4.82×10^{-7}	
$SiO(g) + \frac{1}{2} O_2(g) \rightarrow SiO_2(c)$	5.59×10^{18}	H_2O	10^{-4}	
$Na_2O \cdot SiO_2(c) \rightarrow SiO_2(c) + Na_2O(g)$	7.83×10^{-20}	Na_2O	7.9×10^{-28}	
$Na_2O \cdot SiO_2(c) + H_2O \rightarrow SiO_2(c) + 2Na(g) + 2\ OH(g)$	5.85×10^{-28}	Na	5.02×10^{-14}	
$Na_2O \cdot SiO_2(c) + H_2O \rightarrow SiO(OH)(g) + Na_2O(g) + OH(g)$	1.19×10^{-36}	SiO(OH)	3.13×10^{-15}	
$Na_2O \cdot SiO_2(c) + H_2O \rightarrow Si(OH)_2(g) + \frac{1}{2} O_2(g) + Na_2O(g)$	1.68×10^{-42}	$Si(OH)_2$	2.13×10^{-27}	
$Na_2O \cdot SiO_2(c) + H_2O \rightarrow SiO(OH)_2(g) + Na_2O(g)$	2.72×10^{-26}	$SiO(OH)_2$	3.44×10^{-11}	
$Na_2O \cdot SiO_2(c) + 2H_2O \rightarrow Si(OH)_4(g) + Na_2O(g)$	1.57×10^{-27}	$Si(OH)_4$	2.00×10^{-16}	
$2Na_2O \cdot SiO_2(c) + 3H_2O \rightarrow Si_2O(OH)_6(g) + 2Na_2O(g)$	1.38×10^{-51}	$Si_2O(OH)_6$	2.21×10^{-25}	
$Si(c) + 2H_2O(g) \rightarrow SiO_2(c) + 2H_2(g)$	1.33×10^{13}			
$Si(c) + H_2O(g) \rightarrow SiH(g) + OH(g)$	5.19×10^{-18}	SiH	1.08×10^{-15}	
$Si(c) + 2H_2O(g) \rightarrow SiH_4(g) + O_2(g)$	8.00×10^{-21}	SiH_4	8.00×10^{-29}	
$Si(c) + 3/2\ O_2(g) + 2Na(g) \rightarrow Na_2O \cdot SiO_2(c)$	7.14×10^{45}			
$Si(c) + 5/2\ O_2(g) + 2Na(g) \rightarrow Na_2O \cdot 2SiO_2(c)$	1.21×10^{73}			
$Na_2O \cdot SiO_2(c) + SiO_2(c) \rightarrow Na_2O \cdot 2SiO_2(c)$	0.944			
$Na_2O(g) + \frac{1}{2} O_2(g) \rightarrow 2NaO(g)$	0.42	NaO	1.82×10^{-14}	
$NaO(g) + H_2O(g) \rightarrow NaOH(g) + OH(g)$	4.69	NaOH	1.77×10^{-11}	$9.99 \times 10^{7} \simeq 10^{8}$
$2NaOH(g) \rightarrow Na_2(OH)_2(g)$	4.78	$Na_2(OH)_2$	1.50×10^{-21}	

* Rapid formation of a silica film on the silicon tube.

sphere resulting in a typical silicon oxidation tube operated at 1300°K using pure oxygen at 1 atm plus 100 ppm water. Sodium in the tube wall might be assumed to be sodium metasilicate [$Na_2O \cdot SiO_2(c)$] and sodium silicate [$Na_2O \cdot 2SiO_2(c)$]. Measurements of sodium vaporization from silica glasses (32) indicate that sodium metasilicate might be dominant; deviations of the value $\Delta H°_{f298} = -376.8$ kcal/mole calculated for $Na_2O \cdot SiO_2(c)$ from the JANAF value (33) is ascribed to solution effects of $Na_2O \cdot xSiO_2$ species. Silicon and water react to form $SiO_2(c)$ (equilibrium reaction constant $K = 1.33 \times 10^{13}$). Sodium metasilicate is incorporated in the oxide film developed on the tube wall and evaporates to build up in the oxidation chamber an atmosphere containing about 10^8 sodium atoms/cm^3, including both atomic and molecular species; NaOH is the most abundant compound. If no water is present in the oxidation ambient, the sodium content is negligible [$P(Na_2O) = 7.9 \times 10^{-28}$ atm]. This condition prevails as long as the sodium level in silicon bulk is only 10 ppb.

Oxidation Tube Cleaning

Periodic *in situ* cleaning at oxidation temperature is required to keep silicon oxidation tubes clean under operative conditions. Dilute hydrogen chloride is generally used for rather long periods in the oxidation chamber to assure proper cleaning of the wall. Assuming 100 ppm water (10^{-4} atm) in addition to 10% HCl in a silicon tube operated at 1300°K, the relevant reactions occurring are shown in Table II. Sodium chloride is formed from the interaction with sodium glasses contained in the silica film formed on the silicon tube wall. At equilibrium, the sodium number density in the atmosphere is 3.66×10^{15} atoms/cm^3. This is 10^7 times larger than the equilibrium sodium density normally present in the oxidation ambient. It should be emphasized that these results refer to equilibrium conditions. Although most reactions proceed rapidly at the inner tube wall surface, diffusion effects in the bulk may limit to some extent the applicability of this analysis. However, the enhanced sodium diffusion in polysilicon will reduce this limitation. The density of the resulting species at the surface could be lower, thus reducing the amount of sodium (or other species) actually removed. No attempts are made here to explore the kinetics of these reactions although it can be seen that hydrogen chloride cleaning is predicted to be very effective in agreement with current empirical observation.

The use of dry chlorine as a cleaning agent of silicon tubes should be avoided because of the risk involved due to its high reactivity with silicon. Table III shows that the tube could be severely damaged by chlorine if the protective silica film deposited on the inner tube wall has pinholes through which chlorine may come in contact with silicon to produce quantities of $SiCl_4(g)$, $SiCl_3(g)$, and $SiCl_2(g)$. However, if water is present in the system, hydrogen chloride is generated, moderating the aggressive behavior of dry chlorine.

Oxidation Tube Conditioning

The silica film formed on the tube wall can be removed by hydrogen at oxidation temperature. The formation of water generated through the hydrogen silica interaction contributes to the leaching of sodium from the tube bulk. Table IV shows the relevant reactions taking place in the tube when 100 ppm water (10^{-4} atm) is present in the hydrogen atmosphere. Sodium compounds such as NaO, Na_2O, NaOH, and $Na_2(OH)_2$ are formed in addition to atomic sodium. The total sodium equilibrium pressure in the tube atmosphere is 1.82×10^{-8} atm resulting in a number density of 1.03×10^{11} atoms/cm^3 where the atomic species is the most abundant one due to the reducing action of hydrogen. Although the use of hydrogen around an oxidation facility involves risks and difficulties which may make it impractical, it is of value to observe that the use of diluted (less than 4%) hydrogen in an inert gas carrier could make this procedure feasible by eliminating the risk of forming an explosive air-hydrogen mixture. If such an atmosphere is maintained in silicon oxidation tubes when they are

Table II. Equilibrium atmosphere in silicon oxidation tube cleaned with hydrogen chloride at 1300°K

Sodium content in silicon bulk: 10 ppb, hydrogen chloride at 0.1 atm, water at 10^{-4} atm

Reaction	K	Product	P (atm)	Na (cm^{-3})
$Na_2O \cdot SiO_2(c) + 2HCl(g) \rightarrow SiO_2(c) + 2NaCl(g) + H_2O(g)$	0.42	NaCl	6.48×10^{-4}	3.66×10^{15}
$Na_2O \cdot SiO_2(c) + 2HCl(g) \rightarrow Si(OH)_2(g) + 2NaCl(g) + \frac{1}{2} O_2(g)$	9.03×10^{-24}	$Si(OH)_2$	1.66×10^{-18}	
$Na_2O \cdot SiO_2(c) + 2HCl(g) \rightarrow SiO(OH)(g) + 2NaCl(g) + OH(g)$	6.39×10^{-18}	SiO(OH)	8.45×10^{-11}	
$Na_2O \cdot SiO_2(c) + 2HCl(g) + H_2O(g) \rightarrow Si(OH)_4(g) + 2NaCl(g)$	8.45×10^{-9}	$Si(OH)_4$	2.01×10^{-12}	
$2Na_2O \cdot SiO_2(c) + 4HCl(g) + 1H_2O(g) \rightarrow Si_2O \cdot (OH)_6(g) + 4NaCl(g)$	3.98×10^{-14}	$Si_2O(OH)_6$	2.26×10^{-21}	
$Na_2O \cdot SiO_2(c) + 3HCl(g) \rightarrow SiClH_3(g) + 3/2\ O_2(g) + 2NaCl(g)$	4.98×10^{-36}	$SiClH_3$	5.50×10^{-14}	
$Na_2O \cdot SiO_2(c) + 4HCl(g) \rightarrow SiCl_2H_2(g) + 1\ O_2(g) + 2NaCl(g) + H_2O(g)$	7.38×10^{-29}	$SiCl_2H_2$	1.05×10^{-12}	
$Na_2O \cdot SiO_2(c) + 5HCl(g) \rightarrow SiCl_3H(g) + \frac{1}{2} O_2(g) + 2NaCl(g) + 2H_2O(g)$	3.53×10^{-19}	$SiCl_3H$	6.51×10^{-9}	
$Na_2O \cdot SiO_2(c) + 5HCl(g) \rightarrow SiCl_3(g) + OH(g) + 2NaCl(g) + 2H_2O(g)$	4.14×10^{-20}	$SiCl_3$	5.48×10^{-8}	
$Na_2O \cdot SiO_2(c) + 4HCl(g) \rightarrow SiCl_2(g) + \frac{1}{2} O_2(g) + 2NaCl(g) + 2H_2O(g)$	5.38×10^{-21}	$SiCl_2$	9.91×10^{-10}	
$Na_2O \cdot SiO_2(c) + 6HCl(g) \rightarrow SiCl_2(g) + 2NaCl(g) + 3H_2O(g)$	3.80×10^{-11}	$SiCl_4$	9.04×10^{-7}	
$2NaCl(g) \rightarrow Na_2Cl_2(g)$	27.1	Na_2Cl_2	1.14×10^{-5}	6.43×10^{13}
$Si(c) + HCl(g) \rightarrow SiCl_4(g) + 2H_2(g)$	1.20×10^{3}	$Si(OH)_2$	1.67×10^{-18}	
$SiO_2(c) + H_2O(g) \rightarrow Si(OH)_2 + \frac{1}{2} O_2(g)$	2.15×10^{-23}	O_2	1.67×10^{-18}	
$H_2O(g) + Cl_2(g) \rightarrow 2HCl + \frac{1}{2} O_2$	1.29×10^{27}	HCl	0.1	
$HCl(g) \rightarrow \frac{1}{2}H_2(g) + \frac{1}{2}Cl_2(g)$	7.5×10^{-5}	Cl_2	9.19×10^{-9}	
$HCl(g) \rightarrow H(g) + Cl(g)$	1.0×10^{-12}	Cl	1.17×10^{-6}	
$H_2(g) \rightarrow 2H(g)$	1.2×10^{-12}	H	8.57×10^{-8}	
$H_2O(g) \rightarrow H(g) + OH(g)$	1.54×10^{-14}	H_2	6.12×10^{-3}	
$2H_2O(g) \rightarrow H^2(g) + 2\ OH(g)$	2.0×10^{-16}	OH	1.80×10^{-11}	
$H_2O(g) + \frac{1}{2} O_2(g) \rightarrow 2\ OH(g)$	2.5×10^{-9}	H_2O	10^{-4}	

Table III. Reaction constants resulting in silicon oxidation tubes cleaned with chlorine at 1300°K

Sodium content in silicon bulk: 10 ppb, chlorine at 0.1 atm

Reaction	K	Product	P (atm)
$Si(c) + 2Cl_2(g) \rightarrow SiCl_4(g)$	3.77×10^{19}	$SiCl_4$	3.77×10^{17}*
$2Si(c) + 3Cl_2(g) \rightarrow 2SiCl_3(g)$	4.74×10^{28}	$SiCl_3$	6.91×10^{12}*
$Si(c) + Cl_2(g) \rightarrow SiCl_2(g)$	3.50×10^{8}	$SiCl_2$	3.50×10^{7}
$SiO_2(c) + 2Cl_2(g) \rightarrow SiCl_4(g) + O_2(g)$	2.11×10^{-8}		
$2SiO_2(c) + 3Cl_2(g) \rightarrow 2SiCl_3(g) + 2\ O_2(g)$	1.48×10^{-26}		
$SiO_2(c) + Cl_2(g) \rightarrow SiCl_2 + O_2(g)$	1.96×10^{-19}		
$Na_2O \cdot SiO_2(c) + Cl_2(g) \rightarrow SiO_2(c) + 2NaCl(g) + \frac{1}{2} O_2(g)$	6.43		

* Rapid formation of these compounds.

Table IV. Equilibrium atmosphere in silicon oxidation tube cleaned with wet hydrogen at 1300°K

Sodium content in silicon bulk: 10 ppb, hydrogen at 1 atm, water at 10^{-4} atm

Reaction	K	Product	P (atm)	Na (cm^{-3})
$SiO_2(c) + H_2(g) + H_2O(g) \rightarrow SiH(g) + 3\,OH(g)$	7.86×10^{-47}	SiH	2.80×10^{-15}	
$SiO_2(c) + 2H_2(g) \rightarrow SiH_4(g) + O_2(g)$	6.00×10^{-34}	SiH_4	9.38×10^{-12}	
$Na_2O \cdot SiO_2(c) + H_2(g) \rightarrow SiH(g) + OH(g) + O_2(g) + 2Na(g)$	8.43×10^{-57}	Na	1.82×10^{-8}	1.03×10^{11}
$Na_2O \cdot SiO_2(c) + H_2(g) \rightarrow SiH(g) + OH(g) + 2NaO(g)$	1.10×10^{-57}	NaO	5.28×10^{-20}	
$Na_2O \cdot SiO_2(c) + 5/2H_2(g) \rightarrow SiH(g) + H_2O(g) + 2NaOH(g)$	8.49×10^{-33}	NaOH	1.74×10^{-11}	
$Si(c) + H_2O(g) \rightarrow SiO_2(c) + 2H_2(g)$	1.33×10^{13}			
$2NaOH(g) \rightarrow Na_2(OH)_2(g)$	4.78	$Na_2(OH)_2$	1.45×10^{-21}	
$Na_2O(g) \rightarrow NaO(g) + Na(g)$	1.16	Na_2O	8.28×10^{-28}	
		H_2	1.0	
		H_2O	10^{-4}	
$2H_2O \rightarrow H_2(g) + 2\,OH(g)$	2.0×10^{-12}	OH	1.41×10^{-12}	
$H_2O(g) + ½\,O_2(g) \rightarrow 2\,OH(g)$	2.5×10^{-9}	O_2	6.40×10^{-28}	

Table V. JANAF thermodynamic data used to calculate equilibrium conditions at 1300°K for reactions listed in Tables I-IV

Compound	ΔH°_{f298}[1] (kcal/mole)	$-(G^\circ_T - H^\circ_{298})/T$[2] (cal/°K mole)
$H_2O(g)$	−57.798	51.136
H(g)	52.1	30.879
OH(g)	9.432	48.877
O(g)	59.559	42.044
$O_2(g)$	0.0	54.283
$H_2(g)$	0.0	36.130
Na(g)	25.755	40.201
NaOH(g)	−50.4	63.786
NaO(g)	20.0	60.896
$Na_2(OH)_2(g)$	−154.8	89.141
$Na_2O \cdot SiO_2$(gls)[3]	−376.8	50.565
$Na_2O \cdot 2SiO_2(c)$	−590.36	73.554
$SiO_2(c)$ (quartz)	−217.7	19.918
$Na_2O(g)$[4]	8.7	72.30
HCl(g)	−22.063	49.624
$Cl_2(g)$	0.0	59.318
Cl(g)	28.922	43.226
NaCl(g)	−43.36	61.099
NaCl(liq)	−92.237	32.199
NaCl(c)	−98.26	26.479
$Na_2Cl_2(g)$	−135.3	91.387
Si(g)	107.7	43.715
Si(l)	11.585	15.188
Si(c)	0.0	8.399
SiH(g)	90.0	52.515
$SiH_4(g)$	7.3	58.969
SiO(g)	−24.0	55.994
$SiO_2(g)$	−73.0	63.266
$SiO_2(l)$	−215.74	21.134
SiCl(g)	45.7	62.985
$SiClH_3(g)$	−48.0	71.412
$SiCl_4(g)$	−157.1	95.763
$SiCl_2H_2(g)$	−75.0	81.596
$SiCl_3H(g)$	−119.6	89.722
$SiCl_2(g)$[5]	−39.3	76.581
$SiCl_3(g)$[5]	−96.0	89.134
$SiO \cdot (OH)$[5]	−118.0	73.63
$Si \cdot (OH)_2$[5]	−101.0	74.42
$SiO \cdot (OH)_2$[5]	−222.0	82.65
$Si \cdot (OH)_4$	−322.3	95.43
$SiO_2 \cdot (OH)_6$[5]	−612.1	132.83

[1] ΔH°_{f298} = standard enthalpy of formation.
[2] $(G^\circ_T = H^\circ_{298})/T$ = Gibbs energy function in the standard state at 1300°K.
[3] The value of ΔH°_{f298} for $Na_2O \cdot SiO_2$ (in SiO_2) was calculated using the equilibrium constant from reaction $Na_2O \cdot SiO_2$ (in SiO_2) $\rightarrow 2Na(g) + ½\,O_2(g) + SiO_2(c)$, $K = 2.5 \times 10^{-19}$ [see Ref. (32)]. The free energy function was assumed to be that of $Na_2O \cdot SiO_2$ (gls) given by the JANAF tables.
[4] The Na_2O data were estimated from various lithium, sodium, and potassium oxides data given in the JANAF tables.
[5] The heats of formation were calculated from bond energies as outlined in Ref. (36). The thermodynamic functions were obtained by interpolation of the values given there.

not being used for semiconductor processing, the sodium impurity from the tube wall bulk and the silica film on the tube are constantly removed from the hot zone. The enhanced sodium diffusion in polysilicon increases the sodium migration into the silica film which is being removed by the hydrogen reducing action. This tube conditioning would reduce the need for periodic HCl cleaning and consequently minimize the incidence of other species (such as chlorine) in the oxidation chamber. Experimental evidence shows that chlorine is incorporated into oxide films thermally grown on silicon wafers processed in oxidation tubes previously cleaned with HCl (34). This has proved to be detrimental for radiation-hard devices resulting in electrical instabilities (35).

Conclusions

The above results show that the dominant factor in the preparation of clean thermal oxides is the purity of the oxidation tube wall if other process steps are kept under strict control. Such processes involve the wafer cleaning and handling prior to oxidation and metallization immediately after oxidation. When recently installed, new silicon tubes have a low sodium content and thus constitute an excellent material to enclose the oxidation atmosphere. This is due to the tube fabrication process (chemical vapor deposition) employing highly purified (low alkali) materials (28). Preparation of clean low mobile ion content thermal oxide films by wet oxidation of silicon wafers is in principle possible if silicon oxidation tubes are used, provided that the tube environment is clean enough to avoid inclusion of ambient contamination in the tube. However, a silicon oxidation tube will tend to develop alkali contamination during normal operation unless special care is taken to isolate it from external contamination. These conditions are hard to maintain even in clean production-oriented facilities, so periodic *in situ* tube cleaning is required. At oxidation temperatures sodium deposited on the exterior of the tube diffuses through the wall into the oxidation atmosphere contaminating the thermal oxide films grown on silicon wafers. The contamination process may be originated by the furnace refractories impurity, the room ambient, and other factors external to the tube. The main advantage of employing silicon oxidation tubes lies in the possibility of using temperatures higher than tolerated by fused silica tubes.

Acknowledgment

The authors are very much indebted to Drs. W. Murray Bullis and Kenneth F. Galloway of the Electronic Technology Division for constant stimulus during this work and critical review of the manuscript.

This work was conducted as part of the Semiconductor Technology Program at the National Bureau of Standards and was supported by the Defense Nuclear Agency.

Manuscript submitted June 17, 1977; revised manuscript received Sept. 8, 1977.

Any discussion of this paper will appear in a Discussion Section to be published in the December 1978 JOURNAL. All discussions for the December 1978 Discussion Section should be submitted by Aug. 1, 1978.

Publication costs of this article were assisted by the National Bureau of Standards.

REFERENCES

1. B. E. Deal, *This Journal*, **121**, 198C (1974).
2. T. W. Hickmott, *J. Appl. Phys.*, **46**, 2583 (1975).
3. C. M. Osburn and S. I. Raider, *This Journal*, **120**, 1369 (1973).
4. T. H. DiStefano and J. E. Lewis, *J. Vac. Sci. Technol.*, **11**, 1020 (1974).
5. G. F. Derbenwick, *J. Appl. Phys.*, **48**, 1127 (1977).
6. K. G. Aubuchon, *IEEE Trans. Nucl. Sci.*, **NS-18**, No. 6, 117 (1971).

7. E. H. Snow, A. S. Grove, B. E. Deal, and C. T. Sah, *J. Appl. Phys.*, **36**, 1664 (1965).
8. B. E. Deal, NBS Special Publication 337, Silicon Device Processing, C. P. Marsden, Editor, pp. 36-50, Washington, D.C. (1970).
9. S. I. Raider, L. V. Gregor, and R. Flitsch, *This Journal*, **120**, 425 (1973).
10. B. Yurash and B. E. Deal, *ibid.*, **115**, 1191 (1968).
11. J. E. Barry, H. M. Donega, and T. E. Burgess, *ibid.*, **116**, 257 (1969).
12. W. R. Knolle, *ibid.*, **120**, 987 (1973).
13. W. R. Knolle and T. F. Retajczyk, Jr., *ibid.*, **120**, 1106 (1973).
14. D. R. Fewer and W. L. Gill, Technical Report No. RADC-TR-66-345, pp. 33-46 (1966); also available as NTIS Document AD-489-969.
15. K. G. Aubuchon, Hughes Research Laboratories Final Tech. Rep., contract N00014-71-C-0079 (1971).
16. R. J. Kriegler, *Appl. Phys. Lett.*, **20**, 449 (1972).
17. R. J. Kriegler, Y. C. Cheng, and D. R. Colton, *This Journal*, **119**, 388 (1972).
18. R. J. Kriegler, *Thin Solid Films*, **13**, 11 (1972).
19. R. J. Kriegler, in "Semiconductor Silicon 1973," H. R. Huff and R. R. Burgess, Editors, p. 363, The Electrochemical Society Softbound Symposium Series, Princeton, N.J. (1973).
20. R. J. Kriegler, in "12th Annual Proceedings Reliability Physics 1974," IEEE Catalog No. 74CHO-839-IPHY (1974).
21. A. Rohatgi, S. R. Butler, and F. J. Feigl, *Appl. Phys. Lett.*, **30**, 104 (1977).
22. Y. J. van der Meulen, C. M. Osburn, and J. F. Ziegler, *This Journal*, **122**, 284 (1975).
23. S. Mayo and W. H. Evans, *ibid.*, **124**, 780 (1977).
24. G. Hetherington, G. W. Stephenson, and J. A. Winterburn, *Electronic Engin.*, **41**, No. 495, 52 (1969); *ibid.*, **41**, No. 496, 44 (1969).
25. A. E. Owen and R. W. Douglas, *J. Soc. Glass Technol.*, **43**, 159T (1969).
26. H. F. Wolf, "Silicon Semiconductor Data," pp. 136-137, 526-527 Pergamon Press, Oxford (1969).
27. S. Horiuchi and R. Blanchard, *Solid-State Electron.*, **SC-18**, 529 (1975).
28. W. Dietze, L. P. Hunt, and D. H. Sawyer, *This Journal*, **121**, 1112 (1974).
29. E. S. Schlegel, *IEEE Trans. Electron Devices*, **ed-14**, 728 (1967); *ibid.*, **ed-15**, 951 (1968).
30. A. H. Agajanian, *IBM Tech. Rep.*, **22**, 1559 (1972).
31. E. A. Irene, *This Journal*, **121**, 1613 (1974); E. A. Irene and Y. J. van der Meulen, *ibid.*, **123**, 1380 (1976).
32. G. L. Vidale, "Measurements of the Absorption of Resonance Lines III, Vaporization of Sodium from Sodium Silicate Glasses," Generall Electric Co., Technical Information Series, R60SD390 (1960).
33. JANAF Thermochemical Tables, D. R. Stull and H. Prophet, Editors, Second ed., NSRDS-NBS 37 (1971).
34. N. J. Chou, C. M. Osburn, and Y. J. van der Meulen, *Appl. Phys. Lett.*, **22**, 380 (1973).
35. R. A. Bunghard, B. L. Gregory, C. W. Gwyn, and G. F. Derbenwick, "Process Dependence of Radiation Effects in CMOS Integrated Circuits," Final Report, AFWL Contract 75-198 (1975).
36. O. H. Krikorian, in "Proceedings of the Symposium on Engineering with Nuclear Explosives," Conf. 700101, Vol. 1, p. 481, Las Vegas, Nevada (1970).

Mechanism of CVD Thin Film SnO_2 Formation

R. N. Ghoshtagore*

Westinghouse Research Laboratories, Pittsburgh, Pennsylvania 15235

ABSTRACT

The kinetic mechanism of CVD SnO_2 deposition has been studied for (*i*) $SnCl_4 + O_2$ reaction at 675°-940°C for $p_{SnCl_4} = 1.67 \times 10^{-5}$ to 5.3×10^{-4} atm and $p_{O_2} \geqq 1.04 \times 10^{-3}$ atm, (*ii*) $SnCl_4 + H_2O$ reaction at 400°-807°C for $p_{SnCl_4} = 2.63 \times 10^{-5}$ to 4.2×10^{-4} atm and $p_{H_2O} = 5.2 \times 10^{-5}$ to 4.17×10^{-3} atm, and (*iii*) $Sn(CH_3)_4$ (TMT) + O_2 reaction at 425°-578°C for $p_{TMT} = 3.5 \times 10^{-5}$ to 1.17×10^{-3} atm and $p_{O_2} \geqq 1 \times 10^{-3}$ atm. In combination with the available literature data, the results of the present investigation have been interpreted to show atomic oxygen as the adsorbed species and tin-containing gas as the gaseous reactant in both the direct oxidation reactions (Rideal-Eley mechanism). The hydrolysis reaction is the only thermally unactivated one in the group and proceeds by the collision of $SnCl_4$ molecules on four adsorbed (symmetrically) water molecules on the surface. The open tube cold wall horizontal reactor has been established as an ideal equipment for the kinetic mechanism delineation of all CVD reactions.

The vast influence of solid surfaces on reaction kinetics has been the subject of catalysis for more than a century. But a detailed understanding of the molecular mechanism of such interactions requires a knowledge of chemical reaction equilibria and kinetics, vapor pressures of all the participating species, fluid dynamics of the system, and the adsorption and desorption characteristics (including surface diffusion) of all the chemical entities. So few of these quantities are known for most systems that a complete theoretical and/or experimental analysis of most chemical vapor deposition reactions becomes almost impossible. However, several guidelines are available in this direction (1).

Chemical vapor deposition under large supersaturations or chemical driving force is controlled by growth, producing a fine-grained, roughly random deposit with growth rates tending to approach a maximum as fixed by the slowest (rate-determining) process. Under low supersaturations (fixed by vapor-phase mass transport) nucleation can be rate controlling, preferred-orientation deposits can form (epitaxy or oriented growth), and growth rates can be less than the maximum.

Stannic oxide thin films are currently actively investigated since their high transparency (in the 0.4-1.2μ range) and electrical conductivity would be of unique value in numerous optoelectronic applications (solar cells, MOS sensors, etc.). Although a majority of these films are being formed by CVD, little or no information exists on their heterogeneous deposition kinetics. The kinetics of polycrystalline SnO_2 CVD film deposition explored in this study include O_2 or H_2O vapor reaction of two basic tin sources: (*i*) $SnCl_4$ and (*ii*) tetramethyl tin. The experiments utilize these chemical reactions on a heated amorphous SiO_2 substrate in a conventional horizontal "cold wall" quartz tube reactor at atmospheric pressure. The methodology of the present study has been reported earlier (2).

* Electrochemical Society Active Member.

Experimental Technique

Ultrahigh purity stannic chloride or tetramethyl tin (TMT) (Ventron Corporation) in thermostat-held quartz bottles was used as a tin source bubbler through which a carrier gas of ultrapure oxygen or nitrogen was passed at a controlled rate. This gas (saturated with tin source vapor) was then mixed with additional ultrapure oxygen or water vapor (from a quartz bubbler held at 25° ± 0.5°C) and/or nitrogen through a set of calibrated flowmeters, liquid traps, and filters, and the mixture was reacted on a quartz encapsulated high purity graphite susceptor heated by rf induction. The saturation transport of all liquid reactants in this study was carefully checked for the maximum carrier gas flow used by observing growth rate changes as a function of bubbler bath length change (in a multiple bubbler system). The quartz tube reactor used in this study was of 92 mm ID, with the susceptor being 20 × 65 × 320 mm externally. The over-all reactions employed in this work can be described by

$$SnCl_4(g) + O_2(g) \rightleftarrows SnO_2(s) + 2Cl_2(g) \quad [1]$$

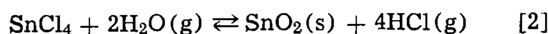

$$SnCl_4 + 2H_2O(g) \rightleftarrows SnO_2(s) + 4HCl(g) \quad [2]$$

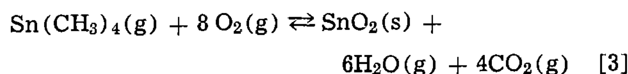

$$Sn(CH_3)_4(g) + 8\,O_2(g) \rightleftarrows SnO_2(s) + 6H_2O(g) + 4CO_2(g) \quad [3]$$

The free energy changes at different temperatures for reactions [1] and [2] have been calculated (3), whereas that for reaction [3] cannot be calculated due to the unavailability of the thermodynamic data for TMT. The vapor pressure of TMT was obtained from the compilation by Dub (4).

Of the three reactions listed above, the direct oxidation of stannic chloride (Eq. [1]) is the highest temperature reaction examined in the present work. It has also been used here for the CVD SnO_2 film growth for the first time. On the other hand, the high temperature hydrolysis of stannic chloride spray (Eq. [2]) is the classic technique of "Nesa" glass coating. A controlled version of this reaction was reported by Aboaf *et al.* (5) for CVD thin film SnO_2 formation on oxidized silicon. Their films were basically reproduced in this study with added emphasis on the surface reaction kinetics. The direct oxidation of TMT (Eq. [3]) on glass slides and deposited SiO_2 (in a hot wall reactor) was recently studied (6) as a means of producing chlorine-free SnO_2 films. The kinetic data in that work was not optimized for mechanism delineation, however.

The substrates used in this work were uniformly (111), 20-30 Ωcm, 9 ± 1 mil single crystal silicon wafers pyrogenically oxidized at 1100°C to 900 ± 5Å. In most experiments the deposited SnO_2 thickness was ~ 1000Å. Film thicknesses were determined by reference to an ellipsometrically calibrated SiO_2 color chart, assuming an effective deposited film refractive index of 2.0 (see later). All the liquid bubblers were maintained at 25° ± 0.5°C and that of the substrates to ± 5°C (with a calibrated IR pyrometer). All experiments were conducted at the atmospheric pressure. All the films grown were randomly oriented polycrystalline (by electron diffraction) with an average grain size of 0.1-0.3 μm.

Results

Flow rate relationships.—In any kinetic investigation of heterogeneous reactions in a flow system, the examination of the dependence of the rate of formation of the solid reaction product on the flow rates of each of the reactants (while the others are kept constant) is the primary order of business. This information provides the fluid dynamic relationships of the particular experimental system and helps to delineate the surface reaction-controlled region from the mass-transfer controlled region (2, 7). In the absence of a nucleation barrier, at low flow rates the reaction rate is controlled by the gas-phase mass-transfer rate. In this region, the CVD deposition rate is proportional to the half-power of the gas flow rate or the average gas velocity (2, 8) and the reaction is not strongly activated. With increasing flow rates (at constant reactant partial pressure), the boundary layer thickness attains a limiting value, and the Reynolds number and the gas-phase mass-transfer coefficient increase to a value where the reaction is controlled by the chemical surface reaction rate constant. Growth rates are no longer dependent on the flow rates and the reaction becomes highly activated.

The dependence of the tin oxide growth rates on the gas velocities were examined and the surface reaction-controlled activated region determined for all the reactions studied in this work. However, no attempt was made to delineate the mass-transfer controlled region in detail. As expected (2), at all temperatures and rate-determining species partial pressures the measured SnO_2 film growth rates attained a constant value at high flow rates. Boundary layer theory predicts that under such circumstances the gas-phase mass-transfer coefficient is much higher than the surface-reaction rate constant and the reaction kinetics is controlled by an activated process (adsorption, desorption, surface reaction, or nucleation). Within the range of reaction temperatures and stannic chloride partial pressures used, the direct oxidation reaction (Eq. [1]) was established to be flow rate independent at average gas velocities (calculated from volume flow rates) over 10 cm/sec. To be safely beyond the mass-transfer-controlled region, all the kinetic mechanism delineation experiments were conducted at 11.3 cm/sec. The stannic chloride hydrolysis reaction (Eq. [2]) was established to be total flow rate independent at gas velocities over 6 cm/sec in the entire range of reaction temperatures and $SnCl_4$ partial pressures used in this study. All the kinetic data for this reaction were accumulated at an average velocity of 7.2 cm/sec. Finally, the direct oxidation of TMT (Eq. [3]) was flow rate independent at gas velocities above 2 cm/sec, and all the kinetic data were obtained at 2.4 cm/sec.

Reactant partial pressure relationships.—$SnCl_4$ + O_2 reaction.—In the surface reaction-controlled region under 873°C, the deposition rate of SnO_2 was an increasing function of oxygen concentration for any fixed $SnCl_4$ concentration. As shown in Fig. 1, at low oxygen concentrations the reaction is of one-half order, but becomes zero order above a minimum p_{O_2} whose value increases with increasing p_{SnCl_4}, but is independent of temperature. This behavior is identical to that of the direct oxidation of $TiCl_4$ (2). Since the saturated growth rates (Fig. 1) at any two temperatures are disproportional to the corresponding enhancement of tin chloride diffusion rates through the boundary layer

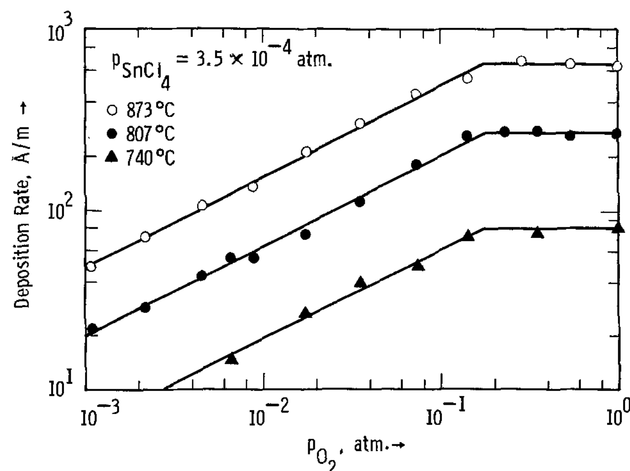

Fig. 1. Oxygen partial pressure dependence of SnO_2 deposition at different temperatures for the $SnCl_4$ + O_2 reaction.

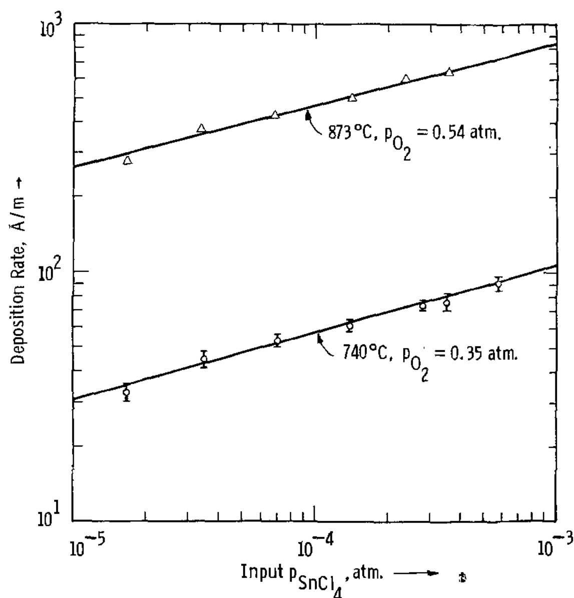

Fig. 2. SnO_2 deposition rate as a function of stannic chloride partial pressure in the p_{O_2} independent range.

(9) and the onset of saturation is not a function of p_{O_2}, it can be concluded that the complete consumption of tin chloride species at the substrate surface is not involved in these experiments.

Figure 2 shows the linear dependence of the SnO_2 deposition rate on the partial pressure of tin chloride at two temperatures and fixed oxygen gas phase concentrations. Since the oxygen partial pressure was fixed high enough in these experiments for the reaction to be of zero order (with respect to oxygen) for the highest p_{SnCl_4} used, no depletion of oxygen is expected in each of these series of experiments. Both at 740° and 873°C, the reaction order is seen to be 0.26 ± 0.01 with respect to $SnCl_4$.

$SnCl_4$ + H_2O reaction.—Figure 3 shows the behavior of the surface deposition rate as a function of water vapor concentration at different p_{SnCl_4}. In the entire range of temperature studied (400°-807°C), the deposition rate increases monotonically with p_{H_2O} to a saturated value at each p_{SnCl_4}. Figure 4 shows the first-order relationship of the surface reaction rate on the stannic chloride concentration. The fixed water vapor concentration (4.17 × 10^{-3} atm) in these experiments was high enough for reaction [2] to be independent of p_{H_2O} (Fig. 3). The data of both Fig. 3 and 4 show no effect of the deposition rate on the substrate temperature. This is further pointed out in Fig. 5, where the minimum water vapor partial pressure required for zero-order SnO_2 deposition (with respect to H_2O) is plotted against the corresponding p_{SnCl_4} at all temperatures studied. In the flow-independent range, the ratio of p_{H_2O} to p_{SnCl_4} is always found to be four.

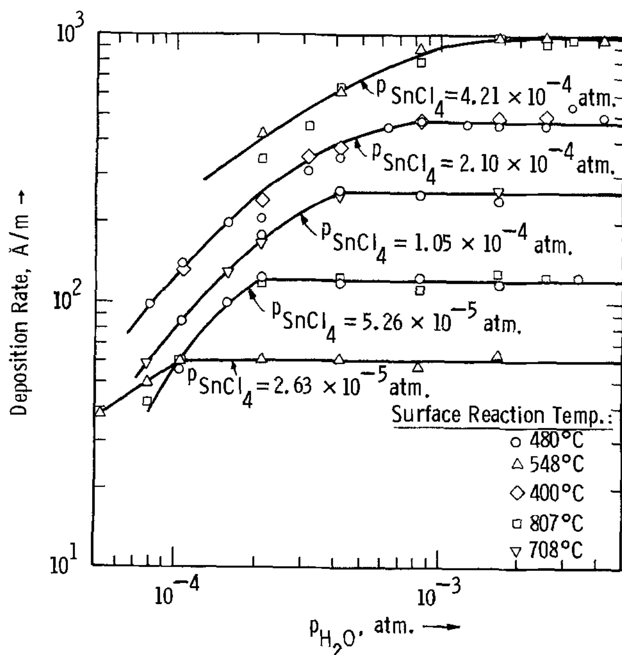

Fig. 3. Deposition rates of SnO_2 films as a function of water vapor and $SnCl_4$ concentration for the $SnCl_4$ + H_2O reaction (at different temperatures).

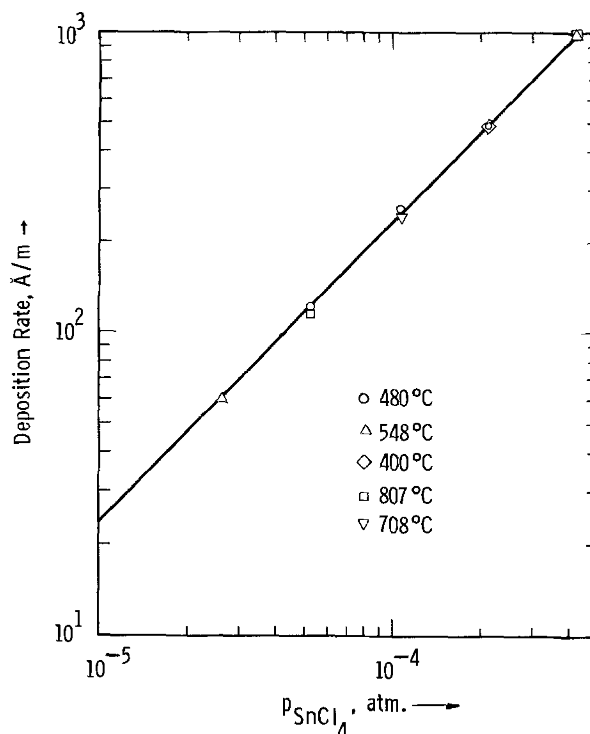

Fig. 4. Stannic chloride concentration dependence on the deposition rate of SnO_2 at p_{H_2O} = 4.17 × 10^{-3} atm.

$Sn(CH_3)_4$ + O_2 reaction.—As has already been demonstrated (6), the direct oxidation of TMT (Eq. [3]) is a very favorable route of SnO_2 CVD film formation. However, the partial pressure relationships of the reactants are not known so far. Figure 6 shows a typical SnO_2 film deposition rate dependence on p_{O_2} at a fixed p_{TMT} at low temperatures. As in the direct oxidation

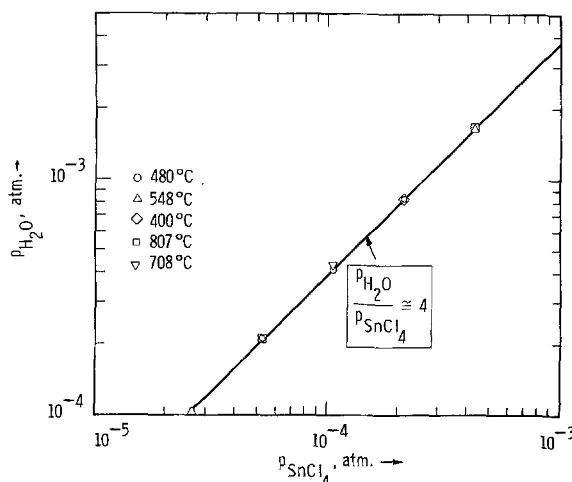

Fig. 5. Minimum water vapor partial pressure required for zero order (with respect to H_2O) SnO_2 deposition at different stannic chloride concentrations.

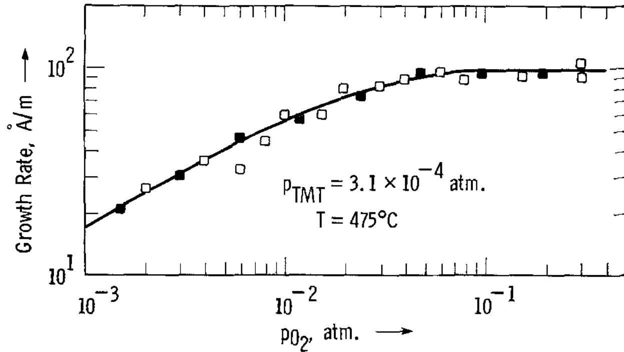

Fig. 6. Growth rate data as a function of oxygen concentration at a temperature where volume reaction is negligible. Open symbols indicate data from the first ~ 1000Å of the film and closed symbols are those from the second ~ 1000Å of the film.

of $SnCl_4$ (Fig. 1) the growth rate is one-half order with respect to oxygen at low p_{O_2} and saturates at higher p_{O_2}. The open symbols indicate macroscopic growth rate data from the first ~ 1000Å of the film and the closed symbols are those from the second ~ 1000Å of the film. The significance of the latter is illustrated in Fig. 7, where these two types of growth rate data differ significantly at higher temperatures. It should also be noted that at low partial pressures the reaction order is no longer one-half with respect to oxygen and goes higher at higher temperatures. Moreover, the growth rate clearly peaks out at higher oxygen pressures for the second kÅ film at both the high temperatures and for the first kÅ of the film at the highest (578°C) temperature shown. As will be seen later, this temperature dependence of p_{O_2} relationship of the growth rate in the surface reaction-controlled region of Eq. [3] is directly related to the high temperature non-Arrhenius behavior of the apparent surface reaction rate. Figure 8 shows the TMT concentration dependence of the growth rate at a so-called "low" and "high" temperature. The fixed oxygen pressure at both these temperatures was maintained high enough for the reaction either to be saturated with respect to oxygen (Fig. 6) or to be beyond the apparent peak (Fig. 7). The deposition rate data of Fig. 8 was obtained macroscopically from the first kÅ of the film. It is clear that the reaction is apparently of first order with respect to TMT at both these temperatures.

Temperature coefficients of CVD SnO_2 formation.—The temperature dependence of a chemical reaction in the activated region provides insight into both the molecular mechanism of the reaction and the sensitivity of the process to temperature variation in the system. Figure 9 shows the Arrhenius behavior of the SnO_2 film formation rate on SiO_2 (by Eq. [1]) at two $SnCl_4$ concentrations up to a maximum temperature of 873°C. Above that temperature the behavior is nonideal. Both sets of data in Fig. 9 were obtained with a fixed p_{O_2} of 0.9975 atm ($\simeq$ 1 atm), well in the region of zero-order dependence of the surface reaction rate with respect to oxygen. Between 675° and 873°C, the surface reaction rate constants can be calculated from the data of Fig. 9 using a relation of the type

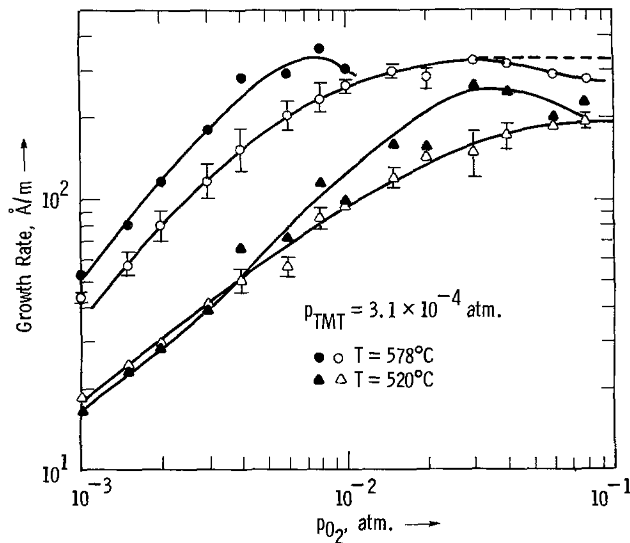

Fig. 7. Growth rate of SnO_2 film from TMT as a function of oxygen concentration. Closed and open symbols have the same significance as in Fig. 6.

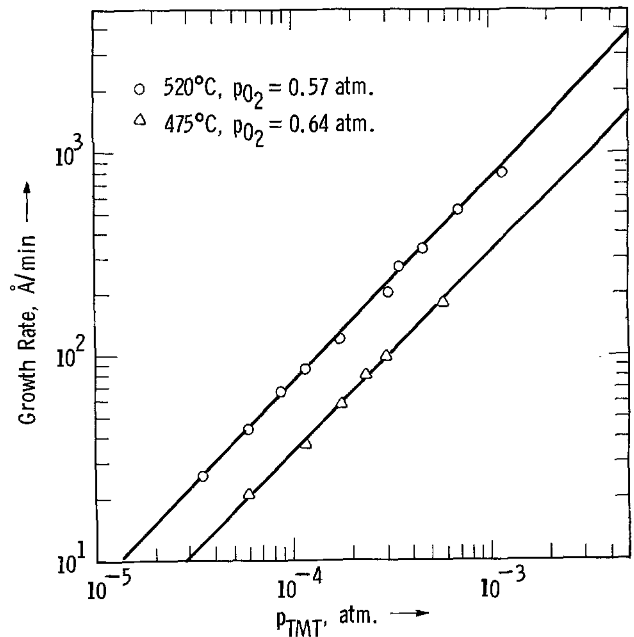

Fig. 8. TMT-produced SnO_2 film growth rate as a function of TMT concentration in the oxygen-saturated region.

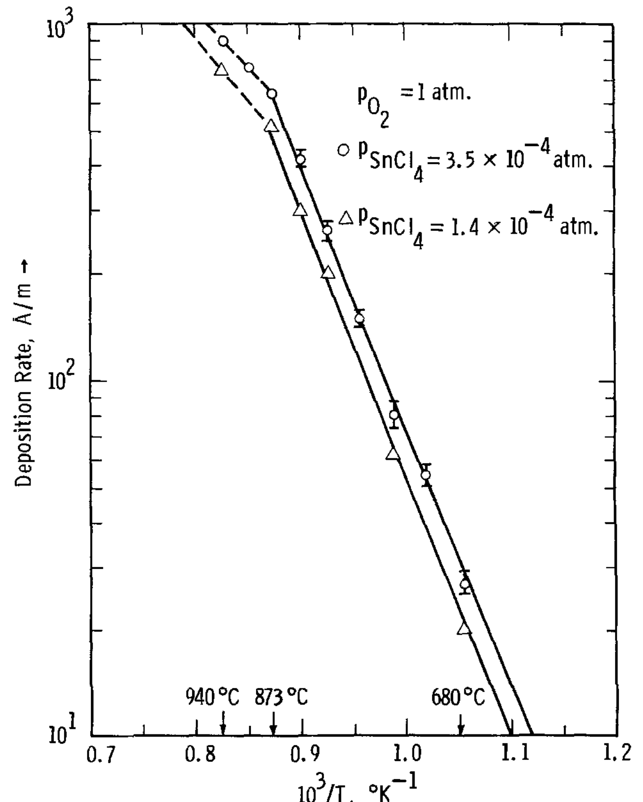

Fig. 9. Temperature dependence of SnO_2 deposition rate by the $SnCl_4 + O_2$ reaction.

$$G = \frac{C_G}{N} k_s \quad [4]$$

where G is the growth rate, C_G is the gas phase $SnCl_4$ concentration, N is the number of SnO_2 molecules per unit volume of the film, and k_s is the surface reaction rate constant. The activation energy of the surface reaction rate is seen to be ~ 1.5 eV from Fig. 9. It should be noted that the normalization of the observed partial pressure relationships of the deposition rate for both the reactants of Eq. [1] (shown in Fig. 1, 2, and 9) at all temperatures below 873°C would result in a single Arrhenius plot for either the specific growth rate or the surface reaction rate constant (2). However, this is not the case in the higher temperature non-Arrhenius region and both these fundamental parameters are directly proportional to the concentration of the rate-determining species (*i.e.*, $SnCl_4$).

In contrast to the direct oxidation of $SnCl_4$ (Eq. [1]), the high temperature hydrolysis of $SnCl_4$ (Eq. [2]) is seen to be thermally nonactivated (Fig. 3-5) even in the so-called flow-independent activated region of the surface reaction. An attempt to explain this phenomenon is made in the Discussion section.

The temperature dependence of the direct oxidation of TMT (Eq. [3]) shown in Fig. 10 is seen to be very similar to that of $SnCl_4$. Below ~ 490°C, the relationship is Arrhenius with an indicated activation energy of ~ 1.8 eV. The growth rate data, shown in Fig. 10, are macroscopic values obtained from the first ~ 1000Å of the film. As has been described before, below 490°C a single Arrhenius plot can be obtained for either the specific growth rate or the surface reaction rate constant of Eq. [3] from Fig. 6, 8, and 10. The non-Arrhenius regions of Fig. 9 and 10 are seen to be very similar.

Microscopic growth characteristics.—For an accurate assertion of the molecular mechanism of a CVD film growth, it is imperative to establish that the macroscopic kinetic data are valid from the microscopic point of view. In the Arrhenius region, deposition rates were determined as a function of film thickness or time for both the reactions involving $SnCl_4$ (Eq. [1] and [2]) at some selected temperature and partial pressure conditions. Within the range of experimental error, film thicknesses (in the range ~ 200 to ~ 2000Å) were found to be linearly proportional to the deposition time with no detectable incubation period. The situation has not been found to be so with Eq. [3]. Figure 11 shows the microscopic growth data for a set of SnO_2 films grown by the direct oxidation of TMT at the highest temperature of the Arrhenius region (Fig. 10). The oxygen pressure was maintained at the onset of the growth rate saturation (Fig. 6) that is independent of temperature (Fig. 1) for similar surface reaction-controlled oxidation reactions (2). The films were ellipsometrically analyzed for individual thickness and refractive index. Both the growth rates and the refractive index attain a constant value after about 400Å of the film have been grown. Since the thin samples did appear to be of low refractive index, one of the thicker samples (1428Å) was argon ion-milled to remove the outer portion of the film to test if the film first deposited was of low refractive index. ψ, Δ values obtained after milling for 1 min and again after a further 35 sec milling fitted the 2.053 refractive index curve well with no indication of lower refractive index for the remaining films of 775 and 183Å, respectively. (Apparently, the first 60 sec milling removed 750Å for a 750Å/min rate; the second 35 sec removed 592Å for a 1015 Å/min rate. Whether this increase in milling rate under identical conditions is significant is unclear.) No evidence of any significant optical adsorption at 546 nM wavelength was discovered. Although the data of Fig. 11 indicate an incubation period of about a minute, no attempt was made either to incorporate it into the macroscopic growth data shown in Fig. 6, 7, 8, and 10 or to delineate its temperature and reactant concentration dependence. Its effect on the kinetic data of TMT oxidation is considered to be small.

Figure 12 shows the resistivity of the same films as a function of the film thickness. Films under 400Å must be defective enough to produce both very low resistivity and refractive index (Fig. 11). However, unlike the refractive index, the resistivity of the thicker films does not saturate above 400Å. That could originate either in mobility or in carrier concentration variation across its thickness.

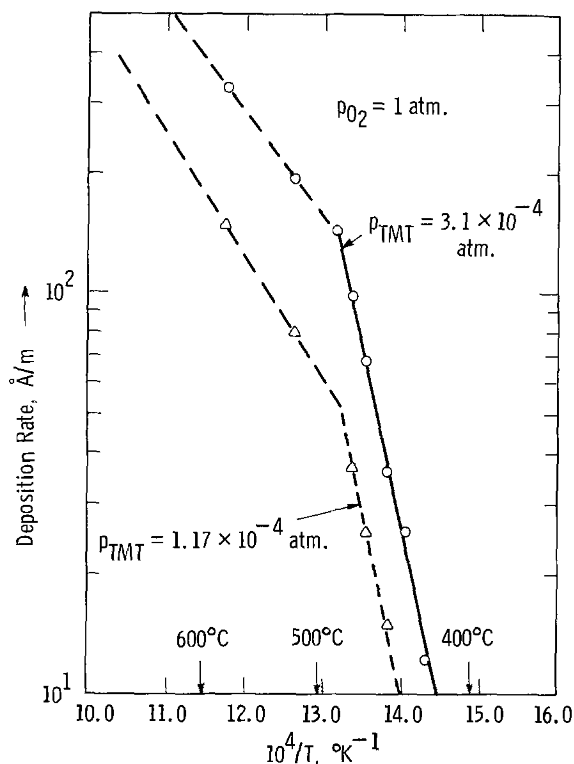

Fig. 10. Temperature coefficient of TMT-produced SnO_2 film growth rate.

Discussion

In general, a heterogeneous reaction involving one or more gaseous species on a solid surface involves the following steps: (*i*) diffusion of reactants to the surface, (*ii*) adsorption of at least one reactant on the surface, (*iii*) formation of critical nuclei by surface reaction preceded by surface diffusion and formation of activated complex, (*iv*) desorption of gaseous products with or without some surface migration, and (*v*) diffusion of products away from the surface. When the

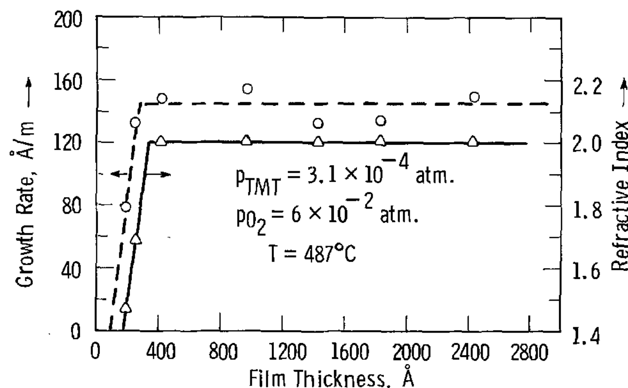

Fig. 11. Over-all growth rate and refractive index of SnO_2 film from TMT as a function of film thickness or growth time in the oxygen-saturated region.

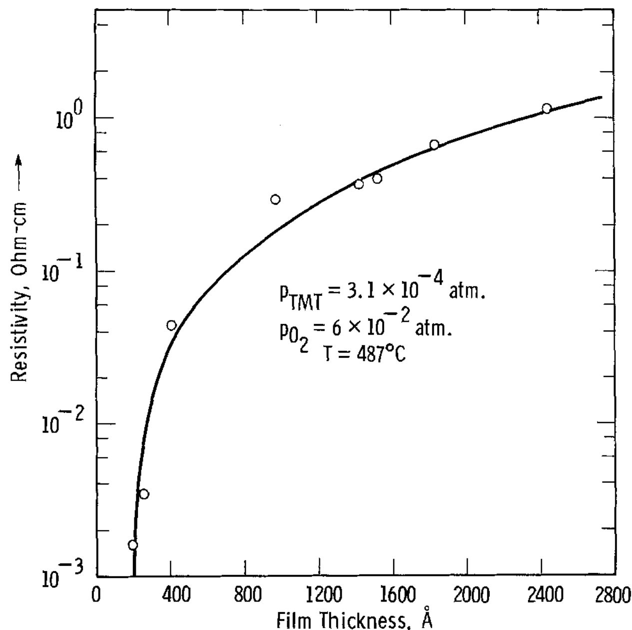

Fig. 12. Resistivity of the same TMT oxidized SnO_2 films as a function of film thickness.

heterogeneous CVD reaction is conducted in the flow-independent activated region (as has been done in this study), steps (*i*) and (*v*) are not rate controlling. Each of the CVD reactions studied in this work (Eq. [1]-[3]) will now be examined in light of step (*ii*), (*iii*), or (*iv*) rate control. It should, however, be noted that there are two basic mechanisms of reactant adsorption-controlled CVD reactions:

(*a*) In the Langmuir-Hinshelwood mechanism the reaction occurs between both the species adsorbed on adjacent sites. This may lead to considerable competition for the adsorption sites as a function of temperature and reactant concentration ratios.

(*b*) In the Rideal-Eley mechanism the CVD reaction is between an adsorbed species and a gaseous species without any competition between them.

The major distinguishing feature of these two mechanisms is that in the former the rate (*R*) will pass through a maximum as the partial pressure of either reactant is varied, whereas in the latter the rate will reach a limiting value when the partial pressure of one of the reactants is varied (which is the one that is adsorbed).

The direct oxidation of $SnCl_4$ shows

$$R \propto (p_{O_2})^{1/2}(p_{SnCl_4})^{0.26\pm0.01} \quad [5]$$

at low p_{O_2} and all p_{SnCl_4}, whereas

$$R \propto (p_{SnCl_4})^{0.26\pm0.01} \quad [6]$$

at high p_{O_2} (depending on p_{SnCl_4}) and all p_{SnCl_4}. Since the surface reaction rate is proportional to the adsorption density of the species involved, it appears that Rideal-Eley mechanism is operating for Eq. [1] with atomic oxygen as the most probable chemisorbed species and some molecular form of tin chloride colliding on the surface from the gas phase. Similar to the direct oxidation of $TiCl_4$ to produce TiO_2 (2), the saturation of surface adsorption of atomic oxygen occurs at the same p_{O_2} at all temperatures. An alternative interpretation of the Eq. [5] p_{O_2} dependence is the partial surface coverage by adsorbed oxygen (10). The value of the exponent of p_{O_2} should then increase with temperature. This is in contradiction to the experimental findings (Fig. 1).

The absence of a maximum in the deposition rate as a function of both p_{O_2} and p_{SnCl_4} (Fig. 1 and 2) indicates the strong possibility that the tin-containing species is not involved in adsorption on the substrate, *i.e.*, it is a gas phase diffusing species. The $p_{SnCl_4}{}^{0.26\pm0.01}$ dependence of the surface deposition rate (Eq. [5] and [6]) is also indicative of the fact that the rate-determining tin species is not the input stannic chloride. Thermodynamic calculations of the major equilibrium tin species in the $SnCl_4$-N_2 system were performed at 1000°-1200°K to check the possibility of a clear connection of the observed p_{SnCl_4} dependence of the deposition rate with the intermediate $SnCl_2$ species. This is shown in Fig. 13(*a*) and (*b*). For any input p_{SnCl_4},

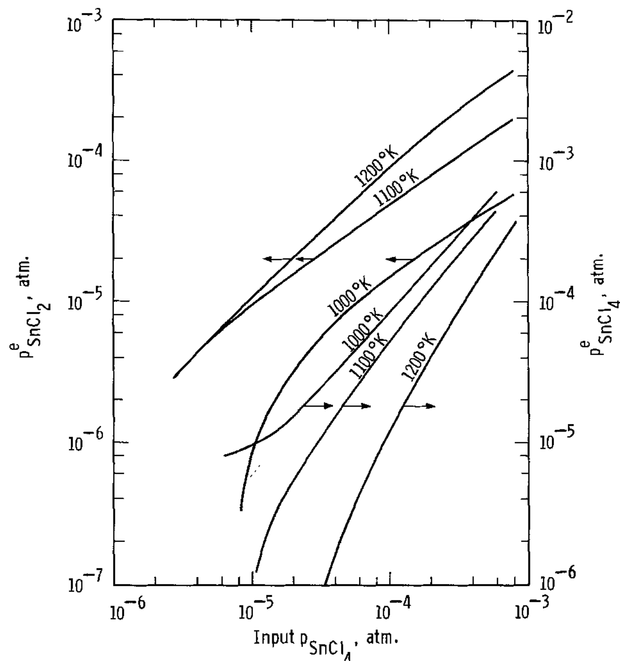

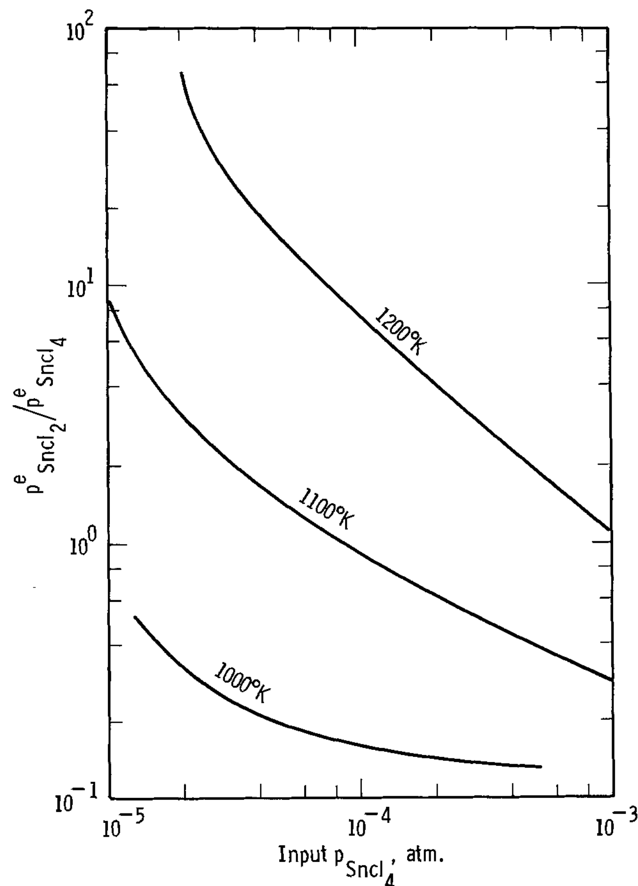

Fig. 13. Calculated equilibrium distributions of $SnCl_2$ and $SnCl_4$ as a function input p_{SnCl_4} at atmospheric pressure. Courtesy of P. Rai-Choudhury.

the equilibrium partial pressure of $SnCl_4$ ($p^e{}_{SnCl_4}$) decreases and that of $SnCl_2$ ($p^e{}_{SnCl_2}$) increases with increasing temperature [Fig. 13(a)]. Alternatively, the ratio of $p^e{}_{SnCl_2}$ to $p^e{}_{SnCl_4}$ always decreases with increasing p_{SnCl_4} in the experimental temperature and input p_{SnCl_4} range [Fig. 13(b)]. Since this is contrary to the experimental findings (Fig. 2), $SnCl_2$ is not the rate-determining species. The major effect of rising p_{SnCl_4} on the surface reaction rate must therefore be of $p^e{}_{SnCl_4}$ with possibly some poisoning effect from the liberated chlorine and/or gas phase oxygen. In Eq. [1] the reverse reaction is fairly active at ~1000°C. As a result, the net reaction rate (obtained from the deposition rate) is the difference between the forward and reverse reactions with reverse being proportional to $p_{Cl_2}{}^2$ or ¼ $p_{SnCl_2}{}^2$. Without an independent determination of the etch rate of SnO_2 films by chlorine, it is, therefore, not possible to identify the $p_{SnCl_4}{}^{0.26\pm0.01}$ dependence of the deposition rate to any single species in the $SnCl_4$-$SnCl_2$-Cl_2-Cl-O_2-O system.

The activation energy of the sufrace reaction process (~1.5 eV), shown in Fig. 9, in the oxygen-saturated region, is too high for the desorption of product chlorine [step (*iv*)] to be rate controlling. At the same time since no incubation period has been detected in the microscopic growth rate studies, the reaction is probably not nucleation controlled. The surface reaction control of this reaction above ~873°C becomes apparently non-Arrhenius due to the significant onset of volume reaction-produced depletion of the rate-determining tin species. It is interesting to compare the fortuitous agreement of this transition temperature of 873°C with that of ~875°C calculated by Tabata (3) where the free energy of reaction [1] becomes positive and thus no longer favored heterogeneously.

As shown in Fig. 6-8, the direct oxidation of TMT below ~490°C is a close analog to that of $SnCl_4$ with the surface deposition rate (R) being expressed by

$$R \propto (p_{O_2})^{1/2}(p_{TMT}) \qquad [7]$$

at low p_{O_2} and all p_{TMT}, whereas

$$R \propto p_{TMT} \qquad [8]$$

at high p_{O_2} (depending on p_{TMT}) and all p_{TMT}. Over and above, there is detectable nucleation-induced(?) incubation period of growth (Fig. 11). Consequently, following the previous logic, it can be inferred that atomic oxygen is also the adsorbed species here with TMT as the virtually undissociated gaseous (unadsorbed) reaction species. The initial nucleation-induced rate limitation presumably has no impact on the equilibrium growth kinetics limited by the surface reaction (under oxygen saturation conditions). The higher activation energy of the surface reaction rate constant, shown in Fig. 10 (~1.8 eV), compared to that of the similar mechanism SnO_2 formation from $SnCl_4$ (~1.5 eV), may originate from the larger activation energy of the surface diffusion of a bigger activated complex (involving methyl groups) in this case. The non-Arrhenius behavior of this surface reaction above ~490°C (Fig. 10) also has the same origin, *i.e.*, volume-reaction induced depletion of the TMT in the gas phase. This fact is further illustrated by the growth rate data above 490°C in Fig. 7. Compared to that in Fig. 6, the p_{O_2} dependence in this region is more than one-half order and the apparent reaction order increases with the temperature (particularly for the second kÅ). This growth enhancement presumably originates from the increasing incorporation of the volume-reacted material in the growing film (at low p_{O_2}). The volume reaction rate, being proportional to p_{O_2}, increases faster than the surface reaction rate at higher p_{O_2}. But at fixed flow rates the fraction of the volume-reacted material collected by the growing film is the same. Consequently, at higher p_{O_2} the gas phase would be homogeneously depleted of TMT and the growth rate would actually drop (instead of saturation) as seen in Fig. 7. This situation apparently gets more severe at longer times of growth (*i.e.*, second kÅ of the film). The apparent enhancement of reaction order at temperatures where significant volume reaction occurs has also been observed in CVD TiO_2 film growth rates (2).

The high temperature hydrolysis reaction (Eq. [2]) is the most interesting process studied. As shown in Fig. 3 and 4, in the entire range of temperature studied (400°-807°C), the surface depositon rate can be expressed by

$$R \propto (p_{H_2O})(p_{SnCl_4}) \qquad [9]$$

at low p_{H_2O} and all p_{SnCl_4}, whereas

$$R \propto p_{SnCl_4} \qquad [10]$$

at high p_{H_2O} (depending on p_{SnCl_4}) and all p_{SnCl_4}. These rate dependences immediately identify H_2O as the undissociated adsorbed species and $SnCl_4$ as the gaseous reactant. Since no growth rate saturation or maximum is achieved with increasing stannic chloride concentration, Langmuir-Hinshelwood mechanism of surface reaction by two adjacently adsorbed species is ruled out. This reaction then appears to be another classic case of Rideal-Eley mechanism where gaseous $SnCl_4$ reacts at the surface with adsorbed H_2O molecules (without any competition for the adsorption sites). The data in Fig. 5 (obtained from Fig. 3) indicate the requirement of four (symmetric?) H_2O molecule adsorptions on oxygen sites (around a tin site) of the rutile lattice for the $SnCl_4$ collision reaction at the surface to be successful in SnO_2 formation at all temperatures. This fact is interestingly in violation of the stoichiometric relation shown in Eq. [2]. From the facts that the calculated free energy change of reaction [2] is less than −10 kcal/molecule (3) and that the net energy change of a catalyzed heterogeneous reaction is the difference between that of homogeneous reaction and adsorption or desorption of the rate-determining species (2) (which is zero for this unactivated reaction in the activated region), it can be concluded that the adsorption energy of H_2O on SnO_2 closely compensates for the energy of reaction [2] in the entire temperature range studied.

Summary and Conclusions

The kinetics of three heterogeneous CVD reactions for SnO_2 thin film formations were studied in this work. Using a horizontal cold-wall reactor, it was demonstrated again (2) that it is possible to reasonably delineate the kinetic mechanism of all such surface reactions. The kinetics of both stannic chloride and tetramethyl tin surface oxidations were found to proceed by the collision of the gas-phase tin species with the adsorbed atomic oxygen. In the case of high temperature hydrolysis of stannic chloride, four adjacent symmetrically adsorbed water molecules are required for every colliding gaseous tin chloride species to be successfully reacted at the surface. The requirement of no activation energy in this case is due to the close balance of the free energies of water adsorption (on SnO_2) and homogeneous volume reaction. Furthermore, in the entire range of temperatures (400°-807°C) and stannic chloride partial pressures (0.26-4.17 $\times$ 10^{-4} atm) examined in this work, no evidence of the homogeneous gas-phase volume reaction has been found. In contrast, this homogeneous reaction becomes very important for stannic chloride oxidation above ~875°C and for TMT oxidation above ~490°C. It should be noted that volume reaction is highly undesirable in all CVD processes. The fractional order kinetics of stannic chloride surface oxidation on its concentration could not be quantitatively explained on any single species.

Manuscript submitted April 25, 1977; revised manuscript received Aug. 18, 1977.

Any discussion of this paper will appear in a Discussion Section to be published in the December 1978 JOURNAL. All discussions for the December 1978 Discussion Section should be submitted by Aug. 1, 1978.

Publication costs of this article were assisted by Westinghouse Research Laboratories.

REFERENCES

1. J. P. Hirth, in "Vapor Deposition," C. F. Powell, J. H. Oxley, and J. M. Blocher, Jr., Editors, p. 126, John Wiley & Sons, Inc., New York (1966).
2. R. N. Ghoshtagore, *This Journal*, **117**, 529 (1970); R. N. Ghoshtagore and A. J. Noreika, *ibid.*, **117**, 1310 (1970).
3. O. Tabata, in "Chemical Vapor Deposition, Fifth International Conference," J. M. Blocher, Jr., H. E. Hintermann, and L. H. Hall, Editors, pp. 681-694, The Electrochemical Society Softbound Symposium Series, Princeton, N.J. (1975).
4. M. Dub, in "Organometallic Compounds," Vol. III, pp. 158-160, Springer-Verlag, New York (1968).
5. J. A. Aboaf, V. C. Marcotte, and N. J. Chou, *This Journal*, **120**, 701 (1973).
6. B. J. Baliga and S. K. Gandhi, *ibid.*, **123**, 941 (1976); Proc. IEEE Electron. Devices Meeting, pp. 105-106 (Dec. 1-3, 1975).
7. A. S. Grove, "Physics and Technology of Semiconductor Devices," pp. 7-21, John Wiley & Sons, Inc., New York (1967).
8. H. Schlichting, in "Boundary Layer Theory," 4th ed., Chap. 7, McGraw-Hill Book Co., New York (1960).
9. W. H. Shepherd, *This Journal*, **112**, 988 (1965).
10. R. R. Monchamp, W. J. McAleer, and P. I. Pollak, *ibid.*, **111**, 879 (1964).

The Role of Energy Levels in Semiconductor-Electrolyte Solar Cells

R. Memming

Philips GmbH Forschungslaboratorium Hamburg, 2000 Hamburg 54, Germany

ABSTRACT

The transfer of minority carriers across the semiconductor-electrolyte interface during illumination has been studied. In particular the parameters which determine the competition between pure redox processes and hydrogen evolution at p-type or anodic dissolution at n-type material have been investigated. In the first case the electron transfer between p-type electrodes and the redox system can simply be interpreted on the basis of an energy scheme. In the case of hole transfer from n-type electrodes across the interface the competition of a pure redox process and anodic dissolution is more complex. It is mainly determined by kinetic parameters. The results obtained with CdS and various III-V compounds are discussed in view of application of n- and p-type semiconductors in solar energy conversion systems.

During the last few years photoelectrochemical processes at semiconductor-electrolyte interfaces found new interest because of their possible application in solar energy conversion systems. Originally the research was mainly devoted to the direct electrolytic decomposition of water which is principally possible with semiconductor electrodes. Corresponding systems have been realized with TiO_2 (1-5), titanates (6), and tantalates (7). In these cases, however, the efficiency of solar energy is very low because of the large bandgaps (>3 eV) of these materials. There are several other semiconductor electrodes of low bandgaps which show large photoeffects. These electrodes, however, are not stable, *i.e.*, instead of oxygen formation electrochemical dissolution occurs.

It has also been suggested to construct self-regenerating photocells containing at least one semiconductor electrode for conversion of solar energy directly into electrical energy. Corresponding cells have been realized consisting of an n-type CdS and a Pt counterelectrode and $[Fe(CN)_6]^{4-}/[Fe(CN)_6]^{3-}$ (8) or $S/S^{=}$ (9) as redox systems. Several aspects make these electrochemical photocells quite attractive in comparison to ordinary solid-state devices such as pn junctions and metal/semiconductor interface. There are three main advantages: (*i*) no complicated technology is required for making electrolyte/semiconductor contacts; (*ii*) the light can easily pass the electrolyte and reach the space charge region without essential losses; (*iii*) several semiconductor electrodes of different bandgap can be combined in one cell.

Key words: charge transfer, redox systems, anodic dissolution, semiconductor photoelectrolysis.

On the other hand problems arise with semiconductors in electrolytic cells as far as the stability of these compounds are concerned (10), although in the two CdS cells mentioned above the corrosion could be reduced to very low levels. However, the bandgap of CdS is still relatively large (2.5 eV) and other semiconducting electrodes of lower bandgaps are required for a high solar energy conversion efficiency. The stability problem arises insofar as holes produced by light excitation in n-type material may not only be transferred to the occupied energy levels of a redox system such as $[Fe(CN)_6]^{4-}$ or $S^{=}$, but could also be consumed for the anodic dissolution of the semiconductor.

The conversion efficiency cannot only be increased by semiconductors of a smaller bandgap but also by choosing a combination of an n-type electrode/redox system in which the difference of flatband and redox potentials is larger than in the case of CdS/$[Fe(CN)_6]^{3-/4-}$. Principally this can be realized by combining n-CdS with a redox system of a more positive normal potential or by using a semiconductor such as n-GaP with energy bands at rather negative energy values (Fig. 1) [negative flatband potential (11)].

For all combinations, however, the stability problem arises (30). It is the purpose of this paper to investigate the parameters which determine the competition between redox process and anodic dissolution during illumination. Moreover, the possibility of combining p-type electrodes with redox systems is investigated in order to avoid the problem of anodic dissolution.

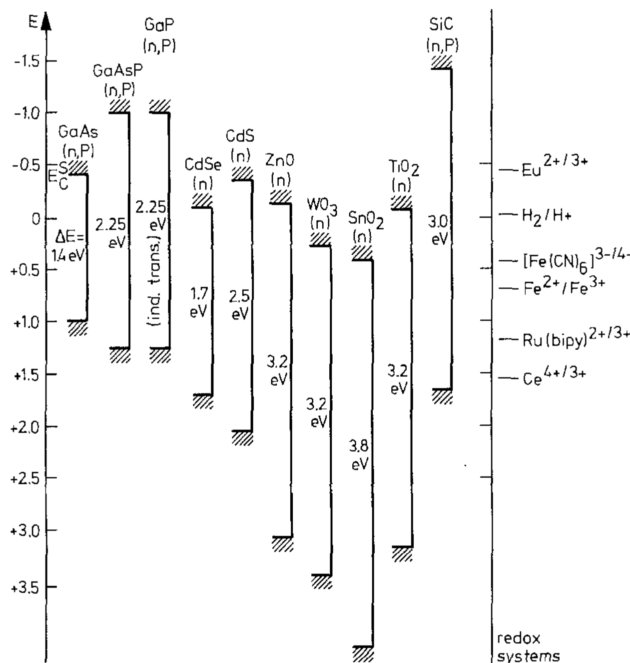

Fig. 1. Energy band at semiconductor-electrolyte interface at pH 1

Experimental

Most experiments were performed with single crystals of CdS, GaP, GaAs, and GaAsP. Their surfaces were carefully polished. In some cases epitaxial layers of GaP and GaAsP on GaP-substrates were investigated too. In order to distinguish between anodic dissolution and pure redox process rotating ring-disk electrodes were used consisting of a semiconductor disk and platinum ring. The semiconductor was illuminated by chopped light. If any charge transfer between semiconductor and redox system occurs during illumination then the oxidized species passed the Pt-ring during rotation where it was reduced back to its original state. The method has been described in detail elsewhere (12). The collection factor was determined by a pure platinum ring-disk electrode of the same dimensions. We obtained $\gamma = (i_{\mathrm{Ring}}/i_{\mathrm{disk}}) = 0.14$.

The current-potential curves were measured under potentiostatic conditions. The potentials refer to the standard calomel electrode if not otherwise indicated. The photo- and ring currents were measured by a lock-in amplifier or displayed on an oscilloscope (signal averager).

Results

Current-potential behavior.—Typical current-potential curves have been obtained with n-type electrodes. The surface preparation or the use of epitaxially grown layers did not have any influence on the value of the anodic limiting current. In the case of cathodic processes at n-type materials it has been observed that the H_2 evolution at epitaxial layers occurs at somewhat more cathodic potentials. As far as p-type electrodes are concerned the treatment of the electrode surface plays an important role. Only for well-polished surfaces or epitaxial layers could the cathodic limiting current be kept at a very low level over a large potential range (>3V).

The doping of the semiconducting material seems only to be important for GaAs as demonstrated at first by Hollan and Tranchart (13). In this case the anodic and cathodic limiting currents remain at a low value only for donor or acceptor densities below 10^{15} cm^{-3}. For higher doping levels the anodic current for n-type and the cathodic current for p-type GaAs increase at certain potentials. The authors (13) interpreted this result as avalanche processes.

As far as the spectral distribution of the photosensitivity is concerned it should be emphasized that

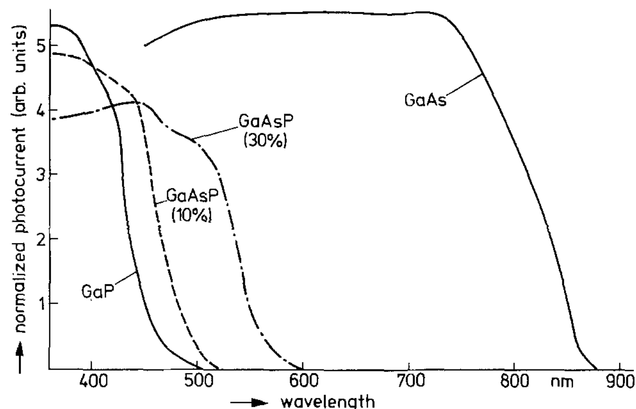

Fig. 2. Spectral distribution of photocurrent at pH 7

the corresponding photocurrent obtained with GaP sets in below 500 nm (2.5 eV) (Fig. 2). *i.e.*, at an energy being much larger than the bandgap of 2.25 eV and comparable with that of CdS. This result is due to the fact that the bandgap of 2.25 eV corresponds to an indirect transition (14), which generally has a lower absorption coefficient ($\alpha \leq 10^3$ cm^{-1}). Since the diffusion length is much smaller ($L = 10^{-4}$ cm) greater photocurrents can only be obtained in the range of direct transitions. The absorption of GaP can be shifted towards longer wavelengths in crystals of GaAsP containing only 10-30% As (90-70% P). In the case of 30% As the direct transition of GaAsP occurs at the energy of the indirect transition of pure GaP.

Redox processes during illumination.—The ring(Pt)-disk (semiconductor) electrode arrangement has been used for studying charge-transfer processes between redox systems and semiconductor during illumination (12). A typical example obtained with the ring-disk electrode using a CdS disk and $[Fe(CN)_6]^{4-}$ as a redox system is shown in Fig. 3. The anodic photocurrent immediately follows the light pulses. The ring current, corresponding to the reduction of Fe(III) formed at CdS during light excitation back into Fe(II), rises and decays rather slowly depending on the speed of the angular rotation. Using the collection factor $\gamma = 0.14$ one obtains for the current i_{ox} equiva-

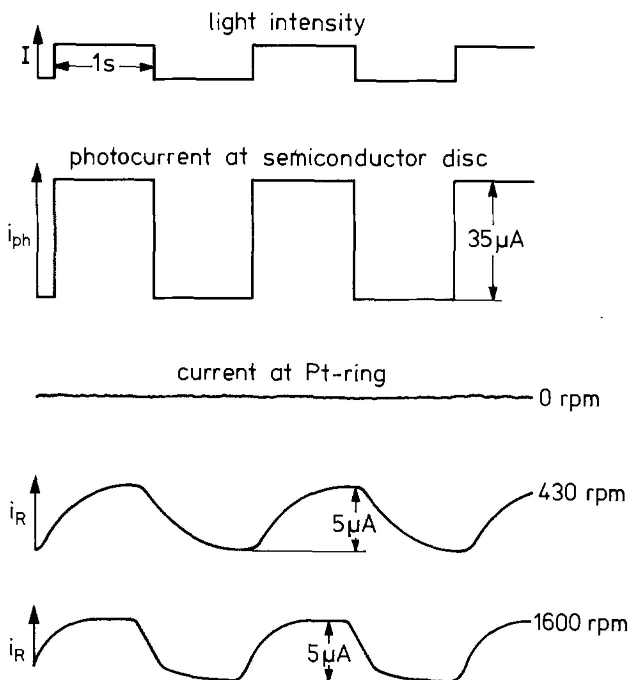

Fig. 3. Photo- and ring current at rotating electrode

Table I. Relative values of oxidation (i_{ox}) and reduction currents (i_{red}) for redox systems (i_{ph} = photocurrent)

Semiconductor	$\frac{i_{ox}}{i_{ph}}$ n-type semiconductor				$\frac{i_{red}}{i_{ph}}$ p-type semiconductor	
Redox syst.	CdS	GaP	GaAsP	GaAs	GaP	GaAs
$[Fe(CN)_6]^{4-/3-}$ U_E = 0.42V	1.0 (pH 6-13)	1.0	0.35	0.35	0.04 (pH 1)	0.25 (pH 1)
$Fe^{2+/3+}$ 0.73	0.13	0.35	0.1	0.1	—	—
$Ce^{3+/4+}$ 1.6	0.08	0.1	0	0	—	—
$Ru(bipy)_3^{2+}$ 1.2	0	0	—	—	—	—
Quinone (Q/QH_2) 0.5	1.0	1.0	0.2	0.2	1.0 duroqu. (pH 1-5)	1.0 duroqu. (pH 1-6)
Fe(II)ox	0.1	0.1	—	—	—	—
$Eu^{2+/3+}$ −0.42	—	—	—	—	1.0 (pH 1-6)	1.0 (pH 1-6)
Fe(II)EDTA	—	—	—	—	0.9	1.0

lent to the oxidation of Fe(II) in the anodic process at the semiconductor electrode

$$\frac{i_{ox}}{i_{ph}} = \frac{i_R}{\gamma i_{ph}} \quad [11]$$

For instance in the case of $[Fe(CN)_6]^{4-}$ we obtained $(i_{ox}/i_{ph}) = 1$ at pH = 6.5. Various other semiconductors and redox systems have been investigated; the results are given in Table I. In some cases also the pH dependence has been determined as given in Fig. 4. It is interesting to note that not only in the case of CdS but also for GaP the oxidation of $[Fe(CN)_6]^{4-}$ is faster than the anodic dissolution. In the latter case, however, the redox process can only sufficiently compete with the dissolution in a pH range between 6.5 and 10. With GaAs and also with GaAsP (30% As) the i_{ox}/i_{ph} ratio was always much lower even in neutral solutions (Fig. 4, Table I). The ratio did not depend on the electrode potential of the semiconductor.

It should be emphasized that large i_{ox}/i_{ph} values have only been obtained with very well-polished surfaces or epitaxial layers. Especially in the case of GaP, GaAsP, and GaAs any deterioration of the surface led to a decrease of the i_{ox}/i_{ph} ratio.

Similar investigations have also been performed with p-type GaP and GaAs. Here the corresponding redox process (reduction) has to compete with the hydrogen evolution. The best results have been obtained with quinone, Eu^{3+} and Fe(III)EDTA. In all cases the ratio i_{red}/i_{ph} was equal to 1, *i.e.*, the redox process competes well with the hydrogen formation. No pH dependence has been found in the range of $6 \leq pH \leq 0$. It should be emphasized that ring currents could only be detected if oxygen was excluded from the electrolyte. Obviously oxygen easily reoxidized the reduction products. The surface pretreatment did not seem to be as important for cathodic processes as for n-type electrodes in the anodic range. The surface roughness should only be sufficiently low in order to keep the dark current at a low value.

It should be mentioned that in some cases information about the cathodic reduction of a redox system such as $Eu^{3+/2+}$ can also be obtained directly from a current-potential curve as determined with an n-type electrode. For instance with an n-type GaAsP electrode the reduction of Eu^{3+} yields higher cathodic currents than that of H^+/H_2 (Fig. 5). This result, however, has only been obtained with epitaxial layers and not with ordinary crystals.

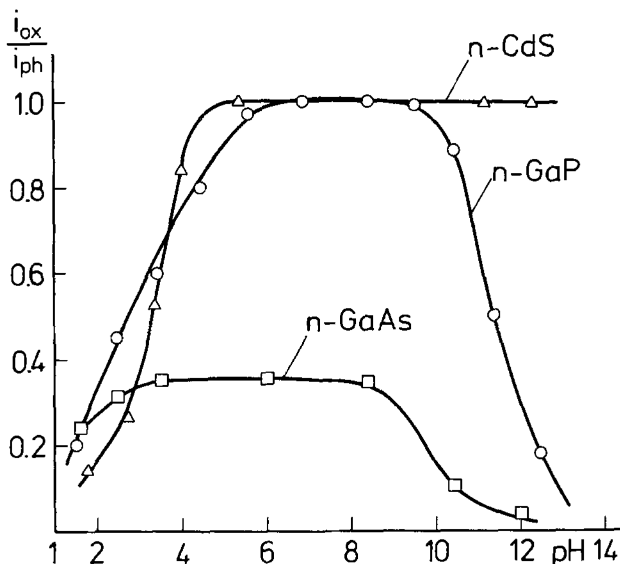

Fig. 4. i_{ox}/i_{photo} vs. pH for $[Fe(CN)_6]^{4-}$

Discussion

The results presented in the previous section show that some redox processes at semiconductor electrodes can occur during illumination without having any anodic dissolution or hydrogen evolution. The question arises, however, which factors are of importance in determining whether a redox process can really compete with the anodic dissolution at n-type and with hydrogen evolution at p-type electrodes. The two cases will be treated separately.

Hole transfer at n-type electrodes.—In the case of n-type electrodes the anodic current is limited to a very low value since no holes are available at the surface. Light excitation leads to the creation of electron-hole pairs. The holes are pushed towards the surface by the electrical field across the space-charge region and consumed for an anodic charge transfer process. In some cases such as SnO_2 (15), TiO_2 (2, 7, 15), and WO_3 (16) the corresponding anodic reaction is oxygen evolution. The semiconductor electrodes such as CdS (17), GaP (18), GaAsP, and GaAs (19, 20) discussed here only show anodic dissolution. Taking GaP as an

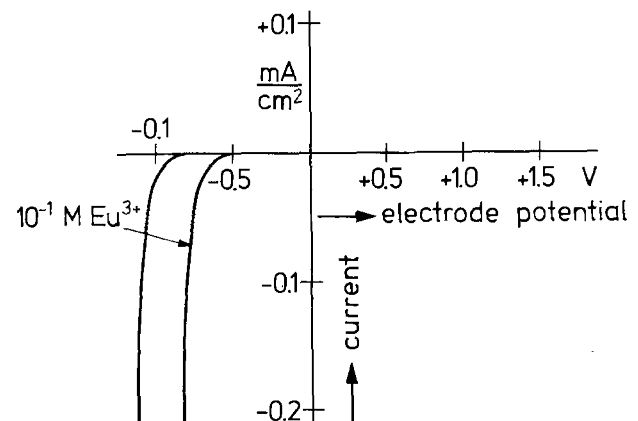

Fig. 5. *I-U* dependence for n-GaAsP (epitaxial layer on GaP) in 0.1*N* H_2SO_4.

example this reaction can be described as (18)

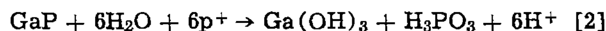

$$GaP + 6H_2O + 6p^+ \rightarrow Ga(OH)_3 + H_3PO_3 + 6H^+ \quad [2]$$

In the case of an oxidation of a redox system which also consumes holes the competing process is given by

$$Red + p^+ \rightarrow Ox \quad [3]$$

It seems to be useful to consider these two competing processes in view of thermodynamic data from which a theoretical value of the potential at which anodic dissolution is expected can be calculated. In order to relate such a value to the normal hydrogen potential we also used the equation

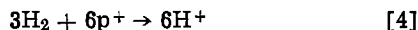

$$3H_2 + 6p^+ \rightarrow 6H^+ \quad [4]$$

Subtracting Eq. [2] and [4] one obtains

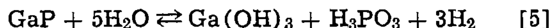

$$GaP + 5H_2O \rightleftarrows Ga(OH)_3 + H_3PO_3 + 3H_2 \quad [5]$$

Free energy values of $Ga(OH)_3$ and H_3PO_3 are tabled in Ref. (21). Some uncertainty exists about the value for GaP (22). We used $\Delta G_{GaP} = -23$ kcal. The free energy of the total reaction (5) is $\Delta G = +40.6$ kcal/mole. The corresponding potential calculated from this ΔG value is given in Fig. 6 for $pH = 7$. In the same way also the potential for the dissolution of GaAs has been determined (Fig. 6). The latter value differs from that already calculated by Harvey (20) who used only an estimated ΔG_{GaAs} value.

According to the thermodynamic data dissolution should be the process preferred over charge-transfer processes with redox systems such as $[Fe(CN)_6]^{4-/3-}$, $Fe^{2+/3+}$, etc. The situation is quite similar for various other semiconductors such as CdS (23), CdSe, and ZnO (Table II). It must be emphasized, however, that thermodynamic data only describe the general tendency of the material and do not take into account the existence of energy bands in the semiconductor, shown in Fig. 6.

An electron transfer across the interface only occurs if energy levels exist at the same energy on both sides of the interface assuming weak interaction between electrode and reactant. Consequently, the most effective hole transfer is expected if the occupied levels D_{red} of a redox couple overlap with the valence band. In order to fulfill this condition one should select a redox system of a sufficiently large normal potential. Taking $[Fe(CN)_6]^{4-/3-}$ as an example the corresponding energy levels of this redox system are given in Fig. 7 assuming a value of the reorientation energy of $\lambda = 0.5$ eV (24, 25). The position of the energy bands at the surface of a few semiconductors are also plotted in this figure for $pH = 7$. Comparing the three semiconductors GaAs, GaP, and CdS the largest density of states of the redox system occurs at the upper edge of the GaP valence band whereas it is much lower at the valence band of CdS. According to this energy scheme one should also expect that a hole transfer across a CdS electrode surface would preferably work (with respect to the dissolution) with a redox system of a higher normal potential such as, *e.g.*, $Fe^{2+/3+}$.

The experimental results indicate, however, that this model is not sufficient. The investigations with the rotating ring-disk electrodes have definitely shown that the oxidation of $[Fe(CN)_6]^{4-}$ at CdS can compete well with the anodic dissolution. In the case of GaP it

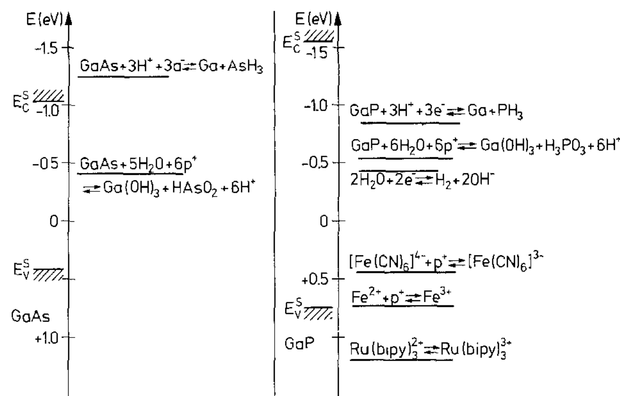

Fig. 6. Thermodynamic data for GaAs and GaP

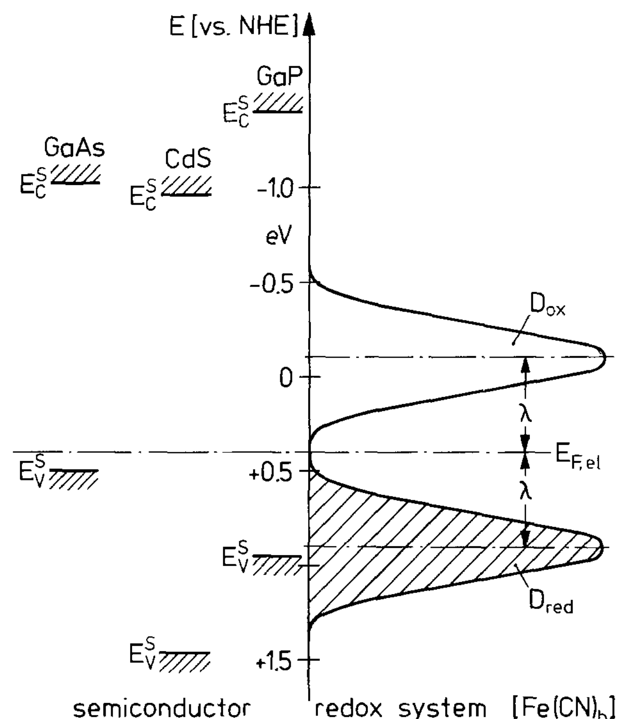

Fig. 7. Energy scheme of semiconductor/$[Fe(CN)_6]^{4-/3-}$ at *p*H 7.

is already critical. The strong pH dependence found with this electrode (Fig. 4) cannot be explained only by a corresponding shift (18) of the energy bands with pH. Moreover, it is not clear from this picture why GaAs and GaAsP dissolve (Table I).

A pure thermodynamic picture is also insufficient because it would never explain any effective hole transfer from one of these semiconductor electrodes to a redox system such as $[Fe(CN)_6]^{4-/3-}$.

Another possibility to interpret the efficient hole transfer from CdS or GaP to $[Fe(CN)_6]^{4-}$ is the assumption that this complex is better adsorbed at the surface than, for instance, Fe^{2+} ions surrounded by a strong solvation shell. Adsorption, however, cannot be the dominant factor in this process because no hole

Table II. Thermodynamic dissolution data (*p*H = 7)

Semiconductor	(eV)	Anodic reaction	$\frac{\Delta G}{nF}$ (V)
GaAs	1.4	$GaAs + 5H_2O + 6p^+ \rightleftarrows Ga(OH)_3 + HAsO_2 + 6H^+$	−0.38
GaP	2.25	$GaP + 6H_2O + 6p^+ \rightleftarrows Ga(OH)_3 + H_3PO_3 + 6H^+$	−0.71
CdS	2.5	$CdS + 2HCl + 2p^+ \rightleftarrows Cd^{2+} + 2Cl^- + 2H^+ + S$	−0.09
TiO_2	3.0	$TiO_2 + 4HCl + 4p^+ \rightleftarrows TiCl_4 + O_2 + 4H^+$	+1.4
ZnO	3.25	$2ZnO + 4H_2O + 4p^+ \rightleftarrows 2Zn(OH)_2 + O_2 + 4H^+$	+0.81
SnO_2	3.8	$SnO_2 + 4HCl + 4p^+ \rightleftarrows SnCl_4 + O_2 + 4H^+$	+1.05

transfer from GaP or CdS to $Ru(bipy)_3^{2+}$ has been detected between pH 1 and 8 although this complex is partly adsorbed at the surface and its redox potential (U_{Redox} = 1.2V) is much larger.

It is interesting to note that besides $[Fe(CN)_6]^{4-}$, hydroquinone (Table I) and polysulfide (9) can effectively compete with the anodic dissolution process too. Both latter systems have rather low normal potentials. In all three cases the density of the corresponding energy levels (D_{red}) is certainly not very large at the upper edge of the CdS valence band. These results lead to the assumption that the essential charge transfer occurs mainly via surface states as shown in Fig. 9. Such a process seems to be reasonable because anodic dissolution occurs also partly via surface states. In most cases several reaction steps are involved in the dissolution process and surface states are formed as intermediate states [see *e.g.*, (10)] The complete dissolution of a surface group can obviously be avoided by a fast electron transfer from a redox system into surface states. This model is supported by recent results obtained by Chang *et al.* (26) who studied the charge transfer between n-GaAs electrodes and a selenide redox system. In this case the standard potential of the redox system is rather negative and the occupied levels of the redox system can only reasonably overlap with surface states within the bandgap of GaAs. The authors found that at high (~1M) selenide concentrations the GaAs surface remains completely stable during illumination.

The *p*H dependence in Fig. 4 is not yet fully understood. It may be partly due to a relative shift of energy levels but it seems to be mainly determined by the change of surface groups (dissociation) which influence strongly the rate of anodic dissolution.

Electron transfer at p-type electrodes.—Transfer of excited electrons from the conduction band to a redox system seems to be much easier, since most redox systems selected on the basis of the normal energy scheme

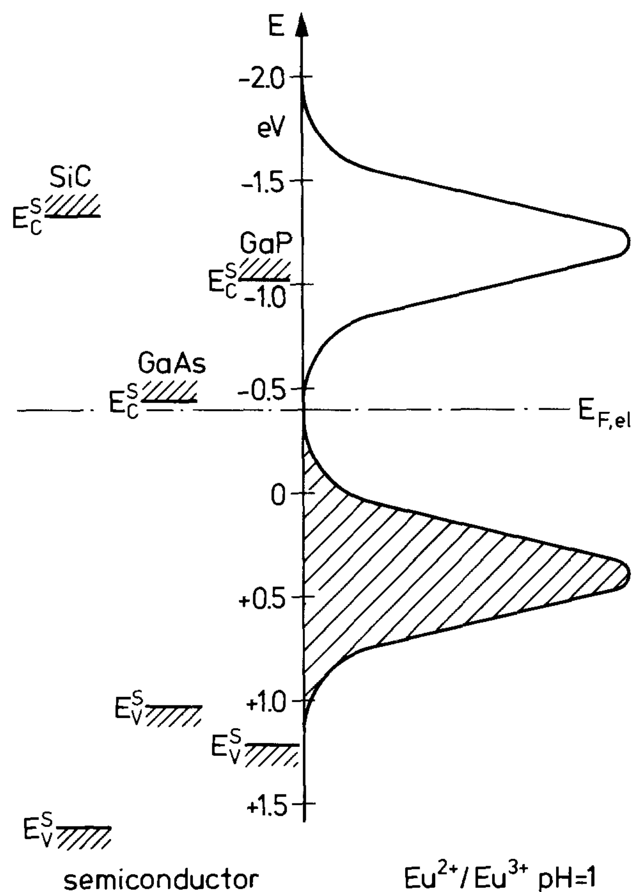

Fig. 8. Energy scheme of semiconductor/Eu^{2+3+} at pH 1

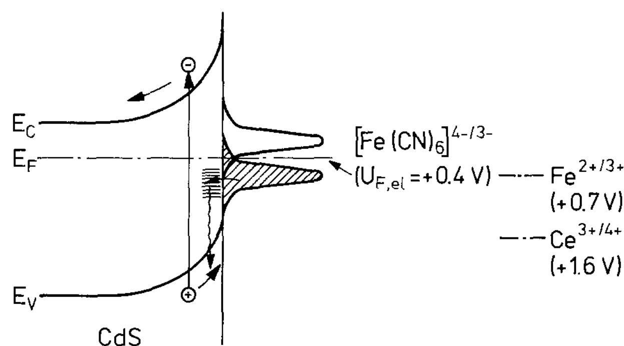

Fig. 9. Energy scheme of $CdS/[Fe(CN)_6]^{4-/3-}$

work even with GaAs (i_{red}/i_{ph} = 1, Table I). Taking Eu^{2+}/Eu^{3+} as an example the corresponding energy diagram of the interface is presented in Fig. 8. The reorientation energy was estimated to be $\lambda \approx 1$ eV, a value being similar to that of Fe^{2+}/Fe^{3+} (24). The unoccupied levels of Eu^{2+}/Eu^{3+} overlap well with the conduction band of several semiconductors. We did not plot any levels of the H_2/H_3O^+ system because it is not known whether it can be treated as a simple redox system or whether other surface reactions are involved (strong interaction). According to the experimental results, however, the reduction of some systems can efficiently compete with the hydrogen evolution. The density of occupied states of $Eu^{2+/3+}$ must be very low at the lower edge of the conduction band because the electron transfer from Eu^{2+} into the conduction band of, *e.g.*, n-GaAs is hard to detect. The corresponding anodic current must be less than $2 \cdot 10^{-7}$ Acm^{-2} (Fig. 10).

It is interesting to note that the photoinduced electron transfer to quinone can also compete with the hydrogen evolution although the normal potential of Q/QH_2 is +0.7V [NHE]. This is due to the fact that two electrons are involved in the redox process of quinones and the normal potential of Q/QH occurs at much more negative values as derived from current-doubling effects observed with p-GaP electrodes (27).

Solar cells.—According to the results obtained with p-type electrodes it would be quite interesting to construct photocells with p-GaAs as a semiconductor and $Eu^{2+/3+}$ as a redox system because p-GaAs should show strong band bending under equilibrium conditions as shown in Fig. 11. In this case a large photopotential of more than 1V is expected. We performed some preliminary experiments with a corresponding cell. As a counterelectrode we used an amalgamated

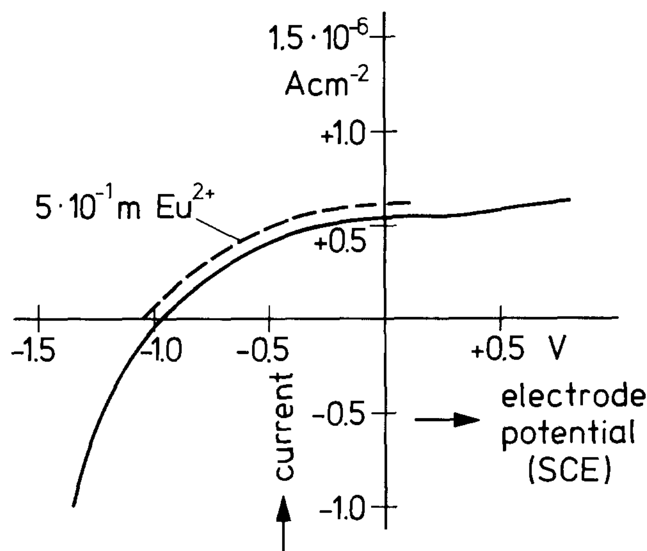

Fig. 10. *I-U* characteristic for n-GaAs in 1*N* H_2SO_4

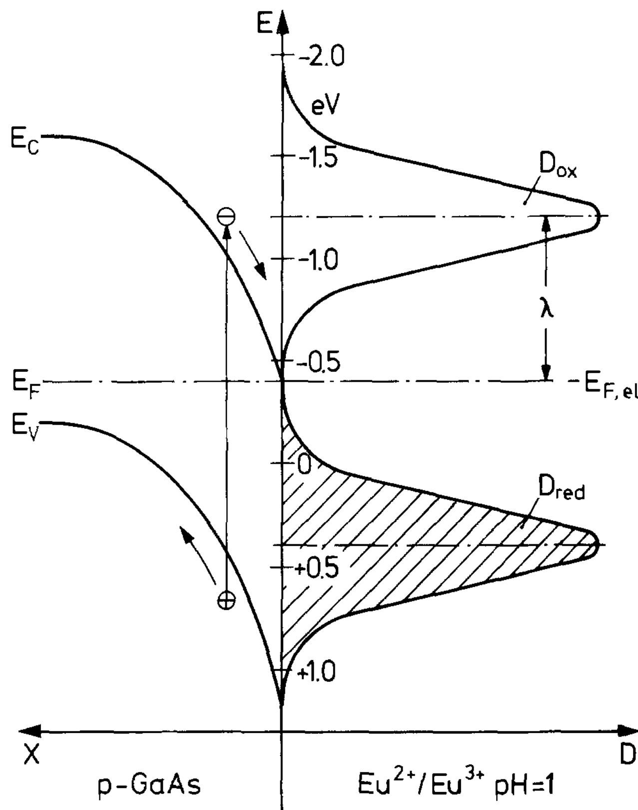

Fig. 11. Energy scheme of p-GaAs/$Eu^{2+/3+}$ at pH 1

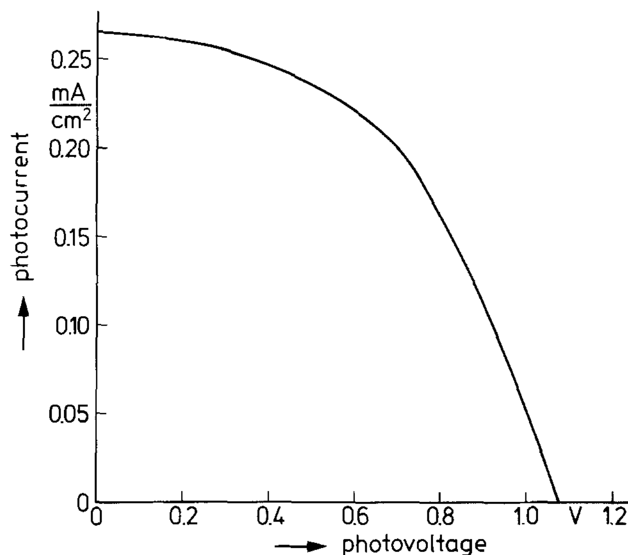

Fig. 12. i_{ph}-U_{ph} for p-GaP/Hg(Au) solar cell with 10^{-1}M Eu^{3+}/2 · 10^{-2}M Eu^{3+} at pH 1.

Au electrode since its large H_2 overpotential defines the potential well. We obtained relatively large photocurrents and a photopotential of 0.7V; the i_{ph}-U_{ph} characteristic, however, was rather poor. This has to be studied in more detail. A better cell performance has been obtained with a cell containing a p-GaP electrode (Fig. 12). The open-circuit photovoltage was 1.07V. The intensity of the incident white light (Xe lamp) was ~6 mW.

In general it seems to be rather easy to find suitable redox systems to be combined with p-type electrodes. The selection is limited, however, by the fact that the energy bands of most semiconductors which can be made p-type are located at relatively high energies (Fig. 1). On the other hand it has been shown by several authors that the light-induced anodic dissolution at n-type electrodes can be avoided by selecting a redox system of which the occupied levels overlap with surface states of the semiconductor. In this case, however, the Fermi level is located at the interface near the middle of the forbidden zone. The maximum value of the photovoltage is given by the difference of the redox potential U_{Redox} and the flatband potential U_{fb} according to

$$U_{ph} \leqq U_{Redox} - U_{fb}$$

Consequently, the photopotential U_{ph} is always much lower than that of the bandgap Eg/e. In most cases one should expect a value of $U_{ph} \approx 0.5$ Eg/e. Accordingly, the maximum quantum efficiency for solar energy conversion in systems containing n-type semiconductors will not be more than half of the theoretical value.

In connection with this problem the question arises whether the sensitivity in the red can be increased by strong doping of the material so that excitation of electrons from acceptor levels into the conduction band also contributes to the photocurrent. Such effects are well known in CdS photoconductors doped with Cu, with which sensitivities up to 700 nm have been found (28). We have tested corresponding CdS(Cu) layers in electrochemical cells but did not find any extrinsic photocurrent. WO_3 is the only material known so far where excitation via interstates causes an anodic photocurrent (16).

It would be quite tempting to combine n- and p-electrodes of different bandgaps in one cell, as it has been suggested by Nozik (28) for the direct decomposition of H_2O. According to the results presented above certainly a self-generating cell can be constructed. One would expect on the first sight that the combination of n- and p-type electrodes which also have different bandgaps would lead to a considerable increase of the efficiency. Such a cell, however, would only show a reasonable characteristic if the anodic and cathodic photocurrents at the n-and p-type electrodes, respectively, are equal. The two currents can be balanced by using electrodes of different surface areas. This is a rather tricky method and we did not test such a system.

Acknowledgments

The author would like to express his gratitude to Dr. L. Hollan (Laboratoires d' Electronique et de Physique Appliquee, Paris) and Dr. Werkhoven (Philips Research Laboratories, Eindhoven The Netherlands) for supplying the GaAs, GaAsP, and GaP single crystals.

Manuscript submitted June 28, 1977; revised manuscript received Sept. 15, 1977. This paper was presented at the Airlie, Virginia, Meeting of the Society, May 1977.

Any discussion of this paper will appear in a Discussion Section to be published in the December 1978 JOURNAL. All discussions for the December 1978 Discussion Section should be submitted by Aug. 1, 1978.

Publication costs of this article were assisted by Philips GmbH Forschungslaboratorium Hamburg.

REFERENCES

1. A. Fujishima and K. Honda, *Bull. Chem. Soc. Jpn.*, **44**, 1148 (1971).
2. D. Laser and A. J. Bard, *Chem. Phys. Lett.*, **34**, 605 (1975); *This Journal*, **123**, 1027 (1976).
3. M. S. Wrighton, D. S. Ginley, P. T. Wolczanski, A. G. Ellis, D. L. Morse, and A. Ling, *Proc. Natl. Acad. Sci. U.S.A.*, **72**, 1518 (1975).
4. T. Ohnishi, Y. Nakato, and H. Tsubomura, *Ber. Bunsenges. Phys. Chem.*, **79**, 523 (1975).
5. W. Gissler, P. L. Lensi, and S. Pizzini, *J. Appl. Electrochem.*, **6**, 9 (1976).
6. J. G. Mavroides, D. I. Tchernev, J. A. Kafalas, and D. F. Kolesar, NBS Publication 455, 221 (1976).
7. A. B. Ellis, S. W. Kaiser, and M. S. Wrighton, *J. Chem. Phys.*, **80**, 1325 (1976).
8. H. Gerischer and J. Gobrecht, *Ber. Bunsenges. Phys. Chem.*, **80**, 327 (1976).

9. M. S. Wrighton, A. B. Ellis, P. T. Wolczanski, D. L. Morse, H. B. Abrahamson, and D. S. Ginley, *J. Am. Chem. Soc.*, **98**, 2774 (1976); B. Miller and A. Heller, *Nature (London)*, **262**, 680 (1976).
10. R. Memming, NBS Publication 455, 267 (1976).
11. R. Memming, *This Journal*, **116**, 785 (1969).
12. R. Memming, *Ber. Bunsenges. Phys. Chem.*, **81**, 732 (1977); B. Miller, S. Menerges, and A. Heller, Paper presented at The Electrochemical Society Meeting in Airlie, Virginia, May 3-5, 1977.
13. L. Hollan and J. C. Tranchart, Submitted to *This Journal*.
14. R. J. Elliot and A. F. Gibson, "Introduction to Solid State Physics," The Macmillan Press (1974).
15. P. J. Boddy, *This Journal*, **115**, 199 (1968).
16. W. Gissler and R. Memming, *ibid.*, **124**, 1710 (1977).
17. J. Williams, *J. Chem. Phys.*, **32**, 1505 (1960).
18. R. Memming and G. Schwandt, *Electrochim. Acta*, **13**, 1299 (1968).
19. H. Gerischer, *Ber. Bunsenges. Phys. Chem.*, **69**, 578 (1965).
20. W. W. Harvey, *This Journal*, **114**, 473 (1967).
21. W. M. Latimer, "Oxidation-Potentials," Prentice Hall, Inc., Englewood Cliffs, N.J. (1959).
22. C. D. Thurmond, *J. Phys. Chem. Solids*, **26**, 785 (1965).
23. H. Gerischer, in Proceedings of Congress on Photochemical Processes, London (1976).
24. R. Memming and F. Möllers, *Ber. Bunsenges. Phys. Chem.*, **76**, 475 (1972).
25. R. A. L. van den Berghe, F. Cardon, and W. P. Gomes, *Surf. Sci.*, **39**, 368 (1973).
26. K. C. Chang, A. Heller, B. Schwartz, S. Menerges, and B. Miller, *Science*, 196, 1097 (1977).
27. R. Memming and F. Möllers, *Ber. Bunsenges. Phys. Chem.*, **76**, 609 (1972).
28. R. H. Bube, "Photoconductivity of Solids," John Wiley & Sons, New York (1960).
29. A. J. Nozik, *Appl. Phys. Lett.*, **29**, 150 (1976).
30. S. N. Frank and A. J. Bard, *J. Am. Chem. Soc.*, **99**, 4662 (1977); A. J. Bard and M. S. Wrighton, in Proceedings of The Electrochemical Society in Airlie, Va., (1977).

Phase Diagram of the In-Ga-As-P Quaternary System and LPE Growth Conditions for Lattice Matching on InP Substrates

Kazuo Nakajima, Toshihiro Kusunoki, Kenzo Akita, and Tsuyoshi Kotani

Fujitsu Laboratories Limited, 1015 Kamikodanaka, Nakahara-ku, Kawasaki, Japan

ABSTRACT

The phase diagram of the In-Ga-As-P quaternary system has been determined experimentally for several As isoconcentration sections at 600° and 650°C. The liquidus data were obtained by the seed dissolution technique, and the solidus data were determined from liquid phase epitaxial layers grown on InP(111)B substrates by using EPMA. Lattice constants of the quaternary solid solutions were measured by an x-ray diffraction technique. The LPE growth conditions of exactly lattice-matched $In_{1-x}Ga_xAs_{1-y}P_y$ ($0 \leq x \leq 0.35$, $0.3 \leq y \leq 1.0$) layers on InP substrates were found from the results of the phase diagram and lattice constant measurements. The phase diagram was also calculated by using a simple solution model and was compared with experimental results.

It has been reported that lasers or LED's emitting in the 1.1-1.3 μm region would provide optimum performance in communication systems using fused silica fibers (1, 2). The InGaAsP quaternary system has received considerable attention because of the advantage that exactly lattice-matched layers can be grown by liquid phase epitaxy (LPE) on InP substrates (3, 4) for such devices giving emission in the wavelength range from 0.9 to 1.6 μm. Recently, Hsieh *et al.* (5) reported that stripe-geometry InGaAsP/InP DH diode lasers operate continuously at room temperature with emission at 1.15 μm.

For producing these InGaAsP/InP quaternary diodes by LPE growth, the accurate In-Ga-As-P equilibrium phase diagram is desired. Antypas *et al.* (6, 7) reported this phase diagram first, however, it did not supply sufficient information required for the growth of lattice-matched quaternary layers giving various emission wavelengths. Sankaran *et al.* (8) measured the Ga and As content in the solid for layers lattice-matched to InP as a function of the Ga and As in the liquid at 650°C.

In this paper, the experimental equilibrium phase diagram of In-Ga-As-P system to facilitate the preparation of closely lattice-matched InGaAsP/InP heterostructure diodes is described. We report 600° and 650°C phase diagram data. These temperatures were selected to permit the LPE growth of the quaternary layers under reasonable conditions. The LPE growth conditions of exactly lattice-matched $In_{1-x}Ga_xAs_{1-y}P_y$ ($0 \leq x \leq 0.35$, $0.3 \leq y \leq 1.0$) layers are also described. The phase diagram calculated by using a simple solution model is compared with experimental results.

Key words: III-V semiconductors, light emitting materials, phase equilibrium, heterojunctions.

Experimental Procedure and Results

Liquidus.—The seed dissolution technique (9-11) was used to determine the 600° and 650°C liquidus isotherms. A ternary undersaturated In-Ga-As solution (the As concentration in the solution was always below the solubility limit) was saturated with P at the fixed temperature by bringing the melt into contact with an InP seed. The melt and the seed were kept in contact at temperature for an hour. The liquidus composition was determined from the weight loss of the seed after removal from the melt. In this work, the materials used were semiconductor grade In, InP, InAs, and GaAs. The experimental apparatus consisted of a horizontal furnace system and a conventional sliding graphite boat.

The experimental 600° and 650°C liquidus results are listed in Table I and II, respectively. Figure 1 shows the 600°C liquidus isotherms at $X_{As}^l = 0.0$ and 0.030, where X_i^l represents the atomic fraction of the element i in the liquid. Figure 2 shows the 650°C liquidus isotherms at $X_{As}^l = 0.030$ and 0.050. These figures indicate that the main effect of the addition of Ga to the melt is to appreciably decrease the solubility of P in the liquid, while the presence of As

Table I. Liquidus and solidus compositions at 600°C determined by the seed dissolution technique and EPMA in the In-Ga-As-P quaternary system, respectively

Liquidus composition (atomic fraction)				Solidus composition	
X_{Ga}^{l}	X_{In}^{l}	X_{As}^{l}	X_{P}^{l}	x	y
0.0	0.9964	0.0	0.0036	0.0	1.00
0.0010	0.9957	0.0	0.0033	—	—
0.0020	0.9948	0.0	0.0032	—	—
0.0030	0.9939	0.0	0.0027	—	—
0.0	0.9914	0.0050	0.0036	0.0	0.915
0.0005	0.9911	0.0050	0.0034	0.045	0.916
0.0010	0.9905	0.0050	0.0035	0.070	0.918
0.0012	0.9903	0.0050	0.0035	0.087	0.911
0.0016	0.9905	0.0050	0.0029	0.130	0.914
0.0020	0.9900	0.0050	0.0030	0.162	0.924
0.0025	0.9897	0.0050	0.0028	0.195	0.925
0.0	0.9866	0.0100	0.0034	0.0	0.780
0.0005	0.9863	0.0100	0.0032	0.044	0.780
0.0010	0.9858	0.0100	0.0032	0.070	0.798
0.0017	0.9850	0.0100	0.0033	0.112	0.755
0.0020	0.9850	0.0100	0.0030	0.125	0.770
0.0025	0.9849	0.0100	0.0026	0.168	0.772
0.0030	0.9845	0.0100	0.0025	0.195	0.770
0.0	0.9814	0.0150	0.0036	0.0	0.656
0.0010	0.9808	0.0150	0.0032	0.067	0.640
0.0020	0.9799	0.0150	0.0031	0.106	0.620
0.0025	0.9797	0.0150	0.0028	0.157	0.625
0.0030	0.9792	0.0150	0.0028	0.170	0.610
0.0035	0.9792	0.0150	0.0023	0.188	0.640
0.0036	0.9789	0.0150	0.0025	0.188	0.640
0.0040	0.9788	0.0150	0.0022	0.223	0.695
0.0050	0.9775	0.0150	0.0025	0.292	0.672
0.0	0.9765	0.0200	0.0035	0.0	0.531
0.0010	0.9756	0.0200	0.0034	0.060	0.530
0.0020	0.9750	0.0200	0.0030	0.102	0.525
0.0030	0.9744	0.0200	0.0026	0.141	0.547
0.0040	0.9736	0.0200	0.0024	0.190	0.545
0.0043	0.9737	0.0200	0.0020	0.192	0.554
0.0045	0.9737	0.0200	0.0018	0.200	0.552
0.0050	0.9732	0.0200	0.0018	0.210	0.500
0.0	0.9666	0.0300	0.0034	—	—
0.0020	0.9652	0.0300	0.0028	0.060	0.250
0.0040	0.9641	0.0300	0.0019	0.115	0.249
0.0060	0.9627	0.0300	0.0013	0.190	0.280
0.0080	0.9608	0.0300	0.0012	0.290	0.295
0.0100	0.9589	0.0300	0.0011	—	—
0.0150	0.9545	0.0300	0.0005	—	—
0.0200	0.9491	0.0300	0.0003	—	—
0.0250	0.9441	0.0300	0.0009	—	—
0.0390	0.9308	0.0300	0.0002	—	—

Table II. Liquidus and solidus compositions at 650°C determined by the seed dissolution technique and EPMA in the In-Ga-As-P quaternary system, respectively

Liquidus composition (atomic fraction)				Solidus composition	
X_{Ga}^{l}	X_{In}^{l}	X_{As}^{l}	X_{P}^{l}	x	y
0.0	0.9638	0.0300	0.0062	0.0	0.670
0.0010	0.9636	0.0300	0.0054	0.060	0.675
0.0020	0.9634	0.0300	0.0046	0.100	0.665
0.0030	0.9624	0.0300	0.0046	0.125	0.685
0.0040	0.9620	0.0300	0.0040	0.160	0.655
0.0050	0.9614	0.0300	0.0036	0.185	0.625
0.0060	0.9605	0.0300	0.0035	0.235	0.655
0.0	0.9536	0.0400	0.0064	0.0	0.560
0.0020	0.9535	0.0400	0.0045	0.065	0.548
0.0030	0.9534	0.0400	0.0036	0.110	0.520
0.0040	0.9520	0.0400	0.0040	0.140	0.540
0.0050	0.9515	0.0400	0.0035	0.165	0.540
0.0055	0.9511	0.0400	0.0034	0.170	0.543
0.0065	0.9503	0.0400	0.0032	0.215	0.520
0.0070	0.9501	0.0400	0.0029	0.220	0.525
0.0077	0.9497	0.0400	0.0026	0.230	0.520
0.0080	0.9494	0.0400	0.0026	0.240	0.530
0.0	0.9441	0.0500	0.0059	0.0	—
0.0020	0.9434	0.0500	0.0046	—	—
00.040	0.9427	0.0500	0.0033	—	—
0.0060	0.9412	0.0500	0.0028	0.135	0.315
0.0080	0.9400	0.0500	0.0020	0.185	0.320
0.0100	0.9382	0.0500	0.0018	0.275	0.325
0.0120	0.9363	0.0500	0.0017	0.275	0.315
0.0140	0.9346	0.0500	0.0014	0.325	0.285
0.0150	0.9336	0.0500	0.0014	0.330	0.290
0.0160	0.9325	0.0500	0.0015	0.375	0.260
0.0200	0.9291	0.0500	0.0009	—	—
0.0250	0.9238	0.0500	0.0012	—	—
0.0300	0.9195	0.0500	0.0005	—	—
0.0350	0.9143	0.0500	0.0007	—	—

has a less pronounced effect in this range. The 650°C liquidus data at $X_{As}^{l} = 0.0145$ by Antypas and Moon (6) shown in Fig. 2 are found to be consistent with this work. Broken lines in these figures are drawn through our experimental points.

Solidus.—The 600° and 650°C solidus isotherms were determined by electron microprobe analysis performed on surfaces of $In_{1-x}Ga_xAs_{1-y}P_y$ epitaxial layers grown on Sn-doped InP(111)B substrates from quaternary solutions. The apparatus used was the same as that used for the saturation experiments. Prior to growth the undersaturated In-Ga-As solutions were held on InP sources for an hour to achieve saturation and then were moved over the substrates while simultaneously the cooling cycle was started. A constant cooling rate of 0.5°C/min was used starting from an initial temperature of 600° ± 0.5°C or 650° ± 0.5°C. Cooling intervals adopted were 25°C at 600°C and 16°C at 650°C. Thicknesses of the layers were in a range of ~2.5 to ~4.0 μm.

Electron microprobe analysis, employing wavelength dispersive x-ray detection, was used to determine the intensities of the Ga-K_α, As-K_α, and P-K_α lines from the sample and from GaP and InAs standards. An electron beam energy of 25 keV was used. The measured intensities were converted to concentrations by performing the atomic number, absorption, and fluorescence corrections.

The experimental 600° and 650°C solidus results are also listed in Tables I and II, respectively. The solidus isotherms in equilibrium with the quaternary liquids containing $X_{Ga}^{l} < 0.016$ and $X_{As}^{l} = 0.005$,

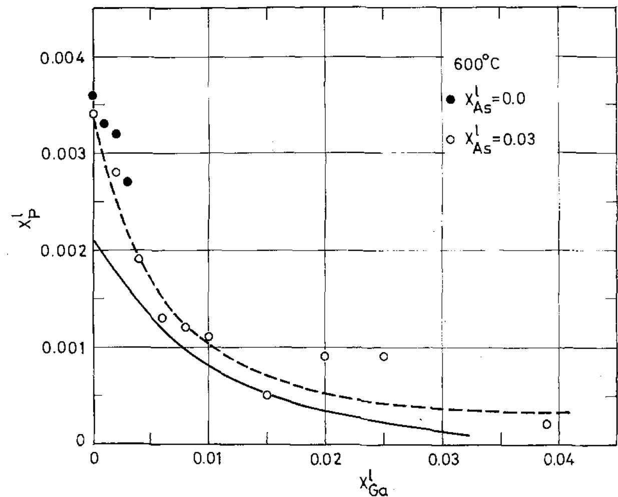

Fig. 1. 600°C liquidus isotherms in the In-Ga-As-P system at $X_{As}^{l} = 0.0$ and 0.030 determined by the seed dissolution technique. ●, $X_{As}^{l} = 0.0$; ○, $X_{As}^{l} = 0.030$. ---- drawn through experimental points at $X_{As}^{l} = 0.030$. —— Represents the calculated liquidus at $X_{As}^{l} = 0.030$.

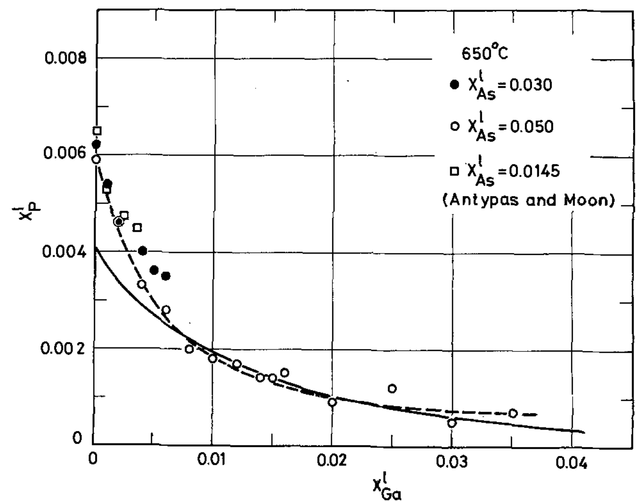

Fig. 2. 650°C liquidus isotherms in the In-Ga-As-P system at $X_{As}^{l} = 0.030$ and 0.050 determined by the seed dissolution technique. ●, $X_{As}^{l} = 0.030$; ○, $X_{As}^{l} = 0.050$, □, $X_{As}^{l} = 0.0145$ by Antypas and Moon (6). ---- Is drawn through experimental points at $X_{As}^{l} = 0.050$. —— Represents the calculated liquidus at $X_{As}^{l} = 0.050$.

0.010, 0.015, 0.020, 0.030, 0.040, and 0.050 were determined. These As compositions and temperatures were selected to permit the LPE growth of $In_{1-x}Ga_xAs_{1-y}P_y$ ($0 \leq x \leq 0.35$, $0.3 \leq y \leq 1.0$) lattice-matched layers on InP substrates under reasonable conditions. Figures 3 and 4 show the solid solubility isotherms for Ga into the quaternary solid solutions at 600° and 650°C, respectively. These solidus isotherms indicate that the distribution coefficient for Ga increases with decreasing growth temperature and/or X_{As}^1. Figures 5 and 6 show the solid solubility isotherms for P into the quaternary solids at 600° and 650°C, respectively. These isotherms indicate that the distribution coefficient for P increases with decreasing X_{As}^1. The 650°C solidus data at $X_{As}^1 = 0.00565$ by Antypas and Moon (6) are also included in Fig. 4 and 6. Present results of the solid solubility for Ga are a little higher than the data reported by them, as shown in Fig. 4.

Lattice constant.—Lattice constants of the quaternary solid solutions were measured by an x-ray diffraction technique. A double crystal x-ray diffraction technique was used for nearly lattice-matched samples. Samples used were 1.5-3 μm thick epitaxial layers on InP(111)B substrates.

The results at 600° and 650°C are shown in Fig. 7 and 8, respectively. The lattice constant is displayed as a function of X_{Ga}^1 at several X_{As}^1. The dashed line represents the lattice constant of InP. The exactly

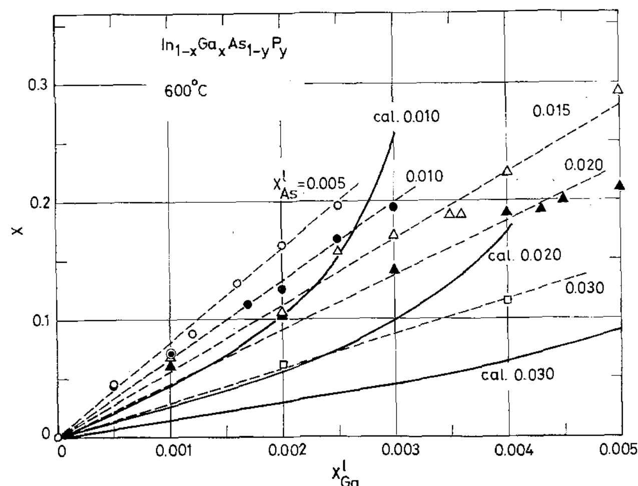

Fig. 3. 600°C solid solubility isotherms for Ga into the $In_{1-x}Ga_xAs_{1-y}P_y$ quaternary solid solutions at $X_{As}^1 = 0.005$, 0.010, 0.015, 0.020, and 0.030. ○, $X_{As}^1 = 0.005$; ●, $X_{As}^1 = 0.010$; △, $X_{As}^1 = 0.015$; ▲, $X_{As}^1 = 0.020$; □, $X_{As}^1 = 0.030$. ---- Is drawn through experimental points. —— Represents the calculated solidus isotherms at $X_{As}^1 = 0.010$, 0.020, and 0.030.

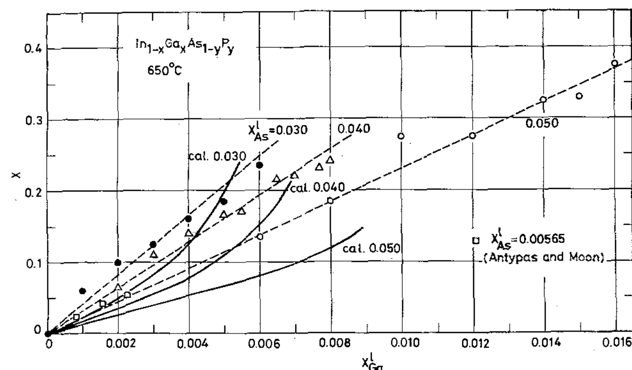

Fig. 4. 650°C solid solubility isotherms for Ga into the $In_{1-x}Ga_xAs_{1-y}P_y$ quaternary solid solutions at $X_{As}^1 = 0.030$, 0.040, and 0.050. ●, $X_{As}^1 = 0.030$; △, $X_{As}^1 = 0.040$; ○, $X_{As}^1 = 0.050$; □, $X_{As}^1 = 0.00565$ by Antypas and Moon (6). ---- Is drawn through experimental points. —— Represents the calculated solidus isotherms at $X_{As}^1 = 0.030$, 0.040, and 0.050.

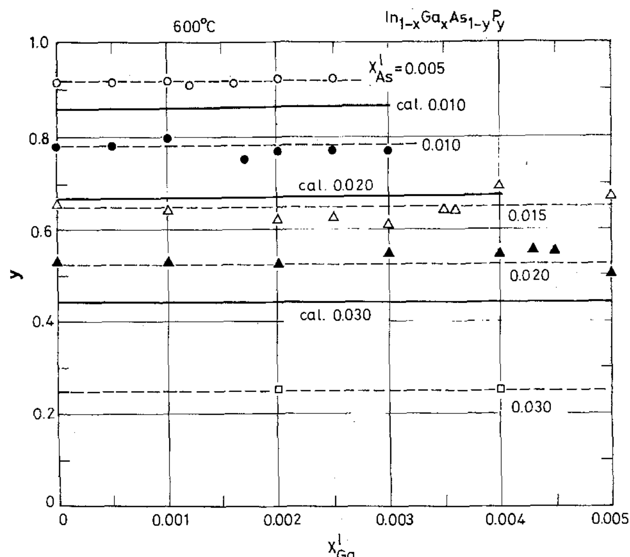

Fig. 5. 600°C solid solubility isotherms for P into the $In_{1-x}Ga_xAs_{1-y}P_y$ quaternary solid solutions at $X_{As}^1 = 0.005$, 0.010, 0.015, 0.020, and 0.030. ○, $X_{As}^1 = 0.005$; ●, $X_{As}^1 = 0.010$; △, $X_{As}^1 = 0.015$; ▲, $X_{As}^1 = 0.020$; □, $X_{As}^1 = 0.030$. ---- Is drawn through experimental points. —— Represents the calculated solidus isotherms at $X_{As}^1 = 0.010$, 0.020, and 0.030.

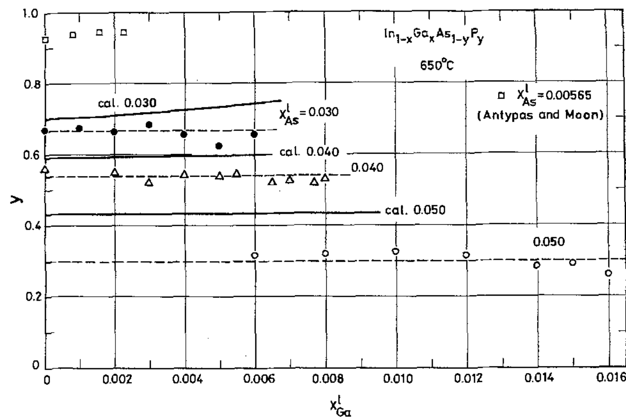

Fig. 6. 650°C solid solubility isotherms for P into the $In_{1-x}Ga_xAs_{1-y}P_y$ quaternary solid solutions at $X_{As}^1 = 0.030$, 0.040, and 0.050. ●, $X_{As}^1 = 0.030$; △, $X_{As}^1 = 0.040$; ○, $X_{As}^1 = 0.050$; □, $X_{As}^1 = 0.00565$ by Antypas and Moon (6). ---- Is drawn through experimental points. —— Represents the calculated solidus isotherms at $X_{As}^1 = 0.030$, 0.040, and 0.050.

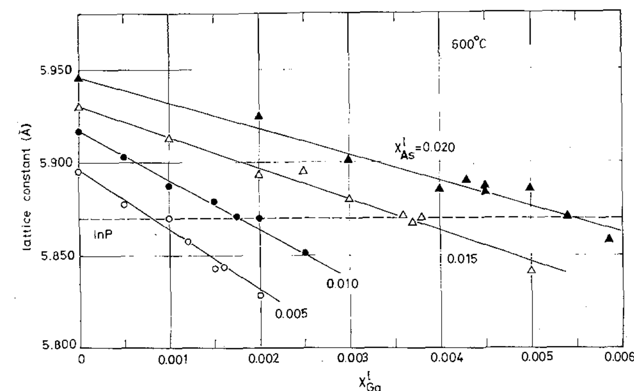

Fig. 7. Lattice constants of the $In_{1-x}Ga_xAs_{1-y}P_y$ quaternary solid solutions grown from 600°C liquids at $X_{As}^1 = 0.005$, 0.010, 0.015, and 0.020. ○, $X_{As}^1 = 0.005$; ●, $X_{As}^1 = 0.010$; △, $X_{As}^1 = 0.015$; ▲, $X_{As}^1 = 0.020$. ---- Represents the lattice constant of InP. —— Is drawn through experimental points.

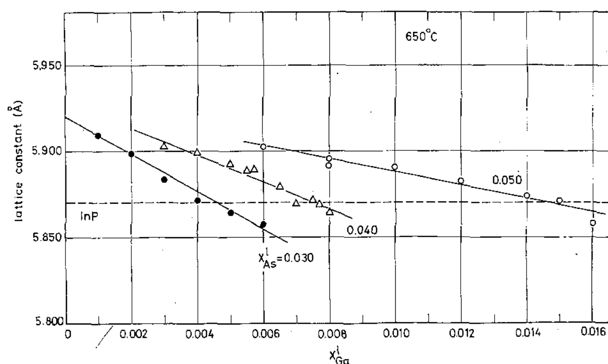

Fig. 8. Lattice constants of the $In_{1-x}Ga_xAs_{1-y}P_y$ quaternary solid solutions grown from 650°C liquids at $X_{As}{}^l = 0.030, 0.040$, and 0.050. ●, $X_{As}{}^l = 0.030$; △, $X_{As}{}^l = 0.040$; ○, $X_{As}{}^l = 0.050$. ---- Represents the lattice constant of InP. —— Is drawn through experimental points.

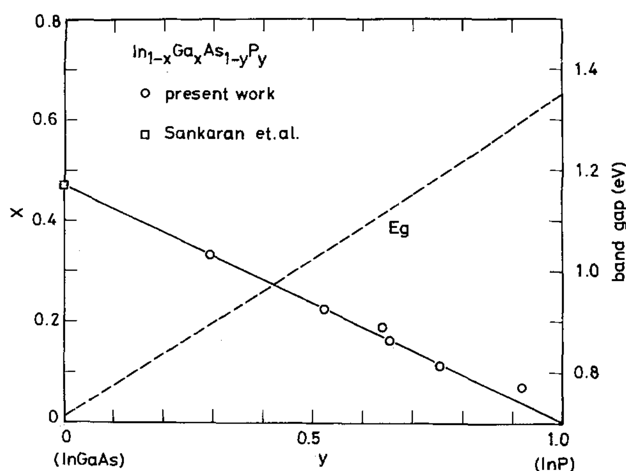

Fig. 9. Compositions of the lattice-matched $In_{1-x}Ga_xAs_{1-y}P_y$ quaternary solids. ○, Present work; □, Sankaran et al. (12). —— Is the calculated result on the basis of Vegard's law. ---- Represents the calculated room temperature bandgap energy of the lattice-matched solid by Moon *et al.*'s expression (13).

lattice-matched layer can be easily grown by using these results. Figure 9 shows the compositions of the lattice-matched quaternary solids. The solid line is the calculated result on the basis of Vegard's law. The experimental points are in good agreement with the calculated line. The broken line is the calculated room temperature bandgap energy of the lattice-matched solid using Moon *et al.*'s expression (13).

Solidus isoconcentration curve.—Figures 10 and 11 show solidus isoconcentration curves of Ga and P at 600° and 650°C, respectively. These curves were obtained by interpolation of the results of solidus isotherms shown in Fig. 3, 4, 5, and 6. The broken line shows the composition of the quaternary liquid ($X_{Ga}{}^l$ and $X_{As}{}^l$) required for the LPE growth of the lattice-matched layer at each temperature. They were derived from the results of lattice constant measurements shown in Fig. 7 and 8. The Ga and As content in the solid for layers lattice-matched to InP measured by Sankaran *et al.* (8) at 650°C are in exact agreement with the results shown in Fig. 11.

Discussion

The experimental phase diagram shows that, in the InP-rich end at constant $X_{As}{}^l$, the solubility of Ga in the quaternary solid is almost linearly dependent on $X_{Ga}{}^l$, and the atomic ratio of P to As in the solid is nearly independent of $X_{Ga}{}^l$. Antypas and Moon (6) reported the same results, *i.e.*, changing Ga in the liquid changed only the Ga in the solid and did not affect the P or As in the solid. Such

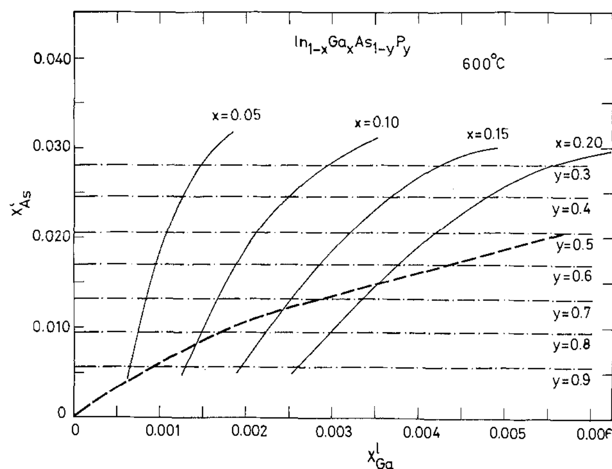

Fig. 10. Solidus isoconcentration curves of Ga and P at 600°C. ---- Represents the composition of the In-Ga-As-P quaternary liquid required for the LPE growth of the lattice-matched layer at 600°C.

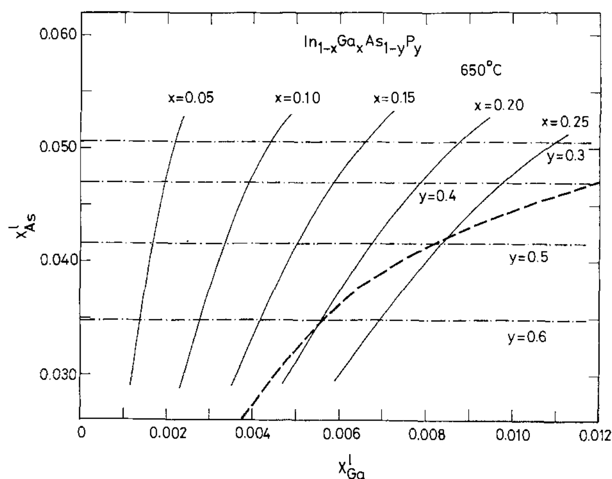

Fig. 11. Solidus isoconcenration curves of Ga and P at 650°C. ---- Represents the composition of the In-Ga-As-P quaternary liquid required for the LPE growth of the lattice-matched layer at 650°C.

phenomena were also observed in other quaternary systems, such as Al-Ga-As-Sb (16), In-Ga-As-Sb (17), and Al-Ga-In-As (18). Therefore, in the In-Ga-As-P system, the lattice constant of the quaternary solid in the InP-rich end is linearly dependent on $X_{Ga}{}^l$ at constant $X_{As}{}^l$ as shown in Fig. 7 and 8. By using the information contained in the phase diagram and the lattice constant measurements, the LPE growth conditions for lattice matching on InP substrates can be easily known.

The In-Ga-As-P phase diagram was calculated by treating the quaternary liquid and solid as simple solutions (14, 15), similar to our previous work (18). Calculation methods to predict the III_A-III_B-V_C-V_D type phase diagram have been derived by Huber (19), Ilegems and Panish (20), and Stringfellow (26). Jordan and Ilegems (27) presented the most rigorous thermodynamic treatment of solid-liquid equilibria in this type of quaternary system. Therefore, we adopted Jordan and Ilegems's model for calculation of the In-Ga-As-P phase diagram. The reasonable values found in the literature were used as the interaction parameters necessary for the calculation. These values are listed in Table III. The calculated results represented by solid lines in Fig. 1-6, however, did not agree well with the experimental ones.

Exact reasons for the disagreement are not known, but it seems that one of the reasons may be the unsuitability of the interaction parameters used for calculation. These parameters have been derived from

Table III. Thermodynamic input data for the In-Ga-As-P phase diagram calculation

T_{AB}^F and ΔS_{AB}^F are the temperature and entropy of fusion of the AB compound, respectively. Ω^l and Ω^s are the interaction parameters in the liquid and solid, respectively.

Input data	
T_{GaP}^F = 1738°K (21)	T_{GaAs}^F = 1511°K (21)
T_{InP}^F = 1343°K (22)	T_{InAs}^F = 1215°K (23)
ΔS_{GaP}^F = 16.8 cal/mole °K (15)	ΔS_{GaAs}^F = 16.64 cal/mole °K (24)
ΔS_{InP}^F = 14.0 cal/mole °K (15)	ΔS_{InAs}^F = 14.52 cal/mole °K (24)
Ω_{GaP}^l = 2800 − 4.8T cal/mole (15)	Ω_{GaAs}^l = 5160 − 9.16T cal/mole (25)
Ω_{InP}^l = 4500 − 4.0T cal/mole (15)	Ω_{InAs}^l = 3860 − 10.0T cal/mole (15)
Ω_{GaIn}^l = 1060 cal/mole (15)	Ω_{AsP}^l = 1500 cal/mole (15)
$\Omega_{GaP-GaAs}^s$ = 400 cal/mole (15)	$\Omega_{InP-InAs}^s$ = 400 cal/mole (15)
$\Omega_{GaP-InP}^s$ = 3500 cal/mole (15)	$\Omega_{GaAs-InAs}^s$ = 3000 cal/mole (15)

curve-fitting with the binary or ternary experimental phase diagrams, but most of them have not been determined at such low temperature as 600° or 650°C. Therefore, it is difficult to entirely fit the calculated results with the experimental data presented in this paper. For obtaining reasonable agreement, values of several parameters need to be changed. This seems to suggest that the departure from regularity in the thermodynamic property of the In-Ga-As-P system cannot be neglected. That is, the interaction parameters may be functions of temperature and composition in the strict sense. For example, Osamura and Murakami (28) reported that the partially associated solution model successfully explains the asymmetric III-V binary phase diagrams of the AlSb, InP, GaP, and InAs systems whose compounds have relatively large ionicity (29). Such an idea gives us a hint for the development of a thermodynamic model which can explain every III-V phase diagram data quite satisfactorily.

Summary

The In-Ga-As-P quaternary equilibrium phase diagram was experimentally determined at 600° and 650°C. From this investigation of the phase diagram and lattice constant measurements, we have found the LPE growth conditions of exactly lattice-matched $In_{1-x}Ga_xAs_{1-y}P_y$ ($0 \leq x \leq 0.35$, $0.3 \leq y \leq 1.0$) layers on InP substrates and also found that the $In_{1-x}Ga_xAs_{1-y}P_y$ quaternary solid solutions obey Vegard's law.

Acknowledgments

The authors are indebted to Mrs. T. Furusawa and Y. Udo for microprobe measurements. They are grateful to Dr. S. Komiya for x-ray diffraction measurements and helpful discussions.

Manuscript submitted April 25, 1977; revised manuscript received Aug. 18, 1977.

Any discussion of this paper will appear in a Discussion Section to be published in the December 1978 JOURNAL. All discussions for the December 1978 Discussion Section should be submitted by Aug. 1, 1978.

Publication costs of this article were assisted by the Fujitsu Laboratories, Limited.

REFERENCES

1. L. G. Cohen, P. Kaiser, J. B. MacChesney, P. B. O'Connor, and H. M. Presby, *Appl. Phys. Lett.*, **26**, 472 (1975).
2. M. Horiguchi and H. Osanai, *Electron. Lett.*, **12**, 310 (1976).
3. J. J. Hsieh, M. C. Finn, and J. A. Rossi, in "Gallium Arsenide and Related Compounds, 1976."
4. G. A. Antypas, R. L. Moon, L. W. James, J. Edgecumbe, and R. L. Bell, in "Gallium Arsenide and Related Compounds, 1972," Conference Series No. 17, Institute of Physics and Physical Society, p. 48, London (1973).
5. J. J. Hsieh, J. A. Rossi, and J. P. Donnelly, in IEEE International Semiconductor Laser Conference at Nemuno-sato, Japan (1976).
6. G. A. Antypas and R. L. Moon, *This Journal*, **120**, 1574 (1973).
7. G. A. Antypas and J. Edgecumbe, *J. Cryst. Growth*, **34**, 132 (1976).
8. R. Sankaran, G. A. Antypas, R. L. Moon, J. S. Escher, and L. W. James, *J. Vac. Sci. Technol.*, **13**, 932 (1976).
9. M. Ilegems and G. L. Pearson, in "Proceedings of 1968 Symposium on GaAs," p. 3.
10. M. Ilegems and M. B. Panish, *J. Cryst. Growth*, **20**, 77 (1973).
11. M. Ilegems and M. B. Panish, *J. Phys. Chem. Solids*, **35**, 409 (1974).
12. R. Sankaran, R. L. Moon, and G. A. Antypas, *J. Cryst. Growth*, **33**, 271 (1976).
13. R. L. Moon, G. A. Antypas, and L. W. James, *J. Electron. Mater.*, **3**, 635 (1974).
14. E. A. Guggenheim, "Thermodynamics," 5th ed., p. 197, North Holland, Amsterdam (1967).
15. M. B. Panish and M. Ilegems, in "Progress in Solid State Chemistry," Vol. 7, H. Reiss and J. O. McCaldin, Editors, p. 39, Pergamon Press, Inc., New York (1972).
16. G. A. Antypas and R. L. Moon, *This Journal*, **121**, 416 (1974).
17. R. Sankaran and G. A. Antypas, *J. Cryst. Growth*, **36**, 198 (1976).
18. K. Nakajima, K. Osamura, and Y. Murakami, *This Journal*, **122**, 1245 (1975).
19. D. Huber, *J. Phys. Chem. Solids*, **34**, 1859 (1973).
20. M. Ilegems and M. B. Panish, *ibid.*, **35**, 409 (1974).
21. C. D. Thurmond, *ibid.*, **26**, 785 (1965).
22. L. M. Foster and J. E. Scardefield, *This Journal*, **117**, 534 (1970).
23. G. A. Antypas, *ibid.*, **117**, 1393 (1970).
24. B. D. Lichter and P. Sommelet, *Trans. AIME*, **245**, 1021 (1969).
25. J. R. Arthur, *J. Phys. Chem. Solids*, **28**, 2257 (1967).
26. G. B. Stringfellow, *J. Cryst. Growth*, **27**, 21 (1974).
27. A. S. Jordan and M. Ilegems, *J. Phys. Chem. Solids*, **36**, 329 (1975).
28. K. Osamura and Y. Murakami, *ibid.*, **36**, 931 (1975).
29. J. C. Phillips, *Rev. Modern Phys.*, **42**, 317 (1970).

High Temperature Annealing Behavior of Oxygen in Silicon

H. J. Ruiz and G. P. Pollack*

Texas Instruments Incorporated, Semiconductor Research and Engineering Laboratories, Dallas, Texas 75222

ABSTRACT

It is well known that the Czochralski-grown silicon commonly used in manufacture of electronic devices contains, as a major impurity, oxygen in excess of 1×10^{18} atoms/cm^3. At typical device-processing temperatures (900°-1300°C) this oxygen is quite mobile and has been shown to interact in a complex manner both with the silicon lattice and the dopant species used to form active regions in the device (1, 2). In this report, the effect of high temperature annealing on the state of oxygen near the surface of silicon wafers is examined. It is shown that, after high temperature annealing, a considerable number of oxygen donors can still be generated at 450°C except in the region near the surface where the oxygen donor concentration is reduced in a manner which suggests out-diffusion of oxygen from the silicon lattice.

Experimental

The substrates used in this study were 2 in. diam <111> silicon wafers, sliced from adjacent sites in the top portion of a Czochralski-grown crystal and mechanically polished on one side to a thickness of 15 mil. The crystal was phosphorus doped with an average resistivity of 5 Ω-cm ±10% in the region selected. The interstitial oxygen concentration, as measured by the 9 μm absorption band in silicon, was 1.4×10^{18} atoms/ cm^3 (3). In addition, several similarly prepared slices were obtained from the top portion of a phosphorus-doped 4 Ω-cm <111> crystal grown by the float-zone method. The oxygen concentration in this crystal was found to be less than 5×10^{15} atoms/cm^3.

The wafers were subjected to various high temperature diffusion, oxidation, and annealing cycles which were designed to simulate the type of environment typically encountered during device processing. The wafers then received a 100 hr 450°C nitrogen anneal in an attempt to form electrically active oxygen donors from those with oxygen still present in its original interstitial state. Spreading resistance measurements were then made on angle-polished samples taken from the center of each wafer. The spreading resistance apparatus consisted of an in-house built spreading resistance probe interfaced to a computer-controlled data acquisition system. This allowed the spreading resistance data to be automatically translated and plotted as resistivity *vs.* depth for each of the samples.

Results and Discussion

As an initial experiment a float-zone and a Czochralski grown-wafer were given a 1 hr deposition from a boron nitride source at 1050°C followed by a 1150°C diffusion cycle consisting of 15 min in O_2 and 2 hr in N_2. The spreading resistance profile obtained on a sample taken from the float-zone wafer is shown in Fig. 1. In this case, no change in the bulk resistivity was observed after the 450°C heat-treatment which indicates that no electrically active oxygen was present in the sample. The spreading resistance profile obtained before and after the 450°C heat-treatment on samples taken from the Czochralski-grown wafer are shown in Fig. 2. Note that, even after considerable high temperature processing, a significant number of oxygen donors were generated by the 450°C heat-treatment as evidenced by the decrease in the bulk resistivity from 5 Ω-cm to approximately 0.55 Ω-cm after heat-treatment. Of particular interest, however, is the increase in the bulk resistivity that is observed in the heat-treated sample in the region near the boron-diffused junction. This surface resistivity gradient has also been observed in the nondiffused surface regions of oxide-patterned Czochralski-grown wafers after 450°C heat-treatment. Thus, this apparent decrease in oxygen donor activity near the surface of Czochralski-grown wafers is not associated with the presence of the boron-diffused junction.

The results suggest that oxygen has outdiffused from the wafer surface during the high temperature processing, thus reducing the amount of oxygen available for donor formation in the region near the surface. The

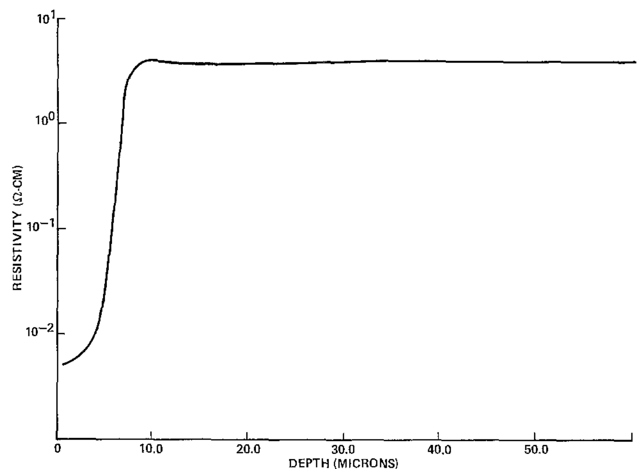

Fig. 1. Resistivity *vs.* depth for a boron-diffused float-zone wafer after annealing at 450°C for 100 hr.

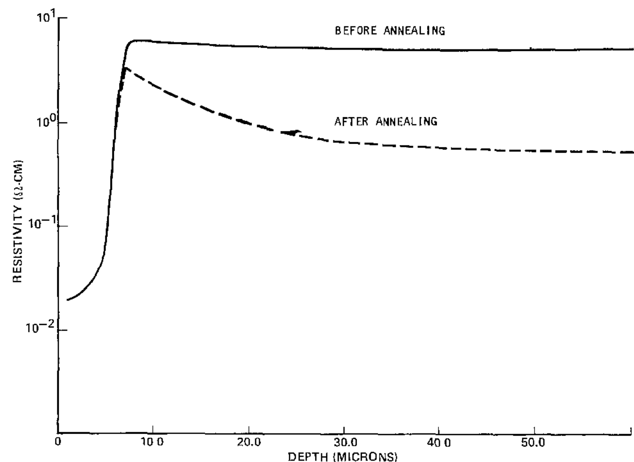

Fig. 2. Resistivity *vs.* depth for a boron-diffused Czochralski-grown wafer before and after annealing at 450°C for 100 hr.

* Electrochemical Society Active Member.

Key words: oxygen donors, oxygen diffusion, silicon wafer processing, spreading resistance.

driving force for this outdiffusion is assumed to be the lower oxygen solubility at these processing temperatures. In order to test this hypothesis, a number of Czochralski-grown wafers were annealed in nitrogen at 1100°C for times ranging from 1-100 hr. At 1100°C the solid solubility of oxygen in silicon is almost an order of magnitude below the measured value of 1.4×10^{18} atoms/cm^3 in these samples (4). The spreading resistance profiles obtained after the 450°C anneal for samples annealed for 1, 9, and 25 hr at 1100°C are shown in Fig. 3. Note that, as the annealing times are increased, the bulk resistivity value is reached asymptotically at increasing depth below the surface. For annealing times greater than approximately 36 hr, the bulk resistivity was found to slowly increase from its minimum range of 0.6-0.7 Ω-cm to 5 Ω-cm, until after 100 hr at 1100°C no change in the bulk resistivity was observed after the 450°C anneal.

These results suggest that, for annealing times less than 36 hr, the center region of the 15 mil thick wafer can be treated as a semi-infinite source of oxygen. A solution of the diffusion equation subject to this boundary condition yields the following expression for the distribution of oxygen in the wafer

$$C = C_F + (C_O - C_F)\ \mathrm{erfc}\left(\frac{\chi}{2\sqrt{Dt}}\right) \quad [1]$$

where C_F is the solid solubility of oxygen in silicon at 1100°C, and C_O is the initial oxygen concentration in the wafer. The relationship between the oxygen donor concentration is believed to follow a power law dependence (1). Since there is some question as to the exact form of this dependence, it will be assumed, for simplicity, that Eq. [1] also reasonably approximates the oxygen donor distribution in the samples. The resistivity distribution in the wafer is then given by the relation

$$\frac{1}{\rho} = \frac{1}{\rho_S} + \frac{1}{\rho_B}\ \mathrm{erf}\left(\frac{\chi}{2\sqrt{Dt}}\right) \quad [2]$$

where ρ_S is the resistivity at the wafer surface, *i.e.*, $x = 0$, and ρ_B is the net decrease in resistivity produced by the oxygen donor formation. The surface resistivity ρ_S can be expressed as

$$\frac{1}{\rho_S} = e\mu_n(N_D - N_A + N_F) \quad [3]$$

where $N_D - N_A$ is the net impurity density other than oxygen donors, N_F is the oxygen donor density at the surface, e is the electronic charge, and μ_n is the electron mobility. The decrease in resistivity produced by oxygen donors, ρ_B, can be expressed as

$$\frac{1}{\rho_B} = e\mu_n(N_o - N_F) \quad [4]$$

where N_o is the oxygen donor density in the semi-infinite bulk region of the wafer.

A curve fit of Eq. [2] to the results shown in Fig. 3, while not exact, has been found to be reasonably good. Average values for ρ_S and ρ_B obtained from the results shown in Fig. 3 are $\rho_S = 4.5$ Ω-cm and $\rho_B = 0.65$ Ω-cm. If, for convenience, $\chi/2\sqrt{Dt}$ is assigned a value of 0.6, Eq. [2] can be solved and yields a value of $\rho = 0.91$ Ω-cm. Values of χ obtained from the spreading resistance plots at $\rho = 0.91$ Ω-cm are shown in Fig. 4 plotted as a function of the square root of the annealing time. As predicted by Eq. [2], a linear dependence between χ and $\sqrt{t}$ is observed. A fit of the expression

$$\chi = 1.2\sqrt{Dt} \quad [5]$$

to the results shown in Fig. 4 yields a value of $D = 1.3 \times 10^{-10}$ cm^2/sec for the diffusion coefficient of oxygen in silicon at 1100C. This is in good agreement with the most recently published value for the diffusion coefficient of oxygen in silicon of $D = 1.4 \times 10^{-10}$ cm^2/sec obtained by Takano and Maki (4).

As a final result, it was found that diode test structures fabricated in this material exhibited no measurable degradation in the form of enhanced reverse leakage after heat-treatment at 450°C. The only measurable change exhibited by these structures was a decrease in both breakdown voltage and reverse leakage as a result of the decreased resistivity in the region of the junction. This low leakage is presumably due to the shallow nature of the oxygen donor levels in silicon, ~0.13 eV, which prevent the oxygen donor from acting as an efficient generation-recombination center.

In summary, it has been shown that even after considerable high temperature processing, a large number of oxygen donors can still be generated in Czochralski-grown silicon wafers after heat-treatment at 450°C. However, in the region near the wafer surface, this oxygen donor activity is considerably reduced due to the effect of oxygen outdiffusion. No change in junction properties is produced by this annealing other than those effects resulting from an increase in donor density.

Acknowledgment

The authors wish to thank Dr. H. Schaake for the many valuable discussions throughout this work.

Manuscript submitted April 7, 1977; revised manuscript received Aug. 12, 1977.

Any discussion of this paper will appear in a Discussion Section to be published in the December 1978 JOURNAL. All discussions for the December 1978 Discussion Section should be submitted by Aug. 1, 1978.

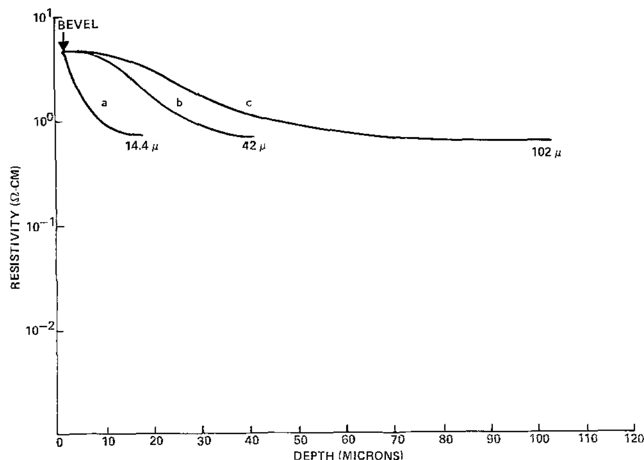

Fig. 3. Resistivity vs. depth for three Czochralski-grown wafers annealed at 1100°C for (a) 1, (b) 9, and (c) 25 hr, and then at 450°C for 100 hr.

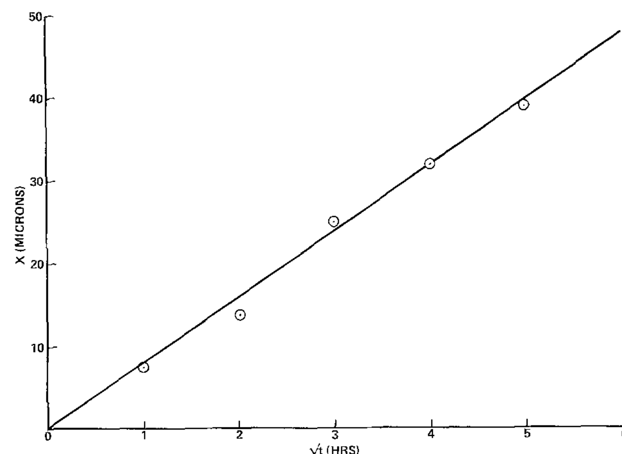

Fig. 4. Depth into the wafer at which $\rho = 0.91$ Ω-cm plotted as a function of the square root of the annealing time.

Publication costs of this article were assisted by Texas Instruments Incorporated.

REFERENCES

1. W. Kaiser, H. L. Frisch, and H. Reiss, *Phys. Rev.*, **112**, 1546 (1958).
2. C. S. Fuller, F. H. Doleiden, and K. Wolfstirn, *J. Phys. Chem. Solids*, **13**, 187 (1960).
3. J. A. Baker, *Solid-State Electron.*, **13**, 1431 (1970).
4. Y. Takano and M. Maki, "Semiconductor Silicon 1973," H. R. Huff and R. R. Burgess, Editors, The Electrochemical Society Softbound Symposium Series, Princeton, N.J. (1973).

Properties of Liquid Phase Epitaxial $In_{1-x}Ga_xAs$ ($x \cong 0.5$) on InP Substrate

Yoshikazu Takeda, Akio Sasaki, Yujiro Imamura, and Toshinori Takagi

Department of Electronics, Kyoto University, Kyoto, Japan

ABSTRACT

Undoped $In_{1-x}Ga_xAs$ ($x \cong 0.5$) crystal films with very homogeneous composition were grown on InP substrates by liquid phase epitaxy. Study was made on physical, electrical, and optical properties of this mixed crystal. The growth temperature was varied between 550° and 750°C. All the crystals were n-type. The electron mobility was found to vary from 5240 to 8500 cm^2 V^{-1} sec^{-1} and the electron concentration from 6.3×10^{16} to 1.3×10^{16} cm^{-3} at 300°K. Etch pit density and half-width of photoluminescence spectra decreased with increasing growth temperature. High quality crystals were grown at around 700°C.

Much interest has been recently focused on $In_{1-x}Ga_xAs$ mixed crystal because of its applications to optical sources (1-3) and detectors (4) in the 1.06 μm low loss region of optical fibers (5). Efficient light-emitting diodes and room temperature laser diodes were fabricated with this material. Another potential application of this mixed crystal is for high frequency devices (6).

The mixed crystal can be designed to have larger bandgaps than InAs and higher mobilities than GaAs. Near middle composition the bandgap, E_g, is about 0.75 eV at which the extrinsic carrier concentration ($>10^{15}$ cm^{-3}) is not affected by the temperature variations of the intrinsic carrier concentration ($\sim 10^{11}$ cm^{-3}) around room temperature. Further, the energy separation, ΔE, between the central and the satellite valleys in the conduction band becomes wider with the increase of the InAs mole fraction. Near $x \cong 0.5$, E_g is expected to equal ΔE. This does not make the electron velocity decreased by the transferred electron effect. Thus, $In_{1-x}Ga_xAs$ ($x \cong 0.5$) can be considered better suited for high frequency field-effect transistors and high speed switching devices than GaAs or InP (6).

The $In_{1-x}Ga_xAs$ epitaxial films of around middle composition ($x \cong 0.5$) have been grown by vapor phase epitaxy on GaAs (7-8) and Al_2O_3 (9) substrates. Fairly high electron mobilities and the electron scattering analysis were reported by Glicksman *et al.* (10) for $In_{1-x}Ga_xAs$ ($0.75 \leqq x \leqq 1$). However, the mobilities around 6000 cm^2 V^{-1} sec^{-1} are not higher than those of GaAs. Bulk $In_{1-x}Ga_xAs$ crystals have shown very high mobilities (11-12) as compared with epitaxial mixed crystals of around middle composition, but it is difficult to grow single crystals uniform in composition. The difficulty is attributed to large difference between the liquidus and solidus. Single crystals with nonuniform composition are not suitable for most device applications.

A uniform and good crystalline $In_{1-x}Ga_xAs$ can be grown on GaAs by using stepwise (2) or continuous (14-15) compositional grading to take up the lattice mismatch between the substrate and the desired composition layers. However, with the grading process it is not easy to reach $In_{1-x}Ga_xAs$ ($x \cong 0.5$) from GaAs substrate nor is it suitable for mass production. The lattice constant of InP lies in the middle of the lattice constants of InAs and GaAs, matching with that of $In_{0.53}Ga_{0.47}As$, when Vegard's law is applied to $In_{1-x}Ga_xAs$. Moreover, semi-insulating InP substrates, although not yet developed enough, are available which facilitate electrical evaluation of the grown layers and device applications. It has been reported by Sasaki *et al.* (16) that $In_{1-x}Ga_xAs$ ($x \cong 0.5$) can be grown directly on InP by liquid phase epitaxy. Recently, the conditions for LPE growth of $In_{0.53}Ga_{0.47}As$ have been discussed by Sankaran *et al.* (17). Electron mobility and energy gap of LPE $In_{0.53}Ga_{0.47}As$ on InP have been reported by Takeda *et al.* (18).

In this paper, we describe a study on the properties of $In_{1-x}Ga_xAs$ ($x \cong 0.5$) grown on InP from a melt with a theoretical solidus composition of $x = 0.5$ at each growth temperature. Single crystals of $x \cong 0.5$ are grown on semi-insulating InP substrates by liquid phase epitaxy. The growth temperature (the initial temperature at which the melt is brought over the substrate is called the growth temperature in this paper, since the temperature is lowered in this growth process) is varied from 500° to 800°C keeping the other conditions, such as the melt-baking temperature and interval, the cooling rate and interval, and the substrate orientation, the same. Thickness, surface morphology, etch pit density, composition, photoluminescence, electron mobility, and electron concentration of the grown layers are examined.

Experimental Procedures

Crystal growth.—Liquid phase epitaxial growth is carried out in a horizontal graphite boat and slider assembly in a Pd-diffused flowing hydrogen ambient. All the mixed crystals are grown on the Cr-doped ($\rho > 10^3$ Ωcm), (111)B-oriented InP substrates. Growth temperatures are chosen at 50°C intervals from 500° to 800°C. The cooling rate is 0.15°C/min, and the cooling interval is about 10°C at each growth temperature.

Starting materials are six 9's pure In, seven 9's pure Ga (Mitsubishi Metal Mining Company, Limited),

Key words: InGaAs, LPE, heteroepitaxy, InP substrate.

and undoped polycrystalline InAs ($n = 1 \sim 3 \times 10^{16}$ cm^{-3} and $\mu = 20{,}000 \sim 23{,}000$ cm^2 V^{-1} sec^{-1}) (Sumitomo Electric Industries, Limited). The Ga is not etched, but the In is etched with a 5% $HCl{:}H_2O_2$ solution, and the InAs with a 1% Br:methanol solution just prior to loading. Polished InP substrates are etched with a 1% Br:methanol solution for 2 min. The melts are about 2g, and a slight excess of InAs is added to ensure As saturation in the melt. The substrate dimensions are $10 \times 5 \times 0.4$ mm^3.

Prior to growth, In and Ga are baked in a flowing hydrogen ambient at 800°C for 3 hr to mix the In atoms and Ga atoms. In order to minimize the thermal etching of the substrate surface and to avoid the deviation of the melt composition due to the loss of As during the baking treatment at a high temperature, the substrate and the InAs are introduced to the furnace after cooling the melt to room temperature. The substrate is placed in a recess of the boat and is covered with the slider to minimize thermal etching during the saturation time of the melt.

The phase diagram was calculated according to Wu and Pearson's model (19), and the ternary melt having a solidus composition of $In_{0.50}Ga_{0.50}As$ is used at each growth temperature. The melt compositions are given in Table I.

Composition.—The composition is determined by x-ray diffraction of the Cu-$K_{\alpha 1}$ radiation using Vegard's law which can be applied to this mixed crystal (20). At high diffraction angles such as for (333) or (444) reflections, both reflections from the epitaxial layer and the substrate are detected. Since the diffraction angle of the InP substrate is known, the precise diffraction angle of the mixed crystal is determined from (333) or (444) reflection using the substrate reflection as an internal standard.

Photoluminescence (PL).—The photoluminescence excited by a He-Ne laser (6328Å) is detected by a PbS photoconductive diode cooled with a Dry Ice: ethanol solution. A conventional lock-in technique is used. The spectral response of the total system is in the range from 1.4 to 2.3 μm (at half-responses). After being lightly etched with a 1% Br:methanol solution, the sample is attached to a copper jig and immersed in liquid nitrogen contained in a double wall Dewar. All the samples are angle-lapped at 3° to examine the spectral variations along the thickness of the grown layers. The sample is moved parallel to the angle-lapped surface by a manipulator to which the copper jig is attached.

Resistivity and Hall coefficient measurement.—The method of van der Pauw (21) is used to determine the resistivity and the Hall coefficient. Typical sample dimensions for the measurements are 4×4 mm^2 and the thickness of the epitaxial layers varied from 3 to 24 μm. Pure indium dots (usually about 300 μm in diameter) are alloyed for contact electrodes at the corners of the grown layers in a flowing hydrogen ambient at 450°C for 1 min. Prior to the alloying, the surface is lightly etched with a 1% Br:methanol solution.

The sample temperature is varied from 77°K (immersed in liquid nitrogen) to 300°K and controlled to be stable within ±0.5°K. The source current is 20 or 100 μA, and the magnetic field for the Hall coefficient measurement is 5 kG.

Table I. Calculated weight of Ga and InAs per gram of In of melt for solidus $In_{0.50}Ga_{0.50}As$

T_G (°C)	In (g)	Ga (mg)	InAs (mg)
500	1.000	10.27	13.80
550	1.000	13.84	29.94
600	1.000	18.08	58.55
650	1.000	23.14	104.67
700	1.000	29.27	174.12
750	1.000	36.82	275.32
800	1.000	46.58	423.96

Results and Discussion

Thermal etching of InP substrate surface.—Examples of the substrate (111)B-surface baked at 500° and 750°C for 1 hr in a flowing hydrogen ambient are shown in Fig. 1, (a) and (b), respectively. The substrates are placed in a recess of the boat and covered with the slider during the heat-treatment. The substrate surface shows evidence of thermal etching. Small droplets remain on the surface at a lower temperature, and larger droplets at a higher temperature. A large droplet is seen to be due the coalescence of small droplets. The droplets are identified to be In by the electron probe microanalyzer (EPMA), and this thermal etching is due to the thermal decomposition of InP at a high temperature. Similar observations have been reported by Pak *et al.* (22). This etching effect influences the thickness and the surface morphology of the grown layer as is shown next.

Thickness and surface morphology.—As-grown surfaces and cleaved cross sections of the epitaxial layers grown at 500° and 700°C are shown in Fig. 2 (a) and (b), respectively. The as-grown surface at 700°C is the smoothest among those grown in the range from 500° to 800°C. At temperatures below 650°C, the surface becomes rough. Melt droplets are left on the as-grown surface during wiping due to the surface roughness. The thickness of epitaxial layer decreases exponentially with decreasing growth temperature. At 500°C no layer is grown, and this can be attributed to the low solubility of As at 500°C. At temperatures above 750°C, the as-grown surface is also rough. This is confirmed to be caused by the roughness of the substrate surface as a result of the thermal etching. At 800°C the melt remains almost over the entire surface after wiping. However, a uniform layer would be grown if the problem of the thermal etching is overcome by keeping the phosphorus over-pressure

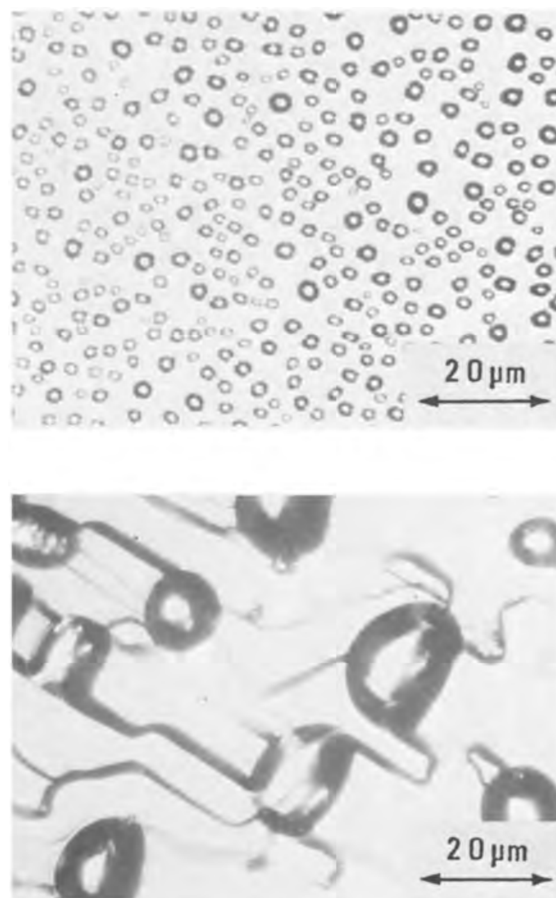

Fig. 1. Examples of the thermal etching of InP substrate surface after 1 hr baking at 550°C (a, top) and 750°C (b, bottom) in a flowing hydrogen ambient.

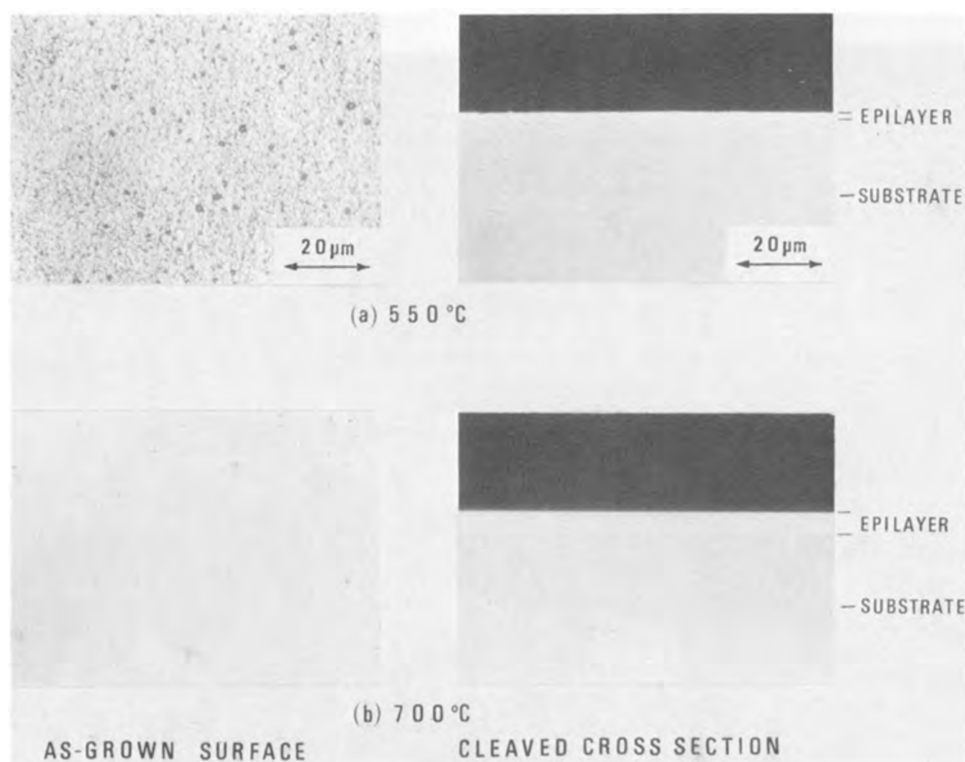

Fig. 2. As-grown surfaces and as-cleaved cross sections of the epitaxial layers grown at 550°C (a) and 700°C (b). Small spots are droplets of melts remaining on rough surface. No inclusions are found in cleaved sections.

or by etching back the InP surface. In the experiments all the mixed crystals grown at 800°C are excluded from the measurements.

In Fig. 3 the temperature dependence of the layer thickness normalized with the In weight in the melt (W_{In}) and the cooling interval (T_c) is shown. Between 550° and 700°C, the curve follows qualitatively the temperature dependence of the As fraction in the melt. The abrupt decrease at 750°C could be explained as follows. A fair amount of In remains on the substrate surface due to the thermal etching, as shown in Fig. 2. The melt when contacted with the substrate is diluted by this In and undersaturated at the interface. Therefore, the initial cooling period is spent in re-equilibration and resaturation and the layer thickness is small. No In inclusions are found at the interface of the layers, indicating that all the In droplets are taken into the contacted melt before the growth begins.

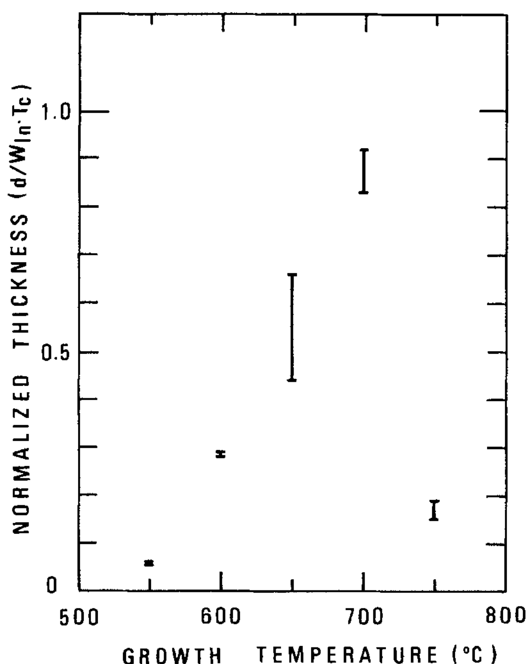

Fig. 3. Layer thickness as a function of growth temperature. The thickness is normalized to In weight (W_{In}) and cooling interval (T_c). The bar length corresponds to variation from sample to sample.

Etch pit density (EPD).—Etch pits in the grown layers are revealed by etching with an A-B solution (23) for 10-30 sec at room temperature. The average density at each growth temperature is listed in Table II. In the sample grown at 550°C the EPD is too high to count, far beyond 10^6 cm^{-2}. This high EPD may be in part due to the relatively large lattice mismatch between the substrate and the layer as is shown in Fig. 4. Better crystals could be grown even at temperatures below 650°C by precisely matching the lattice constant. About 1×10^5 cm^{-2} may be the lower limit of the EPD, because the Cr-doped InP substrate has approximately the same density of etch pits as revealed by etching with an R-C solution (24) for 10 min at 60°C.

Composition.—The composition *vs.* growth temperature is shown in Fig. 4. Although the In-Ga-As solution with the solidus composition of $In_{0.50}Ga_{0.50}As$ at each growth temperature is used, the composition of the mixed crystals grown at temperatures between 650° and 750°C is $In_{0.53}Ga_{0.47}As$ at which the lattice constant of the grown layer matches with that of InP. Below 650°C, the mismatch becomes greater with decreasing temperature.

As pointed out by Wu and Pearson (19) the accuracy of the solidus data in their experiment is ±3 mole percent. In our experiments at 600° and 550°C the deviation is over this range. It is possible that the lower Ga composition obtained at these temperatures is due to the inaccuracy of the Wu and Pearson phase diagram. Only a few experimental

Table II. Average EPD of mixed crystals at each growth temperature

Growth temperature (°C)	Average EPD (cm^{-2})
550	$>>1 \times 10^6$
600	$>1 \times 10^6$
650	$>5 \times 10^5$
700	$\sim 5 \times 10^5$
750	$\sim 1 \times 10^5$

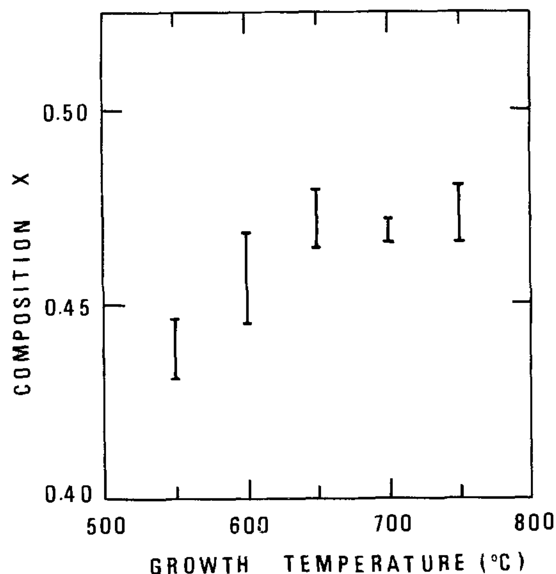

Fig. 4. Composition vs. growth temperature. The In-Ga-As solution of solidus composition $x = 0.5$ is used at each growth temperature.

data were examined in their phase diagram calculation at these lower temperatures.

Between 650° and 750°C the compositions of the grown layers are within the accuracy of the phase diagram and almost lattice-matched ($x \sim 0.47$) to the InP substrate. It could be considered that at these temperatures lattice-matched layers are obtained at the lower limit 0.47 (=0.50-0.03) of the accuracy of the phase diagram, but there may be another possibility that the lattice-matched layer is forcibly grown by the composition latching in the growth of InGaAs on InP in a certain range of composition as was observed by Stringfellow (25) in the LPE growth of InGaP on GaAs. Further investigations are being carried out on these phenomena and on the determination of the optimum melt composition for lattice matching at each growth temperature.

Continuous layers are obtained from melts of slightly deviated composition from 0.50, but from melts of 0.40 and 0.70 at 700°C only island growth, shown in Fig. 5, is observed as reported by Sankaran *et al.* (17).

An example of the (444) reflections is shown in Fig. 6. The reflections from the epitaxial layer and the substrate are detected at this high angle, and from these peaks a mismatch of 6.6×10^{-4} is calculated. The $K_{\alpha 1}$ and $K_{\alpha 2}$ peaks are clearly resolved, indicating good homogeneity of this mixed crystal which is grown at 750°C. The half-width of the peak from the epitaxial layer increases with decreasing growth temperature.

Photoluminescence.—Emission spectra of two epitaxial layer surfaces grown at different temperatures

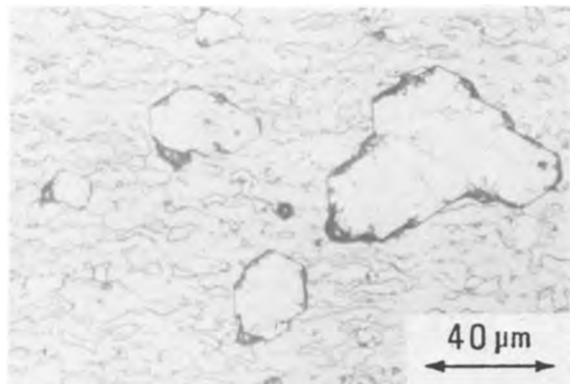

Fig. 5. Island growth of InGaAs on InP substrate grown at 700°C from the melt of a solidus composition $x = 0.4$.

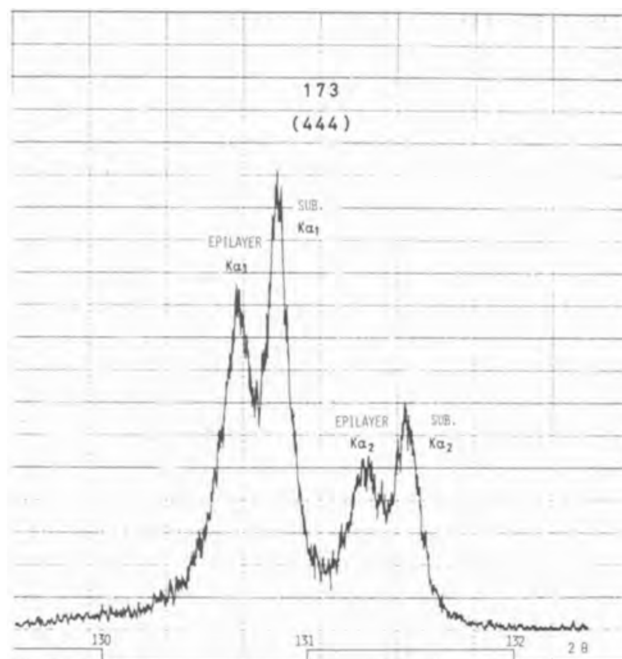

Fig. 6. An example of (444) x-ray reflections from the $In_{1-x}Ga_xAs$ layer and the InP substrate. $K_{\alpha 1}$ and $K_{\alpha 2}$ peaks from both crystals are clearly resolved.

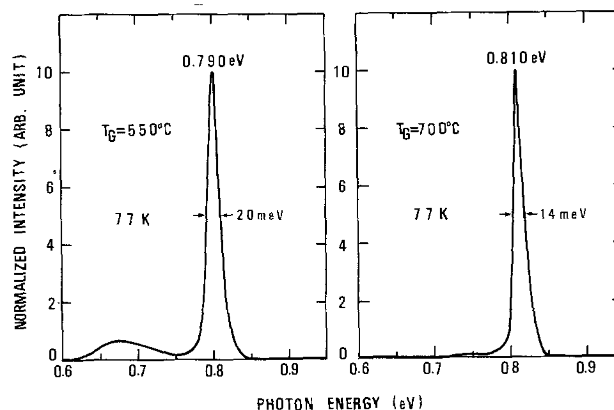

Fig. 7. Photoluminescence spectra (77°K) of two epitaxial layers grown at 550°C (a) and 700°C (b).

are compared in Fig. 7. There are two distinctions in the spectra: the photon energy at peak intensity and the half-width. The compositions determined by the photon energies at peak intensities are close to those in Fig. 4 obtained by x-ray diffraction. A good fit to the photon energy ($h\nu$) *vs.* composition (x), in the region $0.43 < x < 0.48$ and at $x = 0$, InAs, and $x = 1$, GaAs, at 77°K is given by

$$h\nu(\text{eV}) = 0.404 + 0.649x + 0.457x^2$$

The curve gives quite the same values as those by Wu and Pearson at 77°K (19).

The full width at half-maximum (FWHM) of the spectra decreases linearly with the increase of the growth temperature, *i.e.*, from ~20 meV at 550°C to ~14 meV at 750°C. This dependence is not based on the composition variation across the grown layer within the penetration depth of the He-Ne laser beam. Such a composition variation can be expected from the phase diagram (19); however, the lower the growth temperature, the smaller the composition variation for a cooling interval of 10°C at $x \cong 0.5$. Furthermore, in the experiments, the composition variation from near the interface to the surface is measured to be within ±1% by the EPMA and the photoluminescence. Moreover, the penetration depth of the

laser beam is less than 1 μm. Along with the growth temperature dependence of the half-width of x-ray reflection peak, it is understood that mixed crystals of better composition homogeneity are grown at higher temperature.

The variation of the photon energy at peak intensity, the intensity, and the FWHM along the angle-lapped grown layer are shown in Fig. 8 for sample 153 as an example. Constant photon energy indicates the uniformity in the composition, and very small variations of the intensity and the FWHM show a homogeneous crystal quality across the grown layer. Similar results are obtained in every sample at different growth temperatures. A relatively low intensity near the interface is due to the finite diameter of the laser beam (~50 μm), *i.e.*, at distance 0 μm, most of the laser spot irradiates the substrate and at about 3 μm (corresponding to about 50 μm in a layer angle-lapped by 3°) the whole spot is on the grown layer.

Electrical properties.—The highest electron mobilities at different growth temperatures are listed in Table III along with electron concentrations and compositions. In the table, the data of GaAs grown in the same growth system at 800°C are shown for comparison. All the grown mixed crystals are n-type with excess carrier concentrations of the order of 10^{16} cm^{-3}. Our experiments indicate the general tendency that the mobility increases while the concentration decreases with increasing growth temperature. An observation similar to this has been made in the case of InP grown at temperatures between 540°

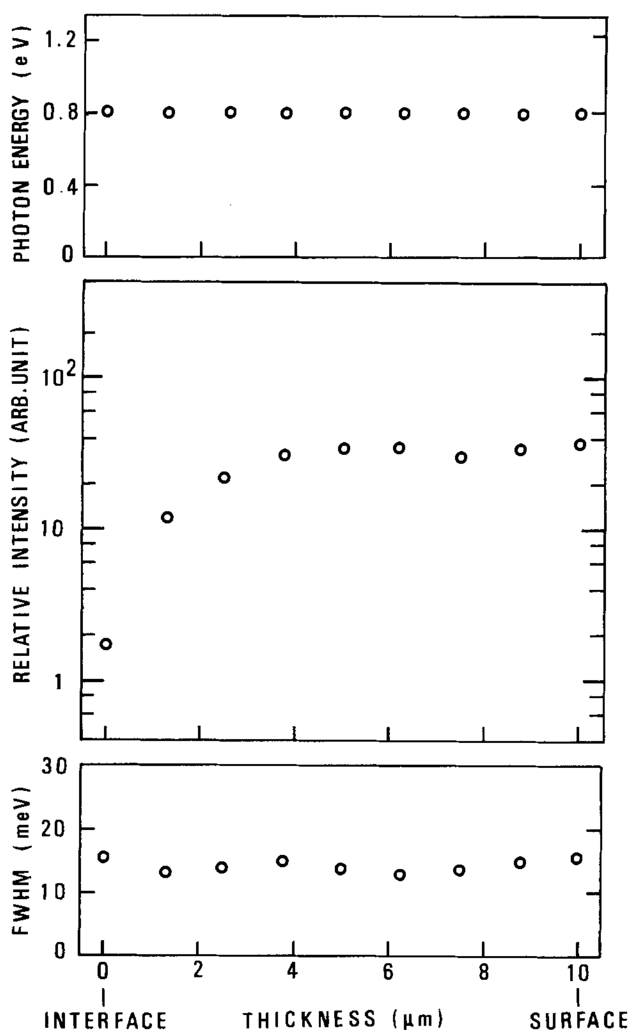

Fig. 8. Variations of the photon energy at peak intensity, the intensity, and the FWHM along the angle-lapped cross section in sample 153, showing good composition homogeneity and uniform crystal quality.

Table III. Composition and electrical properties of mixed crystals and GaAs

T_G (°C)	Sample No.	Composition x	300°K		77°K	
			μ*	n	μ	n
550	183	0.44	5240	6.3×10^{16}	7,400	5.3×10^{16}
600	180	0.46	6590	3.2×10^{16}	11,700	2.7×10^{16}
650	177	0.47	8240	2.3×10^{16}	15,400	2.0×10^{16}
700	153	0.47	7600	5.0×10^{15}	20,200	4.3×10^{15}
750	173	0.47	8500	1.3×10^{16}	22,100	1.1×10^{16}
800	204	1.00	6920	2.0×10^{14}	46,400	1.9×10^{14}
800	211	1.00	6870	2.8×10^{14}	43,300	2.5×10^{14}

* μ (cm^2 V^{-1} sec^{-1}), n (cm^{-3}).

and 780°C by LPE on InP (26). It seems from Table III that better mixed crystals (with higher mobility and lower concentration) can be grown at higher temperatures. But the epitaxial layer is nonuniform at high temperatures due to the thermal etching of the substrate surface. Invariably, the mobility of the mixed crystals increases with decreasing lattice temperature in contrast to Conrad's (7) and Baliga's (8) data. Both 8500 cm^2 V^{-1} sec^{-1} at 300°K and 22,100 cm^2 V^{-1} sec^{-1} at 77°K of sample 173 are significantly high in the epitaxial $In_{1-x}Ga_xAs$ ($x \cong 0.5$) (7-8, 14) and comparable to those of bulk grown mixed crystals (11-13).

Recently, Sankaran *et al.* (17) have reported mobility values of 10,030 cm^2 V^{-1} sec^{-1} at 300°K and 34,620 cm^2 V^{-1} sec^{-1} at 77°K in $In_{0.53}Ga_{0.47}As$ grown at 650°C by LPE on InP substrate, using the In, Ga, and As for the melt which was baked at 725°C for 22 hr. With the In, Ga, and InAs as melt constituents they have obtained 5540 cm^2 V^{-1} sec^{-1} at 300°K and 8430 cm^2 V^{-1} sec^{-1} at 77°K. Using almost the same purity In, Ga, and InAs, we have obtained mobility values of about 8000 cm^2 V^{-1} sec^{-1} at 300°K in the $In_{0.53}Ga_{0.47}As$ grown between 650° and 750°C by baking the In and Ga at 800°C for only 3 hr.

There has been a distinct difference in the value of the mobility between an epitaxial and a bulk $In_{1-x}Ga_xAs$ ($x \cong 0.5$), *i.e.*, the former has been lower and the latter similar to or higher than that of GaAs. Although Conrad *et al.* (7) suspected that the mixed crystal formation *per se* might be responsible in part for the low mobility and its temperature dependence, our results contradict this conclusion. The low mobility of the epitaxial layer grown previously can be considered to be due to a large internal strain and a large number of defects in the layer caused by the lattice mismatch with the substrate.

The electron concentration is calculated from the Hall coefficient using the relation

$$n = 1/eR_H$$

where e is the electron charge and R_H is the Hall coefficient. The Hall factor is assumed to be 1 for simplicity as is usually done. Figure 9 shows the electron concentration *vs.* inverse absolute temperature for three samples. The curve of a low concentration sample 173 shows two distinct regions suggesting two impurity levels at least; a shallow level for $T <$ 200°K and a deeper level for $T >$ 200°K. The distinction is not clear in the higher concentration samples. To find the donor and acceptor concentrations, a wider range of the temperature dependence of the electron concentration has to be measured and analyzed. However, it is evident from the temperature dependence of the mobilities that the impurity concentrations are not very high and the impurity scattering cannot be dominant at room temperature.

Conclusions

Undoped $In_{1-x}Ga_xAs$ ($x \cong 0.5$) films were grown on the InP substrates by liquid phase epitaxy at temperatures between 550° and 750°C by the present growth process. Etch pit density, half-width of the

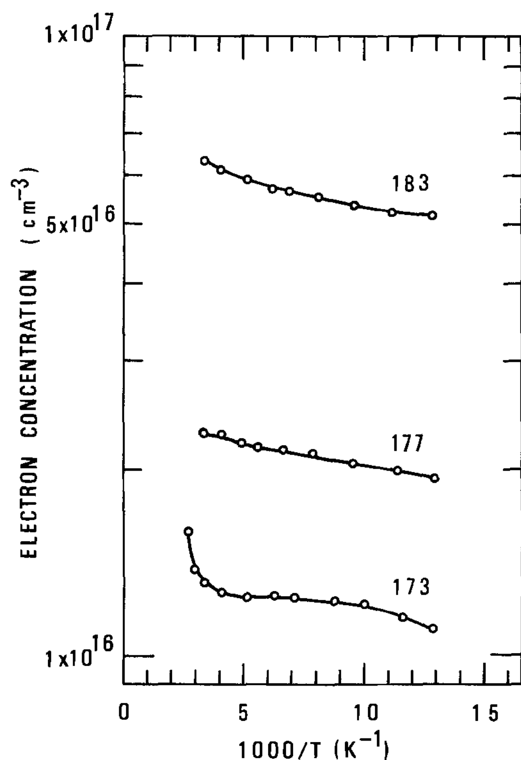

Fig. 9. The electron concentration as a function of inverse absolute temperature. In sample 173, there are at least two impurity levels.

PL spectra, and electron concentration decrease, while the electron mobilities at room temperature and at 77°K increase with increasing growth temperature. Composition and crystal quality are very uniform across the grown layer. The electron mobility is as high as 8500 cm^2 V^{-1} sec^{-1} at 300°K and increases on cooling from 300°K to 77°K in all samples. Although the crystal quality and the electrical properties seem to be better at high growth temperatures, the thermal decomposition of the InP substrate makes it difficult to obtain a uniform growth of the mixed crystal on the substrate. High quality crystals are grown at around 700°C.

Acknowledgment

We are grateful to Dr. Shigeo Fujita for valuable discussions and experimental facilities and to Professor Tanaka's laboratory for x-ray diffractometer. It is a pleasure to acknowledge Mr. Yukio Naito for his assistance in the electrical measurements. This work was supported in part by the Grant-in-Aid for the specified subject "Crystal Growth" from Scientific Research of the Ministry of Education in Japan.

Manuscript submitted Aug. 16, 1976; revised manuscript received Aug. 22, 1977.

Any discussion of this paper will appear in a Discussion Section to be published in the December 1978 JOURNAL. All discussions for the December 1978 Discussion Section should be submitted by Aug. 1, 1978.

REFERENCES

1. C. J. Nuese, M. Ettenberg, R. E. Enstrom, and H. Kressel, *Appl. Phys. Lett.*, **24**, 224 (1974).
2. R. E. Nahory, M. A. Pollack, and J. C. DeWinter, *ibid.*, **25**, 146 (1974).
3. C. J. Nuese and G. H. Olsen, *ibid.*, **26**, 528 (1975).
4. G. E. Stillman, C. M. Wolfe, A. G. Foyt, and W. T. Lindley, *ibid.*, **24**, 8 (1974).
5. L. G. Cohen, P. Kaiser, J. B. MacChesney, P. B. O'Conner, and H. M. Presby, *ibid.*, **26**, 472 (1975).
6. W. Fawcett, C. Hilsum, and H. D. Rees, *Electron. Lett.*, **5**, 313 (1969).
7. R. E. Conrad, P. L. Hoyt, and D. D. Martin, *This Journal*, **114**, 164 (1967).
8. B. J. Baliga and S. K. Ghandhi, *ibid.*, **122**, 683 (1975).
9. H. M. Manasevit and W. I. Simpson, *ibid.*, **120**, 135 (1973).
10. M. Glicksman, R. E. Enstrom, S. A. Mittleman, and J. R. Appert, *Phys. Rev. B*, **9**, 1621 (1974).
11. M. S. Abrahams, R. Braunstein, and F. D. Rosi, *J. Phys. Chem. Solids*, **10**, 204 (1959).
12. J. W. Wagner, *This Journal*, **117**, 1193 (1970).
13. T. V. Dzhakhutashvili, A. A. Mirtskhulava, L. G. Sakvarelidze, A. L. Shkol'nik, and M. S. Matinova, *Sov. Phys.-Semicond. (Engl. Trans.)*, **5**, 190 (1971).
14. R. E. Enstrom, D. Richman, M. S. Abrahams, J. A. Appert, D. G. Fisher, A. H. Sommer, and B. F. Williams, in "Gallium Arsenide and Related Compounds, 1970 Conference," Series 9, p. 30, Institute of Physics, London (1971).
15. H. Nagai and Y. Noguchi, *Appl. Phys. Lett.*, **26**, 108 (1975).
16. A. Sasaki, M. Mohri, T. Takagi, and T. Tanaka, Abstracts of the 4th International Conference on Crystal Growth, Tokyo, 1974, p. 237.
17. R. Sankaran, R. L. Moon, and G. A. Antypas, *J. Cryst. Growth*, **33**, 271 (1976).
18. Y. Takeda, A. Sasaki, Y. Imamura, and T. Takagi, *J. Appl. Phys.*, **47**, 5405 (1976).
19. T. Y. Wu and G. L. Pearson, *J. Phys. Chem. Solids*, **33**, 409 (1972).
20. J. C. Woolley and B. A. Smith, *Proc. Phys. Soc. (London)*, **72**, 214 (1958).
21. L. J. van der Pauw, *Philips Res. Rep.*, **13**, 1 (1958).
22. K. Pak, T. Nishinaga, and S. Uchiyama, *Jpn. J. Appl. Phys.*, **14**, 1613 (1975).
23. M. S. Abrahams and C. J. Buiocchi, *J. Appl. Phys.*, **36**, 2855 (1965).
24. J. L. Richards and A. J. Crocker, *J. Appl. Phys.*, **31**, 611 (1960).
25. G. B. Stringfellow, *ibid.*, **43**, 3455 (1972).
26. M. G. Astles, F. G. H. Smith, and E. W. Williams, *This Journal*, **120**, 1750 (1973).

Polishing of Sapphire with Colloidal Silica

Henry W. Gutsche and Jerry W. Moody

Monsanto Company, Electronic Products Division, St. Peters, Missouri 63376

ABSTRACT

The polishing of sapphire with colloidal silica has been studied. Stock removal rates have been found to vary with the solids content in the polishing fluid and the temperature on the polishing pad. The pH of the polishing fluid has also been found to be a factor influencing removal rate. Because concentrated silica solutions are unstable at high temperatures, a compromise between temperature and concentration must be made. Still, practical removal rates over 25 μ/hr have been achieved. Work damage, an important factor in polishing operations, has been found to extend about 1.0-1.5 mils into the surface of commercially available sawn or ground sapphire blanks. When all embedded diamond from the slicing and grinding operations is removed prior to polishing, a scratch-free, featureless surface is produced on which high quality, epitaxial silicon films can be deposited. C-MOS devices built into the films without the use of any specific processing technique to minimize the effect of the Al_2O_3-Si interface showed n-channel leakage of 1×10^{-10} A/mil with negligible wafer-to-wafer variations (1). The polishing of sapphire by colloidal silica is believed to follow a chemical reaction leading to aluminum silicate dihydrate as described in previous literature. For the reaction

$$Al_2O_3 + 2SiO_2 + 2H_2O \rightarrow Al_2Si_2O_7 \cdot 2H_2O \quad [1]$$

an activation energy of 14.6 kcal/mole has been calculated from the temperature dependency of the removal rate.

Sapphire, *i.e.*, αAl_2O_3, is used to advantage as a dielectric substrate under thin silicon films for integrated circuits and microwave devices with highly desirable features which are difficult or impossible to achieve on bulk silicon. Nonetheless, high material cost and difficulties with leakage currents have limited silicon-on-sapphire electronics to special applications only. The high material cost is related partly to the present low level of production and need not concern us here. The leakage currents, however, are our concern. One source of leakage currents is the Si/Al_2O_3 interface where lattice mismatch is often aggravated by the use of substrate material with mechanically polished surfaces.

Mechanical polishing produces mirror surfaces on the macroscopic scale only. "Semiconductor" polishing, *i.e.*, preparing material for electronic device work, must produce a surface which is whole, flat, and clean on the microscopic scale, better yet, on the atomic scale. Ideally, semiconductor surface preparation should produce a substrate that is enveloped by a natural, low energy, low index crystal plane that contains no remnant work damage and is covered by a well-defined usable or easily removable protective film.

In the case of silicon, polishing with colloidal SiO_2 has gained a reputation for producing a nearly perfect substrate surface for even the most critical integrated circuit application. Polishing with colloidal SiO_2 was patented in 1963 by Walsh and Herzog (2) as a mechanical process, and in 1966 as mechanical-chemical by Lachapelle (3), who found that the alkalinity of the polishing fluid drastically affected the removal rate.

Silicon surfaces polished with colloidal SiO_2 have been investigated by several authors (4-7). Techniques ranging from Sirtl etching before or after oxidation and epitaxial film growth to x-ray diffraction and ion backscattering have been applied. In all cases SiO_2 polished surfaces have been found to be free of damage, free of contour, and free of contamination. As a consequence semiconductor polishing with colloidal SiO_2 is now the worldwide accepted standard method for silicon substrate preparation. Colloidal SiO_2 also works on many other substances: metals and glasses, for example. It is particularly useful for polishing garnets (8).

Because of the success with garnets and silicon, it was therefore tempting to investigate whether colloidal SiO_2 could produce a similar surface on sapphire substrate. At first look such an endeavor seems obviously futile. When polishing silicon, with colloidal SiO_2 the particles may crystallize and reach a hardness sufficient to provide some degree of gentle molecular abrasion (9). Also, the alkalinity of the solution may be sufficient to chemically dissolve the substrate where friction generates enough heat on the surface of silicon. Surfaces of α-aluminum oxide, on the other hand, are extremely hard (Mohs' > 9) and allow even reactive melts at temperatures over 1000°C to dissolve only a few microns per hour (10). It was therefore rather surprising to find that colloidal SiO_2, in the complete absence of diamond particles, does indeed polish sapphire and produce a damage-free surface which is suitable for the growth of thin silicon epitaxial films for device work.

Before SiO_2 polishing of silicon, one physical imperfection in particular has been blamed for many device failures: remnant surface damage, that is to say, work damage left in mechanically shaped slices after inadequate polishing or etching. Especially in epitaxial wafers, surface damage in the substrate has been related to severe crystal disorder in the deposited film, often rendering the material useless for device work. Similarly remnant surface damage in sapphire substrate under thin epitaxial silicon films must make it next to impossible to prepare a good silicon-on-sapphire device. To date little has been published on processes for the preparation of a damage-free, flat, and clean sapphire-polished slices. Authors usually acknowledge the existence of "work" damage in the diamond-polished substrate surfaces they work with but rely then on "healing by annealing" for a remedy.

In silicon-on-silicon epitaxy only a slight lattice mismatch exists between the usually heavily doped substrate and the usually lightly doped film. It still leads to measurable tensile strain in n-on-p wafers however. In silicon-on-sapphire epitaxy, in addition to a considerable lattice mismatch [6% for {100} Si on $(1\bar{1}02)$ sapphire] (11), the large difference in their respective coefficients of thermal expansion cause the silicon film to sustain 8×10^9 dyne/cm^2 strain when grown at 1000°C and cooled to room temperature.

Therefore, for the preparation of usable epitaxial silicon films on sapphire, absence of damage in the substrate surface becomes an extremely important factor.

Experimental Results

Crystals.—The slices used were sawed from 2 in. diam sapphire crystals purchased from Union Carbide, San Diego, California, and from Crystal Systems, Salem, Massachusetts. The slice surfaces were oriented to within ±2° of the $(\bar{1}\bar{1}02)$ plane by Laue back-reflection. Sawing was done on a Silicon Technology saw, Silicon Technology Corporation, Oakland, New Jersey, equipped with a rotating ingot holder.

Slice preparation.—After sawing, the slices are 20 mils thick. They were fine ground to 14 mils on a Mueller grinder, Kugel-Mueller, Nurenberg, Germany, equipped with a 230 grit diamond wheel. To achieve complete absence of diamond which is necessary for scratch-free polish and to minimize bow after polishing, the ground slices are annealed in O_2 at 1100°C for 2-4 hr.

Polishing.—The polishing step was carried out on an Elgin 1-20 machine, Elgin Tool Company, Whitehall, Michigan, equipped with an oscillating pressure arm. A PR-30 polishing cloth, Process Research Products, Pennington, New Jersey, was found suitable, but non-perforated Pellon and Buehler Microcloth was also useful, albeit quick to wear out. Stock removal rate was calculated by measuring the thickness with a dial micrometer at 5 points on the wafer periodically during polishing. The fluid was Syton HT-40, Monsanto Company, St. Louis, Missouri.

It was found that the thin, heavily damaged layer of a freshly ground wafer was removed at stock removal rates of well over 50 μ/hr. The removal rates listed in the following tables and figures were measured after this heavily damaged layer was removed and when the rate became independent of total stock removal. Therefore, the removal rates given are believed to be characteristic of the undamaged $(\bar{1}\bar{1}02)$ sapphire plane under the conditions described.

The influence of various process variables on the speed of polishing expressed as rate of stock removal is shown in Tables I-III. Table I indicates that increasing the solids content of the colloidal SiO_2 solution from about 4 to 25% almost triples the removal rate from 6 to 17 μ/hr. Further increase in solids content does not seem to help matters much, probably because SiO_2 solutions with solid contents over 16% become rather unstable under polishing conditions. The SiO_2 particles agglomerate, precipitate, and finally crystallize thereby reducing the effective concentration of the solution. Therefore, practical removal rates do not exceed 12 μ/hr in strongly basic solutions.

Fortunately, as Table II shows, the speed of polishing is also influenced by the *p*H of the fluid which can be adjusted by carefully adding 0.5*N* HCl. Maximal removal rates occur at *p*H values between 7 and 8. In this manner 10% solid solutions which remove 11-12 μ/hr at *p*H 10.5 will "cut" at 19-20 μ/hr at *p*H 8.

When polishing sapphire with colloidal SiO_2, abrasion can be ruled out as cause for stock removal because sapphire is harder than the SiO_2. Stock removal must occur because of chemical reaction, and it comes

Table II. Removal rate vs. pH of fluid
(Temperature 78°C, solids 10%)

*p*H	Removal rate (μ/hr)
10.5	11.4
10	14.0
9	15.2
8	19.2
7	17.8
6	11.4
5	10.2
2	3.6

as no surprise that the removal rate is also dependent on the temperature at the surface of the polishing pad as shown in Table III. This temperature, as monitored using a Fenwal-Spartan 2040 LTF infrared thermometer, is adjustable by varying the pressure of the polishing arm and the flow and temperature of the polishing fluid onto the turntable. We found that 82°C is about the highest operating temperature compatible with the stability of both the polishing fluid and the pad adhesive. Table III shows that the removal rate increased with temperature up to the maximum temperature employed. For practical, routine work a 16% solids, *p*H 8 fluid is recommended at 82°C pad temperature. This will "cut" the $(\bar{1}102)$ plane sapphire at rates ≧25 μ/hr.

Reaction Mechanism

The surprising fact that SiO_2 reacts at all with the extremely hard and nearly inert sapphire can be explained in part by the thermodynamics of the tripartite system $Al_2O_3/SiO_2/H_2O$. In the simplest case $Al_2O_3 + SiO_2 \rightarrow Al_2SiO_5$ such common, naturally occurring aluminum silicates as kyanite, andalusite, or mullite may form. All three reactions are thermodynamically possible, the mullite formation being the most likely of the three at 400°K, which is about the temperature on the surface of the sapphire during the polishing process. The free energies of these reactions are (T = 400°K): $\Delta\mathbf{F}$ (kyanite) = −18 cal/mole; $\Delta\mathbf{F}$ (andalusite) = −55 cal/mole; and $\Delta\mathbf{F}$ (mullite) = −377 cal/mole calculated from enthalpy and entropy data published by the Bureau of Mines (12). The reaction Al_2O_3 (alpha-alumina) + $SiO_2 \rightarrow Al_2SiO_5$ (mullite) is endothermic as might be expected and requires an enthalpy change of +5100 cal/mole at 400°K.

Naturally these data merely indicate that Al_2O_3 and SiO_2 may react at temperatures only slightly above the boiling point of water. However, what actually happens during polishing probably has been described by Schwartz and Brenner (13) who found that "in a neutral $Al_2O_3/SiO_2/H_2O$ system the stable compound $Al_2Si_2O_7 \cdot 2H_2O$ with a structure identical or very similar to natural kaolin is capable of forming," and, "it is uninfluenced by the presence of an excess of silica. It is formed with particular readiness when at least 6 moles of SiO_2 are present for each mole of Al_2O_3." Since we are observing in our polishing system maximal stock removal rates at *p*H values between 7 and 8, we suggest that the formation of $Al_2Si_2O_7 \cdot 2H_2O$ as described by Schwartz and Brenner can indeed explain the chemistry of polishing sap-

Table I. Removal rate vs. percent solids
(Temperature 78°C, *p*H 10.5)

SiO_2 solids (% weight)	Removal rate (μ/hr)
4	6.1
8	10.7
12	11.4
16	11.7
20	14.7
26	17.3
40	17.8

Table III. Removal rate vs. temperature
(Solids 10%, *p*H 10.5)

Temperature (°C)	Removal rate (μ/hr)
64	5.3
74	9.1
78	11.2
80	13.2
81	15.7
82	16.5
83	26.0 (16% solids)

phire with colloidal silica at or near the boiling point of water. Indeed, a slight loss of weight can be measured when rough sapphire blanks are simply immersed in a boiling silica solution of pH 7-8.

To proceed with measurable speed the reaction must have available three conditions: (*i*) Heat must be supplied to support the reaction; (*ii*) the reaction product must be continually removed from the sapphire surface; and (*iii*) the reactants must be forced into intimate contact at all times. All three conditions are met during the polishing process. The sapphire surface is pressed against a fast-rotating high friction polishing cloth. The polishing cloth serves as vehicle and heater for the polishing fluid and by moving the Syton particles over the surface of the sapphire under pressure, continuously "shaves off" the reaction product thereby constantly exposing fresh sapphire surface to the SiO_2 in the polishing fluid. The reaction product can sometimes be observed under the electron microscope in the form of triangular, apparently oriented, precipitates ~1000Å in diameter which wipe off with a moist cotton swab (Fig. 1).

Stock removal in Syton polishing of αAl_2O_3 is therefore entirely chemical. No abrasive, fracturing, or otherwise mechanical action removes lattice constituents in the system described. Therefore, this system will not produce a flat, featureless surface as long as damage exists in that surface, simply because a damaged surface element will always polish faster than any damage-free surface element next to it. Since good phase-contrast optics make visible adjacent height differences as shallow as 30-50Å, microscopic examination of clean Syton-polished surfaces constitutes a sensitive test for absence of remnant surface damage. In fact, x-ray rocking curves showed absence of damage, indicating strain in all samples that were polished until their surface appeared featureless at 100× and maximum phase contrast position of the Nomarski attachment to a Reichert microscope.

C-MOS devices built into the films without the use of any specific processing technique to minimize the effect of the Al_2O_3-Si interface showed n-channel leakage of 1×10^{-10} A/mil with negligible wafer-to-wafer variations (11).

The activation energy for the polishing reaction was determined from the temperature dependency of the reaction rate as shown in Fig. 2. From the slope of the line the activation energy was calculated as 14.5 kcal/mole.

Conclusions

Silica solutions have been found to be an effective agent for polishing sapphire wafers for S-O-S device work. Under proper conditions of pH and temperature,

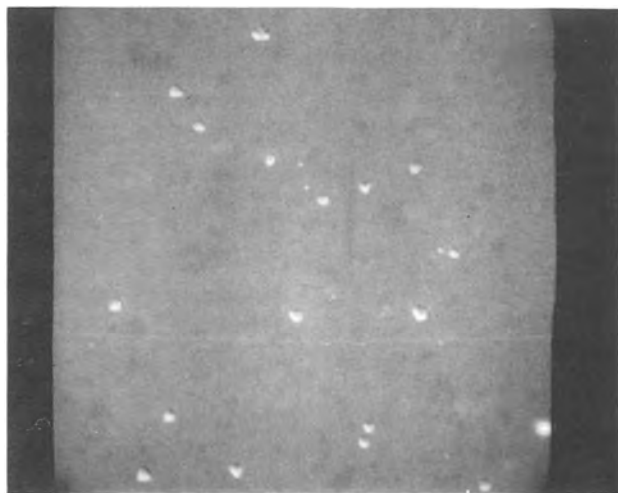

Fig. 1. Reaction products on sapphire surface; electronic microscope 10,000×.

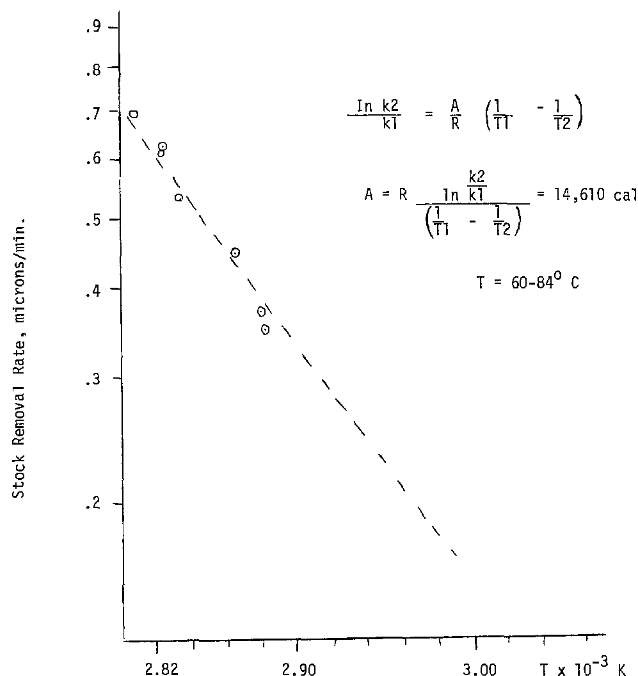

Fig. 2. Removal rate vs. temperature.

stock removal rates ≧25 μ/hr can be realized. It is believed that the polishing results from a chemical reaction between the sapphire and the silica particles in which alumina silicates are formed. Since abrasion can be ruled out completely and a chemical reaction is involved, this polishing procedure produces a surface which must be free of all remnant work damage.

Acknowledgments

The authors wish to thank Mrs. Brenda Schulte for her patience and help with carrying out the experiments. Thanks also go to Drs. J. Fayring and D. Dohm of the Physical Science Center of Monsanto for their valuable EM and x-ray work on the polished-sapphire surface. We also appreciate very much the device work performed by Dr. H. Hawkins of Hughes Aircraft Company to evaluate the influence of the Al_2O_3-Si interface on the electrical characteristics of C-MOS structures.

Manuscript submitted April 25, 1977; revised manuscript received Aug. 19, 1977.

Any discussion of this paper will appear in a Discussion Section to be published in the December 1978 JOURNAL. All discussions for the December 1978 Discussion Section should be submitted by Aug. 1, 1978.

Publication costs of this article were assisted by Monsanto Company.

REFERENCES

1. D. M. Hawkins, Private communication.
2. R. J. Walsh and A. H. Herzog, U.S. Pat. 3,970,273.
3. R. L. Lachapelle, U.S. Pat. 3,323,141.
4. H. W. Gutsche, Paper presented at the 6th IEEE Microelectronics Symposium, Clayton, Mo., June 21, 1967.
5. E. Mendel, *Solid State Technol.*, **10**, 27 (1967).
6. A. Mayer, *RCA Rev.*, **31**, 414 (1970).
7. T. M. Buck and G. H. Wheatley, Paper presented at the American Vacuum Society Fall Meeting, Seattle, Washington, October 1969.
8. M. F. Ehman, *This Journal*, **12**, 1240 (1974).
9. E. Rabinowitz, *Sci. Am.*, **218**, 91 (1968).
10. P. H. Robinson and C. W. Mueller, *Trans. Metall. Soc. AIME*, **236**, 268 (1966).
11. P. A. Larssen, *Acta Crystallogr.*, **20**, 599 (1966); C. Y. Ang and H. M. Manasevit, *Solid-State Electron.*, **8**, 994 (1965).
12. K. K. Kelly, Bull. 584, Bureau of Mines (1966).
13. R. Schwartz and A. Brenner, *Chem. Ber.*, **56**, 1933 (1923).

Physicochemical Properties of Chemical Vapor-Deposited Silicon Oxynitride from a SiH_4-CO_2-NH_3-H_2 System

A. K. Gaind* and E. W. Hearn

IBM System Products Division, East Fishkill Facility, Hopewell Junction, New York 12533

ABSTRACT

The physicochemical properties of amorphous silicon oxynitride ($Si_lO_mN_p$) films deposited from a SiH_4-CO_2-NH_3-H_2 system have been investigated. The properties of CVD Si_3N_4 and SiO_2 deposited from SiH_4-NH_3-H_2 and SiH_4-CO_2-H_2, respectively, were also investigated, wherever appropriate, to determine the end points of the $Si_lO_mN_p$ series. The film stress is a continuous, approximately parabolic function of silicon oxynitride composition. The $Si_lO_mN_p$ composition also determines its resistance to oxidation in steam (950°-1100°C). It is shown that a ~500Å thick film with the composition of Si_2ON_2 is an adequate barrier to steam oxidation for 6 hr at 1000°C. The etch rate of $Si_lO_mN_p$ films is a function of composition in 7:1 BHF. In refluxing H_3PO_4, a peak in etch rate exists at a film composition of ~64% equivalent Si_3N_4. $Si_lO_mN_p$ films deposited between 900° and 1000°C densify 2-3% after "heat-treatment" at 1000°C for 2 hr and their etch rates decrease by ~50%; whereas the stress increases (more tensile) as a result of heat-treatment.

Silicon oxynitride ($Si_lO_mN_p$) films have been chemical vapor deposited from various chemical systems (1-6), and the resulting properties have been reported (1-8). It was shown earlier by Gaind *et al.* (9) that the SiH_4-CO_2-NH_3-H_2 chemical system results in better process control, especially in forming Si_3N_4-rich oxynitride films; *e.g.*, $Si_lO_mN_p$ films with refractive index $\geqq 1.73$ can be formed with NH_3:CO_2 ratio of ~6 at 900°C, whereas for other chemical systems, the NH_3:oxidant ratio must be at least 50, usually ~5000 depending upon the oxidant (1-5).

It is our purpose to show the similarity between the silicon oxynitrides produced by the above system and those reported in the literature. This is done by comparing physicochemical properties wherever possible with the existing data in the literature. We will at the same time be filling in gaps in the knowledge of physicochemical properties of silicon oxynitride, especially those which are important in the processing of devices (bipolar, FET, etc.) which require wet etching, *e.g.*, the oxidation barrier of oxynitrides to steam and the etch rate in refluxing phosphoric acid. There are no available data in the literature regarding these physicochemical properties.

From a device-processing point of view, the importance of the effect of postdeposition "heat-treatment" (which simulates processes like diffusion or oxidation) on physicochemical properties of these dielectric films cannot be overemphasized. Thus we have investigated the effect of heat-treatment on $Si_lO_mN_p$ film stress, etch rate, and changes in density (thickness). We have also investigated the effect of the deposition temperature on $Si_lO_mN_p$ physicochemical properties by investigating these at two deposition temperatures, 900° and 1000°C.

Experimental

The details of the reactor used (10), the sample preparation, thickness measurement procedures, and typical deposition conditions have been described elsewhere (9). During this study, 1000-1500Å films were used for the determination of most properties, except for stress measurements for which film thicknesses ranged between ~600-8000Å. The details of experimental techniques used to measure stress, etch rates, and other properties are given in the results section of this paper.

* Electrochemical Society Active Member.

Key words: silicon nitride, silicon dioxide, barrier to oxidation, film stress.

Results

The dependence of refractive index of $Si_lO_mN_p$ films on NH_3:CO_2 ratio and the relationship of infrared absorption maxima with the refractive index have been previously established (9). Throughout this paper we have reported the physicochemical properties in terms of the composition of $Si_lO_mN_p$ films rather than their refractive indexes. The composition was calculated from the $Si_lO_mN_p$ refractive index, either (*i*) weight fraction averaging, *i.e.*, Lorentz-Lorenz theory (11-13) or (*ii*) mole fraction averaging techniques. The values used here are the mean of the results obtained by either method. If silicon oxynitride were to be represented as $x \cdot SiO_2 y \cdot Si_3N_4$, then "equivalent" SiO_2 (or Si_3N_4) can be calculated by Lorentz-Lorenz theory using Eq. [1]-[3], *i.e.*

$$n_{on}^2 = \frac{\dfrac{a_{ox} n_{ox}^2 W_{ox}}{\rho_{ox}} + \dfrac{a_n n_n^2 W_N}{\rho_N}}{\dfrac{a_{ox} W_{ox}}{\rho_{ox}} + \dfrac{a_n W_n}{\rho_N}} \qquad [1]$$

where

$$a_{ox} = (n_{ox}^2 + 2)^{-1} \quad \text{and} \quad a_n = (n_n^2 + 2)^{-1}$$

and w_{ox} and w_N are weight fractions of equivalent SiO_2 and Si_3N_4. Using n_{ox} (refractive index of SiO_2) = 1.45[1] and n_n (refractive index of Si_3N_4) = 2.025[1], ρ_{ox} = 2.15[1], and ρ_n = 3.09[1] are SiO_2 and Si_3N_4 densities, respectively. Rearranging Eq. [1] and substituting $W_N = 1 - W_{ox}$, we have

$$W_{ox} = \frac{0.217 - 0.053 \cdot n_{on}^2}{0.0605 n_{on}^2 - 0.021} \qquad [2]$$

where n_{on} is the refractive index of $Si_lO_mN_p$. The mole fraction of equivalent SiO_2 in silicon oxynitride is then given by

$$x = \frac{140\ W_{ox}}{60 + 80\ W_{ox}} \qquad [3]$$

Alternately, using the mole fraction averaging technique we have

$$n_{on} = x n_{ox} + y n_n \qquad [4]$$

and substituting $y = 1 - x$ and the values of n_{ox} and n_n we have

$$x = \frac{2.025 - n_{on}}{0.575} \qquad [5]$$

[1] Experimentally determined.

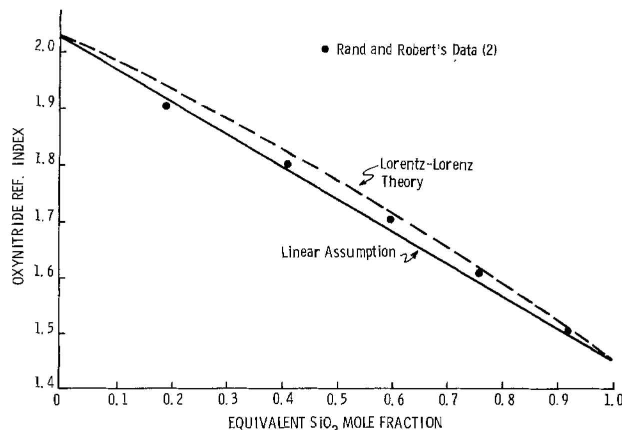

Fig. 1. Silicon oxynitride refractive index vs. equivalent SiO_2 mole fraction in $Si_lO_mN_p$ (composition) showing applicability of Lorentz-Lorenz theory and mole fraction averaging.

Equivalent SiO_2 mole fractions in silicon oxynitride films are plotted against these refractive indexes in Fig. 1. The experimental data of Rand and Roberts (2) is provided as a comparison.

Stress measurement.—The stresses in the films were calculated from measurements of elastic bending of the substrate film combination. In this technique, the substrate of thickness, t_s, is bent to a radius of curvature R by the forces at one surface. If the film thickness $t_f << t_s$, the average stress in the film is given by Eq. [6] (7, 14, 15)

$$\sigma_f = \frac{1}{6}\frac{E_s}{1-\gamma_s}\frac{t_s^2}{t_f}\left(\frac{1}{R_f}-\frac{1}{R_o}\right) \quad [6]$$

where E_s and γ_s are Young's modulus and the Poisson ratio of the substrate, respectively, and R_f and R_o are the radii of curvature of substrate with and without the film. For (100) oriented substrates $E_s/(1 - \gamma_s) = 1.8 \times 10^{12}$ dynes/cm^2 (16, 17).

The radius of curvature was measured by the use of Fe K_α radiation in a double crystal diffractometer. The x-ray beam is Bragg diffracted from (440) planes of [100] silicon monochromator. The diffracted beam is directed onto the sample whose radius of curvature is to be measured. Note that the sample is also (100) Si crystal with or without dielectric films (CVD SiO_2, Si_3N_4, or $Si_lO_mN_p$). If the sample is bent, the resulting topograph of the twice diffracted beam is a narrow vertical line. The sample is then rotated a small amount and another line is diffracted parallel and displaced from the first line on the topograph. (This procedure is schematically shown in Fig. 2.) Such a composite topograph is called a "zebra topograph" (18). In the case where the sample curvature is too small to yield a "zebra" pattern (thus producing overlapping intensities), a pair of pinhole slits is introduced between the monochromator and the sample crystal. The sample crystal is rotated to maximize the intensity of the diffracted beam from the two different diffracting positions and the x-ray films are replaced by an electronic detector which allows separation of overlapping intensities. Thus the radius of curvature is given by $l/\Delta\theta$, where l is the distance between the pinholes or the distance along the film in the zebra topographs, and $\Delta\theta$ is the measured angular distance resulting in separation l. With the above described techniques, the curvatures from a few seconds of arc up to a few degrees of arc can be measured. Several samples were measured with the film and then the film was stripped by etching in 49% HF and the radius of curvature measured again. In all cases $R_o >> R_f$ and therefore $1/R_o$ was neglected in Eq. [6] for all stress calculations.

Stress in Si_3N_4 (as-deposited).—The radius of curvature of samples with an Si_3N_4 film thickness of ~800-

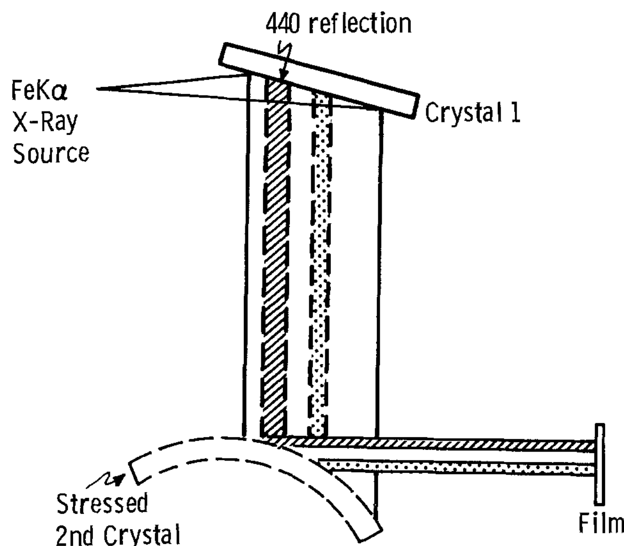

Fig. 2. Schematic of double crystal stress measurement technique

6000Å was measured. The stress in the Si_3N_4 is tensile and independent of film thickness and deposition rate. However, stress is a function of deposition temperature, *i.e.*, stress increases with decreasing deposition temperature. Shown in Table I are the Si_3N_4 refractive index, density, and stress of Si_3N_4 as a function of deposition temperature. The Si_3N_4 stress values reported here are in good agreement with literature values (2, 15).

Stress in SiO_2 (as-deposited).—The SiO_2 films deposited from SiH_4-CO_2-H_2 are under compression. Once again, the stress in CVD SiO_2 is not a function of thickness (~600-6000Å) or deposition rate. However, the stress decreases (*i.e.*, becomes less compressive) as the deposition temperature is decreased; *i.e.*, stress in 1000°C films is ~ 1.3×10^9 dynes/cm^2, where at 900°C it is only ~ 0.8×10^9 dynes/cm^2. These trends are consistent with the trends reported for thermally grown oxides [*e.g.*, (19, 20)]. The magnitude of stress in SiO_2 films deposited at 900°C are in good agreement with the value reported by Rand and Roberts (2).

Stress in silicon oxynitride (as-deposited).—The stress in silicon oxynitride films as a function of the equivalent Si_3N_4 mole fraction is shown in Fig. 3 at two deposition temperatures. The film thicknesses were varied from ~600 to ~8000Å. Consistent with CVD SiO_2 and Si_3N_4, the stress in oxynitride films was independent of film thickness and deposition rate. The strong influence of deposition temperature can be seen in Fig. 3. A 100°C drop in deposition temperature causes the film stress to become more tensile by ~ 2×10^9 dynes/cm^2 in the entire range of composition from near SiO_2 to near Si_3N_4. The stress in silicon oxynitride films does not increase as a linear function of equivalent Si_3N_4 mole fraction. However, stress does appear to be

Table I. Some properties of Si_3N_4 as a function of deposition temperature

Deposition temp. (°C)	RI[a]	Density[b] (g/cm^3)	Stress × 10^9 [c] (dynes/cm^2)
1000	2.025	3.09	8.5 (±1)
950	2.025	—	10.5 (±1)
900	2.023	3.09	11.1 (±1.5)
850	1.981	—	10.7 (±2.0)

[a] Median values shown in table. Distribution is skewed, minimum and maximum value of RI for 900°-1000°C range from 2.005 to 2.03 and for 850°C from 1.97 to 1.99.
[b] Density by weight loss method. The values given are mean values. Sample-to-stample variation ±0.1.
[c] Values in parentheses are twice the standard deviation. The stress in Si_3N_4 is tensile.

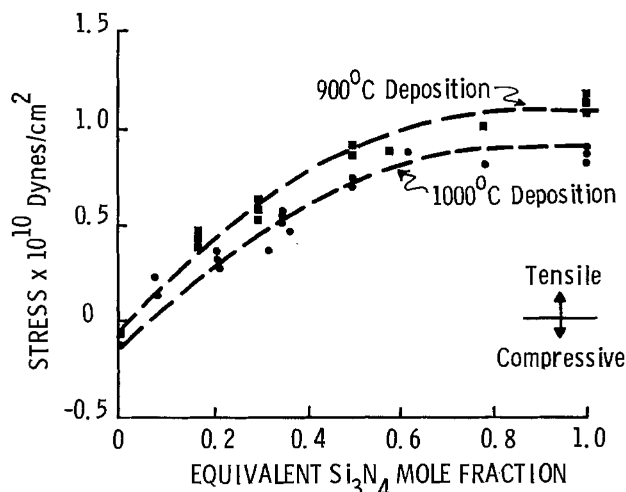

Fig. 3. Film stress as a function of composition and two deposition temperatures.

a continuous function of composition as shown by the broken curves. Unlike Rand and Roberts (2) we did not observe the discontinuity in stress *vs.* composition curve. This discrepancy is due to the fact that Rand and Roberts produced low refractive index silicon oxynitrides (for which they reported stress values) by SiH_4-NO processes and not by SiH_4-NO-NH_3 processes. These authors also attribute this discontinuity to the use of two different chemical systems for the deposition of silicon oxynitride films (2).

Relative oxidation barrier.—Si_3N_4 is known to be a barrier to oxidation in steam. The question then arises as to how this property varies as a function of silicon oxynitride composition. Si_3N_4 and $Si_lO_mN_p$ films (~1000Å on Si) were subjected to steam at 950°C (9.5 hr), 1000°C (6 hr), and 1100 C (2.5 hr). At these temperatures and respective times, ~ 1.15μ of SiO_2 grows on bare (100) Si wafers. The refractive index of Si_3N_4 or $Si_lO_mN_p$ films was measured before and after oxidation. The films were subsequently etched in 7:1 buffered HF and the refractive index measured at 5 sec intervals of etching. This process of etching and ellipsometric measurement was continued until the refractive index stabilized (*i.e.*, reached a constant value very nearly equal to the initial value). Thickness corresponding to stabilized refractive index was thus the thickness of unoxidized $Si_lO_mN_p$ (or Si_3N_4). A typical example of this process is graphically shown in Fig. 4 (initial RI = 1.788). The ratio of the thickness of oxidized Si_3N_4 to the thickness of oxidized $Si_lO_mN_p$ is called the relative oxidation barrier and is a function of $Si_lO_mN_p$ composition at the three temperatures as shown in Fig. 5. The effect of deposition temperature

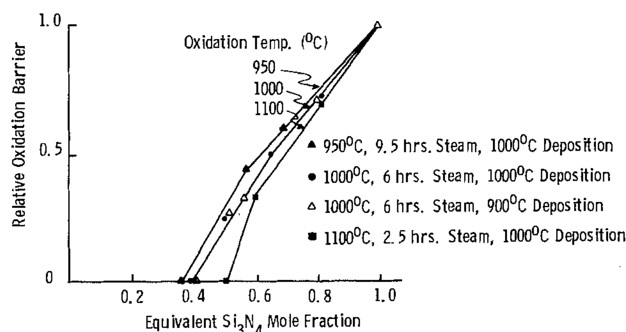

Fig. 5. Relative oxidation barrier of silicon oxynitride as a function of composition at three oxidation temperatures.

was investigated and no significant differences were found between 900° and 1000°C (Fig. 5). Zero oxidation barrier compositions were those which allowed ≧ 8000Å SiO_2 to grow on the film side of the silicon substrate. In other words, when none of the original silicon oxynitride remained on silicon after exposure to steam, the film was completely converted to SiO_2 and additional SiO_2 grew in the usual manner. Thus the minimum equivalent Si_3N_4 required for the film to act as a barrier to oxidation increases from 0.38 (at 950°C) to 0.5 (at 1100°C) when ~ 1.15μ of SiO_2 is grown on silicon. The effect of time on percentage oxidation of the film is shown in Fig. 6. Note that up to ~ 0.6 mole fraction of Si_3N_4, the percentage oxidation is nearly linear with a subsequent steep rise to 100% oxidation at 0.3-0.4 mole fraction of equivalent Si_3N_4. Thus the oxidation barrier study indicates that silicon oxynitride films with composition of ≧ 0.6 equivalent Si_3N_4 behave more like Si_3N_4, whereas films with equivalent Si_3N_4 ≦ 0.3 mole fractions behave like SiO_2. The region from 0.3 to 0.6 mole fraction can be considered a transition region, where the films can be completely oxidized in reasonably short time at 1000°C.

Etch rates.—The etch rates were measured on films of ~ 1000Å thickness. The film thickness was measured by ellipsometry and the sample then etched for fixed amount of time in a given etchant. The thickness was then measured again. This procedure was usually repeated a few times and the etch rate values reported here are an average of these measurements.

Etch rate of Si_3N_4 (as-deposited).—The etch rate of Si_3N_4 was determined in three etchants; *viz,* 49% HF (23° ± 2°C), refluxing H_3PO_4 acid at 180°C, and 7:1 buffered HF at 23° ± 2°C. The values obtained are

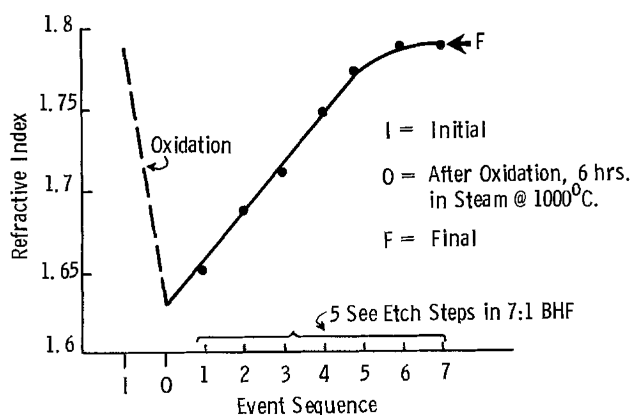

Fig. 4. Change of refractive index as a function of oxidation in steam and subsequent recovery of refractive index after short etch steps in 7:1 BHF.

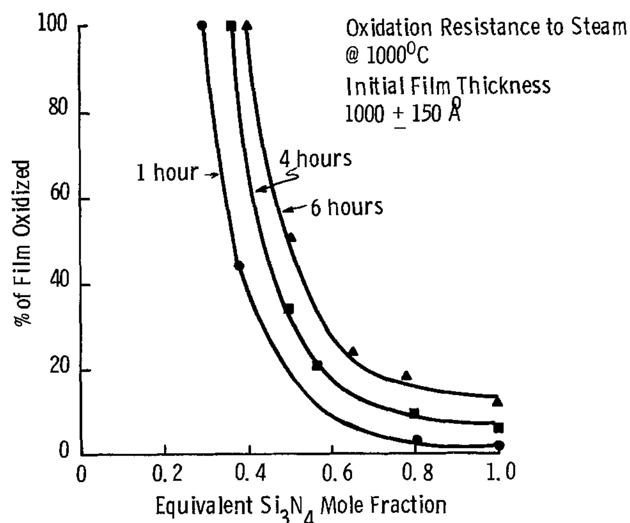

Fig. 6. Oxidation resistance to steam at 1000°C as a function of silicon oxynitride composition.

Table II. Si_3N_4 etch rates

Deposition temp. (°C)	Density	Refractive[1] index	49% HF[1,3] (Å/min)	Ref. 1[2] (49% HF) (Å/min)	7:1 BHF[1] (Å/min)	Ref. 2[2] 7:1 BHF (Å/min)	Refluxing[1] H_3PO_4 (Å/min)	Ref. 23[2] Refluxing H_3PO_4 (Å/min)
1000	3.09	2.025	100 (±10)	140 (2.03)	6.6	—	60	—
950	—	2.025	110 (±15)	330 (—)	7.0	—	—	—
900	3.09	2.023	150 (±35)	750 (—)	7.8	—	65	105 (1.97)[4]
850	—	1.981	250 (±45)	—	12-16	9-13 (1.98)	—	—
800	—	—	—	1000 (—)	—	—	—	—

[1] Present work.
[2] Number in parentheses is the reported refractive index.
[3] Number in parentheses is twice the standard deviation.
[4] Deposition temperature of 880°C.

shown in Table II. Available data from the literature are also shown (1, 2, 21). Note that our Si_3N_4 etch rates in 49% HF are considerably lower than the data reported by Brown *et al.* (1). The etch rates in 7:1 BHF are comparable with the data reported by Rand and Roberts and our Si_3N_4 appears to etch more slowly in refluxing phosphoric acid than that of Van Gelder and Hauser (21).

From Table II it can be seen that the increase in etch rate due to decreasing temperature in as-deposited films is not exclusively due to decrease in density as suggested by Chu *et al.* (22), especially in the temperature range of 900°-1000°C. At these two temperatures, the measured densities, refractive indexes, and infrared absorption spectra are very nearly identical within the error of measurement. The reason for the significantly higher etch rate for 850°C deposited Si_3N_4 appears to be the decrease in refractive index between 900° and 850 C, which may be due to a change in either the density or composition, or both.

Etch rates of silicon oxynitride (as-deposited).—The etch rates of silicon oxynitride as a function of composition in 7:1 buffered HF are shown in Fig. 7 (Rand and Roberts' data are included for comparison). Figure 7 also includes data for oxynitride etch rates after annealing for 2 hr in N_2 at 1000 C. These data are discussed later under annealing. From Fig. 7, the etch rate of as-deposited films is a function of deposition temperature at a fixed composition, *i.e.*, higher etch rates are obtained for 900°C than for 1000°C deposited films. This is consistent with what we found for Si_3N_4 films. Films of identical refractive index and composition (*i.e.*, infrared spectra), deposited at 900° and 1000°C must also have identical density. This can be seen from Lorentz-Lorenz theory (11), which relates density of any material with its refractive index as shown in Eq. [7]

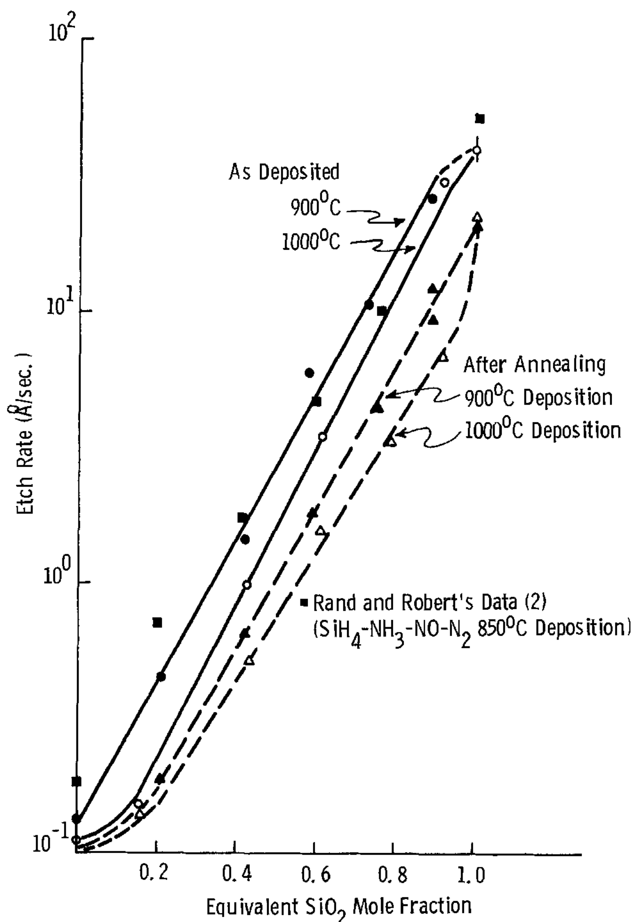

Fig. 7. Etch rate of silicon oxynitride in 7:1 BHF as a function of composition at two deposition temperatures, as-deposited, and after annealing in N_2 at 1000°C for 2 hr.

$$\rho = \frac{M}{A} \frac{n^2 - 1}{n^2 + 2} \quad [7]$$

where M is the molecular weight, n the refractive index, and A the molar refractivity. Since molar refractivity and molecular weight are a constant for a given material (11) the density is a function of the refractive index only (9). Therefore the difference in silicon oxynitride etch rates at two deposition temperatures (*i.e.*, 900° and 1000°C) for films with identical refractive indexes and composition (*i.e.*, infrared spectra) cannot be due to the difference in density.

The etch rates of silicon oxynitride films in refluxing H_3PO_4 (180°C) are presented in Fig. 8. Data are presented for 900° and 1000°C deposited films. Limited data are also shown for samples which were annealed in N_2 for 2 hr at 1000°C (this is discussed under Annealing). From the literature (2) we expected to find a linear relationship between etch rate and composition. This is not the case (Fig. 8). However, these data are consistent with earlier observations that films deposited at 1000°C etch at a slower rate than those deposited at 900°C.

The increase in etch rate with decreasing nitrogen content from 1 to 0.64 mole fraction of equivalent Si_3N_4 suggests that the presence of oxygen aids the dissolution of silicon nitride. This is consistent with the proposed mechanism of attack by hot H_3PO_4 acid on Si_3N_4 in the presence of H_2O (21). That is, if H_2O hydrolyzes (oxidizes) the Si_3N_4 to some form of hydrous silica and ammonia, the ammonia remaining in solution as ammonium phosphate, then the presence of oxygen in nitride films would increase the etch rate in hot phosphoric acid because it has partially accomplished what H_2O is supposed to achieve in the first place. However, as silicon oxynitride approaches pure SiO_2, the etch rate drops to approximately the etch rate of SiO_2 in refluxing H_3PO_4. Therefore the nonlinearity of etch rates as a function of composition can be explained by the mechanism proposed by Van Gelder and Hauser (21).

Etch rates of SiO_2 (as-deposited).—The etch rates of SiO_2 deposited from SiH_4-CO_2-H_2 in 7:1 BHF (23° ± 2°C) are shown in Fig. 7. The etch rate of these films was between 36 and 43 Å/sec independent of the deposition temperature in 900°-1000°C range. The measured density of these films was 2.15 ± 0.15 for 1000°C deposition and 2.15 ± 0.2 for 900°C deposition. The infrared spectra of these films was also identical within the error of measurement.

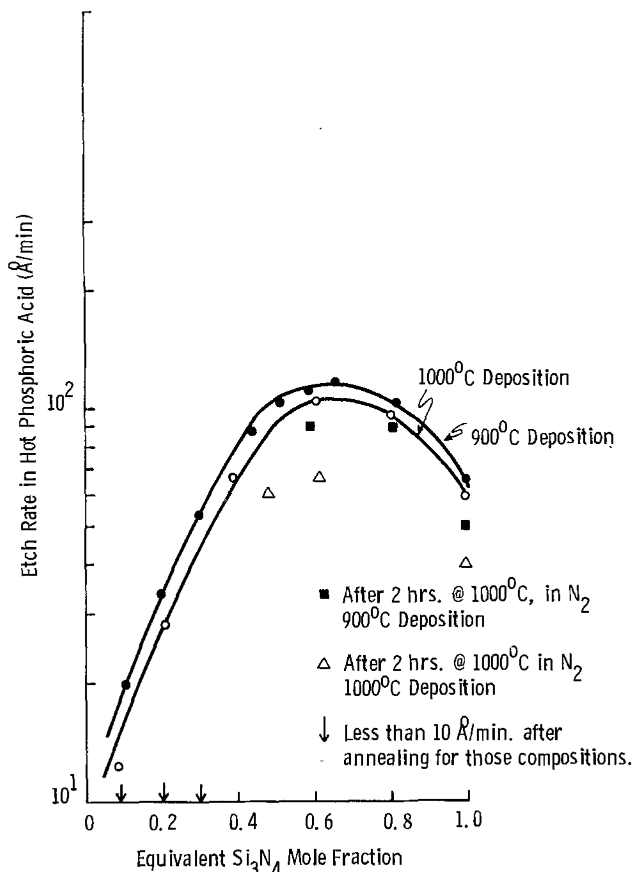

Fig. 8. Silicon oxynitride etch rate in hot refluxing phosphoric acid (180°C) as a function of composition at two deposition temperatures. Also shown is the etch rate after 2 hr annealing at 1000°C for 2 hr in N_2.

Effect of annealing.—The reason for undertaking the investigation of annealing on properties of $Si_lO_mN_p$ films was the experimental observation that the final refractive index (Fig. 4), during the oxidation barrier study, was always somewhat higher (*i.e.*, ~ 0.006 for most $Si_lO_mN_p$ films and ~ 0.008 for Si_3N_4) than the initial value. To determine whether the change in refractive index (and other properties) results from the oxidation or annealing, we carried out the investigation described below.

A single anneal temperature-time combination was first arrived at via preliminary experiments. SiO_2 and Si_3N_4 films (~ 1000Å) deposited both at 900° and 1000°C were annealed in N_2 for time-temperature combinations identical with those used for the barrier to oxidation study. The test samples were withdrawn at 15 min intervals and their refractive indexes and etch rates determined. It was found that these two properties showed no additional change (*i.e.*, "saturated") after a given amount of time at any temperature within the experimental range. The anneal temperature did not influence the saturation values; however, longer times were required to reach the saturation value for lower temperatures. Thus, based on the above experiments, 2 hr at 1000°C appeared to be a reasonable compromise for a temperature-time combination for the annealing experiment. Several samples of SiO_2, Si_3N_4, and $Si_lO_mN_p$ films deposited at both 900° and 1000°C were annealed for 2 hr at 1000°C. Along with investigating the effect of annealing on refractive index and etch rate, we have investigated the effect of annealing on film stress and for a limited number of samples on infrared spectra.

Annealing reduced the films thickness by ≤4% and, correspondingly, the refractive index increased by 0.002-0.015 depending on the composition of the film. The least change in thickness and refractive index occurred at equivalent SiO_2 mole fraction of 0.82 (RI ~ 1.57), *i.e.*, ~1% and 0.002, respectively, for 1000°C deposited films. Other $Si_lO_mN_p$ films deposited at 1000°C showed a decrease in thickness of 1.5-2.0% and refractive index increase of ~0.005. For 900°C deposited films, similar results were obtained except that the magnitude of the changes was somewhat larger; *i.e.*, for most $Si_lO_mN_p$ films, the thickness decreased by 1.5-2.3% and the refractive index increased by ~0.007. The Si_3N_4 films deposited at either temperature showed ~3% decrease in thickness and increase in refractive index of 0.008 ±0.002. The largest increase in refractive index occurred for SiO_2, *i.e.*, 0.012 ± 0.003 for either deposition temperature coupled with decrease in thickness of 3.7 ± 0.3%.

Silicon oxynitride film of thickness ≥4000Å and with a composition of ~25% equivalent Si_3N_4 showed microcracks similar to the ones reported in the literature for pure Si_3N_4 (14), after annealing at 1000°C for 2 hr. These cracks were not present in as-deposited films and they appeared in films after annealing irrespective of the deposition temperature. The stress values after annealing are for those films which did not crack.

For uncracked films, annealing increased the tensile stress in $Si_lO_mN_p$ and Si_3N_4 films and made the stress more compressive for SiO_2 films as shown in Fig. 9 and 10. Again, the least change is seen at equivalent Si_3N_4 mole fraction of ~0.18. However, after annealing, stress remains more tensile in 900°C deposited films than in 1000°C deposited films as shown in Fig. 11. The CVD SiO_2 films are an exception to this rule

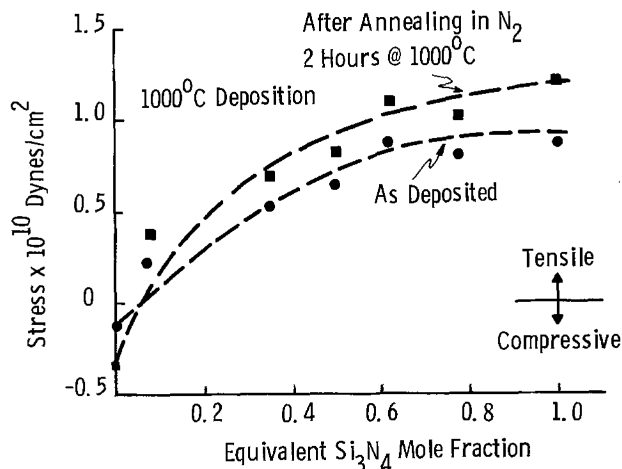

Fig. 9. Film stress as a function of composition and annealing, 1000°C deposited film.

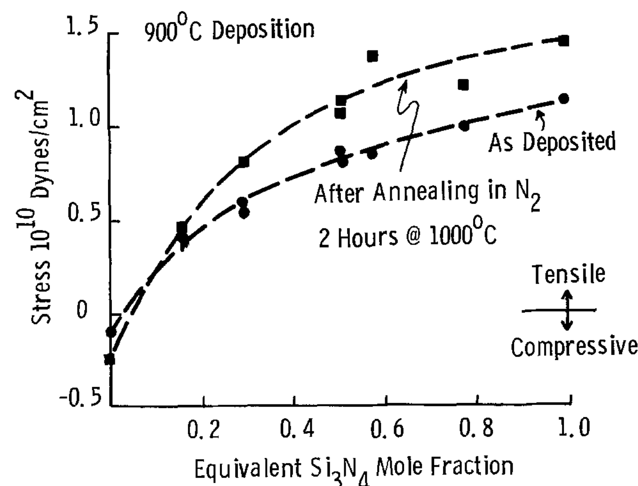

Fig. 10. Film stress as a function of composition and annealing, 900°C deposited film.

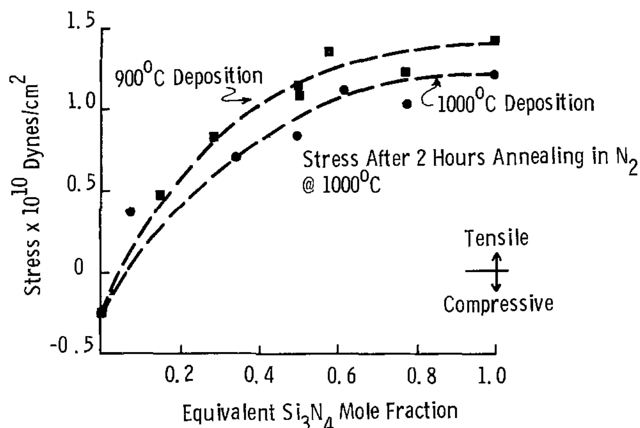

Fig. 11. Film stress as a function of composition after annealing for 900° and 1000°C deposited film.

as can be seen from Fig. 11. The stress in CVD SiO_2 appears to saturate at $\sim 2.5 \times 10^9$ dynes/cm^2 irrespective of the deposition temperature. This strongly suggests that the measured stress in CVD SiO_2 is almost entirely due to the thermal mismatch of the expansion coefficient of SiO_2 and Si. The same conclusion was reached by Jaccodine and Schlegel (19) about the nature of stresses in thermal SiO_2. The stress value for annealed CVD SiO_2 agrees very closely with the one reported for thermal SiO_2 (19).

The etch rates decreased as a result of annealing as shown in Fig. 7 and 8. The Si_3N_4 etch rates for 900° and 1000°C deposited films were nearly identical, within the error of measurement, after annealing in 7:1 buffered HF at 6.3 Å/min, whereas the etch rates of SiO_2 saturated at $\sim$1320 Å/min. However, the silicon oxynitride etch rates were not identical. The 900°C deposited films etched faster in 7:1 buffered HF (Fig. 7). In refluxing H_3PO_4, the Si_3N_4 etch rate of 900° and 1000°C deposited films were not identical either, as shown in Fig. 8. Again, 900°C deposited films etched faster. The infrared spectra of films which had been annealed showed small changes in the location of the major absorption maxima (*i.e.*, between 1100 and 800 cm^{-1}), usually within 5 cm^{-1} of the preannealed absorption maxima. The most striking feature of the postannealed infrared spectra for Si_3N_4 and $Si_lO_mN_p$ films was a near absence of the absorption band at $\sim$3380 cm^{-1}, indicating a marked decrease in the N-H species responsible for this absorption band. This is consistent with the observations of Rand and Roberts (2).

In a final experiment, several wafers of $Si_lO_mN_p$ (RI 1.7-1.9) and Si_3N_4 were broken in half. One half of these wafers was subjected to the annealing treatment (*i.e.*, 2 hr at 1000°C in N_2), and the other half to steam oxidation at 1000°C for 2 hr. The wafers subjected to oxidation were subsequently etched in 7:1 BHF in a sequence shown graphically in Fig. 4. The refractive indexes and etch rates of the unoxidized films were then compared with those of annealed samples. Both refractive indexes and etch rates were found to be identical (within the error of measurement) in the two cases. This last experiment showed to our satisfaction that densification and changes in other properties also occur during the process of steam oxidation.

Discussion

Using Rand and Roberts' (2) composition data, we have demonstrated the validity of two calculation procedures for determination of $Si_lO_mN_p$ composition. The novelty of these procedures lies in the fact that they are both written with the underlying assumption that $Si_lO_mN_p$ films are homogenous mixtures of Si_3N_4 and SiO_2. Silicon oxynitride films are clearly not mixtures for two reasons: (*i*) the infrared spectra do not show the separation of SiO_2 and Si_3N_4 absorption peaks, and (*ii*) the kinetic investigation by Gaind *et al.* (9) clearly shows that the deposition rate constants of $Si_lO_mN_p$ cannot be determined by assuming codeposition of SiO_2 and Si_3N_4. Thus neither the Lorentz-Lorenz theory nor the procedure of molar averaging based solely on the properties of SiO_2 and Si_3N_4 (*i.e.*, refractive index and density) should have yielded any meaningful results. However, the fact remains that by the use of these procedures, the composition of $Si_lO_mN_p$ is determined quite accurately. In view of this, we suggest that these procedures may also be applicable, despite their simplistic approach and assumptions, to other complex films such as aluminum oxynitrides.

The work in this paper was undertaken with an important application in mind, *i.e.*, the use of $Si_lO_mN_p$ films during the formation of recessed oxide isolation (ROX). The details of the ROX process have been published recently by Bassous *et al.* (23). The $Si_lO_mN_p$ can easily replace Si_3N_4 in the combination of thermal SiO_2 and Si_3N_4 during the formation of ROX isolation. For this application, one needs to know the barrier to oxidation for selected $Si_lO_mN_p$ composition. The knowledge of film stress is of significance since it probably determines the dislocation density in the silicon mesa covered by the selected film during the ROX formation (23). The etch rates of $Si_lO_mN_p$ in both BHF and hot phosphoric acid are needed for device application. The changes in these properties after annealing or ROX process are also important since subsequent device processing may require either selective or blanket etching of these films. All the above experimental data are available in this paper.

Besides the pragmatic aspects of this paper, some issues of fundamental importance need to be reviewed. For example, why is the etch rate of thin dielectric films a function of deposition temperature, especially when the infrared absorption spectra (structure) and the refractive indexes are identical? The concept of density difference alone, as an explanation of this etch rate difference as proposed by Chu *et al.* (22), and furthered by Brown *et al.* (1), is not consistent with the experimental data presented here, especially in the case of as-deposited Si_3N_4 films. Also, upon annealing, the change in density is $\sim$3% in most cases. Such a small change in density cannot explain the $\sim$50% change in etch rate. Therefore, there is no satisfactory explanation of changes in the etch rate of dielectric films like Si_3N_4 and $Si_lO_mN_p$ as a function of deposition temperature. It is suggested here that the change in film stress or the amount of H incorporated during film growth, when the deposition temperature is altered, may be some of the causes of observed differences in etch rate as a function of deposition temperature.

Some preliminary experiments (not reported in detail here) also suggest that in the case of Si_3N_4 the etch rate is a function of the NH_3 concentration used in the reactor during deposition, *i.e.*, etch rates increasing with increasing NH_3 concentration. Similar observations have been reported by others (24). The difference in Si_3N_4 etch rates observed in our studies and by Brown *et al.* (see Table II) may be due to the fact that Brown *et al.* used only SiH_4 and NH_3 (*i.e.*, no carrier gas) to deposit Si_3N_4. Therefore the NH_3 concentration in their case would be considerably higher than in our study, and hence the difference in observed etch rates. We have shown that the stresses in $Si_lO_mN_p$ and Si_3N_4 are tensile and that the stress measured at room temperature increases (becomes more tensile) with decreasing deposition temperature. Since the stress measured at room temperature is a sum of intrinsic and thermal stress, an increase in measured stress at room temperature implies that the thermal stress for Si_3N_4 and $Si_lO_mN_p$ is compressive

and that the intrinsic stress is tensile. Same conclusions were drawn by Tamura *et al.* (17) concerning the nature of stresses in Si_3N_4. The nonlinearity of $Si_lO_mN_p$ stress as a function of composition is not surprising since a linear stress *vs.* composition curve would have implied that $Si_lO_mN_p$ are codeposited SiO_2 and Si_3N_4. As already pointed out, $Si_lO_mN_p$ films are not codeposited SiO_2 and Si_3N_4 but are "polymers" of silicon, oxygen, and nitrogen (2, 9).

Summary and Conclusions

We have studied several important properties of silicon oxynitride ($Si_lO_mN_p$) films. The knowledge of these properties is especially useful if the $Si_lO_mN_p$ films are to be used in LSI processing for the formation of recessed oxide isolation (ROX). We have also investigated similar properties of Si_3N_4 and SiO_2 mainly to provide the end points of $Si_lO_mN_p$ series. In general, the physicochemical properties of $Si_lO_mN_p$ do not vary linearly as the composition is altered from SiO_2 to Si_3N_4. For example, the film stress is approximately a parabolic function of composition. The barriers to oxidation in steam, etch rate in 7:1 BHF, and hot refluxing H_3PO_4 all are nonlinear functions of composition. We have also investigated the effect of annealing on the above properties and find that the film stress increases and etch rate decreases for all $Si_lO_mN_p$ films. We have simultaneously studied the properties of $Si_lO_mN_p$ deposited at two deposition temperatures (*i.e.*, 900° and 1000°C) and find that both the stress and etch rates increase as the deposition temperature is reduced from 1000° to 900°C. The effect of deposition temperatures on $Si_lO_mN_p$ properties has not been previously reported. We have also shown that the composition of silicon oxynitride can be calculated most satisfactorily by either weight fraction averaging (Lorentz-Lorenz theory) or by mole fraction averaging knowing only the density and refractive index of Si_3N_4 and SiO_2. The novelty of the above calculation procedures is in the fact that both assume that $Si_lO_mN_p$ films are homogeneous mixtures of SiO_2 and Si_3N_4. It is clear that $Si_lO_mN_p$ are not mixtures but compounds (or polymers) of silicon, nitrogen, and oxygen. Thus the above procedures should not have yielded meaningful results. However, the fact remains that the results of these procedures are most satisfactory in arriving at the composition of $Si_lO_mN_p$ Finally, we have shown that the oxynitride films deposited from SiH_4-CO_2-NH_3-H_2 are in general identical in composition and properties with oxynitride films deposited from other chemical systems.

Acknowledgments

We are grateful to Dr. W. A. Pliskin for his help with infrared absorption data. Our thanks are due to Drs. L. A. Kasprzak and W. A. Pliskin for very stimulating discussions during the course of this work. We are deeply indebted to V. E. Elliott for sample preparations, T. Dicastro for measurements of film properties other than stress, and to C. Hoogendoorn for stress measurements.

Manuscript submitted Oct. 21, 1976; revised manuscript received Sept. 12, 1977.

Any discussion of this paper will appear in a Discussion Section to be published in the December 1978 JOURNAL. All discussions for the December 1978 Discussion Section should be submitted by Aug. 1, 1978.

Publication costs of this article were assisted by IBM Corporation.

REFERENCES

1. D. M. Brown, P. V. Gray, F. K. Heumann, H. R. Philipp, and E. A. Taft, *This Journal,* **115,** 311 (1968).
2. M. J. Rand and J. F. Roberts, *ibid.,* **120,** 446 (1973).
3. T. L. Chu, J. R. Szedon, and C. H. Lee, *ibid.,* **115,** 318 (1968).
4. N. C. Tombs, F. A. Sewell, Jr., and J. J. Comer, *ibid.,* **116,** 862 (1969).
5. Annual Report on Research Project, Ferranti Ltd., RP-1-55, AD-827049 (1967).
6. Y. I. Kol'tsov, N. G. Kol'tsov, G. I. Zhuravler, and I. V. Korober, *Izv. Akad, Nauk SSR,* **7,** 521 (1971).
7. C. M. Drum and M. J. Rand, *J. Appl. Phys.,* **39,** 4458 (1968).
8. P. F. Schmidt, M. J. Rand, J. P. Mitchell, and J. D. Ashner, *IEEE Trans. Nucl. Sci.,* **NS-16,** No. 6, 211 (1969).
9. A. K. Gaind, G. K. Ackerman, V. J. Lucarini, and R. L. Bratter, *This Journal,* **124,** 599 (1977).
10. A. K. Gaind, G. K. Ackerman, V. J. Lucarini, and R. L. Bratter, *ibid.,* **123,** 111 (1976).
11. M. Born and E. Wolf, "Principles of Optics," 5th ed., p. 87, Pergamon Press, New York (1975).
12. K. L. Chopra, S. K. Sharma, and V. N. Yadava, *Thin Solid Films,* **20,** 209 (1974).
13. R. Jacobson, in Proceedings of the Symposium on Optical Properties of Dielectric Films, Boston, Mass. (1968).
14. G. H. Schwuttke and J. K. Howard, *J. Appl. Phys.,* **39,** 3 (1968).
15. M. Tamura and H. Sunami, *Jpn J. Appl. Phys.,* **11,** 1097 (1972).
16. W. A. Westdorp and G. H. Schwuttke, *Thin Film Dielectrics,* 546 (1969).
17. V. E. Bean, P. S. Gleim, and R. L. Yeakley, *This Journal,* **114,** 733 (1967).
18. R. Renninger, *Phys. Lett.,* **1,** 104 (1962).
19. R. J. Jaccodine and W. A. Schlegel, *J. Appl. Phys.,* **37,** 2429 (1966).
20. H. Sunami, Y. Itoh, and K. Sato, *ibid.,* **41,** 5115 (1970).
21. W. Van Gelder and V. E. Hauser, *This Journal,* **114,** 869 (1967).
22. T. L. Chu, C. H. Lee, and G. A. Gruber, *ibid.,* **114,** 717 (1967).
23. E. Bassons, H. N. Yu, and Y. Maniscalco, *ibid.,* **123,** 1729 (1976).
24. V. Y. Doo, D. R. Kerr, and D. R. Nichols, *ibid.,* **115,** 61 (1968).

Kinetics of Lateral Autodoping in Silicon Epitaxy

G. R. Srinivasan

IBM System Products Division, East Fishkill Facility, Hopewell Junction, New York 12533

ABSTRACT

The kinetics of lateral autodoping in silicon epitaxy over silicon substrates containing localized arsenic diffusions was studied as a function of deposition temperature, growth rate, and preepitaxial heat cycling. The lateral autodoping increases either with the decrease of deposition temperature or with the increase in growth rate. The autodoping *vs.* temperature plot yields an enthalpy of ~ -64 kcal/mole for the process in the temperature range 950°-1100°C and at 0.08 μm/min growth rate. Thermodynamic calculations showed that the arsenic redistribution during lateral autodoping cannot be completely described by equilibria considerations and that an incorporation model based on dopant trapping during epitaxy is capable of explaining quantitatively the growth rate and temperature effects observed here. The effect of preepitaxial baking is such that the lateral autodoping decreases with the increase in either the bake temperature for constant bake time or the bake time for constant bake temperature. These results were analyzed in terms of the evaporation of arsenic during prebake and consequent surface depletion in the diffused regions. Arsenic evaporation velocity was calculated for several temperatures, which yields an activation energy of 5.16 eV for arsenic evaporation from (100) silicon surface in an H_2 flow ambient. This high activation barrier pertains to the evaporation of arsenic from the silicon surface through a nearly stagnant boundary layer in a typical CVD epitaxial system.

Autodoping refers to that part of the epitaxial doping which originates from the substrates during the deposition process. Lateral autodoping involves lateral transport of gaseous dopants which are released to the gas stream from the substrates during the preepitaxial and initial stages of the deposition. There have been several studies of autodoping [see Ref. (1) for a brief review] and yet very few of them (2-4) relate to the kinetics of lateral autodoping. We present here the details of such a study using silicon substrates which have localized arsenic diffusions of high surface concentration. Since the dopant diffusions are only at the top surface, contributions to autodoping from the bottom surface of the substrate are negligible. The use of substrates with localized diffusions allows a convenient way of separating the outdiffusion and lateral transport kinetics. Also, these cases are more typical of the processes involved in the fabrication of high performance bipolar integrated circuits.

Thermodynamics of Autodoping

Let us consider an intrinsic epitaxial process (*i.e.*, no external dopants added) during which a redistribution of the arsenic present in the substrate occurs. Just prior to the deposition, a certain concentration of arsenic exists in the vapor phase, and if a thermodynamic equilibrium were to exist between this vapor and the arsenic incorporated into the first few layers of the epitaxy, we can write

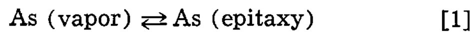

$$\text{As (vapor)} \rightleftarrows \text{As (epitaxy)} \qquad [1]$$

Assuming monatomic species and ideal gas behavior for the arsenic vapor, we obtain an expression for the equilibrium constant for this reaction as given by

$$k_{eq} = \frac{a_{As}}{p_{As}} \qquad [2]$$

where a_{As} is the activity of arsenic in the silicon epitaxial solid solution and p_{As} is the partial pressure of the arsenic vapor. If we now invoke Henry's law for the low arsenic concentrations incorporated into the epitaxy we can write for the dissolution process, assuming no kinetic limitation

$$a_{As} = k' N_{As} \qquad [3]$$

where N_{As} is the concentration of arsenic in the epitaxial solid solution and k' is the proportionality constant. The assumption of Henry's law is valid up to arsenic concentrations of 10^{18} cm^{-3} at typical epitaxial temperatures as pointed out by Rai-Choudhury and Salkovitz (5). The equilibrium constant is, thus

$$k_{eq} = \frac{k' N_{As}}{p_{As}} \qquad [4]$$

The enthalpy change for the above process is given by

$$\frac{-\Delta H}{R} = \frac{d \ln k_{eq}}{d(1/T)} \qquad [5]$$

where R is the gas constant and T is the growth temperature. If we define the standard state of arsenic in the epitaxial solid solution as an infinitely dilute solution of arsenic in silicon (*i.e.*, $k' = 1$), we have from Eq. [4] and [5]

$$\frac{-\Delta H}{R} = \frac{d \ln N_{As}}{d(1/T)} - \frac{d \ln p_{As}}{d(1/T)} \qquad [6]$$

One can also write the enthalpy change for the equilibrium reaction of Eq. [1] as

$$\begin{aligned}\Delta H &= \overline{H}_{As(epi)} - \overline{H}_{As(vap)} \\ &= \{\overline{H}_{As(epi)} - \overline{H}_{As(pure\ solid)}\} + \{\overline{H}_{As(pure\ solid)} - \overline{H}_{As(vap)}\} \\ &= \Delta H_s + \Delta H_c\end{aligned}$$

where ΔH_c is the heat of condensation and ΔH_s is the heat of solution.

Rearranging Eq. [6], we obtain the following expression for the enthalpy change associated with the formation of the epitaxial solid solution of arsenic in silicon

$$\Delta H_s = \frac{R d \ln p_{As}}{d(1/T)} - \frac{R d \ln N_{As}}{d(1/T)} - \Delta H_c \qquad [7]$$

Equation [7] can be used to evaluate ΔH_s from autodoping experiments in which N_{As} is determined for various epitaxial growth temperatures and from a knowledge of the temperature variation of the arsenic vapor pressure in equilibrium with the solid solution and from the heat of condensation of arsenic.

In the above derivation, we have assumed monatomic arsenic in the vapor, and an equivalent expression may

be obtained for any other polyatomic species. The validity of Eq. [7] assumes, of course, an equilibration between the vaporized arsenic and the arsenic incorporated into the initial layers of the epitaxy.

Arsenic Evaporation Kinetics

In a typical CVD epitaxial deposition process, the substrates are subjected to a preepitaxial bake cycle in order to establish stabilized thermal and gas flow conditions prior to the deposition. During this prebake, some of the dopant impurities evaporate from the substrates; and since autodoping mainly arises from these substrate sources, changes in the prebake cycle are expected to cause changes in autodoping. In order to interpret these prebake effects, we developed a theory based on the rate limitation for the evaporation of arsenic from the silicon substrate surface. An expression is derived here which relates the lateral autodoping concentration to the arsenic evaporation velocity, arsenic diffusivity in silicon, and prebake time.

Theory of surface-limited evaporation.—One-dimensional Fick's law solution for the case of dopant evaporation from homogeneously doped crystal into vacuum yields, in the absence of any surface rate limitation, an error function distribution of the dopant in the crystal with zero surface concentration at all times. If a kinetic barrier at the surface were to exist for the evaporation process, however, the solution to the diffusion equation becomes analogous to that for the heat flow with the radiation boundary condition and yields a finite buildup of the dopant at the surface. Miller and Smits (6) have demonstrated this to be the case for the evaporation of dopants from Ge. More recent studies (7, 8) show similar results for the case of dopant evaporation from silicon. The solution for these cases takes the form

$$\frac{C(x,t)}{C_o} = \text{erf}\left(\frac{x}{2\sqrt{Dt}}\right) + \left\{ \exp\left(\frac{K^2t}{D} + K\frac{x}{D}\right) \bullet \text{erfc}\left(\frac{x}{2\sqrt{Dt}} + K\sqrt{\frac{t}{D}}\right)\right\} \quad [8]$$

where $C(x, t)$ is the dopant concentration at time t from the start of evaporation and depth x from the surface of the crystal, C_o is the uniform initial concentration, D is the dopant diffusivity in the crystal, and K is a mass transfer coefficient which has the dimension of velocity and is referred to as evaporation velocity. As $K \to \infty$ the rate-limitation case reduces to one of erf distribution.

For the case of inhomogeneously doped crystal, such as in the case of substrates with dopant diffusions, the one-dimensional solution is given by (9)

$$C(x,t) = \frac{1}{2\sqrt{\pi DT}} \int_0^\infty f(x')\,[\exp\{-(x-x')^2/4Dt\} + \exp\{-(x+x')^2/4Dt\}]dx' - (K/D)\int_0^\infty f(x') \exp\{(K^2t/D) + K(x+x')/D\} \bullet \text{erfc}\{(x+x')/2\sqrt{Dt} + K\sqrt{t/D}\}dx' \quad [9]$$

where $f(x')$ represents the initial dopant distribution prior to evaporation. Equation [8] is a particular case of the above solution for which the initial distribution $f(x')$ is a constant.

For the case of arsenic diffusion used in this study, the initial distribution $f(x')$ of arsenic diffusion in the p-type substrate may be approximated by

$$f(x') = \begin{cases} C_o & \text{for} \quad 0 < x' < x_j \\ 0 & \text{for} \quad x' > x_j \end{cases} \quad [10]$$

where x_j is the junction depth and C_o is the arsenic surface concentration prior to evaporation.

Substituting Eq. [10] in Eq. [9] one obtains for the surface concentration ($x = 0$)

$$\frac{C(0,t)}{C_o} = I_1 - I_2 \quad [10a]$$

where $I_1 = \text{erf}\, x_j/2\sqrt{Dt}$

and

$$I_2 = \frac{K}{D}\int_0^{x_j} \exp\left\{\frac{K^2t}{D} + K\frac{x'}{D}\right\} \left[\text{erfc}\left\{\frac{x'}{2\sqrt{Dt}} + K\sqrt{\frac{t}{D}}\right\}\right]dx'$$

With proper change of variables and integrating by parts, we obtain

$$I_2 = \text{erf}\frac{x_j}{2\sqrt{Dt}} + e^{\frac{K^2t}{D}}\left\{ e^{\frac{Kx_j}{D}} \text{erfc}\left(\frac{x_j}{2\sqrt{Dt}} + K\sqrt{\frac{t}{D}}\right) - \text{erfc}\,K\sqrt{\frac{t}{D}}\right\}$$

Substituting this in Eq. [10a], we get

$$C(0,t)/C_o = \exp\,(K^2t/D)\{\text{erfc}\,K\sqrt{t/D} - \exp(Kx_j/D)\,[\text{erfc}\,(x_j/2\sqrt{Dt} + K\sqrt{t/D})]\} \quad [11]$$

Equation [11] describes the variation of arsenic surface concentration as a function of evaporation time for substrates with initial arsenic diffusion given by Eq. [10]. For the case of evaporation from homogeneously doped substrates for which $x_j \to \infty$, the second term in Eq. [11] approaches zero, so that Eq. [11] reduces to Eq. [8] with $x = 0$. Further, since $\text{erfc}(x_j/2\sqrt{Dt})$ converges to zero for $x_j \gtrsim 4\sqrt{Dt}$, the evaporation from substrates with arsenic diffusions from the top surface becomes equivalent to that from homogeneously doped wafers, provided the evaporation conditions are chosen such that $4\sqrt{Dt} \lesssim x_j$. This condition is satisfied for the experiments reported here, and thus, the variation of arsenic concentration at the substrate surface with evaporation time (bake time) as given by the first term in Eq. [11] is

$$C(0,t) = C_o\{\exp\,(\beta^2 t)\} \bullet \text{erfc}\,(\beta t^{1/2}) \quad [12]$$

where $\beta(T) = K(T)/\sqrt{D}(T)$.

If we assume (6, 7) an Arrhenius behavior for both K and D, such that

$$D(T) = D_o \exp\,(-E_D/kT)$$

and

$$K(T) = K_o \exp\,(-E_K/kT)$$

where E_D and E_K are the activation energy for arsenic diffusion in and evaporation from the silicon substrate, respectively, and k is the Boltzmann constant and T is the evaporation temperature, we can write

$$\beta(T) = \beta_o \exp\,(-\Delta E/kT)$$

where $\Delta E = E_K - E_D/2$. Thus, by measuring the surface concentration as a function of evaporation time for constant temperature or as a function of evaporation temperature for constant time, one can determine β and ΔE. Evaporation velocity K and activation barrier to evaporation E_K can then be evaluated from a knowledge of $D(T)$.

Preepitaxial bake cycle and lateral autodoping.—As mentioned earlier, some of the dopant impurities in the substrate wafers evaporate during the prebake cycle in an epitaxial run. Part of this impurity is carried away in the flow stream, and a part gets redeposited on

the substrate, thereby causing lateral autodoping. Skelly and Adams (10) and Shachnev (11) have shown that the level of autodoping in the epitaxy is directly proportional to the substrate dopant concentration. Thus, changes in the lateral autodoping due to changes in the prebake cycle should reflect the changes in the surface concentration prior to epitaxial deposition. Equation [12] can now be rewritten in terms of lateral autodoping peak concentration, C_{max}, as

$$C_{max}(T, t) = Ae^{\beta^2 t} \bullet \text{erfc}(\beta t^{1/2}) \quad [13]$$

where A is a constant of proportionality which is constant for identical postbake epitaxial deposition conditions. T and t are bake temperature and time, respectively. Since C_{max} is expected to vary with distance from the diffused area, applicability of Eq. [13] requires that lateral autodoping peak concentration be measured at the same distance from the arsenic diffusion and in the same direction relative to the gas flow in all the experiments.

Experimental

The substrates used in this study were p^{-}-silicon wafers (10-20 Ωcm) of (100) orientation. Arsenic diffusions were made on these substrates to cover 20% area in five square regions for the growth temperature studies and 2.5% area in four square regions for the prebake studies. The surface concentration C_o of arsenic over the diffusion was $\sim 1.5 \times 10^{21}$ cm^{-3} and $x_j \sim 1$ μm. (The concentration profile was made using Rutherford backscattering technique.)

All epitaxial depositions were made in an rf heated horizontal reactor with a 3°-inclined, silicon-carbide coated graphite susceptor. The depositions were ~ 2 μm thick and were intrinsic; *i.e.*, no external doping was used. An H_2 carrier gas with a linear flow velocity of ~ 10.5 cm/sec (20.6 liters/min flow rate) was used. $SiCl_4$ flow rates were adjusted to yield different growth rates used in this study; and the growth rates varied linearly with $SiCl_4$ flow rates at all the deposition temperatures used here. A log growth rate *vs.* reciprocal deposition temperature gave a nearly linear region between 950°-1100°C with a slope corresponding to ~ 30 kcal/mole, and a flattening beyond that temperature. Substrate temperatures were read optically with appropriate emissivity corrections including those due to quartz wall absorption.

In the prebake experiments, the deposition conditions were held identical, varying only the preepitaxial bake cycle. In the bake time experiments, the bake temperature and the deposition temperature were chosen to be the same (*i.e.*, 1150°C), and the baketime was varied from 2 min to 2 hr. The growth rate was 0.25 μm/min. In the bake temperature experiments, all depositions were made at 1000°C, which is lower than or equal to the bake temperatures used (1000°-1200°C). Thus, any contribution to evaporation during reequilibration to the deposition temperature was considered to be small. Further, a bake time of 1 hr used in these experiments was believed to be long enough to ignore the transient effects during heat up and cool down cycles. The depositions were made at 0.25 μm/min.

Lateral autodoping was measured by the spreading resistance technique, in which the vertical depth profiles of arsenic in the epitaxy were determined on a beveled surface. The vertical profiles were made at 0.1 mm away from the diffusion square, and the profiles were corrected using a power law interpolation technique (12).

It should be pointed out that the spreading resistance measurements give the donor concentration at room temperature through Irvin's curve. This concentration will be different from the neutral arsenic present at the epitaxial temperatures, and the determination of one from the other involves a model-dependent calculation. In this present study we ignore this difference and intend to present a refinement of the calculation at a later time.

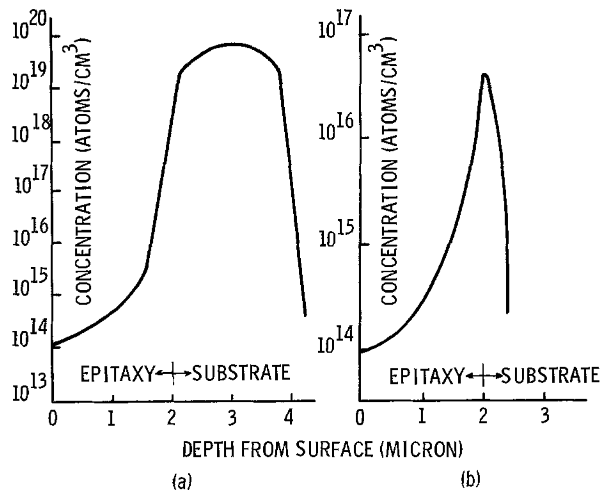

Fig. 1. Vertical depth profiles of arsenic obtained by the spreading resistance technique (a) over diffused region, (b) 0.1 mm away from diffused region. Deposition temperature 1100°C. Growth rate 0.08 μm/min.

Results

Figure 1 shows typical arsenic vertical depth profiles obtained from the corrected spreading resistance data. The vertical profile over the diffused region is shown in Fig. 1(a) and the vertical profile over the nondiffused region (0.1 mm away from the diffused area) is shown in Fig. 1(b). These results are from an 1100°C $SiCl_4$ deposition run for a growth rate of 0.08 μm/min. From Fig. 1(a), it can be seen that the arsenic concentration falls off very rapidly ($\sim 10^8$/cm^4) within the initial layers of the epitaxy and approaches a level of $\sim 10^{14}$/cm^3 toward the end of the epitaxial run, which is typical of the background dopant level in the system. The initial decrease in concentration can be explained by the solid diffusion of arsenic in silicon (13).

Figure 1(b) shows the lateral autodoping effects caused by the transport of vaporized arsenic to regions far removed from the diffused area. A detailed analysis of this lateral distribution as a function of distance from the diffused area will be reported elsewhere (14). Examination of Fig. 1(b) shows that the lateral autodoping reaches a maximum at the initial stages of the epitaxial growth and falls off rapidly in a manner similar to that over the diffused area. In fact, both the on- and off-diffusion profiles superimpose well, once a thickness of a few hundred angstroms of the epitaxy is reached. We summarize these findings in Fig. 2, which shows that out-diffusion

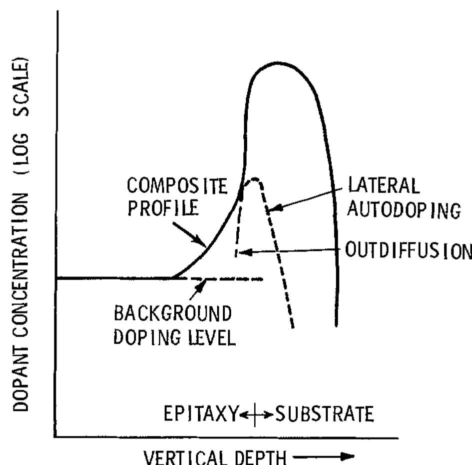

Fig. 2. Vertical profile (schematic) over diffused region

effects predominate in the initial portions of the dopant profiles. Thus, in order to study lateral (*i.e.*, gas phase) autodoping, it is desirable to separate out the out-diffusion effects by obtaining autodoping profiles from nondoped areas such as typified in Fig. 1(b).

Lateral autodoping can be characterized by the maximum concentration, C_{max}, in the vertical profiles over the nondiffused region. We also find that the integrated area under the autodoping profile is an equally valid feature of autodoping, since both this area and the peak concentration vary similarly with the process parameters.

Figure 3 shows the effect of deposition temperature and epitaxial growth rate on the arsenic peak concentration, C_{max}, in the lateral autodoping profiles for the $SiCl_4$ depositions. These results show that (*i*) lateral autodoping increases with decrease in deposition temperature for the same growth rate, (*ii*) lateral autodoping increases with increase in growth rate for the same deposition temperature, and (*iii*) the effect of growth rate is more pronounced at lower deposition temperatures. The 0.25 μm/min growth rate data shows a maximum lateral autodoping at 1000°C deposition temperature. It was also found that, when depositions were made using silane, the autodoping *vs.* temperature curve had nearly identical slope for the 0.08 μm/min growth rate to that of $SiCl_4$ deposition between 950° and 1100°C.

The effect of preepitaxial bake time and bake temperature variations are shown in Fig. 4 and 5. The lateral autodoping decreases by about a factor of 5 when the bake time is increased from 2 min to 2 hr at 1150°C. The solid line is the least squares fit of the data to Eq. [13] which gave the following parameters: $A = 5.03 \times 10^{16}$ cm^{-3} and $\beta = 0.02$ sec$^{-1/2}$.

The effect of bake temperature variation is shown in Fig. 5 as a log C_{max} *vs.* 1/T plot for 1 hr bake time and 0.25 μm/min growth rate depositions. The autodoping increases by about a factor of 4 when the bake temperature is decreased from 1200° to 1000°C. The solid line represents the fit of the data to Eq. [13] using $\beta = 0.02$ at 1150°C as obtained from the bake time experiments. The results of this fit are: $A = 8.834 \times 10^{16}$ cm^{-3} and $\beta = 1.291 \times 10^9 \exp(-3.06/kT)$ sec$^{-1/2}$.

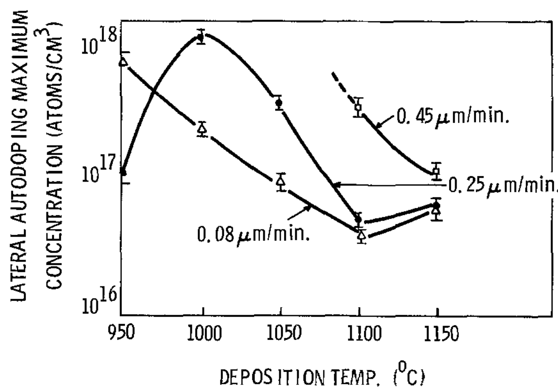

Fig. 3. Effect of growth rate and temperature on lateral autodoping

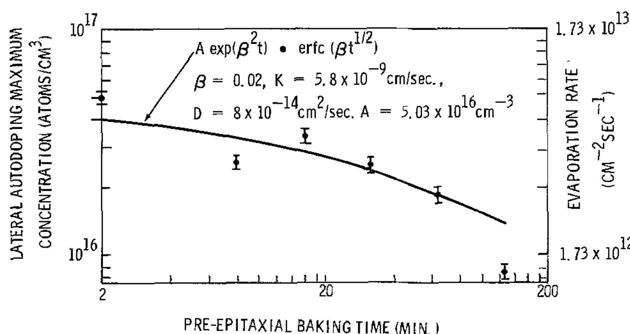

Fig. 4. Effect of bake time variations on arsenic autodoping. Bake temperature 1150°C. Growth rate 0.25 μm/min.

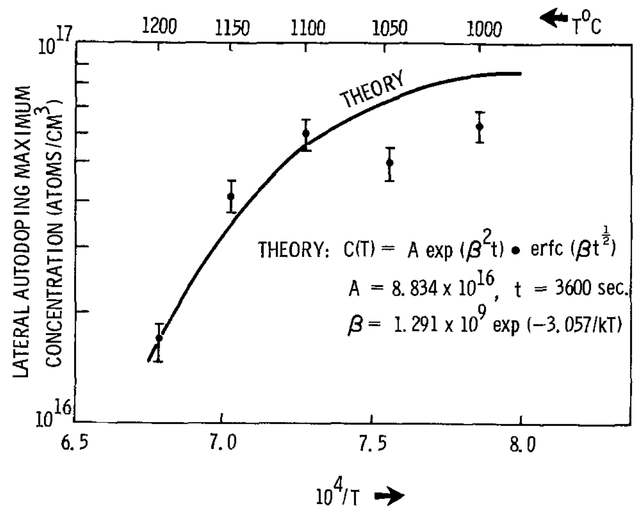

Fig. 5. Effect of preepitaxial bake temperature variations on arsenic autodoping. Bake time 1 hr. Deposition temperature 1000°C. Growth rate 0.25 μm/min.

Discussion

Temperature dependence of lateral autodoping.—In an earlier section we developed an expression (see Eq. [7]) for the enthalpy associated with the formation of the arsenic solid solution in epitaxial silicon, assuming an equilibrium reaction for arsenic incorporation. To evaluate this enthalpy, ΔH_s, we plot the 0.08 μm/min growth rate data in an enthalpy plot as shown in Fig. 6. We chose this growth rate data for the evaluation of ΔH_s for the following reasons: (*i*) The growth rate was considered to be low enough to approach thermodynamic conditions, should they exist in autodoping, (*ii*) silane depositions also exhibited the same linearity and slope as in Fig. 6 under identical growth conditions, so that any complicating halide etching effects in $SiCl_4$ deposition can be neglected, and (*iii*) linearity in the enthalpy plot suggests a single operating mechanism for the incorporation process. The slope of the enthalpy plot yields

$$R \frac{d \ln N_{As}}{d(1/T)} \sim 64 \text{ kcal/mole}$$

In order to evaluate ΔH_s using Eq. [7], it is necessary to know the temperature dependence of the arsenic partial pressure in equilibrium with arsenic solid solution in silicon. Sandhu and Lyons (15) have obtained such data, and their results show that the enthalpy of the process, $-R \frac{d \ln p_{As}}{d(1/T)}$, is 53.52 kcal/mole in the temperature range 800°-1050°C. Using this value and $\Delta H_c = -72.3$ kcal/mole obtained from Honig and

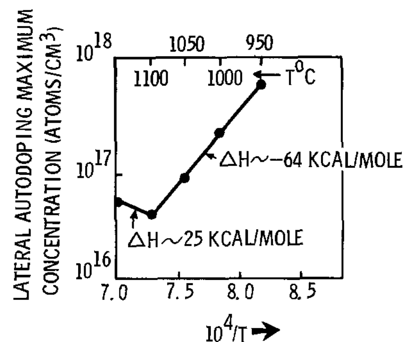

Fig. 6. Temperature dependence of arsenic autodoping. Growth rate 0.08 μm/min.

Kramer's compilation (16) for the heat of condensation of monatomic arsenic, we obtain $\Delta H_s = -45.2$ kcal/mole from Eq. [7].

Rai-Choudhury and Salkovitz (5) have obtained from their doping experiments $\Delta H_s \sim 22.6$ kcal/mole. Their analysis was, however, based on diatomic arsenic in the vapor. If we use a similar argument and assume that arsenic dissolves atomically in epitaxial silicon, we can write

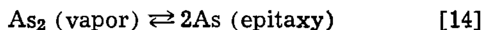

$$As_2 \text{ (vapor)} \rightleftarrows 2As \text{ (epitaxy)} \quad [14]$$

for the incorporation reaction.

The heat of solution for the above reaction is now given by

$$\Delta H_s = \frac{R}{2}\frac{d \ln p_{As2}}{d(1/T)} - R\frac{d \ln N_{As}}{d(1/T)} - \Delta H_c' \quad [15]$$

where $\Delta H_c'$ is the heat of condensation for diatomic arsenic. Taking $\Delta H_c' = -53.1$ kcal/mole again from literature (16), we obtain $\Delta H_s' = -37.7$ kcal/mole from Eq. [15]. (Note that we use 53.52 kcal/mole for the enthalpy of the arsenic equilibration for the diatomic species as well, since the measurement of total arsenic vapor pressure made in these experiments (15) refers to whichever predominant species that is present.) Thus, the heat of solution obtained from autodoping experiments for either the monatomic or the diatomic arsenic species turns out to be a negative value, in contrast with Rai-Choudhury and Salkovitz's value of $+22.6$ kcal/mole. Further, a calculation (5) based on Weiser's model (17) also yields a positive value for ΔH_s of $\sim$7 kcal/mole. The small positive value of ΔH_s is also consistent with the calculations of arsenic activity coefficients in silicon as a function of temperature (18).

In view of the above disagreements with the heat of solution evaluations, we conclude that the arsenic autodoping cannot be described adequately by equilibria considerations alone. It seems likely that other kinetic limitations, such as impurity trapping during the epitaxial growth, play a significant role in the autodoping phenomena.

Growth rate dependence of lateral autodoping.—Since our experiments are in a kinetic region of interface controlled epitaxial growth, we expect the mass transfer limitations to play no important role in the autodoping kinetics. Yet, we see from Fig. 3 that the growth rate has a significant effect on autodoping, especially at lower deposition temperatures.

The theory of Hall (19), which was later extended by Holmes (20), takes into account the effect of growth rate on the solute distribution kinetics in melt-grown crystals. They show that the excess solute concentration in the bulk when solute trapping has occurred is a function of growth rate as given by

$$C_{xs}^* = C_{xs} \exp(-V_i/V) \quad [16]$$

where $C_{xs} = C_s - C_b$ is the equilibrium excess concentration at the surface, C_s and C_b being the equilibrium solute concentration at the surface and in the bulk, respectively. $C_{xs}^* = C_b^* - C_b$ is the excess solute concentration in the bulk due to trapping, where C_b^* is the nonequilibrium bulk concentration due to trapping. V is the growth rate of the crystal, and V_i is the growth velocity for which the relaxation time for diffusion in the interface and the time for the growth of one monolayer are about the same. Thus, Hall's theory predicts that the bulk concentration due to trapping varies from bulk equilibrium concentration at very low growth rates to surface equilibrium concentration at very high growth rates. It should be pointed out here that the deposition temperature should be high enough to permit a diffusional exchange between the buried layer and the growing surface, otherwise the initially adsorbed layer would remain at the surface concentration level for all growth rates.

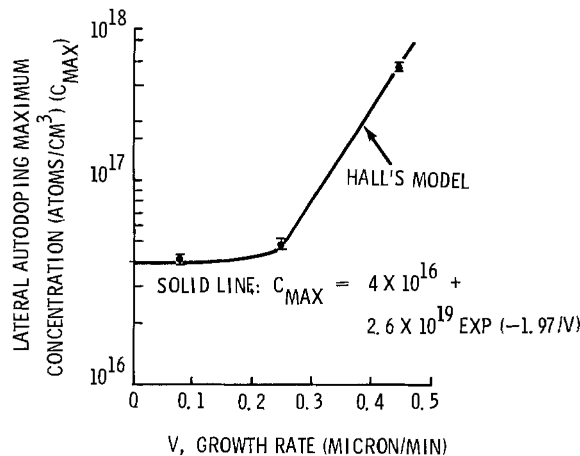

Fig 7. Effect of growth rate on lateral autodoping. Deposition temperature 1100°C.

In view of above considerations. we replot in Fig. 7 the 1100°C autodoping data as log C_{max} *vs.* growth rate. (The 1150°C data has not been used in this analysis since it represents a different slope in the enthalpy plot, which may imply a change in the incorporation mechanism. We take $C_b^* = C_{max}$ to represent the nonequilibrium arsenic concentration.) The data indicate a linear portion for low growth rates up to $\sim$0.25 μ/min with a slope which changes to a higher value at higher growth rates.

Extrapolating our data in Fig. 7 to zero growth rate yields $C_b \approx 4 \times 10^{16}$ cm^{-3}, and if we apply the data to Eq. [16], we obtain $V_i = 1.97$ μm/min and $C_s \approx 2.6 \times 10^{19}$ cm^{-3}. The solid line in Fig. 7 represents the equation: $C_{max} = 4 \times 10^{16} + 2.6 \times 10^{19} \exp(-1.97/V)$. Thus, Hall's theory indicates that the equilibrium surface concentration of arsenic would be $\sim$700 times that in the bulk. This high surface concentration is not untypical of the equilibrium surface segregation observed in many systems (21). Further, taking the relaxation time for diffusion or arsenic at 1100°C to be $\sim$0.07 sec ($t \sim x^2/D$, where $x \sim 4$Å for one monolayer of silicon), we estimate the effective thickness through which the trapped arsenic atoms have to diffuse to exchange with the surface to be $\simeq 0.07V_i$; *i.e.*, $\sim$5 atom layers. The range of this dynamic exchange is about the same as that found by Bloem for phosphorus incorporation in epitaxial silicon (22).

Preepitaxial bake effects on lateral autodoping.—The bake time data yield $\beta = K/\sqrt{D} = 0.02$ sec$^{-1/2}$. Taking $D = 8 \times 10^{-14}$ cm^2/sec for bake temperature of 1150°C from Masters and Fairfield data (23), we obtain the evaporation velocity, K, of arsenic from (100) silicon surface at 1150°C in an H_2 flow ambient to be 5.8×10^{-9} cm/sec. The rate of arsenic evaporation, r, varies with bake time as given by

$$r = KC(o,t) \quad [17]$$

where $C(o,t)$ is the surface concentration of arsenic in the diffused region. From Eq. [12], [13], and [17] we obtain

$$r = \left(\frac{KC_o}{A}\right) C_{max}(T,t) \quad [18]$$

Substituting the values for K and A obtained in the bake experiments, and taking $C_o \simeq 1.5 \times 10^{21}$ cm^{-3}, we obtain the rate of arsenic evaporation from the silicon substrates during prebake to be

$$r_{1150} = 1.73 \times 10^{-4} C_{max}(t) \text{ cm}^{-2}\text{sec}^{-1} \quad [19]$$

where $C_{max}(t)$ is shown in Fig. 4. Since $r \propto C_{max}$, Fig. 4 describes also the variation of arsenic evaporation rate

with bake time at 1150°C. The arsenic evaporation rate varies in present autodoping experiments from 8.75×10^{12} cm^{-2} sec^{-1} at the beginning of the prebake to 1.47×10^{12} cm^{-2} sec^{-1} at the end of 2 hr prebake cycle. This evaporation of arsenic prior to the beginning of the deposition cycle could amount to a substantial depletion of the diffusions in a typical integrated circuit fabrication process.

Arsenic evaporation velocity.—The bake temperature data shown in Fig. 5 gave $\beta = K/\sqrt{D} = 1.291 \times 10^9 \exp(-3.06/kT)$. Using $D = 60 \exp(-4.2/kT)$ for arsenic diffusivity (23), we obtain the following expression for the arsenic evaporation velocity from (100) silicon surface in an H_2 flow ambient

$$K = 1.0 \times 10^{10} \exp(-5.157/kT) \text{ cm sec}^{-1}$$

The evaporation velocity varies from 2.3×10^{-8} cm sec^{-1} at 1200°C to 3.8×10^{-11} cm sec^{-1} at 1000°C. Table I shows this data together with the evaporation velocity values determined by Arai and Terunuma (8) in their vacuum evaporation experiments. Their values are 40-80% lower than our present values, and they obtained an activation energy of 2.92 eV as compared to our value of 5.16 eV. This difference may be related to a possible existence of a stagnant boundary layer (24) in the epitaxial prebake experiments, which would not be the case for the dynamic vacuum evaporation experiments used by Arai and Terunuma. However, in a separate experiment (25), we determined the evaporation velocity of arsenic from (111) surface of a silicon substrate under static vacuum, and this experiment also indicated a higher velocity than that obtained by Arai and Terunuma. It is also possible that at the high C_0 used here nonlinear effects in the diffusivity need to be considered when solving the diffusion equation.

In order to further verify the proportionality assumed in deriving Eq. [13] between the lateral autodoping and the arsenic concentration over the diffusion, we have plotted the sheet (spreading) resistance values, both on and off diffused regions, as a function of bake temperature in Fig. 8. The figure clearly demonstrates a similar variation for these quantities, thus justifying the above assumption.

Conclusions

Kinetics of lateral autodoping is determined, among other factors, by (*i*) preepitaxial bake treatments which determine, in turn, the dopant evaporation kinetics in the epitaxial process, and (*ii*) deposition parameters, such as growth rate and temperature, which imply the existence of nonequilibrium situations in the dopant incorporation process.

Acknowledgments

I would like to express my appreciation to Mr. R. Hoffman for epitaxial depositions, to Mr. W. Patterson for spreading resistance measurements, and to Dr. H. B. Pogge for introducing me to this subject. I would also like to thank Dr. J. Bloem for a critical review of the manuscript.

Manuscript submitted May 11, 1976; revised manuscript received Aug. 10, 1977. This was Paper 191 presented at the Philadelphia, Pennsylvania, Meeting of the Society, May 8-13, 1977.

Table I. Temperature variation of arsenic evaporation velocity

Temp (°C)	Evaporation velocity (cm/sec): Present results of prebake experiments	Arai and Terunuma's results (vacuum evaporation)
1000	4.12×10^{-11}	—
1050	2.42×10^{-10}	—
1100	1.26×10^{-9}	6.0×10^{-10}
1150	5.80×10^{-9}	1.42×10^{-9}
1200	2.41×10^{-8}	3.19×10^{-9}

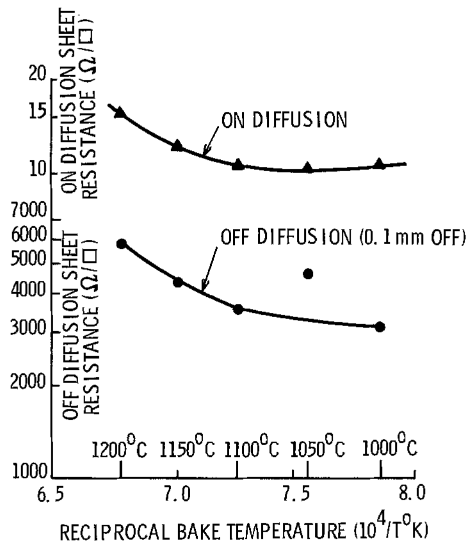

Fig. 8. Bake temperature dependence of sheet resistance

Any discussion of this paper will appear in a Discussion Section to be published in the December 1978 JOURNAL. All discussions for the December 1978 Discussion Section should be submitted by Aug. 1, 1978.

Publication costs of this article were assisted by IBM Corporation.

REFERENCES

1. P. H. Langer and J. I. Goldstein, *This Journal*, **121**, 563 (1974).
2. H. B. Pogge, D. W. Boss, and E. Ebert, in "Fifth International Conference on Chemical Vapor Deposition," J. M. Blocher, H. E. Hintermann, and L. H. Hall, Editors, p. 767, The Electrochemical Society Softbound Symposium Series, Princeton, N.J. (1970).
3. G. Mitsuhashi, *NEC Res. Dev.*, **36**, 68 (1975).
4. L. D. Dyer and F. Padovani, "Semiconductor Silicon 1973," H. R. Huff and R. R. Burgess, Editors, p. 201, The Electrochemical Society Softbound Symposium Series, Princeton, N.J. (1973).
5. P. Rai-Choudhury and E. I. Salkovitz, *J. Cryst. Growth*, **7**, 353 (1970).
6. R. C. Miller and F. M. Smits. *Phys. Rev.*, **107**, 65 (1957).
7. R. N. Ghoshtagore, *Solid State Electron.*, **15**, 1113 (1972).
8. E. Arai and Y. Terunuma, *Jpn. J. Appl. Phys.*, **9**, 410 (1970).
9. H. S. Carslaw and J. C. Jaeger, "Conduction of Heat in Solids," p. 359, Clarendon Press, Oxford (1948).
10. G. Skelly and H. C. Adams, *This Journal*, **120**, 116 (1973).
11. V. I. Shachnev, *Inorg. Mater.*, **10**, 176 (1974).
12. S. M. Hu, *Solid State Electron.*, **15**, 809 (1972); *ibid.*, **16**, 432 (1973).
13. A. S. Grove, A. Roder, and C. T. Sah, *J. Appl. Phys.*, **36**, 802 (1965).
14. G. R. Srinivasan, To be submitted to *J. Cryst. Growth.*
15. J. S. Sandhu and V. J. Lyons, Unpublished work.
16. R. E. Honig and D. A. Kramer, *RCA Rev.*, **30**, 285 (1969).
17. K. Weiser, *J. Phys. Chem. Solids*, **7**, 118 (1958).
18. S. M. Hu, *Phys. Rev.*, **180**, 773 (1969).
19. R. N. Hall, *ibid.*, **88**, 139 (1952); *J. Phys. Chem.*, **57**, 836 (1953).
20. P. J. Holmes, *J. Phys. Chem. Solids*, **24**, 1239 (1963).
21. S. H. Overbury, P. A. Bertrand, and G. A. Somorjai, *Chem. Rev.*, **75**, 547 (1975).
22. J. Bloem, *J. Cryst. Growth*, **13/14**, 302 (1972).
23. B. J. Masters and J. M. Fairfield, *J. Appl. Phys.*, **40**, 2390 (1969).
24. F. C. Eversteyn, P. J. W. Severin, C. H. T. Vanden Brekel, and H. J. Peek, *This Journal*, **117**, 925 (1970).
25. G. R. Srinivasan, To be published.

An Examination of the Chemical Staining of Silicon

D. G. Schimmel and M. J. Elkind

Bell Laboratories, Reading, Pennsylvania 19604

ABSTRACT

Large-scale chemical lapping of diamond-sawed silicon wafers to remove residual mechanical damage results in the formation of wafer stains. Highly doped p-type substrates are particularly susceptible and have been a primary cause of low wafer yields during production. This paper describes an investigation into the cause of silicon staining and a practical solution to the problem. On the premise that the stain is a suboxide of silicon, various nitric-hydrofluoric acid mixtures, as well as mixtures of hydrofluoric acid with oxidizing agents such as Cr^{+6}, Fe^{+3}, Cu^{+2}, and I^0 were used to synthesize silicon stains. Ion-scattering spectroscopy (ISS) and secondary ion mass spectrometry (SIMS) analyses established that all of the stains were suboxides of silicon ($SiO_{<2}$). Their origin is the incomplete oxidation of silicon, which is determined by the nature of the oxidant and its concentration. Although it is not practical to prevent silicon stains from forming, they can readily be removed by a 15 sec immersion in a 2:1 volume ratio of hydrofluoric acid: 0.038M potassium permanganate solution.

Diamond-sawed silicon wafers are chemically thinned, *i.e.*, chemically lapped with solutions of nitric (HNO_3), hydrofluoric (HF), and acetic (HAc) acids to remove residual saw damage. The wafers are then either Syton polished on one side, or, in some instances of discrete devices, subjected directly to production processing without further preparation. A visible stain is generally a reason for rejection of chemically lapped wafers. Staining became more prevalent with the increased usage of boron-doped <100> silicon having resistivities less than 1 Ω-cm (1).

The staining of silicon is not a new phenomenon. Over the years it has been observed to occur under a variety of silicon etching conditions, including anodic dissolution (2, 3), as well as with a variety of etching solutions (4-10). Amorphous silicon (11, 12), silicon hydride (13), mixtures of silicon oxides (14), and silicon monoxide or suboxide (15, 16) have been proposed as compositions to account for the discolorations. Based on these works and further production experience, two characteristics are notable: (*i*) the stain occurs most readily on highly doped p-type silicon; and (*ii*) the stain occurs as a result of treatment with any number of HNO_3-HF-HAc etching compositions.

Chemical lapping consists of immersing the silicon wafers in a temperature-controlled acid etch solution of HNO_3:HF:HAc. A volume ratio of 4:1:2 is a typical example (17). The stains form during removal of the wafers from the acid bath and subsequent immersion in water during the rinse. Because production applications frequently deal with very large etchant volumes, *e.g.*, 35 gallons, it is not feasible to quench the reaction by water dilution.

Silicon staining most readily occurs on highly boron-doped wafers, the degree of staining varying directly with the boron concentration. Staining also occurs on n-type silicon but to a lesser degree. Here again, the staining of n-type silicon varies directly with dopant concentration.

In very general terms the chemical reaction for the dissolution of silicon is as follows

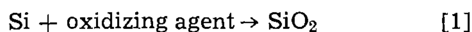

$$Si + \text{oxidizing agent} \rightarrow SiO_2 \quad [1]$$

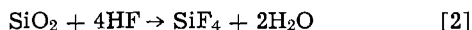

$$SiO_2 + 4HF \rightarrow SiF_4 + 2H_2O \quad [2]$$

In the presence of water and hydrofluoric acid, SiF_4 is converted to H_2SiF_6.

The stain films formed on silicon by HNO_3:HF:HAc etching solutions are insoluble in HF and in HNO_3. They are partially dissolved, however, in ammonium hydroxide (NH_4OH) solutions with some attendant attack on the silicon substrate. The stains can also be dissolved by reimmersion in the 4-1-2 etch solution, or, indeed, in any of the other usual HNO_3-HF etch solutions, such as the 5-3-3. However, during the interval in which the wafer is withdrawn from the etchant and water rinsed, the stain will reform.

Key words: silicon etching, stain films, chemical lapping.

This suggests that HNO_3-HF etchant compositions may favor the formation of some intermediate reaction product, perhaps a silicon oxide other than SiO_2. As an initial approach, the specificity of HNO_3 as the stain initiator can be rejected. Anodic oxidation of silicon in aqueous HF, for example, forms a stain similar to those chemically induced by HNO_3-HF mixtures. Furthermore, highly boron-doped silicon (~0.01 Ω-cm) has also been observed to stain during defect evaluation (18, 19). Here the defect etchant contains only HF and chromic acid (CrO_3) or potassium dichromate ($K_2Cr_2O_7$) as the oxidizing agent. In fact, highly doped p-type silicon will even stain when immersed in only hydrofluoric acid. The reaction is slow, requiring an hour or two to develop, and incident light is essential. In this instance, the oxidant for silicon is the water present in the concentrated hydrofluoric acid (20). The critical factor involved in stain formation on silicon appears to be the nature of the oxidant and probably its concentration.

If it is assumed that the stain is SiO_x, where $x < 2$, then a fast depletion of the oxidizing agent at the silicon-solution interface could be responsible for its formation. This depletion occurs because of the very high oxidation rate of the highly doped silicon surface. Since the stain film varies in thickness with time, the rate of the silicon suboxide formation is greater than the rate of its dissolution or oxidation to Si^{+4}. Once formed, the stain cannot be attacked by HF.

Experimental

In view of the above considerations, it should be possible to select oxidants having the necessary oxidation potential and concentration for the full conversion of silicon to the solubilized Si^{+4} state. Experiments were first performed to determine the range of HNO_3-HF ratios which cause silicon staining. The use of HAc in all of the formulations employed did not influence the formation of the stain. Since its primary function is that of a diluent, its further use was omitted (6, 21). Except where noted all samples were 0.01 Ω-cm p-type silicon.

Vertically oriented silicon test samples, partially submerged in the etchants maintained at 20°-23°C, showed that staining could occur in any of three ways: (*i*) solution staining of the entire immersed silicon; (*ii*) a thin-line stain at the air-liquid interface; or (*iii*) staining above the etch solution (vapor-phase stain). Formation at each of these locations depended

upon the HNO_3-HF volume ratios used. Nevertheless, staining of one type or the other occurred over a very wide range of ratios.

In general, HNO_3-rich solutions of ~12:1 to ~4:1 (HNO_3:HF by volume) caused air-liquid interface staining. Faster etches of ~3:1 to ~1:3 (HNO_3:HF) caused variable staining. For example, if the etch solution was vigorous enough to generate fumes or mist, a vapor-phase stain occurred on the silicon above the etch solution level. Staining was also found to be dependent upon the interval between withdrawal of the silicon from the etch solution and water rinsing. The more active etchant concentrations appeared to enhance stain formation after withdrawal of the substrate from the solution. For etch solutions of 1:4 to as high as 1:250 (HNO_3:HF ratios), the silicon stain formed only in solution. Obviously, the problem of silicon staining would not be solved merely by simple changes in the HNO_3-HF-HAc etchant composition.

Consequently, to learn more of stain formation and chemical composition of the discoloration, a number of typical oxidizing species were selected as substitutes for HNO_3 in combination with HF. As shown in Table I, these oxidants react by generating changes in oxidation state (valence) involving 1-5 electrons (possibly even 7-8). If partial oxidation of silicon is responsible for the stain, then those oxidants with one-, two-, and even three-electron changes should be candidates likely to produce stains. As mentioned above, CrO_3 and $K_2Cr_2O_7$ which undergo a three-electron change when reduced, do indeed stain silicon.

It was not surprising, then, that solutions of ferricyanide (ranging from 0.5-2 parts of 1M $K_3Fe(CN)_6$ to 1 part HF) with a one-electron change in oxidation state (Fe^{+3} to Fe^{+2}) provided very intense examples of staining on silicon. Prolonged immersion of silicon in such solutions merely intensified the discoloration from a brown to bluish-black color. Another single electron change is associated with the reaction of cupric chloride with silicon (0.5 parts of 1.5M $CuCl_2$ to 1 part HF). Again staining was very intense. Copper is not deposited in this case because insoluble CuCl is formed. With $CuSO_4$, however, the two-electron transfer would cause copper to plate out upon the silicon. Still another example is the reaction of KI-I_2 solutions with silicon (5 parts of KI-I_2 solution, containing 2 moles I_2 and 6 moles KI, to 1 part HF). This single electron type oxidation likewise produced very intense staining. Hydrofluoric acid solutions of hydrogen peroxide and ammonium persulfate, respectively, were inactive; and thus, these two-electron transfer reactions could not be effected. One other oxidant which probably involves a two-electron change is aqua regia. A two-part aqua regia:1 part HF mixture did show some activity by forming a stain.

These observations show that one and probably two-electron type oxidants, regardless of concentration, are incapable of completely oxidizing silicon. Those with a three-electron transfer, chromates and probably HNO_3, likewise tend toward staining. However, increasing their concentration in respect to HF in the etchant solution does enhance their oxidizing capability. For example, by increasing the HNO_3:HF from 1:4 by volume [0.135 mequiv. (22) HNO_3:1 mequiv. HF] to 1:3 by volume (0.180 mequiv. HNO_3:1 mequiv. HF), solution staining can be eliminated.

For chromium, which has an oxidation state change of three, no solution staining of silicon occurs in a 1 part 9.4M CrO_3:2.54 HF by volume solution (0.391 mequiv. Cr^{+6}:1 mequiv. HF). However, when the volume ratio is changed to 1 part 9.4M CrO_3:3 HF (0.325 mequiv. Cr^{+6}:1 mequiv. HF) then staining does occur. On a molar basis, therefore, the minimum concentration of each oxidant required to prevent solution staining is a HF solution 2.64M in Cr^{+6} and a HF solution 3.90M in HNO_3, respectively.

Though solution staining can be completely eliminated for the Cr^{+6} and the HNO_3 acid systems, nonuniform staining will occur upon withdrawal of the wafer, particularly from the HNO_3-HF etchants. This is a time-dependent reaction, since any residual acid (thin films, droplets, or vapor) will continue to react with the silicon. In addition, the instability of the HNO_3 in air accelerates the decrease in its effective concentration. That is to say, there is a rapid change in the HNO_3:HF ratio from a nonstaining region to one which stains by the incomplete oxidation of the silicon. In the case of the Cr^{+6} system, a longer time will elapse before staining occurs, simply because the Cr^{+6} is not degraded in air as is the HNO_3; and, hence, its effective concentration remains higher.

For a powerful oxidizing agent, such as $KMnO_4$ with a five-electron change occurring in acid solutions, no silicon staining of any type was encountered throughout a four-order-of-magnitude range of oxidant concentration. In fact, stains were not even apparent in solutions of 6.67×10^{-5} mequiv. Mn^{+7}:1 mequiv. HF. This remarkable performance is violated only when p-n junctions are present. Then the high boron-doped areas become stained when the Mn^{+7} concentration is only 3.27×10^{-3} mequiv. Mn^{+7}:1 mequiv. HF.

With this as a basis, it follows that this powerful oxidant might well be able to interact with residual stains formed on silicon by other etchants. In fact, a solution of 2 parts hydrofluoric acid to 1 part 0.038M potassium permanganate by volume readily dissolves stains formed by HNO_3-HF etchants on silicon within 10-15 sec at room temperature. The silicon etch rate for this solution is ~0.4 μm/min for <100> silicon ranging from 0.002 Ω-cm n-type to 0.01 Ω-cm p-type. The actual etch rates determined for two resistivities each of n- and p-type <100> silicon are listed in Table II.

In view of the results obtained with $KMnO_4$, iodic acid (HIO_3) and periodic acid (HIO_4) with oxidizing capabilities involving at least five-electron changes, respectively, were also evaluated. Both oxidants exhibited strong etch activity. However, they apparently formed some intermediate metastable iodine compounds during their reduction, which interfered with the completeness of the oxidation process. Silicon wafers treated in HF solutions containing each of these iodic acids turned dark and upon exposure to air continuously liberated iodine vapor.

Since the concentration of the oxidant has been shown to be one of the controlling factors in minimizing or eliminating stain formation on silicon, the use of solid fluoride salts in conjunction with HNO_3 and CrO_3, or $K_2Cr_2O_7$, was explored to avoid the dilution

Table I. Oxidizing agents

	Redox reaction	Valence change	Single electrode potential (V)
1.	$Sn^{+2} \rightarrow Sn^0$	$+2e$	−0.14
2.	$HCOOH \rightarrow CHO^-$	$+1e$	+0.06
3.	$SO_4^= \rightarrow SO_3^=$	$+2e$	+0.17
4.	$HCHO \rightarrow CH_3OH$	$+2e$	+0.19
5	$Cu^{+2} \rightarrow Cu^0$	$+2e$	+0.34
6.	$Fe(CN)_6^{-3} \rightarrow Fe(CN)_6^{-4}$	$+1e$	+0.36
7.	$Cu^{+2} \rightarrow Cu^{+1}$	$+1e$	+0.54
8a.	$I_3^- \rightarrow 3I^-$	$+1e$	+0.53
b.	$IO_3^- \rightarrow \frac{1}{2}I_2^0$	$+5e$	+1.19
c.	$HIO \rightarrow \frac{1}{2}I_2^0$	$+1e$	+1.45
d.	$H_5IO_6 \rightarrow IO_3^-$	$+2e$	+1.6
9.	$NO_3^- \rightarrow NO\uparrow$	$+3e$	+0.96
10.	$Cr_2O_7^= \rightarrow 2Cr^{+3}$	$+3e$	+1.33
11.	$MnO_4^- \rightarrow Mn^{+2}$	$+5e$	+1.51
12.	$H_2O_2 \rightarrow H_2O$	$+2e$	+1.77
13.	$S_2O_8^= \rightarrow 2SO_4^=$	$+2e$	+2.01

Table II. $KMnO_4$-HF etch rate for p- and n-type silicon

<100> Si			
Resistivity (Ω-cm)	Type	Etch rate* (μm/min)	Etch solution
0.002	n	0.42	2 parts HF 1 part 0.038M $KMnO_4$
3	n	0.42	
4	p	0.34	
0.01	p	0.32	

* Etch step measured with a Taylor-Hobson Talystep.

effect inherent with the water present in concentrated HF. The results showed clearly that undissociated HF rather than fluoride ions was essential for removing silicon dioxide (23). For example, the Secco etch (2 parts HF:1 part 0.15M $K_2Cr_2O_7$) readily generated a stain on 0.01 Ω-cm p-type <100> silicon. Replacing the HF with the equivalent concentration of potassium fluoride (KF) solution gave no reaction with silicon, even with the KF concentration increased to saturation. However, additions of hydrochloric (HCl) or sulfuric (H_2SO_4) acids to the nonreactive solution resulted in silicon staining. Hydrofluoric acid was evidently formed by the hydrochloric acid addition: $H^+ + Cl^- + K^+ + F^- \rightleftarrows HF + K^+ + Cl^-$.

Potassium fluoride added to HNO_3-HF solutions (1:1 by volume) reduced the normally violent silicon etch reaction to nil. Partial regeneration of the solution reactivity to silicon was achieved with HNO_3 additions. However, additions of water, hydrofluoric acid, or acetic acid were ineffectual. It is presumed that the potassium fluoride in this instance had initially caused massive nitric acid ionization to form undissociated HF and to simultaneously lower the oxidizing capability of the nitric acid.

Ammonium fluoride and potassium fluoride were also used as replacements for HF in HNO_3-HF (1:1 by volume) solutions. Silicon staining resulted in each case, but not the expected violent etch reaction. Nitric acid additions increased the solution etch activity, whereas sulfuric acid additions were not as effective. Violent silicon etching occurred, however, when hydrofluoric acid was added. Thus, it appears that the sulfuric acid did not completely convert all the fluoride ions from the fluoride salts into undissociated hydrofluoric acid.

Silicon stain composition.—Silicon samples with stains generated from hydrofluoric acid solutions containing oxidizing agents of items 6, 7, 8, 9, and 10 of Table I were analyzed for oxygen:silicon ratios and residual metallic contamination (24) with ion-scattering spectroscopy (ISS) and secondary ion mass spectrometry (SIMS). Two oxidized silicon wafers were used to establish the calibration for the oxygen:silicon ratio determination. The oxides of these calibration samples were approximately 50 and 2000Å thick. Figures 1A and 1B show the data obtained from the ISS for each of these oxide thicknesses. As expected, the ratio is essentially 2:1, oxygen:silicon. Figure 1C shows the oxygen:silicon ratio of the HNO_3:HF (1:110) generated stain film. This ratio is constant at about 1.4-1 over a thickness of 100Å. Similar ratios were obtained from the stain samples prepared in the HF solutions of $K_3Fe(CN)_6$, $CuCl_2$, CrO_3, and KI-I_2, respectively.

Figure 1D represents a production-type stain sample. The stain is very thin, probably 20Å or less. Accordingly, there is no extended flat portion above the base line to the oxygen:silicon ratio curve. Nevertheless, the stain is a silicon suboxide with a ratio of <2:1. Figure 1E shows the ISS oxygen:silicon ratio curve for the surface of a clean epi control wafer. As expected, there is only a very small quantity of oxygen present on the surface.

Both ISS and SIMS analyses showed that the elements Fe, Cu, Cr, and I_2 were not significant constituents in any of the stain samples. Though fluoride ions were also present, they were in such low concentrations as to preclude any Si-O-F combinations. It is clear, then, that all of the stain films formed by the 1, 2, and 3 electron change oxidants used in these experiments have a similar composition involving only oxygen and silicon in a ratio of <2:1.

Stain removal.—It is obvious from the results obtained that it is impractical to achieve a stain-free chemically lapped silicon wafer by using the conventional etchants, such as HNO_3-HF, on a large scale. The ease with which the 1 part 0.038M $KMnO_4$:2 parts HF solution completely removes such stains without

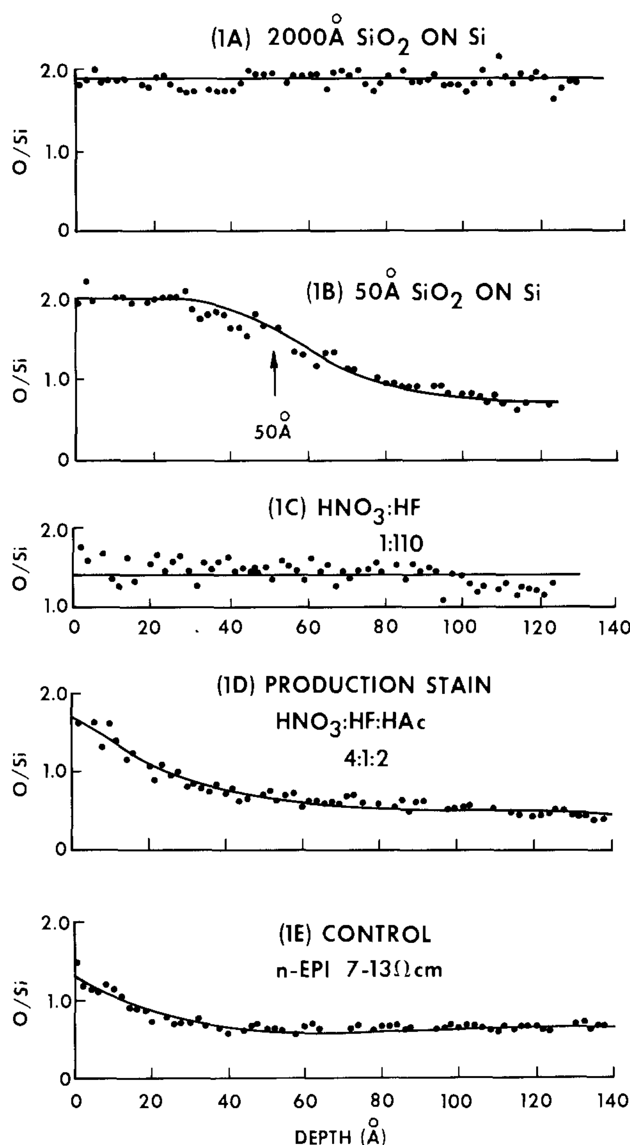

Fig. 1. Oxygen:silicon ratio vs. depth of stain films determined by ion-scattering spectroscopy. 1A, O_2:Si ratio of 2000Å thick 1050°C steam oxide; 1B,* O_2:Si ratio of 50Å thick 900°C dry oxide; 1C, O_2:Si ratio of stain film from 1:110 by volume HNO_3:HF solution; 1D,* O_2:Si ratio of very thin stain film from 4:1:2 by volume HNO_3:HF:HAc production etching; 1E,* O_2:Si ratio of a clean n-epi control wafer surface. * indicates the base line is not zero, since a discriminator was not used to eliminate the crater edge effects.

significant attack on the substrate itself (0.1 μm per side in 10-15 sec) makes it very attractive for post-chemical lapping stain removal.

The possibility of residual manganese and potassium contamination exists for stained wafers treated in the $KMnO_4$-HF stain-removal etch solution. Accordingly, after treatment of a production-stained wafer in the $KMnO_4$-HF solution to remove the stain, water rinsing, and drying, it was analyzed for residual surface contamination by SIMS and ISS. Manganese was not detected, and the residual potassium level was consistent with that normally detected on clean silicon surfaces (<0.1 ppm). A large variety of devices were also fabricated from wafers that had been treated for stain removal on a limited production quantity basis. These device yields were consistent with the regular production yields. Added assurance against residual manganese and/or potassium contamination is that the stain removal treatment is performed prior to the preoxidation and prediffusion cleaning which all wafers receive.

Characteristics of the $KMnO_4$-HF etchant.—Although the silicon etch rate for 2 parts hydrofluoric

acid: 1 part 0.038M potassium permanganate is about 0.4 μm/min, it is not surprising that increasing the permanganate concentration also increases the etch rate. Accordingly, $KMnO_4$-HF solutions were surveyed as possible chemical-lapping etches.

The strongest formulation examined was a solution of 7g $KMnO_4$ in 100 ml HF, which upon mixing produced a very vigorous exothermic reaction. This solution exhibited limited stability, however, and produced inconsistent etching results. A preferred combination for etching silicon was formulated with 3.5g $KMnO_4$, 100 ml HF, and 10 ml H_2O. This etchant produced highly polished surfaces and exhibited an etch rate of 4.4 μm/min. Typically, 4:1:2 (HNO_3:HF:HAc) etches about three times faster and leaves the surface with a matte finish. A matte surface is preferred to provide friction for holding wafers in position during the Syton polishing operation.

Even though a $KMnO_4$-HF formulation contains considerably less oxidant than does a HNO_3-HF solution to stoichiometrically solublize silicon, rejuvenation by simple addition would eventually lead to solution buildup of manganese and potassium salts. The HNO_3-HF etchant, on the other hand, can be readily maintained by routine acid additions. Thus, considering the low etch rate, the polished rather than matte surface finish, and solution by-product buildup, $KMnO_4$-HF is not a suitable direct replacement for HNO_3-HF in a production chemical-lapping operation.

The low surface etch rate, $\sim$0.4 μm/min, of the 2 parts HF: 1 part 0.038M $KMnO_4$ stain-removal solution suggests that this type of etch solution might be adaptable to defect etching (25-27). An advantage of permanganate solutions would be that no special disposal is required, as is the case with the chromium-containing defect etches, such as those of Sirtl and Secco. Solutions containing one part of $KMnO_4$ in concentrations ranging from approximately 0.1-0.004M with 2 parts HF were surveyed for potential defect etchants, both with and without ultrasonic agitation.

The $KMnO_4$-HF defect etch solutions were evaluated on $<100>$ wafer samples with p-n junctions. Stacking faults and some dislocations were nicely delineated by etch pits in the junction areas. However, in the n-epi areas dislocation etch pits did not develop where dislocations were known to exist. This is not too surprising, since Landgren (28) found that $KMnO_4$-HF etchants were almost completely preferential to p-type material when p-n junctions are present.

Conclusions

The causes of the chemical staining of silicon, such as that which occurs during production quantity chemical lapping, have been shown to arise from the incomplete oxidation of silicon in the usual HNO_3-HF etchant compositions. Staining may occur in solution or in the vapor phase prior to rinsing as a result of oxidant depletion. Highly boron-doped $<100>$ silicon is particularly susceptible to stain formation. It has been shown that these stains can occur over a very wide range of HNO_3-HF compositions. Consequently, formulation variations to prevent silicon stain formation in a production process are impracticable.

Silicon stains were also generated with Cr^{+6}, Fe^{+3}, Cu^{+2}, and I^0 as oxidants in hydrofluoric acid solutions. These stains as well as those formed in various HNO_3-HF mixtures have been shown to be a suboxide of silicon, SiO_x, where $x < 2$.

$KMnO_4$-HF solutions do not form any kind of silicon stain over a wide range of permanganate concentrations. Though relatively active as a general silicon etch, the attack rate of the $KMnO_4$-HF solutions is only about 1/3 of that of a typical 4-1-2 HNO_3-HF-HAc solution. Furthermore, the resultant polished rather than matte surface finish and solution by-product buildup preclude its direct substitution for the usual HNO_3-HF-HAc etchants used in large scale chemical lapping operations.

Compositions of $KMnO_4$-HF in dilute form, however, are extremely effective for rapid postchemical lapping HNO_3-HF stain removal. A 2 part HF: 1 part 0.038M $KMnO_4$ solution at 20°-25°C completely dissolves stains in 10-15 sec without any significant silicon dissolution.

Acknowledgments

The authors thank D. L. Malm for the ISS and SIMS analyses.

Manuscript submitted April 18, 1977; revised manuscript received Sept. 6, 1977.

Any discussion of this paper will appear in a Discussion Section to be published in the December 1978 JOURNAL. All discussions for the December 1978 Discussion Section should be submitted by Aug. 1, 1978.

Publication costs of this article were assisted by Bell Telephone Laboratories.

REFERENCES

1. W. W. Gladney, Unpublished.
2. D. R. Turner, *This Journal*, **107**, 810 (1960).
3. D. R. Turner, *ibid.*, **108**, 561 (1961).
4. D. R. Turner, *ibid.*, **106**, 701 (1959).
5. H. Robbins and B. Schwartz, *ibid.*, **106**, 505 (1959).
6. H. Robbins and B. Schwartz, *ibid.*, **107**, 108 (1960).
7. B. Schwartz and H. Robbins, *ibid.*, **108**, 365 (1961).
8. B. Schwartz and H. Robbins, *ibid.*, **123**, 1903 (1976).
9. P. F. Schmidt and G. L. Schnable, *ibid.*, **123**, 3106 (1976).
10. C. S. Fuller and J. A. Ditzenberger, Unpublished.
11. R. J. Archer, *J. Phys. Chem. Solids*, **14**, 104 (1960).
12. M. M. Koltun, *Russ. J. Phys. Chem. (Engl. Transl.)*, **38**, 381 (1964).
13. K. Beckman, *Surf. Sci.*, **3**, 314 (1965).
14. E. A. Efimov, *et al.*, *Russ. J. Phys. Chem. (Engl. Transl.)*, **36**, 645 (1962).
15. A. Uhlir. Jr., *Bell Syst. Tech. J.*, **35**, 323 (1956).
16. C. S. Fuller and J. A. Ditzenberger, *J. Appl. Phys.*, **27**, 544 (1956).
17. R. A. Clapper, Unpublished.
18. T. L. Chu and J. R. Gavaler, *Electrochim. Acta*, **10**, 1141 (1965).
19. D. G. Schimmel, Unpublished.
20. S. M. Hu and D. R. Kerr, *This Journal*, **114**, 414 (1967).
21. M. J. Elkind and D. G. Schimmel, To be published.
22. F. Brescia, *J. Chem. Ed.*, **53**, 362 (1976).
23. J. S. Judge, *This Journal*, **118**, 1772 (1971).
24. M. J. Vasile and D. L. Malm, *Int. J. Mass Spectrom. Ion Phys.*, **21**, 145 (1976).
25. D. G. Schimmel, *This Journal*, **123**, 734 (1976).
26. E. Sirtl and A. Adler, *Z. Metallkd*, **52**, 529 (1961).
27. F. Secco d'Aragona, *This Journal*, **119**, 948 (1972).
28. C. R. Landgren, U.S. Pat. 2,847,287.

Investigation of the Ti-Pt Diffusion Barrier for Gold Beam Leads on Aluminum

S. P. Murarka,* H. J. Levinstein, I. Blech,[1] T. T. Sheng, and M. H. Read

Bell Laboratories, Murray Hill, New Jersey 07974

ABSTRACT

In order to avoid Al-Au interactions and to ensure the electrical and mechanical stability of the Au beam leaded structures using Al metallization, a Ti-Pt diffusion barrier between Al and Au has been investigated. Ti and Pt films of different thicknesses were employed as diffusion barriers. The resulting Al-Ti-Pt-Au thin film sandwich structures were aged at temperatures in the range of 300°-500°C to evaluate the effectiveness of the barrier in preventing Al-Au interaction. The interaction was followed by use of optical and electron microscopy, x-ray diffraction, and sheet resistance measurements. It was found that metallurgical interactions in these structures occurred at preferential sites which were shown to be hillocks in Al. On continued aging, reaction spread around these sites and finally covered the entire surface. The number of such reaction sites increased with decreasing barrier metal thickness and with increasing time and temperature of anneal. The reaction was considerably inhibited (*i*) by annealing Al at 450°C for ½ hr prior to barrier metallization and (*ii*) by using at least 2000Å each of Ti and Pt in the barrier. An understanding of the effectiveness and need of a 2000Å Ti-2000Å Pt diffusion barrier between Al and Au was obtained by additional studies of the metallurgical interactions induced in Al-Pt, Al-Ti, and Al-Ti-Au thin film sandwich structures by aging at temperatures in the range of 200°-500°C. Ti is required to cover Al well so as to prevent Al-Pt interactions and Pt is required to prevent Ti-Au interactions caused by diffusion of Au through Pt to Ti.

Aluminum is most widely used as a practical metallization material in the IC technology. In order to extend the use of aluminum metallization to multichip assemblies it is advantageous to form gold beam leaded sealed structures using such metallization. To avoid gold-aluminum (1) interactions, a suitable diffusion barrier between Al and Au has to be provided. This barrier metallization must prevent Al-Au interactions and must not lead to a loss of electrical conduction between the outside world and the circuit during its operation.

Several barrier metallization schemes—such as Ti-Pd, Ti-Pt, Ti-Rh, Ti-Ni—have been considered in the past (2-9) in one form or the other. Such two metal schemes have been chosen to satisfy both the adherence and barrier criteria and to provide sufficient corrosion resistance. The results of both Melliar-Smith and Polito (7) and DeBonte *et al.* (8) indicate that a Ti-Pt diffusion barrier between Al and Au would be a good choice. Speight and Bill (2), who studied the effects of aging in dry air at 150° and 250°C and in wet and dry air with 10 ppm HCl at 150°C on the contact resistance of Ti-Pt-Au conductor film metallization on Ta_2N, reported such metallization to exhibit by far the greatest stability.

We have investigated the feasibility of using a Ti-Pt diffusion barrier between Al metallization and the Au beams. In order to understand the barrier characterestics and its effectiveness, one must learn about the metallurgical interactions in two (*e.g.*, Al-Pt, Al-Ti, etc.), three (*e.g.*, Al-Ti-Au, Al-Pt-Au, etc.), and four metal (the Al-Ti-Pt-Au) systems. In the temperature range of 200°-600°C there is considerable interdiffusion in Ti-Au (8-9) and Pt-Au (10-11) films although no intermetallics are reported for the latter. Al-Au films are known (1) to react catastrophically. Al-Ti films have been reported (12) to react at higher temperatures, leading to the formation of Al_3Ti which retarded further interaction between Al and Ti. On the other hand, there is very little interdiffusion reported in Ti-Pt (8) films. In a recent paper (13) we have reported the results of our investigations of the metallurgical interactions in thin films of Al and Pt. Al and Pt films were found to interact very rapidly, leading to the formation of several intermetallics. In this paper we report and discuss the results of our studies of the Al-Ti-Pt-Au metallization scheme together with the results of the relevant studies of the metallurgical interactions in Al-Pt, Al-Ti, and Al-Ti-Au thin film structures. It will be shown that Ti-Pt diffusion barrier provides excellent barrier characteristics between Al and Au.

* Electrochemical Society Active Member.

[1] Present address: Technion, Haifa, Israel.

Key words: aluminum metallization, beam leads, diffusion barrier.

Experimental

The metal films were always deposited on oxidized silicon substrates. Throughout this paper the metal deposited first is written first. For example, Al-Ti-Au would mean that Al was deposited on the substrate, followed by Ti deposition on this Al, and Au (the outermost layer) deposition on Ti.

Al-Ti-Pt-Au structures.—Three different test structures were used in this investigation as shown in Fig. 1. The first [Fig. 1(a)] was the simple planar structure formed by depositing various films one after another. 1.5 μm thick Al was evaporated onto hot substrates at 320°C. Ti (or Ti/TiN) and Pt were sputter deposited on chemically cleaned (in 30:1 ammonium fluoride:HF for 30 sec) Al in the desired thicknesses. 5000Å thick Au was then electroplated on top of Pt. (In a typical beam lead about 10-15 μm of Au is electroplated on Pt. Such a thick layer of Au is, however, not suitable for the metallurgical interaction studies.) Most of the initial studies were made by measuring the sheet resistance of the composite film and by following the reaction visually under an optical microscope. A few x-ray diffraction patterns were obtained for the reacted specimens to learn about the possible intermetallics formed.

Based on the results of the studies on the above-mentioned test structures, new test structures of the type shown in Fig. 1b were made using a metallization scheme 2000Å Ti-2000Å Pt-5000Å Au on hot-deposited (320°C) Al. The Al was annealed at 450°C for 0.5 hr in hydrogen to simulate the actual device-fabricating conditions, and to reduce the hillock growth

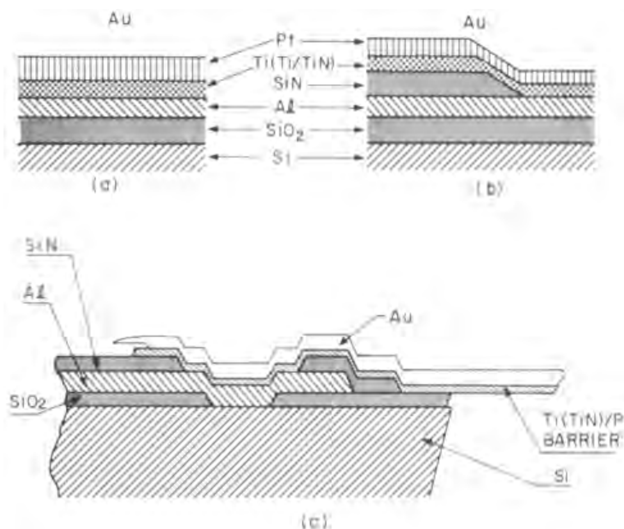

Fig. 1. Schematic drawings of the various Ti/Pt barrier layers between Al and Au.

in subsequent 350°C agings. Also, in some cases half of each wafer was coated with 1 μm of plasma silicon nitride prior to Ti-Pt deposition so that a comparison could be made between the Al-Ti-Pt-Au and Ti-Pt-Au interactions. It may be noted that in the rest of the investigation we have used only hot-deposited (320°C) Al films which were annealed to 450°C for ½ hr in hydrogen prior to any subsequent metallizations.

Al-Pt structures.—In a recent publication (13) we have already reported the results of thin film interactions of Al and Pt. Al and Pt react very rapidly at higher temperatures and Ti is needed to avoid this interaction. In this paper we report the results of our investigation of the hillocks in aluminum as the preferential reaction sites. Since Al-Pt interact very rapidly, a very thin (200Å of Ti) barrier was used between Al and 2000Å of Pt to retard the reaction so it could be followed during heating on a hot stage in the scanning electron microscope in a reasonable length of time. One of these samples was heated on the hot stage of a SEM. A Chromel-Alumel thermocouple connected to the hot stage measured the temperature of the hot stage. The reaction, as it occurred, was recorded as snapshots. The maximum temperature attained during these interactions was 510°C.

Al-Ti-Au structures.—In order to establish the usefulness of Pt in the Al-Ti-Pt-Au metallization scheme, we studied a few Al-Ti-Au thin film sandwich structures. Ti and Au films were deposited on 1.5 μm thick (hot-deposited and preannealed) Al films in two different manners: (*i*) On some wafers Ti and Au films were sequentially sputtered in the same sputtering chamber without breaking vacuum. Samples with 1000, 2000, and 3000Å thick Ti films were prepared. Each had 5000Å Au film on top; (*ii*) In another case, 2000Å of Ti was sputtered on Al and the wafer was taken out in air prior to Au evaporation. In many of these samples Au did not adhere very well to the Ti surface, which could be a serious drawback in using gold directly on Ti if the Ti gets exposed to air before the Au deposition.

Al-Ti-Au samples thus prepared were then annealed at 350°C in forming gas ambient. The interaction between the metallic films was followed by optical examination of the top surface of the structure, four-point probe sheet resistivity measurements, and x-ray diffraction studies.

Results and Discussion

Al-Ti-Pt-Au structures.—Ti film thicknesses of 1000 and 2000Å with or without 100-200Å of TiN and Pt films of 1000, 2000, and 4000Å thicknesses were used. These thicknesses are indicated on the figures. All

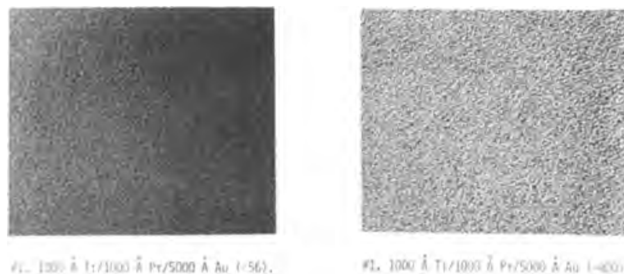

Fig. 2. Top view of the surface of Al/Ti/Pt/Au samples as-prepared

the high temperature agings were carried out in forming gas. Most of the samples were annealed at 350°C, and some were annealed at 300° and 400°C.

All sample surfaces were identical in the as-prepared state. The optical photomicrographs in Fig. 2 show the top view of one as-prepared 1.5 μm Al-Ti-Pt-Au sample. Figure 3 shows the surfaces of various samples annealed at 350°C for 5 hr. As a result of the aging, the metallurgical interaction in these films has become visible. As can be seen in Fig. 3, the reaction appears as black spots (in fact, they were slightly purple hillocks) indicating preferential reaction sites. Very similar spot formation has been reported by Kolesnick *et al.* (14). The number of such sites increased with the increase in aging time. It can be seen that both thicker Ti (≈2000Å) and Pt (≈2000Å) films help to reduce the extent of the interaction. The intermediate layer of TiN would also seem to help in reducing this interaction.

Composite film sheet resistances were monitored as a function of the annealing time and temperature. Figure 4 shows the sheet resistance before and after the annealing for 22 hr at 350°C for various samples. One finds a good qualitative correlation between the results of Fig. 4 and those of Fig. 3. A 2000Å Ti-2000Å Pt barrier between Al and Au films seems to be very effective in controlling the metallurgical interactions which lead to high sheet resistances. Figure 5 shows the sheet resistance of Al-2000Å Ti-2000Å Pt-Au structures as a function of time at several temperatures of anneal.

The number of interaction sites (so-called black spots) increased with increasing time of anneal. Figure 6 shows the number of these sites per square centimeter as a function of time of anneal at 400°, 350°, and 300°C. This result is very similar to one shown in Fig. 5. It may be pointed out that even after 45 hr of aging at 350°C the number of reaction sites on specimen No. 11 (with 2000Å Ti-2000Å Pt)

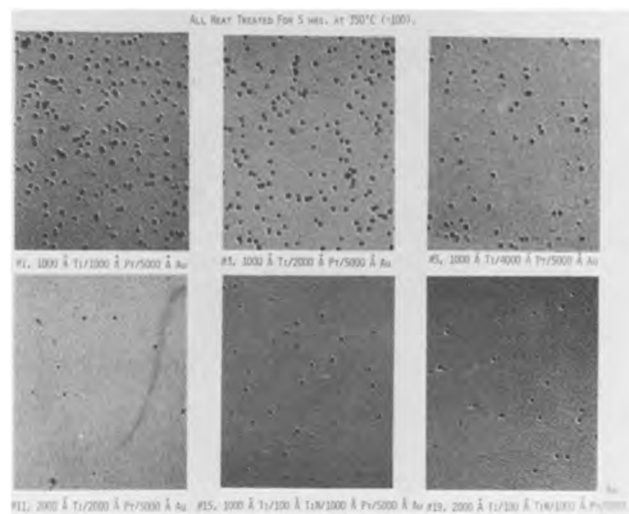

Fig. 3. Top view of the surface of Al/Ti/Pt/Au samples after 5 hr anneal at 350°C.

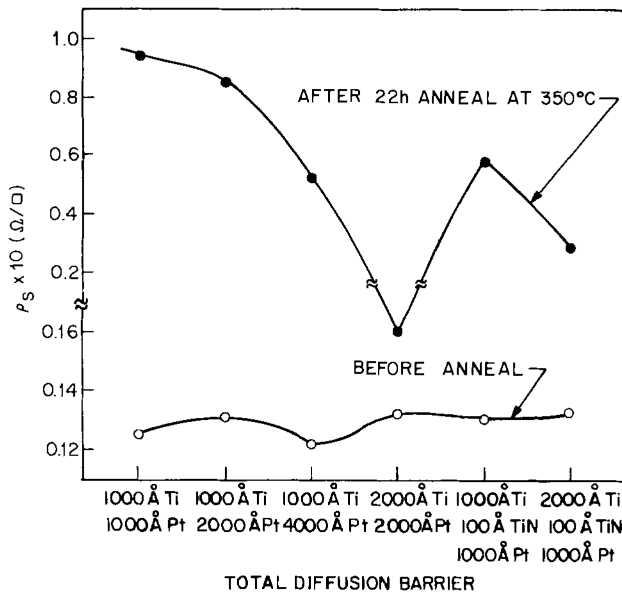

Fig. 4. Effect of a 22 hr anneal at 350°C on the composite film sheet resistance of samples with different barrier thicknesses.

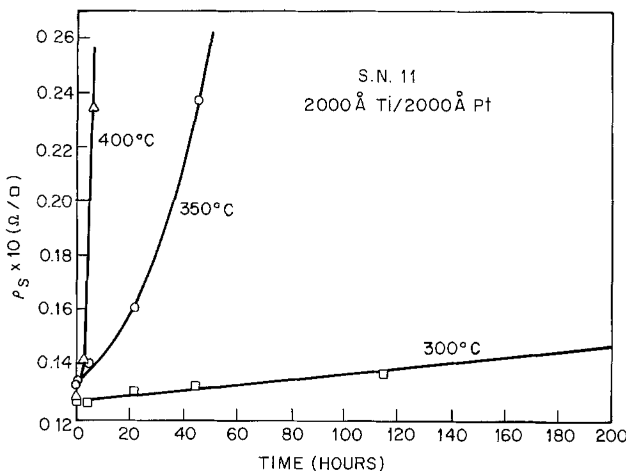

Fig. 5. The sheet resistance of the sample with the 2000Å Ti/2000Å Pt barrier as a function of time and temperature of anneal.

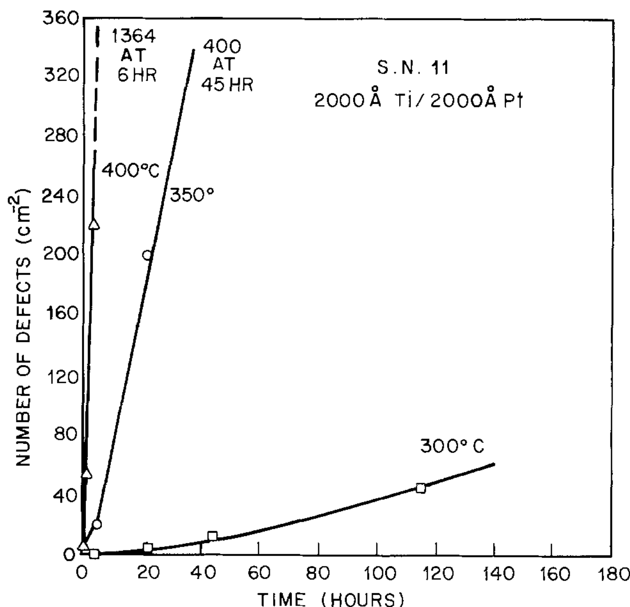

Fig. 6. The number of observed defects in the sample with the 2000Å Ti/2000Å Pt barrier as a function of time and temperature of anneal.

was only 0.08 per 200 μm × 100 μm area, a typical metallization area.

A comparison of the sheet resistances and the number of the black spots appearing after the 400°, 350°, and 300°C anneals (Fig. 5 and 6) shows that the over-all metallurgical interaction in the 1.5 μm Al-2000Å Ti-2000Å Pt-5000Å Au system is a thermally activated process. Although it is not possible to characterize this process, which could be a composite of several thermally activated reactions, one can extract a very useful number in terms of the over-all activation energy as reflected in sheet resistance and number of defect measurements (Fig. 5 and 6). The activation energy in the present case was found to be ~1.5-1.7 eV. Knowledge of this number and of the useful life at the accelerated aging temperature can be utilized to approximate the life of the composite film structure at the operating temperature of the devices.

Results of x-ray diffraction studies of the reacted films are given in Table I. The only reaction product detected was Al_2Au which confirms the observation of purplish color of the reacted spots. Phases other than the purple Al_2Au were optically visible but were undetected by x-rays.

As stated earlier, in all these specimens the Al films were deposited on substrates heated to 320°C, and no postannealing was carried out prior to Ti-Pt-Au depositions. Al is known (15) to form hillocks during annealing. These hillocks may punch through Ti-Pt films during the 350°C anneals, leading to direct contact between Al and Au. Also, the hillocks present at the interface may be high enough that Ti-Pt coverage is poor, leading to thinning of the barrier metal and permitting reaction to occur at these sites in subsequent heat-treatment. To test this hypothesis and to minimize hillock growth during annealing, a few samples were prepared according to the schematic shown in Fig. 1(b). Here, Al was annealed at 450°C for 30 min in hydrogen prior to silicon nitride deposition. Such a heat-treatment of Al prior to further metallization is a common practice during device fabrication.

Figures 7(a) and 7(b) show optical photographs of the surface of two samples (with 200Å Ti-2000Å Pt and 2000Å Ti-100Å TiN-2000Å Pt between Al and Au) annealed for 42 hr at 350°C. The reaction, as represented by black spots, has taken place only in the half where Al was in contact with Ti-Pt-Au. There is very little change in the sheet resistance on this half of these samples. In the other half, where silicon nitride formed a thick barrier between Al and the Ti-Pt-Au metallization, no reaction seemed to have occurred. There is no change in the measured sheet resistivity of Ti-Pt-Au on this half of the wafer. The number of defects on the reacted side (on Al) is considerably less in these samples (even after 42 hr of anneal) compared to those shown in Fig. 3. This difference in reaction rate (compared to that discussed earlier with as-deposited Al, *e.g.*, Fig. 4) could be attributed to the 450°C anneal of

Table I. X-ray diffraction studies of the reacted films

Metallization	Heat treatment (°C)	Intermetallics identified
Al-1000Å Ti-1500Å Pt-5000Å Au	1 hr at 350	None
	3 hr at 350	None
	20 hr at 350	Strong spotty lines due to Al_2Au only
Al-2000Å Ti-2000Å Pt-5000Å Au	5 hr at 350	None
	22 hr at 350	Definite Al_2Au but not as strong as in other sample (above)
	115 hr at 300	A few spots only indicating 2-10% Al_2Au
Al-1000Å Ti-5000Å Au	8 hr at 350	Al_2Au and Au_4Ti
Al-2000Å Ti-5000Å Au	8 hr at 350	Au_4Ti only
Al-3000Å Ti-5000Å Au	8 hr at 350	Au_4Ti only

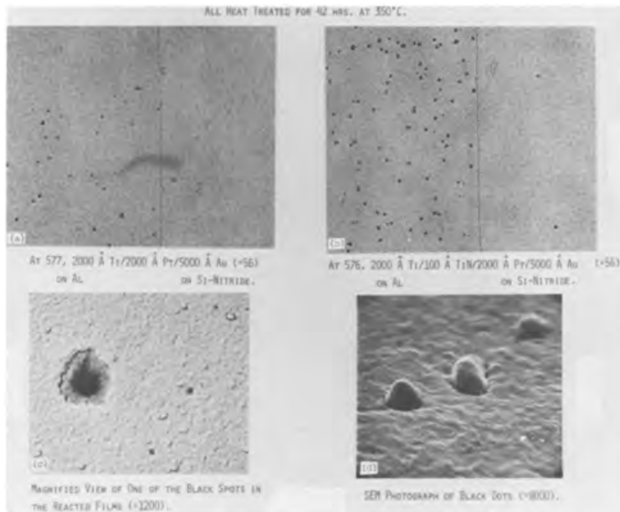

Fig. 7. Top view of heat-treated samples made at 450°C for 1/2 hr prior to barrier metallization. (a) With 2000Å Ti/2000Å Pt/5000Å Au on Al and on Si nitride; (b) with 2000Å Ti/100Å TiN/2000Å Pt/5000Å Au on Al and on Si nitride; (c) one reacted spot as visible in optical microscope and; (d) several reacted spots as visible in SEM.

Al prior to Ti-Pt-Au depositions. Due to this treatment hillock formation in Al is considerably retarded at lower temperatures. Figure 7(c) shows an isolated black spot in high magnification. The periphery of the spot was purple and the central area was protruding out of the surroundings. These spots appear as hillocks in the SEM, as can be seen in Fig. 7(d).

Hillocks as the reaction sites: Al-Pt reaction.—In the absence of Ti, Al and Pt react very rapidly and reaction occurs preferentially at sites which appear as black spots during optical examination. Figure 8 shows a series of SEM snapshots as the Al-Pt interaction (slightly slowed down by a 200Å Ti barrier in between) occurred on the heated stage of the SEM. Figure 8(a) shows a window in the as-prepared sample. The description under each photograph describes the total time since heat-treatment began, as well as temperature and the magnification. Going through the sequence of these photographs it is very clear that there is a one-to-one correspondence between the hillocks present in Al and the reaction site (black dot as it appears in the optical microscope). Some hillocks start to grow early and they are the first to react. Others follow in time. Figure 8(d) shows a cross section of one of these hillocks. In Fig. 8(d) the hillock has the typical conical shape. Such hillocks were subsequently found to have folded on themselves on prolonged heating. From these it is clear that as the hillocks grow in size, a void increasing in volume is created under the top surface of the hillock. The formation of the void is caused by the separation of the intermetallics from the underlying aluminum. It may be noted that the hillock underneath the silicon nitride layer separating Al from Ti-Pt did not grow during this treatment (as shown by the arrows in Fig. 8). These observations clearly establish that the black dot formation in Al-Ti-Pt-Au structures (due to accelerated aging at elevated temperatures) was due to the presence of hillocks in the Al and subsequent growth due to reaction at these hillocks.

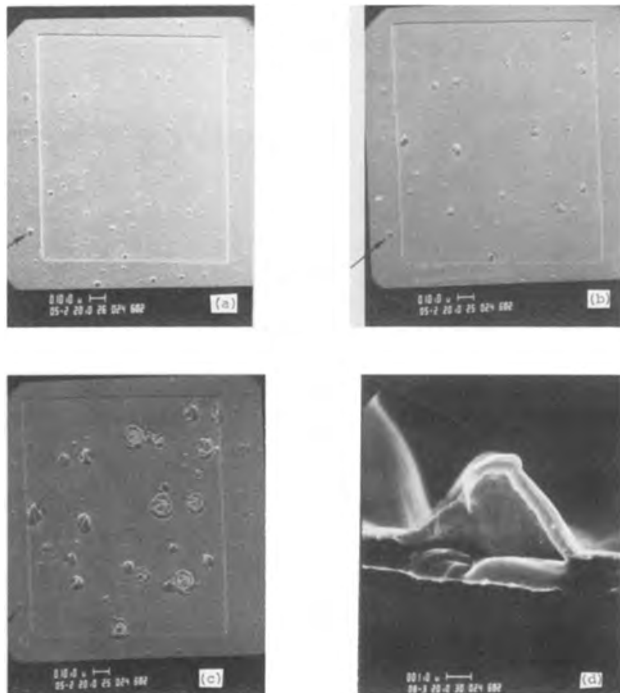

Fig. 8. SEM snapshot photographs of the sample with 200Å Ti/2000Å Pt on 1.5 μm thick annealed Al film (in window). Sample was annealed on the hot stage of the microscope. (a) As-prepared, X500; (b) after 109 min of heating, hot-stage temperature 510°C, X500; (c) after 135 min of heating, hot-stage temperature 510°C, X500; (d) heater shut off after 135 min (510°C), cooled, and cleaved, X8000.

The absence of any Al-Ti, Al-Pt, or Ti-Au intermetallics and the presence of only Al_2Au in the reacted Al-Ti-Pt-Au films can now be explained. Interaction was initiated at the localized Al-hillocks between Al and Ti-Pt. The interaction led to void formation and collapse of the reacted volume leading to metallurgical contact between Al and Au. The rapid delocalization of Al-Au interaction follows leading to the formation of detectable amounts of Al_2Au over the entire surface. Other intermetallics, formed at localized sites, were not present in large enough amounts to be detected by x-ray diffraction in a decisive manner.

Al-Ti-Au structures.—Samples with in situ-deposited Ti and Au.—Figure 9 shows the surface of Al-Ti-Au films after a 4 hr anneal. Intermetallic reaction products are visible in samples with 1000 and 2000Å Ti but not in the sample with 3000Å Ti. In the sample with only a 1000Å Ti barrier between Al and Au, reaction seems to start at preferential sites, which according to Fig. 8 could be the hillocks in Al. The surface away from these black spots has also turned grayish in all samples, indicating some metallurgical interaction. In samples with a 2000Å Ti as barrier, such reaction sites (black spots) are very limited in number and there appears to be interaction occurring everywhere as denuded (or reflecting) regions.

Figure 10 shows the surface of the same samples after 8 hr of anneal. Interaction is now visible even

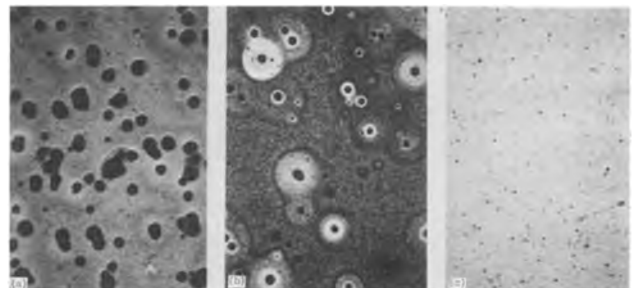

Fig. 9. Photomicrographs showing interaction in samples with *in situ*-deposited Ti/5000Å Au on 1.5 μm thick and annealed Al—after 4 hr/350°C/forming gas anneal. (a) 1000Å Ti; (b) 2000Å Ti; (c) 3000Å Ti.

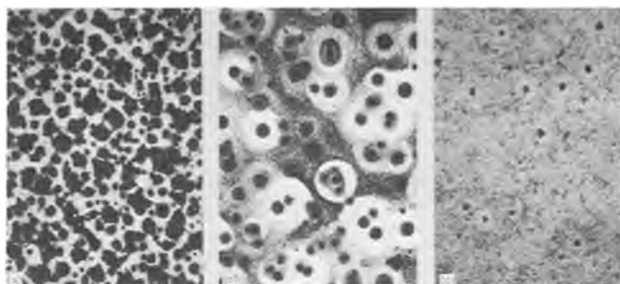

Fig. 10. Photomicrograph showing interaction in samples with *in situ*-deposited Ti/5000Å Au on 1.5 μm thick and annealed Al—after 8 hr/350°C/forming gas anneal. (a) 1000Å Ti; (b) 2000Å Ti; (c) 3000Å Ti.

on the sample with 3000Å Ti. The surface of the sample with 1000Å Ti is now purplish in color, whereas the other two surfaces are increasingly grayish black. Absence of black spots on samples with 2000Å and 3000Å Ti, in as large a number as is visible on sample with 1000Å Ti, would indicate a better coverage of Al hillocks with thicker Ti films.

The sheet resistance of the samples was measured on the top surface (Au layer) at room temperature. Figure 11 shows a plot of the sheet resistance of various Al-Ti-Au samples as a function of time. These results confirm the microscopic observations of Fig. 9 and 10. As seen in the case of Al-Pt samples (13) there is an instantaneous decrease in the sheet resistance of all the samples that could be associated with the annealing of the films. For the sample with 1000Å Ti, there is a gradual increase in the resistivity with time and at the end of 8 hr anneal there has been approximately 100% increase in ρ_s indicating considerable consumption of Al (13). There has been no change in the sheet resistivity of the sample with 3000Å Ti besides the initial decrease. After the initial decrease, there has been only slight (~6%) increase in the resistivity of sample with 2000Å titanium. There has been thus a negligible interaction involving Al since the total sheet resistivity of the Al-Ti-Au samples is largely contributed by Al only.

X-ray diffraction studies of the films after 8 hr of anneal show the intermetallics listed in Table I. In samples with 2000 and 3000Å Ti films the only identified intermetallic is Au_4Ti. On the other hand, in the sample with 1000Å Ti, $AuAl_2$ is predominantly present together with Au_4Ti.

Samples with Au deposited on air-exposed Ti.—Figure 12 shows the optical micrographs of the sample after 350°C anneal in forming gas. Note that in half of this sample Al was covered with plasma silicon nitride. Ti-Au was on top of aluminum in the other half. This enabled us to compare the Ti-Au interaction occurring on one half with Al-Ti-Au interaction on the other. Since nitride as well as Ti and Au replicate

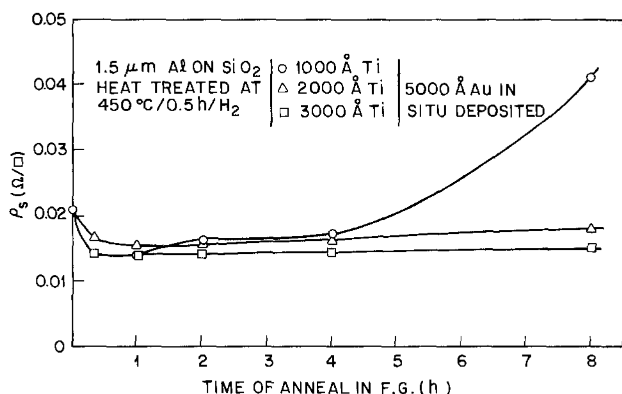

Fig. 11. Sheet resistance of various Al/Ti/Au samples as a function of time of anneal at 350°C in forming gas.

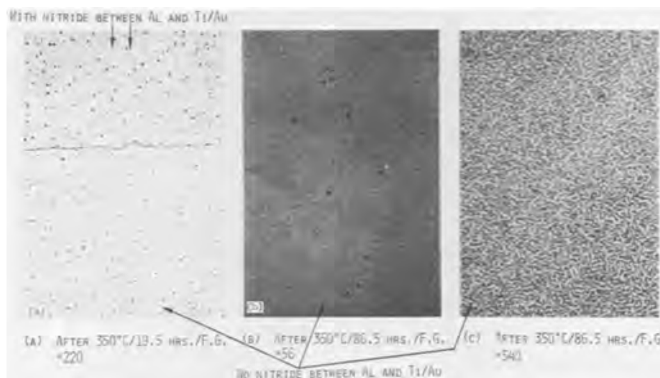

Fig. 12. Photomicrographs showing an absence of interaction on the sample with titanium exposed to air prior to gold evaporation.

the halves, they look identical and any differences in the mode of interaction could be easily detected. As can be seen in Fig. 12, there is no reaction visible even after 19.5 hr of anneal. Surface discoloration only has become visible after 86.5 hr of anneal. A few small black spots are also visible. There was no significant change in the sheet resistance of the sample of Al-Ti-Au or Ti-Au halves. X-ray diffraction study of the two halves does not show anything intermetallic. Only metallic Ti, Au, and Al are detected.

Al-Ti interaction.—We have also investigated samples with 2000Å Ti on Al annealed at 350°C up to 86.5 hr in forming gas. No interaction has been visible at the surface. There has been no significant change in the sheet resistance, indicating absence of any significant reaction. X-ray diffraction study of this sample does not show any intermetallics.

Absence of any Al-Ti intermetallic in all the samples has been unique and surprising. It would appear that under the present circumstances Al and Ti do not interact at any appreciable rate at 350°C. Bower (12) has described an Al-Ti metallization scheme and has reported the formation of $TiAl_3$ at the Ti-Al interface. The amount X of the Ti consumed to produce $TiAl_3$ was given by

$$\frac{X^2}{t} = 0.15 \exp(-1.85 \text{ eV}/kT) \text{ cm}^2/\text{sec}$$

where t is the time of anneal in seconds at the temperature T°K. This expression may be used to calculate the approximate amount of Ti consumed during 86.5 hr anneal at 350°C. Thus if the Al-Ti interaction occurred in our samples, 600Å of Ti should have been consumed to form $TiAl_3$. Such an amount of $TiAl_3$ should have been large enough to be detected by x-ray diffraction studies.

Absence of the formation of any detectable amount of Al-Ti intermetallics could be attributed to either or both of the following. (*i*) In the present case, Al films were preannealed in hydrogen at 450°C prior to Ti deposition, leading to considerable grain growth and hillock formation in Al. Such a heat-treatment of Al will retard the migration of Al in subsequent aging at lower temperatures. (*ii*) The interaction may be considered to be inhibited by the presence of the interfacial oxide layer on Al. The latter, however, would seem unlikely because unlike Pt, Ti is an excellent oxygen getter with the ability to absorb almost half its weight in reaction products interstitially. Ti will thus bond easily with Al and the presence of any oxide layer should not inhibit Al-Ti interaction. It may be noted here that Bower (12) deposited both Ti and Al at 100°C in a single evaporation during one pumpdown of the evaporator. He had thus eliminated the interfacial oxide layer formation and had low temperature Al which could react at a much faster rate than our annealed Al.

Ti-Au and Au-Al interactions.—In samples with *in situ*-deposited Ti-Au on Al, the reaction between Ti and Au seems to occur fairly rapidly in all the samples as indicated by discoloration of Au and presence of $TiAu_4$ in all the samples. Thus given enough time to interact with Ti, Au eventually could get to the Al-Ti interface, and the Al-Au interaction, which is catastrophically fast at these temperatures, would be initiated. That is what happened in the case of the sample with only 1000Å Ti between Al and Au. This amount of Ti may not be enough to cover the hillocks in Al and may have a larger density of pinholes, both of which lead to Al-Au interaction at an early stage of heat-treatment This was the case leading to the formation of $AuAl_2$ in this sample.

In samples where Au was evaporated on Ti exposed which have been annealed prior to Ti-Pt-Au metallization and (*ii*) 2000Å Ti-2000Å Pt (at least) barrier between Al and Au. The first of these two reduces flow in Al and growth of hillocks during subsequent anneals. Thicker Ti-Pt provides a good coverage on the Al hillocks and prevents Al-Pt, Al-Au, interactions any one of which could be catastrophic. The high temperature aging studies of the Al-Ti-Pt-Au composite films have thus clearly established that 2000Å Ti-2000Å Pt barrier between Al (which is annealed at 450°C) and Au beam leads forms metallurgically stable structures.

We now understand the need of a Ti-Pt (with at least ~2000Å of each) diffusion barrier between Al and Au. This understanding can be summarized in the schematic given below.

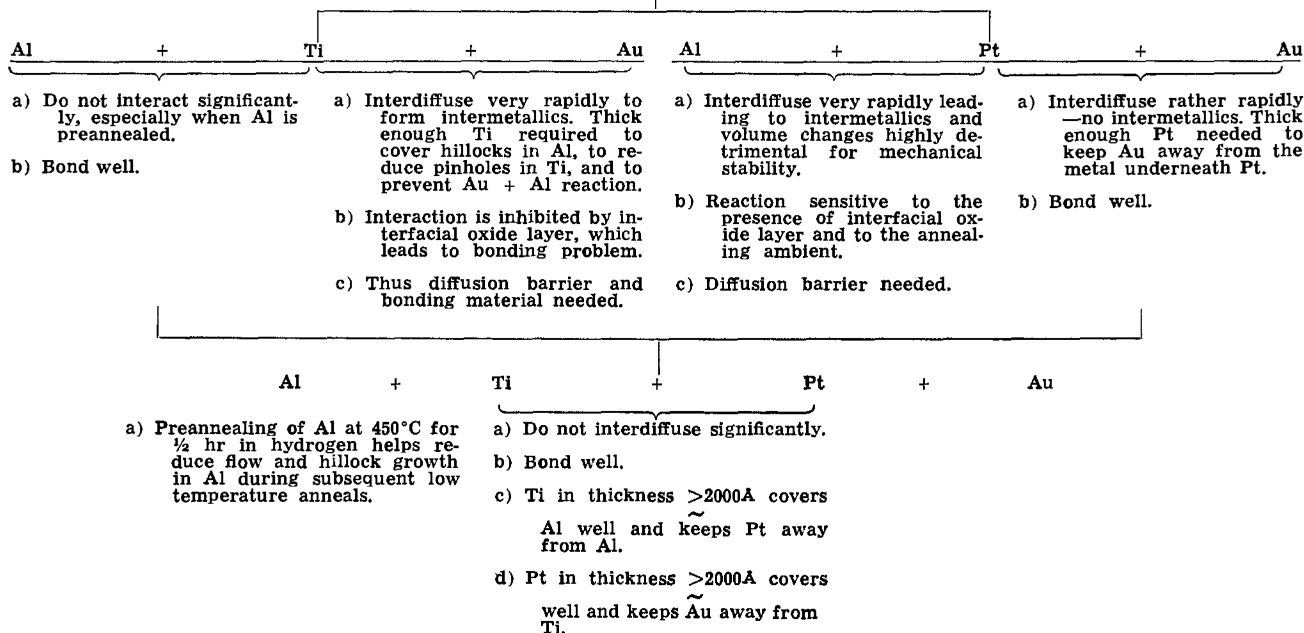

in air (Fig. 12), there was no new phase detected even after 80.5 hr of anneal, indicating absence of any significant Al-Ti, Ti-Au, or Al-Au interactions. Thus the oxidized Ti surface very effectively inhibited the Ti-Au interaction which was otherwise visible in *in situ*-deposited samples. Similar results were reported by Poate *et al.* (9) who found considerable Ti-Au interdiffusion leading to the formation of $TiAu_4$ and $TiAu_2$ in samples annealed in vacuum. For air-annealed samples, the interaction was retarded and Ti was found in oxidized form on top of the gold layer.

During preparation of the samples by evaporation of Au on air-exposed Ti, it was realized that occasionally Au film would not adhere to Ti. Since Au has very poor affinity for oxygen, such a behavior is expected. This would thus provide an additional reason to use Pt not only as the diffusion barrier between Ti and Au, but also as a bonding layer between them.

Conclusion

Results of this investigation show that the high temperature metallurgical interaction in the Al-Ti-Pt-Au composite film structures leads to the formation of several intermetallics, but only Al_2Au was detected in the x-ray diffraction studies. The reaction preferentially occurred at the hillocks in Al leading to black spot formation. The number of such spots increases with time and temperature of anneal and decreases by increasing the thickness of the Ti-Pt barrier. The reaction spreads around such reacted sites and given enough time it covers the whole surface area and entire thickness of both Al and Au. The interaction in Al-Ti-Pt-Au composite structure is drastically slowed down by use of (*i*) Al films

Acknowledgments

The authors would like to thank R. B. Marcus and R. S. Wagner for the encouragement throughout the investigation.

Manuscript submitted May 13, 1977; revised manuscript received Sept. 6, 1977.

Any discussion of this paper will appear in a Discussion Section to be published in the December 1978 JOURNAL. All discussions for the December 1978 Discussion Section should be submitted by Aug. 1, 1978.

Publication costs of this article were assisted by Bell Laboratories.

REFERENCES

1. C. Weaver, *Phys. Thin Films*, **6**, 315 (1971).
2. J. D. Speight and M. J. Bill, *Thin Solid Films*, **15**, 325 (1973).
3. G. K. Herb and E. F. Labuda, Ger. Pat. Offer. 2, 261, 337 (1973); Appl. US 209, 560 (1971).
4. A. T. English and P. A. Turner, *J. Electron. Mater.*, **1**, 1 (1972).
5. G. Lehnert and H. W. Meinhardt, *DEW Tech. Ber.*, **11**, 236 (1971).
6. T. C. Tisone and J. Drobeck, *J. Vac. Sci. Technol.*, **9**, 271 (1972).
7. C. M. Melliar-Smith and W. J. Polito, Unpublished work.
8. W. J. DeBonte, J. M. Poate, C. M. Melliar-Smith, and R. A. Levesque, *J. Appl. Phys.*, **46**, 4284 (1975).
9. J. M. Poate, P. A. Turner, W. J. DeBonte, and J. Yahalom, *ibid.*, **46**, 4275 (1975).
10. A. K. Sinha, T. E. Smith, and T. T. Sheng, *Thin Solid Films*, **22**, 1 (1974).

11. C. C. Chang and G. Quintana, *ibid.*, **31**, 265 (1976).
12. R. W. Bower, *Appl. Phys. Lett.*, **27**, 99 (1973).
13. S. P. Murarka, I. A. Blech, and H. J. Levinstein, *J. Appl. Phys.*, **47**, 5175 (1976).
14. D. P. Kolesnik, A. F. Andrushk, and Y. I. Suklinin, *Phys. Met.*, R(34), **3**, 76 (1972).
15. A. D. Paddock and J. R. Block, *This Journal*, **115**, 70C (1968).

Interaction of Fluorine and Fluorides with Tantalum, Tungsten, and Rhenium at Low Pressures and High Temperatures

J. L. Philippart, J. Y. Caradec, B. Weber, and A. Cassuto

CNRS, Laboratoire de Recherches sur les Interactions Gaz-Solides, Laboratoire Maurice Letort, B.P. 104-54600 Villers-Nancy, France

ABSTRACT

Reactions of fluorine and tantalum fluoride at low pressures with tantalum, tungsten, and rhenium at high temperatures have been investigated using line-of-sight mass spectrometry. Results are interpreted using a model which assumes: dissociative adsorption of incident molecules; surface reactions of adsorbed species; and desorption of products. Dissociative adsorption occurs upon each collision of the gaseous reactant with the surface. The adsorption is followed by the rapid establishment of a thermodynamic surface equilibrium. The model shows that the valency of the products decreases as the substrate temperature is increased in agreement with experimental results. The model has been used to predict the possibility of chemical vapor deposition at low temperatures by means of disproportionation reactions. The prediction has been verified.

In previous studies of reactions on a high temperature tantalum surface involving chlorine (1) and tantalum pentachloride (2) at low pressures, a reaction mechanism was proposed and shown to be consistent with the experimental results. This mechanism assumed dissociative adsorption followed by surface reactions in which the desorption products are formed. Quantitatively, the model is an extension of one proposed for oxidation reactions of transition metals by molecules other than oxygen (3-5). Using this model we were able to explain some chemical vapor deposition reactions involving chlorine and chlorides (2, 6). This study presents similar results for fluorine and tantalum pentafluoride reactions with tantalum, tungsten, and rhenium. The same model has been applied and has been found to be valid.

Experimental

The main apparatus has been described previously (4). Basically it consists of a ribbon, heated by direct current, enclosed in a cooled reactor which is in turn enclosed in the main vacuum chamber. The reactor has a slit directly in front of the ribbon through which it is pumped. This slit defines a molecular beam for unstable and condensible products which then can pass directly into the ionization chamber of the mass spectrometer (Veeco GA5). A second slit, positioned in front of the ionization chamber, prevents any collisions with the walls of the mass spectrometer. A shutter allows interruption of the beam. After bakeout, the system regularly attains vacua of the order of 5×10^{-10} Torr.

The samples (tantalum, tungsten, and rhenium ribbons of dimensions 20 mm × 2 mm × 30 μm supplied by Heraeus, initial purity 99.95%) are recrystallized at high temperature (2200°K) and carbon is removed by heating in oxygen at 10^{-6} Torr for 24 hr. After flashing off the oxygen in vacuum, AES shows less than 1% impurities on the surface. X-ray back-reflection analysis shows {110} orientation parallel to the surface for tantalum with large grains, several centimeters long; {0001} orientation for rhenium with small grains of the order of 0.1 mm with a possible 10° misorientation; and {111}, {100}, {110} orientations for tungsten.

Gaseous reactants (fluorine and pentafluoride, Comurhex) are distilled in a stainless steel inlet system and transferred into a gas reservoir confined between two valves. One of the valves is a leak valve connected directly to the reactor. Because of reactions at the walls of the vacuum system, HF and O_2 levels cannot be decreased below a few percent. Various fluorides are also observed, resulting from parasitic reactions, as well as fluorine atoms, even when the sample is cold. This phenomenon, which was described in a previous study (7), may be interpreted in terms of reactions with the walls and the filament of the mass spectrometer. It restricts the precision of the measurements and the detection limit of the reaction products, particularly fluorine atoms.

Calibration Procedures

From the pumping speed of the main vacuum system, the mass spectrometer is calibrated by a dynamic flow technique. From the dimensions of the slit connecting the reactor to the main system the pressure around the sample is deduced.

When a simple product can be identified in a restricted temperature range its flux is determined from a material balance, and the over-all yield of the reaction B can be written

$$B = 1 - \frac{P}{P_o} \quad [1]$$

where P is the pressure of reactant during the reaction and P_o the reactant pressure without reaction, with the ribbon cold. For a perfect isotropic reactor B can be expressed as $\nu b/1 + \nu b$ (8) where b is the reactive sticking probability and ν the mean number of collisions of the reactant molecules with the surface before being pumped away from the reactor. The net flux per square centimeter and per second is therefore, if fluorine is the reactant

$$Z_{M_xF_y} = \frac{2}{y} p_{F_2} b/\sqrt{2\pi M_{F_2} k T_g} \quad [2]$$

Key words: fluorine, tantalum fluoride, line-of-sight mass spectrometry.

[Corrections to b due to pressure anisotropy are obtained by comparison with oxidation reactions (9)]. Assuming complete equilibrium between desorbed products and surface temperatures, flux values are derived from measured ionic currents using the relation $Z_x = I_x T^{1/2}$.

For the production of fluorine atoms occurring at high substrate temperatures because of the background at m/e = 19, intensities at m/e = 9.5 have been used with the shutter close to the mass spectrometer open. When only fluorine atoms are produced, the atomic flux is strictly proportional to $|I_{F^{++}} - (1 - B) I^{\circ}_{F^{++}}|$. $I_{F^{++}}$ and $I^{\circ}_{F^{++}}$ represent the ion intensities when the ribbon is hot and cold. B is obtained from the fluorine pressure variations between reacting and nonreacting conditions. When monofluoride is also formed at high temperatures (on tantalum), its flux is obtained from the total yield of the reaction and the fluorine atom flux (neglecting the contribution of TaF to m/e = 9.5). TaF desorption corresponds to only 6% of the over-all fluorine reaction yield. Finally this TaF_5 pressure is estimated by comparison with fluorine, using the two observed reactions

$$F_2 + \text{Surface} \rightarrow 2F.$$

$$TaF_5 + \text{Surface} \rightarrow 5F. + Ta$$

Reactions with Fluorine

Reports that high valency fluorides and chlorides do not yield parent peaks in the mass spectrum (10, 11) have been confirmed in this laboratory using $TaCl_5$ and TaF_5, and so TaF_4^+ and WF_5^+ peaks have been used to measure TaF_5 and WF_6 partial pressures. All analyses have been performed using 150 eV electron beam energies to overcome the problem of sensitivity of the mass spectrometer at lower ionization energies.

Fortunately, by varying the temperature, constant mass spectra are obtained for tantalum and rhenium in restricted temperature ranges. Results, given in Fig. 1 and 2, include fluorine atom production. Tables I and II analyze the mass spectra of the observed fluorides; their nature is identified using the quantitative analysis of the data and are presented in the next section.

With tungsten, the separation of WF_6 and WF_5 formation is almost impossible (11); except at very high temperatures where only fluorine atoms are formed, no constant spectrum is observed. However, progressive transfer from production of the high valency fluoride, WF_6, to the lower valency WF_5 is clear as the temperature increases from 1200° to 1500°K.

Fluorine atoms are produced on all three metal surfaces. Figures 3-5 are representative of the results. At high temperatures and low pressures, atomic fluorine

Table I. Mass spectra of tantalum fluorides

(Relative intensities)
(Ionization energy: 150 eV)

Neutral species \ Ions	TaF_5^+	TaF_4^+	TaF_3^+	TaF_2^+	TaF^+	Ta^+
TaF_5	—	100	8	9	10	13
TaF_4	—	100	34	18	10	—
TaF_3	—	—	87	100	30	—
TaF	—	—	—	—	100	~20

Table II. Mass spectra of rhenium fluorides

(Relative intensities)
(Ionization energy: 150 eV)

Neutral species \ Ions	ReF_6^+	ReF_5^+	ReF_4^+	ReF_3^+	ReF_2^+	ReF^+	Re^+
ReF_6	1	40	100	10	15	10	8
ReF_4	—	—	63	100	66	35	67

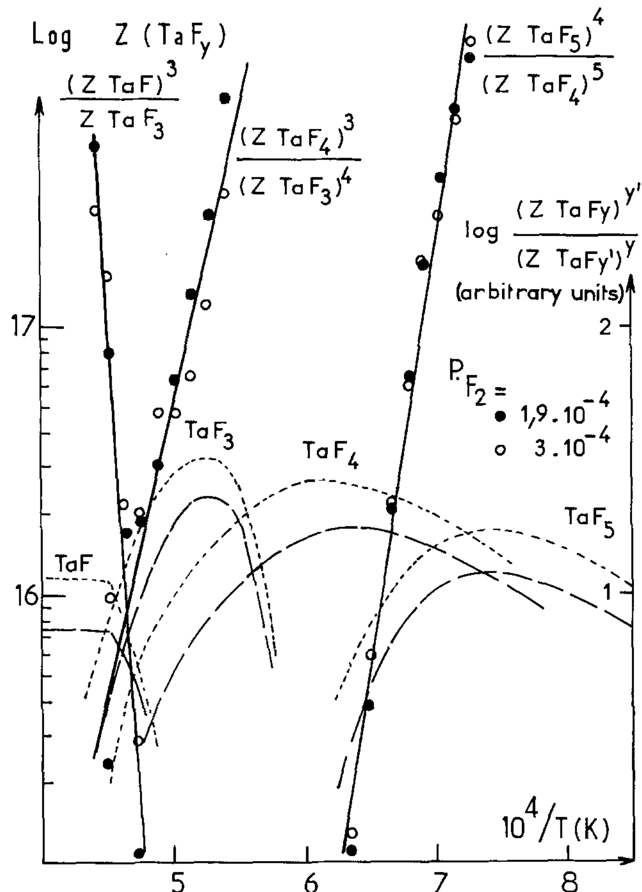

Fig. 1. Desorption of products in the tantalum-fluorine system and values of the ratio $(Z_{TaF_y})^{y'}/Z_{TaF_{y'}})^y$ (see text).

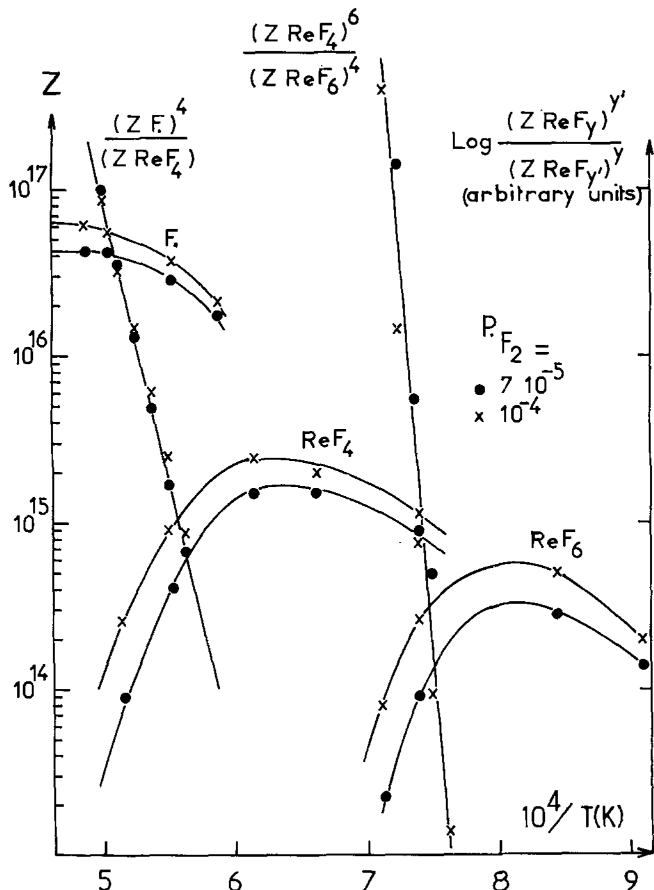

Fig. 2. Desorption of products in the rhenium-fluorine system and values of the ratio $(Z_{F.})^4/(Z_{ReF_4})$ and $(Z_{ReF_4})^6/(Z_{ReF_6})^4$ (see text).

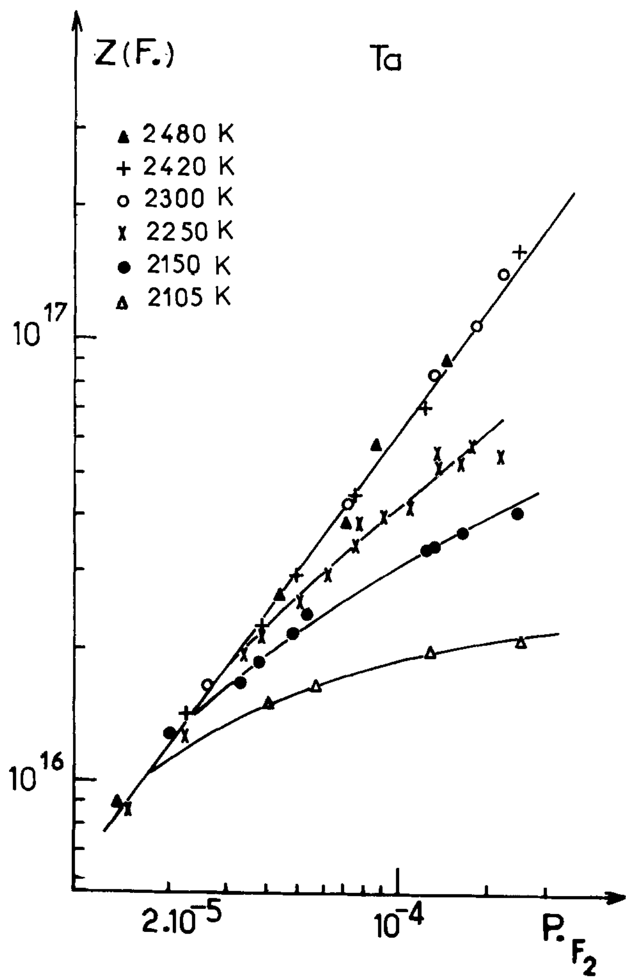

Fig. 3. Desorption isotherms of atomic fluorine during reaction of molecular fluorine with tantalum.

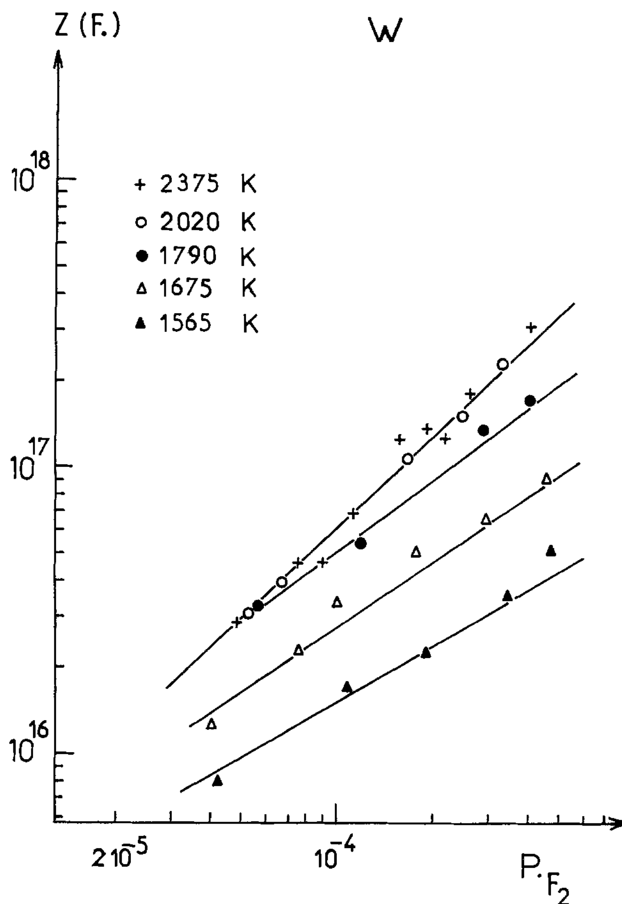

Fig. 4. Desorption isotherms of atomic fluorine during reaction of molecular fluorine with tungten.

production is first order with pressure and is characterized by unit sticking coefficient.

Quantitative interpretation.—The same model which was applied to oxygen-transition metal interactions (5, 12) and more recently to tantalum-chlorine (1) and tantalum-chlorides (2) interactions is developed here. The elementary steps are: a nonactivated dissociative adsorption

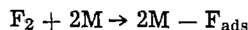

$$F_2 + 2M \rightarrow 2M - F_{ads}$$

followed by desorption of products

$$y(MF)_{ads} \rightarrow M_xF_y + (y - x)M$$

Table III defines x and y values for the various reactions.

Qualitatively, it is clear that as the substrate temperature increases, the valency of the product fluorides must decrease. Taking θ as the fluorine atom coverage, defined as the ratio of the number of fluorine atoms adsorbed to the maximum possible number of fluorine

Table III. Halides formation

Metal	x	y	Product
Ta	0	1	F
	1	1	TaF
	1	3	TaF_3
	1	4	TaF_4
	1	5	TaF_5
Re	0	1	F
	1	4	ReF_4
	1	6	ReF_6
W	0	1	F
	1	5	WF_5
	1	6	WF_6

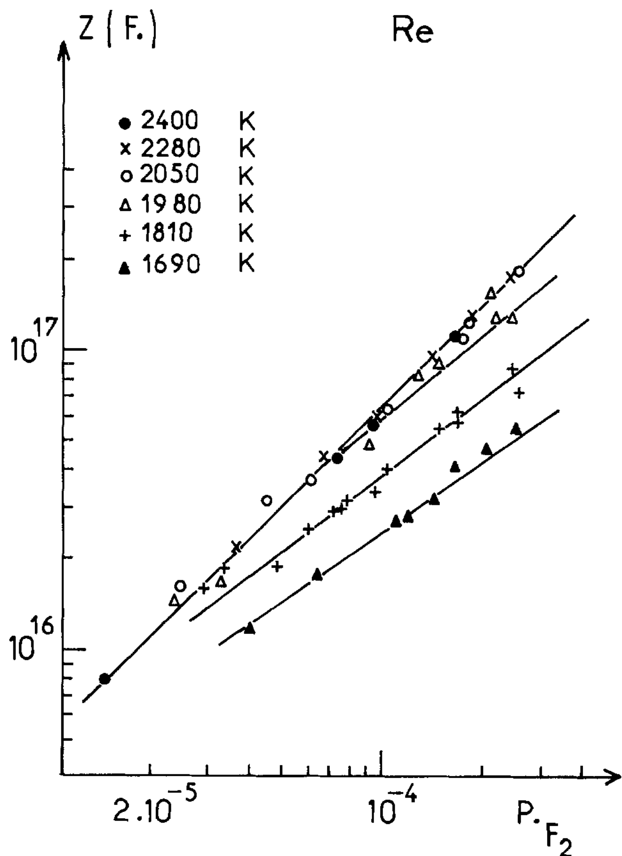

Fig. 5. Desorption isotherms of atomic fluorine during reaction of molecular fluorine with rhenium.

atoms adsorbed, the desorption flux can be written

$$Z_{M_xF_y} = \nu_{M_xF_y}(n_s\theta)^y \exp - \left| \frac{y\chi(\theta) + xL_M - \epsilon_{M_xF_y}}{RT} \right| \quad [3]$$

where $\nu_{M_xF_y}$ represents a preexponential factor, n_s the number of adsorption sites, $\chi(\theta)$ the heat of chemisorption of fluorine atoms, L_M the heat of sublimation of the metal M, and $\epsilon_{M_xF_y}$ the heat of formation of the gaseous product M_xF_y, from gaseous metal and fluorine atoms.

Since the $\epsilon_{M_xF_y}$ values are unknown for most of the fluorides ($y < 4$), direct comparison is difficult. However, using two values of the flux, θ and χ can be eliminated and we obtain expressions of the general form

$$\frac{(Z_{M_xF_y})^{y'}}{(Z_{M_{x'}F_{y'}})^y} = \frac{(\nu_{M_xF_y})^{y'}}{(\nu_{M_{x'}F_{y'}})^y} \cdot \exp \left| \frac{y'\epsilon_{M_xF_y} - y\epsilon_{M_{x'}F_{y'}} - (xy' - x'y)L_M}{RT} \right| \quad [4]$$

The main advantage of these expressions for testing the model is that they are dependent only on temperature and not pressure. A set of such ratios is given in Fig. 1 and 2.

Knowing ϵ_{TaF_5} (13) we calculate, $\epsilon_{TaF_4} = 580$ kcal/mole, $\epsilon_{TaF_3} = 430$ kcal/mole, and $\epsilon_{TaF} = 180$ kcal/mole using relation [4] and compare them with the corresponding values estimated by Zmbov and Margrave (10), (assuming that Ta-F bonds are identical in all fluorides), 576, 432, and 144 kcal/mole, respectively.

There is a discrepancy only for TaF. Experimentally, at high temperatures the ratio $Z_{TaF}/Z_{F.}$ is constant. Our model predicts such a constancy if $\epsilon_{TaF} \simeq L_{Ta} =$ 189 kcal/mole. Two independent determinations ($Z_{TaF}/Z_{F.}$ and $[Z_{TaF_3}/(Z_{TaF})^3]$ confirm that ϵ_{TaF} is of the order of 180 kcal/mole. The agreement between our ϵ' values for TaF_4, TaF_3, and Ref. (10) plus the pure TaF_5 mass spectrum confirm the nature of the tantalum fluorides.

In the case of the high temperature fluoride, an alternative could be TaF_2 production instead of TaF. Using TaF^+ ions as a measure of Z_{TaF_2}, a straight line is indeed obtained when $Z_{TaF_2}/(Z_{F.})^2$ *vs.* $1/T$ is plotted. But ϵ_{TaF_2} then appears to be 380 kcal/mole, an unrealistic value when compared to 430 for ϵ_{TaF_3} and 290 calculated with an average 144 kcal/atom derived from $\epsilon_{TaF_5} = 720$ kcal/mole.

In the case of rhenium, ϵ_{ReF_4} is again determined, by comparison with the ReF_6 or F. flux. The two values are respectively 370 and 350 kcal/mole. The difference between these two values gives an idea of the uncertainties in the measurements. The data have also been analyzed assuming ReF_4 production at high temperatures. To choose between ReF_4 and ReF_5 production, a plot of $Z_{ReF_5}/(Z_{F.})^5$ *vs.* $1/T$ has been made, using the ReF_4^+ ion intensity as a measure of Z_{ReF_5}. The ϵ_{ReF_5} value determined in this way leads to an average value of 60 kcal for the Re-F bond. This value is inconsistent with the 95 kcal per bond, determined from heat of formation of ReF_6 (14). A similar argument holds in the low temperature range. ReF_7 formation instead of ReF_6 formation is excluded because no straight line is obtained when $(Z_{ReF_4})^7/(Z_{ReF_7})^4$ *vs.* $1/T$ is plotted.

In a recent investigation of the fluorine-tantalum system, using a modulated molecular beam, Ollander (15) proposed an alternative mechanism for TaF_5 desorption in a lower temperature range. The main step is the diffusion of fluorine atoms through a subhalide surface layer. In our temperature and pressure range, we are in the submonolayer coverage range and that kind of mechanism may not apply. Agreement of the experimental results with our model when volatile products are formed is therefore again satisfactory as in the case of the formation of oxides and chlorides. Even at higher pressures (10^{-2}-10 Torr) similar products are observed, using infrared spectroscopy (6). The only change is a shift towards higher temperatures at the higher pressures.

Reaction Products Using Fluorides—Application to Chemical Vapor Deposition

Tantalum pentafluoride.—The reaction of TaF_5 and tantalum gives the same products as those observed when fluorine reacts with this metal. As the temperature is increased, TaF_4, TaF_5, and finally fluorine atoms are observed. However, because the incident molecule contains a tantalum atom, the over-all reaction can be either one of attack or of deposition, depending on the temperature range. The reaction can be followed by resistivity measurements.

At low temperatures (~ 1200°K), TaF_5 is produced by reaction of F_2 and tantalum, and therefore no decomposition of TaF_5 occurs. At higher temperatures (above 1300°K) TaF_4 and TaF_3 appear resulting from the attack reactions

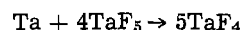

$$Ta + 4TaF_5 \rightarrow 5TaF_4$$

$$2Ta + 3TaF_5 \rightarrow 5TaF_3$$

Finally, at temperatures above 2000°K fluorine atoms are the major product and tantalum deposition is observed.

This result confirms the low value observed for TaF desorption when using fluorine molecules at high temperatures. The reaction of TaF_5 with tantalum leads to deposition only if the TaF flux represents less than 20% of the over-all reaction flux. The experimental value of 6% is consistent with this argument. It also explains, due to the high fragment peak coming from TaF_5, why no measurement of TaF production has been possible when TaF_5 decomposition occurs.

X-ray back-reflection analysis indicates complete epitaxy of the deposited tantalum on recrystallized {110} tantalum, even up to thicknesses of 90 μm (three times the original ribbon thickness). Microscopic examination shows that tantalum crystals develop simply perpendicularly to the surface, keeping the same grain boundaries and crystallite cross sections.

The model proposed for fluorine reactions is therefore still valid if one assumes that after dissociative adsorption and incorporation of tantalum atoms into the lattice, forgetting their origin, reaction products are determined only by the temperature and coverage of fluorine atoms. Such an interpretation has already been proposed in the case of $TaCl_5$ reactions on tantalum (2).

This interpretation is confirmed by observing TaF_5 reactions on tungsten. At low temperatures (~ 900°K), WF_6 is the only product formed. Its production rate decreases with time, simultaneously with the growth of a tantalum layer. If the tantalum is removed from the surface by dissolution into the bulk at high temperatures, the same experiment may be repeated on the now clean surface. In the high temperature range, where tantalum is dissolved in tungsten (> 2000°K), fluorine atoms become the only product. Using this technique, tantalum-tungsten homogeneous alloys have been prepared with a variable tantalum atom concentration between 10 and 40%.

Despite difficulties in interpreting the data due to the complexity of the phase diagrams, TaF_5 reactions with rhenium lead to the same result: it is possible to prepare tantalum-rhenium alloys or compounds with a variable but controlled composition.

Reactions of low valency fluorides.—The model predicts that disproportionation reactions such as

$$5TaF_4 \rightarrow 4TaF_5 + Ta$$

or

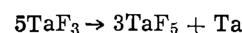

$$5TaF_3 \rightarrow 3TaF_5 + Ta$$

are possible in a temperature gradient and may lead to tantalum deposition at low temperatures, as in the

case of chlorides (6). The principle of the experiment is simple. It consists of the attack by TaF_5, of a tantalum ribbon at a temperature above 1300°K (where TaF_4 or TaF_3 are formed), and consecutive reaction of the low valency fluoride products with a second tantalum sample, maintained at a lower temperature (600°-1000°K), where TaF_5 is the stable product. A double ribbon arrangement has been used to confirm this hypothesis. Resistivity measurements were used as a continuous control of the high temperature ribbon attack and the low temperature ribbon growth. Using such an arrangement tantalum deposits have been formed on substrates in the (600°-1000°K) temperature range. Confirmation of the process was obtained in a higher pressure range (10^{-2}-1 Torr) using gravimetric measurements.

Conclusion

As in the case of reactions with chlorine molecules and chlorides, fluorine and fluoride reactions can be described by a mechanism involving, as a first step, dissociative adsorption and product formation controlled by the halogen atoms surface coverage. This depends on the temperature and the pressure, but is independent of the means to bring halogen atoms to the surface. This mechanism is an extension of the model previously used to describe oxidation reactions of transition metals (3-5, 12).

The model leads to a general method for chemical vapor deposition at low temperatures, without the help of hydrogen for most of the transition metals, which form halides of more than one valency. An arrangement of two samples at different temperatures was used to demonstrate the deposition of tantalum and other metals, using chloride or fluoride reactions on different substrates at low temperatures. The resulting deposits have good adhesion.

Acknowledgments

We should like to thank M. Housley for his help in the translation of this paper.

Manuscript submitted May 19, 1977; revised manuscript received Aug. 29, 1977.

Any discussion of this paper will appear in a Discussion Section to be published in the December 1978 JOURNAL. All discussions for the December 1978 Discussion Section should be submitted by Aug. 1, 1978.

REFERENCES

1. B. Weber, J. L. Philippart, and A. Cassuto, *Surf. Sci.*, **52**, 311 (1975).
2. J. Y. Caradec, J. L. Philippart, B. Weber, and A. Cassuto, *ibid.*, **54**, 593 (1976).
3. J. C. Batty and R. E. Stickney, *J. Chem. Phys.*, **51**, 4475 (1969).
4. B. Weber and A. Cassuto, *Surf. Sci.*, **36**, 81 (1973).
5. B. Weber and A. Cassuto, *ibid.*, **39**, 83 (1973).
6. J. Y. Caradec, J. L. Philippart, G. Piquard, M. Bargues, and G. Metay, *Le Vide*, **182**, 69 (1976).
7. J. D. McKinley, *J. Chem. Phys.*, **45**, 1690 (1966).
8. P. Le Goff, *ibid.*, **53**, 359 (1956).
9. N. Pacia, J. A. Dumesic, B. Weber, and A. Cassuto, *J. Chem. Soc., Faraday Trans. 1*, **72**, 1919 (1976).
10. M. Zmbov and J. L. Margrave, *J. Phys. Chem.*, **72**, 1099 (1968).
11. W. E. Falconer, G. R. Jones, W. A. Sunder, and M. S. Vasile, *J. Fluorine Chem.*, **4**, 213 (1974).
12. B. Weber and A. Cassuto, in "Reaction Kinetics in Heterogeneous Chemical Systems," P. Barret, Editor, p. 353, Elsevier Scientific Publishing Co., Amsterdam (1975).
13. Ya I. Gerassimov, V. I. Lavrentiev, O. Van Goldbeck, D. T. Livey, R. Ferro, and A. L. Dragoo, in "Tantalum: Physico-Chemical Properties of its Compounds and Alloys," O. Kubachewski, Editor, Atomic Energy Review, Special Issue No. 3, International Atomic Energy Agency, Vienna (1972).
14. C. E. Wicks and F. E. Block, in "Thermodynamic Properties of 65 Elements, their Oxides, Halides, Carbides, and Nitrides," Bureau of Mines, Bulletin 605 (1963).
15. A. Machiels and D. R. Ollander, Submitted to *Surf. Sci.*

Technical Notes

Irregular Growths of $B(OH)_3$ on the Surface of Oxidized Silicon

M. Crooke, S. Wittstock, and E. Köck

National Electrical Engineering Research Institute, Solid State Electronics Division, Council for Scientific and Industrial Research, Pretoria 0001, South Africa

During process experimentation for new bipolar logic circuits, growths emanating from the oxidized silicon surface were observed. These growths are tentatively identified as crystalline orthoboric acid, $B(OH)_3$.

To accommodate the requirements of the design engineer for new experimental logic circuits, it was necessary to perform an extra p^+ (boron) deposition (and simultaneous shallow diffusion) at the termination of the normal high temperature processing sequence of the standard npn bipolar process.

About three days later growths were observed on the oxidized silicon wafer surface. Available literature was consulted and a limited number of tests were performed on the sample in the time available, which gave rise to the belief that these growths are composed of orthoboric acid, $B(OH)_3$. Optical photographs and scanning electron micrographs as well as the results of energy dispersive x-ray (EDX) analysis of the growths are provided in support of this tentative supposition.

Key words: crystalline orthoboric acid, orthoboric acid growths, boron deposition, storage conditions.

Experimental

When the additional p^+-window photomask was applied ~18 hr after the diffusion of the n^+ (phosphorus) emitter, no surface irregularities were visible. After a further 18 hr had elapsed, the additional p^+(boron) deposition was performed but not deglazed. The wafer was stored and submitted for further photoprocessing (contact windows) about 66 hr later. It was at this stage that the growths on the

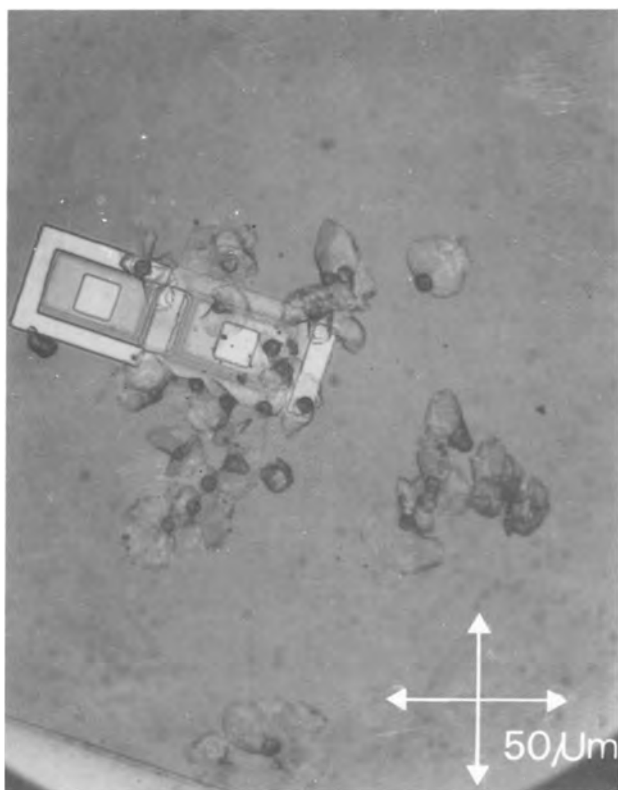

Fig. 1. Optical micrograph showing appearance of the surface irregularities on and around a photoengraved device.

wafer surface were observed through an optical microscope with coaxial illumination in white light.

Figure 1 illustrates the appearance of these growths so observed, which in our laboratories were labeled "butterflies" and "fans". These terms describe in some measure the region of irregularity emanating from a "nucleus" which is not necessarily visible or central to the effect. The fan appears to be relatively thin and largely transparent, particularly where it extends over an opened window in the SiO_2 layer, as the window edge can be seen through it.

With the assistance of a scanning electron microscope (SEM), Fig. 2 and 3 show that the nucleus observed optically now appears to be a surface mound from which the fan emanates. However, only two of these were observed. When observed at high angles of tilt (from the vertical) Fig. 4 indicates fans which have probably collapsed as a result of "rough" handling, or grown so large that they could no longer be supported by the mound. Figure 5 shows a mound without the fan. On this basis, the fans appear to be surface rather than bulk and do not appear to have caused any damage to the surface.

The EDX attachment coupled to the SEM is a rapid qualitative method for determining the presence of elements of atomic number $Z \geq 11$ (Na). (Na represents the lower limit of element detection in this case, due to the low detection efficiency for elements of $Z \leq 11$ caused by detector window absorption of these characteristic x-rays). EDX analysis showed the absence of any element with $Z \geq 11$ in an amount greater than the detection limit [about 0.1-1.0 weight percent (w/o)] which therefore excludes the possibility of phosphorus ($Z = 15$) from the deposition and diffusion for the n^+ (phosphorus) emitter, being a component in either the fan or mound.

Project demands at this stage prevented further sophisticated analyses. It was observed, prior to further photoprocessing, that all the fans had been removed from the surface and only a few mounds of very much reduced size remained after cleaning the wafers in boiling trichloroethylene, cold acetone, and rinsing them in cold water. As a large percentage of the fans were only resting on the surface (see Fig. 4) these could easily be removed, but the continued existence of a few mounds on the surface (see, for example, Fig. 5) after this cleaning process indicates their more permanent character. Attempts to regrow the fan were unsuccessful.

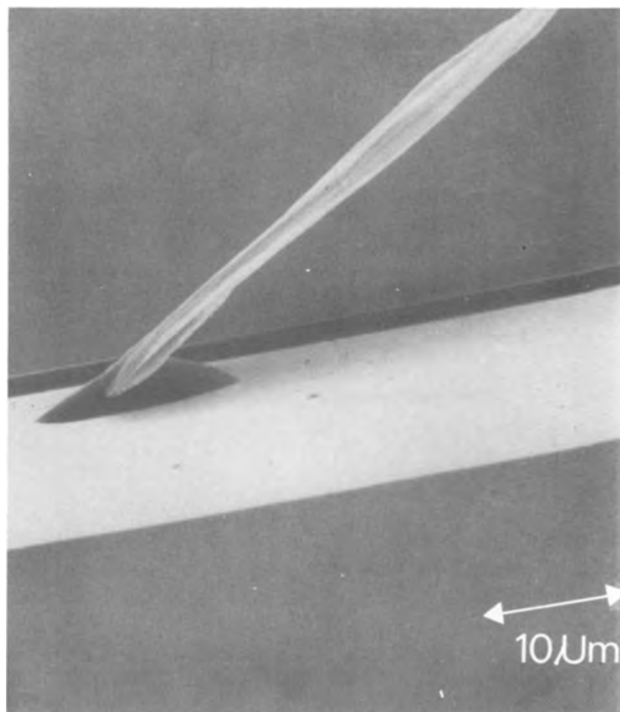

Fig: 2. SEM micrograph of the fan and mound seen edge-on (width of channel is 110 µm).

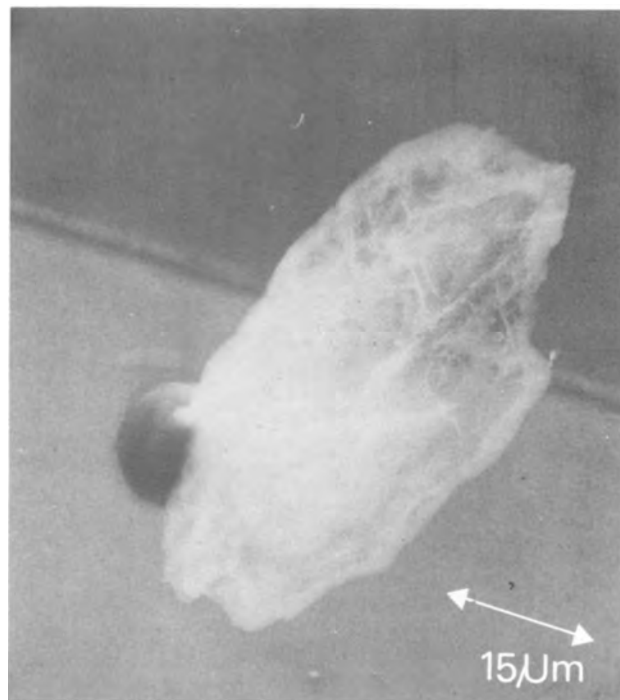

Fig. 3. SEM micrograph of the fan and mound when taken at a low angle of tilt.

Discussion

As EDX has excluded phosphorus and its compounds as a constituent of the fan—certainly in an amount greater than the detection limit—its com-

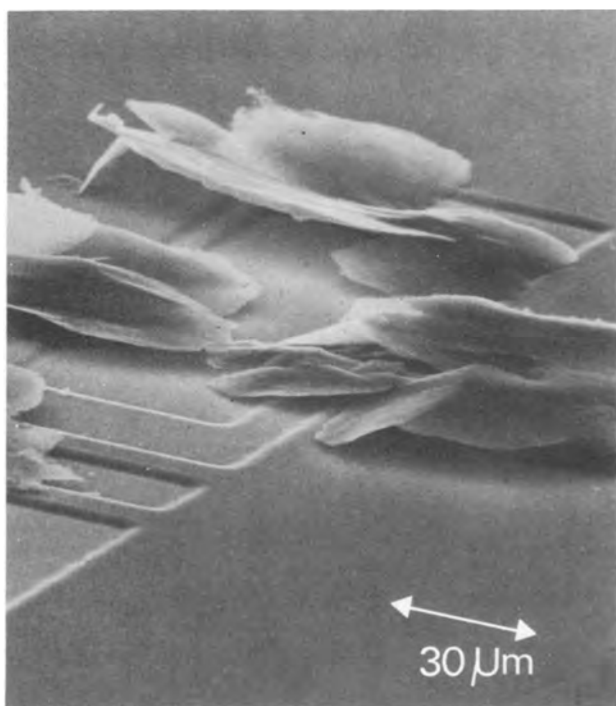

Fig. 4. SEM micrograph showing collapsed fans over a photoengraved device, (76° tilt).

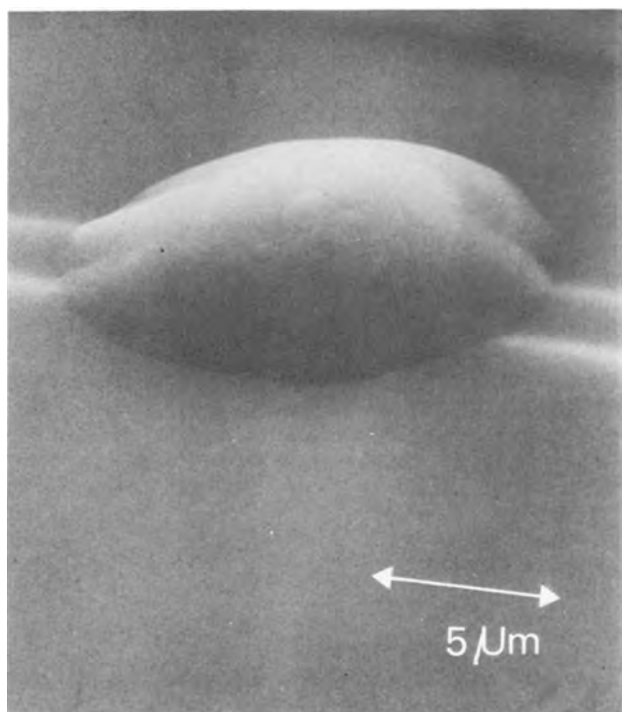

Fig. 5. SEM micrograph of a single mound, (65° tilt)

position is dependent on the major compounds involved at the last high temperature (1323°K) boron deposition stage (involving oxidized boron nitride disks) and the subsequent reaction of these compounds with water vapor of the room air. These include B_2O_3 (1) (boric oxide) and HBO_2 (2, 3) (metaboric acid.[1] Thus the mound and the fan probably contain the element boron ($Z = 5$) in some combination with appropriate elements that were similarly not detected by EDX, *viz.* oxygen and/or hydrogen. Due to the great difficulty in crystallizing (5) glassy B_2O_3 (*i.e.*, transforming a randomly ordered three-dimensional network into an ordered one at room temperature) the possibility that they contain boron and oxygen only, as B_2O_3, was excluded. It was thus inferred that the mound and the fan consist largely of boron and hydroxyl groups from the reaction of the oxide of boron with the water vapor of the room air. Although relatively slow compared to the pure B_2O_3 films, water absorption in the mixed $(yB_2O_3 \cdot zHBO_2)xSiO_2$ (borosilicate) glass film, which forms on the surface of the passivating SiO_2 during the high temperature boron deposition, is rapid in environments of high relative humidity and is largely dependent on the B_2O_3 content of the film (6-8).

[1] Particularly in the presence of water vapor, a small percentage which occurs in the ultrahigh purity argon (99.995% min.) employed, the following reaction takes place preferentially (2, 4)
$B_2O_3(s \text{ or } l) + H_2O(g) \rightarrow 2HBO_2(g) \quad \Delta H^\circ = 47.6$ kcal/mole

Thermodynamic data and hydration reactions of interest concerning the change from the glassy B_2O_3 to the whitish, powdery substance that occurs particularly when the boron nitride deposition system is removed from the furnace and permitted to cool to room temperature in the moist atmosphere of the clean work station before storage, include (9-11)

$$B_2O_3 + H_2O \rightarrow B_2O_3 \cdot H_2O \cdots\cdots 2HBO_2$$

$$HBO_2 + H_2O \rightarrow HBO_2 \cdot H_2O \cdots\cdots B(OH)_3$$

(orthoboric acid)

i.e.

$$B_2O_3(\text{glass}) + 3H_2O(l) \rightarrow 2B(OH)_3(s)$$

$(\Delta H^\circ = -9.1$ kcal/mole$)$

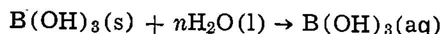

$$B(OH)_3(s) + nH_2O(l) \rightarrow B(OH)_3(aq)$$

$(\Delta H^\circ = -5.2$ kcal/mole$)$

The heat of hydration of amorphous $B_2O_3 \rightarrow$ crystalline $B(OH)_3$ is -18.3 kcal/mole.

During storage in a sealed container that traps a portion of the atmosphere of the same relative humidity as the working area, the hydration reaction proceeds over a period of many hours at a rate that is determined by the diffusion coefficient of water in the borosilicate glass film at room temperature. The reaction continues until the water vapor present in the container is depleted. According to Arai (7) the $B(OH)_3$ migrates out of the boron-rich surface, leaving water behind.

On the basis of this limited information, it is inferred that the fan observed is composed of crystalline orthoboric acid, $B(OH)_3$, and the mound of concentrated aqueous $B(OH)_3$ in which an impurity has provided the seed for crystalline growth of the fan.

Because the logic circuits were experimental in nature, they were exposed to the ambient and stored for periods longer than normal during the p^+ deposition evaluation. Under the proper processing conditions of minimum storage time in a dry ambient, these growths would not normally be observed. The growths of orthoboric acid can be removed by rinsing in pure methanol (8).

Acknowledgments

The authors acknowledge the assistance of Mr. S. A. Smithies, the Electron Microscopy Division of the National Physical Research Laboratory of the CSIR, and the reviewers for their comments and suggestions.

Manuscript submitted June 9, 1977; revised manuscript received Aug. 31, 1977.

Any discussion of this paper will appear in a Discussion Section to be published in the December 1978 JOURNAL. All discussions for the December 1978 Discussion Section should be submitted by Aug. 1, 1978.

Publication costs of this article were assisted by the Council for Scientific and Industrial Research.

REFERENCES
1. "Comprehensive Inorganic Chemistry," Vol. 1, A. F. Trotman-Dickenson *et al.*, Editors, p. 881, Pergamon Press, Oxford (1973).
2. D. J. Meschi, W. A. Chupka, and J. Berkowitz, *J. Phys. Chem.*, **33**, 530 (1960).
3. S. P. Randall and J. L. Margrave, *J. Inorg. Nucl. Chem.*, **16**, 29 (1960).
4. "Comprehensive Inorganic Chemistry," Vol. 1, A. F. Trotman-Dickenson *et al.*, Editors, p. 882, Pergamon Press, Oxford (1973).
5. *ibid.*, p. 880.
6. E. A. Taft, *This Journal*, **118**, 1985 (1971).
7. E. Arai and Y. Terunuma, *ibid.*, **121**, 676 (1974).
8. W. Kern, *RCA Rev.*, **32**, 429 (1971).
9. J. W. Mellor, "A Comprehensive Treatise on Inorganic and Theoretical Chemistry," Vol. V, pp. 43 and 48, Longmans, Green and Co., London (1946).
10. F. A. Cotton and G. Wilkinson, "Advanced Inorganic Chemistry," 2nd ed., p. 266, Wiley Interscience, New York (1966).
11. "Comprehensive Inorganic Chemistry," Vol. 1, A. F. Trotman-Dickenson *et al.*, Editors, pp. 882 and 884, Pergamon Press, Oxford (1973).

The Reduction of Poly-Si Dissolution and Contact Resistance at Al/n-Poly-Si Interfaces in Integrated Circuits

H. M. Naguib* and L. H. Hobbs

Bell-Northern Research, Ottawa, Ontario, Canada K1Y 4H7

In a previous investigation (1), we reported a rapid increase in Al/n-poly-Si contact resistance following 5 min isochronal sintering at temperatures in excess of 450°C. This increase in contact resistance, R_c, was attributed to the precipitation of a p-type (Al-doped) layer on n-poly-Si with the consequent formation of a "quasi-Schottky diode." To minimize this effect, the thickness of this precipitated layer should be kept to a minimum. Practically, this can be achieved by: (*i*) decreasing the amount of Al available for reaction by reducing the thickness of the Al metallization; (*ii*) placing a Ti barrier film between the Al layer and the Si substrate; or (*iii*) using Al-2% Si alloy. The aim of the present investigation is to evaluate the validity of these various metallization techniques for application in the fabrication of Si integrated circuit using standard processing techniques.

Experiments

The phosphorus-doped poly-Si (CVD layer, 0.3 μm thick, sheet resistivity of ~17 $\Omega/\square$) resistors used in the present investigation were prepared using the same resistor structure and the same process sequences as described in the previous paper (1). The metallization systems used were the following: (*i*) Al deposited by electron beam evaporation to thicknesses of 0.25 and 1.0 μm; (*ii*) a 0.25 μm layer of Ti deposited by electron beam evaporation followed by 0.7 μm of Al deposited in the same pumping cycle; and (*iii*) an Al-2 weight percent (w/o) Si layer deposited by magnetron sputtering to a thickness of 1 μm.

The electrical measurements and SEM analysis were carried out after 5 min isochronal sintering at various temperatures in a N_2 ambient. After sintering, all specimens were pulled out of the furnace rapidly (~15 sec) and then left (~5 min) to cool down to room temperature in a N_2 ambient. For SEM analysis, the Al metallization was removed from the contact windows by chemical etching.

Results and Discussion

The effect of Al thickness.—In our previous work (1) we observed that the increase in contact resistance, R_c, is correlated with the increase in barrier heights of Al/Si junctions, ϕ_B, during sintering as reported by Chino (2). The increase arises from the precipitation at the interface of Si dissolved in the Al during sintering. Card (3) reported that the increase in ϕ_B is more pronounced for thicker Al contacts. Accordingly, we anticipated a similar effect of the Al thickness on the contact resistance of Al/n-poly-Si contacts.

The effect of sintering temperature on contact resistance of poly-Si resistors with 1 and 0.25 μm Al metallization is shown in Fig. 1. The average value of the contact resistance before sintering was 5 ± 0.3Ω. The results show that R_c is slightly lower for 0.25 μm Al contacts than for 1 μm Al. The effect is more pronounced at high sintering temperatures in excess of 500°C. However, contacts with 0.25 μm Al layers still exhibit a significant increase in R_c following the high temperature sintering (*e.g.*, a 400% increase in R_c after sintering at 560°C for 5 min).

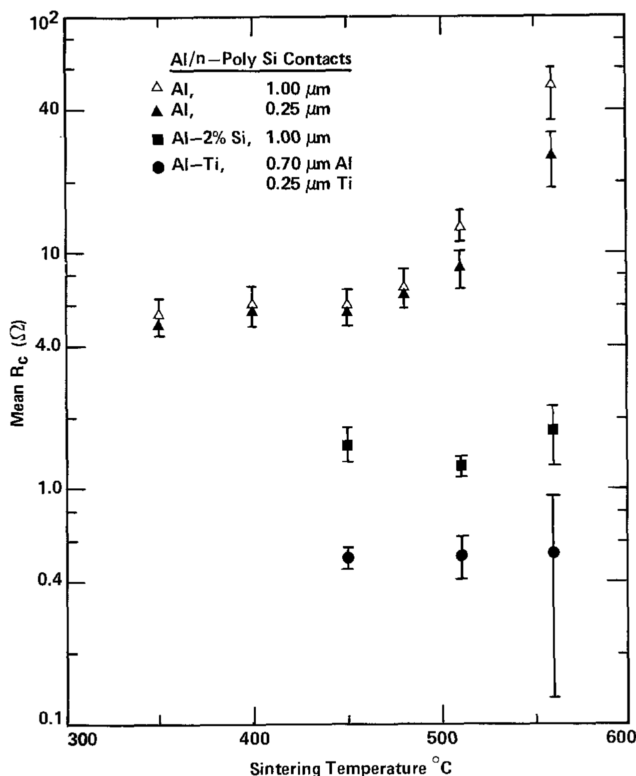

Fig. 1. Al/n-poly-Si contact resistance as a function of sintering temperature for various metallization systems. The sintering was carried out for 5 min in N_2. The electrical measurements were performed on poly-Si resistors having contact windows of 12 × 10 μm^2.

* Electrochemical Society Active Member.

Key words: aluminum metallization, contact characterization, ohmic contacts, silicon technology.

SEM examination showed no significant difference in the amount of poly-Si dissolved for Al thicknesses of 0.25 and 1 μm, as shown in Fig. 2 and 3. In both cases, poly-Si pitting can be observed at contact windows after 5 min sintering at temperatures as low as 350°C. Further reduction in the Al thickness might reduce poly-Si pitting and R_c values, but would also result in poor step coverage over the substrate, creating potential reliability problems (4).

The effect of Al-Ti contacts.—Ti has been used as an intermediate layer between Al and single crystal Si (5) and between Al and poly-Si (6) to prevent the dissolution of Si into Al during sintering. In both cases, this layer effectively acts as a barrier as long as the Ti is not completely consumed in the reaction with Al to form the intermetallic compound $TiAl_3$. If all the Ti is consumed, a Si-rich ternary phase $Ti_7Si_{12}Al_5$ is formed (5) which is virtually transparent to both Al and Si.

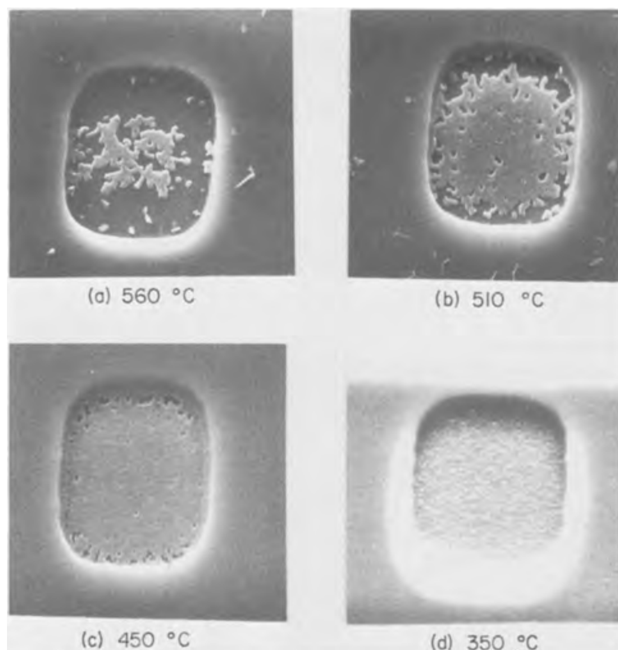

Fig. 2. Poly-Si contacts sintered for 5 min at various temperatures and then etched to remove 1.0 μm Al metallization (X3K).

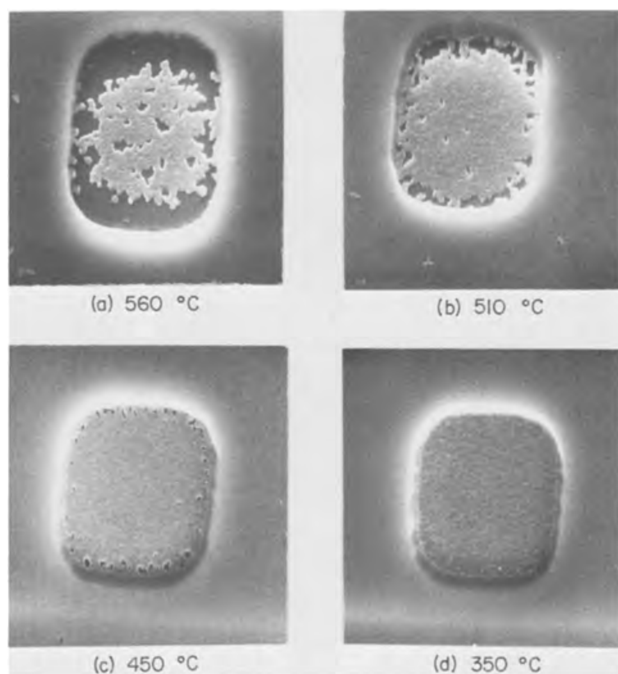

Fig. 3. Poly-Si contacts sintered for 5 min at various temperatures and then etched to remove 0.25 μm Al metallization (X3K).

Before sintering, the contact resistance of Al-Ti contacts on n-poly-Si was $\sim$0.52 $\pm$ 0.05Ω. The average value of R_c remained unchanged after 5 min sintering at temperatures $\geq$450°C. However, the standard deviation increased significantly after the 560°C sintering, as shown in Fig. 1. In addition, poly-Si dissolution was found in contacts sintered at 560°C. Typical SEM results are shown in Fig. 4. To reveal the poly-Si for SEM observations, the samples were first etched in H_3PO_4 to remove the top Al layer, then, in dilute HF solution to etch the Ti layers. Since HF also etches the SiO_2 layer between the contact windows this layer is thinner than the oxide originally covered by the metallization layer as shown in Fig. 4. Energy dispersion x-ray was used in the SEM to confirm the complete removal of Ti from the contact sites.

The time required to consume a 0.25 μm layer of Ti during sintering at 560°C is approximately 11 min (5). Accordingly, the appearance of poly-Si pits at contact windows following sintering at 560°C for a period of 5 min was rather unexpected. However, this may be attributed to local variation of Ti thickness over the wafer resulting in rapid dissolution of Si from contact sites. Also, the Al-Ti reaction may be influenced by the microstructure and the internal stresses of the deposited films, particularly at high sintering temperatures. These parameters were not considered during the course of this investigation.

The use of a Ti barrier layer between Al metallization and poly-Si substrates produces low contact resistance at n-poly Si contacts. However, in agreement with previous work (5, 6), careful consideration must be given to sintering temperature, sintering time, and Ti thickness to avoid the consumption of the barrier layer during sintering. In addition, further studies are needed to evaluate the long term performance and reliability of Si devices with Al-Ti contacts.

The effect of Al-2% Si alloy metallization.—Finally, we have examined the effect of Al-2 w/o Si alloy metallization on Si dissolution and contact resistance of Al/n-poly-Si contacts. This metallization system has been used successfully to reduce the formation of Si pits in single crystal Si substrates (7, 8). In this case, sufficient Si is present in the Al metallization to satisfy the solid solubility limits during high temperature heat-treatment processes.

Figure 1 shows the effect of sintering temperature on contact resistance of poly-Si resistors with 1 μm Al-2% Si alloy metallization. The average values of contact resistance before sintering was 16 $\pm$ 7Ω. After 5 min sintering at temperatures $\geq$450°C, R_c was 1.5 $\pm$ 0.25Ω and was virtually independent of the sintering temperature.

SEM micrographs of poly-Si contacts after removing the Al-Si alloy metallization are shown in Fig. 5. No sign of poly-Si pitting can be observed even after sintering at 560°C. However, a large number of Si precipitates are evident on the surface of the wafer. These

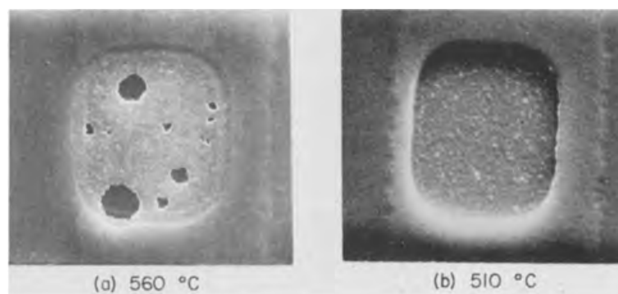

Fig. 4. Poly-Si contacts with a barrier layer of Ti under the Al after sintering and etching of the Al-Ti layers (X3K).

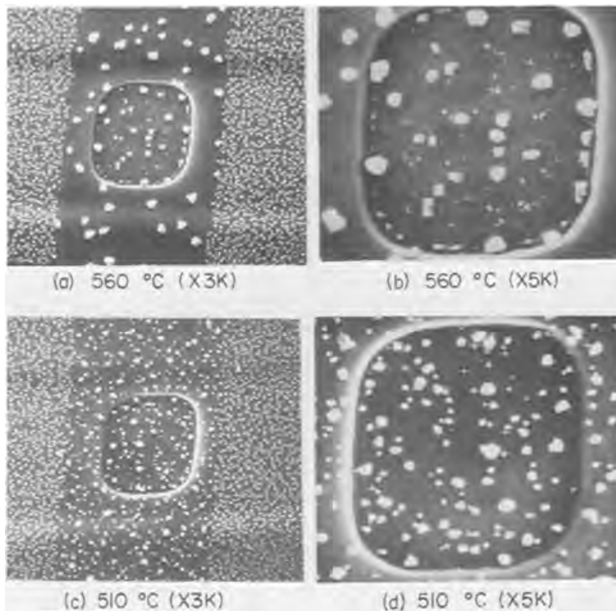

Fig. 5. The effect of Al-2% Si alloy on poly-Si dissolution. The central strip is sintered at 510° and 560°C for 5 min and then etched to remove 1.0 μm Al-2% Si layer. All specimens were subjected to the same standard cooling cycles as described in the text. The metallization film outside the central strip was photoengraved and etched before sintering.

precipitates are formed during the alloy deposition because of the negligible solubility of Si in Al at room temperature (~0.001%). Most of the Si precipitates in as-deposited Al-Si alloy were found predominantly at the surface/film interface and also near the free surface (9). The precipitates at the Al/poly-Si interface may have contributed to the high contact resistance at this interface before sintering.

Si precipitates on Al/SiO_2 interface remained on the oxide surface after the photoengraving and etching of the Al metallization. The Si precipitates present in the metallization are partially redissolved in the Al during sintering. However, since the maximum solubility of Si in Al at 560°C is 1.3 w/o even at this sintering temperature, there is still excess Si present as a second phase in the alloy and these serve as nucleation sites for the reprecipitation of Si during cooling. The size and density of the reprecipitated Si particles are dependent on the sintering temperature, assuming identical cooling cycles after each sinter. After 510°C sintering, the density of Si particles was about $1.8 \times 10^8/cm^2$ with an average diameter of 0.25 μm. A much coarser structure with lower density of $1.0 \times 10^8/cm^2$ and an average diameter of 0.8 μm was observed after 560°C sintering.

These observations of Si precipitates from Al-2% Si alloys are similar to those reported by van Gurp (9) for Si precipitates from Al/Si alloys deposited on single crystal substrates. Although the precipitates at the contact sites are particles of Si doped with Al, the sintering process caused a significant reduction in the area covered by these p-type precipitates, as seen in Fig. 5, which may result in the observed decrease in the contact resistance. It would be interesting to examine the effect of Al-Si alloy metallization on the barrier heights, ϕ_B, at Al-Si junctions to establish their correlation with the contact resistance.

Conclusion

The present results indicate that the use of Al-2% Si metallization is the most practical technique to minimize poly-Si dissolution and reduce the resistance at the Al/n-poly-Si contacts in integrated circuits. A similar conclusion has been reached for the metallization of contacts to single crystal substrates (7, 8). However, Si process technologists have been reluctant to use Al-Si metallization because of the lack of a proper technique for the deposition of alloy films. This problem was greatly minimized recently with the development of the magnetron sputtering technique for the deposition of alloys (10). For Al alloys, this new technique provides high deposition rates, consistent stoichiometry, and minimum radiation damage to dielectric films which can be easily annealed out at temperatures compatible with standard device processing (11).

Acknowledgments

We would like to thank W. D. Westwood and R. J. Kriegler for useful discussions and for reviewing the manuscript and R. Beaulieu for conducting the SEM analysis.

Manuscript submitted June 23, 1977; revised manuscript received Aug. 31, 1977.

Any discussion of this paper will appear in a Discussion Section to be published in the December 1978 JOURNAL. All discussions for the December 1978 Discussion Section should be submitted by Aug. 1, 1978.

Publication costs of this article were assisted by Bell-Northern Research.

REFERENCES

1. H. M. Naguib and L. H. Hobbs, *This Journal*, **124**, 573 (1977).
2. K. Chino, *Solid-State Electron.*, **16**, 119 (1973).
3. H. C. Card, in Proceedings of the IEEE Electronic Devices Meeting, Washington, D.C., p. 288 (1975).
4. T. Yanagawa and I. Takekoshi, *IEEE Trans. Electron. Devices*, **ed-17**, 964 (1970).
5. R. W. Bower, *Appl. Phys. Lett.*, **23**, 99 (1973).
6. N. Nakamura, S. S. Lau, M-A. Nicolet, and J. W. Mayer, *ibid.*, **28**, 277 (1976).
7. P. A. Totta and R. R. Sopher, *IBM J. Res. Dev.*, **13**, 226 (1969).
8. A. J. Learn, *Thin Solid Films*, **20**, 261 (1974).
9. G. J. van Gurp, *J. Appl. Phys.*, **44**, 2040 (1973).
10. V. Hoffman, *Solid State Technol.*, **19**, No. 12, 57 (1976).
11. R. W. Wilson and L. E. Terry, *J. Vac. Sci. Technol.*, **13**, 157 (1976).

JOURNAL OF THE ELECTROCHEMICAL SOCIETY

ACCELERATED

BRIEF COMMUNICATIONS

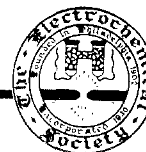

JANUARY 1978

A Computer Study of pH Effect in Electroless Copper Deposition

Milan Paunovic*,[1]

Kollmorgen Corporation, Photocircuits Division, Glen Cove, New York 11542

It was found by Schoenberg (1) that the rate of electroless deposition of copper first increases, passes through a maximum and then decreases when the concentration of formaldehyde, copper ions and copper complexing agent are held constant and that of sodium hydroxide varied. The maximum rate and the falling off of the rate at high pH values was explained (1) on the basis of dissociation of methylene glycol and the change of the relative concentration of the methylene glycolate and the hydroxide ions with pH. In order to contribute to the interpretation of this pH effect we have derived series of mathematical models of electroless copper deposition and obtained computer solutions for the change of the rate of deposition and the mixed potential with pH. The starting point of our derivations was the current (i) potential relationship for the high overvoltage (η) range

$$i = i^\circ \exp(\alpha\eta\, F/RT) \qquad [1]$$

where i°, α, F and T are the exchange current density, the transfer coefficient, faraday constant and temperature, respectively. On the basis of this equation, using the basic principles of the mixed potential theory (2), we have derived the following equations, for the mixed potential E_{MP}

$$E_{MP} = (b_M b_{Red}/b_M + b_{Red}) \ln(Q/R) \qquad [2]$$

where

$$Q = i^\circ_M \exp(E_{RM}/b_{RM}) \qquad [3]$$

$$R = i^\circ_{Red} \exp(-E_{RRed}/b_{Red}) \qquad [4]$$

$$b_M = RT/\alpha_M n_M F,\quad b_{Red} = RT/\alpha_{Red} n_{Red} F$$

and the rate of deposition i_{dep}

$$i_{dep} = (i^\circ_M)^p\, (i^\circ_{Red})^q \exp(V) \qquad [5]$$

$$\text{where } V = [(E_{RM} - E_{RRed})/(b_M + b_{Red})] \qquad [6]$$

$$p = b_M/(b_M + b_{Red}),\quad q = b_{Red}/(b_M + b_{Red})$$

and the meaning of other symbols are as follows: i°_M, i°_{Red}, E_{RM}, and E_{RRed} are the exchange current densities and the rest (equilibrium) potentials for the cathodic and anodic partial reactions, respectively.

This communication discusses only two mathematical models. In both models the dissociation of methylene glycolate (formaldehyde) is taken into account using for the dissociation constant $K = 1.62\times10^{-13}$ (1). In Model I it is assumed that the electrochemical kinetic parameter α_{Red} (the transfer coefficient) is independent of pH. The variation of the exchange current density i°_{Red}, with pH, was calculated on the basis of the theoretical equation (3)

$$i^\circ = nFk^\circ\, (c^\circ_{Ox})^{1-\alpha} (c^\circ_{Red})^{\alpha} \qquad [7]$$

as applied to this case (introduction of OH^- factor).

Previous interpretation did not consider that α_{Red} and i°_{Red} could vary with pH. However, Paunovic and Pearson (4) have determined experimentally that these parameters are pH dependent. Analytical expressions derived from these data, with the use of Newton's interpolation formula (5) are given as follows

$$\alpha_{Red} = -10.59 + 1.784\text{pH} - 7.40\times10^{-2}(\text{pH})^2 \qquad [8]$$

*Electrochemical Society Active Member

Key words: copper, electroless plating, formaldehyde, mixed potential

$$i^{\circ}_{Red}=\text{const}+9.26\times10^{-3}\text{pH}-3.85\times10^{-4}(\text{pH})^2$$

$$\text{const}=-5.52\times10^{-2} \qquad [9]$$

for the 0.2M CH_2O at 25°C.

In both models it was assumed that i°_M and α_M are independent of pH. Results obtained from equations [2-9] are shown in Fig. 1 and 2. For Model I a value of 0.15 was taken for α_{Red}. It is seen that only Model II gives the same pH effect as the experimentally observed relationship: the initial increase, a maximum and fall off of the rate with increasing pH. Model I gives continuously increasing rate of deposition when plotted vs. pH.

From these results we can conclude that the maximum and the falling off of the rate at high pH values are caused by the pH dependence of the kinetic parameters α_{Red} and i°_{Red} for formaldehyde. Dissociation of methylene glycol is an important factor in electroless deposition of copper but it is not sufficient to explain the pH effect.

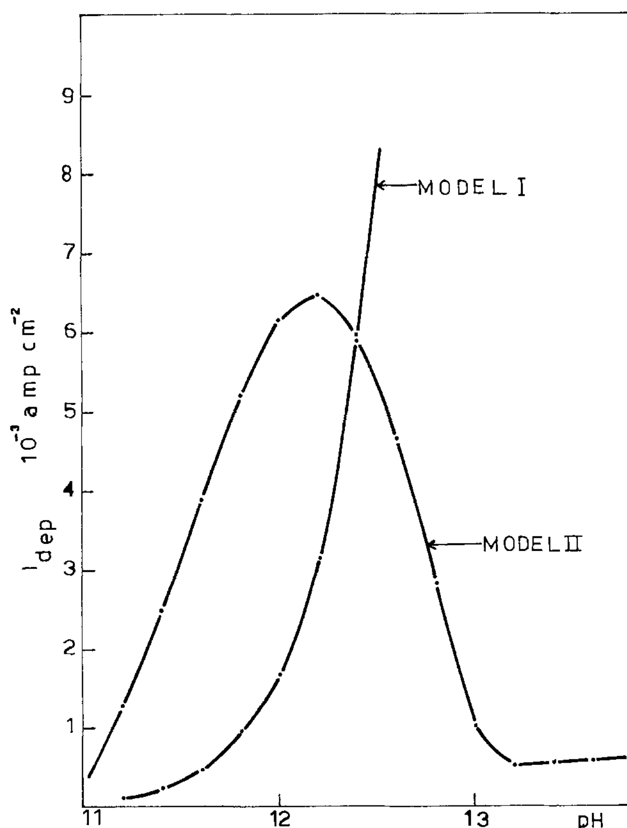

Fig. 1 - Variation of the rate of electroless deposition with pH for c_{CH_2O}= 0.2 M and $i^{\circ}_M=3.4\times10^{-5}$ amp $cm.^{-2}$

ACKNOWLEDGMENTS

The author would like to thank Dr. Karl Egerer, Vice-President and J. McCormack, Director of Research, Photocircuits for permission to publish this communication.

REFERENCES

1. L. N. Schoenberg, J. Electrochem. Soc., 118, 1571 (1971).
2. M. Paunovic, Plating, 55, 1161 (1968).
3. P. Delahay, "Double Layer and Electrode Kinetics", Interscience, New York (1965).
4. M. Paunovic and L. J. Pearson, to be published.
5. H. Margenau and G. M. Murphy, The Mathematics of Physics and Chemistry, D. Van Nostrand Co., Inc., Princeton, New Jersey, 1956, Volume 1.

Manuscript submitted Oct. 12, 1977; revised manuscript received Oct. 18, 1977.

Publication costs of this article were assisted by Kollmorgen Corporation.

[1]Present address: Department of Chemistry, Adelphi University, Garden City, New York 11530.

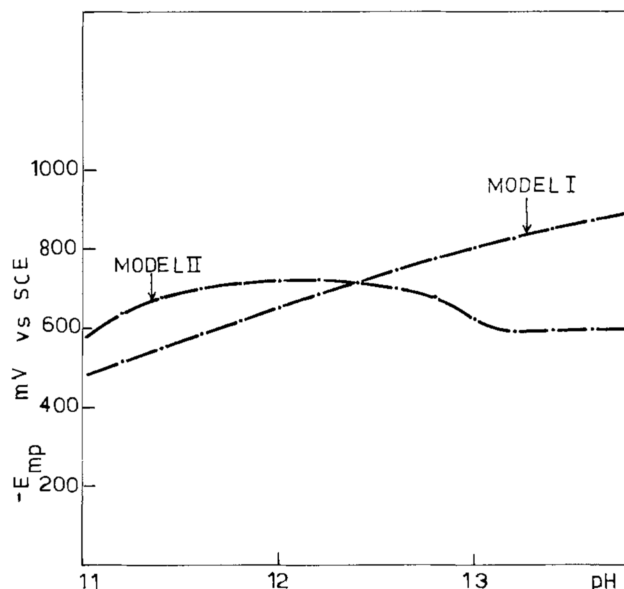

Fig. 2 - Variation of the mixed potential with pH for c_{CH_2O}= 0. 2M and $i^{\circ}_M=3.4\times10^{-5}$ amp $cm.^{-2}$

JOURNAL OF THE ELECTROCHEMICAL SOCIETY

ELECTROCHEMICAL SCIENCE AND TECHNOLOGY

FEBRUARY 1978

Electrochemical Determination of Activities in Cr_2O_3-Al_2O_3 Solid Solution

K. T. Jacob

Department of Metallurgy and Materials Science, University of Toronto, Toronto, Ontario, Canada, M5S 1A4

ABSTRACT

The activity of Cr_2O_3 in Cr_2O_3-Al_2O_3 solid solution has been determined in the temperature range 800°-1320°C from electromotive force measurements on the solid oxide galvanic cell

$$Pt,Cr + Cr_2O_3/Y_2O_3\text{-}ThO_2/Cr + Cr_xAl_{2-x}O_3,Pt$$

The activities of Cr_2O_3 and Al_2O_3 in the solid solution show both positive and negative deviations from Raoult's law. The heat and entropy of mixing of the solid solution obtained from the temperature dependence of the emf can be expressed as

$$\Delta H = X_{Cr_2O_3}X_{Al_2O_3}[31{,}700X_{Cr_2O_3} + 37{,}470X_{Al_2O_3}] \text{ J mole}^{-1}$$

$$\Delta S = -1.8R[X_{Cr_2O_3} \ln X_{Cr_2O_3} + X_{Al_2O_3} \ln X_{Al_2O_3}]$$

The entropy of mixing is 10% lower than that predicted by the Temkin model. The large positive heat of mixing in the Cr_2O_3-Al_2O_3 solid solution, however, suggests that this apparent entropy discrepancy originates with the clustering of positive ions on the cation sublattice. The asymmetric miscibility gap exhibited in the Cr_2O_3-Al_2O_3 system below 900°C is consistent with the thermodynamic data trends recorded at the more elevated temperatures.

Base metal catalysts such as copper chromite ($CuCr_2O_4$) supported on alumina have recently been considered for the oxidation of carbon monoxide and hydrocarbons to carbon dioxide and water vapor (1). A knowledge of phase relations in ternary systems of the type MO-Al_2O_3-Cr_2O_3, where MO is a divalent oxide like FeO, CoO, NiO, or CuO, would be useful for evaluating the interaction between chromium ion containing catalysts and alumina supports. Such systems often contain two series of solid solutions at high temperatures, one with the spinel structure ($MCr_xAl_{2-x}O_4$) and the other with the corundum structure ($Cr_xAl_{2-x}O_3$). The conjugate lines which connect these two solid solution regions on the ternary diagram have their directions determined by the ion exchange reaction

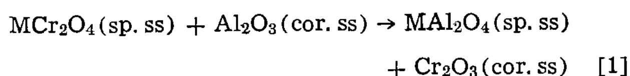

$$MCr_2O_4(\text{sp. ss}) + Al_2O_3(\text{cor. ss}) \rightarrow MAl_2O_4(\text{sp. ss}) + Cr_2O_3(\text{cor. ss}) \quad [1]$$

The composition of the conjugate phases can be calculated from a knowledge of the relative stability of the two pure spinel phases (MAl_2O_4 and MCr_2O_4) and activities in the two solid solutions. Some progress has recently been made in relating activities in spinel solid solutions to the distribution of cations between the tetrahedral and octahedral sites of the spinel lattice, and to the site preference energies of the cations (2). This paper reports measurements of the thermodynamic properties of Cr_2O_3-Al_2O_3 solid solutions using a solid oxide galvanic cell.

Key words: alumina-chromium sesquioxide solid solution, thermodynamics, solid electrolyte, galvanic cell, entropy of mixing, enthalpy of mixing, activities, miscibility gap.

Information on activities in Cr_2O_3-Al_2O_3 solid and liquid solutions are of interest in the physical chemistry of the aluminothermic reduction of Cr_2O_3. The high temperature phase diagram of the Cr_2O_3-Al_2O_3 system (3) is of the isomorphous type, in which the two oxides are mutually soluble in all proportions in the solid and liquid state. Knapp (4) has shown that the calculated separation between the solidus and the liquidus curves based on the assumption that activities are equal to mole fractions in both solid and liquid solutions, and using estimated heats of fusion of oxides, is smaller than experimentally observed. A miscibility gap has been reported (5, 6) in this system at temperatures below 900°C, and under high pressures or hydrothermal conditions. The lattice parameters a and c show slight positive departure from the linearity predicted by Vegard's rule (6).

Experimental Methods

Materials.—Fine powders of Cr,Cr_2O_3 and α-Al_2O_3, each 99.99% pure, were obtained from Alfa Inorganics. The $Cr_xAl_{2-x}O_3$ solid solutions were prepared by mixing fine powders of component oxides in the required ratio, compacting the mixture into pellets and sintering at 1450°C under a flowing stream of argon gas for 65 hr. One composition of the spinel solid solution ($x = 0.74$) was also synthesized at 1600°C. The formation of homogeneous solid solutions was confirmed by x-ray diffraction analysis and microscopic examination. Thoria pellets doped with 15 mole percent (m/o) $YO_{1.5}$ were supplied by Cerac Incorporated. This composition is close to that of maximum ionic conductivity. The Y_2O_3-ThO_2 material was chosen as the electrolyte because its ionic transport number is greater than

0.995 at the low oxygen potentials encountered in this study.

Apparatus and Procedure

The apparatus was identical to that used for the measurements of the free energy of formation of $MgCr_2O_4$, and has been described earlier (7).

The $Cr + Cr_2O_3$ and $Cr + Cr_xAl_{2-x}O_3$ electrodes were prepared by compacting a mixture of their powders in the molar ratio 1.5:1. Preliminary experiments indicated a slight tendency for the oxidation of chromium in the pellet despite the use of titanium internal getters. Electron microprobe examination of the surface of a pellet in contact with the electrolyte showed a slightly lower metal concentration at the end of the experiment than at the start. To compensate for this effect, excess chromium was used in the pellets. The pellets were sintered at 1300°C in prepurified argon stream for 35 hr. Titanium internal getters were placed 2.5 cm above and below the pellets to remove any residual oxygen in the argon or oxygen bearing species desorbing from the refractory tubes. The reversible electromotive force (emf) of the cell

$$Pt,Cr + Cr_2O_3/Y_2O_3\text{-}ThO_2/Cr + Cr_xAl_{2-x}O_3,Pt \quad [1]$$

was measured in the temperature range 800°-1320°C with a "Solatron" digital voltmeter, which had an input impedance of $10^{12}\Omega$. The reversibility of the cell was checked by passing a small current ($\approx$ 50 μA) through the cell for 1-2 min in either direction, and it was found that the emf returned to its initial value in approximately 30 min, after which it remained constant for up to 5 hr. The emf's were also found to be independent of the flow rate of inert gas through the cell.

Some contamination of platinum wires in contact with the electrodes was observed. The extent of contamination was similar at both electrodes. To check for possible errors caused by the thermal emf of the contaminated platinum leads, the emf of a junction made from two contaminated wires, used as leads in one experiment, was measured as a function of temperature. The highest emf obtained was 0.15 mV.

Results and Discussion

The emf of the cell is shown as a function of temperature in Fig. 1, for different compositions of the solid solution. Reproducible emf's could not be measured below 800°C in experiments in which the compositions of the solid solution were given by $x = 0.2$, 0.48, 1.54, and 1.8. This is probably related to the sluggish reaction between Cr and Cr_2O_3 to establish the equilibrium oxygen potential. In experiments with solid solutions characterized by values of $x = 0.74$, 1.0, and 1.28, steady emf's could not be obtained below 900°C. The slow exsolution of the solid solution below 900°C probably contributed to this drift in the emf. It was also observed that in order to yield reproducible emf's the cell had to be heated initially to 1100°C. After this initial heat-treatment, steady emf's were obtained in 20-60 min after the cell had attained a contant temperature. The reproducibility of the emf's varied from 0.5 to 1.5 mV depending on the composition of the solid solution; the reproducibility was better when the solid solution contained more Cr_2O_3. Almost identical emf's were obtained for $x = 0.74$ using samples synthesized at 1450° and 1600°C. This observation and the reproducibility of emf's after repeated temperature cycling confirm the homogeneity of the solid solutions. The equations representing the variation of the emf with temperature for each composition of the solid solution, obtained by the least mean squares regression analysis, are summarized in Table I.

The activity or the partial free energy of mixing of Cr_2O_3 in the solid solution is simply related to the emf of the cell

$$\Delta G_{Cr_2O_3} = RT \ln a_{Cr_2O_3} = -6\mathbf{FE} \quad [2]$$

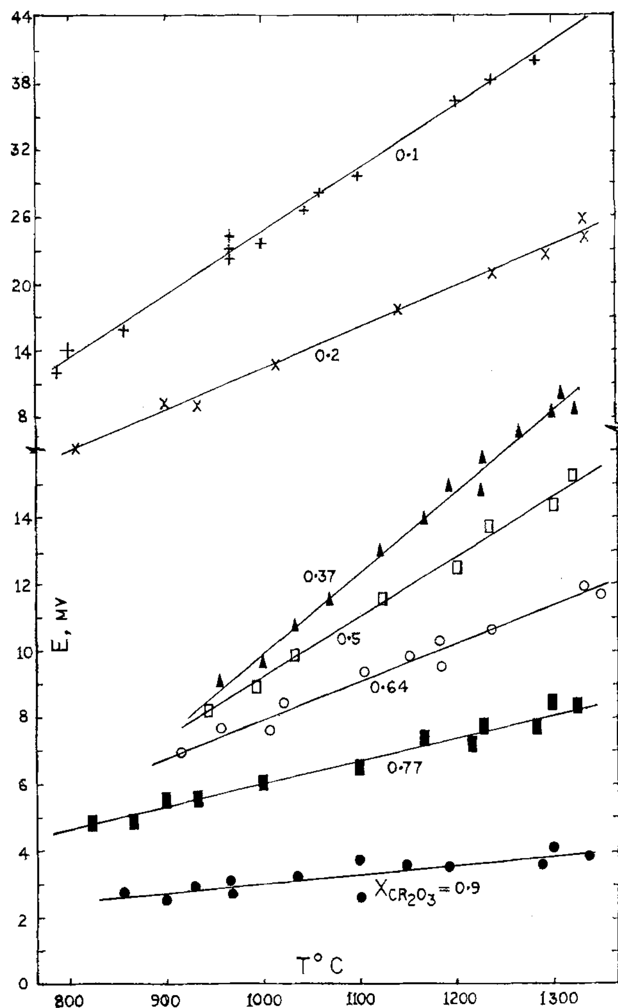

Fig. 1. Variation of the emf of cell [1] with temperature for different compositions of the corundum solid solution. $X_{Cr_2O_3}$ is the mole fraction of Cr_2O_3 in the solid solution.

where **F** is the Faraday constant (96,500 J V^{-1} mol^{-1}) and E is the emf in volts. The activity of Cr_2O_3 at 1000° and 1300°C is plotted against the composition of the solution in Fig. 2. The activity coefficient of Al_2O_3 is calculated using the Gibbs-Duhem relation

$$\ln \gamma_{Al_2O_3} = -\int_{X_{Al_2O_3}=1}^{X_{Al_2O_3}} \frac{X_{Cr_2O_3}}{X_{Al_2O_3}} d \ln \gamma_{Cr_2O_3} \quad [3]$$

where $\gamma(= a/X)$ is the activity coefficient. The activities of both components of the solid solution show positive deviations from Raoult's law at low concentrations and negative deviations at high concentrations. The integral free energy of mixing of the solid solution at 1000°C given by

$$\Delta G = RT\,[X_{Cr_2O_3} \ln a_{Cr_2O_3} + X_{Al_2O_3} \ln a_{Al_2O_3}] \quad [4]$$

is shown in Table I.

The partial heat of mixing of Cr_2O_3 in the solid solution is calculated directly from the temperature de-

Table I. The temperature dependence of the emf of cell [1] and the integral free energy of mixing of the $Cr_xAl_{2-x}O_3$ solid solution

x	$X_{Cr_2O_3}$	$E = a + bT$ (°K) mV	ΔG (1000°C) J mol^{-1}
0.2	0.1	$-50.8 + 5.95 \times 10^{-2}T$ ($\pm$0.7)	−2870
0.48	0.24	$-34.6 + 3.69 \times 10^{-2}T$ ($\pm$0.6)	−3920
0.74	0.37	$-22.8 + 2.57 \times 10^{-2}T$ ($\pm$0.5)	−4320
1.00	0.50	$-13.7 + 1.79 \times 10^{-2}T$ ($\pm$0.4)	−4560
1.28	0.64	$-6.73 + 1.15 \times 10^{-2}T$ ($\pm$0.4)	−4670
1.54	0.77	$-2.61 + 6.76 \times 10^{-3}T$ ($\pm$0.4)	−4430
1.80	0.90	$-0.47 + 2.72 \times 10^{-3}T$ ($\pm$0.5)	−3290

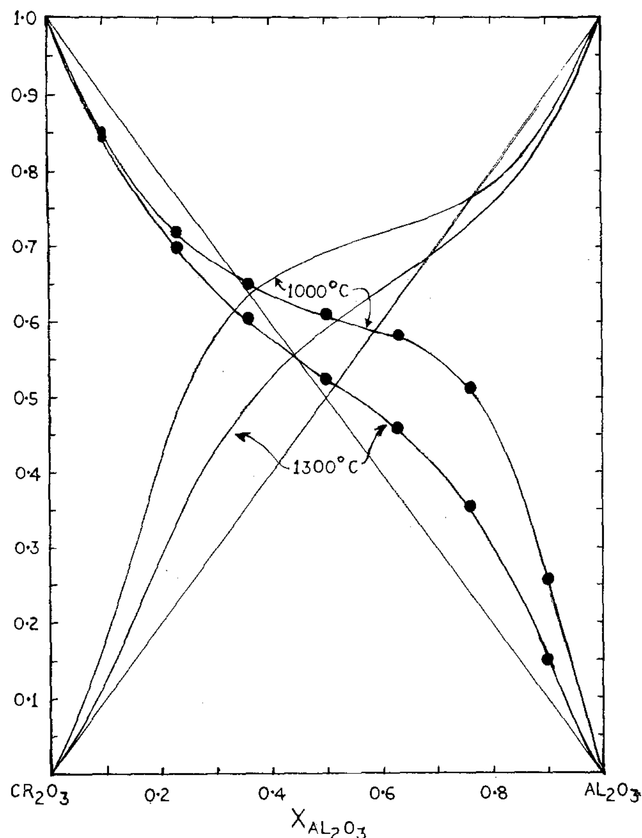

Fig. 2. Activities of Cr_2O_3 and Al_2O_3 in the Cr_2O_3-Al_2O_3 solid solution at 1000° and 1300°C.

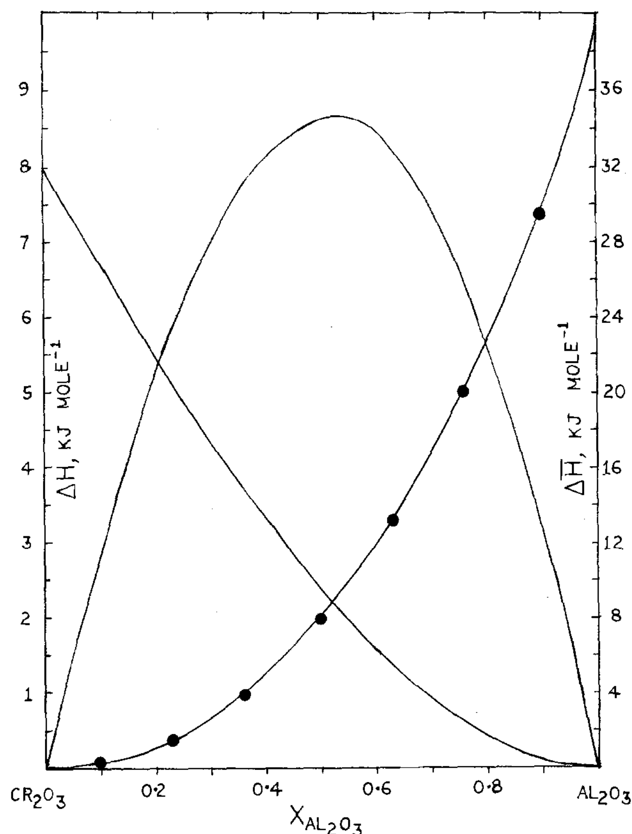

Fig. 3. Partial and integral molar heat of mixing of the Cr_2O_3-Al_2O_3 solid solution.

pendence of the emf

$$\Delta H_{Cr_2O_3} = -6F\,[E - T(\partial E/\partial T)_P] \quad [5]$$

The partial heat of mixing of Al_2O_3 is calculated from the composition dependence of the partial heat of Cr_2O_3 using the Gibbs-Duhem relation. The integral heat of mixing is given by

$$\Delta H = X_{Cr_2O_3}\Delta H_{Cr_2O_3} + X_{Al_2O_3}\Delta H_{Al_2O_3} \quad [6]$$

The variation of the partial and integral heats of mixing with the composition of the solid solution is shown in Fig. 3.

The integral heat of mixing is not a symmetric function of composition. However, the plot of $\Delta H/X_{Cr_2O_3}X_{Al_2O_3}$ *vs.* composition, shown in Fig. 4, yields a straight line. The integral and partial heats of mixing can therefore be expressed analytically

$$\Delta H = X_{Cr_2O_3}X_{Al_2O_3}\,[31{,}700\,X_{Cr_2O_3} + 37{,}470\,X_{Al_2O_3}]\,\text{J mol}^{-1} \quad [7]$$

$$\Delta H_{Cr_2O_3} = 25{,}910\,X^2_{Al_2O_3} + 11{,}560\,X^3_{Al_2O_3}\,\text{J mol}^{-1} \quad [8]$$

$$\Delta H_{Al_2O_3} = 43{,}250\,X^2_{Cr_2O_3} - 11{,}560\,X^3_{Cr_2O_3}\,\text{J mol}^{-1} \quad [9]$$

These equations are similar to the "subregular" model suggested by Hardy (8). The positive heat of mixing probably arises from the difference in ionic radii of Al^{3+} and Cr^{3+} ions. On the Shannon and Prewitt (9) scale the ionic radii of Al^{3+} and Cr^{3+} ions are 0.67 and 0.755Å, respectively, for sixfold coordination. It is conceivable that the introduction of a larger ion in a lattice of smaller ions would cause a larger positive heat effect than the incorporation of a smaller ion in a host lattice of larger ions.

The entropy of mixing of the solid solution is calculated from the values of free energy and heat of mixing discussed above

$$\Delta S = -(\Delta G - \Delta H)/T \quad [10]$$

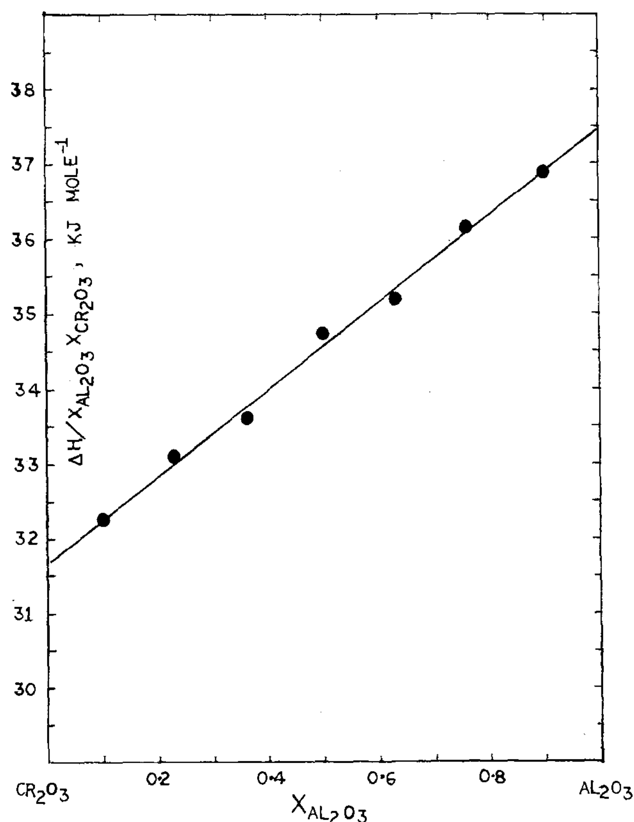

Fig. 4. Variation of the function, $\Delta H/X_{Cr_2O_3}X_{Al_2O_3}$, with composition in the Cr_2O_3-Al_2O_3 system.

The entropy of mixing is compared with that calculated using Temkin's model in Fig. 5. The corundum structure is basically a hexagonal close-packed oxygen lattice with the two trivalent cations occupying two-thirds of the available octahedral sites. Since two cat-

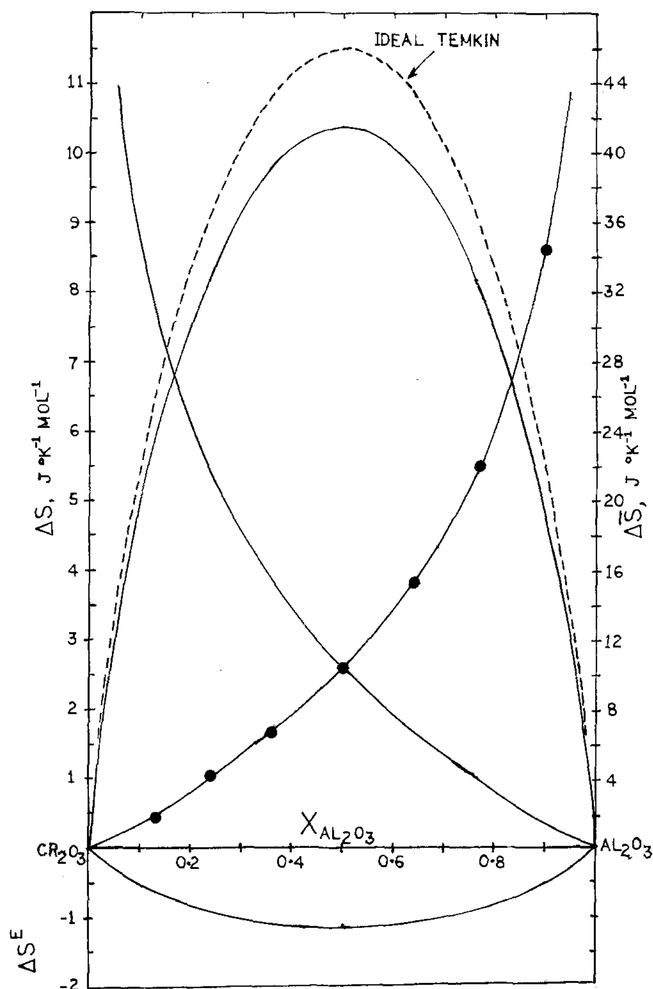

Fig. 5. Comparison of the entropy of mixing of Cr_2O_3-Al_2O_3 solid solution with that predicted by Temkin's model. The composition dependence of partial and excess entropies are also shown. ——— Results obtained in this study; ---- Temkin's model.

ions are involved in the mixing process on the octahedral sublattice per mole of oxide solid solution, the Temkin entropy of mixing is given by

$$\Delta S_{\text{Temkin}} = -2R\,[X_{Cr_2O_3} \ln X_{Cr_2O_3} + X_{Al_2O_3} \ln X_{Al_2O_3}] \quad [11]$$

The experimental entropy of mixing of the solid solution is 10% lower than the Temkin entropy of mixing, although both are symmetric functions of composition. The experimental entropy of mixing can be expressed as

$$\Delta S = -1.8R\,[X_{Cr_2O_3} \ln X_{Cr_2O_3} + X_{Al_2O_3} \ln X_{Al_2O_3}] \quad [12]$$

Similarly the partial molar entropy of Cr_2O_3 and Al_2O_3 can be expressed as

$$\Delta \bar{S}_{Cr_2O_3} = -1.8R \ln X_{Cr_2O_3} \quad [13]$$

$$\Delta \bar{S}_{Al_2O_3} = -1.8R \ln X_{Al_2O_3} \quad [14]$$

The partial molar entropy of Cr_2O_3 obtained directly from the temperature dependence of the emf

$$\Delta \bar{S}_{Cr_2O_3} = 6\mathbf{F}(\partial E/\partial T)_P \quad [15]$$

is in almost exact agreement with Eq. [13].

The excess entropy of mixing on the Temkin model is negative

$$\Delta S^{E}_{\text{Temkin}} = \Delta S - \Delta S_{\text{Temkin}} = 0.2R\,[X_{Cr_2O_3} \ln X_{Cr_2O_3} + X_{Al_2O_3} \ln X_{Al_2O_3}] \quad [16]$$

The large positive heat of mixing suggests that the origin of the negative excess entropy on the Temkin model lies in the clustering of positive ions on the octahedral cation sublattice. It is obvious from Eq. [12] that the Raoultian excess entropy of mixing is positive. However, for ionic solids the concept of Raoult's law has little physical significance.

At the critical point corresponding to the appearance of a miscibility gap

$$\frac{\partial \Delta \bar{G}_{Cr_2O_3}}{\partial X_{Cr_2O_3}} = \frac{\partial \Delta \bar{G}_{Al_2O_3}}{\partial X_{Al_2O_3}} = 0 \quad [17]$$

$$\frac{\partial \Delta \bar{G}_{Cr_2O_3}}{\partial X^2_{Cr_2O_3}} = \frac{\partial \Delta \bar{G}_{Al_2O_3}}{\partial X^2_{Al_2O_3}} = 0 \quad [18]$$

Expressing the partial free energies in terms of partial heats (Eq. [8] and [9]) and partial entropies (Eq. [13] and [14]) and solving Eq. [17] and [18] gives the following relations between the temperature (T_c) and composition ($X_{Cr_2O_3(c)}$ and $X_{Al_2O_3(c)}$) of the critical point

$$T_c = \frac{190{,}140\, X^2_{Cr_2O_3(c)} X^2_{Al_2O_3(c)}}{1.8R\,(-9X^2_{Cr_2O_3(c)} + 10X_{Cr_2O_3(c)} - 2)} \quad [19]$$

$$T_c = \frac{224{,}820\, X^2_{Cr_2O_3(c)} X^2_{Al_2O_3(c)}}{1.8R\,(-9X^2_{Al_2O_3(c)} + 10X_{Al_2O_3(c)} - 2)} \quad [20]$$

Remembering that

$$X_{Cr_2O_3(c)} + X_{Al_2O_3(c)} = 1 \quad [21]$$

numerical values characterizing the critical point, where the miscibility gap is imminent, can be evaluated

$T_c = 1173°K\,(900°C)$, $X_{Cr_2O_3(c)} = 0.44$, $X_{Al_2O_3(c)} = 0.56$

The solubility limits at temperatures below 900°C can be determined by drawing common tangents to

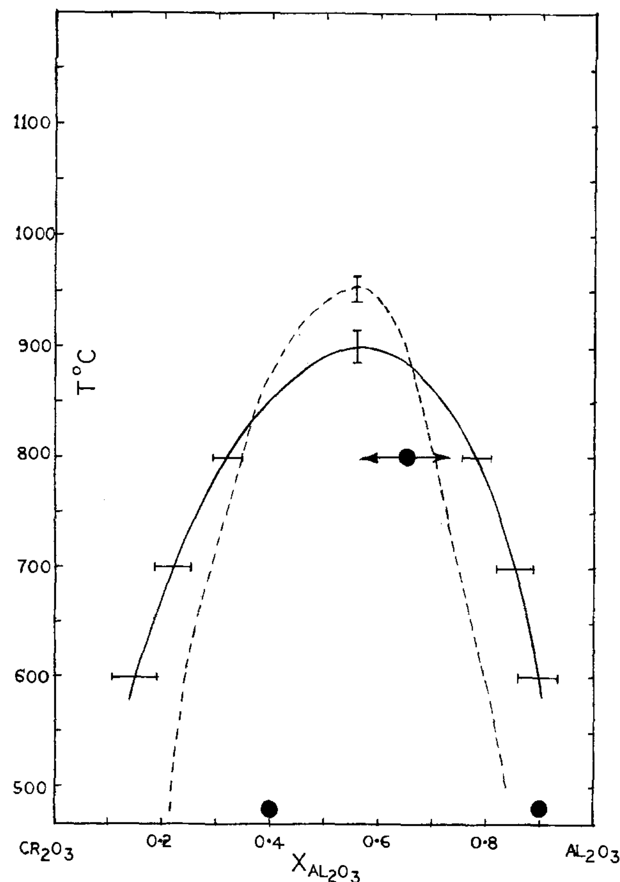

Fig. 6. Comparison of the miscibility gap derived from thermodynamic data obtained in this study with direct measurements at high pressures. ——— This study; ● Neuhaus et al. (5); ---- Roy and Barks (6).

the free energy composition curves. The results so obtained are compared with direct measurements of Neuhaus *et al.* (5) at 2000 atm pressure and Roy and Barks (6) at 988 atm (hydrothermal). The critical temperature calculated from the present results lies between the values 800° (5) and 945°C (6) reported at higher pressures. There is also qualitative agreement between the three sets of data regarding the asymmetry of the miscibility gap. The solubility limits at lower temperatures differ significantly. Since the formation of the solid solution is accompanied by an increase in molar volume, the miscibility gap may be expected to be narrower at high pressures.

Manuscript submitted May 6, 1977; revised manuscript received Aug 30, 1977.

Any discussion of this paper will appear in a Discussion Section to be published in the December 1978 JOURNAL. All discussions for the December 1978 Discussion Section should be submitted by Aug. 1, 1978.

REFERENCES

1. R. D. Shoup, K. E. Hoekstra, and R. J. Farrtauto, *Bull. Am. Ceram. Soc.*, **54**, 564 (1975).
2. K. T. Jacob and C. B. Alcock, *J. Solid State Chem.*, **20**, 79 (1977).
3. E. N. Bunting, *J. Res. Natl. Bur. Std.*, **6**, 947 (1931).
4. W. J. Knapp, *J. Am. Ceram. Soc.*, **36**, 43 (1953).
5. A. Neuhaus, E. Jumperty, and P. Brenner, *Fortschr. Mineral.*, **40**, 60 (1963).
6. D. M. Roy and R. E. Barks, *Nature (London) Phys. Sci.*, **235**, 118 (1972).
7. K. T. Jacob, *This Journal*, **124**, 1827 (1977).
8. H. K. Hardy, *Acta Metall.*, **1**, 202 (1953).
9. R. D. Shannon and C. T. Prewitt, *Acta Crystallogr. Sect. B*, **52**, 925 (1969).
10. M. Temkin, *Acta Physicochim. URSS*, **20**, 411 (1945).

Effects of Composition Changes, Substitutions, and Hydrostatic Pressure on the Ionic Conductivity in Lithium Aluminosilicate and Related Beta-Eucryptite Materials

R. M. Biefeld,* R. T. Johnson, Jr., and R. J. Baughman

Sandia Laboratories, Albuquerque, New Mexico 87115

ABSTRACT

The effects of selected compositional changes, substitutions, and hydrostatic pressure on the lithium ion conductivity in lithium aluminosilicate solid electrolytes which exhibit the β-eucryptite ($LiAlSiO_4$) structure when in crystalline form have been determined. Substitutions of Ga_2O_3 for Al_2O_3 and GeO_2 for SiO_2 in glass and glass-ceramic materials have no significant effect on the ionic conductivity; however, the addition of Li_2O and substitution of B_2O_3 for Al_2O_3 increases the conductivity. The highest conductivities [2×10^{-2} (Ω-cm)$^{-1}$ at 500°C] were obtained for glasses with enhanced Li_2O concentrations (*e.g.*, $3.1Li_2O \cdot Al_2O_3 \cdot 3.8SiO_2$), and for glass-ceramics with both enhanced Li_2O concentrations and B_2O_3 substitutions (*e.g.*, $3.1Li_2O \cdot B_2O_3 \cdot 3.8SiO_2$). Generally, the glass-ceramics have a lower conductivity than the glass except for certain B_2O_3 substituted glass-ceramics where this trend is reversed. Hydrostatic pressure experiments (to 2.0 GPa) on various glasses and glass-ceramics showed only slight variations in the ionic conductivity characteristics. All of the results can be consistently interpreted in terms of the existence of glass-crystalline interfacial layers in the glass-ceramics. Ionic conductivity data are also presented on $LiAlSiO_4$ single crystals.

Lithium aluminosilicate glasses and glass-ceramics with the stoichiometric β-eucryptite (1, 2) composition $Li_2O \cdot Al_2O_3 \cdot 2SiO_2$ ($LiAlSiO_4$) have been shown to have high Li ion conductivities [$\sigma > 10^{-3}$ (Ω-cm)$^{-1}$] at temperatures above 400°C (3). Thus these materials are of interest as possible high temperature solid electrolytes. We have previously examined the effects of the degree of crystallinity on the ionic conductivity in the stoichiometric β-eucryptite composition (4). The studies reported here examine the effects of compositional changes from stoichiometric $LiAlSiO_4$ and the effects of pressure on the ionic conductivity in glasses and glass-ceramics with emphasis on determining the extent to which the ionic conductivity can be increased. Since glass-ceramics consist of crystallites grown within a glass matrix the conductivity of $LiAlSiO_4$ (β-eucryptite) single crystals is also reported.

In β-eucryptite the Li ions reside in one-dimensional channels parallel to the c-axis and are most easily transported along these channels (2, 5, 6). In this ordered crystalline phase as well as in the disordered glassy phase the size of the conductive pathways (or channels) through which the ions move probably influences the ionic conductivity. The channel size can be varied both by changing the composition of the material by replacing some of the ions in $LiAlSiO_4$ with ions of different sizes and by applying high pressure. In this investigation, a large number of glasses and glass-ceramics with composition changes and substitutions were prepared and their electrical, thermal, and structural characteristics were examined. The ionic conductivity of several of these materials was also determined under hydrostatic pressure to 2.0 GPa. Compositional substitutions into $Li_2O \cdot Al_2O_3 \cdot 2SiO_2$ included B_2O_3 and Ga_2O_3 for Al_2O_3, and GeO_2 for SiO_2. The effect of changing the Li_2O concentration (and thus the number of ionic carriers) on the ionic conductivity was also examined.

Materials Preparation and Characterization

The glasses used in this investigation are listed in Table I and were prepared from reagent grade Li_2CO_3 and the required oxides following procedures previ-

* Electrochemical Society Active Member.

Key words: solid electrolytes, lithium ion conductors, ionic conductivity, lithium aluminosilicate based glasses and glass-ceramics, β-eucryptite single crystals.

Table I. Compositions, glass transition (annealing) temperatures, T_g, crystallization temperatures, T_c, and structural types observed for materials based on the lithium aluminosilicate ($Li_2O \cdot Al_2O_3 \cdot 2SiO_2$) system

Composition	T_g (°C)	T_c (°C)	Crystalline phase(s)
Stoichiometric			
$Li_2O \cdot Al_2O_3 \cdot 2SiO_2$*	650	760-960	β-eucryptite
Ge substituted			
$Li_2O \cdot Al_2O_3 \cdot GeO_2 \cdot SiO_2$*	600	760-950	β-eucryptite
$2Li_2O \cdot 2Al_2O_3 \cdot GeO_2 \cdot 3SiO_2$†	400	750-800	β-eucryptite
Ga substituted			
$2Li_2O \cdot Al_2O_3 \cdot Ga_2O_3 \cdot 4SiO_2$*	600	745-900	α- and β-eucryptite
$4Li_2O \cdot 3Al_2O_3 \cdot Ga_2O \cdot 8SiO_2$†	620	760-770	β-eucryptite
Ge and Ga substituted			
$2Li_2O \cdot Al_2O_3 \cdot Ga_2O_3 \cdot 2GeO_2 \cdot 2SiO_2$	450		
B substituted			
$Li_2O \cdot 3B_2O_3$	500		
$Li_2O \cdot B_2O_3 \cdot 2SiO_2$‡	450		
$2Li_2O \cdot Al_2O_3 \cdot B_2O_3 \cdot 4SiO_2$†	500	550	β-eucryptite
$4Li_2O \cdot 3Al_2O_3 \cdot B_2O_3 \cdot 8SiO_2$†	560	630-715	β-eucryptite
Li enhanced			
$Li_2O \cdot Al_2O_3 \cdot 1.3SiO_2$	630		
$1.3Li_2O \cdot Al_2O_3 \cdot 2SiO_2$	570		
$3.1Li_2O \cdot Al_2O_3 \cdot 3.8SiO_2$†	490	620-650	β-eucryptite and lithium orthosilicate
$4.3Li_2O \cdot Al_2O_3 \cdot 7SiO_2$	480	630-650	β-eucryptite
$2Li_2O \cdot 3SiO_2$	500		
Li enhanced and Ge substituted			
$3.1Li_2O \cdot Al_2O_3 \cdot 1.9GeO_2 \cdot 1.9SiO_2$†	510	580-610	β-eucryptite and lithium metasilicate
Li enhanced and Ga substituted			
$6.2Li_2O \cdot Al_2O_3$ $Ga_2O_3 \cdot 7.6SiO_2$†	460	530	α- and β-eucryptite
Li enhanced and Ge and Ga substituted			
$6.2Li_2O \cdot Al_2O_3 \cdot Ga_2O_3 \cdot 3.8GeO_2 \cdot 3.8SiO_2$	450		
Li enhanced and B substituted			
$3.1Li_2O \cdot B_2O_3 \cdot 3.8SiO_2$†	460	580-770	Lithium metasilicate and lithium metadisilicate
$6.2Li_2O \cdot B_2O_3 \cdot Al_2O_3 \cdot 7.6SiO_2$†	480	640	β-eucryptite and lithium metasilicate

* Contains 3 w/o TiO_2 as a nucleating agent.
† Contains 3 w/o TiO_2 + 1 w/o ZrO_2 as nucleating agents.
‡ Partially crystallized during the initial preparation.

ously described (3). After melting at ~ 1600°C the glasses were quenched and then annealed in the temperature range of 400°-650°C for 5-10 min to remove strain. X-ray powder diffraction photographs of the glasses revealed no crystalline structure. The annealing temperatures, which were the glass transition temperatures (T_g), are listed in Table I and were determined from differential thermal analysis (DTA) performed on unannealed glass samples. The results show that the T_g values decrease as the composition deviates from $Li_2O \cdot Al_2O_3 \cdot 2SiO_2$.

The glass-ceramics were prepared by controlled devitrification of the glasses. The heat-treatments used to devitrify the glasses (Table I) were also determined from DTA. These heat-treatments involved annealing the glasses from slightly below to slightly above the crystallization exotherms over a period of 1-4 hr. TiO_2 and/or ZrO_2 [concentrations to ~ 4 weight percent (w/o)] were added to the glasses as nucleating agents to aid in the formation of the glass-ceramics. Attempts to crystallize the glass without any nucleating agent(s) resulted in preferential surface crystallization and cracking of the samples. X-ray powder diffraction photographs were taken of the glass-ceramics to determine the phase or phases present. In most of the glass-ceramics examined, β-eucryptite was the only crystalline phase present or the most predominant crystalline phase. Other phases such as α-eucryptite, lithium metadisilicate, $Li_2Si_2O_5$, lithium orthosilicate, Li_4SiO_4, and lithium metasilicate, Li_2SiO_3, were also found in some samples. The phase(s) observed for each composition are given in Table I.

Single crystals of β-eucryptite were grown by the flux technique (7). The starting materials were Li_2CO_3, Al_2O_3, and SiO_2 powders mixed in the appropriate proportions. This material (46.4 w/o) was mixed with LiF (29.2 w/o), AlF_3 (10.3 w/o), and V_2O_5 (14.1 w/o) powder as fluxing agents. The mixture was ball milled in ethyl alcohol for 12 hr and dried in a convection oven. The ball-milled material was then charged in a 7.6 cm diam × 7.6 cm high platinum crucible with a tight fitting lid. The loaded crucible was placed in a furnace and the temperature raised to 1200°C. This temperature was held for 4 hr. The temperature was then immediately lowered to 1130°C. From this point, the temperature was driven down to 900°C at a constant rate of 1.25°C/hr. The crucible was then removed from the furnace, opened, and the molten flux decanted from the crucible and the solid $LiAlSiO_4$ (8). The crucible, which contained the $LiAlSiO_4$, was then returned to the furnace and allowed to slowly cool. The resulting single crystals had dimensions of the order of several millimeters.

Electrical Measurement Techniques

The glass and glass-ceramic samples used for the ionic conductivity measurements had dimensions of about 1 × 1 × 0.1 cm^3. Evaporated Cr electrodes were applied to the 1 × 1 cm^2 faces. The methods for sample preparation and contacting have been described (3). The single crystal samples were cut so that electrical measurements could be made normal to the (00·1) plane (*i.e.*, parallel to the c-axis and the Li ion containing channels). The single crystal specimens were ~ 1 mm thick and were (nearly) visually free of imperfections (*e.g.*, flux inclusions). No measurements were made in directions parallel to the (00·1) plane (*i.e.*, perpendicular to the c-axis) because of difficulties encountered in obtaining a large sample with this orientation that was free of imperfections. Evaporated Cr electrodes were also used on these samples.

The high pressure experiments were under hydrostatic pressure conditions and utilized a 3.0 GPa Harwood pressure system with a heater coil (9). The sample was emersed in pentane which was the pressure transmitting medium. The pressure was determined from a calibrated manganin coil. The temperature was determined by using thermocouples.

The ionic conductivity measurements were made by using 2-terminal and 3-terminal a-c techniques over the frequency range from 5 to 5 × 10^5 Hz (3). Previous work showed that the measured conductance and thus the conductivity is that associated with Li ions in the bulk material (3). A least squares method was used for analyzing the temperature dependent data.

Results

Stoichiometric $LiAlSiO_4$.—The ionic conductivity results for stoichiometric $LiAlSiO_4$ glass, glass-ceramic

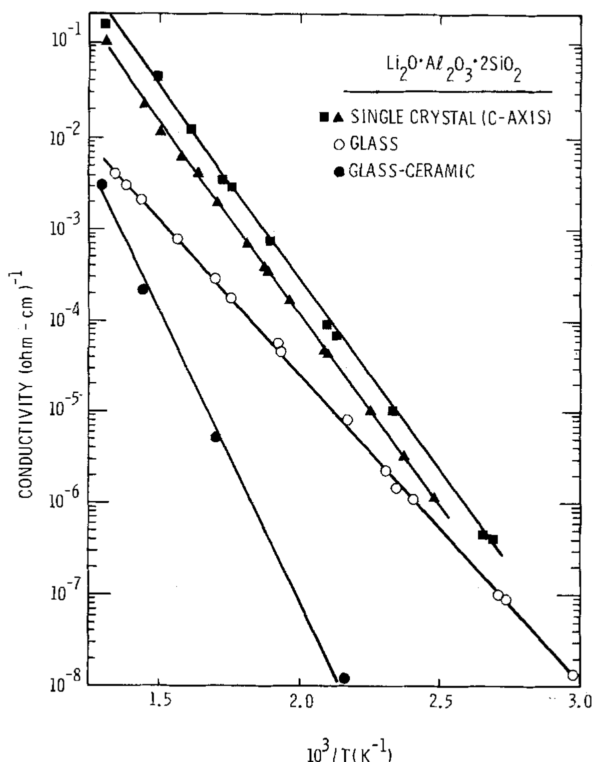

Fig. 1. Ionic conductivity temperature dependence for $LiAlSiO_4$ single crystals (c-axis), glass, and glass-ceramic (88% crystallinity). The single crystals (β-eucryptite) are one-dimensional conductors parallel to the c-axis, whereas the glass is a three-dimensional conductor. The glass-ceramic is polycrystalline material in a glass matrix prepared by devitrification of the glass.

[88 volume percent (v/o) crystalline] and single crystals (parallel to the c-axis) are shown in Fig. 1. The ionic conductivity, σ, for these materials is thermally activated ($\sigma = \sigma_0 e^{-E/kT}$) over the temperature range examined. The activation energies, E, and the preexponential factors, σ_0, are given in Table II.

The results obtained from two different single crystal samples are given in Fig. 1. The activation energy for the Li ion conductivity along the one-dimensional (c-axis) channels is nearly the same for both of these crystals but the σ_0 values are somewhat different. The crystal with the higher σ_0 value appeared by visual examination to be a nearly perfect crystal, whereas the crystal with the lower σ_0 value appeared to contain some flux inclusions which probably blocked ionic transport in some of the channels. This would account for the different σ_0 values observed for these two crystals. Our results are in reasonable agreement with those of van Alpen *et al.* (6) and suggest that the ionic conductivity for Li ion transport along the one-dimensional channels in single crystal β-eucryptite is described by $E \approx 0.83$ eV and $\sigma_0 \gtrsim 8 \times 10^4$ (Ω-cm)$^{-1}$.

Table II. Ionic conductivity activation energies, E, and preexponential factors, σ_0, for stoichiometric $LiAlSiO_4$ determined from $\sigma = \sigma_0 e^{-E/kT}$

Material	E (eV)	σ_0 (Ω-cm)$^{-1}$
Single crystal*		
Sample 1	0.81 ± 0.01	$1.70 \times 10^4 \begin{pmatrix} +0.26 \\ -0.22 \end{pmatrix} \times 10^4$
Sample 2	0.84 ± 0.01	$7.84 \times 10^4 \begin{pmatrix} +1.93 \\ -1.55 \end{pmatrix} \times 10^4$
Glass	0.68 ± 0.01	$1.83 \times 10^2 \begin{pmatrix} +0.11 \\ -0.11 \end{pmatrix} \times 10^2$
Glass-ceramic†	1.23 ± 0.05	$2.60 \times 10^5 \begin{pmatrix} +3.60 \\ -1.51 \end{pmatrix} \times 10^5$

* Parallel to c-axis.
† 88 v/o crystallinity.

The ionic conductivity for $LiAlSiO_4$ glass is characterized by $E = 0.68$ eV and $\sigma_0 = 1.8 \times 10^2$ (Ω-cm)$^{-1}$. Previous studies have shown that the nucleating agent(s) do not significantly affect these results, at least for the concentrations used here (*i.e.*, ≤ 4 w/o) (3). The conductivity of the glass is somewhat less than that for the single crystal (c-axis) over the temperature range examined. The interesting feature of these results, however, is that the glass is a good conductor for Li ions in three dimensions (with no long-range structural order) when compared to the single crystal where the Li ions reside in the one-dimensional c-axis channels and are transported along these channels.

The results in Fig. 1 (and Table II) for the $LiAlSiO_4$ glass-ceramic show that the conductivity decreased on conversion of the glass to the glass-ceramic. Furthermore, E for the glass-ceramic ($E = 1.23$ eV for 88% crystallinity) does not approach the value found for single crystal β-eucryptite ($E \sim 0.83$ eV). Several explanations for this discrepancy have been presented including the probable existence of an interfacial layer between the glass and the crystallites in the glass-ceramic which retards ionic transport through the crystalline regions (4). Such an interface would make the crystalline regions appear as insulating regions. This explanation has been advanced in conjunction with a continuum percolation model for describing the dependence of the ionic conductivity on the degree of crystallinity in these materials (4).

Composition variations and substitutions.—The effects of compositional variations and substitutions on the ionic conductivity were examined in the glass and glass-ceramic materials. In the glass-ceramics with compositions which differ from that of stoichiometric $LiAlSiO_4$, the composition of the glass and crystalline phases are generally not the same. In these materials, the volume fraction of crystalline material was not determined. The presence of substituents or other crystalline phases would change the x-ray results from those expected for stoichiometric mixtures of $LiAlSiO_4$ (β-eucryptite) crystallites in a $LiAlSiO_4$ glass matrix (4). Although a detailed dependence of conductivity on degree of crystallinity was not obtained for each composition, the results of the electrical measurements do give the general trend in ionic conductivity changes associated with compositional variations and substitutions.

Ionic conductivity results on a variety of glasses and glass-ceramics which contain GeO_2 and Ga_2O_3 are shown in Fig. 2. A complete listing of the materials examined and the corresponding values for E and σ_0 are presented in Table III. Substitution of GeO_2 for SiO_2 or Ga_2O_3 for Al_2O_3 causes a slight decrease in the conductivity of the glasses. This effect is not very large and the conductivities of these substituted glasses and glass-ceramics are very similar to those of stoichiometric $LiAlSiO_4$ glass and glass-ceramic (Fig. 1). This suggests that if there is a resistive glass-crystalline interfacial layer in these substituted glass-ceramics as in the $LiAlSiO_4$ glass-ceramics, the composition substitutions do not significantly influence the interfacial resistance. The results of the x-ray diffraction experiments indicated that the β-eucryptite lattice constants increased in the Ga_2O_3 or GeO_2 substituted glass-ceramics. For example, the lattice constants for $Li_2O \cdot Al_2O_3 \cdot GeO_2 \cdot SiO_2$ are a = 10.61(3) and c = 11.44(6) Å while for $LiAlSiO_4$, they are a = 10.49(1) and c = 11.18(1) Å (1, 2). This increase of the lattice constants in the crystalline phase did not appear to affect the ionic conductivity for the GeO_2 and Ga_2O_3 substituted glass-ceramics. It should be noted, however, that any conductivity changes within the crys-

Table III. Ionic conductivity activation energies, E, and preexponential factors, σ_o, obtained from $\sigma = \sigma_o \exp(-E/kT)$ for glasses and glass-ceramics with compositions based on $Li_2O \cdot Al_2O \cdot 2SiO_2$. For an indication of the magnitude of the errors, see Tables II and IV.

Composition	Glass		Glass-ceramic*	
	E (eV)	σ_o $(\Omega\text{-cm})^{-1}$	E (eV)	σ_o $(\Omega\text{-cm})^{-1}$
Stoichiometric				
$Li_2O \cdot Al_2O_3 \cdot 2SiO_2$	0.68	1.8×10^2	1.23	2.6×10^5†
Ge substituted				
$Li_2O \cdot Al_2O_3 \cdot GeO_2 \cdot SiO_2$	0.69	1.1×10^2	1.13	1.1×10^4
$2Li_2O \cdot 2Al_2O_3 \cdot GeO_2 \cdot 3SiO_2$	0.70	1.8×10^2	0.90	9.0×10^1
Ga substituted				
$2Li_2O \cdot Al_2O_3 \cdot Ga_2O_3 \cdot 4SiO_2$	0.72	1.7×10^2	1.18	1.3×10^3
$4Li_2O \cdot 3Al_2O_3 \cdot Ga_2O_3 \cdot 8SiO_2$	0.69	1.3×10^3	0.82	2.4×10^2
Ge + Ga substituted				
$2Li_2O \cdot Al_2O_3 \cdot Ga_2O_3 \cdot 2GeO_2 \cdot 2SiO_2$	0.76	2.6×10^2	—	—
B substituted				
$Li_2O \cdot 3B_2O_3$	0.84	2.8×10^3	—	—
$Li_2O \cdot B_2O_3 \cdot 2SiO_2$‡	—	—	0.65	6.7×10^1
$2Li_2O \cdot Al_2O_3 \cdot B_2O_3 \cdot 4SiO_2$	0.77	2.8×10^2	0.77	3.0×10^2
$4Li_2O \cdot 3Al_2O_3 \cdot B_2O_3 \cdot 8SiO_2$	0.72	1.9×10^2	0.72	5.2×10^2
Li enhanced				
$Li_2O \cdot Al_2O_3 \cdot 1.3SiO_2$	0.68	2.7×10^2	—	—
$1.3Li_2O \cdot Al_2O_3 \cdot 2SiO_2$	0.68	2.5×10^2	—	—
$3.1Li_2O \cdot Al_2O_3 \cdot 3.8SiO_2$	0.63	1.9×10^2	0.85	1.8×10^3
$4.3Li_2O \cdot Al_2O_3 \cdot 7SiO_2$	0.63	1.0×10^2	0.81	2.1×10^3
$2Li_2O \cdot 3SiO_2$	0.59	1.6×10^2	—	—
Li enhanced and Ge substituted				
$3.1Li_2O \cdot Al_2O_3 \cdot 1.9GeO_2 \cdot 1.9SiO_2$	0.66	1.3×10^3	0.85	4.2×10^1
Li enhanced and Ga substituted				
$6.2Li_2O \cdot Al_2O_3 \cdot Ga_2O_3 \cdot 7.6SiO_2$	0.64	2.1×10^3	0.95	2.1×10^2
Li enhanced and Ge and Ga substituted				
$6.2Li_2O \cdot Al_2O_3 \cdot Ga_2O_3 \cdot 3.8GeO_2 \cdot 3.8SiO_2$	0.69	3.8×10^2	—	—
Li enhanced and B substituted				
$3.1Li_2O \cdot B_2O_3 \cdot 3.8SiO_2$	0.60	1.4×10^2	0.60	1.0×10^3
$6.2Li_2O \cdot B_2O_3 \cdot Al_2O_3 \cdot 7.6SiO_2$	0.70	1.1×10^3	0.95	1.1×10^2

* Values depend on the volume fraction of crystallinity.
† 88 v/o crystallinity.
‡ Partially crystallized during the initial preparation.

tallites may have been masked by a resistive interfacial layer.

The ionic conductivity results for the B_2O_3 substituted glasses and glass-ceramics are given in Fig. 3 and 4 and Table III. Comparison of the results for $Li_2O \cdot Al_2O_3 \cdot 2SiO_2$ glass with the results of the B_2O_3 substituted glasses (Fig. 3) indicates that B_2O_3 substitution causes a net decrease in the ionic conductivity of the glass. However, the results in Fig. 4 show that the ionic conductivities of some B_2O_3 substituted glass-ceramics are similar to or in some instances, even greater than, the conductivities for the corresponding

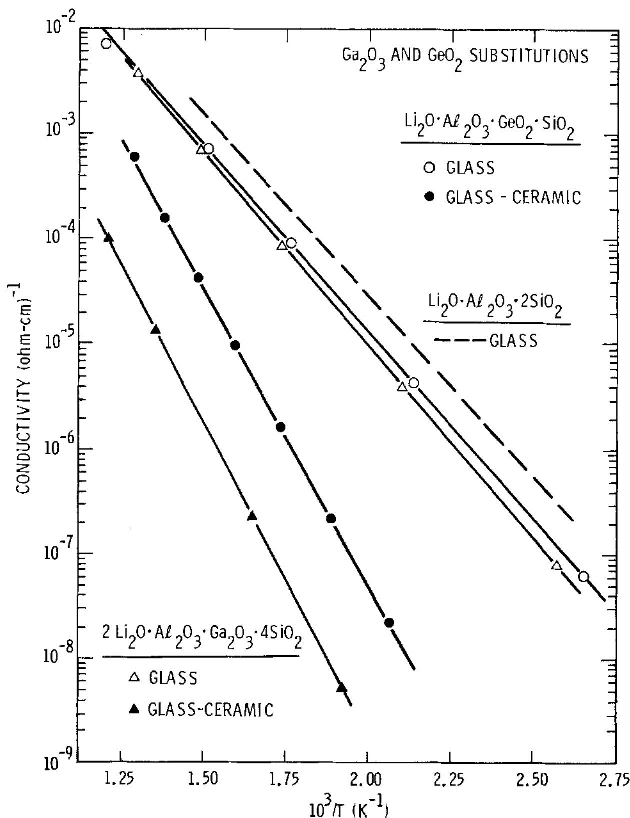

Fig. 2. Ionic conductivity temperature dependence for substitutions of GeO_2 for SiO_2 and Ga_2O_3 for Al_2O_3 in lithium aluminosilicate glasses and glass-ceramics. Results are compared with stoichiometric $Li_2O \cdot Al_2O_3 \cdot 2SiO_2$ glass (dashed line) and show that these substitutions do not significantly affect the conductivity when compared wih $Li_2O \cdot Al_2O_3 \cdot 2SiO_2$ glass and glass-ceramic (see Fig. 1).

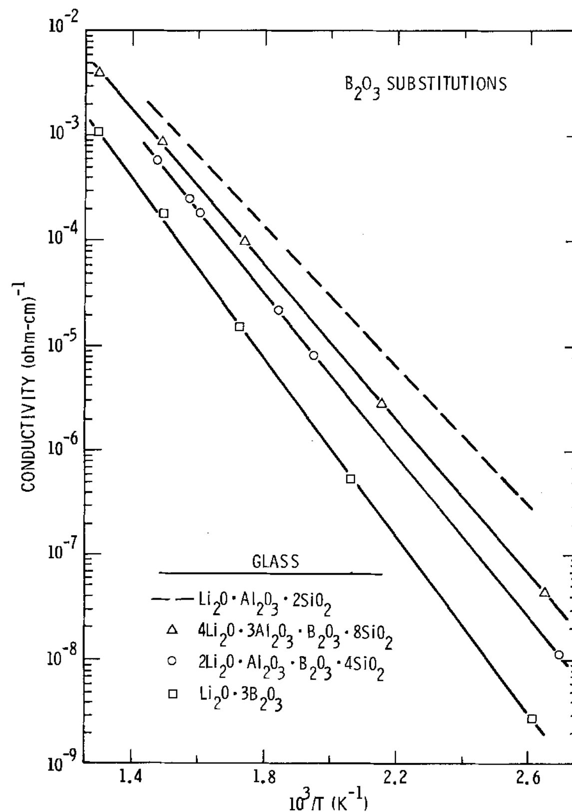

Fig. 3. Ionic conductivity temperature dependence for B_2O_3 substitutions for Al_2O_3 in $Li_2O \cdot Al_2O_3 \cdot 2SiO_2$ (*i.e.*, $LiAlSiO_4$) glass. Results show that substitution of B_2O_3 causes a net decrease in the ionic conductivity of the glass.

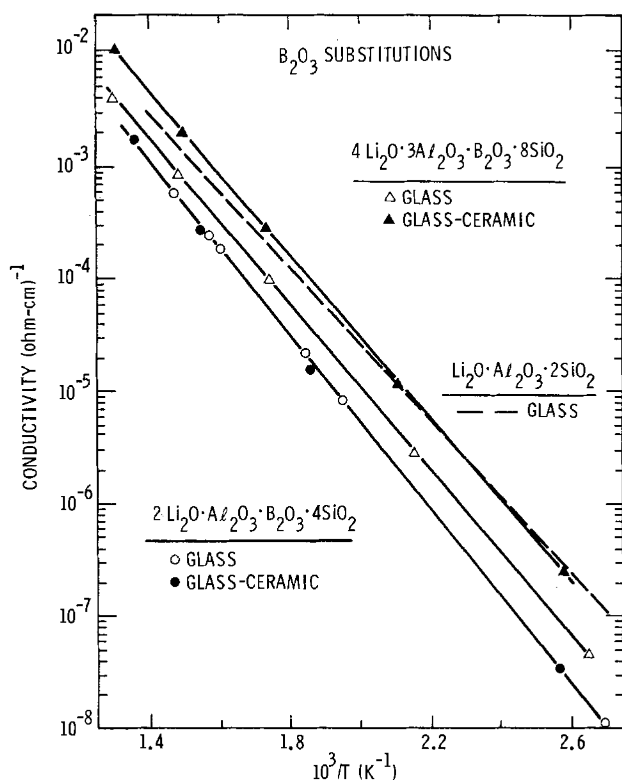

Fig. 4. Ionic conductivity temperature dependence for B_2O_3 substituted lithium aluminosilicate glasses and glass-ceramics. The conductivities of the glass-ceramics are similar to (or greater than) the conductivities for the corresponding glass. This is in contrast to the trends observed for stoichiometric $Li_2O \cdot Al_2O_3 \cdot 2SiO_2$ and for the GeO_2 and Ga_2O_3 substituted materials (see Fig. 1 and 2).

glasses. This is exactly opposite to the behavior observed for the stoichiometric $LiAlSiO_4$ glass-ceramics, for the GeO_2 and Ga_2O_3 substituted glass-ceramics, and for several other glass-ceramic systems (10-13). To our knowledge, this is the first reported observation of an increase in ionic conductivity in a Li_2O containing system upon conversion from a glass to a glass-ceramic.

In interpreting these results, the degree of crystallinity must be considered. For the composition $2Li_2O \cdot Al_2O_3 \cdot B_2O_3 \cdot 4SiO_2$ in Fig. 4 the glass and glass-ceramic are observed to have the same conductivity. The x-ray data on this particular glass-ceramic indicated that it is only slightly crystalline as evidenced by both the long exposure time needed to obtain the x-ray diffraction photograph and the presence of a large amount of low angle scattered x-rays associated with the glass phase. From the previous results for the dependence of the ionic conductivity on the percent crystallinity in the ($LiAlSiO_4$) glass-ceramics (4), it is reasonable to expect that a low crystallinity glass-ceramic would have a conductivity similar to that for the corresponding glass. Thus for the $2Li_2O \cdot Al_2O_3 \cdot B_2O_3 \cdot 4SiO_2$ material, it is not possible, with the present data, to determine whether the observed conductivity effects are due to the B_2O_3 substitution or the low degree of crystallinity. The situation is a little clearer, however, for $4Li_2O \cdot 3Al_2O_3 \cdot B_2O_3 \cdot 8SiO_2$ (Fig. 4). The glass-ceramic of this composition had a relatively high degree of crystallinity. The conductivity data indicate an increase in conductivity above that for the corresponding glass. We interpret this behavior as due to a compositional change (*i.e.*, substitution of B_2O_3). The magnitude of the conductivity increase observed in Fig. 4 is of the order of what might be expected if the β-eucryptite crystalline regions began to contribute to the conductivity. It is possible that boron may be lowering the resistance of the glass-crystalline interfacial layer in the glass-ceramic.

X-ray diffraction results on these boron containing glass-ceramics showed that they contained β-eucryptite crystallites (see Table I); however, the lattice constants [a = 10.45(1) and c = 11.13(4)Å] are smaller than those for $LiAlSiO_4$. Since the crystallite lattice constants are smaller, the size of the channels through which the Li ions move should be reduced. Whether this actually causes an increase or decrease in conductivity is not known. There does appear to be an optimum channel-to-ion size ratio for maximizing the conductivity in crystallographic tunnels in solid electrolytes (14, 15).

Studies were also pursued on compositions for which the Li_2O content of the material is greater than that in stoichiometric $LiAlSiO_4$. The results of the ionic conductivity measurements on these lithium enriched glasses and glass-ceramics are presented in Fig. 5, 6, and 7 and in Table III. Increasing the Li_2O content of the Al, Ga, or Ge containing glasses, Fig. 5 and 6, causes an increase in the ionic conductivity of the glasses. [This has also been observed for Li_2O-SiO_2 glasses (11, 13).] However, the corresponding glass-ceramics have ionic conductivities that are similar to or even lower than the ionic conductivities for $LiAlSiO_4$ glass-ceramics. The results for B_2O_3 substituted glasses and glass-ceramics with an enhanced Li_2O content are given in Fig. 7. The ionic conductivities of the glasses are greater than that of $LiAlSiO_4$ glass, which is consistent with the results for the other Li_2O enhanced glasses. The conductivity of these Li_2O enriched glasses does not appear to be significantly affected by B_2O_3

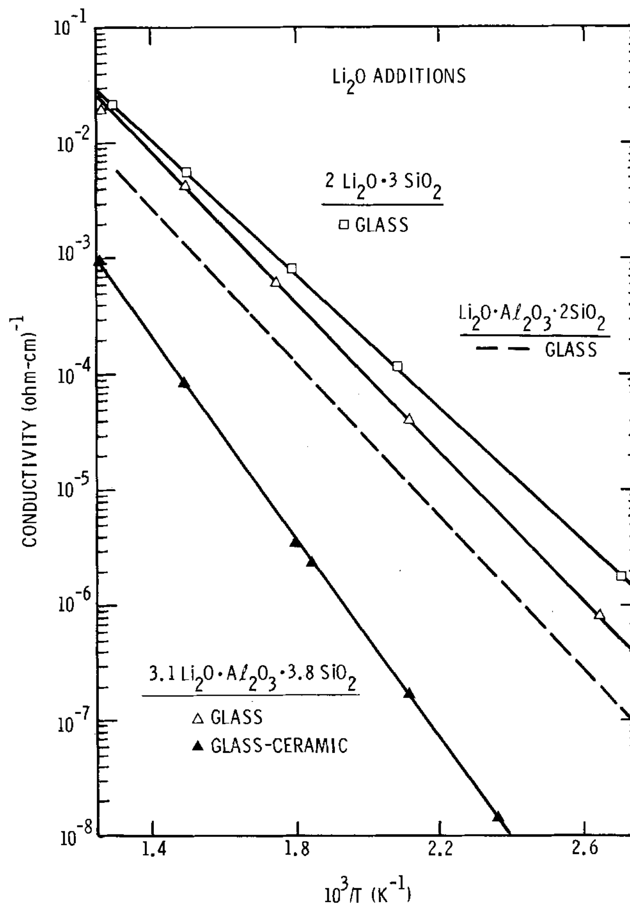

Fig. 5. Ionic conductivity temperature dependence for lithium silicate and lithium aluminosilicate glass and glass-ceramic with enhanced Li_2O concentrations. Results are compared with stoichiometric $Li_2O \cdot Al_2O_3 \cdot 2SiO_2$ glass (dashed line) and show that the addition of Li_2O increases the conductivity of the glass. The decrease in conductivity upon forming a glass-ceramic is similar to that observed in $Li_2O \cdot Al_2O_3 \cdot 2SiO_2$ glass-ceramics (Fig. 1).

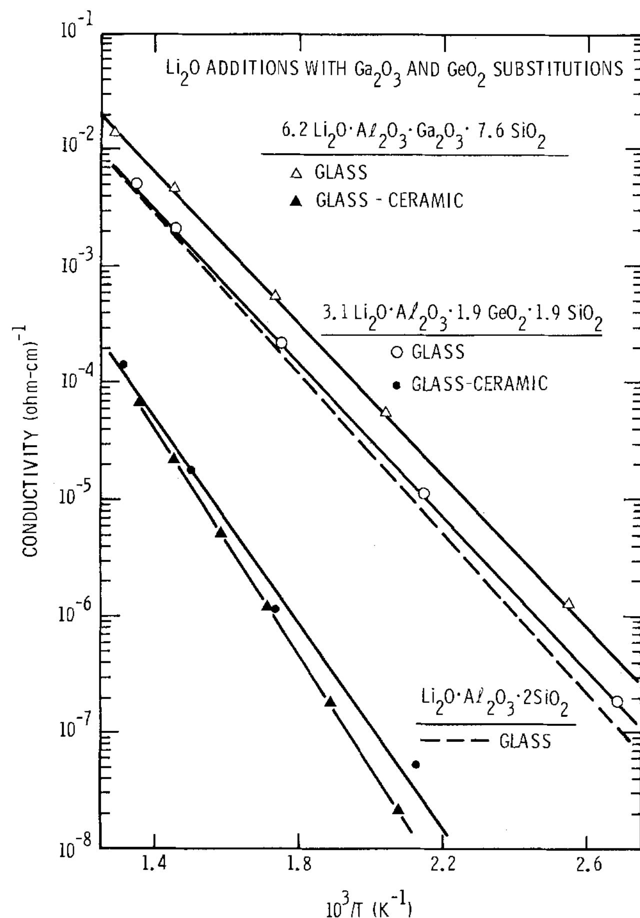

Fig. 6. Ionic conductivity temperature dependence for Li_2O additions to lithium aluminosilicate glasses and glass-ceramics with GeO_2 and Ga_2O_3 substitutions for SiO_2 and Al_2O_3, respectively. Results are compared with stoichiometric $Li_2O \cdot Al_2O_3 \cdot 2SiO_2$ glass (dashed line) and show that the conductivity of the glasses is increased by Li_2O additions. The conductivity decrease upon forming a glass-ceramic is similar to that observed for $Li_2O \cdot Al_2O_3 \cdot 2SiO_2$ glass-ceramics (Fig. 1).

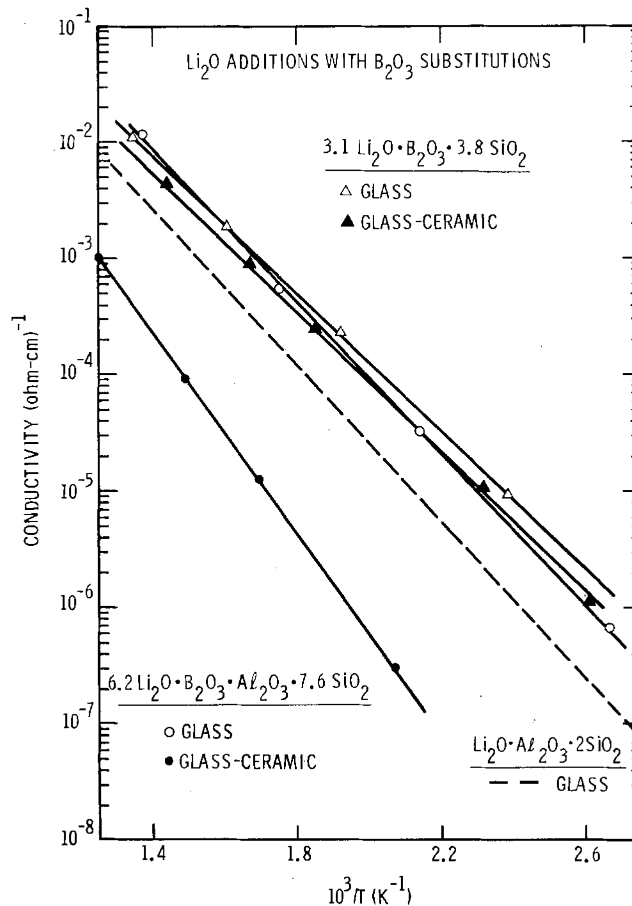

Fig. 7. Ionic conductivity temperature dependence for lithium aluminosilicate glasses and glass-ceramics with Li_2O additions and B_2O_3 substitutions for Al_2O_3. Results are compared with those for $Li_2O \cdot Al_2O_3 \cdot 2SiO_2$ glass (dashed line) and show that Li_2O additions enhance the conductivity and that some B_2O_3 containing glass-ceramics ($3.1Li_2O \cdot B_2O_3 \cdot 3.8SiO_2$) exhibit a conductivity which is greater than that for the corresponding glass.

substitutions, at least for the compositions examined in Fig. 5 and 7. The most striking effects of B_2O_3 substitutions, however, are seen for the glass-ceramic materials. Some of the B containing Li_2O enriched glass-ceramics ($3.1 Li_2O \cdot B_2O_3 \cdot 3.8 SiO_2$) have conductivities very similar to those of the glass. These results further emphasize the anomalous behavior of some boron containing glass-ceramics. Both of the glass-ceramics examined in Fig. 7 have a high degree of crystallinity. As seen in this figure, the $6.2 Li_2O \cdot B_2O_3 \cdot Al_2O_3 \cdot 7.6 SiO_2$ glass-ceramic has a much lower conductivity than the glass. It is not clear why some of the boron containing glass-ceramics do not show the anomalous behavior. A good comparison between the conductivities of glasses and glass-ceramics with and without B_2O_3 substitution is seen by comparing the results for $3.1 Li_2O \cdot Al_2O_3 \cdot 3.8 SiO_2$ in Fig. 5 with those for the corresponding B_2O_3 substituted material, $3.1 Li_2O \cdot B_2O_3 \cdot 3.8 SiO_2$, in Fig. 7. In contrast to the Al_2O_3 containing materials the B_2O_3 substituted glass-ceramic has a conductivity which is nearly the same as that of the glass. This glass-ceramic $3.1 Li_2O \cdot B_2O_3 \cdot 3.8 SiO_2$, (Fig. 7) contains largely lithium metasilicate (Li_2SiO_3) crystallites instead of β-eucryptite crystallites. The sample is mostly crystalline as evidenced by its opaqueness, absence of low angle scattering, and the short exposure time needed to obtain the x-ray diffraction photograph. The anomalously high conductivity can be explained by assuming that glass-ceramics with only lithium metasilicate crystallites have higher conductivities than glass-ceramics which also have β-eucryptite crystallites. However, this appears to be unlikely since results reported by Kinser and Hench (13) indicate that Li_2O-SiO_2 glass-ceramics which contain lithium metasilicate crystallites also have conductivities that are lower than those of the starting glass. Another possible way to explain the high conductivity in some of the boron containing glass-ceramics is to assume that the boron reduces the glass-crystalline interfacial resistance.

It appears from all of these experimental results that the glass-crystalline interfaces play a very important role in influencing the ionic conductivity characteristics of glass-ceramics based on the lithium aluminosilicate (β-eucryptite) system.

Pressure dependence.—The effect of hydrostatic pressure on the ionic conductivity was examined in a glass and glass-ceramic (81% crystallinity) of the basic β-eucryptite composition ($LiAlSiO_4$), in a glass which exhibits one of the highest conductivities resulting from an enhanced Li_2O content ($3.1 Li_2O \cdot Al_2O_3 \cdot 3.8 SiO_2$), and in a B_2O_3 substituted glass-ceramic which has a conductivity greater than that of the corresponding glass ($4 LiO_2 \cdot 3 Al_2O_3 \cdot B_2O_3 \cdot 8 SiO_2$). The ionic conductivity was first measured at 250°C as a function of pressure to 2.0 GPa and the results showed only slight (20-50%) variations with pressure. The temperature dependence of the conductivity was then measured at 2.0 GPa. The E and σ_o values determined from these experiments are given in Table IV and are compared to similar data obtained at atmospheric pressure on "sister" samples. The results show that E and σ_o were not significantly affected by pressure. There does appear to be a slight lowering of σ_o at 2.0 GPa, but these differences are nearly within experimental

Table IV. Ionic conductivity activation energies, E, and preexponential factors, σ_0, at pressures of ~0 and 2.0 GPa as determined from $\sigma = \sigma_0{}^{-E/kT}$ for lithium aluminosilicate and related glass and glass-ceramic materials.*

Material	~0 GPa E (eV)	~0 GPa σ_0 $(\Omega\text{-cm})^{-1}$	2.0 GPa E (eV)	2.0 GPa σ_0 $(\Omega\text{-cm})^{-1}$
$Li_2O \cdot Al_2O_3 \cdot 2SiO_2$ glass	0.68 ± 0.01	$1.83 \times 10^2 \left(\begin{smallmatrix}+0.11\\-0.11\end{smallmatrix}\right) \times 10^2$	0.68 ± 0.01	$1.19 \times 10^2 \left(\begin{smallmatrix}+0.35\\-0.27\end{smallmatrix}\right) \times 10^2$
$Li_2O \cdot Al_2O_3 \cdot 2SiO_2$ glass-ceramic†	1.14 ± 0.04	$8.50 \times 10^4 \left(\begin{smallmatrix}+7.2\\-3.9\end{smallmatrix}\right) \times 10^4$	1.14 ± 0.01	$2.05 \times 10^4 \left(\begin{smallmatrix}+0.17\\-0.15\end{smallmatrix}\right) \times 10^4$
$3.1Li_2O \cdot Al_2O_3 \cdot 3.8SiO_2$ glass	0.64 ± 0.01	$3.02 \times 10^2 \left(\begin{smallmatrix}+0.32\\-0.29\end{smallmatrix}\right) \times 10^2$	0.61 ± 0.01	$1.17 \times 10^2 \left(\begin{smallmatrix}+0.33\\-0.25\end{smallmatrix}\right) \times 10^2$
$4Li_2O \cdot 3Al_2O_3 \cdot B_2O_3 \cdot 8SiO_2$ glass-ceramic	0.72 ± 0.01	$5.18 \times 10^2 \left(\begin{smallmatrix}+0.78\\-0.68\end{smallmatrix}\right) \times 10^2$	0.69 ± 0.02	$2.65 \times 10^2 \left(\begin{smallmatrix}+1.19\\-0.82\end{smallmatrix}\right) \times 10^2$

* The ~ 0 and the 2.0 GPa pressure data were obtained on different ("sister") samples.
† 81 v/o crystallinity.

error. This is consistent with results on sodium aluminosilicate glasses where only a small pressure effect on ionic conductivity was observed (16).

Although there is no significant pressure effect on the glasses examined here, it is reasonable to expect more of an effect in the crystalline material since the β-eucryptite lattice does change with pressure (17). However, the conductivity of the crystalline grains in the glass-ceramics may be masked by a resistive interfacial layer. The lack of a significant pressure effect on the glass-ceramics examined here could be explained by assuming that an increase in pressure has no effect on the conductivity of the glass-crystalline interface.

Summary

The ionic conductivities of stoichiometric $LiAlSiO_4$ glass, glass-ceramic, and single crystal show that the glass is a good three-dimensional conductor when compared to the single crystal (along the one-dimensional conducting channels) and is a considerably better conductor than the glass-ceramics (for high degrees of crystallinity and at low temperatures). Substitution of Ga_2O_3 or GeO_2 for Al_2O_3 or SiO_2, respectively, in $Li_2O \cdot Al_2O_3 \cdot 2SiO_2$ glass and glass-ceramic has little effect on the ionic conductivity. However, substitution of B_2O_3 for Al_2O_3 increases the ionic conductivity in some of the glass-ceramics when compared to that of the starting glass. This effect is opposite to the trend observed for the Al, Ga, or Ge containing glass-ceramics. When the Li_2O content of a glass is increased over that for $LiAlSiO_4$, an increase in the ionic conductivity results. When B_2O_3 is substituted into the enhanced lithium materials an anomalous effect on the conductivity is again observed for some of the glass-ceramics. The anomalous enhancement of the ionic conductivity in some boron containing glass-ceramics is explained by its effect on the glass-crystalline interface. The existence of glass-crystalline interfacial layers which significantly affect the conductivity of the glass-ceramics provides a consistent interpretation for all of the results.

The effect of hydrostatic pressure (to 2.0 GPa) on the ionic conductivity in glass and glass-ceramic materials was determined for a number of samples with different compositions and conductivities. No significant pressure effect was observed. This is consistent with the results for other glasses (16) and with the important role thought to be played by the interfacial layers in the glass-ceramics.

At the present time the highest ionic conductivities [$\sim 2 \times 10^{-2}$ $(\Omega\text{-cm})^{-1}$ at 500°C] have been obtained in the glasses with enhanced lithium concentrations and in the glass-ceramics with both enhanced lithium concentrations and B_2O_3 substitutions for Al_2O_3. It is possible that the ionic conductivity of a glass-ceramic may be increased further by orienting the crystallites within the glass-ceramic. Atkinson and McMillan (18) have reported an increase of up to a factor of 38 in the conductivity of aligned Li_2O-SiO_2 glass-ceramics when compared to the conductivity of the unaligned glass-ceramics. By aligning the crystallites in the boron containing lithium aluminosilicate glass-ceramics, higher ionic conductivities than those reported here may be obtainable at high temperatures.

Acknowledgments

The authors are indebted to D. L. Stewart for preparing some of the glass and glass-ceramic samples and to D. D. Drummond and P. B. Bolwahnn for the ionic conductivity measurements. This work was done for the U.S. Energy Research and Development Administration under Contract At(29-1)-789.

Manuscript submitted June 23, 1977; revised manuscript received Sept. 21, 1977.

Any discussion of this paper will appear in a Discussion Section to be published in the December 1978 JOURNAL. All discussions for the December 1978 Discussion Section should be received by Aug. 1, 1978.

Publication costs of this article were assisted by Sandia Laboratories.

REFERENCES

1. V. Tscherry, H. Schulz, and F. Laves, *Z. Krist.*, **135**, 161 (1972); *ibid.*, **135**, 175 (1972).
2. H. Schulz, *J. Am. Ceram. Soc.*, **57**, 313 (1974).
3. R. T. Johnson, Jr., R. M. Biefeld, M. L. Knotek, and B. Morosin, *This Journal*, **123**, 680 (1976).
4. R. M. Biefeld, G. E. Pike, and R. T. Johnson, Jr., *Phys. Rev. B*, **15**, 5912 (1977).
5. H. Böhm, *Phys. Status Solidi A*, **30**, 531 (1975).
6. U. v. Alpen, E. Schönherr, H. Schulz, and G. H. Talat, *Electrochim. Acta*, **22**, 805 (1977).
7. V. Tscherry and R. Schmid, *Z. Krist.*, **133**, 110 (1971).
8. J. P. Remeika, *J. Am. Chem. Soc.*, **76**, 940 (1954).
9. R. T. Johnson, Jr., and B. Morosin, *High Temp.-High Pressures*, **8**, 31 (1976).
10. P. W McMillan, "Glass-Ceramics," p. 158, Academic Press, New York (1964).
11. P. W. McMillan, *Glass Technol.*, **15**, 5 (1974).
12. P. W. McMillan, S. V. Phillips, and G. Partridge, *J. Mater. Sci.*, **1**, 269 (1966).
13. D. L. Kinser and L. L. Hench, *J. Am. Ceram. Soc.*, **51**, 445 (1968).
14. W. H. Flygare and R. A. Huggins, *J. Phys. Chem. Solids*, **34**, 1199 (1973).
15. R. H. Radzilowski and J. T. Kummer, *This Journal*, **118**, 714 (1971).
16. D. Chakravorty and L. E. Cross, *J. Am. Ceram. Soc.*, **47** 370 (1965).
17. B. Morosin and P. S. Peercy, *Phys. Lett. A*, **53**, 147 (1975).
18. D. I. Atkinson and P. W. McMillan, *J. Mater. Sci.*, **10**, 2012 (1975); *ibid.*, **12**, 443 (1977).

Efficiencies of Cycling Lithium on a Lithium Substrate in Propylene Carbonate

R. D. Rauh,* T. F. Reise, and S. B. Brummer*

EIC Corporation, Newton, Massachusetts 02158

ABSTRACT

To assess the cycling efficiency of the Li electrode in a positive-limited secondary battery, Li has been plated and stripped from a Li substrate. This has been carried out in a specially designed cell containing a Li electrode of known volume: Li is plated and stripped from this electrode until the substrate is depleted. Individual efficiencies can also be determined from inflections in the stripping curves. Average efficiencies were best for PC, 1M $LiAsF_6$ which had been preelectrolyzed and treated with activated neutral alumina. Here, for 10 C/cm² cycles about 85% cycling efficiency was obtained, essentially without change until the substrate was depleted. In general, $LiClO_4$ showed inferior behavior to $LiAsF_6$.

Secondary Li batteries have generated renewed interest over the last several years (1-6). One type of system under investigation is the ambient temperature cell with an aprotic solvent-based electrolyte. A principal difficulty in the development of such a battery is the inefficiency of the Li electrode (7-10). Studies to date of the Li electrode have concentrated on a negative-limited system in which the Li is plated from solution onto an inert or alloying substrate (11-13) and then either removed immediately or following a waiting period. By such experiments, the cycling efficiency and rate of activity loss could be measured.

The over-all efficiency of the cycling process in such experiments appears to be a multidetermined variable. Variations in efficiency have been noted for plating and stripping current density, charge density, supporting electrolyte, electrolyte additive, substrate (12), and cycle number (7-9, 14). In the propylene carbonate (PC), $LiClO_4$ system, and probably in many other systems, the efficiency of the plating step is nearly 100% (10). All of the inefficiencies are realized in the stripping process. Following such inefficient stripping, most of the unaccounted Li remains on the electrode, and is electrically insulated from it. On stand, the rate of capacity loss has been observed to exceed by roughly a factor of 10 the rate of Li oxidation (10). For both types of activity loss, insulation of Li granules through encapsulation by resistive Li-electrolyte reaction products has been suggested (7, 8). Finally the efficiency of the plating-stripping process decreases markedly with cycle, apparently due to blockage of portions of the substrate with reaction products, and accumulations of insulated Li (7, 8, 14).

In practice, then, the efficiency of the Li electrode is diminished by encapsulation of active material and by associated deterioration of the substrate. Approaches to the encapsulation problem are to eliminate all reactivity of the electrolyte with Li, to alter the morphology of the Li so it is less susceptible to attack, and to add a material to the electrolyte which will form a protective Li^+-permeable film on the electrodeposit. The latter idea is in analogy to the $Li/SOCl_2$ (15-17) and Li/SO_2 (18, 19) primary batteries, in which the Li is obviously protected from the highly oxidizing liquid cathode by a passivating film, yet can be discharged.

Most of the secondary Li battery systems which have been studied have been positive electrode-limited devices. However, the relative merits of positive and negative limitation have not been discussed in the open literature. A positive-limited system would be the better arrangement to achieve highest energy density, and this is why all primary systems are positive-limited. Indeed, if a battery contains an insoluble positive with 100% cycling efficiency and there is zero self-discharge rate, a negative-limited system with a less efficient Li electrode would not be feasible. With a soluble-positive system, in which much or all of the Li capacity loss can be attributed to self-discharge, such as the Li/Br_2 battery described by Weininger (20), a negative-limited system is feasible and perhaps even desirable.

It is the purpose of this study to investigate the cycling behavior in PC of Li on a dense Li substrate. This is the situation which would be present in a positive-limited Li secondary battery. Better deposit morphology might be expected in plating a metal onto itself than onto a foreign substrate. Correspondingly, the effect of cycle number on the efficiency should be improved, although this is not easily predictable.

Experimental

Propylene carbonate (PC) obtained from Burdick and Jackson Laboratories was used as-received. The latter material was characterized by lot analysis to contain 0.005% H_2O, and to be of otherwise high purity ("distilled in glass").

Lithium perchlorate ($LiClO_4$, Foote Mineral Company, anhydrous) was dried for 24 hours *in vacuo* (< 0.1 mm) at its fusion point (230°C). Lithium hexafluoroarsenate ($LiAsF_6$, electrochemical grade) was obtained from United States Steel, Agri-Chemicals Division, Decatur, Georgia, and was used as-received. It was indicated by the manufacturer to contain from 50 to 100 ppm H_2O (Karl Fischer method). Details concerning the preparation and analysis of high purity anhydrous $LiAsF_6$ have been discussed by Lawless *et al.* (21).

Neutral alumina (Fisher) was activated at 350°C in an argon stream overnight. The desiccant was immediately transferred to the dry box antechamber and allowed to cool under vacuum. Linde 5A molecular sieves were used as-received. All desiccants were used only in the dry box. In the appropriate experiments, 50 ml of electrolyte were slowly percolated through a chromatograph column containing 10g of desiccant. The first 10% through the column was discarded; the remainder was collected and stored in a tightly capped flask in the glove box.

All cycling studies were conducted at room temperature in a Vacuum/Atmospheres Company dry box. The argon atmosphere was continuously recirculated through a column containing molecular sieves and an activated Cu gettering material (BASF catalyst R3-11), for removing moisture and O_2.

Plating and stripping of Li were carried out galvanostatically using either a specially constructed constant current power supply or a Wenking Model LT 73 po-

* Electrochemical Society Active Member.

Key words: lithium batteries, lithium electrodeposition, propylene carbonate.

tentiostat operating in the constant current mode. Cycles were performed continuously, without waiting periods between half cycles.

Results

Using a Li substrate for Li cycling studies is not as straightforward as using an inert substrate, chiefly due to the difficulty of determining the electrochemical stripping end point. An experiment for determining the average Li cycling efficiency over 10 or more cycles was therefore designed. The substrate consisted of a well-defined area of commercially available 0.13 mm (5 mil) thick Li foil. Exactly 10 C/cm^2 of Li were first deposited, then stripped from this substrate. If the process were not 100% efficient, some of the substrate would be oxidized during the stripping process. From the number of cycles required to deplete the substrate, the average efficiency per cycle could be calculated.

The cell used for these studies is illustrated in Fig. 1. The working and counterelectrodes were 0.13 mm and 0.39 mm (15 mil) thick Li disks, respectively. The reference electrode consisted of Li in 1M Li^+/PC in a Luggin capillary with fiberglass filter paper plugging the tip. Counter and working electrodes were pressed against Ni backings. The cell body was made of Teflon and was held together using a C clamp.

The reproducibility of the capacity of the 0.13 mm Li was determined by totally stripping several electrodes taken from various parts of the Li ribbon. The electrolyte was PC/1M $LiClO_4$; stripping was carried out at 5 mA/cm^2. Theoretically, 0.13 mm Li contains 91.6 C/cm^2. The experimentally determined value was 82.9 $\pm$ 7.0 C/cm^2 for 10 samples taken at random from this particular roll of foil. This experimental value was used in calculating average cycling efficiencies.

Li cycling experiments were carried out using a plating and stripping current density of 2.5 mA/cm^2. The average efficiency per cycle, $\overline{E}$, was calculated from the equation

$$\overline{E} = 1 - \frac{N}{nQ} \quad [1]$$

Here, N is the number of coulombs/square centimeter of Li present initially on the substrate, Q is the number of coulombs/square centimeter plated and stripped in each cycle (10 in these experiments), and n is the number of cycles until Li substrate depletion.

Before the initial plating cycle, 1 C/cm^2 was stripped from the substrate to remove any surface films. The chronopotentiogram for this initial stripping step showed an anodic overshoot, then a leveling off of potential at a less anodic value. This latter potential was taken to be the stripping potential of substrate Li, uncorrected for IR, but constant within a given cell. Li surface films could also be removed by abrading the Li substrate with a paper towel before introduction into the cell. The initial stripping chronopotentiograms for nonabraded and abraded Li are reproduced in Fig. 2. The curves are uncorrected for IR, explaining the differences in the limiting Li stripping potentials in the two cells.

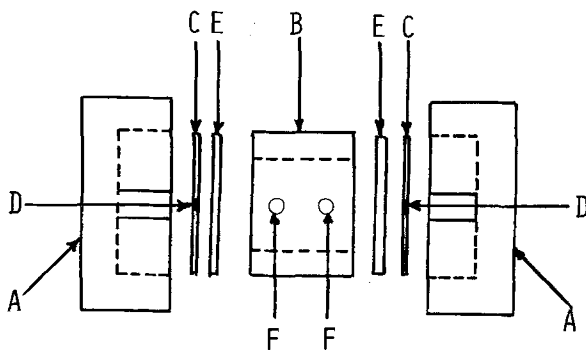

Fig. 1. Cell for cycling Li on a Li substrate drawn approximately to scale. A, Teflon end pieces; B, cylindrical Teflon center piece; C, Ni disk contact; D, contact tab; E, 5 mil Li disk (working electrode); E', 15 mil Li disk (counterelectrode); F, reference electrode and filling holes. The entire apparatus is held together with a C clamp.

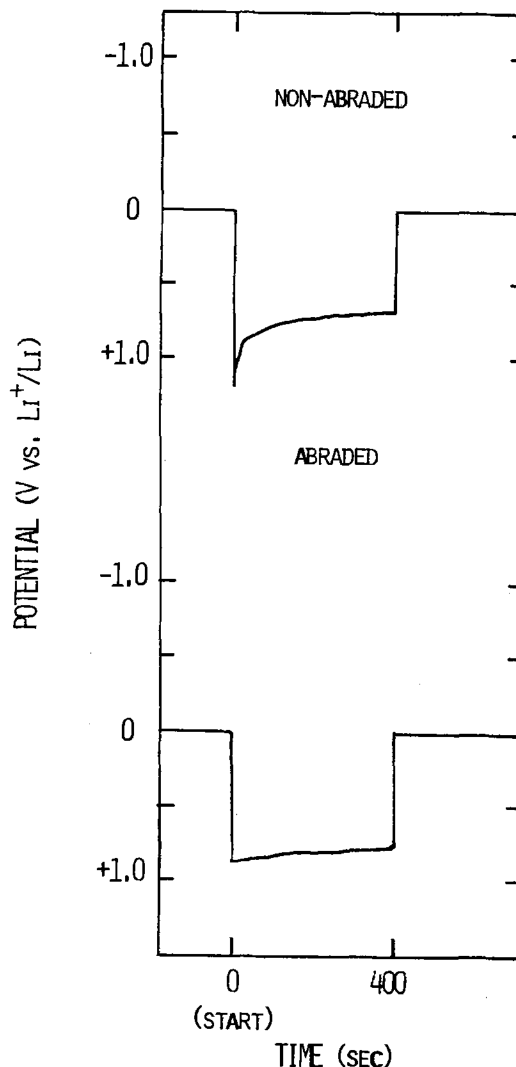

Fig. 2. Chronopotentiograms showing the initial stripping of a Li substrate, comparing abraded and nonabraded surfaces. i_s = 2.5 mA/cm^2, Q_s = 1 C/cm^2. Electrolyte is 1M $LiClO_4$ in PC.

The cycling efficiency of Li on a Li substrate was studied as a function of electrolyte purification and of electrolyte salt ($LiClO_4$ or $LiAsF_6$).

PC/$LiClO_4$.—The results of cycling Li on Li in PC/1M $LiClO_4$ solutions are summarized in Table I. In

Table I. Effect of electrolyte preparation and purification procedures on the efficiency of cycling Li on a Li substrate. Electrolyte is 1M in Li salt. $Q_p = Q_s$ = 10 C/cm^2; $i_p = i_s$ = 2.5 mA/cm^2.

Solution	Purification procedure	Average cycling efficiency
PC, 1M $LiClO_4$	/	44.2, 34.0
	A/	44.2
	A/A	44.2
	S/	40.0
	S/S	40.0
	S/S 500 ppm H_2O	44.0
	/P	44.0
	/PA	65.0
PC, 1M $LiAsF_6$	/	79.0
	A/	82.0
	A/A	83.0
	S/S	68.0
	S/	81.0
	/P	77.3
	/PA	84.2

A/ — Pass through column of activated neutral Al_2O_3.
S/ — Pass through column of activated molecular sieves.
/ — Add fuse-dried $LiClO_4$ or anhydrous $LiAsF_6$.
P/ — Preelectrolyze between Li electrodes.

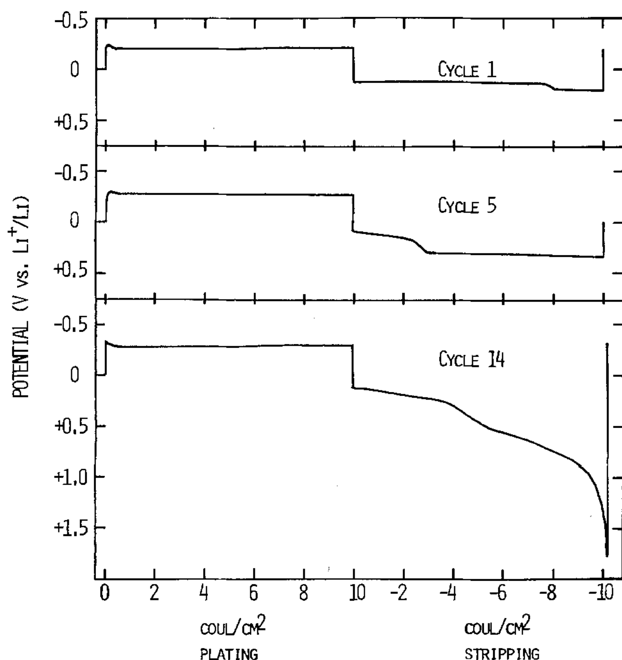

Fig. 3. Chronopotentiograms for plating and stripping Li on a Li substrate: $i_p = i_s = 2.5$ mA/cm²; $Q_p = Q_s = 10$ C/cm². Electrolyte is 1M $LiClO_4$ in PC.

general, inspection of the individual stripping chronopotentiograms allowed an estimate of the single cycle efficiencies. As shown in Fig. 3, the stripping curve following electrodeposition has two components, separated by about 100 mV. The more cathodic component, which is recorded initially, is ascribed to removal of the electrochemically accessible portion of the deposit, with its high surface area. The low surface area substrate is removed at the more positive potential, because of the higher effective current density. This latter potential corresponds to the stripping potential of the substrate, as determined at the beginning of each run.

The average efficiencies over 10-20 cycles showed some sensitivity to electrolyte purification. Electrolyte prepared by adding the $LiClO_4$ to as-received solvent gave an average efficiency of only 40%. Treatment of the electrolyte or solvent with molecular sieve led to no improvement. Addition of 500 ppm H_2O to sieve-treated electrolyte even yielded slightly higher efficiencies, in accordance with earlier results utilizing a Ni substrate (7). Alumina treatment of the electrolyte or solvent yielded a slightly improved 44%. The only significant enhancement of cycling efficiency was observed for electrolyte which had been preelectrolyzed between Li electrodes, then passed through alumina. This procedure resulted in a 65% average cycling efficiency. Similar effects of purification have been observed on a Ni substrate (14).

Figure 4 shows the single cycle efficiency profile for the PC/$LiClO_4$ system. The cell containing the untreated electrolyte showed an initial efficiency of 74%. This dropped rapidly over the next five cycles, yielding around 30% until electrode failure. The sieve-treated material gave only 44% on the first cycle, and cycled between 24 and 38% thereafter. Similarly, the preelectrolyzed electrolyte maintained a single cycle efficiency of ~40% over the 13 cycles needed to exhaust the substrate. When this same solution was passed over activated neutral alumina, the first cycle was 78%, dropping gradually to about 40% over 10 cycles, and staying at this level until the final cycle.

PC/$LiAsF_6$.—It has been reported that Li in contact with solutions of esters and $LiAsF_6$ is quite stable even at elevated temperatures (22). Higgins has also demonstrated a higher stability of Li to several aprotic solvent electrolytes if $LiAsF_6$ is used as the supporting electrolyte compared to $LiAlCl_4$ (23). In addition, studies of the Li electrode in MA, utilizing an inert substrate, indicate higher efficiencies for $LiAsF_6$ solutions than for those containing $LiClO_4$ (24). Galvanostatic cycling experiments were therefore undertaken using PC, 1M $LiAsF_6$.

Results of the cycling studies, reported in Table I, show generally higher efficiencies than obtained for PC, 1M $LiClO_4$. Thus, the untreated solution gave an average efficiency of 79%, going 34 cycles before the substrate was exhausted. As with PC, $LiClO_4$, alumina treatment enhanced this efficiency. Treatment of just the solvent with molecular sieves also improved the average cycling efficiency, while treatment with sieves after the addition of the salt gave poorer results. Again, the best cycling efficiency, 84.2%, was obtained using electrolyte which had been preelectrolyzed, then passed through a column of alumina.

The single cycle efficiencies, plotted *vs.* cycle in Fig. 5, confirm the high average efficiencies. Compared to the $LiClO_4$ solutions, the stripping plateaus were usually separated by a smaller potential, indicating a more compact, lower surface area deposit. With the preelectrolyzed solvent, plateaus were not even discernable until the 9th cycle. The average of the single cycle efficiencies was generally a few percent lower than the average efficiency computed from Eq. [1]. Probably, some stripping of electrodeposited Li continued into the second plateau. It is particularly noteworthy that the deterioration in efficiency with cycle, so evident when a Ni substrate is used with similar preparations (14), is much reduced on Li.

Discussion

Compared to $LiClO_4$, $LiAsF_6$ enhances the cycling efficiency of Li on a Li substrate in PC. This has also been observed on a Ni substrate in PC (14) and in MA

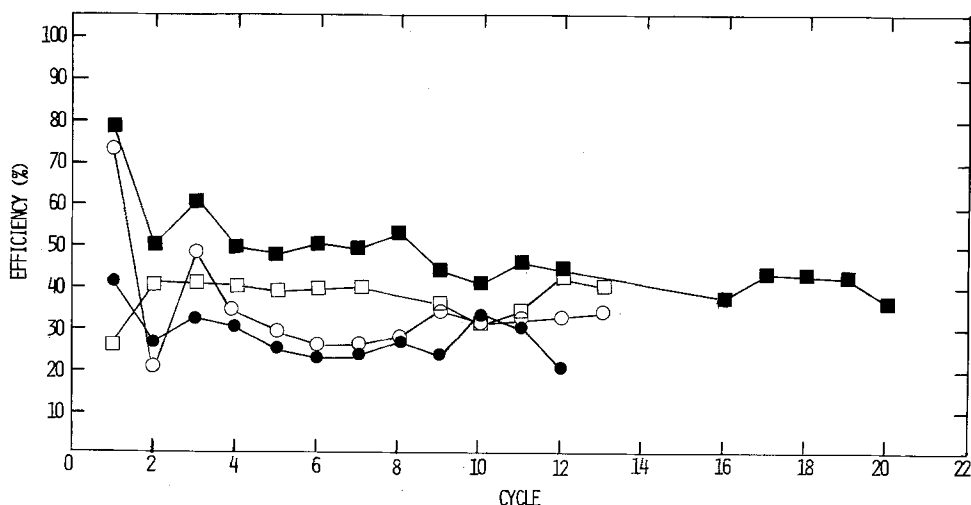

Fig. 4. Efficiencies of cycling Li on a Li substrate, as a function of cycle and electrolyte purification, in PC, 1M $LiClO_4$. $i_p = i_s = 2.5$ mA/cm²; $Q_p = Q_s = 10$ C/cm². ○ No purification. ●, Solvent and electrolyte solution passed through a column of Linde 5A molecular sieves. □, Electrolyte solution electrolyzed between Li electrodes. ■, Electrolyte solution electrolyzed between Li electrodes, then filtered through Al_2O_3.

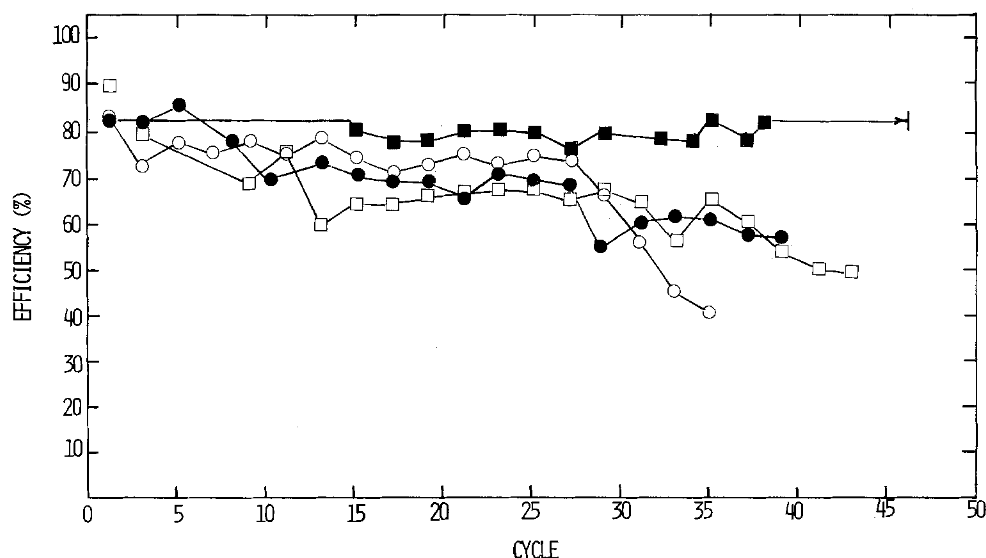

Fig. 5. Efficiencies of cycling Li on a Li substrate, as a function of cycle and electrolyte purification in PC, 1M $LiAsF_6$. $i_p = i_s = 2.5$ mA/cm²; $Q_p = Q_s = 10$ C/cm². ○, No purification. ●, Solvent only passed through a column of Linde 5A molecular sieves. □, Solvent and electrolyte solution passed through a column of activated neutral Al_2O_3. ■, Electrolyte solution electrolyzed between Li electrodes, then filtered through Al_2O_3.

(24). The main cause of inefficiency appears to be encapsulation of electrodeposited Li, leading to its insulation from the substrate.

Studies of 1 C/cm² plates on Ni show in general a more catastrophic drop of efficiency with cycle (14) than the 10 C/cm² plates in the present paper. This may reflect the more efficient reduction of solvent or impurities on Ni (at the Li potential) than on Li. As already mentioned, such reaction products and/or insulated Li remaining from previous cycles could lead to a lower effective substrate surface area and a poorer morphology. Perhaps as important, stripping away part of the Li substrate on each cycle probably provides new nucleation centers for each succeeding cycle, which is not possible on an inert substrate.

Examination of Li plated on a Li substrate reveals a dendritic habit similar to that found on Ni. However, electrodeposits are considerably more adherent with $LiAsF_6$ than with $LiClO_4$. In cycled half-cells, more Li was found floating in the electrolyte in the presence of the latter salt, and the individual granules appeared smaller. A mechanism presented by us for dendrite growth involved the filming of as-deposited Li with insulating reaction products, preventing the growth of large granules and, rather, enhancing the formation of trees and dendrites (7, 8). However, as described in the introduction, films selectively permeable to small ions, namely Li^+, may actually help grain growth, by allowing Li plating while preventing the intrusion of insulating-film-forming reactants. It is possible that $LiAsF_6$ contains, as an impurity, a substance which reacts with the Li to form such a semipermeable film, or that adsorption of AsF_6^- has the same function. It is also possible that we have been unable to rid $LiClO_4$ of certain oxidizing impurities not found in $LiAsF_6$.

The implications of these results for the construction of a practical battery based on this electrolyte are readily apparent. We estimate that a typical charge for a Li D cell (25) would be approximately 50 C/cm². Even if 85% cycling efficiency could be achieved, our best results for only 10 C/cm², a Li loss of 7.5 C/cm² per cycle would result. An extravagant tenfold excess of Li would allow only 67 complete cycles before anode failure. Correspondingly, 100 full capacity cycles would require a 90% cycling efficiency and 1000 cycles a 99% cycling efficiency. Losses can also be incurred due to isolation of electrodeposited Li on open-circuit stand. Since the phenomena of efficiency loss and Li isolation appear to result from the intrinsic reactivity of Li with the solution, improvements would surely be noted if a more inert electrolyte were found. However, since a certain amount of Li encapsulation may be inevitable, methods should be sought of recontacting the isolated dendrites or resolubilizing them via a controlled self-discharge reaction to avoid using large excesses of Li in cell construction. Such approaches are currently under investigation in our laboratory.

Acknowledgment

The authors wish to acknowledge NSF-RANN for their support of this research under Grant No. AER75-03779.

Manuscript submitted June 29, 1977; revised manuscript received Oct. 6, 1977.

Any discussion of this paper will appear in a Discussion Section to be published in the December 1978 JOURNAL. All discussions for the December 1978 Discussion Section should be submitted by Aug. 1, 1978.

REFERENCES

1. For a review of earlier work, see R. Jasinski, "High Energy Batteries," Plenum Press, New York (1967).
2. J. Birk and R. Steunenberg, in "New Uses of Sulfur," J. West, Editor, American Chemical Society, Advances in Chemistry Series No. 40, Washington, D.C. (1975).
3. J. Broadhead, F. DiSalvo, and F. Trumbore, U.S. Pat. 3,864,167 (1975).
4. M. S. Wittingham, *Science*, **192**, 1126 (1976).
5. G. L. Holleck, F. S. Shuker, and S. B. Brummer, Proceedings of 10th 1ECEC, Newark, Delaware (1975); G. L. Holleck and J. R. Driscoll, *Electrochim. Acta*, In press.
6. R. D. Rauh, F. S. Shuker, J. M. Marston, and S. B. Brummer, Paper 6 presented at The Electrochemical Society Meeting, Washington, D.C., May 2-7, 1976.
7. R. D. Rauh and S. B. Brummer, *Electrochim. Acta*, **22**, 75 (1977).
8. R. D. Rauh and S. B. Brummer, *ibid.*, **22**, 85 (1977).
9. J. Gabano, G. Gerbier, and J. Laurent, Proceedings 23rd Power Sources Conf., p. 80 (1969).
10. R. Selim and P. Bro, *This Journal*, **121**, 1457 (1974).
11. M. Nicholson, *ibid.*, **121**, 734 (1974).
12. B. M. L. Rao and K. Hill, Paper 14 presented at The Electrochemical Society Meeting, Buffalo, N.Y., Oct. 10-14, 1965.
13. B. M. L. Rao, R. W. Francis, and H. Christopher, Paper 68 presented at The Electrochemical Society Meeting, Las Vegas, Nevada, Oct. 17-22, 1976.
14. V. R. Koch and S. B. Brummer, Paper 4 presented at The Electrochemical Society Meeting, Washington, D.C., May 2-7, 1976.
15. J. J. Auborn, K. W. French, S. I. Lieberman, V. K. Shah, and A. Heller, *This Journal*, **120**, 1613 (1973).
16. W. K. Behl, J. A. Christopulas, M. Ramirez, and S. Gilman, *ibid.*, **120**, 1619 (1973).
17. J. R. Driscoll, G. L. Holleck, and D. E. Toland, Proceedings 27th Power Sources Symposium, Atlantic City, N.J., June 1976.
18. A. H. Taylor, P. Bro, and A. N. Dey, *Power Sources 4*, D. N. Collins, Editor, (1973).

19. D. L. Maricle and J. P. Mohns, Fr. Demandé 2,015,-160 (1970).
20. J. L. Weininger and F. W. Secor, *This Journal*, **121**, 315 (1974).
21. E. W. Lawless, C. J. Wiegand, Y. Mizumoto, and C. Weis, *J. Inorg. Chem.*, **10**, 1084 (1971).
22. F. W. Dampier and P. E. Krouse, Paper 23 presented at The Electrochemical Society Meeting, New York, Oct. 13-17, 1974.
23. R. L. Higgins, Final Report, Contract AFAPL-TR-75-63, July 1975.
24. F. W. Dampier and S. B. Brummer, Unpublished results.
25. N. Marincic, *J. Appl. Electrochem.*, **6**, 51 (1976).

Behavior of Maleic Acid during the Anodization of Aluminum

Michiko Shimura

Faculty of Engineering, Tokyo Metropolitan University, Tokyo, Japan

ABSTRACT

Anodization of aluminum in aqueous maleic acid at constant current densities showed that the formation of the anodic film took place competitively with the oxidation of maleic acid. In dilute electrolyte, except for the initial short period where the colorless thin film was formed, the over-all current served to oxidize the double bond of maleic acid into glyoxal or carbon monoxide. In concentrated electrolyte, the brownish anodic film was readily formed and became black as it thickened. The colored film was shown to favor the passage of ionic current and was made up of aluminum oxide complexed with maleate. The coloration of the film was considered to be induced from carboxylate anion radicals, which were coordinated to the aluminum ion as a ligand, as in the case of oxalic acid film reported previously.

The properties of aluminum anodic films differ according to the electrolytes employed. For instance, the change of the activity of hydronium ions near the anodic film is considered to affect the properties of the film because the hydronium ions react with the aluminum oxide to give an unstable soluble substance resulting in the formation of a porous film (1). However, the effect of the anion species of the acids has been scarcely explained in spite of the important fact that anodic film cannot be formed in electrolytes containing acetate or other specific anions.

Recently, the author studied the behavior of oxalic acid during the anodization of aluminum and found that oxalate ions coordinate to aluminum ions competitively with water to form aluminum complexes such as $[Al(C_2O_4)_n(H_2O)_{6-2n}]^{m-}$ which changes to $[Al \cdot O_x \cdot (C_2O_4)_y]_z$ polymer by deprotonation and olation, and that the aluminum anodization process scarcely involves Kolbe's reaction for the oxalic acid (2, 3). The coloration of the oxalic acid anodic film was suggested to have come from $C_2O_4^{2\cdot-}$ radical which should be produced by transferring charges from central low-valency aluminum ion to the oxalato ligand.

As the continuation of these studies, this paper deals with the behavior of maleic acid in the aluminum anodization process.

Experimental

Anodization.—Aqueous maleic acid electrolyte of 0.1-1.0 moles/liter was prepared from analytical grade reagent and distilled water. Cleaned 99.99% aluminum sheets and wires were anodized at 15°-45°C in vessels filled with stirred electrolytes with current supplied from a galvanostat or selenium rectifier.

Measurement of ESR spectra.—For the anodized aluminum wire, ESR spectra were measured in air using a JEOL, JES-PE 3X instrument.

Analysis of gases generated at the anode.—In order to prevent mixing of gases generated at the anode and cathode, a closed vessel with two compartments, each of which was fitted with a silicone rubber stopper, was used as the anodizing cell (4). Prior to anodization, the electrolyte was flushed with argon for several minutes. During galvanostatic anodization at 20 mA/cm², gaseous products at the anode (1 × 1 cm) were collected in a 0.1 ml syringe through the silicone rubber stopper and successively were injected to a gas chromatograph (Shimazau GC-4 AIT) equipped with molecular sieve 5A columns (Nishio Industry). Reference and sample columns were maintained at 65°C, and the helium flow was adjusted to ∼8.14 ml/min.

Detection of aldehyde.—A small ceramic beaker was inserted in a glass beaker. Into the space between the two beakers was poured 200 ml of the anolyte. The catholyte of 100 ml was poured into the ceramic beaker. A cleaned aluminum sheet of 3.5 × 8 cm was dipped in the anolyte, and 5 mA/cm² current was supplied from a selenium rectifier. The total amount of charge was measured with a copper-coulometer which was connected in series to the anodizing circuit. Every 2 hr the anodization was interrupted for a minute, the sample was replaced with another new one, and water was added to the anolyte and catholyte so as to attain initial levels. The anodization was stopped when the total amount of charge reached 10,000C. Small parts of the used anolyte and catholyte were tested with Schiff's reagent. Aldehyde was found in the anolyte but not in the catholyte. The whole anolyte was reacted with dinitrophenylhydrazine to separate the aldehyde as insoluble dinitrophenylhydrazone-derivative, which was identified by infrared absorption spectra, melting point, and so on. The yield of the aldehyde

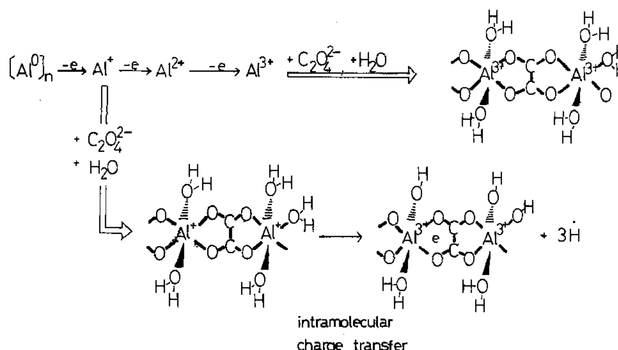

Fig. 1. Formation of aluminum complexes during anodization

Key words: anodic oxidation, aluminum, carbon monoxide.

was calculated on the basis of charge passed as electron transfer at the interface of the anode/electrolyte.

Gravimetric measurement of oxidized aluminum.—The amount of aluminum oxidized during the anodization at a given number of Faradays was measured in the following way: Al samples were weighed, to an accuracy of 10^{-4}g, before anodization and after dissolving anodized layers with H_3PO_4-CrO_3 solution. The difference of the two values, *i.e.*, the amount of aluminum anodized by a certain number of Faradays, is taken as the measure of the anodic oxidation.

Detection of succinic acid.—To investigate the behavior of maleic acid at the cathode, the catholyte after prolonged anodization was separated with paper-chromatograph using butanol-formic acid solution as developer. The separated substance was confirmed to be succinic acid from its R_f value and infrared absorption spectrum.

Results and Discussion

Profiles of the anodization.—Anodization in maleic acid electrolyte shows some unique phenomena such as vigorous evolution of gases, sharp increase of voltage accompanying the browning of the anodic film, and unusual *V-t* behaviors.

Figure 2 shows the *V-t* curves for 0.2, 0.5, and 1.0 mole/liter of maleic acid at 20 mA/cm², 20° ± 1°C. In the beginning of the anodization, all *V-t* curves increased rapidly up to about 80V, likely due to barrier layer formation. Then, they either maintained constant values, decreased, or increased depending on the concentration of maleic acid. In 0.2 mole/liter maleic acid, the voltage decreased to a steady value where bubbles were constantly produced throughout the course of anodization. Colored film was not formed even at 60 min anodization. In 1.0 mole/liter maleic acid, the voltage increased progressively in accordance with the growth of brownish anodic film. It saturated at about 160V due to the occurrence of breakdown of the film. At this voltage the anodic film started to become black and finally became completely black. In 0.5 mole/liter maleic acid, the voltage decreased to reach amost steady state as in the case of 0.2 mole/liter maleic acid but, after 10 min, it again increased suddenly up to 170V with the appearance of brownish anodic film. At the end of the anodization (60 min), the color of the film was as black as in the case of 1.0 mole/liter maleic acid.

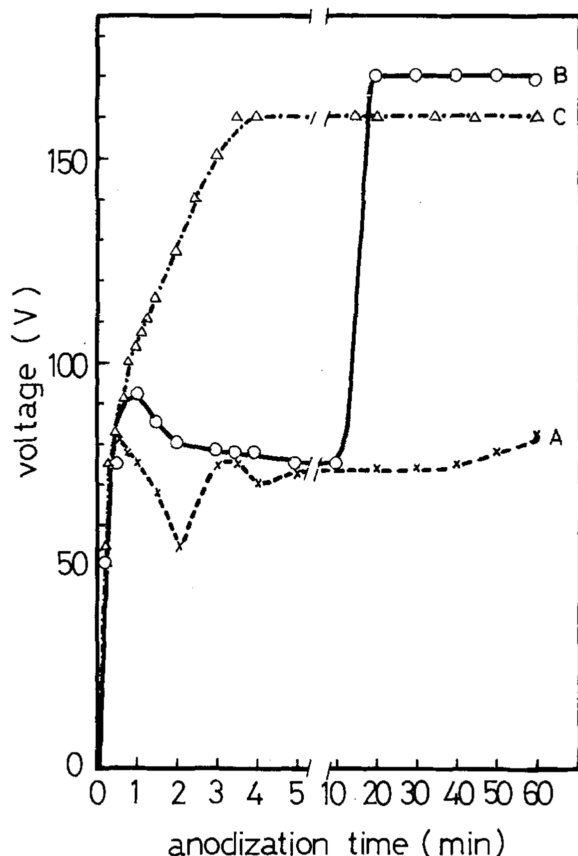

Fig. 2. Voltage-time curves in anodization. 20 mA/cm², aqueous maleic acid electrolyte. Curve A, 0.2; curve B, 0.5; curve C, 1.0 mole/liter.

The black anodic film was lusterless, rough, and loosely adhered on the aluminum substrate[1] unlike the brown anodic films formed in oxalic and malonic acids. Occasionally, it adsorbed slightly yellowish deposits at the surface of the maleic electrolyte.

The aluminum substrate after stripping off the black anodic film with H_3PO_4-CrO_3 solution was remarkably rugged, indicating that the aluminum substrate did not dissociate uniformly during the anodization. It is assumed that the uneven dissociation is caused by the heterogeneous incorporation of maleate in the anodic film and the different ionic conductances with sites.

Anodic dissociation of aluminum.—The aluminum consumption during the anodic oxidation (or anodic dissociation) was remarkably smaller than the estimated value from Faraday's law. This means that the efficiency of the ionic current was extremely small and dependent upon the concentration of the electrolyte (Table I). In 0.2 mole/liter maleic acid, the efficiency was no more than 0.01 and violent gas evolution occurred as mentioned above. In case of 0.5 mole/liter, the efficiency was 0.30; however, it can be corrected to 0.39, the same value as in 1.0 mole/liter, if the charge passed at the initial gas evolution period was substracted. Thus, the same efficiencies for the colored films suggest that the efficiency was determined mainly by the ionic conductivity of the anodic film, into which maleate was incorporated, and not by the electrolyte concentration.

Infrared spectra of the anodic films.—Figure 3 shows infrared absorption spectra by KBr disk method for the slightly yellowed deposits adsorbed at the black anodic film during prolonged anodization (curve A) and for a sample of maleic acid (curve B). It is found that the deposit is identical with maleic acid except for additional absorption peaks at 3650, 1570, 1450, 1010, 830, 680, 580, and 500 cm^{-1}. Since the aluminum ion has been detected from HCl solution of the deposit by the aluminon colorimetry method, and the foreign absorptions at 3650, 1010, 830, 680, 580, and 500 cm^{-1} can be assigned to the vibrations of M-OH or M-H_2O (5), it is considered that the deposit partly contains hydroxides of aluminum. The other foreign absorptions (at 1570 and 1450 cm^{-1}) can be assigned to COO^- stretching vibration of maleate because the same absorption has been found for H_2SO_4 anodic film after prolonged immersion in aqueous maleic acid, and assigned to COO^- of maleate chemisorbed at acidic sites of the H_2SO_4 anodic film (curve C). From these results, the deposit is considered as a mixture of maleic acid in a free state and aluminum hydroxide complexed with maleate. The deposition of maleic acid on the anode is explained in the following way: most of the maleate ions, which are migrated to the anode

[1] The black anodic film was discolored gray when it was scraped off from the aluminum substrate. The blackness was not completely inherent to chemical composition but changed with physical states.

Table I. Ionic current efficiency of the anodization
20 mA/cm², 20°C, 60 min, 4 cm²

Mole/liter	Anodically dissociated aluminum (mg)	Ionic current efficiency	Color of the anodic film
0.2	0.3	0.01	Colorless
0.5	8.2	0.30	Black
1.0	10.5	0.39	Black

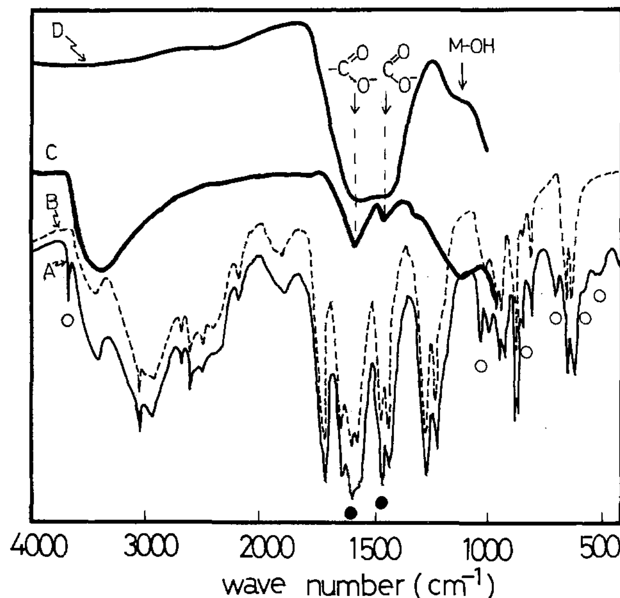

Fig. 3. Infrared absorption spectra. Curve A, yellowish deposit; curve B, maleic acid; curve C, H_2SO_4 anodic film after immersion in aqueous maleic acid; curve D, black anodic film.

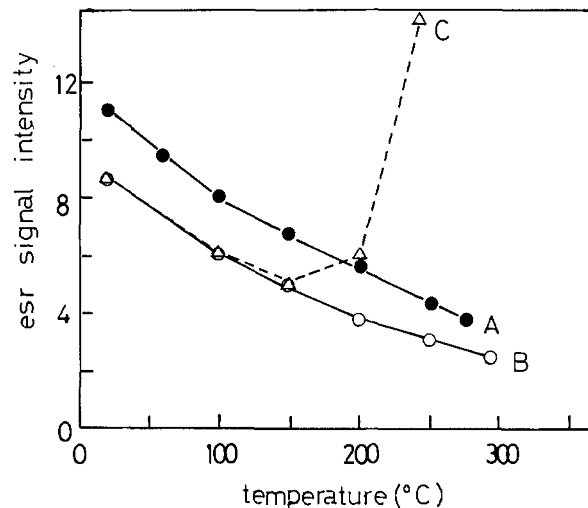

Fig. 4. Temperature dependence of ESR signals for anodic films and aluminum complex. Curve A, black anodic film formed in aqueous maleic acid; curve B, anodic film formed in aqueous oxalic acid; curve C, aluminum complex separated from oxalic acid anodic film.

in the electric field, combine with the protons which are released from the aluminum hydroxides on the anode, and become neutral acid molecules. When the concentration of the neutral molecules becomes high, they deposit on the anode. A small part of the maleate ions would be brought into the aluminum oxide and coordinate to Al^{n+} ions as can be seen in the following description.

At curve D of Fig. 3 another infrared spectrum for the black anodic film by KBr disk method is shown. The spectrum is characterized by intense and broad absorption in the region 1570-1450 cm^{-1} and below 900 cm^{-1} but has no absorption in the region 3500-3000 cm^{-1} which is commonly observed as water for usual aluminum anodic film (5). The broad absorption in 1570-1450 cm^{-1} probably indicates various states of carboxylate incorporated in the anodic film, *i.e.*, the carboxylate adsorbed on the surface of the film, coordinated to Al^{3+} ion as ligand, or combined with Al^{3+} ion electrostatically during the anodization. It is deduced that the black anodic film is composed of well-dehydrated aluminum oxide with maleate incorporated in complicated ways. It can be considered that there is a relationship between the development of the dehydration and the incorporation of maleate in the anodic film. When the anodic film grows, the electrochemical circuit has to be closed so as to allow the flow of anodizing current. At the interface of the barrier layer/electrolyte, ionic species should migrate instead of the Al^{3+} ion, as the Al^{3+} ion stays on the anode as the anodic film. The ionic migration is known to be induced by protons which are released from the anodic film (aluminum hydroxide) in the electric field. In the aluminum complexes intricately incorporated with maleate, ligand water should be deprotonated completely with the progress of the anodization.

ESR spectra of the anodic film.—The black anodic film showed a singlet ESR signal at $g = 2.004$ with $\Delta H_{msl} = 8G$. The signal intensity was saturated at small microwave output (0.8 mW), indicating that the relaxation time T_1 was long and therefore the signal was from organic radicals.[2] It was found that the signal intensity decreased uniformly with the increase of temperature up to 298°C (Fig. 4), but at room temperature it remained unchanged for several months. These facts agree precisely with the observations for the anodic film prepared in oxalic acid (2, 3), for which the ESR signal was considered attributable to $C_2O_4^{2-}$ radical coordinated to aluminum ions. The results obtained for the black anodic film seem indicative of carboxylate radicals coordinated to Al^{3+} ion. Generation of hydrogen at the anode supports this consideration and is explained in the following section.

Gaseous products at the anode.—Generation of gases at the anode during anodization was much more brisk in aqueous maleic acid than in common electrolytes (*i.e.*, sulfuric, oxalic, or malonic acid). This was a side reaction (6) because electronic current was about 60-99% of the charge passed across the anodic film (Table I).

Analysis of the gases in three experimental runs gave average volume ratios as shown in Table II.[3] An important observation was that the major part of the anode gases was carbon monoxide, whereas the gases were hydrogen (98%) and oxygen (2%) and scarcely contained carbon monoxide or carbon dioxide in the case of aqueous oxalic and malonic acids. The percentage of carbon monoxide became larger with the decrease of the concentration of maleic acid in the electrolyte. The increase of the side reaction is responsible for it, since the electronic current became predominant over the ionic current with the decrease of the concentration (see Table I) coincident with a trifling growth of the anodic film.

Another important observation was the generation of hydrogen truly collected in the anodic compartment and not leaked from the cathodic compartment. The volume ratio of the hydrogen increased remarkably with the concentration of maleic acid in the electrolyte, coincidently with the increase of ionic current. The generation of hydrogen is induced to accompany the

[2] T_1 is spin-lattice relaxation time. It is indicated by Bloch's equation as follows

$$\frac{dM_z}{dt} - \gamma(M_xH_y - M_yH_x) + \frac{M_z - M_o}{T_1} = 0$$

where M_x, M_y, and M_z are components of magnetic moment, γ is gyromagnetic factor, and H_x, H_y, and H_z are components of magnetic field

[3] Nitrogen is considered from the air leaked in when sampling. The value for oxygen also contain the one for leaked air.

Table II. Composition of anode gases

Mole/liter	C.D. (mA/cm^2)	H_2 (%)	CO (%)	O_2 (%)	N_2 (%)
0.2	20	1.5	74.7	11.1	12.7
0.5	20	37.0	41.2	10.0	13.0
1.0	20	45.0	35.0	8.7	11.3

formation of the anodic film. In previous papers (2, 3), the generation of hydrogen has been inferred as due to "anodic reduction" in the following way: providing that aluminum oxidation proceeds by three steps as $Al^{0} \xrightarrow{-e} Al^{+} \xrightarrow{-e} Al^{2+} \xrightarrow{-e} Al^{3+}$ and water can coordinate to the low valency aluminum ions to make aluminum aquo-complexes, intramolecular charge transfer will take place from the aluminum ions to the ligand water, resulting in the production of hydrogen atoms (see Fig. 1).

The anodic gases, carbon monoxide, hydrogen, and oxygen,[3] are thought to have arisen from different processes. Carbon monoxide and oxygen[3] are produced by the electrochemical oxidation of maleic acid and water, respectively. Hydrogen is probably produced from "anodic reduction" of ligand water with the low valency aluminum ions.

Formation of aldehyde at the anode.—A water insoluble substance was isolated from the reaction product of used anolyte and 2,4-dinitrophenylhydrazine. The substance was identified as 2,4-dinitrophenylhydrazone of glyoxal from its infrared absorption spectrum and melting point. From the whole precipitate of 78.9 mg, the amount of glyoxal was estimated 10.9 mg for the anodization of the passed charge of 10,000C. While aldehyde formation at an aluminum anode in the case of saturated carboxylic acid has been explained by the "anodic reduction" of the carboxylic acid (2, 3) (Eq. [1]), the glyoxal production is considered due to the oxidation of easily oxidizable —C=C— double bond of maleate (Eq. [2]). Reduction of carboxyl groups to aldehyde does not seem likely in maleic acid electrolyte since the reaction of maleic acid with hydrogen was found favorable to the formation of succinic acid through the analysis of the infrared absorption spectrum of the substance isolated from the used maleic acid catholyte by paper-chromatography (Eq. [3])

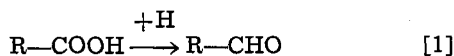

$$R\text{—}COOH \xrightarrow{+H} R\text{—}CHO \qquad [1]$$

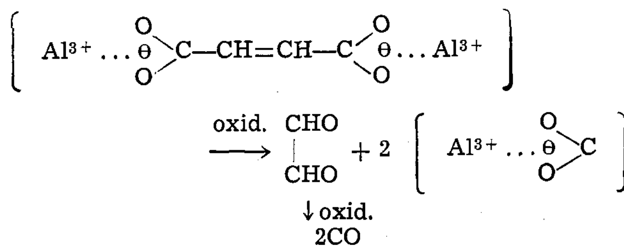

[2]

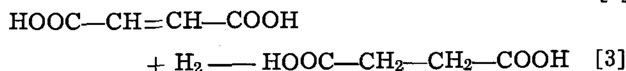

$$HOOC\text{—}CH{=}CH\text{—}COOH + H_2 \text{——} HOOC\text{—}CH_2\text{—}CH_2\text{—}COOH \qquad [3]$$

Assuming that the electronic current is one-half of the total current, yield of the glyoxal is only 1.4% for the passed charge of 10,000C. Most of the oxidation product of maleate should be carbon monoxide. The formation of carbon monoxide can not be explained by the reaction of carbon dioxide with hydrogen (Eq. [4]) because the formation of carbon dioxide or Kolbe's reaction (Eq. [5]) did not take place at the aluminum oxide anode

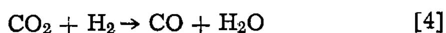

$$CO_2 + H_2 \rightarrow CO + H_2O \qquad [4]$$

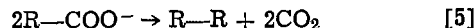

$$2R\text{—}COO^- \rightarrow R\text{—}R + 2CO_2 \qquad [5]$$

Vijh has suggested that the greater the bandgap of oxides, the smaller the electronic conductivity and the larger the relative ionic conductivity due to the lack of electronic carrier (7). Aluminum oxides are indeed high bandgap oxides and show relatively higher ionic conductivity than electronic conductivity. In order to transfer electrons from COO^- of maleate to the interior (or conduction band) of the aluminum oxide film across the barrier of the conduction band of the oxide/H.O.M.O. levels of the COO^-, the anodic field should be intensely supplied with external voltage. In such high field, however, Al^{n+} ions can easily migrate from the aluminum substrate towards the surface of the oxide film, resulting in the formation of the anodic film. The —C=C— double bond of maleic acid, of which energy levels are located at the higher state, is considered easily oxidizable at low anodic field.

Conclusions

At the anodization of aluminum in aqueous maleic acid, various *V-t* curves were observed in accordance with the concentration of maleic acid. In case of 1.0 mole/liter, the *V-t* curve increased rapidly up to about 170V resulting in a breakdown of the anodic film. In case of 0.2 mole/liter, the *V-t* curve stayed at about 80V with a violent gas evolution.

Ratios of ionic current against the total current were 0.39 and 0.01 for 1.0 mole/liter and 0.2 mole/liter, respectively.

When the ionic current ratio was 0.39, black anodic film with rough and rugged surface was formed. The anodic film was dissimilar to the ones formed in aqueous oxalic and malonic acids. It was found with infrared absorption spectra that the black anodic film was incorporated with maleate ion in complicated ways, coordinated to Al^{3+}, combined electrostatically with Al^{3+}, and adsorbed on the surface of the anodic film. The blackness of the film was assumed to have come from carboxylate radicals. It should be noticed that hydrogen evolution at the anode accompanied the anodic film formation. The "anodic reduction" is presumably related to the formation of the carboxylate radical.

The oxidation product of maleic acid on the aluminum anodic film was mainly carbon monoxide.

Ionic conductivity of the anodic film is assumed to vary with the amount of maleate incorporated.

Manuscript submitted May 11, 1977; revised manuscript received Sept. 12, 1977.

Any discussion of this paper will appear in a Discussion Section to be published in the December 1978 JOURNAL. All discussions for the December 1978 Discussion Section should be submitted by Aug. 1, 1978.

REFERENCES

1. M. Shimura, *Denki Kagaku*, **38**, 100 (1970).
2. M. Shimura, *J. Chem. Soc. Faraday Trans. 1*, **72**, 2248 (1976).
3. M. Shimura and S. Tajima, *Denki Kagaku*, **44**, 39, 726 (1976).
4. N. Baba, *J. Met. Finish. Soc. Jpn.*, **24**, 34 (1973).
5. G. A. Dorsey, Jr., *This Journal*, **115**, 1053 (1968).
6. R. W. Santway and R. S. Alwitt, *ibid.*, **117**, 1282 (1970).
7. A. K. Vijh, *Electrochim. Acta*, **14**, 921 (1969).

A New Voltammetric Stripping Method Applied to the Determination of the Brightener Concentration in Copper Pyrophosphate Plating Baths

Dennis Tench* and Cameron Ogden

Rockwell International, Science Center, Thousand Oaks, California 91360

ABSTRACT

A new voltammetric stripping method for determining the concentration of brightening or leveling additives in plating baths is described. The method is based on the effect that such additives exert on the rate of metal electrodeposition. To determine the latter, the potential of an inert rotating electrode is cycled in the bath, so that a small amount of metal is alternately deposited on the surface and then stripped off, *i.e.*, anodically dissolved. The charge required to strip the copper is related to the deposition rate and, thus, to the concentration of additive in the plating bath. Errors caused by changes in the electrode surface or bath composition are mitigated by using the internal standard provided by the static electrode. Results are reported for the determination of both 2,5-dimercapto-1,3,4-thiadiazole and proprietary brightener PY61-H in copper pyrophosphate baths, for which a precision of about 0.1 ppm (0.1 ml/liter of PY61-H) was attained in the concentration range from 0.0 to 2.5 ppm (0.0-2.0 ml/liter). The effect of bath contamination is also considered and a model is proposed to explain the effectiveness of dimercapto-thiadiazoles as leveling agents.

A key process in the manufacture of multilayer printed circuit boards is the plating of through-hole interconnections, which involves both electroless and electrodeposition methods. When high reliability is required, as in military and space applications, through-holes are usually electroplated from copper pyrophosphate baths (1). An organic additive generally used is proprietary brightener PY61-H (2, 3), whose active ingredient is a dimercaptothiadiazole.

A major difficulty with the plated through-hole process is maintaining constancy of the brightener concentration in the low ppm range necessary to obtain acceptable deposits. Its concentration fluctuates because of oxidation at the anode, reduction and inclusion at the cathode, and chemical reactions. When the brightener level is insufficient, deposits are burnt and powdery, whereas, excess brightener induces brittleness and nonuniform deposition (4). Hull cell and ductility tests, combined with periodic additions of fresh additive, have been the only methods available to maintain a controlled brightener concentration. Since these methods are unreliable, circuit board quality has suffered and rejection rates have been objectionably high. The voltammetric stripping method described here is a new means of monitoring the brightener concentration in copper pyrophosphate baths and the technique should be applicable to other plating systems.

Voltammetric Stripping Method

In performing their functions, brightening and leveling additives affect the rate of metal electrodeposition at a given electrode potential (5) and this effect can be used to determine the concentrations of such additives in plating baths. In the simplest case, the deposition current would simply be followed at a particular cathodic potential, with sufficient solution agitation to maintain an adequate concentration of additive at the electrode. Obtaining and maintaining a reproducible electrode surface, however, are formidable problems, and the latter is complicated at longer deposition times by changes in the surface area of the electrode. In addition, the current measured may include contributions from competing processes like hydrogen evolution and reduction of oxygen and impurities.

* Electrochemical Society Active Member.

Key words: electroplating, copper pyrophosphate, brightener determination, voltammetric stripping analysis.

In the voltammetric stripping method, the potential of an inert electrode (*e.g.*, Pt) is cycled as a function of time, so that a small amount of metal is alternately deposited on the electrode and stripped off by anodic dissolution. This is illustrated in Fig. 1 by the steady-state voltammetry curve for a Pt disk electrode rotated at 2500 rpm and swept continuously at 50 mV/sec between −0.700 and 1.000V *vs.* SCE (saturated calomel electrode) in copper pyrophosphate baths with 1.0 and 2.0 ml/liter of brightener PY61-H added. The electrode rotation maintains an adequate, reproducible concentration of brightener at the electrode surface (6). Deposition of copper occurs between −0.3 and −0.7V for both sweep directions and the copper deposit is removed by oxidation, *i.e.*, stripped, on the anodic sweep between −0.3 and −0.05V *vs.* SCE. The area under the stripping peak corresponds to the charge required to oxidize the copper deposit and is proportional to the average deposition rate for that cycle. Comparison of the peak areas for baths containing 1.0 and 2.0 ml/liter of PY61-H shows that the brightener in this concentration range exerts a strong decelerating effect on the rate of copper deposition. The area of the stripping peak can therefore be related to the concentration of PY61-H in the bath.

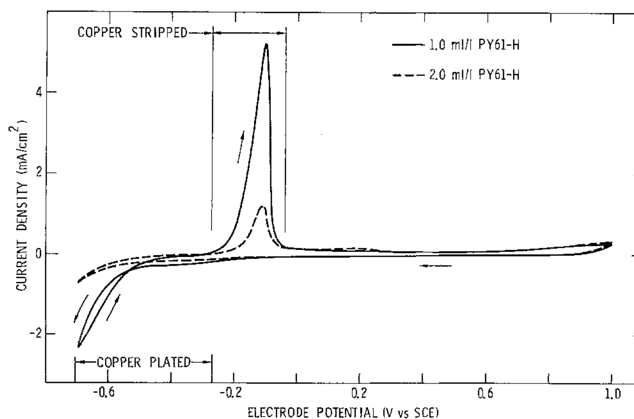

Fig. 1. Steady-state linear sweep cyclic voltammograms at 50 mV/sec for a Pt disk electrode rotating at 2500 rpm in argon-saturated copper pyrophosphate plating baths (22°C) containing 1.0 and 2.0 ml/liter of PY61-H.

Although copper stripping is essentially completed by −0.050V (see Fig. 1), the sweep is extended to 1.000V since this procedure was found to give more reproducible results. This probably relates to the state of oxidation of the Pt electrode surface. The small oxidation peak at 0.2V and the corresponding reduction peak at −0.3V (hardly discernible on the current scale of Fig. 1) presumably indicate a somewhat irreversible oxidation of the Pt surface since they are dependent on the sweep rate, but not the electrode rotation (in the absence of brightener). If the anodic sweep is not extended past the oxidation peak at 0.2V, the surface is slowly reduced on each subsequent sweep and a steady state for the stripping peak is not attained even after 20-30 cycles. The extended anodic sweep probably maintains the state of oxidation of the Pt surface at a steady-state level. In addition, the small current plateau beginning at 0.8V presumably results from brightener oxidation since it is only observed in solutions containing PY61-H. Thus, another beneficial effect of the more anodic sweeps may be removal of accumulated brightener on the electrode surface. Since this plateau depends only slightly on electrode rotation rate or brightener concentration in the range of interest, the oxidation of brightener is kinetically controlled and cannot itself be used as an indication of PY61-H level.

When brightener breakdown products are present in the bath, they oxidize in the same potential region as the brightener, producing a well-defined current plateau. A plot of the current on this plateau *vs.* the square root of the rotation rate is linear but does not pass through the origin. This indicates some kinetic limitation. Thus, the current in this potential region can be used as an indication of the bath purity, but the proportionality to the concentration of breakdown products will not be unity. As will be shown later, bath impurities and breakdown products of the brightener also seem to interfere somewhat with its functioning, but the voltammetric method yields an effective concentration, which can be used directly to adjust the additive level of the bath.

Experimental Details

Unless otherwise noted, measurements were made at room temperature in electrolytes prepared from plating bath concentrates C10XB, C11XB, and PY61-H obtained from M&T Chemicals Inc. Baths typically had a pH of 8.3 and contained 22.5 g/liter Cu^{++}, 173 g/liter $(P_2O_7)^{-4}$, and 2.25 g/liter NH_3. Argon gas was always bubbled through the solution via a glass frit for at least 15 min before making measurements. The controlled-atmosphere cell was Pyrex glass with a Teflon top and had a volume of 100 ml. The Pt-40% Rh counterelectrode and commercial SCE were dipped directly in the cell. Although no Luggin capillary was used, ohmic losses should be negligible considering the concentrated electrolyte and current levels involved.

The indicator electrode was a 99.95% Pt disk (The Wilkinson Company) of 0.13 cm^2, which was mounted concentric and flush with the end of a 12 mm diam Kel-F cylinder by compression molding at elevated temperature. After mounting, the electrode was polished on successively finer aqueous alumina powder slurries to 0.05 μm particle size and then was cycled at 50 mV/sec from −0.700 to 1.000V *vs.* SCE in the argon-saturated plating bath without brightener until a steady-state voltammogram was obtained. Subsequently, the electrode was always stored in the copper pyrophosphate solution without brightener.

The indicator electrode potential was controlled, relative to the SCE reference, with a PAR (Princeton Applied Research Corporation) Model 173 potentiostat/galvanostat in conjunction with a PAR Model 175 Universal programmer. Anodic current peaks were integrated electronically to −0.05V *vs.* SCE using a PAR Model 179 digital coulometer. For the data reported, the sweep rate was always 50 mV/sec and the sweep limits were −0.700 and 1.000V *vs.* SCE. At faster sweep rates the stripping peaks were broader and less reproducible, whereas slower sweeps were unnecessarily time consuming. Sweeps to a more cathodic limit than −0.7V resulted in broader stripping peaks and a loss in brightener sensitivity, possibly because of mass transport limitations at the higher current densities.

To achieve maximum sensitivity, the electrode rotation must be sufficiently fast to maintain an adequate supply of brightener at the electrode surface. The effect of rotation rate (ω) on the integrated peak area (A_r) is shown in Fig. 2 for a previously heat-treated bath (16 hr at 50°C) containing 2.0 ml/liter of PY61-H concentrate. At lower rotation rates, the brightener becomes depleted at the surface and exerts an accelerating effect on the deposition rate. With faster electrode rotation, the brightener surface concentration approaches the bulk solution value and decelerates the deposition rate, producing the observed peak. At the PY61-H concentration used here (2.0 ml/liter), further deceleration above 2500 rpm is small. For convenience, this value for the electrode rotation rate was used for all data reported here, but a faster rotation rate might prove advantageous, especially at lower brightener concentrations.

Care must be exercised in preparing brightener standard solutions from PY61-H concentrate. For freshly prepared baths, the brightener activity at room temperature is very low, but increases over a period of several hours upon heating at 50°C. This is illustrated in Fig. 3, which shows the stripping peak area at 2500 rpm and room temperature as a function of heating time at 50° ± 2°C before quenching of a copper pyrophosphate bath containing 2.0 ml/liter of PY61-H concentrate. The heating may be necessary to depolymerize the brightener to an active form or promote formation of a complex species. In any case, other bath constituents are involved in the activation process since heating PY61-H alone, or solutions of 2,5-dimercapto-1,3,4-thiadiazole, does not produce active brightener. At room temperature, activated solutions slowly lose activity, possibly because of repolymerization or chemical degradation. To minimize errors, standards were

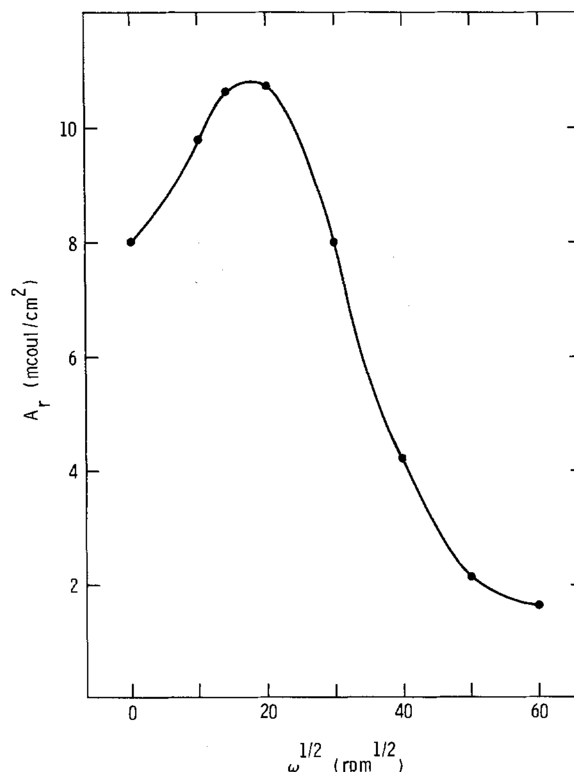

Fig. 2. Effect of rotation rate (ω) on the steady-state Cu stripping peak area (A_r) for a Pt disk electrode cycled at 5 mV/sec between −0.700 and 1.000V *vs.* SCE in an argon-saturated copper pyrophosphate bath (22°C) containing 2.0 ml/liter of PY61-H.

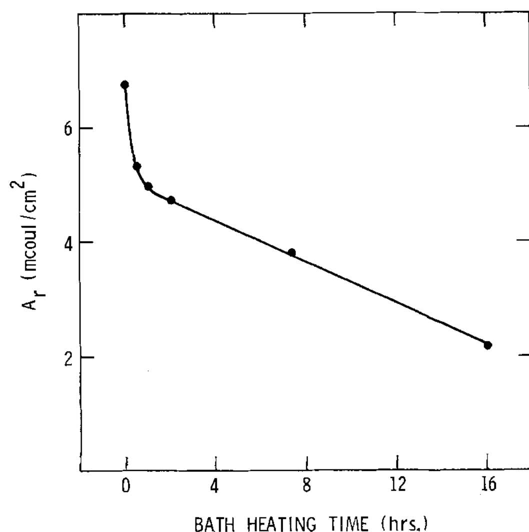

Fig. 3. Effect of bath heating time at 50° ± 2°C on the steady-state Cu stripping peak area (A_r) for a rotating Pt disk electrode (2500 rpm) cycled at 50 mV/sec between −0.700 and 1.000V vs. SCE in argon-saturated copper pyrophosphate baths (22°C) containing 2.0 ml/liter PY61-H.

always heat-treated at 50° ± 2°C for 16 hr and run at room temperature (22°C) within a few hours of preparation.

To generate standard curves, steady-state stripping peak areas were determined with electrode rotation at both 2500 rpm (A_r) and 0 rpm (A_s) for a series of baths containing (*i*) no brightener, (*ii*) a standard amount, and (*iii*) 1.0 ml/liter of PY61-H. After immersing the rotating electrode in the bath or after stopping rotation, steady-state voltammograms were usually obtained after 3-5 cycles.

Results and Discussion

A plot of the Cu stripping peak area at 2500 rpm (A_r) *vs.* the brightener concentration is shown in Fig. 4. There is considerable scatter in the data which seems to result from changes in the electrode surface from experiment to experiment. Such variations can be mitigated by measuring a fixed standard immediately before or after each data point and plotting the ratio. This is shown in Fig. 5 for a rotation rate of 2500 rpm and a fixed standard of 1.0 ml/liter. From 0.6 to 2.0 ml/liter of PY61-H, which covers the actual operating range, the curve is practically linear. Reproducibility is illustrated by the dual data points which show that a precision of about 0.1 ml/liter can be attained at PY61-H concentrations between about 1.0 and 2.0 ml/liter. Some error in the PY61-H determination results from the dependence of $A_r(x)$ on the bath composition. Variations in the NH_3 concentration over the range 1.12-2.81 g/liter were found to introduce a maximum error in the measured brightener concentration of 20% for a bath containing 1.0 ml/liter of PY61-H. The corresponding maximum error for $(P_2O_7)^{-4}$ variations over the concentration range 164-190 g/liter was also 20%. Since these bath fluctuations would represent extremes, these errors are not too serious.

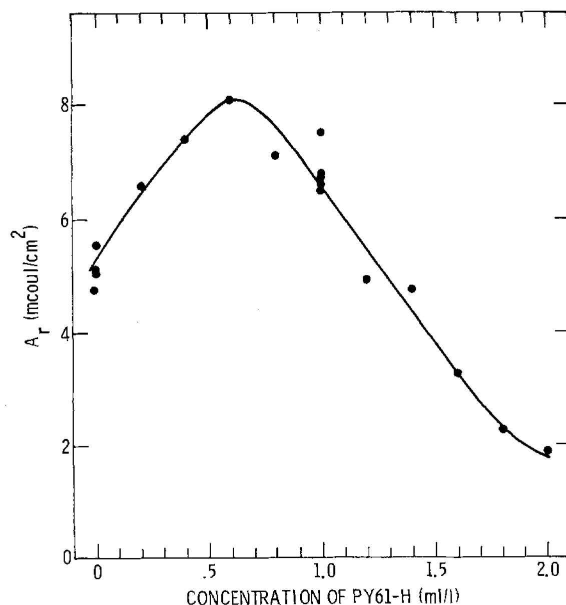

Fig. 4. Dependence of the Cu stripping peak area (A_r) on PY61-H concentration (other conditions always the same as for Fig. 1).

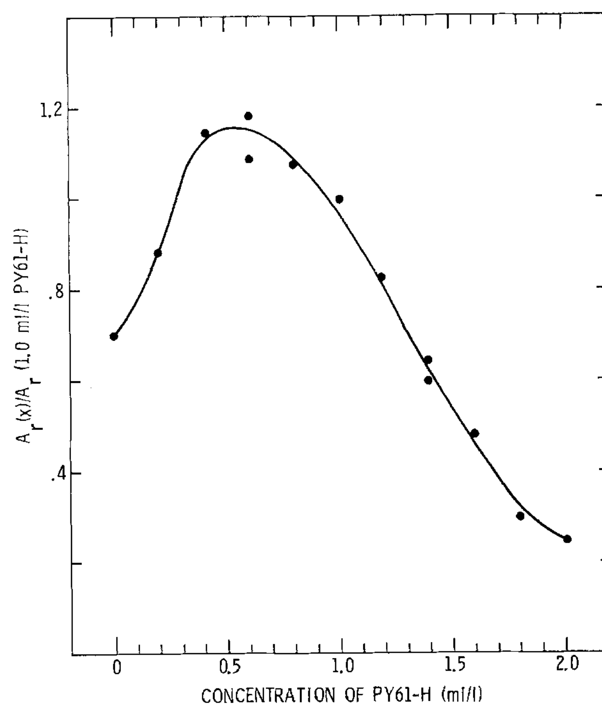

Fig. 5. Brightener concentration dependence of the ratio of the Cu stripping peak area for a given PY61-H concentration [$A_r(x)$] to that for a 1.0 ml/liter standard [A_r(1.0 ml/liter PY61-H)] determined immediately after each $A_r(x)$ measurement (other conditions always the same as for Fig. 1).

Variations in A_r caused by changes in the electrode surface can more conveniently be mitigated by using the internal standard provided by the static electrode in the same bath. When the electrode rotation is stopped, the concentration of brightener at the surface decreases with continued potential cycling until a small steady-state level, determined by diffusion, is established. Steady-state curves with and without electrode rotation are shown in Fig. 6. The larger static peak area (A_s), corresponding to nearly zero brightener concentration at the electrode, can be used as an internal standard. A plot of A_r/A_s *vs.* brightener concentration is shown in Fig. 7. The reproducibility is somewhat better than that obtained using the 1.0 ml/liter fixed external standard, so that a precision of 0.1 ml/liter is attained even at the lower PY61-H concentrations.

As would be expected, the use of the static electrode as an internal standard also tends to lessen the effects of changes in bath composition. Percent variations in the measured A_r/A_s values and the corresponding percent error in the brightener determination are shown in Table I for the maximum variations in both parameters expected for copper pyrophosphate baths. The percent errors are seen to be usually small (<10%). It should also be mentioned that errors introduced by *p*H fluctuations from 8.0 to 8.5 are small (<10%), but become appreciable at significantly higher *p*H values. This is not a serious problem since *p*H can be easily adjusted. These effects produced by variations in the bath com-

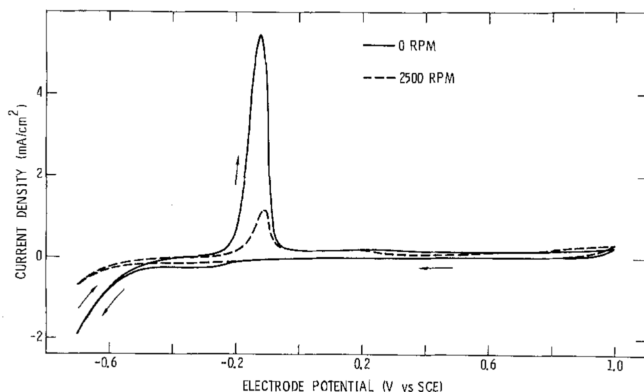

Fig. 6. Steady-state linear sweep cyclic voltammograms at 50 mV/sec for a Pt disk electrode rotating at 0 and 2500 rpm in an argon-saturated copper pyrophosphate plating bath (22°C) containing 2.0 ml/liter of PY61-H.

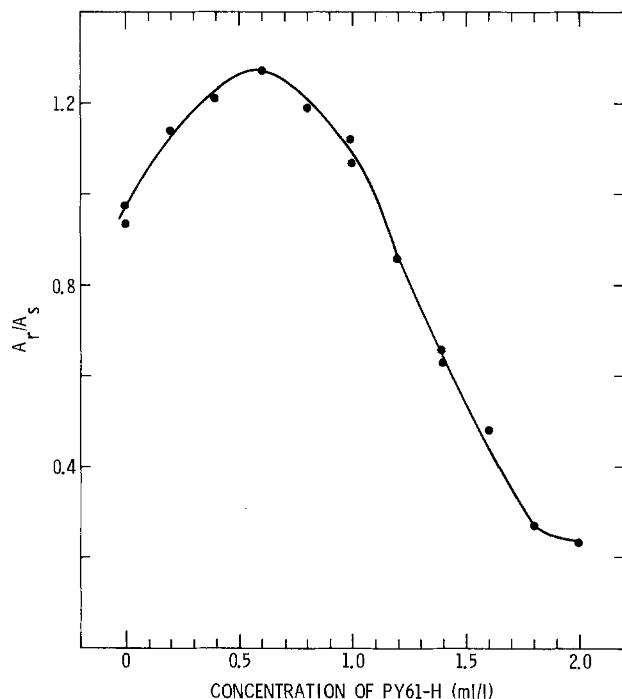

Fig. 7. Dependence of the ratio of the Cu stripping peak area with (A_r) and without (A_s) electrode rotation on the concentration of PY61-H (other conditions always the same as for Fig. 6).

position may to some extent reflect changes in the effective brightener concentration.

As was indicated by the variation in A_r with rotation rate, the brightener is seen to accelerate deposition at lower concentrations while decelerating it at higher levels. This results in a peak in the standard curves, so that two concentrations correspond to the same A_r or ratio value. The correct concentration can be determined, however, since the voltammetry peak is shifted cathodically by as much as 50 mV for brightener concentrations less than about 0.5 ml/liter.

Table I. Changes in A_r/A_s and the corresponding error in PY61-H concentration at 1.0 ml/liter resulting from variations in the copper pyrophosphate bath composition

Bath variation		Change in A_r/A_s (%)	Corresponding error in PY61-H concentration (%)
Low NH_3	(1.13 g/liter)	−19.5	20.0
Low NH_3	(1.69 g/liter)	9.2	−10.0
High NH_3	(2.81 g/liter)	0.4	0.0
Low $(P_2O_7)^{-4}$	(164 g/liter)	−3.1	3.0
High $(P_2O_7)^{-4}$	(181 g/liter)	−1.7	2.0
High $(P_2O_7)^{-4}$	(190 g/liter)	−4.5	5.0

All of the results reported here were obtained using standards prepared from the same batch of PY61-H, but for four other batches tested the effective concentrations of brightener measured by the voltammetric stripping method were 30-70% smaller. These variations could reflect aging effects or actual differences in the concentrations or properties of the brightener concentrates obtained from the supplier.

To provide a better defined reference, standard brightener solutions were prepared using 2,5-dimercapto-1,3,4-thiadiazole (Aldrich Chemical Company, Incorporated). The solid was first dissolved in 6*N* KOH which was then diluted 3:1 with water before addition to freshly prepared copper pyrophosphate plating solution. Before use, samples were heat-treated as described earlier (50° ± 2°C for 16 hr). Standard curves of A_r/A_s *vs.* concentration of solid brightener are shown in Fig. 8 for both freshly prepared and contaminated baths. For the freshly prepared bath, the pure 2,5-dimercapto-1,3,4-thiadiazole is seen to accelerate the Cu electrodeposition rate at the lower concentrations to a greater extent than PY61-H, but above 1.3 ppm a constant relationship obtains such that the incremental effect on the electrodeposition rate of 0.12-0.14 ppm of the pure compound is equivalent to 0.1 ml/liter of the proprietary additive. Based on a few data points, the pure brightener seems also to reach its maximum effective concentration more quickly, after only about 4 hr at 50°C.

To investigate the effect of bath contaminants on the voltammetric stripping analysis, standards were prepared by addition of 2,5-dimercapto-1,3,4-thiadiazole to samples of a production bath which had been used to plate circuit board through-holes for several years and had then stood at room temperature for several weeks to allow residual brightener to decompose. The procedure used was the same as that described in the preceding paragraph. A relatively large level of bath contamination was apparent from the voltammetric curves which, for electrode rotation of 2500 rpm, ex-

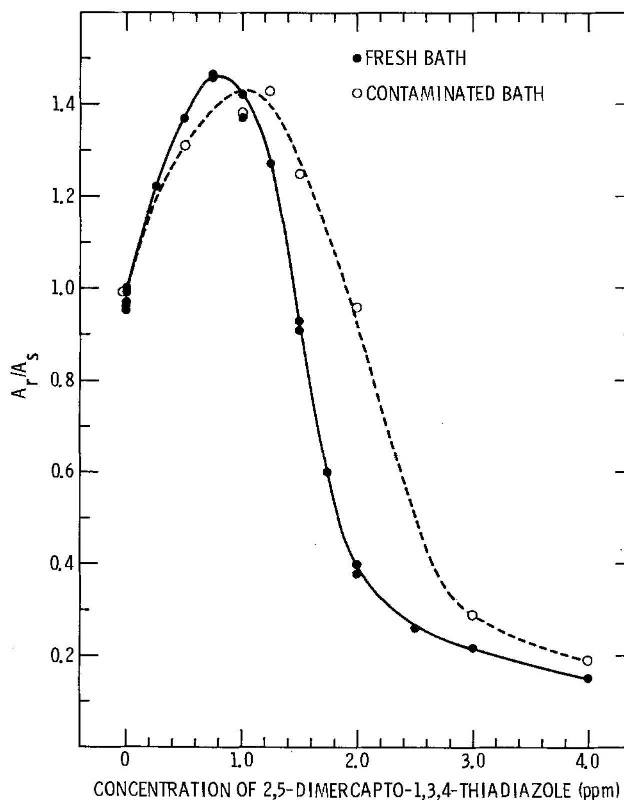

Fig. 8. Dependence of the ratio of the Cu stripping peak area with (A_r) and without (A_s) electrode rotation on the concentration of 2,5-dimercapto-1, 3, 4-thiadiazole in freshly prepared and contaminated copper pyrophosphate baths (other conditions always the same as for Fig. 6).

hibited anodic current plateaus of 26 mA/cm^2 in the potential range from 0.8 to 1.0V *vs.* SCE. Contaminants are expected to include brightener breakdown products, residues from photoresist and solvents used in circuit development, oils from pumps and drilling equipment, epoxy laminant residues, substances leached from plating tanks and other cell components, and airborne impurities.

A plot of the A_r/A_s ratio *vs.* concentration of pure solid brightener added to the contaminated bath is also shown in Fig. 8. By comparison with the curve for the freshly prepared bath, it is evident that the contaminants interfere somewhat with the functioning of the brightener, diminishing the decelerating effect which the latter exerts on the electrodeposition rate. For additive levels of more than 1.5 ppm, the effective concentration of the brightener is reduced by a constant amount of 0.6 ppm for this degree of contamination, which represents an extreme. It should be mentioned that proper conditioning of the Pt electrode is even more important when bath impurities are present. To obtain reproducible voltammetric stripping results, the electrode must be conditioned after polishing by potential cycling in a clean bath with no brightener before being introduced into contaminated baths.

The voltammetric stripping data reported here are for argon-saturated baths at 22°C, but similar results are obtained at 55°C in air-saturated solutions, which represent normal production conditions. Thus, the technique should be applicable to on-line monitoring. At 55°C, the cross-over point between the accelerating and decelerating effect of PY61-H occurs at lower concentrations compared to that at 22°C. Thus, at some concentrations the brightener will exert an accelerating effect on the electrodeposition rate at room temperature, but a decelerating effect under operating conditions. The opposite of the last two statements is observed for 2,5-dimercapto-1,3,4-thiadiazole.

As a side issue, the present results, establishing the dual accelerating-decelerating effects of the brightener, provide the basis for understanding why the dimercaptothiadiazoles are so effective in inducing uniform deposition of copper (leveling). In actual circuit board plating, freshly prepared baths generally contain 2.0 ml/liter of PY61-H, so that the bulk brightener concentration presumably exerts a decelerating effect on the electrodeposition rate. Thus, as brightener is depleted at the electrode by inclusion in the deposit, its concentration at micro and macro peaks on the electrode remains sufficient to inhibit deposition, as long as solution agitation and bulk brightener level are adequate. At the same time, because of reduced solution agitation in recesses, the brightener concentration becomes sufficiently depleted that acceleration of deposition occurs. Hence, peaks are plated more slowly than without brightener and recesses are plated more rapidly, so that very efficient leveling results. Of course, either acceleration or deceleration alone would also level the deposit, but the two operating together should be most effective.

Conclusions

The voltammetric stripping method described in this paper is a sensitive means for determining the concentration of brightener additive in copper pyrophosphate plating baths. For the greatest precision, measurements of the steady-state Cu stripping peak areas for a Pt disk electrode should be made with and without electrode rotation. This permits the effects of changes in the electrode surface and bath composition to be minimized by using the ratio of the two measurements to determine the brightener concentration. With this ratio technique, a precision of about 0.1 ppm can be attained in the concentration range from 0.0 to 2.5 ppm of 2,5-dimercapto-1,3,4-thiadiazole. The voltammetric stripping method should also be applicable to the determination of brightening and leveling additives in other plating systems.

This voltammetric technique has the advantage over conventional analytical methods of yielding a parameter (A_r or A_r/A_s) which reflects the effectiveness of the additive in performing its function, rather than simply an absolute concentration. Thus, the effects of breakdown products or impurities which interfere with the functioning of the addition agent can automatically be taken into account. Also, inactive forms of the additive which are chemically similar, such as polymers and breakdown products, are not measured with the voltammetric stripping method.

Manuscript submitted Aug. 15, 1977; revised manuscript received Sept. 29, 1977.

Any discussion of this paper will appear in a Discussion Section to be published in the December 1978 JOURNAL. All discussions for the December 1978 Discussion Section should be submitted by Aug. 1, 1978.

Publication costs of this article were assisted by Rockwell International.

REFERENCES

1. J. W. Dini, in "Modern Electroplating," 3rd ed., F. A. Lowenheim, Editor, p. 205, Wiley-Interscience, New York (1974).
2. F. H. Wells and D. M. Lyde, British Pat. 939,997 (1960).
3. P. Hinton, M.S. Thesis, University of Arizona (1968).
4. D. A. Luke, *Trans. Inst. Met. Finish.*, **47**, 36 (1969).
5. S. S. Krugilov, N. T. Kudriavtsev, G. F. Vorobiova, and A. Ya. Antonov, *Electrochim. Acta*, **10**, 253 (1965).
6. V. G. Levich, "Physicochemical Hydrodynamics," Prentice-Hall, Englewood Cliffs, N.J. (1962).

A Mechanism for the Effect of Heat-Treatment on the Accelerated Corrosion of Zircaloy-4 in High Temperature, High Pressure Steam

A. W. Urquhart,* D. A. Vermilyea,* and W. A. Rocco

General Electric Company, Corporate Research and Development, Schenectady, New York 12301

ABSTRACT

Potential differences which develop across growing oxide films and effects of applied electric fields on oxide growth have been measured on specimens of Zircaloy-4 corroding in high temperature, high pressure steam. From these results it is concluded that the accelerated corrosion process observed in this environment is associated with the development of metal-negative potential differences across the oxide (analogous to potential differences associated with cathodic polarization in aqueous corrosion). Initiation of this form of attack is inhibited on suitably heat-treated material because the relatively high effective electronic conductivity of the oxide film growing on this material shifts these potential differences toward the metal-positive direction. The effect of alloy heat-treatment on the oxide conduction characteristics is explained in terms of the microstructure of the metal, and it is suggested that hydrogen absorption into the oxide under metal-negative potential differences leads to initiation of the accelerated attack.

In a previous publication (1) it was noted that the accelerated corrosion of Zircaloy[1] in high temperature, high pressure steam may correlate with an accelerated corrosion process found during exposure in a neutron flux in oxygenated water. While this correlation is not established on the strength of existing in-reactor data, it was suggested (1) that studies of the mechanism of accelerated corrosion in 500°C, 1500 psi steam may be useful. This paper reports some of the results of such a study.

The accelerated corrosion process that occurs in high temperature, high pressure steam (*e.g.*, 500°C, 1500 psi) has been described previously (1-4). The phenomenon involves the nucleation of a relatively nonprotective oxide which grows at a much faster rate than would be expected for the normal linear (post-transition) oxidation kinetics of Zircaloy at 500°C, as measured in other environments such as low pressure steam or oxygen. It has also been observed that the resistance of Zircaloy to this accelerated corrosion phenomenon is very dependent on the heat-treatment of the alloy. Specifically, heat-treatments in the β-phase field followed by reasonably rapid cooling to room temperature provide greatly improved resistance to accelerated steam corrosion. In fact, data from Ref. (3), when plotted to reveal the corrosion kinetics, indicate that β heat-treated Zircaloy in 500°C, 1500 psi steam follows approximately the normal oxidation processes expected from other 500°C tests. The purpose of this research is to gain some insight into the mechanisms which result in the nucleation of a fast-growing, nonprotective oxide film in high temperature, high pressure steam tests and to clarify the reasons for the beneficial effects of β heat-treatments on corrosion resistance.

This paper presents evidence that initiation of the accelerated corrosion process is associated with the development of potential differences across the initially protective oxide barrier film in the metal (zirconium) negative direction, as measured with an electronically conducting electrode on the oxide surface. These potential differences are assumed to be associated with anion diffusion potentials which arise naturally when the effective ionic conductivity of the oxide is comparable to or greater than the electronic conductivity. The possible effect of proton currents on these diffusion potentials is ignored as a first approximation.

Metal negative potential differences across the oxide do not lead to accelerated corrosion by direct enhancement of anion transport in a barrier-type oxide, since the resulting electric fields actually oppose this process. Rather, the accelerated corrosion phenomenon is associated with some sort of disruption of the barrier film giving a loss of protectiveness due to porosity or other damage to the oxide. It will be argued that this results from proton migration into the oxide when the electric fields are favorable to this process.

Thus, the present experimental work is primarily concerned with measurements of the open-circuit potential differences across growing oxide films, correlation of the results with susceptibility of the material to accelerated corrosion, and observation of the effects of applied potential differences on corrosion rates.

Experimental Procedure

The test environment of 500°C, 1500 psi steam was produced in a one liter stainless steel autoclave connected to a flowing water loop. The replenishment rate was 5-10 cm^3/min of degassed, deionized water. Corrosion test samples for weight gain measurements were supported on stainless steel hooks; separate experiments have shown that insulating the specimens from the autoclave structure does not affect the results, as might be expected from the low conductivity of the steam environment and the tendency of the samples to become isolated from the support hooks by the growing oxide films. During start-up the samples were initially covered with water which was boiled away at atmospheric pressure to degas the autoclave. The desired test pressure was established at ~350°-400°C during the heat-up process. For comparison purposes, some testing was also done in the same apparatus using pure oxygen gas at 500°C and 1500 psi.

Because the steam phase is a poor conductor under the specified test conditions, it is necessary to make contact directly with the surface of the oxide film for electrical measurements. Sputtered platinum electrode spots were used for this purpose. One contact was made by spot-welding a Pt lead directly to the specimen while mechanical contact was made to the electrode

* Electrochemical Society Active Member.

* Key words: electric field effects, hydrogen effects.

[1] Two Zircaloy compositions are of practical interest. The experimental work in this paper was performed with Zircaloy-4 which contains nominally 1.5% tin, 0.2% iron, and 0.1% chromium (by weight) in addition to zirconium. Zircaloy-2 is a similar zirconium alloy, containing 1.5% tin, 0.15% iron, 0.1% chromium, and 0.05% nickel. The latter alloy is somewhat more resistant to accelerated corrosion in steam, but it responds to heat-treatment similarly to Zircaloy-4.

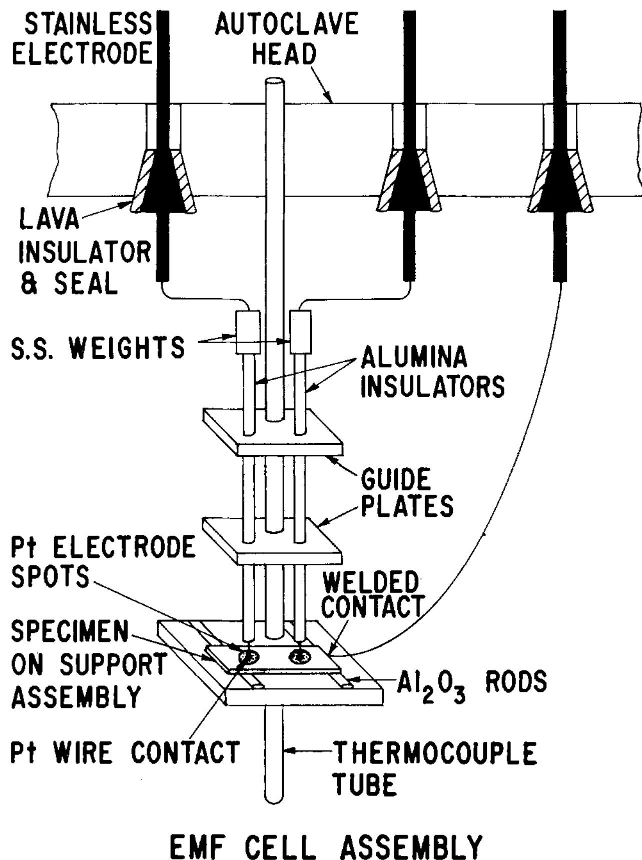

Fig. 1. Electrode arrangement for open-circuit potential measurements and experiments on the effects of applied potential differences.

spots with contact forces maintained by weights of 5-9g. This arrangement is illustrated in Fig. 1. Each specimen contained two independent Pt spots which were ~6 mm in diameter and ~150Å thick. At this thickness the platinum is both electrically continuous and permeable, such that oxidation of the underlying metal is not prevented by lack of access of the oxidant.

It should be noted that electronically conducting potential probes measure only the difference in the electrochemical potential for electrons across the oxide. The actual electric fields in the oxide are related to these observed potential differences through contact potentials which are in general unknown but are assumed to be constant. Thus, the experimental observations are limited to relative changes in the potential differences in one direction or the other for different cases, without attempting to specify the actual field in the oxide. A review of these techniques with references to the original literature has been given by Kröger (5).

An important concern is the possibility that the Pt electrodes may not be reversible with respect to the charge transfer reactions occurring on the surface of the oxide. If reversibility is not achieved, then reaction overpotentials will tend to reduce both the observed open-circuit potential differences and the extent to which applied potential differences actually appear across the oxide. Literature data (5) suggest that the test temperature of 500°C may be marginal for platinum electrode reversibility, although in the present experiments it was found that observed open-circuit potential differences were rapidly regained following a deliberate perturbation. In the absence of definitive information on this point, it will be assumed only that comparisons between observations from different specimens provide indications of differences in the relative balance between effective ionic and electronic conductivities; no quantitative interpretation will be attempted. Some other possible effects of the electrodes which might influence the interpretation of the test results are discussed in later sections.

All specimens were pickled in the usual H_2O-HNO_3-HF pickling solution prior to application of electrodes or autoclave testing. In one case the specimen was preoxidized prior to electrode sputtering.

The potentials developed across the growing oxide were monitored using Keithley 602 electrometers with a high input impedance. The specimen resistance was measured in an approximate way by periodically adding in shunt resistors across the electrometer input and observing the resistance at which the specimen potential was reduced appreciably. It was sometimes found that the parallel resistance of the electrode feedthrough insulation in the autoclave head (~50,000Ω) was limiting, and it will be noted below when the data may have been affected. In some experiments a d-c power supply was used to impose potentials from the electrode spots to the zirconium metal to determine the influence of applied electric fields.

All of the experiments were carried out with specimens cut from the same piece of Zircaloy-4 strip. The metallurgical condition of the starting material is the result of a conventional process involving β-quenching at the large forging stage with subsequent hot working in the α-phase field and final coldworking with intermediate and final anneals at 732°C (1350°F), also in the α-field. This metallurgical condition is referred to below as the starting material or initial material. Pieces of this material were also given further heat-treatments at several temperatures as listed in Table I. These treatments involved 15 min exposures at temperature under vacuum with cooling in helium to produce an estimated cooling rate of ~10°C/sec.

The heat-treated material used in evaluating the effects of applied electric fields was given a β-phase treatment at 1020°C followed by relatively slow cooling. This was accomplished by heating the specimens in evacuated capsules which were immersed intact in cold water after the heat-treatment. The resulting relatively coarse structure provided reasonably good protection (weight gain of 69 mg/dm²) in a 24 hr test in 500°C, 1500 psi steam. However, some small nodules of thicker oxide were found on the wider lamellae of the Widmanstätten structure. This material condition of intermediate corrosion resistance was selected in order to allow observation of either favorable or unfavorable response to applied electric fields.

Results

Corrosion weight gains.—Table I illustrates the influence of various heat-treatment temperatures on the weight gains of Zircaloy-4 specimens after 24 hr in 500°C, 1500 psi steam. These results are entirely consistent with earlier work in which it was noted that heat-treatments in the β-phase field followed by reasonably rapid cooling produce a substantial improvement in the resistance of the material to accelerated corrosion in steam (2-4). In fact, these heat-treatments reduced the weight gains from ~3000 to <50 mg/dm². As discussed above, the large weight gains found on the starting material (or after α-phase annealing) correspond to a much more rapid corrosion process than would be expected for the normal oxidation of Zircaloy at 500°C, based on measurements in other environments such as low pressure steam or oxygen. Other tests have shown that all of the material conditions listed in Table I show good corrosion resistance at lower temperatures, such as 400°C, 1500 psi steam.

Table I. Effect of heat-treatment on corrosion weight gains

(24 hr in 500°C, 1500 psi steam)

Heat-treatment temperature (°C)	Weight gain (mg/dm²)
Starting material	2930
600	2830
700	2550
1000	47
1050	49

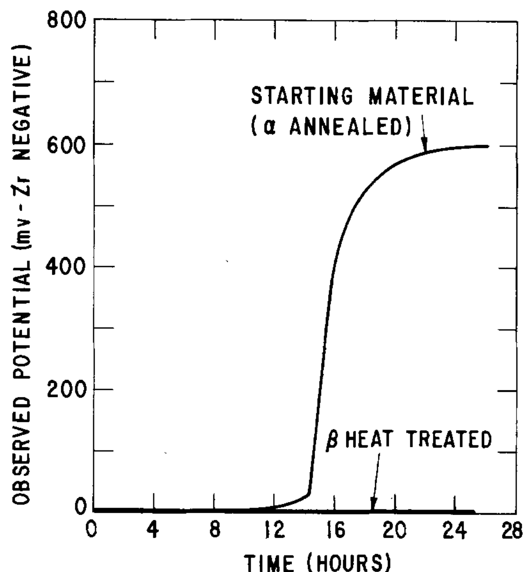

Fig. 2. Potential differences observed across oxide films growing in steam at 500°C, 1500 psi. Potentials for which the Zircaloy becomes negative relative to the oxide surface are plotted as positive along the potential difference axis.

Potential difference measurements.—Figure 2 shows typical results obtained by monitoring the potential differences which develop across the growing oxide films. On the starting material one initially finds low potential differences which, after several hours, increase quite rapidly to about 600-700 mV (Zr negative). During this time the resistance of the oxide is also increasing, and at the final potential the results may be limited by the insulation resistance of the electrode feed throughs. Thus, it can be concluded that significant potentials develop across the oxide on the starting material, but that the final measured potential values may be lower than the actual values by some unknown amount.

For the heat-treated materials the observed potentials never exceed a few millivolts, and in this case the oxide resistance was always very much less than the feed-through resistance. These potential values are therefore considered to be reasonably accurate.

The experiments reported in Fig. 2 have been repeated several times with very reproducible results. Varying the probe contact force from 5 to 9g did not affect the results, and exposure of a specimen of the starting material with electrode spots for 6 hr prior to establishing the mechanical contact produced the same values of potential difference *vs.* total oxidation time as given in Fig. 2. In addition, potential measurements on a heat-treated specimen which had been preoxidized in the test environment for 24 hr prior to application of the sputtered electrodes resulted in low measured potential differences comparable to those found on similar specimens oxidized with the Pt electrode spots present from the outset. These observations tend to suggest that the results given in Fig. 2 do not depend on mechanical damage to the oxide by the contact probe or on the continuous presence of the Pt layer possibly inhibiting some step in the initial oxidation process.

However, it is clear that the presence of the electrodes does influence the oxidation process under open-circuit conditions. Thus, by metallography it has been found that the thick oxide (~250 μm) which normally forms on the starting material during a one-day test has been suppressed under the open-circuit electrodes; here one finds only a relatively uniform oxide ~3 μm thick. For the β heat-treated material there is little difference between the oxide thicknesses (also ~3 μm) found with and without electrodes on the surface, although even in this case the oxidation process may be more uniform under the electrode material as previously suggested by Cox (6). These observations are interpreted in a later section. For the present it is noted that all of the potential difference measurements were obtained across thin, barrier-type oxide films, and it is suggested below that these values are indicative of differences in the relative ionic and electronic conduction characteristics of the thin oxides which form initially and which control the initiation of the accelerated corrosion process.

Effect of applied potential differences.—Since the accelerated corrosion process is being correlated with the occurrence of metal-negative potential differences across the oxide film, it should be possible to apply an external potential source to induce the accelerated attack process where it otherwise would not occur. This has in fact been accomplished in the experiments summarized in Fig. 3, where it is found that applied potential differences in the Zr-negative direction are harmful, while smaller Zr-negative or Zr-positive potentials are beneficial. The oxide thickness data given in Fig. 3 were obtained by metallographic examination of the oxide formed directly under the electrode spot.

Similar experiments were also done in pure oxygen gas at 500°C and 1500 psi. In this case no accelerated corrosion was observed even under large applied potential differences; the resulting oxide films were estimated at about 3 μm in thickness. Trowse *et al.* (7) have also reported that accelerated corrosion does not occur in high temperature, high pressure oxygen.

The currents associated with the applied voltages were monitored during each of these tests. The initial currents were found to be quite high (as much as 350 mA/cm^2), and it was initially thought that high local currents might be causing disruption of the oxide and initiating an enhanced corrosion process. However, this seems rather unlikely, since comparable currents were passed during the application of potential differences in both directions and in oxygen as well as steam, while accelerated corrosion was found only in steam under Zr-negative potentials. In addition, in one experiment the potential difference was not applied for several hours after test initiation. In this case accelerated corrosion was still observed, despite the passage of very much smaller currents (maximum of ~15 mA/cm^2) due to the growth of a more resistive oxide prior to applying the voltage.

Discussion

The open-circuit potential difference measurements (Fig. 2) indicate that the starting material tends to develop a large metal-negative potential drop across the oxide; this material is highly susceptible to accelerated corrosion. The heat-treated material shows very small potential differences and is resistant to accelerated at-

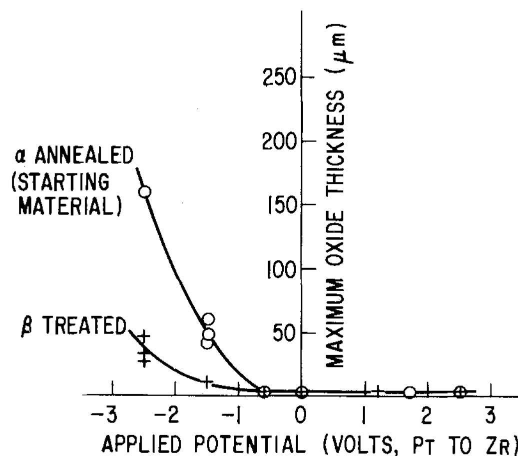

Fig. 3. Effect of applied potential differences on the maximum oxide thickness measured under the electrodes. For comparison, it is noted that away from the electrodes, the maximum oxide thicknesses observed were 220 μm on the starting material and ~10 μm on heat-treated specimens. Further details on the metallurgical condition of these specimens are given in the text.

tack. Furthermore, the accelerated corrosion process can be induced or inhibited by artificially imposing external potentials, with large Zr-negative potentials leading to accelerated attack and smaller negative or positive potential differences inhibiting it. Taken together, these results provide good support for a model in which accelerated corrosion is prevented on suitably heat-treated Zircaloy by a shift in the potential difference across the oxide toward the metal-positive direction. This results from the relatively good electronic conductivity of oxides growing on the heat-treated material.

The oxide conductivity characteristics observed with different heat-treatments can be rationalized in terms of the effect of heat-treatment on the microstructure of the alloy. Since there is evidence (8) that intermetallic precipitates in the Zircaloy provide sites for electron transport through the zirconium oxide, it is suggested that the distribution of these particles is the critical parameter. As shown in Fig. 4a, the starting material contains a random array of intermetallic particles distributed throughout the α-zirconium matrix. In the heat-treated condition, Fig. 4b, the particles tend to form two-dimensional networks along grain boundaries or subgrain boundaries, again in an α-zirconium matrix.

A possible model for the effect of these particle distributions on electron conduction through the oxide is shown schematically in Fig. 5. On the starting material, intermetallic particles initially provide adequate sites for electron transport through the oxide (Fig. 5a). One would therefore expect to observe during initial film growth the relatively low film resistance and small potential drops that are displayed in Fig. 2. At a later stage (Fig. 5b), after growing an oxide which is thicker by some amount than the larger intermetallic precipitates, the particles tend to become isolated by the growing oxide and insulated from the underlying metal. Under these conditions the oxide resistance should increase and the potential drop across the oxide should drift in the metal negative direction, as is indeed observed after about 15 hr. At this time the average oxide thickness is about 2 μm, which compares reasonably well with the size of the intermetallic particles (as much as about 1 μm in diameter).

On heat-treated material the intermetallic particles tend to be quite closely spaced along grain boundaries, and Fig. 5c is intended to suggest that in this case the particles never become insulated from either the metal or the oxide surface. In this case, both the oxide resistance and the observed potential differences should remain low indefinitely as was found experimentally (Fig. 2). This argument assumes that the precipitates, identified as $Zr(Fe, Cr)_2$ in Zircaloy-4 (9, 10), remain reasonably conductive even when oxidized (8), a point requiring further confirmation. In addition, observations at higher resolution by transmission electron microscopy (11) show that the precipitates are not actually in contact, and it must therefore be argued that the few hundred angstroms of ZrO_2 which may form between the particles is also a relatively good electron conductor due to doping effects from the nearby particles. Nevertheless, it is suggested that the microstructural changes produced by the heat-treatment process may provide a quite natural explanation for the effect of heat-treatment on the observed potentials and on the improved resistance of heat-treated Zircaloy to accelerated corrosion in steam.

It was noted above that the Pt electrode spots are permeable, and this point is confirmed by the occurrence of accelerated corrosion under the electrodes when suitable potential differences are applied. Nevertheless, in the absence of applied voltages the electrodes do tend to inhibit the accelerated corrosion process. This is believed to result from the imposition of an equipotential on the oxide surface due to the high conductivity of the sputtered platinum. In the absence of an electrode, it is suggested that surface iR potential drops can result in increased metal-negative potential differences as one moves along the surface away from localized sites for electron conduction through the oxide. With no electrode these high local potentials probably control initiation of the accelerated corrosion process. Under the electrodes the maximum potential differences are reduced because the electrodes average the oxide transport characteristics over macroscopic areas of the surface. It is suggested that these average potentials are not negative enough to initiate the accelerated oxidation. For the same reason, one cannot expect a direct correlation between the measured potential differences on the starting material (which is susceptible to accelerated attack away from the elec-

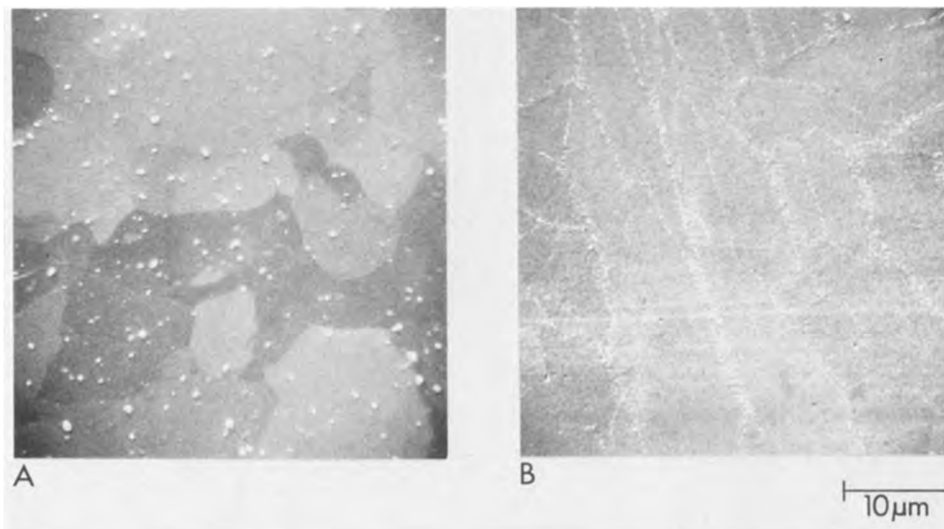

Fig. 4. Effect of heat-treatment on the distribution of intermetallic precipitates in Zircaloy-4: (a) material typical of the starting condition described in the text, and (b) material heated at 1025°C (β-phase field) and cooled at ~10°C/sec.

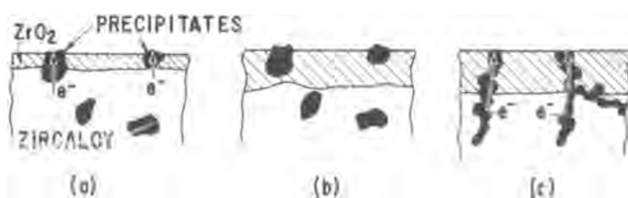

Fig. 5. Schematic of model for effect of intermetallic precipitate distribution on electronic conductivity of oxide film: (a) starting material after short exposure, good electronic conductivity because precipitates span the oxide; (b) starting material after longer exposure, poor electronic conductivity because precipitates are isolated by the oxide; and (c) heat-treated material, good electronic conductivity because precipitates arrayed along grain boundaries do not become isolated.

trodes) and the applied potentials necessary to initiate the process under the electrodes for either of the material conditions tested.

This argument leads naturally to an explanation for the necessity (2) of relatively rapid cooling rates after β heat-treatments to maintain good corrosion resistance. As shown in Fig. 4b, the intermetallic particles after β heat-treatment reside at the boundaries between lamellae in a Widmanstätten or platelike structure. These lamellae become progressively coarser as the cooling rate is reduced, so that the sites for electron transport become more widely separated across the surface. It is suggested that this results in local potentials near the center of the lamellae (at a maximum distance from the intermetallic particles) which, when the structure is sufficiently coarse, can become large enough to initiate the accelerated attack. In fact, examination of the β heat-treated specimens in these tests indicates that accelerated corrosion often initiates on the larger lamellae and tends to be confined initially to individual lamellae until spreading occurs in the more extreme cases.

The nodular oxide morphology commonly observed on the starting material during accelerated corrosion in steam is also consistent with the occurrence of localized conditions favorable to the initiation of the process. It is suggested that these may be sites of lower intermetallic particle concentration, such that the necessary local control of the potential difference across the oxide is not maintained.

An alternative explanation (6) for the effect of the electrodes involves the production of a more uniform oxide (due to the imposition of equipotential surfaces on both sides of the film) which is more resistant to breakdown simply because of its uniformity. However, the above explanation in terms of the reduction of local potential differences seems to fit more naturally with the observed effects of applied voltages.

There is at present no firm evidence to indicate why the development of metal-negative potential differences across the film results in initiation of accelerated corrosion. The electric fields associated with these potential differences are in fact opposite to the direction which tends to promote anion transport through a barrier-type oxide as in normal oxide growth processes. Thus, the phenomena being observed in these experiments are not the same as the much smaller effects reported (12) from experiments on pure zirconium in oxygen gas, where short-circuiting the growing oxide produced an increase in the oxidation rate. Small effects in the opposite direction were reported (13) on short-circuiting Zircaloy-2 specimens oxidizing in molten salt baths. While similar, relatively minor effects may be occurring in the present experiments within the uncertainty of the oxide thickness measurements, these processes seem unrelated to the much more dramatically accelerated corrosion phenomenon of present interest.

What is required is a process leading to the breakdown of the normally protective oxide scale and the nucleation of a rapidly growing, nonprotective oxide. Since the phenomenon of interest is observed in steam but not in oxygen, it is suggested that hydrogen liberated by the corrosion reaction may play a role. In fact, the migration of protons into the oxide under the favorable electric fields associated with metal-negative potential differences fits naturally with all of the reported observations. This could lead to disruption of the oxide film and loss of protectiveness perhaps through an effect of hydrogen on the phase transformation or recrystallization processes that occur in the oxide. Measurements made with a capillary condensation technique described previously (14) have shown that the oxide grown under accelerated conditions in steam contains more fine porosity (per unit weight) than a normal post-transition film, and this may be related to its less protective character. In any case, it is clear that further work is necessary to establish the mechanism by which hydrogen in the oxide might reduce its protectiveness and accelerate the oxidation process.

In arguing that hydrogen migration into the oxide leads to accelerated corrosion, the present model resembles some aspects of previously suggested (15, 16) mechanisms for various accelerated corrosion processes in zirconium and other alloys. However, these earlier studies were not focused on heat-treatment effects or on the particular accelerated corrosion phenomenon which occurs with Zircaloy in high temperature, high pressure steam. A more recently proposed (17) model for nodular corrosion based on cathodic depolarization at intermetallic particles is in some respects opposite to the mechanism suggested here.

Conclusions

1. Large potential differences in the Zr-negative direction are observed across oxide films growing on Zircaloy which is susceptible to accelerated attack in 500°C, 1500 psi steam. When the material has been heat-treated for resistance to such attack, the observed potential differences are much smaller.

2. On Zircaloy with different metallurgical treatments, accelerated attack may be initiated by applied external potential differences (Zr-negative) and inhibited by imposing smaller or oppositely directed electric fields.

3. The data support a model in which accelerated corrosion is prevented on suitably heat-treated Zircaloy by the reduction of unfavorable (metal-negative) potential differences due to the relatively good electronic conductivity of oxides growing on heat-treated materials.

4. The electronic conduction characteristics of the oxide can be explained by differences in the distribution of intermetallic precipitates for different heat-treatments. These differences determine how long during the oxidation process the precipitates can serve as paths for electron conduction through the oxide.

5. Because of the lack of similar effects in pure oxygen gas, it is suggested that proton migration into the oxide film under favorable electric fields causes a loss of protectiveness, although the details of this process cannot be specified at this time.

Acknowledgments

The authors would like to acknowledge J. L. Walker for helpful discussions concerning phase transformations in Zircaloy and metallographic procedures, D. E. Broecker for assistance with the experimental work, B. M. Beach, S. R. Hayashi, and M. D. McConnell for scanning electron microscopy, and C. R. Rodd for metallography. H. S. Spacil contributed a critical review of the manuscript with helpful comments, and several useful suggestions were provided by anonymous reviewers.

Manuscript submitted Feb. 25, 1977; revised manuscript received Sept. 12, 1977.

Any discussion of this paper will appear in a Discussion Section to be published in the December 1978 JOURNAL. All discussions for the December 1978 Discussion Section should be submitted by Aug. 1, 1978.

Publication costs of this article were assisted by General Electric Company.

REFERENCES

1. A. W. Urquhart and D. A. Vermilyea, *J. Nucl. Mater.*, **62**, 111 (1976).
2. S. Kass, *ASTM STP*, **368**, 3 (1974).
3. A. B. Johnson, Jr., *ibid.*, **458**, 271 (1969).
4. B. Cox, *AECL*, 4448 (1973).
5. F. A. Kröger, "The Chemistry of Imperfect Crystals," 2nd ed., chap. 23 and 24, American Elsevier, New York (1974).
6. B. Cox, *This Journal*, **115**, 1259 (1968).
7. F. W Trowse, R. Sumerling, and A. Garlick, Paper presented at the Symposium on Zirconium in the Nuclear Industry, Quebec, Canada (August 1976).
8. N. Ramasubramanian, *J. Nucl. Mater.*, **55**, 134 (1975).

9. J. B. Vander Sande and A. L. Bement, *ibid.*, **52**, 115 (1974).
10. P. Rao and J. L. Walker, *ibid.*, In Press.
11. P. Rao, Unpublished data.
12. J. H. Eriksen and K. Hauffe, *Z. Phys. Chem. N.F.*, **59**, 332 (1968).
13. B. Cox, *J. Nucl. Mater.*, **31**, 48 (1969).
14. A. W. Urquhart and D. A. Vermilyea, *ASTM STP*, **551**, 463 (1974).
15. J. E. Draley and W. E. Ruther, *This Journal*, **104**, 329 (1957).
16. J. N. Wanklyn and B. E. Hopkinson, *J. Appl. Chem.*, **8**, 496 (1958).
17. M. F. Sheppard and C. Tyzack, Paper presented at the Symposium on Zirconium in The Nuclear Industry, Quebec, Canada (August 1976).

Electrolytic Purification of Nickel Plating Solutions

Luther E. Vaaler

Battelle Columbus Laboratories, Columbus, Ohio 43201

ABSTRACT

Data from published and unpublished sources on electrolytic removal of small quantities of copper, zinc, and iron from nickel-plating baths have been compared. As expected the more noble copper plates out preferentially at a rate limited only by diffusion to the cathode. Zinc ions increase the cathodic potential for nickel deposition to the point that zinc plates out with nickel at a diffusion-limited rate. Removal of iron may also be diffusion limited but results are less clear than for copper and zinc.

Nickel plating solutions become contaminated with metal ions, such as copper, zinc, and iron which are brought into a bath by solution clinging to the work or by dissolution of the surface of the work. A convenient and efficient way of removing these impurities is by low current density electrolysis (dummying), either directly in the plating bath during nonproduction periods or in a separate electrolysis unit to which the plating solution is pumped and from which it is returned to the cell.

The objective of the present study was to reduce the data available (obtained under widely varying conditions) to a common basis for comparison. Some previously unreported experimental data were considered along with published information. Then the effect of such independent variables as the current density and degree of agitation on the rate of impurity removal could be more accurately ascertained.

Sources of Data

Max and Whitehurst (1) studied the removal of copper and iron from nickel plating solutions using a channel cell with vertical anodes and cathodes 5.08 cm high and 38 cm long spaced 2.54 cm apart. Flow rate was varied from 3.15 to 25.4 cm/sec and the current density from 5.38×10^{-4} to 1.72×10^{-2} A/cm^2. The concentration of impurity was followed as a function of time. Plots of log copper concentration *vs.* time were linear indicating that removal of the copper follows first-order kinetics. The authors measured the time for removal of half of the 100 mg/liter of copper originally present and used this value as an index of performance for a given set of conditions.

Schaer and Layer (2) used a rotating-rod cathode 10 cm in diameter to remove copper, iron, and zinc from a nickel plating solution at constant current density. They plotted the impurity concentration in milligrams per liter *vs.* the ampere-minutes/liter and obtained a curve whose negative slope became smaller as electrolysis proceeded.

Other investigators were less precise in defining the conditions of agitation used during electrolysis. Case (3) and Ewing *et al.* (4) used impellers to stir small volumes of nickel plating solution past flat-panel cathodes, and made rough estimates of the linear flow rate. They removed copper, iron, zinc, and nickel at constant current density. Curves of concentrations *vs.* ampere-minutes or ampere-hours/gallon also showed smaller negative slopes as electrolysis proceeded. Raub (5) electrolyzed nickel plating solutions containing small but approximately constant concentrations of zinc. The solution was stirred but no details were reported. A range of current densities was used with each bath. The composition of the deposits was determined. Plots of zinc content of the deposit *vs.* current density for each bath showed negative slopes that became smaller with continued electrolysis.

Treatment of Data

Following Max and Whitehurst's plots of log concentration *vs.* time, other data (3-5) were replotted in terms of log concentration *vs.* ampere-seconds/cubic centimeter. Since amperes and volume for any experiment are fixed the abscissa is proportional to time. Least squares plots are shown in Fig. 1-9. Most of the data are approximated by the straight lines with some exceptions, *e.g.*, Fig. 2. Data were available only as plots rather than as tabulations. Therefore, an error in estimating these points was added to any error in the original experiments.

Raub's (5) data were replotted in a different manner since the bulk concentration of the zinc was maintained constant during the experiment and the deposit rather than the bath was analyzed. The curves of zinc content *vs.* current density had a hyperbolic shape suggesting that a plot of the reciprocal of the zinc content *vs.* current density would be linear. Such plots are shown Fig. 10. The larger reciprocal values were particularly hard to estimate from the original plot so that these points are more scattered.

Discussion

Basis for comparing results.—Comparing the curves from the various sources obtained under a variety of conditions is difficult. To make comparison easier a simple model was assumed that would give a directly comparable rate constant for each curve independent of the impurity concentration, C_b, in the bulk solution. The model assumes that the impurity ions diffuse through a uniform layer to the cathode and that migration is negligible by comparison. It also assumes that the current for depositing the impurity is proportional to its concentration at the electrode. Current in excess of that for impurity deposition plates out nickel.

$$i_d = n\mathbf{F}k_c(C_b - C_i) = n\mathbf{F}k_iC_i \quad [1]$$

Where i_d = current density for impurity deposition,

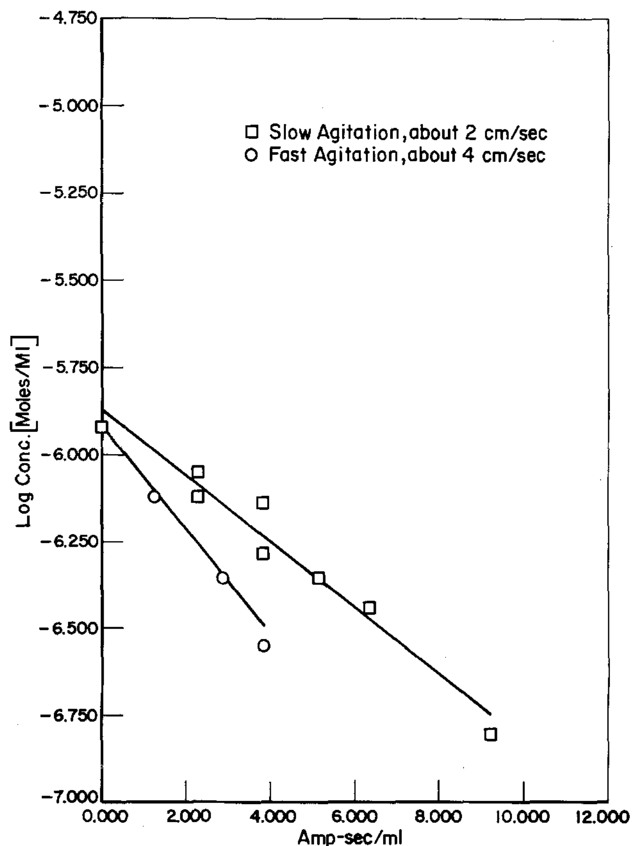

Fig. 1. Copper; Case (3), 0.00538 A/cm²

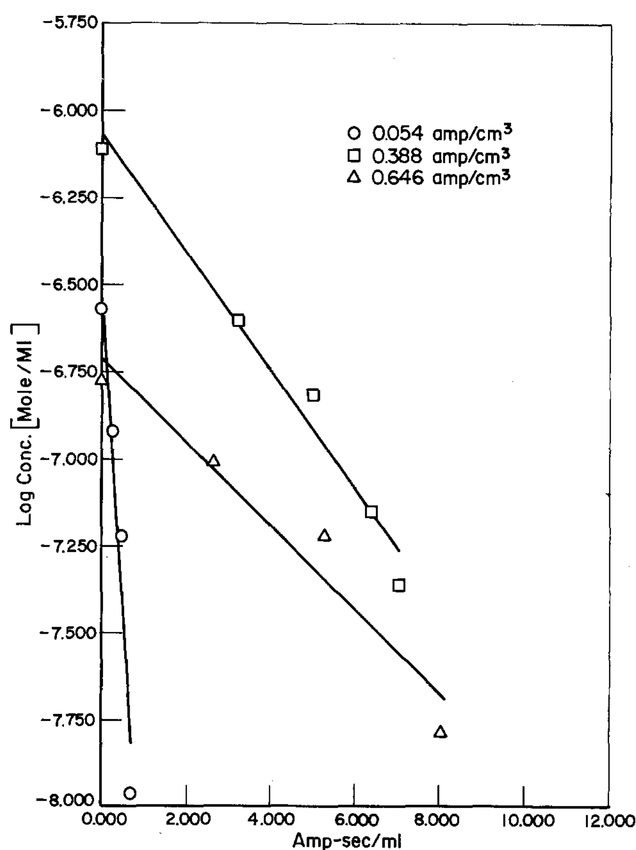

Fig. 3. Copper; Schaer and Layer (2), 10 cm diam. cylinder rotated at 7.6 rps.

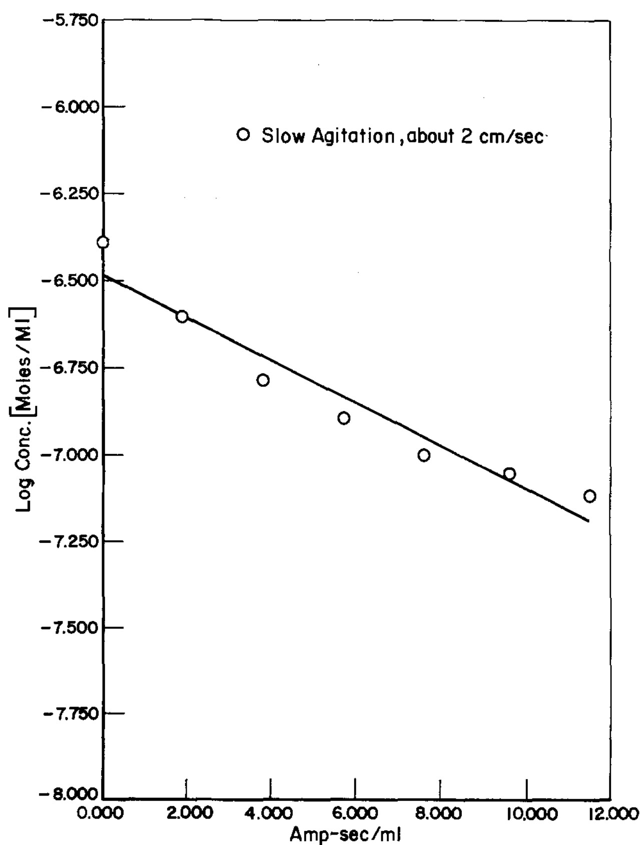

Fig. 2. Copper; Ewing *et al.*, (4), 0.00215 A/cm²

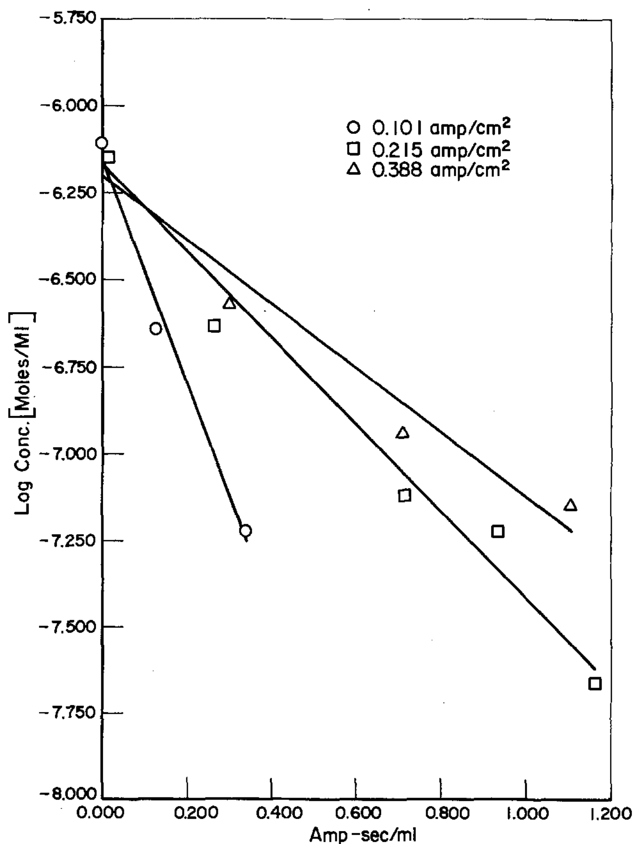

Fig. 4. Copper; Schaer and Layer (2), 10 cm diam cylinder rotated at 11.5 rps.

A/cm²; k_c = mass transfer coefficient through the diffusion layer, cm/sec; C_b = bulk concentration of impurity, moles/ml; C_i = concentration of impurity at the electrode, moles/ml; and k_i = constant relating i_d and C_i, cm/sec.

Using k_i as a constant strongly implies that the cathode potential is constant as C_i changes. If the current density for nickel deposition is much larger than that

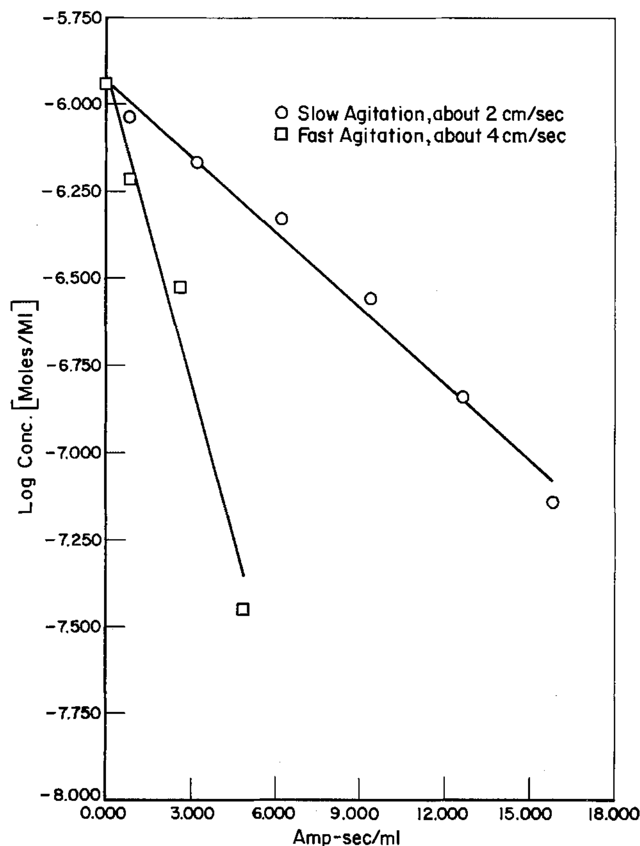

Fig. 5. Zinc; Case (3), 0.00538 A/cm²

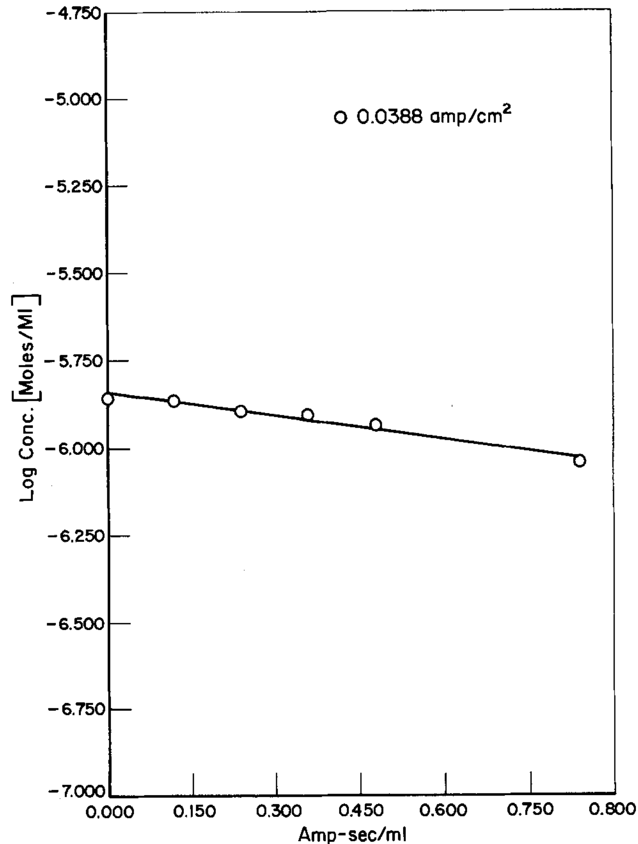

Fig. 7. Zinc; Schaer and Layer (2), 0.63 cm diam cylinder rotated at 183 rps.

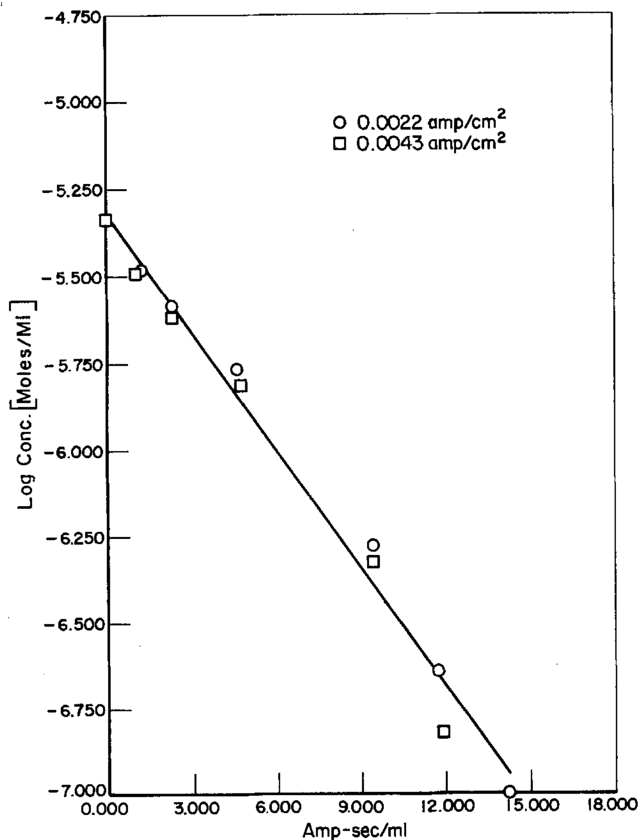

Fig. 6. Zinc; Ewing *et al.* (4), agitation about 2 cm/sec

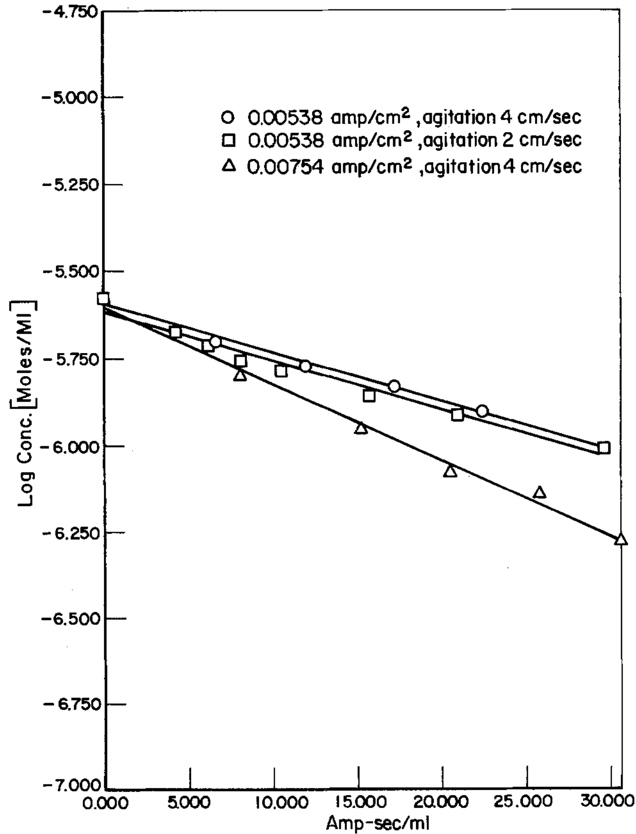

Fig. 8. Iron; Case (3)

for impurity deposition and therefore approximately constant at a constant total current density, the cathode potential will remain approximately constant. In many of the experiments reported the amount of nickel deposited greatly exceeded that of the impurity. Equation [1] can be rearranged to give

$$i_d = n\mathbf{F}(k_i k_c / k_1 + k_c) C_b = n\mathbf{F}KC_b \qquad [2]$$

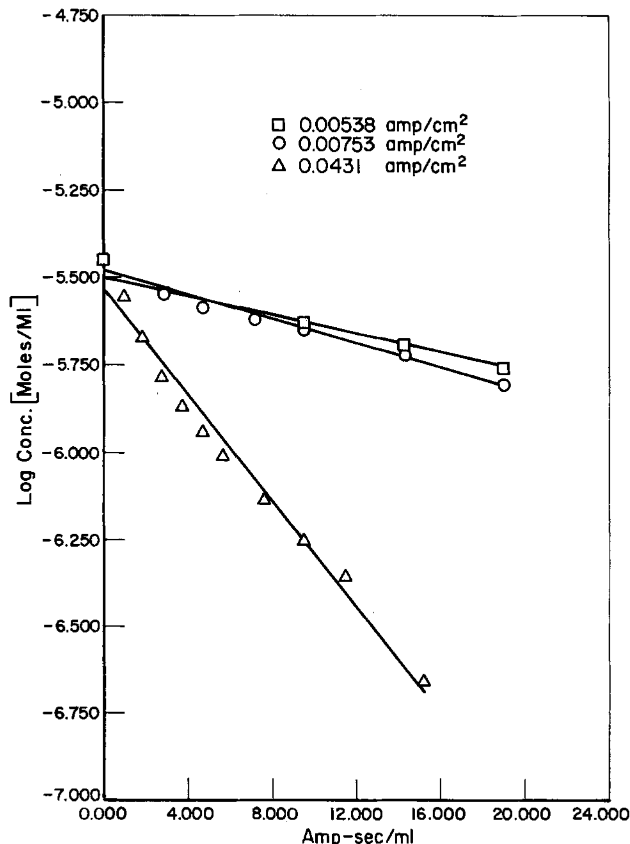

Fig. 9. Iron; Ewing *et al.* (4), agitation 2 cm/sec

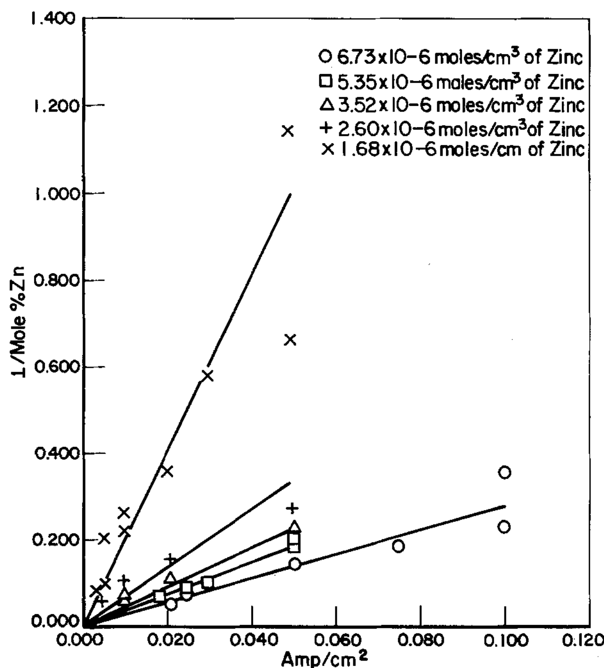

Fig. 10. Zinc; Raub (5), agitated bath at 50°C

If the current density for deposition of an impurity is diffusion limited ($C_i \approx 0$)

$$i_d = n\mathbf{F}k_cC_b \quad [3]$$

However, a linear relation between i_d and C_b does not imply a diffusion limitation and further evidence is needed to establish such a limitation.

Experiments were run at a constant total current density i_T so that i_d was not actually measured. Therefore, the value of K cannot be determined from Eq. [2] or [3]. The following derivation makes feasible the evaluation of K from the available data.

A balance between the rate at which the impurity is deposited and removed from solution can be written as follows

$$i_dA = -n\mathbf{F}v\frac{dC_b}{dt} \quad [4]$$

A is the cathode area, cm^2 and v is the solution volume, cm^3. Combining Eq. [2] and [4]

$$\frac{dC_b}{dt} = -KAC_{b/v} \quad [5]$$

and integrating

$$-\ln(C_{bt}/C_{bo}) = KAt/v \quad [6]$$

C_{bt} is the bulk concentration at t, moles/ml and C_{bo} is the bulk concentration at $t = 0$, moles/ml.

The ampere-time/volume units C_T, *i.e.*, coulombs/cubic centimeter, in which the experimental data of Fig. 1-8 are reported are equivalent to

$$C_T = i_TAt/v \quad [7]$$

combining Eq. [6] and [7]

$$-\ln(C_{bt}/C_{bo}) = KC_T/i_T$$

Therefore K can be determined from the slope $-K/i_T$ of the plots in Fig. 1-8 since i_T is known.

The same rate constant can be derived from Max and Whitehurst's values for the time required to remove one-half of the copper originally present. Substituting in Eq. [7]

$$C_T = i_TAt_{1/2}/v \quad [9]$$

and Eq. [8]

$$-\ln 0.5 = KAt_{1/2}/v \quad [10]$$

$$K = 0.693v/At_{1/2} \quad [11]$$

Where $t_{1/2}$ is the half-time in seconds.

A rate constant can also be obtained from the plot of Fig. 9, of reciprocal zinc content of the deposit *vs.* current density.

The mole fraction of zinc in the deposit M_b is

$$\frac{1}{M_b} = \frac{i_T}{i_d} = \frac{i_T}{n\mathbf{F}KC_{bl}}$$

The linearity of the $1/M_b$ *vs.* i_T plots indicates a constant value for i_d, or that zinc is being deposited at a limiting current density.

From Eq. [2] a value of i_d can be determined knowing K and C_b and the composition of the deposit calculated from the ratio i_d/i_T. The maximum mole fraction, M_b, of the impurity deposited during an experiment was calculated and included in the results. M_b is highest at the beginning of electrolysis and decreases as C_b is lowered during the electrolysis.

Results

The composition of the nickel bath for which the rate constants for removal of copper, zinc, and iron have been determined are shown in Table I. Case and Ewing *et al.* and Raub used essentially the same bath. Max and Whitehurst used a more concentrated bath. Experiments of Schaer and Layer were with the most concentrated bath but without chloride.

Table I. Concentration of nickel baths and temperature

Source	Nickel (moles/ml)	$SO_4^=$ (moles/ml)	Cl^- (moles/ml)	H_3BO_3 (moles/ml)	Temperature (°C)
Max (1)	1.27×10^{-3}	1.14×10^{-3}	2.52×10^{-4}	6.7×10^{-4}	60
Schaer (2)	1.75×10^{-3}	1.75×10^{-3}	0.0	1.6×10^{-4}	60
Case (3)[a]	1.10×10^{-3}	9.1×10^{-4}	3.8×10^{-4}	4.9×10^{-4}	70
Ewing (4)	1.10×10^{-3}	9.1×10^{-4}	3.8×10^{-4}	4.9×10^{-4}	50-55
Raub (5)[b]	1.10×10^{-3}	9.1×10^{-4}	2.7×10^{-4}	4.9×10^{-4}	50

[a] Assume composition of Weisberg (8), Co 9.7×10^{-6} moles/ml, sodium formate 5.14×10^{-4} moles/ml.
[b] 10^{-3} g/ml of toluolsulfonamide.

Table II. Removal of copper

Data origin	Metal conc (moles/ml)	Current density (A/cm^2)	Agitation (flow) (cm/sec)	Slope (cm^3/A-sec)	K (cm/sec)	Std error of K (%)	Max M_b (m/o)
Case (3)	1.20×10^{-6}	5.38×10^{-3}	4.0	−0.369	1.93×10^{-3}	3.2	16
Case (3)	1.20×10^{-6}	5.38×10^{-3}	2.0	−0.220	1.18×10^{-3}	7.6	5
Max (1)	7.87×10^{-7}	5.38×10^{-4}	3.15		6.81×10^{-4}	9.4	19
Max (1)	7.87×10^{-7}	to	6.35		8.12×10^{-4}	8.6	23
Max (1)	7.87×10^{-7}	1.72×10^{-3}	12.7		1.32×10^{-3}	10.2	37
Max (1)	7.87×10^{-7}		25.4		2.52×10^{-3}	20.4	71
Ewing (4)	4.07×10^{-7}	2.15×10^{-3}	2.0	−0.0141	3.03×10^{-5}	10.4	0.11
Schaer (2)	2.71×10^{-7}	5.38×10^{-2}	243 (7.6 rps)	−4.69	2.53×10^{-2}	14.6	24.5
Schaer (2)	7.86×10^{-7}	3.88×10^{-2}	243 (7.6 rps)	−0.394	1.52×10^{-2}	7.9	6.0
Schaer (2)	7.81×10^{-7}	6.46×10^{-2}	243 (7.6 rps)	−0.279	1.80×10^{-2}	14.6	0.9
Schaer (2)	7.81×10^{-7}	1.08×10^{-2}	366 (11.5 rps)	−7.39	7.95×10^{-2}	8.5	111
Schaer (2)	7.81×10^{-7}	2.15×10^{-2}	366 (11.5 rps)	−2.89	6.21×10^{-2}	6.4	44
Schaer (2)	7.81×10^{-7}	3.88×10^{-2}	366 (11.5 rps)	−2.13	8.26×10^{-3}	12.8	32

Copper.—Values of K were calculated from the $t_{1/2}$ values of Max and Whitehurst as a function of flow rate and current density. An analysis of variance showed that flow rate was significant but current density was not. Results obtained from the plots of the other investigators and from $t_{1/2}$ values for copper are summarized in Table II. Accuracies of K's in term of standard error were determined from the variance of line slopes or, in the case of Max and Whitehurst's data, from the values of K for the six current densities at each flow rate. The independence of K and current density in data of Max and Whitehurst and in that of Schaer and Layer with the rotating cathode strongly suggest that copper is being plated out at its limiting current density.

This result is expected for the more noble copper present in low concentrations. However, in the experiment with the rotating cathode the mass transport rate was high enough to allow essentially 100% deposition of copper (the calculated value of 111% is probably due to the inherent error of the slope from which K was calculated). Ettel, Tilak, and Gendron (6) added small amounts of silver ion to a copper electrowinning bath and measured the limiting current density of silver deposition by analysis of the silver content of the copper deposit: From the measurement they were able to define the mass transfer rate for copper deposition. Limiting deposition rates for copper in a nickel plating bath provide a similar measurement of mass transfer conditions and are a function of the degree of agitation as found experimentally by Max and Whitehurst (1) and Schaer and Layer (2).

Agitation conditions for experiments of Case (3) and Ewing *et al.* (4) are poorly defined. Case's results, by comparison with Max and Whitehurst's, indicate a fairly high degree of mass transfer, while Ewing's results indicate very poor mass transfer conditions. The results as a whole show the importance of agitation in obtaining rapid removal of impurities at a high current efficiency.

Zinc.—The calculated K values for zinc removal are shown in Table III. Values for Case (3), Ewing (4), and Raub (5) are within the same order of magnitude. The reciprocal relation between zinc content of the deposit and the total current density strongly suggests that zinc is plated out at its limiting current density. The K values with the rotating cylinder used by Schaer and Layer (2) are significantly higher, showing the improvement possible by increasing the mass transfer rate. The zinc content of the nickel deposits is relatively high for such an active metal, and Knodler (7) has suggested that this is due to the pronounced effect that zinc exerts upon the potential for nickel deposition. Nickel is plated out at a cathode potential of −500 to −600 *vs.* SHE in the absence of zinc. In the absence of nickel zinc deposits at −800 to −900 mV *vs.* SHE. Small additions of zinc to a nickel bath shift the deposition potential for nickel to that for zinc. Knodler suggests that the shift is due to adsorption of a zinc hydroxide layer on the cathode surface.

Iron.—Results for iron are shown in Table IV. The removal of iron from nickel baths would appear to involve a more complex mechanism than for copper and even than for zinc. K values are generally lower than for copper and zinc and are not increased to the same extent as for copper by enhancing mass transfer by using a rotating cathode. Max (1) found that no iron was removed at less than 4.3×10^{-3} A/cm^2 and that results at 8.6×10^{-3} A/cm^2 were uncertain. Only at

Table III. Removal of zinc

Data origin	Metal	Metal conc (moles/ml)	Current density (A/cm^2)	Agitation (flow) (cm/sec)	Slope (cm^3/A-sec)	K (cm/sec)	Std error of K (%)	Max Mb_1 (m/o)
Case (3)	Zn	1.14×10^{-6}	5.38×10^{-3}	4	−0.69	3.71×10^{-3}	11	15.2
Case (3)	Zn	1.14×10^{-6}	5.38×10^{-3}	2	−0.17	9.03×10^{-4}	4	3.7
Ewing (4)	Zn	4.59×10^{-6}	2.2×10^{-3}	2	−0.26	5.77×10^{-4}	4	23.0
Ewing (4)	Zn	4.59×10^{-6}	4.3×10^{-3}	2	−0.26	1.13×10^{-3}	4	23.0
Raub (5)	Zn		10^{-3} to 10^{-1}			2.7×10^{-3}	12	
Schaer (2)	Zn	1.39×10^{-6}	3.87×10^{-2}	362 (183 rps)*	−0.52	2.01×10^{-2}	12	14.0

* 0.63 cm diam cylinder.

Table IV. Removal of iron

Data origin	Metal	Metal conc (moles/ml)	Current density (A/cm^2)	Agitation (cm/sec)	Slope (cm^3/A-sec)	K (cm/sec)	Std error of K (%)	Max Mb_1 (m/o)
Case (3)	Fe	2.63×10^{-6}	5.38×10^{-3}	4	−0.033	1.77×10^{-4}	3	1.66
Case (3)	Fe	2.63×10^{-6}	5.38×10^{-3}	2	−0.033	1.75×10^{-4}	6	1.65
Case (3)	Fe	2.63×10^{-6}	7.54×10^{-3}	4	−0.051	3.85×10^{-4}	4	2.59
Max (1)	Fe	8.95×10^{-7}	1.72×10^{-3}	3.05	—	2.54×10^{-4}		
Max (1)	Fe	8.95×10^{-7}	1.72×10^{-3}	6.35	—	4.37×10^{-4}		—
Max (1)	Fe	8.95×10^{-7}	1.72×10^{-3}	25.4	—	9.58×10^{-4}		—
Schaer (2)								
Ewing (4)	Fe	3.58×10^{-6}	5.38×10^{-3}	2	−0.035	1.62×10^{-4}	9.0	2.08
	Fe	3.58×10^{-6}	7.53×10^{-3}	2	−0.040	3.01×10^{-4}	6.6	2.76
	Fe	3.58×10^{-6}	4.31×10^{-2}	2	−0.175	7.56×10^{-3}	4.2	12.1

1.72×10^{-2} A/cm^2 was consistent removal obtained. Ewing *et al.* (4) show a drastic increase in K when current density is raised to 4.3×10^{-2} A/cm^2. Iron offers the possible complication of forming Fe(III) at the anode and Fe(II) at the cathode rather than elemental iron, so that the current efficiency of iron removal can be very low.

Removal of Impurities in Electroplating and Electrowinning

Electrolytic purification has been successfully used but considerably more nickel than impurity is removed. It is evident that more agitation and lower current densities, at least for copper and zinc removal, would be beneficial and possibly a separate divided cell to prevent anodic oxidation of the iron would aid its removal. A certain amount of nickel deposition is probably beneficial in maintaining a deposit that is coherent so that it will not fall back into the bath. While removal of the three impurity elements have been considered separately, in actual practice they are removed together and how zinc hydroxide adsorption, for example, affects deposition of copper and iron in this system has not been well defined. Codeposition of small concentrations of copper, zinc, and iron in the presence of much higher concentrations of nickel requires some additional careful experimental work to elucidate mechanisms, and would be of considerable interest not only for impurity removal but also for the plating of alloys.

Much development work is now going on to increase current density and mass transfer in the electrowinning of metals. Increasing agitation and mass transfer increases the deposition of impurities that are mass transfer limited. Thus, the total current density must be increased proportionately to keep impurity levels low. On the other hand, if it is desirable to recover one of two metals in solutions without contamination from the other, increased mass transfer can increase the limiting current density to a point that a single metal can be selectively removed to a low concentration at practical current densities provided one metal does not affect the deposition kinetics of the other. Thus, it is possible to separate copper from nickel to a concentration of 10 mg/l of copper without significant deposition of nickel. While considerable effort has been devoted to electrowinning dilute solutions of copper under high mass transfer-high surface area conditions, *i.e.*, forced flow, rotating-cylinder cathodes, packed and fluidized beds, less attention has been devoted to these techniques for selective recovery of metals from solutions containing more than one metal ion.

Manuscript submitted Dec. 16, 1976; revised manuscript received Aug. 8, 1977.

Any discussion of this paper will appear in a Discussion Section to be published in the December 1978 JOURNAL. All discussions for the December 1978 Discussion Section should be submitted by Aug. 1, 1978.

Publication costs of this article were assisted by Battelle Columbus Laboratories.

REFERENCES

1. A. M. Max and M. L. Whitehurst, *Tech. Proc. Am. Electroplat. Soc.*, **40**, 181 (1959).
2. G. R. Schaer and C. A. Layer, Battelle's Columbus Laboratories, Unpublished data (1966).
3. B. C. Case, *Tech. Proc. Am. Electroplat. Soc.*, **34**, 228 (1947).
4. D. T. Ewing, R. J. Rominski, and W. M. King, *Plating*, East Orange, N.J., **36**, 1137 (1949).
5. E. Raub and F. Elser, *Metalloberflaeche*, **11**, 1377 (1957).
6. V. A. Ettel, B. V. Tilak, and A. S. Gendron, *This Journal*, **121**, 867 (1974).
7. A. Knödler, *Metalloberflaeche*, **21**, 321 (1967).
8. L. Weisberg, *Trans. Electrochem. Soc.*, **73**, 435 (1938).

Current Distribution Leveling Resulting from Auxiliary Bipolar Electrodes[1]

Werner Engelmaier* and Thomas Kessler[2]

Bell Laboratories, Whippany, New Jersey 07981

and Richard Alkire*

Department of Chemical Engineering, University of Illinois, Urbana, Illinois 61801

ABSTRACT

The effect of auxiliary electrodes on cathodic current distribution is determined both in terms of visual characteristics of plated copper and direct measurements. Experiments are carried out using a Hull cell with high conductivity $CuSO_4/H_2SO_4$ electrolyte. The results indicate that leveling of the distribution takes place when certain types of conductive auxiliary electrodes are placed within an electrolysis cell even though the auxiliary electrodes are not connected to an external source of current. Experiments are described which compare the leveling power of several geometric arrangements of auxiliary electrodes within a cell, as well as the effect of chemical composition of the auxiliary electrodes. The study clarifies the fundamental nature of the process by which leveling is obtained.

The desirability of uniform cathodic current distributions during copper electroplating of multilayer printed wiring boards (MLB's) has been discussed (1-3). MLB's contain plated through-holes (PTH's) which provide electrical connections between the various circuit layers of the MLB. During the electroplating step, copper is deposited in the drilled PTH's as well as on the outer MLB surfaces. Uniform deposit thickness in the PTH's over the whole MLB is critical for connector pin inser-

* Electrochemical Society Active Member.
[1] United States Patent No. 4,043,891 has been granted on this concept.
[2] Present address: Xerox Corporation, Webster, New York, 14580.

Key words: electroplating, electrodeposition, current density, copper plating, printed wiring boards.

tion on the one hand, and functional integrity on the other (1-4). Methods for achieving uniform distributions include: (*i*) modification of electrode and cell configuration, (*ii*) variation of electrolyte composition, and (*iii*) use of auxiliary aids such as dielectric shields and conductive thieves to redistribute the current within the cell. Configuration changes to improve current distribution uniformity have recently been discussed (5). Only a slight increase in the electrolyte conductivity can be achieved by increasing the H_2SO_4 concentration in the 0.27 molar $CuSO_4$/1.76 molar H_2SO_4 baths. This beneficial increase would not lead to a major improvement in plating uniformity on the MLB's. Since methods (*i*) and (*ii*) offer only limited possibilities, method (*iii*) is the most likely method for achieving more uniform copper. References (6) and (7) contain examples of the extensive use of auxiliary aids to improve the uniformity of cathodic current distributions.

The following studies describe a new type of auxiliary aid, a bipolar screen auxiliary double electrode, which consists of two metal pieces immersed in the cell and connected to each other but not to any external source of current. With proper choice of material and position within the cell, such double auxiliary electrodes can provide highly uniform current distributions under highly adverse operating conditions.

The purpose of this investigation is to conduct experiments to demonstrate the effect of auxiliary metal aids and to assess which materials and geometries are most effective in leveling the current distribution. The cell geometry chosen for study is the Hull cell; it is designed to give a highly nonuniform current distribution at the cathode and is the traditional test cell configuration used to illustrate current distribution effects.

Apparatus

The geometry and dimensions of the Hull cell used in this study are shown in Fig. 1(a). A copper anode was positioned perpendicular to the insulating side walls of the cell; the cathode was placed at a 40° angle with respect to the anode. The following tests were conducted: (*i*) conventional Hull cell tests with visual inspection of the plating on a 6.9 × 10.0 cm brass cathode and (*ii*) measurements of cathodic current distributions with segmented cathodes.

The segmented cathode was divided into ten sections as shown schematically in Fig. 2. Note that the width of segment 10 is 0.5 cm whereas the other segments are 0.9 cm wide. The segmented cathode was fabricated from 2-oz copper-plated epoxy board which was pattern-etched to remove strips between segments.

Within the Hull cell were placed metal pieces of several types acting as auxiliary electrodes: copper screen (Cu), copper-plated platinized titanium expanded mesh (Cu/Pt-Ti), platinized titanium expanded mesh (Pt-Ti), and titanium screen (Ti). These auxiliary electrodes were placed, two by two, in three geometrical arrangements within the Hull cell as indicated in Fig. 1(b), (c), and (d). For geometry III the dimension L was 1.25 cm with the solid cathodes and 0.6 cm with the segmented cathodes. Parametric calculations for the dimensional requirements are given in the Appendix.

The electrolytic solution used in the study was copper sulfate in sulfuric acid and distilled water without plating additives. As discussed below, measurements by Baker (8) show that the cathode current distribution is independent of additives presently in use. The approximate concentration of the solution was 0.3M $CuSO_4$, 1.5M H_2SO_4; the nature of the experiments was such that determination of the precise composition was unnecessary.

The electrical circuit used for supplying power and making measurements is given in Fig. 3. The power supply (Hewlett-Packard, 6281A) was deployed in constant current mode. Measurement of the applied current and the current passing between auxiliary electrodes was made with a multimeter (Keithley, 160).

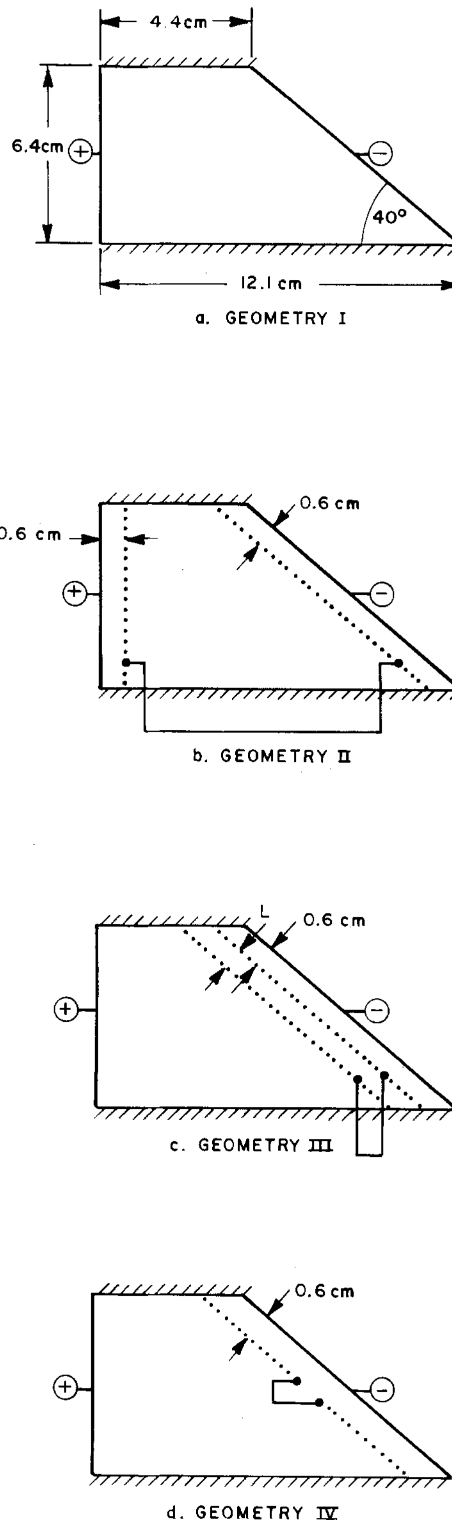

Fig. 1. Hull cell and auxiliary electrode geometries and dimensions

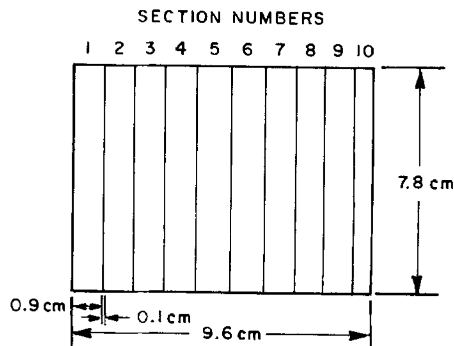

Fig. 2. Segmented cathode for current distribution measurements

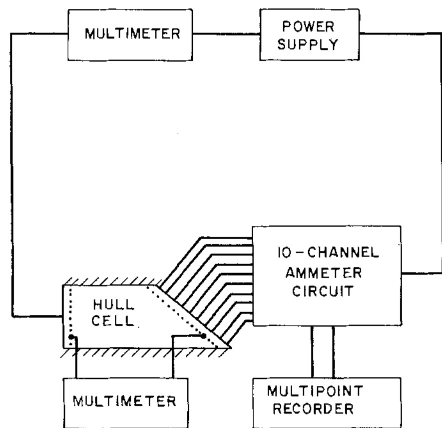

Fig. 3. Circuitry for plating current supply and current distribution measurements.

For the tests with segmented cathodes the section currents were measured with a 10-channel operational amplifier zero-resistance ammeter circuit which supplied a voltage signal to a potentiostatic multipoint recorder (Esterline Angus). The zero-resistance ammeter circuit maintained the potentials of the ten electrode sections to within $\pm 20\ \mu V$.

Procedure

The Hull cell was filled with solution to an approximate depth of 5 cm for the conventional cathodes and to a depth of 2.5 cm for the segmented cathode studies. For the solid cathode experiments the plating times ranged from 1-30 min, with the length of plating time inversely dependent on the applied current. Experiments were carried out at the applied currents given in Table I.

The procedure for making measurements consisted of turning on the current, measuring the section currents, the current flowing between auxiliary electrodes, and the total applied current. Because the solid cathode experiments indicated that mass transfer effects were important at the higher applied currents, measurements of the current distribution was initiated within 1 sec of switching on the current. The section currents were measured in order of section number (see Fig. 2), beginning with No. 1; that is, the current to the most reactive section was measured within about 2 sec of circuit activation. Measurements were conducted for a period of about 40 sec after which the current was switched off. Between experiments, at least 30 sec was allowed before reinitiating current in order to allow for the relaxation of concentration gradients within the cell, should they exist. Measurements were made at the applied currents indicated in Table I.

Results and Discussion

A compilation of experiments performed is given in Table I, in which the geometries, materials, and currents are indicated. From the geometry of the cell, the applied current is related to the average cathodic current density by

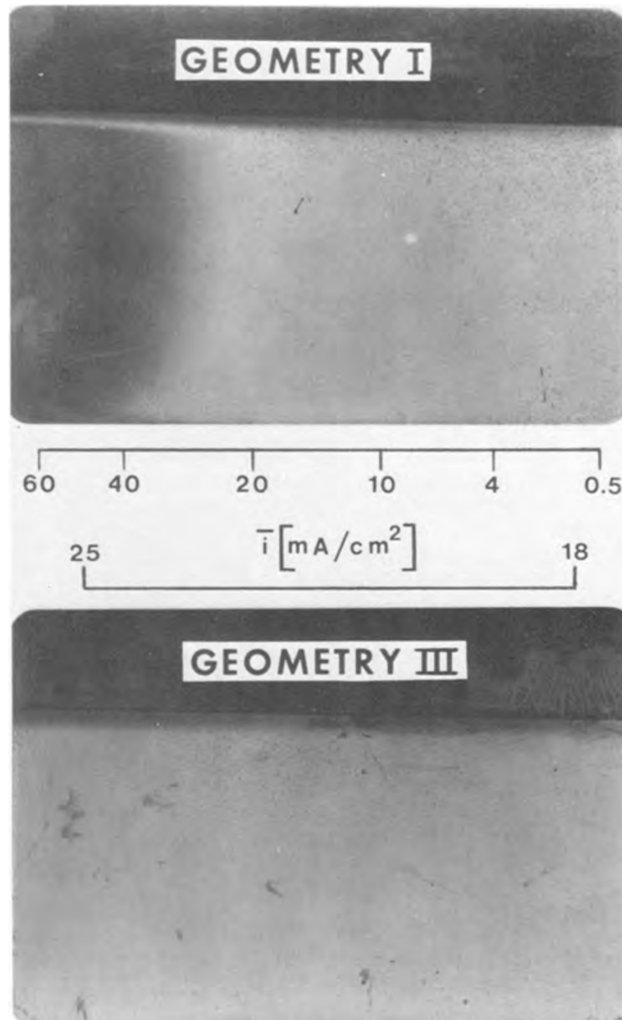

Fig. 4. Visual appearance of Hull cell copper deposit at I = 1000 mA without (geometry I) and with (geometry III) bipolar auxiliary electrodes.

$$\bar{i}_{cath}(mA/cm^2) = 0.0200 I (mA)$$

for the solid cathodes and for the segmented cathodes by

$$\bar{i}_{cath}(mA/cm^2) = 0.0465 I (mA)$$

Conventional Hull cell cathodes.—The effect of the auxiliary electrodes was investigated by observing the visual characteristics of the plated copper for several of the geometries of Fig. 1 by plating on conventional brass Hull cell cathodes. From the experiments listed in Table I it was found that current densities greater than 25 mA/cm² result in a brownish powdery deposit for geometry I; such deposits are characteristic of plating at or near the limiting current density.

Figure 4 shows the difference in visual appearance of the deposit for plating at 1000 mA with two different

Table I. Summary of experimental cathodes

Geometry \ Auxiliary electrodes	Cu screen	Cu/Pt-Ti mesh	Pt-Ti mesh	Ti screen	Applied current, I (mA)
		Solid brass cathodes			
I					500, 1000, 1500
III	X	X	X	X	500, 1000, 1500
IV	X		X		500, 1000, 1500
		Segmented cathodes			
I					100, 200, 300, 400, 500, 2100
II	X	X		X	100, 200, 300, 400, 500
III	X				100, 200, 300, 400, 500
IV	X				100, 200, 300, 400, 500

geometries. A sample plated using geometry I is shown in Fig. 4(a) with the standard Hull cell current density scale to indicate the current density gradient present. Figure 4(b) shows a sample plated using geometry III with copper screens; the current density scale shown for geometry III is estimated from the segmented cathode data (see Fig. 11). As can be seen, for geometry III, the plating is quite uniform; the auxiliary electrodes average out the current densities and all plating takes place at the average current density which for the applied current of 1000 mA is below the limiting current density.

Table II lists the test results for the various electrode material/geometry combinations. From the materials tested it is clear that only auxiliary electrodes that have copper surfaces, and thus facilitate bipolar anodic and cathodic electrochemical processes to take place at the auxiliary electrodes, will be useful in leveling the current distribution. The placement of auxiliary electrodes made of platinized titanium or titanium had no discernible effect on producing more uniform plating.

Segmented cathodes.—Segmented cathode experiments were carried out to place the qualitative results found with the conventional Hull cell cathodes on a quantitative basis. The current flowing between the auxiliary electrodes was measured and is shown in Table III. It is seen that the current flowing between the auxiliary electrodes depends on the applied current, the material of the electrodes, and the geometric positions of the electrodes within the cell. The significance of these variations is discussed below.

The following paragraphs discuss results of experiments on four different geometric configurations shown in Fig. 1.

Geometry I: no auxiliary aids.—Figure 5 provides current distribution data measured at five different applied currents in the absence of aids. Recall that the width of segment 10 is 5/9 of the width of the other segments; none of the data have been adjusted to compensate for this difference in area. The dashed line corresponds to the theoretical primary current distribution (for a total applied current, $I = 350$ mA) which would be observed if electrolyte conduction processes alone controlled the current distribution. It is seen that the measured current distributions are more uniform than the primary distribution, indicating a small resistive contribution from perhaps charge transfer or mass transfer processes. However, the most important resistance is the ohmic resistance of the electrolytic solution. All measured distributions are highly nonuniform, indicating that deposition under these geometric conditions represents a stringent configuration for testing the effectiveness of auxiliary aids for leveling the distribution.

Previously unpublished measurements in an identical Hull cell by Baker (8), presented in Fig. 6, show simi-

Table II. Leveling effect of electrode material/geometry combinations using solid brass cathodes

Geometry \ Auxiliary electrodes	Cu screen	Cu/Pt-Ti mesh	Pt-Ti mesh	Ti screen
I		None		
III	Leveled	Levelled	None	None
IV	Leveled		None	

Table III. Current flowing between auxiliary electrodes (in mA)

Geometry (electrode material)	Applied current, I (mA)				
	100	200	300	400	500
II (Cu)	30	112	205	286	372
II (Cu/Pt-Ti)	67	140	215	288	366
II (Ti)	0.0	0.0	0.3	0.5	0.5
III (Cu)	35	76	121	165	200
IV (Cu)	2.2	19	46	79	108

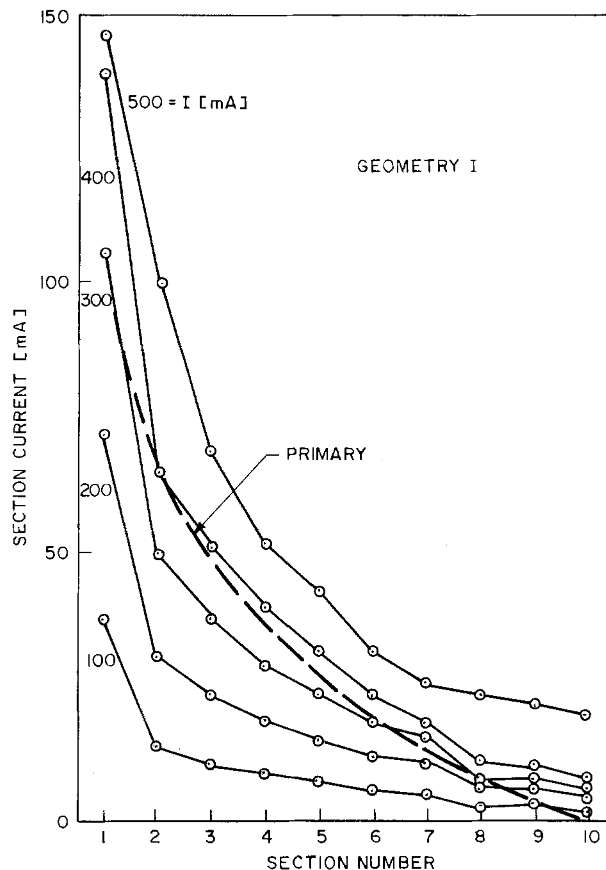

Fig. 5. Hull cell current distributions without leveling aids. The theoretical primary current distribution for $I = 350$ mA is superimposed.

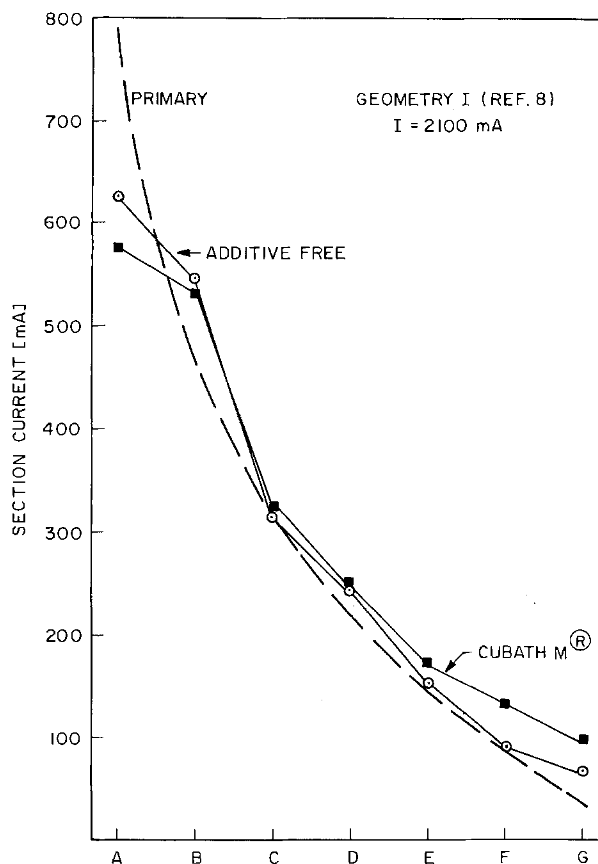

Fig. 6. Hull cell current distribution without leveling aids for electrolyte with and without brightening additives.

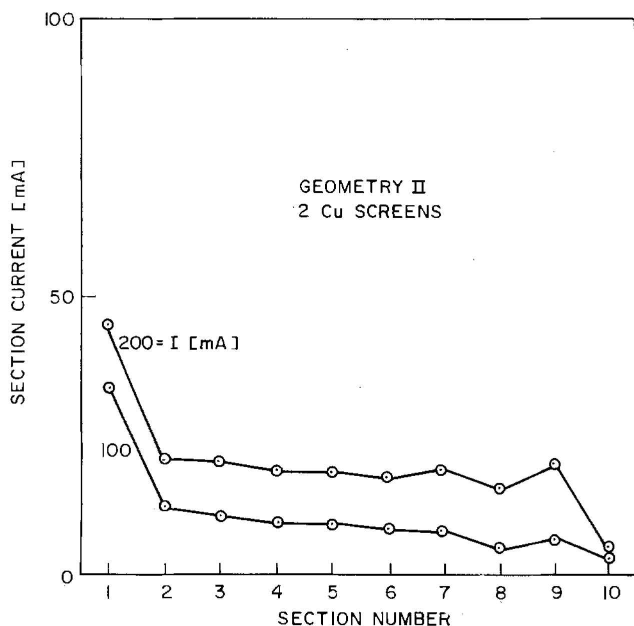

Fig. 7. Current distributions in Hull cell with copper screen auxiliary electrodes arranged in geometry II.

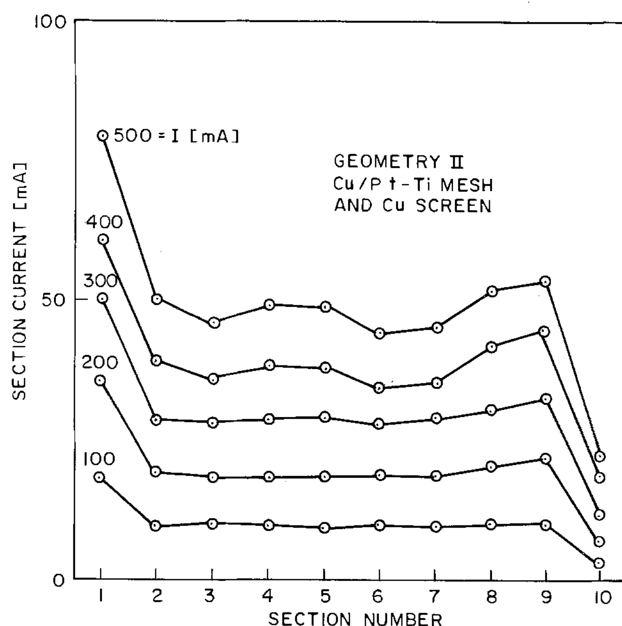

Fig. 9. Current distributions in Hull cell with copper-plated platinized titanium mesh and copper screen auxiliary electrodes arranged in geometry II.

lar distributions. Baker's experiments were conducted with a 2100 mA total cell current, a solution depth of approximately 5 cm, and a cathode divided into seven equal segments. Note the negligible effect of additives on the current distribution.

Geometry II: two screens, each parallel to the adjacent electrodes.—Figure 7 shows experimental current distribution data for two auxiliary copper screens. The magnitude of current flowing between auxiliary screens is given in Table III. It is seen from these data that the function of the two screens is to remove the current from the anolyte region and redistribute it in the catholyte region. If 100% of the applied current were to pass between the auxiliary electrodes, then the electrical path would be equivalent to the two-compartment cell depicted in Fig. 8; if the distance denoted d is small, then the primary current distribution at the cathode would be highly uniform.

Figure 9 gives current distribution data for the Cu/Pt-Ti mesh near the cathode and the Cu screen near the anode. It is seen that the electrochemical properties of the copper-plated titanium mesh are such that virtually the same current distribution is obtained as with the copper screen.

Figure 10 gives current distribution data for a Ti screen near the cathode and a Cu screen near the anode. No leveling is obtained and the current distributions are essentially identical to those measured in the absence of auxiliary aids (Fig. 5). Further, it is seen from Table III that no electrical current is induced to flow between the Ti and Cu screens. The reason that the screens do not support reaction is that there is no anodic electrochemical reaction possible, under these conditions, at the Ti screen so that current is thereby blocked from flowing through it. All of the current is

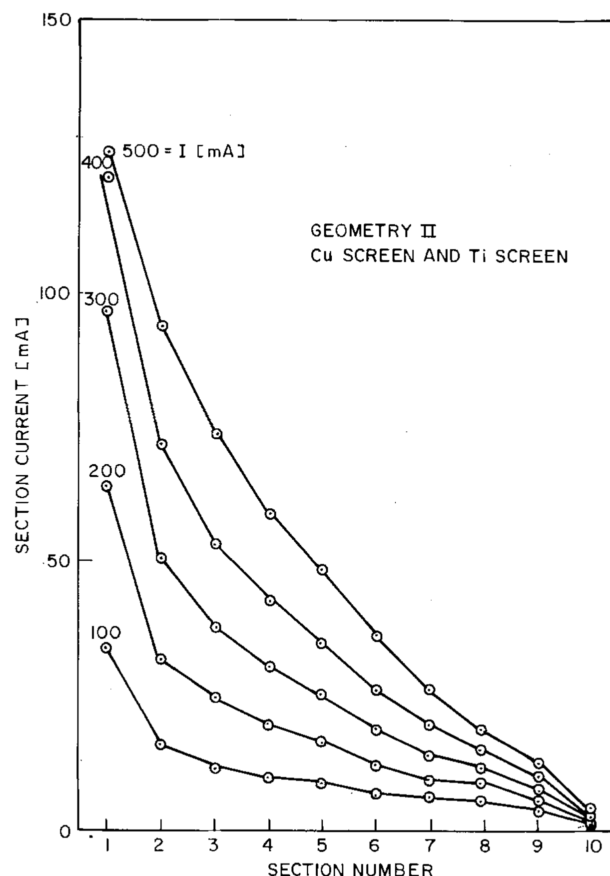

Fig. 10. Current distributions in Hull cell with titanium screen and copper screen auxiliary electrodes arranged in geometry II.

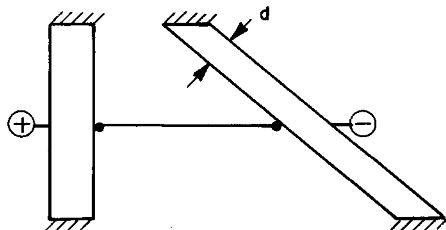

Fig. 8. Double cell geometry nominally equivalent to auxiliary electrode geometry II.

forced to remain in the electrolyte phase, as is the case in geometry I.

Geometry III: two screens, each parallel to the cathode.—Figure 11 gives current distribution data for two auxiliary copper screens. Generally speaking, the cathodic distributions are nearly identical to those provided in Fig. 7, where one screen was parallel to the anode. These observations indicate that the screen near the cathode is important in controlling the cathodic

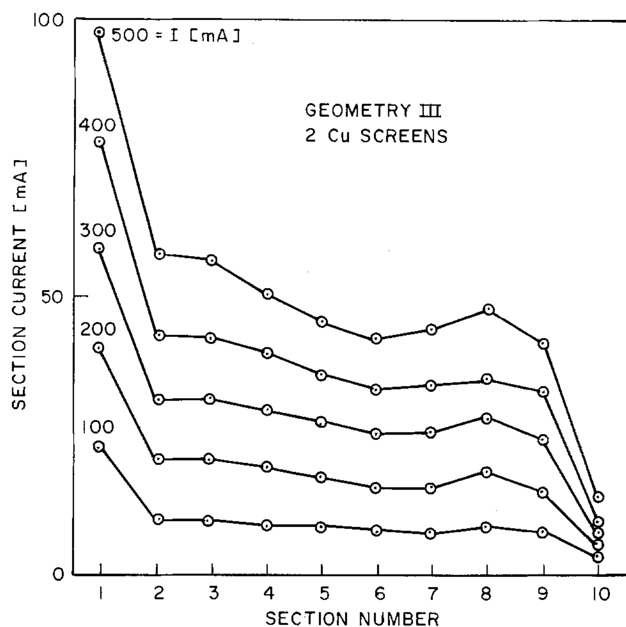

Fig. 11. Current distributions in Hull cell with copper auxiliary electrodes arranged in geometry III.

current distribution. The screen near the anode must merely be positioned sufficiently far from the other screen that an appreciable fraction of the applied current flows between the two screens (see Appendix). Otherwise, redistribution of current will not occur.

Geometry IV: two screens parallel to and equidistant from the cathode.—Current distribution data for the geometry of Fig. 1(d) are given in Fig. 12. It should be recognized that geometry IV corresponds to the conducting shield device reported by Rousselot (6). Figure 12 shows that the conducting shield geometry improves the current distribution with respect to the nonaided case (Fig. 5), but that the improvement is not as good as with either geometry II or III. The screen used in geometry IV was segmented into two adjacent sections, and the current flowing between sections is indicated in Table III.

Comparison of segmented cathode results.—The results of the current distribution measurements for geometries I through IV can best be compared by a cross plot of the data. Such a plot is shown in Fig. 13 for two currents: $I = 100$ mA and $I = 500$ mA. For this plot, the measured I for section 10 has been multiplied by 1.8 so that all I's are for the same surface area.

The results quantitatively substantiate the findings from the conventional Hull cell experiments. A single auxiliary electrode (geometry IV) offers some improvement in the distribution from geometry I. However, the improvement in uniformity with two auxiliary electrodes (geometries II and III) is seen to be substantial.

The foregoing data clarify events which occur when auxiliary metal electrodes are placed in electrolysis cells. When electrical current passes through the electrolyte, a potential field arises owing to the ohmic resistance of the electrolyte. If auxiliary electrodes are placed such that they cut across equipotential surfaces in the electrolyte, the possibility of induced cocurrent electronic conduction arises. In order that cocurrent conduction can occur in the auxiliary electrodes, both anodic and cathodic electrochemical reactions must occur on the auxiliary electrodes in a bipolar mode to provide a source and sink for electrons.

Conclusions

1. The current distribution at the cathode of a Hull cell can be made substantially more uniform by placing suitably reactive metal electrodes between the anode and the cathode.

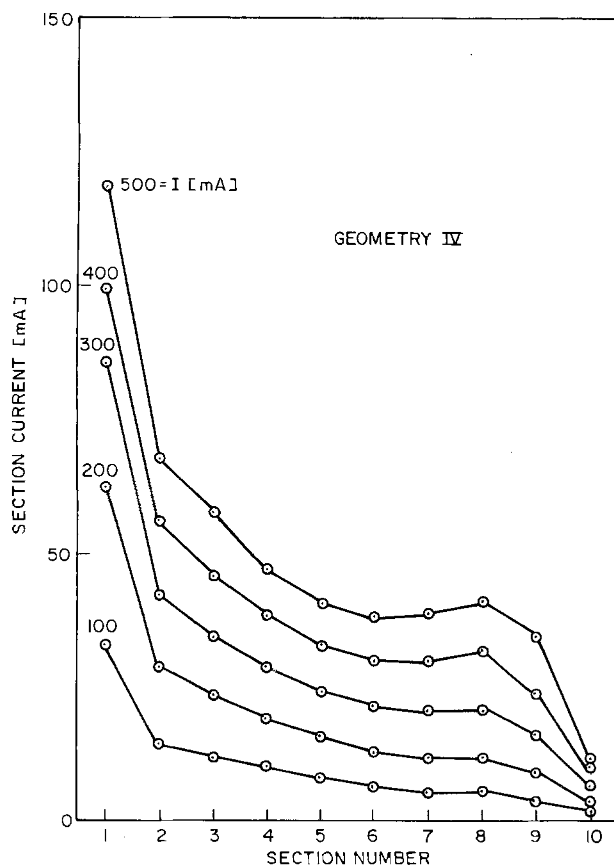

Fig. 12. Current distributions in Hull cell with auxiliary electrodes arranged in geometry IV.

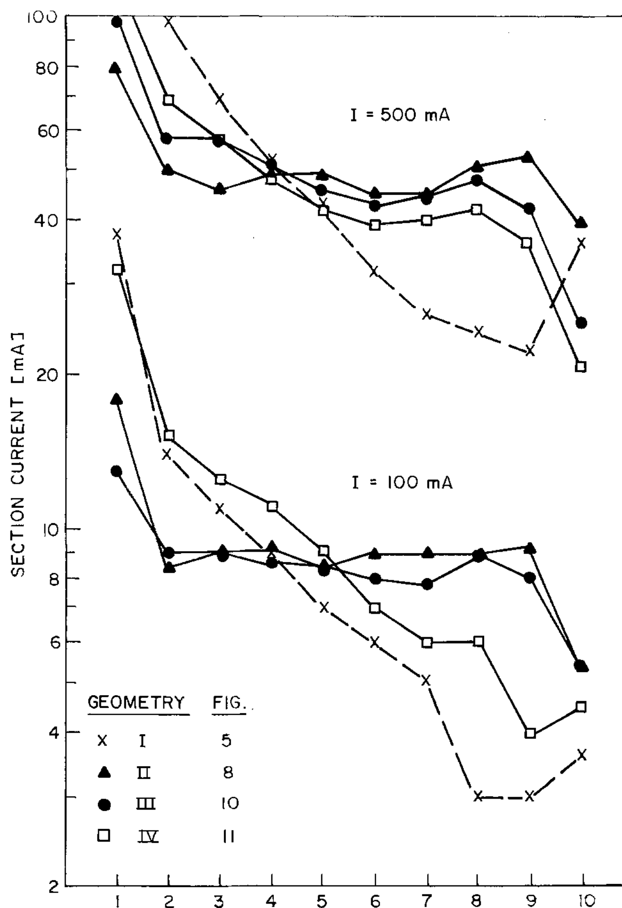

Fig. 13. Comparison of current distributions resulting from geometry I through IV ploting arrangements.

2. With appropriate choice of geometries, two electrically connected auxiliary electrodes can be made more effective in leveling the cathodic current distribution than a single screen placed near the cathode.
3. Material other than screen could be used such as mesh, wires, rods, metal brushes, porous metal sheets, etc.
4. Auxiliary electrodes must be of such material, *i.e.*, for copper plating the electrode surface has to be copper, and of sufficient surface area that both anodic and cathodic electrochemical processes occur in a bipolar mode within the potential difference resulting at the screens.
5. The potential difference induced between the screens is determined by the distance along the path of current flow (in the electrolytic phase) which separates the auxiliary electrodes.
6. For leveling to occur, the current flowing between the two auxiliary electrodes must be an appreciable fraction of the total applied current.
7. A Hull cell is a convenient test configuration to assess the effectiveness of current leveling aids and with a sectioned cathode for direct measurement of the current distribution.

Acknowledgment

The authors are grateful to R. T. Baker for the use of previously unpublished data; and to G. T. Gass and A. J. Long for the experimental measurements.

Manuscript submitted June 27, 1977; revised manuscript received Sept. 20, 1977. This was Paper 279 presented at the Atlanta, Georgia, Meeting of the Society, Oct. 9-14, 1977.

Any discussion of this paper will appear in a Discussion Section to be published in December 1978 JOURNAL. All discussions for the December 1978 Discussion Section should be submitted by Aug. 1, 1978.

Publication costs of this article were assisted by Bell Laboratories.

APPENDIX

To produce the desired leveling effect for the cathodic current distribution, it is necessary for an appreciable fraction of the applied current to flow between the two auxiliary electrodes. To obtain this bipolar operation, it is necessary for the following criteria to be met

$$R_\Omega << R_{CT} << R_{\Omega S} \quad [A-1]$$

These criteria establish dimensional requirements for the auxiliary electrode system.

The charge transfer resistance (3)

$$R_{CT} = \frac{R_g T}{\alpha_c \mathbf{F} \bar{i} A} \quad [A-2]$$

the ohmic solution resistance

$$R_{\Omega S} = \frac{L}{\kappa A_s} \quad [A-3]$$

using the most conservative model, and the ohmic electrode resistance

$$R_\Omega = \frac{\bar{t}}{\sigma A_\phi} \quad [A-4]$$

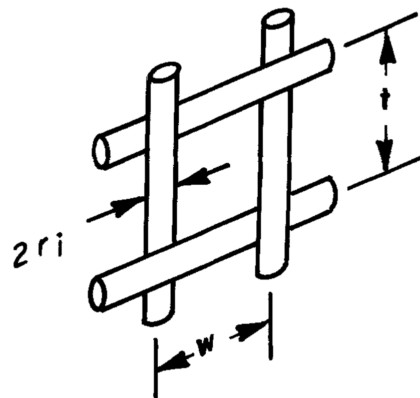

Fig. 14. Geometry of screen used for auxiliary electrodes

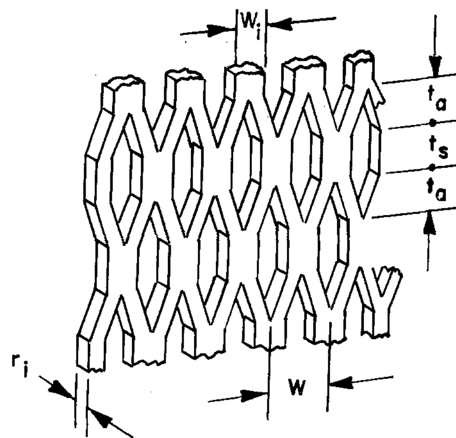

Fig. 15. Geometry of mesh used for auxiliary electrodes

Using the screen geometry indicated in Fig. 14, the criteria of Eq. [A-1] become the following dimensional criteria

$$r_i >> \frac{2\bar{t}^2}{\sigma}\left(1 + \frac{w}{t}\right)\frac{\alpha_c \mathbf{F}}{R_g T}\bar{i} \quad [A-5]$$

and

$$L >> \frac{1}{2\pi r_i\left(\frac{1}{w} + \frac{1}{t}\right)}\frac{R_g T}{\alpha_c \mathbf{F}}\frac{\kappa}{\bar{i}} \quad [A-6]$$

Similarly, from the geometry of the expanded mesh shown in Fig. 15 follows

$$r_i >> \frac{2\bar{t}^2}{\sigma}\left[1 + \frac{r_i}{w_i}\frac{2t_a + t_s}{t_a + t_s}\right]\frac{\alpha_c \mathbf{F}}{R_g T}\bar{i} \quad [A-7]$$

and

$$L >> \frac{w}{2w_i\left[1 + \frac{r_i}{w_i}\frac{2t_a + t_s}{t_a + t_s}\right]}\frac{R_g T}{\alpha_c \mathbf{F}}\frac{\kappa}{\bar{i}} \quad [A-8]$$

Using Eq. [A-5]-[A-8], Table IV gives the dimensional criteria for the three auxiliary dual electrode geometries used in the experiments.

Table IV. Dimensional criteria status for Hull cell experiments

Auxiliary electrode	Criteria: $r_i >>$ (μm)	Criteria: $L >>$ (cm)	Actual: r_i (μm)	Actual: L (cm)	Criteria status
Copper screen	0.8	0.42	108		o.k.
				L (II) = 3.0	o.k.
				L (III) = 1.3	o.k.
				L (III) = 0.6	?
Titanium screen	1.6	1.08	140		o.k.
				L (II) = 3.0	o.k.
				L (III) = 1.3	?
Titanium expanded mesh	3.3	0.24	7870		o.k.
				L (II) = 3.0	o.k.
				L (III) = 1.3	o.k.

LIST OF SYMBOLS

- A active surface area of the auxiliary electrodes, cm^2
- A_s $\overline{w} \cdot \overline{t}$, projected area between auxiliary electrodes, cm^2
- A_ϕ horizontal cross-sectional area of auxiliary electrodes, cm^2
- d distance between electrodes in double cell (Fig. 8)
- $\mathbf{F}$ Faraday's constant, 96,494 C/g-equiv.
- I total applied cell current, mA
- $\overline{i}$ average plating current density, mA/cm^2
- L distance between auxiliary electrodes, cm
- r_i screen wire diameter (Fig. 14) or expanded mesh thickness (Fig. 15), cm
- R_{CT} charge transfer resistance from the solution to the auxiliary electrodes, Ω
- R_g gas constant, 8.21 J/gmole-°K
- R_Ω ohmic resistance in the auxiliary electrodes, Ω
- $R_{\Omega s}$ ohmic resistance of the solution between the auxiliary electrodes, Ω
- T temperature, °K
- t vertical screen dimension (Fig. 14), cm
- $\overline{t}$ immersion depth of auxiliary electrodes, cm
- t_a vertical expanded mesh dimension (Fig. 15), cm
- t_s vertical expanded mesh dimension (Fig. 15), cm
- w horizontal screen (Fig. 14) or expanded mesh (Fig. 15) dimension, cm
- $\overline{w}$ width of auxiliary electrodes, cm
- w_l horizontal expanded mesh dimension (Fig. 15), cm
- α_c cathodic transfer coefficient, 0.5 dimensionless
- κ electrolyte conductivity, 0.55 Ω^{-1} cm^{-1}
- σ electrode conductivity, 0.58 $\times$ 10^{-6} Ω^{-1} cm^{-1} for copper, 0.31 $\times$ 10^{-6} Ω^{-1} cm^{-1} for titanium

REFERENCES

1. W. Engelmaier and T. Kessler, *This Journal*, **125**, 36 (1978).
2. T. Kessler and R. Alkire, *ibid.*, **123**, 990 (1976).
3. T. Kessler and R. Alkire, *Plating*, **63**, 22 (1976).
4. W. Engelmaier, T. J. Kessler, and A. J. Colucci, Paper 150 presented at the Electrochemical Society Meeting, Dallas, Texas, Oct. 5-9, 1975.
5. D. A. Rudy, Paper 264 presented at the Electrochemical Society Meeting, Washington, D.C., May 2-7, 1976.
6. R. H. Rousselot, *Metal Finishing*, **57**, (1961).
7. H. L. Pinkerton, "Electroplating Engineering Handbook," 3rd ed. K. A. Graham, Editor, chap. 16, Van Nostrand Reinhold Co., New York (1971).
8. R. T. Baker, Unpublished work (1974).

Electrochemical Studies of β-Carotene, all-*trans*-Retinal and all-*trans*-Retinol in Tetrahydrofuran

Su-Moon Park*

Department of Chemistry, The University of New Mexico, Albuquerque, New Mexico 87131

ABSTRACT

Detailed electrode mechanisms involved in oxidations and reductions of all-*trans*-β-carotene, all-*trans*-retinal, and all-*trans*-retinol have been investigated employing cyclic voltammetry, chronoamperometry, chronopotentiometry, and controlled potential coulometry at the platinum electrode in rigorously dried tetrahydrofuran (THF) solutions with *tetra*-n-butylammonium perchlorate (TBAP) as a supporting electrolyte, and the results are described. Pseudo first-order decay rate constants of intermediate species of β-carotene and retinal reductions are obtained and reported. β-Carotene was oxidized to β-apo-12-carotenal in the presence of water and was reduced mainly to 15,15′-dihydro-β-carotene in dry THF. Retinal was reduced at various double bonds, resulting in many products including retinol, both in dry and wet THF.

Carotenoid compounds, especially β-carotene, play a very important role in plants for the transfer of the energy absorbed from solar radiation to chlorophyls for the photosynthetic processes. β-Carotene is also important as a source of vitamin A, since it is absorbed in the animal systems and undergoes an oxidative cleavage at the 15,15′-double bond in the liver to all-*trans*-retinal, which eventually is reduced to vitamin A alcohol (1). There has been a large amount of effort (2-6) to elucidate the reaction mechanisms involved in this sequence of reactions and to reproduce this reaction *in vitro*. Chemical oxidation of β-carotene, however, did not generally show the same specificity as in the *in vivo* reaction. Since this sequence of the reaction is a redox one, we thought it would be very interesting to carry out an electrochemical investigation on this system and compare the result with those occurring *in vivo* systems and those obtained by the oxidation of β-carotene with chemical oxidants.

Electrochemistry of β-carotene and retinal was first reported by Takahashi *et al.* (7, 8), in which reduction potentials, the number of electrons transferred, and diffusion coefficients were measured with polarographic methods in the benzene-acetonitrile mixed solvent. Some of these results were shown to be erroneous later by Mairanovsky *et al.* (9) from their more refined studies. There have also been reports on controlled electrolysis of carotenoid compounds (10, 11).

In our present report, we have carried out a detailed study on electrode mechanisms of β-carotene, retinal, and retinol employing chronoamperometry, chronopotentiometry, cyclic voltammetry, and controlled potential coulometry in rigorously dried tetrahydrofuran solutions, and the results obtained are presented.

Experimental

Mallinckrodt A. R. tetrahydrofuran (THF) was dried over sodium metal under the vacuum for at least half a week and was distilled directly into the electrochemical cell *in vacuo* by the vapor transfer method without being exposed to the air to make up the solution. Eastman Organic's (E.O.) polarographic grade *tetra*-n-butylammonium perchlorate (TBAP) was dried at approximately 100°C under vacuum for at least

* Electrochemical Society Active Member.

Key words: β-carotene, all-*trans*-retinal, all-*trans*-retinol (vitamin A).

Table I. Electrode potentials*,†

Substances	Reduction (V)	Oxidation, (V)
β-Carotene	−1.63 (1.0), −1.78, −2.46, −2.70	0.74 (2.0), 1.01
Retinal	−1.42 (1.0), −1.89	1.20 (4.0)
Retinol	−2.19 (1.0)	0.95 (1.0)

° Cyclic voltammetric peak potentials *vs.* the aqueous saturated calomel electrode (SCE) in THF at the platinum disk electrode ($A \simeq 0.017$ cm²) with TBAP as a supporting electrolyte. The scan rate was 100 mV/sec in all measurements.
† Numbers in parentheses are n_{app} determined voltammetrically using 9,10-diphenylanthracene as a reference compound under the same experimental conditions.

24 hr and was used as a supporting electrolyte throughout the study. β-Carotene (E.O.) was recrystallized from diethyl ether three times and stored in the freezer. All-*trans*-retinal (E.O.) and all-*trans*-retinol (E.O.) were used without further purification but were stored in the freezer.

Solutions were prepared by distilling the solvent (THF) into the cell directly under vacuum, which contained the preweighed sample and the supporting electrolyte (TBAP) corresponding to 0.1*M* solution. This solution was degassed by 3∼5 freeze-pump-thaw cycles by pumping down to a vacuum of 10^{-6} Torr.

A three-electrode cell, where the platinum disk (area ≅ 0.017 cm²) and a platinum wire were used as working and auxiliary electrodes, respectively, was used for the voltammetric and potentiostatic measurements. For most of the electrochemical measurements, a shielded silver wire pseudo-reference electrode was used, while an SCE electrode was used as a reference for the measurements of the electrode potentials reported in Table I. In coulometry experiments, a three compartment cell described by Childs *et al.* (12) with a large platinum gauze electrode was used. All experiments were carried out at room temperatures. In all cyclic voltammetric measurements, the *iR* drop was compensated by the positive feedback built in the potentiostat used.

A Princeton Applied Research (PAR) 173 (potentiostat-galvanostat) with a PAR 175 (Universal programmer) was used for chronoamperometric, chronopotentiometric, and cyclic voltammetric measurements. For coulometric experiments, a PAR 179 (digital coulometer) attached to the PAR 173 was used. A Cary-14 UV-VIS spectrophotometer was used for recording electronic absorption spectra of the electrolysis products.

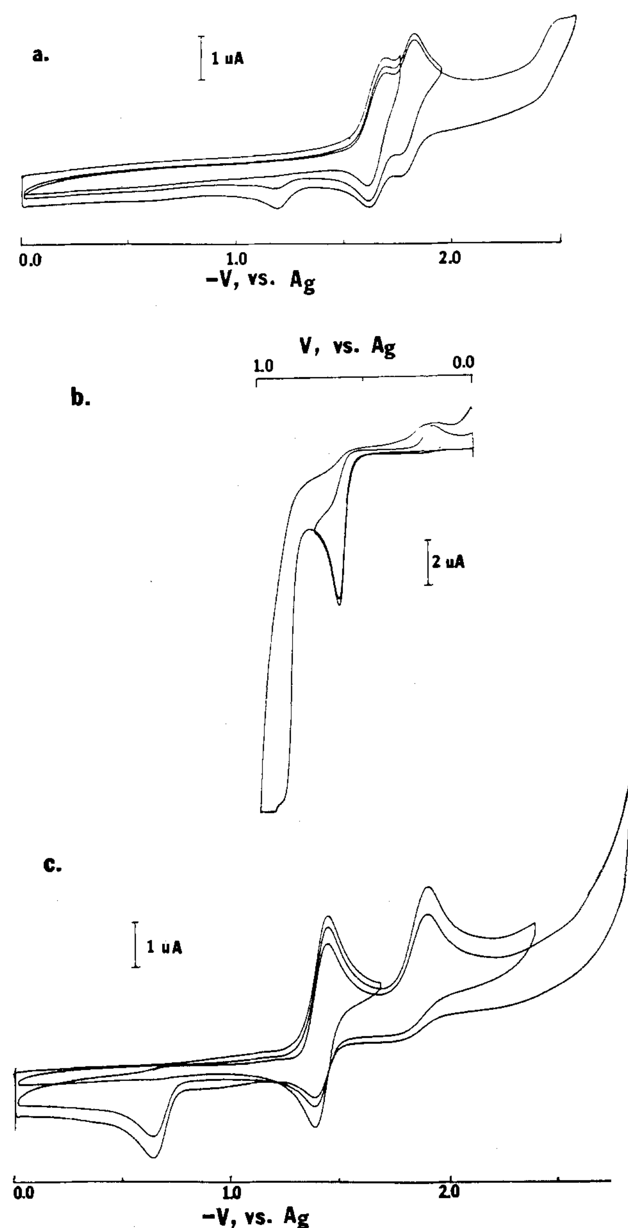

Fig. 1. (a) Cyclic voltammogram of β-carotene reduction at Pt disk electrode in THF solution with TBAP (0.1*M*) as a supporting electrolyte. The solution was 0.94 mV in β-carotene. (b) Cyclic voltammogram of β-carotene oxidation (1.0 m*M* in β-carotene). (c) Cyclic voltammogram of retinal reduction (1.1 m*M* is retinal). Scan rates were 100 mM/sec in all cases.

Results and Discussion

Electrode potentials of these compounds, cyclic voltammetric data of β-carotene and retinal reductions, and coulometric data are summarized in Tables I-IV. Part of the cyclic voltammetric results are reproduced in Fig. 1(a)-(c). Electrode potentials listed in Table I are in good agreement with the literature values (8, 9) within experimental error. More detailed observations and discussion follow.

Cyclic voltammetric results.—Cyclic voltammograms (CV) of selected redox systems are shown in Fig. 1. As is evident from Fig. 1(a) and (c), reductions of β-carotene and retinal are reversible, one-electron transfer processes, while oxidations of β-carotene and retinal (not shown) are irreversible. Oxidation and reduction of retinol, however, were totally irreversible, and the redox potentials were further beyond those of β-carotene and retinal (Table I). In the cases of β-carotene and retinal reductions, the electrogenerated species (radical anions) decay to some other product slowly, as can be seen from Tables II and III (i_{pa}/i_{pc}) and from CV's in Fig. 1. The number of electrons transferred, listed in Table I, was obtained by comparison of the current functions of these compounds with that of a known one, *i.e.*, 9,10-diphenylanthracene under the same experimental conditions, assuming that diffusion coefficients are not very different.

Table II. Cyclic voltammetric data for β-carotene in THF*

	Reduction**					Oxidation†
	First wave			Second wave		
Scan rate (V/sec)	i_{p_c}/$V^{1/2}C$	ΔE_{p_c},mv‡	i_{p_a}/i_{p_c}	i_{p_c}/$V^{1/2}C$	ΔE_{p_c},mv‡	i_{p_a}/$V^{1/2}C$
0.01	17.5	69	0.90	8.5	32	33.3
0.02	16.5	72	0.84	6.5	32	32.3
0.05	15.8	79	0.88	6.5	32	32.2
0.10	15.4	83	1.01	5.6	48	31.1
0.20	15.2	85	0.97	5.4	51	31.4
0.50	14.7	87	—	6.3	53	—
1.00	—	—	—	4.8	63	—

* Measured at the platinum disk electrode with the area of ∼0.017 cm². The solution was 1.04 m*M* in β-carotene with 0.1*M* TBAP present.
** In addition to these two reduction waves listed, there were 3rd and 4th reduction waves within the background.
† Second oxidation wave was observed and the height was approximately twice of the first wave.
‡ $\Delta E_{p_c} = E_{p_c} - E_{p_a}$ for the first or second cyclic voltammetric waves.

Table III. Cyclic voltammetric data for all-*trans*-retinal in THF*

Rate (V/sec)	Reduction† First wave $i_{p_c}/V^{1/2}C$	ΔE_{p_c}, mV	i_{p_a}/i_{p_c}	Second wave $i_{p_c}/V^{1/2}C$	Oxidation $i_{p_a}/V^{1/2}C$
0.01	13.0	65	0.87	8.1	—
0.02	12.3	67	0.93	8.0	—
0.05	11.7	70	0.99	8.1	—
0.10	11.4	71	1.01	8.1	48.2
0.20	11.2	73	0.99	8.2	—
0.50	11.0	72	1.00	8.2	—
1.00	11.5	135	1.02	8.8	—

* Measured at the platinum disk electrode ($A \sim 0.017$ cm²). The solution was 1.14 m*M* in all-*trans*-retinal with 0.1*M* TBAP present.
† In acetonitrile, the oxidation wave heights were almost the same as those of reduction waves, indicating 1e-transfer process.

Cyclic voltammetric data listed in Tables II and III indicate that reductions of β-carotene and retinal are characteristic of EC or ECE. It is not clear from these tables, however, whether the electrode reaction has the EC or ECE character.

Peak separations between the cathodic and anodic waves of β-carotene and retinal reductions are approximately 60 mV, consistent with the one-electron transfer process. Employing the diffusion coefficients reported by Takahashi *et al.* (8), the heterogeneous electron transfer rate constant (k_s) at the platinum electrode is estimated to be $(3.3 \pm 2.7) \times 10^{-3}$ and $(2.4 \pm 1.3) \times 10^{-2}$ cm/sec for β-carotene and retinal, respectively, from the formula given by Nicholson (13). The aldehyde group on retinal seems to affect the k_s value by approximately one order of magnitude, even though the length of the carbon chain is only a half of β-carotene.

It is apparent from the cyclic voltammogram shown in Fig. 1(b) and the CV data that the oxidation of β-carotene is a two-electron transfer process, followed by rapid chemical reaction. Retinal, however, undergoes four-electron, irreversible oxidation.

Retinol, as already pointed out, undergoes one-electron reduction and oxidation at the platinum electrode in THF. The electrode reaction product, however, rapidly blocks the electrode surface, making further measurements difficult. We therefore did not pursue a detailed study on this system.

Chronoamperometric results.—Chronoamperometric data on β-carotene and retinal reduction are shown in Fig. 2, where $i \cdot t^{1/2}$ is plotted for the different time durations. In both cases, the potential was controlled such that the current at the first reduction waves was monitored. For the reduction of β-carotene, the plot is characteristic of a reversible, diffusion-controlled reaction, with a possible slow following reaction. The plot shown for the retinal reduction is more characteristic of an ECE reaction, since $i \cdot t^{1/2}$ increases with time. This result, along with CV data, may establish an EC nature for the β-carotene reduction and an ECE nature for the retinal reduction, although it is not so clear-cut.

Chronopotentiometric results.—Since it is certain from CV and chronoamperometric data that the reduction of both β-carotene and retinal has either EC or ECE character, it would be interesting to see how fast the electrogenerated species, *i.e.*, the radical anion, decays to the products or other intermediate species. To determine this pseudo-first-order decay rate constant, reversal (or cyclic) chronopotentiometric experiments were performed and the results are presented in Fig. 3(a) and (b). Here kt_1, obtained from the table prepared according to Testa and Reinmuth (14) was plotted against t_1, where k is the pseudo first-order decay rate constant and t_1 is the current reversal time. For a reversible electron transfer reaction, in which

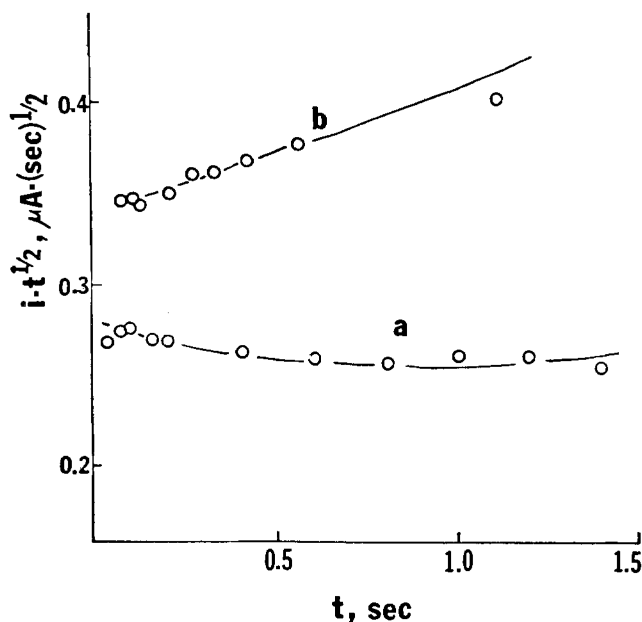

Fig. 2. Chronoamperometric data. Plot of $i \cdot t^{1/2}$ vs. t for the potential step at the first reduction potential for (a) β-carotene and (b) retinal.

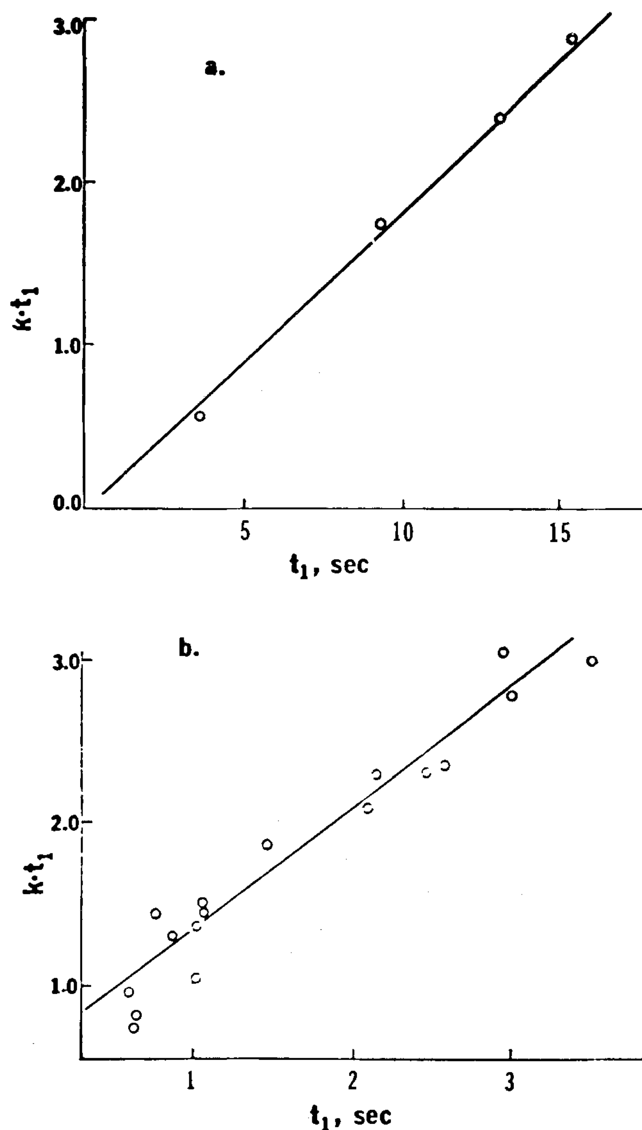

Fig. 3. Chronopotentiometric determination of pseudo-first-order decay rate constant. Plot of kt_1 vs. t_1 for (a) β-carotene and (b) retinal reduction.

the electrogenerated species is very stable (or k is practically 0), the ratio of τ_2/t_1, where τ_2 is the chronopotentiometric transition time after the current reversal, should be 1/3 irrespective of the reversal time (14, 15). When there is a kinetic complication, this ratio is a function of the reversal time, and from the ratio of τ_2/t_1, one can read kt_1 from the tabulated values or the working curve. If one plots kt_1 thus obtained against t_1, a straight line should result with the slope equal to the pseudo first-order decay rate constant. The slopes thus obtained from Fig. 3(a) and (b) are 0.21 and 0.74 sec^{-1} for radical anions of β-carotene and retinal, respectively. Mairanovsky *et al.* (9) reported that the rate constant of the anion radical of β-carotene was 0.21 and 0.76 sec^{-1} in a THF solution with 0.3% H_2O present.

A suggested route of the decay process could be the abstraction of and combination with the hydrogen ion, H^+, either from the solvent or a trace amount of water present in the solvent, *i.e.*

$$R^{\bar{\cdot}} + H^+ \rightarrow RH\cdot \qquad [I]$$

This reaction path is further rationalized by coulometric experiments. The fate of RH· thus produced is discussed in the next section.

Coulometric results.—The number of electrons transferred for reductions or oxidations of these compounds was determined from the CV data and shown in Table I. To further study the electrode mechanisms, coulometric measurements were made and the results are listed in Table IV. Apparently the coulometric results shown in Table IV are not in agreement with n_{app} obtained voltammetrically. This indicates that the reductions and oxidations of these compounds at the electrode are very complicated. The coulometric result obtained here can be explained by the reduction mechanism proposed by Mairanovsky *et al.* (9) as follows

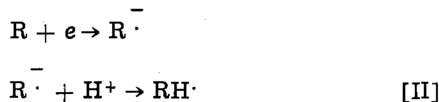

$$R + e \rightarrow R^{\bar{\cdot}}$$

$$R^{\bar{\cdot}} + H^+ \rightarrow RH\cdot \qquad [II]$$

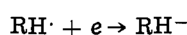

$$RH\cdot + e \rightarrow RH^-$$

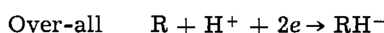

$$\text{Over-all} \quad R + H^+ + 2e \rightarrow RH^-$$

or

$$R + e \rightarrow R^{\bar{\cdot}}$$

$$R^{\bar{\cdot}} + H^+ \rightarrow RH\cdot \qquad [III]$$

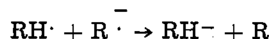

$$RH\cdot + R^{\bar{\cdot}} \rightarrow RH^- + R$$

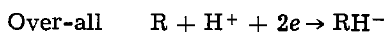

$$\text{Over-all} \quad R + H^+ + 2e \rightarrow RH^-$$

The coulometric result does not distinguish whether the reaction sequence [II] or [III] is really occurring in the reduction. The chronoamperometric results presented above seem to indicate that β-carotene reduction may have an EC character and retinal ECE. One may therefore conclude that β-carotene may follow route [III], while retinal follows route [II]. This is not clear, for even route [III], it is a catalytic process.

Table IV. Coulometric data, n_{app}*

	Reduction		Oxidation	
Substances	First wave	Second wave	w/o H_2O	w/H_2O‡
β-Carotene	2.2	2.7†	4.7†	10.1
Retinal	2.0†	2.7†	—	—

* See potentials listed in Table I.
† Average values of more than two measurements.
‡ Water was about 20% of the solution.

These two reactions are too close to be distinguished, although the above argument is reasonable.

These results indicate that an intermediate RH^- is produced regardless of whether one has $R^=$ or $R^{\bar{\cdot}}$ as a product of the reduction. Inspection of CV's in Fig. 1(a) and (c) suggests that the anodic wave observed at about $-1.2V$ ($\sim -0.65V$ for retinal) on potential reversal results only from the scan to the second reduction wave. Since the dianion ($R^=$) is formed on scanning to the second wave, we attribute this wave to the reaction

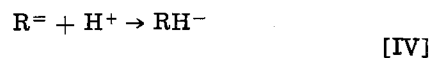

$$R^= + H^+ \rightarrow RH^- \qquad [IV]$$

$$R^- - e \rightarrow RH\cdot$$

after the second electron transfer

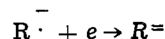

$$R^{\bar{\cdot}} + e \rightarrow R^=$$

at the second reduction wave. According to reaction path [II] or [III] above, one should have the same result, even if one generates $R^{\bar{\cdot}}$ at the first reduction potential. Indeed, this was found to be true for reductions of β-carotene and retinal, as is demonstrated in Fig. 4. When the potential is reversed after the first reduction wave, there is no discernable RH^- oxidation wave observed [(a) in Fig. 4]. If, however, one holds for a while at the first reduction potential before the reversal, the RH^- oxidation peak is observed. This peak height is also found to be a function of the electrolysis time [see (b) and (c) in Fig. 4]. This was true even when the scan was reversed at the peak potential of the first reduction wave. The same behavior was observed for the reduction of retinal, where the first and second waves are separated by about 400 mV. This result confirms that either reaction [II] or [III] is occurring at the electrode. This also indicates that the rate of combination with H^+ is faster for $R^=$ than for $R^{\bar{\cdot}}$. One can therefore readily see that, in the long-term electrolysis as in the coulometric experiment, the product is RH^-. This is clearly shown in Fig. 5, where CV's are recorded during the exhaustive electrolysis. As the electrolysis proceeds, the third and fourth reduction waves as well as the one attributable to RH^- oxidation at about $-1.2V$ increase at the expense of the first and the second reduction waves, even the potential is controlled so that only the first electron is transferred. The CV recorded after the electrolysis has been completed is shown in Fig. 5(b), where the anodic wave at $-1.2V$ as well as the third and fourth cathodic waves remained with improved shapes. We also found that the anodic wave appearing at $-1.2V$ decayed slowly as a function of time. The decay curve

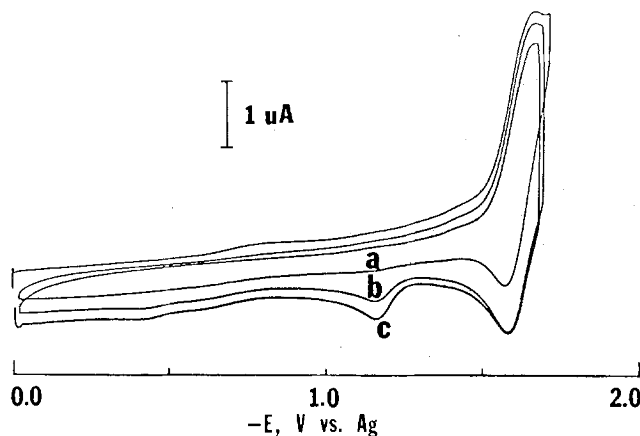

Fig. 4. Time dependence of RH^- generation. (a) Scan reversed without delay. (b) Scan reversed after 15 sec delay at the reversal potential. (c) Scan reversed after 30 sec delay. This was the reduction of β-carotene. Scan rates were 100 mV/sec.

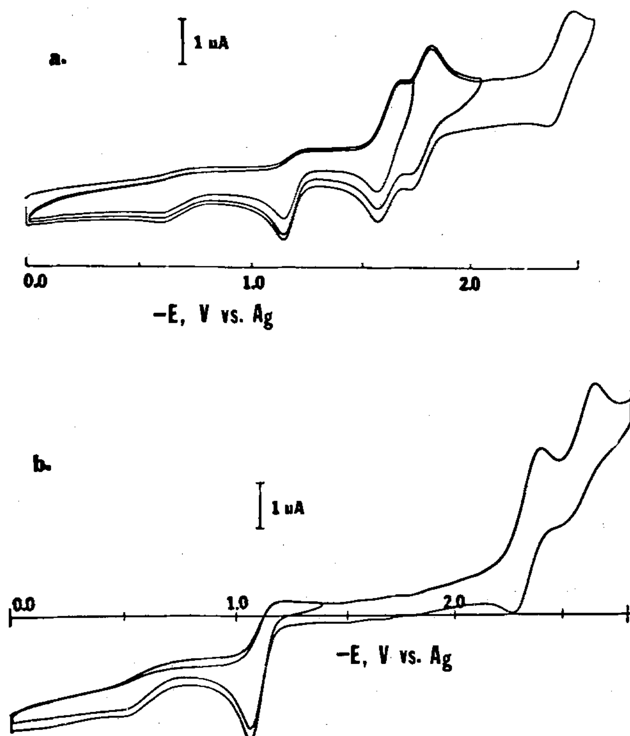

Fig. 5. (a) Voltammogram of β-carotene after about 40% exhaustive electrolysis at the first reduction potential with a scan rate of 100 mV/sec. (b) Cyclic voltammogram of β-carotene after complete electrolysis. Scan rate was 100 mV/sec.

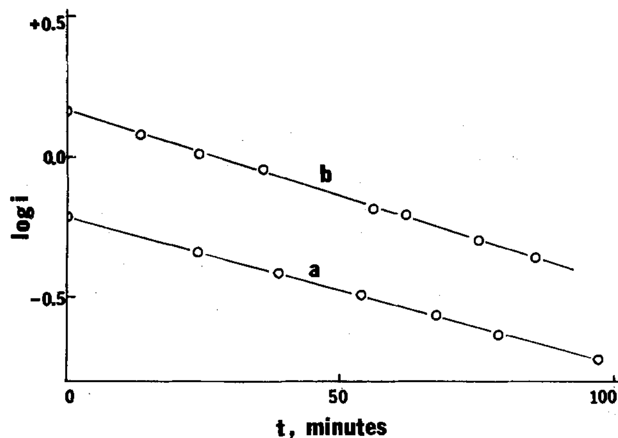

Fig. 6. Log i vs. t plot for the oxidation of RH^- (i in μA). Species RH^- derived from (a) β-carotene and (b) from retinal.

(log i vs. t plot) is shown in Fig. 6. The excellent linearity of this plot clearly demonstrates that the decay is a first-order process. The slope of these lines gives the pseudo first-order decay rate constants of 0.0052 min^{-1} for RH^- species derived from β-carotene and 0.0060 min^{-1} for retinal. Even after these RH^- peaks disappeared, the third and fourth waves remained. This leads us to conclude that these reduction waves, which resemble the first and the second waves of the parent compound, respectively, can be attributed to the reduction of the other carotenoid compound produced by the reduction of β-carotene, *i.e.*

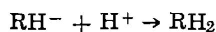

$$RH^- + H^+ \rightarrow RH_2$$

$$RH_2 + e \rightarrow \overset{-}{RH_2}\cdot \qquad [V]$$

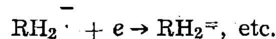

$$\overset{-}{RH_2}\cdot + e \rightarrow RH_2^{=}, \text{ etc.}$$

We also notice that the CV current corresponding to RH_2 reduction recorded after electrolysis at the first reduction potential is approximately 1.5 times higher than the reduction current observed for the parent molecule before electrolysis. The higher current of the product reduction wave can be explained by assuming that two identical molecules are produced by exhaustive electrolysis and reduced. This observation along with those to be described below may answer the question as to the identity of the reduced product. The most reasonable conclusion could be that the reduction occurred at 15,15′-positions, resulting in two isolated identical olefinic hydrocarbons, *i.e.*, two axerophtenes linked with an ethylene bridge among others. Theoretically, one should have exactly two times the current by having this 15,15′-dihydro-β-carotene, since one generates two identical molecules by reduction. The fact that we have only 1.5 times the current indicates that there should be another product(s). In order to confirm this, an absorption spectrum was recorded for the product in the THF solution. The λ_{max}'s were 336 and 399 nm with fine vibration structures at 321 nm (shoulder) and 356 nm, and 369 and 424 nm, respectively. According to an empirical formula devised by Hirayama (17) for the calculation of λ_{max} of this type of compounds

$$\lambda_{max}^2 = (37.56 - 39.68 \times 0.920^N) \times 10^4 \text{ nm}^2 (\text{in THF})$$

where N is a constant determined by the number of effective double bonds and the nature and number of substituents the prospective product, *i.e.*, two axerophtenes, should have the λ_{max} of 332 nm in THF. If, instead, some portion of β-carotene is reduced at either the 11,12- or the 11′,12′-position, the product has one more double bond than axerophtene, and is expected to have the λ_{max} of 393 nm. Both λ_{max}'s observed are in good agreement with those calculated and one may therefore conclude that the major reduction product is 15,15′-dihydro-β-carotene and the by-product may be 11,12-dihydro-β-carotene. Further, the reduction potential of this product is −2.46V *vs.* SCE (Table I) and the reduction potential of axerophtene (9) is reported to be −2.32V *vs.* SCE. There was always some current observed between the second and the third reduction peaks, although the wave was not well defined. This may be due to the reduction of 11,12-dihydro-product, since this compound is expected to reduce at lower potential than 15,15′-dihydro-product.

When the exhaustive electrolysis was carried out at the second reduction potential, where only $R^=$ is produced instead of $\overset{-}{R}\cdot$, the result was exactly the same. The number of faradays per mole of the parent molecule at the first reduction potential is also the same as the one obtained by the electrolysis at the second reduction potential within experimental error (Table IV). These results are justified by the electrode mechanisms already described.

In the case of retinal reduction, the result was the same except that the reduction current corresponding to the product was much lower. The reduction wave corresponding to that of the product appeared at approximately the same potential as those of retinol, but the yield was quite low, judging from the current observed after reduction. When the absorption spectrum was obtained from the electrolyzed product, there apparently was a component corresponding to the absorption of an alcohol (~ 325 nm retinol), but this was not the major band. The major absorption bands were at 245 and 292 nm. This indicates that the reduction occurred mostly at the double bond of the hydrocarbon rather than at the carbonyl group. From the same calculations as above, one can deduce that the most reduction occurred at 11,12- and 13,14-positions, whose calculated λ_{max} are 243 and 290 nm, respectively. The alcohol, apparently a by-prodcut of the reduction of retinal, could be simply retinol or a glycol, as already reported (10, 11). Addition of H_2O to the solution (~20%) did not change the reduction product dras-

tically. The same result was obtained by electrolysis at the second reduction potential.

In summary, the following electrode mechanisms are consistent with results presented

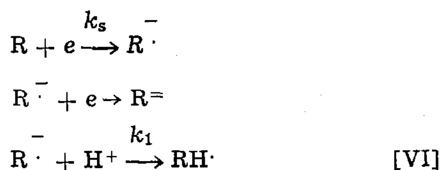

$$R + e \xrightarrow{k_s} \bar{R}\cdot$$

$$\bar{R}\cdot + e \rightarrow R^{=}$$

$$\bar{R}\cdot + H^+ \xrightarrow{k_1} RH\cdot \quad [VI]$$

$$RH\cdot + e \rightarrow RH^-$$

or

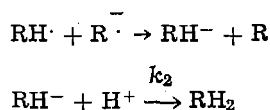

$$RH\cdot + \bar{R}\cdot \rightarrow RH^- + R$$

$$RH^- + H^+ \xrightarrow{k_2} RH_2$$

where k_1 is 0.21 and 0.74 sec^{-1} and k_2 is 5.2×10^{-3} and 6.0×10^{-3} min^{-1} for β-carotene and retinal, respectively.

Oxidation of β-carotene.—Since the oxidation of β-carotene is of a major interest in terms of the *in vivo* reaction, our study is limited to that of β-carotene only. No attempts were made to study oxidation processes of retinal and retinol in detail.

Two electrons were found to be involved in oxidation of β-carotene at the electrode by both our result and the one reported by Mairanovsky *et al.* These authors proposed an oxidation mechanism, where RH_2 is a parent molecule

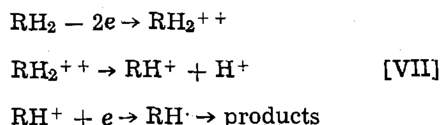

$$RH_2 - 2e \rightarrow RH_2^{++}$$

$$RH_2^{++} \rightarrow RH^+ + H^+ \quad [VII]$$

$$RH^+ + e \rightarrow RH\cdot \rightarrow \text{products}$$

i.e., β-carotene. The most probable product could be a dimer, and/or polymers, if the above mechanism describes the electro-oxidation, since the free radical would initiate dimerization. This reaction, however, was found to be more complex than the one postulated above. The controlled potential coulometry result shows that 4 or 5 electrons may actually be involved in the over-all oxidation reaction. With water present, approximately 10 electrons are involved as shown in Table IV.

Inspection of CV shown in Fig. 1(b) indicates that there are two reductions of either a product or an intermediate species at ~ 0.20 and ~ −0.10V on reversal scan. The reduction wave at about −0.10V is not apparent from the figure shown, but this was true in all of our observations. This voltammetric behavior is different from the one reported by Mairanovsky *et al.*, where they had only one reduction wave on reversal, which they attributed to H^+ reduction. We have carried out the exhaustive electrolysis and the CV's were recorded, while the electro-oxidation was being carried out (not shown). On electrolysis at the large platinum electrode, the two reduction waves behaved differently: The cathodic current at 0.20V was decreased as the concentration of β-carotene was depleted, while the one at −0.10V increased as the electrolysis proceeds. The increase in the cathodic current at −0.10V was much faster than the decrease in β-carotene concentration. This result indicates that the former must be a reduction of an intermediate, while the latter should be a product, *e.g.*, H^+. After the electrolysis was completed, the current at −0.10V was approximately twice the oxidation current or four times the reduction current of β-carotene before electrolysis. Assuming that this is the H^+ reduction, the amount of H^+ was determined coulometrically and the number of H^+ released was about 4.1 moles for each mole of β-carotene. After this was completely reduced coulometrically, no major reduction peaks appear within the background potential of THF. There were, however, low currents observed at potentials which might correspond to reduction of alcohols. Products, therefore, seem to be the cleaved hydrocarbons having fewer double bonds, and/or the alcohol derived from the carbonium ion with the trace of water.

Absorption spectrum of the electrolyzed solution without water shows that there are many products absorbing at wavelengths ranging 240 ~ 400 nm. Dimerization, therefore, is not a likely process and oxidative cleavages seem to be the main ones occurring instead. No attempts were made to analyze the products.

When water was added (~ 20%) and electrolyzed, there seemed to be a single product formed, or at least a large amount of a single compound with small or trace amounts of by-products. The CV recorded after exhaustive electrolysis at the first oxidation potential in the presence of water is shown in Fig. 7, and we notice that this resembles the reductions of both retinal and β-carotene. The fact that the reduction potential is lower suggests that this compound should be an aldehyde with longer chains than retinal. The absorption spectrum of this solution was obtained and λ_{max} was at 406 nm with two vibrational structures at 383 and 428 nm (408 nm in petroleum ether and 409 nm in ethyl alcohol). This product is identified to be β-apo-12′-carotenal by comparison with absorption spectra in the literature (2, 18, 19).

We do not have data to conclude the electrode mechanism of this process, but the over-all reaction is found to be

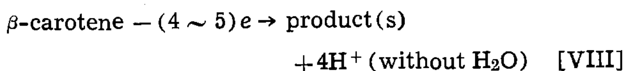

$$\beta\text{-carotene} - (4 \sim 5)e \rightarrow \text{product(s)} + 4H^+ \text{ (without } H_2O\text{)} \quad [VIII]$$

and

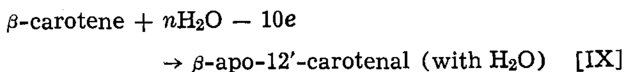

$$\beta\text{-carotene} + nH_2O - 10e \rightarrow \beta\text{-apo-12'-carotenal (with } H_2O\text{)} \quad [IX]$$

Since the one-step oxidative cleavage at 11,12-position to form the above product from reaction [IX] would require a four-electron process, we can conclude that reaction [IX] is a multistep process.

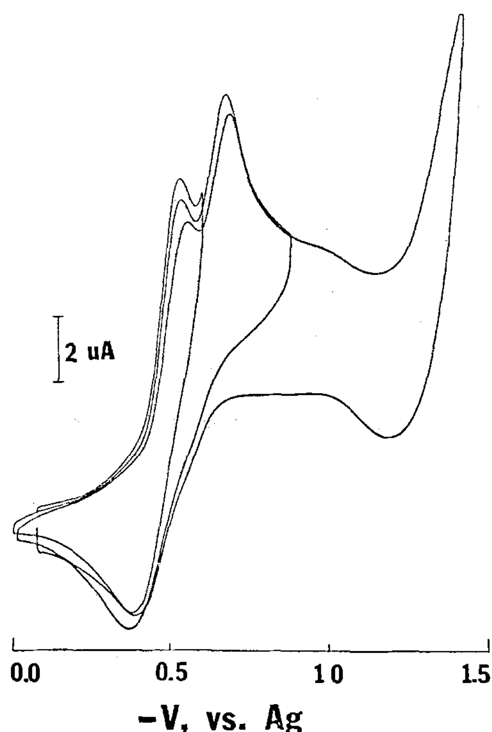

Fig. 7. Cyclic voltammogram after exhaustive oxidation of β-carotene in the presence of H_2O (~20%) with a scan rate of 100 mV/sec.

Conclusion

The results of both oxidation and reduction of selected carotenoids in THF solutions indicate that electrode reactions do not have the same specificities shown by *in vivo* reactions. The reaction specificities cannot be explained by the theoretical indexes, either. Quantum mechanical indexes calculated by Pullman (20, 21) with the LCAO method are reproduced in Fig. 8. All of these indexes indicate that the double bond at the 5,6- or terminal position has a higher reactivity than those inside; yet the result we obtained is not in agreement with theoretical predictions. As the Pullmans discuss (21), the terminal attack is more likely than the attack at the central double bonds. This might have been what has happened in the β-carotene oxidation as suggested by the number of electrons transferred for reaction [IX], as already pointed out. There have been some evidences that β-apo-12′-carotenal is an intermediate in rat metabolism (6) of β-carotene. We still cannot offer any explanation as to why the electrochemical reaction stops at the 12-position, while *in vivo* reaction stops at the 15-position to produce the retinal. There is also no reasonable explanation for the reduction of β-carotene at either the 15,15′- or 11,12-position. Since the LCAO method of Pullman (20, 21) failed to explain the reactivities, a more elaborate theoretical treatment may be desired.

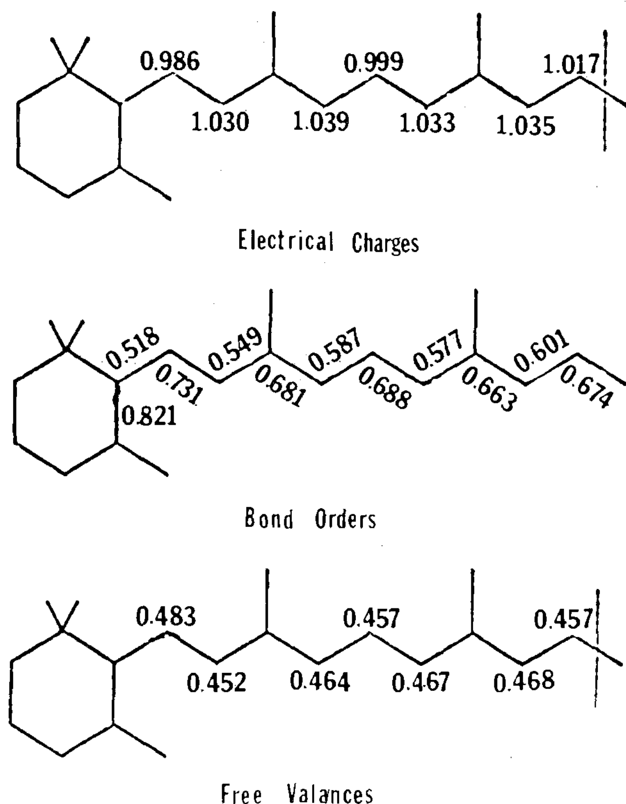

Fig. 8. Quantum mechanical index of β-carotene. Taken from Ref. (21).

Although we did not reproduce the *in vivo* reaction at the electrode surface, the electro-oxidation of β-carotene in the presence of water may find some synthetic applications, since β-apo-12-carotenal is known to be a good vitamin A precursor (22).

Acknowledgment

The author gratefully acknowledges the grants-in-aid from the Research Allocations Committee of the University of New Mexico for the purchase of PAR 179 digital coulometer.

Manuscript submitted July 19, 1977; revised manuscript received Sept. 21, 1977. This was Paper 257 presented at the Philadelphia, Pennsylvania, Meeting of the Society, May 8-13, 1977.

Any discussion of this paper will appear in a Discussion Section to be published in the December 1978 JOURNAL. All discussions for the December 1978 Discussion Section should be submitted by Aug. 1, 1978.

REFERENCES

1. See, for example, A. L. Lehninger, "Biochemistry," 2nd ed., pp. 352-355, Worth Publishers, Inc., New York (1970).
2. P. Karrer and U. Solmssen, *Helv. Chim. Acta*, **20**, 682 (1937).
3. P. Karrer, U. Solmssen, and W. Gugelmann, *ibid.*, **20**, 1020 (1937).
4. R. F. Hunter and N. E. Williams, *J. Chem. Soc.*, **1945**, 554.
5. N. L. Wendler, C. Rosenblum, and M. Tishler, *J. Am. Chem. Soc.*, **72**, 234 (1950).
6. J. Glover and E. R. Redfearn, *Biochem. J.*, **58**, XV (1954).
7. R. Takahashi, *Rev. Polarogr.*, **9**, 247 (1961).
8. R. Takahashi and I. Tachi, *Agr. Biol. Chem.*, **26**, 771, 777 (1962).
9. V. G. Mairanovsky, A. A. Engovator, N. T. Ioffe, and G. I. Samokhvalov, *J. Electroanal. Chem.*, **66**, 123 (1975).
10. R. E. Sioda, B. Terem, J. H. P. Utley, and B. C. L. Weedon, *J. Chem. Soc., Perkin Trans. 1*, 561 (1976).
11. E. A. H. Hall, G. P. Moss, J. H. P. Utley, and B. C. L. Weedon, *J. Chem. Soc., Chem. Commun.*, **1976**, 586.
12. W. V. Childs, J. T. Maloy, C. P. Keszthelyi, and A. J. Bard, *This Journal*, **118**, 874 (1971).
13. R. S. Nicholson, *Anal. Chem.*, **37**, 1351 (1965).
14. A. C. Testa and W. H. Reinmuth, *ibid.*, **32**, 1512 (1960).
15. H. B. Herman and A. J. Bard, *ibid.*, **36**, 510 (1964).
16. See, for example, S.-M. Park and A. J. Bard, *J. Electroanal. Chem.*, **77**, 137 (1977).
17. K. Hirayama, *J. Am. Chem. Soc.*, **77**, 373, 379, 382, and 383 (1955).
18. O. Isler, R. Rüegg, and U. Schwieter, *Pure Appl. Chem.*, **14**, 245 (1967).
19. W. Vetter, G. Englert, N. Rigassi, and U. Schieter, in "Carotenoids," O. Isler, Editor, pp. 189-266, Halstead Press, New York 1971.
20. A. Pullman, *Comp. Rend.*, **251**, 1430 (1960).
21. B. Pullman and A. Pullman, "Quantum Biochemistry," pp. 435-470, Interscience Publishers, New York (1963).
22. S. Fazakerley and J. Glover, *Biochem. J.*, **65**, 38P (1957).

The Theory of the Light-Induced Evolution of Hydrogen at Semiconductor Electrodes

J. O'M. Bockris* and K. Uosaki[1]

School of Physical Sciences, Flinders University of South Australia, Adelaide, Australia

ABSTRACT

The photoelectrode kinetics of the hydrogen evolution reaction is considered, using the WKB approximation for the penetration of the barrier at the semiconductor-solution interface. The absorption characteristics of photons in the electrode are introduced and the number of electrons produced at the surface is obtained as a function of the semiconductor statistics, and also diffusion and field effects. The model makes use of the conclusion that the photo-produced electrons have been deactivated to the bottom of the conduction band by the time they have diffused from the point of photon absorption to the surface. Image energy and the potential difference in the double layer at the semiconductor-solution interface are taken into account. The expression obtained for the photo hydrogen current density is tested in its ability to predict the photo-current-potential curves at the gallium phosphide cathode. Agreement with experiment is fair. Discrepancies are discussed.

Although photoeffects on electrochemical reactions at semiconductor-solution interfaces have been studied intensively (1-3), few theoretical analyses have been given (4-6). These all have the substantial defect that they consider the activation of electrons arising from interactions within the semiconductor and neglect an analysis of transfer through the electric double layer at the semiconductor-solution interface.

Photoeffects on electron transfer reactions at the metal/solution interfaces have been studied by Brodsky *et al.* (7). Bockris *et al.* (8) have treated photoeffects in hydrogen evolution reaction at metals, using the WKB approximation for electron tunneling through the double layer (9, 10).

In the present paper, we apply this approach to photoeffects in the hydrogen evolution reaction at p-type semiconductors, taking into account the activation and transport of photogenerated electrons to the electrode surface. The approach made is quasi-phenomenological and does not attempt a general solution, independent of any assumption as to a rate-determining step.

Assumptions

In the absence of evidence to the contrary (11, 12), it is assumed that charge-transfer is the rate-determining step for the semiconductors used

$$\text{p-SC}(e) + H_3O^+ \rightarrow \text{p-SC—H—}H_2O \qquad [1]$$

The cathodic current, i_c, is given by (8, 13)

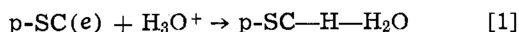

$$i_c = e_o \frac{C_A}{C_T} \int_o^\infty N(E) W(E) G(E) dE \qquad [2]$$

where e_o is the unit charge; $N(E)$ is the number of electrons arriving at the surface per unit area per unit time with energy, E; $W(E)$ is the WKB tunneling probability of electrons through the potential barrier at energy, E; $G(E)$ is the distribution function of the vibrational-rotational states of an acceptor, H_3O^+, at energy, E; C_A is the number of acceptors per unit area in the Outer Helmholtz Plane (OHP); C_T is the total number of sites per unit area in the OHP. Energy levels are counted as zero in value at the bottom of the conduction band.

In p-type electrodes, the absorption of photons activates electrons in the conduction band where they are available for cathodic reactions. (Contrast thermal electrochemical reactions at the semiconductor-solution interface, where p-type electrodes usually function as anodes).

The validity of the use of the WKB approximation was examined by Sen and Bockris (9), who compared the approach with that of the time-dependent perturbation theory, the results showing that the WKB approximation does not differ in order of magnitude from a time-dependent perturbation calculation for electron transfer (though there are significant discrepancies for proton transfer calculations).

Photon Absorption and Electron Excitation

The number of photons, the energy of which is $h\nu$, absorbed by the semiconductor between x and $x + dx$ from the surface, $N_{ph}(x)dx$, is given by

$$N_{ph}(x)dx = I_o(1 - R_\lambda)\alpha_\lambda e^{-\alpha_\lambda x}dx \qquad [3]$$

where I_o is the total number of photons of incident light of energy $h\nu$ per unit area per unit time ($cm^{-2} \cdot sec^{-1}$); R_λ and α_λ are, respectively, the reflectivity and the absorption coefficient of the semiconductor for the wavelength λ.

Each absorbed photon, the energy of which is greater than the energy gap of the semiconductor, makes an excited electron in the conduction band and a hole in the valence band. Therefore, the number of electrons excited between x and $x + dx$, $N_e(x)dx$, is equal to the number of photons absorbed between x and $x + dx$, $N_{ph}(x)dx$, and also to the number of holes produced in the valency band. From Eq. [3], $N_e(x)dx$ is given by

$$N_e(x)dx = N_h(x)dx = N_{ph}(x)dx \qquad [4]$$

Number of Electrons Arriving at the Electrode Surface

The electric field at the surface of a semiconductor is well known from the work of Kingston and Neustädter (14). It is possible to extend their result in finding an expression for the field at any point within the semiconductor.

* Electrochemical Society Active Member.
[1] Present address: Mitsubishi Petrochemical Company Limited, Ami, Ibaraki, Japan.
Key words: hydrogen, semiconductor, photoeffect, energy level.

One finds

$$\left(\frac{dV}{dx}\right)_x = \pm\sqrt{\frac{8\pi kT}{\epsilon}\left[-(N_D - N_A)y + p_0(e^{-y} - 1) + n_0(e^{y} - 1)\right]} \quad [5]$$

where

$$y = \frac{e_0(V_x - V_b)}{kT} \quad [6]$$

and the + sign is for $y < 0$.

The number of photoexcited electrons, originally expressed for $x = x$ in Eq. [3] and [4], decreases to $N_{e,x=x-dx}(x)dx$, after traveling dx. Then

$$N_{e,x=x-dx}(x)dx = N_e(x)e^{-\frac{1}{L(x)}dx}dx \quad [7]$$

where $L(x)$, the mean free path of electrons at x, is given by (15)

$$L(x) = \frac{2l_D^2}{\sqrt{l_E^2 + 4l_D^2} - l_E} \quad [8]$$

where l_D is the diffusion length and l_E is the drift length. The terms l_D and l_E are given by[2]

$$l_D = \sqrt{D\tau_e} = \sqrt{300\mu_e\tau_e kT/e_0} \quad [9]$$

$$l_E = \tau_e\mu_e V'(x) \quad [10]$$

respectively, where μ_e is the mobility of the electron $cm^2\ V^{-1}\ sec^{-1}$, τ_e is the lifetime of the electron, and $V'(x)$ is the potential gradient at $x(-(dV/dx)_x$ in $V\ cm^{-1})$.

Similarly

$$N_{e,x=x-2dx}(x)dx = N_{e,x=x-dx}(x)e^{-\frac{1}{L(x-dx)}dx}dx$$

$$= N_e(x)e^{-\left(\frac{1}{L(x)} + \frac{1}{L(x-dx)}\right)dx}dx \quad [11]$$

After N steps ($N = x/dx$), at the surface

$$N_{e,x=0}(x)dx = N_{e,x=dx}e^{-\frac{1}{L(dx)}dx}dx$$

$$= N_e(x)e^{-\left(\frac{1}{L(x)} + \frac{1}{L(x-dx)} + \cdots + \frac{1}{L(dx)}\right)dx}dx \quad [12]$$

$N_{e,x=0}(x)dx$ is the number of electrons excited between x and $x + dx$ arriving at the surface per unit area per unit time. Therefore, the total number of electrons arriving at the surface per unit area per unit time $N_e(h\nu,V)$, is given by

$$N_e(h\nu,V) = \int_0^\infty N_{e,x=0}(x)dx \quad [13]$$

which represents all the electrons excited by photons at any distance inside the semiconductor and which reach the surface, where V is the p.d. inside the semiconductor.

The Energy of an Electron Arriving at the Surface

The experimentally observed independence of the so-called critical potential (*i.e.*, the potential at which, for light of a given wavelength, the current begins) with the energy of the exciting photons, Fig. 1 (16), suggests that the energies of all the photoexcited electrons are the same by the time they reach the surface. It seems reasonable to postulate that this energy is the bottom of the conduction band. Thus, the average path length of an electron is $1/\alpha \simeq 10^{-4}$ cm. A typical mean free path for an electron-phonon collision is (17) 60Å. Hence, a typical energy loss for electrons in reaching the surface is $(10^4/60)$. 0.025 eV ($\simeq$ 4 eV). Thus, the photoexcited electron is effectively deactivated to the energy at the bottom of the conduction band before it reaches the surface (though it does not cross the energy gap, which would need a deactivating cause equivalent in energy to several electron volts).

[2] k and e_0 must be in gaussian units.

Electron Transfer Process

Energy level of an acceptor in solution.—The enthalpy change for electron transfer from a semiconductor to H_3O^+.—The standard enthalpy change, $\Delta H(e)$, for an electron transfer reaction corresponding to Eq. [1] from the bottom of the conduction band of the semiconductor at the surface to the proton in solution when the proton-solvent system is in its ground state and no potential drop it in the electric double layer can be obtained by using the following thermodynamic cycle

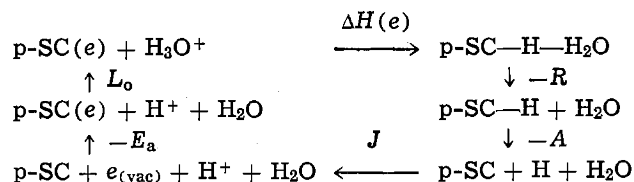

where R, A, J, E_a and L_0 represent the H-H_2O repulsive force, the heat of adsorption of a hydrogen atom on the semiconductor, the ionization potential of the hydrogen atom, the electron affinity of the semiconductor, and the hydration energy of proton, respectively. In respect to R and A, these quantities are distance dependent and the distance assumed was that appropriate to their state at neutralization. Therefore

$$\Delta H(e) = -L_0 + E_a - J + A + R \quad [14]$$

The energy level of an electron in the ground state of the H_3O^+ ion.—By taking into account the potential drop in the electric double layer at the flatband potential (Fig. 2), the energy level of an electron in the ground state of H_3O^+ with respect to the bottom of the conduction band at the flatband potential, $\Delta H'(e)$, is given by

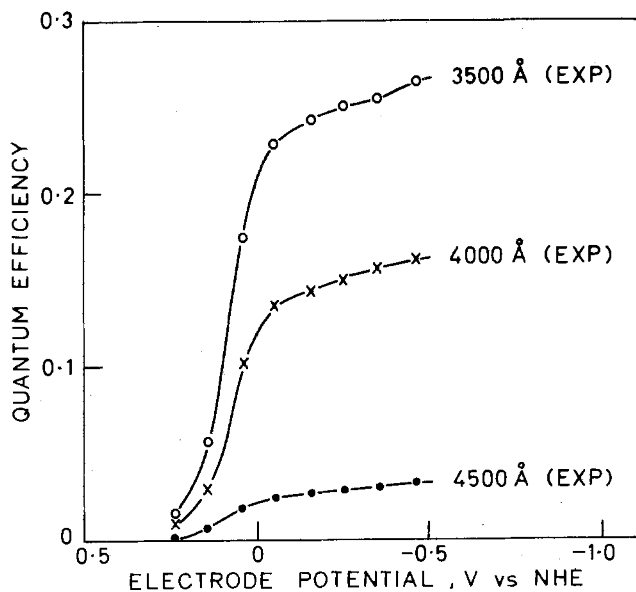

Fig. 1. The experimental quantum efficiency-potential relations of p-GaP in 1N H_2SO_4.

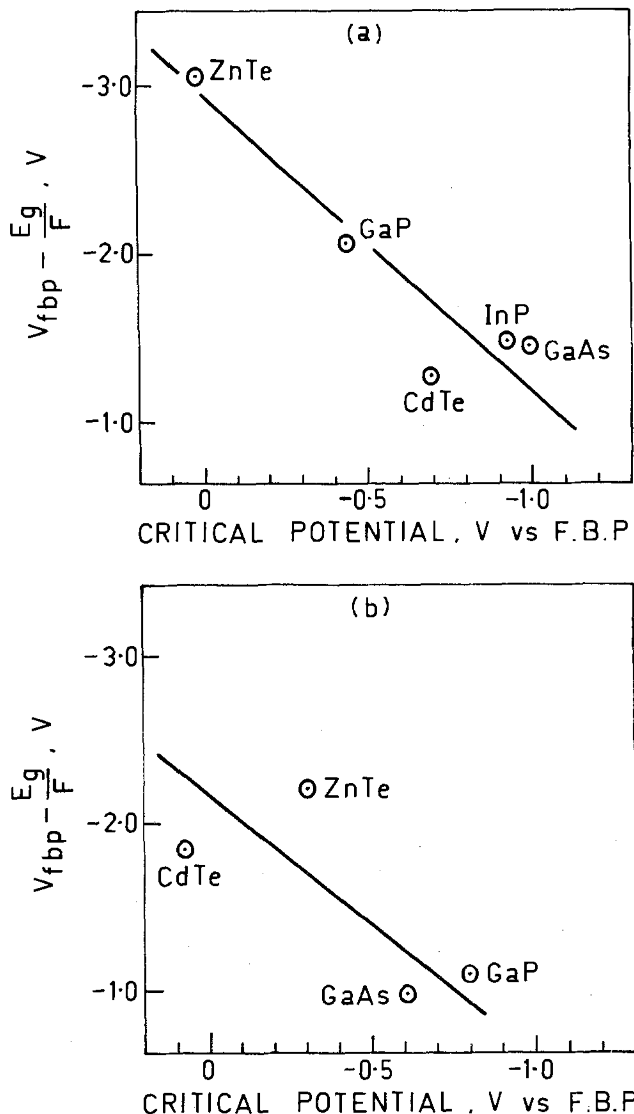

Fig. 2. The relations between (V_{fbp} $-E_g/F$) and the critical potential with respect to the flatband potential in 1N NaOH (a) and 1N H_2SO_4 (b).

$$\Delta H'(e) = \Delta H(e) + F(^{SC}\Delta^{S}\phi)_{fbp}$$

$$= -L_o + E_a - J + A + R + F(^{SC}\Delta^{S}\phi)_{fbp} \quad [15]$$

where $^{SC}\Delta^{S}\phi$ is an absolute potential (18, 19).

The barrier for electron transfer.—Image interaction and the dielectric constant of water.—We have neglected the interaction energy between an emitted electron and its image in a metal in the barrier construction for the photoeffect at metal electrodes (8). In these calculations, the optical dielectric constant was used for the dielectric constant of water. The reason for the neglect of the image interaction was that the emitted electrons travel across the barrier too quickly to make an image in the semiconductor. The optical dielectric constant was used for the same reason.

However, there was some misunderstanding in these considerations. When one wants to construct a potential barrier, one should consider an ideal test charge, *i.e.*, a ("classical") electron moving slowly enough to make its image in the semiconductor. Thus, the interaction energy between the emitted electron and its image should be taken into account in determining the energy barrier and the static dielectric constant of water [=6 for the oriented water molecules adsorbed on the electric double layer (20, 21)].

The image interaction, $U_{im}(x)$, is given by

$$U_{im}(x) = \frac{e_o^2}{4x\epsilon_{st}} \frac{\epsilon_{st} - \epsilon}{\epsilon_{st} + \epsilon} \quad [16]$$

Interaction with ions in the OHP and their images.—When a photoexcited electron leaves the semiconductor surface, it interacts with all ions in the OHP and their electrical images in the semiconductor. The Coulombic force between this electron (x from electrode) and all ions in OHP and their images, $F(x)$, is given by (8)

$$F(x) = -\frac{e_o^2}{(\delta_r - d_{O\text{-}H} - x)^2\epsilon_{st}} + \frac{e_o^2}{(\delta_r - d_{OH} + x)^2\epsilon_{st}} \frac{\epsilon - \epsilon_{st}}{\epsilon + \epsilon_{st}} - \frac{2\pi e_o^2}{\epsilon_{st}} \sum_{n=1}^{\infty} \left\{ \frac{d - x}{\{(d-x)^2 + n^2R_i^2\}^{3/2}} - \frac{d + x}{\{(d+x)^2 + n^2R_i^2\}^{3/2}} \frac{\epsilon - \epsilon_{st}}{\epsilon + \epsilon_{st}} \right\} \quad [17]$$

where δ_r is the distance between the electrode surface and the nearest proton of the H_3O^+ ion, $d_{O\text{-}H}$ is the distance between hydrogen and oxygen atom in water, d is the distance between the semiconductor surface and OHP, ϵ_{st} is the static dielectric constant of water, n = 1, 2, 3 and represents the succession of rings of ions around a given central ion, and R_i is the distance between two ions in the OHP, depending on its coverage with ions and determined by $R_i = 4r_i/(\pi\theta)^{1/2}$, where θ is the coverage and r_i is the radius of the ions. *Potential barrier.*—From the above considerations, the potential energy barrier for electron transfer, $U(x)$, from the surface of the semiconductor surface to the H_3O^+ is given by

$$U(x) = U_{im}(x) + \int_0^x F(x)dx + e_oX_xx \quad [18]$$

where X_x is the field in the double layer.

Potential Drop in the Semiconductor and in the Double Layer

The potential drop in the electric double layer at the SC-solution interface is often considered to be negligible (22). However, when the carrier density of the semiconductor is high, or the density of the surface states is high, the potential drop in the electric double layer cannot be ignored. We can obtain this quantity from an analysis of the Mott-Schottky plot (23, 24).

The Mott-Schottky relation is given by

$$\frac{1}{C_{SC}^2} = \frac{8\pi}{\epsilon e_o N_A}\left(\psi_{SC} - \frac{kT}{e_o}\right) \quad [19]$$

where C_{SC} is the space charge capacity, N_A is the concentration of ionized acceptors, and ψ_{SC} is the potential drop in the space charge layer.

The appropriate relation in the case of measurements in solution is[3]

$$\frac{1}{C^2} = \frac{8\pi}{\epsilon e_o N_A}\left(V - V_{fbp} - \frac{kT}{e_o}\right) \quad [20]$$

where C is the total capacity of the electrode (neglecting the roughness factor) and V and V_{fbp} are the electrode potential and the flatband potential with respect to a reference electrode, respectively.

Since (see Fig. 2)

$$V - V_{fbp} = \psi_{SC} + \Delta\Delta\phi_H \quad [21]$$

[3] C_{SC} has been assumed equal to $C_{measured}$ because other capacitances (*e.g.*, that of the counterelectrode and Helmholtz layer) are much larger than C_{SC} and hence negligible in series array.

where

$$\Delta\Delta\phi_H = ({}^{SC}\Delta^S\phi)_V - ({}^{SC}\Delta^S\phi)_{fbp} \quad [22]$$

and $\Delta\phi$ is the Galvani p.d. in the double layer at V and the fbp, respectively, then, Eq. [21] becomes

$$\frac{1}{C^2} = \frac{8\pi}{\epsilon e_o N_A}\left(\psi_{SC} + \Delta\Delta\phi_H - \frac{kT}{e_o}\right) \quad [23]$$

Only when $\Delta\Delta\phi_H = 0$ or $\Delta\Delta\phi_H = c\psi_{sc}$, where c is a proportional constant, does the plot between $(1/C^2)$ and V become linear (23, 24).

If $\Delta\Delta\phi_H = 0$, Eq. [21] becomes Eq. [20] and the slope of the experimental plot (Eq. [21]) must be the same as that of the theoretical plot.

In the case of $\Delta\Delta\phi_H = c\psi_{SC}$, Eq. [24] becomes

$$\frac{1}{C^2} = \frac{8\pi}{\epsilon e_o N_A}\left\{\psi_{SC}(1 + c) - \frac{kT}{e_o}\right\} \quad [24]$$

and thus, c can be calculated by comparing the experimental slope with the theoretical one. This is the case found in recent experimental work (16). $(V - V_{fbp})/(1 + c)$ gives the potential drop in the space charge layer in the semiconductor.

De Gryse *et al* (25) criticized reasoning of this type by showing that the slope of the plot has the same value whether the potential drop occurred in the electric double layer or not. However, in their treatment they assumed an absence of surface charge and this assumption limits the applicability of the interpretation.[4] The experimental *p*H dependence of the flatband potential can only be interpreted by assuming the existence of surface states, and the discussion of de Gryse *et al.* on this matter is no longer directly applicable to situations of this kind.

Photocurrent Expression

By taking into account the above considerations and Eq. [2], the photocurrent, i_p, is given by

$$i_p = e_o \frac{C_A}{C_T}\int_0^\infty N(E)W(E)G(E)dE$$

$$= e_o \frac{C_A}{C_T} N_e(h\nu,\psi_{SC})$$

$$\exp\left\{-\frac{\pi^2 l}{h}\sqrt{2m_e(U_m + e_o\Delta\Delta\phi_H)}\right\}$$

$$\exp\{-\beta(\Delta H(e) + e_o\Delta\Delta\phi_H)/kT\} \quad [25]$$

where $N_e(h\nu,\psi_{SC})$ is the number of electrons arriving at the surface when the potential drop in the semiconductor is ψ_{SC} and can be obtained from Eq. [13] replacing V by ψ_{SC}; U_{max} is the barrier maximum with respect to the bottom of the conduction band at the flatband potential; $\Delta\Delta\phi_H$ is defined in Eq. [22]; and V is defined in Eq. [21]. The use of $e_o\Delta\Delta\phi_H$ for the electron energy in the tunneling expression is consistent with a model in which the electrons arrive with a uniform energy at the bottom of the conduction band, *i.e.*, $E_e = 0$; and the barrier is then influenced by the p.d. in the double layer in the sense that the barrier is reduced when $\Delta\Delta\phi_H$ is negative.[5,6]

Computation of the Photocurrent-Potential Relation and Comparison with Experimental Results

Photocurrents were calculated for the example of GaP for different wavelengths of light as a function of potential. A schematic energy diagram, which shows the shape of the barrier, is shown in Fig. 3. It was constructed by the use of Eq. [16] and [17] in Eq. [18].

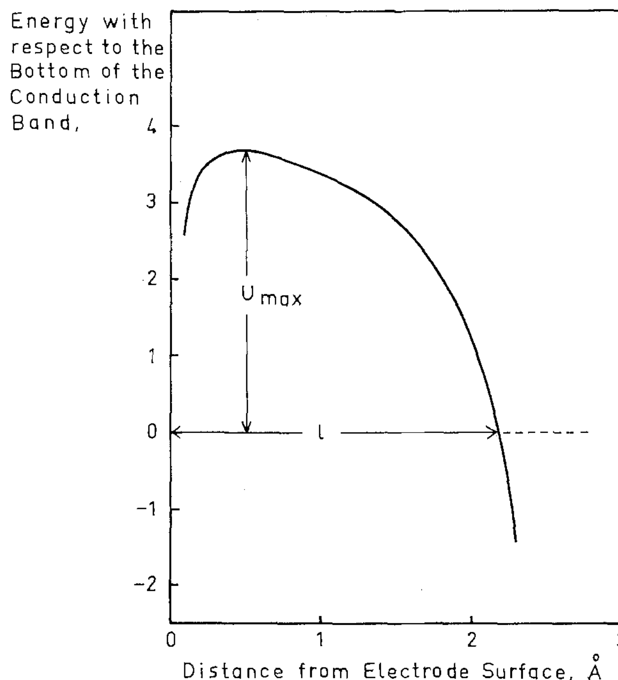

Fig. 3. Schematic diagram of the potential energy barrier for electron transfer from GaP electrode at flatband potential to an acceptor. (E_g is the energy gap; critical potential = potential at which photocurrent commences.)

The values used for the calculation of i_p through such a barrier by the use of [25] are: $\tau_e = 10^{-10}$ sec (26), $\mu_e = 300$ cm^2/V · sec (27), $L_o = -11.3$ eV (28), $E_a = 4.3$ eV (27), $J = 13.6$ eV (28), $A = -0.3$ eV (29), $R = -0.1$ eV (30), $\epsilon = 11$ (31), $E_g = 2.25$ eV (27), $V_{fbp} = 1.13$V (NHE) (16), and $c = 1.32$ (16). $({}^{SC}\Delta^S\phi)_{fbp}$ is taken from values given in the paper of Bockris and Uosaki (32). The theoretical results are shown in Fig. 4(a), (b), and (c) and are compared with experimental results. The calculated and experimental results agree fairly in respect to the position and shape of the quantum efficiency-potential relation. The potential at which the photocurrent commences (the so-called critical potential) is predicted to be 0.2-0.4 too positive.

Discussion of Discrepancies Between Theory and Experiment

Discrepancies between theory and experiment exist as follows:

1. Theoretically estimated quantum efficiencies are only 20-30% of the experimental quantum efficiencies.
2. The position of the theoretical quantum efficiency-potential relations appear at about 0.2-0.4V more positive than those of experiment.

These discrepancies may be due to cumulative uncertainties in the quantities of Eq. [17] which give the energy levels of electrons in the neutralized H_3O^+; $\Delta H(e)$ at the flatband potential and uncertainties in the value of the barrier width, which has been taken at 2.2Å, following the reasoning of Matthews and Bockris (28).

In respect to the determination of $\Delta H(e)$, the difference betwen the Fermi level and the top of the valency band was assumed to be zero. However, this quantity depends on the carrier density and has the order of 0.01 ~ 0.2 eV. Were this taken into account, the theoretical quantum efficiency-potential relations would shift toward more negative potentials (*i.e.*, an improvement) by 0.01-0.2V, depending on the carrier density.

[4] In general, the p.d. at a semiconductor-solution interface will be partly in the solution if the doping is very high or there is a significant concentration of surface states.

[5] Equation [25] is no longer an integral because transfer is seen as occurring only from electrons at the bottom of the conduction band (*i.e.*, photogenerated electrons have been deactivated until they arrive at the interface at a potential V_c).

[6] A rough computation for GaP-NaOH at 0 on the NH scale suggests that about 50% of the electrons activated by light reach the surface. Those which do not tunnel to the solution deactivate at the surface to the valence band.

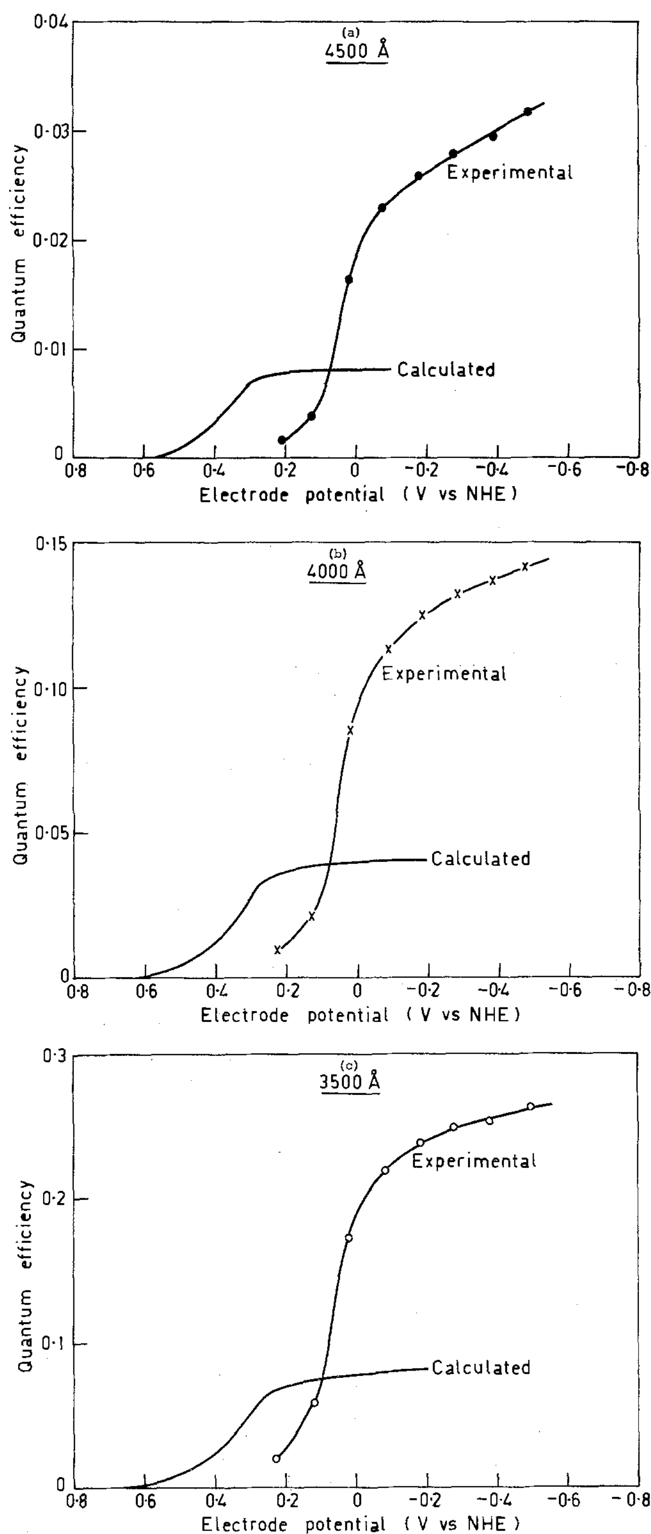

Fig. 4. Calculated and experimental quantum efficiency vs. electrode potential curves for GaP in 1*N* NaOH at the three monochromatic wavelengths (a) 4500; (b) 4000; and (c) 3500.

In respect to the determination of the barrier dimension, the electron was assumed to transfer to a proton in the second layer of water, to which a proton transfers from H_3O^+ in the OHP prior to electron transfer (28).[7] However, it may be possible that a proton transfers to water attached to the electrode surface, and electrons transfer to that. In this case, the barrier thickness becomes much smaller than that assumed and, therefore, higher quantum efficiency than those calculated in the present model would be expected.

[7] The origin of this model lies in the interpretation of the values observed for the dependence of the separation factor on the potential (11). Much lower barrier widths give separation factors which are too large.

Acknowledgment

We would like to thank Dr. M. A. Habib and Mr. S. U. M. Khan for their useful discussions. One of us (K.U.) thanks Flinders University for a scholarship.

Manuscript submitted Dec. 21, 1976; revised manuscript received Aug. 10, 1977.

Any discussion of this paper will appear in a Discussion Section to be published in the December 1978 JOURNAL. All discussions for the December 1978 Discussion Section should be submitted by Aug. 1, 1978.

Publication costs of this article were assisted by the Flinders University of South Australia.

REFERENCES

1. H. Gerischer and I. Mattes, *Z. Phys. Chem. (N.F.)*, **49**, 112 (1966).
2. Yu. V. Pleskov and V. V. Eletsky, *Electrochim. Acta*, **12**, 707 (1967).
3. R. Memming and G. Schwandt, *ibid.*, **13**, 1299 (1968).
4. H. Gerischer, *This Journal*, **113**, 1174 (1966).
5. V. A. Myamlin and Yu. V. Pleskov, "Electrochemistry of Semiconductors," (English ed.), Chap. II, Plenum Press, New York (1967).
6. D. Laser and A. J. Bard, Paper submitted to *This Journal*.
7. A. M. Brodsky and Yu. Ya. Grevich, *Electrochim. Acta*, **13**, 1245 (1968).
8. J. O'M. Bockris, S. U. M. Khan, and K. Uosaki, *J. Res. Inst. Catal., Hokkaido Univ.*, **24**, 1 (1976).
9. R. K. Sen and J. O'M. Bockris, *Chem. Phys. Lett.*, **18**, 166 (1973).
10. A. J. Appleby, J. O'M. Bockris, R. K. Sen, and B. E. Conway, in "Physical Chemistry," Vol. 6, J. O'M. Bockris, Editor, MTP Int. Rev. Sci., Butterworths, London (1973).
11. J. O'M. Bockris, S. Srinivasan, and D. B. Matthews, *Discuss. Faraday Soc.*, **39**, 239 (1965).
12. M. Enyo, in "Modern Aspects of Electrochemistry," Vol. 11, Chap. 4, J. O'M. Bockris and B. E. Conway, Editors Plenum Press, New York (1975).
13. R. W. Gurney, *Proc. R. Soc. London, Ser. A*, **134**, 137 (1932).
14. R. H. Kingston and S. F. Neustädter, *J. Appl. Phys.*, **26**, 718 (1955).
15. S. M. Ryvkin, "Photoelectric Effects in Semiconductors," (English ed.), Chap. XIII, Consultants Bureau, New York (1964).
16. K. Uosaki, Ph.D. Thesis, The Flinders University of South Australia (1976).
17. J. I. Pankove, "Optical Processes in Semiconductors," Prentice-Hall, Inc., New Jersey (1971).
18. J. O'M. Bockris and S. Argade, *J. Chem. Phys.*, **49**, 5133 (1968).
19. S. Trasatti, *J. Electroanal. Chem.*, **52**, 313 (1974).
20. J. O'M. Bockris, M. A. V. Devanathan, and K. Müller, *Proc. R. Soc. London, Ser. A*. **274**, 55 (1963).
21. J. O'M. Bockris and M. A. Habib, *J. Electroanal. Chem.*, **65**, 473 (1975).
22. F. Möllers and R. Memming, *Ber. Bunsenges. Phys. Chem.*, **76**, 469 (1972).
23. T. O. Rouse and J. L. Weininger, *This Journal*, **113**, 184 (1966).
24. T. P. Biriutseva and Yu. V. Pleskov, *Izv. Akad. Nauk. SSSR, Ser. Khim.*, 251 (1965).
25. R. De Gryse, W. P. Gomes, F. Cardon, and J. Vennik, *This Journal*, **122**, 711 (1975).
26. R. A. Logan and A. G. Chynoweth, *J. Appl. Phys.*, **33**, 1649 (1968).
27. "Handbook of Chemistry and Physics," R. C. Weast, Editor, CRC, 55th ed., E-103 (1974).
28. D. B. Matthews and J. O'M. Bockris, in "Modern Aspects of Electrochemistry," Vol. 6, Chap. 4, J. O'M. Bockris and B. E. Conway, Editors, Plenum Press, New York (1971).
29. J. O'M. Bockris and K. Uosaki, Paper submitted to *Adv. Chem. Ser.*
30. R. Schroeder and E. R. Lippincott, *J. Phys. Chem.*, **61**, 921 (1959).
31. A. S. Barker, Jr., *Phys. Rev.*, **165**, 1674 (1965).
32. J. O'M. Bockris and K. Uosaki, Paper submitted to *This Journal*.

Prediction of Flatband Potentials at Semiconductor-Electrolyte Interfaces from Atomic Electronegativities

M. A. Butler* and D. S. Ginley*

Sandia Laboratories, Albuquerque, New Mexico 87115

ABSTRACT

The electron affinities of several metal oxide semiconductors that have been used as anodes in photoelectrochemical cells are calculated using the atomic electronegativities of the constituent atoms. These electron affinities are quantitatively related to the measured flatband potentials by considering the effects of specific adsorption of potential-determining ions (for metal oxides used in photoelectrolysis, these are usually OH^- and H^+). Methods are discussed for determining the *p*H at which net adsorbed surface charge and thus potential across the Helmholtz layer is zero (point of zero zeta potential, pzzp). This *p*H value is shown to correlate with the electronegativity of the metal oxides. The application of these ideas to other semiconductor-electrolyte systems is discussed.

The use of semiconducting metal oxides to decompose water photoelectrolytically is a process which has recently attracted considerable interest (1). The ability of the photoelectrolysis cell to operate with little or no external bias in the system is a function of the degree to which the flatband potential is more negative than the hydrogen evolution potential. Thus it is very useful to be able to predict the flatband potentials of possible semiconducting metal oxide electrodes. In a recent publication (2) we showed that a correlation existed between the atomic electronegativities of the constituent atoms in titanates of the form $MTiO_3$ and the flatband potentials. In this paper, we extend this idea to all metal oxides and show it is capable of quantitatively predicting the flatband potentials.

In actuality, the quantity predicted from the atomic electronegativities is the electron affinity, *EA*, of the semiconductor. However, since the semiconductor's flatband potential, V_{fb}, and its electron affinity, *EA*, are essentially measures of the position of the intrinsic conduction band with respect to different references (standard calomel reference electrode and vacuum, respectively), they can be directly related by

$$EA = E_o + V_{fb} + \Delta_{fc} + \Delta_{pH} \quad [1]$$

where E_o is a constant relating the reference electrode to the vacuum level ($E_o = 4.75$ eV for SCE) (3), Δ_{fc} corrects for the difference between the doped Fermi level and the bottom of the conduction band ($\Delta_{fc} \sim 0.1$ eV for heavily doped metal oxides) (2), and Δ_{pH} is the potential drop across the Helmholtz layer due to specific adsorption of OH^- and H^+ ions. There exists some unique point for each semiconductor where the number of positively and negatively charged potential-determining ions at the interface are equivalent. At this point, the potential drop across the Helmholtz layer due to adsorbed ions is zero and Δ_{pH} or its equivalent for other adsorbed ions is zero. This point, called the point of zero zeta potential (pzzp) (4), is the only point at which truly meaningful flatbands can be measured and it is this flatband to which the calculated electron affinities should be compared. We will discuss the determination of the pzzp for several metal oxides and show that it correlates to the Fermi energy of the undoped metal oxide semiconductor. With these two correction factors (Δ_{fc} and Δ_{pH}) taken into account, the predicted and measured flatband potentials are in excellent agreement. Additionally, we will discuss some of the implications of these ideas to nonoxide electrodes and other than aqueous redox couples.

Calculation of Semiconductor Electron Affinity

Considerable success has been achieved in calculating Fermi energies and photoelectric thresholds for several classes of compounds (5) using the atomic electronegativities of the constituent atoms. Mulliken's definition of the electronegativity of a neutral atom is the arithmetic mean of the atomic electron affinity and the first ionization energy

$$\chi(M) = \tfrac{1}{2}\,(A_f + I_1) \quad [2]$$

where, for clarity's sake, we use A_f for the atomic electron affinity and I_1 is the first ionization potential. Since the ionization potentials (6) and electron affinities (7) for most atoms are tabulated, the Mulliken electronegativities $\chi(M)$ form a readily evaluated absolute electronegativity scale based only on measurable physical parameters. In a sense, $\chi(M)$ is the electrochemical potential of the electron in the neutral atom. When atoms are brought together to form compounds, charge will flow until the electrochemical potentials (electronegativities) are equalized. Sanderson (8) and more recently Nethercot (5), have postulated, based on bond length arguments, that the resulting bulk electronegativity of the compound is the geometric mean of the electronegativities of the constituent atoms. This assumption appears to be valid for a large number of compounds (5, 9). For a semiconductor the bulk electronegativity corresponds to the undoped Fermi level or halfway between the bottom of the conduction band and the top of the valence band. Thus the electron affinity of the compound will be given by

$$EA = \chi - \tfrac{1}{2}\,E_g \quad [3]$$

where E_g is the bandgap energy. Applying this equation and the postulate of the geometric mean, we find, for example, that for TiO_2, the electron affinity is

$$EA(TiO_2) = \chi(TiO_2) - \tfrac{1}{2}\,E_g = [\chi(Ti)\,\chi^2(O)]^{1/3} - \tfrac{1}{2}\,E_g = 4.33\ \text{eV} \quad [4]$$

relative to the vacuum level. We have calculated the electron affinities for a number of metal oxides and they are listed in Table I. Even without considering the correction terms in Eq. [1], there is obviously a strong correlation between the measured flatband potentials and calculated electron affinities as is illus-

* Electrochemical Society Active Member.

Key words: photoelectrolysis, zeta potential, electron affinity.

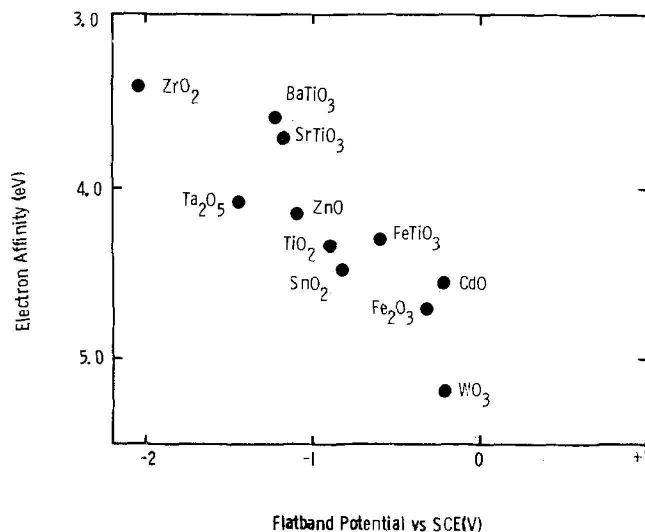

Fig. 1. The electron affinity calculated using atomic electronegativities vs. the flatband potentials measured at pH = 13.3 (1M NaOH).

strated in Fig. 1. As expected (10), the more negative flatband potentials come from semiconductors with smaller electron affinities. The correction for the difference between the doped Fermi level and the bottom of the conduction band depends, naturally, on doping level. However, for heavily doped metal oxides, commonly employed for photoelectrolysis, this term is only about 0.1 eV. Such a small correction cannot account for the scatter observed in Fig. 1. This must come from the specific adsorption of ions.

Point of Zero Zeta Potential (PZZP)

A brief discussion of the nature of the pzzp and the techniques employed for its measurement are in order due to the importance and magnitude of Δ_{pH}. There is a sizeable literature on the pzzp of metal oxides (4, 11-17), which colloidal chemists have traditionally referred to as the point of zero charge (pzc). This terminology is clearly inappropriate in the context of semiconductor electrochemistry where pzc refers to the flatband potential. Thus we adopt the notation of the point of zero zeta potential (pzzp) (18). Historically, the determination of the pzzp for materials has had important ramifications in the area of flotation processes (4). While several ionic species may be specifically adsorbed, for metal oxides, the point of zero zeta potential usually refers to specific adsorption of OH and H^+ ions. The pzzp is then the pH at which the net surface charge is zero or the concentration of adsorbed OH^- and H^+ ions is equal. Under these conditions, there is no net potential across the Helmholtz layer other than the small dipole contribution of the solvent. The energetics of this condition can be examined by considering the electrochemical potential ($\bar{\mu}$) of the ions in the adsorbed layer and in the solution.

Any adsorbed ion in equilibrium with the same ion in solution will have

$$\bar{\mu}_{ad} = \bar{\mu}_{sol} \quad [5]$$

and under equilibrium situations this should apply to all adsorbed ions. Thus at the pzzp we can write

$$\bar{\mu}_{ad}^{OH^-} - \bar{\mu}_{ad}^{H^+} = \bar{\mu}_{sol}^{OH^-} - \bar{\mu}_{sol}^{H^+} \quad [6]$$

The chemical potential of any component, A, in solution can be written as

$$\bar{\mu}_{sol}^{A} = {}_{0}\bar{\mu}_{sol}^{A} + RT \ln (a_A) \quad [7]$$

where ${}_{0}\bar{\mu}_{sol}^{A}$ is the electrochemical potential in the standard state, a_A is the activity of A in the solution phase, R is the ideal gas constant, and T is the absolute temperature. Normally the assumption is made that the solution is close to ideal and a_A can be replaced by C_A, the concentration of A. In the adsorbed phase at pzzp the concentration of OH^- and H^+ are equal; thus we may write

$${}_{0}\bar{\mu}_{ad}^{OH^-} - {}_{0}\bar{\mu}_{ad}^{H^+} = {}_{0}\bar{\mu}_{sol}^{OH^-} - {}_{0}\bar{\mu}_{sol}^{H^+} + RT \ln C_{OH^-sol} - RT \ln C_{H^+sol} \quad [8]$$

Since (2.303) pH = $-\ln C_{H^+sol}$ and the difference in standard state electrochemical potentials in solution for OH^- and H^+ is 1.23 eV, this may finally be written

$${}_{0}\bar{\mu}_{ad}^{OH^-} - {}_{0}\bar{\mu}_{ad}^{H^+} = 1.23 \text{ eV} + 4.606\, RT\, (pH_{pzzp} - 7) \quad [9]$$

It is possible to determine the standard-state electrochemical potentials for the adsorbed species if the appropriate hydroxylated and protonated species and their standard free energies of formation are known. In this case, the pzzp may be calculated directly using Eq. [9]. In general, this information is not known and the pzzp must be measured experimentally or estimated from knowing the semiconductor electronegativities. We show in Fig. 2 the pzzp for several metal oxides *vs.* the electronegativity of those oxides. The data suggest that there is a strong correlation. The observed slope has the same pH_{pzzp} dependence as in Eq. [9]. However, the quantitative relationship between Eq. [9] and Fig. 2 is not clear. The scatter in the data undoubtedly arises from the difficulty in measuring pzzp's. Measured pzzp's seem to depend somewhat on the method of preparation of the oxide (4).

Several techniques have been used to determine pzzp's (4). The simplest is just addition of the metal oxide powder to an aqueous solution of a known pH with no other adsorbable species present. The pH of the solution will shift on addition of the powder toward the pzzp. At the pzzp the pH of the solution is independent of the amount of metal oxide added. A more quantitative measure of specific ion adsorption is obtained from the potentiometric titration of a metal oxide suspension with either acid or base for solutions of specific ionic strength. Since the ions added must either go to changing the pH of the solution or be adsorbed on the metal oxide surface, it is possible to determine the surface charge density as a function of pH for several concentrations of supporting electro-

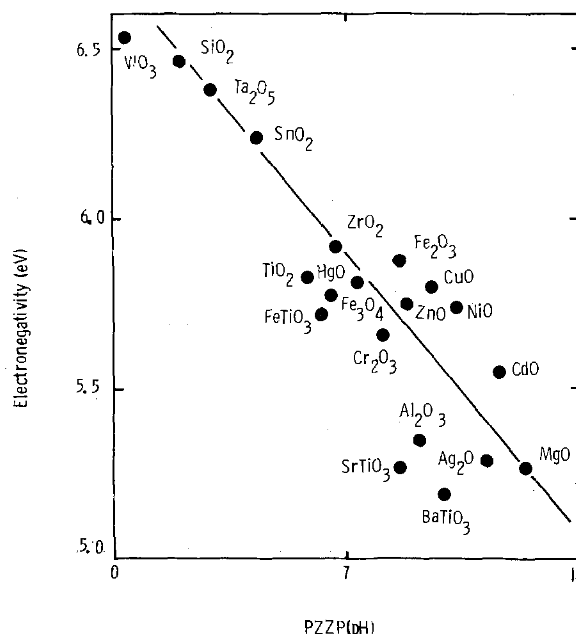

Fig. 2. Plot of the pH where the zeta potential is zero (pzzp) vs. calculated electronegativity for the bulk semiconductor in electron volts. The line is drawn through the data and has a slope of 0.12 eV/pH.

lyte. The point at which these curves intersect is the pzzp.

We have found that a simple differential potentiometric titration of an aqueous suspension of the semiconductor of interest in a solution of known ionic strength gives good peaks for the pzzp on plots of $\Delta pH/\Delta ml$ *vs.* pH.

In general this technique is similar to that employed for obtaining the fast adsorption isotherms but is somewhat less complex as only one titration is required. A procedural outline is included so as to clarify the experimental parameters. All glassware was cleaned by boiling in distilled water, from an all-glass Autostill, after an Alconox wash and distilled water rinse, then subsequently rinsed five times with distilled water. Reagents used were of the highest available purity and all of the oxide powders were four nines or better purity. The pH was measured with a Markson Electromark pH analyzer equipped with an Orion combination pH electrode and a digital readout. All titrations were performed in argon purged, stirred solutions. Typically, 1-10g of the oxide of interest were added to 600 ml of deionized, distilled water typically 0.001M in KNO_3, which is a nonadsorbing species. The KNO_3 was found to be unnecessary, but some ionic strength in the solution helped stabilize pH readings near the equivalence point. The pH of the solution was then adjusted to near 10-11 with 1M KOH. The solution was back titrated with HNO_3 first with 1M and then with 0.1M as was indicated by the rate of change of pH with additional increments of titrant. All additions were carried out with microburettes and typical accuracies were ±0.002 ml and ±0.005 pH units. The reproducibility of the peaks corresponding to the pzzp was excellent.

On the addition of titrant, conservation of charge requires that

$$A(\Gamma_{H^+} - \Gamma_{OH^-}) = xC_1 - V[(C_{H^+} - C_{OH^-}) - (C_{H^+} - C_{OH^-})_{\text{initial}}] \quad [10]$$

where A is the surface area of the suspended metal oxide, Γ is the surface density of the appropriate ion, x is the volume of titrant added, C_1 is the concentration of titrant, V is the volume of the suspension, and C is the appropriate concentration of ions in solution. This equation assumes that total added volume due to titration is negligible compared to the total suspension volume. If we differentiate this equation with respect to x, we find

$$\frac{A}{V}\frac{\partial(\Gamma_{H^+} - \Gamma_{OH^-})}{\partial x} = \frac{C_1}{V} - \frac{\partial C_{H^+}}{\partial x}[1 + k_w/C_{H^+}{}^2] \quad [11]$$

where k_w is the ionization constant for water. By expanding the partial of the surface charge density, we obtain

$$\frac{\partial C_{H^+}}{\partial x} = (C_1/V)\left[1 + \frac{A}{V}\frac{\partial \Gamma}{\partial C_{H^+}} + \frac{k_w}{C_{H^+}{}^2}\right]^{-1} \quad [12]$$

where $\Gamma \equiv (\Gamma_{H^+} - \Gamma_{OH^-})$. Now $C_{H^+} = \exp(-2.303\ pH)$. This equation and its derivative with respect to x allows us to convert Eq. [12] to a pH dependence. Finally we find

$$\frac{\partial pH}{\partial x} = \frac{-(C_1/V)\exp(2.303\,pH)}{2.303\left[1 + k_w \exp(4.606\,pH) - (A/2.303V)\dfrac{\partial\Gamma}{\partial pH}\exp(2.303\,pH)\right]} \quad [13]$$

The behavior of this equation is displayed in Fig. 3 for pure water and for 10^{-3}M KNO_3 solution with two different amounts of TiO_2 powder added. The solid curve for pure water is just Eq. [13] with A the surface area of suspended metal oxide set equal to zero. In general, the data agree excellently with the theory

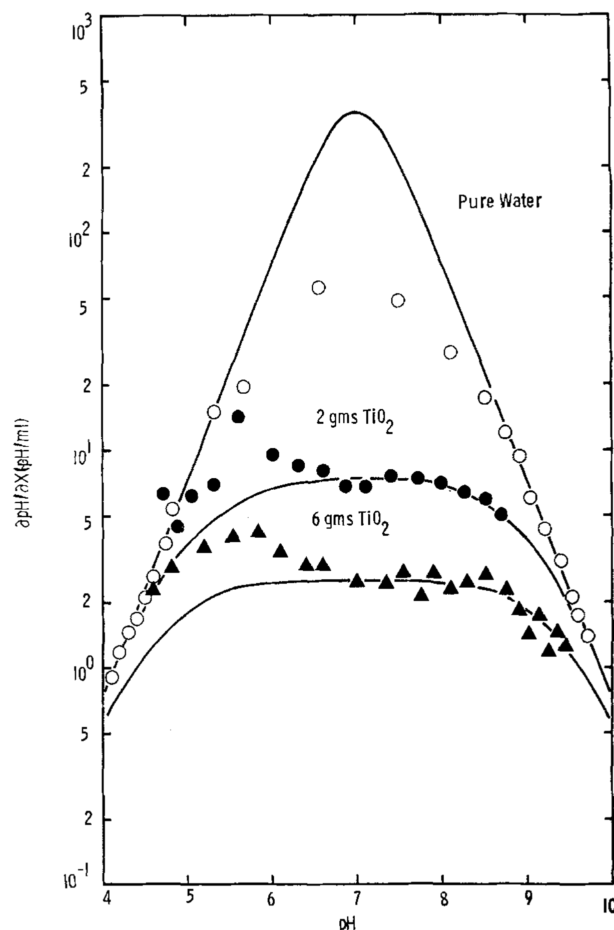

Fig. 3. Differential potentiometric titrations plotted as $\partial pH/\partial X$ (Δ_{pH}/Δ_{ml}) vs. pH for 3 solutions: ○○○ 600 ml distilled-deionized water, initial pH adjusted with 0.1M KOH, ●●● 600 ml distilled-deionized water 0.001M in KNO_3 with 2g of suspended TiO_2 (99.995%) initial pH adjusted with 0.1M KOH, ▲▲▲ 600 ml distilled-deionized water 0.001M in KNO_3 with 6g of suspended TiO_2 (99.995%). The solid lines represent theoretical fits of the data from Eq. [13] in the text. All solutions were stirred under a constant purge of argon and all titrations were performed with 0.1M HNO_3.

(no adjustable parameters) except where the rate of change of pH becomes quite large (near the equivalence point). Here, adsorption onto the glass surface and small amounts of impurities can buffer the solution to significantly lower the rate of change in pH. The "theoretical" curves for the TiO_2 suspensions were calculated from Eq. [13] with an assumed constant value for $\partial\Gamma/\partial pH$ of 4×10^{-11} moles/cm² (13). The surface area was then adjusted to fit the data at pH = 7. Note that the rate of change in pH at pH = 7 scales inversely with the amount of TiO_2 added. This indicates that the particle size was the same for two powders. We find from the fit a surface area for the powder of ~ 17.3 m²/g. This may be compared to the results of Berube and DeBruyn (13) who used TiO_2 powder of 43 m²/g. If we assume spherical particles, our surface area corresponds to diameters of ~ 900Å. These numbers are quite reasonable. At the pzzp it is evident (4) that $\partial\Gamma/\partial pH$ becomes small. From Eq. [13] we would thus expect a peak in the derivative curve at the pzzp. As you can see in Fig. 3, this is indeed the

Table I. Calculated electronegativity and electron affinity and measured flatband potential and point of zero zeta potential for several metal oxides

Compound*	χ (eV)	EA (eV)	V_{fb} (SCE)**	Ref.	PZZP (pH)†	Ref.
WO_3	6.53	5.18	−0.20	(19)	0.43	(17)
SiO_2 (a)	6.46	—	—	—	2.0	(24)
Ta_2O_5	6.38	4.08	−1.44	(20)	2.9	This work
SnO_2	6.24	4.49	−0.82	(21)	4.3	(14)
ZrO_2	5.92	3.42	−2.04	(20)	6.7	(12)
Fe_2O_3 (b)	5.88	4.71	−0.32	(9)	8.6	(16)
TiO_2	5.83	4.33	−0.90	(10)	5.8	(13) and this work
HgO	5.81	4.57	—	—	7.3	(24)
CuO	5.80	—	—	—	9.5	(24)
Fe_3O_4	5.77	—	—	—	6.5	(25)
ZnO	5.75	4.15	−1.09	(22)	8.8	(11)
NiO	5.74	3.89	—	—	10.3	(24)
$FeTiO_3$ (c)	5.72	4.30	−0.59	(2)	6.3	This work
Cr_2O_3	5.66	4.80	—	—	8.1	(26)
CdO	5.55	4.55	−0.22	(23)	11.6	(24)
Al_2O_3	5.35	—	—	—	9.2	(24)
Ag_2O	5.29	4.69	—	—	11.2	(27)
MgO	5.27	1.42	—	—	12.4	(28)
$SrTiO_3$ (d)	5.27	3.71	−1.19	(2)	8.6	This work
$BaTiO_3$ (e)	5.19	3.60	−1.22	(2)	9.9	This work

* The sources for these materials were: (a) Johnson Matthey Chemicals Limited, purity 99.999%. (b) Johnson Matthey Chemicals Limited, 99.999%; Fisher, 99.95%; and Matheson Coleman Bell, 99.5%; all gave comparable results. (c) See D. S. Ginley and R. J. Baughman, *Mater. Res. Bull.*, **11**, 1539 (1976). (d) National Lead Company, Research Department, "High purity reagent". (e) National Lead Company, purity 99.99%.
** Measured or corrected to pH = 13.3. Measurement accuracy is about ±0.1V.
† There is a great deal of scatter in the measured pzzp's. These are believed to be the most reliable values.

case for TiO_2 whose pzzp is ~ 5.8. A word of caution is perhaps relevant at this point. Contamination of the suspension by a buffer or other metal oxides will result in spurious peaks in the curve. The reality of the peak can be checked by using the simple method of direction of pH change with addition of additional metal oxide. The pzzp's for several metal oxides are shown in Table I. In general, we have found that this simple technique yields results in good agreement with previously published results.

Discussion

Since both of the correction terms can now be evaluated, we can compare the measured flatband potentials directly to the calculated electron affinities as is shown in Fig. 4. The solid line is the behavior expected from Eq. [1] with no adjustable parameters. One expects a unitary slope and an intercept at zero flatband potential of E_0. The agreement with theory is excellent and

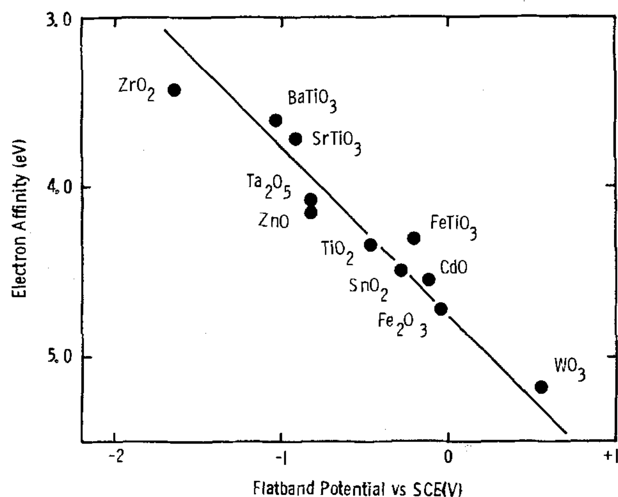

Fig. 4. The electron affinity calculated using atomic electronegativities vs. the measured flatband potentials for the labeled semiconductors corrected to their respective pzzp's. The solid line is that expected from Eq. [1] if the correction term, Δ_{fc}, is ignored. The flatband potentials and pzzp's not measured by us are those listed in Table I.

shows that the flatband potentials for metal oxides can be calculated with an accuracy of ~ 0.2V from the atomic electronegativities of the constituent atoms if specific adsorption of potential-determining ions is properly taken into account. Even without an accurate accounting for the pzzp the predicted flatbands are close enough so as to act as a guideline for electrode selection.

While most of the considerations in this paper have been concerned specifically with OH^- and H^+ as the potential-determining ions, the results certainly are more generally applicable. It is possible, for instance, that the flatband could be shifted by the addition of other ions which are specifically absorbed while not changing the pH and consequently the H_2 and O_2 evolution reaction potentials. The effect of specific ion adsorption on the cathode should also be evaluated since this may result in an additional potential drop in the circuit.

These ideas are of considerable importance with respect to wet photovoltaic cells and other systems employing nonoxide electrodes with nonaqueous redox couples (29-31). Many of these systems show no pH dependence of the flatband potential but do show a Nernstian type dependence on the concentration of potential determining ion. For example, in the cadmium sulfide, sulfur, sulfide ion cell ($CdS/S-S^{-2}-OH^-/Pt$), the flatband potential of the CdS depends on the S^{-2} concentration. Thus, there will be a Δ_{pS} correction term in Eq. [1] and a pzzp for sulfide ion, since the potential across the Helmholtz layer will depend on (S^{-2}). Therefore, in general, one must correct the measured flatband potentials to the respective pzzp of the potential-determining ions to obtain a measure of the intrinsic flatband potential. We are currently in the process of evaluating some of these numbers for nonoxide systems.

Acknowledgments

The authors are indebted to W. H. Smyrl for helpful discussions. The work reported in this paper was done for the U.S. Energy Research and Development Administration under Contract AT(29-1)-789.

Manuscript submitted June 20, 1977; revised manuscript received Sept. 17, 1977.

Any discussion of this paper will appear in a Discussion Section to be published in the December 1978 JOURNAL. All discussions for the December 1978 Discussion Section should be submitted by Aug. 1, 1978.

Publication costs of this article were assisted by Sandia Laboratories.

REFERENCES

1. A. Fujishima and K. Honda, *Nature*, **238**, 37 (1972); M. Wrighton, D. S. Ginley, P. T. Wolczanski, A. B. Ellis, D. L. Morse, and A. Linz, *Proc. Natl. Acad. Sci.*, **72**, 1518 (1975); G. Hodes, D. Cahen, and J. Manassen, *Nature*, **260**, 313 (1976); A. J. Nozik, *Appl. Phys. Lett.*, **29**, 150 (1976); K. L. Hardee and A. J. Bard, *This Journal*, **122**, 139 (1975); J. G. Mavroides, J. A. Kafalas, and D. F. Kolesar, *Appl. Phys. Lett.*, **28**, 241 (1976); L. A. Harris and R. H. Wilson, *This Journal*, **123**, 1010 (1976); and R. M. Candea, M. Kostner, R. Goodman, and N. Hickok, *J. Appl. Phys.*, **47**, 2724 (1976).
2. M. A. Butler and D. S. Ginley, *Chem. Phys. Lett.*, **47**, 319 (1977).
3. F. Lohmann, *Z. Naturforsch., Teil A*, **22**, 843 (1967).
4. G. A. Parks and P. L. DeBruyn, *J. Phys. Chem.*, **66**, 967 (1962).
5. A. H. Nethercot, Jr., *Phys. Rev. Lett.*, **33**, 1088 (1974); R. T. Poole, D. R. Williams, J. D. Riley, J. G. Jenkins, J. Liesegang, and R. C. G. Leckey, *Chem. Phys. Lett.*, **36**, 401 (1975).
6. F. A. White, "Mass Spectrometry in Science and Technology," p. 343, John Wiley & Sons, Inc., New York (1968).
7. H. Hotop and W. C. Lineberger, *J. Phys. Chem. Ref. Data*, **4**, 539 (1975).
8. R. T. Sanderson, "Chemical Periodicity," pp. 37-38, Reinhold, New York (1960).

9. M. A. Butler, D. S. Ginley, and M. Eibschutz, *J. Appl. Phys.*, **48**, 3070 (1977).
10. J. G. Mavroides, D. I. Tchernev, J. A. Kafalas, and D. F. Kolesar, *Mater. Res. Bull.*, **10**, 1023 (1975).
11. L. Blok and P. L. DeBruyn, *J. Colloid. Interfac. Sci.*, **32**, 518 (1970).
12. K. C. Ray and S. Khan, *Ind. J. Chem.*, **13**, 577 (1975).
13. Y. G. Berube and P. L. DeBruyn, *J. Colloid. Interfac. Sci.*, **27**, 305 (1968).
14. S. Mukai, Y. Yokoyama, T. Wakamatsu, and N. Narazaki, *Suiyokai-Shi*, **17**, 49 (1970).
15. J. Bjerrum, G. Schwarreenbach, and L. G. Sillen, "Stability Constants—Part II, Inorganic Ligands," The Chemical Society, London (1958).
16. R. J. Atkinson, A. M. Posner, and J. P. Quirk, *J. Phys. Chem.*, **71**, 550 (1967).
17. R. K. S. El. Wakkad and H. A. Risk, *ibid.*, **61**, 494 (1957).
18. S. H. Maron and C. F. Prutton, "Principles of Physical Chemistry," pp. 848-849, MacMillan Co., London (1965).
19. M. A. Butler, *J. Appl. Phys.*, **48**, 1914 (1977).
20. P. Clechet, J. Martin, R. Oliver, and C. Vallony, *C. R. Acad. Sci., Ser. C*, **282**, 887 (1976).
21. M. S. Wrighton, D. L. Morse, A. B. Ellis, D. S. Ginley, and H. B. Abrahamson, *J. Am. Chem. Soc.*, **98**, 44 (1976).
22. F. Lohmann, *Ber. Bunsenges. Phys. Chem.*, **70**, 428 (1966).
23. H. H. Kung, H. S. Jarrett, A. W. Sleight, and A. Ferretti, *J. Appl. Phys.*, **48**, 2463 (1977).
24. G. A. Park, *Chem. Rev.*, **65**, 177 (1965).
25. I. Iwasaki, S. R. B. Cooke, and Y. S. Kim, *Trans. AIME*, **223**, 113 (1962).
26. K. Emerson and W. M. Gravea, *J. Inorg. Nucl. Chem.*, **11**, 309 (1959).
27. H. R. Kruyt, "Colloid Science," Vol. 1, p. 231, Elsevier, New York (1952).
28. M. Robinson, J. A. Pask, and D. W. Fuerstenau, *J. Am. Ceram. Soc.*, **47**, 516 (1964).
29. A. B. Ellis, S. W. Kaiser, and M. S. Wrighton, *J. Am. Chem. Soc.*, **98**, 1635 (1976); *ibid.*, **98**, 6418 (1976); *ibid.*, **98**, 6855 (1976).
30. G. Hodes, J. Manassen, and D. Cahen, *Nature (London)*, **261**, 403 (1976).
31. B. Miller and A. Heller, *ibid.*, **262**, 680 (1976).

Behavior of Polymeric Sulfur Nitride, $(SN)_x$, Electrodes in Aqueous Media

Robert J. Nowak,* Wlodzimierz Kutner,[1] and Harry B. Mark, Jr.**

Department of Chemistry, University of Cincinnati, Cincinnati, Ohio 45221

and Alan G. MacDiarmid

Department of Chemistry, University of Pennsylvania, Philadelphia, Pennsylvania 19174

ABSTRACT

Polymeric sulfur nitride, $(SN)_x$, has been characterized as an electrode material in aqueous solution by cyclic voltammetry and cyclic chronoamperometry. Background currents, resulting from oxidation and reduction of electrode surface functional groups, were studied in different supporting electrolytes and pH values. A large influence of the nature of the alkali metal cations and Ca^{2+} of supporting electrolytes on the magnitude of background currents and cathodic breakdown potentials was found. This was interpreted in terms of differences in the interaction strength between these cations and electrode surface functional groups. The ferro-ferricyanide couple was used to determine relevant electrochemical parameters as well as electrode surface areas. Other redox couples which are active at $(SN)_x$ electrodes are discussed, *e.g.*, Pb^{2+}/Pb^{0}, $Ru(NH_3)_6^{3+}/Ru(NH_3)_6^{2+}$, quinone/hydroquinone. It was not possible to reduce Cr^{3+} at $(SN)_x$ electrodes. Furthermore, a dramatic decrease in background currents was observed for Cr^{3+} electrolyte solutions. The $(SN)_x$ was found to be remarkably stable in aqueous solutions under a wide variety of conditions and a suitable electrode material for chemical modification.

Polymeric sulfur nitride, $(SN)_x$, has been reported recently (1) as a new electrode material. This substance has been classified as a metal even though there are no metal atoms present in its structure (2). The $(SN)_x$ exhibits electrical and chemical anisotropy and its surfaces make available numerous types of functional groups and surface types for possible chemical modification (3). In order to use $(SN)_x$ in this capacity, it is of primary importance to characterize its general electrochemical behavior before any modification experiments are performed. Therefore, we report here systematic fundamental studies using $(SN)_x$ as a working electrode in order to evaluate it with respect to the criteria suggested by Mueller and Adams (4).

* Electrochemical Society Student Member.
** Electrochemical Society Active Member.
[1] Permanent address: Institute of Fundamental Problems of Chemistry, Warsaw University, Warsaw, Poland.

Key words: polythiazyl, polymeric electrodes, chemically modified electrodes, lead deposition, ferri-ferrocyanide.

Experimental

Reagents.—All chemicals were of reagent grade and were used without further purification. Chromium(III) perchlorate was obtained from Ventron Corporation. Solutions were prepared with distilled water which was passed through ion exchanger and, finally, activated carbon columns. Solutions were deoxygenated with argon or high purity nitrogen.

Instrumentation.—Cyclic voltammetric and chronoamperometric experiments were carried out with the use of PAR™ Model 173 potentiostat/galvanostat equipped with a PAR™ Model 176 current to voltage converter, a PAR™ Model 175 universal programmer, and a Hewlett Packard Model 2D-2M X-Y recorder or alternatively, a PAR™ Model 170 electrochemistry system. Micrographs were obtained with a Coates and Welter Cwikscan 100-4 or International Scientific Instruments Model 7 scanning electron microscope.

Electrode preparation.—High purity crystals of $(SN)_x$ (*ca.* 10^{-6}-10^{-3} cm^3) were prepared from S_4N_4 by a published method (2). Elemental analysis (Galbraith Laboratories, Incorporated) yielded the following results: Calc for $(SN)_x$: S, 30.41; N, 69.59. Found: S, 30.32; N, 69.73. Crystals were cemented to the end of a silver wire (0.040 cm radius, sealed in glass) with conducting silver paint (GC Electronics) and all but the crystal face of interest was masked off with Torr Seal® (Varian Associates). In this way electrodes could be constructed which had the $(SN)_x$ fiber bundles parallel or perpendicular to the electrode/solution interface. Thus, electrodes are designated as being "parallel" or "perpendicular" henceforth.[2] Projected surface areas for electrodes prepared in this way as measured by a calibrated microscope were in the range: 1-50 $\times$ 10^{-3} cm^2. New mounted electrodes with over-all resistances of less than 20Ω were used for each type of electrochemical experiment. It was not possible to renew the surface of a used electrode by polishing without severely damaging the crystal. All electrodes were stored in a vacuum desiccator as $(SN)_x$ crystals begin to tarnish after exposure to air for many weeks, although there appears to be little decomposition of $(SN)_x$ when it is immersed in water for six days (5).

Working electrodes made from platinum, palladium, and silver wires, having areas comparable to $(SN)_x$ electrodes, as well as a Kemula type hanging mercury drop electrode (radius = 0.043 cm) were used to compare the electrochemical behavior of selected redox couples on $(SN)_x$ or modified $(SN)_x$ with that on the metallic electrodes.

Platinum wire and KCl or NaCl saturated calomel electrodes served as counter and reference electrodes, respectively. All experiments were carried out at room temperature (*ca.* 25°C) unless otherwise mentioned.

Results and Discussion

Studies in supporting electrolyte.—The first step in evaluating $(SN)_x$ electrodes involved cyclic voltammetric studies in aqueous media in the absence of electrochemically active substances. In this way background and breakdown currents could be studied, and the feasibility of using $(SN)_x$ electrodes to study solutions containing electroactive materials could be determined. The electrochemical behavior of $(SN)_x$ electrodes was found to be dependent on *p*H, ionic strength, scan rate, scan number, and the nature of the supporting electrolyte. All experiments were performed with both parallel and perpendicular electrodes. A distinction between experimental results obtained with parallel or perpendicular electrodes is made here only if their electrochemical behavior was significantly different under identical experimental conditions.

Many different supporting electrolytes were used to characterize the nature of background currents. Cyclic voltammograms recorded in supporting electrolytes such as MCl (M = Li^+, Na^+, K^+, Cs^+), NaX (X = ClO_4^-, $SO_4^=$, NO_3^-, F^-, Cl^-, Br^-, N_3^-, SCN^-) or $Ca(NO_3)_2$ varied as a function of scan number. NaI was not used as it is electrochemically active at $(SN)_x$ electrodes (6). Usually, residual currents were very high on the first scan and gradually decreased on subsequent scans (Fig. 1). When negative and positive reversal potentials were kept constant, background currents fell to constant, reproducible values after five to ten scans. However, whenever the potential was held at positive values for a few seconds, high cathodic currents, typical of the first scan (Fig. 1), were observed. The magnitude of these cathodic currents was also directly proportional to the value of the positive reversal potential. Hysteresis of the cathodic current

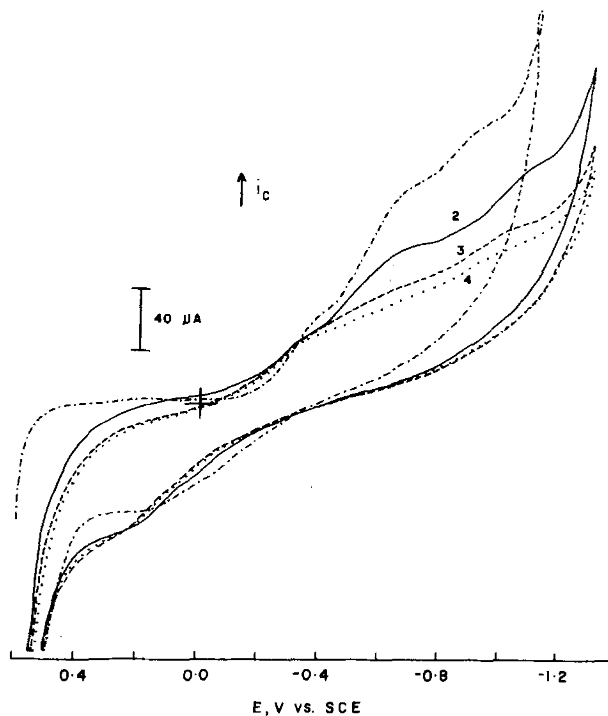

Fig. 1. Cyclic voltammogram in 0.5M $NaClO_4$. Scan number is indicated on each curve. Scan rate 0.05 V sec^{-1}.

was observed in the negative breakdown region for all electrolytes (unless otherwise noted) provided the current was allowed to reach negative enough values. (In Fig. 1 [scans 2-4], the potential reversal occurred prior to values necessary to cause this hysteresis.)

In order to investigate the nature of the cathodic breakdown process, the *p*H was varied. With perpendicular electrodes in the presence of acetate (*p*H = 4.75) or phosphate (*p*H = 7.3) buffers (sodium or potassium salts) the cathodic peaks attributed to surface redox processes of $(SN)_x$ itself (*vide infra*) were diminished or not present but the cathodic hysteresis still remained.

Using perpendicular electrodes, the *p*H was varied from 7 to 0 with H_2SO_4 solutions. The cathodic hysteresis disappeared only for acid concentrations of 0.5M (Fig. 2). Bubbles of hydrogen gas were observed on the electrode surface in the latter solution after negative polarization into the breakdown region. The high cathodic overvoltage of 0.5M H_2SO_4 solutions

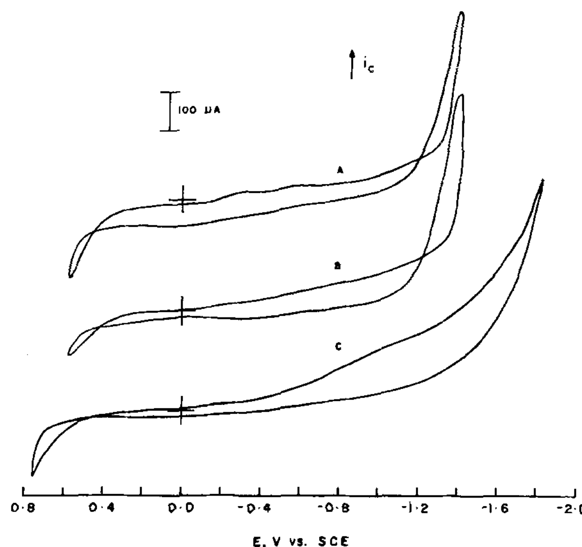

Fig. 2. Cathodic current breakdown dependence on solution acidity (A) 0.5M Na_2SO_4, (B) 0.45M Na_2SO_4 + 0.05M H_2SO_4, (C) 0.5M H_2SO_4. Scan rate 0.05 V sec^{-1}.

[2] Torr Seal resin appears to dissolve or decompose the $(SN)_x$ when fibers were mixed with it forming a paste. The latter material was found to be insulating. The larger $(SN)_x$ crystals used in this study were not significantly affected by Torr Seal.

might result from the increase in the electrode resistance due to gaseous hydrogen adsorption.

In similar experiments both parallel and perpendicular electrodes were used in solutions of 3M KCl with 10^{-3}, 10^{-2}, 10^{-1}, and 1M HCl added. There were no significant differences in (*i*) the cathodic breakdown potential (which was the same for 3M KCl without added HCl), (*ii*) the magnitude and form of the background currents, and (*iii*) the cathodic hysteresis (which was observed on all scans). If only HCl was present (0.1 or 1M) there was no cathodic hysteresis and an increase in background currents with increased concentration was observed. These results, plus the observation of visible dissolution and corrosion of the surface, indicate that the cathodic current breakdown is predominately a result of the decomposition of the electrode material rather than water electrolysis in solutions of $pH > 1$.

At least three cathodic peaks at *ca.* −0.35, −0.65, and −0.85V and three anodic peaks at *ca.* 0.10, 0.30, and 0.40V could be distinguished when the potential was scanned negatively and positively, respectively, in neutral unbuffered solution (Fig. 3). A mutual dependence of anodic and cathodic peaks was noted from scan reversal experiments (Fig. 3). If the negative scan was reversed at −0.65V prior to the cathodic process at the most negative potential before breakdown, the subsequent anodic peaks were shifted negatively with a simultaneous decrease in current magnitudes (Fig. 3C). Similar results were obtained as the reverse potential was made more positive on subsequent scans (Fig. 3D) until no anodic peaks were observed when the scan reversal was at +0.05V (Fig. 3E). These results demonstrate the faradaic and irreversible character of background currents which are probably due to the electrochemical oxidation and reduction of surface functional groups of the $(SN)_x$ itself. The observed peaks were better developed at lower scan rates (10-20 mV sec^{-1}) presumably due to the decrease in capacitance currents and/or the increase in the extent of oxidation or reduction of surface functional groups resulting from longer electrolysis times (cf. Fig. 3A, B).

Generally, background currents were higher for higher ionic strength electrolytes for all salts used. The values of potentials of anodic and cathodic current breakdown (*ca.* 0.5 and −1.2V, respectively) as well as the magnitude of the faradaic currents appeared to be independent of the cation or anion of the supporting electrolyte for perpendicular electrodes. However, background currents showed a marked dependence on the type of cation with only minor effects observed with different anions when parallel electrodes were used. Changing the cation of the supporting electrolyte from lithium through cesium resulted in a large shift in the cathodic breakdown potential to less negative values (*i.e.*, $Li^+ = -1.54$, $Na^+ = -1.25$, $K^+ = -1.15$, and $Cs^+ = -1.20V$), an increase in the hysteresis of the current on the reverse (positive) scan and an increase in background currents. In the experiment shown in Fig. 4 the same electrode was used for all of the cyclic voltammograms and results were identical if the experiments were performed by changing the cation in the reverse order, *i.e.*, cesium

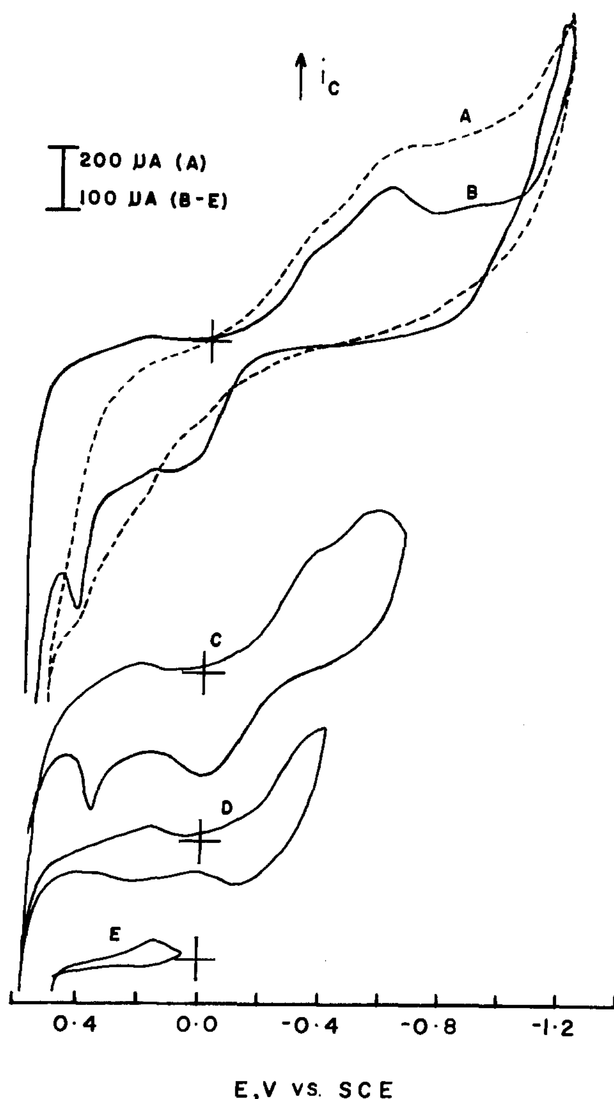

Fig. 3. Dependence of anodic peaks on cathodic reverse potential in 3M CsCl. (A, B) −1.200V, (C) −0.650V, (D) −0.400V, (E) +0.050V. Scan rate: (A) 0.2 V sec^{-1}; (B-E) 0.01 V sec^{-1}.

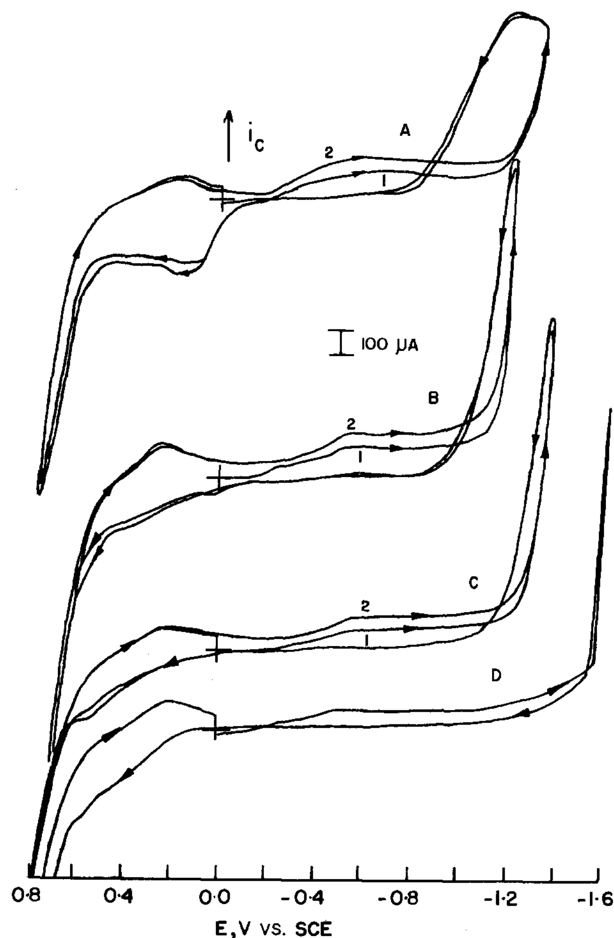

Fig. 4. Dependence of background currents on the cation of supporting electrolyte for parallel electrode in 3M solution of (A) CsCl, (B) KCl, (C) NaCl. (D) LiCl. Scan rate 0.02 V sec^{-1}.

through lithium. Furthermore, the cathodic breakdown potential for CsCl solutions was dependent on the scan rate (varied between 5 and 200 mV sec^{-1}) whereas with LiCl, the scan rate did not substantially affect this potential. At lower scan rates (5 mV sec^{-1}) the cathodic breakdown potential in CsCl solutions was approximately −1.20V but approached −1.50V at higher scan rates (100 mV sec^{-1}). Nonetheless, the slope of the *i-E* curves at cathodic breakdown was much less for CsCl than LiCl at all scan rates. From the above, one might conclude that Li^+ interacts most strongly with the parallel $(SN)_x$ surface, inhibiting redox transformation of surface functional groups. The order of magnitude of these interactions, increasing in the series $Cs^+ < K^+ < Na^+ < Li^+$, is exactly opposite to the order of adsorptivity of these cations on mercury (7).

The current hysteresis observed in the cathodic breakdown region was completely eliminated in $Ca(NO_3)_2$ supporting electrolyte on both parallel and perpendicular $(SN)_x$ electrodes (Fig. 5). On perpendicular electrodes, an increase in the concentration of $Ca(NO_3)_2$ resulted in the disappearance of the background current peaks (normally observed in alkali metal ion solutions) with a concomitant appearance of new reduction peaks at −1.0 and −1.25V (Fig. 5). In 5M $Ca(NO_3)_2$, where the activity of water is only 0.58, two reduction peaks at +0.1 and −0.7V, and one oxidation peak at +0.5V appeared. Furthermore, the potential of cathodic breakdown remained the same as for solutions of the alkali metal cations.

Cathodic breakdown in $Ca(NO_3)_2$ solutions using parallel electrodes was not detected as far negatively as −2.0V. A single cathodic peak at *ca.* −1.7V appeared during the first scan only, and there was no evidence of hysteresis upon scan reversal. There was no effect observed upon changing the concentration of $Ca(NO_3)_2$. These results are consistent with the previous studies with the alkali metal cations in that cathodic breakdown is extended more negatively using parallel electrodes with supporting electrolytes containing cations with increasingly higher charge densities. Perpendicular electrodes showed no extension of the cathodic limit. The additional cathodic peaks observed with perpendicular electrodes might be related to nitrate ion reduction.

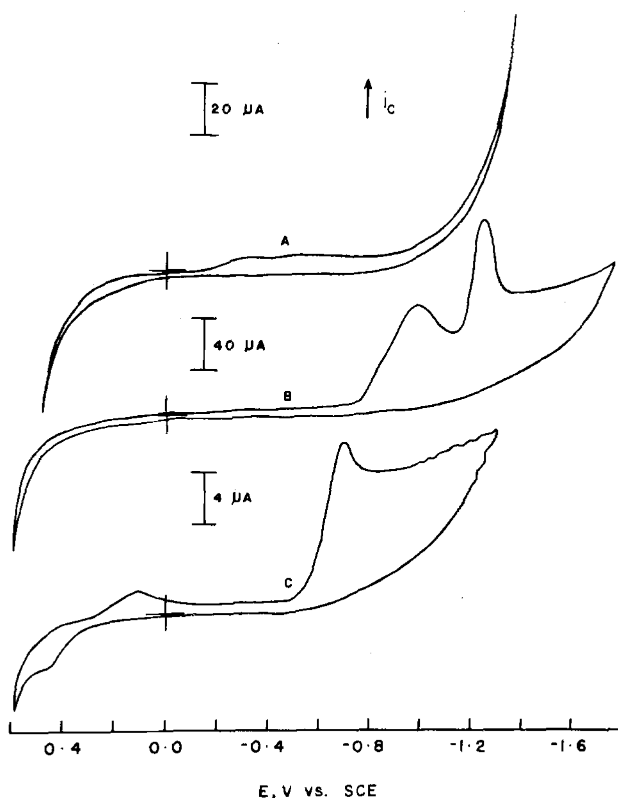

Fig. 5. Cyclic voltammogram for perpendicular electrode in $Ca(NO_3)_2$: (A) 0.1. (B) 1, (C) 5M. Scan rate 0.05 V sec^{-1}.

Finally, the faradaic background currents decreased and the cathodic breakdown potential became more negative when chromium(III) perchlorate or chromium(III) chloride was added to a solution of supporting electrolyte (Fig. 6). It is of interest to note that no chromium(III) reduction peaks were observed on either surface. Chromium(III) may interact strongly with the $(SN)_x$ surface at these potentials which increased the overvoltage necessary to reduce it. The nature of this interaction and why chromium(III) reduction may be inhibited by it is not understood at this time. It is interesting to note, however, that the electrode is not poisoned. The presence of chromium(III) in the interface did not influence charge transfer in the ferri-ferrocyanide system. Normal cyclic voltammograms are observed.

The differences in interactions with respect to alkali metal cation solutions between mercury and parallel $(SN)_x$ electrodes might be related to the type of process occurring. Clearly, adsorption is the predominant electrochemical process occurring on mercury electrodes but this may not be true at $(SN)_x$ electrodes. In this case some specific chemical interaction might be present. In general, the higher the charge density of the cation (when crystallographic radii are used), the lower the background currents and the more negative is the potential of the cathodic decomposition of $(SN)_x$. These effects are noticed only at parallel electrodes in the alkali metal cation series. A much higher charge density ion, *e.g.*, chromium(III), is needed to produce similar effects on the perpendicular surface. These results indicate that the parallel surface could be considered to be chemically softer (8) than the perpendicular surface. This is not surprising as the parallel surface consists predominantly of a conjugated π-electron system but the perpendicular surface presumably has harder functional groups.

Ferri/ferrocyanide.—The ferri-ferrocyanide couple has been previously recommended (9) and widely used (4, 9-11) for the study of solid electrodes because of its polarographic reversibility and the availability of the diffusion coefficients for both the oxidized and reduced forms under a variety of solution conditions (12). We also found this couple to be very useful in cyclic voltammetric and cyclic chronoamperometric studies with $(SN)_x$ electrodes even though the electron transfer mechanism has been shown recently (13) to be more complex than once thought. Formal poten-

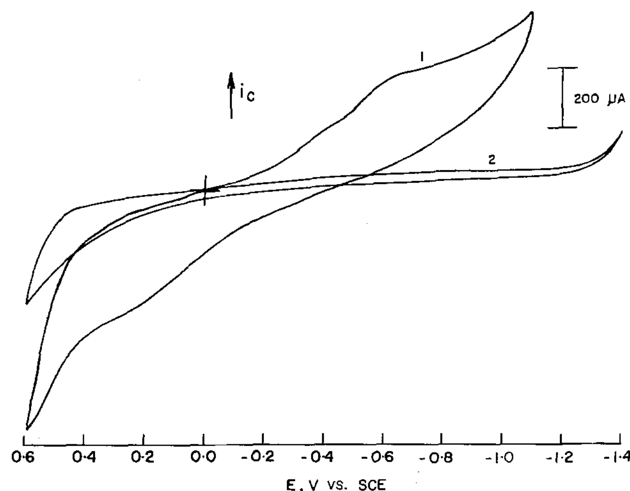

Fig. 6. Effect of the addition of $Cr(ClO_4)_3$ to 0.5M $NaClO_4$ on cyclic voltammogram recorded with perpendicular $(SN)_x$ electrode: (1) 0.5M $NaClO_4$, (2) 0.5M $NaClO_4$ + 0.01M $Cr(ClO_4)_3$. Scan rate 0.05 V sec^{-1}.

Table I. Electrochemical characterization of $(SN)_x$ electrodes with respect to $Fe(CN)_6^{3-}$ solutions

				Electrode surface area × 10^3 cm^2				
				Cyclic chronoamperometry				
Electrode	KCl (moles/liter)	$K_3Fe(CN)_6$ (moles/liter)	$\frac{E_{p_a} + E_{p_c}}{2}$ (V)	Cathodic decay (10 sec)	Anodic decay (10 sec)	Projected-calibrated microscope	$\frac{i_{p_c}}{i_{p_a}}$	$\left(\frac{\partial \log i_p}{\partial \log V}\right)$
$(SN)_x \parallel$	3.0	0.03	+0.260	4.57	4.47	2.31	0.96	0.44
$(SN)_x \parallel$	3.0	0.03	+0.265	8.71	8.10		0.99	0.54
$(SN)_x \perp$	0.5	0.1	+0.215	5.70	5.76	3.08	1.03	0.50
$(SN)_x \perp$	0.5	0.1	+0.215	8.22	8.02	7.01	1.09	0.50
Pt disk*	0.5	0.1	+0.215	5.01	4.87	4.95	1.05	0.47
Pt disk	3.0	0.03	+0.270	5.59		4.95	1.00	0.50

* Torr Seal mounted.

tials, $E_f{}^\circ$, were calculated as the mean of the cathodic and anodic peak potentials obtained from cyclic voltammetric experiments in KCl supporting electrolyte solutions. Typical results for two parallel and two perpendicular $(SN)_x$ electrodes are shown in Table I. At moderate potential scan rates (0.01-0.2 V sec^{-1}) the separation of the oxidation and reduction peak potentials for both electrode orientations was close to the theoretical value for a reversible system (57 mV at 25 °C).

The diffusion-controlled nature of the currents for the ferri-ferrocyanide couple at $(SN)_x$ electrodes was demonstrated by the following results (Table I): (*i*) the ratio of the cathodic to anodic peak currents was close to 1.09 which is the predicted value for a diffusion controlled process (taking into account the differences in diffusion coefficients of the ferri- and ferrocyanide), (*ii*) the dependence of peak currents on scan rate yielded the expected result of $\partial \log i_p / \partial \log V = 0.5$, and (*iii*) the temperature dependence of the cathodic peak currents in the temperature range 15°-75°C, *i.e.*, $(2.303/\Delta T)\Delta \log i_{pc} \cdot 100\% = 0.4\%$. It should be noted that the platinum disk electrode yielded similar values of the formal potential, i_{pc}/i_{pa} and $\partial \log i_p/\partial \log V$ under the same experimental conditions.

The dependence of the peak current and formal potential on *p*H was also found to be the same for both platinum and perpendicular $(SN)_x$ electrodes (Table II). The results obtained with parallel electrodes (not shown) were identical.

As $(SN)_x$ electrodes varied markedly in projected area and macroscopic surface roughness it was difficult to compare the electrochemical behavior of individual $(SN)_x$ electrodes. In order to obtain current densities so that results could be normalized, cyclic chronoamperometry was used to determine the electrochemically active surface area of $(SN)_x$ electrodes. For this reason a 10 sec current decay period was chosen so that the diffusion layer thickness in chronoamperometry experiments was comparable to that in cyclic voltammetry experiments under the scan rates employed. Ferricyanide was chosen as it was shown above to be well behaved at $(SN)_x$ electrodes. The potentials chosen were 0.1V more negative and positive than the reduction and oxidation peak potentials, respectively. Using the Cottrell equation (14, 15), the electrochemical area was calculated from the slopes

Table II. *p*H dependence of peak current and $E_f{}^\circ$ for $Fe(CN)_6^{3-}/Fe(CN)_6^{4-}$

	Pt (disk)		$(SN)_x \perp$	
pH	i_{p_c} (μA)	$\frac{E_{p_a} + E_{p_c}}{2}$ (V)	i_{p_c} (μA)	$\frac{E_{p_a} + E_{p_c}}{2}$ (V)
1.5	38.4	0.250	20.0	0.260
2.5	40.0	0.225	21.2	0.230
4.6	38.2	0.215	18.5	0.215
7.0	40.0	0.215	18.5	0.220
10.7	35.7	0.215	17.0	0.215

of linear i *vs.* $t^{-1/2}$ (14) and i *vs.* $\{(t - 10)^{-1/2} - t^{-1/2}\}$ (15) plots for the cathodic and subsequent anodic decay curves, respectively. The results indicate that the electrochemical area is significantly larger than the area obtained by using a calibrated microscope (Table I). This is not surprising as the surface roughness of $(SN)_x$ electrodes can often be seen with a magnifying glass. Similar chronoamperometric studies with a platinum disk electrode, having a surface area comparable to those of the $(SN)_x$ electrodes, yielded areas which were nearly identical to those obtained with the calibrated microscope (Table I). Thus, it is recommended that the $(SN)_x$ electrode areas be determined using the chronoamperometric technique with ferricyanide solutions, as it is not possible to polish $(SN)_x$ crystals in order to produce a smooth surface because of the delicate nature of this material.

After the potential scan experiments in ferricyanide solution, the $(SN)_x$ electrodes were rinsed with water and scanned in supporting electrolyte solution. There was no evidence of reduction or oxidation peaks of ferri- or ferrocyanide, respectively. This indicates that there is no permanent alteration of the surface due to exposure to ferricyanide solution, *i.e.*, these electrodes were considered to be unmodified in subsequent studies.

Cyclic voltammetry in ferricyanide solutions was also found to be useful in assessing the condition of $(SN)_x$ electrodes. After extended exposure to air or solutions containing adsorbing species, voltammograms of ferricyanide solutions occasionally appeared ill defined (Fig. 7A) with larger peak potential separations than for the reversible case. These electrodes were not used for further study. Thus, the cyclic voltammetric behavior in ferricyanide solution served as a selection criterion for electrodes which were to be used.

Although the $(SN)_x$ crystals used were somewhat porous (Fig. 8) it is doubtful that electrolysis occurs deep within the fibers because: (*i*) there is no "memory effect" for ferricyanide solutions, (*ii*) the solution resistance in the "pores" is much greater than at the surface, and (*iii*) the data fit equations which assumed linear diffusion conditions.

Lead(II) deposition.—Parallel and perpendicular $(SN)_x$ electrodes were used in lead deposition studies (1-40 mM $Pb(NO_3)_2$) in the *p*H range 3.5-4.5 using 0.1M KNO_3 as the supporting electrolyte. Typical results are shown in Fig. 9. Cyclic voltammograms obtained with perpendicular (Fig. 9A) and parallel (Fig. 9B) $(SN)_x$ electrodes differ markedly in the separation between cathodic and anodic peak potentials. There is a pronounced current hysteresis (following potential reversal at −0.72V) for parallel electrodes only (Fig. 9B) which is not uncommon in cyclic voltammetric studies of metal depositions on carbon (16, 17) and mercury (18, 19) electrodes. No well-defined underpotential deposition or stripping peaks were observed with either perpendicular or parallel $(SN)_x$ electrodes. Instead, a gradual increase in the current was observed prior to the bulk lead deposition peak. The voltammetric behavior of parallel $(SN)_x$ elec-

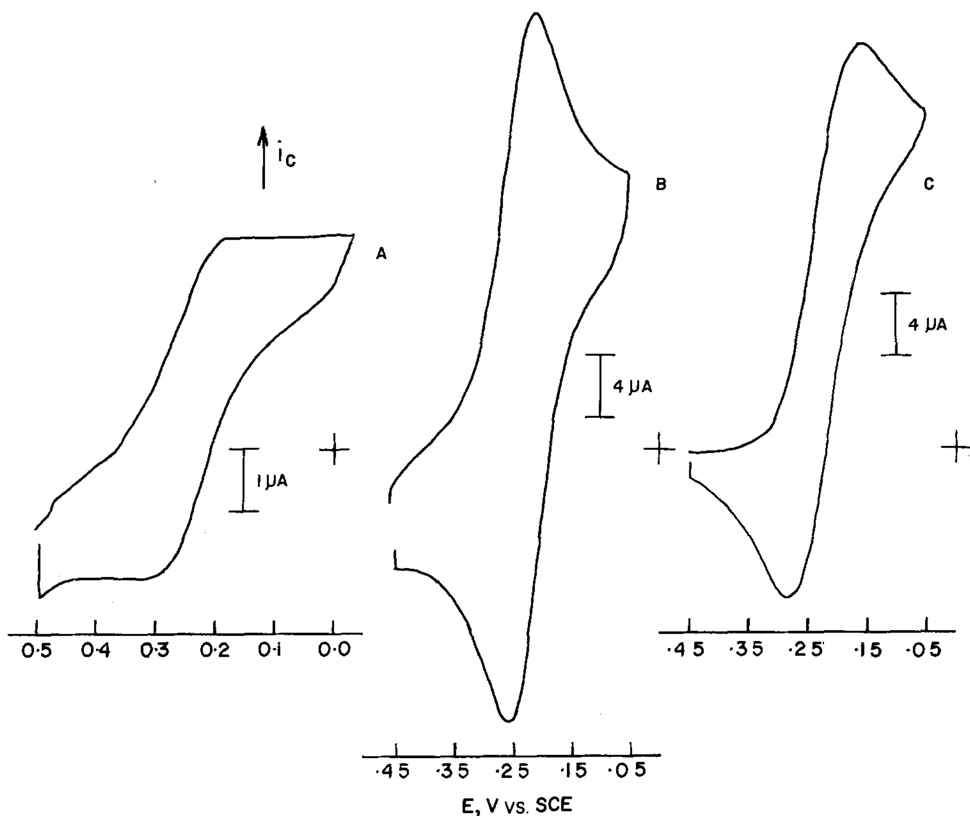

Fig. 7. Cyclic voltammogram of $K_3Fe(CN)_6$ in 0.5M KCl: (A) damaged or extensively used $(SN)_x$ electrode, 0.02M $K_3Fe(CN)_6$, 0.10 V sec^{-1}; (B) new $(SN)_x$ electrode, 0.05M $K_3Fe(CN)_6$, 0.020 V sec^{-1}; (C) Pt disk electrode, same conditions as (B).

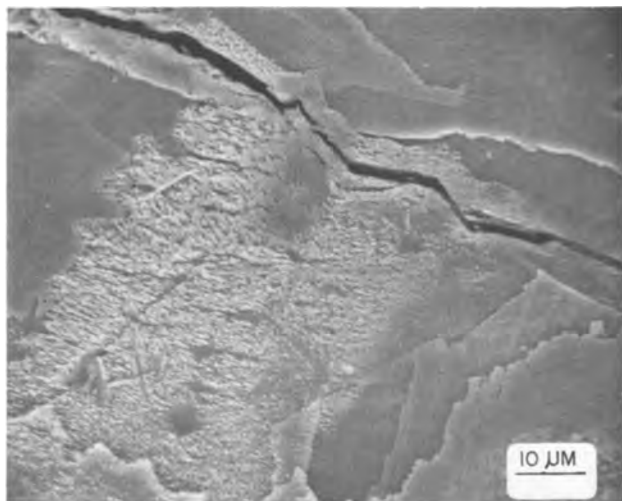

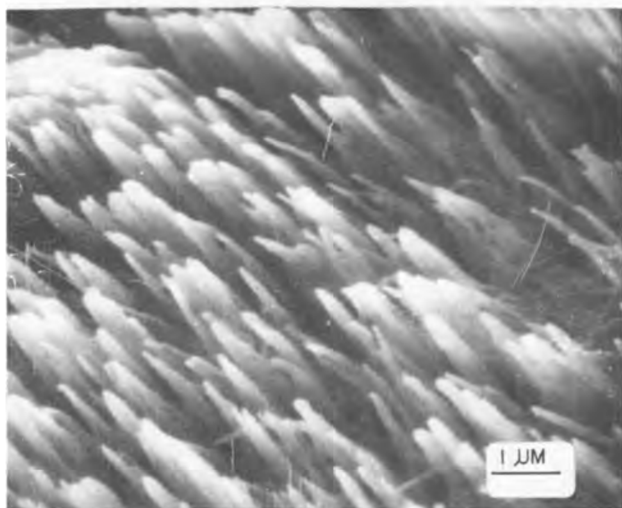

Fig. 8. Scanning electron micrograph of ends of $(SN)_x$ fiber bundles of an $(SN)_x$ crystal.

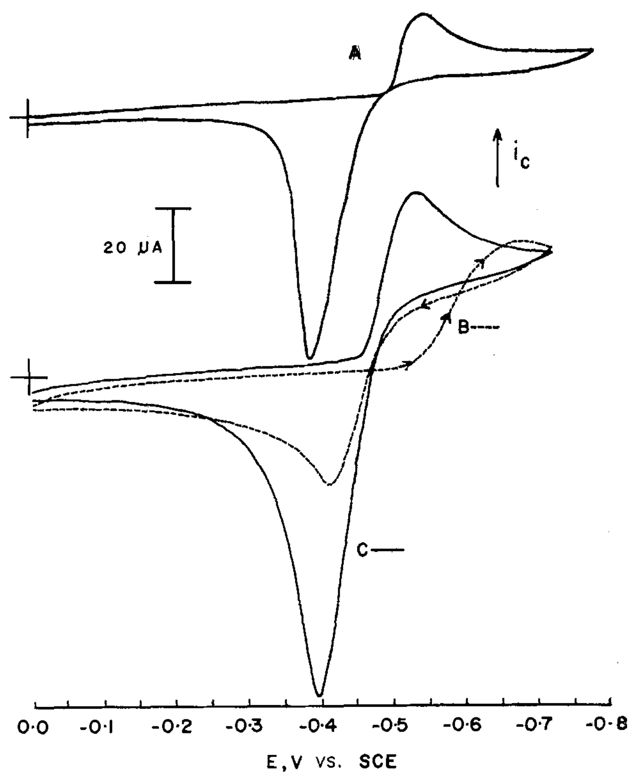

Fig. 9. Cyclic voltammograms in 0.1M KNO_3: (A) 0.005M $Pb(NO_3)_2$ at perpendicular electrode; (B) 0.01M $Pb(NO_3)_2$ at parallel electrode, (C) 0.01M $Pb(NO_3)_2$ at pretreated (see text) parallel electrode. Scan rates 0.015 V sec^{-1}.

trodes in lead ion solutions became nearly identical to that of perpendicular electrodes when the former are pretreated by immersion into a 0.1M $Hg(NO_3)_2$ solution ($pH = 2.5$) for 1 min followed by thorough rinsing with distilled water before the voltammetric experiment (Fig. 9C). That is, the potentials for the deposition and stripping peaks are the same as for perpendicular electrodes, and there is no hysteresis of

the current on the positive scan. These effects do not depend on whether or not lead has been previously deposited on the parallel surface. Parallel electrodes were also treated by exposure to air or to solutions of the same composition and pH as the mercuric ion solution, but without mercury(II) present. Such pretreatment had no effect on lead cyclic voltammograms obtained with parallel electrodes. Further studies dealing with the chemical modification of $(SN)_x$ surfaces with metal cations will be reported in the future.

No significant differences in the appearance of the lead waves were observed between mercuric ion pretreated and untreated perpendicular $(SN)_x$ electrodes. There was, however, an additional cathodic wave observed of similar magnitude on the first scan only at more positive potentials (between −0.1 and −0.2V). This additional wave was not observed with similarly treated parallel electrodes.

When $(SN)_x$ crystals were placed in 0.1M $Hg(NO_3)_2$ solution, small droplets of metallic mercury formed almost exclusively on the perpendicular surface after 5-10 min. Thus, mercury(II) chemically oxidizes functional groups on the ends of the fiber bundles with a concomitant production of mercury metal which coalesces on the perpendicular surface. The additional cathodic peak observed in voltammograms after mercury(II) pretreatment of perpendicular electrodes is probably due to the reduction of chemically oxidized functional groups or of unreacted absorbed mercury(II).

The presence of mercury on the parallel $(SN)_x$ surface affects the cyclic voltammograms of lead dramatically and reproducibly upon indefinite cycling. Stripping experiments were carried out in order to determine if mercury was present in the metallic state on mercuric ion pretreated parallel electrodes. Attempts to electrochemically oxidize metallic mercury which may have been present on these surfaces were not successful. No oxidation peak of mercury was observed and there were no differences in voltammograms obtained in 0.1M KCl for untreated and mercury(II) pretreated parallel $(SN)_x$ electrodes when the potential was scanned from 0V to the anodic current breakdown potential (*ca.* +0.7V). If mercury(II) is present in solution and is electrochemically reduced, the metallic mercury produced is oxidized at *ca.* +0.7V (20). Thus, the amount of metallic mercury on on the parallel surface, if present, is small. Scanning electron micrographs have revealed the presence of mercury droplets on perpendicular but not parallel mercuric ion pretreated electrodes. Mercury is thought to be present on parallel surfaces as a thin metallic film rather than in a strongly adsorbed or complexed ionic form.

The cathodic and anodic currents for cyclic voltammograms obtained in lead ion solutions were integrated in order to determine the ratio of charge exchanged in each of these processes. For a platinum disk electrode, $Q_c/Q_a = 1.07$. For $(SN)_x$ electrodes this ratio was always greater than unity typically being between 1.25 and 4.0. This might be due to (*i*) cathodic background currents in this potential region, but this source of excess cathodic current seemed too small; (*ii*) the irreversible formation of sulfur and/or nitrogen containing Pb^{2+} compounds, *e.g.*, thionitrosyls (21), caused by the catalytic reduction of the $(SN)_x$ surface; or (*iii*) the initial deposition of metallic lead which is not subsequently stripped off. Scanning electron micrographs were obtained after the deposition and subsequent stripping of lead at parallel and perpendicular electrodes (Fig. 10, 11). Some material remained on the surface despite attempts to oxidize it electrochemically. On perpendicular electrodes, the deposit is restricted to the ends of the fibers (Fig. 10). Most of the remaining material on the parallel electrodes was found to be at breaks in the fiber bundles (Fig. 11) which are, of course, perpendicular ends.

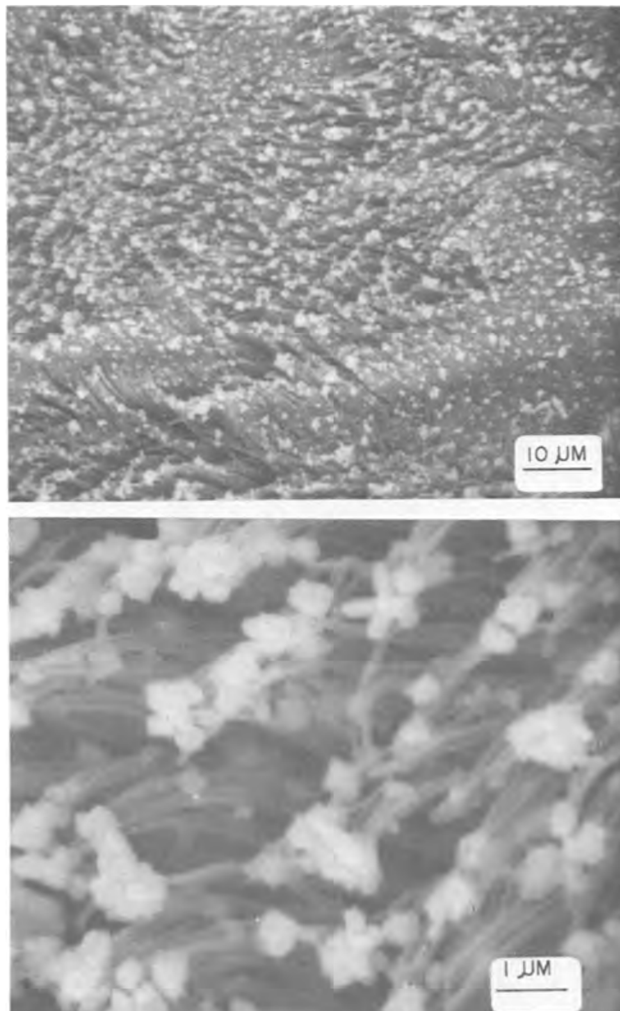

Fig. 10. Scanning electron micrograph of lead deposit on perpendicular electrode or fiber bundle ends.

In order to investigate the mechanism of the lead deposition reaction at $(SN)_x$ electrodes, the procedure developed by Mamantov (22) was employed. It has been suggested that plots of log $(i_p - i)$ *vs.* E (in the potential region 0.5 i_p to 0.9 i_p) and values of $\Delta E = E_p - E_{p/2}$ be used to assess the reversibility of metal deposition reactions at solid electrodes (22). Although plots of log $(i_p - i)$ *vs.* E were linear in the appropriate region for $(SN)_x$ electrodes, the slopes (*ca.* 8-40) and the values of ΔE (*ca.* 0.032-0.118V) indicated that lead deposition at $(SN)_x$ electrodes was not a reversible, diffusion-controlled process. Under the same experimental conditions slopes of these plots for lead deposition on a platinum disk electrode were $\partial \log (i_p - i)/\partial E = 91$ (theoretical $\partial \log (i_p - i)/\partial E = 75$) and the value of ΔE was 0.020V (theoretical $\Delta E = 0.010$V).

As the effect of alkali metal cations of the supporting electrolyte on background currents and breakdown potentials was so pronounced on parallel electrodes, the lead deposition reaction was also studied in the presence of 1M $LiNO_3$ or 1M $CsNO_3$ supporting electrolyte solutions (Fig. 12). A platinum disk electrode was used for comparison. The $E_{pc/2}$ for the deposition of lead was found to be more negative in $LiNO_3$ than $CsNO_3$ for the two parallel electrodes studied. This is consistent with earlier results which indicated a stronger interaction of parallel $(SN)_x$ with Li^+ than Cs^+. The effect of cation on the deposition at the platinum electrode, if any, was just the opposite.

Other systems.—The electrochemical behavior of hydroquinone on $(SN)_x$ electrodes appeared to be

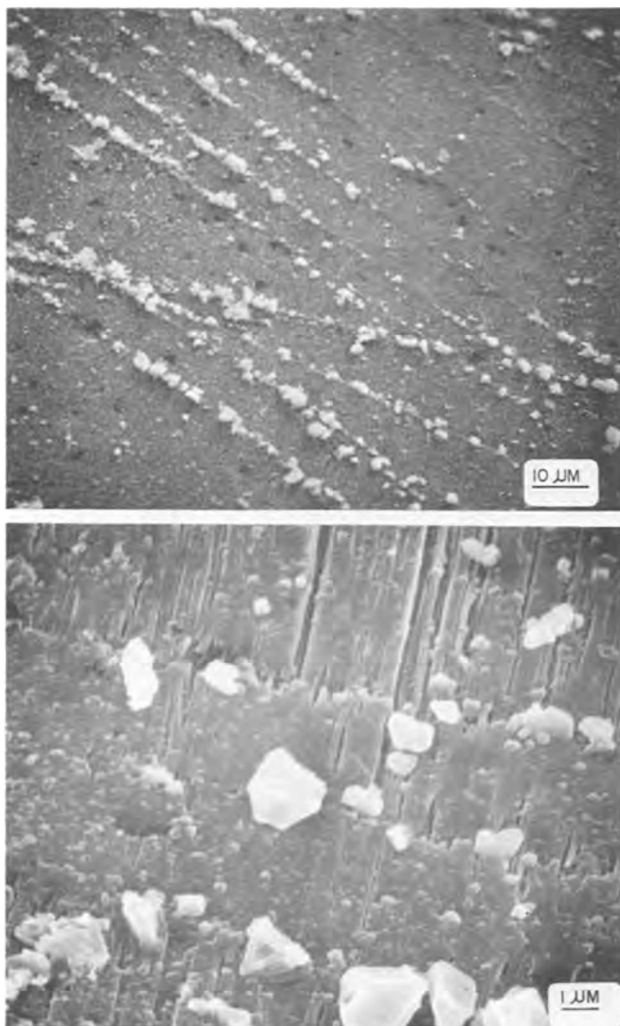

Fig. 11. Scanning electron micrograph of lead deposit on parallel electrode.

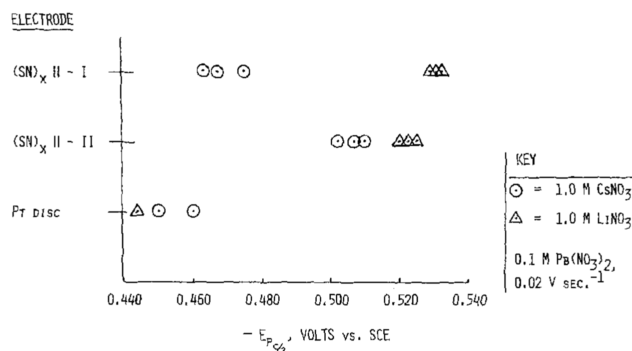

Fig. 12. Effect of nature of cation of supporting electrolyte on $E_{pc/2}$ for lead(II) deposition on two different parallel electrodes.

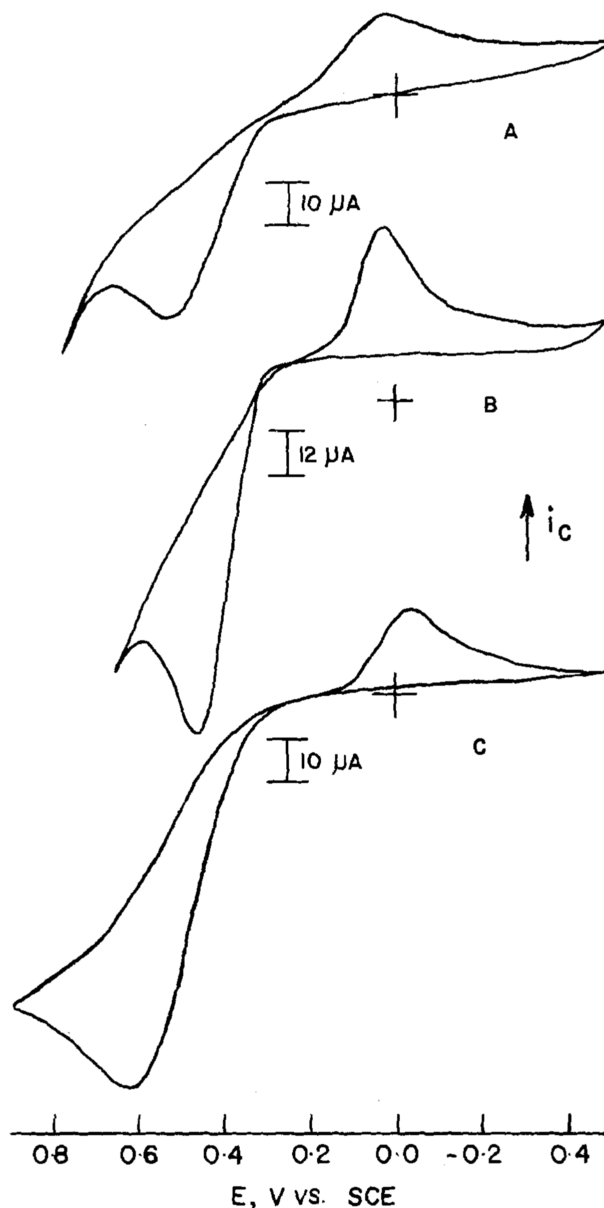

Fig. 13. Cyclic voltammogram in 0.1M hydroquinone solution in 0.5M acetic buffer (pH = 4.75): (A) parallel, (B) perpendicular, (C) Pt disk electrode. Scan rate 0.02 V sec^{-1}.

nearly the same as on Pt-disk electrodes. In 0.5M acetate buffer (pH = 4.75) one irreversible oxidation and reduction peak at $E_{pa} = 0.45V$ and $E_{pc} = 0.03V$, respectively, at scan rate 0.02 V sec^{-1} was obtained (Fig. 13). Anodic, βn_β, and cathodic, αn_α, transfer coefficients calculated from equations $\beta n_\beta = 0.048/(E_{pa} - E_{pa/2})$ and $\alpha n_\alpha = 0.048/(E_{pc/2} - E_{pc})$ were equal to 0.4 and 0.5, respectively, for both $(SN)_x$ and Pt electrodes.

Also, no differences in behavior on $(SN)_x$ and Pt electrodes were found for ruthenium(III)hexammine trichloride reduction being reversible with $E_f° = -0.210V$ in 0.5M KCl (Fig. 14).

Finally, it has to be noted that several redox systems appear to be electrochemically inactive on $(SN)_x$ electrodes. Among them were: $Co(CN)_6^{3}$, $Cr(SCN)_6^{3-}$, $S_4O_6^{2-}$, $S_2O_8^{2-}$, Fe^{3+}, Eu^{3+}, BrO_4^-. The reasons for this inactivity are not known at this time, and are the subject of further investigation.

Summary and Conclusions

In conclusion, $(SN)_x$ appears to be a suitable electrode material for chemical modification studies in aqueous solutions. Thus, regarding the behavior of $(SN)_x$ electrodes in aqueous media: (*i*) Both parallel and perpendicular $(SN)_x$ surfaces exhibit a useful overvoltage region in aqueous media and fulfill the criteria presented for the use of working electrodes in voltammetric studies (4). (*ii*) Surface rather than bulk physiocochemical features of the material govern its electrochemical properties. (*iii*) Electrochemically active surface functional groups undergo irreversible charge transfer reactions. Electrochemical transformations in the bulk of the material are not likely. (*iv*) In addition to typical metallic electrode behavior, $(SN)_x$ exhibits some very unusual surface properties. Metal cations interact more strongly with the $(SN)_x$ surface than other metal electrodes. This is particularly true for the interaction of the alkali metal cations with the parallel surface and of Cr^{3+} with both surfaces. (*v*) Lead cyclic voltammograms

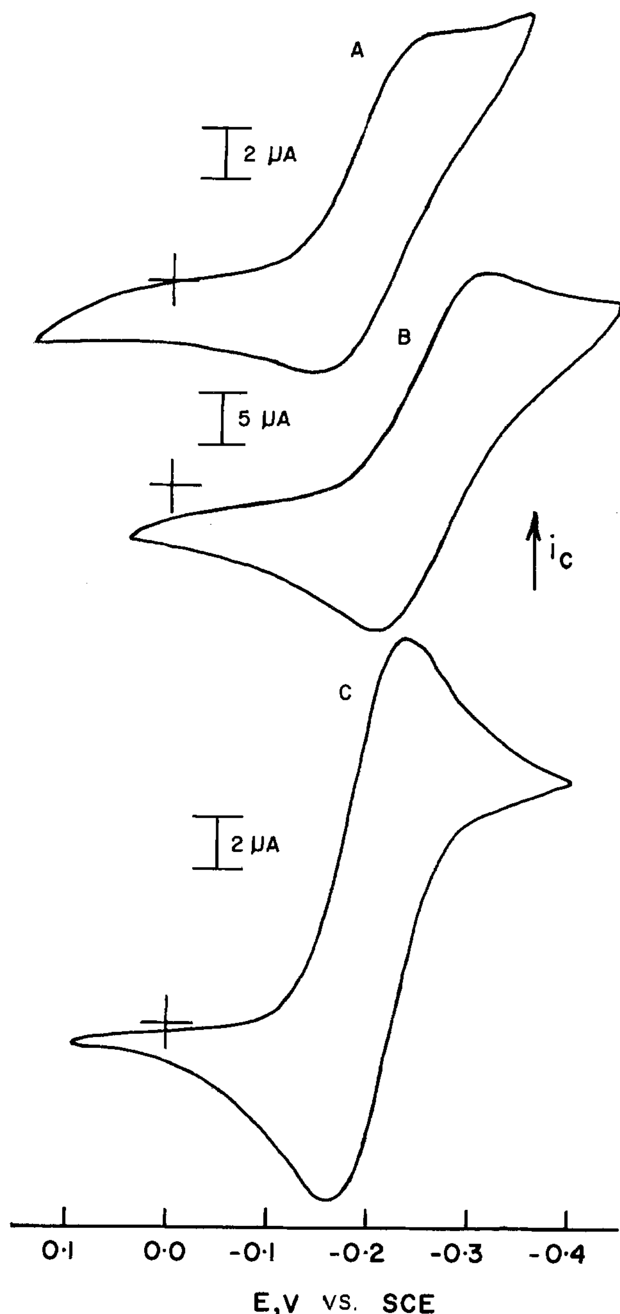

Fig. 14. Cyclic voltammogram in 0.02M $Ru(NH_3)_6Cl_3$ in 0.5M KCl. (A) parallel, (B) perpendicular, (C) platinum disk electrode. Scan rate: (A), (C) 0.02 V sec^{-1}; (B) 0.05 V sec^{-1}.

are dependent on electrode orientation. It is not possible to remove all of the electrodeposited lead by anodic polarization. (*vi*) Mercury(II) chemically oxidized $(SN)_x$ with the simultaneous reduction of mercury(II) to metallic mercury. Mercury droplets form on the perpendicular surface, but mercury metal is probably present on the parallel surface in the form of a thin film.

Acknowledgments

The authors gratefully acknowledge the National Science Foundation for financial support, and one of us (R.J.N.) wishes to thank The Electrochemical Society for financial assistance through the Edward Weston Fellowship (1976).

The technical assistance of Merle Ferry of the Procter and Gamble Company and International Scientific Instruments for scanning electron microscopy studies is gratefully acknowledged. We would also like to thank Dr. E. H. Appelman of Argonne National Laboratories for generously supplying $KBrO_4$.

Manuscript submitted July 11, 1977, revised manuscript received Aug. 31, 1977.

Any discussion of this paper will appear in a Discussion Section to be published in the December 1978 JOURNAL. All discussions for the December 1978 Discussion Section should be submitted by Aug. 1, 1978.

Publication costs of this article were assisted by the University of Cincinnati.

REFERENCES

1. R. J. Nowak, H. B. Mark, Jr., A. G. MacDiarmid, and D. Weber, *J. Chem. Soc. Chem. Commun.*, 9 (1977).
2. C. M. Mikulski, P. J. Russo, M. S. Saran, A. G. MacDiarmid, A. F. Garito, and A. J. Heeger, *J. Am. Chem. Soc.*, **97**, 6358 (1975).
3. P. R. Moses and R. W. Murray, *J. Electroanal. Chem.*, **77**, 393 (1977) and references therein.
4. T. R. Mueller and R. N. Adams, *Anal. Chim. Acta.*, **23**, 467 (1960).
5. C. M. Mikulski, A. G. MacDiarmid, A. F. Gariot, and A. J. Heeger, *Inorg. Chem.*, **15**, 2943 (1976).
6. R. J. Nowak, W. Kutner, H. B. Mark, Jr., A. G. MacDiarmid, In preparation.
7. L. Gierst, E. Nicolas, and L. Tytgat-Vanderberghen, *Croat. Chem. Acta.*, **42**, 117 (1970).
8. R. G. Pearson, *Chemistry in Britan*, **3**, 103 (1967); D. J. Barclay, *J. Electroanal. Chem.*, **19**, 318 (1968).
9. R. N. Adams, "Electrochemistry at Solid Electrodes," Marcel Dekker, New York (1969).
10. L. Lindquist, *J. Electroanal. Chem.*, **52**, 37 (1974).
11. R. E. Panzer and P. J. Elving, *This Journal*, **119**, 864 (1972).
12. M. von Stackelberg and V. Toome, *Z. Electrochem.*, **57**, 342 (1953).
13. L. M. Peter, W. Dürr, P. Bindra, and H. Gerischer, *J. Electroanal. Chem.*, **71**, 31 (1976), and references therein.
14. P. J. Lingane, *Anal. Chem.*, **36**, 1723 (1964).
15. Z. Galus, "Fundamentals of Electrochemical Analysis," Ellis Norwood, Ltd., Winchester (1976).
16. J. A. Harrison, R. P. J. Hill, and J. Thompson, *J. Electroanal. Chem.*, **44**, 445 (1973).
17. M. F. Bell and J. A. Harrison, *ibid.*, **41**, 15 (1973).
18. E. Itabashi and M. Tan, *ibid.*, **60**, 299 (1975).
19. L. Janiszewska and Z. Galus, *Chemia Anal.*, **17**, 691 (1972).
20. Unpublished results.
21. J. Weiss and D. Neubauer, *Z. Naturforsch.*, **13b**, 459 (1958); J. Weiss, *Z. Anorg. Allg. Chem.*, **343**, 315 (1966).
22. G. Mamontov, D. L. Manning, and J. M. Dale, *J. Electroanal. Chem.*, **9**, 253 (1965).

Electrochemistry of 2,2'-Bipyridine Complexes of Cobalt in the Presence of Acrylonitrile

Shlomo Margel, Wayne Smith, and Fred C. Anson*

Arthur Amos Noyes Laboratory, California Institute of Technology, Pasadena, California 91125

ABSTRACT

The previously claimed (1) catalysis of the electroreduction of acrylonitrile by means of a complex of Co(I) and 2,2'-bipyridine is shown to be erroneous. The "catalytic currents" result instead from the two-electron reduction of a mixed complex of Co(I) acrylonitrile and 2,2'-bipyridine. The equilibrium and forward rate constants for the formation of the mixed complex have been estimated and its spectrum is given. The behavior of a number of other vinyl monomers, which mimic acrylonitrile, is described.

Some time ago Tanaka and Sato described experiments (1) in which they claimed to have shown that a low valent complex of cobalt with 2,2'-bipyridine, generated electrochemically in acetonitrile as solvent, was an effective catalyst for the electrochemical reduction of acrylonitrile. We were intrigued by this report for three reasons: (*i*) The claimed catalysis was very notable ($E_{1/2}$ for the wave attributed to acrylonitrile reduction is shifted from −2.3 to −1.3V *vs.* SCE); (*ii*) the reduction of acrylonitrile is a reaction of considerable industrial importance; and (*iii*) the catalytic mechanism was speculated to involve the adsorption of a low valent complex on the surface of the mercury electrode. We have therefore examined this system in more detail at both mercury and platinum electrodes by means of controlled potential electrolysis, cyclic voltammetry, and polarography. Contrary to the previous report (1) we find that the cobalt-2,2'bipyridine complexes do not function as catalysts for the reduction of acrylonitrile. The increase in current that results when both reactants are present arises instead from the reduction of a complex containing bipyridine, acrylonitrile, and cobalt(I) to a new complex containing cobalt in the (−I) oxidation state. Several other vinyl monomers which form complexes with cobalt(1), *e.g.*, 2,2'-bipyridine, also facilitate the reduction to cobalt(−I). This report summarizes the experimental evidence which has led us to these conclusions.

Experimental

Apparatus.—Polarograms were obtained with a Princeton Applied Research (PAR) Model 174 polarographic analyzer and recorded with a Hewlett-Packard Model 7004 X-Y recorder. Cyclic voltammograms were obtained by means of a PAR Model 173 potentiostat driven by a conventional signal generator. The voltammograms were recorded with the X-Y recorder or by photographing the screen of a Tektronix 564 oscilloscope. Controlled potential coulometry was conducted with the PAR Model 173 potentiostat equipped with a Model 179 digital coulometer. Gas chromatographic analyses for acrylonitrile in acetonitrile were obtained with a Hewlett-Packard Model 5830 A gas chromatograph with an 18 ft column containing Carbowax 20 M on Chromosorb W. Spectra were recorded with a Cary 11 spectrophotometer using cuvettes capped with rubber septums which were deoxygenated by purging with argon.

Measurements were conducted in a three-compartment cell. The reference electrode was a silver wire immersed in 0.1M $AgNO_3$ in acetonitrile which was double isolated by fritted glass disks from the main cell compartment. The potential of this reference electrode was 392 mV more positive than an aqueous SCE when both were immersed in 0.01M aqueous KNO_3. All potentials are given with respect to the Ag/0.1M $AgNO_3$ reference electrode.

The platinum indicator electrode was a platinum wire (diameter = 0.076 cm) sealed in soft glass and cut and polished to expose a 0.045 cm^2 disk flush with the glass surface. The working electrode for the controlled potential electrolyses was a cylindrical platinum gauze electrode supported with stout platinum wire.

Solutions were deoxygenated with prepurified argon which was passed successively through an aqueous chromous chloride solution, purified acetonitrile, and a calcium chloride drying tower before entering the test solution.

Materials.—Polarographic grade tetraethylammonium perchlorate (TEAP) (Southwestern Analytical Company) was used as supporting electrolyte without additional purification. Spectroquality acetonitrile was stirred over CaH_2 for 24 hr, distilled under reduced pressure, and stored under argon.

$Co(bipy)_3(ClO_4)_3$ and $Co(bipy)_3(ClO_4)_2$ (bipy ≡ 2,2'-bipyridine) were prepared by standard methods (2), $Co(phen)_3(ClO_4)_2$ (phen ≡ 1,10-phenanthroline) was prepared by mixing a slight excess of 1,10-phenanthroline monohydrate with $CoCl_2 \cdot 6H_2O$ in ethanol in the absence of air. Addition of a concentrated aqueous solution of $NaClO_4$ followed by cooling to 0°C produced the desired solid. Ethyl cinnamate, cinnamonitrile, and 4-vinyl pyridine were distilled before use. Vinyl monomers used as received included ethyl acrylate, methyl methacrylate, styrene, and methacrylonitrile.

Preparation and properties of $[Co(bipy)_2CH_2CHCN]ClO_4$.—Solid $Co(bipy)_3ClO_4$ has been isolated by reduction of $Co(bipy)_3^{3+}$ with Na(Hg) (3) or $NaBH_4$ 4) followed by precipitation with excess perchlorate. To obtain the corresponding acrylonitrile complex 100 mg of $Co(bipy)_3(ClO_4)_2$ was dissolved in 20 ml of a 1:3 mixture of water and ethanol containing 200 mg of acrylonitrile. The mixture was freed of oxygen and all subsequent steps were conducted in an atmosphere of argon. Addition of 2 ml of a 0.7M solution of $NaBH_4$ in water produced a deep purple solution from which a black solid was precipitated by adding a large excess of $NaClO_4$. The solid was filtered, washed with oxygen-free water and ether, and dried at room temperature under vacuum. Elemental analysis of the solid (percentages): C, 49.0; H, 3.5; N, 12.0; Co, 11.9; Cl, 7.2. Calculated for $Co(bipy)_2(CH_2CHCN)ClO_4$: C, 52.8; H, 3.6; N, 13.3; Co, 11.3; Cl, 6.8.

The black solid is oxidized much more slowly by oxygen than is $Co(bipy)_3ClO_4$. The infrared spectrum of the solid (Nujol mull) shows a band at 2210 cm^{-1} (carbon-nitrogen stretch) which is not far removed from the same band in free acrylonitrile, indicating that the nitrile group is not directly involved in the bonding to the cobalt(I). The acrylonitrile-cobalt(I) bond is most likely centered on the double bond.

* Electrochemical Society Active Member.
Key words: catalysis, mixed complexes, vinyl monomers.

Results

Polarography: Comparison with the results of Tanaka and Sato (1).—In agreement with Ref. (1), we observed four reduction waves for $Co(bipy)_3^{3+}$ corresponding to the successive formation of complexes containing cobalt in the oxidation states (II), (I), and (−I) followed by the reduction of liberated 2,2′-bipyridine. The half-wave potentials also agreed with those listed in Ref. (1). The addition of acrylonitrile to solutions of $Co(bipy)_3^{3+}$ resulted in the "catalytic wave" described by Tanaka and Sato (1) but the properties of this wave are very sensitive to the concentration of the supporting electrolyte. With the rather low supporting electrolyte concentration employed in Ref. (1) (0.05M tetraethylammonium perchlorate), the "catalytic wave" exhibited the properties described by Tanaka and Sato, *i.e.*, the limiting current of the catalytic wave was approximately proportional to the acrylonitrile concentration up to concentrations as large as 5 times the concentration of the cobalt complex. However, if the concentration of supporting electrolyte is increased, this behavior changes: The magnitude of the catalytic wave is no longer proportional to the concentration of acrylonitrile. Instead it tends toward a limiting value close to that of the wave corresponding to the reduction of Co(I) to Co(−I) in the absence of acrylonitrile (Fig. 1). Even when neat acrylonitrile is used in place of acetonitrile as the solvent the magnitude of the limiting current of the catalytic wave remains about the same (Fig. 1).

In agreement with Tanaka and Sato (1) we observed that the addition of free 2,2′-bipyridine to solutions of $Co(bipy)_3^{3+}$ causes no shift in the half-wave potentials of the waves corresponding to the reduction of Co(III) to Co(II) and of Co(II) to Co(I) while the wave for the reduction of Co(I) to Co(−I) shifts to more negative potentials. In the presence of acrylonitrile the value of $E_{1/2}$ for the reduction of Co(II) to Co(I) does respond to the addition of 2,2′-bipyridine until its concentration is increased sufficiently to cause the value of $E_{1/2}$ to match its value in the absence of acrylonitrile, whereupon further additions of 2,2′-bipyridine are without effect (Table I).

Spectral observations.—The intensely blue complex formed by reducing cobalt(II) in the presence of 2,2′-bipyridine has a visible absorption spectrum with a maximum at 600 nm (5). Since the cobalt(II)-bipy complexes show essentially no absorption in this region of the spectrum, it proved possible to utilize the absorbance at 600 nm to determine the number of molecules of 2,2′-bipyridine coordinated to cobalt in the Co(I) complex by means of the method of continuous variations (6). Figure 2 shows a plot of the absorbance at 600 nm as a function of the ratio of 2,2′-bipyridine to cobalt in solutions prepared by mixing $Co(ClO_4)_2$ and the ligand in oxygen-free methanol and adding a slight excess of $NaBH_4$ dissolved in oxygen-free methanol. The two straight lines drawn through the data points intersect at a ratio of 2,2′-bipyridine to cobalt of 2.95 indicating that the cobalt(I) complex present is predominately $Co(bipy)_3^+$.

Table I. Half-wave potentials for the reduction of Co(II) to Co(I) in acetonitrile solutions containing 2,2′-bipyridine and acrylonitrile. All solutions contained 0.6 mM $Co(bipy)_3(ClO_4)_2$ and 0.1M TEAP

Conc of acrylonitrile (mM)	Added bipy conc (mM)	$-E_{1/2}$ (V *vs.* Ag/0.1M $AgNO_3$)
0	0	1.340
0.8	0	1.336
1.6	0	1.327
2.4	0	1.324
4.0	0	1.320
6.0	0	1.318
14.0	0	1.317
22.0	0	1.315
22.0	1.2	1.318
22.0	2.4	1.320
22.0	3.6	1.323
22.0	6.0	1.325
22.0	14.0	1.331
22.0	34.0	1.338

The spectral changes accompanying the conversion of $Co(bipy)_3^+$ to the mixed complex containing acrylonitrile are shown in Fig. 3. It did not prove possible to obtain reliable estimates of the relative concentrations of complexes present from the spectra, but the large spectral changes make it clear that there is substantial complexation of acrylonitrile by cobalt(I). Tanaka and Sato (1) reached the opposite conclusion, but they did not examine the visible spectra of their solutions.

Cyclic voltammetry.—Our observation that the polarographic wave which Tanaka and Sato attributed to the catalyzed reduction of acrylonitrile had a magnitude that was quite sensitive to the ionic strength of the supporting electrolyte suggested that the wave might have been exalted by polarographic streaming maxima in the dilute supporting electrolyte employed in Ref. (1). The system was therefore examined by cyclic voltammetry with a platinum electrode replacing the dropping mercury electrode. The cyclic voltammograms for $Co(bipy)_3^{3+}$ in the absence of acrylonitrile exhibit the same three waves [Co(III) → Co(II), Co(II) → Co(I), Co(I) → Co(−I)] that were observed in the polarographic experiments. The first two waves exhibit reversible behavior at all scan rates with peak

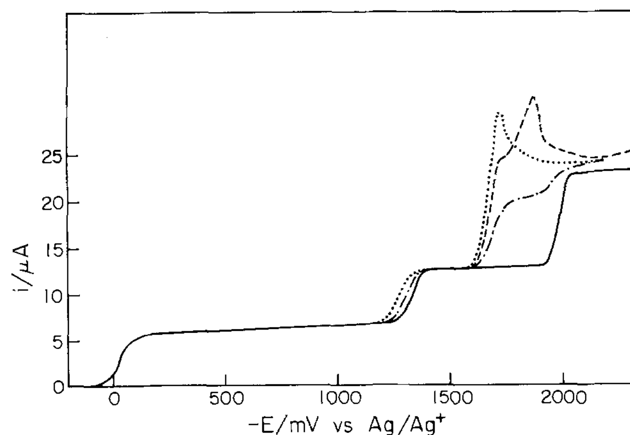

Fig. 1. D-C polarograms for 1 mM $Co(bipy)_3^{3+}$ in acetonitrile: (—) no acrylonitrile; (·—·—·—) 1 mM acrylonitrile; (— — —) 2 mM acrylonitrile; (· · · · ·) pure acrylonitrile as solvent. Supporting electrolyte: 0.1M TEAP. Capillary characteristics: drop time 1 sec, mercury flow rate —1.26 mg sec^{-1}.

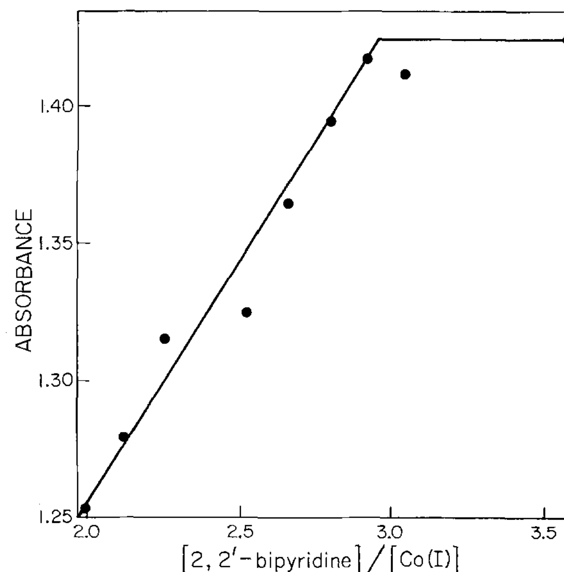

Fig. 2. Absorbance at 600 nm *vs.* the ratio of 2,2′-bipyridine to Co(I) in methanol.

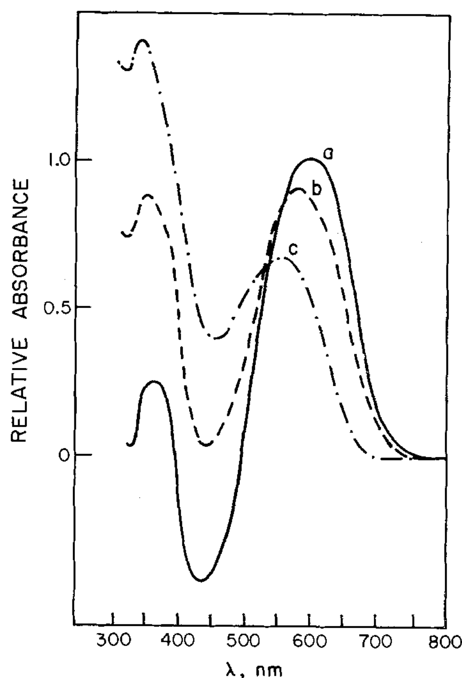

Fig. 3. Effect of acrylonitrile on the absorption spectrum of 0.1 mM Co(I) in a methanol solution containing 0.9 mM 2,2′-bipyridine: (——) no acrylonitrile; (— — —) 0.2 mM acrylonitrile (—·—·—) 1.6 mM acrylonitrile. The Co(I) was obtained by reduction of Co(II) with a slight excess of $NaBH_4$.

potential separations of *ca.* 60 mV and no dependence of peak potentials on scan rate or the addition of 2,2′-bipyridine. The third wave exhibits reversible behavior at moderate scan rates (1 V sec^{-1}) with peak potentials and anodic-cathodic peak potential separations that depend on the concentration of added 2,2′-bipyridine. Figure 4 shows the dependence of the average of the anodic and cathodic peak potentials of all three waves on the concentration of 2,2′-bipyridine. The slope of the line drawn through the points for the Co(I)-to-Co(−I) wave is 25 mV/decade which indicates that one molecule of 2,2′-bipyridine is lost when the Co(I) complex is reduced to Co(−I).

Figure 5 contains a representative set of voltammograms for the second and third reduction steps in

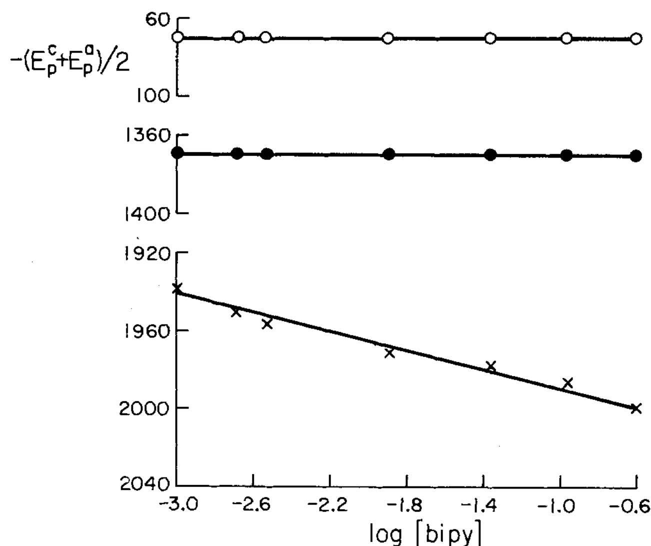

Fig. 4. Average of cathodic and anodic peak potentials for cyclic voltammograms: (○), Co(III) ⇌ Co(II); (●), Co(II) ⇌ Co(I); (×), Co(I) ⇌ Co (−I) in acetonitrile solutions of 2,2′-bipyridine. Concentration of cobalt: 1 mM. Supporting electrolyte: 0.1M TEAP. Scan rate: 1 V sec^{-1}.

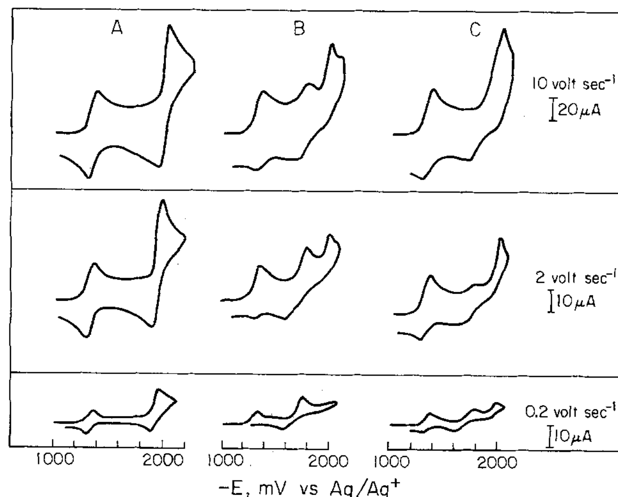

Fig. 5. Cyclic voltammograms for $Co(bipy)_3(ClO_4)_2$ in acetonitrile: A, no acrylonitrile present; B, 2.5 mM acrylonitrile present; C, 2.5 mM acrylonitrile and 2.0 mM 2,2′-bipyridine present. Supporting electrolyte: 0.1M TEAP. Platinum microelectrode: 0.045 cm^2.

the absence and presence of acrylonitrile. As acrylonitrile is added to the solution of $Co(bipy)_3{}^{3+}$ a new wave appears (Fig. 5B), but its magnitude never exceeds that of the wave corresponding to the reduction of Co(I) to Co(−I) in the absence of acrylonitrile. This wave merely diminishes at the same rate as the new wave grows. Both waves correspond to the two-electron reduction of cobalt(I) without any apparent reduction of acrylonitrile.

The relative magnitude of the two cyclic voltammetric waves depends on the rate of potential scan: The less negative wave is suppressed and the more negative wave is enhanced the higher the scan rate. The less negative wave is reversible at high scan rates but becomes progressively less so as the scan rate is diminished. The wave can also be suppressed or eliminated by addition of 2,2′-bipyridine to solutions containing $Co(bipy)_3{}^{3+}$ and acrylonitrile (Fig. 5C). The behavior is consistent with the presence of a sluggishly established equilibrium as indicated in reaction [1]

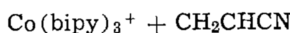

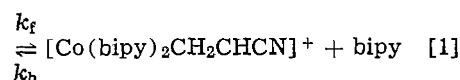

$$Co(bipy)_3{}^+ + CH_2CHCN \underset{k_b}{\overset{k_f}{\rightleftharpoons}} [Co(bipy)_2CH_2CHCN]^+ + bipy \quad [1]$$

The new wave resulting from the addition of acrylonitrile can then be understood as the reduction of the mixed Co(I) complex, $[Co(bipy)_2CH_2CHCN]^+$, to the Co(−I) state.

An estimate of the equilibrium constant for reaction [1] was obtained by preparing solutions of $Co(bipy)_3{}^{3+}$ containing various concentrations of acrylonitrile and 2,2′-bipyridine and adjusting the potential of a platinum indicator electrode to −1400 mV [where the cobalt(III) complex was reduced to a mixture of the two cobalt(I) complexes] for 60 sec to allow the equilibrium in reaction [1] to be established. The electrode potential was then scanned toward more negative values and the peak currents for the two waves corresponding to the reduction of Co(I) to Co(−I) were measured. At scan rates of 5 V sec^{-1} or greater the ratio of the two peak currents became essentially independent of scan rate and thus provided a direct measure of the equilibrium concentrations of $Co(bipy)_3{}^+$ and $[Co(bipy)_2CH_2CHCN]^+$. Table II summarizes the results obtained from a series of such measurements and the resulting values of the equilibrium constant for reaction [1]. The reasonable constancy of the equilibrium constants obtained support the stoichiometry indicated in reaction [1], *i.e.*, one molecule of 2,2′-bipyridine is replaced by one molecule of acrylonitrile to form the more easily reduced complex.

Table II. Equilibrium constant for reaction [1], K_1, evaluated from voltammetric peak current ratios

Scan rate (V sec^{-1})	Conc of 2,2'-bipyridine* (mM)	Conc of acrylonitrile (mM)	Peak current ratio†	K_1 (calc)
5	5.0	5.0	1.00	1.0
10	5.0	5.0	1.05	1.1
5	12.5	5.0	0.47	1.2
10	12.5	5.0	0.52	1.3
5	2.5	5.0	0.22	1.1
10	2.5	5.0	0.27	1.3
20	2.5	5.0	0.25	1.3
5	5.0	10.0	2.07	1.0
10	5.0	10.0	2.0	1.0
			Average:	1.1

* The concentration of $Co(bipy)_3^{3+}$ was 0.5 mM.
† The ratio is of the peak current corresponding to the reduction of the acrylonitrile complex to that for the reduction of $Co(bipy)_3^+$. A platinum microelectrode (0.045 cm^2) was employed.

Kinetics of reaction [1].—The cyclic voltammetric behavior of the pair of waves corresponding to the reduction of $Co(bipy)_3^{2+}$ and the oxidation of $Co(bipy)_3^+$ can be utilized to inspect the kinetics of reaction [1]. In the absence of acrylonitrile the cathodic and anodic peak currents for these two waves are equal, but the anodic peak current is diminished by the addition of acrylonitrile as reaction [1] proceeds from left to right (Fig. 5B). By working in the presence of excess acrylonitrile the reaction can be made pseudo first order and essentially irreversible. Under these conditions the forward rate constant for reaction [1] can be evaluated from the sweep rate dependence of the peak current ratio (7). Table III summarizes the data obtained from which an average value for k_f of 8×10^3 M^{-1} sec^{-1} was calculated.

Controlled potential electrolysis.—Successive electrolysis of acetonitrile solutions of $Co(bipy)_3^{3+}$ with mercury pool or platinum gauze electrodes at potentials on the plateau of the first and then of the second polarograph waves (*i.e.*, −100 and −1400 mV, respectively) results in the consumption of 1F/mole for each wave as expected for successive reductions to $Co(bipy)_3^{2+}$ and $Co(bipy)_3^+$. During the reduction to $Co(bipy)_3^+$ the solution develops the deep blue color characteristic of this complex (3, 4). If the electrolysis is continued at the same potential an additional faraday per mole of electricity is slowly consumed over a period of a few hours, the blue color fades, and a dark precipitate resembling metallic cobalt appears. This slow, electrolytic decomposition of the complex is diminished by the addition of excess 2,2'-bipyridine.

Acrylonitrile is without effect on the course of the controlled potential reduction of $Co(bipy)_3^{3+}$ and $Co(bipy)_3^{2+}$. However, if sufficient acrylonitrile is present the color developed as Co(I) is produced and is

Table III. Forward rate constant for reaction [1], k_f, estimated from cyclic voltammetric peak current ratios

Scan rate (V sec^{-1})	Conc of acrylonitrile* (mM)	Peak current ratio†	$k_{app}\tau$‡	k_{app} (sec^{-1})	10^{-3} k_f (M^{-1} sec^{-1})
2	0.5	0.74	0.34	4.3	8.6
5	0.5	0.87	0.14	4.2	8.4
5	1.0	0.79	0.24	6.5	6.5
5	1.0	0.77	0.28	8.8	8.8
5	2.0	0.70	0.40	12.6	6.3
10	2.0	0.77	0.28	17.5	8.8
				Average:	8×10^3

* The concentration of $Co(bipy)_3(ClO_4)_2$ was 0.5 mM. Supporting electrolyte: 0.1M TEAP.
† The ratio is of the peak current for the oxidation of $Co(bipy)_3^+$ to that for the reduction of $Co(bipy)_3^{2+}$.
‡ Read from a plot of the data in Table XI in Ref. (7). The negligibility of the reverse of reaction [1] under the experimental conditions employed was demonstrated by the lack of significant changes in the peak current ratio when small amounts of 2,2'-bipyridine were added to the solutions.

deep purple rather than the characteristic blue of $Co(bipy)_3^+$. The same color can be produced by adding acrylonitrile to a previously electrogenerated solution of $Co(bipy)_3^+$. It is apparently the color of the mixed complex, $Co(bipy)_2(CH_2CHCN)^+$.

Controlled potential reduction of the purple solution at a potential on the plateau of the new wave now present (Fig. 5B) results in the consumption of almost exactly two additional faradays per mole of Co and yields a brownish yellow solution. This result is independent of the excess of acrylonitrile present: The same behavior is obtained if acrylonitrile is substituted for acetonitrile as the solvent.

That no reduction of the acrylonitrile occurs during the controlled potential reduction was confirmed by gas chromatographic analysis of the solution before and after the electrolysis: Only a negligible loss of acrylonitrile was observed by the time that 2F/mole of cobalt had been consumed and the current had decayed to its background level.

If the controlled potential electrolysis is carried out with a solution containing $Co(bipy)_3^{2+}$ and acrylonitrile the total charge consumed at −1.7V is 3F/mole of cobalt(II), as expected, but the initial current is not as large as would correspond to the simple, direct reduction of cobalt(II) to cobalt(−I). The behavior is consistent with the intervention of a slow chemical step along the electrolytic pathway. A likely candidate for such a slow step is reaction [1]. If the electrolysis is continued beyond the point at which the cobalt has been converted to Co(−I) the current falls to the background level but the concentration of acrylonitrile monitored by gas chromatography decreases slowly over a period of several hours. However, there is no detectable loss of acrylonitrile before this stage of the electrolysis. We found no evidence of acrylonitrile reduction accompanying the reduction of the cobalt.

Reaction of $Co(bipy)_3^+$ with vinyl monomers.—The apparent propensity for acrylonitrile to coordinate to Co(I) and thereby facilitate its further reduction suggested that other vinyl monomers might exhibit similar behavior. This proved to be the case for a number of vinyl monomers which all produce the same wave near −1.7V that results when acrylonitrile is added to solutions of $Co(bipy)_3^{2+}$. The wave height in each case corresponds to the reduction of Co(I) to Co(−I). The equilibrium and forward rate constants for the formation of the assumed cobalt(I)-vinyl monomer complexes according to reaction [2]

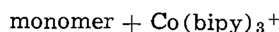
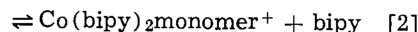

$$\text{monomer} + Co(bipy)_3^+ \rightleftharpoons Co(bipy)_2\text{monomer}^+ + \text{bipy} \quad [2]$$

were evaluated by the same cyclic voltammetric procedures employed with acrylonitrile and the results are given in Table IV. Note that the stability of the cobalt(I)-vinyl monomer complexes increases with the ease of reduction of the monomer itself ($E_{1/2}$ values are given in Table IV).

Discussion

The results that have been described can all be accommodated on the basis of the set of reaction se-

Table IV. Forward rate constants, k_f, and equilibrium constants, K_2, for reaction [2] estimated from voltammetric peak current ratios

Vinyl monomer	k_f (M^{-1} sec^{-1})	K_2	Half-wave potential of the monomer, $-E_{1/2}$ (V)
Ethyl cinnamate	9×10	4.5×10^{-3}	2.2
Cinnamonitrile	4×10^2	5.0×10^{-2}	2.2
Ethyl acrylate	5×10^2	6.0×10^{-2}	2.5
Acrylonitrile	5×10^{-1}	1.3×10^{-5}	2.57
4-Vinyl pyridine	8×10^3	1.1	2.55
Methacrylonitrile	2	7.0×10^{-4}	2.62
Methyl methacrylate	$<10^{-1}$	*	2.63
Styrene	$\sim 3 \times 10^{-1}$	*	2.83

* Too small to measure, *i.e.*, $<10^{-5}$.

Scheme I

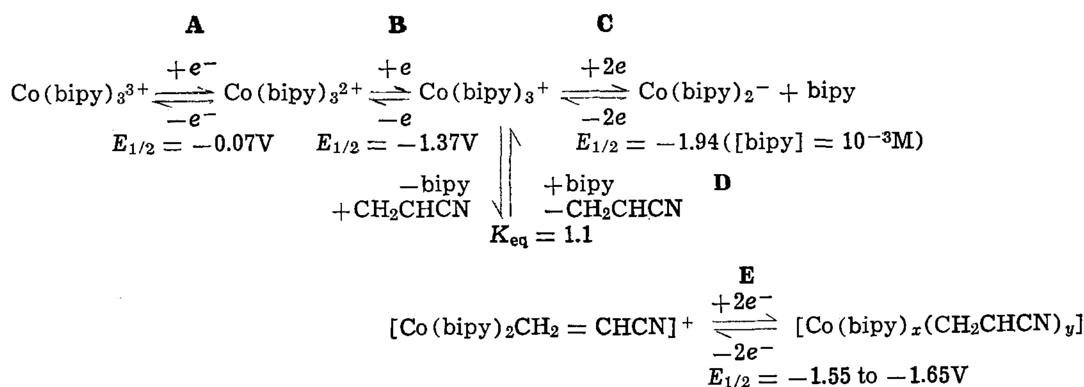

quences given in Scheme I. The evidence to support the conclusion that there is no loss of coordinated 2,2′-bipyridine as Co $(bipy)_3^{3+}$ is reduced to $Co(bipy)_3^{+}$ is the fact that both the polarographic half-wave potentials and the cyclic voltammetric peak potentials corresponding to the reversible steps **A** and **B** in Scheme I show no dependence on the concentration of free 2,2′-bipyridine (Table I; Fig. 4). However, this does not require that the 2,2′-bipyridine retain its bidentate chelation of the cobalt center when the latter is reduced to the Co(I) state. The resulting d^8 complex could well become five-coordinate by the breaking of one of the cobalt-bipy bonds.

Both step **C** and steps **D** + **E** in Scheme I show half-wave and peak potentials which depend on the concentration of 2,2′-bipyridine in the way to be expected if a loss of coordinated 2,2′-bipyridine accompanied the electrode reaction. It is noteworthy that step D could not be observed with the $Co(phen)_3^{+}$ complex even in the presence of large excesses of acrylonitrile. Apparently the steric constraints imposed by the larger and more rigid 1, 10-phenanthroline ligands which cannot become monodentate as readily as can 2,2′-bipyridine, impedes the formation of the π-bonded acrylonitrile complex.

The composition of the product of step **E** was not definitely established. However, it is not the same as the product of step **C** because solutions resulting from the reduction of $Co(bipy)_3^{2+}$ by three electrons in the absence of acrylonitrile are noticeably bluer than those obtained when acrylonitrile is present. Moreover, the latter solutions can be converted to what appears to be the same blue color by the addition of excess 2,2′-bipyridine following the reduction. The Co(−I) complex may contain more than a single acrylonitrile molecule and fewer than two 2,2′-bipyridine molecules but the available data are inadequate to permit a definitive assignment of its composition.

The primary differences between the interpretations offered by Tanaka and Sato and that given in Scheme I are the lack of any reduction of acrylonitrile and the proposed formation in step **D** of a stable, mixed complex of acrylonitrile and 2,2′-bipyridine which undergoes reduction to the Co(−I) state at less negative potentials than does the $Co(bipy)_3^{+}$ complex. That the mixed complex has the composition given in Scheme I is supported by the spectral data, cyclic voltammetric data from which reasonably constant values for the equilibrium constant for step **D** were obtained (Table II), and the fact that a perchlorate salt was isolated which gave an elemental analysis that corresponded reasonably well to that calculated for $[Co(bipy)_2CH_2CHCN]ClO_4$.

Tanaka and Sato concluded that $Co(bipy)_3^{+}$ and CH_2CHCN do not react with each other in the bulk of solution because the height of the polarographic wave they attributed to the reduction of the product of this reaction did not increase linearly with the concentration of $Co(bipy)_3^{+}$. On this basis they argued that the mixed complex was formed only at the mercury electrode surface where it was adsorbed. As mentioned earlier, we believe Tanaka and Sato were misled by the presence of polarographic maxima under the conditions of their experiments. By employing higher supporting electrolyte concentrations or by substituting a platinum electrode for the DME we observed wave heights that remained linearly proportional to the concentration of cobalt(I) throughout the range from 0.1 to 10 mM. We found no evidence of adsorption of $Co(bipy)_3^{2+}$ or $Co(bipy)_3^{3+}$ in the cyclic voltammetric data at mercury electrodes: The cathodic and anodic peak currents for the Co(II)/Co(I) waves remained proportional to the square root of the scan rate and equal to each other up to scan rates of 20 V sec^{-1}. Chronocoulometric measurements indicated some possible adsorption of $Co(bipy)_3^{+}$, but it was not possible to distinguish between adsorption and precipitation of the slightly soluble $Co(bipy)_3ClO_4$ on the electrode surface.

Polarographic maxima were apparently also responsible for the erroneous assertion (1) that acrylonitrile reduction is catalyzed in the presence of $Co(bipy)_3^{+}$. Limiting currents that exceed two electrons per Co(I), the sole basis for the conclusions of Tanaka and Sato, are not observed with larger supporting electrolyte concentrations or at platinum electrodes. Of course, the controlled potential electrolytic reduction of solutions containing both $Co(bipy)_3^{2+}$ and acrylonitrile in which the charge consumed corresponds to precisely three electrons per Co(II) and is independent of the amount of acrylonitrile present provides the clearest proof that acrylonitrile is not reduced. Gas chromatographic monitoring of the concentration of acrylonitrile throughout the electrolysis confirms that none is consumed. Thus, the extremely interesting results of Tanaka and Sato do not constitute an example of a relatively slow electrode reaction being catalyzed by an electrogenerated organometallic intermediate. [The reduction of Co(I) to Co(−I) is "catalyzed" by coordinated acrylonitrile but since the reduction does not lead to the same product in the absence and presence of acrylonitrile, the latter is not functioning as a true catalyst.]

That many vinyl monomers mimic the behavior of acrylonitrile (Table IV) despite having widely different electrochemistry of their own in the absence of $Co(bipy)_3^{+}$ adds support to the notion that one is dealing with a general type of coordination chemistry involving a low valent transition metal center and activated olefins as ligands. Ethylene and acetylene were without effect on the polarography of $Co(bipy)_3^{2+}$. Carbon monoxide appeared to react with $Co(bipy)_3^{+}$ and facilitate its further reduction but the reaction was not examined in detail.

Very recently we observed that electrogenerated $Co(bipy)_3^{+}$ can function as an effective catalyst for the reductive dimerization of allyl halides to produce hexadienes in a reaction having many of the features Tanaka and Sato believed they had observed in the case of acrylonitrile. The details of these experiments will be described in a forthcoming publication.

Acknowledgments

This work was supported by the National Science Foundation. Shlomo Margel gratefully acknowledges a Chaim Weizmann Fellowship.

Manuscript submitted July 12, 1977; revised manuscript received Sept. 19, 1977.

Any discussion of this paper will appear in a Discussion Section to be published in the December 1978 JOURNAL. All discussions for the December 1978 Discussion Section should be submitted by Aug. 1, 1978.

Publication costs of this article were assisted by the California Institute of Technology.

REFERENCES

1. N. Tanaka and Y. Sato, *Bull. Chem. Soc., Jpn.*, **41**, 2059 (1968).
2. F. H. Burstall and R. S. Nyholm, *J. Chem. Soc.*, **1952**, 3570.
3. B. Martin, W. R. McWhinnie, and G. M. Waind, *J. Inorg. Nucl. Chem.*, **23**, 207 (1961).
4. A. A. Vloek, *Nature*, **180**, 753 (1957).
5. Y. Kaizu, Y. Torii, and H. Kobayashi, *Bull. Chem. Soc. Jpn.*, **43**, 3296 (1970).
6. F. J. C. Rossotti and H. Rossotti, "The Determination of Stability Constants," p. 47, McGraw-Hill Book Co., New York (1961).
7. R. S. Nicholson and I. Shain, *Anal. Chem.*, **36**, 706 (1964).

Semiconductor Electrodes

XIV. Electrochemistry and Electroluminescence at n-Type TiO_2 in Aqueous Solutions

Rommel N. Noufi,* Paul A. Kohl,* Steven N. Frank, and Allen J. Bard****

Department of Chemistry, The University of Texas, Austin, Texas 78712

ABSTRACT

The electrochemical behavior of single crystal n-TiO_2 was investigated in aqueous solutions. Charge transfer at the semiconductor/electrolyte interface was probed with several redox couples with standard redox potentials spanning a wide range. Most reductions occurred at potentials close to V_{fb}, the flatband potential and the current-voltage behavior suggested involvement of surface states in the charge transfer process. Evidence for the adsorption of phosphate ion and its effect on the reduction of $Fe(CN)_6^{3-}$ is also presented. Electroluminescence was observed during reduction of $S_2O_8^{2-}$ at wavelengths longer than 700 nm, suggesting the existence of intermediate levels.

The electrochemical behavior of n-TiO_2 has been the subject of several recent investigations including a previous report in this series (1), which utilized an aprotic solvent, acetonitrile (ACN), and which postulated that electron transfer can occur via intermediate levels or surface states within the bandgap region. Studies in aqueous solutions with TiO_2 (2) and other semiconductors (3, 4) have also investigated the mechanism of charge transfer of added redox couples at the semiconductor/solution interface. Although not as many Nernstian, one-electron redox couples are available in aqueous, as compared to nonaqueous solutions, the relative location of the energy levels of TiO_2 at the semiconductor/solution interface (*i.e.*, the flatband potential) can be changed in aqueous solutions by relatively large amounts by changing the solution pH. This provides another variable for investigating the band structure. This approach has previously been used to study SiC (4) and SnO_2 (5).

In the present study the semiconductor/solution interface was investigated by several techniques. Electron transfer reactions of couples, including some with standard redox potential well positive of those used in a previous study (2), were investigated at different pH's. To probe the existence and role of intermediate levels within the bandgap, electroluminescence of the n-TiO_2 semiconductor caused by electron-hole recombination from minority carrier injection from the electrolyte was studied. Hole injection into n-type semiconductors leading to radiative recombination has previously been demonstrated for GaP (6), SnO_2, ZnO, CdS, and GaAs (7).

In addition a study of the space charge capacitance, C_{sc}, as a function of potential, E, was undertaken in an attempt to determine the donor density (N_D) and flatband potential (V_{fb}), via the Schottky-Mott equation (Eq. [1]) (8)

$$1/C_{sc}^2 = (\Delta\phi_s - kT/e)\ 2/(\epsilon\epsilon_0 e N_D) \qquad [1]$$

where C_{sc} is the space charge capacitance, $\Delta\phi_s$ is the amount of band bending, k is the Boltzmann constant, T is the absolute temperature, e is the electronic charge, ϵ is the dielectric constant of the semiconductor, and ϵ_0 is the permittivity of free space. In several previous studies these plots of C_{sc}^{-2} *vs.* E showed deviations from the behavior predicted by Eq. [1] [see, for example, (2, 9, 10) and references therein]. In this work, two independent methods were used to calculate N_D for several n-TiO_2 crystals: (*i*) capacitance determined by a-c methods and cyclic voltammetry via Eq. [1] and (*ii*) conductance. Ohmic contacts were made by four different methods to determine their effect on the capacitance-potential behavior.

Experimental

The single crystal n-TiO_2 semiconductors used for the electrochemical investigation of redox couples were obtained from National Lead (Niagara Falls, New York). Two of the crystals were cut perpendicular to the C_2 axis and one of these was heated to 650°C in vacuum at 10^{-4} Torr for 3 hr and will be called "the moderately doped sample" with $N_D \simeq 10^{18}/cm^3$, as determined from a Schottky-Mott plot. The other was heated at 650°C in a hydrogen atmosphere for 15 min and will be denoted "the highly doped sample," with $N_D \cong 10^{20}/cm^3$. An ohmic contact was made to one side of each crystal by electrochemically depositing In from a 0.1M $InCl_3$ solution.

The capacitance measurements were made with four crystals cut perpendicular to the C_2 axis from a boule

* Electrochemical Society Student Member.
** Electrochemical Society Active Member.

Key words: semiconductors, luminescence, surface states.

generously donated by Fuji Titanium (Hiratsuka, Japan). The 1.5 mm thick crystals were heated in a hydrogen atmosphere for 15 min at 650°C. Two ohmic contacts were made to each crystal by one of the following methods:

1. Electrochemical deposition of indium from a 0.1M $InCl_3$ solution.
2. Electrochemical deposition of indium from a 0.1M $InCl_3$ solution followed by heating in vacuum (10^{-4} Torr) for 1 hr at 650°C.
3. Soldering a copper wire to the rear of the crystal with indium solder.
4. Smearing with In-Ga alloy (1:1 by volume mixture). In methods 1, 2, and 3, copper wires were attached to the contacts with conducting silver epoxy cement (Allied Corporation, New Haven, Connecticut).

The crystals were insulated, except for the (001) face, with Devcon epoxy cement (Devcon Corporation, Danvers, Massachusetts) and mounted on glass rods for use as electrodes as described previously (1). Each crystal was etched for about 15 sec in an HF/HNO_3 solution (11) prior to use except when special etchants were employed, as noted.

All compounds used in this study were reagent grade obtained from commercial sources. Solution concentrations were usually 1 and 10 m*M* in electroactive species. The solutions were prepared with triply distilled water and deaerated with prepurified nitrogen for 30 min. The electrochemical cell, similar to previous design (1), contained an optically flat Pyrex window for illuminating the semiconductor working electrode. A conventional three electrode design was used with an aqueous saturated calomel reference electrode (SCE) and a coiled platinum wire counterelectrode separated from the main compartment by a medium porosity glass frit. The capacitance measurements were performed in the dark with a platinum counterelectrode with an area at least ten times that of the working electrode. The d-c faradaic current was less than 0.2 $\mu A/cm^2$ in the voltage range used for capacitance measurements.

A PAR Model 173 potentiostat (Princeton Applied Research, Princeton, New Jersey) and PAR Model 175 universal programmer were used for the electrochemical measurements. Positive feedback was used to compensate for the *iR* drop in the solution and semiconductor working electrode. The cyclic voltammetric (*i-E*) curves were recorded on a Houston Instruments (Austin, Texas) Model 2000 X-Y recorder for scan rates less than 1 V/sec. For faster scan rates the *i-E* curves were recorded on a Tektronix Model 564 (Tektronix, Incorporated, Beaverton, Oregon) storage oscilloscope. The semiconductor electrodes were illuminated with a 450W xenon lamp (Oriel Corporation, Stamford, Connecticut) employing a Model 6242 power supply. The cell capacitance was measured by an a-c method which superimposed a 5 mV sine wave (500-10,000 Hz) on a d-c voltage, and corresponding phase shift between the current and voltage was measured with a PAR Model HR-8 lock-in amplifier. The potentiostat in these measurements was a Wenking Model 61 RH (G. Bank Electronik, Germany), and the instrumental setup has been described previously (12). The capacitance was also estimated by measuring the charging current of the cyclic voltammograms in the absence of electroactive species as discussed in the next section.

The electroluminescence emitted in the ultraviolet and visible region was detected with a Barr and Stroud (Glasgow, United Kingdom) circular interference filter and a sensitive photomultiplier tube (Dumont 6467). The near infrared light was detected with an Oriel Model 7240 grating monochromator (grating blazed at 1 μm) in conjunction with an ultraviolet cut off filter and Radiometer/photometer (E. G. & G. Incorporated, Salem, Massachusetts).

Results

Capacitance measurements.—The d-c and a-c current measured between the two contacts made on the crystals was directly proportional to the applied voltage and independent of polarity and frequency over the range 100-10,000 Hz for all of the contacts. Thus these can be taken as purely ohmic contacts.

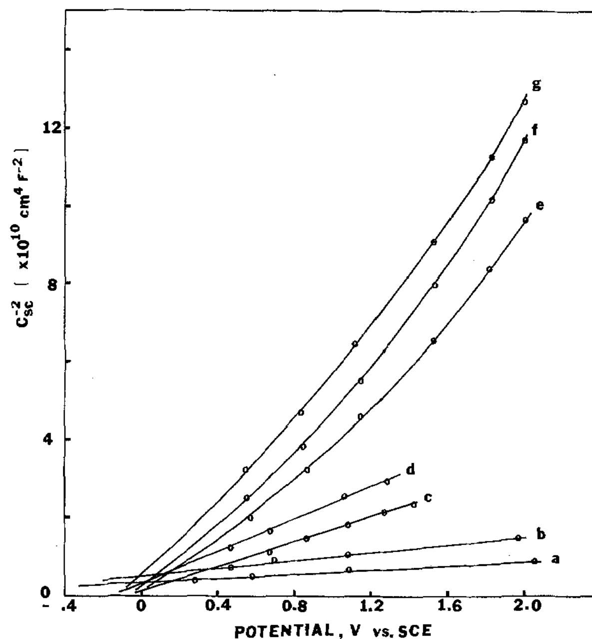

Fig. 1. Plot of C_{sc}^{-2} (cm^4F^{-2}) *vs.* *E* (V, vs. SCE) in 1.0*M* H_2SO_4. Capacitance measured by (a) a-c method at 500 Hz, (b) a-c method at 1000 Hz, (c) cyclic voltammetric method at 5 V/sec (reactivated crystal), (d) cyclic voltammetric method at 500 V/sec (reactivated crystal), (e) a-c method 1000 Hz (reactivated crystal), (f) a-c method 2000 Hz (reactivated crystal), (g) a-c method 5000 Hz (reactivated crystal).

Plots of C_{sc}^{-2} *vs.* *E* (Eq. [1]) of a moderately doped TiO_2 crystal under various conditions are shown in Fig. 1. Curves a and b were obtained by a-c methods at 500 and 1000 Hz, respectively, after the crystal had been used for extended periods as a photoanode in a 1.0M H_2SO_4 solution. The current density of these photoanodes decreased with time during irradiation, as previously reported (10). When the crystal was reactivated in vacuum (10^{-4} Torr) at 650°C for 5 min, the C_{sc}^{-2} *vs.* *E* plots shown in Fig. 1, curves e, f, and g resulted. C_{sc} was also estimated from the charging current measured in the cyclic voltammograms in the dark at various scan rates (0.2-500 V/sec) with no electroactive species in solution. The capacitance was calculated by dividing the current at a given potential by the scan rate. Curves c and d (Fig. 1) show the C_{sc}^{-2} *vs.* *E* plots at 5 and 500 V/sec respectively, for a reactivated crystal.

The Schottky-Mott plots for the four crystals with the different types of contacts (see experimental section) were all very similar with the exception of contact b which yielded a smaller slope, apparently because the doping level increased during the heating in vacuum. The donor densities calculated from the a-c measurements (500-10,000 Hz) for contacts a, c, and d were $1 \times 10^{20}/cm^3$ to $2 \times 10^{20}/cm^3$, while the cyclic voltammetry results (0.2-500 V/sec) gave values of $2 \times 10^{20}/cm^2$ to $3 \times 10^{20}/cm^3$. In all cases, frequency dispersion of the C_{sc}^{-2} *vs.* *E* plots was observed with both the a-c and cyclic voltammetric results.

The intersection of the C_{sc}^{-2} *vs.* *E* plot with the x-axis, yielding V_{fb}, was very similar for the a-c methods and cyclic voltammetric results but there was appreciable scatter and frequency dependence in the V_{fb} values obtained by extrapolation. The origin of the frequency dispersion has been studied extensively and several reasons have been given for the observed results, *e.g.*, dielectric relaxation, crystal imperfections, adsorbed species, and filling and emptying of localized levels in the bandgap (2, 9, 10).

N_D was also estimated by making an ohmic contact of known area to opposite sides of the crystal and measuring the conductivity using Eq. [2]

$$\sigma = N_D e \mu_e \quad [2]$$

where σ is the conductivity, e is the electronic charge, and μ_e is the mobility (13). The value of N_D for crystals with contacts a, c, and d determined by this method was about $7 \times 10^{19}/cm^3$.

Redox processes.—Prior to the addition of an electroactive species, the background oxidation of water in 0.5M H_2SO_4 in the dark did not appear at the moderately doped TiO_2 ($N_D = 10^{18}/cm^3$) until +4.5V and with the highly doped ($N_D = 10^{20}/cm^3$) electrode until +4.0V. During dark water oxidation, bubbles were observed at the electrode surface. Only a small charging current, which was directly proportional to scan rate, was observed for scans from about 0V to potentials for the oxidation of water in 0.5M H_2SO_4. When the scan rate was toward negative potentials, two waves with peak heights directly proportional to scan rate and with peak potentials at −0.45 and −0.85V occurred, followed by a large wave attributed to hydrogen ion reduction. On the reverse scan towards positive potentials, an oxidation wave with a peak potential about 30 mV positive of the first reduction peak appeared; this was attributed to the oxidation of hydrogen. These reduction and oxidation peaks shifted towards negative potentials by about 30 mV/pH unit with increasing pH.

The charge transfer processes at the n-TiO_2/electrolyte interface were studied using several redox systems, listed in Table I. Representative examples of cyclic voltammograms for reductions are shown in Fig. 2. The reduction of $Fe(CN)_6^{3-}$, Ce^{4+}, Fe^{3+}, Ag^{2+}, and $IrCl_6^{2-}$ did not start until the electrode potential was well negative of the corresponding $E_{1/2}$ value ($E_{1/2}$ is taken here as $(E_{pc} + E_{pa})/2$) determined at Pt. In all cases the wave was shifted towards V_{fb} which was not changed by the addition of any of the redox systems, but some current flow occurred at potentials positive of V_{fb}. No reversal anodic waves were found for any reduction. For all waves the reduction peak currents varied with the square root of the scan rate, $v^{1/2}$, and the cathodic peak potentials (E_{pc}) shifted negative by about 54 mV/pH unit. The E_{pc} values for the moderately doped TiO_2 electrode were always 20-70 mV more negative of those for the highly doped one at the same pH. The cathodic current density depended exponentially on the applied potential in a region at the foot of the wave near, but positive of V_{fb}. From Tafel plots, *i.e.*, log i_c *vs.* E, as shown in Fig. 3, which were obtained from the exponential current rise in a stirred solution where there was no contribution from mass transfer, the transfer coefficient, α, was calculated, assuming Eq. [3] applies

Table I. Peak potentials (vs. SCE) for the reduction and reoxidation of compounds used in this study. The scan rate was 0.1 V/sec the donor density of the n-TiO_2 was $N_D = 10^{18}/cm^3$

Compound	Electrolyte	Pt E_{pc}	Pt E_{pa}	n-TiO_2 E_{pc}
$IrCl_6^{2-}$	6M HCl	0.98	1.36	0.02
Ag^{2+}	4M HNO_3	1.08	1.21	−0.02
Ce^{4+}	0.5M H_2SO_4	0.70	—	−0.12
$Fe(CN)_6^{3-}$	0.5M H_2SO_4	0.40	0.52	−0.24
Fe^{3+}	0.5M H_2SO_4	0.36	0.48	−0.31

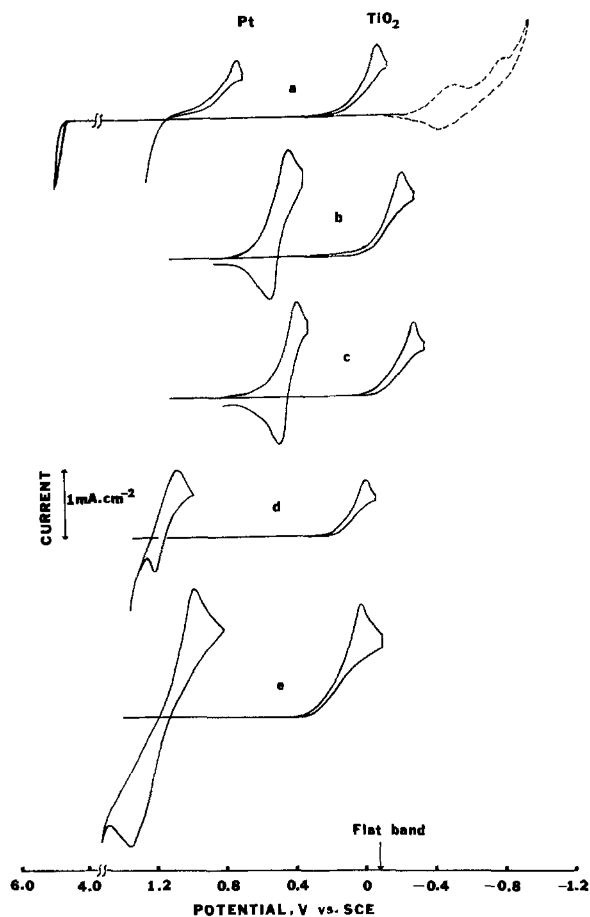

Fig. 2. Cyclic voltammograms for moderately doped ($N_D = 10^{18}/cm^3$) TiO_2 and Pt disk electrodes in (− − − −) 0.5M H_2SO_4 and (———) 0.5M H_2SO_4 with (a) $10^{-2}M$ Ce^{4+}, (b) $10^{-2}M$ $Fe(CN)_6^{3-}$, (c) $10^{-2}M$ Fe^{3+}, (d) $10^{-2}M$ Ag^{2+}, (e) $10^{-2}M$ $IrCl_6^{2-}$ at a sweep rate of 0.1 V/sec.

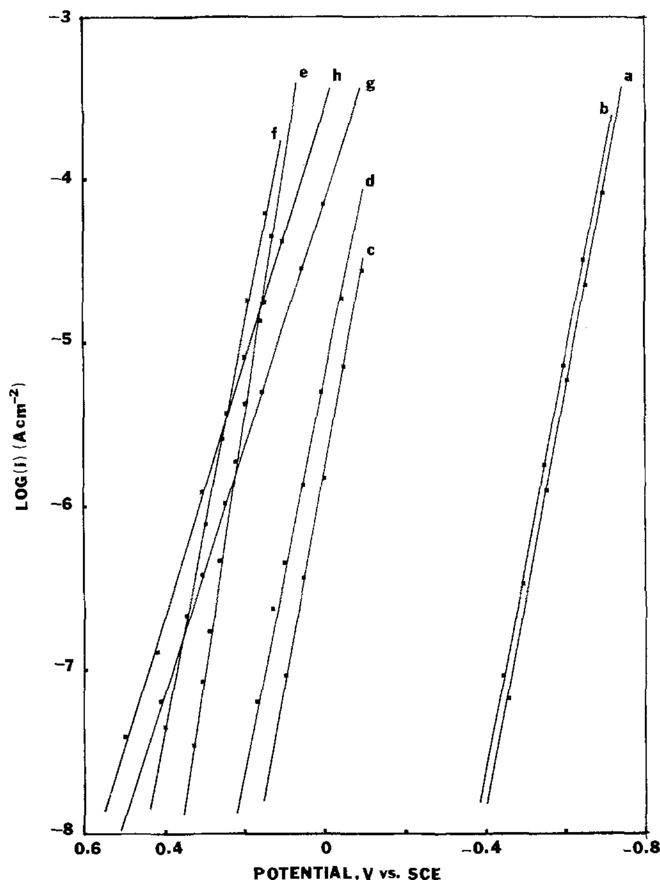

Fig. 3. Logarithm of the dark cathodic current vs. applied potential for the highly doped (H.D.) ($N_D = 10^{20}/cm^3$) and moderately doped (M.D.) ($N_D = 10^{18}/cm^3$) n-TiO_2 electrodes. (a) $10^{-2}M$ $Fe(CN)_6^{3-}$, 0.1M KOH, M.D. (b) $10^{-2}M$ $Fe(CN)_6^{3-}$, 0.1M KOH, H.D. (c) $10^{-2}M$ $Fe(CN)_6^{3-}$, 0.5M H_2SO_4, M.D. (d) $10^{-2}M$ $Fe(CN)_6^{3-}$, 0.5M H_2SO_4, H.D. (e) $10^{-1}M$ Ag^{2+}, 4M HNO_3, M.D. (f) $10^{-1}M$ Ag^{2+}, 4M NHO_3, H.D. (g) $10^{-2}M$ Ce^{4+}, 0.5M H_2SO_4, M.D. (h) $10^{-2}M$ Ce^{4+}, 0.5M H_2SO_4, H.D.

Table II. Comparison of the dark cathodic behavior of oxidizing agents at highly doped (H.D.) and moderately doped (M.D.) n-TiO_2 single crystals[a]

Oxidizing agent	Conc	$E_{1/2}$[b] on Pt (V *vs.* SCE)	Electrolyte	α H.D.	α M.D.	$i°$ ($A\ cm^{-2}$) H.D.	$i°$ ($A\ cm^{-2}$) M.D.
Ag^{2+}	0.1*M*	1.14	4*M* HNO_3	0.75	0.85	$<10^{-15}$	
$IrCl_6^{2-}$	0.01*M*	1.17	6*M* HCl	0.35	0.35	4×10^{-10}	6×10^{-11}
Ce^{4+}	0.01*M*	0.82[c]	0.5*M* H_2SO_4	0.42	0.42	2×10^{-10}	1×10^{-11}
$Fe(CN)_6^{3-}$	0.01*M*	0.46	0.5*M* H_2SO_4	0.75	0.80	8×10^{-10}	7×10^{-11}
Fe^{3+}	0.01*M*	0.42	0.5*M* H_2SO_4	0.44	0.46	2×10^{-7}	4×10^{-8}

[a] H.D., highly doped ($N_D \sim 10^{20}\ cm^{-3}$); M.D., moderately doped ($N_D \sim 10^{18}\ cm^{-3}$).
[b] $E_{1/2}$ is taken here as $(E_{pc} + E_{pa})/2$.
[c] Half-peak potential.

$$\log i_c = \log i° - \frac{\alpha n \mathbf{F}(E - E_{1/2})}{2.3\,RT} \quad [3]$$

where n is the number of equivalents per mole, **F** is Faraday's constant, R is the ideal gas constant, and T is the absolute temperature. The exchange current, $i°$, was estimated by extrapolation of log i_c to the $E_{1/2}$ value found with a platinum electrode for the redox couple. A summary of the Tafel plot results is given in Table II. The values of the Tafel slope, (dE/d log i), for the different couples were relatively high for TiO_2 compared to values found with other semiconductors as was also observed by Gomes *et al.* (2). The accepted model (8), which assumes isoenergetic electron transfer of an electron from the semiconductor conduction band to unoccupied solution levels predicts a slope of 60 mV ($\alpha = 1$) for a pure conduction band process at potentials positive of V_{fb}.

Effect of supporting electrolyte.—The cyclic voltammetric reduction of $Fe(CN)_6^{3-}$ in buffers containing phosphate in the *p*H range 5-9.5 showed two peaks at TiO_2 (Fig. 4a), but only one at Pt in this buffer. The relative height of the two peaks was a function of scan rate (Fig. 4b) and also of the etchant employed. The more positive peak (P_1) was higher at lower scan rates and also when the electrode was etched in 5*M* NaOH as compared to a concentrated HNO_3 etchant. The second peak was more pronounced after etching in concentrated HNO_3 and at higher scan rates. Addition of Na_2SO_4 or KI to the phosphate electrolyte suppressed the second wave (P_2) until only the first wave appeared during reduction. Only the first wave was observed with other electrolytes (*e.g.*, 0.5*M* H_2SO_4, 0.1*M* KOH). Addition of Na_2SO_4 to produce a solution concentration of 0.2*M* totally suppressed the second wave in 0.33*M* phosphate buffer with an electrode etched in HNO_3. The addition of KCl to the buffer however did not have any effect on the double wave. Other redox couples such as $CuCl_2$, Ce^{4+}, and $IrCl_6^{2-}$ did not exhibit the double wave phenomenon in the phosphate buffers. However, experiments with these required acidic media, and at these *p*H's even $Fe(CN)_6^{3-}$ did not show the double wave. $Fe(C_2O_4)_3^{3-}$ and Fe^{3+} also exhibited a similar double wave behavior. However, for these the two waves were not as well defined as those found with $Fe(CN)_6^{3-}$; in this case the first wave was shifted towards negative potentials, so that it appeared as a prewave on the second wave and quantitative data on the relative peak heights was not possible. A systematic change of the total phosphate concentration from 0.01 to 0.5*M* at a fixed *p*H did not appear to change V_{fb}, as determined by the onset of photoanodic current.

Oxidation.—When the electrode was scanned to potentials positive of V_{fb}, a blocking region was observed in the dark extending to +4.5 and +4.0V *vs.* SCE for the moderately and highly doped electrodes respectively, where no oxidation currents appeared. In Fig. 5 the effect of addition of the reduced forms of several redox couples on the dark anodic current is shown and the behavior of the highly doped electrode is compared to that of the moderately doped one. At the highly doped electrode the blocking region was smaller than that of the moderately doped one with no reducing agent in solution. Upon addition of a reducing agent, an anodic current started at less positive potentials than background oxidation for all species tried at the highly doped electrode. At the moderately doped electrode only $Fe(CN)_6^{4-}$ produced significant anodic current at potentials less positive than the background oxidation; the oxidations of Ce^{3+} and Fe^{2+}, if they occurred, took place along with the background oxidation.

Illumination of the electrode did not have any effect on the reduction processes. Oxidation of the reduced species occurred upon illumination which was evident by the increase in the anodic current at a given potential on the rising portion of the wave for photooxidation of water, which commences positive of V_{fb}. A decrease in the amount of O_2 evolved was observed, indicating competition of the reduced species with water for the photogenerated holes. These types of

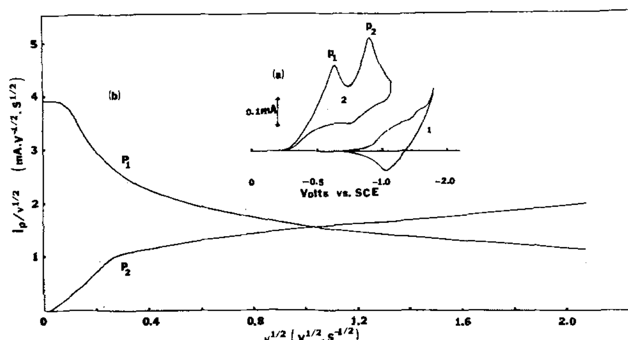

Fig. 4. (a) Cyclic voltammogram at 0.1 V/sec of n-TiO_2 ($N_D = 10^{18}/cm^3$) (etched in concentrated HNO_3), 0.33*M* phosphate buffer, *p*H = 7.3. (1) alone and (2) containing 10 mM $Fe(CN)_6^{3-}$; (b) peak current dependence *vs.* scan rate, conditions as (a) (2).

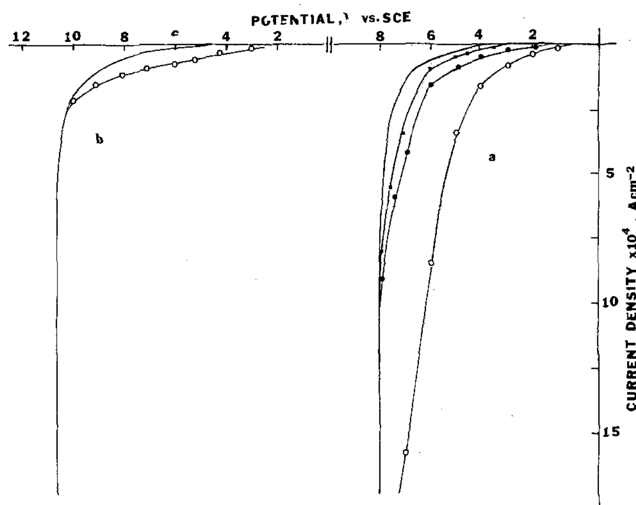

Fig. 5. Linear potential sweep in (——) 0.5*M* H_2SO_4 containing (○) 0.2*M* $Fe(CN)_6^{3-}$, (●) 0.2*M* Fe^{2+}, (■) 0.2*M* Ce^{3+} at TiO_2. (a) Highly doped ($N_D = 10^{20}/cm^3$), (b) moderately doped ($N_D = 10^{18}/cm^3$).

experiments on photoprocesses for different redox couples in aqueous solutions at TiO_2 have been discussed elsewhere (14, 15).

Polycrystalline TiO_2 prepared by chemical vapor deposition (16) showed identical electrochemical behavior in aqueous solution to that of the moderately doped single crystal. Similar results have already been demonstrated in acetonitrile (1). However, the photocurrents on the polycrystalline electrodes were smaller than those for the single crystals.

Light emission.—The electroluminescence observed during reduction of persulfate and H_2O_2 at several semiconductors in aqueous solutions has been used to interpret the mechanism of charge transfer and to obtain information about energy levels in the gap (6, 7). Luminescence produced by recombination of an electron with a hole in the semiconductor was also observed with n-TiO_2 electrodes when persulfate was reduced. The mechanism for luminescence probably follows that proposed for other semiconductors (6, 7) with an initial step being transfer of an electron from the conduction band or a surface state below the conduction band to $S_2O_8^{2-}$ (Eq. [4])

$$S_2O_8^{2-} + e^-(CB) \rightarrow SO_4^{2-} + SO_4^{\overline{\cdot}} \qquad [4]$$

Since $SO_4^{\overline{\cdot}}$ is very easily reduced, the $SO_4^{\overline{\cdot}}/SO_4^{2-}$ energy level lies below the valence bandedge, and thus electron transfer to the radical causes injection of a hole into the valence band or a state just above the valence band (Eq. [5])

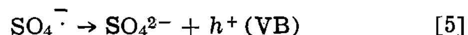

$$SO_4^{\overline{\cdot}} \rightarrow SO_4^{2-} + h^+(VB) \qquad [5]$$

Electron-hole recombinations then cause emission of radiation. The i-E curve (Fig. 6a) shows that the reduction of persulfate occurs about 100 mV positive of the background reduction of water. The light emission did not start when the reduction of persulfate first occurred. Luminescence began when the electrode potential was pulsed to -1.5V, a value negative of V_{fb}. The emission intensity increased with pulsing to more negative potentials and attained a maximum value at -3.0V. At this potential the intensity was a function of pulse duration and was largest with a 100 msec pulse. Shorter pulses gave weak emission; longer pulses gave an emission with intensity equal to that of the 100 msec pulse which then decayed to a steady state (Fig. 6b). The TiO_2 electroluminescence spectra (Fig. 7) were different than those observed with ZnO (7), although both materials have similar bandgaps and flatband potentials. Most of the light emission occurred at photon energies smaller than that of the bandgap, *i.e.*, only a very small fraction of the emitted light corresponded to bandgap energy (3.2 eV), while most of the emitted light extended into the near infrared region

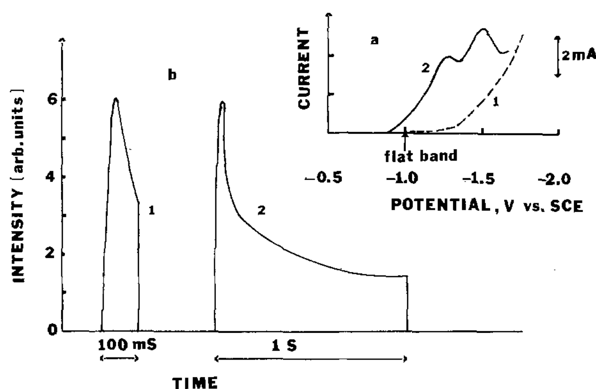

Fig. 6. (a) Linear potential sweep of highly doped n-TiO_2 at 0.1 V/sec in (1) 5M NaOH solution, (2) 0.1M $S_2O_8^{2-}$, 5M NaOH solution, (b) Intensity vs. time curve of the electroluminescence of n-TiO_2 at -3.0V in 0.1M $Na_2S_2O_8$, 5M NaOH (1) 0.1 sec pulse, (2) 1 sec pulse.

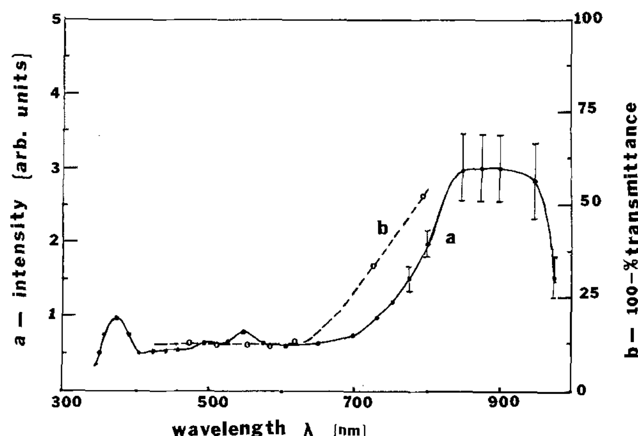

Fig. 7. (a) Spectral distribution of electroluminescence of n-TiO_2 at -3.0V with grating monochromator, (b) percent transmission of electroluminescence at -3.0V with cut-on filters.

with photon energies of 1.5-1.24 eV. This behavior is similar to that exhibited by n-GaAs (7).

The spectral distribution of the luminescence with n-TiO_2 clearly suggests the existence of surface states or intermediate levels located within the bandgap. As in the previous studies (6, 7), the quantum efficiency for the emission is very low suggesting that the extent of nonradiative recombination or reduction of $SO_4^{\overline{\cdot}}$ directly via surface states rather than via the valence band is significant. Previous studies of TiO_2 (1, 14) and other semiconductors (17) in nonaqueous solvents have provided evidence of the importance of levels within the gap in explaining the electrochemical properties of semiconductor materials.

Discussion

Reduction.—The reduction of solution species in the absence of surface states should occur at a wide bandgap semiconductor through either the conduction band or valence band depending upon the standard potential of the redox couple (8). The position of the energy levels and distribution maxima of the solution species investigated and TiO_2 are shown in Fig. 8, where W_{Ox} is the maximum of the distribution for the oxidized form in solution, W_{Red} is the maximum of the distribution for the reduced form, and $E°_{redox}$ is the Fermi level of the redox couple (8). The separation between

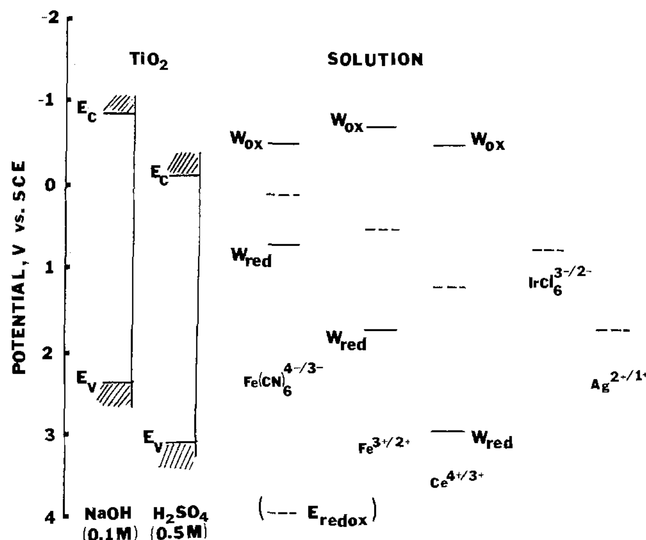

Fig. 8. Relative energy positions of n-TiO_2 and various redox couples where $E°_{redox}$ is the standard redox potential, W_{Red} is the distribution maximum of the reduced species, W_{Ox} is the distribution maximum of the oxidized species, E_c and E_v are the conduction and valence bandedges, respectively.

W_{Ox} and W_{Red} is essential 2λ, where λ is the solvent reorganizational energy during electron transfer. The λ values estimated for several couples by Memming *et al.* (5) have been used in Fig. 8. For all of the couples in this study the distribution of the oxidized form at the valence bandedge, $W_{Ox}(E_v)$, is small so that reduction by hole injection into the valence band should be small. However, for reduction only via the conduction band for a couple where $E°_{redox}$ is below E_c the reduction current should be proportional to the electron density at the surface, n_s, and the overlap of the unoccupied solution levels with the conduction band, $W_{Ox}(E_c)$. The potential dependence of the reduction current should then follow that of n_s and hence the apparent exchange parameter, α (as defined in Eq. [3]) should be equal to unity at potentials positive of V_{fb}. Since α values less than one were observed, a pure conduction band process seems unlikely. We do not think that reduction via tunneling from the conduction band to the oxidized species, as discussed by Pettinger *et al.* (18) is likely in this case. Our results show that the reduction current for $Fe(CN)_6^{3-}$ in both 0.5*M* H_2SO_4 and 0.1*M* KOH starts positive of V_{fb} by about 0.45V. Tunneling from the conduction band to solution, which is a function of the space charge thickness at the energy level distribution of the unoccupied species (18), should give a larger difference between the onset of the reduction current and V_{fb} (because of the negative shift in V_{fb}) in base as compared to acid while the distribution W_{Ox} remains fixed. The onset of reduction on both the highly and moderately doped TiO_2 crystals occurs at potentials where the extent of band bending appears to be too small to satisfy the conditions for such tunneling. Thus the α values measured probably represent involvement of surface states or intermediate levels in the reduction processes. Dutoit *et al.* (2) also found anomalously large Tafel slopes for the reduction of several couples at *n*-TiO_2 and presented strong arguments against variation of the Helmholtz layer potential as the origin of this effect.

The reduction of electroactive species with redox potentials well positive of V_{fb} at both moderately and highly doped TiO_2, in aqueous solutions is different from the behavior found in ACN (1). In ACN couples with redox potentials more than 1.5V positive of V_{fb} were all reduced at potentials about 1V below the conduction bandedge; this was attributed to the location of intermediate levels in the semiconductor near this energy. The redox couples used in this study with $|E_{redox} - V_{fb}|$ greater than 1.2V all showed reduction waves close to V_{fb} (Fig. 2). However, the solvent interaction energy, λ, is larger in water than in ACN. This broadens the W_{Ox} distribution and shifts it closer to the conduction band, making better overlap possible even for couples with very positive values of E_{redox} (Fig. 8). Couples with potentials as positive as those used in ACN could not be employed because they are not stable in water. It is also possible that the different extent of interaction of the water with the TiO_2 surface causes the energy level of surface states to be located closer to the conduction band than in ACN.

The double wave for the reduction of $Fe(CN)_6^{3-}$ in the phosphate-containing media can be attributed to the adsorption of phosphate on the TiO_2 surface and reduction of $Fe(CN)_6^{3-}$ at both phosphate-free and phosphate-covered sites. At the free sites the reduction occurs at similar potentials as found in other supporting electrolytes while at the covered sites the reduction takes place at more negative potentials. The double wave cannot be attributed to solution chemistry, since the behavior at the platinum electrode is the same as in other media, and no type of interaction between $Fe(CN)_6^{3-}$ and a phosphate is apparent. The effect of etchant noted on the double-wave behavior can probably be explained by changes in the extent of adsorption of phosphate with surface treatment with the acidic etchant (concentrated HNO_3) enhancing the adsorption of phosphate as compared to the basic one (5*M* NaOH). The scan rate dependence of the two peaks can be explained qualitatively by considering the two site reduction as analogous to a reversible preceding chemical reaction (CE). P_1 represents the reduction of $Fe(CN)_6^{3-}$ on free sites and P_2 represents the reduction on phosphate-covered ones. At slow scan rates reduction occurs mainly via the free sites, since $Fe(CN)_6^{3-}$ has time to diffuse to these locations; thus $P_1 > P_2$. At fast scan rates reduction occurs via both sites and the ratio of P_2 to P_1 increases (Fig. 4). Note, however, that the total peak height $(P_1 + P_2)$ is constant, proportional to the total electrode area at all scan rates.

Oxidations.—The oxidation of a number of couples in the dark at TiO_2 and other wide bandgap semiconductors (2, 18-20) has been explained by tunneling from filled levels in the electrolyte to empty levels at the same energy in the conduction band. Our results are in agreement with this explanation. The tunneling of electrons from solution species does not occur until the thickness of the space charge region, X, (which is a function of the surface field strength and N_D as shown in Eq. [6]) at the energy level of the reduced species becomes sufficiently thin (18, 21). The steep increase in the anodic current for water oxidation beyond a band bending equivalent to the bandgap of TiO_2 (3.2 eV) is a result of interband tunneling (22)

$$X = (2\epsilon_0\epsilon\Delta\phi/eN_D)^{1/2} \quad [6]$$

The anodic current in the blocking region upon the addition of a reducing agent increases as a result of a tunneling process at an energy where the distribution for reduced form in solution is sufficiently large and the extent of band bending is such that the space charge thickness is sufficiently small. The observed results agree very well with previous studies and with the relative energy positions of the occupied levels (Fig. 8) below the conduction band.

Acknowledgment

The support of this research by the National Science Foundation and the Army Research Office is gratefully acknowledged.

Manuscript submitted July 15, 1977; revised manuscript received Sept. 2, 1977.

Any discussion of this paper will appear in a Discussion Section to be published in the December 1978 JOURNAL. All discussions for the December 1978 Discussion Section should be submitted by Aug. 1, 1978.

Publication costs of this article were assisted by the National Science Foundation and Army Research Office.

REFERENCES

1. S. N. Frank and A. J. Bard, *J. Am. Chem. Soc.*, **97**, 7427 (1975).
2. E. C. Dutoit, F. Cardon, and W. P. Gomes, *Ber. Bunsenges. Phys. Chem.*, **80**, 475 (1976).
3. W. P. Gomes and F. Cardon, *Z. Phys. Chem.*, **86**, 330 (1973).
4. M. Gleria and R. Memming, *J. Electroanal. Chem.*, **65**, 163 (1975).
5. R. Memming and F. Mollers, *Ber. Bunsenges. Phys. Chem.*, **76**, 475 (1972).
6. K. H. Beckman and R. Memming, *This Journal*, **116**, 368 (1969).
7. B. Pettinger, H. R. Schoppel, and H. Gerischer, *Ber. Bunsenges. Phys. Chem.*, **80**, 849 (1976).
8. (a) H. Gerischer, in "Physical Chemistry: An Advance Treatise," Vol. 9A, H. Eyring, D. Henderson, and W. Jost, Editors, Academic Press, New York (1970); (b) H. Gerischer, *Adv. Electrochem. Electrochem. Eng.*, **1**, 139 (1961).
9. E. C. Dutoit, R. L. Van Meirhaege, F. Cardon, and W. P. Gomes, *Ber. Bunsenges. Phys. Chem.*, **79**, 1206 (1976).
10. L. A. Harris and R. H. Wilson, *This Journal*, **123**, 1010 (1976).
11. A. Fujishima, K. Honda, and S. Kikuchi, *Chem. Soc. Jpn.*, **72**, 108 (1969).
12. H. Kojima and A. J. Bard, *J. Electroanal. Chem.*, **63**, 117 (1975).

13. R. G. Breckenridge and W. R. Hosler, *Phys. Rev.*, **91**, 793 (1953).
14. S. N. Frank and A. J. Bard, *J. Am. Chem. Soc.*, **99**, 4669 (1977).
15. E. C. Dutoit, F. Cardon, and W. P. Gomes, *Ber. Bunsenges. Phys. Chem.*, **80**, 1285 (1976).
16. K. L. Hardee and A. J. Bard, *This Journal*, **122**, 739 (1975).
17. P. A. Kohl and A. J. Bard. *J. Am. Chem. Soc.*, **99**, 7531 (1977).
18. B. Pettinger, H. R. Schoppel, and H. Gerischer, *Ber. Bunsenges. Phys. Chem.*, **78**, 450 (1974).
19. P. J. Boddy, *This Journal*, **115**, 199 (1968).
20. F. Mollers and R. Memming, *Ber. Bunsenges. Phys. Chem.*, **76**, 469 (1972).
21. J. F. Dewald, *J. Phys. Chem. Solids*, **14**, 155 (1960).
22. B. Pettinger, H. R. Schoppel, T. Yokoyama, and H. Gerischer, *Ber. Bunsenges. Phys. Chem.*, **78**, 1024 (1974).

Significance of Effects of High Pressure on Kinetics of Electrode Reactions

I. Applications to Transition States in Hydrogen Evolution Reaction Mechanisms

B. E. Conway and J. C. Currie

Chemistry Department, University of Ottawa, Ottawa, Ontario, Canada

ABSTRACT

The effects of high hydraulic pressures on electrode reactions are complex because of (*i*) the variation of reference electrode potentials with pressure so that only an apparent volume of activation can be directly measured experimentally, and (*ii*) dependence of coverage by adsorbed intermediates, such as H, with pressure. Methods of dealing with these problems are treated and the significance of measured apparent volumes of activation for the hydrogen evolution reaction is discussed in terms of the nature of the transition state for proton transfer and neutralization. The negative true volumes of activation found for the cathodic H_2 evolution reaction under some conditions are attributed to increasing electrostriction of the proton in the $H_9O_4^+$ complex as the transition state is formed. The significance of applications to ionic redox reactions is pointed out where pressure effects may be able to distinguish activation associated with long-range Born polarization from that associated more specifically with reorganization of the primary solvation shell or inner coordination sphere of ions.

Studies on the effects of pressure on condensed-phase chemical reactions (1), ionic conductance (2), and ionic equilibria (3) have produced useful new information on the volume changes which occur in these processes and in the activation process in their kinetics. The method is especially useful for studying reactions in which changes of charge, and corresponding changes of electrostriction, occur, *e.g.*, in reactions where polar transition states are developed or in ionic reactions involving a change of charge.

Processes involving elimination or diminution of charge of ions are usually associated with an increase of volume of the system due to decrease or removal of the electrostriction in the over-all reaction. Examples in homogeneous processes are redox reactions, ion-pair association, and the reverse of quaternization of tertiary amines (Menschutkin reaction) (1, 4, 5). In the latter case, it is known that the decrease of electrostriction in the over-all reaction is accompanied by a positive volume of activation, as may be expected. Similar considerations apply to electrochemical reactions where discharge or reduction of cations occurs, giving a decrease in electrostriction in the over-all reaction; *e.g.*, elsewhere (6) we have shown experimentally that the simple electrochemical reaction $H_3O^+ + Pt + e \rightarrow PtH_{ads} + H_2O$ is accompanied by a positive volume change of 7.4 ± 2 cm³ mole⁻¹.

In recent years, some interesting experimental studies have been reported on effects of pressure on the cathodic H_2 evolution reaction where the charge on two protons is lost. The results indicated negative volumes of activation which, in comparison with the behavior in the cases mentioned above, must be regarded as unexpected.

In the case of electrochemical reactions, a number of other factors, besides the true volume of activation, determine the measured values of $(\partial \ln i/\partial p)_{T,\eta}$ and complicate the interpretation of observed pressure effects in kinetics, *e.g.*, of the H_2 evolution reaction. It is, therefore, necessary first to establish their effects before considering the kinetic significance of negative volumes of activation.

It will be shown that, for several reasons, the pressure derivative of the log of exchange currents or currents at finite overpotential η does not give a true volume of activation for the electrode process which can be interpreted like volumes of activation for homogeneous, nonelectrochemical reactions (1). This complication gave rise to an erroneous [see Ref. (7) and the discussion in Ref. (8)] interpretation of the significance of the observed pressure effect in the kinetics of H_2 evolution in Ref. (9).

In this paper, we examine in some detail the significance of effects of high pressure on the kinetics of the hydrogen evolution reaction for several cases and attempt to use the conclusions to clarify conflicting deductions which have hitherto been made regarding the significance of pressure effects on this reaction. The behavior of other types of reaction, *e.g.*, ionic redox processes, is also mentioned (see also Part II which follows).

Pressure Effects Arising for Various Reaction Mechanisms of Cathodic H₂ Evolution

The reaction mechanisms considered (10) are

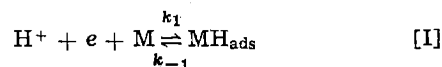

$$H^+ + e + M \underset{k_{-1}}{\overset{k_1}{\rightleftharpoons}} MH_{ads} \qquad [I]$$

followed by

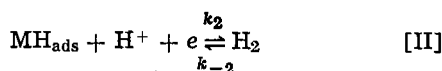

$$MH_{ads} + H^+ + e \underset{k_{-2}}{\overset{k_2}{\rightleftharpoons}} H_2 \quad [II]$$

or

$$2MH_{ads} \underset{k_{-3}}{\overset{k_3}{\rightleftharpoons}} H_2 \quad [III]$$

as the desorption pathways. The reaction equations [I], [II], and [III] as written above also serve to define the respective rate constants k_1, k_{-1}, k_2, k_{-2}, k_3, and k_{-3} which are required in the discussion which follows.

Case 1: The problem of pressure-dependence of the reference electrode potential.—The simplest case arises for a rate-controlling discharge step [I] for which

$$i_t = 2\mathbf{F}k_1C_{H^+}(1-\theta_H)\exp - \beta\phi\mathbf{F}/RT \quad [1]$$

where i_t is the total current density passing in the rate-determining step plus that in a subsequent desorption step and θ_H is the steady-state coverage by H. The term ϕ is the metal-solution potential drop. Here, the detailed form of ϕ as determined by double layer ion-distribution and specific adsorption effects will not be considered because the small pressure effects which may arise in the structure of the double layer will divert attention away from the main factors to be discussed here. ϕ can be expressed in the usual way in terms of the experimentally accessible overpotential, η defined by

$$\phi = \eta + \phi_e \quad [2]$$

where ϕ_e in the reversible potential for the over-all reaction

$$H_3O^+ + e \rightleftharpoons \tfrac{1}{2} H_2 + H_2O \quad [IV]$$

The pressure derivative of i_t in Eq. [1] is then

$$\left(\frac{\partial \ln i_t}{\partial p}\right)_{\eta,T} = \left(\frac{\partial \ln k_1}{\partial p}\right)_T - \frac{\beta\mathbf{F}}{RT}\left(\frac{\partial \phi_e}{\partial p}\right)_T \quad [3]$$

noting that $\theta_H \rightarrow 0$ when *I* is rate controlling.

Since $\phi_e = -\Delta G_e/z\mathbf{F}$ for the electrode process [IV] at equilibrium and $\partial(\Delta G_e/\partial p)_T = \Delta V_o$, the volume change per e for the over-all reaction [IV], and because k_1 can be written in terms of the exponential $e^{-\Delta G_1^{\ddagger}/RT}$ it follows that the experimentally measured $\left(\frac{\partial \ln i_t}{\partial p}\right)_{\eta,T}$ does not give the true volume of activation, $\Delta V_t^{\ddagger}$, but rather an apparent quantity, $\Delta V_a^{\ddagger}$, given [cf., (7, 8, 11)] by

$$\Delta V_a^{\ddagger} = \Delta V_{t,1}^{\ddagger} - \beta\Delta V_o \quad [4]$$

Thus, as first pointed out by Conway (7) [cf. Ref. (8, 12)], the true volume of activation, $\Delta V_{t,1}^{\ddagger}$ differs from the apparent value $\Delta V_a^{\ddagger}$ (determined by the pressure-dependence of rate of an electrochemical reaction at constant η) by β times the equilibrium volume change ΔV_o in the over-all reaction ([IV] in this case). Also the molar concentration of reactant ions, C_{H^+}, will increase with pressure, but this is a trivial effect that can easily be allowed for if the compressibility of the solution is known. At 10^4 bars in aqueous solution it gives a 20% effect on rates but appears to have been neglected in previous work.

It is seen that evaluation of $\Delta V_t^{\ddagger}$ for an electrode process involves problems similar to those arising (13, 14) in evaluation of the activation energy of electrode processes from determinations of the temperature dependence of currents at a given η as pointed out in Ref. (7).

The result (9), derived here for case 1, is generally applicable to any electron-transfer reaction (*e.g.*, the redox reaction treated in Part II) in which the kinetics are not influenced by a prior or subsequent step, or in which an intermediate, whose coverage could be pressure dependent, does not arise.

Case 2: The mechanisms [I] and [II] controlled by the rate constant of the desorption step [II].—Here, and for other cases to be treated below, θ_H can be appreciable so that pressure dependence of θ_H, as well as of the rate constant and ϕ_e, determines the value of $\Delta V_a^{\ddagger}$ measured experimentally. For interpretation of pressure effects, the relation between $\Delta V_a^{\ddagger}$ and $\Delta V_t^{\ddagger}$ for various conditions is required.

For mechanisms [I] and [II], the total current i_t is

$$i_t = i_1 - i_{-1} + i_2 = 2i_2 \text{ (in the steady state)} \quad [5]$$

Thus

$$i_t = 2\mathbf{F}k_2C_{H^+}\theta_H \exp(-\beta\phi\mathbf{F}/RT) \quad [6]$$

Then

$$\left(\frac{\partial \ln i_t}{\partial p}\right)_{\eta,T} = \left(\frac{\partial \ln k_2}{\partial p}\right)_T + \left(\frac{\partial \ln \theta_H}{\partial p}\right)_{\eta,T} - \frac{\beta\mathbf{F}}{RT}\left(\frac{\partial \phi_e}{\partial p}\right)_T \quad [7]$$

at constant η, using Eq. [2] to introduce ϕ_e.

Introducing the volume terms that arise from the pressure dependencies of the k_2 and ϕ_e terms, as in Eq. [4], gives the expression for $\Delta V_a^{\ddagger}$

$$\left(\frac{\partial \ln i_t}{\partial p}\right)_{\eta,T} = -\frac{\Delta V_{a,2}^{\ddagger}}{RT} = -\frac{\Delta V_{t,2}^{\ddagger}}{RT} + \left(\frac{\partial \ln \theta_H}{\partial p}\right)_{\eta,T} + \frac{\beta\Delta V_o}{RT} \quad [8]$$

where $\Delta V_{t,2}^{\ddagger}$ is the true activation volume of step [II] and ΔV_o is as in Eq. [4].

The effect of pressure on θ_H at a given η may be derived from the condition that $i_1 \doteq i_{-1}$ when [II] is rate controlling, *i.e.*

$$k_1C_{H^+}(1-\theta_H)\exp(-\beta\phi\mathbf{F}/RT) = k_{-1}\theta_H\exp(1-\beta)\phi\mathbf{F}/RT \quad [9]$$

so that in the usual way (15)

$$\theta_H = \frac{K_1C_{H^+}\exp(-\phi\mathbf{F}/RT)}{1 + K_1C_{H^+}\exp(-\phi\mathbf{F}/RT)} \quad [10]$$

where $K_1 = k_1/k_{-1}$ is the quasi-equilibrium constant for step [I]. Then the pressure derivative of θ_H can be written as

$$\frac{1}{\theta_H}\left(\frac{\partial \theta_H}{\partial p}\right)_{\eta,T} = \left(\frac{\partial \ln \theta_H}{\partial p}\right)_{\eta,T} = \left(\frac{\partial \ln K_1}{\partial p}\right)_T - \frac{\mathbf{F}}{RT}\left(\frac{\partial \phi_e}{\partial p}\right)_T - \frac{1}{1 + K_1C_{H^+}\exp(-\phi\mathbf{F}/RT)} \left[C_{H^+}K_1\left(-\frac{\mathbf{F}}{RT}\right)\exp(-\phi\mathbf{F}/RT)\left(\frac{\partial \phi_e}{\partial p}\right)_T + C_{H^+}\exp(-\phi\mathbf{F}/RT)(\partial K_1/\partial p)_T \right] \quad [11]$$

so that

$$\left(\frac{\partial \ln \theta_H}{\partial p}\right)_{\eta,T} = -\frac{\Delta V_1}{RT} + \frac{\Delta V_o}{RT} - \frac{\theta_H}{RT}(\Delta V_o - \Delta V_1) \quad [12]$$

With further rearrangements of Eq. [12]

$$\left(\frac{\partial \ln \theta_H}{\partial p}\right)_{\eta,T} = (1-\theta_H)(\Delta V_o - \Delta V_1)/RT \quad [13]$$

where ΔV_1 is the volume change in step [I] and $\Delta V_o - \Delta V_1$ is the volume of adsorption of H from ½ H_2 which we have recently determined experimentally at Pt (6) as 7.4 ± 2 cm^3 mole^{-1}.

Then from Eq. [8]

$$\Delta V_{t,2}^{\ddagger} = \Delta V_{a,2}^{\ddagger} + \Delta V_o(1 + \beta - \theta_H)\Delta V_1 \quad [14]$$

Under (experimentally inaccessible) conditions of constant ϕ, the true volume of activation for the over-all processes [I] and [II], with [II] rate controlling, would therefore be[1]

$$\Delta V_{t,2}^{\ddagger} = \Delta V_2^{\ddagger} + (1 - \theta_H)\Delta V_1 \quad [15]$$

or with Eq.]14]

$$\Delta V_{t,2}^{\ddagger} = \Delta V_{a,2}^{\ddagger} + \Delta V_o(1 + \beta - \theta_H) \quad [16]$$

evaluated at a constant η for a corresponding value of θ_H at the given η. It is seen from Eq. [16] that the $\Delta V_t^{\ddagger}$ differs from the measured $\Delta V_a^{\ddagger}$ in this case by one term derived from $(\partial\theta_H/\partial p)_\eta$ and another from $(\partial\phi_e/\partial p)_T$. If $\Delta V_{t,2}^{\ddagger}$ is desired for step [II] itself, information on θ_H and the volume change ΔV_1 in step [I] (6) is evidently required.

Two limiting conditions can usefully be considered: (*i*) If $k_1 >> k_{-1}$, $k_1 >> k_2$, then $\theta_H \rightarrow 1$ so that θ_H is pressure independent. Hence

$$\Delta V_{a,2}^{\ddagger} = \Delta V_{t,2}^{\ddagger} - \beta\Delta V_o \quad [17]$$

(*ii*) $k_{-1} >> k_1$ and $k_{-1} >> k_2$ so that $\theta_H \rightarrow 0$ but is $f(p)$, then

$$\Delta V_{a,2}^{\ddagger} = \Delta V_{t,2}^{\ddagger} + \Delta V_1 - (1 + \beta)\Delta V_o \quad [18]$$

Cases for other mechanisms or conditions follow the same kind of treatment in terms of $(\partial\phi_e/\partial p)_T$ and $(\partial\theta_H/\partial p)_{\eta,T}$ and the results are therefore presented only briefly, as follows:

Case 3: Mechanisms [I] and [II] when [I] is rate controlling and [II] is in quasi-equilibrium as a rapid desorption step.—For some metals, the discharge step [I] can be rate controlling but a coverage by H greater than "zero" can be established through step [II] in quasi-equilibrium. For this case

$$i_t = 2\mathbf{F}k_1C_{H^+}(1 - \theta_H)\exp(-\beta\phi\mathbf{F}/RT) \quad [19]$$

with θ_H determined mainly by step [II]. The steady-state condition gives then

$$1 - \theta_H = \frac{k_2C_{H^+}}{k_1C_{H^+} + k_2C_{H^+} + k_{-2}p_{H_2}\exp(\phi\mathbf{F}/RT)} \quad [20]$$

Taking logarithms and with further rearrangements, the pressure derivative of $1 - \theta_H$ can be obtained, so that from Eq. [19], $(\partial \ln i_t/\partial p)_{\eta,T}$ gives

$$\Delta V_{a,1}^{\ddagger} = \Delta V_1^{\ddagger} - \Delta V_o(1 + \beta) + \Delta V_2(1 - \theta_H)$$
$$\left[\Delta V_o - \Delta V_2 + \frac{k_1k_{-2}p_{H_2}}{k_2^2}(\Delta V_o - \Delta V_1^{\ddagger} + \Delta V_2^{\ddagger})\right] \quad [21]$$

The over-all true volume of activation $\Delta V_{t,1}^{\ddagger}$ for this case is

$$\Delta V_{t,1}^{\ddagger} = \Delta V_1^{\ddagger} + \Delta V_2\theta_H + K'\Delta V_2^{\ddagger}$$
$$- K'\Delta V_1^{\ddagger} - K'\theta_H\Delta V_2^{\ddagger} + K'\theta_H\Delta V_1^{\ddagger} \quad [22]$$

where $K' = (k_1k_{-2}p_{H_2})/(k_2^2)$. Then Eq. [22] can be expressed in terms of the experimental volume of activation, $\Delta V_{a,1}^{\ddagger}$, and ΔV_o by

$$\Delta V_{t,1}^{\ddagger} = \Delta V_{a,1}^{\ddagger} + \Delta V_o(1 + \beta)$$
$$- \Delta V_o(1 - \theta_H) - \Delta V_oK'(1 - \theta_H) \quad [23]$$

Again two limiting conditions may usefully be examined:

(*i*) If $k_1 << k_2 >> k_{-2}p_{H_2}$, then $(k_1k_{-2}p_{H_2})/(k_2^2) \rightarrow 0$ and $\theta_H \rightarrow 0$; then Eq. [21] can be written (cf. Eq. [4]) as

$$\Delta V_{a,1}^{\ddagger} = \Delta V_1^{\ddagger} - \beta\Delta V_o \quad [24]$$

which is, as expected, simply the result for step [I] without any following equilibrium step [II].

(*ii*) If $k_1 << k_{-2} >> k_2$, then $\theta_H \rightarrow 1$ and Eq. [23] reduces to

$$\Delta V_{a,1}^{\ddagger} = \Delta V_1^{\ddagger} - \Delta V_o(1 + \beta) + \Delta V_2 \quad [25]$$

Therefore the over-all true volume of activation can be written as

$$\Delta V_{t,1}^{\ddagger} = \Delta V_1^{\ddagger} + \Delta V_2 = \Delta V_a^{\ddagger} + (1 + \beta)\Delta V_o \quad [26]$$

It is of interest that Eq. [16] becomes identical with Eq. [26] when $\theta_H = 0$ in [16] and 1 in Eq. [23], although of course Eq. [16] applies when step [II] is rate controlling while Eq. [26] applies when step [I] is the limiting process.

Case 4: Recombination step [III] is rate determining.—In this case, step [I] (at quasi-equilibrium) is followed by [III]. This case arises for H_2 evolution at certain noble metals and for Cl_2 evolution on oxidized Pt and Ru surfaces. The total current i_t is given by

$$i_t = 2(i_1 - i_{-1}) = 2\mathbf{F}k_3\theta_H^2 \quad [27]$$

Following the procedures used in the previous cases, the pressure coefficient $(\partial \ln i_t/\partial p)_{\eta T}$, gives

$$\Delta V_{a,3}^{\ddagger} = \Delta V_3^{\ddagger} - 2(1 - \theta_H)(\Delta V_o - \Delta V_1) \quad [28]$$

and the over-all true volume of activation, $\Delta V_t^{\ddagger}$, is

$$\Delta V_{t,3}^{\ddagger} = \Delta V_3^{\ddagger} + 2\Delta V_1[1 - \theta_H]$$
$$= \Delta V_a^{\ddagger} + 2(1 - \theta_H)\Delta V_o \quad [29]$$

The limiting conditions for case 4, are as follows:
(*i*) $K_1C_{H^+}\exp(-\phi\mathbf{F}/RT) >> 1$ in Eq. [10], so that $\theta_H \rightarrow 1$, *i.e.*, when the $i \sim \phi$ relation corresponds to a limiting current, as at high η. Then

$$\Delta V_{t,3}^{\ddagger} = \Delta V_{a,3}^{\ddagger} = \Delta V_3^{\ddagger} \quad [30]$$

(*ii*) $K_1C_{H^+}\exp(-\phi\mathbf{F}/RT) << 1$ in Eq. [10], so that $\theta_H << 1$ and is potential dependent. This corresponds to the $i \sim \phi$ relation having a Tafel slope of $RT/2\mathbf{F}$. Then.

$$\Delta V_{t,3}^{\ddagger} = \Delta V_{a,3}^{\ddagger} + 2\Delta V_o \text{ where } \Delta V_{t,3}^{\ddagger} \equiv \Delta V_3^{\ddagger} \quad [31]$$

Case 5: Coupled mechanism [I] and [II] at high η.—At sufficiently high η, the reverse reaction currents for these steps are negligible, so that the total current is given by

$$i_t = i_1 + i_2 = 2\mathbf{F}k_2C_{H^+}\theta_H\exp(-\beta\phi\mathbf{F}/RT) \quad [32]$$

θ_H is now determined by a steady-state condition $i_1 = i_2$ rather than by Eq. [10], so that $\theta_H = k_1/(k_1 + k_2)$. Then proceeding as in previous cases to obtain $(\partial \ln \theta_H/\partial p)_{\eta,T}$ and deriving $(\partial \ln i_t/\partial p)_{\eta,T}$, we find

$$\Delta V_a^{\ddagger} = \theta_H\Delta V_2^{\ddagger} + (1 - \theta_H)\Delta V_1^{\ddagger} - \beta\Delta V_o \quad [33]$$

The over-all true volume of activation is represented by

$$\Delta V_t^{\ddagger} = \theta_H\Delta V_2^{\ddagger} + (1 - \theta_H)\Delta V_1^{\ddagger} = \Delta V_a^{\ddagger} + \beta\Delta V_o \quad [34]$$

[1] It is convenient to distinguish a quantity, $\Delta V_t^{\ddagger}$, as the over-all true volume of activation from the true $\Delta V_n^{\ddagger}$ for the rate-determining step n, derived from the pressure derivative of the log of the rate constant. ΔV_t differs from $\Delta V_n^{\ddagger}$ when pressure-dependent coverage terms are significant. Both ΔV_t and $\Delta V_n^{\ddagger}$ differ from $\Delta V_a^{\ddagger}$ due to the pressure dependence of ϕ_e. In complex cases, such as that here where θ_H can be $f(p)$, $\Delta V_t^{\ddagger}$ can be expressed either in terms of the true $\Delta V^{\ddagger}$ for the rate-determining step or in terms of $\Delta V_a^{\ddagger}$ with $\Delta V_o^{\ddagger}$ and θ_H.

Table I. Relation between true ($\Delta V_t^{\ddagger}$) and apparent ($\Delta V_a^{\ddagger}$) volumes of activation for various mechanisms or conditions in the hydrogen evolution reaction

Case	Rate-determining step or condition	$\Delta V^{\ddagger}$ relation	Observed or derived values of $\Delta V^{\ddagger}$ (cm³ mole⁻¹) for constant η
1	H_3O^+ discharge step [I]; $\theta_H << 1$	$\Delta V_1^{\ddagger} = +\Delta V_a^{\ddagger} + \beta\Delta V_o$*	$\Delta V_a^{\ddagger} \simeq -3.4$ (Hg) $\Delta V_t^{\ddagger} \simeq +5.6$ (Hg)
2	Desorption of H in step [II]; $\theta_H > 0$ and potential and pressure dependent	$\Delta V_t^{\ddagger} = \Delta V_a^{\ddagger} + (1 + \beta - \theta_H)\,\Delta V_o$ $= \Delta V_2^{\ddagger} + (1 - \theta_H)\,\Delta V_t$	
Limiting cases	$\theta_H \to 1$	$\Delta V_a^{\ddagger} = \Delta V_2^{\ddagger} - \beta\Delta V_o$	$\Delta V_a^{\ddagger} \simeq -12.5$ (Cu, Ag, Au)
	$\theta_H << 1$	$\Delta V_a^{\ddagger} = \Delta V_1 - (1 + \beta)\,\Delta V_o + \Delta V_2^{\ddagger}$	$\Delta V_t^{\ddagger} \simeq +2$ (Cu, Ag, Au) for $\phi_H << 1$
3	Step [I], with θ_H determined by quasi-equilibrium in step [II]	$\Delta V_t^{\ddagger} = \Delta V_a^{\ddagger} + [1 + \beta - (1 - \theta_H)]\,\Delta V_o - K'(1 - \theta_H)\,\Delta V_o$	
Limiting cases	$\theta_H \to 1$	$\Delta V_a^{\ddagger} = \Delta V_1^{\ddagger} - (1 + \beta)\,\Delta V_o + \Delta V_2$ or $\Delta V_t^{\ddagger} = \Delta V_1^{\ddagger} + \Delta V_2 = \Delta V_a^{\ddagger} + (1 + \beta)\,\Delta V_o$	
	$\theta_H << 1$	$\Delta V_a^{\ddagger} = \Delta V_1^{\ddagger} - \beta\Delta V_o$	$\Delta V_a^{\ddagger} \simeq -12.5$ (Cu, Ag, Au) $\Delta V_t^{\ddagger} \simeq \Delta V_1^{\ddagger} = -7.6$ (Cu, Ag, Au)
4	Recombination step [III]	$\Delta V_t^{\ddagger} = \Delta V_3^{\ddagger} + 2\Delta V_1\,(1 - \theta_H)$ $= \Delta V_a^{\ddagger} + 2\,(1 - \theta_H)\,\Delta V_o$ or $\Delta V_a^{\ddagger} = \Delta V_3^{\ddagger} - 2\,(1 - \theta_H)\,(\Delta V_o - \Delta V_1)$	
Limiting cases	$\theta_H \to 1$	$\Delta V_t^{\ddagger} = \Delta V_a^{\ddagger} = \Delta V_3^{\ddagger}$	
	$\theta_H << 1$	$\Delta V_t^{\ddagger} = \Delta V_a^{\ddagger} + 2\Delta V_o\ (\equiv \Delta V_3^{\ddagger})$	
5	Coupled [I] and [II]; high η	$\Delta V_t^{\ddagger} = \theta_H\Delta V_2^{\ddagger} + (1 - \theta_H)\,\Delta V_1^{\ddagger}$ $= \Delta V_a^{\ddagger} + \beta\Delta V_o$	$\Delta V_a^{\ddagger} \simeq -12.5$ (Cu, Ag, Au) $\Delta V_t^{\ddagger} \simeq -7.6$ (Cu, Ag, Au)
Limiting cases	$\theta_H \to 1$	$\Delta V_a^{\ddagger} = \Delta V_2^{\ddagger} - \beta\Delta V_o$	
	$\theta_H << 1$	$\Delta V_a^{\ddagger} = \Delta V_1^{\ddagger} - \beta\Delta V_o$	

* This type of relation also applies to any simple discharge step, *e.g.*, as in an ionic redox reaction (see Part II).

The limiting steady-state cases are:

(*i*) If $k_2 >> k_1$, $\theta_H \to 0$; then

$$\Delta V_a^{\ddagger} = \Delta V_1^{\ddagger} - \beta\Delta V_o \quad [35]$$

which is the same result as that derived for the condition that step [I] is rate determining (*i.e.*, case 1); and

(*ii*) If $k_1 >> k_2$, $\theta_H \to 1$; then

$$\Delta V_a^{\ddagger} = \Delta V_2^{\ddagger} - \beta\Delta V_o \quad [36]$$

A summary of the results obtained for the various cases is given in Table I.

Discussion of Previously Published Experimental Results

The proton discharge reaction at Hg.—It is generally agreed that the rate-determining step in H_2 evolution at Hg is step [I] with desorption by [II]. Hills and Kinnibrugh's work (9) on this reaction gave data[2] for $(\partial \ln i/\partial p)_{T,\phi\ \text{calomel}}$ which they assumed corresponded to the true volume of activation; a negative value of -3.4 cm³ mole⁻¹ was found. As shown in case 1, this value is, in fact, the apparent volume of activation [cf. Ref. (7, 8)], *i.e.*, $\Delta V_{t,1}^{\ddagger} = \Delta V_{a,1}^{\ddagger} + \beta\Delta V_o$, where $\Delta V_a^{\ddagger} = -3.4$ cm³ mole⁻¹, $\Delta V_o = 18$ cm³ mole⁻¹, and $\beta = 0.5$. Hence the true activation volume is $-3.40 + 0.5 \times 18$, *i.e.*, a positive value of 5.6 cm³ mole⁻¹. $\Delta V_a^{\ddagger}$ was obtained from $(\partial \ln i/\partial p)_{T,\eta}$ measured at $p > 250$ bars. It appears that a steeper slope would have been measured if $(\partial \ln i/\partial p)_{T,\eta}$ had been derived limitingly at $p = 1$ bar (data at atmospheric pressure were not given). $\Delta V_{t,1}^{\ddagger}$ could then be appreciably smaller than 5.6 cm³ mole⁻¹.

[2] Hills and Kinnibrugh's results were obtained from measurements at "constant electrode potential" *vs.* a calomel reference. They corrected their results to constant overpotential but did not take into account the further correction to constant "metal-solution p.d." which is also required (see Eq. [3] and [4]).

The H_2-evolution reaction at Cu, Ag, and Au.—Heusler and Gaiser (16) measured the pressure-dependence of H_2 evolution currents at Cu, Ag, and Au. Their derived volumes were based on $(\partial \ln i/\partial p)_{\eta,T}$ evaluated at $p > 500$ bars where the derivative is independent of p. Under these conditions, ΔV_o for the over-all reaction [IV] is 8.7 cm³ mole⁻¹ based on Ref. (13); $\overline{V}_{H_2} = 15.0$ cm³ mole⁻¹ at these pressures and including $V_e = 3$ cm³ Faraday⁻¹; $\overline{V}_{H^{+o}}$ was taken (16) as -5.2 cm³ mole⁻¹. The measured $\Delta V_a^{\ddagger}$ is -12.5 cm³ mole⁻¹. Therefore the over-all $\Delta V_t^{\ddagger} = 12.5 + 1/2\,(9.7) = -7.6$ cm³ mole⁻¹.

In Heusler and Gaiser's treatment (16) of their results, allowance was correctly made for $(\partial\phi_e/\partial p)_T$ and the back-reaction of step [I] was neglected (case 5 above). For these conditions, the true volume of activation is given by Eq. [4]

$$\Delta V_t^{\ddagger} = \theta_H\Delta V_2^{\ddagger} + (1 - \theta_H)\,\Delta V_1^{\ddagger} = \Delta V_a^{\ddagger} + \beta\Delta V_o$$

There is no evidence for any substantial coverage by chemisorbed H at Cu, Ag, or Au at normal overpotentials nor is underpotential deposition observed. Thus, $\theta_H \simeq 0$ so that $\Delta V_t^{\ddagger} \doteq \Delta V_1^{\ddagger} = -7.6$ cm³ mole⁻¹. This negative value is surprising since it might be expected that in the electrochemical reaction, when the proton charge is neutralized, a positive volume of activation would arise as for the corrected results at Hg (8).

However, if case 2 (*i.e.*, with quasi-equilibrium in step I) is examined, then from Eq. [16] with $\theta_H \simeq 0$, the over-all $\Delta V_t^{\ddagger}$ is given by

$$\Delta V_t^{\ddagger} = -12.5 + 3/2\,(9.7) = +2 \text{ cm}^3 \text{ mole}^{-1}$$

Then the volume of activation for step [II], $\Delta V_2^{\ddagger} = 2 - \Delta V_1$ from Eq. [15], where ΔV_1 is the quasi-equilibrium volume change in step [I]. If ΔV_1 is positive and greater than 2 for this case, then $\Delta V_2^{\ddagger}$, the true volume of activation for step [II] will have again a negative value. Experimentally (6), at Pt, $\Delta V_1 = 7.4 \pm 2$ cm^3 mole^{-1}.

If case 3 applied, a complicated expression is generated if $\theta_H > 0$. Thus, combining Eq. [21] and [22]

$$\Delta V_t^{\ddagger} = \Delta V_a^{\ddagger} + (1 + \beta)\,\Delta V_o - (1 - \theta_H)\Delta V_o - K'(1 - \theta_H)V_o \quad [37]$$

However, if $\theta_H \rightarrow 0$, case 1 would be recovered giving $\Delta V_t^{\ddagger} = \Delta V_1^{\ddagger} = -7.6$ cm^3 mole^{-1}.

It is useful to establish the sign of $\Delta V_t^{\ddagger}$ for an appreciable value of θ_H, say 0.5. Then, from Eq. [37], taking $K' = 0$, $\Delta V_t^{\ddagger} = \Delta V_a^{\ddagger} + \Delta V_o = 12.6 + 9.7 = -3$ cm^3 mole^{-1}. Also with $\beta = 0.5$ and $\theta_H = 0.5$, $\Delta V_t^{\ddagger} = \Delta V_1^{\ddagger} + \Delta V_2/2$. Hence, $\Delta V_1^{\ddagger} = -3 - \Delta V_2/2$. But the quantity ΔV_2, which is the equilibrium volume change in the process $MH_{ads} + H^+ + e\ (M) \rightleftharpoons H_2$ (step [II]), is expected [cf. (6)] to be positive. Hence, $\Delta V_1^{\ddagger}$ will still be negative for intermediate coverages of the metal.

The above discussion shows, surprisingly, that negative values of the true volume of activation of the HER arise at certain metals, after allowance for the complicating factors is made.

Significance of negative or small positive values of $\Delta V_t^{\ddagger}$.—On the basis of their original uncorrected results, it was concluded by Hills and Kinnibrugh (9) and by Hills (12) that the observed negative volume of activation (really $\Delta V_{a,1}^{\ddagger}$) indicated electrochemical formation of the hydrated electron as the primary step in the HER at Hg. Various objections to this mechanism, apart from those connected with the difference between $\Delta V_{t,1}^{\ddagger}$ and $\Delta V_{a,1}^{\ddagger}$, were, however, pointed out by Conway (7) (15) and by Bewick and Conway (17).

It is very difficult to see how a negative value of the true volume of activation can arise in the discharge of a cation, here H_3O^+. We show in Part II that the true volume of activation for an ionic redox reaction $Fe(CN)_6^{4-} \rightarrow Fe(CN)_6^{3-} + e$ does have the expected sign (positive for the direction written above). Hence, it may be suggested that the anomalous behavior of H_3O^+ arises from the special nature of the hydrated proton in solution. Thus, good evidence exists (18, 19) that H^+_{aq} exists as the $H_9O_4^+$ ion in which proton charge is decentralized by joint proton tunneling between $4H_2O$ molecules + H^+ and delocalized at any momentarily existing H_3O^+ center. The transition state for classical proton transfer must presumably arise by a reorganization (23) of the $H_9O_4^+$ aqueous complex. If the activation process involves localization of the proton on one of the H_2O molecules in $H_9O_4^+$ in the double layer to produce an excited state to which electron transfer occurs by the usual radiationless transfer (Fig. 1), then it can be seen that a negative volume of activation could arise since more electrostriction could be developed temporarily in the double layer at the localized proton state than in the initial $H_9O_4^+$ ion in which proton charge-density is diffused. The relaxation time of the water structure H-bonding in relation to the lifetime of the proton being discharged will determine the electrostriction in the transition state. That the proton in water has relatively an unusually large partial molal volume is indicated when the volume of ionization of water is compared with that for NH_3 aqueous in the processes

$$H_2O + H_2O \rightarrow \text{“}H_3O^+\text{”} + OH^-$$

$$\Delta V^o = -21.8;\ -22.1\ \text{cm}^3\ \text{mole}^{-1}$$

and

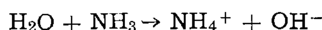

$$H_2O + NH_3 \rightarrow NH_4^+ + OH^-$$

$$\Delta V^o = -28.9;\ -28.5\ \text{cm}^3\ \text{mole}^{-1}$$

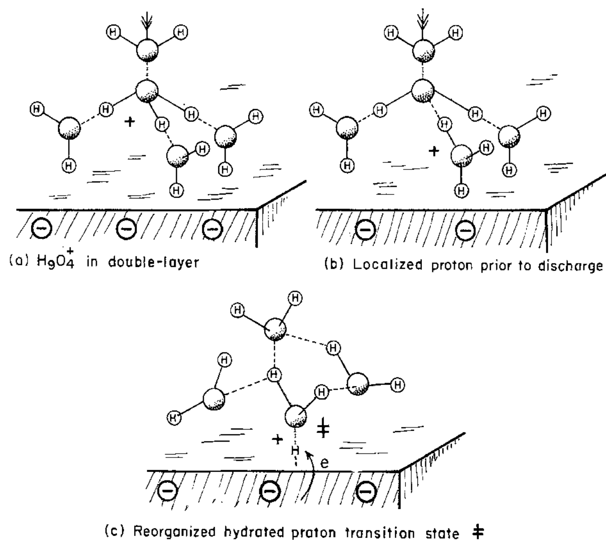

Fig. 1. Configurations of the hydrated proton, as $H_9O_4^+$ + $1H_2O$ in the double layer in the course of the activation process in electrochemical proton discharge (schematic).

in which NH_3 is isoelectronic with H_2O and NH_4^+ with “H_3O^+.” (The first values of ΔV^o are derived from pressure effects on the ionization constant and the second from volumetric measurements; data are from Ref. (20). Assuming that the difference of intrinsic volume of NH_4^+ and “H_3O^+” would be close to the corresponding difference between NH_3 and H_2O, due to the extra H atom, it seems reasonable to conclude that the electrostriction at “H_3O^+” is *ca.* 6.5 – 7 cm^3 mole^{-1} smaller than at the isoelectronic NH_4^+ ion. This is consistent with diffusion of the proton charge in $H_9O_4^+$ which cannot occur in the hydrated NH_4^+ ion. The difference of 6.5-7 cm^3 mole^{-1} is of the correct magnitude to account for the negative $\Delta V_t^{\ddagger}$ values.

While the volume of activation for H_2 evolution from H_{aq}^+ evidently exhibits unusual behavior, that for ionic redox reactions should help to elucidate the nature of the activation process involving solvent reorganization in such cases. In particular, the question arises whether short-range reorganization of the hydration shell is involved or whether less specific fluctuations of the long-range dielectric polarization are mainly operative. These questions will be dealt with in Part II on the $Fe(CN)_6^{3-}$ redox reaction.

Acknowledgments

Grateful acknowledgment is made to the National Research Council of Canada for support of this work and to the Defence Research Board for support in its earlier stages.

Manuscript submitted April 11, 1977; revised manuscript received July 14, 1977.

Any discussion of this paper will appear in a Discussion Section to be published in the December 1978 JOURNAL. All discussions for the December 1978 Discussion Section should be submitted by Aug. 1, 1978.

REFERENCES

1. K. J. Laidler and R. Martin, *Int. J. Chem. Kinetics*, **1**, 113 (1969); see also *Disc. Faraday Soc.*, **22**, 88 (1956).
2. G. J. Hills, in “Chemical Physics of Ionic Solutions,” B. E. Conway and R. G. Barradas, Editors, chap. 23, John Wiley & Sons, Inc., New York (1966).
3. S. D. Hamann, P. J. Pearce, and W. Strauss, *J. Phys. Chem.*, **68**, 375 (1964).
4. K. J. Laidler, “Chemical Kinetics,” p. 234, McGraw Hill Book Co., New York (1969).
5. C. T. Burris and K. J. Laidler, *Trans. Faraday Soc.*, **51**, 1497 (1955) and *Can. J. Chem.*, **37**, 599 (1959).
6. B. E. Conway and J. C. Currie, *J. Chem. Soc., Faraday Trans. 1*, In course of publication.
7. B. E. Conway, in “Chemical Physics of Ionic Solu-

tions," B. E. Conway and R. G. Barradas, Editors, pp. 577-578, John Wiley & Sons, Inc., New York (1966).
8. B. E. Conway, *This Journal*, **113**, 1118 (1966); L. I. Krishtalik, **113**, 1117 (1966).
9. G. J. Hills and D. R. Kinnibrugh, *ibid.*, **113**, 1111 (1966).
10. *E.g.*, see R. Parsons, *Trans. Faraday Soc.*, **47**, 1332 (1951).
11. S. Barnartt, *Electrochim. Acta*, **13**, 901 (1968).
12. G. H. Hills, *Disc. Faraday Soc.*, **39**, 207 (1965).
13. M. I. Temkin, *Zh. Fiz. Khim.*, **22**, 1081 (1948).
14. B. E. Conway and D. J. MacKinnon, *This Journal*, **116**, 1665 (1969).
15. *E.g.*, see B. E. Conway, "Theory and Principles of Electrode Processes," Ronald Press, New York (1965).
16. K. E. Heusler and L. Gaiser, *Ber. Bunsenges.*, **72**, 1059 (1969).
17. A. Bewick, B. E. Conway, and A. Tuxford, *J. Electroanal. Chem.*, **42**, pp. 11-15 (1973).
18. A. Wicke, M. Eigen, and Th. Ackermann, *Z. Phys. Chem., N.F.*, **1**, 340 (1956).
19. A. J. Cunningham, J. D. Paysant, and P. Kebarle, *J. Am. Chem. Soc.*, **94**, 7627 (1972); see also, *ibid.*, **89**, 6393 (1967).
20. S. D. Hamann, in "Modern Aspects of Electrochemistry," Vol. 9, B. E. Conway and J. O'M. Bockris, Editors, Tables 17 and 18, Plenum Publishing Corp., New York (1974).
21. E. W. Tiepel and K. E. Gubbins, *J. Phys. Chem.*, **76**, 3044 (1972).
22. B. E. Conway and D. J. MacKinnon, *ibid.*, **74**, 3363 (1970).
23. L. I. Krishtalik, *Elektrokhimiya*, **11**, 184 (1975).

Significance of Effects of High Pressure on Kinetics of Electrode Reactions

II. The Nature of Solvent Reorganization in the Activation Process of an Electrochemical Redox Reaction

B. E. Conway and J. C. Currie

Chemistry Department, University of Ottawa, Ottawa, Ontario, Canada

ABSTRACT

New information on the nature of the solvent reorganization process involved in formation of the transition state in an electrochemical redox reaction [the $Fe(CN)_6^{3-}/Fe(CN)_6^{4-}$ couple] is given by studies of the kinetics of this process at high pressures in aqueous solutions at Au. The apparent activation volume is evaluated together with the true volumes of activation for the forward and reverse directions of the redox reaction. By means of calculations of the electrostriction associated with the long-range dielectric polarization in comparison with that associated with ion-solvent interaction in the primary hydration shell, it is shown that the activation process must be mainly (75%) due to short-range solvent reorganization in the primary shell. This is contrary to what has often been assumed in the interpretation of the energy of activation of ionic redox reactions. The experiments also allow some deduction to be made about the "symmetry" of the transition states in the electrochemical reaction in comparison with that in the corresponding homogeneous reaction, in so far as solvent reorganization is concerned.

In Part I (1), some of the general problems of interpretation of effects of pressure on the kinetics of electrode reactions were discussed and exemplified with respect to the hydrogen evolution reaction. It was shown that investigations of pressure effects on the latter reaction are complicated by (*i*) the mechanism having more than one step; (*ii*) the consequent adsorption of an intermediate H; and (*iii*) the unusual properties of the hydrated proton, referred to in Part I, as well as the general point that reference electrode potentials required in all measurements are themselves pressure dependent (2).

It is therefore desirable to examine pressure effects on a simpler reaction where only an electron-transfer step is involved, *e.g.*, as in a redox reaction. Hitherto, studies of electrochemical redox reactions have been concerned with (*i*) evaluation of absolute values of standard electrochemical rate constants (3, 4); (*ii*) their comparison with values for corresponding homogeneous solution reactions (5); and (*iii*) the role of the substrate metal (6) (its work function and the state of its surface) in determining the rate constant.

In the present paper, pressure effects on the $Fe(CN)_6^{3-} + e \rightleftharpoons Fe(CN)_6^{4-}$ reaction at a gold electrode are reported. This type of reaction is of special interest with regard to current theories of electron transfer (7-14) where the reorganization (10) of the initial state is involved in the activation process for electron transfer. One of the questions involved is the extent to which the activation process involves long-range solvent polarization fluctuations (10, 11) around the initial state ion, or more specific short-range changes of hydration shell configuration or inner coordination shell reorganization (7, 8, 12). It may be expected that study of pressure effects on the kinetics of a simple electrochemical redox reaction may provide a means of distinguishing these effects, *e.g.*, in terms of the anticipated changes of electrostriction involved in the reorganization process. Examination of the effect of pressure on the kinetics of a redox reaction thus provides a further dimension from which new data of a useful kind can be derived. Previous high pressure work on a redox reaction has been restricted to a report of values of $\Delta V_t^{\ddagger}$ for the ferro-ferricyanide reaction in a review (15) but no experimental details or commentary on the data have been published. The results quoted are inconsistent with the known electrostrictions at the two ions in this reaction.

A second point, of general interest, is whether a chemically symmetrical reaction such as the ferro-ferricyanide one behaves in a kinetically symmetrical

way (symmetry factor $\beta = 0.5$) when established at an electrode surface.

Experimental

General.—The kinetics of the $Fe(CN)_6^{3-} + e \rightleftharpoons Fe(CN)_6^{4-}$ reaction were studied at a gold electrode. The latter was chosen as the substrate metal because it is known to have a wide range of potentials over which neither H nor O species is chemisorbed (under-potentially deposited). The exchange rate constants for the ferri-ferrocyanide reaction are relatively large (4), so that a nonsteady-state method is required for their proper evaluation. In the present work, the kinetics of the reaction were studied by a-c impedance measurements based on well-known principles (16) which lead to evaluation of the reaction resistance and hence the exchange current density i_o. From this the standard rate constant can be obtained knowing the concentrations of the reactant species.

Method.—The faradaic impedance was measured by means of phase-sensitive a-c voltammetry at phase angles $\phi = 0$ and $\phi = 90°$ which directly give the real and imaginary components of the impedance, that is, the ohmic and capacitative contributions. This method has been referred to in previous literature (17) and provides a convenient way of performing a-c impedance experiments. It is quite precise providing that one component of the impedance is not very much smaller than the other.

Electrical measurements.—The present system employed a Wenking potentiostat and a Servomex function generator which provided a controlled repetitive linear sweep of potential. A small alternating voltage signal, modulating the sweep, was provided from an auxiliary oscillator at various frequencies and mixed with a linear sweep in an operational amplifier. A PAR phase-sensitive amplifier was employed to effect resolution of the ohmic and capacitative components of the impedance. The satisfactory operation of this system was first established by test measurements on dummy series and parallel *C-R* circuits (the phase-sensitive amplifier measures *C* and *R* components in terms of admitted a-c currents in a "parallel" combination). The range of frequencies employed in the measurements was from 25 to 250 Hz. The a-c "polarograms" and the d-c current-potential profiles generated by the linear sweeps were recorded simultaneously.

Cell for high-pressure measurements.—A cell suitable for use in a high pressure environment (Fig. 1) under oil was constructed from glass and shrinkable Teflon tubing. The latter provides a flexible section of the cell that can adjust to the electrolyte volume changes that arise at elevated pressures. This system is preferable to the use of a mercury piston which gives rise to contamination in electrochemical experiments on metals other than mercury itself. The cell is provided with a large gauze counterelectrode for the a-c measurements and the gold test electrode is sealed into the glass head. After filling the cell with deoxygenated solution in a N_2 glove bag, it is closed with a screw cap and set up in the high pressure bomb under the hydraulic fluid.

Complete absence of contamination and of leaks was indicated by demonstrating that the cyclic-voltammetry current-potential profile for a Pt electrode in the high pressure cell could be maintained for many hours with as perfect a form as that previously reported (18) for ultraclean solutions at ambient pressures in a regular glass cell. "Clean electrochemistry" could therefore be satisfactorily performed in the system described over many hours and at elevated pressures.

High pressure system.—The small electrochemical cell, fabricated from glass and shrinkable Teflon, was set up in a 10 in. diam (OD) thermostated high pressure bomb containing hydraulic oil. Electrical connections to exterior instruments are provided through a special head. A manual pumping system enabled pressures up to 3000 bars to be attained. They were recorded on a Heise gauge calibrated at the National Research Council Laboratories. Measurements were made at several increasing and decreasing series of pressures. At each pressure, at least 1 hr was allowed for thermal equilibium to be attained since compression or decompression of the hydraulic fluid causes substantial changes of temperature.

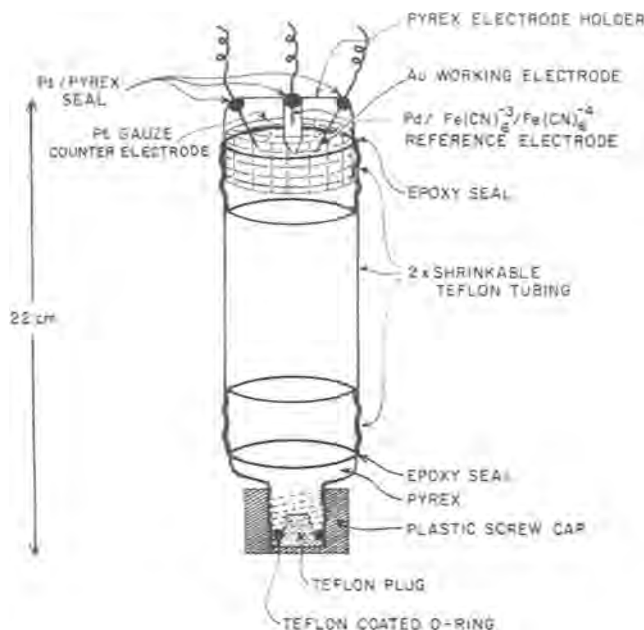

Fig. 1. Electrochemical cell with flexible shrinkable Teflon section for high pressure work.

Solutions.—All measurements were made in a supporting electrolyte of 0.5M K_2SO_4 at 25°C. The ambient-pressure concentrations of $K_3Fe(CN)_6$ and $K_4Fe(CN)_6$ were 5×10^{-3}M. Some experiments were carried out with one only of these components at this concentration and other experiments with both components at this concentration. As noted elsewhere in this paper, corrections to these concentrations, which are required as the pressure is increased, were made in all experiments although in other high pressure work this point has often been ignored.

Results

The impedance behavior.—Analysis of the a-c impedance was made in the usual way (19) by means of Randles plots (16) in which the "series" faradaic resistance $R_{F,s}$ and the diffusional capacitance $(1/\omega C_{F,s})$ contributions are plotted as a function of $\omega^{-1/2}$ after separation of the double layer capacity and solution resistance impedance components determined in experiments in the absence of the redox couple. The double layer capacity was also determined from the results at $\phi = 90°$ at potentials well away from the half-wave potentials, *i.e.*, where the Warburg diffusional capacitance is negligible. The faradaic reaction resistance, R_r, was then evaluated by extrapolation of the Randles plots to infinite frequency, as shown in Fig. 2, giving

$$R_r = RT/z\mathbf{F}i_o \quad [1]$$

where the exchange current i_o is related to the standard electrochemical rate constant $\overline{k}_o$ by

$$i_o = z\mathbf{F}\overline{k}_oCA \quad [2]$$

where A is the electrode area, z is the number of

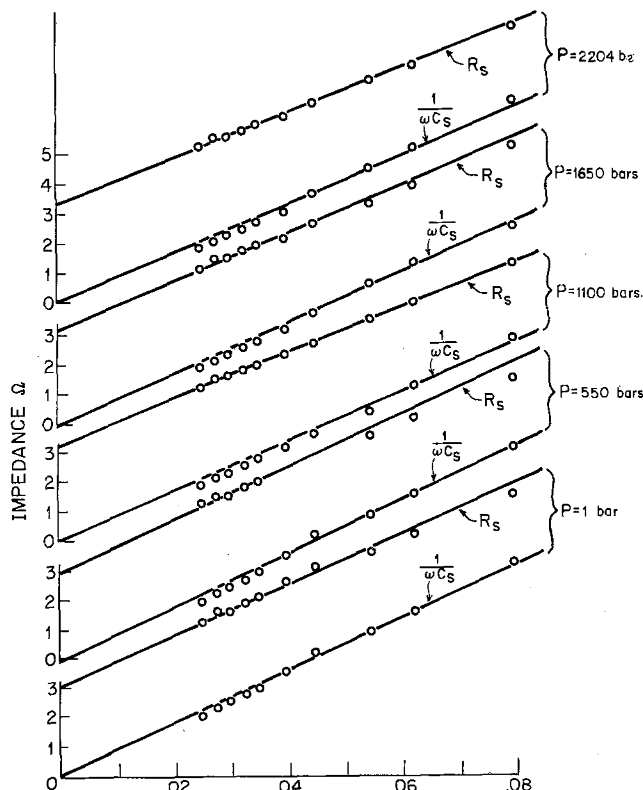

Fig. 2. Randles plots for the impedance behavior of the $Fe(CN)_6^{3-}/Fe(CN)_6^{4-}$ reaction at Au at 25°C.

electrons ($z = 1$ here) in the exchange reaction, and C the concentration in mole cm^{-3} of the reactant species. The measured "a-c" currents were evaluated for unit area of the substrate metal and, for high pressures, corrections were made to the ambient pressure concentration using the known compressibility of the solutions.

A test of the satisfactory operation of the electronic measurement system is that the $R_{F,s}$ and $1/\omega C_{F,s}$ quantities should give parallel lines in a plot against $\omega^{-1/2}$ and the $1/\omega C_{F,s}$ relation should pass through the origin.

Figure 2 shows the results at pressures 1, 550, 1100, 1650, and 2204 bars. The plots of $R_{F,s}$ and $1/\omega C_{F,s}$ *vs.* $\omega^{-1/2}$ at each pressure are satisfactorily parallel, with the out-of-phase component passing through the origin as required from the treatment of Randles

$$\frac{1}{\omega C_{F,s}} = \frac{RT}{z^2\mathbf{F}^2AC}\sqrt{\frac{2}{\omega D}} \quad [3]$$

where A is the area of the electrode, C the bulk concentration of the "depolarizer," *i.e.*, $Fe(CN)_6^{-4}/Fe(CN)_6^{-3}$, and D the mean diffusion coefficient of the redox couple ions.

The intercept of the in-phase component line is related to the heterogeneous rate constant $\overline{k}_o$ by the following relation

$$R_{F,s} = \frac{RT}{z^2\mathbf{F}^2AC}\left(\sqrt{\frac{2}{\omega D}} + \frac{1}{k_o}\right) \quad [4]$$

At $\omega^{-1/2} = 0$, the faradaic resistance becomes the reaction resistance, R_r, as represented by the equation (cf. Eq. [1])

$$R_r = \frac{RT}{z^2\mathbf{F}^2AC}\left(\frac{1}{k_o}\right) = \frac{RT}{z\mathbf{F}i_o} \quad [5]$$

The numerical results are recorded in Table I. The results are fitted to a second-order polynomial of the form

$$\ln i_o = a + bp + cp^2$$

then plotted as $\ln i_o$ *vs.* p as in Fig. 3. Also included

Table I. Impedance and kinetic results for the $Fe(CN)_6^{3-}/Fe(CN)_6^{4-}$ couple at a gold electrode at 25°C as a function of pressure

Pressure (bars)	R_r (Ω)	$i_o \times 10^2$ ($A \cdot cm^{-2}$)	$\ln i_o$	$\overline{k}_o \times 10^2$* ($cm \cdot sec^{-1}$)
1	3.24	1.13	−4.481	2.34
550	3.35	1.11	−4.514	2.30
1100	3.51	1.05	−4.561	2.18
1650	3.58	1.02	−4.581	2.11
2204	3.70	0.99	−4.614	2.05

Initial slope $(\partial \ln i_o/\partial p)_{p\to 0\ bar} = -7.47 \times 10^{-5}\ bar^{-1}$

* Derived from i_o values after allowance for pressure-dependent concentration of reactant ions.

are the error limits of the best-fit data. The limiting slope $(\partial \ln i_o/\partial p)_{\eta=0}$ at $p \to 0$ bars is evaluated from the coefficient b as $-7.47 \pm 0.4 \times 10^{-5}\ bar^{-1}$. The significance of this finite, rather than zero, value for $(\partial \ln i_o/\partial p)_{\eta=0}$ for the symmetry of the activation process is discussed later.

Relation to volumes of activation.—The pressure coefficient derived above is related to the apparent [see Ref. (1, 2)] volume of activation $\Delta V_a^{\ddagger}$ given by

$$\left(\frac{\partial \ln i_o}{\partial p}\right)_{\eta=0} = -\frac{\Delta V_a^{\ddagger}}{RT} = -7.47 \times 10^{-5}\ bar^{-1} \quad [6]$$

Hence

$$\Delta V_a^{\ddagger} = 1.9 \pm 0.1\ cm^3\ mole^{-1} \quad [7]$$

for the ferri/ferrocyanide couple at its equilibrium potential.

Discussion

Significance of the kinetic data derived from the a-c impedance measurements.—The reaction resistance determined gives the exchange current density, i_o, as indicated by Eq. [1]. It is thus the i_o values which are obtained in a low amplitude a-c electrochemical experiment as a function of pressure. The exchange current density is given by

$$i_o = \overrightarrow{i} = z\mathbf{F}\overrightarrow{k}C_{O,e} \exp -\beta\mathbf{F}\phi_e/RT \quad [8]$$

$$= \overleftarrow{i} = z\mathbf{F}\overleftarrow{k}C_{R,e} \exp (1-\beta)\mathbf{F}\phi_e/RT \quad [9]$$

written for an ionic redox reaction

$$O + ze \underset{\overleftarrow{k}}{\overset{\overrightarrow{k}}{\rightleftharpoons}} R \quad [10]$$

where $C_{O,e}$ and $C_{R,e}$ are the concentrations of O and R at the electrode interface, and $\overrightarrow{k}$ and $\overleftarrow{k}$ are the rate

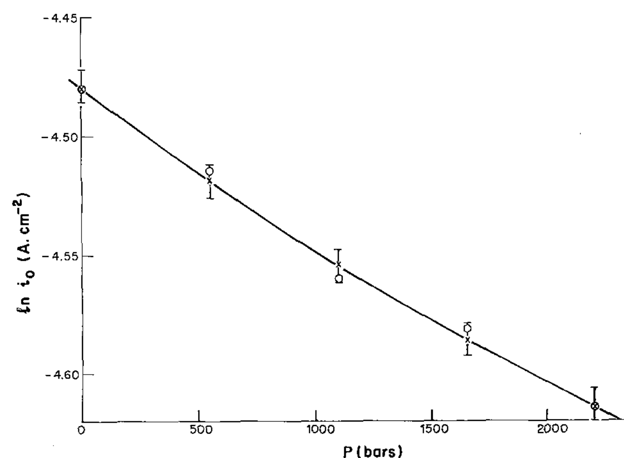

Fig. 3. Plot of ln i_o against pressure for the $Fe(CN)_6^{3-}/Fe(CN)_6^{4-}$ reaction at Au at 25°C at a concentration of 5×10^{-3}M.

constants for the forward and backward directions of the reaction. Experimental studies of pressure effects on i_o lead to evaluation of the pressure-dependence of the electrochemical rate constants $\vec{k}$ $(= \vec{k} \exp -\beta \mathbf{F}\phi_e/RT)$ or $\overleftarrow{k}$ $(= \overleftarrow{k} \exp (1-\beta) \mathbf{F}\phi_e/RT)$, *i.e.*, from the experimental derivative $(\partial \ln i_o/\partial p)_{T,\eta=0}$. Then, neglecting pressure-dependence of molar concentration and of double layer effects as in Part I (1)

$$\left(\frac{\partial \ln \vec{k}}{\partial p}\right)_T + \left[\frac{\partial}{\partial p}\left(\frac{-\beta\phi_e\mathbf{F}}{RT}\right)\right]_T = \left(\frac{\partial \ln i_o}{\partial p}\right)_T \quad [11]$$

or

$$\left(\frac{\partial \ln \overleftarrow{k}}{\partial p}\right)_T + \left[\frac{\partial}{\partial p}\left(\frac{(1-\beta)\phi_e\mathbf{F}}{RT}\right)\right]_T = \left(\frac{\partial \ln i_o}{\partial p}\right)_T \quad [12]$$

Hence the apparent volume of activation, $\Delta V_a^{\ddagger}$, which is found experimentally from $(\partial \ln i_o/\partial p)_T$, is given either by

$$\Delta V_a^{\ddagger} = \Delta \vec{V}_t^{\ddagger} - \beta \Delta V_o \quad [13]$$

or by

$$\Delta V_a^{\ddagger} = \Delta \overleftarrow{V}_t^{\ddagger} + (1-\beta)\Delta V_o \quad [14]$$

where $\Delta V_a^{\ddagger}$ applies to either direction of the reaction at $\eta = 0$, since at the reversible potential, the electrochemical free energies of the reactant and product species are at identical levels. In Eq. [13], ΔV_o is the equilibrium volume change in the over-all reaction [10] corresponding to $(\partial\phi_e/\partial p)_T$. The situation corresponding to Eq. [13] is illustrated schematically in Fig. 4b for volume changes at the reversible potential $(\phi = \phi_e)$ in relation to that in Fig. 4a representing the true volumes of activation $\Delta \vec{V}_t^{\ddagger}$ and $\Delta \overleftarrow{V}_t^{\ddagger}$ for hypothetical $\phi = 0$.

Since (see Part I) a relatively accurate nonthermodynamic estimate can usually be made of the volume change, ΔV_o, for the over-all reaction, both $\vec{V}_t^{\ddagger}$ and $\overleftarrow{V}_t^{\ddagger}$ can be separately evaluated from $\Delta V_a^{\ddagger}$ derived from $(\partial \ln i_o/\partial p)_{T,\eta=0}$.

It is to be noted that by the nature of the equations representing $\vec{k}$ and $\overleftarrow{k}$, the experimental pressure derivative will always give a small or zero (depending on β) apparent volume of activation from which the $\Delta V_t^{\ddagger}$ values for the forward or backward reaction must be obtained by addition or subtraction of about half of the over-all reaction volume (Eq. [13], [14]). This situation is thermodynamically unavoidable.

A relation obtainable from Eq. [13] and [14] is

$$2\Delta V_a^{\ddagger} = \Delta \vec{V}_t^{\ddagger} + \Delta \overleftarrow{V}_t^{\ddagger} + (1-2\beta)\Delta V_o \quad [15]$$

giving

$$(1-2\beta) = [2\Delta V_a^{\ddagger} - (\Delta \vec{V}_t^{\ddagger} + \Delta \overleftarrow{V}_t^{\ddagger})]/\Delta V_o \quad [16]$$

which would enable β to be evaluated if $\Delta \vec{V}_t^{\ddagger}$ and $\Delta \overleftarrow{V}_t^{\ddagger}$, or their sum, were independently available. A symmetrical transition state, $\beta = \frac{1}{2}$, corresponds, of course, to $\Delta V_a^{\ddagger} = \frac{1}{2}(\Delta \vec{V}_t^{\ddagger} + \Delta \overleftarrow{V}_t^{\ddagger}) = 0$. It is evident that with $\beta = \frac{1}{2}$, the true volumes of activation for the forward and backward reactions differ symmetrically from the common apparent volume of activation $\Delta V_a^{\ddagger}$ by $\pm \frac{1}{2}\Delta V_o$; also, as thermodynamically required, $\Delta \overleftarrow{V}_t^{\ddagger} - \Delta \vec{V}_t^{\ddagger} = \Delta V_o$. Hence, $\Delta V_a^{\ddagger} = 0$ for a symmetrical reaction. In the general case, $V^{\ddagger}$, the actual volume of the transition state is, however, not necessarily the mean of the initial and final state volumes in a reaction at an electrode since different adsorption effects can arise. An example is the $Fe(CN)_6^{3-}/Fe(CN)_6^{4-}$ redox reaction treated in the present paper. Unfortunately, it is clear from the foregoing that $\Delta \vec{V}_t^{\ddagger}$ and $\Delta \overleftarrow{V}_t^{\ddagger}$ can be evaluated through Eq. [14] from the measured $\Delta V_a^{\ddagger}$ and a nonthermodynamic value of ΔV_o only by choosing a reasonable value for β which would be presumed to be ½ for a "symmetrical" redox reaction (but see later section on transition state symmetry).

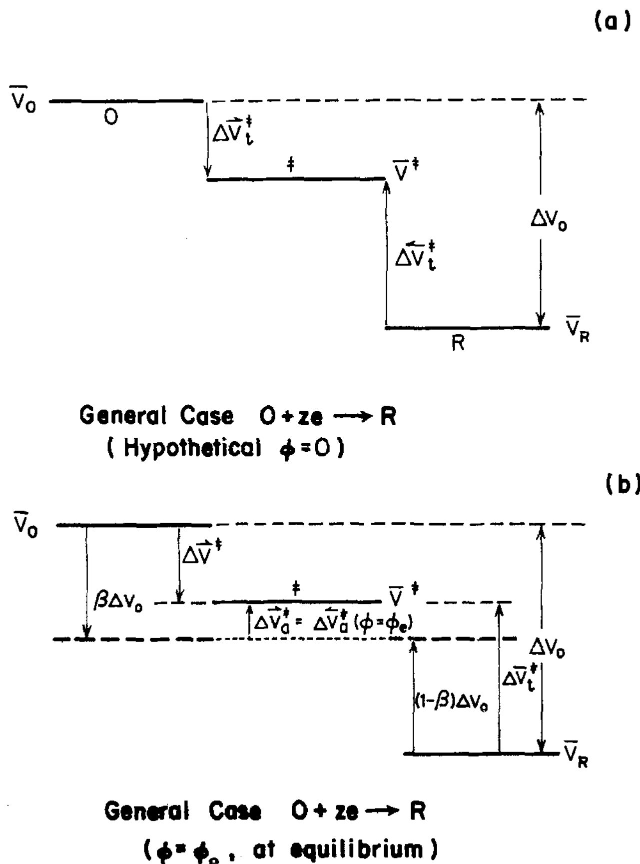

Fig. 4. Schematic relations between the true and apparent volumes of activation for the backward and forward directions of a general electron transfer reaction at $\phi = 0$ (hypothetical) and $\phi = \phi_r$, *i.e.*, at equilibrium, and the over-all partial molar volume difference $\Delta V°$, between products and reactants. $\bar{V}^{\ddagger}$ is the partial molar volume of the transition state.

Applications to the results for the $Fe(CN)_6^{3-}/Fe(CN)_6^{4-}$ couple.—In order to interpret the solvent reorganization behavior in this reaction, we require the change of electrostriction volume between the initial state and the transition state. The apparent volume of activation $\Delta V_a^{\ddagger}$ is available from the measurement of $(\partial \ln i_o/\partial p)$. Hence we first require ΔV_o (Eq. [13], [14]) for the reaction $Fe(CN)_6^{3-} + e \rightarrow Fe(CN)_6^{4-}$.

For the systems studied here, the individual partial molar volumes for the ions of the couple are (20)

$$\bar{V}°_{Fe(CN)_6^{4-}} = 95.6 \text{ and } \bar{V}°_{Fe(CN)_6^{3-}} = 137.0 \text{ cm}^3 \text{ mole}^{-1}$$

These values are based on the well-established individual ionic volume of the proton $(\bar{V}°_{H^+} = -5.4$ $\text{cm}^3 \text{ mole}^{-1})$ derived in at least two ways which give concordant results, as discussed in previously published literature (21, 22). The volume of the electron V_{e^-} in the half-cell redox reaction should be taken into account. It is difficult to find a reliable value for this term but Heusler and Gaiser (23) have suggested a value of 3 cm³ Faraday⁻¹ in a metal in their work on the H_2-evolution reaction. Using this value

$$\Delta V_o = \bar{V}°_{Fe(CN)_6^{4-}} - \bar{V}°_{Fe(CN)_6^{3-}} - V_{e^-} = -44.4 \text{ cm}^3 \text{ mole}^{-1}$$

Then, following Eq. [14], the true volumes of activation for the forward and backward directions of the reaction can be calculated from the common apparent volume of activation, $\Delta V_a^{\ddagger} = 1.9$ cm³ mole⁻¹

(Eq. [7]). Thus, for the reaction written in the direction $Fe(CN)_6^{3-} + e \rightarrow Fe(CN)_6^{4-}$

$$\overrightarrow{\Delta V}_t^{\ddagger} = 1.9 + \tfrac{1}{2}(-44.4) = -20.3 \text{ cm}^3 \text{ mole}^{-1} \quad [17a]$$

and

$$\overleftarrow{\Delta V}_t^{\ddagger} = 1.9 - \tfrac{1}{2}(-44.4) = 24.1 \text{ cm}^3 \text{ mole}^{-1} \quad [17b]$$

assuming β for this reaction can be taken [see below and Ref. (11)] as ½. The partial molar volume of the transition state, $\overline{V}^{\ddagger}$, is estimated from the relationship

$$\overline{V}^{\ddagger} - \overline{V}^{\circ}_{Fe(CN)_6^{3-}} = \overline{V}_e + \overrightarrow{\Delta V}_t^{\ddagger} + 119.7 \text{ cm}^3 \text{ mole}^{-1} \quad [18]$$

As in Fig. 4a, the changes of volume in the system as it passes from its initial state, through the transition state, to the final state can be represented schematically as shown in Fig. 5.

While the main changes in volume of conjugate ions in a redox couple are associated with the difference of electrostriction between the pair of ions, significant effects which must be considered can also arise from the change of ionic radius or ligand-to-metal bond length (24, 25). Thus, in an isoelectronic series, *e.g.*, Na^+, Ne, and F^-, changes of charge produce appreciable changes, Δr, of radii, from 0.95, through 1.1-1.36Å, respectively, for these three elements. Similarly, for Pb^{4+} to Pb^{2+}, the difference of radii is 0.36Å for 2*e*. It is more difficult to judge the effects of change of charge in $Fe(CN)_6^{3-}/Fe(CN)_6^{4-}$ because it is a complex ion with some charge delocalization (26). Based on the above figures for simple ions, a reasonable estimate of Δr would be 0.1Å per electron. However, recent crystallographic data (27, 28) on $Fe(CN)_6^{3-}$ and $Fe(CN)_6^{4-}$ (as their acids or salts) indicate, in fact, that there is very little difference in radius of these two ions and M.O. calculations show that the effective charges on Fe are almost identical. Thus the total Fe-to-N length is 3.07Å in $LaFe(CN)_6 \cdot 5H_2O$ (27) and 3.04Å in $H_4[Fe(CN)_6]$ (28), the value for the 4- ion being surprisingly the smaller of the two. This is consistent with a difference of 0.1Å taken by Mathieson (29) in that direction. The similar sizes of the two ions of the couple are also borne out by the similarity of their ionic mobilities (30-32) at infinite dilution, which indicates they have almost the same Stokes hydration radii.

Bearing in mind that it has been assumed that $\beta = 0.5$ for the $Fe(CN)_6^{3-}/Fe(CN)_6^{4-}$ system, then the transition state for an adiabatic electron transfer [cf. (11)] should bear a charge of $-3.5e$. Taking the radius of $Fe(CN)_6^{3-}$ as 3.31Å (29) an intrinsic volume of 91 cm³ mole⁻¹ is calculated. With $\Delta r = -0.03$Å per *e* (27, 28), the intrinsic volume of the transition state ion (charge $-3.5e$) would be 90 cm³ mole⁻¹, *i.e.*, 1 cm³ mole⁻¹ smaller than the initial state ion. Therefore the volume change due to solvent reorganization ($\overrightarrow{\Delta V}_{t,r}^{\ddagger}$) will be somewhat less than $\overrightarrow{\Delta V}_t^{\ddagger}$ and takes the value $-20.3 + 1$ in cm³ mole⁻¹, *i.e.*, -19.3 cm³ mole⁻¹, since $\overrightarrow{\Delta V}_t^{\ddagger}$ measures the total of all volume contributions associated with the formation of the transition state. Correspondingly $\overleftarrow{\Delta V}_{t,r}^{\ddagger}$ will be 23.1 cm³ mole⁻¹.

The main point to be emphasized is that these figures of -19.3 and 23.1 cm³ mole⁻¹ are relatively large volume changes and are associated mainly with the change of electrostriction about the ion since the small change of intrinsic volume has been allowed for. It is to be noted that the $\overrightarrow{\Delta V}_t^{\ddagger}$ differ significantly, but by a small amount, from half the volume change, ΔV_o, in the over-all reaction. This behavior originates from the fact that $\Delta V_a^{\ddagger}$ differs significantly from zero. The significance of the volume changes in Fig. 5 for the "symmetry" of the reaction will be examined later.

From the above data and Fig. 5, it is seen that the total volume of activation, less the contribution associated with ½*e* that remains in the metal, is -18.8 cm³ mole⁻¹. This is the volume change associated with solvent reorganization about the ion (including any contribution locally in the double layer) plus the change of intrinsic volume of the ion in the activation process in which ½*e* is transferred. Therefore the solvent electrostriction volume change in the activation process is $-18.8 - (-1)$ cm³ mole⁻¹ $= -17.8$ cm³ mole⁻¹ for the forward direction of the reaction and 21.6 cm³ mole⁻¹ for the backward direction. This is to be compared with the solvent electrostriction change in the over-all reaction which is $-41.4 - (-2) = -39.4$ cm³ mole⁻¹. Although the numerical value of the volume of activation depends on the effective volume of the electron, it is to be noted that the evaluation of the solvent electrostriction volume from $\Delta V_a^{\ddagger}$ is independent of the value assigned to V_{e^-}. Values of the electrostriction volumes[1] derived for the present case are illustrated in Fig. 6.

Electrostriction change and the nature of the activation process.—The electrostriction contributions, ΔV_{el}, to the volumes of activation derived above are quite large. In previous theoretical considerations (7, 8), it

[1] The ions of the ferro-ferricyanide couple exhibit unusual partial molal volume behavior (29) as there is evidently an appreciable structure-forming volume in $Fe(CN)_6^{3-}$ aq. like that for R_4N^+ ions (21). There is, however, the expected large electrostriction increase (−39.4 cm³ mole⁻¹) in going from the 3- to the 4-ion (Fig. 6).

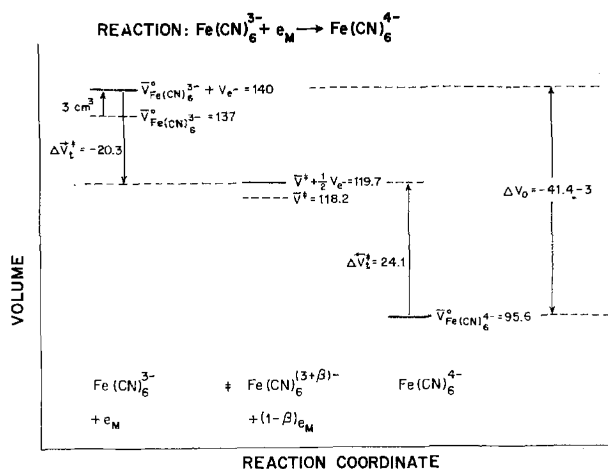

Fig. 5. Schematic relation for the volume changes in the $Fe(CN)_6^{3-} + e \rightarrow Fe(CN)_6^{4-}$ reaction showing the true volumes of activation in relation to the partial molar volumes of the initial, final, and transition state (‡). All volume data are in cm³ mole⁻¹. Volume data including a finite volume of the electron are shown.

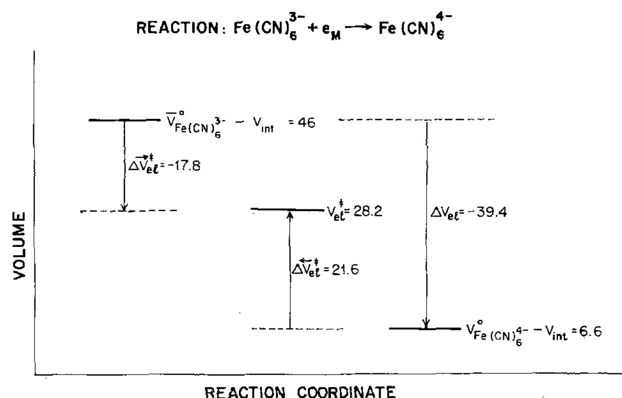

Fig. 6. Schematic relation for the electrostriction volume changes in the $Fe(CN)_6^{3-} + e \rightarrow Fe(CN)_6^{4-}$ reaction. *i.e.*, after the intrinsic volumes of the ions and the e-volume have been subtracted out.

has been pointed out that there are difficulties in accepting the view (10-12) that the solvent reorganization process is associated only with organized fluctuations of long-range (Born) dielectric polarization. The quantum-mechanical objections to primary hydration sphere reorganization being involved in the activation process on the basis that the $h\nu$ values for the modes involved are much larger than kT are weakened by the known (33) important contributions which such solvation-sphere modes make to the heat capacities of solvated ions in aqueous media at ordinary temperatures. Sufficient low frequency vibration and intermolecular modes are available. More recently, the role of inner-shell activation processes has been recognized (34) and treated by Schmickler (35).

It is therefore important to attempt to estimate the relative contributions to the electrostriction, ΔV_{el}, at an ion in water from successive spherical annular elements of the solvent out from the periphery of the ion; especially the contribution to ΔV_{el} from the solvent volume within 3-4Å from the ion in comparison with that further out, viz., 5-50Å, will be of interest.

While it would be desirable to calculate the volume changes associated with charge-transfer from recent quantum statistical calculations (12-14, 34-36) on this process, the required pressure derivatives of the quantities involved in such treatments of $\Delta G^{\ddagger}$ are mostly quite unknown; indeed reliable *ab-initio* numerical evaluations of $\Delta G^{\ddagger}$ quantities themselves have yet to be given. Even for solvation of simple ions (36), quantum statistical calculations of electrostriction have not yet been developed. On the other hand, relatively sophisticated electrostatic calculations have been published (37-40) which give electrostriction volumes at ions within 10-15% of values derived from experimental data. Hence the electrostatic model treatment is pursued here.

The simplest approach for calculation of electrostriction would be through the specific compressibility γ given by

$$-\gamma = \frac{1}{V}\left(\frac{dV}{dp}\right) \quad [19]$$

and the electrostrictive pressure p

$$p = \epsilon_r E^2/8\pi = (ze)^2/8\pi\epsilon_r r^4 \quad [20]$$

where E is the field $ze/\epsilon_r r^2$ due to the ion in the dielectric taking into account the fact that the relative permittivity, ϵ_r, is a function of r, the distance from the ion.

Then, from Eq. [20]

$$\frac{dp}{dr} = -[(ze)^2/2\pi\epsilon_r r^5] - [(ze)^2/8\pi\epsilon_r^2 r^4] \Big/ \left(\frac{d\epsilon_r^{-1}}{dr}\right) \quad [21]$$

The relative volume change dV in a spherical volume element $4\pi r^2 \cdot dr$ about the ion will be given by Eq. [19] as

$$dV = -\gamma 4\pi r^2 \cdot dr \cdot dp \quad [22]$$

Then, introducing dp as $f(r \cdot dr)$ from Eq. [21]

$$dV = [2\gamma(ze)^2/\epsilon_r r^3]dr \cdot dr + [\gamma(ze)^2/2r^2\epsilon_r^2]dr \cdot d\epsilon_r \quad [23]$$

from which changes of volume due to electrostrictive tension in successive annular elements of volume could be calculated by integration. In Eq. [23], it is to be expected (37) that γ as well as ϵ will be a function of r. Hence, integration of Eq. [23] with both γ and ϵ as a function of r is obviously difficult. However, a better approach may be made using the calculations previously published from this laboratory, based on empirical equations for pressure and field effects on ϵ and the thermodynamic theory of electrostriction given by Frank (38).

It is convenient to consider the permittivity near an ion in terms of a step-function (39) related to the semiempirical expression (41) for the differential dielectric constant ϵ_d as $f(E)$

$$\epsilon_d = [(\epsilon_o - n_o^2)/(1 + bE^2)] + n_o^2 \quad [24]$$

where n_o^2 is the square of the refractive index, ϵ_o is the static, zero-field dielectric constant, and b is a coefficient related to field-dependence of ϵ_d derived in Booth's theory (42). Two cases of interest arise in electrostriction theory (37): when $bE^2 << 1$ and $bE^2 >> 1$, *i.e.*, for low and high fields.

The high field approximation gives (37) for the relative volumes of normal (v_o) and electrostricted (v) water

$$\log v_o/v = G \log (KE^2 + 1) \quad [25]$$

where

$$G = D/(1 - C) = 0.1469$$

and

$$K = C(1 - C)n_o^2/8\pi\beta D = 1.102 \times 10^{-11}$$

and β, C, and D are known empirical constants (37) determining the pressure dependence of n_o^2 and ϵ.

The following model of the hydration of the $Fe(CN)_6^{3-}$ and $Fe(CN)_6^{4-}$ ions will be considered: Eight hydration shell water molecules can be accommodated in the faces of the octahedral 6CN/Fe arrangement and will be firmly bound electrostatically; another shell, one H_2O molecule in thickness, is also firmly associated ($\epsilon \rightarrow n_o^2$) with the complex further out. Both types of ions presumably will have a similar inner layer of the 8 water molecules. This model seems reasonable since the two kinds of ions have 3 and 4 times the charge of a simple ion like Na^+ but have a hydration radius about twice as great so that, although the field is 2½ times smaller per charge, the net electrostrictive field near the periphery of both ions will be larger than that near a small univalent ion.

Under low field conditions, beyond the primary hydration shell, the equation for dV can be analytically integrated since ϵ can then be assumed (39) to be almost independent of E as can γ. Then Eq. [23] can be integrated to give the electrostriction volume

$$\Delta V_{el} = \int_{r_h}^{\infty} dV = -\int_{r_h}^{\infty}\int_{r_h}^{\infty} \frac{2(ze)^2\gamma}{\epsilon r^3} dr \cdot dr = \frac{-(ze)^2\gamma}{\epsilon}\left[\frac{1}{r}\right]_{r_h}^{\infty} \quad [26]$$

where r_h is the radius of the outer periphery of the primary hydration shell. Taking $\gamma = 4.57 \times 10^{-11}$ cm² dyne⁻¹ for water and $r_h = 6.09$Å (where $r_i = 3.31$Å) for $Fe(CN)_6^{3-}$ and 6.06Å for $Fe(CN)_6^{4-}$ ($r_i = 3.28$Å), enables the Born electrostriction volume, ΔV_{el}, arising beyond the primary hydration shells of these ions to be evaluated as

$$\Delta V_{el,Fe(CN)_6^{3-}} = -12.0; \quad \Delta V_{el,Fe(CN)_6^{4-}} = -21.0 \text{ cm}^3 \text{ mole}^{-1} \quad [27]$$

The relative contributions to the ΔV_{el} in annular volume elements of increasing thicknesses over the first 50Å from the periphery of the primary hydration shells of the ions can be evaluated from Eq. [26] using successively different integration limits and are shown in Fig. 7. The total difference of the long-range electrostriction, which corresponds to the figures in Eq. [27] with ∞ taken as the upper limit in the integrals of Eq. [26], is -9 cm³ mole⁻¹, *i.e.*, -4.5 cm³ mole⁻¹ for the electrostriction change upon activation ($\beta = ½$). It is important to note that this is only *ca.* 25% of the total real volume of activation.

The primary hydration shell volume differences $\delta\Delta V_{el,1}$ in $Fe(CN)_6^{3-}$ and $Fe(CN)_6^{4-}$ are evaluated using Eq. [25] assuming the field E is given by $E = (ze)^2/\epsilon(r_h')^2$ where r_h' is the mean radius of the hydration shell (*i.e.*, $r_h' \doteq r_i + ½\, d_{H_2O}$, where r_i is the

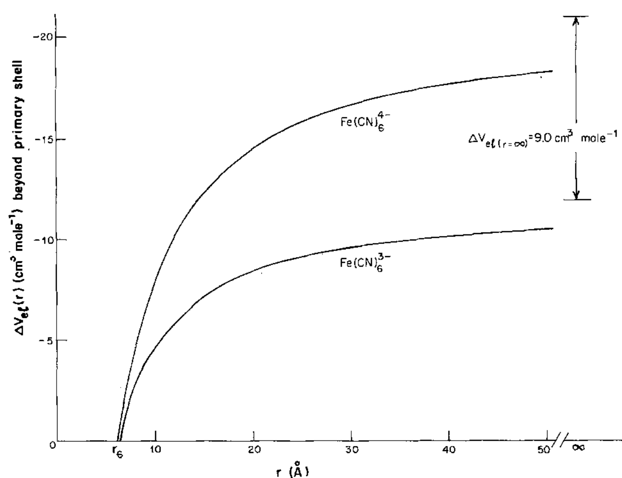

Fig. 7. Calculated Born polarization electrostriction volume changes ΔV_{el} (from Eq. [26]) beyond the primary hydration shells as a function of distance r from the periphery of those shells at $Fe(CN)_6^{4-}$ and $Fe(CN)_6^{3-}$ ions.

ionic radius and d the diameter (=1.39Å) of a water molecule; also r_h' is related to r_h in Eq. [26] by $r_h' = r_h - \frac{1}{2} d_{H_2O}$. ϵ for the primary hydration shell is taken as 2 [cf. Ref. (39, 41, 42)]. The volume differences will depend (*i*) on the ionic radii taken for the ions themselves, and (*ii*) on the field E in the primary shell.

In order to try to make an objective evaluation of the electrostriction, we have made several estimates of the primary shell contribution to ΔV_{el} based on one assumed and various available values of the differences of ionic radii. The volumes of the primary hydration shells are calculated, the field is estimated as above and then application of Eq. [25] gives the compression ratio (38) v/v_0 to be applied to these volumes for the two ions; hence ΔV_{el} is evaluated. The results of these calculations are given in Table II. Calculations of this kind have been given in Ref. (37) where the uncertainties were examined. However, here, differences in volumes are involved so the reliability of their evaluation may be better than that in calculations for individual ions.

Relation to theories of electron transfer.—Evidence for reorganization in the primary hydration shell.—The experimental value for the over-all volume change in reaction [28] (−44.4 cm^3 mole^{-1}) when corrected for the change of intrinsic volume of the ion and for the finite volume of the electron gives an electrostriction volume change of −39.4 cm^3 mole^{-1}. This agrees best with the total electrostriction change (−40 cm^3 mole^{-1}) calculated for the case where there is a small contraction of ionic radius from $Fe(CN)_6^{3-}$ to $Fe(CN)_6^{4-}$ as indicated by the x-ray diffraction results (Table II). Other assignments of ionic radii differences, except that where $r_{Fe(CN)_6^{4-}} > r_{Fe(CN)_6^{3-}}$, give the right order of magnitude but not such good agreement with experiment. It can be concluded from these calculations that the main contribution (*ca.* 75%) to ΔV_{el} arises from changes in primary hydration shell volume and only *ca.* 25% from volume changes due to long-range polarization (Fig. 7). The latter calculations are relatively reliable since they depend on near normal values of ϵ and γ.

It has been shown above that the activation volume $\Delta V_t^{\ddagger}$ for the forward direction of the reaction is about 40% of the total volume change. Hence the activation volume involves a contribution of about 40% of 9.0 cm^3 mole^{-1} in the long-range polarization effect plus about 40% of 32.4 cm^3 for the primary hydration shell volume change, assuming (11) in an adiabatic reaction there is a progressive change of electron charge density as the transition state configuration is developed from the initial state.

These results lead to the important conclusion that the activation process is associated mostly with a change of state of the primary hydration shell of the reactant ion rather than with fluctuations in the long-range polarization co-sphere of the ion. The latter effect has formed the basis of most theories of the activation process in redox reactions. Were it the main factor, as implied with respect to energies of activation, only a small volume of activation calculated from β times the result given by Eq. [26] would be observed; it is much smaller than that found experimentally.

It is to be noted that whatever is the actual value of β, *e.g.*, 0.5 ± 0.1, it will not materially change the conclusion that the real volume of activation will be *ca.* half the equilibrium volume change in the over-all reaction and thus substantially larger than the Born polarization electrostriction and, of course, much larger than the $\Delta V_a^{\ddagger}$. This conclusion is of a rather general kind, as is seen from Eq. [14].

Symmetry of the transition states.—For a homogeneous reaction between ferri- and ferrocyanide, the transition state must be a symmetrical complex between the ions with each having an intermediate charge −3.5*e*. While the over-all equilibrium in a redox couple established at an electrode, referred to some other reference electrode, will be identical with that in the corresponding homogeneous reaction, a symmetrical transfer of charge will not necessarily occur in the transition states involved in the electrochemical reactions

Table II. Electrostriction volume difference in primary hydration shells of $Fe(CN)_6^{3-}$ and $Fe(CN)_6^{4-}$ ions in water for various assumed radii

Ion	Ionic radii (A)	Hydration shell volumes (cm^3 mole^{-1})	Field in shell (esu)	Electrostriction factor v_0/v from Eq. [25]	Electrostriction volume difference ΔV_{el} (cm^3 mole^{-1})	Total electrostriction volume difference: primary shell + Born electrostriction beyond
$Fe(CN)_6^{3-}$	3.31*	484	3.3×10^5	1.12	−22	−31
$Fe(CN)_6^{4-}$	3.31*	484	4.4×10^5	1.18		
$Fe(CN)_6^{3-}$	3.31*	484	3.3×10^5	1.12	−31	−40 (in best agreement with expt.)
$Fe(CN)_6^{4-}$	3.28‡	478	4.48×10^5	1.19		
$Fe(CN)_6^{3-}$	3.31*	484	3.3×10^5	1.12	−42	−51
$Fe(CN)_6^{4-}$	3.21	464	4.6×10^5	1.19		
$Fe(CN)_6^{3-}$	3.31†	484	3.3×10^5	1.12	~−1	~−10
$Fe(CN)_6^{4-}$	3.41†	504	4.23×10^5	1.17		
$Fe(CN)_6^{3-}$	3.28**	478	3.35×10^5	1.13	−41	−50
$Fe(CN)_6^{4-}$	3.18**	458	4.65×10^5	1.20		

* From Mathieson (29) based on space-filling models with V_i = 2.52, r^3 = 91 cm^3 mole^{-1}.
† Based on an assumption (see text) that Δr = 0.1A increase per e added.
** Based on empirical relations for effective ionic radii (43).
‡ Difference based on x-ray diffraction data on the solid salts (27, 28).

$$Fe(CN)_6^{3-} + e_M \rightarrow Fe(CN)_6^{4-} \quad [28]$$

or

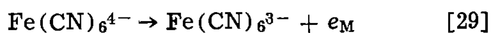

$$Fe(CN)_6^{4-} \rightarrow Fe(CN)_6^{3-} + e_M \quad [29]$$

which occur at an electrode as distinct events at a common potential. The reason is that the ferri- and ferrocyanide ions will probably not interact with the electrode in the same way [cf. Ref. (6)] nor is this interaction likely to be negligible; for example, at Pt and Au, even simple ions such as SO_4^{2-} and ClO_4^- are quite strongly adsorbed. This situation means, of course, that β need not necessarily be exactly 0.5. This does not involve any conflict with the principle of microscopic reversibility, of course, since the equilibrium condition will always involve electrode potential terms in both exp $(-\beta\phi_e\mathbf{F}/RT)$ and exp $(1 - \beta)\phi_e\mathbf{F}/RT$ in the usual way where ϕ_e is the metal/solution p.d. at equilibrium.

The present experimental results, treated in the first approximation with the assumption that $\beta = 0.5$ [cf. Ref. (11)], show that the activation process, from the point of view of the volume changes involved, is not "symmetrical" since the $\Delta \overrightarrow{V}_t^{\ddagger}$ is appreciably less than the $\Delta \overleftarrow{V}_t^{\ddagger}$. This result arises principally from the experimental fact that $\Delta V_t^{\ddagger}$ is not zero (see Eq. [7] and [14]). From the point of view of solvent reorganization in the activation process (10, 11), this means that the hydration shell configurations of the transition states in Eq. [28] and [29] are not symmetrical with respect to those of reactant and product ions as would be the case in the corresponding homogeneous reaction. Presumably this could be due to different adsorption of $Fe(CN)_6^{3-}$ and $Fe(CN)_6^{4-}$ anions at Au, *i.e.*, different interactions of the two ions with the Au surface and with adsorbed water in the inner Helmholtz layer (44). It is of interest to note that the asymmetry is less at higher pressures since $\Delta V_a^{\ddagger}$ decreases with pressure (Fig. 3).

If, in Eq. [14], a value of β were sought that gave equal numerical values for $\Delta \overrightarrow{V}_t^{\ddagger}$ and $\Delta \overleftarrow{V}_t^{\ddagger}$, it would not be 0.5, again indicating asymmetry in the activation processes for the forward and backward directions of the redox reaction at the electrode surface. It is to be noted that values of β for this reaction, differing significantly from 0.5, have been reported in the literature (4, 45).

That the deviation of $\Delta V_a^{\ddagger}$ from zero is connected, in part, with the effect of pressure on the ion-pairing in this system cannot be excluded, *e.g.*, see Bindra *et al.* (46).

Acknowledgments

Grateful acknowledgment is made to the National Research Council of Canada for support of this work and to the Defence Research Board for a grant in the earlier stages of this research.

Manuscript submitted April 11, 1977; revised manuscript received July 14, 1977.

Any discussions of this paper will appear in a Discussion Section to be published in the December 1978 JOURNAL. All discussions for the December 1978 Discussion Section should be submitted by Aug. 1, 1978.

REFERENCES

1. B. E. Conway and J. C. Currie, *This Journal*, **125**, 252 (1978).
2. B. E. Conway, in "Chemical Physics of Ionic Solutions," B. E. Conway and R. G. Barradas, Editors, pp. 577-578, John Wiley & Sons, Inc., New York (1966).
3. R. Parsons and E. Passeron, *J. Electroanal. Chem.*, **12**, 524 (1966).
4. D. H. Angell and T. Dickinson, *ibid.*, **35**, 55 (1972).
5. R. A. Marcus, *Ann. Rev. Phys. Chem.*, **16**, 155 (1964).
6. J. O. M. Bockris, R. J. Mannan, and A. Damjanovič, *J. Chem. Phys.*, **48**, 1898 (1968).
7. A. J. Appelby, J. O'M. Bockris, R. K. Sen, and B. E. Conway, "MTP International Review of Science," Series 1, Vol. 6, J. O'M. Bockris, Editor, chap. 1, Butterworths, London (1973).
8. J. O'M. Bockris, R. K. Sen, and B. E. Conway, *Nature (London), Phys. Sci.*, **240**, 143 (1972).
9. V. G. Levich, in "Physical Chemistry, An Advanced Treatise," Vol. IX B, H. Eyring, D. Henderson, and W. Just, Editors, chap. 12, Academic Press, New York (1970).
10. R. A. Marcus, *J. Chem. Phys.*, **24**, 966 (1956).
11. N. S. Hush, *ibid.*, **28**, 962 (1958); *Z. Elektrochem.*, **61**, 734 (1957).
12. V. G. Levich and R. R. Dogonadze, *Dokl. Acad. Nauk, SSSR*, **133**, 158 (1960).
13. R. R. Dogonadze, *ibid.*, **142**, 1108 (1961).
14. R. R. Dogonadze and Y. A. Chizmadzhev, *ibid.*, **144**, 1077 (1962); *ibid.*, **145**, 848 (1962).
15. G. J. Hills and S. Hsieh, *Chem. Ing. Tech.*, **44**, 216 (1972).
16. J. E. B. Randles, *Discus. Faraday Soc.*, **1**, 269 (1947).
17. A. M. Bond, *Anal. Chem.*, **44**, 315 (1972). See also, A. M. Bond, *J. Electroanal. Chem.*, **50**, 285 (1974); A. N. Fleming and J. A. Harrison, *Electrochim. Acta*, **21**, 905 (1976).
18. B. E. Conway, H. Angerstein-Kozlowska, W. B. A. Sharp, and E. Criddle, *Anal. Chem.*, **45**, 1331 (1973).
19. J. O'M. Bockris and B. E. Conway, *J. Chem. Phys.*, **28**, 707 (1958).
20. (a) L. G. Hepler, J. M. Stokes, and R. H. Stokes, *Trans. Faraday Soc.*, **61**, 20, (1965).
(b) F. J. Millero, in "Water and Aqueous Solutions," R. A. Horne, Editor, chap. 13, Interscience, New York (1972).
21. B. E. Conway, R. E. Verrall, and J. E. Desnoyers, *Trans. Faraday Soc.*, **62**, 2738 (1966).
22. R. Zana and E. Yeager, *J. Phys. Chem.*, **70**, 954 (1966); *ibid.*, **71**, 521 (1967); *ibid.*, **71**, 4241 (1967).
23. K. E. Heusler and L. Gaiser, *Ber Bunsenges.*, **72**, 1059 (1969).
24. H. C. Brown, *J. Phys. Chem.*, **56**, 868 (1952).
25. R. A. Marcus, *Ann. Rev. Phys. Chem.*, **15**, 156, 159 (1964).
26. R. G. Shulman and S. Sugano, *J. Chem. Phys.*, **42**, 39 (1965).
27. W. E. Bailey, R. J. Williams, and W. O. Milligan, *Acta Crystallogr., Sect. B*, **29**, 1365 (1973).
28. M. Pierrot, R. Kern, and R. Weiss, *Acta Crystallogr.*, **20**, 425 (1966).
29. J. G. Mathieson, Ph.D. Thesis, 1972, University of Newcastle, N.S.W. Australia; In course of publication with R. Curthoys.
30. G. S. Hartley and G. W. Donaldson, *Trans. Faraday Soc.*, **33**, 457 (1937).
31. G. Jones and F. C. Jelen, *J. Am. Chem. Soc.*, **59**, 1760 (1937).
32. C. W. Davies, *ibid.*, **58**, 2581 (1936).
33. Th. Ackermann, *Discuss. Faraday Soc.*, **24**, 180 (1957).
34. R. R. Dogonadze and A. M. Kuznetsov, *Elektrokhimiya*, **3**, 1324 (1967).
35. W. Smickler, *Electrochim. Acta*, **21**, 161 (1976); *ibid.*, **21**, 777 (1976).
36. R. R. Dogonadze and A. A. Kornyshev, *J. Chem. Soc., Faraday Trans. 2*, **70**, 1121 (1974).
37. J. E. Desnoyers, R. E. Verrall, and B. E. Conway, *J. Chem. Phys.*, **43**, 243 (1965).
38. H. S. Frank, *ibid.*, **23**, 2023 (1955).
39. B. E. Conway, J. E. Desnoyers, and A. C. Smith, *Phil. Trans. R. Soc. London, Ser A*, **256**, 389 (1964).
40. J. Padova, *J. Chem. Phys.*, **39**, 1552 (1963); *ibid.*, **39**, 2599 (1963); *ibid.*, **40**, 691 (1964).
41. D. C. Grahame, *ibid.*, **21**, 1054 (1951).
42. P. Booth, *ibid.*, **19**, 391 (1951); *ibid.*, **19**, 1327 (1951); *ibid.*, **19**, 1615 (1951).
43. L. Hepler, *J. Phys. Chem.*, **61**, 1426 (1957).
44. B. E. Conway, *Elektrokhimiya* (Frumkin Memorial Issue) **13**, 822 (1977).
45. D. Jahn and W. Vielstich, *This Journal*, **109**, 849 (1962).
46. P. Bindra, H. Gerischer, and L. M. Peter, *J. Electroanal. Chem.*, **57**, 435 (1974).

Nickel-Based Alloys as Electrocatalysts for Oxygen Evolution from Alkaline Solutions

P. W. T. Lu* and S. Srinivasan*

Department of Applied Science, Brookhaven National Laboratory, Upton, New York 11973

ABSTRACT

The oxygen evolution reaction on the alloys of Ni with Ir, Ru, or W and on Ni-Ti intermetallic compounds was studied in 30 weight percent (w/o) KOH at 80°C using steady-state potentiostatic and slow potentiodynamic (at 0.1 mV/sec) methods. Since this reaction always takes place on film-covered surfaces, the nature of oxide films formed on these alloys was investigated using cyclic voltammetry. The peaks for the formation and reduction of oxygen-containing layers appearing on the pure metals are not always found on these alloys. Oxygen overpotentials at an apparent current density of 20 mA/cm^2, on the alloys of 50Ni-50Ir and 75Ni-25Ru (in atomic percent, a/o) and the intermetallic compound Ni_3Ti were less than on Ni by about 40, 30, and 20 mV, respectively. On long-term polarization at potentials in the oxygen evolution region, the oxygen-containing films on Ni-Ir and Ni-Ru alloys are predominantly composed of nickel oxide and independent of the bulk composition of the alloys themselves. This accounts for the absence of any direct dependence of electrocatalytic activities for oxygen evolution on their electronic properties. The effects of relative activities of the individual components in the alloys are however detectable on the oxide formation reactions on the surfaces of freshly prepared electrodes.

One of the more difficult problems which limit the operation efficiency of the water electrolyzers and secondary metal-air batteries is the slowness of the oxygen electrode reaction (OER) (1-3). Of the metals, nickel is the best known electrocatalyst for oxygen evolution from alkaline solutions. The metal nickel has 0.54 unpaired electrons in the 3d band (4). Alloying nickel with other transition elements having more unfilled d shells (*e.g.*, Ir) can result in more d-band vacancies (5). Thus, it is possible to deduce significant alteration in other electronic properties such as density of surface states, work function, and Fermi level. In a recent review regarding hydrogen evolution on alloys (6), it was emphasized that the electrocatalytic properties of an alloy parallel changes in its electronic properties.

Data on the kinetics of the OER on alloys and intermetallic compounds are sparse (3). Historically, the only studies of the oxygen overpotential on nickel alloys in alkaline solution have been with Ni-Fe (7, 8), Ni-Co (8), and Ni-Cr systems (9). These investigations on Ni-based alloys provided no evidence of correlation between the electrochemical activities for the OER and the alloy composition. The possible effect of the electronic properties of the alloys on their electrocatalytic properties was not considered.

In the present work, alloys of Ni with Ir, Ru, or W and Ni-Ti intermetallic compounds were investigated as anodes for oxygen evolution from 30 w/o KOH at 80°C. Anodic oxide films formed on the electrode surfaces of these alloys or intermetallic compounds were also characterized. The major purposes of this study are (*i*) to elucidate any possible effect of the electronic properties of the alloys or intermetallic compounds on their electrocatalytic properties, (*ii*) to understand the dependence of the kinetics of electrode reactions on the nature of oxide films, and (*iii*) to find better electrode materials to replace the conventional nickel anodes for oxygen evolution from alkaline solutions.

Experimental

Specimen preparation.—Three Ni-Ti intermetallic compounds, *i.e.*, Ni_3Ti, NiTi, and $NiTi_2$, were prepared in an electric arc furnace under an Ar atmosphere. The alloys of Ni with Ir, Ru, or W were prepared by Paul D. Merica Research Laboratory, International Nickel Company—three alloys of nominal compositions 25, 50, and 75 a/o Ni in the Ni-Ir or Ni-Ru system and two alloys (50 and 75 a/o Ni) in the Ni-W system. These alloys were annealed at 1400°C in a H_2 atmosphere for about 24 hr. The examination of chemical composition and homogeneity of these alloys and intermetallic compounds was carried out using electron microprobe analysis and metallurgical microscopy. The specimens were cut in the shape of cylinders using the electric discharge machine. The electrodes were prepared by sealing the cylindrical specimens and their lead wires into shrinkable Teflon tubes using heat-treatment. Finally, each electrode having a geometric area of 0.20 cm^2 was mechanically polished as described elsewhere (10).

Solution.—The 30 w/o KOH solution was prepared from Baker analyzed reagent grade potassium hydroxide and triply distilled water. The solution was purified by anodic preelectrolysis for 24 hr or more at a C.D. of 2 mA/cm^2. After each experiment, the measuring solution was analyzed using atomic absorption spectroscopy.

Apparatus.—A three-compartment Teflon cell, placed in an air thermostat, was used to carry out the electrochemical study of electrode materials. A saturated calomel electrode (SCE) was employed as a reference. The potentials are referred to the reversible hydrogen electrode (RHE), which is approximately −1.16V *vs.* SCE as obtained by measurement in this investigation. The electrochemical measurements were conducted using a PAR Model 173 potentiostat coupled with a PAR Model 175 programmer and a PAR Model 376 "log converter." When carrying out potentiodynamic measurements, Tafel plots and cyclic voltammograms were recorded by use of an HP Model 7047A X-Y recorder. A Tektronix Model 7623A oscilloscope was used to measure ohmic overpotentials (*i.e.*, *iR* drops) between the edge of Luggin capillary and the working electrode.

Electrochemical measurements.—Tafel plots for the OER on test electrodes were determined using steady-state potentiostatic and slow potentiodynamic (at 0.1 mV/sec) methods. Each electrode was preanodized at a constant C.D. of 200 mA/cm^2 for 2 hr or more to form stable oxide films on its surface. In the potentiodynamic measurements, "log *I* output" signals from the log converter were connected to an X-Y recorder so that Tafel plots appeared directly on the semilogarith-

* Electrochemical Society Active Member.

Key words: electrocatalysis, Ni-based alloys, oxide films, oxygen evolution, Tafel parameters, mechanism.

mic paper. During each run, the electrolyte was deaerated with purified O_2 and magnetically stirred. Experiments were conducted at 80°C in the direction of high currents to low currents. On each electrode, at least two individual steady-state potentiostatic and one slow potentiodynamic measurements were carried out. Ohmic overpotentials were measured by use of an interruptor technique (11).

The formation and reduction of oxide films on the freshly polished electrodes of Ni, Ir, and Ni-Ir alloys were studied using cyclic voltammetric techniques. Each electrode was initially maintained at -0.05V in N_2-saturated 30 w/o KOH at 80°C for 20 min to remove oxide films possibly formed on its surface during polishing. A linear potential sweep at 20 mV/sec was applied between -0.05 and $+1.50$V. The cyclic voltammograms for the first two sweeps on each electrode were recorded.

After long term polarization (up to 80 hr) for oxygen evolution at an apparent C.D. of 20 mA/cm^2 on Ni, Ni_3Ti, and on the alloys of 50Ni-50Ir and 75Ni-25Ru, the potential of each electrode was stepped instantaneously to 1.60V. Then, cyclic voltammograms on the preanodized electrodes were recorded between -0.05 and 1.60V at a sweep rate of 20 mV/sec. The first ten traces of the continuous cyclic voltammograms on each electrode were recorded on an X-Y recorder.

Results and Discussion

Composition and homogeneity of specimens.—The chemical compositions of these Ni-based alloys or intermetallic compounds, determined by the electron microprobe, are slightly different from the nominal compositions with deviations of less than 7 a/o. Figure 1 shows the microstructures of these specimens in the Ni-Ti system. The nominal intermetallic compounds NiTi and $NiTi_2$ exhibit two phases, while Ni_3Ti appears to be a single phase system. As illustrated in Fig. 2, two phases appear on each of Ni-W alloys, being β (*i.e.*, NiW) and one W-rich phase. In the Ni-Ru system, the alloy of 50Ni-50Ru appears to be composed of two phases as expected from the phase diagram, while the other two alloys exhibit only a single phase. Unfortunately, no phase diagram for the Ni-Ir system could be attained. The metallographic examination revealed that two phases appear in the alloys of 50Ni-50Ir and 25Ni-75Ir whereas only one in the alloy of 75Ni-25Ir.

Automation of measurement of Tafel plots.—A typical Tafel plot for oxygen evolution determined with potentiodynamic techniques at a slow potential sweep of 0.1 mV/sec, is shown in Fig. 3. Data from two independent, steady-state potentiostatic measurements for the OER on the same electrode and under the same experimental conditions are also presented for comparison. As illustrated in Fig. 3, the maximum potential deviation (at the same C.D.) between any two individual measurements is about 5 mV in the linear region. The Tafel plot obtained by use of the slow potentiodynamic method exhibits a slightly higher exchange C.D. than that from the steady-state potentiostatic measurements (9.2×10^{-7} and 6.0×10^{-7} A/cm^2, respectively). The potentiodynamic measurements also provide a slightly higher Tafel slope (70 mV, compared to 66 mV obtained from the steady-state potentiostatic measurements). In general, however, Tafel plots determined using both the steady-state potentiostatic and

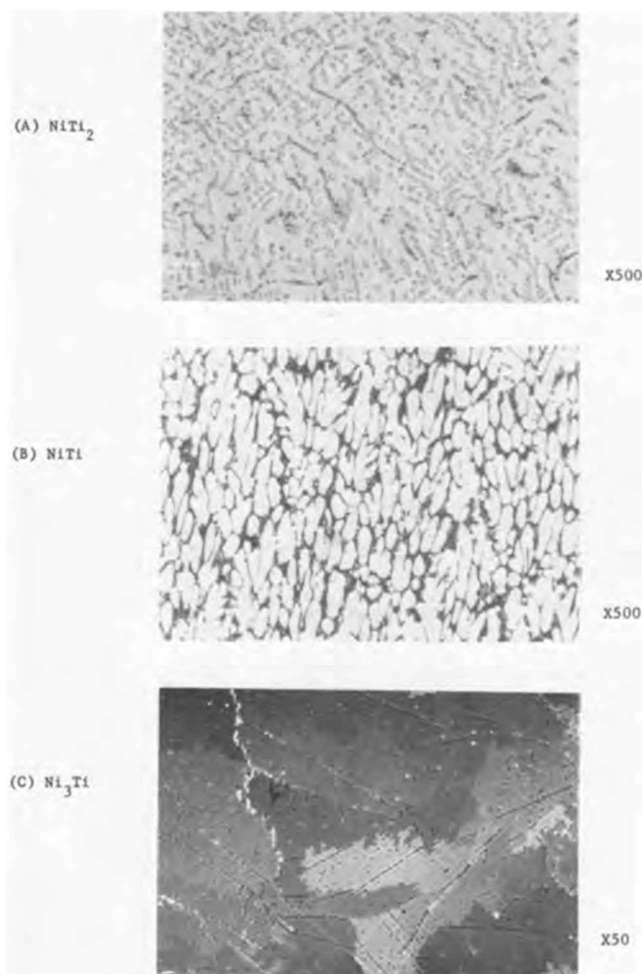

Fig. 1. Microstructures of three intermetallic compounds in the Ni-Ti system.

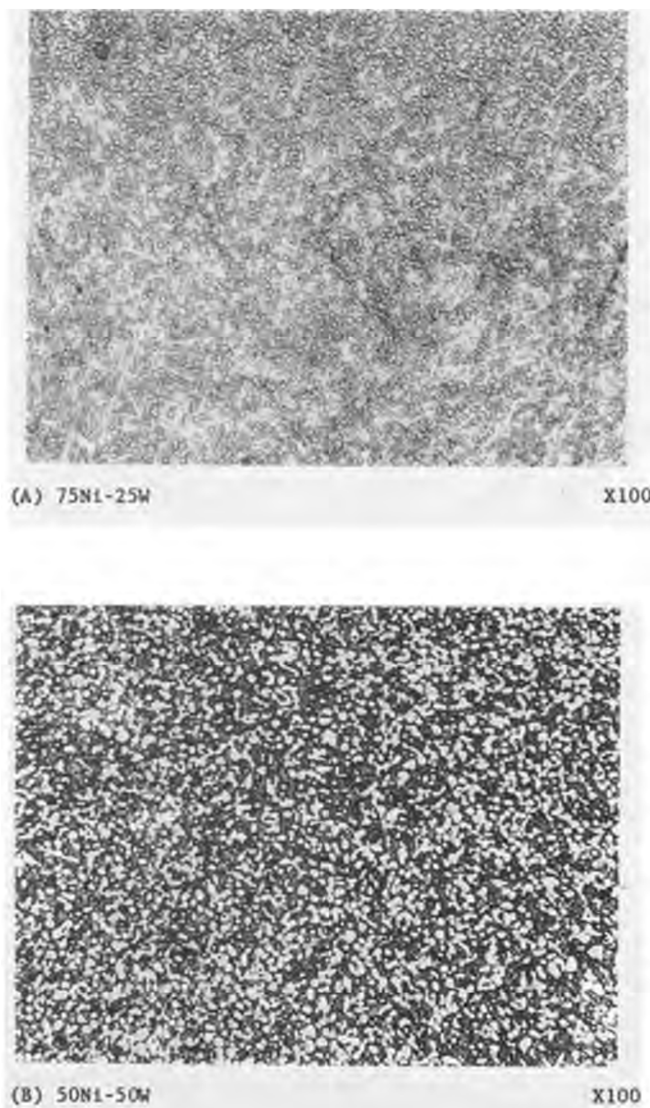

Fig. 2. Microstructures of two Ni-W alloys after annealing at 1400°C in hydrogen atmosphere for 24 hr.

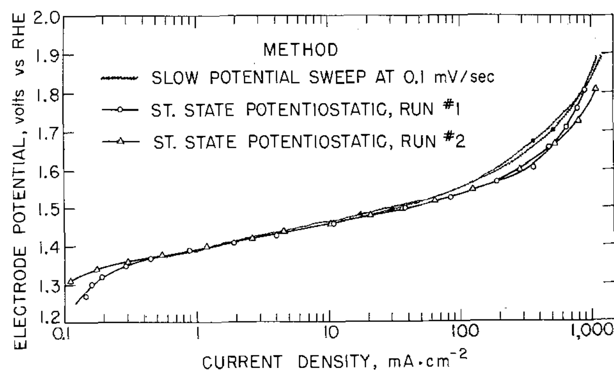

Fig. 3. Comparison of Tafel plots for oxygen evolution on the alloy of 25Ni-75Ir in 30 w/o KOH at 80°C, obtained from the steady-state potentiostatic and slow potentiodynamic (at 0.1 mV/sec) measurements.

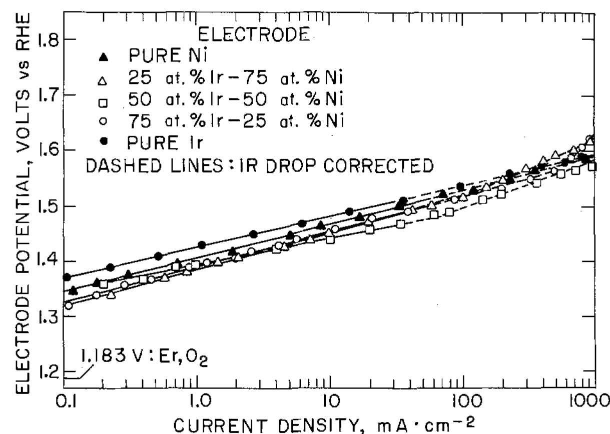

Fig. 4. Tafel plots for oxygen evolution on Ni, Ir, and three Ni-Ir alloys in 30 w/o KOH at 80°C.

the slow potentiodynamic methods are in fair agreement with each other.

Conventional steady-state potentiostatic or galvanostatic techniques used to determine electrode kinetic parameters are time consuming. It has been noted (12) that, using the potentiodynamic method at slow sweep rate (<10 mV/sec), a steady-state condition can be approached. Furthermore, the present work indicates that the slow potentiodynamic technique is efficient, timesaving and, most importantly, accurate in determining electrode kinetic parameters.

Kinetics of oxygen evolution reaction.—The reversible potential of the oxygen electrode in 30 w/o KOH at 80°C was determined empirically to be 1.183V *vs.* RHE. Electrode kinetic parameters for the OER on the various electrodes investigated are summarized in Table I. It is noted that each parameter represents the average value of two independent steady-state potentiostatic and one slow potentiodynamic measurements.

Ni-Ir system.—Figure 4 shows the Tafel plots for the OER on Ni, Ir, and Ni-Ir alloys. The Ni and Ni-Ir alloys are better electrocatalysts than Ir for oxygen evolution from alkaline solution. At an apparent C.D. of 20 mA/cm^2, the oxygen overpotential on any of these Ni-Ir alloys is slightly lower than that on Ni (see Table I). The lowest oxygen overpotential, which is about 40 mV lower than that on Ni at this current, is observed on the alloy of 50Ni-50Ir. As shown in Table I, Tafel slopes and exchange C.D. for the OER on these alloys are very similar to those on Ni. According to thermodynamic data (13), iridium oxide formed on electrode surfaces of Ni-Ir alloys probably tends to dissolve at such high potentials for the anodic evolution of oxygen.[1] Consequently, oxide films on these alloys, on which the OER takes place, are predominantly composed of nickel oxides despite the bulk composition of the alloys themselves. Therefore, the Ni-Ir alloys are expected to exhibit approximately the same electrochemical activities for oxygen evolution as those on pure Ni.

[1] The alternative explanation is that nickel is preferentially anodized in the alloys. However, recent ellipsometric investigations of the iridium electrodes, polarized at potentials over 1.65V, strongly supported the viewpoint of anodic dissolution of iridium oxide in the OER region (14).

Regarding the OER on nickel from alkaline solutions, it has been reported (15-17) that dual Tafel regions of $2RT/\mathbf{F}$ and $RT/2\mathbf{F}$ are observed at high and low current densities, respectively. Further, the discharge of adsorbed OH^- ions and the spontaneous decomposition of NiO_2 are generally accepted as the rate-determining steps at high and low overpotential, respectively. As indicated in Table I, Tafel slopes of $\sim RT/\mathbf{F}$ are observed on Ni and Ni-Ir alloys. Referring to the reaction scheme proposed by Krasil'shchikov (17), a Tafel slope of $RT/\mathbf{F}$ is possible, if the step for the formation of O^- intermediates, on the substrate S, that is

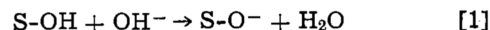

$$S\text{-}OH + OH^- \rightarrow S\text{-}O^- + H_2O \qquad [1]$$

is rate determining. However, since proton transfer between hydroxylic species is generally rapid (18, 19), this step is unlikely to be rate controlling. Recent work of Tilak and Conway (20) indicates that an "electrochemical desorption" type of mechanism leads to a Tafel slope of $\sim RT/\mathbf{F}$, when the lateral interaction parameter (g) for the adsorbed O^- intermediates is large ($g > 20\ RT$).

Ni-Ru system.—On preanodization, Ni-Ru alloys containing 50 a/o Ru or higher tended to dissolve anodically in KOH solution. Consequently, the colorless electrolyte became straw yellow and fine black particles were found to leach out of the solid electrode. Similar results have been observed by Stoyanovskaya, Khomchenko, and Vovchenko (21), who investigated Ru as anode at the potentials of oxygen evolution. The corrosion of Ru electrode essentially arises from the

Table I. Electrode kinetic parameters for the oxygen evolution reaction on Ni, Ir, and some nickel-based alloys from 30 w/o KOH at 80°C

Electrode	Tafel slope (V) Low η	Tafel slope (V) High η	Transfer[b] coefficient Low η	Transfer[b] coefficient High η	Exchange current density (A/cm^2) Low η	Exchange current density (A/cm^2) High η	Oxygen overpotential at 20 mA/cm^2 (V)
Pure Ni	0.062		1.1		2.3×10^{-7}		0.31
75Ni-25Ir[a]	0.067		1.0		8.8×10^{-7}		0.29
50Ni-50Ir[a]	0.047	0.086	1.5	0.81	3.4×10^{-8}	2.0×10^{-5}	0.27
25Ni-75Ir[a]	0.064		1.1		6.0×10^{-7}		0.29
Pure Ir	0.055		1.3		5.0×10^{-8}		0.32
75Ni-25Ru[a]	0.056		1.3		2.4×10^{-8}		0.28
75Ni-25W[a]	0.114		0.61		4.6×10^{-5}		0.30
50Ni-50W[a]	0.125		0.56		2.5×10^{-4}		—[c]
Ni_3Ti	0.064		1.1		4.7×10^{-7}		0.29
NiTi	0.057	0.094	1.3	0.74	6.0×10^{-8}	2.8×10^{-6}	0.35
$NiTi_2$	0.383		0.18		6.5×10^{-5}		—[d]

[a] In atomic percent.
[b] Transfer coefficient = 2.303 $RT/b\mathbf{F}$ where b is the Tafel slope.
[c] The observed current densities in the Tafel region for oxygen evolution on the alloy of 50Ni-50W are above 40 mA/cm^2.
[d] Limiting current density for oxygen evolution on $NiTi_2$ is less than 10 mA/cm^2 (see Fig. 5).

formation soluble ruthenate (RuO_4^{--}) or perruthenate (RuO_4^-) ions during anodic polarization (22, 23). The atomic absorption spectroscopic analysis of the solutions, in which the Ni-Ru alloys are preanodized, reveals that the concentration of Ru-containing ions in each solution is about 1.2 mg/ml after 2 hr of preanodization.

Surprisingly, the electrode of 75Ni-25Ru alloy is quite stable on anodization even in long-term studies. As demonstrated in Table I, the alloy of 75Ni-25Ru exhibits slightly lower Tafel slope ($\sim 2RT/3F$) and exchange C.D. in comparison with these on pure Ni. At an apparent C.D. of 20 mA/cm^2, the oxygen overpotential on this alloy is about 30 mV lower than that on Ni.

Ni-W system.—As indicated in Table I, Tafel slopes observed on the alloys of 75Ni-25W and 50Ni-50W are much higher than that on Ni. On polarization in the oxygen evolution region, tungsten oxide is formed on the surfaces of Ni-W alloys. This oxide film, with a low electronic conductivity leads to the barrier-layer effects (24), and thus results in low transfer coefficients (*i.e.*, high Tafel slopes). Further, the transfer coefficient observed for the OER on Ni-W alloys decreases with increasing tungsten content.

Ni-Ti system.—Tafel plots for the OER on the intermetallic compounds Ni_3Ti, NiTi, and $NiTi_2$ are given in Fig. 5. Except for a lower oxygen overpotential of about 20 mV at an apparent C.D. of 20 mA/cm^2, the intermetallic compound Ni_3Ti behaves very similarly to Ni. Two distinct, linear regions corresponding to Tafel slopes of RT/F and $2RT/F$ are observed on the electrode of NiTi. The OER on this electrode exhibits a higher overpotential than that on Ni. The Tafel plot for oxygen evolution on the intermetallic compound $NiTi_2$ shows an unusually high Tafel slope (close to $5RT/F$) and a limiting current density of about 3 mA/cm^2. According to thermodynamic data (13), TiO_2 is formed in the potential range for oxygen evolution. The species TiO_2 has high corrosion resistance but is a poor conductor for electron transfer (25). Thus, the unusually high slope arises from the barrier-layer effect (24).

Cyclic voltammetric studies on freshly polished electrode surfaces.—The first and second traces of cyclic *i-V* curves on the freshly prepared electrodes of Ni, Ir, and Ni-Ir alloys in N_2-saturated 30 w/o KOH at 80°C are shown in Fig. 6. Prior to the determination of cyclic voltammograms, each electrode was maintained at -50 mV for 20 min. The cathodic evolution of H_2 at this potential may result in the chemisorption of hydrogen atoms on the electrode surface. In the first potential sweep on Ni, Ir, or Ni-Ir alloys, the anodic peak between 0.15 and 0.25V is observed to increase with the length of time of the cathodic pretreatment. Thus, this peak is obviously attributed to the oxidation of the chemisorbed hydrogen atoms on the substrate S, namely

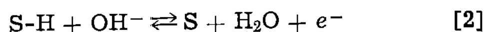

$$S\text{-}H + OH^- \rightleftarrows S + H_2O + e^- \qquad [2]$$

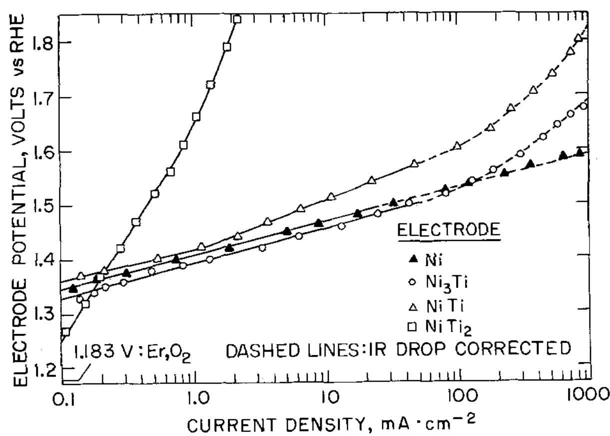

Fig. 5. Tafel plots for oxygen evolution on Ni and three Ni-Ti intermetallic compounds in 30 w/o KOH at 80°C.

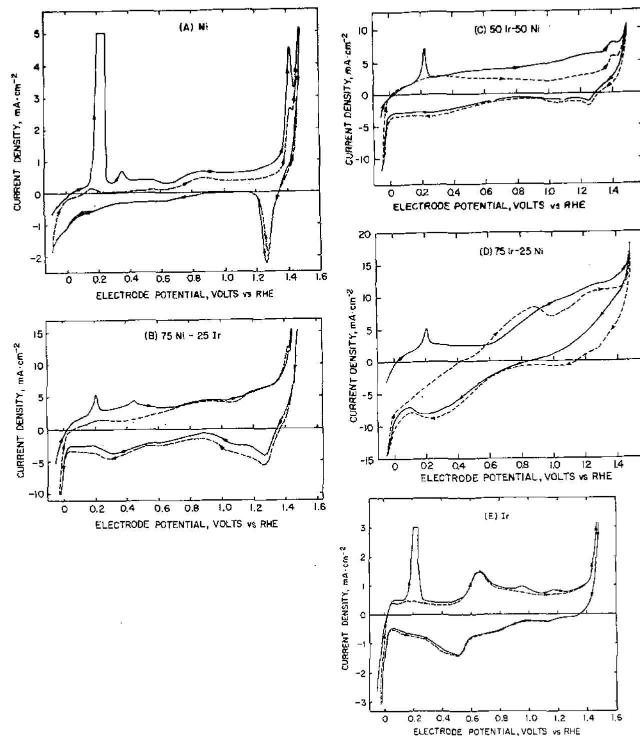

Fig. 6. Cyclic *i-V* curves for freshly prepared electrodes of Ni, Ir, and Ni-Ir alloys in N_2-saturated 30 w/o KOH at 80°C. The solid and dashed lines represent the first and second sweeps (at a rate of 20 mV/sec), respectively.

As seen in Figure 6(A), the second anodic peak on Ni at a potential of $\sim$0.36V disappears on the second trace of the cyclic potential sweep. Furthermore, the position of this peak is found to be independent of the magnitude of potential and the length of time of the cathodic pretreatment. It has been noted (26) that the species $Ni(OH)_2$ is not reduced by the cathodic potential sweep, and thus no peak corresponding to the formation of $Ni(OH)_2$ can be detectable on the second sweep. Therefore, the second anodic peak observed on Ni is no doubt due to the formation of $Ni(OH)_2$ On the electrode surfaces of Ni-Ir alloys, this peak is superimposed by the anodic reaction occurring on Ir sites, and consequently appears not distinguishable.

As has been pointed out (18, 19), the species $Ni(OH)_2$ is further oxidized to β-NiOOH by a proton transfer process at potentials above 0.4V. Following the work of Weininger and Breiter (27), the broad peak observed on Ni (see Fig. 6) in the intermediate potential region of 0.6-1.0V arises from the composite electrode reaction of the growth of $Ni(OH)_2$ and the transformation of $Ni(OH)_2$ to β-NiOOH occurring simultaneously or consecutively. On the Ni-Ir alloys, anodic peaks in the potential region of 0.4-1.2V appear considerably different from those on Ni or Ir. Obviously, these peaks result from the superposition of the anodic peaks on Ni sites with those on Ir sites.

At sufficiently high potential, the species β-NiOOH is formed directly from the substrate Ni (27). As seen in Fig. 6, the formation and reduction of β-NiOOH on Ni take place at potentials of about 1.42 and 1.26V, respectively. The small difference (about 0.16V) between the potentials for the formation and reduction peaks of β-NiOOH implies that the reaction for the formation of β-NiOOH is approximately reversible. These couples for the formation and reduction of β-NiOOH are also detectable on the alloys of 75Ni-25Ir and 50Ni-50Ir, but not on the alloy of 25Ni-75Ir. Consequently, the relative activities of the individual components in the alloys do play a significant role in the reaction of oxide formation on these alloys. Similar results have been reported on smooth noble metal alloys in the work of Rand and Woods (28), who noted that the electrocatalytic activities of the alloys vary with their surface

composition. The latter is in turn strongly dependent on the electrochemical pretreatment of the alloys.

Cyclic voltammetric studies on preanodized electrode surfaces.—Investigations of the cathodic *i-V* curves on preanodized electrodes may lead to important complementary information to identify the major species in oxygen-containing films formed on its surface during the OER. After anodization at an apparent C.D. of 20 mA/cm^2 for 80 hr, the first, second, and tenth cathodic *i-V* curves, obtained from the continued cyclic voltammograms on Ni, Ni_3Ti, and the alloys of 50Ni-50Ir and 75Ni-25Ru, are shown in Fig. 7. Only one reduction peak corresponding to β-NiOOH is observed on Ni electrode. This result is consistent with the work by McIntyre and Kolb (26).

As illustrated in Fig. 7, the first cathodic sweeps on 50Ni-50Ir, 75Ni-25Ru, and Ni_3Ti exhibit electrochemical behavior similar to that on Ni. No distinguishable reduction peak is detected on the first cathodic sweep except for the one corresponding to the reduction of β-NiOOH at about 1.26V. On the preanodized alloy of 50Ni-50Ir, two additional peaks, which are due to the reduction of oxide layer on Ir sites as reported by Böld are Breiter (28), are detectable starting in the third sweep. The second cathodic *i-V* curve on the alloy of 75Ni-25Ru also exhibits two additional peaks which are probably attributed to the reduction of oxide layers on Ru sites. Further, the heights of these reduction peaks on the alloy of 50Ni-50Ir or 75Ni-25Ru increase with increasing the number of potential sweeps. These observations indicate that the oxide film on the preanodized electrodes of Ni-Ir or Ni-Ru alloys is predominantly composed of nickel oxides rather than a mixed oxide of the same composition as the alloy itself. According to the Pourbaix diagrams (13), the oxides of iridium or ruthenium on anodized electrode surfaces of these alloys are expected to dissolve at the potentials in the range for oxygen evolution from alkaline media. Conversely, nickel oxide is extremely stable in alkaline solutions. Thus, when Ni-Ir or Ni-Ru alloys are utilized as anodes, the OER takes place substantially on a layer of nickel oxide. This is the reason for Ni-Ir and Ni-Ru

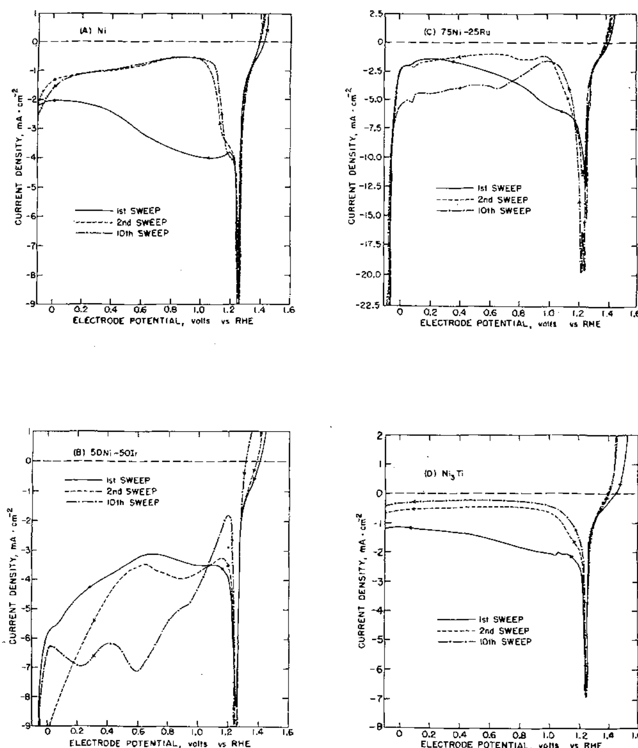

Fig. 7. Cathodic *i-V* curves obtained from the continuous cyclic voltammograms on Ni, Ni_3Ti, and the alloys of 50Ni-50Ir and 75Ni-25Ru in 30 w/o KOH at 80°C with a potential sweep rate of 20 mV/sec. Each electrode was preanodized at a constant C.D. of 20 mA/cm^2 for 80 hr.

alloys to exhibit the same electrocatalytic activities for oxygen evolution as on Ni. The stability of oxide films, formed on metals or alloys under the operating conditions is a significant criterion in the selection and evaluation of oxygen evolving electrodes.

Conclusions

In the potential range for oxygen evolution from alkaline solutions, Ni-Ru alloys containing 50 a/o or more Ru are unstable, while oxide films with extremely low conductivity are formed on the electrode surfaces of Ni-W alloys and $NiTi_2$. Most of stable Ni-based alloys or intermetallic compounds investigated exhibit practically the same electrocatalytic activities as pure Ni. Decreases in oxygen overpotential at an apparent C.D. of 20 mA/cm^2 on the alloys of 50Ni-50Ir, 75Ni-25Ru, and Ni_3Ti are about 40, 30, and 20 mV, respectively, in comparison with that on Ni. With the Ni-W alloys and the $NiTi_2$ intermetallic compound on which poorly conducting oxide films are formed, the relatively higher Tafel slopes observed arise due to barrier layer effect.

Iridium oxide or ruthenium oxide formed on the electrode surfaces of Ni-Ir or Ni-Ru alloys tend to dissolve in the potential region for oxygen evolution. Cyclic voltammetric studies reveal that the electrode surfaces of these alloys after prolonged anodization are predominantly composed of nickel oxide, which consequently determines the kinetic parameters of the oxygen evolution reaction. Therefore, in addition to the electronic conductivity and catalytic properties of oxide films, the stability of these films under the operating conditions is an extremely significant criterion in the selection and evaluation of electrocatalysts for the oxygen evolution reaction.

The present work confirms that, for the anodic evolution of oxygen, there is no simple dependence of the electrocatalytic activities of the alloys on their electronic properties, because of coverage of the alloy electrode surface by films predominantly composed of nickel oxide. However, the effects of relative activities of the individual components in the alloys on the oxide formation reaction on the bare surface of the alloys, are indeed detectable. It was also shown in this study that the potentiodynamic technique at slow sweep rates (say, 0.1 mV/sec) is an efficient, time-saving, and accurate method in determining kinetic parameters of an electrode reaction.

Acknowledgments

The authors wish to thank Mr. F. J. Salzano and Dr. R. H. Wiswall for their constant interest and encouragement throughout this study. Special thanks are due to Professor B. E. Conway and Dr. S. Gottesfeld for their helpful discussions. The authors are also grateful to Mr. G. Kissel for his useful suggestions and invaluable assistance in the design and construction of experimental equipment.

This work was carried out under the auspices of the U.S. Energy Research and Development Administration.

This work was carried out by one of the authors (P.W.T.L.) in partial fulfillment of requirements for the Ph.D degree from the Department of Material Science, State University of New York at Stony Brook, Stony Brook, New York.

Manuscript submitted April 11, 1977; revised manuscript received Aug. 20, 1977. This was Paper 328 presented at the Washington, D.C., Meeting of the Society, May 2-7, 1976.

Any discussion of this paper will appear in a Discussion Section to be published in the December 1978 JOURNAL. All discussions for the December 1978 Discussion Section should be submitted by Aug. 1, 1978.

Publication costs of this article were assisted by Brookhaven National Laboratory.

REFERENCES

1. M. W. Breiter, in "Advances in Electrochemistry and Electrochemical Engineering," P. Delahey and C. W. Tobias, Editors, Vol. 1, Chap. 3, Inter-

science, New York (1961).
2. J. O'M. Bockris and S. Srinivasan, "Fuel Cells: Their Electrochemistry," Chap. 8, McGraw-Hill Book Co., New York (1969).
3. J. P. Hoare, "The Electrochemistry of Oxygen," Interscience, New York (1968).
4. N. F. Mott and H. Jones, "The Theory of Metals and Alloys," Oxford University Press, Fair Lawn, N.J. (1940).
5. F. E. Hoare, in "Electronic Structure and Alloy Chemistry of the Transition Elements," P. A. Beck, Editor, John Wiley & Sons, Inc., New York (1963).
6. E. W. Brooman and A. T. Kuhn, *J. Electroanal. Chem.*, **49**, 325 (1974).
7. M. de K. Thompson and A. L. Kaye, *Trans. Electrochem. Soc.*, **60**, 229 (1931).
8. G. Grube and W. Gaupp, *Z. Elektrochem.*, **45**, 290 (1939).
9. M. de K. Thompson and G. H. Sistare, Jr., *Trans. Electrochem. Soc.*, **78**, 259 (1940).
10. M. H. Miles, G. Kissel, P. W. T. Lu, and S. Srinivasan, *This Journal*, **123**, 332 (1976).
11. K. R. Williams, "Introduction to Fuel Cells," pp. 57-63, Elsevier, New York (1966).
12. D. M. MacArthur, in "Characterization of Solid Surfaces," P. F. Kane and G. B. Larrabee, Editors, Chap. 8, Plenum Press, New York (1974).
13. M. Pourbaix, "Atlas of Electrochemical Equilibria in Aqueous Solutions," Pergamon Press, London (1966).
14. S. Gottesfeld and S. Srinivasan, *J. Electroanal. Chem.*, In press.
15. V. N. Fiseiskii and Ya. I. Tur'yan, *Zh. Fiz. Khim.*, **24**, 567 (1950).
16. L. M. Elina, T. I. Borisova, and Ts. I. Zalkind, *ibid.*, **28**, 785 (1954).
17. A. I. Krasil'shchikov, *ibid.*, **37**, 531 (1963).
18. G. W. D. Briggs, E. Jones, and W. F. K. Wynne-Jones, *Trans. Faraday Soc.*, **51**, 1433 (1955).
19. E. Jones and W. F. K. Wynne-Jones, *ibid.*, **52**, 1260 (1956).
20. B. V. Tilak and B. E Conway, Private communication.
21. T. N. Stoyanovskaya, G. P. Khomchenko, and G. D. Vovchenko, *Vestn. Mosk. Univ. II Khim.*, **18**, 20 (1963).
22. J. Llopis and M. Vazquez, *Electrochim. Acta*, **11**, 633 (1966).
23. D. N. Buckley and L. D. Burke, *J. Electroanal. Chem.*, **52**, 433 (1974).
24. R. E. Meyer, *This Journal*, **107**, 847 (1960).
25. L. Young, "Anodic Oxide Films," Academic Press, New York (1961).
26. J. D. E. McIntyre and D. M. Kolb, *Symp. Faraday Soc.*, No. 4, 99 (1970).
27. J. L. Weininger and M. W. Breiter, *This Journal*, **110**, 484 (1963).
28. D. A. J. Rand and R. Woods, *J. Electroanal. Chem.*, **36**, 57 (1972).
29. W. Böld and M. W. Breiter, *Electrochim. Acta*, **5**, 169 (1961).

SOLID-STATE SCIENCE
AND TECHNOLOGY

FEBRUARY
1978

Hot Corrosion Resistance of Nickel-Chromium-Aluminum Alloys

Gilbert J. Santoro and Charles A. Barrett

National Aeronautics and Space Administration, Lewis Research Center, Cleveland, Ohio 44135

ABSTRACT

The hot corrosion resistance of nickel-chromium-aluminum alloys was examined by cyclically oxidizing sodium sulfate-coated specimens in still air at 900°, 1000°, and 1100°C. The compositions tested were within the ternary region: Ni; Ni-50 atom percent (a/o) Cr; and Ni-50 a/o Al. At each temperature the corrosion data were statistically fitted to a third-order regression equation as a function of chromium and aluminum contents. From these equations corrosion isopleths were prepared. Compositional regions with the best hot corrosion resistance were identified.

In recent years many promising compositions have been identified in the nickel-chromium-aluminum (Ni-Cr-Al) system for use in application requiring a high degree of high temperature corrosion resistance. Such applications have included coatings for many types of alloys (1) and as the matrices for oxide dispersion-strengthened alloys (2). Recently a program was initiated at NASA-Lewis to determine the optimum compositions with the best balance of cyclic oxidation and hot corrosion resistance, tensile properties, ductility, and strategic element content. In pursuit of this objective an investigation was completed (3) wherein nickel-rich alloys in the Ni-Cr-Al system were evaluated for their cyclic oxidation resistance in still air at 1100° and 1200°C. A first approximation oxidation attack parameter was derived which was related to the Cr and Al content by a multiple linear regression analysis. The resultant equations were translated into contour diagrams showing regions with minimum oxidation attack. This paper is the second step in the over-all program. The same alloys as were used in Ref. (3) were examined in this study for their hot corrosion resistance by cyclically oxidizing sodium sulfate (Na_2SO_4) coated specimens in still air at 900°, 1000°, and 1100°C. The compositions tested were within the ternary region: Ni; Ni-50Cr; and Ni-50Al [all compositions are given in atomic percent (a/o) in this paper]. A limited number of alloys were coated with Na_2SO_4 containing 10 weight percent (w/o) sodium chloride (NaCl) in order to determine the effect of NaCl on the corrosion process. The extent of the corrosion was determined by the specimen's net weight change, the maximum depth of attack, and by the weight of its spalls. The maximum depth of attack data, being the least ambiguous measure of the corrosion, were related to Cr and Al content at each temperature by a multiple linear regression analysis. The resultant third-order regression equations were translated into corrosion isopleths which indicated compositional regions of minimum attack. The corrosion contours from this study were compared to those from Ref. (3) for oxidation resistance, and regions of simultaneously good oxidation and hot corrosion resistance were identified.

Materials

All of the alloys specifically prepared for this program were vacuum melted in zirconia (ZrO_2) crucibles and cast in zirconia shell molds. The zirconium (Zr) pickup of up to 0.6 w/o was detected. Each mold consisted of a tree of ten 2.5 × 5.1 × 0.25 cm coupons, each with its own riser. For each coupon used the risers were removed and analyzed by atomic absorption for chromium and aluminum. The composition of these alloys are given in Table I, castings 1-11.

Most of the supplement alloys used in this study were obtained from a previous program (4) and had been melted in alumina (Al_2O_3) crucibles and cast into 1.9 cm diam cyclindrical ZrO_2 molds. These castings had been annealed 24 hr at 1200°C in quartz tubes which had been evacuated and backfilled with argon and sealed. Their compositions are given in Table I, castings 15-27. Another supplemental alloy was arc melted in a copper mold (casting 13 of Table I). Finally the commerical alloy, IN-671, was also tested as its composition is essentially Ni-50.9Cr, see Table I.

All the specimens used in this investigation were glass-bead blasted, ultrasonically cleaned in alcohol, and weighed prior to testing.

Metallographic examination of the as-cast materials revealed four general types of structures. Figure

Table I. Chemistry and phases of the alloys

Alloys	Composition (a/o) Cr	Al	As-cast phases
1	15.98	17.54	γ',β
2a	11.50	25.58	γ',β,α
2b	12.44	22.72	γ',β,α
3	13.19	12.07	γ,γ'
4	18.42	11.06	γ,γ'
5a	14.35	23.65	γ',β,α
5b	16.89	29.19	γ',β,α
6a	19.15	24.16	γ',β,α
6b	19.19	24.24	γ',β,α
7	15.81	5.77	γ
8a	18.87	26.99	γ',β,α
8b	20.84	16.52	γ',β,α
9	9.73	17.18	γ,γ'
10	19.87	—	γ
11	38.70	—	γ
13*	—	41.78	β
15†	0.78	24.50	γ'
16†	2.86	22.60	γ'
17†	9.98	15.73	γ'
20†	2.60	47.60	β
21†	10.30	39.10	β
22†	2.80	7.10	γ
23†	1.20	8.90	γ
27†	Remelted and cast nickel-200 (99.6%)		γ
IN-671‡	50.90	(0.39Ti-0.23C)	γ,α

* Arc melted ingots in copper molds.
† Melted in Al_2O_3 crucibles and annealed.
‡ Commercial alloy, nominal composition.

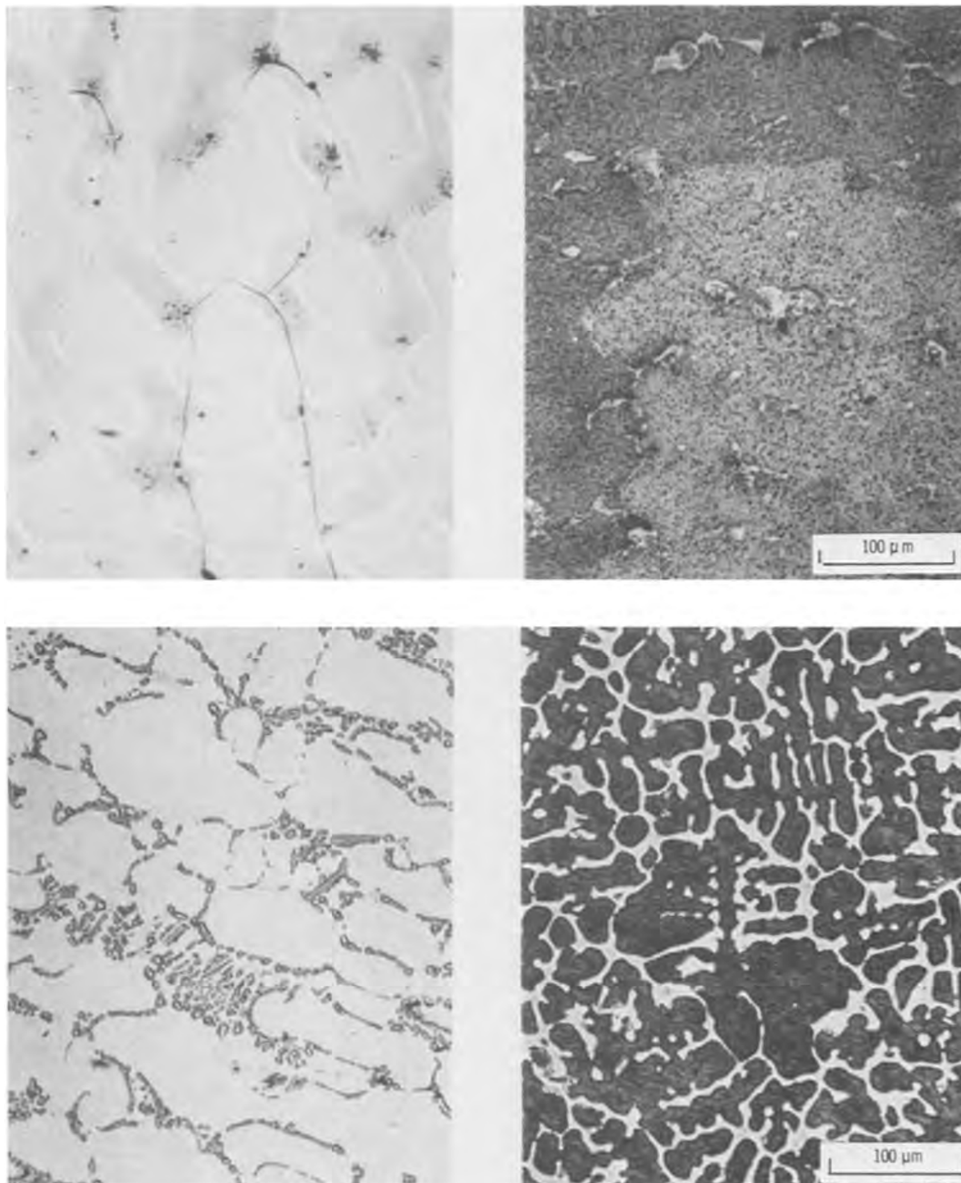

Fig. 1. Representative microstructures in the Ni-Cr-Al system. (a, upper left) Ni-15.81Cr-5.77Al; γ phase. (b, upper right) Ni-9.73Cr-17.18Al; $\gamma + \gamma'$ phase. (c, lower left) Ni-15.98Cr-17.54Al; $\gamma' + \beta$ phase. (d, lower right) Ni-11.5Cr-25.58Al; $\gamma' + \beta + \alpha$ phase.

1(a) is a single-phase structure typical of γ-nickel solid solution, of γ'-(Ni_3Al), and of β-(NiAl). Figure 1(b) shows the $\gamma + \gamma'$ structure found in most nickel base superalloys. Figure 1(c) represents the $\gamma' + \beta$ structure and finally Fig. 1(d) consists of a blocky structure of γ' and β with small particles of chromium solid solution (α-Cr) in the β. Tables I lists the as-cast phases of the alloys tested in this study and Fig. 2 is a phase diagram of the region of interest (5).

Procedures

Test procedures.—Prior to testing sample dimensions were measured and in particular the thickness was measured to a precision of ± 1 μm. Prior to exposure in the furnace, samples were coated with 1 mg/cm^2 of Na_2SO_4, or in some cases 1 mg/cm^2 of the mixture Na_2SO_4 + 10 w/o NaCl. Application of the salt coating was accomplished by heating a weighed sample on a hot plate set at about 200°C and spraying one side with a saturated solution of salt using an airbrush. The sample was then cooled and weighed to check for the correct amount of salt deposition. The same procedure was used to coat the other side of the specimen. The samples were then ready for the cyclic specimen furnace which has been described in detail (6). Samples were thermally cycled to allow 1 hr at temperature and a minimum of 40 min cooling in static air. A typical temperature profile is shown in Fig. 3. Samples reached

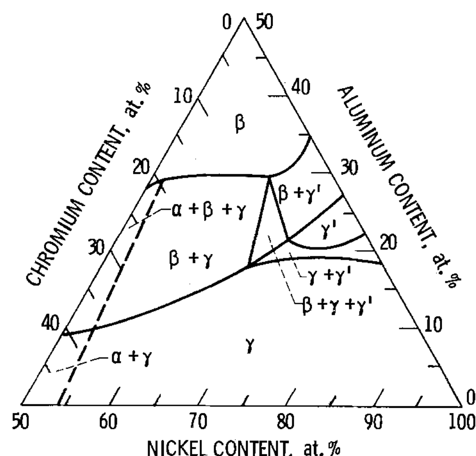

Fig. 2. Phase diagram in the Ni-Cr-Al system at 1100°C after Taylor and Floyd (5).

the highest test temperature in less than 2 min after insertion into the furnace and cooled to ambient temperature in less than 20 min after removal from the furnace. Samples of each alloy were exposed for 100 cycles at 900°, 1000°, and 1100°C. Weight change was determined at regular intervals throughout the test. At

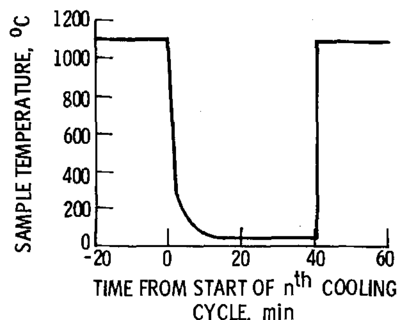

Fig. 3. Temperature profile of typical thermal cycle

the conclusion of the furnace testing the accumulated spall for each sample was weighed and examined by x-ray diffraction. Each corroded sample was also examined by x-ray diffraction and by metallography. The thickness of the alloy visibly unaffected by the corrosion attack was measured on metallographically prepared cross sections with a microscope cathetometer at a magnification of 100X. The original thickness minus the above measurement all divided by two then is defined here as the maximum depth of penetration of the corrosion attack.

Statistical procedures.—A digital computer program, NEWRAP, was used to perform the regression analyses (7). A two independent variable polynomial model was *a priori* judged as suitable for this data. The dependent variable was the maximum depth of corrosion, D, and the two independent variables were C and A, the atomic percent concentrations of chromium and aluminum, respectively, in the alloy. The approach was to begin with a first-order polynomial and to go to higher order equations if necessary. The decision as to which order polynomial provided the best fit was judged from the fraction of total variation (total sum of squares) accounted for by a particular regression equation and how reasonable were the predictions of this equation at locations away from the data points. This fraction of the total variation explained by the regression equation is called the coefficient of determination, R^2

Nonsignificant terms were deleted from the model by the back-rejection technique where the critical significance level is supplied as input. The strategy used here for a given order equation was to minimize the standard error of estimate and still predict reasonable values over the composition range.

It is possible to significantly increase the R^2 of a regression equation by including other factors that might account for a significant added fraction of variability. This is accomplished by the addition of a dummy variable, Z, and setting it either to 0 or 1. Thus in Ref. (3) the alloys were divided into two groups: those melted in zirconia crucibles and not annealed, $Z = 1$, and those that were melted in alumina crucibles and annealed, $Z = 0$. The addition of the dummy variable significantly raised the R^2 and lowered the standard error of estimate. From this result it was inferred that zirconia impurity affected the oxidation resistance. The dummy variable approach was included in this study for each of the three temperature regression runs.

In corrosion studies of this type the dependent variable (in this case the maximum depth of attack, D) usually has the same relative error over a wide range of values. This situation requires the dependent variable to be transformed to the logarithm of the variable. The process is termed homogenizing the error variance.

Results

Measure of corrosion.—The extent of corrosion was measured by the net specific weight change, the accumulated weight of spall, and the maximum depth of attack. In general all three measures gave consistent results. Samples which changed little in weight usually spalled only slightly and had relatively little depth of attack. The reverse statement is also generally true. Figure 4(a) to (c), contains the weight change data

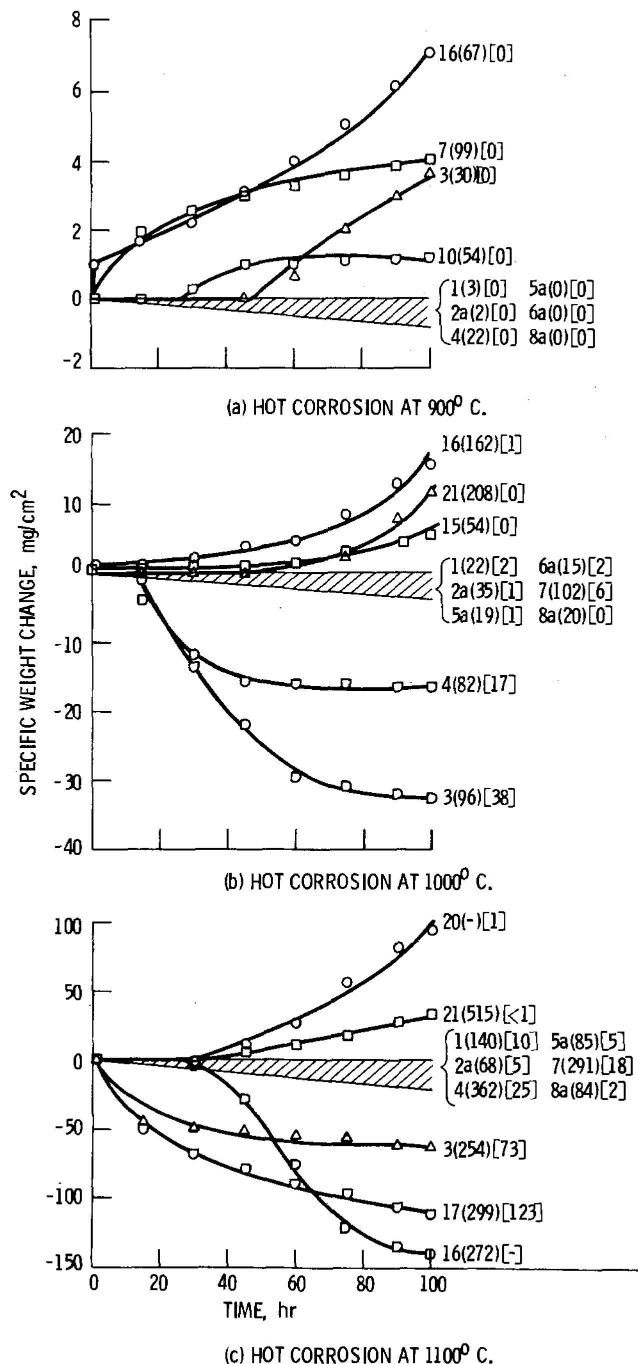

Fig. 4. The first number designates the alloy; the number in parentheses is the maximum depth of attack μm; the number in brackets is the specific accumulated spall weight, mg/cm^2.

from 900° to 1100°C of a random selection of the alloys tested. The values in parentheses following the alloy designations are the maximum depth of attack in micrometers and the values in brackets are the specific accumulated spall weight in milligrams per centimeter squared. The data can be classified into three categories: (*i*) alloys with relatively little weight change, (*ii*) alloys with substantial weight gains, and (*iii*) alloys with substantial weight losses.

A complete set of the corrosion data is presented in tabular form in Table II where the temperature dependence for each alloy is readily discernable. Thus at 900°C only alloy 17 spalled (and then but slightly) while many samples spalled at 1100°C. Comparing the last two columns of Table II, specific net weight change and specific weight of accumulated spall, a negative weight change in the former column ought to be accompanied by a nearly equal weight of spall in the latter column. A fair comparison is observed in this re-

Table II. Cyclic hot corrosion of nickel-chromium-aluminum alloys
[Specimens coated with 1 mg/cm² of sodium sulfate (Na_2SO_4); 100 hr at temperature.]

Alloy	Temperature (°C)	Maximum depth of attack (μm)	Specific weight change (mg/cm²)	Specific weight of accumulated spall (mg/cm²)
1	900	3	0	0
	1000	22	−2	2
	1100	140	−7	10
2a	900	2	0	0
	1000	35	0	1
	1100	68	−14	5
2b	1000	0	−1	0
	1100	168	−14	13
3	900	30	4	0
	1000	96	−33	38
	1100	254	−61	73
4	900	22	0	0
	1000	82	−16	17
	1100	362	−18	25
5a	900	0	0	0
	1000	19	−2	1
	1100	85	−10	5
5b	900	0	0	0
	1000	0	0	0
	1100	90	−6	0
6a	900	0	0	0
	1000	15	−4	2
6b	900	0	0	0
	1000	0	0	0
	1100	163	−6	4
7	900	99	4	0
	1000	102	−4	6
	1100	291	−15	18
8a	900	0	0	0
	1000	20	0	0
	1100	84	−2	2
8b	900	6	0	0
	1000	4	−2	0
	1100	231	−7	7
9	900	18	0	0
	1000	138	−35	49
	1100	187	−58	70
10	900	54	0	0
	1100	155	−106	107
11	1100	113	−3	3
13	900	20	29	0
	1000	52	10	7
	1100	164	1	2
15	900	50	4	0
	1000	54	6	0
	1100	153	−59	66
16	900	67	7	0
	1000	162	16	1
	1100	272	−138	—
17	900	14	4	1
	1000	131	−47	52
	1100	299	−111	123
20	900	2	1	0
	1000	125	9	0
	1100	—	114	1
20	900	—	1	0
	1000	156	4	0
	1100	—	97	1
21	900	0	0	0
	1000	208	12	0
	1100	—	34	2
21	900	0	0	0
	1000	156	7	0
	1100	515	24	0
22	900	87	6	0
	1000	233	23	7
	1100	709	−515	0
23	900	94	6	0
	1000	150	20	0
	1100	373	−267	0
27 (Ni-200)	900	55	18	0
	1000	—	11	4
	1100	205	20	3
IN-671	900	68	2	0
	1000	98	−1	1
	1100	139	1	1

spect for most of the alloys with the notable exception of alloys 22 and 23. For these two alloys there is a large net weight loss but no detectable spall. Since a spall shield surrounded the specimens when they were cooling, a large fraction of the spall should have been collected even if the specimens spalled explosively. Thus it must be assumed these two specimens had spalled either at temperature or while being raised out of the furnace.

X-ray diffraction and metallography.—After the furnace exposure both the retained and the spalled oxides were identified by x-ray diffraction. These oxide phases are listed in Table III. With but few exceptions all specimens formed multioxide phases. Figure 5(a) to (c) is a graphical presentation of the x-ray diffraction data. For the purpose of this figure the spalled and retained oxide data were combined. The figure illustrates two major points. The presence of chromium in the alloy decreases the aluminum content needed for Al_2O_3 formation in the scale. An explanation of this result is given Ref. (8). The other point is that with increased temperature more aluminum is required in the alloy for Al_2O_3 formation. The opposite behavior occurs in straight oxidation because of the increased diffusivity of the aluminum ion with temperature. But under the hot corrosion conditions of this study the spalling increased with temperature and overshadowed

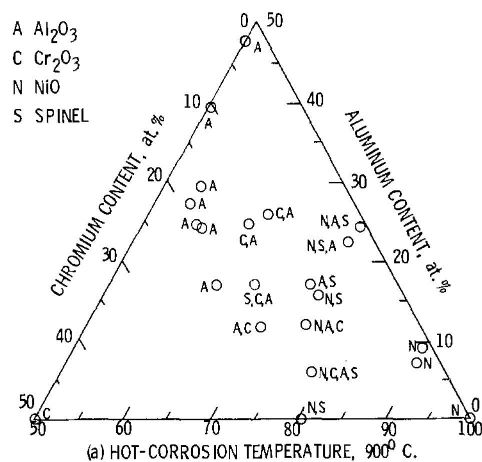

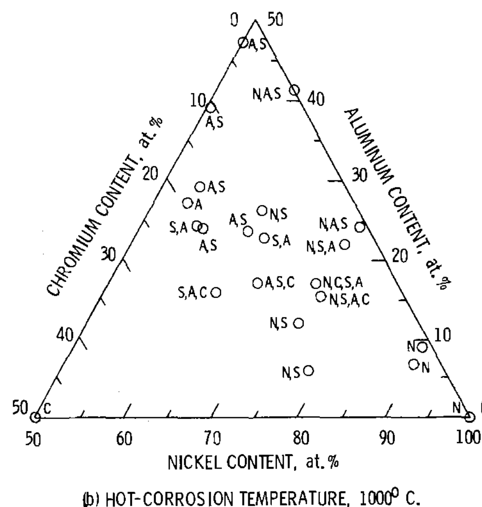

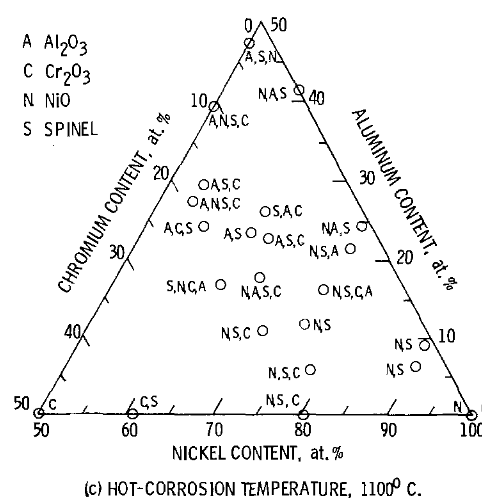

Fig. 5. Oxide phases in the scale of hot-corroded specimens. (Phases are listed in order of decreasing line intensities.)

Table III. Oxide phases and mode of microstructural attack

Alloy	Temp (°C)	Oxide phases*		Mode of attack		
		Retained scale	Spalled scale	Oxide penetration	Depleted zone	Internal corrosion or voids
1	900	Spinel, Cr_2O_3, Al_2O_3	No spall detected	No	No	No
	1000	Cr_2O_3	Al_2O_3, spinel, Cr_2O_3	No	Yes	No
	1100	Cr_2O_3, spinel	NiO, Al_2O_3, spinel	No	Yes	Yes
2a	900	Cr_2O_3, Al_2O_3	No spall detected	No	No	No
	1000	—	NiO, spinel	No	Yes	No
	1100	Al_2O_3, Cr_2O_3	Spinel, Al_2O_3	No	Yes	No
2b	1000	Spinel, Al_2O_3, Cr_2O_3(?)	Spinel, Al_2O_3	No	No	No
	1100	Al_2O_3, spinel, Cr_2O_3	Spinel, Al_2O_3	No	Yes	Yes
3	900	NiO, Al_2O_3, Cr_2O_3	No spalls detected	No	Yes	No
	1000	NiO	NiO, spinel	No	Yes	No
	1100	NiO, spinel	NiO, spinel	Yes	Yes	Yes
4	900	Al_2O_3, Cr_2O_3	No spalls detected	No	Yes	No
	1000	Cr_2O_3	NiO, spinel	Yes	Yes	Yes
	1100	Spinel, Cr_2O_3	NiO, spinel, Cr_2O_3	Yes	Yes	Yes
5a	900	Cr_2O_3, Al_2O_3	No spalls detected	No	No	No
	1000	—	Al_2O_3, spinel	No	Yes	No
	1100	Al_2O_3, spinel	Al_2O_3, spinel	No	Yes	Yes
5b	900	Al_2O_3	No spalls detected	No	No	No
	1000	Al_2O_3, spinel	No spalls detected	No	No	No
	1100	Al_2O_3, spinel	Al_2O_3, spinel, Cr_2O_3	Yes	Yes	No
6a	900	Al_2O_3	No spalls detected	No	No	No
	1000	—	Al_2O_3, spinel	No	Slight	No
7	900	NiO, Cr_2O_3, Al_2O_3, spinel	NiO, spinel	Yes	No	No
	1000	NiO, spinel	NiO, spinel	Yes	No	Yes
	1100	NiO, spinel, Cr_2O_3	NiO, spinel, Cr_2O_3	Yes	No	Yes
8a	900	Al_2O_3	No spalls detected	No	No	No
	1000	Al_2O_3	No spalls detected	No	Yes	No
	1100	Al_2O_3, spinel, Cr_2O_3	Al_2O_3, NiO	Yes	Yes	Yes
8b	900	Al_2O_3	No spalls detected	No	No	No
	1000	Al_2O_3, Cr_2O_3	Spinel, Al_2O_3	No	No	No
	1100	Cr_2O_3, Al_2O_3, spinel	Spinel, NiO, Al_2O_3, Cr_2O_3	No	Yes	Yes
9	900	Al_2O_3, spinel	No spalls detected	No	Slight	No
	1000	NiO, spinel, Al_2O_3, Cr_2O_3	NiO, Cr_2O_3	No	Yes	No
	1100	Al_2O_3, Cr_2O_3	NiO, spinel	Some	Yes	Yes
10	900	NiO, spinel	No spalls detected	No	No	Yes
	1100	NiO, spinel, Cr_2O_3	NiO, spinel, Cr_2O_3	No	No	Yes
11	1100	Cr_2O_3, spinel	Cr_2O_3	No	No	Yes
13	900	NiO, Al_2O_3	No spalls detected	No	No	No
	1000	Al_2O_3, NiO	NiO, Al_2O_3, spinel	Yes	Yes	No
	1100	NiO, Al_2O_3, spinel	NiO, Al_2O_3, spinel	Yes	Yes	No
15	900	NiO, Al_2O_3, spinel	NiO, Al_2O_3	No	No	No
	1000	NiO, spinel, Al_2O_3	NiO, Al_2O_3, spinel	No	Slight	No
	1100	NiO, spinel, Al_2O_3	NiO, Al_2O_3	Yes	Yes	No
16	900	NiO, spinel, Al_2O_3	NiO	No	No	No
	1000	NiO, spinel, Al_2O_3	NiO	No	No	No
	1100	NiO, spinel, Al_2O_3	NiO, Al_2O_3	Yes	Yes	Yes
17	900	NiO, spinel	NiO	No	Yes	No
	1000	NiO, spinel, Al_2O_3, Cr_2O_3	NiO	No	Yes	Yes
	1100	NiO, spinel, Al_2O_3, Cr_2O_3	NiO	Yes	Yes	Yes
20	900	Al_2O_3	No spalls detected	No	No	No
	1000	Al_2O_3	NiO, Al_2O_3,spinel	Some	Yes	No
	1100	Al_2O_3, spinel	NiO, spinel(?)	Yes	Yes	No
21	900	Al_2O_3	No spalls detected	No	No	No
	1000	Al_2O_3, spinel	No spalls detected	Yes	Yes	No
	1100	Al_2O_3, Cr_2O_3, spinel	Al_2O_3, NiO	Yes	Yes	No
22	900	NiO	No spalls detected	No	No	No
	1000	NiO	NiO	No	No	No
	1100	NiO	NiO, spinel	No	No	No
23	900	NiO	No spalls detected	No	No	No
	1000	NiO	No spalls detected	No	No	No
	1100	NiO, spinel(?)	NiO, spinel	No	No	No
27	900	NiO	No spalls detected	No	No	No
(Ni-200)	1000	NiO	NiO	No	No	No
	1100	NiO	NiO	No	No	No
IN-671	900	Cr_2O_3	No spalls detected	No	Yes	Yes
	1000	Cr_2O_3	Cr_2O_3	No	Yes	Yes
	1100	Cr_2O_3, spinel(?)	Cr_2O_3	No	Yes	Yes

* Listed in order of decreasing line intensities. (?) Insufficient lines for positive identification.

this effect. Thus at higher temperatures a greater aluminum content in an alloy is necessary to maintain a sufficient level to compensate for that lost due to the increased spalling.

The modes of attack during hot corrosion are described in Table III by listing three major morphological aspects frequently observed in corroded alloys and by identifying which ones are applicable to each of the alloys tested. The three modes are: (*i*) oxide penetration, often along grain boundaries; (*ii*) formation of a depleted zone immediately beneath the scale; and (*iii*) internal corrosion products and/or void formation. Examples of these corrosion modes are presented in Fig. 6(a) and (b).

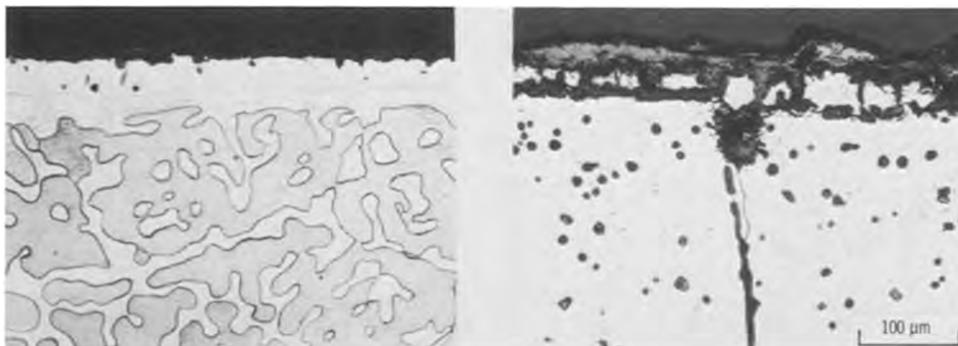

Fig. 6. Hot corroded Ni-Cr-Al alloys at 1100°C showing typical corrosion morphologies. (a, left) $\gamma' + \beta + \alpha$ alloy, Ni-11.50Cr-25.58Al shows a thin retained scale, a depleted zone, and the unaffected alloy. (b, right) γ alloy, Ni-15.81Cr-5.77 Al shows a thick retained scale, oxide penetration, and internal corrosion extending deep into the alloy.

Table IV. Effect of sodium chloride (NaCl) on the corrosion attack

Alloy	900°C						1100°C					
	Na_2SO_4			Na_2SO_4 + 10 w/o NaCl			Na_2SO_4			Na_2SO_4 + 10 w/o NaCl		
	MDA*	S**	ΔW***	MDA	S	ΔW	MDA	S	ΔW	MDA	S	ΔW
						A. Amount of corrosion						
1	3	0	0	19	2	−2	140	10	−7	232	36	−31
2a	2	0	0	21	<1	0	68	5	−14	46	18	−21
3	30	0	4	28	2	8	254	73	−61	295	59	−49
4	22	0	0	29	10	−2	362	25	−18	326	37	−27
5a	0	0	0	9	<1	−1	85	5	−10	65	9	−18
9	18	0	0	16	<1	3	187	70	−58	247	87	−73

Alloy	Na_2SO_4		Na_2SO_3 + 10 w/o NaCl	
	Retained scale	Spalled scale	Retained scale	Spalled scale
		B. Oxide phases in the scale† — 900°C		
1	Spinel, Cr_2O_3, Al_2O_3	None detected	Spinel, Al_2O_3, Cr_2O_3, NiO	NiO, spinel, Cr_2O_3
2a	Cr_2O_3, Al_2O_3	None detected	Al_2O_3, spinel, NiO, Cr_2O_3(?)	NiO, spinel
3	NiO, Al_2O_3, Cr_2O_3	None detected	NiO, spinel, Al_2O_3, Cr_2O_3	NiO, spinel, Cr_2O_3(?)
4	Al_2O_3, Cr_2O_3	None detected	NiO, spinel, Cr_2O_3, Al_2O_3	NiO, spinel
5a	Cr_2O_3, Al_2O_3	None detected	NiO, spinel, Al_2O_3	NiO, spinel
9	Al_2O_3, spinel	None detected	NiO, spinel, Al_2O_3	NiO, spinel
		C. Oxide phases in the scale† — 1100°C		
1	Cr_2O_3, spinel	NiO, Al_2O_3, spinel	Spinel, NiO, Cr_2O_3, Al_2O_3	NiO, spinel
2a	Al_2O_3, Cr_2O_3	Spinel, Cr_2O_3	NiO, spinel, Al_2O_3, Cr_2O_3	NiO, spinel
3	NiO, spinel	NiO, spinel	Spinel, NiO, Al_2O_3, Cr_2O_3	NiO, spinel
4	Spinel, Cr_2O_3	NiO, spinel, Cr_2O_3	Spinel, NiO, Cr_2O_3, Al_2O_3	NiO, spinel
5a	Al_2O_3, spinel	Al_2O_3, spinel	Spinel, Al_2O_3, NiO, Cr_2O_3	NiO, Cr_2O_3, spinel
9	Al_2O_3, Cr_2O_3	NiO, spinel	NiO, spinel, Al_2O_3, Cr_2O_3	NiO, spinel

* MDA = maximum depth of attack, μm.
** S = specific weight of accumulated spall, mg/cm².
*** ΔW = specific weight change, mg/cm².
† Listed in order of decreasing line intensities. (?) Insufficient lines for positive identification.

Sodium chloride effect.—Table IV summarizes the data concerning the effect of adding NaCl to the Na_2SO_4 on the hot corrosion of a limited number of alloys. At 900°C the effect is quite apparent. The NaCl caused the scale to spall and thereby accelerated the attack. Also NiO was a prominent phase in the spall of all specimens indicating a depletion in their surface concentration of aluminum and chromium. This result agrees with literature reports indicating sodium chloride vapors can disrupt the protective scale of alloys (9, 10).

At 1100°C the effect of the NaCl is not so evident. NiO was consistently a predominant phase of the spall of specimens with NaCl in their coating but was not always detected in the spalls of specimens corroded in the absence of NaCl. However at 1100°C the presence of NaCl did not seem to be consistently detrimental to the corrosion resistance of the alloys.

Discussion

How a material corrodes depends not only on its composition but also on the testing parameters used. Since there are many hot corrosion testing procedures in use today (11) it would be very difficult to directly compare the corrosion results obtained here with those of other laboratories. Of course the ultimate test procedure would be to test the material in actual application, *e.g.*, in a gas turbine engine. This procedure is not practical for use with all candidate materials and a number of screening-type tests are required so that only a few

Table V. Analysis of variance

Source	Sums of squares	Degrees of freedom	Mean squares	Calculated F value
		A. Data at 900°C		
Regression	31.126461	4	7.7816153	78.80 (compared to F(4, 19, 0.95) ≈ 5.81)
Residual	1.876195	19	0.0987471	
Total	33.002656	23		
		B. Data at 1000°C		
Regression	2.087594	5	0.4175188	9.97 (compared to F(5, 14, 0.95) ≈ 4.63)
Residual	0.586315	14	0.0418796	
Total	2.673909	19		
		C. Data at 1100°C		
Regression	1.097560	5	0.2195120	10.09 (compared to F(5, 17, 0.95) ≈ 4.59)
Residual	0.369896	17	0.0217586	
Total	1.467456	22		
		D. Data at 1100°C with dummy variable		
Regression	1.230196	8	0.1537745	9.07 (compared to F(8, 14, 0.95) ≈ 3.23)
Residual	0.237260	14	0.0169471	
Total	1.467456	22		

A. Data at 900°C:

R^2 = SSQ(REG)/SSQ(TOT) = 0.943150
Standard error of estimate = 0.314241

$$\log D = 1.81689 + 9.11839 \times 10^{-2}A - 5.26785 \times 10^{-3}A^2 - 5.65473 \times 10^{-3}CA + 6.45260 \times 10^{-5}A^3$$

B. Data at 1000°C:

R^2 = SSQ(REG)/SSQ(TOT) = 0.780727
Standard error of estimate = 0.204645

$$\log D = 2.20239 + 8.18814 \times 10^{-2}C - 1.69504 \times 10^{-3}C^2 - 2.10706 \times 10^{-4}A^2 - 9.28978 \times 10^{-3}CA + 2.18724 \times 10^{-4}CA^2$$

C. Data at 1100°C:

R^2 = SSQ(REG)/SSQ(TOT) = 0.747934
Standard error of estimate = 0.147508

$$\log D = 2.17186 + 0.143390A - 9.52439 \times 10^{-3}A^2 - 3.05352 \times 10^{-3}CA + 1.47265 \times 10^{-4}A^3 + 1.14503 \times 10^{-4}CA^2$$

D. Data at 1100°C with dummy variable:

R^2 = SSQ(REG)/SSQ(TOT) = 0.838319
Standard error of estimate = 0.130181

$$\log D = 2.29753 + 2.41902 \times 10^{-2}C + 0.101384A - 5.34642 \times 10^{-4}C^2 - 7.20886 \times 10^{-3}A^2 - 1.42786 \times 10^{-3}CA + 1.14005 \times 10^{-4}A^3 + 6.04861 \times 10^{-5}CA^2 - 0.363850Z$$

D = maximum depth of corrosion, μm.
C = a/o chromium.
A = a/o aluminum.
Z = dummy variable: Z = 0, melted in Al_2O_3 crucible and annealed.
Z = 1, melted in ZrO_2 crucible and not annealed.

"best" candidates are chosen for the actual application test. The procedure used in this investigation must be considered as a screening-type test. Its value lies in the identification of those "best" compositions for further testing.

Based on the data collected in this study, a multiple linear regression analysis was used to identify the "best" compositions in the Ni-rich end of the Ni-Cr-Al system. The procedure used was discussed earlier. The maximum depth of attack data, being the least ambiguous measure of the corrosion, were chosen to relate corrosion to the Cr and Al content of the alloys at each temperature. A summary of the statistical data appears in Table V(a) to (c), and is called the analysis of variance table (ANOVA). Included are the final regression equations. The third order, two independent variables regression equations were translated by a computer program into corrosion isopleths. Figure 7(a) to (c) are the resultant contours at 900°, 1000°, and 1100°C, respectively. Although the contours are related to the logarithm of the maximum depth of attack in micrometers, log D, the values listed in Fig. 7 within the contours are D directly. At 900°C a large minimum attack area exists at the higher chromium, higher aluminum compositions. At 1000°C this area decreases in size. At 1100°C two small areas of minimum attack exist at the edges of the diagram, one centered at about Ni-30Cr-20Al and the other centered at Ni-33Al. These two areas overlap areas of minimum oxidation attack observed in Ref. (3) and are shown here in Fig. 8.

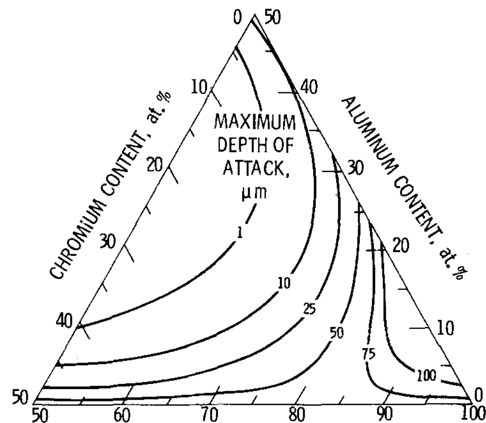

(a) AT 900° C. (EQUATION FOR CONTOURS GIVEN IN TABLE V(a).)

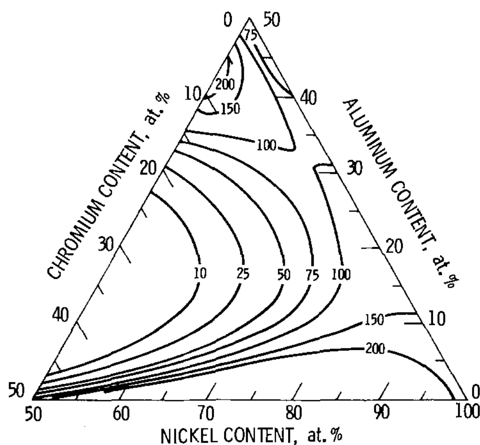

(b) AT 1000° C. (EQUATION FOR CONTOURS GIVEN IN TABLE V(b).)

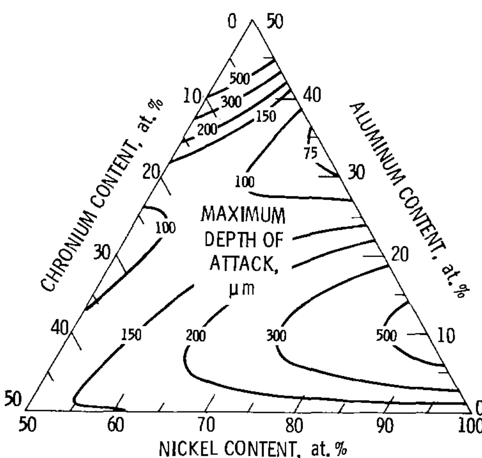

(c) AT 1100° C. (EQUATION FOR CONTOURS GIVEN IN TABLE V(c).)

Fig. 7. Hot corrosion isopleths

One effect of increasing temperature is to increase the rate of corrosion which in turn provides a better separation of the corrosion resistance of the alloys. But a surprising feature of Fig. 7 is that alloys with very low aluminum content corroded more at 1000°C than they did at 1100°C. Since the vapor pressure of Na_2SO_4 at 1100°C is moderate, 10^{-1} Nm^{-2} (10^{-6} atm) (12), the decrease in corrosion at 1100°C for these low aluminum-containing alloys cannot be attributed entirely to the loss of Na_2SO_4 via vaporization.[1] The entire Na_2SO_4 coating can be lost, however, by the spalling of the outer portion of the scale. Having lost their Na_2SO_4 coatings the alloys could then heal themselves and further corrosion would be by pure oxidation and at a much lower rate. Figure 7(c) then could represent the recovery ability of those hot corroded alloys that spalled. And most of the alloys at 1100°C did spall. Since the best hot corrosion resistant compositions in Fig. 7(c) overlap the best oxidation resistant compositions in Fig. 8, it can be generalized that for these alloys the ones with the best oxidation resistance have the best hot corrosion recovery ability. In gas turbines the exposure to hot corrosion conditions is thought to be intermittent (10). Thus the ability of material to recover from an hot corrosion attack could be an important factor in the life of that material when used in gas turbine engines.

As was done in Ref. (3) a dummy variable was used to determine if a significant variation could be ascribed to differences in the preparation of the alloys. One set of alloys came from a previous program (4) and were

[1] Fred J. Kohl (NASA-Lewis) extrapolated his 900°C rate data from slowly flowing oxygen and calculated a rate of vaporization of 3.5×10^{-2} mg/cm^2 hr^{-1} for 1100°C. This value would represent an upper limit as the tests in this paper were conducted in still air. Thus sodium sulfate (or perhaps more correctly its reacted products) ought to be present throughout most of the 100 hr duration of these tests.

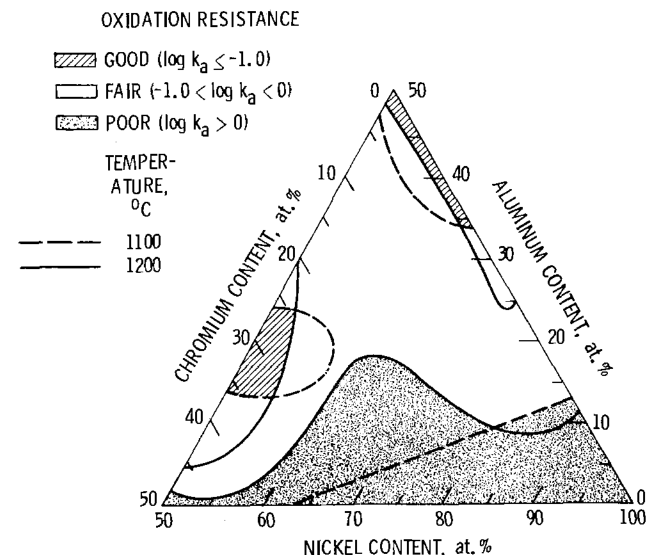

Fig. 8. Over-all cyclic oxidation resistance for Ni-Cr-Al alloys at 1100° and 1200°C in still air; Ref. (3).

melted in Al_2O_3 crucibles and annealed. The alloys prepared specifically for this program were melted in zirconia crucibles and were not annealed. No significant preparation effect could be detected for the 900°C data, *i.e.*, there was not a significant rise in R^2 or lowering of the standard error of estimate. Only a small effect could be detected for the 1000°C data. But at 1100°C a marked difference was detected. The statistical data and the regression equations are listed in Table V (d). Figure 9(a) and (b) are the resultant corrosion isopleths. Figure 9(a), where the dummy variable was set to zero, applies to alloys melted in Al_2O_3 crucibles and annealed. Figure 9(b), where the dummy variable was set to one, applies to alloys melted in ZrO_2 crucibles and not annealed. Analogous to the oxidation of these alloys (3) the latter preparation of the alloys provided superior corrosion resistance. Thus either trace amounts of ZrO_2 and/or the absence of annealing has a significant beneficial effect on the hot corrosion resistance of Ni-Cr-Al alloys.

Summary of Results

Alloys in the nickel-chromium-aluminum system were cyclically hot corroded at 900°, 1000°, and 1100°C for 100 hr. The data were statistically treated to obtain corrosion isopleths at each temperature as a function composition. The hot corrosion results were compared with previous work on the oxidation of these same alloys. The results of this work are summarized as follows:

1. Compositions with simultaneously good oxidation and hot corrosion resistance were found to be centered at about Ni-33Al and Ni-30Cr-20Al.

2. Alloys melted in zirconia crucibles and not annealed had significantly greater hot corrosion resistance at 1100°C than alloys melted in alumina crucibles and annealed. At lower temperatures differences in the preparation of the alloys did not significantly affect their hot corrosion resistance.

3. At low temperatures, the presence of NaCl in the Na_2SO_4 caused the scales of the samples to spall and thereby to increase their rate of corrosion.

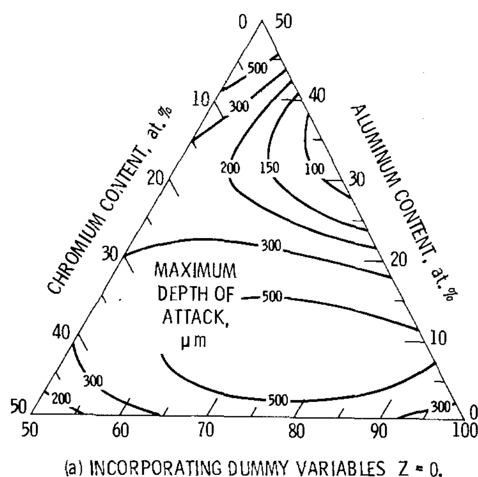

(a) INCORPORATING DUMMY VARIABLES Z = 0.

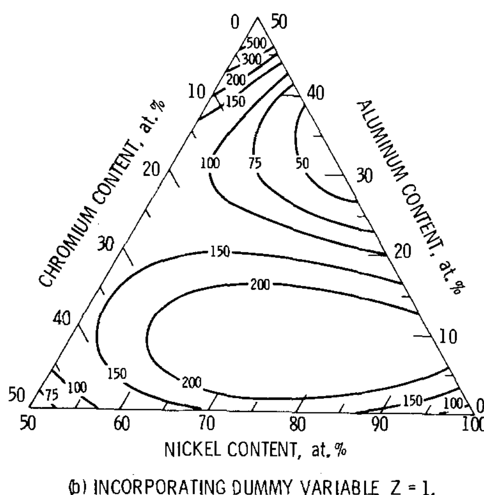

(b) INCORPORATING DUMMY VARIABLE Z = 1.

Fig. 9. Hot corrosion isopleths at 1100°C. (Equation for contours given in Table Vd.)

Manuscript submitted Aug. 1, 1977; revised manuscript received Sept. 8, 1977. This was Paper 34 presented at the Philadelphia, Pennsylvania, Meeting of the Society, May 8-13, 1977.

Any discussion of this paper will appear in a Discussion Section to be published in the December 1978 JOURNAL. All discussions for the December 1978 Discussion Section should be submitted by Aug. 1, 1978.

Publication costs of this article were assisted by NASA/Lewis Research Center.

REFERENCES

1. E. J. Felten, T. E. Strangman, and N. E. Ulion, PWA-5091, Pratt and Whitney Aircraft, East Hartford, Conn. (1974); also NASA CR-134735.
2. D. H. Timbres, L. F. Norris, and M. A. Glegg, Sherritt Gordon Mines, Ltd. (AD-748266; AFML-TR-72-50), Fort Saskatchewan, Alberta (1972).
3. C. A. Barrett and C. E. Lowell, NASA Tech. Note D-8255 (1976).
4. G. J. Santoro, D. L. Deadmore, and C. E. Lowell, NASA Tech. Note D-6414 (1971).
5. A. Taylor and R. A. Floyd, *J. Inst. Met.*, **81**, 451 (1952-1953).
6. C. A. Barrett and C. E. Lowell, *Oxid. Met.*, **9**, 307 (1975).
7. S. M. Sidik, NASA Tech. Note D-6770 (1972).
8. R. Kosak, Jr., Ph.D. Thesis, Ohio State Univ., Columbus (1969).
9. P. Hancock, in "Proceedings of 1974 Gas Turbine Materials in the Marine Environment Conference," MCIC-75-27, J. W. Fairbanks and I. Machlin, Editors, p. 225, Metals and Ceramics Information Center, Battelle Columbus Laboratories, Columbus, Ohio (1975).
10. J. F. G. Conde and B. A. Wareham, in "Proceedings of 1974 Gas Turbine Materials in the Marine Environment Conference," MCIC-75-27, J. W. Fairbanks and I. Machlin, Editors, p. 73, Metals and Ceramics Information Center, Battelle Columbus Laboratories, Columbus, Ohio (1975).
11. J. Stringer, MCIC-72-08, Metals and Ceramics Information Center (AD-745474), Battelle Columbus Laboratories, Columbus, Ohio (1972).
12. F. J. Kohl, C. A. Stearns, and G. C. Fryburg, in "Metal-Slag-Gas Reactions and Processes," Z. A. Foroulis and W. W. Smeltzer, Editors, p. 649, The Electrochemical Society Softbound Symposium Series, Princeton, N.J. (1975).

Oxidation of an Fe-9 w/o Ni Alloy in CO_2 at 700°-1000°C

W. J. Tomlinson[1] and I. A. Menzies[2]

Corrosion and Protection Centre,
University of Manchester Institute of Science and Technology, Manchester, England

ABSTRACT

The oxidation of an Fe-9.21% Ni alloy in dry CO_2 has been studied at 700°-1000°C using thermogravimetry, metallography, and electron-probe microanalysis. At all temperatures the kinetics for oxygen consumption (weight gain) followed a linear-parabolic-linear sequence. During the initial linear stage the scale consisted mainly of magnetite with pockets of wustite at the scale/alloy interface, and the observed activation energy of 193 ± 74 kJ $mole^{-1}$ is considered to be due to the dissociation of CO_2 into CO and adsorbed oxygen on the outer magnetite surface. During the parabolic oxidation stage a continuous alloy layer containing ≈60% Ni at the scale/alloy interface forms a barrier to Fe diffusion, and the associated activation energy of 207 ± 33 kJ $mole^{-1}$ is for the diffusion of Fe through the layer. The final linear kinetic stage corresponds to the breakdown of the barrier layer and a return to linear oxidation kinetics with an activation energy of 155 ± 13 kJ $mole^{-1}$ for the dissociation of CO_2 on the outer surface. During the final linear stage extensive subscale formation with pronounced intergranular penetration occurs and alloy particles containing ≈55-60% Ni are isolated in the wustite matrix. The wustite of the scale and subscale are continuous and contain ≈1.0 w/o Ni. Detailed information is presented of the Ni redistribution during oxidation and its correlation with the morphological structures and the oxidation kinetics. The associated oxidation processes are discussed.

Reviews on the oxidation of Fe-Ni alloys (1, 2) showed a considerable amount of information on their high temperature behavior in oxygen and air, but relatively little was known about their oxidation behavior in other gases. Morris and Smeltzer (3) have determined the kinetics and general morphological structures on Fe-Ni alloys containing up to 40% Ni oxidized in CO_2 at 1000°C. However, except for alloys containing 2, 36, and 48% Ni (4, 5, 6) there have been no investigations involving detailed and systematic information on the changing Fe and Ni distribution during oxidation of Fe-Ni alloys in CO_2 over a range of temperatures. The objects of the present investigation were to study the kinetics of oxidation of an Fe-9.21% Ni alloy at 700°-1000°C in CO_2, to examine the scale and subscale morphology as a function of temperature and time, and to determine qualitatively and quantitatively the Fe and Ni composition changes during the oxidation process.

Experimental

The chemical analysis (w/o) of the alloy was: Ni, 9.21; C, 0.0014; N, 0.0017; Si, 0.01; S, 0.005; P, 0.002; Cr, 0.02; Cu, 0.011; Al, 0.01; and Mn, Mo, W, V, Ti, and Co all < 0.01, and the CO_2 was special analytic grade which after drying had impurities less than (ppm): O_2, 6; N_2, 20; H_2O, 10. Full experimental details of the specimen preparation, kinetic, metallographic, and EPMA techniques have been given elsewhere (4). The essential features of the quartz spring thermobalance were that the weight gains were measured to <0.2 mg cm^{-2} and the temperature variation was <4° at 1000°C. The P_{O_2} due to dissociation of CO_2 at 1000°C is only 1.2×10^{-5} atm (20) with the values being less at the lower temperatures.

Results

Kinetics of oxidation.—At all temperatures in the range 700°-1000°C the kinetic behavior was broadly similar and followed the sequence linear, parabolic, linear (Fig. 1-3). Note that in Fig. 2 some points near the origin have been omitted for clarity. The initial linear stage is seen at 800°-950°C, while below 800°C the initial linear stage was absent or not well defined, and at 1000°C the rate of oxidation in the early stages was too fast to allow the kinetic pattern to be clearly

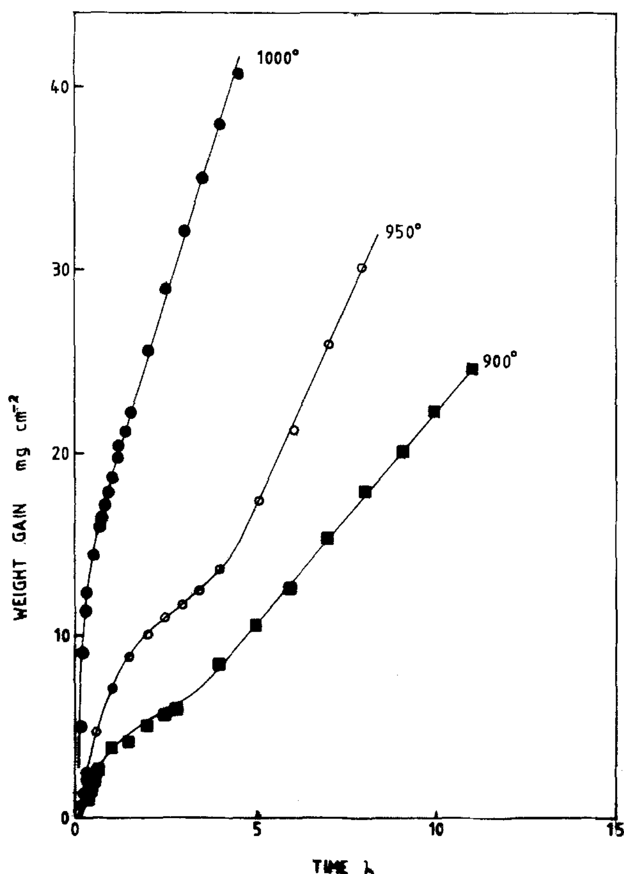

Fig. 1. Oxidation kinetics of an Fe-9.21% Ni alloy in CO_2 at 1 atm.

[1] Present address: Department Applied Science, Lanchester Polytechnic, Eastlands, Rugby CV21 3TG, England.
[2] Present address: Department Materials Technology, Loughborough University of Technology, Loughborough, England.

Key words: oxidation, iron-nickel alloys, kinetics, oxide morphology, electron probe microanalysis.

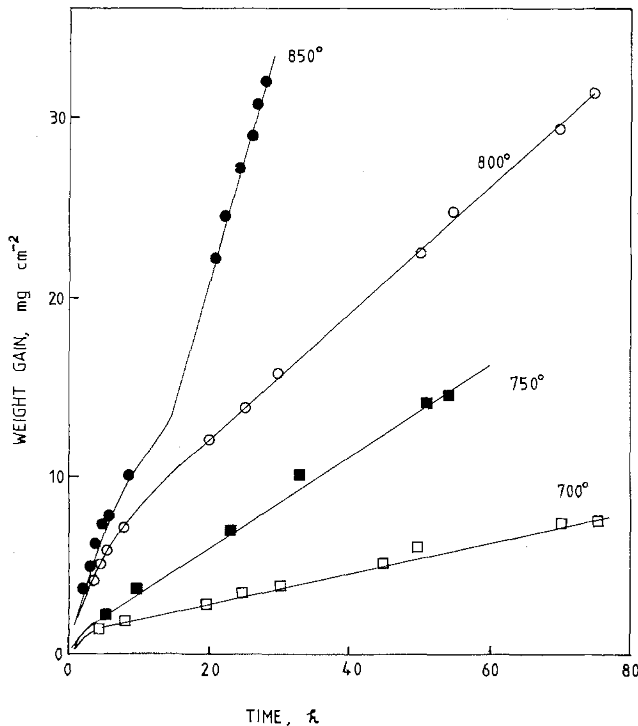

Fig. 2. Oxidation kinetics of an Fe-9.21% Ni alloy in CO_2 at 1 atm.

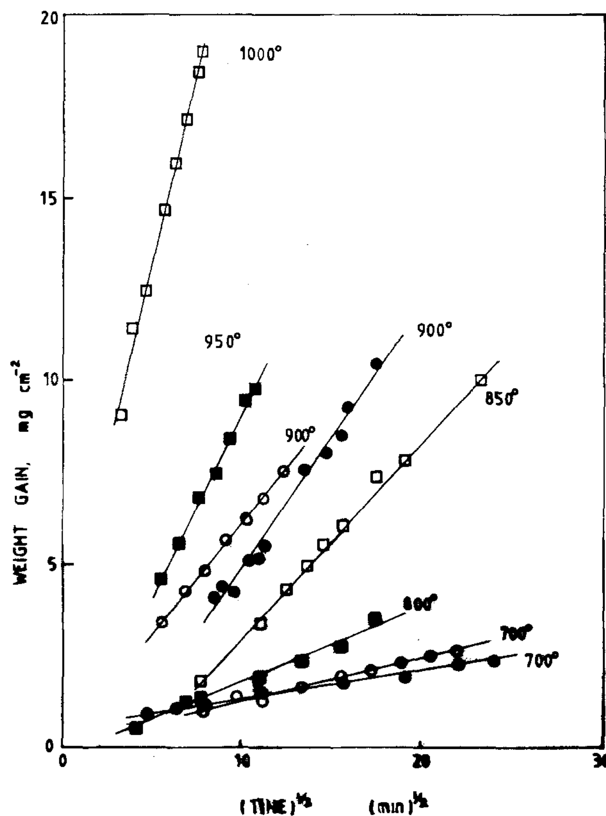

Fig. 3. Oxidation kinetics in parabolic form of an Fe-9.21% Ni alloy in CO_2 at 1 atm.

established. The parabolic region occurred over the whole temperature range (Fig. 3) although the kinetics were not strictly parabolic at 750° and 800°C. The final stage of oxidation was always linear. The clearest over-all pattern of kinetics is seen at 850°-950°C. The weight gains and times of transitions were difficult to define accurately and the best values are shown in Table I. It is seen that the duration of the

Table I. Specimen weight gain and time of exposure at the start of the parabolic and final linear oxidation stages

	Parabolic stage		Final linear stage	
Temperature (°C)	Wt. gain (mg cm^{-2})	Time (hr)	Wt. gain (mg cm^{-2})	Time (hr)
1000	9	0.25	19	1
950	4	0.5	15	4.5
900	2	0.25	26	6
850	5	3	12	15
825	—	—	18	18
800	—	—	12	15
800	6	5	10	18
700	1	0.5	2	5
700	1	1	4	20

initial linear stage tended to decrease, and the transition to the final linear stage occurred at higher weight gains and shorter exposure times as the temperature of oxidation increased. Typically the oxidation rate in the second linear stage was about half that in the first linear stage. Arrhenius functions for the three stages are shown in Fig. 4 and the calculated (95% confidence limit) activation energies were 193 ± 74, 207 ± 33, and 155 + 13 kJ mole^{-1} for the initial linear, parabolic, and final linear oxidation stages, respectively.

Morphology.—Specimens exposed for 5, 10, 20, 30, and 45 min and 1, 2, 4, 6, and 8 hr at 1000°C for 0.5, 1, 3, 6, and 10 hr at 900°C, and for 5, 10, and 25 hr at 800°C were examined, and at all temperatures the same sequence of structures was observed (Fig. 5-8). In the early stages of oxidation the scale consisted essentially of magnetite, and Ni accumulated in the alloy as a layer at the metal/scale interface and showed marked intergranular penetration which eventually enveloped grains. Subsequent formation of pockets of wustite in the magnetite at the scale/alloy interface and precipitation of subscale oxide were both associated with the greater accumulation of Ni at grain boundaries (Fig. 5a). Growth of the wustite pockets to form a continuous thick inner layer (here shown with magnetite precipitated during cooling) was associated with the breakdown of the Ni-enriched layer to form isolated metal particles in the subscale wustite which became smaller as the distance from the subscale/alloy interface into the subscale increased (Fig. 5b). A mature subscale is shown in Fig. 6b where it is seen that the subscale and scale wustite is continuous and that the metal particles are uniformly dispersed. The unevenness of the interfaces made it difficult to determine the thickness of the layers. However, after the early stages, particularly at 1000°C, it was possible to obtain a reasonable estimate of the magnetite layer thickness and this is shown in Fig. 7a and 8. With the ancillary information incorporated in the figures concerning the continuity of the Ni-rich layer and the

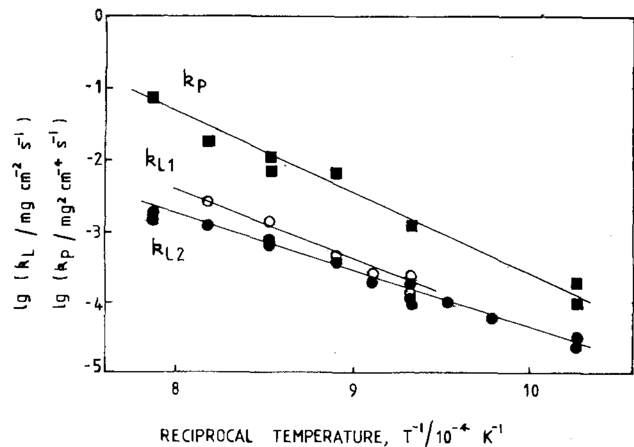

Fig. 4. Arrhenius functions of the linear and parabolic oxidation kinetics.

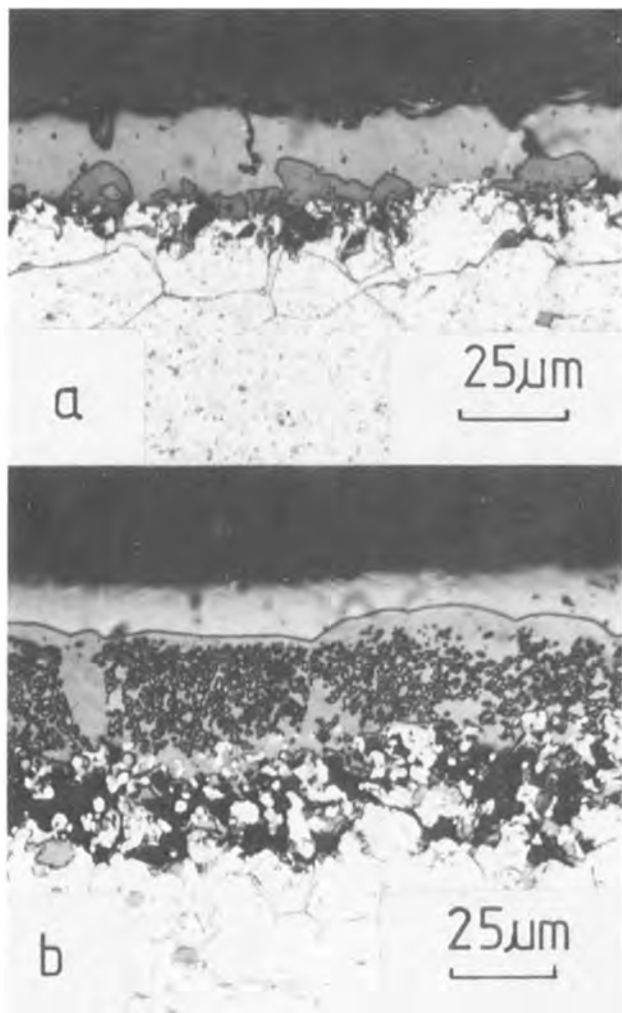

Fig. 5. Scale (at top) and subscale on the alloy oxidized at 800°C. Etched nital. (a) 5 hr exposure, pockets of darker wustite in magnetite scale opposite largest part of oxide subscale regions; (b) 10 hr exposure, magnetite now a layer on the outside, wustite (with precipitated magnetite) between magnetite and subscale.

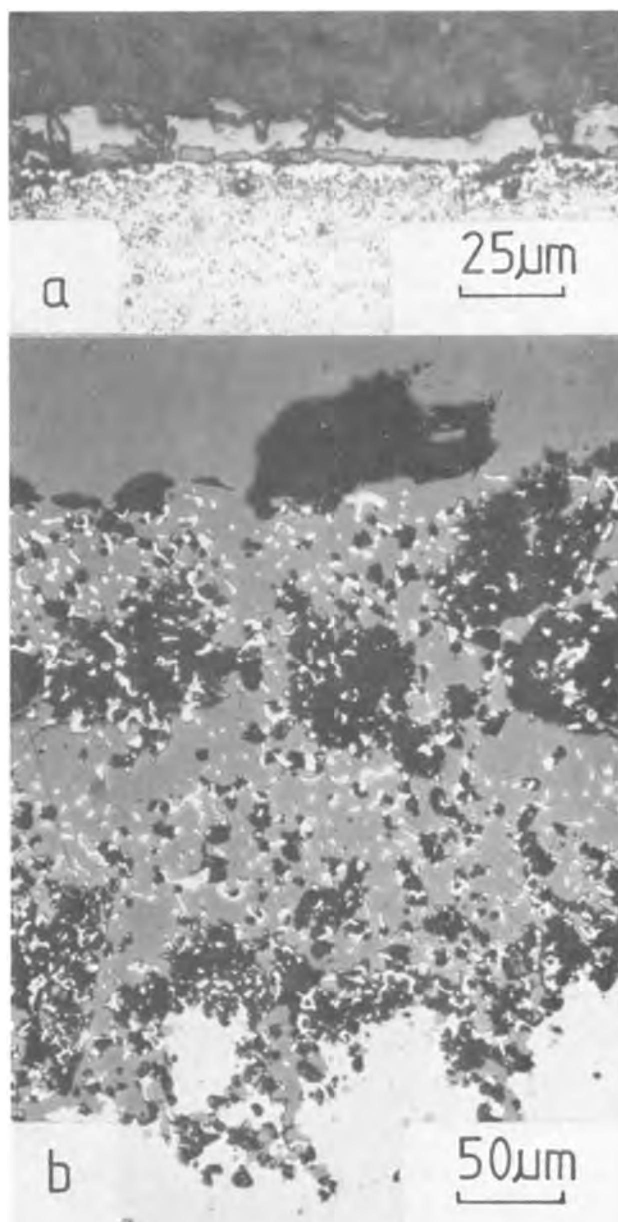

Fig. 6. Scale (at top) and subscale on the alloy oxidized at 1000°C. (a) 10 min exposure; etched nital; nearly continuous pockets of darker wustite in the magnetite at the alloy surface opposite the unetched Ni-enriched layer (light region at alloy surface) in the alloy: (b) 10 hr exposure; unetched; metal particles in the wustite subscale.

kinetics of oxidation (*cf* Table I) it is seen that the magnetite thickness increased during the initial linear stage, decreased during the parabolic stage, and remained constant during the final linear stage when the Ni-rich layer had been dispersed. Owing to the very uneven interfaces, the maximum thicknesses of the wustite layer and the subscale are of limited value. However, they do show that the breakdown of the Ni-rich layer is associated with the start of subscale oxide precipitation, and also give an indication of the relative thicknesses of the layers (Fig. 7a).

Electron probe microanalysis.—The distribution and concentration of Fe and Ni were determined in the scale and subscales of specimens oxidized for 10 and 30 min, and for 1, 2, 4, 6, 8, and 10 hr at 1000°C (Fig. 9, 10, 7b, 7c). Figure 9 shows some of the data for the changing general distribution. Iron phases are difficult to distinguish owing to limited contrast, but the Ni shows clearly the limited amount uniformly dispersed in the scale and the substantial amount segregated within the subscale. It is seen (Fig. 9) that the Ni-rich layer started to breakdown after 1 hr and subsequently metal particles were isolated in the subscale. Pronounced intergranular penetration of Ni occurred. On each specimen many linear scans were examined and Fig. 10 showing the considerable variation along line X of Fig. 9c is typical. The Ni concentration about the grain boundary oxide at B is high (at F and G). It was always observed that Ni accumulation preceded oxide precipitation. Variation parallel to the surface was also considerable, *e.g.*, after 2 hr exposure, within 100 µm along the surface the Ni concentration was 40 and 80%. The maximum Ni concentration in each subscale is shown in Fig. 7b where the rapid accumulation of Ni in the early part of oxidation and its peak nonequilibrium concentration in isolated metal particles is clear. The Ni concentration in the scale was small and decreased during oxidation (Fig. 7c); also the Ni concentration in the subscale wustite tended to be higher than in the scale.

Discussion

The most significant feature of the present work is the correlation between the linear-parabolic-linear stages of the kinetics and the reaction morphologies established by metallographic and EPMA techniques. Most of the processes and sequence of events observed by the different techniques are displayed for comparison in Fig. 7 and 8.

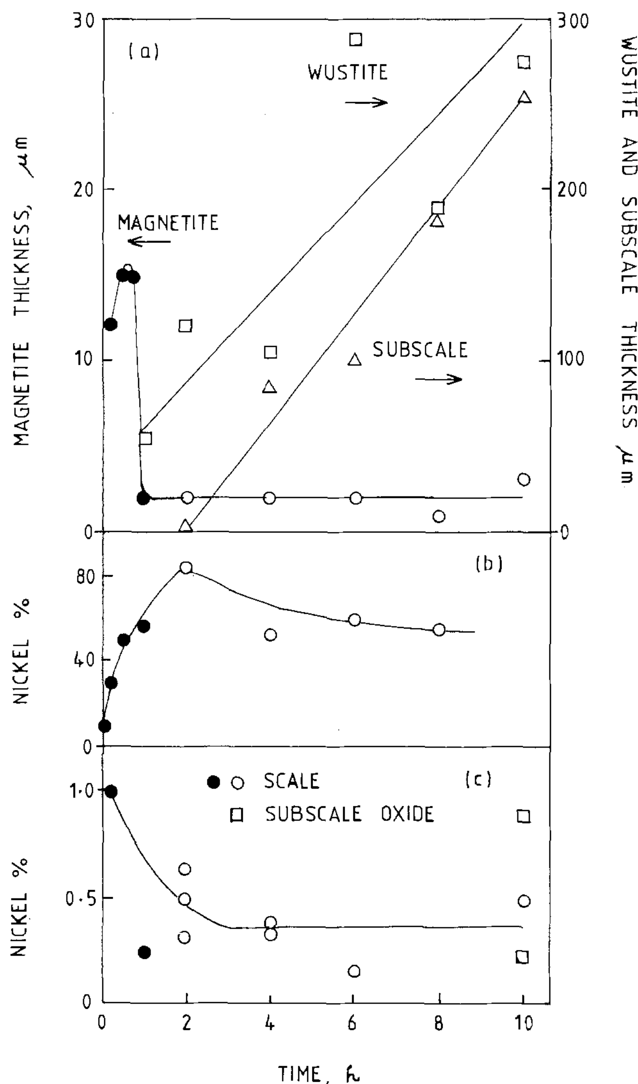

Fig. 7. Oxidation at 1000°C. (a) The scale magnetite and wustite, and subscale thicknesses: (b) the maximum Ni concentration in the subscale: (c) the Ni concentration in the scale and subscale oxide; closed and open symbols show the period when the Ni rich layer was continuous or discontinuous, respectively. Note: the kinetics were linear for 10 min, then parabolic up to 1 hr, then again linear.

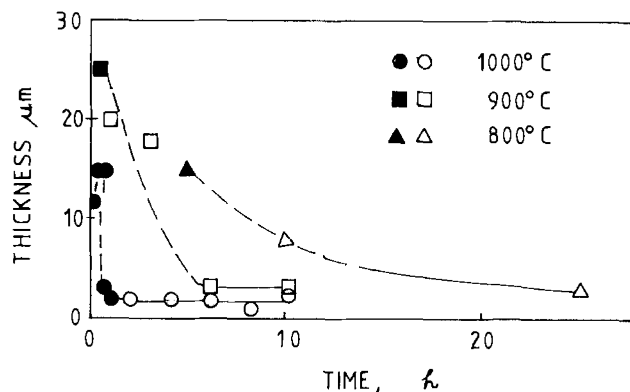

Fig. 8. Magnetite scale thickness formed at 800°-1000°C. Closed and open symbols show the period when the Ni-rich layer was continuous and discontinuous, respectively. Full and dashed lines show the period when the kinetics were in the final linear and parabolic stages, respectively.

During the initial linear stage the scale consists predominantly of magnetite with pockets of wustite at the scale/alloy interface and contains only about 1.0% Ni. The occurrence of magnetite as the predominant

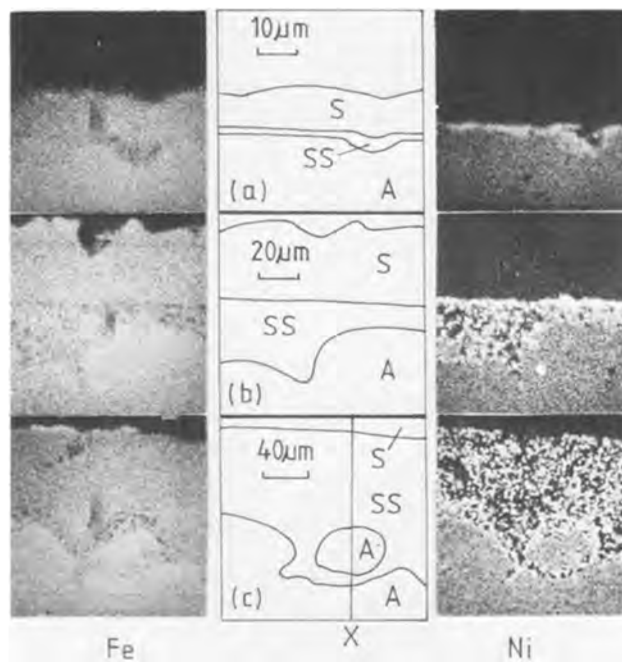

Fig. 9. Fe and Ni distributions on cross sections of specimens oxidized at 1000°C for (a) 10 min; (b) 1 hr; and (c) 8 hr. (Light for relatively higher concentrations). S = Scale; SS = subscale; A = alloy.

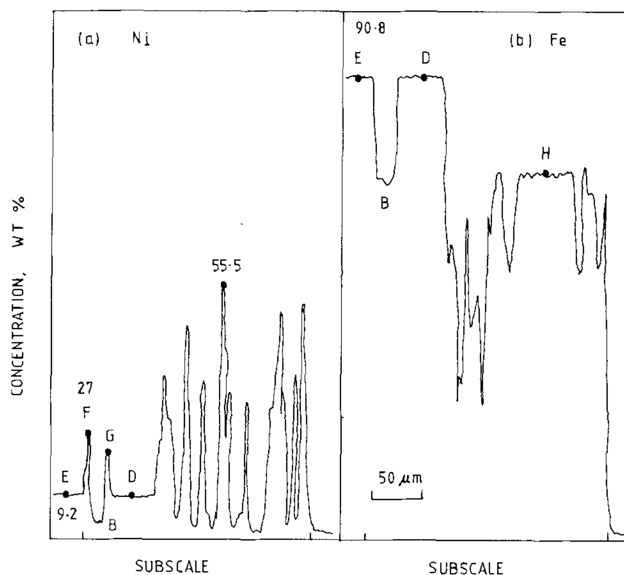

Fig. 10. Fe and Ni concentration profiles along the line X of Fig. 9c.

phase in the scale is unexpected and is discussed later. The selective oxidation of Fe accumulates Ni as a layer in the alloy at its surfaces, and the faster grain boundary diffusion leaves the alloy with an intergranular accumulation of Ni which is sufficiently marked to envelop grains. The linear kinetic law observed here is thought to reflect a phase boundary reaction. A similar linear law has been observed for the oxidation of Fe in CO_2 (7) and it was established (7) that the rate-controlling step was the reaction

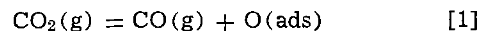

$$CO_2(g) = CO(g) + O(ads) \quad [1]$$

on the outer surface of wustite to form adsorbed oxygen. It is probable that a similar mechanism occurs in the present case. The activation energy for the dissociation of CO_2 during Fe oxidation is 211 kJ mole^{-1} (7) compared with the present value of 193 ±

74 kJ $mole^{-1}$. Thus the linear oxidation stage is controlled by the supply of oxygen and the supply of Fe from the alloy is relatively fast.

Continued depletion of Fe from the surface of the alloys means that eventually Fe must be transported from the interior by diffusion through the Ni-rich layer. This process corresponds to the parabolic oxidation stage where the activation energy of 207 ± 33 kJ $mole^{-1}$ is taken to represent the rate-controlling process of diffusion of Fe through the Ni-rich rim. However, this value compares poorly with the activation energy of about 300 kJ $mole^{-1}$ observed for the diffusion of Fe in Fe-Ni alloys (8), and it is thought that the much lower value observed in the present case is due to the changing microstructure and Fe and oxygen concentrations in the Ni-rich layer during oxidation.

Whatever the mechanism of magnetite formation in the early stages of oxidation, it is unstable and decomposes to form wustite

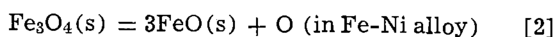

$$Fe_3O_4(s) = 3FeO(s) + O \text{ (in Fe-Ni alloy)} \quad [2]$$

This occurs during the later stages of the linear oxidation period and during the parabolic period (Fig. 7, 8), and is associated with the regions of highest Ni accumulation at the grain boundaries (Fig. 5a). At 1000°C the solubility of oxygen in Fe and Ni is 3 ppm (9) and 150 ppm (10), respectively, and since solid Fe-Ni alloys are nearly ideal (11), as a first approximation we may assume that the solubility of oxygen in the alloy is directly proportional to the Ni concentration. It appears that the increased solubility for oxygen, by the higher amounts of Ni enriched alloy at grain boundaries, is the cause for magnetite decomposition (Eq. [2]) and the disposition of the wustite pockets. The dissolved oxygen diffuses inwards and at the furthest extent of Fe depletion (and Ni accumulation) reacts with the higher Fe activity of the alloy and precipitates wustite. Subscale formation starts after the formation of the Ni-rich layer and its advance is approximately linear and extrapolates to zero time (Fig. 7). The preprecipitation period is the time needed to saturate the Ni-rich layer with oxygen, and the growth of the subscale is linear over-all because it occurs by a repeated process of wustite precipitation enriching the alloy with Ni, and oxygen dissolving and diffusing in the enriched Ni layer till it precipitates more wustite. The decomposition of magnetite (Eq. [2]) causes its thickness to decrease rapidly during the parabolic stage (Fig. 7 and 8). Oxygen solution, diffusion, and precipitation as subscale wustite is the cause of the breakdown of the Ni-rich layer and the end of the parabolic oxidation stage. Once the subscale wustite is continuous, the supply of Fe via the highly nonstoichiometric FeO (12) is faster than the supply of oxygen by CO_2 dissociation and linear kinetics are again observed. The different activation energies of 193 ± 74 and 155 ± 13 kJ $mole^{-1}$ for the initial and final linear stages are considered to be due to the different catalytic activities of the two magnetite surfaces. For example, Kobayashi and C. Wagner (13) showed that the catalytic activity of a surface was a sensitive function of its concentration of electronic defects, and the initial unstable magnetite is unlikely to have the same defect structure, and hence electronic structure, as the later stable magnetite. In addition, Fueki and J. Wagner (14) observed a pronounced effect of the scale composition on the activation energy: with pure Ni oxidized in CO_2 at 1000°-1300°C it was 113 kJ $mole^{-1}$, but with 0.37% Cr in the alloy the value had changed to 54 kJ $mole^{-1}$ (900°-1200°C) and 159 kJ $mole^{-1}$ (1200°-1300°C). When the magnetite is decomposing, the supply of oxygen to the metal is by reaction [2], but during the final linear oxidation stage the magnetite thickness is constant (Fig. 8) and another mechanism must operate. The subscale wustite must supply the oxygen by the process

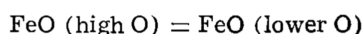

$$FeO \text{ (high O)} = FeO \text{ (lower O)} + O \text{ (dissolved in alloy)} \quad [3]$$

since oxygen does not diffuse in FeO (12). The wide nonstoichiometry range of FeO (12) may make this a relatively easy process.

The greater reactivity of Fe and its selective oxidation and the subsequent readjustment towards the stable phases of the Fe-Ni-O system are responsible for the sequence of reaction morphologies and kinetics observed. The changes in the early stages are so fast that highly nonequilibrium states are formed. At the start of oxidation at 1000°C the Ni concentration in the scale is ≈1.0% and this adjusts to a constant value of ≈0.3% as oxidation continues (Fig. 7c). A similar pattern occurred during the oxidation of a 2% Ni alloy in CO_2 but in that case (4) the final value was ≈0.2%. The concentration of Ni in FeO in equilibrium with a 60% Ni alloy at 1000°C is 0.13% (15) and this is in reasonable agreement with the present value of ≈0.20%. However, in the present case the Ni concentration of ≈1.0% in the early stages of oxidation when the Ni concentration of the alloy is lower is opposite to what is expected and must represent a condition way out of equilibrium. The most rapid rise in Ni concentration in the alloy is during the initial linear and parabolic stages (Fig. 7b) but the greatest increase occurs once the metal particles are isolated. After 2 hr at 1000°C the Ni concentration adjusted to ≈55-60%, which is similar to the value observed in a 2% Ni alloy oxidized in CO_2 at 1000°C (4), and compares with 54% on a 2.9% Ni alloy oxidized at 1200°C (16) and 45% Ni obtained on 10% Ni alloy at 700°C (17). At 1000°C the concentration of Ni in an Fe-Ni alloy in equilibrium with FeO containing maximum oxygen is 80% (15). The present value of ≈60% Ni is not inconsistent with this value since in a growing scale the oxygen potential of the FeO decreases from the outer surface inwards, and the subscale metal particles are positioned some distance in from the outer surface where the oxygen content of the FeO will be lower and hence the corresponding equilibrium concentration of Ni in the alloy will be less.

Finally we return to consider why the scale is predominantly magnetite in the early stages of oxidation. The magnetite is unstable and appears to form for kinetic reasons (Fig. 7 and 8). Arkharov (18) observed the formation of magnetite during the later stages of oxidation of Fe in CO_2 and attributed this to the lower supply of Fe. However, the situation is opposite in the present case: the magnetite forms when the supply of Fe is fastest. It appears that the magnetite nucleates preferentially. Brauns *et al.* (19) showed that the temperature below which wustite formed in the scale increased as the Ni concentration increased: 21% Ni raised the temperature from 570° to 680°C and this may indicate a tendency to form magnetite under conditions of rapid Ni enrichment. However, it appears likely that magnetite forms because it can dissolve up to 25% Ni whereas wustite can only dissolve a maximum of 0.84% (15). In the initial very fast reaction, diffusion of Ni away from the reaction zone may not be fast enough to avoid a concentration higher than the equilibrium amount for wustite being incorporated in the growing scale, and this would make the formation of magnetite with Ni in solid solution energetically preferred. Evidence that such a process has occurred is supported by the high Ni concentration in the scale in the early stages of oxidation and its subsequent adjustment toward lower values appropriate to a wustite equilibrium as oxidation continues (Fig. 7c). However, these considerations are mere possibilities; the reason for the occurrence of magnetite in the scale is unknown.

Acknowledgment

W. J. Tomlinson is grateful to the Department of Scientific and Industrial Research (now the Science Research Council) for the provision of a research studentship. The authors also wish to thank Mr. B. Lambert for his valuable assistance with the E.P.M.A., and B.I.S.R.A. for analyzed samples of the alloy.

Manuscript submitted May 2, 1977; revised manuscript received Sept. 19, 1977.

Any discussion of this paper will appear in a Discussion Section to be published in the December 1978 JOURNAL. All discussions for the December 1978 Discussion Section should be submitted by Aug. 1, 1978.

REFERENCES

1. R. T. Foley, *This Journal*, **109**, 1202 (1962).
2. W. J. Tomlinson, PhD Thesis, Univ. Manchester, Manchester, U.K. (1965).
3. L. A. Morris and W. W. Smeltzer, *Acta Metall.*, **15**, 1591 (1967).
4. I. A. Menzies and W. J. Tomlinson, *J. Iron Steel Inst., London*, **204**, 1239 (1966).
5. I. A. Menzies and W. J. Tomlinson, *Br. Corr. J.*, **2**, 235 (1967).
6. I. A. Menzies and W. J. Tomlinson, *J. Mater. Sci.*, **2**, 529 (1967).
7. F. Pettit, R. Yinger, and J. B. Wagner, *Acta Metall.*, **8**, 617 (1960).
8. "Metals Reference Book," 5th ed., C. J. Smithells, Editor, p. 913, Butterworths, London (1976).
9. J. Swisher and E. T. Turkdogan, *Trans. AIME*, **239**, 626 (1967).
10. M. Hansen, "Constitution of Binary Alloys," p. 1024, McGraw-Hill, New York (1958).
11. R. A. Oriani, *Acta Metall.*, **1**, 448 (1953).
12. P. Kofstad, "Nonstoichiometry, Diffusion and Electrical Conductivity in Binary Metal Oxides," p. 221, Wiley, New York (1972).
13. H. Kobayashi and C. Wagner, *J. Chem. Phys.*, **26**, 1609 (1957).
14. K. Fueki and J. B. Wagner, *This Journal*, **112**, 1079 (1965).
15. A. D. Dalvi and W. W. Smeltzer, *ibid.*, **117**, 1431 (1970).
16. K. Sachs, *J. Iron Steel Inst., London*, **185**, 348 (1957).
17. J. Benard and J. Moreau, *Rev. Metall.*, **47**, 317 (1950).
18. V. I. Arkharov, *Fiz. Met. Metallov.*, **5**, 251 (1957).
19. E. Brauns, A. Rahmel, and H. Christmann, *Arch. Eisenhuttenwes*, **30**, 553 (1959).
20. B. Swaroop and J. B. Wagner, Jr., *This Journal*, **114**, 685 (1967).

Electrochromism in Li_xWO_3

S. K. Mohapatra*,[1]

Bell Laboratories, Holmdel, New Jersey 07733

ABSTRACT

The electrochromic behavior of Li_xWO_3 has been studied by potentiostatic and galvanostatic measurements for both symmetric and asymmetric cells. The kinetics of coloration and bleaching are ascribed to barrier-limited and space charge-limited current flow, respectively, similar to the case of H_xWO_3. Galvanostatic measurements indicate linearity of optical density with injected charge at low injection levels. At high injection levels a nonlinear response is observed which is attributed to the approach of a phase boundary with increasing x in Li_xWO_3. A general comparison of Li_xWO_3 and H_xWO_3 in H_2SO_4: H_2O indicates greater stability for open-circuit memory of the Li_xWO_3 cells. Response times for various symmetric cells are tabulated.

Electrochromism in WO_3 is due to the formation of W-bronze, M_xWO_3, where M^{z+} is a cation in the octahedral interstitial site and z is different from six. Charge neutrality is maintained by the formation of W^{5+} or by a free electron in the conduction band. The coloration in M_xWO_3 is attributed to the shift of the plasma edge in single crystals and to the intervalence transfer transition ($W^{5+} \rightleftharpoons W^{6+}$) (1) in amorphous material where the electron is more localized.

In principle electrochromism in WO_3 is reversible and therefore has promise for passive display applications. Speed of response and contrast are the primary considerations for display applications. The ensuing criteria for cation selection are: (*i*) high solubility, (*ii*) high diffusion coefficient, (*iii*) low injection potential, and (*iv*) high deposition potential. Protons satisfy most of the criteria. However, the thermodynamic stability of H_xWO_3 at room temperature is poor (2). In addition, the electrode (WO_3) tends to dissolve in the electrolyte ($H_2SO_4 + H_2O$), and the electrolyte has a comparatively low decomposition potential of 1.5V. As is shown later, these difficulties can be circumvented by the use of alkali metal ions despite the smaller diffusion coefficients (Table I) of alkali ions compared to protons.

Although there has been considerable work on the electrochromism in WO_3 using protons (5, 8-12) little is known about the electrochromic behavior of Li_xWO_3. Hersh, McGee, and Kramer (13) initiated work on electrochromic aspects of alkali metal tungsten-bronzes. From the coloration and bleaching experiments Green *et al.* (14) postulated a diffusion-controlled process for $WO_3|MClO_4$ in PC|M (where M is Li or Na) cells. In the present paper, the characteristics of electrochromic coloration and bleaching of Li_xWO_3 are reported and compared with that of H_xWO_3. Criteria for stability and reversibility of these electrochromic cells are also discussed.

* Electrochemical Society Active Member.
[1] Present address: Coulter Information Systems, Bedford, Massachusetts 01730.
Key words: electrochromism, potentiostatic measurements, galvanostatic measurements.

Sample Preparation and Experimental Procedure

Thin films of WO_3 were prepared by electron beam evaporation of reagent grade WO_3 powder (Ventron

Table I. Impurity diffusion in WO_3 at 25°C

Diffusing species	Diffusion coefficient, D (μ^2/hr)	Remarks	Ref.
H^+	$2\ 52 \times 10^6$	NMR	3)
H^+	10^{-1}-10^{-2}	NMR on single crystal	(4)
H^+	7.2×10^3	Bleaching experiments on amorphous film	(5)
H^+	2.7×10^4	NMR on polycrystal	(6)
H^+	1.9×10^4	Table II	Present work
Li^+	1.9×10^3	Table II	Present work
Na^+	10^{-20}	From high temperature diffusion data on $Na_{0.78}WO_3$	(7)

Corporation, 99.7% purity) on transparent In_2O_3 coated glass substrates (PPG Nesatron). The thickness of the films was determined with a Taylor-Hobson Talysurf. Li was injected into WO_3 from a 1M $LiClO_4$-propylene carbonate (PC) electrolyte. $LiClO_4$ was dried for 7-8 hr at 100°C and then dissolved in PC.

Two-electrode potentiostatic measurements were carried out in a cylindrical glass cell with optical windows on opposite sides. Galvanostatic or constant current measurements were carried out with the same cell placed inside a Cary-14 spectrophotometer. A Keithley 225 current source was used for applying a constant current. Two types of cell geometries were studied: (*i*) the asymmetric cell $In_2O_3|WO_3|$electrolyte|metal electrode, and (*ii*) the symmetric configuration $In_2O_3|WO_3|$electrolyte$|M_xWO_3|In_2O_3$. Indium was used as the counterelectrode in the asymmetric configuration. For a practical electrochromic display the symmetric cell type is more favorable. Even though such a symmetric arrangement has been proposed (15), the cell characteristics have not been reported.

Since H^+ rather than Li^+ might possibly be injected into WO_3 in the presence of small quantity of H_2O in the electrolyte, a symmetric cell of H_xWO_3 and WO_3 separated by the electrolyte 1M $LiClO_4$-PC was set up. A bias of 1.5V applied to this cell did not transfer any color (*i.e.*, H^+) from H_xWO_3 to WO_3. In addition, it follows from the galvanostatic measurements (discussed below) that the variation of the optical density with injected charge at high injection levels differs for H^+ and Li^+. Therefore, proton injection in these experiments is unlikely.

Results and Discussion

Characteristics of coloration.—Coloration characteristics of an asymmetrical cell of WO_3 in $LiClO_4$-PC are similar to that of H_xWO_3. As in H_xWO_3, at a constant applied bias the current drops with time, because of the increase in chemical potential of the injected cation with time. Crandall and Faughnan (9) performed an analysis of the kinetics of H^+ incorporation in WO_3 according to which the kinetics is essentially controlled by the proton transport across the WO_3-electrolyte interface. It obeys the well-known Butler-Volmer relation (16)

$$j = j_0 \left[\exp\left(\frac{(1-\beta)e\eta}{kT}\right) - \exp\left(-\frac{\beta e\eta}{kT}\right) \right] \quad [1]$$

where j_0 is the exchange current density, β the barrier symmetry factor, and η the overpotential, *i.e.*, the applied potential minus the reversible potential.

One of three processes may control the kinetics of coloration: (*i*) charge transport across the electrode-electrolyte interface, (*ii*) diffusion in the electrolyte, and (*iii*) diffusion in the WO_3. The barrier-controlled process leads to the current-voltage behavior presented by Eq. [1]. If diffusion in the electrolyte is the dominant process, the current density is represented by (17)

$$j = \pi^{-1/2} n \mathbf{F} D_0^{1/2} C^0 t^{-1/2} \quad [2]$$

where $n = 1$ is the number of electrons participating in the reduction, $\mathbf{F}$ the Faraday constant, D_0 the diffusion coefficient, and C^0, the concentration of the redox species, Li^+. From the equivalent conductance data of Keller *et al.* (18) D_0 of Li^+ in $LiClO_4$:PC can be obtained, which when substituted in Eq. [2] with a C^0 of 10^{-3} mole/cm³ would give a j value two orders of magnitude higher than observed in electrochromic experiments. Therefore, diffusion in the electrolyte cannot control the rate of coloration.

The rate of diffusion in the neutral WO_3 bulk does not depend on voltage. But at elevated levels of charge injection it is possible to go from a barrier-controlled process to a diffusion-controlled process. If a diffusion-controlled process is assumed, concentration of the injected cation at a distance y ($y = 0$ at In_2O_3-WO_3 interface; l is the thickness of the film) and at time t can be expressed as (14, 19)

$$C(y,t) = \frac{J_0 t}{l} + \frac{J_0 l}{D} \mathbf{F}(y,t) \quad [3]$$

where J_0 is the flux at the film-electrolyte interface and D the diffusion coefficient of the cation. The function $\mathbf{F}(y,t)$ depends upon Dt/l^2 and y/l. $\mathbf{F}(y,t)$ values can be obtained from plots (14) of $\mathbf{F}(y,t)$ *vs.* y/l for various Dt/l^2 values. Using $J_0 = 2$ mA cm² (close to the maximum value in our experiments), $D_{Li} \simeq 10^{-9}$ cm²/sec (Table I), $l = 3 \times 10^{-5}$ cm and considering a time $t = 1$ sec, $C(y = 0)/C(y = l) \simeq 0.80$. Therefore a diffusion-dependent coloration process can be ruled out.

Having eliminated diffusion in the electrolyte and in WO_3, it is reasonable to attribute the coloration process to a barrier-controlled process. In such a case j in Eq. [1] can be translated into the time domain if the reversible potential V_0 as a function of the composition parameter x (in M_xWO_3) is known. For $x \leq 0.2$ the emf E of the cell $Li_xWO_3|$1M $LiClO_4$ in PC|Li (20) can be fitted to an analytical expression given by Crandall *et al.* (9).

After substitution of this expression for the equilibrium emf in η, the current density j in the Butler-Volmer relation can be translated to the time domain as $j = kt^{-1/2}$ with a barrier symmetry factor $\beta \sim 0.5$. A typical plot of j *vs.* t for Li incorporation in WO_3 is shown in Fig. 1. The solid line represents $j = kt^{-1/2}$ for $k = 1.6$ mA (sec)$^{1/2}$ cm^{-2}. A reasonable fit with the experimental values is obtained in the initial stage of coloration. It should be mentioned at this point that $j = kt^{-1/2}$ is valid only for short times t and for small x values. For high x values Eq. [1] must be solved numerically. In addition, Arnoldussen (21) has pointed out that j_0 contains the reversible potential which would change as a function of x. Therefore, j_0 would change as a function of x and t. Thus a deviation of the simple relationship of $j \propto t^{-1/2}$ from the experimental points at long coloration times is to be expected.

Characteristics of bleaching.—Faughnan *et al.* (5) have shown that for an asymmetric cell consisting of H_xWO_3:H_2SO_4:In the bleaching of H_xWO_3 is governed by a space-charge limited (SCL) current of H^+ and

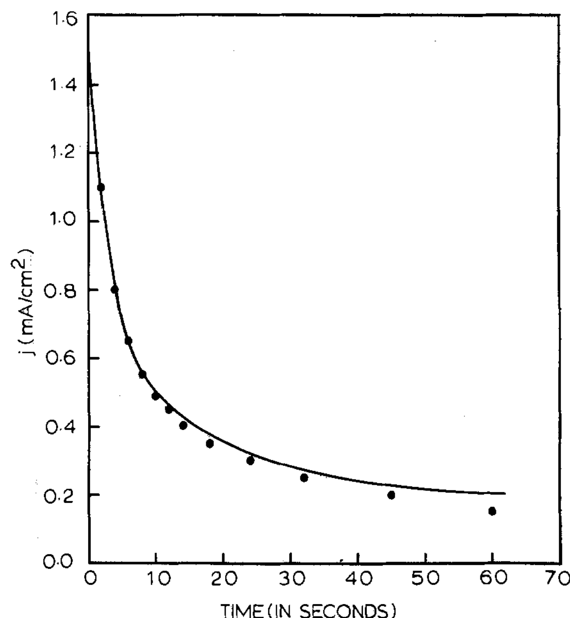

Fig. 1. Current density-time plot for the cell WO_3:1M $LiClO_4$-PC:In during coloration. The solid circles are the experimental points and the solid line is drawn for $j = 1.6t^{-1/2}$.

electrons. The space charge builds up because of the enormous difference between electron and cation mobilities ($D_e \sim 2.5 \times 10^{-1}$ cm²/sec (8) and $D_{M^+} < 10^{-8}$ cm²/sec). The voltage dependence normally observed rules out simple diffusion-limited bleaching.

The SCL current equation of Faughnan *et al.* is expressed as

$$J(t) = (p^3 \epsilon \epsilon_o \mu_p)^{1/4} V^{1/2} / (4t)^{3/4} \quad [4]$$

where p is the volume density of the cations in the intermediate neutral plasma region, ϵ the relative dielectric constant of WO_3, ϵ_o the permittivity of free space, μ_p the mobility of the cation, V the applied voltage, and t the time. The end of the bleaching peroid, or the finish time, t_f is expressed as

$$t_f = ps^4 / (4 \epsilon \epsilon_o \mu_p V^2) \quad [5]$$

s marking the boundary of the cation space charge with respect to the electrolyte-WO_3 interface. Figure 2 represents a $j(t)$ plot for both the symmetric and asymmetric cells of H_xWO_3 and Fig. 3 is that of Li_xWO_3. It is interesting to see that both for symmetric and asymmetric cells of H_xWO_3 and Li_xWO_3 a ¾ slope is obtained according to Eq. [4]. A plot

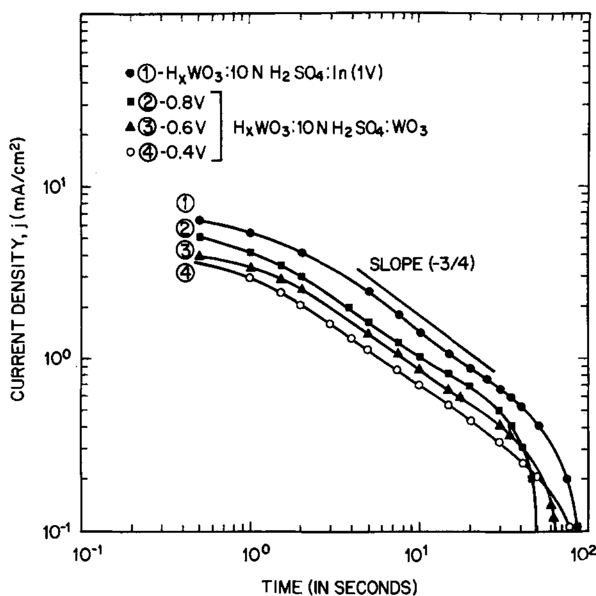

Fig. 2. Bleaching characteristics of symmetric and asymmetric cells for H_xWO_3 in the presence of 10N H_2SO_4.

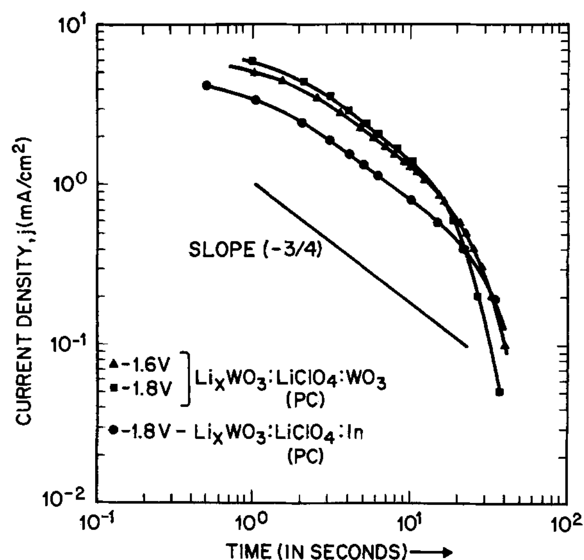

Fig. 3. Bleaching characteristics of symmetric and asymmetric. cells for Li_xWO_3 in the presence of 1M $LiClO_4$-PC.

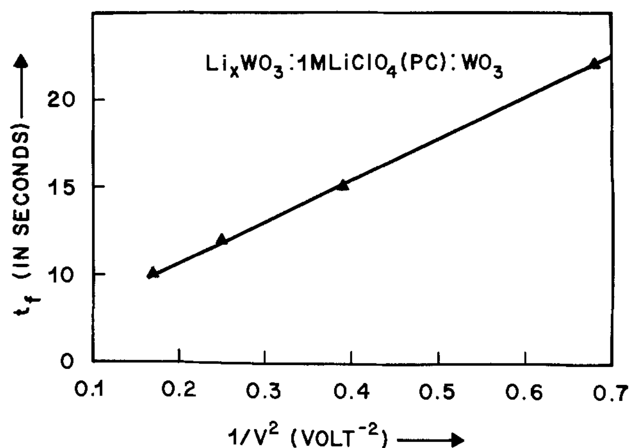

Fig. 4. Plot of response time t_f vs. $1/V^2$ for symmetric cells of Li_xWO_3.

of t_f *vs.* $1/V^2$ for symmetric cells of Li_xWO_3 is shown in Fig. 4, t_f being obtained from the intersection of the −¾ slope with the faster decreasing current slope toward the end of the bleach pulse. Therefore, in analogy with H_xWO_3, it seems appropriate to attribute a SCL current flow model to symmetric cells of Li_xWO_3. The electrochromic characteristic of symmetric cells is then essentially determined by the bleaching kinetics.

From bleaching experiments it is possible to calculate the Li^+ mobility according to Eq. [5]. The arguments given in the previous section make it likely that under the operating current conditions the films will be homogeneous in cation concentration. Using the data of Table II in Eq. [5] with $\epsilon = 50$ and $s = 2.8 \times 10^{-7}$ cm the values of $D = kT\mu/e$ have been calculated and are tabulated in Table I. It is seen that D_{Li^+} in WO_3 is about an order of magnitude smaller than the D_{H^+}. The decomposition potential of the 1M $LiClO_4$:PC electrolyte is 3V (with respect to SCE) compared to that of H_2SO_4:H_2O which is about 1.5V. Since bleaching response $t_f \propto 1/V^2$ it is possible to decrease the response time in the Li_xWO_3 electrochromic cell by increasing the bias voltage.

Constant current measurements.—Constant current measurements were carried out to determine the relationship between the optical density, O.D., and the injected charge. A linear relationship between the two would be expected since

$$\text{O.D.} = k(\lambda) Cl$$

where $k(\lambda)$ is the extinction coefficient, C the concentration of the absorbing species, and l the thickness of the sample. A plot of optical density as a function of injected charge is shown in Fig. 5 for Li_xWO_3 and H_xWO_3 for several current levels. The optical density was measured at a wavelength of 6300Å in the Cary spectrophotometer. Nonlinearity between O.D. and injected charge is observed for Li_xWO_3 beyond an O.D. $\simeq$ 1, whereas linearity up to 1.8 O.D. has been observed in the case of H_xWO_3. Not all the O.D. *vs.* injected charge points lie on the same line because of different film thicknesses.

It is important to note that there is a drop in O.D. with higher injected charge in the case of Li_xWO_3. If we take the apex of the O.D. curve at 35 mC/cm² a

Table II. Response of symmetric cells of H_xWO_3 and Li_xWO_3

Optical density	Cells	Applied bias (V)	Response time, t_f (sec)
0.6	H_xWO_3:10N H_2SO_4:WO_3	1	4
0.6	H_xWO_3:10% H_2SO_4-gylcerol:WO_3	1	40
0.6	Li_xWO_3:1M $LiClO_4$-PC:WO_3	1	40

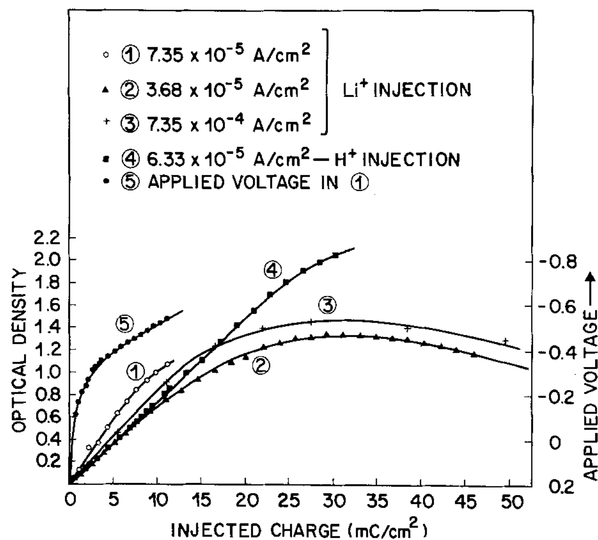

Fig. 5. Injected charge vs. optical density at various current levels for Li^+ and H^+ injection.

Li concentration $x = 0.39$ is calculated for a 3000Å thick film of Li_xWO_3. WO_3 films with $x < 0.4$ are blue in color and turn pink for $x > 0.4$. The optical absorption spectra taken with respect to an uncolored film are shown in Fig. 6. The films with $x > 0.4$ show an increasing absorption toward u.v. It should be mentioned that the extra peak around 1750 nm increased in intensity with increasing coloration (either by H^+ or Li^+). Whether it is a true absorption band or an interference effect is presently under investigation. Dickens and Whittingham (22) have given the stability phase fields of various alkali metal ion tungsten bronzes, according to which $0 < x < 0.4$ seems to be the existence region for Li_xWO_3. Recent emf measurements (20) also indicate a Li-rich phase in equilibrium with $Li_{0.4}WO_3$, supporting the results of galvanostatic measurements. Irreversible coloration at $x > 0.4$ does not pose a serious problem since for a reasonable contrast (O.D. ~0.6 at 600 nm for a film ~3000Å thick) an x value of 0.1 is sufficient.

Stability and response of the electrochromic films.— One of the primary concerns in the performance characteristics of electrochromic display is the long-term stability of the thin films and the persistence of open-circuit memory (long-term persistence of coloration). This is a particularly important consideration for the symmetric cell configuration. The two degradation processes so far as the storage life is concerned are: (*i*) dissolution of the WO_3 film in H_2O and H_2SO_4, and (*ii*) oxidation of M_xWO_3 by dissolved oxygen in the electrolyte.

Dissolution is a process of chemical attack. Thin films of WO_3 are normally attacked by H_2O. Therefore, the present trend in H_xWO_3 electrochromic cells is to use an organic solvent, glycerol or PVA (polyvinyl alcohol) (23, 24) to increase the stability of the film. Likewise, the aprotic Li electrolyte (1M $LiClO_4$ in PC) imparts greater stability to the WO_3 film. The role of dissolved oxygen in limiting the open-circuit memory of H_xWO_3 and Li_xWO_3 is shown in Fig. 7. All the films were colored at a constant current to the same optical density at 630 nm inside the Cary spectrophotometer. Then the optical density was recorded as a function of time. H_xWO_3 in the presence of O_2-saturated H_2SO_4 is unstable compared to H_2SO_4 saturated with argon. Li_xWO_3 was highly stable even in the oxygen-saturated electrolyte. Therefore, the stability of Li_xWO_3 is superior to that of its hydrogen counterpart.

The response times of some of the symmetric cells are tabulated in Table II. An optical density of 0.6 was arbitrarily chosen to give a reasonable contrast. It can be seen that H_xWO_3 with H_2SO_4-glycerol medium and Li_xWO_3 in 1M $LiClO_4$-PC medium have similar response characteristics at a given applied voltage. It should be pointed out that the fast responding cells with H_2SO_4-H_2O are not very stable. The response of the stable electrochromic cells of H_xWO_3 and Li_xWO_3 are essentially the same. An additional advantage in the case of Li_xWO_3 would be the low temperature operation of the cell because of the lower melting point of PC (−20°C) compared to H_2SO_4-glycerol cell (20°C).

Conclusion

Electrochromic coloration in Li_xWO_3 is governed by charge transport across the WO_3-electrolyte interface. Bleaching response of Li_xWO_3 is governed by a space charge limited current flow. The kinetics of symmetric Li_xWO_3 cells appear to be determined by the bleaching cycle, in analogy to H_xWO_3 cells. Galvanostatic measurements indicate a phase boundary of Li_xWO_3 at $x \sim 0.4$. Reversible coloration and bleaching of Li_xWO_3 can be obtained with lower concentrations of Li. Li_xWO_3 electrochromic cells have better memory and resistance to oxidation than its proton counterparts. The response times of stable electrochromic cells of H_xWO_3 and Li_xWO_3 are similar but the lower melting point of the electrolyte 1M $LiClO_4$-PC may facilitate the operation of Li_xWO_3 electrochromics at low temperature.

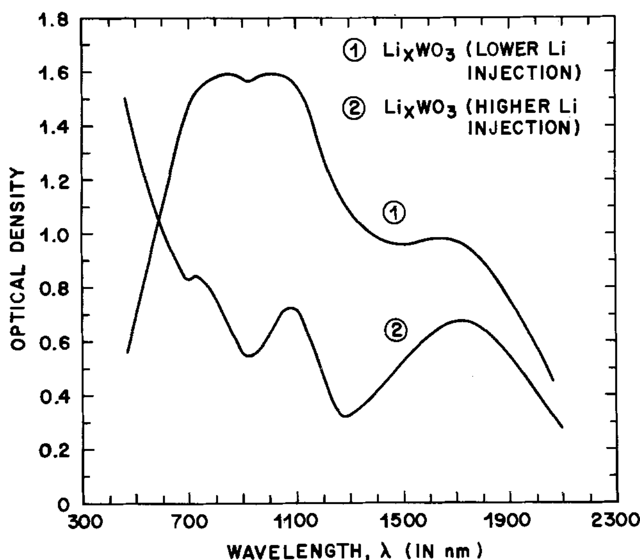

Fig. 6. Absorption spectra of Li_xWO_3 after the drop in optical density.

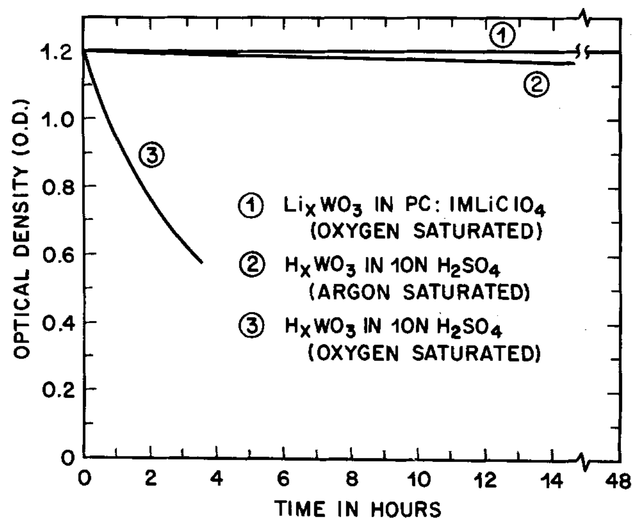

Fig. 7. Optical density change with storage time for H_xWO_3 and Li_xWO_3.

Acknowledgments

I wish to thank Drs. G. D. Boyd, R. A. Lemons, and S. Wagner for fruitful discussions and their useful comments on the paper, D. W. Doughty for preparing the thin films, and D. H. Olson for his constant help in preparing my experiments.

Manuscript submitted April 4, 1977; revised manuscript received Sept. 12, 1977. This was Paper 125 presented at the Philadelphia, Pennsylvania, Meeting of the Society, May 8-13, 1977.

Any discussion of this paper will appear in a Discussion Section to be published in the December 1978 JOURNAL. All discussions for the December 1978 Discussion Section should be submitted by Aug. 1, 1978.

Publication costs of this article were assisted by Bell Laboratories.

REFERENCES

1. B. W. Faughnan, R. S. Crandall, and P. M. Heyman, *RCA Rev.*, **36**, 177 (1965).
2. P. G. Dickens, J. H. Moore, and D. J. Neild, *J. Solid State Chem.*, **7**, 241 (1973).
3. M. A. Vanice, M. Boudart, and J. J. Fripiat, *J. Catal.*, **17**, 359 (1970).
4. P. G. Dickens, D. J. Murphy, and T. K. Halstead, *J. Solid State Chem.*, **6**, 370 (1973).
5. B. W. Faughnan, R. S. Crandall, and M. A. Lampert, *Appl. Phys. Lett.*, **27**, 275 (1975).
6. N. Nishimura, *Solid State Commun.*, **20**, 523 (1976).
7. J. F. Smith and G. C. Danielson, *J. Chem. Phys.*, **22**, 266 (1954).
8. R. S. Crandall and B. W. Faughnan, *Appl. Phys. Lett.*, **26**, 120 (1975).
9. R. S. Crandall and B. W. Faughnan, *ibid.*, **28**, 95 (1976).
10. I. F. Chang, B. L. Gilbert, and T. I. Sun, *This Journal*, **122**, 955 (1975).
11. P. G. Dickens and R. J. Hurditch, in "Chemistry of Extended Defects in Nonmetallic Solids," LeRoy Eyring and Michael O'Keefe, Editors, p. 555, North-Holland/American Elsevier, Amsterdam (1970).
12. G. Hollinger, J. M. Duc, and A. Deneuville, *Phys. Rev. Lett.*, **37**, 1564 (1976).
13. H. N. Hersh, W. E. Kramer, and J. H. McGee, *Appl. Phys. Lett.*, **27**, 646 (1975).
14. M. Green, W. C. Smith, and J. A. Weiner, *Thin Solid Films*, **38**, 89 (1976).
15. H. Witzke and S. E. Schnatterly, U.S. Pat. 3,840,-287 (1974).
16. J. O'M Bockris and A. K. N. Reddy, "Modern Electrochemistry," Vol. 2, chap. 8, Plenum Press, New York (1973).
17. P. Delahay, "New Instrumental Methods in Electrochemistry," chap. 3, Interscience Publishers, (1954).
18. R. Keller, J. N. Foster, D. C. Hanson, J. F. Hon, and J. S. Muirhead, NASA Rep., December 1968, Contract NAS3-8521.
19. H. S. Carslaw and J. C. Jaeger, "Conduction of Heat in Solids," 2nd ed., p. 112, Oxford University Press, Oxford (1959).
20. S. K. Mohapatra and S. Wagner, To be published.
21. T. C. Arnoldussen, Paper 199 presented at The Electrochemical Society Meeting, Las Vegas, Nevada, Oct. 17-22, 1976.
22. P. G. Dickens and M. S. Whittingham, *Quart. Rev. Chem. Soc.*, **22**, 30 (1968).
23. M. D. Meyers, U.S. Pat. 3,708,220 (1973).
24. D. J. Berets, U.S. Pat. 3,879,108 (1975).

Cathodoluminescence Measurement Techniques

Michael T. Stevens*

Zenith Radio Corporation, Glenview, Illinois 60025

ABSTRACT

A comparison is made of the three modes of cathodoluminescence excitation: continuous, pulsed, and raster. The proper excitation density needed to correctly analyze data obtained in each mode is discussed. The effects of a shrunken raster are investigated, and a new concept, multiexcitation, is presented. It is shown that the lack of correlation between brightness measurements made on small screens in demountable systems and full-size television picture tubes is due to multiexcitation. Furthermore, multiexcitation tends to linearize sublinear phosphors, such as the sulfides, masking their saturation at high excitation density. It is proposed that, to avoid multiexcitation, phosphor evaluation measurements be made with either pulsed or single line scan rasters.

Although the field of cathodoluminescence is quite old (Braun assembled the display device which bears his name back in 1897), and nonlinearities in the luminescence *vs.* excitation curves have been known for at least forty years, it is only recently that the necessity for more discriminating measurements of cathodoluminescent phosphors has been appreciated.

In the early days of cathodoluminescence, excitation was via a continuous stationary electron beam which was not necessarily even focused. It was soon discovered that a focused beam is capable of damaging the phosphor; the heat generated by the beam can physically destroy the screen. Thus, one had to either keep the beam intensity very low (which ruled out high intensity excitation experiments) or somehow modulate the excitation. Modulation could be achieved by pulsing the beam, thus decreasing the average power input to the phosphor by the duty factor. However, the average current and the average luminescence are also reduced, making them harder to measure. An alternative to time modulation is spatial modulation, *i.e.*, deflect the beam in a regular manner such that each phosphor crystallite is exposed to the electron beam for only a short fraction of the total time. This is achieved via a raster (as used in television) wherein the beam is swept over the screen in a series of scan lines.

We show that raster excitation is not the best scheme in terms of gaining knowledge about the physics of cathodoluminescence. We will also explain why there is, in general, no correlation between measurements made in demountable cathode ray tubes on small area screens and data on full-size picture tubes.

Statement of the Problem

In general, a cathodoluminescence experiment requires (*i*) excitation of a phosphor, (*ii*) measure-

* Electrochemical Society Active Member.

Key words: phosphors, multiexcitation, saturation properties, shrunken rasters.

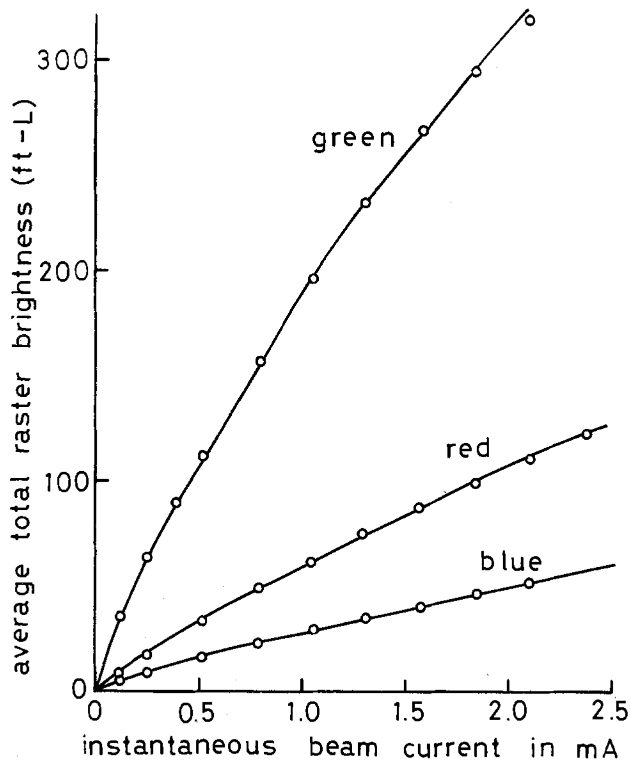

Fig. 1. Dependence of average total raster brightness (ft-L) on beam current (mA), measured on 19 in. cathode ray tubes with a full raster.

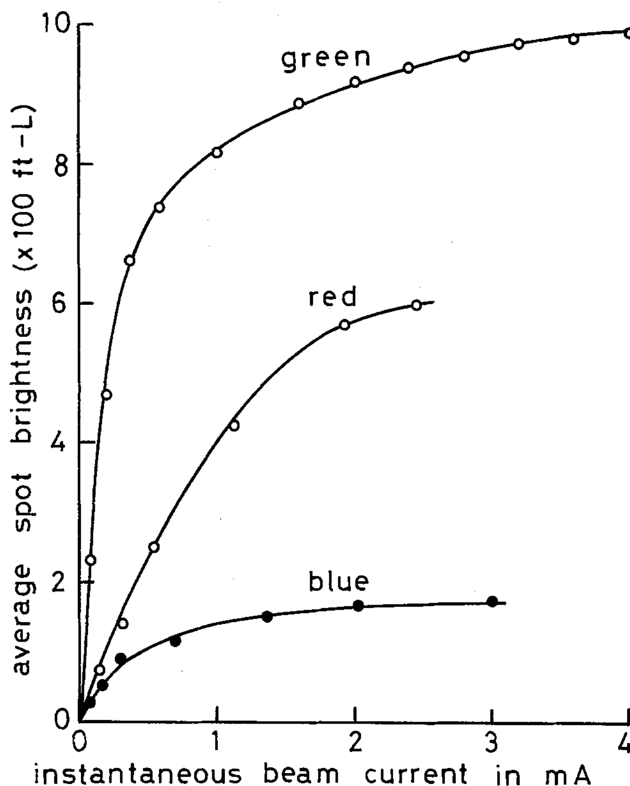

Fig. 2. Dependence of average spot brightness (ft-L) on beam current (mA), measured on 19 in. cathode ray tubes with a single line scan raster.

ment of the resulting luminescence, and (*iii*) interpretation of the results. Both excitation and measurement can be done by one of various techniques, each of which has its advantages and disadvantages, and the particular techniques utilized will influence the results and hence the interpretation.

In Fig. 1 and 2 we present data taken in our laboratory on brightness *vs.* excitation of the red (Y_2O_2S:Eu), blue (ZnS:Ag), and green (ZnCdS:Cu) phosphors used currently in color television picture tubes. (The data were taken on 19 in. tubes with aluminized screens.) The excitation is similar in both cases; only the optical measurement details differ. In Fig. 1 we show the dependence on beam current of the average raster brightness, *i.e.*, the time-averaged brightness of a phosphor screen excited by an electron beam swept across in a regular manner, as in a television display. It is obvious from the data that all three phosphors are reasonably linear; and one would never consider phosphor saturation as a cause of poor picture fidelity, or as being the culprit in gray scale imbalance.

In Fig. 2 we present a spot brightness measurement. This is done with a telephotometer capable of measuring the brightness of an area much smaller than a phosphor dot. Instead of a full raster, here only a single line scan per frame period was used. It is quite obvious that the luminescence is quite sublinear for all three color fields, and one could very easily draw the conclusion that all three phosphors are nonlinear.

The reason Fig. 1 and 2 present misleading results is that they present characteristics of the excitation-deflection-luminescence system, not merely of the phosphor. At high currents, the diameter of the electron beam increases; this causes the brightness data in Fig. 2 to be too low at high excitation levels, and hence, the rare earth red, which is known to be a linear phosphor, appears to be sublinear.

We can correct for the variation in beam diameter by utilizing the excitation density as the independent variable in a brightness *vs.* excitation curve. We shall assume a "pill-box" current distribution, *i.e.*, the current density is uniform over the entire beam. Although the excitation density calculated on the basis of this assumption will not be numerically correct, it will be proportional to the true value, and as such is sufficient for our purposes.

The spot brightness data of Fig. 2 can now be plotted *vs.* excitation density in Fig. 3. We see that the green and blue sulfides saturate at high excitation densities and the red rare earth phosphor remains linear.

Thus, we have shown that there is more than one way to make a cathodoluminescence measurement, and hence, it is quite possible to obtain more than one set

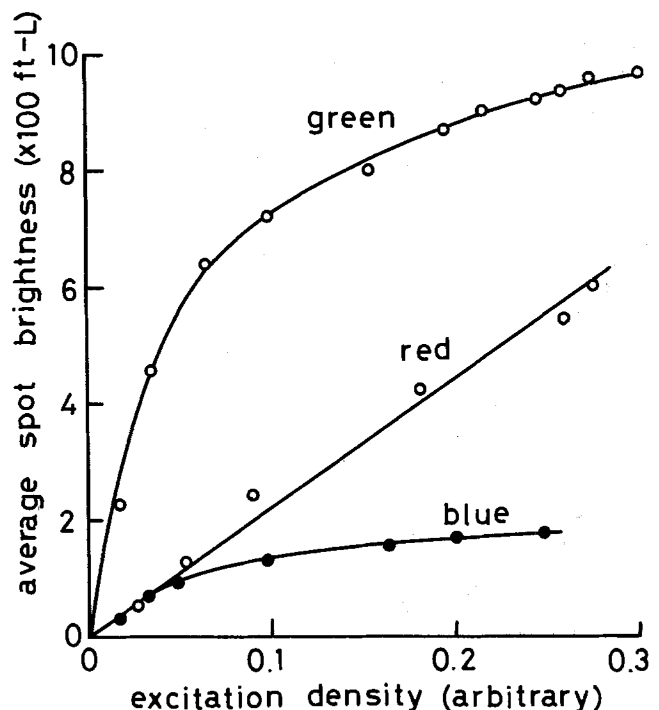

Fig. 3. Dependence of average spot brightness on beam excitation density, measured on 19 in. cathode ray tubes with a single line scan raster.

of data for a particular phosphor. The problem then can be stated in the following way: What is the difference between the various schemes of taking cathodoluminescence data, and which method is the best in terms of understanding phosphor physics?

Excitation Techniques

Three excitation methods currently in use are continuous (or d.c.), pulsed, and raster. The first two are really defined by the characteristic times of the phosphor under study: the rise and decay times of the phosphor must be compared to the excitation pulse length and the period between pulses. These characteristic times can vary from nanoseconds for flying spot scanner phosphors, to microseconds for the materials used in television picture tubes, to milliseconds for oscilloscope phosphors, and to seconds for day-glow phosphors.

To simplify matters, we will consider only those cases where the phosphor rise and decay times are both very short compared to the time between excitation pulses. (One can always arrange an experiment such that this requirement is met.) Then, depending on whether the duration of excitation, *i.e.*, the excitation pulse length, is long or short compared to the phosphor response time, *i.e.*, the phosphor rise time, one has either continuous or pulsed excitation, respectively. We note that a cathode ray tube capable of generating a fixed pulse length electron beam will excite some materials in a pulsed mode and others continuously. It is obvious that the approximations which are possible at these two extreme cases are not valid if the excitation time is the same as the response time of the phosphor. This does not mean that such a situation is not amenable to interpretation, only that interpretation is more difficult. This also holds if the simplifying assumption made above is invalid.

In continuous excitation, a steady-state condition is achieved wherein a constant fraction of the luminescent centers in the phosphor are in an excited state at all times. As excited centers decay (radiatively or nonradiatively), other centers are excited from the ground state by the incident electron beam. Hence, the required input parameter is current density j, which is a measure of the time rate of incident electrons.

In pulsed excitation, the input parameter of interest is charge density, σ. Because the entire excitation takes place in a very short time, the phosphor does not begin to respond to the incident electron beam until the pulse has ended. Thus, the details of the electron beam pulse waveshape are unimportant; the only meaningful measure of excitation is the integral

$$\sigma = \int_{\tau} j \, dt \quad [1]$$

Then, provided the excitation duty factor is low enough, we can conceive of the phosphor as being suddenly excited as the entire charge of the pulsed electron beam is dumped into the crystallites all at once, and then slowly relaxing as the phosphor luminesces and returns to the ground state.

Let us now turn our attention to raster excitation. This is a variant of pulsed excitation which is different enough to warrant special treatment. Rasters are technologically important (as in television) and are easy to generate. A raster is also an easy method of exciting a phosphor screen to uniform brightness. Each phosphor crystallite is excited by the electron beam as it is swept past, so in effect the excitation is a pulse of length τ where

$$\tau = d/v \quad [2]$$

d is the electron beam diameter and v the velocity of the scanned beam. For typical television rasters, this is in the submicrosecond range. Each element of the phosphor screen is excited at a different time, and the light output of the screen appears constant. Hence, a

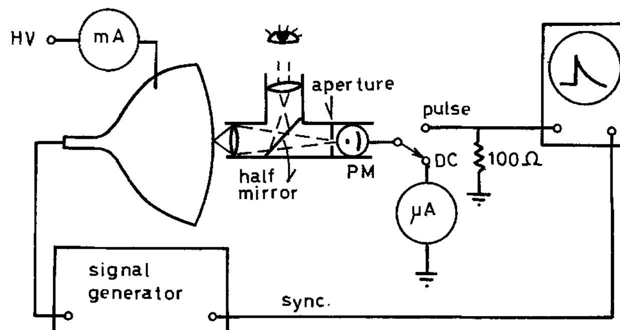

Fig. 4. Experimental arrangement for observing time-averaged and time-resolved luminescence.

measurement of the luminescence of a large area of the screen will show minimal time dependence; if the photodetector can see the entire raster the sensor output will be essentially constant. If, however, the photodetector is illuminated by only a very small region of the screen (smaller than the diameter of the electron beam) then the output signal will be a pulse.

Figure 4 shows the experimental arrangement used to measure the luminance of a phosphor screen. The brightness is measured in relative units by the photomultiplier; the microammeter measures the ordinary time-averaged brightness and the oscilloscope displays the time-resolved brightness. The microscope allows one to measure the brightness of a small region of one phosphor dot; this we call the spot brightness. When the microscope is not present, the photomultiplier measures the brightness over many phosphor dots; we call this the raster brightness. In a television display, the viewer sees the raster brightness. The spot brightness, the brightness of an infinitesimally small area, is needed for analytical purposes if one is to understand the phosphor contribution to the display system.

Excitation Density

We can compute the excitation density for each of the three modes for two different assumed current profiles. We will consider a "pill-box" current distribution and a Gaussian, as shown in Fig. 5.

A word on notation: The first subscript indicates the mode of excitation (continuous, pulsed, or raster), and the second specifies the assumed current profile (pill-box or Gaussian). The radial distance from the center of the beam is r, and the parameter a is the usual measure of width of the Gaussian. The observed electron beam diameter is d.

If the total beam current is i, then for the pill-box

$$j_{cp} = \frac{4}{\pi} \frac{i}{d^2} \quad [3]$$

and for the Gaussian

$$j_{cg} = \frac{i}{\pi a^2} \exp\left[-(r/a)^2\right] \quad [4]$$

These are the excitation densities for continuous excitation.

When $r = 2a$, the exponential term is 0.018, so we will define the effective radius of the Gaussian distribution as $2a$. Hence we have

$$j_{cg} = \frac{16}{\pi} \frac{i}{d^2} \exp\left[-(4r/d)^2\right] \quad [5]$$

which for

$$4r/d < 0.1$$

i.e., at the center of the beam, reduces to

$$j_{cg} = \frac{16}{\pi} \frac{i}{d^2} \quad [6]$$

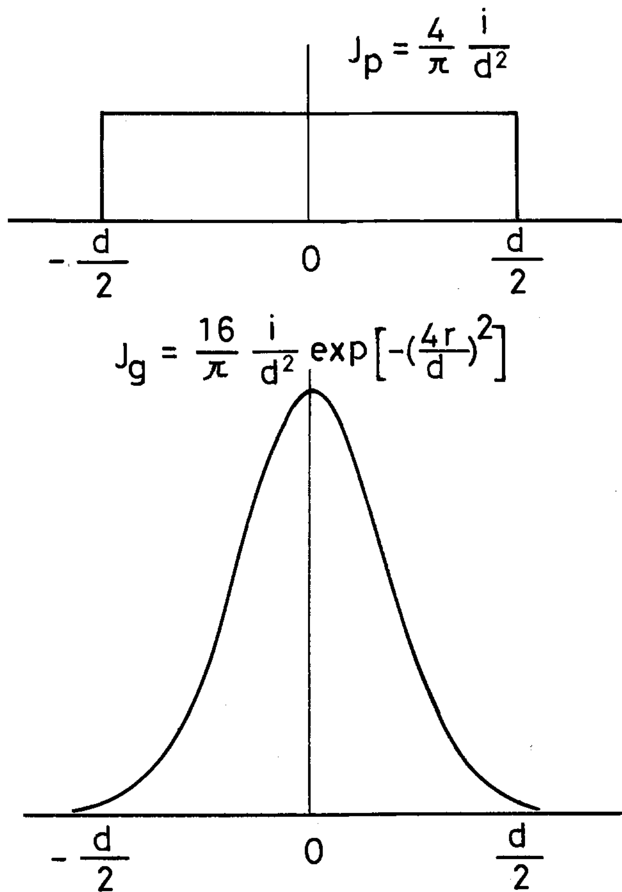

Fig. 5. Current density distributions for a pill box model (top) and a Gaussian (bottom).

For pulsed excitation, the excitation density is the time integral

$$\sigma_p = \int_\tau j\, dt \qquad [7]$$

which, for the pill-box distribution is

$$\sigma_{pp} = \frac{4}{\pi}\frac{i}{d^2}\tau \qquad [8]$$

and is

$$\sigma_{pg} = \frac{16}{\pi}\frac{i}{d^2}\tau \qquad [9]$$

for the Gaussian.

For raster excitation, one performs an integration

$$\sigma_r = \int_{d/v} j\, dt = \int_d \frac{1}{v} j\, dx \qquad [10]$$

which is (for the pill-box)

$$\sigma_{rp} = \frac{4}{\pi}\frac{i}{vd} \qquad [11]$$

where v is the beam-scanning velocity. For the Gaussian

$$\sigma_{rg} = \frac{4}{\sqrt{\pi}}\frac{i}{vd}\exp\left[-(4y/d)^2\right] \qquad [12]$$

which, for

$$4y/d < 0.1$$

reduces to

$$\sigma_{rg} = \frac{4}{\sqrt{\pi}}\frac{i}{vd} \qquad [13]$$

The functional dependence of excitation density on the beam diameter is independent of the assumed distribution. The excitation densities for pulsed and raster excitation differ in their dependence on beam diameter, as in the latter the beam is integrated as it sweeps past the phosphor crystallite being studied.

Inspection of the expressions above shows that for continuous and pulsed excitation, the peak value for the Gaussian is four times that of the pill-box model. For a typical high resolution 19 in. color television picture tube, which has a 1 mm diam spot at a beam current of 1 mA, the current density is 127 mA/cm^2 for an assumed pill-box distribution, and for a Gaussian, the peak current density is over 500 mA/cm^2. For raster excitation, the density for the Gaussian is only $\sqrt{\pi} = 1.77$ times the pill-box value. For the same 19 in. tube, the charge density is therefore 1.91×10^{-8} C/cm^2 for the pill-box model and 3.39×10^{-8} C/cm^2 for the Gaussian.

Multiexcitation Effects in Raster Excitation

There is one complication in raster excitation; this is related to the fact that the distance between scan lines of the raster is not unique. By making appropriate adjustments in the vertical and horizontal deflection fields it is possible to change the size and shape of a raster by an arbitrary amount. The raster brightness will, of course, vary inversely with raster size. Figure 6 shows such behavior. At each value of beam current, as the size of the raster is reduced, the raster brightness goes up. In Fig. 7 we present spot brightness data. The curves are roughly similar to the raster brightness curves, but there is a sharp break in each curve at which the slope changes. This is indicated by the dashed line. This change in slope indicates that two processes may be at work.

To separate these two processes, we show in Fig. 8 the spot brightness as separate functions of raster width and raster height. In the upper set of curves, where only the raster width has been changed, there

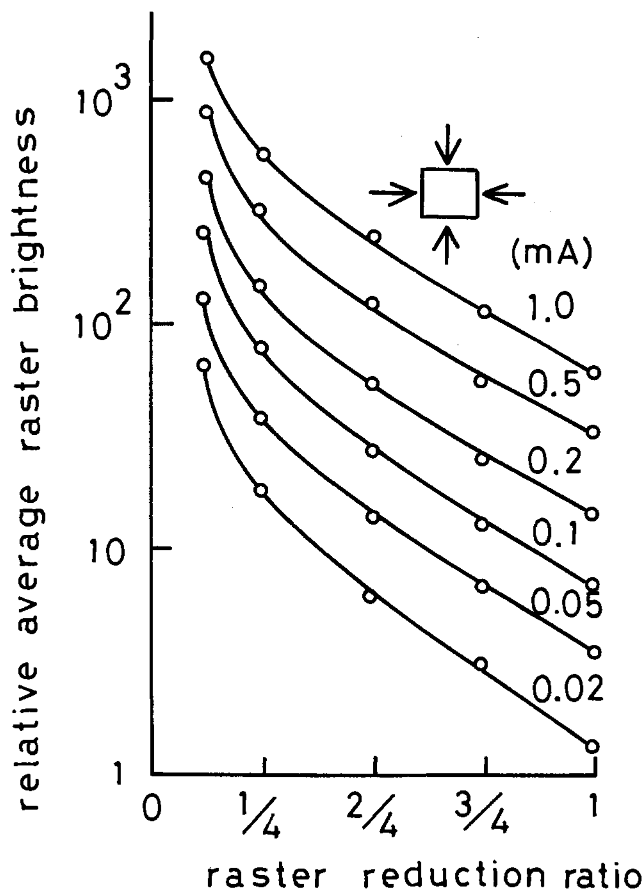

Fig. 6. Dependence of average raster brightness on raster size, simultaneous variation of raster height and width, on 19 in. tube.

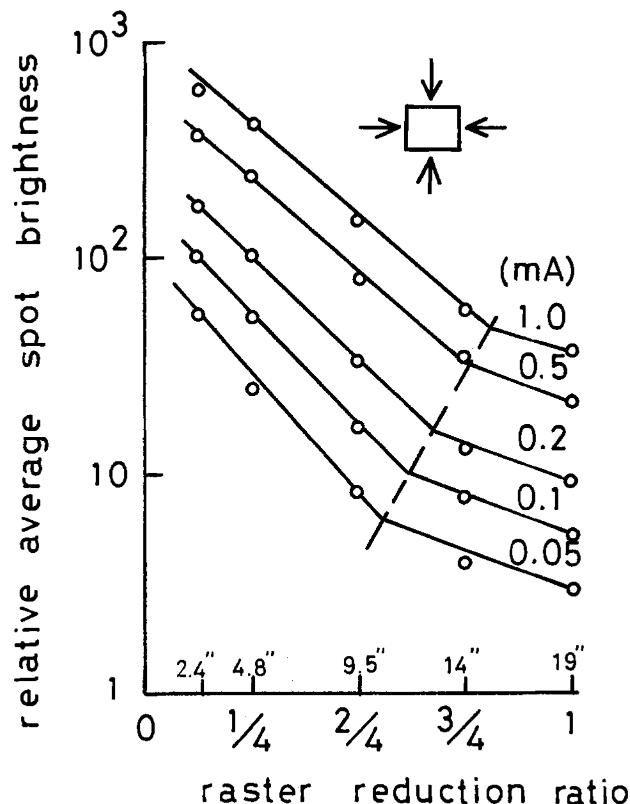

Fig. 7. Dependence of average spot brightness on raster size, simultaneous variation of raster height and width, on 19 in. tube.

is only one slope, indicating only one process. The slope is essentially that of the right-hand lines in Fig. 7. As the raster width is decreased, because the time per scan line is fixed, the beam scanning velocity decreases also, so the effective pulse length of the beam as it excites the small area under study increases. Thus, the increase in brightness as the raster width is reduced is due to the increase in the total time during which the phosphor is excited.

Let us now look at the way the slope changes when the raster height is changed. For small reductions there is no change in spot brightness, but upon further reduction the slope increases, and this increase is sharper than for the same relative decrease in raster width. The explanation is as follows: for a given electron beam current, as the raster height is reduced, the vertical separation between the horizontal scanning lines becomes smaller. If the electron beam diameter is less than this distance there is no effect, and there is no change in the spot brightness. However, when the beam diameter is greater than the raster-line spacing, *i.e.*, when the ratio of the diameter to the spacing is greater than unity, the phosphor dot will be excited more than once per frame period, and the spot brightness will increase. The greater the ratio, the greater the increase in spot brightness. The ratio can be increased either by reducing the raster height or by enlarging the electron beam diameter. Because the beam diameter increases with current, the onset of multiple excitation occurs sooner at higher currents. This multiple excitation phenomenon can be visualized by studying the idealized spot brightness waveshapes of Fig. 9. The upper part shows the photodetector output for a single excitation per frame time, while the lower sketch indicates five excitations per frame. The middle pulse is the result of the center of the electron beam passing the screen element under observation; the two to the left are due to excitation by the bottom of the two previous scans and the two peaks to the right are due to excitation by the top of the next two scans.

A family of oscillograms of the time resolved brightness curves is shown in Fig. 10. The upper left corner

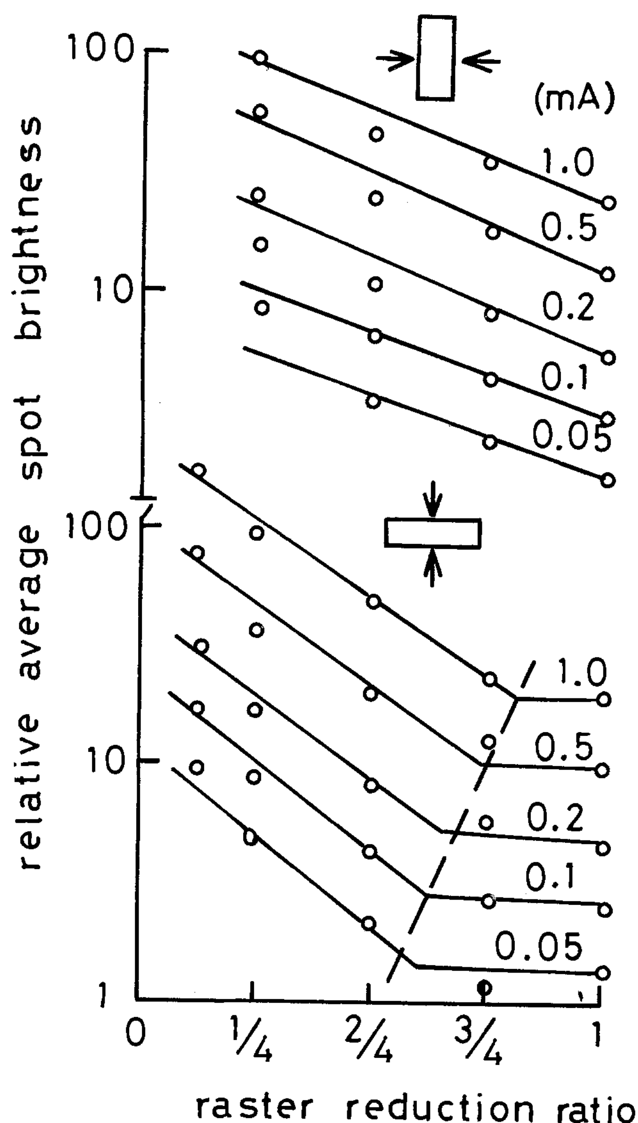

Fig. 8. Dependence of average spot brightness on raster width at full height (top), and on raster height at full width (bottom), on 19 in. tube.

shows one excitation per frame time for the conditions of low current (and hence small beam diameter) and full raster (when the vertical separation between adjacent scan lines is the largest). The photographs clearly show the onset of multiexcitation as the beam current increases and/or the raster size is reduced.

From the viewpoint of the television design engineer, when the degree of multiexcitation is excessive, picture quality will be reduced. From the viewpoint of phosphor physicists who make cathodoluminescence measurements using shrunken rasters, results may be meaningless unless the degree of multiexcitation and current density are specified.

In typical demountable cathode ray tubes, the sample area (which is the same as the raster area) is 10 cm^2 or less, the beam diameter is about 0.1 cm, yielding an effective pulse length of 1.5 μsec, and there may be 100 scan lines per centimeter. This can be compared with a 19 in. color picture tube, which has an area of 1200 cm^2, the same beam diameter of 0.1 cm, an effective pulse length of 150 nsec, and only 8 scan lines per cm.

This then is the reason why there is typically no correlation between demountable tube measurements and data taken on full-size picture tubes. As was shown in Fig. 10, the full size raster will show no multiexcitation effects, whereas the demountable raster, which is about one-tenth full size, will show considerable multiexcita-

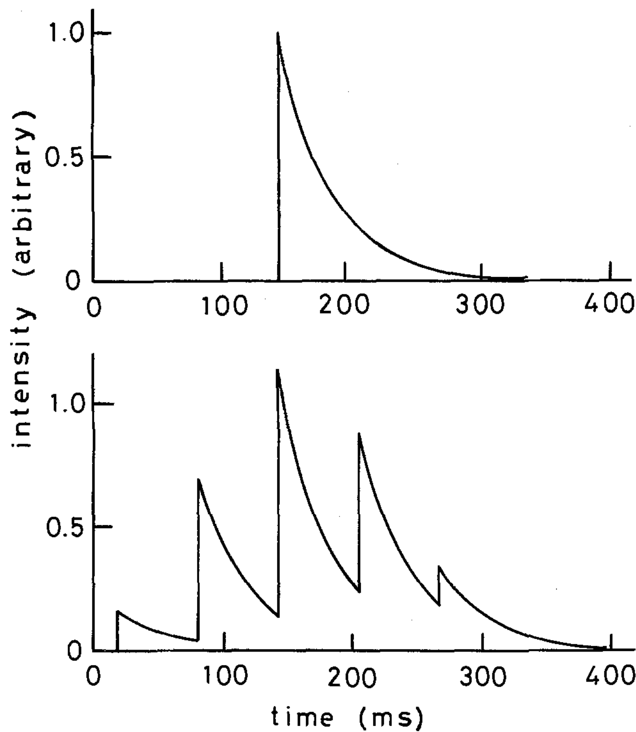

Fig. 9. Idealized time-resolved luminescence without (top) and with (bottom) multiexcitation.

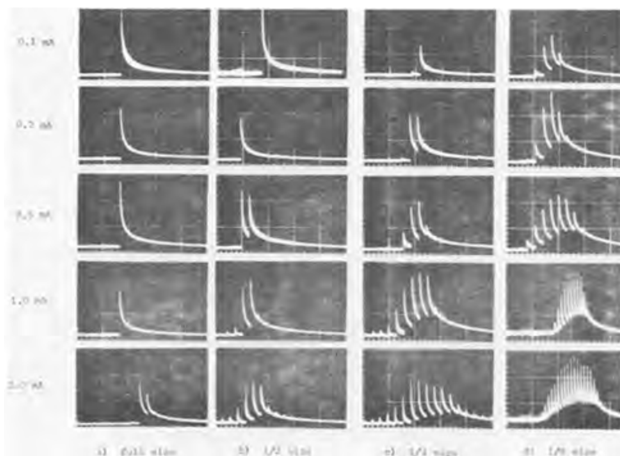

Fig. 10. Actual time-resolved luminescence curves for a 19 in. cathode ray tube at various raster sizes and beam currents.

tion. It is found that multiexcitation tends to linearize raster brightness data, and hides the true degree of saturation (or sublinearity) of the phosphor. In addition, the effective pulse length in the small raster excitation is an order of magnitude longer than in the large area raster, making the impulse approximation invalid for many phosphors.

Determination of Beam Current Density

To calculate the current density requires a knowledge of the current profile, which is determined by the electron gun. The electron beam "diameter" is usually determined by visual observation of the light spot produced by a phosphor. It is possible to use the profile of the oscillograms of a multiply excited phosphor screen to calculate the profile of the electron beam. Figure 11 shows oscillograms of electron beams of different beam profiles, which were created by deliberately defocusing the beam. The envelope of the pulses in the oscillogram is a representation of the electron beam profile, and by an appropriate analytical treatment the beam shape can be extracted. Figure 12 shows a comparison of the beam "diameters" obtained by visual observation (through a telescope) and from multiple excitation oscillograms.

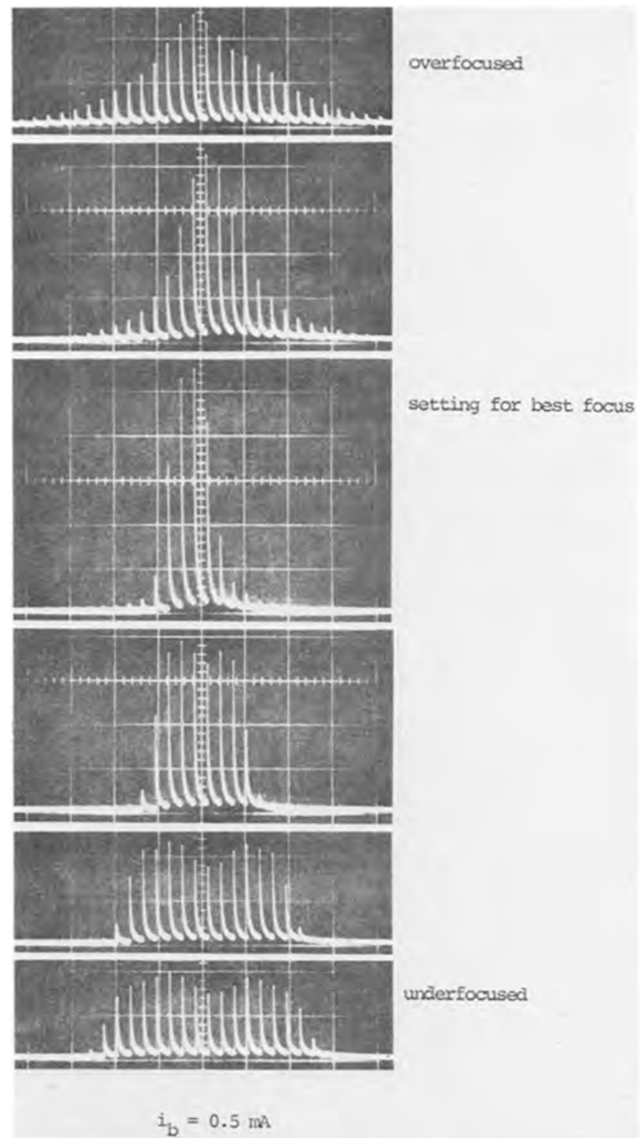

Fig. 11. Multiexcitation effects for a 19 in. cathode ray tube under conditions of focus (center) and defocus (top and bottom).

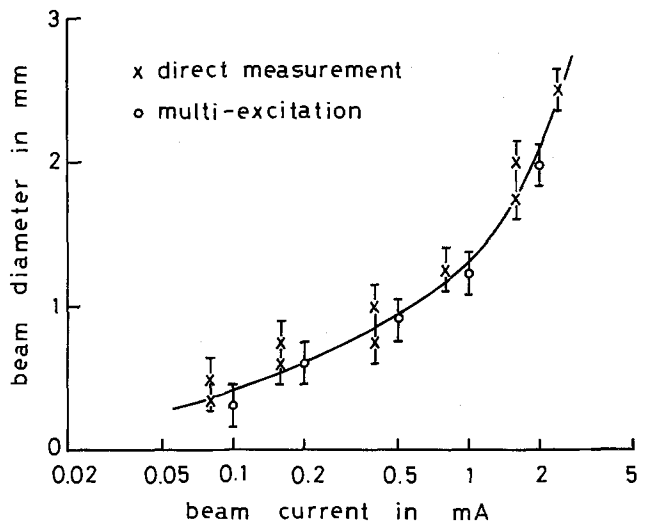

Fig. 12. Dependence of beam diameter upon beam current for a 19 in. cathode ray tube, measured either directly with a microscope or inferred from the number of multiexcitation pulses in a 1/10 height, full-width raster.

One point commonly overlooked is the question of how to define current density. The phosphor crystallites are exposed to an instantaneous current density given by (assuming a "pill-box" current distribution)

$$j = \frac{4}{\pi}\frac{i}{d^2} \quad [14]$$

A common error is to call

$$j' = \frac{i}{A} \quad [15]$$

(where A is the raster area) the current density, while in actuality it is the time-averaged current density. This is not the value to which the phosphor responds. The instantaneous value j, or the integral $\sigma = \int j\,dt$, are the only meaningful quantities if one wishes to study phosphor physics.

Conclusion

Thus we have seen that in a raster excitation experiment, multiexcitation can cause a considerable effect. Any experiment which permits multiexcitation to occur will yield misleading results, as the current density of the excitation pulse will be unknown and the number of excitation pulses per frame will vary as the beam current, and hence beam diameter, varies. It should be pointed out that a raster-scanning experiment wherein only raster brightness measurements are made cannot be properly used even for crude evaluation experiments, for the degree of nonlinearity differs for various phosphors, preventing any comparison, even if the same excitation means (electron gun, deflection yoke, etc.) are used. Hence raster brightness measurements are a poor way to characterize cathodoluminescent phosphors: a much more meaningful technique is a spot brightness measurement as a function of beam excitation density on a single line scan raster, or on a stationary pulsed beam (meeting the criteria discussed above) as a function of current density.

Acknowledgment

The author acknowledges helpful discussions with H. N. Hersh and L. Ozawa, the assistance of G. Ban, and the encouragement of G. E. Weibel in the work presented here.

Manuscript submitted July 15, 1977; revised manuscript received Oct. 5, 1977.

Any discussion of this paper will appear in a Discussion Section to be published in the December 1978 JOURNAL. All discussions for the December 1978 Discussion Section should be submitted by Aug. 1, 1978.

Publication costs of this article were assisted by Zenith Radio Corporation.

Preparation of Pure and Doped Silicon Carbide by Pyrolysis of Silane Compounds

W. von Muench* and E. Pettenpaul

Institut A für Werkstoffkunde, Technische Universität, D-3000 Hannover, Germany

ABSTRACT

Polycrystalline β-SiC is prepared from three different silane compounds (methyl-trichlorosilane, dimethyl-dichlorosilane, and trimethyl-chlorosilane) by the van Arkel process. The influence of the growth parameters (flow rates, vapor pressures, and deposition temperature) on the growth rate and the stoichiometry of the deposit is investigated. The most satisfactory results in terms of stoichiometry are obtained in the 1400°-1600°C temperature range. Doping is accomplished by adding trimethyl-aluminum and diborane. The 6H silicon carbide crystals are grown by the sublimation technique using doped and undoped polycrystalline material.

The 6H polytype of silicon carbide is considered a potentially useful material for special semiconductor devices, *e.g.*, for light-emitting diodes, high temperature rectifiers, and avalanche diodes. The 6H silicon carbide crystals for electronic applications are produced by sublimation of polycrystalline silicon carbide or elementary silicon and carbon at temperatures around 2500°C (Lely process). In most cases, so far, commercial (green or black) grinding powder has been used as a feed material (1-3); the synthesis from the elements is generally less efficient in terms of crystal size and perfection. With the grinding powder, however, a large amount of various impurities is introduced into the growth system. The resulting (n- or p-type) crystals, therefore, contain compensating (acceptor or donor) impurities and also deep traps. These crystals cannot be directly used for junction formation in most applications. They may serve as a substrate material for VPE or LPE processes; some impurity transfer (autodoping) from the substrate to the epitaxial layer then must be taken into account (4).

The realization of blue light-emitting diodes with a rather high efficiency has prompted the present investigation on the preparation of polycrystalline silicon carbide as a starting material in the Lely process (5). Previous studies on vapor-phase reactions involving silicon carbide were performed with emphasis on single crystal growth of different polytypes (6-13). Knippenberg, Kapteyns, and Hagen were the first to introduce presynthesized (CVD) silicon carbide in the Lely process (14, 15); this material was obtained with a methyl-dichlorosilane source at a low deposition rate (3g/hr). The main purpose of this study is the optimization of the growth rate, the yield, and the stoichiometry of the vapor-grown material. This has been accomplished by proper reactor design, choice of reactants, and deposition conditions. In addition, some observations on the surface morphology are included.

A major problem in the Lely process is the reproducibility of the incorporation of acceptors (mainly aluminum and boron). Previously, these dopants have been added in solid form to the (undoped) feed mate-

* Electrochemical Society Active Member.
Key words: silicon carbide, van Arkel process, methyltrichlorosilane, dimethyl-dichlorosilane, trimethyl-chlorosilane.

rial in the Lely process. It is difficult, however, to obtain uniformly doped crystals in this manner, because of large differences in the vapor pressures of the dopants and the dissociation products of silicon carbide. This problem can be overcome by introduction of dopants during the pyrolysis of the silane compounds. Doping with diborane and trimethyl-aluminum has been investigated in this study.

Experimental

The principle of the van Arkel process is shown in Fig. 1a. Details of the reaction chamber can be seen in Fig. 1b. The (water-cooled) base plate is made from silver-plated copper, the current leads and the gas inlet (nozzles) are of pure silver. It is important that the gas streams ejected from the nozzles are hitting both carbon heater rods uniformly and with high velocity. This can be accomplished by appropriate shaping and adjustment of the nozzles. The carbon rods (6 mm diam, 150-300 mm length) are heated with a.c. under constant voltage conditions. Exact measurements of the temperature (by pyrometry) are possible only in the initial stage of the growth experiment, since reaction by-products are deposited at the inside of the quartz bell jar. It is estimated that the surface temperature of the silicon carbide decreases by about 100°C during the 6 hr growth period. The reaction chamber is carefully evacuated and flushed with pure hydrogen (50 min, at least) before each run. The deposition takes place in hydrogen at atmospheric pressure.

The carrier gas can be saturated with silane compounds kept at (thermostatically controlled) temperatures in the 13°-35°C range. The following compounds have been used: methyl-trichlorosilane, CH_3SiCl_3

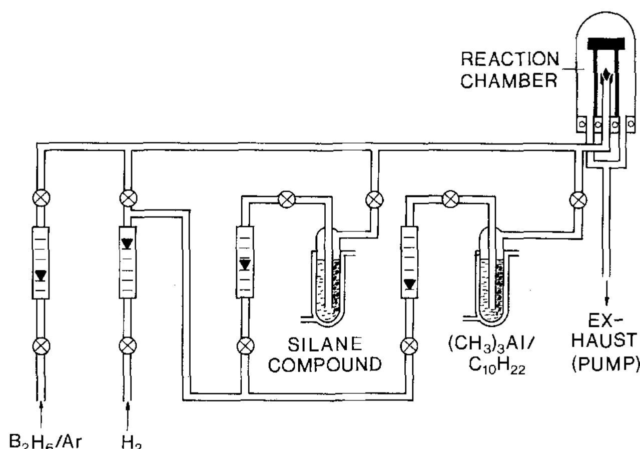

Fig. 1a. Apparatus for the growth of doped and undoped silicon carbide by the van Arkel process.

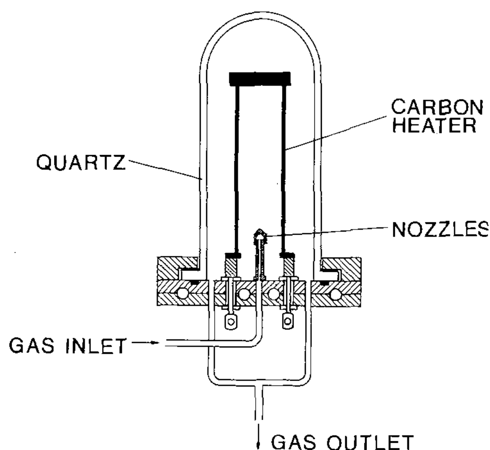

Fig. 1b. Design of reaction chamber

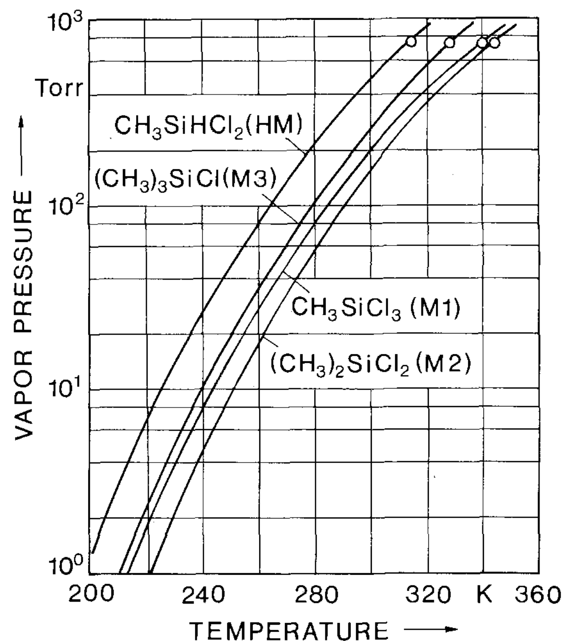

Fig. 2. Vapor pressure of silane compounds. From Landolt-Börnstein (16).

(M1); dimethyl-dichlorosilane, $(CH_3)_2SiCl_2$ (M2); and trimethyl-chlorosilane, $(CH_3)_3SiCl$ (M3). The vapor pressures of these compounds are shown in Fig. 2. The use of methyl-dichlorosilane (HM) appears to be impractical, due to the high vapor pressure at room temperature.

Doping of polycrystalline material with boron is accomplished by adding a metered flow of diborane (diluted in argon) during the deposition cycle. A separate bubbler containing a 10-20% solution of trimethyl-aluminum in n-decane ($C_{10}H_{22}$) serves as the source for aluminum doping; the vapor pressure of n-decane is negligible in the temperature range involved.

The carbon rods and excess carbon (if any) are removed by heat-treatment in oxygen. Any excess of silicon is removed by evaporation in vacuum. Thus, both an excess of carbon and an excess of silicon can be determined quantitatively by simple gravimetric means.

The silicon carbide rods (doped and undoped) are broken into lumps of suitable size and cleaned in hydrofluoric acid. These lumps serve as a feed material for the modified Lely process described previously (5, 14). The 6H silicon carbide crystals are obtained in the form of platelets with flat surface perpendicular to the c-axis. Hall and resistivity measurements are performed by the van der Pauw method.

Growth of Polycrystalline SiC

The growth of polycrystalline silicon carbide from silane compounds can be described in terms of the following reactions (17). At low temperatures (~ 1200°C)

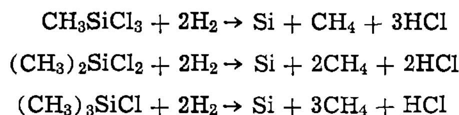

$$CH_3SiCl_3 + 2H_2 \rightarrow Si + CH_4 + 3HCl$$
$$(CH_3)_2SiCl_2 + 2H_2 \rightarrow Si + 2CH_4 + 2HCl$$
$$(CH_3)_3SiCl + 2H_2 \rightarrow Si + 3CH_4 + HCl$$

$$CH_4 \rightarrow C + 2H_2$$

$$Si + C \rightarrow SiC$$

At high temperatures (~ 1800°C)

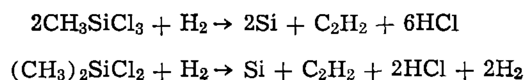

$$2CH_3SiCl_3 + H_2 \rightarrow 2Si + C_2H_2 + 6HCl$$
$$(CH_3)_2SiCl_2 + H_2 \rightarrow Si + C_2H_2 + 2HCl + 2H_2$$

$$2(CH_3)_3SiCl + H_2 \rightarrow 2Si + 3C_2H_2 + 2HCl + 6H_2$$

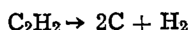

$$C_2H_2 \rightarrow 2C + H_2$$

$$Si + C \rightarrow SiC$$

In the intermediate temperature range both methane and acetylene can be formed.

The amount of excess silicon or carbon resulting from the above reactions is dependent on the silane composition and the growth temperature. As shown in Fig. 3, an essentially stoichiometric growth of silicon carbide is possible with all three silane compounds in the 1450°-1550°C temperature range. Methyl-trichlorosilane (M1) yields a relatively large excess of silicon at temperatures below 1400°C. The results obtained with dimethyl-dichlorosilane (M2) and trimethyl-chlorosilane (M3) are quite similar in the 1400°-1500°C temperature range.

The temperature dependence of the over-all growth rate is shown in Fig. 4. With the process parameters fixed as follows: bubbler temperature, 12°C; bubbler flow rate, 60 liters/hr; and total flow rate, 300 liters/hr; one obtains the highest deposition rate with silane M3 (15 g/hr at 1600°C) due to the high vapor pressure of this compound (see Fig. 2). The deposition rates achieved with the silane compounds M1 and M2 are quite similar (6 g/hr. approximately). These figures are valid for a simultaneous deposition on two carbon rods of 150 mm length each. The yield can be increased by 50%, approximately, by using carbon rods of 300 mm length.

A higher growth rate can also be achieved by increasing the bubbler flow rate, at the expense of the bypass flow. An example is shown in Fig. 4 (top curve) for silicon carbide growth using silane M2 (bubbler flow rate 100 liters/hr, no bypass).

Figure 5 demonstrates the influence of the growth temperature on the morphology of silicon carbide (with excess silicon or carbon) produced from dimethyl-dichlorosilane. High density material with small grain size and uniformly distributed excess silicon is obtained at low temperatures. The grain size increases with increasing growth temperature. The excess carbon which is formed at temperatures above 1600°C, is concentrated mainly between particles of silicon carbide. Similar results are obtained with the other silane compounds.

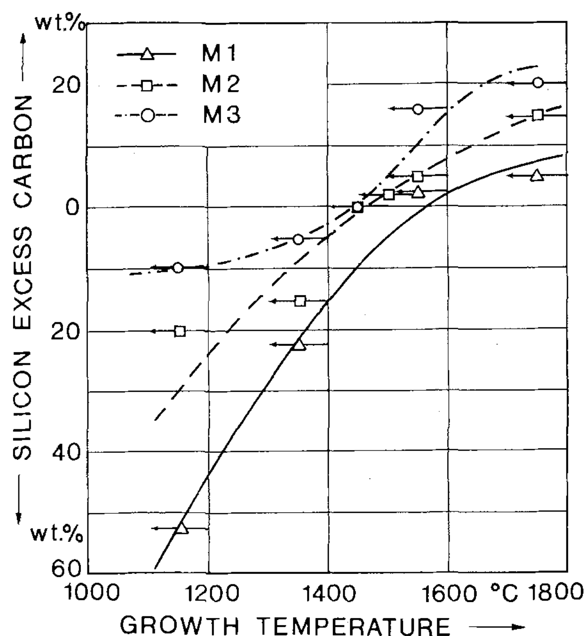

Fig. 3. Deviation from stoichiometry (excess carbon or silicon) vs. growth temperature. Arrows are pointing from the initial growth temperature to the (estimated) temperature at the end of the growth process.

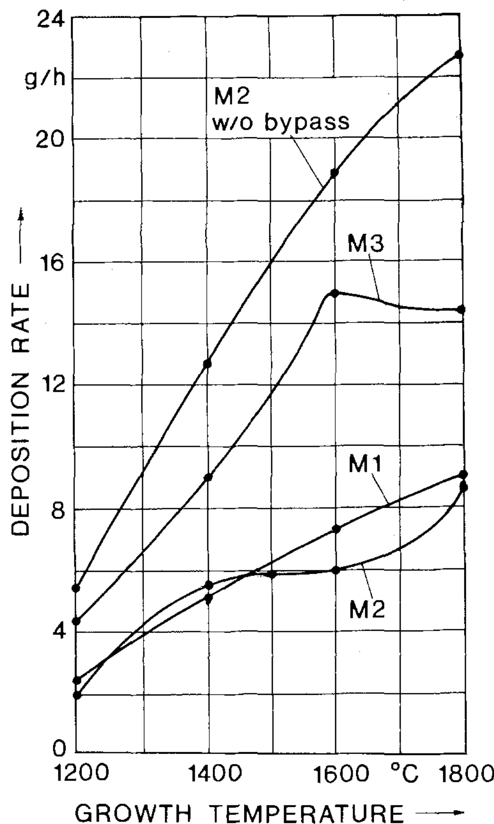

Fig. 4. Temperature dependence of the over-all growth rate. (See text for other growth parameters).

The influence of various process parameters (silane temperature, gas flow) on the growth rate is shown in Fig. 6. As expected, there is a monotonic increase of the growth rate with increasing saturation temperature (silane vapor pressure, Fig. 6a). A higher growth rate can also be achieved by increasing the flow rate through the silane bubbler (Fig. 6b). At flow rates exceeding 60 liters/hr, however, there is only a small further increase of the growth rate. The dependence of the growth rate on the total hydrogen flow (bubbler plus bypass) is shown in Fig. 6c. There is a maximum at 300 liters/hr. Obviously, the deposition reaction will be incomplete if the gas velocity in the vicinity of the carbon rods is too high.

Properties of Silicon Carbide Crystals Grown from the Van Arkel Material

The 6H silicon carbide crystals have been grown by the sublimation technique (Lely process) using commercial "green grit" abrasive and silicon carbide synthesized by the van Arkel process. The electronic properties of these crystals are summarized in Table I. Crystals grown from the abrasive powder are usually p-type and highly compensated; the hole mobility is in the 10-15 cm^2/V sec range. An addition of nitrogen during the Lely process yields n-type crystals with a mobility around 120 cm^2/V sec. Crystals grown from undoped van Arkel material are n-type, with a mobility up to 200 cm^2/V sec. Doping with aluminum and boron has been achieved by adding trimethylaluminum and diborane during the van Arkel process. Using 10 and 20% solutions of $(CH_3)_3Al$ in $C_{10}H_{22}$ (n-decane), hole concentrations between 10^{16} and 10^{18} cm^{-3} have been obtained. The mobility is in the range from 10 to 35 cm^2/V sec.

The dependence of the hole concentration on the partial pressure of the dopant during the van Arkel process is shown in Fig. 7. There is a linear relation-

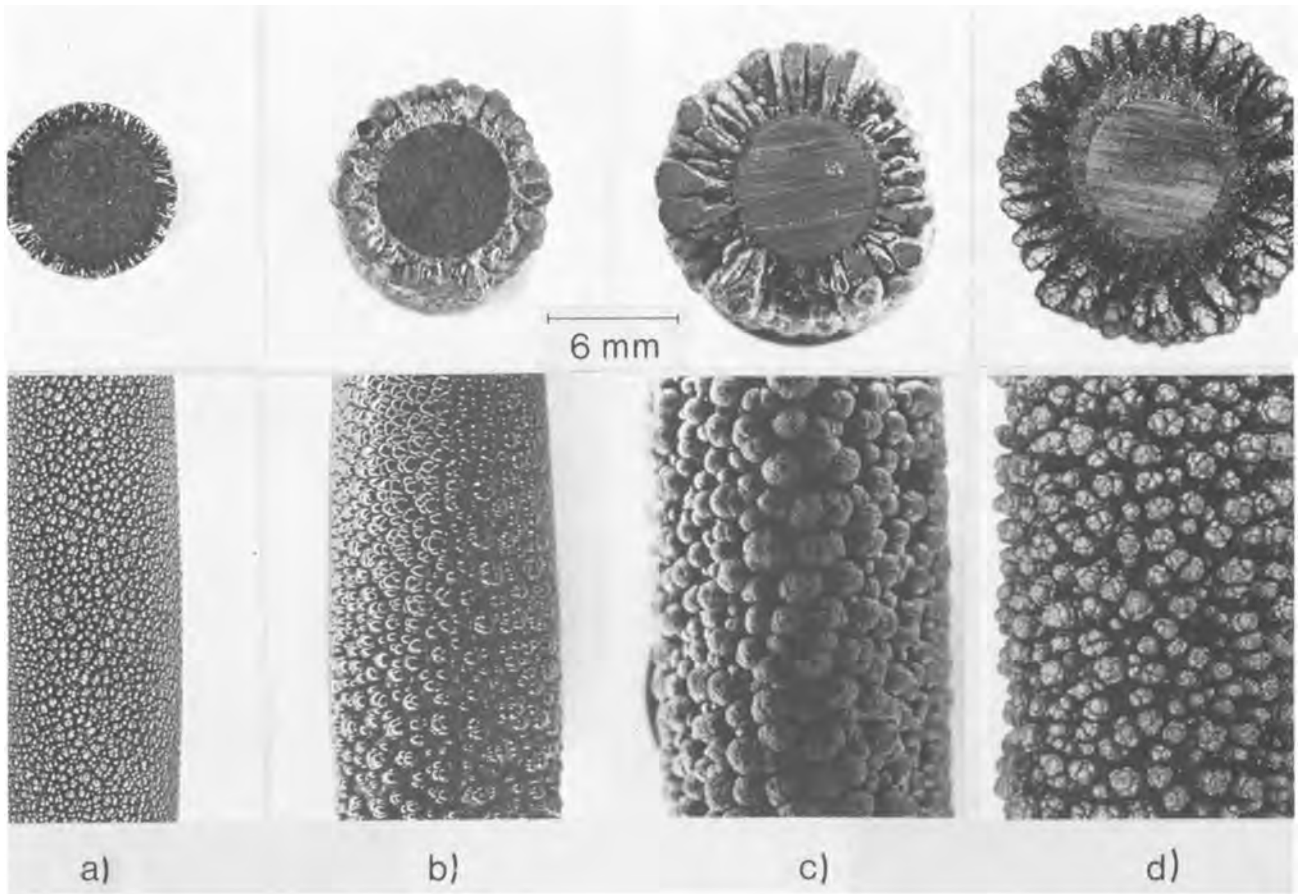

Fig. 5. Morphology of silicon carbide grown by the van Arkel process at different temperatures (silane M2). (a) 1200°C, (b) 1400°C, (c) 1600°C, (d) 1800°C (initial temperatures).

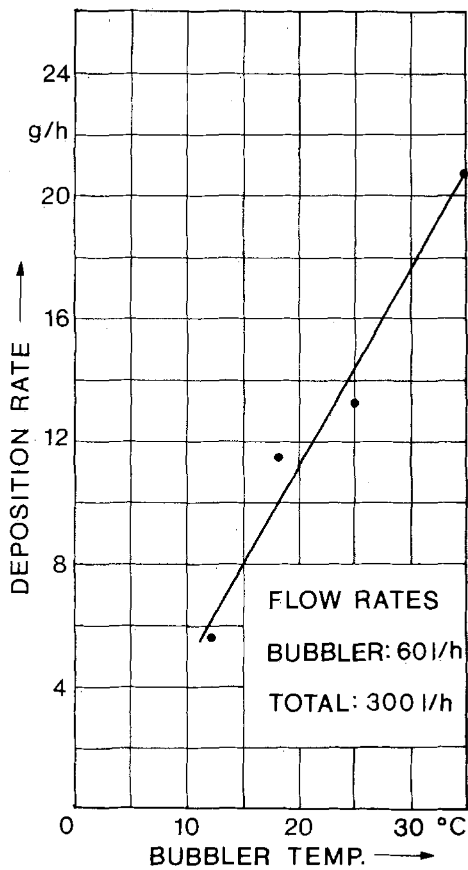

Fig. 6a. Dependence of the growth rate on the saturation temperature (silane M2).

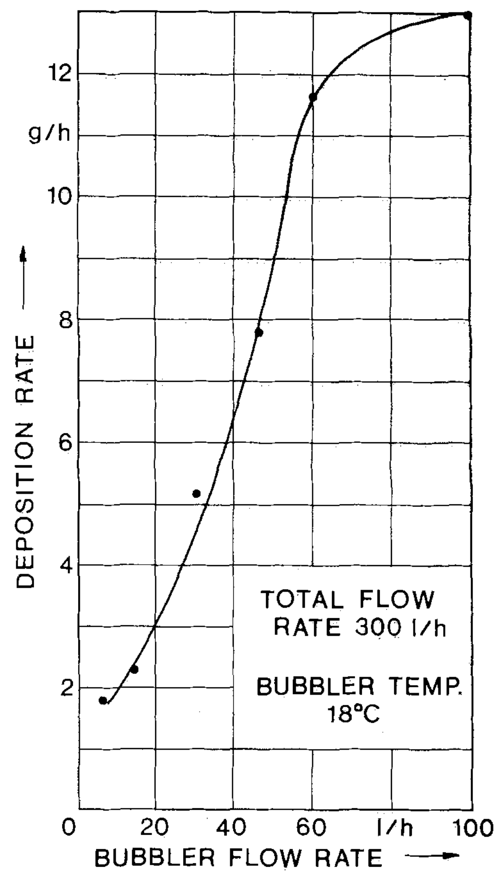

Fig. 6b. Dependence of the growth rate on the bubbler flow rate (silane M2).

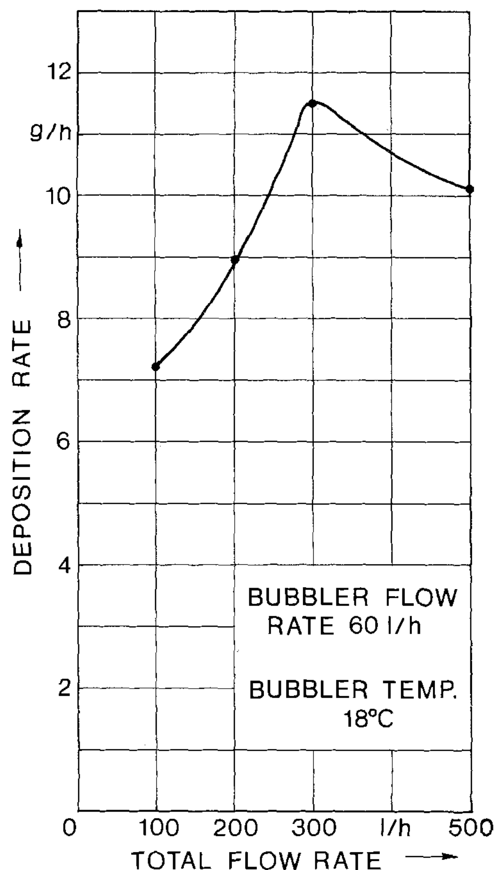

Fig. 6c. Dependence of the growth rate on the total hydrogen flow rate (silane M2).

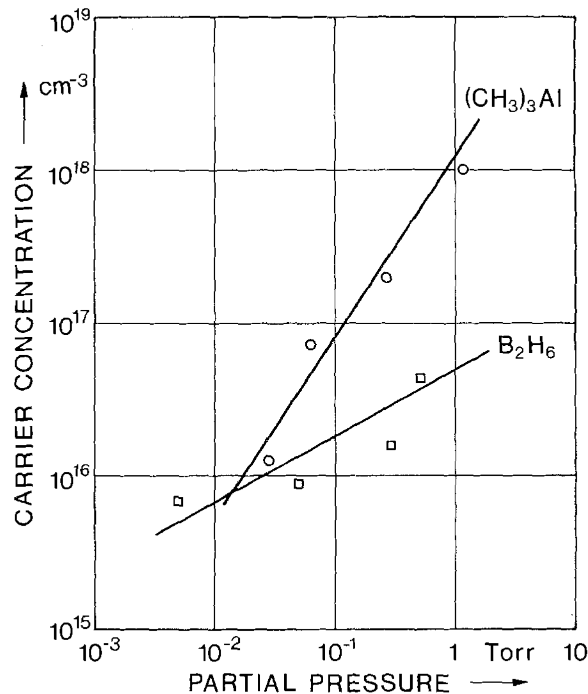

Fig. 7. Hole concentration in Lely-grown silicon carbide crystals vs. partial pressure of doping compound in the van Arkel process.

ship (approximately) for the doping with aluminum. The over-all doping efficiency is much smaller than unity, because of losses of aluminum during the van Arkel process and during the sublimation of silicon carbide (*i.e.*, high vapor pressure of aluminum as compared to silicon carbide). The incorporation of boron exhibits a sublinear behavior. A visual inspection of the polycrystalline material indicates that a large part of the boron is deposited as elementary boron particles. Thus, most of the boron is probably lost during the oxidation and degassing cycles.

The 77°K photoluminescence spectra of silicon carbide crystals grown from different types of polycrystalline material are shown in Fig. 8. Crystals produced from abrasive powder exhibit a broad emission spectrum with a maximum around 640 nm and additional peaks at 505 and 535 nm. The emission spectrum of crystals grown from undoped van Arkel material is dominated by the 640 nm peak. A relatively weak emission peak is found at 475 nm; this peak may be due to a "memory effect" resulting from previous doping experiments with aluminum. Crystals grown from Al-doped van Arkel material exhibit a strong emission peak at 490 nm; the 640 nm peak is also present.

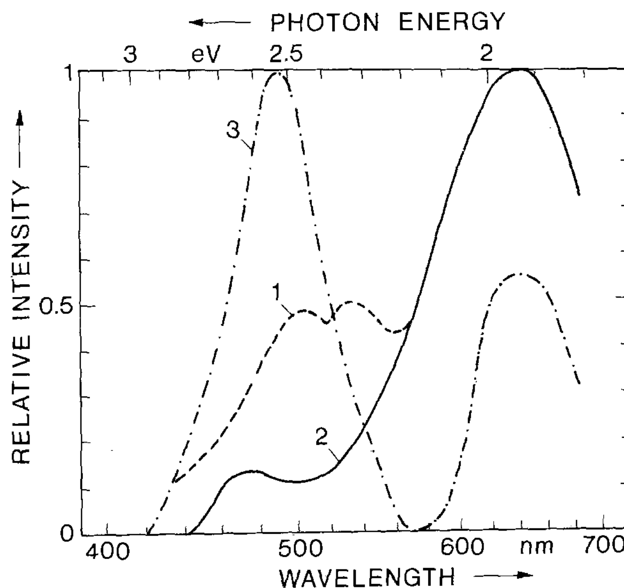

Fig. 8. Photoluminescence spectra (77°K) of silicon carbide crystals grown from different kinds of polycrystalline material: curve 1, "green grit" commercial silicon carbide abrasive; curve 2, undoped silicon carbide produced by the van Arkel process; curve 3, Al-doped silicon carbide produced by the van Arkel process.

The 640 nm peak is also observed for all boron-doped crystals. It is not clear, however, whether boron

Table I. Properties of silicon carbide crystals

Starting material	Dopant	Carrier concentration (cm^{-3}) Room temperature	High temperature	Mobility (cm^2/V sec)	Activation energy (meV)
Abrasive	None	$p = 1 \ldots 5 \times 10^{15}$	2×10^{18}	10 . . . 15	270
Abrasive	N_2*	$n = 1 \ldots 5 \times 10^{16}$	2×10^{17}	120	70
van Arkel mat.	None	$n = 1 \times 10^{16}$	3×10^{16}	200	70
van Arkel mat.	$(CH_3)_3Al$**	$p = 1.5 \times 10^{16}$	6×10^{18}	35	270
		$p = 8 \times 10^{16}$	1×10^{19}	28	270
		$p = 3 \times 10^{17}$	2×10^{19}	22	270
		$p = 1 \times 10^{18}$	2.5×10^{19}	10	270

* Doping during Lely process.
** Doping during van Arkel process.

incorporation is the only reason for the occurrence of this peak; crystal defects may also contribute to the 640 nm emission. The latter process is suggested by the results obtained with crystals of extremely high purity.

Conclusion

Pure and doped polycrystalline silicon carbide can be produced by the van Arkel process using silane compounds. A reasonable growth rate (in the order of 40 g/hr) can be achieved by proper choice of the growth conditions; a stoichiometric deposit is obtained in the 1400°-1600°C temperature range. The polycrystalline SiC material can serve as feed material for the Lely process, *i.e.*, for the growth of 6H silicon carbide crystals. A substantial improvement of the electrical properties (*i.e.*, higher carrier mobility) has been achieved. The process is particularly useful for doping with aluminum; hole concentrations in the 10^{16}-10^{18} cm^{-3} range are obtained reproducibly in this manner.

Manuscript submitted June 17, 1977; revised manuscript received Sept. 7, 1977.

Any discussion of this paper will appear in a Discussion Section to be published in the December 1978 JOURNAL. All discussions for the December 1978 Discussion Section should be submitted by Aug. 1, 1978.

Publication costs of this article were assisted by the Institut A für Werkstoffkunde der Technische Universität Hannover.

REFERENCES

1. J. A. Lely, *Ber. Deutsch. Keram. Ges.*, **32**, 229 (1955).
2. W. F. Knippenberg, *Philips Res. Rep.*, **18**, 205 (1963).
3. R. M. Potter and J. H. Sattele, *J. Cryst. Growth*, **12**, 245 (1972).
4. W. von Muench, W. Kuerzinger, and I. Pfaffeneder, *Solid-State Electron.*, **19**, 871 (1976).
5. W. von Muench, *J. Electron. Mater.*, **6**, 449 (1977).
6. J. T. Kendall, *J. Chem. Phys.*, **21**, 821 (1953).
7. R. F. Adamsky and K. M. Merz, *Z. Kristallogr.*, **111**, 350 (1959).
8. V. E. Straughan and E. F. Mayer, in "Silicon Carbide, J. R. O'Connor and J. Smiltens, Editors, p. 94, Pergamon Press, New York (1960).
9. S. Susman, R. A. Spriggs, and H. S. Weber, in *ibid.*, p. 94.
10. H. W. Huggins and C. H. Pitt, *Am. Ceram. Soc. Bull.*, **46**, 266 (1967).
11. I. Berman and C. E. Ryan, *J. Cryst. Growth*, **9**, 314 (1971).
12. A. W. C. van Kemenade and C. F. Stemfoort, *ibid.*, **12**, 13 (1972).
13. F. Kobayashi, K. Ikawa, and K. Iwamoto, *ibid.*, **28**, 395 (1975).
14. C. J. Kapteyns and W. F. Knippenberg, *ibid.*, **7**, 20 (1970).
15. S. H. Hagen and C. J. Kapteyns, *Philips Res. Rep.*, **25**, 1 (1970).
16. "Landolt-Boernstein, Zahlenwerte und Funktionen," Vol. II. 2a, p. 44 Springer-Verlag, Berlin (1960).
17. P. Rai-Choudhury and N. P. Formigoni, *This Journal*, **116**, 1440 (1969).

Optical Reflectance Method for Determining the Surface Quality of Sapphire (Al_2O_3)

P. J. Zanzucchi,* M. T. Duffy,* and R. C. Alig

RCA Laboratories, Princeton, New Jersey 08540

ABSTRACT

Polished sapphire wafers are used as substrates for the growth of crystalline silicon. The quality of the substrate surface is an important factor in determining the crystalline quality of the silicon film and, in turn, relates to silicon device performance and reliability. To improve silicon-on-sapphire device manufacture, a sensitive and nondestructive optical reflectance technique has been developed to determine the quality of polished sapphire surfaces. The correlation between surface damage and single or multiple specular reflectance of sapphire in the lattice mode region, 900-300 cm^{-1}, is reported. As a result of surface damage, the Al_2O_3 vibrational modes of sapphire are distorted and the optical constants associated with these modes change. To interpret the single and multiple reflectance spectra the optical constants of undamaged and damaged ($1\bar{1}02$) sapphire surfaces have been calculated from reflectance data using the Kramers-Kronig method. From this analysis, the reflectance of sapphire at about 600 cm^{-1} is found to be very sensitive to surface quality. In this spectral region multiple reflectance can be used to measure the surface quality of sapphire with a high degree of sensitivity. The technique can, in principle, be used to measure the quality of any semiconductor or dielectric surface in spectral regions of high reflectance, such as regions of lattice band or bandgap absorption.

The crystalline perfection of thin, epitaxial layers is strongly influenced by the crystalline perfection of the substrate surface. From studies of the growth of silicon films (1, 2) on silicon substrates it is well known that defects on the substrate surface lead to crystal growth defects in the epitaxial layer. By the use of Lang topographic techniques, McFarlane and Wang (3) have shown that the crystalline perfection of III-V semiconductor films on sapphire or spinel substrates is significantly altered by defects on the substrate surface. These defects, which often are not visible, are usually scratches introduced in the polishing of the substrate. Defects can cause the epitaxial film to be misoriented in localized regions. As a consequence, this introduces lattice imperfections in the epitaxial film and these imperfections are particularly evident when the epitaxial film is relatively thin, *i.e.*, a micrometer or less in thickness. With the increased use of semiconductors and dielectrics prepared as thin epitaxial films by

* Electrochemical Society Active Member.

Key words: quality control, ($1\bar{1}02$) sapphire, multiple reflectance, Kramers-Kronig method.

chemical vapor deposition, there is a need for a fast and nondestructive technique for determining the quality of polished sapphire surfaces.

An optical multiple-reflectance technique for determining the quality of sapphire surfaces used in silicon-on-sapphire (SOS) device manufacture is described in this paper. It is known from the work of Barker (4) that the procedures used to polish sapphire can introduce lattice damage or strain at the sapphire surface. According to Barker (4), this surface damage deforms the normal modes of Al_2O_3 (sapphire), the associated optical constants change, and forbidden modes appear in the specular reflection spectrum of the lattice modes. Thus optical reflectance can be used to detect polishing-related lattice damage and the magnitude of the optical constants of the sapphire surface can be used to provide a quantitative measure of the damage.

To interpret the reflectance spectrum of sapphire, it is very useful to know the optical constants. These constants are not known for the $(1\bar{1}02)$ orientation, Fig. 1, of sapphire. Since they are important to an over-all understanding of the features of a single and multiple reflectance spectra, we have used the Kramers-Kronig method to determine the optical constants of damaged and undamaged $(1\bar{1}02)$ sapphire surfaces in the lattice mode region. Based on this, lattice mode regions can be selected where the optical properties of sapphire correlate with surface damage. We have used the technique of multiple reflectance to enhance the sensitivity of measuring changes in reflectance associated with surface damage.

Experimental

Materials.—Polished sapphire substrates were obtained from different commercial vendors. Although a best quality "epi" grade polish was specified, the quality of the surface finish varied widely on these substrates. To perform controlled experiments, the observed variation in surface quality was simulated by sapphire substrates which were polished at RCA Laboratories. By using a number of polishing agents with various grit sizes, different degrees of work damage were obtained on the substrate surfaces. Diamond grit, ranging from 1 to 6 μm particle size on a Bakelite base, was used to provide the final surface finish for some. Alumina (Linde A) or colloidal silica (Syton), on a Pellon or Corfam pad, were used to provide better quality surface finish for others. The actual degree of surface damage depended on both the type of agent used and the grit size. For the same grit size, diamond polishes produced more damage at the surface than, for example, alumina polishes. The substrates were 1.5 in.

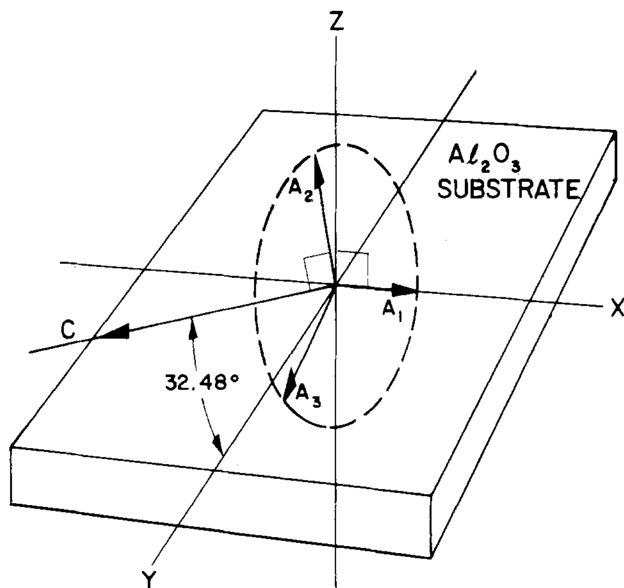

Fig. 1. Vectorial presentation of c and a axes in $(1\bar{1}02)$ sapphire

in diameter with a ground-back surface, and were usually $(1\bar{1}02)$ oriented. In some cases (0001) and $(11\bar{2}0)$ oriented sapphire substrates were examined.

Sapphire is birefringent. The optical constants are measured with the electric vector of light parallel p and perpendicular s to the c-axis. In (0001) oriented sapphire the c-axis is perpendicular to the polished surface. In this case the p and s components are identical. As Barker (4) noted, polishing-related surface damage on the (0001) surface cannot be detected by optical reflectance. With $(11\bar{2}0)$ oriented sapphire the c-axis is in the plane of the polished surface. In the $(1\bar{1}02)$ orientation, the c-axis is about 32° from the polished surface, Fig. 1. For the Kramers-Kronig analysis the polarization of the light with respect to the c-axis must be known. In multiple-reflection measurement the polarization of the light is unnecessary and average effects are measured with unpolarized light.

Evaluation.—As a basis for developing a multiple reflection method to measure surface perfection, it is important to know how the refractive index n and the absorption index k vary in the wavelength region of interest. The values of n and k are related to the measured reflectance, Eq. [1]

$$R = \frac{(n-1)^2 + k^2}{(n+1)^2 + k^2} \quad [1]$$

As these constants are altered by the presence of lattice damage, a change in reflectivity occurs and this can be used as a measure of the lattice damage at the reflecting surface. The optical constants for the surface material of the variously polished sapphire substrates were calculated from specular reflectance data using Kramers-Kronig analysis (5-7). The reflectance measurements were made using a Perkin Elmer 457 infrared spectrophotometer and specially designed reflectance jigs. A computer program written by Klucker and Nielsen (6), which is available through the Journal Library at the School of Physics and Applied Mathematics, Queen's University, Belfast BT7, North Ireland, was used to calculate n and k. The program was obtained on tape and used without significant modification.

The calculated optical constants for (0001) Al_2O_3 are similar in magnitude to published data (8). Although optical constants calculated by the Kramers-Kronig method can be inaccurate (9), data from the published work of Arakawa and Williams (10) is used to obtain a reasonable high energy limit of about 25 eV. Our calculated refractive indexes agree well with extrapolated values of the index from the reported data of Malitson *et al.* (11) and Russell and Bell (12).

The absolute reflectance spectra were obtained for the variously polished surfaces using either p or s polarization with respect to the c-axis orientation of the substrate. The direction of the crystallographic axes was determined by Laue x-ray back-reflection. As indicated $(1\bar{1}02)$ is the orientation of sapphire which is of primary interest in silicon-on-sapphire device manufacture and, therefore, this study.

Results and Discussion

Reflectance measurements.—Reflectance spectra obtained on variously polished $(1\bar{1}02)$-oriented sapphire substrates are shown in Fig. 2 which corresponds to p polarization. In this figure, spectrum (a) is used as a reference corresponding to the best surface finish attainable by polishing with silica sol (Sytôn). Spectrum (b) corresponds to a Linde A (Al_2O_3, 0.3 μm grit) polish, and spectra (c), (d), and (e), correspond to surface finishing with 1, 3, and 6 μm diamond grit, respectively. For both polarizations, the spectra show that there is a significant change in the reflectivity near 600 cm^{-1} with increasing grit size, or hardness, of the polishing medium. For other spectral regions, the effect of polishing damage on the reflectance of the sapphire is less evident though clearly present. Similar features occur

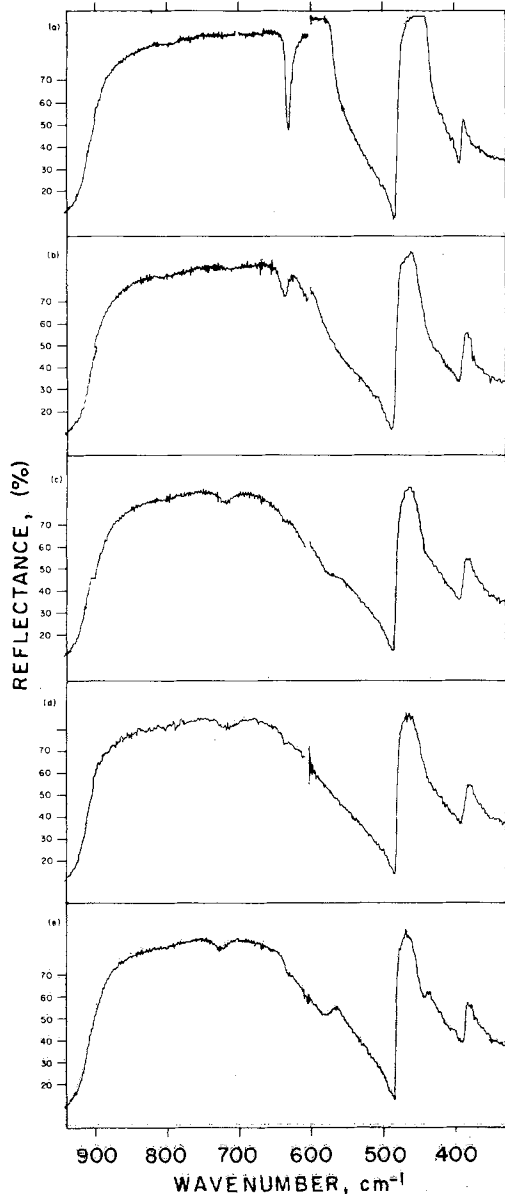

Fig. 2. Comparison of sapphire reflection spectra for variously polished $(1\bar{1}02)$ sapphire, p polarization: (a) Syton polished (best surface), (b) 0.3 μm Al_2O_3, Linde A, (c) 1 μm diamond, (d) 3 μm diamond, and (e) 6 μm diamond.

in the reflectance spectra using s polarization. Using the Kramers-Kronig method, the phase angle θ, refractive index n, and absorption index k, were calculated from the data in Fig. 2. Between 300 and 400 points in the region 250-900 cm^{-1} were used in the calculation.

The computed optical constants corresponding to the different vibrational modes for the variously polished surfaces are summarized in Table I. It is apparent from the data that the surface damage associated with the different sizes of the polishing grit is large. This indicates that any mechanical abrasion, not involving a chemical polishing action as with Syton, is likely to result in a considerable change in the computed values of the optical constants for the sapphire surface. The computed values of the optical constants for a Syton polished (0001)-oriented Al_2O_3 sample are also summarized in Table I.

A basic question concerning these data is their accuracy. Based on the work of Spitzer and Kleinman (7) it is known that the Kramers-Kronig analysis is accurate to better than 10% of "true" value for $k > 0.1$. For lower values of k the accuracy tends to be poor. We observed this. The calculated phase angle for small phase changes was sometimes negative, which is

Table I. Optical constants for $(1\bar{1}02)$ sapphire, p polarization, with various surface polishes

Orientation and final polish	Absorption index, k: λ (μm)	σ (cm^{-1})	eV	k	Refractive index, n: λ (μm)	σ (cm^{-1})	eV	n
(0001) Standard	25.9	385	0.0478	1.93	26.1	382	0.0474	6.25
	22.6	442	0.0548	20.1	22.7	440	0.0546	27.7
	17.5	572	0.0709	20.9	17.6	568	0.0704	28.3
	15.9	629	0.078	6.3	15.8	634	0.0786	3.57
$(1\bar{1}02)$ Standard	25.6	390	0.0484	1.77	25.9	386	0.0478	6.02
	22.8	440	0.0545	30.1	22.8	438	0.0543	28.3
	17.3	578	0.0717	26.4	17.5	572	0.0709	37.4
	15.7	636	0.0789	8.08	15.7	636	0.0786	5.67
$(1\bar{1}02)$ Linde A	26.4	379	0.047	2.86	26.6	375	0.0466	6.34
	22.1	452	0.056	9.64	22.3	448	0.0555	9.98
	16.3	613	0.076	8.12	16.98	589	0.073	9.62
	15.7	637	0.079	6.2	15.9	629	0.078	2.48
$(1\bar{1}02)$ 1 μm diamond	26.2	382	0.0474	2.89	26.7	374	0.0464	6.04
	22.1	452	0.056	7.09	22.5	444	0.055	8.28
	16.0	623	0.0773	6.14	17.97	556	0.069	4.72
	15.7	637	0.079	6.14	16.6	602	0.0746	7.09
$(1\bar{1}02)$ 3 μm diamond	26.3	380	0.0471	2.67	26.7	375	0.0464	5.59
	22.0	454	0.0563	6.81	22.5	444	0.055	7.53
	16.1	620	0.0769	6.72	16.7	598	0.0741	8.79
$(1\bar{1}02)$ 6 μm diamond	26.2	382	0.0474	2.95	26.3	379	0.047	5.75
	22.96	435	0.054	2.90	22.96	435	0.054	6.3
	17.7	565	0.070	2.32	17.97	556	0.069	5.5
	15.7	637	0.079	6.75	16.6	602	0.0746	6.62

physically meaningless. In the Kramers-Kronig calculation, the program does not consider the sign of the phase angle. Gross errors are thus expected for small values of the phase angle and correspondingly small values of k. This is not significant at the lattice modes where n and k are very large and, correspondingly, the phase change is large. In comparison to published data (8), the optical constants for the (0001) Al_2O_3 lattice modes reported here are significantly larger in general. However in approximating the limits to the Kramers-Kronig integral, errors can be introduced (7, 9). Simple experimental errors such as determining the angle of incidence, the c-axis orientation, and the polarizer position are not critical. Small errors in these orientations, *e.g.*, a few degrees, do not appear to significantly affect the calculated optical constants, at least not in comparison with the degree the values are affected by the high energy limit selected in the Kramers-Kronig integration. For example, the nominal angle of incidence in these measurements is 10°. If the value is 10° in error, *e.g.*, 20° is used, the error in the optical constants is less than about 5%. The orientation of the c-axis in each crystal was determined by the Laue x-ray technique and the orientations are accurate within a few degrees. Similarly, the polarizer orientation can be accurately adjusted.

Errors in measuring the absolute reflectance are, however, critical in determining the magnitude of the optical constants. When the measured reflectance, R, of our reference sample was deliberately diminished by 0.005, 0.01, and 0.02, respectively, the influence of these small changes on the computed values of the optical constants was considerable as shown in Table II. In this case, the reflectance was measured for s polarization. Thus, small changes in surface reflectance due to residual polishing damage can grossly affect the magnitude of the calculated optical constants. The reflectance data must be accurate to much better than 1% before attempting to determine absolute values of the optical constants. For our purposes, relative changes in the magnitude of these constants gives a reasonable insight into the effects of polishing damage and the absolute values are not critical.

In summary, it is apparent that deliberately introduced polishing damage significantly changes the optical constants of the Al_2O_3 surface. For sapphire with considerably less damage than introduced by our selective polishing, we can expect to measure significant changes in the infrared optical properties of sapphire. However, Kramers-Kronig analysis is not practical for testing the surface quality where frequent testing of many samples is required as in a production facility.

Table II. Effect of constant reflectance error, ΔR, introduced in calculation of optical constants for "standard" ($1\bar{1}02$) sapphire, s-polarization

ΔR	eV	n	k
zero	0.05158	44.4	
	0.05183		28.9
	0.06026	4.5	
	0.06051		5.2
	0.07192	29.3	
	0.07217		21.8
0.005	0.05158	34.0	
	0.05183		25.2
	0.06026	4.2	
	0.06051		5.0
	0.07192	26.3	
	0.07217		19.6
0.01	0.05134	29.9	
	0.05158	25.6	23.6
	0.06026	3.9	
	0.06051		4.8
	0.07192	22.3	
	0.07217		17.5
0.02	0.05134	24.1	
	0.05158		19.7
	0.06026	3.3	
	0.06051		4.3
	0.07167	14.7	
	0.07192	13.9	
	0.07217		13.5

The experimental procedures and the mathematical calculation are time consuming. More significantly, the magnitude of the difference between undamaged and slightly damaged surfaces, while not small, is still not sufficient for detecting lightly damaged surfaces. Based on the data reported here, it is desirable to have a technique with an order of magnitude more sensitivity to surface damage which can be obtained using the technique of multiple reflection as discussed in the following section. It should be emphasized, however, that interpretation of the multiple reflection spectra is not possible without knowing the behavior of the optical constants in the region of interest.

Multiple reflection measurements.—Multiple reflection techniques are well known and are often used to amplify small changes in reflectance. At least two conditions can be specified for the multiple reflection of light: (*i*) multiple external reflection where the light is external to a medium of higher refractive index, and (*ii*) multiple internal reflection where the light is contained by a medium of higher refractive index. For either multiple external or internal reflection, it is well known that surface defects diminish the intensity of the reflected light beam. The loss may be very small for a single reflection but becomes amplified with multiple reflection. For example, the reflectance R_m after m reflections from a pair of parallel metal surfaces (external reflections) is given by

$$R_m = R^m \qquad [2]$$

where R is the absolute reflectance of the surface, *i.e.*, the reflectance measured with a single specular reflection. For 10 reflections between two metal surfaces of 0.96 reflectance, the measured reflectance is 0.66. If damage introduces a 0.01 change in reflectance of the metal surface, *i.e.*, $R = 0.95$, the measured reflectance after 10 reflections is 0.60. A 0.01 change in reflectance is amplified to a 0.06 difference. Obviously, as the surface damage of a good reflector increases, the larger the change in R_m for a given value of R. It is also apparent that the effect of multiple reflection in regions of low reflectivity is to rapidly diminish the measured reflectance. Thus, a multiple reflection spectrum retains only a portion of the spectrum where the reflectance is close to one.

This technique can be applied to dielectrics and semiconductors in spectral regions where the optical constants are very large and the reflectance of the materials is very high. This follows from the relation between R and the optical constants for reflection from single surface at normal incidence, Eq. [1]. For large n and k, R is large. For sapphire this occurs at the lattice modes and R can be as large as 0.96. Thus, as

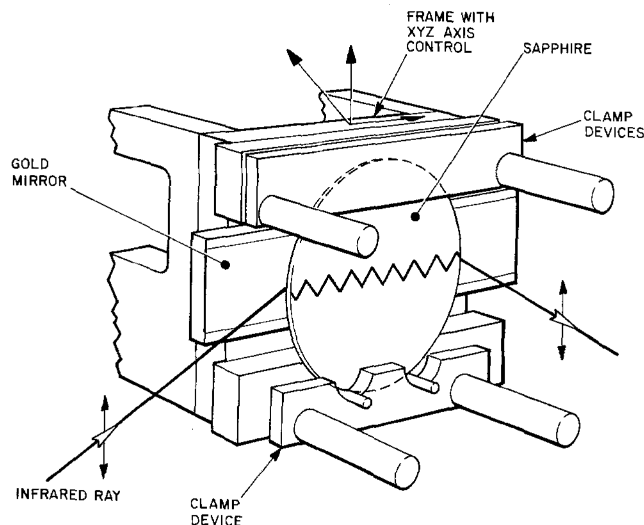

Fig. 3. Schematic representation of multiple reflections between a gold-surfaced mirror and a sapphire substrate.

shown in Fig. 3, multiple external reflections are obtained from a sapphire surface by using a gold mirror. Reproducible mounting of the sapphire wafers is required. As shown by Fig. 3, the sapphire wafer is mounted at a fixed distance from a gold-surface mirror. The distance is selected to produce about 10 reflections. All components are rigid and fixed. The sapphire wafer is demountable. The multiple reflection jig is mounted on a three-axis micrometer stage to precisely position the jig in the infrared beam. The sapphire is strongly reflecting in regions of large n and k and poorly reflecting in regions of small values for the optical constants. The effects of surface damage in relation to the optical constants of the surface material will be amplified by changes in the measured multiple reflectance. The reflectance is measured with unpolarized radiation without regard to the c-axis orientation of the sapphire substrates.

The qualitative features of the resulting single and multiple reflection spectra are shown in Fig. 4. In the multiple reflection spectra, note the loss of weak band structure, the frequency shift, and the decrease in amplitude of the band at 600 cm^{-1} for the damaged

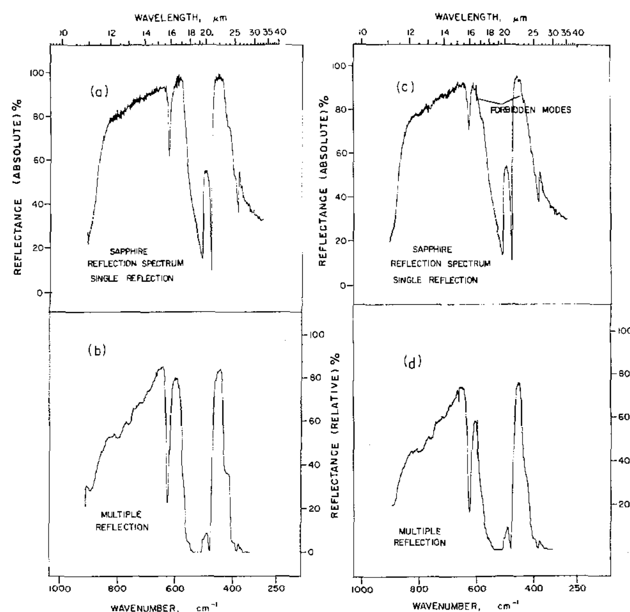

Fig. 4. Reflection spectra of undamaged and damaged sapphire: (a) undamaged, a single reflection spectrum; (b) undamaged, a multiple reflection spectrum; (c) damaged (as received), a single reflection spectrum; and (d) damaged (as received), a multiple reflection spectrum.

sample in comparison with the undamaged sample. The correlation between surface damage and the measured reflectance near 600 cm^{-1} in the multiple reflection spectrum gives a relative, quantitative, and rapid evaluation of surface damage.

Multiple reflection measurements on an absolute scale were performed on the set of variously polished substrates characterized by the Kramers-Kronig analysis. The reflectance scale was calibrated by a gold mirror reflector and a reference trace was obtained by scanning the spectral region 400-900 cm^{-1} using a gold-coated polished sapphire substrate of the same diameter as test samples in the sample beam. The reflectance, after an estimated 10 reflections between the gold mirror and gold-coated sapphire sample, is shown in the upper trace (a), of Fig. 5. The curve shows a sharp discontinuity at 600 cm^{-1} due to instrumental effects. A grating change occurs here which causes a shift in the curves due to grating tilt. All curves show this discontinuity, which is reproducible and does not affect the interpretation of data. After the reference trace was established, the variously polished samples were substituted for the gold-coated sample, and the spectra obtained are sequentially presented in Fig. 5. An analysis of the spectra show that, with diamond polishing, irrespective of grit size, the surface is so badly damaged that the vibrational modes of Al_2O_3 are not detected. In the case of Linde A (0.3 μm alumina grit), a band at 600 cm^{-1} has shifted to approximately 610 cm^{-1} and the amplitude is diminished to less than half the magnitude corresponding to a silica sol surface finish. This is consistent with the previous Kramers-Kronig dispersion analysis of these damaged surfaces. Thus, we expect to be able to detect damage caused by polishes much finer than studied here. After the infrared analysis, the substrates were etched in aqueous KOH at about 300°C to delineate polishing damage. Comparison of etch data with the infrared data in Table I shows the same quantitative trends as observed in the values of the optical constants. Multiple reflectance measurements were also performed on about 30 as-received sapphire wafers obtained from different vendors. Multiple reflection spectra for the best and worst surfaces together with photographs of the corresponding etched surfaces are shown in Fig. 6 and 7, respectively. It is evident from these figures that a wide variation in surface finishing can occur among samples from the different vendors.

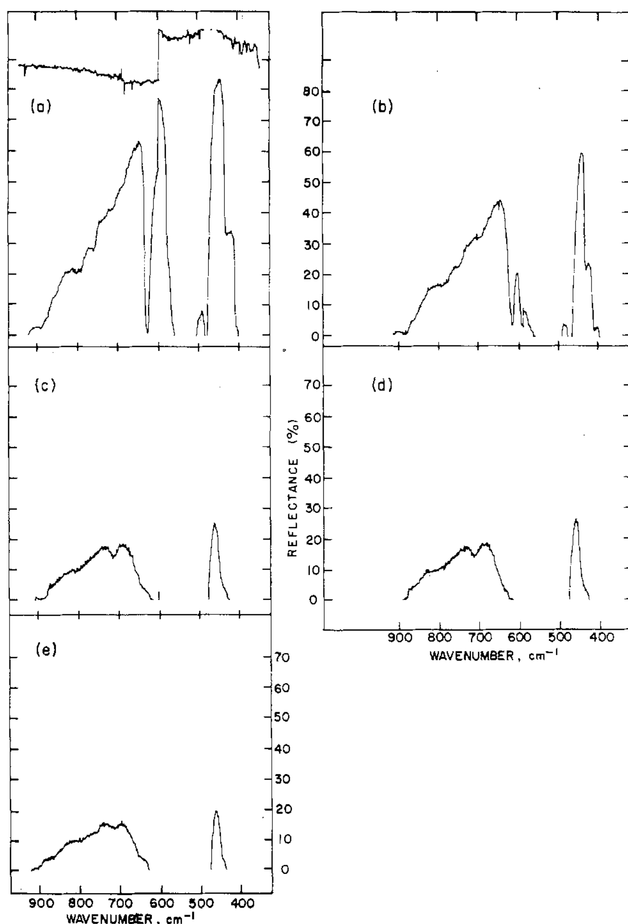

Fig. 5. Absolute multiple reflection measurements for variously polished sapphire surfaces: (a) upper trace gold standard vs. gold mirror normally present, lower trace sapphire wafer with "best" finish, (b) sapphire wafer with a 0.3 μm (Al_2O_3) polish (c) sapphire wafer with a 1 μm diamond polish, (d) sapphire wafer with a 3 μm diamond polish, and (e) sapphire wafer with a 6 μm diamond polish.

Differential methods to evaluate polished surfaces were also examined. However, with this technique it is difficult to obtain a true null signal due to the sharp and widely varying reflectance of the Al_2O_3 vibrational modes.

Factors influencing reflectance measurements.—The symmetry properties of sapphire strongly influence vibrational mode frequency and amplitude. It should be noted that the infrared technique is specifically measuring a molecular distortion which is characteristic of surface damage (4). If this distortion in sapphire is eliminated by an annealing treatment, evidence of such damage is no longer apparent in the infrared reflectance spectra even though etch striations may still appear in chemical etch treatments. It is important, therefore, that the reflectance technique be used prior to sample annealing. Even relatively low temperature annealing, 1000°C, is effective in this respect. Note such anneals may not remove damage but remove the characteristic optical features of the damage. When the surface damage in sapphire is not measurable, due for example, to prior annealing of the material, using the same principles outlined here, the surface quality of the epitaxial semiconductor can be measured in regions well above bandgap. The features of this measurement, and the correlation to electrical properties, will be reported (13).

The external multiple reflectance technique requires reproducible mounting of sapphire samples. For absolute measurements and for comparison purposes, alignment of the various components is important and reflecting surfaces should be very clean. Failure to observe these conditions can result in diminished reflectance throughout the spectral region of interest. Thus, if the reflectance is measured at a given wave number near 600 cm^{-1}, there may be some doubt as to whether the measured value is representative of the degree of surface perfection. For in-line quality control purposes a preferable procedure is to represent the surface condition of a given sample by the ratio of the reflectance at 600 and 450 cm^{-1}, *i.e.*, $R_{600}\ cm^{-1}/R_{450}\ cm^{-1}$. This minimizes errors due to misalignment and surface cleanliness. In addition, for lightly damaged samples the reflectance at 450 cm^{-1} is not noticeably influenced by the presence of damage.

Summary

A quantitative, sensitive, and nondestructive multiple reflectance technique to detect small changes in the surface quality of sapphire has been described. As shown, commercially polished sapphire will have wide variation in surface perfection. The effect of this is to cause wide variation in the crystalline perfection of epitaxial semiconductors grown on these substrates.

The multiple reflectance technique described is based on changes in the optical constants, and thus reflectance, with surface damage in the 600 cm^{-1} spectral region. To interpret the multiple reflectance spectrum, we have obtained the optical constants for $(1\bar{1}02)$ sapphire, with various surface finishes, using the Kramers-Kronig method. The accuracy of this technique has been discussed. From this analysis, the reflectance of sapphire at about 600 cm^{-1} is found to be very sensitive to surface quality. For unannealed sapphire substrates, multiple reflection in this spectral region can be used to

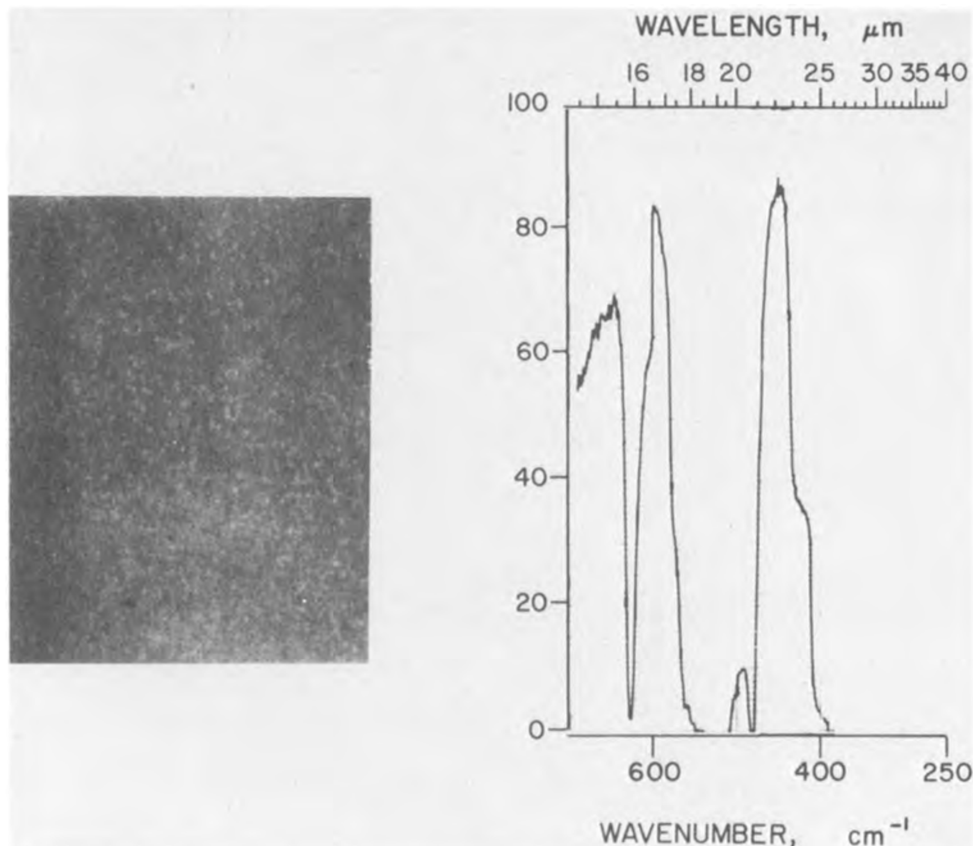

Fig. 6. As-received commercial sample of sapphire, best sample. Comparison of multiple reflection and chemical etch data.

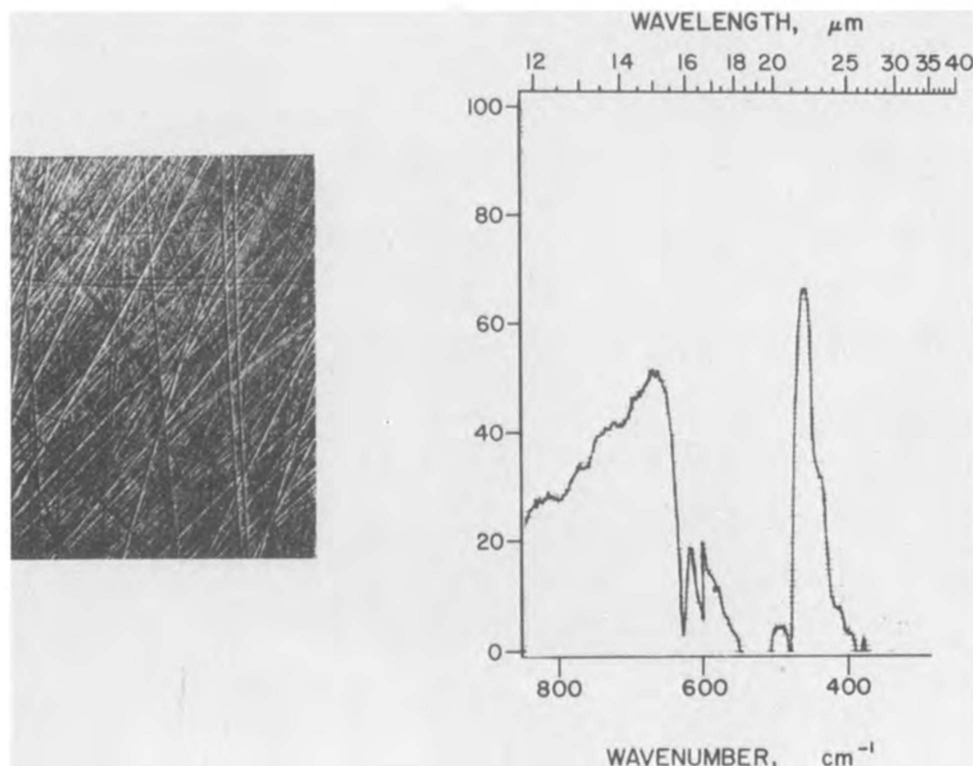

Fig. 7. As-received commercial sample of sapphire, worst sample. Comparison of multiple reflection and chemical etch data.

measure the surface quality of sapphire with a high degree of sensitivity. For clean substrates, the technique is adaptable to quality-control evaluation of substrates used in silicon device manufacture. In principle, the multiple reflectance technique can be used to measure the surface quality of polished semiconductors or dielectrics in spectral regions of high reflectance, *i.e.*, regions of lattice band or bandgap absorption.

Acknowledgments

We greatly appreciate the technical assistance of E. M. Botnick for assisting with the computer calculation and R. A. Soltis and D. A. Kramer for preparing samples and obtaining many of the measured values reported here. Technical discussions with J. I. Gittleman at RCA Laboratories and with K. Galloway and W. M. Bullis at NBS have been helpful and are also appreciated. This research was funded by the Advanced Research Project Agency Order 2397 through the National Bureau of Standard's Semiconductor Technology Program Contract 5-35915. Funding was also provided by RCA Laboratories.

Manuscript submitted July 18, 1977; revised manuscript received Sept. 19, 1977. This was Paper 171 pre-

sented at the Las Vegas, Nevada, Meeting of the Society, Oct. 17-22, 1976.

Any discussion of this paper will appear in a Discussion Section to be published in the December 1978 JOURNAL. All discussions for the December 1978 Discussion Section should be submitted by Aug. 1, 1978.

Publication costs of this article were assisted by RCA Laboratories.

REFERENCES

1. S. Mendelson, *J. Appl. Phys.*, **35**, 1570 (1964).
2. D. J. Dumin and W. N. Henry, *Metall. Trans.*, **2**, 677 (1971).
3. S. H. McFarlane and C. C. Wang, *J. Appl. Phys.*, **43**, 1724 (1972).
4. A. S. Barker, Jr., *Phys. Rev.*, **132**, 1474 (1963).
5. D. M. Roessler, *Br. J. Appl. Phys.*, **16**, 1119 (1965).
6. R. Klucker and U. Nielsen, *Computer Phys. Commun.*, **6**, 187 (1973).
7. W. G. Spitzer and D. A. Kleinman, *Phys. Rev.*, **121**, 1324 (1961).
8. B. Piriou, *C. R. Acad. Sci., Paris*, **259**, 1052 (1964).
9. P. O. Nilsson and L. Munkby, *Phys. Kondens. Mater.*, **10**, 290 (1969).
10. E. T. Arakawa and M. W. Williams, *J. Phys. Chem. Solids*, **29**, 735 (1968).
11. I. H. Malitson, F. V. Murphy, Jr., and W. S. Rodney, *J. Opt. Soc. Am.*, **48**, 72 (1958); I. H. Malitson, *ibid.*, **52**, 1377 (1962).
12. E. E. Russell and E. E. Bell, *ibid.*, **57**, 543 (1967).
13. M. T. Duffy and P. J. Zanzucchi, Presented at the IEEE SOS Technical Workshop, Vail, Colorado (Sept. 28-30, 1977).

Selective Studies of Chemical Vapor-Deposited Aluminum Nitride-Silicon Nitride Mixture Films

S. Zirinsky and E. A. Irene*

IBM Thomas J. Watson Research Center, Yorktown Heights, New York 10598

ABSTRACT

Films of aluminum nitride and mixtures of aluminum nitride and silicon nitride have been chemically vapor deposited upon silicon and sapphire substrates within the temperature range of 600°-1100°C by the ammonolysis of gaseous aluminum trichloride and silane. Characterization of film properties included; film morphology as observed by transmission electron microscopy (TEM), optical properties, dissolution rate, residual stresses, electrical conduction, and charge-storage behavior, as a function of composition and deposition parameters. Some compositions appeared promising for programmable read only memory applications (MIOS-FET) based upon low write-erase voltages, good fatigue, and charge retention properties.

The potential for aluminum nitride (AlN) as a useful dielectric material for device applications has been frequently alluded to, and includes MIS charge storage (1, 2) and surface acoustic wave devices (3). The preparation and properties of polycrystalline films have been thoroughly explored and well documented (4, 5). Their crystalline structure under all reported conditions of vapor deposition minimizes their utility for MIS applications, since amorphous films are considered to show more uniform electrical and physical properties and lower permeability to the diffusion of impurities (6).

Amorphism can be achieved by low temperature sputter deposition (1), but annealing causes reversion to a crystalline structure (1). Oxygen additions [25-45 weight percent (w/o)] will produce amorphous mixtures of AlN and Al_2O_3 (7). Some of these compositions exhibit significant charge-storage hysteresis with bipolar pulse biasing (7, 8). MNOS-type charge-storage devices made with these compositions exhibited instabilities with regard to multiple pulse stressing and read biasing during long-term storage (8).

The thrust of the present study is to obtain candidate materials from which to construct metal-insulator-oxide-silicon, MIOS charge-storage devices which exhibit better charge storage capability than MNOS (metal-Si_3N_4-SiO_2-Si) or MAOS (metal-Al_2O_3-SiO_2-Si) systems. For this purpose candidate insulator films must meet many physical properties' criteria. For example, the electrical conduction characteristics must show charge storage, the films must be etchable in order to be able to fabricate devices, film stress must be low enough so as not to damage other films or silicon, and the morphology is best if amorphous, so as to avoid grain boundary effects. It is also desirable that the dielectric properties be similar to those exhibited by silicon nitride. Therefore these properties are measured in the present study to select the best compositions for charge storage applications. The measurements utilized are those previously applied for the study of materials and processing parameters associated with MNOS structure (11).

Only limited miscibility between AlN and Si_3N_4 has been reported (9) at high temperatures. However, it may be possible to obtain single phase films over a wider composition range by producing metastable amorphous solutions by chemical vapor deposition (CVD). Such solutions have been previously prepared by CVD in the AlN-Al_2O_3 system (7). These compositions exhibited lower electrical conductivity values and enhanced dielectric reliability as compared to the starting materials. Therefore, CVD in the AlN-Si_3N_4 system will be used for film preparation in the present study.

Although the preparation of materials by CVD in the ternary system Al, N, Si in principle involves the control of many parameters (*e.g.*, flow rate, purity, concentrations of reacting species, temperature, etc.), it was reported (5, 6) that AlN and Si_3N_4 can both be prepared similarly by the ammonolysis of $AlCl_3$ and silane, respectively. The deposits even show nearly equivalent deposition rates under the same conditions. These relationships will be utilized to characterize and explore the CVD of mixtures of AlN and Si_3N_4.

Experimental Procedures

Film preparation.—Chem-mechanically polished silicon wafers measuring 3.2 cm in diameter and 0.025

* Electrochemical Society Active Member.

Key words: memory, charge storage, physiochemical properties.

cm thick with <100> orientation were utilized in this study. Typically, 2 Ω-cm p-type Si was used unless otherwise stated. Each Si wafer was thoroughly cleaned by a procedure previously described (10).

Chemical vapor deposition (CVD) was used to prepare the individual and mixed films of AlN and Si_3N_4 by ammonolysis of gaseous $AlCl_3$ and SiH_4, respectively, in an N_2 ambient. The procedures and apparatus for the preparation of the individual AlN and Si_3N_4 films as well as mixed films of AlN and Al_2O_3 were previously described (11, 12). The present study utilized an RF heated furnace (11) with gas handling equipment capable of transpiring $AlCl_3$ with N_2 along with SiH_4 and NH_3 into the reaction zone of the furnace. Final mixing of all the reactants occurred just prior to the entrance into the deposition tube. The deposition chamber consisted of a rectangular (30 mm high by 70 mm wide) fused silica liner. The silicon wafer carrier was heated by radiation from an RF heated graphite susceptor, separated from the wafer carrier by a sealed quartz envelope so as to prevent contamination of the heated wafers from graphite reaction products. The deposition uniformity was also improved by use of a tapered fused silica canopy, positioned so as to compensate for rear position depletion of the gaseous reactants (11). The film compositions were determined by electron microprobe analysis.

Electron microscopy.—The films of interest (AlN, Si_3N_4, and mixtures) were prepared for transmission electron microscopy, TEM, by etching holes through the silicon while leaving free-standing ~500Å films for TEM study. The details of this procedure were previously reported (7). Films prepared in this way were readily transparent to 100 kV electrons.

Optical properties.—The film thicknesses were measured by ellipsometry. The refractive indexes obtained from ellipsometry for both AlN and Si_3N_4 for 5461Å light were ~ 2.0. The AlN and mixtures of AlN and Si_3N_4 were optically absorptive within the visible region, and therefore necessitated the evaluation of their optical absorption coefficients. These were determined, for AlN, Si_3N_4, and the mixtures, with a double beam Cary 14 spectrophotometer. Films on the order of 5000Å were deposited at 900°C on sapphire substrates. Transmission measurements (referenced to a blank sapphire substrate) were carried out to determine the film absorption within the wavelength range of 2800-6000Å. Measurements were carried out with AlN and several AlN/Si_3N_4 mixtures prepared at low NH_3/($AlCl_3$, SiH_4) reactants ratios, all deposited at 900°C. The absorption edges were calculated for all the films examined using the direct transition hypothesis (13).

Stress measurements.—Selective stress studies were carried out as a function of deposition temperature for AlN (using a fixed deposition rate of 250 Å/min), and with varying AlN/Si_3N_4 mixture ratios deposited at 800 °C. All films were prepared with high NH_3/($AlCl_3$, SiH_4) reactants ratio. These were deposited upon <111> oriented silicon substrates with calibration of their radii of curvature prior to film deposition using Taleysurf diametric profile measurements. The change in radius of curvative of the substrate with film deposition permitted the determination of the net stress within the film (14). The weight of the Taleysurf stylus during the surface profiling did not introduce any error from induced surface deflection, since it can be shown analytically (15) that the induced deflection of the substrate (considered as a membrane or cantilever supported at one point) varies linearly with the distance traversed by the stylus. This results in a correctable orientation bias for the stylus displacement and the recorded stylus measurement indicates true radius of curvature.

The stress within the film is then determined to be (14)

$$\Delta_T = \frac{E_{Si}}{(1 - \nu_{Si})} \cdot \frac{t^2_{Si}}{t_f} \cdot \frac{1}{R_{Si}} \quad [1]$$

Δ_T is the total room temperature film stress; E_{Si} and ν_{Si} are the Young's modulus and Poisson's ratio for the silicon substrate, respectively; t_{Si}, the silicon substrate thickness; t_f, the film thickness; R_{Si}, the radius of curvature of the silicon substrate measured along the normal to the coated surface. Measurable radii of curvature are obtainable with 3.2 cm silicon substrates, 0.025 cm thick, and films under 0.5 μm thick. Three radii measurements are required in the order indicated; (*i*) the orginal uncoated substrate, (*ii*) the coated substrate, and (*iii*) the bare substrate after etch removal of the film. The last measurement is required to confirm that no plastic deformation of the substrate has occurred as a result of the high temperature film deposition. For the <111> oriented Si, E_{Si} and ν_{Si} are symmetrical in all directions within the plane of the Si surface. The value, 2.305 × 10^{12} dyne/cm² was used for $E_{Si}/(1 - \nu_{Si})$ (16). The calculated stress values for Si_3N_4 films were found to correlate with stresses evaluated from optically determined radii of curvature (similarly deposited films) (17).

The stress contribution arising from differences in thermal expansion can be calculated by use of the approximate relation

$$\Delta_{Th} = (\alpha_f - \alpha_{Si}) \frac{\overline{E}_f}{(1 - \nu_f)} (T_{dep.} - T_{RT}) \quad [2]$$

Δ_{Th} is the thermal stress contribution to the total film stress at room temperature and is tensile if the thermal expansion of the film is greater than that of the substrate. $(\alpha_f - \alpha_{Si})$ is the algebraic difference in the mean thermal expansion values between room (T_{RT}) and the deposition temperature ($T_{dep.}$). $\overline{E}_f/(1 - \nu_f)$ is the appropriate elastic stiffness term using averaged coefficients over the temperature range evaluated. The appropriate values for the thermal stress calculation are indicated within Table I. The thermal stresses for the mixtures were assumed to be additive in proportion to the volume ratio of the mixed components. The intrinsic stress can then be calculated from knowledge of the measured total room temperature stress and the calculated thermal stress.

Chemical etching behavior.—The chemical etching behavior of the AlN and mixtures was examined in several solvents. For the AlN, rapid solubility was observed in strongly oxidizing acidic and basic solutions (frequently used for Si substrate cleaning), but the films were found to be insoluble in both HF and HF plus HNO_3 mixtures. Quantitative measurement of etch rate in 85% H_3PO_4 was carried out (using ellipsometric measurements for thickness change) for AlN and the AlN-Si_3N_4 mixtures. These measurements

Table I. Mean thermal stress parameters

Material	$T_{Dep.}$ (°C)	Thermal expansion coeff. (×10^{-6} °C^{-1}) $\alpha_\perp$	$\alpha_\parallel$	$\alpha_{Av.}$*	$\overline{E}$ (×10^{12} dynes/cm²)	ν	$\frac{\overline{E}}{(1-\nu)}$ (×10^{12} dynes/cm²)
AlN (18, 19)							
	800	5.27	4.15	4.89	3.35	0.25	4.46
	900	5.29	4.17	4.90	3.31	0.25	4.41
	1000	5.31	4.19	4.91	3.25	0.25	4.34
Si (20)							
	800			3.59			
	900			3.61			
	1000			3.63			
Si_3N_4 (21, 22)							
	800			2.69	2.25	0.25	3.00

* For hexagonal crystal, $\alpha_{Av} = 1/3\ (\alpha_\parallel + 2\alpha_\perp)$ with $\alpha_\parallel$ measured along a axes, and $\alpha_\perp$ measured along the c axes.

are useful for device processing because of the insolubility of SiO_2 within H_3PO_4 (up to 200° C).

Electrical measurements.—D-c electrical conduction measurements were carried out in the range of 20°-200°C for AlN and Si_3N_4 films as a function of deposition temperature, and with varying composition mixtures at a single deposition temperature. Other deposition parameters were the same as those for the TEM and stress studies. Test devices were simple MIS dot capacitors, using Al gate electrodes and both n and p low resistivity Si substrates. No significant difference in conduction was observed for alternate gate electrode polarity, or change of substrate. Additionally, no thickness dependence was observed for films within the range of 500-3000Å. The log J/E *vs.* $E^{1/2}$ dependence is linear above approximately 1 MV/cm. Linearity of log $J/E|E \rightarrow$ o *vs.* $1/T(o_K)$ was observed between RT and approximately 200°C, above which significant decrease in slope was observed.

The charge storage behavior of AlN and various mixtures were evaluated utilizing MNOS-type configurations as was previously used to study Si_3N_4 (11). The capacitive type test structure used n^+-diffused lines in a grid pattern in 2Ω cm p-type Si substrates that allowed for pulse injection of electrons and holes, yielding high frequency *C-V* traces similar to those observed with low frequency traces, *i.e.*, the V-shaped traces. The *C-V* minima correspond to the "turn on" threshold voltage for FET's.

The charge window is defined by the voltage displacement of the *C-V* trace following application of a sufficiently high voltage to the capacitor gate. The voltage displacement is measured at either capacitive flatband for nongridded substrates or at C_{min} with the gridded substrates (11). The theory of this behavior with "MNOS"-type structures has been well documented (23-25). Two suitable reference charge states are obtained by either positive or negative bias saturation, which is defined as the longest pulse width, at constant voltage, that does not result in additional displacement of the *C-V* trace, and additionally does not result in electrical breakdown, by shorting, of the capacitor. This type of biasing is considered the "erase" mode. "Writing" is carried out by immediate (milliseconds to seconds) application of voltage pulses, shorter than the "saturation" pulse, and of opposite polarity. "Read" measurements are obtained with voltage biasing only within the substrate range of accumulation to inversion, with care observed not to extend the bias into deep depletion, otherwise the state of charge will be changed. This aspect is important for long-term charge leakage (memory life) measurements (26). The dynamic charge window is obtained with the following sequence: erase-read-write-read. The write pulses are applied at varying time lengths at constant voltage. Measurements are made for both positive "write" from negative "erase" (injection of electrons from the substrate into the insulator charge trapping layer) and negative "write" from positive "erase" (injection of holes). Reverse leakage to the substrate (discharge) after "write" biasing (26) results in shrinkage of the dynamic charge window. Therefore, "read" sensing (11) of the charge window was carried out with time delays (following application of the "write" pulse) between 35 and 100 msec. The electrical apparatus for carrying out the procedure has been described previously (11). The same apparatus was used for multiple pulse endurance testing. For these latter studies, the broadening of the V-shaped *C-V* trace, measured at flatband, gave qualitative indication of interface state generation with excessive single, or multiple pulse ("fatigue") stressing. This condition generally presaged device failure (11, 27).

Long-time charge retention behavior was evaluated with the same structures utilized for the dynamic charge window measurements. Chips containing these structures were bonded to TO-5 headers and stored in room ambients for periods up to 15 months. The gate and substrate leads were always shorted except when interrogating the state of the charge. All devices on long term test were pre-exercised over approximately 10^5 cycles and put on standby in either the "write" or "erase" mode.

Experimental Results

Chemical vapor deposition.—Because of the reactivity of $AlCl_3$ and NH_3, prereaction and depletion of these reactants occur in the upstream portion of the heated susceptor. This factor, previously reported for the preparation of $Al_xO_yN_z$ films (13), caused difficulty in obtaining axial uniformity. Higher carrier gas flow rates and the use of tapered canopies over the susceptor were helpful in improving uniformity. However, the most useful solution was obtained by lowering the ratio $NH_3/AlCl_3$ from 170/1 ($HiNH_3$) to 1.7/1 ($LoNH_3$) for the AlN preparation. The improvement is shown in Fig. 1.

A similar effect can be realized for the Si_3N_4 preparation wherein the NH_3/SiH_4 ratio becomes important. However, in both of these cases caution must be exercised, since the films may contain excess Al or Si if the amount of NH_3 is too low. Additionally it is seen in Fig. 1 that for high $NH_3/AlCl_3$ ratio the axial uniformity degrades with increasing temperature. This is due to prereaction as stated above which is enhanced at higher temperature. As expected under these conditions, prereaction upstream depletes the reactants so that a lower deposition rate is observed in the susceptor region containing the test wafers (12).

Ellipsometry measurements on films with mixed compositions [prepared using the high $NH_3/(AlCl_3,$

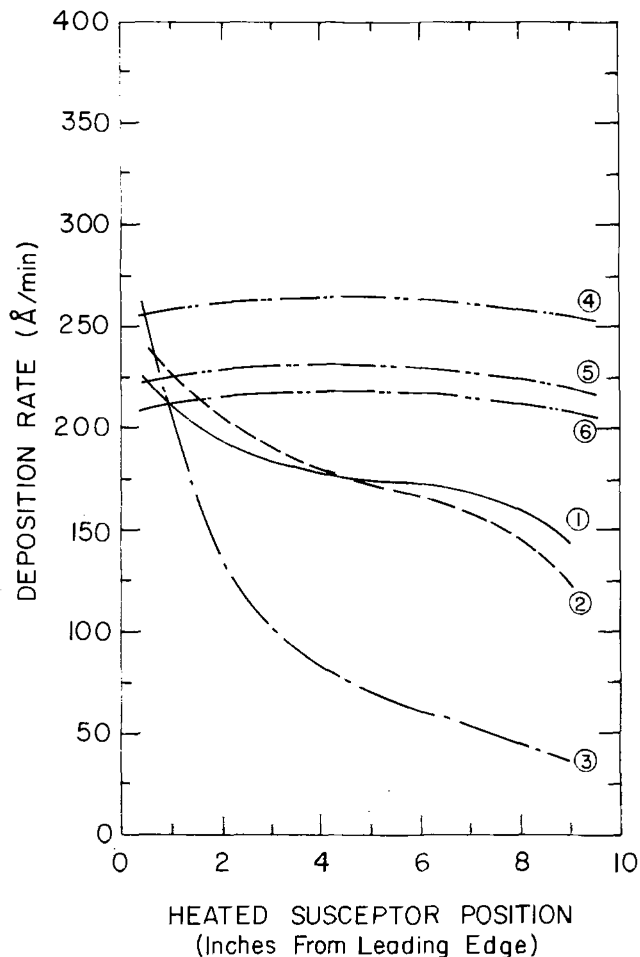

Fig. 1. Deposition rate of AlN along axis of susceptor. 1, 800°C ($HiNH_3$); 2, 900°C ($HiNH_3$); 3. 1000°C ($HiNH_3$); 4, 1000°C ($LoNH_3$); 5, 900°C ($LoNH_3$); 6, 800°C ($LoNH_3$) (See text for definition of high and low NH_3).

SiH_4) reactants ratio] have shown that the film thickness was the sum of the thicknesses which would result from independent deposition of AlN and Si_3N_4, while maintaining the 170/1 NH_3/($AlCl_3$ or SiH_4) reactants ratio. The volume fractions of each component were then additive. Figure 2 shows the calibration of the volume fraction plotted and weight fraction (as determined by electron microprobe analysis) plotted *vs.* the gas phase composition. Such a plot allows control of film thickness and composition for all mixtures and conditions based only on a knowledge of the individual deposition rates of the film components under the prescribed set of film deposition conditions. This finding indicates that the deposition of the AlN and Si_3N_4 components are uncoupled and suggests that the resultant morphology for the mixed composition film will be two phase, *i.e.*, an AlN and a Si_3N_4 phase. The microstructure studies to follow bear out this reasoning.

Film morphologies.—TEM has shown all the AlN films prepared in this study to be polycrystalline. Figure 3 shows that there is a variation of AlN grain size with film deposition temperature. For the films prepared at 650°C, the grains are ~250-350Å and the grain boundaries are not sharp. At 850°C, the grains are somewhat smaller, ~150-250Å, and the grain boundaries are well defined. However, at 1075°C the grains are ~500Å in size and possess well-defined boundaries. A previous study (7) found that the AlN grain size decreased from 770° to 900°C for similarly prepared films. This was explained (7) by invoking the competition between grain growth, which would enable larger grains to grow at higher temperatures due to increased surface mobility of reactants, and the increased nucleation rate with increasing temperature. Apparently, in the 650°-850°C temperature interval, nucleation is dominant. However, for the 1075°C films there is sufficient surface mobility to reverse the competition and render grain growth the dominant mechanism. Furthermore, the lack of sharpness in both diffraction and imaging modes for the low temperature AlN probably indicates that the grains were formed by direct attachment. At high temperatures grains were formed by atoms which would diffuse to more energetically favorable sites.

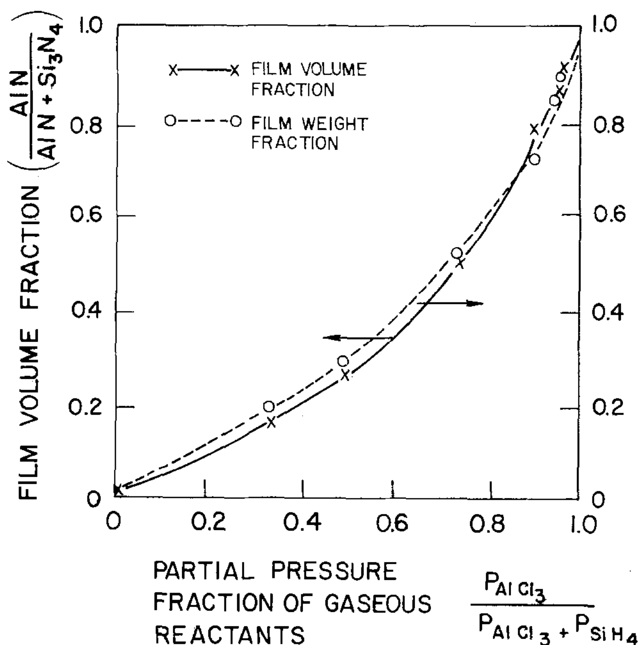

Fig. 2. Prediction of composition of mixed AlN-Si_3N_4 films. Carrier flow velocity = 19 cm/sec, N_2; $NH_3 + H_2 \simeq 0.05$ mole fraction; Al Cl_3 reactor temp. = 120°C with N_2 flush; $SiH_4 + AlCl_3 \simeq 0.01$ mole fraction.

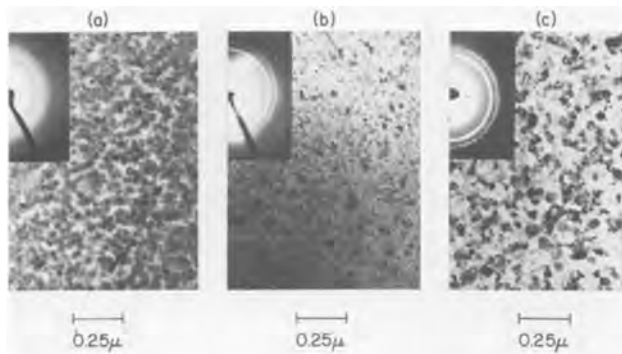

Fig. 3. TEM microstructures of AlN as a function of deposition temperature (a) 650°C; (b) 850°C; (c) 1075°C.

All the Si_3N_4 films prepared in this study were found to be amorphous. Films prepared at lower temperatures were found to contain considerable amounts of particulate matter and this is shown in Fig. 4. The particulates are thought to be Si_3N_4 formed by gas-phase nucleation, carried to the substrate surface by the moving gas stream, and occluded in the growing film. There is more occluded particulate at lower temperatures. We believe that the particulate occurs preferentially for the lower temperature CVD processes because less gas phase depletion of reactants occurs upstream at the lower temperatures. Therefore, within the substrate region, there exists larger concentrations of gas phase reactants, thereby enabling more gas phase nucleation of particulate. A similar phenomena related to film growth rates has been previously reported (12).

The films of mixed composition prepared by codeposition of AlN and Si_3N_4 have been found to contain two phases. The AlN phase is usually polycrystalline and the Si_3N_4 phase is amorphous. When the AlN predominates, grains of AlN are discernible by TEM but the grain boundaries are not sharp. This appears to be due to the Si_3N_4 which surrounds the AlN grains as seen in Fig. 5a. As the amount of AlN in the mixture decreases the AlN grains become smaller as evidenced by the diffuseness of the diffraction patterns for Fig. 5b. In addition, it becomes more difficult to discern grains from particulate or other irregularities. When the Si_3N_4 phase is ~90% or more the mixture appears to be amorphous as seen in Fig. 5c.

Optical properties.—The ellipsometric index of refraction (at 5461Å) for all films deposited at 800°C and above remained constant at 1.99 ± 0.02. Lower dep-

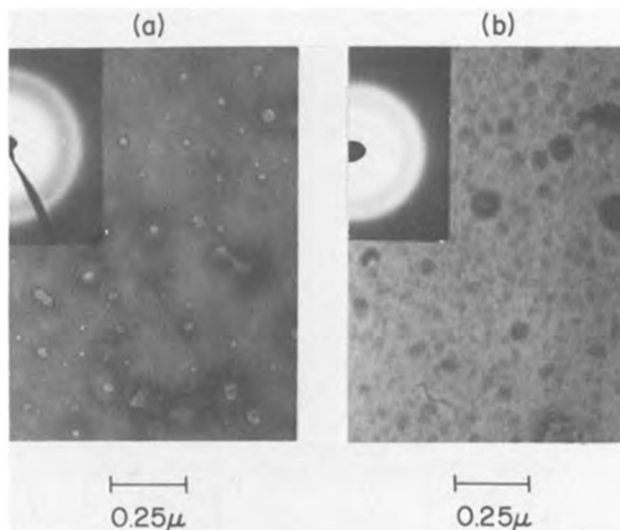

Fig. 4. TEM microstructures of Si_3N_4: (a) 850°C; (b) 1100°C

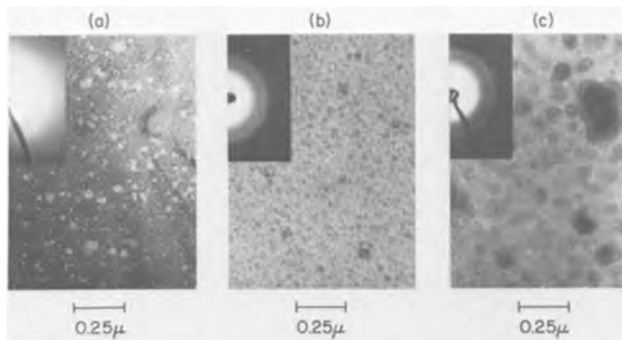

Fig. 5. TEM microstructures of $AlN-Si_3N_4$ mixtures deposited at 850°C: (a) 3/1 volume ratio AlN/Si_3N_4; (b) 1/3; (c) 1/9.

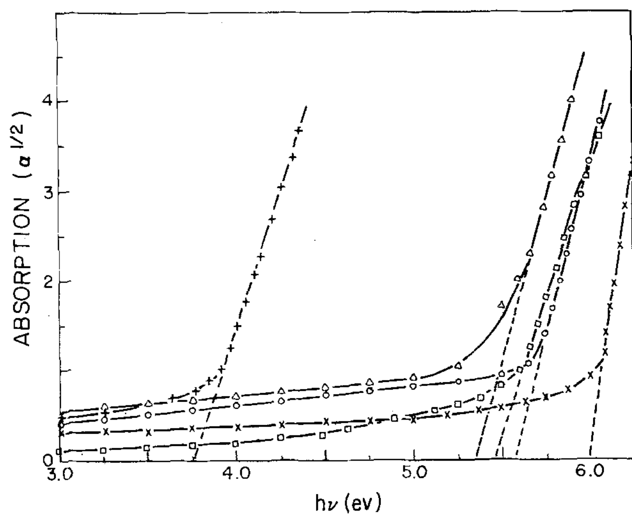

Fig. 6. Wavelength dependence of u.v. and visible optical absorption. ×, AlN ($HiNH_3$); ○, AlN ($LoNH_3$ + H_2); △, AlN ($LoNH_3$, No H_2); □, Si_3N_4 ($HiNH_3$); +Si_3N_4 ($LoNH_3$); 900°C deposition.

osition temperatures for AlN yielded lower refractive indexes, decreasing to 1.70 for 600°C depositions. The wavelength dependence of the absorption for AlN and Si_3N_4 is shown in Fig. 6 as a function of the gaseous reactants composition. Significant differences are observed when varying the NH_3/SiH_4 ratio for the Si_3N_4, as has been reported elsewhere (28). For the low $NH_3/AlCl_3$ ratio films, the addition of H_2 to the reaction also changes the films' absorptive properties. This effect was not evident with the deposition rates and electron microprobe-determined stoichiometry. Though in principle it may be feasible to extract mixture composition data from the absorption coefficient measurements, the sensitivity of the optical absorption values to film microstructural variations (*i.e.*, grain size, inclusions, etc.), and Si or Al enrichment renders this measurement unreliable for AlN/Si_3N_4 mixture ratio calibration. The calculated absorption edges (13) for the low $NH_3/(AlCl_3,SiH_4)$ ratio films are plotted in Fig. 7 and are compared to the values indicated for high $NH_3/(AlCl_3,SiH_4)$ ratio films of AlN and Si_3N_4.

Apparently the shift in the absorption edge to lower values with less NH_3 correspond with a metal enrichment of the film (either Al or Si). This would cause a reduced bandgap, higher conductivity, and an increased density of states near the conduction band. Such properties have been found to be undesirable for charge-storage layers (8). For devices made using Si-rich Si_3N_4 (8), "read" windows were large for low "write" voltages (15-25V) but charge loss was rapid (seconds) unless thick tunneling oxides were used (50-75Å). However, such thick oxide would require larger "write" voltages and therefore effectively counter the potential advantage of the device. Therefore, it was decided to use compositions prepared with high $NH_3/(AlCl_3, SiH_4)$ ratios for the electrical studies.

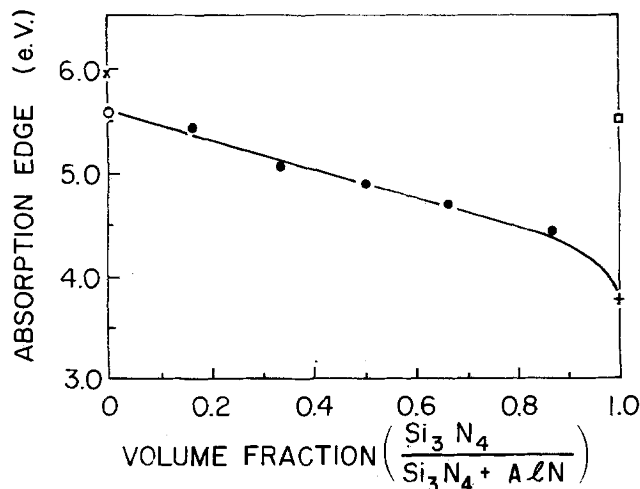

Fig. 7. Calculated optical absorption edges for $AlN-Si_3N_4$ mixtures ×, AlN ($HiNH_3$); ○, AlN ($LoNH_3$); □, Si_3N_4 ($HiNH_3$); ●, mixtures ($LoNH_3$); ⊕, Si_3N_4 ($LoNH_3$).

Stress measurements.—Figure 8 shows the variation of the components of AlN film stress with film deposition temperature. It can be seen that the AlN net tensile stress is dominated by the differential thermal expansion stress component (arising during cooling from the deposition temperature) which is tensile. The intrinsic stress component (17) deduced from the measured net and calculated thermal components is compressive and apparently increases with film deposition temperature. The increase is slight and may be only an indirect result of an increase in the anisotropic Youngs modulus with the development of some preferred orientation, as shown in Fig. 3b and 3c and reported elsewhere (5, 6).

Similar stress measurements for the mixed AlN, Si_3N_4 films are shown in Fig. 9. The addition of Si_3N_4 to the AlN results in a strong influence upon the total net stress. The morphological studies have shown that the Si_3N_4 deposits around the AlN grains thereby forming the connective phase. Therefore, it is expected that the intrinsic stresses within films of the

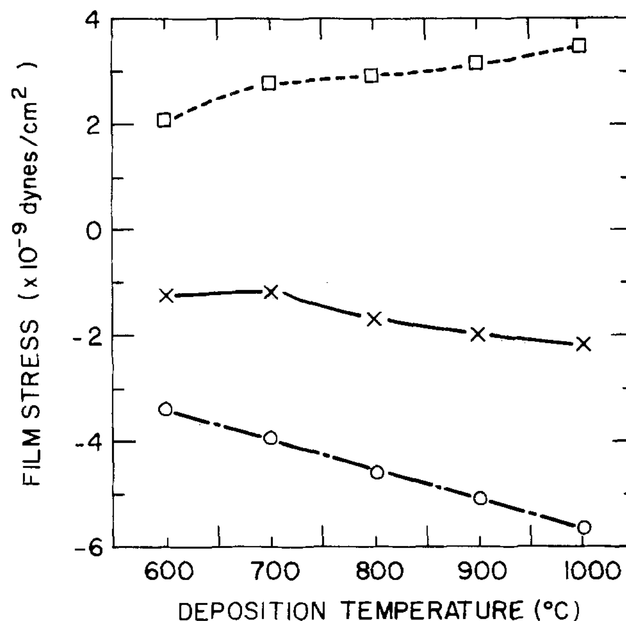

Fig. 8. Stress in AlN films as a function of deposition temperature. ×, measured at room temperature; ○, calculated thermal stress (at room temperature); □, net intrinsic stress.

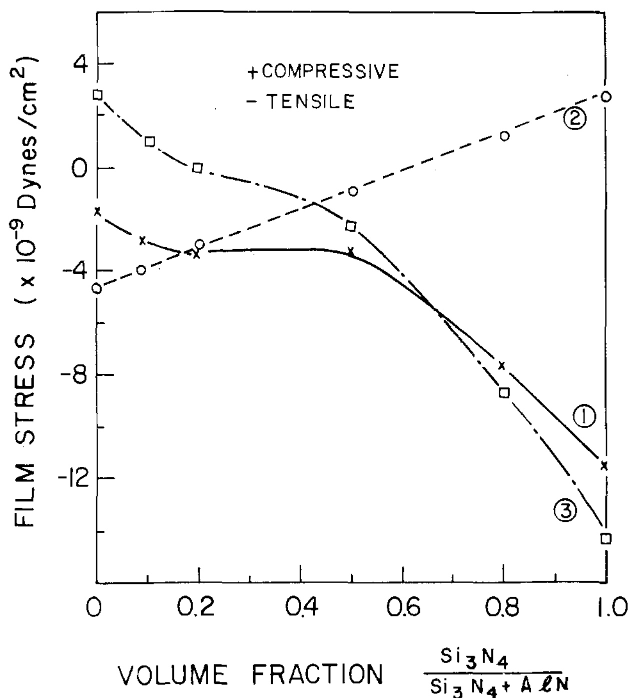

Fig. 9. Stresses in $AlN-Si_3N_4$ mixtures ($T_{dep.} = 850°C$). ×, measured at room temperature; ○. calculated thermal stress; □, net intrinsic stress.

mixed components would be due primarily to the connective Si_3N_4 phase.

Etching behavior.—Both the AlN and $AlN-Si_3N_4$ mixtures show varying solubility within hot 85% H_3PO_4, depending upon film composition and the deposition parameters, as shown in Fig. 10. The mixtures are much more resistant to etching by hot H_3PO_4 than is the pure AlN. This is most likely due to the shielding of the AlN by the matrix of amorphous Si_3N_4 surrounding the AlN grains. The dependence of the deposition temperature for the etch rate of AlN is shown in Fig. 10. Higher deposition temperatures yield lower etch rates as has been reported (5). The influence of the $NH_3/AlCl_3$ reactants ratio is shown for the example of a 4/1 film mixture (AlN/Si_3N_4). The low reactants ratio (1.7/1) causes enrichment of the mixture with silicon. This is known to reduce the etch rate for silicon nitride (29). This factor is more clearly indicated for the apparently anomalous difference in etch rate observed for the film mixture prepared with low $NH_3/(AlCl_3, SiH_4)$ ratio at 800° and 1000°C. The film prepared at lower deposition temperatures contains relatively more excess Si, thereby becoming more etch resistant.

Electrical properties.—The d-c conduction behavior appears to be similar to Poole-Frenkel bulk-limited-type in accordance to the following relationship (30)

$$J/E = \Delta_0 \exp -\{[\psi_d - (B_{P\text{-}F}E)^{1/2}]/rkT\} \quad [3]$$

with J = current density, E = averaged steady-state electric field across the insulator, ψ_d = energy of the coulombic trap below the conduction band, $B_{P\text{-}F}$ = Frenkel-Poole constant, k = Boltzmann constant, T = absolute temperature. Δ_0 is a conduction term at zero field that is interpreted according to assumed distribution, types, and occupany of the traps associated with the P-F type of conduction (31-33). r takes on values of 2 or 1 depending upon whether a donor-trap model (29,32) is applied to the data, or a model invoking both donor traps (which are coulombic) and neutral traps (32) (noncoulombic). For the former case Eq. [3] is as follows

$$J/E = \Delta_0 \exp - [\psi_d - (B_{P\text{-}F}E)^{1/2}]/2kT \quad [4]$$

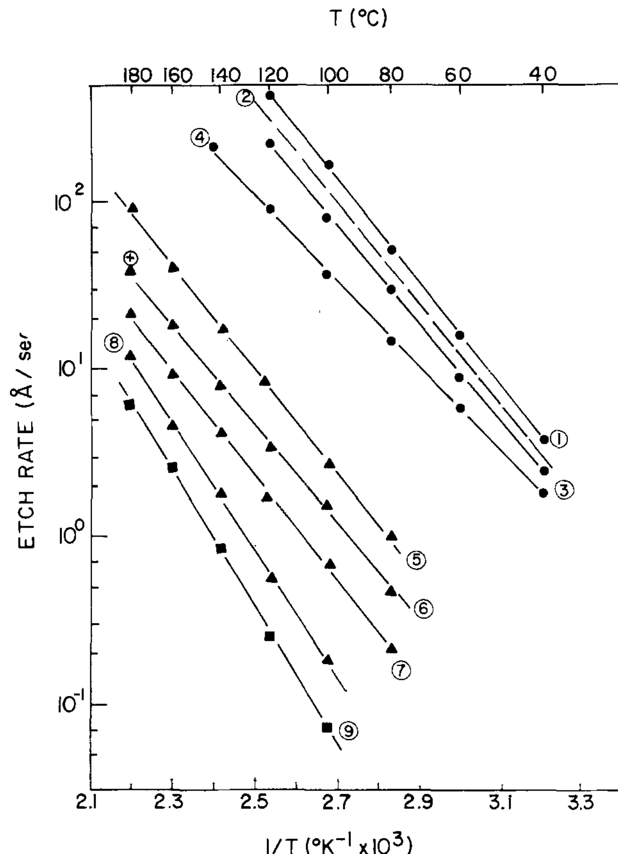

Fig. 10. The etching characteristics of AlN and $AlN-Si_3N_4$ mixtures in hot H_3PO_4. 1, AlN (800°C, $LoNH_3$); 2, AlN [900°C. Ref. (5)]; 3, AlN (900°C, $LoNH_3$); 4, AlN (1000°C, $LoNH_3$); Si_3N_4 (900°C, $HiNH_3$). ⊕ mixtures (volume ratio AlN/Si_3N_4); 5, 4/1 (1000°C, $HiNH_3$); 6, 4/1 (1000°C, $LoNH_3$); 7, 1/1 (1000°C, $LoNH_3$); 8, 1/4 (1000°C, $LoNH_3$); 9, 1/1 (800°C, $LoNH_3$).

with: $\Delta_0 = e_\mu (N_c N_d)^{1/2}$
and for the latter case

$$J/E = \Delta_0 \exp - [\psi_d - (B_{P\text{-}F}E)^{1/2}]/kT \quad [5]$$

with: $\Delta_0 = e_\mu N_c (N_d/N_t)^{1/2}$
μ = carrier mobility (single carrier injection); N_c = density of states within the insulator film's conduction band; N_d = density of film's coulombic traps; and N_t = density of films neutral traps.

The theoretical value for $B_{P\text{-}F}$ is calculated as follows

$$B_{P\text{-}F} = \frac{e^3}{\pi \epsilon_0 \epsilon_f} \quad [6]$$

with e = electronic charge, ϵ_0 = free space permittivity and is approximately equal to the optical index of refraction squared. For room temperature measurements, Eq. [3] can be utilized in the following form

$$\ln (J/E) = \left[\ln \Delta_0 - \frac{\psi_d}{rkT} \right] + \frac{B_{P\text{-}F}^{1/2}}{rkT} (E^{1/2}) \quad [7]$$

which allows for a determination of $[B_{P\text{-}F}^{1/2}/rkT]$ from the slope of the ln (J/E) *vs.* $E^{1/2}$ plot. Isothermal plots at several temperatures were then used to obtain plots of $(1/T°K)$ *vs.* ln $(J/E)_{E=0}$. The slope of this plot then yields values of ψ_d.

The calculated conduction parameters of Eq. [3] are plotted in Table II, from conduction data obtained with (*i*) AlN as a function of deposition temperature, (*ii*) Si_3N_4, as a function of deposition temperature, and (*iii*) several $AlN-Si_3N_4$ mixtures deposited at 850°C. The experimental (J/E) *vs.* $E^{1/2}$ slope ($B_{P\text{-}F}$) for the AlN implies that the coulombic trap model applies and r = 2. The experimetal $B_{P\text{-}F}$ slope for both

Table II. Electrical conduction as a function of composition

Film* composition (volume ratio AlN/Si_3N_4)	Extrapolated zero field conduction Δ_0 (a/V cm at RT)	Poole-Frenkel slope (RT)	r	Trap depth below conduction band ψ_d (eV)
1/0 (600°C)	10^{-19}	0.0044	2	1.28
1/0 (725°C)	10^{-16}	0.0081	2	1.17
1/0 (850°C)	10^{-16}	0.0070	2	1.60
1/0 (975°C)	10^{-16}	0.0088	2	2.05
1/0 (1075°C)	10^{-17}	0.0135	2	2.13
0/1 (700°C)	10^{-24}	0.0195	1	0.98
0/1 (850°C)	10^{-33}	0.020	1	1.06
0/1 (1100°C)	10^{-23}	0.0167	1	1.10
3/1 (850°C)	10^{-18}	0.0197	1	1.30
1/1 (850°C)	10^{-26}	0.0190	1	1.38
1/3 (850°C)	10^{-25}	0.0232	1	1.45
1/9 (850°C)	10^{-33}	0.0256	1	1.65
		0.00738**	2	

* Deposition temperature in bracket, and using high $NH_3/(AlCl_3, SiH_4)$ reactants ratio.
** Theoretical for index of refraction = 2.0 and r = 2.

the Si_3N_4 and mixtures imply a mix of coulombic and neutral traps, and therefore $r = 1$. The calculated values for ψ_d from the experimental $(J/E)_{E=0}$ *vs.* $1/T$ slopes take into account the conduction model invoked, and value of "r" used. A more comprehensive $B_{P\text{-}F}$ conduction model [*i.e.*, see, for example Arnett (34)], is beyond the scope of this paper, because of the limited amount of conduction data available. The conduction measurements were in fact initiated mainly for the purpose of providing a useful precursor to selection of the best compositions and deposition conditions for charge storage application. A suitable reference guideline would be the conduction parameters associated with Si_3N_4, deposited at 850°C.

The AlN data show significant variation of the conduction constants with varying deposition temperature. All conduction parameters increase with increased deposition temperature. The major variant is the $B_{P\text{-}F}$ slope for 600°C deposition. When comparing the conduction parameters of the AlN with those for the Si_3N_4 deposited at 850°C, it can be noted that the Δ_0 values are significantly higher and $B_{P\text{-}F}$ slopes lower. Charge storage structures with pure AlN yielded smaller storage windows and rapid charge decay compared to equivalent Si_3N_4 structures. The conduction parameters for the mixtures between (1/1) AlN/Si_3N_4 and (1/9) AlN/Si_3N_4 appeared more similar to those for the Si_3N_4. Both of these compositions were therefore selected for more comprehensive evaluation of charge storage properties.

Charge storage measurements were carried out using standard configurations of the tunneling oxide (thickness range 25-50Å SiO_2) plus the charge storage layer contained within single dielectric films (~500Å). Storage layer compositions evaluated included AlN and $AlN\text{-}Si_3N_4$ mixtures within the volume range of 1/1-1/9. For all oxide thicknesses, charge windows comparable to those observed with Si_3N_4 (11) were obtained, when using "write" pulses (15-25V) in the msec range. These storage windows exhibited very short lifetimes due to rapid charge decay. The storage layer configuration was subsequently modified to include a CVD Al_2O_3 layer. The layer thicknesses were adjusted to yield a total thickness of 500Å (~250Å apiece). The AlN films (deposited at 850°C) exhibited no change in charging behavior and only moderate improvement in charge window lifetime. Si_3N_4 films (deposited at 850°C) exhibited both charging and discharge behavior similar to that exhibited by monolithic Si_3N_4 films (11).

The mixed film compositions, 1/1 and 1/9 volume ratio of AlN/Si_3N_4 were evaluated with the dual dielectric storage structure. Both exhibited similar charging and discharge behavior, therefore the subsequent data for the 1/1 volume ratio are representative of both compositions.

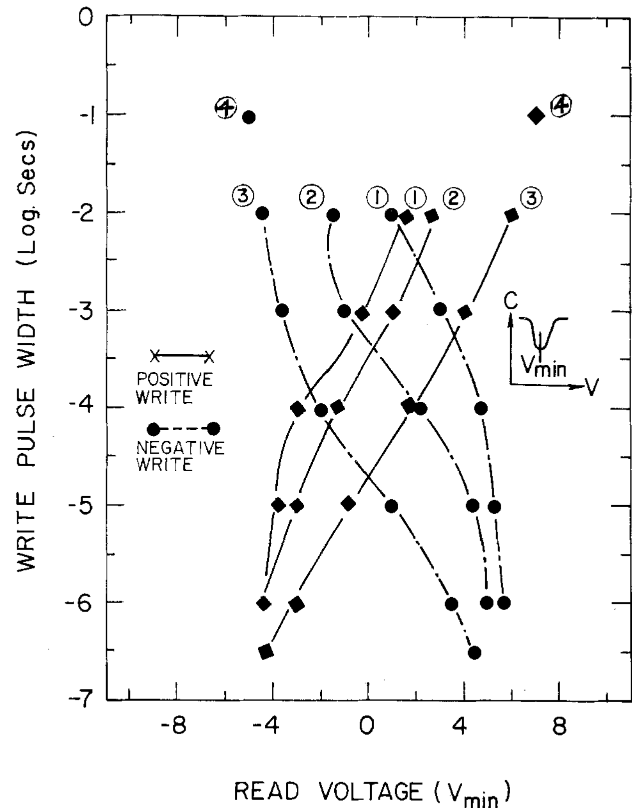

Fig. 11. Charge window using 1/1 volume ratio AlN/Si_3N_4 for charge storage layer (n^+-gridded Si substrate. 24Å SiO_2, 250Å $AlN\text{-}Si_3N_4$, 250Å Al_2O_3, Al gate) (1, 7.5V; 2, 10V; 3, 15V; 4, 25V; saturation erase; 35 μsec read delay).

The dynamic-charge injection behavior as a function of tunnel oxide thickness is indicated in Fig. 11-13. The shift in V_{min} from opposite polarity saturation is shown for varying pulse widths and several voltage levels. Figure 11 indicates that symmetric charge windows can be obtained over a wide range of "low" voltages (7½-25V) for "thin" oxide devices (<30Å SiO_2). These can be used for either n- or p-channel depletion-mode devices (35). For oxide thicknesses between 30 and 40Å, there is a shift to the median of charge polarity to the positive mode (Fig. 12). All positive mode operation is achieved for oxide thicknesses greater than 40Å, as is indicated in Fig. 13. This type of operation is useful for enhancement mode n-channel operation, such as, for example, has been explored with MAOS structures (36). The charge window for 48Å SiO_2 is similar to that for Al_2O_3 with a 30Å tunnel oxide thickness (Fig. 14), excepting that higher write-erase voltages are required for the Al_2O_3 device. Limited multiple cycling studies have indicated good window stability (no window shift, interface state buildup, or device failure) with up to 10^7 for 25V, and at least 10^8 (test cutoff) write-erase cycles for 15-20V. The absolute magnitude of the charge window, as written from "erase" saturation is plotted in Fig. 15, as a function of tunnel oxide thickness for "write" voltages of 15 and 25V. Comparison is also presented with similar Si_3N_4 devices (11). Significantly larger charge windows are observed with the use of the $AlN\text{-}Si_3N_4$ mixtures. Additionally, the observation of large charge windows over a wide range of tunneling oxide thickness (up to 48Å SiO_2) is advantageous from a device fabrication point of view. The relaxation of close oxide thickness tolerances contributes to increased device yield and lowered manufacturing costs.

The long-term charge retention behavior has been monitored with test devices of both 1/1 and 1/9 volume ratio AlN/Si_3N_4, in both the "write" and "erase" mode. Typical results are indicated in Fig. 16 for three

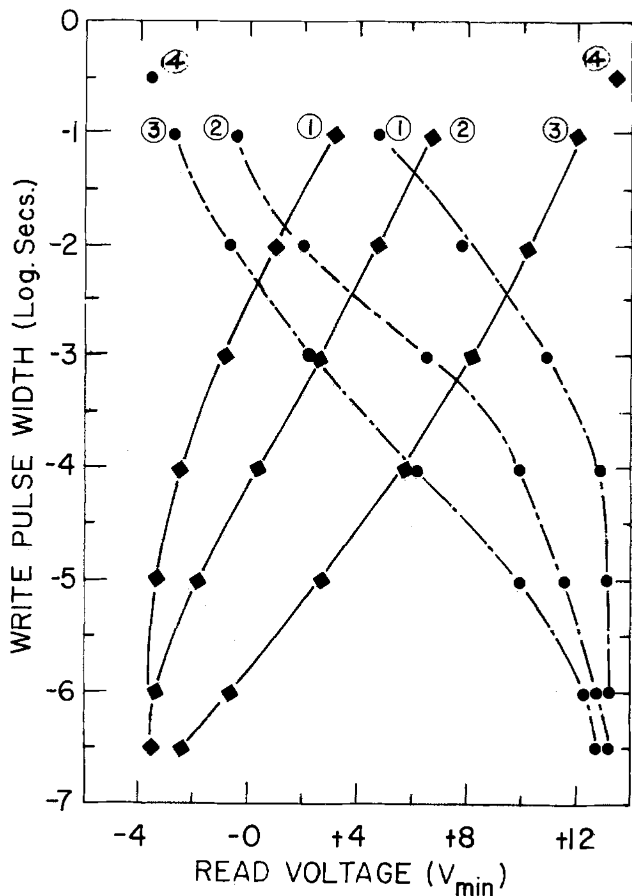

Fig. 12. Charge window, 35Å SiO_2. (1, 15V; 2, 20V; 3, 25V; 4, 25V. Saturation erase; 0.1 min read delay).

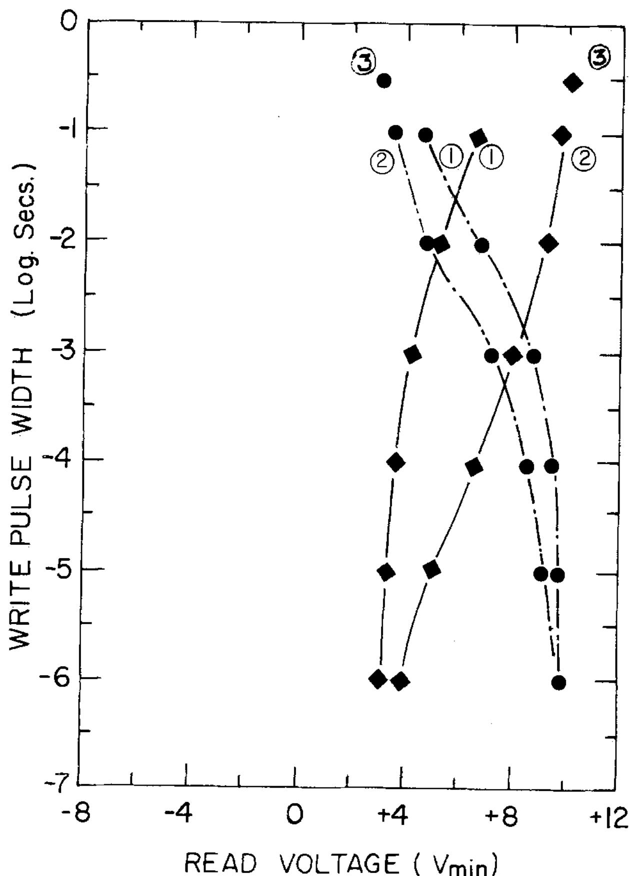

Fig. 13. Charge window, 48Å SiO_2. (1, 20V; 2, 25V; 3, 25V; saturation erase; 0.1 min read delay).

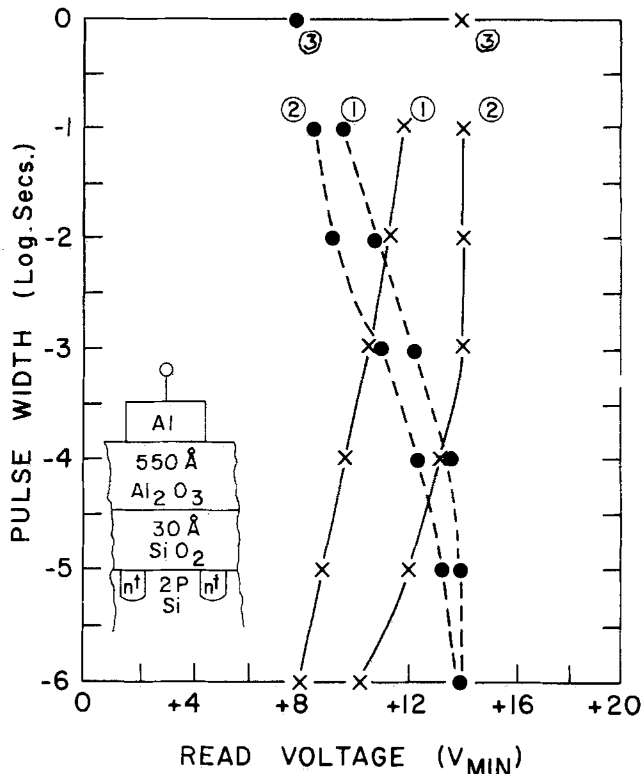

Fig. 14. Charge window with Al_2O_3 storage layer. (1, 25V; 2, 30V; 3, 30V. Saturation erase; 0.1 min read delay).

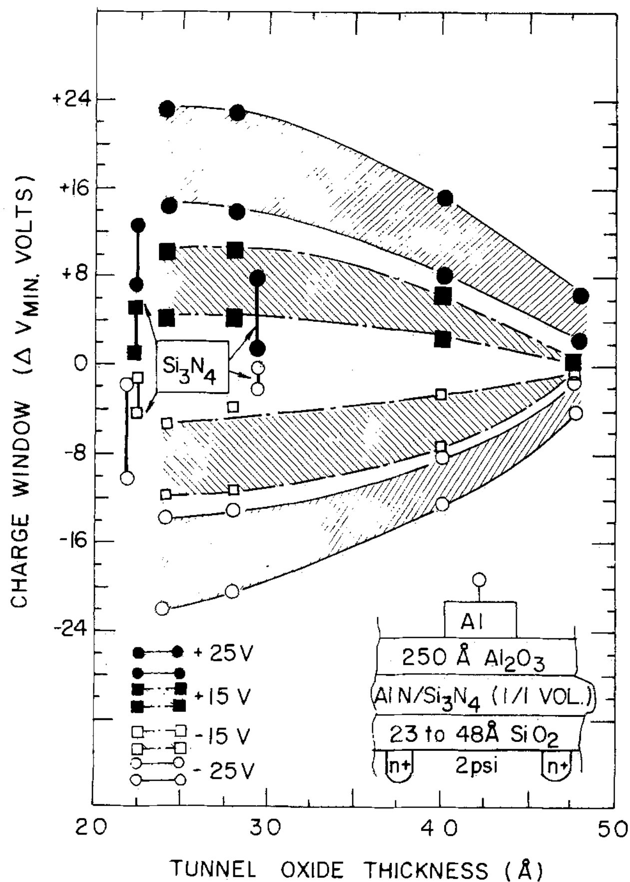

Fig. 15. Absolute magnitude of positive and negative charge windows as a function of SiO_2 thickness. [Write pulse width range: 10^{-5} to 10^{-1} sec; Si_3N_4 data. Ref. (11)].

"erase-write" conditions. Six devices are required since the initial state of charge (in either "write" or "erase" mode) is maintained on long-term test. The pairing of "erase-write" data points result from pulse

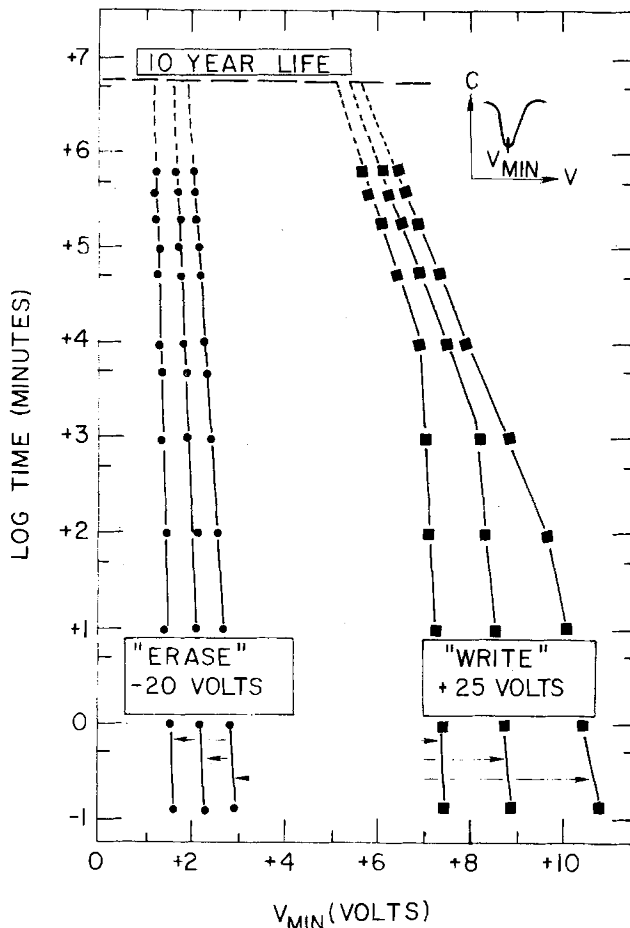

Fig. 16. Long time charge-retention behavior (43Å SiO_2)

width selection during initial charging to yield different windows. The initial "erase" positions differ since saturation pulse widths were not used, otherwise the "erase" data points would merge. It was observed that the discharge behavior is qualitatively similar to that observed for Si_3N_4 (11, 26, 35). The initial discharge rate increases with increased "write" bias, as was also observed with devices made from Si_3N_4 (11). Additionally, when comparing devices of varying tunnel oxide thickness, "writing" to the same charge level yields initial discharge rates that decrease with increased oxide thickness (26). For all initial V_{min} values the shift in V_{min} is linear with $\Delta V_{min}/\Delta ln\ t$, and always in a direction toward shrinkage of the charge window. This, of course, arises from loss of charge through the tunneling oxide to the Si substrate (26). When "erasing" to a negative V_{min} (not shown in Fig. 16), the shift in V_{min} is toward 0V. The time duration of the constancy of the $\Delta min/\Delta ln\ t$ slope, after "writing," varies qualitatively and inversely with the initial value of V_{min}. A discontinuous increase in the $\Delta V_{min}/\Delta ln\ t$ slope then occurs. The net result is eventual convergence of the V_{min} values, even with large differences in the initial written V_{min} values (for constant tunneling oxide thickness). Since this behavior was also observed with Si_3N_4 storage devices (11) the storage behavior of the mixture is most likely governed by the Si_3N_4 matrix within the two-phased structure of the AlN-Si_3N_4 mixture. The data indicated in Fig. 16 for devices with 1/1 volume ratio of AlN/Si_3N_4 and 43Å SiO_2 show that even with initial "read" windows of 5-8V, the final "read" window after 10 years is projected to be of the order of 3-4V. The indicated data points were acquired over a 15 month period.

Discussion

The rise in the Poole-Frenkel conduction slope values ($\beta_{P\text{-}F}$), with increased deposition temperature, can perhaps be reconciled with an increased density of neutral traps, in accordance with the Yeargan-Taylor compensation model (32). With increased deposition temperatures the microstructure (as observed with TEM) tends toward more well-defined grain boundaries and crystallinity (see Fig. 3). We speculate that these higher angle grain boundaries possibly contribute toward increased density of neutral traps. On the other hand, the relative insensitivity of the extrapolated zero-field conduction term (Δ_0), with deposition temperature, would then imply that even with the increase of the neutral traps the total number of traps (neutral plus coulombic) remains essentially the same. Additionally, we postulate that the well-defined crystallinity with increased deposition temperature tends to yield deeper traps, as indicated by the ψ_d values for AlN in Table II.

The $\beta_{P\text{-}F}$ slope values for the Si_3N_4 and mixtures are higher than indicated by the above compensation model and must be reconciled by alternate schemes. The presence of particulates with the lower deposition temperatures (see Fig. 4) may contribute to the excess low field conduction, leading to higher Δ_0 conduction values. The high Δ_0 with deposition at 1100°C could be due to the presence of crystalline Si_3N_4 at and above this temperature (37, 38).

The increasing concentration of Si_3N_4 with the mixtures causes a rapid lowering of the Δ_0 conduction term. The high field conduction behavior, as shown by the $\beta_{P\text{-}F}$ slope values, is similar to that indicated by the Si_3N_4. The conduction behavior of the mixtures, then, appears to be influenced mainly by the enveloping matrix of Si_3N_4 surrounding the AlN grains. This factor is significant regarding the charge storage behavior. We propose the following:

During the charging cycle, the higher $\beta_{B\text{-}F}$ values indicate essentially uniform conduction within the matrix of the Si_3N_4 envelope and AlN grains. Trap filling occurs mostly within the AlN grains and at the AlN-Si_3N_4 interface. With removal of the high external voltage a reversed lower internal field remains due to the high concentration of trapped charge. With the dual dielectric storage structure the trapped charge tends to leak toward the silicon substrate. The rate of discharge is restricted by the Si_3N_4 matrix and the "thick"-tunneling thermal SiO_2.

From energy band considerations, the presence of the Al_2O_3 provides an energy barrier, as shown in Fig. 17, which would cause additional charge pileup at the

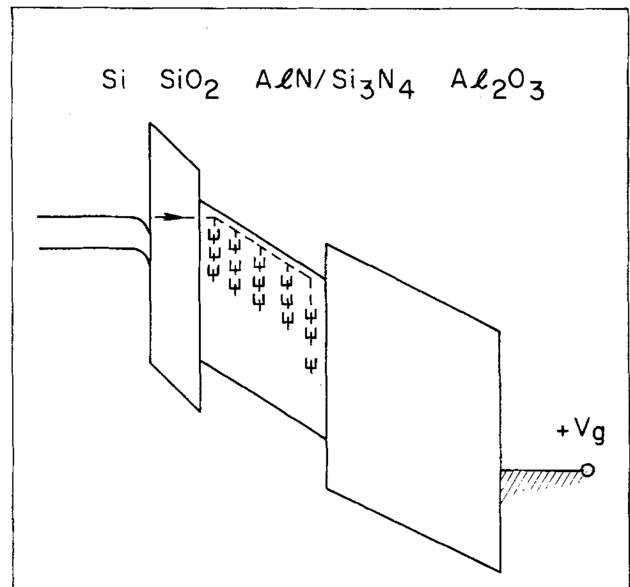

Fig. 17. Energy band diagram for thick oxide charge storage device with AlN-Si_3N_4 mixture within the charge-storage layer (positive write case).

$(AlN-Si_3N_4)-Al_2O_3$ interface. Dual dielectric structures of Si_3N_4 plus Al_2O_3 do not behave differently from single Si_3N_4 charge storage structures (8). This would imply that, perhaps, the mixtures do indeed contain a higher concentration of trapping sites than does Si_3N_4. In addition, high concentration of relatively deep traps with the mixtures (as implied by the larger ψ_d values for the mixtures in Table II) would minimize charge tunneling at the $(AlN-Si_3N_4)-Al_2O_3$ interface into the Al_2O_3 conduction band. This could happen when using Si_3N_4 as a replacement for the Al_2O_3. These devices show smaller charge windows than comparably "written" $(AlN-Si_3N_4)Al_2O_3$ devices.

The influence of varying the tunneling oxide thickness upon the long term discharge behavior is similar to that exhibited by other storage layers (39). Therefore, devices exhibiting long-time charge retention properties, require thick tunneling oxides (between 40 and 50Å).

Summary and Conclusions

The preparation of films of mixtures of AlN and Si_3N_4 has been carried out by the thermal ammonialysis of gaseous $AlCl_3$ and SiH_4. The deposition kinetics and film thickness uniformity is significantly influenced by the $NH_3/(AlCl_3, SiH_4)$ reactants ratio. Some physiochemical properties have been characterized as a function of composition and deposition parameters and compared to those observed with AlN and Si_3N_4. Charge storage structures analogous to MNOS and MAOS devices have been prepared using a dual dielectric storage layer. These devices provide superior electrical performance compared to both MNOS and MAOS devices. The large charge windows obtained with low (under 25V) "write" voltages and the adequate charge retention over long periods of time make these devices potentially useful with read mostly and read only memory devices.

A new concept has been attempted in this work, *i.e.,* the use of a two-phase dielectric layer to enhance charge storage properties. The measurement of several physical properties indicates that the mixed film of $AlN-Si_3N_4$ behaves electrically similarly to Si_3N_4, except that the charge trapping behavior is enhanced due to the addition of the AlN phase. A simple energy band model utilizing a finite width potential well analogue is invoked to qualitatively explain the charge storage behavior of the $(AlN-Si_3N_4)-Al_2O_3$ dual dielectric layer.

Acknowledgments

The authors gratefully acknowledge Dr. A. B. Fowler for his helpful suggestions and continual support of this work, and Drs. P. Arnett and D. DiMaria for stimulating and informative discussions. Additionally, we appreciate Dr. T. Sedgewick's critical review of this manuscript. And finally we wish to acknowledge the experimental support provided by H. Ripke for the electrical apparatus, D. Dong for CVD and ellipsometry support, and J. Kuptsis for electron microprobe analytical support.

Manuscript submitted June 1, 1977; revised manuscript received Oct. 3, 1977. This was Paper 248 presented at the Las Vegas, Nevada, Meeting of the Society, Oct. 17-22, 1976.

Any discussion of this paper will appear in a Discussion Section to be published in the December 1978 JOURNAL. All discussions for the December 1978 Discussion Section should be submitted by Aug. 1, 1978.

Publication costs of this article were assisted by IBM Corporation.

REFERENCES

1. S. Mirsch and H. Reimer, *Phys. Status Solidi A,* **11,** 631 (1972).
2. G. Lewicki and J. Maserjian, *Metall. Trans.,* **2,** 673 (1971).
3. J. K. Lieu, K. M. Lakin, and K. L. Wang, *J. Appl. Phys.,* **46,** 3703 (1975).
4. A. J. Noreika and D. W. Ing, *ibid.,* **3,** 5578 (1968).
5. T. L. Chu and R. W. Kelm, Jr., *This Journal,* **122,** 995 (1975).
6. T. L. Chu, C. H. Lee, and G. A. Gruber, *ibid.,* **114,** 717 (1967).
7. E. A. Irene, V. J. Silvestri, and G. R. Woolhouse, *J. Electron. Mater.,* **4,** 409 (1975).
8. S. Zirinsky, Unpublished data.
9. V. M. Kamyshov and A. G. Gorbatov, *Sb. Naukchn. Tr. Sverdl.,* Inst. Nar. Koz., No. 18, 31 (1970).
10. E. A. Irene, *This Journal,* **121,** 1613 (1974).
11. S. Zirinsky, *J. Electron. Mater.,* **4,** 591 (1975).
12. V. J. Silvestri, E. A. Irene, S. Zirinsky, and J. D. Kuptsis, *ibid.,* **4,** 429 (1975).
13. W. M. Yim, E. T. Stofko, P. J. Zanzucchi, J. I. Pankove, M. Ettenberg, and S. L. Gilbert, *J. Appl. Phys.,* **44,** 291 (1973).
14. A. Brenner and S. Senderoff, *J. Natl. Bur. Stnds.,* **42,** 105 (1949).
15. R. J. Roark, "Formulas for Stress and Strain," p. 98, McGraw-Hill Co., New York (1943).
16. J. J. Wortman, *J. Appl. Phys.,* **36,** 153 (1965).
17. E. A. Irene, *J. Electron. Mater.,* **5,** 287 (1976).
18. W. M. Yim and R. J. Paff, Jr., *J. Appl. Phys.,* **45,** 1456 (1974).
19. K. M. Taylor and C. Lenie, *This Journal,* **107,** 308 (1960).
20. J. P. Dismukes, L. Ekstrom, and R. J. Paff, Jr., *J. Phys. Chem.,* **68,** 3021 (1964).
21. W. A. Fate, *J. Appl. Phys.,* **46,** 2375 (1975).
22. P. J. Burkhardt and R. F. Marvel, *This Journal,* **116,** 864 (1969).
23. E. C. Ross and J. T. Wallmark, *RCA Rev.,* **30,** 366 (1969).
24. D. Frohman-Bentchkowsky, *J. Appl. Phys.,* **40,** 3307 (1969).
25. K. I. Lundström and C. M. Svennson, *IEEE Trans. Electron. Devices,* **ed-19,** 826 (1972).
26. L. Lundkvist, I. Lundström, and C. Svensenn, *Solid State Electron.,* **16,** 811 (1973).
27. M. H. Woods and J. W. Treska, "Degradation of MNOS Memory Transistors," Physics of Failure Meeting, Las Vegas, Nevada (1972).
28. G. A. Brown, W. C. Robinette, Jr., and H. G. Carlson, *This Journal,* **115,** 948 (1968).
29. V. Y. Doo, D. R. Kerr, and D. R. Nicholls, *ibid.,* **115,** 61 (1968).
30. D. R. Lamb, "Electrical Conduction Mechanisms in Thin Insulating Films," p. 74, Methuen and Co., Ltd., London (1967).
31. J. G. Simmons, *Phys. Rev.,* **155,** 657 (1967).
32. J. R. Yeargan and H. L. Taylor, *J. Appl. Phys.,* **39,** 5600 (1968).
33. P. S. Tsang, R. M. Anderson, and S. Cvikevich, *This Journal,* **123,** 57 (1976).
34. P. C. Arnett, *J. Appl. Phys.,* **46,** 5236 (1975).
35. M. H. White and J. R. Cricchi, *IEEE Trans. Electron Devices,* **ed-19,** 1280 (1972).
36. M. T. Duffy and A. G. Revesz, *This Journal,* **117,** 372 (1970).
37. V. Y. Doo, D. R. Nicholls, and G. A. Silvey, *ibid.,* **113,** 1279 (1966).
38. K. E. Beam, P. S. Gleins, and R. L. Yeakley, *ibid.,* **114,** 733 (1967).
39. D. Kahng, W. J. Sundberg, D. M. Boulin, and J. R. Ligenza, *Bell Syst. Tech. J.,* **53,** 1723 (1974).

A Possible Method for the Growth of Homogeneous Mercury Cadmium Telluride Single Crystals

G. Fiorito, G. Gasparrini, and D. Passoni
CISE, Segrate, Milan, Italy

ABSTRACT

A new procedure for preparing homogeneous single crystals of $Hg_{1-x}Cd_xTe$ alloys over a wide range of compositions is proposed. The method, based on a modification of the usual Bridgman technique, promises to overcome variations in composition resulting from the high segregation rate of CdTe with respect to HgTe. During most of the growth period the melt composition is controlled by means of a second solid phase. In particular some results are reported in connection with a composition of significant interest for application as an infrared detector and spin flip laser material.

In recent years the Mercury Cadmium Telluride pseudobinary alloys ($Hg_{1-x}Cd_xTe$) have proved to be uniquely suitable for preparation of high quality medium and far infrared detectors. The reason stems from the various basic material peculiarities (1) such as an energy gap which can be adjusted from 0 to 1.5 eV varying the composition (x). The detector spectral response can be matched to any wavelength in the 1-14 μm range at working temperatures at or above 77°K. In addition to the compositional dependence of the bandgap, $Hg_{1-x}Cd_xTe$ alloys are direct gap semiconductors having high absorption coefficients with low intrinsic carrier concentrations and with high electron mobilities.

Though very high performance photoconductive and photovoltaic detectors have been made for many years, either as single detectors or as arrays, up to now the potentialities of such alloys have been limited by the difficulties of growing crystals with long-range homogeneity of reasonable size. Moreover, to achieve economic fabrication of devices, high yields of useful material are required. For these reasons, present research on the material will be concerned primarily with improved methods of growing large single crystals of adequate compositional uniformity.

To achieve this goal, several techniques have been proposed and used. Most of them are based on the existence of a liquid phase even for thin layer depositions. However most thin layers have been grown by an evaporation-diffusion mechanism, using a close-spaced configuration, or in a mercury plasma using a triode sputtering arrangement. These layers of the compounds have been successfully used for fabricating photovoltaic detectors (2-4).

The main problem in $Hg_{1-x}Cd_xTe$ growth from the melt is the compositional inhomogeneities which result along the growth direction because of strong segregation of its binary components, due to the wide separation of the liquidus and solidus lines in the phase diagram (5, 6). Melt stoichiometry maintenance during the growth is also a problem because of the high mercury vapor pressure in equilibrium with the melt. Moreover a tellurium excess may introduce a remarkable constitutional supercooling (7).

By a modified Bridgman approach, the CdTe segregation with respect to HgTe has been prevented utilizing high speeds of growth (Burton-Prim-Slichter mechanism). Because of the rapid solidification, the resulting ingot contains a dendritic substructure, and a subsequent high temperature anneal must be used to remove such a structure (8). The preparation of suitable crystals has been also attempted by a two-step technique (9) employing a quenching from the liquid state under appropriate conditions followed by heat-treatment for a long time in mercury vapor just below the solidus temperature. Homogeneous crystals have also been obtained by the vertical zone melting method (10), although composition fluctuations are generally observed due to hot-zone instability. The vertical-zone melting method has also been employed for solution growth of $Hg_{1-x}Cd_xTe$ using Te as a solvent (11). Finally, some amount of high quality material has been obtained using a method involving crystallization from a two-phase mixture followed by a solid recrystallization (12).

These methods generally labeled as modified Bridgman techniques, solid-state recrystallization, vertical-zone melting, and "slush" recrystallization have been applied with varying degrees of success. In addition, we propose and have experimentally tested another method for obtaining large single crystal portions having a high composition homogeneity starting from a two-phase system. We have taken advantage of the marked difference between the liquidus and the solidus curves in the HgTe-CdTe pseudobinary system.

Proposed Method and Some Experimental Results

Consider in Fig. 1 the schematic temperature profile of a vertical furnace (not to scale) and the sketch of the phase diagram for the $Hg_{1-x}Cd_xTe$ single pseudobinary alloy system. Assume an ampul filled with an alloy charge of over-all composition x_0 to be placed in the furnace in region 1 (not to scale) at temperature T_0. The charge will be entirely melted since the temperature T_0 is slightly above the liquidus line, as shown in the figure. Assume further that the ampul containing the charge is quickly lowered to region 2 (not to scale) at temperature T, intermediate between liquidus and solidus lines for the x_0 composition. This procedure will produce a liquid and solid two-phase mixture of composition x_L and x_S, respectively. At this point the directional freezing is actuated by lowering the ampul to region 3.

If freezing occurs slowly as it is assumed for the time being, the liquid phase composition remains constant at value x_L as long as the solid phase x_S is present which supplies the liquid marking up for the depletion due to the crystal growth in the ampul tip. As soon as the x_S composition phase is exhausted, normal freezing occurs. In these idealized conditions, what is expected is a crystal with constant composition equal to x_S for a length corresponding to the steady-state region for the melt composition and finally a transient with rapidly decreasing cadmium telluride concentration. This schematic situation occurs only if directional freezing of liquid alloy occurs in equilibrium conditions with complete mixing in the liquid. This condition can be approached by selecting a freezing rate which is small as compared with x_S solid dissolution rate in the liquid

Key words: modified Bridgman, compositional uniformity, infrared material.

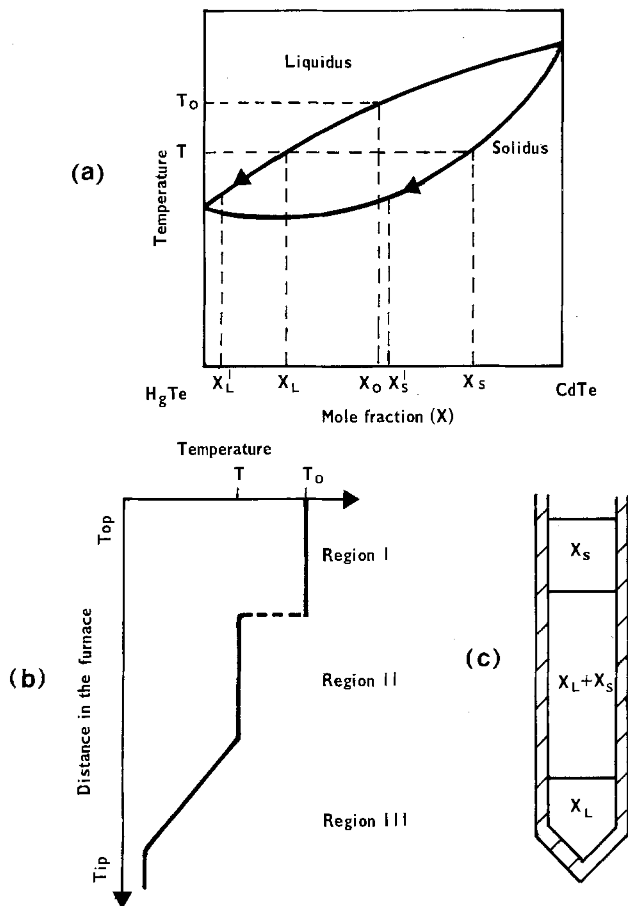

Fig. 1. Sketches of: (a) phase diagram of the pseudobinary alloy system HgTe-CdTe; (b) Temperature profile of growth apparatus; (c) x_L and x_S phase distribution at the growth starting.

and in particular if comparable with the diffusion rate in the liquid.

On the other hand the requirement of producing useful material with high yield at a reasonable rate suggests that the freezing rate be adjusted to a value not very far from the constitutional supercooling limit related to the actual thermal gradient operating at the solid liquid crystallization interface. In this connection, it has already been reported elsewhere (7) that the possibility of constitutional supercooling arising from both segregation of CdTe with respect to HgTe exists as well as the segregation of any Te excess in the melt. This latter effect proved to be the most restrictive as to growth rate, as it appears even at very low growth speeds. It is therefore necessary to assure the melt stoichiometry to get better Te segregation conditions and to be able to approach the limit imposed by the constitutional supercooling.

The speed of 0.5 mm/hr, if used for growths from melts with carefully adjusted metal to Te ratio, may be considered as reasonably close to the mentioned limit which can also be calculated by Tiller's relation (13). In addition to an accelerated growth rate as above described, mixing in the liquid phase is never complete and in particular in our experimental configuration, because of the rather poor actual temperature gradient distribution at the solidification interface (40°C/cm), because of the charge diameter (12-13 mm) and because of the charge length (up to 25 cm).

Finally it is not convenient to keep the x_S solid-phase distribution uniform. In fact the presence of unmelted particles at the growth interface will activate undesirable spurious nucleations with consequent worsening of the crystal quality. The drawback can be avoided if the distribution of the liquid and solid phases occur as schematized in Fig. 1c. This is realized in the actual method by quenching to room temperature the T_0 homogenized charge, taking care that the ampul end, where the directional freezing has to start, be directed upwards. Thus, as the filling coefficient is necessarily less than unity, the solid will not occupy the empty end. The subsequent overturn of the ampul and heating at T temperature will make, by gravity, the liquid phase occupy the lower volume free form the solid phase, as schematized in Fig. 1c. Then it is obvious that at the start of a growth the charge end part will now essentially consist of an extremely spongy self-supporting solid emerging from the liquid. The extension of the liquid zone, free from the solid, is an adjustable parameter depending on the ampul total length to content ratio. Under these conditions, because of poor mixing, the advancing crystal rejects solvent more rapidly than the x_S solid reserve can refill by dissolution and diffusion. As a consequence, the liquid composition at the growth interface tends to become lower than the starting x_L value, reaching after a transient, a $x_L' < x_L$ value. In this case, the solidified crystal will be characterized by an initial composition transient with decreasing solute concentration from the x_S value, a quasisteady-state region with a constant composition, and a final composition transient with rapidly varying solute concentration.

This is just what happens as shown in Fig. 2 for the two different growth runs. The composition values were determined both by measuring the 77°K cutoff wavelengths of a set of photovoltaic detectors prepared by ion implantation (14) on the surface of wafers cut at right angles to the growth direction and by measuring the absorption edges of the same samples at room temperature. The latter analysis method, rather integral, was used once the solidification interface, under the experimental conditions, was proved to be flat (15) and radially symmetric (16) as to allow $\Delta x < 0.01$ composition variations over 80% of the solidification interface diameter.

Table I reports the composition values along a wafer diameter (position 1-12) as obtained from the cutoff wavelengths of a set of photovoltaic detectors (the devices were 200 μm in diam and taken 800 μm apart center-to-center distance). The wafer center corresponds to position 6.

The synthesis of $Hg_{1-x}Cd_xTe$ alloys was accomplished by melting together the appropriate quantities of HgTe and CdTe binary compounds in evacuated thick-walled quartz ampuls with enough excess mercury to maintain a $\simeq$ 16 atm pressure at operating temperature T. Starting materials for binary compound preparations were Cd and Te 6N purity in a stoichiometric mixture to prepare CdTe, Hg, and Te 6N purity with an excess Hg in the case of HgTe. In $Hg_{1-x}Cd_xTe$ alloy synthesis we preferred to start from binary components rather than from single elements to avoid Hg-Cd direct contact, since the amalgama formed readily oxidize. The ampul containing the ternary mixture was first treated at 500°C; then the temperature was carefully raised just above the liq-

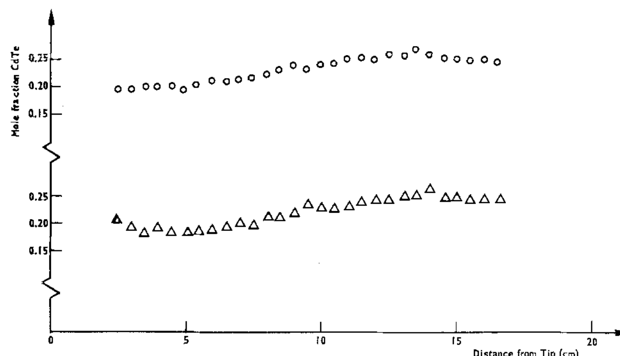

Fig. 2. Composition profile of the staedy-state region for two different growth runs.

Table I

Position No.	x	Position No.	x
1	0.239	7	0.232
2	0.239	8	0.235
3	0.237	9	0.235
4	0.234	10	0.236
5	0.232	11	0.239
6	0.232	12	0.240

uidus line for the actual over-all composition. The melt was then left to homogenize for at least 24 hr. At this point the above suggested procedure could be started. Figure 3 shows an as-grown crystal.

Conclusions

Though several growth techniques have already been proposed and applied for $Hg_{1-x}Cd_xTe$ single crystal production having long-range homogeneity and reasonable size, from the detector manufacturers stand point, the problem is not fully solved. At present the research in the field should be primarily concerned with improved methods of large single crystal growth as well as development of thin-film techniques. In this connection we think that our suggestion, if suitably developed, may lead to positive improvements. The results presented are in fact to be intended more as capabilities rather than as technique limits. On the other hand, the yield obtained can be considered as rather satisfactory for suitable material even if it is too early to be definite in this point. Further work along the described line is now under way.

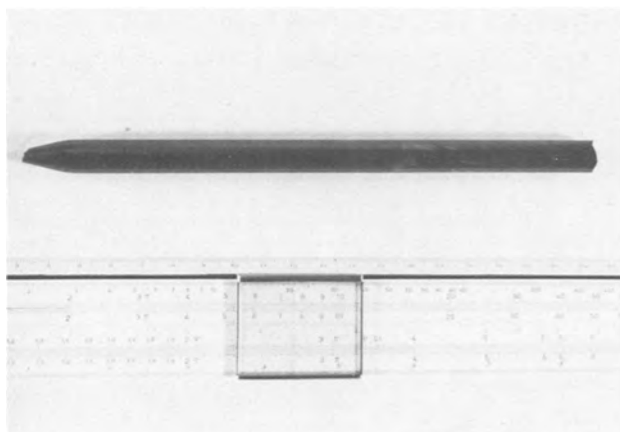

Fig. 3. An as-grown crystal

Acknowledgments

The authors wish to thank G. M. Schiavini for helpful discussions and valuable suggestions during the course of this work. This work was supported by CNR-CISE contract no. 73.01435.

Manuscript submitted June 21, 1977; revised manuscript received Sept. 24, 1977.

Any discussion of this paper will appear in a Discussion Section to be published in the December 1978 JOURNAL. All discussions for the December 1978 Discussion Section should be submitted by Aug. 1, 1978.

Publication costs of this article were assisted by CISE.

REFERENCES

1. D. Long and J. L. Schmit, "Semiconductors and Semimetals, "Vol. 5, p. 175, Academic Press, New York (1970).
2. O. N. Tufte and E. L. Stelzer, *J. Appl. Phys.*, **40**, 4559 (1969).
3. G. Cohen-Solal and Y. Riant, *Appl. Phys. Lett.*, **10**, 436 (1971).
4. G. Cohen-Solal, A. Zozinie, C. Motte, and Y. Riant, *Infrared Phys.*, **16**, 555 (1976).
5. J. L. Schmit and C. J. Speerschneider, *ibid.*, **8**, 247 (1968).
6. A. Langier, *Rev. Phys. Appl.*, **8**, 259 (1973).
7. B. E. Bartett, J. Deans, and P. C. Ellen, *J. Mater. Sci.*, **4**, 266 (1969).
8. E. L. Stelzer, J. L. Schmit, and O. N. Tufte: IEEE Trans. Electron. Devices, **ed 16,** 880 (1969).
9. L. N. Swink and M. J. Brau, *Metall. Trans.*, **1**, 629 (1970).
10. E. Z. Dziuba, *This Journal*, **116**, 104 (1969).
11. R. Ueda, O. Ohtsuki, K. Shinohara, and Y. Ueda, *J. Cryst. Growth*, **13/14**, 668 (1972).
12. T. C. Harman, *J. Electron. Mater.*, **1**, 230 (1972).
13. W. A. Tiller, "The Art and Science of Growing Crystals," J. Wiley, New York (1963).
14. G. Fiorito, G. Gasparrini, and F. Svelto, *Infrared Phys.*, **15**, 287 (1975).
15. Y. Takase, *J. Appl. Phys.*, **13**, 539 (1974).
16. G. Gasparrini, M. Mangialajo, D. Passoni, and B. Pirovano, *Infrared Phys.*, **14**, 145 (1974).

Transport Phenomena Measurements in Epitaxial Reactors

Vladimir S. Ban*

RCA Laboratories, Princeton, New Jersey 08540

ABSTRACT

The deposition rates and uniformity in CVD reactors are functions of transport phenomena. It is necessary to understand these phenomena as completely as possible in order to design and use reactors properly. In the last few years several, mostly theoretical, discussions of transport phenomena in CVD reactors appeared. In the present study we discuss the results of the experimental measurements of these phenomena by means of flow visualization techniques and temperature and concentration measurements. These measurements suggest a model of flow somewhat different than models suggested by other authors. The importance of entry effects and influences on the development of velocity and temperature profiles are illustrated. Such a model is more complex than models where the fully developed velocity and/or temperature fields are assumed, but it is also more descriptive of the true situation in the reactor.

Today's multiwafer epitaxial reactors must fulfill requirements of satisfactory deposition rates and of stringent thickness and doping uniformity. This means that sufficient and equal amounts of gaseous reactants (*e.g.*, $SiCl_4$, SiH_4, etc.) and dopants (*e.g.*, PH_3, B_2H_6, etc.) must be supplied to all wafers in the reactor. Good understanding of the gas phase transport phenomena is thus important for reactor designers and users.

* Electrochemical Society Active Member.
Key words: CVD, epitaxial reactor, transport phenomena silicon deposition.

In the last few years several theoretical treatments of transport phenomena in epitaxial reactors appeared (1-4). The purpose of this work is to present the results of experimental studies of transport phenomena in a horizontal silicon epitaxy reactor. The apparatus itself and the preliminary results have been described previously (5). Briefly, the somewhat modified laboratory size horizontal reactor (susceptor was 5 $\times$ 15 cm; rectangular quartz tube length was 60 cm, cross section was 7.5 $\times$ 5.0 cm) was equipped with an instrument introduction port. A specially designed mass spectrometric probe was used to determine qualitatively and quantitatively the vapor species present, as well as their spatial distribution. The temperature and its spatial distribution was measured by means of specially designed thermocouples, and the gas flow patterns were observed by means of the TiO_2 smoke visualization. In this work we present some additional results of these studies as well as a brief discussion of these results.

Results

Flow visualization experiments.—The flow visualization experiments provide an insight into the momentum transfer of the gas phase. The nature of flow in epitaxial reactors is difficult to predict. The low values of Reynolds number (typically < 200) suggest a laminar flow, but on the other hand, the steep transverse temperature gradients caused by the hot susceptor imply possible disturbance of the laminar nature. Furthermore, the entry effects must be considered, because susceptors are relatively short and the velocity and thermal profiles might not be completely developed. Sparrow *et al.* (6) studied a similar problem of simultaneous action of buoyancy and viscous forces and devised the Gr/Re^2 ratio as a criterion for assessing the relative influences of the above two forces (Gr = Grashof number; Re = Reynolds number; see Table I for definition). We observed flow patterns by means of TiO_2 smoke for Gr/Re^2 ratios ranging from 0.16 to 12.5 and susceptor temperatures from 500° to 1200°C. The results of these observations are summarized in Fig. 1. At $Gr/Re^2 \geqq 0.5$ one observed a fully developed spiral, and at lower values upward deflection of the streamline was observed. Both of these observations clearly show the effect of buoyancy forces. A spiral flow was also observed by Takahashi *et al.* (7) in their observations of flow in epitaxial reactors. Some fluid mechanics workers report different behavior (8, 9), but in their experiments special effort has been made to eliminate the entry effects.

Temperature measurements.—The temperature and the temperature distribution in the reactor is a function of several variables, such as the gas velocity, the nature of the gas, and the geometry of the reactor. We measured temperature in the x-y plane above the susceptor (x = direction of the gas flow; y = direction perpendicular to the susceptor; $y = 0$ at the susceptor; $y = 3$ cm at upper wall) as a function of those variables.

Table I. Definition of dimensionless numbers

Number	Symbol	Physical meaning	Definition*
Reynolds	Re	Inertia force / Viscous force	$\rho Vl / \mu$
Grashof	Gr	(Inertia force) (Buoyant force) / (Inertia force)^2	$\rho^2 g l^3 \beta \Delta T / \mu^2$
Prandtl	Pr	Momentum diffusivity / Thermal diffusivity	$C_p \mu / h_c$

* Nomenclature: ρ = mass density (g/cm^3), V = flow velocity (cm/sec), l = linear dimension (cm), μ = absolute viscosity (g/cm-sec), g = gravitational constant (cm/sec^2), β = expansion coefficient (liter/°K), and ΔT = temperature difference (°K), C_p = specific heat (cm^2/sec^2°K), h_c = thermal conductivity (g cm/sec^3°K).

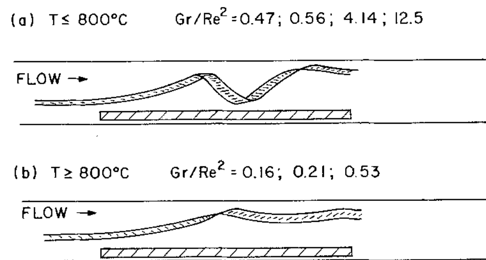

Fig. 1. TiO_2 smoke streamlines observed at various Gr/Re^2 ratios and susceptor temperatures (these drawings were obtained by tracing the actual photograph of the flow patterns).

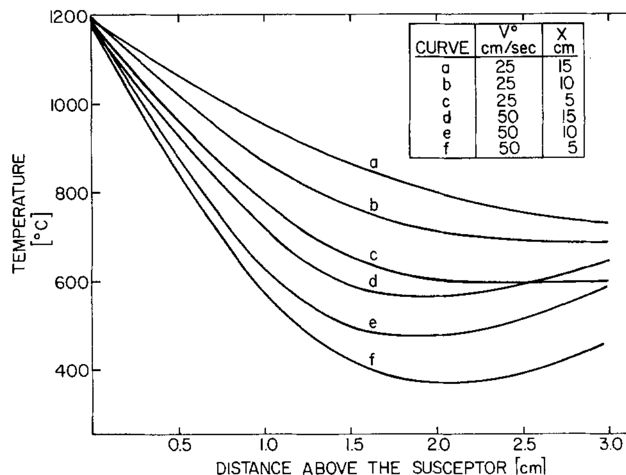

Fig. 2. Temperature profiles in He for various experimental conditions.

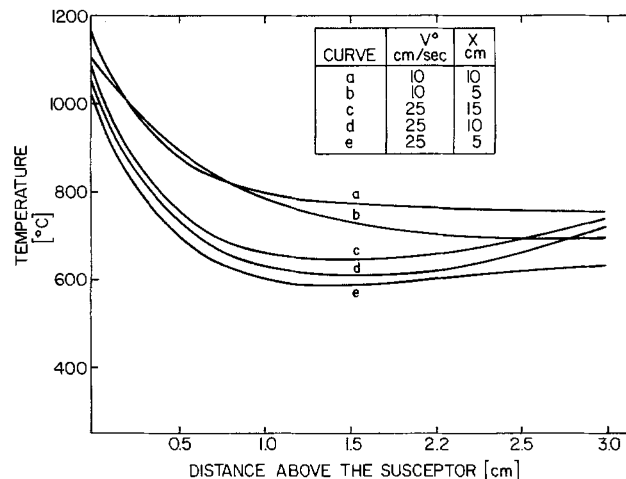

Fig. 3. Temperature profiles in N_2 for various experimental conditions.

Figure 2 shows temperature profiles in the y direction in helium. These profiles were taken at x = 5, 10, and 15 cm. Two different gas velocities were used $V° \approx 25$ cm/sec and ~ 50 cm/sec ($V°$ = velocity at room temperature). The susceptor temperature, T_s, was 1200°C. Figure 3 shows similar profiles taken in N_2. All relevant data are specified in the figure.

There are several things to notice in the above curves: (*i*) There is a steep temperature gradient in the first 1.5 cm above the susceptor, and a practically flat gradient above it; (*ii*) for the same velocity and susceptor temperature, gradients are steeper in N_2 than in He (H_2 behaves similarly to He); and (*iii*) the temperature of the upper portion of the gas increases with x and with decreasing V, thus resulting in shallower gradients under those conditions. Figure 4 shows the isotherms in the horizontal reactor. In this

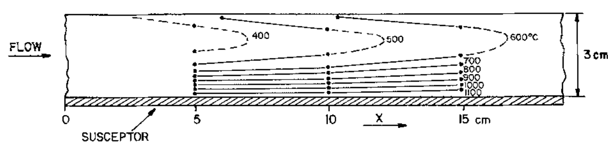

Fig. 4. Isotherms in the horizontal reactor ($V° = 50$ cm/sec; $T_s = 1200$°C).

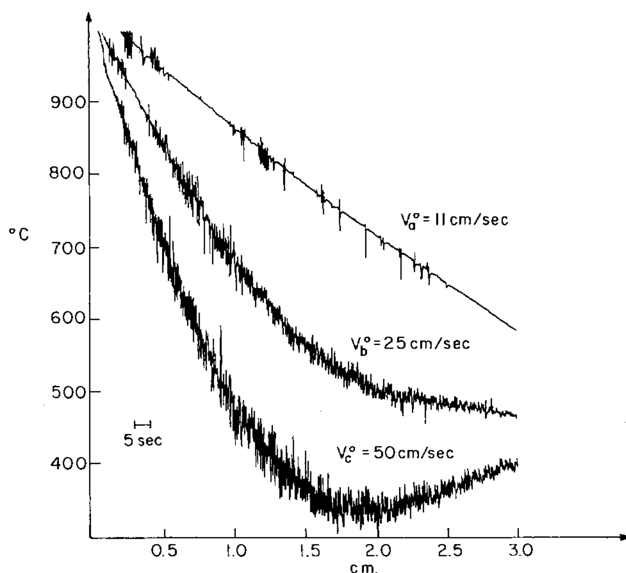

Fig. 5. Direct recordings of temperature profiles in He showing oscillations. $T_s = 1000$°C, $x = 15$ cm.

case $V° = 50$ cm/sec, $T_s = 1200$°C, gas is helium. Again, two different temperature areas are visible.

Another interesting observation in these measurements is the existence of large temperature fluctuations. Figure 5 shows the direct temperature profile recording. The relevant data are specified in the figure. These oscillations have a frequency of about 3-5 Hz and amplitudes as large as ± 30°C. Similar fluctuations were observed by Curtis and Dismukes (10).

Partial pressure measurements.—Mass spectrometric experiments determined the following species in the vapor phase: H_2, $SiCl_4$, HCl, and $SiCl_2$; $SiCl_2$ is at least an order of magnitude less abundant than the other species. The H_2 and $SiCl_4$ are, of course, the input gases, while the HCl and $SiCl_2$ are products of chemical reactions occurring in the system. In addition to the above gases, about 1% of Ar was added to the input mixture; Ar served as an internal standard so that the quantitative measurements of partial pressures of other gases can be made by comparison with the known Ar pressure.

The spatial variation of partial pressures of $SiCl_4$ and HCl in the x-y plane were given in Ref. (5). From these data it is possible to construct the $SiCl_4$ isobars, which are shown in Fig. 6. Again in the upper area a flatter concentration gradient exists than in the lower area, where isobars are closer together. There is also a partial pressure gradient in the x direction, due to the depletion of the reactant. If uncorrected (*e.g.*, by tilting the susceptor) this depletion would cause the downstream wafers to be thinner than the upstream wafers. The HCl isobars would show the opposite tendencies: an increase in pressure close to the susceptor and also in the x direction.

Figure 7 is the direct mass spectrometric recording of the $SiCl_4$ partial pressure profile. Again, one notices fluctuations in the middle section of this curve; the frequency is around 3-4 Hz and the amplitude is about ± 10% of the mean value.

Discussion

The above-described results allow us to make some conclusions on the nature of transport phenomena in the epitaxial reactors. First of all, one deals with not fully developed temperature and velocity profiles. The full development of the temperature field in a horizontal channel heated from below occurs when $x > L = 0.4$ DPe, where D = height of the channel and Pe = Peclet number (Pe = Pr × Re where Pr = Prandtl number) (8). In our case Re ≈ 50, Pr = 0.7, $D = 3$ cm. Therefore, temperature is fully developed when $x > 40$ cm, which is considerably longer than the susceptor itself.

A criterion for the elimination of entry effects from the velocity profiles is that $x > L = 0.029$ ReD. In our case $L \approx 45$, and thus again much longer than the susceptor itself. In the entry region boundary layers start to form on the walls of the channel, but between these layers one has a central core of the fluid with different temperature and velocity characteristics as evidenced by the observed flat temperature and concentration profiles and the recorded oscillations. These oscillations increase with a value of Re, which is consistent with the entry effect explanation presented here. The entry effects disappear when the upper and lower boundary layer met and a fully developed laminar flow velocity profile is formed. The lower layer increases in thickness faster, because the viscosity of the gas increases with temperature. The flat concentration and temperature gradients mean that relatively good mixing occurs in the central core. This mixing is due to the transverse gas movement caused by buoyancy effects, which were observed in the flow visualization experiments. The core can be thus considered a reservoir of reactant gaseous species from which they diffuse through the boundary layer to reach the growth interface. The core itself changes in the x direction. It becomes narrower due to the development of boundary layers, its temperature increases, the partial pressure of reactants decreases and of products increases. These ideas are pictorially presented in Fig. 8, where the qualitative changes in velocity, temperature, and concentration profiles are shown.

It is important to note that the model which emerges from our experiments is more complex than models used in theoretical calculations referenced earlier. In these works either the fully developed laminar velocity profiles and/or the constant temperature in the

CURVE	a	b	c	d	e	f	g
$SiCl_4$ PRESSURE $\times 10^{-3}$ atm	3.6	3.2	2.8	2.4	2.0	1.6	1.2

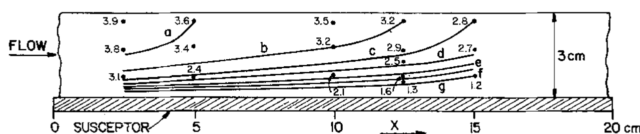

Fig. 6. $SiCl_4$ isobars in the horizontal reactor ($V° = 25$ cm/sec, $T_s = 1200$°C, $p°_{SiCl_4} = 6.1 \times 10^{-3}$ atm).

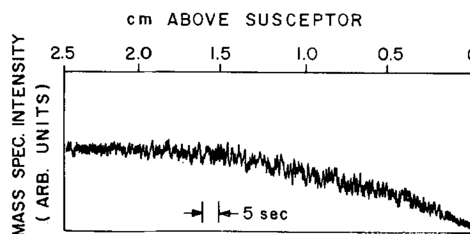

Fig. 7. Direct mass spectrometric recording of the partial pressure profile of $SiCl_4$ showing oscillations. $T_s = 1140$°C, $p°_{SiCl_4} = 6.1 \times 10^{-3}$ atm, $V° = 25$ cm/sec).

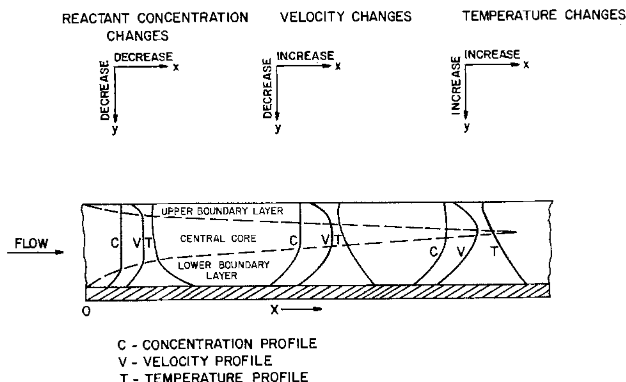

Fig. 8. A qualitative depiction of a transport model suggested by our experiments. Entry effects and the resulting influences on the velocity, temperature, and partial pressure gradients are shown.

x direction are assumed. The real situation is, however, different and a more realistic model should take into account the above complications. We intend to develop a mathematical treatment of such a model in the near future.

Acknowledgment

The author would like to acknowledge helpful discussions with D. Richman, S. Berkman, and Y. S. Chiang.

Manuscript submitted June 16, 1977; revised manuscript received Sept. 23, 1977. This was Paper 232 presented at the Atlanta, Georgia, Meeting of the Society, Oct. 9-14, 1977.

Any discussion of this paper will appear in a Discussion Section to be published in the December 1978 JOURNAL. All discussions for the December 1978 Discussion Section should be submitted by Aug. 1, 1978.

Publication costs of this article were assisted by RCA Laboratories.

REFERENCES

1. S. E. Bradshaw, *Int. J. Electron.*, **23**, 381 (1967).
2. F. C. Eversteyn and H. L. Peek, *Philips Res. Rept.*, **25**, 472 (1970).
3. S. Berkman, V. S. Ban and N. Goldsmith, in "Heteroepitaxial Semiconductors for Electronic Devices," G. W. Cullen and C. C. Wang, Editors, Springer-Verlag, New York (1977).
4. C. W. Manke and L. F. Donaghey, *This Journal*, **124**, 561 (1977).
5. V. S. Ban and S. L. Gilbert, *J. Cryst. Growth*, **31**, 284 (1975).
6. E. M. Sparrow, R. Eichorn, and J. L. Greg, *Phys. Fluids*, **2**, 319 (1959).
7. R. Takahashi, Y. Koga, and K. Sugawara, *This Journal*, **119**, 1406 (1972).
8. G. J. Hwang and K. C. Cheng, *J. Heat Transfer, ASME*, **95**, 72 (1973).
9. Y. Kamotani and S. Ostrach, *ibid.*, **98**, 62 (1976).
10. J. P. Dismukes and B. J. Curtis, in "Semiconductor Silicon 1973," H. R. Huff and R. R. Burgess, Editors, p. 250, The Electrochemical Society Softbound Symposium Series, Princeton, N.J. (1973).

Etching of CVD Si_3N_4 in Acidic Fluoride Media

Cheryl A. Deckert*

RCA Laboratories, Princeton, New Jersey 08540

ABSTRACT

The process whereby CVD Si_3N_4 films are etched in acidic fluoride solutions has been investigated at 25° and 60°C by use of a series of well-characterized etchants. The rate law for the dissolution process has been identified and is found to be linear in both [HF] and $[HF_2^-]$, but independent of $[F^-]$. Although the exact magnitude of the etch rates of CVD Si_3N_4 is known to depend on the deposition conditions used, it is thought that the general form of the rate law will remain constant. Comparison between the rate constants for Si_3N_4 and those previously reported for SiO_2 suggests that the etch rate of Si_3N_4 can be increased relative to that of SiO_2 by use of elevated temperatures and very low pH solutions, and by adjustment of the nitride deposition parameters so as to increase the NH_3/Si ratio in the reaction mixture.

Removal of silicon nitride from semiconductor device wafers is usually carried out using a hot (180°C) phosphoric acid etchant (1). As has been pointed out previously (2), this process is rather inconvenient to utilize both because of the high temperature which must be maintained and because water tends to become depleted from the etchant mixture. Etch rates of Si_3N_4 films in buffered hydrofluoric acid and in concentrated HF have been reported; more recently, dissolution studies of Si_3N_4 in various dilutions of HF over a range of temperature have appeared (2, 3). In all these cases, comparison with etch rates of SiO_2 films has been made; the etch rates of nitride are lower than those of oxide in all the cases reported except for very dilute ($\gtrsim$ 0.3%) HF solutions at high temperatures ($\geq$90°C). The implementation of processes based upon such data is hampered by two main difficulties: first, unlike thermally grown SiO_2, which gives readily reproducible etch rates in a given medium, CVD Si_3N_4 displays varying etch rates depending on the exact deposition parameters; and second, the mechanism of etching Si_3N_4 has never been investigated in a series of well-characterized etchants, as has been done for SiO_2 (4), so as to yield a simple rate law based on one or more chemical species.

In this study we have examined the dissolution of CVD Si_3N_4 films of a "typical" formulation in a variety of well-characterized fluoride etchants, in an attempt to deduce the dependence of etch rate on the various chemical species present. Although such a rate law will vary somewhat depending on the film deposition conditions, the general form of the rate equation will most likely be constant and can thus be of general use in nitride patterning processes.

Experimental

The silicon nitride films were prepared by chemical vapor deposition techniques on silicon wafers of [111] orientation. The flow rate of N_2 carrier gas through $SiCl_4$ at ~25°C was 110 cm³/min resulting in transport of 0.21 g/min $SiCl_4$. The flow rate of NH_3 was 600 cm³/min. The nitrogen main flow was 225 liters/min,

* Electrochemical Society Active Member.

Key words: CVD Si_3N_4 films, acidic fluoride solutions, etching.

and the reactor temperature was 875°C. Nitride deposition rate was 120-130 Å/min. Thicknesses of deposited nitride were limited to approximately 2100Å in order to avoid excessive stress buildup. The material was found to dissolve at 10-12 Å/min in a p-etch (30 parts conc. HF, 20 parts conc. HNO_3, 600 parts H_2O). The etching experiments were terminated at about 800Å remaining nitride so that possible occurrence of oxy-nitride species near the Si_3N_4/Si interface would not alter the observed etch rates. The etching tests were conducted in a constant temperature bath controlled to within ±0.5°C. Thicknesses, both before and after etching, were measured by a technique based on relative reflectivity of a monochromatic beam of light (5). Two different wavelengths of light were employed and duplicate samples were tested in each experiment. The usual assumption was made that etch rate is linear with time. Estimated error in etch rates was ±5%.

Either reagent- or electronic-grade chemicals were used throughout the experiments. The NH_4F stock solution was analyzed for % fluorine content by Schwarzkopf Microanalytical Laboratory using a volumetric procedure with La^{3+}.

Results

The etchant solutions were prepared similarly to those of Judge (4). Simplistically, formulation of the etchant solutions can be described as follows: NH_4F was used to control the total fluoride content, HCl to lower the *p*H, and NH_4Cl to bring the total solution ionic strength up to 1M. The composition of the etchant solutions, expressed in terms of formality of reagents added, is given in Table I. The exact concentrations of the various fluoride-containing species were determined from the known dissociation constants for HF in 1M ionic strength media (6)

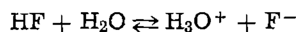

$$HF + H_2O \rightleftarrows H_3O^+ + F^-$$

$$K_1\ (25°C) = 1.30 \times 10^{-3}$$
$$(60°C) = 6.57 \times 10^{-4} \quad [1]$$

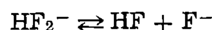

$$HF_2^- \rightleftarrows HF + F^-$$

$$K_2\ (25°C) = 1.04 \times 10^{-1}$$
$$(60°C) = 3.66 \times 10^{-2} \quad [2]$$

The calculated equilibrium concentrations and observed etch rates are given in Tables II and III.

In order to deduce the rate law for Si_3N_4 dissolution, the correlation of etch rate with concentration of the various fluoride-containing species was examined. Simple perusal of the data indicates that etch rate is independent of concentration of "free" fluoride ion, F^-, whereas both protonated fluoride species, HF and HF_2^-, appear to be involved in the rate law. Characterization of the SiO_2 etching process has revealed (4) a linear dependence of etch rate on both [HF] and [HF_2^-]; thus we performed a multiple regression analysis on the data to determine whether a good straight line fit could be obtained using the equation

$$R = A[HF] + B[HF_2^-] + C \quad [3]$$

When R is expressed in Å/sec and concentrations are in molarity, the values of the constants A, B, and C calculated for the Si_3N_4 etching process are those given in Table IV. For comparison, the constants previously reported (4) for SiO_2 are also given. As a check on the assumption that the data would fit the linear Eq. [3], a plot was made of etch rate *vs.* the calculated function for each temperature. These plots are shown in Fig. 1 and 2. It is seen that the data do fall close to the plotted straight lines and that the intercept is very close to the origin in each case (since parameter C is close to zero), thus increasing confidence in the validity of the calculated rate law.

Table I. Composition of fluoride etchants

Etchant No.	Concentration of reagent added (F) [HCl]	[NH_4F]	[NH_4Cl]
1	0.900	0.0945	0.100
2	0.800	0.190	0.200
3	0.600	0.380	0.400
4	0.900	0.922	0.000
5	0.450	0.445	0.500
6	0.400	0.572	0.400
7	0.250	0.380	0.600
8	0.350	0.618	0.350
9	0.150	0.284	0.700
10	0.300	0.665	0.300
11	0.270	0.695	0.270
12	0.200	0.761	0.200
13	0.100	0.855	0.100
14	0.050	0.941	0.050
15	0.010	0.981	0.010

Table II. Calculated equilibrium concentrations and observed Si_3N_4 etch rates in 1M ionic strength etchant solutions at 25°C

Etchant No.	Calculated concentrations (M) [HF]	[HF_2^-]	[F^-]	[H_3O^+]	Calculated *p*H	Etch rate (Å/sec)
1	0.0941	0.00014	0.00015	8.06×10^{-1}	0.09	0.013
2	0.189	0.00073	0.00040	6.11×10^{-1}	0.21	0.025
3	0.364	0.0072	0.00206	2.29×10^{-1}	0.64	0.053
4	0.735	0.0872	0.0123	7.75×10^{-2}	1.11	0.14
5	0.367	0.0343	0.00972	4.90×10^{-2}	1.31	0.076
6	0.265	0.128	0.0505	6.81×10^{-3}	2.17	0.089
7	0.164	0.0820	0.0520	4.10×10^{-3}	2.39	0.053
8	0.178	0.170	0.0397	2.32×10^{-3}	2.64	0.078
9	0.0874	0.0616	0.0734	1.55×10^{-3}	2.81	0.040
10	0.111	0.189	0.176	8.21×10^{-4}	3.09	0.076
11	0.0823	0.188	0.237	4.51×10^{-4}	3.35	0.069
12	0.0410	0.159	0.402	1.33×10^{-4}	3.88	0.051
13	0.0134	0.0866	0.668	2.62×10^{-5}	4.58	0.029
14	0.00547	0.0445	0.846	8.40×10^{-6}	5.08	0.016
15	0.00095	0.00905	0.962	1.28×10^{-6}	5.89	0.0045

Table III. Calculated equilibrium concentrations and observed Si_3N_4 etch rates in 1M ionic strength etchant solutions at 60°C

Etchant No.	Calculated concentration (M) [HF]	[HF_2^-]	[F^-]	[H_3O^+]	Calculated *p*H	Etch rate (Å/sec)
1	0.0940	0.00020	0.000077	8.06×10^{-1}	0.09	0.13
2	0.188	0.00109	0.000202	6.11×10^{-1}	0.21	0.26
3	0.359	0.0100	0.00102	2.31×10^{-1}	0.64	0.56
4	0.709	0.104	0.00535	8.71×10^{-2}	1.06	1.8
5	0.354	0.0431	0.00445	5.23×10^{-2}	1.28	0.89
6	0.238	0.155	0.0239	6.54×10^{-3}	2.18	1.1
7	0.141	0.106	0.0274	3.40×10^{-3}	2.47	0.76
8	0.137	0.212	0.0568	1.58×10^{-3}	2.80	1.0
9	0.0634	0.0856	0.0494	8.43×10^{-4}	3.07	0.52
10	0.0657	0.234	0.131	3.30×10^{-4}	3.48	0.96
11	0.0422	0.228	0.197	1.41×10^{-4}	3.85	0.84
12	0.0176	0.182	0.379	3.05×10^{-5}	4.52	0.61
13	0.00525	0.0948	0.660	5.22×10^{-6}	5.28	0.34
14	0.00208	0.479	0.843	1.62×10^{-6}	5.79	0.19
15	0.000367	0.00963	0.961	2.51×10^{-7}	6.60	0.060

Table IV. Calculated values of the parameters in the rate law equation $R = A[HF] + B[HF_2^-] + C$, where R is expressed in Å/sec and the concentrations are in molarity

Film	Temperature, °C	A	B	C
Si_3N_4	25	0.16	0.31	<0.0001
	60	1.9	3.7	−0.02
SiO_2[a]	25	2.50	9.66	−0.14
	60	10.4	48.6	−1.02

[a] Ref. (4).

Discussion

It is interesting that the rate laws for etching of SiO_2 and Si_3N_4 are so similar, and that the unprotonated species, F^-, is unreactive in each case. One might hypothesize an etching mechanism which involves an intermediate hydrogen-bonded species (I)

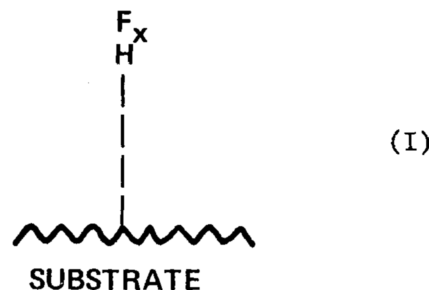

(I)

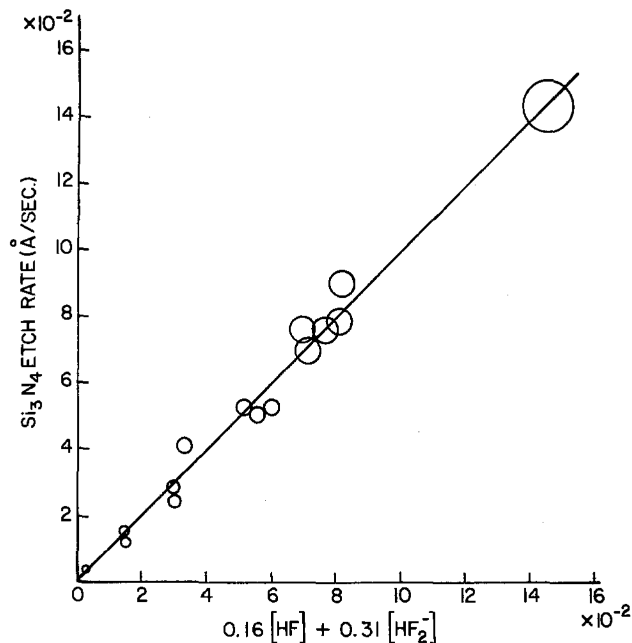

Fig. 1. Si_3N_4 etch rate at 25°C *vs.* the function $\{A[HF] + B[HF_2^-]\}$. The diameters of the circles reflect the experimental error in the etch rates.

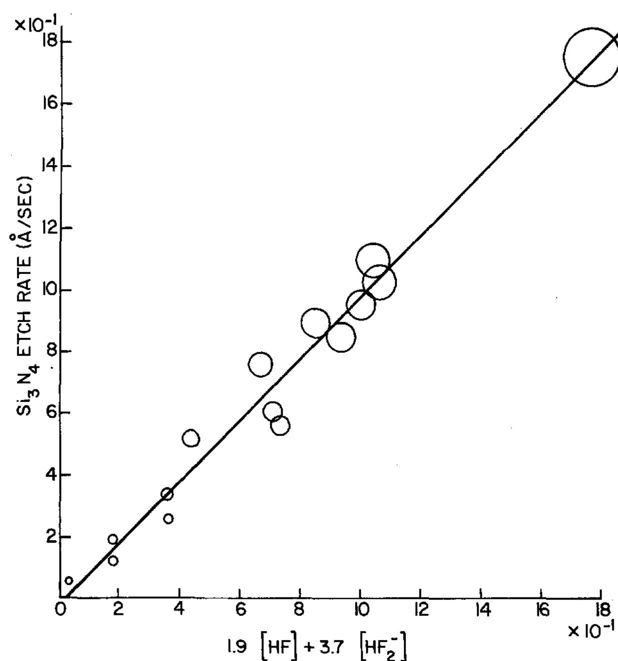

Fig. 2. Si_3N_4 etch rate at 60°C *vs.* the function $\{A[HF] + B[HF_2^-]\}$. The diameters of the circles reflect the experimental error in the etch rates.

Initial formation of such a species might hold the fluorine atoms close to the substrate for a long enough period of time so that they could achieve a favorable orientation and could thus successfully attack the substrate.

Regarding the relative rates of oxide *vs.* nitride etching, it can be seen from the data in Table IV that although at both temperatures studied Si_3N_4 etches much more slowly than does SiO_2, nevertheless the nitride rate constants appear to be increasing somewhat faster with temperature than those of oxide. This behavior indicates higher activation energies for the nitride etching process than for oxide, as is shown graphically in Fig. 3. Since the slopes of these lines are equal to $-E_A/R$, we can calculate the apparent activation energies shown in Table V, in kcal/mole.

Table V

	Si_3N_4	SiO_2
A term (HF dependent)	14	8.0
B term (HF_2^- dependent)	14	9.1

From these activation energies, it can be determined that, although keeping the HF/HF_2^- ratio large (by buffering at a low pH) should favor the nitride etch rate as much as possible, the SiO_2 and Si_3N_4 etch rates in 1M ionic strength etchants will not become equal at temperatures below the boiling point of the etchants. This result is in contrast to those of Harrap (2), who found that under certain conditions, namely at high temperatures (~90°C) and in very dilute hydrofluoric acid solutions, the nitride etch rate could be favored over that of oxide. This difference may be in part due to the particular nitride deposition process used: our process involved a smaller NH_3/Si (Si from $SiCl_4$) molar ratio (22) than did Harrap's (75 or 250, Si from SiH_4), a change which is expected to decrease nitride etch rate. Unfortunately, the fact that Harrap's work was done in solutions of undetermined ionic strength hampers direct comparison of his results and ours. It is quite likely, however, that use of dilute solutions and high temperatures favor HF formation relative to HF_2^-; this would be the case if the 1M ionic strength acid dissociation constants are applicable, and would give qualitative agreement between the two sets of results. However, more detailed comparisons of the two studies, particularly where the more highly concentrated fluoride media are concerned, will require further information concerning higher associated fluoride species and acid dissociation constants.

Acknowledgment

The comments and helpful suggestions of G. L. Schnable, W. Kern, and R. Williams, who reviewed the manuscript, are gratefully acknowledged. We also wish to thank Kurt Strater of RCA Solid State Division, who deposited the silicon nitride films.

Manuscript submitted June 8, 1977; revised manuscript received Sept. 1, 1977. This was Paper 112 presented at the Philadelphia, Pennsylvania, Meeting of the Society, May 8-13, 1977.

Any discussion of this article will appear in a Discussion Section to be published in the December 1978

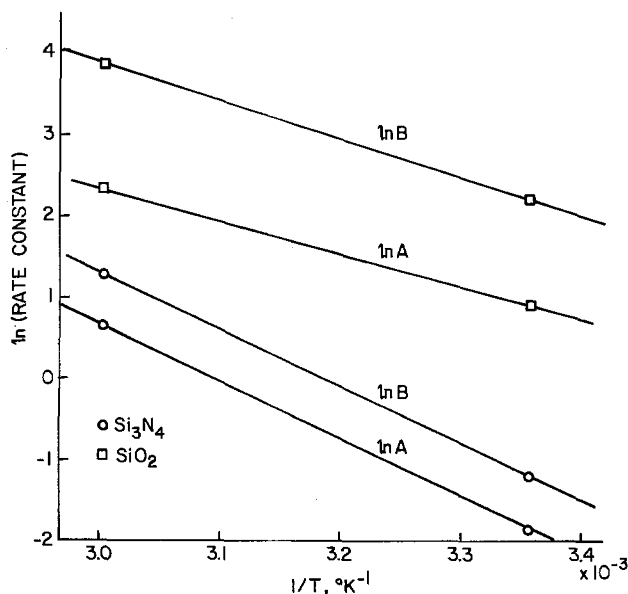

Fig. 3. Plots of ln (rate constant) *vs.* reciprocal of absolute temperature.

JOURNAL. All discussions for the December 1978 Discussion Section should be submitted by Aug. 1, 1978.

Publication costs of this article were assisted by RCA Laboratories.

REFERENCES

1. W. Van Gelder and V. E. Hauser, *This Journal*, **114**, 869 (1967).
2. V. Harrap, in "Semiconductor Silicon 1973," H. R. Huff and R. R. Burgess, Editors, p. 354, The Electrochemical Society Softbound Symposium Series, Princeton, N.J. (1973), Paper 124 presented at The Electrochemical Society Meeting, Chicago, Illinois, May 13-18, 1973.
3. R. Herring and J. B. Price, Paper 160 presented at The Electrochemical Society Meeting, Chicago, Illinois, May 13-18, 1973.
4. J. S. Judge, *This Journal*, **118**, 1772 (1971); Paper 42 presented at The Electrochemical Society Meeting, Washington, D.C. May 2-7, 1976.
5. (a) I. Franz and W. Langheinrich, *Solid-State Electron.*, **11**, 59, 987 (1968); M. J. Rand, *J. Appl. Phys.*, **41**, 787 (1970).
6. R. E. Mesmer and C. F. Baes, Jr., *Inorg. Chem.*, **8**, 618 (1969).
7. L. Jones and R. Penneman, *J. Chem. Phys.*, **22**, 781 (1954).

Analysis of Phosphorus-Diffused Layers in Silicon

Richard B. Fair*

Bell Laboratories, Reading, Pennsylvania 19604

ABSTRACT

Using the Fair-Tsai model of P diffusion in Si, equations have been derived which relate the total P concentration, electron concentration, sheet resistance, and junction depth of a P-diffused layer. Curves are presented which show surface concentration as a function of the $R_S \cdot x_J$ product, percentage of electrically active P as a function of surface concentration, and R_S *vs.* x_J for P-implant doses ranging from 1×10^{14} to 5×10^{16} cm^{-2}.

At high concentrations the diffusion of phosphorus in silicon produces an impurity atom distribution that differs considerably from the Gaussian or complementary error-function distributions. For this reason it has not been known how to calculate curves that relate P surface concentration and electron concentration to the average resistivity ($R_S \cdot x_J$ product) of the layer, etc.

Recently, Fair and Tsai (1) reported on a model of P diffusion in Si which accounts quantitatively for the existence of electrically inactive P, the "kink" and the tail regions of the P profile, and the emitter dip effect. This model is based upon the idea that P diffuses with vacancies in the V^x, V^-, and $V^=$ charge states. In the high concentration surface region ($n \geqq 10^{20}$ cm^{-3}) equilibrium concentrations of $P^+V^=$ pairs dominate. At lower concentrations when the Fermi level is ~0.11 eV below the conduction band, the $V^=$ vacancy gives up an electron, and the 0.3 eV lower binding energy of the resulting P^+V^- pairs enhances the probability for pair dissociation by a factor of 10-35, depending on the temperature. This effect creates a steady-state excess vacancy concentration which flows to the bulk and the surface. The concentration of excess vacancies is proportional to the number of $P^+V^=$ pairs in the surface region times the probability for pair dissociation. These V^- vacancies interact with P to create the enhanced tail diffusion. Three diffusion coefficients are required to describe P diffusion [see Fig. 1 taken from Ref. (1)].

Analysis

In this section simplifying assumptions are introduced into the physics governing P diffusion in Si. In this way approximate expressions are developed for estimating the important profile parameters in P diffusion; sheet resistance, junction depth, and surface concentration. To begin it it necessary to calculate the electrically active P/cm² concentration, Q_{el}, for any diffusion condition.

Total and electrically active phosphorus per square centimeter.—It was shown in Ref. (1) that the implication of the three phosphorus diffusion coefficients means that high concentration phosphorus diffusion yields a profile similar to the one shown in Fig. 2. This profile can be divided into two parts; one associated with the highly doped surface region with total doping per square centimeter of Q_{ST}, and one associated with the tail region with total doping per square centimeter of Q_{TAIL}. Not all of the P in the surface region is electrically active. The inactive doping, Q_{sn}, is in the form of $P^+V^=$ pairs while the active doping is labeled Q_{se}. The total electrically active P/cm² under the profile is

$$Q_{el} = Q_{se} + Q_{TAIL} \qquad [1]$$

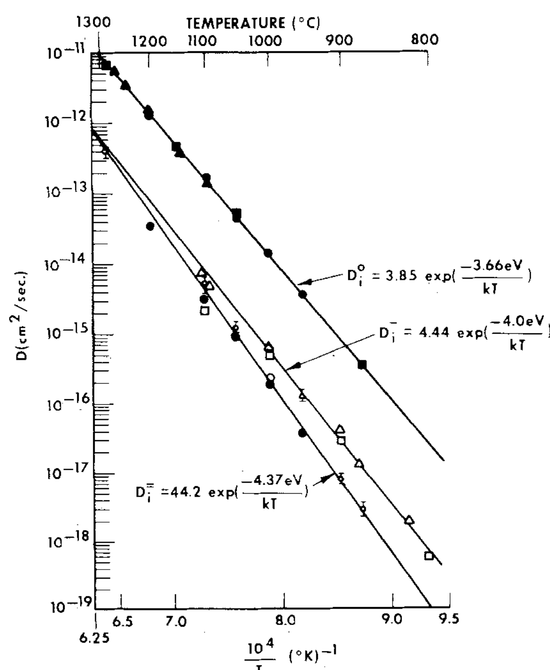

Fig. 1. Intrinsic diffusivities of phosphorus in silicon [after Ref. (1)].

* Electrochemical Society Active Member.

Key words: electrical activity, diffusion in silicon, ion implantation.

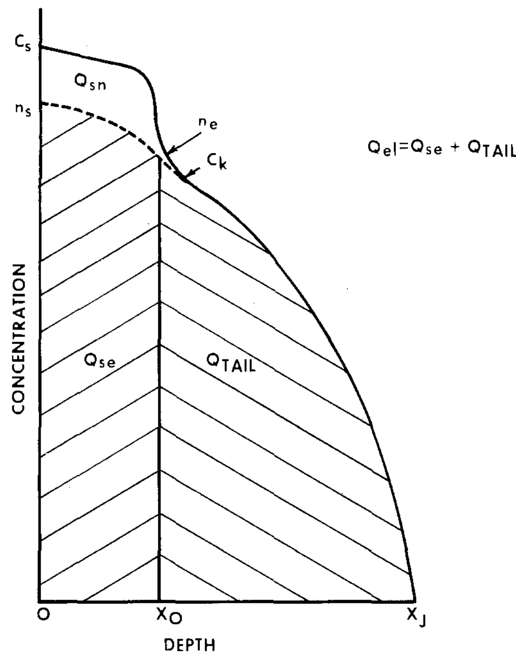

Fig. 2. A typical high concentration phosphorus diffusion profile in silicon.

The tail profile is a complementary error function with a "surface" concentration, C_k, occurring at the profile kink. The integrated concentration of P in the tail is

$$Q_{TAIL} = \frac{2}{\sqrt{\pi}} \sqrt{D_{TAIL} t}\, C_k \quad [2]$$

D_{TAIL} is the tail diffusivity given by

$$D_{TAIL} = D_i^x + \frac{D_i^- n_s^3}{n_e^2 n_i} \left[1 + \exp\left(\frac{0.3 \text{ eV}}{kT}\right) \right] \quad [3]$$

where n_s is the electron concentration at the Si surface, n_e is the concentration at which $P^+V^=$ pairs dissociate to create excess V^- vacancies, and D_i^- is the intrinsic diffusivity of P when diffusion occurs with V^- vacancies. The 0.3 eV term in the exponential refers to the binding energy difference between $P^+V^=$ pairs and P^+V^- pairs. Arrhenius plots of the diffusion coefficients for P are shown in Fig. 1. The data from which these diffusion coefficients were obtained are referenced in Ref. (1) as are values of C_k, n_e, and n_s as a function of temperature.

Making use of the observation that $C_k/n_e \simeq 0.4$ for many profiles and assuming that the second term on the right in Eq. [3] is dominant if $n_s \gtrsim 5 \times 10^{19}$ cm^{-3}, then

$$Q_{TAIL} \simeq \frac{n_s^{3/2}}{2} \sqrt{\frac{D_i^-}{n_i} \left[1 + \exp\left(\frac{0.3 \text{ eV}}{kT}\right) \right] t} \quad [4]$$

At surface concentrations below $n_s = 2 \times 10^{19}$ cm^{-3}, $D_{TAIL} \simeq D_i^x$. In this concentration range neutral vacancies control P diffusion.

In the high concentration surface region it has been observed that the total P/cm² concentration is

$$Q_{ST} = Q_{se} + Q_{sn},$$

$$\simeq \frac{C_s x_o}{2} \quad [5]$$

where Q_{sn} is the number of nonelectrically active P atoms/cm², C_s is the total P surface doping density, and x_o is the depth at which $n \simeq n_e$. An approximate expression for x_o, sometimes referred to as the width of the "flat region," is

$$x_o = 2 \sqrt{D_i^= \left(\frac{n_s}{n_i}\right)^2 ht} \quad [6]$$

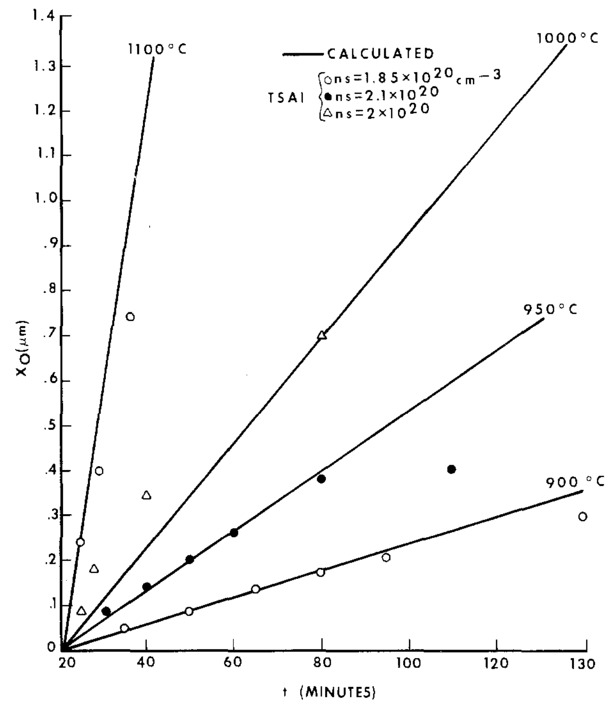

Fig. 3. Calculated "flat" region width of a phosphorus profile vs. diffusion time.

In Eq. [6] $D_i^=$ is the surface region P diffusivity ($P^+V^=$ pair diffusion), and h is the electric-field enhancement factor ($h \simeq 2$). Equation [6] is shown plotted in Fig. 3 for several temperatures. The data are from Tsai (2) and represent the flat region width for P diffusions with $n_s \simeq 2 \times 10^{20}$ cm^{-3}. Good agreement is obtained with these measured data. C_s is related to n_s through the equation (1)

$$C_s = n_s(1 + 2.04 \times 10^{-41} n_s^2) \quad [7]$$

This equation results because at high concentrations a fraction of the P is not electrically active. The "inactive" P is contained in $P^+V^=$ pairs.

Equation [5] can be solved for Q_{ST} in terms of n_s. Adding this result to Eq. [4] for Q_{TAIL} gives the total P atoms/cm² in a diffused profile as

$$Q_T = Q_{ST} + Q_{TAIL} = n_s^{3/2} \sqrt{\frac{t}{n_i}} \left[(1 + 2.04 \times 10^{-41} n_s^2) \sqrt{\frac{D_i^= n_s h}{n_i}} + \frac{1}{2} \sqrt{D_i^- \left(1 + \exp\left(\frac{0.3 \text{ eV}}{kT}\right)\right)} \right] \quad [8]$$

and the electrically active P/cm² as

$$Q_{el} = Q_{se} + Q_{TAIL} = n_s^{3/2} \sqrt{\frac{t}{n_i}} \left[\sqrt{\frac{D_i^= n_s h}{n_i}} + \frac{1}{2} \sqrt{D_i^- \left(1 + \exp\left(\frac{0.3 \text{ eV}}{kT}\right)\right)} \right] \quad [9]$$

Equations [8] and [9] are shown plotted in Fig. 4 where Q_T and Q_{el} *vs.* n_s are the coordinates. The data shown were taken from measured P profiles in which the $POCl_3$ source flow rates were adjusted to achieve different surface concentrations for the 875°C 45 min diffusions (3). Reasonably good agreement is obtained between the data and the calculated curves.

It can be seen that Eq. [8] is of the form $Q_T = \sqrt{KT}$ which agrees with the experimentally observed parabolic law behavior of P predeposition (4). At very

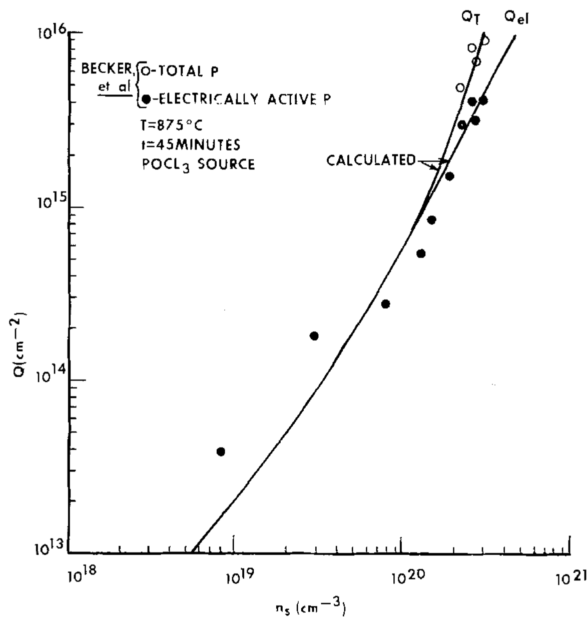

Fig. 4. Total and electrically active P/cm² vs. surface electron concentration.

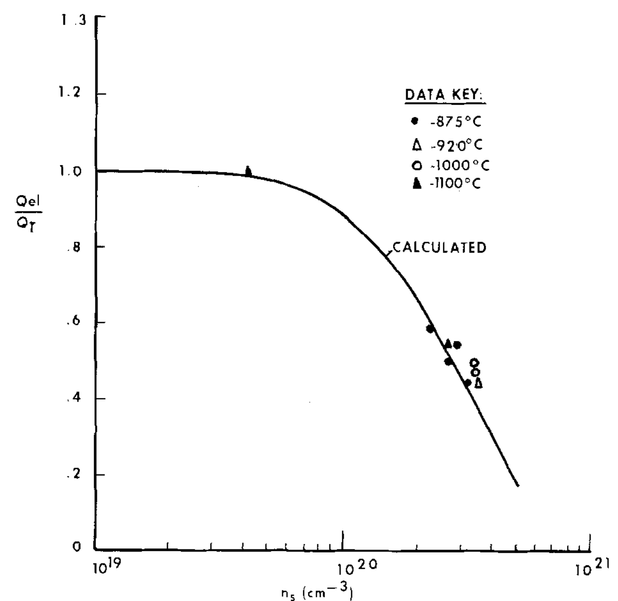

Fig. 5. Electrically active phosphorus fraction vs. surface electron concentration for all diffusion temperatures.

large surface concentrations, Eq. [8] reduces to

$$Q_T = n_s^{3/2}\sqrt{\frac{t}{n_i}}\,(1 + 2.04 \times 10^{-41} n_s^2)\sqrt{\frac{D_{i^=} n_s h}{n_i}} \quad [10]$$

The diffusivity of the $P^+V^=$ pair controls the rate of introduction of P into Si, so that from Fig. 1 with n_s independent of temperature

$$Q_T \propto \sqrt{\exp\left(\frac{-4.37\text{ eV}}{kT}\right) \Big/ n_i^2}$$

$$\propto \exp\left(\frac{-1.49\text{ eV}}{kT}\right)$$

where 1.49 eV is the calculated energy term in the temperature dependence of Q_T. Negrini *et al.* (4) have measured this energy to be 1.1 eV. However, it is evident from their published profiles (5) that for a fixed $POCl_3$ flow rate, n_s is a function of temperature. Also, Eq. [8] for Q_T is only valid for P concentrations below solid solubility, whereas Negrini's work concentrates on the region above solid solubility.

The parabolic constant K can be calculated from Eq. [10] for low $POCl_3$ flow rates. For example, for a 920°C deposition with 0.06% $POCl_3$ in 1.3% O_2 for 27 min, Negrini measures $K = 1.5 \times 10^{32}$ cm^{-4} hr^{-1}. From Ref. (5) this predeposition corresponds to a P profile with $n_s \simeq 2.8 \times 10^{20}$ cm^{-3}. From Eq. [10], the calculated K value is 1.8×10^{32} cm^{-4} hr^{-1}, in good agreement.

Taking the ratio of Q_{el} (Eq. [9]) to Q_T (Eq. [8]) and plotting the result as a function of n_s yields a single curve which is independent of temperature and diffusion conditions (source ambient) etc. This curve is shown in Fig. 5 and is particularly useful in predicting the percent electrically active P following implantation and subsequent diffusion. This curve is only valid for P concentrations below the P solid solubility limit in Si. Care must be taken in comparing this curve with P diffusion data where P precipitation has occurred. The data shown in Fig. 5 (1, 4-6) were selected on this basis and show good agreement with the calculated curve.

Sheet resistance and surface concentration.—The expression for the sheet resistance of a diffused impurity layer in Si is

$$R_S = \frac{1}{q\,\bar{u}\,Q_{el}} \quad [11]$$

where $\bar{u}$ is the effective bulk carrier mobility (cm²/V-sec) given by

$$\bar{u} = \frac{\int_0^{x_J} u\,n(x)\,dx}{Q_{el}} \quad [12]$$

An approximate expression for mobility can be obtained from the data of Mousty *et al.* (7). Thus

$$u = 75 + \frac{1.8 \times 10^{20}}{n} \quad [13]$$

where n is the electron concentration. Substitution of Eq. [13] into Eq. [12] and using the resulting expression for $\bar{u}$ in Eq. [11] yields

$$R_S = \frac{1}{q(75\,Q_{el} + 1.8 \times 10^{20}\,x_J)} \quad [14]$$

The units of electrically active P, Q_{el}, are (atoms cm^{-2}) and x_J is in cm.

By eliminating time from the expression for Q_{el} in Eq. [9] and solving for Q_{el} as a function of x_J, then the $R_S \cdot x_J$ product can be determined from Eq. [14]. The junction depth is the sum of the "flat region" width, x_o, and the depth of the tail region profile

$$x_J = x_o + 2\sqrt{D_{TAIL}t}\,\text{erfc}^{-1}\left(\frac{C_B}{C_K}\right) \quad [15]$$

C_B is the substrate background doping and C_K is the concentration at the kink in the P profile. Thus, Eq. [9] becomes

$$Q_{el} \sim \frac{x_J(1 + 2.04 \times 10^{-41} n_s^2)}{\text{erfc}^{-1}\left(\frac{C_B}{C_K}\right)} \left[3.5 \times 10^{10}\sqrt{\frac{D_{i^=} n_s}{D_{i^-}\left[1 + \exp\left(\frac{0.3\text{ eV}}{kT}\right)\right]}} + \frac{C_K}{\sqrt{\pi}}\right] \quad [16]$$

for $n_s >> C_K$ and

$$Q_{el} \sim \frac{n_s x_J}{\mathrm{erfc}^{-1}\left(\frac{C_B}{n_s}\right)\sqrt{\pi}} \quad [17]$$

for $n_s < C_K$. These equations are valid for the temperature range $T \lesssim 1050°C$. Above 1050°C the kink in the profile disappears.

Equations [16] and [17] have been used in Eq. [14] for estimating the $R_S \cdot x_J$ product for a background doping of 1×10^{17} cm^{-3}. The results are plotted *vs.* total P doping, C_S, and n_s for 800°, 900°, and 1050°C in Fig. 6. The C_S and n_s curves stop at the respective solid solubility limits. Data taken from measured profiles (8) are also included in Fig. 6 to support the calculations. Similarly, for the 1100°-1300°C range average $R_S x_J$ *vs.* C_S and n_s curves are shown in Fig. 7. In this temperature range the resistivity *vs.* surface concentration curves do not show the temperature dependence of the 800°-1050°C curves shown in Fig. 6.

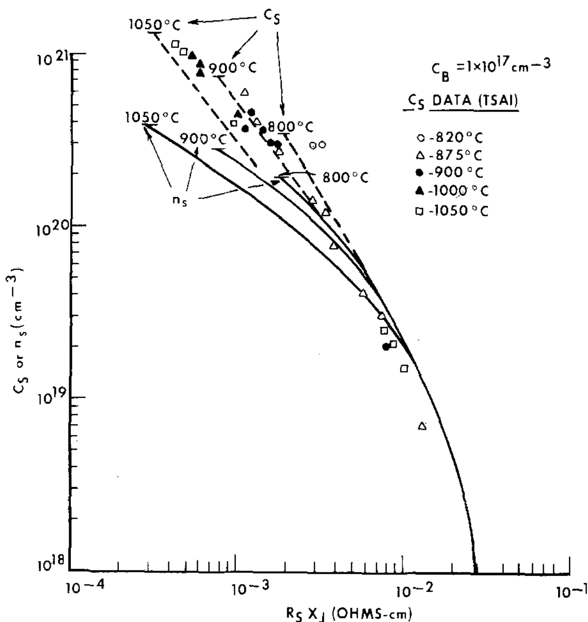

Fig. 6. Total and electrically active P surface concentrations *vs.* average resistivity for the 800°-1050°C temperature range.

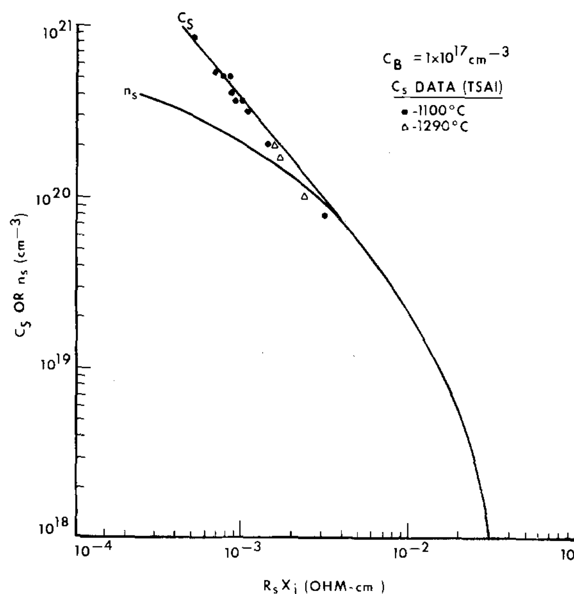

Fig. 7. Total and electrically active P surface concentration for the 1100°-1300°C temperature range.

Drive-in of implanted or predeposited P layers.—In the case of an ion-implanted P layer, the total dose, Q_T, is known. In order to determine R_S as a function of x_J, Q_{el} must be calculated. If the final surface concentration, n_s, is known, then Q_{el} can be determined from Fig. 5 for any diffused P layer in Si, regardless of the diffusion temperature. Rewriting Eq. [14], the sheet resistance becomes (Ω/□)

$$R_S = \frac{8.3 \times 10^{16}(1 - 28.8 R_S x_J)}{Q_{el}} \quad [18]$$

Curves of R_S *vs.* x_J at a background doping of 1×10^{17} cm^{-3} can now be generated. For a given P implant dose, values of n_s can be selected from which Q_{el} (Fig. 5) and $R_S x_J$ (Fig. 6 and 7) can be determined. Equation [18] can then be solved for R_S. Calculated curves which have been averaged over the temperature range of 900°-1300°C are shown plotted in Fig. 8. For example, a 1×16 cm^{-2} P implant with a junction depth of 3 μm will have a sheet resistance of approximately 8.5 Ω/□. The data shown in Fig. 8 were obtained from 50 keV P implants and support the approximate curves for the doses shown. However, these curves do not depend on implant energy since the unique relationship between R_S and x_J is only a function of Q_{el}. This assumes that the initial implant quickly redistributes during thermal processing so that this unique relationship can occur rapidly.

Conversely, the surface concentration can be determined from R_S measurements if the implant dose and diffusion temperature range are known. For example, a 20 Ω/□, 5×10^{15} cm^{-2} P implant diffused in the temperature range $T > 1100°C$ yields $x_J \simeq 1$ μm at 10^{17} cm^{-3}. Thus, $R_S x_J = 2 \times 10^{-3}$ Ω-cm. From Fig. 7, $C_S = 1.2 \times 10^{20}$ cm^{-3} and $n_s = 1 \times 10^{20}$ cm^{-3}.

Discussion

At least one phenomenon in P diffusion has not been treated in this paper, *i.e.*, precipitation on dislocations. Generally, it is found that if the surface concentration is limited to solid solubility values, precipitation is negligible in its effect on diffusion. At higher surface concentrations significant precipitation can occur in the Si, depending to some extent on the initial dislocation density of the Si crystal (9). The effect of P precipitation on dislocations is to introduce nonequilibrium processes into the diffusion mechanisms which can significantly reduce the depth to which

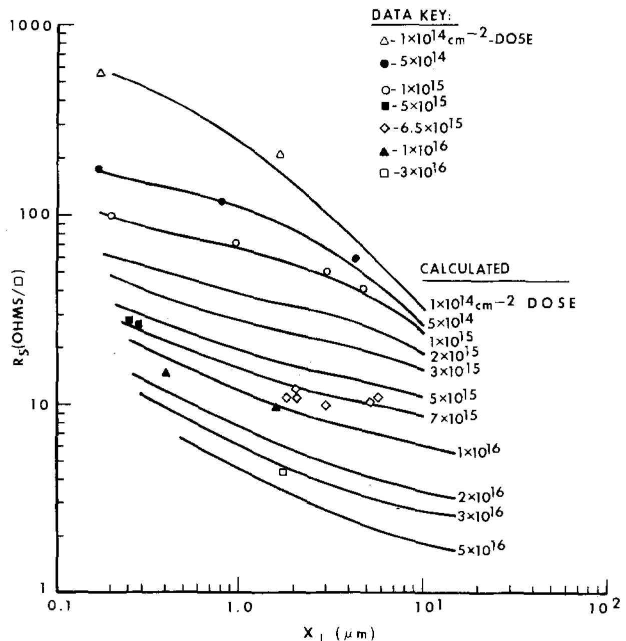

Fig. 8. Sheet resistance *vs.* junction depth at 10^{17}cm^{-3} curves for P implanted-diffused layers in Si.

P diffuses for a given time and temperature. The curves presented in this paper do not account for precipitation. As a result, diffusions with C_S greater than solid solubility will show a smaller junction depth and larger C_S than predicted by the analysis.

Summary and Conclusions

The complex diffusion of phosphorus in silicon has been analyzed in simplified terms. By calculating the relationship between total P/cm^2 and electrically active P/cm^2, curves have been generated which relate P and electron surface concentrations to the average diffused-layer resistivity. For the case of an ion-implanted P layer which is subsequently diffused, it has been shown that well-defined curves of R_S *vs.* x_J can be generated for a particular implant dose, regardless of the diffusion time and temperature.

Manuscript submitted June 14, 1977; revised manuscript received Sept. 21, 1977.

Any discussion of this paper will appear in a Discussion Section to be published in the December 1978 JOURNAL. All discussions for the December 1978 Discussion Section should be submitted by Aug. 1, 1978.

Publication costs of this article were assisted by Bell Laboratories.

REFERENCES

1. R. B. Fair and J. C. C. Tsai, *This Journal*, **124**, 1107 (1977).
2. J. C. C. Tsai, *Proc. IEEE*, **57**, 1499 (1969).
3. W. H. Becker, W. H. Eckton, and G. A. Kelley, Jr., Unpublished.
4. P. Negrini, D. Nobili, and S. Solmi, *This Journal*, **122**, 1254 (1975).
5. G. Masetti, D. Nobili, and S. Solmi, in "Semiconductor Silicon 1977," H. R. Huff and E. Sirtl, Editors, p. 648, The Electrochemical Society Softbound Symposium Series, Princeton, N.J. (1977).
6. R. A. McDonald, G. G. Ehlenberger, and T. R. Huffman, *Solid State Electron.*, **9**, 807 (1966).
7. F. Mousty, P. Ostoja, and L. Passari, *J. Appl. Phys.*, **45**, 4576 (1974).
8. J. C. C. Tsai, Unpublished.
9. M. Watanabe, H. Muroka, and T. Yonezawa, Proceedings of 6th Conference on Solid State Developments, Tokyo, 1974, p. 269.

Characterization of the Gaseous and Solid Products of Aluminum Sulfate Decomposition

Gary F. Knutsen and Alan W. Searcy

Materials and Molecular Research Division, Lawrence Berkeley Laboratory and Department of Materials Science and Mineral Engineering, University of California, Berkeley, California 94720

ABSTRACT

Measurements of SO_2^+/SO_3^+ mass spectrometer ion ratios and of weight losses when $Al_2(SO_4)_3$ is decomposed in an effusion cell show that equilibrium is achieved. Measurements of H_2O^+/SO_3^+ mass spectrometer ion intensities as a function of time shows that "anhydrous" aluminum sulfate contains about 0.03 moles of water per mole of sulfate ion. The solid decomposition product in the range of effusion studies, below 600°C, is an amorphous Al_2O_3 which has a surface area of 165 M^2/g and internal pores that average about 100Å in diameter. The experimentally measured decomposition pressures are higher by more than a factor of 4 than would be expected from thermochemical calculations, probably because the heat of formation of $Al_2(SO_4)_3$ is 7-9 kcal per mole more positive than reported.

Many metal sulfates, when heated, decompose to a solid oxide plus a mixture of SO_3, SO_2, and O_2 gases in proportions that depend on the temperature necessary to cause decomposition. Among reactions investigated in our laboratory in recent years were the decomposition of barium and strontium sulfates (1, 2). These reactions yielded SO_2 and O_2 as the primary gas products in both Knudsen (equilibrium) and Langmuir (kinetic) studies. But recently, by means of a combined weight loss, torsion effusion and mass spectrometry study, Lau, Cubicciotti, and Hildenbrand (3) showed that although $CaSO_4$ yields equilibrium SO_2 and O_2 pressures relatively readily, $MgSO_4$ does not. With large orifices the principal gaseous product of $MgSO_4$ decomposition was SO_3. When the orifices of the cell were made sufficiently small or when Fe_2O_3 was added as a catalyst, the principal gaseous products became SO_2 and oxygen.

The temperatures suitable for effusion measurements with $MgSO_4$ are lower than for $CaSO_4$, $SrSO_4$, or $BaSO_4$. It appeared of interest to investigate a sulfate decomposition that occurred at a still lower temperature to determine if, under conditions for which equilibrium decomposition pressures of SO_2, O_2, and SO_3 are calculated to be nearly equal, the equilibrium partial pressures of SO_2 can be obtained.

Key words: sulfur dioxide; sulfur trioxide; aluminum sulfate decomposition; aluminum oxide, amorphous; aluminum sulfate, heat of formation, of; aluminum sulfate, water content of.

From available data (4, 5) it could be predicted that aluminum sulfate decomposition would be suitable for such a study. Furthermore, recent investigations by Beruto and Searcy (6, 7) of the calcium oxide produced by vacuum decomposition of $CaCO_3$ suggest that it should be of particular interest to investigate the crystal structure, morphology, and surface area of the solid product of the reaction sequence $Al_2(SO_4)_3 \cdot 17H_2O_{(s)} = Al_2(SO_4)_{3(s)} + 17H_2O(g) = Al_2O_{3(s)} + 3SO_{2(g)} + 3/2\ O_{2(g)}$.

Vacuum decomposition of $CaCO_3$ yields a CaO that is poorly crystalline, has particles with an internal porosity of more than 50%, and has surface areas of the order of 50 M^2/g. That oxide is much more reactive toward water vapor than is the oxide produced by decomposition of $CaCO_3$ in air or dry nitrogen.

The molar volume of Al_2O_3 formed from $Al_2(SO_4)_3 \cdot 17H_2O$ can be calculated to be only 10% that of the starting material. Thermal decomposition of $Al_2(SO_4)_3$ in air at temperatures less than 750°K yields an alumina that x-ray powder diffraction studies show to be amorphous (4-6). A study by Kalinina and Pori-Koshits (8) shows that $Al_2(SO_4)_3$ decom-

poses to γ-Al_2O_3 at approximately 1170°K and then transforms to the thermodynamically more stable form α-Al_2O_3 at temperatures greater than 1420°K. Therefore analogy with the results of $CaCO_3$ decomposition suggests that the alumina from $Al_2(SO_4)_3 \cdot 17H_2O$ decomposition in vacuum might well be both metastable and highly porous. If so it might, like the oxide produced by calcite decomposition, show unusually high reactivity.

Experimental

The mass spectrometer used to investigate the gaseous products of $Al_2(SO_4)_3$ decomposition was a 24 cm radius, Atlas CH4 magnetic deflection device equipped with a 16 stage, Cu-Be, electron multiplier for use as an ion current detector. Reagent grade $Al_2(SO_4)_3$ powder was purchased from the J. F. Baker Company. The only listed impurities were 0.01% Cl, 0.001% Fe, and 0.001% Pb. The powder, a hydrated form of $Al_2(SO_4)_3$, was heated for 24 hr at 620°K to drive the water off. The product then showed the expected powder x-ray pattern for anhydrous $Al_2(SO_4)_3$.

The dried $Al_2(SO_4)_3$ was stored in a vacuum desiccator until it was transferred to a 99.5% Al_2O_3 effusion cell. The cell was heated in the mass spectrometer by radiation from a 0.025 cm diameter tungsten wire surrounded by a tantalum heat shield. Temperatures were measured with a Pt-Pt 10% Rh thermocouple inserted in the bottom of a platinum cell holder which contained the Al_2O_3 cell.

Experiments were performed with cell lids of three different orifice diameters in order to test whether equilibrium is achieved inside the cells and to correct for nonequilibrium if necessary (9, 10). Orifice diameters were 0.31, 0.51, and 0.78 mm, respectively, and the thickness of each lid was 2.31 mm.

Background pressures below 10^{-7} Torr were established before each run. The intensities of SO_3^+ and SO_2^+ were followed using 70 or 17 eV electrons. In all the decomposition runs the temperature variations were less than 2°K, and the temperatures were stable at the midpoints for long periods of time. The total fluxes of SO_3 + (SO_2 + 1/2 O_2) were calculated from the weight changes produced in known periods of heating. The relative amounts of SO_3 and SO_2 effused were determined by monitoring the mass 80 peak, which corresponds to $S^{34}O_3{}^{16}$, and both the mass 64 which corresponds to $S^{32}O_2{}^{16}$ and the mass 66 peak for $S^{34}O_2{}^{16}$.

The Al_2O_3 that formed on the decomposition of $Al_2(SO_4)_3$ was examined by the powder x-ray diffraction method and a scanning electron microscope was used to determine the characteristic particle sizes and shapes for the $Al_2(SO_4)_3$ and the Al_2O_3 product. The surface area of the Al_2O_3 and the $Al_2(SO_4)_3$ were measured using a Quantasorb surface area analyzer. The samples were out-gassed for 1-2 hr at 625°K prior to surface area determination to desorb water or other contaminates on the surfaces.

Pore size distributions were studied for thoroughly out-gassed samples using a high pressure (60,000 lb) American Instrument mercury porosimeter.

Results and Discussion

It has been reported (11) that fragmentation of SO_3 to SO_2^+ is considerable. In order to determine accurate gas composition data, the ion current ratios were measured at 17 eV (about 5 eV above appearance potentials for both ions). The effective cross section σ_{eff} for a molecule at less than maximum potential values is given by the equation

$$\sigma_{eff} = \frac{(E - AP)\sigma}{(E_{MAX} - AP)}$$

where AP is the appearance potential. For SO_2, σ_{eff} is 0.52 and for SO_3 it is 0.54 based on cross sections by Mann (12) and appearance potentials determined by Lau *et al.* (3). When 17V electrons are used, fragmentation of both SO_2 and SO_3 is minimal, and the vapor effused from orifices of diameters 0.31, 0.51, and 0.78 mm all give SO_2^+/SO_3^+ ratios of 1.8/1 at 673°K. The fact that the ion ratios and calculated total pressures were independent of orifice area shows that equilibrium was attained more readily than for $MgSO_4$ decomposition (3). Fragmentation of SO_3 to SO_2^+ does have a significant effect when 70V electrons are used in studies of decomposition of $Al_2(SO_4)_3$; the SO_2^+/SO_3^+ ratio measured with 70V electrons was 2.7/1 at 673°K.

Our early SO_2^+/SO_3^+ ratios measured at 70 eV were higher than 2.7/1, and a scan of the mass spectrometer peaks showed the H_2O^+/SO_2^+ intensity ratio was approximately 1.1/1. After some 20% of the sulfur oxide had been driven out by heating, the H_2O^+ intensity decreased to about 10-15% of the SO_2^+ intensity. The relative intensities then remained at 1.8/1 until the sulfate was nearly decomposed (Fig. 1).

The initial high H_2O^+ intensity probably resulted from escape of adsorbed water. When the powder was exposed to air for more than 20 min the ratios of SO_2^+ to SO_3^+ measured with 70 eV electrons increased to 5/1. High SO_2^+/SO_3^+ ratios were accompanied by high H_2O^+ intensities and a peak corresponding to $H_2SO_4^+$ which was about 10% of the intensity of H_2O^+. Reaction of water with SO_3 is evidently the cause of the high SO_2^+/SO_3^+ ratios.

At longer times of heating, the intensities of SO_2^+, SO_3^+, and H_2O^+ all decreased at essentially the same rate, until about 95% of the sulfur oxide content of the sample had been exhausted. The intensities then decreased at a faster rate and SO_2^+/SO_3^+ ratios increased as expected when insufficient $Al_2(SO_4)_3$ remains to provide the equilibrium pressures of gaseous products. The gradual decrease in ion intensities that characterized most of the period of a run is probably a consequence of poisoning of the electron multiplier by the sulfur oxides.

The fact that an H_2O^+ peak persisted at some 3% of the SO_2^+ + SO_3^+ intensity throughout sample decomposition appears to mean that water is a significant component of "anhydrous" aluminum sulfate, as usually prepared. This conclusion is consistent with the report by Young (13) that he was unable to lower the water content of $Al_2(SO_4)_3$ below 0.3 weight percent of his sample, or about 2.4 mole percent, of the sulfur oxide content.

Decomposition of $Al_2(SO_4)_3$ in vacuum at 720°K produced a solid product that gave no discernable x-ray pattern, which indicates an amorphous material. Decomposition in vacuum at 1020°K produced a solid that showed only three broad x-ray peaks of

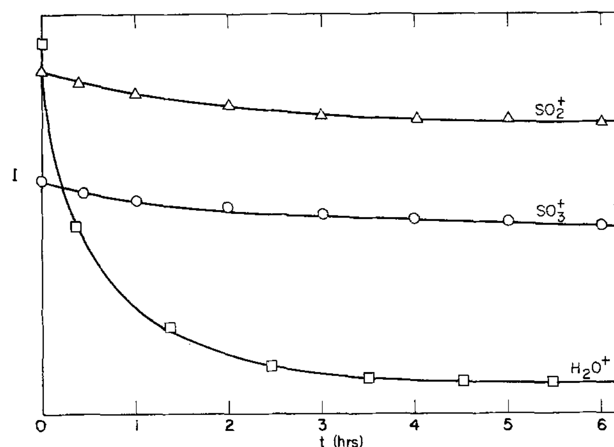

Fig. 1. Ion intensity vs. time at 800°K

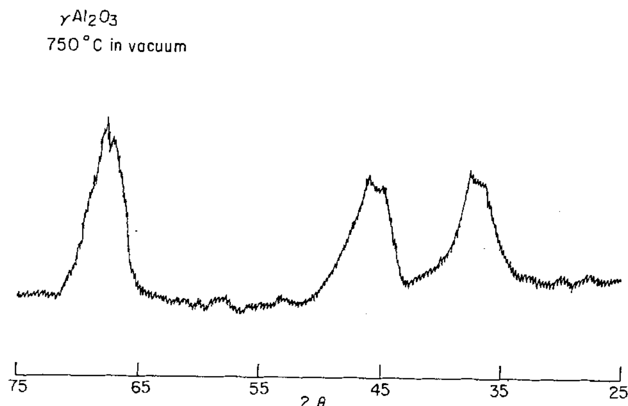

Fig. 2. X-ray pattern of γ-Al_2O_3 from decomposition at 750°C

γ-Al_2O_3 (Fig. 2). Decomposition in vacuum at 1370°K produced well-crystallized α-Al_2O_3. These results are consistent with earlier results for $Al_2(SO_4)_3$ decomposition in air (8).

Total decomposition pressures were calculated from isothermal Knudsen effusion weight loss experiments of at least several hours duration. The vapor was assumed to be a mixture of SO_3, SO_2, and O_2 which was at equilibrium for each temperature and total mass flux. Water, which is estimated to account for less than 2% of total weight losses, was neglected. The equilibrium assumption is supported by the fact that consistent total pressures were calculated from measurements with orifices of three different diameters (Fig. 3).

Because the alumina produced in our experiments was amorphous the corresponding decomposition pressures must be lower than those when γ-Al_2O_3 is the product (14). But our measured pressures are higher than the pressure calculated for decomposition to γ-Al_2O_3 by about a factor of 4 (5, 15). Furthermore, in the $Al_2(SO_4)_3$, the sulfur oxide activities should be reduced by the presence of water by an amount of the order of 3%, in accordance with Raoult's law, regardless of the form in which the water is present.

The heat of formation of $Al_2(SO_4)_3$ has been estimated to be uncertain by 5 kcal. The discrepancy between calculated and measured pressures is accounted for if it is assumed that the true heat of formation of $Al_2(SO_4)_3$ is, in fact, $5 + n$ kcal more negative than reported, where n is the heat of formation of amorphous alumina from γ-Al_2O_3. Probably n is 1-3 kcal.

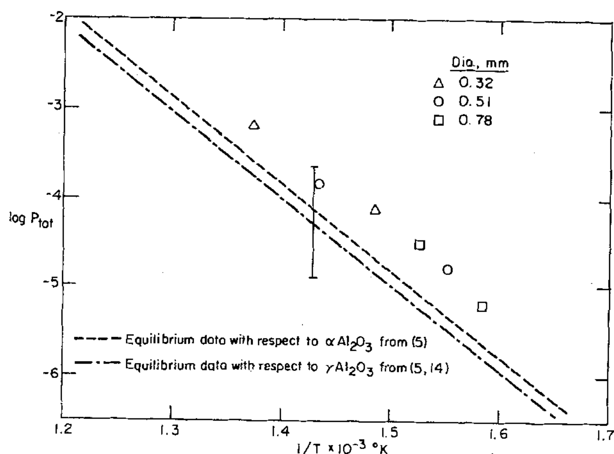

Fig. 3. Variation of p_{tot}, the total equilibrium decomposition pressure in atmospheres, with temperature. 5 kcal error bar is included on γ-Al_2O_3 line.

Table I. Surface areas

Material	Surface areas (M^2/g)
$Al_2(SO_4)_3 \cdot 17H_2O$	1.5
$Al_2(SO_4)_3$	35
Al_2O_3	165

Scanning electron micrographs of $Al_2(SO_4)_3 \cdot 17H_2O$ and Al_2O_3 show the hydrate and product oxide particles to be of the same shapes and dimensions, approximately 20 μm in typical cross section. Molar volume calculations indicate that the alumina particles must have more than 85% internal porosity. The fact that the pores could not be resolved in SEM pictures shows that either their diameters must be less than 0.1 μm or that reaction with water vapor during the short time of exposure to the atmosphere before SEM pictures could be made obscured the pore mouths.

Surface areas were obtained using the dynamic BET method on $Al_2(SO_4)_3 \cdot 17H_2O$, $Al_2(SO_4)_3$, and Al_2O_3. The results are given in Table I. These results coupled with the scanning electron micrographs prove that the alumina particles have very high internal surface areas.

A high pressure mercury porosimeter was used to measure the pore size distribution for the Al_2O_3 (Fig. 4). The average pore size is calculated to be 100Å.

Because the surface area of 165 M^2/g is nearly as high as areas of catalyst supports (16), we have initiated studies to determine if the Al_2O_3 produced from $Al_2(SO_4)_3 \cdot 17H_2O$ decomposition may be an effective reactant for removal of SO_2 and/or SO_3 from gas streams.

Acknowledgments

We thank Dr. David Meschi and Dr. Jim Roberts for their technical assistance and numerous helpful suggestions and thank Jim Severns, Emery Kozak, and Gay Brazil for technical assistance. This work was supported by the U.S. Energy Research and Development Administration.

Manuscript submitted Aug. 1, 1977; revised manuscript received Sept. 29, 1977.

Any discussion of this paper will appear in a Discussion Section to be published in the December 1978 JOURNAL. All discussions for the December 1978 Discussion Section should be submitted by Aug. 1, 1978.

Publication costs of this article were assisted by the University of California.

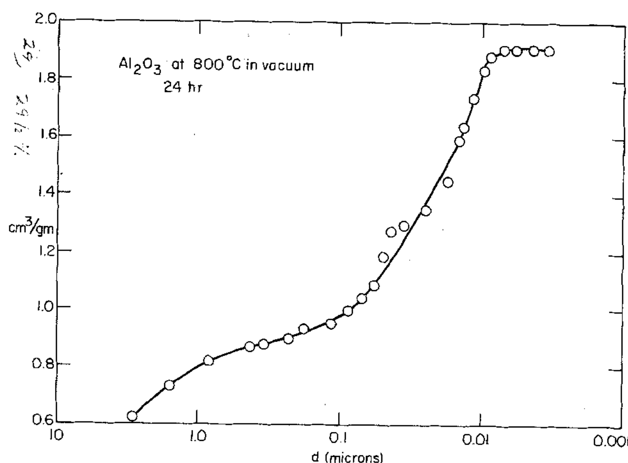

Fig. 4. Pore size distribution of Al_2O_3

REFERENCES

1. P. Mohazzabi and A. W. Searcy, *J. Chem. Soc., Faraday Trans. 1*, **72**, 290 (1976).
2. T. K. Basu and A. W. Searcy, Unpublished work.
3. K. H. Lau, D. Cubicciotti, and D. L. Hildenbrand, *J. Chem. Phys.*, **66**, 4532 (1977).
4. H. H. Kellogg, *Trans. Met. Soc., AIME*, **230**, 1622 (1964).
5. K. H. Stern and E. L. Weise, National Bureau of Standards Report NSRDA-NBS 7, U.S. Government Printing Office, Washington, D.C. (1966).
6. D. Beruto and A. W. Searcy, *J. Chem. Soc., Faraday Trans., 1*, **70**, 2145 (1974).
7. D. Beruto and A. W. Searcy, *Nature*, **263**, 221 (1976).
8. A. M. Kalinina and E. A. Porai-Koshits, *Proc. Acad. Sci. USSR, Phys. Chem. Sect., (Engl. Transl.)*, **114**, 297 (1957).
9. C. I. Whitman, *J. Chem. Phys.*, **20**, 161 (1952).
10. K. Motzfelt, *J. Phys. Chem.*, **59**, 139 (1955).
11. J. P. Briggs, R. R. Hudgins, and P. L. Stevenson, *Inter. J. Mass Spec. Ion Phys.*, **20**, 1 (1976).
12. J. H. Mann, in "Recent Development in Mass Spectroscopy," K. Ogata and T. Hayakawa, Editors, p. 5, University Park Press, Baltimore, Md. (1970).
13. F. E. Young, *J. Am. Chem. Soc.*, **67**, 257 (1945).
14. A. W. Searcy and D. Beruto, *J. Phys. Chem.*, **80**, 425 (1976).
15. JANAF Thermochemical Tables, 2nd ed., D. R. Stull and H. Prophet, Editors NSRDS-NBS 37, U.S. Government Printing Office, Washington, D.C. (1971).
16. J. H. Sinfelt, *Science*, **195**, 644 (1977).

Kinetics of the Transformation of Metastable Tin-Nickel Deposits

I. Determination of the Avrami Equation Parameters by DSC or DTA

J. A. Augis and J. E. Bennett

Bell Laboratories, Columbus, Ohio 43213

ABSTRACT

Using both differential scanning calorimetry (DSC) and differential thermal analysis (DTA), the kinetics of the transformation upon heating of the metastable tin-nickel alloy were studied. The solid-state reaction proceeds according to a classical Avrami equation. The parameters of the reaction equation were determined, and it is shown that the metastable alloy will not revert to the stable state, for all practical purpose, if kept at temperatures below 100°C. Variations of the kinetic parameters were observed which can explain most of the different stability evaluations reported by different authors.

The electrodeposited equiatomic [approximately 65 weight percent (w/o) Sn-35 w/o Ni] tin-nickel alloy has been used in various practical applications because of its corrosion resistance or passivity and its thermal stability. Its remarkable corrosion resistance (1) has been the subject of several recent studies (2-4). Thermal stability has been reexamined by one of the authors (5). The equiatomic alloy is not an equilibrium phase of the nickel-tin binary system (6) and can only be prepared either by electroplating (7) or from more recent results by sputtering (8). The electroplated and sputtered deposits are metastable and are known to revert upon heat-treatment to the two phases Ni_3Sn_4 and Ni_3Sn_2 which constitute the room temperature equilibrium state of the equiatomic alloy of tin and nickel. The metastable phase is what is normally electrodeposited, and if conditions are such that transformation could occur during service life it is important to be able to predict it. However the morphology of this phase and the reason for its stability are still unknown. In this paper a study of the transformation kinetics was performed to derive a prediction equation. This study also provided information on the mechanism of the transformation which is reported in a companion paper (9).

Using the technique of differential thermal analysis (DTA), the metastable phase was shown to decompose exothermically at around 365°C, when heated at 5°C/min, into the equilibrium intermetallic compounds Ni_3Sn_2 and Ni_3Sn_4 (5). In the same article a brief review of previous work on "SnNi" thermal stability was presented. Some workers observed the decomposition from isothermal annealing at temperatures as low as 250°C (10) while others report stability at temperatures as high as 500°C (11). While Bennett and Tompkins (5) utilized a different method (DTA) from that of previous investigators in their thermal stability study, it was apparent that a more detailed study of the transformation kinetics was needed. By using either a differential scanning calorimeter (Perkin-Elmer Model DSC-1B) or a differential thermal analysis apparatus (CSI, R. L. Stone Company), we determined the parameters for the Avrami equation (12) describing the transformation as well as the range of activation energies observed for different deposits.

Theory and Experiments

DTA is a dynamic technique where the time variable and the temperature variable are intermixed, so that no true isothermal experiment can be performed with DTA equipment. While DTA measures a temperature difference between the investigated sample and a reference material, DSC works on a different principle whereby the apparatus provides heat to either the sample or the reference container in order to keep their temperatures equal. The instantaneous power delivered to sample and reference is available as an analog signal. In a single step reaction the fraction of material transformed *vs.* time is proportional to the quantity of heat evolved or absorbed. Isothermal experiments can be conducted with a differential scanning calorimeter.

Most reactions in solid metallic phases are empirically described by the Avrami equation where x is the fraction of material transformed at the time t

$$x = 1 - \exp[-(kt)^n] \quad [1]$$

n is a dimensionless exponent, k has the dimensions of reaction rate and is generally given by an Arrhenius type of relation

$$k = \nu \exp - \frac{\Delta E}{RT} \qquad [2]$$

where ν = frequency factor, ΔE = activation energy, R = gas constant, and T = Kelvin temperature.

The rate of transformation at any instant is given by differentiating Eq. [1] with respect to time at constant temperature

$$\frac{dx}{dt} = nk^n t^{n-1} (1 - x) \qquad [3]$$

For a given temperature, k is constant and Eq. [3] yields a characteristic rate curve. As mentioned above, isothermal experiments cannot be performed with DTA equipment, but such rate curves can be obtained from isothermal DSC experiments.

Although the DSC equipment measures dx/dt directly, the data can be more conveniently analyzed by the integral of Eq. [3], *i.e.*, Eq. [1] which can be rewritten as

$$\ln \frac{1}{1 - x} = (kt)^n \qquad [4]$$

This expression is used to determine n and k at a given temperature by least squares fitting the natural logarithm of expression [4] to ln t. By repeating the same procedure at different temperatures one can generate k as a function of T. The activation energy and the frequency factor are then determined by the standard method of plotting ln k *vs.* the reciprocal of T.

The advantage of DSC is obvious as one considers Eq. [4]; although all the terms necessary to solve for k in [4] are available in a DTA run there are no unambiguous ways to choose the exponent n since DTA cannot be done isothermally.

In this study DSC measurements were taken on two different deposits in order to determine precisely the parameters, n, ΔE, and ν for these two particular cases. Since no variation of n was found in the DSC experiments, previous DTA results on various other deposits were then used to estimate the range of variation of the parameters ΔE and ν.

The materials used for the DSC runs were a thick electrodeposit (40-100 μm) plated under conditions similar to the ones described in Ref. (5) and a sputtered film (15-20 μm) prepared as in Ref. (8). Both films were deposited on a stainless steel foil and were freed from their substrate prior to the thermal experiments by bending the foil. Both types of samples were first run in the scanning mode (20°C/min) in order to determine the temperature range where transformation could be detected. Several fixed temperatures were selected in these ranges to perform isothermal experiments. During the runs the temperature of the calorimeter was first increased linearly at 40°C/min to the vicinity of the selected temperature. This final temperature was then adjusted manually and the rate curve was traced on a time chart recorder until the vertical deflection remained stable, thus indicating the end of the reaction. A typical rate curve is shown in Fig. 1a. For each temperature, the area under the curve was measured until a given time t by using a planimeter. The amount transformed x, ratio of this area to the total area under the curve was then used in a least squares fitting procedure for Eq. [4]. The "ln-ln plot" of Eq. [4] is shown in Fig. 1b for the rate curve of Fig. 1a.

The procedure for the DTA experiments has been presented previously (5). Numerous DTA experiments were run on "SnNi" produced during different electroplating operations. A typical DTA trace is shown in Fig. 2.

Results

The values of the exponent n and the rate constant k at various temperatures are shown in Tables I and II for the electroplated and the sputtered samples, respectively. The plot of ln k *vs.* T^{-1} is linear in both cases (Fig. 3a and b). From a least squares fit of these data the activation energies and the frequency factors shown in Table III were derived. The parameters are given with their 95% confidence intervals. The value of n is rather constant over the range of temperature investigated which justifies the use of an Avrami type of equation and indicates that probably only one mechanism is operative during the transformation. Although the 95% confidence intervals for the activation energies overlap slightly, the difference in the mean values for ΔE between electroplated and sputtered samples is probably genuine (both ΔE and ν are distinct within the "one sigma" limit); it is only the limited number of isothermal experiments available which leads to such relatively large confidence intervals at the 95% level.

In order to obtain information on the variability of the activation energy for different plating operations we next used the DTA data of Table IV. The platings are identified by their date. The average temperatures T_M at which the peak of the DTA trace occurs, and their confidence intervals are given for the constant

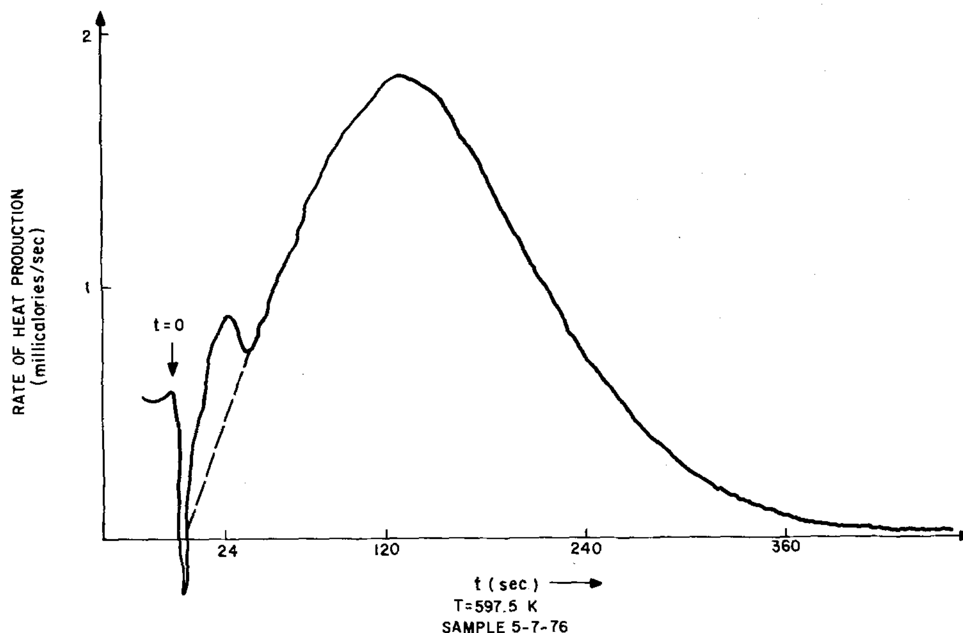

Fig. 1a. DSC rate curve obtained with plated "SnNi" (5-7-76) at 597.5°K. The time is measured from the instant the temperature 597.5°K is reached. The transient behavior seen at the beginning of the curve is due to the calorimeter and is disregarded.

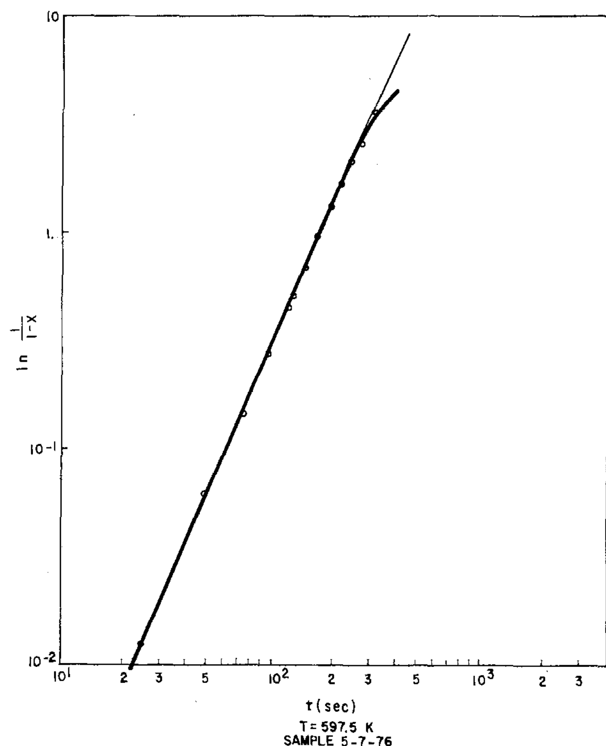

Fig. 1b. ln-ln plot of Eq. [4] applied to the rate curve of Fig. 1a. The least square fitting gives $n = 2.20$ and $k = 5.81 \times 10^{-3}\ s^{-1}$.

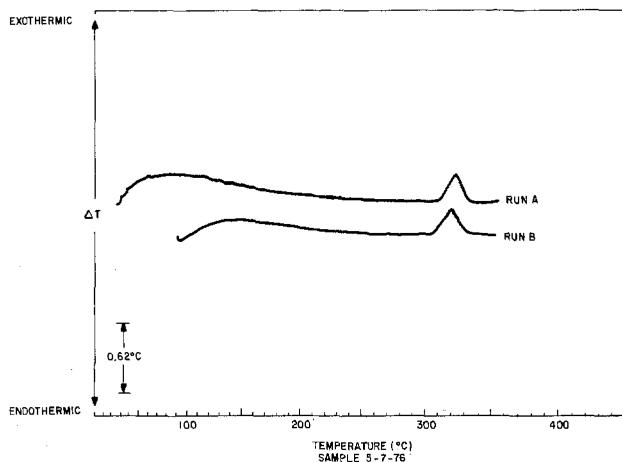

Fig. 2. Differential thermal analysis curve for sample 5-7-76. Sample wt. 0.007g, program rate $\alpha = 5°C/min$, $T_M \simeq 598°K$.

heating rate of 5°C/min. Using a graphical method the activation energies for the different platings were calculated assuming n equal to 2.1 and a constant ν equal to $2 \times 10^{14}\ sec^{-1}$. The results are shown in Table V. The margin of error given in Table V is not a true confidence interval but merely represents the shift in intersection in the graphical solution by using the confidence interval for the various T_M values.

The graphical method employed led us to modify the Kissinger method commonly used for kinetic analysis of DTA data for homogeneous systems (13). This

Table I. Values of the exponent n and rate constant k at different temperatures for an electroplated "SnNi" sample

T (°K)	n	k (sec^{-1})
610	2.07	13.20×10^{-3}
605	2.07	10.75×10^{-3}
600	2.02	7.33×10^{-3}
597.5	2.20	5.81×10^{-3}
595	2.07	5.68×10^{-3}
590	2.23	3.79×10^{-3}
585	2.12	2.72×10^{-3}

Table II. Values of the exponent n and rate constant k at different temperatures for a sputtered "SnNi" sample

T (°K)	n	k (sec^{-1})
700	2.01	11.56×10^{-3}
695	2.18	7.75×10^{-3}
690	2.07	6.54×10^{-3}
685	2.02	5.01×10^{-3}
680	2.13	3.64×10^{-3}

method enables determination of the kinetic parameters (ΔE and ν) from the influence of the heating rate on the position of the DTA peak. However, this method is applicable only when the exponent in the Avrami equation, n, equals unity. Our modification,

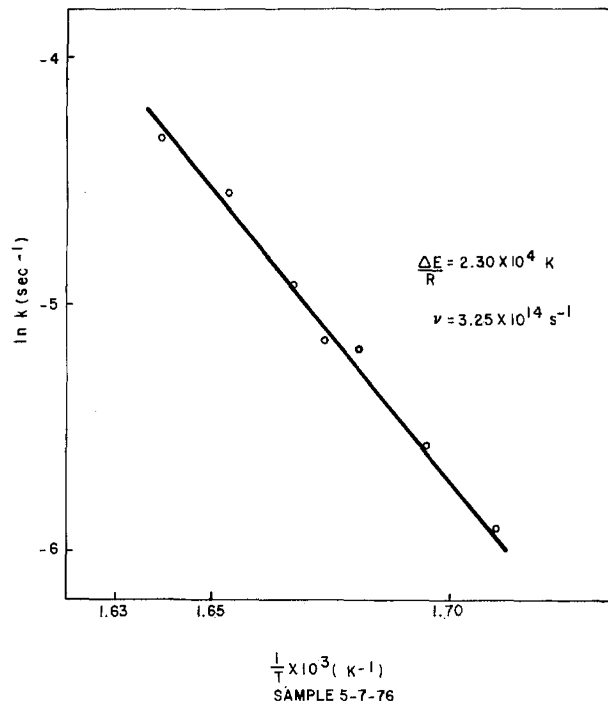

Fig. 3a. Arrhenius plot for the rate constant of the transformation of the plated sample 5-7-76.

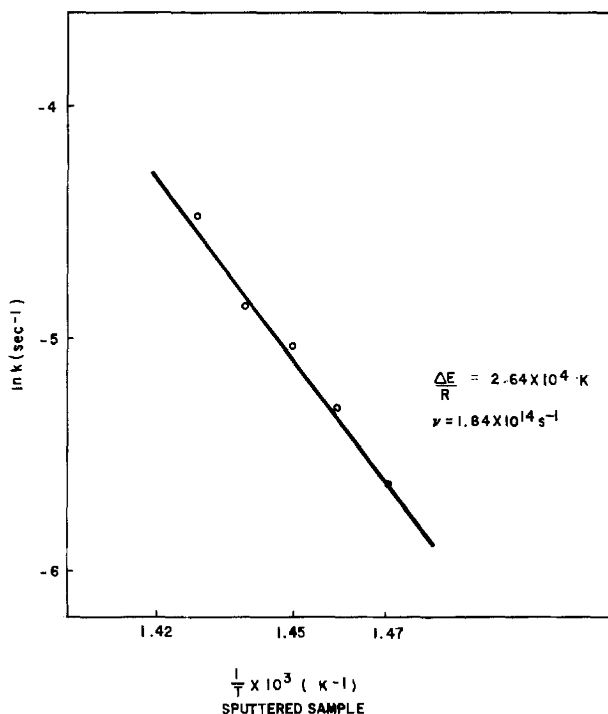

Fig. 3b. The same as Fig. 3a for the sputtered sample

Table III. Reaction kinetic parameters derived from DSC experiment

		$\bar{n}$	ν (sec^{-1})	$\frac{\Delta E}{R}$ (K)	E (kcal/mol)
Plated		2.11	3.25×10^{14}	2.30×10^4	46.0
95% confidence interval	—from	2.05	8.2×10^{15}	2.10×10^4	42.0
	—to	2.17	1.3×10^{13}	2.49×10^4	49.8
Sputtered		2.08	1.84×10^{14}	2.64×10^4	52.8
95% confidence interval	—from	2.01	3.3×10^{16}	2.28×10^4	45.6
	—to	2.15	1.2×10^{13}	2.99×10^4	59.9

Table IV. Temperature of the DTA peak for different "SnNi" platings

Plating identification	Average T_M (°K)	90% confidence interval
2-3-75	636	644 ⟷ 628
4-8-75	655	661 ⟷ 649
7-2-75	640	649 ⟷ 632
4-28-76	619	626 ⟷ 612
5-7-76	598	602 ⟷ 593
Sputtered	684	688 ⟷ 679

Table V. Activation energy for different platings calculated from DTA results

Plating identification	ΔE (kcal/mol)
2-3-75	51.5 ± 1.0
4-8-75	53.2 ± 1.5
7-2-75	52.0 ± 2.5
4-28-76	50.3 ± 2.5
5-7-76	48.0 ± 2.0
Sputtered	55.6 ± 2.5

reported in detail elsewhere (14), is applicable to heterogeneous systems which follow a general Avrami law for any value of n, and enabled us to independently calculate ΔE and ν solely from DTA data. The values obtained ($n = 2.2$, $\Delta E = 56$ kcal/mol, $\nu = 2.3 \times 10^{17}$ sec^{-1}) are in reasonable agreement with our DSC results.

Discussion

The decomposition kinetics of various deposits of "SnNi" can all be described by an Avrami equation (Eq. [1]) with a constant exponent n equal to 2.1. The rate constant follows an Arrhenius equation (Eq. [2]) with a frequency factor of the order of 10^{14} sec^{-1} and an activation energy varying between 42 kcal/mole – 60 kcal/mole (1.83-2.61 eV).

From the values of these parameters and by using Eq. [1] and [2] we can calculate the fraction of transformed material as a function of time at isothermal conditions. Taking the central values in Table III found for the plating (5-7-76), we plotted in Fig. 4 the fraction x of transformed material for various temperatures. It is observed that transformation occurs very rapidly close to 320°C (almost complete transformation in a few minutes). The time to transformation increases rapidly with lowering of the temperature, for example, no detectable amount of material is transformed in one day at 200°C, and about 120 days are required for complete transformation at this temperature. The activation energy of this particular electroplate is the lowest that we have observed, and it is then the least stable of our samples. In Fig. 5 the time necessary to reach 10% (t_{10}) and 90% (t_{90}) decomposition as a function of temperature is shown. We have included in this figure the maximal variation of parameters encountered in this study (cf. Table III $\Delta E/R$ min. $= 2.1 \times 10^4$K^{-1}, $\Delta E/R$ max $= 3 \times 10^4$K^{-1}, ν min. $= 1.2 \times 10^{13}$ sec^{-1}, ν max $= 8.2 \times 10^{15}$ sec^{-1}). Here again one can note that no amount of transformation is expected in 40 yr at temperatures below 125°C.

However, there are wide variations from sample to sample in the time necessary to achieve a certain percentage of transformation; for instance, at 320°C 10% decomposition can be reached in a minimum of 1 min for samples having the lowest ΔE, or a maximum of 4 days for samples having the highest ΔE (sputtered). Regardless of the values of ΔE and ν, t_{90} is roughly four times longer than t_{10}. Ten percent transformation is roughly the minimum amount which can be detected by x-ray means. The variation in activation energy and the consequent variation in t_{10} that we show in this paper are more or less consistent with the reported variations of thermal stability (5) if one excludes the 500°C value of Smart and Robins (11).

Summary

The transformation kinetics of several samples of electroplated or sputtered equiatomic tin-nickel alloy have been investigated. The transformation follows an Avrami law with an exponent n equal to 2.1, an activation energy ranging from 42 to 60 kcal/mol, and a frequency factor ranging from 1.2×10^{13} sec^{-1} to 3.3×10^{16} sec^{-1}. These numbers predict a very steep influence of the temperature on the transformation rate.

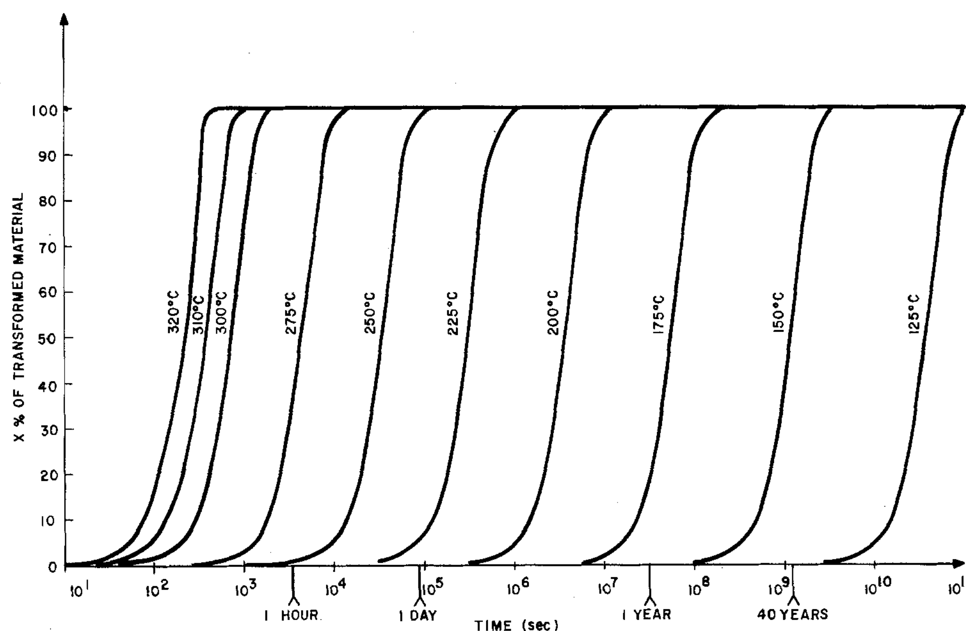

Fig. 4. Sigmoidal curves for the decomposition of sample 5-7-76. The percentage of transformed material is plotted against time for various temperatures (in °C). The plot was generated using the central values determined for 5-7-76.

$$x = 1 - \exp\left[-(kt)^{2.1}\right]$$
$$k = 3.25 \times 10^{14} \exp - \left[\frac{2.30 \times 10^4}{T}\right] \text{sec}^{-1}$$

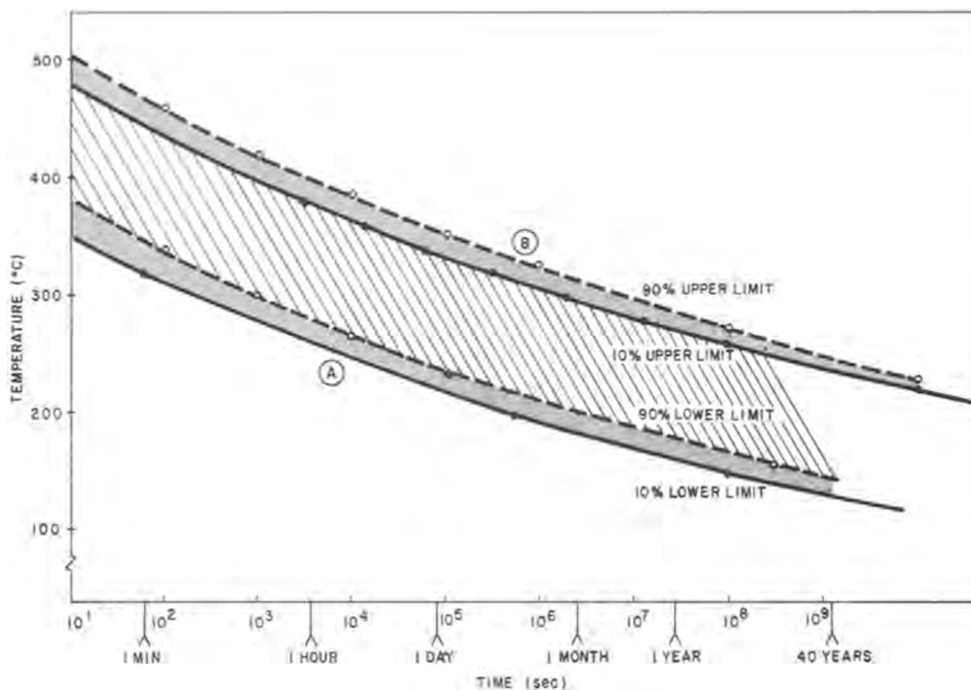

Fig. 5. Time-temperature-transformation curves for the "Sn-Ni" transformation. Curve A corresponds to the lower limits of the scatter of the parameters ΔE and ν, Curve B corresponds to the upper limits of the same parameters. For both A and B the lower curves correspond to 10% transformation (t_{10}) the upper curves to 90% transformation (t_{90}).

While 40 yr at 125°C will be insufficient to lead to transformation, 1 min at 475°C completely transforms all samples. The value of n makes the influence of the observed variations of ΔE and μ large enough to explain most of the varied stability results previously acknowledged.

Acknowledgments

The authors wish to thank B. G. Bagley for use of the DSC equipment, T. M. Paskowski for diligently taking the DSC and DTA data, and M. R. Pinnel for stimulating discussions.

Manuscript submitted June 10, 1977; revised manuscript received Sept. 28, 1977.

Any discussion of this paper will appear in a Discussion Section to be published in the December 1978 JOURNAL. All discussions for the December 1978 Discussion Section should be submitted by Aug. 1, 1978.

Publication costs of this article were assisted by Bell Laboratories.

REFERENCES

1. M. Antler, *IEEE Trans. Parts, Hybrids, Packag.*, **php-11**, 216 (1975).
2. H. G. Tompkins and J. E. Bennett, *This Journal*, **123**, 1003 (1976).
3. J. H. Thomas, III and S. P. Sharma, Submitted to *J. Vac. Sci. Technol.*
4. H. G. Tompkins and G. K. Wertheim, Submitted to *This Journal.*
5. J. E. Bennett and H. G. Tompkins, *This Journal*, **123**, 999 (1976).
6. M. Hansen "Constitution of Binary Alloys," p. 1042, McGraw-Hill Book Co., New York (1958).
7. N. Parkinson, *J. Electrodepositors' Tech. Soc.*, **27**, 129 (1951).
8. J. A. Augis and J. E. Bennett, *This Journal*, **124**, 1455 (1977).
9. J. A. Augis and J. E. Bennett, *This Journal*, **125**, 335 (1978).
10. P. K. Dutta and M. Clarke, *Trans. Inst. Met. Finish.*, **46**, 20 (1968).
11. R. F. Smart and D. F. Robins, *ibid.*, **37**, 108 (1960).
12. M. Avrami, *J. Chem. Phys.*, **7**, 1103 (1939); **8**, 212 (1940).
13. H. E. Kissinger, *Anal. Chem.*, **29**, 1702 (1957).
14. J. A. Augis and J. E. Bennett, *J. Thermal Anal.*, Accepted for publication.

Kinetics of the Transformation of Metastable Tin-Nickel Deposits

II. Formation and Transformation Mechanisms

J. A. Augis and J. E. Bennett

Bell Laboratories, Columbus, Ohio 43213

ABSTRACT

The nature of as plated metastable tin-nickel phase is reexamined. From x-ray, scanning electron microscope studies, and measurement of the enthalpy of transformation of the metastable alloy, it is concluded that the deposited alloy is a metastable extension of the composition range of the equilibrium phase Ni_3Sn_2 and not a distinct low temperature phase. It forms as a result of more favorable nucleation kinetics at the low deposition temperature. Its metastability is due to its morphology, and its decomposition upon heating is interpreted as precipitation and growth of the second equilibrium phase Ni_3Sn_4 from the supersaturated metastable configuration.

In a previous paper (1) the authors found that the solid-state transformation of a metastable equiatomic [approximately 65 weight percent (w/o) Sn-35 w/o Ni] tin-nickel alloy into the equilibrium compounds Ni_3Sn_2 and Ni_3Sn_4 (2) proceeds according to a classical Avrami equation

$$x = 1 - \exp[-(kt)^n] \quad [1]$$

where x is the fraction of material transformed at the time t, and n is a dimensionless exponent. k has the dimensions of reaction rate and is generally given by an Arrhenius expression

$$k = \nu \exp\left[-\frac{\Delta E}{RT}\right] \quad [2]$$

where ν = frequency factor, ΔE = activation energy, R = gas constant, and T = temperature.

Analysis of DSC data, and analysis of DTA data using our modification (3) of Kissinger's method (4), enabled determination of the following values for the Avrami and Arrhenius parameters

$n = 2.1$

$\Delta E = 42\text{-}60$ kcal/mol

$\nu = 1.2 \times 10^{13}\text{-}3.3 \times 10^{16}$ sec^{-1}

While our data allows a prediction for the conditions of the decomposition of "SnNi," the morphology of this nonequilibrium phase and its transformation mechanism are still uncertain. Rooksby (5) considered "SnNi" to be the result of an extension of the composition range of the equilibrium phase Ni_3Sn_2. Such extensions are quite often found during the rapid deposition of alloys by various techniques such as plating (6), sputtering (7), and splat-cooling (8). On the other hand, Dutta and Clarke (9) on the basis of solution calorimetry data argue that the electrodeposit is a new phase which is thermodynamically stable at the temperature of electrodeposition (72°C). To resolve this uncertainty we do reexamine the x-ray data, use SEM examination, and measure the enthalpy of formation of "SnNi."

Experimental Results

X-ray.—The methods and results are similar to those already presented in Ref. (10) and (11). The crystal structures of "SnNi" and Ni_3Sn_2 are very similar and all x-ray diffraction lines of the deposited alloy are nearly coincident with the more intense lines of Ni_3Sn_2. The structure of Ni_3Sn_4 is markedly different (12). In Fig. 1 we show a portion of the x-ray spectra for a powdered sample of electroplated "SnNi" before and after heat-treatment (500°C, 1 hr). We also show

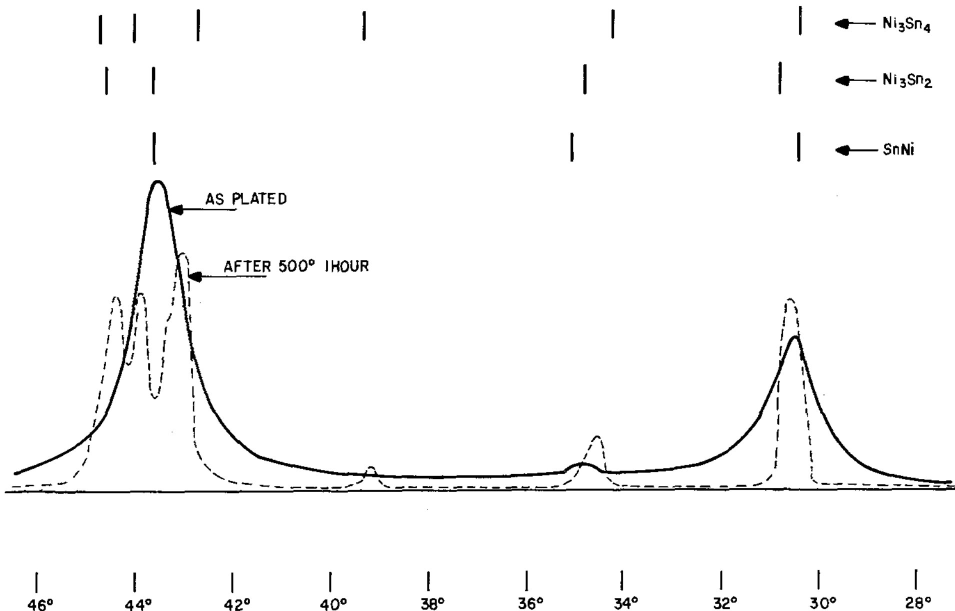

Fig. 1. Part of x-ray diffraction pattern for as-plated and heat-treated "SnNi" powders. Filtered copper radiation 50 kV, 30 mA. Also shown are the positions of the major peaks for "SnNi," Ni_3Sn_2. Ni_3Sn_4.

the characteristic positions of the main diffraction lines (relative intensity greater than 40) for "SnNi," Ni_3Sn_2, and Ni_3Sn_4. Besides the observation that upon heat-treatment the lines of Ni_3Sn_4 become apparent in addition to the lines of Ni_3Sn_2, one can observe the obvious sharpening of the lines. On the as-deposited samples the corrected full width at half-maximum is as large as 1.4×10^{-2} radian. X-ray line broadening is known to be due to small grain size, internal microstresses, and/or lattice defects. While it is not possible in the present case to separate the three factors, the line breadth is nonetheless an indication of small grain size; by assigning all the broadening to this effect and using the Scherrer formula, we predict the main dimension of the crystallites to be around 15 nm.

SEM examination.—To confirm the conclusion of the x-ray work, a metallographic study was attempted. Electrodeposited "SnNi" is known to be passive in respect to attack by most chemicals, and we were unable to reveal any structure by conventional metallographic methods. Better results were obtained by ion etching followed by scanning electron microscopy. Figure 2a shows the etched surface of a "SnNi" sample prior to heat-treatment. Although a nodular structure is present we were unable to detect any grain structure at any magnification, which suggests grain sizes of the order of tens of nanometers.

After heat-treatment (500°C, 24 hr) the transformed alloys show grain sizes of the order of 1 μm (Fig. 2b) within the wall of the nodular structure.

Free energy of formation of "SnNi".—The heats of transformation $-\Delta H_{TM}$ were measured using the differential scanning calorimeter on several samples of different deposits. The results and their scatter are shown in Table I along with the results of compositional analyses obtained using wavelength dispersive x-ray analysis and pure metal standards on a scanning electron microscope.

Regardless of the morphology of "SiNi," the transformation can be written

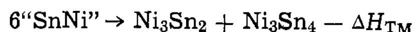

$$6\text{"SnNi"} \rightarrow Ni_3Sn_2 + Ni_3Sn_4 - \Delta H_{TM}$$

or, more exactly, since we have departure from stoichiometry

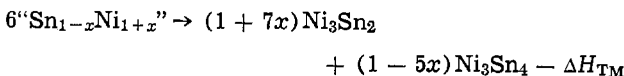

$$6\text{"}Sn_{1-x}Ni_{1+x}\text{"} \rightarrow (1 + 7x)Ni_3Sn_2 + (1 - 5x)Ni_3Sn_4 - \Delta H_{TM}$$

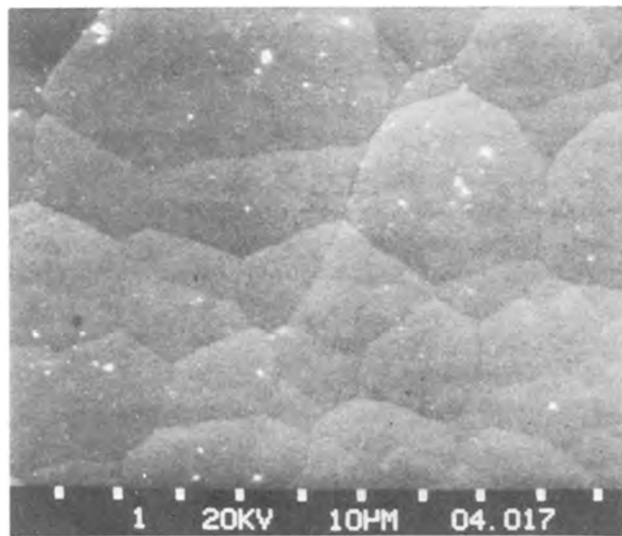

Fig. 2a. Scanning electron micrograph of the surface of an unannealed sample of plated SnNi (5-7-76) after 15 min of argon ion etching. There is no evidence of grain structure; the boundaries shown are those of plating nodules. The interval between the scan marks is 10 μm. 1150×.

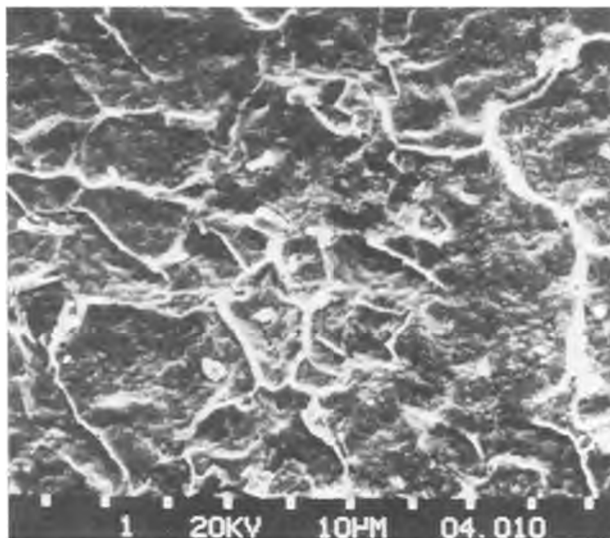

Fig. 2b. The same as Fig. 2a for the same sample after heat-treatment at 500°C for 24 hr. The grain structure is now evident (grain size of the order of 1 μm). 1150×.

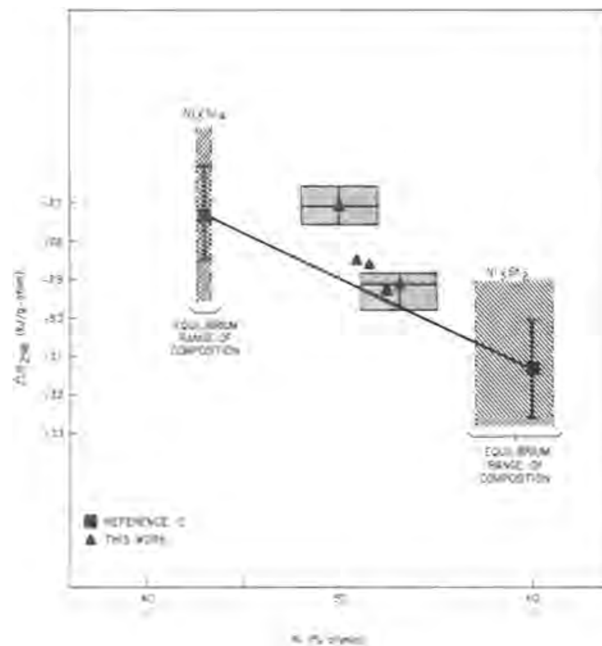

Fig. 3. Calculated standard enthalpies of formation of the "SnNi" alloys as a function of the nickel concentration. The values (△) are derived from the measured heat of reaction. The values for Ni_3Sn_2 and Ni_3Sn_4 are taken from Korber and Oelsen (14).

Using a similar analysis to the one of Dutta and Clarke (9) we can estimate the heat of formation of "$Sn_{1-x}Ni_{1+x}$" as a function of the Ni content.

To convert our experimental $-\Delta H_{TM}$ to the standard convention $-\Delta H_{298}$, we assumed the Kopp-Neuman rule of mixtures (13) concerning the specific heat. The results for our deposits are plotted in Fig. 3

Table I. Measured heats of transformation and composition analysis for several samples

Deposit identification	T_M (°K)	$-\Delta H_{T_M}$ (kJ/g-atom)	Composition (a/o) Ni	Composition (a/o) Sn
2-3-75	636	0.315 ± 0.300	52.5 ± 2	47.5 ± 2
7-2-75	640	0.817 ± 0.290	53.0	47.0
4-28-76	619	1.100 ± 0.160	51.4	48.6
5-7-76	598	1.26 ± 0.160	51.0	49.0
Sputtered	684	3.45 ± 0.465	49.8	50.2

vs. atomic composition, along with the enthalpies of formation of the equilibrium compounds (14). The vertical error bars are due to standard errors both in the calorimetric experiments and the composition analyses. For the composition range of our deposits (which is narrower than that used by Dutta and Clarke) the heat of formation of "SnNi" is not very different from the heat of formation of the corresponding mixture of the equilibrium compounds.

No data are available on the standard entropy of these compounds but if we assume these values to be similar (not too different entropy of mixing, similar vibrational entropy due to similar lattice), the ΔH_{298} values should show the relative positions of the free energy ΔG_{298} values in a free energy diagram. Within the limits of our assumptions, the experimental results do not indicate a substantial lowering of the free energy in the vicinity of the "SnNi" composition. Consequently the existence of "SnNi" as a new equilibrium phase at low temperatures is not indicated. A probable chemical free energy diagram for this system at a given low temperature, near ambient, is sketched in Fig. 4: the wider range of composition of the Ni_3Sn_2 phase (2) is consistent with a shallower free energy curve than that for Ni_3Sn_4.

Discussion

The experimental data have shown that: there is seemingly no minimum in the free energy diagram in the vicinity of the equiatomic composition, the crystal structure of "SnNi" is close to that of Ni_3Sn_2, and the microstructure of the deposit is characterized by very small grains. We will show how these facts are sufficient to consider "SnNi" as an extension of the composition range of Ni_3Sn_2 (5) and not a new low temperature equilibrium phase (9). The chemical free energy of a Ni_3Sn_2-like phase having an equiatomic composition would be represented by the point A, (ΔG_A), in Fig. 4. The equilibrium state for the equiatomic composition would be point B, (ΔG_B), corresponding to a mixture of the two equilibrium compounds (Ni_3Sn_2, Ni_3Sn_4). This diagram shows that, thermodynamically, state B should be more stable than state A, and this is known to be true from metallurgical preparation of the equiatomic composition alloy. However, the diagram in Fig. 4 representing equilibrium conditions cannot be used to ascertain the formation of phases obtained by electrodeposition and sputter-deposition at low temperatures.

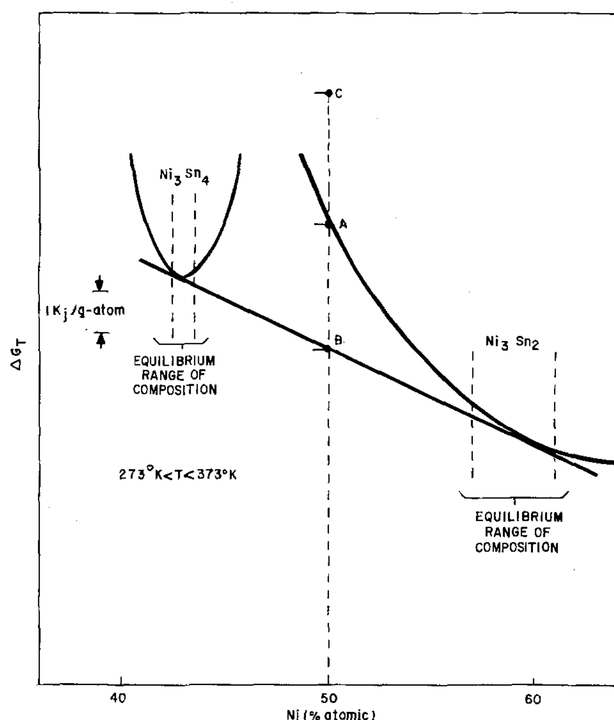

Fig. 4. Probable low temperature chemical free energy diagram for the "Sn-Ni" system between the compositions Ni_3Sn_4 and Ni_3Sn_2. B corresponds to the equilibrium mixture, A to the metastable state, C to the equilibrium state taking into account the grain boundaries energy.

The conditions during deposition are such that nucleating a mixture of the two phases would raise the free energy of the system to $\Delta G_C > \Delta G_A$. Consequently the system chose the metastable state A, with a barrier $\Delta G_C - \Delta G_A$ which can be overcome by heat-treatment to return to the equilibrium state B. The term which raises the free energy from ΔG_B to ΔG_C comes from the elastic energy stored at the grain boundaries.

To form the equilibrium configuration, *i.e.*, Ni_3Sn_2 and Ni_3Sn_4, corresponding to point B in Fig. 2, by electrodeposition would require simultaneous nucleation of these two compounds which have different crystal structures. In an ideal (most favorable) nucleation situation, both phases would differ in composition but have the same lattice structure and parameters. The boundary between two such phases would be coherent, *i.e.*, the structures would meet at an interface whose lattice points are common to both. The interface energy factor in this ideal two-phase situation would tend toward a minimum. Any factor which limits or decreases the degree of coherency, such as crystal structure or lattice parameter differences, leads to appreciably higher values of the interface energy term. Thus, any structural assembly with lower coherency of the boundaries is more difficult to nucleate.

Typical interface energies for incoherent boundaries fall in the range of 0.5-1 J/m^2 while for coherent boundaries the values are between 0.02 and 0.2 J/m^2 (14). For an average grain size of 15 nm the total boundary internal energy can be as large as 4 kJ/g-atom for the incoherent case and as low as 0.08 kJ/g-atom for the coherent one. This additional term makes the total free energy of the equilibrium mixture with small grains higher than that of the metastable phase.

The authors postulate that during electrodeposition (or sputtering) of the equiatomic alloy, nucleation of a metastable supersaturated form of Ni_3Sn_2 is then favored; it is, in essence, an intermediate stage between the aqueous plating bath or sputtering vapor phase and the equilibrium two-phase structure. From classical nucleation theory (15) the free energy of formation of a nucleus in the heterogeneous case is still of the form $W \propto \gamma^3$, where γ is the interfacial energy per unit area. The lower coherency raises the free energy of formation of stable nuclei ($W_B > W_A$), and this barrier to nucleation of the equilibrium configuration is accentuated by the low temperature deposition techniques since nucleation rate is proportional to exp $(-W/kT)$. The metastable phase, although it is less stable ($\Delta G_A > \Delta G_B$), forms preferentially since it can be nucleated at a significantly greater rate at the low temperatures of deposition (345°K) than the equilibrium mixture of Ni_3Sn_4 and Ni_3Sn_2; higher plating temperatures result in two-phased equilibrium deposits. The results of Polesya *et al.* (16) on splat-quenching of liquid nickel-tin alloys showed that this technique of low-temperature rapid crystallization substantially increased the composition range (33.1-54.8 a/o Sn) of the Ni_3Sn_2 phase. Furthermore, even with a melt having the stoichiometric Ni_3Sn_4 composition, they still found Ni_3Sn_2 in the quenched product, which they attributed to the high rate of formation of Ni_3Sn_2 nuclei.

Transformation of the Metastable Structure

The model for "SnNi" proposed in the preceding paragraph must be consistent with the kinetics of its transformation presented in the companion paper (1).

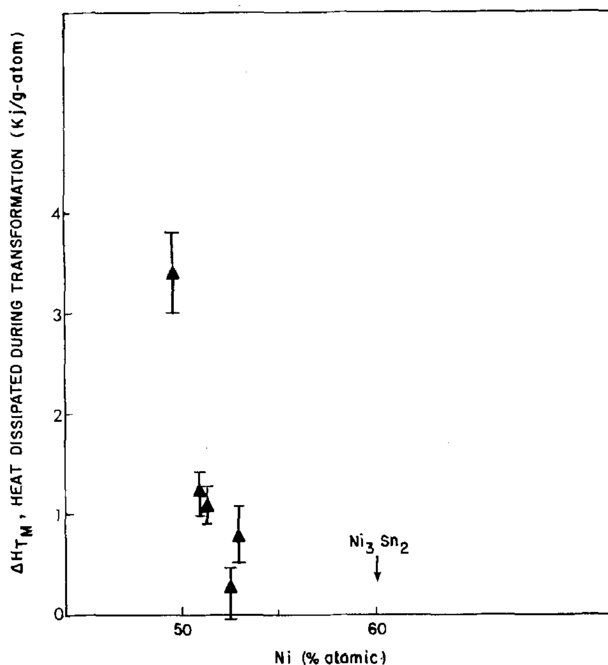

Fig. 5. Heat dissipated during transformation as measured with the DSC. The heat measured close to the temperature of maximum rate of reaction T_M is plotted as a function of the nickel concentration.

Upon heat-treatment of the supersaturated metastable deposit, transformation to the equilibrium configuration becomes feasible and a maximum energy $-\Delta H_{TM}$ is released which is the sum of the difference of enthalpies between state A and state B, and of the contribution due to the boundaries. This model could explain the trend observed in Table I or Fig. 5, where the exothermic heat of transformation increases as the sample composition departs further from the Ni_3Sn_2 stoichiometry. The kinetic data (1) should be consistent with a transformation consisting of a nucleation and diffusion-controlled growth of a second phase (Ni_3Sn_4) from a supersaturated alloy ("extended Ni_3Sn_2").

The Avrami equation for such a precipitation process with a constant nucleation rate has been calculated (17) and can be represented approximately by

$$x = 1 - \exp [-(2.76D^{3/2}It^{5/2})] \qquad [3]$$

where $D = D_o \exp(-\Delta E_D/RT)$ is the diffusion constant with an activation energy equal to ΔE_D and $I = I_o \exp(-\Delta E_N/RT)$ is the nucleation rate with an activation energy equal to ΔE_N.

Equation [3] predicts an Avrami exponent n equal to 2.5; our experimental value of 2.1 is close but indicates a somewhat decreasing nucleation rate (in the absence of nucleation, n should be equal to 1.5) (17). The rate constant of Eq. [2] should be given according to Eq. [3] by

$$k \simeq 1.5D^{0.6}I^{0.4} \qquad [4]$$

which leads to

$$\Delta E = 0.6\Delta E_D + 0.4\Delta E_N \qquad [5a]$$

$$\nu = 1.5D_o^{0.6}I_o^{0.4} \qquad [5b]$$

No values for the diffusion rate of Sn or Ni in "SnNi" or in the equilibrium compounds were found in the literature. An order of magnitude calculation using the diffusion constants of Sn in copper-tin alloys ($\Delta E_D = 50$ kcal/mol [2.17 eV], $D_o = 2400$ cm²/sec) (17), requires the activation energy for nucleation of the second phase to be of the order of 50 kcal/mol to agree with Eq. [5a] and [5b] and our experimental value of the activation energy for the transformation. With this simplified model the rate of nucleation of the second phase would be given using Eq. [5a] and [5b] and $\nu = 10^{14}$ s^{-1} by

$$I \simeq 10^{30} \exp - \frac{2.5 \times 10^4}{T} \qquad [6]$$

Thus, at a typical service temperature (100°C)

$$I = 7.8 \text{ nuclei/cm}^3\text{/s}$$

whereas, at the observed transformation temperature (345°C)

$$I = 2.7 \times 10^{12} \text{ nuclei/cm}^3\text{/s}$$

Our model is evidently not sophisticated enough to hope to be more quantitative in the use of Eq. [6] and to determine the free energy of nucleation or the value of the interfacial energy γ. However, it shows how the nucleation rate increases dramatically between deposition temperature and temperature where the transformation is observable. With the barrier to nucleation overcome, the elevated temperature also favors diffusion to obtain grains of the order of 1 μm as observed in the SEM experiment. Due to the value of the Avrami exponent and the order of magnitudes of the activation energies encountered, the presented model for the morphology of the plated "SnNi" phase is at least not in contradiction with the kinetic data of its transformation.

The morphology of the deposit gives it its metastable character so that the height of the barrier to transformation, ΔE, must be related to this morphology and particularly to the grain size. The elastic energy stored in grain boundaries, which can be released upon heating, is also a function of the grain size. Therefore, a correlation was expected between the heat of transformation, $-\Delta H_{298}$, reported herein and the activation energy, ΔE, reported in a companion paper (1). Our calorimetric procedure was sensitive enough to reveal only a weak correlation.

Summary

The morphology of metastable "SnNi" and the mechanism of its transformation upon heating have been studied. The metastable phase belongs to an extended composition range of the equilibrium Ni_3Sn_2 phase as suggested by Rooksby; it is not a thermodynamically stable low temperature phase as theorized by Clarke and Dutta. The mechanism for the formation of the extended Ni_3Sn_2 morphology was attributed to its more favored nucleation kinetics at the deposition temperature, and the resistance of this deposit to transformation at low temperatures (<100°C) was attributed to the lower energy configuration of the fine grained single phase deposit. The transformation at higher temperature is interpreted as the precipitation and growth of the second phase Ni_3Sn_4 from the supersaturated alloy. The parameters which described the kinetics of this transformation are given.

Acknowledgments

The authors wish to thank B. G. Bagley for the use of the DSC, T. M. Paskowski for diligently taking the DSC data, R. Schroeder and H. G. Tompkins for ion etching of the deposits, and C. C. Lo and M. R. Pinnel for stimulating discussions.

Manuscript submitted June 10, 1977; revised manuscript received Sept. 28, 1977.

Any discussion of this paper will appear in a Discussion Section to be published in the December 1978 JOURNAL. All discussions for the December 1978 Discussion Section should be submitted by Aug. 1, 1978.

Publication costs of this article were assisted by Bell Laboratories.

REFERENCES

1. J. A. Augis and J. E. Bennett, *This Journal*, **125**, 330 (1978).

2. M. Hansen, "Constitution of Binary Alloys," p. 1042, McGraw-Hill Book Co., New York (1958).
3. J. A. Augis and J. E. Bennett, *J. Thermal Anal.* Accepted for publication.
4. H. E. Kissinger, *Anal. Chem.*, **29**, 1702 (1957).
5. H. P. Rooksby, *J. Electrodepositors' Tech. Soc.*, **27**, 153 (1951).
6. N. P. Fedot 'ev and P. M. Vyacheslavov, *Plating*, **57**, 700 (1970).
7. J. W. Martin and R. D. Doherty, "Stability of Microstructure in Metallic Systems," p. 72, Cambridge University Press, London (1976).
8. B. C. Giessen and R. H. Willens, "Phase Diagrams: Material Sciences and Technology," Vol. 3, p. 103, Academic Press, New York (1970).
9. M. Clarke and P. K. Dutta, *J. Phys. D. Appl. Phys*, **4**, 1652 (1971).
10. J. A. Augis and J. E. Bennett, *This Journal*, **124**, 1455 (1977).
11. J. E. Bennett and H. G. Tompkins, *ibid.*, **123**, 999 (1976).
12. X-ray Power Diffraction File, Joint Committee on Powder Diffraction Standards, Swarthmore, Pennsylvania, Cards 7-256, 6-0141, and 4-0845.
13. O. Kubaschewski and E. Evans, "Metallurgical Thermochemistry," 3rd. ed., p 185, Pergamon Press, London (1958).
14. F. Korber and W. Oelsen, Mitt. K-Wilhem-Inst. Eisenforsch, Dusseld, **19**, 209 (1937).
15. J. Burke, "The Kinetics of Phase Transformations in Metals," p 108, Pergamon Press, Oxford (1965).
16. A. F. Polesya and L. S. Slipchenko, Tsvetnaya Metallurgiya No. 3, 1972 Joint Publication Research Service, Transl. No. 58681 Arlington, Va., 1973.
17. Burke, *ibid.*, 15, p. 180.
18. R. Ebeling and H. Wever, *Z. Metallk.*, **53** (3): 222 (1968).

Kinetics of the Thermal Oxidation of Silicon in O_2/H_2O and O_2/Cl_2 Mixtures

B. E. Deal* and D. W. Hess*,[1]

Research and Development Laboratory, Fairchild Camera and Instrument Corporation, Palo Alto, California 94304

and J. D. Plummer and C. P. Ho**

Integrated Circuits Laboratory, Stanford University, Stanford, California 94305

ABSTRACT

The kinetics of the thermal oxidation of (111) and (100) oriented silicon in O_2/H_2O (2-10 v/o H_2O) and O_2/Cl_2 (1-3 v/o Cl_2) mixtures were investigated over the temperature range 900°-1100°C. Effective values of the parabolic and linear rate constants in the general oxidation relationship and therefore over-all oxidation rates were found to increase with increasing concentrations of H_2O. Additions of Cl_2 to O_2 also increased the oxidation rates, but results were more erratic. The experimental oxide thickness-oxidation time data for the O_2/H_2O ambients were compared with those calculated from a relationship involving the simultaneous oxidation of silicon by two independent oxidation species. Since H_2O and Cl_2 are possible reaction products of O_2 and HCl, the results of this investigation were compared with those previously obtained for O_2/HCl silicon oxidations. Reaction mechanisms of the O_2/HCl silicon oxidations, including possible effects due to the presence of H_2O and Cl_2, are discussed.

The addition of a chlorine species to the oxidation ambient used to passivate silicon device structures continues to be an important factor in semiconductor technology (1-3). In a recent paper (4), the thermal oxidation kinetics of (111) and (100) oriented silicon in oxygen containing 0-10 volume percent (v/o) hydrochloric acid were investigated over the temperature range 900°-1100°C. For a given silicon orientation and temperature, the rate of oxidation increased with increasing HCl concentration, and corresponding changes in the effective parabolic and linear rate constants were determined. No detailed mechanisms were devised which would account for the observed rate increases, but it was suggested that water and chlorine, possible reaction products, could well contribute to the change in the oxidation process. These two species may be produced by the reaction of oxygen with hydrochloric acid as follows (5-7)

$$4HCl + O_2 \leftrightarrows 2H_2O + 2Cl_2 \quad [1]$$

The exact equilibrium conditions are not known, especially when possible catalytic effects at the SiO_2 surface are considered.

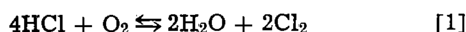

* Electrochemical Society Active Member.
** Electrochemical Society Student Member.
[1] Present address: Department of Chemical Engineering, University of California, Berkeley, California 94720.
Key words: silicon, kinetics, oxidation, chlorine.

In view of the possible contributions resulting from the presence of either H_2O or Cl_2 to the O_2/HCl oxidation process, a short program was carried out to determine silicon oxidation kinetics in oxygen containing either 2-10% H_2O or 1 and 3% Cl_2. The same temperature range (900°-1100°C) and silicon orientations [(111) and (100)] were employed as in the previous O_2/HCl investigation. It was hoped that the results of these studies would provide a better insight into the mechanisms involved in the thermal oxidation of silicon in O_2/HCl mixtures.

Experimental

The experimental conditions and procedures employed in this program were very similar to those reported previously (4). Silicon wafers were (111) and (100) oriented, 4-6 Ω-cm n-type. The wafers were cleaned following the same procedure described earlier (8). Similarly, the oxidation systems utilized were the same as previously described (8) with the following modifications. For the water additions, initially, oxygen was bubbled through a quartz flask containing deionized water whose temperature was controlled to ±0.1°C. The vapor pressure and thus the percentage of water in the oxygen was controlled by the temperature employed. It was determined, however, that this method was not satisfactory, since

oxidation rates were not reproducible. Also, it appeared that at higher percentages of water (corresponding to $T > 30°C$), the partial pressures of water were much lower than calculated, probably due to condensation in the tubing leading to the furnace. For these reasons, a pyrogenic system involving water generation from O_2 and H_2 was employed for all data reported here. The system was manufactured by Corso-Gray Instruments, Sunnyvale, California, Model D-101. Concentrations of water in oxygen varied from 2 to 10 v/o. Silicon oxides were prepared at 900°, 1000°, and 1100°C.

For the O_2/Cl_2 oxidations, procedures were identical to those reported for the O_2/HCl experiments (4); in addition, chlorine of 99.9% purity was used. Due to severe corrosion of the plumbing and duct work, oxidations were limited to temperatures of 1000° and 1100°C and to concentrations of Cl_2 in O_2 of 1.0 and 3.0 v/o.

In the case of O_2/H_2O oxidations the wafers were pushed rapidly into the furnace after the appropriate O_2/H_2O mixture had been established and was flowing at approximately 2 liters/min (~44 cm/min). The wafers were rapidly pulled from this ambient at the end of the oxidation time. The push-pull conditions for O_2/Cl_2 oxidations were the same as for the O_2/HCl work (4). That is, the wafers were rapidly pushed into the furnace in oxygen, the appropriate Cl_2 flow was started, and when the oxidation was completed, the O_2/Cl_2 flow was stopped, the wafers were purged in nitrogen for 15 min, and the wafers were pulled out of the furnace at ~15 cm/min.

Oxidation times for the O_2/H_2O mixtures at 900°C ranged from 1 to 48 hr; at 1000° and 1100°C times were 0.25-16 hr. For the O_2/Cl_2 mixtures the times were 0.25-7 hr. Oxide thicknesses were measured using a Rudolph Model 436-200E ellipsometer with a helium-neon laser source. Measurement reproducibility was ±3%. Mobile ion concentrations in all oxides, including those produced by the H_2-O_2 system were typically less than 2×10^{10} cm^{-2} as determined by C-V analysis.

Data Evaluation

Following the same procedure as for the O_2/HCl data reported previously (4), the oxidation rate data for the O_2/H_2O and O_2/Cl_2 oxidations were evaluated using the general relationship (9)

$$x_o^2 + Ax_o = B(t + \tau) \qquad [2]$$

where x_o = oxide thickness in micrometers, A = constant in micrometers, B = parabolic rate constant in square micrometers per hour, B/A = linear rate constant in micrometers per hour, t = oxidation time in hours, and τ = correction factor, which accounts for an observed initial accelerated growth rate in dry oxygen, in hours. Equation [2] may also be written in the form

$$\frac{x_o^2 - x_i^2}{B} + \frac{x_o - x_i}{B/A} = t \qquad [2a]$$

where $x_i = x_o$ at $t = 0$, and the other terms are the same as defined in Eq. [2]. The effective rate constants B and B/A were determined from x_o vs. $(t + \tau)/x_o$ plots as described earlier (9).

Since these oxidations were due to more than one reacting gas species (O_2 and H_2O or O_2 and Cl_2) the above relationship is not truly valid. Therefore a combination general relationship was derived based on one reported earlier by Hirabayashi and Iwamura (5). It is as follows

$$t = \frac{1}{E}\left\{ (x_o^2 - x_i^2) + C(x_o - x_i) - D \ln\left[\frac{2Ex_o + F}{2Ex_i + F}\right]\right\} \qquad [3]$$

where $C = (A_1B_1 + A_2B_2)/(B_1 + B_2)$, $D = [B_1B_2(A_1 - A_2)^2]/[2(B_1 + B_2)^2]$, $E = B_1 + B_2$, $F = A_1B_2 + A_2B_1$, and A_1 and B_1 are the constants in Eq. [2] for one oxidation species and A_2 and B_2 the constants for the second species. B_1 and B_2 are proportional to the partial pressure of components 1 and 2 in the oxidation ambient.

In deriving the type of combination oxidation relationship as given by Eq. [3], Hirabayashi and Iwamura assumed that the fluxes of the two reacting species (representing diffusion through the oxide as well as a reaction at the Si-SiO_2 interface) are parallel but independent. This assumption of complete independence may or may not be valid, as will be discussed later. The over-all oxide growth rate is therefore a function of the sum of these fluxes.

An important difference between the relationship derived by Hirabayashi and Iwamura and Eq. [3] above is the inclusion of x_i in Eq. [3]. As indicated, $x_i = x_o$ at $t = 0$, but alternately can take into account the rapid initial oxidation rate observed for dry oxygen oxidation of silicon (9). If this constant ($x_i \sim 200$Å for dry O_2) is not included, then it is almost impossible to analyze the data properly. Not known, however, is how x_i changes as H_2O is added to O_2. In this work a constant value of $x_i = 180 \pm 20$Å was assumed for all mixtures, with values of τ determined from extrapolated linear plots of x_o vs. t.

If the values of A and B in Eq. [3] are known from single-component, oxidation studies, then t can be calculated as a function of x_o and compared with experimental results. As indicated earlier (4), the parabolic rate constants in either Eq. [2] or [2a] and thus Eq. [3] should be independent of silicon orientation, while the linear rate constants B/A should vary with orientation.

Previous work (9) has indicated that the constant in Eq. [2] that is most difficult to determine is τ, and care must be taken to assure that $\tau << t$ for the data used to determine the constants A and B. More recently, Irene and van der Meulen (10) have investigated in detail the application of Eq. [2] to silicon oxidation at lower temperatures.

In order to determine activation energies using an Arrhenius-type expression, the effective rate constants from Eq. [2] had to be used, since Eq. [3] is too complex for this analysis.

Hirabayashi and Iwamura (5) pointed out that if the conditions are such that $A_1 \approx A_2$, then Eq. [3] may be approximated by

$$B^*t = (x_o^2 - x_i^2) + A(x_o - x_i) \qquad [4]$$

where $B^* = B_1 + B_2$. This is the same form as Eq. [2] and experimentally determined effective values of B and A may be compared with those calculated from earlier experimental results of one-component oxidations, assuming B_1 and B_2 are proportional to partial pressures of the two components in the mixture. For O_2/H_2O oxidation of silicon, $A_{O_2} \approx A_{H_2O}$ at 1100°C. Thus, experimental results may be evaluated at this temperature using Eq. [4].

Finally, if the reaction of O_2 and HCl presented in Eq. [1] is valid and is assumed to go primarily to completion (to the right), then 2 moles of HCl will produce 1 mole each of H_2O and Cl_2. The O_2/HCl data can therefore be compared with the results obtained from the equivalent O_2/H_2O or O_2/Cl_2 oxidations.

Results and Discussion

Oxidation rate data.—O_2/H_2O and O_2/Cl_2 mixtures.— As indicated above, oxidation rate data were obtained for O_2/H_2O and O_2/Cl_2 mixtures as a function of silicon orientation, oxidation temperature and H_2O and Cl_2 concentration. Typical results are indicated in Fig. 1 and 2 where plots of log x_o vs. log t at 1000°C for various ambient concentrations and the two silicon orientations are presented. It can be noted that the oxidation rates for all cases increase with increasing

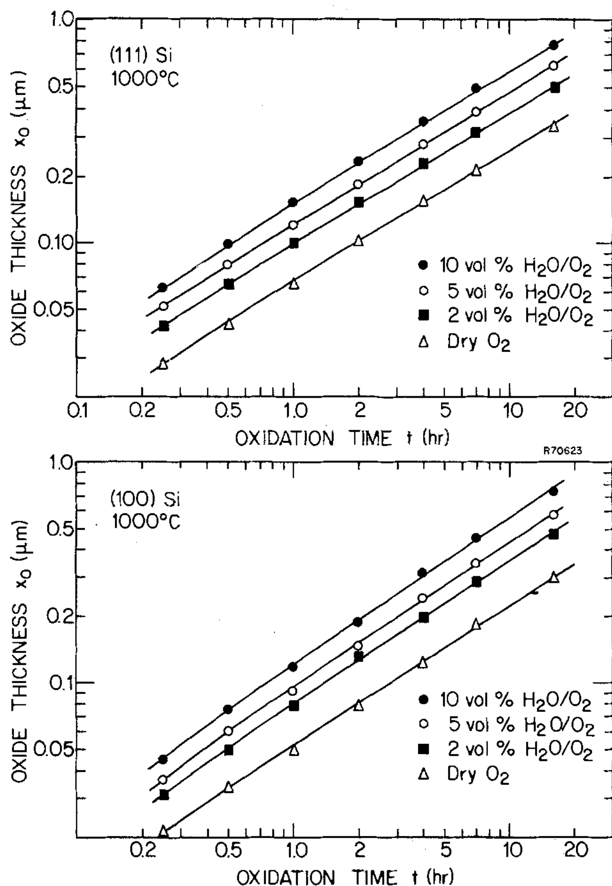

Fig. 1. Oxide thickness *vs.* oxidation time for the oxidation of (111) and (100) oriented n-type silicon in various O_2/H_2O mixtures at 1000°C.

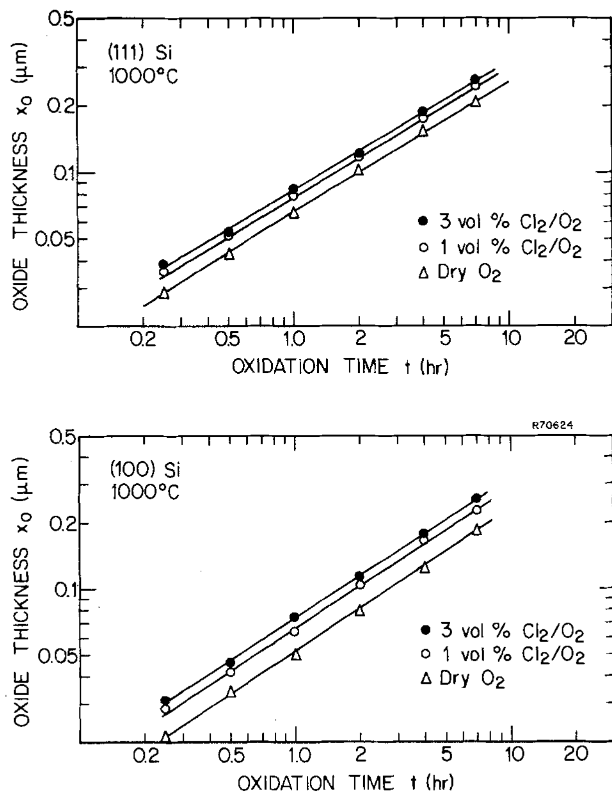

Fig. 2. Oxide thickness *vs.* oxidation time for the oxidation of (111) and (100) oriented n-type silicon in various O_2/Cl_2 mixtures at 1000°C.

H_2O or Cl_2 concentrations and that the plots are very similar to those for O_2/HCl oxidations presented in

Table I. Rate constants for silicon oxidation in O_2/Cl_2 mixtures at 1000°C. Data for O_2 and O_2/1% HCl mixtures are included for comparison.

(n-type, 4-6 Ω-cm Si)

Ambient	Silicon orientation	τ (hr)	A (μm)	B (μm²/hr)	B/A (μm/hr)
O_2	(100)	0.35	0.195	0.00913	0.0467
	(111)	0.35	0.120	0.00956	0.0797
O_2/1% Cl_2	(100)	0.1	0.125	0.0113	0.0901
	(111)	0.1	0.0766	0.0108	0.141
O_2/3% Cl_2	(100)	0.1	0.157	0.0143	0.0911
	(111)	0.1	0.109	0.0135	0.123
O_2/1% HCl	(100)	0.2	0.253	0.0157	0.0622
	(111)	0.2	0.172	0.0156	0.0906

Table II. Rate constants for silicon oxidation in O_2/Cl_2 mixtures at 1000°C. Data for O_2 and O_2/1% HCl mixtures are included for comparison.

(n-type, 4-6 Ω-cm Si)

Ambient	Silicon orientation	τ (hr)	A (μm)	B (μm²/hr)	B/A (μm/hr)
O_2	(100)	0.09	0.101	0.0247	0.246
	(111)	0.09	0.0845	0.0244	0.289
O_2/1% Cl_2	(100)	0.05	0.0512	0.0381	0.745
	(111)	0.05	0.0635	0.0391	0.615
O_2/3% Cl_2	(100)	0.05	0.0245	0.0400	1.63
	(111)	0.05	0.0393	0.0416	1.06
O_2/1% HCl	(100)	0.04	0.0886	0.0341	0.385
	(111)	0.04	0.0741	0.0341	0.461

Fig. 2 in Ref. (4) which also are for 1000°C. Similar trends were found for the O_2/H_2O and O_2/Cl_2 oxidations at the other temperatures investigated.

Values of the constants A, B, and B/A were determined as indicated in the previous section. These data for O_2/Cl_2 oxidations at 1000° and 1100°C are tabulated in Tables I and II. Also included for comparison in the tables are the data for 100% dry O_2 and 1% HCl in O_2 oxidations, as well as the values of τ used in these determinations. The significance of τ will be discussed later. The variations of the effective parabolic rate constant B and the effective linear rate constant B/A for O_2/H_2O mixtures with H_2O concentration are indicated by the plots in Fig. 3 and 4. Here, it can be observed that gradual increases of both B and B/A values occur with increasing H_2O concentrations. The trends are somewhat different than those reported for O_2/HCl oxidations (4), where, in the latter case considerable less dependence of B and especially B/A on HCl concentration was found. These differences will be discussed later.

Arrhenius-type plots of log B and log B/A *vs.* $1/T$ were prepared and activation energies determined. For the linear rate constants all activation energies, for both (111) and (100) silicon orientation, ranged from 1.95 to 2.05 eV. This value of approximately 2 eV has been found (9) for both dry oxygen and wet oxygen (95°C H_2O) and is believed to be associated with the Si-Si bond energy: It is therefore expected that all mixtures of O_2 and H_2O would have the same activation energy associated with the linear rate constant.

The parabolic rate constant activation energy for 10% H_2O in O_2 was found to be 0.9 eV, compared to 1.2 eV for dry O_2 and 0.7 eV for wet O_2 (95°C H_2O). Values of 0.93 eV and 1.07 eV were calculated for 5% and 2% H_2O in O_2, respectively. It is apparent that relatively small amounts of water have considerable effect on the activated process associated with the diffusion of the oxidizing species through the oxide; similar effects have been reported by Irene (11). It should be pointed out that, unlike the data for O_2/HCl oxidation (4), all Arrhenius plots for the O_2/H_2O oxidations were straight lines over the temperature range 900°-1100°C.

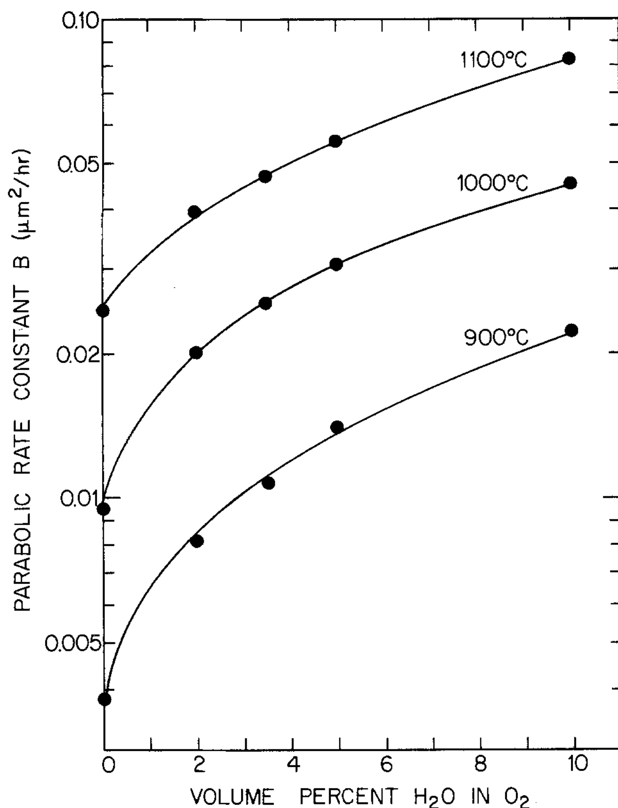

Fig. 3. Parabolic rate constant *vs.* volume percent H_2O in O_2 for oxidation of n-type silicon at 900°, 1000°, and 1100°C. Data are for (111) silicon orientation; values of B for (100) silicon are essentially equal to those of (111) silicon.

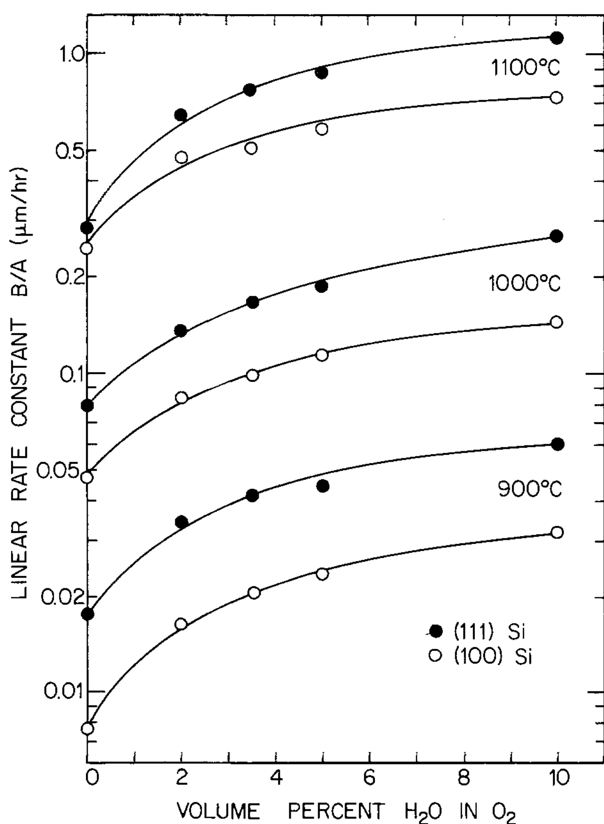

Fig. 4. Linear rate constant *vs.* volume percent H_2O in O_2 for oxidation of (111) and (100) oriented n-type silicon at 900°, 1000°, and 1100°C.

In the previous section a complex relationship (Eq. [3]) for silicon oxidation involving simultaneous oxidation by two reactants was presented. It was noted, however, at 1100°C, the values of A_{H_2O} and A_{O_2} are approximately equal, and thus Eq. [3] takes the form of Eq. [4] with $B^* = B_1 + B_2$. Since B_1 and B_2 in the case of O_2/H_2O mixtures are equal to the B values at atmospheric pressure multiplied by their partial pressures in the mixture, the experimental results of t *vs.* x_o at 1100°C can readily be compared to calculated values. This comparison is shown in Table III, where the times (t) required to obtain particular oxide thicknesses are listed, along with the corresponding times calculated from Eq. [4] for those same oxide thicknesses. Also included in Table III are the times calculated from Eq. [3], and the ratios of the two calculated values of t. Data are included for 900° and 1000°C, in addition to 1100°C. It can be observed that t from the full calculation, Eq. [3], is identical to the t from Eq. [4] at 1100°C, but the agreement becomes worse as the oxidation temperature decreases. Also, in all cases, the experimental time required to obtain a particular oxide thickness is less than that calculated by either equation. This latter finding would imply that some interaction between O_2 and H_2O is occurring which is increasing the oxidation rate compared to that predicted by Eq. [3].

Table III. Comparison of experimental oxidation times (t) and those calculated from Eq. [3] and [4]
[n-type, 4-6 Ω-cm, (111) Si]

Oxidation temperature (°C)	A_{O_2}/A_{H_2O}	x_o (μm)	t_{exp} (hr)	$t_{Eq. [3]}$ (hr)	$t_{Eq. [4]}$ (hr)	$t_{[4]}/t_{[3]}$
900	0.44	0.245	10.0	10.83	11.33	1.046
1000	0.65	0.278	4.0	4.34	4.36	1.005
1100	0.90	0.446	4.0	4.56	4.56	1.000

To determine which rate constant might reflect the above-mentioned acceleration of the oxidation reaction in O_2/H_2O mixtures, experimentally determined values of B and B/A (at 1100°C) are plotted against H_2O concentration in Fig. 5 and 6. Also plotted in

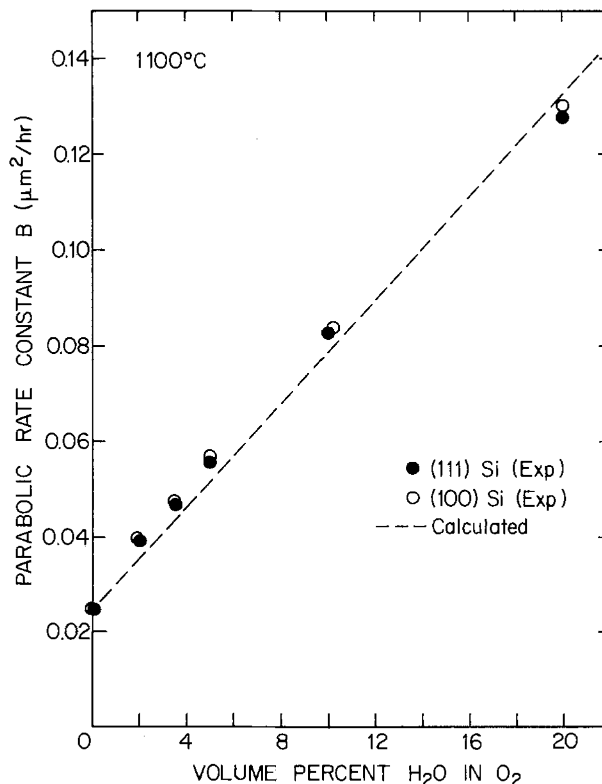

Fig. 5. Comparison of experimental and calculated values of the parabolic rate constant *vs.* volume percent H_2O in O_2 for the oxidation of (111) and (100) oriented n-type silicon at 1100°C. Dashed line represents data calculated using Eq. [4].

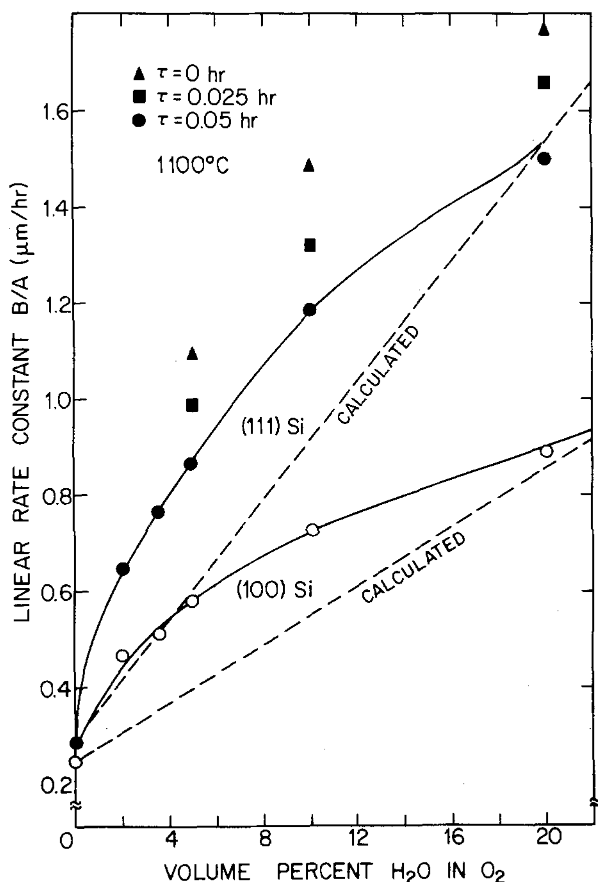

Fig. 6. Comparison of experimental and calculated values of the linear rate constant vs. volume percent H_2O in O_2 for the oxidation of (111) and (100) oriented n-type silicon at 1100°C. Dashed line represents data calculated using Eq. [4]. Also included for selected H_2O concentrations are data for various values of τ in general relationship.

Fig. 5 and 6 are values of B^* and B^*/A, which are obtained from the relationship $B^* = \gamma B_{H_2O} + (1 - \gamma)B_{O_2}$, where γ = mole fraction of H_2O, $(1 - \gamma)$ = mole fraction of O_2, and B_{H_2O} and B_{O_2} are the parabolic rate constants at atmospheric pressure. The values of A are those determined at atmospheric pressure and do not change with concentration. As observed in Fig. 5, the values of B^* and B_{exp} agree quite closely up to 20% H_2O (a 20% H_2O/O_2 mixture was included at 1100°C only). However, there is considerable deviation between experimental and calculated B/A values up to about 20% H_2O. At this concentration, the O_2 contribution is negligible compared to that of the H_2O and above 20% H_2O it is anticipated that the two curves will be the same. Similar results are noted for both (111) and (100) silicon orientations.

Some mention should be made of the value of τ used for the data in Fig. 6. In determining the values of the rate constants B and B/A tabulated in Table III using Eq. [2], τ was set equal to 0.05 hr for the H_2O/O_2 data at 1100°C (a value of τ = 0.04 hr was used for 20% H_2O). Normally the exact value of τ used at the higher temperatures is not critical, especially in regards to its effect on B, the parabolic rate constant, and the over-all oxidation kinetics. However, in plotting the linear rate constant data in Fig. 6, it was observed that A and thus B/A is quite dependent on the value of τ used. For this reason, values of B/A are indicated in Fig. 6 with τ = 0, 0.025, and 0.05 hr. Close examination of the x_o vs. $(t + \tau)/x_o$ plots used to determine the rate constants indicated the true value of t lies between 0.025 and 0.05 hr. Thus, if anything, the difference between experimental and calculated values of B/A in the H_2O concentration range 0-20% is even a little greater than originally determined. The net general trend is the same, with the two curves coming together at about 20% H_2O concentration. As mentioned above, B in Fig. 5 is not dependent to any great extent on τ.

The reason for the accelerated oxidation rate resulting from small additions of water to oxygen is not known. Since the effect is mainly through the linear rate constant B/A, it is possible that a catalytic reaction due to the water affects the breaking of Si-Si bonds. Such an effect apparently does not, however, change the activation energy as indicated above. This would suggest that the enhanced oxidation rate, relative to that calculated, is associated with the pre-exponential term in the Arrhenius expression (12).

Comparison of O_2/H_2O and O_2/Cl_2 oxidation data with O_2/HCl results.—If it is assumed that the reaction of HCl with O_2 (Eq. [1]) goes to completion, *i.e.*, 2 moles HCl produces 1 mole each of H_2O and Cl_2, then the kinetic oxidation results of various concentrations of HCl in O_2 can be compared with those of half the same concentrations of H_2O and/or Cl_2 in O_2.[2] This was done in the case of H_2O by plotting log x_o vs. log t data for 10% HCl in O_2 and 5% H_2O in O_2 at 900°, 1000°, and 1100°C. These plots for (111) oriented silicon are presented in Fig. 7-9. Also in-

[2] Exact calculations indicate that 10% HCl will produce 5.13% each of H_2O and Cl_2 due to a difference in total moles gas produced. Similarly 2.0% HCl produces 1.005% of H_2O and Cl_2.

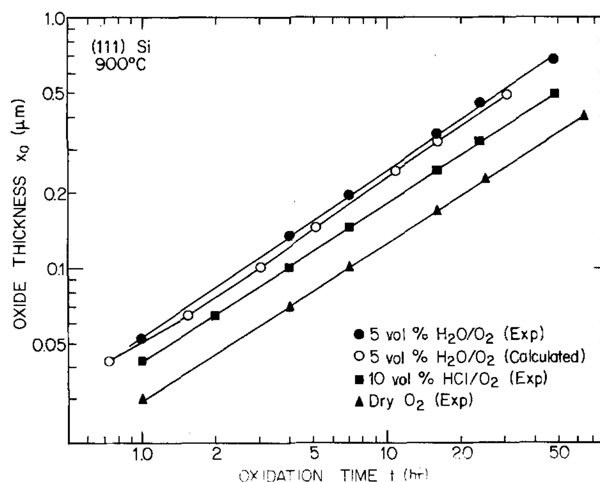

Fig. 7. Oxide temperature vs. oxidation time for the oxidation of (111) oriented n-type silicon at 900°C in 5 v/o H_2O/O_2, 10 v/o HCl/O_2, and dry O_2 mixtures. Also included are data for 5 v/o H_2O/O_2 mixtures calculated from Eq. [3].

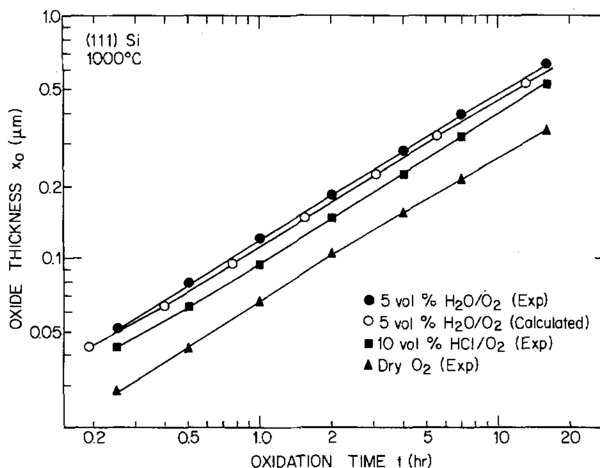

Fig. 8. Oxide thickness vs. oxidation time for the oxidation of (111) oriented n-type silicon at 1000°C in 5 v/o H_2O/O_2, 10 v/o HCl/O_2, and dry O_2 mixtures. Also included are data for 5 v/o H_2O/O_2 mixtures calculated from Eq. [3].

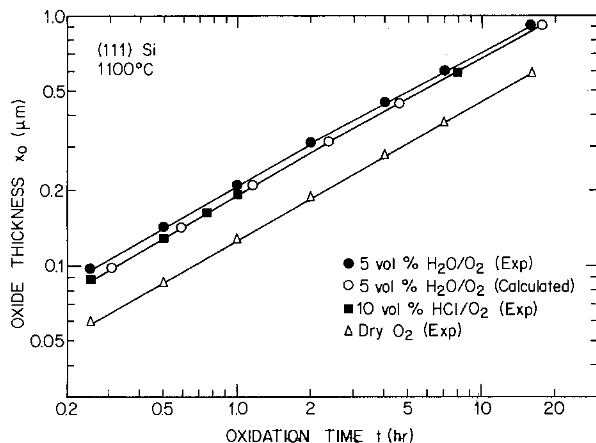

Fig. 9. Oxide thickness vs. oxidation time for the oxidation of (111) oriented n-type silicon at 1100°C in 5 v/o H_2O/O_2, 10 v/o HCl/O_2, and dry O_2 mixtures. Also included are data for 5 v/o H_2O/O_2 mixtures calculated from Eq. [3].

cluded for comparison are the calculated data for 5% H_2O in O_2 using Eq. [3], and previous data obtained for dry oxygen (9). It can be observed that, as indicated earlier, the experimental H_2O oxidation rates are slightly greater than the calculated ones. Also, the 5% H_2O rates are significantly greater than those of 10% HCl, although the difference becomes much less at 1100°C (about 10%) as compared to 900°C (30%).

Another way of comparing O_2/HCl oxidation data with those of O_2/H_2O and O_2/Cl_2 mixtures is to observe variation of oxidation rate constants of the three mixtures as a function of equivalent gas compositions. This comparison is shown in Fig. 10 and 11 where values of B and B/A for O_2/HCl oxidations at 1000°C are plotted for 0-10% HCl concentrations, and corresponding B and B/A values are included for 0-5% H_2O and Cl_2 in O_2. The data in Fig. 10 represent both (111) and (100) silicon orientations, since the parabolic rate constant is independent of silicon orientation. In Fig. 11, separate plots for (111) and (100) orientation are presented, reflecting

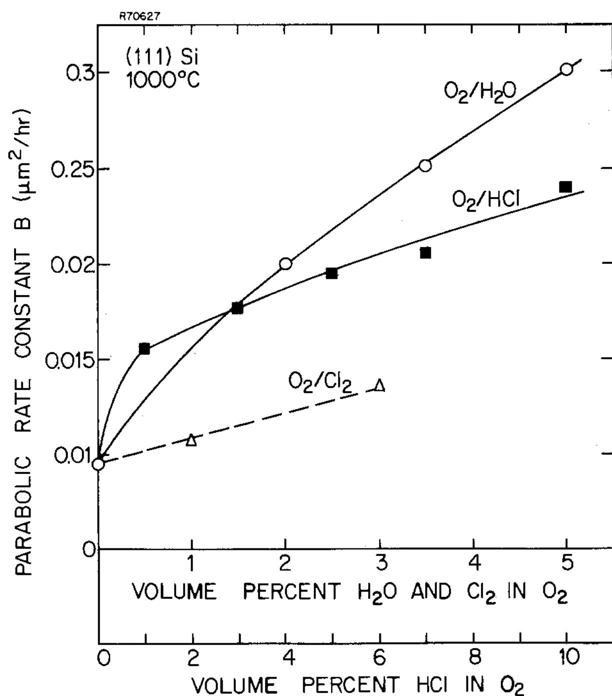

Fig. 10. Parabolic rate constants vs. 0-5 v/o H_2O and Cl_2 in O_2 and 0-10 v/o HCl in O_2 for the oxidation of (111) oriented n-type silicon at 1000°C.

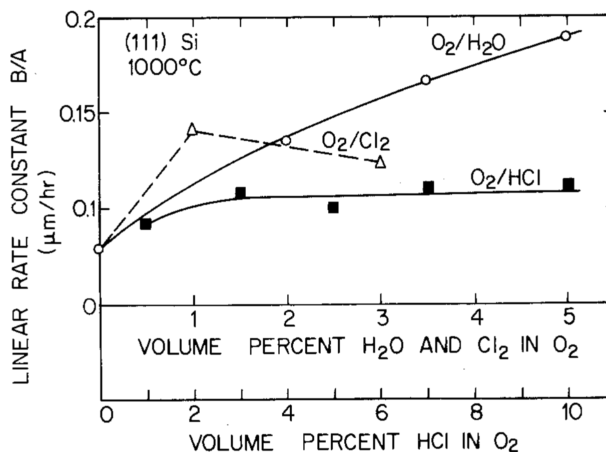

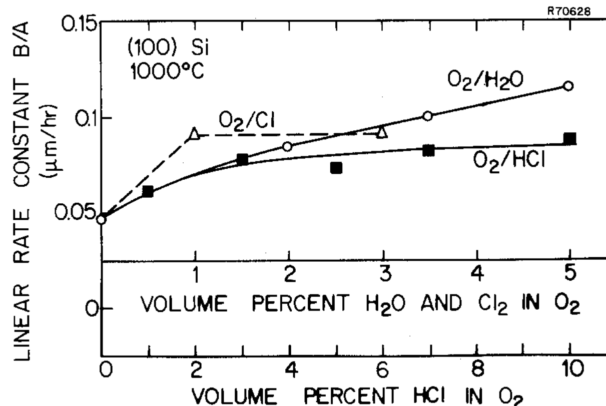

Fig. 11. Linear rate constants vs. 0-5 v/o H_2O and Cl_2 in O_2 and 0-10 v/o HCl in O_2 for the oxidation of (111) and (100) oriented n-type silicon at 1000°C.

the dependence of the linear rate constant on orientation.

Figures 10 and 11 indicate that the 2:1 ratio for HCl:H_2O predicted by the O_2-HCl reaction (Eq. [1]) is too small, at least at 1000°C. It would appear from the parabolic rate constant data (Fig. 10) that a 3:1 ratio at 1000°C would be more likely. From similar 1100°C plots (not shown) the ratio is about 2½:1, while at 900°C it is approximately 5:1. An extrapolation of these data would indicate that the 2:1 ratio might be obtained at about 1250°C. The data for the linear rate constant (Fig. 11) are more confusing, however. For both orientations, and for the other two temperatures, the value of B/A levels off with increasing HCl concentrations. Thus, it is not possible to compare this curve in a quantitative manner with that of the O_2/H_2O oxidation.

The general effects due to B and B/A variations with HCl concentration on the over-all kinetic rate data for O_2/HCl oxidations may be observed in another type of plot. This involves the change of oxide thickness with increasing HCl concentration for a given oxidation time. Such a plot is given in Fig. 12 for O_2/HCl oxidations at 1000°C and for an oxidation time of 2 hr. The HCl concentration in O_2 varies from 0 to 10%. Corresponding data are also shown for O_2/H_2O oxidations, with the equivalent concentration range of H_2O in O_2 being 0-5%.

In the case of O_2/HCl oxidations, it can be observed quite clearly in Fig. 12 that the increase of oxide thickness tends to level off somewhat at an HCl concentration of about 3%. This corresponds to a similar leveling off of the O_2/HCl linear rate constant observed in Fig. 11 for both orientations. Above 6% HCl, the oxide thickness again slowly increases, which corresponds to the increase of the O_2/HCl parabolic rate constant B in Fig. 10. Similar results were observed for other temperatures and oxidation times.

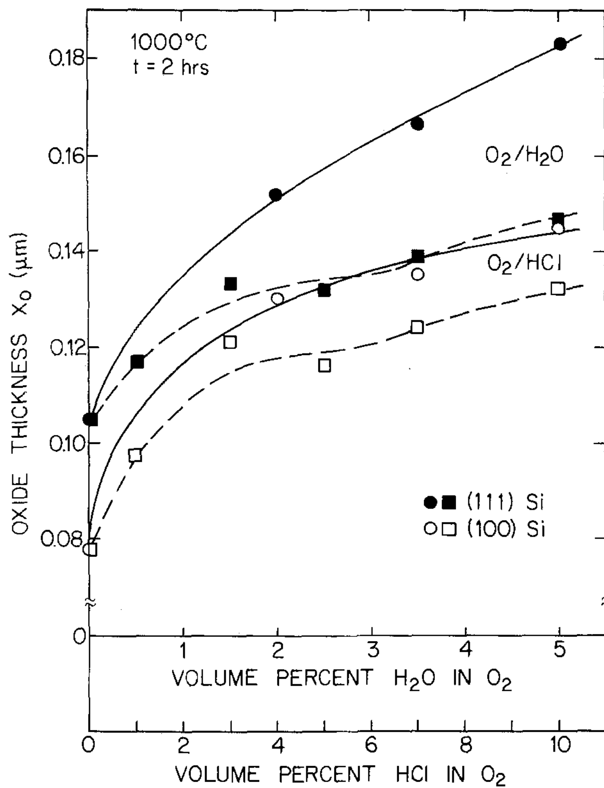

Fig. 12. Oxide thickness vs. v/o H_2O and HCl in O_2 for the oxidation of (111) and (100) oriented n-type silicon at 1000°C for 2 hr.

The O_2/H_2O data in Fig. 12 indicate a regular increasing oxidation rate with H_2O concentration. This trend was noted for all temperatures, times, and both orientations.

It can be observed from Fig. 10 and 11 that the oxidation rate constant data for O_2/Cl_2 mixtures are somewhat erratic. This was also the case at 1100°C (no O_2/Cl_2 data were obtained at 900°C). Thus, no real comparisons with the O_2/HCl results can be made, although speculation of the effect of Cl_2 on the over-all oxidation reaction will be included in the next section.

Mechanism for O_2-HCl silicon oxidation.—The results obtained from the O_2/H_2O and O_2/Cl_2 oxidation experiments seem to provide some insight into the mechanism involved in O_2/HCl silicon oxidation processes. First, the observed effects on the general kinetics due to either H_2O or Cl_2 additions to O_2 (Fig. 1-2) are very similar to those previously obtained for HCl additions (4). Also, the variation of parabolic rate constants B with increased HCl or H_2O content are quite similar [Fig. 3 and Ref. (4)]. Finally, the relationships in Fig. 7-11 also show similarities in effects due to H_2O (and Cl_2) additions as compared to oxidations in O_2/HCl mixtures. The main differences between O_2/HCl and O_2/H_2O results are primarily reflected in the linear rate constant results (Fig. 4 and 11).

If the parabolic rate constant B is first considered, the data indicate that the assumed reaction of 2 moles HCl with 1/2 mole O_2 to produce 1 mole H_2O (*i.e.*, Eq. [1]) goes to completion at some temperature above 1100°C (Fig. 10). Since the parabolic rate constant becomes dominant at higher temperatures [from the general relationship (9)], the assumed 2HCl:1 H_2O relationship becomes more apparent in the over-all oxidation kinetic data, as indicated in Fig. 9. At lower temperatures, however, much less water is produced, and at 900°C the ratio of HCl to H_2O produced was found to be 5:1. Thus, the parabolic rate constant data would predict, as shown in Fig. 7, that the reaction of HCl with O_2 is much more efficient as the oxidation temperature increases.

The ratio of change between HCl- and H_2O-containing oxygen ambients is greater at all temperatures for the linear rate constants B/A than for the parabolic rate constants, especially for higher HCl concentrations. Therefore, effects of the Si-SiO_2 interface reaction on the deviation from the assumed 2:1 HCl:H_2O ratio should be evident at lower temperatures where the oxidation reaction is more surface controlled. Why the B/A values level off with increasing HCl concentrations is not clear. The effect may well be due to the Cl_2 also produced by the O_2/HCl reaction. This species may interact or interfere with the other oxidizing species at the Si-SiO_2 interface where it has been reported to pile up (3, 13), and thus might actually retard the reaction at higher HCl concentrations. In addition, more recent data involving H_2O/HCl oxidations (14) indicate that little or no effect on oxidation kinetics in H_2O is observed due to the HCl. This would agree with earlier reports (15) that higher water concentrations repress the formation of Cl_2 (or at least its presence in the oxide), and thus Cl_2 may not be a factor in the oxidation reaction at higher HCl concentrations in O_2 since more H_2O is produced according to Eq. [1]. Such a mechanism might indicate a maximum effect on the Si-SiO_2 interface reaction occurs somewhere in the 0-10% HCl concentration range. This would tend to complicate even further the already complex mechanism for the O_2/HCl oxidation of silicon.

Much of this discussion has been based on the assumption that at oxidation temperatures the reaction of O_2 and HCl produces H_2O and Cl_2, as per Eq. [1]. The exact amounts of H_2O and Cl_2 produced depend on the equilibrium constant associated with Eq. [1], which can be affected by several factors. In order to verify the above assumption, an oxidation at 1000°C in O_2 containing 2% H_2O plus 2% Cl_2 was carried out. The kinetic results of this oxidation can be compared to those obtained from an oxidation in a 96% O_2/4% HCl mixture, and this is done in Table IV. Also included in the table are the 98% O_2/2% H_2O results. The first part of Table IV gives oxide thicknesses (x_o) after 2 and 4 hr oxidation. It can be observed that the oxide thicknesses for both the 4% HCl and the 2% H_2O/2% Cl_2 ambients are in good agreement for both orientations, while all the 2% H_2O values are significantly higher.

Values of the rate constants at 1000°C, B and B/A, are also listed in Table IV. The 2% H_2O/2% Cl_2 values of B, the parabolic rate constant, are in be-

Table IV. Comparison of silicon oxidation kinetic data at 1000°C in O_2 with 4% HCl, 2% H_2O + 2% Cl_2, and 2% H_2O additions

	Silicon orientation	O_2/4% HCl	O_2/2% Cl_2/ 2% H_2O	O_2/2% H_2O
Oxide thickness x_o (μm) at t = 2 hr	(111)	0.133	0.132	0.152
	(100)	0.118	0.115	0.130
Oxide thickness x_o (μm) at t = 4 hr	(111)	0.202	0.207	0.230
	(100)	0.182	0.186	0.198
Parabolic rate constant B (μm²/hr)	(111)	0.0185	0.0199	0.0200
	(100)	0.0185	0.0197	0.0205
Linear rate constant B/A (μm/hr)	(111)	0.103	0.101	0.135
	(100)	0.0780	0.0743	0.0837

tween those of the 4% HCl and the 2% H_2O mixtures. This is expected if the data in Fig. 10 are examined, since for these concentrations the curves for the two mixtures are fairly close together. On the other hand, values of the linear rate constant, B/A, for the 2% H_2O/2% Cl_2 mixture are very close to those of the 4% HCl ambient, and much lower than the 2% H_2O value.

These results tend to confirm that Eq. [1] is valid for the oxidation of silicon in O_2 with small additions of HCl. Also, the equilibrium of the reaction (Eq. [1]) is approached very rapidly whether starting with either O_2 + HCl or H_2O + Cl_2.

Summary

The kinetics of the thermal oxidation of (111) and (100) oriented silicon in O_2/H_2O and O_2/Cl_2 mixtures have been investigated over the temperature range 900°-1100°C. The concentrations of H_2O in O_2 were varied from 2 to 10 v/o, while those of Cl_2 were 1 and 3 v/o. Effective values of the parabolic (B) and linear (B/A) rate constants in the silicon oxidation general relationship were determined and both increased with increasing H_2O concentration in O_2. Results for O_2/Cl_2 oxidations were more erratic, however, although the addition of Cl_2 to O_2 also increased the over-all silicon oxidation rate. The experimentally determined O_2/H_2O oxide thickness oxidation time data were compared with similar data calculated from a combination general relationship involving simultaneous but independent oxidation of silicon by two species. Good agreement between experimental and calculated values of parabolic rate constants was obtained. However, below 20% H_2O, the experimentally determined linear rate constants B/A were significantly greater than the corresponding calculated values. This implies that some catalytic effect or interaction between H_2O and O_2 occurs at the Si-SiO_2 interface to accelerate the silicon oxidation reaction.

The O_2/H_2O and O_2/Cl_2 oxidation processes described above were studied in part because H_2O and Cl_2 are possible products of the O_2-HCl reaction in this temperature range, and their presence may affect the O_2/HCl silicon oxidation kinetics. A comparison between the results obtained here and those reported previously for O_2/HCl oxidation kinetics indicates that the increases found for parabolic and linear rate constants and over-all oxidation rates with varying H_2O concentrations in O_2 are greater than corresponding increases for equivalent HCl additions. It appears, however, that effective values of the parabolic rate constant B for O_2/H_2O mixtures approach the B values for O_2/HCl oxidations at some temperature above 1100°C. The over-all oxidation rates are also similar for these two systems at 1100°C or above, which is expected, since the oxidation process is controlled primarily by the parabolic rate constant at these higher temperatures. These results suggest that the assumed relationship $4HCl + O_2 \leftrightarrows 2H_2O + 2Cl_2$ may go to completion at higher temperatures. While the O_2/Cl_2 data are somewhat erratic, a reaction or interference by Cl_2 at the silicon surface (where it probably accumulates) may lead to the observed decrease in oxidation rate in O_2/HCl mixtures at lower temperatures, reflected in the lack of dependence of the linear rate constant on increasing HCl concentration.

A special experiment involving silicon oxidation in O_2 with 2% H_2O + 2% Cl_2 gave identical results to those obtained with a 96% O_2/4% HCl ambient. This helps to confirm the assumption that O_2 reacts with HCl to form Cl_2 and H_2O, and also indicates that the equilibrium of the reaction and product species occurs rather rapidly under these oxidation conditions.

The effect of increasing amounts of H_2O produced by higher HCl concentrations on chlorine incorporation in the oxide and thus on the subsequent oxidation kinetics is not known. Accurate chlorine concentration profiles in the oxide for various oxidation conditions would be highly desirable, and should provide additional insight into O_2/HCl oxidation mechanisms

Acknowledgments

The authors wish to thank Dr. James M. Early and Mr. Tarsaim L. Batra for helpful suggestions and for critically reviewing the manuscript. Also, Julia Bien performed many of the experiments and measurements required for this program. A portion of this work was supported by ARPA Contract No. DAAB07-77-C-2684.

Manuscript submitted July 6, 1977; revised manuscript received Sept. 15, 1977.

Any discussion of this paper will appear in a Discussion Section to be published in the December 1978 JOURNAL. All discussions for the December 1978 Discussion Section should be submitted by Aug. 1, 1977.

Publication costs of this article were assisted by the Fairchild Camera and Instrument Corporation.

REFERENCES

1. R. J. Kriegler, *Denki Kagaku*, **41**, 466 (1973).
2. A. Rohatgi, S. R. Butler, F. J. Feigl, H. W. Kraner, and K. W. Jones, *Appl. Phys. Lett.*, **30**, 104 (1977).
3. Y. J. van der Meulen, C. M. Osburn, and J. F. Ziegler, *This Journal*, **122**, 284 (1975).
4. D. W. Hess and B. E. Deal, *ibid.*, **124**, 735 (1977).
5. K. Hirabayashi and J. Iwamura, *ibid.*, **120**, 1595 (1973).
6. Y. J. van der Meulen and J. G. Cahill, *J. Electron. Mater.*, **3**, 371 (1974).
7. R. E. Tressler, J. Stach, and D. M. Metz, *This Journal*, **124**, 607 (1977).
8. D. W. Hess and B. E. Deal, *ibid.*, **122**, 579 (1975).
9. B. E. Deal and A. S. Grove, *J. Appl. Phys.*, **36**, 3770 (1965).
10. E. A. Irene and Y. J. van der Meulen, *This Journal*, **123**, 1380 (1976).
11. E. A. Irene and R. Ghez, in "Semiconductor Silicon," H. R. Huff and E. Sirtl, Editors Proceedings Volume 77-2, p. 313, The Electrochemical Society, Inc., Princeton, N.J. (1977).
12. J. R. Ligenza, *J. Phys. Chem.*, **65**, 2011 (1961).
13. R. L. Meek, *This Journal*, **120**, 308 (1973).
14. B. E. Deal, To be published.
15. R. J. Kriegler, "Semiconductor Silicon," H. R. Huff and R. R. Burgess, Editors, p. 363, The Electrochemical Society Softbound Symposium Series, Princeton, N.J. (1973).

Technical Note

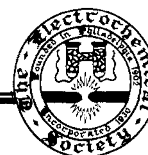

A Technique for Uniform Etching of Polished Gallium Phosphide

B. C. Dobbs

Air Force Materials Laboratory, Wright-Patterson Air Force Base, Ohio 45433

Takao Miyazaki

Central Research Laboratory, Hitachi Limited, Tokyo, Japan

and Y. S. Park

Air Force Avionics Laboratory, Wright-Patterson Air Force Base, Ohio 45433

Although several etchants (1-4) exist for gallium phosphide, in general, etch rates are greater than 100 Å/min, and often the resulting surface is not uniform and smooth. A new technique has been developed for etching gallium phosphide which permits a nearly constant etch rate, uniform etching across the sample surface, and a moderately slow etch rate that allows thin layers (a few hundred angstroms) of the sample to be removed in reasonable time. Such an etchant is desirable in order to determine the depth distribution of the dopants in thin layers of ion-implanted gallium phosphide.

The 5 × 5 × 0.5 mm polished gallium phosphide samples were washed separately in trichloroethylene, acetone, and methanol rinses before etching. A coating of black wax was applied to the sample to permit approximately one-half of the sample to be exposed to the etchant. The wax dissolved in the trichloroethylene to reveal the necessary etch step which was measured with a Sloan Dektak Surface Profile Measuring System. Once the sample had been etched, all wax was removed with cleaning solvents; then the sample was glued to a glass microscopy slide which facilitated edge-step measurements. Measurements were made of the step height at four evenly spaced locations across the sample surface.

A mixture of 2g $K_3Fe(CN)_6$, 6 ml 45% KOH, and sufficient deionized water to bring the final volume to 150 ml proved to be a most satisfactory etchant. The etching solution was placed in an ice-water bath 30 min before use in order to stabilize the temperature at a constant 0°C. Since the etch rate varies with temperature this particular temperature was chosen because it is stable and entirely reproducible. Magnetic stirring at 10 Hz was used and our etchant emitted only small amounts of noxious gases when retained at 0°C.

The etched gallium phosphide surfaces were smooth and uniform. Dislocations in the GaP material affect the surface smoothness since these regions etch at a different rate (3) than the uniform material; however, the low temperature and dilute etchant solution minimize this effect. It was found that 150 ml of solution will last ~8 hr with the samples used in our experiments. The etchant must be fresh if stable rates are to be achieved. Sulfur-doped n-type GaP and zinc-doped p-type GaP were etched simultaneously to eliminate variations due to etching conditions. The p-type material was found to etch 37% faster than the n-type material. Table I illustrates the type of GaP used. All samples were oriented along the <100> direction.

Table I. Type of GaP used

Dopant	Carrier concentration (cm^{-3})	Mobility ($cm^2 v^{-1} sec^{-1}$)	Resistivity (Ω-cm)
S	2.3×10^{17}	132	0.207
Zn	1.2×10^{17}	73	0.42

When the etch step was measured, it was found that the center of the sample etched at a slightly slower rate than the edges. Generally, this was found to be ~5% of the total edge step. The Dektak was found to be accurate to better than 1% for ideal samples; however, usually some variation was found in the four measurements made on each GaP sample. This error was found to be negligible in most cases.

Acknowledgments

The authors wish to thank Drs. Phil W. Yu and Darrel Hopper for helpful discussions.

Manuscript submitted April 28, 1977; revised manuscript received Sept. 7, 1977.

Any discussion of this paper will appear in a Discussion Section to be published in the December 1978 JOURNAL. All discussions for the December 1978 Discussion Section should be submitted by Aug. 1, 1978.

Publication costs of this article were assisted by the U.S. Air Force.

REFERENCES

1. J. L. Richards, in "Compound Semiconductors," Vol. 1, R. K. Willardson and H. L. Goering, Editors, p. 297, Reinhold Publishing Corp., New York (1962); O. Lindberg and J. W. Faust, Jr., *ibid.*, p. 308; and J. W. Faust Jr., *ibid.*, p. 454.
2. A. Milch, *This Journal*, **123**, 1256 (1976).
3. R. H. Saul, *ibid.*, **115**, 1184 (1968).
4. L. R. Plauger, *ibid.*, **121**, 455 (1974).

Hydrogen Adsorption on Single Crystal Platinum

E. Yeager,* W. E. O'Grady,* M. Y. C. Woo,* and P. Hagans*

Case Laboratories for Electrochemical Studies and Department of Chemistry, Case Western Reserve University, Cleveland, Ohio 44106

Various electrochemists (1-5) have examined the role of surface structure in electrocatalysis but the results have not been highly conclusive. Recently more sophisticated efforts have been made to determine the role of crystal orientation (6-8). This note reports the results of studies of H electrosorption on Pt(111), (100) and (110) as well as the effect of cycling the potential of polycrystalline Pt.

The LEED-Auger-electrochemical system used in these studies has been described elsewhere (6). The Pt surfaces were cleaned by argon ion sputtering at 350eV and annealed at 900°C to obtain sharp LEED patterns. The principal surface contaminant is carbon which diffuses to the surface from the bulk of the Pt. This procedure was repeated a number of times until no further C or other impurity was detectable in the Auger spectrum (sensitive to ∿0.01 monolayer). The same procedure was used for polycrystalline Pt without the LEED examination. The sample was next transferred under vacuum into a second vacuum chamber which was back-filled with ultra-pure argon (99.9999%, further purified by Ti gettering). The sample was then examined electrochemically in a thin-layer cell with an α Pd-H counter electrode in 0.05M H_2SO_4, prepared with ultra-pure acid (Baker Ultrex H_2SO_4) and pyrolyzed water. The Pt was brought into contact with the electrolyte under controlled potential (0.4V vs. RHE) to minimize the possibility of surface reconstruction.

Figure 1 presents the voltammetry curves for Pt(100) and (111) obtained on the first cathodic scan, starting at 0.4V (RHE) and the reverse anodic sweep. H_2 formation is observed in the cathodic sweep at ∿0.05V and the complementary H_2 oxidation peak in the anodic sweep. The (111) surface exhibits a small H peak in the anodic and cathodic sweeps at ∿0.10V. The charge under the anodic peak is estimated to be ∿7μC/cm^2. Assuming 15.0×10^{14}atoms/cm^2 on Pt(111) and one H per Pt atom, this corresponds to a low coverage of ∿0.03. The first sweep on the Pt(110) surface also exhibits a quite small H peak at ∿0.1V and is similar to that for Pt(111). This is not surprising since a (2x1) LEED pattern was obtained for the Pt(110) surface as a result of a reconstructed surface composed of Pt(111) facets (9).

The first sweep for the Pt(100) surface indicates a much larger H peak at ∿0.25V, corresponding to more strongly adsorbed H. Although the anodic and cathodic peaks differ in width, the charge ratio Q(cath)/Q(anod)=∿1 and the charge is ∿50μC/cm^2. Assuming 13.1×10^{14} atoms/cm^2 on the Pt(100) surface, this corresponds to a coverage of ∿0.3. There may also be a small contribution from weakly adsorbed H. The LEED pattern for the clean Pt (100) surface indicated a (5x1) overlayer as reported in the literature (10) but this surface probably reconstructed to (1x1) upon introduction into the electrolyte.

The H coverages on these surfaces are surprisingly low compared to those found in conventional electrochemical experiments on polycrystalline Pt. The 0.3 coverage for strongly adsorbed H on Pt(100), however, compares favorably with flash desorption studies (11) in the gas phase on Pt(100) which also yield coverages of ∿0.3 at room temperature. The low coverage (∿0.03) for the weakly adsorbed H peaks on the Pt(110) and (111) may not be associated with these surfaces but rather edge effects in the thin-layer cell. They may also arise from portions of the surface which are not the orientation indicated by the LEED pattern. The LEED patterns are sharp and up to literature standards but this does not necessarily insure a very high degree of surface perfection. Samples annealed at high temperatures as in the present study, however, usually have relatively defect free surfaces (12). A third possibility is that the low coverage is the result of surface contamination. This is unlikely in view of the extensive precautions to prevent contamination. Reexamination of the surfaces with Auger after the electrochemical measurements was complicated by the non-volatility of the

*Electrochemical Society Member

Key words: hydrogen adsorption, platinum single crystal, LEED, Auger.

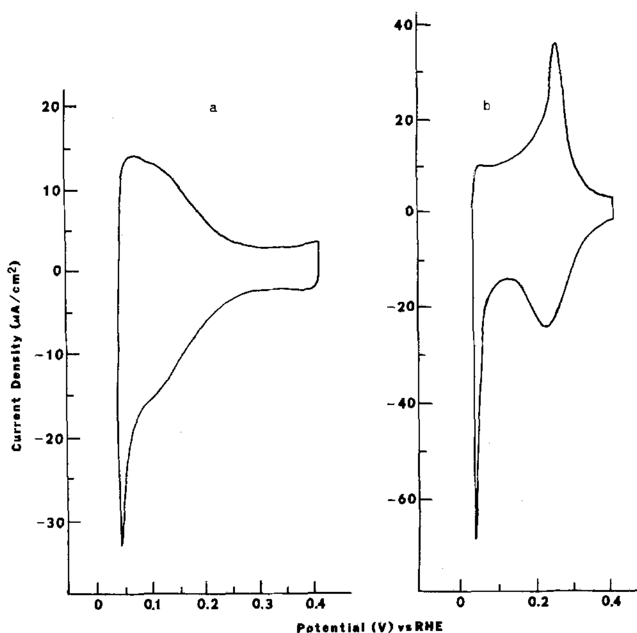

Fig. 1. Voltammograms for a) clean Pt(111) - (1x1) and b) clean Pt(100) - (5x1) in 0.05M H_2SO_4. Sweep rate: a) 100mV/s; b) 50mV/s.

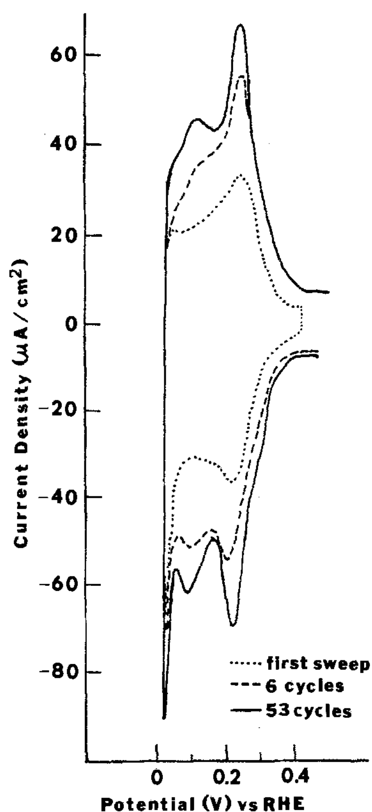

Fig. 2. Voltammograms for polycrystalline Pt in 0.05M H_2SO_4. Sweep rate: 100mV/s.

Manuscript received Nov. 22, 1977; revised manuscript received Dec. 7, 1977.

electrolyte. Post-Auger measurements indicated large sulfur peaks from the sulfate electrolyte and only a minor C peak. On the basis of the ratio of the C to Pt peaks, the C coverage was less than ∿0.1 monolayer.

In Figure 2 is shown the initial scan in 0.5M H_2SO_4 for polycrystalline Pt. The scan was begun at 0.4V and swept cathodically. A predominate H peak appears at ∿0.25V corresponding to stronger adsorbed H with only a minor contribution due to the weakly adsorbed hydrogen. The high temperature annealed polycrystalline Pt resembled quite closely the (100) surface. Cycling of the polycrystalline Pt out to 1.3V in the anodic film region leads to increases in the areas of the H peaks already present as well as the development of additional peaks. After 53 cycles the voltammogram begins to take on the appearance normally found in conventional studies of Pt. The most likely explanation is the reconstruction of the Pt surface.

Acknowledgement.— This research has been supported by ONR, NASA-Ames and the Diamond Shamrock Corporation, the latter through a fellowship to one of the authors (M.Y.C.W.). The authors express thanks to the General Motors and Union Carbide Corporations for grants which helped with the purchase of equipment.

REFERENCES

1. F. G. Will, This Journal, 112, 451 (1965).
2. S. Schuldiner, M. Rosen, and D. R. Flinn, ibid., 117, 1251 (1970).
3. V. S. Bagotzky, Yu. B. Vassiliev, and I. I. Pyshnograeva, Electrochim. Acta, 16, 2141 (1971).
4. K. Kinoshita and P. Stonehart, ibid., 20, 101, (1975).
5. H. Angerstein-Kozlowska, W. B. A. Sharp, and B. E. Conway, in Proceedings of the Symposium on Electrocatalysis, ed. M. W. Breiter, (Electrochemical Society, N.J. 1974), p.94.
6. W. E. O'Grady, M. Y. C. Woo, P. L. Hagans, and E. Yeager, J. Vac. Sci. Technol., 14, 365 (1977).
7. P. N. Ross, Jr., J. Electroanal. Chem., 76, 139 (1977).
8. R. W. Ishikawa and A. T. Hubbard, ibid., 69, 317 (1976).
9. R. Ducros and R. P. Merrill, Surface Sci., 55, 227 (1977).
10. e.g., G. A. Somorjai, "Principles of Surface Chemistry," Chapt. 1, Prentice-Hall, New York (1972).
11. K. E. Lu and R. R. Rye, Surface Sci., 45, 677 (1974).
12. F. Jona, ibid., 8, 478 (1967).

Publication costs of this article were assisted by Case Western Reserve University.

Application of Neutron Transmutation Doping for Production of Homogeneous Epitaxial Layers

S. Prussin*

TRW Semiconductors, Lawndale, California 90260

and J. W. Cleland

Oak Ridge National Laboratory, Solid State Division, Oak Ridge, Tennessee 37830

Neutron transmutation doping (NTD) is being applied to convert ingots of high resistivity float-zoned silicon into homogeneously and precisely phosphorus doped n-type material (1-6). Such neutron transmutation doped material is being successfully used in high voltage thyristors and diodes (7,8).

This communication describes the application of NTD to the generation of precisely and homogeneously doped n-type epitaxial layers. Such starting material would result in a greater yield of devices of desired electrical parameters. It would be especially desirable for large area devices consisting of a group of adjacent cells which must all be as identical as possible in order to operate more effectively.

In the method conventionally used, doped silicon is epitaxially laid down on a prepared heated silicon substrate by the decomposition of a flowing gas containing a silicon compound such as silane, dichlorsilane, trichlorsilane or silicon tetrachloride, together with a doping agent such as PH_3. The concentration of the dopant in the epitaxially deposited silicon layer, here phosphorus, is affected by variations in gas flow, by temperature gradients and by autodoping, the pickup of impurities from the doped substrate and their redeposition with the epitaxial silicon. Schuman (9) has published a detailed description of the impurity profile found in a conventionally produced n/n^+ epitaxial wafer, using spreading resistance measurement techniques. He found significant inhomogeneities across the surface as well as in depth of the epitaxial layer.

The process utilizing NTD began with the deposition of an undoped silicon epitaxial layer on a heavily arsenic doped substrate at 1050°C using undoped silane as the silicon source. These wafers were subjected to an irradiation of 250 hours in an in-core position of the Bulk Shielding Reactor at Oak Ridge National Laboratory. The thermal neutron flux was measured as 1.3×10^{13} n cm^{-2} sec^{-1}, the fast neutron flux using a Ni detector was found to be 1.7×10^{12} n cm^{-2} sec^{-1}.

This results in the reaction,

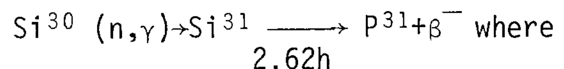

$$Si^{30}\ (n,\gamma) \rightarrow Si^{31} \xrightarrow[2.62h]{} P^{31} + \beta^{-}$$ where

the stable silicon isotope Si^{30} is converted to the stable phosphorus isotope P^{31}, thereby doping the material n-type. The effective decay length for silicon is sufficiently large to limit variation in resistivity due to neutron flux absorption to 1%. The continuously uniform neutron flux at any position in a nuclear reactor permits us by controlling the time of exposure to obtain a reproducibility of doping from lot to lot. Thus reproducibilities and uniformities of ±2% are possible compared to the ±10% normally specified for the resistivity of epitaxial layers prepared by conventional techniques.

The final step in the process consisted of an annealing treatment of 20h at 750°C in dry N_2. This permits the newly created P atoms to take substitutional positions in the silicon crystal lattice and to reduce the lattice damage so that

---

*Electrochemical Society Active Member. Key words: neutron irradiation, neutron transmutation doping, homogeneous epitaxial layers, epitaxial wafers.

full electrical activity can be observed (3,5).

Figure 1 illustrates the resistivity profiles obtained before and after neutron bombardment and annealing. The profile was obtained by a spreading resistance probe technique, utilizing a Hartman ε conducting correction. This correction was found to give consistently good agreement with C/V data on n/n^+ epitaxial structures (10). We note that while the deposited silicon varies in resistivity over the range of 20 to 100Ωcm, the neutron bombarded epitaxial resistivity is quite uniform at 2.7Ωcm.

The half-life for Si^{31} of 2.6h insures that the neutron bombarded silicon decays to an undetectable level in 3 to 5 days (5). The doping level required in epitaxial layers are normally one to two orders of magnitude greater than are encountered in power devices prepared by NTD. This raises a question with regard to the P^{31} atoms generated by NTD which are subject to the secondary transmutation,

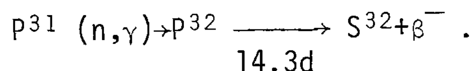

$$P^{31}\ (n,\gamma)\rightarrow P^{32} \xrightarrow[14.3d]{} S^{32}+\beta^- .$$

Because of the longer half-life of P^{32}, there is the possibility of significant residual radioactivity. However, after a 25 day cool down period the unetched wafers were found with a radioactivity of less than $2mRh^{-1}$, well within acceptable safe limits.

The possible donor substrate dopants are antimony and arsenic. Phosphorus is precluded because of its excessive autodoping tendencies. The neutron transmutations of these elements are given as,

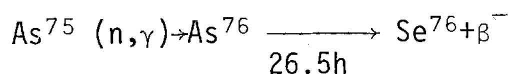

$$As^{75}\ (n,\gamma)\rightarrow As^{76} \xrightarrow[26.5h]{} Se^{76}+\beta^-$$

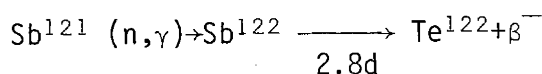

$$Sb^{121}\ (n,\gamma)\rightarrow Sb^{122} \xrightarrow[2.8d]{} Te^{122}+\beta^-$$

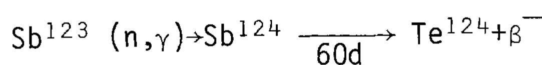

$$Sb^{123}\ (n,\gamma)\rightarrow Sb^{124} \xrightarrow[60d]{} Te^{124}+\beta^-$$

Although As^{75} has a much larger thermal neutron capture cross section than Sb^{121} or Sb^{123}, the much longer half-life of the Sb^{123} (60.2d) precludes its use as a substrate dopant for the neutron fluence of $5x10^{18}$ to $1x10^{20}$ cm^{-2} normally required. The use of As permits radioactive decay in a reasonable period. Similarly, Ga represents an acceptable acceptor type substrate dopant, while B does not, since B^{10} (19.6% abundant) has a large (3,840 barn) cross section, and fissions to introduce He^4 and donor type Li^7.

ACKNOWLEDGMENTS

The authors would like to thank Jay Levine for carrying out the epitaxial deposition, and Dr. Arthur Hochberg and Robert Etchells for the computer program.

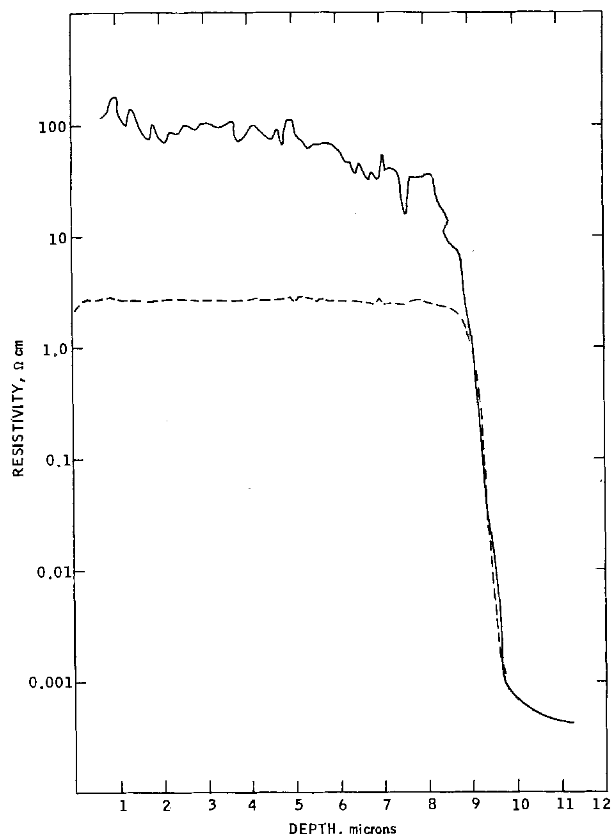

Figure 1. Resistivity Profile Before and After Neutron Transmutation Doping.

REFERENCES

1. M. Tanenbaum and A. D. Mills, This Journal 108, 171 (1961).
2. H. A. Herrman and H. Herzer, This Journal 122, 156B (1975).
3. H. Herzer, Semiconductor Silicon 1977, H. R. Huff and E. Sirtl, eds. The Electrochemical Society, Princeton, N.J. p. 106.
4. See also p 116 ff. *ibid.*
5. Hans Mark Janus and Olof Malmros, IEEE Trans. Electron Devices ED-23, 797 (1976).
6. Ernst W. Haas and Manfred S. Schnoller, *ibid.* ED-23, 803(1976).
7. Karl Platzoder and Karl Leinz Loch, *ibid* ED-23, 805 (1976).
8. Martin J. Hill, Paul M. Van Iseghem, and Wolfgang Zimmerman, *ibid* ED-23, 809 (1976).
9. P. A. Schuman, Jr., C. P. Schneider and L. A. Pietrogallo, Solid State Technology 16, 54 (September, 1973).
10. Gilbert Gruber, Solid State Measurements, personal communication.

Manuscript submitted Aug. 29, 1977; revised manuscript received Nov. 23, 1977.

Publication costs of this article were assisted by TRW Semiconductors.

JOURNAL OF THE ELECTROCHEMICAL SOCIETY

ELECTROCHEMICAL SCIENCE
AND TECHNOLOGY

MARCH
1978

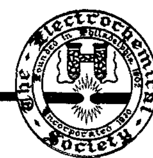

Thermal Properties of Battery Systems

H. Frank Gibbard*

Gould Laboratories, Rolling Meadows, Illinois 60008

ABSTRACT

A compact expression is derived for the change in any extensive thermodynamic state variable which accompanies an electrochemical reaction. The distinction between an electrochemical reaction and the complete thermodynamic change in state is clearly drawn. The cases in which every reactant is in a single, pure phase and that in which some reactants are dissolved in solution are discussed. Detailed calculations of ΔH, ΔG, the cell potential, and the thermal efficiency of the lead/acid battery are presented as examples. Practical thermal efficiencies of 11 other systems are calculated and compared, where possible, with theoretical thermal efficiencies. Equations for the rate of heat flow from batteries are developed and applied to a typical duty cycle of a lead/acid battery for vehicular propulsion.

The measurement and calculation of thermodynamic properties of battery systems have many practical applications. For example, engineering analyses of plants for utility load leveling and peak shaving require heat balances. For some military applications, thermal efficiencies for battery discharge must be known. Thermodynamic calculations are straightforward for cell reactions in which each reactant and each product is present in a single, pure, condensed phase. However, the thermodynamics of electrochemical cells in which some of the constituents are dissolved in a liquid solution is more complicated. For both cases, it is convenient to have a simple expression which describes the change in any extensive thermodynamic state function for a given extent of the cell reaction. The purpose of this paper is not only to present the results of some calculations of discharge efficiencies but also to show in some detail how such calculations are done.

Equations for Thermodynamic Properties

The stoichiometry of the net cell reaction is specified by numbering the reactants and products and defining a quantity υ_i which is equal to the stoichiometric coefficient of the ith species, if it is a product, and is equal to the negative of the stoichiometric coefficient of the ith species, if it is a reactant. The amount (in moles) of any substance i present at the beginning of the cell reaction is designated by n_i°. After some extent of reaction has occurred, the amount of substance i present is $n_i^\circ + \upsilon_i\xi$, where ξ is the reaction progress variable for the cell reaction. The υ_i are pure numbers and ξ has units of moles. If X is any extensive state variable, *e.g.*, Gibbs energy G, enthalpy H, or entropy S, then

$$X = \Sigma_i n_i \overline{X}_i \quad [1]$$

where $\overline{X}_i$ is the partial molar X of the ith component, and the summation is taken over all components present, not only those which appear in the cell reaction. For the change from the initial state, taken as $\xi = 0$, to the final state, taken as $\xi = 1$ mole, the change in X is given by

$$\Delta X = \Sigma_i n_i^\circ [\overline{X}_i(\xi = 1) - \overline{X}_i(\xi = 0)] + \Sigma_i \upsilon_i \overline{X}_i(\xi = 1) \quad [2]$$

which is the desired general relation. For reactions in which all of the components are present in single, pure phases, the first summation vanishes, and $\overline{X}_i$ is simply the molar X of pure substance i. For reactions involving solutions, the first summation does not vanish and will include terms for every substance present in the solution, even if some substances do not take part in the chemical reaction.

Here it should be mentioned that the notation "ΔX" in the literature often does not mean the change in X for a finite change in state. It is rather the derivative of X with respect to ξ

$$(\partial X/\partial \xi)_{P,T} = \Sigma_i \upsilon_i \overline{X}_i(\xi) \quad [3]$$

For reactions in solution, generally $\overline{X}_i$ is not the molar quantity of pure substance i, and the substitution of "ΔX" for $(\partial X/\partial \xi)_{P,T}$ is poor nomenclature.

If X is G, then $\overline{X}_i$ is μ_i, the chemical potential of component i, which may be expressed in terms of the activity of i

$$\mu_i = \mu_i^\circ + RT \ln a_i \quad [4]$$

Then Eq. [2] becomes

$$\Delta G = \Sigma_i \upsilon_i \mu_i^\circ + RT \ln \Pi_i [a_i(\xi = 1)]^{\upsilon_i} + RT \ln \Pi_i [a_i(\xi = 1)/a_i(\xi = 0)]^{n_i^\circ} \quad [5]$$

where $\Sigma_i \upsilon_i \mu_i^\circ$ is the so-called "standard Gibbs energy change" for the cell reaction. If X is the enthalpy function H, then

$$\Delta H = \Sigma_i \upsilon_i \overline{H}_i^\circ + \Sigma_i n_i^\circ [\overline{L}_i(\xi = 1) - \overline{L}_i(\xi = 0)] + \Sigma_i \upsilon_i \overline{L}_i(\xi = 1) \quad [6]$$

where $\Sigma_i \upsilon_i \overline{H}_i^\circ$ is the standard enthalpy change for the cell reaction, and $\overline{L}_i$ is the relative partial molar enthalpy of substance i

$$\overline{L}_i = \overline{H}_i - \overline{H}_i^\circ \quad [7]$$

* Electrochemical Society Active Member.

The thermal efficiency of a battery system is defined as the negative of the electrical work divided by the enthalpy change which accompanies the cell reaction. For the case of reversible operation, the thermodynamic thermal efficiency ϵ_{th} is given by

$$\epsilon_{th} = \Delta G/\Delta H \quad [8]$$

in which the change in state to which ΔG and ΔH refer is the discharge of the battery between known initial and final states. Equations [5] and [6] show that ϵ_{th} can be calculated if the activities and relative partial molar enthalpies of each constituent are known. As is shown below, the calculation is simple, provided that careful attention is given to writing the correct over-all change in state.

For most batteries accurate activity coefficients and relative partial molar enthalpies are not known. In these cases Eq. [3] provides an alternate, but usually less accurate, method to find ΔG and ΔH. For an electrochemical cell $\Sigma_i \upsilon_i \overline{G}_i = -n\mathbf{F}E$ and integration of Eq. [3] with respect to ξ gives

$$\Delta G = -n\mathbf{F}\int_0^1 E(\xi)d\xi \quad [9]$$

so that ΔG can be calculated if the open-circuit voltage (taken to be the cell potential E) of the battery is measured during discharge. Values of ΔH can be derived from measurements of the temperature dependence of the cell potential and the Gibbs-Helmholtz equation, written in the form

$$\Delta H = -n\mathbf{F}\int_0^1 [E - T(\partial E/\partial T)_{\xi,P}]d\xi \quad [10]$$

Examples of the use of Eq. [5] and [6] and the alternative Eq. [9] and [10] to calculate thermal efficiencies will be given for the lead/acid battery, for which all of the relevant properties are well known.

For some applications it may be useful to know the "instantaneous thermal efficiency" ϵ'. This quantity, which at any time represents the fraction of total energy[1] output which is electrical work, is defined by

$$\epsilon' = -n\mathbf{F}V_i/(\partial H/\partial \xi)_{P,T} \quad [11]$$

where V_i is the operating voltage of the cell. For the case of reversible operation the thermal efficiency is

$$\epsilon'_r = (\partial G/\partial H)_{P,T,\xi} = (\partial G/\partial \xi)_{P,T}/(\partial H/\partial \xi)_{P,T} \quad [12]$$

which can be computed by using the differential forms of Eq. [5] and [6] or Eq. [9] and [10], which are

$$(\partial G/\partial \xi)_{P,T} = \Sigma_i \upsilon_i \mu_i^\circ + RT \ln \Pi_i [a_i(\xi)]^{\upsilon_i} \quad [13]$$

$$(\partial G/\partial \xi)_{P,T} = -n\mathbf{F}E(\xi) \quad [14]$$

$$(\partial H/\partial \xi)_{P,T} = \Sigma_i \upsilon_i \overline{H}_i^\circ + \Sigma_i \upsilon_i \overline{L}_i(\xi) \quad [15]$$

$$(\partial H/\partial \xi)_{P,T} = -n\mathbf{F}[E - T(\partial E/\partial T)_{\xi,P}] \quad [16]$$

If values of ΔS or $(\partial S/\partial \xi)_{P,T}$ are desired, they may be calculated using the equation

$$\Delta S = (\Delta H - \Delta G)/T \quad [17]$$

or its differential form

$$(\partial S/\partial \xi)_{P,T} = [(\partial H/\partial \xi)_{P,T} - (\partial G/\partial \xi)_{P,T}]/T \quad [18]$$

Calculation of Thermal Efficiencies

Application to the lead/acid battery.—The lead/acid battery provides an excellent example for the calculation of thermal efficiencies, because the solute and solvent activities (1) and relative partial molar enthalpies (2) are known accurately, and the cell potential and its temperature derivative have been measured by various authors (3-5). Also the lead/acid system clearly shows the large role which concentration changes in the electrolyte can play.

To write the complete change in state it is useful to begin with the general equation for the molality of a solute species

$$m_i = (n_i^\circ + \upsilon_i \xi)/(n_1^\circ + \upsilon_1 \xi)M_1 \quad [19]$$

in which n_i° is the number of moles of species i when $\xi = 0$, component 1 is the solvent, and M_1 is the molar mass of the solvent in kilograms per mole. For the special case in which the solvent does not participate in the cell reaction, Eq. [19] reduces to

$$m_i = m_i^\circ + (\upsilon_i/n_1^\circ M_1)\xi \quad [20]$$

The cell reaction for the lead/acid battery may be written

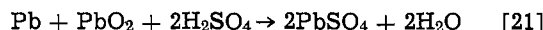

$$Pb + PbO_2 + 2H_2SO_4 \rightarrow 2PbSO_4 + 2H_2O \quad [21]$$

The constituents are numbered as shown in Table I. To write a specific change in state the initial and final molalities of sulfuric acid are chosen as 5.989 and 1.135 mole/kg, which are representative of batteries in the charged and discharged states. Substitution of these values into Eq. [19] and solution of the two equations for n_1° and n_2° gives enough information to write the complete change in state for one mole of reaction

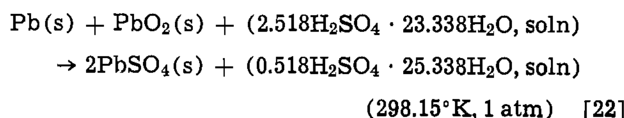

$$Pb(s) + PbO_2(s) + (2.518H_2SO_4 \cdot 23.338H_2O, soln) \rightarrow 2PbSO_4(s) + (0.518H_2SO_4 \cdot 25.338H_2O, soln) \quad (298.15°K, 1\ atm) \quad [22]$$

To calculate ΔG and ΔH for the change in state [22], values for the terms $\Sigma_i \upsilon_i \mu_i^\circ$ and $\Sigma_i \upsilon_i \overline{H}_i^\circ$ are required. From tabulations of the National Bureau of Standards (6) these are calculated to be −394.15 and −315.60 kJ/mole, respectively. The activity of sulfuric acid is $4m^3\ \gamma_\pm^3$, and from the values of $\gamma_\pm$, a_1, $\overline{L}_2$, and $\overline{L}_1$ from Table II for $\xi = 0$ and $\xi = 1$ mole, Eq. [5] and [6] give $\Delta G = -391.05$ kJ and $\Delta H = -378.02$ kJ. Thus the over-all thermal efficiency of the lead/acid battery for the change in state [22] is 1.0345. This value indicates that the lead/acid battery tends to absorb heat during a slow, nearly reversible, discharge.

It is interesting to examine not only the over-all thermal efficiency but also the instantaneous thermal efficiency at each stage of the discharge process. For this reason the data of Table II are given in steps of 0.1 mole in ξ, and Fig. 1 shows the values of ϵ'_{th} cal-

Table I.

Substance	i	υ_i
Pb	3	−1
PbO_2	4	−1
H_2SO_4	2	−2
$PbSO_4$	5	2
H_2O	1	2

Table II. Data used in calculations on the lead/acid system at 298.15°K

ξ/mole	m/(mole/kg)	$\gamma_\pm$*	a_1*	$\overline{L}_2$/(kJ/mole)**	$\overline{L}_1$/(kJ/mole)**
0.0	5.989	0.2364	0.6269	40.02	−1.142
0.1	5.466	0.2120	0.6673	38.11	−0.947
0.2	4.952	0.1904	0.7073	36.15	−0.760
0.3	4.447	0.1717	0.7463	34.19	−0.597
0.4	3.951	0.1556	0.7838	32.19	−0.440
0.5	3.462	0.1422	0.8194	30.34	−0.317
0.6	2.981	0.1314	0.8526	28.62	−0.216
0.7	2.508	0.1234	0.8830	27.04	−0.136
0.8	2.043	0.1181	0.9104	25.69	−0.082
0.9	1.585	0.1162	0.9347	24.66	−0.048
1.0	1.135	0.1196	0.9560	23.80	−0.027

* From Ref. (1).
** From Ref. (2).

[1] Expansion work against the pressure of the atmosphere is ignored, as is customary.

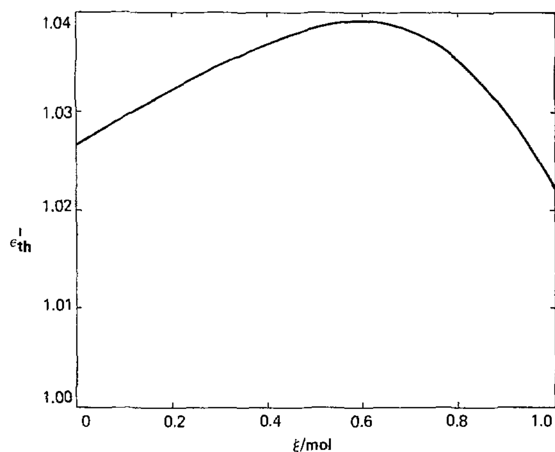

Fig. 1. Differential thermal efficiency of the lead/acid battery at 298.15°K.

culated from Eq. [12], [13], and [15]. The curve shows that the maximum absorption of heat occurs at $\xi = 0.6$ mole, or at a sulfuric acid molality of about 3.0 mole/kg. This sort of plot and its irreversible counterpart might be useful to a battery design engineer if thermal efficiency were important in a particular application; for it clearly shows in which parts of the discharge the greatest and least absorptions of heat occur.

The calculations required to prepare Fig. 1 also permit comparison of the present work with previous studies of the lead/acid battery. Figure 2 shows the cell potential calculated from values of $(\partial G/\partial \xi)_{P,T}$ for the data in Table II, along with measurements on storage batteries and electrochemical cells by Vinal and his co-workers (7). Since the molalities selected for the charged and discharged states in this paper are arbitrary, some of the points for other studies lie outside the range $0 \leq \xi \leq 1.0$ mole. Over the range of the present calculations, the agreement with Vinal and Altrup (7) is within 0.001V, while Craig and Vinal's (5) measurements lie 0.003 to 0.008V higher. The dotted curve shows the mean value of cell potential measurements of Vosburg and Craig (3), Harned and Hamer (4), and Craig and Vinal (5). Integration of the dotted curve serves to determine ΔG for the change in state [22] from cell potentials alone. The value obtained from Eq. [9] is -391.8 kJ, which is 0.19% lower than that determined by Eq. [5]. Integration of the curve for this work yields -391.08 kJ, which shows

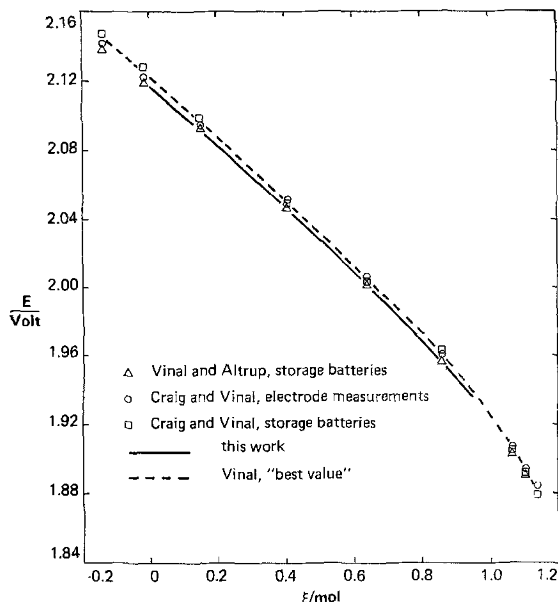

Fig. 2. Cell potential of the lead/acid battery at 298.15°K

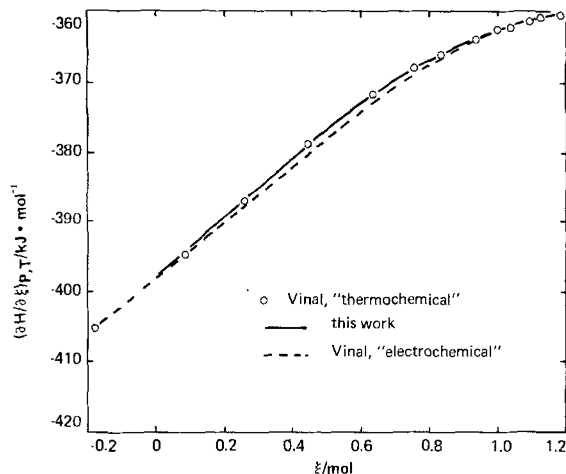

Fig. 3. $(\partial H/\partial \xi)_{P,T}$ for the lead/acid battery at 298.15°K

good consistency of the solute and solvent activities through the Gibbs-Duhem equation.

Figure 3 shows values of $(\partial H/\partial \xi)_{P,T}$ calculated from the $\overline{L_i}$ data in Table II, and the corresponding values determined by Vinal (7) from cell potentials and from the thermal data available to him. The value of ΔH from Eq. [10] for the change in state [22] is -378.45 kJ, which is 0.11% lower than that found from Eq. [6]. Thus the over-all thermal efficiency calculated from cell potentials alone is $-391.08/-378.45$ or 1.0353, and due to a cancellation of errors this differs by only 0.08% from the value obtained from activity and thermal data.

In concluding this section it is important to note that the results for the lead/acid battery are by no means typical of most battery systems. First, the thermal efficiency of most batteries is in the range of 0.8-0.95, while that of lead/acid is greater than unity. Second, for no other practical battery system are data available which are as numerous and precise as those of the lead/acid battery. This is to be expected because of the practical importance, the long history, and the relatively simple and reversible cell reaction of the lead storage battery. However, many advanced battery systems are currently under development for vehicular propulsion, utility off-peak storage, and other applications. The more successful of these will be carefully studied, and it may be expected that the data needed for the calculations presented here will become available for several systems.

Practical Thermal Efficiencies

Results for other systems.—The terminal voltage V_i of any battery being discharged at a finite rate is less than its reversible cell potential E. Because of the dissipative processes in the battery the electrical work must be less than $-\Delta G$. For a battery undergoing discharge at voltage V_i and current I for a period of time t we write

$$\epsilon = -(n\mathbf{F}/\Delta H) \int_0^t V_i(\tau)I(\tau)d\tau \Bigg/ \int_0^t I(\tau)d\tau \quad [23]$$

Equation [23] is a general relation of which Eq. [8] represents the special case of reversible discharge. For constant-current discharge Eq. [23] reduces to

$$\epsilon = -n\mathbf{F}V_i(\text{avg})/\Delta H \quad [24]$$

where V_i(avg) is the average discharge voltage.

Equation [24] is a very convenient form for the calculation of practical thermal efficiencies; all that is needed is a discharge curve and the enthalpy change for the cell reaction. Table III shows the thermal efficiencies of 12 systems, calculated by Eq. [24] with ΔH's from Ref. (6), and the average discharge voltage taken from typical discharge curves in the literature. The exact values obtained for ϵ and V_i(avg) are not

Table III. Thermal efficiencies of 12 battery systems at 298.15°K*

System	Assumed cell reaction	V_i(avg)/V	ϵ	ϵ_{th}
1. Ag/Zn	$2AgO + Zn + H_2O \rightarrow Ag_2O + Zn(OH)_2$; $Ag_2O + Zn \rightarrow 2Ag + ZnO$ **	1.55	0.90	0.94
2. Ni/Zn	$2NiOOH + Zn + H_2O \rightarrow 2Ni(OH)_2 + ZnO$	1.54	0.83	0.93
3. Ni/Cd	$2NiOOH + Cd + 2H_2O \rightarrow 2Ni(OH)_2 + Cd(OH)_2$	1.21	0.84	0.94
4. Pb/acid	$Pb + PbO_2 + 2H_2SO_4 \rightarrow 2PbSO_4 + 2H_2O$	1.97	1.00	1.03
5. Zn/Br_2	$Zn + Br_2 \rightarrow ZnBr_2$	1.60	0.78	0.91
6. $Li/SOCl_2$	$8Li + 4SOCl_2 \rightarrow Li_2S_2O_4 + 6LiCl$	3.40	0.90	—†
7. Li/SO_2	$2Li + 2SO_2 \rightarrow Li_2S_2O_4$	3.30	0.83	—†
8. Zn/O_2	$Zn + (½) O_2 \rightarrow ZnO$	1.28	0.71	0.91
9. Li/H_2O_2	$4Li + O_2 + 2H_2O \rightarrow 4LiOH$	2.90	0.77	0.91
10. H_2/Br_2	$H_2 + Br_2 \rightarrow 2HBr$	0.90*	0.73*	0.83*
11. Zn/MnO_2	$2Zn + 3MnO_2 \rightarrow 2ZnO + Mn_3O_4$	1.20	0.88	1.00
12. Zn/HgO	$Zn + HgO \rightarrow ZnO + Hg$	1.28	0.95	1.01

* The data for system 10 are for 391.4°K.
** Two-step discharge.
† Gibbs energy data lacking.

especially significant, because they depend on the discharge rate. However, the systems with high and low thermal efficiencies are readily identified, and the results are easily converted to other observed average voltages by multiplication of the table entry for ϵ by the ratio of the observed average voltage to the average voltage in the table. A detailed treatment of solution effects was possible only in the cases of the lead/acid and H_2/Br_2 systems. A description of the computations for the latter system has been reported elsewhere (8).

To perform the calculations in Table III it was necessary to assume unit coulombic efficiency of each electrode. This is certainly not true for some systems, but it is the only approximation which can be made in the absence of detailed information on the nature and extent of any nonfaradaic reactions. The formalism developed here can be extended to systems in which nonfaradaic reactions occur, as is shown below. Consider the case in which one electrochemical and p chemical reactions occur simultaneously. Then $p + 1$ reaction progress variables $\xi_j (j = 1, \ldots, p + 1)$ are required to specify the state of the battery. Assume that the battery contains m substances; then the jth reaction can be written

$$\sum_{i=1}^{m} \upsilon_i^{(j)} S_i = 0 \quad (j = 1, \ldots, p + 1) \qquad [25]$$

where S_i represents substance i. Of course, if S_k is not a reactant or product of reaction j, then $\upsilon_k^{(j)} = 0$. If one nonfaradaic reaction is the chemical path for the cell reaction, then the reaction must be written twice, with two independent reaction progress variables, to include the effect of self-discharge.

The change in an extensive state variable X is now written

$$\Delta X = \sum_{i=1}^{m} \left(n_i^\circ + \sum_{j=1}^{p+1} \upsilon_i^{(j)} \xi_j \right) \overline{X}_i(\{1, \xi_2, \ldots, \xi_{p+1}\}) - \sum_{i=1}^{m} n_i^\circ \overline{X}_i(\{0\}) \qquad [26]$$

in which $\{\xi_j\}$ represents the set of reaction progress variables, and $\{0\}$ is the set in which each reaction progress variable is zero. If Eq. [26] is written for ΔH, as in Eq. [6], and if each ξ_j is measured for the battery's discharge, then Eq. [23] can be used for the calculation of thermal efficiency. In the practically important case where the only significant chemical reaction is self-discharge, the result is simply the replacement of ΔH for $\xi = 1$ mole by the ΔH for $\xi = (\epsilon_C)^{-1}$ mole, where ϵ_C is the coulombic discharge efficiency.

Rates of Heat Flow in Battery Systems

To the battery engineer a quantity which may be more useful than the thermal efficiency is the rate of heat flow during charge and discharge. The rate of heat flow $-q'$ from the battery to its surroundings can be written as a derivative either with respect to the reaction progress variable or with respect to time. We write

$$-q'_\xi = \begin{cases} -dq/d\xi \text{ for discharge } (d\xi > 0) \\ dq/d\xi \text{ for charge } (d\xi < 0) \end{cases} \qquad [27]$$

where

$$-dq/d\xi = -T(\partial S/\partial \xi)_{P,T} + n\mathbf{F}(E - V_i) - C_p dT/d\xi \qquad [28]$$

and C_p is the average constant-pressure heat capacity of the battery, or

$$-q'_t = -dq/dt = I\,[-(T/n\mathbf{F})(\partial S/\partial \xi)_{P,T} + E - V_i] - C_p dT/dt \qquad [29]$$

with the convention that $I > 0$ for discharge and $I < 0$ for charge.

Several special cases of Eq. [28] and [29] are of interest. For reversible, isothermal operation the second and third terms of Eq. [28] vanish, and $q'_\xi = T(\partial S/\partial \xi)_{P,T}$. Figure 4 shows, for example, the reversible absorption of heat by the lead/acid battery at 298°K as a function of state of charge.

For isothermal operation the heat capacity terms drop out of Eq. [28] and [29], and the net heat flow depends on the intrinsic entropy change and the overpotential. In Fig. 5 the rate of heat flow $-q'_\xi$ for iso-

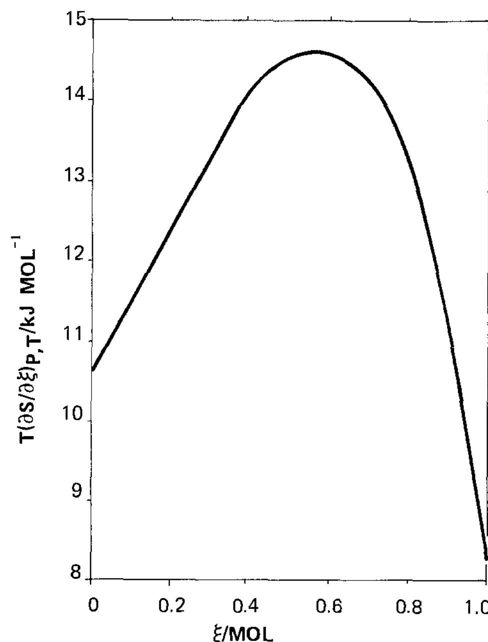

Fig. 4. Absorption of heat for reversible operation of the lead/acid battery at 298°K.

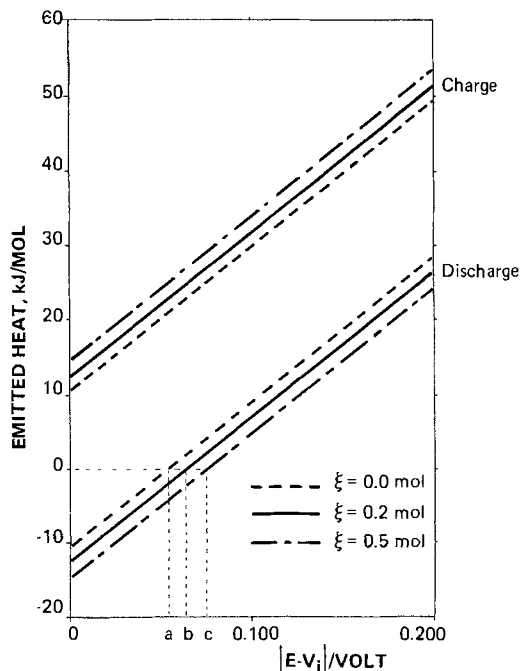

Fig. 5. Dependence of heat flow from the lead/acid battery on overpotential at 298°K.

thermal operation of the lead/acid battery is shown as a function of overpotential. This figure clearly illustrates the facts that the lead/acid battery evolves heat at all potentials on charge, while on discharge heat may be absorbed or emitted. At a certain overpotential which depends on the state of charge the battery neither absorbs nor emits heat. This "thermoneutral" overpotential is shown for three states of charge by the abscissas a, b, and c in Fig. 5. For most other battery systems $T(\partial S/\partial \xi)_{P,T} < 0$, so the relative positions of the charge and discharge lines in Fig. 5 are reversed, and the thermoneutral overpotential applies to the charge mode of the battery.

A final limiting case of interest is the adiabatic one, in which the left-hand sides of Eq. [28] and [29] are zero. Here the internal energy which would flow to the surroundings in isothermal operation remains in the battery, and the temperature rises accordingly. Figure 6 shows the change in temperature calculated from Eq. [29] for a fully charged 281 A·hr (3 hr rate) battery subjected to the load cycle shown. This current profile resembles that observed in a test of electric vehicles for postal service (9). Repetition of the 1 min cycle in Fig. 6 leads to an adiabatic heating rate of 2.64°K/hr; for a half-discharged battery the rate is

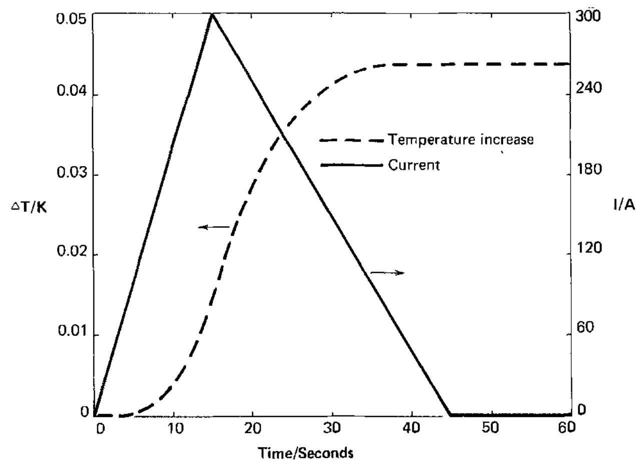

Fig. 6. Calculated temperature rise in an adiabatically insulated lead/acid battery subjected to a vehicular propulsion load cycle.

3.56°K/hr and at the end of discharge it has risen to 4.10°K/hr. Temperature rises of the magnitude calculated are actually observed for the first few hours of service in vehicular propulsion applications (10), before heat loss to the surroundings brings about a steady state at 45°-50°C.

For purposes of comparison we note that the thermodynamic treatment of Gross (11, 12) can be expressed in terms of the formalism developed here. His "enthalpy voltage" $E_{\Delta H}$ is given by

$$E_{\Delta H} = E - (T/n\mathbf{F})(\partial S/\partial \xi)_{P,T} \qquad [30]$$

Gross (11) treated the case of more than one electrochemical reaction and discussed alternatives to the thermodynamic approach for the study of thermal energy in battery systems. He did not give a detailed treatment of solution effects.

Manuscript submitted Aug. 3, 1977; revised manuscript received Oct. 6, 1977. This was Paper 370 presented at the Philadelphia, Pennsylvania, Meeting of the Society, May 8-13, 1977.

Any discussion of this paper will appear in a Discussion Section to be published in the December 1978 JOURNAL. All discussions for the December 1978 Discussion Section should be submitted by Aug. 1, 1978.

Publication costs of this article were assisted by Gould Laboratories.

LIST OF SYMBOLS

a_i	activity of substance i
E	reversible cell potential, V
$\mathbf{F}$	Faraday constant, C/mole
G	Gibbs energy, J
$\overline{G}_i$, $\overline{G}_i^\circ$	partial molar Gibbs energy, standard partial molar Gibbs energy of substance i, J/mole
H	enthalpy, J
I	current, A
$\overline{H}_i$, $\overline{H}_i^\circ$	partial molar enthalpy, standard partial molar enthalpy of substance i, J/mole
$\overline{L}_i$	relative partial molar enthalpy of substance i, J/mole
m_i, m_i°	molality, initial molality of substance i
M_1	molar mass of solvent, kg/mole
n	number of electrons in cell reaction
n_i, n_i°	quantity of substance i, initial quantity of substance i, mole
P	pressure, N/m²
q	heat flow to the system, J
q'_t	rate of heat flow, W
q'_ξ	heat flow per mole of reaction, J/mole
R	gas constant, J/mole·°K
S	entropy, J/mole·°K
t	discharge time, sec
T	temperature, °K
V_i, V_i(avg)	cell voltage, average cell voltage, V
X	any extensive thermodynamic state function
$\gamma_\pm$	mean ionic activity coefficient
ϵ	thermal efficiency
ϵ_C	coulombic efficiency
ϵ_{th}	reversible thermal efficiency for a finite process
ϵ'_r	differential reversible thermal efficiency
μ_i, μ_i°	chemical potential, standard chemical potential of substance i, J/mole
υ_i	generalized stoichiometric coefficient
ξ	reaction progress variable, mole
τ	dummy variable of integration

REFERENCES

1. J. A. Rard, A. Habenschuss, and F. H. Spedding, *J. Chem. Eng. Data*, **21**, 374 (1976).
2. Y. C. Wu, Ph.D. Thesis, University of Chicago (1957).
3. W. C. Vosburgh and D. N. Craig, *J. Am. Chem. Soc.*, **51**, 2009 (1929).
4. H. S. Harned and W. J. Hamer, *ibid*, **57**, 33 (1935).
5. D. N. Craig and G. W. Vinal, *J. Res. Natl. Bur. Stds.*, **24**, 475 (1940).
6. D. D. Wagman, W. H. Evans, and V. B. Parker in, and (in various individual parts) I. Halow, S. M. Bailey, R. H. Schumm, and K. L. Churney, in

"Selected Values of Chemical Thermodynamic Properties," National Bureau of Standards Technical Notes 270-3 (1968), 270-4 (1969), 270-5 (1971), and 270-6 (1971).
7. G. W. Vinal, "Storage Batteries," 4th ed., John Wiley & Sons, Inc., New York (1955).
8. H. F. Gibbard, M. J. Montgomery, J. E. Oxley, and R. A. Putt, Final Report to Brookhaven National Laboratory, Contract 387324-S (Sept. 1976).
9. J. R. Willhite, Personal communication.
10. J. Mandil, Proceedings of the Fourth International Electric Vehicle Symposium, Vol. 2, 31.2 Dusseldorf, Aug. 31-Sept. 2, 1976.
11. S. Gross, *Energy Conversion*, **9**, 55 (1969).
12. S. Gross, "Rapid Charging of Lead Acid Batteries," IEEE Industrial Applications Society Eighth Annual Meeting, October 1973.

Electrochemical and Optical Properties of Thin Oxide Layers Formed on Fresh Titanium Surfaces in Acid Solutions

D. Laser, M. Yaniv, and S. Gottesfeld

Institute of Chemistry, Tel-Aviv University, Ramat Aviv, Israel

ABSTRACT

Optical properties and thicknesses of thin oxide layers formed electrochemically on Ti surfaces which were exposed by abrasion *in situ* were evaluated according to results of ellipsometric and reflectometric measurements. It is shown that the optical as well as some other physical properties of the thin ($d < 100$Å) oxide films are close to those of bulk Ti oxides and, hence, deviations of their electrochemical characteristics from those of bulk TiO_2 are most probably due only to their small thicknesses. Electroreduction of such films was also traced by the optical means and could be shown to result, under certain conditions, in some thinning and, especially, in the increase of the extinction coefficient of the film. The effect of such a reductive treatment on the electrochemical characteristics of the oxide layer is also discussed.

The physical properties of TiO_2 films formed electrochemically on Ti substrates are of interest in relation to the stability of Ti in corrosive environments. Furthermore, since the activity of TiO_2 as a photoanode has become the subject of intensive recent efforts, analysis of such properties and their bearing on the electrochemical and photoelectrochemical reactivity of the Ti/TiO_2/electrolyte system seems to be of importance. In this work thin TiO_2 films ($d < 150$Å) were grown on fresh Ti surfaces exposed by the abrasion *in situ* of Ti electrodes in aqueous H_2SO_4 solutions. While the films formed by anodization of Ti in appropriate solvents may be much thicker (1), the formation of such thin films following exposure of the fresh metal surface probably simulates the process of film repair at sites of protective film failure. The optical properties (thickness and complex refractive index) were determined according to combined reflectometric and ellipsometric measurements taken for films formed anodically following abrasion, as well as for the same films after their partial reduction. The optical-electrochemical cell was equipped with an arrangement for the abrasion *in situ* of the Ti surfaces, which allowed the monitoring of the films optically (*in situ*) immediately following abrasion. The unit employed for the abrasion *in situ* was an improved version of the system originally developed by Ambrose and Kruger (2). A combination of the optical measurements with various electrochemical measurements of the capacity and the behavior of some redox systems, as well as the photooxidation of water at the Ti/TiO_2/electrolyte interface, should allow some insight into the relationship between thickness and optical properties of such films and their electrochemical characteristics.

Experimental

Experiments were carried out with the L119 Gaertner ellipsometer at a wavelength of 5460Å, using a 150W tungsten lamp as a power source, a Bausch and Lomb high intensity monochromator, a mica quarter-wave plate as a retarder prior to the sample, and a Hamamatsu Type R585 photomultiplier. Power suppliers to the lamp and photomultiplier were, respectively, Kepco Model JQE 36V/15A and J. Fluke Model 412B. The photomultiplier output current was converted by a current to voltage converter and monitored on an X-Y recorder. The cylindrical electrochemical cell which served for *in situ* ellipsometric and reflectometric measurements has been employed before (3) and was made of Teflon with a brass envelope in which quartz windows were mounted for an angle of incidence of 65°. A Teflon lid with a central hole for the electrode holder was clamped to an X-Y-Z micrometer positioner attached to the ellipsometer base. The flat surface Teflon electrode holder was attached to a glass tube passing through the lid's central hole, thus allowing rotation around the optical axis.

The *in situ* abrasion unit attached to the optical-electrochemical cell is shown schematically in Fig. 1. A shaft (made of steel with a front Kel-F part) was rotated by an a-c motor at a speed of 300 rpm, as determined by the radius of the large transmission wheel. A linear motion bearing at the center of the large wheel allowed the free linear motion of the shaft along its axis. The rotating shaft (front Kel-F part)

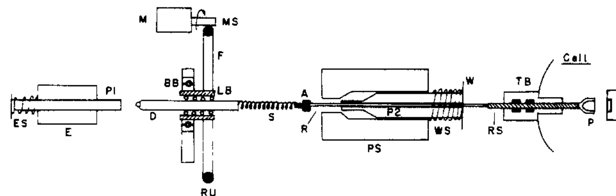

Fig. 1. Schematic presentation of the apparatus for abrasion *in situ* followed by optical and electrochemical examination: E, electroportional solenoid; LB, linear motion bearing; BB, ball bearing; D, drive shaft; F, fly wheel; RU, Neoprene O-ring; M, a-c motor; A, anvil; PS, pull solenoid; R, rotating shaft; W, washer; TB, Teflon bearing; RS, Kel-F rotating shaft; P, polishing head.

Key words: ellipsometry, corrosion, semiconductor electrodes.

entered the electrochemical-optical cell through a Teflon bearing (braided Teflon permeated with Kel-F oil) and carried on its end the polishing head. To produce an efficient and durable polishing head, which allowed numerous consecutive efficient abrasions before replacement while leaving specularly reflecting metal substrates and clear solutions, a 3μ diamond paste (Struers Scientific Instruments) was applied to a suitable polishing cloth (Struers DP cloth Type DUR) and thermally treated (1-2 hr at 100°C). The thermal treatment left the diamond powder embedded in the cloth and active for 20-50 consecutive abrasions of Ti electrodes. This impregnated cloth was glued by silicon rubber cement to a silicon rubber support casted in a Kel-F hollow cone. The threaded apex of this conical "cushion" holder could be connected to the rotating shaft and, thus, the whole polishing head easily replaced without misalignment.

While rotating the shaft, the polishing head could be pressed against the metal electrode sample, applying a controllable pressure by means of an electroproportional solenoid. After the completion of the abrasion the polishing head could be quickly retracted by applying a strong knock to the rotating shaft along its axis by means of a fast solenoid. To allow the fast retraction, the electroproportional solenoid was switched off simultaneously, the "on" and "off" commands to the pair of solenoids being appropriately synchronized by an electronic unit. By using this approach for retracting the rotating shaft, the optical path was found to be completely cleared within 0.5 msec after the termination of polishing. Thus optical readings of film growth on exposed metal surfaces could be taken in the millisecond time scale. The possibility of following such early stages of film growth is significant (2), and the resulting advantages of faster retraction will be demonstrated in a forthcoming contribution.

The Ti specimens were prepared by cutting disks 6 mm in diameter from Ti rods (99.7% pure, Ventron, Alfa Products, Beverly, Massachusetts) and were mounted by pressure in a Teflon holder exposing a single surface to the solution. Samples within the holder were mechanically polished prior to the electrochemical experiments with silicon-carbide paper grades 300 and 600 followed by diamond paste size 15 and 3μ successively, using ethanol as lubricant. After polishing the samples were immersed in sulfochromic acid solution and then thoroughly rinsed and soaked in an ultrasonic triply distilled water bath. The working solution was 0.5M Na_2SO_4 with pH adjusted to 1.7 with H_2SO_4. A commercial saturated calomel electrode with a sealed porous glass bridge served as a reference electrode. The assembled cell, containing the mounted sample but without solution and windows, served for the alignment procedure according to McCrackin *et al.* (4). Allowance was made for window birefringence.

Samples were abraded in the cell under controlled potential, preselected as described in the next section. Δ and Ψ null readings were taken when the current, under potentiostatic conditions, has attained a steady state. Continuous changes in the reflectivity were recorded in linear potential scanning experiments by monitoring the exit beam intensity with the ellipsometer set at P = A = 0° or P = A = 90° for variations in reflectance at parallel and perpendicular polarization, respectively. Continuous variations of Δ were recorded in such experiments as off-null intensity transients. The off-null settings of the ellipsometer were selected according to the criteria described elsewhere (5), but the variations of Δ followed in this work were too large to allow a perfectly linear dependence of $\delta I_{\rm refl.}$ on $\delta\Delta$ at constant off-null settings. Further calibrations of such off-null intensity curves were, therefore, performed by separate constant voltage growth experiments, in which the same off-null settings were used. Changes of the exit beam intensity due to the application of several constant anodic voltages were fitted to the shifts of Δ measured at the same applied voltages by the regular method of nulling. This fitting yielded the required (slightly nonlinear) $\delta\Delta$ *vs.* $\delta I_{\rm refl.}$ curve, which is suitable for the specific film/substrate system under the off-null settings employed. (The growth of films with identical optical properties in constant voltage and in linear scanning experiments is assumed in such a calibration.) The convention: $\hat{n} = n - ik$ will be used throughout for the presentation of the complex refractive index.

Results and Discussion

Ellipsometric and reflectometric measurements of oxide film growth on titanium.—The initial state of the "film free" Ti surface.—The nature of the "clean Ti surface," left in contact with an acid solution following the abrasion *in situ*, was first examined. Figure 2 shows the current-potential curve recorded while the abrasion of a Ti electrode immersed in an acidic Na_2SO_4 solution (pH adjusted to 1.7 with H_2SO_4) was taking place. The corrosion potential, V_c, is identified as the potential at which zero net current is observed for the fresh exposed Ti surface. According to previous reports (6, 7), the net current in the whole region shown in Fig. 2 is expected to be the sum of partial cathodic and anodic currents. The cathodic processes involved may be H_2 evolution and Ti hydride formation (8), while the anodic processes are the electrooxidation of Ti to some soluble products and to the surface oxide. The overlap of the oxide and hydride stability regions (7) means that, in principle, it should be impossible to obtain at equilibrium in solution a Ti surface which is perfectly free of any adsorbed (or absorbed) species by a combination of abrasion and cathodic polarization. However, for the wavelength employed (5460Å) the optical effects due to the H surface layer could be shown to be negligible in the potential range covered. For the polished Ti surface no significant change in any optical parameter could be detected as the voltage was scanned between V_c and the cathodic limit set by the beginning of H_2 evolution. (Onset of gas evolution could be identified optically by very unstable readings due to the bubbles formed in the light path.) The optical effects caused by adsorbed H layers on other metals in the visible

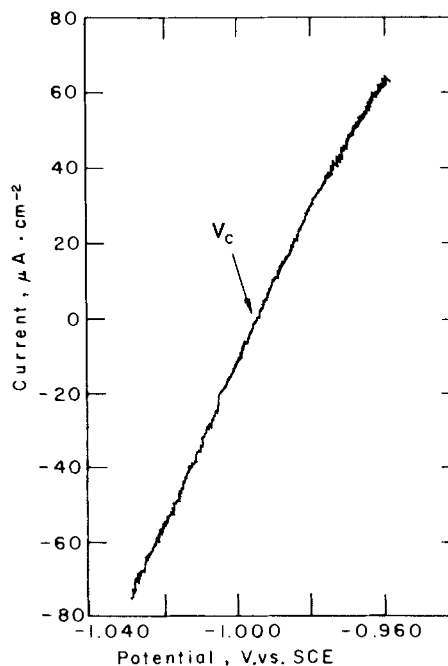

Fig. 2. Current-voltage curve for a Ti electrode taken during mechanical polishing *in situ*. Solution: 0.5M Na_2SO_4, 0.075M H_2SO_4 (pH = 1.65).

region are already known to be at least an order of magnitude smaller than the effects due to similar coverages of oxygen (9). It was thus concluded that, as far as the optical reference state is concerned, the existence of some form of H coverage prior to oxide formation had probably a very minor influence at 5460Å. [Stronger optical effects due to H ad- or absorption may be obtained at shorter wavelengths (10).]

Abrasion under cathodic polarization seems, according to these results, to produce a Ti surface which is quite suitable to serve as the reference "film-free" substrate. The apparent optical properties of such substrates were measured ellipsometrically, taking null readings for abraded Ti electrode surfaces, which, following abrasion, were kept at potentials between V_c and the H_2 evolution region. The results obtained at 5460Å were: $n_{Ti} = 2.7\text{-}2.8$; $k_{Ti} = 3.20\text{-}3.25$.

The large scatter in the results reported in the literature for $\hat{n}_{Ti}$ has been discussed by Smith (11). The last author obtained at 5460Å for a mechanically polished polycrystalline Ti sample which was carefully cleaned in vacuum: $n_{Ti} = 3.1$; $k_{Ti} = 3.4$.

The fit between the results for Ti surfaces as obtained by abrasion *in situ* and those given by Smith for samples cleaned in vacuum is not perfect, but the deviation is not large when compared with the scatter found in some sets of experimental data for "clean metal substrates" quoted in the literature. This order of deviation is most probably a result of a slightly different "damaged layer" which is left on the metal surface in each of the cases, as a result of mechanical polishing, although a residual H or O coverage cannot be completely ruled out. In some cases mechanical polishing outside the cell prior to the optical measurements left a relatively rough surface, which could not be improved by abrasion *in situ* with cathodic applied potentials. This was manifested by the value of Δ_0, measured at -0.9V following abrasion, being several degrees lower than usual. In such cases, it was found that abrasion under anodic applied potentials (0.0V) had a favorable effect, apparently caused by the electropolishing of the exposed metal surface under the positive applied potential. Following such a treatment the smoothed surface exhibited the higher regular Δ values at -0.9V.

Electrochemical and optical results recorded during film growth.—The combination of ellipsometric and reflectometric measurements was shown in previous contributions to constitute an effective tool for following the growth and evaluating the properties of thin films (12). Figure 3 shows the dependence on potential of the current and of three optical parameters Δ, $R_{||}$, and $R_{\perp}$, for a Ti electrode to which a triangular potential scan was applied following abrasion *in situ*. (The most reproducible optical and electrochemical results, as well as simple and regular growth kinetics, were obtained when such continuous linear changes of the potential were employed.) The continuous recording of the changes in Δ was performed with off-null settings of the ellipsometer. The pair of symmetrical intensity transients obtained at two symmetrical off-null settings [curves a and b in Fig. 3 indicate that transients thus recorded closely approximate the variation of Δ as a function of applied potential (5).] Any deviation from linearity in the dependence of $\delta I_{refl.}$ was further corrected, however, prior to the computer analysis, according to the procedure described above (see Experimental). In the anodic branch of the current cycle a "dissolution peak" is first observed, followed by a region of film growth in which the current is practically constant during the linear potential scan. The beginning of the change in optical properties can be observed to occur at the foot of the "dissolution peak," as the net current becomes positive. In the constant current range all three optical parameters seem to change linearly with applied potential. For the thin

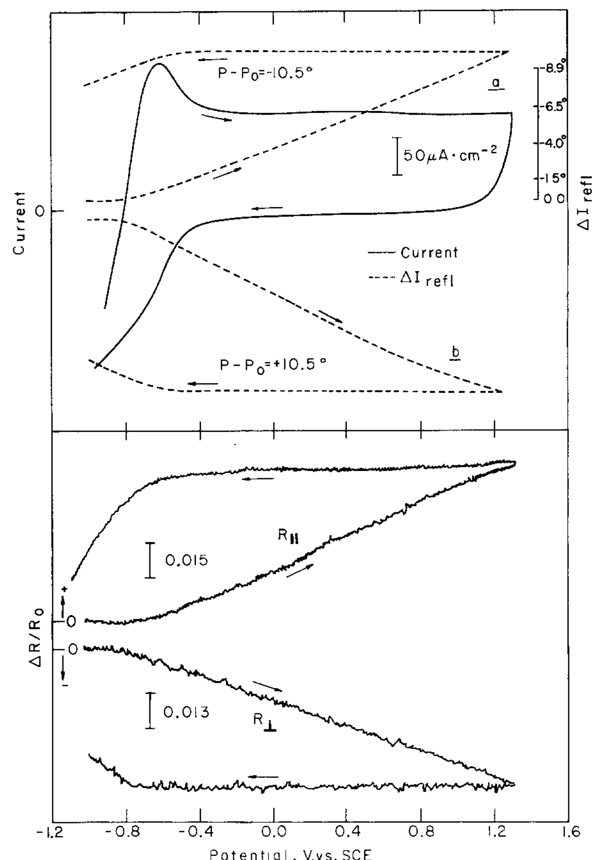

Fig. 3. Current-voltage curve and the associated optical changes recorded during oxide film growth and its subsequent reduction in a triangular potential scanning experiment: a and b, light intensity changes recorded at two symmetrical off-null settings: the scale in the upper right-hand corner shows the calibration of curve a in terms of changes in Δ (see Experimental). Solution as in Fig. 2; scan rate, 15 mV sec^{-1}; $\lambda = 5460$Å.

films involved, this immediately proves the linear dependence of thickness on applied potential, and, more significantly, it proves the growth of a film with practically uniform properties in the potential range covered in this figure. As shown in some previous contributions on combined ellipsometric-reflectometric measurements (12), if the optical properties of such a film change with thickness this would cause appreciable changes in the ratio $\delta\Delta/(\delta R/R)$, which were not observed here in practice.

In the cathodic half-cycle very low currents were recorded and no change in the optical properties of the film-covered Ti surface could be observed until a potential of ~ -0.5V was reached (see Fig. 3). A cathodic current then started to develop and was accompanied by appreciable changes in the thickness and properties of the oxide. These changes are discussed later.

Analysis of the optical properties of the film.—Two approaches were attempted in the analysis of the optical properties for thin films produced on Ti in the potential region -0.9 to $+1.5$V in the acidic solutions employed. In the first approach (method 1) it was assumed that the Ti surface kept under cathodic polarization following abrasion *in situ* is indeed a perfect film-free substrate and may be, therefore, taken as an ideal optical reference state for film growth. Results of combined ellipsometric and reflectometric measurements taken at different potentials were fitted to a uniform film growth model by a minimization computer program (13). A minimum for the function

$$F = \Sigma \{ (\delta\Delta_{meas} - \delta\Delta_{calc})^2 + (\delta\Psi_{meas} - \delta\Psi_{calc})^2 + [(\delta R/R)_{||, meas} - (\delta R/R)_{||, calc}]^2 + [(\delta R/R)_{\perp, meas} - (\delta R/R)_{\perp, calc}]^2 \} \quad [1]$$

was searched, assuming that a film-free Ti surface, with optical properties calculated according to the Δ_0 and Ψ_0 readings following abrasion, indeed existed at -0.9V.

Another computational approach (method 2) was also tested, the use of which allowed the avoidance of the rigid assumption of a perfectly film-free surface in the initial state. If it was assumed, rather, that an initial very thin film did exist on the surface following abrasion (and prior to anodization), the parameters of the substrate became two additional unknowns. These could be solved, however, if it was further assumed that the optical properties of the "initial film" resembled those of the film grown by anodization. (This approach is capable, in principle, of avoiding the complications when the buildup of some surface film is very fast at any applied potential following abrasion, *i.e.*, due to the overlap of oxide and hydride stability regions, thus making the state of a perfectly clean substrate unachievable.) A total $4 + j$ unknowns: n_{metal}, k_{metal}, n_{film}, k_{film}, and j thicknesses including that of the initial film, could be solved according to the ellipsometric and reflectometric readings taken at each point during anodization, using the same minimization computer program (13). Since for thin films such as those investigated here an interplay between the optical properties of substrates and film may yield different local minima, the (Δ_0, Ψ_0) readings taken at -0.9V were always used for the initial guess of the metal's properties in such a search for a minimum of F.

Both isotropic and nonisotropic uniform film models were tested. In the nonisotropic model different values were assumed for n_{film} in the direction normal to the surface, $(n_f)_n$, and parallel to it, $(n_f)_t$, with the same k_f in both directions. Results of the computer analysis based on a growth experiment extending up to 1.5V are summarized in Table I. It can be seen that method 2 of computation generated a better fit, *i.e.*, that solving the substrate is to be preferred to an assumption of film-free surface at any potential. It also shows that an absorption coefficient slightly different than zero in an isotropic film could be "traded-off" for a slightly anisotropic but transparent film. The refractive index evaluated is similar to that reported recently for much thicker anodic oxide films on Ti, the structure of which was shown to be that of crystalline anatase (40).

Figure 4 demonstrates the fit between the solution obtained for the single isotropic film model and the experimental optical results of another growth experiment conducted with a series of constant applied voltages. The curves in Fig. 4 which gave the best fit were due to the following optical properties of substrate and film: $n_{Ti} = 2.80$; $k_{Ti} = 3.25$; $n_{oxide} = 2.43$; $k_{oxide} = 0.0$. Some difference in the properties of the film as a function of the method of growth (linear potential scanning or large potential steps) can be seen to occur.

Since metal dissolution may have occurred to a small extent during the anodic scans employed (see current peak in Fig. 3), changes in the morphology of the metal substrate which could affect the optical parameters were possible in principle. The results obtained revealed, however, that film growth was not accompanied by appreciable changes in the optical properties of the Ti substrate surface under the experimental

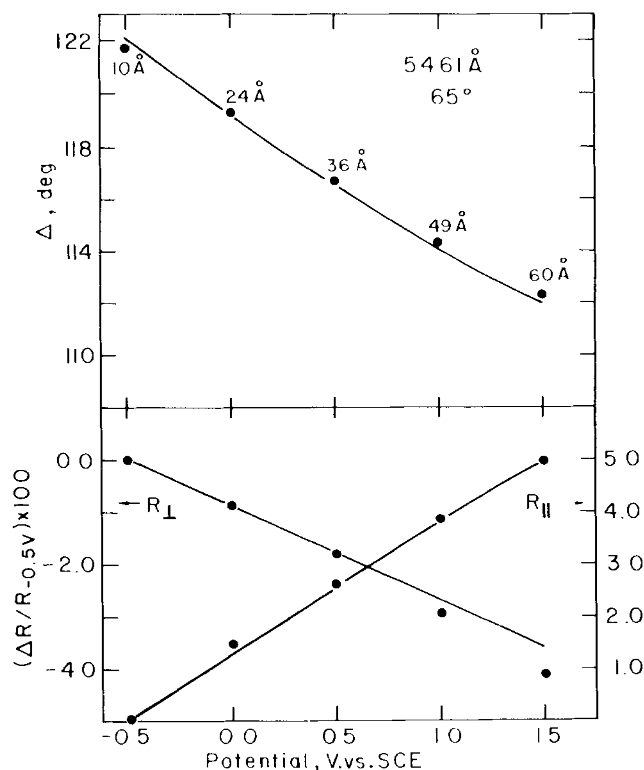

Fig. 4. Experimental and calculated optical changes during film growth. Points = experimental readings, solid lines = the computer solution for a single isotropic film model fitted according to all the optical measurements, with $\hat{n}_{film} = 2.43-0.0i$, $\hat{n}_{Ti} = 2.80-3.25i$.

conditions described above. Smoothing of the surface, which is to be expected when metal dissolution occurs simultaneously with oxide growth, should have brought about an increase of both $R_{||}$ and $R_{\perp}$, while in fact $R_{\perp}$ was found to decrease regularly (see Fig. 3). Any other type of a significant change in the optical properties of the metal substrate during anodization should have caused severe difficulties in the fitting of results of combined ellipsometric and reflectometric measurements to a model of single uniform film growth. Thus it seems that, under the experimental conditions employed, the optical effects must have been almost exclusively determined by the process of oxide growth, the contribution from a simultaneous limited metal dissolution process being minor.

The analysis of the optical results as presented above shows that "as-grown" thin TiO_2 films are found to be uniform and to have optical properties close to those of much thicker TiO_2 layers (1, 14, 40). Deviation of the electrochemical behavior of such thin films from that of bulk TiO_2 samples must be traced, therefore, to the sole effect of thickness. This is true provided, however, that the film has not undergone any further treatment following its growth (see below).

Table I. Optical properties and thicknesses of thin oxide layers on titanium

Model for film and calc method	n_M	k_M	$(n_F)_t$	$(n_F)_n$	k_F	$d_{-0.5V}$ (A)	A/V*	$\sum \frac{(X - X')^2}{\sigma^2}$**
Isotropic; method 1	2.76	3.22	2.35	2.35	0.02	7.5	22.9	$3 \cdot 10^{-1}$
Isotropic; method 2	2.79	3.22	2.33	2.33	0.03	9.8	23.1	$5 \cdot 10^{-3}$
Nonisotropic; method 1	2.75	3.22	2.39	2.47	0.0	7.3	22.1	$2 \cdot 10^{-1}$
Nonisotropic; method 2	2.82	3.24	2.38	2.46	0.0	11.4	22.1	$2 \cdot 10^{-4}$

* The increase of oxide film thickness per 1V of anodic applied voltage in the region of growth under constant field (see next section).

** X = measured parameter; X' = calc parameter; σ = experimental precision.

Evaluation of some physical properties of the thin films and kinetic parameters related to their growth according to the combined electrochemical and optical results.—For a mechanism of ionic migration under a high field, the current due to oxide growth depends on the field strength inside the film through Eq. [2], the theoretical foundation of which was given by Verwey (15) and Mott and Cabrera (16)

$$i = A \exp(\beta E) \quad [2]$$

where A and β are constants characteristic of the film, and E is the electrical field within the film. The parameters A and β could be solved according to the combined electrochemical and optical results obtained in linear scan experiments in the constant current region. Since in this region both the current and the growth rate (determined optically) were found to be constant, it could be safely assumed that the current efficiency for oxide growth was practically 100%. Furthermore, according to Vetter (17) a constant current implies no change in the potential drop across the oxide-electrolyte interface, and, hence, the total change of V apparently falls across the film. Therefore, in the region of constant current obtained in the linear potential scan experiments, the field across the film is given by

$$E = \frac{\Delta V}{\Delta e} = \frac{(dv/dt)\Delta t}{\int kidt} = \frac{(dv/dt)\Delta t}{ki\int dt} = \frac{dv/dt}{ki} \quad [3]$$

where dv/dt is the scan rate and k is the factor relating charge density to film thickness. The value of k could be easily determined according to film thicknesses obtained and the corresponding measured anodic charges. (Since uniform film growth was established optically, this implied a constant k, and, therefore, it could be taken, together with the constant measured current i outside the integral which appears in the denominator.) The final form of Eq. [3] implies that growth actually occurs under constant field conditions in the region in question, and Eq. [2] becomes

$$i = A \exp\left(\beta \frac{dv/dt}{ki}\right) \quad [4]$$

and a plot of ln i *vs.* $[(dv/dt)/i]$ gives β/k as the slope. Having determined k, β can be thus evaluated and A is computed next from Eq. [4]. Growth under constant field conditions could also be confirmed by some complementary constant current experiments shown in Fig. 5 in which the practically linear change with

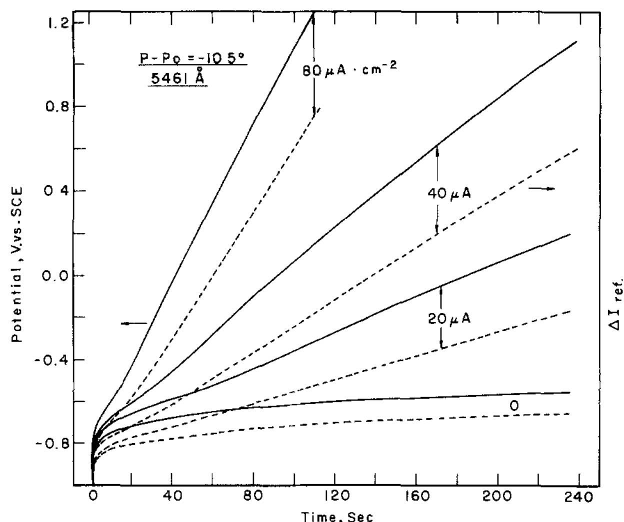

Fig. 5. Changes of the potential and of the light intensity under off-null settings in galvanostatic experiments of oxide growth on Ti (solution as in Fig. 2). The value of constant current applied in each case is designated in the figure.

time of both potential and thickness testify to this behavior. If k is known, two properties of the films grown may be further estimated: the density and the thickness of a monolayer

$$d \text{ monolayer} = kQ \text{ monolayer} \quad [5]$$

$$\rho \text{ film} = \frac{M}{n\mathrm{F}k} \quad [6]$$

where M is the molecular weight assumed for the surface compound (the value for TiO_2 was used) and Q monolayer may be taken as 880 μCb (4e process per Ti atom). The kinetic and physical parameters calculated from our measurements in thin oxide films may be compared to values given in the literature for thicker TiO_2 films, according to Table II.

Capacity measurements and the dielectric constant of the film.—Combined impedance and (optical) thickness measurements yield the dielectric constant of the film. Assuming that the admittance of the interface is due to the oxide film alone (*i.e.*, that the capacity of the Helmholz layer is much larger), it is given by

$$Z^{-1} = \omega\epsilon''\epsilon_0/d + i\,\omega\epsilon'\epsilon_0/d \quad [7]$$

where d is film thickness, ω is the angular frequency, ϵ', ϵ'' are the real and imaginary parts of the complex dielectric constant, and ϵ_0 the permittivity of free space. For a parallel circuit presentation

$$Z^{-1} = R_p^{-1} + i\,\omega\,C_p \quad [8]$$

hence

$$C_p = \epsilon'\epsilon_0/d \quad [9]$$

and a linear dependence of $1/C_p$ on d is expected.

C_p was determined for different stages of film growth as $(1/\omega)I_m(Z^{-1})$. A lock-in amplifier equipped with a phase-sensitive detector was used for this measurement to determine the component of the current at 90°C to the (10 mV ptp) sinusoidal voltage perturbation. The plot of $1/C$ *vs.* d (where d was found from the optical measurements) is given in Fig. 6. The linear dependence obtained is quite satisfactory, lending support to the optically evaluated thicknesses. It could be shown (Fig. 6) that $1/C_p$ was dependent on ω even at such low frequencies, which meant that the measured $\epsilon'(\omega)$ was somewhat lower than the static dielectric constant, due to some very slow dielectric relaxation processes in the film. The measured slope at ω = 100 Hz (Fig. 6) gave: ϵ' = 47. This value is inside the range quoted earlier for thicker TiO_2 films (1).

Electron transfer through the TiO_2 film.—Since it is not expected that thin films of TiO_2 such as those analyzed in this work should exhibit electron transfer properties identical with those of much thicker semiconductor (SC) films, and since the ease of electron transfer through the film may be an important condition for the interaction of the (TiO_2 covered) Ti metal with different oxidizing or reducing components of the electrolyte, possible deviations from the behavior predicted for thicker TiO_2 layers seemed worth looking into.

Rectification properties of thick anodic oxide films were observed long ago (20). While oxidation reactions appear to be inhibited by the oxide, H_2 evolution as well as some other reductions were found to proceed through the film (21, 22). The essential requirement for charge transfer between various redox sys-

Table II. Kinetic parameters and physical properties for oxide films on titanium

Quantity	This work	Other works	
β, cm V^{-1}	$6.8 \pm 0.2 \cdot 10^{-6}$	$5.6\text{-}6.8 \cdot 10^{-6}$	(18)
A, A cm^{-2}	$5 \cdot 10^{-15}\text{-}7 \cdot 10^{-17}$	$1 \cdot 10^{-13}\text{-}5 \cdot 10^{-14}$	(18)
d_o, monolayer thickness, cm	$5.2 \pm 0.2 \cdot 10^{-8}$	$5.0 \cdot 10^{-8}$	(19)
ρ, film density, g cm^{-3}	3.4 ± 0.2	2.5-4.0	(14)

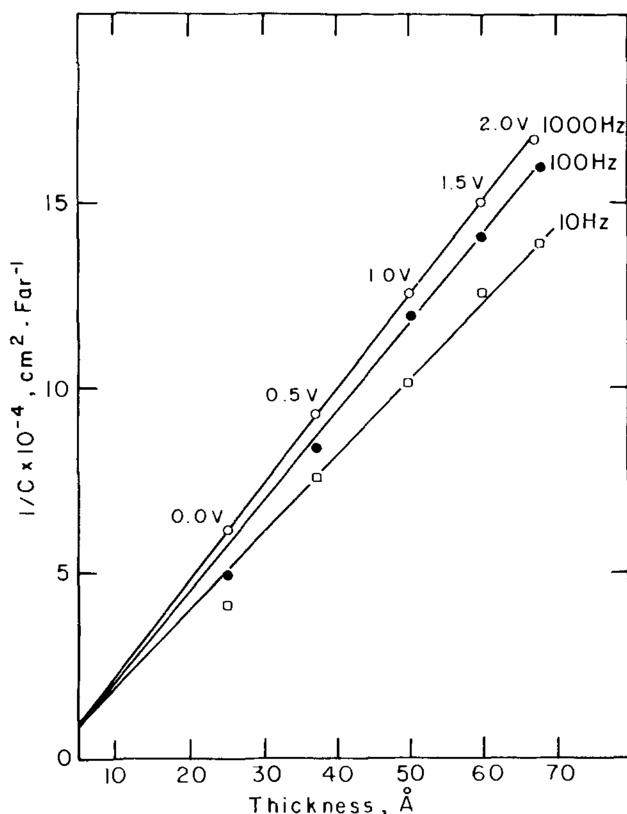

Fig. 6. The reciprocal capacitance for an oxide-covered Ti electrode, as obtained with these modulation frequencies, plotted against the optically determined thickness. (Solution as in Fig. 2).

tems in solution and the bands of a thick SC electrode is the energetic overlap between the SC bands at the surface and the so-called "Fermi level in solution" [which, to a first approximation, coincides with the standard redox potential of the relevant couple in solution (23)]. The energetic overlap condition and the magnitude of the potential gradient in the Helmholtz layer are expected to determine together the characteristics of thick n-type SC-aqueous electrolyte systems, which are expected to exhibit the following behavior (24): (*i*) Redox couples with standard potentials more negative than the flatband potential (FBP) should be able to exchange electrons with the conduction band of the SC in both directions, under small applied overvoltages. [The FBP nearly coincides with the energetic location of the SC conduction band relative to the reference electrode used (25).] (*ii*) Redox couples with nobler standard potentials (*i.e.*, energetically located within the SC bandgap) should not be able to exchange electrons with a n-type SC unless potentials more negative than the FBP are imposed, at which a cathodic process may occur. No anodic process is expected, however, for the last type of redox systems at a thick n-type SC electrode.

All the above-mentioned arguments have been put forward and shown to apply for thick n-type SC electrodes (26), including n-TiO_2 (27) [diagrams of electron energy levels in TiO_2 and in various redox couples in solution are given in Ref. (27)]. From recent measurements the value of the FBP has been evaluated for the single crystal TiO_2 as -0.3 ± 0.1V *vs.* SCE (28) and may be assumed as a first approximation to apply to the TiO_2 films dealt with here as well.

It was found in this work that any species which is known to be reducible at a gold or Pt electrode could be reduced also through the thin oxide films grown on the Ti electrodes (by the injection of electrons from the conduction band of the SC). Since this can be achieved only at electrode potentials more nega-

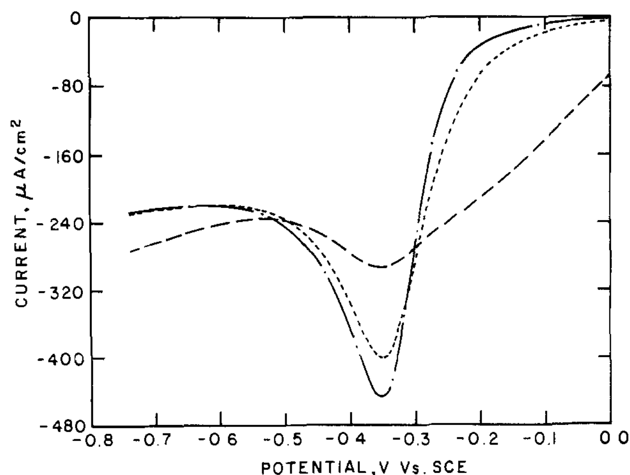

Fig. 7. Reduction of $Fe(CN)_6^{-3}$ at an oxide covered Ti. Solution as in Fig. 2 $+5\cdot10^{-3}$M $K_3Fe(CN)_6$; scan rate, 40 mV sec^{-1}. Curves a, b, and c correspond to films grown to 1.0, 1.5, and 5.0V vs. SCE, respectively.

tive than the FBP, an "overvoltage" for such reactions was always found for systems with standard redox potentials more positive than -0.3V *vs.* SCE. This behavior, as presented for the reduction of $Fe(CN)_6^{-3}$ in Fig. 7 was found to be independent of film thickness for $d > 20$Å, and is consistent with the general behavior of bulk n-TiO_2 electrodes. It could also be shown that a couple such as Cd/Cd^{+2}, with a standard redox potential of -0.75V (more negative than the FBP), indeed exhibited both the reduction and oxidation current peaks at the TiO_2 film electrode, while cupric and silver ions (E° of 0.05 and 0.34V, respectively) were reduced at the Ti/TiO_2 electrode but the corresponding metals were not oxidized (Fig. 8).

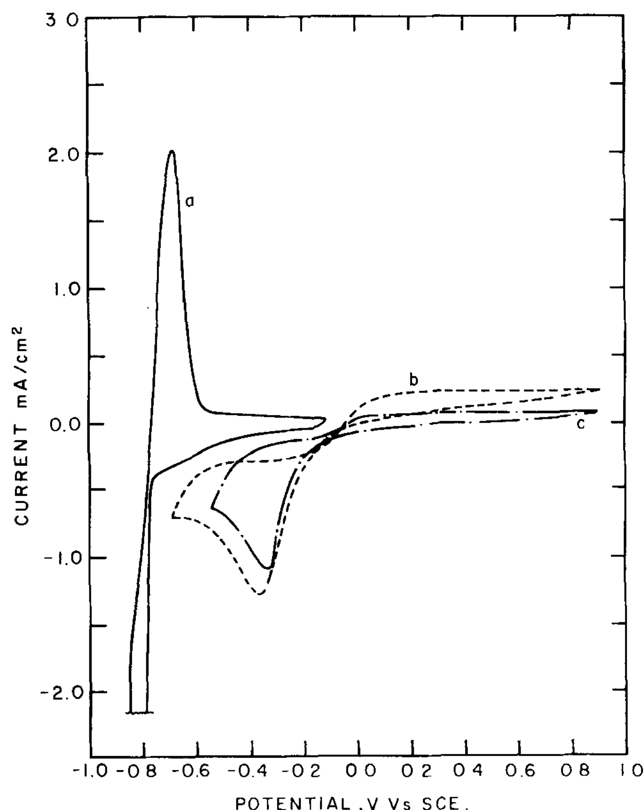

Fig. 8. Deposition and dissolution of metals at an oxide-covered Ti electrode. Solution as in Fig. 2 + 10^{-2}M of Cd^{+2} (curve a), Cu^{+2} (curve b), or Ag^{+} (curve c). Oxide film grown to 5.0V for the experiment with Cd^{+2} and to 2.0V for the experiments with the Cu^{+2} or Ag^{+} ions.

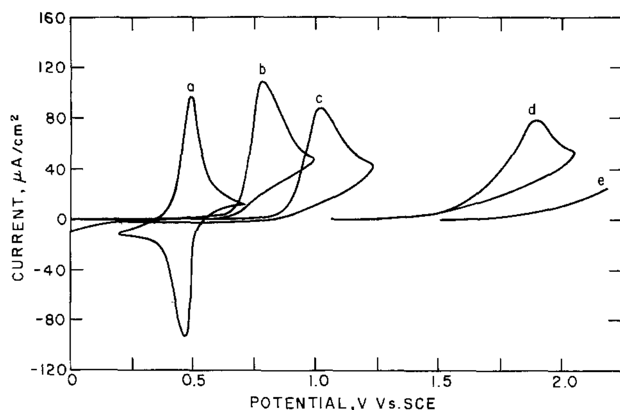

Fig. 9. Oxidation of I^- at an oxide-covered Ti electrode, with oxide films of different thicknesses. Solution as in Fig. 2 + 10^{-3}M NaI; scan rate, 20 mV sec^{-1}. Curve a, reference curve recorded at a gold electrode; curves b-e, at oxide films on Ti grown to 1.0, 1.5, 2.0, and 2.5V, respectively.

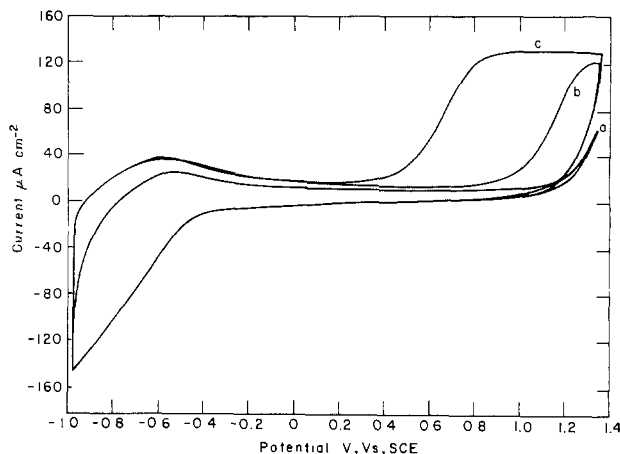

Fig. 10. Current-voltage curves for the reoxidation of reduced oxide layers on Ti. Curve a, continuous scanning; curve b, after 5 min holding at −1.0V; curve c, after 10 min holding at −1.0V. Solution as in Fig. 2; scan rate, 20 mV sec^{-1}.

Deviations from the regular behavior predicted for thick SC electrodes were also found, however, as presented for example by the oxidation of I^- ($E°_{I^-/I_2}$ = 0.5) in Fig. 9. Such oxidations were found to take place through the thin TiO_2 films, although they were shifted to higher anodic potentials with the increase of film thickness. Similar behavior was also found for oxidations of the $Fe(CN)_6^{-2}$ ion and of hydroquinone, both of which are not expected to undergo oxidation at thick TiO_2 electrodes. The effect of film thickness has an important role in such charge transfer processes, which apparently do not involve an electron transfer to the conduction bandedge, but rather the tunneling of an electron through the thin film to the Ti substrate. Such effects were observed before at highly doped SC electrodes with a narrow space charge region (29). It seems, therefore, that the oxidation of Ti_{aq}^{+3} at a TiO_2 (thin film) covered Ti electrode (30), which was shown to have a possible role in the self-repair mechanism of Ti, is not unique, and other oxidations may also take place through such thin TiO_2 films, although they are not expected to occur at thicker TiO_2 layers.

Oxide film reduction.—Recent contributions have dealt with changes in the optical properties of oxide films on metal electrodes, such as W (31), Mo (32), V (33), Ni (34), and Ir (35), which can be induced by modulation of the electrode potential. Such changes in the apparent optical properties indicate some changes in composition and structure of the oxide which may have a significant bearing on its electrochemical characteristics, including, possibly, its corrosion resistance (33). Figure 3 reveals that as the potential of the Ti electrode covered by an anodically grown TiO_2 film is scanned in the negative direction a reduction current appears at ~ −0.5V and the optical parameters start to change. The negative change of $R_{||}$ (the reflectivity at parallel polarization) associated with the cathodic current is found to be more pronounced than the changes of either Δ or $R_{\perp}$. This testifies to an increase of light absorption in the film as one of the results of the cathodic process, since oxide dissolution alone should return all the parameters evenly toward their original values while the increase of κ_{film} is expected to affect more strongly the value of $R_{||}$. The current recorded during a second anodic sweep, following the cathodic process (Fig. 10), shows, however, that reductive dissolution does occur to some extent: The current in the second anodic sweep is quite small at first, rising steeply at some voltage which is found to depend on the potential and duration of the cathodic treatment. This shows that the film has reached a smaller thickness by cathodic dissolution. As the voltage corresponding to that thickness is passed in the next anodic sweep, the field strength in the film exceeds the value required for renewed growth, resulting in the sudden increase of the anodic current.

In order to characterize completely the changes in the optical constants of the film caused by the reductive process, oxide films were grown at steady applied potentials of 3.0 or 4.0V, then reduced at −0.9V, further reduced at −1.2V, and at the end the electrode returned to the original anodic growth potential. The film's optical constants and thicknesses at each potential were determined according to the measured changes of the pair of ellipsometric and pair of reflectometric parameters. Table III illustrates results of two experiments of this kind. At −0.9V an increase of the refractive index is observed and at the more cathodic potential of −1.2V a significant increase in the absorption coefficient occurs. As may be seen, the reduction is also accompanied by some film dissolution.

Thermal reduction of TiO_2 (films or single crystals) by hydrogen has been reported to convert the TiO_2 from intrinsic to n-type semiconductors. This was explained by partial reduction of the TiO_2 to form a nonstoichiometric compound ("n-type TiO_2") in which the excess of Ti atoms acts as electron donors to the conduction band. The same effect was obtained by heating a vapor-deposited TiO_2 film in vacuum (36). On the other hand, the annealing of vapor-deposited TiO_2 in air was shown to increase its refractive index and specific gravity (14). This was explained by the conversion of the film from polycrystalline to the crystalline rutile form. It seems that electrochemical reduction of the oxide causes the same apparent changes as those which result from a combination of heat-treatment and thermal reduction.

The electrochemical reduction of the oxide and the associated increase in light absorption may most probably be explained in terms of a double-injection mechanism, such as that suggested by Faughnan, Crandall, and Heyman (31) to explain the electrochromism of WO_3:H^+ ions are injected into the oxide

Table III. Optical constants for the oxide on Ti at various potentials (at 5460Å)

Applied voltage (V)	i (μA cm⁻²)	n_f	k_f	d_f (A)
+3.0	+50	2.45	0.0	113
−0.9	−20	2.56	0.0	83
+3.0	+50	2.47	0.0	107
+4.0	+60	2.43	0.0	138
−0.9	−20	2.58	0.0	100
−1.2	−200	2.60	0.14	86
4.0	+60	2.40	0.0	135

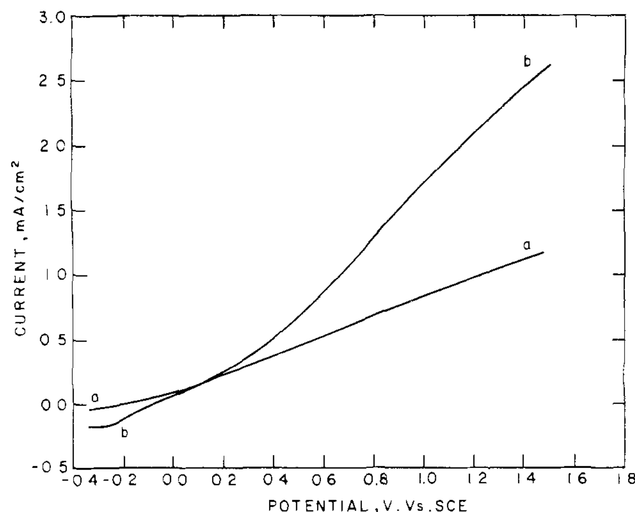

Fig. 11. Photocurrent at the oxide film on Ti, recorded when illuminated with u.v. light. Solution as in Fig. 2; scan rate, 10 mV sec^{-1}. Curve a, at the anodic film as grown; curve b, at the same film following its reduction at −1.3V for 5 min.

from the aqueous solution and electrons from the metal. Thus H atoms are introduced into the oxide and are probably bound to $O^{=}$ ions to form OH groups. Such incorporated H atoms lower the valence of some of the Ti ions to +3. The mixed valence oxide formed may exhibit either an intervalence transfer absorption or free carrier absorption, depending on the extent of the delocalization of the electrons due to the incorporated H atoms (31).

Figure 11 shows that electroreduction of the TiO_2 film resulted in a significant increase of its activity in the photooxidation of water (36). This result is quite understandable, since the increase in defect concentration as well as in the number of conduction electrons, both of which may cause the recorded increase of κ_f, is believed to assist in the photooxidation process (28, 37). It has to be noticed, however, that the anodic photocurrent obtained following film reduction is quite low for potentials smaller than 0.3V: curve b in Fig. 11 has a sigmoidal shape rather than increase quite steeply from 0.0V (38). This behavior depends on the applied potential and duration of the oxide film reduction and is probably associated with excessive trapping of photocarriers, as described in more detail elsewhere (39).

Acknowledgment

This work was supported by a grant from the U.S.-Israel Binational Science Foundation (BSF), Jerusalem.

Manuscript submitted July 13, 1977; revised manuscript received Oct. 31, 1977.

Any discussion of this paper will appear in a Discussion Section to be published in the December 1978 JOURNAL. All discussions for the December 1978 Discussion Section should be submitted by Aug. 1, 1978.

REFERENCES

1. F. Koover and M. J. Musselin, *Thin Solid Films*, **2**, 211 (1968).
2. J. R. Ambrose and J. Kruger, *Corrosion*, **28**, 30 (1972); *This Journal*, **121**, 599 (1974).
3. S. Gottesfeld and B. Reichman, *J. Electroanal. Chem.*, **67**, 169 (1976).
4. F. L. McCrackin, E. Passaglia, R. R. Stromberg, and H. L. Steinberg, *J. Res. A, Natl. Bur. Stds.*, **67**, 363 (1963).
5. S. Gottesfeld and B. Reichman, *Surface Sci.*, **44**, 377 (1974).
6. T. R. Beck, *This Journal*, **115**, 890 (1968).
7. T. R. Beck, *Electrochim. Acta*, **18**, 807 (1973).
8. E. L. Owen *et al.*, *Corrosion*, **28**, 292 (1972).
9. See, for example, S. Gottesfeld, M. Babai, and B. Reichman, *Surface Sci.*, **56**, 373 (1976).
10. W. Paatsch, *Ber. Bunsenges. Phys. Chem.*, **79**, 922 (1975).
11. T. Smith, *J. Opt. Soc. Am.*, **62**, 774 (1972).
12. S. Gottesfeld, M. Babai, and B. Reichman, *Surface Sci.*, **57**, 251 (1976).
13. F. James and M. Roos, *Comput. Phys. Commun.*, **10**, 343 (1975).
14. E. T. Fitzgibbons and W. H. Hartwig, NASA Tech. Rep. No. 86 (1970).
15. E. J. Verwey, *Physica*, **2**, 1059 (1935).
16. N. Cabrera and N. F. Mott, *Rep. Prog. Phys., N.F.*, **12**, 163 (1948).
17. K. J. Vetter, *Electrochim. Acta*, **16**, 1923 (1971).
18. H. A. Johnson, G. B. Adams, and P. Van Rysselberghe, *This Journal*, **104**, 339 (1957).
19. E. N. Paleolog, A. Z. Fedotova, and V. D. Fitulina, *Electrokhimiya*, **4**, 700 (1968).
20. L. Young, "Anodic Oxide Films," Academic Press, New York (1961).
21. P. F. Schmidt, F. Huber, and R. F. Schwartz, *J. Phys. Chem. Solids*, **15**, 270 (1960).
22. S. Shibamori, S. Yoshizawa, and F. Hine, *J. Electrochem. Soc. Jpn.*, **35**, 197 (1967).
23. H. Gerischer, *Photochem. Photobiol.*, **10**, 243 (1972).
24. H. Gerischer, in "Advances in Electrochemistry and Electrochemical Engineering," Vol. 1, P. Delahay and C. W. Tobias, Editors, Interscience Publishers, New York (1961).
25. W. P. Gomes and F. Cardona, *Z. Phys. Chem. N.F.*, **86**, 330 (1973).
26. D. Laser and A. J. Bard, *J. Phys. Chem.*, **80**, 459 (1976).
27. S. N. Frank and A. J. Bard, *J. Am. Chem. Soc.*, **97**, 7427 (1975).
28. J. M. Bolts and M. S. Wrighton, *J. Phys. Chem.*, **80**, 459 (1976).
29. B. Pettinger, H. R. Schöppel, and H. Gerischer, *Ber. Bunsenges. Phys. Chem.*, **78**, 450 (1974).
30. E. J. Kelly, *This Journal*, **123**, 162 (1976).
31. B. W. Faughnan, R. S. Crandall, and P. M. Heyman, *RCA Rev.*, **36**, 177 (1975).
32. T. C. Arnoldussen, *This Journal*, **123**, 527 (1976).
33. D. J. DeSmet, *Electrochim. Acta*, **21**, 1137 (1976).
34. M. A. Hopper and J. L. Ord, *This Journal*, **120**, 183 (1973).
35. S. Gottesfeld and S. Srinivasan, *J. Electroanal. Chem.*, In press.
36. K. L. Hardee and A. J. Bard, *This Journal*, **122**, 739 (1975).
37. S. M. Lu, F. H. Pollak, and R. M. Raccah, in Proceedings of the Workshop on Electrocatalysis on Non-metallic Surfaces, National Bureau of Standards, Gaithersberg, Md. (December 1975).
38. A. Fujishima and K. Honda, *Nature (London)*, **238**, 32 (1972).
39. S. Gottesfeld, S. Srinivasan, M. Yaniv, and D. Laser, *J. Phys.*, In press.
40. G. Blondeau, M. Froelicher, M. Froment, and A. Hugot-Leboff, *Thin Solid Films*, **38**, 261 (1976).

Anodic Polarization Behavior of Fe-Cr Surface Alloys Formed by Ion Implantation

B. S. Covino, Jr.,* B. D. Sartwell, and P. B. Needham, Jr.

Bureau of Mines, U.S. Department of the Interior, College Park Metallurgy Research Center, College Park, Maryland 20740

ABSTRACT

A new class of alloys has been fabricated by implantation of 25 keV chromium ions into the surface regions of iron in doses ranging from 1.0×10^{16} to 4.0×10^{16} Cr atoms/cm^2. The aqueous corrosion characteristics of these "surface alloys" have been studied under conditions of anodic polarization at 30°C in a helium-deaerated, sodium borate-buffered boric acid solution at a pH of 8.5 containing 2400 ppm Cl^-. The active-and passive-region corrosion characteristics are shown to be comparable to those of nominally equivalent standard bulk alloys. In addition, the electrochemical properties of one of the Fe-Cr surface alloys are compared with those obtained for the equivalent Fe-Ni surface alloy, and the results are interpreted as indicating that these corrosion characteristics are not due to defect production during implantation.

The formation of alloyed regions near the surfaces of metals using ion implantation is being investigated by the Bureau of Mines as a means of providing corrosion resistance while realizing a substantial reduction in the consumption of expensive alloying materials that are in limited supply (1). To date, these "surface alloys" have been fabricated by implanting chromium, nickel, aluminum, and cadmium ions into iron and by implanting aluminum ions into titanium. The concentrations of the alloy elements in the surface region have ranged from 3 to 30 atomic percent (a/o). These surface alloys have been tested for gaseous, electrochemical, and galvanic corrosion characteristics.

The surface alloys described in this paper were fabricated by implantation of the desired total implant dose, D, of 25 keV chromium ions into polycrystalline iron targets. In order to facilitate comparison of the anodic polarization characteristics of the implanted samples to those of standard bulk alloys, we have designated the surface alloys by the average chromium implant concentration a/o over the depth, δ (cm), containing 95% of the implanted chromium. The chromium depth distributions were determined experimentally using proton-excited x-ray analysis (PEX) coupled with argon-ion sputtering. From these distributions, δ was determined and the surface-alloy designation was calculated from N (atoms/cm^3) $= D/\delta$ and written as Fe-X(s)Cr where $X(a/o) = (N/8.5 \times 10^{22}) \times 10^2$ for iron.

Reported in this paper are anodic polarization results comparing the corrosion resistance of Fe-6(s)Cr, Fe-10(s)Cr, and Fe-19(s)Cr surface alloys with Fe, Fe-5%Cr, Fe-12%Cr, and Fe-18%Cr bulk alloys. The corresponding measured total ion doses for these surface alloys were 1.25×10^{16}, 2.20×10^{16}, and 4.0×10^{16} ions/cm^2, respectively. In addition, in order to make a preliminary determination as to whether the observed electrochemical corrosion characteristics were due to the formation of an alloy structure or to the production of radiation damage-type defects during the implantation process, the polarization characteristics of an Fe-Cr surface alloy are compared with those for an Fe-Ni surface alloy.

Experimental Techniques

The surfaces of the iron samples used in the fabrication of the surface alloys and the surfaces of the iron and iron-chromium bulk alloys used for anodic polarization studies were prepared using identical techniques. Each sample was cut from a high purity (99.95%) 1.5 mm thick sheet, polished through 600 grit paper, stress relieved at 600°C for 2 hr in an argon atmosphere, and then water quenched to prevent grain boundary precipitation of carbon. The samples were then cleaned in a dilute solution of sulfuric acid, rinsed thoroughly in distilled water, electropolished in a 9:1 ratio of glacial acetic acid/70% perchloric acid, rinsed in 18 MΩ water, and dried in a stream of dry nitrogen. The iron samples intended for implantation were immediately transferred to the vacuum chamber. The iron-chromium alloy samples intended for anodic polarization were placed into the electrochemical cells within minutes of the electropolishing step.

The polycrystalline iron samples were implanted in a vacuum chamber that had a base pressure of 1.33×10^{-6} Pa. During implantation, the pressure was $<6.6 \times 10^{-5}$ Pa. Twelve 2.5 cm diam samples were mounted on a carousel that continuously rotated through the 1.3 cm diam ion beam during implantation, resulting in a laterally uniform implanted strip. The samples were maintained at +150V for suppression of secondary electrons, and the total number of ions implanted into the samples was determined by an integrating current digitizer. Following implantation, at least two of the twelve samples were analyzed for residual carbon, oxygen, and other surface impurities using PEX prior to both the profiling and the electrochemical studies.

The composition depth profiles of the surface alloys were obtained using a technique, designated PEX-IS, that combined PEX with 1 keV argon ion sputtering. The argon ions were incident at an angle of 30° with respect to the sample surface, and 180 keV protons were used to excite Cr-K x-rays from the chromium implant region. This profiling technique has been described in detail elsewhere (2).

The anodic polarization characteristics of the surface alloys and bulk alloys were studied using standard electrochemical cells (3) modified to permit maximum agitation of the solution in front of the working electrode. The solution was 0.15N boric acid (H_3BO_3) buffered to pH 8.5 with sodium borate ($Na_2B_4O_7 \cdot 10H_2O$) and containing 2400 ppm Cl^- (as NaCl). The solution, consisting of reagent-grade chemicals mixed with 18 MΩ water, was maintained at a temperature of 30°C. High purity helium was bubbled through the solution at a rate of 6 liters per min to deaerate the solution and to minimize, by agitation, the effects of diffusion on the anodic polarization results. The surface and bulk alloys were mounted in Lexan compression-type holders using Viton O-rings with only

* Electrochemical Society Active Member.

Key words: ion implantation, anodic polarization, pitting potential, surface alloys, Fe-Cr.

0.8 cm^2 of the implant region exposed to the solution. The electrochemical parameters were measured using a Wenking 70TSI potentiostat, a Keithley 165 multimeter, and an X-Y recorder. Potentials were measured using a saturated calomel electrode/Luggin probe combination and are reported here *vs.* the normal hydrogen electrode (NHE).

The anodic polarization measurements were performed identically for iron, the bulk alloys, and the surface alloys. Prior to beginning the potential scan, the sample was cathodically reduced using the potentiostat in the galvanostatic mode. A cathodic current density of 5×10^{-4} A/cm^2 was used to reduce the air-formed oxide film on the metal surface. The sample was then allowed to achieve a steady-state open-circuit rest potential (E_R) for 10-15 min, following which the anodic polarization test was initiated at -100 mV with respect to E_R with the potential scanned at a rate of 10 mV/min.

Results

Prior to performing the anodic polarization measurements, representative surface alloy, bulk alloy, and electropolished iron samples were analyzed by PEX (1) to characterize the surface impurities. These measurements indicated that, for the electropolished iron and bulk alloys, the residual carbon coverage was approximately 1×10^{16} atoms/cm^2 (equivalent to about 9Å as graphite) and that the air-formed oxide film was less than 12Å thick.

After implantation, the surface alloys had residual carbon, silicon, and chlorine surface impurities as shown in Table I. These impurities were a result of neutrals drifting into the vacuum chamber from the ion source assembly in the ion-implantation system. The silicon originated in the silicon-based fluid used in the ion-implantation system oil diffusion pump. From the composition depth-profiling measurements, it was determined that about one-half of the measured carbon impurity concentration was actually distributed throughout the implant region, presumably due to recoil implantation of surface carbon atoms resulting from collisions with the incident ions. The chlorine and silicon, on the other hand, were found only on the sample surface.

Figure 1 shows the chromium implant profile obtained experimentally using PEX-IS for Fe-10(s)Cr ($D = 2.2 \times 10^{16}$ ions/cm^2) with the concentration plotted as a function of the sample depth in angstroms. The depth scale in angstroms was obtained by normalization of the experimental sputtering charge (*i.e.*, microcoulombs of incident argon ions) scale with an appropriate sputtering yield (4) for the sputtering of iron by 1.0 keV argon ions.

Figures 2-4 show the anodic polarization behavior of the Fe-6(s)Cr, Fe-10(s)Cr, and Fe-19(s)Cr alloys individually compared to all of the bulk metals and alloys. Each curve represents the average of six samples polarized at 10 mV/min. The electrochemical data presented in this report, relating surface alloys to bulk alloys, are interpreted under the boundary condition that an equivalent i_c means equivalent general corrosion resistance, an equivalent E_p means equivalent pitting corrosion resistance, and that these interpretations hold true only as long as the alloyed surface region remains intact. These three figures indicate that, in general, increasing the chromium content of both the surface and bulk alloys causes a decrease in the critical corrosion current, i_c, and shifts the pitting potential, E_p, toward more positive potentials. A comparison of Fe-6(s)Cr with Fe-5%Cr, Fig. 2, indicates that in the region generally attributed to anodic dissolution the alloys are quite similar electrochemically. The i_c's were identical, although the E_p for the Fe-5% Cr alloy was more positive. At

Table I. Average impurity coverages of carbon, chlorine, and silicon as determined by PEX for the Fe-Cr surface alloys used in the polarization studies

Surface alloy	Carbon (atoms/cm^2)	Chlorine (atoms/cm^2)	Silicon (atoms/cm^2)
Fe-6(s)Cr	7.0×10^{16}	5.5×10^{15}	1.1×10^{16}
Fe-10(s)Cr	3.0×10^{16}	1.3×10^{15}	ND[1]
Fe-19(s)Cr	8.0×10^{16}	ND	ND

[1] ND = Not detected.

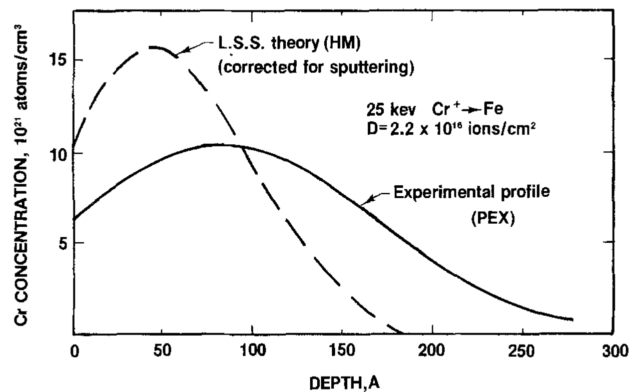

Fig. 1. Comparison of the depth distribution for 25 keV chromium ions implanted into iron as predicted by LSS theory modified to include sputtering of the substrate during implantation to that determined experimentally using PEX and low energy argon ion sputtering (IS).

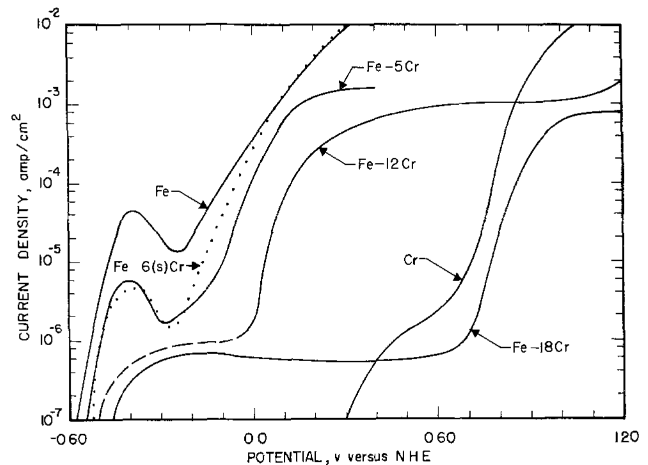

Fig. 2. Anodic polarization behavior (in borate-buffered *p*H 8.5 solution with 2400 ppm Cl^- addition) of Fe-6(s)Cr compared to polycrystalline Fe, Cr, and three Fe-Cr bulk alloys.

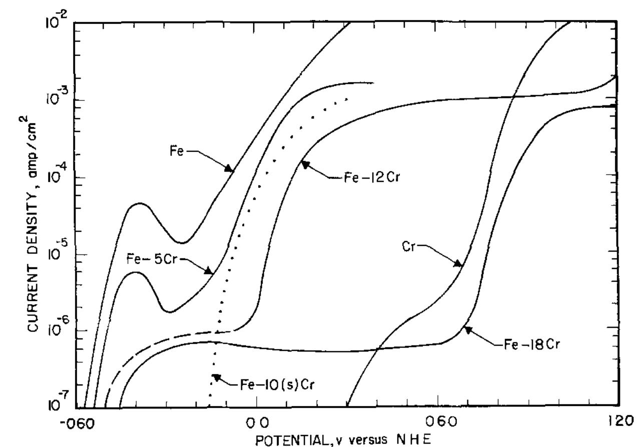

Fig. 3. Anodic polarization behavior (in a borate-buffered *p*H 8.5 solution with 2400 ppm Cl^- addition) of Fe-10(s)Cr compared to polycrystalline Fe, Cr, and three Fe-Cr bulk alloys.

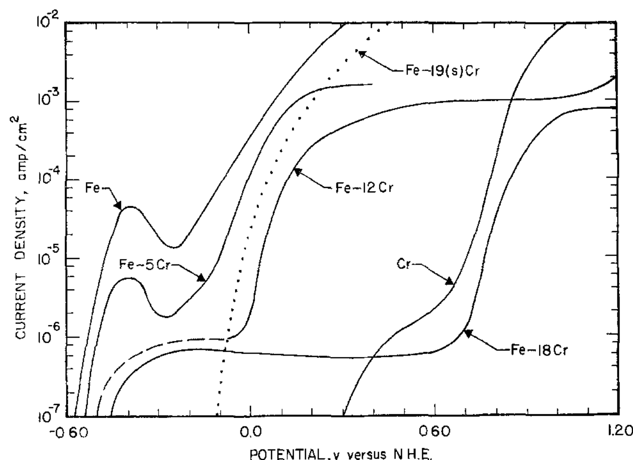

Fig. 4. Anodic polarization behavior (in a borate-buffered pH 8.5 solution with 2400 ppm Cl^- addition) of Fe-19(s)Cr compared to polycrystalline Fe, Cr, and three Fe-Cr bulk alloys.

the potentials associated with the transpassive region, the electrochemical behavior of the Fe-6(s)Cr was quite similar to that of iron.

In Fig. 3 and 4 the implantation of chromium ions to a concentration greater than 6 a/o is shown to not only shift the crossover potential, E_o, in the positive direction but to completely eliminate the region of anodic dissolution. For metals exhibiting this type of behavior, we have taken E_p as being equivalent to E_o. Compared with the bulk Fe-Cr alloys the surface alloys appear to be more protective at potentials negative with respect to the E_o's of the surface alloys. In addition, the sharp rise in current density associated with the surface alloys is attributed to the rapid pitting of the thin surface alloyed region while the bulk alloys exhibit a wide, low current density passive region.

Both the Fe-10(s)Cr, Fig. 3, and Fe-19(s)Cr, Fig. 4, indicate the onset of pitting corrosion without a prior region of anodic dissolution. Both alloys exhibit a pitting potential more negative than that of the Fe-12%Cr bulk alloy, implying a lower resistance to pitting corrosion. As the polarization proceeded into the transpassive region, the Fe-19(s)Cr shows a dissolution rate many orders of magnitude higher than the Fe-18%Cr; at a potential of +0.5V *vs.* NHE, the Fe-19(s)Cr dissolution rate is significantly higher than even that of the Fe-12%Cr.

Several iron and surface alloy samples were anodically polarized to +0.30V and then removed from the electrochemical cells for analysis by scanning electron microscopy (SEM). Figure 5 shows the resulting SEM analyses of iron and an Fe-10(s)Cr alloy. For iron, the dissolution occurred over the entire surface, whereas the dissolution of the Fe-10(s)Cr occurred only as a result of pit nucleation and propagation at inclusions, defects, and grain boundaries. Using an x-ray attachment on the SEM, it was determined that the chromium concentration outside the pits was the same as that for an unpolarized sample. No chromium was detected inside the pits.

Discussion

In Fig. 1 we have compared the experimentally determined chromium depth profile for the implanted iron samples to that predicted by the theory of Lindard, Sharff, and Schiott (LSS) (5). In using the LSS theory we have made a slight modification in the method of calculation in order to include the effects of sputtering of the iron samples by the chromium ions during implantation (1). Although for the present case of chromium this tends to shift the predicted distribution somewhat closer to the surface than is observed experimentally, for the case of nickel the method resulted in excellent agreement (2). From the experimental profile, the depth δ required in the calculation of the surface alloy concentration was determined to be 250Å.

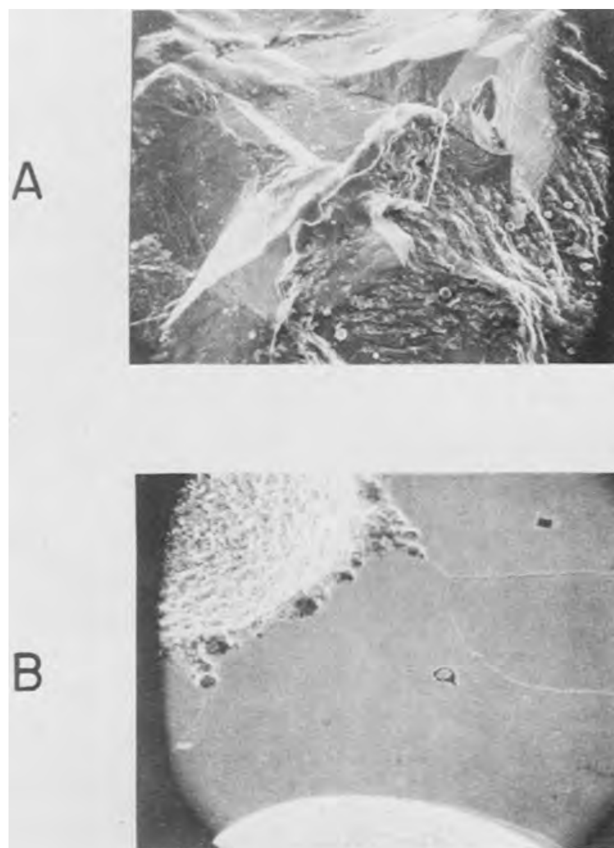

Fig. 5. SEM photomicrographs of (A) iron (magnification 600×) and (B) Fe-10(s)Cr alloy (magnification 1200×) polarized to +0.3V vs. NHE in a borate-buffered pH 8.5 solution with 2400 ppm Cl^- addition.

The polarization curves shown in Fig. 2 and 3 for the Fe-6(s)Cr and Fe-10(s)Cr alloys are shifted, with respect to iron, by an amount that is very close to that for the respective equivalent bulk alloy. The major difference is, as might be expected, their behavior in the high potential transpassive regions where dissolution resulting from pit nucleation at defects and grain boundaries has largely destroyed the nearby regions of the 250Å implant, with resulting dissolution kinetics approximating those of iron. The Fe-19(s)Cr is only slightly lower in pitting potential than the Fe-12%Cr, and the subsequent transpassive dissolution currents are substantially different than those of either Fe-12%Cr or Fe-18%Cr. The large difference between the pitting potential of Fe-19(s)Cr and Fe-18%Cr and the fact that the current density of Fe-19(s)Cr rises rapidly to that of pure iron indicate that the effect of the implanted chromium is, as might be expected, rapidly negated when the pits progress beyond the implanted region. Thus, in terms of pitting corrosion, the implanted chromium improves the resistance to pitting corrosion, but the amount of improvement cannot be directly correlated with nominally equivalent bulk alloy compositions. Since the definition used here for the surface-alloy concentration is somewhat arbitrary, caution must be exercised in making direct correlations between the observed corrosion characteristics for the surface and bulk alloys. From preliminary observations on the depth profiles, a more logical correlation may be between the amount of chromium in the first few tens of angstroms and the bulk alloy chromium concentration. The implication of such a correlation would be that substantially lower ion beam energies and smaller implant dosages would yield the same elec-

trochemical results as reported here. Such investigations are continuing.

In addition, the residual surface impurities present on the surface alloys should be taken into account in any interpretation of the anodic polarization results. The results presented here have indicated that the over-all corrosion resistance of the surface alloys increased with increasing chromium concentration. On the other hand, the quantities of the surface impurities were not a function of ion beam dose D, and, as shown in Table I, varied considerably for each type of surface alloy studied. It was concluded, therefore, that the corrosion resistances of the surface alloys were due principally to the effects of the implanted chromium and that the effects of the initial impurity coverages were at least minimal.

Finally, since other laboratories have demonstrated that corrosion behavior can be altered by radiation damage due to high rate, high dose ion implantation (6), it is desirable to determine whether the increased corrosion resistance obtained in these experiments was due to the formation of a specific alloy structure or was simply due to the production of defects caused by the collisions between the incoming ions and the lattice atoms. The ion current densities used in these studies have been kept below 500 nA/cm^2 to minimize the production of "dose-rate"-caused defects. Figure 6 compares anodic polarization data obtained for Fe-6(s)Cr to that obtained for Fe-6(s)Ni under identical electrochemical conditions. The Fe-6(s)Ni alloys were fabricated with 8.5×10^{15}, 25 keV Ni^+ $ions/cm^2$. If the shift in the effective pitting potential resulting from the implantation process was due to defect production, the Fe-6(s)Cr and Fe-6(s)Ni data would be expected to be essentially identical since defect production rates for Cr^+ and Ni^+ ions of the same energy are about the same (5). Clearly,

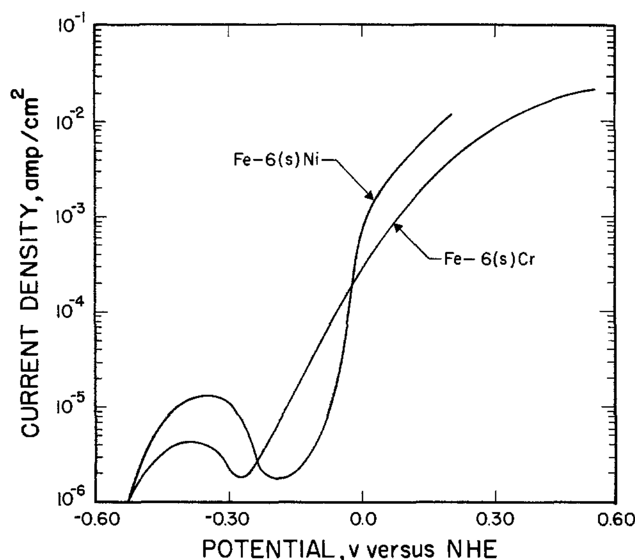

Fig. 6. Anodic polarization behavior (in a borate-buffered pH 8.5 solution with 2400 ppm Cl^- addition) of Fe-6(s)Cr compared to Fe-6(s)Ni.

the chromium and nickel surface alloys exhibit substantial differences in both the values of the i_c and E_p. We have attributed these differences to some, as yet undefined, alloy characteristics.

Summary

Surface alloys have been fabricated using the implantation of energetic chromium and nickel ions into the surface region of iron. The composition depth profiles of the Fe-Cr surface alloys have been compared to theoretical profiles modified to include sputtering of the iron during implantation.

Anodic polarization studies at 30°C in a borate-buffered boric acid solution (pH 8.5) containing 2400 ppm Cl^- to enhance pitting corrosion have demonstrated that electrochemical corrosion characteristics comparable to those of bulk Fe-Cr alloys are obtained through fabrication of Fe-Cr surface alloys. The mechanism of corrosion for the surface alloys was shown to be pit nucleation and propagation at crystal defects or grain boundaries, a result similar to that for bulk alloys. In the transpassive regions where pitting corrosion had largely destroyed the implant regions, however, the surface alloys, particularly the Fe-19(s)Cr, exhibited dissolution currents significantly higher than those of the equivalent nominal bulk alloys.

The results of a comparison of the anodic polarization behavior of Fe-6(s)Cr and Fe-6(s)Ni alloys have been interpreted as demonstrating that the improved corrosion characteristics obtained by surface alloying are due primarily to some unspecified alloy characteristics and are not due to the production of radiation damage-type defects.

Manuscript submitted July 25, 1977; revised manuscript received Oct. 18, 1977. This was Paper 58 presented at the Dallas, Texas, Meeting of the Society, Oct. 5-11, 1975.

Any discussion of this paper will appear in a Discussion Section to be published in the December 1978 JOURNAL. All discussions for the December 1978 Discussion Section should be submitted by Aug. 1, 1978.

Publication costs of this article were assisted by the Bureau of Mines, U.S. Department of the Interior.

REFERENCES

1. B. D. Sartwell, P. B. Needham, Jr., A. B. Campbell, and W. C. Lederer, "The Development of a New Class of Alloys Using the Techniques of Ion Implantation: Theory, Fabrication, and Physical Properties," To be published by the U.S. Bureau of Mines.
2. B. D. Sartwell, A. B. Campbell, and P. B. Needham, Jr., in "Ion Implantation in Semiconductors and Other Materials," F. Chernow, Editor, p. 201, Plenum Press, New York (1977).
3. N. D. Greene, "Experimental Electrode Kinetics," Rensselaer Polytechnic Institute, Troy, N.Y. (1965).
4. P. B. Needham, Jr. and T. J. Driscoll, Unpublished.
5. K. Bruce Winterbon, "Ion Implantation Range and Energy Deposition Distributions," Vol. 2, Plenum Press, New York (1975).
6. G. Dearnaley, P. D. Goode, W. S. Miller, and J. F. Turner, in "Ion Implantation in Semiconductors and Other Materials," B. L. Crowder, Editor, p. 405, Plenum Press, New York (1973).

Anodic Polarization Behavior of Fe-Ni Alloys Fabricated by Ion Implantation

B. S. Covino, Jr.,* P. B. Needham, Jr., and G. R. Conner*,[1]

Bureau of Mines, U.S. Department of the Interior, College Park Metallurgy Research Center, College Park, Maryland 20740

ABSTRACT

Surface alloys have been fabricated by implantation of 25 keV nickel ions into polycrystalline iron to doses ranging from 8.5×10^{15} to 3.4×10^{16} ions/cm^2. Their aqueous corrosion characteristics have been studied under conditions of anodic polarization at 30°C in a helium-deaerated sodium borate buffered boric acid solution (pH 8.5) containing 2400 ppm chloride ion. The pitting- and general-corrosion characteristics are comparable to nominally equivalent bulk commercial alloys and are superior to those of pure iron. A high strength maraging steel is shown to exhibit an increase in pitting-corrosion resistance due to the implantation of chromium ions.

Ensuring an adequate supply of critical materials such as nickel to meet national economic and strategic needs is a goal of the Bureau of Mines metallurgy research program. Ion implantation offers the potential of extending the usefulness of our supply of critical materials without sacrificing chemical or physical properties.

A group of iron-nickel alloys has been fabricated by the implantation of low energy metallic ions into the surface regions of polycrystalline iron. These alloys have been designated as surface (s) alloys (1) since the alloyed region extends only to a depth of 200Å below the iron surface. A potentiodynamic study of the characteristics of these alloys has been conducted in order to determine their characteristic critical current densities (i_c) and pitting potentials (E_p). These two parameters are an indication of the relative general- and pitting-corrosion resistances, respectively, and can be compared to equivalent parameters determined for commercial bulk alloys of known corrosion resistance. E_p is an operational parameter measured in an identical manner for all of the data reported here and is equivalent to the "critical breakdown potential" reported by other authors (2).

The surface alloys were prepared by implanting 25 keV nickel ions into 99.99% purity polycrystalline iron samples. The details of the technique have been extensively described elsewhere (3), and only a few brief remarks are made here. Prior to implantation, the iron surfaces were prepared using mechanical grinding, electropolishing, and high vacuum treatments that also have been described elsewhere (1, 4). The result of these surface preparations was a residual oxide coverage less than 10Å in thickness and a residual carbon surface impurity coverage of less than 1×10^{16} atoms/cm^2. The 25 keV nickel ions had a mean penetration depth of 38Å, and the final implant depth distribution was shown experimentally to be essentially Gaussian in character, with approximately 99% of the nickel located within the first 150Å (3). The surface alloy concentration has been defined, therefore, as the average concentration over this 150Å implant region. Implantation of nickel ions was used to fabricate surface alloys of 6 atom percent (a/o) (a dose of 8.50×10^{15} Ni^+ ions/cm^2), designated as Fe-6(s)Ni, and 25 a/o (a dose of 3.40×10^{16} Ni^+ ions/cm^2), designated as Fe-25(s)Ni. Tertiary surface alloys containing 15 a/o Ni (a dose of 2.05×10^{16} Ni^+ ions/cm^2) and 10 a/o Cr (a dose of 2.08×10^{16} Cr^+ ions/cm^2), designated as Fe-10(s)Cr-15(s)Ni, also were fabricated and studied. A commercial maraging steel, Vascomax 250 (V-250), was implanted with 25 keV chromium ions to a total dose of 2.08×10^{16} Cr^+ ions/cm^2. This resulted in an average concentration of 10 a/o chromium over the first 200Å.

The potentiodynamic polarization studies of both the surface and the bulk alloys were conducted in a high purity boric acid solution buffered to pH 8.5 with the addition of sodium tetraborate decahydrate and containing 2400 ppm Cl^- (as NaCl). The solutions were deaerated with helium, and the area in front of the electrode was rapidly stirred with the same gas to minimize the effects of diffusion on the polarization results. The polarization tests were conducted in standard 1-liter glass polarization cells that were cleaned with boiling HNO_3. The planar electrodes (test alloys) were mounted in an O-ring sealed Lexan electrode holder. The tests were conducted at 30°C with a polarization scan rate of 10 mV/min. The initial applied potential was −100 mV with respect to E_R, where E_R was the rest potential recorded after the electrode had stabilized following a cathodic reduction process. The electrode potential was maintained using a Wenking 70TSI potentiostat and was scanned with a Wenking VSG72 scan generator.

Results

The surface alloys, bulk alloys, and metals reported here were studied under identical electrochemical con-

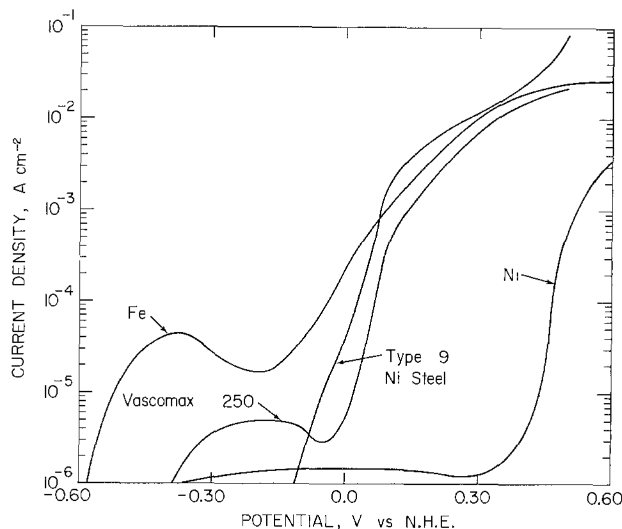

Fig. 1. Anodic polarization behavior (in a borate-buffered solution with 2400 ppm Cl^- addition) of polycrystalline iron and nickel and two commercial alloys.

* Electrochemical Society Active Member.

[1] Present address: Inficon, Inficon Leybold-Heraeus Incorporated, East Syracuse, New York 13057.

Key words: ion implantation, surface alloys, anodic polarization, pitting potential, Fe-Ni.

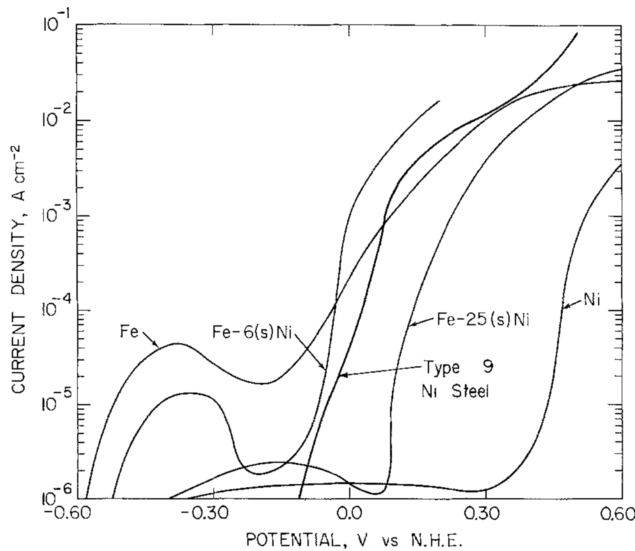

Fig. 2. Anodic polarization behavior (in a borate-buffered solution with 2400 ppm Cl$^-$ addition) of the surface alloys Fe-6(s)Ni and Fe-25(s)Ni compared with that for polycrystalline iron and nickel and one commercial alloy.

ditions. Figure 1 shows the results obtained for polycrystalline iron (99.99%), nickel (99.5%), V-250 (18% Ni), and Type 9 nickel steel (9% Ni) under these specific conditions. Each curve in this figure and in subsequent figures represents the average of a minimum of four tests. Figure 2 shows the results obtained for the Fe-6(s)Ni and Fe-25(s)Ni alloys compared with those obtained for pure iron, nickel, and Type 9 nickel steel. The electrochemical behavior of iron in a borate-buffered solution of pH 8.5 without the presence of Cl$^-$ indicates an i_c of 1-3 $\times$ 10^{-5} A/cm^2 with a definite passivation region extending from -0.20 to $+1.10$V *vs.* NHE (5, 6), the normal hydrogen reference electrode. The addition of 2400 ppm Cl$^-$ reduces the length of the passive region, increases i_c to 4.5 $\times$ 10^{-5} A/cm^2, and shifts E_p to -0.14V *vs.* NHE. E_p was determined graphically for each alloy by the intersection of tangents drawn from the passive region and the region of the current density *vs.* applied potential curve that exhibited the steepest slope. For those polarization curves that did not exhibit active dissolution regions, E_p was determined as the potential at which the current density was equal to 1 $\times$ 10^{-6} A/cm^2, generally the lowest measurable current density in these experiments. A comparison of the results obtained for iron with the results obtained for the Fe-Ni surface alloys shows three effects due to the surface alloying: (*i*) a substantial reduction in i_c; (*ii*) a shift of the crossover potential, E_o, toward the noble direction; and (*iii*) a shift of E_p toward the noble direction. The values for these parameters obtained directly from the curves in Fig. 2 are summarized in Table I.

Figure 3 contains the results for the Fe-10(s)Cr-15(s)Ni alloy, 316 L stainless steel (18% Cr, 12% Ni), Inconel 625 (61% Ni, 21.5% Cr), and the iron and nickel data from Fig. 1. The electrochemical parameters of interest are summarized in Table II and again indicate that the resistance to pitting corrosion is enhanced by surface alloying. In Fig. 4 results are shown

Table I. Electrochemical parameters from Fig. 2 where i_c ≡ critical current density, E_o ≡ the crossover potential, and E_p ≡ the pitting potential

Metal	i_c (A/cm^2)	E_o (V *vs.* NHE)	E_p (V *vs.* NHE)
Iron	4.5 × 10^{-5}	−0.58	−0.14
Fe-6(s)Ni	1.3 × 10^{-5}	−0.52	−0.12
Type 9 Ni steel	<<10^{-6}	−0.12	−0.12
Fe-25(s)Ni	2.5 × 10^{-6}	−0.40	0.08
Nickel	1.5 × 10^{-6}	−0.36	0.41

Table II. Electrochemical parameters from Fig. 3

Metal	i_c (A/cm^2)	E_o (V *vs.* NHE)	E_p (V *vs.* NHE)
Fe-10(s)Cr-15(s)Ni	<<10^{-6}	−0.09	−0.09
316 L SS	1.5 × 10^{-6}	−0.30	0.52
Inconel 625	1.1 × 10^{-6}	−0.20	0.59

Table III. Electrochemical parameters from Fig. 4

Metal	i_c (A/cm^2)	E_o (V *vs.* NHE)	E_p (V *vs.* NHE)
Iron	4.5 × 10^{-5}	−0.58	−0.14
Vascomax 250	5.0 × 10^{-6}	−0.39	0.01
Vascomax 250 + 10(s)Cr	2.0 × 10^{-6}	−0.13	0.05

for the electrochemical behavior of V-250 + 10(s)Cr, as compared with V-250 and pure iron. The relevant electrochemical parameters are summarized in Table III.

Discussion

The implantation of nickel ions into polycrystalline iron has been shown (Fig. 2) to produce results similar to those previously reported for Fe-Cr surface alloys (1). These results indicate a general trend, similar to those observed for Fe-Cr and Fe-Ni bulk alloys, for E_p to become more noble with increasing concentration of the alloying element. A similar type of behavior in bulk alloys has been interpreted by many in-

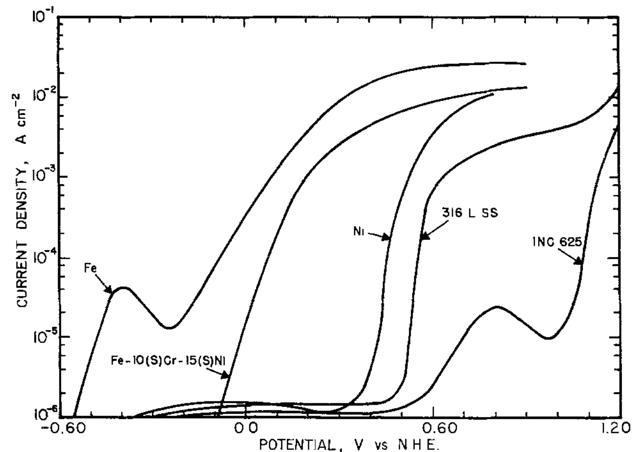

Fig. 3. Anodic polarization behavior (in a borate-buffered solution with 2400 ppm Cl$^-$ addition) of a tertiary surface alloy, Fe-10(s)Cr-15(s)Ni, compared with that for polycrystalline iron and nickel and two commercial alloys.

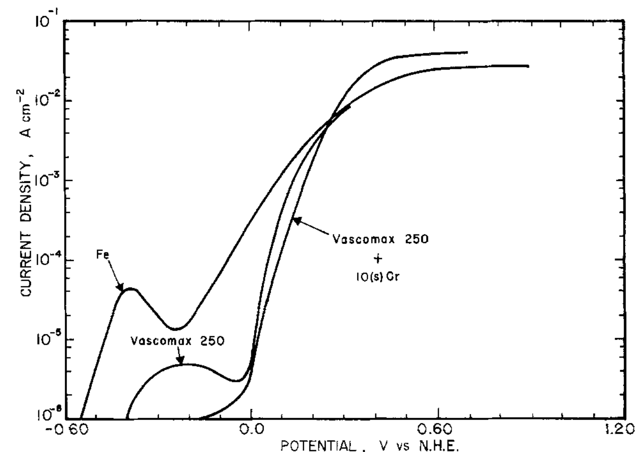

Fig. 4. Anodic polarization behavior (in a borate-buffered solution with 2400 ppm Cl$^-$ addition) of a maraging steel, after implantation of 25 keV Cr$^+$ ions to an average concentration of 10 a/o.

vestigators (2, 7, 8) to indicate an increase in the resistance of the alloy to pitting corrosion. Increasing the resistance to general corrosion by increasing either the nickel and/or the chromium concentration in bulk alloys is a well-known phenomenon. The electrochemical data reported here for the Fe-Ni surface alloys are interpreted as indicating that, since the active, passive, and transpassive regions for the surface alloys are similar to those for the equivalent bulk alloys, the over-all corrosion behavior could be expected to be the same. It has been reported previously (1) that the electrochemical results for an Fe-5% Cr bulk alloy were essentially identical to those for an Fe-6(s)Cr alloy up to a potential of +0.20V *vs.* NHE. At more anodic potentials, the implanted region was completely dissolved and the subsequent electrochemical behavior of the Fe-6(s)Cr alloy resembled that of pure iron. This was interpreted as indicating that as long as the alloyed surface region remains intact, the over-all corrosion resistance properties are the same. Similar conclusions are reached in this paper for the Fe-Ni surface alloys.

Table I shows that there is a decrease in i_c and an increase in E_p with increasing nickel implant concentration. The i_c approached a limiting value of 1.5×10^{-6} A/cm^2, the same value measured for pure nickel. The effect of the implanted nickel can be seen also as a shift of E_0 toward the same value as that for pure nickel. The decreasing i_c reflects the decreasing anodic dissolution; the increasingly more noble E_p reflects an increased resistance to pitting corrosion. The Fe-25(s)Ni alloy exhibits a more noble E_p than that measured for an Fe-19(s)Cr alloy (1) and has a pitting-corrosion resistance approximately equal to that of an Fe-12% Cr bulk alloy (1) (assuming that the surface alloyed region remains intact).

Two Fe-Ni commercial alloys, V-250 and Type 9 nickel steel, were tested. In addition to iron and nickel, the V-250 contains significant amounts of Co, Mo, Mn, and Ti. These additional alloying elements are probably detrimental to the over-all corrosion resistance since i_c for the V-250 was higher than that for the Fe-25(s)Ni alloy and the E_p was less noble than that for the surface alloy. The addition of the chromium, via implantation into the V-250, resulted in a decrease in i_c and a more noble value of E_p. The results for the V-250 + 10(s)Cr are interpreted as indicating a region of anodic dissolution, followed by pitting (indicated by the rapid rise in current density). The i_c was determined as the highest current density measured before the applied potential reached the value of E_p. A comparison of the results for the Fe-6(s)Ni alloy with those for the Type 9 nickel steel shows that the surface alloy exhibited a substantially higher i_c than the Type 9 nickel steel (which in fact exhibited no i_c at all). Also, the Type 9 nickel steel had an E_p slightly greater than that of the Fe-6(s)Ni alloy.

The commercial alloys, Inconel 625 and 316 L stainless steel (with an i_c of approximately 1.0×10^{-6} A/cm^2), each exhibited a much more noble E_p than the Fe-10(s)Cr-15(s)Ni alloy. The results for this multiple implant are comparable to those for the Type 9 nickel steel and the Fe-19(s)Cr alloy (1).

The implantation of nickel and chromium ions into iron and steels has been shown to have the potential for fabricating alloys with good general- and pitting-corrosion characteristics. In addition, high strength steels such as V-250 can have their surfaces alloyed to increase resistance to corrosion while at the same time retaining their designed bulk strength characteristics.

Manuscript submitted July 25, 1977; revised manuscript received Sept. 21, 1977. This was Paper 88 presented at the Las Vegas, Nevada, Meeting of the Society, Oct. 17-22, 1976.

Any discussion of this paper will appear in a Discussion Section to be published in the December 1978 JOURNAL. All discussions for the December 1978 Discussion Section should be submitted by Aug. 1, 1978.

Publication costs of this article were assisted by the Bureau of Mines, U.S. Department of the Interior.

REFERENCES

1. P. B. Needham, Jr., B. D. Sartwell, and B. S. Covino, Jr., *This Journal*, **125**, 366 (1978).
2. Ja. M. Kolotyrkin, *Corrosion*, **19**, (8), 261t (1963).
3. B. D. Sartwell, A. B. Campbell, and P. B. Needham, Jr., in "Proceedings of Fifth International Conference on Ion Implantation in Semiconductors and Other Materials," Plenum Press, New York (1977).
4. P. B. Needham, Jr., H. W. Leavenworth, Jr., and T. J. Driscoll, *This Journal*, **120**, 778 (1973).
5. T. Noda, K. Kudo, and N. Sato, *J. Jpn. Inst. Metals*, **37**, 951 (1973).
6. "The Development of a New Class of Alloys Using the Techniques of Ion Implantation," U.S. Bureau of Mines Report of Investigations, To be published.
7. Z. Szklarska-Smialowska, *Corrosion*, **27**, (6), 223 (1971).
8. A. A. Seys and A. A. Van Haute, *ibid.*, **29**, (8), 329 (1973).

HPLC Analysis of the Stereoisomers Obtained by Electrohydrodimerization of *p*-Hydroxybenzaldehyde

David F. Tomkins and John H. Wagenknecht*

Monsanto Company, Corporate Research Department, St. Louis, Missouri 63166

ABSTRACT

In contrast to previous reports, high pressure liquid chromatographic analysis (HPLC) of the 4,4′-dihydroxyhydrobenzoin formed by the electrohydrodimerization of *p*-hydroxybenzaldehyde showed that the ratio of *dl*- and *meso*-isomers did not vary significantly with various reduction mediums, the cathode material, or the concentration of aldehyde.

The electrochemical reduction of aldehydes and ketones in a divided cell leads to glycol/pinacol dimers in good yield under a variety of conditions (1, 2). Aldehydes and nonsymmetrically substituted ketones dimerize to form a mixture of stereoisomers and, by varying the reaction conditions, the ratio of *dl*/*meso*-isomers can be varied (1, 2). Also, the use of an

* Electrochemical Society Active Member.
Key words: electrohydrodimerization, *p*-hydroxybenzaldehyde, high pressure liquid chromatography, *dl*/*meso* ratio, glycol formation.

optically active solvent allows the *d* to *l* ratio to be varied (3).

The *dl*/*meso* ratio of the glycols from aromatic aldehydes can be varied over a small range with many aldehydes. However, *p*-hydroxybenzaldehyde seems unique in that it is reported to give pure *meso*-dimer in aqueous base (4, 5) and nearly pure *dl*-dimer in acidic solution (6). Our results with *p*-hydroxybenzaldehyde indicated that a nearly equal amount of *dl*- and *meso*-isomers of 4,4'-dihydroxyhydrobenzoin was formed under a wide variety of conditions, including those previously reported. However, an important difference was in the sample workup. Previous workers isolated the dimers before analysis; we developed a high pressure, liquid chromatographic procedure for analysis of the catholyte. The fact that no isolation was required eliminated possible preferential loss of one of the isomers (which have quite different solubility properties) during workup.

Experimental

The electrolyses were carried out in a glass frit divided H cell with a platinum foil anode and SCE reference electrode. The cathode materials are listed in Table I. Electrolyses at constant potential were carried out with a Wenking Model PCA 72H Potential Control Amplifier. Constant current electrolyses were carried out with a Lambda Model LP-412A-FM power supply. NMR spectra were obtained on a Varian T-60 spectrometer.

The HPLC was carried out with a du Pont Model 830 high performance, liquid chromatograph equipped with a gradient elution accessory and u.v. (254 nm) detector. The system was modified by the addition of a Waters Model U6K injector system and coupled with a Hewlett-Packard 7132A recorder and Autolab System IV (Spectra-Physics) integrator. The column was a μ-Bondapak C_{18} analytical (Waters Associates) reversed-phase column (4 mm ID × 30 cm). μ-Bondapak C_{18} is an octadecyltrichlorosilane permanently bonded to μ-silica particles. A mobile-phase gradient from pH = 3 H_2O—adjusted with H_3PO_4 (initial) to 50% MeOH pH = 3 H_2O (final)—using the concave gradient No. 3 at 5%/min was utilized for the determinations. The flow rate was adjusted to 2 ml/min. The suggested conditions for analysis required modification (reduced final methanol composition) depending upon column performance.

Analytical

An internal standard solution was prepared by the addition of 100 ml acetone to 1 liter methanol. The same internal standard solution was used for standards and samples.

A standard solution was prepared by accurately weighing 18 mg *p*-hydroxybenzaldehyde, 2 mg *p*-hydroxybenzoic acid, 9 mg *p*-hydroxybenzyl alcohol, and 40 mg 4,4'-dihydroxyhydrobenzoin and dissolving the mixture in 10 ml of 10% acetone/methanol solution (internal standard solution) and adding 2 ml of glacial acetic acid.

The sample reaction products were determined by pippeting a 1 ml sample into a 15 ml screw-capped vial and adding 10 ml internal standard solution and 2 ml glacial acetic acid.

The determination was accomplished by injecting 5 μl of standard solution, starting the gradient, and monitoring the effluent at 254 nm. The integrator was set to measure the peak areas accurately. The sample solution (5 μl) was injected after an approximately 15 min reequilibration time. The calculations were made utilizing the System IV integrator with established procedures employing the internal standard.

Reagents.—Solvents used for HPLC were methanol (u.v. grade "distilled in glass" [Burdick and Jackson]), water (obtained from Mili-Q system [Millipore Corporation]) acidified to pH 3.0 with H_3PO_4, acetone (reagent grade), and glacial acetic acid (reagent grade). Eastman *p*-hydroxybenzaldehyde was used for the electrolyses.

Electrolysis procedure.—The electrolyses carried out at Hg (6 cm^2) were stirred with a very small magnetic stirrer which did not cause large waves on the Hg surface which would give widely varying values of cathode potential because of the changing distance between the SCE and the Hg pool. The volume of the catholyte was 75 ml and the composition is listed in Table I. Electrolyses were carried to completion under N_2 and the quantity of electricity passed was measured by an in-series d-c motor attached to an odometer. Approximately 1**F** of electricity per mole of aldehyde was passed in each case. Analyses of the products formed in 80% ethanol were carried out at partial conversion, because at complete conversion the *meso*-isomer precipitated from solution, thus complicating the analyses. Analysis of the *dl*/*meso* ratio at periods throughout the electrolyses in aqueous base showed that no change in ratio occurred during the electrolyses.

The electrolyses at constant current (see Table I) were carried out with 30 ml of weil-stirrd, deaerated catholyte for sufficient time to dimerize 85% of the aldehyde. The only physical product isolation carried out is indicated below.

Product isolation and characterization.—The optimum product isolation from an electrolysis of 0.8*M* *p*-hydroxybenzaldehyde carried to completion in 1*M* NaOH was achieved by adjusting the pH to 9.0 with acetic acid and cooling the solution to 5°C. About 80% of the 4,4'-dihydroxyhydrobenzoin present will precipitate, giving a solid with a *dl*-*meso* ratio of approximately 0.45. The *dl*-*meso* ratio in the original solution was 0.77. Analysis of the filtrate by HPLC showed that the *dl*-isomer predominated in that solution. The dried solid melted at 215°C as observed by Allen (4). Recrystallization from pyridine gave *meso*-isomer, mp 242°C [lit. mp 244°-245° (5)]; NMR (pyridine d_5) δ 5.33 (s, 2, CHOH) and 7.42 (m, 8, aromatic). The tetraacetate of this isomer melted at 176°-177°C; NMR ($CDCl_3$) δ 2.00 (s, 6, OAc), 2.26 (s, 6, OAc), 6.05 (s, 2, CHOAc), and 7.13 (m, 8, aromatic) and had the proper elemental analysis. A sample of *meso* 4,4'-dihydroxybenzoin was neutralized with NaOH in water. The solution was concentrated until crystals formed. The assignment of the *meso* structure to this isomer was verified by x-ray crystallography. The full crystal structure will be published elsewhere.

A predominately *dl*-isomer of 4,4'-dihydroxyhydrobenzoin was obtained from the filtrate of the original isolation by concentrating the solution. Several recrystallizations and reprecipitations did not yield pure *dl*-isomer. However, by comparison with the spectrum of the *meso*-isomer it could be determined that the

Table I. Electrochemical hydrodimerization of *p*-hydroxybenzaldehyde

Cathode[a]	Solvent-electrolyte	*p*-Hydroxybenzaldehyde concentration	Cathode potential (V *vs.* SCE)	*dl*/*meso* ratio[b]
Hg	80/20 EtOH/H_2O-2*M* KO_2CCH_3	0.68*M*	−1.75	0.94
Hg	80/20 EtOH/H_2O-1*M* HO_2CCH_3, 1.3*M* LiCl	0.25*M*	−1.3	0.93
Hg	H_2O-1*M* NaOH	0.1*M*	−1.8	0.77
Hg	H_2O-1*M* NaOH	0.01*M*	−1.8	0.80
Hg	H_2O-1*M* NaOH	0.001*M*	−1.8	0.78
Hg	H_2O-0.38*M* Tetrabutylammonium hydroxide	0.1*M*	−1.8	0.89
Various[c]	H_2O-1*M* NaOH	0.8*M*	—[c]	0.77-0.81

[a] All electrolyses were carried out in a divided cell with a Pt foil anode.
[b] *dl*/*meso* ratio of 4-4'-dihydroxyhydrobenzoin formed in the reaction.
[c] Constant current electrolysis at Hg, Pb, Cd, Sn, glassy carbon and graphite. Current density of 100 mA/cm^2.

NMR absorption for the benzylidyne hydrogens in the *dl*-isomer occurs at $\delta = 5.14$ in pyridine d_5. We were unable to obtain the *dl*-tetraacetate free of *meso*-isomer by recrystallization; however, the predominately *dl*-tetraacetate had a satisfactory elemental analysis, and, by comparison with the NMR spectrum of the *meso*-tetraacetate, it could be determined that the NMR spectrum of the *dl*-tetraacetate in $CDCl_3$ was δ 2.08 (s, 6, OAc), 2.24 (s, 6, OAc), 6.03 (s, 2, C*H*OAc), and 7.04 (m, 8, aromatic).

Results and Discussion

The electrochemical reduction of *p*-hydroxybenzaldehyde was carried out under a variety of conditions. The results of the individual experiments are shown in Table I. The ratio of *dl/meso* was within an experimental error of 0.79 in all experiments carried out in 1*M* NaOH. In less basic media, the ratio was significantly higher. Although the change in ratio at various pH's was the same order of magnitude as reported by Stocker and Jenevein (7), the direction was opposite. The fact that changing electrode material and aldehyde concentration did not change the *dl-meso* ratio, and changing *p*H did, was consistent with previously reported results (3, 7).

A small effect on the *dl/meso* ratio was observed when tetrabutylammonium hydroxide was used in place of NaOH. The change is opposite in direction and much smaller, compared to the result obtained by Puglisi *et al.* (8), when quaternary ammonium ions were added to the electrolyte during reduction of benzaldehyde in acidic solution. Our results do not allow one to determine whether these dimerizations occur in the immediate vicinity of the electrode-solution interface or in the bulk solution, but they should eliminate the use of *p*-hydroxybenzaldehyde as an example of a highly stereoselective reaction.

A major difference between our results and those reported by others (4-6) seemed to be related to the new sample workup. The different solubilities of the *dl*- and *meso*-isomers caused separation of isomers during sample workup. Our analytical procedure (high pressure liquid chromatography) avoided separations prior to the analysis. The procedure is described in the Experimental section, and a sample chromatogram is shown in Fig. 1.

A reversed-phase system was employed using a nonpolar (octadecyltrichlorosilane) stationary phase with a polar solvent in the gradient elution mode. The *p*H of the initial H_2O solution was adjusted to *p*H 3 with H_3PO_4 to suppress the ionization of the phenolic compounds, thus enhancing the partition between the stationary and mobile phases. This ion-suppression technique increased the retention characteristics of the reaction products and allowed complete separation of components of interest using the gradient elution mode. Water, free of organic contaminants, was used to prevent extraneous peaks in the reversed phase mode.

The column needed special care to maintain separation efficiency. Useful column life was normally limited to approximately one month of continuous operation before resolution was irreversibly lost. During use, the column packing settled, producing a void at the column head and causing loss of efficiency. This void was refilled with μ-Bondapak C_{18} packing and the column was restored to nearly original efficiency.

Acetone was used as the internal standard of choice because its elution was in an area that was free from interferences. The high volatility and low absorbance of acetone limit its use as an internal standard, but other compounds tested as internal standards, including phenol and *o*-chlorobenzoic acid, were more affected by interferents and *p*H changes. These compounds, when used on an efficient column, also were satisfactory internal standards.

The pure *meso*-isomer was isolated and the tetraacetate prepared; however, the pure *dl* mixture could not be isolated. Pyridine d_5 proved to be an excellent

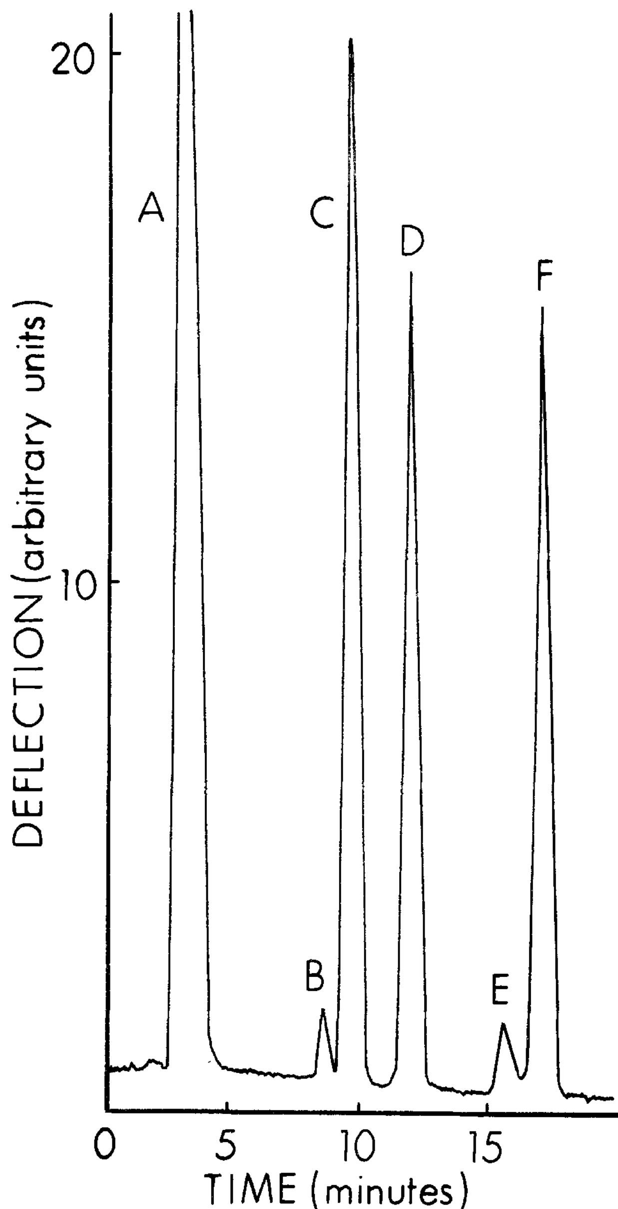

Fig. 1. HPLC analysis of the products of the electrohydrodimerization of *p*-hydroxybenzaldehyde. A, acetone (internal standard); B, *p*-hydroxybenzyl alcohol; C, meso-4,4'dihydroxyhydrobenzoin; D, *dl*-4,4'-dihydroxyhydrobenzoin; E, *p*-hydroxybenzoic acid (impurity in *p*-hydroxybenzaldehyde); F, *p*-hydroxybenzaldehyde.

solvent for NMR analyses of the dimers [as suggested by Snowden (2)] because of the widely differing chemical shifts of the benzylidyne hydrogen of the *dl*- and *meso*-isomers.

It has been shown previously (9) that when pinacols are treated with strong base the molecule may cleave to form two ion radicals (reaction [1]). If that reaction were to occur in aqueous base, it could explain the constant

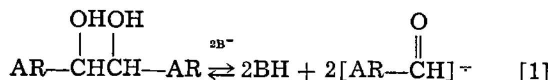

$$\text{AR—}\overset{\text{OH}}{\overset{|}{\text{C}}}\text{H}\overset{\text{OH}}{\overset{|}{\text{C}}}\text{H—AR} \underset{}{\overset{2B^-}{\rightleftarrows}} 2BH + 2[\text{AR—}\overset{\text{O}}{\overset{\|}{\text{C}}}\text{H}]^{\dot{-}} \quad [1]$$

dl/meso ratio in basic electrolyses. This was tested by warming the *meso*-isomer in 1*M* NaOH followed by HPLC analysis. No *dl*-isomer was detected in the sample.

We concluded from our results that changing the electrolysis conditions does not grossly affect the stereochemistry of the dimeric product obtained from the electroreduction of *p*-hydroxybenzaldehyde. The use of HPLC to analyze the products was an extremely useful tool for this type of study because isomer

losses in product isolation and/or derivatization were avoided.

Acknowledgment

The authors would like to thank Kenneth F. Koncki and John A. Long who carried out many of the experiments and analyses and Ray B. Stultz who performed the crystal structure analysis.

Manuscript submitted Oct. 13, 1976; revised manuscript received Nov. 7, 1977.

Any discussion of this paper will appear in a Discussion Section to be published in the December 1978 JOURNAL. All discussions for the December 1978 Discussion Section should be submitted by Aug. 1, 1978.

Publication costs of this article were assisted by Monsanto Company.

REFERENCES

1. L. G. Feoktistov, H. Lund, L. Eberson, and L. Horner, "Organic Electrochemistry," M. M. Baizer, Editor, pp. 355-366, 891-893, and references therein, Marcel Dekker, Inc., New York (1973).
2. F. W. Snowden, Ph.D. thesis, University of New Orleans (1975). Xerox University Microfilms, 75-23, 110, and references therein.
3. D. Seebach and H. A. Oei, *Angew. Chem. Int. Ed. Engl. Transl.*, **14**, 634 (1975).
4. M. J. Allen, *J. Am. Chem. Soc.*, **72**, 3797 (1950).
5. J. Grimshaw and J. S. Ramsey, *J. Chem. Soc.* (C), **1966**, 653.
6. F. W. Snowden, Ph.D. thesis, University of New Orleans (1975). Xerox University Microfilms, p. 100.
7. J. H. Stocker and R. M. Jenevein, *J. Org. Chem.*, **33**, 2145 (1968).
8. V. J. Puglisi, G. L. Clapper, and D. H. Evans, *Anal. Chem.*, **41**, 279 (1969).
9. M. A. Michel, G. Mousset, J. Simonet, and H. Lund, *Electrochim. Acta*, **20**, 143 (1975).

Semiconductor Electrodes XV. Photoelectrochemical Cells with Mixed Polycrystalline n-Type CdS-CdSe Electrodes

Rommel N. Noufi,* Paul A. Kohl,* and Allen J. Bard**

Department of Chemistry, The University of Texas at Austin, Austin, Texas 78712

ABSTRACT

Solid solutions of CdS and CdSe of different compositions were prepared by sintering pressed pellets and vacuum evaporation. The bandgap of the mixtures varied monotonically with percent composition between that of CdS and CdSe. Studies of the photoassisted oxidation of sulfide with these electrodes with a 1*M* Na_2S, 0.1*M* NaOH electrolyte showed that the flatband potentials (V_{fb}) of the mixtures were shifted toward negative potentials with respect to pure CdS and CdSe. Solar cells using these electrodes formulated as (x)n-CdS $(1 - x)$CdSe/1*M* Na_2S, 0.2*M* S, 0.1*M* NaOH/Pt are described. When $x = 0.9$, for a sintered pellet electrode, a power efficiency of 9% at a cell voltage of 202 mV (irradiation with 577 nm light of 1 mW/cm^2 intensity) was obtained.

There has been much recent interest in the application of n-type cadmium chalcogenide (CdX, where X = S, Se, or Te) electrodes to the construction of photoelectrochemical cells for the conversion of solar to electrical energy (1-14). These materials have bandgap energies (E_g) which are small enough ($\leq$2.4 eV) to capture a reasonable fraction of the solar spectrum and can be operated for long time periods with little or no decomposition of the semiconductor electrode in suitable electrolytes (*e.g.*, S^{2-}/S_x^{2-}). Cells with solar energy power conversion efficiencies ($\eta_{p,s}$) of 7-8% (9) and monochromatic light efficiencies ($\eta_{p,m}$) of 9-10% (4) using single crystal CdX electrodes have been reported.

The maximum efficiency of a photoelectrochemical cell utilizing a redox couple with an equilibrium potential, V_{redox}, for conversion of light to electrical energy with no over-all change in electrolyte composition depends upon the flatband potential of the semiconductor, V_{fb}. For a cell with an n-type semiconductor photoanode, the more negative the value of V_{fb}, the greater the possible output voltage (which has a maximum value $V_{redox} - V_{fb}$) and the larger the maximum efficiency. Thus optimization of the semiconductor-electrolyte characteristics involves variation of E_g for optimum match with the solar energy spectrum (15) and V_{fb}. Other semiconductor characteristics of importance include the doping level, which governs the material resistivity and the thickness of the space charge region at a given bias, the minority carrier lifetime in the bulk and at the surface, and the location and properties of intermediate levels within the gap region. We report here studies of electrodes produced by forming solid solutions of CdS and CdSe of different compositions prepared from sintered, pressed pellets or by vacuum evaporation and used as photoanodes in S^{2-}/S_x^{2-} electrolytes. The effect of composition and sample preparation on V_{fb}, E_g, efficiency and stability were of particular interest.

Experimental

The pellet semiconductor electrodes used in this study were prepared from high purity, reagent grade polycrystalline CdS and CdSe powder (Ventron, Beverly, Massachusetts). Mixtures of the two compounds, which are known to form solid solutions after sintering (16), were milled in acetone for 30 min prior to use. The 0.5 mm thick pellets were pressed at 5000 psi, sintered in a nitrogen atmosphere at 450°C for 12 hr, and then heated in a hydrogen atmosphere for 5 min. The densities of the pellets were about 87-89% of single crystal densities. An ohmic contact was made to the rear of each pellet with gallium-indium alloy. The resistance between the two faces of the pellet after sintering was generally less than 100Ω.

Electrodes were also prepared in a vacuum evaporation apparatus by vacuum deposition of the pure compounds and their mixtures on Pt and SnO_2-

* Electrochemical Society Student Member.
** Electrochemical Society Active Member.
Key words: photoelectrochemistry, solar cells, photovoltaic cells, semiconductors.

coated glass substrates (donated by Texas Instruments, Dallas, Texas). Before the deposition, the Pt substrates were boiled in concentrated nitric acid for 5 min followed by several rinsings with water and then with ethyl alcohol. The SnO_2-coated glass substrates were soaked in alcoholic KOH for 1 hr and rinsed several times with distilled water, followed by baking in an oven at 200°C for 2 hr. The semiconductor films, which were about 1.5 μm thick as determined by weighing the electrode before and after deposition, were annealed first in a nitrogen atmosphere at 400°C for 2 hr and then in a hydrogen atmosphere at 400°C for 5 min. The resistance between the film surface and conducting substrate was less than 1Ω.

A copper wire was attached to the electrodes with conducting silver epoxy cement (Allied Chemicals, New Haven, Connecticut). The back and sides of the electrodes were insulated with epoxy resin cement (Devcon Corporation, Danvers, Massachusetts). The exposed areas of the electrodes were 0.25-1.0 cm^2. The electrodes were etched in 6M HCl prior to use. The etching times for the sintered and film electrodes were about 15 and 5 sec, respectively. Both polycrystalline CdS and CdSe electrodes show a comparable increase in photocurrent after a similar etching step.

The semiconductors were used as the working electrode in a conventional three-electrode cell with a platinum foil counterelectrode and an aqueous saturated calomel reference electrode (SCE). The semiconductor electrodes were irradiated through an optically flat Pyrex window. The two-electrode, single compartment solar cell contained a platinum foil counterelectrode (about 10 cm^2) which was spaced about 0.5 cm from the semiconductor electrode. With this cell the current was measured as a function of load resistance under irradiation with no external power source.

The electrolyte solution (1M Na_2S, 0.2M S, and 0.1M NaOH) was yellow in color and a correction for absorption of the incident radiation by the solution was performed when calculating efficiencies.

For voltammetric measurements, a PAR (Princeton Applied Research, Princeton, New Jersey) Model 173 potentiostat and Model 175 universal programmer were employed. The current-voltage (i-V) curves were recorded using IR compensation on a Houston Instruments (Austin, Texas) Model 2000 X-Y recorder for scan rates less than 1 V/sec. Current-voltage curves at greater than 1 V/sec, obtained for capacitance measurements, were recorded on a Nicolet (Madison, Wisconsin) digital oscilloscope. An Oriel Corporation (Stamford, Connecticut) 450W xenon lamp and Model 7240 grating monochrometer were used to illuminate the electrodes. The radiant power was measured with a Model 550-1 Radiometer/Photometer (E.G. & G., Salem, Massachusetts).

ESCA and Auger electron analysis of the electrodes were carried out with a Physical Electronics Model 548 (Eden Prairie, Minnesota) instrument. The relative amounts of S and Se were determined from the area of the Se $3d_{5/2}$ peak at 54.18 eV as the amount of S increased in the mixture. Small amounts of carbon impurities were detected in the mixtures by Auger electron analysis. The x-ray diffraction spectrum (obtained with a Norelco x-ray diffractometer) of the mixed compound electrodes gave no lines characteristic of either of the pure components, indicating the mixtures were substitutional solid solutions.

Results

Electrode composition.—The composition of the electrodes prepared by sintering was known from the relative quantities of CdS and CdSe employed. The composition of the vacuum-deposited material was known approximately from the amounts of CdS and CdSe used as the source material and the known relative evaporation rates (16); the CdS content of the films was always higher than its relative amount in the source material. These films were analyzed by ESCA and x-ray diffraction, and the results, reported in Table I, are probably accurate to within 5% of the values listed. In general, the electrochemical behavior of sintered and vacuum-evaporated film electrodes of about the same composition was very similar, except where noted.

Table I. Properties of mixtures of CdS and CdSe[a]

Composition				
% CdS	% CdSe	E_g (eV)	$-V_{fb}$ (V vs. SCE)	V_{oc} (V)
Sintered pellets				
0	100	1.70	1.34	0.60
36	64	1.81	1.40	0.66
58	42	1.90	1.45	0.70
67	33	2.05	1.48	0.75
77	23	2.11	1.55	0.91
90	10	2.18	1.65	0.96
95	5	2.25	1.60	0.79
99	1	2.30	1.50	0.75
100	0	2.38	1.42	0.77
Vacuum-deposited films				
0	100	1.75	1.30	—
40	60	1.82	1.40	
63	37	2.00	1.50	
83	17	2.12	1.58	
100	0	2.40	1.40	

[a] For solution of 1.0M Na_2S and 0.1M NaOH under irradiation with white light.

E_g and V_{fb}.—The bandgap energy was determined by noting the longest wavelength (λ) which produced a photoanodic current with the electrode held at potentials 0.60-0.95V positive of V_{fb}. V_{fb} was estimated from the i-V curves and was taken as the potential for the onset of the photoanodic current. Typical i-V and i-λ curves for a film electrode are given in Fig. 1 and the rising portion of the photocurrent-V curves as a function of electrode composition is shown in Fig. 2. The shapes of the i-V curves were similar in solutions of 1M Na_2S and 0.1M NaOH, with and without dissolved sulfur. Values of E_g and V_{fb} for the

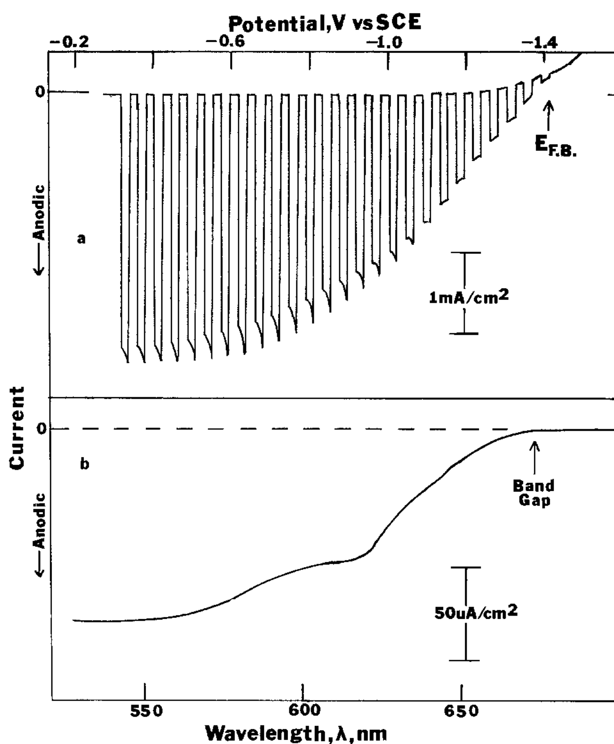

Fig. 1. (a) Photocurrent-potential curve (light chopped at 0.23 Hz); (b) photocurrent vs. wavelength at −0.8V vs. SCE, for the 40% CdS-60% CdSe evaporated film electrode in 1M Na_2S, 0.1M NaOH.

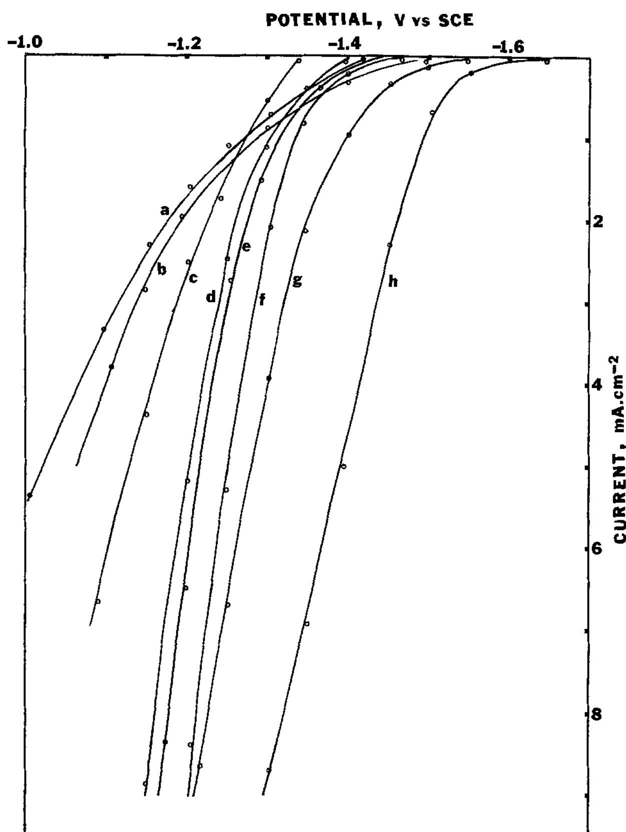

Fig. 2. Photocurrent-potential curves for pressed pellets of the following composition (illuminated with white in 1.0M Na_2S, 0.1M NaOH): (a) 100%CdS, 0%CdSe; (b) 99%CdS, 1%CdSe; (c) 0%CdS, 100%CdSe; (d) 36%CdS, 64%CdSe; (e) 58%CdS, 42%CdSe; (f) 67%CdS, 33%CdSe; (g) 77%CdS, 23%CdSe; (h) 90%CdS, 10%CdSe.

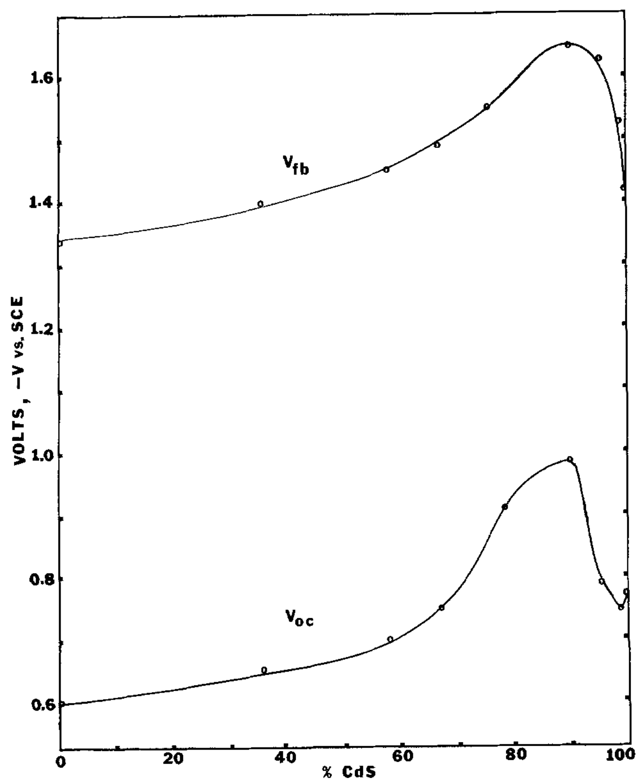

Fig. 3. Values of the flatband potential (V_{fb}) and open-circuit potential (V_{OC}) for pressed pellets containing different amounts of CdS and CdSe in a 1M Na_2S, 0.1M NaOH solution with Pt counter-electrode.

different electrodes are given in Table I; the variation of V_{fb} with electrode composition is shown in Fig. 3. Butler (17) has recommended that V_{fb} be determined not from the potential of onset of the photocurrent but from the extrapolated value of a plot of V *vs.* (photocurrent).[2] The trend in such extrapolated values with composition generally is the same as that in Fig. 3 but displaced to more positive values. Similar i-V behavior was observed in 0.1*M* NaOH alone, with the onset of photooxidation shifted in a positive direction by about 0.5V compared to the sulfide-containing solutions. In these solutions the electrodes underwent photodissolution to Cd^{2+}, S, and Se (with the appearance of a yellowish film in the case of CdS-containing electrodes and a gray film on the CdSe electrode) and the photocurrent decreased with time.

The dark anodic curent in 0.1*M* NaOH at the film electrodes appeared at potentials positive of 0V *vs.* SCE and bubbles were observed forming on the electrode surface. No dark anodic current was found at the sintered electrodes until potentials well positive of +1.0V *vs.* SCE. A cathodic current in 0.1*M* NaOH was observed at potentials just negative of V_{fb}, occurring at slightly more positive potentials at the film electrodes. Attempts to determine V_{fb} from Mott-Schottky plots (18), with the capacitance determined by cyclic voltammetry (19) over a potential range where no dark faradaic current was observed led to intercepts that were frequency dependent. The slopes of these plots showed doping levels between 10^{18} and 10^{20} cm^{-3}.

Efficiency and solar cells.—The quantum efficiency for electron flow, Φ_e, defined as the number of electrons flowing in the external circuit divided by the number of photons impinging on the electrode, was 100 ± 2% for all electrodes maintained at −0.70V *vs.* SCE. The open-circuit voltages, V_{oc}, of the two-electrode solar cells (x)n-CdS $(1 - x)$CdSe/1*M* Na_2S, 0.2*M* S, 0.1*M* NaOH/Pt measured between the illuminated sintered semiconductor electrode and the platinum cathode are listed in Table I. The maximum value of V_{oc} is $V_{fb} - V_{redox}$, where V_{redox} is −0.7V *vs.* SCE (4, 20-23). The trend in V_{oc} with electrode composition followed very closely that of V_{fb} determined from the i-V curves, with a maximum with an electrode composition of about 90% CdS-10% CdSe (Fig. 3). The open-circuit photopotentials were dependent on light intensity. For example, in the case of the measurement made using the 67% CdS-33% CdSe, when white light from the 450W xenon lamp was reduced by 50%, the open-circuit potential, V_{oc}, decreased from 0.75 to 0.66V; at intensities reduced to 10 and 1%, V_{oc} was 0.58 and 0.45V, respectively. Similar dependence was observed when measuring the potential drop through a 1000Ω resistor. This dependence on light intensity was also evident when measuring solar cell efficiencies. The $\eta_{p,s}$ of the 90% CdS-10% CdSe sintered material electrode was measured to be about 1% for solar intensities of about 75 mW·cm^{-2} compared to 5.9% with an attenuated solar intensity (using neutral density filters) of 1.1 mW·cm^{-2}. A similar decrease of efficiency with increasing irradiation intensity was also observed by Wrighton *et al.* (3, 4) in CdS and CdSe cells. The monochromatic light power efficiency, $\eta_{p,m}$, of the photoelectrochemical cell, defined as the ratio of the output power across the external load resistor to the incident radiant power, was determined with 577 nm light (12 nm bandpass) with an intensity of 1 mW·cm^{-2}. For the 90% CdS-10% CdSe sintered pellet with a 1000Ω load resistor, the output voltage was 202 mV and the current was 0.45 mA·cm^{-2}, yielding $\eta_{p,m}$ = 9%. The maximum value of $\eta_{p,m}$ found with the film electrodes was with the 60% CdS-40% CdSe material on Pt substrate with an 800Ω load resistor, and incident power of 0.4 mW·cm^{-2}. $\eta_{p,m}$ was 7% with an output voltage of 157 mV. The measured $\eta_{p,m}$ and $\eta_{p,s}$ values were quite vari-

able from electrode to electrode; this can be attributed to the high and variable internal resistance of the sintered electrodes and the poor adhesion of the vacuum evaporated films to the substrates, particularly the SnO_2-coated glass. Separate experiments in which the sintered electrodes were used as photoanodes in stirred solutions containing 1*M* NaS, 0.2*M* S, and 0.1*M* NaOH for periods (about 14 hr) which would have been sufficient to dissolve all the electrode material by photooxidation of the lattice showed weight loss of about 1%. This small loss was attributed to surface erosion of the pressed pellets during the long periods of stirring and soaking of the electrode. The stability of the cell current was dependent on the sulfide-polysulfide concentration. For example, when the solution contained 1*M* S and the initial current density was 16 $mA \cdot cm^{-2}$ (100Ω load) the current dropped to about 55% of its initial value in 14 hr. With 0.2*M* S, the current dropped to 26% of its initial value after the same period of time. Furthermore, when illumination was interrupted for several minutes and then resumed the onset current would reach a value slightly smaller than its initial value. After a 10 sec etch in 6*M* HCl, the current would attain almost its initial value.

Discussion

The mixtures (x)CdS $(1 - x)$CdSe gave the expected monotonic variation of E_g as the composition was changed from pure CdS to pure CdSe (16, 24). It is particularly interesting that the variation of V_{fb} with x shows a maximum (Fig. 3) with the mixture where $x = 0.9$ having a V_{fb} *ca.* 0.2V more negative than either pure CdS or CdSe. To seek the reason for this behavior let us consider the factors that affect V_{fb}. These include the electron affinity of the semiconductor (EA), the potential drop through the Helmholtz layer (V_H), the potential drop across the diffuse double layer (V_d), and the difference between the Fermi level and the conduction band ($E_F - E_C$); to put V_{fb} on a scale relative to a given reference electrode using the absolute EA (in eV), a constant term, E_{ref}, usually taken as *ca.* 4.75 eV for the SCE *vs.* the vacuum level (25) is used. The following equation, which is an extension of one given by Butler and Ginley (26), can then be written

$$V_{fb} = \frac{EA}{e} - \frac{E_{ref}}{e} - (V_H + V_d) + \frac{(E_F - E_c)}{e} \quad [1]$$

Taking $E_F - E_c$ as 0.10 eV, $E_{ref} \simeq 4.75$ eV, and assuming a negligible drop across the diffuse double layer ($V_d \sim 0$) this can be written

$$V_{fb}(V) \simeq \frac{EA}{e} - 4.7 - V_H \quad [2]$$

The values of V_{fb} for CdS and CdSe in NaOH and in the presence of S^{2-} taken from various sources are shown in Table II. The V_{fb} values for CdS and CdSe in sulfate media are independent of *p*H (4, 27) and the relative values agree quite well with those predicted from E_g and the intrinsic Fermi level ($E_F{}^i$) calculated by Nethercot (28) from electronegativities. In the latter case $E_F{}^i$ is calculated from the Pauling electronegativities for the atoms A and B (χ_A and χ_B) using the equation (28, 29)

$$E_F{}^i = 2.86(\chi_A\chi_B)^{1/2} \quad [3]$$

If one takes EA as the difference in energy between the conduction bandedge and vacuum (26), then

$$EA = E_F{}^i - E_g/2 \quad [4]$$

Calculated EA values are shown in Table II. When these values are used in Eq. [2], a V_H of about 0.9 (±0.1)V is obtained for both CdS and CdSe in the NaOH medium. The addition of S^{2-} causes the V_{fb} values to shift toward negative values by about 0.5V for CdS and 0.7V for CdSe (4) presumably because specific adsorption of S^{2-} causes a change in the voltage drop across the Helmholtz layer (to about 1.4 and 1.6V for CdS and CdSe, respectively).

Thus the change in V_{fb} with composition could be ascribed to changes in the EA or specific adsorption (V_H). The fact that the same sort of maximum of V_{fb} with composition is observed for NaOH solutions in the absence of S^{2-} suggests that this variation can be attributed to changes in the EA and that the introduction of small amounts of CdSe into the CdS lattice yields a material with a significantly smaller EA. However it is also possible that the composition of the surface layer of these electrodes changes upon immersion or operation in the sulfide electrolyte medium. Under these conditions a junction potential could arise between the surface layer and the bulk semiconductor which would affect the observed V_{fb} values obtained under illumination. Investigations of the changes in the electrode surfaces by ESCA and Auger electron spectroscopy are currently underway in this laboratory.

It is of interest to consider in a general way how the efficiency of a photoelectrochemical solar cell varies with E_g and V_{fb}. For irradiation with light of energy equal to that of the bandgap the maximum efficiency, or the so-called open-circuit voltage efficiency (15), is

$$\eta_{p,m}(\max) = \frac{(V_{redox} - V_{fb})e}{E_g} \quad [5]$$

Thus both the maximum output voltage and efficiency depend upon V_{fb}. When one considers the solar energy efficiency of a threshold semiconductor device the ultimate power efficiency, η_{ult}, depends upon the value of E_g [as given in Ref. (15), Eq. [2], and Fig. 3]. Thus, considering the variation of both V_{fb} and E_g, the maximum (open-circuit voltage) efficiency for solar irradiation is $\eta_{p,m}(\max)\ \eta_{ult}$; typical curves showing the efficiency (for AM1 sunlight) are given in Fig. 4. With these curves and the V_{fb} and E_g values

Table II. Characteristic data for CdS and CdSe

	V_{fb} (0.1 *M* NaOH) (V *vs.* SCE)	V_{fb} (1.0*M* Na_2S) (V *vs.* SCE)	$E_F{}^i$ [d] (eV)	E_g [e] (eV)	EA [f] (eV)
CdS	−0.90[a] −0.80[b]	−1.4[a] −1.42[c]	5.90	2.46	4.67
CdSe	−0.70[a]	−1.45[a] −1.34[c]	5.78	1.68	4.94

[a] From Ref. (4).
[b] From Ref. (4) and (27).
[c] This work.
[d] From Ref. (28), calculated using the following Pauling electronegativities (χ_P): Cd, 1.7; S, 2.5; Se, 2.4.
[e] From Ref. (28)
[f] Calculated using Eq. [4].

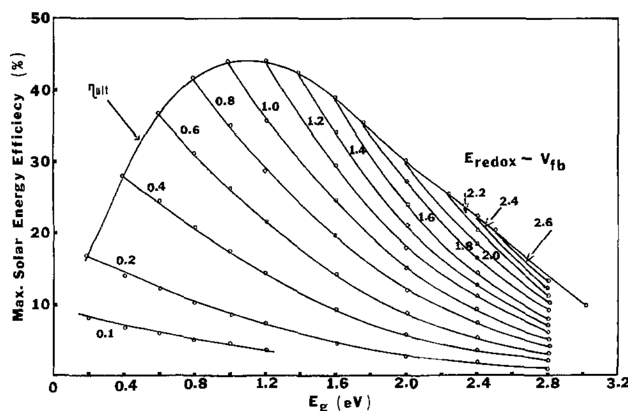

Fig. 4. Maximum solar efficiency (AM1 sunlight) for various values of E_g and ($V_{redox} - V_{fb}$). Values of η_{ult} used in preparing this figure from (15).

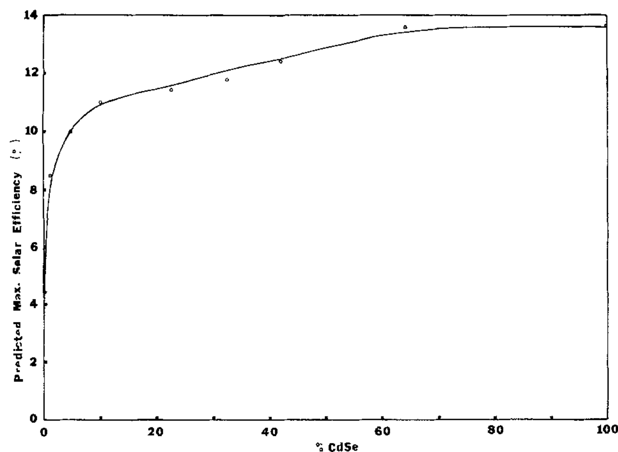

Fig. 5. Predicted maximum solar efficiency vs. composition for the (x)CdS $(1 - x)$CdSe system with S^{2-}, S_x^{2-} electrolyte.

of the various CdS-CdSe mixtures a plot of maximum solar efficiency as a function of composition can be derived (Fig. 5). The results suggest that the addition of only a small amount of CdSe greatly improves the maximum efficiency of a CdS electrode. Although the efficiency in this case is smaller than that of CdSe alone, this principle when applied to other systems could, by suitable manipulation of V_{fb} and E_g, yield higher efficiencies than the pure compounds.

Solid solutions such as (x)CdS $(1 - x)$CdSe may also be utilized in preparing a film electrode with a gradient composition, *i.e.*, an increasing CdSe content with depth. This would allow one to take advantage of the negative shift in V_{fb} at the solution interface (with high CdS content), and to absorb a greater fraction of the visible spectrum further into the space charge region (with the higher CdSe content). Work is currently being carried out in our laboratory to improve the conductivity of the pellets and extend the concept of solid-state solutions to other semiconductor systems.

Acknowledgment

The support of this research by the National Science Foundation and the Robert A. Welch Foundation is gratefully acknowledged.

Manuscript submitted Aug. 15, 1977; revised manuscript received Oct. 27, 1977.

Any discussion of this paper will appear in a Discussion Section to be published in the December 1978 JOURNAL. All discussions for the December 1978 Discussion Section should be submitted by Aug. 1, 1978.

Publication costs of this article were assisted by The University of Texas at Austin.

REFERENCES

1. A. B. Ellis, S. W. Kaiser, and M. S. Wrighton, *J. Am. Chem. Soc.*, **98**, 1635 (1976).
2. A. B. Ellis, S. W. Kaiser, and M. S. Wrighton, *ibid.*, p. 6418.
3. A. B. Ellis, S. W. Kaiser, and M. S. Wrighton, *ibid.*, p. 6855.
4. A. B. Ellis, S. W. Kaiser, J. M. Botts, and M. S. Wrighton, *ibid.*, **99**, 2839 (1977).
5. G. Hodes, J. Manassen, and D. Cahen, *Nature (London)*, **261**, 403 (1976).
6. C. Hodes, D. Cahen, and J. Manassen, *ibid.*, **260**, 312 (1976).
7. J. Manassen, G. Hodes, and D. Cahen, *This Journal*, **124**, 532 (1977).
8. B. Miller and A. Heller, *Nature (London)*, **262**, 680 (1976).
9. A. Heller, K. C. Chang, and B. Miller, *This Journal*, **124**, 697 (1977).
10. T. Inoue, T. Watanabe, A. Fujishima, K. Honda, and K. Kohayakawa, *ibid.*, **124**, 719 (1977).
11. H. Minoura, T. Oki, and M. Tsuiki, *Chem. Lett.*, **1279** (1976).
12. Y. G. Chai and W. W. Anderson, *Appl. Phys. Lett.*, **27**, 183 (1975).
13. H. Gerischer, *J. Electroanal. Chem.*, **58**, 263 (1975).
14. H. Gerischer and J. Gobrecht, *Ber. Bunsenges. Physik. Chem.*, **80**, 327 (1976).
15. M. D. Archer, *J. Appl. Electrochem.*, **5**, 17 (1975).
16. N. I. Vitrikhouskii and I. B. Mizetskaya, in "Growth of Crystals," Vol. 3, p. 247, Consultants Bureau, New York (1962).
17. M. A. Butler, *J. Appl. Phys.*, **48**, 1914 (1977).
18. H. Gerischer and W. Mindt, *Electrochim. Acta.*, **13**, 1329 (1968).
19. R. N. Noufi, P. A. Kohl, S. N. Frank, and A. J. Bard, *This Journal*, **125**, 246 (1978).
20. W. M. Latimer, "The Oxidation States of the Elements and Their Potentials in Aqueous Solutions," Prentice Hall Inc., New York, (1952).
21. J. J. Lingane and L. W. Niedrach, *J. Am. Chem. Soc.*, **70**, 4115 (1948).
22. A. J. Panson, *J. Phys. Chem.*, **67**, 2177 (1963).
23. P. L. Allen and A. Hickling, *Trans. Faraday Soc.*, **53**, 1626 (1957).
24. E. T. Handelman and W. Kaiser, *J. Appl. Phys.*, **35**, 3519 (1964).
25. F. Lohmann, *Z. Naturforschg.*, **22A**, 843 (1967).
26. M. A. Butler and D. S. Ginley, Private communication (1977).
27. T. Watanabe, A. Fujishima, and K. Honda, *Chem. Lett.*, 897 (1974).
28. A. H. Nethercot, Jr., *Phys. Rev. Lett.*, **33**, 1088 (1974).
29. R. T. Pool, D. R. Williams, J. D. Riley, and J. G. Jenkin, J. Liesengang, and R. C. G. Leckey, *Chem. Phys. Lett.*, **36**, 401 (1975).

Coulostatic Deposition of Metals at Underpotential

I. Potential Relaxation in the Absence of Chemical Reactions

D. F. Untereker,*[,1] W. G. Sherwood,*[,2] and Stanley Bruckenstein*

Chemistry Department, State University of New York at Buffalo, Buffalo, New York 14214

ABSTRACT

Under commonly occurring conditions, coulostatic processes can lead to underpotential deposition of a metal on a foreign metal substrate. These deposition processes are described quantitatively in terms of the isotherm for underpotential metal deposition, the double layer capacitance of the electrode surface, and the initial potential of the electrode. Coulostatically controlled underpotential deposition is demonstrated for silver on gold and platinum and for mercury on gold.

The process of underpotential deposition (UPD) of metals has been studied by a number of workers (1) since the original studies of Haissinsky (2) and Rogers (3). An understanding of UPD can give insight into the nature of the interactions occurring at the interface between two metals. Such insight can be used for a variety of purposes, such as to produce electrocatalytic surfaces of controlled activity. Thus, it is important to know when UPD has occurred. To date, UPD phenomena have been assumed to occur only when charge flows in the external circuit and no recognition was given to the possibility of unsuspected UPD processes occurring under zero current conditions. Several years ago we discovered a zero current UPD phenomenon in the course of rotating platinum ring-platinum disk electrode studies. It was noted (4) that some shielding of Ag^+ ion could be detected at the ring electrode of a rotating platinum ring-disk electrode when it was immersed in $\sim 10^{-5}M$ Ag^+ dissolved in 0.2*M* H_2SO_4, even though the disk electrode was at open circuit. In addition, after the shielding ceased, electrooxidation of the disk produced a collection current at the ring for a species having the properties of Ag^+. As is shown below, these phenomena are the result of UPD of silver occurring via coulostatic discharge of the double layer capacitance.

The purpose of this work is to quantitatively describe the coulostatic mechanism of UPD. Our theoretical description has been confirmed using the rotating ring-disk electrode (RRDE) on the systems Ag^+/Ag on Pt, Ag^+/Ag on Au, and Hg^{2+}/Hg on Au.

Theoretical

Coulostatic discharge processes for the electrochemical reaction

$$A \pm ne = B \quad [1]$$

are well understood when A and B are both soluble species. However, no treatment exists for the case where A is soluble and B deposits on a solid electrode surface in a uniform layer such as occurs in UPD of metals.

Let us carry out a coulostatic experiment at a solid electrode in the presence of M^{n+} which can deposit at underpotential. Assume that the isotherm for UPD of M is given by curve 1 of Fig. 1 and is represented by Eq. [2]

$$\theta = \mathbf{F}(E) \quad [2]$$

At potentials anodic to $E_{\theta=0}$, the surface coverage, θ, of M is zero and at potentials more cathodic than $E_{\theta=0}$, θ increases to one at $E_{\theta=1}$. We make no assumptions concerning the net charge on the UPD species other than it lies between n and 0. If the electrode potential is set originally so that $\theta = 0$, and then it is stepped to E_i, UPD of M will eventually occur if $E_i < E_{\theta=0}$. However, if before any significant UPD can take place, this electrode is disconnected from the external circuit, only coulostatic processes can be operative. The key points of our argument are that once the potential of the electrode is made more cathodic than $E_{\theta=0}$, and the electrode is disconnected from the circuit: (*i*) UPD of M must occur on the electrode by removal of cathodic charge from the double layer capacitance and (*ii*) the electrode will reach equilibrium when θ and E correspond to some point on the UPD isotherm. These points are formulated below, first without specifying any particular model and second for a linear combination model.

The charge in the double layer capacitance, Q_{E_i}, at the instant of disconnect is

$$Q_{E_i} = AC_{E_i,\theta=0}(E_{\theta=0}{}^* - E_i) \quad [3]$$

where A is the microscopic electrode area, $C_{E_i,\theta=0}$ is the integral (double layer) capacitance per unit area at the potential E_i of the substrate metal electrode before any UPD of M has occurred, *i.e.*, the surface coverage of M, θ, is zero, and $E_{\theta=0}{}^*$ is the point of zero charge (pzc) of the substrate metal.

As UPD of M proceeds, the relationship between E and θ is governed by Eq. [4]

$$Q_{E_i} = AC_{E,\theta}(E_\theta{}^* - E) + q_{E,\theta} \quad [4]$$

where $C_{E,\theta}$ is the integral capacitance per unit area. $C_{E,\theta}$ is defined with respect to the θ-dependent potential of zero charge, $E_\theta{}^*$, and is a function of E and θ. $q_{E,\theta}$ is the charge required by the UPD process to pro-

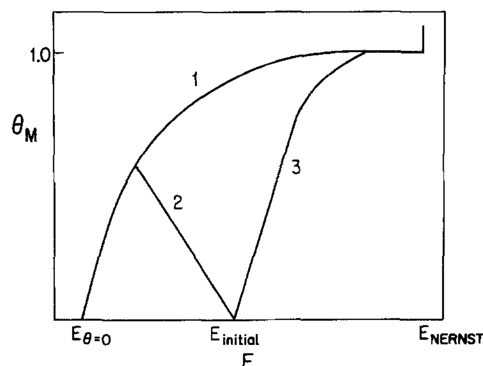

Fig. 1. Hypothetical θ-E relaxation responses for coulostatic UPD phenomenon. Curve 1, UPD isotherm for metal M on substrate; curve 2, response where relaxation path has a negative slope at point of intersections with UPD isotherm; curve 3, response where relaxation path has a positive slope at point of intersection with UPD isotherm. It is assumed $E_{\text{Nernst}} = E_{\theta=1}$.

* Electrochemical Society Active Member.
[1] Medtronic, Incorporated, Power Sources R & D Department, Minneapolis, Minnesota 55418.
[2] AMAX Incorporated, Extractive Metallurgy Department, Golden, Colorado 80401.

Key words: coulostatic, underpotential deposition.

duce coverage θ at a potential E, starting from E_i where $\theta = 0$.

The particular functional form of $C_{E,\theta}$, E_θ^*, and $q_{E,\theta}$ depends on the model chosen. However, it is not necessary to specify a particular model in order to discuss the potential path taken as θ increases. For E_i more cathodic than $E_{\theta=0}$ the coulostatic discharge process will change the electrode potential, for example, along the path shown by curve 2 of Fig. 1, or perhaps along the path taken by curve 3. All of the possible paths are described by Eq. [4], which can be rewritten as

$$\theta = \mathbf{G}(E, Q_{E_i}) \quad [5]$$

The potential of the electrode will change according to the path described by Eq. [5] until Eq. [2] is also satisfied

$$\mathbf{G}(E, Q_{E_i}) = \mathbf{F}(E) \quad [6]$$

i.e., until the coulostatic relaxation path and the UPD isotherm intersect. At the intersection point of curves 1 and 2 the system is in equilibrium for path 2.

Curve 3 of Fig. 1 represents that path followed when the change in E_θ^* and/or $C_{E,\theta}$ with θ as such that it overcomes the tendency of $q_{E,\theta}$ (the charge taken from the double layer capacitance in the reduction case of Eq. [1]) to shift the electrode's potential anodic. In this situation, even after E and θ correspond to a point on the UPD isotherm, the electrode's potential will spontaneously shift cathodically along the isotherm until the Nernst potential is reached $(\theta = 1)$.

The RRDE technique provides data of the form of Eq. [5]; thus, we use this functional form to compare the experimental data with the predictions arising from a specific model. A remarkably simple one leads to good agreement with experiment. In this model: (*i*) The electrode is assumed to consist of two electrode regions, of area θA for the UPD material and $(1 - \theta)A$ for the substrate metal, where A is independent of θ; (*ii*) the integral double layer capacitance per unit area and the point of zero charge of each area are assumed to be unique and independent of θ; and (*iii*) $q_{E,\theta}$ is assumed to be given by

$$q_{E,\theta} = kA\theta \quad [7]$$

where k still may be a function of θ and E. k represents the charge per square centimeter required by the UPD process to produce a coverage, θ, starting at coverage $\theta = 0$. Then the expression equivalent to Eq. [4] is

$$Q_{E_i} = AC_S(1-\theta)(E_S^* - E) + A\theta C_M(E_M^* - E) + kA\theta \quad [8]$$

where the subscripts S and M refer to the substrate region and UPD region coated with M, respectively. At $\theta = 0$, $E = E_i$ and

$$Q_{E_i} = AC_S(E_S^* - E_i) \quad [9]$$

Thus, equating Eq. [8] and [9] yields

$$\theta = \frac{C_S(E - E_i)}{k + [C_M(E_M^* - E) - C_S(E_S^* - E)]} \quad [10]$$

as the explicit form of Eq. [5]. Now, the terms in the braces in the denominator tend to be of the same magnitude and can cancel each other. Then, when M^{n+} is discharged as M, k will be the predominant term in the denominator. Thus, not infrequently, a limiting form of Eq. [10] may hold, *i.e.*

$$\theta = C_S(E - E_i)/k \quad [11]$$

The actual oxidation state of the UPD species cannot be determined from electrochemical data unless a model is chosen. This can be seen by writing Eq. [4] in the form

$$Q_{E_i} = AC_{E,\theta}([E_\theta^* + k\theta/C_{E,\theta}] - E) \quad [12]$$

by substituting Eq. [7] into Eq. [4]. Since E_θ^* and k may both be functions of E and θ, there is no model-free way to distinguish E_θ^* from k.

A model, such as that used to derive Eq. [10], permits evaluating k, and thus $q_{E,\theta}$. The value of $q_{E,\theta}$ yields the average charge, $\bar{a}$, carried by a single UPD species. In principle, for the reduction case of Eq. [1], $0 \leq \bar{a} \leq n$. We prefer to interpret nonzero values of $\bar{a}$ as signifying an underpotential deposit consisting of a mixture of zero valent (adatom) and ionic metal species (adion), although we recognize that others prefer to regard such a result as evidence for a single surface species carrying a partial ionic charge. No experimental evidence exists which has distinguished between these two models. Theoretical arguments favoring the single surface species have not considered the possibility of stabilization of surface ions by solvent interactions and we regard the choice between these two views still to be a matter of personal preference.

Experimental

Chemicals.—Supporting electrolyte solutions were prepared from triply distilled water and Baker analyzed reagent grade sulfuric acid. Mercuric and silver sulfate stock solutions were prepared by dissolving the appropriate Mallinckrodt reagent grade sulfates in $0.2M$ H_2SO_4. The stock solutions were diluted to the working concentration just before an experiment was performed.

Equipment.—Standard laboratory equipment was used for these experiments. The rotator, electrochemical cell, and potentiostat are all of conventional design. The digital data acquisition and control system is described elsewhere (5). The rotating ring-disk electrodes were constructed in our laboratory (6).

Data acquisition.—A six-step digital data acquisition sequence was used to acquire data for the zero current experiments in $2.0 \times 10^{-5}M$ Hg^{2+} solution with a gold RRDE. In the first step the disk electrode potential was scanned at 100 mV/sec between -0.4 and $+1.6$V for 3 min at $\omega = 2500$ rpm. Simultaneously, the ring electrode was potentiostated at 1.0V. The disk electrode potential was then stepped to 0.0V at $\omega = 0$ rpm for 10 sec to ensure complete reduction of gold oxide formed during the previous step. Then the electrode rotator was started ($\omega = 2500$ rpm) and the disk electrode was potentiostated at 1.05V for 20 sec. At this potential, no mercury deposits and no gold oxide forms. Simultaneously, the ring electrode was potentiostated at 0.0V. Finally, the disk electrode potential was stepped to the desired initial potential for 0.2 sec, after which the current was set to zero and data acquisition was begun.

The Ag^+/Ag data on gold and platinum were obtained by a similar procedure using manual techniques.

In all cases it was possible to begin the zero current part of the experiments before any significant UPD could occur via a conventional faradaic mechanism. All potentials are reported *vs.* the saturated calomel electrode (SCE).

Au double layer capacitance determination.—To determine the capacitance of a gold electrode, a stationary gold disk electrode was scanned from 1.0 to 0.0V in $0.2M$ H_2SO_4 to obtain the *i-E* curve from which the charge-potential (*q-E*) plot was calculated. The *q-E* plot was normalized to the microscopic electrode area (see below) and the average integral double layer capacitance of the gold electrode over this potential region was calculated to be 57 $\mu F/cm^2$. Values for the pzc of Au and Hg in dilute sulfuric acid have been given in the literature as -0.042 and -0.442V (*vs.* SCE), respectively (7), and these are the values used in our model.

Determination of the isotherm for UPD metal on Au and Pt.—The quantity of UPD metal that was de-

posited on the substrate (Au or Pt) at a particular potential was determined as follows.

The gold electrode was first pretreated according to the sequence described above in the section on Data acquisition. Explicitly, the final steps in these experiments were to step to the UPD potential of interest and initiate rotation at 2500 rpm. After 10 min when UPD was complete the electrode was oxidized by means of a linear anodic potential scan at 100 mV/sec. The Hg^{2+} produced in this anodic scan was collected at the ring electrode. The charge required to oxidize the UPD deposit from the gold disk electrode was measured and compared with the simultaneously acquired ring electrode data. From these two sets of data, both θ and the fraction of θ that exists as adatoms were estimated as a function of potential. These techniques were also used after coulostatic experiments to determine the coverage of Hg on the Au surface.

Similar experiments were also performed to determine the UPD isotherm for Ag^+ on Pt. The situation of Pt is somewhat more complicated than on Au, in that part of the Ag on Pt isotherm superimposes on the Pt oxidation region in 0.2*M* H_2SO_4. Also, as is the case for Hg(II) on Au, there is adsorption of Ag(I) on Pt, and $\bar{a} \neq 0$ in the potential region of interest. Separate charge balance experiments were used to estimate the amount of Ag(I) which adsorbs. At 0.64V, the rest potential attained after the Pt disk was open-circuited at 0.2V, the fraction of total adsorbate present as Ag(I) was about 0.5 ($\bar{a} \approx 0.5$). In the Ag^+/Ag on Au system, the silver deposited almost entirely as Ag(O).

Microscopic electrode area.—The microscopic area of gold disk electrode was determined in order to permit charge density calculations required to interpret the coulostatic relaxation experiments performed in Hg^{2+} and Ag^+ solutions. After potentiostating a pretreated and reduced stationary Au disk electrode at 1.20V for 5 min the charge required to reduce the oxidized surface was used as a measure of the true microscopic Au area. This method has been described elsewhere (8). The microscopic area of the platinum disk electrode was calculated from hydrogen adsorption curves, assuming hydrogen adsorbs to the extent of 210 $\mu C/cm^2$ (9).

Results and Discussion

Coulostatic relaxation experiments involving Hg^{2+} were performed using a rotating gold ring-gold disk electrode, and both gold-gold and platinum-platinum ring-disk electrodes were used in the Ag^+ experiments. Representative disk potential-time (E_D-t) responses for these cases are shown in Fig. 2. In each case, following pretreatment, the electrode was open-circuited at an initial potential, E_i; E_D drifted anodically and finally reached its equilibrium potential, E_{eq}. Although not shown in this figure, E_{eq} depends on E_i. Note that the E_D-t curves for Hg^{2+} and Ag^+ on a Au are linear, while the Ag^+ on Pt curve has two linear parts and has a definite change in slope at about 0.5V.

Ring electrode shielding responses for each system show that metal ion is being consumed at the disk electrode while E_D drifts anodically. The ring electrode current, i_R, returns to the unshielded value at the time the E_D drift ceases. The ring electrode shielding curves also show that metal ion consumption occurs at a convective-diffusion controlled rate during most of the E_D relaxation. Also, the Ag^+/Ag on Pt system is diffusion controlled over at least the Ag^+ concentration range of 10^{-5}-$10^{-7}M$.

Hg^{2+}/Hg on Au.—The ring electrode shielding curve corresponding to the Hg^{2+}/Hg on Au E_D-t curve in Fig. 2 is shown in Fig. 3. The ring electrode in Fig. 3 is potentiostated at 0.0V. When the disk electrode is open-circuited the ring electrode becomes shielded (see Experimental section) until the disk electrode reaches E_{eq}. The shaded area represents Hg(II) that has deposited both as adatoms and adions on the disk

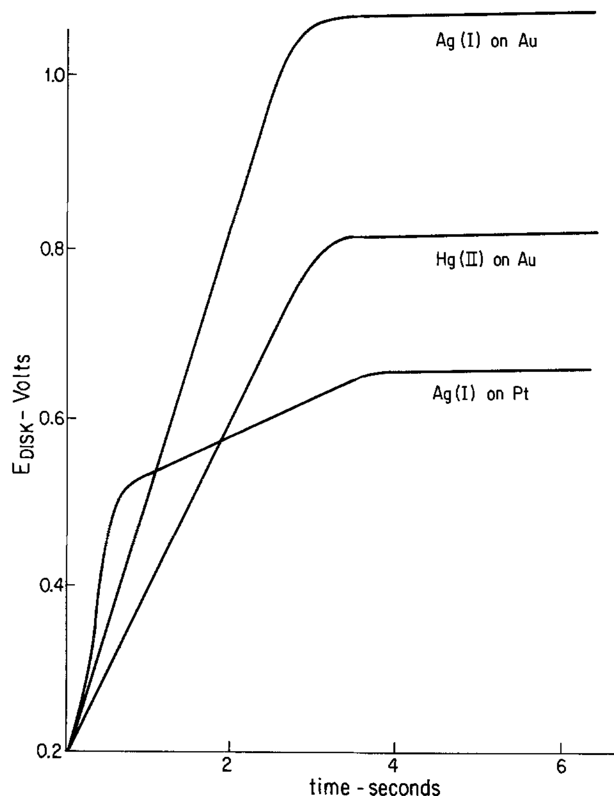

Fig. 2. Coulostatic potential-time curves for three UPD systems. $C_{M^{n+}} = 2 \times 10^{-5}M$, $\omega = 2500$ rpm, 0.2M H_2SO_4, geometric area of disk electrode = 0.46 cm^2. $E_{initial} = 0.2V$ in each case.

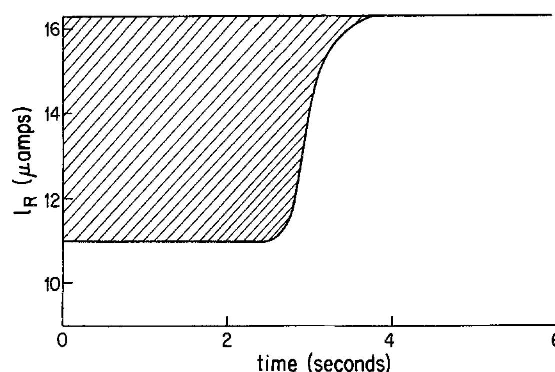

Fig. 3. Ring electrode current-time curve corresponding to the coulostatic E_D-t curve for the Hg(II)/Hg on Au system in Fig. 2. $E_R = 0.00V$.

electrode surface. 54 $\mu C/cm^2$ of Hg(II) did not reach the ring electrode because the equivalent of this amount (2.8×10^{-10} g·atoms/cm^2) of Hg species adsorbed on the disk electrode. Analogous i_R-t curves were observed in each system studied.

If, after attaining E_{eq}, the disk electrode is swept in the anodic direction, oxidation peaks identical to those obtained for stripping conventionally prepared UPD deposits of Hg (5, 6) are observed.

Ring electrode shielding data of the kind shown in Fig. 3 were used to determine the UPD coverage of Hg as a function of E for various E_i's. The time integral of i_R, divided by the collection efficiency, N, of the RRDE yields the total quantity of Hg(II) species consumed at the disk as a function of time (and thus E_D). The maximum adsorbate that can be formed is determined in a separate potentiostatic RRDE experiment performed a few tenths of a millivolt anodic of the Nernst potential. At $\theta = 1$, 2.0×10^{-9} g·atom/cm^2 of total mercury adsorbate forms, of which only 87% is present as Hg(0). Using this maximum value we calculate θ as a function of E. Three of these E *vs.* θ

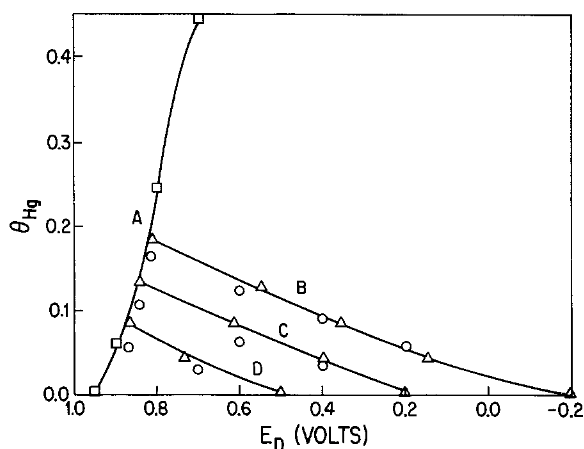

Fig. 4. θ_M vs. E plots for the Hg(II)/Hg on Au system. Three initial potentials −0.2, +0.2, and +0.5V vs. SCE. ω = 2500 rpm, 0.2M H_2SO_4, $C_{Hg(II)} = 2 \times 10^{-5}M$. Curve A experimental UPD isotherm, curve B is the theoretical θ-E path for E_i = −0.2V, curve C is the theoretical path for E_i = 0.2V, curve D is the theoretical path for E_i = +0.5V. △ are experimental points, ○ are calculated points using Eq. [11].

plots (curves B-D) are shown in Fig. 4 for the Hg^{2+}/Hg on Au systems. Note that as E_i is made more cathodic, θ at E increases and, also, that the slope of the E-θ plots appear to be independent of E_i. It can be seen from the plots shown in Fig. 4 that the θ-E behavior is consistent with Eq. [1]-[4]. Note that each of the θ-E paths terminates within experimental error, at the isotherm, curve A. These plots are similar to path 2 in the example discussed in the Theoretical section and, as shown below, are consistent with the view that adatom formation, by reduction of Hg(II) using charge stored in the double layer, is the main potential-determining process.

The experimental θ-E plots calculated from the coulostatic data agree well with Eq. [11]. As stated above, this would be the case when the bracketed term in the denominator of Eq. [10] is insignificant with respect to k. Thus, the bracketed term in Eq. [10] must be almost zero, and

$$C_M \simeq C_S(E_S^* - E)/(E_M^* - E) \qquad [13]$$

Values of C_M, calculated from Eq. [13], range from 30 to 40 $\mu C/m^2$ for nearly all the experimental data if E_M^* is taken to be equal to that of bulk mercury. Thus, the value of C_M is surprisingly similar to that of mercury at anodic potentials.

The value of k in Eq. [11] (as determined coulometrically) is 295 $\mu C/cm^2$ in the UPD coverage range of mercury, $0.06 \leq \theta \leq 0.2$. This coulometric value was calculated from the charge required to oxidize the UPD mercury from the disk electrode. The value of k calculated from the "straight" lines plots in Fig. 4 were: curve B, 300 $\mu C/cm^2$ and curves C and D, both 295 $\mu C/cm^2$. Thus, the predictions of the coulostatic relaxation mechanism agree well with independent coulometric data for Hg(II) UPD as Hg(0).

Ag^+/Ag on Au and Pt.—Two other systems were studied to investigate the generality of the coulostatic UPD phenomena. The E_D-t curve shown in Fig. 2 for the Ag^+/Ag system on Au and Pt shows that coulostatic deposition occurs on these two metals. For the Ag^+/Ag on Au system, the UPD isotherm is very steep in the range $0 \leq \theta \leq 0.3$, and E_{eq} was observed to be nearly independent of E_i. Ag^+ does not appear to absorb on Au appreciably in the potential range studied and Eq. [11] adequately describes the E-θ paths. The Ag^+/Ag on Pt system shows more complex behavior than the other systems during coulostatic relaxation experiments. The isotherm for Ag on Pt is shown in Fig. 5. These data are presented in terms of microcoulombs per square centimeter of Ag(I) consumed at the disk in order to clarify the discussion that follows.

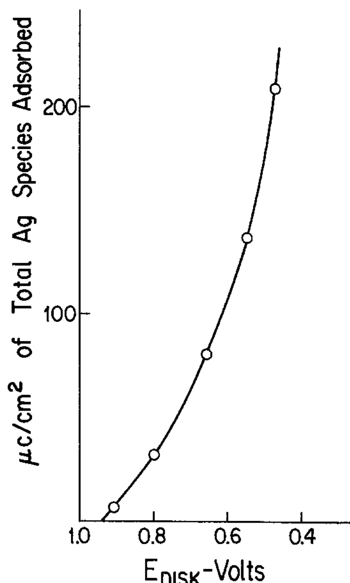

Fig. 5. UPD isotherm for Ag(I)/Ag on Pt in 0.2M H_2SO_4

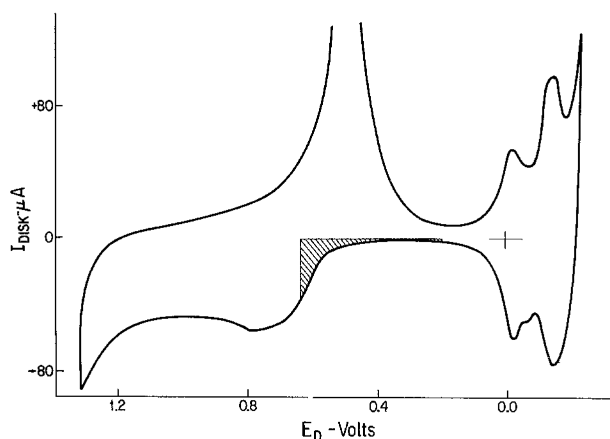

Fig. 6. Current-potential curve for Pt disk electrode in 0.2M H_2SO_4. Area of disk = 0.46 cm^2, roughness factor = 1.6, dE_d/dt = 100 mV/sec.

A comparison of the isotherm with the current-potential curve for platinum in 0.2M H_2SO_4 (Fig. 6) indicates that a significant quantity of a silver species exists on the platinum surface in the potential region where some surface oxidation has occurred.

Figure 7 represents the charge-potential curve calculated from the anodic current-potential scan in Fig. 6. In going from 0.2 to 0.64V, 90 $\mu C/cm^2$ are required for double layer charging and electrode oxidation. A RRDE experiment, conducted during a coulo-

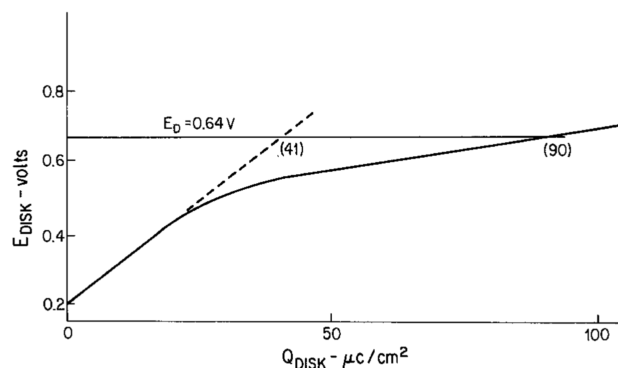

Fig. 7. Charge-potential curve for anodic portion of Fig. 6

static relaxation experiment in $2 \times 10^{-5}M$ Ag^+ in $0.2M$ H_2SO_4 (Fig. 2), showed that 88 $\mu C/cm^2$ of Ag^+ was consumed at the disk between 0.2 and 0.64V. The agreement between the amount of Ag^+ consumed and the charge data in Fig. 7 is most simply explained by the reduction of Ag^+ to Ag(0) on platinum during the coulostatic relaxation. The charge required for this reduction was supplied from the double layer and by electrochemical oxidation of the platinum surface, just as is the case when anodic charge flows in the external circuit.

It should be noted that the fraction of the platinum surface that may be oxidized at E_{eq} is not large. However, the conclusion that some platinum surface oxidation occurs as a result of the couples

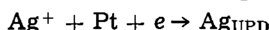

$$Ag^+ + Pt + e \rightarrow Ag_{UPD}$$

$$Pt \rightarrow Pt(oxidized) + e$$

is an indication of the strength of the interaction between UPD silver and surface platinum atoms.

Conclusion

The coulostatic process can lead to significant surface coverages of species which can be underpotentially deposited. Thus, when an open-circuited electrode is immersed in a solution containing metal ions which can underpotentially deposit, the electrode potential will drift to a potential determined by the UPD isotherm for the metal ion/substrate system. Changing the concentration of the metal ion present in solution will then produce another shift in potential to a new point on the UPD isotherm. This phenomenon provides a mechanism that explains how "noble" metal electrodes such as platinum and gold can act as indicator electrodes in potentiometric titrations involving certain metal ions, such as Ag^+. Also, given the UPD isotherm for a particular metal ion at different metal substrates, the coulostatic theory predicts which metal substrate will yield the largest change in end-point potential during a potentiometric titration. The coulostatic UPD process also provides another way to alter the characteristics of electrocatalysts by (unsuspected) trace metal ion impurities and should be added to the catalog of mechanisms by which electrode processes can be unintentionally inhibited or accelerated.

Acknowledgment

This work was supported by the Air Force Office of Scientific Research under Grant No. 74-2572.

Manuscript submitted Aug. 19, 1977; revised manuscript received Oct. 27 1977.

Any discussion of this paper will appear in a Discussion Section to be published in the December 1978 JOURNAL. All discussions for the December 1978 Discussion Section should be submitted by Aug. 1, 1978.

Publication costs of this article were assisted by the State University of New York at Buffalo.

REFERENCES

1. W. J. Lorenz, H. D. Hermann, N. Wüthrich, and F. Hilbert, *This Journal*, **121**, 1187 (1974).
2. M. Haissinsky and A. Coche, *J. Chem. Soc.*, **1949**, 5397.
3. J. T. Byrne, L. B. Rogers, and J. Griese, Jr., *This Journal*, **98**, 452 (1951).
4. G. W. Tindall, Private communication.
5. W. G. Sherwood, Ph.D. Thesis, State University of New York at Buffalo (1977).
6. D. F. Untereker, Ph.D. Thesis, State University of New York at Buffalo (1973).
7. J. O. M. Bockris and B. E. Conway, "Modern Aspects of Electrochemistry," Vol. 5, Plenum Press, New York (1969).
8. S. B. Brummer and H. C. Makrides, *This Journal*, **111**, 1122 (1964).
9. F. G. Will, *ibid.*, **112**, 451 (1965).
10. G. W. Tindall and S. Bruckenstein, *Electrochim. Acta*, **16**, 245 (1971).
11. S. H. Cadle, Ph.D. Thesis, State University of New York at Buffalo (1972).

Coulostatic Deposition of Metals at Underpotential

II. The Effect of Heterogeneous Chemical Reactions on the Potential Relaxation Process

W. G. Sherwood,*[,1] D. F. Untereker,**[,2] and Stanley Bruckenstein**

Chemistry Department, State University of New York at Buffalo, Buffalo, New York 14214

ABSTRACT

The coulostatically controlled underpotential deposition (UPD) processes Ag(I) + e = Ag on gold and platinum and Hg(II) + $2e$ = Hg on gold have been shown to lead to anodic potential excursions (1). Chemical reactions that precede and/or accompany coulostatic underpotential deposition can produce two other kinds of potential relaxation. For example, the potential of an oxidized gold electrode, on being open-circuited in Hg(I) solutions, shifts continuously to a more cathodic potential until equilibrium is reached. The Hg(I) reduces the gold oxide and then produces a UPD mercury layer on the gold surface through the disproportionation reaction

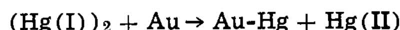

$$(Hg(I))_2 + Au \rightarrow Au\text{-}Hg + Hg(II)$$

The potential shift ceases when the Nernst potential is reached. The potential of a reduced gold electrode, on being open-circuited in a Hg(I) solution, initially shifts anodically and then shifts cathodically until equilibrium is reached. The initial anodic shift is due to a conventional coulostatic deposition mechanism while the subsequent cathodic shift is due to the disproportionation mechanism given above.

In a previous paper dealing with potential relaxations occurring at open-circuited metal electrodes, a theory for coulostatic underpotential metal deposition (UPD) was developed (1). Experimental evidence was given for zero-current UPD in the systems Ag^+/Ag on Pt, Ag^+/Ag on Au, and Hg^{2+}/Hg on Au. In these systems, the coulostatic process causes a monotonic anodic potential excursion that stops when the UPD surface coverage and electrode potential reach the UPD isotherm for the system. In this paper, two

* Electrochemical Society Student Member.
** Electrochemical Society Active Member.
[1] AMAX, Incorporated, Extractive Metallurgy Department, Golden, Colorado 80401.
[2] Medtronic, Incorporated, Power Sources R & D Department, Minneapolis, Minnesota 55418.

Key words: coulostatic, underpotential deposition, heterogeneous reaction.

situations are considered that exhibit cathodic potential excursions, both taking place in dilute Hg(I) solutions in $0.2M\ H_2SO_4$. In the first case, an oxidized gold electrode is open-circuited, and in the second case an oxidized gold electrode surface is electrochemically reduced and then open-circuited at a cathodic potential. The (initially) anodically poised system exhibits a monotonic cathodic potential excursion, while the (initially) cathodically poised system first undergoes an anodic potential shift, which is then followed by a cathodic potential excursion. The concepts developed previously (1) are valid in these more complicated systems where heterogeneous chemical reactions also occur.

We show below that: (*i*) when an oxidized gold electrode is open-circuited in a Hg(I) solution, the electrode surface is first reduced by the oxidation of Hg(I) to Hg(II), and then covered with UPD Hg resulting from the disproportionation reaction

$$(\mathrm{Hg(I)})_2 + \mathrm{Au} \rightleftharpoons \mathrm{Au\text{-}Hg} + \mathrm{Hg(II)} \qquad [1]$$

and (*ii*) when a reduced gold electrode is open-circuited in a Hg(I) solution, coulostatic UPD of Hg first shifts the potential anodically then the disproportionation reaction shifts the potential cathodically. In both cases the potential relaxation ceases when the Nernst potential is reached.

Theoretical

Double layer charging in the presence of surface chemical reactions.—If an electrode is potentiostated at a potential, E_i, and then open-circuited, and a chemical process occurs to produce or remove a monolayer film of coverage, θ, the equilibrium electrode potential will correspond to a point on the isotherm of the adsorbate being formed or removed. The charge in the double layer may be expressed by

$$Q_{E_i} - q_{E,\theta} = AC_{E,\theta}\,(E_\theta{}^* - E) \qquad [2]$$

where Q_{E_i} is the charge in the double layer at the potential of disconnect, E_i, A is the microscopic electrode area, and $C_{E,\theta}$ is the integral double layer capacitance per unit area. $C_{E,\theta}$ is defined with respect to the θ-dependent potential of zero charge, $E_\theta{}^*$, and is a function of E and θ. $q_{E,\theta}$ is the charge injected into or removed from the double layer on "adsorbing" one or more solution species in going from E_i to E. A part of $q_{E,\theta}$ may involve one or more species detectable at the ring electrode of a ring-disk electrode. When this is the case, it becomes possible to quantitate the change in the flux of these species to or from the disk electrode surface and to describe these flux changes in terms of adsorption. Using disk electrode charge data obtained in experiments subsequent to the open-circuit (coulostatic) experiment and making assumptions concerning the double layer capacitance, the net charge of the adsorbate can be estimated.

Interpretation of ring electrode currents.—The ring-disk electrode is used to determine the presence, generation, or removal of the Hg(I) and Hg(II) species.

At $E_R = 1.0\text{V}$, the reaction

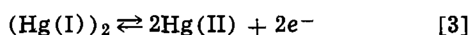

$$(\mathrm{Hg(I)})_2 \rightleftharpoons 2\mathrm{Hg(II)} + 2e^- \qquad [3]$$

occurs, while at $E_R = 0.0\text{V}$, the reactions

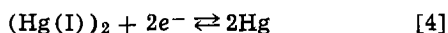

$$(\mathrm{Hg(I)})_2 + 2e^- \rightleftharpoons 2\mathrm{Hg} \qquad [4]$$

and

$$\mathrm{Hg(II)} + 2e^- \rightleftharpoons \mathrm{Hg} \qquad [5]$$

occur. Thus, ring electrode current measurements at $E_R = 1.0\text{V}$ and 0.0V allow us to determine the disk electrode surface concentrations of Hg(I) and Hg(II) in a Hg(I) solution, using the fundamental definition of the collection efficiency, N, at both ring electrode potentials.

In the discussion that follows, $C_{II}{}^S$ represents the concentration of Hg(II) at the disk electrode surface and $C_I{}^S$ and $C_I{}^b$ represent the disk electrode surface and bulk concentrations of $(\mathrm{Hg(I)})_2$, respectively.

For $E_R = 1.0\text{V}$, the flux of Hg(I) to the ring equals the flux of Hg(I) from solution plus the flux of Hg(I) from the disk, or

$$\frac{(i_R)_{1.0}}{2\mathbf{F}} = \beta^{2/3} L C_I{}^b - NL(C_I{}^b - C_I{}^S)$$

and

$$(i_R)_{1.0} = -2\mathbf{F}L\{(\beta^{2/3} - N)C_I{}^b + NC_I{}^S\} \qquad [6]$$

where L is the Levich constant relating flux and species concentration (2), $\mathbf{F}$ is the Faraday, $\beta^{2/3}$ the ratio of the convective-diffusion controlled ring to disk electrode currents when the ring operates in the absence of a disk current, and $(i_R)_{1.0}$ is the ring electrode current when $E_R = 1.0\text{V}$.

For $E_R = 0.0\text{V}$, the flux of Hg(II) to the ring electrode is the RRDE collection efficiency times the flux of Hg(II) leaving the disk electrode; hence the part of the ring current at $E_R = 0.0\text{V}$ due to reduction of Hg(II) is

$$(i_{R,II})_{0.0} = 2\mathbf{F}LNC^S{}_{\mathrm{Hg(II)}} \qquad [7]$$

The Hg(I) flux balance leads to

$$\frac{(i_{R,I})_{0.0}}{2\mathbf{F}} = \beta^{2/3} < C_I{}^b - NL(C_I{}^b - C_I{}^S)$$

or

$$(i_{R,I})_{0.0} = 2\mathbf{F}L\{(\beta^{2/3} - N)C_I{}^b + NC_I{}^S\} \qquad [8]$$

where $(i_{R,I})_{0.0}$ is the part of the ring current at $E_R = 0.0\text{V}$ due to Hg(I) reduction. Equation [8] describes the Hg(I) shielding process. The observed ring current, $(i_R)_{0.0}$ in a solution containing $(\mathrm{Hg(I)})_2$ and in which Hg(II) is generated at the disk is

$$(i_R)_{0.0} = (i_{R,II})_{0.0} + (i_{R,I})_{0.0}$$

or

$$(i_R)_{0.0} = 2\mathbf{F}L\{(\beta^{2/3} - N)C_I{}^b + N(C_{II}{}^S + C_I{}^S)\} \qquad [9]$$

where it is assumed that $D_I = D_{II}$, as observed to a very good approximation (3).

Experimental

Reagents.—Supporting electrolyte solutions were prepared from triply distilled water and Baker Analyzed Reagent Grade sulfuric acid. Stock $0.1M\,(\mathrm{Hg(I)})_2$ was prepared according to a procedure described elsewhere (4, 5). The solution was initially standardized using Pugh's method (4) and was later restandardized via amperometric titration with standard chloride solution.

Equipment.—Standard laboratory equipment was used for these experiments. The rotator, electrochemical cell, potentiostat, and the digital data acquisition and control system have been described elsewhere (6).

Data acquisition.—The data acquisition sequence used to obtain data for zero current experiments initiated on reduced gold electrodes ($0.9\text{V} > E_i > -0.2\text{V}$) is identical to that described previously for the Hg(II)/Hg on Au system (1). However, for the Hg(I) system it was necessary to perform rotating ring-disk electrode experiments with the ring electrode potentiostated at two ring potentials, *i.e.*, at 0.0V where both Hg(II) and Hg(I) are reduced at convective diffusion control and at 1.0V where Hg(I) is oxidized and can be selectively monitored in the presence of Hg(II).

The data acquisition sequence for zero current experiments initiated on an oxidized electrode was similar to the one described in Ref. (1). Following pretreatment of the gold disk electrode, the potential was stepped to 1.2V and maintained there for 5 min at $\omega = 0$ rpm. After potentiostating the ring electrode at the appropriate potential (1.0 or 0.0V), the electrode was rotated at $\omega = 2500$ rpm, the disk electrode current was set to zero, and the disk electrode potential-time and the ring electrode current-time responses were simultaneously recorded.

The charge required to electrochemically reduce the oxidized gold electrode surface formed at 1.2V was determined by separate linear voltage scan experiments and was related to the microscopic surface area according to the procedure of Brummer and Makrides (7). The value of the "real" surface area was needed to relate experiments done using different electrodes, since the electrode roughness determines both the double layer capacitance and the charge corresponding to one monolayer of UPD mercury.

Results and Discussion

Zero current reduction of oxidized gold: $E_D > 0.95V$. —*Disk electrode potential-time curves.*—Coulostatic relaxation experiments in the presence of Hg(I) were performed at an oxidized gold electrode poised at an initial potential, E_i, of 1.2V. The zero current disk electrode potential-time, E_D-t, response obtained is shown in curve A of Fig. 1.

After open circuiting the oxidized gold electrode, the potential rapidly shifts cathodically from 1.2 to 0.95V. Gold oxide reduction occurs at these potentials, and, therefore, the initially oxidized gold surface must be undergoing reduction. Hg(I) is oxidized at potentials where the gold oxide surface is reduced (3). Therefore, oxidation of Hg(I) by surface gold oxide is a thermodynamically spontaneous process. Since the Au electrode is open-circuited, it is plausible that reduction of the oxide occurs via the heterogeneous chemical reaction

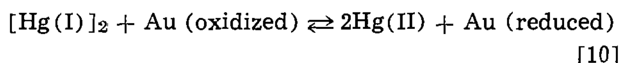

$$[Hg(I)]_2 + Au\ (oxidized) \rightleftarrows 2Hg(II) + Au\ (reduced) \quad [10]$$

Since 0.95V is slightly anodic of the UPD isotherm, no UPD Hg deposition can occur (1, 8).

Ring electrode current-time curves.—The ring electrode current-time responses accompanying the cathodic disk potential drift of Fig. 1, curve A, are shown in Fig. 2. The shielding response curve for Hg(I) (E_R = 1.0V, curve A) shows that it is being consumed at all disk potentials more anodic than ~0.4V (times less than 75 sec). However, the ring electrode collection current for Hg(II) and Hg(I) (E_R = 0.0V, curve B) is initially greater than its unshielded value. It returns to the limiting value about the time the Au disk electrode potential drops below ~0.95V, the potential corresponding to complete reduction of gold oxide. The i_R-t curves are consistent with reaction [10] since the Hg(I) ring shielding response shows that it is consumed quantitatively at the disk electrode. If reaction [10] is quantitative, $C_I^S = 0$. Thus according to Eq. [6], the change in ring current in going from a surface concentration of zero, when there is reaction according

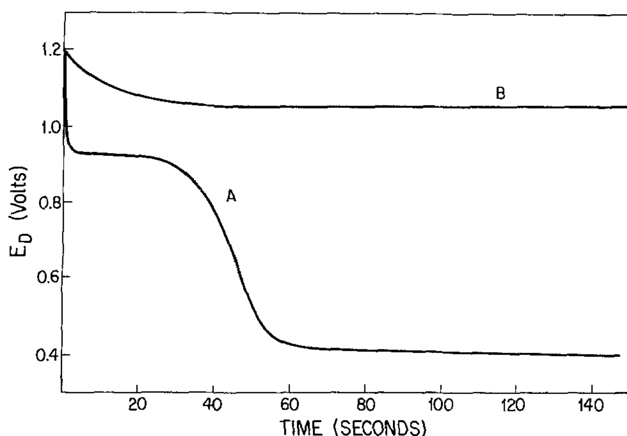

Fig. 1. Zero current potential-time responses at an oxidized gold disk electrode in: curve A. 0.2M H_2SO_4-2.0 × 10^{-5}M Hg_2^{2+}; and curve B, 0.2M H_2SO_4. ω = 2500 rpm.

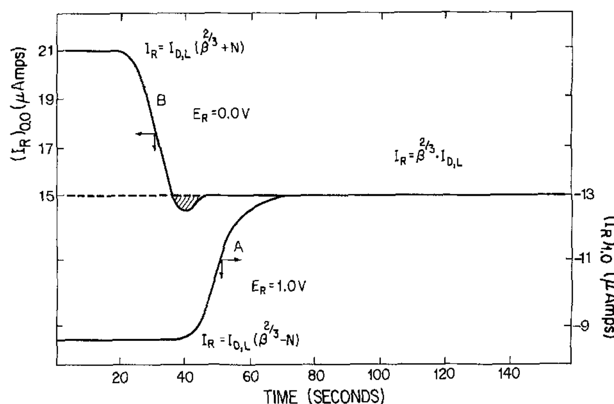

Fig. 2. Ring electrode current-time responses accompanying curve A of Fig. 1, curve A, E_R = 1.0V; curve B, E_R = 0.0V. I_{DL} is the appropriate disk-limiting current.

to Eq. [10], to a value of C_I^S when there is no reaction, is

$$(\Delta i_R)_{1.0} = 2\mathbf{F}LNC_I^S$$

The disk electrode limiting current for the oxidation of Hg(I) to Hg(II) (reaction [3]) is

$$(i_L)_{1.0} = -2\mathbf{F}LC_I^S$$

Hence

$$(\Delta i_R)_{1.0} = -N(i_L)_{1.0} \quad [11]$$

The average value of Δi_R for 10 experiments of the kind shown in Fig. 2, curve A, was 4.9 ± 0.2 μA. The value of $(i_L)_{1.0}$ was −14.2 and N = 0.341, yielding 4.8 μA for the product $N(i_L)_{1.0}$, in good agreement with the observed values of Δi_R. Note that the experimental value of $(i_L)_{1.0}$ is only 90% of the theoretical value. This low value of $(i_L)_{1.0}$ also occurs at platinum electrodes (7), appears to be associated with kinetic complication in the oxidation of Hg(I), and in no way affects our interpretation.

The ring collection response shows a cathodic current greater than the unshielded Hg(I) reduction current when $E_D > 0.95V$, *i.e.*, during the reduction of oxidized gold. We calculate the change in ring current, $(\Delta i_R)_{0.0}$, when the reaction given by Eq. [10] occurs as compared to when there is no reaction, as follows. Initially in the absence of reaction, the surface concentrations of Hg(I) and Hg(II) are C_I^b and 0, respectively, and they are 0 and C_I^S, respectively during the reaction. Thus

$$(\Delta i_R)_{0.0} = 2\mathbf{F}NL(C_{II}^S - C_I^b)$$

If Eq. [8] is quantitative, and $D_I = D_{II}$, $C_{II}^S = 2C_I^b$, and

$$(\Delta i_R)_{0.0} = 2\mathbf{F}NLC_I^b \quad [12]$$

The cathodic disk limiting current for reduction of Hg(I) to Hg is

$$(i_L)_{0.0} = 2\mathbf{F}LC_I^b$$

thus

$$(\Delta i_R)_{0.0} = N(i_L)_{0.0} \quad [13]$$

We found Δi_R = 5.9 ± 0.4 μA from 10 experiments of the type shown in Fig. 2, curve B. The value $(i_L)_{0.0}$ is 16.0 μA and N = 0.341 yielding a calculated value for the product of $N(i_L)_{0.0}$ of 5.5 μA, in satisfactory agreement with the assumption that reaction [10] occurs quantitatively at an oxidized gold electrode.

Charge balance.—The open-circuit potential relaxation must simultaneously satisfy Eq. [2] and the isotherm for oxygen coverage on gold. Since Q_{E_i} is constant and $C_{E,\theta}$ and E_θ are predetermined (but unknown) functions of E and θ, $q_{E,\theta}$ must adjust to satisfy the requirements of Eq. [2]. Therefore, charge balances between the quantity of gold oxide existing on the electrode surface and the various mercury species were made at 1.2V. All our experiments started at 1.2V, and it

was assumed that $\theta = 1$ for oxygen coverage (2.1×10^{-9} g-atoms O/cm^2), as stated by Brummer and Makrides (7).

Writing the reduction reaction as

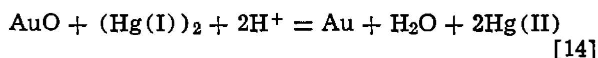

$$AuO + (Hg(I))_2 + 2H^+ = Au + H_2O + 2Hg(II) \quad [14]$$

we see that $N_O = N_{(Hg(I))_2} = -\frac{1}{2}N_{Hg(II)}$, where N is the number of gram-atoms of the subscript species consumed. Eight replicate coulostatic relaxation experiments were performed in $2.0 \times 10^{-5}M$ $(Hg(I))_2$ solution. Ring electrode experiments at $E_R = 0.0$ and 1.0V showed that in going from 1.2 to 0.95V (oxidized to reduced surface) $4.0 \pm 0.1 \times 10^{-9}$ g-atoms/cm^2 of Hg(II) were produced and $2.1 \pm 0.2 \times 10^{-9}$ g-atoms/cm^2 of $(Hg(I))_2$ were consumed. Any discrepancies between these values and the number of O atoms on the initially oxidized gold surface (2.1×10^{-9} g-atoms/cm^2) are within experimental error, and there is no evidence for any Hg species contributing to the value of $q_{E,\theta}$ (Eq. [2]) in the potential range 1.2-0.95V.

Formation of UPD mercury by disproportionation of (Hg(II))$_2$.—In the material that follows we will demonstrate that during the disk potential relaxation process that occurs after the reduction of AuO ($E < 0.95$V), the surface concentrations of $[Hg(I)]_2$ and Hg(II) are in quantitative agreement with Eq. [1], and also that the amount of UPD Hg deposited agrees with the stoichiometry required by Eq. [1].

Ring current responses.—After the gold oxide surface is reduced, curve A of Fig. 1 shows that E_D shifts cathodically to 0.40V, the equilibrium potential we found for a Hg-covered gold electrode in the solution used. The accompanying ring current responses are given in Fig. 2. At 1.0V, the ring current remains completely shielded, as it was during the reduction of the oxidized gold surface. Clearly, Hg(I) continues to be removed at the disk electrode surface. Also, at $E_R = 0.0$V, the cathodic ring current changes in a direction corresponding to a decrease in the reducible flux reaching the ring electrode. Both ring current responses agree with the quantitative surface disproportionation of Eq. [13].

As shown above, if $C_I^S = 0$, Eq. [6] predicts a shielded ring current given by Eq. [11], and there should be no change in i_R between 0.95 and 0.40V since Eq. [1] continues to hold $C_I^S = 0$.

Further according to Eq. [1] and assuming $D_I = D_{II}$

$$C_{II}^S = C_I^b$$

Substituting this result and $C_I^S = 0$ into Eq. [9], the expression for the ring current at 0.0V is

$$(i_R)_{0.0} = 2FL\beta^{2/3}C_I^b$$

or

$$(i_R)_{0.0} = \beta^{2/3}(i_L)_{0.0} \quad [15]$$

In a $2.7 \times 10^{-5}M$ $(Hg(I))_2$ solution, $(i_L)_{0.0} = 21.6$ μA. Using the value, $\beta^{2/3} = 0.94$, we calculate the product $\beta^{2/3}$ $(i_L)_{0.0}$ to be 20.3 μA (9 experiments), in agreement with Eq. [15].

Thus the ring current responses at 1.0 and 0.0V are in quantitative agreement with the assumed heterogeneous disproportionation reaction.

Anodic stripping behavior.—Equation [1] also predicts that UPD mercury will deposit on the electrode surface. Curve A, Fig. 3, is an anodic current-potential curve seen on a gold disk electrode that has relaxed from 1.2 to 0.4V at open circuit. It yields anodic stripping peaks not found on a bare gold electrode. Ring electrode collection curves at $E_R = 1.0$V (not shown) and 0.0V (curve B, Fig. 3) demonstrate the collection of a species whose electrochemistry is that of Hg(II). Identical behavior is found for UPD Hg on Au.

The amount of UPD Hg assumed to be stripped was calculated from the disk anodic charge. In one particular experiment this charge corresponded to 1.7×10^{-9} g-atoms/cm^2, while 2.0×10^{-9} g-atoms/cm^2 of Hg(II) were formed, as calculated from the ring electrode collection. The discrepancy between the disk stripping and ring collection values is caused by adsorption of a charged Hg species at the disk (see below).

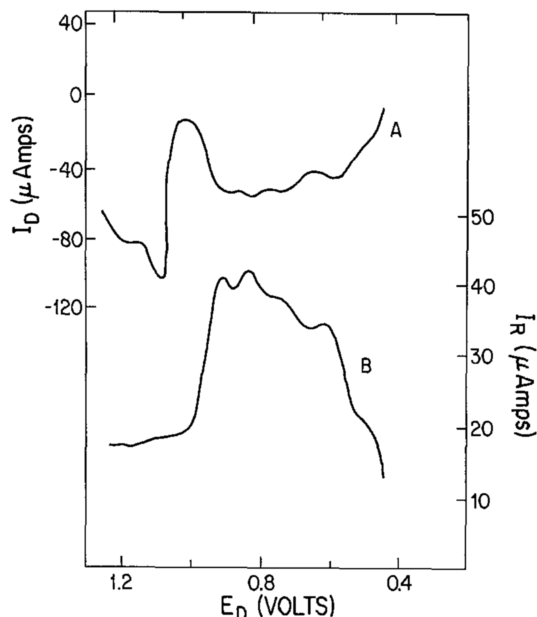

Fig. 3. Disk electrode stripping (curve A) and ring electrode collection response (curve B) obtained during anodic potential sweep after the zero-current experiment of Fig. 1, $\omega = 2500$ rpm, $E_R = 0.0$V.

The spontaneous formation of UPD mercury by Eq. [1] is not really surprising despite the unfavorable thermodynamics for this process at a bulk mercury surface. The strong interaction of Hg with Au on the formation of UPD mercury supplies the necessary driving force. The disproportionation reaction should cease when the UPD mercury surface becomes the same as that of bulk mercury. This proves to be the case since the "equilibrium" potential of a gold electrode in $[Hg(I)]_2$ solutions is the same as that of a bulk mercury surface (5). Note that the effect of the disproportionation reaction on the potential of the Hg/$(Hg(I))_2$ interface is negligible under our experimental conditions.

In eight replicate experiments at $E_R = 1.0$V, it was found that $1.9 \pm 0.2 \times 10^{-9}$ g-atoms/cm^2 of $[Hg(I)]_2$ were consumed in going from 0.95 to 0.40V (bare gold electrode to Hg-coated electrode). The stoichiometry of the disproportionation reaction (Eq. [1]) requires that $N_{(Hg(I))_2} = N_{Hg(UPD)}$. This relationship is consistent with the ring electrode collection data obtained during anodic stripping of UPD Hg, 1.9×10^{-9} g-atoms/cm^2 (3). The discrepancy between the quantity of Hg stripped from the disk electrode (1.7×10^{-9} g-atom/cm^2) and the quantity consumed at open circuit and collected at the ring electrode during the disk electrode anodic stripping experiment can again be attributed to the adsorption of a charged mercury species on the disk electrode surface (8). The small shielding response at $E_R = 0.0$ immediately after gold oxide reduction (shaded area, curve B, Fig. 2) is also consistent with the adsorption of a charged mercury species on the disk electrode since neither Eq. [1] nor Eq. [10] predict electrode shielding when $E_R = 0.0$V. The area of the shaded portion of curve A corresponds to only 1.6×10^{-10} g-atoms/cm^2 of adsorbed mercury species, compared to a difference between ring electrode collection and disk electrode stripping values of 5.4×10^{-10} g-atoms/cm^2. The additional charged mercury species adsorbed on the electrode surface at open circuit may be produced via a coulostatic discharge (oxidation) process, indicating that $q_{E,\theta}$ (Eq.

Table I. UPD Hg coverage for $0.95 > E_D > 0.40V$ obtained using $E_R = 1.0V$ data ($\theta_{1.0,R}$)

E_D(V)	$\theta_{1.0,R}$	θ_{iso}
0.80	0.20	0.25
0.70	0.42	0.45
0.60	0.55	0.58
0.50	0.78	0.76
0.40	0.97	1.00

[2]) has a nonzero value in the potential range 0.95-0.40V.

Hg coverage vs. E.—The coverage of gold with UPD Hg after reduction of the oxidized gold should, according to Eq. [2], obey the E-θ isotherm for UPD Hg. Table I shows the coverages determined at various intervals in the potential range $0.95V > E_D > 0.40V$ using $E_R = 1.0V$ data.

The isotherm coverage, θ_{iso}, (column 3) determined independently (8) agrees well with that obtained using the ring electrode. This result confirms that the disproportionation reaction determines the potential relaxation response during the cathodic shift at potentials between 0.95 and 0.40V.

Potential relaxation of a reduced Au electrode $+0.9V > E_i > 0.2V$.—If a reduced gold electrode potentiostated at 1.0V is stepped to a potential in the region +0.9 to −0.2V, and then open-circuited the electrode potential initially relaxes anodically and then relaxes cathodically, stopping at 0.40V in a $2 \times 10^{-5}M$ $(Hg(I))_2$ solution. Typical experiments are shown in Fig. 4.

Our interpretation of this relaxation response is: (*i*) During the anodic potential shift, coulostatic discharge of $(Hg(I))_2$ occurs, producing UPD mercury on the gold electrode surface. The explanation of this process is identical to that given earlier (1) in Hg(II) solutions. (*ii*) The anodic potential excursion ceases when θ_{Hg} and E correspond to the UPD isotherm for Hg on Au. (*iii*) The cathodic potential excursion proceeds via the disproportionation reaction of Eq. [1].

Anodic potential shift region.—As the electrode potential shifts from E_i to a maximum anodic value, the i_R-t curves show that $[Hg(I)]_2$ is quantitatively consumed at the disk electrode and no Hg(II) is produced (Fig. 5). We calculate the electrode coverage with mercury species from the total amount of shielded Hg(I) (Fig. 5, curve A), and calculate θ assuming that 2.0×10^{-9} g-atom/cm^2 of total mercury species corresponds to $\theta = 1$ (3). Typical E_i-$\theta_{R,0.0}$ data are reported in columns 1 and 3 of Table II. The maximum anodic disk potential (E_D^P, column 2) obtained during the potential-time relaxation should correspond to a point on the UPD-Hg isotherm, if the mercury species being produced is UPD mercury. The last column of Table II corresponds to the value of θ_{iso} according to the previously determined UPD-Hg isotherm (8). The agreement between θ_{iso} and $\theta_{R,0.0}$ data is excellent and thus confirms the mechanism of the coulostatic discharge process. Note that as E_i is made more anodic, E_D^P becomes more anodic and the coverage obtained by coulostatic deposition decreases. At $E_i = 0.9V$, the anodic excursion and resultant coulostatic coverage are nearly zero, implying that all UPD-Hg is formed according to the disproportionation reaction, Eq. [3].

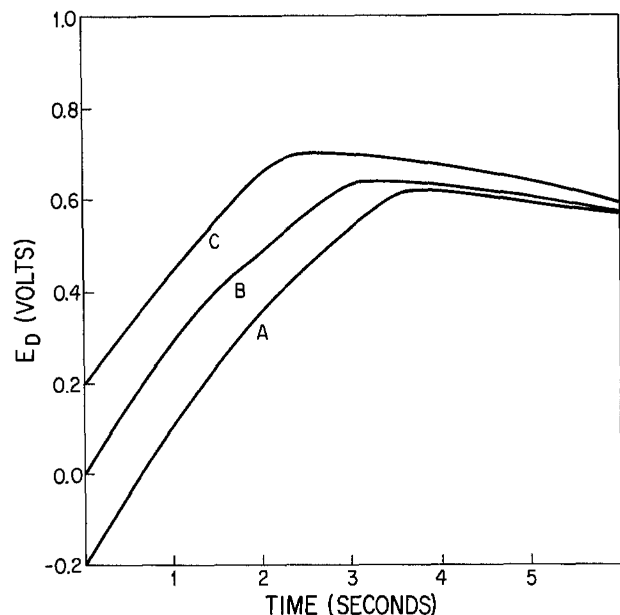

Fig. 4. Coulostatic E_D-t responses in 0.2M H_2SO_4-$2.0 \times 10^{-5}M$ Hg_2^{2+}. Curve A, $E_i = -0.20V$; curve B, $E_i = 0.0V$; curve C, $E_i = 0.20V$. $\omega = 2500$ rpm.

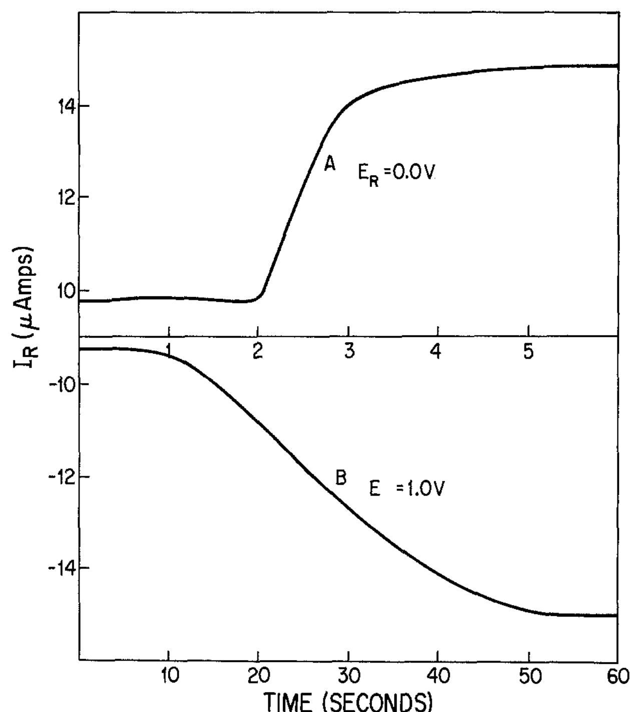

Fig. 5. Ring electrode current-time responses accompanying curve B of Fig. 4. Curve A, $E_R = 0.0V$; curve B, $E_R = 1.0V$.

Cathodic potential shift region.—Table III presents cathodic E-θ data obtained for an electrode initially potentiostated at 0.5V. The electrode potential first shifts anodically to a maximum of 0.78V, and then shifts cathodically. The potentials observed during this cathodic excursion E_D^C, are given in column 1 of Table III. Column 2, $\theta_{1.0,R}$, is the coverage calculated from ring data at $E_R = 1.0V$, and the third column, θ_{iso}, is the value of coverage taken from the previously determined isotherm (8). Again, agreement between $\theta_{1.0}$ and θ_{iso} is excellent, confirming that the dispropor-

Table II. A comparison of the coverages ($\theta_{R,0.0}$) obtained at E_D^P under zero-current conditions to isotherm coverages at the same potential

E_i(V)	E_D^P(V)	$\theta_{R,0.0}$	θ_{iso}
−0.2	0.63	0.53	0.55
−0.1	0.65	0.53	0.53
0.0	0.66	0.47	0.51
0.1	0.70	0.41	0.44
0.2	0.71	0.39	0.43
0.3	0.75	0.38	0.36
0.4	0.76	0.32	0.33
0.5	0.78	0.28	0.28
0.6	0.80	0.25	0.24
0.7	0.81	0.22	0.22
0.8	0.84	0.19	0.17
0.9	0.90	0.03	0.05

Table III. A comparison of the coverages ($\theta_{1.0,R}$) obtained during the cathodic potential shift of an electrode initial open circuit at 0.5V

E_D^C(V)	$\theta_{1.0}$	θ_{iso}
0.78	0.28	0.28
0.70	0.42	0.45
0.60	0.59	0.58
0.50	0.77	0.76
0.40	0.98	1.00

tionation mechanism governs the cathodic part of the open-circuit discharge process that follows the initial anodic potential excursion.

Conclusions

The occurrence of two independent processes, namely, spontaneous reduction of gold oxide by $(Hg(I))_2$ and disproportionation of $(Hg(I))_2$, produces a cathodic potential shift on an initially oxidized gold disk electrode under open-circuit conditions. When open-circuit experiments are performed on an initially reduced gold disk electrode, there is first an anodic potential excursion, during which UPD Hg deposits coulostatically, and then there is a cathodic potential excursion as the UPD Hg coverage increases via disproportionation of $(Hg(I))_2$ along the UPD isotherm. The point at which the potential excursion changes direction corresponds to a UPD mercury coverage relationship of the UPD isotherm. The final mercury coverage obtained for all initial potentials of open circuiting was $\theta = 1$, as predicted from the theory developed in Ref. (1).

Acknowledgment

This work was supported by the Air Force Office of Scientific Research under Grant No. 74-2572.

Manuscript submitted Aug. 19, 1977; revised manuscript received Oct. 27, 1977.

Any discussion of this paper will appear in a Discussion Section to be published in the December 1978 JOURNAL. All discussions for the December 1978 Discussion Section should be submitted by Aug. 1, 1978.

REFERENCES

1. D. F. Untereker, W. G. Sherwood and S. Bruckenstein, *This Journal*, **125**, 384 (1978).
2. V. G. Levich, *Acta. Physiochem. USRR*, **17**, 257 (1942).
3. W. G. Sherwood, Ph.D. Thesis, SUNY at Buffalo, chap. IV (1977).
4. M. Z. Hassan, Ph.D. Thesis, University of Minnesota (1973).
5. W. Pugh, *J. Chem. Soc., (London)*, 1824 (1937).
6. W. G. Sherwood, Ph.D. Thesis, SUNY at Buffalo, chap. II (1977).
7. S. B. Brummer and A. C. Makrides, *This Journal*, **111**, 1122 (1964).
8. W. G. Sherwood, Ph.D. Thesis, SUNY at Buffalo, chap. V (1977).

The Fe(II)-Fe(III) and Hydroquinone-Quinone Reactions on Oxygen-Covered Rhodium Electrodes

K. G. Everett, L. A. Drew, and S. J. Ericson

Department of Chemistry, Stetson University, DeLand, Florida 32720

and G. M. Schmid*

Department of Chemistry, University of Florida, Gainesville, Florida 32611

ABSTRACT

The kinetics of the Fe(II)-Fe(III) and of the hydroquinone-quinone reaction were investigated on smooth rhodium covered with oxygen to the extent of $\theta = 0$ to 1.5 monolayer charge equivalents (2 electrons per oxygen atom). For the Fe(II)-Fe(III) system the apparent rate constant varies systematically from $k_a^o = 4.60 \times 10^{-4}$ cm sec^{-1} at $\theta = 0$ to $k_a^o = 2 \times 10^{-5}$ cm sec^{-1} at $\Theta = 1.40$ and it does not seem to decrease significantly after that. The charge transfer coefficient is 0.55 ± 0.04 independent of θ. For the hydroquinone-quinone system, $k_a^o = 2.42 \times 10^{-4}$ cm sec^{-1} at $\theta = 0$ and $k_a^o = 1.87 \times 10^{-5}$ cm sec^{-1} at $\theta = 0.75$ and it varies only little for $\theta \geqq 0.75$. The charge transfer coefficient is 0.53 ± 0.07. Data are interpreted on the basis of a blocking effect, the charge transfer rate on oxygen-covered rhodium being negligible as compared to that on the free surface.

There is ample evidence in electrochemical literature that materials adsorbed on electrode surfaces can substantially influence the rate of electrochemical reactions (1). Several possible mechanisms for this influence have been discussed (2-5). The effect may arise from a simple geometric blocking effect in which the electrochemical reaction occurs only at the free surface, or from a field effect in which the adsorbed material alters the potential at the outer Helmholtz plane, or, alternatively, changes the position of the plane in the double layer at which reaction occurs.

One of the most common materials adsorbed on electrode surfaces is oxygen. The adsorbed oxygen or oxide film on a metal electrode generally inhibits the rate of an electrochemical reaction. It causes passivation on some metals, inhibiting metal dissolution reactions (6), and prevents electron transfer reaction on others, *e.g.*, oxalic acid oxidation on platinum (7). But while this effect of adsorbed oxygen is widely acknowledged, its mechanism is not well understood. It was our intent in the present study to focus upon the quantitative features of oxide film inhibition of charge transfer reactions and the mechanism responsible for the effect.

Previous efforts in this direction are those of Schmid and co-workers (8, 9), who studied the effect of adsorbed oxygen on the gold dissolution reaction and on the Ce(III)-Ce(IV) reaction kinetics at a gold electrode. They point out that the amount of adsorbed oxygen on a noble metal electrode can be controlled

* Electrochemical Society Active Member.
Key words: electrode kinetics, oxygen coverage, double layer, blocking effects.

and determined through its charge equivalent upon electroreduction. Moreover, the oxygen adsorption-desorption behavior at such electrodes exhibits a hysteresis which makes it possible to have various coverages on the surface at a fixed potential. This allows the kinetics of a charge transfer reaction to be studied as a function of oxygen coverage alone, all other experimental conditions being held constant. However, Bonewitz and Schmid's (9) choice of gold as the test electrode limited the scope of their study in two respects. Firstly, oxygen adsorbs on gold only at a potential above 1.2V *vs.* NHE, and the number of simple electron transfer reactions with equilibrium potentials in the range of 1.2-1.4V is small. Secondly, relative to the oxygen adsorption curves of gold, the equilibrium (formal) potential of the Ce(III)-Ce(IV) couple is such as to permit kinetic data to be taken only at coverages equivalent to or greater than about 0.6 of a monolayer. Trends at $0.6 \leq \theta \leq 1$ indicate the possibility of a more dramatic rate change in the $\theta = 0$ to $\theta = 0.6$ range of coverage.

In the present study rhodium was chosen as the test electrode material. Although the hysteresis of oxygen adsorption on rhodium is not as pronounced as on gold, the potential range over which adsorption occurs begins at 0.6V, making it possible to choose some simple redox couples whose rates can be studied as a function of oxygen coverage in the $\theta = 0$ to $\theta = 1$ range. Accordingly, the test systems chosen were the Fe(II)-Fe(III) and hydroquinone-quinone couples, the kinetics of which have been thoroughly studied by other workers and are well known to be free of undue complications (6).

Experimental

Solutions and materials.—The water employed throughout this work was distilled once from alkaline permanganate, then twice more in an all-quartz still. The 1.0*M* $HClO_4$ was made up directly from standardized reagent grade 70% $HClO_4$ solutions. 0.1*M* ferrous and ferric perchlorate stock solutions were prepared in 1.0*M* $HClO_4$ from the reagent grade salts once recrystallized from 1.0*M* $HClO_4$. The ferrous and ferric ion concentrations were determined by titrating aliquots of each solution with standard permanganate, both with and without prereduction with stannous chloride. When kept in closed flasks, periodic restandardization showed the 0.1*M* ferrous solutions to be stable with respect to air oxidation over the two to three week periods of usage. All hydroquinone and quinone test solutions were prepared gravimetrically from the reagent grade materials without further purification.

The all-Pyrex electrochemical cell was of standard design and contained in the main compartment a rhodium wire test electrode (Englehard Industries) of 0.100 cm^2 apparent surface area and a large-area platinum wire gauze auxiliary electrode. The main compartment was connected via a Haber-Luggin capillary to a side compartment containing a saturated calomel reference electrode. The capillary contained a normally closed ground glass stopcock to prevent chloride contamination of the test solution. In addition, the cell was fitted with gas lines to allow purging of dissolved oxygen from the test solutions with helium. The lines were made of Pyrex glass and 5/16 in. Teflon tubing connected with Teflon Swageloks.

Experimental procedures.—At the outset of this work, the test electrode was cleaned by brief immersion in aqua regia followed by washing with copious amounts of water. Thereafter, and preceding each run, the electrode was cleaned by immersion in chromosulfuric cleaning solution for 10 min and then thoroughly rinsed with water. To purge the test solutions of oxygen, a constant stream of helium (99.99% pure) was bubbled through the cell for at least 8 hr prior to and during a run. Solutions were stirred with a magnetic stirrer.

The oxygen coverage of the test electrode was determined by constant current cathodic stripping. To determine the ascending coverage (*i.e.*, coverage established coming from more cathodic potentials) the electrode was first set to 0.25V, where the surface is free of adsorbed oxygen, for at least 5 min using a Wenking Model 70TS1 potentiostat. The electrode was then set to a value in the range of 0.65-1.65V and held there for 10 min to allow for the oxygen coverage to reach steady state. The potentiostat, which was bucking the current from a Kepco Model ABC 40-0.5M power supply, was then disconnected from the circuit using a Potter and Brumfield mercury-wetted relay, which simultaneously triggered a storage oscilloscope (Tektronix, Model 564B). The potential-time function produced by the stripping current was displayed on the oscilloscope screen. "Transition times" were read from inflection point to inflection point and the charge calculated as the product of stripping current and time. For determination of the descending coverage (*i.e.*, coverage established coming from more anodic potentials) the electrode was held at 0.25V and then at some value in the 0.65-1.65V range for 5 and 10 min, respectively. The potential was then lowered to a value between 1.65 and 0.40V and held there for another 10 min, after which stripping was carried out as above. The constant stripping current from the power supply was found by measuring the potential drop across a standard resistor with a Hewlett Packard 425A electrometer.

Apparent exchange currents, i_o^a, for the Fe(II)-Fe(III) and hydroquinone-quinone reactions were obtained at various equilibrium potentials and various oxygen coverages of the electrode and were computed from the slopes of low overpotential *vs.* current density data. Prior to the application of overpotentials about a given equilibrium potential the oxygen coverage was always established as described above. Overvoltages were applied in steps of ±5 and ±4 mV about the equilibrium potentials of the hydroquinone-quinone and Fe(II)-Fe(III) systems, respectively, with the total applied overvoltages for the two systems being ±15 and ±16 mV, respectively. Again, the currents were determined by measuring the potential drop across a standard resistor with a Hewlett Packard 425A electrometer. Typical plots are shown in Fig. 1.

Results and Discussion

Cathodic stripping.—In the cathodic stripping of rhodium in acidic solutions, the removal of adsorbed

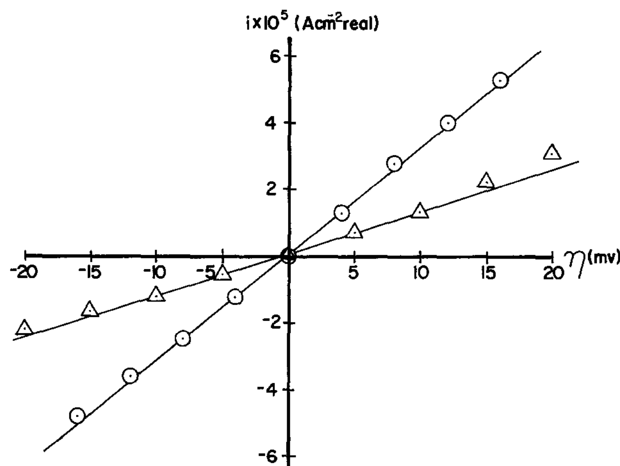

Fig. 1. Typical plots of current density *vs.* overpotential. ○: Fe(II)-Fe(III) reaction ($5.41 \times 10^{-3}M$ Fe(II), $1.786 \times 10^{-3}M$ Fe(III), $E_{eq} = 0.731V$, $\theta = 0.76$); △: hydroquinone-quinone reaction ($1.010 \times 10^{-3}M$ H_2Q, $0.1303 \times 10^{-3}M$ Q, $E_{eq} = 0.616V$, $\theta = 0.26$).

oxygen is followed by the adsorption of hydrogen. The potential of oxygen removal is more negative the higher the potential at which the coverage is established and the larger the stripping current density, making it increasingly more difficult to separate oxygen removal from hydrogen adsorption (10, 11). However, no major difficulties were encountered with current densities of less than 10 mA cm^{-2}. In the experiments reported here the stripping current density was 5 mA cm^{-2}. The results are shown in Fig. 2. The hysteresis frequently found for oxygen adsorption on noble metals is evident, *i.e.*, the coverage depends on the highest potential reached prior to stripping. It is assumed, as in the case of gold (9), that the change in slope of the ascending curve at +0.95V indicates the point at which a monolayer of oxygen atoms is adsorbed on the surface. The charge corresponding to this break is 2700 $\mu C\ cm^{-2}$ apparent. Taking 560 $\mu C\ cm^{-2}$ real (two electrons per rhodium surface atom and 1.74×10^{15} atoms cm^{-2}), the roughness factor calculated is approximately 5, a value not unreasonable for an etched electrode. Fractional coverages, θ, were calculated using 2700 $\mu C\ cm^{-2}$ apparent as representing monolayer coverage. All kinetic parameters reported in this paper are reported in terms of real area using a roughness factor of 5.

A charge of 560 $\mu C\ cm^{-2}$ real for a monolayer and a roughness factor of 5 agree well with the results of other workers. Thus, Böld and Breiter (10) find a charge of about 1.3 mC cm^{-2} apparent with oxygen uptake starting at 0.55V in acidic solution. Icenhower *et al.* (11) report approximately 0.5 mC at 1.0V *vs.* RHE in acidic solution on what appears to be a smooth Rh wire of 0.4 cm^2 apparent area. Will and Knorr (12) show a change of slope of the oxygen uptake curve at about 0.9V and a charge of about 0.4 mC cm^{-2} in good agreement with the results presented here.

The Fe(II)-Fe(III) reaction.—Ten ferrous-ferric mixtures, varying from 5.35×10^{-4}M to 5.41×10^{-3}M in Fe^{++} and 4.82×10^{-4}M to 5.73×10^{-3}M in Fe^{+++} (Table I), all 1.0*M* in $HClO_4$, were used in studying the reaction kinetics of this system. The equilibrium potentials showed good Nernstian behavior.

For each solution the apparent exchange current, i_o^a, was determined as a function of oxygen coverage of the electrode in the range of $0.3 \leq \theta \leq 1.6$ by appropriate selection of the initial anodic potential of the electrode. The experimental data are listed in Table I. A representative plot is shown in Fig. 3. Typically, i_o^a decreased linearly with increasing θ down to a coverage of $\theta = \sim 1.3$, beyond which point i_o^a appeared to decline at a much slower rate.

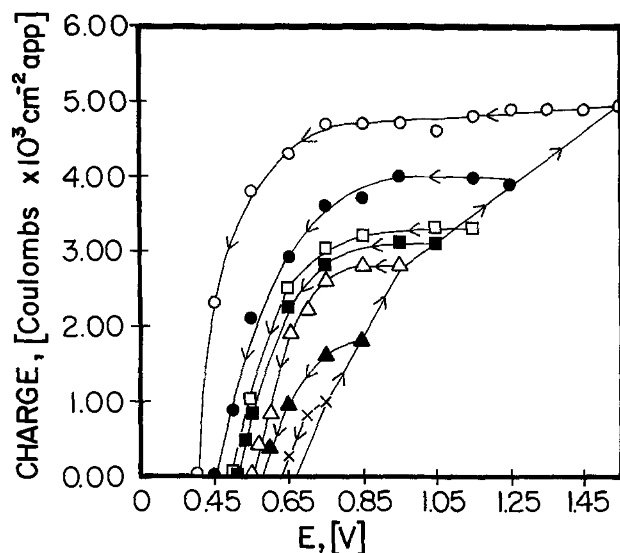

Fig. 2. Cathodic stripping curves for oxygen on rhodium in 1*M* $HClO_4$. Decay from ⊙, 1.55V; ●, 1.25V; ⊡, 1.15V; ■, 1.05V; △, 0.95V; ▲, 0.85V; x, 0.75V.

Table I. Exchange current vs. fractional coverage for the Fe(II)-Fe(III) system

Solution	Equilibrium potential (V *vs.* NHE)	θ	$i_o^a \times 10^5$ (A cm^{-2} real)
5.37×10^{-3}M Fe^{++} and 3.992×10^{-3}M Fe^{+++}	0.733	0.29	6.76
		0.57	5.58
		0.76	5.44
		0.94	5.02
		1.09	1.80
		1.30	0.824
		1.56	0.500
5.35×10^{-3}M Fe^{++} and 0.4817×10^{-3}M Fe^{+++}	0.712	0.33	7.04
		0.53	4.92
		0.72	4.74
		0.91	3.60
		0.98	1.72
		1.26	0.432
		1.53	0.244
0.535×10^{-3}M Fe^{++} and 3.926×10^{-3}M Fe^{+++}	0.797	0.64	3.14
		0.83	4.00
		1.03	2.42
		1.11	2.08
		1.39	0.450
		1.60	0.210
1.605×10^{-3}M Fe^{++} and 3.944×10^{-3}M Fe^{+++}	0.771	0.51	8.00
		0.63	6.22
		0.81	5.90
		1.00	4.96
		1.08	2.90
		1.36	0.572
		1.59	0.284
5.35×10^{-3}M Fe^{++} and 1.265×10^{-3}M Fe^{+++}	0.732	0.37	13.28
		0.46	11.90
		0.57	10.32
		0.77	8.58
		0.95	6.56
		1.03	2.70
		1.30	0.672
		1.55	0.356
5.41×10^{-3}M Fe^{++} and 5.73×10^{-3}M Fe^{+++}	0.740	0.47	19.34
		0.58	15.72
		0.77	13.22
		0.96	10.26
		1.04	4.50
		1.30	1.15
		1.56	0.648
5.41×10^{-3}M Fe^{++} and 0.659×10^{-3}M Fe^{+++}	0.696	0.30	5.12
		0.40	4.38
		0.49	3.52
		0.69	3.64
		0.87	2.76
		0.96	1.34
		1.21	0.444
		1.51	0.316
0.541×10^{-3}M Fe^{++} and 5.64×10^{-3}M Fe^{+++}	0.809	0.66	2.74
		0.84	2.52
		1.03	2.12
		1.11	1.44
		1.40	0.436
		1.61	0.228
$1.62 \times 10M^{-3}$ Fe^{++} and 5.66×10^{-3}M Fe^{+++}	0.781	0.54	9.68
		0.64	8.74
		0.81	7.12
		1.01	6.20
		1.09	3.40
		1.37	0.768
		1.59	0.398
5.41×10^{-3}M Fe^{++} and 1.786×10^{-3}M Fe^{+++}	0.731	0.40	14.14
		0.58	10.18
		0.76	8.16
		0.95	6.18
		1.03	2.70
		1.29	0.674
		1.55	0.418

Values of the apparent charge transfer coefficient, α, and the standard rate constant, k_o^a, were obtained at various oxygen coverages by using the expression (13)

$$\ln (i_o^a/c_o) = -(n\mathbf{F}\alpha/RT)E_{eq} + \ln n\mathbf{F}Ak_o^a$$

where c_o is the concentration of the oxidized species, in this case Fe(III). Thus, α values were calculated from the slopes and k_o^a values from the intercepts of plots in $\ln (i_o^a/c_o)$ *vs.* E_{eq}, keeping the coverage of adsorbed oxygen constant for any one plot. Such plots were made for oxygen coverages of $\theta = 0$, 0.25, 0.50, 0.75, 1.00, 1.25, and 1.50 with the appropriate i_o^a values being obtained by interpolation or extrapolation from the i_o^a *vs.* θ plots. Two representative plots are shown in Fig. 4. The slopes and intercepts were obtained by a least squares analysis, assuming E_{eq} to be known precisely. The results are summarized in Table II, from which it can be seen that α remains fairly constant with oxygen coverage $0 \leq \theta \leq 1.5$. Figure 5 shows the plot of the least

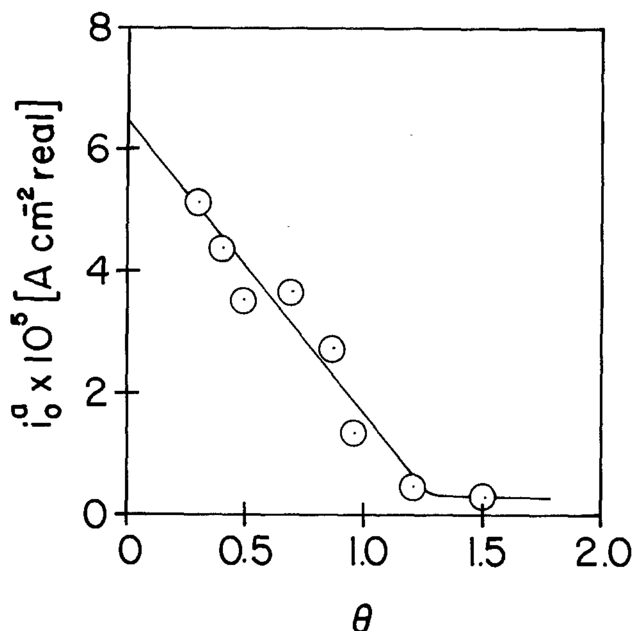

Fig. 3. Effect of θ on i_o^a for the Fe(II)-Fe(III) reaction. Solution 1.0M in $HClO_4$, 5.41 × $10^{-3}M$ in Fe^{++}, and 0.659 × $10^{-3}M$ in Fe^{+++}.

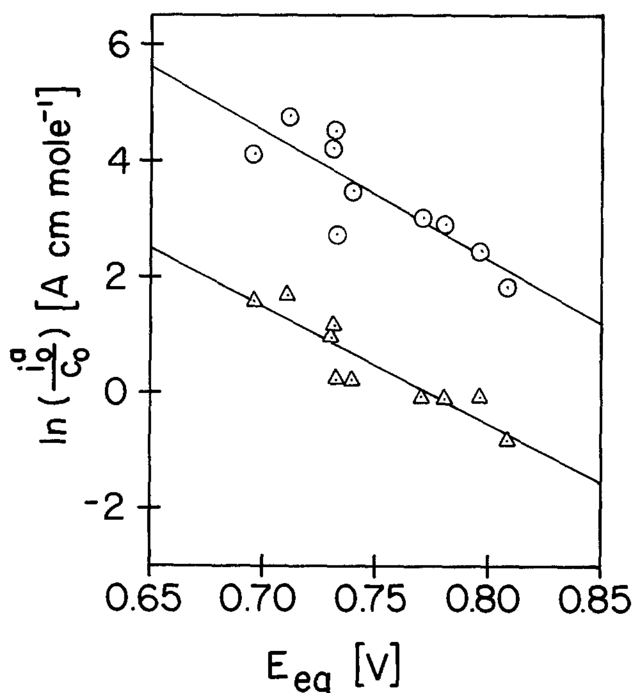

Fig. 4. Plots of $\ln(i_o^a/c_o)$ vs. E_{eq} for the Fe(II)-Fe(III) reaction. ⊙: $\theta = 0.5$; △: $\theta = 1.5$.

squares k_o^a values *vs.* oxygen coverage. k_o^a decreases linearly up to $\theta = 1.4$, but then seems to diminish much more slowly.

Standard rate constants quoted in the literature for the Fe(II)/Fe(III) reaction in both 1M $HClO_4$ and 1M H_2SO_4 on Pt are generally between 5 × 10^{-3} and 2 × 10^{-2} cm sec^{-1} and are thus higher by a factor of 6-10 than the values reported here (14-19). On glassy carbon in $HClO_4$ they are > 10^{-2} cm sec^{-1} (20), on carbon paste in H_2SO_4 ~10^{-5} cm sec^{-1} (21, 22). In view of the dependence of the rate on electrode material the k_o^a for Rh at $\theta = 0$ is quite reasonable. The values of α are in good agreement with Stulikova's and Gerischer's work (14, 20) on Pt in H_2SO_4 and $HClO_4$.

The hydroquinone-quinone reaction.—Five different hydroquinone-quinone solutions varying from 8.57 × $10^{-5}M$ to 1.06 × $10^{-2}M$ in hydroquinone and from 9.26 × $10^{-5}M$ to 4.46 × $10^{-3}M$ in quinone were used in studying the kinetics of this reaction. Apparent exchange currents were determined in the same way as for the Fe(II)-Fe(III) system, with values being obtained for oxygen coverages ranging from $\theta = 0$ to $\theta = 1.65$. Table III contains these data for all solutions. A typical plot of i_o^a *vs.* θ is shown in Fig. 6, and indicates a linear variation of i_o^a with oxygen coverage over the range of $\theta = 0$ to $\theta = $ ~0.7. At higher values of θ, i_o^a is constant within experimental error.

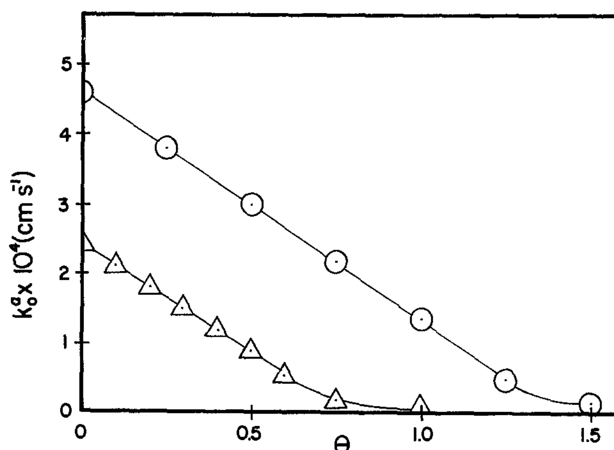

Fig. 5. Effect of θ on k_o^a. Data from Table II. ○: Fe(II)-Fe(III) reaction; △: hydroquinone-quinone reaction.

Values for α and k_o^a at various oxygen coverages were obtained using the same procedures employed for the Fe(II)-Fe(III) system. Plots of ln (i_o^a/c_o) *vs.* E_{eq} were constructed for oxygen coverages of θ = 0.0, 0.10, 0.20, 0.30, 0.40, 0.50, 0.60, 0.75, 1.00, 1.25, and 1.50. The plots at $\theta = 0$ and $\theta = 1.0$ are shown in Fig. 7. Table II lists the least squares values of α and k_o^a obtained from these plots. Over the entire range of coverages α is reasonably constant although a slight downward drift is noted in the $\theta = 0$ to $\theta = 1.0$ segment. In the k_o^a *vs.* θ plot given in Fig. 5, the decline in k_o^a is seen to occur in the $\theta = 0$ to $\theta = 0.75$ region of coverage. The decrease is parallel to the one observed for the Fe(II)-Fe(III) system, where it occurs over the more extensive range $0 \leq \theta \leq 1.40$.

According to Vetter (23) and to Hale and Parsons (24), the hydroquinone-quinone reaction is a two one-electron step reaction, with approximately equal activation energy for each step. In acetonitrile the reaction is one two-electron step (25) and there is evidence in the literature that this is so in aqueous solutions also (26). At pH 3.9, Parsons (24) finds α

Table II. Kinetic parameters as a function of θ for the Fe(II)-Fe(III) and the hydroquinone-quinone system

	Fe(II)-Fe(III)		Hydroquinone-quinone	
θ	α	k_o^a × 10^4 (cm sec^{-1})	α	k_o^a × 10^4 (cm sec^{-1})
0.00	0.59	4.60	0.61	2.42
0.10			0.60	2.11
0.20			0.59	1.82
0.25	0.58	3.79		
0.30			0.58	1.51
0.40			0.55	1.20
0.50	0.57	2.99	0.51	0.889
0.60			0.40	0.544
0.75	0.54	2.18	(0.28)*	0.187
1.00	0.49	1.35	0.48	0.0581
1.25	(0.25)*	0.480	0.45	0.0377
1.50	0.52	0.159	0.49	0.0319
	average α = 0.55 ± 0.04		average α = 0.53 ± 0.07	

* Omitted from average.

Table III. Exchange current vs. fractional coverage for the hydroquinone-quinone system

Solution	Equilibrium potential (potential vs. NHE)	θ	$i_o^a \times 10^6$ (A cm^{-2} real)
1.018 × 10^{-3}M H_2Q[a] and 1.015 × 10^{-3}M Q	0.643	0.00	63.4
		0.33	46.2
		0.70	14.3
		0.81	3.26
		1.15	0.748
		1.33	0.642
		1.59	0.658
1.010 × 10^{-3}M H_2Q and 0.1303 × 10^{-3}M Q	0.616	0.00	23.2
		0.26	16.3
		0.52	5.54
		0.70	1.32
		1.07	0.232
		1.26	0.191
		1.56	0.224
0.08573 × 10^{-3}M H_2Q and 1.060 × 10^{-3}M Q	0.659	0.07	21.6
		0.39	11.4
		0.74	3.30
		0.85	1.01
		1.22	0.432
		1.37	0.240
		1.62	0.236
10.63 × 10^{-3}M H_2Q and 0.0926 × 10^{-3}M Q	0.580	0.00	34.6
		0.01	31.4
		0.19	22.4
		0.48	9.30
		0.95	0.568
		1.19	0.396
		1.47	0.378
0.0908 × 10^{-3}M H_2Q and 4.461 × 10^{-3}M Q	0.674	0.11	10.84
		0.44	6.10
		0.80	2.44
		0.90	1.07
		1.25	0.576
		1.40	0.616
		1.65	0.580

[a] H_2Q = hydroquinone.
Q = quinone.

= 0.58 and a standard rate constant, k_o^a = 1.4 × 10^{-3} cm sec^{-1}, about six times larger than the one reported here on oxygen-free rhodium.

Interpretation of Results and Conclusions

The dominant and most interesting feature of the charge transfer rate data presented in this paper is that most of the inhibitive effect produced by oxygen adsorption occurs during the buildup of the first monolayer of coverage. This behavior could be attributed to (*i*) a change in the reaction mechanism, which would cause changes in both α and k_o^a; (*ii*) a double layer field effect; or possibly (*iii*) a simple geometric blocking effect.

Possibility (*i*) can be excluded because α is essentially independent of oxygen coverage in the range in which the major decrease occurs in k_o^a both for the Fe(II)-Fe(III) and the hydroquinone-quinone reaction systems.

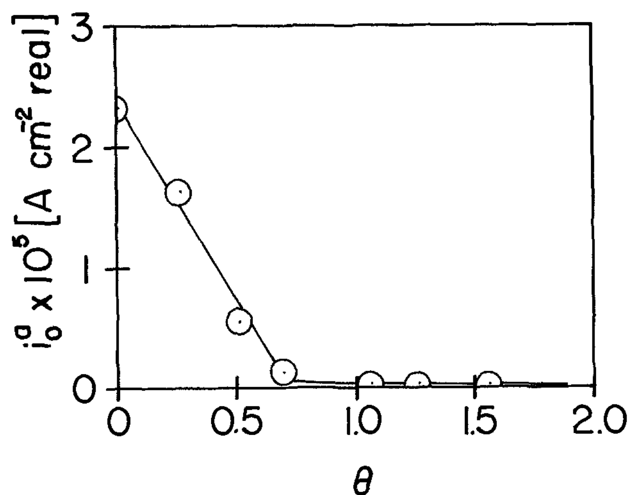

Fig. 6. Effect of θ on i_o^a for the hydroquinone-quinone reaction. Solution 1.0M in $HClO_4$, 1.010 × 10^{-3}M in hydroquinone and 0.1303 × 10^{-3}M in quinone.

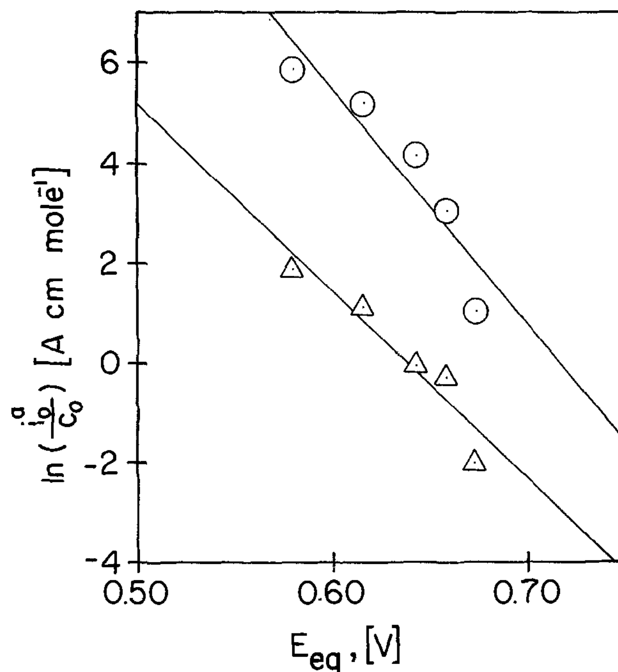

Fig. 7. Plots of $\ln(i_o^a/c_o)$ vs. E_{eq} for the hydroquinone-quinone system. ⊙: θ = 0.0; △: θ = 1.0.

The field effect explanation (*ii*) of the data involves the assumption that the presence of adsorbed oxygen on the electrode surface causes, at constant electrode potential, a change in ϕ_c, the potential drop across the compact double layer with a concomitant change in ϕ_2, the potential drop across the diffuse double layer. This changes the electric field at the site of the reaction, affecting k_o^a but not α. The change in ϕ_2 caused by a monolayer of oxygen coverage can be estimated by assuming that there is an apparent standard rate constant for the oxygen-covered surface, $k_{o}^{a}{}_{,\theta=1}$ and one for the bare surface, $k_{o}^{a}{}_{,\theta=0}$. We can then write (13)

$$k_{o}^{a}{}_{,\theta=0} = k_o^t \exp[-(z_R + \alpha)(F/RT)\phi_{2,\theta=0}]$$

and

$$k_{o}^{a}{}_{,\theta=1} = k_o^t \exp[-(z_R + \alpha)(F/RT)\phi_{2,\theta=1}]$$

where k_o^t is the true standard rate constant and z_R is the charge of the reduced species. Therefore, for a given reaction

$$k_{o}^{a}{}_{,\theta=0}/k_{o}^{a}{}_{,\theta=1} = \exp[-(z_R + \alpha)(F/RT)\Delta\phi_2]$$

where $\Delta\phi_2 = (\phi_{2,\theta=0} - \phi_{2,\theta=1})$ is the change sought. For the Fe(II)-Fe(III) couple, $k_o^a{}_{\theta=0}$ = 4.60 × 10^{-4} cm sec^{-1}, $k_{o}^{a}{}_{,\theta=1}$ = 2 × 10^{-5} cm sec^{-1} (at θ = 1.40), and $\Delta\phi_2$ = (−)32 mV. For the hydroquinone-quinone couple, $k_{o}^{a}{}_{,\theta=0}$ = 2.42 × 10^{-4} cm sec^{-1}, $k_{o}^{a}{}_{,\theta=1}$ = 1.87 × 10^{-5} cm sec^{-1} (at θ = 0.75), and $\Delta\phi_2$ = (−)124 mV. The discrepancy between the $\Delta\phi_2$ values for the two reaction couples, 32 *vs.* 124 mV, is too great to be rationalized on the basis of the difference in θ (1.40 *vs.* 0.75). Alternatively, the presence of adsorbed oxygen could cause changes in the plane of closest approach of the reactants, *i.e.*, changes in the value of the activity coefficient of the activated complex (2). This requires $\ln(k_{o}^{a}{}_{,\theta}/k_{o}^{a}{}_{,\theta=0})$ to be linear in θ. Such plots are convex for Fe(II)-Fe(III) and sigmoid in shape for the hydroquinone-quinone system. The results strongly argue that over the θ = 0 to θ = 1 coverage range, the data cannot adequately be explained as due to a double layer field effect.

The geometric blocking model (*iii*) together with the assumption that charge transfer is much more rapid at free rhodium than at oxygen-covered rho-

dium accounts particularly well for the marked linearity of the k_o^a *vs.* θ plots and for the fact that they are parallel for the two systems studied. Furthermore, these plots show that while for the Fe(II)-Fe(III) system the major decline in rate occurs over the $\theta = 0$ to $\theta = 1.4$ coverage range, the corresponding decline for the hydroquinone-quinone system occurs over only half that range, from $\theta = 0$ to $\theta = 0.75$. At $\theta = 0.75$, the rate for the Fe(II)-Fe(III) reaction is about half its value at $\theta = 0$, indicating that at $\theta = 0.75$ the remaining free rhodium surface atoms are sterically accessible to ferrous and ferric ions. In the hydroquinone-quinone system, however, the rhodium atoms that are still uncovered at $\theta = 0.75$ are apparently sterically inaccessible to hydroquinone and/or quinone molecules. If the planar quinone (or hydroquinone) molecule must lie flat on the free electrode surface to react, then its dimensions (5.5Å from oxygen to oxygen) require a free surface equivalent to that provided by at least two adjacent free rhodium surface atoms, and this is a very unlikely occurrence beyond $\theta = 0.75$. Organic compounds containing ring systems are frequently found to lie flat on electrode surfaces (28). Apparently in order to be blocking the Fe(II)-Fe(III) reaction the film must be slightly thicker than a monolayer.

In both reaction systems charge transfer occurs at greater than monolayer coverage, albeit at a much slower rate. Generally, the data indicate that at coverages beyond $\theta = 1.40$ for the Fe(II)-Fe(III) couple and beyond $\theta = 0.75$ for the hydroquinone-quinone couple, the charge transfer rate is not much affected by increasing oxygen coverage. This is especially obvious in the hydroquinone-quinone system, and is in agreement with Bonewitz and Schmid's observations (3) for the Ce(IV)-Ce(III) reaction on gold from $\theta = 1$ to $\theta = 2$.

Summary

Oxygen coverages on rhodium in 1M $HClO_4$ were determined as a function of potential. Working with increasing potential, the uptake begins at 0.65V, has reached a monolayer, $\theta = 1$ at 0.95V and $\theta = 1.8$ at 1.55V. The uptake is linear with potential. Hysteresis is pronounced; when working with decreasing potentials rhodium becomes oxygen free at potentials from 0.65 to 0.35V as the highest potential reached varies from 0.65 to 1.55V.

Apparent rate constants, k_o^a, and charge transfer coefficients, α, were measured for the Fe(II)-Fe(III) system for solutions having equilibrium potentials 0.809 to 0.696V as a function of oxygen coverage $0 \leq \theta \leq 1.5$. At $\theta = 0$, $k_a^o = 4.60 \times 10^{-4}$ cm sec^{-1} and shows a systematic decrease to $k_a^o = 2 \times 10^{-5}$ cm sec^{-1} at $\theta = 1.40$, decreasing only slightly to $\theta = 1.50$. In the range $0 \leq \theta \leq 1.5$ α has values $0.59 > \alpha > 0.49$, generally decreasing slightly with θ. It is considered to be constant over the range studied.

For the quinone-hydroquinone system, solutions had equilibrium potentials 0.580-0.674V. At $\theta = 0$, $k_a^o = 2.42 \times 10^{-4}$ cm sec^{-1}, decreasing to 1.87×10^{-5} cm sec^{-1} at $\theta = 0.75$. The decrease in k_a^o at $\theta > 0.75$ is minor. A decrease is apparent in α which varies from 0.61 at $\theta = 0$ to 0.49 at $\theta = 1.5$. The mean is 0.53 ± 0.07 and α is considered constant, the variation not being consistent enough to justify the assumption of a coverage dependence. The approximate constancy of α indicates that the reaction mechanism is independent of θ.

The effect of oxygen coverage on the apparent rate constant could be caused by a double layer effect. Accordingly $\Delta\phi_2$ potentials were calculated for the two systems, $\Delta\phi_2 = \phi_{2,\theta=1} - \phi_{2,\theta=0}$. The values are 37 mV for Fe and 124 mV for quinone. The two values seem inconsistent with each other, even taking into account the difference in the values of θ at which blocking is at its maximum.

The assumption of a blocking effect is consistent with the observed variation of k_a^o with θ and with the steric requirements of the reactants at the rhodium surface.

Manuscript submitted May 13, 1977; revised manuscript received Nov. 7, 1977.

Any discussion of this paper will appear in a Discussion Section to be published in the December 1978 JOURNAL. All discussions for the December 1978 Discussion Section should be submitted by Aug. 1, 1978.

REFERENCES

1. R. Parsons, in "Advances in Electrochemistry and Electrochemical Engineering," Vol. 1, P. Delahay and C. W. Tobias, Editors, pp. 1ff, Interscience Publishers, New York (1961).
2. R. Parsons, *J. Electroanal. Chem. Interfacial Electrochem.*, **21**, 35 (1969).
3. R. DeLevie, *This Journal*, **118**, 185C (1971).
4. R. Guidelli and M. L. Foresti, *Electrochim. Acta*, **18**, 301 (1973).
5. M. L. Foresti and R. Guidelli, *J. Electroanal. Chem. Interfacial Electrochem.*, **53**, 219 (1974).
6. K. Vetter, "Electrochemical Kinetics," Academic Press, New York (1967).
7. A. G. Kormienko, L. A. Mirkind, and M. Ya. Fioshin, *Elektrokhimiya*, **3**, 1370 (1967).
8. J. N. Gaur and G. M. Schmid, *J. Electroanal. Chem. Interfacial Electrochem.*, **24**, 279 (1970).
9. R. A. Bonewitz and G. M. Schmid, *This Journal*, **117**, 1367 (1970).
10. W. Böld and M. Breiter, *Electrochim. Acta*, **5**, 169 (1961).
11. D. E. Icenhower, H. B. Urbach, and J. H. Harrison, *This Journal*, **117**, 1500 (1970).
12. F. G. Will and C. A. Knorr, *Z. Elektrochem.*, **64**, 270 (1960).
13. P. Delahay, "Double Layer and Electrode Kinetics," Interscience Publishers, New York (1965).
14. H. Gerischer, *Z. Elektrochem.*, **54**, 366 (1950).
15. J. E. B. Randles and K. W. Somerton, *Trans. Faraday Soc.*, **48**, 937 (1952).
16. M. D. Wijnen and W. M. Smit, *Recl. Trav. Chim. Pays-Bas.*, **79**, 289 (1952).
17. F. C. Anson, *Anal. Chem.*, **33**, 939 (1961).
18. D. Jahn and W. Vielstich, *This Journal*, **109**, 849 (1962).
19. J. Jordan and R. A. Javick, *Electrochim. Acta*, **6**, 23 (1962).
20. M. Stulikova and F. Vydra, *J. Electroanal. Chem. Interfacial Electrochem.*, **38**, 349 (1972).
21. R. J. Lawrence and J. A. Chambers, *Anal. Chem.*, **39**, 134 (1967).
22. Z. Galus and R. N. Adams, *J. Phys. Chem.*, **67**, 866 (1963).
23. K. J. Vetter, *Z. Elektrochem.*, **56**, 797 (1952).
24. J. M. Hale and R. Parsons, *Trans. Faraday Soc.*, **59**, 1429 (1963).
25. B. R. Eggins and J. Q. Chambers, *This Journal*, **117**, 186 (1970).
26. M. A. Loshkarev and B. I. Tomilov, *Russ. J. Phys. Chem. (Engl. Transl.)*, **34**, 836 (1960); **36**, 66 (1962).
27. W. Lorenz and K.-H. Lubert, *Z. Phys. Chem. (Leipzig)*, **241**, 285 (1969).
28. B. B. Damaskin, O. A. Petrii, and V. V. Batrakov, "Adsorption of Organic Compounds on Electrodes," Plenum Press, New York (1971).

Electrochemical Determination of Interdiffusivity of Cations in Liquid Li_2O-SiO_2 System at 1100° to 1350°C

M. Kawakami,* K. Nagata,[1] and K. S. Goto

Department of Metallurgical Engineering, Tokyo Institute of Technology, Tokyo, Japan

ABSTRACT

An electrochemical polarization method was proposed to obtain the interdiffusivity in molten binary ionic melts at high temperature. The following galvanic cell was constructed using molten Li_2O-SiO_2 as an electrolyte

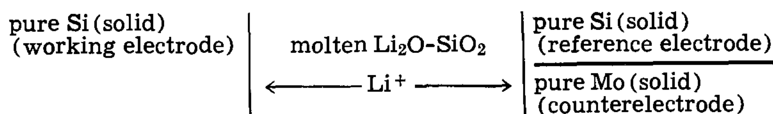

A small direct current was supplied for a very short time through the left silicon electrode and pure molybdenum electrode, while the overpotential was measured between both silicon electrodes. The overpotential induced at the left silicon electrode was related to the interdiffusion of Li_2O-SiO_2 at the electrode interface. From the time dependency of the overpotential, the interdiffusivities at definite composition were obtained as follows:

For 20 weight percent (w/o) Li_2O-80 w/o SiO_2

$D = 7.2 \times 10^{-3} \exp(-33 \times 10^3/RT$ (cm²/sec) 1100°-1350°C

For 30 w/o Li_2O-70 w/o SiO_2

$D = 3.0 \times 10^{-3} \exp(-29 \times 10^3/RT$ (cm²/sec) 1200°-1350°C

These results are quite reasonable compared with other interdiffusivity data in other molten binary silicates obtained by the conventional method.

The experimental technique of high temperature electrochemistry has been developed extensively since a discovery of very stable solid electrolytes by Kiukkola and Wagner (1) in 1957. Many papers have been published on thermodynamic studies at 500° ~ 1600°C with the aid of these zirconia- and thoria-based electrolytes. Recently, Fischer and Janke (2) documented all the papers up to 1975 in their comprehensive monograph. The studies were exclusively made on thermodynamic properties up to 1967. However, Rickert and Steiner (3) in 1966 and Pastorek and Rapp (4) in 1969 used the solid electrolytes to determine the diffusivity of oxygen dissolved in silver and copper, respectively. The principle of the measurement is based on the electrical current limited by the diffusion of oxygen dissolved in the metallic electrode. The same principle was used by Sasabe and Goto (5) to determine the diffusion of molecular oxygen dissolved in liquid oxide mixtures. As another application of this principle the present authors (6, 7) proposed the method of determining the interdiffusivity of ions in liquid oxide mixtures from the variation of the potential or current with time. In this method, the current is supplied to the following type of the cell

$$\text{solid metal, B/liquid } AO_m\text{-}BO_n\text{/solid metal B} \quad [1]$$

where A and B mean metals, and the liquid oxide mixture AO_m-BO_n has an exclusive cationic conduction by A^{2m+} and AO_m is thermodynamically much stabler than BO_n. The details of the measurement are given in the following section, but the principle is based on the current limited by the interdiffusion of cations of A^{2m+} and B^{2n+} in the oxide melts. A similar idea has been proposed also by Nowak and Schwerdtfeger (8).

This new principle does not need cumbersome analyses of the oxide mixture quenched after a diffusion run. Further, this method suffers from no effect of the convection in the oxide melt, because the diffusion distance is very limited from the surface of the solid electrode. Thus it seems very interesting to prove its universal applicability to many oxide melts. The present paper reports the results on the system of Li_2O-SiO_2.

Experimental Method of Determining the Interdiffusivity

Principle.—The following cell is constructed using molten oxide itself as an electrolyte

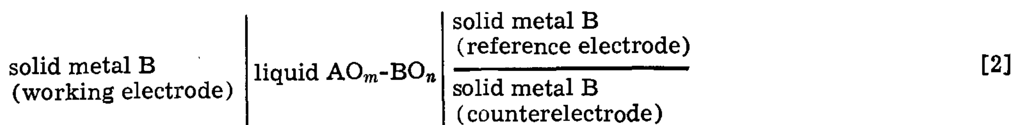

Essential requirements for the interdiffusivity measurement are: (*i*) the transference number of A^{2m+} should be unity (*ii*) the standard free energy of formation of AO_m should be much smaller than that of BO_n, and (*iii*) activity data in the molten AO_m-BO_n are available.

Wagner (9) derived a general equation for electromotive force of any galvanic cells in terms of the chemical potential of electrically neutral species, based on only two assumptions of local equilibrium and of electrical neutrality throughout the cell,

$$E = -\frac{1}{\mathbf{F}}[-\tilde{\mu}''_{[B]} + \tilde{\mu}'_{[B]} + \Sigma_\alpha \int t_\alpha d\tilde{\mu}_{\alpha B} - \Sigma_{\beta=e} \int t_\beta d\tilde{\mu}_{A\beta}$$

$$+ \int (\Sigma_{\beta=e} t_\beta) d\tilde{\mu}_{AB} + \int t_e d\tilde{\mu}_{[B]} + \Sigma_\gamma \int t^*_\gamma d\mu_\gamma] \quad [3]$$

* Electrochemical Society Active Member.
[1] Present address: Centro de Ingenierial y Computacion, I.V.I.C., Caracas, Venezuela.

Key words: polarization, galvanostat, alkali, silicates.

where $\tilde{\mu}$ is the chemical potential per equivalent, t is transference number, α and β denote cation and anion, respectively. The prime and double prime show different electrode interfaces. The other symbols are the same as those in Ref. (9). Equation [3] is appropriate to apply to the expression of electromotive force or potential difference in ionic solutions at high temperature such as molten oxides and molten halides, because the local equilibrium condition is very easily satisfied and no other arbitrary conventions are needed. In the present case of molten binary silicates with the transference number $t_{A^{2m+}}$ of unity, the equation can be simplified as

$$E = \frac{RT}{4\mathbf{F}} \ln \frac{P''_{O_2}}{P'_{O_2}} - \frac{RT}{2m\mathbf{F}} \ln \frac{a''_{AO_m}}{a'_{AO_m}} \quad [4]$$

At each electrode interface in the above cell, P_{O_2} is determined by the following reaction equilibrium as long as AO_m is much stabler than BO_n

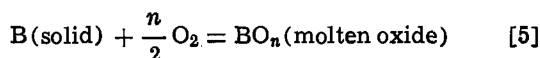

$$B(\text{solid}) + \frac{n}{2} O_2 = BO_n(\text{molten oxide}) \quad [5]$$

Further, the activity of pure metal B is taken as unity. Then, P_{O_2} in Eq. [4] can be replaced by the activity of BO_n in the molten oxide

$$E = \frac{RT}{2n\mathbf{F}} \ln \frac{a''_{BO_n}}{a'_{BO_n}} - \frac{RT}{2m\mathbf{F}} \ln \frac{a''_{AO_m}}{a'_{AO_m}} \quad [6]$$

When the whole of the cell is in equilibrium before supplying a current, the potential differences between three electrodes should be zero.

When a finite cathodic current is supplied to the working electrode, the following series of reactions will take place

$$A^{2m+} + ame \rightarrow A(\text{metal}) \quad [7]$$

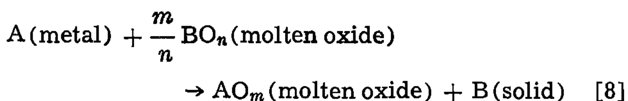

$$A(\text{metal}) + \frac{m}{n} BO_n(\text{molten oxide}) \rightarrow AO_m(\text{molten oxide}) + B(\text{solid}) \quad [8]$$

because the transference number of A^{2m+} is unity and AO_m is much stabler than BO_n. As the result, the concentration of BO_n is reduced and that of AO_m is enriched at the interface with the bulk composition unchanged. Conversely, when an anodic current is supplied

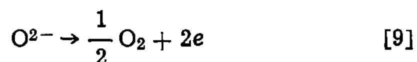

$$O^{2-} \rightarrow \frac{1}{2} O_2 + 2e \quad [9]$$

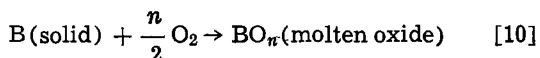

$$B(\text{solid}) + \frac{n}{2} O_2 \rightarrow BO_n(\text{molten oxide}) \quad [10]$$

The composition of the molten oxide at the interface changes conversely. The fact that such kinds of reactions really take place was proved in the previous paper (6) by the microanalyses of oxides after the current supply in the molten CaO-SiO_2-Al_2O_3 system, where CaO and Al_2O_3 are much stabler than SiO_2. Therefore, the virtual cell reaction induced by the current supply can be summarized as

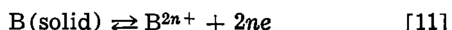

$$B(\text{solid}) \rightleftarrows B^{2n+} + 2ne \quad [11]$$

as long as AO_m is much stabler than BO_n. The overpotential η is induced by the difference of the composition between the interface and the bulk and can be expressed in terms of the activities of constituent oxides in each phase

$$\eta = \frac{RT}{4\mathbf{F}} \ln \frac{a_{BO_2}{}^{i}}{a_{BO_2}{}^{b}} - \frac{RT}{2\mathbf{F}} \ln \frac{a_{AO}{}^{i}}{a_{AO}{}^{b}} = \frac{RT}{4\mathbf{F}} \ln \left\{ \left(\frac{a_{BO_2}}{a_{AO}{}^2} \right)^{i} \Big/ \left(\frac{a_{BO_2}}{a_{AO}{}^2} \right)^{b} \right\} \quad [12]$$

where m and n are assumed as 1 and 2, respectively, for brevity.

$\ln(a_{BO_2}/a_{AO}{}^2)$ can be empirically expressed as a linear function of weight percent of BO_2, if the change of BO_2 concentration induced by the current supply is relatively small

$$\ln(a_{BO_2}/a_{AO}{}^2) = a + b[\text{w/o } BO_2] \quad [13]$$

where constants a and b can be obtained graphically using the activity data. Then Eq. [12] can be simplified as

$$\eta = \frac{bRT}{4\mathbf{F}} ([\text{w/o } BO_2]^{i} - [\text{w/o } BO_2]^{b}) \quad [14]$$

When the current is supplied galvanostatically, the time dependency of BO_2 concentration at the interface can be given, assuming unidirectional diffusion in a semi-infinite medium and under the following conditions

$$c_{BO_2}{}^{i} = c_{BO_2}{}^{b} \qquad 0 \leqq x, \quad t = 0$$

$$-D_{AO\text{-}BO_2} \frac{dc_{BO_2}}{dx} = \frac{i}{4\mathbf{F}} \ (\text{const.}) \qquad x = 0, \quad t > 0$$

$$c_{BO_2}{}^{b} = \text{const.} \qquad x = \infty, \ t > 0 \quad [15]$$

Consequently, the equation of Fick's second law is solved as

$$c_{BO_2}{}^{i} - c_{BO_2}{}^{b} = \frac{i}{2\mathbf{F}\sqrt{\pi D_{AO\text{-}BO_2}}} \sqrt{t} \quad [16]$$

where c_{BO_2} is molar concentration (mole/cm^3), i is current density (A/cm^2), $\mathbf{F}$ is Faraday constant (C/equiv.), $D_{AO\text{-}BO_2}$ is the interdiffusivity (cm^2/sec), and t is time (sec). Molar concentration can be converted to weight percent with density data of the system. Substitution of Eq. [16] for Eq. [14] will give the time dependency of η as

$$\eta = \frac{100 b i M_{BO_2} RT}{8\mathbf{F}^2 \rho \sqrt{\pi D_{AO\text{-}BO_2}}} \sqrt{t} \quad [17]$$

where ρ is the density and M_{BO_2} is the molar weight of BO_2. Thus, the interdiffusivity will be obtained from the slope of plots of η against $\sqrt{t}$.

In reality, A^{2+} and B^{4+} would migrate, satisfying the electrical neutrality condition by the movement of O^{2-}. However, the micromechanism of the diffusion process in ionic melts is not yet clarified. Thus, the interdiffusivity is simply written as $D_{AO\text{-}BO_2}$ in the present paper. The diffusivity is determined in the external coordinate frame of reference, whose origin was taken at the electrode interface of B. Therefore, the diffusivity would be slightly different from that determined by Matano-Boltzmann method from the penetration curves. However, the difference would be much smaller than the error estimated in the subsequent section.

Under the potentiostatic condition, on the other hand, the diffusion equation will be solved under the boundary condition that molar concentration of BO_2 at the electrode interface is kept constant, to give the time dependency of current density as

$$i = 4\mathbf{F}j = 4\mathbf{F}(c_{BO_2}{}^{i} - c_{BO_2}{}^{b}) \sqrt{\frac{D_{AO\text{-}BO_2}}{\pi}} \frac{1}{\sqrt{t}} \quad [18]$$

Again, converting molar concentration to weight percent, substitution of Eq. [14] for Eq. [18] will give the following equation

$$i = \frac{16\mathbf{F}^2 \rho}{100 b M_{BO_2} RT} \eta \sqrt{\frac{D_{AO\text{-}BO_2}}{\pi}} \frac{1}{\sqrt{t}} \quad [19]$$

The interdiffusivity will be obtained from the slope of plots of i against $1/\sqrt{t}$.

This principle can be applied to obtain the interdiffusivity in any binary or quasibinary ionic solutions, regardless of liquid or solid oxides (or halides), as long as the above requisitions are fulfilled. Among silicate systems, CaO-SiO_2, CaO-SiO_2-Al_2O_3, Li_2O-SiO_2, etc., are considered as the appropriate systems, because SiO_2 is very unstable in all cases with unit transference number of Ca^{2+} and Li^+.

In the present paper, Li_2O-SiO_2 was taken because no interdiffusivity data was reported on the system. A measurement of transference number on this system was carried out by Bockris *et al.* (10). From the measurement, the present authors concluded the transference number of Li^+ as unity. The experiment was carried out under galvanostatic condition. Then, with appropriate numerical values, Eq. [17] was simplified as

$$\eta = 8.69 \times 10^{-7} \frac{biT}{\rho \sqrt{D_{Li_2O\text{-}SiO_2}}} \sqrt{t} \qquad [20]$$

Experimental procedure.—As shown in Fig. 1, the cell assembly consisted of molten oxide contained in a dense alumina crucible, into which a working electrode W, a counterelectrode C, and a reference electrode R were dipped. The working electrode was a rod of pure silicon with 1.5 mm diam and 30 mm length. The upper end of the rod was connected with a molybdenum wire used as lead wire. A piece of molybdenum sheet was immersed so as to cover the sidewall of the crucible and was used as the counterelectrode, which is not necessarily made of silicon as seen in Eq. [2]. Another rod of pure solid silicon with about 3 mm diam was immersed in the molten oxide and used as the reference electrode. The cell assembly and lead wires were shielded by an earthed iron net from the noise induced by the stray electric field. Argon containing 10% hydrogen was introduced into the furnace tube at 500 cm^3/min in order to prevent oxidation of silicon rods. The temperature was measured at the surface of the molten oxide with a Pt-13% Rh·Pt thermocouple. The crucible was placed so that the temperature at the upper part was a few degrees higher than at the bottom in order to avoid thermal convection in the molten oxide phase.

Compositions of the oxide were 70 w/o SiO_2-30 w/o Li_2O and 80 w/o SiO_2-20 w/o Li_2O by charge. The

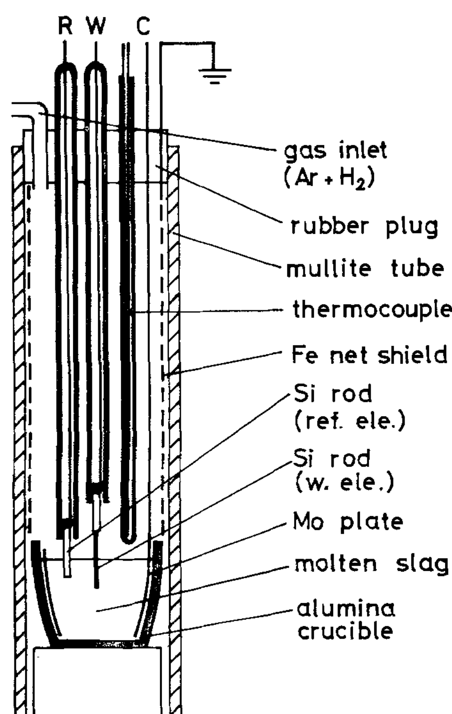

Fig. 1. Schematic diagram of cell assembly

commercial 99.9% silica powder (Merck, Kieselgel 60) was heated at 1000°C to obtain a constant weight. The commercial >99.0% lithium carbonate powder was kept at over 200°C for several days to obtain a constant weight. These powders were mixed to have the above composition and were melted in the alumina crucible. The molten oxide solution was carefully mixed and quenched on a water-cooled copper plate. The quenched oxide was crushed finely, mixed carefully, and then served for the experiment. Dissolution of the alumina crucible into the molten oxide was negligibly small, because the solidified oxide could be easily split away from the crucible, showing no reaction between them.

A constant current was generated with a commercial potentiostat and a known resistance and was supplied between the working and counterelectrodes. The potential difference between the working and reference electrodes was measured by a commercial potential recorder with input impedance of 2 MΩ. When the current was supplied for a very short time, the potential change was followed by a memory-type oscilloscope. The electrical circuits to generate a rectangular single pulse of current and to measure the potential changes over a very short time were detailed in Ref. (7).

After the oxide powder was remelted in the cell assembly the working and reference electrodes were dipped into the molten oxide. The surface level was detected by taking electrical connection between the counter and above electrodes. The depth of the electrodes were fixed to the desired position from the surface. After dipping the electrodes, it took several hours to obtain steadily zero potential difference between the working and reference electrodes. The constant current was supplied to the working electrode thereafter. Since the value of b in Eq. [20] was estimated as 0.110 for 80 w/o SiO_2 and 0.147 for 70 w/o SiO_2 from the activity data (11), and the value of ρ was obtained at the experimental temperature from published data (12), the interdiffusivity was obtained using Eq. (20).

Experimental Results

When the current was supplied, the potential jumped immediately corresponding to the *IR* drop. Then, the potential changed parabolically with time. Figure 2 shows three examples of the potential change with time recorded by the oscilloscope for different time scales. A circuit for the *IR*-drop compensator was used to record only the parabolic potential change in the scope on a large scale. Although the *IR* drop could not be estimated with sufficient accuracy from the figure, it could be obtained accurately by plotting the potential against square root of time and extrapolating to zero. In Fig. 3, subtracting the *IR* drop from the potential change, the overpotential η was plotted against square root of time with different anodic and cathodic current densities. It is seen that the time dependency of the potential was well expressed by Eq. [20], regardless of current directions and densities. In Fig. 4, the slope of the above lines were plotted against current densities, showing a very good proportionality. Thus, Eq. [20] was proved to be satisfied by the experiments with respect to current density. Figure 5 shows the change of the slope with the depth of the working electrode keeping a constant current density. At smaller depths the slope increases with the depth, but over 10 mm, it seems virtually constant. When the depth is small, a part of the current would be consumed by a side reaction such as

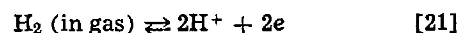

$$H_2 \text{ (in gas)} \rightleftarrows 2H^+ + 2e \qquad [21]$$

at the three-phase boundary of gas-molten oxide-electrode. Over 10 mm depth, however, the effect of the above reaction can be neglected. Therefore, the interdiffusivities were estimated from the data for over

10 mm depth. The diffusion distance from the interface would increase with duration of current supply. If there exists a convection in the molten oxide and, further, if the distance exceds the diffusion boundary layer, the time dependency of the potential would be changed with the duration of current supply. The duration was changed from 100 msec to 10 sec. Results are shown in Fig. 6. The slope of η *vs.* $\sqrt{t}$ plot is vir-

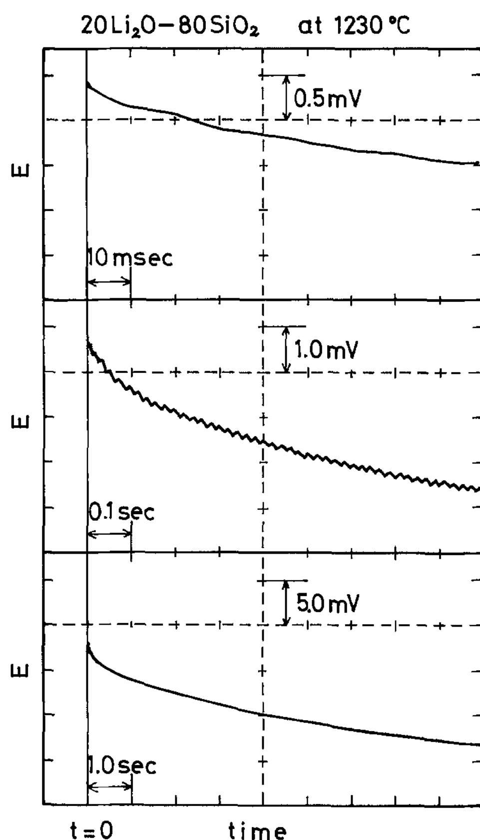

Fig. 2. Change of the overpotential with time recorded on the oscilloscope.

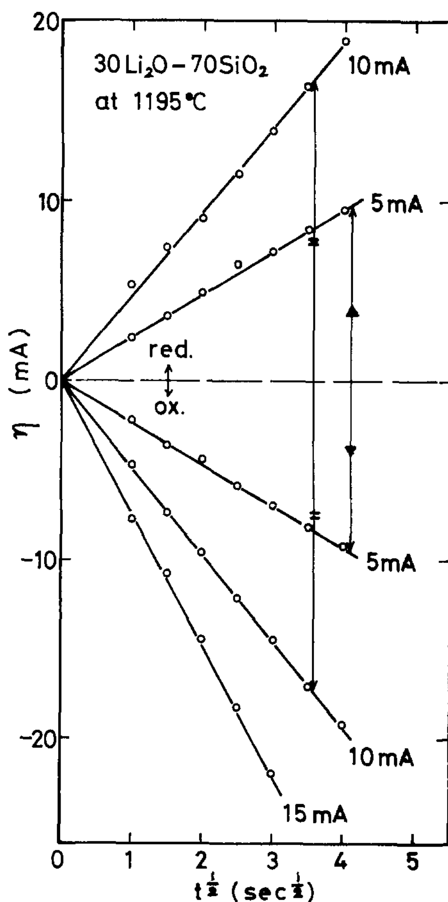

Fig. 3. Plots of the overpotential against square root of time with different current values and directions.

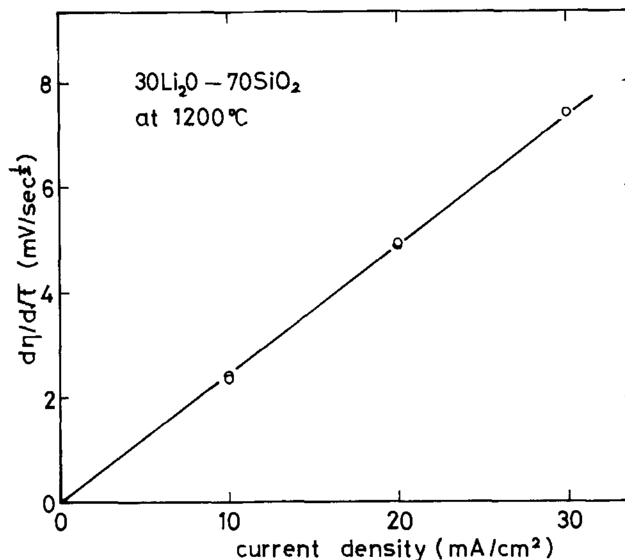

Fig. 4. Plot of the slope of overpotential over square root of time against current density.

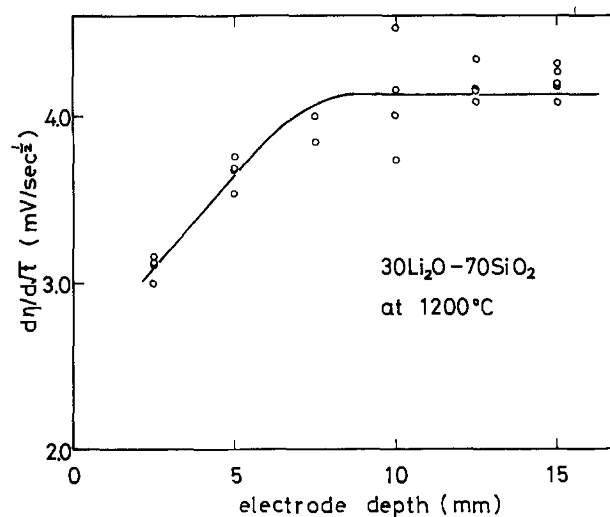

Fig. 5. Plot of the slope of overpotential over square root of time against electrode depth.

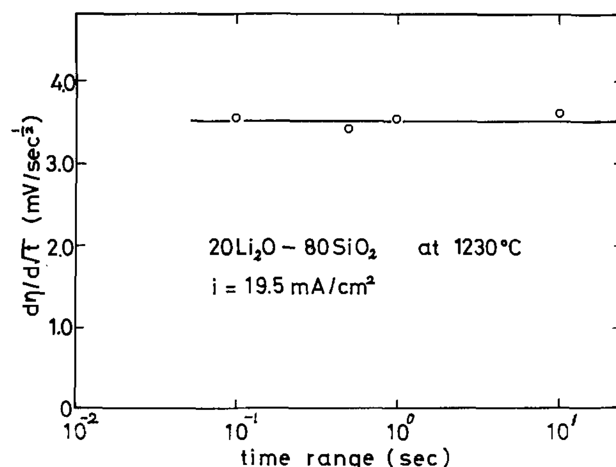

Fig. 6. Plot of the slope of overpotential over square root of time against electrolysis time range.

tually constant regardless of the duration, showing no effect of convection on the polarization.

By these precautions, it was proved that the time dependency of the overpotential was completely due to the unsteady interdiffusion in the stagnant molten oxide. Thus, the interdiffusivities were estimated from 31 polarization curves for $30Li_2O$-$70SiO_2$ and 21 curves for $20Li_2O$-$80SiO_2$ at different temperatures, using Eq. [20]. They are plotted against reciprocal of absolute temperature in Fig. 7 and are formulated by a least squares method as follows:

For 20 w/o Li_2O-80 w/o SiO_2

$$D_{Li_2O\text{-}SiO_2} = 7.2 \times 10^{-3} \exp(-33 \times 10^3/RT) \quad (\text{cm}^2/\text{sec}) \quad 1100°\text{-}1350°\text{C}$$

For 30 w/o Li_2O-70 w/o SiO_2

$$D_{Li_2O\text{-}SiO_2} = 3.0 \times 10^{-3} \exp(-29 \times 10^3/RT) \quad (\text{cm}^2/\text{sec}) \quad 1200°\text{-}1350°\text{C}$$

The standard deviation for activation energies were 1.6 kcal/mole for $20Li_2O$-$80SiO_2$ and 2.7 kcal/mole for $30Li_2O$-$70SiO_2$, respectively. Higher Li_2O content gave higher interdiffusivity within the experimental temperature range, but lower activation energy.

Discussion

Estimation of errors.—The "mean error" of the determination of the interdiffusivity can be defined as the following equation

$$\left|\frac{\Delta D}{D}\right| = \sqrt{\left|\frac{\Delta(\eta/\sqrt{t})}{\eta/\sqrt{t}}\right|^2 + \left|\frac{\Delta I}{I}\right|^2 + \left|\frac{\Delta A}{A}\right|^2 + \left|\frac{\Delta T}{T}\right|^2 + \left|\frac{\Delta b}{b}\right|^2} \quad [22]$$

where I is the total current and A is the interfacial area. The largest error was included in the estimation of the value of b, *i.e.*, $\Delta b/b = \pm 10\%$. The next largest were $\Delta A/A$ of $\pm 5\%$ and $\Delta I/I$ of $\pm 5\%$. The slope of the overpotential *vs.* square root of time has a very small error of $\pm 1\%$ as seen in Fig. 3. Measurement of temperature has also a very small error of $\pm 1\%$. The mean error, then, can be estimated as $\pm 13\%$.

Although the electrode had cylindrical geometry, a planar interface was assumed on solving the diffusion equation. The solution for cylindrical coordinates under the same initial and boundary conditions as those of Eq. [15] is given for a short time as

$$c_{BO_2}{}^i - c_{BO_2}{}^b = \frac{i}{4F}\left(\frac{t}{D_{AO\text{-}BO_2}}\right)^{1/2} \left[\frac{2}{\sqrt{\pi}} - \frac{1}{2}\left(\frac{D_{AO\text{-}BO_2}t}{a^2}\right)^{1/2} + \ldots\right] \quad [23]$$

where a is the radius of the electrode (13). Comparing Eq. [16] with [23], the error induced by the assumption of the planar interface geometry is given as

$$\left[\frac{1}{2}\left(\frac{D_{AO\text{-}BO_2}t}{a^2}\right)^{1/2} + \ldots\right] \quad [24]$$

Using the largest $D_{AO\text{-}BO_2}$ value of 4×10^{-7} cm²/sec, the radius of the electrode of 0.05 cm and the longest time of 20 sec in Eq. [24], the error is estimated as 2.8×10^{-2}, which corresponds to 2.5% of $2/\sqrt{\pi}$. Consequently, the error from the assumption of the planar interface geometry was estimated less than 2.5%.

The activity data (11) was estimated at 1400°C from the measurement of vaporization rate of Li_2O (14). Therefore, the use of such data would cause a certain error, but the magnitude of it could not be estimated in the present work. If more accurate data were available, the interdiffusivity obtained would be more accurate, because the slope of η *vs.* $\sqrt{t}$ was obtained very accurately in the present experiment.

Comparison of the present data with those of others.—Interdiffusivities in other molten binary silicates are cited in Fig. 8 together with the present data. Number 1 shows the interdiffusivities of Li_2O-SiO_2 obtained in the present work, numbers 2-5 for Na_2O-SiO_2, number 6 and 7 for K_2O-SiO_2, and finally, number 8 for PbO-SiO_2.

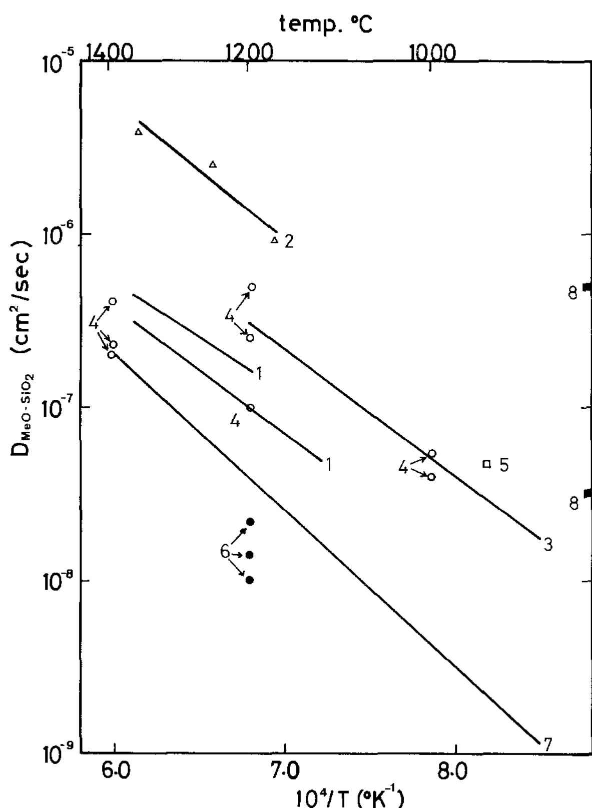

Fig. 7. Interdiffusivities in molten binary silicates. Li_2O-SiO_2: 1, the present work. Na_2O-SiO_2: 2, Shurygin *et al.* (17); 3, Hlavac and Nademlynska (18); 4, Schwerdtfeger (16); 5, Kreider and Cooper (19). K_2O-SiO_2: 6, Schwerdtfeger (16); 7, May and Wollast (20). PbO-SiO_2: 8, Kosaka *et al.* (14).

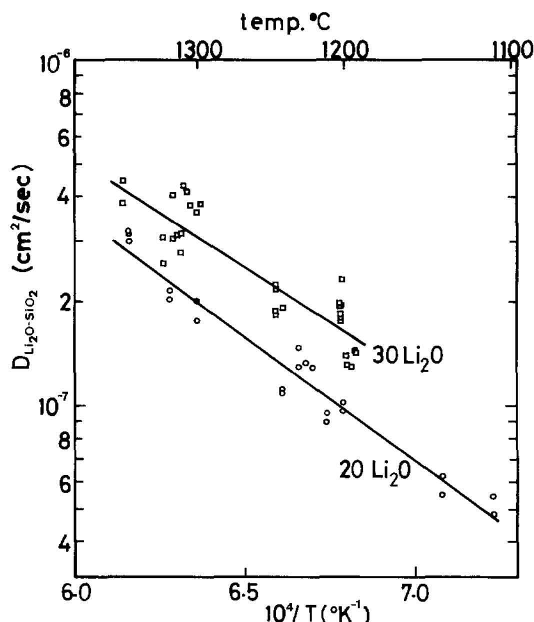

Fig. 8. Interdiffusivities of Li_2O-SiO_2 obtained in the present work

May and Wollast (20) reported no composition dependency of the interdiffusivity from their experiments on K_2O-SiO_2 system at SiO_2 mole fractions from 0.74 to 0.84. Schwerdtfeger (16), however, suggested that the diffusivity would decrease by a factor of 2 from SiO_2 mole fraction of 0.77-0.88 in K_2O-SiO_2 system at 1200°C. On Na_2O-SiO_2 system, Schwerdtfeger (16) suggested large decrease by a factor of 5 from SiO_2 mole fraction of 0.65-0.75. Kosaka *et al.* (15) reported a large decrease of an order of magnitude on the PbO-SiO_2 system at 850°C. In the present work, small dependency by a factor of 1.5 from 0.54 to 0.67 SiO_2 mole fraction was obtained at 1200°C. As a whole, it might be concluded that there exists a moderate dependency of the interdiffusivity on SiO_2 mole fraction, *i.e.*, by a factor of 2 ~ 3 from 0.60 to 0.80 SiO_2 mole fraction at 1200°C.

In the present work, the activation energy was obtained 33 and 29 kcal/mole for 0.67 and 0.54 SiO_2 mole fraction, respectively. The others reported about 35 kcal/mole, although SiO_2 mole fractions are different. Thus, it might be concluded that the activation energy for the interdiffusion in molten alkali silicate is 30-40 kcal/mole, regardless of alkali element and compositions.

Conclusion

The interdiffusivity of Li_2O-SiO_2 in molten binary Li_2O-SiO_2 was determined by an electrochemical polarization method from 1100° to 1350°C. Li_2O-SiO_2 was selected because of no data on the diffusivity and because SiO_2 is stabler with unit transference number of Li^+. The results are summarized as follows.

For 20 w/o Li_2O-80 w/o SiO_2

$$D_{Li_2O\text{-}SiO_2} = 7.2 \times 10^{-3} \exp(-33 \times 10^3/RT) \quad (cm^2/sec) \quad 1100°\text{-}1350°C$$

For 30 w/o Li_2O-70 w/o SiO_2

$$D_{Li_2O\text{-}SiO_2} = 3.0 \times 10^{-3} \exp(-29 \times 10^3/RT) \quad (cm^2/sec) \quad 1200°\text{-}1350°C$$

The interdiffusivity is larger by a factor of 1.5 for $30Li_2O$-$70SiO_2$ than for $20Li_2O$-$80SiO_2$ at 1200°C. The activation energies are 33 and 29 kcal/mole for $20Li_2O$-$80SiO_2$ and $30Li_2O$-$70SiO_2$, respectively.

These results are quite reasonable compared with published interdiffusivity data in other molten binary silicates. Thus, the present method was proved to be applied successfully to determine the interdiffusivity in molten Li_2O-SiO_2 system.

Manuscript submitted April 18, 1977; revised manuscript received Sept. 12, 1977. This was Paper 241 presented at the Toronto, Canada, Meeting of the Society, May 11-16, 1975.

Any discussion of this paper will appear in a Discussion Section to be published in the December 1978 JOURNAL. All discussions for the December 1978 Discussion Section should be submitted by Aug. 1, 1978.

Publication costs of this article were assisted by K. S. Goto.

REFERENCES

1. K. Kiukkola and C. Wagner, *This Journal*, **104**, 379 (1957).
2. W. A. Fischer and D. Janke, "Metallurgische Electrochemie," Springer-Verlag (1975).
3. H. Rickert and R. Steiner, *Z. Phys. Chem.*, **49**, 127 (1966).
4. R. L. Pastorek and R. A. Rapp, *Trans. Metall. Soc. AIME*, **245**, 1711 (1969).
5. M. Sasabe and K. S. Goto, *Metall. Trans.*, **5**, 2225 (1974).
6. K. Nagata, M. Kawakami, and K. S. Goto, Proceedings of the Metal-Slag-Gas Reactions and Processes Symposium, American Electrochemical Society, pp. 183-198, Toronto, Canada (1975).
7. K. Nagata and K. S. Goto, *Ironmaking and Steel making*, **4**, 23 (1977).
8. N. Nowak and K. Schwerdtfeger, Proceedings of the Metal-Slag-Gas Reactions and Processes Symposium, American Electrochemical Society, pp. 98-110, Toronto, Canada (1975).
9. C. Wagner, in "Advances in Electrochemistry and Electrochemical Engineering," Vol. 4, P. Delahay, Editor, pp. 1-46 (1966).
10. J. O'M Bockris, J. A. Kitchener, and A. E. Davies, *Trans. Faraday Soc.*, **48**, 536 (1952).
11. R. J. Callow, *ibid.*, **46**, 663 (1950).
12. J. O'M Bockris, J. W. Tomlinson, and J. L. White, *ibid.*, **52**, 299 (1956).
13. H. S. Carslaw and J. C. Jaeger, "Conduction of Heat in Solid," p. 338, Oxford University Press, Oxford, England (1959).
14. E. Preston and W. E. S. Turner, *J. Soc. Glass Technol.*, **18**, 143 (1934).
15. M. Kosaka, H. Hayashi, S. Sakakibara, and H. Shimizu, Report of the Government Industrial Research Institute Nagoya, Japan, 22, 205 (1973).
16. K. Schwerdtfeger, *J. Phys. Chem.*, **70**, 2131 (1966).
17. P. M. Shurygin, L. N. Barmin, and O. A. Esin, *Izv. Vysshikh. Uchebn. Zavedenii Chernaya Met.*, **5**, 5 (1962).
18. J. Hlavac and H. Nademlynska, *Glass Technol.*, **10**, 54 (1969).
19. K. G. Kreider and A. R. Cooper, *ibid.*, **8**, 71 (1967).
20. H. B. May and R. Wollast, *J. Am. Ceram. Soc.*, **57**, 30 (1974).

Technical Notes

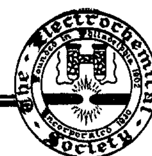

The Four-Point Bend Test for Measuring the Ductility of Brittle Coatings

C. C. Lo

Bell Laboratories, Columbus, Ohio 43213

Electroplated metals are often much harder and less ductile than the same metals obtained from the melts. One of the primary causes for the reduction of ductility is the codeposits of gaseous and other impurities in many electroplates. ASTM recommends (1) that the

Key words: ductility, brittle coatings.

ductility (the strain to fracture) be determined by a bend test for brittle plates on a substrate, and a tensile test for ductile plates with the substrate removed.

The procedure of the bend test (1, 2) is to press the specimen onto a series of mandrels of various diameters with the substrate side against the mandrel. When visible cracks are observed under a 10X magnifier, the ductility is then calculated over a range from the two adjacent mandrel diameters and the specimen thickness. This technique is simple. However, with the 10X magnifier one can never be sure about the occurrence of cracks until they are extensive. Other major deficiencies of this method are the uncertainty with the rate and the force distribution during the bending.

The bulge test has also been used in determining the ductility of electroplates (3). However, the bulge is not shaped like a spherical cap as frequently assumed (4), hence the uncertainty arises from the strain calculation based on the bulge height measurement, particularly if the bulge height is small as is the case for a brittle material. Because the biaxial stress in a bulge test resists necking which is seen in a conventional uniaxial tensile test for a ductile material, the bulge test has been used successfully for obtaining the stress-strain relationship over the large plastic strain region. The strain to fracture obtained in a bulge test usually is much larger than that of the uniaxial tensile test.

A different, simple bend test method is presented here, which avoids the problems just described. The technique is sometimes called the four-point method as used by the ceramic industry, where the specimen, without a substrate, is bent and fractured into two or more pieces. This tester can be used to evaluate the ductility of a brittle coating with a strain to fracture between 0 and 2%. Cracks are revealed under an optical microscope at 50X with oblique illumination. Cracks as revealed by this optical technique are also compared with those by two other techniques commonly used for porosity testing: HNO_3 vapor and electrography.

Four-Point Bend Test

The basic mechanisms of the four-point bend test include a simply supported beam subjected to two loads, symmetrical over the central span (Fig. 1). Since the bending moment is constant between the two loads, the plastic hinge is not likely to develop. Samples are placed on two tool steel knife edge supports located 50.8 mm apart. Two line loads are applied by two 3.2 mm diam steel cylinders spaced 12.7 mm apart, or 19.1 mm from the supports, and controlled by a micrometer which indicates the displacement. After every 0.1 mm increment (or any selected distance) of the loading cylinders, the specimen is removed from the testing frame and examined at 50X magnification under oblique dark field illumination. If the specimen is bent at a rate of about 0.1 mm in 1 or 2 sec, we obtain a strain rate of about 10^{-4}/sec, which can be considered as a static rate The rod which connects the loading cylinders and the micrometer can be made long enough that the specimen can be placed inside an oven while the micrometer is outside for measuring the ductility at elevated temperatures.

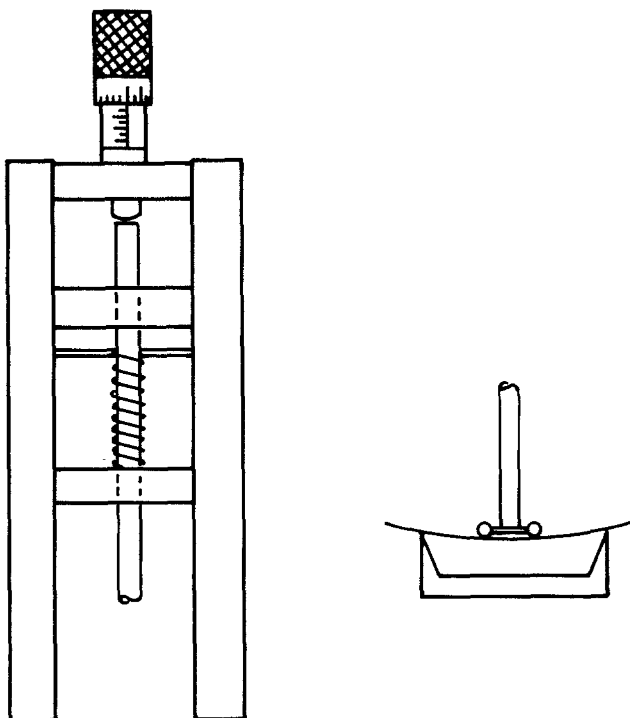

Fig. 1. Schematic of the four-point bend test apparatus

The errors of the measurement depend on whether the two loading cylinders are parallel to the knife edge supports, are making contact at the same time, and are at the right positions, and whether the specimen has a uniform thickness and width, as discussed by Hoagland *et al.* (5) for the elastic bending case. To evaluate the reliability of the four-point bend test, they compared the Young's modulus of a steel beam measured in the bend test with tests in uniaxial loading. The difference was only about 1%. The single most important error in the bend test is that due to the twisting action when the specimen is not flat so that the supporting edges and the loading cylinders do not make the initial parallel contact with the specimen simultaneously. This error is inversely proportional to the beam deflection. The typical deflection for a brittle coating on a metallic substrate is much larger than that for a ceramic specimen, hence the error for the former is smaller. In conclusion, it seems to be reasonable to assume that, with standard laboratory precaution, the total error can be kept within 5%.

For brittle nonmetallic materials without the substrate the strain to fracture obtained by the four-point bend method appears to be 15-30% higher than that obtained by a tensile test (6, 7). This can be explained by the fact that all the flaws in the tensile specimen are subjected to the maximum tensile stress to cause crack initiation and growth, while in the bend test only the flaws near the tensile side surface of the specimen are. A statistical treatment of this case was given in Ref. (6). For a thin coating on a ductile substrate, all the flaws in the coating can nucleate cracking for both the tensile test and the bend test, so the strain to fracture should be the same for both tests. However, an experimental proof is still needed.

Strain to Fracture

After cracks appear, the ductility can be determined from the measured displacement at the loading cylinders. If the substrate material is within its elastic limit and the distance between the two loads is 1/4 of the span, the maximum strain in the specimen is

$$= \frac{16}{3}\frac{h\delta}{l^2} \quad [1]$$

where h, l and δ are the total thickness, distance between the two supports, and the displacement under the loads, respectively. If the ductility of the coating is less than 0.5%, it is advantageous to choose a substrate with a high yielding strain so that Eq. [1] can be used. One of the suggested substrates is a phosphor bronze strip 10 mm wide and 0.3-0.4 mm thick. The coating thickness can vary between 5 and 20 μm.

However, if the substrate material deforms plastically, the strain cannot be calculated easily. First, the stress-strain curve for the substrate should be obtained from a tensile test machine. Then the displacement-strain curve is usually obtained by a tedious numerical integration method. As an alternative, an approximate simple solution was given in Ref. (8) for maximum strains of 1-2%, depending on the stress-strain curve. For a half-hard copper substrate, the strain-displacement curves based on this nonlinear theory (8), as well

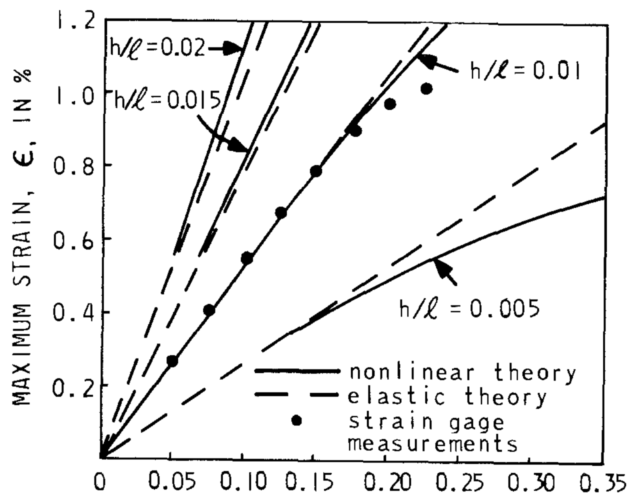

Fig. 2. Strain-displacement curves for a half-hard copper substrate.

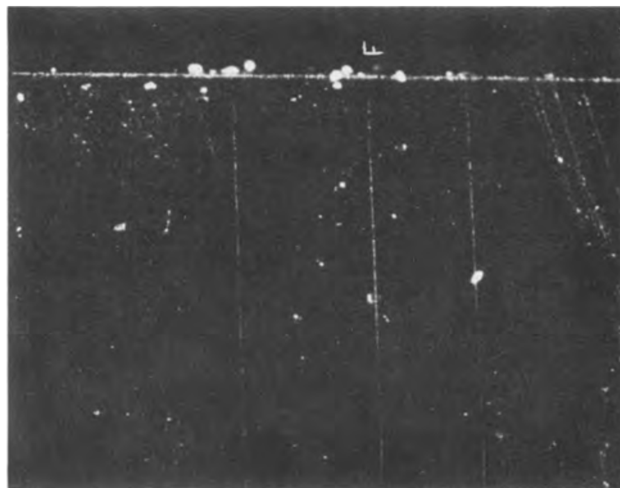

Fig. 3. Cracks on a 10 μm NiSn plate as revealed at 50X under oblique illumination.

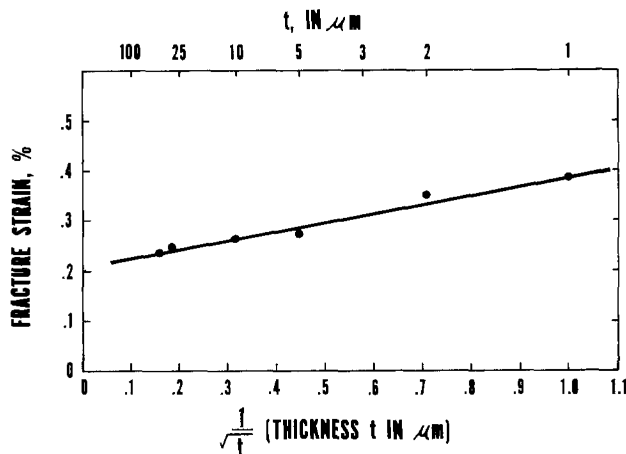

Fig. 4. Ductility of NiSn plate versus the plate thickness

as that based on the simple elastic theory, are shown in Fig. 2. It is interesting to note that, when the ratio of the total thickness (coating and the substrate) to the distance between the two supports is about 0.01, the strain obtained from the simple theory of Eq. [1] is nearly the same as that obtained from the nonlinear theory for strains up to 1%.

The displacement-strain curve can also be calibrated experimentally by measuring the strain optically. However, none of the optical techniques is simple or readily available. The strain gauge method is not desirable because it affects the stiffness of the sample, so that plastic hinges are likely to develop which will lower the measured strain. To prove this point, we used the smallest strain gauge available, which had a thickness of less than 25 μm, on a 0.5 mm half-hard copper strip. The displacement *vs.* strain curve based on these strain gauge measurements is shown in Fig. 2 as dots (h/l = 0.01). At about 0.9% strain, plastic hinges started to appear, and the measured strain became smaller than the calculated value.

Methods to Reveal Cracks

Oblique illumination.—In this study, we chose NiSn alloy (9) coating as an example because it is rather brittle and resistant to most etching chemicals. NiSn alloy was electrodeposited on both sides of a half-hard copper strip, 12.5 mm wide and 0.5 mm thick. The copper strip was not polished; its surface scratches were also apparent on the plated surface. The NiSn plate had a nonuniform thickness varying from about 15 μm at the edge to 7 μm near the center. When a cracked specimen was placed under a microscope at 50X with oblique lighting perpendicular to the cracks, cracks could be seen easily. The internal oblique illumination provided by some microscopes does not reveal the cracks as clearly as an external light can. When the incidence angle was low, the background was dark, and cracks were shown as fine straight lines perpendicular to the edges, whereas the scratches were seen as coarse lines at random orientations as shown in the upper right corner of Fig. 3. It is also interesting to see that the ductility for NiSn varies linearly at a low slope with the reciprocal of the square root of the plate thickness over 1-40 μm as shown in Fig. 4. The dependence of ductility on the coating thickness has long been suspected (2). For brittle coatings, this can be explained by the increased number of flaws in the coating with thickness as discussed earlier.

Though fine cracks can be seen easily using oblique dark field illumination, the same cracks can be seen only at much higher magnifications under normal incidence bright field illumination. At high magnification, it becomes difficult to distinguish cracks from scratches. Under normal incidence illumination, both the resolution and the perception limits are proportional to the ratio of the wavelength of light to the numerical aperture of the microscope. On the other hand, under the oblique dark field illumination, perception depends only on the total light reflected from the cracks (10).

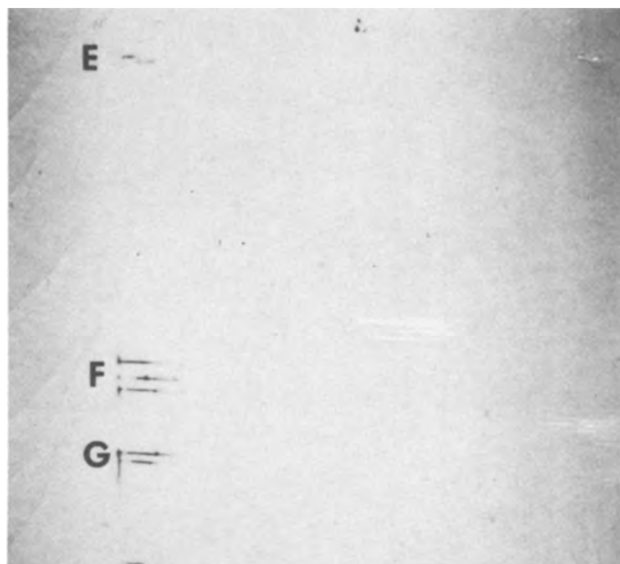

Fig. 5. Cracks on a 10 μm NiSn plate as revealed by electrographic technique, 5X.

Electrography.—After a specimen was examined using a microscope with oblique illumination, the same sample was tested by the electrographic technique (11-13). Kodak Type F dye transfer paper was cut into strips 2 by 7 cm and soaked for 15-45 min in a solution of 20 g/liter of disodium salt of dimethylglyoxime and 20 g/liter of NaCl. A roller was used to remove the excess solution from the printing paper. The specimen was held firmly against the printing paper between two aluminum electrodes which were pressed together in a hydraulic press. A current was passed through the specimen and paper for 1 min at a constant voltage of 2.0V. The result is shown in Fig. 5. The electrographic method in this case has revealed about 1/3 of cracks found by oblique illumination. Other samples with plating thicknesses from 4 to 40 μm of NiSn alloy gave similar results. Unrevealed cracks indicate that the electrolyte does not fill all cracks but depends on the crack dimension, the NiSn plating thickness, and the wetting angle between the alloy and the solution. Figure 5 shows that the electrographic technique revealed some cracks near the edge, but none in the center area even though the former had a plating thickness twice as large as the latter. The electrolyte used here is effective for revealing pores in a gold plate. However, it is possible that some other electrolytes may be more effective for NiSn alloy plates due to different wetting angles.

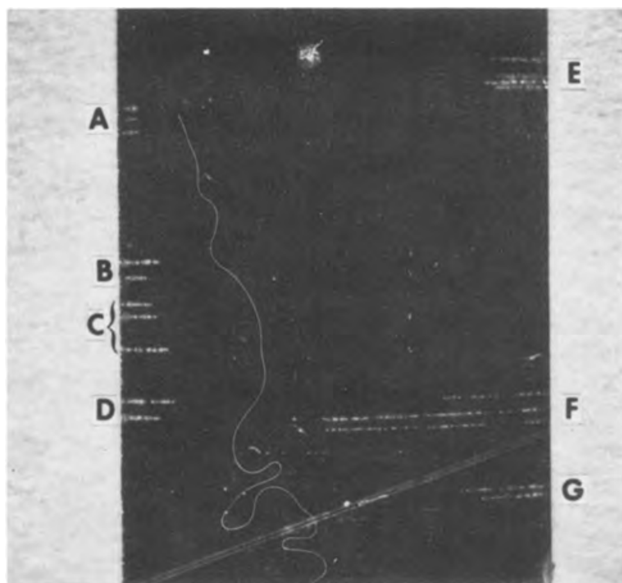

Fig. 6. Cracks on a 10 μm NiSn plate as revealed by HNO_3 vapor, 5X.

HNO_3 vapor.—After the electrographic test, samples were placed in a desiccator over a pool of HNO_3 of 70% concentration for 1 hr. Cracks were manifested by copper corrosion products as shown in Fig. 6 at 5X. In Fig. 6, cracks were marked as areas A to G so that they may be compared to the same cracks shown in Fig. 3 and 5. Cracks revealed by HNO_3 vapor were identical to those revealed by oblique illumination.

Manuscript submitted Aug. 23, 1977; revised manuscript received Oct. 20, 1977.

Any discussion of this paper will appear in a Discussion Section to be published in the December 1978 JOURNAL. All discussions for the December 1978 Discussion Section should be submitted by Aug. 1, 1978.

Publication costs of this article were assisted by Bell Laboratories.

REFERENCES

1. ASTM B489-68, "Standard Recommended Practice for Bend Test for Ductility of Plated Metals."
2. A. F. Mohrnheim, *Plating (East Orange, N.J.)*, **50**, 1094 (1963).
3. T. A. Prater and H. J. Reed, *ibid.*, **36**, 1221 (1949); **38**, 142 (150).
4. T. D. Dudderar, F. B. Koch, and E. M. Doerries, *Exp. Mech.*, **133** (1977).
5. R. G. Hoagland, C. W. Marschall, and W. H. Duckworth, *J. Am. Ceram. Soc.*, **59**, 189 (1976).
6. J. Campo, TR-75-17, Army Material and Mechanics Research Center, Watertown, Mass. (1975).
7. H. E. Schull, *Am. Ceram. Soc. Bull.*, **55**, 202 (1976).
8. C. C. Lo and S. Das Gupta, Submitted to *J. Appl. Mech.*
9. J. W. Cuthbertson, N. Parkinson, and H. P. Rooksby, *This Journal*, **100**, 107 (1953).
10. R. C. Grifkins, "Optical Microscopy of Metals, "American Elsevier Publishing Co., New York (1970).
11. ASTM B583-73, "Standard Methods of Test for Porosity in Gold Coating on Metal Substrates."
12. H. J. Noonan, *Plating (East Orange, N.J.)*, **53**, 461 (1966).
13. WE Manufacturing Standard 17000, Section 1275, (1975).

Surface Composition of Equiatomic Electrodeposited Tin-Nickel Alloy

G. C. Nelson

Sandia Laboratories, Albuquerque, New Mexico 87115

The surface passivity of an equiatomic tin-nickel alloy has been studied with Auger electron spectroscopy by Tompkins and Bennett (1). They conclude that the air-formed surface layer is tin rich. However, due to the escape depth of the Auger electrons used for the analysis, it was not possible to clearly state whether the layer is devoid of nickel. They do conclude however, that the least complex model consistent with their results is a tin oxide containing no nickel. To clarify this point, the surface composition of equiatomic electrodeposited tin-nickel alloy has been determined by low energy ion-scattering spectroscopy. Since this technique is more surface sensitive than Auger electron spectroscopy, it is possible to unambiguously determine the composition of the first few monolayers.

Key words: tin-nickel alloy, surface passivity, equiatomic.

Experimental Results

The ion-scattering spectrometer used for these measurements is a modified commercial instrument. A 2 keV $^4He^+$ beam was used for the analysis and for obtaining a sputter profile of the near surface region. The ion beam was rastered over a 4 mm^2 area with only the signal originating in the center 1 mm^2 accepted in the pulse-counting system. The 1 μm thick tin-nickel samples were obtained from Tompkins and Schubert and were electroplated on Cu and stainless steel, respectively. Rutherford backscattering was used to deter-

mine the composition of the films at a depth of 1000Å. This composition was considered to represent that of the bulk. It was found that the composition of these samples deviated slightly from being equiatomic. The sample on stainless steel was found to contain 51 a/o (atomic percent) Sn while the one on Cu contained 45 a/o Sn. By using these bulk composition values and the relative Ni/Sn peak height obtained from the sputter profiles, sensitivity factors for Ni and Sn were obtained. With the sensitivity factors, the depth profile data were converted to a concentration profile. These data for Sn/Ni on Cu are shown in Fig. 1. The initial rise in the Sn signal is due to the removal of carbonaceous material and the tin oxide layer as discussed by Tompkins (1). The delay in the Ni signal clearly indicates that the Ni is absent in the surface region. By measuring the current density and estimating the sputtering yield, the depleted surface layer was found to be 5-10Å thick which is in agreement with the value of 5Å reported by Tompkins. Similar results were obtained from the sample electroplated on stainless steel. These results confirm the speculation of Tompkins and are consistent with the idea that since tin is more readily oxidized than nickel, a tin oxide will form on the surface. It should be pointed out, however, that a tin-rich surface may also form in the absence of oxygen due to differences in surface-free energies (2).

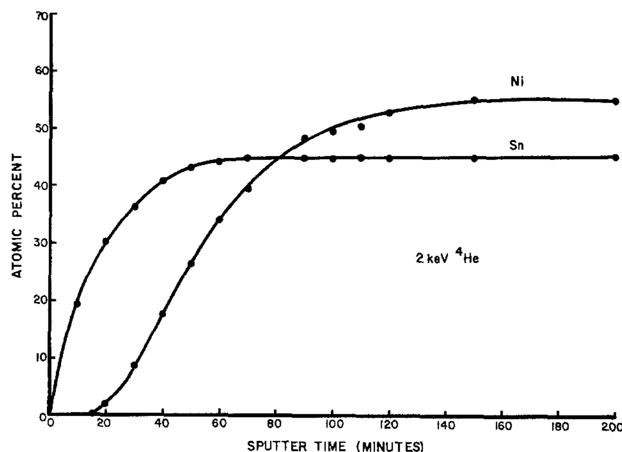

Fig. 1. Depth profile of electrodeposited tin-nickel sample. The absence of Ni in the surface region is clearly evident.

Acknowledgments

The author would like to thank H. G. Tompkins and R. Schubert for supplying the samples and J. A. Borders for the RBS measurements. This work was supported by the U.S. Energy Research and Development Administration.

Manuscript submitted Sept. 19, 1977; revised manuscript received Oct. 21, 1977.

Any discussion of this paper will appear in a Discussion Section to be published in the December 1978 JOURNAL. All discussions for the December 1978 Discussion Section should be submitted by Aug. 1, 1978.

Publication costs of this article were assisted by Sandia Laboratories.

REFERENCES

1. H. G. Tompkins and J. E. Bennett, *This Journal*, **123**, 1003 (1976).
2. G. A. Somorjai, "Principles of Surface Chemistry," p. 64, Prentice-Hall, Englewood Cliffs, N.J. (1972).

Oxygen Reduction on Platinum in Trifluoromethane Sulfonic Acid

A. J. Appleby*

CNRS Bellevue, Laboratoire d'Electrolyse, 92-Bellevue, France

and B. S. Baker*

Energy Research Corporation, Danbury, Connecticut 06810

In strongly acidic solution, the rate of the electrolytic reduction of oxygen on oxide-free platinum appears to be determined by the heat of adsorption of the product of the rate-determining step, which may be identified with the primary electron- and atom-transfer process (1-3)

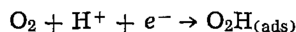

$$O_2 + H^+ + e^- \rightarrow O_2H_{(ads)}$$

A further effect on the rate may result from the coverage of adsorbed molecular oxygen initially present on the electrode surface (2, 3), which may be a function of the heat of adsorption of the anion in the solution.

Acid fuel cells, which currently operate at temperatures on the order of 150°-180°C to ensure adequate reaction rates, use concentrated orthophosphoric acid as the electrolyte. This material has not only poor mass-transport properties (oxygen solubility and diffusivity together with ionic conductivity) but also very low exchange currents for oxygen reduction at temperatures less than *ca.* 100°C (2, 4) when comparison is made with, *e.g.*, perchloric acid (1) or sulfuric acid. The latter acids are insufficiently stable for use in fuel cells at temperatures above about 80°C. Consequently, starting in 1971, a search was made for other possible acid electrolytes with higher stability than perchloric and sulfuric acids, and improved kinetics for oxygen reduction compared with orthophosphoric acid. At that time, trifluoromethane sulfonic acid was examined; it was later shown elsewhere that it demonstrated improved kinetics for hydrocarbon oxidation compared with orthophosphoric acid (5). After initial work on oxygen reduction kinetics and performance of trifluoromethane sulfonic acid in a fuel cell, less volatile higher homologs were examined, particularly tetrafluoroethane 1-2 disulfonic acid (6). The kinetics of the oxygen reduction process on platinum in trifluoromethane sulfonic acid solution are described in this paper.

Experimental

A 10% solution of trifluoromethane sulfonic acid (Eastman Kodak) in distilled water was used. This corresponded to a molarity of about 1.1M. The electrochemical cell was of conventional 3-compartment type, and was fitted with a platinum-black fuel cell electrode

* Electrochemical Society Active Member.

Key words: oxygen reduction, electrocatalysis, platinum, trifluoromethane sulfonic acid.

on a tantalum exmet screen as counterelectrode, a dynamic hydrogen reference electrode (7) which used a similar cathode (area 1 cm^2) together with a smooth platinum anode in a compartment fitted with a Luggin capillary, and a bright platinum working electrode 2 cm^2 in area. The polarizing current for the dynamic hydrogen electrode was 1 mA and its potential was determined to be +5 mV with respect to a bubbling hydrogen electrode in the same electrolyte. This value was independent of temperature in the range studied. The cell contained a further electrode in the working electrode compartment which was identical with the counterelectrode and was used for preelectrolysis of the trifluoromethane sulfonic acid solution.

The solution as first prepared had a pale straw color which slowly cleared as oxygen was bubbled through the cell. A slight precipitate formed during this period. Accordingly, all solutions were first pretreated using this procedure for a period of about 48 hr after which the solution was filtered and preelectrolysis was started. Stable electrochemical results were obtained after 60-72 hr of preelectrolysis at 1 mA-cm^{-2}. Shorter periods than this were insufficient to remove oxidizable impurities and resulted in considerable deactivation of V-log i curves for oxygen reduction (see below). Oxygen (ultrapure grade) was bubbled through the solution during the preelectrolysis period. After preelectrolysis, the platinum-black anode was removed from the solution in the working compartment and the oxygen flow was reduced. The working electrode, prepared as in previous work (2), was then lowered into the cell. It was activated by the anodic and cathodic pulsing procedure described earlier (2). After the final cathodic pulse into the hydrogen adsorption region, a galvanostatic current of the value desired was applied and the electrode was allowed to reach the potential corresponding to this value. Since relatively rapid deactivation of the bright platinum electrode due to adsorption of impurities occurred [*cf.* Ref. (2)] the maximum potential registered was taken to be that corresponding to the reduction of oxygen on the clean, oxide-free platinum surface. Potentials and currents were measured using a Wenking potentiostat with digital voltmeter readout.

Results were obtained on two bright platinum working electrodes, which were consistently within 5 mV of each other. All results reported below refer to a single electrode. The Tafel plots shown could be traced forwards and backwards fairly reproducibly (±5 mV). Temperatures were maintained to ±0.3°C using a water or ice bath.

Results

Tafel plots after 72 hr of preelectrolysis at 0°, 20°, 36°, and 62°C are shown in Fig. 1. Open-circuit poten-

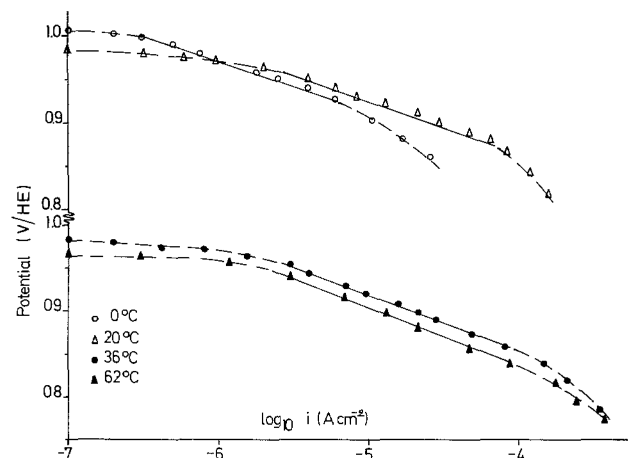

Fig. 1. Tafel plots for oxygen reduction on smooth oxide-free platinum in 1.1*N* trifluoromethane sulfonic acid solutions (after 72 hr preelectrolysis).

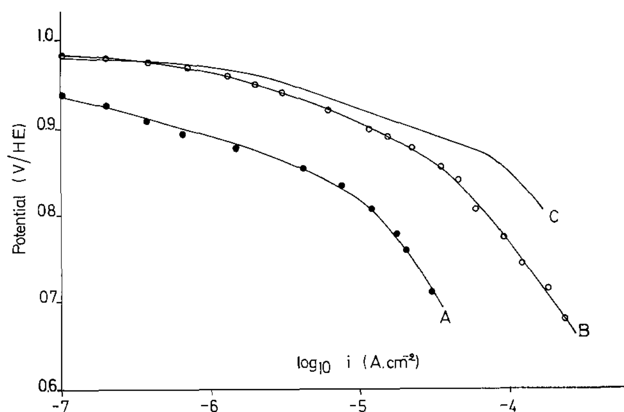

Fig. 2. Tafel plots as in Fig. 1, as a function of preelectrolysis time. A, no preelectrolysis; B, 12 hr; C, 72 hr.

tials (measured after completion of the Tafel plots) varied from 1025 mV *vs.* hydrogen at 0°C to 990 mV at 62°C. Figure 2 shows the effect of preelectrolysis on the results obtained at 20°C. Tafel slopes in the potential range above 920 mV (at 0°C) and 850 mV (at 62°C) appear to be close to $RT/\mathbf{F}$ (54-66 mV/decade depending on temperature). At lower potentials, just before the limiting current region, higher slopes seem to occur. Although this secondary Tafel range is never long enough for accurate slope determination, results may be on the order of 2 $RT/\mathbf{F}$, as has been observed elsewhere (8, 9). The Tafel slopes have been extrapolated back to the calculated reversible oxygen electrode potentials [taking into account the temperature and the gas and water-vapor partial pressures (2)] to obtain the apparent exchange current values shown in Table I. Values shown are for 1 atm oxygen partial pressure, the extrapolated values from the Tafel plots being corrected as necessary for the effect of water vapor pressure, assuming the oxygen reduction reaction to be first order (1, 2).

An Arrhenius plot of the exchange current density values is shown in Fig. 3. Experimental activation energy is 12.6 (±2) kcal/mole under 1 atm oxygen pressure conditions.

Discussion

The Tafel slope observed, as in other acids (1, 2, 9), is $RT/\mathbf{F}$. This suggests that the same rate-determining step occurs as in perchloric and orthophosphoric acids (1, 2). While support from order of reaction determinations is required for a positive confirmation, evidence points to the primary electron transfer step

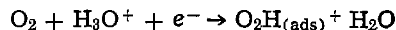

$$O_2 + H_3O^+ + e^- \rightarrow O_2H_{(ads)}{}^+ H_2O$$

as rate-limiting. Due to the presence of adsorbed —OH or —O radicals derived from the oxidation of water, which have a heat of adsorption that is linearly dependent on coverage (1) (Temkin conditions), the environment of adsorption of the reaction intermediate is affected (10). When coverage of reversibly adsorbed —OH or —O radicals is low (*i.e.*, when Langmuir adsorption occurs) the characteristic slope of $RT/\beta\mathbf{F}$, where β is the symmetry factor, should be observed [*i.e.*, 2 $RT/\mathbf{F}$, or about 120 mV, with a typical value for β equal to ½ (8, 9)]. This is consistent with the results obtained.

The probable 25°C exchange current for reduction of oxygen at 1 atm pressure is 9 × 10^{-11} A/cm^2. The

Table I. Exchange currents for oxygen reduction in 1.1*N* CF_3SO_3H

Temp, °C (±0.3)	Calculated theoretical $E°$ (mV *vs.* H_2)	i_o, A/cm^2 (1 atm O_2)
0	1248	8.0 × 10^{-12}
20	1231	6.0 × 10^{-11}
36	1216	1.7 × 10^{-10}
62	1192	5.8 × 10^{-10}

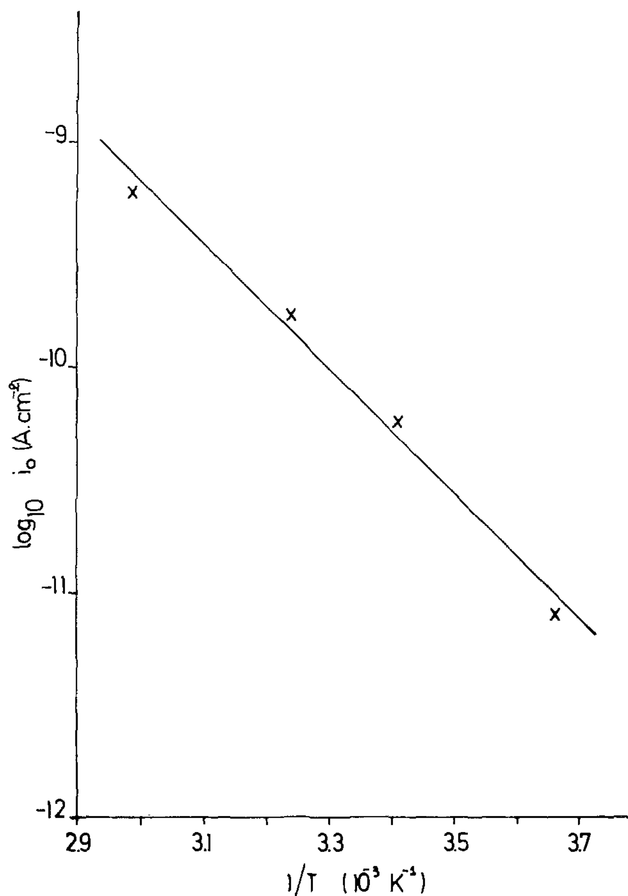

Fig. 3. Arrhenius plot for extrapolated exchange current densities (1 atm O_2).

corresponding value in perchloric acid (0.1N) is about 8×10^{-11} (1), whereas that in 85% orthophosphoric acid (14.5M) is about 4×10^{-13} A/cm^2 (2). A compensation effect between the activation energy and the Arrhenius preexponential term is noted for oxygen reduction on bright platinum in trifluoromethane sulfonic and orthophosphoric acids. The corresponding preexponential terms for the exchange currents are -0.94 and $+2.17$, respectively, when expressed as $\log_{10} i_o$ (A/cm^2). The temperature at which the oxygen reduction reaction has the same rate in both acids is about 135°C, the i_o value being *ca.* 2×10^{-8} A/cm^2.

Conclusions

1.1M trifluoromethane sulfonic acid shows an exchange current density for oxygen reduction at 1 atm pressure and ordinary temperature that is about 2 orders of magnitude greater than that in 85% orthophosphoric acid, the electrolyte normally used in acid fuel cells. It shows a particularly low activation energy (about ~10.3 kcal/mole less than that in orthophosphoric acid) which renders it particularly interesting for use at lower temperatures. This difference in activation energy probably results from the combined effect of heat of adsorption of anions and differences in the heat of solution of oxygen. As noted elsewhere for oxygen reduction in acid solution, a compensation effect (3) is observed between the Arrhenius preexponential terms and activation energies in the two acids, with an extrapolated crossover temperature of about 135°C. Such compensation effects may be of great theoretical significance for oxygen electrode processes.

Manuscript submitted Nov. 1, 1976; revised manuscript received Nov. 21, 1977.

Any discussion of this paper will appear in the December 1978 JOURNAL. All discussions for the December 1978 Discussion Section should be submitted by Aug. 1, 1978.

Publication costs of this article were assisted by Energy Research Corporation.

REFERENCES

1. A. Damjanovic and V. Brusic, *Electrochim. Acta*, **12**, 615 (1967).
2. A. J. Appleby, *This Journal*, **117**, 328 (1970).
3. A. J. Appleby, "Modern Aspects of Electrochemistry," Vol. 9, B. E. Conway and J. O'M. Bockris, Editors, p. 369, Plenum Press, New York (1974).
4. H. R. Kunz and G. A. Gruver, *This Journal*, **122**, 1279 (1975).
5. A. A. Adams and H. J. Barger, *ibid.*, **121**, 987 (1974).
6. R. N. Camp and B. S. Baker, Contract DAAKO2-73-C-0084, AD 766 313/1, N.T.I.S., Springfield, Va., 1973.
7. J. Giner, *This Journal*, **111**, 376 (1964).
8. A. Damjanovic and M. Genshaw, *Electrochim. Acta*, **15**, 1281 (1970).
9. M. R. Tarasevich, *Elektrokhimiya*, **9**, 599 (1973).
10. E. Gileadi and B. E. Conway, "Modern Aspects of Electrochemistry," Vol. 3, J. O'M. Bockris and B. E. Conway, Editors, p. 347, Butterworth, London (1964).

Photoanodic Behavior of n-type Cadmium Sulfide in Acetonitrile Solutions Containing Iodide Ion

Kenji Nakatani,[1] Shigeyuki Matsudaira, and Hiroshi Tsubomura

Department of Chemistry, Faculty of Engineering Science, Osaka University, Toyonaka, Osaka, Japan

The conversion of light energy to electrical and chemical energy in electrochemical systems equipped with semiconductor electrodes has attracted wide attention. Unfortunately, many semiconductors having appropriate bandgaps, *e.g.*, CdS, GaP, etc., are subject to undesirable dissolution or decomposition by photoelectrochemical reactions in aqueous solutions (1). Recently, some photoelectrodes, *e.g.*, CdS, CdTe, have been reported to be stabilized in aqueous solutions containing reducing agents such as ferrocyanide, sulfide, and selenide (2).

We thought that the dissolution or decomposition could be prevented, or suppressed by employing nonaqueous solvents. It turned out that the photoanodic dissolution of CdS could not be fully avoided in various organic solvents, such as acetonitrile, nitromethane, and dimethylformamide. But the onset potential for the anodic dissolution current of CdS was found to change with solvent basicity (3). In this paper, we report the results on stable CdS photocells using nonaqueous solution containing iodide ion. The photoelec-

[1] Present address: Teijin Limited, Central Research Institute, Hino, Tokyo, Japan.

Key words: semiconductor, photocell, photocurrent, solar energy conversion.

tric behavior of semiconductor electrodes in nonaqueous solutions has also been extensively studied by Bard *et al.* (4).

Experimental

The structure of the electrochemical photocell and the measuring devices used are of a conventional type, reported in our previous paper (5). In some cases, a two-compartment cell separated by an agar bridge was used. Some of the experiments were made under the potentiostatic conditions using a Hokutodenko HA 101 potentiostat. CdS single crystal electrodes with the (0001) face polished with alumina abrasive and etched in a 3M HCl solution for 5 sec were used together with a platinum plate counterelectrode. Acetonitrile and nitromethane were purified according to the literature (5, 6). Lithium perchlorate (0.1 mole · $liter^{-1}$) was used as a supporting electrolyte. A 250W high pressure mercury lamp combined with Toshiba glass filters, UV-35 and UB-46, or a 500W halogen lamp monochromatized by an MC-20 monochromator of Ritsu Oyo Company Limited was used as the light source, and the light intensity was measured with an Eppley thermopile. The intensity of the light incident upon the sample is *ca.* $1.40 \cdot 10^{-2}$W cm^{-2} for the former and $1.20 \cdot 10^{-4}$W cm^{-2} at λ: 475 nm for the latter.

In order to check the dissolution of CdS after the passage of photocurrent under potentiostatic conditions (0V *vs.* SCE), solutions were ashed with a suitable amount of concentrated nitric acid and analyzed for Cd^{2+} by either colorimetry with dithizone (7) or atomic absorption method. The differential capacitance of the electrode was measured with an a-c bridge at 1 kHz.

Results and Discussion

No steady photocurrent was obtained between an illuminated CdS electrode and a directly connected counterelectrode in an acetonitrile solution containing only $LiClO_4$. The surface of the CdS electrode became rough and yellow by the anodic photocurrent, owing to the deposition of sulfur. The amount of the Cd^{2+} ion produced, measured by the colorimetric analysis, was almost equivalent to the electrical quantity passed (0.3-18C, for periods of 20 min to 9 hr).

The decomposition of CdS was prevented by addition of sodium iodide into the solution even for the case of strong illumination, and a photocurrent as shown by curve a in Fig. 1 was obtained. The solution became yellow by passage of the current, suggesting the oxidation of I^- ion on the surface of the electrode to I_3^-. By employing an H-shaped cell, with the cathode and anode being separated, the formation of I_3^- was confirmed from the absorption spectrum of the solution in the CdS half-cell. The amount of I_3^- calculated from the absorbance and the molar extinction coefficient of I_3^-, 2.9×10^4, agreed well with the theoretical value obtained according to the following reaction

$$3I^- + 2p \rightarrow I_3^- \quad [1]$$

When the photocurrent experiments were carried out using an H-shaped photocell containing I^- in both sides, with oxygen bubbled into the cathodic (Pt) half-cell and nitrogen into the anodic (CdS) half-cell, the photocurrent under the short-circuit condition increased, as shown by the dotted curve in Fig. 1, probably because of the reduction of oxygen. No effect was observed by bubbling oxygen into the CdS half-cell.

With more than 10^{-4} mole · $liter^{-1}$ of I_2 added into the cathodic half-cell, the photocurrent was not affected by oxygen. The initial drop of the photocurrent as shown by curve a of Fig. 1 was avoided by addition of I_2 in the solution before illumination (curve b, Fig. 1), I_2 being mostly changed to I_3^-, owing to the large equilibrium constant for $I^- + I_2 \rightleftarrows I_3^-$ (8). These results arise undoubtedly by the reaction at the cathode

$$I_3^- + 2e \rightarrow 3I^- \quad [2]$$

With an undivided cell, the intensity of the I_3^- absorption band in the solution did not change even after long illumination, showing that equal amounts of I^- and I_3^- are generated at the anode and the cathode, respectively.

Quantitative analysis of the Cd^{2+} ion was carried out for the photoreacted acetonitrile solution containing various quantities of sodium iodide, and the "dissolution ratio," that is, the ratio of the observed Cd^{2+} concentration *vs.* that calculated from the total electric quantity of the photocurrent was plotted against the NaI concentration (Fig. 2). When the concentration of NaI was above 0.2 mole · $liter^{-1}$, the Cd^{2+} ion concentration in the solution became very small as found from colorimetric and atomic absorption analysis, and no weight loss of the CdS electrode was detected even after long illumination with an intensity of up to 0.135 W/cm^2.

Honda *et al.* (2) reported that the photoanodic dissolution of CdS in aqueous solutions could not be fully avoided by addition of I^-. The present favorable result can be attributed to the following two reasons. Firstly, the photodissolution current of CdS arises only at a more positive potential (− 0.3 ~ − 0.6V *vs.* SCE) in acetonitrile than in water (3). Secondly, the redox potential of I^-/I_3^- in acetonitrile (+ 0.03V *vs.* SCE) is more negative than that in water (+ 0.29V) (9), probably because of the smaller solvation energy of I^- in acetonitrile than in water. According to these

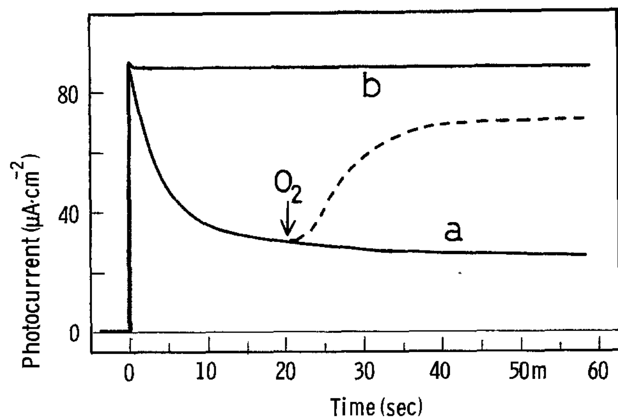

Fig. 1. Photocurrent curves *vs.* time under nitrogen gas bubbling. *a*, CH_3CN solution containing 0.285M NaI and 0.1M $LiClO_4$ (------: O_2 bubbling started at 20 sec); b, CH_3CN solution containing 0.285M NaI, 6×10^{-4}M I_2, and 0.1M $LiClO_4$.

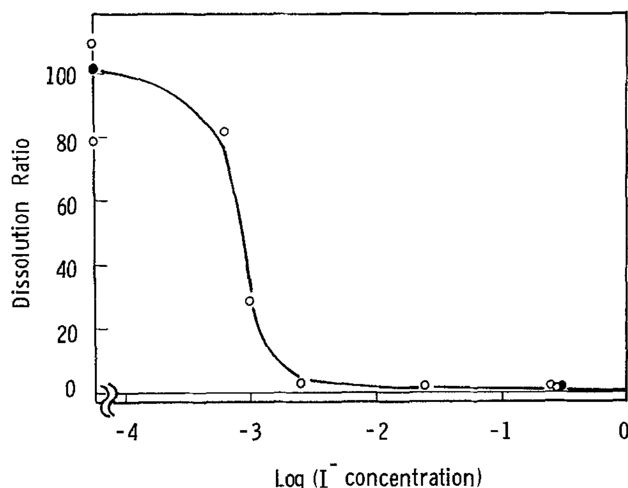

Fig. 2. "Dissolution ratio" for a CdS electrode under light from a filtered mercury lamp at various concentrations of NaI in acetonitrile solutions of $LiClO_4$. ○, By the colorimetric analysis: ●, by the atomic absorption analysis.

two reasons, CdS becomes stable in acetonitrile in the presence of an I^-/I_3^- couple.

An attempt was made to use nitromethane instead of acetonitrile, which was expected to stabilize CdS electrodes by its weak basicity (3). This was unsuccessful due to the small solubility of NaI in nitromethane. Even when a saturated solution of NaI was used, *ca.* 6% of the photocurrent arose from the dissolution of CdS.

The above-mentioned satisfactory result for acetonitrile solutions has led us to check the efficiency of the conversion of light to electrical energy by the photocell <CdS|NaI-acetonitrile|Pt> with variable load resistance (R) inserted into the external circuit and with light from a Xe lamp monochromatized at 475 nm. The acetonitrile solutions of NaI/I_2 redox couple, in spite of their yellow color, have little effect of retarding light coming toward the CdS electrode, as shown in Fig. 3.

Van den Berghe *et al.* reported that the etching of the electrode is very important for getting a large photocurrent (10). We have also observed that the photocurrent was enhanced by etching in a 3M HCl solution for 3 min (Fig. 4). Longer etching caused no further increase. The best power-conversion efficiency (electrical power, $i_p \cdot V_p$, produced divided by incident light power) obtained was 9.5% at $R = 100$ kΩ with an output potential of 0.70V and the highest photocurrent quantum efficiency (number of electrons in the short-circuit current ($R = 0$) divided by number of incident photons) was 69%, both for incident monochromatic light, 0.120 mW cm^{-1} at wavelength 475 nm. The dissolution of CdS was inhibited by I^- irrespective of the etching time.

The etching has been found to influence the differential capacitance in acetonitrile (Fig. 5). The $1/C^2$ *vs.* potential plot for a sufficiently etched (for 10 min) CdS electrode resulted in a straight line, while the plots for insufficiently etched CdS electrodes deviated from it. As the capacitance of the Helmholtz layer is thought to be much larger than the capacitance measured ($< 0.3\ \mu F/cm^2$), the observed capacitance should have arisen mostly from inside the semiconductor. The result in Fig. 5 shows that a part of the capacitance is brought about by a surface layer which can be removed by the etching. It is therefore concluded that the improvement of the photocurrent by etching is due to the removal of the current-retarding interfacial material.

Acknowledgment

The authors are grateful for the many kind suggestions of Professor A. J. Bard. The present work was partially supported by a Grant-in-Aid for Scientific Research from the Ministry of Education (No. 911504).

Manuscript submitted Aug. 23, 1977; revised manuscript received Oct. 13, 1977.

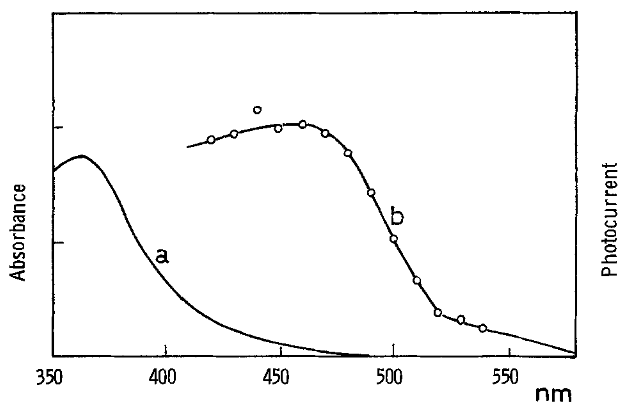

Fig. 3. a, Absorption spectrum of a CH_3CN solution of 0.285M NaI, 6×10^{-4}M I_2, and 0.1M $LiClO_4$. b, Action spectrum of photocurrent in the same solution.

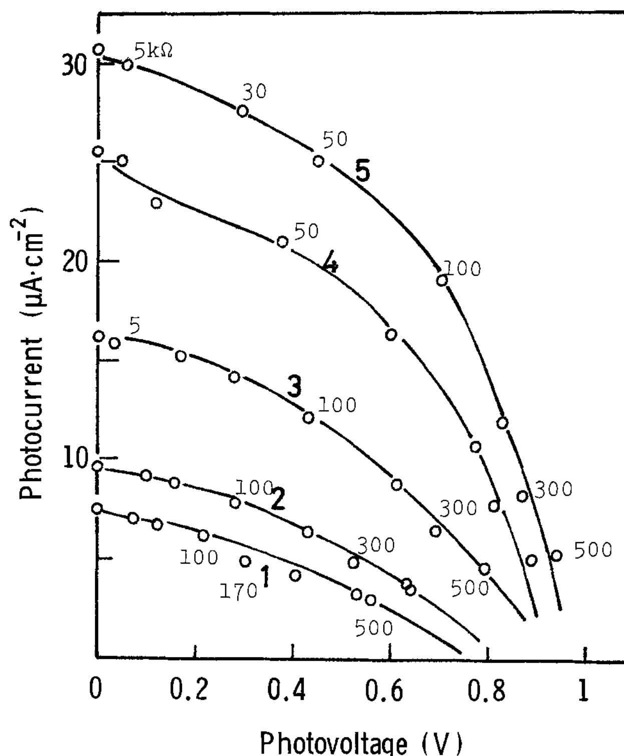

Fig. 4. The i-V curves for <n-type CdS|0.285M $I^-/3 \times 10^{-4}$M I_2/CH_3|Pt> on the time of etching in 3M HCl (λ 475 nm). 1, 5 sec; 2, 30 sec; 3, 1 min; 4, 2 min; 5, 3 min. The numbers in the figure denote the load resistances in kΩ.

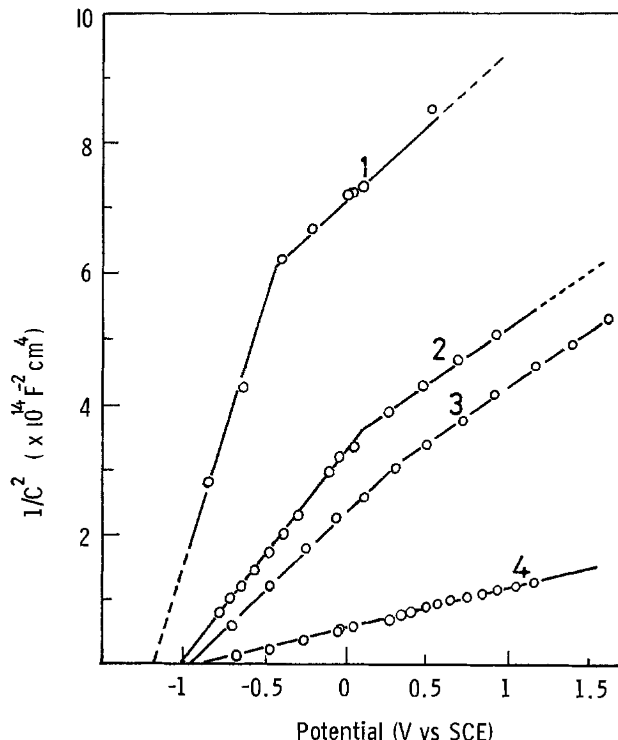

Fig. 5. The Mott-Schottky plots of the differential capacitances for the electrodes etched in 3N HCl. 1, 5 sec; 2, 3 min; 3, 5 min; 4, 10 min.

Any discussion of this paper will appear in a Discussion Section to be published in the December 1978 JOURNAL. All discussions for the December 1978 Discussion Section should be submitted by Feb. 1, 1978.

Publication costs of this article were assisted by Osaka University.

REFERENCES

1. H. Gerischer, *J. Electroanal. Chem. Interfacial Electrochem.*, **58**, 263 (1975); M. Matsumura, K. Yamamoto, and H. Tsubomura, *J. Chem. Soc. Jpn.*, **399**, (1976).
2. A. Fujishima, E. Sugiyama, and K. Honda, *Bull. Chem. Soc. Jpn.*, **44**, 304 (1971); T. Inoue, T. Watanabe, A. Fujishima, and K. Honda, *This Journal*, **124**, 719 (1977); A. B. Ellis, S. W. Kaiser, and M. S. Wrighton, *J. Am. Chem. Soc.*, **98**, 1635, 6855 (1976); A. B. Ellis, S. W. Kaiser. J. M. Bolts, and M. S. Wrighton, *ibid.*, **99**, 2839 (1977). A. B. Ellis, J. M. Bolts, S. W. Kaiser, and M. S. Wrighton, *ibid.*, **99**, 2848 (1977); G. Hodes, J. Manassen, and D. Cahen, *Nature (London)*, **261**, 403 (1976); J. Manassen, G. Hodes, and D. Cahen, *This Journal*, **124**, 532 (1977); H. Gerischer and J. Gobrecht, *Ber. Bunsenges. Phys. Chem.*, **80**, 327 (1976); B. Miller and A. Heller, *Nature (London)*, **262**, 680 (1976); A. Heller, K. C. Chang, and B. Miller, *This Journal*, **124**, 967 (1977).
3. K. Nakatani and H. Tsubomura, Unpublished results.
4. S. N. Frank and A. J. Bard, *J. Am. Chem. Soc.*, **97**, 7427 (1975); D. Laser and A. J. Bard, *J. Phys. Chem.*, **80**, 459 (1976); P. A. Kohl and A. J. Bard, Private communication.
5. K. Nakatani and H. Tsubomura, *Bull. Chem. Soc. Jpn.*, **50**, 783 (1977).
6. C. K. Mann, "Electroanalytical Chemistry," Vol. 3, A. J. Bard, Editor, Marcel Dekker, Inc., New York (1969).
7. B. E. Saltzman, *Anal. Chem.*, **25**, 493 (1953).
8. V. A. Macagno, M. C. Giordano, and A. J. Arvia, *Electrochim. Acta.*, **14**, 335 (1969).
9. A. I. Popov and D. H. Geske, *J. Am. Chem. Soc.*, **80**, 1340 (1958).
10. R. A. L. Van den Berghe, W. P. Gomes, and F. Cardon, *Ber. Bunsenges. Phys. Chem.*, **77**, 289 (1973); R. A. L. Van den Berghe, F. Cardon, and W. P. Gomes, *ibid.*, **78**, 331 (1974).

Brief Communication

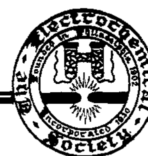

Persistent Polarization of Polyelectrolyte Membranes in an Aqueous Environment

G. A. Bornzin and I. F. Miller*

Bioengineering Program, University of Illinois, Chicago, Illinois 60680

Over the past several years, a number of attempts have been made to model neural excitation and conduction phenomena using a dipole orientation and stabilization model (1-4). Evidence for the involvement of dipole orientation comes from measurements of axonal surface charges (5), birefringence changes (6, 7), and infrared emission measurements during action potential propagation (8).

Although the dipole orientation and stabilization models used are considered to be heterocharged electret models, there are important differences between axonal membranes and the systems usually used in electret studies. Most experimental studies of heterocharged electrets have involved dry electrical insulators and workers have postulated their formation to involve electron trapping (9) in some cases or displacement of ionic impurities in other cases (10). Such electrets have been shown to involve volume polarization (11) and have been shown to decay by mechanisms of dielectric relaxation (12, 13). Of course, axonal membranes are highly swollen with water, contain mobile ions, and cannot be considered to be electrical insulators.

Recently, we reported on a system in which strong heterocharged electrets were shown to exist in polyelectrolyte membranes (14-17). These membranes were electrical conductors and, in fact, it was shown that the amount of persistent polarization actually increased with electrical conductivity. The process involved was modeled by assuming mobile ion displacement down the electric field and stabilization of the dipoles thus induced by hydrogen bonding. The polyelectrolyte membranes contained sodium polystyrene sulfonate and polyvinyl alcohol, were studied in vacuum, and were dry.

* Electrochemical Society Active Member.

Key words: electret, polarization, polyelectrolyte, nerve, water.

In using the results of various electret studies to model the neural axon membrane, the role of water must be taken into account. Water swelling of dielectric membranes would destabilize any electret present. Similarly, if hydrogen bonding is involved, as apparently occurs in the polyelectrolyte systems, water should also have a disruptive effect here, unless water is excluded from the hydrogen bonding regions as probably occurs in certain polypeptide systems (18).

In this work, we have attempted to assess the effect of water and aqueous solution swelling on polarization stability in a polyelectrolyte membrane system. In the membrane formulation studied, the components were sodium polystyrene sulfonate (PSSNa), (Dow SA-1291.1, avg. mol. wt. $\simeq$ 2-4 $\times$ 10^6), polyvinyl alcohol (PVA) (Dupont Elvanol 71-30), crosslinked by hexamethoxymelamine (American Cyanamid Cymel 303). In addition, a small amount of *para*-toluenesulfonic acid (p-TSA) was added as an acid catalyst. All ingredients were washed several times and dialyzed against distilled water for purification purposes. The ingredients were dissolved in a methanol-water mixture, cast on glass plates, and cured at 70°C in a circulating oven. The finished membranes were clear, flexible, and fairly tough, had thicknesses ranging from 0.05 to 0.07 mm, and had an ion exchange capacity averaging 1.08 Mequiv./dry gram. They also could absorb substantial amounts of water. When dry, the membranes contained 15.2 weight percent (w/o) PSSNa, 30.9 w/o PVA, 51.7 w/o Cymel, and 2.2 w/o *p*-TSA. This formulation corresponds to a mole fraction of 0.08 in sulfonate groups.

Thermoelectrets were formed in these membranes by the methods reported earlier (14), except that the membranes and electrodes were previously coated with purified colloidal graphite to reduce contact resistance (17). Polarization was carried out at 65°-75°C in vac-

uum for at least 24 hr. After cooling to room temperature, four different experiments were carried out:

(*i*). The first, a control experiment, involved a removal of the charging field and a reheating of the membrane (following a capacitive discharge) to 15°C above the charging temperature, while monitoring the discharge current with a Keithley 610C electrometer. Integration of the discharge current over time yielded the total charge stored.

(*ii*). This was similar to (*i*) above, except that after cooling the charged electret to room temperature, the seal was broken, the electrode removed, and the membrane exposed to 100% relative humidity air at 20°C for 24 hr. The electrode was then replaced and the chamber resealed, evacuated, and thermally discharged.

(*iii*). This was similar to (*ii*) above, except that instead of exposure to high humidity air, the membrane was soaked in distilled water for 2 min.

(*iv*). This was similar to (*ii*) above, except that the membrane was soaked in 0.2M KCl solution for 24 hr, followed by a distilled water wash.

The results of these experiments are shown in Table I. As may be seen from the data, exposure to humid air or aqueous solution leads to substantial water swelling of the membranes. However, apparently it does not significantly destabilize the thermoelectrets formed. In fact, the water swelling appears to lead to substantially more charge storage than the control experiments (it should be noted that the control numbers are essentially the same as those reported by Linder (14) for a similar system). This is even true for the experiments in which the membrane is soaked in salt solution.

It is possible to explain the role of water in apparently stabilizing the electrets formed by considering its effect on the local field surrounding an electret forming group. In forming a heterocharged electret, the local field opposes the polarization, and anything that can reduce the effect of the local field within the membrane should lead to enhanced electret stability. When water enters the membrane, its polarization vector is in the same direction as the local electric field, thereby reducing the local field. Another effect of the water might be to reduce the attractive forces between separated charges in any induced dipoles present. This effect is, of course, counterbalanced by the disruptive effect of the water on the hydrogen bonding which stabilizes the separated charges.

Table I

	Experiment	Charge-stored C/cm² × 10⁸ two experiments
(*i*)	Control—negligible water content	0.052, 0.026
(*ii*)	Humid air—18.0% water (by weight)	0.92, 0.42
(*iii*)	Distilled water—20.2% water (by weight)	0.10, 0.26
(*iv*)	0.2M KCl—24.4% water (by weight)	0.14, 0.15

Thus, one might expect that there is an optimum amount of water that will maximize electret stability beyond which the electrets become less stable. The possibility of such an optimum may be inferred from the data reported, but the data is too sparse to reach a firm conclusion. If these reported effects also occur in neural axon membranes, perhaps it is easier to understand how persistent polarization can occur in a membrane so heavily loaded with water and mobile ions.

In the axon membrane, of course, ionic permeability changes accompany polarization changes. An attempt (using K^+ as the permeant) to determine if significant permeability changes occur in the polyelectrolyte membranes as a function of charge storage and degree of water swelling resulted in no significant changes being observed.

Acknowledgment

The authors wish to thank the National Science Foundation for support for this work, under grant no. GK 43294. This work is based on a thesis submitted by G. A. Bornzin in partial fulfillment of the requirements for the M.S. degree in Bioengineering at the University of Illinois at Chicago Circle.

Manuscript submitted Oct. 14, 1977; revised manuscript received Nov. 3, 1977.

Any discussion of this paper will appear in a Discussion Section to be published in the December 1978 JOURNAL. All discussions for the December 1978 Discussion Section should be submitted by Aug. 1, 1978.

REFERENCES

1. D. Wobshall, *J. Theor. Biol.*, **21**, 439 (1968).
2. L. Y. Wei, *Bull. Math. Biophys.*, **31**, 39 (1969).
3. C-Y Lee and C. Chiang, *Bull. Math. Biol.*, **38**, 59 (1976).
4. B. Hamel and I. Zimmerman, *Biophys. J.*, **10**, 1029 (1970).
5. J. R. Segal, *ibid.*, **8**, 470 (1968).
6. L. B. Cohen, R. D. Keynes, and B. Hill, *Nature (London)*, **218**, 438 (1968).
7. A. von Hippel, "Dielectrics and Waves," J. Wiley & Sons, New York (1954).
8. A. Fraser and A. H. Frey, *Biophys. J.*, **8**, 731 (1968).
9. R. Gerson and J. H. Rohrbaugh, *J. Chem. Phys.*, **23**, 238 (1955).
10. M. L. Miller, *J. Polym. Sci., Part A2*, **4**, 685 (1966).
11. B. Gross and R. J. De Moraes, *J. Chem. Phys.*, **37**, 710 (1962).
12. H. C. Berg, *Biophys. J.*, **8**, 1051 (1968).
13. B. Gross, "Charge Storage in Solid Dielectrics," Elsevier, Amsterdam (1964).
14. C. Linder and I. F. Miller, *J. Phys. Chem.*, **76**, 3434 (1972).
15. C. Linder and I. F. Miller, *This Journal*, **120**, 498 (1973).
16. C. Linder and I. F. Miller, *J. Polym. Sci., Part A1*, **11**, 1119 (1973).
17. I. F. Miller and J. Mayoral, *J. Phys. Chem.*, **80**, 1387 (1976).
18. B. D. Ratner and I. F. Miller, *J. Polym. Sci., Part A1*, **10**, 2425 (1972).

JOURNAL OF THE ELECTROCHEMICAL SOCIETY

SOLID-STATE SCIENCE
AND TECHNOLOGY

MARCH
1978

The Effect of SO_2 and NaCl on High Temperature Hot Corrosion

D. W. McKee, D. A. Shores,* and K. L. Luthra*

General Electric Company, Corporate Research and Development, Schenectady, New York 12301

ABSTRACT

Sea salt ingested into gas turbines in a marine environment may result in the transient deposition of NaCl in a Na_2SO_4 film on hot gas path components under certain conditions. It has been found in laboratory studies that the corrosion behavior of high temperature alloys, such as IN 738, IN 713C, IN 100, and Ni-30Al (NiAl), toward such salt deposits is strongly influenced by the chemical composition of the gaseous environment. When SO_2 is present together with small concentrations of NaCl in Na_2SO_4 in an oxidizing atmosphere, these alloys are rapidly attacked at around 750°C, whereas much less corrosion occurs when either SO_2 or NaCl is absent. It appears that gaseous chlorine formed during sulfation of NaCl plays an important role in initiating attack which is subsequently propagated by the presence of a liquid phase.

The role of NaCl in the hot corrosion of gas turbines operating in a marine environment has been the subject of several investigations (1-7) and was discussed extensively in a recent conference (8). The controversy is not over the effect of NaCl, its ability to accelerate Na_2SO_4-induced attack has been demonstrated repeatedly, but whether NaCl is a relevant species in a gas turbine environment and by what mechanism it can accelerate attack by a predominantly Na_2SO_4 deposit.

In a marine environment NaCl is ingested into a gas turbine predominantly as an aerosol of sea salt along with the intake air. With normal engine operation and low-to-moderate salt levels, thermodynamic calculations predict that NaCl should not condense on first stage buckets; indeed, NaCl should be converted to Na_2SO_4 by reaction with SO_2 in the combustion gas (9, 10). However, because of the short residence times of the combustion gases, kinetic limitation of the sulfation and evaporation reactions may allow some NaCl particles from the compressor deposits to survive long enough to reach the first stage buckets (3, 11, 12). Thus, according to these arguments, NaCl may deposit by impaction along with Na_2SO_4 and other salts on turbine blades, but will be removed eventually by evaporation or sulfation. Operation of the gas turbine at low or moderate power will enhance the likelihood for the deposition of NaCl particles and, because of the lower blade temperatures, the average residence time of a deposited NaCl particle will be longer than at high power. Unfortunately, it has proved to be difficult to confirm the existence of NaCl on turbine blades. Careful chemical analysis of deposits or corroded regions on turbine blades only rarely reveals chlorides (13), but this may be simply a reflection of the transient nature of the deposited NaCl particle owing to sulfation and evaporation or, as others have proposed, due to the formation of volatile products by reaction with components of the scale (1-7). The deposition of NaCl particles under particular circumstances such as low power operation, appears likely but not well substantiated.

Earlier published work, especially by Hancock *et al.* (4, 5) and Condé (1, 3), has demonstrated that Cr_2O_3-forming alloys are particularly susceptible to attack in the presence of NaCl, with corrosion rates generally increasing with temperature. By contrast, Al_2O_3-forming alloys and aluminide coatings without Cr were reported to be much less affected by chloride. These observations were made using the dynamic vibration modulus technique (5, 14, 15), hot stage microscopy (4) and salt-sprayed specimen testing in atmospheres of air or oxygen to which NaCl was introduced (3). Recently, burner-rig data have been presented which show quite a different pattern of behavior for MCrAlY-type coatings and high temperature alloys such as IN-738 and Nimonic 105 (8). In these cases, when SO_2 was present in the gaseous combustion products, the alloys and coatings showed much more extensive chloride-induced corrosion at 750°C than at 900°C.

The present report concerns the role of NaCl in the mechanism of Na_2SO_4-induced hot corrosion attack of several alloys at moderate temperatures (700°-800°C). In particular, the synergistic effect of SO_2 and NaCl, reported previously (16), is considered in some further detail. Another mechanism of attack at moderate temperatures, which is dependent on SO_2 and SO_3 but not NaCl, will be described in a subsequent paper.

Experimental Procedure

Three kinds of kinetic experiments have been carried out: (*i*) studies of the interaction of Na_2SO_4-NaCl mixtures with O_2 and $O_2 + SO_2$ environments, (*ii*) studies of the oxidation of IN-738 and Ni-30Al in O_2 and in $O_2 + Cl_2$ mixtures, and (*iii*) crucible-type hot corrosion tests of several alloys in Na_2SO_4, NaCl, and Na_2SO_4-NaCl mixtures with various environments. The kinetics of evaporation and sulfation of NaCl in Na_2SO_4-NaCl mixtures were measured wtih a Mettler

* Electrochemical Society Active Member.

Thermoanalyzer-2 balance. This instrument recorded weight changes as a function of time at various temperatures in a controlled environment. The sensitivity of this balance could be varied over a wide range up to maximum sensitivity of $\pm$ 5 μg for a 5g load. The salt mixtures were prepared from Fisher Certified A.C.S. grades of NaCl and anhydrous Na_2SO_4, and were premelted at 900°C in air for 1 hr, then cooled, ground, and thoroughly mixed before use. Experiments were carried out at temperatures from 600° to 1000°C in O_2 (dried by passage through Drierite) or in various O_2-SO_2 mixtures. Gas mixtures (analyzed grade) were prepared by Union Carbide Corporation (Linde Division) from gases of the following purity: oxygen 99.6%, sulfur dioxide 99.9%, chlorine 99.5%, and hydrogen chloride 99%. Because of the expected slow attainment of equilibrium between SO_2, O_2, and SO_3 at moderate temperatures, a few corrosion tests were carried out in the presence of a Pt catalyst. This was accomplished with the specimen and salt contained in a Pt crucible which was covered with a few layers of Pt gauze. The Ni-30Al (NiAl) alloy was prepared by induction melting and casting in argon 1 in. diam bars from which rectangular coupons were cut. Similar specimens of superalloys were machined from cast ingots which had been given the appropriate heat-treatments as suggested in the literature (17). The compositions of the alloys used in the hot corrosion experiments are listed in Table I. The alloy specimens for both the oxidation and hot corrosion tests were polished through 600 grit SiC paper and degreased with alcohol and acetone before use. Oxidized and corroded specimens were examined metallographically and with the scanning electron microscope.

In the hot corrosion tests alloy coupons (typically 6.4 $\times$ 12.8 $\times$ 1 mm) were placed in small, glazed porcelain crucibles containing 1.0g of either Na_2SO_4, NaCl, or premelted mixtures containing small concentrations of NaCl in Na_2SO_4. In this configuration the specimen was about half-immersed in the salt. For those conditions in which the salt melted, the upper half of the specimen was also covered with a thin film of salt because of capillarity. The crucible and contents were placed in the Chevenard thermobalance previously described (18) and brought to temperature within an hour in a flowing stream of the desired environment, which included O_2, $O_2 + SO_2$, $O_2 + Cl_2$, or O_2 + HCl. Many of the runs were carried out in 76%O_2-0.1%SO_2-bal N_2 which simulates the chemical potentials of oxygen and sulfur typical of the combustion products in a gas turbine operating at 5 atm with a 50:1 air/fuel ratio, and this composition will be referred to subsequently as simulated combustion gas (SCG). Since evaporation and sulfation of the salt were significant under some conditions, the measured weight changes were corrected by data from blank runs under identical conditions but containing no specimen. The sensitivity of the Chevenard balance was approximately $\pm$ 0.2 mg. Hot corrosion tests were carried out at a variety of temperatures between 600° and 950°C on Ni-30Al, IN-738, IN-713C, and IN-100. Some of the alloys were preoxidized in O_2 at 700°-900°C before the hot corrosion test. No appreciable corrosion of the glazed porcelain crucibles by the Na_2SO_4-NaCl melt could be detected during the duration of the experiments.

Results

Gas/salt interactions.—The combustion gas produced by burning petroleum-based fuels in a gas turbine contains N_2, O_2, CO_2, H_2O, small amounts of nitrogen oxides, CO, SO_2, hydrocarbons, and various airborne or fuel-borne impurities. The interaction of these various impurities with O_2, SO_2, and H_2O are significant to hot corrosion. Thus, the study of the effect of NaCl on hot corrosion under conditions which simulate a gas turbine environment necessarily involve evaporation and sulfation reactions

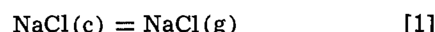

$$NaCl(c) = NaCl(g) \quad [1]$$

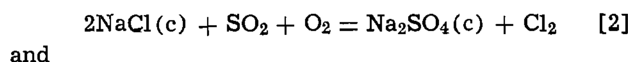

$$2NaCl(c) + SO_2 + O_2 = Na_2SO_4(c) + Cl_2 \quad [2]$$

and

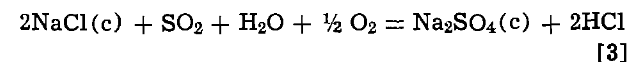

$$2NaCl(c) + SO_2 + H_2O + \tfrac{1}{2} O_2 = Na_2SO_4(c) + 2HCl \quad [3]$$

and

$$Na_2SO_4(c) = Na_2SO_4(g) \quad [4]$$

The rate at which reactions proceed to the right under our experimental conditions was measured by TGA in some preliminary runs. In slowly flowing dry O_2 at 800°C a Na_2SO_4-10 w/o NaCl melt lost weight steadily as a result of evaporation and no Cl_2 could be detected in the exhaust gas. With $O_2 + SO_2$ or $O_2 + SO_2 + H_2O$ the melt either lost weight less rapidly or gained weight indicating that sulfation was taking place concurrently with evaporation. Analysis of the exhaust gas for the $O_2 + SO_2$ run revealed copious amounts of Cl_2 as expected from Eq. [2]. As will be shown later, Cl_2 can have a substantial influence on rates of hot corrosion.

At lower temperatures the rates of evaporation and sulfation were reduced, but the same response was observed, *i.e.*, weight losses due to evaporation in O_2 and weight gains in $O_2 + SO_2$. Even at the highest temperature used in the hot corrosion tests, 950°C, a major portion of the NaCl remained after 6 hr. In Table II are reported analyses of Na_2SO_4-NaCl mixtures after

Table I. Composition of alloys

Alloy*	Weight per cent									
	Ni	Co	Cr	Al	Ti	Mo	W	Cb	Ta	C
Ni-30Al	Bal	—	—	29.3	—	—	—	—	—	—
IN-738	Bal	8	16	3.4	3.4	1.75	2.6	0.9	1.75	0.11
IN-713C	Bal	—	12.5	6.1	0.8	4.1	—	2.0	—	0.12
IN-100	Bal	15	10	5.5	4.7	3.0	—	—	—	0.18

* Except for Ni-30% Al, the alloys were heat-treated as appropriate for service.

Table II. Stability of NaCl in crucible tests with SO_2*

Initial mixture	Temperature (°C)	Time (hr)	Atmosphere	Final mixture
Na_2SO_4-10% NaCl	750	5	76% O_2-0.1% SO_2-N_2	Na_2SO_4-9.0% NaCl
Na_2SO_4-20% NaCl	850	6	50% O_2-1% SO_2-N_2	Na_2SO_4-16.2% NaCl
Na_2SO_4-25% NaCl	950	6	50% O_2-1% SO_2-N_2	Na_2SO_4-15.7% NaCl

* The gas flow rate was 250 ml/min with a 1g sample.

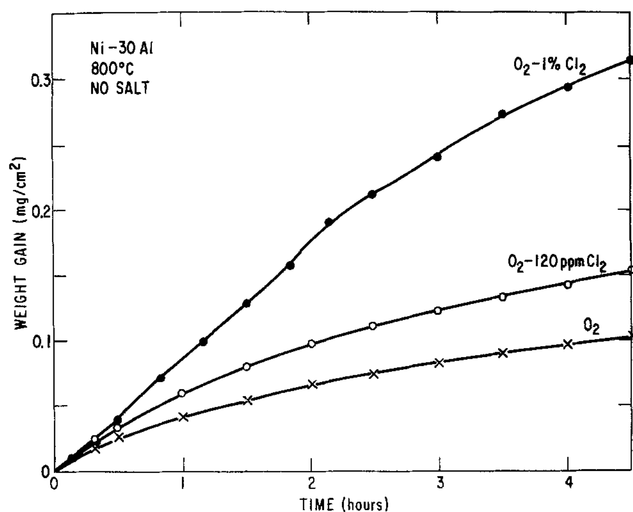

Fig. 1. Effect of gaseous Cl_2 on oxidation rate of Ni-30Al in O_2 at 800°C. Weight gains vs. time.

heating in atmospheres containing O_2 + SO_2 (but not H_2O) at three temperatures.

Oxidation.—IN-738 and Ni-30Al are resistant to oxidation at 800°C in pure O_2; however, for Ni-30Al the addition of a small amount of Cl_2, 120 ppm, to O_2 resulted in a measurable increase in the rate of weight gain, as shown in Fig. 1. With the addition of 1% Cl_2 the rate of weight gain was further increased. For IN-738 120 ppm Cl_2 also produced a slow but steady weight gain, but when the oxygen contained 1% Cl_2, the sample of IN-738 developed an oxide scale yet it lost weight steadily (Fig. 2), indicating the formation of a volatile product. However, of greater significance is the effect of Cl_2 on the integrity of the protective scale. With pure O_2 IN-738 formed a dense, protective scale at 800°C with an overgrowth of fine crystallites as shown in the SEM photographs in Fig. 3. Another specimen, exposed under identical conditions except that the gas contained 1% Cl_2, developed a much different scale morphology that was badly cracked and spalled as shown in Fig. 4. The appearance of the latter sample is very similar to that in Fig. 5 which is typical of a sample exposed in the crucible test to Na_2SO_4-1% NaCl in the SCG at 750°C.

Hot corrosion tests.—Some preliminary crucible-type tests were carried out with IN-738 in pure NaCl at 750°C in various environments, and the results are shown in Fig. 6 and 7. These tests were not intended to simulate conditions in a gas turbine, but rather to provide information on alloy/NaCl interactions. With pure O_2 IN-738 gained weight very slowly, but at a rate

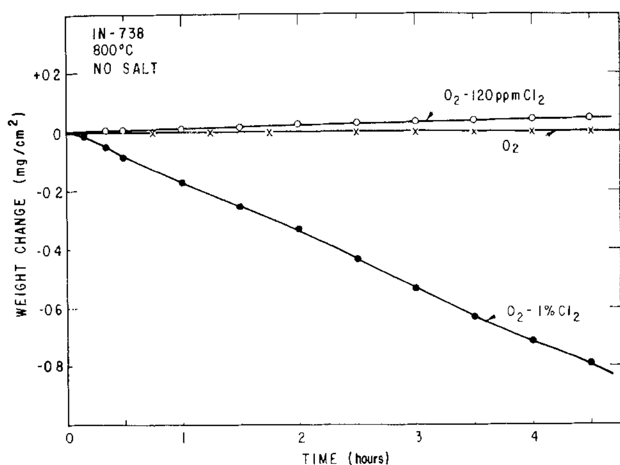

Fig. 2. Effect of gaseous Cl_2 on oxidation of IN-738 in O_2 at 800°C. Weight change vs. time.

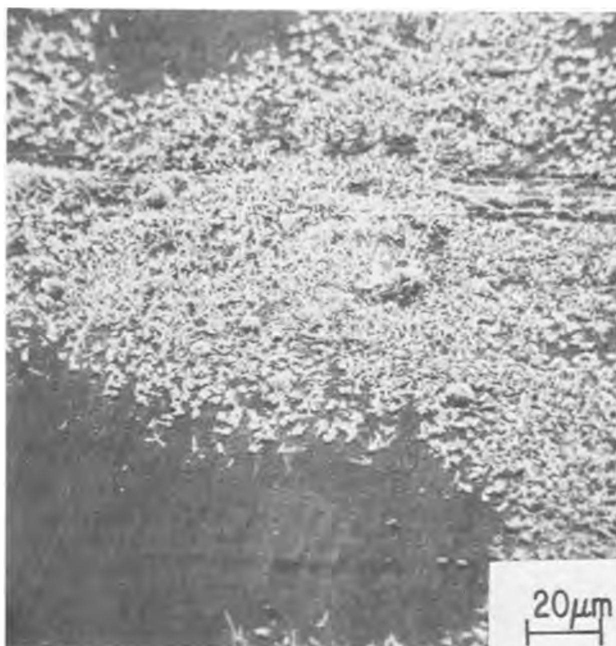

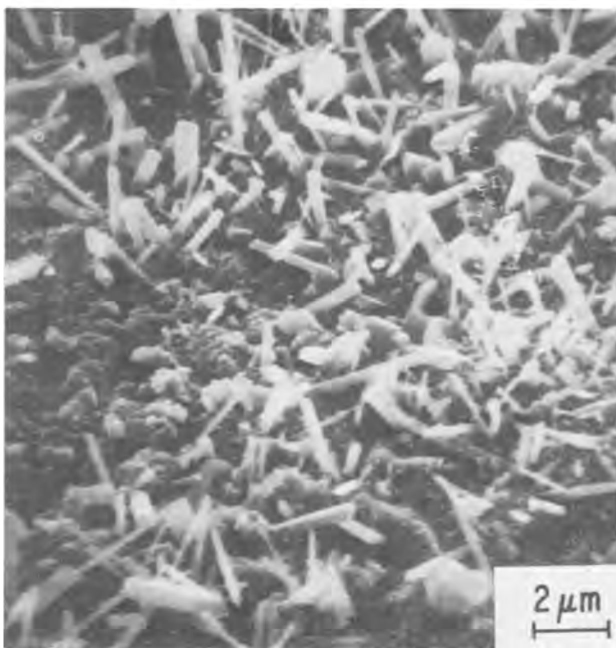

Fig. 3. SEM micrographs of the surface of IN-738 after oxidation in O_2 for 120 hr at 800°C.

somewhat faster than for simple oxidation. Although the salt was not melted at this temperature, the normally protective oxide scale was cracked and spalled, probably by NaCl vapor. Hancock *et al.* (4) have demonstrated that NaCl vapor will crack the protective oxide scale on Ni-base superalloys. With the addition of 120 ppm Cl_2 to O_2 IN-738 initially lost weight but subsequently was attacked considerably faster than in O_2. Very rapid rates of attack were observed in O_2-60 ppm HCl and in O_2-1% Cl_2. To distinguish the effect of NaCl vapor from that due to condensed NaCl in contact with the specimen, two runs were carried out with specimens suspended over, but not in contact with, NaCl. These data are reported as dashed curves in Fig. 6. In both O_2 and in O_2-1% Cl_2 the rate of attack in these tests was much lower than that when condensed NaCl was in contact with the specimen.

Although the test temperature was ~ 50°C below the melting point of NaCl, a liquid phase may have

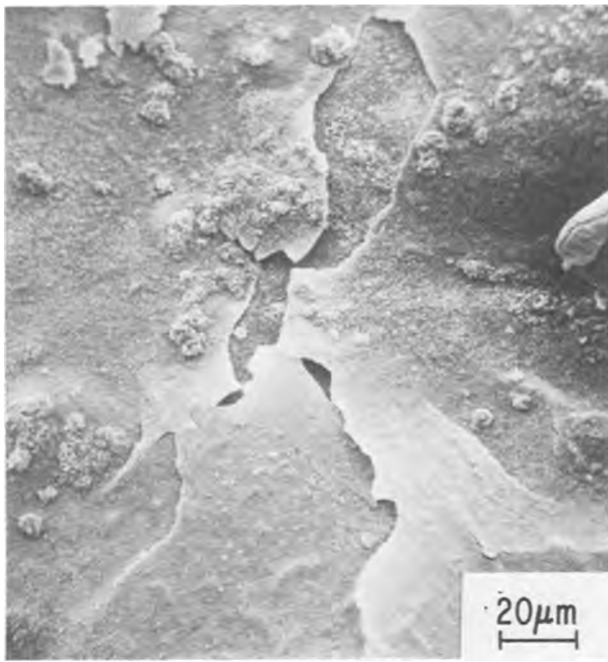

Fig. 4. SEM micrograph of the surface of IN-738 after oxidation in O_2-1% Cl_2 for 120 hr at 800°C.

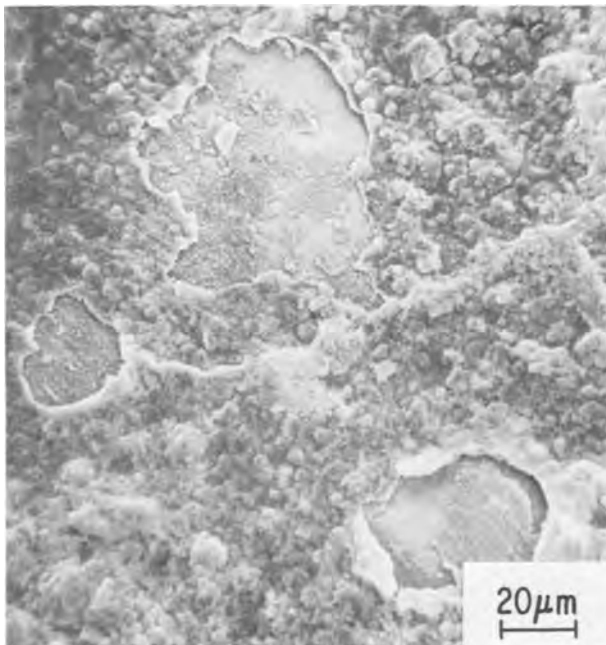

Fig. 5. SEM micrograph of the surface of IN-738 after 6 hr exposure to Na_2SO_4-1% NaCl at 750°C in 0.1% SO_2-76% O_2-N_2.

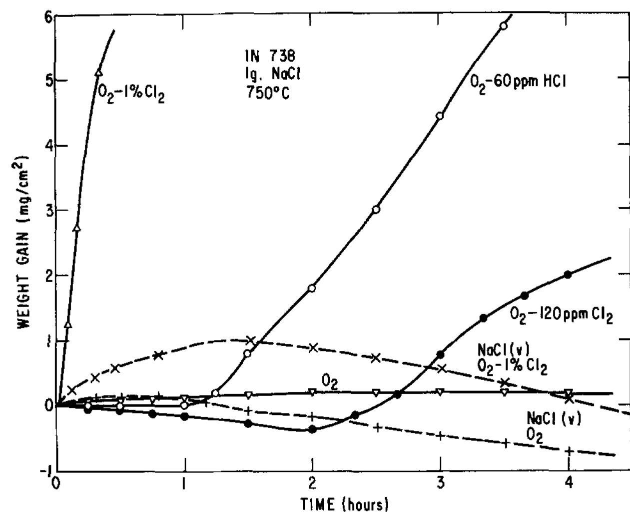

Fig. 6. Effect of Cl_2 or HCl in O_2 on the corrosion of IN-738 by pure NaCl at 750°C in the crucible tests. Weight changes vs. time. Solid curves are for solid NaCl, dashed curves are for NaCl vapor.

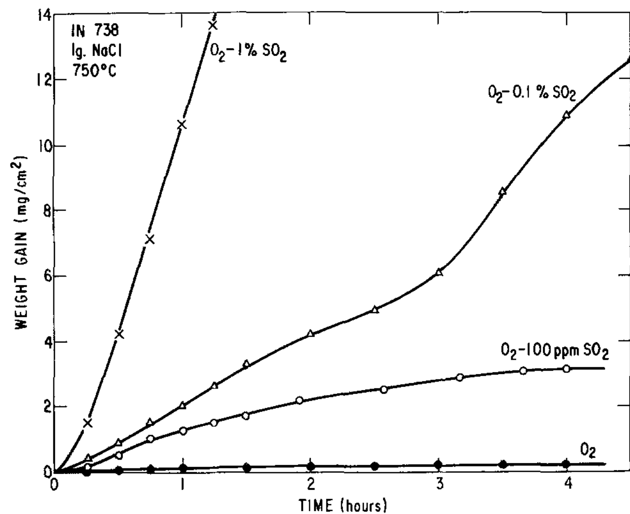

Fig. 7. Effect of SO_2 in O_2 on the corrosion of IN-738 by pure NaCl at 750°C in the crucible test. Weight gains vs. time.

formed in the crucible tests with O_2 + Cl_2 by the interaction of condensed NaCl with transition metal chlorides, which themselves are formed by the reaction of Cl_2 with components of the oxide scale. As is shown later some transition metal chlorides are thermodynamically stable in the presence of relatively high oxygen activities. Atomic absorption analysis revealed significant quantities of water soluble Ni and Co in the salt which is evidence for the formation of $NiCl_2$ and $CoCl_2$ during the test.

The presence of small concentrations of SO_2 in place of Cl_2 invoked a similar response of IN-738 in pure NaCl at 750°C, *e.g.*, 0.1% SO_2 approximately doubled the corrosion rate and in O_2-1% SO_2 the weight increases were linear and about an order of magnitude faster than in pure O_2. These data are reported in Fig. 7. One important effect of SO_2 is to convert NaCl to Na_2SO_4 and to generate Cl_2. The concentration of Cl_2 at the sample surface would be difficult to estimate because the rate-limiting step for reaction [2] is unknown. Nevertheless, in O_2 + 1% SO_2 the value of the activity of Cl_2 corresponding to thermodynamic equilibrium was estimated to be 0.16 atm when the activity of Na_2SO_4 was 1. Thus, it seems not unreasonable to suppose that at the specimen surface fairly high levels of Cl_2 were possible which could crack the oxide scale. In addition, the reaction of SO_2 with NaCl produces Na_2SO_4, again by Eq. [2], which eventually could form an aggressive liquid NaCl-Na_2SO_4 eutectic melt. In the present tests with either O_2-SO_2 or O_2-Cl_2 environments the bulk of the salt did not melt, but it appeared that the salt grains in contact with the sample had formed a small amount of liquid phase. From the runs in which the specimen was suspended above the salt (thereby excluding the possibility of a liquid phase) it was apparent that NaCl vapor together with Cl_2 in the presence of O_2 was insufficient to induce rapid attack.

A series of crucible tests have been carried out with several alloys in Na_2SO_4-NaCl mixtures, and the rate of attack was found to be strongly dependent on temperature, SO_2 in the gas and concentration of NaCl in the salt. In Fig. 8 are shown weight gain *vs.* time data for IN-100 at 750°C. In O_2 the rate of attack in

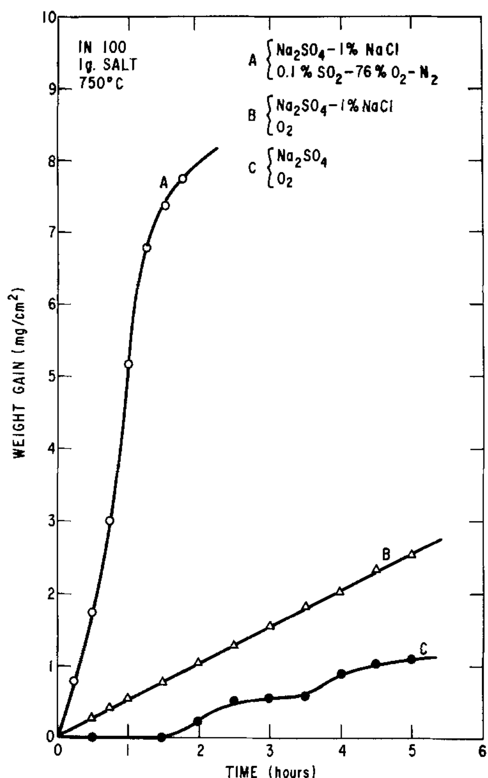

Fig. 8. Effect of NaCl and SO_2 on Na_2SO_4-induced corrosion in the crucible test of IN-100 at 750°C. Weight gains vs. time with Na_2SO_4 and Na_2SO_4-1% NaCl in O_2 or simulated combustion gas.

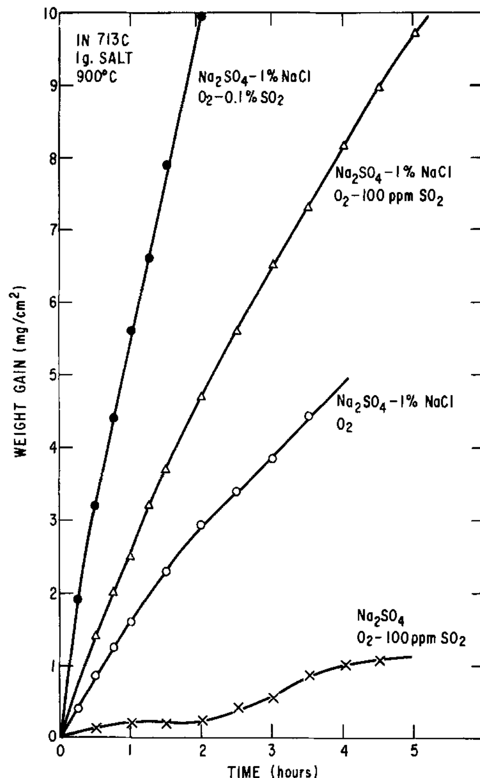

Fig. 10. Effect of NaCl and SO_2 on Na_2SO_4-induced corrosion of IN-713C in the crucible test at 900°C. Weight gains vs. time.

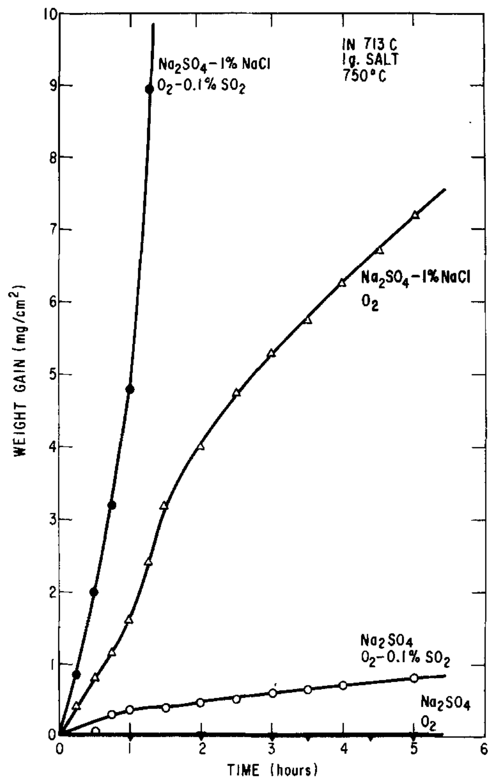

Fig. 9. Effect of NaCl and SO_2 on Na_2SO_4-induced corrosion of IN-713C at 750°C. Weight gains vs. time.

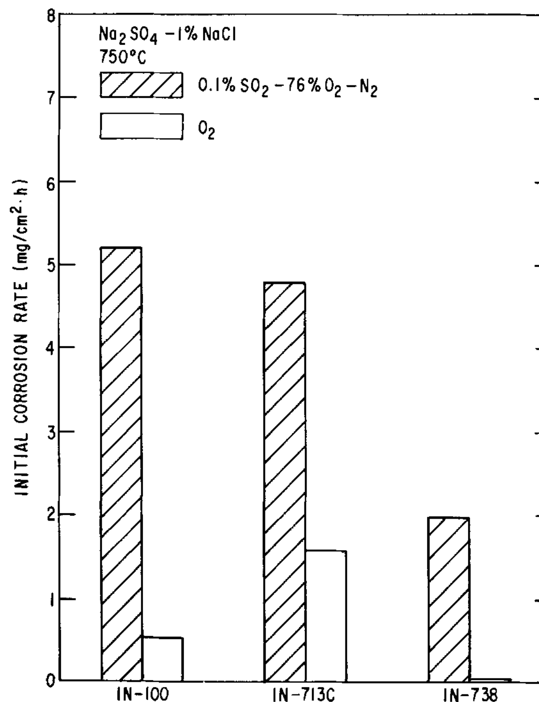

Fig. 11. Comparison of initial corrosion rates of several alloys in Na_2SO_4-1% NaCl melts at 750°C.

Na_2SO_4-1% NaCl was increased over that in Na_2SO_4 alone; when SO_2 was added to the environment a further substantial increase in the rate of attack occurred. IN-713C responded in a similar way at both 750° and 900°C, as shown in Fig. 9 and 10. The latter data also demonstrated that as little as 100 ppm SO_2 with NaCl in the salt was able to accelerate the rate of attack over that in O_2. Both of these alloys have been shown to have rather poor resistance to Na_2SO_4-induced hot corrosion at elevated temperatures (19). Figure 11 shows a comparison of the initial corrosion rates (during the first hour of exposure) of the three superalloys in Na_2SO_4-1% NaCl at 750°C. In both oxygen and simulated combustion gas, IN-738 was the most resistant.

More extensive crucible tests as a function of temperature and composition of the environment were car-

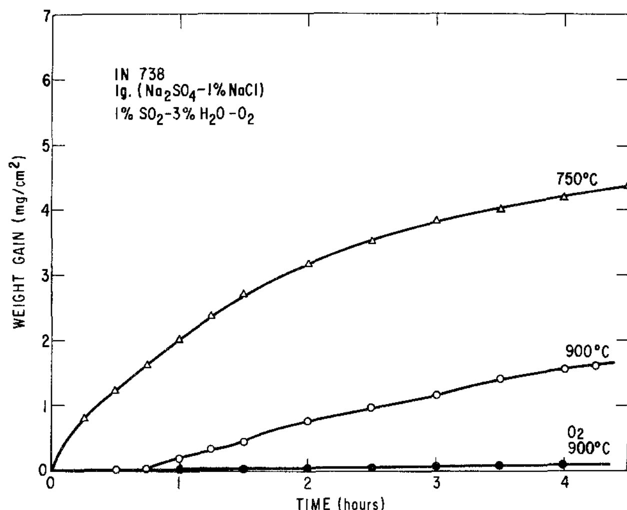

Fig. 12. Corrosion of IN-738 in the crucible test by Na_2SO_4-1% NaCl in O_2 and 1% SO_2-3% H_2O-O_2. Weight gains vs. time at 750° and 900°C.

ried out in Na_2SO_4-1% NaCl mixtures with IN-738. Figure 12 shows that environments containing O_2-SO_2-H_2O (which generate HCl by reaction with NaCl via Eq. [3]) also accelerated the rate of attack. Under these conditions the attack was faster at 750° than at 900°C. In a series of tests at temperatures between 600° and 900°C in the SCG the rate of attack of IN-738 became noticeable at 600°C, reached a maximum at about 750°C, and declined at higher temperatures. The data from these runs are summarized in Fig. 13 as a plot of initial corrosion rate (averaged over the first 1-2 hr) *vs.* temperature. Although most tests lasted only 5-6 hr, a 48 hr test at 850°C in O_2-SO_2 maintained a reasonably uniform rate of attack for the entire duration. Thus, the lower rates of attack between 800° and 900°C are not the result of a prolonged incubation period; rather, they represent steady-state corrosion under those test conditions. A similar, but less intense, peak in corrosion rate was found with O_2-100 ppm SO_2. For comparison Fig. 13 also shows that the rates of attack were relatively low over that temperature range when the test involved either 1% NaCl in O_2 or Na_2SO_4 in O_2-0.1% SO_2; only when both SO_2 and NaCl were present together were high rates achieved.

In a separate series of crucible tests at 750°C with IN-738 a Pt catalyst was used with SCG to insure a p_{SO_3} close to the equilibrium value. In these tests IN-738 was attacked by Na_2SO_4 alone and at a substantially faster rate by Na_2SO_4-10% NaCl. The effect of chloride was still marked in the presence of O_2-SO_2-SO_3 at 750°C. In the previously described tests without a Pt catalyst p_{SO_3} was unknown but was somewhat less than the equilibrium value. The main effect of SO_3 was to enhance attack by Na_2SO_4 at moderate temperatures but by a different mechanism which will be discussed in a subsequent paper.

Alloy coupons that had been intensely corroded by Na_2SO_4-NaCl-SO_2 at 750°C exhibited a flaky, spalled surface scale shown previously in the SEM photograph in Fig. 5. Metallographic examination of that specimen revealed a thick nonprotective oxide scale and numerous internal Cr_xS precipitates (Fig. 14a). On the other hand, when SO_2 was absent, a test in Na_2SO_4-1% NaCl at 750°C produced only a thin, dense scale with no internal precipitates (Fig. 14b).

With Ni-30Al the combined effects of NaCl and gaseous SO_2 again produced a maximum in the rate of attack at intermediate temperatures. Figure 15 summarizes the results of several crucible tests on Ni-30Al in a variety of Na_2SO_4 mixtures over a range of temperatures. With 1% NaCl the maximum rate occurred at about 850°C, but with higher concentrations of NaCl the maximum shifted to lower temperatures. The rates of attack in the range of 700°-850°C were extremely rapid (note that the ordinate in Fig. 15 encompasses a range more than ten times that of Fig. 13). Under these conditions the samples gained weight linearly with time and formed thick, porous, layered scales as shown in Fig. 16. As with IN-738, crucible tests with Na_2SO_4 alone yielded relatively low rates of attack. Preoxidation was effective in delaying the onset of rapid attack,

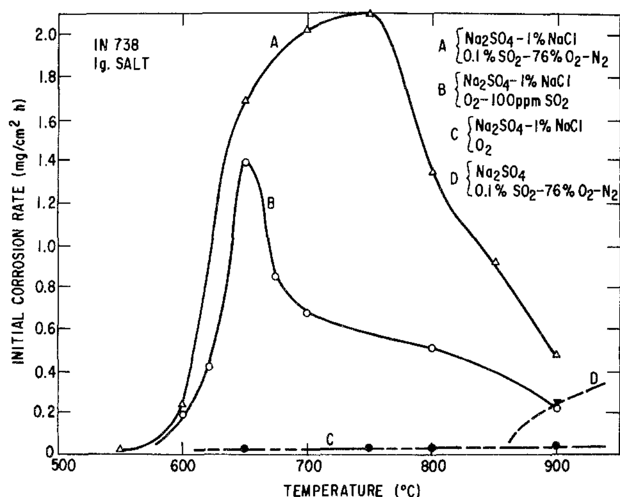

Fig. 13. Combined effects of NaCl and SO_2 on the corrosion behavior of IN-738 toward Na_2SO_4-1% NaCl. Initial corrosion rates (after 1 hr) vs. temperature for various atmospheres.

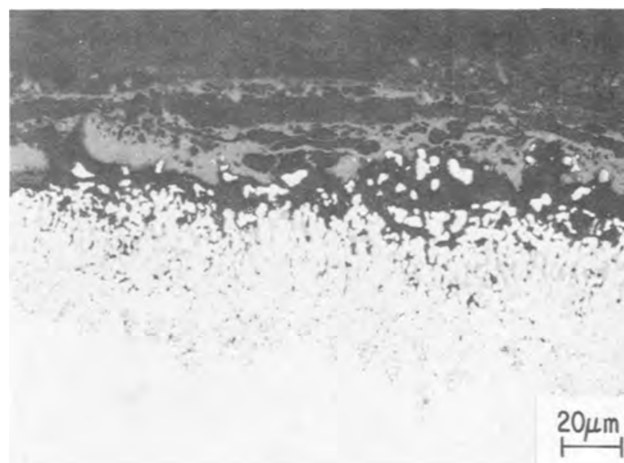

Fig. 14. Photomicrograph of a section of IN-738 after exposure to Na_2SO_4-1% NaCl for 6 hr at 750°C in (a, top) simulated combustion gas and (b, bottom) O_2.

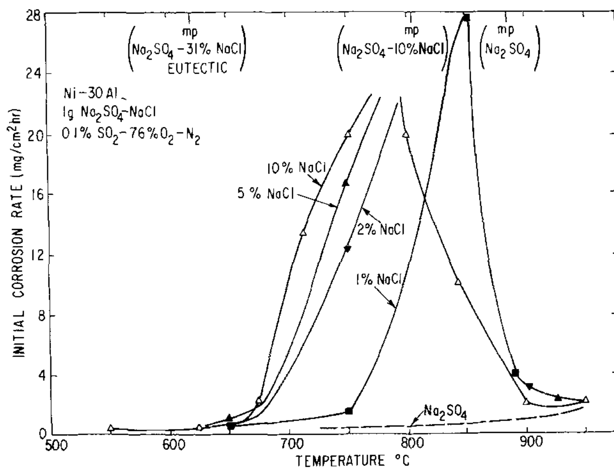

Fig. 15. Effect of NaCl concentration on the corrosion behavior of Ni-30% Al in Na_2SO_4-NaCl. Initial corrosion rates (after 1 hr) vs. temperature in simulated combustion gas.

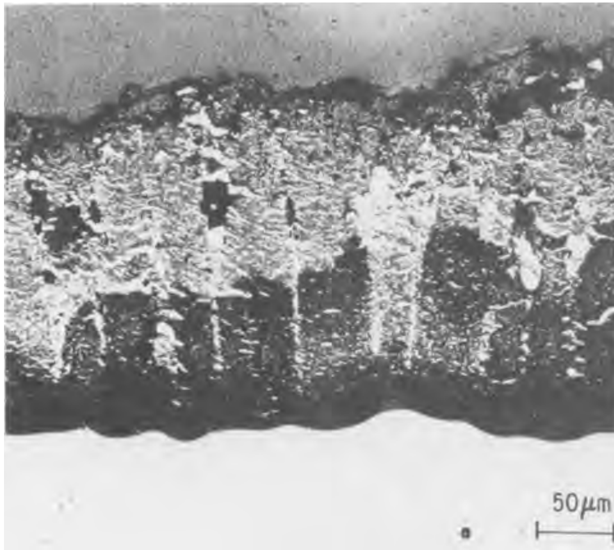

Fig. 16. Photomicrograph of porous oxide scale formed on Ni-30A after exposure to Na_2SO_4-10% NaCl for 1 hr in the crucible test at 750°C in simulated combustion gas.

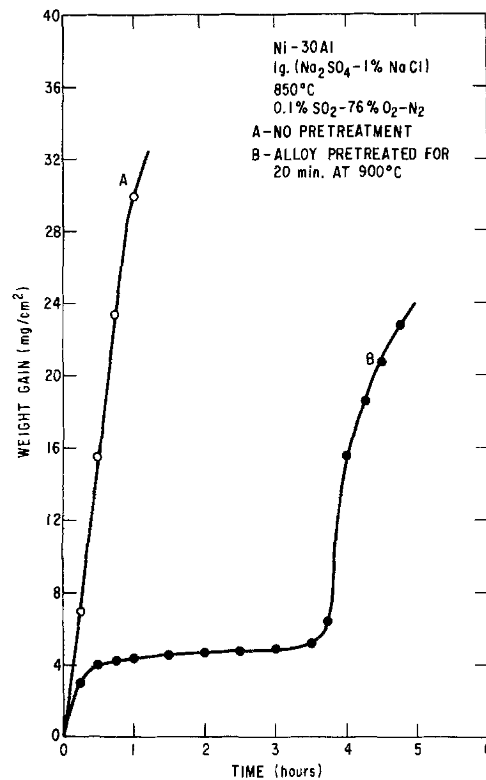

Fig. 17. Effect of preoxidation at 900°C on the corrosion of Ni-30% Al by Na_2SO_4-1% NaCl at 850°C in simulated combustion gas. Weight gains vs. time.

as shown in Fig. 17, but could not prevent it. This appeared to be a general effect for all the alloys tested and has been observed before (3, 4). The rapid attack of Ni-30Al in the presence of NaCl and SO_2 is in contrast to previous generalizations that alloys forming Al_2O_3 scales are less susceptible to chloride-induced attack. However, the synergistic effect of NaCl and SO_2 was not recognized previously.

Discussion

There seems to be wide agreement that the principal role of small concentrations of NaCl in hot corrosion induced by Na_2SO_4-NaCl mixtures is to crack or break the protective oxide scale, thereby drastically reducing the initiation or incubation period (1-7). When the salt mixture gains direct access to the alloy beneath the oxide scale, the subsequent rapid hot corrosion reactions proceed much as if access were accomplished by any other alternate mechanism; such as by cracking from thermal cycling or by fluxing. Corrosion morphologies and corrosion reaction products from deposits containing small concentrations of NaCl are much the same as in the absence of NaCl, Cl is usually not detected among the corrosion products (6). There is, however, much less concurrence on explanations of how NaCl breaks the protective scale.

In the present work attention has been focused on the role of Cl_2, and in particular on Cl_2 generated by the interaction of SO_2 in the environment with NaCl in a salt mixture. (HCl is expected to have a similar effect.) Chlorine has been found to play a much more aggressive role in hot corrosion than NaCl; *e.g.,* in corrosion tests with small concentrations of NaCl, low Cl_2 activities produced low rates of attack whereas high Cl_2 activities produced aggressive attack. In fact, Cl_2 was able to crack oxide scales whether or not NaCl was also present. A detailed explanation of the mechanism of Cl-induced cracking of oxide scales cannot be offered at present. However, some possible reactions involving chlorine and oxides are discussed below. It should be recognized, however, that in some laboratory tests, as well as in marine gas turbines, mass transport through salt layers or through gas boundary layers may limit the activities of some species at the reaction site.

At the usual temperatures for hot corrosion testing (900°-1000°C) rapid rates of attack can be sustained because a liquid film of salt prevents the formation of a barrier oxide at the alloy surface. For the same reason it is quite likely that a liquid salt is also a necessary (but perhaps not sufficient) condition for rapid attack at lower temperatures. Consider the kinetic data for IN-738 in pure NaCl at 750°C, which is about 50°C below the melting point of the salt. When a sample was exposed to only gaseous reactants, O_2-1% Cl_2 plus NaCl vapor, the rate of attack was rather low (Fig. 6). However, when the run was repeated with essentially the same activities of reactants, except that the specimen was in contact with condensed NaCl, rapid attack occurred. If it is presumed that a liquid film is required, the question then becomes how a molten phase can occur at temperatures below the melting point of pure NaCl. The possibility of forming low melting eutectics between NaCl and transition metal chlorides was examined by first calculating the thermodynamic stability of several transition metal chlorides which might form by reaction of Cl_2 with components of the oxide scale. These results, which are summarized in

Table III. Calculated partial pressures of O_2 and Cl_2 in O_2-Cl_2 mixture in equilibrium with liquid NaCl-M Cl_x mixtures at 750°C

System	Stable oxide	Liquid phase	MCl_x activity in melt	p_{O_2} (atm)	p_{Cl_2} (atm)**
Na-Al-Cl	Al_2O_3	Na_3AlCl_6	0.016 ($AlCl_3$)	1.2×10^{-9}	1.00
Na-Cr-Cl	Cr_2O_3	Na_3CrCl_6	0.016 ($CrCl_3$)***	8.1×10^{-7}	1.00
Na-Co-Cl	Co_3O_4	NaCl-18.3% $CoCl_2$	0.183†	0.89	0.11
Na-Ni-Cl	NiO	NaCl-20% $NiCl_2$	0.021‡	0.94	0.06
Na-Ti-Cl	TiO_2	—	—	$<10^{-8}$	1.00

* Pure liquid MCl_x as the standard state.
** Assuming p_{O_2}-p_{Cl_2} = 1 atm.
*** Activity of $CrCl_3$ assumed equal to that of $AlCl_3$ because of similar liquid phase.
† Based on ideal behavior of MCl_x and NaCl in liquid.
‡ Activity coefficient was estimated from the phase diagram (20).

Table III, reveal that only $NiCl_2$ and $CoCl_2$ are sufficiently stable in an oxidizing environment to be possible candidates. Second, the NaCl-$NiCl_2$ and NaCl-$CoCl_2$ phase diagrams (20) reveal low melting eutectics and, equally importantly, the uptake by NaCl of relatively small amounts of these chlorides is sufficient to cause melting at 750°C. Thus, liquid could form where NaCl crystals contact the samples, and subsequent cracking of the oxide by Cl_2 could provide access for the liquid phase to attack the alloy.

Evidence for the formation of such transition metal chlorides was obtained by analysis of salt that had been in contact with IN-738 during a crucible test. Atomic absorption analysis of the salt revealed significant concentrations of water-soluble Ni and Co and very low concentrations of Cr and Al in agreement with the thermodynamic estimates in Table III. It is noted that runs in pure O_2 (Fig. 6), where transition metal chlorides would not be stable, produced quite low rates of attack. In principle, the same arguments apply to Na_2SO_4-NaCl mixtures. However, because the concentrations of NaCl were low and because most of the tests were run above the Na_2SO_4-NaCl eutectic temperature, the effect of $NiCl_2$ or $CoCl_2$ (if present) is expected to be very small. All the data are consistent with the proposal that a liquid phase is necessary to sustain rapid attack.

In a series of tests with Na_2SO_4-NaCl mixtures over a range of temperatures a maximum in the corrosion rate was found at intermediate temperatures when the environment contained O_2 and SO_2 (Fig. 13 and 15). In contrast to this, low corrosion rates were found over the whole temperature range with Na_2SO_4-NaCl mixtures in O_2 or with Na_2SO_4 in O_2 and SO_2. Both an Al_2O_3-forming alloy (Ni-30Al) and a Cr_2O_3-forming alloy (IN-738) exhibited this pattern. For Ni-30Al the maximum corrosion rate shifted from about 850°C to about 700°C as the concentration of NaCl was increased from 1 to 10%. It is proposed that these observations can be rationalized in the following way.

According to the phase diagram the Na_2SO_4-NaCl system forms a simple eutectic with a melting point of about 625°C. There is negligible solid solubility of NaCl in Na_2SO_4 (20). Therefore, aside from any possible interactions with the oxide, in tests above 625°C some liquid salt would be present, the amount increasing at higher temperatures. In addition, those environments containing SO_2 will generate Cl_2, which can accelerate the attack in the presence of liquid salt by cracking and disrupting the oxide scale. However, the activity of Cl_2 so generated will be strongly dependent on temperature, as indicated by the estimates from thermodynamic considerations in Table IV. Clearly the activity of Cl_2 could be quite high at the lower range of temperatures but will decline with increasing temperatures to rather low values at 900°C.

Thus, it is proposed that the corrosion rate is affected by two opposing factors: with increasing temperature the increasing amount of liquid tends to accelerate the rate, but at the same time the declining activities of Cl_2 tend to lower the rate, approaching

Table IV. Calculated pressure of Cl_2 in equilibrium with Na_2SO_4-NaCl mixtures*

Temperature (°C)	Mole fraction NaCl	Pressure Cl_2 (atm)**	Pressure Cl_2 (atm)†
1000	0.01	5.4×10^{-8}	3.6×10^{-8}
1000	0.10	5.9×10^{-6}	6.7×10^{-6}
900	0.01	4.4×10^{-7}	5.6×10^{-7}
900	0.10	4.8×10^{-5}	6.2×10^{-5}
800	0.214‡	2.6×10^{-3}	4.5×10^{-3}
750	0.30‡	0.02	0.045
700	0.387‡	0.14	0.46

* Based on the assumption of an ideal solution between Na_2SO_4 and NaCl. Initial values of p_{O_2} and p_{SO_2} were 0.76 and 0.001 atm, respectively.
** Based on the assumption that the SO_2-SO_3 equilibrium was established in the gas.
† Based on no conversion of SO_2 to SO_3.
‡ Mole fraction of NaCl was obtained from the phase diagram (20).

that in Cl_2-free environments above 900°C. As the test temperature increases from the eutectic temperature, the effect of the increasing amount of liquid is offset by the declining activity of Cl_2, and the rate passes through a maximum. Although the liquid is initially rich in NaCl, with increasing temperature the concentration of NaCl diminishes; however, the consequences of this appear to be less important than the declining activity of Cl_2. The activity of Cl_2 at the alloy surface may be further limited by diffusion when the sample is covered by a continuous film of liquid salt or is submerged in a melt. Chlorine transport through a liquid salt is likely to be slow, as is thought to be the case with O_2 in Na_2SO_4 (21). Hence, at high temperatures the liquid may effectively shield the specimen from Cl_2, and thereby further contribute to a reduction in corrosion rate.

Increasing the concentration of NaCl from 1 to 10% in $O_2 + SO_2$ environments shifted the maximum corrosion rate of Ni-30Al to lower temperatures (see Fig. 15). This behavior is understandable because the amount of liquid formed at a given temperature will increase as the concentration of NaCl is increased; or to put it another way, as the NaCl concentration is raised the minimum amount of liquid for substantial attack will be formed at lower temperatures. At a given temperature the liquid phase will have the same composition whether the over-all concentration of NaCl is 1 or 10%. By the same reasoning, complete coverage by a liquid film will occur at lower temperatures with high NaCl concentrations, and hence the decline of corrosion rates will commence at lower temperatures. Thus, the entire curve of corrosion rate *vs.* temperature will be shifted to lower temperatures with increasing NaCl concentrations, as shown in Fig. 15.

Chlorine and NaCl vapor have been shown to be effective in cracking oxide scales on alloys, but the mechanism by which this occurs is not known. Because alloys forming Cr_2O_3 scales were found to be more susceptible to Cl-induced hot corrosion than those forming Al_2O_3 scales (3-7), the evolution of volatile chromium chlorides or oxychlorides has been sug-

gested as a means of lifting and breaking the oxide scale. However, the vapor pressures of these species are considerably less than 1 atm in the temperature range where chloride effects are observed. On the other hand, the boiling points of $AlCl_3$ and $TiCl_4$ are quite low, and these species could generate considerable pressure if they were to form in a region of low oxygen activity at the metal/scale interface.

For example, at the alloy/scale interface (choosing $a_{Ni} = 0.65$, $a_{NiO} = 1$, $a_{Al_2O_3} = 1$) the chlorine activity required to generate 1 atm of $AlCl_3 + Al_2Cl_6$ is only 0.0025 atm. However, as mentioned before, with p_{Cl_2} at the oxide/salt interface on the order of 0.16 atm (for $p_{SO_2} = 0.001$ atm, $a_{NaCl} = 1$ and $a_{Na_2SO_4} = 1$), clearly a $p_{AlCl_3} + p_{Al_2Cl_6}$ greater than 1 atm is feasible. Thus, if cracking is due to mechanical lifting by gaseous chlorides, Al or Ti chlorides are more feasible. On diffusing out of cracks in the scale into a region of high oxygen activity, both $AlCl_3$ and $TiCl_4$ would be quickly converted to their respective oxides leaving little evidence of Cl in subsequent analysis.

Conclusions

The present studies, which were designed to elucidate the corrosive effects of NaCl in Na_2SO_4 deposits, have shown that it is important to include the active components of the combustion environments. In particular:

(*i*) Small concentrations of Cl_2 in O_2 produced extensive fracturing and spalling of oxide scales in the absence of a salt deposit.

(*ii*) The reaction of SO_2 with NaCl in a deposit can produce substantial partial pressures of Cl_2.

(*iii*) In the presence of a liquid salt phase, cracking of the oxide scale by gaseous halogens is accompanied by rapid attack.

(*iv*) With a Na_2SO_4 deposit containing small (1-10%) concentrations of NaCl, the corrosion rate attained a maximum at temperatures around 750°C when SO_2 was present. This behavior was observed with a binary alloy and three superalloys which included both Al_2O_3 and Cr_2O_3 formers; IN-738 was the least affected. When either SO_2 or NaCl was absent the rates of attack were much lower on all the alloys in this temperature range.

Some possible reasons for the observed behavior have been discussed.

Acknowledgment

The authors are indebted to H. S. Spacil for helpful discussions and for the use of a computer program for calculating the multicomponent thermodynamic equilibria, to J. Jackowski for help with the experimental work, and to C. Rodd and M. Gill for the metallography and scanning electron microscopy.

Manuscript submitted June 6, 1977; revised manuscript received Oct. 21, 1977.

Any discussion of this paper will appear in a Discussion Section to be published in the December 1978 JOURNAL. All discussions for the December 1978 Discussion Section should be submitted by Aug. 1, 1978.

Publication costs of this article were assisted by General Electric Company.

REFERENCES

1. J. F. G. Condé, in Proceedings of the AGARD Conference on High Temperature Corrosion of Aerospace Alloys, p. 204, AGARD-CP-120 Copenhagen, Denmark (1972).
2. J. F. G. Condé, in "Gas Turbine Materials Conference Proceedings," p. 17, Naval Ship Engr. Center/Naval Air Systems Comm. (1972).
3. J. F. G. Condé, in Proceedings of the 1974 Gas Turbine Materials in the Marine Environment Conference, J. W. Fairbanks and I. Machlin, Editors, p. 73, M.C.I.C. Report 75-27 Castine, Me. (1974).
4. R. C. Hurst, J. B. Johnson, M. Davies, and P. Hancock, in "Deposition and Corrosion in Gas Turbines," A. B. Hart and A. J. B. Cutler, Editors, p. 143, Halstead Press (1973).
5. P. Hancock, in Proceedings of the 1974 Gas Turbine Materials in the Marine Environment Conference, J. W. Fairbanks and I. Machlin, Editors, p. 225, M.C.I.C. Report 75-27 (1974).
6. D. J. Johnson, D. P. Whittle, and J. Stringer, *Corros. Sci.*, **15**, 721 (1975).
7. Y. Bourhis and C. St. John, *Oxid. Metals*, **9**, 507 (1975).
8. A. F. Taylor, B. A. Wareham, G. C. Booth, and J. F. G. Condé, Third Conference on Gas Turbine Materials in the Marine Environment, Bath, England, 1976, To be published.
9. M. A. DeCrescente and N. S. Bornstein, *Corrosion*, **24**, 127 (1968).
10. R. E. Fryxell, C. A. Trythall, and R. J. Perkins, *ibid.*, **29**, 423 (1973).
11. V. I. Hanby, *J. Engr. Power*, **96**, 129 (1974).
12. C. G. McCreath, in Third Conference on Gas Turbine Materials in the Marine Environment, Bath, England (1976).
13. R. L. Jones. in Proceedings of the 1974 Gas Turbine Materials in the Marine Environment Conference, J. W. Fairbanks and I. Machlin, Editors, p. 219, M.C.I.C. Report 75-27 (1974).
14. D. Bruce and P. Hancock, *J. Inst. Metals*, **97**, 140 (1969).
15. R. C. Hurst, M. Davies, and P. Hancock, *Oxid. Metals*, **9**, 161 (1975).
16. D. A. Shores, D. W. McKee, and H. S. Spacil, in Proceedings of the Symposium on the Properties of High Temperature Alloys, The Electrochemical Society, pp. 649-654, Las Vegas, Oct. 17-22, 1976.
17. Handbook of Materials Science, Vol. II, CRC Press, Cleveland, Ohio (1975).
18. D. W. McKee and G. Romeo, *Met. Trans.*, **5**, 1127 (1974).
19. J. F. Stringer, "High Temperature Corrosion of Aerospace Alloys," AGARD Publication AG-200 (1975).
20. E. M. Levin, C. R. Robbins, and H. F. McMurdie, "Phase Diagrams for Ceramists," The American Ceramic Society, 1964, 1969, and 1975 supplements.
21. A. J. B. Cutler and C. J. Grant, in "Deposition and Corrosion in Gas Turbines," A. B. Hart and A. J. B. Cutler, Editors, p. 178, Halstead Press, (1973).

Contact Resistance of Tin-Nickel Alloy Electrodeposits

M. Antler

Bell Laboratories, Columbus, Ohio 43213

ABSTRACT

The atmospheric corrosion resistance of equiatomic tin-nickel alloy having the weight percent composition, 65Sn-35Ni, increases with time due to the growth of a protective oxide. Tin-nickel is used as a material for wiping electric contacts, usually as an underplate for gold, and during use can become exposed as the gold is worn through. In this study, the contact resistance of tin-nickel was found to be initially low and to change on aging as the oxide forms at a rate which depends on relative humidity and temperature. Contact resistance increases very slowly in dry air and quickly in humid air with little rate difference between 15 and 88% relative humidity. The increase of contact resistance when tin-nickel is in contact with water has the same kinetics initially as when it is aged in humid air, but resistance continues to grow with time well beyond the air-limiting value. The initial kinetics of contact resistance increase at 100°C are the same as at room temperature, although much higher levels are attained on prolonged aging at 100°C. The contact resistance of tin-nickel is also inversely related to its surface roughness.

Electrodeposited tin-nickel alloy is a single phase equiatomic intermetallic compound (SnNi) having the weight percent composition, 65Sn-35Ni. It is considered to be thermodynamically unstable, since it does not appear in the phase diagram for the two metals (1). Practical experience, however, has shown SnNi to be kinetically stable, transforming rapidly to Ni_3Sn_4 and Ni_3Sn_2 only above *ca.* 300°C (2-5). Coherent electrodeposits that are mixtures of SnNi, Ni_3Sn_4, and Ni_3Sn_2 with chemical and physical properties similar to those of the single phase plating have also been prepared (6).

Tin-nickel can be corroded by HNO_3 vapor and other reagents if it is exposed immediately after removal from the electroplating bath (7). However, it quickly becomes corrosion resistant in air, a characteristic which improves on continued air exposure for several thousand hours, after which there is no further change (7). This long recognized (8) chemical stability is due to a protective oxide (9, 10) that grows on its surface to a limiting thickness, believed to be about 30Å, and to consist of tin oxide mixed with some tin and nickel hydroxides (11).

Among the applications of SnNi are its use as a chemical etch resist for the fabrication of printed wiring boards from copper-clad laminate (12, 13). When the board has electric contacts along its edge which engage separable connectors, a gold overplating is usually applied to lower contact resistance, and even thin (less than 1 μm) gold is effective for this purpose. Furthermore, the corrosion resistance of gold on SnNi is equivalent to that of SnNi alone, because a galvanic couple does not persist at pores and other discontinuities in the gold once the protective oxide is formed (6, 7). When in service as a contact material, the gold plate may gradually become worn through by the wiping of the opposing contact thereby exposing the SnNi underplate. As the area of exposed SnNi enlarges and as it becomes oxidized, contact resistance increases and can become unacceptable. It is, therefore, of interest to determine environmental factors which affect the growth of the oxide and thereby its contact resistance.

The objective of this investigation was to determine whether the contact resistance of SnNi is controlled by the relative humidity (RH) of the air in which it is aged. This work is an expansion of a preliminary study (7) of the dependence of contact resistance with time of aging which was conducted at 15-20% RH. Experiments with SnNi in contact with water or in air at elevated temperature were also made. In this work, the SnNi samples were etched in HCl to assure that they were free of films prior to aging. Observations were also made of the contact resistance of unetched SnNi that had been aged for up to 10 years. The dependence of contact resistance of SnNi on its surface roughness was examined.

Key words: passivation, oxidation, corrosion resistance, electric contacts.

Experimental

Sample preparation.—Electropolished, oxygen-free copper panels, 3.8 cm square by 0.16 cm thick, were plated with 12 μm of SnNi from a fluoride bath (14). Samples were etched in 18% HCl (1:1 mixture of water and concentrated HCl, sp gr = 1.18) to remove any air-formed film that was present, washed well in distilled water, blown dry with nitrogen, and inserted immediately into various controlled environments, described below, in which they were aged. A few samples were not etched, including some that had been prepared by abrasion of the substrate surface rather than by electropolishing. One of these panels was brass plated with 15 μm of SnNi.

The completeness of removal of air-formed oxide could be determined by contact resistance measurement after etching. Treatment for a minimum of 1 min with 18% HCl at room temperature was adequate to reduce contact resistance to a low and reproducible level of 5-6 mΩ (7) when measured in a prescribed way, discussed later. Some samples were etched in HCl for less than 1 min, which gave a contact resistance intermediate to the initial value and 5-6 mΩ. Their change of contact resistance on air aging was then determined.

Additional samples, obtained from commercial sources, were printed wiring boards having 5 or 12 μm of SnNi on copper substrates without a gold overplate and were plated from a fluoride bath (14). These samples were not etched prior to plating.

Roughness was measured with a diamond stylus instrument; the polished panels were too smooth to give meaningful readings and are presumed to have been below *ca.* 0.03 μm center line average (CLA). The printed wiring boards had comparably smooth surfaces.

Aging.—Panel samples in loosely covered petri dishes were aged at room temperature and ambient conditions (25-60% RH) or in an oven at 100°C. The samples aged at controlled RH and room temperature were in sealed desiccators over slurries in water of CP salts: 15% RH, LiCl; 51% RH, $Ca(NO_3)_2$; 88% RH, $BaCl_2$. Silica gel, which leaves 0.03 mg residual water/liter air at 30.5°C (15), was also used (0% RH). The water-aged sample was immersed in deionized water in a sealed vessel. The SnNi-plated printed wiring boards were aged in laboratory air without humidity control.

The panel samples were removed periodically for contact resistance measurement and then were returned to their aging environments. The water-aged sample was dried in nitrogen prior to probing. The RH of the room air in which probing was done was 15-20%.

Contact resistance.—An automated contact resistance probe ("Autoprobe") (16) was used. The probe was a 3.2 mm diam smooth hemispherically ended solid gold rod. Open-circuit voltage was 0.03V. Nine or more measurements were made on each sample at each time interval with load continuously increasing from 0 to 200g.

Observations and Discussion

Aging in air at room temperature.—Figure 1 is a plot of the median contact resistances at 100g from etched samples aged at 0, 15, 51, and 88% RH including 9000 hr data for an 88% RH aged panel. The bands include 95% of all of the measurements that were made; *i.e.*, 5% of the determinations were outliers. Shown also in Fig. 1 are the median contact resistances for unetched samples aged for 3, 6, 8, 18, 72, and 120 months at ambient conditions. Newly plated, unetched samples had about the same contact resistance, 5-7 mΩ, as freshly etched specimens. These contact resistance determinations were made within 10 min of removal from the plating bath or etching solution.

The maximum resistance value from the 500 determinations made with all samples was 15Ω. Contact resistances at loads other than 100g are not presented because the trends were the same, with only the absolute values being different. This is illustrated in Fig. 2, typical median contact resistances at 25, 50, 100, and 200g for the etched sample in Fig. 1 which was aged at 15% RH.

The data in Fig. 1 can be grouped into two categories, resistances for etched samples aged at 0% RH, and those from etched samples aged at 15-88% RH. Resistance increases with air aging, but much more quickly when water vapor is present, attaining values of 1-10Ω in several thousand hours. There is no significant difference in rate of resistance change in aging at 15, 51, and 88% RH. It is possible that etched SnNi attains a limiting contact resistance which is the same as that for as-plated samples. This trend in contact resistance parallels an increasing ability of SnNi on air aging to resist attack by corrosive environments (7).

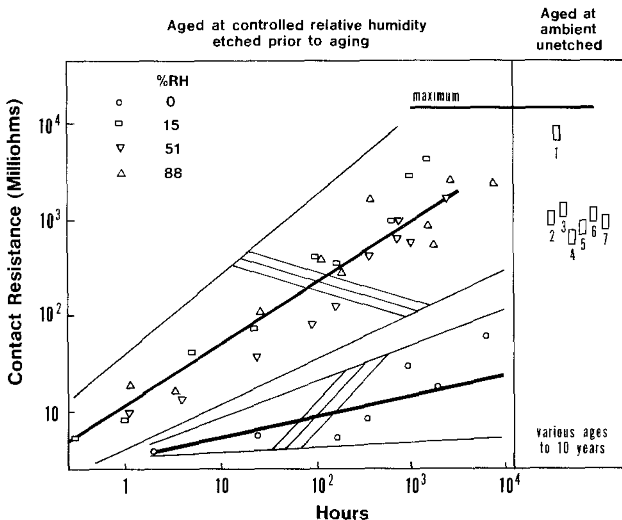

Fig. 1. Contact resistance at 100g of smooth SnNi electrodeposits. Left: Aged in air at room temperature and controlled RH. Samples were 12 μm thick on copper. Etched in 18% HCl prior to aging. Right: Aged indoors at ambient uncontrolled RH. Samples 1, 2, 3, and 7 were coupons of 12-15 μm SnNi on copper or brass; 4, 5, and 6 were printed wiring boards with 5-12 μm SnNi on copper. Not etched. Sample 1, 3 months old; sample 2, 6 months old; sample 3, 8 months old; sample 4, 18 months old; sample 5, 18 months old; sample 6, 72 months old; and sample 7, 120 months old. Probed with a hemispherically ended gold rod. Each point is the median of 9 or more measurements. 95% of all measurements are within the bands, with a maximum value of 15Ω from 500 determinations.

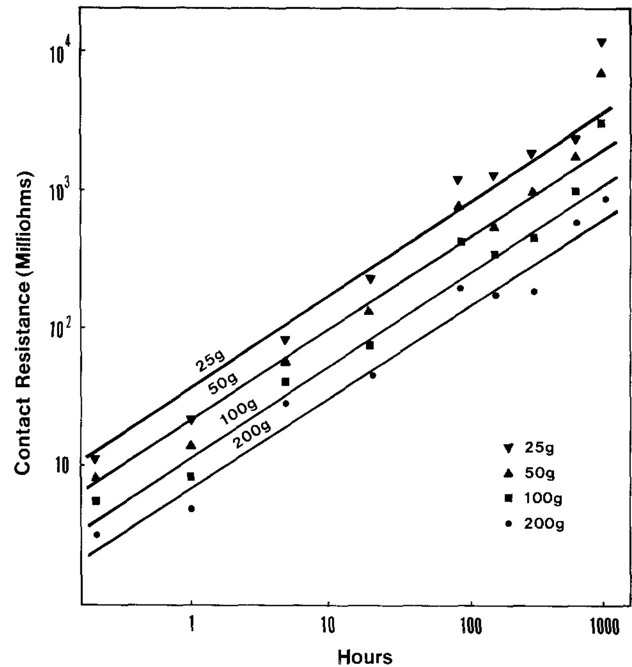

Fig. 2. Typical dependence of contact resistance on load. Etched SnNi aged in air at room temperature and 15% RH. Data at 100g are replotted from Fig. 1.

The sample aged at 0% RH was observed for 7000 hr during which contact resistance slowly increased. Nevertheless, contact resistance was still relatively low, only 0.01-0.1 of the value in humid air.

The different rates of contact resistance change between aging SnNi in water vapor and aging in dry air suggest either that different films formed or that the film at anhydrous conditions grew less quickly. Earlier work (17) in which SnNi had been freed of its air-formed film by sputtering, then exposed to dry oxygen, showed that a different film (believed to be a mixture of anhydrous nickel stannate [$NiSnO_3$] with oxides of tin and nickel) formed and grew more rapidly than the one produced in humid air. Additional experiments are necessary to determine whether the contrasting contact resistance behaviors of the dry air and humid air grown films in the present work are attributable to differences in film thickness or in their mechanical and electrical properties.

Aging in water.—Contact resistance data for the etched sample aged in deionized water are given in Fig. 3, including the range of values at each time interval and the median contact resistances. The contact resistance after about 100 hr of immersion was within the range observed for SnNi aged in humid air, but on longer immersion the median contact resistances attained higher values and the spread was larger than in the air-aged case, with some resistances greater than 1000Ω.

The film on the water-aged sample after 1000 hr was mottled gray, unlike the thin, invisible films on all of the other specimens. It is likely that the film formed in water was heterogeneous as well as different in composition from those obtained on air exposure. Apparently, water can slowly corrode SnNi that does not have its "natural" passive layer.

The rate of contact resistance change depends on the water content of the environment, increasing from dry air, to humid air, to water immersion. These observations, as pointed out earlier, can be explained by assuming that the primary determinant of contact resistance is film thickness and that the rate of growth of films on SnNi is markedly different in these environ-

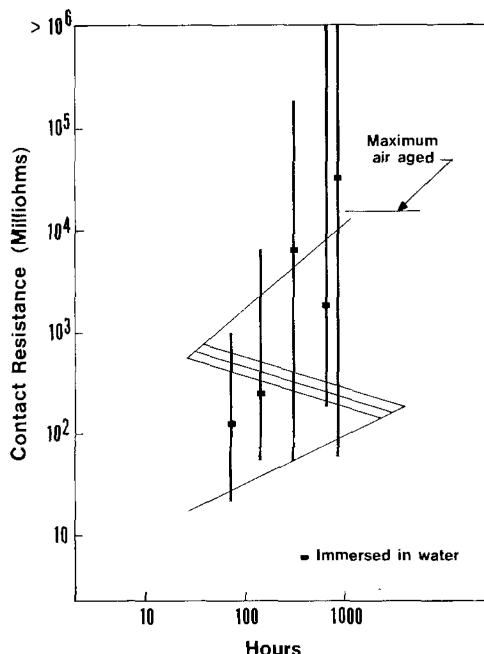

Fig. 3. Median contact resistance of smooth SnNi electrodeposit, 12 μm thick, on copper. Aged in deionized water. Etched in 18% HCl prior to aging. Probed at 100g with a hemispherically ended gold rod. Nine measurements at each time interval. The range of values is indicated by the vertical lines. The band encompasses 95% of all points obtained on air aging from 15-88% RH (see Fig. 1).

ments. Differences in film resistivity, attributable to different film compositions, may be a contributing factor.

Air aging of partially etched tin-nickel.—It was of interest to determine the contact resistance change with time of SnNi having a natural air-formed film which was incompletely removed by brief etching in 18% HCl, sufficient to lower contact resistance partially from its initial value. Figure 4 is a plot of contact resistance on aging at 51 and 88% RH for two specimens having initial (1 hr aged after etching) median contact resistances, respectively, of 240 and 550 mΩ. Contact resistance increases in this case, achieving the same value in approximately 100 hr as that of oxide-free SnNi after several thousand hours.

These observations cannot be explained by assuming that abbreviated etching removed only part of the air-formed film, which then reformed to its initial state on resumption of air aging. It has been found (18) that the initial decrease in contact resistance on brief etching is not accompanied by a change in mass. Perhaps chemical changes of the films were promoted by contact with HCl, which in turn altered its electrical characteristics.

Aging at 100°C.—A sample was etched and then aged at 100°C in the laboratory atmosphere having a RH calculated to be 1-2% at this temperature. Figure 5 shows that the contact resistance dependence closely parallels that for aging at room temperature from 15-88% RH for 1000 hr. Heating was continued for 2200 hr and a median contact resistance greater than 1000Ω was obtained. All values of resistance were greater than 15Ω, the largest value attained by both etched and unetched room temperature aged SnNi (Fig. 1).

These results can be understood by assuming that the kinetics of early growth and the electrical-mechanical characteristics of the film at 100°C are similar to those for the room temperature films, but that it grows thicker on prolonged aging.

Dependence of contact resistance on surface roughness.—Most oxide films have low plasticity and strains sufficient to rupture then on probing can increase the extent of metallic contact of the two surfaces. Film fracture is roughness dependent, demonstrated in studies with various materials (19-22). In the present work, surfaces were very smooth which accentuates the effects of films on contact resistance.

It is useful, however, to illustrate the contact resistance dependence on roughness of SnNi, and Fig. 6 shows this relationship with unetched specimens aged in excess of 50 months having three different roughnesses, polished (less than 0.03), 0.06, and 0.38 μm CLA. At 100g the median contact resistance was 130 mΩ for the rough sample compared to 1000 mΩ for the polished specimen. As suggested earlier (20), rough sur-

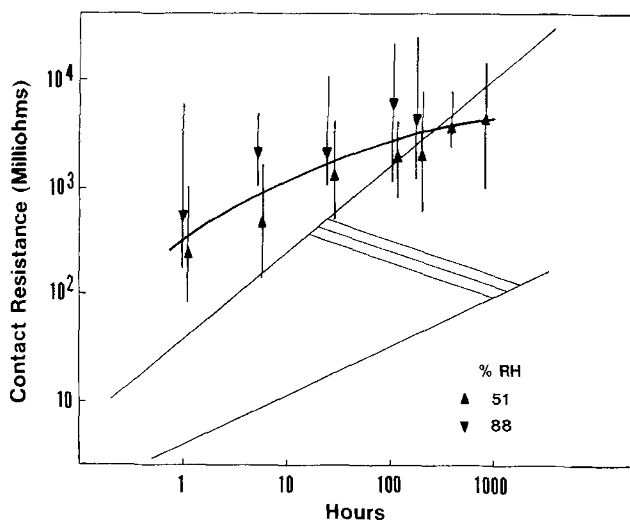

Fig. 4. Contact resistance of smooth SnNi electrodeposits, 12 μm thick, on copper. Aged in air at room temperature and controlled RH. Natural oxide incompletely removed by brief etching in 18% HCl prior to aging. Each point is the median of 9 measurements at 100g, with the range of values indicated by the vertical lines. The band encompasses 95% of all points obtained on aging fully etched samples in air at controlled RH, from 15-88% (see Fig. 1).

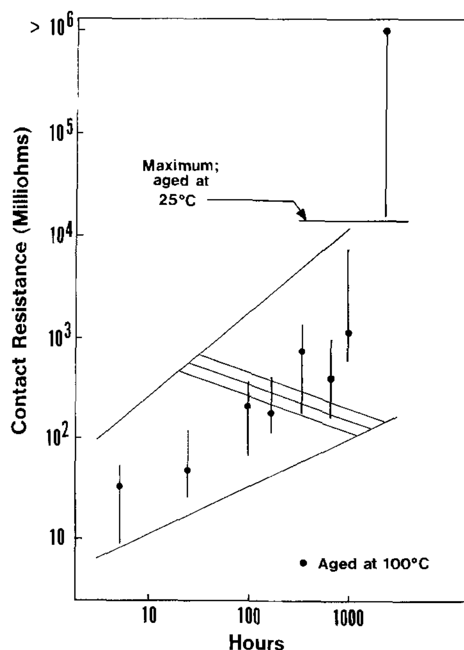

Fig. 5. Median contact resistance of smooth SnNi electrodeposit, 12 μm thick, on copper. Aged in air at 100°C. Etched in 18% HCl prior to aging. Probed at 100g with a smooth hemispherically ended gold rod. Nine measurements at each time interval. The range of values is indicated by the vertical lines. The band encompasses 95% of all points obtained on air aging at room temperature with a maximum value from 500 determinations of 15Ω (see Fig. 1).

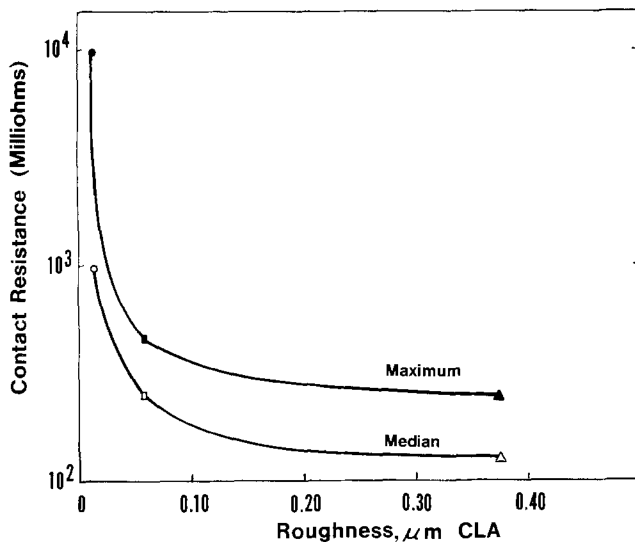

Fig. 6. Contact resistance of SnNi as function of center line average surface roughness. Not etched. Aged indoors at ambient RH in excess of 50 months. Probed at 100g with a hemispherically ended gold rod. Nine determinations at each load. ○, ●, polished surface; □, ■, abraded surface; △, ▲, abraded surface.

faces can probably be designed for base metal contacts which will permit them to be utilized in practical connector applications, probably with nonwiping designs to avoid high sliding friction and wear.

With conventional wiping contacts made of gold on a SnNi underplate, the contribution to contact resistance by SnNi through a worn gold layer can also be expected to depend on surface roughness.

Summary and Conclusions

It is necessary to understand factors which control the contact resistance of metals in order to be able to use them as contact materials. The SnNi system was chosen for study because of its unusual corrosion stability and its acceptance as a material for separable contacts, in most cases with a thin (0.1-1.0 μm) gold overplate. If the gold becomes worn through during use, the SnNi is exposed and its contact resistance characteristics contribute to the behavior of the system. Tin-nickel develops a self-limiting oxide film in air which is responsible for the increase in its contact resistance as well as its passivity.

In this study, it was determined that the contact resistance of SnNi, freed of oxide by etching in HCl, depends on the RH of the air in which it is aged. In dry air at room temperature, contact resistance rises very slowly for 7000 hr or more; in humid air (from 15-88% RH), contact resistance rises more rapidly and achieves a value of 1-10Ω at 100g for polished surfaces against a gold probe in several thousand hours. The contact resistance of unetched SnNi aged in air for up to 10 years likewise is in the range, 1-10Ω. The limiting contact resistance is less with rough surfaces, typically 0.1-0.2Ω with a finish of 0.4 μm CLA. The contact resistance increase of etched SnNi immersed in water or heated in air at 100°C follows the same initial kinetics as in humid air at room temperature, but ultimately attains much higher levels. The contact resistance of SnNi whose natural oxide is incompletely removed by brief etching in HCl is slowly restored to its equilibrium level when re-exposed to air.

Acknowledgments

The cooperation of C. F. Hornig, P. T. Woodberry, Hewlett-Packard Company, Singer Business Machines, Incorporated, and the Tin Research Institute, Incorporated is acknowledged for providing the SnNi samples used in this study. Valuable discussions were had with K. F. Bradford and J. H. Thomas, III. M. Drozdowicz obtained most of the experimental data.

Manuscript submitted July 15, 1977; revised manuscript received Oct. 7, 1977.

Any discussion of this paper will appear in a Discussion Section to be published in the December 1978 JOURNAL. All discussions for the December 1978 Discussion Section should be submitted by Aug. 1, 1978.

Publication costs of this article were assisted by Bell Laboratories.

REFERENCES

1. M. Hansen, "Constitution of Binary Alloys," p. 1042, McGraw-Hill Book Co., New York (1958).
2. P. K. Dutta and M. Clarke, *Trans. Inst. Met. Fin.*, **46**, 20 (1968).
3. J. E. Bennett and H. G. Tompkins, *This Journal*, **123**, 999 (1976).
4. C. F. Hornig and J. F. Bohland, *Scrip. Metall.*, **11**, 301 (1977).
5. J. A. Augis and J. E. Bennett, Private communication.
6. M. Antler, M. Feder, C. F. Hornig, and J. Bohland, *Plating Surf. Fin.*, **63**, 30 (1976).
7. M. Antler, M. H. Drozdowicz, and C. F. Hornig, *This Journal*, **124**, 1069 (1977).
8. N. Parkinson, S. C. Britton, and R. M. Angles, *Sheet Metal Industries*, 757 (Aug. 1951).
9. T. P. Hoar, M. Talerman, and E. Trad, *Nature Physical Sci.*, **244**, 41 (July 16, 1973).
10. H. G. Tompkins and J. E. Bennett, *This Journal*, **123**, 1003 (1976).
11. J. H. Thomas, III and S. P. Sharma, *J. Vac. Sci. Technol.*, **14**, 1168 (1977).
12. G. C. Wilson, *Trans. Inst. Met. Fin.*, **50**, 109 (1972).
13. G. T. Robinson, *Products Fin.*, 38 (Nov. 1976).
14. "Electroplated Tin-Nickel Alloy," Publication 235, 4th ed., Tin Research Institute (1962).
15. J. H. Bower, *Bur. Stds. J. Research*, **12**, 241 (1934).
16. M. Antler, in "Gold Plating Technology," F. H. Reid and W. Goldie, Editors, chap. 26, pp. 334-344, Electrochemical Publications, Ltd., Ayr, Scotland (1974).
17. S. P. Sharma and J. H. Thomas, III, *Anal. Chem.*, **49**, 987 (1977).
18. J. H. Thomas, III, *This Journal*, **124**, 677 (1977).
19. J. B. P. Williamson, Proceedings of the International Conference on Electromagnetic Relays, Tohoku University, Sendai, Japan, Oct. 8-11, 1963, pp. 33-37.
20. M. Antler and S. J. Krumbein, in Proceedings of the Seminar on Electric Contact Phenomena, University of Maine, Orono, Maine, 1965, pp. 103-137.
21. J. R. Osias and J. H. Tripp, *Wear*, **9**, 388 (1966).
22. M. Antler, *Plating*, **56**, 1139 (1969).

Composition, Chemical Bonding, and Contamination of Low Temperature SiO_xN_y Insulating Films

Gordon Wood Anderson, William A. Schmidt,* and James Comas

Naval Research Laboratory, Washington, D. C. 20375

ABSTRACT

The stoichiometry and contamination of low temperature SiO_xN_y layers grown by the pyrolytic decomposition of silane in an ammonia- and oxygen-rich atmosphere on InSb and Si substrates are reported. The chemical composition and chemical bonding properties of the films have been analyzed by Auger, nuclear reaction analysis, optical, Rutherford backscattering, and SIMS techniques. Capacitors were fabricated on Si and InSb substrates, and the electrical characteristics were measured. The layers exhibited physical characteristics similar to those of thermally grown SiO_2 layers. Analysis of the SiO_xN_y films indicated a uniform distribution of Si and O throughout the films. The N concentration measured in the films ranged from 1 to 3% of the O concentration, depending on the growth parameters. The optical results indicated some evidence of small amounts of Si-N and N-H bonding. All films grown on Si substrates in the presence of InSb or on InSb substrates had In and Sb contamination throughout, with the In and Sb content increasing from the film/substrate interface to the SiO_xN_y surface.

Significant interest currently exists in developing high quality metal-insulator semiconductor (MIS) devices using narrow bandgap semiconductors as substrates, in particular InSb, for utilization in infrared imaging systems (1-6). Typically, the insulating films for MIS capacitors on InSb contain Si, O, and N and are grown at low temperatures (200°-250°C) by the pyrolytic decomposition of silane in the presence of oxygen, nitrogen, and ammonia. Low temperature processing is necessary in the case of InSb because the material is thermally unstable above 400°C (7). The electrical properties of these MIS devices have been studied extensively (1-5), but no efforts have been made to characterize the stoichiometric, chemical, and other physical properties of these low temperature insulating films. It is the purpose of this paper to present the results of a series of spectroscopic studies of these SiO_xN_y insulating films on both InSb and Si substrates, including Auger, nuclear reaction analysis, optical, Rutherford backscattering (RBS), and secondary ion mass spectroscopy (SIMS) techniques. These studies are the first extended effort to characterize the stoichiometric, chemical bonding, and structural properties of these technologically important, low temperature SiO_xN_y films.

Insulator Growth

Processing.—The low temperature (200°-250°C) silicon-oxy-nitride (SiO_xN_y) system for insulator growth is conventional in design and similar to those used by others (1-5). A schematic of the reaction system is shown in Fig. 1. A Matheson gas mixture of 3% silane in nitrogen was used as the silane source. The silane mixture, oxygen, and ammonia used were ultrahigh purity "electronic grade" gases. Boil-off from a liquid nitrogen tank was the source for the nitrogen carrier gas. Flow rates were controlled by manually set needle valves and monitored by mass flowmeters. The silane mixture was further diluted with nitrogen in a mixing manifold prior to being introduced into the reaction chamber. Nitrogen, ammonia, and oxygen were combined in a second mixing manifold before introduction into the chamber.

The reaction chamber was enclosed by a stainless steel base plate and a Pyrex bell jar which was O-ring sealed to the base plate (Fig. 1). Substrates were supported on a rotating (~20 rpm) carbon platen which rested on a resistively heated aluminum block.

* Electrochemical Society Active Member.

Key words: silicon-oxy-nitride films, chemical vapor deposition, film composition and contamination, optical, spectroscopic properties.

Numerous other designs were tried, but this design gave the most reliable service.

InSb samples were prepared for passivation by chem-mechanical polishing on a Pellon cloth pad with a solution of bromine in methanol, etching in a solution consisting of 50 parts lactic acid, 8 parts HNO_3, and 2 parts HF, and briefly dipping in HF. Silicon wafers were used as delivered from the manufacturer after cleaning with organic solvents followed by a short HF dip. Low Na content electronic grade reagents and high resistivity water rinses (18 MΩ-cm) were used. Cleaned, polished samples were loaded onto the carbon platen, and the system was flushed with nitrogen for 30 min. The samples were then heated for 20 min in a nitrogen atmosphere to achieve thermal stability at the growth temperature. The reactive gases then were turned on to initiate growth. After a preselected time, the heat and reactant gases were shut off simultaneously, terminating growth.

The temperature of the stationary heated block was measured with thermocouples mounted directly in the block. Under growth thermal conditions but with no growth reaction taking place, substrate surface temperatures were measured optically and with phase altering indicators. These temperature values were compared with the block thermocouple readout. Because of difficulties in making substrate surface temperature measurements during film growth, this procedure was used to estimate substrate surface tem-

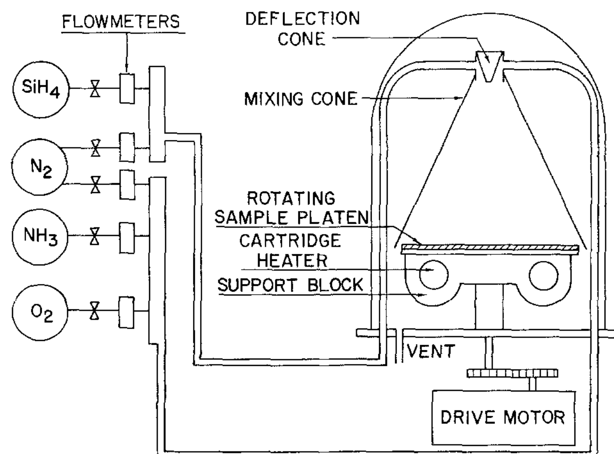

Fig. 1. Schematic illustration of sample preparation system

peratures during growth. This procedure indicated that substrate surface temperatures during growth were 23° ± 4°C lower than the temperature of the stationary block.

Processing variations.—Layer thickness uniformity was such that only one interference color extended over the entire surface of a 38 mm diam Si wafer. Sample thickness, growth rate, rotation rate of the sample holder, and uneven heating were the major factors affecting the thickness, uniformity, and reproducibility of the films. The growth rate decreased with increases in the nitrogen carrier gas flow rate. Variation of other parameters including temperature, ammonia, oxygen, and silane gas flow rates, and rotation rate had less predictable effects on the growth rate because of competing effects. Typical growth conditions were: temperature, 250°C; nitrogen carrier gas and 3% silane in nitrogen introduced into one mixing manifold at flow rates of 1700 and 275 cm^3/min, respectively, and the mixture introduced into the chamber; and nitrogen carrier gas, oxygen, and ammonia introduced into a second mixing manifold at flow rates of 1700, 50, and 50 cm^3/min, respectively, and the second mixture introduced into the chamber separately from the first mixture.

The growth rate using the conditions listed above was about 50 Å/min. Growth rates were insensitive to ±70% variations of the oxygen flow rate. Variations of the remaining parameters about the values listed above caused significant changes in the film characteristics. Increasing or decreasing the silane flow rate resulted in an increase or decrease, respectively, in the film growth rate. With an increase of as little as 25% in the silane flow rate, growth occurred throughout the chamber, and an excessive amount of particulates were formed which caused spots and defects in the films. With an equivalent decrease in the silane flow rate, film growth was effectively stopped.

The variation of the growth rate with the ammonia flow rate was nonlinear (Fig. 2). The growth rate changed from about 160 Å/min at a flow rate of 20 cm^3/min to about 15 Å/min at a flow rate of 130 cm^3/min. While the film growth rate increased sharply at lower flow rates, at flow rates below about 15 cm^3/min the film growth was uncontrollable, and the growth resulted in the formation of whiskers, platelets, and other irregularly shaped structures.

Variation of the substrate temperature also had a significant effect on the growth rate. A 20°C decrease in temperature effectively stopped growth on the substrate, while a similar temperature increase resulted in an increase in the growth rate by a factor of 3-5.

Etching techniques have been developed (8) which permit a comparison of the quality of SiO_2 and SiO_xN_y

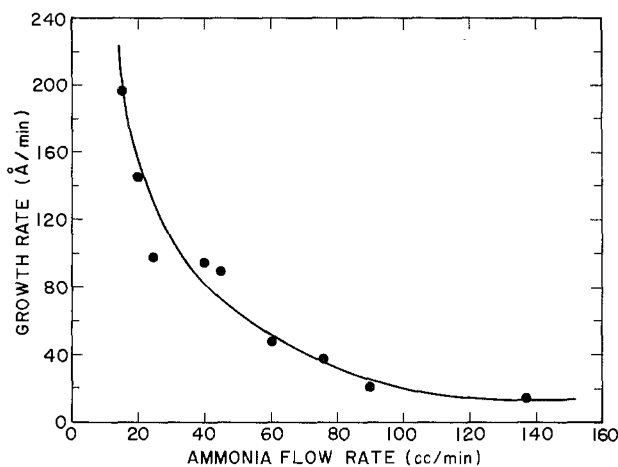

Fig. 2. Relation of film growth rate to ammonia flow rate during film growth for the typical growth conditions listed in the text.

films grown by various processes. The "P" etch used in the work discussed below consisted of 15 parts HF, 10 parts HNO_3, and 300 parts H_2O. Films grown under the conditions listed above had etch rates of 20 Å/sec. This etch rate is similar to that for undensified SiO_2 films grown at 405°C. In comparison, SiO_2 films grown by the thermal oxidation of Si at 1000°C are etched at a rate of 2 Å/sec. There was no significant variation in the etch rates for different SiO_xN_y films etched with "P" etch. Variation of the film growth rate by as much as a factor of 5 by means of ammonia flow rate adjustments did not affect the density of the films as determined by the etching measurements.

No adverse reactions were detected with any of the materials used for substrates. Uniform, insulating films were grown on a range of different substrate materials including quartz, metal wafers, and various elemental, III-V, and II-VI semiconductors. Excellent results were achieved with normal photoresist and etching processes on films used as dielectric isolation layers in devices where low temperature processing was required.

Diagnostic Techniques

Auger.—Auger electron spectroscopy measurements were made to determine the N content of the SiO_xN_y films utilizing a Physical Electronics Industries system. An SiO_2 film implanted to a peak N concentration of 10^{21} ions/cm^3 was used as a standard. The depth distributions in the films were obtained by sputter-etching the samples with a 5 keV Ar ion beam and simultaneously recording the Auger energy spectrum. An Si_3N_4 sample and a dry thermal oxide were also examined for comparison with the N-implanted SiO_2 film and the SiO_xN_y grown films. The limit of sensitivity of the Auger technique is approximately 0.1 atomic percent (a/o)

Nuclear reaction analysis.—Nuclear reaction measurements were made for both N and O in the SiO_xN_y films. A 900 keV deuteron beam from the Naval Research Laboratory (NRL) 5 MV Van de Graaff accelerator was incident on the film, and protons and alpha particles were detected. In the case of N, a $^{14}N(d, \alpha)^{12}C$ reaction was analyzed, and, in the case of O, a $^{16}O(d, p)^{17}O$ reaction was analyzed. The areas under the N and O reaction curves are directly related to the number of atoms in the layer for a given sample. The ratio of these areas for a given sample is directly related to the composition of the film. Comparisons between samples were made on the basis of the values of these ratios. A Si surface barrier detector was used with an 0.059 mm Ni foil placed in front of the detector to absorb elastically scattered deuterons.

Optical.—Optical transmission experiments were made utilizing two spectrophotometers, a Beckman IR-7 and a Perkin-Elmer 521, in the range of 250-4000 cm^{-1} (40.0-2.5 μm). The measurements were double beam measurements, and a beam condenser was used for small samples. Attenuated total reflection (ATR) experiments were made in the same range using the Perkin-Elmer instrument. Ellipsometry measurements were made at 6328Å using a Rudolph 43702-200E ellipsometer. All measurements were made at room temperature.

RBS.—RBS techniques were used to determine the major constituents and to evaluate the thickness of films grown on both Si and InSb substrates. Due to the irregular surfaces on InSb substrates, mechanical and ellipsometry measurements of film thicknesses on these substrates were difficult to obtain. The RBS system employed 2 MeV He ions from the NRL 5 MV Van de Graaff accelerator and a Si solid-state detector. The depth resolution for these films utilizing this technique was ~150-200Å. Reviews of the technique and its usefulness for analysis of insulating films are given elsewhere (9, 10).

Table I. Summary of RBS, thickness, nuclear reaction analysis, and processing gas ratio data

Sample	Substrate	RBS (keV)	RBS (A)	Dektak* (A)	Ellipsometry* (A)	Ellipsometry* n	A(N)/A(O)**	Gas ratio, $NH_3:O_2$
Thermal SiO_2								
Std	Si	56	1287***	1275	1287***	1.46	0	
N implant	Si	57	1310	1350	1321	1.54	8.3×10^{-3}	
SiO_xN_y								
1 NRL†	Si	62	1425	1620	1600	1.46	3.5×10^{-3}	1:1
2 NRL†	InSb	84	2025				4.0×10^{-3}	1:1
3 NRL†	Si	60	1379	1450	1563	1.46	1.9×10^{-3}	1:2
4 NRL†	InSb	72	1736				1.6×10^{-3}	1:2
5 NRL†	Si	300	6895	6025			2.3×10^{-3}	1:4
6 NRL†	InSb	345	8316				1.9×10^{-3}	1:4
7 GE‡	InSb	124	2989				0.66×10^{-3}	

* Ellipsometry measurements made at 6328A. Ellipsometry and Dektak values listed are averages of several measurements for each sample.
** Ratio of the area under the N nuclear reaction spectrum to the area under the O nuclear reaction spectrum for the particular reactions stated in the text.
*** Thickness for RBS data obtained from this sample was arbitrarily set equal to the value measured by ellipsometry in order to determine thickness values of all other samples from the RBS data
† 1 NRL and 2 NRL grown simultaneously, 3 NRL and 4 NRL grown simultaneously, and 5 NRL and 6 NRL grown simultaneously.
‡ 7 GE prepared by the General Electric Company.

SIMS.—Profiles of Si, SiO, SiO_2, Sb, and In were measured by SIMS techniques using a Cameca IMS-300. SIMS experimental techniques and instrumentation details are described elsewhere (11). Due to surface-related effects associated with the SIMS analysis, data from the near surface region (~100Å) were omitted. Depth scales were established from thickness measurements of the SiO_xN_y films. SIMS depth measurements and atomic concentration profiles were reproducible within about 25% for a given sample.

To ensure that the SIMS signal at mass 115 was due to In contamination and not a Si-type complex, the isotopic ratios (113 and 115) of In in the films and substrates were measured. It was established using this approach that the films grown on InSb substrates or in the presence of InSb contained In. The N content in these films could not be determined by the SIMS technique due to competing signals from Si and its complexes. Impurities in SiO_xN_y films grown on Si were determined by mass spectra analyses.

Electrical.—Electrical evaluations of these layers were made by measuring *C-V*, *G-V*, and *I-V* characteristics of MIS test capacitors having chromium-gold gates and back side contacts. Measurements were made using either probes or gold wires bonded to individual pads. Gate areas were 2×10^{-3} cm². All samples with d-c leakage currents greater than about 10^{-13}A at +1V gate bias (~10^5 V/cm) at 80°K were discarded. The discarded samples included approximately 50% of all samples and generally exhibited shorts associated with bonding problems or pin holes. *C-V* and *G-V* measurements for Si substrate capacitors were made at 295°K and 80°K and for InSb substrate capacitors at 80°K. These samples were bonded to transistor headers. To eliminate extraneous lead capacitance and enhance cooling efficiency, the InSb chips were mounted on gold-plated beryllium oxide heat sink pads on headers which in turn were mounted directly to a cold finger. High frequency (1 MHz) *C-V* measurements were made with a Boonton capacitance meter, and lower frequency *C-V* and *G-V* measurements were made using a PAR 129A lock-in amplifier. Leakage current measurements were made using Keithley 602 and 616 electrometers.

Diagnostic Results

Auger.—An estimate of the N concentration in the SiO_xN_y films, based on the comparison of the N Auger signals from the SiO_xN_y films and the reference N-implanted, thermally grown SiO_2 film, gave a value of <5 a/o throughout the layers. The N content estimated from the Auger data was in qualitative agreement with the nuclear reaction results.

Nuclear reaction analysis.—The nuclear reaction results were utilized to give a quantitative measurement of the amount of N incorporated in the insulating films. A portion of the same N-implanted, thermally oxidized Si wafer discussed above was used as a reference. The results are shown in Table I in the next to last column for several films. These films included the reference sample and several SiO_xN_y films grown on both Si and InSb substrates. The major point of these data is that the total amounts of N incorporated in the SiO_xN_y films grown in this study were over a factor of two less than the amount implanted in the reference thermal oxide. If the N implanted in the thermal oxide were of uniform concentration through the oxide, that concentration would be approximately 5% of the O concentration on an atomic basis. Thus, the N concentrations in the SiO_xN_y films were low, about 1 to 2% of the O concentration on an atomic basis.

Optical.—Optical transmission experiments were carried out on a series of samples including thermal oxides grown on Si substrates and SiO_xN_y films grown on both InSb and Si substrates. The transmission spectra of the SiO_xN_y films grown on Si were very similar to those of thermal SiO_2 films grown on Si; the spectra of the SiO_xN_y films on InSb differed from those of the thermal oxides on Si primarily in the effects of the different substrates on these spectra. The results for two typical SiO_xN_y films, one deposited on a Si substrate and the other on an InSb substrate, are shown in Fig. 3, and results for all spectra are

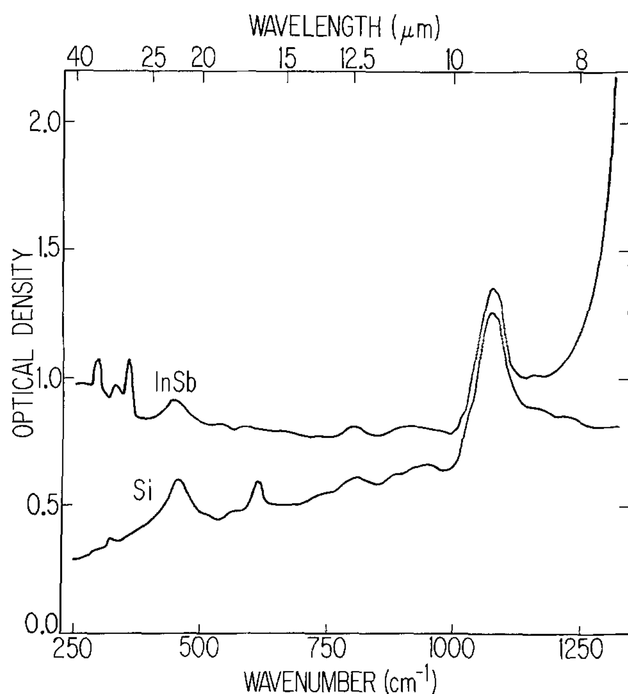

Fig. 3. Optical absorption spectra of SiO_xN_y films. Upper curve, film on InSb substrate, sample 6 NRL. Lower curve, film on Si substrate, sample 5 NRL. Room temperature measurements.

Table II. Summary of vibrational modes of SiO_xN_y films

Energy (cm⁻¹)	Strength*,†	Breadth*,†	Source†	References	Experiment
450	s	b	SiO_2	(8, 14-17)	Transmission
560	w	n	Si LO + TA	(14, 15, 18)	Transmission
810	m	b	SiO_2	(8, 14-17)	Transmission
880	w	n	Si-N ?	(12, 13, 22, 26)	Transmission
930	w	vb	SiO_2 ?	(14, 15, 17)	Transmission
1080	vs	b	SiO_2	(8, 12-17)	Transmission
1160	s	b	SiO_2	(8, 14-17)	Transmission
1615	vw	b	SiO_2	(19)	ATR
1700 ?	vw	b	SiO_2 ?		ATR
1830	vw	b	SiO_2	(19)	ATR
1980	vw	b	SiO_2	(19)	ATR
2115	vw	b	Si-H or SiH . . . O ?	(20-23)	ATR
2260	vw	b	Si-H or SiH . . . O	(20-23)	ATR
2415	vw	b	Si-H or SiH . . . O ?	(20-23)	ATR
2590	vw	b	Unknown		ATR
3255	w	vb	N-H or O-H	(20-23)	ATR
3600	m	n	O-H or N-H	(20-23)	ATR and transmission

* vs = very strong, s = strong, m = medium, w = weak, vw = very weak, n = narrow (sharp), b = broad, vb = very broad.
† See text.

briefly summarized in Table II. The four major bands observed in bulk SiO_2 glass and thermally grown films on Si were observed in the SiO_xN_y films as well (8, 12-17). The broad shoulder on the high energy side of the major 1080 cm^{-1} band at about 1160 cm^{-1} was not as pronounced in the spectra of films on InSb because of the onset of the fundamental absorption edge (Fig. 3).

The very broad 930 cm^{-1} band observed in the SiO_xN_y films was at the energy at which bands have been observed in some bulk SiO_2 glasses and thermal oxide films and may be a SiO_2 band (14, 15, 17). In addition, the weak 560 cm^{-1} shoulder was observed in the SiO_xN_y films on Si but not clearly observed in films on InSb. This band very likely was the Si LO + TA combination band (18), though a weak band at this energy also has been observed in some bulk SiO_2 glasses (14, 15). The weak band near 3500 cm^{-1} was observed in the SiO_xN_y films on Si substrates but not in the thermal oxides.

ATR spectra of SiO_xN_y films grown on Si exhibited several bands in the range 1300-4000 cm^{-1} (Fig. 4 and Table II). Only the bands at 3255 and 3600 cm^{-1} may be related to N in the films. Four of the eight other bands previously have been assigned to SiO_2, Si-H, or SiH . . . O type bonding as indicated in Table II (19-23). The unreported and/or unidentified bands are described briefly below.

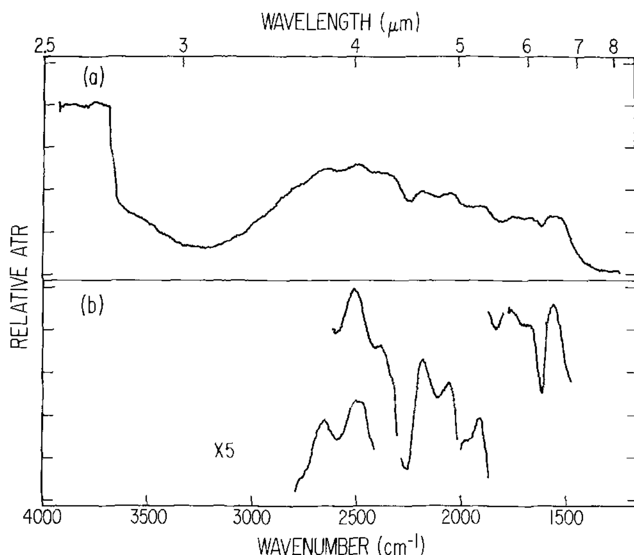

Fig. 4. Typical ATR spectra of SiO_xN_y films on Si. (a) Relative ATR spectra. (b) Scale expansion factor ×5. Vertical position of each section in (b) is relative to itself. Vertical position of different sections in (b) cannot be compared quantitatively. Room temperature measurements.

The very weak and previously unreported band at 1700 cm^{-1}, if real, is thought to be a SiO_2 band. The 1830 cm^{-1} band is shifted to a position lower in energy than that observed in thermal SiO_2 probably due to the different composition and stoichiometry of the two types of films (19). The 2115 and 2415 cm^{-1} bands appear to be satellites of the main 2260 cm^{-1} Si-H band (20-23) and are thought to be Si-H or SiH . . . O type bands, the 2415 cm^{-1} band being slightly removed in energy from the position of the atmospheric CO_2 band. The origin of the 2590 cm^{-1} band is not known.

Values of the thickness and real part, n, of the index of refraction of films on Si substrates determined by ellipsometry at 6328A are given in Table I. It was assumed that the value of the imaginary part of the index of refraction of the films was zero in calculating these results from the ellipsometry data.

RBS.—The RBS spectra for SiO_xN_y films on Si substrates were very similar to those of thermal oxides on Si substrates. In addition, the absence of a resolvable N peak in the RBS data in films on Si substrates demonstrated that the N content of the films was very low (less than 5% of the O content atomically).

The film thickness values obtained from RBS, mechanical (Dektak), and ellipsometry techniques are presented in Table I. It should be noted that the RBS measurements are presented as qualitative comparisons of the films, and it was assumed for the thickness analyses that the films were of uniform and equal density, an assumption substantiated by the chemical etch rates of films on Si substrates. The unimplanted SiO_2 thermal oxide film was used as a reference to estimate the film thicknesses from the RBS data in order to compare these values with the mechanical (Dektak) and ellipsometry measurements. In the cases of films grown on InSb substrates, corrections for dE/dx of the He ions were made to determine the thicknesses from the energy shifts of the edge of the onset of scattering as shown in columns 3 and 4 of Table I. These energy shifts were with reference to the position of the edge for a clean InSb substrate with no film on its surface.

The RBS data include results obtained from three pairs of samples, one substrate being Si and one InSb for each pair. The films were grown simultaneously on the two substrates of each pair. These RBS results indicated that for films grown simultaneously on InSb and Si substrates, the films on InSb substrates contained more mass as shown in column 3 of Table I.

SIMS.—The SIMS data obtained from an SiO_xN_y film are shown in Fig. 5. The results indicate a uniform distribution of Si and O throughout the SiO_xN_y film. Films grown on InSb also had uniform distributions of Si and O throughout. In addition, the SIMS Si:SiO:SiO_2 ion sputtering yield ratios for individual

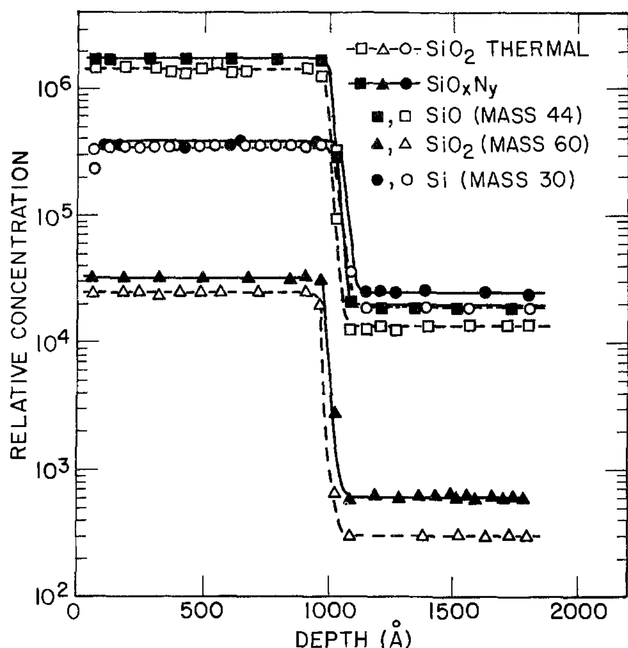

Fig. 5. Relative concentrations of SiO (■, □)-atomic mass 44, SiO_2 (▲, △)-atomic mass 60, and Si (●, ○)-atomic mass 30 in SiO_xN_y (closed data points) and thermal SiO_2 (open data points) films on Si substrates determined by SIMS. Steps at about 1000Å depth represent insulator-substrate interfaces. Samples grown at same times and in same chambers with sample 1 NRL and thermal SiO_2 standard (unimplanted).

SiO_xN_y films on Si substrates and for individual thermal SiO_2 films were similar (Fig. 5). These ratios were also within 25% or better of the ratios of yields of films grown on InSb substrates. Thus, the stoichiometry of SiO_xN_y films grown on both InSb and Si substrates and of thermal SiO_2 films was similar. The Si, SiO, and SiO_2 signals decreased beyond the film/substrate interface due to the decrease in the secondary ion yields in Si as compared to those in SiO_xN_y and SiO_2 (Fig. 5).

The atomic profiles of In in SiO_xN_y films grown simultaneously on Si and InSb substrates are shown in Fig. 6. Films grown on InSb substrates had a significantly higher In content than films grown simultaneously on Si substrates. Films subsequently grown on Si substrates in the absence of InSb showed

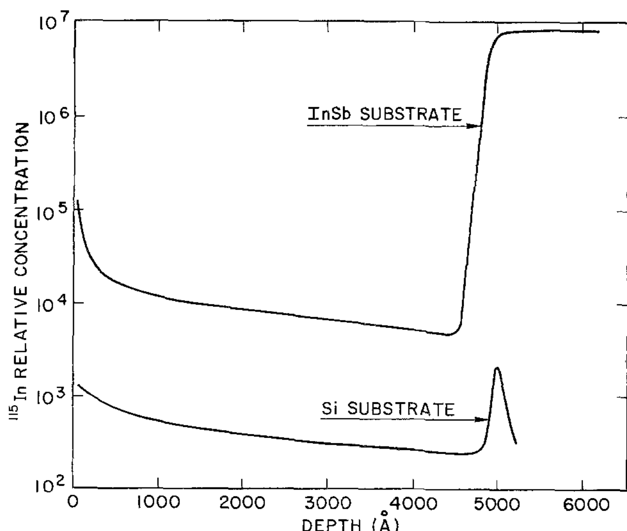

Fig. 6. Relative concentrations of In in SiO_xN_y films grown simultaneously on Si and InSb substrates. Steps at about 5000Å represent insulator-substrate interfaces. Growth conditions similar to those of samples 5 NRL and 6 NRL.

significantly less In content. An estimate of the ^{115}In concentration in the SiO_xN_y films grown on InSb substrates was approximately 10^{16}-10^{17} cm^{-3}. This estimate was based on a comparison between the SIMS ^{115}In signals from a ^{115}In implanted reference sample and from the SiO_xN_y films. To investigate the possibility of decomposition of InSb from the back surface during film growth, several samples were coated on the back surface with sputter-deposited Si_3N_4 prior to being placed in the reactor which had been cleaned and flushed. The SIMS analysis of the films grown in this manner indicated a significant decrease in the In and Sb content. Antimony was also detected and showed the same general behavior as In, although the concentration levels were not determined.

Mass spectra analyses of two classes of samples were carried out to determine the relative Na concentrations in the two classes. One class, samples of which were rejected for further measurements because of anomalously broad hysteresis loops (7-15V) in their C-V curves, had at least three orders of magnitude more Na content than the second class, samples which were retained for further electrical measurements. The Na concentration as a function of depth in the films could not be determined due to the high mobility of Na in insulating films subjected to ion bombardment (24). All films analyzed contained traces of hydrocarbons, K, and Ca.

Electrical.—The dielectric constant determined by correlating the measured values of gate oxide capacitance, insulator thickness, and gate area for given MIS capacitors was typically about 3.3 for the low temperature SiO_xN_y films. Though the measured values were in a range 2.2-4.6, increased with film thickness, and varied from film to film, they generally were less than 3.9, the dielectric constant of thermally grown SiO_2. These measured values are believed to be correct within about 20%. In addition, the dielectric constant values of the low temperature SiO_xN_y films were consistently less than the range 4-9 reported for higher temperature SiO_xN_y films with various x/y ratios (12, 13).

The *C-V* curves for capacitors on Si and InSb substrates showed that the flatband voltage values typically were -1 to -2V [Fig. 7(a) and (b)]. Hysteresis was observed for about 95% of the samples measured, and hysteresis of both clockwise and counterclockwise sense was observed. An example of a *C-V* curve with essentially no hysteresis is shown [Fig. 7(c)]. The flatband voltage could be varied by applying a negative bias voltage at room temperature and cooling the samples to 80°K under bias. Flatband voltage shifts as large as +5V have been observed when samples were cooled under negative bias voltage, and this process was reversible.

Discussion

The results of the experiments indicate that the low temperature SiO_xN_y films were very much like thermal SiO_2 films but with a very small N concentration, about 1-2% of the O concentration on an atomic basis. The spectroscopic results for samples prepared in this study and for industrial samples (2, 3) were very similar for each technique employed. The value of the real part of the index of refraction of the SiO_xN_y films was the same as that of dry, thermal SiO_2 films. This value was not intermediate between that of SiO_2 and that of Si_3N_4 as in the case of higher temperature SiO_xN_y films which contain significant amounts of nitrogen (25).

The optical results also demonstrated that there was very little N present in the low temperature SiO_xN_y films. The major 1080 cm^{-1} band did not shift to lower energy for these films, as observed for higher temperature SiO_xN_y films (12, 13), indicating little or no evidence of Si-N bonding. The Si-N band reported at ~ 475-500 cm^{-1} was not observed with certainty in the present work (22, 26).

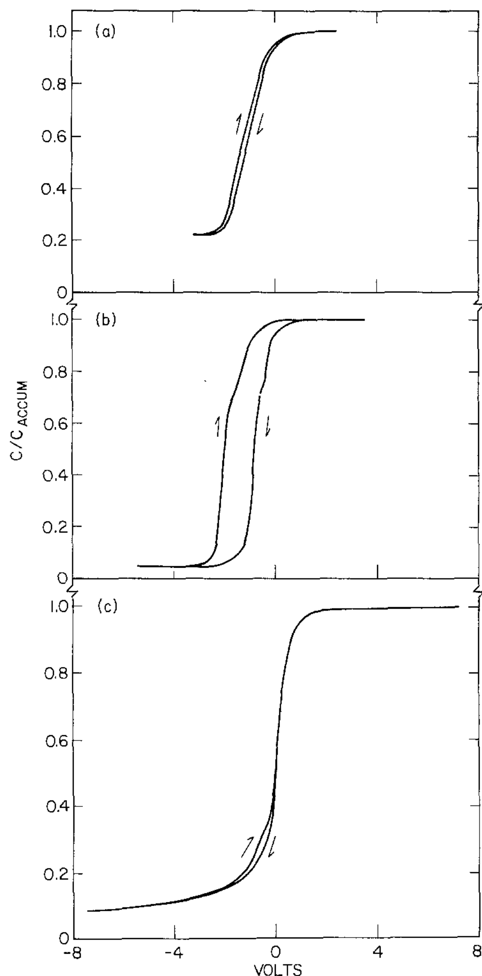

Fig. 7. One MHz C-V curves for three MIS capacitors having SiO_xN_y insulating films. (a) InSb substrate measured at low temperature. (b) Si substrate measured at room temperature. (c) Si substrate measured at 80°K. About 5% of capacitors tested exhibited essentially no hysteresis as shown in (c).

The weak band observed at about 880 cm^{-1} may be due to Si-N type vibrations. The sharpness of this band in comparison to those observed at this energy in other studies of SiO_xN_y films deposited at higher temperatures and of Si_3N_4 (12, 13, 22, 26), however, casts some doubt on this identification.

The 3255 and 3600 cm^{-1} ATR bands and the 3500 cm^{-1} transmission band, which probably is the same as the 3600 cm^{-1} ATR band, may be either N-H type or O-H type vibrational bands as reported for thermal oxides, Si_3N_4 films, and higher temperature SiO_xN_y films (20-23). It is reasonable to postulate that the 3600 cm^{-1} band may be an O-H type vibrational band and the 3255 cm^{-1} band an N-H type band (20-23). The N-H band reported (22, 23) at about 1200 cm^{-1}, if present in these films, was obscured by the strong SiO_2 type bands at 1080 and 1160 cm^{-1}.

The optical evidence for little N bonding and the close similarity of the spectra to those of thermal SiO_2 films are consistent with the general observation that little N is present in these low temperature films and that the films are like SiO_2 in many observable respects. Thus, the role of the ammonia in the film growth reaction is not clear. The presence of the ammonia in the reaction chamber was necessary, however, or uniform and controllable film growth would not occur. The growth rate variations indicate that the primary role of the ammonia may be that of a modifying agent in retarding the low-temperature pyrolytic decomposition rate of the silane in the presence of oxygen (Fig. 2).

The SIMS results (Fig. 5) also demonstrated that the low temperature SiO_xN_y films are uniform in composition and similar to thermal SiO_2 films. Because the concentrations of In and Sb impurities detected in films grown on InSb substrates or on Si substrates in the presence of an InSb substrate increased with distance away from the semiconductor-insulator interface (Fig. 6) and because significantly less contamination was present in films grown on InSb substrates having the back sides coated with Si_3N_4 prior to film growth, it is believed that this contamination resulted from the decomposition of InSb at the back surface of the InSb substrates.

The hysteresis observed in many C-V measurements could have been due to one or more of several causes (27-32), and hysteresis of both cyclic senses was observed in different samples. At present it is not possible to identify which one or more of these potential causes were responsible for the hysteresis.

The thickness values of films on Si substrates as determined mechanically, by RBS, and by ellipsometry were in agreement within 13.5% or better (Table I). The RBS data, however, indicated that the SiO_xN_y films on InSb substrates had more mass and thus were thicker or denser or both than the corresponding films deposited simultaneously on Si substrates. This observation is not understood at present. The etching rate values described in the processing section indicated, in addition, that the SiO_xN_y films were less dense than dry, thermal SiO_2 films grown on Si substrates, and the measured dielectric constant values were consistent with this observation.

Thus, it has been demonstrated that low temperature SiO_xN_y films successfully grown on InSb and Si substrates are uniform in composition, are very much like thermal SiO_2 films grown on Si substrates, and contain only small amounts of N. The SiO_xN_y films, moreover, show significant promise for use in electronic devices.

Acknowledgments

The authors thank H. M. Day and J. K. Hirvonen for carrying out several experiments and W. D. Baker, R. E. Dehl, E. D. Palik, M. L. Rebbert, N. S. Saks, and L. E. Smith for numerous, valuable technical discussions. The cooperation of L. Plew of the Naval Weapons Support Center, Crane, Indiana, in obtaining the SIMS data is gratefully acknowledged. The authors also thank J. C. Kim for providing chips of an SiO_xN_y film grown on an InSb substrate at the General Electric Company.

Manuscript submitted Oct. 19, 1976; revised manuscript received Oct. 9, 1977. This was Papers 89 and 90 presented at the Washington, D. C., Meeting of the Society, May 2-7, 1976 and Papers 203 and 365 presented at the Atlanta, Georgia, Meeting of the Society, Oct. 9-14, 1977.

Any discussion of this paper will appear in a Discussion Section to be published in the December 1978 JOURNAL. All discussions for the December 1978 Discussion Section should be submitted by Aug. 1, 1978.

Publication costs of this article were assisted by the Naval Research Laboratory.

REFERENCES

1. C. E. Hurwitz and J. P. Donnelly, *Solid-State Electron.*, **18**, 753 (1975).
2. J. C. Kim, IEEE Trans. Parts, Hybrids, Packag., **php-10**, 200 (1974).
3. J. C. Kim, "InSb MOS Detector," Final Technical Report, U.S. Army Electronics Command, Night Vision Laboratory, Fort Belvoir, Va., Contract No. DAAK02-73-C-0006, Feb. 1975, Department of Defence Documentation Center, AD No. B004428L; and J. C. Kim, "Fabrication and Evaluation of InSb CID Arrays," Final Report, Naval Electronic Systems Command, Defense Advanced Research Projects Agency, and Naval Research Laboratory, Contract No. N00014-75-C-0124, Aug. 1976, National Technical Information Service, AD No. A030 022/8GI.
4. Solid State Research Report, Lincoln Laboratory, M.I.T. (1971:4), p. 1, Electronic Systems Division Contract F 19628-70-C-0230.

5. J. Shappir, S. Margalit, and I. Kidron, *IEEE Trans. Electron Devices*, **ed-22**, 960 (1975).
6. G. W. Anderson, W. A. Schmidt, and J. Comas, in "Proceedings of the Symposium on Thin Film Phenomena: Interfaces and Interactions," J. E. Baglin and J. M. Poate, Editors, The Electrochemical Society, Inc., Princeton, N.J., To be published.
7. K. Schmid, H. Ryssel, H. Müller, K. H. Wiedeburg, and H. Betz, *Thin Solid Films*, **16**, S11 (1973).
8. W. A. Pliskin and H. S. Lehman, *This Journal*, **112**, 1013 (1965).
9. W. D. Mackintosh, in "Characterization of Solid Surfaces," P. F. Kane and G. B. Larrabee, Editors, p. 403, Plenum Press, New York (1974).
10. W. K. Chu, J. W. Mayer, M-A. Nicolet, T. M. Buck, G. Amsel, and F. Eisen, *Thin Solid Films*, **17**, 1 (1973).
11. J. M. Morabito and R. K. Lewis, *Anal. Chem.*, **45**, 869 (1973).
12. R. I. Frank and W. L. Moberg, *This Journal*, **117**, 524 (1970).
13. T. L. Chu, J. R. Szedon, and C. H. Lee, *ibid.*, **115**, 318 (1968).
14. M. Hass, *J. Phys. Chem. Solids*, **31**, 415 (1970).
15. M. Miler, *Czech. J. Phys.*, **B18**, 354 (1968).
16. G. Hoffmann, M. Németh-Sallay, and J. Schanda, *Acta Phys. Acad. Sci. Hung.*, **36**, 349 (1974).
17. V. Gopal and M. Gopal Rao, *Phys. Status Solidi a*, **11**, 783 (1972).
18. F. A. Johnson, *Proc. Phys. Soc. (London)*, **73**, 265 (1959).
19. G. A. Haas, T. Pankey, Jr., and R. T. Holm, *J. Appl. Phys.*, **47**, 1185 (1976).
20. K. H. Beckmann and N. J. Harrick, *This Journal*, **118**, 614 (1971).
21. H. J. Stein, *J. Electron. Mater.*, **5**, 161 (1976).
22. E. A. Taft, *This Journal*, **118**, 1341 (1971).
23. H. J. Stein and H. A. R. Wegener, *ibid.*, **124**, 908 (1977).
24. H. L. Hughes, R. D. Baxter, and B. Phillips, *IEEE Trans. Nucl. Sci.*, **ns-19**, No. 6, 256 (1972).
25. D. M. Brown, P. V. Gray, F. .K Heumann, H. R. Philipp, and E. A. Taft, *This Journal*, **115**, 311 (1968).
26. Yu N. Volgin and Yu. I. Ukhanov, *Opt. Spektrosk.*, **38**, 727 (1975).
27. P. V. Gray, *Proc. IEEE*, **57**, 1543 (1969).
28. E. H. Snow, A. S. Grove, B. E. Deal, and C. T. Sah, *J. Appl. Phys.*, **36**, 1664 (1965).
29. A. S. Grove, "Physics and Technology of Semiconductor Devices," pp. 337-340, John Wiley & Sons, Inc., New York (1967).
30. S. M. Sze, "Physics of Semiconductor Devices," pp. 460-464, John Wiley & Sons, Inc., New York (1969).
31. A. Many, Y. Goldstein, and N. B. Grover, "Semiconductor Surfaces," chap. 5 and 9, John Wiley & Sons, Inc., New York (1965).
32. F. P. Heiman, Ph.D. Thesis, Department of Electrical Engineering, Princeton University, 1964 (University Microfilms, Ann Arbor), pp. 67 ff.

On Thermally Stimulated Space-Charge Decay in Sn^{2+}-doped Sodium Chloride and Potassium Chloride Crystals

Ah Mee Hor*,[1] and P. W. M. Jacobs

Department of Chemistry, University of Western Ontario, London, Ontario N6A 5B7, Canada

ABSTRACT

When quenched crystals of NaCl:Sn^{2+} or KCl:Sn^{2+} are warmed at a constant rate and the voltage appearing across platinum electrodes in contact with the crystal is monitored, as in a thermal depolarization experiment, large d-c currents are measured even when the crystals have not previously been polarized. This charge release is believed to be associated with the crystallization of precipitates of $SnCl_2$ within the crystal. The appearance of depolarization currents of the "wrong" sign during heating of previously polarized crystals is commented upon briefly.

The purpose of this brief paper is to report on the strange behavior of quenched NaCl:Sn^{2+} and KCl:Sn^{2+} crystals during thermal depolarization. RbBr:Sn^{2+} crystals (1) behave "normally," that is to say, whereas untreated crystals or crystals annealed at 250°C for 20 hr display no depolarization currents, crystals annealed at 500°C for 4 hr and then at 400°C for 13 hr prior to quenching in liquid nitrogen, exhibit after polarization and warming at a steady rate of 4°K/min a characteristic double peak in the temperature range 182°-212°K. If the polarization temperature T_p is low enough (215°K) this is the only peak observed. With higher polarization temperatures a more-or-less complicated series of depolarization bands are observed on the high temperature side of the 182°-212°K double peak. The structure of these bands depends on T_p and hence on the polarization current. The bands have tentatively been assigned to the release of macroscopic space charge associated with electrode processes occurring during polarization. The double peak is ascribed to the occurrence of Sn^{2+}-cation vacancy complexes. Broadly similar behavior occurs in RbBr:Ba^{2+} (1), RbCl:Sr^{2+} (2), and in many other doped alkali halides.

The behavior of NaCl:Sn^{2+} and KCl:Sn^{2+} is quite different and includes a feature we believe not to have been previously reported. An unpolarized NaCl:Sn^{2+} crystal which had not received any thermal pretreatment showed zero "depolarization" current j on warming from 100°K to room temperature. j was similarly negligible if this crystal was subjected to a polarization voltage of 200V at 255°K. The same behavior was observed after annealing for 16 hr at 360°K but if T_p was increased to 295°K a sharp inverted peak occurred at 255°K (Fig. 1).

During polarization the top platinum lead was connected to the input of a Cary 401 electrometer and the lower platinum electrode resting on the sapphire insulator was connected to the + terminal of a Hewlett Packard 6100 A d-c voltage supply (see Fig. 2). During depolarization the top electrode remained connected to the input of the electrometer and the bottom electrode was grounded. Both surfaces of the crystal in contact with leads were coated with silver paint to en-

* Electrochemical Society Student Member.
[1] Present address: Tunku Abdul Rahman College, Kuala Lumpur, Malaysia.

Key words: thermal depolarization, ionic thermoconductivity, doped alkali halides.

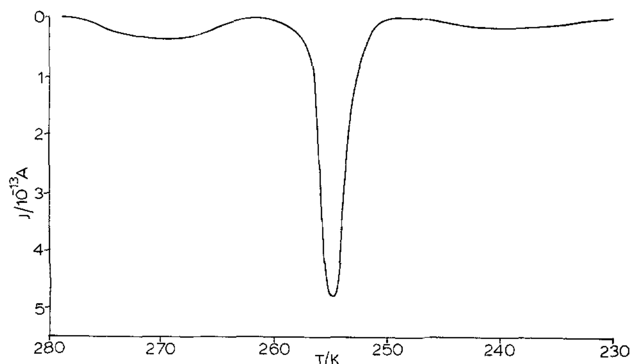

Fig. 1. Large "inverted" peak in the $j(T)$ depolarization curve for a NaCl:Sn^{2+} crystal that had been polarized at 295°K. Two broad smaller peaks are also found at 239° and 269°K, respectively.

(a) During polarization

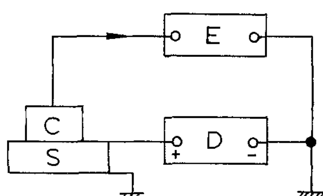

(b) During depolarization

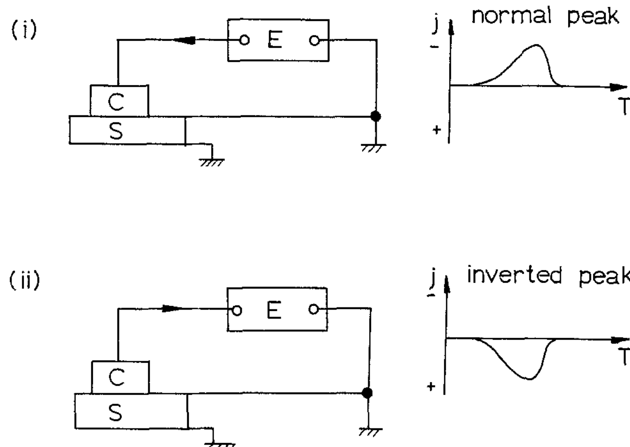

Fig. 2. Schematic circuit diagrams for (a) polarization; and (b) depolarization measurements. C = crystal; E = electrometer; D = d-c power supply; S = sapphire insulator. Arrows show direction of flow of positive current through the external circuit. In (b):(i) the direction of current flow is as expected, and obtained, for randomization of dipoles and the depolarization current peak is referred to as "normal"; (ii) For "inverted" peaks the electrometer records a positive voltage instead of a negative one, *i.e.*, the current flow through the external circuit is in the same direction as that during polarization. The terms "normal" and "inverted" have their same significance even when the polarization voltage $V_p = 0$.

sure good electrical contact with the platinum leads. During depolarization both sides of the sapphire insulator were grounded. One anticipates, and normally measures, a negative voltage with the electrometer due to the reorientation of dipoles aligned preferentially in the d-c field during polarization. An "inverted peak" means that the polarity of the voltage across the crystal was positive instead of negative. Inverted peaks have been observed previously during thermally stimulated depolarization measurements and have generally been ascribed, rather loosely, to precipitates or space charge. However, a space charge consisting of carriers that have piled up in front of one or both of the electrodes should, as it decays, yield a "normal" depolarization current in the opposite direction to that flowing during polarization. In alkali halides at or below room temperature and particularly in these Sn^{2+}-doped crystals we anticipate an excess of cation vacancies and that an excess of vacancies will have accumulated adjacent to the (lower) positive electrode during polarization. The migration of these vacancies to restore the equilibrium distribution should give a normal (negative) depolarization peak.

However, the above facile explanation of a space charge peak overlooks the possibility that the potential distribution in the crystal may be more complicated than just described. In unpolarized crystals the potential is not uniform due to the Frenkel (3) space charge. If the polarized crystal contains specifically adsorbed carriers plus diffuse double layers of neutralizing charge, then the perturbation of these double layers by the polarizing field could result in a nonequilibrium charge distribution whose relaxation would give a current flow in the opposite direction to that associated with the randomization of dipoles. Specific detailed models of the decay of macroscopic space charge during thermal depolarization in ionic crystals, including the occurrence of inverted peaks, have not yet been developed although the existence and importance of the macroscopic space charge has been pointed out, for example, by Kessler (4). Possibly, double layers at precipitates, as well as at surfaces and dislocations, contribute to the space charge.

A second NaCl:Sn^{2+} crystal was annealed for 31 hr at 400°C, quenched in liquid nitrogen, and then allowed to warm to room temperature before mounting in the polarization cell. The crystal was shorted at room temperature, cooled to ~100°K, and then warmed at a constant rate of 4°K/min. No polarizing voltage had been applied, yet substantial inverted peaks were observed in the 205°-250°K range. The cooling and warming sequence was repeated twice without any application of a voltage to the crystal. No depolarization was observed on cooling but on each warming cycle a small inverted peak followed by large "normal" peaks were observed. Figure 3 shows that this behavior is qualitatively reproducible in the same crystal. The maximum currents are large: 1.5 and 2.3 $\times$ 10^{-12}A, respectively, and are much larger than would normally be observed in the thermally activated randomization of M^{2+}-cation vacancy dipoles, for instance (~3 $\times$ 10^{-14}A).

A possible explanation of this phenomenon is that during cooling of the crystal from room temperature to 100°K, Sn^{2+}-cation vacancy dipoles aggregate but maintain the NaCl structure. On warming recrystallization to $SnCl_2$ precipitates takes place with ejection

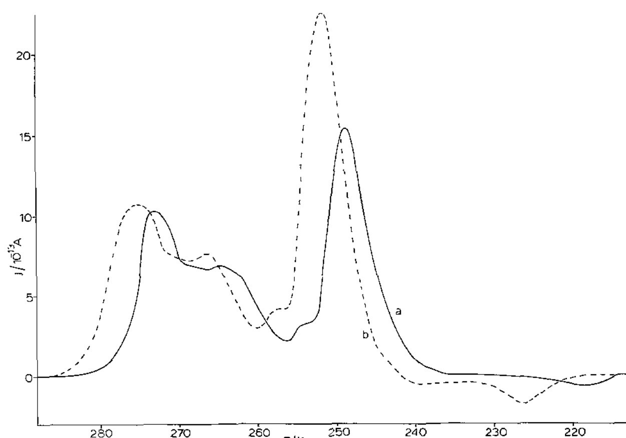

Fig. 3. Large "depolarization" currents observed on warming a previously annealed and quenched NaCl:Sn^{2+} crystal from ~ 100°K to room temperature. (a) Second warming cycle; (b) third warming cycle. No polarizing field has been applied to this crystal.

of cation vacancies. The concentration of cation vacancies now locally exceeds the equilibrium value and is reduced by the diffusion of vacancies to sinks (dislocations). The net displacement current is the vectorial sum of all the microscopic current flows. It would be entirely fortuitous if this sum were zero. Clearly it might have either sign depending upon the actual dislocation structure of the crystal. This tentative explanation requires an unusually high mobility for Sn^{2+} ions in NaCl, which we know to be so because of the relative rapidity with which precipitation occurs in freshly quenched crystals of NaCl: Sn^{2+} compared to, say, RbBr: Sn^{2+}.

Broadly similar behavior was observed for KCl: Sn^{2+}. Figure 4 shows the TD curve on warming a crystal that had been quenched in liquid nitrogen after 2 hr at 550°C, allowed to warm to room temperature, and then cooled to ~100°K in the polarization cell without any application of a polarization voltage. There was no current flow during cooling but in the heating cycle strong inverted peaks occurred in the range 230°-280°K. The crystal was then polarized at 215°K (V_p = 300V) when it showed a qualitatively similar charge release on the warming cycle. This implies either that this charge release has little to do with the attempt to polarize the crystal or that the crystal was

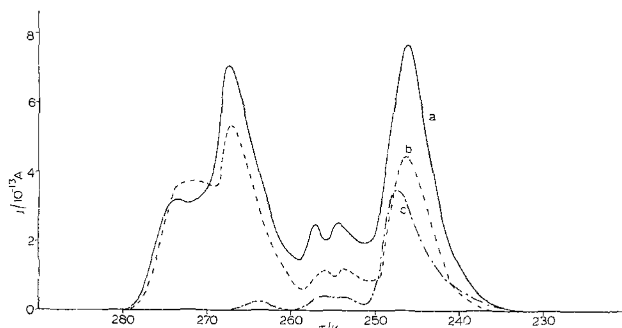

Fig. 4. Depolarization currents observed on warming a previously annealed and quenched KCl: Sn^{2+} crystal from ~ 100°K to room temperature. (a) First run V_p = 0V; (b) second run, V_p = 300V, T_p = 215°K; (c) third run, after annealing for 3 hr at 313°K, V_p = 0V (× 3.33).

somehow self-polarized prior to the first run. It is known (5) that freshly cleaved ionic crystals may contain nonuniform charge distributions but the resulting voltage across the crystal is of the order of magnitude of hundreds of millivolts rather than hundreds of volts. Thus self-polarization seems to be unlikely. This crystal was then annealed at 310°K for 3 hr, cooled to ~100°K without further polarization, and warmed at a constant rate. There was no charge release during cooling but in the warming cycle a small (j_{max} ~ 10^{-13}A) inverted peak occurred in the same temperature region as the large peak in the previous run. This behavior is of a similar nature to that observed for NaCl: Sn^{2+} and the explanation is probably similar.

It seems likely that related effects to those discussed here may have been observed by other research workers in the field but not pursued because of their complexity and irreproducibility. Indeed, the high temperature side of the dipole relaxation peaks has been referred to in the literature (2) as "dielectric chaos." We trust that these modest beginnings may encourage the more detailed investigation of a region of the dielectric behavior of ionic crystals that is important in aiding our knowledge and understanding of dipole aggregation, precipitation, and electrode processes.

Acknowledgment

We thank the National Research Council of Canada for its support of this research program.

Manuscript submitted Sept. 2, 1977; revised manuscript received Oct. 10, 1977.

Any discussion of this paper will appear in a Discussion Section to be published in the December 1978 JOURNAL. All discussions for the December 1978 Discussion Section should be submitted by Aug. 1, 1978.

Publication costs of this article were assisted by the University of Western Ontario.

REFERENCES

1. A. M. Hor and P. W. M. Jacobs, To be published.
2. G. P. Williams and D. Mullis, *Phys. Status. Solidi. A*, **28**, 539 (1975).
3. J. Frenkel, "The Kinetic Theory of Liquids," Oxford University Press, New York (1946).
4. A. Kessler, *This Journal*, **123**, 1236 (1976).
5. A. R. Allnatt and P. W. M. Jacobs, *Proc. R. Soc. London, Ser. A*, **267**, 31 (1962).

Gate Oxide Thinning at the Isolation Oxide Wall

T. T. Sheng and R. B. Marcus

Bell Laboratories, Murray Hill, New Jersey 07974

ABSTRACT

Transmission electron micrographs of cross sections of MOS devices have shown thinning of the gate oxide at the isolation oxide wall. It is shown that the thinning is related to the slope of that wall which is in turn affected by the time of overetch in BHF during window photolithography. A 7 min overetch produces a thinning of ~25% and cases of 30% thinning have been found in device samples. The thinning is caused by the wall acting as a partial barrier to local oxidation at that site.

During the transmission electron microscope study of cross sections of MOS test devices, it was noticed that gate oxides were sometimes thinned by 20-30% in regions very close to the field oxide wall. Some experiments were carried out to help understand the origin (and control) of this anomalous thinning, and results are reported in this paper.

Key words: MOS devices, gate oxides, oxide wall.

Experimental

The main method used to study the profile of gate oxides was to prepare thin film sections orthogonal to the isolation oxide wall and sample surface, and study these samples by transmission electron microscopy (TEM). A number of authors have described cross-sectional techniques for preparing simple (*e.g.*, non-device) semiconductor structures for TEM study (1-3).

Table I. List of samples

[All samples (100) orientation]

Sample	Description
A	CMOS device
B	CMOS device
C	CMOS device
D	CMOS device
E	CMOS device
F	Tester: 7 min BHF, no gate SiO_2
G	Tester: 7 min BHF, 500Å SiO_2
H	Tester: 7 min BHF, 1500Å SiO_2
I	Tester: 14 min BHF, no gate SiO_2
J	Tester: 14 min BHF, 500Å SiO_2
K	Tester: 14 min BHF, 1500Å SiO_2

Table II. Processing of tester samples

1. Clean
2. Oxidize 1050°C wet O_2 10,000Å
3. Window photolithography
4. 7 min BHF, Resist strip | 14 min BHF, Resist strip
5. Oxidize 1000°C dry O_2 500Å | Oxidize 1000°C dry O_2 1500Å

Sheng and Chang (3) described a method for sectioning device samples where particular device features need to be examined; their technique was used to prepare samples for the present study. Samples were either CMOS device structures or structures specifically prepared for this study. All samples were (100) orientation and contained ~1μ field oxide formed by wet oxidation at 1050°C and 500-1500Å gate oxide formed by dry oxidation at 1000°-1100°C. The samples are listed in Table I.

The structures specifically prepared for this study were designed to test the effects of variations in window wall geometry on the occurrence of anomalous thinning. They were formed according to the processing scheme shown in Table II. 7 min BHF was needed to clear windows down to the Si substrate; some wafers received a 14 min etch to produce a change in slope of the side wall (see below). Gate oxides were grown to 500 and 1500Å thicknesses to test the effect of gate oxide thickness on anomalous thinning.

Results

Representative transmission electron micrographs of cross sections are shown in Fig. 1 and 2. The electron beam is normal to a (110) surface. The angle formed between the isolation oxide wall and the horizontal surface at the base of the wall are shown in the figures. This angle changes only slightly before and after gate oxidation (compare Fig. 1a with 1c and Fig. 2a with 2c). The relationship between wall angle and percent gate oxide thinning obtained from these measurements is shown in Fig. 3. It can be seen that ~25% thinning occurs on samples which have been 100% overetched (samples J, K) whereas samples which received no overetch (samples G, H) show very little or no thinning. Of the five device samples examined, two (C and D) show 20% gate oxide thinning; these samples probably received a severe overetch in BHF. The percentage oxide thinning is not correlated with gate thickness over the range 500-1500Å (compare J with K and G with H).

The gate oxide thinning is apparently due to the geometrical effect of the isolation oxide wall acting as

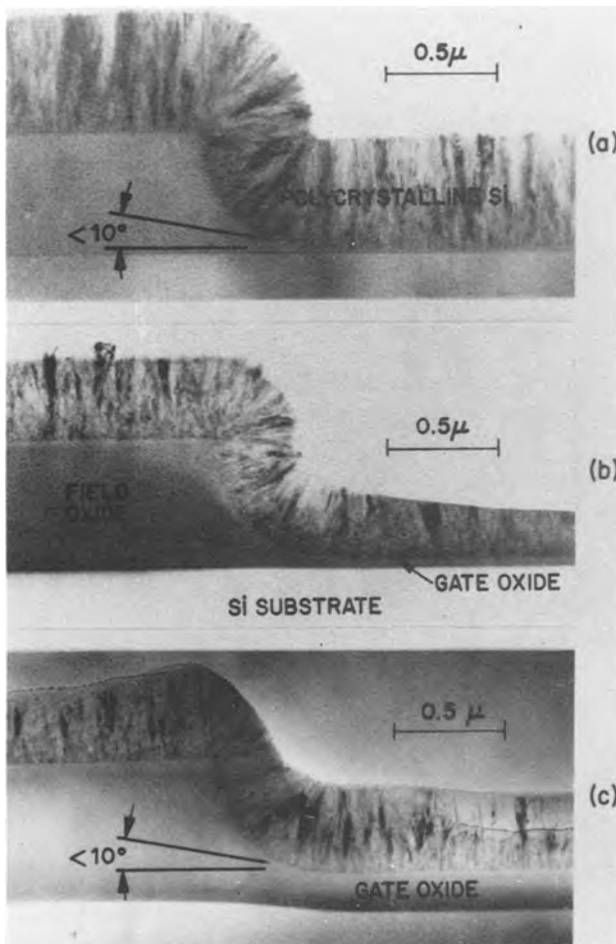

Fig. 1. TEM photos of cross sections of tester samples with 7 min BHF. Sample F, no gate oxide (a); sample G, 500Å SiO_2 (b); sample H, 1500Å SiO_2 (c).

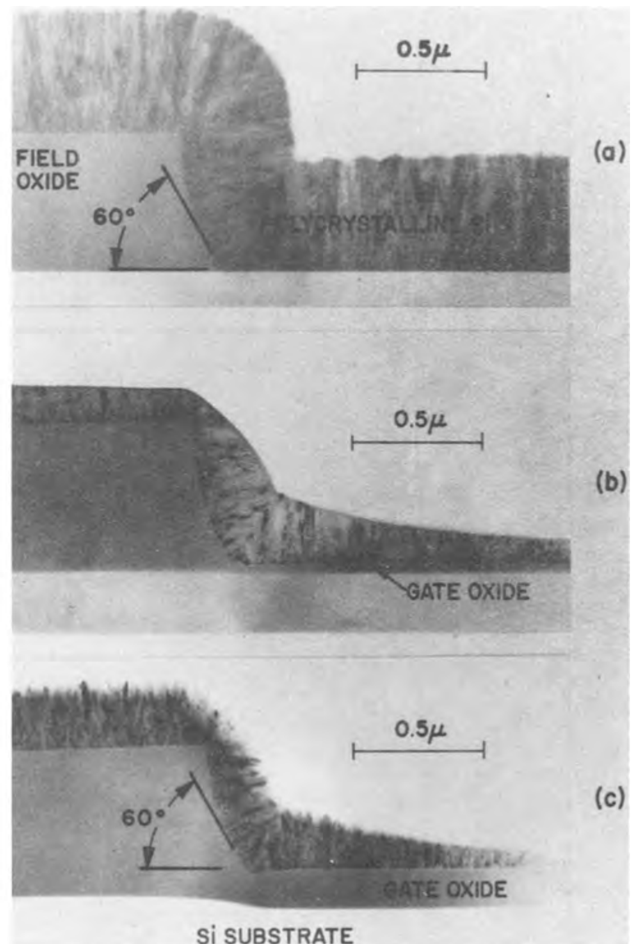

Fig. 2. TEM photos of cross sections of tester samples with 14 min BHF. Sample I, no gate oxide (a), sample J, 500Å SiO_2 (b); sample K, 1500Å SiO_2 (c).

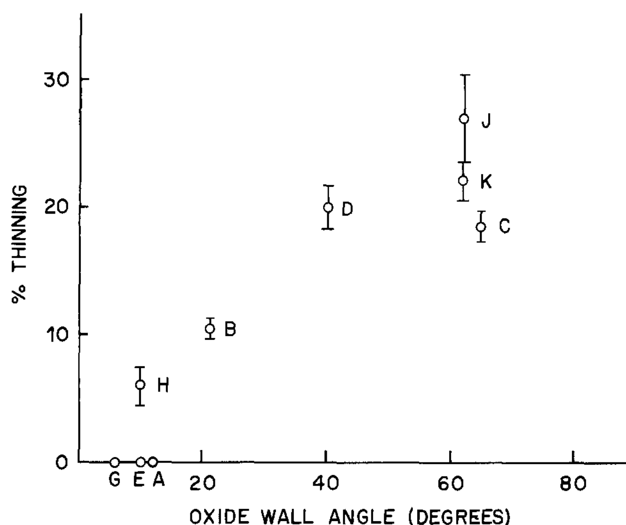

Fig. 3. Relation between angle at base of isolation oxide wall and gate oxide thinning.

a partial barrier which limits the oxidation rate in that local region. This mechanism is now being mathematically modeled. It is clear that as long as oxide thickness and oxide etch rate nonuniformities occur among the wafers in a lot undergoing processing and overetch is required, gate oxide thinning will occur. Assuming a linear relation between time of overetch, isolation oxide wall slope, and gate oxide thinning (Fig. 3), it would appear that $\lesssim$ 10% thinning would occur if the overetch time of thermal oxide in BHF could be kept less than 2 min (~30% overetch). Tighter requirements would occur for faster etching oxides.

Manuscript submitted June 20, 1977; revised manuscript received Aug. 11, 1977.

Any discussion of this paper will appear in a Discussion Section to be published in the December 1978 JOURNAL. All discussions for the December 1978 Discussion Section should be submitted by Aug. 1, 1978.

Publication costs of this article were assisted by Bell Laboratories.

REFERENCES

1. D. P. E. Lidbury, H. R. Pettit, and G. R. Booker, *Electron. Engin.*, **43**, 50 (1971).
2. M. S. Abrahams and C. J. Buiocchi, *J. Appl. Phys.*, **45**, 3315 (1974).
3. T. T. Sheng and C. C. Chang, *IEEE Trans. Electron. Devices*, **ed 23**, 531 (1976).

Thermally Stimulated Depolarization Studies of PVC Polymer Electrets

I. M. Talwar and D. L. Sharma

Department of Physics, Punjab Agricultural University, Ludhiana-141004, India

ABSTRACT

Thermally stimulated depolarization (TSD) of polyvinyl chloride thermoelectrets prepared at polarizing temperatures of 80°, 100°, and 120°C with field strengths 10, 12.5, and 15 kV/cm has been studied. A very sharp peak appears at 97°C. The activation energy associated with the trap at a depth of a 0.44 ± 0.03 eV has been calculated by the initial rise method. The characteristics of the TSD spectra are in agreement with the theory and are explained on the basis of theoretical predictions.

The thermally stimulated depolarization (TSD) of polar dielectrics usually shows several bands or peaks, indicating thereby that the depolarization of thermoelectrets is realized by several different processes. Two of these processes that are well known are the relaxation of aligned impurity-point defect complexes (1) and the relaxation of a space charge caused by mobile defects accumulated at the electrodes (2, 3). But there are still unidentified processes which cause TSD peaks (1, 4), and one of the fundamental aims of TSD studies is to establish a correspondance between the observed peaks and the specific polarization processes.

Polyvinyl chloride (PVC) has been selected as a typical example to study the conduction mechanism in polymers. The electret behavior (5, 6) and isothermal electrical conductivity (7) of this polymer have already been reported. The present communication deals with nonisothermal thermally stimulated conductivity of PVC thermoelectrets.

Theory

TSD studies are generally carried out by heating a polarized sample of thickness d and area of cross section a to measure the depolarization current $I_d(t, T)$. The measured current density $i_d(t, T) = I_d(t, T)/a$ is equal to the sum of the charge transport rate density $e \cdot j(x, t)$ and the displacement current density $dD(x, t)/dt$ at any arbitrary cross section of the sample. The current measurement is generally carried out by a sensitive current-measuring device keeping no bias voltage, *i.e.*

$$V = \int_0^d E(x, t)\, dx = 0 \quad [1]$$

and without any charge transfer to the electrodes, so that

$$j(0, t) = j(d, t) = \text{zero} \quad [2]$$

Consequently, the measured current density is simply the displacement current density due to the redistribution of charges inside the sample

$$i_d(t, T) = \frac{dD(x, t)}{dt} \quad [3]$$

Of various different mechanisms of polarization only the following two are important: the polarization due to an accumulation and/or depletion of mobile defects (8) and the depolarization due to the orientation of dipoles. Both of these processes are heat dependent. The rate of depolarization current i_d for such processes is expected to be proportional to some charac-

Key words: thermally stimulated depolarization, thermoelectret, activation energy, trap depth, initial rise method.

teristic rate constant $K(T) = K_0 \exp(-U/kT)$ with a pertinent activation energy U, and to some driving force $F(t)$ (9), *i.e.*

$$i_d \propto K(T)\ F(t) \quad [4]$$

where temperature T is a function of time t, *i.e.*, $T = \phi(t)$.

These conditions satisfy the requisites of Bucci's dipolar theory. If the instantaneous polarization of the sample is P, the decay rate can be expressed as

$$P = P_0 \exp\left(-\int_0^t \frac{dt}{\tau}\right) \quad [5]$$

where τ is the relaxation time and depends on temperature and hence time. If the initial polarization P_0 is due to electric field E_p and temperature T_p, then for freely rotating dipoles

$$P_0 = \frac{N\,b^2\,E_p}{3\,k\,T_p} \quad [6]$$

where N is the dipole volume density and b the dipole moment of the dielectric. The current density is due to redistribution of charges and dipoles. For dipolar solids, such as PVC, the relaxation of polar side group is given by

$$\tau = \tau_0 \exp(U/kT) \quad [7]$$

where τ_0 is a constant. When the dielectric is heated at a linear rate the depolarization current density is given by

$$i_d(T) = \frac{N\,b^2\,E_p}{3k\,T_pT_0} \mathrm{Exp} \left| -\frac{U}{kT} - \frac{1}{\beta\,\tau_0}\int_{T_0}^{T} \exp(-U/kT)\,dT \right| \quad [8]$$

Discharge current from the release of charge carriers from traps has the similar expressions, except for the preexponential factor.

The temperature (T_m) at which maximum current (i_m) occurs can be obtained by differentiating Eq. [8] with respect to T and putting $d\ i_d/dT = 0$. This gives

$$\tau_0 = k\,T_m^2/\beta U \exp(U/kT_m) \quad [9]$$

where β is the heating rate. According to the initial rise method (10), the low temperature tail of i_d can be written as

$$\ln i_d(t) = \text{const.} - U/kT \quad [10]$$

Experimental

The electret material (polyvinyl chloride) used in the present investigation was in the form of a sheet 0.092 cm thick procured from M/S Bhor Industries, Bombay. In addition to containing PVC resin the material had certain copolymers, stabilizers, plasticizers, lubricants etc., which certainly affect the dielectric properties. The glass-transition temperature T_g of PVC is reported to be 80°C, however T_g is drastically affected by the plasticizers, etc. The material does not melt, however; its softening range was 90°-100°C (5) and it gets roasted above 140°C. After 120°C thermal decomposition of the material may possibly set in, as evidenced by disproportionately large current, so only three temperatures 80°C (T_g), 100°C (softening-range temperature), and 120°C (above softening range) were selected. The specimen used was 1 × 1 cm² and was fitted tightly in a 1 × 1 cm² cavity in a 6 × 4 × 0.9 cm³ mica holder. Copper foil was used for electrodes. Two electrodes 1 × 1 cm² were placed one each above and below the specimen. In order to have an ohmic contact, as far as possible between the dielectric and the electrodes they were sandwiched between two glass slabs. The glass slabs were further held between four iron strips and tightened by four screws. So as to ensure a uniform pressure the screws were tightened to the same number of threads. After each set of observations a look at the specimen revealed that the electrodes had left permanent impressions on its faces. Moreover, there was no visible sputtering (as seen under a microscope × 430) on the surfaces of either the electrodes or the dielectric. This rules out the possibility of air-gap breakdown. One of the protruding terminals of the electrodes was earthed, while the other was connected to a d-c power supply capable of giving 500-1500V. The electret assembly was placed in a thermostat capable of measuring 250°C to an accuracy of ± 1°C. In order to control the temperature precisely, the thermostat was maintained at the required temperature for ½ hr and then the field was switched on. After 3 hr of heating the specimen was brought to room temperature in 1 hr. The controlled rate of heating ensured uniform polarization. The specimen was then kept in a shorted position overnight at room temperature to eliminate the frictional and stray charges. The polarizing field was 10.0, 12.5, and 15.0 kV/cm.

The electret was then heated in the same assembly at the uniform rate of 1°C/min by adjusting the input to the thermostat. The electrometer and thermometer readings were taken after every 5 min. For noting the discharge current an electrometer amplifier Model EA 812 manufactured by M/S Electronics Corporation of India, Hyderabad was used. This can measure current of the order of 10^{-12}A to an accuracy of ± 2%. A new specimen was made for every run.

Results

The curves of discharge current *vs.* temperature were plotted to obtain position of current maximum (i_m). The current was measured from 30° to 140°C. Only one peak which is very sharp at 97°C is observed (Fig. 1). The peak temperature (T_m) does not shift with temperature and field. However, the value of i_m increases with field (Table I). The charge is calculated from the area under the curve using a planimeter and is plotted as a function of field along with i_m (Fig. 2). The activation energy was calculated by plotting i_d *vs.* $1000/T$, employing a least squares fit. These values are shown in Table II along with those obtained from Takamatsu *et al.* (12) and Pillai *et al.* (13) through TSD studies and those of Matsuka *et al.* (14) obtained with dielectric measurement on PVC. The values obtained here are in close agreement with those obtained from the dielectric

Table I. Variation of i_m with E_p at different T_p's

E_p (kV/cm)	i_m ($\times 10^{-11}$A)	T_m (°C)
	T_p = 80°C	
10	12	97
12.5	13.7	97
15	15	97
	T_p = 100°C	
10	8.6	97
12.5	12	97
15	15	97
	T_p = 120°C	
10	14	95, 100
12.5	16	95, 100
15	19	95

Table II

T_p (°C)	E_p (kV/cm)	T_m (°C)	U (eV)
80	10	97	0.41
80	12.5	97	0.44
80	15	97	0.43
100	10	97	0.43
100	12.5	97	0.44
100	15	97	0.47
Takamatsu *et al.*			0.60
Pillai *et al.*			0.23
Matsuoka *et al.*			0.43

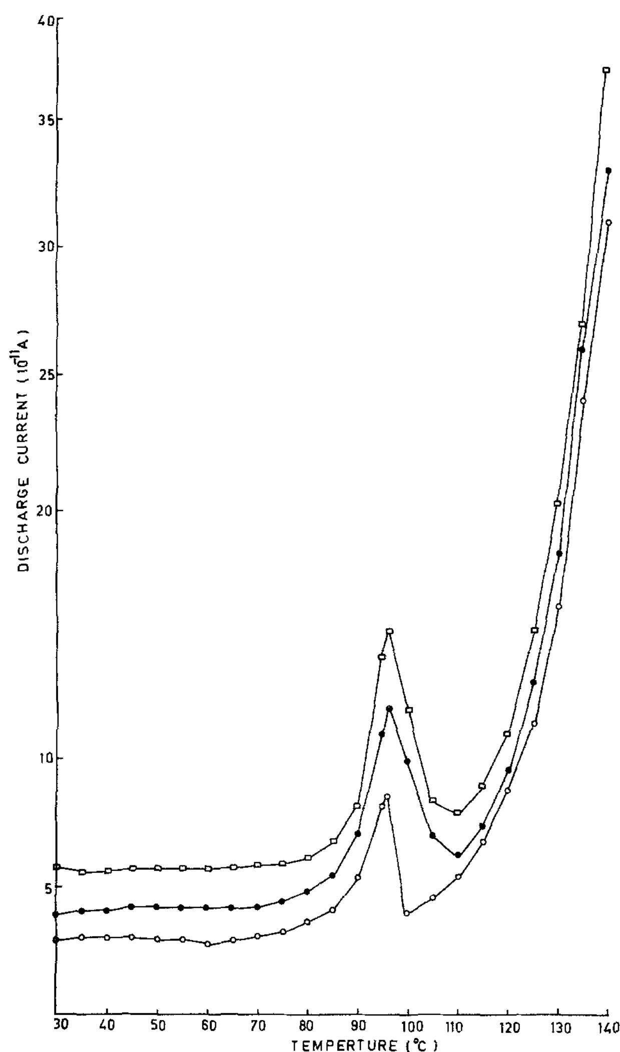

Fig. 1. Discharge current vs. temperature for various polarizing fields E_p ⊙, ●, □ corresponding to E_p 10, 12.5, and 15 kV/cm, respectively. $T_p = 100$°C.

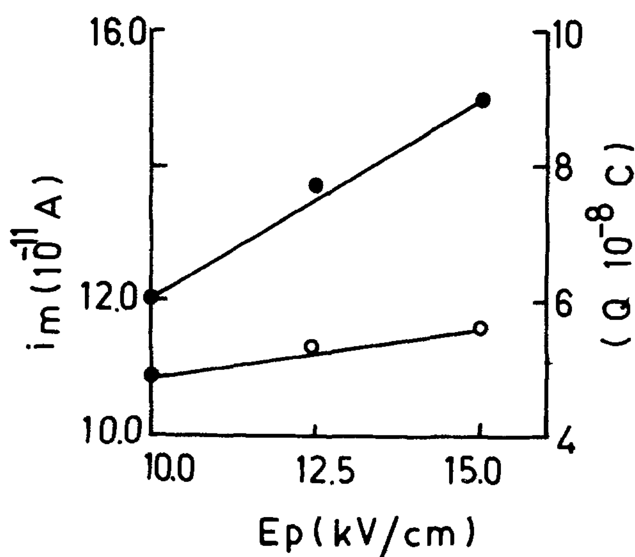

Fig. 2. Peak current (i_m) and total charge (Q) released to the external circuit vs. polarizing field, ● current, ⊙ charge. T_p 80°C.

measurement. However, the values disagree with those obtained from the TSD studies of Takamatsu *et al.* and Pillai *et al.* This may be attributed to different composition of the materials used by different

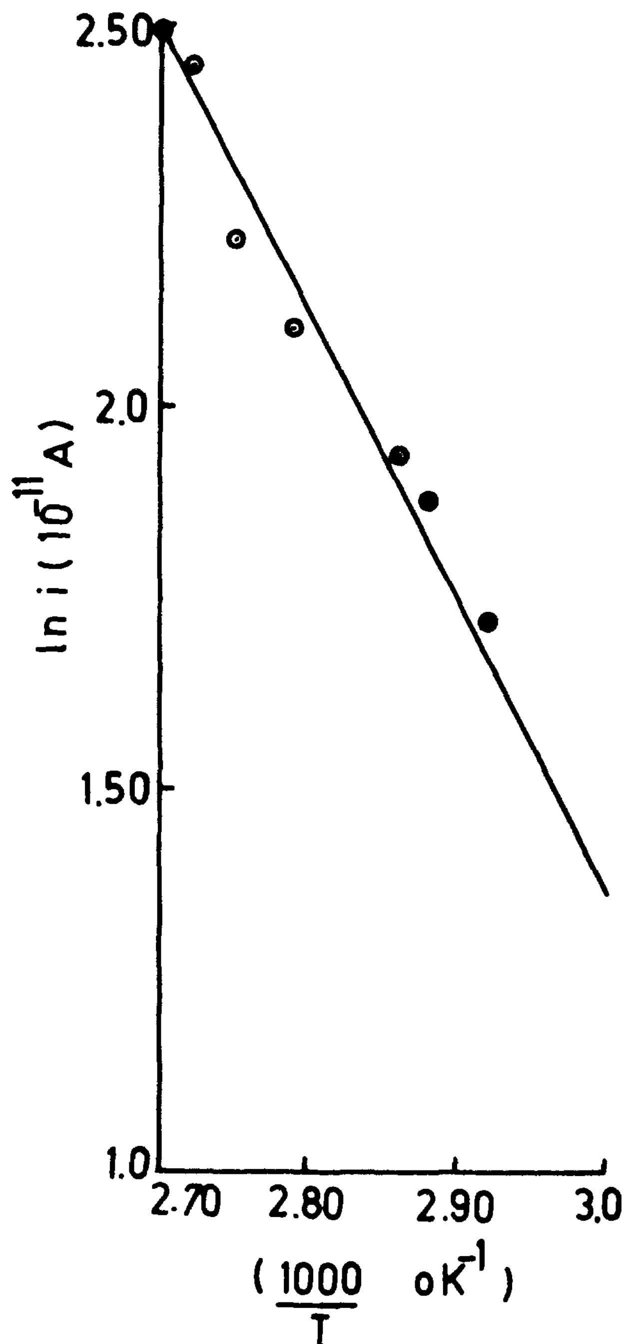

Fig. 3. Calculation of activation energy from initial rise plot of Fig. 1; least squares fit, ⊙ experimental.

workers. Takamatsu *et al.* used films prepared by hot pressing, whereas Pillai *et al.* made use of pure resin. The material used here for the present studies had a complex composition.

Discussion

The sharp peak at 97°C corresponds to primary relaxations, as suggested by Takamatsu (12). As already seen, there is no shift of T_m with E_p and T_p (except a slight shift in the 120°C series). Moreover, the shape of curves is identical as per the prediction of Eq. [8]. A space-charge polarization is ruled out because in such cases T_m is strongly T_p dependent, as shown by several workers for the electrets of ionic crystals (15), ice (16), and certain polymers (17). While the results of TSD current show many of the characteristics expected for dipolar disorientation, this cannot be the major component of heterocharge. This is evident from the following observation:

From Eq. [6], the charge is given by

$$P_o \equiv Q_{cal} = N\,b^2\,E_p/3kT_p$$

for $E_p = 10$ kV/cm and $T_p = 357°K$ the charge calculated by finding the area under the curve comes out to be 4.98×10^{-8}C. Assuming dipole moment to be 1.73*D* (11), the volume density of dipoles is found to be 2.18×10^{23} dipoles/cm^3. Taking approximate molecular weight of PVC as 60,000 (18) and calculated density as 1.41 g/cm^3, we get 1.41×10^{19} molecules/cm^3, which corresponds to 15,600 dipoles/molecule.

The structure of polyvinyl chloride can be represented as

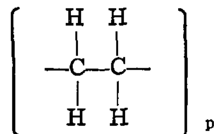

The molecular weight of each monomer of polyvinyl chloride (*i.e.*, vinylchloride) is 62.5, therefore the number of monomers in one polymer of PVC is approximately 1000, thus giving 15.6 ($\approx$16) dipoles per monomer of PVC which is about three times the number of bonds available.

So the depolarization current cannot be explained solely by thermal disorientation of aligned dipoles. As suggested by Perlman (19), ions trapped in the defects or dislocations in crystalline regions present in the amorphous structure of PVC could give rise to heterocharge and the associated current.

However, the thermally stimulated depolarization current may be qualitatively explained by the stepwise superposition of various phenomena responsible for persistent polarization in electrets (20). When heating is started space charges of opposite polarity combine to give rise to depolarization current. Then the current is contributed by the disorientation of dipoles and the release of ionic charges from the defects or dislocations. As the thermal treatment is carried on the charge carriers injected on the dielectric surfaces, the electrodes also disappear and become the source of TSD current.

In order to know the cause of depolarization current, work is going on in our laboratory. To differentiate between the space-charge polarization and uniform polarization due to dipoles, it is one of the future plans to study the TSD current spectra of vacuum-formed films of different thicknesses. Such studies have already been undertaken by Fischer and Rohl (21).

Acknowledgment

The authors gratefully acknowledge the help received from Dr. Vishwamittar, Pool Officer, Department of Physics, Punjab Agricultural University, in the writing of this paper. One of the authors (IMT) thanks UGC, New Delhi, for the award of a grant.

Manuscript submitted July 11, 1977; revised manuscript received Aug. 30, 1977.

Any discussion of this paper will appear in a Discussion Section to be published in the December 1978 JOURNAL. All discussions for the December 1978 Discussion Section should be submitted by Aug. 1, 1978.

REFERENCES

1. C. Bucci and R. Fieschi, *Phys. Rev. Lett.*, **12**, 1 (1964); *Phys. Rev.*, **148**, 816 (1966).
2. I. Kunze and P. Muller, *Phys. Status Solidi A*, **13**, 197 (1972).
3. A. Kessler and J. F. Caffyn, *J. Phys. C*, **5**, 1134 (1972).
4. C. Bucci and S. C. Riva, *J. Phys. Chem. Solids*, **26**, 363 (1965).
5. I. M. Talwar and D. R. Bhawalkar, *Indian J. Pure Appl. Phys.*, **7**, 685 (1969).
6. I. M. Talwar, *ibid.*, **11**, 334 (1973); *Solid State Commun.*, **17**, 1343 (1975).
7. I. M. Talwar and D. R. Bhawalkar, *Indian J. Pure Appl. Phys.*, **7**, 681 (1969); **9**, 436 (1971).
8. A. B. Lidiard, in "Encyclopedia of Physics," Vol. XXII, Springer Verlag, Berlin (1957).
9. A. Kessler, *This Journal*, **123**, 1236 (1976).
10. G. F. J. Garlick and A. F. Gibson, *Proc. Phys. Soc. London*, **60**, 574 (1948).
11. A. Tager, "Physical Chemistry of Polymers," Mir Pub., Moscow (1968).
12. T. Takamatsu, Y. Nakajima, and E. Fukada, "Reports in Progress in Polymer Physics in Japan," Vol. XVIII, p. 371 (1975).
13. P. K. C. Pillai, K. Jain, and V. K. Jain, *Indian J. Pure Appl. Phys.*, **11**, 597 (1973).
14. S. Matsuoka *et al.*, "Dielectric Properties of Polymers," F. E. Karasz, Editor, Plenum Press, New York (1972).
15. A. Gubkin and W. Sovokin, *Trans. Bull. Acad. Sci. USSR*, **24**, 246 (1960).
16. S. Mascarenhas, in "Physics of Ice," R. Bullemer and E. Haidt, Editors, p. 483, Plenum Press, New York (1969).
17. G. Sessler and J. West, *Appl. Phys. Lett.*, **17**, 507 (1970).
18. G. Mathews, "Vinyl and Allied Polymers Vol. 2, Vinyl Chloride Vinyl Acetate Polymers," Iliffe Books, London (1971).
19. M. M. Perlman, *J. Appl. Phys.*, **42**, 2645 (1971).
20. T. Takamatsu and E. Fukada, in "Electrets, Charge Storage and Transport in Dielectrics," M. M. Perlman, Editor, p. 134, The Electrochemical Society Softbound Symposium Series, Princeton, N.J. (1973).
21. P. Fischer and P. Rohl, *J. Polym. Sci., Polym. Phys. Ed.*, **14**, 531 (1976).

Structure and Stability of Anodic Films Formed on Aluminum Containing Dispersed Al_3Fe Phase

J. Zahavi

Israel Institute of Metals, Technion, Haifa, Israel

A. Zangvil

Ben-Gurion University, Beersheva, Israel

and M. Metzger*

University of Illinois at Urbana-Champaign, Urbana, Illinois 61801

ABSTRACT

Al-Fe alloys containing Al_3Fe particles of micron size were anodized at 5 mA/cm² in 2.4M H_2SO_4 and film growth was studied by electron microscopy. It was deduced that the particles were removed by pitting of the matrix progressing preferentially around their margins followed by reanodization of the pit to form a loose pocket of film around the particle. The particle may fall out or be retained depending on the geometry.

The structure and mechanisms of formation of films on alloys containing a finely dispersed phase have not received much attention. This question is particularly pertinent to the behavior of commercial aluminum alloys which are able to form stable films and which exhibit passive behavior despite the presence of numerous microconstituents and (usually) precipitates or zones providing strengthening. Some attention to this question has been given at a relatively macroscopic level for anodizing. However, questions of local film character and its relation to heterogeneities in the substrate and to breakdown processes will require high magnification microscopy and related tools. The authors have employed electron microscopy to study film stability and breakdown models during anodic film growth on single phase 99.999% Al in sulfuric acid (1). In the present work, this approach is applied to alloys containing dispersed Al_3Fe phase. This constituent was of interest for a first study in part because there is some disagreement in previous work as to whether it dissolves, anodizes, or passes into the film unchanged. An attractive feature of the Al-Fe system is that there is limited solid solubility so that the extensive results on high purity aluminum (1) should be applicable to the behavior of the matrix in the alloy.

Previous work on the behavior of Al_3Fe in sulfuric acid involved large, sometimes massive (20 μm), particles and thick films ($\gtrsim$20 μm) in which sections through particle and film were prepared for optical, SEM, or electron-microprobe examination. Keller *et al.* (2) reported that this constituent tended to dissolve but sometimes appeared in the coating, which they explained as the result of an effective cessation of the dissolution when the growing film happened to electrically isolate the particle from the substrate. Wood and Brock (3) found that Al_3Fe particles were incorporated into the oxide without apparently being oxidized or dissolved. Cote *et al.* (4) found that Al_3Fe "oxidized" (*i.e.*, anodized) at about the same rate as the aluminum matrix. They explained Wood and Brock's result (for which the anodizing conditions were not very different) on the electrical isolation model. This was not a strong explanation since the former's sample contained an 8 μm particle which would, on Cote *et al.*'s model, have had substantial time to anodize before becoming isolated.

For the present work, observation of localized processes was sought and the requirement was for small particles and thin films growing up to the depth to which the particles were embedded so that processes in particle and matrix would be visible simultaneously side by side. Procedures were directed toward particle sizes near 1 μm and films of no more than a few microns. Anodizing conditions were the same as in the authors' previous electron-microscopic studies, and this meant that current densities and cell voltages were substantially lower than those employed in the previous studies of Al_3Fe.

Experimental

Alloy preparation.—Binary 0.4 and 1.0% Fe alloys were prepared by melting 99.999% Al and 99.99% Fe in a high purity graphite mold degassed at $\leq 10^{-5}$ Torr and sealed in a Vycor capsule. This was quenched in water to speed solidification. The 2.5 cm diam ingots were swaged to 1.2 cm, recrystallized at 500°C, and cold rolled with one intermediate anneal to 1.0 mm sheet. This procedure was devised to yield Al_3Fe particles of suitable size near 1 μm. Blanks were cut with a working area 20 × 5 mm and a narrow tab and these were annealed in air at 645°C for 6 hr and cooled in an air stream. The final high temperature anneal was given to dissolve any tiny precipitates and promote a more homogeneous matrix (solid solution of 0.05% Fe). A check by optical emission spectroscopy of the impurities in the Fe alloys showed only small increases from the original 99.999% Al, which was from the lot used in authors' previous studies (1), Table I.

Surface preparation.—An initial surface was required which was smooth and undeformed and in which the Al_3Fe intermetallic particles were retained. Three electrochemical treatments were found to yield acceptable particle retention (in each case the oxide film formed during annealing was first etched off with 10% HF): (*i*) electropolishing in 20 volume percent (v/o) 70% $HClO_4$ in ethanol at 0.1 A/cm² for 10 min at −10° to −15°C and rinsing with a jet of ethanol (treatment A of Ref. 1); (*ii*) electropolishing in 33 v/o

Table I

Alloy	Impurities detected, ppm wt				
	Cu	Si	Mg	Mn	Ca
0.4% Fe	2	3	2	1	1
1.0% Fe	2	3	2	1	1
Al, Lot III-A*	1.0	1.5	0.6	0.1	0.2

* By mass spectrograph.

* Electrochemical Society Active Member.

Key words: anodizing, film growth, pitting, Al, Al_3Fe.

70% HNO_3 in methanol at 0.15 A/cm^2 at −30°C for 20 min and rinsing in a jet of methanol (treatment F); (*iii*) chemical polishing in a solution containing 150 ml of 96% H_2SO_4, 800 ml of 85% H_3PO_4, and 50 ml of 70% HNO_3 at 85°-90°C for 6 min and rinsing in water (treatment D of Ref. 1).

Anodizing.—As in the authors' previous studies (1), films were formed at 5 mA/cm^2 in 2.4M H_2SO_4 at 25.0 ± 0.2°C with a ~50 cm^2 Pt cathode. Anodizing times of 25-2700 sec were used with more attention to 84-300 sec when the film was still thin enough to be examined in transmission.

Microscopy.—The synthesis of information from a variety of techniques including scanning, transmission, and replica microscopy was found essential for investigating the film and particle geometries. Carbon replicas preshadowed at ~35° with platinum were employed. In these two-phase alloys a serious particle retention problem also arose in the question to what degree the particles present after anodizing were attacked and altered during the chemical treatments employed to detach the film for either observation in transmission or preparation of a film-underside replica. For film detachment from the substrate, both 0.3% $HgCl_2$ solution and 10% iodine in methanol at ~50°C (5) were employed with results as discussed later.

The shapes and sizes of particles were examined by SEM of as-polished specimens and also by TEM after preparing thin foils of the alloy by conventional jet thinning and electropolishing in sulfuric acid-ethanol and perchloric acid-ethanol solutions. The particles were retained, mostly protruding from the foil and opaque to the electron beam with a sharp silhouette. The particles in the 1% Fe alloy were found to be mainly well distributed euhedral crystals of lath or rod shape with minimum lateral dimensions typically 1-1½ μm and lengths up to ~5 μm and with edges and corners faceted. The particles in the 0.4% Fe alloy were less geometric and more equiaxed with typical dimensions from ~½ to 1½ μm, and they lay preferentially in bands. Diffraction patterns were consistent with the crystallography of Al_3Fe (6); the analysis is described below for particles in detached anodic films.

Results and Discussion

The cell voltage measured with respect to the platinum cathode showed at 5 mA/cm^2 substantially the same variation with time for the two-phase 1% Fe alloy as for single phase 99.999% Al. This is shown for chemically polished specimens (treatment D) in Fig. 1. It was also true for electropolished specimens (treatment A or F) and for chemically polished Al-0.4% Fe.

SEM observations.—Scanning electron microscopy was used for a preliminary survey of the behavior of the Al_3Fe particles during anodizing. Figure 2 shows the backcattered electron image of the surface as chemically polished. The particles appear as light patches (due to greater electron scattering than the matrix). The particles protruded various distances above the matrix surface as indicated by the variation of the "shadow" in the adjacent matrix where the particle shielded backscattered electrons from the collector. The dark patches were cavities at the locations of particles removed during chemical polishing. Figure 2 shows that a minor but significant fraction of the particles at the surface were removed during surface preparation, presumably those less deeply embedded. For electropolishing treatment F, this fraction was about the same as shown in Fig. 2; for the perchloric acid-ethanol electropolish (A), the fraction removed tended to be somewhat larger. The nature of the phenomena occurring during surface preparation or subsequent anodizing appeared to be the same for all treatments.

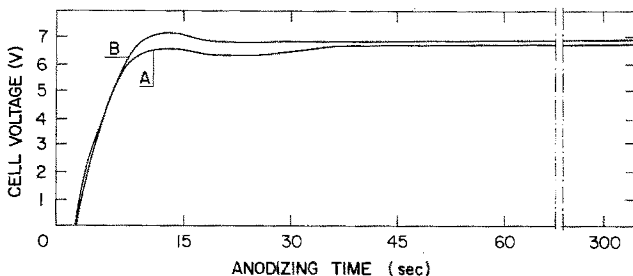

Fig. 1. Cell voltage vs. time for anodizing chemically polished specimens in 2.4M H_2SO_4 at 5 mA/cm^2. A. Al-1% Fe alloy; B. 99.999% Al.

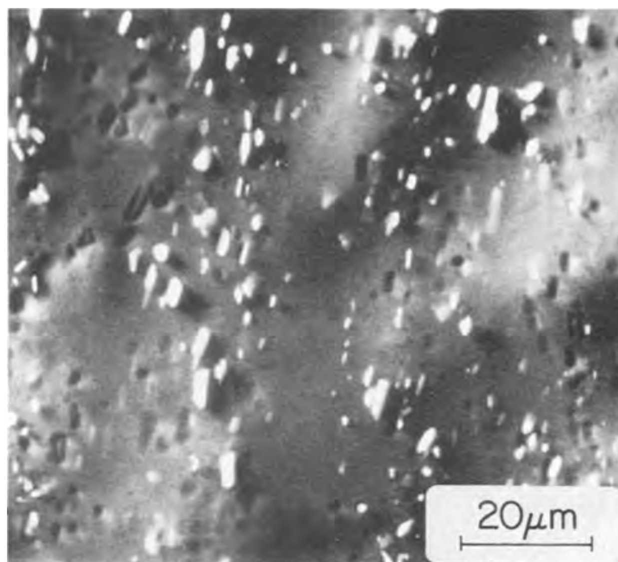

Fig. 2. Scanning electron micrograph showing Al_3Fe particles and cavities in chemically polished Al-1% Fe specimen. Backscattered electron image.

In the course of anodizing, the particles at the surface were gradually removed leaving cavities in the surface, as illustrated in Fig. 3. It was noted that the particles did not continuously shrink in size, which would point to a dissolution process, but appeared to remain at their original size and to be substantially unaffected so long as they were present. A process consistent with this observation would be undermining of the particles by some type of localized or crevice corrosion at their margins. Examination of the surface at higher magnification did reveal that some particles were partially bordered by dark strips that were not shadowing effects, but the resolution of SEM was far below that required for closer study.

TEM observations.—Films examined by transmission electron microscopy after having been detached from the substrate in aqueous $HgCl_2$ or I_2-CH_3OH solutions usually showed structures as in Fig. 4a, b, and c. Some rounded fully anodized cavities, such as in Fig. 4a, are thought to have been cavities present before anodizing from a particle removed during the polishing treatment. More typical was a dark band surrounding a strip of thin film with a gap in the center, occasionally with an almost complete thin film window, Fig. 4b and 4c. These are thought to have represented the sites of particles still attached during anodizing. Since it appeared that an anodic film was forming around the particle, one would expect that some of the many particles visible in SEM would be held by this film and would be seen in the detached film, as in an extraction replica. This was rarely the case. Evidence indicated that either of the solutions used to dissolve the Al substrate and so detach the film also attacked the Al_3Fe phase although at a lower rate.

The residual intermetallic particles in the film were examined, as follows. Figure 5 shows a scanning transmission electron micrograph of a field in which two cavities are visible. In one cavity, the particle had evidently been removed earlier during anodizing since

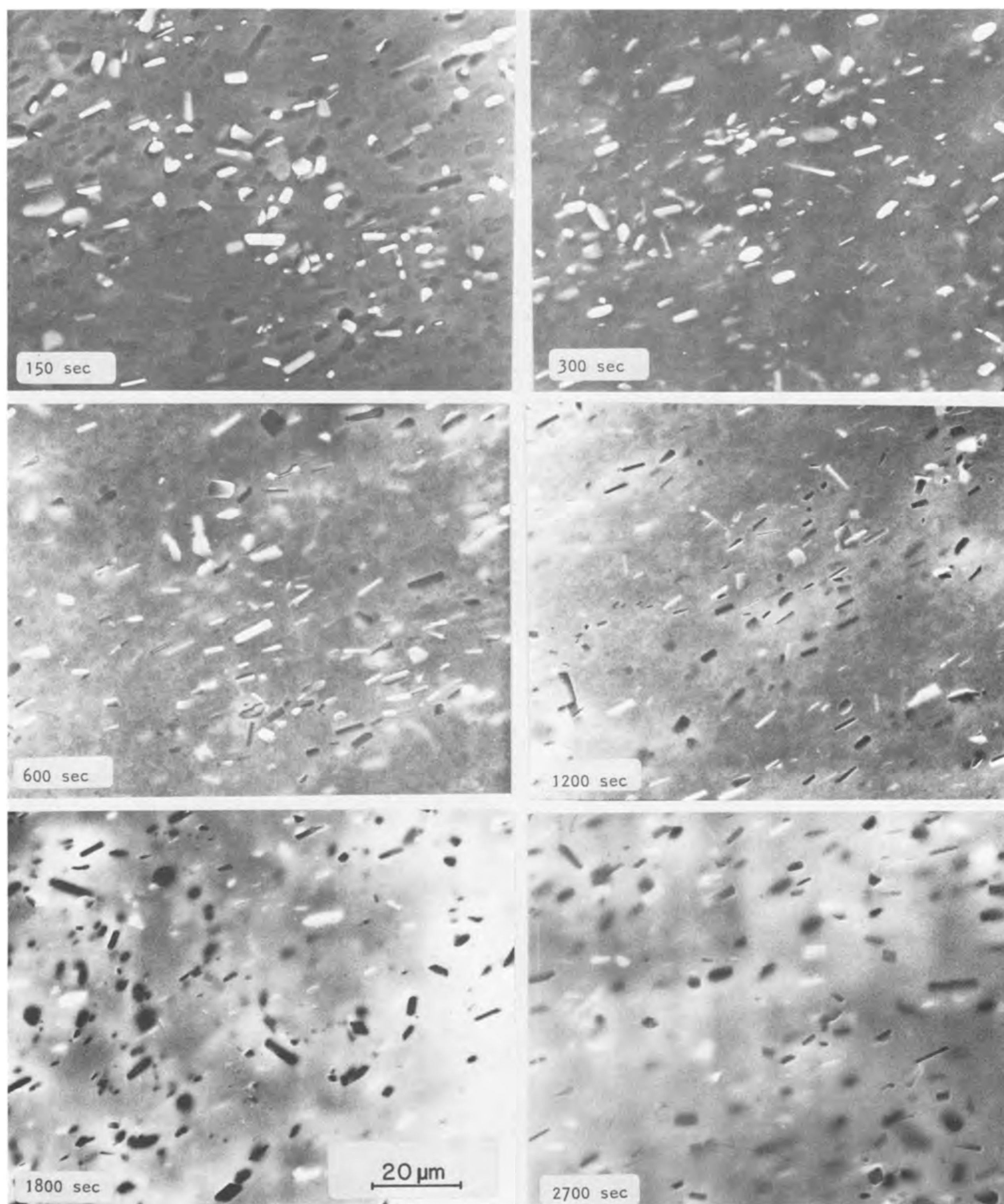

Fig. 3. Progressive removal of Al_3Fe particles during anodizing of chemically polished specimens of Al-1% Fe. Secondary electron images.

the cavity shows the pattern of small dark patches seen throughout this field. This pattern was the result of the micropitting phenomenon which is prominent in single phase aluminum at about this time of anodizing (1) (this pattern was present in the two-phase alloys of the present work but was normally much less prominent). The second cavity contained what was thought to be an incompletely dissolved particle and selected area diffraction did yield a few spots indicating the presence of material other than the amorphous film. Similar results were obtained for the dark cavity (P) in the center of Fig. 4b. Figure 6 shows a case in which an incompletely dissolved particle gave a substantial transmission diffraction pattern when the film was appropriately tilted, Fig. 6b. With a tilt-rotation stage, patterns from this particle in the 1% Fe alloy and one in the 0.4% Fe alloy were analyzed. These were found to be consistent with the monoclinic structure of Al_3Fe as given by Black (6) with $a = 1.5489$ nm, $b = 0.8083$ nm, $c = 1.2476$ nm, and $\beta = 107.14°$. A set of diffraction patterns was recorded while tilting around an axis found to be the normal to $(11\bar{1})$. Each pattern could be analyzed and

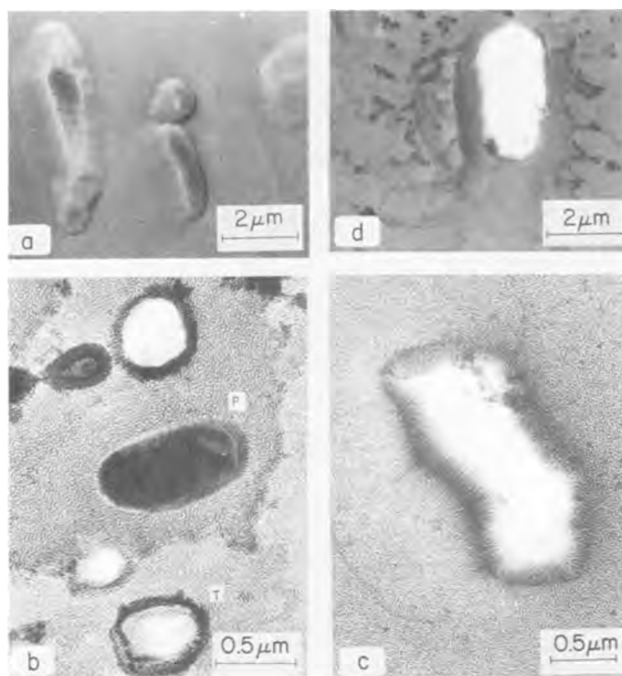

Fig. 4. Transmission electron micrographs showing various details associated with the formation of anodized cavities where particles had been present. b, c, and d show "cavities" in the process of formation where the particle was still partly attached to the substrate at the termination of anodizing. Specimens were chemically polished Al-1% Fe and films were detached in $HgCl_2$ except as noted. a. Rounded fully anodized cavities. Electropolish A and 84 sec anodizing; b. Variation in detail at different "cavities" in 0.4% Fe alloy anodized 84 sec; "T", typical or most common type; "P", part of the original particle present; c. Typical "cavity." Film detached in iodine-methanol solution after 150 sec anodizing; d. Extended region of micropitting-repair associated with "cavity" in specimen anodized 150 sec.

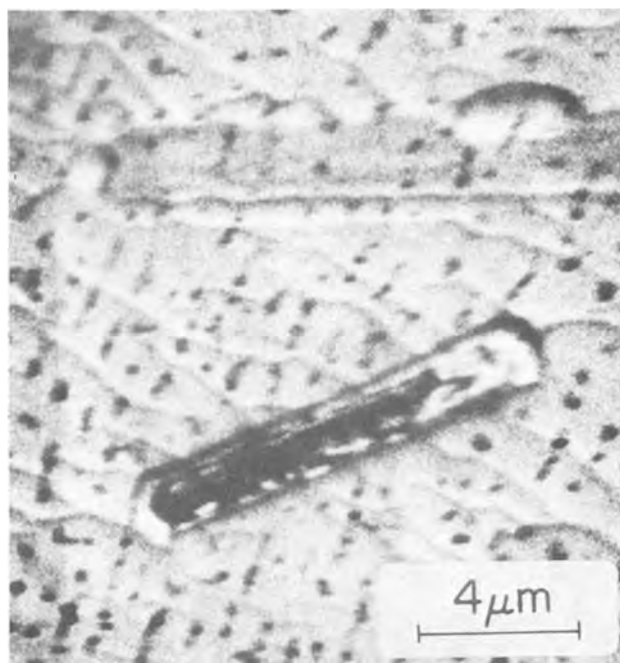

Fig. 5. Part of particle retained in one cavity in Al-1% Fe electropolished (A) and anodized 84 sec. Scanning transmission electron micrograph of film detached in $HgCl_2$.

its zone normal found. The angles between the different zone normals were calculated and found to be in close agreement with the actual increments of tilt. These checks seemed sufficient to conclude that these particles were Al_3Fe phase and neither artifacts introduced in film preparation nor the metastable orthorhombic Al_6Fe phase which can form in the Al-Fe system (7). The sides of the particle in Fig. 6a appear to be parallel to the (001) plane. The wavy top and bottom edges of

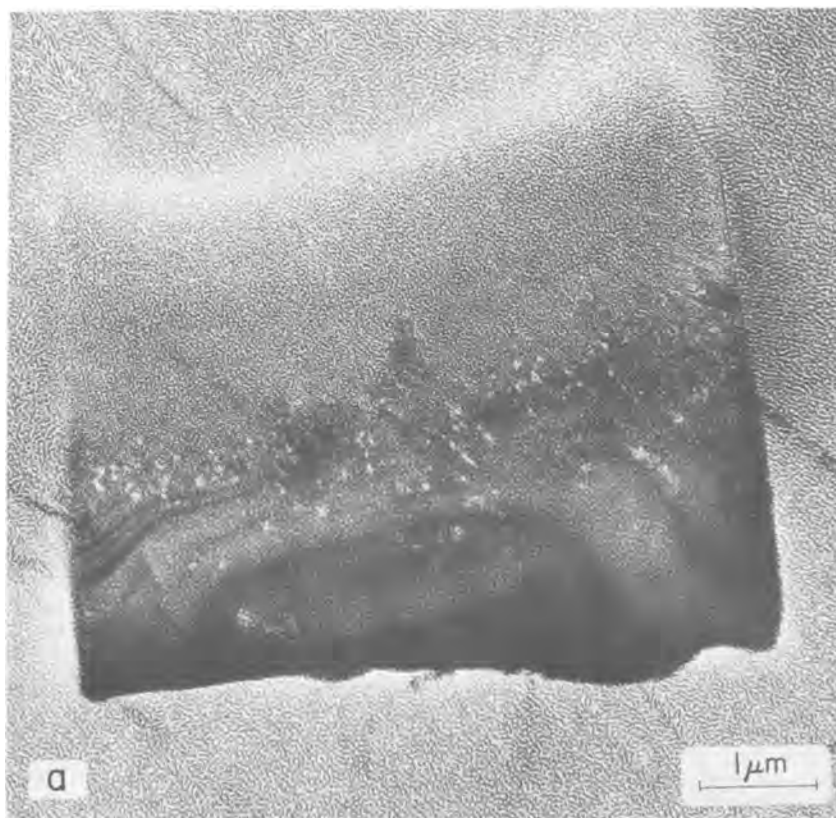

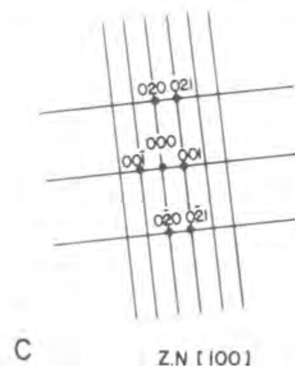

Fig. 6. Examination of part of particle retained in 84 sec film on electropolished (F) Al-1% Fe detached in $HgCl_2$. a. Transmission electron micrograph; b. Diffraction pattern; c. Partial indexing of diffraction pattern.

the particle silhouette and the thickness fringes are interpreted as the result of atack by the $HgCl_2$ solution used to detach the film. The conclusion that this attack occurred during film detachment and not during anodizing was not drawn from this photograph but from the SEM observations plus the surface replica observations discussed below.

A film was presumed present on the particle during anodizing. It was thought that this film would, like the anodic film on the aluminum matrix, resist dissolution during the detachment process. This film could not be identified in the transmission micrographs, perhaps because it was not thick enough or strong enough to survive.

A typical "cavity" in transmission, *e.g.*, Fig. 4c or *T* in Fig. 4b, had a dark rim, a patch of thin film window, and a gap in the center. The origin of the contrast was deduced with the aid of the replica observations discussed below.

Replica observations.—It is to be noted that replicas of the film underside are made after detaching the film, and since the particle is generally removed during this process the replica will show a gap over the region where the particle was still attached to the substrate after anodizing. On the other hand, surface replicas are made without further treatment of the specimen and a particle present at the surface after anodizing will be replicated. Some surface-replica micrographs are given in Fig. 7. Figure 7a shows for the 0.4% Fe alloy particles at the surface which appear substantially complete, *i.e.*, no evidence of substantial dissolution in 10 min of anodizing. Figure 7b shows for the 1% Fe alloy a particle peeking out from under a flap of anodic film, and this also appears substantially unattacked after 30 min of anodizing. These observations support the interpretation given above of the transmission micrographs, *i.e.*, there were many regions where substantially complete particles had been present after anodizing but had been completely removed or partly dissolved in the process of film detachment.

The interpretation of thin film windows in the transmission micrographs was that a shell of anodic film was growing around the particles. If so, the film-underside replicas should show the steeply inclined sides of this shell with a more or less flat bottom if the shell were complete. If the shell were incomplete at the termination of anodizing, there would be a hole in the replica where the particle had been dissolved out in the

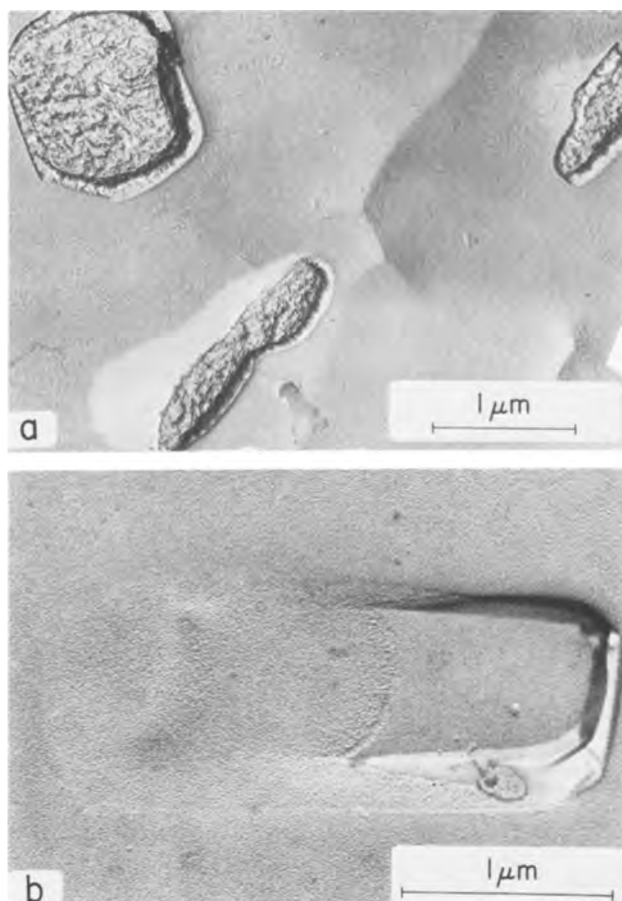

Fig. 7. Surface replicas of specimens anodized after chemical polishing. a. Ditching around particles in 10 min specimen of Al-0.4% Fe; b. Particle lying at a small angle to the surface perhaps detached but retained by overlying film. Al-1% Fe, 30 min.

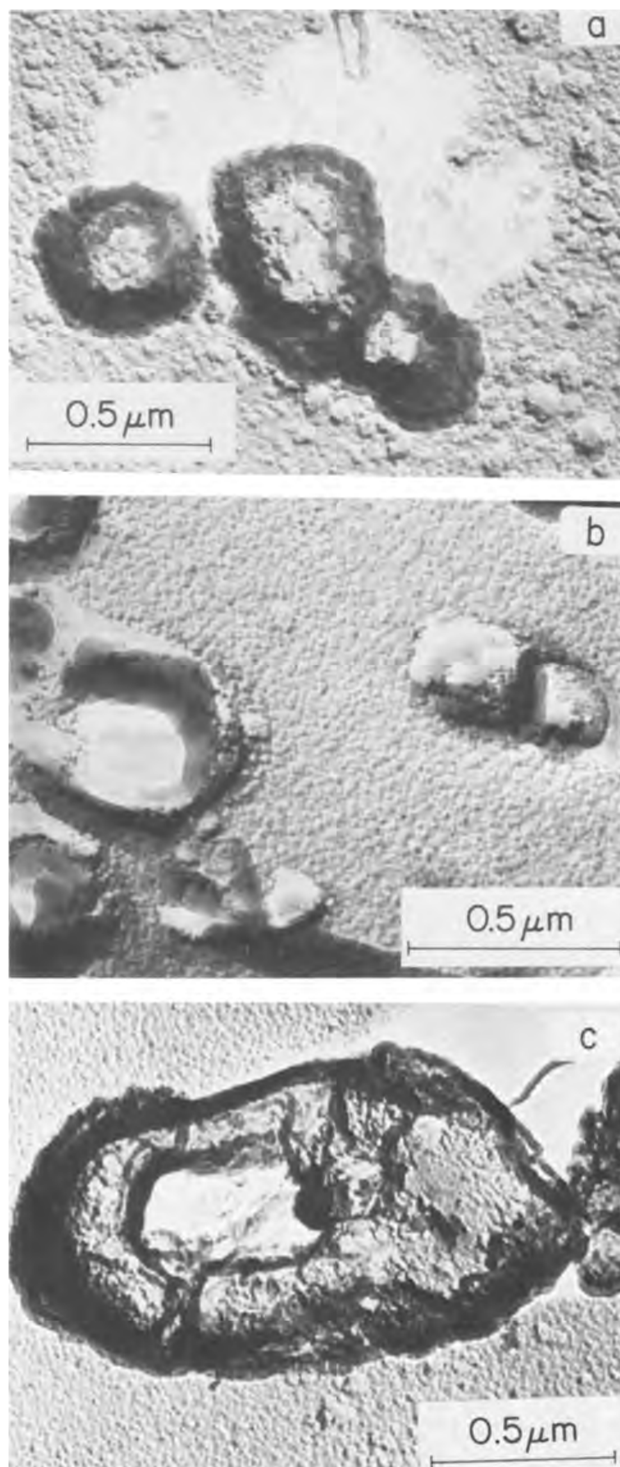

Fig. 8. Film underside replicas of "cavities" in Al-0.4% Fe anodized 300 or 600 sec. a. No gap in replica, cavity fully anodized; b. and c. Gaps in replicas—particles had still been attached to substrate at their bases before preparation of replica.

film-detachment operation. The underside replicas of the 0.4% Fe alloy in Fig. 8 show the sides of the shell of film as a dark ring, sometimes with a considerable shadow. The cell-base pattern of the classical pore structure visible in the background of these micrographs is visible on the flat bottoms of the shells in Fig. 8a, *i.e.*, these were complete. In Fig. 8b and c, gaps in the center of the shells indicate that the bottoms of the particles were still partly attached to the substrate at the termination of anodizing. From these and many other fields of observation, the topography of the film and the nature of contrast in the replicas was deduced to be that presented schematically in Fig. 9 for a partially detached particle. In the center is shown the anodic film containing a particle around which a shell of anodic film is forming progressively during anodizing. It is suggested that this occurs by pitting of the matrix following the particle margins with reanodization of the pit surface behind the pit front; this is discussed further below and the main concern at this point is the contrast in the micrographs. When the film underside replica, shown below in Fig. 9, is prepared, the particle is not present as noted above. The steeply inclined part of the replica around the particle appears thick to the electron beam even without help from shadowing by Pt and so gives a full dark ring as in Fig. 8a, b, and c. Where the film extends over the bottom surface of the particle, the replica is sloping only gently and the density in the micrograph will be comparable to that of the background.

It is to be noted that the scheme of film topography in Fig. 9 is consistent with the typical contrast in the transmission micrographs, *e.g.*, Fig. 4c or *T* in Fig. 4b. There will be a gap where the particle had been removed during film detachment, a thin film window will be visible at the leading edge of the shell of film when the particle axis lies at an angle to the film normal, and this will be surrounded by a dark ring from the steeply sloping part of the shell of film around the particle.

The scheme presented in Fig. 9 of a pitting which tended to follow particle margins is not intended to be specific or unique as regards pit geometry, which varied in detail as well as could be ascertained. As to the size of the gap between the particle and the shell of anodic film, direct observation could be made only at the external surface, as, for example, in Fig. 7a and b. Some use could be made of the observation that many anodized cavities where the particle had been removed during anodizing were quite uniform with widths approximately the same as the typical particle width. This indicated that in these cases the gap had been only a fraction of the particle width. However, the geometry of the transient pitting and thus the extent and shape of the shell of repair film was frequently larger or less regular than represented in Fig. 9. Evidence of this was, for example, the broad shell of repair film in the underside replica of Fig. 8c (*cf.* Fig. 8a and b) or in the transmission micrograph of Fig. 4d, where instead of the relatively uniform dark ring of the typical cavity there was an irregular spreading dark patch. One also notes the large darkish patch in Fig. 4b, which included a number of cavities clustered near one another. None of these observations contradicted the conclusion that there was a strong tendency for the pitting to follow particle margins.

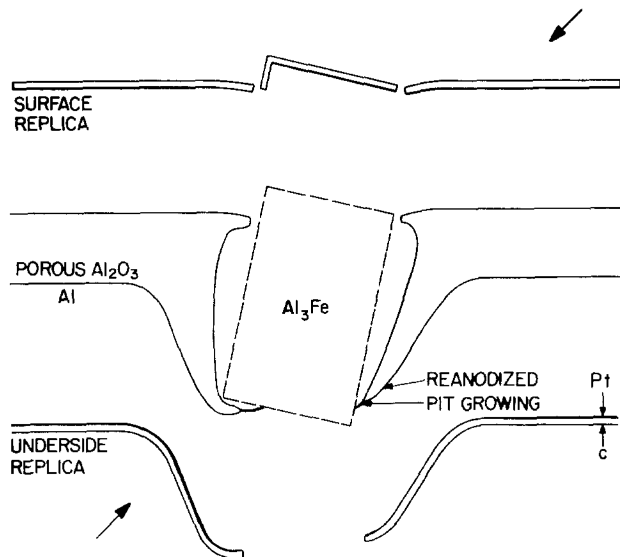

Fig. 9. Schematic of film configuration produced by excavation process illustrating the origin of the contrast. The preshadowed surface and underside carbon replicas are shown. The particle was absent during examination of film in transmission or during preparation of the underside replica.

According to the analysis presented above, the Al_3Fe particles were excavated and undermined by preferential pitting of the adjacent matrix. The continuation of the process represented in Fig. 9 would lead to a configuration in which the particle is only loosely held in a pocket of anodic film and can fall out during anodizing or be removed during subsequent rinsing. Note that the surface geometry might be such that the final configuration would include a flap of film preventing the undermined particle from falling out of its pocket. The particle in Fig. 7b may be such a case. Presumably many of the particles remaining in the film after long anodizing times (Fig. 3) were retained in this manner. A particle initially buried and exposed in the course of anodizing would of course be trapped in the film.

Further Discussion

Electrochemical considerations.—The electrochemical processes implied by the present results and conclusions are examined briefly below for plausibility and consistency.

The conclusion that the Al_3Fe particles did not suffer substantial corrosion during anodizing required that this phase be passive under the conditions employed. An independent examination of the behavior of this phase is in order and has been initiated.

The result that the voltage-time curves for the two-phase alloys were substantially the same as that for single phase aluminum required that those anodic currents associated with the presence of the particles were small. In principle, these currents included (*i*) the ion current of film growth or dissolution of the Al_3Fe particles; (*ii*) the electron current going to the production of oxygen at the surface of the film over the particles; and (*iii*) the local pitting current on the matrix at the particle margins. The first of these was small, as concluded above. A rough check for the presence of a significant oxygen evolution current was made by observing the bubble evolution on the specimen with a $40\times$ microscope during anodizing of the 1% Fe alloy. Very little bubble evolution was noted. The absence of a substantial oxygen evolution current in this alloy at potentials far above the oxygen reversible potential implies that the film over the Al_3Fe phase was a poor electronic conductor, as is the film over the aluminum matrix. The magnitude of the third current, the local pitting current, was viewed as follows. The excavation of the particles by local pitting took place over a time interval of many minutes so that on a time-average basis this particular pitting current need not have been large. A rough estimate for the 1% Fe alloy is as follows. If, say, at most 10 μm^3 of matrix had to be dissolved to excavate a particle and if this took on average only 10 min, then the $\sim 10^6$ particles exposed over 1 cm^2 of the alloy surface needed to draw local pitting currents totaling at most ½ mA/cm^2 to effect the excavation. This current was thus at most 1/10 of the applied current, *i.e.*, it was significant but perhaps not large enough to produce a substantial decrease in cell voltage. The argument given in this paragraph shows that it was not implausible that the

presence of the particles had little effect on cell voltage.

Nature of the local pitting.—The microscopic observations did not give a clear indication of the nature of the pitting around the particle. If the growth of the pit around the margin of the particle is continuous and slow, this cannot be active-mode pitting at low potential with no film. The process might then be a type of high potential pitting perhaps similar to the one suggested earlier by the authors in which dissolution occurs through a soluble film (referred to in a general way as an electropolishing-type film) (1). The presence of some film over the dissolving surface is suggested in Fig. 9. An alternative possibility is that the pit growth is intermittent and the relatively slow time-average growth of the pit around the particle is the result of short periods of rapid partly active pitting interrupted by repair. Such a scheme has the attractive feature that it is analogous to the micropitting phenomenon, *i.e.*, repeated breakdown-pitting-repair events, known to occur over the surface of the matrix. A possible scheme for particle excavation by such a process is given schematically in Fig. 10. After a short initial period of film growth, breakdown occurs at the margin of the particle and a very short period of active-mode pitting gives the geometrical situation shown in Fig. 10b. The active-mode pitting is presumed unstable so the pit surface becomes reanodized. A subsequent breakdown and short period of pit growth, Fig. 10c, starts a repetition of the cycle. This process would produce the geometrical features required to explain the micrographs. It is to be noted that the particle is not necessarily inert as was represented for simplicity in Fig. 10.

Figure 10 represents a geometrical interpretation of particle excavation employing the previous interpretation of the micropitting phenomenon as the point of departure. The special feature introduced here is the assumption of preferential film breakdown or pit initiation at the particle margin. No specific explanation for this is proposed. Local stresses in the anodic film, also transient breakdown or slow dissolution of the particle are conceivable contributing factors. Although it was deduced that the particle was passive at the high potential of its external surface, a different behavior at points within a cavity where the potential was temporarily lower was not precluded. Studies which have been initiated of the behavior of isolated Al_3Fe phase may provide guidance in these matters.

Relation to other work.—Previous work on Al_3Fe involved larger particles and higher cell voltages than used here, and little information was available to indicate how these differences should be taken into account. It was noted that in the 0.4% Fe alloy, which had slightly smaller particles than the 1% Fe alloy, particle removal during anodizing progressed somewhat faster, consistent with the model. Among a few observations made after anodizing at 10 mA/cm^2 (plateau voltage 10-11V, about the same as for 99.999% Al), a check was made on the conclusion that the Al_3Fe did not dissolve. The solution was analyzed for dissolved Fe after anodizing 1 hr. The charge passed here was sufficient to oxidize to the +3 state a layer of alloy contributing 0.67 ppm Fe to the solution if the Al_3Fe dissolved, but there was no increase in dissolved iron within the accuracy of measurement, 0.1 ppm.

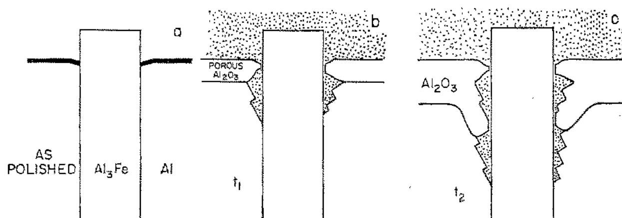

Fig. 10. Schematic of particle excavation by an intermittent local breakdown-pitting-repair process analogous to the micropitting phenomenon.

The larger particles used by previous workers would have required longer anodizing for excavation and they would have been less likely to fall out especially if the gap between particle and pocket of film was narrow as in the present work. Thus, according to the present model, these workers would have tended to observe the particles retained in the film, as noted by Wood and Brock (3). With the light microscopy they employed, Wood and Brock would not have detected a narrow gap between particle and film indicating the excavation process. The present results can thus be reconciled with theirs although a reconciliation is not strictly required since their cell voltages were substantially higher—19.1-19.8V at 25 mA/cm^2. For the same reason, since Cote *et al.* (4) anodized at 16V, their observation that Al_3Fe anodized at the same rate as the matrix is not necessarily incompatible with the present results although their disagreement with Wood and Brock remains to be clarified. In general, it seems not unlikely that the processes occurring will often be more complex than encompassed in the simple alternatives of particle dissolution, anodization, or "inert" behavior and that detailed observations with higher resolution need to be made at various stages of film growth instead of limiting the studies of constituent behavior to thick films.

Acknowledgments

This work was sponsored by the U.S.-Israel Binational Science Foundation. Supplementary support was provided by the U.S. Army Research Office and by the U.S. Energy Research and Development Administration through the Materials Research Laboratory. Thanks are due J. B. Woodhouse for discussion of contrast in SEM and I.D. Ward for advice on the STEM technique.

Manuscript submitted Aug. 8, 1977; revised manuscript received Oct. 21, 1977. This was Paper 54 presented at the Philadelphia, Pennsylvania, Meeting of the Society, May 8-13, 1977.

Any discussion of this paper will appear in a Discussion Section to be published in the December 1978 JOURNAL. All discussions for the December 1978 Discussion Section should be submitted by Aug. 1, 1978.

Publication costs of this article were assisted by the University of Illinois at Urbana-Champaign.

REFERENCES

1. J. Zahavi and M. Metzger, *This Journal*, **121**, 268 (1974).
2. F. Keller, G. W. Wilcox, M. Tosterud, and C. J. Slunder, *Met. Alloys*, **10**, 219 (1939).
3. G. C. Wood and A. J. Brock, *Trans. Inst. Met. Finish.*, **44**, 189 (1966).
4. J. Cote, E. E. Howlett, M. J. Wheeler, and H. J. Lamb, *Plating*, **56**, 386 (1969).
5. M. J. Pryor and D. S. Keir, *This Journal*, **102**, 370 (1955).
6. P. J. Black, *Acta Crystallogr.*, **8**, 43 and 175 (1955).
7. E. H. Hollingsworth, G. R. Frank, Jr., and R. F. Willett, *Trans. Metall. Soc. AIME*, **224**, 188 (1962).

Lanthanum and Yttrium Halo-Silicate Phosphors

W. Lehmann* **and Th. J. Isaacs**

Westinghouse Research and Development Center, Pittsburgh, Pennsylvania 15235

ABSTRACT

Lanthanum and yttrium halo-silicates of the approximate composition $LnSiO_3X$ (Ln = La, Y; X = F, Cl, Br) have been discovered as new chemical compounds and as phosphor host materials. Luminescence activators are some of the trivalent rare earth elements. The crystallographic symmetry of $LaSiO_3F$ has tentatively been identified.

Halo-silicates, *i.e.*, silicates containing halide ions as essential part of their crystal structures, are relatively little known in general, and as phosphor host materials in particular. Burrus, Nicholson, and Rooksby (1) report Eu^{2+} emission in a material of the approximate composition $Sr_2Si_3O_8 \cdot 2SrCl_2$. Wanmaker and Verriet (2) describe luminescence due to Pb^{2+} and Eu^{2+} in $CaSiO_3 \cdot CaCl$. Wilke, Albers, and Mannheim (3) report $CaSiO_3 \cdot 2CaF_2$ and $CaSi_2O_5 \cdot 2CaF_2$ activated by Pb^{2+}, Bi^{3+}, and Mn^{2+}. A magnesium fluoro-silicate of the approximate composition $MgSiO_3 \cdot 2MgF_2$ activated by Ti^{4+} and Mn^{2+} is described by Ranby and Henderson (4). We want to report about structural and luminescent propertiese of lanthanum and yttrium halo-silicates which, to the best of our knowledge, have not been reported before. The composition of these materials is approximately $LaSiO_3X$ or $YSiO_3X$, respectively (X = F, Cl, Br). The luminescent properties of the lanthanum compounds were observed to be superior to those of the corresponding yttrium compounds. Hence, most experimental work was limited to lanthanum halo-silicates.

Preparation

The materials are prepared by conventional firing. The technique is described below using (La, Ce) SiO_3Cl as an example.

A uniform blend of La_2O_3, CeO_2, a slight excess of silicic acid, and a somewhat larger excess of NH_4Cl is slurried in water to obtain the reaction

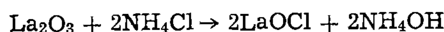

$$La_2O_3 + 2NH_4Cl \rightarrow 2LaOCl + 2NH_4OH$$

A typical molar ratio between La, Ce, Si, and Cl to be used may be about 0.85:0.15:1.1:1.5. The slurry is dried in air. The dry powder is fired first in loosely capped quartz tubes surrounded by a slightly reducing atmosphere (*e.g.*, 99% N_2 + 1% H_2) at 1200°C for about 1 hr. It is then ground to a fine powder and refired in open quartz boats for 15 min at 1200°C, again in a reducing atmosphere. The material is then washed in water to remove any traces of water-soluble halides which may remain after the second firing. The final phosphor is a free-flowing white powder of particles in the 5-20 μm size range. It is stable in air and water although attacked by strong mineral acids.

Lanthanum can be replaced by yttrium. Chlorine can be replaced by fluorine or bromine, but not by iodine. SiO_2 appears to be unique; it cannot be replaced by GeO_2, SnO_2, ZrO_2, or by ½ $AlPO_4$ and ½ BPO_4.

Structural Properties

Microscopic examination of a phosphor prepared as described above reveals irregularly shaped particles which do not display crystal faces. Illumination by ultraviolet shows the particles to be uniformly luminescent throughout. Hence, the phosphor is not a heterogeneous halide-silica system as reported elsewhere for different materials (5).

Powder x-ray diffraction spectra show two different patterns depending on the halide used. Materials containing chlorine or bromine are almost identical, having very small changes in lattice spacings, but they differ from those containing fluorine. We were not able to identify either line pattern by comparison with published data of known materials (6).

Attempts to grow single crystals from the melt of lanthanum chloro-silicate failed; the halide escapes at the melting temperature (~ 1550°C) leaving lanthanum silicate behind. Some success was achieved with lanthanum fluoro-silicate, however, although there was still an appreciable loss of the added halide which escaped as SiF_4. Portions of the boule were pulverized and the x-ray powder diffraction pattern was seen to be essentially the same as that of $LaSiO_3F$ phosphor powder. While the boule itself was not a single crystal, we were able to chip from it small pieces (> 1 mm) which were single crystals. These were studied by the Burger precession method using Mo k α radiation. The compound is orthorhombic. Extinction conditions give the diffraction aspect Pn*n, with the possible space groups being Pnmn or Pn2n. The lattice parameters are: $a = 8.828 \pm 0.005$Å; $b = 13.121 \pm 0.005$Å; $c = 5.397 \pm 0.005$Å. The number of molecules per unit cell was determined to be eight. The density was measured by means of a pycnometer and found to be 4.86 g/cm³. The calculated density based on the formula $LaSiO_3F$ is 4.97 g/cm³.

The molecular formula is still somewhat uncertain. The materials were made with the expectation of obtaining $LaSiO_3X$ (X = F, Cl, Br), giving a La:Si:X ratio of 1:1:1. We used somewhat different proportions in the raw mix to allow for the unavoidable loss of volatile halide and, possibly, silicon (as silicon halide) during firing. The ratio of La:Si:X in the final phosphor therefore differs from that used in the raw mix.

We tried to determine the exact composition by wet chemical analysis. The melt-grown boule mentioned above gave a La:Si:F ratio of 1:0.48:0.19, whereas a normal lanthanum chloro-silicate phosphor powder gave a La:Si:Cl ratio of 1:1.1:0.61. Although the 1:1 ratio between La and Si was essentially maintained in one case, the halide content was appreciably lower in both cases, and the two differed from each other.

We believe that the ideal composition of our halo-silicates is given by the formula $LaSiO_3X$ although the materials appear to tolerate appreciable deviation. This conclusion is supported by the close agreement between the theoretical and measured density mentioned above.

Luminescence Due to Various Activators

Cerium.—Pure lanthanum halo-silicates are white powders without significant luminescence under either 254 or 365 nm u.v. radiation. Replacement of about 15-20% of the La^{3+} by Ce^{3+} produces a phosphor which luminesces efficiently in the near ultraviolet under excitation by short-wave ultraviolet. The emission and optical absorption spectra of fluoro- and chloro-silicates differ from each other (Fig. 1 and 2) reflecting the different crystal structures of the mate-

* Electrochemical Society Active Member.

Key words: phosphor, luminescence, lanthanum, yttrium, silicate, halo-silicate.

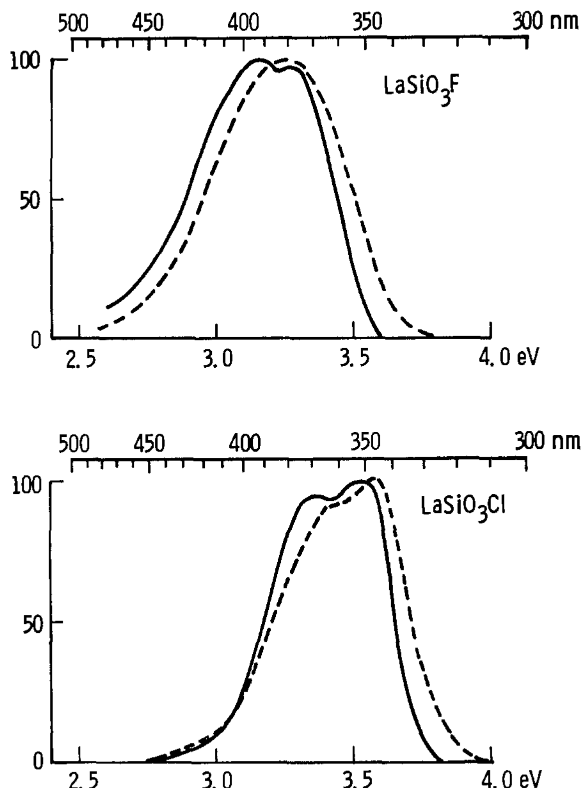

Fig. 1. Emission spectra of Ce^{3+} in lanthanum halo-silicates. Solid lines: excitation by 254 nm u.v. Dashed lines: excitation by 10 kV cathode ray.

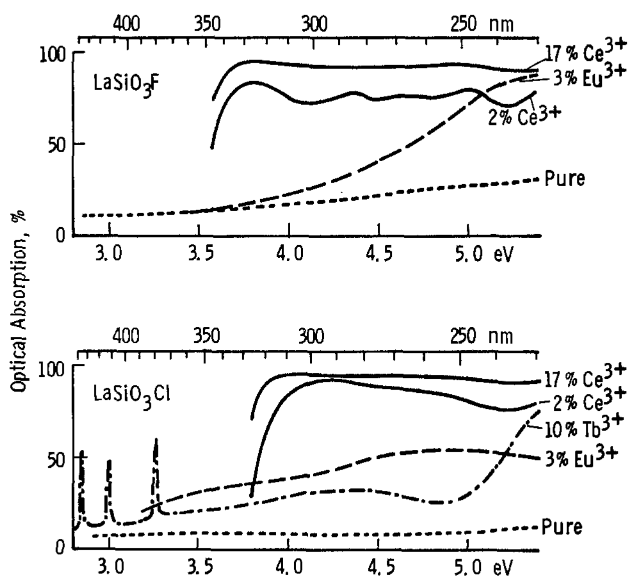

Fig. 2. Optical absorption spectra of lanthanum halo-silicate phosphors containing different activators.

rials. The spectra obtained on bromo-silicates are identical to those of chloro-silicates. Corresponding emission spectra of yttrium halo-silicates (Fig. 3) differ slightly from those of the lanthanum compounds. Two overlapping emission bands about 0.2 eV apart, reflecting recombination into the two ground states $^2F_{5/2}$ and $^2F_{7/2}$ of the Ce^{3+} ion, are frequently discernible. All emission spectra depend somewhat on the mode of excitation; they are shifted to higher energies in cathodoluminescence (Fig. 1). We do not as yet understand the reason of this effect.

Terbium.—The Tb^{3+}-emission in these halo-silicates consists of the usual pattern, a strong line group in the green at about 543 nm corresponding to the $^5D_4 \rightarrow {}^7F_5$

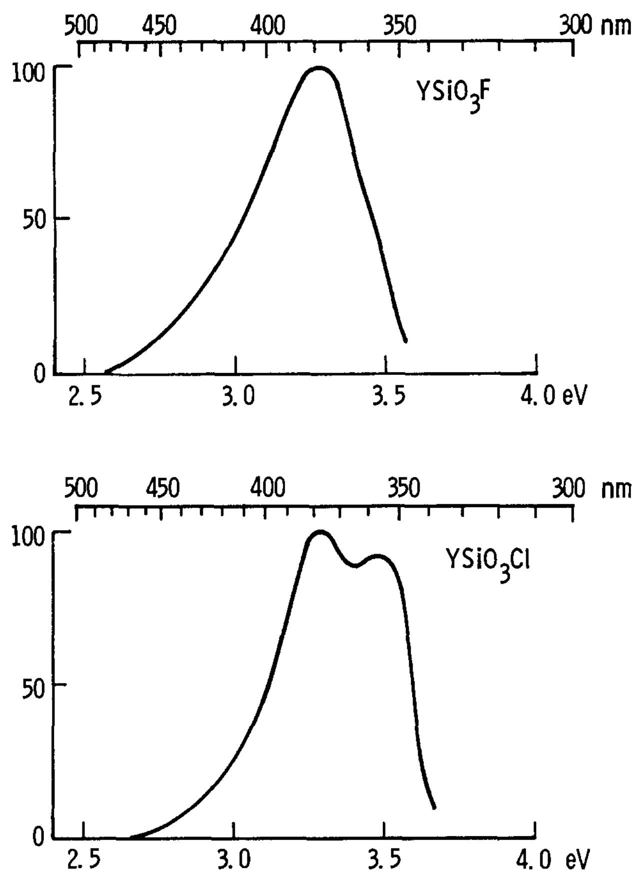

Fig. 3. Emission spectra of Ce^{3+} in yttrium halo-silicates. Excitation by 254 nm u.v.

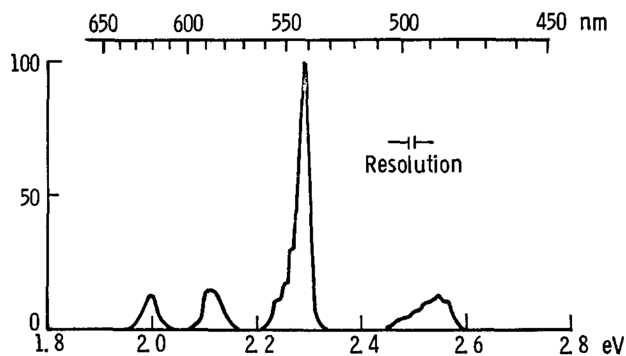

Fig. 4. Emission spectrum of La(0.7), Ce(0.2), Tb(0.1) SiO_3Cl. Excitation by 254 nm u.v.

electron transition, and several weaker ones to both sides (Fig. 4). It is not well excited by either 254 or 365 nm ultraviolet because of the absence of strong optical excitation at these wavelengths (Fig. 2). However, the Tb^{3+} is very efficiently sensitized for 254 nm excitation by Ce^{3+}. The obvious reason of this perfect energy transfer, $Ce^{3+} \rightarrow Tb^{3+}$, is the spectral overlap of the Ce^{3+} emission with several strong absorption lines of the Tb^{3+} (Fig. 1, 2, 3). The quantum efficiency (ratio of emitted/absorbed quanta) of La(0.7) Ce(0.2) Tb(0.1) SiO_3Cl phosphor under excitation by 254 nm ultraviolet was determined (by comparison to NBS-1021) to be about 90% (we believe the efficiency of the ultraviolet Ce^{3+} emission in a similar phosphor without Tb at least as high). The energy efficiency of cathodoluminescence is less impressive, however. We obtained ~4-5% under steady excitation by 10 kV electrons of low current density. This phosphor tolerates very high cerium concentration. While the optimum efficiency requires ~15-20% cerium and 10% terbium, replacement of all lanthanum by cerium,

[*i.e.*, Ce(0.9) Tb(0.1) SiO_3Cl] still gives a phosphor measured to have a quantum efficiency of the Tb^{3+} emission of about 70% under 254 nm excitation.

Samarium and dysprosium.—Both Sm^{3+} and Dy^{3+} in lanthanum and yttrium halo-silicates require sensitization by Ce^{3+} to respond to 254 nm ultraviolet. The energy transfer is not good, however. We observed quantum yields of about 5% for Sm^{3+} and about 30% for Dy^{3+} emission in (La, Ce) SiO_3Cl. These phosphors show the typical line emission and colors of the respective activator ions, *i.e.*, Sm^{3+} orange and Dy^{3+} yellowish-white.

Europium.—As in many other materials, trivalent europium requires an oxidizing atmosphere during preparation of halo-silicates to prevent reduction to Eu^{2+}. Thus we cannot sensitize Eu^{3+} with Ce^{3+}, as the latter requires a reducing atmosphere. Spectra showing the red Eu^{3+} emission in $LaSiO_3X$ are given in Fig. 5. They differ upon the halide used, which reflects the difference in structure. These spectra show relatively many lines between ~580 and 630 nm. The $^5D_0 \rightarrow {}^7F_2$ electron transition obviously is responsible for the strongest emission between ~610 and 620 nm, but a detailed line identification has not yet been possible. The optical absorption spectra due to Eu^{3+} in the lanthanum halo-silicates are relatively flat over a wide spectral range. We measured quantum yields of photoluminescence of ~25-30% for $LaSiO_3F$ and ~45-50% for $LaSiO_3Cl$, both materials containing an optimum europium concentration of about 3%. For reasons which we do not understand, we were unable to obtain Eu^{3+} emission in yttrium halo-silicate phosphors. The latter persistently showed only the Eu^{2+}, not the Eu^{3+}, emission.

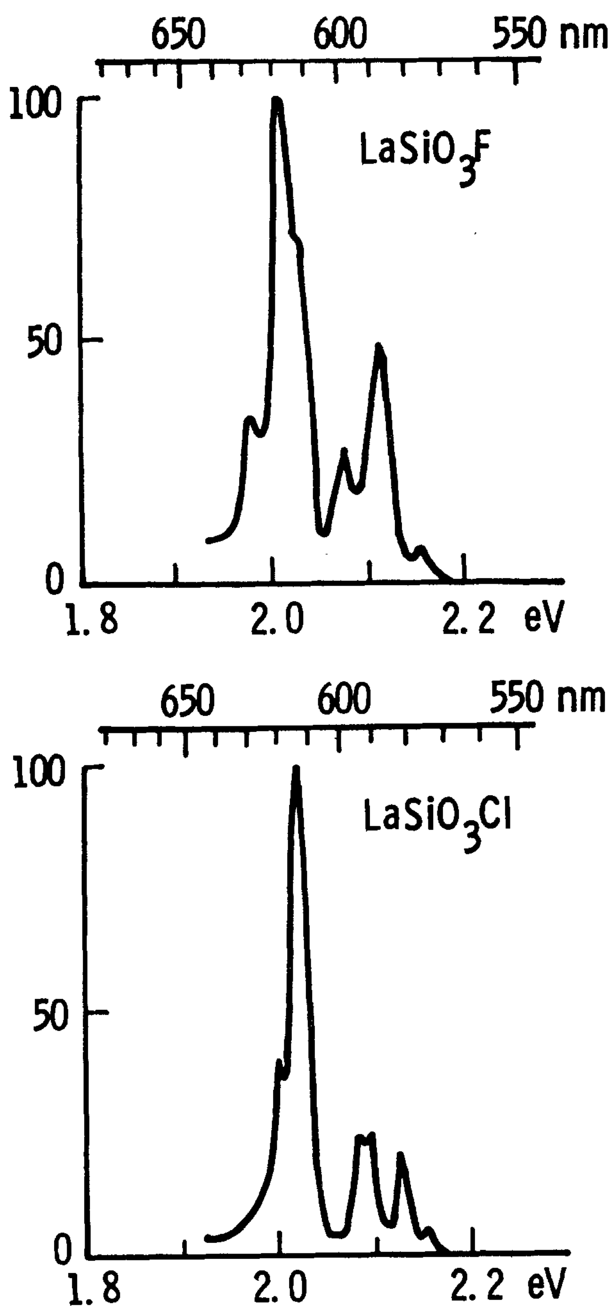

Fig 5. Emission spectra of Eu^{3+} in $LaSiO_3F$ and $LaSiO_3Cl$. Excitation by 254 nm u.v.

Luminescence due to Eu^{2+} in the halo-silicates consists of two diffuse emission bands suggestive of Eu^{2+} ions incorporated in two different lattice sites. A narrow band in the blue to violet dominates, while a very broad band centered in the green is weaker in intensity. Representative spectra of some chloro- and bromo-silicates are shown in Fig. 6. We were not able to obtain unambiguously similar spectra of fluorosilicates because of possible presence of Eu^{2+}-activated fluorides which, being insoluble in water, cannot be removed by washing. Attempts of charge compensation (*e.g.*, Eu^{2+} + Th^{4+} replacing two La^{3+}) had no visible effect on the phosphors. The optical absorption spectra of the materials contain a strong and very broad absorption band from close to the narrow emission band to below 220 nm in the shorter ultraviolet.

Discussion

Lanthanum and yttrium halo-silicates have been prepared and demonstrated as host materials of phosphors. The crystallographic symmetry of $LaSiO_3F$ has tentatively been identified to be orthorhombic. We believe the symmetries of the other compounds of this family to be not much different. More details of the crystal structures of the new compounds are not yet certain. The appearance of two emission bands due to Eu^{2+} activation (Fig. 6) suggests that the lattice provides two different sites with different symmetries for the Eu^{2+} to occupy and, consequently, the same two different sites conceivably are available also for RE^{3+} ions. Although this is far from certain, it seems to be supported by the numerous emission lines observed in the Eu^{3+} spectra (Fig. 5) which may easily be a superposition of emissions from Eu^{3+} ions on two different sites. The Tb^{3+} emission (Fig. 4) is much less sensitive to differences in site symmetry and does not show this line proliferation. More conclusions appear to be too speculative at the moment.

The usefulness of the new halo-silicates as phosphors is relatively limited since only two activators, Ce^{3+} and Tb^{3+} (the latter in combination with Ce^{3+}), provide efficiencies high enough to warrant application in lamps, etc. A systematic evaluation in this respect is not yet available.

Acknowledgment

The writers want to express their appreciation to A. Wachtel for chemical analyses of these materials.

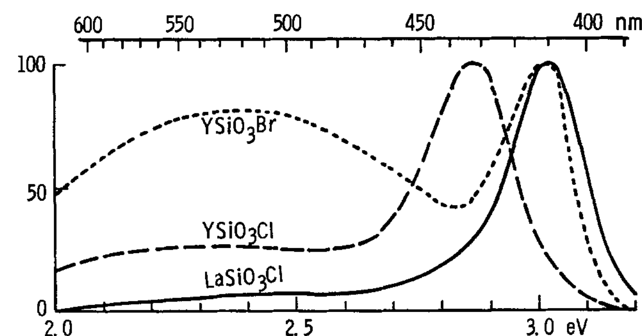

Fig. 6. Emission spectra of Eu^{2+} in chloro- and bromo-silicates. Excitation by 365 nm u.v.

Manuscript submitted Aug. 29, 1977; revised manuscript received Oct. 5, 1977.

Any discussion of this paper will appear in a Discussion Section to be published in the December 1978 JOURNAL. All discussions for the December 1978 Discussion Section should be submitted by Aug. 1, 1978.

Publication costs of this article were assisted by Westinghouse Research and Development Center.

REFERENCES

1. H. L. Burrus, K. P. Nicholson, and H. P. Rooksby, *J. Lumin.*, **2**, 467 (1971).
2. W. L. Wanmaker and J. G. Verriet *Philips Res. Rep.*, **28**, 80 (1973).
3. K. Th. Wilke, K. Albers, and R. Mannheim, *Z. Phys. Chem. (Leipzig)*, **213**, 191 (1960).
4. P. W. Ranby and S. T. Henderson, *This Journal*, **102**, 631 (1955).
5. W. Lehmann, *ibid.*, **122**, 748 (1975).
6. Powder Diffraction File, ASTM Joint Committee on Powder Diffraction Standards, Philadelphia (1970).

Very Thin Silicon Nitride Films Grown by Direct Thermal Reaction with Nitrogen

T. Ito,* S. Hijiya, T. Nozaki, H. Arakawa, M. Shinoda, and Y. Fukukawa

Semiconductor Laboratory, Fujitsu Laboratories Limited, 1015 Kamikodanaka, Kawasaki, Japan

ABSTRACT

Very thin uniform silicon nitride films less than 100Å have been obtained on silicon wafers by direct thermal reaction with nitrogen at temperatures ranging from 1200° to 1300°C. Small amounts of water or oxygen in reaction mixture caused vapor etching which gave rise to local crystallization. By eliminating both from the reaction ambient to less than 1 ppm, amorphous silicon nitride films can be deposited. These films have been found to have properties similar to those of CVD Si_3N_4 by investigations of Auger electron spectroscopy, infrared spectroscopy, and ellipsometry. Remarkable masking effects of the films against oxidation and phosphorus diffusion have been found.

Silicon nitride films have been widely used in integrated circuit processing as dual dielectric gate films, local oxidation masks, and surface passivation films. This is because silicon nitride has a higher dielectric constant, a higher density, more resistance to radiation, and a higher barrier against alkali-ion migration than silicon dioxide. However, it is well known that the films directly deposited on silicon cause interfacial instabilities between silicon nitride and the substrate (1).

Direct nitridation of silicon wafers was thought to be a profitable technique to obtain a good interfacial structure. Knoop and Stickler (2) examined thermal reaction of silicon wafers packed in quartz ampule with gases containing nitrogen. Brown patches, whiskers, and aggregates of silicon nitride appeared on the wafers. Hu (3) reported that direct nitridation of silicon at temperatures ranging from 1300° to 1400°C yielded polycrystalline silicon nitride in the form of either small or microcrystals. Frieser (4) also observed that directly nitrided silicon films in nitrogen were polycrystalline and were a mixture of α and β Si_3N_4. Electrical properties of these films could hardly be measured because they were nonuniform.

The reasons why it was difficult to react silicon with nitrogen by direct thermal reaction are as follows: binding energy of nitrogen molecules is fairly large, diffusion of nitrogen atoms in silicon or silicon nitride is very slow, and standard free energy of reaction between silicon and nitrogen is small. However, we thought this process would be feasible at a lower temperature than ones mentioned above and uniform thin films of silicon nitride might be obtained if oxidizing impurities in a reactor tube were effectively eliminated. Our efforts were primarily directed at obtaining uniform films of silicon nitride by improving conditions of reaction.

* Electrochemical Society Active Member.

Key words: thermal nitridation, elimination of oxidant, surface morphologies, masking effects.

In this paper, we describe thermal reaction conditions for uniform thin silicon nitride films. The films were characterized using Auger electron spectroscopy (AES), infrared transmittance spectroscopy (IRS), and ellipsometry, and masking effects against oxidation and phosphorus diffusion were studied.

Experimental

Wafer treatment procedure.—Silicon p-type (100) or (111) oriented CZ wafers with boron doping concentrations of 1×10^{15}-2×10^{16} cm^{-3} were used as a starting material. The wafers were chemically cleaned by degreasing, etching in hydrofluoric acid, and rinsing with deionized water. They were then dipped into 48% hydrofluoric acid for 1 min, dried by nitrogen gas flowing, loaded on a silicon carbide-coated susceptor in a nitrogen atmosphere, and inserted into a quartz reactor tube heated at a temperature ranging from 1200° to 1300°C. This process seems to be useful to remove natural oxide on silicon. Vapor etching with hydrochloric or hydrogen gases is also effective to remove the natural oxide, but it is not appropriate to this experiment because some mixture of these gases with nitrogen cause nonuniformities on the surfaces.

Growth apparatus.—The ambient nitrogen gas, flowing continuously through the reactor tube, was highly purified using a specially constructed purifier with catalysis. The experimental apparatus is shown in Fig. 1. Amounts of water and oxygen contained in the nitrogen gas were measured at the outlet of the reactor tube by a dew point meter and an oxygen detector, respectively. Flow rates of the nitrogen were measured with a flowmeter.

Measurement.—Both film thicknesses and refractive indexes were measured by an ellipsometric technique. These values were self-consistently calculated by a computer. Film properties were analyzed by AES and infrared spectroscopy. AES spectra were taken with a cylindrical mirror analyzer. Further, masking effects

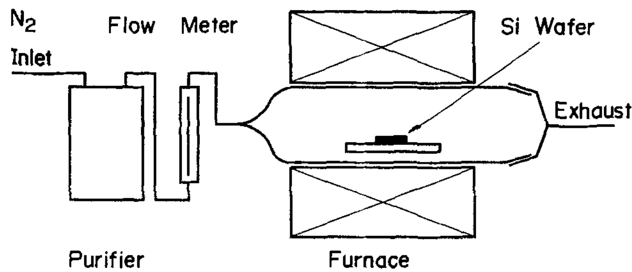

Fig. 1. Apparatus for directly thermal nitridation of a silicon wafer.

of the films grown on silicon wafers against oxidation and phosphorus diffusion were examined. Thermally nitrided silicon wafers were oxidized step by step in an oxidation tube heated at 1010°C. Film thicknesses on the wafers were measured after each oxidation. Donor concentration profiles after diffusing phosphorus into silicon masked by thermally grown silicon nitride films were determined by measuring sheet resistivities of surface layers and step-by-step etching after anodic oxidation.

Results

Growth conditions.—Figure 2 shows boundary conditions in which different surface morphologies are specified. In this case, the ambient nitrogen gas contained no more than 1 ppm water and 0.1 ppm oxygen. The reaction was tried at temperatures ranging from 1200° to 1300°C. The recovery time of the susceptor was nearly 15 sec at those temperatures and is shown as a broken line in the figure. The growth conditions for uniform silicon nitride films with smooth surfaces were restricted to a region between the solid line and the broken one. Rough surfaces with a crystalline morphology were observed for reaction times above the solid line. Small spots just like shallow etch pits appeared for reaction times near the line. If the purity of the ambient is improved, uniform films might be obtained in a wider region than that one shown in Fig. 2. To the contrary, if it contains more water or oxygen, uniform silicon nitride films would hardly be obtained.

Various surface morphologies of the silicon nitride films grown under conditions corresponding to three different regions in Fig. 2 are shown in Fig. 3. These wafers were nitrided at 1250°C for 10, 3, and 1 min, respectively. (a) shows the surface morphology of a partially crystallized silicon nitride film. Such a pattern has previously been reported by others (4). (b) shows a small spots pattern. These small spots seem

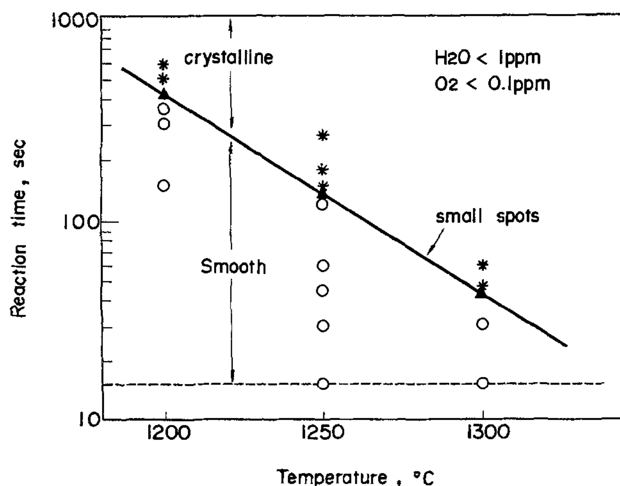

Fig. 2. Reaction conditions in which various surface morphologies of the grown films are specified. Experimental conditions are indicated as star, triangular, and open-circle marks, respectively.

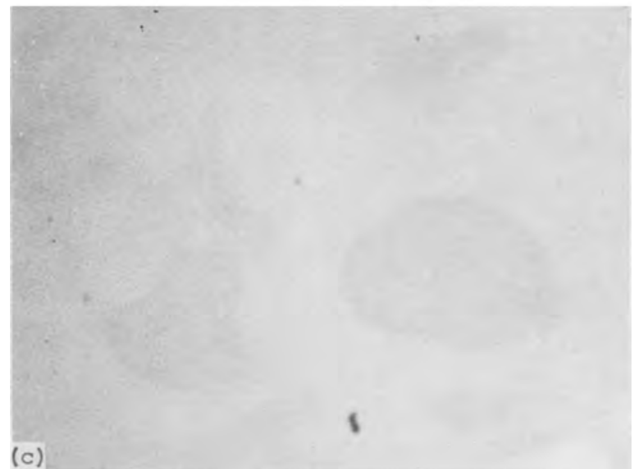

Fig. 3. Photographs of the film surfaces grown at 1250°C. (a) 10 min reaction, crystalline pattern; (b) 3 min reaction, small spots; (c) 1 min reaction, smooth and uniform surface.

to act as nuclei for crystallization. Figure 4 is an electron micrograph of the surface of the small spots sample (b) in Fig. 3, taken by a carbon replica technique. These small spots seem to grow in 3 dimensions. The surrounding plain region is as smooth as a silicon surface chemically etched by a conventional method. It exhibits no extra structural textures. This smooth region corresponds to the surface of the sample (c) in Fig. 3.

Figure 5 shows a relation between the film thickness and the reaction time at a temperature of 1250°C. Nitrogen gas of 5 liters/min flows continuously through the reactor tube. The growth rate varied up to 2.8Å/

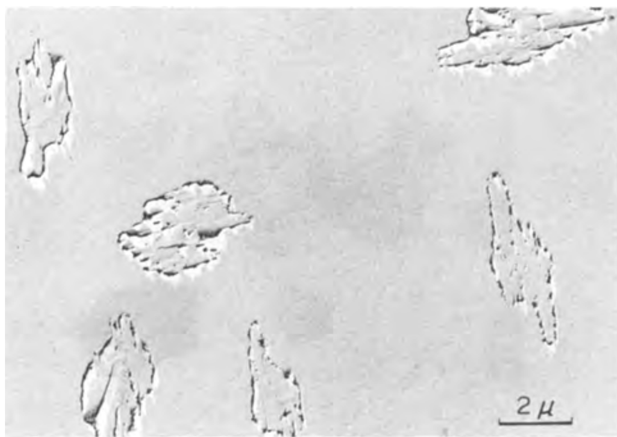

Fig. 5. Relation between film thickness and reaction time

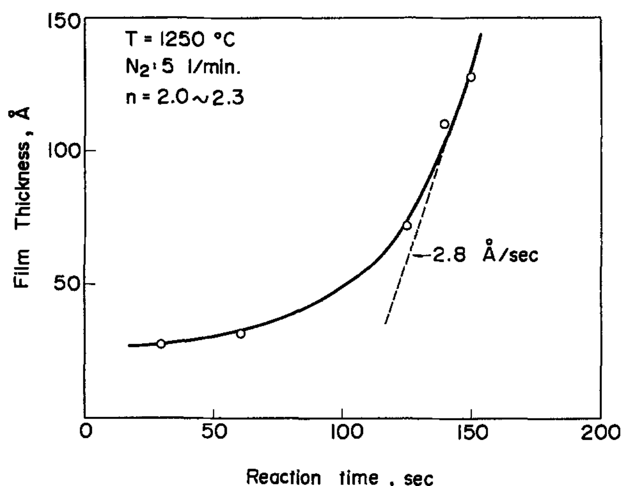

Fig. 5. Relation between film thickness and reaction time

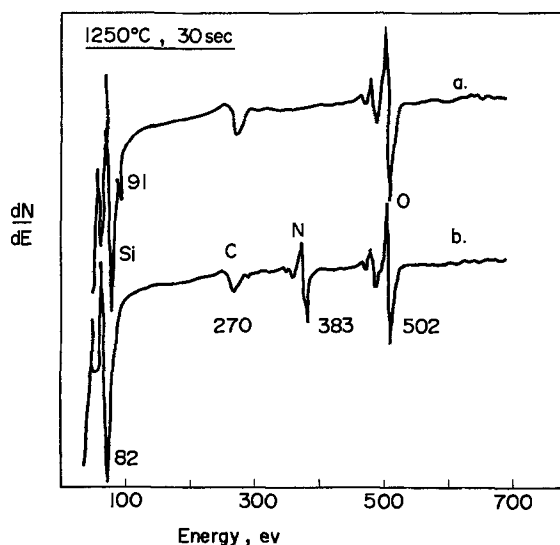

Fig. 6. AES spectra of films grown in different ambient gases. (a) Water, 5 ppm; oxygen, 4 ppm; (b) 1 ppm, 0.1 ppm, respectively.

sec and uniform films with thicknesses less than 100Å could be obtained. Refractive indexes of these films ranged from 2.0 to 2.3, which are slightly higher than those of the CVD materials. This shows a little deviation of stoichiometry of silicon nitride.

Film structural analysis.—Figure 6 shows Auger spectra of typical silicon nitride films. Both wafers were nitrided at a temperature of 1250°C for 30 sec. The upper spectrum (a) is of a film grown in nitrogen gas containing 5 ppm water and 4 ppm oxygen. The lower (b) is 1 ppm and 0.1 ppm, respectively.

The only detectable contaminants in these silicon nitrides are carbon and oxygen, which appear at 270 and 502 eV, respectively. In the upper spectrum, little nitrogen is detected and an elemental silicon peak still remains at 91 eV. This surface seems to be partly oxidized and to have partly remained bare silicon. In the case of improved ambient, the intense nitrogen KLL peak at 383 eV appears and the elemental silicon peak at 91 eV disappears. The chemically shifted silicon peak at 82 eV is believed to be associated with silicon nitride.

Figure 7 shows infrared absorption spectra of samples with different surface morphologies. These wafers were isothermally nitrided at 1250°C for 2, 2.5, and 4.5 min, respectively. Peaks at wavelengths of 9 and 16.4 μm seemed to be attributed to the substrate because they were noticed even in a bare silicon and did not change after the film growth. The surface of the 1 min sample was fairly uniform. But some small spots appeared on the 2.5 min sample and a crystalline pattern generated in the 4.5 min sample. These aspects have been mentioned in Fig. 3. A noticeable peak was recognized at 11.2 μm. The peak height increased with the reaction time.

For samples with the small spots or the crystalline pattern, a peak at 11.8 μm appeared and then overwhelmed the 11.2 μm. The 11.8 μm peak is due to stretching vibration of Si-N bond (5) and seemed to be associated with undesirable crystallization of silicon nitride, because the peak height increased with increasing the crystalline size. A shift of an absorption peak in silicon oxinitride was previously reported by Brown *et al.* (1, 6). According to their data, this uniform silicon nitride film, which only shows the absorption peak at 11.2 μm, would have a composition of 85% nitride and 15% oxide on the average if the band shift could be used in composition calibration. According to electron diffraction the uniform films showed a halo pattern and Kikuchi Lines reflected from the substrates as shown in Fig. 8. These films were surely amorphous.

Masking effects against oxidation and diffusion.—Direct thermal nitrided silicon wafers were inserted into a dry oxidation tube. Figure 9 shows a typical relation between the change of the film thickness on the silicon substrate and the oxidation time at a temperature of 1010°C. The thickness of the initial film, which was silicon nitride, was 75Å. It gradually increased with the oxidation time. After 5 hr the change was less than 50Å.

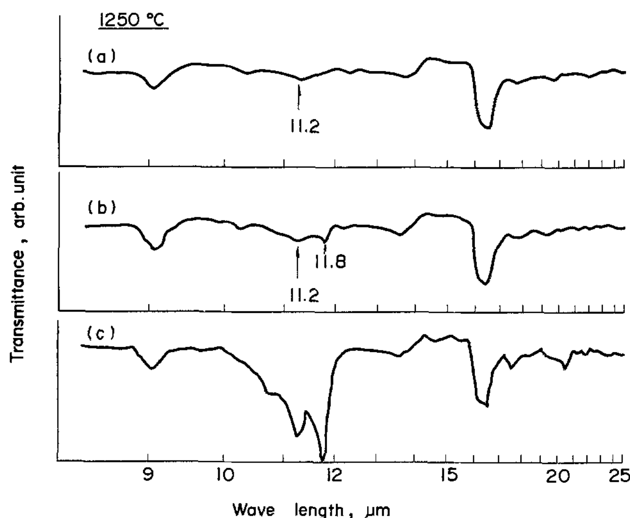

Fig. 7. Infrared absorption spectra of samples with different surface morphologies. (a) Uniform; (b) with small spots; (c) crystalline.

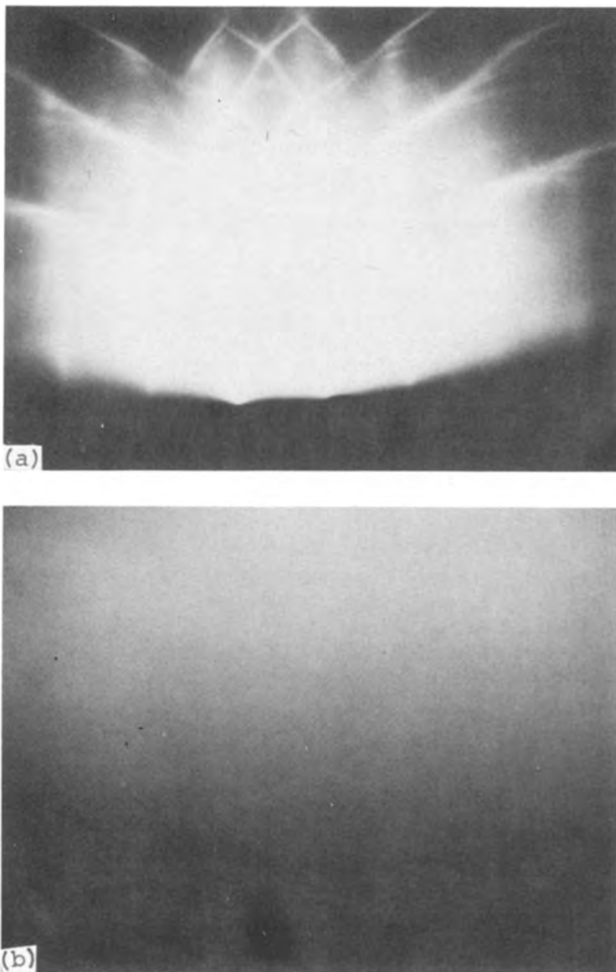

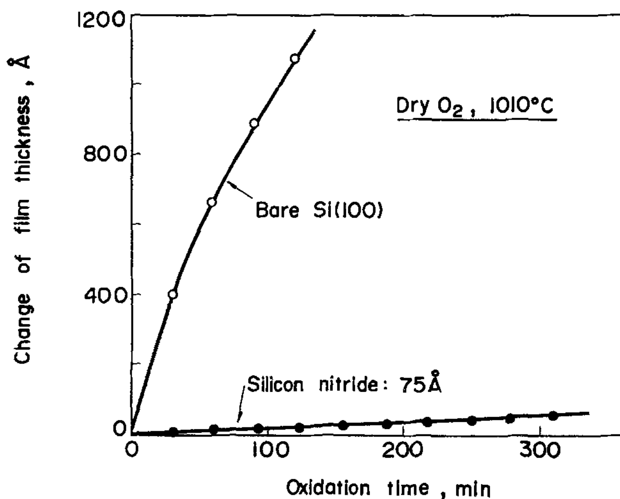

Fig. 8. Electron diffraction patterns. (a) Si surface etched; (b) directly nitrided Si surface.

Fig. 9. Change of film thickness vs. oxidation time. The silicon wafers with the silicon nitride film were heated in dry oxygen.

The mean oxidation rate is about 10Å per hour. For a comparison, a bare silicon wafer was also oxidized under the same conditions. The growth of silicon dioxide on the wafer is indicated as open circles in the figure.

Figure 10 shows carrier concentration profiles after diffusing phosphorus into p-type silicon substrates. Silicon nitride films with film thicknesses of 34 and 92Å were grown on silicon wafers. Subsequently a

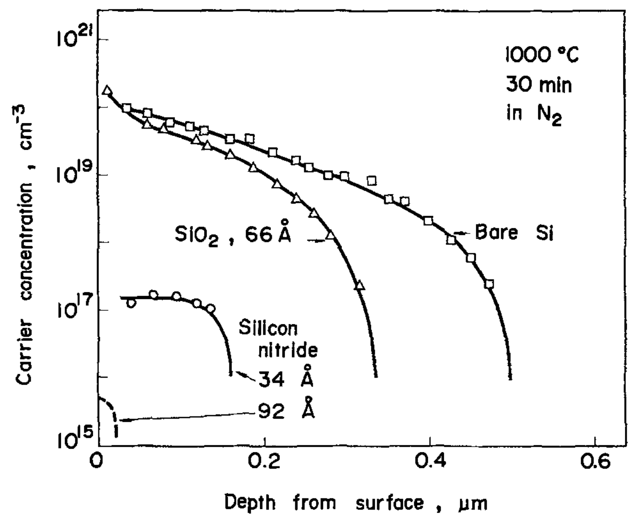

Fig. 10. Phosphorus diffusion profiles in silicon wafers with different protection-masks.

CVD phosphosilicate glass film was deposited by oxidation of silane and phosphine at a temperature of 450°C. Phosphorus concentration was 1.5 weight percent (w/o) and the film thickness was about 1000Å. The diffusion was carried out at 1000°C for 30 min in pure nitrogen ambient. The phosphorus doping profiles were compared with those of diffusions into bare silicon and thermally oxidized silicon with 66Å silicon dioxide. The depths after diffusing through the silicon nitride films are much smaller than those of the references. Especially, the silicon nitride film with 92Å thickness acts almost perfectly as a mask against the diffusion.

Figure 11 shows dependencies of surface-carrier concentrations on mask film thicknesses. The phosphorus diffusion was carried out under the same conditions as that in Fig. 10 and the diffusion times were 30, 60, and 120 min, respectively. The surface-carrier concentrations increase with increasing the diffusion time. However, all of the experimental values in Fig. 11 are smaller than that of a reference sample using a 66Å silicon dioxide film. Comparing one of silicon nitride samples with the reference at the same mask film thickness and under the same diffusion time, this silicon nitride film has more than four orders smaller values than the silicon dioxide film.

Discussion

The object of this work is to obtain stoichiometric silicon nitride films by direct thermal nitridation with

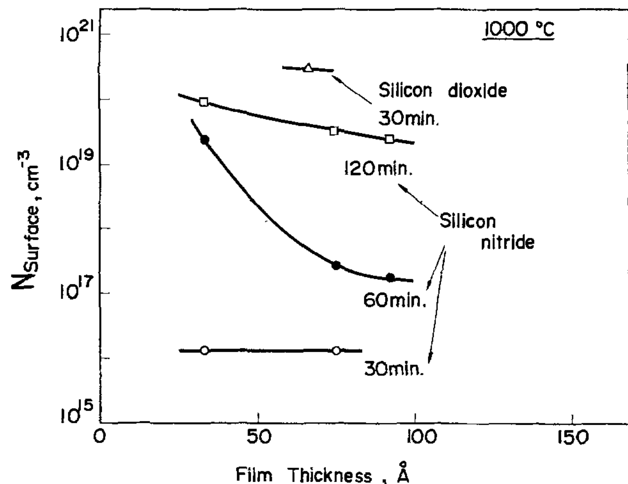

Fig. 11. Carrier concentrations at silicon surfaces vs. mask film thicknesses.

nitrogen. Since oxidation of silicon is thermodynamically more feasible than nitridation, it is necessary to reduce the amount of oxidant such as oxygen and water in reaction ambient. Those amounts have been reduced to less than 1 ppm water and 0.1 ppm oxygen measured at the outlet of the reaction tube, if absorbed gases in the wall of the quartz tube were fully taken out and the above-mentioned experimental conditions were established. However silicon nitride films obtained here have appeared to contain unintentional oxygen by the observations of AES and IRS. To attain the stoichiometry of Si_3N_4 it is necessary to improve further the experimental conditions. The origins of oxygen contained in the films are thought to be backstreaming of air while inserting wafers, penetrating through a quartz tube, and unremoved natural oxide on silicon surfaces besides impurities in the ambient reactive gas. Influences of these oxidants in the reaction process are observed in Fig. 5 which shows the film growth. The growth rate of silicon nitride increases with the increase of reaction time till the film thickness is nearly 100Å. We had expected that the process would obey a self-limiting reaction because the diffusion of nitrogen in silicon nitride is very slow. However the present result does not seem to support it. This is probably because the initial growth would be influenced by natural oxide on silicon and a backstreaming of air from the outlet. These would cause vapor etching of the silicon surface as the wafer temperature gradually elevates. The vapor etching would be caused by silicon monoxide structure.

After the initial reaction occurs, nitridation would become easier than the earlier, even though the nitrogen diffusion becomes slower. The refractive indexes of the films were a little higher than that of chemically vapor-deposited silicon nitride films. This seems to be caused by excess silicon atoms in the film because films grown in less pure ambient had refractive indexes ranging from 2.5 to 3.5. This ambient would cause much vapor etching of silicon and then, more excess silicon would remain in the grown film. The Auger electron peak of bare silicon in Fig. 6 also shows the existence of free silicon. Excess silicon atoms and oxidants contained in the film would become nuclei for local crystallization as indicated in Fig. 3(a). These regions have been ascertained to act hardly as masks against oxidation and impurities diffusion.

Chemically deposited silicon nitride films generally deviate from the expected Si_3N_4 stoichiometry over a wide range of deposition conditions. Johannessen *et al.* (7) analyzed them by AES and reported that an approximately 20% excess of silicon would be the general trend. According to Holloway and Stein (8), oxygen concentrations in various CVD silicon nitride films were observed to range from 0.4 to 7 atomic percent (a/o), where carbon was below the detection limits. Considering these results, some deviations from the stoichiometry in the grown nitride might become less important to certain applications. Deviations of film thicknesses of uniform silicon nitride among wafers and over a wafer were less than 5%, respectively.

Recently, Vromen (9) described that enough nitrogen could penetrate over a 52.6 nm oxide film at a temperature of 1050°C in 20 min to generate a large defect density. The degradation in dielectric strength was due to the generation of defects rather than to a change in intrinsic dielectric strength. Raider *et al.* (10) also reported nitrogen gas diffused to an oxide silicon interface, where it chemically reacts with silicon at elevated temperatures. They found that nitrogen would degrade the electrical properties of structures with the oxide during annealing. Further, Kooi *et al.* (11) observed the formation of some nitride at the silicon surface along the selective oxidation edge by steam oxidation. These phenomena did not show any feasibility in improving surface properties of silicon. However, the directly nitrided silicon films reported here would have far different properties from some nitrides examined by above-mentioned authors, and they would have some important advantages. For example, for the high performance of a short channel MOS transistor in LSI, the thinner gate insulator with a large dielectric constant is effective in eliminating so-called short channel effects and in decreasing the area. A further advantage of the films as a gate insulator is that a poly-Si gate can be highly doped without any impurities diffusing through the film to the channel region.

Conclusions

Very thin uniform silicon nitride films have been obtained by direct thermal reaction with nitrogen at temperatures ranging from 1200° to 1300°C. The film thicknesses were limited to less than 100Å because the reaction was inhibited by the growth of dense silicon nitride films. Small amounts of water or oxygen cause vapor etching and then give rise to local crystallization of the films, so that it has been found to be especially important to control them in ambient nitrogen to less than 1 ppm. The film properties have been investigated by AES, infrared spectroscopy, and ellipsometry. The very thin silicon nitride films had properties similar to those of a thick chemically vapor-deposited one. However, they appeared to contain a little excess silicon and oxygen. Masking effects of the films against oxidation and phosphorus diffusion were remarkable. This very thin silicon nitride film and the direct thermal nitridation process may be used in various integrated circuit technologies.

Acknowledgments

The authors would like to express their appreciation to Drs. S. Kojima, T. Oshida, and T. Misugi for their encouragement during this research.

Manuscript submitted May 2, 1977; revised manuscript received Aug. 5, 1977. This was Paper 310 presented at the Las Vegas, Nevada, Meeting of the Society, Oct. 17-22, 1976.

Any discussion of this paper will appear in a Discussion Section to be published in the December 1978 JOURNAL. All discussions for the December 1978 Discussion Section should be submitted by Aug. 1, 1978.

Publication costs of this article were assisted by Fujitsu Laboratories Limited.

REFERENCES

1. F. K. Heumann, D. M. Brown, and E. Mets, *This Journal,* **115**, 331 (1968).
2. A. N. Knoop and R. Sticker, *Electrochem. Technol.,* **3**, 84 (1965).
3. S. M. Hu, *This Journal,* **113**, 7, 693 (1966).
4. R. G. Frieser, *ibid.,* **115**, 10, 1092 (1968).
5. J. Wong, *J. Electron. Mater.,* **5**, 2, 113 (1976).
6. E. A. Taft, *This Journal,* **118**, 1341 (1971).
7. J. S. Johannessen, W. E. Spicer, and Y. E. Strausser, *Thin Solid Films,* **32**, 311 (1976).
8. P. H. Holloway and H. J. Stein, *This Journal,* **123**, 5, 723 (1976).
9. B. H. Vromen, *Appl. Phys. Lett.,* **27**, 3, 152 (1975).
10. S. I. Raider, R. A. Gdula, and J. R. Petrak, *ibid.,* **27**, 3, 150 (1975).
11. E. Kooi, J. G. Van Lierop, and J. A. Appels, *This Journal,* **123**, 7, 1117 (1976).

Oxidation of Silicon in the Presence of Chlorine and Chlorine Compounds

B. R. Singh[1] **and P. Balk***

Institute of Semiconductor Electronics/SFB 56 "Festkörperelektronik"
Technical University, 5100 Aachen, Germany

ABSTRACT

The need for higher manufacturing yields and improved operational reliability of semiconductor devices and circuits has led to a continuing scrutiny of all processing steps. Topic of the present paper is the effect of addition of chlorine or one of its compounds during silicon oxidation. After discussing oxidation kinetics in the presence of halogens and the metallurgical aspects of the process, a comprehensive review of the electrical effects is given. Attention is paid to the elimination of oxide charge centers and interface states, surface stabilization and enhanced dielectric behavior in MOS structures, and to the increased minority carrier lifetime in the silicon substrate. The improvements in device characteristics which have been attained using this method are summarized.

Adequate control of the threshold voltage and the breakdown strength of the gate insulator are essential conditions for the successful manufacture of field effect transistors. A decade ago alkali ions were found to be a major cause of instability of the surface potential in MOS structures; thus elimination of this form of oxide contamination was imperative (1-5). Since working under ultraclean manufacturing conditions presented some practical problems, the PSG stabilization process was developed where the impurities are gettered in a thin phosphosilicate glass layer directly at the metal electrode (6-9). Another possible solution is sealing off the SiO_2 film with a Si_3N_4 layer which is impenetrable to alkali ions (10-11). In both cases the breakdown behavior of the gate insulator is also improved, however, at the price of obtaining a polarizable (PSG) or an electronically somewhat unstable (SiO_2-Si_3N_4) system.

Given this situation the discovery that the addition of chlorine-containing species to the oxidation ambient during growth of the gate oxide may lead to improved stability and breakdown strength of the straightforward MOS structure was of considerable importance. In addition, lowering of the interface state density, elimination of stacking faults, and improvement in the minority carrier lifetime in the substrate on using these processes have been reported. Because of the great technological interest of the method different chlorine-containing species have been explored. However, these do not always lead to the same results.

It is the purpose of the present paper to review our level of understanding of the technique and of the mechanism involved in these processes. Discrepancies in the results and areas requiring further investigation are identified.

Chemistry of Chlorine Processes

Kinetics of oxide growth.—The thermal oxidation of silicon in the presence of O_2 or H_2O for SiO_2 thicknesses beyond 20 nm is generally described by a combined linear-parabolic equation which can be written as (12, 13)

$$\frac{x^2 - x_o^2}{k_{par}} + \frac{x - x_o}{k_{lin}} = t$$

where x is the oxide thickness, t the oxidation time, and k_{par} and k_{lin} are the parabolic and linear rate constants, respectively. For thin films the growth rate is determined by the reaction at the Si/SiO_2 interface. After an initial phase, characterized by the oxide thickness value x_o, the process proceeds at constant rate, yielding a linear increase of oxide thickness with time. For larger oxide thicknesses the growth is determined by the diffusion of the oxidizing species through the oxide layer and thus a parabolic rate equation results. Chlorine oxidation[2] also follows a linear-parabolic law (14-19). However, the values of the constants and their temperature dependences are affected by these additions to the O_2 ambient (Table I) (15): x_o appears to increase in all cases; k_{lin} increases strongly on addition of Cl_2 but is only weakly dependent on p_{HCl}; k_{par} increases with p_{HCl}, whereas the effect of p_{Cl_2} depends on the temperature.

The results for k_{par} with O_2/HCl at 1100°C were confirmed by Hirabayashi and Iwamura (16, 20). However, for k_{lin} these authors found the opposite trend as Van der Meulen and Cahill (15). At least at 1150°C Cl_2 has a stronger effect on growth rate than HCl (Fig. 1). In virtually all cases of practical interest thicker films are obtained with chlorine or chlorine compounds than without. Similarly, addition of trichloroethylene (TCE) to the oxidation ambient causes the rate to increase (Fig. 2) (17, 19, 21, 22).

To interpret the effect of chlorine and its compounds one has to keep in mind that the compounds will at least partially react with oxygen to form Cl_2 and H_2O (19, 23). For example, as may be seen from Fig. 3, a 5% HCl/O_2 mixture will yield approximately 3.5% HCl, 0.7% H_2O, and 0.7% Cl_2 according to the reaction

$$4HCl + O_2 \rightleftharpoons 2Cl_2 + 2H_2O$$

at 1100°C (23). At lower temperatures, the equilibrium shifts slightly to the right. Similarly, at 1100°C the reaction

* Electrochemical Society Active Member.
[1] Alexander von Humboldt Fellow 1976-1978.
[2] Here and in the following we will designate the oxidation in an ambient containing Cl_2 or a chlorine compound by "chlorine oxidation." Similarly, "chlorine oxide" designates the film obtained in such a process. To refer to specific processes (oxides) we will use the term Cl_2, HCl, or TCE oxidation (oxides).

Key words: chlorine oxidation, Si/SiO_2 interface, MOS, gettering.

Table I. Dependence of x_0 and of parabolic and linear rate constants on temperature (15)

Oxidant	T (°C)	k_{par} (nm²/min)	k_{lin} (nm/min)	x_o (nm)
O_2	900	39.4	0.220	6.4
	1000	169.0	0.805	19.2
	1100	414.0	3.25	33
O_2 + 4.5% HCl	900	64.2	0.217	11.4
	1000	440.0	1.02	25
	1100	540.0	?	?
O_2 + 0.5% Cl_2	900	18.46	0.31	17.5
	1000	180.0	0.83	24

$$4C_2HCl_3 + 9\,O_2 \rightarrow 2H_2O + 6Cl_2 + 8CO_2$$

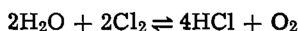

$$2H_2O + 2Cl_2 \rightleftharpoons 4HCl + O_2$$

will yield for a 1% TCE/O_2 ambient approximately 0.95% HCl, 0.05% H_2O, and 1.0% Cl_2. Again, at lower temperatures somewhat more Cl_2 and H_2O are being formed.

Originally it was thought that the water formed in the above reaction would be responsible for the enhanced oxidation rates in the O_2/HCl system. However, the effect is larger than that which one would expect in a comparable O_2/H_2O ambient (14). It appears that the Cl_2 formed will also affect the oxidation process (particularly k_{lin}) as may be seen from the O_2/Cl_2 data (Table I). Furthermore, an enhanced diffusion of O_2 and H_2O during chlorine oxidation cannot be ruled out (16, 20). On the other hand, at least at 900°C the effect of the O_2/HCl ratio on k_{lin} is negligible (Table II). It would appear that in this area more extensive studies are required.

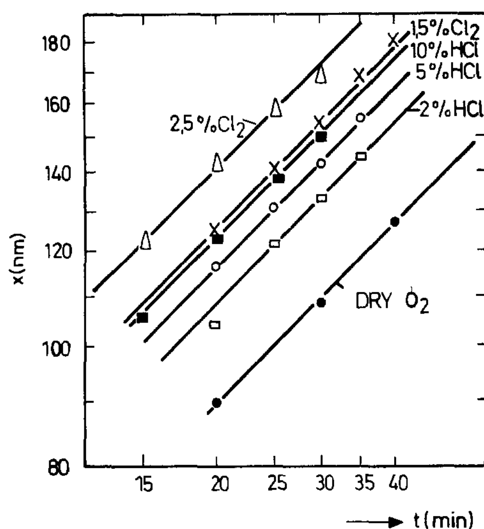

Fig. 1. Effect of HCl and Cl_2 additions on the oxidation rate of <100> silicon in O_2 at 1150°C (14).

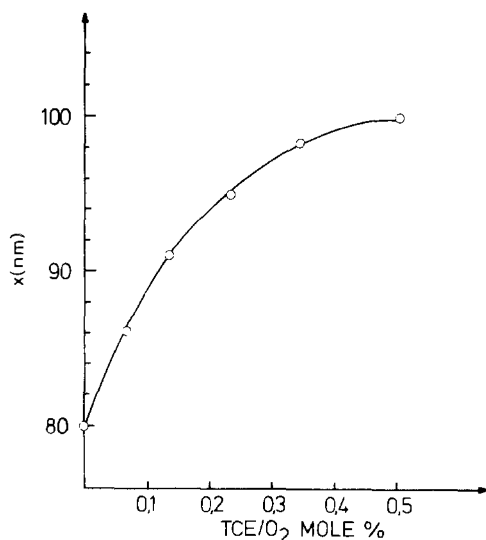

Fig. 2. Oxide thickness vs. TCE concentration (n-type Si, <100>, 4-5 Ωcm; T, 1200°C; t_{ox}, 11 min) (21).

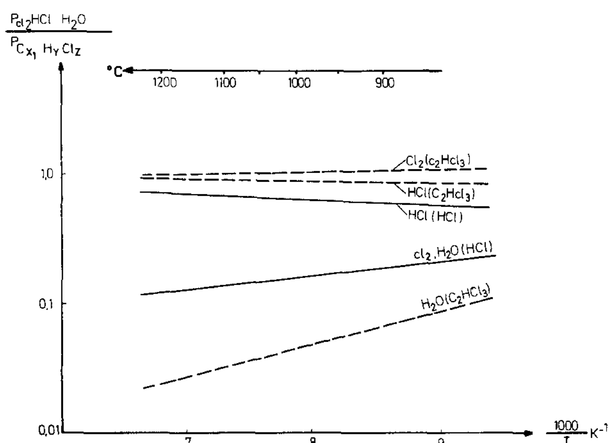

Fig. 3. Relative concentrations of Cl_2, HCl, and H_2O in O_2/HCl and O_2/TCE oxidation ambients at various temperatures. Values have been normalized with respect to the HCl and TCE input concentrations (23).

Chlorine distribution.—To gain insight in the chlorine incorporation and the distribution of this element in chlorine oxides, different analytical experiments using secondary ion mass-spectroscopy (24), Auger (25, 26), x-ray fluorescence (XFS), nuclear back scattering (NBS) (27-29), and electron microprobe analysis (EMA) have been performed. Of all the techniques employed, EMA was found to be the most sensitive, but detailed results are only available from the NBS technique which also yields the chlorine profile in a quantitative and nondestructive manner as a function of depth. A comparison of the amounts of chlorine detected in differently grown chlorine oxide films using various analytical methods is presented in Table III. Even though there may be some doubt about the quantitative nature of the results, almost all analytical techniques show large chlorine concentrations very near to the Si/SiO_2 interface and low concentrations in the rest of the oxide (24-29). The Auger data of Fig. 4 are an example of an experimentally found profile. In this case the Cl tail in the silicon may be an artifact of the Auger analysis method. The profile has the same shape regardless of SiO_2 thickness, growth temperature, and chlorine concentration in the gas phase (28, 29). From the observed large chlorine concentration at the Si/SiO_2 interface it appears that incorporation of chlorine takes place at the oxidation front. As the reaction proceeds, chlorine is expected to be slowly released and perhaps replaced by oxygen. The direct formation of Si-Cl instead of Si-O bonds at the interface has been proposed by Kriegler (26).

In Cl_2 oxides, the chlorine profile was found to be broadly peaked and more homogeneous compared to

Table II. The effect of additive concentration on x_o and on parabolic and linear rate constants during oxidation at 900°C (15)

Oxidant	k_{par} (nm^2/min)	k_{lin} (nm/min)	x_o (nm)
O_2	39.4	0.220	6.4
O_2 + 1% HCl	42.75	0.213	11.4
2	54.9	0.221	11.1
4.5	64.2	0.217	11.4
9	84.0	0.211	13.7
O_2 + 0.5% Cl_2	18.46	0.31	17.5

Table III. Amount of chlorine (μg-cm^{-2}*) detected using different analytical techniques in oxide films prepared by O_2/Cl_2 or O_2/HCl oxidation (29)

Halide addition	Oxid. temp (°C)	Thickness (nm)	EMA	XFS	NBS
0.5% Cl_2	1000	99.5	0.085	0.12	NA†
2% Cl_2	1000	94.2	0.27	0.60	0.27
3% HCl	1000	103	0.21	0.020	NA†
9% HCl	1000	105	0.023	0.020	0.022
3% HCl	1150	92.8	0.067	0.090	0.092
9% HCl	1150	93.7	0.13	0.21	0.17

* 0.60 μg-cm^{-2} corresponds to 1.0 × 10^{16} atoms/cm^2.
† NA: not available.

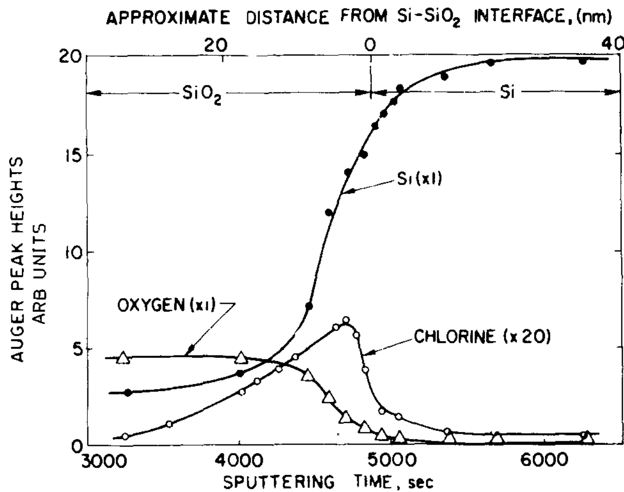

Fig. 4. Chlorine distribution in HCl oxide film determined by sputter etching. The silicon and oxygen profiles have also been indicated (25).

HCl oxides. Also, a higher level of chlorine incorporation was observed in comparison to HCl oxides for comparable concentrations of chlorine in the gas phase (28). Sequential growth studies in which a chlorine species was added during the later part of the oxidation process indicate that in Cl_2 oxides significant chlorine concentrations occur only near the Si/SiO_2 interface, whereas in regular Cl_2 oxides (Cl_2 added throughout the oxidation process) the element was distributed over a much wider range. In HCl oxides the same sequence yields chlorine profiles similar to those for regular HCl oxides. During N_2 annealing at 1200°C a slow chlorine removal takes place in Cl_2 oxides, whereas a rapid loss (to approximately 50%) and a change in the chlorine profile were found in HCl oxides. The above-mentioned differences in chlorine profiles for Cl_2 and HCl oxide and their behavior under annealing may be caused by H_2O which is only present during HCl oxidation. Both with Cl_2 and with HCl as a chlorine source average chlorine concentrations of the order of 10^{20} atoms/cm^3 can easily be achieved (27).

In spite of these differences, a number of similarities in the behavior of both Cl_2 and HCl oxides have also been observed. In both types of chlorine oxides chlorine is reported to be completely removed during further steam oxidation (26, 28, 30). However, some chlorine was found in oxides grown in regular steam/HCl ambient at 1200°C (31). Vacuum annealing at 100°C for about 60 min and also annealing at 1000°C in N_2 ambient do not result in any significant loss in chlorine concentration for both types of oxides.

Metallurgical Characteristics

Surface roughening.—The SiO_2 films grown in large concentrations of chlorine and chlorine compounds, or at smaller concentrations for longer duration show a grainy appearance when viewed through an optical microscope (16, 24, 26). Transmission and scanning electron microscopy results indicate that this is caused by roughening of the Si/SiO_2 interface. It has been suggested that development of smooth rounded bumps takes place and that their height and diameter increase with the HCl concentration (24).

Elimination of stacking faults.—Chlorine oxidation will cause suppression of stacking fault generation. The elimination or shrinkage of stacking faults which were already present have also been realized (32-37). This improvement has been attributed to interaction of these defects with vacancies probably created by removal of silicon atoms during high temperature chlorine oxidation. The diffusion of phosphorus and boron takes place at a reduced rate in O_2/chlorine ambients (38). Such studies related to stacking fault elimination have recently gained considerable importance because of the possible correlation of these defects with dark current spikes in CCD's (39). The existence of a strong correlation has been confirmed by Declerck *et al.* (37, 40).

Optimizing the process may cause some difficulty since the elimination of stacking faults which are already present requires growth conditions (1150°-1240°C, 3-6%) which will result in surface roughening and degradation of other beneficial properties like the attainment of low interface state density, high dielectric breakdown strength, and good stability under room temperature bias. These adverse effects are avoided by working at somewhat more moderate temperatures (1100°-1150°C) and concentrations (3-4% HCl), but under these conditions only generation of new stacking faults is prevented. Thus combination with other methods, like the POGO technique [gettering of defects using a phosphorus or Si_3N_4 deposition on the back of the silicon wafer (41-43)] or damaging the back by ion implantation (which has a similar gettering effect) may be necessary to eliminate the stacking faults (37).

Electrical Properties

In this section the effect of chlorine oxidation on different electrical properties of MOS structures, silicon substrates, and devices are discussed and a comparison between oxides grown in different chlorine-containing species made. In general, all chlorine species tend to have similar effects in improving the Si/SiO_2 interface properties. Nonetheless, some important differences have been observed for typical growth conditions.

Interface state density.—It is now well established that a one order of magnitude reduction in interface state density can easily be obtained in the case of chlorine oxides as compared to oxides grown in chlorine-free atmospheres (Fig. 5) (44-47). In TCE oxides the effect reverses for TCE/O_2 mole ratios of more than 0.6%, where an increase in interface state density is obtained (17). It has been suspected that the reduction is due to the presence of highly active hydrogen or OH^- groups produced during HCl or TCE oxidation which tie up some or all of the dangling bonds at the interface (44, 46, 48, 49). The reduction in interface state density has also been attributed to the gettering of the chemical impurities (21).

The orientation dependence of the interface state density for samples oxidized in O_2 with 3%HCl is similar to that for oxides grown in a chlorine-free atmosphere (47). The results indicate a higher density of states for <111> than for <100> oriented surfaces. Upon postmetallization annealing in N_2 at 525°C the densities reduce for both orientations to the same small value (47). There is no information on the dependence of the state density on the temperature and HCl additive concentration.

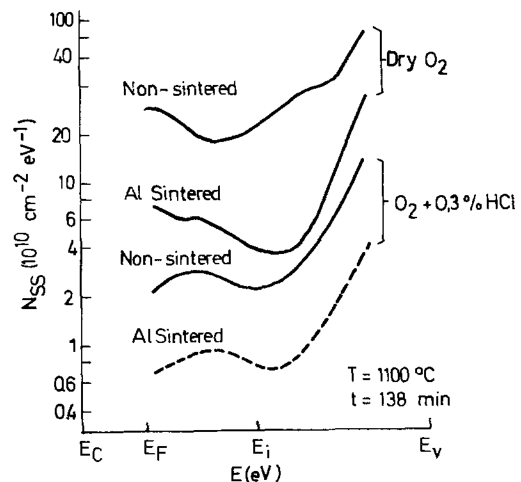

Fig. 5. Surface state distribution at the Si/SiO_2 interface for <111> oriented silicon oxidized in dry O_2 and in HCl ambients (44).

Fixed oxide charge density.—Most authors agree that chlorine oxides do not show significantly reduced fixed oxide charge densities (14, 21, 44-46, 50). However, for TCE the situation is not quite clear (51). Recently a detailed analysis of the dependence of the flatband voltage on the TCE concentration has been conducted. Minimum oxide charge was observed for TCE concentrations of 0.3-0.4% (22). The charge density was found to increase for higher TCE concentrations.

Cleaning effect.—Alkali ion contamination, mainly in the form of sodium ions introduced during high temperature processing of semiconductor devices, results in erratic turn-on voltages and instability of device parameters under operational stresses. These ions move through the insulator film under operational stresses and accumulate at the Si/SiO_2 interface, inducing an equal amount of negative charge in the silicon.

It has been observed that the addition of chlorine during high temperature oxidation has a significant effect in removing sodium ions by forming volatile chlorides (21, 26). Clean oxides have also been obtained by simply oxidizing the wafer in O_2 or steam in a furnace tube which has been precleaned by prolonged exposure to an O_2/chlorine mixture. In this case, the cleaning effect might have been caused by the release of trace amounts of chlorine from the furnace tube into the oxidizing ambient during further oxidation in the chlorine-free atmosphere. However, the fact that the same level of stability was observed for oxides grown in chlorine-free atmosphere (after 15 hr O_2/HCl and 30 min steam purge) and regular HCl oxides (6% HCl, after 15 hr O_2/HCl purge) indicates that prevention of contamination from the tube is the essential point (Table IV). It is also shown in this table that oxidations in 6% HCl/O_2 and in 0.75% TCE/O_2 (which yields approximately the same Cl_2 concentration, see Fig. 3) are comparable in their effectiveness in reducing the mobile ion density (21, 26). This suggests that pure Cl_2 will be equally or perhaps more effective than hydrogen-containing chlorine compounds in this respect.

From the significant reduction in the radiation-induced oxide charge obtained for steam/HCl oxides at 875°C it may be concluded that even under these conditions clean oxides can be obtained (52). This radiation-induced charge buildup is believed to be due to the liberation during irradiation of neutral sodium (not mobile with BT stress) bonded with coulombic forces to oxygen vacancies (53). A similar reduction in the amount of radiation-induced oxide charge was observed by Aubuchon *et al.* (54) in oxides grown in an HCl-purged furnace. On the other hand, oxides with high chlorine concentration show an increased radiation-induced charge. This may be partly due to chlorine migration during irradiation.

In thermally grown oxide, sodium is present both as ionic and as neutral species (4). The instability due to incorporated mobile Na^+ ions caused by involuntary Na^+ contamination, observed after "standard furnace cleaning" (Table IV) appears to be in sharp contrast with the findings of Revesz and Evans (13). After intentionally doping the SiO_2 films with 10^{20} Na atoms cm^{-3} during oxidation, they observed no significant instability. Their oxidation conditions and those in Ref. (21, 26) appear to be quite similar. It thus appears that in Revesz and Evan's films, Na was incorporated in an immobile form, whereas in the experiments of Table IV this element was in mobile form. Most likely a transition between these two forms may occur, but it is not clear under which conditions. The question still remains unanswered if the cleaning effect is due to the formation of volatile chloride or to the neutralization of Na^+ ions during chlorine oxidation.

Passivation effect.—As discussed in the previous section, the incorporation of sodium ions can be prevented either by precleaning the furnace tube or by simply adding a small percentage of chlorine to the oxidation ambient. By definition, the cleaning action of chlorine cannot extend beyond the thermal oxidation step. However, for the fabrication of devices a number of additional steps, like photolithography and metallization, are required which can again introduce significant amounts of sodium and result in device degradation.

It has been observed that chlorine oxides grown under appropriate conditions, *i.e.*, at a reasonably high temperature with a fairly large chlorine concentration and for a sufficient length of time, can effectively alleviate the undesirable electrical effects of sodium even if the contaminant is introduced after high temperature oxidation (24, 26, 55, 56). This will most likely result in the high chlorine concentration near the Si/SiO_2 interface which is apparently necessary to passivate the SiO_2 film, *i.e.*, to neutralize Na^+ ions at the interface. The conclusion about Na^+ neutralization at the Si/SiO_2 interface is based on radiotracer and C-V data obtained on intentionally contaminated chlorine oxide films (6% HCl at 1150°C) after BT stress. The radiotracer data show a relatively high sodium concentration near the interface (Fig. 6) (56). The C-V characteristics measured on identical devices show no appreciable shift. This indicates that sodium ions lose their charge after interacting with chlorine already present at the Si/SiO_2 interface and that the charge must be transferred to the silicon electrode. Once sodium ions lose their charge, they are believed to be strongly trapped or bonded with chlorine. Van der Meulen *et al.* (27) are of the view that sodium ions after interacting with chlorine may be neutralized, but that they are not necessarily immobile. The exact mechanism of charge transfer to the silicon electrode is not understood (26, 55, 57).

The development of passivation takes place suddenly in a narrow range of HCl concentrations between 3 and 4% for devices having sodium contamination levels of the order of 10^{12} ions/cm^2 (Fig. 7). A significant incorporation of chlorine (10-15 $\times$ 10^{14} atoms/cm^2) particularly for 3-4% HCl at 1200°C has recently been observed and its possible correlation with threshold behavior in passivation discussed (Fig. 8) (58). This indicates that passivation is achieved once a certain minimum level of chlorine is incorporated in the SiO_2 film. However, this thresholdlike behavior of passivation is not understood. A similar thresholdlike behavior has been found for TCE oxides (17). Kriegler (24) observed that the passivation efficiency is independent of the sodium contamination level up to a value of 4 $\times$ 10^{12} ions/cm^2. The findings of Van der Meulen *et al.* (27) for higher contamination levels (10^{12}-10^{14} ions/cm^2) indicate that only one-third of the total so-

Table IV. Effect of HCl (26) and TCE (21) on mobile ion density in thermally grown SiO_2

HCl — 1200°C, 2-10-2 min dry-wet-dry cycle, N_2 anneal, 10 min

Sample description	Ion density (ion/cm^2)
No HCl, grown after standard (HF rinse, 6 hr steam purge at 1200°C) cleaning of furnace tube	26×10^{10}
6% HCl, grown without any previous exposure of tube to HCl	12×10^{10}
6% HCl, grown after 15 hr purge with 6% HCl/O_2	1.2×10^{10}
No HCl, grown after further 30 min steam purge	1.4×10^{10}

TCE — 1100°C, 30 min dry oxidation, N_2 anneal, 10 min

Sample description	Ion density (ion/cm^2)
No TCE, grown after standard (HF and H_2O rinse) furnace tube cleaning	3×10^{10}
No TCE, grown after 30 min purge with 0.75% TCE/O_2	10^{10}
No TCE, grown after 2 hr purge with 0.75% TCE/O_2	$3\text{-}6 \times 10^{10}$
No TCE, grown after 15 hr purge with 0.75% TCE/O_2	2×10^{9}

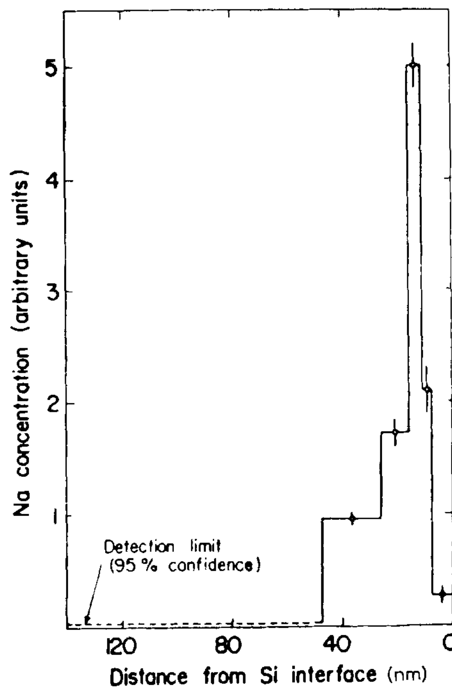

Fig. 6. Radiatracer data on Na^{22} distribution in a 6% HCl oxide after BT stress (56).

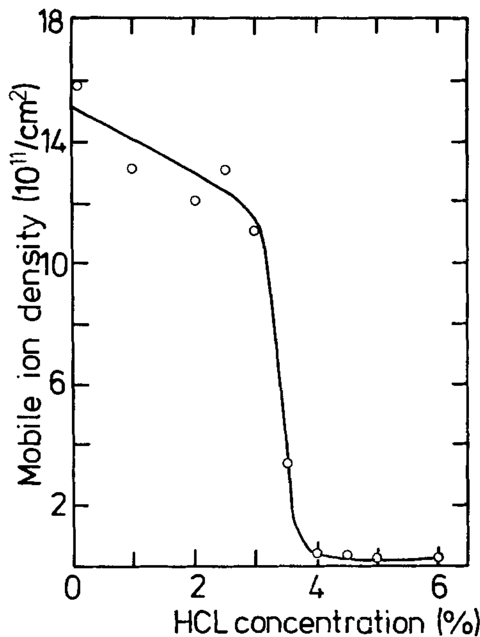

Fig. 7. Dependence of effective mobile ion density in Na-contaminated HCl oxide films on HCl concentration added during oxidation (T, 1150°C; t_{ox}, 34 min) (24).

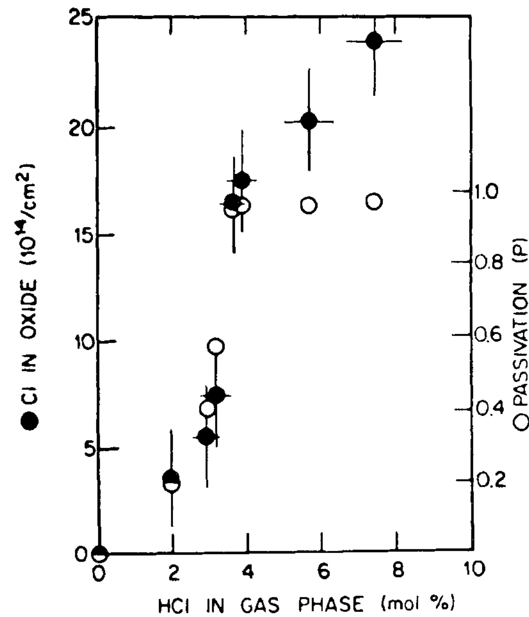

Fig. 8. Dependence of chlorine concentration (solid circles) and sodium passivation (open circles) on HCl concentration added to O_2 ambient during oxidation (T = 1200°C; t_{ox} = 30 min; contamination level, 3×10^{12} Na ions/cm^2). $p = (N_{Mob} - N_{fc})/N_{Mob}$. N_{Mob}, mobile ion density; N_{fc}, number of unneutralized Na^+ ions after BT stress (58).

dium ions are immobile in the SiO_2 films with high chlorine concentrations ($\gtrsim 10^{20}$ atoms/cm^3, 1150°C, 9% HCl). It thus appears that complete neutralization and immobilization of sodium ions are possible only up to a certain level of contamination ($\approx 10^{12}$ ions/cm^2) and that at higher Na^+ levels the effectiveness of the chlorine in the film to trap Na^+ drops off markedly. The observation that TCE oxides are not effective at high levels of contamination ($>10^{12}$ ions/cm^2) can be attributed to this fact (21). A systematic study with different chlorine and sodium concentrations would be required to obtain better understanding of the phenomenon.

The same order of equivalent ion density, which is indicative of the level of passivation, can be achieved for HCl and Cl_2 at a given temperature and oxidation time when the total amount of chlorine in the gas phase is the same (Table V). A minimum temperature larger than 1050°C is required to obtain any effect at all. Raising the temperature to 1150° or 1200°C does not result in a significant improvement in passivation property at least for devices having a sodium ion density of the order of 10^{12} ions/cm^2 (Table VI) (26).

Room temperature bias instability.—At very high fields (>5 MV cm^{-1}) chlorine oxide films exhibit instability of a magnitude not found for the oxides grown in a chlorine-free atmosphere (28, 59, 60). O_2/HCl grown layers exhibit only negative flatband voltage shifts for negative gate voltages (Fig. 9) along with a distortion of the C-V curves indicating generation of surface states (28-59). These effects show a pronounced dependence on the stressing field and on the chlorine concentration (28, 60).

More complex shifts have been reported for Cl_2 oxide (Fig. 10). They occur for both polarities of the

Table V. Effectiveness of HCl and Cl_2 concentrations on the passivation characteristics of the oxide films grown at 1150°C for 30 min on <100> Si. Na^+-contaminated aluminum electrode. Stressing condition: 250°C, 5 min, 5×10^5 V/cm (26)

Sample description	Thickness (nm)	V_{FB^-} (V)	V_{FB^+} (V)	Equivalent ion density (10^{10}/cm^2)
Dry O_2	105	−0.18	−2.1	41.4
1.5% Cl_2	156	−0.74	−0.9	11.9
3.0% HCl	134	−0.22	−0.65	10.0
2.5% Cl_2	167	−0.16	−0.1	1.2
5.0% HCl	148	−0.23	−0.1	1.4

Table VI. Dependence of HCl passivation on oxidation temperature. Na^+-contaminated aluminum electrode. Stressing condition: 250°C, 5 min, 5×10^5 V/cm (26)

HCl:O_2 (mole %)	Temperature (°C)	Time (min)	Thickness (nm)	V_{FB^+} (V)
0	1150	48	148	−8.5
6	1200	24.5	148	−0.05
6	1150	34	151	−0.1
6	1100	44	146	−0.4
6	1050	76	149	−5.9
6	1000	150	146	−6.3

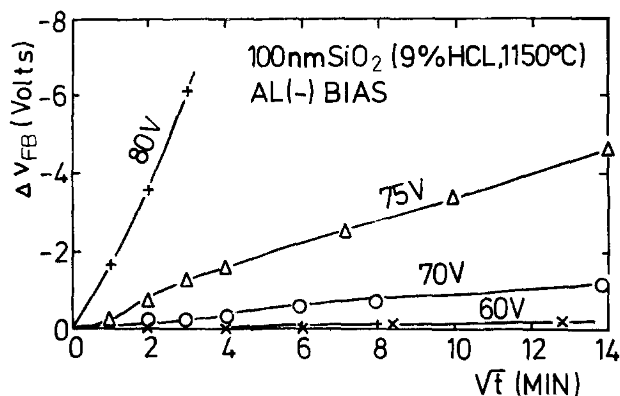

Fig. 9. Change of flatband voltage with time under negative bias in HCl oxide film. Parameter: applied voltage (28).

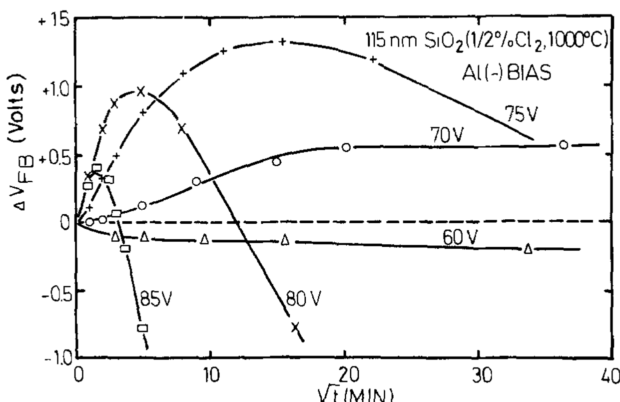

Fig. 10. Change of flatband voltage with time under negative bias in Cl_2 oxide film. Parameter: applied voltage (28).

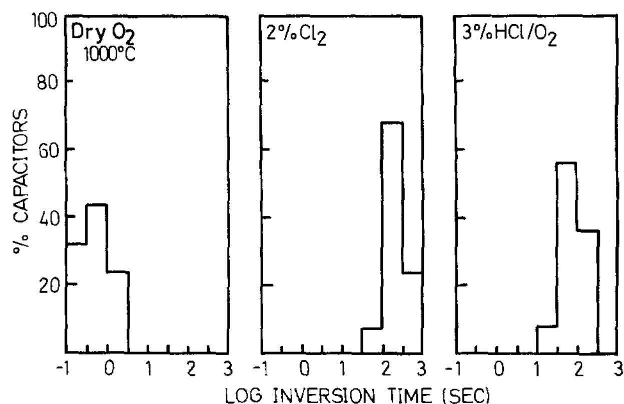

Fig. 11. Effect of Cl_2 and HCl oxidation on statistical distribution of inversion times (66).

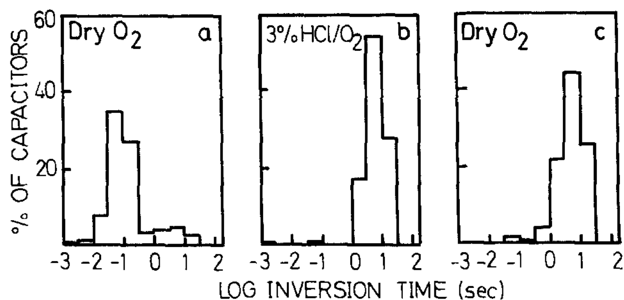

Fig. 12. Permanence of improvement in inversion times after HCl gettering at 1000°C. (a) After dry O_2 oxidation; (b) after oxidation in 3% HCl/O_2; (c) after HCl oxide etching, regrowth in O_2 (66).

stressing voltage and their direction depends on that of the bias, suggesting that both negative and positive charges must be present. However, NBS measurements on such samples failed to show any changes in the Cl profiles on stressing. At very high fields (8 MV cm^{-1}) again interface states are being generated (28, 59). The mechanism behind these shifts is as yet unknown. A similar but less pronounced instability has been observed in TCE oxides (22).

Minority carrier lifetime.—It is now well established that many high temperature processing step in silicon device fabrication result in decreased minority carrier lifetimes. This adversely affects device characteristics like storage time and leakage currents. The reduction in minority carrier lifetime is believed due to the presence of heavy metal impurities, *e.g.*, Au, Cu, Fe, and Mg, which create recombination generation centers in the forbidden energy gap of silicon. Different gettering techniques with KCN, V_2O_5, boron, or phosphorus have been used to control this parameter (61-63).

Recent studies have shown that the minority carrier lifetime can be improved by two to three orders of magnitude using a chlorine oxidation technique (64-67) (Fig. 11). This process probably removes the metallic impurities in the form of volatile chlorides. Cl_2 (2%) is more effective than HCl (3%) in removing the metals (Fig. 11). The significant effect of TCE can be concluded from storage time data. This parameter is found to increase from seconds to minutes after TCE oxidation (19, 22).

Results of experiments with a HCl oxidation source indicate that the improvement can be retained during oxidation in a chlorine-free atmosphere once the impurities are removed by HCl oxidation (Fig. 12). Sequential growth studies, *i.e.*, growth of oxide in chlorine-free atmosphere (25 nm) followed by HCl oxidation have shown improvements similar to those observed in oxides grown completely with O_2/HCl. However, annealing of oxide films grown in chlorine-free atmosphere (50 nm) in 3% HCl/N_2, *i.e.*, in an oxygen-free ambient, leads to short inversion times. An increase in lifetime was observed with the increase in oxidation temperature from 850° to 1150°C and additive concentration from 1 to 6% HCl (66). However, a low additive concentration is desirable to have good control over oxidation rates and to prevent surface roughening.

Ronen and Robinson (65) have suggested that the above-mentioned improvements can only be realized when good quality bulk crystals with low oxygen content are being used to begin with. This point deserves further study. Also, the optimization of the process temperature and of the additive concentration for different compounds is still to be carried out.

Dielectric breakdown.—Oxide defects and alkali ion contamination are the main factors responsible for poor breakdown characteristics of MOSFET gates. While studying the effects of different process variations on oxide defects, *i.e.*, spots with low breakdown strength, it was first observed that the defect density is considerably reduced by oxidizing the silicon wafers in a mixture of HCl and O_2. Even prior cleaning of the furnace tube with 6% O_2/HCl at 1150°C, followed by oxidation, results in a 60% reduction of the defect density (68, 69).

A detailed study using different halogen-containing species like HCl, Cl_2, TCE, HBr, and CCl_4 has been carried out by Osburn (69). All additives lead to reduced defect densities. A minimum defect density was observed for the oxides grown in a 3% HCl ambient (Fig. 13). This ambient gives a pronounced effect at 1%. In general, the results indicate that for all additives the lowest defect density can be achieved at concentrations about a factor of two below those which produce nonuniform films. Figure 14 indicates the improvement observed in the statistical distribution of the breakdown voltages for oxides grown in 3% HCl or 2% Cl_2.

Analogous to oxides grown in chlorine-free atmosphere, the defect density in HCl oxide increases with

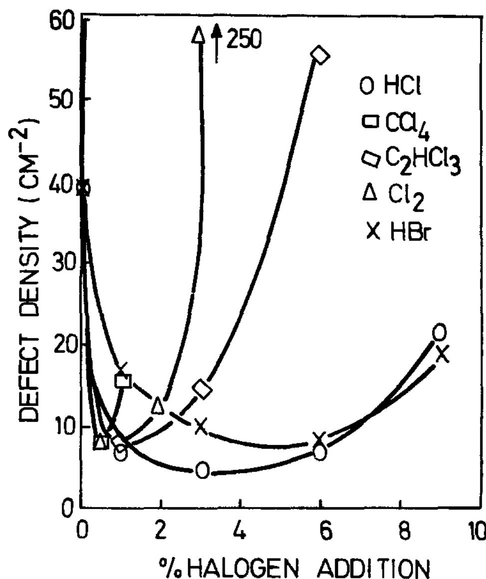

Fig. 13. Effect of halogen concentration during oxidation on defect density of SiO_2 films (T, 1000°C) (69).

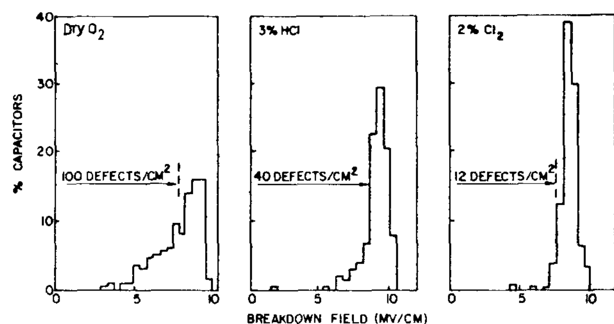

Fig. 14. Distribution of dielectric breakdown strength in HCl and Cl_2 oxides grown at 1000°C (69).

oxidation temperature, as can be seen from the Fig. 15. This enhancement in defect density becomes very pronounced at 1150°C; HCl oxides grown at this temperature or higher lose their favorable breakdown characteristics (69).

For 2% HCl oxides accelerated breakdown tests have shown an increase in wear-out time of up to two orders of magnitude over those grown in pure O_2 at 1000°C. Also, the spread in failure times is reduced. This increase in wear-out times is believed to be due to a retardation of the so-called electrochemical-type degradation during accelerated stressing (69).

Cl_2 oxides grown at 1000 C showed shorter wear-out times than oxides grown in a chlorine-free atmosphere. This result is somewhat surprising because Cl_2 oxides are superior to HCl oxides with regard to improving the initial breakdown characteristics (69).

Investigations of the dependence of the wear-out time on the additive concentration have shown that this dependence is almost linear up to 3% HCl. The positive dependence continues up to 6% HCl and saturates only at this concentration. The wear-out time also increases with oxidation temperature. To obtain any improvement at all an oxidation temperature above 850°C is required. At the same temperature (850°C) a minimum defect density (Fig. 15) is observed. In contrast, the films grown at 1150°C show poor initial breakdown characteristics but maximum wear-out times. This indicates that these two parameters are influenced differently by the presence of HCl in the oxidation ambient (69).

In general, additives like HBr and C_2HCl_3 which contain both halogen and hydrogen improve the dielectric integrity of the SiO_2 films. On the other hand, Cl_2 and CCl_4 also cause adverse effects like shorter wear-out times. It seems reasonable to suspect that the difference between the two groups of additives is due to the presence of the reaction product H_2O in the ambient for the first group of materials. This may reduce the attack of chlorine on the silicon surface. As expected, chlorine oxidation also yields improved breakdown characteristics in devices intentionally contaminated with sodium (69).

Device performance.—In this section we summarize the improvements in characteristics observed for devices fabricated using chlorine oxidation. Mesa-type epitaxial SOS bipolar transistors have shown low leakage current, improved forward and reverse characteristics, and increased breakdown voltage. This effect is probably due to the removal of metallic impurities which results in increased minority carrier lifetimes, as demonstrated in Fig. 16. The low frequency gain of the devices was increased by a factor of two to ten after chlorine oxidation. A significant increase in the base transit time and the minority carrier lifetime has also been noted (65).

Al- and Si-gate MOS transistors have been fabricated to compare the over-all performance of chlorine-oxidized devices with those with oxides grown in a chlorine-free atmosphere and also to see the possible effect of further processing on properties of chlorine oxides. The devices having chlorine gate oxides were found to be more stable (23).

Three phase polysilicon CCD's, delay lines, analog memories, and image sensors using TCE oxide/Si_3N_4 as a gate insulator exhibit improved performance (40). CCD's fabricated with TCE oxide as a gate insulator show significantly higher storage time (by one to two order of magnitude) than oxides grown in a chlorine-free atmosphere (70). The increase in bulk generation lifetime to 300-350 μsec and the low surface generation velocity (0.3-0.4 cm/sec) results in dark currents as low as 5 nA/cm^2 for normal CCD operation. Dark current spikes are considerably reduced.

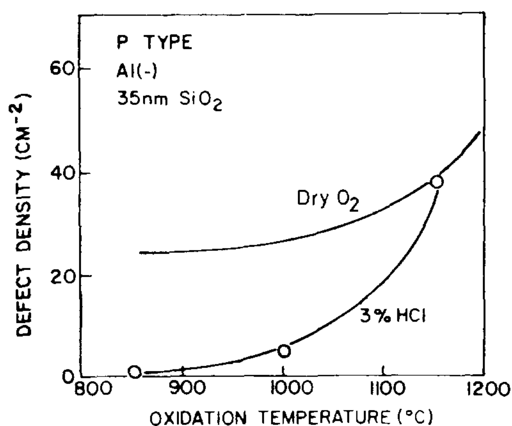

Fig. 15. Dependence of defect density on oxidation temperature for dry and HCl oxide (69).

Conclusions

The wide improvement observed in Si/SiO_2 interface properties using HCl with the oxidation process clearly indicates its superiority over other chlorine-containing species. Even though Cl_2 is one of the more effective gettering agents, its large reactivity toward the silicon surface even at moderate temperatures and concentrations is a drawback. The corrosive nature of HCl and the problems with handling this material have instigated the search for more manageable chlorine additives with similar properties. Here TCE appears to be rather attractive since it is much easier to handle, contains sufficient chlorine to show effective gettering, and also provides a source of hydrogen. However, the available data on TCE oxidation are still rather limited.

It may be seen from this review that it is impossible to optimize the process conditions for all parameters at

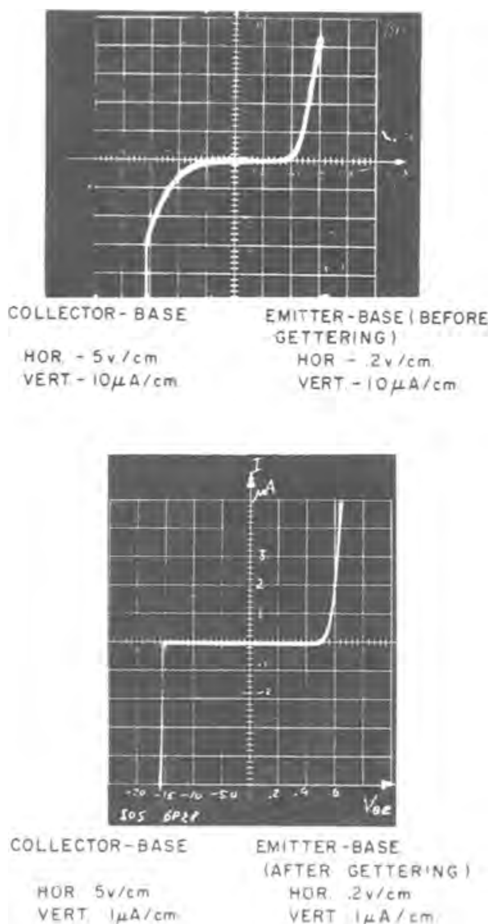

Fig. 16. Improvement in the *I-V* characteristics of collector-base and emitter-base junctions in SOS bipolar transistor after HCl_2 gettering (1% Cl_2, 2 hr at 950°C) (65).

the same time. Specifically, rather different growth conditions are required for achieving good dielectric breakdown characteristics and for passivation and elimination of as-grown stacking faults or defects. Here one has to compromise depending on the nature of the devices. Except for the last two effects, all possible improvements can be realized to a reasonable extent by growing the oxide at 1100°C with 3% HCl. Furthermore, one may expect that if the furnace tube has been precleaned and relatively little contamination will occur during further processing, addition of 4-5% HCl at the same temperature may yield a reasonably good passivation.

With TCE all improvements could be realized in the temperature range of 1100°-1200°C and at concentrations of 0.3-0.4% TCE. Only the high process temperature is a disadvantage of this chlorine compound.

Note added in proof.—Since this manuscript was completed a few publications pertinent to the subject matter of this review appeared. References (71-73) present more extensive data on the effect of Cl_2 and HCl on oxidation kinetics, roughening of the silicon surface, and negative bias instability, respectively. Particularly interesting is the conclusion of Monkowski *et* al. (74) that a second phase is formed near the Si/SiO_2 interface during chlorine oxidation. A study by Pearce and Rozgonyi (75) appears to indicate that the effectiveness of chlorine in suppressing or eliminating oxidation-induced stacking faults is mainly due to the gettering of interstitial oxygen from the bulk of the silicon by this element.

Acknowledgments

The authors wish to thank Dr. G. J. Declerck, Katholieke Universiteit, Leuven, Belgium, for useful discussions and also for making available some of his unpublished results. They are indebted to Dr. C. M. Osburn, IBM Research Center, Yorktown Heights, New York, for bringing to their attention some very recent publications on chlorine oxidation.

Manuscript submitted June 27, 1977; revised manuscript received Oct. 26, 1977.

Any discussion of this paper will appear in a Discussion Section to be published in the December 1978 JOURNAL. All discussions for the December 1978 Discussion Section should be submitted by Aug. 1, 1978.

Publication costs of this article were assisted by the Technical University of Aachen.

REFERENCES

1. E. H. Snow and B. E. Deal, *Trans. Metall. Soc. AIME*, **242**, 512 (1968).
2. D. R. Kerr, *Proceedings of 8th Reliability Physics Symposium*, 1 (1970).
3. J. R. Szedon and R. M. Handy, *J. Vac. Sci. Technol.*, **6**, 1 (1969).
4. B. E. Deal, *This Journal*, **121**, 198C (1974).
5. B. R. Singh and K. Singh, *Microelectron. Reliab.*, **15**, 385 (1976)
6. D. R. Kerr, J. S. Logan, P. J. Burkhardt, and W. A. Pliskin, *IBM Res. Dev.*, **8**, 376 (1964).
7. P. Balk and J. M. Eldridge, *Proc. IEEE*, **57**, 1558 (1969)
8. E. H. Snow and B. E. Deal, *This Journal*, **113**, 263 (1966).
9. J. M. Eldridge, R. B. Laibowitz, and P. Balk, *J. Appl. Phys.*, **40**, 1922 (1969).
10. T. L. Chu, J. R. Szedon, and C. H. Lee, *Solid State Electron.*, **18**, 867 (1968).
11. J. V. Dalton and J. Drobek, *This Journal*, **115**, 865 (1968).
12. B. E. Deal and A. S. Grove, *J. Appl. Phys.*, **36**, 3770 (1965).
13. R. G. Revesz and R. J. Evans, *J. Phys. Chem. Solids*, **30**, 551 (1969).
14. R. J. Kriegler, Y. C. Cheng, and D. R. Colton, *This Journal*, **119**, 388 (1972).
15. Y. J. Van der Meulen and J. G. Cahill, *J. Electron. Mat.*, **3**, 371 (1974)
16. K. Hirabayashi and J. Iwamura, *This Journal*, **120**, 1595 (1973).
17. G. J. Declerck, T. Hattori, G. A. May, J. Beaudouin, and J. D. Meindl, *ibid.*, **122**, 436 (1975).
18. D. W. Hess and B. E. Deal, Paper 323 presented at the Electrochemical Society Meeting, Las Vegas, Nevada, Oct. 17-22, 1976.
19. W. M. Grubbs, M. B. Das, J. Stach, and R. E. Tressler, Paper 325 presented at the Electrochemical Society Meeting, Las Vegas, Nevada Oct. 17-22, 1976.
20. K. Hirabayashi and J. Iwamura, International Conference on Solid State Devices, Tokyo, Aug. 29-31, 1973
21. E. J. Janssens and G. J. Declerck, ESSDERC Grenoble, Sept. 8-12 1975.
22. D. L. Heald, R. M. Das, and R. P. Khosla, *This Journal*, **123**, 302 (1975).
23. G. J Declerck, Private communication.
24. R. J. Kriegler, A. Aitken, and J. D. Morris, *Suppl. J. Jpn. Soc. Appl. Phys.*, **43**, 341 (1974).
25. N. J Chou, C. M. Osburn, Y. J. Van der Meulen, and R. Hammer, *Appl. Phys. Lett.*, **22**, 380 (1973).
26. R. J. Kriegler, in "Semiconductor Silicon 1973," H. R. Hoff and R. R. Burgess, Editors, p. 363, The Electrochemical Society Softbound Symposium Series, Princeton, N.J. (1973).
27. R. L. Meek, *This Journal*, **120**, 308 (1973)
28. Y. J. Van der Meulen, C. M. Osburn, and J. F. Ziegler, *ibid.*, **122**, 284 (1975).
29. Y. J. Van der Meulen, C. M. Osburn, and J. F. Ziegler, Paper 54 presented at The Electrochemical Society Meeting, Chicago, Illinois, May 13-18, 1973.
30. P. Ritchey and J. Stach, Paper 127 presented at The Electrochemical Society Meeting, Dallas, Texas, Oct. 5-9, 1975.
31. H. Shibayama, H. Masaki, H. Ishikawa, and H. Hashimoto, *Appl. Phys Lett.*, **29**, 136 (1976).
32. M. Shiraki, *Jpn. J. Appl. Phys.*, **14**, 147 (1975).
33. M. Shiraki, *ibid.*, **15**, 1 (1976).
34. M. Shiraki, *ibid.*, **15**, 83 (1976).
35 T. Hattori, *This Journal*, **123**, 945 (1976).
36. T. Hattori, *Appl. Phys. Lett.*, **30**, 312 (1977).

37. C. L. Claeys, E. E. Laes, G. J. Declerk, and R. J. van Overstraeten, Paper 224 presented at The Electrochemical Society Meeting, Philadelphia, Pa., May 8-13, 1977.
38. Y. Nabeta, T. Uni, S. Kubo, and M. Tsukanoto, *This Journal*, **123**, 1416 (1976).
39. K. Tanikawa, Y. Ito, and M. Sei, *Appl. Phys. Lett.*, **28**, 205 (1976).
40. G. J. Declerck, K. M. De Meyer, E. J. Janssens, E. E. Laes, J. Van der Spiegel, and C. L. Claeys, International Conference on the application of CCD's, Edinburgh, Sept. 28-30, 1976.
41. G. A. Rozgonyi, P. M. Petroff, and M. H. Read, *This Journal*, **122**, 1725 (1975).
42. P. M. Petroff, G. A. Rozgonyi, and T. T. Sheng, *ibid.*, **123**, 565 (1976).
43. G. A. Rozgonyi and R. A. Kushner, *ibid.*, **123**, 510 (1976).
44. M. Severi and G. Soncini, *Electron. Lett.*, **8**, 402 (1972).
45. E. A. Fogels and C. A. T. Salama, *This Journal*, **118**, 2002 (1971).
46. B. R. Singh, B. D. Tyagi, A. N. Chandorkar, and B. R. Marathe, Paper 42 presented at The Electrochemical Society Meeting, San Francisco, Calif., May 12-17, 1974.
47. G. Baccarni, M. Severi, and G. Soncini, *This Journal*, **170**, 1436 (1973).
48. E. Kooi, *Philips Res. Rep.*, **20**, 518 (1965).
49. F. Montillo and P. Balk, *This Journal*, **118**, 1463 (1971).
50. S. Brojdo, J. V. Dalton, W. J. Polito, and M. A. Waggner, Paper 244 presented at The Electrochemical Society Meeting, Miami Beach, Fla., Oct. 8-13, 1972.
51. M. C. Chen and J. W. Hile, *This Journal*, **119**, 223 (1972).
52. J. L. Peel, R. K. Pancholy, G. J. Knhlmann, T. J. Oki, and R. A. Williams, IEEE Annual Conference on Nuclear and Space Radiation Effects, California, July 14-17, 1975.
53. H. L. Hughes, R. D. Baxter, and B. Phillips, *IEEE Trans. Nucl. Sci.*, **ns-19**, 256 (1972).
54. K. G. Aubuchon, E. Harari, D. H. Leong, and C. P. Chang, *ibid.*, **ns-21**, 167 (1974).
55. R. J. Kriegler, *Thin Solid Films*, **13**, 11 (1972).
56. R. J. Kriegler, *Appl. Phys. Lett.*, **20**, 449 (1972).
57. R. J. Kriegler and T. F. Devenyi, Reliability Physics Symposium, Las Vegas, Nevada, April 3-5, 1973.
58. A. Rohatgi, S. R. Butler, and F. J. Feigl, *Appl. Phys. Lett.*, **30**, 104 (1977).
59. A. Bhattacharya, P. K. Choudhary, and D. Beyar, Paper 41 presented at The Electrochemical Society Meeting, San Francisco, Calif., May 12-17, 1974.
60. P. M. Ritchey, J. Stack, and R. E. Tressler, Paper 324 presented at The Electrochemical Society Meeting, Las Vegas, Nevada, Oct. 17-22, 1976.
61. S. W. Ing, Jr., R. E. Morrison, L. L. Alt, and R. W. Aldrich, *This Journal*, **110**, 533 (1963).
62. R. N. Hall and J. H. Racette, *J. App. Phys.*, **35**, 379 (1964).
63. J. E. Lawrence, *Trans. AIME*, **242**, 484 (1968).
64. P. H. Robinson and F. P. Heiman, *This Journal*, **118**, 141 (1971).
65. R. S. Ronen and P. H. Robinson, *ibid.*, **119**, **747** (1972).
66. D. R. Young and C. M. Osburn, *ibid.*, **170**, 1578 (1973).
67. J. M. Green, C. M. Osburn, and J. O. Sedgwick, *J. Electron. Mat.*, **3**, 579 (1974).
68. C. M. Osburn and D. W. Ormond, *This Journal*, **119**, 597 (1972).
69. C. M. Osburn, *ibid.*, **121**, 809 (1974).
70. G. J. Declerck, K. M. De Meyer, E. J. Janssens, E. E. Laes, and J. Van der Spiegel, *IEEE Trans. Solid State Circuits*, **sc-II**, 229 (1976).
71. D. W. Hess and B. E. Deal, *This Journal*, **124**, 735 (1977).
72. D. W. Hess and R. C. Macdonald, *Thin Solid Films*, **42**, 127 (1977).
73. D. W. Hess, *This Journal*, **124**, 740 (1977).
74. J. Monkowski, J. Stach, and R. E. Tressler, "Semiconductor Silicon 1977," H. R. Huff and E. Sirtl, Editors, p. 324, The Electrochemical Society Softbound Symposium Series, Princeton, N.J. (1977).
75. C. W. Pearce and G. A. Rozgonyi, *ibid.*, p. 606.

Electrical Activation of Implanted Arsenic in Silicon during Low Temperature Anneal

Hidetoshi Nishi, Teruo Sakurai, and Tsuneo Furuya

Fujitsu Laboratories Limited, 1015 Kamikodanaka, Nakaharaku, Kawasaki 211, Japan

ABSTRACT

The correlation between the electrical activation of implanted As in Si and the recrystallization of the amorphous layers during low temperature anneals at 440°-650°C is studied by Hall effect measurements and glancing incidence channeling analysis. The results show that the activation process is described well by a simple epitaxial regrowth model. Implanted As atoms are electrically activated during the recrystallization with an activation energy ~2.7 eV. The electrical activation depends strongly on the crystal orientation of the wafer. In (100) oriented wafers the activation rate is highest, and we can achieve almost complete activity. However, in (110) and (111) oriented wafers, about 20 and 35% of As atoms are unactivated, respectively. It is confirmed from channeling analysis that lattice disorder remains in (110) and (111) oriented wafers. It is speculated that these defects act possibly as carrier compensating centers, thereby reducing the electrical activity.

Many investigators have been interested in a detailed understanding of the correlation between electrical activation of implanted dopants and the reordering of lattice damage created by ion implantation after annealing (1-4). For high dose implantation, if a continuous amorphous layer to the surface is formed during implantation, this layer will regrow epitaxially on the underlying crystalline substrate during annealing at temperatures around 600°C (5). A simultaneous reduction of the sheet resistivity is observed in this temperature range, indicating that the implanted dopants are incorporated onto lattice sites (6).

Channeling effect measurement is a useful tool for directly observing reordering of lattice disorder. Recent works of Csepregi *et al.* show that the regrowth of amorphous Si layers formed by self-ion (Si^+) im-

Key words: ion implantation, orientation dependence, epitaxial regrowth, recrystallization.

plantations is linear with time with an activation energy of 2.3 eV (7). It has also been observed that there are marked differences in the regrowth behavior depending on the crystal orientation of the wafers (8). It is reasonable to believe that the orientation-dependent regrowth behavior will affect the electrical activation of an implanted dopant, and will also be reflected in the annealing behavior at high temperature around 1000°C (9).

The purpose of the present paper, then, is to study the electrical activation of high dose implanted As in Si during the recrystallization process and the effect of crystal orientation on electrical activation. The electrical evaluation of the implanted layers, such as annealing characteristics of sheet carrier concentrations or carrier profiles, were made by Hall effect measurements. Glancing incidence channeling analysis was employed to observe recrystallization occurring some hundreds of angstroms beneath the surface for comparison with the electrical activation behavior. The glancing incidence channeling technique has recently been demonstrated by Williams to be a powerful method for investigating disorder distributions with a depth resolution of a few tens of angstroms (10).

First we discuss the electrical activation behavior which can be explained by a simple epitaxial regrowth model. Next, we discuss the effect of crystal orientation of the wafers on the electrical activation.

Experimental

The samples used in the present work were epitaxially grown p-type Si with resistivities of 1-5 Ω-cm. The crystal orientations of the wafers were (100), (110), and (111). The As implantations were carried out at 100 keV with substrate at room temperature. The implanted dose was 1×10^{15} cm^{-2}, and the dose rates ranged from 0.5 to 1.0×10^{12} cm^{-2} sec^{-1}. The critical dose for forming an amorphous layer by 100 keV As implantation is around 3×10^{14} cm^{-2} (6), so the dose studied in these experiments was sufficient to create continuous amorphous layers. Annealing of the implanted specimens was done in a dry nitrogen atmosphere at temperatures ranging from 440° to 650°C.

Electrical evaluation of the implanted layer was made using Hall effect and sheet resistivity measurements using a van der Pauw structure. Before As implantation the electrical contact areas for the Hall measurements were formed by a phosphorus diffusion with a surface concentration of 1×10^{20} cm^{-3} and a junction depth of about 1.5 μm. Carrier profiles were then determined from Hall effect and sheet resistivity measurements utilizing anodic oxidation and HF stripping methods. The thickness of anodic oxides was estimated by ellipsometry. The conversion ratio from SiO_2 thickness to etched layer thickness was determined using a Talystep and was found to be 0.58 ± 0.03.

The glancing incidence backscattering and channeling analysis were performed using 1.5 MeV He^+ ions. The incident direction of a beam was aligned with the <101> axis of a (110) oriented sample by tilting the sample 60° away from the <110> axis along the $(\bar{1}11)$ plane. The backscattered ions through an angle of 165° (of about 75° with respect to the surface normal) were detected by a solid-state detector. The directions of the <110> axes of the (110) samples deviated 5° at maximum from the surface normal of the samples. The energy resolution of the measuring system was about 13 keV. Corresponding depth resolution depended on the deviation of the direction of <110> axis from that of the surface normal and was 90-65Å. The thickness of the amorphous layers was determined using the stopping power data by Ziegler and Chu (11).

Results and Discussions

Recrystallization of amorphous layers.—Recrystallization behavior of the amorphous layers created by 100 keV As implantation to a dose of 1×10^{15} cm^{-2} was observed using glancing incidence channeling analysis. The upper part of Fig. 1 shows the backscattering spectra resulting from 1.5 MeV He ions directed along the <101> axis of (110) oriented specimens. Data indicated by the open circles and by + marks correspond to the spectrum obtained after anneals at 500°C for 60 and 200 min, respectively, and the closed circles correspond to as-implanted. The aligned spectra for <110> directions of the same samples were also measured and the results are shown in the lower part of Fig. 1 for comparison. As can be seen from the figure, the amorphous layer on the underlying crystalline substrate is characterized by a steplike shape. The thickness of the amorphous layer can be estimated from the energy width at half-height of the step using the stopping power data (11).

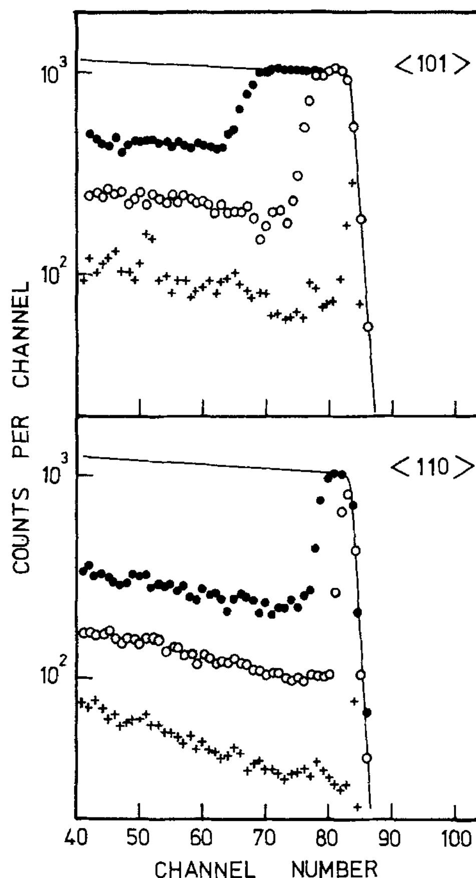

Fig. 1. Backscattering energy spectra for 1.5 MeV He ions directed along the <101> (upper) and the <110> (lower) of the (110) oriented Si. The spectrum indicated by the closed circles corresponds As 1×10^{15} cm^{-2} as-implanted. The open circles and + marks show the spectra after anneal at 500°C for 60 and 200 min, respectively.

The improvement of the depth resolution offered by utilizing the glancing incidence channeling technique can be easily seen by comparing the two corresponding spectra shown in the upper and the lower parts of Fig. 1. For example, in the <110> spectrum for the 60 min annealed sample, the surface peak does not coincide with random yield, however, in <101> spectrum we can clearly observe that a thin amorphous layer still remains.

From the spectrum indicated by the closed circles in Fig. 1, it is seen that a continuous amorphous layer of thickness 1100 ± 90Å was formed due to the implantation. After the anneal for 60 min at 500°C, this amorphous layer was reduced to 440 ± 70Å, indicating that the amorphous layer regrew epitaxially from the crystalline substrate to the surface with a regrowth velocity of about 11 Å/min. The amorphous layer is fully annealed as shown in the spectrum for 200 min anneal, however, the spectrum still indicates that a small frac-

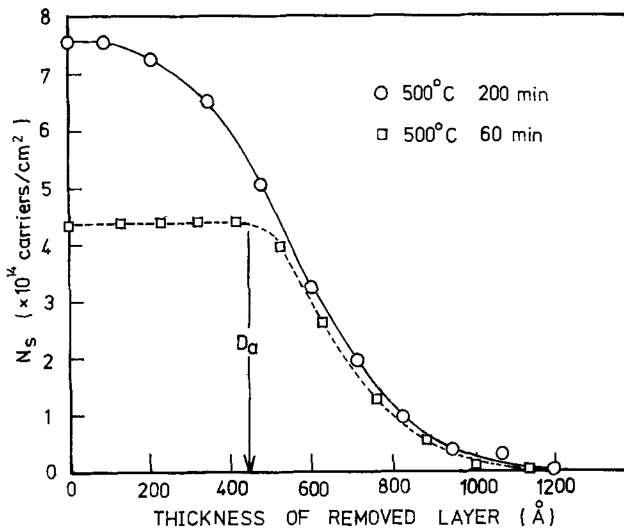

Fig. 2. The variations of the measured N_S's for the (110) oriented samples annealed at 500°C for 60 min (□) and for 200 min (○) as a function of the etched depth. The thickness of the residual amorphous layer after the 60 min anneal is indicated by D_A.

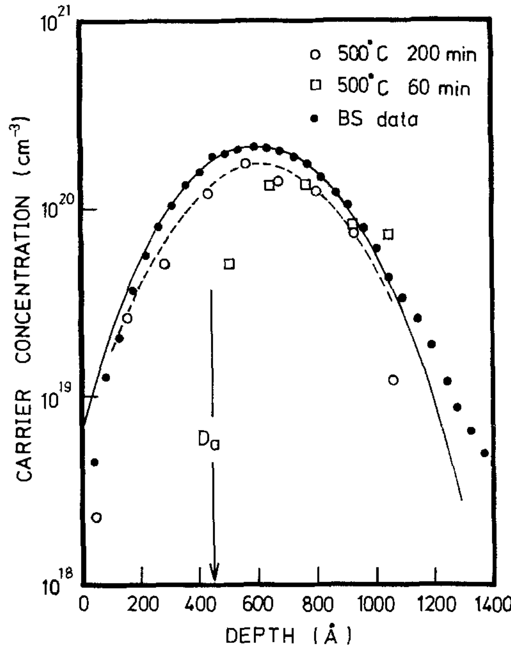

Fig. 3. Carrier profiles obtained from the data shown in Fig. 2. The depth distribution of As atoms is also shown indicated by the closed circles. The solid line represents the Gaussian profile with R_p 600Å and ΔR_p 240Å.

tion of disorder remains in the recrystallized layer; this is mentioned in a later section relating to the orientation-dependent electrical activity.

Carrier profiles were obtained from the same set of samples used in the channeling analysis. In Fig. 2, the measured N_s's are plotted as a function of the etched depth. The resulting carrier profiles are shown in Fig. 3 together with the depth distribution of As atoms obtained by the glancing incidence backscattering analysis. In both figures the data indicated by the squares and the open circles represent the results for 60 and 200 min anneals, respectively. As is seen in Fig. 2, the measured N_s's for the 60 min annealed sample exhibited no change from the surface to a depth of around 440Å, denoted by D_A in the figure. In the region deeper than 440Å, however, the N_s's for the 60 min annealed sample coincide well with that of the 200 min annealed sample. Considering that the amorphous layer regrew to a reduced thickness of about 440Å after the 60 min anneal at 500°C, it is seen that the ionized carriers exist only in the recrystallized layer, with the activation occurring from the amorphous/crystalline interface to the surface corresponding to the regrowth of the amorphous layer. We now introduce an epitaxial regrowth model and compare it with the electrical activation behavior.

Epitaxial regrowth model.—Based on the conclusion, as described above, that electrical activation of implanted As atoms occurs only in the recrystallized layer, we make the following three assumptions: (*i*) electrical activation ratio, η (the number of carriers in unit area per implanted dose), is constant throughout a recrystallized layer; (*ii*) amorphous layer created by As implantation regrows with a constant velocity, v, at annealing temperature, T_A; and (*iii*) v is independent of As concentrations. Therefore, for an As atom distribution with a Gaussian profile represented by the range parameters R_p and ΔR_p, the sheet carrier concentration, $N_s(t)$, after an anneal for time t at a temperature T_A is described by the following equation

$$N_s(t) = \frac{\Phi\eta}{\sqrt{2\pi}\Delta R_p}\int_{\infty}^{D_A} \exp\left\{-\frac{(x-R_p)^2}{2\Delta R_p^2}\right\} dx \quad [1]$$

where $D_A = D_O - vt$, Φ is the implanted dose, and D_O and D_A represent the thicknesses of the amorphous layer after the implantation and the anneal, respectively.

To compare this model with experimental results, the range parameters, R_p and ΔR_p, were estimated from the glancing incidence backscattering data shown in Fig. 3 indicated by the closed circles. The solid line in the figure represents a Gaussian profile with R_p 600Å and ΔR_p 240Å. These values agree well with those reported by Sigmon *et al.* (12). The distribution of As atoms fits well to the Gaussian profile except close to the surface and the region deeper than 1000Å.

Comparison of the experimental results with the calculated ones for a (100) oriented sample annealed isothermally at 460°C is shown in Fig. 4. The calculated curve (solid line) was derived from Eq. [1] using range parameters, R_p = 600Å and ΔR_p = 240Å, which were determined by the glancing incidence backscattering analysis and by using other parameters such as D_O = 1400Å, η = 0.95, and v = 3.5 Å/min. The value of η depends strongly on the crystal orientation of the wafer; this is described in the next section. In every calculation η was determined from the saturation value of N_s obtained after a sufficiently long anneal. The value of D_o used in every calculation is about 300Å

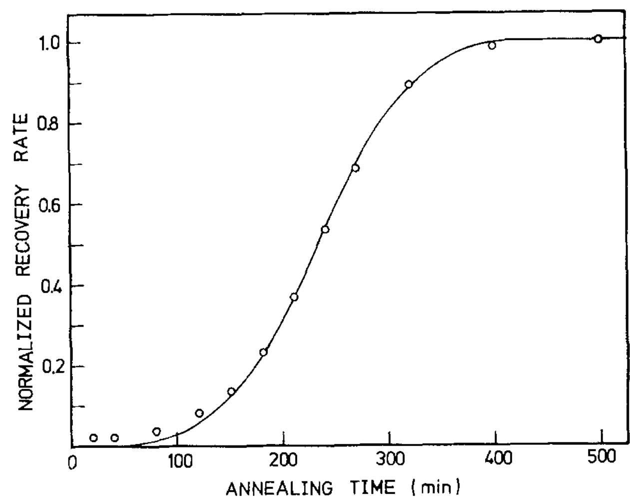

Fig. 4. Comparison of the experimental results with the calculated using the epitaxial regrowth model. The sample was (100) oriented and annealed at 460°C

larger than that obtained by glancing incidence channeling analysis; this is also discussed later. Agreement between the experimental and calculated values are quite good, except at the initial stage of the annealing.

For the epitaxial regrowth model, we adopt the assumption that As atoms are activated with a constant activation ratio in the whole regrown layer. To justify this assumption we examine (111) oriented wafers in which the activity, η, is only about 65% as is described in the next section. The results for annealing at 500°C are shown in Fig. 5. The solid line in the figure represents the calculated result from Eq. [1] with the condition that η is 0.65 and v is 1.3 Å/min. Calculation was also made for the assumption that the carrier concentration is limited to a certain value. To obtain the same activity, 65%, for the whole recrystallized layer, we assume that this limit is 1.2×10^{20} cm^{-3} and the activity is 100% for As concentration below this limit. The calculated result is shown by the dashed line in Fig. 5. The solid line fits the experimental results better than the dashed line, proving that the activation ratio is constant in the whole region and no observable saturation of carriers occurs for the dose of 1×10^{15} cm^{-2}.

Calculations were also made using the equation based on the epitaxial regrowth model and compared with the experimental results for (100), (110), and (111) oriented wafers annealed isothermally in the temperature range 440°-650°C. Good agreement was obtained in every case using the parameter $D_O = 1400$Å while only changing the assumed value of the epitaxial regrowth velocity, v, and assuming η to be equal to the final activity obtained when the regrowth is completed. The value D_O used in every calculation is about 300Å larger than that observed by glancing incidence channeling analysis. The regrowth velocity is actually dependent on impurity concentration (13), therefore, it is reasonable to assume that the v used in the calculations reflects the regrowth velocity in highly As-doped layer. In the initial stage of annealing, the amorphous layer regrows with slower velocity than that used in the calculations because of low As concentrations. This effect, together with a fact that a small number of implanted As atoms are located beyond the amorphous region (see the As distribution in Fig. 3), leads to a smaller calculated value than the experimental ones in the initial stage of annealing as can be seen in Fig. 4 and 5. Furthermore, the quantity η may not be constant throughout the whole regrown layer; however, this factor is not sufficiently large to be detected in the experiments studied here.

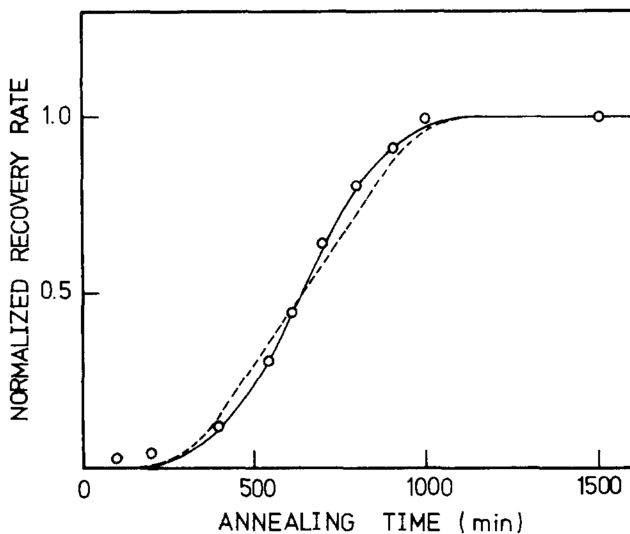

Fig. 5. Comparison of the experimental results with the calculated for the (111) oriented sample annealed at 500°C. The solid and the dashed curves represent the calculated results assuming that the activity is constant in the whole recrystallized layer and that the carrier concentration is limited at 1.2×10^{20} cm^{-3} and the activity is 100% below this value, respectively. In both calculations v is taken to be 1.3Å/min.

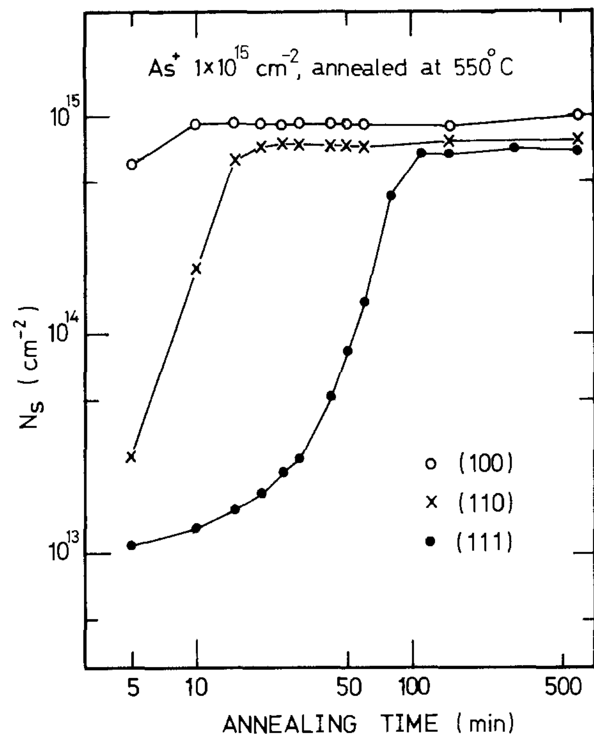

Fig. 6. Orientation dependence of isothermal annealing behaviors of N_S's at 550°C.

Crystal orientation dependence.—In this section we study the effect of crystal orientation of a wafer on the electrical activation of As implanted in silicon.

Isothermal annealing characteristics of the measured N_S's are shown in Fig. 6, comparing the results for (100), (110), and (111) oriented samples. Implanted dose was 1×10^{15} cm^{-2}, and annealing was carried out

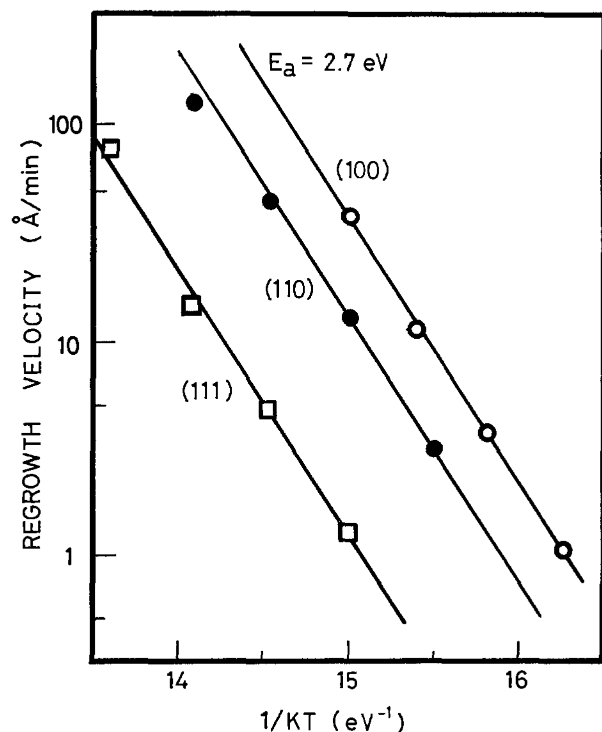

Fig. 7. Arrhenius plot of a regrowth velocity used in the calculations based on the epitaxial regrowth model.

at 550°C. It can be seen from the data that both the activation rate and the final activity are strongly dependent on the crystal orientation of the wafer. For the (100) oriented wafer, the electrical activation progresses most rapidly and results in almost complete activity, however, it progresses most slowly and results in the lowest activity (~65%) for the (111) oriented wafer. The (110) oriented sample exhibits an intermediate characteristic to the (100) and the (111) oriented samples. For 1×10^{14} As ions cm^{-2} implanted Si, the annealing characteristics of measured N_s's did not depend on the crystal orientation of the wafer, indicating that the orientation dependence is due to the formation of the amorphous layer by As implantation. Activation behavior showed similar tendencies at the other annealing temperature studied (440°-650°C).

Figure 7 shows Arrhenius plot of v used in the calculations of the previous section. It is found from this figure that v is about 3 and 29 times higher for (100) wafers than for (110) and (111) oriented wafers, respectively. The orientation dependence of the activation rate is, therefore, attributed to the difference in the regrowth velocity for the various orientations. The activation energy was determined from the data to be 2.8 ± 0.2 eV for (100), 2.6 ± 0.3 eV for (110), and 2.7 ± 0.2 eV for (111) oriented samples. The activation energy for the three different orientations can be regarded to be equivalent, ~2.7 eV. The value obtained from this work is close to the activation energy for the regrowth of intrinsic amorphous Si (2.3 eV) measured by Csepregi *et al.* (7).

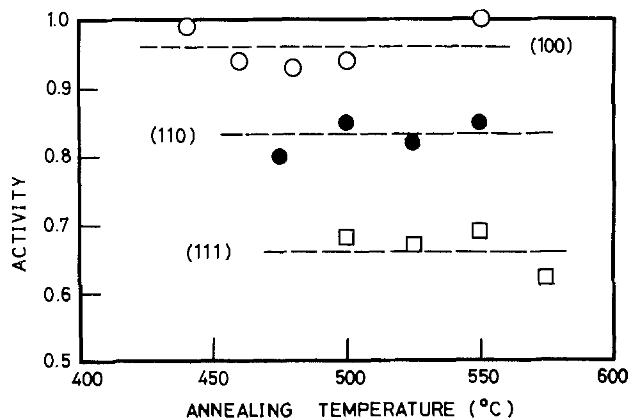

Fig. 8. Temperature dependence of the final activity obtained when the regrowth completes at each temperature.

Figure 8 shows the temperature dependence of the final activity obtained after an anneal sufficiently long so that the regrowth is completed at each temperature. It can be seen from the figure that the electrical activity depends only on the crystal orientation. In (100) oriented wafers nearly complete activity (0.96 ± 0.04) can be achieved, however, the activities are fairly low in (110) and (111) oriented wafers, 0.83 ± 0.04 for (110) and 0.66 ± 0.04 for (111). To compare with these results, the crystalline properties of the recrystallized layers were examined by channeling analysis.

Backscattering spectra for 1.5 MeV He^+ ions incident on <100> for (100) oriented, <110> for (110) oriented, and <111> for (111) oriented samples are shown in Fig. 9A, B, and C, respectively, along with that of an unimplanted sample. All the samples were annealed at 500°C for a sufficiently long time so that the regrowth proceeded to completion as shown in Table I. Data for the recrystallized layers are indicated by the closed circles and the solid lines represent the aligned spectra for the unimplanted samples. The surface peak for the unimplanted samples around the channel number of 84 corresponds to native silicon dioxide. In the (100) oriented sample (Fig. 9A) we cannot observe any difference between the aligned spectra for the recrystallized and unimplanted layers. The aligned spectrum for the recrystallized (110) oriented sample (Fig. 9B) exhibits a slightly higher scattering yield than for the unimplanted, except the surface peak. Discrepancy between the aligned spectra of the recrystallized and the unimplanted samples is quite remarkable for (111) oriented samples as is seen in Fig. 9C. This spectrum shows that lattice disorder remains in the recrystallized layer of (111) oriented sample. The surface peak of the spectrum is larger than the unimplanted sample, indicating that ~1.6×10^{16} displaced Si atoms per cm^{-2} exist at the surface layer.

The minimum yields for these samples are determined from the channeling spectra shown in Fig. 9A, B, and C, and are listed in Table I together with the measured N_s's for the same samples. The minimum yield listed is the averaged value corresponding to a depth 500-600Å beneath the surface. In the (100) oriented sample the minimum yield is equivalent to that of the unimplanted sample. For the (110) orientation the difference in the minimum yield between the recrystallized and unimplanted samples is within ex-

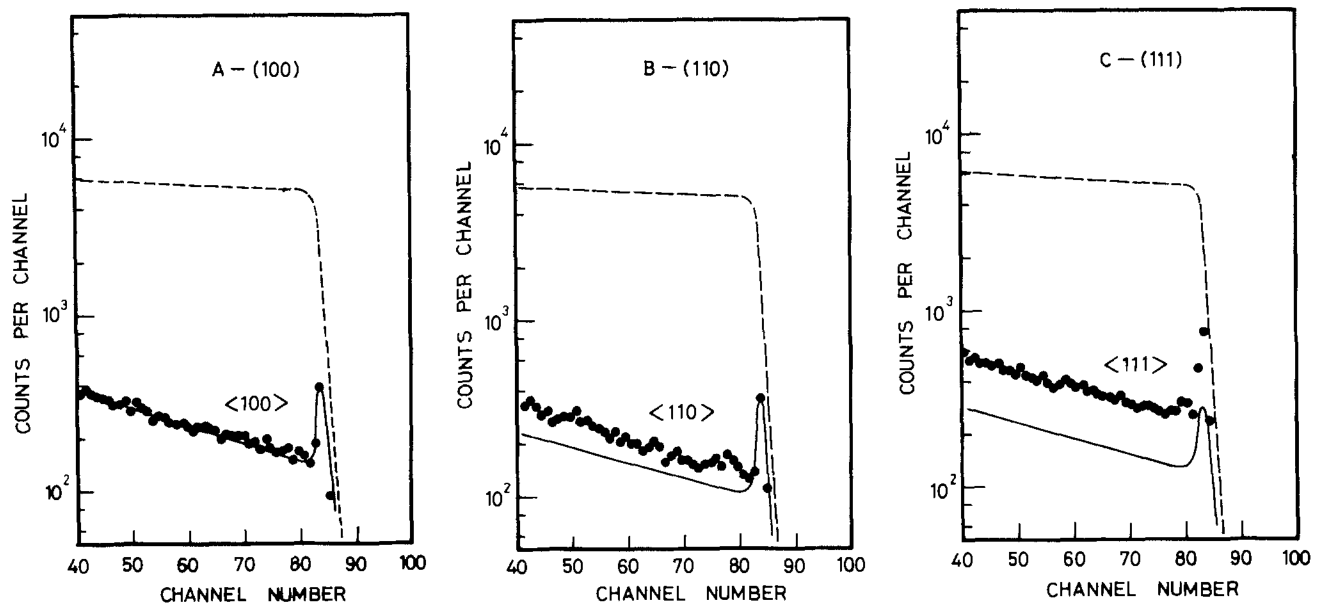

Fig. 9. Comparison of the aligned spectra between the recrystallized and the unimplanted samples. The results for the (100), (110), and (111) oriented samples are shown in A, B, and C, respectively.

Table I. Comparison of the minimum yields for channeling with the measured N_S.
The minimum yields are obtained at the depth 500-600A

Sample orientation	Axis	x_{min} (%) Implanted	x_{min} (%) Unimplanted	N_s (cm^{-2})	Annealing
(100)	<100>	3.1 ± 0.3	3.1 ± 0.5	9.5 × 10^{14}	500°C 85 min
(110)	<110>	2.7 ± 0.3	2.2 ± 0.2	8.4 × 10^{14}	500°C 200 min
	<101>	6.1 ± 0.3	2.0 ± 0.3		
(111)	<111>	5.1 ± 0.4	2.5 ± 0.6	6.8 × 10^{14}	500°C 1500 min

perimental error. However, the result from the glancing incidence channeling analysis clearly show that lattice disorder remains in the recrystallized (110) layers. This can be seen because of the improvement of sensitivity in detecting lattice disorder available using the glancing incidence technique (10). The minimum yield for the recrystallized (111) oriented sample is about twice as large as for the unimplanted sample. Increase in the scattering yield due to lattice disorder observed at the surface of (111) oriented sample is calculated to be less than 10^{-3} according to the single scattering model (14). Therefore, the difference in minimum yields is caused by disorder remaining in the recrystallized layer. The minimum yield for <110> channeling for the recrystallized (111) oriented sample was also measured and it showed about twice as large a value as for the unimplanted sample. The orientation dependence observed in the minimum yield corresponds well with that of the N_S's listed in Table I. The lattice location of implanted As atoms might be different in the differently oriented samples, however, the correlation between the channeling measurements and the activation of implanted As in samples of different orientation indicates that the lower activity for (110) and (111) oriented samples could be due to carrier compensation by residual defects remaining in the recrystallized layers.

Summary

The electrical activation behavior of implanted As in Si during recrystallization of amorphous layers has been studied. The results obtained in this study are summarized as follows:

1. The activation behavior is described well by the epitaxial regrowth model. The activation occurs from the amorphous/crystalline interface to the surface corresponding to the regrowth of the amorphous layer.
2. The activation energy of implanted As is ~2.7 eV, close to that reported for the regrowth of intrinsic amorphous Si.
3. The activation rate depends on the crystal orientation of the wafer, being highest for (100) orientation (about 3 and 29 times larger than for (110) and (111), respectively). This is attributed to the difference in the regrowth velocity for the orientations.
4. Lattice disorder remains in the recrystallized amorphous layer on (111) and (110) wafers, and these residual defects possibly act as carrier compensating centers, thereby reducing the electrical activities by about 17 and 34% in (110) and (111) oriented wafers, respectively.

Acknowledgments

The authors would like to express their thanks to Dr. T. Oshida and Dr. O. Ryuzan for their encouragements throughout this work, to T. Hisatsugu, S. Hashimoto, and T. Kaneda for valuable discussions and comments on this work. They also thank T. Sato, S. Tatsuta, T. Inada, and H. Kawata for their experimental help, and to S. Yamamoto for Talystep measurements. One of the authors (H.N.) would like to thank Dr. A. Revesz for helpful comments on this work.

Channeling experiments were performed using the 2.0 MeV Van der Graaff accelerator at Government Industrial Research Institute, Osaka. The authors greatly appreciate I. Fukui and M. Sato for affording the use of the facility.

Manuscript submitted May 13, 1977; revised manuscript received Oct. 17, 1977.

Any discussion of this paper will appear in a Discussion Section to be published in the December 1978 JOURNAL. All discussions for the December 1978 Discussion Section should be submitted by Aug. 1, 1978.

Publication costs of this article were assisted by Fujitsu Laboratories Limited.

REFERENCES

1. L. Eriksson, G. R. Bellavance, and J. A. Davies, *Radiat. Eff.*, **1**, 71 (1969).
2. L. Eriksson, J. A. Davies, N. G. Johanson, and J. W. Mayer, *J. Appl. Phys.*, **40**, 842 (1969).
3. G. Fladda, K. Bjorkqvist, L. Eriksson, and D. Sigurd, *Appl. Phys. Lett.*, **16**, 313 (1970).
4. J. C. North and W. M. Gibbons, *ibid.*, **16**, 126 (1970).
5. J. W. Mayer, L. Eriksson, S. T. Picraux, and J. A. Davies, *Can. J. Phys.*, **46**, 663 (1968).
6. B. L. Crowder, *This Journal*, **118**, 943 (1971).
7. L. Csepregi, J. W. Mayer, and T. W. Sigmon, *Phys. Lett. A*, **54**, 157 (1975).
8. L. Csepregi, J. W. Mayer, and T. W. Sigmon, *Appl. Phys. Lett.*, **29**, 92 (1976).
9. H. Müller, W. K. Chu, J. Gyulai, J. W. Mayer, T. W. Sigmon, and T. R. Cass, *ibid.*, **26**, 292 (1975).
10. J. S. Williams, in "Ion Beam Surface Layer Analysis," Vol. 1, O. Meyer, G. Linker, and F. Kappeler, Editors, p. 223, Plenum Press, New York (1975).
11. J. F. Ziegler and W. K. Chu, *At. Data Nucl. Data Tables*, **13**, 463 (1973).
12. T. W. Sigmon, W. K. Chu, H. Müller, and J. W. Mayer, *Appl. Phys.*, **5**, 347 (1975).
13. L. Csepregi, Private communication.
14. L. C. Feldman and J. W. Rodgers, *J. Appl. Phys.* **41**, 3776 (1970).

Controlling the Interfacial Oxide Layer of Ti-Al Contacts with the CrO_3-H_3PO_4 Etch

T. A. Shankoff, C. C. Chang, and S. E. Haszko

Bell Laboratories, Murray Hill, New Jersey 07974

ABSTRACT

The cause of high resistance contacts between Al integrated circuit metallization and subsequently applied Ti/Pt/Au beam leads has been evaluated by direct measurement of the surface Al-oxide thickness at various steps in the processing sequence. The Al-oxide layer thicknesses were estimated using Auger electron spectroscopy and gravimetric measurements and were correlated with Hg-probe voltage breakdown observations. Processed MOS wafers incorporating ethylene glycol-buffered HF cleans typically contain 50-60Å of Al oxide in bonding pad regions just prior to Ti deposition. It was demonstrated that the Ti nullifies about 45Å of the oxide by interfacial reaction; therefore, products having >50Å oxide will be yield-limited by high resistance beam-to-Al contacts. A dielectric breakdown strength of 0.09 V/Å was found for the surface Al oxide obtained during processing, and the effective electron tunneling distance was estimated to be 12Å. A convenient method of eliminating surface Al oxide just prior to Ti deposition was demonstrated. An Al-oxide etchant containing CrO_3-H_3PO_4-H_2O removes Al oxide, leaving only an equilibrium final film of 25-30Å thickness, and does not attack underlying Al metal. The effectiveness of such a surface treatment has been confirmed by the excellent contact yields obtained with two MOS split device lots.

Electrical contact to Al metallization in Si integrated circuits is sometimes difficult to establish because of the rapid growth of a surface oxide layer during processing. If this oxide is sufficiently thick, a contact will be open until enough voltage is applied to cause dielectric breakdown.[1] Two approaches that can be considered as potential solutions to this problem are backsputtering and chemical etching. Backsputtering has the advantage that the oxide thickness can in principle be reduced to zero if the subsequent metallization is applied without exposure to air. The disadvantages include: possibility of radiation induced MOS damage; potential for contamination of the sputtering system; redeposition of previously sputtered material, especially from the substrate table; and the need for frequent monitoring of system cleanliness. The chemical etch procedure does not have these disadvantages, but the oxide thickness can never be reduced to zero.

We show below that because of a finite electron tunneling distance and because a Ti film deposited onto Al will effectively consume a certain amount of Al oxide, it is not necessary to reduce the oxide thickness to zero to obtain Ti-Al contacts with zero breakdown voltage. The present study was conducted in order to carefully define Al-oxide thickness tolerances for subsequent Ti metallization, and to optimize a chemical etching procedure based on the CrO_3-H_3PO_4-H_2O Al-oxide solvent system (1). Oxide thicknesses were determined using Auger spectroscopy and gravimetric measurements, while breakdown voltages were obtained using the Hg probe. We describe our model of the Ti-Al contact, and the procedures for preparing Ti-Al contacts with zero breakdown voltage, using the chemical treatment.

Experimental

The Al test films used in this work were 1.5 μm thick, deposited on oxidized 3 in. Si wafers by E-gun evaporation without intentional substrate heating. The Al was doped with 1 weight percent (w/o) Cu. Patterning was accomplished using negative photoresist and A-30 stripping (Allied Chemical proprietary solvent system). Several wafers were also examined after removal from MOS device lots at appropriate points during processing. The Al processing sequence investigated for this work is shown on the left-hand side of Table I.

Ti dots were filament evaporated onto the Al surface through a shadow mask for the experiments on the effect of Ti on the surface Al-oxide. Other methods of Ti dot preparation for this evaluation (evaporated and sputtered Ti patterned by photolithography and chemical or plasma etching) resulted in data that were difficult to interpret, apparently owing to etching residues from the interaction of the Al-oxide surface with the uniformly deposited Ti.

Oxide breakdown voltages were measured using a Hg probe, which was simply a drop of Hg, about 1 mm in diameter, held over the position of interest by a Pt wire loop. The Pt wire also served as part of the electrical circuit for the probe. Contact to the Al film was established by pushing a second Pt wire directly into the Al. The breakdown voltage was obtained from *I-V* curves, generated on a Tektronix 576 curve tracer. A sufficient number of measurements were made (between 5 and 10) so that the standard deviation was less than ±5%.

The etchant used for surface Al-oxide removal is the CrO_3-H_3PO_4-H_2O system. Although the effect of this etch on both Al and Al-oxide surfaces has been extensively investigated (1, 2), the effects on actual LSI MOS circuits was not known, and the useful

Table I. Aluminum oxide thicknesses during processing*

Processing step	Al-oxide thickness (A)
1. Deposit Al	20-30
2. Al photolithography, A-30 resist strip	25-35
3. EG:BHF:H_2O clean 1**	35-45
4. 30 min, 450°C hydrogen anneal	40-80
5. EG:BHF:H_2O clean 2	40-60
6. O_2 plasma clean	
7. Plasma silicon nitride window etch (plasma)	40-60
8. EG:BHF:H_2O clean 3	40-60
9. Ti deposition	

* The processing sequence tabulated here is incomplete in the sense that steps not directly relevant to the Al-oxide problem have been deleted.

** EG:BHF:H_2O is an equivolume mixture of ethylene glycol, 7:1 buffered HF, and water.

[1] For example, contact failures on some MOS devices were characterized by open Al-Ti contacts detected with 1-1.5V test voltage, which "healed" when the voltage was raised to 2-3V, indicating a thin dielectric barrier.

etchant compositions and thickness variations of the final, equilibrium Al oxide over different areas of a given device chip have not been previously measured. Therefore, we investigated these factors to determine the optimum process conditions for the present applications.

One of the methods used to determine the amount of surface Al oxide was an extension of an established ASTM gravimetric procedure (3) wherein a sample is weighed, exposed to a CrO_3-H_3PO_4-H_2O solution to dissolve the oxide surface, and is reweighed. Since it has been established (3) that the equilibrium loss of Al metal in the etchant is about 2 Å/min, the weight loss is due to etched Al oxide once correction for Al loss is made. In the ASTM method, typical weight losses in the milligram range corresponded to Al-oxide thicknesses in the micrometer range. We have been able to extend the method into the angstrom range by measuring weight losses of less than 100 μg. The assumptions made in applying this method to our case include: (*i*) that the mechanism of the CrO_3-H_3PO_4-H_2O Al-oxide clean is such that all of the initially present surface Al oxide is removed and an equilibrium final film containing both Cr and P is then formed [this is in general agreement with earlier observations (1)]; (*ii*) that although the density range of Al oxide can be from 2.5 to 4.0 g/cm^3, the surface oxide we are dealing with which was formed in solution, probably is a form of alumina with a density close to 3.0 [note that the ASTM method clearly defines a density of 3.0 for Al oxides determined using the gravimetric method as does previous work at Bell Laboratories (4) regarding Al oxide formed in water]; and (*iii*) that the equilibrium Al etch rate of 3 Å/min found in this work is applied against the weight loss found for each sample. A solution containing 2g CrO_3, 5 ml 85% H_3PO_4, and 100 ml of water was used for 5 min at 80°C. As with the Hg probe data, a sufficient number of readings were taken for each weighing until the results were statistically meaningful (usually 20). Extreme care had to be taken to ensure neither the addition of, nor the removal of, material from the 3 in. Si wafer used as the Al film substrate, because of the small weight losses being measured.

The surface compositions and oxide thicknesses were also determined using Auger analysis (5, 6). Oxide thicknesses were estimated using the chemically shifted Auger peaks (6) so that ion mill depth-profiling was not necessary. The Auger apparatus was a Varian cylindrical mirror analyzer with a 10 kV electron gun and comparatively high energy resolution (0.25%) which enabled the chemically shifted Auger peaks to be effectively resolved. The spatial resolution of this technique is limited by the incident electron beam diameter and was less than 10 μm.

Results and Discussion

Typical oxide thicknesses.—The right hand portion of Table I shows typical Al-oxide thicknesses at various stages of Al processing. An important point to note is that, as processing of as-deposited Al proceeds, the oxide thickness can increase. Unless one is acutely aware of the effect of each processing step on the surface Al-oxide thickness, reasonable amounts can build up which later make electrical contact of a subsequent metallization difficult or impossible. The Auger thickness data in Table I are supported by the gravimetric and Hg-probe data as shown in Table II.

Table II. Surface aluminum oxide thickness by various methods

Sample	Thickness in Å found by Hg-probe	Auger	Weight loss
1	51	56	58 ± 18
2	47	47	39 ± 18

Note: Close agreement between Auger and Hg probe data is expected because the latter was calibrated using Auger thickness data. However, it is to be pointed out that the resultant dielectric breakdown strength for the Al-oxide turned out to be almost exactly the value for bulk Al-oxide which provides an independent confirmation of the correctness of the calibration.

An attempt to check the thickness data given in Table II with yet another technique, ellipsometry (7), resulted in data indicating significantly thicker films (>100Å) compared to the other three methods. It should be noted that the samples used for Table II were processed through a final cleaning solution containing one part ethylene glycol, one part 7:1 buffered-HF (7 parts 40 w/o NH_4F in water to 1 part 49% HF) and one part water (EG:BHF:H_2O). For most other processing treatments ellipsometric results tended to be in good agreement with the Auger values. We consider it unlikely that all of the other methods could be in error by the amount indicated by the ellipsometric results. Moreover the ellipsometric data can be sensitive to the exact degree of oxide hydration, porosity, and physical surface structure (*i.e.*, platelet, filamentary, crystalline, etc.) (8). Therefore, we have based the present investigation on the Auger, gravimetric, and Hg-probe results, which are quite self-consistent, and sufficiently understood.

As discussed above, the Al surface which is obtained in the EG:BHF:H_2O solution proved the most difficult to reconcile among the four measurement techniques. This solution affords a convenient means of etching and cleaning dielectrics (SiO_2, Si_3N_4, Al_2O_3) in the presence of Al metal without significant attack on the metal (9). This treatment was recently being evaluated for routine MOS processing as a preplasma SiN clean. Recent Auger analysis showed that Al surfaces treated with an EG:BHF:H_2O solution contain besides Al and O, significant amounts of F, and trace amounts of N, suggesting the possibility of an Al-oxyfluoride surface compound rather than a simple Al oxide. The underlying Al film tends to be slightly attacked and roughened. These factors are probably responsible for the discrepancy between ellipsometric data and the other measurements.

Dielectric breakdown strength of oxide on aluminum.—The dielectric strength of the oxides of interest here were determined using the Hg probe, and the results are presented in Fig. 1. Al-oxide thicknesses were all determined using the Auger method except for the two gravimetric points (1G and 2G). We obtained a dielectric breakdown strength of 0.09 V/Å, which is typical of good quality dielectrics, *e.g.*, SiO_2 is ~0.08 V/Å. The zero intercept for the straight line plotted in Fig. 1 corresponds to an effective electron tunneling distance of 12Å.

Effect of titanium.—One of the practical objectives of the present study was to prepare an Al surface to which Ti (the initial metal in the trimetal beam lead process) can make proper contact. Thus, the next area considered was the effect of Ti on the Al-oxide breakdown voltage. A sample of Al having 90Å surface oxide (Auger) that was grown in 60°C water was used; Ti dots were filament evaporated through a shadow mask. The 90Å thickness was selected to ensure residual Al oxide after surface interaction with the Ti, since the goal of the experiment was to accurately determine the decrease in effective dielectric thickness of the Al oxide upon Ti deposition. Prior to Ti deposition the oxide breakdown voltage was measured with the Hg probe to be 7.5V, which as can be seen from point 9 in Fig. 1 is in excellent agreement with the 90Å Auger thickness value. After Ti deposition, the uncovered Al areas were still found to break down at 7.5V, whereas the Ti areas required only 3.5V, corresponding to the annihilation of about 45Å of Al oxide. This conclusion is valid because the Ti dot surface does not contribute to the breakdown voltage as evidenced by

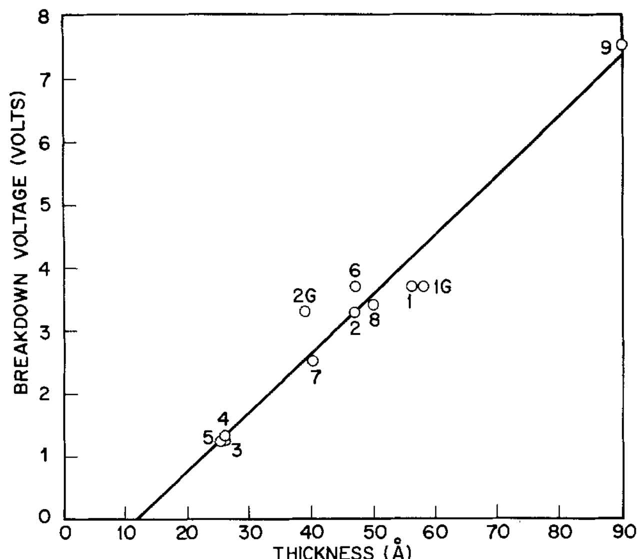

Fig. 1. Breakdown voltage (Hg probe) vs. Al-oxide thickness (Auger and gravimetric). The slope of the straight line gives a dielectric breakdown strength of 0.09 V/Å, and the zero intercept gives an electron tunneling distance of 12Å. Sample numbers are indicated at each data point and correspond to the following processing:

No.	Thickness	Processing sequence (see Table I)
1.	Auger	No. 1, 2, 3, 4, 5
1G.	Gravimetric	No. 1, 2, 3, 4, 5
2.	Auger	No. 1, 2, 3, 4, 5
2G.	Gravimetric	No. 1, 2, 3, 4, 5
3.	Auger	Sample 1 + CrO_3-H_3PO_4 + 15 min in air
4.	Auger	Sample 3 + 30 hr in air
5.	Auger	Sample 2 + CrO_3-H_3PO_4 + 15 min in air
6.	Auger	No. 1 + 30 days
7.	Auger	No. 1, 4
8.	Auger	No. 1, 4, 5
9.	Auger	No. 1 + 60°C H_2O; sample used in Ti expt

the zero breakdown voltage found between a Hg probe and a large area Ti film. The following Al-oxide reduction reaction can be noted

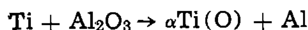

$$Ti + Al_2O_3 \rightarrow \alpha Ti(O) + Al$$

where the O is in solid solution in Ti. Note that the solid solubility of O in the αTi phase is about 33% (10). If the 12Å tunneling range found earlier is added to this 45Å, then it is suggested that Al films having about 55Å of surface oxide will make ohmic contact to Ti metal on a statistically marginal basis. It is clear that the processing sequence of Table I produces an Al surface whose average oxide thickness is close to the marginal value (step 8). Therefore, it is not surprising that the final aspect of this program involved developing a chemical treatment which effectively reduces the Al-oxide thickness to "safe" low values.

The CrO_3-H_3PO_4-H_2O Al-oxide etching system.—It has been reported (1) that the aqueous CrO_3-H_3PO_4 solution passivates the Al surface first by dissolving the surface oxide and then by subsequent reaction with the metal to form a thin surface layer. Estimates of the thickness range of this passivating layer fall in the 10-30Å range (1, 2). In Ref. (1), an estimate of 10-20Å was obtained by use of radioactive CrO_3 and H_3PO_4 to label the thin Al surface film. It was found that the atomic concentration ratio of P to Cr was 0.85 ± 0.2. Using the assumption of a mixed Al-Cr phosphate surface compound having a density about that of $AlPO_4$ (2.6 g/cm^3), it was concluded that a typical film would be 10-20Å thick. Several other results (1) of interest include: (*i*) a 5 min treatment of an Al surface at 85°C is sufficient to establish an equilibrium film condition; (*ii*) the equilibrium dissolution rate of the underlying metal is no more than 2 Å/min (we found 3 Å/min); (*iii*) the initial Al-oxide thickness prior to CrO_3-H_3PO_4-H_2O treatment has little effect on the final thickness of the passivation layer.

Application of the CrO_3-H_3PO_4-H_2O etchant as described in the literature (5 v/o H_3PO_4, 2 w/o CrO_3 at 80°-85°C) showed that certain regions of every device chip on MOS wafers developed a brownish coloration, suggesting a form of electrochemical corrosion. Clearly the above composition is not an optimum one for obtaining the thinnest possible surface film for our application. Therefore, additional experiments whose results are set out in Table III were performed to determine this optimum composition and also to minimize the browning attack. In addition, actual device wafers processed up to step 8 of Table I were treated, and individual contact pads were surveyed, in order to determine the pad-to-pad Al-oxide thickness differences.

In Table III, samples no. 1-18 were full-surface Al films with a 60Å surface oxide grown in 40°C water. Etchant composition, solution temperature, and etch times were varied, and the resultant oxide thicknesses were measured using Auger spectroscopy. Samples no. 1 and no. 2 show that the browning is caused by CrO_3. The brown coloration was visually impossible to discern with any of the remaining full surface samples. The table also shows that the etch composition is clearly not an important variable over a wide range. The solution temperature is obviously important, although the effect of a lower temperature can be compensated by an increased etch time. In general, the more dilute solutions with respect to CrO_3 produced thinner surface films. However. sample no. 1, 17, and 18 show that Al attack and dissolution become severe if the CrO_3 content is too low.

An approximate calculation of the surface atomic composition using the Auger data indicated no large differences in surface composition as a function of the variables investigated. However, some variation was noted as a function of depth. The surface composition in the outer half (~10Å) of the surface layer was in good agreement with the literature (1) in that P and Cr amounts are consistent with mixed phosphates and oxide of trivalent Al and Cr. How-

Table III. The H_3PO_4-CrO_3-H_2O etch

No.	H_3PO_4 (ml)	CrO_3 (g)	Temp (°C)	Time (min)	Oxide (Å)	Remarks
Full surface Al samples						
1	10	0	80	5	—	Al etches
2	0	5	80	5	—	Al gets brown
3	10	5	20	5	43	Al etches ~3Å/min
4	30	15	20	5	38	Al etches ~3Å/min
5	10	5	20	30	34	Al etches ~3Å/min
6	30	15	20	30	34	Al etches ~3Å/min
7	10	5	50	10	33	Al etches ~3Å/min
8	3.5	2	50	10	35	Al etches ~3Å/min
9	30	15	50	10	35	Al etches ~3Å/min
10	10	5	80	2	33	Al etches ~3Å/min
11	3.5	2	80	2	33	Al etches ~3Å/min
12	30	15	80	2	34	Al etches ~3Å/min
13	10	1	80	2	34	Al etches ~3Å/min
14	10	0.5	80	2	32	Al etches ~3Å/min
15	10	0.25	80	2	30	Al etches ~3Å/min
16	10	0.20	80	15	—	Al etches ~3Å/min
17	10	0.10	80	15	—	Al etches <1000Å/min
18	10	0.05	80	5	—	Al etches >3000Å/min
MOS device chips						
19	30	15	20	5	31	2 contact pads examined
20	10	5	80	2	28	2 contact pads examined
21	10	5	50	10	28	2 contact pads examined
22	10	1	80	2	28	2 contact pads examined
23	10	0.5	80	2	27	2 contact pads examined
24	10	0.25	80	2	(27)	35 contact pads examined

Starting material was an Al film with 60Å of surface oxide for the full surface samples, while device chips were after step 8 of Table I and had typically 50Å of oxide.

The H_3PO_4 was an 85% solution and all etches were prepared by mixing the listed contents with 100 ml of water.

ever, the remaining 10Å or more appeared to be deficient in P and Cr and was therefore essentially Al oxide. This result explains why the thicknesses we measured are somewhat larger than those previously calculated (1) assuming a single Al-Cr phosphate-oxide layer. With these initial results, then, some actual device chips were treated and the oxide thicknesses on the bonding pad areas were measured.

The device chosen was a MOS code processed up to step 8 of Table I, when typical oxide thicknesses should be near 50Å; for example, the thicknesses over devices from two different lots were 54 and 60Å. The results are displayed in no. 19-24; all of the experiments were performed using chips taken from the same wafer. For the last sample, all 42 pads were examined; while for the remaining samples, the two pads at the pad locations in no. 24 which evidenced the thickest films, were measured. The distribution of oxide thicknesses on the pads of sample no. 24 is shown in Fig. 2. The thicknesses ranged from 24 to 29Å with a sharp distribution peak at 27Å. Note that the data from only 35 of the 42 pads could be obtained; all of the remaining 7 pads were floating pads (not connected to the Si substrate), and data could not be obtained from them because of electrostatic charging problems caused by the incident electron beam. For this etch procedure then, the oxide thickness was about 27 ± 3Å which is considerably less than the marginal value of 55Å we determined earlier. Therefore, this etch should be quite acceptable for routine application because of the rather large safety margin of a factor of two in oxide thickness.

The brown coloration due to the presence of CrO_3 was more easily seen on the device chips than on full surface Al films because of the preferential coloration over certain areas in the metallization pattern. Coloration was clearly evident within the Al circuitry (although not on contact pads) for no. 22, perhaps present for no. 23, and not discernable at all for no. 24. Therefore, CrO_3 concentrations below that used for no. 22 appears requisite if all discoloration is to be avoided.

Based on the aforementioned quantitative surface oxide thickness data and on qualitative (gas evolution, surface attack) and quantitative (etch rates) observations regarding Al attack, we decided that the optimum Al-oxide etchant contains 3.5-10 ml 85% H_3PO_4 and 0.25-0.50g CrO_3 for each 100 ml of water. Typical etching times are between 2 and 10 min at 80°C. Reduction of CrO_3 below 0.2g encourages Al attack by H_3PO_4, while amounts of CrO_3 in excess of 0.5g results in visible browning of various portions of the integrated circuit metallization pattern. Quantities of CrO_3 well in excess of 0.5g (5-15g) appear to have little effect on electrically floating Al metal.

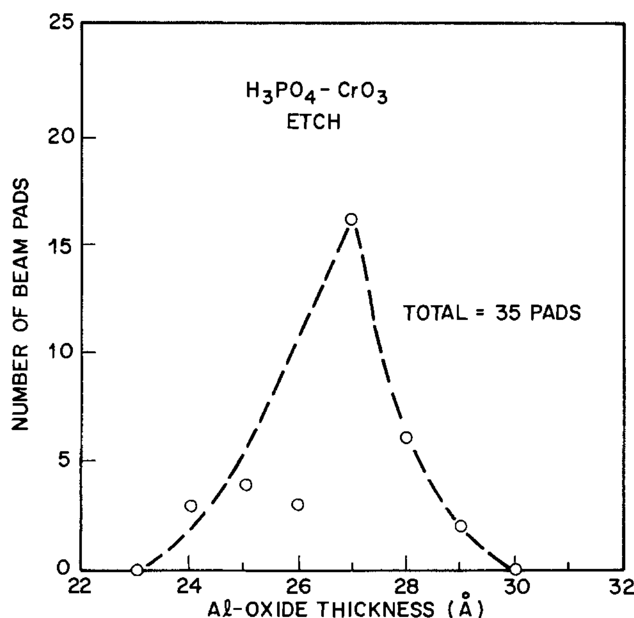

Fig. 2. Al-oxide thickness distribution over 35 contact pads on one integrated circuit chip. The distribution is fairly narrow (±3Å) and is sharply peaked at 27Å.

Split-lot testing of the CrO_3-H_3PO_4-H_2O system.—As a final test, a solution containing 5 ml 85% H_3PO_4, 0.30g CrO_3, and 100 ml of water was used for 5 min at 80°C to clean one-half of the wafers in each of two device lots designated for in-process split-lot evaluation of the CrO_3-H_3PO_4 etchant. Split lot no. 1 consisted of 7 MOS device wafers that had been processed through step 8 of Table I. Three wafers were cleaned as described above immediately prior to Ti deposition, while 4 control wafers received no extra treatment. The contact yield data for the 7 wafer lot are presented in Table IVA. The number of contact failures in the control half of the lot was fairly typical of the standard product processed according to Table I. An over-all contact yield of 94% was found for the etched group *vs.* 78% for the controls.

The second split lot also involved MOS devices, but in this instance the control group was comprised of wafers that received a backsputter etch treatment prior to Ti deposition. The backsputter clean was done in one unit prior to Ti sputter-deposition in a second unit, thus resulting in air exposure of the samples. A typical Auger analysis of this type of Al surface indicates 30-40Å of Al oxide. In addition to the change in controls for this lot, the EG:BHF:H_2O cleans were also omitted for all of the wafers. The resultant contact yields are presented in Table IVB. The backsputtered control group yield of 91.8% can be compared to the 90.8% yield for the CrO_3-H_3PO_4-H_2O cleaned half of the lot. Note that all contact yields quoted here are probably somewhat low since other factors (*e.g.*, closed beam to Al via holes and photolithographic defects) can limit contact yield. Thus, those yields between 90-100% probably reflect contact yields of nearly 100%.

The split lot data show that CrO_3-H_3PO_4-H_2O treatment furnishes an Al surface to which subsequent Ti metallization can make good electrical contact after normal device line processing. The second split lot data suggest little difference between the etching treatment and *ex situ* backsputtering (*i.e.*, use of a separate sputtering unit for cleaning prior to Ti deposition in a second unit). The results from lot no. 1 imply that the CrO_3-H_3PO_4-H_2O treatment can be used successfully even in the Table I Al processing sequence which contains the EG:BHF:H_2O clean-

Table IV. Split lot contact yields in evaluation of the CrO_3-H_3PO_4-H_2O etch

Wafer No.	Processing	Contact yield (%)
A. Lot No. 1		
1	etched	96
2	etched	94
3	etched	93
Average—	etched	94
4	control	72
5	control	73
6	control	83
7	control	85
Average—	control	78
B. Lot No. 2		
1	etched	91.3
2	etched	87.5
3	etched	92.0
4	etched	92.3
5	etched	92.3
6	etched	92.9
7	etched	87.5
Average—	etched	90.8
8	backsputtered	90.7
9	backsputtered	92.9
10	backsputtered	92.9
11	backsputtered	91.0
12	backsputtered	91.7
Average—	backsputtered	91.8

ing procedure. It seems safe to conclude that the availability of the CrO_3-H_3PO_4-H_2O etching system relaxes the requirement of "acute awareness" of the Al metal surface condition during each processing step as long as the etchant is used immediately prior to Ti deposition in the beam lead process.

Summary and Conclusions

We have evaluated the Al metal surface during its processing in integrated circuit manufacture by monitoring the thickness of the surface oxide as a function of various processing steps. It is clearly shown that Al oxide can become too thick for ohmic contact to subsequent metallization if the Al surface is not properly treated during processing. It was found that when the Al-oxide thickness is in the 50-60Å range, contacts between Al and Ti are marginal, and Al-Ti contact failures become a prime cause for poor device yields. We estimate that the critical tolerable Al-oxide thickness is about 55Å which is the sum of the estimated electron tunneling distance (12Å) and the amount of dielectric that is "nullified" by the Ti upon deposition (~45Å). The dielectric breakdown strength for the surface Al oxide during processing was found to be 0.09 V/Å.

A practical method of avoiding Al contact problems involves use of a treatment in CrO_3-H_3PO_4-H_2O (0.2-0.5g CrO_3, 3.5-10 ml H_3PO_4, 100 ml H_2O) for 2-10 min at 80°C prior to Ti metallization. This etch removes surface oxide, leaving only an equilibrium final film of 25-30Å thickness, and it does not attack underlying Al metal. The CrO_3 concentration is particularly critical; too little CrO_3 results in Al attack by the H_3PO_4, whereas too much CrO_3 induces selective electrochemical corrosion of Al in certain areas of a device chip. Practical application was clearly demonstrated through the use of two split lots undergoing actual MOS device processing. Additionally, the etching treatment minimizes the requirement for surface Al-oxide monitoring during processing provided it is used just prior to Ti metallization.

Acknowledgments

The authors are grateful to W. R. Costello for help in processing experimental wafers and for ellipsometric data, to A. Tretola for coordination and control of many of the experimental wafers, to L. C. Parrillo for contact measurements and data interpretation for split lots, and to A. K. Sinha and R. B. Marcus for reviewing the manuscript.

Manuscript submitted June 15, 1977; revised manuscript received Oct. 3, 1977.

Any discussion of this paper will appear in a Discussion Section to be published in the December 1978 JOURNAL. All discussions for the December 1978 Discussion Section should be submitted by Aug. 1, 1978.

Publication costs of this article were assisted by Bell Laboratories.

REFERENCES

1. J. E. Lewis and R. C. Plumb, *Int. J. Appl. Radiat. Iso.*, **1**, 33 (1956).
2. R. C. Plumb, *This Journal*, **105**, 498 (1958).
3. J. D. Edwards, *Proc. Am. Soc. Test. Mater.*, **40**, 959 (1940).
4. C. C. Chang, D. B. Fraser, M. J. Grieco, S. E. Haszko, R. E. Kerwin, R. B. Marcus, T. T. Sheng, and A. K. Sinha, Submitted to *This Journal.*
5. C. C. Chang, in "Characterization of Solid Surfaces," P. F. Kane and G. B. Larrabee, Editors, Chap. 20, Plenum Publishing Corp., New York (1974).
6. C. C. Chang and D. M. Boulin, *Surf. Sci.*, **69**, 385 (1977).
7. W. R. Costello, Unpublished results.
8. T. Smith, *Surf. Sci.*, **56**, 252 (1976).
9. T. F. Retajczyk and T. A. Shankoff, Unpublished report.
10. A. D. McQuillan and M. K. McQuillan, "Titanium," p. 250, Butterworths, London (1956).

A New Self-Aligned Contact Technology

Y. Tanigaki, S. Iwamatsu, and K. Hirobe

Hitachi, Limited, Semiconductor and Integrated Circuits Division, Kodaira, Tokyo, Japan

ABSTRACT

A new self-aligned contact technology for high density MIS LSI is described in this paper. The technology does not need any alignment tolerances of contact regions which have been indispensable for the conventional Si gate technology. Therefore the technology makes a grate reduction in contact areas. An R-S flip-flop circuit was designed by the technology. The packing density has been increased about 20% compared with that of the conventional circuit structure.

A variety of technologies have been developed in order to increase the packing density of MIS LSI. These are the local oxidation of silicon (LOCOS) and the self-aligned Si-gate technology. The isolation area is reduced by the LOCOS technology because of forming channel stopper under the thick oxide region, and the gate area is reduced by the Si-gate technology forming the self-aligned gate structure. Even if these technologies are applied to the MIS fabrication steps, the contact region still occupies large area because sufficient tolerances are needed for a mask alignment. A new self-aligned contact technology is developed with high packing density of MIS LSI to solve the problem.

The steps involved in fabricating a Si-gate n-channel MIS LSI are as follows. The starting materials are 8-12 Ω-cm, (100) oriented, p-type silicon wafers. Active regions are formed by the LOCOS technology (Fig. 1a) first, and then the gate oxide is thermally grown in dry oxygen ambient for 105 min at 1000°C with an oxide thickness of 750Å. Then silicon nitride is deposited at 850°C by the reaction of silane (SiH_4) and ammonia (NH_4) gases. After the deposition, about 150Å of oxide is thermally grown on the silicon nitride film with steam ambient of 110 min at 1000°C, and polycrystalline Si (poly-Si) is deposited at 600°C (Fig. 1b). This is followed by the gate formation and the poly-Si layer is plasma-etched, and then phosphorus ions are implanted at an energy of 180 keV, a dose of 8×10^{15} cm^{-2} (Fig. 1c). The next processing step is the steam oxidation for 45 min at 1000°C. In this treatment, about 3000Å thick oxide film is formed only on the poly-Si gate because of using the silicon

Key words: MOS, integrated circuit, self-alignment.

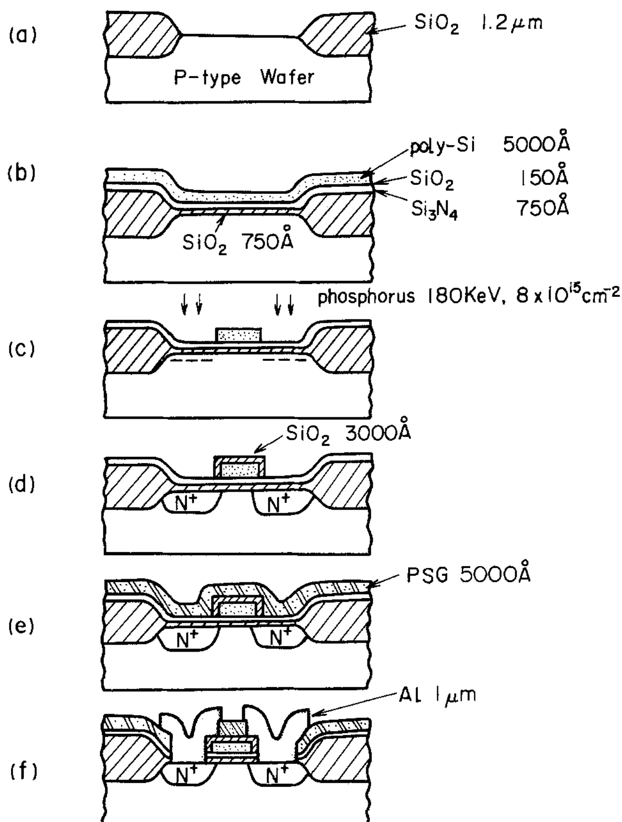

Fig. 1. Steps during fabrication of a Si gate n-channel MIS LSI by the self-aligned contact technology.

nitride film as a mask for oxidation, and the phosphorus drive-in diffusion is carried out simultaneously to form the diffused regions (Fig. 1d).

In the subsequent steps, PSG (phosphosilicate glass) is deposited, followed by annealing in N_2 ambient for 10 min at 1050°C and opening the contact windows. The contact windows on source or drain region and the contact windows on gate region must be opened separately because of the difference of oxide thickness on each region. Therefore we need 2 masks for opening contact windows. The process is completed by depositing aluminum (1 μm in thickness), defining the metal interconnect pattern, and annealing in H_2 ambient for 30 min at 400°C (Fig. 1f).

The new and conventional structures are compared in Fig. 2, where three kinds of alignment tolerances L_1, L_2, and L_3 are defined as follows: L_1, tolerance between the gate and the contact; L_2, tolerance between the isolation region and the contact; and L_3, tolerance between the isolation region and the contact, respectively. Overlapping of the contact to the gate can be tolerated on this technology since the oxide on the gate is thick enough to insulate the gate

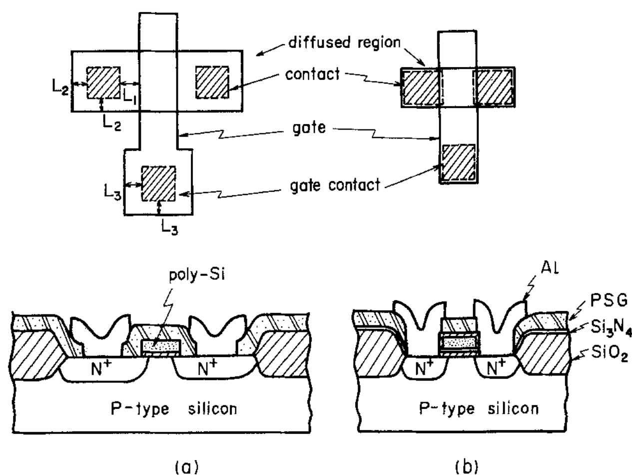

Fig. 2. Structures of Si gate MIS FET's fabricated by (a) conventional technology, and (b) self-aligned contact technology.

from the electrodes of source and drain after opening contact windows. When the contact windows on source and drain regions overlapped to the isolation regions, the silicon nitride layer under PSG (phosphosilicate-glass) prevents overetching of the thick oxide of the isolation region. Therefore, at the edge of the isolation region, thickness of the thick oxide is not reduced. No deterioration of p-n junction in electric characteristics was observed after annealing for aluminum metallization. Misalignment of gate contacts over the isolation region can be also tolerated since the silicon nitride film under PSG layer protects the thick oxide against reduction in thickness during overetching PSG film. There is no increase in step height at the edge of poly-Si on the isolation region, therefore opening does not occur in the aluminum metallization.

An n-channel Si-gate MIS FET was fabricated by the new technology. There was no reduction in electron mobility (μ_n = 600 cm^2/V-sec) and in breakdown voltage (80V) between the gate and source or drain. An R-S flip-flop circuit was designed and compared by the new and conventional technology. The packing density of the new circuits has been increased about 20% compared with that fabricated by the conventional technology. These results showed that the technology is very effective for achieving high packing density in MIS LSI.

Manuscript submitted April 1, 1977; revised manuscript received Sept. 21, 1977.

Any discussion of this paper will appear in a Discussion Section to be published in the December 1978 JOURNAL. All discussions for the December 1978 Discussion Section should be submitted by Aug. 1, 1978.

Publication costs of this article were assisted by Hitachi, Limited.

Ohmic Contacts to GaAs Transferred Electron Devices

B. P. Johnson*

Electrical Engineering Department, University of Nevada, Reno, Nevada 89507

and C. I. Huang

Air Force Avionics Laboratory, WPAFB, Ohio 45433

ABSTRACT

The specific contact resistance of Au/Ge/Ni alloy contacts to GaAs for transferred electron devices has been measured. It is found that a shallow sulfur diffusion under the contact is effective in reducing the specific contact resistance by up to two orders of magnitude. This procedure is expected to improve the uniformity of threshold and bias voltages in integrated circuit configurations by making the contact resistance only 1-10% of the total device resistance.

Because of the low doping found in GaAs transferred electron devices (TED's) for microwave applications, the contact resistance to the device is the major part of the total device resistance. A survey of the literature indicates that for a given doping level, the contact resistance can vary up to two orders of magnitude as the processing parameters are varied (1-5). Significant variation can also occur across a wafer in a given run. This situation is allowable for discrete device configurations where postsorting is possible. In integrated circuit configurations, however, local variations are intolerable because threshold and bias voltages must be uniform from one device to the next in the same circuit. The purpose of this paper is to show that a shallow sulfur diffusion under the metallization pads can reduce the contact resistance to 1-10% of the total device resistance. The specific contact resistance is lowered by approximately two orders of magnitude over that measured on nondiffused samples.

The metallurgical and electrical properties of alloyed Au-Ge/Ni films on n-type GaAs are relatively well understood (1). Edwards, Hartman, and Torrens (2) have summarized specific contact resistance data of this and other contact alloys to GaAs through mid-1971. In general, their data show two order of magnitude variation in the specific contact resistance which ranges from a mean of 3×10^{-3} Ω-cm at a doping level of mid-10^{15}/cm^3 to 10^{-4} Ω-cm at 10^{17}/cm^3. Robinson (3) and Yu (4) have independently confirmed that by process optimization, the mean specific contact resistance can be lowered by up to one order of magnitude. For GaAs TED's doped from mid-10^{15}/cm^3 to mid-10^{16}/cm^3, the specific contact resistance values reported as well as those measured in our laboratories give a device contact resistance far greater than the intrinsic device resistance (typically 3000Ω). To lower the contact resistance to 1-10% of the total device resistance, a specific contact resistance of $\sim 10^{-5}$ Ω-cm is required. The exact value depends on the specific device configuration. This value is two orders of magnitude lower than that reported, and hence can only be achieved by the formation of a shallow n+ layer below the contact to give a doping level of mid-10^{17}/cm^3 to mid-10^{18}/cm^3.

The samples used in this experiment were semi-insulating GaAs substrates on which 25 μm vapor phase epitaxy layers were grown. The typical doping range was mid-10^{15}/cm^3 to mid-10^{16}/cm^3 n-type (Si). Ohmic contacts were formed by evaporation of a gold/12 weight percent (w/o) germanium alloy followed by nickel. The contacts were fused for 30 sec at 475°C in a hydrogen ambient. Figure 1 shows the experimental configuration used to measure the contact resistance. It was chosen to provide dimensions comparable to that of actual devices being constructed. The resistance between pads 1 and 2, 2 and 3, and 3 and 4 was measured, and the contact resistance R_c determined by elimination of the bulk GaAs and probe resistances. The specific contact resistance was then evaluated from (6)

$$r_c = \frac{(ZR_c)^2 \alpha}{\rho}$$

where Z and α are defined in Fig. 1 and ρ is the resistivity of the epitaxial material. This model assumes that the ohmic region is shallow in comparison to the total epitaxial layer thickness. Measurements were made on both as grown epitaxy layers, which were used as a control, and on epitaxy layers which had a shallow sulfur diffusion under the contact pads. Pattern definition was achieved by mesa isolation as indicated in the figure.

Donor diffusion into GaAs has been reported by several authors. Reeves and Donovan (5) have summarized the work through 1972, while Matino (7) presents more recent sulfur results. Germanium and

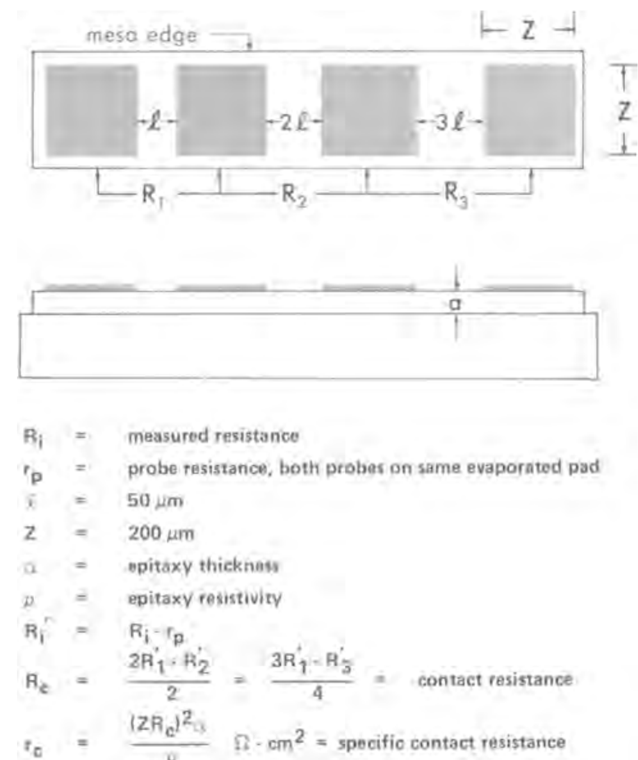

Fig. 1. Contact resistance measurement configuration

* Electrochemical Society Active Member.

Key words: gallium arsenide, transferred electron devices, specific contact resistance, sulfur diffusion.

silicon were not considered for this work because of their amphoteric behavior. Sulfur was chosen over selenium and tellurium because of its higher diffusion coefficient and reported reproducible behavior (7). Diffusion calibration runs using Ga_2S_2 and As were carried out at 800° and 900°C in vacuum-sealed quartz capsules using a 5:1 by weight gallium sulfide to arsenic ratio. Uniform temperature was maintained over the entire length of the capsule ($\Delta T < 0.1°C$). Upon withdrawal from the furnace, the source end of the capsule was quenched to prevent deposition of the vapor on the sample surface during cooling. The results are compared to the data reported by Matino in Fig. 2. The curve gives a D_o of 1.34×10^5 cm^2/sec with an activation energy of 3.98 eV. The 5:1 ratio was chosen to minimize surface compound formation and yet maintain a high surface sulfur concentration. Surface compound formation was observed at 900°C using a 10:1 ratio.

Contact resistance samples were diffused at 800° and 900°C and processed along with nondiffused control samples to measure specific contact resistance. The diffusion depth was typically between 1 and 2 μm. The results are presented in Fig. 3. Each diffused sample data point represents the average value of measurements on 30 samples. The shaded area represents the two order of magnitude variation in specific contact resistance reported in the literature. The optimized values of Robinson (3) and Yu *et al.* (4) are indicated as well as the range of values measured in our laboratories on nondiffused samples.

Capacitance-voltage measurements on the diffused samples indicated a doping level (1×10^{18} cm^{-3} at 898°C and 4×10^{17} cm^{-3} at 789°C) corresponding to the solid solubility of sulfur in GaAs at these temperatures (8, 9). The mean specific contact resistance at these values is in good agreement with that actually measured on the diffused samples. The point at 898°C

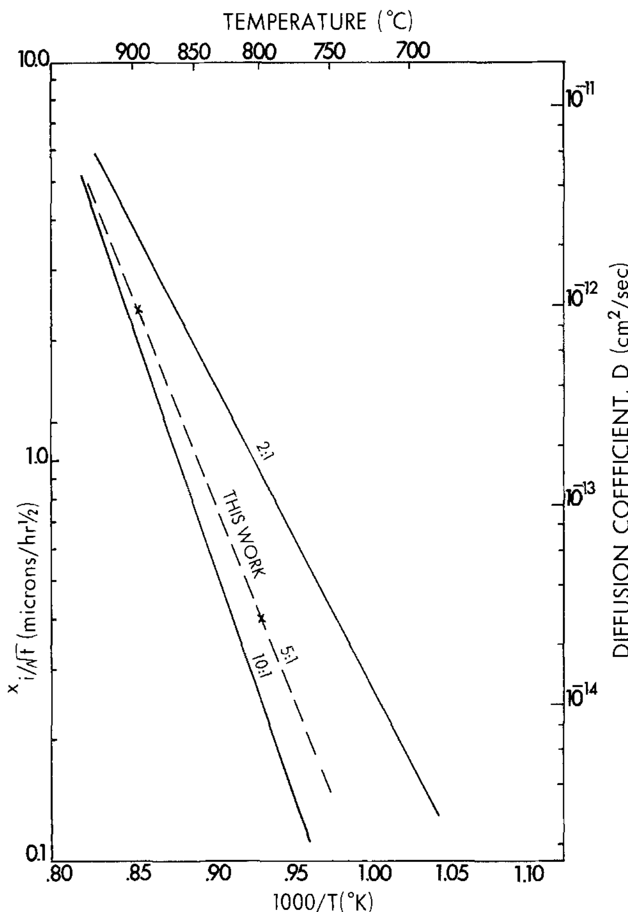

Fig. 2. Diffusion coefficient of sulfur into GaAs. 2:1 and 10:1 are from Matino (6).

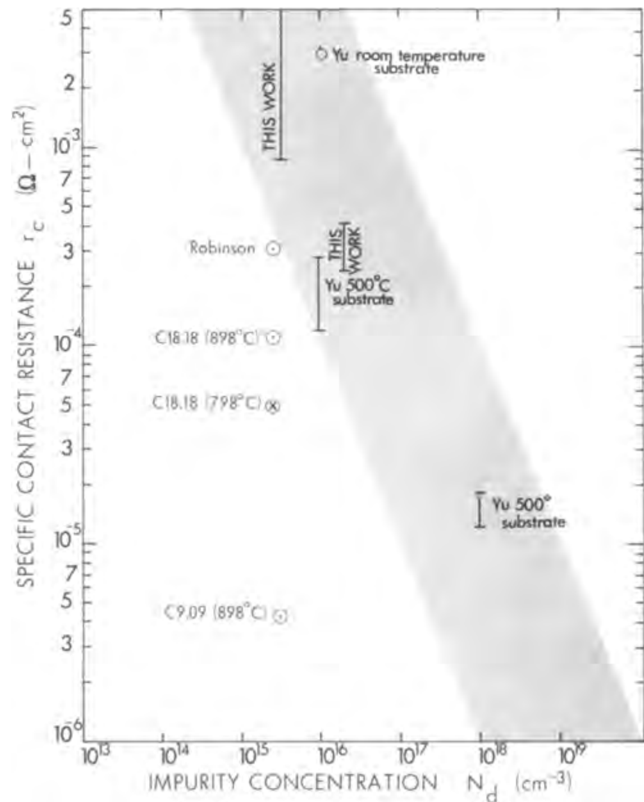

Fig. 3. Specific contact resistance measured on samples which were sulfur diffused at 898°C (⊙) and at 798°C (⊗). The shaded area represents the two order of magnitude variation in specific contact resistance reported in the literature. The optimized values of Robinson (3) and Yu *et al.* (4) are indicated as well as the range of values measured in our laboratories on nondiffused samples.

for sample no. C18.18 is included to illustrate the need for process monitoring. In this particular processing sequence, the problem was tracked down to a leak in the vacuum system during the run.

This work demonstrates that a shallow sulfur diffusion [as well as ion implantation (10)] should be successful in lowering the contact resistance of GaAs TED's from being the major part of the total device resistance, to a value that is 1-10% of the total device resistance. This is crucial for uniform device parameters and reduced power dissipation in integrated circuit applications of TED's.

Acknowledgment

Part of this work was performed while one of the authors (Johnson) was on an USAF-ASEE Summer Faculty Fellowship Program.

Manuscript submitted July 25, 1977; revised manuscript received Oct. 7, 1977. This was Recent News Paper 373 presented at the Las Vegas, Nevada, Meeting of the Society, Oct. 17-22, 1976.

Any discussion of this paper will appear in a Discussion Section to be published in the December 1978 JOURNAL. All discussions for the December 1978 Discussion Section should be submitted by Feb. 1, 1978.

REFERENCES

1. V. L. Rideout, *Solid-State Electron.*, **18**, 541 (1975).
2. W. D. Edwards, W. A. Hartman, and A. B. Torrens, *ibid.*, **15**, 387 (1972).
3. G. Y. Robinson, *ibid.*, **18**, 331 (1975).
4. A. Y. Yu, H. J. Gopen, and R. K. Waits, Fairchild Camera and Instrument Corp., Technical Rep. AFAL-TR-70-196 (AD875591) (1970).
5. G. G. Reeves and R. P. Donovan, Air Force Avionics Lab., Technical Rep. AFAL-TR-72-312 (AD-908834), (1973).
6. "Semiconductors and Semimetals," Vol. 7A, R. K. Willardson and A. C. Beer, Editors, pp. 179-180, Academic Press, New York (1971).
7. H. Matino, *Solid-State Electron.*, **17**, 35 (1974).

8. R. K. Willardson and W. P. Allred, in "Proceedings of the International Symposium on GaAs, 1966," pp. 35-40, Inst. Phys, and Phys. Soc., London (1967).
9. A. B. Y. Young and G. L. Pearson, *J. Phys. Chem. Solids*, 31, 517 (1970).
10. D. H. Lee, J. J. Berenz, and R. L. Bernick, *Electron Lett.*, 11, 189 (1975).

Quantitative Analysis of the Effects of Destabilizing Vertical Thermal Gradients on Crystal Growth and Segregation: Ga-Doped Ge

K. M. Kim

RCA Laboratories, Princeton, New Jersey 08540

and A. F. Witt,* M. Lichtensteiger, and H. C. Gatos*

Department of Materials Science and Engineering and Center for Materials Science and Engineering, Massachusetts Institute of Technology, Cambridge, Massachusetts 02139

ABSTRACT

The effects of destabilizing vertical thermal gradients on crystal growth and segregation in an inverted Bridgman configuration were investigated in Ga-doped Ge melts by monitoring the thermal characteristics of the melt and relating them through interface demarcation directly to growth and segregation. It was found, consistent with established thermohydrodynamic criteria, that as solidification progressed the melt exhibited successively turbulent convection, oscillatory thermal instabilities, and, finally, thermal stability. Growth under turbulent melt convection is characterized by pronounced and rapid fluctuations with the rate changing within 1 sec from negative to more than 30 μm/sec. A quantitative microsegregation analysis based on interface demarcation for the determination of dopant concentrations was performed. It showed that segregation under turbulent convection is in basic agreement with the BPS theory: Dopant incorporation is controlled by the microscopic rate of growth while convection-induced boundary layer perturbations constitute a second-order effect.

Time-dependent convective melt flow caused by unavoidable destabilizing thermal gradients has been identified as the primary cause of random compositional variations in semiconductor single crystals grown from the melt (1). The exact nature of such thermohydrodynamic instabilities in crystal growth systems (2) and their functional dependence on growth parameters have not as yet been established; more importantly, quantitative cause and effect relationships between convective flow and microsegregation are still not available.

Recently, the nature of convective instabilities associated with destabilizing thermal gradients was systematically studied for the growth of InSb (3). This study established the effects of convection in the melt on crystal growth characteristics and revealed some basic relationships between convection and dopant incorporation. The present investigation is concerned with the study of convective melt flow in a germanium growth system with destabilizing vertical thermal gradients and its effect on dopant (Ga) incorporation with primary emphasis on a quantitative analysis of segregation under turbulent convection.

Experimental Procedures

All growth experiments were carried out in an apparatus shown schematically in Fig. 1. The Ge charge and the Ga dopant (4×10^{19} atoms/cm^3 in the melt) were placed in a quartz tube of 1.3 cm ID, heated to slightly above the melting point with a cylindrical resistance heater, and brought into contact with an <111> Ge seed. The height of the molten zone at the start of the growth experiment was about 2.5 cm. Growth in the downward direction was achieved by controlled furnace power reduction. At a constant cooling rate of 0.43°C/min (obtained with a nominal

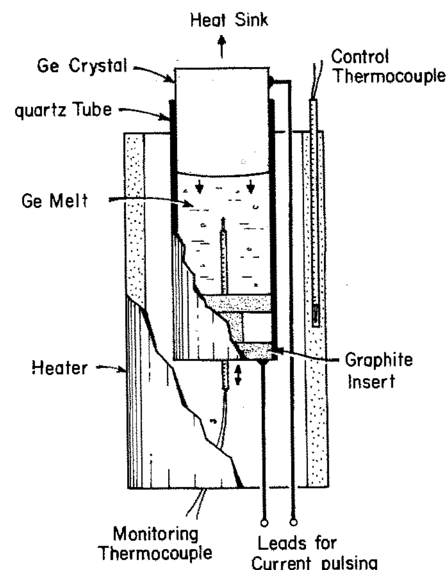

Fig. 1. Schematic diagram of experimental setup used for the study of crystal growth under destabilizing vertical thermal gradients.

* Electrochemical Society Active Member.

Table I. Data characterizing the different modes of convective instability in confined Ge and InSb melts

	Turbulent convection		Oscillatory instability		Time independent convection	
	Ge	InSb	Ge	InSb	Ge	InSb
Melt height range (cm)	2.4-1.8	3.0-2.0	~1.8-1.2	~1.8-1.0	1.2-0	1.0-0
Aspect ratio range	1.8-1.4	2.3-1.5	1.4-0.9	~1.1-0.75	0.9-0	0.75-0
Frequency of thermal instabilities (Hz)	A* 1-0.2 B* 0.01-0.02	A* 1-0.2 B* 0.008-0.004	0.4	0.29, 0.38	—	—
Amplitude of thermal instabilities (±°C)	A ~5 B <5	A ~7 B <5	0.06-0	0.1-0	—	—
Rayleigh No. range	5×10^5-9×10^4	3×10^5-4×10^3	9×10^4-2×10^4	4×10^3-2×10^3	2×10^4-0	2×10^3-0
Grashof No. range	7×10^7-$\sim 1 \times 10^7$	4×10^7-5×10^5	1×10^7-3×10^6	5×10^5-2.5×10^5	3×10^6-0	2.5×10^5-0

Vertical destabilizing thermal gradients: Ge = 27°C/cm at 2.5 cm melt height; InSb = 19°C/cm at 3.3 cm melt height; and 8°C/cm at 1.2 cm melt height.
* A and B refer to the simultaneously present modes of thermal instability (see text).

destabilizing vertical thermal gradient of 27°C/cm taken from the temperature difference between the growth interface and the bottom of the melt at the onset of the growth experiment) an average macroscopic growth rate of 2.8 μm/sec was established. Volume expansion during solidification was accommodated by a special graphite insert near the bottom of the quartz tube.

For the purpose of interface demarcation by current pulsing (4), electrical contacts were made with the seed crystal and the graphite pedestal. Current pulses (18A) of 50 msec duration were transmitted at intervals of 0.6 sec during growth under turbulent convection conditions; the interval between pulses was increased to 30 sec under oscillatory thermal instability and under thermal stability conditions.

Temperature measurements in the melt were obtained with a Chromel-Alumel thermocouple inserted through the graphite pedestal. During growth the location of the thermocouple junction was adjusted so that temperature measurements for various melt heights could be taken at a constant distance of approximately 5 mm from the growth interface. Since displacements of the thermocouple did not alter the growth and segregation behavior it is concluded that its presence did not noticeably affect the thermal behavior of the melt. Current pulsing was stopped prior to the termination of growth so that the last interface demarcation line could be identified and serve as a direct time reference between the temperature recording and the corresponding growth region [the current pulses were inductively registered by the thermocouple; see also Ref. (3)].

The growth and segregation analyses were performed on crystal segments cut along the growth axis; the segments were polished and etched (8 sec in 1HF + $1CH_3COOH$ + $1H_2O_2$) to reveal segregation effects and interface demarcation by interference contrast microscopy; for quantitative microsegregation analysis, dopant concentration profiles were determined by single-point probe spreading resistance measurements.

Experimental Results and Discussion

Thermohydrodynamics and growth behavior.—The nature of the thermohydrodynamic instabilities in the Ge melt under the present growth configuration and their effect on the growth characteristics were investigated through temperature measurements in the melt and through an analysis of the segregation inhomogeneities (striation patterns) in the grown crystal. The results indicated that the convective melt flow behavior depends strongly on the melt height and is in principle analogous to that encountered in an InSb growth system of similar configuration (3). Thus, with continuing growth in the downward direction (with decreasing melt height) the melt experienced successively turbulent, oscillatory, and laminar convection with correspondingly different growth and segregation behavior.

While the presently observed convective flow behavior is basically the same as that observed in InSb and consistent with established thermohydrodynamic criteria, it differs in detail as seen in Table I. At large Ge-melt heights (2.4-1.8 cm) a turbulent convective roll is established (Fig. 2) which rotates slowly about its vertical axis (3) (as indicated by large amplitude-low frequency variations). The temperature measurements and the characteristics of the corresponding segregation inhomogeneities in the grown crystal showed that the rotation of the convective roll about its vertical axis was arrested as the melt height decreased below 1.8 cm. Thus, the large amplitude-low frequency temperature variations in the melt ceased and concurrently the pronounced remelt striations in the growing crystal (which at larger melt heights overlap in the center of the crystal as a result of the

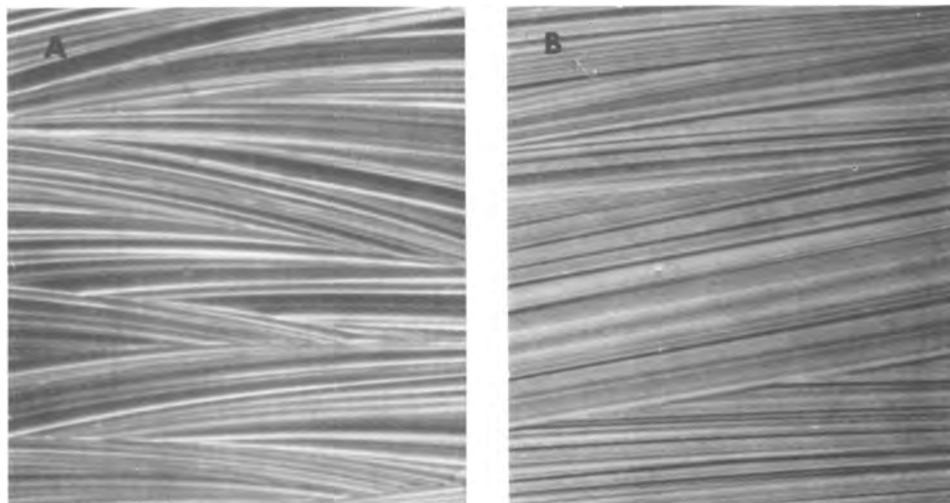

Fig. 2. Comparison of etched segments of Te-doped InSb (A) and Ga-doped Ge (B) crystals grown under turbulent convective melt flow. 20X.

vertical rotation of the convective roll) no longer form; the random non-remelt striations of higher frequency persist and assume an orientation normal to the growth direction (see below). It is of interest to note that coincident with this change in the convective flow pattern the average microscopic growth rate decreases from 24 to 2.8 μm/sec. The similarity of the convective melt flow behavior for Ge and InSb is evident in Fig. 2 which shows comparable crystal segments grown under turbulent convection.

The random temperature fluctuations changed to oscillatory instabilities as the melt height decreased to 1.7 cm. Temperature oscillations with a constant frequency of 0.4 Hz and an amplitude decreasing continuously from a value of ± 0.06°C were observed to a melt height of 1.2 cm. The oscillatory melt instability in germanium is different from that observed in InSb insofar as its frequency (although constant over significant time intervals) exhibits noticeable irregularities, particularly prior to transition to thermal stability at a melt height of 1.2 cm.

Dopant Segregation

Macrosegregation.—The macrosegregation behavior of the Ge-Ga system in the form of a compositional profile obtained by spreading resistance measurements (4) at spacings of 25 μm along the axis of the grown crystal is shown in Fig. 3. It can be seen that dopant segregation during growth under turbulent convection (left portion of the diagram) led to compositional variations in excess of about $\pm 10\%$. In contrast, segregation under both oscillatory instability (central portion) and thermal stability (right portion) exhibited compositional fluctuations of less than $\pm 2\%$. Figure 3 shows further that the Ga concentration in the Ge crystal increases steadily in the direction of growth (with the exception of one decrease which is followed by a rapid recovery). This finding is significant since the solidifying melt was subjected to abruptly changing convective flows which resulted in pronounced changes of the microscopic growth rate.

It would be desirable to make use of this compositional profile for a quantitative segregation analysis on the basis of the normal freezing equation (5). However, the average dopant concentration computed for the initial segment (turbulent convection) is not reliable since the measurements were taken at spacings of 25 μm and major compositional fluctuations associated with intermittent backmelting occur at comparative spacings (20-80 μm). Moreover, radial segregation cannot be ignored.

Microsegregation.—Segregation under turbulent convection (with extensive backmelting).—A quantitative analysis of the growth and segregation behavior on a microscale for a crystal segment grown at a melt height of 2.4 cm under turbulent convection is presented in Fig. 4. The growth rate analysis (curve B in Fig. 4), obtained from the spacing of successive interface demarcations,[1] shows that the average microscopic growth rate (24 μm/sec) is larger than the average macroscopic growth rate (2.8 μm/sec) by a factor of about 10 as a result of turbulent convection; the growth rate between the irregularly spaced periods of backmelting fluctuates significantly with maximum values in excess of 50 μm/sec; more importantly, the microscopic growth rate changes very rapidly, increasing after backmelting (negative rate) to more than 30 μm/sec within less than 1 sec.

In the context of the present microscopic growth rate analysis the inherent limitation of the interface demarcation technique for growth rate determination should be considered: The frequency of the interface demarcation (presently 1.7 Hz) was selected to yield optimum accuracy at the expected average growth rate; rapid growth rate excursions to very high and very low levels introduce, by necessity, uncertainties originating from limited growth rate resolution for high rates and spatial resolution for low growth rates. (in the present study the rate determination was optimized for the range of 10 to 30 μm/sec.)

The compositional profile obtained from spreading resistance measurements at 5 μm spacings is given by curve C of Fig. 4. The data indicate an average Ga concentration of $4.6 \times 10^{18}/\text{cm}^3$ with compositional fluctuations of $\pm 10\%$. A comparison of curves B and C in Fig. 4 shows that maxima and minima in dopant concentration are associated with corresponding maxima and minima in the microscopic growth rate. The observed coincidence of the growth rate and compositional maxima and minima shows that the major variations in dopant concentration originate from microscopic growth rate fluctuations; it also indicates that melt flow-induced fluctuations in the thickness of the diffusion boundary layer constitute a second-order effect under the present growth conditions.

BPS-segregation analysis.—In view of the preceding phenomenological considerations it is of interest to investigate the applicability of the Burton, Prim, and Slichter relationship (7) to segregation under turbulent convective melt flow; thus, the Ga concentration in the solid is given by

$$C_s = \frac{C_L k_o}{k_o + (1 - k_o) \exp(-V\delta/D)}$$

where C_s is the Ga concentration in the crystal C_L is the Ga concentration in the bulk of the melt, k_o is the

[1] The growth rate curve was obtained by fitting all spacings of interface demarcations to a computer-generated expression for the growth rate *vs.* growth distance employing a cubic (spline) interpolating polynomial (6).

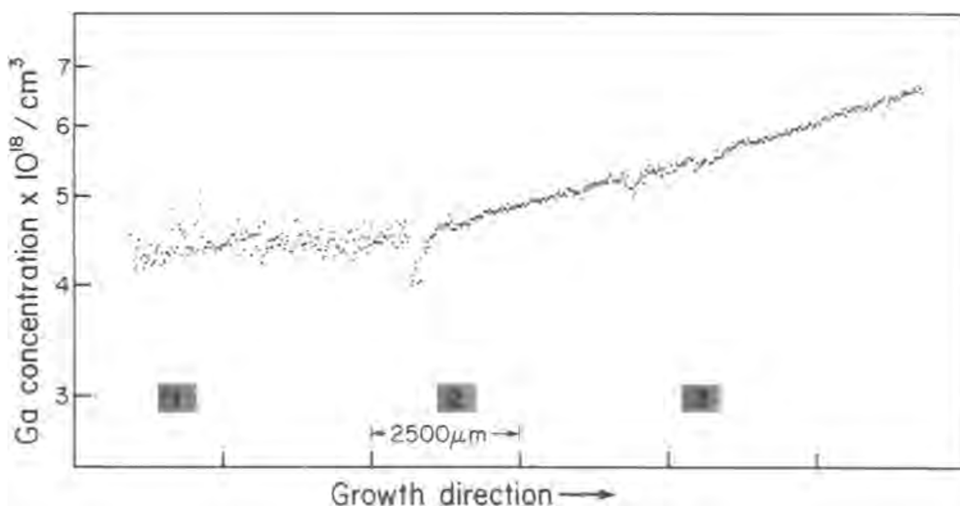

Fig. 3. Macroscopic longitudinal Ga-concentration obtained from single point spreading resistance measurements at spacings of 25 μm. Regions 1, 2, and 3, grown under turbulent convection, oscillatory instability, and laminar convection, respectively, were subjected to segregation analysis on a microscale (see Fig. 4, 6, and 7).

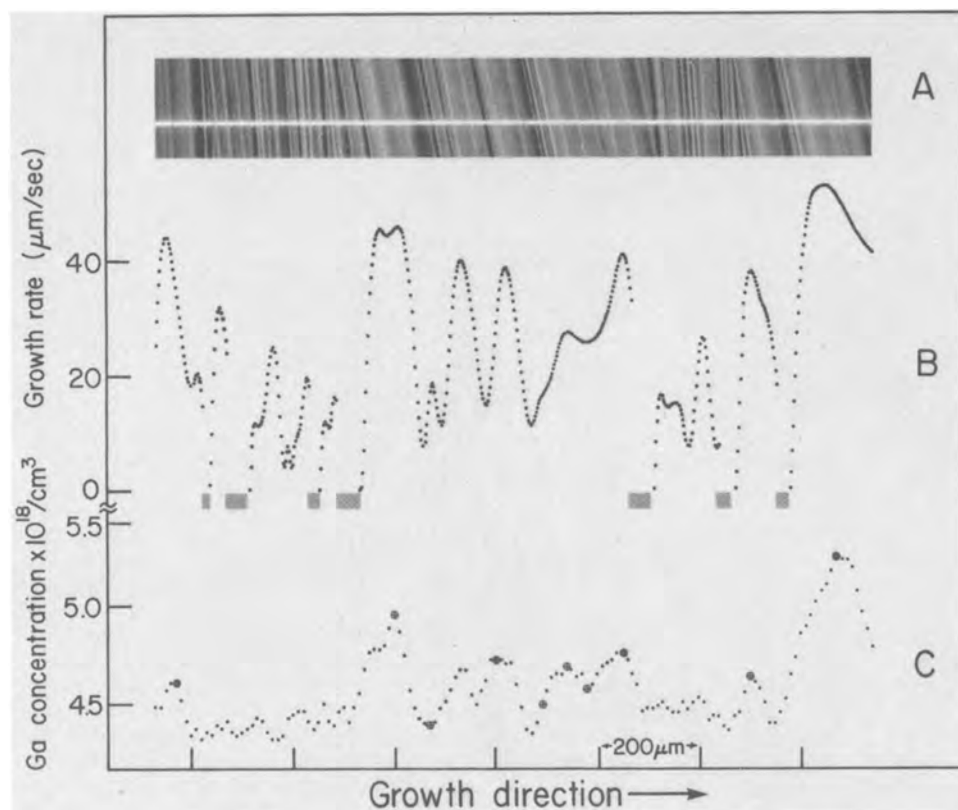

Fig. 4. Microsegregation analysis of Ge crystal grown under turbulent melt convection: (a) photomicrograph of etched crystal segment, (b) growth rate analysis, (c) compositional analysis. Ten randomly selected dopant concentrations on curve C (⊕) with the corresponding growth rates in curve B were subjected to a BPS analysis in Fig. 5. (Experimental points, indicated as ●, correspond to concentrations for which the growth rates are associated with potentially high measurement error because of limited rate resolution under turbulent growth conditions.)

equilibrium distribution coefficient, V is the microscopic growth rate, δ is the diffusion boundary layer thickness, and D is the diffusion coefficient of Ga in the melt. For the purpose of this analysis the Ga concentration in the melt is taken to be identical with the normal concentration in the original charge, since the grown region shown in Fig. 4 is located only 2 mm below the original regrowth interface. Considering the limited resolution of interface demarcation and the necessarily transient segregation behavior associated with pronounced growth rate accelerations and decelerations, the data points considered for analysis (indicated in curve C of Fig. 4) were randomly selected from regions of intermediate maxima and minima for which the reliability of the corresponding growth rates (12-42 μm/sec) is highest; some less reliable data involving growth rates in excess of 42 μm/sec are also included; excluded, for reasons to be discussed later, are data from regions immediately following remelting. The results are shown in Fig. 5; they are considered as indicative of basic compliance of the segregation behavior with the BPS theory; deviations from theoretical behavior at rates in excess of 42 μm/sec reflect in part the error associated with the determination of the growth rate due to limited resolution at the applied demarcation frequency (see above).

In view of the observed agreement between experiment and theory it is meaningful to analyze further

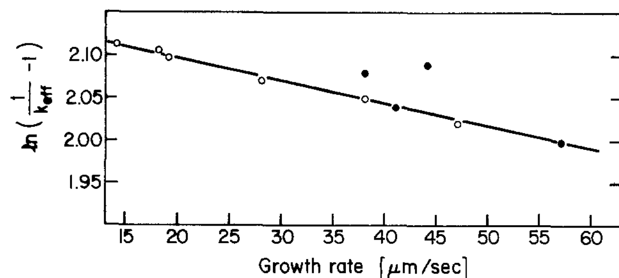

Fig. 5. BPS segregation analysis for growth under turbulent convection based on data in Fig. 4. (For points indicated as ●, see Fig. 4).

the results in Fig. 5. The slope of the BPS plot (δ/D) is found to be 26.3 sec/cm and the thickness of the convection-controlled diffusion boundary layer is computed to be 40 μm (taking $D = 1.5 \times 10^{-4}$ cm^2/sec). Extrapolating the Ga concentration in Fig. 5 to zero growth rate the equilibrium distribution coefficient, k_0, is found to be 0.108. This value is significantly higher than the one generally used (0.087) (8) but identical with that most recently obtained through extensive, as yet unpublished, segregation studies.

The applicability of the BPS theory to segregation under conditions of turbulent convection is surprising in view of the transient nature of the growth conditions; it can, however, be rationalized as a direct consequence of the prevailing high convective melt flow rates. Thus, the convection-controlled diffusion boundary layer thickness is rather small and diffusional adjustment of the segregated Ga to its steady-state value takes place within a short time interval. Taking $\delta^2/D = 0.106$ sec as the characteristic time constant for diffusional segregation readjustment following a growth rate perturbation (9), it must be concluded that the observed intermediate compositional maxima and minima are reasonably close to steady-state values. It is clear, on the other hand, that growth immediately following backmelting exhibits a segregation behavior to which the BPS theory cannot be applied; the dopant concentration profile adjacent to the growth interface is modified by the backmelt process and is most likely affected by a temporary reversal of concentration gradients (the backmelting solid is of lower Ga concentration than the bulk melt) leading to backdiffusion from the bulk melt into the diffusion boundary layer. Because of extensive backmelting the measured temperature fluctuations could not be qualitatively related to the microscopic growth rate and thus it was not possible to apply the Hurle, Jakeman, and Pike theory (10).

On the basis of the present analysis it is concluded that dopant segregation under conditions of turbulent convection (characterized by pronounced and rapid growth rate variations) is in good agreement with the BPS relationship; segregation variations due to con-

vection-induced boundary layer perturbations appear to be a second-order effect.

Segregation under turbulent convection (without extensive backmelting).—At a melt height of 1.8 cm both the growth and segregation behavior undergo a fundamental change. As discussed above the convection roll ceases to rotate about its vertical axis; however, high frequency temperature fluctuations characteristic for turbulent convection persist. Concurrent with the change in convective melt flow behavior, the pronounced remelt striations disappear (see Fig. 2). Since interface demarcation was applied intermittently only, a quantitative growth rate analysis at this transition region cannot be carried out. However, decreased spacing of impurity striations of the non-remelt type are taken as indicative of a pronounced decrease in the microscopic growth rate. This decrease could be quantitatively confirmed through interface demarcation applied again 2 mm below the transition region where growth took place without noticeable backmelting. At this region the average microscopic growth rate is found to be 2.8 μm/sec and thus virtually identical with the macroscopic rate of growth.

In the absence of detailed growth rate information it is of interest to consider phenomenologically the segregation behavior in the above transition region on the basis of the macrosegregation profile given in Fig. 3. It is seen that concurrent with the arrest of extensive backmelting, an abrupt drop of the dopant concentration to about $4.05 \times 10^{18}/cm^3$ takes place. This concentration change, although larger than expected, is consistent with a decrease of the microscopic growth rate from an average of 24 to 2.8 μm/sec expected for this region. (Experimental verification of this assumption could not presently be achieved.) The ensuing gradual dopant concentration increase, which takes place under a constant microscopic rate of growth, is clearly the result of a steady increase in the thickness of the diffusion boundary layer and thus reflects an abrupt decrease in the convective flow velocity. In the later stages of this transition region (location 2 in Fig. 3), a gradual attenuation of the compositional fluctuations from $\pm 10\%$ to about $\pm 2\%$ takes place as seen in Fig. 6.

Segregation under oscillatory thermal instability and under thermal stability (laminar convection).—The dopant segregation under oscillatory instability is characterized by virtual microscopic compositional homogeneities (fluctuations in Ga-concentration are less than $\pm 2\%$). This segregation behavior reflects both a constant microscopic growth rate (2.7-2.8 μm/sec) and relatively stable diffusion boundary layer characteristics.

A crystal segment grown during the transition from oscillatory thermal instability to thermal stability in the melt (location 3 in Fig. 3), together with the corresponding compositional profile, are shown in Fig. 7. It can be seen that in this transition region the microscopic growth rate remained constant while the dopant segregation increased gradually. It must therefore be concluded that the convective flow characteristics, in particular the flow velocity, contrary to the previously discussed transition region, did not change abruptly during the transition from oscillatory instability to thermal stability. The data must be taken as indirect evidence of the presence of laminar convective flow under conditions of thermal stability. No attempts, however, were made to confirm these conclusions through a calculation of the diffusion boundary layer thickness, for example (by applying the Burton, Prim, and Slichter relationship), since the required determination of the Ga concentration in the melt on the basis of the directional freezing equation was considered as unreliable for these late stages of growth.

Summary and Conclusions

The nature of thermohydrodynamic instabilities in Ga-doped Ge melts under destabilizing vertical thermal gradients was determined over a wide range of melt aspect ratios during crystal growth in an inverted Bridgman configuration. It was found that the nature of the convective instabilities (similar to those observed in InSb) changes with decreasing aspect ratio in agreement with theory. The effects of the various modes of convection in the melt on the growth characteristics were studied by high resolution etching analyses of the grown crystal. It was shown that the average microscopic growth rate for growth under time-independent convection melt flow and under oscillatory thermal instability was identical with the average macroscopic growth rate whereas that observed during growth under turbulent convection (because of extensive backmelting) was by about one order of magnitude higher.

Using high resolution spreading resistance measurements for compositional profiling on a microscale together with the microscopic growth rate data obtained through interface demarcation it was for the first time possible to perform a quantitative segregation analysis for crystal growth under turbulent melt convection. This analysis revealed that the dopant incorporation is primarily controlled by the microscopic rate of growth and segregation (with the exception of regions affected

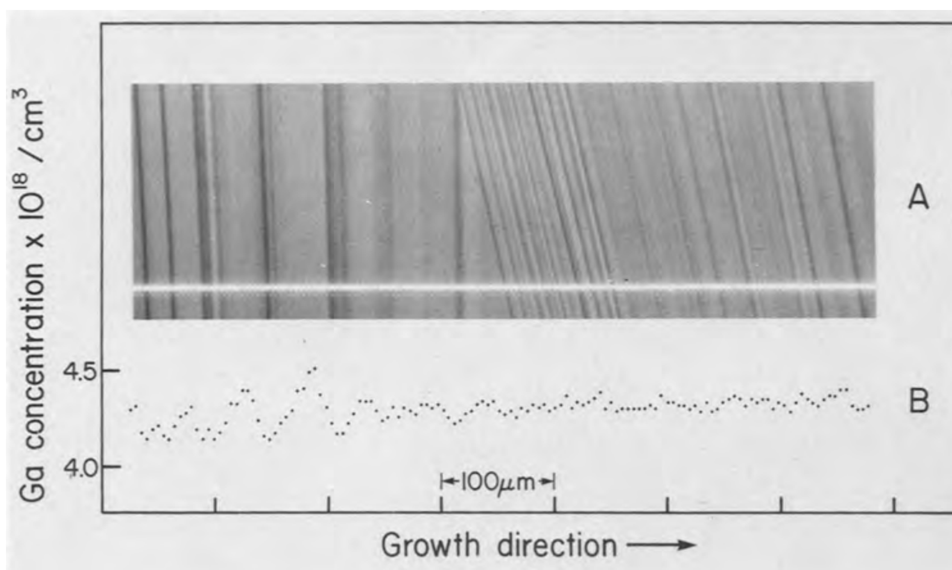

Fig. 6. Dopant incorporation in the transition region from turbulent convection to oscillatory instability (segment 2 in Fig. 2). Notice the attenuation of compositional fluctuations from $\pm 5\%$ to about $\pm 2\%$.

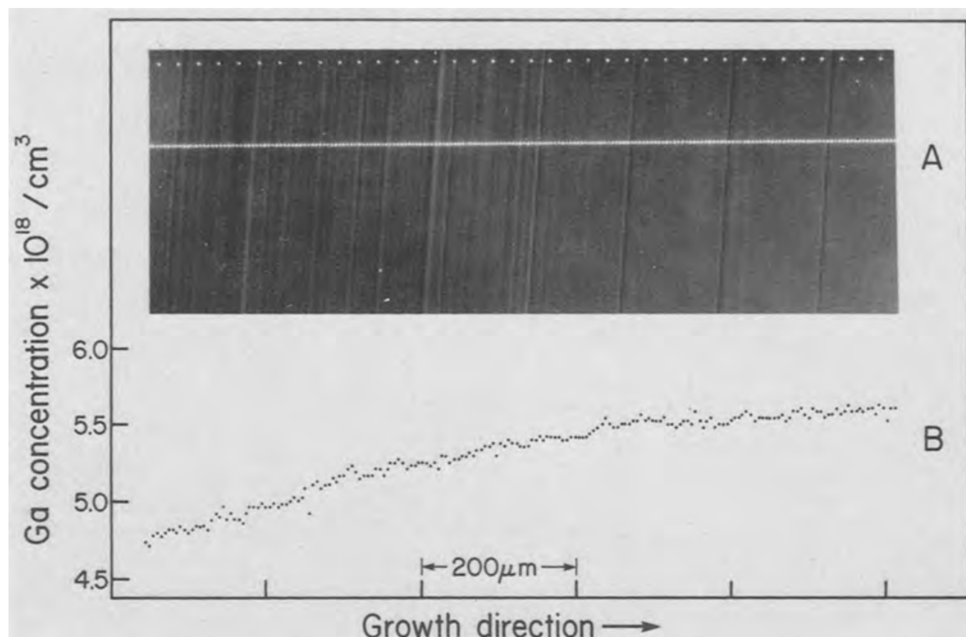

Fig. 7. Dopant incorporation in the transition region from oscillatory instability of time independent laminar convective flow (segment 3 in Fig. 2). See text.

by backmelting) is in basic compliance with the BPS theory. Convection-induced solute boundary layer perturbations were found to be a second-order effect. The applicability of the BPS theory to segregation under pronounced growth rate variations is attributed to the establishment of a small solute boundary layer thickness resulting from relatively high convective flow rates in the melt. Thus, growth rate controlled diffusional solute adjustment within the solute boundary layer is rapid and segregation can adjust without noticeable transient effects to randomly changing growth rates.

Acknowledgments

The authors are grateful to the National Aeronautics and Space Administration and to the National Science Foundation (MRL) for their financial support of this work. They are also indebted to Mr. C. J. Herman and Mr. J. Baker for their skillful assistance with the analysis of the experiments.

Manuscript submitted March 3, 1977; revised manuscript received Oct. 20, 1977.

Any discussion of this paper will appear in a Discussion Section to be published in the December 1978 JOURNAL. All discussions for the December 1978 Discussion Section should be submitted by Aug. 1, 1978.

Publication costs of this article were assisted by Massachusetts Institute of Technology.

REFERENCES

1. A. Müller and M. Wilhelm, *Z. Naturforsch., Teil A*, **19**, 254 (1964); A. F. Witt and H. C. Gatos, *This Journal*, **113**, 808 (1966).
2. J. R. Carruthers, *J. Cryst. Growth*, **2**, 1 (1968).
3. K. M. Kim, A. F. Witt, and H. C. Gatos, *This Journal*, **119**, 1218 (1972).
4. M. Lichtensteiger, A. F. Witt, and H. C. Gatos, *ibid.*, **120**, 1119 (1973).
5. W. G. Pfann, *Trans AIME*, **194**, 747 (1952).
6. I. J. Schoenberg, *Bull. Am. Math. Soc.*, **77**, 1039 (1971).
7. J. A. Burton, R. C. Prim, and W. P. Slichter, *J. Chem. Phys.*, **21**, 1987 (1953).
8. F. A. Trumbore, E. M. Porbausky, and A. A. Tartaglia, *J. Phys. Chem. Soc.*, **11**, 239 (1959).
9. W. P. Slichter and J. A. Burton, in "Transistor Technology," H. E. Bridgers, J. H. Scaff, and N. J. Shive, Editors, p. 107, Van Nostrand, New York (1955).
10. D. T. J. Hurle, E. Jakeman, and E. R. Pike, *J. Cryst. Growth*, **3, 4**, 633 (1968).

Plasma-Grown Oxide on GaAs

Semiquantitative Chemical Depth Profiles Obtained Using Auger Spectroscopy and Neutron Activation Analysis

C. C. Chang, R. P. H. Chang,* and S. P. Murarka*

Bell Laboratories, Murray Hill, New Jersey 07974

ABSTRACT

Plasma oxidation of GaAs is a low temperature oxide growth technique with possible electronics device applications. Chemical depth profiles through 600-3000Å thick plasma-grown oxides were obtained using Auger spectroscopy combined with ion milling and were calibrated using neutron activation analysis. The "bulk" compositions of these oxides were uniform with depth and equivalent to those of mixtures of Ga_2O_3 and As_2O_3. Approximately the first 200Å of the oxide surfaces were always As-rich, but each oxide as a whole was As deficient and the Ga/As concentration ratio increased with oxide thickness from 1.1_8 at 600Å to 1.4_5 at 2780Å. The mechanism of As loss is the faster out-diffusion of As compared to Ga during oxidation and volatilization of surface As-containing species. A sheet of elemental As, amounting to about 10^{15} atoms/cm²/1000Å of oxide growth, was found at the oxide-GaAs interface. The interface widths were <30 and <70Å at oxide thicknesses of 600 and 2780Å, respectively.

Recent demonstration of the growth of native oxides on GaAs using a magnetically confined plasma medium suggested that the plasma oxidation technique may be of practical interest to electronics device technology (1). This technique has certain advantages over other methods, such as thermal oxidation or anodization. With thermal oxidation, the growth rate is too slow at low temperatures, and at temperatures sufficiently high for reasonably fast growth rates, there are the problems of As loss and recrystallization of Ga_2O_3 (2). Anodic oxides require various postgrowth anneals for stabilization and improvement of film properties, and the growth process is sensitive to the semiconducting properties of the GaAs. These oxides are also characterized by either a wide film thickness distribution or a diffuse oxide-GaAs interface that span a mean width of approximately 700Å for oxides 2500Å thick (3, 4). On the other hand, plasma oxide films were found to be uniform, homogeneous, dense, nearly stoichiometric, and amorphous in nature (1). Preliminary electrical measurements have shown that the GaAs MOS capacitors have relatively stable *C-V* characteristics as well as high breakdown voltages (1). The present paper reports on Auger spectroscopy studies of the plasma-grown oxide on GaAs in the thickness range between 600 and 3000Å. Knowledge of the oxide chemistry and depth profile should provide a better understanding of the chemical and physical processes involved in the oxide growth, as well as some idea of the "quality" of these oxides compared to other types of oxides.

Experimental

The plasma oxidation process was carried out in a linear plasma device described elsewhere (1, 5). An oxygen plasma (density $\cong 10^{10}$ particles/cm³, $T_e \cong$ 4 eV) was formed at a background pressure of 2×10^{-3} Torr and an ambient temperature of $\cong$40°C with a pair of rf aluminum electrodes which were driven in balance at the same d-c potential with a typical rf power of 300W at 20-30 MHz. The plasma thus formed (in the source region of the plasma device) was confined by an external magnetic field of 500G. The magnetic confinement also reduced the contamination from the chamber walls. The plasma column was 5 cm in diam and 50 cm long. The GaAs wafer, (100) orientation, Te doped, with a carrier concentration of 2×10^{17}/cm³, was first cleaned in dilute HCl and then mounted on a Monel substrate holder. The wafer surface was mounted normal to the magnetic field lines and at least 30 cm away from the electrodes to avoid sputtering contamination from the aluminum electrodes. The substrate was then biased at up to 90V positive with respect to the plasma for collecting electrons and negatively charged oxygen species.

Four samples were investigated for this report and they are listed in Table I together with the oxide thickness which ranged from about 600Å to almost 3000Å. The oxide thicknesses were determined using Rutherford backscattering. All the oxides were grown under essentially similar conditions except for No. 1782, which was grown at a slightly faster rate. Detailed descriptions of the growth conditions are outside the intended scope of this paper and will be presented in a forthcoming report.

Chemical analyses were performed by measuring the surface composition by Auger electron spectroscopy (6, 7), using a (Varian) cylindrical analyzer with an energy resolution of 0.25%. Typical operating conditions were 10 μA incident electron beam at 6 keV, 50μ beam diameter, and 2 eV a-c modulation; data were taken in the $d[EN(E)]/dE$ mode and multiplexed over only the relevant Auger peaks. Complete scans from 0 to 1800 eV were also taken from time to time to ensure that the multiplexed elements were the only species present in the oxide. Since hydrogen is not detectable by Auger electron spectroscopy, its possible presence was ignored in this work. Depth profiles were generated by measuring the surface composition while simultaneously milling the surface with a (Varian) Ar ion gun operated at 2 keV. The times required for ion milling the oxide from the surface to the oxide-GaAs interface are plotted against oxide thickness in Fig. 1 (filled points). As expected, the relationship is linear; the solid line drawn through the points represents a milling rate of 100 Å/min.

Table I. List of samples

Sample No.	Thickness (A)*
1931	640
1771	1400
1782	1750
1816	2780

* Determined using Rutherford backscattering.

* Electrochemical Society Active Member.

Key words: GaAs plasma-grown oxide, Auger spectroscopy, neutron activation analysis.

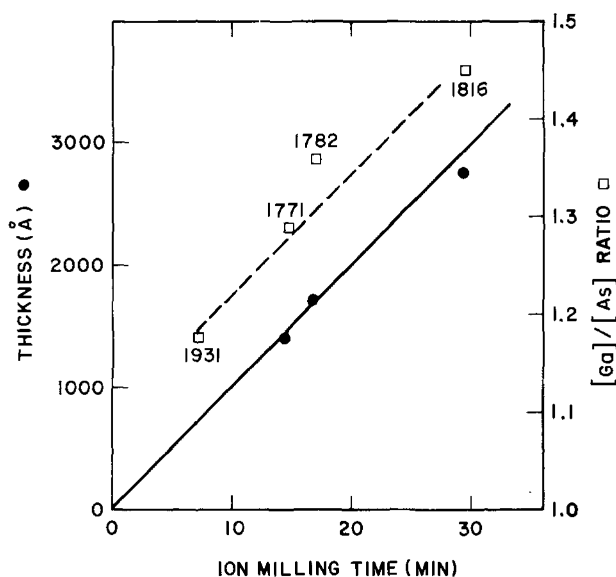

Fig. 1. The oxide thickness (filled points) and Ga/As concentration ratio (open squares) as functions of ion milling time. The over-all Ga/As concentration ratio increases with oxide thickness.

Neutron activation analysis was utilized to calibrate the concentration ratio of Ga and As in the oxide because this ratio was the only quantity for which a calibration could not be obtained from Auger data alone. Details are further described below.

Results

Calibration of the Auger data.—Quantitative Auger analysis (6, 7) can be accomplished by experimentally determining the coefficients for all of the known factors that affect the Auger signal intensity, so that the measured heights of peaks in the Auger spectra can be converted to composition in atom percent. This procedure of calibrating the Auger intensity is quite involved. Only an outline of the procedures followed in this work is presented here, with the appropriate references. We define quantitative analysis as one in which numerical results are calculated, together with some well-defined error limits. In the Discussion section, we describe some of the difficulties encountered in estimating meaningful error limits for the present work. Because of a lack of the statement of error limits, these analyses can only be considered semiquantitative.

Numerical evaluations of certain parameters and corrections for all experimental artifacts must be completed before quantitative depth profiles can be calculated. A description of these evaluations is now presented, organized into the five items discussed below. The first two items concern (*i*) the Auger sensitivity factors, and (*ii*) the correction factors for compositional changes induced by the ion beam used for ion milling and the electron beam used for Auger excitation. Three additional problems had to be considered. Item (*iii*): At the start of ion milling, the ion and electron beam interactions have not had time to establish steady-state conditions; in fact, at time t = 0 min, the surfaces are not perturbed at all, so that (*ii*) above does not apply at the oxide surface. Item (*iv*): At the oxide-GaAs interface, signals from the oxide and GaAs both contribute simultaneously to the Auger peak. Since the correction factors for GaAs and the oxide are different, these signals must first be separated before application of the correction factors. Item (*v*): We demonstrate below that some of the oxide-GaAs interfaces investigated here were only about 30Å wide; for such narrow interfaces, data normalization cannot be performed using peak heights measured at different times because of the rapid change of the Auger peak heights with time. Peaks

Table II. Parameters for quantitative Auger analysis

	Element		
	O	Ga	As
Auger electron energy (eV)	507	1067	1228
Inverse Auger sensitivity factors:			
Ion milled GaAs	—	1.0	1.6
Ion milled oxide	1.6	1.0	1.6
Ion, electron beam correction (oxide only)	1.0	1.0	2.0

Notes:
The inverse Auger sensitivity factors are applicable under the following conditions: 6 keV incident electron energy, 2V, a-c modulation, and analyzer resolution of 0.25%.
The inverse Auger sensitivity factors for Ga and As in the oxide and in GaAs were found to be the same in this work, in contrast to the different values found in Ref. (4). The new values are consequences of the higher energy resolution of the present apparatus. When the derivative-type spectra are used, the higher resolution results in (*a*) a reduced interference from the plasmon loss peak, and (*b*) a reduced interference among the closely spaced (<5 eV) multiplets which comprise each of the Ga and As peaks.

measured at the same instant must somehow be obtained. Each of the above five items will now be considered in greater detail.

Item (i): the Auger sensitivity factors.—The Auger sensitivity factors for Ga and As were determined (8) by an analysis of four reference GaAs surfaces: (*a*) cleaved in vacuum, (*b*) ion milled, (*c*) molecular-beam grown (Ga stabilized), and (*d*) molecular-beam grown (As stabilized). The sensitivity factor for O was taken from a previous calibration obtained by use of a single crystal of Ga_2O_3 (4). The resulting sensitivity factors are shown in Table II, together with the transition energies of the peaks selected for these analyses. The value of 1.6 for the O sensitivity factor was computed by multiplying the value of 0.64 [from Ref. (4), normalized to the Ga sensitivity factor of 1.0] by two transform factors, one for the difference in energy resolution and the other for the different incidence energy. These two transform factors were determined using the present apparatus by decreasing the energy resolution (increasing the a-c oscillation) and decreasing the incidence energy to 3 keV to simulate the operating conditions of Ref. (4).

Item (ii): ion and electron beam induced artifacts.—The ion and electron beam induced compositional changes were investigated by measuring the Ga and As concentration ratios for our plasma-grown oxides by neutron activation analysis. Although this correction factor had been previously obtained using an identical procedure applied to anodic oxides on GaAs (4), this factor might be different for the plasma-grown oxide because of the different physical and chemical properties of the two kinds of oxides. For the neutron activation analysis, one crystal of GaAs with about 1500Å of plasma-grown oxide was irradiated in a neutron flux, and then the oxide was etched off in a known volume of 1:1 solution of $HCl:H_2O$. A precise volume of this solution was then transferred to a 2 in. diam filter paper since the Li drifted Ge detector was calibrated for this geometry. Counting was performed as a function of time to determine the half-life of the detected radiation, and the concentrations of Ga and As were then calculated using known efficiencies. The amount of Ga was found to be constant with time but the amount of As decreased, as observed previously (4). We used the Ga and As concentrations extrapolated back to the time of dissolution as the value in the oxide. This procedure assumes no concentration change between the time of irradiation and the time of dissolution, no precipitation in the HCl solution, and no preferential adsorption at container walls. To minimize wall adsorption, micropipettes and beakers made from nonwetting polypropylene were used.

The desired correction factor for the Auger data was obtained by dividing the Ga/As concentration

ratio from neutron activation analysis, which was 1.2_9, by the apparent concentration ratio from Auger analysis. The latter was obtained as the ratio of areas under the curves for oxidized Ga and As in the depth profiles through sample No. 1771, with 1400Å oxide (possible errors caused by the 100Å difference between this sample and the one analyzed by neutron activation analysis are expected to be small and have been neglected).

The correction factors for the ion and electron beam induced compositional changes are listed in Table II. The value of 1.0 for the ion and electron beam correction of Table II for Ga was assumed to be that found for Ga_2O_3 (4). The value of 2.0 for the As correction factor, which derives from the neutron activation analysis measurement, is significantly different from the 1.6 determined earlier for anodic oxides (4). Although the reason for this difference is not known, there is no requirement, as stated earlier, that these values should be identical. The value of 1.0 for O is explained in Ref. (4).

To determine whether the ion or electron beam produced the larger effect, the result from electron bombardment alone was investigated and is shown in Fig. 2. It was found that under the present operating conditions, the decomposition of Ga oxide was negligibly slow, but the As oxide was rapidly decomposed and a new As peak, near the energy of As in GaAs, appeared in the spectra. Because of the relatively high energy resolution of the Auger apparatus, these chemically shifted (by about 7 eV) and unshifted peaks could be effectively resolved. The total As Auger signal could be measured as the sum of these two peaks. The open points in the figure indicate the change with time of the total Ga/As Auger signal ratio, which is seen to increase by a factor of two and level off in about 2 min. This increase suggests that some As is lost from the surface. The factor of two increase is equal to the correction factor of two found above using neutron activation analysis. Therefore, the major contribution to the correction factor comes from the electron bombardment and very little from the ion bombardment. This conclusion is consistent with the fact that the curves of Fig. 2 remain essentially the same when the data are taken with or without simultaneous ion milling. This last observation is somewhat unexpected because the ion milling should remove the decomposed As, and indicates that much more can be learned about the electron and ion beam interactions with these oxides by further Auger studies.

Item (iii): the nonsteady-state problem at start of ion milling.—The possible errors caused by the initial nonsteady-state conditions were reduced by varying the preferential sputtering correction linearly from 1.0 to 2.0 between 0 and 2 min during data acquisition. There should be nothing fundamental about the 2 min interval; this time was simply the interval to attain steady state as illustrated in Fig. 2 for the present operating conditions. Under different conditions (*e.g.*, electron beam intensity), this time interval is expected to be different.

Item (iv): separation of signals from the oxide and from the GaAs at the interface.—The Auger signals from the oxide and from GaAs could be distinguished in one of three ways. These are the use of: (*a*) the chemical shift, (*b*) the O Auger signal, and (*c*) the plasmon loss peak. We have tried all three methods and they gave essentially the same results within experimental error. Each method has its particular advantages and disadvantages and there was no one technique that was clearly more accurate than the other two. Typical results from the last two methods are compared in Fig. 3 for data from two samples with different interface widths. In the figure, the amount of GaAs was estimated using the oxygen peak by assuming that only Ga_2O_3, As_2O_3, and GaAs are present at the interface (open points), and by use of the Ga plasmon loss peak (filled points). From the close agreement of the two curves, it is concluded that the amount of interface material is too small to be detected using this type of analysis. For example, if large amounts of excess As or suboxides were present, the open points would lie to the left of the filled points in Fig. 3. Therefore, either method is equally useful for determining the amount of GaAs. Because use of the O peak was the simplest and the scatter in the data was least, this method was adopted for this work.

Item (v): obtaining simultaneous peak heights.—With the present apparatus, it was not possible to monitor several Auger peaks simultaneously. Therefore, one peak from each element was multiplexed and each element was recorded sequentially as a function of time. Then continuous curves were drawn, one through the maxima, and one through the minima, of the peaks from each element, defining an "envelope" describing the peak height variation of that element with time. The value of peak heights determined by the envelope for each element present at one given instant was then used for the computations. For sample No. 1931, several envelopes were obtained using data from different areas of the sample and superposed

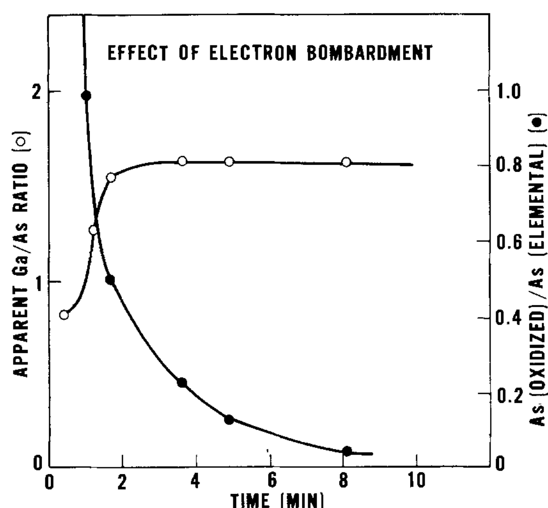

Fig. 2. Decomposition of As-oxide by electron bombardment. The decomposition is incomplete even after 4 min (filled points), but the method of peak height measurement adopted in this work (addition of the chemically shifted and unshifted peaks) gives the final steady-state value of the Ga/As ratio after only 2 min.

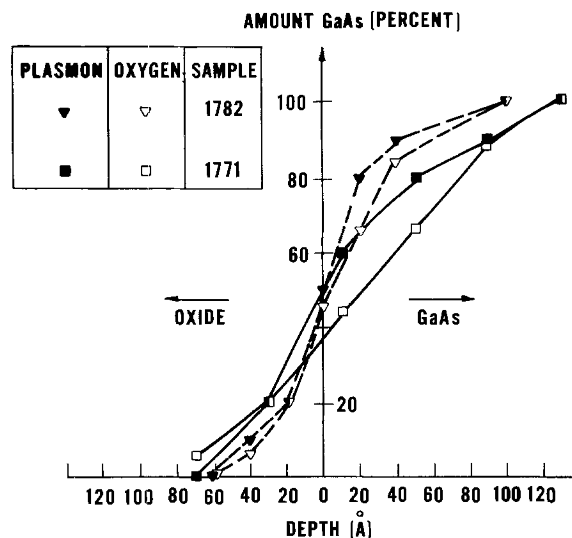

Fig. 3. Comparison of the use of the plasmon loss peak and the oxygen Auger signal for separating the Auger signals from oxidized and unoxidized Ga and As atoms at the oxide-GaAs interface.

(by matching the envelopes) to increase the density of data points and reduce the amount of envelope extrapolation between them.

Using the above correction factors and methodology, the chemical depth profiles of this work were obtained. The Auger intensities were measured as the peak-to-peak heights of the "derivative" spectra. Calculations were performed in the homogeneous approximation, *i.e.*, ignoring the oxide-GaAs layer sequence, since the details of the layer geometry were not sufficiently known. Compositions (in atom percent) were calculated as the normalized Auger signal (6, 7) A_i, for each element i, which includes the corrections for the Auger sensitivity factors of Table II. In addition, the Auger intensities were multiplied (4) by their proper preferential sputtering coefficients. The question of error limits is taken up in the Discussion.

The chemical depth profiles.—Chemical depth profiles from the four samples of Table I are displayed in Fig. 4-7. The interface regions are shown expanded in Fig. 5b-7b so that details of these abrupt interfaces can be seen. For the sample of Fig. 4, nonstandard ion milling conditions were used up to about 350Å, and that part of the data is not shown. All the depth profiles exhibit very similar general features, which are described in the following paragraphs.

The "bulk" of the oxides contained about 60% O; therefore, the oxide compositions are consistent with those of mixtures of Ga_2O_3 and As_2O_3. The bulk of each oxide had a constant composition with depth, but with varying over-all Ga/As concentration ratios for each sample. The variation of this ratio with oxide thickness is illustrated in Fig. 1 (open squares). There appears to be a linear increase in this ratio with thickness, from 1.1_8 at 600Å to 1.4_5 at 2780Å; only sample No. 1782 deviates slightly from the linear relationship, presumably because it was grown under somewhat different conditions from the rest.

The oxide as a whole was always As deficient and, therefore, As must have been lost during growth. We describe below one possible mechanism for oxide growth which leads to a larger diffusion coefficient for As than for Ga. Since oxides of As are more volatile than oxides of Ga, the As deficiency is a reasonable consequence of the faster out-diffusion of As and the higher volatility of the As oxides.

The surfaces of the oxides always contained more As than Ga. Thus the faster out-diffusing species, not surprisingly, pile up at the surface. The significance of the apparent rise of the O concentration near the surface is presently not clear. It could arise from an error in our calibration scheme, or else it may be a real effect caused by the formation of As_2O_5. This compound has been identified from x-ray photoemission spectra on air-exposed GaAs surfaces (8). However, no distinct peak attributable to As_2O_5 could be discerned in the Auger spectra. Therefore, further interpretation of the apparent rise in the O concentration near the surface cannot be provided until Auger spectra from As_2O_5 are examined.

There is a region near the surface of approximately 200Å in which the As concentration decreases from about 20% to a value below the Ga concentration, in the direction away from the surface. This higher As concentration is opposite to that observed for anodic oxides, since the surface layer in the anodic oxide was As deficient (4). Therefore, it is most unlikely that both layers are experimental artifacts of the same method of analysis. This argument lends further credence to the validity of these depth profiles.

The interfaces between these oxides and GaAs are surprisingly abrupt. The interface width as a function of oxide thickness is plotted in Fig. 8. The convention used here to determine the interface width was to define the apparent width as two times the depth spanned in the profile between 85 and 50% of the

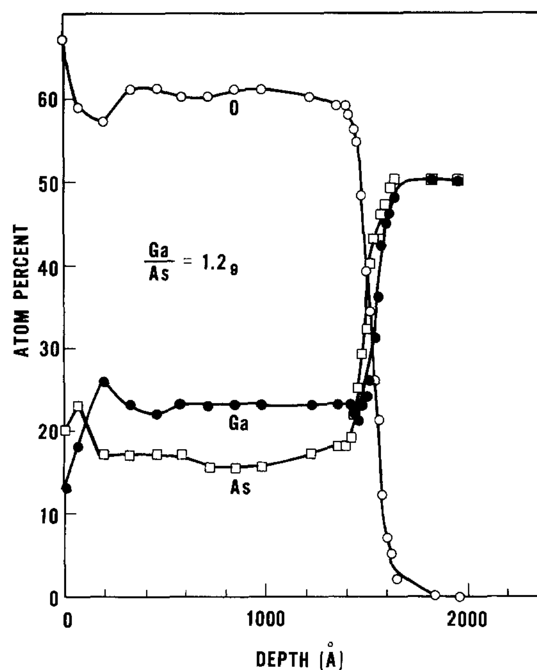

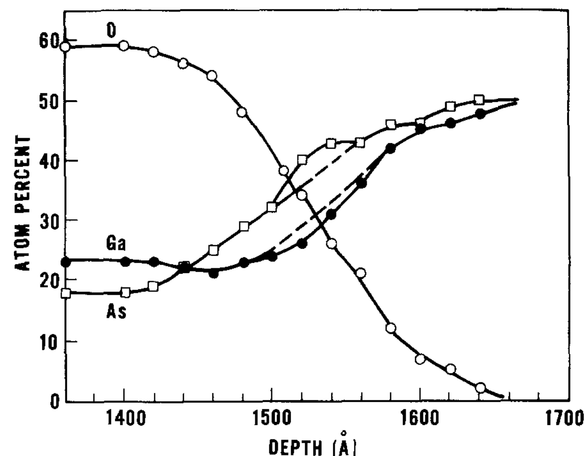

Fig. 5. (a, top) Chemical depth profile of sample No. 1771. (b, bottom) Expanded view of the oxide-GaAs interface region revealing details of the interface.

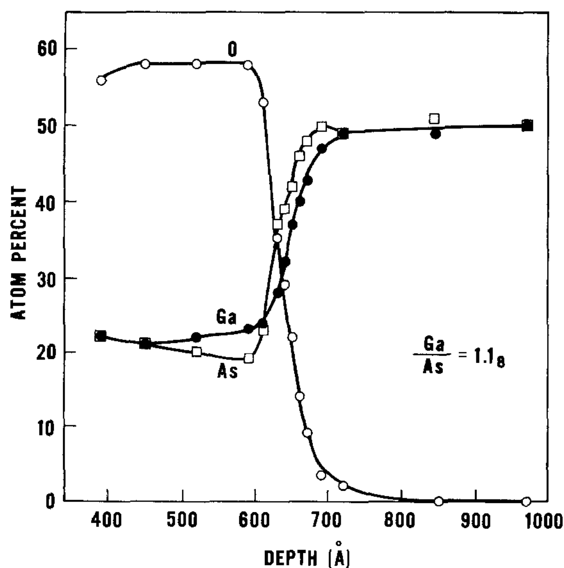

Fig. 4. Chemical depth profile of sample No. 1931. Note that the compositions for all three elements were computed for the same instant in time (see text).

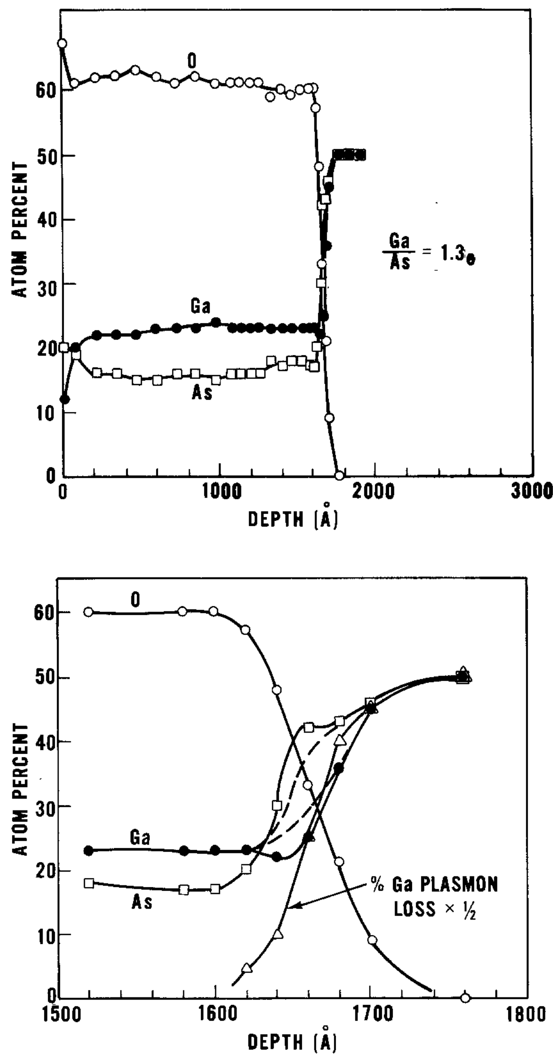

Fig. 6. (a, top), (b, bottom), Same as Fig. 5, sample No. 1782

"bulk" oxygen signal. The width thus defined is called the "symmetric mean width" [see Ref. (9) for the reasons for adoption of this convention, which provides the most reliable estimate of the width from the depth profiles and minimizes errors from ion milling artifacts, etc.]. This procedure does not take into account various broadening factors, the largest of which is due to the finite escape depth of Auger electrons. Data from SiO_2-Si interfaces (9) indicate that use of the apparent symmetric mean width of the oxygen profile leads to a broadening factor of at least 30Å. The estimated true interface width of Fig. 8 was therefore obtained by subtracting this 30Å from the measured apparent symmetric mean width. This procedure should be valid provided that the escape depth of 507 eV electrons in SiO_2 and in the present oxides are equal. The resultant widths ranged from <30 to <70Å. How much less will depend on how much worse the experimental broadening factors are for the GaAs systems studied here compared to the Si systems from which the 30Å broadening contribution was estimated. It is inconceivable that the broadening factors are less for the present systems, because these factors were minimally small for the Si systems (9).

The final topic we consider in detail is the As excess at the oxide-GaAs interface. "Excess As" is defined here simply as the amount of As in excess of the amount of Ga at a given depth. The interface regions are shown expanded in the b-figures (Fig. 5b-7b). Even for the thinnest oxide film, sample No. 1931, a clear As excess was detected (Fig. 4). For the next thicker film, a "bulge" appeared in the As profile near the depth at which the O signal is one-half of its bulk value. This suggests that the As responsible for the bulge is located at the interface because it has been shown (9) that the interface is within several angstroms of the point where the O signal is at half-maximum for the SiO_2-Si system.

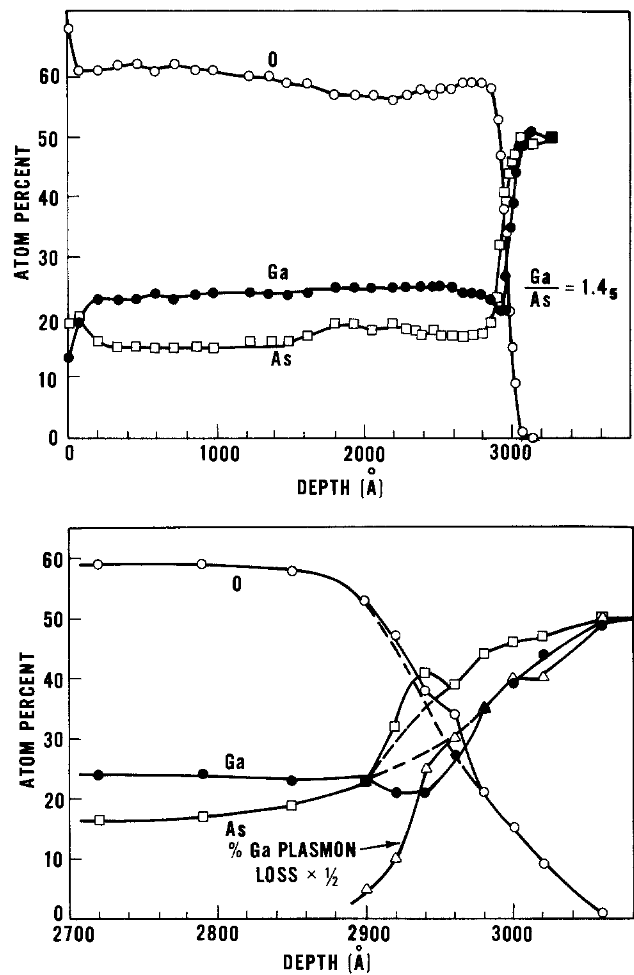

Fig. 7. (a, top), (b, bottom), Same as Fig. 5, sample No. 1816

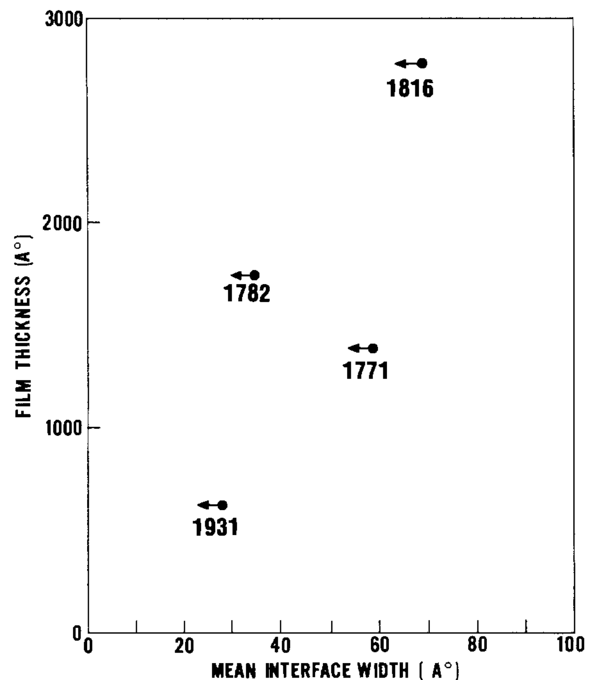

Fig. 8. Measured symmetric mean interface widths. The arrows indicate that the actual widths are expected to be smaller than the values indicated.

This bulge was visible in all of the profiles and was largest for the thickest film, No. 1816. Part of this apparent bulge may be an artifact due to an underestimate of the Ga peak height caused by mutual interference of the chemically shifted and unshifted Ga peaks in the oxide and GaAs, respectively. When the Ga peak is underestimated, the As (and O) peak heights become overestimated during the normalization process. Because the two Ga peaks were summed in the peak height measurement, we estimate that the megnitude of the bulge (amount of deviation from the dashed lines) is too large to be caused by spectral overlap alone. In addition, errors from spectral overlap should be the same for all the depth profiles, whereas the bulge increases with oxide thickness. Therefore, from the large magnitude of the bulge and its increase with oxide thickness, we conclude that the bulge is mostly real and must represent a thin layer of excess As at the exact location of the oxide-GaAs interface. The apparent mean width of this layer on the depth profile is only about 40Å and the true layer thickness is much less. The amount of excess As should be equal to the area between the As and Ga profiles at the interface. For the three thicker films, this amount was approximately 5Å or about two atom layers, if the bulge is ignored. For the thickest film, No. 1816, the bulge adds another monolayer of excess As. These amounts correspond to an As accumulation rate of approximately 10^{15} atoms/cm^2/1000Å of oxide growth. Because the plasmon loss peak associated with the excess As was prominent while the plasmon loss peak for Ga (and for As throughout the oxide) was much smaller, we conclude that the As is in elemental form, similarly to the case for the anodic oxide (4, 8).

Discussion

Some comments on the expected error limits of the present semiquantitative results are in order. All we can claim here is that we have incorporated into our analysis most of the known correction factors that could be numerically calculated. However, a meaningful estimate of the error limit is not possible for the present system because of insufficient experimental data. For depth profiles of SiO_2 on Si, an estimate of the error limits was attempted (9), but even for such a well-studied system, it was clear that the final answer was not unique because of several basic unknowns, such as the amount of suboxide at the interface. To illustrate some of the difficulties, we discuss here a few points of particular concern. (*i*) The accuracy of the neutron activation analysis for the Ga/As concentration ratio has not been tested. Since the depth profile and neutron activation data cannot obviously be obtained from the same sample, the sample-to-sample variations become important. The possible preferential loss of some chemical components during liquid transfer, are also not sufficiently known. (*ii*) An accurate determination of the Auger sensitivity factor for O in an oxide containing Ga and As has not yet been satisfactorily performed for lack of a good standard. We point out that the sensitivity factor of 1.6 used here should be compared to a value of approximately 0.6 in Ref. (10) (pp. 14-15; data were transformed to conform to the conventions, definitions, and operating conditions of this work). This is a disagreement of over a factor of 2 and represents one of the largest discrepancies of the Auger sensitivity factor in the literature. This disagreement results largely from the sensitivity of the O Auger peak shape to chemical environment [a different oxide was used in Ref. (10)]. This comparison illustrates the variability of the O Auger sensitivity factor depending on the chemical environment; however, there is presently insufficient experimental data to statistically establish the typical variations in the sensitivity factor with variations in properties of the Ga-As-oxide. (*iii*) Another source of uncertainty arises from the complexity of the interface structure. No provision was made in the above analyses for the presence of the As layer. Moreover, the formalism adopted effectively assumed that the proportion of oxidized Ga to oxidized As remained the same at the interface as in the bulk of the oxide. This assumption is probably not strictly valid because of the presence of the elemental As. Because of the various artifacts that cloud the As Auger data, all of the three methods for separating the Auger signals from the oxide and GaAs described in item (*ii*) above apply mostly to Ga. In fact, little is presently known about the precise distribution of the As atoms in the oxidized, elemental, and GaAs phases. In summary, we have clearly demonstrated that certain corrections must be applied to the Auger data for obtaining more quantitative depth profiles and that some of these corrections can be rather large; however, additional experimental work will be required before meaningful error limits can be estimated. Nevertheless, the reproducibility of the data was sufficiently high (about $\pm 5\%$) to justify those conclusions of this work based on what might appear, from these disclaimers, to be small differences between profiles from different samples.

The O concentrations in the oxide measured in this work are in agreement with those from studies of similar films using ion-induced x-ray analysis (11). However, there is significant disagreement for the Ga/As concentration ratio; the discrepancy is about 13% at oxide thickness of 1000Å but increases to about 30% near 3000Å. In the work of Ref. (11), no increase in the Ga/As ratio was found with oxide thickness. The reason for this discrepancy is presently being investigated. Although the possibility of an error in the absolute calibration of the present work cannot be ruled out, there is no known artifact which would cause the error to increase with oxide thickness.

The present understanding of the ion-mill depth profiling technique is insufficient to provide unequivocal proof that the excess As observed at the interface is real. However, a mounting quantity of evidence supporting the correctness of the depth profiles is accumulating, making it increasingly difficult to maintain a skeptical attitude. The existence of a sheet of As near the oxide-GaAs interface has already been hypothesized on the basis of anomalous ellipsometric results (12). The excess As seen in depth profiles of anodic oxides on GaAs has been directly examined after etch removal of the oxide to expose the As layer (4). Evidence for the elemental nature of this As was supplied both from x-ray photoemission data (8) and from the observation of prominent plasmon losses in Ref. (4) and in this work. Unless a phase separation had occurred, the different behavior of As from that of Ga cannot be explained. Finally, the presence of the sharp "bulge" described above and its increase with oxide thickness are difficult to explain away on the basis of an experimental artifact. The importance of the excess As idea cannot be overemphasized because if excess As does exist, it can provide the answers to many previously unanswered questions concerning oxides on GaAs. The As layer can (*i*) dominate important MOS properties of these oxides, (*ii*) control the surface potential of the semiconductor, and (*iii*) determine the semiconducting properties of the underlying GaAs by influencing the Ga vacancy concentration, etc.

The over-all As deficiency found in this work contrasts sharply with the nearly stoichiometric composition of the oxides obtained when an aluminum-oxide layer is used as a surface "filter" to confine the As within the growing oxide (13). Therefore, in addition to the ability to grow these oxides at low temperatures as demonstrated here, ways have also been found to control the relative amounts of Ga and As within the oxide.

Conclusions

The major conclusions of this investigation are:

1. The composition of the plasma-grown oxide is uniform with depth over 90% of its total thickness; the

oxide as a whole is As deficient and the Ga/As concentration ratio increased with oxide thickness from 1.1_8 at 600Å to 1.4_5 at 2780Å. There is a surface region almost 200Å thick which is As rich. The oxide composition is equivalent to that of a mixture of Ga_2O_3 and As_2O_3.

2. We propose that the mechanism for As loss derives from the faster out-diffusion of As compared to Ga during oxide growth (8) and the higher volatility of As oxides compared to Ga oxides. This conclusion means, of course, that there is a finite As out-diffusion during oxide growth.

3. A pile-up of elemental As was observed at the oxide-GaAs interface. The mechanism (4, 8) for the formation of the As layer is the preferential oxidation of Ga due to the higher heat of formation of Ga_2O_3 compared to As_2O_3. The As pile-up increased with oxide thickness, at the rate of approximately 10^{15} atoms/cm^2/1000Å of oxide growth.

4. The oxide-GaAs interface width was extremely narrow, ranging from <30Å at oxide thickness of 600Å to <70Å at 2780Å.

5. The electron beam produces a larger effect in decomposing the Ga-As-oxide than the ion beam and it is the As oxide that is rapidly decomposed; the decomposition of Ga oxide was not detected.

Acknowledgments

The authors are grateful to R. L. Kaufman, L. C. Feldman, and J. M. Poate for some very useful discussions and for the measurements of the oxide thicknesses using Rutherford backscattering.

Manuscript submitted July 27, 1977; revised manuscript received Oct. 25, 1977.

Any discussion of this paper will appear in a Discussion Section to be published in the December 1978 JOURNAL. All discussions for the December 1978 Discussion Section should be submitted by Aug. 1, 1978.

Publication costs of this article were assisted by Bell Laboratories.

REFERENCES

1. R. P. H. Chang and A. K. Sinha, *Appl. Phys. Lett.*, **29**, 56 (1976).
2. S. P. Murarka, *ibid.*, **26**, 180 (1975).
3. B. Schwartz, F. Ermanis, and M. Brastad, *This Journal*, **123**, 1089 (1976).
4. C. C. Chang, B. Schwartz, and S. P. Murarka, *ibid.*, **124**, 922 (1977).
5. R. P. H. Chang, *J. Vac. Sci. Technol.*, **14**, 278 (1977).
6. C. C. Chang, in "Characterization of Solid Surfaces," P. F. Kane and G. B. Larrabee, Editors, Chap. 20, Plenum Press, New York (1974).
7. C. C. Chang, *Surf. Sci.*, 48, 9 (1975).
8. C. C. Chang, P. H. Citrin, and B. Schwartz, *J. Vac. Sci. Technol.*, **14**, 943 (1977).
9. C. C. Chang and D. M. Boulin, *Surf. Sci.*, **69**, 385 (1977).
10. L. E. Davis, N. C. MacDonald, P. W. Palmberg, G. E. Riach, and R. E. Weber, "Handbook of Auger Electron Spectroscopy," 2nd ed., Physical Electronics Ind., (1976).
11. R. L. Kaufman, L. C. Feldman, J. M. Poate, and R. P. H. Chang, *Appl. Phys. Lett.*, **30**, 319 (1977).
12. K. H. Zaininger and A. G. Revesz, *J. Phys. (Paris)*, **25**, 208 (1964).
13. R. P. H. Chang, C. C. Chang, and T. T. Sheng, *Appl. Phys. Lett.*, **30**, 657 (1977).

Experimental Investigation of the Gas Phase in a Chemical Vapor Deposition Reaction

Application to the Silane-Ammonia Reaction Leading to Silicon Nitride Deposits

G. Cochet, H. Mellottée, and R. Delbourgo

CNRS, Centre de Recherches sur la Chimie de la Combustion et des Hautes Températures, 45045 Orléans Cédex, France

ABSTRACT

The investigation of the gas phase composition of a CVD system was carried out applying a method derived from flame front structure research and implying a point-to-point analysis of concentrations and temperature profiles. A finely drawn nozzle-shaped probe is used to draw stable species samples out of the gas phase. They are subsequently compressed into a VPC analyzer. A fine silica-coated thermocouple is used to draw the temperature profiles. The method was applied to the co-pyrolysis of silane and ammonia forming silicon nitride on a vitreous sintered silica substrate heated at 950°, 1000°, and 1050°C at different values of the ratio of silane to ammonia. The results obtained localize the space, in the gas phase, and relatively to the substrate, where the solid phase starts condensing as the initial reactants are consumed. The method is reproducible and reliable. If properly developed it should lead to interesting applications in the interpretation of CVD aerothermochemistry and chemical kinetics.

One of the main problems raised by the interpretation of chemical vapor deposition mechanisms lies in the accurate space and time resolution of the reaction species and parameters. The question is not yet fully settled as to whether the reaction is localized in the gas phase or on the heated substrate or occurs simultaneously in the gas phase and on the substrate. Any attempt to interpret quantitatively CVD data should first aim at obtaining experimental evidence on the relative contribution of the gas phase and of the substrate reactions especially if the objective is one of obtaining theoretical models more satisfactory and general than those presently found in the literature (1, 2). The efforts made in this direction appear how-

Key words: chemical vapor deposition, silicon nitride, gas phase investigation.

ever to have been limited by experimental difficulties due to the necessity of controlling a high temperature reactive system under flow conditions.

This paper describes an attempt to apply to CVD systems a point-to-point probe and thermocouple analysis to determine concentrations and temperature profiles in a system leading to silicon nitride deposited on vitreous sintered silica by the co-pyrolysis reaction of silane and ammonia.

Experimental

The method used is an extension of the Fristrom and Westenberg (3) technique originally developed for flame front structure studies. Gas samples are withdrawn from the reaction zone at different points of the gas flow and a consistent profile can be drawn for each species by moving the probe from the unburned gas to the products and through the flame front. It has been shown that with adequate care and equipment (finely drawn quartz probes) minimum perturbation of the gas flow is achieved and that samples can be withdrawn from the reaction zone sufficiently rapidly to ensure quenching of the products. With minor modifications we have attempted to apply the same method to a CVD reactor.

Temperature profiles.—In order to establish temperature profiles one is led to introduce a fine thermocouple in the gas flow. If the diameter of the wires and junction are kept small (*ca.* 10-50 μm) no instability is added to the flow aerodynamics. Catalytic effects can be offset by coating the thermocouple with a fine silica coat. Radiative loss can be a source of error, the thermocouple behaving as a radiant heat sink. To account for this factor implies knowing the emissivity of the thermocouple and properties such as the thermal conductivity, specific gravity, viscosity, and flow rate of the gas phase. In a CVD system, at temperatures of the order of 1000°C, it appears that radiative loss can be neglected since the temperature drops very rapidly as one moves away from the substrate. Accounting for a proportionality of radiation loss with the fourth power of temperature, one obtains for a 20 μm probe, a gas phase in which hydrogen is the main carrier and a temperature of 1100°K, a correction of only 8°K value which is considered affecting only negligibly the temperature profiles drawn.

Pt/Pt-Rh 10% thermocouples were used throughout this work. The size of the thermocouple junction is less than 0.1 mm. A coat of SiO_2 obtained by dipping the thermocouple in silicone oil and flaming reduces catalytic effects.

Concentration profiles.—Sampling in the gas phase is obtained by a finely tapered quartz probe. Samples are drawn into the nozzle under reduced pressure (4-10 Torr), the orifice diameter is small (10-100 μm). The gases are drawn in rapidly and rapid flow rate quenches the species out of the reaction zone satisfying both representative and reproducible results.

Satisfactory quenching of samples is borne out by the application of this method to flame structure studies and the agreement obtained with mass spectrograph and EPR data (3). Also, the sample is essentially gaseous, no solid deposit being apparent in the probe except for traces similar to the Si_3N_4 deposited on the cold walls of the reactor (same color, ammonia smell, and Si-N bands found by infrared spectroscopy). There seems to be no reason to believe that these traces imply a variation in composition of the gas phase. As in the case of the thermocouple, the introduction of a fine probe in the gas flow does not affect the stability of the system. The emissivity of quartz is 2×10^{-2} (3) and, therefore, thermal effect can be considered negligible. Catalytic effects are also not significant and the only source of error seems to be the difference in diffusion rates of the various species present. In a CVD system in which a carrier gas is in most cases in excess the problem is limited to a binary system for which the diffusion coefficients can be calculated.

The samples are transferred to a gas chromatograph or to a mass spectrometer by any convenient means and the analyses of the gas phase can therefore be accomplished at least for all stable species.

Combining temperature profiles and concentration profiles, one can draw a point-to-point map of the gas phase and obtain important information on the evolution of the reactants from their inlet at the top of the CVD reactor down to the heated substrate where the condensed phase is deposited.

In applying these techniques to a CVD system heated by a high frequency device, one must be aware of the possible influence of the HF on the thermocouple. The relative dimension of the inductor and the susceptor (in this case the thermocouple) is such that the error appears to be small. The temperature recorded by the thermocouple has been compared to a reading obtained by infrared pyrometry. The maximum difference obtained, near the substrate, is less than 10°C. This does not affect significantly the profiles and gradients which were obtained.

CVD reactor.—The method described above was applied to the following system

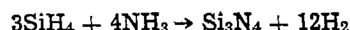

$$3SiH_4 + 4NH_3 \rightarrow Si_3N_4 + 12H_2$$

depositing silicon nitride films on a vitreous sintered silica substrate.

The setup used is shown in Fig. 1. It consists of a panel comprising the different manometers, flowmeters, and needle valves. The reactants are mixed in a tube filled with glass beads. The reactor consists mainly of a graphite susceptor, protected by a coat of silicon nitride and heated by high frequency under 1 MHz. The substrate is a plane disk 1 mm thick, 28 mm diam made of sintered silica and adjusted on the susceptor.

The susceptor was designed to obtain a constant temperature (± 2°C) across a diameter. The temperature was measured by infrared pyrometry. The temperature of the graphite was kept constant by a regulating system connected to a thermocouple W 97%-Re 3%/W 75%-Re 25%. The top of the reactor is fitted with a mobile head designed to monitor the simultaneous lateral and vertical movement of the probe or thermocouple (Fig. 2). The positioning can be adjusted to 5×10^{-2} mm and readings can be taken every 0.1 mm along the vertical axis and radially every 1.0 mm. Samples were taken down to a distance equal to 0.5 mm from the substrate. Any attempt to probe at smaller distances from the substrate results in rapid clogging of the probe. The thermocouple wires were coated with SiO_2 by burning with a silicone oil.

The gas samples are drawn into a piston under a reduced pressure of the order of 10 Torr then compressed into a VPC analyzer fitted with a catharometer (4). The following gases were analyzed: SiH_4, H_2, N_2,

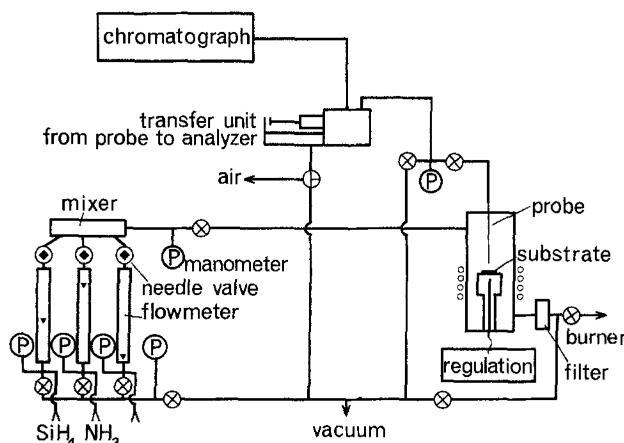

Fig. 1. Schematic layout of the apparatus

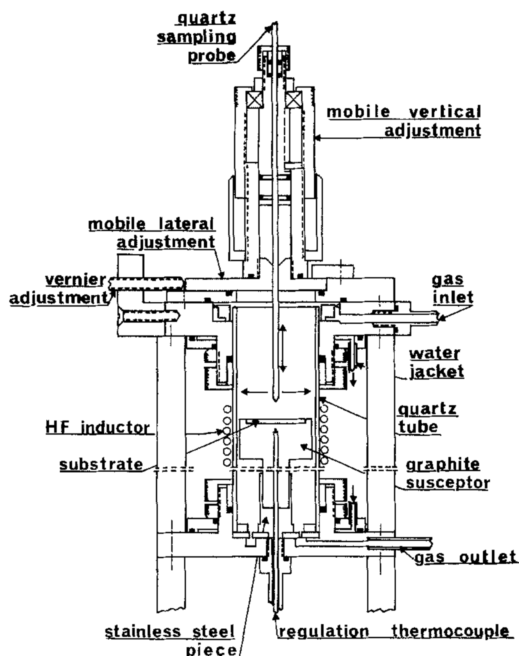

Fig. 2. Mobile probing head for thermocouple readings and gas samples.

NH_3, and Ar. Two columns were placed in series, one 2m long filled with Porapak T, heated at 110°C, the other, outside the chromatograph, 3m long fitted with 13*X*, molecular sieve, was kept at room temperature.

Down flow of the reactor, a metal grid filters the solid particles formed around the substrate. The flow gases are ultimately burned in a diffusion gas burner.

Reaction conditions.—The optimum conditions for obtaining Si_3N_4 from the co-pyrolysis of SiH_4 and NH_3 are given elsewhere (5). In the present case three temperatures of the substrate were systematically investigated: 950°, 1000°, and 1050°C.

We will recall that favorable conditions for Si_3N_4 require large values of the ratio of NH_3/SiH_4, at least of the order of 30 (6) and varying with the experimental conditions. In this investigation the mixtures studied were in the ratios 50/1, 100/1, 200/1, and no Si in excess nor any trace of Si-H bands as detected by infrared spectrometry were observed, as would be the case for lower values of the NH_3/SiH_4 ratio. The gas flow rates were set at 11, 22, and 44 liter/hr, corresponding to linear velocities of 0.25, 0.5, and 1.0 cm/sec.

Results

Temperature profiles.—The temperature profiles which were obtained are shown in Fig. 3. They refer to a mixture flow rate of 22 liters/hr with a ratio of NH_3/SiH_4 equal to 100/1 and a substrate temperature of 950°C. The y axis represents distances from the substrate along its axis and the walls of the reactor and the substrate are shown at the right and lower part of the figure. The profiles shown are isotherms drawn every 20°C.

The temperatures recorded are mean values and similar instabilities to the ones reported by Curtis and Dismukes (7) were observed. The frequency of these oscillations is of the order of 0.5 Hz with an amplitude depending on the carrier gas. It is of the order of 25°C for nitrogen or argon but is reduced to 4°-5°C in the case of hydrogen. Ammonia would lie in between hydrogen and nitrogen. These oscillations, like those observed by Curtis and Dismukes, could be interpreted in terms of perturbations due to convection and related to the number of Rayleigh ($R = Gr \cdot Pr$).

Two areas are clearly seen: At the center and approximately for 80% of the plate radial distance, the isotherms are nearly horizontal and the gradients small

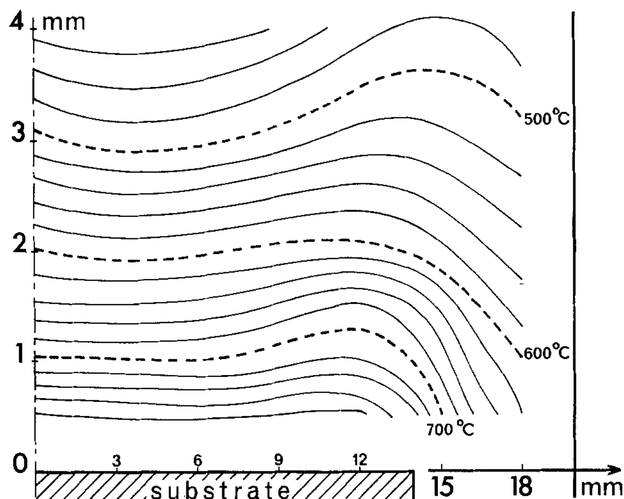

Fig. 3. Temperature profile map. NH_3/SiH_4 ratio = 100, total flow rate 22 liters/hr.

and practically negligible, near the walls the temperature is lower and the gradient steeper. In both situations the vertical gradient is also steep, especially near the heated substrate, as one would expect. Whereas little information can be drawn from the perturbated annulus near the walls, the study of the central radially isothermal core gives an estimate of the influence of the total flow rate and of the ratio of NH_3/SiH_4 or that of the inert gas eventually added.

Influence of the variation of the total flow rate.—The temperature gradients can be deduced from the temperature profiles along the axis of the reactor. The following figures present the variation of the temperature along the axis under a certain number of parameters. The substrate temperature is in all cases equal to 950°C.

Figure 4 shows the influence of the total flow rate in a case where the NH_3/SiH_4 ratio is equal to 100/1. The gradient appears to remain constant as close as 1 mm from the substrate. For smaller distances, between 0 and 1 mm, the gradient becomes steeper when the total flow rate increases. Analogous variations are obtained for other temperatures of the substrate and various NH_3/SiH_4 ratios.

Influence of the gas.—The temperature of the gas phase above the substrate is related to the nature of

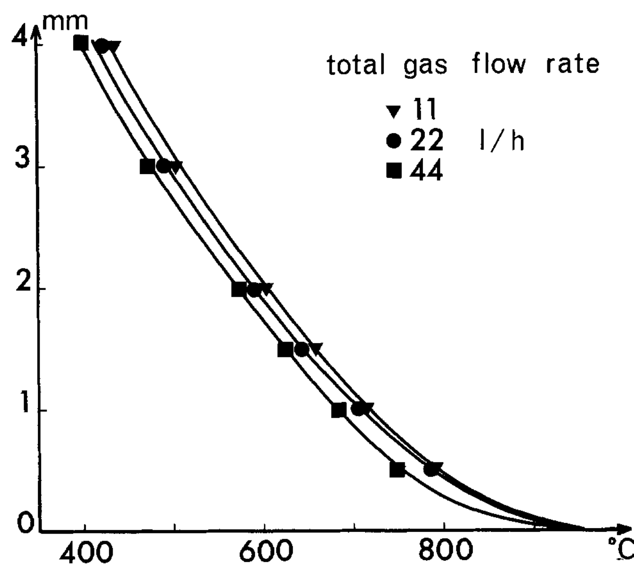

Fig. 4. Influence of the total flow rate on the gas temperature along the axis of the reactor. Substrate at 950°C, NH_3/SiH_4 = 100.

the gas mixture. This is especially important in the case of various carrier gases. This point is illustrated in Fig. 5 showing temperature profiles taken along the axis for a substrate temperature of 950°C and various gases flowing at 22 liters/hr. The temperature in the gas phase is a function of the thermal conductivity of the gas and is highest for gases exhibiting high conductivities. The ammonia curve which should normally lie between those of nitrogen and argon is shifted toward that of hydrogen. This is probably due to spatial thermal decomposition of NH_3 producing some hydrogen.

It follows that the knowledge of these profiles and gradients and the use of an appropriate gas or mixture of gases can be of help in optimizing the conditions for a satisfactory process of deposition.

Influence of the ammonia/silane ratio.—The influence of various ratios has been studied. Figure 6 shows the results obtained at 950°C and 44 liters/hr for three ratios of NH_3/SiH_4, 50/1, 100/1, and 200/1.

Two competitive parameters must be considered: the endothermicity of the reaction and the production of hydrogen. Immediately on the surface of the substrate, the temperatures are high enough to favor the syntheses of Si_3N_4. This also is favored by small values of NH_3/SiH_4. One notes also that vertical thermal gradients increase when this ratio decreases. In this area the influence resulting from the chemical reactions offsets the heat effect added to the gas phase by the hydrogen formed. On the other hand, above this hot zone, the vertical gradients increase along with NH_3/SiH_4 ratios. In this area the chemical reaction is reduced but the rapid diffusion of the hydrogen formed in the hot zone contributes to the heating of the gas phase.

Concentration profiles.—The following figures give the concentration profiles of the various species as a function of distance from the substrate and along the axis of the reactor. The substrate is heated to 950°C, total flow rate is 22 liters/hr, and the same three ratios 50/1, 100/1, and 200/1 were kept. The results are given for silane (Fig. 7), hydrogen (Fig. 8), and nitrogen (Fig. 9) without correction for diffusion coefficients. Correcting for diffusion would slightly shift the values along the x axis without significantly altering the trends shown. It follows from examining the curves that as one moves nearer to the substrate hy-

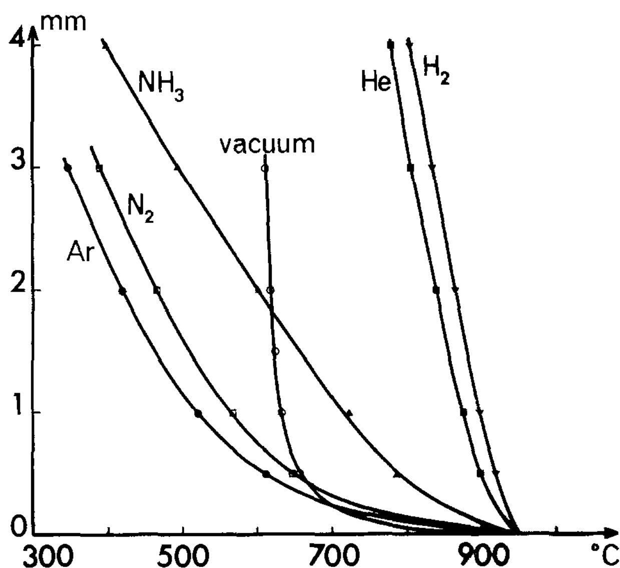

Fig. 5. Influence of the nature of the gas on the temperature measures along the axis. Substrate at 950°C, flow rate 22 liters/hr.

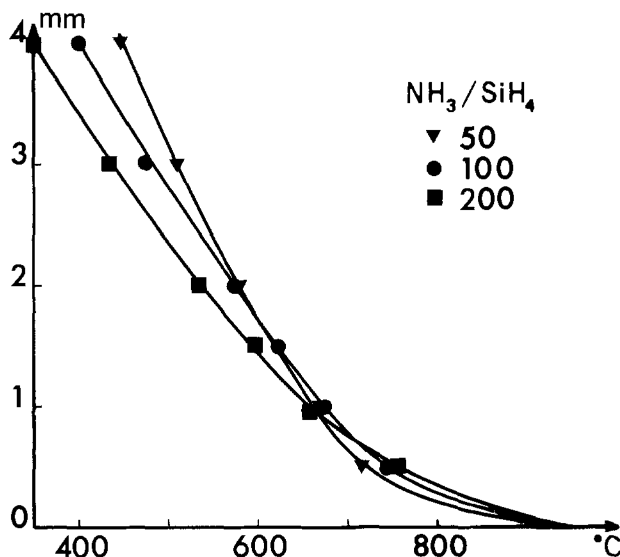

Fig. 6. Influence of NH_3/SiH_4 ratio on the temperature along the axis. Substrate at 950°C, flow rate 44 liters/hr.

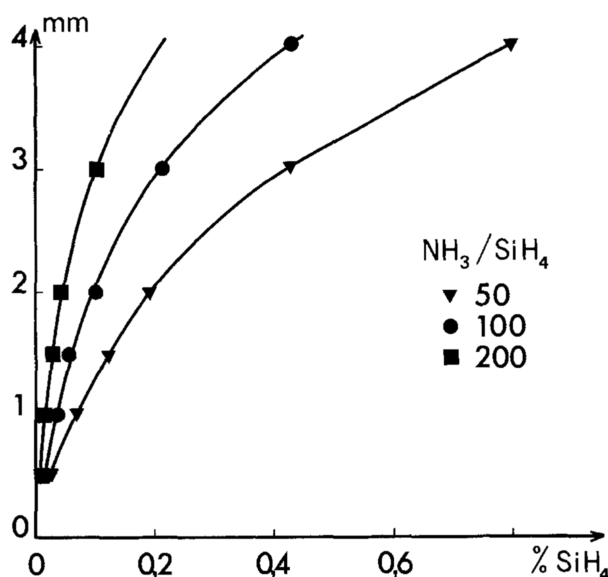

Fig. 7. Silane concentration in the mixture as a function of distance from substrate. Substrate at 950°C, total flow rate 22 liters/hr.

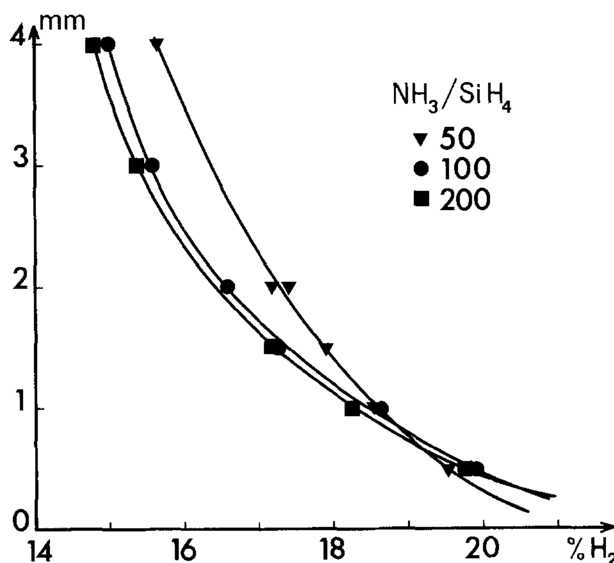

Fig. 8. Hydrogen concentration in the mixture as a function of distance from substrate. Substrate at 950°C, total flow rate 22 liters/hr.

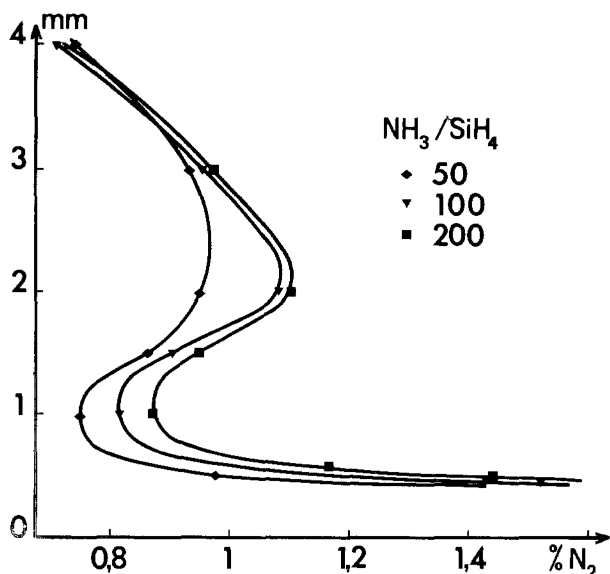

Fig. 9. Nitrogen concentration in the mixture as a function of distance from substrate. Substrate at 950°C, total flow rate 22 liters/hr.

drogen is steadily produced. Silane is practically totally dissociated at 0.5 mm from the substrate. Whatever the SiH_4/NH_3 ratio at this distance no more than 1% of SiH_4 is present.

The nitrogen curves offer some interesting features. They show the competition between the two main phenomena: first, the production of N_2 by the thermal decomposition of NH_3, slow at first but becoming very rapid as the temperature increases near the substrate; second, at 1-2 mm from the substrate, the depletion of the N_2 concentration which must be ascribed to its progressive combination with the products resulting from the decomposition of silane and mainly silicon to form at least some of the silicon nitride which will deposit on the substrate.

The results reported here are uncorrected for diffusion. Considering one in dealing with a large excess of one of the reactants, correction can be easily operated applying Hirshfelder, Bird, and Curtis (8) relations. This shows that close to the substrate the general mapping of the concentration curves is not significantly affected. Only their position relative to the substrate is slightly altered without any implication on the conclusions drawn.

Discussion

Silane is thermally unstable and decomposes rapidly as soon as temperatures of the order of 450°C are reached. At high temperatures the mechanism is partly homogeneous leading to compounds of the type Si_nH_{2n+2} and to their products of dehydrogenation. It is also heterogeneous leading to the formation of Si and H_2. This mechanism becomes predominant as temperature increases (9). Although the presence of hydrogen in large quantities tends to inhibit the decomposition, a cloud of fine particles of silicon or other condensed phases containing Si and H is clearly visible. When nitrogen, produced from the decomposition of ammonia, is present, they tend to react with it. It would be interesting to compare the amounts of free N_2 to the N_2 produced by the NH_3 decomposition and thus have an estimate of the nitrogen bonded. This is not easy because of the large excess of NH_3 and its moderate decomposition ratio resulting in an unsatisfactory accuracy in the analysis. Hydrogen however can be measured accurately and is produced by the silane decomposition. The fraction due to ammonia can be calculated and hence the nitrogen concentration. The difference between the nitrogen produced and the free nitrogen can be used to estimate the nitrogen bonded. These calculations, which are under the process of being carried out, require precise knowledge of the binary diffusion coefficients.

No direct evidence is available to support the contention that the nitrogen consumed is entirely converted to Si_3N_4 exclusively, other compounds are possible, such as $Si(NH)_2$, $Si_2(NH)_3$, and Si_2N_2.

However, equilibrium calculations on the system Si-N-H lead to limited information on the composition of compounds containing Si and N (except Si_3N_4) or containing Si, N, and H (10). The thermodynamic values for such compounds (in the condensed state) are not available and their theoretical formation cannot be estimated. On the other hand, although thermodynamic constants are known for SiN and Si_2N in the gas phase, these species are never present at equilibrium under CVD pressure, temperature, and concentration conditions. If compounds containing Si and N other than Si_3N_4 are formed, they are converted into Si_3N_4 on reaching the substrate as temperature increases, as witnessed by their absence in the deposit (11).

The most probable model would therefore be a consumption of nitrogen formed by the pyrolysis of ammonia at a distance approximately less than 2 mm from the substrate at temperatures reaching 600°C for which silane is already strongly decomposed. At this stage all that can be inferred is that the consumption of nitrogen can be due to its reaction with silane and with its degradation products without implying any specific stage in the kinetic mechanism.

Conclusion

The method described in the above study is now fully reproducible and reliable. It offers the possibility to localize in the gas phase above the substrate the point-to-point evolution of the gaseous reactants and their products of pyrolysis. In bringing evidence that the silane depletes steadily while flowing downward and is practically totally decomposed at 1 mm from the substrate, it seriously invalidates models in which the reaction is strictly localized on the substrate. It also allows the drawing of the temperature profiles in the gas phase and could be extended to establish an aerothermochemical model for CVD reactors combining kinetics data to heat and mass transport balances.

It should however not be underestimated that the system chosen to illustrate the method, $SiH_4 + NH_3$, lends itself to an analytical study which does not offer major difficulties. Other CVD systems may not be as easy to treat by this method, especially those leading to samples partially condensable as would be the case for systems for which one at least of the reactants is a liquid and is introduced under its own partial pressure. Its condensation in the probe or during compression before entering the VPC analyzer would lead to erratic values (*e.g.*, deposits using $SiCl_4$ or $TiCl_4$ as vectors for Si and Ti). However cases such as those which produce or consume hydrocarbons, boranes, hydrogen, hydrogen cyanide, hydrogen chloride, or fluoride should be able to be processed along very similar lines and cast some new light on the chemical vapor deposition mechanisms.

Manuscript submitted May 20, 1975; revised manuscript received Oct. 31, 1977.

Any discussion of this paper will appear in a Discussion Section to be published in the December 1978 JOURNAL. All discussions for the December 1978 Discussion Section should be submitted by Aug. 1, 1978.

REFERENCES

1. K. J. Sladek, *This Journal*, **118**, 654 (1971).
2. F. C. Eversteyn, *Philips Res. Rep.*, **86**, 134 (1971).
3. R. M. Fristrom and A. A. Westenberg, "Flame Structure," McGraw-Hill Book Co., New York (1965).

4. C. Vovelle, R. Foulatier, and R. Delbourgo, *Methodes Phys. Anal.*, **1971**, (4) 353.
5. H. Mellottée and R. Delbourgo, *Bull. Soc. Fr. Céram.*, **102**, 65 (1974).
6. J. Gyulai, O. Meyer, J. W. Mayer, and V. Rodriguez, *J. Appl. Phys.*, **42**, 451 (1971).
7. B. J. Curtis and J. P. Dismukes, *J. Cryst. Growth* **17**, 128 (1972).
8. J. O. Hirshfelder, C. F. Curtis, and R. B. Bird, "Molecular Theory of Gases and Liquids," John Wiley & Sons, Inc., New York (1967).
9. G. Cochet, H. Mellottée, and R. Delbourgo, *J. Chim. Phys.*, **71**, 1363 (1974).
10. H. Mellottée and G. Cochet, *Rev. Int. Hautes Temp. et Réfract.*, **13**, 31 (1976).
11. H. Mellottée, G. Cochet, and R. Delbourgo, *Rev. Chim. Minérale*, **13** (4), 273 (1976).

Crystallization in Copper-Containing Solder Glasses

R. G. Frieser,* J. L. Powell, and R. R. Tummala

IBM System Products Division, East Fishkill Facility, Hopewell Junction, New York 12533

ABSTRACT

A study of copper-containing lead glasses showed that heating such glass above 750°C produced significant amounts of Cu^+ ions, which, on subsequent thermal exposure, produced Cu_2O precipitation in the glass. This effect was found to be cumulative with respect to time and temperature. Bubbling oxygen through the glass melt below 1100°C reduced the Cu^+ ion concentration. Surface contamination both of the lead glass rods and of the substrate to which they were sealed enhanced the growth of Cu_2O. The mechanism of the Cu_2O precipitation is described.

High lead copper-containing glasses are frequently used to form seals between other glasses. During a study of such glasses, some crystallization was noted in the glass after the sealing step. Under a variety of sealing conditions, a reddish-brown precipitate was observed in these lead glasses. Precipitates were observed at the interface of the seal and the substrate glass, but primarily in the center of the bulk of the seal. The morphology of these crystals varied with the state of crystallization (Fig. 1). Their symmetry was found to be fourfold. The cited references provided a background for this study.

The CuO-Cu_2O Equilibrium

An examination of the literature revealed the following information. The decomposition temperature for CuO going to Cu_2O at a pressure of 1 atm is usually reported to be 1064°C. Though CuO is known to be triclinic, Cu_2O is face-centered cubic. However, the reported melting and transformation temperatures vary considerably (1). Thus, for CuO the decomposition temperature is given as 1064°C and the melting point as 1233°C, whereas a CuO/Cu_2O eutectic temperature is given as 1082°C. For Cu_2O, the reported melting points are 1210°, 1235°, and a range from 1084° to 1162°C. A 3.5% CuO/Cu_2O eutectic temperature is recorded at 1065°C. Furthermore, reported decomposition temperatures are higher for a 1:1 mixture of CuO and Cu_2O at the same oxygen pressures than for pure CuO (2).

A more recent critical review (3) of these equilibria (Cu/CuO and CuO/Cu_2O) lists a CuO/Cu_2O (68/32%) eutectic temperature at 1075°C. It points out that Cu_2O is unstable below 375°C and appears to break down into Cu and CuO. CuO, when heated to ~1110°C, melts at pressures less than 1 atm, with loss of oxygen and forming an oxygen-deficient liquid. The same article reports the dissociation pressure at the eutectic temperature to be ~0.5 atm. This implies that, when heated at oxygen pressures less than 0.5 atm, CuO will dissociate to Cu_2O in the solid state before melting. Melting will occur then, at the eutectic temperature at this pressure, with the formation of oxygen.

The data variations in the literature can be attributed to the variation of purity in the reported samples. Thus, the reported temperatures are only a guide. In view of the involved equilibria, it seemed pertinent to examine our starting materials at various temperatures. To ensure good thermal equilibrium we used powdered copper oxides. The oxides, CuO, Cu_2O, and a 1:1 mixture of each, were heated in a platinum crucible in air at 1110°, 800°, and 500°C for 1 hr and quenched (~500°C/min) in air to room temperature. We analyzed these materials by x-ray diffraction both before and after heating. The oxides were reagent grade chemicals used in the glass-making process. Table I summarizes the essential results of this investigation. The results of differential thermal analysis (DTA) of the original oxides are shown in Table II and Fig. 2.

Our preliminary experiments led to the following observations:

(*i*) The reagent grade Cu_2O contained some CuO and, possibly, even metallic Cu. (*ii*) The CuO material showed no contamination. (Contaminants less than

* Electrochemical Society Active Member.

Key words: Cu_2O precipitation, crystallization, copper-containing solder glasses.

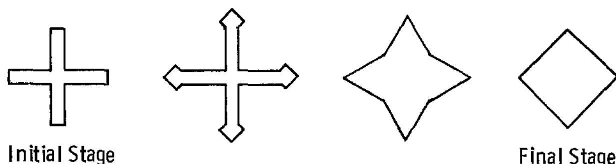

Fig. 1. Progress of crystallization

Table I. CuO/Cu_2O conversion

Nominal starting material	X-ray composition: Before heating	X-ray composition: After heating at 1100°C
CuO	CuO	Cu_2O + ~6% CuO
Cu_2O	Cu_2O + 2-3% CuO + 3% Cu	Cu_2O + ~10% CuO
CuO/Cu_2O (1:1)	CuO + Cu_2O + 3% Cu	Cu_2O + ~12% CuO
		800°C
CuO		CuO
Cu_2O		CuO
		500°C
Cu_2O		CuO + 2% Cu_2O

Table II. DTA endotherms of original oxides (±4°C)

Starting material	Major peak (°C) (CuO)	Minor peak (°C) (Cu_2O)	Area ratio of peaks [(CuO)/(Cu_2O)]
CuO	1068	1168	10:1
Cu_2O	1084	1158	4:1
CuO/Cu_2O (1:1)	1081	1154	2:1

~2% by weight do not show up on an x-ray diffractogram.)

(*ii*) Once copper oxide was heated to 1100°C in air, at least 90% was converted into Cu_2O, as indicated by x-ray data. Any metallic copper also present originally was eventually oxidized to Cu_2O (via CuO, with subsequent loss of oxygen).

(*iii*) Heating the same oxides to 800°C, however, oxidized the Cu_2O (and Cu) to CuO. At 500°C, apparently, the oxidation was not complete; thus, some Cu_2O remained.

(*iv*) The DTA traces (Fig. 2) supported the x-ray observations. The observed decomposition temperature for CuO was 1068°C, while, for the mixture, the expected eutectic melting temperature (1081°-1084°C) was observed. The precision of our DTA data is taken to be +3°-4°C. The minor peaks are apparently the Cu_2O melting point. The area enclosed by the curve is proportional to the amount of crystalline material present that melted at that temperature. The ratios (see Table II) of these areas indicate that the relative amount of Cu_2O was greater in the Cu_2O and mixed samples. The small peak attributed to Cu_2O in the DTA trace of the CuO samples was, presumably, not present originally, but can be attributed to the heating of the sample in the DTA system. From the x-ray work, we know that ~6% of the CuO samples was not reduced on heating above 1000°C.

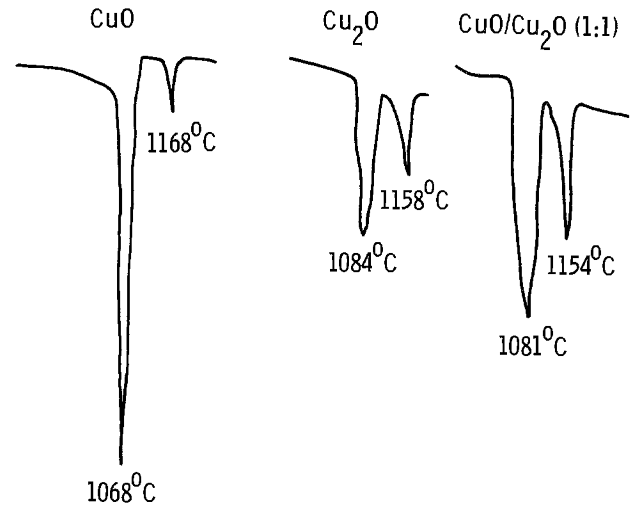

Fig. 2. Differential thermal analysis of copper oxides

Precipitation of Cu_2O in Copper Glass

Because the activity coefficients of the Cu^{++} and Cu^{+} ions in the glass are not known the exact equilibrium cannot be calculated but it is reasonable to

Fig. 3. Photomicrographs of cullet and rods of both standard (a and c) and modified (b and d) glass used as seal, showing crystallization or phase separation (220X).

Table III. Nominal composition of glasses*

Standard glass**	Wt %	Modified glass***
SiO_2	2.0	SiO_2
PbO	66.0	PbO
B_2O_3	14.0	B_2O_3
Al_2O_3	3.5	Al_2O_3
ZnO	10.5	ZnO
Bi_2O_3	1.5	Bi_2O_3
CuO	2.5	Cu_2O

* Ref. (4).
** Tg, 371°C; Ts, 413°C; α, 83.5 × 10^{-7}/°C; foaming T > 750°C.
*** No foaming.

assume that, though the kinetics may differ, the equilibria in the glass are similar to those of the oxides. One might expect a slower rate of conversion (CuO to Cu_2O) in the glass. On the basis of these considerations, the primary species of copper ion to be expected in the glass should be Cu^+, regardless of the starting oxide, if the glass is heated above 1000°C during manufacture. Subsequent work, described later, indicates that conversion of CuO to Cu_2O starts at ~750°C at an undetermined, but very slow rate. To check this assumption, a modified glass was made by substituting Cu_2O for CuO on a weight basis in the standard glass. Table III gives the nominal weight composition (4). We used the standard manufacturing procedure, which was to mix all oxides, shown in Table III, completely in the dry state in a V-blender. Then the material was transferred to a Pt crucible (in 3 or 4 states) and heated slowly to 1080°C.

It should be mentioned at this point that initial heating of the standard glass above 750°C was carried out very slowly because of serious foaming once the charge reached 800°C. No foaming was noted, however, when Cu_2O was the copper source.

Glass Processing

Conventional fining time was ~2.5 hr at ~1080°C. The batch was cooled to ~500°-600°C, and sample rods were pulled for physical measurements. The glass was then remelted to 1080°C for 1 hr of fining. The charge was finally quenched in deionized water through which nitrogen gas was bubbled.

To make rods for subsequent seals, the cullet was reheated to 1080°C and then cooled to 500°-600°C, at which temperature the rods were pulled. Seals were made with such rods by heating the assembly (two rods between two pieces of soda lime glass) to 480°C for 15 min and cooling it to room temperature. The subsequent degree of crystallization in the seal is related to the thermal history of both the cullet and the rod. To assess the influence of both time and temperature on the precipitation in the seal, we conducted the following experiments: (*i*) In the conventional manner, rods were pulled from the cullet of both the standard glass and the modified glass. Seals were subsequently made from these rods at 480°C for 15 min. (*ii*) Other portions of the cullet were preheated at 500°C for 30 min and for 2 hr. Rods were not drawn from these preheated glasses, but seals were formed directly from the cullet.

From photomicrographs of these seals (Fig. 3 and 4), we drew the following summary observations: (*i*) All the crystals had fourfold symmetry and were reddish-brown under the microscope. (*ii*) Seals made from the rod had greater crystal density for each glass

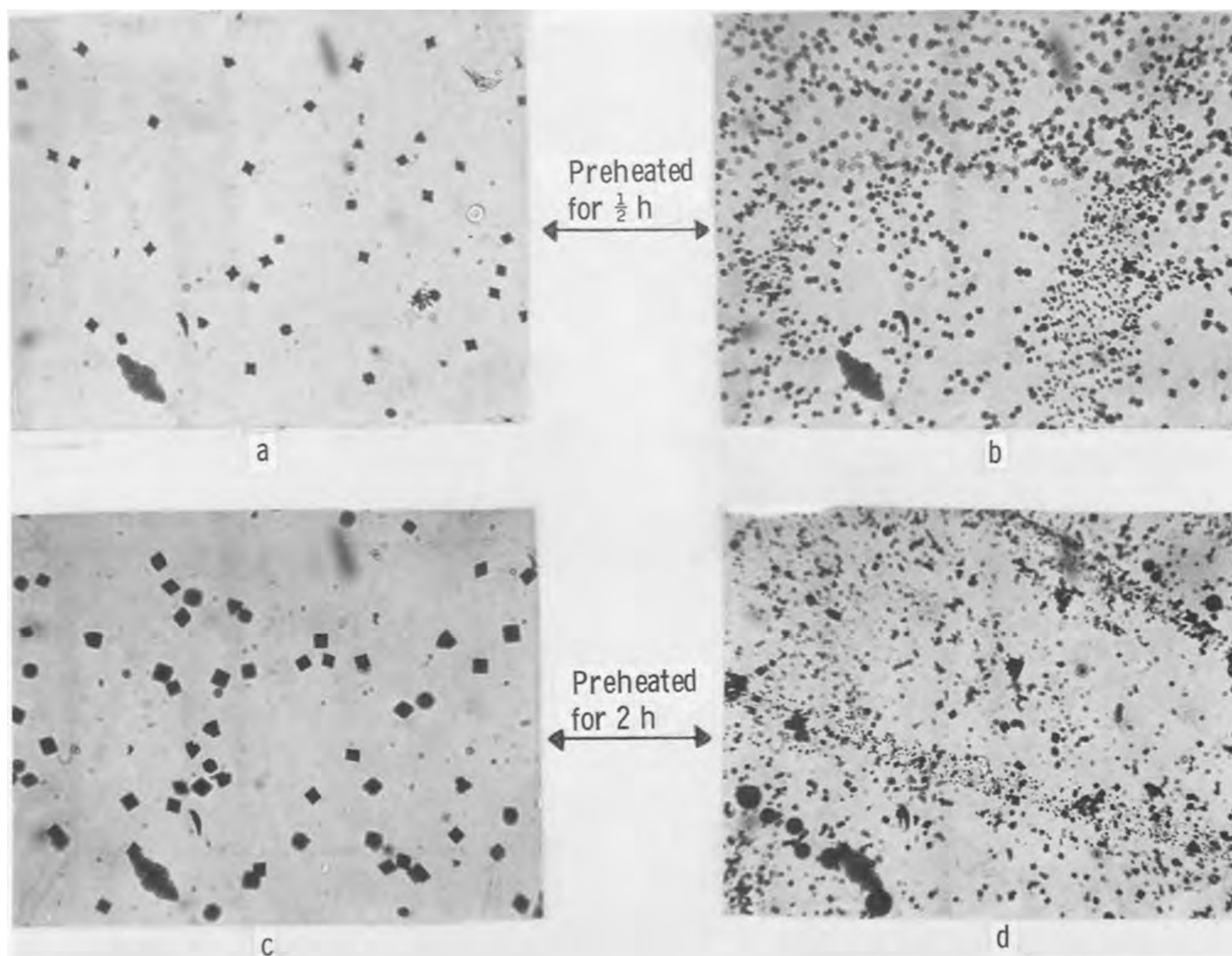

Fig. 4. Photomicrographs of standard-glass (a and c) and modified-glass (b and d) seals made after preheating for ½ or 2 hr (220X).

Table IV. Wet analysis of copper glass

Glass type	Copper oxide Type	Wt %	Fining Time (hr)	Fining Temp (°C)	Total (%) Cu^{++}	Total (%) Cu^{+}
Modified	Cu_2O	2.50	3.5	1060	40.0	60.0
Standard	CuO	2.50	3.5	1040	64.0	36.0
Standard	Above glass reheated		6.75	770	63.0	37.0
Standard	CuO	2.50*	3.5	1020	71.0	29.0
Modified	CuO	4.30	3.0	750	84.0	16.0
Modified	CuO	4.30	14.0	1080	38.0	62.0

* O_2 bubbled through charge during fining.

than seals made from the cullet. (*iii*) Substituting Cu_2O for CuO in the original standard glass vastly increased the amount of brown precipitate in the seals made from modified glass. (*iv*) Preheating either glass before sealing decreased the number of crystals but increased their size. This effect was found to be proportional to the preheating time and was more pronounced in the modified glass than in the standard glass.

After carefully crushing the crystallized glass in alcohol and separating the brown precipitate from the matrix, we used x-ray analysis to show that the precipitate was Cu_2O.

We interpreted the preceding observations as follows: (*i*) The decomposition of CuO (*i.e.*, $2CuO \rightarrow Cu_2O + \frac{1}{2} O_2$) in glass is similar to that in the oxide. (*ii*) Nucleation of Cu_2O appears to depend on the length of fining time above 750°C in the glass (Fig. 4). (*iii*) The eventual size of the Cu_2O crystal, however, depends on the thermal treatment of the glass after fining.

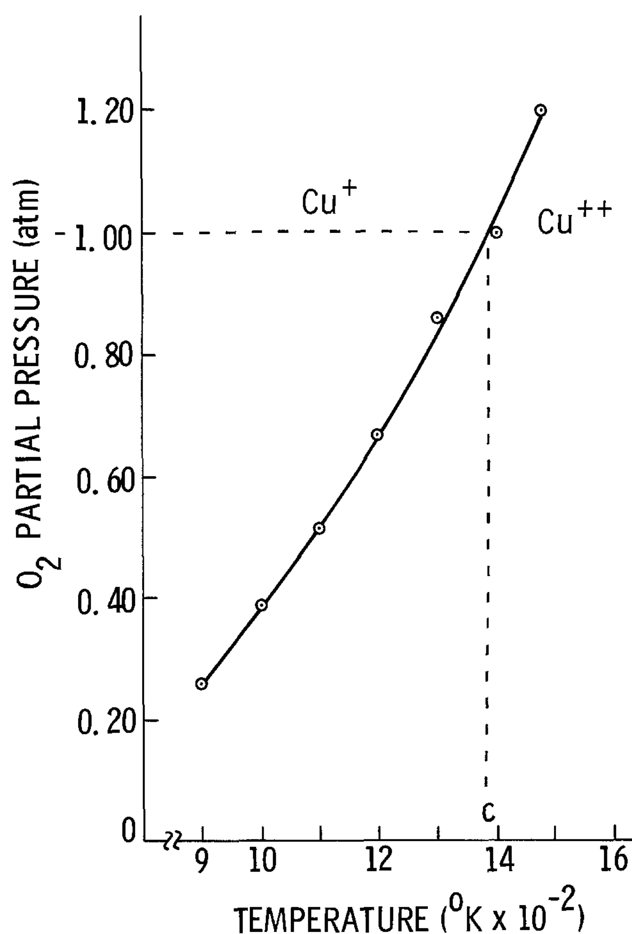

Fig. 5. Partial pressure of O_2 vs. temperature

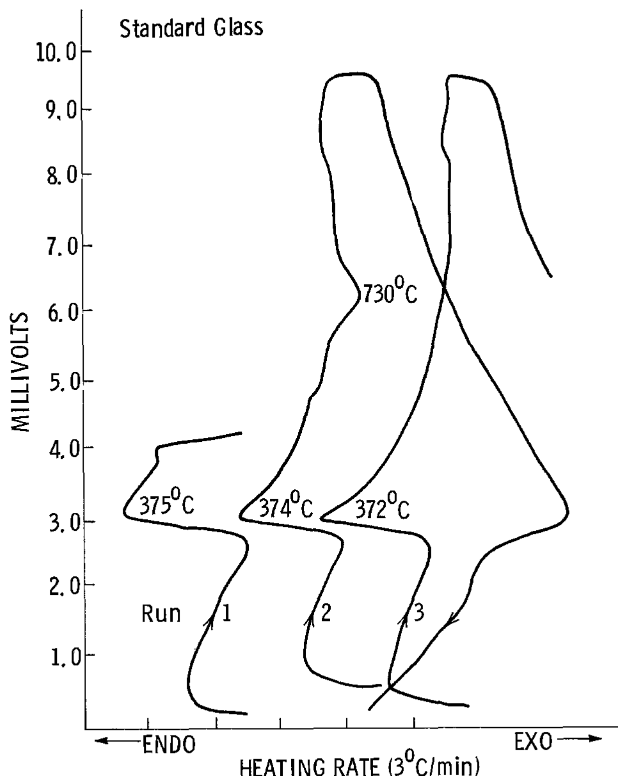

Fig. 6. Differential thermal analysis trace of standard glass

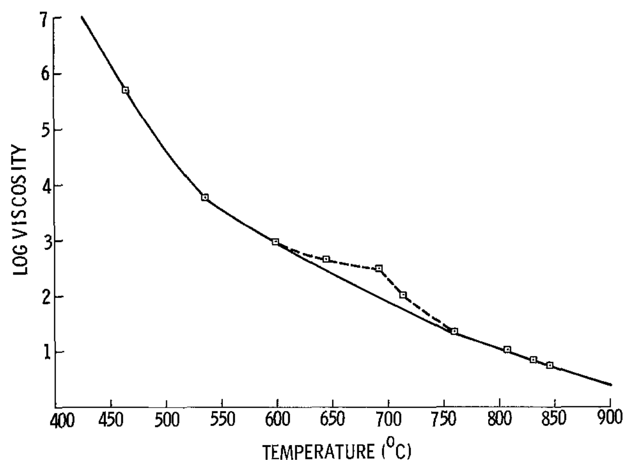

Fig. 7. Standard glass viscosity vs. temperature

Wet Analysis

The interpretations drawn from our experiments were supported by analytical work. A petrological technique was adapted to glass. Total copper (*i.e.*, Cu^+ and Cu^{++}) and Cu^{++} were determined separately, and Cu^+ was obtained by difference. Table IV summarizes pertinent data showing that a considerable portion of Cu^{++} was converted into Cu^+ when the glass was fired above 750°C. Reheating the glass for an extended period of time below 800°C, however, did not seem to change the Cu^+/Cu^{++} equilibrium in the glass. The data seem to indicate that bubbling oxygen through the molten glass at or below 1080°C shifted the equilibrium back to Cu^{++} ion in the glass. The maximum theoretical, rather than the reported value of Cu^{++}, was used to calculate Cu^+ when more than 100% theoretical was reported, because the precision of this technique is $\sim \pm 10\%$. Still the trend is apparent. Other oxygen-bubbling experiments showed a color shift from green to blue in the resulting glass. Such a shift at constant glass composition, especially in lead glasses, can be taken as an oxidative change

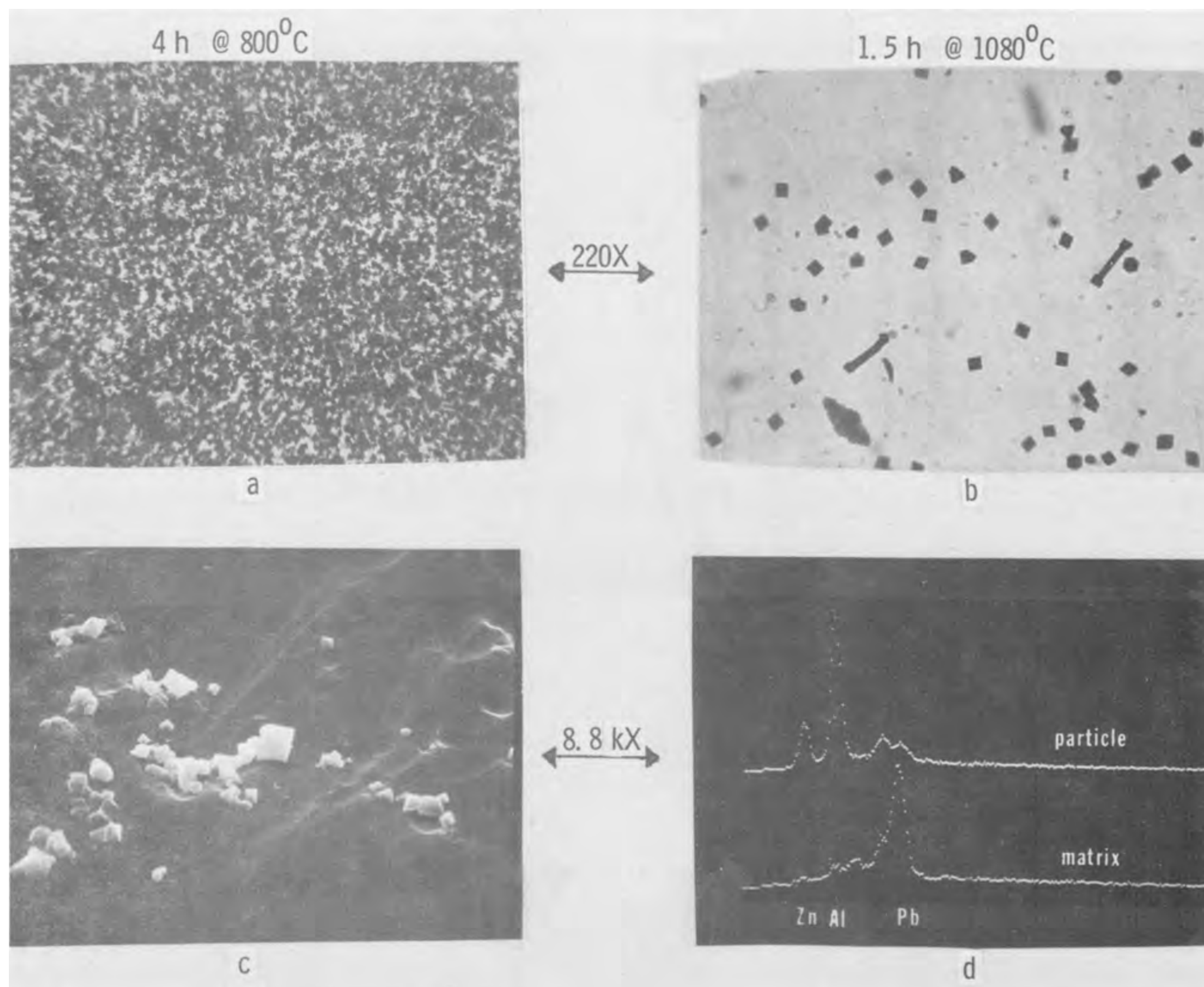

Fig. 8. Photomicrographs and SEM micrographs of standard glass, showing crystallization or phase separation.

from Cu^{+} to Cu^{++} (5). The O_2-bubbling experiments were based on the decomposition pressures of CuO (Fig. 5), which were calculated from the thermodynamic data of the Gibbs free energy (6). Figure 5 shows that maintaining both the partial pressure of oxygen above the glass melt at 1 atm and the melt temperature at 1100°C, causes the equilibrium to shift from Cu^{+} to Cu^{++}.

Thermogravimetric and Differential Thermal Analysis

Two samples of the standard glass were subjected to thermogravimetric (TG) analysis. The data did not correlate with any possible oxygen loss or gain as a result of the Cu^{++} to Cu^{+} shift. A reasonable conclusion was that whatever loss or gain of oxygen was experienced was overshadowed by losses of volatile constituents of the glass. From this experiment, we draw the inference that heating this glass above 750°C for prolonged times can change its composition and, possibly, the solubility of copper oxide in the remaining glass.

Phase Separation

Figure 6 shows a typical DTA trace of the standard glass. The first trace was taken to ~480°-500°C, and the glass was kept at this temperature for 30 min before being cooled to room temperature to simulate conventional sealing conditions. On the second and third traces the samples were taken to 1000°C. In addition to the transformation temperature at about 372°C, the second trace shows a broad exotherm at ~6.5 mV (730°C) which was either lost or reduced and shifted to a considerably higher temperature (8.5 mV or 910°C) on the third trace. This "bump" has been found to be characteristic of all standard glass DTA curves. A similar jog is noted on a viscosity curve supplied by Corning Glass Works on the standard glass billet in the temperature range 650°-750°C (Fig. 7).

The same temperature region is a potentially troublesome area for pulling rods. Our experience has shown that, once the glass is properly fined and cooled to room temperature, it should be brought back to ~1080°C before being cooled to 500°-600°C to get the proper viscosity to pull a 40 mil diameter rod. Unless the heat-treatment exceeded 1080°C, the rods turned out lumpy and rough and contained crystals. Under these conditions it was impossible to maintain a uniform and desired rod diameter. This phenomenon was called, for want of a better term, "phase separation." It was not clear, however, whether it was phase separated in the conventional sense, which would be two or more immiscible "liquids." Some crystalline matter was observed in this "phase." Figure 8a is an electron micrograph (220×) of a cullet sample of the standard glass, which was held at 800°C for 4 hr and examined. Reheating this sample to 1080°C for 1.5 hr, cooling it to 600°C, and pulling rods showed a large number of Cu_2O crystals in subsequent seals made from it (Fig. 8b). Scanning electron microscope (SEM) pictures of standard glass made at 800°C and subsequently heated to 500°C showed some indication of crystalline material. This was brought out by a dilute HNO_3 etch (Fig. 8c). Figure 8d is a mass spectrogram comparison of one of these crystals with that of the neighboring surface. It is clear (Fig. 8b) that these crystals were not

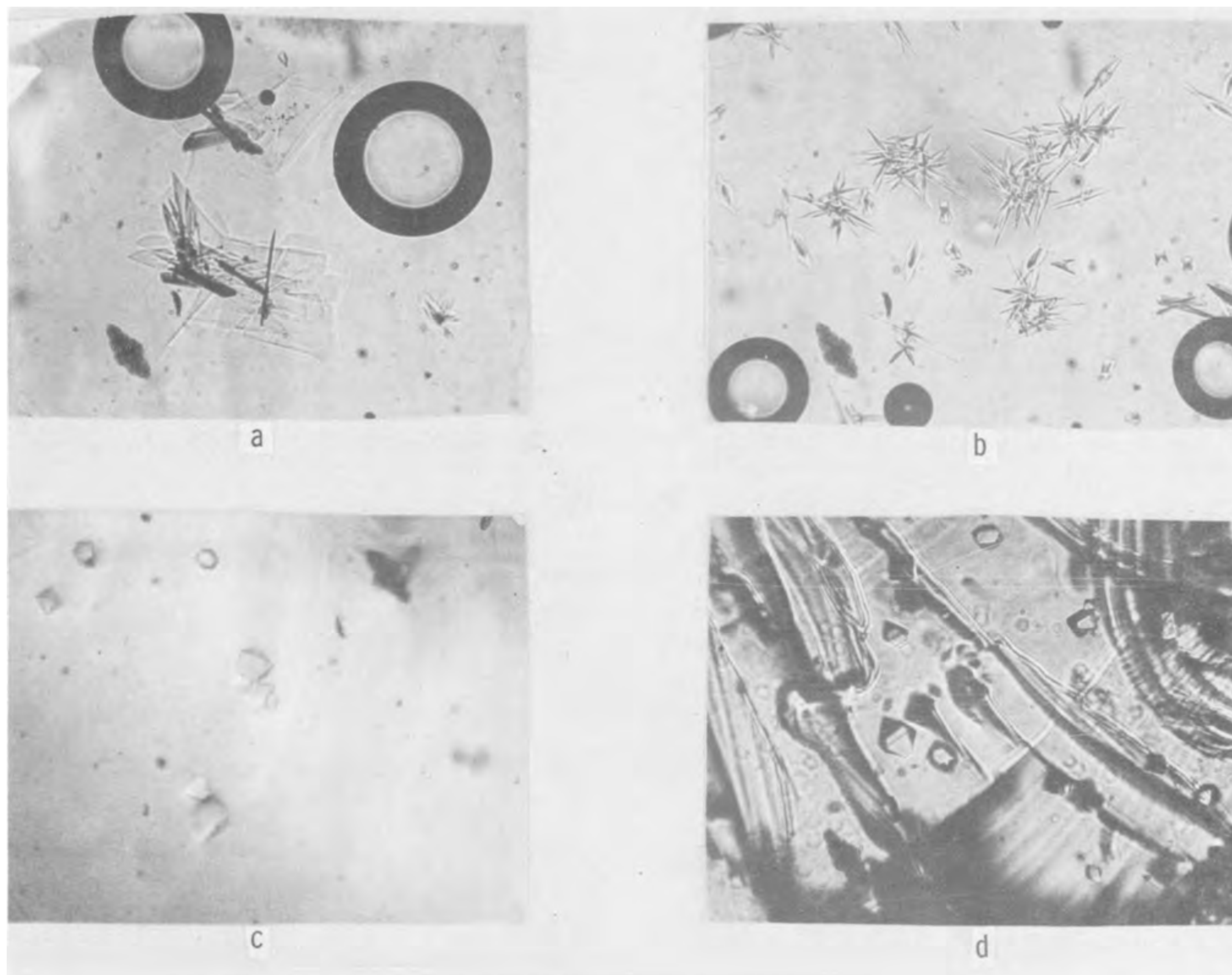

Fig. 9. Photomicrographs of noncopper-containing crystals in seal glass (220X).

Cu_2O but contained an increased amount of Al and Zn and were probably zinc aluminates.

During the course of these experiments, colorless, flat, circular crystals as well as octahedra crystals were occasionally noted in some of our experimental seals, which were made from cullets and rods. Powder x-ray and transmission electron microscopy (TEM) with an x-ray nondispersive analyzer disclosed the following crystalline materials: Al_2O_3 and $ZnAl_2O_4$ (octahedra), and $PbZnB_2O_6$ and $ZnPbO_3$ (plates and circular forms). Figure 9 shows representative samples of the variety of crystals observed. In a few cases, undissolved oxides of the original glass components (Table III) were observed as well.

Surface Effect

Figure 3c shows a definite surface influence on the crystallization pattern, if not on the nucleation, of the standard glass. Various acidic, basic, and organic surface treatments, both on the seal rods and on the substrates, did not seem to eliminate the brown precipitate, although some minimization was evident. It was apparent from observed patterns like those shown in Fig. 3c that surface contamination did enhance and orient the crystal growth of Cu_2O.

Conclusions

The following conclusions are drawn from the preceding study and apply only to the glass composition and techniques described herein:

1. Heating a copper-containing glass above 750°C produces a significant number of Cu^+ ions. The amount of Cu^+ formed appears to be directly proportional to the temperature and to the length of heating time at any temperature above 750°C. The higher the temperature, the faster the Cu^+ to Cu^{++} conversion. This reduction is irreversible, for practical purposes, and can lead eventually to the precipitation of brown Cu_2O.

2. The heat effect is cumulative. Prolonged and/or repeated exposure to subsequent temperatures, even as low as 480°C, can cause the Cu^+ ions present to grow into observable crystals, resulting in the brown Cu_2O precipitate.

3. Bubbling oxygen through the glass melt reduces Cu^+ concentration. A decrease in the Cu^+ concentration was noted when oxygen was bubbled through the glass melt in the temperature range of 600°-1080°C. However, some Cu^+ ions were still present; furthermore, the phase-separation problem appeared to be aggravated.

4. Surface contamination of the rod and substrate enhances the formation and growth of Cu_2O but apparently does not affect its autonucleation.

5. Surface treatment of the rod does not eliminate the Cu_2O crystallization in the final seal but does cause a small reduction in the Cu_2O content of the seal. We believe the reason that the Cu_2O crystallization was not eliminated was that the primary nucleation was a bulk nucleation.

Acknowledgments

The authors are indebted to numerous persons for data on this project. We should like to mention W. Fedrowitz and S. Teed for differential-thermal and thermogravimetric analyses, respectively, F. A. Toman and S. Lawhorne for x-ray analysis, R. M. Anderson for electron differential analysis, D. Cameron for

scanning electron microscopy, and R. T. Vineski for development of the analytical technique.

Manuscript submitted July 13, 1976; revised manuscript received Oct. 31, 1977.

Any discussion of this paper will appear in a Discussion Section to be published in the December 1978 JOURNAL. All discussions for the December 1978 Discussion Section should be submitted by Aug. 1, 1978.

Publication costs of this article were assisted by IBM Corporation.

REFERENCES

1. J. W. Mellor, "A Comprehensive Treatise on Inorganic and Theoretical Chemistry," Vol. III, pp. 118, 122, and 133, John Wiley & Sons, Inc., New York (1922-37).
2. J. W. Mellor, *ibid.*, p. 120.
3. A. M. M. Gadalla, W. F. Ford, and J. White, *Trans. J. Br. Ceram. Soc.*, **62**, 45 (1962).
4. R. G. Frieser, J. L. Powell, and R. R. Tummala, U.S. Pat. 3,904,426 (1975).
5. W. A. Weyl, "Coloured Glasses," pp. 159 and 161, Dawson's of Pall Mall, London (1959).
6. JANAF Thermochemical Tables, Second Ed., National Bureau of Standards, Washington, D.C. (1971).

High Temperature Kinetics of Refractory Metal Gasification by Atomic Fluorine

Paul C. Nordine

Chemical Engineering Section, Department of Engineering and Applied Science, Yale University, New Haven, Connecticut 06520

ABSTRACT

Intrinsic kinetics for the F/Ir, Pt, Ta reactions were measured using microwave discharge, low pressure, transonic flow reactor techniques with filament gasification rates deduced from specimen resistance *vs.* time measurements. Data were obtained in the temperature ranges 1000°-1450°K for Ir, 600°-1430°K for Pt, and 1100°-3030°K for Ta, at F-atom partial pressures between 0.65-7.4 Pa. Also, transient filament resistance and temperature changes could be observed which lead to the conclusion that condensed fluoride films occur on the metals on exposure to atomic fluorine. These films do not inhibit the gasification reaction. The F/Pt data at $T > 800$°K and the F/Ir data agree within experimental error with kinetic models which assume a reactant pressure independent F-atom sticking coefficient and competitive first-order F-atom desorption, nth order (in the F-atom surface concentration) product molecule formation-desorption. The product species formation-desorption reactions are third order in the F/Ir system and are second order at higher temperatures and are fourth order at lower temperatures in the F/Pt system. Quasi-equilibrium preexponential rate law parameters based on the product species, IrF_3, PtF_2, and PtF_4, agree with those derived from the rate measurements. At lower temperature the F/Pt reaction is zero order in the incident F-atom flux. The F/Ta kinetics are qualitatively similar to the F/Ir, Pt kinetics but reaction persists to much higher temperature and nonintegral reaction order is obtained at the highest temperatures. A quantitative model of the F/Ta reaction kinetics is not proposed. Although this work confirms the condensed fluoride film model for the F_2/Ta reaction which was proposed by Machiels and Olander (8), the Ta gasification rates measured here exceed those predicted by their model. This disagreement suggests a change in the condensed fluoride stoichiometry between their experiments, at $p_{F_2} < 10^{-2}$ Pa and the present results obtained at $p_F > 0.6$ Pa. Instructive comparisons are made between the results obtained for these and the F/W, Mo, Ti systems (5, 14), and the implications of quantitative results from F/Ir, Pt models are discussed.

Fluorine is a mono-isotopic, highly electronegative element whose bond energy (157 kJ/mole) (1) is unusually low. However, it forms strong chemical bonds to other elements and will react with nearly every (nonfluoride) substance. Many polyvalent binary fluorides are volatile. These and other unusual properties of fluorine and fluorides lead to useful applications [*e.g.*, uranium isotope separation, chemical and excimer lasers, semiconductor etching reactions (2), and chemical rocket propellants (3)] but are also the source of difficult corrosion problems.

The chemical, physical, and thermodynamic properties of fluorine and fluorides and the kinetics of homogeneous fluorine reactions (4) have been studied in much detail. Heterogeneous reactions have received less attention, despite their importance to corrosion problems and the direct applications of fluorine gasification reactions, *e.g.*, to semiconductor etching (2). Heterogeneous reactions of atomic fluorine are of special interest because fluorine is easily dissociated and atoms usually undergo heterogeneous reaction more rapidly than do molecules (5, 6, 12).

Several recent papers have appeared on the intrinsic kinetics of fluorine gas/solid reactions. Studies of F_2 reactions include McKinley's investigation of the F_2/Ni reaction in a mass spectrometer (7), the modulated beam studies of F_2/Ta and F_2/UO_2 reactions by Machiels and Olander (8, 9), and a paper by Philippart *et al.* on the reactions of fluorine and metal fluorides with Ta, W, and Re (10). Sheer *et al.* studied the desorption of atomic fluorine from molybdenum at high temperature (11). Heterogeneous reactions of atomic fluorine were first investigated by Rosner *et al.*, who report kinetic measurements for the F, F_2/Mo, W

Key words: heterogeneous kinetics, iridium, platinum, tantalum, vaporization, kinetics, metals, refractory.

reactions (5) and the F, F_2 reactions with basal and edge planes of pyrolytic graphite (6). The F, F_2/BN reactions were studied near room temperature (12) and allow the gravimetric measurement of F-atom concentrations in flow systems. Also, F-atom heterogeneous recombination/reaction probabilities have been measured on several materials of construction near room temperature (13). Although this list is brief, the papers cited reveal a growing interest in heterogeneous fluorine reactions and document important new techniques by which these reactions may be studied. They provide some assistance in the selection of corrosion resistant materials of construction and begin to reveal the mechanisms by which fluorine gasifies solids.

This paper presents new kinetic data for the F-atom reactions with iridium, platinum, and tantalum. The principal conclusions include a verification of fluoride film formation (8) during the F/Ta reaction and the discovery of fluoride films during F/Ir and F/Pt reaction as well. The F/Ir, Pt gasification rates are accurately predicted by a kinetic model which contains derived kinetic parameters that agree with values predicted by the quasi-equilibrium model (33, 34). Comparison of the F/Ta data with the modulated beam results of Machiels and Olander (8) provides new insight regarding the surface kinetics. A comparison of Arrhenius diagrams for the F/Ir, Pt, Ta, W (5), Mo (5), Ti (14) reactions at equal reactant pressure demonstrates general trends common to all high temperature F/metal reactions which have been studied.

Experimental

The rate measurements reported here were obtained by use of the low pressure, transonic flow reactor illustrated in Fig. 1. The side-mounted probe was used in these experiments. In this flow reactor, metered Ar/F_2 mixtures pass through a 0.98 cm ID alumina tube where a 2450 MHz, ≈100W microwave discharge dissociates the fluorine molecules. The dissociated mixture then enters a Pyrex section and passes over an electrically heated metal filament mounted transverse to the gas flow. Average flow velocity at the discharge tube exhaust was 2.5×10^4 cm/sec at a total pressure of 133 Pa. Gaseous F, F_2 concentrations were computed from the measured Ar and F_2 flow rates, total pressure, and known (15, 16) microwave discharge dissociation efficiencies (*ca.* 90% for F_2).

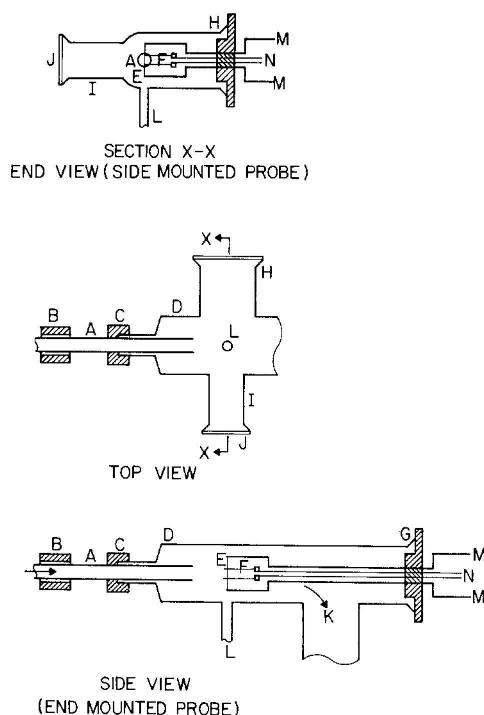

Fig. 1. Filament fluorination apparatus (schematic). A, Discharge tube (alumina); B, microwave cavity; C, O-ring coupling; D, test section (Pyrex); E, filament (specimen); F, voltage taps; G, O-ring joint (end mounted probe); H, O-ring joint (side mounted probe); I, pyrometer; J, optical flat; K, to fluorine trap, pump; L, pressure tap; M, to d-c power supply; N, to voltage-to-frequency converter.

Gasification rates were computed from the resistance-time curves for the central 0.3-0.4 cm of 0.038 cm diam filaments. In most experiments the filament temperature was allowed to increase by 200°-400°K during the experiment and rate *vs.* temperature was computed from resistance-time, temperature-time, and previously measured resistance *vs.* temperature data in the absence of reaction. These procedures are fully described elsewhere (17).

Specimen temperatures above 1000°K were measured with an optical pyrometer. Emittance corrections at $\lambda = 0.665\mu$ for Pt (18), Ir (19), and Ta (20) were obtained from the literature. The Pyrex windows were frequently changed to avoid temperature errors due to etching by fluorine and the window transmission corrections were checked by measuring specimen temperature with or without the window in the light path, using a second window to seal the system. Window corrections always agreed with an expected 5% reflection loss at each window surface.

The F/Pt reaction was also studied below 1000°K. In these lower temperature experiments the filament diameter was computed from measured room temperature resistance before and after reaction. Temperature at the beginning and end of reaction was determined from the high temperature to room temperature resistance ratio, using the known temperature coefficient of resistance. Temperature control was achieved by operating the power supply at constant voltage output with a resistance in series with the filament whose value was chosen to give approximately constant filament power dissipation per unit filament area. Inferred temperatures at the beginning and end of reaction usually agreed to ±10°K.

Most high temperature experiments were performed by setting the gas flow rates, discharge power, and reactant pressure and then heating the filament to the temperature of interest. However, for experiments below 1000°K it was necessary to adjust the filament temperature before its exposure to fluorine, and valves were provided to divert fluorine to the reactor exhaust or allow it to pass through the reactor. A few higher temperature experiments were also performed after these valves were installed. If the heating current was held constant, increases and then decreases in filament temperature (and resistivity) could be observed during a transient period at the start of reaction with fluorine. Following these initial temperature transients, a steady increase of resistance and temperature with time was observed, due to consumption of the filament by the gasification reactions.

Measurements of specimen resistivity provided a check on the temperature measurements. For platinum, the room temperature resistivity agreed to 0.7% with the literature value (21) and corrected pyrometer readings agreed to ±3°K with temperature deduced from resistance measurements. These measurements also show the platinum to be quite pure, for the room temperature resistivity of Pt is typically doubled by the addition of a few percent of an alloying element (22). For iridium, our room temperature resistivity measurement exceeded the literature value (23) by 13% and the temperature coefficient was about 6% low. These differences, which are probably caused by impurities, prevented a check on our iridium temperature measurements. However, no change in iridium specimen resistivity was observed after more than 30% material loss by F-atom gasification. After outgassing at 2500°K, temperatures of Ta filaments deduced from resistance or pyrometer mea-

surements agreed within 1%. However, during reaction with atomic fluorine, a small increase in resistivity and decrease in the temperature coefficient of resistivity were observed. Outgassing at 2500°K in Ar would reverse this effect. These resistivity changes are attributed to dissolution of oxygen and nitrogen impurities in the Ta filaments during reaction with fluorine. The high temperature kinetic studies of the O_2, O, N_2, N/Ta reactions reported by Rosner *et al.* (24, 25) and Feng (39) predict resistivity changes at the prevailing F_2 impurity levels which agree well with those observed here.

Polycrystalline platinum and iridium filaments were obtained from Engelhard Industries, Carteret, New Jersey, who stated the respective Pt and Ir purities to be 99.95 and 99.8%. A spectrographic analysis was supplied for Ir and showed (in parts per million): W, 1740; Re, 400; Pt, 240; Rh, 58; Al, 46; Ni, 32; Pd, 26; Cu, 23; Si, 21; and eleven other elements which added up to 28 ppm. The polycrystalline tantalum filaments (Thermionic Products Company, Plainfield, New Jersey) were stated to be at least 99.97% pure.

Fluorine (Matheson) was quoted to be 98% pure. After NaF trap removal of HF, we found total impurity content to be 1.8% (by volume) by the method of reaction with mercury (26). The argon (99.998% pure) was further purified by use of Oxisorb cartridges from MG Scientific Gases, which reduce O_2 content to *ca.* 1 ppm. The background impurity level in our flow system, due to leaks, outgassing, and argon impurity was checked by measuring the rate of Ta resistance change at *ca.* 2500°K in argon. Since the O_2/Ta gasification kinetics are known (25), we could demonstrate in this way that background O_2 pressures were about 5×10^{-3} Pa. After these experiments had been completed, a supply of 99.9+% pure fluorine was obtained from Argonne National Laboratory. We obtained a few data points for each metal with this high purity fluorine which gave the same reaction rates as did the commercial product.

Specimens were examined with a microscope before and after reaction. Molecular fluorine revealed a strong preference for attack at platinum grain boundaries but the surfaces of the grains showed a smooth recession. Atomic fluorine produced a uniform, smooth recession with Pt filaments with no perceptible preference for grain boundary attack. The rate of the F_2/Pt reaction was about 20 times less than that of the F/Pt reaction at 1100°K and equal reactant pressure, as determined by direct measurement of specimen diameters with the microscope. Reaction of F or F_2 with Ta at temperatures below 2100°K produced slight grain boundary etching and a streaked appearance on the surfaces of individual grains. At higher temperatures fluorine did not etch Ta grain boundaries but shallow undulations of irregular shape appeared on the filament surface. The tantalum grains were of irregular shape with typical dimensions between 0.02-0.08 mm. The streaked pattern on individual grains was often nearly parallel to a grain boundary over the entire grain with a streak spacing *ca.* 0.003 mm. The dimensions of the shallow undulations were typically 0.02 mm in a direction parallel to the filament axis and half that in the other direction. Observations on Ir filaments reacted with atomic fluorine between 1000° and 1400°K were similar to those reported for Ta below 2100°K, except grain boundary etching was not observed. Despite the somewhat nonuniform surface observed for Ta and Ir filaments and grain boundary etching of Ta, the specimen diameter change inferred from resistance measurements always agreed with that measured with a microscope.

Reactant and Product Fluxes

The method by which filament resistance and temperature *vs.* time data are reduced to yield product fluxes has been discussed (17). Necessary auxiliary data include the metal thermal expansion coefficients, which were obtained from Espe (22).

The incident flux, Z_i, of reactant species i, was calculated from the Hertz-Knudsen equation

$$Z_i = \overline{p_{i,w}}(2\pi m_i k \overline{T_{gw}})^{-1/2} \quad [1]$$

However, due to transport effects, the (perimeter mean) gas temperature at the filament, $\overline{T_{gw}}$, will differ from the ambient (T_∞) and filament (T_w) temperatures. Also, for sufficiently large reaction probabilities, the (perimeter mean) reactant pressure at the filament $\overline{p_{i,w}}$, will differ from the known ambient reactant pressure, $p_{i,\infty}$. It is necessary to consider the effects of energy, momentum, and mass transfer between the filament and gas stream to determine the values of $\overline{p_{i,w}}$ and $\overline{T_{g,w}}$ to be used in Eq. [1] and the resulting accuracy of calculated reactant fluxes.

Transport effects under the flow conditions chosen for these experiments are characterized by the dimensionless Mach, M, and Reynolds, Re, numbers. At the exit of the discharge tube these are Re = 224 (based on discharge tube diameter), M = 0.79. However, the centerline velocity in the jet issuing from the discharge tube should approach $3.22 \cdot 10^4$, *i.e.*, M = 1, and the Reynolds number at the filament, which samples the centerline velocity is thus Re ≅ 11.4 (based on filament diameter and free stream gas properties). Slip flow occurs at the filament, for the Knudsen number (ratio of ambient gas mean free path to filament diameter) is Kn ≅ 0.16. If, however, we neglect the effect of slip on gas phase convective energy transfer, the Nusselt number for convective energy transfer from the filament is (27) $\overline{Nu_h} = 2.1$ at Re = 11.4.

Energy transfer.—The perimeter mean convective energy flux from the filament (27), $\dot{q}''$, can be equated to the intrinsic heating of incident atoms (28)

$$\dot{q}'' = \overline{Nu_h} \cdot k_f \cdot (T_{g,w} - T_r)/d = \overline{N_{g,w}} \cdot \overline{c_{g,w}} \cdot R \cdot (T_w - \overline{T_{g,w}})\alpha/2 \quad [2]$$

where k_f is the gas thermal conductivity evaluated at the mean "film" thermal boundary layer temperature $[(\overline{T_{g,w}} + T_r)/2]$, $\overline{N_{g,w}}$, and $\overline{c_{g,w}}$ are the (perimeter mean) gas density and mean thermal speed at the filament (at $\overline{T_{g,w}}$) and α is the thermal accommodation coefficient. The gas dynamic recovery temperature, T_r, exceeds the ambient temperature (300°K) but, due to slip flow, should be less than the stagnation temperature of the free stream (≈380°K). The validity of Eq. [2] was checked by measuring the heat flux from a platinum filament in argon and in vacuum at $1260° < T_w < 1730°K$ from which we compute $0.41 \leq \alpha \leq 0.45$ if $300°K \leq T_r \leq 380°K$. The reported value (30) $\alpha(Ar/Pt) = 0.38$ at $1180° < T_w < 1590°K$ agrees well with these results as do the values obtained ($\alpha \approx 0.40$-0.45) by extrapolating lower temperature measurements (29) to the temperature range of interest here.

The accuracy of values for $T_{g,w}$ computed *via* Eq. [2] is limited by uncertainty in the appropriate gas dynamic recovery temperature and thermal accommodation coefficient. The maximum uncertainty in $T_{g,w}$ can, however, be evaluated from known limits on the values of these quantities. We assume $300°K < T_r < 380°K$ and $0.3 < \alpha < 1.0$. These limits on α represent the approximate lower limit of observed values for argon on bare metal surfaces and the maximum value, unity, which may obtain on gas or metal fluoride covered surfaces (28). Values of $T_{g,w}$ computed for the above limits on T_r and α were found to agree within ±25% with the convenient empirical equation

$$T_{g,w} = 24.1 \cdot T_w^{0.43} \quad [3]$$

which was used for subsequent data reduction. The uncertainty in reactant flux, computed from Eq. [1],

is about half the uncertainty in reactant temperature, *i.e.*, *ca.* ±12%.

Momentum transfer.—Since slip occurs in convective energy transfer it must also occur in momentum transfer, and the gas pressure at the stagnation line of the filament should be less than the stagnation pressure in the free stream. Heating of the gas by the hot filament would also tend to reduce the local stagnation pressure. Therefore, we measured the peripheral variation in recession rate of a Pt filament under conditions where the rate is first order in reactant pressure to deduce the peripheral variation in reactant arrival rate. It was found that the rate of diameter change was 1.33 ± 0.05 times greater for the diameter parallel to the direction of flow than for the diameter perpendicular to the flow. This rate difference equals that predicted by Pitot tube measurements at lower flow velocities ($\overline{M} \cong 0.41$ at discharge tube exit) where the ratio of local to ambient pressure was 1.41 at the leading edge, 0.98 at the trailing edge, and 0.90 at the sides of the Pitot tube and the peripheral average pressure exceeded the ambient pressure by *ca.* 2%. Thus, we conclude that momentum effects influence the pressure distribution around the filament but have a negligible effect on the average reactant pressure. This nonuniform pressure distribution allows an approximate measurement of reaction order. At higher temperatures the Pt filament diameter recession rate ratio is 1.90 ± 0.10, in agreement with that predicted for second-order kinetics.

Mass transfer.—If one neglects thermal diffusion, mass transfer due to irreversible surface reaction is described by an equation similar to that for energy transfer. The (perimeter mean) reactant consumption rate is

$$\dot{m}''_r = \overline{Nu}_m \cdot \overline{D\rho} \cdot (\omega_{r,\infty} - \omega_{r,w})/d = \omega_{r,w}\overline{\rho_{g,w}}\overline{c_{r,w}}\epsilon_r/4 \quad [4]$$

where ω_r is the reactant mass fraction in the free stream (∞) or at the filament (w), $\overline{c_{r,w}}$ and $\overline{\rho_{g,w}}$ are the reactant mean thermal speed and gas density at $\overline{T_{g,w}}$, and ϵ_r is the reaction probability. The product, $\overline{D\rho}$, of the binary reactant-argon diffusivity, D, and the gas density, ρ, is evaluated at the mean boundary layer (film) temperature, $\overline{T}$. Thus, if the apparent reaction probability, ϵ_a, is defined as the value which would be obtained when diffusion effects are neglected

$$\epsilon_a/\epsilon_r = \omega_{r,w}/\omega_{r,\infty} = [1 + (\overline{c_{r,w}}d/4D\overline{Nu}_m)(\overline{T}/T_{g,w})\epsilon_r]^{-1} \quad [5]$$

Estimated diffusion coefficients and the assumption $\overline{Nu}_m \approx \overline{Nu}_h = 2.1$ predict a correction due to mass transport effects equal to *ca.* 40% at $\epsilon_r = 1.0$ and about 8% at $\epsilon_r = 0.1$.

Although mass transport corrections to ϵ_a are clearly small, they are also uncertain due, for example, to errors in (*i*) estimated diffusion coefficients, (*ii*) gas temperatures from Eq. [3], and (*iii*) the effect of slip flow on $\overline{Nu}_m$. In fact, experiments performed at an F-atom reaction probability, $\epsilon_a(F) \approx 0.3$ show the corrections to be smaller than would be estimated from Eq. [5]. Figure 2 shows the rate of Pt gasification by atomic fluorine at 1100°K *vs.* total gas flow rate at constant reactant and total pressure. Diffusion limitations at low flow rates disappear as the flow rate increases and a flow rate independent rate of reaction is observed. Flow rate under normal operating conditions was 1300 cm³ (STP)/min. Above 1620 cm³(STP)/min flow from the discharge tube is choked (M = 1), leading to a local increase of pressure in the underexpanded gas jet at the filament and, thus, an increase in the rate of reaction. From these measurements we conclude that mass transport rates do not significantly influence reactant arrival rate

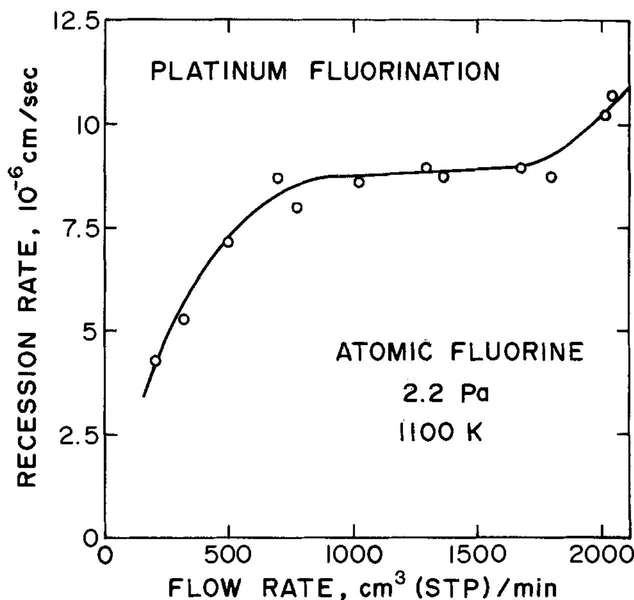

Fig. 2. Platinum gasification rate vs. gas flow rate at T = 1100°K, p_F = 2.2 Pa.

and neglect such corrections in the interpretation of rate measurements.

Results

Filament energy balance.—Transient effects on the filament energy balance are more precisely illustrated by the resistance-time curves (with measurements every 0.5 or 1.0 sec) than by the temperature-time curves which include fewer data points. The initial parts of resistance- and temperature-time curves for three F/Ta experiments using a constant current power supply are illustrated in Fig. 3. Each experiment shows a transient temperature increase followed by a temperature decrease prior to the continuous temperature and resistance increase with time associated with specimen diameter change. The initial temperature rise reflects the increased energy release which accompanies the exothermic gasification reaction. The subsequent temperature decrease reveals a less direct, reaction-induced increase of the specimen heat transfer coefficient, *i.e.*, an increase in its total emittance, ϵ_t, and/or thermal accommodation coefficient, α. If one assumes $\epsilon_t = 0.2$ and $\alpha = 0.3$ prior to F-atom exposure, the observed decrease in specimen temperature can then be explained by $\Delta\epsilon_t \cong 0.1$ or $\Delta\alpha \cong 0.5$. This reaction-induced increase in heat transfer coefficient was observed in all ex-

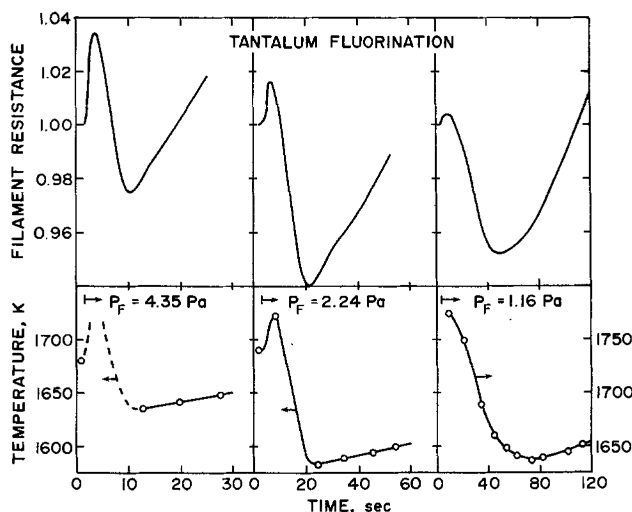

Fig. 3. Tantalum filament resistance and temperature transients on exposure to atomic fluorine with constant current heating.

periments with Ta filaments under conditions where the rate of Ta gasification increases with temperature but was absent in experiments at high temperature, where the rate of gasification decreases with temperature. Transient effects in the F/Pt and F/Ir experiments at 1000°-1200°K were similar to those illustrated in Fig. 3. At higher temperatures, the rates of F/Ir and F/Pt gasification decrease. The transient temperature increase due to the heat of reaction then becomes negligible but the increase in specimen heat transfer coefficient remains. Figure 4 illustrates resistance- and temperature-time effects for two higher temperature F/Ir experiments. These data show the transient effect to reverse in the absence of fluorine as illustrated by the temperature increase at the conclusion of each experiment. All rate data reported here were obtained from measurements subsequent to the initial transient effects. Experiments which employed a constant voltage power supply gave nearly constant temperature and rate data which agree with those obtained under constant current heating.

Gasification rate data.—It will be demonstrated that the order of F/Pt and F/Ir gasification reactions exceeds unity at high temperatures where the rate of reaction decreases rapidly with temperature. Under these conditions, more rapid gasification near the colder ends of the filament controls the duration of an experiment and eventually prevents further rate measurements. The order of reaction has been deduced from nth order Arrhenius diagrams, *i.e.*, plots of log $[\xi_{Me}/Z_F^n]$ *vs.* reciprocal temperature, where ξ_{Me} is the Pt or Ir gasification flux and Z_F is the incident flux of atomic fluorine. Such diagrams reveal nth order kinetics when data obtained at different pressures and temperatures merge into a single curve.

F/Ir kinetics.—The F/Ir data reveal first-order kinetics near 1000°-1100°K and a transition to third-order kinetics at higher temperature. The data, obtained at three different F-atom pressures are illustrated in Fig. 5, a third-order Arrhenius diagram. The lines drawn through the data were derived from the following empirical model of the reaction kinetics. It was assumed that:

1. A temperature and pressure independent fraction, $S_F(Ir)$, of the incident F-atoms stick on the surface and participate in the surface reactions.
2. The adsorbed F-atoms may (*i*) desorb or (*ii*) react with the substrate to produce IrF_3 product molecules.
3. The product molecule and F-atom desorption fluxes are given by the following Arrhenius-type rate laws

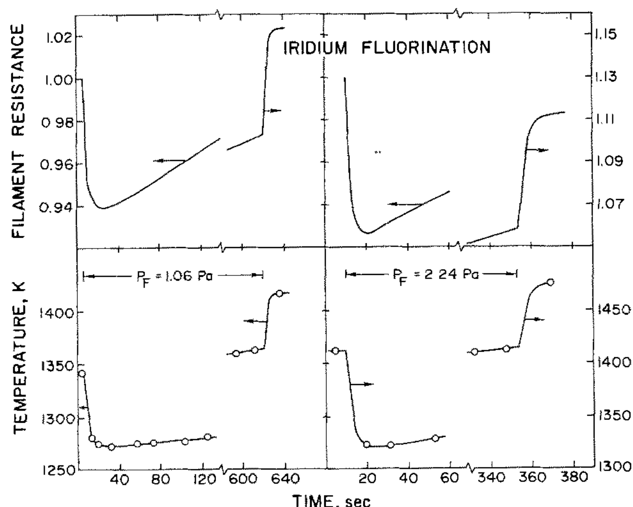

Fig. 4. Iridium filament resistance and temperature transients on exposure to atomic fluorine with constant current heating.

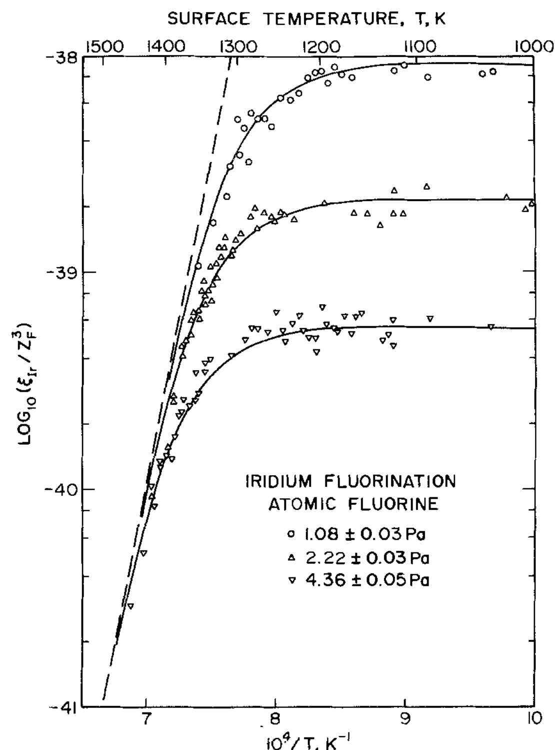

Fig. 5. Third-order Arrhenius diagram for F/Ir gasification reaction. Units for ξ_{Ir}, Z_F are atoms/cm^2 · sec.

$$\xi_F = A_F\theta_F \exp(-\Delta E^{\neq}_F/kT) \quad [6]$$

$$\xi_{IrF_3} = A_{IrF_3}\theta_{IrF_3} \exp(-\Delta E^{\neq}_{IrF_3}/kT) \quad [7]$$

where A, θ, and $\Delta E^{\neq}$ denote temperature independent pre-exponential constants, fractional surface coverage, and desorption activation energies, respectively.

4. The surface reaction by which adsorbed IrF_3 molecules are formed have the net effect that θ_{IrF_3} is proportional to θ_F^3 according to the following Arrhenius-type expression

$$\theta_{IrF_3}/\theta_F^3 = A_S \exp(-\Delta E^{\neq}_S/kT) \quad [8]$$

The constants, A_S, $\Delta E^{\neq}_S$ which appear in Eq. [8] are not elementary rate constants but, rather, reflect the net kinetic effect of several surface reactions or of a third-order surface equilibrium, as discussed below.

It is evident (see Discussion) that a fluoride film forms on the metal surface during reaction. However, the composition, porosity, and even the state (solid or liquid) of this film is unknown and the net surface reaction may occur *via* several different mechanisms. Langmuir-Hinshelwood type surface reactions can lead to Eq. [8], as could an equilibrium between adsorbed species and those dissolved in the fluoride film with a third-order reaction in the film. Also, the product species stoichiometry has not been established by independent measurements and no studies of the lower gaseous fluorides of iridium appear in the literature. However, if it is assumed that third-order kinetics derive from an equilibrium between adsorbed species, *i.e.*, that product desorption is the rate-limiting step, then the present results suggest that $IrF_3(g)$ is the product molecule.

To match the kinetic data, the constants in Eq. [6], [7], and [8] can be chosen so ξ_F is negligible at low temperature and all F-atoms which stick react to produce IrF_3 molecules. Therefore, at low temperature we take

$$S_F = 3\epsilon_{Ir} \text{ (low temperature)} \quad [9]$$

At higher temperatures, the surface F-atom mass balance, is

$$S_F Z_F = 3\xi_{Ir} + \xi_F \quad [10]$$

The sticking coefficient (from Eq. [9] and measured Ir gasification rates, yield the flux quotient

$$\xi_{IrF_3}/\xi_F^3 = \xi_{Ir}/(Z_F S_F - 3\xi_{Ir})^3 \quad [11]$$

which can be fit to

$$\xi_{IrF_3}/\xi_F^3 = A_{Ir} \exp(-\Delta E^{\neq}_{Ir}/kT) \quad [12]$$

Here, A_{Ir} and $\Delta E^{\neq}_{Ir}$ are the appropriate combinations of pre-exponentials and activation energies from Eq. [6]-[8]. The data were fit to Eq. [11] and [12] by (*i*) choosing a value of the sticking coefficient, (*ii*) calculating ξ_{IrF_3}/ξ_F^3 for all high temperature data for which $\epsilon_{Ir} < 0.037$ from Eq. [11], (*iii*) fitting these flux quotients to Eq. [12] by least squares, and (*iv*) repeating the calculation to find the value of S which minimized the variance for all data points. Numerical results are presented in Table I; the flux quotients computed from these results are shown by the solid lines drawn through the data in Fig. 5. The dashed line in Fig. 5 illustrates the limiting high temperature rate constant, $\xi_{Ir}/Z_F^3 = (\xi_{Ir}/\xi_F^3)S_F^3$, which may be used to calculate the Ir gasification rate from the F-atom flux when $\xi_{Ir} << Z_F$.

F/Pt kinetics.—The F/Pt data were obtained over a wider temperature range (600°-1430°K) than were the F/Ir data (1000°-1450°K) and show a greater variety of kinetic behavior. Included are zero-order kinetics at low temperature (600°-650°K), first-order kinetics between 800°-900°K, and second-order kinetics at high temperatures. A pressure and temperature dependent increase in reaction probability is observed between 900°-1300°K which suggests a change in product species. Also, at temperatures below 1000°K the rate of reaction depends on reactant purity as illustrated by experiments in which 35% O_2 was deliberately added to the fluorine.

The low temperature, zero-order kinetics are illustrated in Fig. 6, which plots the rate *vs.* temperature data in a zero-order Arrhenius diagram. Although the number of low temperature data points is small, they clearly merge into a single reactant pressure independent line in the 600°-650°K temperature range. It can be seen that addition of 35% O_2 to the reactant fluorine produces a pronounced decrease in the reaction rate below about 1000°K. However, data obtained with high purity (>99.9%) or commercial (≈98%) fluorine agree at all temperatures investigated. The line drawn through the low temperature F/Pt data is given by the equation

$$\xi_{Pt}(LT) = A \cdot \exp(-\Delta E^{\neq}/kT) \quad [13]$$

The coefficients in Eq. [13] were determined graphically and are reported (with estimated uncertainties) in Table I.

Table I. Fit of iridium and platinum gasification data

Metal	Quantity	Preexponential constant, $\log_{10}$ (A)	Activation energy $\Delta E^{\neq}$(kJ/mole)
Iridium	S_F	−0.616 ± 0.044	—
	ξ_{IrF_3}/ξ_F^3	−59.32 ± 0.87	−577 ± 25
	$(\xi_{Ir}/Z_F^3)_{HT}$	−61.19 ± 0.87	−577 ± 25
Platinum	$\xi_{Pt}(LT)$	30.8 ± 2.4	176 ± 29
	S_F	−0.178 ± 0.069	6.8 ± 1.1
	ξ_{PtF_2}/ξ_F^2	−28.88 ± 0.13	−238 ± 3
	$\xi_{PtF_4}/\xi_{PtF_2}^2$	−31.97 ± 1.70	−287 ± 32
	$(\xi_{Pt}/Z_F^2)_{HT}$	−29.24 ± 0.16	−251 ± 4

Figure 7 illustrates the first-order region between about 750°-900°K where the F/Pt reaction probability is independent of reactant pressure. A slow increase of ϵ_{Pt} with temperature is noted, which indicates a temperature dependent sticking coefficient, S_F(Pt). At about 900°K, depending on reactant pressure, the reaction probability exceeds that given by an extrapolation of the lower temperature first-order data. This effect is interpreted as a change in the product species, with fewer F-atoms required to gasify one Pt-atom rather than a nonlinear variation in log [S_F(Pt)] with reciprocal temperature. At even higher temperatures, a decrease in the rate of gasification is observed. The reaction is second order in this high temperature region, as illustrated in Fig. 8, a second-order Arrhenius diagram. In Fig. 6-8, the lines drawn through the data at temperatures above 750°K were derived from the following empirical model of the reaction kinetics. It was assumed that:

1. A temperature dependent, reactant pressure independent fraction, S_F(Pt), of the incident F-atoms stick on the surface and participate in the surface reactions. The sticking coefficient is given by the Arrhenius rate law

$$S_F(\text{Pt}) = A_F \exp(-\Delta E^{\neq}_F/kT) \quad [14]$$

2. The adsorbed F-atoms may (*i*) desorb or (*ii*) react with the substrate to produce PtF_2 or PtF_4 molecules.

3. The PtF_4, PtF_2, and F-atom desorption fluxes are given by Arrhenius-type rate laws similar to those written for the F/Ir reaction.

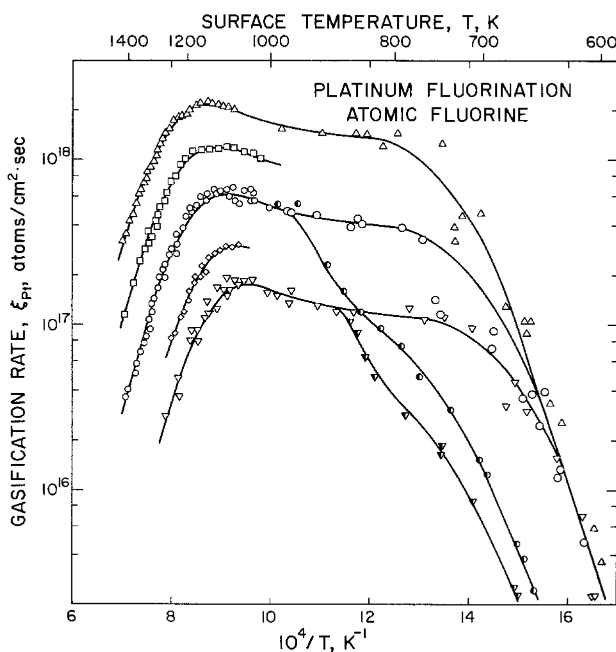

Fig. 6. Rate of platinum gasification by atomic fluorine vs. reciprocal temperature. △, p_F = 7.37 ± 0.03 Pa; □, p_F = 4.19 ± 0.15 Pa; ○, p_F = 2.20 ± 0.05 Pa; ◇, p_F = 1.08 ± 0.03 Pa; ▽, p_F = 0.65 ± 0.04 Pa. Half-filled symbols, 35% O_2 added to fluorine.

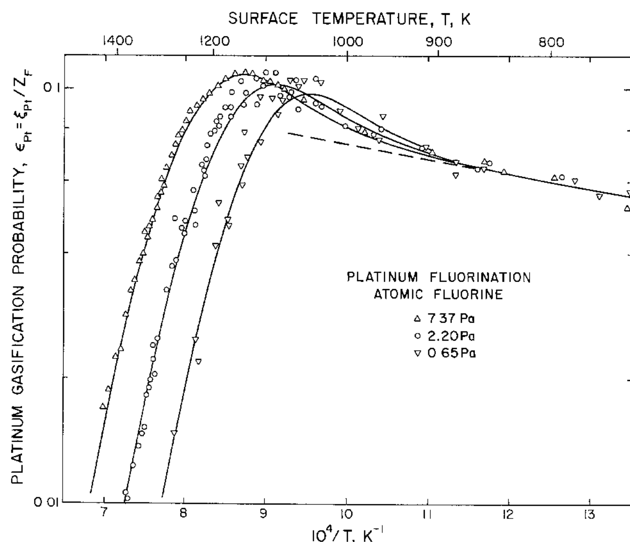

Fig. 7. F/Pt gasification probability vs. reciprocal temperature

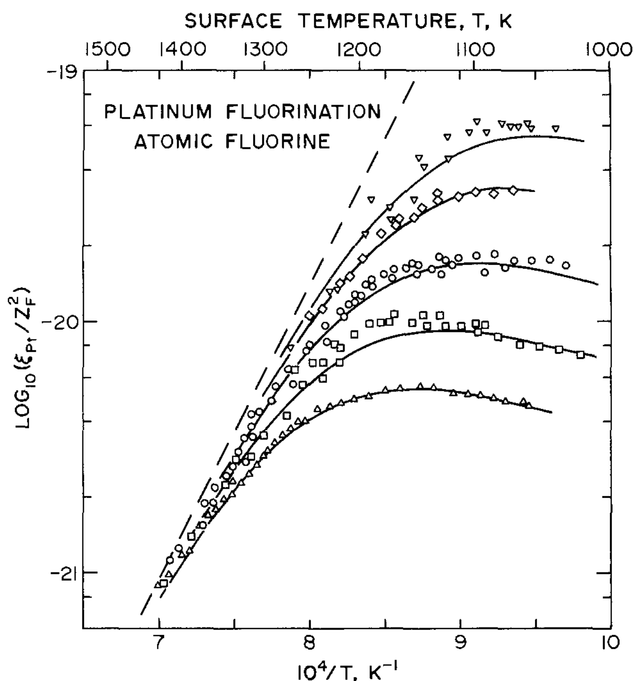

Fig. 8. Second-order Arrhenius diagram for F/Pt gasification reaction (symbols and units as in Fig. 6).

4. The surface reactions by which adsorbed PtF_4 and PtF_2 molecules are formed have the net effect that $\theta_{PtF_4} \propto \theta_F{}^4$ and $\theta_{PtF_2} \propto \theta_F{}^2$.

Proceeding as before, Arrhenius expressions can be written for flux quotients which do not involve the unknown surface concentrations.

The same comments in regard to product stoichiometry and the platinum fluoride film are appropriate here as were made earlier concerning the F/Ir reaction.

The F/Pt data were fit by least squares to the above model by the following method. At temperatures between 750°-900°K, almost all F-atoms which stick react to produce PtF_4, leading to

$$S_F(Pt) = 4\epsilon_{Pt} \quad [15]$$

Thus, A_F and $\Delta E^{\neq}{}_F$ were computed by a least squares fit of the first-order data to Eq. [14]. Above *ca.* 1200°K, ξ_{PtF_4} is negligible and

$$\xi_{PtF_2}/\xi_F{}^2 = \xi_{Pt}/(Z_F \cdot S_F - 2\xi_{Pt})^2$$

may be computed using extrapolated values of $S_F(Pt)$. The derived high temperature flux quotients were fit to the equation

$$\xi_{PtF_2}/\xi_F{}^2 = A_{2F} \exp(-\Delta E^{\neq}{}_{2F}/kT) \quad [16]$$

Finally, the complete F-atom mass balance

$$Z_F \cdot S_F = \xi_F + 2\xi_{PtF_2} + 4\xi_{PtF_4} \quad [17]$$

and Pt mass balance

$$\xi_{Pt} = \xi_{PtF_2} + \xi_{PtF_4} \quad [18]$$

can be solved in the intermediate temperature range, using values of $S_F(Pt)$ from Eq. [14] and $\xi_{PtF_2}/\xi_F{}^2$ from Eq. [16]. The resulting PtF_2 and PtF_4 fluxes were fit to

$$\xi_{PtF_4}/\xi_{PtF_2}{}^2 = A_{42} \exp(-\Delta E^{\neq}{}_{42}/kT) \quad [19]$$

The above calculation was iterated, with small corrections in the higher and lower temperature regions according to the results of the first calculation. Small changes in the computed preexponentials and activation energies were obtained but no further significant change occurred on repeated iterations. The numerical results are presented in Table I and illustrated by the lines drawn through the data in Fig. 6-8. It can be seen that the quantity $\xi_{PtF_4}/\xi_{PtF_2}{}^2$ is obtained with least accuracy. The calculation of this quantity was restricted to those data for which $0.2 < \xi_{PtF_2}/\xi_{PtF_4} < 5$; the fit of these data to Eq. [19] is illustrated in Fig. 9.

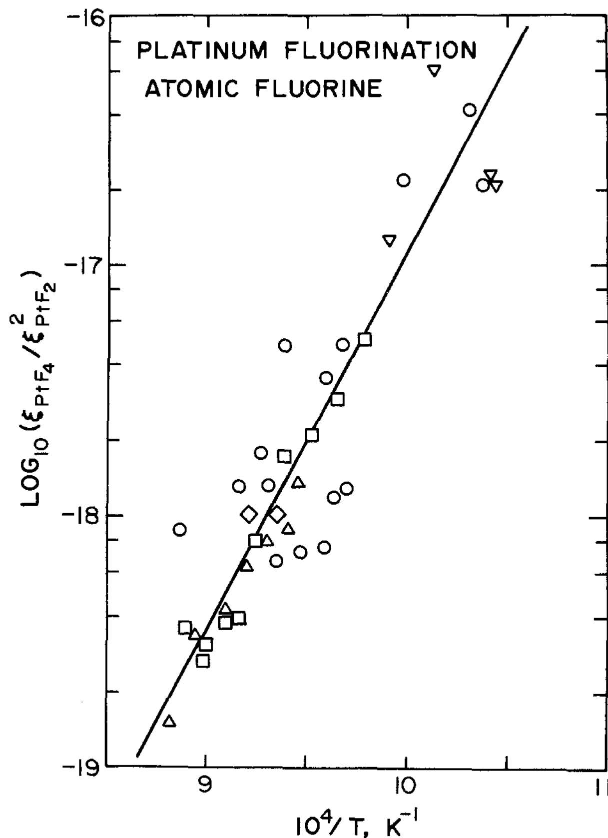

Fig. 9. Derived flux quotient $\xi_{PtF_4}/\xi^2{}_{PtF_2}$ vs. reciprocal temperature (symbols and units as in Fig. 6).

F, F_2/Ta kinetics.—Tantalum reacts with atomic fluorine over a greater range of temperatures than any other metal which has been studied. The exothermic gasification reaction quickly heats a Ta filament from 300°K to $T \cong 600$°K where $\xi_{Ta} = 6.6 \times 10^{16}$ cm^{-2} · sec^{-1} at $p_F = 2.26$ Pa, *i.e.*, $\epsilon_{Ta} \cong 9.4 \times 10^{-3}$. The F/Ta reaction also persists to very high temperature and was measured to $T = 3030$°K in these experiments. The F_2/Ta rate was not measurable at room temperature. Figure 10 illustrates the

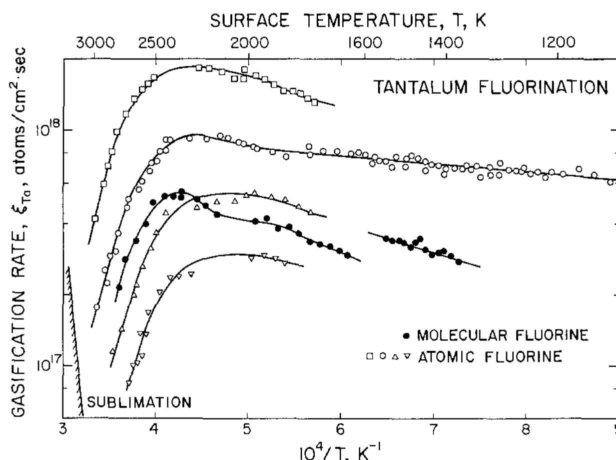

Fig. 10. Rate of tantalum gasification by atomic and molecular fluorine vs. reciprocal temperature. □, $p_F = 4.39 \pm 0.06$ Pa; ○, $p_F = 2.20 \pm 0.04$ Pa; △, $p_F = 1.167 \pm 0.004$ Pa; ▽, $p_F = 0.605 \pm 0.007$ Pa; ●, $p_{F_2} = 1.26 \pm 0.03$ Pa.

F/Ta rate data, obtained at four F-atom reactant pressures and F_2/Ta data at $p_F = 1.26$ Pa.

The lower temperature portion of the F/Ta Arrhenius diagram is easily explained by a temperature dependent, pressure independent sticking coefficient with reaction of all F-atoms which stick on the surface. If the product species is $TaF_5(g)$ one obtains $S_F(\text{Ta}) = 1.28 \exp(-1010/T)$. At 1850°K the reaction order is actually 0.84. Values less than unity are characteristic of a change in product species, as for the F/Pt reaction near 1000°K. At high temperatures the F/Ta reaction order is approximately 1.5 and the Arrhenius activation energy is $\Delta E^{\neq} \approx -290$ kJ/mole. The nonintegral reaction order cannot be explained by competitive desorption of atomic fluorine and a single tantalum fluoride. Further, it was noted that energy balance effects associated with the fluoride film disappear when the temperature coefficient of reaction rate becomes negative. Thus, a changing surface and the possible contribution of several gaseous species complicate the interpretation of high temperature F/Ta data, which was not carried further.

The F_2/Ta data seem to show a small influence of impurities in the fluorine on the rate of reaction. Fluorine purity for the data between 1370°-1540°K was 98% while the higher temperature data were obtained with 96% fluorine. However, no differences in F/Ta rate data were observed for fluorine of 96%, 98%, or 99.9% purity.

Errors in F/Ir and F/Pt kinetics.—The uncertainty in $S_F(\text{Ir})$ listed in Table I is an estimated value, ±10%. All other uncertainties were obtained from the data analysis. The largest contribution to error in the derived coefficients is the standard deviation of the mean values obtained in least squares calculations. However, each calculation gave two coefficients under the assumption that other derived constants in the model were equal to the values listed in Table I. Additional errors in the derived coefficients result from the uncertainty in all (6 for Pt, 3 for Ir) constants in the model; this effect has been included in computing the listed errors.

The rms deviation of the measured values of $\ln \xi_{Pt}$ or $\ln \xi_{Ir}$ from those given by the models is 0.080 for Pt, 0.117 for Ir, corresponding to deviations of 8% and 12% in the respective rates. The greater deviations obtained in the Ir data are mainly due to the larger slope of the high temperature region in the Arrhenius diagram. For example, if the only error were a temperature uncertainty of ±2°K, the consequent errors between measured and computed high temperature rates of reaction would be about ±3.4% for Pt, ±7.4% for Ir. Other sources of error have been discussed (17). It is concluded that the model fits the data within the precision of the measurements. This is not the case if one assumes the lower temperature F/Pt product is $PtF_3(g)$, formed by a third-order surface reaction. Then, the resulting coefficients of the model predict rate data to only 12.4%, largely due to a much poorer fit in the 950°-1250°K temperature range.

It may be remarked that the method of analysis nearly eliminates errors due to the uncertainty in the incident flux if the assumed product species are the actual product species. This is true because $Z_F \cdot S_F$ measures correctly the number of F-atoms which stick on the surface even though Z_F is uncertain by about 10%. The uncertainty in Z_F produces an additional error in S_F (which is not included in Table I) but not in the other coefficients.

Discussion

Fluoride film formation.—The mechanism by which the specimen heat transfer coefficient increases on exposure to fluorine must be consistent with the magnitude, rate, and reversibility of the induced specimen temperature decrease. Roughening of the metal surface is inconsistent with the reversibility and adsorption of an atomic fluorine monolayer would occur too quickly to explain the duration of the transient effect. The observed changes in heat transfer coefficient are thus attributed to formation of condensed metal fluoride films on the metal surfaces. The film presumably has a greater emissivity, thermal accommodation coefficient, and/or roughness than does the bare metal. Reaction under steady-state conditions then occurs *via* F-atom gasification of the fluoride film at a rate equal to that at which it is formed by F-atom diffusion to the underlying metal and/or metal atom diffusion to the surface.

The formation of fluoride films on tantalum has already been proposed by Machiels and Olander (8) for the F_2/Ta reaction on the basis of their modulated beam results at 690° and 930°K. This independent evidence for fluoride films confirms the present explanation of the transient temperature effects for tantalum and leads directly to the conclusion that fluoride films also form on Ir and Pt during reaction with atomic fluorine.

McIntyre and McTaggart (31) studied the kinetics of Cl, Br, I/Ag scale forming reactions by direct measurement of scale growth rates and report near unit reaction probabilities even at a scale thickness of several hundred nanometers. McTaggart (32) obtained similar results for the F/Ag reaction. Thus, the formation of fluoride films need not inhibit the rate of reaction as does oxide scale formation in many metal oxidation reactions. We note that the formation of fluoride films is not a necessary consequence of the present steady-state rate measurements. Indeed, the same mathematical analysis of rate data could be based on low coverage Langmuir-Hinshelwood type surface reactions on the bare metal surface. However, this hypothesis could not explain modulation experiments which more directly probe the surface kinetics, as Machiels and Olander have demonstrated for the F_2/Ta reaction (8).

Quasi-equilibrium F/Ir and F/Pt preexponential quotients.—The preexponential quotients listed in Table I agree well with values computed by a simple, quasi-equilibrium (QE) model (33, 34). If an adsorbed state equilibrium is assumed with unit metal activity and the surfaces are smooth, the measured desorption flux quotients will equal the adsorption flux quotients which obtain under gas/surface equilibrium conditions. For example, $\xi_{PtF_2}/\xi_F{}^2$ will be given by

$$\xi_{PtF_2}/\xi_F{}^2 = (Z_{PtF_2}/Z_F{}^2)_{EQ}(S_{PtF_2}/S_F{}^2) \qquad [20]$$

where $(Z_{PtF_2}/Z_F{}^2)_{EQ}$ is the quotient of equilibrium fluxes and S_{PtF_2} is the PtF_2 sticking coefficient. If, further, activation entropy effects are absent in PtF_2 or F-atom sticking (or cancel out of the following equation), thermodynamics and the Hertz-Knudsen equation yield

$$A_{2F} = (2\pi kT/m_{PtF_2})^{1/2}(m_F/1.013 \times 10^6)\exp(\Delta S°_{RX}/R) \qquad [21]$$

Here, m is the mass of a PtF_2 molecule or F-atom, the numerical factor provides appropriate conversion of units, and $\Delta S°_{RX}$ is the standard entropy of the reaction

$$Pt(s) + 2F(g) = PtF_2(g) \qquad [22]$$

Equation [21] and analogous expressions for the other gasification reactions yield the preexponential quotients reported in Table II. Entropies were obtained from Hultgren (35) for the metals, Janaf Tables (1) for atomic fluorine, and were computed for the iridium and platinum fluorides using the molecular parameters estimated for tungsten fluorides by Hildenbrand (36). In addition to the good agreement between experimental and QE preexponential quotients, thermodynamic property estimates for iridium fluorides by Wallace, Feber, and Hauth (40) also support the QE model. For example, they com-

Table II. Calculation of preexponential quotients

Flux quotient*	$\xi_{PtF_2}/\xi_F{}^2$	$\xi_{PtF_4}/\xi_{PtF_2}{}^2$	$\xi_{IrF_3}/\xi_F{}^3$
Mean temperature (°K)	1290	1040	1370
$\Delta S°_{RX}$(joule/mole · °K)	-114 ± 13	-149 ± 23	-235 ± 15
$Log_{10}(A)$:			
Experimental	-28.88 ± 0.13	-31.97 ± 1.70	-59.32 ± 0.87
Quasi-equilibrium	-29.75 ± 0.66	-30.53 ± 1.18	-59.28 ± 0.81

* Flux units are molecules/square centimeter · second or atoms/square centimeter · second.

pute equilibrium pressures of F and IrF_3 in equilibrium with solid iridium at 1500°K from which one obtains a value for $\xi(IrF_3)/\xi(F)^3$ within 50% of that given by the present results. There are, however, a sufficient number of unproved assumptions in the QE model (adsorbed state equilibrium, unit metal activity, absence of entropy effects in the molecular sticking coefficients) that its success should be viewed with caution, at least until the product species have been independently confirmed and their thermodynamic properties measured.

F, F_2/Ta kinetics.—The present F, F_2/Ta rate measurements can be compared with values predicted with the model and kinetic parameters derived by Machiels and Olander (8) from their modulated molecular beam study of the F_2/Ta reaction. At 690° and 930°K, respectively, they obtained second-order rate constants $k_R = 7.4 \times 10^{-14}$ and 7.9×10^{-14} cm²/sec and site densities $N_S = 5 \times 10^{14}$ and 8×10^{14} cm^{-2}. The rate of reaction to produce TaF_5 on the assumed TaF_3 film is then given by the second-order equation

$$\xi_{TaF_5} = k_R(N_S\theta)^2 \quad [23]$$

where θ is the fractional coverage of atomic fluorine. In the model the source (F or F_2) of the adsorbed fluorine does not influence the rate and all fluorine which is chemisorbed reacts to produce TaF_5(g). If we take $\theta \leq 1.0$ the above results predict $\xi_{TaF_5}(max) = 1.8 \times 10^{16}\ cm^{-2} \cdot sec^{-1}$ at 690°K and $5.1 \times 10^{16}\ cm^{-2} \cdot sec^{-1}$ at 930°K. These values are considerably smaller than the extrapolated higher temperature F/Ta or F_2/Ta rate data obtained here. Further, the one datum at $T \cong 600$°K gave $\xi_{Ta} = 6.6 \times 10^{16}\ cm^{-2}\ sec^{-1}$, also in excess of the predicted values.

The linear extrapolation of present F_2/Ta data over a large temperature range is a source of error which could produce the above discrepancy but no such error is present in the comparison of F/Ta data with the maximum predicted rates. The discrepancy in F/Ta rates may arise in the use of the Machiels and Olander mechanism at the much higher reactant fluxes of the present experiments. As the F-atom coverage of a TaF_3 film increases it is possible that the film stoichiometry changes, *e.g.*, to TaF_4, with a consequent influence on the mechanism and reaction rate. On the other hand, the film might already be TaF_4 (as suggested by Machiels and Olander) and a fit of their data to a TaF_4 film model might give better agreement with the present rate measurements. In either case, the qualitative features of the F_2/Ta and F/Ta reaction mechanism are the same in these two studies: Fluoride films form on the metal surface but these films do not produce a large reduction in the rate of reaction.

General features of metal fluorination reactions.—Kinetic data are now available for F-atom gasification of six metals: Pt, Ir, W (5), Mo (5), Ti (14), and Ta. The first-order Arrhenius diagrams for these reactions at an F-atom reactant pressure of *ca.* 2.2 Pa are illustrated in Fig. 11. The F/Mo and F/W curves are recalculated from the data reported by Rosner and Allendorf (5) using Eq. [1] and [3] to obtain the incident reactant fluxes. Except for Ir, each reaction shows the positive curvature in ln ϵ *vs.* reciprocal temperature characteristic of changes in product species. A change in product species with temperature is also suggested by the observation (5) of less than unit reaction order at 1350°, 1950°K for the F/W reaction, and at 1280°K for the F/Mo reaction.

The observed increase in Ti gasification rate at higher temperature contrasts with the decrease found with all other systems. This effect can be qualitatively understood by thermodynamic considerations. The over-all gasification reactions

$$Me(s) + nF(g) = MeF_n(g) \quad [24]$$

are endoentropic unless $n = 1$ in which case $\Delta S° \cong 0$. Therefore, if the reaction

$$Me(s) + F(g) = MeF(g) \quad [25]$$

is endothermic, the standard Gibbs free energies of all gasification reactions will become positive at sufficiently high temperature and a rate decrease will occur. The enthalpy of reaction [25] is positive if the vaporization enthalpy for the metal exceeds the monofluoride dissociation enthalpy. Known (1, 35-37) and estimated (38) thermodynamic data predict the observed high temperature behavior: at sufficiently high temperature, only titanium [$\Delta H°_v(Ti) = 439$ kJ/mole, $D°(TiF) \cong 630$ kJ/mole] can be gasified by atomic fluorine.

Summary

This paper presents new experimental results pertaining to reactant arrival rates in the low pressure, transonic flow reactor, the F/Ir, Pt, and Ta gasification kinetics, and the occurrence of fluoride films on Ir, Pt, and Ta metals during their reaction with fluorine. These results permit a more detailed interpretation of steady-state F/metal gasification kinetics than has been previously possible, chiefly through the quantitative agreement between F/Ir, Pt rate measurements and a model of the reaction kinetics. The principal results and conclusions are summarized below.

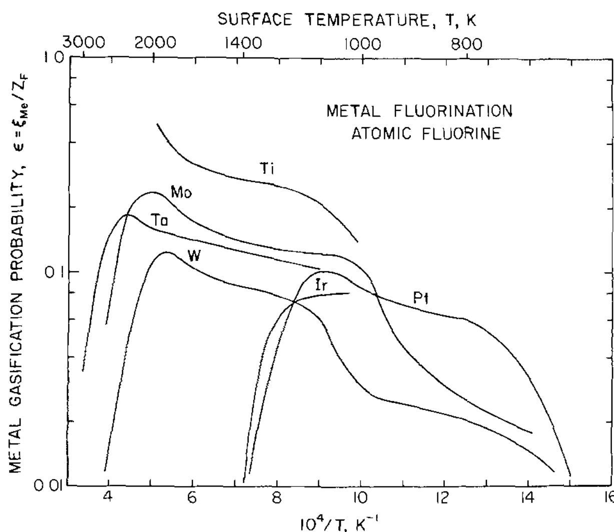

Fig. 11. Temperature dependence of reaction probabilities for the attack of iridium, platinum, tantalum, tungsten, molybdenum, and titanium by atomic fluorine, $p_F \approx 2.2$ Pa.

1. Gas phase mass transport does not significantly influence reactant arrival rate in the transonic flow reactor at near-sonic flow velocities, 130 Pa total pressure, and 0.038 cm filament diameters, even when the intrinsic gas/solid reaction probability approaches unity. However, the temperature of incident atoms exceeds the ambient temperature by an amount which depends on the filament thermal accommodation coefficient, α. Due to uncertainties in α, the gas temperature (given by Eq. [3]) is uncertain by 11-22% in the 1000°-3000°K temperature range which leads to a 6-11% uncertainty in incident reactant flux.

2. An increase in the Ir, Pt, and Ta filament heat transfer coefficient occurs on exposure to fluorine due to an increase in its total emissivity or thermal accommodation coefficient. The time required, magnitude, and reversibility of this effect imply that it is a result of the formation of a fluoride film on the metal surfaces. Adsorption of a single F-atom monolayer or roughening of the bare metal surface are inconsistent with the time required or the reversibility of the change in heat transfer coefficient.

3. The F/Ir reaction kinetics are first order in the incident F-atom flux below 1150°K, and third order at higher temperatures. The data fit, within experimental error, a model which assumes a temperature and reactant pressure independent sticking coefficient with competitive desorption of atomic fluorine and IrF_3 product molecules.

4. The F/Pt kinetics above 800°K are similar to the F/Ir kinetics except: (*i*) the sticking coefficient is slightly temperature dependent and (*ii*) PtF_2 and PtF_4 product molecules may be produced, each being the major product species in a different temperature range. At lower temperatures the F/Pt rate decreases and is zero order below 650°K. Oxygen (35%) added to the flourine reduces the rate of reaction below 1000°K but has no influence on higher temperature rate data. Further study of the corrosive properties of oxygen-fluorine mixtures would be of interest.

5. Quasi-equilibrium preexponential factors for the F/Pt and F/Ir rate laws agree with preexponential quotients derived from the data, and thus lend support to the assumption that second-, third-, fourth-order reactions imply PtF_2, IrF_3, and PtF_4 as the product species. However, independent verification of product species identity and other assumptions of the quasi-equilibrium model is not available and this agreement could be fortuitous.

6. The F/Ta data do not permit a simple quantitative interpretation as do the F/Ir, Pt data. Interpretation of the F/Ta results is complicated by the possible simultaneous occurrence of several gaseous species at the highest temperatures. Also, evidence from heat balance measurements indicates the fluoride film does not occur on tantalum at high temperature where the temperature coefficient of reaction rate is negative. The measured F/Ta rates do not agree with maximum values predicted by the F_2/Ta kinetic model of Machiels and Olander (8). This discrepancy may be due to a change in mechanism which results with reactant dissociation and a 100-200-fold increase of reactant pressure.

The successful fit of F/Ir, Pt data to kinetic models suggests these systems as promising candidates for further detailed study. Thermodynamic data for gaseous fluorides, molecular species sticking coefficients, and modulated beam studies of the surface kinetics would confirm or extend some of the present conclusions. Without such data, the mechanistic conclusions remain unconfirmed, but the simple mathematical models of F/Ir, Pt kinetics retain the significance that they faithfully reproduce the actual F-atom/metal gasification rates.

Acknowledgments

I thank Professor D. E. Rosner for the unpublished F/Ti data illustrated in Fig. 11 and also for valuable discussions of many aspects of this research. Argonne National Laboratory was most helpful in supplying the purified fluorine used in some of these experiments. The confidence and encouragement of Dr. H. M. Davis, Director of the Metallurgy and Ceramics Division of the U.S. Army Research Office, were essential to the success of this research program.

Manuscript submitted June 20, 1977; revised manuscript received Oct. 25, 1977. This was Paper 391 presented at the Atlanta, Georgia, Meeting of the Society, Oct. 9-14, 1977.

Any discussion of this paper will appear in a Discussion Section to be published in the December 1978 JOURNAL. All discussions for the December 1978 Discussion Section should be submitted by Aug. 1, 1978.

REFERENCES

1. D. R. Stull and H. Prophet, "JANAF Thermochemical Tables," 2nd ed., Natl. Stand. Ref. System, NBS Publication 37, U.S. Govt. Printing Office, Washington, D.C. (1971).
2. R. L. Bersin, *Solid State Technol.*, p. 31 (May 1976).
3. M. Farber, *Astronautics*, **34**, 40 (1960).
4. R. Foon and M. Kaufman, *Prog. React. Kinet.*, **8**, 81 (1975).
5. D. E. Rosner and H. D. Allendorf, *J. Phys. Chem.*, **75**, 308 (1971).
6. D. E. Rosner and J. P. Strakey, *ibid.*, **77**, 690 (1973).
7. J. D. McKinley, *J. Chem. Phys.*, **45**, 1690 (1966).
8. A. Machiels and D. R. Olander, *Surf. Sci.*, **65**, 325 (1977).
9. A. J. Machiels and D. R. Olander, *High Temp. Sci.*, **9**, 3 (1977).
10. J. L. Philippart, J. Y. Caradec, B. Weber, and A. Cassuto, Paper 240 presented at The Electrochemical Society Meeting, Atlanta, Georgia, Oct. 9-14, 1977.
11. M. D. Scheer, R. Klein, and J. D. McKinley, *Surf. Sci.*, **30**, 251 (1972).
12. D. A. Winborne and P. C. Nordine, *AIAA J.*, **14**, 1488 (1976).
13. P. C. Nordine and J. D. LeGrange, *ibid.*, **14**, 644 (1976).
14. D. E. Rosner, Unpublished results.
15. P. C. Nordine, *J. Chem. Phys.*, **61**, 224 (1974).
16. P. C. Nordine and D. E. Rosner, *J. Chem. Soc., Faraday Trans. 1*, **72**, 1526 (1976).
17. P. C. Nordine, D. E. Rosner, and P. J. Kindlmann, *Rev. Sci. Instrum.*, **44**, 821 (1973).
18. A. G. Worthing, *Phys. Rev.*, **28**, 174 (1926).
19. Y. S. Touloukian and D. P. DeWitt, Editors, "Thermophysical Properties of Matter," Vol. 7, 8, "Thermal Radiative Properties," IFI Plenum, New York (1970).
20. L. Malter and D. B. Langmuir, *Phys. Rev.*, **55**, 743 (1939).
21. "International Critical Tables," Vol. VI, McGraw-Hill Book Co., New York (1929).
22. W. Espe, "Materials of High Vacuum Technology," Vol. 1, Pergamon, New York (1966).
23. R. T. Wimber and J. J. Halvorson, *J. Mater.*, **7**, 564 (1972).
24. D. E. Rosner, E. Steinheil, and D. P. McArthur, *Met. Trans.*, **4**, 2221 (1973).
25. D. E. Rosner, H. M. Chung, and H. H. Feng, *J. Chem. Soc., Faraday Trans. I*, **72**, 842 (1976); *ibid.*, **72**, 858 (1976).
26. L. A. Bigelow, *Chem. Rev.*, **40**, 110 (1947).
27. J. R. Welty, C. E. Wicks, and R. E. Wilson, "Fundamentals of Momentum, Heat and Mass Transfer," John Wiley & Sons, Inc., New York (1969).
28. L. B. Thomas, in "Fundamentals of Gas-Surface Interactions, p. 346, H. Saltsburg, J. N. Smith and M. Rogers, Editors, Academic Press, New York (1967).
29. W. B. Mann, *Proc. R. Soc. London, Ser. A*, **146**, 776 (1934).
30. W. Watt and R. Moreton, U.S. Dept. Comm. AD453256 (1964). (See Chem. Abs. Vol. 66, No. 98731z, 1967).
31. R. J. McIntyre and F. K. McTaggart, *J. Phys. Chem.*, **74**, 866 (1970).
32. F. K. McTaggart, Private communication.
33. J. C. Batty and R. E. Stickney, *J. Chem. Phys.*, **51**, 4475 (1969).
34. J. C. Batty and R. E. Stickney, *Oxid. Metals*, **3**, 331 (1971).

35. R. Hultgren, R. L. Orr, P. D. Anderson, and K. K. Kelley, "Selected Values of Thermodynamic Properties of Metals and Alloys," John Wiley & Sons, Inc., New York (1963).
36. D. L. Hildenbrand, *J. Chem. Phys.*, **62**, 3074 (1975).
37. D. L. Hildenbrand, *ibid.*, **65**, 614 (1976).
38. R. A. Kent *et al*, *Proc. Nucl. Appl. Nonfissionable Ceram.*, 249 (1966).
39. H. H. Feng, Ph.D. Dissertation, Yale University (July 1975).
40. T. C. Wallace, R. C. Feber, and W. E. Hauth, Los Alamos Scientific Lab. Rep. LA-6780-MS (1977).

Technical Notes

A Pulse Method for the Measurement of Contact Resistance and Bulk Resistance of Semiconductors Samples

S. Dhar and B. R. Nag

Centre of Advanced Study in Radio Physics and Electronics, Calcutta-700 009, India

The contact resistivity of metal-semiconductor contacts, a property of current interest (1-4), is usually obtained from measurements on samples with different contact areas (5) or by subtracting the bulk resistance (determined in a separate experiment) from the sample resistance (1). We describe in this note a method of pulse measurement which may be used to determine the contact resistance and the bulk resistance individually in one experiment. The method has been applied to determine the contact resistance for room temperature electroless nickel contacts and evaporated aluminum contacts to n- and p-type silicon samples having resistivities between 5 and 350 Ω-cm. Values of contact resistance, contact capacitance, and bulk resistivity obtained from the experiments are also presented.

The method is based on the equivalent circuit of a semiconductor sample with contacts as shown in Fig. 1(a). The bulk resistance is represented by R_B and the contact resistance and capacitances by R_{C1}, R_{C2} and C_{C1}, C_{C2}, respectively. A voltage pulse is applied to the sample through a resistance larger than the sample resistance and the resultant voltage across the sample is displayed on an oscilloscope. The voltage displayed on the oscilloscope near the initial end of the pulse (for the conditions stated below) is given by

$$V(t) = [R_B + (aL - R_B)e^{-at} + R_C(1 - e^{-t/R_CC_C})] \frac{V_p}{(R_B + R_S)}$$

where V_p is the applied voltage, R_s is the resistance connected in series with the sample, L is the inductance of the lead connecting the sample to the ground plane, and $1/a$ is the oscilloscope amplifier time constant. C_C and R_C are, respectively, the lumped contact capacitance and resistance (see Fig. 1(b)). It has been assumed that $R_CC_C > 1/a$ and also that $1/ac_i >> R_B$, c_i being the input capacitance of the oscilloscope.

The voltage for large values of t is, on the other hand

$$V(t \to \infty) = V_p(R_B + R_C)/R_B + R_C + R_S)$$

The expected voltage wave shape is as shown in Fig. 1(c). We also find that the initial voltage is a step of height $V_pR_B/(R_B + R_S)$ if the length of the lead

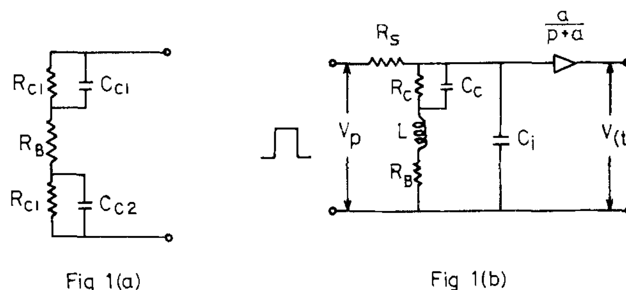

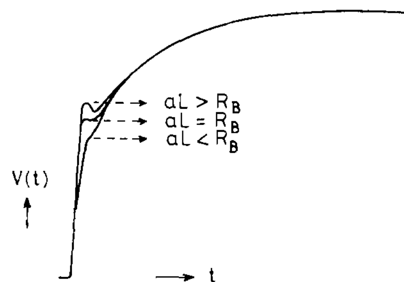

Fig. 1. (a) Equivalent circuit of a semiconductor sample with contacts; (b) actual circuit involved in the measurements; (c) expected wave shape of the voltage across the semiconductor.

is so chosen that the lead inductance satisfies the relation $aL = R_B$. (The length of the lead required for this adjustment in our experiment was between 1 and 7.5 cm.)

It is evident from the above relations that the contact resistance R_C and the sample resistance R_B may be obtained from separate measurements of the initial and the final voltage step. The value of C_c may also be estimated from the rise time of the initial exponential part.

This method has been applied to study the contact resistance of contacts made to silicon samples of both conductivity types (resistivity from 5 to 350 Ω-cm) prepared by the room temperature electroless nickel-plating technique (7) using the following procedure. Samples were first lapped with 800 mesh carborundum powder washed in deionized water, and degreased in boiling methanol. The degreased sample was cleaned in an ultrasonic cleaner and rewashed in methanol

Key words: interfaces, metal-semiconductor contact, electrical properties.

and deionized water. It was then dipped in 48% HF for 1 min and dropped in the nickel-plating bath. The deposition occurred in 8-10 min. Some vacuum-evaporated aluminum contacts were also studied for comparison.

Values of R_s, a, and C_l used in our experiment were, respectively, 100Ω, 2×10^8 sec^{-1}, and 10 pF. The sample dimensions were chosen so that R_B was in the range 5-20Ω. The voltage across the sample had the wave shape schematically presented in Fig. 1(c) and measurements were taken by adjusting the lead length to achieve the condition $aL = R_B$ in all the cases. The required values of L for satisfying this condition lie between 0.025 and 0.1 μH for the experimental values of $a = 2 \times 10^8$ sec^{-1} and R_B = (5-20Ω). This was realized by adjusting the length of the lead connecting the sample to the ground plane between 1 and 7.5 cm. Oscillograms showing the voltage wave shape under different conditions of adjustment are shown in Fig. 2. Our measured values of contact resistivity, bulk resistivity, and contact capacitance for samples of different nominal bulk resistivity are presented in Table I.

The contacts to all the n-type samples gave linear current-voltage characteristics, but for the p-type samples the relation was nonlinear. However, it is found from the pulse measurements that in all the cases significant contact resistance was present. Thus a linear current-voltage characteristic is not always an indication of a low resistance contact as is often assumed (8, 9).

The contact resistance for a freshly prepared contact made by the Ni-plating technique was found to be low for n-type samples, the contact being almost ohmic. The values of contact resistance for such contacts as obtained in our experiment are of the same order as reported by other workers (2, 10). It was observed, however, that the contact resistance of such contacts increased with aging or when a lead is attached to it by the usual process of soldering. Some results for aged contacts are also presented in Table I.

Results of Table I also show that the values of bulk resistivity obtained by the method for high resistivity and long-length low resistivity samples agree fairly well with the nominal values, which were obtained by the four-probe method for low resistivity samples and by the two-probe method (11) for the high resistivity samples. The resistivity of small length low resistivity samples obtained by the method does not, however, agree with the nominal values or vary with the length of the sample. It was found from studies on such samples of the same resistivity but of different lengths that the sample resistance corresponding to the same face area and excluding the contact resistance varied linearly with length, and the slope of the line correctly gave the bulk resistivity. These results indicated that there exists an additional contact resistance of about 0.2 Ω-cm^2 in series with the parallel combination of the contact resistance and capacitance contributed by the semiconductor surface layer. The value of this resistance, in contrast to that of the semiconductor surface layer, was always the same and was of such magnitude that it was negligible in comparison to the sample resistance for high resistivity and long-length low resistivity samples. It was important only in small-length low resistivity samples, but as it is reproducible, it could be eliminated by taking measurements on samples of different lengths as mentioned above. It should be noted in this connection that the other part of the contact resistance cannot be

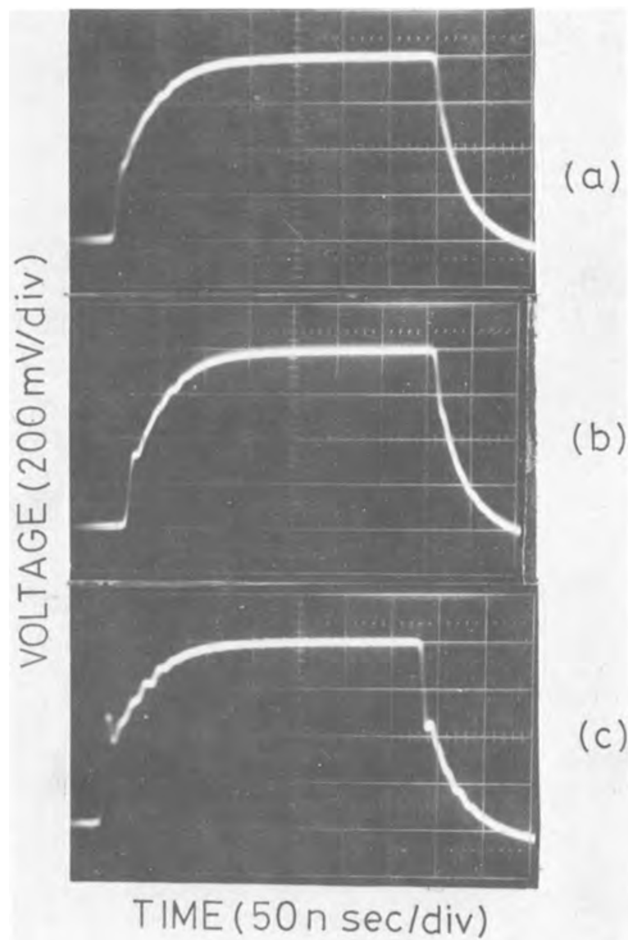

Fig. 2. Experimental wave shape of the voltage across the semiconductor sample (R_B =5.6 Ω); (a) Lead length = 0.5 cm; (b) lead length = 2.5 cm; (c) lead length = 3.5 cm.

Table I. Experimental results on contact and bulk resistance

Sample No.	Dimension of the sample: Length (cm)	Dimension of the sample: Area (cm^2)	Sample type	Nominal bulk resistivity (Ω-cm)	Experimental bulk resistivity (Ω-cm)	Contact resistivity (Ω-cm^2)	Contact capacitance (pF/cm^2)	Nature of contact
1	0.07	0.25	p	350	343	130	400	Electroless Ni
2	0.061	0.123	p	350	341	22	1600	Vapor-deposited Al (Aged for 15 days)
3	0.089	0.390	n	144	146	3	—	Electroless Ni
4	0.078	0.136	n	144	140	13	4700	Vapor-deposited Al
5	0.089	0.176	p	46	48	44	3100	Electroless Ni
6	0.112	0.110	p	46	49	88	—	Vapor-deposited Al
7	0.048	0.10	n	50	51	1.4	23,000	Electroless Ni (Aged sample; soldered leads)
8	0.053	0.073	n	5	9.6	0.36	54,000	Electroless Ni (Stored in methanol for two days; pressed leads)
9	0.074	0.094	n	5	7.9	0.06	46,000	Electroless Ni (Freshly prepared; pressed leads)
10	0.074	0.117	n	5	8.2	4.0	—	Vapor-deposited Al
11	0.175	0.98	n	5	5.8	0.5	50,000	Electroless Ni (Aged sample; soldered leads)
12	0.293	0.092	n	5	5.4	1.3	37,000	Same as above
13	0.398	0.090	n	5	5.2	1.1	40,000	Same as above

easily determined by measurements on samples of different lengths as its value is sensitive to the conditions of contact processing and is not exactly reproducible.

The method described here thus directly gives us the values of contact resistance and capacitance due to the semiconductor surface layer as well as the correct values of bulk resistivity of high resistivity and long-length low resistivity samples. It may also be used to correctly obtain the resistivity of small-length low resistivity samples by taking measurements on samples of different lengths.

Acknowledgment

This work was supported by the Jawaharlal Nehru Memorial Fund.

Manuscript submitted March 4, 1977; revised manuscript received Oct. 14, 1977.

Any discussion of this paper will appear in a Discussion Section to be published in the December 1978 JOURNAL. All discussions for the December 1978 Discussion Section should be submitted by Aug. 1, 1978.

REFERENCES

1. I. Teramoto, *This Journal,* **115**, 912 (1968).
2. R. C. Hooper, J. G. Harper, and J. A. Canningham *Solid-State Electron.,* **8**, 831 (1965).
3. J. Bertoti and K. Somagyi, *Phys. Status Solidi A,* **6**, No. 2, 439 (1971).
4. H. Tippmann and R. Trimbuch, *Z. Tech. Hocksch. Ilmenan,* **20**, No. 3, 133 (1974).
5. R. H. Cox and H. Stack, *Solid-State Electron.,* **10**, 1213 (1967).
6. J. Bardeen, *Bell Syst. Tech. J.,* **28**, 428 (1949).
7. N. Feldestein, *RCA Rev.,* **31**, 317 (1970).
8. W. Siegel, E. Ziegler, and G. Kuhnel, *Phys. Status Solidi A,* **15**, 521 (1973).
9. H. M. Kasper and B. Tell, *J. Appl. Phys.,* **46**, 931 (1975).
10. B. Pellegrini and G. Salardi, *Solid-State Electron.,* **18**, 791 (1975).
11. P. E. Kane and G. B. Larrabee, "Characterization of Semiconductor Materials," p. 90, McGraw-Hill Book Co., New York (1970).

JOURNAL OF THE ELECTROCHEMICAL SOCIETY

ELECTROCHEMICAL SCIENCE

—AND TECHNOLOGY—

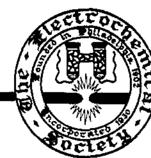

APRIL

1978

Nonaqueous Batteries with BiF_3 Cathodes

P. Fiordiponti, S. Panero, G. Pistoia, and C. Temperoni

Centro di Studio sulla Elettrochimica e la Chimica Fisica delle Interfasi del C.N.R., Istituto di Chimica della Facoltà di Ingegneria, Università di Roma, Rome, Italy

ABSTRACT

Li cells based on BiF_3 cathodes have been tested. In particular, the effect of cathode formulation and compacting pressure, nature of the solution, temperature, and current density have been evaluated. Through x-ray analysis, cyclic voltammetry, and coulometric analysis it was possible to ascertain that BiF_3 is reduced to Bi and then to Li_3Bi. During the first reduction process, ternary phases of the Li_xBiF_3 type are probably formed. Li/BiF_3 cells can give practical energy densities in excess of 200 W-hr/kg at the rate of 0.5 mA/cm^2.

The improvement brought about in the field of lithium primary batteries by the use of liquid or gaseous depolarizers, such as SO_2Cl_2 or $SOCl_2$ (1, 2), SO_2 (3), and O_2 (4), has not stopped the search for solid cathode materials for high energy, low rate cells. Indeed, for low rate applications the performances of the latter compare well with those of the former. On the other hand, problems such as safety, material corrosion, and chemical handling, often encountered with the first type of depolarizers, are almost irrelevant for cells based on solid cathodes.

Several new solid materials have been proposed for Li primary cells in the last few years. Two of them, namely, Ag_2CrO_4 (5) and fluorographite (6), are now used in commercial cells. In addition, several interesting compounds, especially chalcogenides, have been examined and some of them show promise of practical utilization (7).

Recently, in this laboratory, the behavior of Bi_2O_3 cathodes in Li button cells has been investigated (8). This oxide has a high specific capacity, *i.e.*, 0.345 A-hr/g for the reduction to Bi, and may be reduced down to Li_3Bi. Also its specific energy is of interest in spite of the relatively low load voltage (1.5V at 0.5 mA/cm^2 to 1.0V cutoff).

Following this line of research, BiF_3 has been subsequently examined. This fluoride has a specific capacity a little lower than that of Bi_2O_3, *i.e.*, 0.302 A-hr/g. On the other hand, Li/BiF_3 cells have higher mean discharge voltages (*ca.* 2.0V) and lower polarization losses at current densities above 1.0 mA/cm^2.

Experimental Aspects

Materials.—BiF_3 was prepared by dissolving Bi_2O_3 in excess hot HF solution. The fluoride tended to precipitate from the above solution, so that it was filtered out, washed to neutral *p*H, and dried at 150°C. During this preparation, BiOF is also reported to be formed (9) through a hydrolysis reaction. We checked with x-ray analysis (see Table I) that our compound was solely BiF_3. No lines attributable to BiOF or any other Bi compounds are present in the diffraction spectrum.

$LiAsF_6$ and $LiPF_6$ were special reagents used without any further purification. $LiClO_4$ was melted under vacuum at 250°C to eliminate residual water (10). $LiAlCl_4$ was prepared by melting at 200°C under N_2 atmosphere equimolecular amounts of predried LiCl and $AlCl_3$ (11).

All the solvents were purified by fractional distillation [propylene carbonate (PC) and butyrolactone (BL) under reduced pressure]. Methyl formate (MF) was distilled over Merck 4Å molecular sieve. The purification of tetrahydrofuran (THF) proved to be critical due to the possible formation of peroxides which could easily attack Li anodes (12). THF was kept several days on $LiAlH_4$, then poured into a still pot containing Li ribbon, and distilled under N_2 atmosphere. Even after this treatment, the Barnes test (13) revealed the presence of some peroxides. However, leaving the distillate in a dry box on lithium ribbon (in the dark) was effective in reducing the peroxide content below a detectable limit. The solvent so purified was stable toward Li.

Cathode preparation.—BiF_3 is a nonconducting material to which additives have to be added to ensure electronic conductivity. Graphite acetylene black, silver, and bismuth were used for this purpose. Some cathodes were prepared by adding binders such as Teflon and polyethylene. With the first binder, it was not necessary to heat the cathodic mixture before pressing the powder into a pellet, due to the cold flow property of Teflon. As for polyethylene, the mixture

Table I. X-ray diffraction data for BiF_3 obtained by methatetic reaction between Bi_2O_3 and HF

Experimental (dA)*	Literature values (dA)†
3.36 (S)	3.38 (VS)
2.91 (MW)	2.93 (S)
	2.62 (MW)
2.06 (S)	2.07 (S)
1.76 (VS)	1.76 (S)
1.69 (W)	1.69 (MW)
	1.63 (MW)
1.46 (W)	1.46 (MW)
	1.42 (MW)
1.34 (MW)	1.34 (MS)
1.31 (W)	1.31 (M)

* VS, very strong; S, strong; MS, medium strong; M, medium; MW, medium weak; W, weak.
† ASTM X-Ray Powder Data File, 11-10.

Key words: Li batteries, BiF_3, nonaqueous solvents, cyclic voltammetry.

was heated at 120°C to allow flowing of the polymer prior to pressing. The cathode pellets (area, 1.26 cm^2) were supported on Ag powder pelletized at 500 kg/cm^2.

Cell assembly and discharge curves.—The cells (of the button type) were built by putting the lithium anode, three layers of a glass fiber separator (Whatman 934 AH) soaked with electrolyte, and the cathode pellet into a Teflon container with stainless steel terminals. Felt, cotton, and porous polypropylene separators were also tested, but unsatisfactory results were obtained. The cells, having capacities typically around 15 mA-hr, were kept in a dry box during the galvanostatic discharges.

Cell polarization curves.—Galvanostatic polarization curves were done on cells similar to those to be discharged by using an apparatus based on a function generator, a potentiostat, and a X-Y recorder. The decrease in cell voltage was recorded in various solutions as a function of the current, which was varied at the rate of 1.2 mA/min.

Cyclic voltammetry.—The working electrode was formed by pressing the test material (BiF_3 + C or Bi) on a tiny Ag net, so as to obtain a planar microelectrode. A Li rod hung to a Ag wire was used as a reference and was separated from the working electrode by a Luggin capillary. A Ag net counterelectrode completely surrounded the cathode material. Potentiostatic *I-V* curves were recorded at the sweep rate of 20 mV/sec.

Solubility.—BiF_3 was kept 10 days in various solutions to ascertain its solubility. After this time, the solutions were filtered and the amount of BiF_3 was titrated with the EDTA technique (14). Thiourea was used as an indicator at *p*H values 1.5-2.0. Blank experiments with known amounts of soluble Bi salts have allowed the accuracy of this technique in the presence of organic solvents to be ascertained.

Compatibility tests.—BiF_3 and organic solutions were put in large test tubes fitted with manometers in order to test the development of a pressure due to decomposition reactions. After a 5 day observation, neither discoloration nor gassing was observed in $LiClO_4$-PC and $LiClO_4$-THF solutions.

X-ray analysis.—The x-ray powder pattern was obtained on BiF_3 and on the discharged cathodes by using Mo Kα radiation filtered by Zr.

Experimental Results

The galvanostatic cell polarizations of Fig. 1 show that BiF_3 may sustain relatively high current densities. In this sense it is superior to Bi_2O_3 which could not be discharged without marked polarization at current densities over 1.0 mA/cm^2 (8). The shape of the curves is not the typical one, *i.e.*, a linear portion followed by a nonlinear drop. This would indicate that the reduction process is not single step, as is later confirmed by the analysis of the discharge curves.

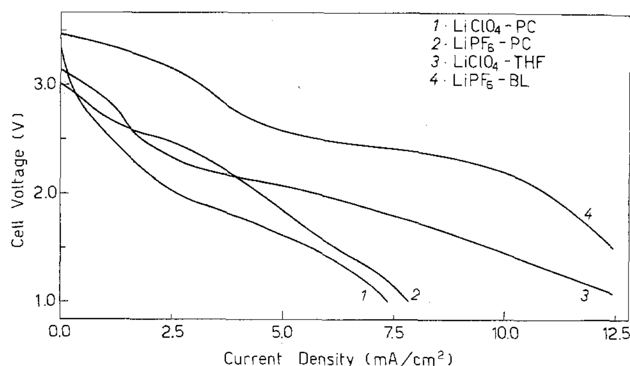

Fig. 1. Cell polarization curves in various electrolytes. Scanning rate. 1.2 mA/min.

Table II reports the effect of various electrolytes on the performance of the Li/BiF_3 cell. Four electrolytes, namely, $LiPF_6$-THF, $LiClO_4$-THF, $LiPF_6$-BL, and $LiClO_4$-PC, give satisfactory results both in terms of capacity and energy. However, the next screening test, *i.e.*, solubility, has allowed us to exclude the suitability of electrolytes containing F^- anions. Indeed, it was found that BiF_3 has no detectable solubility in $LiClO_4$-THF and $LiClO_4$-PC solutions, for the sensitive thiourea test did not show development of the typical yellow color. On the other hand, in $LiPF_6$-PC and in $LiAsF_6$-BL, the solubility of BiF_3 was $1.0 \cdot 10^{-3}$M and $2.2 \cdot 10^{-3}$M, respectively, due to the formation of soluble complexes of the BiF_4^- type. These values would not allow satisfactory shelf life. Therefore, the remainder of this investigation has been restricted to cells containing $LiClO_4$-PC or $LiClO_4$-THF.

The effect of the cathode formulation on cell performance is shown in Table III. Taking the specific energy as a reference parameter, cathodes containing polyethylene+graphite, Teflon+graphite, and more than 10% graphite are the most efficient ones. The specific capacities were only slightly affected by other formulations, but a decrease of potential was observed, this indicating *IR* losses (especially above 1.5V) due to unsatisfactory electronic conductivity. BiF_3, polyethylene+graphite hot pressed cathodes, and BiF_3+10% graphite cathodes were selected for further experiments on the effect of compacting pressure.

In Fig. 2 the variation of the specific capacity as a function of cathodic pressure is reported. In $LiClO_4$-THF solutions, BiF_3+C cathodes are almost insensitive to pressure variations in the range 2000-6000 kg/cm^2. On the other hand, in $LiClO_4$-PC solutions, the performances of BiF_3 cathodes, with or without polyethylene, are largely pressure dependent. These results confirm the importance of the cathode porosity (15) and also stress the interrelation between the porosity and the nature of the solution. This is hardly surprising

Table II. Effect of various electrolytes on the performances of of Li/BiF_3 cells. Current density, 0.5 mA/cm^2. 1.0V cutoff. Compacting pressure, 1500 kg/cm^2

Electrolyte	M	Specific capacity* (A-hr/g)	Mean discharge voltage (V)	Specific energy* (W-hr/g)
$LiClO_4$-PC	1.0	0.21	2.0	0.42
$LiClO_4$-THF	1.3	0.27	1.8	0.49
$LiClO_4$-BL	0.8	0.17	1.8	0.31
$LiClO_4$-MF	2.0	0.16	2.1	0.33
$LiPF_6$-PC	0.5	0.19	1.9	0.38
$LiPF_6$-THF	1.0	0.30	1.9	0.55
$LiPF_6$-BL	1.5	0.26	2.0	0.53
$LiAsF_6$-THF	1.5	0.13	1.8	0.24
$LiAsF_6$-BL	1.5	0.19	1.8	0.34
$LiAlCl_4$-BL	1.0	0.17	1.9	0.32

* Values obtained by dividing the experimental cell performances (A-hr and W-hr) by the weight of BiF_3 (additives excluded).

Table III. Effect of various additives on the performances of Li/BiF_3 cells in $LiClO_4$-PC. Current density, 0.5 mA/cm^2. 1.0V cutoff. Compacting pressure, 1500 kg/cm^2

Additive	Amount (%)	Specific capacity (A-hr/g)	Mean discharge voltage (V)	Specific energy (W-hr/g)
Acetylene black	6	0.21	1.8	0.37
Polyethylene/graphite	5/10	0.25	1.9	0.47
Teflon/graphite	1/9	0.22	2.0	0.43
Bi	10	0.22	1.9	0.41
Ag	10	0.17	1.5	0.25
Graphite	3	0.22	1.5	0.32
Graphite	5	0.21	1.7	0.36
Graphite	10	0.21	2.0	0.42
Graphite	20	0.21	2.0	0.42

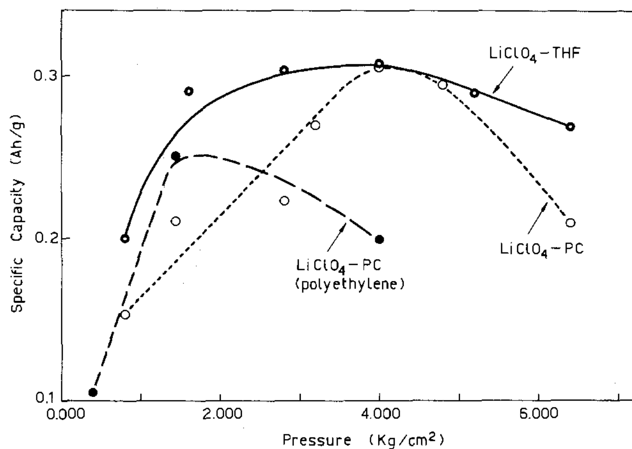

Fig. 2. Dependence of the specific capacity of BiF_3 cathodes on the compacting pressure. Current density, 1.0 mA/cm^2 in $LiClO_4$-THF and 0.5 mA/cm^2 in $LiClO_4$-PC. 1.0V cutoff.

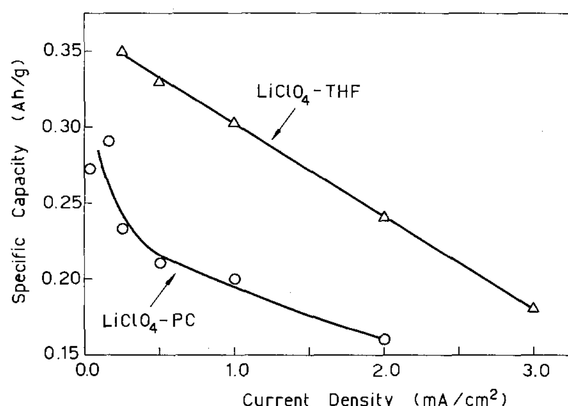

Fig. 3. Dependence of the specific capacity of BiF_3 cathodes on the discharge current density in $LiClO_4$-PC (compacting pressure, 1500 kg/cm^2) and in $LiClO_4$-THF (4000 kg/cm^2). 1.0V cutoff.

when considering that each cathode-electrolyte couple has its own interfacial structure.

Figure 3 shows the decrease of specific capacity as the current density is increased. As expected from the results of the polarization experiments, Li/BiF_3 cells containing $LiClO_4$ (1.3M)-THF solutions behave better in the current range examined. However, the gap between $LiClO_4$-PC and $LiClO_4$-THF is enhanced by the use of a more favorable compacting pressure for the cathodes used in the latter solution.

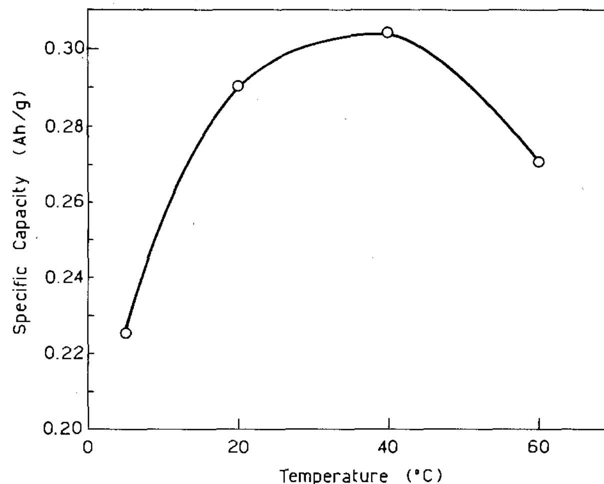

Fig. 4. Dependence of the specific capacity of BiF_3 cathodes on the temperature in $LiClO_4$-PC solutions. Current density, 0.5 mA/cm^2. 1.0V cutoff.

The behavior of Li/BiF_3 cells was also examined in the temperature range 20°-60°C (Fig. 4). Raising the temperature results in an increased capacity due to enhanced mass transfer. In particular, the theoretical value of specific capacity (0.302 A-hr/g) is reached at 40°C. The decrease observed above 40°C may be traced back to mechanical failure of the unoptimized positive electrode (BiF_3 + 10% graphite). Plastic-bonded electrodes should not present this shortcoming.

The effect of the volume of electrolyte was finally investigated in $LiClO_4$-PC solutions. As the electrolyte does not participate in the discharge process, the observed independence of the performances on the number of separator layers had to be expected.

Discussion

The reduction of Bi_2O_3 in organic solutions was found to be a two-step process giving rise to Bi and Li_3Bi, respectively (8). The reduction of BiF_3 leads to the same products. X-ray analysis on BiF_3 cathodes discharged down to 0.9V (Table IV) shows the formation of Bi and LiF through the over-all reaction

$$BiF_3 + 3Li \rightarrow 3LiF + Bi \quad \Delta G = -216 \text{ kcal/mole} \quad [1]$$

In the discharge curves of Fig. 5, an abrupt change in slope occurs around 1.0V, where the formation of Bi is supposed to end. A cell based on reaction [1] has the following characteristic values: E_o, 3.13V; specific

Table IV. X-ray diffraction data for BiF_3 cathodes discharged in $LiClO_4$-PC and $LiClO_4$-THF solutions (to 0.9V cutoff). See Table I for abbreviations

Experimental (dA)		Literature values (dA)		
$LiClO_4$-PC	$LiClO_4$-THF	BiF_3*	Bi**	LiF†
3.28 (M)	3.25 (VS)	3.38 (VS)	3.95 (W)	2.32 (VS)
2.91 (W)	2.32 (S)	2.93 (S)	3.28 (VS)	2.01 (VS)
2.63 (MW)	2.22 (M)	2.62 (MW)	2.38 (M)	1.42 (M)
2.33 (VS)	2.02 (W)	2.07 (S)	2.27 (M)	1.21 (W)
2.02 (S)	1.85 (MW)	1.76 (S)	2.03 (W)	1.16 (W)
1.60 (W)	1.63 (M)	1.69 (MW)	1.97 (W)	1.00 (W)
1.43 (M)	1.48 (W)	1.63 (MW)	1.87 (MW)	0.92 (W)
1.37 (W)	1.42 (MW)	1.46 (MW)	1.64 (W)	0.90 (MW)
1.31 (W)	1.31 (W)	1.42 (MW)	1.49 (W)	0.82 (MW)
1.22 (MS)		1.34 (MS)	1.44 (W)	No more data →
1.17 (MW)		1.31 (M)	1.33 (W)	
1.01 (W)		No more data →	1.31 (W)	
0.93 (M)			1.14 (W)	
0.91 (MW)			1.09 (W)	
0.83 (W)			1.07 (W)	
0.78 (W)			0.98 (W)	
0.69 (W)			0.93 (W)	

* ASTM X-Ray Powder Data File, 11-10.
** ASTM X-Ray Powder Data File, 5-0519.
† ASTM X-Ray Powder Data File, 4-0857.

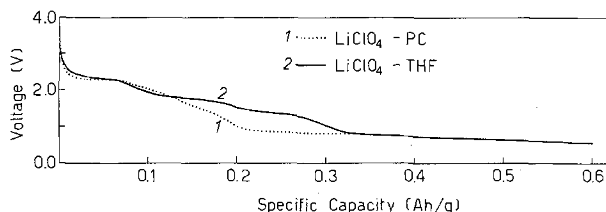

Fig. 5. Discharge curves of Li/BiF_3 cells at 1.0 mA/cm^2. Cathode pressed at 4000 kg/cm^2 for $LiClO_4$-THF (31.4 mg) and 1500 kg/cm^2 for $LiClO_4$-PC (55.6 mg).

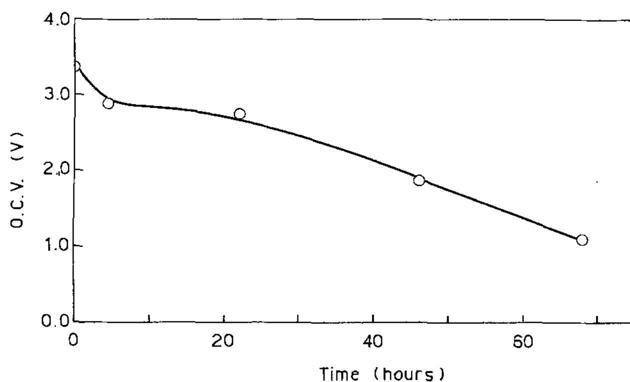

Fig. 6. Open-circuit voltage vs. time of a cell $Li/LiClO_4$-PC/BiF_3, C discharged at 0.16 mA/cm^2.

capacity (referred to BiF_3 only), 0.302 A-hr/g; specific energy (referred to Li + BiF_3), 0.876 W-hr/g.

If reaction [1] gave rise directly to LiF and Bi, these compounds would be in equilibrium with BiF_3, so that an OCV near 3.13V and independent of the state of discharge could be measured. Figure 6 shows that this is not the case for the present system, where the OCV's decrease as a function of discharge, finally reaching values far below 3.13V. X-ray analysis, done on a cathode discharged to 1.7V *vs.* Li/Li^+, confirms these results, showing that BiF_3 only is present as a crystalline phase. This may point to the formation of ternary phase (16) which, for BiF_3, may be written as Li_xBiF_3, where $0 < x < 3$. The final phase Li_3BiF_3 would decompose into Bi and LiF.

The crystalline structure of BiF_3 is not being retained during discharge (see Table IV). According to Whittingham (16), this would exclude reversibility of reaction [1], as was indeed ascertained by cyclic voltammetry experiments.

The shape of the discharge curves in THF-containing solutions is different from that of the curves obtained with all other electrolytes. Indeed, three distinct plateaus are visible in the range 2.5-0.9V, this being independent of the salt used.

The theoretical value of specific capacity is frequently reached in $LiClO_4$-THF solutions. As for $LiClO_4$-PC, the value is approached to optimum conditions, *i.e.*, low current density and medium-low cathode porosity. When working at current densities below 1.0 mA/cm^2 with BiF_3 cathodes pressed at 4000 kg/cm^2 in $LiClO_4$-THF, the theoretical capacity is somewhat exceeded (Fig. 3). The hypothesis of solvent decomposition at the cathode, sometimes observed for low potential values (17, 18), was made and checked by discharges and cyclic voltammetry experiments with graphite cathodes. The discharge curves have shown that above 1.0V decomposition of PC and THF on graphite is of relative importance. This was confirmed by cyclic voltammetry showing the typical spiked trend of solvent reduction only at high scan rates and below 1.0V *vs.* Li/Li^+. The explanation of this apparent discrepancy may reside in the consideration that the positive material formed by slow discharge is neither pure graphite nor the almost pure BiF_3 used in cyclic voltammetry. On the multicomponent cathode material, solvent decomposition may somehow be catalyzed above 1.0V.

The final part of the discharge curves of Fig. 7 is due to the reduction of Bi, according to the reaction

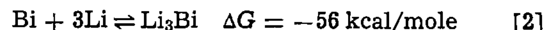

$$Bi + 3Li \rightleftharpoons Li_3Bi \quad \Delta G = -56 \text{ kcal/mole} \qquad [2]$$

This reaction was observed with Bi_2O_3, too, (8) and studied by Besenhard and Fritz (19), who were able to show its reversibility in the cell $Li/LiClO_4$-PC/Bi. Its features are the following: E_o, 0.81V; specific capacity (Bi only), 0.385 A-hr/g; specific energy (Li + Bi), 0.283 W-hr/g. Due to the potential of the Li/Bi couple, some solvent decomposition may also occur. However, we obtained evidence that the plateau below 1.0V in the discharge curve is mainly attributable to reaction [2]. In a first experiment, we discharged $Li/LiClO_4$-THF/Bi cells with and without graphite at the cathode, obtaining the same trend and nearly the same capacity. Cyclic voltammetry on a BiF_3+C electrode in $LiClO_4$-PC (Fig. 7) confirms the reduction of Bi. The peak starting at about 1.0V *vs.* Li/Li^+, to which an anodic peak at about 1.2V *vs.* Li/Li^+ corresponds, is equal to that observed during cyclic voltammetry experiments on a $Li/LiClO_4$-PC/Bi cell. Also with Bi cathode, an anodic peak at *ca.* 1.2V *vs.* Li/Li^+ was observed, thus confirming the results of Besenhard and Fritz (19).

The peak occurring at *ca.* 1.8V *vs.* Li/Li^+ corresponds to the reduction of Bi^{+3} to Bi. In $LiClO_4$-THF solutions, this peak tends to split, thus confirming the trend of the discharge curves.

Obviously, for practical cells only reaction [1] is important. We attempted to see which values of specific capacities and energies (based on the weight of anode, cathode, separators, and solution) could be attained at the end of this reaction. A $Li/LiClO_4$-PC/BiF_3, C cell partially optimized gave 100 A-hr/kg and 200 W-hr/kg at 0.5 mA/cm^2 (1.0V cutoff). These values are expected to increase through a more substantial optimization of the cathode, as may be inferred by Marincic's studies (15). Also the volumetric energies should have interesting values in view of the high density of BiF_3 [8.6 g/cm^3 (20)].

Conclusion

The investigation on BiF_3 as a cathode for lithium cells confirms that some Bi salts may be of interest in this field. BiF_3 has the same advantages shown by other fluorides with respect to the corresponding oxides, *i.e.*, higher voltages and lower polarization losses. Unlike the fluorides investigated heretofore, namely, CuF_2, AgF_2, and NiF_2, BiF_3 does not show an appreciable solubility in $LiClO_4$-containing electrolytes, thus allowing the prediction of a long shelf life for Li/BiF_3 cells. Lack of any interaction with the electrolytes substantiates this prevision.

The major disadvantage connected with the use of BiF_3 resides in its poor voltage regulation, which makes it unsuitable for powering watches or cardiac

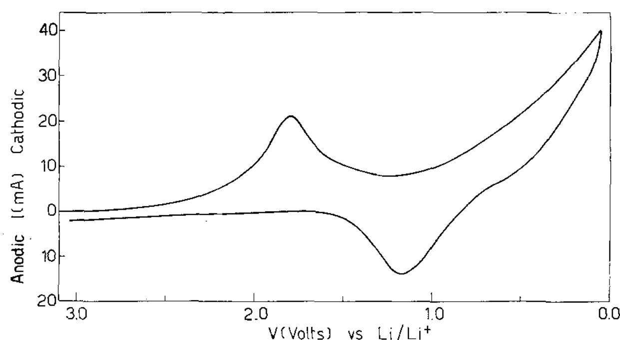

Fig. 7. Cyclic voltammetry of a BiF_3 electrode (with 2% graphite) in $LiClO_4$-PC. Sweep rate, 20 mV/sec.

pacemakers. On the other hand, in terms of energy density, rate capability, safety, and economy, this material seems to merit some attention for possible use in variable-resistance devices.

Acknowledgment

This work was carried out with the financial support of the Consiglio Nazionale delle Ricerche of Italy (C.N.R.). The authors are indebted to Dr. P. Cignini for the x-ray analyses.

Manuscript submitted Aug. 9, 1977; revised manuscript received Nov. 6, 1977.

Any discussion of this paper will appear in a Discussion Section to be published in the December 1978 JOURNAL. All discussions for the December 1978 Discussion Section should be submitted by Aug. 1, 1978.

Publication costs of this article were assisted by the University of Rome.

REFERENCES

1. S. Gilman, in "Proceedings of the 26th Power Sources Conference," p. 28 (1974).
2. N. Marincic, A. Lombardi, and C. R. Schlaikjer, in Proceedings of the 27th Power Sources Conference, p. 37 (1976).
3. P. Bro, H. Y. Yang, C. Schlaikjer, and H. Taylor, in Proceedings of the 10th I.E.C.E.C., Newark, Delaware, 1975, p 432.
4. I. Y. Borg and L. G. O'Connell, *Energy Sources*, **2**, 347 (1976).
5. G. Lehmann, T. Rassinoux, G. Gerbier, and J. P. Gabano, in 8th International Power Sources Symposium, Paper 21, Brighton, England (1972).
6. M. Fukuda and T. Iijima, in 9th International Power Sources Symposium, Paper 45, Brighton, England (1974).
7. G. L. Holleck and J. R. Driscoll, *Electrochim. Acta*, **22**, 647 (1977).
8. P. Fiordiponti, G. Pistoia, and C. Temperoni, *This Journal*, **125**, 14 (1978).
9. J. Mellor, "A Comprehensive Treatise on Inorganic and Theoretical Chemistry," Vol. IX, p. 659, Longmans, Green and Co., London (1952).
10. B. Burrows and R. J. Jasinski, *This Journal*, **115**, 365 (1968).
11. M. B. Rao, *ibid.*, **114**, 13 (1967)
12. J. N. Butler, R. J. Jasinski, D. R. Cogley, H. L. Jones, J. C. Synnott, and S. Carroll, Final Report, Contract No. F 19628-68-C-0056, Tyco (Oct. 1967-Sept. 1970).
13. C. E. Barnes, *J. Am. Chem Soc.*, **67**, 217 (1945).
14. N. H. Furman, "Standard Methods of Chemical Analysis," Vol. I, p. 199, D. Van Nostrand Co., Inc., New York (1962).
15. N. Marincic, *J. Appl. Electrochem*, **6**, 463 (1976).
16. M. S. Whittingham, *This Journal*, **122**, 526 (1975).
17. J. Quobex and J. P. Gabano, *Rev. Gen. Electr.*, **84**, 491 (1975).
18. A. N. Dey and B. P. Sullivan, *This Journal*, **117**, 222 (1970).
19. J. O. Besenhard and H. P. Fritz, *Electrochim. Acta*, **20**, 513 (1975).
20. U. Croatto, *Gazz. Chim. It.*, **74**, 20 (1944).

Analysis of Electrolyte Shunt Currents in Fuel Cell Power Plants

Murray Katz*

United Technologies Corporation, Power Systems Division, South Windsor, Connecticut 06074

ABSTRACT

A general mathematical model is presented for calculating the shunt currents and effective operating potentials of the materials in multicell stacks which have electrolyte interconnections between the individual fuel cells. The analysis takes into account the electrochemical polarizations that occur at the positive and negative ends of each shunt path. Numerical results are presented for an acid electrolyte fuel cell stack design.

Various types of fuel cell power plants use electrolyte or coolant paths interconnected to the individual cells of stacks. Electrolyte circulation is required in some types of fuel cells to distribute dissolved reactants or redox species or to remove reaction products and contaminants. In other fuel cell designs, the interconnected electrolyte is not a necessity, but is a design choice to perform such functions as heat removal, water removal, or to provide tolerance to electrolyte volume changes.

Proper design of these systems requires estimation of the magnitude of the inevitable nonuseful shunt currents through the various liquid paths. In addition, identification of the appropriate electrochemical reactions and effective corrosion potentials of the materials is required at the critical points of the shunt current circuits. This information is needed to assess the magnitude of the power loss, additional reactant consumption, material corrosion, and gas evolution rates, and to conduct tradeoff studies with other design requirements such as pumping power and uniformity of the distribution of fluids.

Previous analysis of such systems [Ref. (1-3)] considered only resistive effects and did not take into account the oxidation-reduction polarization processes that must occur at the positive and negative ends of each shunt path. Although useful for initial estimates of the shunt currents, the models in Ref. (1-3) could not be used to calculate the effective operating potentials of the wall materials since the polarization processes also affect the magnitude of the shunt currents. The purpose of this study was to extend the general mathematical model to include these polarization processes and to develop a general computer program for design purposes. A description of the model and its application to an acid fuel cell stack design is presented.

Theory

A fuel cell stack with interconnected anolyte is shown schematically in Fig. 1 at "open circuit" with respect to its useful load. However, the presence of the high potential across the common electrolyte path results in a set of ionic short circuits which are nonuseful electrical loads on the stack. The ionic current through each fluid port, hereafter called the "shunt current," is the direct result of an electrochemical charge transfer process for which the electrical energy is provided by the fuel cells. The shunt currents through the electrolyte cause a short or current drain on each cell in the stack since all the cells are elec-

* Electrochemical Society Active Member.

Key words: module design, fuel cell assembly, parasitic currents, manifold models, electrical analog.

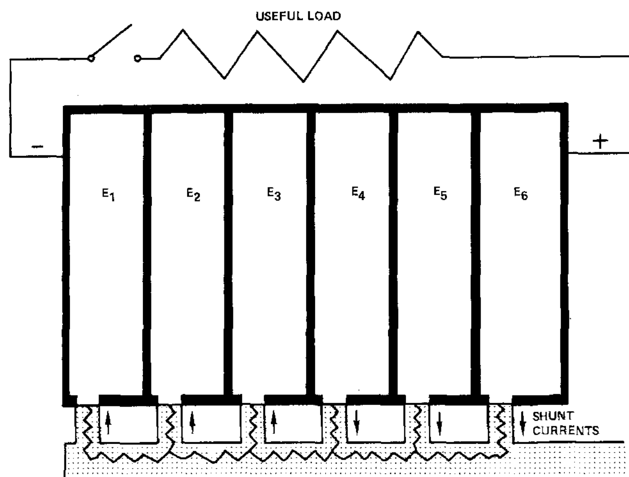

Fig. 1. Shunt paths through interconnected electrolyte

trically connected. The magnitude of the nonuseful current through each of the electrically connected cells is hereafter called the "current drain." The current drain on each cell is a measure of the nonuseful electrical load or additional reactant consumption imposed on each cell as a direct result of the ionic shunt currents through the fluid ports. The current drain on each cell varies with the cell position in the stack, and is a function of the cell voltage, the conductivity of the electrolyte, the ionic resistance of the ports and manifold, and the magnitude of the polarizations of the electrochemical processes involved at the positive and negative ends of each shunt current path. Each shunt current is somewhat dependent on the shunt currents emanating from adjacent cells since the effective ionic resistance of the manifold path is shared.

An electrical analog of the various electronic and ionic paths is shown in Fig. 2 to model the potential distribution of this system. Each cell is schematically represented as a battery with a terminal voltage E and a linear polarization characteristic denoted by a resistance R_c. This should be a good representation of the fuel cell performance with a small current drain. The external load is assumed to be disconnected. The ionic path resistances in the anolyte system are represented by R_p for the fluid distribution ports and R_m for the manifold. It is assumed that the surfaces of the manifold and ports are nonconducting. The conducting surfaces on which the ionic shunt currents exit or enter the cell are schematically represented by an imaginary Zener diode with a polarization characteristic $\phi(I)$ which is different in the forward and backward current direction. The diode simulates the different polarizations for the anodic reactions at the positive end of the cell stack and the cathodic polarizations at the negative end of the cell stack. For example, the polarization characteristic $\phi(I)$ for the decomposition of water is shown in Fig. 3. This fulfills the requirement of essentially zero current flow until the Nernst potential ϕ_o is exceeded (*e.g.*, 1.23V for water electrolysis).

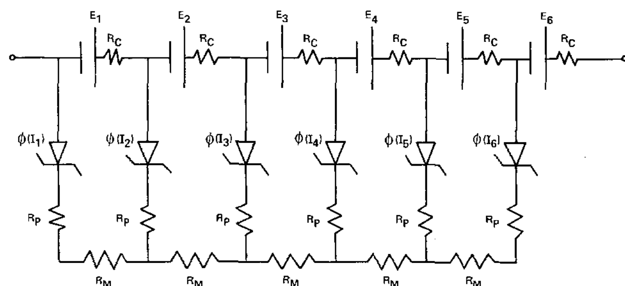

Fig. 2. Electrical analog of fuel cell stack

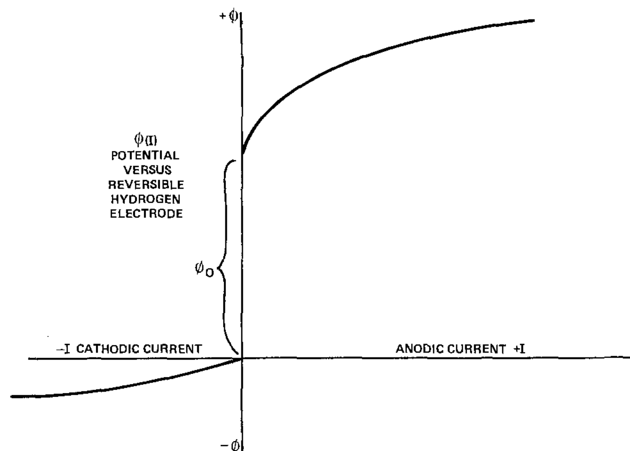

Fig. 3. Polarization function for decomposition of water

The mathematical solution of the individual shunt currents, I_j, depends on specifying the information for the polarization characteristic $\phi(I)$. This requires identification of the possible reactions at the reaction sites and prior experimental data or theoretical estimation of the polarization for the particular design being studied.

Typical anodic reactions at the positive end of the cell assembly are:

(*i*) Material corrosion
$M \rightarrow M^+ + e$
$C + 2H_2O \rightarrow CO_2 + 4H^+ + 4e$

(*ii*) Electrolysis of H_2O to O_2
$H_2O \rightarrow \frac{1}{2} O_2 + 2H^+ + 2e$

(*iii*) Oxidation of fuel
$H_2 \rightarrow 2H^+ + 2e$

(*iv*) Oxidation of ionic species
$M^z \rightarrow M^{z+n} + ne$

(*v*) Combinations of the above.

Some of the possible cathodic electrochemical reactions at the negative end of the cell assembly are:

(*i*) Electrolysis of H_2O to H_2
$2H^+ + 2e \rightarrow H_2$

(*ii*) Metal deposition
$M^+ + e \rightarrow M$

(*iii*) Reduction of O_2 (air)
$\frac{1}{2} O_2 + 2H^+ + 2e \rightarrow H_2O$

(*iv*) Reduction of ionic species
$M^{z+n} + ne \rightarrow M^z$

(*v*) Combinations of the above.

As an example of the application of this approach to an engineering design, let us consider the probable reactions and polarizations we might expect in a multicell assembly of acid electrolyte cells using carbon as a structural material and with an interconnected anolyte. A design of this type was considered for development by United Technologies Corporation early in the TARGET program but was dropped in favor of designs which preclude shunt currents. The polarization characteristic of a carbon surface exposed to a hydrogen-saturated anolyte, Fig. 4, shows schematically that three anodic electrochemical reactions occur as the potential difference between the carbon surface and the electrolyte varies from 0.0 to 2.0V. A small current due to hydrogen oxidation is possible in the potential range from 0 to 1.0V (*vs.* a reversible hydrogen electrode) because carbon is a poor hydrogen oxidation catalyst. Between 1.0 and 1.4V, a larger anodic current

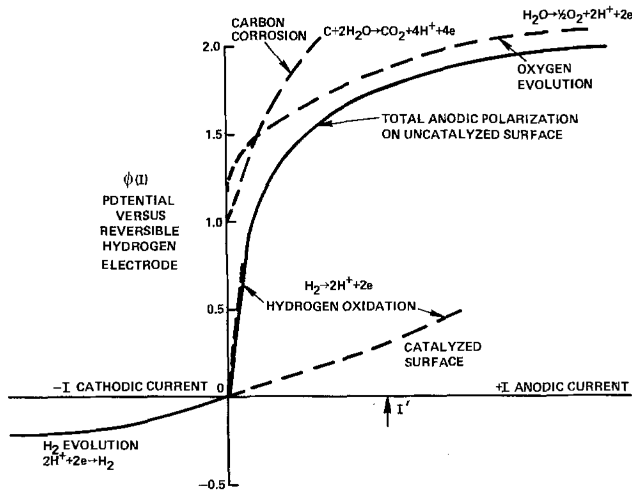

Fig. 4. Typical electrochemical reactions on a carbon surface with hydrogen present.

is possible from carbon oxidation whereas above 1.4V most of the current is due to oxygen evolution even though the carbon oxidation current continues to increase. Alternatively, if the carbon surface is catalyzed with platinum, the anodic current will be much higher at low potential since platinum is an excellent hydrogen oxidation catalyst.

Thus, it can be seen that the likelihood of carbon oxidation at the positive end of the stack assembly is dependent on the magnitude of the anodic shunt current and the nature of the surface. For example, a shunt current of magnitude I' will result in oxidation of uncatalyzed carbon surfaces, but no oxidation should occur with catalyzed carbon surfaces since the rate of hydrogen oxidation is sufficient to maintain the carbon in a safe potential region.

The likely cathodic electrochemical reaction associated with the shunt currents in the cells at the low potential end of the cell assembly is hydrogen evolution since no oxygen or air is present in the anolyte. Large cathodic currents are shown in Fig. 4 since carbon is a fairly good catalyst for hydrogen evolution. No carbon oxidation is expected at the negative ends of the shunt current circuits.

Mathematical Analysis

Application of Ohm's and Kirchoff's laws to the electrical network of an assembly of N fuels cells shown in Fig. 2 will yield N simultaneous equations with N unknown shunt currents. Consider the simple case of a four-cell stack shown in Fig. 5 where the ionic shunt currents $I_1, I_2, \ldots, I_N$ are defined as positive although it is quite evident that most of the shunt currents at the negative end will be in the reverse direction.

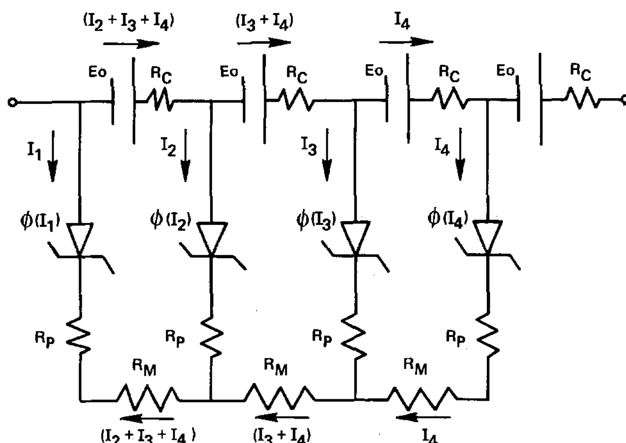

Fig. 5. Electrical analog of four-cell stack

Application of Kirchoff's law yields the first equation for $N = 4$

$$\sum_{j=1}^{j=4} I_j = 0 = I_1 + I_2 + I_3 + I_4$$

Three more equations may be written by applying Ohm's law to each loop starting at the zero voltage end of the network each time. For a four-cell stack, these equations are

$$E_o - \phi(I_2) + \phi(I_1) = -I_1R_p + I_2(R_p + R_c + R_m) + I_3(R_c + R_m) + I_4(R_c + R_m)$$

$$2E_o - \phi(I_3) + \phi(I_1) = -I_1R_p + I_2(R_c + R_m) + I_3(R_p + 2R_c + R_m) + I_4(2R_c + 2R_m)$$

$$3E_o - \phi(I_4) + \phi(I_1) = -I_1R_p + I_2(R_c + R_m) + I_3(2R_c + 2R_m) + I_4(R_p + 3R_c + 2R_m)$$

In order to use standard matrix techniques for solving N simultaneous equations, it is desirable to keep the equations linear. Thus, the polarization function $\phi(I)$, which is typically nonlinear, can be approximated by a series of straight lines.

$$\phi(I_j) = a_j + b_jI_j$$

where a_j and b_j represent the intercept and slope of the linear section containing I_j. Substituting the linear expression for the polarization and letting $R_m + R_c = R_{mc}$ produces the following set of four simultaneous equations for the four-cell stack of fuel cells

$$0 = I_1 + I_2 + I_3 + I_4$$

$$[1E_o - a_2 + a_1] = -I_1(R_p + b_1) + I_2(R_p + R_{mc} + b_2) + I_3R_{mc} + I_4(R_{mc})$$

$$[2E_o - a_3 + a_1] = -I_1(R_p + b_1) + I_2(R_{mc}) + I_3(R_p + 2R_{mc} + b_3) + I_4(2R_{mc})$$

$$[3E_o - a_4 + a_1] = -I_1(R_p + b_1) + I_2(R_{mc}) + I_3(2R_{mc}) + I_4(R_p + 3R_{mc} + b_4)$$

The general solution for N cells with $j = 1,2,\ldots,N$ shunt currents I_j can be written in terms of $i = 1,2,\ldots,N$ linear algebraic equations of the general form.

Equation $i = 1$

$$\sum_{j=1}^{j=N} I_j = 0$$

Equations $i = 2 \ldots\ldots N$

$$[(i-1)E_o - a_i + a_1] = [-(R_p + b_1)]I_1 + [R_p + (i-1)R_{mc} + b_i]I_i + \sum_{\substack{j=2 \\ i>2}}^{j=i-1} [(j-1)R_{mc}]I_j + \sum_{j=i+1}^{j=N} [(i-1)R_{mc}]I_j$$

A computer program was developed to solve for the unknown shunt current I_j in the above set of N simultaneous linear equations. The computer program employs a general usage computer subprogram which uses the Gauss-Jordan reduction scheme with the maximum pivot criterion to solve the equations. The computer program internally computes the matrix coefficients from the above general equations, thus requiring only E_o, N, R_m, R_c, and R_p and $\phi(I)$ as input items. The anodic and cathodic polarization data are input as a table and the slope and intercepts are

automatically calculated assuming a straight line between each pair of data points.

An iteration procedure is required in the computer solution because the polarization $\phi(I)$ is not known *a priori*. The calculation is initiated by computing the shunt currents with zero polarization by setting the polarization function constants a and b equal to zero. This establishes a first guess for the polarization function constants a and b to be used for each shunt current. A new array of coefficients is calculated and the shunt currents are recalculated until all the polarization constants remain unchanged from the last calculated value of the shunt currents. When the iteration is concluded, the polarization and shunt current at each cell are printed out.

The current drain in each fuel cell can be seen by inspection of Fig. 5 to be equal to the ionic current in the electrolyte manifold of the same cell. The current drain $(I_D)_n$ of the nth cell in a stack with N cells can be calculated from the shunt currents I_j from the following expression which holds for all cells except the (N)th or end cell which has no current drain

$$(I_D)_n = \sum_{j=n+1}^{j=N} I_j \text{ or } = \sum_{j=1}^{j=n} I_j$$

The average current drain per cell in a stack of N cells may be expressed as

$$\overline{I}_D = \sum_{n=1}^{n=N-1} (I_D)_n/N$$

The quantity $\overline{I}_D$, by Faraday's law, is proportional to the average quantity of reactants consumed by the fuel cells as a result of the shunt currents. The average power loss per cell, P_D, is then

$$\overline{P}_D = E_o \cdot \overline{I}_D - \overline{I}_D{}^2 R_c$$

The mathematical model can be used with or without the external load connected. When the external load is connected the appropriate values of cell voltage E and the effective over-all cell resistance R_c are required from the fuel cell performance curve. The model can also be applied to an interconnected catholyte system simply by reversing the sign of the fuel cell potential.

Application of the Mathematical Model

The mathematical model was used to predict the shunt currents and effective wall potentials of the carbon structural materials in an experimental 50 cell assembly of phosphoric acid cells with interconnected anolyte reservoirs which was being considered for development as a power plant component. The anode compartment side of the carbon plate which separates the cells of this stack is shown in Fig. 6. The electrolyte reservoir was located in the bottom section of the anode compartment of each cell in the space between the bottom ribs of the carbon plates and an uncatalyzed extension of the hydrogen electrode. The manifold and branch feed ports were designed to provide a high ionic resistance path and were coated with an electrically nonconducting resin to prevent electrochemical reaction. The electrolyte in each cell was connected through the manifold to a reservoir external to this stack. A mathematical analysis of this configuration was conducted to determine the current drain on the stack and to estimate the probability of carbon oxidation.

The contact bars in the pool region offer significant resistance to ion flow and this resistance is in series with the port resistance. It was assumed that the shunt currents originate primarily from the reservoir region near the feed port. An average ionic path length on each side of the port was estimated and this ionic

Fig. 6. Anode side of fuel cell separator plate

resistance, called the field resistance, was added to the actual port resistance to obtain the effective port resistance R_p. The following resistances were calculated for this design using a resistivity of 2.22 Ω-cm for 96% H_3PO_4 at 135° C: manifold resistance $R_m = 21.3\Omega$; port resistance, 113Ω; field resistance, 61Ω; effective port resistance, $R_p = 113 + 61 = 174\Omega$.

The effective cell resistance is obtained from the slope of the voltage-current characteristic which is typically nonlinear for hydrogen-air fuel cells. The effective cell resistance for this design varies from 0.002 to 0.02Ω depending on the external load and was considered to be negligible compared to the manifold and port resistances.

The polarization data for input to the computer program was obtained experimentally. A representative section of the hydrogen electrode was tested in a half-cell apparatus containing a hydrogen reference electrode. A strip ½ in. wide was immersed ½ in. into phosphoric acid electrolyte with hydrogen above the electrolyte to simulate the hydrogen saturated reservoir. Since the active width in the cell design being studied was ten times greater than the test sample, the current obtained at any given polarization was appropriately scaled.

The experimental anodic and cathodic polarization data used in the computer analysis are presented in Fig. 7. The anodic current data for the uncatalyzed carbon electrode show virtually no hydrogen oxidation in the potential range from zero to 1.0V, but carbon oxidation and oxygen evolution proceed rapidly at high overvoltage. A carbon strip catalyzed with trace quantities of platinum was also tested to compare with the uncatalyzed strip. The anodic current data shown in Fig. 7 for the catalyzed strip indicates significant hydrogen oxidation compared to the uncatalyzed carbon strip. The cathodic polarization data indicates that the rate of hydrogen evolution is much faster than the rate of hydrogen oxidation on carbon.

The polarization data shown in Fig. 7 and the calculated resistances presented above were used as input in the computer program. The calculated results of the current drain in each cell, ionic shunt currents

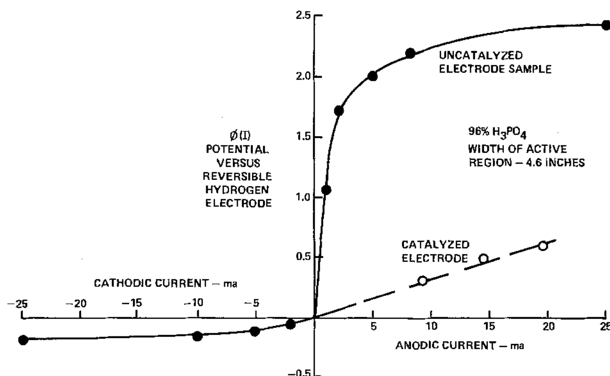

Fig. 7. Polarization data on carbon electrode in phosphoric acid

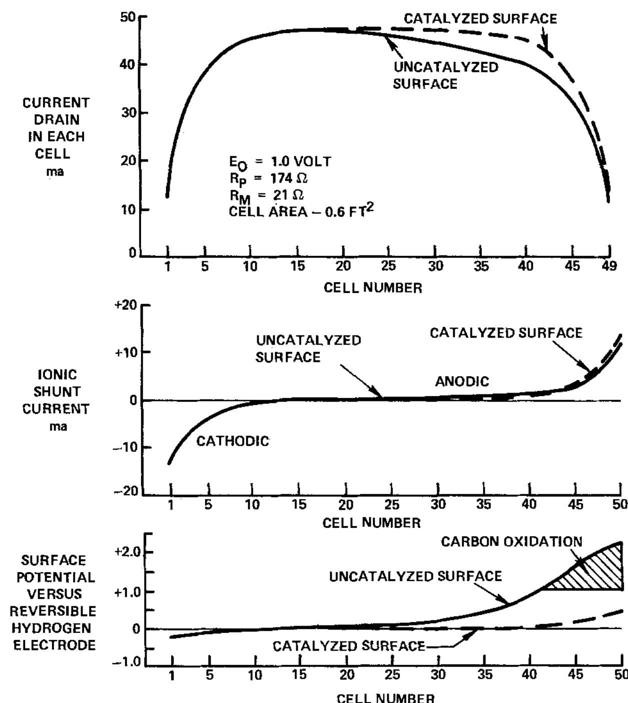

Fig. 8. Calculated results for a 50 cell stack

through the liquid ports, and the effective material potential as a function of cell position are shown in Fig. 8 for the 50 cell assembly of phosphoric acid cells. The calculated results are presented for the cases of uncatalyzed carbon and catalyzed carbon surfaces in the reservoir region to demonstrate the effect of the nature of the surface material on the polarization processes.

The calculated results indicate that the largest shunt currents occur through the electrolyte in the ports at the ends of the stack while the largest current drain occurs in the center cells of the stack. Thus, the rates of electrochemical reactions ocurring in the pool region are highest in the end cells whereas the reactant consumption is highest in the center cells of the stack. The shunt currents from the cells in the center portion of the stack are practically zero because of the balanced or low potential gradients between the surface and the electrolyte.

The calculated magnitude of the current drain on the 50 cell stack is very small and represents a negligible loss of power. For example, the maximum current drain which occurs on the center cell was calculated to be only 47 mA, which represents a current density of only 0.078 A/ft^2 based on the cell area of 0.6 ft^2. This value is calculated when the stack is at open external circuit and the cell voltage is the highest; approximately 1.0V per cell. When the external load is applied, the stack voltage is lower and the current drain will be proportionately lower.

The calculations predict that carbon oxidation should occur on the uncatalyzed carbon surfaces in the pool region of cells 41-50 since the effective surface potential in these cells falls in the range of 1.0-2.2 V *vs.* a reversible hydrogen electrode. The calculated results of the surface potential for catalyzed surfaces indicate that no carbon oxidation should occur since the rate of hydrogen oxidation is sufficient to maintain the carbon in a safe potential region. At the negative end of the stack hydrogen evolution is predicted in cells 1-10. A dielectric coating is required in the port and manifold region to prevent electrochemical reactions. It was calculated that a potential difference as high as 4.7V can exist across the coating in the manifold region of the cells at the positive end of the stack. Any slight dielectric breakdown of the coating in the most positive end cells is likely to result in simultaneous material oxidation and oxygen evolution which would further destroy the coating. Since any corrosion of structural components is inconsistent with the long life requirement for commercial fuel cell power plants, the interconnected anolyte design has not been considered for commercial development.

The mathematical model described above may be applied to many types of fuel cell power plants. Some examples are (*i*) circulating base electrolyte fuel cells (*ii*) circulating hydrazine or peroxide fuel cells, and (*iii*) circulating redox energy storage systems. In each case, the impact of the electrochemical processes occurring on the materials of construction at the critical points of the shunt current circuits can be evaluated with this mathematical model. In addition, the magnitude of the power loss due to the shunt currents through the electrolyte can be calculated for a specific design.

Conclusions

A general mathematical model has been developed for calculating the electrolyte shunt currents and effective operating potentials of the materials in multicell assemblies with interconnected electrolyte. The analysis takes into account the electrochemical polarizations at the positive and negative ends of each shunt current path. By linearizing the polarization function, the mathematical model is reduced to the solution of N simultaneous linear equations for an assembly of N cells.

In the application of this model to an aqueous acid electrolyte fuel cell power plant, some general observations can be made. The maximum electrolyte shunt currents usually occur in the end cells of the stack where the greatest potential gradient exists. This results in a current drain in all the cells, with the largest current drain occurring in the center cells of the stack. Material corrosion and oxygen evolution processes are likely to occur in the cells at the positive end of the stack unless another oxidation process is available to maintain the materials at a low potential level. Hydrogen evolution is the likely electrochemical process at the critical points of the shunt currents in the end cells at the negative end of the stack in the absence of other reducing agents. By proper design of the ionic resistance of the manifold and feed ports, the power loss due to electrolyte shunt currents can be maintained at very low levels.

Acknowledgment

The author wishes to thank Mrs. Linda S. Hoeffer for her valuable effort in developing the computer program.

Manuscript submitted June 13, 1977; revised manuscript received Oct. 7, 1977. This was Paper 390 presented at the Philadelphia, Pennsylvania, Meeting of the Society, May 8-13, 1977.

Any discussion of this paper will appear in a Discussion Section to be published in the December 1978 JOURNAL. All discussions for the December 1978 Discussion Section should be submitted by Aug. 1, 1978.

Publication costs of this article were assisted by United Technologies Corporation.

REFERENCES

1. Wright-Patterson Air Force Base Technical Documentary Report ASD-TDR-62-1044 (1963).
2. I. Rousar, *This Journal*, **116**, 676 (1969).
3. I. Rousar and V. Ceznar, *ibid.*, **121**, 648 (1974).

Measurement of Battery Separator Resistances in Low Impedance Conductivity Cells by A-C Bridge Techniques

W. P. Kilroy* and C. T. Moynihan

Naval Surface Weapons Center, Electrochemistry Branch, White Oak, Silver Spring, Maryland 20910

ABSTRACT

Measurement of the resistance of battery separator membranes is frequently accomplished by taking the difference between the resistances of an electrolyte-filled conductivity cell with and without the separator inserted between the electrodes. For low resistance separators this may involve measurements of impedances of a few tenths of an ohm. It is shown via equivalent circuit analysis and experimental data on a low impedance cell filled with 45% aqueous KOH solution that a-c bridge measurements of separator resistances can be seriously in error if proper account is not taken of electrode impedance.

Efforts to improve battery performance are often centered on the development of a stable separator which contributes relatively little to the internal resistance. An approximate measure of the contribution of a separator material to the battery internal resistance is typically made (1) first by determining the resistance of the electrolyte solution, R_{sol}, between two plane parallel electrodes in a conductivity cell. After this the separator is inserted between the two electrodes and a new resistance, a combination of R_{sol} and the separator resistance, is measured. The contribution of the separator, R_{sep}, to the net resistance of the cell is then the difference between the two measurements. Plainly an accurate measurement of R_{sep} requires that R_{sep} contribute an accurately measurable increment to the sum of the resistances.

A case in point for the present paper is a separator for silver-zinc batteries using 30-45% KOH solution as electrolyte in which a good separator material may contribute as little as 0.01 Ω/in.^{2} to the internal resistance. An accurate measurement of R_{sep} thus requires that R_{sol} be of the order of 0.1 Ω/in.^{2} or smaller.

The usual method of carrying out resistance measurements of this type is by means of a conventional a-c Wheatstone bridge at audio frequencies. The cell impedance is balanced against a parallel resistance-capacitance combination (R_p, C_p). The balancing resistance R_p is usually identified with the cell resistance, R_{sol} or ($R_{sep} + R_{sol}$). As has been pointed out in the literature (2), the equivalent a-c circuit of the cell is not a parallel resistance-capacitance combination. This in turn can lead to large errors in the measurement of R_{sol} and ($R_{sep} + R_{sol}$), as shown below.

The simplest approximations (2) to the true equivalent circuits of a low impedance conductivity cell containing an electrolyte and an electrolyte plus separator are the series circuits shown, respectively, in Fig. 1a and 1b. R_L is the resistance of the leads between the bridge and conductivity cell, and C_{dl} represents the capacitance due to interfacial effects at the electrode surfaces (frequently referred to as "double layer capacitance").

If the circuit of Fig. 1a were measured on an a-c bridge, the equivalent parallel resistance would be (2)

$$R_p^{(a)} = \frac{1}{Re(1/Z^{(a)})} = \frac{(R_L + R_{sol})^2 + (1/\omega C_{dl})^2}{R_L + R_{sol}} \quad [1]$$

where $Re(1/Z^{(a)})$ is the real part of the complex impedance of circuit 1a. In the usual procedure for determination of the separator resistance using a conventional a-c bridge, the apparent resistance would be taken to be

$$R_{sep,\,app} = \frac{1}{Re(1/Z^{(b)})} - \frac{1}{Re(1/Z^{(a)})}$$

$$= R_{sep}\left[1 - \frac{1}{(R_L + R_{sol} + R_{sep})(R_L + R_{sol})(\omega C_{dl})^2}\right] \quad [2]$$

Equations [1] and [2] show that $R_p^{(a)} = R_L + R_{sol}$ and $R_{sep,\,app} = R_{sep}$ only in the limit of large values of ωC_{dl}. That is, neglect of a proper treatment of electrode impedances can lead to errors not only in the total resistance of the cell, but also to errors, in R_{sep} obtained

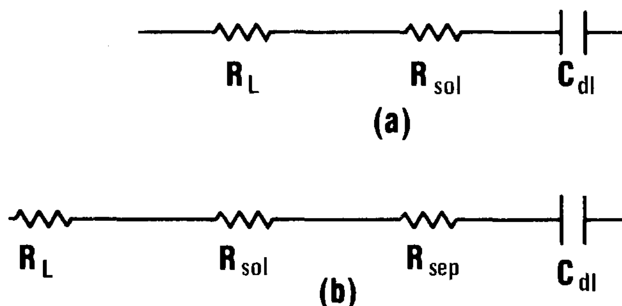

Fig. 1. Approximate equivalent circuits of a conductivity cell containing (a) electrolyte solution; (b) electrolyte solution plus separator.

* Electrochemical Society Active Member.

Key words: capacitance, resistivity, battery separator.

by difference. However, a correct determination of $(R_L + R_{sol})$ should guarantee a correct determination of R_{sep}. Consequently, in the present study we have carried out a series of resistance and capacitance measurements at various frequencies in order to determine what errors, if any, may arise in determinations of separator resistances for cells with 45% KOH electrolyte.

Experimental Section

The conductivity cell obtained from RAI Research Corporation consisted of two heavy gauge plane parallel square Pt electrodes, 2.54 cm on a side and 0.25 cm apart mounted in a Lucite holder. The cell also contained a provision for inserting film between the two electrodes. This feature was not used in the present study.

In order to assess the effect of electrode double layer capacitance, measurements were carried out for two electrode conditions; polished unplatinized platinum and heavily platinized electrodes.

The assembled cell was filled with Fisher Scientific 45 weight percent (w/o) aqueous KOH solution and allowed to stand overnight, refilled with fresh solution and the equivalent parallel resistance and capacitance, R_p and C_p, and measured at 25.0° ± 0.1°C over the frequency range 50-5000 Hz. Resistance measurements (accuracy 1%) were made using a General Radio 1650B impedance bridge with an external capacitance balancing decade box adjustable in steps of 10^{-4} μF and an external Hewlett Packard 200 CD audio oscillator.

A similar set of measurements of R_p and C_p were made at 25°C with the conductivity cell with platinized electrodes filled with 0.01M KCl aqueous solution in order to obtain the calibration constant for the cell. To obtain the resistance of the leads to the cell, R_L, the cell was filled with mercury to short circuit the two electrodes and the resistance measured; this gave a value of $R_L = 0.173\Omega$.

A calibrated capillary conductivity cell with platinized platinum electrodes was used to measure the conductivity of the 45% KOH solution. The equivalent parallel resistance of this cell filled with the KOH solution was 47.9Ω at 25.0°C and 1 kHz.

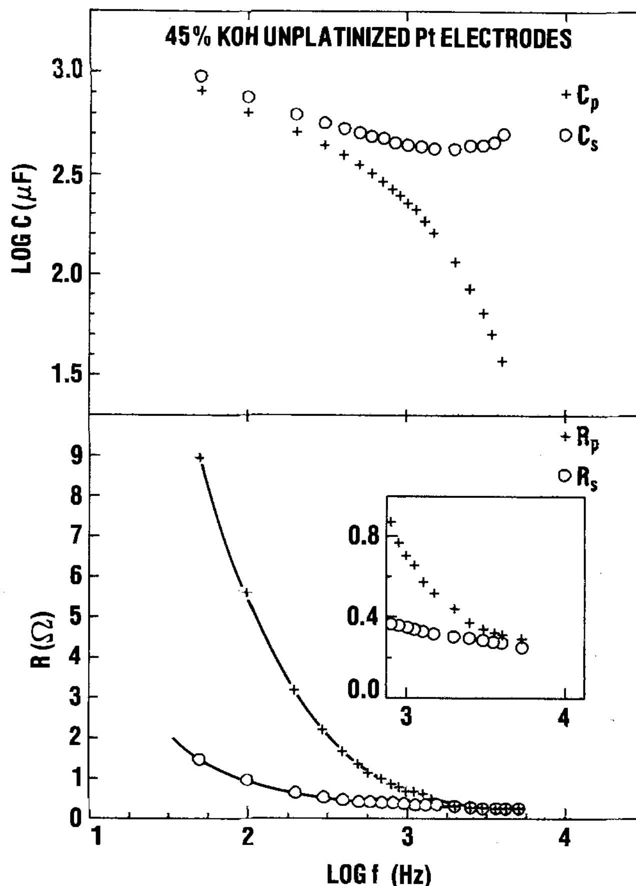

Fig. 2. Equivalent parallel and series resistances and capacitances vs. frequency of a conductivity cell filled with 45% KOH solution at 25.0°C using unplatinized Pt electrodes. Insert is an enlarged plot of the resistance data at high frequency.

Results and Discussion

The resistance, R_p, of the cell filled with 0.01M KCl solution was 27.5 ± 0.1Ω and independent of frequency over the entire frequency range. This indicates (*cf.* Eq. [1]) that contributions to R_p from frequency-dependent electrode impedance terms such as $(1/\omega C_{dl})$ are negligible, so that $(R_L + R_{sol})$ may be taken as the measured R_p value. Subtracting the measured value of R_L from this gives $R_{sol} = 27.3\Omega$. The cell constant, (L/A), obtained using the conductivity of 0.01M KCl solution (3), is 0.0386 cm^{-1}, which is in good agreement with the less precise (L/A) value of 0.039 cm^{-1} calculated from the electrode geometry.

$$R_s = R_L + R_{sol} + \frac{\{[R_F + R_W(\omega)]^2 + [1/\omega C_W(\omega)]^2\}[R_F + R_W(\omega)]}{[R_F + R_W(\omega)]^2 + \{\omega C_{dl}[(R_F + R_W(\omega))^2 + [1/\omega C_W(\omega)]^2] + (1/\omega C_W(\omega))\}^2} \quad [3]$$

Similarly the resistance R of the 45% KOH solution in the capillary conductivity cell is sufficiently large that it may be used directly to calculate the conductivity, 0.465 Ω^{-1} cm^{-1}, of the 45% KOH solution at 25°C.

In Fig. 2 and 3 the bridge measurements of R_p and C_p, respectively, are plotted *vs.* frequency for the 45% KOH solution in the conductivity cell with unplatinized and platinized electrodes. Also plotted are the equivalent series resistance R_s and capacitance C_s calculated from the complex admittance (2).

If the circuit of Fig. 1a were an accurate representation of the cell equivalent circuit, R_s and C_s would be frequency independent and equal, respectively, to $(R_L + R_{sol})$ and C_{dl}. R_s and C_s are frequency dependent, but are less so than R_p and C_p, so that the equivalent circuit of Fig. 1a is clearly a better approximation to the cell circuit than a parallel R_p, C_p combination.

A more realistic representation (2, 4, 5) of the equivalent cell circuit is shown in Fig. 4. $R_W(\omega) + C_W(\omega)$ are the resistive and capacitive components of the Warburg impedance, and R_F is the Faradaic impedance. In Fig. 4 we have neglected capacitance between the conductivity cell leads and the capacitance due to the dielectric constant of the electrolyte, since these contribute a negligible amount to the audio frequency impedance of the low impedance cell under consideration (2).

Equivalent circuit analysis of Fig. 4 gives for the equivalent series resistance [3].

Both $R_W(\omega)$ and $(1/\omega C_W(\omega))$ are frequency dependent with an $\omega^{-1/2}$ dependence (4), so that the high frequency limit of R_s is

$$\lim_{\omega \to \infty} R_s = R_L + R_{sol} \quad [4]$$

Equivalent circuit analysis of Fig. 4 shows that R_p approaches an identical high frequency limit, but at a slower rate (compare Eq. [1]).

The data of Fig. 2 and 3 exhibit this predicted behavior, that is: (*i*) both R_s and R_p approach the same limiting value at high frequencies, R_s more quickly than R_p; and (*ii*) the resistance values for both platinized and unplatinized electrodes approach the same frequency limit.

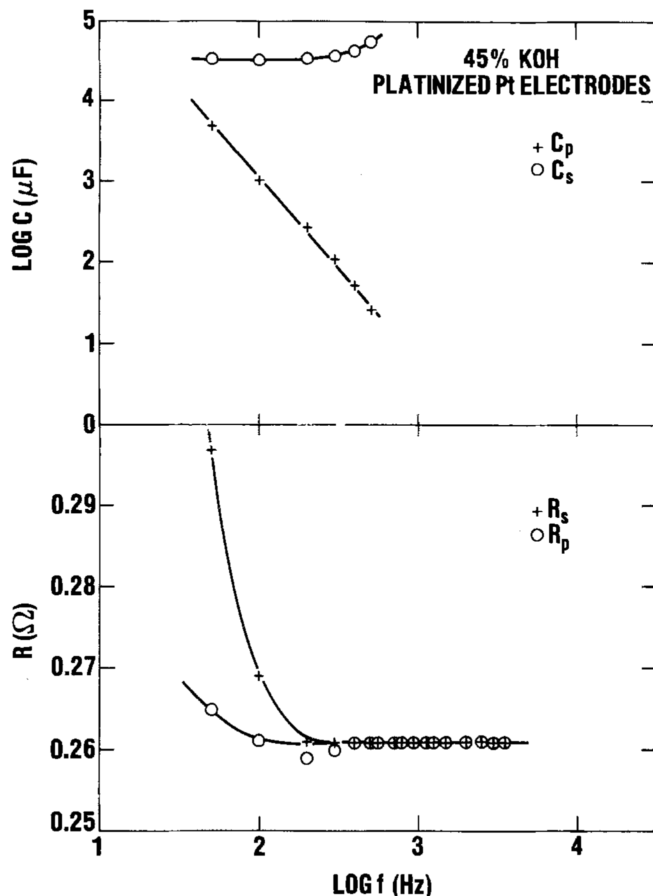

Fig. 3. Equivalent parallel and series resistances and capacitances vs. frequency of a conductivity cell filled with 45% KOH solution at 25.0°C using platinized Pt electrodes.

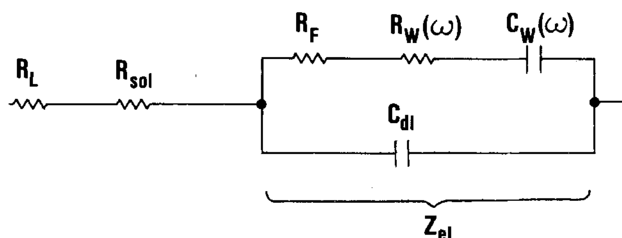

Fig. 4. Equivalent circuit of conductivity cell containing electrolyte

We may take the observed limiting high frequency value of $R_s = 0.261\Omega$ for the platinized electrodes and identify it with $(R_L + R_{sol})$. This agrees within experimental error with the value of $(R_L + R_{sol}) = 0.256\Omega$ calculated from the independently measured values of R_L, (L/A), and the conductivity of the 45% KOH solution.

Conclusions

One may obtain correct measurements of $(R_L + R_{sol})$ and of $(R_L + R_{sol} + R_{sep})$ and therefore of R_{sep} by audio frequency a-c bridge measurements on low impedance conductivity cells only if some precautions are observed. With platinized electrodes (cf. Fig. 3), R_p and R_s reach their limiting high frequency values only at the higher frequency end of the audio range, therefore, it is plainly not sufficient to make a measurement of R_p at a single frequency and assume it equal to $(R_L + R_{sol})$ or $(R_L + R_{sol} + R_{sep})$. Rather it is recommended that for low impedance cells, R_p and C_p measurements be made as a function of frequency, that R_s be calculated from R_p and C_p, and that the limiting high frequency value of R_s be identified with $(R_L + R_{sol})$ or $(R_L + R_{sol} + R_{sep})$. Platinized electrodes should be used, since their use leads to the approach of R_s to its limiting value within the observable frequency range (Fig. 3), while unplatinized electrodes may require extrapolation of R_s beyond the audio range in order to obtain the high frequency limit.

Manuscript submitted Sept. 15, 1977; revised manuscript received Nov. 21, 1977.

Any discussion of this paper will appear in a Discussion Section to be published in the December 1978 JOURNAL. All discussions for the December 1978 Discussion Section should be submitted by Aug. 1, 1978.

Publication costs of this article were assisted by the Naval Surface Weapons Center.

REFERENCES

1. A. J. Salkind and J. J. Kelley, in "Characteristics of Separators for Alkaline Silver Oxide Zinc Secondary Batteries—Screening Methods," J. E. Cooper and A. Fleisher, Editors, pp. 69-75, Air Force Aero Propulsion Laboratory, WPAFB, Ohio (1964).
2. J. Braunstein and G. D. Robbins, *J. Chem. Educ.*, **48**, 52 (1971).
3. R. A. Robinson and R. H. Stokes, "Electrolyte Solutions," p. 466, Butterworths, London (1965).
4. G. J. Hills and S. Dordjevic, *Electrochim. Acta.*, **13**, 1721 (1968).
5. G. D. Robbins, *This Journal*, **116**, 813 (1969).

Electroless Gold Metallization for Polyvinylidene Fluoride Films

L. M. Schiavone

Bell Laboratories, Holmdel, New Jersey 07733

ABSTRACT

A method for metallizing polyvinylidene fluoride films with gold has been developed using an electroless plating process.

Metallized polyvinylidene fluoride (PDVF) has been found to be a good material for making piezoelectric devices once it has been poled. For this purpose, poled and aluminized PVDF is commercially available, but due to the rapid oxidation of the aluminum it is very difficult to make contact to it.

This paper describes a method of gold electroless plating used to metallize PVDF films. Since gold does not become oxidized it is an excellent choice for piezoelectric devices as well as for other uses such as flexible printed circuit boards.

Key words: PVDF films, electroless-plating process, piezoelectric devices.

Procedure and Experimental Data

Several important steps must be followed to achieve electroless plating: namely cleaning, sensitizing, activating, plating, and post cleaning.

Cleaning.—This is probably the most important step since a surface that is not free of grease and dirt will

not plate evenly and there may be areas where no metal will adhere.

Sensitizing.—This is achieved by immersing the PVDF film into a bath made of photosensitive salts such as $AgNO_3$, AgBr, $SnCl_2$, etc. The film is then exposed to light which reduces the salts to the metal in the bath.

Activating.—This process deposits a microthin layer of a catalyst needed to reduce the metal being plated. Palladium is an excellent catalyst for gold.

Plating.—Plating is done by immersing the film into an aqueous solution containing the desired metal. A layer will be deposited on the activated surface. Its thickness is determined by the amount of time the film is in the solution.

Post cleaning.—This is the final rinse and is used to remove any remaining solutions.

Gold-metallized PVDF was produced on 0.005 in. thick PVDF film using the following five steps:

(*i*) Cleaning in trichlorethylene for 4 min, acetone for 3 min, and n,n-dimethylformamide for 3 min and, finally, rinsing in distilled water.

(*ii*) Sensitizing by immersing the film in a 2.5*N* $SnCl_2$ solution and a 2.5*N* $AgNO_3$ solution for 10 min each. Both solutions were held at a temperature of 70°C. The sample was rinsed thoroughly in distilled water between solutions to avoid bath contamination. After the $AgNO_3$ bath the sample was again rinsed in distilled water, dried using nitrogen gas, and then exposed with a xenon lamp.

(*iii*) Activating in a $PdCl_2$, acetic acid bath (1) at 50°C for 30 min. Again the sample was rinsed in distilled water to be sure all of the solution was removed, leaving only a microthin film of palladium.

(*iv*) Plating by immersing the sample in a gold bath (2) at 85°C for 30 min. A magnetic stirrer was used to agitate the bath.

(*v*) Post cleaning by rinsing the film in distilled water several times following with two rinsings in warm methanol, and then thoroughly drying with nitrogen gas.

The result was a gold layer ~1 μm thick with a resistivity $\rho \approx 2.5 \times 10^{-6}\ \Omega$ cm which adhered to the PVDF and passed the "scotch-tape" test. It was possible to buff the layer using a Linde "C" impregnated felt pad with no adverse effects. A scanning electron microscope analysis showed the layer contained only gold. A second sample was made by the same procedure with a test pattern formed using Kodak-thin film resist (KTFR), see Fig. 1.

After initial cleaning, a thin layer of KTFR was spun on the sample and heated to 60°C for 15 min in a hot plate oven. The pattern was exposed using a xenon lamp and again heated to 60°C for 15 min. The KTFR was developed and rinsed in methanol.

Once the pattern was printed on the sample it was sensitized, activated, and gold plated. The KTFR was not affected by the different solutions and had to be removed with J-100 resist strip leaving a gold pattern on the PVDF. If the KTFR were removed after activating, the gold film would only plate on the remaining activated pattern, eliminating any gold waste.

Conclusions

The results of these tests show that PVDF can be metallized by using an electroless gold-plating process. Advantages of this method are that it is simple and economical because photoresist masking can be used with very little gold wasted, the need for expensive evaporating equipment is eliminated, and roll-to-roll processing is possible.

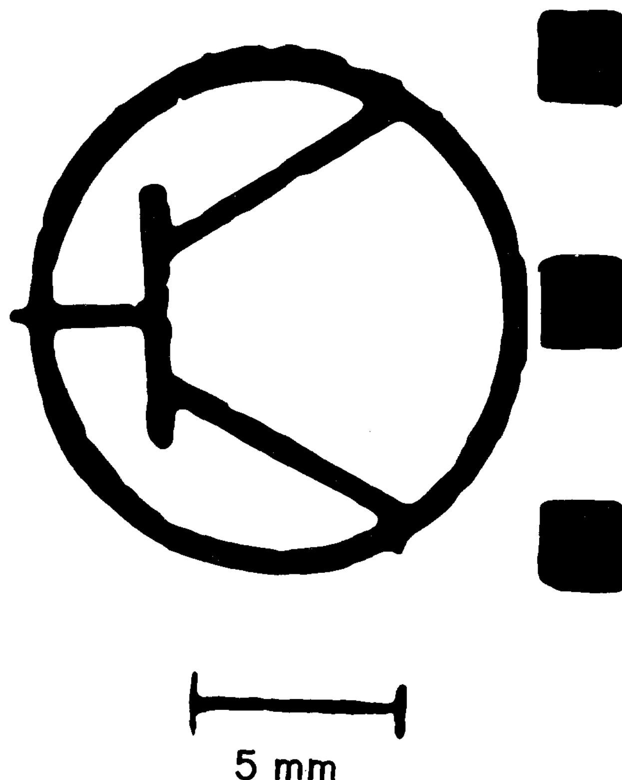

Fig. 1. Gold pattern formed on a 0.75 × 0.75 in. piece of PVDF film using Kodak-thin film resist.

Acknowledgments

The author is grateful to S. Wagner and G. R. Crane for their helpful discussions, and to E. D. Beebe and R. J. Martin for the use of their photoresist equipment.

Manuscript submitted Aug. 8, 1977; revised manuscript received Nov. 9, 1977.

Any discussion of this paper will appear in a Discussion Section to be published in the December 1978 JOURNAL. All discussions for the December 1978 Discussion Section should be submitted by Aug. 1, 1978.

Publication costs of this article were assisted by Bell Laboratories.

APPENDIX.

$PdCl_2$ Activator Solution (after Ref. 1)

Dissolve 0.3g $PdCl_2$ in 9 ml conc. HCl and dilute it with 9 ml H_2O. Add this mixture to 882 ml glacial acetic acid.

Au Plating Solution (after Ref. 2)

To make one liter of a 5× concentrate use: $KAu(CN)_2$, 4.3 g/l; KOH, 56.0 g/l; KCN, 32.5 g/l; KBH_4, 54.0 g/l. (*i*) Dissolve KOH in 500 ml of H_2O. Add KBH_4 and stir until dissolved; (*ii*) Dissolve KCN in 200 ml of H_2O. Add $KAu(CN)_2$ and stir until dissolved; (*iii*) Add solution No. 1 to solution No. 2 in a volumetric flask and make up to volume with distilled H_2O. Filter through Whatman filter paper No. 41. Store in a Teflon or polypropylene bottle. Do not tighten cap because hydrogen is liberated during storage.

REFERENCES

1. M. A. DeAngelo, M. W. Sagal, and D. J. Sharp, U.S Pat 3,485,665 (1962).
2. Y. Okinaka, *Plating (East Orange, N.J.)*, **57**, 914 (1970).

Corrosion of Steel in Concentrated Sulfuric Acid

B. T. Ellison and W. R. Schmeal

Shell Development Company, Houston, Texas 77001

ABSTRACT

A model is presented for corrosion of carbon steel in 60-96% weight sulfuric acid with correlations and data to facilitate quantitative use of the model for mechanical and process design. Corrosion is limited by the rate of convective mass transfer of ferrous ion from a ferrous sulfate (corrosion product) film-liquid interface into bulk acid. This interface is saturated with ferrous ion. The model has been verified in both laboratory and plant acids with rotating cylinder and pipeline geometries and with a variety of carbon and low alloy steels. Ferrous ion is an inhibitor for corrosion, and sacrificial corrosion in certain equipment in plants in which acid is recirculated can protect other critical items in the system. Changing liquid levels in storage tanks, acid purges, addition of iron, and lining of vessels can affect corrosion rate in a plant system.

Sulfuric acid is an industrial catalyst for numerous organic chemical reactions, such as hydrations and alkylations, to produce many important commodities, such as alcohols, ethers, and gasoline. It is desirable to design plants so that carbon steel can be utilized in preference to more expensive materials as much as possible. Toward this end, quantitative corrosion models valid under chemical and fluid flow conditions anticipated for the plant are most useful. These conditions include presence of various chemical reactants in the acid as well as corrosion products which build up in the system because acid is continuously separated from desired chemical products and recirculated.

Much has been written about the corrosion of steel in concentrated sulfuric acid (1). An overview of the corrosion system can be gained by measuring the density of current supplied to a vertical rectangular specimen of AISI 1020 steel in stirred 70% weight acid in order to maintain the electrochemical potential of the specimen fixed (see Fig. 1). Two distinct regions appear in the anodic portion of this current potential curve. One is the "sulfation" range (−0.3 to +0.3V with respect to Ag/AgCl 1M Cl) where the current is independent of potential. Hines and Williamson found the film formed in this range to be duplex, the inside layer being a thin compact film and the outside layer a thick porous ferrous sulfate film (2). At 50 mV negative to the corrosion potential (here about −0.4V), the anodic rate measured by weight loss is identical to this rate in the sulfation region. The independence of anodic current density on potential near (both positive and negative) the corrosion potential implies that the anodic current, in the sulfation range, is also equal to the free corrosion rate. That is, the anodic process limits the corrosion rate.

The second distinct region appearing in the current potential diagram is the passive range, greater than +0.5V, where the steel is apparently covered by a ferric sulfate film over a passive oxide film (3, 4). The sharp peak at about +0.5V in Fig. 1 results from the change in oxidation states of the iron sulfate film already existing on the metal surface.

Donat (5) [see also Putilova (6)] and Poluboyartseva *et al.* (7) discovered that corrosion depends on flow rate and, for 94-96% sulfuric acid, probably on rate of mass transfer of iron sulfate, respectively. Wachter *et al.* (8) and Novakovskii (9) recognized a correspondence between the functionality of corrosion rate upon acid strength and ferrous sulfate solubility and concluded that corrosion rate depends directly on solubility. The objective of the present work is to develop, verify, and define a range of validity of a model to predict corrosion rates of carbon steel in concentrated sulfuric acid for geometries and conditions of industrial significance.

Key words: convective mass transfer, sacrificial corrosion, ferrous sulfate, corrosion inhibition.

Experimental Tools and Methods

Two well-defined turbulent flow fields were studied by means of a rotating cylinder and a pipeline apparatus. Corrosion rates were measured in the former apparatus by the two techniques involving measurement of loss of weight for a given time period and anodic dissolution rate. Corrosion rates were measured directly from weight loss for the pipeline apparatus. Tests could be carried out and environments changed rapidly with the rotating cylinder. Therefore, this device was used for investigating proposed models and the pipeline apparatus was employed for confirmation.

The rotating cylinder apparatus, except for the cylinder itself, was purchased from the Pine Instrument Company. Cylinder rotational speed of 400, 900, and 1600 rpm were obtained with a synchronous motor coupled to the cylinder through stepped pulleys. The rotational speeds were verified with a tachometer. The rotating cylinder was electrically insulated from its support. Electrical current was supplied to the cylinder through an external graphite brush for the anodic dissolution experiments.

The test solution was contained in a 15.24 cm diam Pyrex beaker. The temperature of the solution was adjusted with an electrical heating tape wrapped around the outside of the beaker. The heating tape was coupled to a Thermo Electric Model 400 pulse burst temperature control unit. This combination enabled test solution temperatures of 27°, 40°, and 60°C to be maintained to within ±1°C.

The cylinder shaft was fabricated from Monel alloy 400. The corrosion test specimens were sleeves slipped over this shaft. The specimens were 1.904 ± 0.001 cm

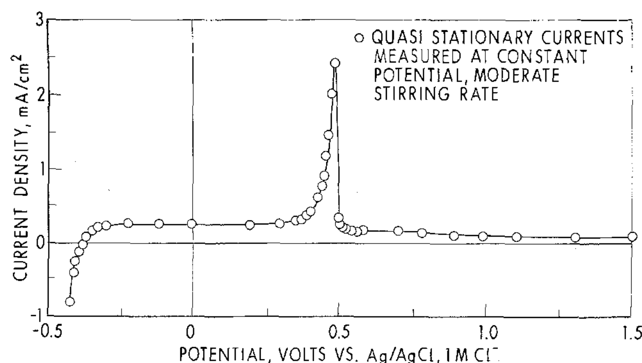

Fig. 1. Current potential curve of SAE 1020 carbon steel in 70% weight H_2SO_4 at 30°C.

in outside diameter by 2.54 ± 0.005 cm long. A 1.905 cm diam Teflon sleeve surrounded the shaft above the test specimen, and a 1.905 cm diam Teflon cap was threaded onto the shaft below the specimen, holding the specimen in place and isolating the shaft from the acid. The Teflon cap held the test specimen in place.

The weight loss experiments were 24 hr long. Cylinders were fabricated from AISI 1113 steel. Microstructure was equiaxed and consisted of lamellar pearlite and ferrite. Ferrovac E cylinders were also used; there was no difference in corrosion performance. The test specimens were sanded with 600 emery paper, degreased, and then weighed. After the experiment, the cylinders were removed, washed in distilled water, and then abraded lightly with a rubber eraser to remove any remaining $FeSO_4 \cdot H_2O$ film. The specimens were then reweighed.

For the anodic dissolution experiments, current-time curves were obtained while the specimens were maintained at a constant potential of 0.0V with respect to a Ag/AgCl 1M Cl^-, cracked glass seal reference electrode. A platinum gauze counterelectrode surrounded the rotating cylinder. Anodic dissolution currents were recorded on a strip chart recorder. The specimens were prepared as for the weight loss experiments; in addition, some specimens were electropolished in an acetic acid-perchlorate solution. Both of these methods of preparation led to the same experimental results.

The closed loop pipeline apparatus was constructed to permit measurement of corrosion rates of pipe walls under flow conditions typical of chemical plant environments. Corrosion test specimens were short pieces of 1 in. pipe fitted between upstream and downstream runs of 1 in. pipe, designed to assure that the velocity profile was fully developed at the test specimens. These entry and exit sections consisted of 1-in. Schedule 40 CPVC plastic pipe extending 183 cm upstream and 122 cm downstream from the test specimens. Steel transition pieces were screwed (with 1-7/16 NF threads and appropriate washers) to the plastic entry and exit lengths. The test specimens were bolted between these transition pieces (see Fig. 2). The transition pieces permitted development of the mass transfer characteristics of the flow before the acid contacted the test specimens. The test specimens and the transition pieces were machined with close internal diameter and concentricity tolerances which assured alignment between specimens to within 0.0025 cm. The specimens were fabricated from AISI 1015 steel tube and were 2.664 cm internal diameter by 7.62 cm long.

The basic components of the pipeline apparatus were the vessel, pump, flow metering and control equipment, and the test section (Fig. 3). The vessel was a 113.7 liter Pfaudler glass-lined steel autoclave. A Worthington 1CNG-32 Worthite pump took suction from the vessel through 2-in. CPVC pipe. A Hills-McCanna 1 in. Penton-lined control valve downstream from the pump maintained 0.03 liter/sec control over a 0.19-2.21 liter/sec range. Downstream of the valve, flows were sensed with either a 3.023 or 1.27 cm tantalum orifice and transmitted to a Foxboro controller (FRC) by a differential pressure cell. The flow recording and control system was calibrated with glycerol-water mixtures as well as with water alone. Downstream from the orifice, the acid entered the 1 in. Schedule 40 test section. The flow discharged from the test section back to the Pfaudler vessel. The temperature control system enabled an acid temperature of 60°C to be maintained to within ±2°C.

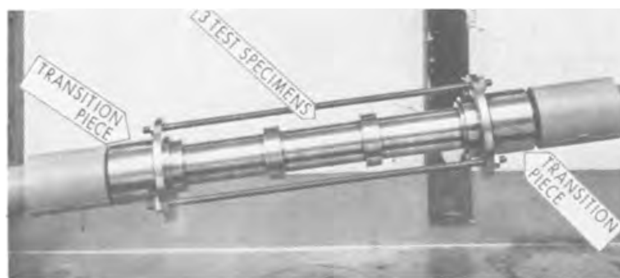

Fig. 2. Pipeline test specimens

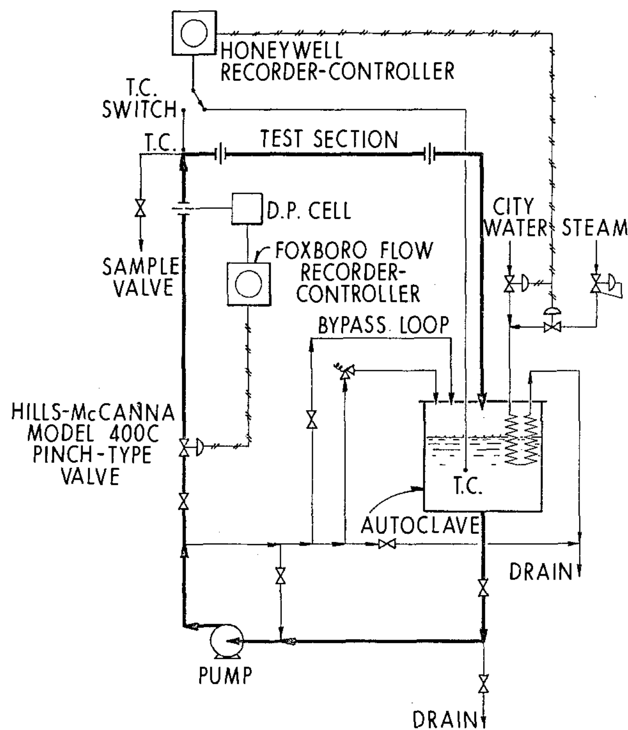

Fig. 3. Schematic diagram of pipeline corrosion test apparatus

Two Hastelloy B sheathed iron-constant thermocouples were available for temperature control. The first was located in the Pfaudler vessel, and the second was located at the entrance to the test section. The temperature difference between the two locations was always less than 1°C. Either of these thermocouples could be connected to a Honeywell temperature controller (TRC). This controller operated steam and water control valves which were on a line to the jacket side of the Pfaudler vessel. The temperature control system enabled an acid temperature of 60°C to be maintained to within ±2°C.

The day before an experiment the test specimens were degreased in acetone, cleaned by gentle abrasion (with a pencil eraser), weighed, and then the test section was assembled. The test section was tested for leaks with low pressure compressed air, then connected to the remainder of the pipeline apparatus.

Reagent grade H_2SO_4 (96% weight) was mixed with distilled water in the Pfaudler vessel to make 68% weight H_2SO_4. The acid strength was determined with a hydrometer. After mixing, the acid was cooled to 60° ± 2°C and the experiment begun. Periodically, acid samples were withdrawn for ferrous ion determination by titration with MnO_4^-. The test period was 24 hr.

At the end of the test, the specimens were cleaned and reweighed. The corrosion rate was calculated from the weight loss of the specimens. Three test specimens were used during each experiment.

Formulation of the Model

Anodic dissolution currents for AISI 1113 rotating cylinder, measured in 68% weight sulfuric acid at 27°, 40°, and 60°C at 400, 900, and 1600 rpm, were found to increase in proportion to velocity to the nth power where $0.6 < n < 0.8$, indicating that convective mass transfer is the likely rate-limiting step in corrosion (see Fig. 4). Next, experiments to identify the species whose mass transfer step is the slow step in the corrosion process in 68% weight H_2SO_4 demonstrated

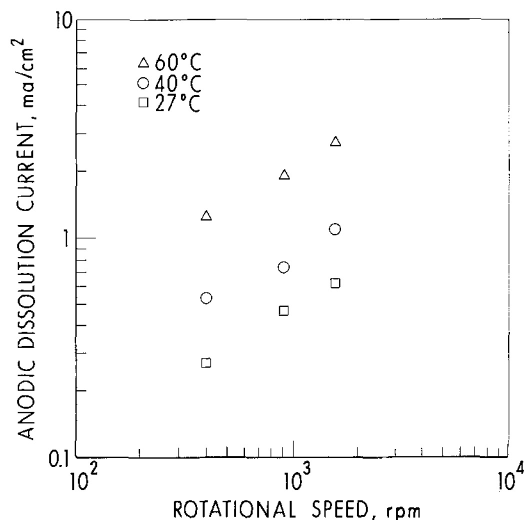

Fig. 4. Anodic dissolution currents vs. rotational speed for 1.905 cm diam cylinder in 68% weight H_2SO_4.

what Poluboyarteseva asserted for 94-96% weight H_2SO_4, that this species is ferrous ion.

The corrosion rate (C.R.) is proportional to the convective mass transfer rate of one of the species

$$\text{C.R.} = \pm Ah(C_f - C_{bulk}) \qquad [1]$$

where A is the conversion factor between moles per square centimeter-second and centimeter per year corrosion rate, h is the convective mass transfer coefficient, C_f is the concentration of the species at the corrosion product film-solution interface, and C_{bulk} is the concentration of the species in the bulk solution.

Anodic dissolution experiments were conducted with different concentrations of ferrous ion in the bulk and the anodic dissolution currents were observed to decrease linearly with the ferrous ion concentration (see Fig. 5). This indicates that the convective mass transfer of ferrous ions is indeed the slow step in the corrosion process.

Next, it was established that the appropriate value for C_f in Eq. [1] is the saturation concentration in acid of the salt, $FeSO_4$-H_2O, which is found on the metal wall. The mass transfer rate to a rotating cylinder is usually expressed as (10)

$$\text{Sh} = 7.91 \times 10^{-2}\text{Re}^{0.7}\text{Sc}^{0.356} \qquad [2]$$

Sh (Sherwood number) is a dimensionless mass transfer rate, Re is the Reynolds number, the dimensionless rotational velocity of the cylinder, and Sc is the Schmidt number, a fluid property characterizing the relative thicknesses of the momentum and mass transfer boundary layers (see List of Symbols for definitions). We determined the mass transfer characteristics of the rotating cylinder used in the present work by measuring the mass transfer limited current for oxygen dissolved in salt water and found that Eq. [2] fit these data to within 5%.

We computed C_f from Eq. [1] using measured values of the corrosion rate, C.R., and C_{bulk}, values of h calculated from Eq. [2], and a value of A of 2.24×10^8 (cm/yr) (moles/cm²-sec). Results given in Fig. 6 show that the computed C_f is independent of Reynolds number and strongly dependent on temperature, consistent with theory. Furthermore, the computed values of C_f are about equal to the saturation concentration of ferrous ion which was measured independently (see Fig. 7) by methods discussed in the Appendix.

A model of the corrosion process is formulated which is based on the corrosion rate of carbon steel in concentrated sulfuric acid being equal to the mass transfer rate of ferrous ions from a ferrous saturated fer-

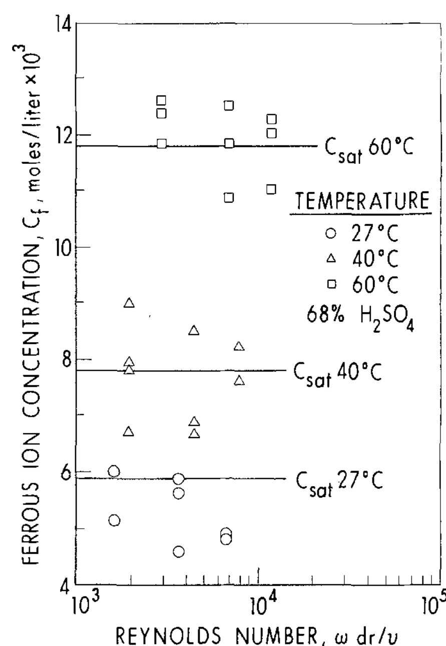

Fig. 6. Interfacial concentration of ferrous ions vs. Reynolds number measured during corrosion of steel in 68% weight H_2SO_4 with rotating cylinder.

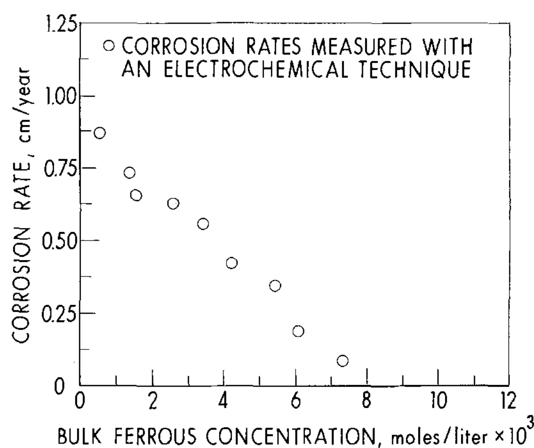

Fig. 5. Measured corrosion rate of a 1.905 cm diam carbon steel cylinder rotating in 68% weight H_2SO_4, 40°C, 900 rpm, vs. bulk concentration of ferrous ions.

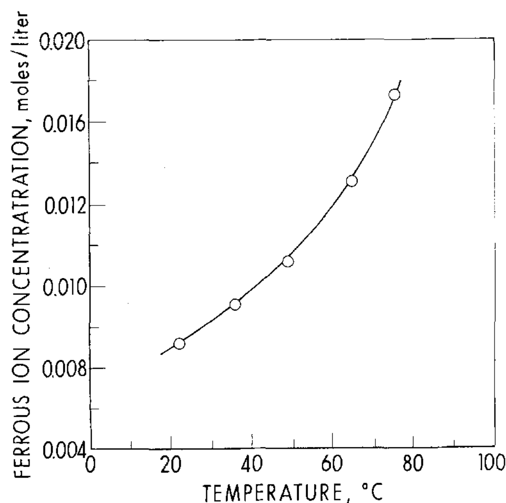

Fig. 7. Solubility of ferrous ion measured in 68% weight H_2SO_4 vs. temperature.

rous sulfate film-sulfuric acid interface to the solution bulk, *i.e.*

$$C.R. = Ah(C_{sat} - C_{bulk}) \quad [3]$$

All of the information required to predict corrosion rates with this model are obtained from sources other than corrosion measurements. The mass transfer coefficient, h, can be obtained from standard engineering formulas in conjunction with diffusion coefficient and viscosity data. The saturation concentration of ferrous ions is obtained from thermodynamic measurements, and the bulk concentration of ferrous ion can be measured or calculated.

Confirmation and Use of the Model for 68% Sulfuric Acid

It is useful to express corrosion rates as dimensionless corrosion Sherwood numbers, Sh*

$$Sh^* = \frac{C.R.\, d}{A(C_{sat} - C_{bulk})D}$$

where C.R. is the measured corrosion rate (centimeter per year), d is the diameter of the rotating cylinder (or the diameter of the pipe), $(C_{sat} - C_{bulk})$ is the difference between the independently measured saturation concentration of ferrous ion and the measured bulk concentration of ferrous ion, A is the conversion factor previously defined, and D is the independently measured diffusion coefficient of ferrous ions in H_2SO_4 (see Appendix). Over the range of validity of the model, plots of Sh* *vs.* dimensionless parameters are the same as the corresponding plots using the mass transfer Sherwood number, Sh, found in the literature (see Fig. 8). For any geometry, plots such as Fig. 8 are universal relations of great utility, since one relation describes corrosion rate over a range of values of all parameters.

From Fig. 8, it can be seen that ±20% is about the limit on the accuracy of the predictions of the model. The cumulative errors in the measurement of diffusion coefficient, ferrous ions solubility, ferrous ion concentration in the bulk acid, and corrosion rate all influence the agreement between the measured corrosion rate and the predictions of the model. Ferrous solubility, in particular, is a difficult measurement so that the scatter in the data is understandable. (Data shown in Fig. 8 include tests with acid 40-70% weight saturated with ferrous ion.)

It is important that results obtained from anodic dissolution experiments be confirmed by weight loss measurements because it is possible that anodic dissolution currents are not equal to corrosion rates in this system. The reason that the anodic dissolution currents could be unrepresentative of free corrosion rates is that the film formed at the corrosion potential may differ from the film formed at 0.0V. For example, hydrogen gas evolution during free corrosion may affect the corrosion rate.

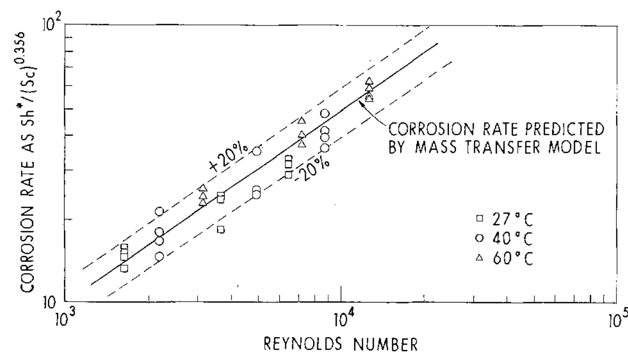

Fig. 8. Anodic dissolution rate (corrosion rate) of AISI 1113 cylinder in 68% weight H_2SO_4.

Twenty-four hour weight loss experiments were conducted with the AISI 1113 cylinder in lean 68% weight acid to verify the corrosion model in these conditions. The corrosion rate should be inversely proportional to the ferrous ion concentration in the acid and, therefore, should decrease as the corrosion product builds up in the acid. Ferrous ion concentrations in the acid were determined periodically so that a mean value with respect to time of the bulk ferrous ion concentration could be determined. This mean value was used as C_{bulk} to formulate the Sherwood number from the measured weight loss.

When the clean specimens (not covered with protective corrosion product film) were first immersed in the acid, they corroded vigorously. The corrosion model is only applicable after steady-state corrosion rates are obtained. The anodic dissolution experiments indicated that steady state is obtained within 30 min. The weight loss of a specimen after the first 30 min was subtracted from the total weight loss of a specimen to determine the Sherwood number. The weight loss during the first 30 min was determined from the ferrous ion concentration in the solution at that time. These weight losses usually accounted for about 5% of the total weight loss.

The results of the weight loss experiments are shown in Fig. 9. These corrosion rates are slightly higher than the predicted corrosion rates but the measurements agree with the predicted corrosion rates to within 20%. The rotating cylinder experiments were run over a range of temperatures from 27° to 60°C and a range of mass transfer coefficients equivalent to those in flows of from 91.5 to 336 cm/sec in a 10.16 cm ID pipe.

The model was confirmed in experiments in the pipeline apparatus. Twenty-four hour weight loss data were taken on the pipe specimens. These data were obtained with 68% weight acid at 60°C. Each reported weight loss is the mean of three weight losses under the same conditions. No weight loss deviated by more than 10% from the mean weight loss; typical deviations were 4%. The weight losses were formulated into a Sherwood number in the same way as the rotating cylinder weight losses were treated. The results are shown in Fig. 10 and are compared with mass transfer correlations proposed by several investigators. The data fit best the correlation of Harriott and Hamilton (11) for the conditions tested

$$Sh = 9.6 \times 10^{-3} Re^{0.913} Sc^{0.346}$$

The measured corrosion rates agree with the mass transfer correlation to within 5%.

The mass transfer model of the corrosion of carbon steel in 68% weight H_2SO_4, which was developed from rotating cylinder experiments, remains valid in pipe

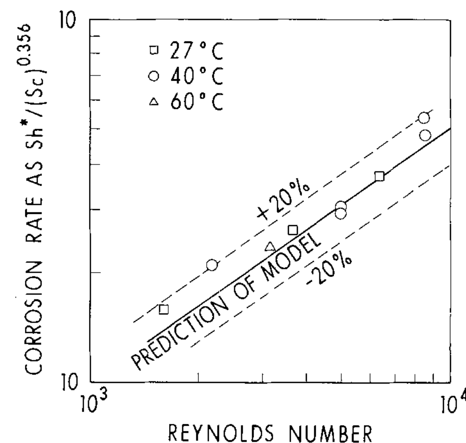

Fig. 9. Corrosion rates measured in 24 hr weight loss experiments of a 1.905 cm diam AISI 1113 cylinder rotating in 68% weight H_2SO_4.

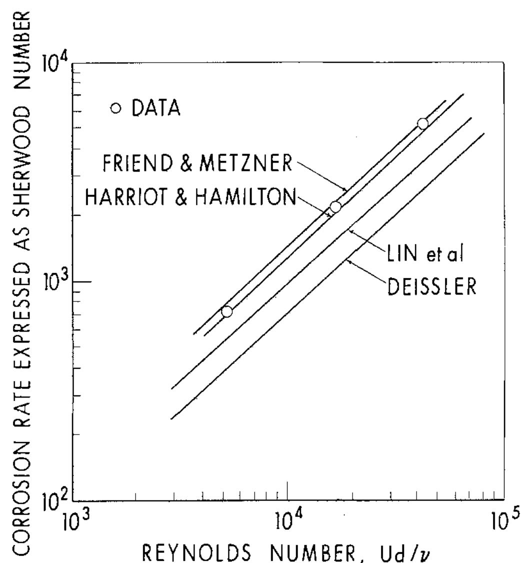

Fig. 10. Corrosion rate of carbon steel pipe walls in 68% weight H_2SO_4 at 60°C.

flow. The model can be expected to remain valid in other hydrodynamic situations.

Range of Validity

It is important to examine the validity of the model under a range of conditions of industrial significance. The model was formulated using 68% weight sulfuric acid. A few experiments were conducted with 78% weight H_2SO_4 to determine if the model is valid at this acid strength. The results of both weight loss and anodic dissolution experiments are shown in Fig. 11. It is seen that the predicted corrosion rates generally agree within 20% with the measured corrosion rates.

It had been believed previously (8) that the acid strength affected corrosion rate primarily by changing ferrous ion solubility (the higher the solubility the greater the corrosion rate). It is now apparent that the important parameters which are a function of acid strength are not only ferrous ion solubility, but also acid viscosity and ferrous ion diffusion coefficient. Even though the ferrous ion solubility in 78% weight acid is higher than in 68% weight acid, the corrosion rate is lower because the diffusion coefficient is lower and the viscosity is higher.

Literature data indicate that the mass transfer corrosion model should be valid over the acid strength range between 60 and 100%. The work of Poluboyartseva *et al.* (7) indicates that the model is valid for 96% weight H_2SO_4. Damon's data on the effects of carbon content and acid strength on the corrosion of carbon steel in sulfuric acid (12) indicate that the rate-controlling mechanism is the same for acid strengths between 60 and 100%.

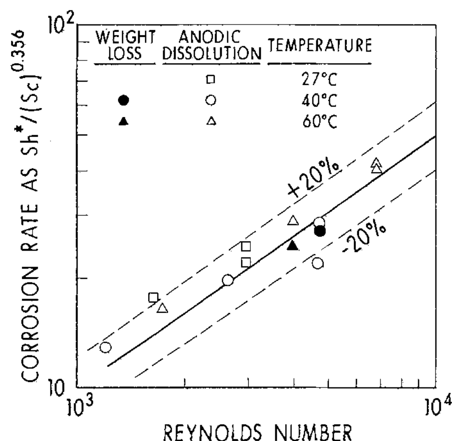

Fig. 11. Anodic dissolution currents and weight losses in 78% weight H_2SO_4.

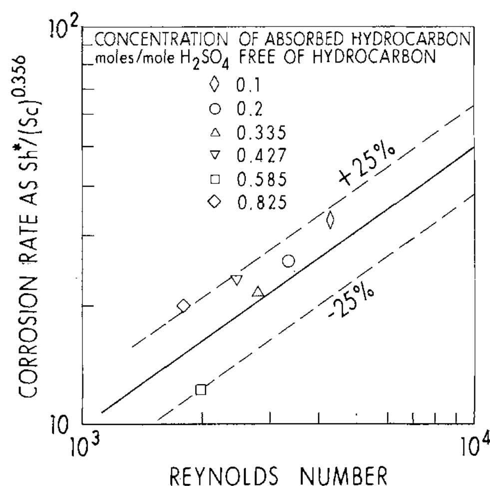

Fig. 12. Corrosion rates measured in 24 hr weight loss experiments in IPA fat 68% weight H_2SO_4 at 38°C, 900 rpm.

To determine the validity of the corrosion model in hydrocarbon fat acids,[1] a series of weight loss experiments was conducted in laboratory-fattened acid and plant acid. Weight loss experiments were conducted with the AISI 1113 cylinders over a range of isopropyl alcohol fatnesses[2] from 0 to 0.825. The weight loss tests were all conducted at 38°C, 900 rpm. The results are shown in Fig. 12. It is seen that the predictions of the model are not as accurate as for lean acids; however, ± 25% accuracy can be expected.

Some weight loss experiments were run with steels of varying composition to determine the effects of carbon content and copper content on corrosion steel in 68% weight H_2SO_4. The steels considered were AISI 1113, AISI 1018, AISI 1045, and U.S. Steel Corten (0.10 C maximum, 0.30 minimum Cu). All experiments were conducted at 900 rpm, 40°C with 68% weight H_2SO_4 free of organics. The results are shown in Table I. It is seen that the predicted corrosion rates agree with the measured corrosion rates to within 5%. These results indicate that steel composition is a minor variable in determining the corrosion resistance of carbon steel to concentrated sulfuric acid. The results are consistent with Damon's results (12). For acid strengths below

[1] Fat acids mean acids containing hydrocarbon and fatness means the concentration of absorbed hydrocarbon in moles per mole of H_2SO_4. Note that absorbed olefins react to form alcohols and other species. It is thus often possible to create desired equilibrium mixtures in the laboratory simply by adding alcohol to acid.

[2] Isopropyl alcohol is the primary equilibrium reaction product which exists when propylene is absorbed in sulfuric acid.

Table I. Effect of steel composition on corrosion rate of carbon steel in 68% weight H_2SO_4

Conditions: Tests were conducted at 900 rpm, temperature 40°C with 1.905 cm diam cylinders in 68% weight H_2SO_4.

Steel	Measured corrosion rate (cm/yr)	Predicted steady-state corrosion rate* (cm/yr)
AISI 1018	0.635	0.602
Corten	0.576	0.587
AISI 1045	0.691	0.673
AISI 1045	0.648	0.655
AISI 1113	0.640	0.653

* Changes in the predicted corrosion rate do not reflect a dependence of steady-state corrosion rate on steel composition but rather varying amounts of corrosion in the first half-hour. These variations produce differing amounts of dissolved ferrous ion in the acid when steady-state corrosion begins. Predictions are made with Eq. [4] using the mean concentration of ferrous ion in the solution during the experiment excluding corrosion in the first half-hour.

60%, steel composition is an important variable [see Ref. (12)].

Systems Aspects of Corrosion

The model for corrosion, Eq. [3], shows that the corrosion rate depends on physical properties of the local environment (temperature, acid strength, and concentration of absorbed species), geometry and flow conditions, and one parameter which reflects events at other times and places, the bulk ferrous ion concentration, C_{bulk}. In many commercial uses of sulfuric acid, the acid recirculates through a plant via absorbers, desorbers, reactors, exchangers, and intermediate storage vessels. Thus, events in some of these vessels which affect ferrous ion concentration in recirculating acid can have a dominant effect on the corrosion rate in other vessels and pipes.

A plant may be visualized as consisting of nodes representing vessels, exchangers, or pipes which are connected by lines representing flow of acid in a network or signal flow diagram. These nodes are connected to adjacent nodes consistent with the route of flow of acid. There will be a purge location represented by a node. For each node the concentration of ferrous ion in the exit stream (C^o_{bulk}) exceeds the concentration in the entering stream (C^i_{bulk}) by an amount proportional to the average corrosion rate ($\overline{C.R.}$) expressed as weight loss of iron per unit area and time

$$C^o_{bulk} - C^i_{bulk} = (\overline{C.R.})\alpha\theta \quad [6]$$

where α is the area per unit volume of the node and θ is the holding time of the node. If ($\overline{C.R.}$) is negative a precipitation rate is indicated. Notice also that the driving force for corrosion or precipitation is proportional to ($C_{bulk} - C_{sat}$) in the node.

The nodes and purge are sources and sinks for ferrous ion. They tend to pull the bulk ferrous concentration in the stream entering toward their saturation ferrous concentration as determined by local temperature and acid composition by corrosion or precipitation. The purge node has a saturation concentration of zero. The steady-state ferrous ion concentration will be determined by the most "influential" nodes, those with large residence times, large surface to volume areas, or large driving forces for corrosion or precipitation. Thus, ferrous ion concentration and, therefore, corrosion rates in pipes, vessels, and exchangers are determined by conditions in large storage tanks or very large heat exchangers.

If one node is dominant it is easy to predict the system bulk ferrous ion concentration by assuming it is the saturation condition in the dominant node. Conservative estimates of ferrous ion concentration which give an upper bound for corrosion rates can be made by assuming the bulk ferrous ion concentration is zero or, more realistically, equal to the saturation concentration in the "influential" node in which it is lowest.

From this it is apparent that lining or lowering the liquid level in an acid storage tank, raising the liquid level in a storage tank containing acid with absorbed hydrocarbon, or upgrading materials in an "influential" node can result in an increase in corrosion rate elsewhere in the system which is often thought to be mysterious. Inhibition of corrosion of downstream equipment has been effected by lowering steel chains into an acid storage tank in the same acid system to create a more "influential" node.

Conclusions

The corrosion rate of carbon steel or iron in 68-78% weight sulfuric acid is limited by the rate of convective mass transfer of ferrous ion from a ferrous sulfate film-liquid interface into bulk acid. The works of Damon (12) and Poluboyartseva *et al.* (7) indicate this model is probably valid for 60-96% weight sulfuric acid. The ferrous ion concentration at the interface is the saturation concentration of ferrous sulfate in the acid. The corrosion rate is, therefore, positively influenced by this saturation concentration, which increases with temperature, decreases with concentration of absorbed hydrocarbon in acid, and depends on acid strength in a complex way [see Ref. (8)]. The bulk concentration of ferrous ion is determined by events elsewhere in the acid system. Thus, inhibition of corrosion can be purposefully effected by sacrificial corrosion in large storage tanks, by addition of iron, or by lowering the liquid level in tanks containing supersaturated solutions to minimize ferrous sulfate precipitation. Inhibition has been accomplished successfully in a petrochemical plant by the intentional introduction of steel chains to a tank to increase the ferrous concentration in the acid. Accidental increases in corrosion of critical items can occur after increases in acid purge rate, lining of storage vessels, or lowering of liquid level in storage vessels. Corrosion rate is influenced by all variables which determine mass transfer coefficient, especially velocity, viscosity, and diffusivity of ferrous ion. The dependence of the latter two on acid strength is more significant than commonly appreciated. For example, the corrosion rate for 78% weight acid is generally lower than for 68% weight acid, despite the fact the ferrous solubility is higher, because the viscosity is higher and the diffusivity of ferrous ion is lower.

Manuscript submitted July 6, 1977; revised manuscript received Oct 31, 1977.

Any discussion of this paper will appear in a Discussion Section to be published in the December 1978 JOURNAL. All discussions for the December 1978 Discussion Section should be submitted by Aug. 1, 1978.

Publication costs of this article were assisted by Shell Development Company.

APPENDIX

It is appropriate to discuss briefly the prediction of physical properties required to use the model: ferrous ion solubility, viscosity, density, and ferrous ion diffusion coefficient in acid. Dependence of these on acid strength and concentration of absorbed hydrocarbon species is important.

Published values for the saturation concentration of ferrous ion in sulfuric acid are in considerable disagreement. For example, at 55°-65°C and 65-70% weight H_2SO_4, the following values for ferrous saturation concentration were found: 0.61% weight (13) and 0.17% weight (14). Solubility measurements were made in 68% weight lean acid at 23°, 38°, 48°, 65°, and 75°C. The results shown in Fig. 7 were obtained after allowing 8 days for equilibration from an initially supersaturated solution. To verify these results, 68% weight acid initially free of ferrous ion was equilibrated with solid $FeSO_4 \cdot H_2O$ at room temperature (about 25°C) for a month. The ferrous concentration was then measured as 5.8×10^{-3} moles/liter, which is in substantial agreement with the concentrations measured in the initially supersaturated solution. Solubilities measured in 78% weight acid as a function of temperature after 7 days equilibration are shown in Fig. 13. It is seen that these solubilities are about 1.5 times as high as those in 68% weight acid. Solubilities of ferrous ion were measured in acid containing isopropyl alcohol, the primary equilibrium reaction product when propylene is absorbed. About a month was required to obtain reasonably steady values of the saturation concentration. The solubility measurements for 38°C are shown in Fig. 14.

Viscosities for the lean acids were obtained from the literature (15, 16) for use in our calculations. Viscosities for the fat acids were determined at 25° and 60°C with a capillary viscometer according to ASTM D445. Viscosities at intermediate temperatures were obtained from Andrade's equation (17) where the constants were obtained from the 25° and 60°C data

$$\mu = Ee^{B/T}$$

For 67% weight acid, viscosities measured at 25° and 60°C are shown *vs.* concentration of absorbed propylene in Table II.

Densities may be found in the literature or measured directly with a hydrometer. In general densities de-

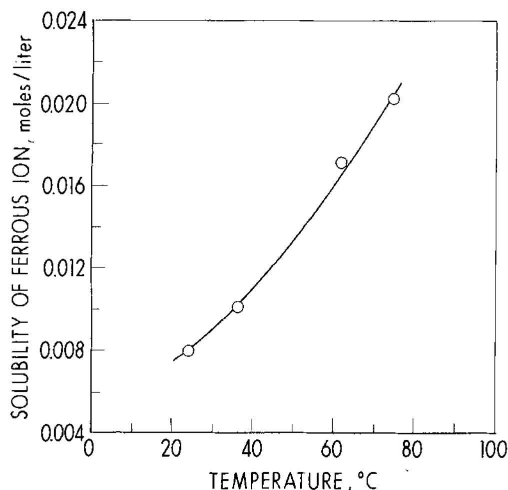

Fig. 13. Solubility of ferrous ion in 78% weight H_2SO_4 vs. temperature.

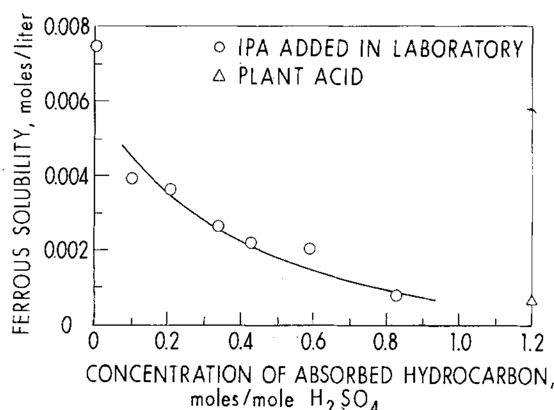

Fig. 14. Solubility of ferrous ion in 68% weight H_2SO_4 containing isopropyl alcohol.

crease with increasing concentration of hydrocarbons. For example, for propylene systems we used

$$\frac{d\rho}{df} = -0.12(\rho - 0.684 - 86/T)$$

where f is the moles of absorbed olefin per mole of H_2SO_4 and T is temperature in °K.

Diffusion coefficients for ferrous ion were measured with a rotating platinum disk electrode. The mass transfer limited current for the oxidation of ferrous ion to ferric ion was determined in an acid of known ferrous concentration. This current was then related to the diffusion coefficient for ferrous ion with Levich's equation (18).

The measured diffusion coefficient of ferrous ion in 68% and 78% weight lean acids are shown in Fig. 15. The diffusion coefficients measured at 24°C (68% weight H_2SO_4) and 30°C (78% weight H_2SO_4) were used with Wilke's formula (17)

$$D\alpha T/\mu$$

to compute the diffusion coefficient at other temperatures. The measured diffusion coefficient at 60°C (68% weight H_2SO_4) agrees within 8% of the value calculated from Wilke's formula.

Table II. Viscosities of 68% weight IPA fat sulfuric acid

Concentration of absorbed hydrocarbon	Viscosity (centistokes) 25°C	60°C
0	—	—
0.1	5.50	2.55
0.2	6.86	3.18
0.335	8.47	3.81
0.427	9.48	4.22
0.585	12.03	5.05
0.825	13.27	5.33

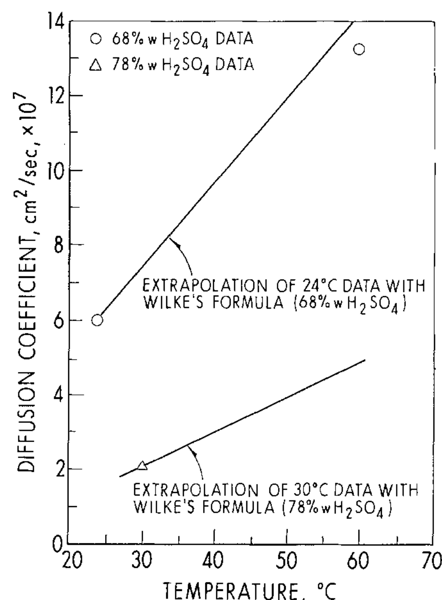

Fig. 15. Diffusion coefficient of ferrous ion in H_2SO_4 vs. temperature.

The diffusion coefficients of ferrous ion in the hydrocarbon fat acid were computed by extrapolating with Wilke's formula (19) the data obtained for 68% weight H_2SO_4. The extrapolation formula was

$$D = 1.68 \times 10^{-10}\, T/\mu$$

where T is in °K, μ in poise, and D in square centimeters per second. This equation can also be used to predict the ferrous ion diffusion coefficient in acids of differing strength. This equation overpredicts (about 30%) the measured diffusion coefficient in 78% weight acid. Although this extrapolation technique is not ideal, use of it did lead to results which were consistent with the other data taken in this research.

LIST OF SYMBOLS[3]

A	conversion factor between mass transfer flux of iron (II) and corrosion rate 2.24×10^8 cm³ sec/yr mole
C	concentration moles/L³
C.R.	corrosion rate, cm/yr
d	diameter, L
D	diffusion coefficient, L²/t
f	concentration of absorbed hydrocarbon, moles/mole H_2SO_4
h	mass transfer coefficient, L/t
l	characteristic length of pipe
M	mass transfer rate, moles/L²-t
r	radius, L
Re	Reynolds number, Vd/ν (dimensionless)
Sc	Schmidt number, ν/D (dimensionless)
Sh	Sherwood number, hd/D (dimensionless)
St	Stanton number, Sh/ReSc (dimensionless)
T	temperature, θ
V	velocity, L/t
δ	effective diffusion layer thickness
μ	viscosity, M/Lt
ν	kinematic viscosity, L²/t
ρ	density, M/L³
ω	angular velocity, 1/t

Subscripts

f	film-solution interface
sat	saturation

[3] Dimensions given in mass (M), length (L), time (t), and temperature (θ).

REFERENCES

1. M. G. Fontana and N. D. Greene, "Corrosion Engineering," McGraw-Hill Book Co., New York (1967).
2. J. G. Hines and R. C. Williamson, *Corros. Sci.*, **4**, 201 (1964).
3 G. Gilli and F. Zucchi, *ibid.*, **8**, 801 (1969).
4. R. C. Williamson and J. G. Hines, *ibid.*, **4**, 221 (1964).

5. E. V. Donat, "Influence of the Speed of Flow of Monohydrate on the Corrosion of Cast Iron and Steel Under Industrial Conditions," Moskow University dissertation (1949).
6. I. N. Putilova, S. A. Balezin, and V. P. Barannik, "Metallic Corrosion Inhibitors," Pergamon Press, New York (1960).
7. L. A. Poluboyarteseva, P. I. Zarubin, and V. M. Novakovskii, *J. Appl. Chem.*, **36**, 1210 (1963).
8. A. Wachter, R. S. Treseder, and M. K. Weber, *Corrosion*, **3**, 3 (1947).
9. V. M. Novakovskii, *Zh. Prikl. Khim. (Leningrad)*, **25**, 325 (1952).
10. M. Eisenberg, C. W. Tobias, and C. R. Wilke, *This Journal*, **101**, 306 (1954).
11. P. Harriott and R. M. Hamilton, *Chem. Eng. Sci.*, **20**, 1073 (1965).
12. G. H. Damon, *Ind. Eng. Chem.*, **33**, 67 (1941).
13. J. W. Mellor, "A Comprehensive Treatise on Inorganic and Theoretical Chemistry," Vol. XIV, p. 272, Longmans, Green and Company, London (1935).
14. K. A. Kobe and R. E. Fredrickson, *Chem. Eng. Data Series*, **1**, 12 (1956).
15. Bright *et al.*, *J. Soc. Chem. Ind.*, **65**, 385 (1946).
16. "International Critical Tables," Vol. 5, pp. 11-13, McGraw-Hill Book Co., New York (1929).
17. R. C. Reid and T. K. Sherwood, "The Properties of Gases and Liquids," McGraw-Hill Book Co., New York (1958).
18. V. G. Levich, "Physicochemical Hydrodynamics," Prentice-Hall, Inc., Englewood Cliffs, N.J. (1962).
19. C. R. Wilke, *Chem. Eng. Prog.*, **45**, 219 (March 1949).

Preparative Electrolyses at Graphite Paste Anodes

Kevin D. Wolter and John T. Stock*

Department of Chemistry, University of Connecticut, Storrs, Connecticut 06268

ABSTRACT

Two forms of thin-layer graphite-paste anodic preparative electrolysis systems have been developed. The rotating counterelectrode chamber of the simpler form provides the stirring action. In the other form, the surface of the paste is continuously reactivated. With this device, electrolysis of the highly anode-deactivating system tyramine in NaOH solution has been shown to yield a carbon-carbon "dimer."

Because graphite paste has been found to give very low anodic residual currents, this is a suitable electrode material for analytical-scale oxidation studies (1). A graphite paste preparative-scale anode has been described by Colaruotolo (2). He used a layer of paste that was spread on a platinum contact at the bottom of a beaker. Although simple, this design makes controlled spreading almost impossible, so that the resulting paste layer is uneven and usually quite thick.

Although electrolysis systems of quite high electrical resistance can be used successfully on the analytical scale, the resistance should be as low as possible when the large quantities of electricity needed for preparative work are involved. Conventional electrode materials have much lower specific resistances than has graphite paste. This suggests that a thin layer of paste should be spread on a low resistance substrate. The paste is made from graphite powder (G) and a nonconducting binder (B) such as Nujol. Accordingly, the B/G ratio (ml of binder per gram of graphite) should significantly affect the resistance of the paste. The paste must be coherent so that it will not break down under the motion of the cell solution or of the cell components. Adams (1) recommended a B/G ratio of 0.6:1 for voltammetric work.

Experimental

A single batch of Fisher Scientific Company grade No. 38 graphite powder was used throughout. Measurements of the electrical resistances of graphite-Nujol pastes gave poorly reproducible results. In general, the application of quite light pressure caused a considerable decrease in resistance. However, three facts become obvious (*i*) high B/G ratios give high resistance pastes, (*ii*) below a certain B/G ratio, the resistance of the past falls quite rapidly as this ratio is further diminished, (*iii*) when the B/G ratio is small, the resistance is comparatively low and is relatively insensitive to changes in this ratio. However, pastes of very low B/G ratio are friable. A B/G ratio of 1.2:1 was chosen as giving the best compromise of electrical and mechanical properties. The specific resistance of this paste was approximately 500 Ω cm.

In an attempt to quantify these conclusions, experiments were made with "frozen" pastes. These were made by mixing graphite powder with molten paraffin wax and allowing the mixtures to cool. After measuring resistances, several of the samples were thin sectioned for photomicrography. This showed that small graphite particles were much more numerous than large ones. Particle size analysis (Imanco Quantimet 720 Image Analyzer) of the stock of graphite powder confirmed this conclusion.

Two thin-layer graphite paste electrolysis systems were constructed. The graphite block cell (GBC) is shown schematically in Fig. 1. Block A is a 2.5 cm length of a 7.5 cm diam graphite rod. A circular groove was cut in the upper face to accept cell B, which is a 150 ml beaker with the bottom cut off. Graphite paste was spread to a uniform thickness of 1 mm or less on the graphite surface enclosed by the groove. The cell was then inserted and sealed into the groove with molten paraffin wax. Stirring was provided by a rotating chamber C, made from a Nafion® ion-exchange sheet (3). This chamber contained the counterelectrode and the catholyte, which was usually saturated KCl solution. All potentials were referred to a saturated calomel electrode through a thread-type salt bridge (4) and were controlled by a McKee-Pedersen Type MP-1026 potentiostat.

Figure 2 shows the essentials of the rotating drum cell (RDC). The reference electrode and counterelectrode compartment (3) are not included. The normal level of solution is indicated by the broken line. Horizontal graphite drum is 6.5 cm in diameter and 6.3 cm long. It has a Lucite axle that runs in U-shaped bearings mounted on the insides of opposing walls of the Lucite cell. This cell is 13 cm long, 12 cm wide, and 11 cm high. Electrical connection to the graphite drum

* Electrochemical Society Active Member.

Key words: electrooxidation, electrosynthesis, graphite paste electrode, electrode activation, tyramine.

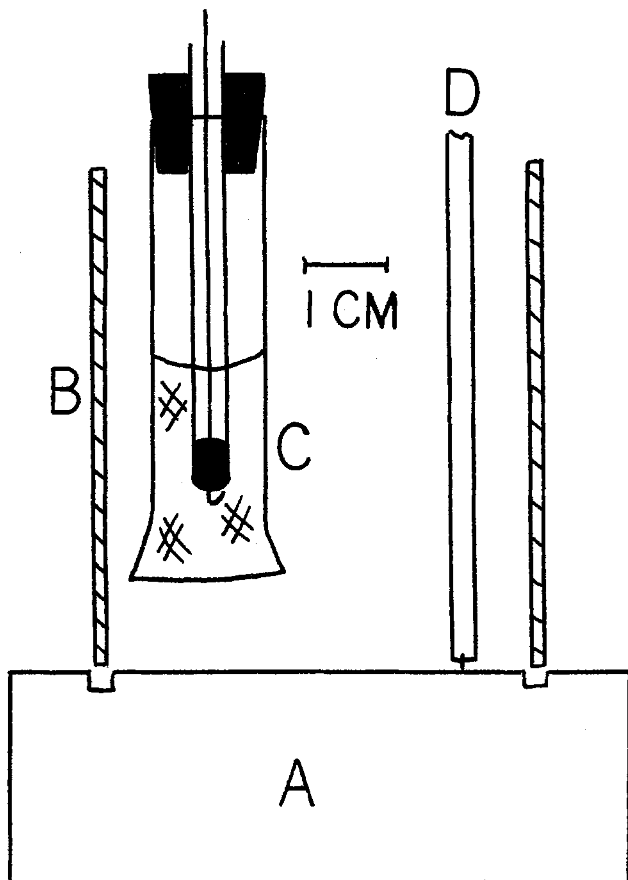

Fig. 1. Graphite block cell. A, graphite block; B, cut-down beaker; C, counterelectrode chamber; D, salt bridge.

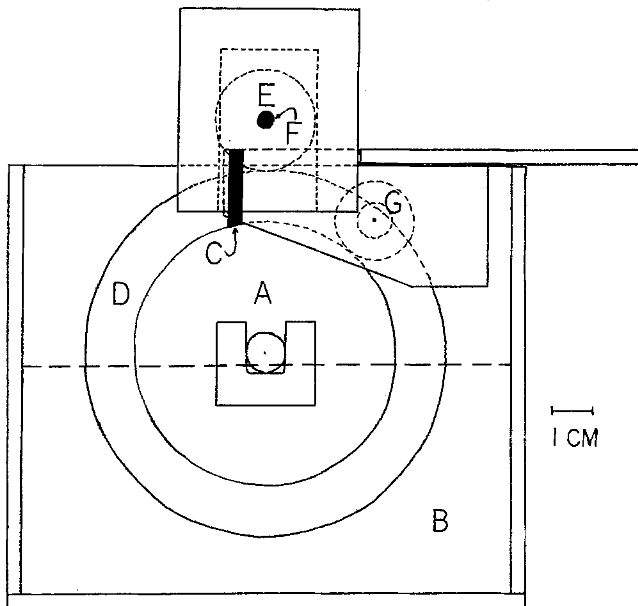

Fig. 2. Rotating drum cell. A, graphite drum; B, Lucite cell; C, carbon brush; D, knurled Lucite wheel; E, rubber drive wheel; F, steel drive shaft; G, reactivation roller.

is made through a small spring-loaded carbon brush that presses near the edge of the periphery of the drum. A knurled Lucite wheel attached to the drum is driven by small rubber wheel which is mounted on stainless-steel drive shaft. This is driven through an 8:1 reduction gear by a 1725 rpm motor. The drive shaft also carries a sprocket that allows reactivation roller to be chain driven. This Lucite roller, which is 1.9 cm in diameter and slightly shorter than the graphite drum, has two functions. First, it controls the thickness of the paste layer on the submerged portion of the drum. To this end, the reactivation roller is mounted on a movable inner housing so that the reactivation roller to graphite drum clearance can be changed. Normally, the clearance was 1 mm. In operation, the system sheds some paste, which falls to the bottom of the cell. Automatic paste feed was tried, but periodic manual application of paste to the drum works very well.

The second function of the reactivation roller is to restore the activity of the paste when an anode deactivator is to be electrolyzed. Some organic compounds form poorly conducting products that coat the anode and hence reduce or cut off the cell current (5). A preparative cell in which a rotating graphite drum reactivates a graphite cloth anode has been described (6). In the RDC, the approximate surface speeds of drum and roller are 1290 cm min^{-1} and 960 cm min^{-1}, respectively. The shear created by this difference in speeds resurfaces the paste before it reenters the solution.

Results and Discussion

Figure 3 shows the effect of the B/G ratio upon the electrical resistance of paraffin wax-graphite "frozen" paste. Resistance readings are relative only, and were obtained with a probe consisting of two 1 mm diam sharp-pointed steel pins fixed 3 mm apart. The pins were inserted in the "paste" to a depth of 5 mm. These results, in line with the general behavior noted for Nujol-bound pastes, were interpreted with the aid of the particle size analysis as follows. In region I, essentially all adjacent particles are in contact, so that the paste has a resistance that is both low and relatively insensitive to shifts in the B/G ratio. When, in region II, this ratio has become larger, the randomly distributed large particles are no longer in mutual contact but are bridged by the more numerous small particles. These provide conductive pathways that become less effective as the dispersion becomes more dilute. In region III the graphite particles fail to make effective contact and the resistance becomes very high.

Solutions of $K_4\,Fe(CN)_6$ in 0.1*M* KCl were used at a potential of +0.80V to check the capabilities of the electrolysis systems. With 0.25*M* $K_4Fe(CN)_6$ in the GBC, the highest current density, obtained with a very thin paste layer, was 68 mA cm^{-1} for a total paste area of 20 cm^2. Titration of residual $K_4Fe(CN)_6$ with standard $KMnO_4$ solution was used to estimate current efficiencies. Values were close to 100% with

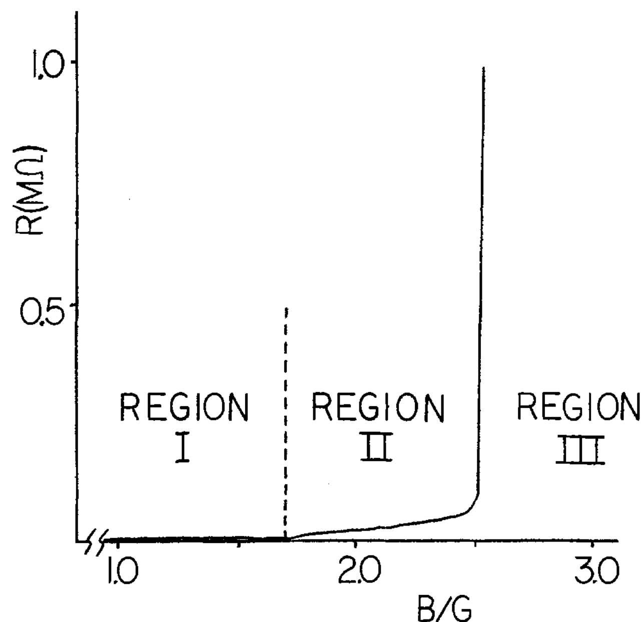

Fig. 3. Resistance as a function of B/G ratio for graphite-wax composites.

$K_4Fe(CN)_6$ concentrations up to approximately 8 m*M*, but became lower at higher concentrations.

Both systems have been used for the oxidative coupling of corypalline (7-hydroxy-6-methoxy-*N*-methyl-1,2,3,4-tetrahydroisoquinoline) and related compounds in aqueous media, with yields comparable to those obtained at graphite cloth or graphite felt electrodes (7). In particular, the simplicity of construction of the GBC and the ease with which its paste layer can be renewed make this system potentially useful for general oxidative syntheses. Experiments are now being made in which chiral and other liquids are used as binders in place of Nujol.

The GBC was used in an attempt to oxidize 1g of the hydrochloride of tyramine [*p*-(2-aminoethyl)-phenol] in 50 ml of 0.1*M* NaOH. At a potential of +0.80V, the current dropped from 80 mA to less that 1 mA within 2 sec. Several runs with the RDC under similar conditions showed that reasonable but somewhat fluctuating currents of 50-60 mA could be maintained for several hours, decreasing only when the substrate concentration was allowed to fall significantly.

In a preliminary report, Papouchado (8) concluded that 90-95% of the electrolytic oxidation products of tyramine were polymeric. On the basis of voltammetric and color-test data, these workers postulated that the nonpolymeric product was *p*-(2-aminoethyl)-*ortho*quinone. A run in the RDC with 3g of tyramine hydrochloride in 400 ml of 0.1*M* NaOH gave a current in the range 60-100 mA. The process was stopped when electricity equivalent to 2*e* per molecule of tyramine had been passed. The reaction mixture was rotary evaporated to dryness, using a hot water bath and reduced pressure (filter pump), and the residue was extracted with 50 ml of methanol. This solution was evaporated to a volume of approximately 5 ml, filtered, and the filtrate was transferred to four silica gel GF254 preparative TLC plates. Using 5% NH_4OH in methanol as developer, the presence of six products was inferred. The one preponderating was recovered in 0.4% over-all yield as a glass that softened at approximately 150°C. This material was identified by infrared and mass spectroscopy as a carbon-carbon "dimer" of tyramine, probably that shown at (a) in Fig. 4. (*IR*: peaks for aromatic C = C and O-H; ms: parent peak at m/e 272 and large peak at m/e 243). To support this identification, 7 mg of the product were acetylated and its mass spectrum was examined (parent peak at m/e 440, in line with formula (b) in Fig. 4; large peak at m/e 381.)

It appears that most of the tyramine is converted to dark-colored products that are probably polymers of the melanin type (9). The maintenance of the current by use of the RDC thus allowed an isolable quantity of a nonpolymeric product to be obtained in this extremely unfavorable case.

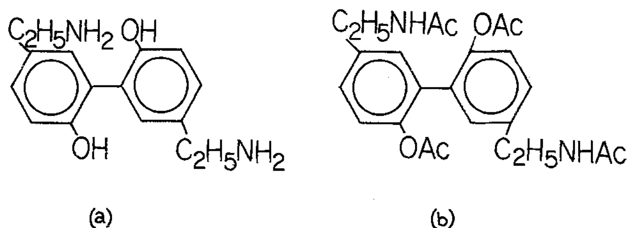

Fig. 4. (a) Carbon-carbon "dimer" of tyramine (b) acetylated "dimer."

Acknowledgments

This work was supported in part by the University of Connecticut Research Foundation. The feasibility of the thin-layer graphite paste electrode was demonstrated by Professor Takeo Hisano while Visiting Research Associate at this University. He also made preliminary designs for the rotating drum cell. The authors thank Professor J. M. Bobbitt for valuable discussions.

Manuscript submitted Sept. 26, 1977; revised manuscript received Nov. 6, 1977.

Any discussion of this paper will appear in a Discussion Section to be published in the December 1978 JOURNAL. All discussions for the December 1978 Discussion Section should be submitted by Aug. 1, 1978.

Publication costs of this article were assisted by the University of Connecticut.

REFERENCES

1. R. N. Adams, "Electrochemistry at Solid Electrodes," p. 280, Marcel Dekker, Inc., New York (1969).
2. J. F. Colaruotolo, Ph.D. dissertation, University of Connecticut (1974).
3. J. T. Stock, in "Topics in Chemical Instrumentation," Vol. II, G. W. Ewing, Editor, p. 244, American Chemical Society, Washington, D.C. (1977).
4. J. T. Stock, *Chemist Analyst*, **48**, 8 ((1959).
5. J. T. Stock, *Anal. Chem.*, **43**, 289 (1971).
6. J. T. Stock and J P. Sapio, *This Journal*, **120**, 1331 (1973).
7. J. M. Bobbitt, H. Yagi, S. Shibuya, and J. T. Stock, *J. Org. Chem.*, **36**, 3006 (1971).
8. L. Papouchado, *This Journal*, **117**, 50C (1970).
9. M. E. Friedman and H. H. Daron, *J. Chem. Educ.*, **54**, 256 (1977).

Electrochemical Studies of Antitumor Antibiotics

III. Daunorubicin and Adriamycin

Gopalakrishna M. Rao,* J. William Lown, and James A. Plambeck*

Department of Chemistry, University of Alberta, Edmonton, Alberta, Canada T6G 2G2

ABSTRACT

Daunorubicin and adriamycin, anthracycline antibiotics, have been investigated by polarography, cyclic voltammetry, and chronopotentiometry in aqueous media at 37.5°C, as have their aglycones daunomycinone and adriamycinone. A mechanism is proposed to explain the complex reduction behavior observed. The significance of the mechanism is discussed in relation to the antineoplastic and cardiotoxic activity of the clinically useful daunorubicin and adriamycin.

Daunorubicin, **1**, a fungal metabolite isolated from *streptomyces peucetius* (which also produces the related tetracyclines) is a member of the anthracycline class of antitumor antibiotics which includes adriamycin, cinerubin, rhodomycin, rutilantine, pyrromycin, nogalamycin, and carminomycin (1). These glycosidic antibiotics are among the most effective antineoplastic agents and show activity against a variety of experimental tumors and certain types of human cancer (1, 2). Daunorubicin was the first compound to show therapeutic effect in the treatment of acute leukemia in man (2). Biochemical evidence indicates that daunorubicin and adriamycin are metabolized in rat liver by an NADPH-mediated "daunorubicin reductase," an aldo-keto reductase, to daunorubicinol and adriamycinol, respectively (3, 4). Enzymatic reduction of the carbonyl group of daunorubicin occurs more readily than does that of adriamycin (5, 6). Daunorubicinol is the major excretion form of daunorubicin and is a major form of the drug in tissues (3); it has cytotoxic properties and is an important component in the action of the drug (3). Another important metabolic pathway leads to reductive cleavage of the glycosidic linkage to produce the 7-deoxyaglycones (6). The anthracyclines are currently considered to act by selective inhibition of both DNA-directed DNA synthesis and DNA-directed RNA synthesis in part by strong intercalative binding to duplex DNA in the cell nucleus; this binding prevents unwinding and strand separation during the semiconservative replication process (1).

There have been reports of chromosomal damage as a result of daunorubicin administration (7, 8). Similarly the marked immunosuppressive action of the anthracyclines appears to be related to the degradation of nucleic acids in blood lymphocytes (9-11). The chemical mechanism of this degradation of nucleic acids has not been investigated. However, there is a structural similarity between the quinone moiety of the anthracyclines and that of streptonigrin (12), mitomycins B and C (13), and certain 5:8-quinolinediones (14) which show antitumor properties and which we have shown cleave DNA after reduction by a common mechanism involving generation of superoxide radical anion and hydroxyl radicals (15-18). One therefore anticipated that a similar mechanism operates for the anthracyclines, which would have the added advantage of being firmly bound to the target DNA. We have recently confirmed that this process occurs between daunorubicin or adriamycin and supercoiled covalently closed circular DNA in the presence of a reducing agent (19).

Chemotherapeutic treatment of cancer employing daunorubicin and adriamycin is hampered by dose-related cardiotoxic effects (20-23) which have been shown to be associated with their inhibition of coenzyme Q_{10} mediated enzymes in mitochondria of the myocardium and with interference of electron transport processes and oxidative phosphorylation and which clearly involve the oxidative power of the anthracyclines (24-29).

For these three separate reasons a detailed study of the redox behavior of the anthracyclines is of interest. An earlier polarographic study of Calendi *et al.* shows a polarographic reduction wave with a formal potential of -0.6V for daunorubicin; however, depolarizer concentration and other polarographic parameters were not reported (30). Moreover, these authors argued that the disappearance of this polarographic wave when DNA was added to daunorubicin was evidence for the formation of a DNA-daunorubicin complex. It is well known that DNA adsorbs on mercury at this potential range (31), which makes this explanation unlikely. Therefore, we report the electrochemical reduction of daunorubicin (**1**), adriamycin (**1b**), and their aglycones *in vitro*, together with such related processes as are accessible to electroanalytical investigations. The structures of **1**, **1a**, and **2** (7-deoxydaunomycinone) are given in Fig. 1; the structure of adriamycin, **1b**, is identical to that of daunorubicin, **1**, except that the $—COCH_3$ ketone side-chain of daunorubicin is replaced by $—COCH_2OH$ in adriamycin.

Experimental

Daunorubicin hydrochloride (daunomycin), **1**, obtained from Calbiochem, was used without further purification. Experimental studies were carried out at three concentrations, 1.9×10^{-4}, 7.8×10^{-5}, and 1.9×10^{-5}M. The concentrations were determined spectrophotometrically on a Cary 118 spectrophotometer using the molar extinction coefficient of 11.4×10^3 at 485 nm (3). The solution was buffered at *p*H 7.1 with 0.1M phosphate buffer in 0.1M KCl in most of the experiments; however, the *p*H of the solution was varied from 6 to 8 in the *p*H-dependence study. The absorption spectrum includes a broad peak around 480 nm in the visible region which was used for analysis and three peaks at 290, 253, and 233 nm in the ultraviolet region.

The aglycone daunomycinone, **1a**, was prepared by acid hydrolysis of the antibiotic according to a literature procedure (32). The absorption spectrum of **1a** differs from that of **1**; the peak at 480 nm is broadened, the peaks at 233 and 290 nm are displaced to 228 and 310 nm, and the 253 nm peak is unchanged. The sample solution of **1a** was prepared as were the sample solutions of **1**. Its concentration was measured spectrophotometrically as 1×10^{-5}M, the maximum concentration which could be achieved due to the low solubility of this compound (33).

* Electrochemical Society Active Member.
Key words: polarography, cyclic voltammetry, antibiotic, daunomycin, daunorubicin.

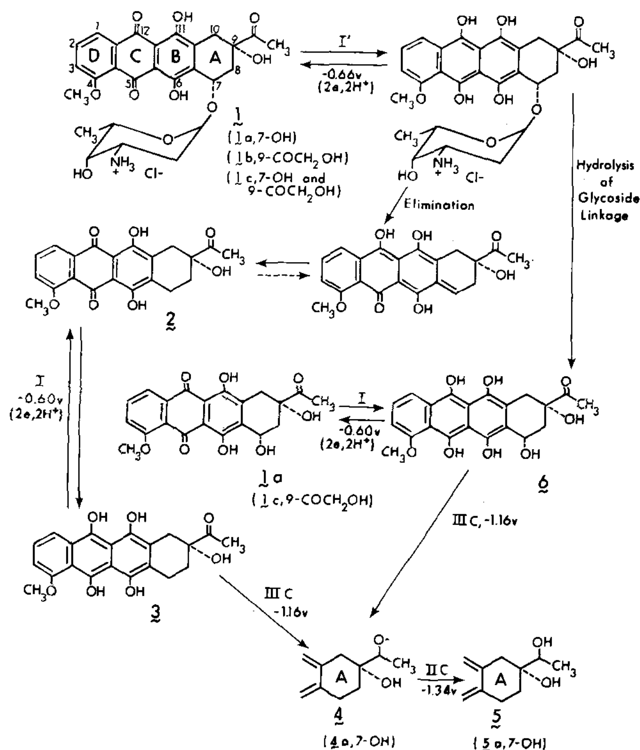

Fig. 1. Electrochemical reduction mechanism proposed. Only the part of the molecule involved in IIIC and IIC is shown for these steps. Potential of processes I and I′ are those for reversible behavior while potentials of IIC and IIIC are experimental peak potentials.

Solutions of the more soluble adriamycin, **1b**, (NCI sample) were 4.0×10^{-4}M and were otherwise prepared and used in the same manner as those of daunorubicin. The aglycone adriamycinone, **1c**, was prepared by acid hydrolysis (32) of adriamycin.

All other experimental conditions were as previously described (34); all potentials were measured and are given with respect to the aqueous saturated calomel electrode.

Results

Daunorubicin, **1**.—The classical d-c polarogram of 1.9×10^{-4}M daunorubicin at 5 sec drop time (0.0-−0.9V) showed two waves with a surface-complicated second wave plateau (Fig. 2) unlike the previously reported two-electron reversible single wave (30). The approximate half-wave potentials of these peaks are, for IC, −0.58V and, for I′C, −0.63V at *p*H 7.1; the average of these two values is close to the literature value of −0.6V (30).

Differential pulse polarography (0.0-−1.6V) gave four peaks depending upon both the drop time and the concentration (Fig. 3). The peak IC appeared at −0.59 ± 0.01V for all drop times 0.5-5 sec. Increasing the concentration had no effect on the peak potential at drop times 0.5-2 sec; at a drop time of 5 sec, however, a shoulder replaced peak IC as the concentration increased. The peak I′C appeared at −0.655 and −0.630V in the solution of 1.9×10^{-4} and 7.8×10^{-5}M, respectively. This peak was always a shoulder at 2 sec and almost undetectable at 0.5 sec even for the 1.9×10^{-4}M solution. Peak IIIC appeared at −1.14V at higher concentrations; the same process appeared as a wave in 1.9×10^{-5}M solution. The peak IIC appeared at −1.32V at all concentrations and drop times.

Chronopotentiometric studies confirmed the presence of all the processes mentioned above. The process that corresponds to the potential of wave IC influences the chronopotentiometric wave I′C. The combined wave has $E_{\tau/4} = -0.63 \pm 0.01$V; $E_{\tau/4}$ is the chronopotentiometric equivalent of the polarographic half-wave potential. The $i\tau^{-1/2}$ product for this wave increases with the increase in current; its chronopotentiometric constant $i\tau^{1/2}$ is proportional to $C^{0.67}$.

Figure 4 is a typical cyclic voltammogram of a *p*H 7.1 daunorubicin solution at 500 mV/sec. It shows three cathodic peaks (IC-IIIC) and one anodic peak (IA). A broad anodic peak also appears close to −0.2V. Multicycle runs showed, in addition to I′C, two more cathodic peaks at about −1.08 and −1.25V; the peak at −1.25V is better defined in alkaline solutions. These two additional cathodic peaks may appear during the first cycle at slow scan rates and, at higher scan rates, in alkaline solution. The cathodic peaks IIIC and IIC appeared at −1.16 ± 0.02V and −1.34 ± 0.02V at $\nu = 500$ mV/sec for solutions of *p*H 6-7.5; both these peaks were barely visible at *p*H > 7.5. No characterizable peaks appeared between −0.9V and the supporting electrolyte discharge in the

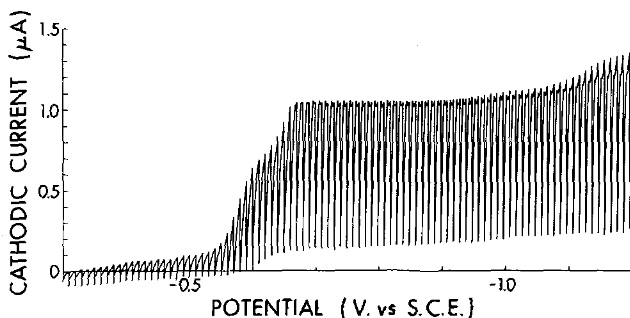

Fig. 2. D-c polarogram of **1** (1.9×10^{-4}M), *p*H = 7.1 in phosphate buffer, 37.5°C, ν = 2 mV/sec, drop time 5 sec.

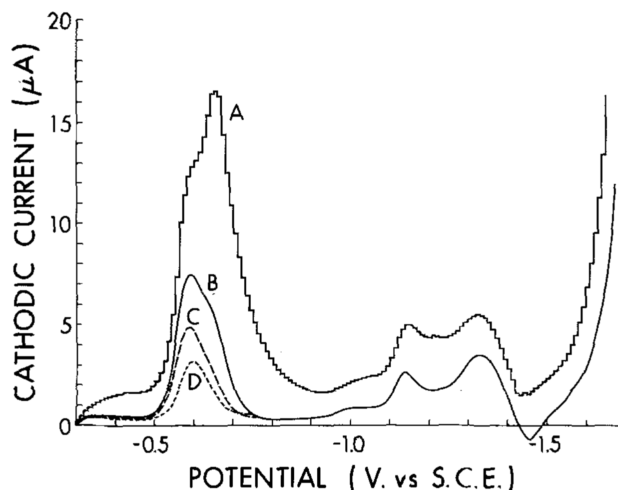

Fig. 3. Differential pulse polarogram of **1** (1.9×10^{-4}M), pH 7.1 in phosphate buffer, 37.5°C, ν = 2 mV/sec; drop times: A, 5 sec; B, 2 sec; C, 1 sec; D, 0.5 sec.

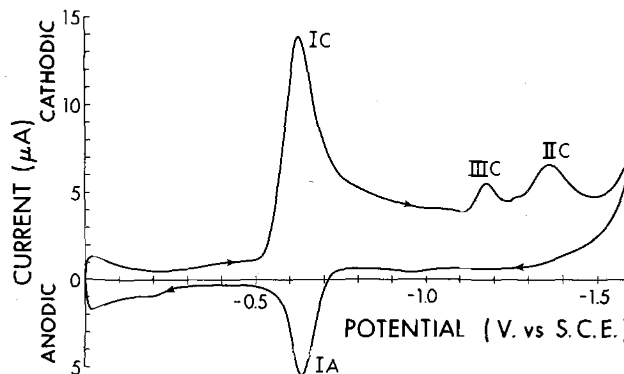

Fig. 4. Cyclic voltammogram of **1** (1.9×10^{-4}M), *p*H 7.1 in phosphate buffer, 37.5°C, ν = 500 mV/sec.

vicinity of −1.2V when the *p*H of the solution was changed from 6.52 to 3.1. Restoring the *p*H of this solution to neutral caused these peaks to reappear. All these cathodic peaks appeared to shift anodic as the scan rate decreased; the relative shift for IIC was greater than IIIC. The appearance of these cathodic peaks and the absence of the corresponding anodic peaks indicates that these processes are not reversible.

Most of the cyclic voltammetric studies were restricted to the potential range of −0.3-−0.9V to avoid complications arising from the processes outside this potential range. With the range thus restricted, only IC, I′C, and IA were visible depending on the scan rate, concentration, and the *p*H of the solution.

The cathodic peak IC is prominent in 1.9×10^{-4}M solution of *p*H 7.1 at scan rates above 100 mV/sec. Below 100 mV/sec, the peak IC appeared either as a small peak or a shoulder (Fig. 5). The scan rate at which IC first appeared as a shoulder decreased as the concentration decreased and increased as the *p*H of the solution increased. The peak potential of IC is −0.62 ± 0.01V, independent of scan rate, up to 2 V/sec, and thereafter is shifted cathodic by 30-40 mV for each tenfold increase in scan rate. The $I_p\nu^{-1/2}$ product increased with the increase in scan rate; an approximate relationship of $I_p\nu^{-1/2}$ proportional to $C^{0.4}$ is obtained from the concentration dependence. Such a concentration dependence on current was observed for anthraquinones by Broadbent and Zollinger (35). According to these authors, the limiting current for the more positive wave was independent of concentration only above 10^{-4}M, the upper limit of the present study. A value of αn of approximately 1.4 can be calculated from the difference between the peak potential and the half-peak potential. This, and the *p*H dependence of peak potential of 58 mV/*p*H-unit for IC, suggests that the electrode process taking place at this peak potential may be an irreversible two-electron, two-proton process.

The potential of the anodic peak IA is −0.64 ± 0.01V, independent of scan rate, up to 500 mV/sec, and thereafter is shifted anodic by 30-40 mV for each tenfold increase in scan rate. The $I_p\nu^{-1/2}$ product increased with increase in scan rate. This peak potential has a *p*H dependence of 58 mV/*p*H unit. The peak IA appeared cathodic to IC at $\nu \leqq 2$ V/sec and anodic to IC at $\nu \geqq 2$ V/sec. The anodic peak sometimes became sharp, especially in 7.8×10^{-5}M solution (Fig. 6), in the vicinity of scan rate 100 mV/sec when I′C is approximately equal to IC, during the multicycle run at slower scan rates (Fig. 5), or upon excursion to very negative potential in a single cycle. The ratio of anodic to cathodic current of process I is constant at about 0.4 for $\nu \leqq 50$ mV/sec and then increases, reaching a value of 0.9 at 50 V/sec (except when IA is sharp or the solution is very acidic). This ratio passes through a maximum in the scan rate region where IA is sharp. In acidic solution, say *p*H = 3.1, the ratio I_p (IA)/I_p (IC) is almost unity at 100 mV/sec $< \nu <$ 50 V/sec, which is the scan rate limit at this *p*H. All these facts suggest that the process or processes giving rise to peak IA show the combined influence of the two cathodic processes of I and I′. The observed single anodic peak IA may arise from two separate but indistinguishable anodic processes, those of I and I′. In 1.9×10^{-4}M solution of *p*H 7.1, the height of the peak I′C is greater than that of the peak IC at $\nu <$ 100 mV/sec. The peak I′C began to become noticeable at slower scan rates as the concentration of the solution decreased and at higher scan rates as the solution *p*H increased. The peak I′C appeared as a shoulder to the peak IC in the solution of *p*H 6.5 at ν = 100 mV/sec; it disappeared upon acidification to *p*H 3.1 and reappeared when the solution *p*H was restored to neutral. The peak potential of I′C is −0.67 ± 0.01V independent of scan rate. The separation of peak potential between I′C and IA is about 30 ± 5 mV. This, and the *p*H dependence of 58 mV/*p*H unit for the peak I′C, suggests that the process occurring at the potential correspond-

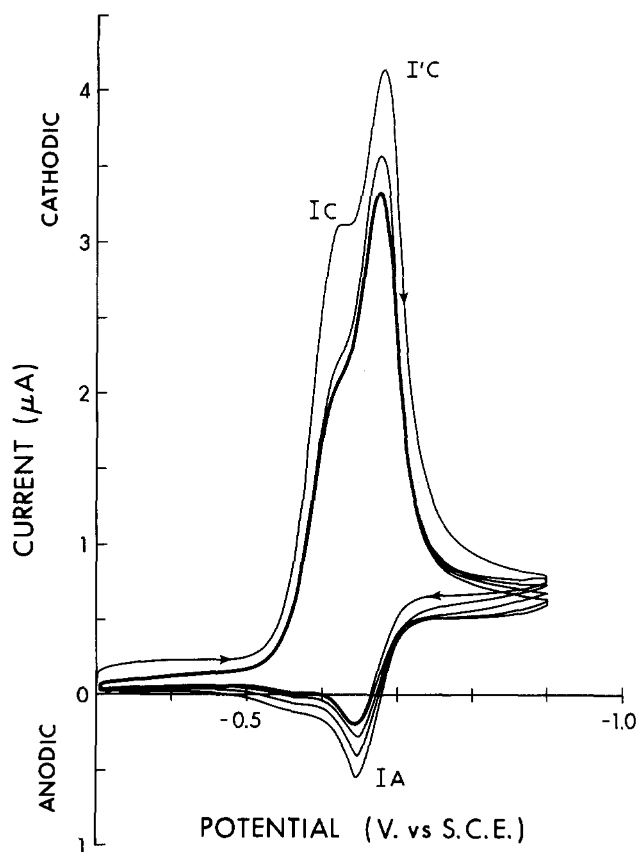

Fig. 5. Multicycle voltammogram of 1 (1.9×10^{-4}M), *p*H 7.1 in phosphate buffer, 37.5°C, ν = 50 mV/sec. Cathodic peaks decrease and peak IA increases with cycling.

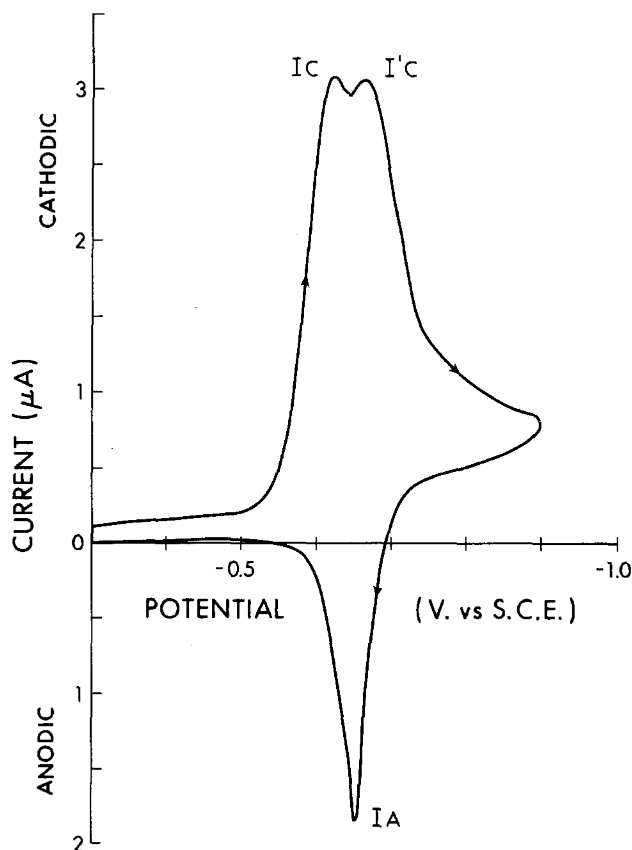

Fig. 6. Cyclic voltammogram of 1 (7.8×10^{-5}M), *p*H 7.1 in phosphate buffer, 37.5°C, ν = 100 mV/sec.

ing to the I′C is a two-electron, two-proton process. The $I_p\nu^{-1/2}$ product increased with the decrease in scan rate and the concentration dependence of $I_p\nu^{-1/2}$ is proportional to $C^{0.67}$, a similar relationship to that observed in the chronopotentiometric studies.

In multicycle runs, the peak IC observed on the first cycle disappeared in the second and subsequent cycles (Fig. 5 and 7). In the second cycle (at ν = 500 mV/sec for the solution of 1.9 × 10^{-4}M of pH 7.1), the height of the peak IA is increased, the height of the new peak I′C is greater than that observed for IC in the first cycle, and the peak separation between the peaks I′C and IA is 30 ± 5 mV. This value of 30 mV peak separation suggests a reversible two-electron process as explained above. Further cycling shows normal behavior, which is a slow decrease in peak height, with a slight or no change in peak potential, as the number of cycles increases. In ten times diluted solution, the height of the new peak I′C in the second cycle is, however, smaller than that of the peak IC in the first cycle (Fig. 7). Multicycle runs at slower scan rate showed similar behavior, but the peak IA grew sharper as the number of cycles increased (Fig. 5).

Daunomycinone, **1a**.—Solutions of daunomycinone at pH 6.86 gave three cathodic-anodic couples (Fig. 8), and two additional cathodic peaks.

Couple I has a cathodic peak IC (−0.60 ± 0.01V, independent of scan rate up to 20 V/sec) and an anodic peak IA (−0.604 ± 0.01V independent of scan rate up to 5 V/sec). At faster scan rates, the cathodic peak

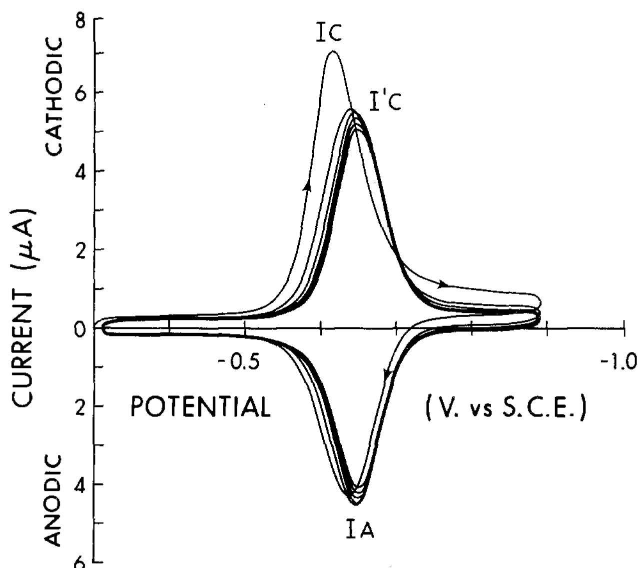

Fig. 7. Multicycle voltammogram of **1** (1.9 × 10^{-5}M), pH 7.1 in phosphate buffer, 37.5°C, ν = 500 mV/sec. First cycle indicated by arrows.

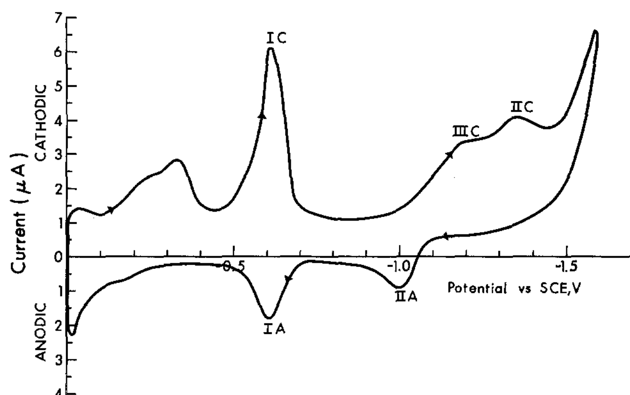

Fig. 8. Cyclic voltammogram of **1a** (approximately 1 × 10^{-5}M), pH 6.86 in phosphate buffer, 37.5°C, ν = 500 mV/sec.

shifted more negative and the anodic peak shifted more positive with increase in scan rate. The ratio of the anodic current to the cathodic current is closer to unity above 500 mV/sec, but this ratio decreased with decrease in scan rate. When the potential range was restricted (−0.4-−0.8V) a current ratio of unity was obtained. The potential difference between the peak potential and the half-peak potential for the cathodic peak is approximately as expected for a two-electron process.

The cathodic peak IIC of couple II appeared at −1.35 ± 0.02V for ν = 500 mV/sec and shifted anodic as the scan rate decreased. The corresponding anodic peak IIA appeared at −1.00 ± 0.01V at ν < 1 V/sec.

A new couple not visible in daunomycin voltammograms, designated IV, was clearly present in those of **1a**, daunomycinone. This couple consisted of a broad cathodic peak IVC which at 50 mV/sec had a potential of −0.195V; a shoulder was present on the positive side. The peak potential became more negative and the peak became better defined as the scan rate was increased. The corresponding but smaller anodic peak IVA had a peak potential of −0.130V at ν = 50 mV/sec (shoulder on negative side). The peak potential became more positive with increasing scan rate and could no longer be distinguished from mercury dissolution at ν > 200 V/sec.

The cathodic peak IIIC was visible at scan rates below 1 V/sec, had a cathodic peak potential of −1.16 ± 0.01V and shifted slightly anodic as the scan rate decreased. Multicycle runs (0-−1.6V) did not show any additional peaks, but IC shifted cathodic with continued cycling until the peak potential of IC equaled that of I′C.

Adriamycin, **1b**.—The behavior of adriamycin was very similar to that of daunorubicin; the major peaks IC, IA, I′C, IIC, and IIIC, as well as the minor peaks, were observed. The slight differences in peak potential are summarized in Table I.

With adriamycin, repeated cyclic voltammetry to −1.6V gave rise to a new process (cathodic E_p −0.26V and anodic E_p −0.17V) which was barely observable on the curves. These are similar to the process IV which appear on the cyclic voltammetric curves of daunomycinone. Corresponding processes IV can barely be distinguished on a few of the curves for the most concentrated solutions of daunorubicin.

Adriamycinone, **1c**.—Solutions of adriamycinone at pH 7.04 gave cyclic voltammograms very similar to those of daunomycinone. Well-defined peaks were observed for IC, IA, IVC, and IVA (peak potentials −0.604, −0.600, −0.194, −0.123V at ν = 100 mV/sec). The cathodic processes IIC and IIIC, though present, were extremely ill defined; a peak IIA was distinguishable at −0.99V. Process I′ was clearly absent in both daunomycinone and adriamycinone.

Discussion

The mechanism proposed to account for the observed behavior of these compounds is shown in Fig. 1. The process I′ is ascribed to the reversible two-electron,

Table I. Peak potentials observed for antibiotics (against aqueous SCE)

Process	Peak potential		
	Daunomycinone (Volts)	Daunorubicin (Volts)	Adriamycin (Volts)
IC	−0.600 ± 0.01	−0.620 ± 0.01	−0.620 ± 0.01
IA	−0.604 ± 0.01	−0.640 ± 0.01	−0.625 ± 0.01
I′C	Absent	−0.670 ± 0.01	−0.660 ± 0.01
IIC	−1.35 ± 0.02	−1.34 ± 0.02*	−1.41 ± 0.02*
IIIC	−1.16 ± 0.01	−1.16 ± 0.02*	−1.18 ± 0.02*

* pH independent; all other processes at pH 7.0 ± 0.1. Scan rate in all cases 100 mV/sec.

two-proton reduction of the quinone group of daunorubicin, **1**, and adriamycin, **1b**, at a formal potential of -0.66 ± 0.02V against SCE. Precise measurement of this reversible process is prevented by two competing subsequent irreversible processes. First, rapid and irreversible elimination of the amino sugar moiety occurs, giving rise to 7-deoxydaunomycinone, **2**. This process parallels the principal pathway for human metabolism of the anthracyclines (36, 37). Like the parent antibiotic, **2** is capable of a reversible two-electron, two-proton reduction of the quinone group. Mild chemical reduction ($Na_2S_2O_4$) of **1** results in quantitative conversion to **2**, supporting this proposed process (38). Second, hydrolytic cleavage of the hydroquinone of **1** gives rise to the reduced form of the aglycone **1a**.

By either route, a system is formed (**2-3** or **1a-6**) which is a quinone-hydroquinone system capable of reversible two-electron, two-proton reduction. A further possible step would be dehydration at C_7 and C_9 of ring A to introduce aromaticity. In all of these three cases the structures are very similar, and the redox process I may involve contributions from them all. However, we believe that the elimination-tautomerism route through **2** is the most probable. The formal potential of I is -0.62 ± 0.02V, the potential being slightly less negative when the amino sugar is absent (**1a**, **1c**) than when it is present (**1**, **1b**), so that following reduction the hydroquinone forms will be present.

Once formed the hydroquinones such as **3** and **6** are capable of further reduction only at considerably more negative potentials where reduction of the side-chain carbonyl group on ring A can take place. This occurs in two irreversible one-electron steps designated IIIC (-1.16V) and IIC (-1.34V) to produce the final product alcohol. Such a mechanism is consistent with the experimental electrochemical data. The mechanism for adriamycin is identical to that for daunorubicin.

Quinone redox processes I and I'.—The two waves observed in the classical polarographic measurements correspond to the process I' and I, reduction of **1** and of **1a** or **2**, respectively, and represent kinetic rather than equilibrium reduction of the latter; the close similarity of half-wave potentials may explain why the separation was not observed by earlier workers (30) since differential pulse polarography is required to distinguish them clearly. The kinetic nature of I' is clearly evident from the effect of drop time shown for the two differential pulse polarograms of Fig. 3; the chemical steps take place within 3 sec, and the half-times of these heterogeneous steps (which are not directly comparable to similar homogeneous chemical kinetic steps) are 1 sec or less, since at such speeds their effect disappears.

The appearance of the combined waves IC and I'C in chronopotentiometry confirms the complication in separating the two processes. Moreover, the increase in $i\tau^{1/2}$ with increasing current is evidence for ECE mechanisms (39) such as are proposed here.

Cyclic voltammetry further characterizes the chemical step between the two charge-transfer steps for the reduction of **1** and **2**. The solubility of daunomycinone in water is low (32) as evident from the observation reported in this work such as low absorption in spectrophotometry and the smaller peak currents in cyclic voltammetry of **1a** compared to **1**. The charge transfer process I' appears to be an irreversible two-electron, two-proton process, but the irreversibility is due to the influence of the following chemical step. The facts to account for by the chemical step are: (*i*) the reversibility of process I for **1a** and **1c**, and the apparent reversibility of I at high scan rates for **1** and **1b**; (*ii*) the continued appearance of I'C and disappearance of IC in the subsequent cycles of a multicycle voltammogram of **1** (Fig. 7); and (*iii*) the influence of cathodic peaks IC and I'C on the anodic peak IA. In consideration of the last point, the anodic peak IA, at least at lower scan rates, behaves as the anodic counterpart of both. Under these conditions of slower speed, the charge-transfer process I' can have no anodic counterpart since the corresponding hydroquinone undergoes chemical reaction and is not available for reoxidation, and an anodic peak I'A should not be observed.

The rate of the irreversible chemical reaction that follows the initial reduction of **1**, breakage of the glycoside linkage, and tautomerization can be estimated from the cyclic voltammetry (34). Use of the anodic/cathodic peak current ratios of the voltammetric curves does not give a satisfactory value of k_f. However, the rate constant k_f can be estimated from the scan rate at which the peak I'C appears and the time required to scan between IC and I'C. The value is about 1 sec^{-1} and comparable with the half-time of 1 sec or less estimated from polarography.

Sidechain carbonyl reduction processes IIC and IIIC.—The nonreversible reduction processes IIC and IIIC are ascribed to the reduction of the side-chain carbonyl groups on the basis of their similarity to the reduction processes of acetophenone and 1'-acetonaphthone (40) and our observation that these peaks are absent when the side-chain carbonyl is protected by a ketal group. With the additional benzene ring in 1'-acetonaphthone, two separate peaks are observed (40). We attribute the peaks IIIC (-1.16V) and IIC (-1.34V) to the reduction of the side-chain carbonyl group on ring A as shown in Fig. 1.

The generally accepted reduction mechanism for the side-chain carbonyl compounds (aryl alkyl ketones) in neutral media (41) is:

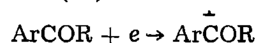

$$ArCOR + e \rightarrow Ar\overset{\dot{-}}{C}OR$$

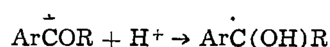

$$Ar\overset{\dot{-}}{C}OR + H^+ \rightarrow Ar\dot{C}(OH)R$$

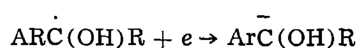

$$AR\dot{C}(OH)R + e \rightarrow Ar\overset{-}{C}(OH)R$$

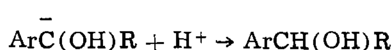

$$Ar\overset{-}{C}(OH)R + H^+ \rightarrow ArCH(OH)R$$

which is two one-electron processes each followed by a protonation step. Our data do not unambiguously show two one-electron steps each followed by protonation, and the mechanism shown in Fig. 1 therefore does not distinguish the protonation process.

Adriamycin gives peak IIC some 70 mV more cathodic than does daunorubicin, indicating that the reduction to the alcohol is considerably easier for daunorubicin than for adriamycin. This is consistent with the observed greater metabolic reduction to daunorubicinol (50-60%) than to the corresponding adriamycinol (15-20%) (3).

Other processes.—The surface complication on the diffusion-limited plateau apparent from the shape of the *i-t* profiles of the individual drops in the classical d-c polarography (Fig. 2) at potentials more negative than -0.7V may well be adsorption of **3** or **6** since the shape of the drops below this plateau is the normal rise expected for $t^{1/6}$ dependence. Sharp peaks observed in cyclic voltammetry at the slower scan rates or in the subsequent cycles of the multicycle run (Fig. 5 and 6) confirm the adsorption of **3** as these sharp peaks were attributed to two-dimensional phase transitions in the adsorbed layer or to lateral interactions between the adsorbed atoms (42).

The process IV occurring at potentials more positive than IC for **1a** and **1c** cannot be unambiguously defined, although it is discussed further in the following paper (40). This process was not found in the parent antibiotics at other than the trace level expected for very slight hydrolysis.

Conclusions

The proposed mechanism for the electrochemical reduction of daunorubicin is consistent with the view of Di Marco *et al.* (1). The metabolic transformation con-

sists of reductive modification of the chromophore associated with breakage of the glycosidic linkage with the formation of the 7-deoxydaunomycinone and similar species. Our experimental findings do not demonstrate the formation of daunorubicinol. Our observations, however, do not preclude the formation of daunorubicinol during enzymatic reduction (3), since the aldo-keto reductase involved in the side-chain reduction is unable to reduce the quinone functional group to its hydroquinone. Moreover, the quinone group hydrogen-bonded to adjacent hydroxyl groups, as in the present case of intramolecular hydrogen bonding between the C_5, C_{12} quinones and the C_6, C_{11} hydroquinones, is known to remain unaffected by some chemical reducing agents; for example, reduction of 1-hydroxyanthraquinone by zinc in the presence of acetic acid yields 1-hydroxyanthrone (43). The effect of hydrogen bonding upon the redox chemistry of these compounds is discussed further in the following paper (40).

The electrochemical results demonstrate that the quinone ring C of the anthracycline is more difficult to reduce than for example mitomycin C (32) (redox potentials of −0.600, −0.650, and −0.385, −0.468V respectively). The identical ring C redox potentials of daunorubicin and daunomycinone confirm that the more extensive degradation of DNA by the parent antibiotic than of the aglycone is due to the strong binding of the amino sugar moiety of the former to the DNA target (19).

In summary the present studies provide an electrochemical basis for interpreting the degradation of DNA that accompanies clinical administration of daunomycin, of the cardiotoxic side effects that depend directly on the oxidative capacity of the chromophore, and of its reductive enzymatic metabolism to 7-deoxydaunomycinone.

Acknowledgment

We are grateful to Dr. S. K. Sim of this Department for the preparation of **1a** and **1c** and to the National Research Council of Canada for support of this research through Operating Grants to J.W.L. and J.A.P. and to the National Cancer Institute of Canada for a research grant to J.W.L.

Manuscript submitted June 1, 1977; revised manuscript received Dec. 13, 1977. This was presented in part as Paper 273 at the Philadelphia, Pennsylvania, Meeting of the Society, May 8-13, 1977.

Any discussion of this paper will appear in a Discussion Section to be published in the December 1978 JOURNAL. All discussions for the December 1978 Discussion Section should be submitted by Aug. 1, 1978.

Publication costs of this article were assisted by The University of Alberta.

REFERENCES

1. A. DiMarco, F. Arcamone, and F. Zunino, in "Antibiotics III-Mechanism of Action of Antimicrobial and Antitumor Agents," J. W. Corcoran and F. E. Hahn, Editors, pp. 101-128 and references therein, Springer-Verlag, New York (1975).
2. D. W. Henry, *Cancer Chemother. Rep.*, Part 2, **4**, No. 4 (1974).
3. R. L. Felsted, M. Gee, and N. R. Bachur, *J. Biol., Chem.*, **249**, 3672 (1974).
4. N. R. Bachur, M. Steele, W. D. Meriweather, and R. C. Hildebrand, *J. Med. Chem.*, **19**, 651 (1967).
5. N. R. Bachur, R. C. Hildebrand, and T. Taenke, *J. Pharmacol. Exp. Ther.*, **191**, 331 (1974).
6. V. P. Marshall, E. A. Reisender, L. M. Reinecke, J. H. Johnson, and P. F. Wiley, *Biochemistry*, **15**, 4139 (1976).
7. A. Di Marco, M. Gaetani, L. Dorigotti, M. Soldati, and O. Bellini, *Cancer Chemotherapy Rep.*, **38**, 31 (1964).
8. A. Di Marco, M. Gaetani, P. Orezzi, B. Scarpinato, R. Silvestrini, M. Soldati, T. Dasdia, and L. Valentini, *Nature (London)*, **201**, 706 (1964).
9. A. M. Isolta, C. Intini, and M. Soldati, *Experentia*, **27**, 202 (1971).
10. A. M. Casazza, A. DiMarco, and G. DiAronzo, *Cancer Res.*, **31**, 1971 (1971).
11. N. Natale and P. Mocorelli, *Tumori*, **55**, 409 (1969).
12. K. V. Rao, K. Beimann, and R. B. Woodward, *J. Am. Chem. Soc.*, **85**, 2532 (1963).
13. W. Szybalski and V. N. Iyer, in "Antibiotics I-Mechanism of Action," D. D. Gottlieb and P. D. Shaw, Editors, pp. 221-245, Springer-Verlag, New York (1967).
14. J. S. Driscoll, G. F. Hazard, H. B. Wood, and A. Goldin, *Cancer Chemother. Rep.*, Part 2, **4**, No. 2, 1 (1974).
15. R. Cone, S. K. Hasan, J. W. Lown, and A. R. Morgan, *Can. J. Biochem.*, **54**, 219 (1976).
16. J. W. Lown, A. Begleiter, D. Johnson, and A. R. Morgan, *ibid.*, **54**, 110 (1976).
17. J. W. Lown and S. K. Sim, *Can. J. Chem.*, **54**, 2563 (1976).
18. J. W. Lown and S. K. Sim, *ibid.*, **54**, 446 (1976).
19. J. W. Lown, K. C. Majumdar, S. K. Sim, and R. Y. Chang, *Biochem. Biophys. Res. Commun.*, **70**, 705 (1977).
20. G. Rosen, N. Wollner, C. Tan, S. J. Wu, S. I. Hadju, W. Cham, G. J. D'Angio, and M. L. Murphy, *Cancer*, **33**, 384 (1974).
21. J. F. Halazun, H. R. Wagner, J. F. Gaeta, and L. F. Sinks, *ibid.*, **33**, 545 (1974).
22. E. A. Lefrak, J. Pitha, S. Rosenheim, and J. A. Gottlieb, *ibid.*, **32**, 302 (1973).
23. J. J. Rinehart, R. P. Lewis, and S. P. Balcerzak, *Ann. Intern. Med.*, **81**, 475 (1974).
24. T. Kishi, T. Watanabe, and K. Folkers, *Proc. Natl. Acad. Sci.*, **73**, 4653 (1976).
25. T. Kishi and K. Folkers, *Cancer Treat. Rep.*, **60**, 223 (1976).
26. Y. Iwamoto, I. L. Hansen, T. H. Porter, and K. Folkers, *Biochem. Biophys. Res. Commun.*, **58**, 633 (1974).
27. E. Bachmann, E. Weber, and G. Zbinden, *Agents and Actions*, **5/4**, 383 (1975).
28. W. R. Bachur, S. L. Gordon, and M. V. Gee, *Mol. Pharmacol.*, **13**, 901 (1977).
29. T. Goodman and P. Hochstein, *Biochem. Biophys. Res. Commun.*, **77**, 797 (1977).
30. E. Calendi, A. DiMarco, M. Reggiani, B. Scarpinto, and L. Valentini, *Biochem. Biophys. Acta*, **103**, 25 (1965).
31. B. Malfoy and J. A. Reynaud, *J. Electroanal. Chem.*, **67**, 359 (1976).
32. F. Arcamone, G. Francesschi, P. Orezzi, G. Cassinelli, W. Barbieri, and R. Mondelli, *J. Am. Chem. Soc.*, **86**, 5334 (1964).
33. S. Takanashi and N. R. Bachur, *J. Pharmacol. Exp. Ther.*, **195**, 41 (1975).
34. G. M. Rao, A. Begleiter, J. W. Lown, and J. A. Plambeck, *This Journal*, **124**, 199 (1977).
35. A. D. Broadbent and H. Zollinger, *Helv. Chim. Acta*, **49**, 1729 (1966).
36. S. Takanashi and N. R. Bachur, *J. Pharmacol. Exptl. Ther.*, **195**, 41 (1975).
37. N. R. Bachur, in "Cancer Chemotherapy," A. C. Sartorelli, Editor, ACS Symposium Series 30, p. 58 (1976).
38. J. H. Smith, A. N. Fujiwara, D. W. Henry, and W. W. Lu, *J. Am. Chem. Soc.*, **98**, 1969 (1976).
39. P. J. Lingane, *Crit. Rev. Anal. Chem.*, **2**, 587 (1971).
40. G. M. Rao, J. W. Lown, and J. A. Plambeck, *This Journal*, **125**, 540 (1978).
41. L. G. Feoktistov and H. Lund, in "Organic Electrochemistry," M. M. Baizer, Editor, pp. 374, Marcel Dekker, Inc., New York (1973).
42. D. Dickertmann and J. W. Schultze, *Electrochim. Acta*, **22**, 117 (1977).
43. L. A. Wiles, *J. Chem. Soc.*, 1358 (1952).

Electrochemical Studies of Antitumor Antibiotics

IV. Electrochemical Studies of Daunomycinone Analogues

Gopalakrishna M. Rao,* J. William Lown, and James A. Plambeck*

Department of Chemistry, University of Alberta, Edmonton, Alberta, Canada T6G 2G2

ABSTRACT

Certain synthetic analogues of daunomycinone have been investigated by cyclic voltammetry in aqueous media at 37.5°C. The experimental results have been of significance in establishing the electrochemical reduction behavior of daunomycinone and the related compounds daunorubicin and adriamycin described in the preceding paper.

Daunorubicin[1] and adriamycin are members of the anthracycline class of antibiotics which are among the most promising for the alleviation of cancerous conditions in humans (1). A serious disadvantage of these drugs is their cardiotoxicity or congestive heart failure, which occurs in 20-30% of patients treated (2-6) and also their currently high price since the isolation yield from the fungus *streptomyces peucetius* is low. Consequently there is considerable current interest in developing viable synthetic approaches to these valuable drugs and the preparation of analogues having improved therapeutic indices.

To date research has concentrated on modifications of the anthracycline or aglycone portion of the molecule, since it has been shown that the amino sugar daunosamine is essential for anticancer activity. Substitution of other molecules for the amino sugar, such as a β-alanine ester of the 7-hydroxy group on the anthracycline, destroyed antitumor activity *in vivo* (7). Two independent total syntheses of the aglycone of daunorubicin and carminomycinone have been reported (8, 9) as well as the subsequent glycosidation with daunosamine (10). Adriamycin may also be prepared from the synthetic daunomycinone (7, 11) and some adriamycin analogues have been described (12).

Recent work has shown that microbial biomodification is useful in the preparation of analogues. Thus bacterial metabolism of daunorubicin by *streptomyces steffisburgensis* produced 7-deoxydaunomycinone and its carbonyl-reduced counterpart by NADPH mediated enzymatic side-chain reduction of the antibiotic (13). This work demonstrated that microbial metabolism of anthracyclines follows the same pathway previously demonstrated for mammalian metabolism.

In the preceding paper (14) we examined the redox behavior of daunorubicin by electroanalytical techniques as it pertains to three separate aspects of chemotherapy by the drug: (*i*) Metabolism by daunorubicin reductase which reduces the side-chain acetyl group and produces biologically active metabolites; (*ii*) cardiotoxicity which is associated with the interference with electron transport processes and oxidative phosphorylation; and (*iii*) chromosomal degradation which may result from single strand cleavage of nucleic acids by radicals produced by the drug *in vivo*.

To further characterize the effects of structural changes in the anthracycline moiety on these processes, we describe in the present paper the electroanalytical examination of a series of synthetic daunomycinone analogues which may prove useful in the prescreening of potential antitumor agents and assist in the molecular interpretation of the electrochemical behavior of daunomycin as reported in the preceding paper (14).

* Electrochemical Society Active Member.

Key words: cyclic voltammetry, antibiotic, daunomycin, quinone, antitumor, adriamycin.

[1] The parent antibiotic is currently called daunorubicin, but its aglycone is referred to as daunomycinone.

Experimental

Compounds **1**, **2**, and **3** were obtained from Dr. C. M. Wong, University of Manitoba, Canada, and were used as received. Reagent grade acetophenone (compound **5**) from Fisher Scientific Company was used without further purification. Technical grade 1'-acetonaphthone (compound **6**) from Eastman Kodak Chemicals was distilled under reduced pressure before use. Compound **4** was prepared by Dr. C. K. Majumdar of this department from **3** by refluxing 4 mg with a trace of *para*-toluenesulfonic acid in 3 ml toluene for 16 hr. Toluene was removed *in vacuo* and the residue was dissolved in 1 ml of chloroform, passed through a neutral alumina column (4 × 1 cm), and eluted with chloroform. Removal of the chloroform *in vacuo* gave about 3 mg of **4** as an orange solid. Its characteristics were: mp 197°-199°C, pmr δ ($CDCl_3$): 2.77 (s, 3H); 4.02 (s, 3H), 4.12 (s, 3H), 7.20-8.94 (m, 6H); infrared (KBr disk): 1680, 1670 cm^{-1} (=C=O); molecular ion (mass spectrum): 390.1108; calculated for $C_{23}H_{18}O_6$ 390.1116. The structures of these compounds are shown in Fig. 1. The solubility of these compounds in water is very low, and increases in the order $1 < 4 < 2 < 3 < 6 < 5$. Therefore, a known amount of the samples (400-700 μg

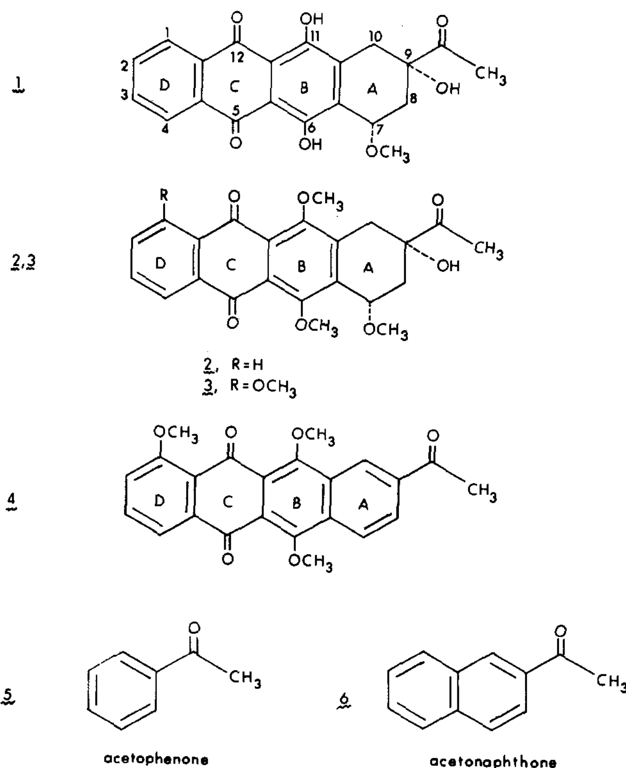

Fig. 1. Structures of compounds studied

for 1-4 and 1 mg for 5-6) were directly weighed into 5 ml of solution buffered at pH 7.04 ± 0.03 with 0.1M phosphate buffer in 0.1M KCl. However, not all of this material dissolved so that the actual concentrations correspond to saturated solutions of each of these compounds. These solutions were deaerated with nitrogen gas and stirred for 15 min prior to each experiment at 37.5° ± 0.02°C. Cyclic voltammetry, which was used in this study, and other procedures were described previously (15); all potentials were measured and are given with respect to the aqueous SCE.

Results

The peaks and processes described here follow the identification I, II, III, ... of the preceding paper (14).

Compound **1**.—At 500 mV/sec, compound **1** gives four cathodic peaks at −0.465V (I*C), −1.095V, −1.170V (IIIC), and −1.47V (IIC) and two anodic peaks at −0.438V (I*A) and −0.682V (IA) (Fig. 2). In the second cycle, two additional cathodic peaks appeared, one at about −0.2V and one at −0.687V (IC) (Fig. 3). In one of the experiments, about 2 mg of **1**, a relatively large amount compared to 430 μg in the above mentioned study was added to the 5 ml of buffer. A broad cathodic peak at a potential less negative than −0.2V, a cathodic peak at −1.27V, and one or two anodic peaks (or waves) at potentials more positive than −0.2V were observed, of which the first broad cathodic peak disappeared in the subsequent cycles. The peaks IC and IA appeared only when the cathodic-to-anodic scan reversal potential was more negative than −1.1V. The peak potentials of I*C and I*A shift, the cathodic peak shifting anodic and the anodic peak shifting cathodic, by 10 mV for each tenfold decrease in scan rate. The $I_p\nu^{-1/2}$ product for both I*C and IC decreases with decrease in scan rate. It is apparent from Fig. 3 that the ratio of anodic-to-cathodic peak currents for both processes I* and I are slightly greater than unity at ν = 500 mV/sec. Dependence of these ratios on scan rates, including 500 mV/sec, may not be of much value due to extreme difficulty in locating the base lines for IC and I*A.

Compound **2**.—The compound **2** gives two cathodic peaks (I*C, IIC) and two anodic peaks (I*A, IIA)

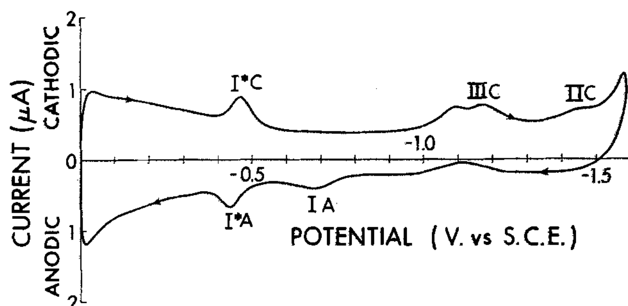

Fig. 2. Cyclic voltammogram of **1**, pH 7.04 in phosphate buffer, 37.5°C, ν = 500 mV/sec.

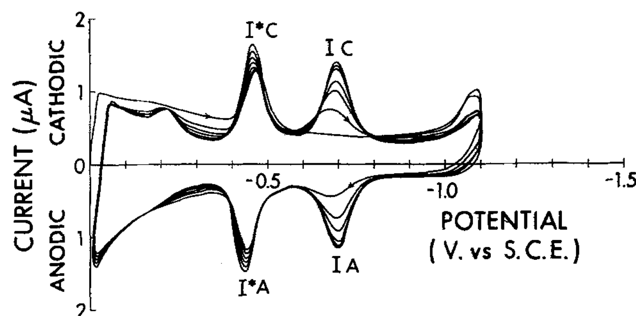

Fig. 3. Multicycle voltammogram of **1**, pH 7.04 in phosphate buffer, 37.5°C, ν = 500 mV/sec. The system I*C-I*A decreases, while IC-IA increases, with cycling.

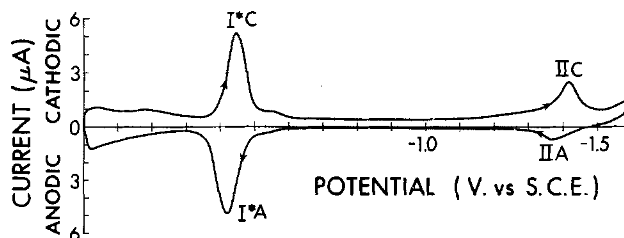

Fig. 4. Cyclic voltammogram of **2**, pH 7.06 in phosphate buffer, 37.5°C, ν = 500 mV/sec.

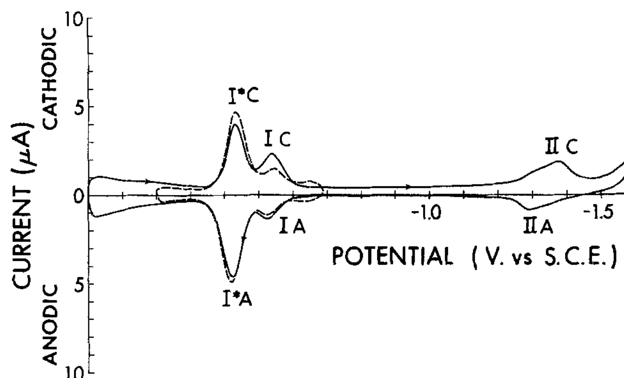

Fig. 5. Cyclic voltammogram of **2**, pH 7.06 in phosphate buffer, 37.5°C, ν = 500 mV/sec, solid line 0-—1.6V scan range, dotted line —0.3-—0.8V scan range. Solution of Fig. 4 after considerable cycling.

during the early part of the experiment at ν = 500 mV/sec (Fig. 4). In the later part of the experiment, *i.e.*, after making cyclic voltammetry measurements at slower scan rates up to 10 mV/sec, two additional peaks (IA and IC) appear as shown in Fig. 5. It is apparent from Fig. 4 and 5 that the presence of peak IC reduced the concentration of the material responsible for the peak I*C, *i.e.*, the peak height of I*C. The appearance of peaks I may be explained due to the formation of material responsible for peak I in the course of cyclic voltammetry at slow scan rates since our experimental solution was very dilute. Careful observation of Fig. 4 shows a very small peak at about −0.2V which disappeared in subsequent cycles of the multicycle runs. If the cell potential was held at −0.2V for different times between cycles, the height of I*C decreased exponentially with electrolysis time while that of IC simultaneously increased; the sum of the peak heights remained approximately constant. For example, electrolysis for 5 min decreased the height of I*C from 4.4 to 1.8 μA while the height of IC increased from 1.7 to 4.8 μA.

The peak potentials for I*C and IC are −0.442 ± 0.01V and −0.552 ± 0.01V, independent of scan rate up to ν = 1 V/sec; then shifted slightly cathodic with further increase in scan rate. The $I_p\nu^{-1/2}$ product decreases with decrease in scan rate for both peaks; however, this decrease is small for IC. On the other hand, the peak potential for I*A depends on the scan rate; for example, E_p = −0.425 ± 0.01V at ν = 500 mV/sec. As the scan rate is increased, the peak potential shifted to more anodic values by about 10-15 mV for each tenfold increase in scan rate up to 1 V/sec and then by a large extent. However, the peak potential of IA is −0.540 ± 0.01V, independent of scan rate up to 1 V/sec, and then shifted to anodic by a large extent with further increase in scan rate. It is apparent from Fig. 4 and 5 that the ratio of anodic to cathodic peak currents for both peaks I* and I are slightly greater than unity at ν = 500 mV/sec. The validity of these ratios is limited for the reasons mentioned above for compound **1**.

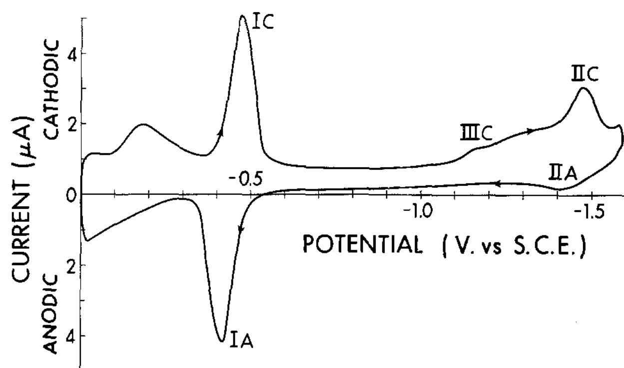

Fig. 6. Cyclic voltammogram of 3, pH 7.05 in phosphate buffer, 37.5°C, ν = 500 mV/sec.

Small peaks IIC and IIA appear at most scan speeds and their peak potentials are −1.40 ± 0.02 and −1.34 ± 0.03V.

Compound **3**.—As shown in Fig. 6, compound **3** gives mainly two cathodic peaks (IC, IIC) and two anodic peaks (IA and IIA) at ν = 500 mV/sec. In addition, a broad cathodic peak at −0.184V (independent of scan rate) disappears in subsequent cycles of the multicycle runs. Very close observation of Fig. 6 indicates also the presence of two very small cathodic peaks (or waves) approximately at −1.17V (IIIC) and at −1.36V.

The cathodic peak (IC) at −0.472V for ν = 500 mV/sec shifts anodic by 15-20 mV for each tenfold decrease in scan rate. The corresponding anodic peak (IA) at −0.398V (when scanning range was restricted between 0 and −0.8V) for ν = 500 mV/sec shifts cathodic by 20-25 mV for each tenfold decrease in scan rate. The $I_p\nu^{-1/2}$ product for IC decreased with decrease in scan rate. The ratio of anodic to cathodic peak currents are approximately 1.2 at ν = 500 mV/sec and increased with decrease in scan rate.

Although the cathodic peak IIC appearing at −1.46 ± 0.01V is independent of scan rate, its anodic counterpart IIA, appearing at −1.42V and ν = 500 mV/sec, is less prominent at slower scan speeds.

Compound **4**.—Figure 7 is a typical cyclic voltammogram of compound **4** at 500 mV/sec. It shows three cathodic peaks (IC-IIIC) and three anodic peaks (IA, IIA, IIIA). Also, a broad cathodic peak, at −0.135V for ν = 500 mV/sec, shifts anodic by 30 mV for tenfold decrease in scan rate. This peak disappears in the second cycle of the multicycle runs as observed for the compounds discussed above. There are three more small cathodic peaks approximately at −0.360, −0.990, and −1.065V (Fig. 7).

Other than a cathodic peak at potentials more positive than −0.2V, only IC and IA are observed when the potential range is restricted to between 0 and −0.8V. Both IC and IA are independent of scan rate and appear at −0.506 ± 0.005V and −0.499 ± 0.005V. The $I_p\nu^{-1/2}$ product for IC decreases with decrease in scan rate. The ratio of anodic to cathodic peak currents and its scan dependence are similar to those for **3**.

The peak potential of IIIC is −1.16V at ν = 500 mV/sec and shifts anodic by about 30-40 mV for each tenfold decrease in scan rate. The anodic peak IIIA is better defined if the switching potential is more negative than −1.2V. The peak potential of IIIA is −0.40 ± 0.005V independent of scan rate. Small peaks IIC and IIA appear at most scan speeds; their peak potentials are −1.35 ± 0.01 and −1.30 ± 0.01V.

Compound **5**.—Acetophenone, **5**, gives only one cathodic peak (IIIC) at −1.53V for ν = 500 mV/sec and shifted anodic by 30-35 mV for each tenfold decrease in scan rate (Fig. 8). A very small anodic peak (IIIA) appears around −0.41V at 500 mV/sec; it is barely visible at lower scan speeds.

Compound **6**.—At ν = 500 mV/sec, 1′-acetonaphthone, **6**, gives two cathodic peaks (IIC, IIIC) and two anodic peaks (IIA, IIIA). A small anodic peak IIIA was visible around −0.39 ± 0.01V up to 100 mV/sec. The corresponding cathodic peak IIIC appears at −1.35 ± 0.01V, independent of scan rate. However, this peak becomes sharp and/or showed as a wavelike appearance on the anodic side of the peak. The cathodic peak IIC has a peak potential of −1.43V at 500 mV/sec and shifts anodic by 40-50 mV for each tenfold decrease in scan rate. The anodic peak IIA, better defined at slower scan speeds, has a peak potential of −1.26V at 500 mV/sec. This peak shifted cathodic by 30-40 mV for each tenfold decrease in scan rate.

Discussion

The quinone moiety (processes I, I)*.—The mechanism of the reduction of the daunomycinone analogues is similar to that for daunomycinone (14). The initial electrochemical two-electron, two-proton reversible electrochemical steps designated "I" are due to reduction of the respective quinones. An irreversible chemical reaction complicates the electrochemical step I. The absence of the cathodic peak I′C present in daunomycinone for **1-4** may arise because the analogues were less soluble than daunomycinone; peak I′C was observed only for an appreciable concentration of daunorubicin in solution (14).

The difference in the IC peak potentials of **3** and **4** is about 40 mV. Therefore, aromatization of the ring A shifts the formal potential of process I for **3** 40 mV more negative.

Wiles (16) has observed that methoxyanthraquinones are more readily reducible than the corresponding hydroxyanthraquinones. Comparison of the voltammograms of **1** and **2**, or of **3** and daunomycinone, shows an apparent anodic shift of I by substitution of methoxy for hydroxy in positions 6 and 11. The pres-

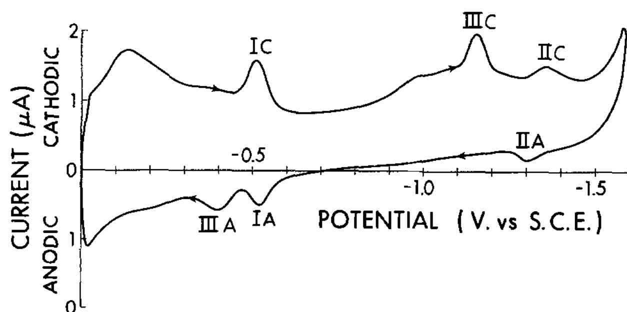

Fig. 7. Cyclic voltammogram of **4**, pH 7.03 in phosphate buffer, 37.5°C, ν = 500 mV/sec.

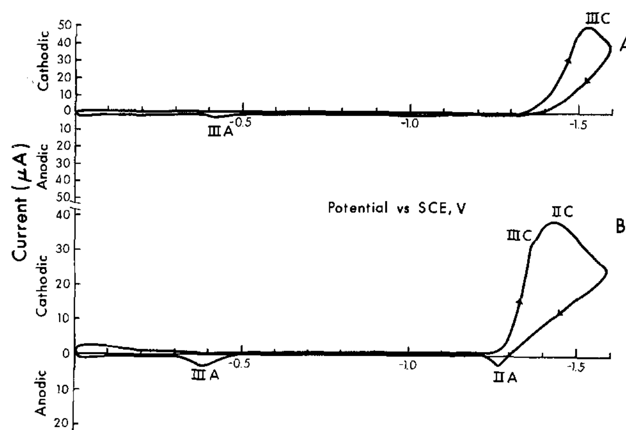

Fig. 8. Cyclic voltammograms of A, **5**, and B, **6**; pH 7.06 in phosphate buffer, 37.5°C, ν = 500 mV/sec.

ence of either a hydroxyl group or sugar linkage at C_7 appears to have little direct influence upon the quinone reduction. Comparison of the IC peak potentials of compounds **1-4** indicates a positive ortho effect, probably due to the regular polar effect of the methoxy group. Contrarily, such an effect was not reported when a second methoxy was substituted affecting the same carbonyl group, in 1,8-dimethoxyanthraquinone (16).

The major phenomena exhibited in this study, however, are the peaks I* and the considerable shift in potential of I between the different analogues. Intramolecular hydrogen bonding in **1** and daunomycinone between the quinone oxygens at C_5, C_{12} and the hydroxyl hydrogens at C_6, C_8 is responsible for shifting the formal potential of these compounds about 150 $\pm$ 15 mV more negative than their respective methoxy derivatives. The difference in half-wave potential between 1,8-dimethoxyanthraquinone and 1,8-dihydroxyanthraquinone of 160 mV observed by Starka *et al.* (17) agrees well with our value of 150 $\pm$ 15 mV.

In compound **1**, an apparently reversible process designated I* appeared at a potential more positive than I. The process I* appeared to decrease with time, which indicates its nature is kinetic. This process I* was also observed for **2**, in which it was initially the only process present; the appearance of I, at lower height than I*, came only after continued cycling or upon reduction at -0.2V. With sufficient reduction at -0.2V, I* could be virtually removed. Process I* cannot be clearly distinguished for compounds **3** and **4** in which it may be hidden in the broad peaks. The difference in potential of peak I*C between **1** and **2** is only 23 mV, far less than the 135 mV difference for IC between **1** and **2** which we believe arises because the contribution of hydrogen bonding in **1** is appreciable while in **2** it is not. The distinction of the process I* from I as that of a more easily reducible tautomer is consistent with this behavior as the partial or complete loss of the 6,11 methoxy groups would reduce the difference for I*C between **1** and **2** if not eliminate it entirely. We then attribute process I* to the formation of more easily reducible tautomers such as the 6,12- or 5,11-dicarbonyl compounds. Such an explanation can be valid only if the methoxy groups can be removed to give access to the 6,11 positions. This removal is known to occur upon oxidation of *p*-methoxyphenol (20).

A process negative to all of the processes I-III, designated IV, was observed neither for daunorubicin nor for adriamycin (14), but was clearly present for both their aglycones, daunomycinone, and adriamycinone. This may be a redox process of the quinone structure which is inhibited by the presence of daunosamine in the parent antibiotics and hence appears only for the aglycones.

The daunosamine may influence the hydrogen bonding in the antibiotics so that the more easily reducible tautomers are not formed until it is removed. In this connection Yesair and McNitt (21) have commented upon the inhibition of reductive glycosidic cleavage by chelation of the dihydroquinone systems of anthracyclines and its relation to daunosamine.

The carbonyl side chain (processes II, III).—The reduction mechanism of the side-chain carbonyl group shown in Fig. 8 of (14), two irreversible one-electron processes (14), can be shown from behavior of compounds **4**, **5**, and **6**; separate protonation steps cannot be distinguished. We observe only one irreversible cathodic peak IIIC for acetophenone, which is consistent with the earlier work of Elving who observed one two-electron process due to the merging of the two one-electron reduction steps (19). However, we have observed two cathodic peaks, IIIC and IIC (both positive to the single cathodic peak for acetophenone, IIIC), and two anodic peaks (IIIA and IIA) for 1′-acetonaphthone and compound **4**.

The carbonyl group in acetophenone is more easily reduced than in acetone due to the strong inductive effect of the phenyl group (19). The increase in inductive effect as the number of benzene rings in a compound increases may explain the observed shift in the cathodic peaks (IIC and IIIC) toward more anodic potential as observed in componunds **4-6**.

Considering only ring A and its side-chain carbonyl group, the aromatic ring structure is equivalent to that of acetophenone while the alicyclic ring structure is equivalent to that of cyclohexanone. Acetophenone is more easily reduced than cyclohexane (18, 19). Thus our observation that reduction of the side chain carbonyl group in compounds **1**, **2**, and **3** occurs at more negative potentials than in compound **4** indicates that ring A of compounds **1**, **2**, and **3** has not achieved aromatic character (by dehydration and demethoxylation) prior to carbonyl reduction.

Acknowledgment

We are grateful to Dr. C. K. Majumdar of this department for the preparation of **4** and to Dr. C. M. Wong of the University of Manitoba for gifts of **1**, **2**, and **3**. This work was supported by the National Research Council of Canada through Operating Grants to J. W. L. and J. A. P. and by the National Cancer Institute of Canada through a research grant to J. W. L.

Manuscript submitted June 1, 1977; revised manuscript received Dec. 28, 1977. This was presented in part as Paper 273 at the Philadelphia, Pennsylvania, Meeting of the Society, May 8-13, 1977.

Any discussion of this paper will appear in a Discussion Section to be published in the December 1978 JOURNAL. All discussions for the December 1978 Dission Section should be submitted by Aug. 1, 1978.

Publication costs of this article were assisted by The University of Alberta.

REFERENCES

1. A. Di Marco, F. Arcamone, and F. Zunino, in "Antibiotics III—Mechanism of Action of Antimicrobial and Antitumor Agents," J. W. Corcoran and F. E. Hahn, Editors, pp. 101-128 and references therein, Springer-Verlag, New York (1975).
2. R. H. Blum and S. K. Carter, *Ann. Intern. Med.*, **80**, 249 (1974).
3. E. A. Lefrak, J. Pitha, S. Rosenheim, and J. A. Gottlieb, *Cancer*, **32**, 302 (1973).
4. J. P. Rinehart, R. P. Lewis, and S. P. Balcerzak, *Ann. Intern. Med.*, **81**, 475 (1974).
5. G. Rosen, N. Wollner, C. Tan, S. J. Wu, S. I. Hajdu, W. Cham, G. J. D'Angio, and M. L. Murphy, *Cancer*, **33**, 384 (1974).
6. J. F. Halazun, H. R. Wagner, J. F. Gaeta, and L. F Sinks, *ibid.*, **33**, 545 (1974).
7. D. W. Henry, *Chem. Eng. News*, **54**, 18 (1976).
8. C. M. Wong, R. Schwenk, D. Popien, and T-L. Ho, *Can. J. Chem.*, **51**, 466 (1973).
9. A. S. Kende, Y-G. Tsay, and J. E. Mills, *J. Am. Chem. Soc.*, **98**, 1967 (1976).
10. E. M. Acton, A. N. Fujiwara, and D. W. Henry, *J. Med. Chem.*, **17**, 659 (1974).
11. T. H. Smith, A. N. Fujiwara, D. W. Henry, and W. E. Lee, *J. Am. Chem. Soc.*, **98**, 1969 (1976).
12. T. Tong, W. W. Lee, D. R. Black, and D. W. Henry, *ibid.*, **19**, 395 (1976).
13. V. P. Marshall, E. A. Reisender, and P. F. Wiley, *J. Antibiot.*, **29**, 966 (1976).
14. G. M. Rao, J. W. Lown, and J. A. Plambeck, *This Journal*, **125**, 534 (1978).
15. G. M. Rao, J. W. Lown, and J. A. Plambeck, *ibid.*, **124**, 195 (1977).
16. L. A. Wiles, *J. Chem. Soc.*, 1358 (1952).
17. L. Stárka, L. Vystrćil, and B. Stárková, *Chem. Listy*, **51**, 1440 (1957).
18. P. Kabasakalian and J. McGlotten, *Anal. Chem.*, **31**, 1091 (1959).
19. P. J. Elving and J. T. Leone, *J. Am. Chem. Soc.*, **80**, 1021 (1958).
20. D. Hawley and R. N. Adams, *J. Electroanal. Chem.*, **8**, 163 (1964).
21. D. W. Yesair and S. McNitt, *Z. Phys. Chem.*, **357**, 1066 (1976).

The Electrochemical Oxidation of Hydrogen Sulfide in the Tafel Region and under Mass Transport Control

M. Farooque and T. Z. Fahidy*

Department of Chemical Engineering, University of Waterloo, Waterloo, Ontario, Canada, N2L 3G1

ABSTRACT

H_2S can be continuously oxidized about 1.21V (RHE) anode potential range at about 93% efficiency, according to the reaction scheme $H_2S \rightarrow S + 2H^+ + 2e^-$ which most probably involves the formation of an SH-chemisorbate on the (platinum) anode surface. At mass transfer-controlled conditions a limiting current is observed; rotating tripolar electrode cell experiments yield the value of 1.94×10^{-5} cm²/sec for the diffusion coefficient of H_2S in a 0.5 mole/dm³ aqueous H_2SO_4 solution, at 23°C.

In a previous publication (1) the oxidation of hydrogen sulfide at low potentials was described in a rotating tripolar wiper-blade electrode (RTE) system via continuous anode reactivation. At potentials less than about 0.5V (RHE) the most likely oxidation mechanism involves two first-order consecutive electrochemical reactions with the SH-chemisorbate as the intermediate product, responsible for the relatively rapid passivation (about 30 sec on an initially fresh anode surface); the RTE system was shown (1, 2) to be an efficient anode "reactivator" in the low potential range.

The extension of this study into the Tafel region and the mass transport-controlled region was stipulated by two major reasons. Firstly very little information about the nature of this reaction in these regions is available in the literature; the establishment of the most likely reaction mechanism is all the more intriguing as H_2S can be oxidized continuously past the range of passivation, characteristic of low potential oxidation. Secondly, oxidation at elevated potentials yields colloidal sulfur as the anode product, which is potentially useful for medicinal purposes, etc., apart from the obvious application in pollution control. Experiments in the mass transfer control regions may also be used to estimate the apparent diffusion coefficient pertaining to the electrochemical system. The present paper summarizes the results of such an investigation and is intended to offer a better understanding of the electrochemical oxidation of hydrogen sulfide over a relatively wide range of electrode potentials.

Basic Characteristics of the Oxidation Process

In the potential range of ~0.7-1.21V (RHE), where H_2S may continuously be oxidized on a platinum surface without noticeable passivation, the gaseous product evolved at the cathode is hydrogen (determined by a gas-chromatography analysis using a thermal conductivity detector and a 5A molecular sieve absorbent) and the anode product is powdery elemental sulfur: the latter is eventually suspended in the anolyte as a milky substance and coagulates after several hours of standing with sedimentation at the bottom. About 20 hr after oxidation, nearly 60% of the sulfur is insoluble in CS_2, the percentage of the CS_2-insoluble substance decreasing gradually with the aging of the product. It appears that the electrochemically produced sulfur is an unstable allotrope which is gradually transformed into a more stable form. Scanning electron microscope tests indicate that the average diameter of the sulfur particles in the milky substance is less than 10^{-4} cm. Chemical analysis of the electrolyte failed to detect any sulfate, sulfite, thiosulfate, or dissolved SO_2. Standard controlled-potential coulometry indicates that the oxidation reaction is a two-electron transfer process

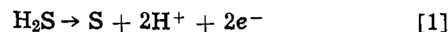

$$H_2S \rightarrow S + 2H^+ + 2e^- \quad [1]$$

of about 93% current efficiency. In H_2SO_4 solutions the rest potential depends on the acid concentration and the partial pressure of H_2S as (3)

$$E \cong 165 - (59 \pm 2)pH - (40 \pm 15)P_{H_2S}\ \text{mV}$$

In cathodic polarization of a 0.5 mole/dm³ electrolyte with H_2 and H_2S bubbling, the Tafel slope is 0.12 ± 0.01V at potentials less than −100 mV on platinized Pt (<−150 mV at bright Pt) and the exchange current density is about 0.1 mA/cm² (bright Pt) and 0.4 mA/cm² (platinized Pt) (3, 4). In anodic polarization the Tafel slope is about 1.38V at ascending potentials and about 0.64V at descending potentials on bright Pt, whereas on platinized Pt, camel hump-like polarization is observed at ascending potentials and no reliable measure of the Tafel slope is obtained. The anodic peak has been ascribed (5) to delayed release of H atoms due to the porous structure of the electrode surface. The anodic exchange current density on bright Pt is about 0.2 μA/cm² from ascending potential *vs.* current curves, and about 0.068 μA/cm² from descending potential *vs.* current curves; the anodic polarization behavior of this system is not well understood.

The Mechanism of Oxidation

The preparation of the electrolyte and pretreatment of the platinum anode was the same as described earlier (1, 2). The electrolyte contained 0.00499 mole/dm³ H_2S dissolved in a 0.1 mole/dm³ H_2SO_4 solution. The potential of oxidation was varied from 1.15 to 1.21V (RHE) at a 22.5°C electrolyte temperature and the steady-state oxidation rate at each potential setting was measured, while the anode was rotated continuously at a speed of 2.0 rad/sec; the true anode area was measured (6) to be 210 cm². The experimentally observed steady-state oxidation rates are shown in Fig. 1. In Table I the results of a previously described (1, 2) likelihood-ratio analysis are presented for a number of plausible mechanisms, where the formulation of the intermediates was made on the basis that sulfur is known to form chain- and ring-molecules (in the following equations M denotes the surface of the platinum anode, and x and y denote the number of sulfur atoms associated with an active site on the platinum surface)

* Electrochemical Society Active Member.

Key words: diffusion, kinetics, chemisorption, rotating electrode.

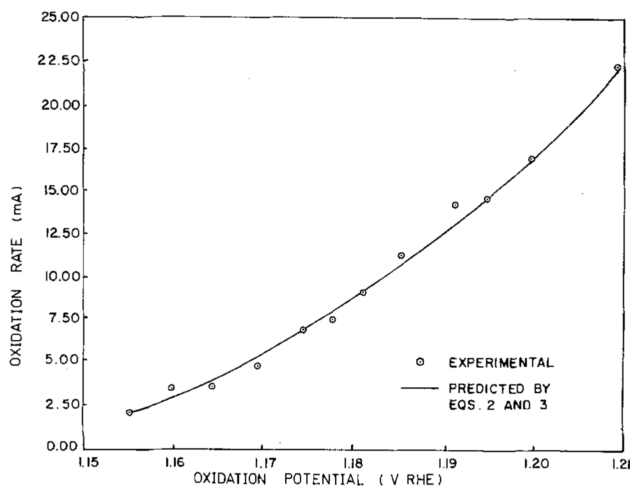

Fig. 1. Oxidation rate vs. oxidation potential. Electrolyte: 4.99 × 10^{-3} mole/dm^3 H_2S in 0.1 mole/dm^3 H_2SO_4 at 22.5°C. Electrode rotation rate: 2 rad/sec.

Mechanism 1

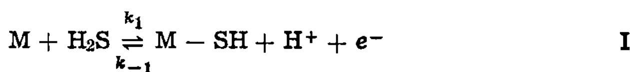

$$M + H_2S \underset{k_{-1}}{\overset{k_1}{\rightleftharpoons}} M - SH + H^+ + e^- \quad \text{I}$$

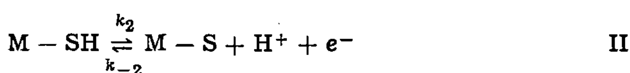

$$M - SH \underset{k_{-2}}{\overset{k_2}{\rightleftharpoons}} M - S + H^+ + e^- \quad \text{II}$$

Mechanism 2

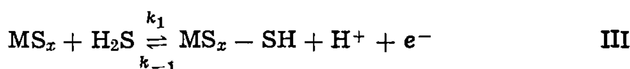

$$MS_x + H_2S \underset{k_{-1}}{\overset{k_1}{\rightleftharpoons}} MS_x - SH + H^+ + e^- \quad \text{III}$$

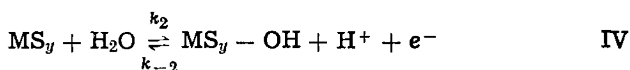

$$MS_y + H_2O \underset{k_{-2}}{\overset{k_2}{\rightleftharpoons}} MS_y - OH + H^+ + e^- \quad \text{IV}$$

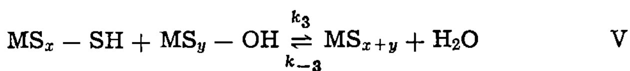

$$MS_x - SH + MS_y - OH \underset{k_{-3}}{\overset{k_3}{\rightleftharpoons}} MS_{x+y} + H_2O \quad \text{V}$$

Mechanism 3

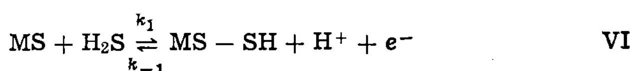

$$MS + H_2S \underset{k_{-1}}{\overset{k_1}{\rightleftharpoons}} MS - SH + H^+ + e^- \quad \text{VI}$$

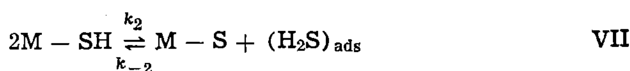

$$2M - SH \underset{k_{-2}}{\overset{k_2}{\rightleftharpoons}} M - S + (H_2S)_{ads} \quad \text{VII}$$

Mechanism 4

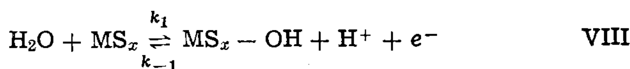

$$H_2O + MS_x \underset{k_{-1}}{\overset{k_1}{\rightleftharpoons}} MS_x - OH + H^+ + e^- \quad \text{VIII}$$

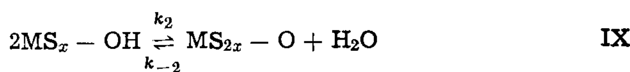

$$2MS_x - OH \underset{k_{-2}}{\overset{k_2}{\rightleftharpoons}} MS_{2x} - O + H_2O \quad \text{IX}$$

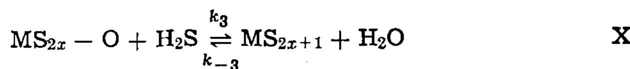

$$MS_{2x} - O + H_2S \underset{k_{-3}}{\overset{k_3}{\rightleftharpoons}} MS_{2x+1} + H_2O \quad \text{X}$$

Table I. Summary of the likelihood analysis of various mechanisms of H_2S oxidation in the Tafel region. Electrolyte: 4.99 × 10^{-3} mole/dm^3 H_2S in 0.1 mole/dm^3 H_2SO_4 at 22.5°C. Experimental error variance: $S_e^2 = 0.20838$

Mechanism	Rate determining step	Residual sum of squares, R_j	$L_j = e^{-R_j/2S_e^2}$	$\lambda_{3j} = L_{3,VII}/L_j$
1	II	19.936	1.679 × 10^{-21}	5.43 × 10^{17}
2	III	3.4949	2.281 × 10^{-4}	3.9978
2	IV	3.4949	2.281 × 10^{-4}	3.9978
3	VII	2.9173	9.119 × 10^{-4}	1.0000
5	XII	35.2610	1.801 × 10^{-37}	5.063 × 10^{33}

Mechanism 5

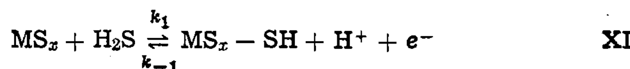

$$MS_x + H_2S \underset{k_{-1}}{\overset{k_1}{\rightleftharpoons}} MS_x - SH + H^+ + e^- \quad \text{XI}$$

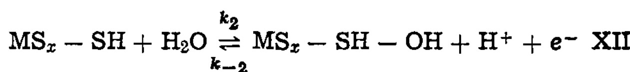

$$MS_x - SH + H_2O \underset{k_{-2}}{\overset{k_2}{\rightleftharpoons}} MS_x - SH - OH + H^+ + e^- \quad \text{XII}$$

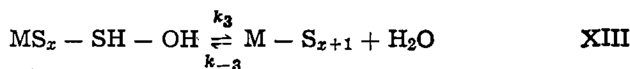

$$MS_x - SH - OH \underset{k_{-3}}{\overset{k_3}{\rightleftharpoons}} M - S_{x+1} + H_2O \quad \text{XIII}$$

The table does not contain those mechanism/rate-determining step combinations (models) whose residuals have been found much higher (*i.e.*, whose associated L_j values are much lower) than the five contenders shown. From a statistical point of view, Model 3-VII represents the most probable reaction mechanism, in spite of the fact that $\lambda_{32} \cong 4$ is less than 10 [which is the ordinarily accepted value to show "real difference in plausibility" (7)], since Model 2 carries four parameters in the associated rate expressions, and Model 3-VII carries only three parameters. Pertinent residual analysis shows no discernible trend, hence Model 3-VII is statistically adequate. The model equations are

$$I = a\theta_{MSH}^2 - b(1 - \theta_{MSH}) \quad [2]$$

$$\theta_{MSH} = 1/[1 + ce^{-VF/RT}] \quad [3]$$

where $a \equiv 2A_oFk_2$; $b \equiv 2A_oFk_{-2}C_{H_2S}$; and $c \equiv \frac{k_{-1}}{k_1} C_{H^+}C_{H_2S}^{-1}$. The numerical estimates of the three parameters, obtained by this regression analysis, are: $a = 38.846$ mA; $b = 0.91275$ mA; and $c = 1.3557 \times 10^{20}$. The model equations associated with the rest of the models have been given in detail elsewhere (2). The solid line in Fig. 1 represents the oxidation rate/oxidation potential relationship expressed by Eq. [2] and [3]. The apparent Tafel slope, computed via a linear regression analysis relating the experimental (V-E) *vs.* $\log_{10}I$ data is about 0.05V and the corresponding exchange current density, using the true electrode area of 210 cm^2, is estimated at the approximate value of 1.9×10^{-5} $\mu A/cm^2$ ($E \sim 0.3V$; residual sum of squares $\sim 2.067 \times 10^{-4}$; standard error of estimate $\sim 3.49 \times 10^{-3}$). The Tafel parameters are a function of the electrode rotation rate; comparison with Ijzermann's data (3) clearly shows the depolarization effect of rotation and surface renewal by wiping.

H_2S Oxidation in the Mass Transport-Control Region

The oxidation rate of H_2S was measured at different anode rotation rates in electrolytes containing 3.44, 11.2, and 12.5 mmole/dm^3 H_2S dissolved in a 0.5 mole/dm^3 H_2SO_4 solution, at an anode potential of 1.45V (RHE). Prior to each set of readings the apparatus was subjected to the following treatment: The cell was washed with deionized water, piperidine, and again with deionized water. The anode was subjected to a potential sweep from 40 mV to 1.6V at a sweep rate of 0.15 V/sec in a 0.5 mole/dm^3 H_2SO_4 solution. Finally the cell was washed with the experimental electrolyte and filled with it. Figures 2 and 3 show the effect of the anode rotation rate on the experimental limiting current density. According to a previous theoretical treatment of mass transport phenomena in a rotating multipolar cell equipped with wiper blades (8,9), the limiting current and the speed of rotation are related as

$$I_{L,avg} = A_o'zFDc_b \left[\frac{2}{\sqrt{\pi D t_s}} - \frac{4}{3\pi\sqrt{\pi \nu t_s}} \right] \quad [4]$$

A slightly improved relationship, developed recently (2, 10), yields

$$I_{L,avg} = \frac{2A_o'zFDc_b}{\sqrt{t_s}} \left[\frac{1}{\sqrt{\pi D}} + \frac{1}{\psi(\sqrt{\pi\nu})} \right] \quad [5]$$

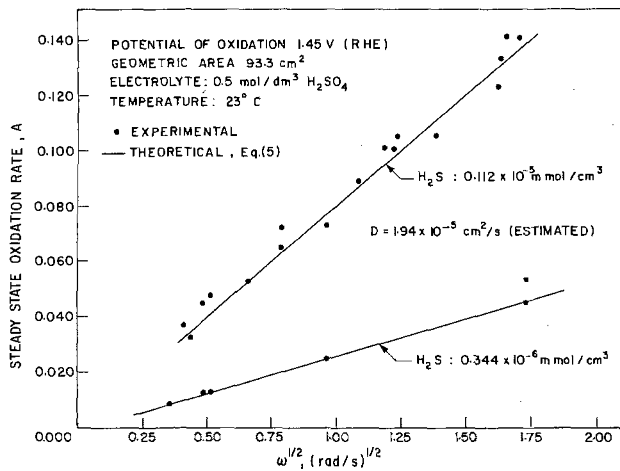

Fig. 2. Oxidation rate vs. rotation rate in the mass transport-controlled region.

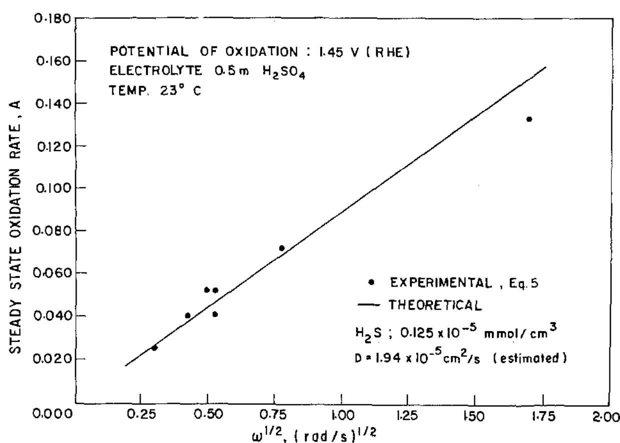

Fig. 3. Oxidation rate vs. rotation rate in the mass transport-controlled region.

where

$$\psi(\sqrt{\pi\nu}) \equiv \int_0^{\sqrt{\pi\nu}} \epsilon^{(y^3/6D\sqrt{\pi\nu} - y^2/4D)} dy$$

and t_s, the time required for the electrode surface to pass from one wiper blade to the next, is related to the rotation rate ω by the expression

$$t_s = \frac{2\pi r_1 - Wd}{\omega W r_1} \qquad [6]$$

Equation [5] was fitted to the experimentally observed rates, employing 30 experimental points and using Powell's least-squares algorithm (11). The regression lines, given by the solid curves in Fig. 2 and 3, possess an average absolute error of 7%, the residual analysis yielding again no discernible trend. Using the experimental values of $A_0' = 93.3$ cm² and $\nu = 1.0457$ mm²/sec, the diffusion coefficient of H_2S in H_2SO_4 is estimated to be 1.9425×10^{-5} cm²/sec with an associated variance of 1.25×10^{-10} cm²/sec.

Conclusions

The electrochemical oxidation of H_2S proceeds without passivation as a two-electron transfer process producing elemental hydrogen and a colloidal dispersion of sulfur at a current efficiency of about 93%.

The statistically most probable mechanism involves sulfohydrogen and sulfur-chemisorbates on the platinum anode with an M-SH → M-S recombination being the rate-controlling step. At high oxidation potential the reaction is mass transfer controlled and its rate is linearly proportional to the square root of the rotation speed of the anode in an RTE cell. The process appears to be a potentially useful means of H_2S pollution control.

Acknowledgment

This project was supported by the National Research Council of Canada and a Canadian Commonwealth Fellowship.

Manuscript submitted Sept. 14, 1977; revised manuscript received Nov. 21, 1977.

Any discussion of this paper will appear in a Discussion Section to be published in the December 1978 JOURNAL. All discussions for the December 1978 Discussion Section should be submitted by Aug. 1, 1978.

Publication costs of this article were assisted by the University of Waterloo.

LIST OF SYMBOLS

- A_0 effective electrode area at zero time
- A_0' geometric area of the electrode
- C_b bulk electrolyte concentration
- D diffusion coefficient
- d wiper blade width
- E rest potential
- F Faraday's constant (96,487 C/mole)
- I current flow
- L_j likelihood function of model j
- R universal gas constant (8.3143 J/K · mole)
- R_j residual sum of squares of model j after estimating the model parameters
- r_1 electrode radius
- z number of electrons transferred in electrode reaction
- V oxidation potential
- W number of wiper blades in cell
- θ_{MSH} electrode coverage by M-SH intermediate
- λ_{ij} likelihood ratio of model i with respect to model j
- ν electrolyte kinematic viscosity
- ω electrode rotation rate

REFERENCES

1. M. Farooque and T. Z. Fahidy, *This Journal*, **124**, 1191 (1977).
2. M. Farooque, Ph.D. Thesis, University of Waterloo, Waterloo, Ont., Canada (1977).
3. A. B. Ijzerman, *Rev. Trav. Chim.*, **88**, 334 (1969).
4. K. J. Vetter, *Angew. Chem.*, **73**, 277 (1961).
5. P. Drossbach and P. Schmittinger, *Electrochim. Acta*, **11**, 687 (1966).
6. T. Biegler, D. A. J. Rand, and R. Woods, *J. Electroanal. Interfacial Electrochem.*, **29**, 269 (1971).
7. P. M. Reilly, *Can. J. Chem. Eng.*, **48**, 168 (1970).
8. P. R. Nadebaum, Ph.D. Thesis, University of Waterloo, Waterloo, Ont., Canada (1974).
9. P. R. Nadebaum and T. Z. Fahidy, *Can. J. Chem. Eng.*, **53**, 259 (1975).
10. M. Farooque and T. Z. Fahidy, *ibid.*, **55**, 355 (1977).
11. M. J. D. Powell, *Comput. J.*, **7**, 303 (1965).

The Effect of Slow Two-Electron Transfers and Disproportionation on Cyclic Voltammograms

Michael D. Ryan*

Marquette University, Department of Chemistry, Milwaukee, Wisconsin 53233

ABSTRACT

The EE mechanism (two-electron transfer) for cyclic voltammetry was investigated in considerable detail along with the effect of disproportionation. The theory was developed for either the first or second electron transfer being slow while the other one was reversible. It was possible to develop generalized working curves for the height and shape of the wave regardless of the difference in E°'s and the values of α and k_s. This theory was then applied to the analysis of the reduction of benzil in the presence of alkaline earth ions in dimethylformamide.

The theory for reversible and irreversible electron transfer has been examined in some detail previously for cyclic voltammetry (CV). The problem of multi-electron transfers in CV was studied first by Polcyn and Shain (1). The main quantitative emphasis was placed on the deconvolution of separated waves and only qualitative results were given for multi-electron waves. Myers and Shain (2) were able to quantitatively correlate the shape and peak current function of reversible voltammetric waves to their difference in $E^{o\prime}$s if the $E^{o\prime}$s were close together. It was found that the shape of the wave was independent of the relative values of the $E^{o\prime}$s only if the difference in $E^{o\prime}$s was greater than 180 mV. Otherwise, the wave will be broader than expected, even though it is still reversible. In addition, its shape and position are independent of scan rate. No correlations were made for quasi-reversible or irreversible electron transfers.

Multi-electron transfers can put a much more stringent demand on the rate of electron transfers if the wave is shifted significantly from its E^o because of the second electron transfer. Ruzic (3) has shown that, for polarography, the apparent heterogeneous electron transfer rate constant, k_s', for the over-all two-electron transfer is less than either of the individual rate constants, $k_{s,1}$ or $k_{s,2}$, if the second E^o, E_2, is more positive than the first E^o, E_1. In particular, the rate constant that is calculated using conventional theory is not the individual rate constant but an apparent one. Thus, the theory for quasireversible electron transfers in CV (4) yields the value of k_s'.

Competing with the multielectron transfer mechnism is the disproportionation mechanism. If the second electron transfer is so slow as to not be important and if E_2 is positive of E_1, the classical disproportionation mechanism can then occur. The theory for this mechanism has been developed and verified by Saveant (5). But very little work has been done in trying to assess the relative importance of the electron transfer mechanism (EE) as compared to the disproportionation (DISP) mechanism. For reversible electron transfers the cyclic voltammograms will not distinguish between these two mechanisms.

It is the purpose of this work to develop the cyclic voltammetric theory more generally for the EE mechanism, including the possibility of disproportionation, and to verify it experimentally. The emphasis will be placed on those cases where only one wave is observed, and either the first or second electron transfer is slow. Recent studies have shown several reductions that are now known to follow the EE mechanism (6). In this study, the electrochemical reduction of benzil in dimethylformamide (DMF) in the presence of alkaline earth salts, which is known to be a quasireversible two-electron transfer (6), is investigated in more detail in this work using the theory that is presented.

* Electrochemical Society Active Member.

Key words: EE mechanism, cyclic voltammetry, disproportionation.

Experimental

Spectroquality N,N-dimethylformamide was obtained from Matheson, Coleman, and Bell. The solvents were dried as required using activated molecular sieves. Strontium and barium perchlorate were obtained from G. F. Smith Chemical Company and were vacuum dried at 250°C for 6 hr (7). Benzil was recrystallized from ethanol. The reference electrode is the same as was described in Ref. (6). Positive feedback resistance compensation was used in all of the fast scan rate experiments. A hanging mercury drop electrode was used as the working electrode. All solutions were deaerated with dry nitrogen. The diffusion equations were solved numerically using the technique of digital simulation (8). The flux equations for a two-electron transfer that were derived by Feldberg (9) were used to calculate the current.

Theory

The generalized EE mechanism that is discussed in this paper is given by reactions [1]-[3]

$$A + e \overset{E_1}{\rightleftharpoons} B \quad [1]$$

$$B + e \overset{E_2}{\rightleftharpoons} C \quad [2]$$

$$2B \overset{k_d}{\rightarrow} A + C \quad [3]$$

Each electron transfer has associated with it a $k_{s,i}$ and α_i value, where i = 1 or 2, for the first or second electron transfer, respectively. The analysis of the mechanism is divided into two major sections, depending upon whether the first or second electron transfer is rate limiting. In both cases, the mechanism is studied in the regions where only one wave is seen.

While each individual step has an α_i associated with it, the over-all electron transfer coefficient that is observed if one wave is seen has been derived by Mohilner (10). If the first electron transfer is limiting, then

$$\alpha n = \alpha_1 \quad [4]$$

If the second electron transfer step is limiting, the observed αn is

$$\alpha n = 1 + \alpha_2 \quad [5]$$

First-electron transfer limiting.— Reversible electron transfer.—Using the theory that was derived for polarography (3) and verified by digital simulation in this work for CV, the value of k_s' can be calculated as follows

$$k_s' = k_{s,1} \exp[-\alpha_1 \mathbf{F} \Delta E / 2RT] \quad [6]$$

where $\Delta E = E_2 - E_1$. As stated earlier, it is the k_s' value that is experimentally measured. Thus, α_1 and ΔE must be known in order to calculate $k_{s,1}$. In order to generalize the results, the dimensionless electron transfer rate parameter, ψ, will be used and is defined as follows

$$\psi = k_s/\sqrt{\pi a D_A} \quad [7]$$

and

$$a = n\mathbf{F}v/RT \quad [8]$$

where v is the scan rate and the other terms have either been defined or have their usual electrochemical significance. Combining Eq. [6] and [7], we obtain

$$\psi_1' = \psi_1 \exp\left[\frac{-\alpha_1 \mathbf{F}\Delta E}{2RT}\right] \quad [9]$$

The shape of the cyclic voltammogram depends on its reversibility (ψ_1') and on the difference in E^{o}'s (ΔE). These are two different parameters which must be evaluated separately. Cyclic voltammograms can be divided into three general classes depending on the value of ψ_1'. These classes are: (*i*) reversible, $\psi_1' > 7$, (*ii*) quasireversible, $0.1 < \psi_1' < 7$; and (*iii*) irreversible, $\psi_1' < 0.1$. Within these three classes, the shape of the wave is also dependent upon ΔE. In this paper, for each of the three classes, the effect of ΔE on these classes is examined. Several limiting cases have already been described. For the reversible and irreversible classes, Nicholson and Shain (11) have derived the shape and behavior of the wave if $\Delta E > 180$ mV. Myers and Shain (2) and Polcyn and Shain (1) have investigated the reversible case if $\Delta E < 180$ mV. These papers can be consulted to determine the shape of the wave and the value of ΔE. The irreversible case was also studied by Polcyn and Shain (1) for $\Delta E <$ 180 mV but quantitative analysis was possible only if two waves were seen.

The disproportionation reaction (reaction [3]) has no effect on the shape of the wave if the first electron transfer is the slow step. This is because B is rapidly reduced to C at the electrode surface. This is not to say that the disproportionation reaction does not occur but only that the reaction has no effect on the wave when it occurs in this situation. This was verified by digital simulation.

Quasireversible electron transfer.—For quasireversible electron transfers, the shape of the wave depends upon ψ_1' and ΔE, and is not very dependent upon α_1. If ΔE is larger than 180 mV, the value of k_s' can be calculated from the theory for quasireversible waves given by Nicholson (4). But even for $\Delta E > 180$ mV, noticeable deviations occur when the waves are simulated by the digital simulation technique (8, 9). The results are shown in Table I for ψ_1' less than 1. The deviations are due to the greater effect of α_1 on the peak potentials for the same value of ψ.

To calculate $k_{s,1}$, ΔE and α_1 must be known. The value of α_1 cannot be accurately determined unless scan rates large enough to make the wave irreversible are used. At these large scan rates, the theory presented in the next subsection on irreversible electron transfers can be used to calculate α_1. The value of ΔE can be calculated using the reversible theory if slow enough scan rates can be achieved or by using the irreversible theory that is described for fast scan rates. For ΔE values less than 180 mV, the working curve will depend upon ΔE in addition to ψ_1'. This effect is not large and can be corrected for in the same way as shown in Eq. [32] later in this paper.

Table I. Variation of ΔE_p values as a function of ψ_1' ($\alpha_1 = 0.5$)

ψ_1'	ΔE_p (mV) EE mechanism	Ref. (4)
1.0	45	42
0.5	61	53
0.2	107	79
0.1	156	106

Irreversible electron transfer.—In the case where single scan is used, the position, shape, and size of the reduction wave depends on the value of ψ_1', α_1, and ΔE. The wave does not occur at its thermodynamically defined E^o but at a more negative potential depending upon scan rate. In the theory as derived by Nicholson and Shain (11) for multielectron irreversible transfer, it was assumed that all the electron transfers except the slow one were fast, at least at the potentials where the reduction wave occurs. Polcyn and Shain (1) have shown that the wave will be affected if this assumption does not hold true but no quantitative theory was derived if one wave is observed. In order to provide a quantitative measure of the relative difference in reduction potentials, the parameter, ΔE_{AB}, is defined as

$$\Delta E_{AB} = \Delta E - \frac{59}{\alpha_1} \log \psi_1 \quad [10]$$

This equation is derived from the fact that an irreversible reduction is shifted to more negative potentials by a rate of $59/\alpha_1 \log \psi_1$. This parameter corrects ΔE for the fact that irreversible reductions do not occur at their thermodynamically defined potential but at some more negative potential depending upon α_1 and $k_{s,1}$. Similar to reversible electron transfer, only one wave is seen if ΔE_{AB} is positive and two waves are seen if ΔE_{AB} is negative enough. The exact values of these regions are shown later. By combining Eq. [9] and [10], ΔE_{AB} can be defined in terms of ψ_1', which is experimentally measured

$$\Delta E_{AB} = \Delta E/2 - \frac{59}{\alpha_1} \log \psi_1' \quad [11]$$

By using digital simulation (8), it was found that the theory for irreversible electron transfers derived by Nicholson and Shain (11) can be used if ΔE_{AB} is greater than $75/\alpha_1$ mV. In this case, the following diagnostic criteria for the cathodic peak potential, E_{pc}, the cathodic peak current, i_{pc}, and the peak $E_{pp/2}$ values can be calculated

$$i_{pc} = 0.992\, \mathbf{F} A C_A^* \sqrt{\alpha_1 D_A a_1} \quad [12]$$

$$E_{pp/2} = E_{pc} - E_{p/2} = 47.7/\alpha_1 \text{ mV} \quad [13]$$

$$dE_{pc}/d \log v = 30/\alpha_1 \text{ mV} \quad [14]$$

and

$$a_1 = \mathbf{F}v/RT \quad [15]$$

and where $E_{p/2}$ is the half-peak potential.

If ΔE_{AB} is less than $75/\alpha_1$ mV and only one wave is seen, the shape of the wave is changed from that predicted for an irreversible electron transfer and depends upon the scan rate. This is shown in Fig. 1 for three different values of ΔE_{AB}. As the scan rate is increased (ΔE_{AB} larger), the value of ΔE_{AB} will increase so as to make the wave approach the irreversible theory as given in Eq. [12]-[14]. The $E_{pp/2}$ value is most strongly dependent upon ΔE_{AB} for ΔE_{AB} values less than $75/\alpha_1$ mV. The variation of $E_{pp/2}$ values with ΔE_{AB} is shown in Fig. 2 for various values of α_1, where the $E_{pp/2}$ values have been normalized in the following manner

$$E^*_{pp/2} = \alpha_1 E_{pp/2} \quad [16]$$

For large negative values of ΔE_{AB} two waves are seen and each wave can be analyzed individually because A will reduce prior to the potential for the B wave. For intermediate values of ΔE_{AB}, the A reduction wave will overlap the B wave and hence a broaden wave will be seen. There is a maximum value for which ΔE can have and still see the behavior as described in Fig. 2. For the wave to begin to broaden, ΔE_{AB} must be less than $75/\alpha_1$ mV and ψ_1' must be less than 0.1. Thus, rearranging Eq. [11], we obtain

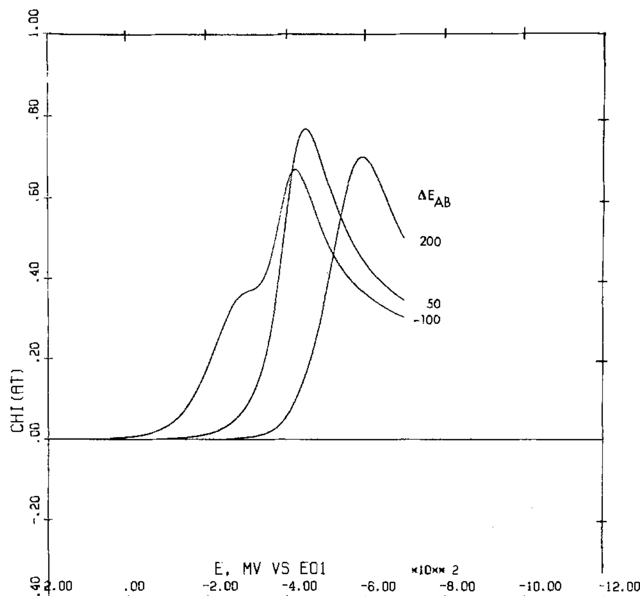

Fig. 1. The simulated cathodic scan for three different values of ΔE_{AB} (first-electron transfer irreversible).

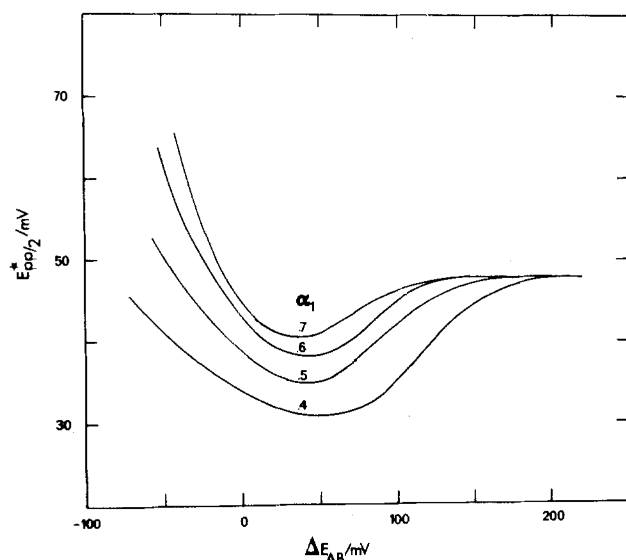

Fig. 2. The variation of $E_{pp/2}^*$ as a function of ΔE_{AB} for various values of α_1 in the case where the first electron transfer is irreversible.

$$\Delta E < \frac{32}{\alpha_1}\text{mV} \quad [17]$$

Otherwise, Eq. [12]-[14] will always hold when the wave is irreversible. In the limit of very slow scan rates, the $E_{pp/2}$ value is limited by the value derived by Myers and Shain (2). The peak current function goes through a maximum at the same point that the $E_{pp/2}$ values go through a minimum but the change in this parameter is not very large with the maximum change on the order of 20%, making this parameter less useful.

In the cyclic experiment, on the anodic scan, the reverse of reactions [1] and [2] occurs

$$\text{C} \overset{E_2}{\rightleftharpoons} \text{B} + e \quad [18]$$

$$\text{B} \overset{E_1}{\rightleftharpoons} \text{A} + e \quad [19]$$

For the return peak, reaction [19] is rate limiting, which is the second-electron transfer. A full discussion of this case is given in the next section and only a few pertinent details are given here. Either one or two waves can be seen on the return scan. The experimental conditions for the number of peaks that are seen are given in the next section.

With the information from the reverse scan, it is possible to determine all the parameters for the two-electron transfer. There are four unknowns which need to be evaluated from the experimental data. They are: E_1, E_2, $k_{s,1}$ and α_1. There are two other parameters that are related to these and are calculated during the analysis. They are

$$E_{1,2} = (E_1 + E_2)/2 \quad [20]$$

and ΔE. It is the aim of the rest of this section to develop the equations necessary to calculate these parameters from the data.

If two anodic peaks are seen, E_2 can be found directly from the most negative peak potential, $E_{pa(2)}$, because that wave will occur at its thermodynamically defined potential

$$E_2 = E_{pa(2)} - 0.0285 \quad [21]$$

The value of α_1 can be determined from several methods depending on the value of ΔE_{AB}. If Eq. [12]-[14] are obeyed, α_1 can be determined from the shift in E_{pc} or by the $E_{pp/2}$ value. If ΔE_{AB} is less than $75/\alpha_1$ mV (in other words, the shape depends upon scan rate), the value of α_1 can be determined from the more positive anodic peak potential, $E_{pa(1)}$. Thus

$$\frac{dE_{pa(1)}}{d\log v} = \frac{30}{1-\alpha_1}\text{mV} \quad [22]$$

The cathodic peak potential can be related to the $E_{1,2}$ value by the following equation (11) if $\Delta E_{AB} > 75/\alpha_1$ mV

$$E_{pc} = E_{1,2} - \frac{RT}{\alpha_1 \mathbf{F}}\left(0.339 - \log \psi_1' + \sqrt{\frac{\alpha_1}{2\pi}}\right) \quad [23]$$

and $E_{pa(1)}$ is

$$E_{pa} = E_{1,2} + \frac{RT}{(1-\alpha_1)\mathbf{F}}\left(0.339 - \log \psi_1' + \log\sqrt{\frac{1-\alpha_1}{\pi}}\right) \quad [24]$$

By taking the difference in the peak potentials, we obtain

$$\Delta E_p = \frac{0.059}{\alpha_1(1-\alpha_1)}(0.339 - \log\psi_1') + \frac{0.059}{1-\alpha_1}\log\sqrt{\frac{1-\alpha_1}{\pi}} + \frac{0.059}{\alpha_1}\log\sqrt{\frac{\alpha_1}{2\pi}} \quad [25]$$

Thus, since α_1 is known, ψ_1' can be calculated from the ΔE_p values. If ψ_1' is now substituted in Eq. [23], $E_{1,2}$ can be found. The value of E_2 is known from Eq. [21] so E_1 can be calculated by using Eq. [20].

If only one anodic peak is seen, α_1 can be found from the anodic or cathodic wave. If the anodic peak potential is used to calculate α_1, then as will be described in the next section, Eq. [26] must be used

$$\frac{dE_{pa}}{d\log v} = 30/(2-\alpha_1)\text{mV} \quad [26]$$

The value of ψ_1' can be found, as before, from the ΔE_p value but Eq. [28] must be used because E_{pa} is given by

$$E_{pa} = E_{1,2} + \frac{0.059}{2-\alpha_1}\left[0.339 + \log\psi_1' + \log\sqrt{\frac{1-\alpha_1}{2\pi}}\right] \quad [27]$$

Using Eq. [27], the variation of ΔE_p with ψ_1' is given by

$$\Delta E_p = \frac{0.118}{\alpha_1(2-\alpha_1)}(0.339 + \log \psi_1') + \frac{0.059}{2-\alpha_1}\log\sqrt{\frac{1-\alpha_1}{2\pi}} + \frac{0.059}{\alpha_1}\log\sqrt{\frac{\alpha_1}{2\pi}} \quad [28]$$

The value of $E_{1,2}$ can be found from Eq. [23]. The final problem is to find a method to determine E_1 and E_2 from $E_{1,2}$. To do this, either fast or slow scan rates must be used to separate either the anodic or cathodic peaks into two waves. It is theoretically possible to cause the cathodic peak to split apart if ΔE is less than -60 mV. If this is not possible, then scan rates fast enough to split the anodic peak apart must be used. If the cathodic peak begins to split apart, Fig. 2 can be used to calculate the value of ΔE_{AB} from the $E_{pp/2}$ values. From Eq. [11], it is possible to determine ΔE because α_1 and ψ_1' are known

$$\Delta E = 2\left(\Delta E_{AB} + \frac{59}{\alpha_1}\log \psi_1'\right) \quad [29]$$

Unless there is some change in the shape of either the anodic or cathodic wave it is impossible to determine E_1 and E_2.

Second-electron transfer limiting.—No disproportionation.—If the disproportionation reaction (reaction [3]) does not occur, the only way of producing C is by the direct reduction of B at the electrode surface. As with the previous case, an apparent electron transfer rate constant, k_s', is observed experimentally rather than the actual k_s value of the second step. The value of k_s' is given by

$$k_s' = k_{s,2}\exp\left(-(1-\alpha_2)\frac{F}{RT}\frac{\Delta E}{2}\right) \quad [30]$$

or

$$\psi_2' = \psi_2 \exp\left[-(1-\alpha_2)\frac{F}{RT}\frac{\Delta E}{2}\right] \quad [31]$$

As before, reversible behavior is observed if ψ_2' is greater than 7. If ψ_2' is less than 0.1, an irreversible wave is seen. For reversible waves, the shape of the wave (2) depends only on ΔE and is independent of ΔE if ΔE is greater than 180 mV.

Quasireversible electron transfer.—For quasireversible waves, the shape of the wave depends upon ψ_2' and ΔE and is not very dependent upon α_2. If ΔE is larger than 180 mV and ψ_2' greater than 0.5, the value of k_s' can be calculated from the theory for quasireversible waves given by Nicholson (4). The ΔE_p values as calculated by digital simulation for different α_2 values are given in Table II for several ψ_2' values less than 1.

If ΔE is less than 180 mV, the ΔE_p values are larger than predicted by Ref. (4). To a close approximation, the working curves for $\Delta E < 180$ mV can be obtained by adding the excess broadness, E_{exc}, as defined in Eq. [32] to the data in Table II

$$E_{exc} = \Delta E_{pr} - 29 \text{ mV} \quad [32]$$

where ΔE_{pr} is the ΔE_p value for a given ΔE (reversible case).

Irreversible case.—With a single scan, as defined earlier, the wave is irreversible if ψ_2' is less than 0.1.

Table II. Variation of ΔE_p values as a function of ψ_2'

ψ_2'	ΔE_p (mV) $\alpha_2 =$ 0.35	0.5	0.65	Ref. (4)
1.0	44	44	43	42
0.5	58	56	53	53
0.2	91	88	85	79
0.1	128	135	147	106

Irreversibility of the second electron transfer makes the second electron transfer occur at more negative potentials. In order to correct for this, we can define a parameter, ΔE_{BC}, which takes into account the effect of the slow electron transfer

$$\Delta E_{BC} = \Delta E/2 + \frac{59}{1+\alpha_2}\log \psi_2' \quad [33]$$

This parameter normalizes the combined effects of ΔE and ψ_2' on the relative positions of the two waves. From digital simulation, it was found that, if ΔE_{BC} is greater than 50 mV, the shape of the wave is given by the theory derived by Nicholson and Shain (11). Substituting $n = 2$ and $\alpha n = 1 + \alpha_2$, the following diagnostic parameters can be calculated

$$i_p = 0.992\,FA\sqrt{(1+\alpha_2)Da_1C_A^*} \quad [34]$$

$$E_{pp/2} = 47.7/(1+\alpha_2)\text{mV} \quad [35]$$

$$dE_p/d\log v = 30/(1+\alpha_2)\text{mV} \quad [36]$$

If ΔE_{BC} is less than 50 mV the wave will broaden and the peak current function will decrease. This effect can be seen in Fig. 3 for three different values of ΔE_{BC}. The variation in χ_p and $E_{pp/2}$ values can be calculated as a function of α_2 by the following normalizations

$$\chi_p^* = \chi_p/(1+\alpha_2)^{1/2} \quad [37]$$

$$E_{pp/2}^* = E_{pp/2}(1+\alpha_2) \quad [38]$$

The effect of ΔE_{BC} on χ_p^* and $E_{pp/2}^*$ is shown in Fig. 4 and 5. The variations in these parameters are qualitatively similar to the ECE and DISP mechanisms. It is only at fast scan rates that the χ_p and $E_{pp/2}$ values differ significantly from the ECE and DISP mechanism. But chronoamperometry will easily distinguish between these mechanisms because a two-electron diffusion-controlled wave can be obtained if a negative enough potential is used. In contrast, an ECE or DISP mechanism will show the slow kinetic step regardless of applied potential.

In a cyclic experiment, since the B to C reduction is limiting in this case, the C to B oxidation will be limiting on the reverse scan. Thus, the theory for the first-step limiting must be used to evaluate the oxidation peak.

As before, there are four parameters which must be determined: E_1, E_2, $k_{s,2}$, and α_2. Thus, four indepen-

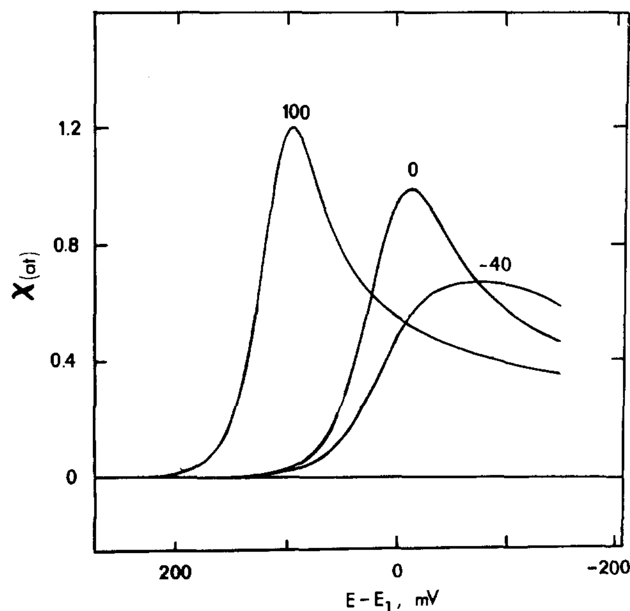

Fig. 3. The simulated cathodic scan for three different values of ΔE_{BC} (second-electron transfer irreversible).

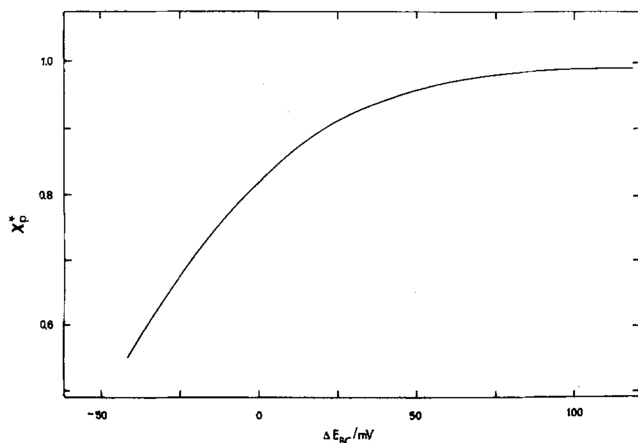

Fig. 4. The variation of χ_p^* as a function of ΔE_{BC} for the case where the second electron transfer is irreversible.

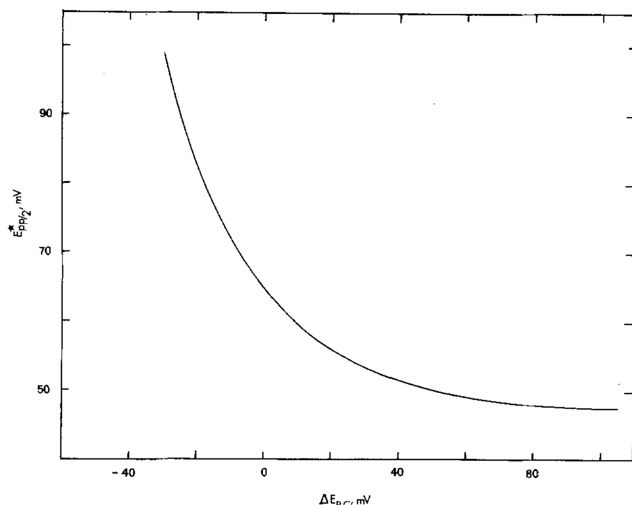

Fig. 5. The variation of $E_{pp/2}^*$ as a function of ΔE_{BC} for the case where the second electron transfer is irreversible.

dent equations must be derived. Only one anodic peak can be seen under practically any conditions where only one cathodic peak is seen as a consequence of Eq. [17]. This limits the existence of two peaks to ΔE values which are close to zero or negative. The value of α_2 can be calculated from Eq. [35] or [36]. The second equation that can be used to calculate these parameters is the cathodic peak potential (11), which is

$$E_{pc} = E_{1,2} - \frac{0.059}{1+\alpha_2}\left[0.339 - \log \psi_2' + \log\sqrt{\frac{\alpha_2}{2\pi}}\right] \quad [39]$$

In addition, E_{pa} is given by (11)

$$E_{pa} = E_{1,2} + \frac{0.059}{1-\alpha_2}\left[0.339 - \log \psi_2' + \log\sqrt{\frac{1-\alpha_2}{2\pi}}\right] \quad [40]$$

Combining Eq. [39] and [40], the ΔE_p values can be derived as a function of ψ_2'

$$\Delta E_p = \frac{0.118}{1-\alpha_2}(0.339 - \log \psi_2') + \frac{0.059}{1+\alpha_2}\log\sqrt{\frac{\alpha_2}{2\pi}} + \frac{0.059}{1-\alpha_2}\log\sqrt{\frac{1-\alpha_2}{2\pi}} \quad [41]$$

Once ψ_2' is calculated, $E_{1,2}$ can be calculated from Eq. [39]. The final determination of E_1 or E_2 requires that ΔE_{BC} be less than 50 mV so that the wave will begin to split apart. If ΔE_{BC} can be determined from the $E_{pp/2}$ or χ_p values, then

$$\Delta E = 2\left(\Delta E_{BC} - \frac{59}{1+\alpha_2}\log \psi_2'\right) \quad [42]$$

If ΔE is such that the wave does not begin to split apart, then a lower limit on ΔE can be established because ΔE_{BC} must be greater than 50 mV

$$\Delta E > 100 - \frac{118}{1+\alpha_2}\log \psi_2' \quad [43]$$

Thus, from Eq. [35] or [36], [39], and [41] and [42], we have four independent equations which allow one to calculate $k_{s,2}$, α_2, E_1 and E_2. The solution is simple because there is only one new unknown in each equation. It is important to obtain a good determination of α_2 since this is critical in all the equations. If the wave is beginning to split apart, it is probably more accurate to use the anodic peak potential to determine α_2 because that will not be affected. But fortunately, it turns out that unless the wave has broadened considerably, the calculation of α_2 from Eq. [36] is also not seriously affected even though Eq. [35] cannot be used.

Disproportionation.—For $\Delta E > 0$, the disproportionation reaction is favorable and can compete with the electron transfer if it is fast enough. In order to discuss this mechanism quantitatively, the rate constant, k_d, is normalized as follows

$$\lambda_d = k_d C_A^*/a \quad [44]$$

where λ_d is the disproportionation kinetic parameter. It is important to keep in mind that λ_d depends upon C_A^* while ψ_2 does not. Thus, it is possible to change λ_d without changing ψ_2 at the same time. In Fig. 6, the effect of the disproportionation reaction can be seen quite clearly. In this figure, the wave becomes dependent upon the disproportionation reaction and not on the second electron transfer. The same type of behavior is demonstrated in Fig. 7, where the electron transfer predominates if it is large enough in spite of a fairly significant rate for the disproportionation reaction. Qualitatively, the DISP mechanism is most important for negative values of ΔE_{BC}. If ΔE_{BC} is positive, the difference in the shape and height of the wave due to these two mechanisms is not large.

The effect of the disproportionation reaction on the EE mechanism was determined by the use of digital simulation (8). The results are shown in Fig. 8 and 9 for the χ_p and E_{pc} values for $\alpha_2 = 0.5$ as a function of ΔE_{BC}. It is assumed in this case that the wave is ir-

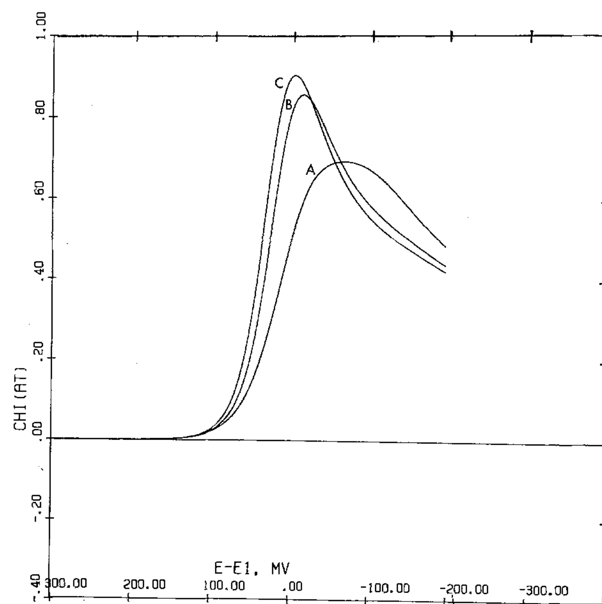

Fig. 6. The simulated cathodic scan for $\Delta E_{BC} = -20$ mV and (a) $\lambda_d = 0$; (b) $\lambda_d = 10$; and (c) $\lambda_d = 30$.

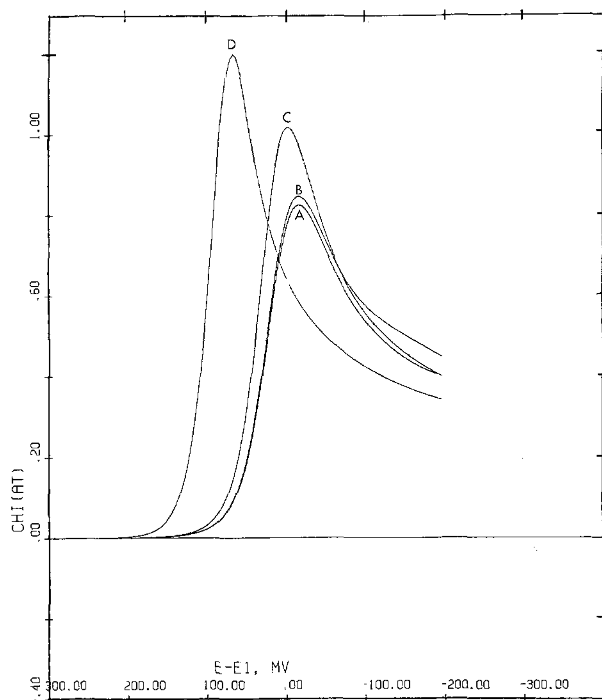

Fig. 7. The simulated cathodic scan for $\lambda_d = 10$, and ΔE_{BC} equal to (a) -100 mV; (b) -50 mV; (c) 0; (d) $+75$ mV.

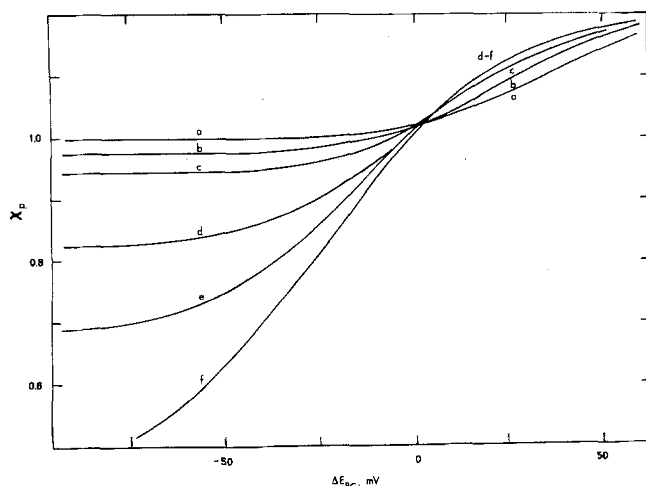

Fig. 8. The variation of χ_p as a function of ΔE_{BC} for various values of λ_d (second-electron transfer irreversible). (a) $\lambda_d = 1000$; (b) $\lambda_d = 300$; (c) $\lambda_d = 100$; (d) $\lambda_d = 30$; (e) $\lambda_d = 10$; (f) $\lambda_d = 0.1$.

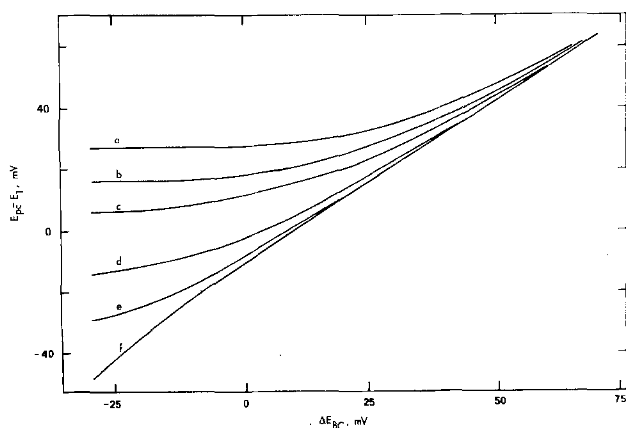

Fig. 9. The variation of $E_{pc} - E_1$ as a function of ΔE_{BC} for various values of λ_d. Values of λ_d given in Fig. 2.

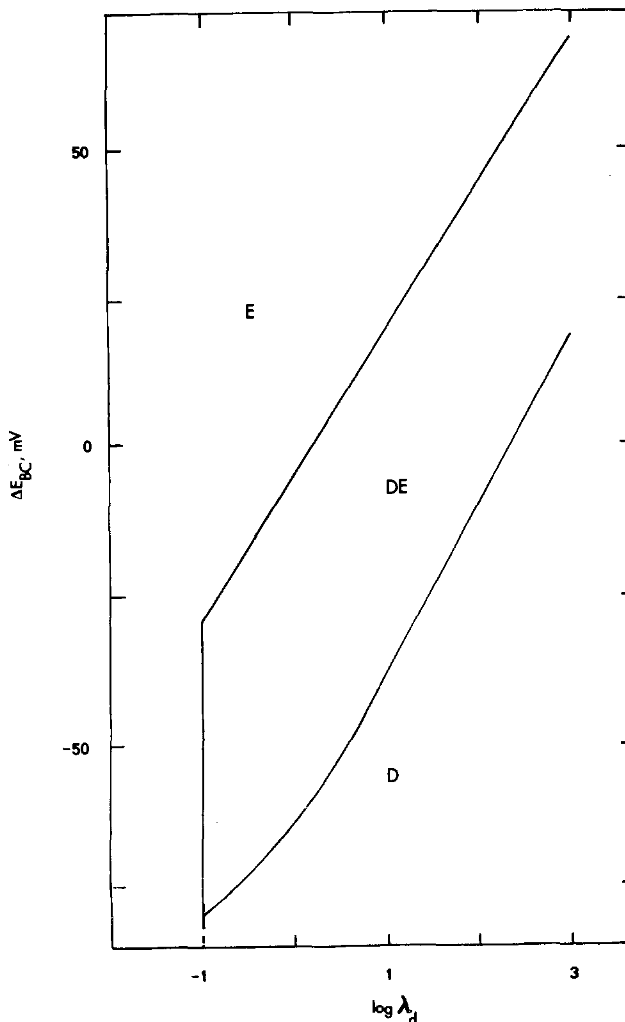

Fig. 10. Values of ΔE_{BC} and λ_d where various mechanisms are applicable. E = EE Mechanism, D = DISP Mechanism, DE = Mixture of EE, and DISP Mechanism.

reversible ($\psi_2' < 0.1$). For quasireversible and reversible waves, the effect of the DISP mechanism is small. Using the criteria that the DISP mechanism predominates if χ_p is within 5% of the value for the wave when $\psi_2' = 0$, a range of ΔE_{BC} values can be calculated and the results are shown in Fig. 10. At the other extreme, the wave is defined by the EE mechanism if the E_{pc} value is within 2 mV of the value obtained when $\lambda_d = 0$. These values are also shown in Fig. 10. Between these two limits, the wave is controlled by both the EE and DISP mechanism and Fig. 8 and 9 can be used. These limits can be expressed as follows

DISP mechanism predominates if

$$\Delta E_{BC} < 25 \log \lambda_d - 70 \text{ mV} \quad [45]$$

EE mechanism predominates if

$$\Delta E_{BC} > 25 \log \lambda_d - 5 \text{ mV} \quad [46]$$

While these results were obtained for $\alpha_2 = 0.5$, the same conclusions were obtained for $\alpha_2 = 0.35$ and 0.65. The E_{pc} curve shown in Fig. 9 is almost independent of α_2. The χ_p curve (Fig. 8) does depend upon α_2 because the limiting value of χ_p when ΔE_{BC} is large does depend upon α_2. In general, this dependence is small and varies by only 10%, at most, for α_2 between 0.35 and 0.65. But the limits given by Eq. [45] do not depend upon α_2. This can be seen in Fig. 11 for $\alpha_2 = 0.35$, 0.5, and 0.65 and $\lambda_d = 10$.

Diagnostic Criteria and Data Analysis

The key to the analysis of cyclic voltammetric data for this case is a systematic approach. The analysis can

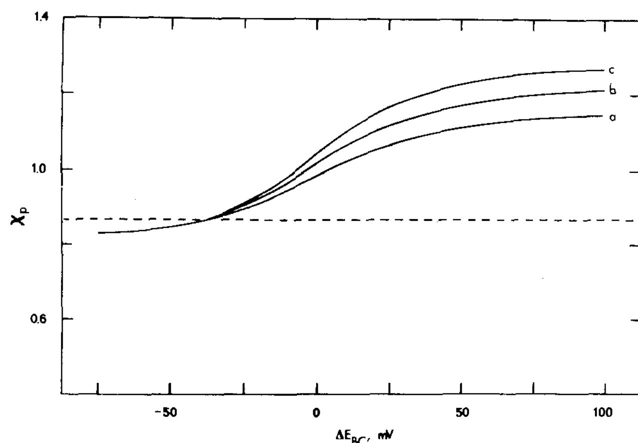

Fig. 11. Variation of χ_p as a function of ΔE_{BC} for $\lambda_d = 10$ and α_2 equal to (a) 0.35; (b) 0.50; and (c) 0.65. Dashed line indicates the value where χ_p has increased by 5%.

be segregated into the following steps:
1. determination that EE mechanism is occurring
2. determine if disproportionation is occurring
3. determination of the reversibility of electron transfer
4. identification of the slow step
5. calculation of electron transfer parameters

Step 1.—The determination that an EE mechanism is occurring is most easily done by double-potential step chronoamperometry. By comparison of the diffusion current with compounds of known electrochemical behavior, the n value can be calculated. Second, from the i_a/i_c ratio, the stability of the product can be verified and one can verify that no irreversible chemical reactions are occurring. Third, the $i_c\sqrt{t}/C_A{}^*$ value should be constant, indicating that no new electroactive products are formed. The value of the final potential must be negative enough so that the slow electron transfer step does not affect the $i_c\sqrt{t}/C_A{}^*$ value.

Step 2.—Since the value of λ_d depends upon $C_A{}^*$, the shape and position of the wave should be dependent upon $C_A{}^*$. Conversely, ψ' is independent of $C_A{}^*$, so one can determine if disproportionation is important under the conditions used.

Step 3.—If the shape or position of the wave is independent of scan rate, then the electron transfers are reversible. If the values of ΔE_p are between 30 and 150 mV, at least one of the electron transfers is slow and the wave is quasireversible. If the ΔE_p values are greater than 150 mV, the electron transfer is irreversible.

Step 4.—The identity of the slow step can be surmised from several ways depending upon the rate of the electron transfers. If the wave is quasireversible, it is difficult to determine the slow step because of the similarities in working curves. Only if scan rates large enough so that ψ' is < 0.1, (*i.e.*, the wave is irreversible) are used can one determine which step is slow.

If the electron transfer is irreversible, the identity of the slow step can be easily determined from the ratio of the peak currents, $i_{p,a}/i_{p,c}$, where $i_{p,a}$ is measured from a baseline calculated from the $t^{-1/2}$ decay of the cathodic current. If the first step is slow, then from Eq. [12] and [34]

$$i_{p,a}/i_{p,c} = \sqrt{(2-\alpha_1)/\alpha_1} \qquad [47]$$

Since $\alpha_1 < 1$

$$i_{p,a}/i_{p,c} > 1 \qquad [48]$$

for all values of α_1. Conversely, if the second electron transfer is slow

$$i_{p,a}/i_{p,c} = \sqrt{(1-\alpha_2)/(1+\alpha_2)} \qquad [49]$$

Once again, α_2 is less than one. Thus

$$i_{p,a}/i_{p,c} < 1 \qquad [50]$$

Substitution of typical values of α into Eq. [47] or [49] will show that there will be significant deviations from unity for the peak current ratio. In order to use this criterion with confidence, ψ' should be less than 0.1 ($\Delta E_p > 150$ mV) and reduced product must be stable.

Step 5.—The calculation of the parameters related to the electron transfer can now be determined once the previous steps have been completed. If the wave is reversible, only the $E_{1,2}$ value can be determined for sure. If ΔE is less than 180 mV, E_1 and E_2 can also be found. If the wave is quasireversible, then ψ' and $E_{1,2}$ can be calculated. Once again, if ΔE is less than 180 mV, E_1 and E_2 can also be found. If scan rates large enough to make the wave irreversible are used, α can be determined (and hence ψ if E_1 and E_2 are known). If the wave is irreversible, α can be calculated from the shape or shift in the wave and ψ' can be calculated from the ΔE_p values. Finally, $E_{1,2}$ can be found. If the values of ΔE_{AB} or ΔE_{BC} are appropriate, then E_1, E_2, and ψ can be found. In all this analysis, it is assumed that the other electron transfer remains reversible. This, in practice, limits the maximum scan rates which can be used to analyze the data by this method.

Results and Conclusions

The reduction of benzil (Bn) in 0.10F barium perchlorate with DMF as solvent is a two-electron quasireversible electron transfer. The cyclic voltammetric data for this solution is shown in Table III. Using the criteria discussed earlier, single and double step chronoamperometry verified that the reduction was a two-electron transfer for times at least as short as 1 msec and that the reduction product was stable. The second step in the analysis was to vary the concentration of benzil to determine if disproportionation was occurring. It was found that for C_{Bn} equal to 0.75 and 5.0 mM no change in the shape of the wave was observed (6). Thus, one could analyze the data in Table III without including the disproportionation reaction. The third step is to determine the reversibility of the electron transfer. Since ΔE_p is greater than 150 mV for all scan rates studied, the electron transfer is irreversible. Finally, because the $i_{p,a}/i_{p,c}$ ratios are much less than 1.0, the second electron transfer must be the slow step.

For the data below 1 V/sec, the experimental data fits quite well with the theory for an EE mechanism. From the ΔE_p values, it was possible to find α_2, which is equal to 0.66. Equation [39], [41] and [42] can then be expressed in the following manner

$$\log \psi_2' = -4.78(\Delta E_p + 0.021) \qquad [47]$$

$$E_{1,2} = E_{pc} + 0.0355\,(0.355 - \log \psi_2') \qquad [48]$$

$$\Delta E = 2(\Delta E_{BC} - 0.0355 \log \psi_2') \qquad [49]$$

The results obtained by these equations are shown in Table IV. Using these values as estimates, it was possible to generate theoretical voltammograms and compare them with the experimental data. This is shown in Fig. 12 for benzil at 100 mV/sec. The best values given in Table IV are obtained from the best fits of

Table III. Cyclic voltammetry of 0.75 mM benzil in DMF containing 0.10F $Ba(ClO_4)_2$

V (V/sec)	E_{pc}*	ΔE_p (mV)	$E_{pp/2}$ (mV)
0.05	−1.419	156	39
0.1	−1.428	190	44
0.2	−1.438	221	48
0.5	−1.448	260	54
1.0	−1.457	285	58
5.0	−1.477	365	61
10.0	−1.500		63
20.0	−1.528		68

* V *vs.* SRE (silver reference electrode).

Table IV. Determination of second-electron transfer rate in 0.1F $Ba(ClO_4)_2$

V (V/sec)	ΔE_{BC} (mV)	ψ'	E_1*	ΔE (mV)	K (M^{-1})	$k_{s,2}$ (cm/sec)
0.05	0	0.143	−1.407	60	1200	5.5×10^{-4}
0.1	−12	0.0983	−1.404	48	1350	5.0×10^{-4}
0.2	−18	0.0699	−1.412	46	1000	4.9×10^{-4}
0.5	−26	0.0455	−1.410	43	1060	5.0×10^{-4}
Best value			−1.408	55	1150	5.0×10^{-4}
Ref. (6)			−1.415	100	880	5×10^{-4}

* V *vs.* SRE.

the experimental data with the simulated voltammograms.

There occur significant deviations at scan rates above 1V/sec due to the slow rate of the first electron transfer. The values of $k_{s,1}$ and α_1 were determined by digital simulation, using the values already calculated for the second electron transfer. It was found that α_1 was equal to 0.7, and $k_{s,1}$ was equal to 6.5×10^{-3} cm/sec. The experimental data along with the theoretical curves are shown in Fig. 13 for the $E_{pp/2}$ values. An experimental voltammogram with the simulated wave is shown in Fig. 14 for benzil at 1.0 V/sec.

The rate of the first electron transfer appears to be unusually slow when compared to the rate of reduction with tetrabutylammonium perchlorate (TBAP) as a supporting electrolyte. But once again we are dealing with an apparent electron transfer rate constant, $k_{s,1}$*,

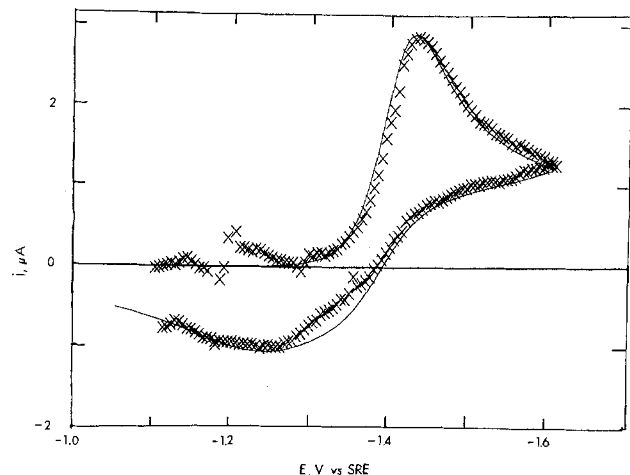

Fig. 12. Cyclic voltammogram for the reduction of 0.75 mM benzil in DMF with 0.10F $Ba(ClO_4)_2$. Scan rate = 100 mV/sec; solid line, theoretical; x, experimental points.

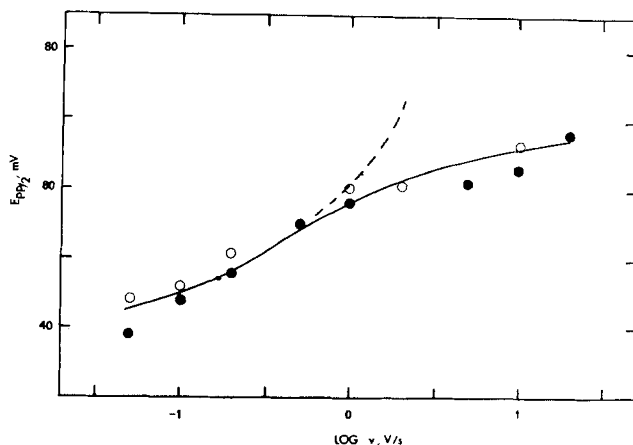

Fig. 13. The variation of $E_{pp/2}$ as a function of scan rate. Solid line, $k_{s,1}$ = 0.10 cm/sec, α_1 = 0.7, $k_{s,2} = 5.0 \times 10^{-4}$ cm/sec, α_2 = 0.66; dashed line, first-electron transfer reversible; closed circles, C_{Bn} = 0.75 mM; open circles, C_{Bn} = 5.0 mM.

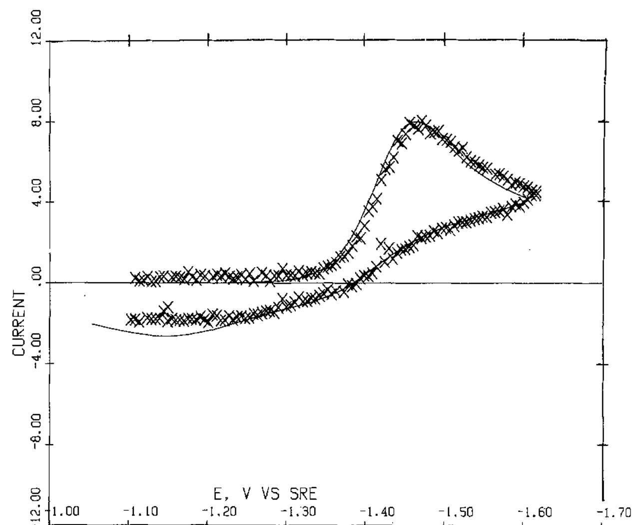

Fig. 14. Cyclic voltammogram for the reduction of 0.75 mM benzil in DMF with 0.10F $Ba(ClO_4)_2$. Scan rate = 1 V/sec; solid line, theoretical; x, experimental points.

instead of the true $k_{s,1}$. This is caused by the shift of the benzil

$$Bn + e \rightleftharpoons Bn^{\overline{\cdot}} \quad [50]$$

$$Bn^{\overline{\cdot}} + Ba^{2+} \overset{K}{\rightleftharpoons} BnBa^{\overset{+}{\cdot}} \quad [51]$$

reduction from its equilibrium position being due to the ion-pairing reaction. Since the wave occurs positive of the potential where benzil alone is reduced, the heterogeneous forward rate constant, k_{hf}, at the peak potential is less than $k_{s,1}$ due to the exponential relationship between k_{hf} and $k_{s,1}$

$$k_{hf} = k_{s,1} \exp \left[-\alpha_1 \frac{nF}{RT} (E - E^o) \right] \quad [52]$$

If one solves the boundary value problem for the above reaction, it turns out that $k_{s,1}$* is related to $k_{s,1}$ by the following equation

$$k_{s,1} = k_{s,1}^* (1 + KC_{Ba})^{\alpha_1} \quad [53]$$

where C_{Ba} is the concentration of the barium ion. For KC_{Ba} = 115 and α_1 = 0.7, $k_{s,1}$ is 0.18 cm/sec. This value of $k_{s,1}$ is within the range that has been observed for several quinones recently (12). This value is still smaller than the minimum value estimated in the presence of TBAP only. This difference cannot be due to ion pairing between the barium and perchlorate ions. While this will reduce [Ba^{2+}], it will at the same time increase the value of K because the K[Ba^{2+}] value was observed experimentally. In addition, estimations of the Ba-ClO_4 ion pair constant from Bjerrum's theory (13) and from data for Mg-ClO_4 in acetonitrile and acetone (14) indicate that ion pairing of the barium perchlorate electrolyte is insignificant in DMF. This lower rate constant could be due, though, to double layer changes caused by the presence of barium ions.

Using the information in Table IV, it is possible to estimate the maximum value for the disproportionation rate constant, k_d, using Eq. [45]. The maximum value of k_d depends upon scan rate, with the disproportionation reaction being more important at faster scan rates because ΔE_{BC} is decreasing. For C_{Bn} = 0.75 mM, it was found that k_d must be less than 700 M^{-1} sec^{-1}. This maximum value may be too small to see. A more practical value is probably 3×10^3 M^{-1} sec^{-1}. Since no disproportionation reaction is seen for the 5 mM solution, k_d must be less than 750 M^{-1} sec^{-1}. It is interesting to note that if ψ_2' were zero, a value of k_d = 750 M^{-1} sec^{-1} could be easily seen and calculated. Thus, for C_{Bn} = 5 mM and v = 50 mV/sec; λ_d

would be 2.7. But this reaction, if it occurs, is obscured by the second electron transfer.

The determination of $k_{s,2}$ for the reduction of benzil in the presence of strontium ion can be accomplished in the same way. The α_2 value was again found to be 0.65. Thus, Eq. [47]-[49] could be used. The results are shown in Table V. The calculated values for the benzil reduction with the strontium ion present agree well with the values determined by trial-and-error simulation. As was seen before (6), the second-electron transfer is somewhat slower with the strontium ion pair than with the barium ion pair. This difference, though, could be due to double layer effects.

The simplicity of this method of analysis is quite evident. Previously, it was necessary to perform a considerable number of trial and error simulations before the best fit could be obtained in order to determine the electron transfer parameters for the EE mechanism. But by use of the equations given in the paper, it was possible to directly calculate the parameters. A second advantage is that it is possible to identify significant deviations from the EE mechanism, as was shown in this case for scan rates in excess of 1 V/sec with barium ions present. If an EE mechanism is occurring with only one of the k_s values being slow, the shape of the wave should follow the criteria given previously. In particular, a good diagnostic criteria is the shift in the anodic and cathodic peak potentials with scan rates. Consistent α values should be obtained from these calculations. A factor complicating the analysis is the situation where both electron transfers may be slow. The diagnostic criteria will obey qualitatively the analysis given in this paper, but will fail seriously upon quantitative analysis. Work is in progress in this laboratory to present similar methods for the analysis of this case.

Table V. Cyclic voltammetry of benzil in DMF containing 0.10F $Sr(ClO_4)_2$

V (V/sec)	$E_{pp/2}$ (mV)	ΔE_p (mV)	E_1*	ΔE (mV)	$k_{s,2}$ (cm/sec)	K (M^{-1})
0.05	47	285	−1.372	72	1.4×10^{-4}	4800
0.1	49	322	−1.370	76	1.4×10^{-4}	5140
0.5	58	350	−1.383	80	1.7×10^{-4}	3100
Best value			−1.375	80	1.6×10^{-4}	4300
Ref. (6)			−1.397	135	2.0×10^{-4}	1800

* V *vs.* SRE.

Acknowledgment

This research was supported by the Petroleum Research Fund, administered by the American Chemical Society. I would also thank Dennis Evans for his help. In addition, the Computer Services Division of Marquette is acknowledged for providing computer time for this work.

Manuscript submitted April 11, 1977; revised manuscript received Oct. 31, 1977.

Any discussion of this paper will appear in a Discussion Section to be published in the December 1978 JOURNAL. All discussions for the December 1978 Discussion Section should be submitted by Aug. 1, 1978.

Publication costs of this article were assisted by Petroleum Research fund.

REFERENCES

1. D. S. Polcyn and I. Shain, *Anal. Chem.*, **38**, 370 (1966).
2. R. L. Myers and I. Shain, *ibid.*, **41**, 980 (1969).
3. I. Ruzic, *J. Electroanal. Chem.*, **52**, 331 (1974).
4. R. S. Nicholson, *Anal. Chem.*, **37**, 1351 (1965).
5. M. Mastragostino, L. Nadjo, and J. M. Saveant, *Electrochimica Acta*, **13**, 721 (1968).
6. M. D. Ryan and D. H. Evans, *J. Electroanal. Chem.*, **67**, 333 (1976); W. H. Smith and A. J. Bard, *ibid.*, **76**, 19 (1977).
7. V. Gutmann, M. Michlmayr, and G. Peychal-Heiling, *J. Electroanal. Chem.*, **17**, 153 (1968).
8. S. W. Feldberg in "Electroanalytical Chemistry," Vol. 3, A. J. Bard, Editor, pp. 199-296, Marcel Dekker, Inc., New York (1969).
9. S. W. Feldberg, in "Electrochemistry," J. S. Mattson, H. B. Mark, Jr., and H. C. McDonald, Jr., Editors, pp. 185-215, Marcel Dekker, Inc., New York (1972).
10. D. M. Mohliner, *J. Phys. Chem.*, **68**, 623 (1964).
11. R. S. Nicholson and I. Shain, *Anal. Chem.*, **36**, 706 (1964).
12. T. W. Rosanske and D. H. Evans, *J. Electroanal. Chem.*, **72**, 277 (1976).
13. J. O'M. Bockris and A. K. N. Reddy, "Modern Electrochemistry," p. 265, Plenum Press, New York (1973).
14. I. S. Perehygin and M. A. Klimchuk, *Russ. J. Phys. Chem. (Engl. Transl.)*, **47**, 1402 (1973); *ibid.*, **48**, 1466 (1974).

Transport Parameters for Potassium Hydroxide-Water Solution in a Cation Exchange Membrane

Manojit Sinha and Douglas N. Bennion*

Chemical, Nuclear, and Thermal Engineering Department, School of Engineering and Applied Science, University of California, Los Angeles, California 90024

ABSTRACT

The salt transport parameter L_e, the water transport parameter L_o, and the cation transference number $t_+{}^m$ have been measured for an RAI P2291 cation exchange membrane for aqueous KOH solutions. The transference number decreases with increase in concentration. For the concentration range 1.0-10.0M a straight line fit was obtained by linear regression. A correction to $t_+{}^m$ in the range of 0.453-0.846 has been used to compensate for the concentration gradient buildup in the porous electrodes due to the passage of current. The L parameters are not constant during the course of a dialysis experiment. An optimization procedure has been used to select the most accurate set of values of L_e ($=2.924 \times 10^{-5}$ cm/sec) and L_o ($=2.057 \times 10^{-4}$ cm/sec) for a single run.

An important application of ion-exchange membranes is in the field of batteries. Synthetic polymers were widely used as battery separators when attempts were being made to improve the performance and life of batteries. These were mostly commercially available films such as cellophane. In the past few years serious attempts have been made to make such films specifically for use as battery separators (1).

RAI-Permion 2291 membranes tested in this work are mainly for use in zinc-silver oxide batteries as an argentistatic spacer. The purpose of the argentistatic spacer is to inhibit the migration of $Ag(OH)_2^-$ in the alkaline solution. Cellophane was used in the early stages of practical zinc-silver oxide cells. Silver reacts with cellophane, thus deteriorating the film. There is an initial low rate of permeation of silver through the membrane (cellophane). After an appreciable period of time the rate of permeation increases. This is apparently caused because the membrane capacity for silver is reached. Permion membranes are more stable.

Permion membranes are made using a 1 mil thick low density polyethylene film made from a Bakelit DFD0602 resin (2). This resin has a narrow molecular weight distribution which is desirable since this gives the most efficient crosslinking per unit of energy used. The extruded film is crosslinked using high energy beta radiation to give a distance between crosslinked sites of 3000-5000 (that is the molecular weight between sites). Permion 2291 40/30 is then made from the crosslinked film by radiation grafting approximately 40% methacrylic acid onto the base film using a chain transfer agent to limit the chain length. (When a reactive monomer is present during irradiation, it may react with the free radicals giving a "grafted" side chain). This grafted film is finally converted to the potassium form by washing in 5% potassium hydroxide solution at 95°C for 3-4 min.

Permion 2291 is a weak cation exchange membrane meant to be used in alkaline electrolyte. It also appears to be useful in situations where high temperature, long wet stand, oxidation resistance, and high rate of charge/discharge are required.

The transference number of the K^+ ion and the L parameters are important in predicting shape change in the zinc electrode of zinc-silver oxide secondary electrodes (3). In this work the transference number of the K^+ ion has been experimentally determined through the RAI P2291 membrane in KOH solutions. The concentration range of measurement is 1.0-10.0M. The average diffusion coefficients of the electrolyte and solvent through the membrane have been measured in the range of concentration 4.95-7.63M. The specific conductivity and the fixed ion concentration of the ion-exchange membrane have also been measured.

Theory

Bennion and Rhee (4) define driving forces as a revised form of Stefan-Maxwell equation

$$d_i = \sum_j K_{ij}(v_j - v_i) \quad [1]$$

and, after a rigorous derivation arrive at flux equations written below

$$N_+ = c_+v_+ = z_-\mathcal{L}_e\nabla\mu_e + z_-\mathcal{L}_{eo}\nabla\mu_o + \frac{t_+i}{z_+\mathbf{F}} \quad [2]$$

$$N_- = c_-v_- = -z_+\mathcal{L}_e\nabla\mu_e - z_+\mathcal{L}_{eo}\nabla\mu_o + \frac{t_-i}{z_-\mathbf{F}} \quad [3]$$

$$N_o = c_ov_o = -\frac{z_+}{\nu}\mathcal{L}_{oe}\nabla\mu_e - \mathcal{L}_o\nabla\mu_o + \frac{t_oi}{\mathbf{F}} \quad [4]$$

Equations [2]-[4] define five independent parameters $\mathcal{L}_e$, $\mathcal{L}_o$, $\mathcal{L}_{eo}$, t_+, t_-. It must be kept in mind that $t_+ = (1 - t_-)$. Also, $\mathcal{L}_{eo} = \mathcal{L}_{oe}$. The sixth independent parameter is the electrical conductivity, κ, which appears in the current equation

$$i = -\kappa\nabla\Phi - \frac{\kappa}{n\mathbf{F}}\left(\frac{s_+t_-}{\nu_+} + \frac{s_-t_+}{\nu_-}\right)\nabla\mu_e - \frac{\kappa}{n\mathbf{F}}(nt_o + s_o)\nabla\mu_o \quad [5]$$

These flux equations need to be integrated across the membrane. It is easier to perform the integration if chemical potentials are replaced by concentration and pressure terms. At this point it should be mentioned that some investigators have used activity instead of concentration. Concentration is a quantity easy to understand and to measure, and hence it has been preferred to activity in this derivation.

Let us consider μ_e and μ_o to be functions of c_e and P, T being assumed constant. From first principles

$$\nabla\mu_e = \frac{\partial\mu_e}{\partial c_e}\nabla c_e + \frac{\partial\mu_e}{\partial P}\nabla P \quad [6]$$

$$\nabla\mu_o = \frac{\partial\mu_o}{\partial c_e}\nabla c_e + \frac{\partial\mu_o}{\partial P}\nabla P \quad [7]$$

* Electrochemical Society Active Member.
Key words: batteries, transference numbers, diffusion coefficients.

Also, the partial differentials may be written as

$$\frac{\partial \mu_e}{\partial c_e} = \frac{RT}{c_e}\left(1 + \frac{d \ln f_\pm}{d \ln c_e}\right) \nabla c_e \quad [8]$$

$$\frac{\partial \mu_o}{\partial \mu_e} = \frac{RT}{c_o}\left(1 + \frac{d \ln f_o}{d \ln c_o}\right) \frac{\partial c_o}{\partial c_e} \nabla c_e \quad [9]$$

And, using a simple, linearized equation of state $c_o = c_o^\circ - ac_e - b(P^\circ - P)$, we arrive at

$$\frac{\partial c_o}{\partial c_e} = -a \quad [10]$$

Substitution of Eq. [8]-[10] into Eq. [6] and [7] gives us

$$\nabla \mu_e = \frac{RT}{c_e}\left(1 + \frac{d \ln f_\pm}{d \ln c_e}\right) \nabla c_e + \overline{V}_e \nabla P \quad [11]$$

$$\nabla \mu_o = -\frac{RT}{c_o}\left(1 + \frac{d \ln f_o}{d \ln c_o}\right) a \nabla c_e + \overline{V}_o VP \quad [12]$$

If δ is the effective membrane thickness across which the integration is performed and when the electric current density is zero (the salt flux, N_e, can be defined as $N_e = N_+/\nu_+ = N_-/\nu_-$), the flux equations can be integrated to yield the following

$$N_e = -L_e \Delta c_e - L_{ep} \Delta P \quad [13]$$

$$N_o = L_o \Delta c_e + L_{op} \Delta P \quad [14]$$

The expressions for the L parameters are given below

$$L_e = -\frac{z_- RT}{\nu_+ \overline{c}_e}\left(1 + \frac{d \ln f_\pm}{d \ln c_e}\right)\frac{\mathcal{L}_e}{\delta} + \frac{z_- RT}{\nu_+ \overline{c}_o}\left(1 + \frac{d \ln f_o}{d \ln c_o}\right) a \frac{\mathcal{L}_{eo}}{\delta} \quad [15]$$

$$L_{ep} = -\left(\frac{z_- \overline{V}_e}{\nu_+}\frac{\mathcal{L}_e}{\delta} + \frac{z_- \overline{V}_o}{\nu_+}\frac{\mathcal{L}_{eo}}{\delta}\right) \quad [16]$$

$$L_o = -\frac{z_+}{\nu_-}\frac{RT}{\overline{c}_e}\left(1 + \frac{d \ln f_\pm}{d \ln c_e}\right)\frac{\mathcal{L}_{oe}}{\delta} + \frac{RT}{\overline{c}_o}\left(1 + \frac{d \ln f_o}{d \ln c_o}\right)\frac{a \mathcal{L}_o}{\delta} \quad [17]$$

$$L_{op} = -\left(\frac{z_+ \overline{V}_e}{\nu_-}\frac{\mathcal{L}_{oe}}{\delta} + \frac{\overline{V}_o \mathcal{L}_o}{\delta}\right) \quad [18]$$

Equations [15]-[18] are important because they show how the four transport parameters L_e, L_o, L_{ep}, and L_{op} are related to three independent transport parameters $\mathcal{L}_e$, $\mathcal{L}_o$, and $\mathcal{L}_{eo}$.

When the driving force ΔP is zero and the current density is not zero, the flux equations may be written in the following form

$$N_+ = -L_e \Delta c_e + \frac{t_+ i}{\mathbf{F}} \quad [19]$$

$$N_o = L_o \Delta c_e + \frac{t_o i}{\mathbf{F}} \quad [20]$$

In certain cases when concentrations inside the ion-exchange membrane are desired, an estimate can be made by using the Donnan exclusion principle. An ion-exchange membrane has fixed ions in the structure. Let us denote this fixed ion concentration by X. Then, the electroneutrality condition yields

$$c_+ = X + c_- \quad [21]$$

Treating both internal and external solutions as ideal, that is, neglecting activity coefficient correction, equality of potentials according to Gibbs-Donnan principle requires that at equilibrium

$$c_+ c_- = c^2 \quad [22]$$

where c = concentration of external solution. Combination of Eq. [21] and [22] yields

$$c_+ = \left[\left(\frac{X}{2}\right)^2 + c^2\right]^{1/2} + \frac{X}{2} \quad [23]$$

$$c_- = \left[\left(\frac{X}{2}\right)^2 + c^2\right]^{1/2} - \frac{X}{2} \quad [24]$$

where c_+ and c_- in this case denote concentrations of the respective ions inside the membrane.

The experimental cell is a dialysis-type cell fitted with capillary tubes to measure volume flows and electrodes to measure transference numbers and electrical conductivity, see Fig. 1.

The sign convention being used is: (*i*) Any flow into a compartment is positive; (*ii*) Any flow out of a compartment is negative.

Thus, a mass balance of compartment 2 is given by the equation

$$N_{e2} = \frac{V}{A}\frac{dc_{e2}}{dt} + \frac{c'_{e2}s}{A}\frac{dl_2}{dt} \quad [25]$$

where s = cross sectional area of capillaries; V = volume of compartment; A = area of cross section of membrane; and c'_{e2} = concentration in capillary if flow is into the compartment or, concentration in the compartment (c_{e2}) if flow is out of the compartment. Thus, when transport across the membrane is only by migration in an electric field

$$N_{e2} = \frac{V}{A}\frac{dc_{e2}}{dt} + \frac{c'_{e2}s}{A}\frac{dl_2}{dt} = \frac{t_+ i}{z_+ \mathbf{F}}$$

Since $dl_2/dt\ c'_{e2}s/A$ is very small it can be neglected. Hence

$$t_+ = \frac{V\mathbf{F}z_+}{iA}\frac{dc_{e2}}{dt} \quad [26]$$

When the solutions on both sides of the membrane have the same concentration (same electrolyte), from Eq. [10]

$$i = -\kappa \nabla \Phi \quad [27]$$

This is Ohm's law. The specific conductivity of the membrane, κ, is defined from Eq. [27] as

$$\kappa = \frac{i}{\nabla \Phi} = \left(\frac{I}{A}\right)\left(\frac{\delta}{\Delta \Phi}\right) \quad [28]$$

where $\Delta\Phi$ is the voltage drop across the membrane as measured by two Hg/HgO reference electrodes.

Equipment.—The major equipment used for the experiments are the cell (Fig. 2 and 3) and Hg/HgO reference electrodes which were made according to the procedure suggested by Bennion (5). Two cells were constructed. In the first one (referred to as the larger cell) each compartment had a volume of 50 cm³, and a cross-sectional area of 20 cm². The second cell (referred to as the smaller cell) had a compartment volume of 4 cm³ and a cross-sectional area of 3 cm². The basic design of both cells were the same.

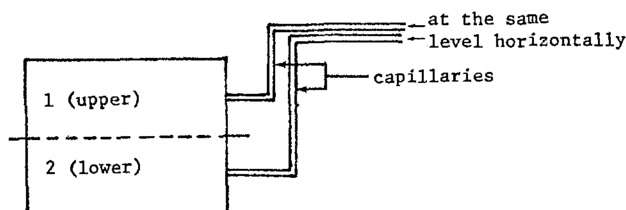

Fig. 1. Schematic diagram of cell assembly

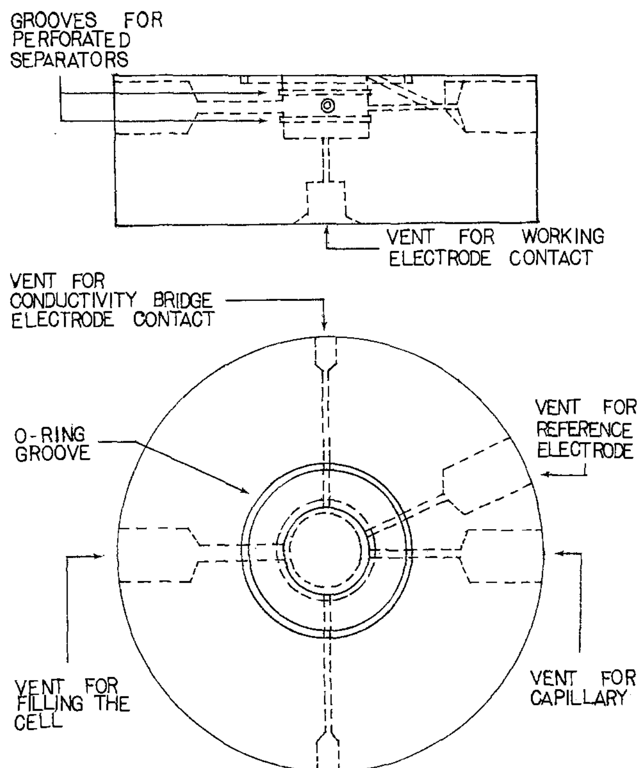

Fig. 2. Schematic diagram of a cell compartment

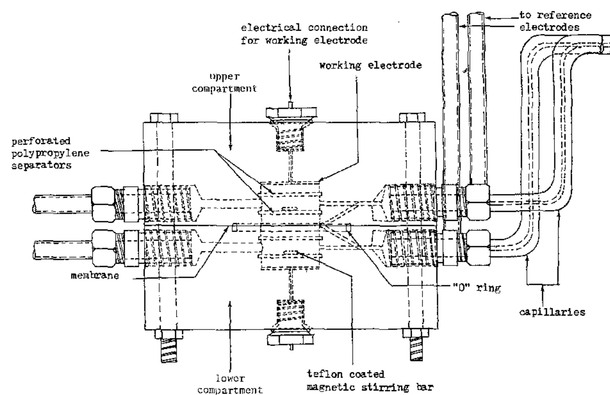

Fig. 3. Assembled cell

Experiments.—Two different experiments were conducted to find the diffusion coefficients, transference numbers, and specific conductivity of the membrane.

Hittorf experiment.—In this experiment both the cell compartments were filled with the same KOH solution. The working electrodes used were Ag/AgO porous electrodes or $Ni(OH)_2$/NiOOH porous electrodes (supplied by the Air Force Aero Propulsion Laboratory, Wright Patterson AFB). The cell compartments were separated by a Permion 2291 membrane (supplied by RAI Corporation). A precalculated current is passed for a predetermined time. This calculation is done assuming a transference number of 0.5, selecting a concentration that can be accurately measured, and determining current and time to give the change. During the course of the experiment the flow rates in the capillaries (horizontally placed tubes) were observed. At the end of the experiment the cell was taken apart and the solution concentrations in the two compartments were analyzed to give the change in concentration. The analysis of the solution was done by titrating with a standard HCl solution using as indicators a pH-meter and phenolphthalein.

At the start of the Hittorf experiment, the potential drop across the membrane was measured with Hg/HgO

Table I. Results of Hittorf experiments

Run No.	Starting conc. (mole/liter)	Final conc. (mole/liter)	Time of run (min)	Current (mA)	t_+^m (K^+)*	t_+^m (K^+)**
1a	1.9362	1.8446	360	2.0	0.824	0.863
b		1.8575			0.798	0.836
c		1.8422			0.846	0.886
2a	2.8674	2.7802	360	2.0	0.785	0.822
b		2.7783			0.802	0.840
c		2.7836			0.754	0.790
3a	3.8779	3.7917	360	2.0	0.775	0.812
b		3.7945			0.750	0.786
c		3.8003			0.698	0.731
4a	4.7280	4.6504	360	2.0	0.698	0.731
b		4.6367			0.821	0.860
c		4.6475			0.724	0.757
5a	5.9328	5.8607	360	2.0	0.649	0.679
b		5.8496			0.748	0.783
c		5.8523			0.724	0.757
6a	8.3993	8.2493	100	250.0	0.453	0.454
b		8.2062			0.583	0.585
c		8.2086			0.576	0.578
7a	9.421	9.1630	130	250.0	0.599	0.601
b		9.1618			0.602	0.604
8	9.508	9.3540	120	200.0	0.504	0.486
9a	9.9947	9.8598	90	200.0	0.620	0.568
b		9.8547			0.587	0.590
c		9.8569			0.581	0.583

Runs 1 to 5: volume of cell compartment = 4.0274 cm^3 (small)
Runs 6 to 9: volume of cell compartment = 46.9161 cm^3 (large)
Runs 1 to 7: porous nickel electrodes used as working electrodes
Runs 8 & 9: porous silver electrodes used as working electrodes

The above results are plotted in Fig. 4.

$$t_+^m \text{ (corr.)} = \frac{V_t c^\circ - (V_c c^f + V_{el} c_{av})}{I\,(\Delta t)}\, F \quad \text{(Appendix I)}$$

* Uncorrected.
** Corrected.
a, b, c are separate runs with the same starting concentration.

reference electrodes, and thus the specific conductivity of the membrane was obtained.

Dialysis experiment.—This experiment is based upon a concentration difference imposed across the membrane and this difference decreasing due to diffusion across the membrane. The concentrations of KOH solution on either side of the membrane were known at the start of the experiment and were measured during the course of the experiment, as described later. Observation was also made of the flow in the capillary. It may be mentioned at this point that the concentration of the KOH solution in a compartment may be measured by an a-c conductivity bridge or by titrating samples. The latter method was used in this case.

Results

The results of the Hittorf experiments are summarized in Table I and Fig. 4. The mass transfer coefficients are calculated on the basis of observations

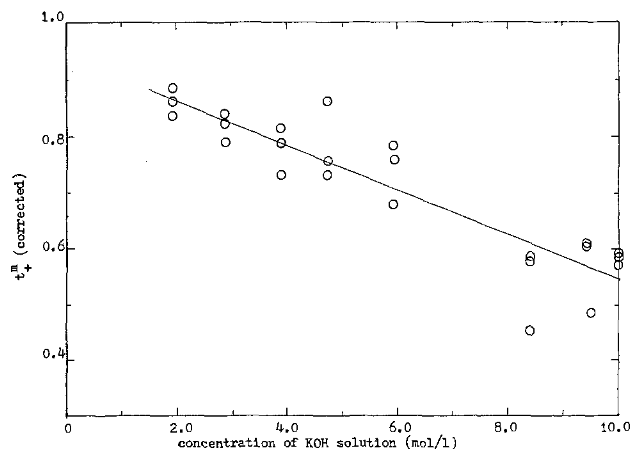

Fig. 4. Corrected transference numbers of K^+ ions through RAI P2291 membrane.

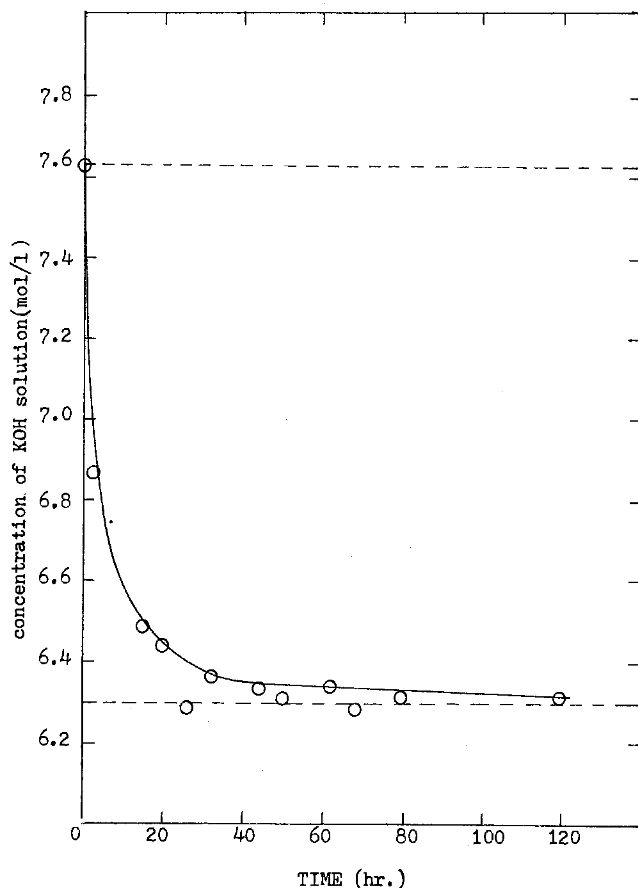

Fig. 5. Concentration profile of KOH solution in upper compartment during a dialysis experiment.

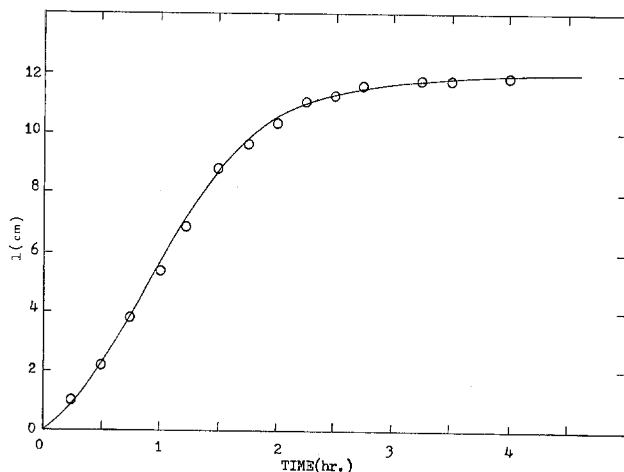

Fig. 6. Volumetric flow observed in the capillary corresponding to the upper compartment (solution flowing in) in dialysis experiment.

shown in Fig 5 and 6, and the procedure outlined in Appendix II. The results of the calculation are summarized in Table II. The specific conductivities are given in Table III.

From the data shown in Fig. 5 and 6 and the procedure outlined in Appendix II, the values of L parameters obtained are shown in Table II.

Discussion

Use of porous electrodes.—Porous electrodes were used instead of a plain metal sheet because their capacity is much higher. As a result, a much higher current can be passed without causing the electrode to "gas." Gassing is undesired because there is no outlet from the cell for the gas to escape and it builds up pressure forcing liquid out of the cell. There is one

Table II. Mass transfer coefficients

Starting concentration Upper compartment (mole/liter)	Lower compartment (mole/liter)	L_e (cm/sec)	L_o (cm/sec)	D_e (cm²/sec)	D_o (cm²/sec)
7.6295	4.9557	2.924×10^{-5}	2.057×10^{-4}	7.428×10^{-8}	5.225×10^{-7}

It should be noted that the L parameters are mass transfer coefficients, while the D's are diffusion coefficients. The conversion from one to the other is simple and is given below.

$$D_i = \delta L_i$$

where δ = thickness of the membrane = 2.54×10^{-3} cm.

Table III. Specific conductivity of membrane

Conc. of KOH on both sides of membrane (mole/liter)	Current (A)	Voltage drop (V)	Sp. conductivity (Ω cm)$^{-1}$
8.3993	0.250	0.01600	2.006×10^{-3}
9.4210	0.250	0.00965	3.326×10^{-3}
9.5080	0.200	0.00955	2.689×10^{-3}
9.9947	0.200	0.00975	2.634×10^{-3}

From the above table κ (av) = 2.664×10^{-3} (Ω cm)$^{-1}$.

disadvantage in using porous electrodes, however. As the electrodes are charged/discharged, a concentration gradient builds up within the thickness of the electrode. If the cell compartment is small, this difference, unaccounted for in the solution analysis, could be significant. Hence, simple corrections were made.

Preference of Ni electrodes over Ag electrodes.—$Ni(OH)_2/NiOOH$ electrodes were used in later experiments instead of Ag/AgO. When Ag/AgO electrodes were used, in a very short time the working area of the membrane (exposed to KOH solution) became colored dark brown. Two things may have happened which could cause the membrane to turn brown. It could have been attacked by KOH solution, which seemed unlikely. Another possibility was AgO going into solution and depositing in the membrane. This was verified by observing the membrane under a microscope. It looked as if some particles had deposited on the membrane and actually got enmeshed with it. The particles could be AgO or Ag, the silver being reduced by the membrane. A possible consequence of such a happening was membrane pores getting clogged or membrane molecules being oxidized and the properties of the membrane changing. So ($Ni(OH)_2/NiOOH$ porous electrodes were tried and they seemed to leave the membrane surface clear.

Comparison of L parameters with previous investigators.—Knowledge of the L parameters is necessary for the analysis of shape change in zinc secondary electrodes (3, 6). It is interesting to compare the values obtained in this work to the values estimated by Choi *et al.* in the above reference. In the analysis by Choi *et al.* there was one more species (Zn^{+2}) than in this analysis. Consequently, the flux equations for the K^+ and water were

$$N_{K,x}m = L_{kk}(c_K{}^n - c_K{}^p) + L_{kz}(c_{Zn}{}^n - c_{Zn}{}^p) + \frac{t_K m i}{\mathbf{F}}$$

$$N_{O,x}m = -L_{oz}(c_{Zn}{}^n - c_{Zn}{}^p) - L_{ok}(c_K{}^n - c_K{}^p) + \frac{t_o m i}{\mathbf{F}}$$

where L_{kk} = mass transfer coefficient of electrolyte and L_{ok} = mass transfer coefficient of water. These two equations may be compared with the Eq. [19] and [20].

Numerical values estimated by Choi *et al.* are given below for comparison with values in parentheses for this work.

$$L_{kk} = 1.0 \times 10^{-5} \text{ cm/sec } (L_e = 2.9 \times 10^{-5} \text{ cm/sec})$$

$$L_{ok} = 2.0 \times 10^{-5} \text{ cm/sec } (L_o = 2.0 \times 10^{-4} \text{ cm/sec})$$

It should be mentioned at this point that in the work by Choi *et al.* a lot of emphasis was laid on determining the cause of shape change. In the process not too much attention was focused on the exact values of the L parameters.

Comparison of electroosmotic flow with previous investigators.—The electroosmotic coefficient, t_o, played a very important role in the shape change in zinc secondary electrodes (3, 6). The values of electroosmotic flow observed in this work has been reported below for comparison with that observed by Choi *et al.*

The electroosmotic coefficient is defined as

$$N_o = t_o^m (i\,\mathbf{F}) \quad \text{for } \Delta P \text{ and } \Delta c_e \text{ zero}$$

where N_o = water flux (mole/cm^2/sec); i = current density = I/A (A/cm^2); I = current (A); and A = area of cross section (cm^2). Hence, we can also write

$$AN_o = t_o^m I/\mathbf{F} \quad \text{(mole/sec)}$$

Multiplication of both sides by partial molar volume of water gives the volume of water flowing (V_{fo}). Similarly, there is a volumetric salt flux (V_{fe}). These fluxes are given by the following equations

$$V_{fo} = AN_o\overline{V}_o = t_o^m I\overline{V}_o/\mathbf{F} \quad \text{(cm}^3\text{/sec)}$$

$$V_{fe} = AN_e\overline{V}_e = t_+^m I\overline{V}_e/\mathbf{F}n \quad \text{(cm}^3\text{/sec)}$$

Thus, the total flux (in the same direction due to electroosmosis) is

$$V_{ft} = V_{fo} + V_{fe} = \frac{I}{\mathbf{F}}\left(t_o^m\overline{V}_o + \frac{1}{n} t_+^m\overline{V}_e \right) \quad \text{(cm}^3\text{/sec)}$$

This is what Choi *et al.* have reported (6). From the above equation $V_{ft} \propto I$, provided everything else is constant, and V_{ft} is independent of A if I is constant. Taking the data for the case when initial solution concentration was 9.9947M, volume change observed (capillary flow) = 2.02167×10^{-5} cm^3/sec (volume flow inward for the anodic compartment). Change in volume due to the reaction at the electrode = $\Delta V_{el}/\Delta t$ = $(\frac{1}{2}\,\overline{V}_{Ag_2O} - \overline{V}_{Ag})\,(I/\mathbf{F}) = 1.232704 \times 10^{-5}$ cm^3/sec. (This has been calculated for the Ag electrode for a current of 200 mA. It should also be noted that the volume of the anode increases.)

Total volumetric flow (200 mA) = 3.254374×10^{-5} cm^3/sec

Total volumetric flow (1A) = 1.627187×10^{-4} cm^3/sec

The values reported by Choi *et al.* for 1A current were in the range of 1.5 to 2.0×10^{-4} cm^3/sec, and as we can see, the value observed in this work is comparable in magnitude.

Acknowledgment

Financial support for this work was provided by the United States Air Force through the Air Force Office of Scientific Research.

Manuscript submitted Oct. 21, 1977; revised manuscript received Nov. 29, 1977.

Any discussion of this paper will appear in a Discussion Section to be published in the December 1978 JOURNAL. All discussions for the December 1978 Discussion Section should be submitted by Aug. 1, 1978.

Publication costs of this article were assisted by the University of California.

APPENDIX I

Derivation of Concentration Profile in the Porous Electrode Due to Passage of Current and Correction for Transference Number

During the course of the Hittorf experiment a concentration gradient builds up in the porous electrodes. This necessitates a correction to Eq. [26]. As a result of this concentration gradient, the concentration in the compartment does not reflect the actual change produced due to the current alone.

The differential equation governing the concentration inside the electrode is

$$D_1 \frac{\partial^2 c}{\partial x^2} + (k_1 a)c = \frac{\partial c}{\partial t} \qquad \text{[A-1]}$$

Initial condition: at $t = 0$, $c = c^o$ for all x; boundary conditions: at $t > 0$, $c = c^o - At$ for $x = 0$; $\partial c/\partial x = 0$ for $x = L$; $D_1 = \mathfrak{D}(1 - d \ln c_o/d \ln c)$ = diffusion coefficient.

$k_1 a$ is an average reaction constant, which is calculated on the assumption that transference number of the positive ion (K^+) is ½, and the reaction is first order. The other assumptions made in this derivation are that the initial concentration is known and it is a steady-state process (current is constant throughout).

Using a change of variable as given below and following the procedure as given by Carslaw and Jaeger (7), a series solution is obtained

$$c/c^o = u \exp(k_1 at) \qquad \text{[A-2]}$$

$$\frac{c}{c^o} = \left(1 - \frac{At}{c^o}\right) + \frac{4}{\pi} e^{k_1 at} \sum_{n=1}^{\infty} \frac{1}{m} \sin\left(\frac{m\pi x}{2L}\right) + \frac{D_1 \pi}{L^2} \sum_{n=1}^{\infty} m \sin\left(\frac{m\pi x}{2L}\right) \left\{ \frac{(A/c^o)t}{D_1 m^2\pi^2/l^2 - k_1 a} \right.$$
$$\left. \frac{[1 - e^{(k_1 a - D_1 n^2\pi^2/l^2)t}]\left[\left(\frac{A}{c^o} - k_1 a\right) + (D_1 m^2\pi^2/4L^2)\right]}{(D_1 m^2\pi^2/l^2 - k_1 a)^2} \right\} \qquad \text{[A-3]}$$

This is the final solution for the concentration profile in the electrode. It should be noted that the solution is valid only for an open interval, and the solution is good for odd values of n only; thus, $m = 2n - 1$. Also, $L = \frac{1}{2}\, l$ = electrode thickness.

The actual transference number is

$$t_+^m(\text{corrected}) = \frac{V_t C^o - (V_c c^f + V_{el} C_{av})}{I(\Delta t)} \mathbf{F} \qquad \text{[A-4]}$$

APPENDIX II

Calculation of Average L Parameters from the Experimental Values

Since the concentration of KOH in a compartment varies during the course of a dialysis experiment, the values of L_e and L_o are not constant either. To find the average values of the L parameters with the least error, the procedure adopted is outlined below.

1. Choose values of L_e and L_o as estimated from experiment.
2. (*i*) Theoretically derive expressions for concentration profile with time as independent variable.
3. (*ii*) Compare this theoretical profile with the experimental profile.
4. Define an error function and calculate the error (E)

$$E = \sum \left[\frac{c_{em}(i) - c_{el}(i)}{c_{em}(i)} \right]^2$$

5. Vary L_e and L_o within the experimental limits and choose the set which gives the least error.

The derivation for concentration profile is given below: Subscript 1, 2 denote concentrations in the respective compartments. c_{eo} = total starting concentration = $c_{eo1} + c_{eo2}$; c_{eoi} = starting concentration in compartment i.

Assumptions used are as follows: (*i*) The total number of moles in the system is constant; (*ii*) The volumetric flow of solution in the capillaries is small enough to be neglected; thus, $dl_i/dt = 0$.

The electrolyte continuity equation can be easily integrated now, with the initial condition: at $t = 0$, $C_{e1} = C^o_{e1}$, yielding the result

$$C_{e1} = \frac{C^o_{e1} + C^o_{e2}}{2} - \frac{(C^o_{e2} - C^o_{e1})}{2} \exp\left(-2\frac{A}{V}L_e t\right) \quad [A\text{-}5]$$

A similar but more complicated expression can be derived if assumption (*ii*) is not valid (8).

LIST OF SYMBOLS

a_i activity of species i, dimensionless
A cross-sectional area of membrane, cm^2
c concentration of electrolyte outside the membrane mole/cm^3
c_i concentration of species i in the membrane, mole/cm^3
c_{ij} concentration of species i in compartment j, mole/cm^3
c_T total concentration, mole/cm^3
c^o concentration at time zero, mole/cm^3
d_i vector driving force per unit volume on species i, dyne/cm^3
$\mathcal{D}_{ij}$ diffusion parameter, cm^2/sec
e^- symbol representing an electron
F Faraday constant, 96,487 C/eq
i electric current density, A/cm^2
I total current, A
K_{ij} friction coefficient, g/cm^3/sec
l membrane thickness, cm
L_e, L_o, L_{eD}, L_{oD} mass transfer coefficients, cm/sec
$\mathcal{L}_e$, $\mathcal{L}_o$, $\mathcal{L}_{eo}$, $\mathcal{L}_{oe}$ transport parameters, $mole^2$/sec cm erg
M_i molecular weight of species i, g/mole
N_i molar flux of species i, mole/cm^2/sec
n number of electrons transferred
P pressure, g/cm^2
R gas constant erg/mole K°
s_i stoichiometric coefficient of species i, dimensionless
T absolute temperature, °K
t^j_i transference number of species i relative to j
t_o electroosmotic coefficient (transport parameter)
V volume, cm^3
$\overline{V}_i$ partial molar volume of species i, cm^3/mole
v_i velocity of species i, cm/sec
X fixed ion concentration of charged group in the membrane, mole/cm^3
z_i charge number of species i

Greek letters
δ membrane thickness, cm
κ electrical conductivity, mho/cm
μ_i chemical potential of species i, erg/mole
ν_i number of species i ions per molecule of electrolyte
ϕ flux of particles
Φ potential of a reference electrode, V

Subscripts
av average
c compartment
e electrolyte as a neutral species
el electrode pores
i any arbitrary species
j any arbitrary species
m measured value
t total
o solvent
1 compartment 1
2 compartment 2
+ positive ion
− negative ion

Superscripts
m implies the quantity is relative to the membrane
o at time $t = 0$

Note: For transference numbers, if no superscript exists, it is implicitly assumed relative to the membrane.

REFERENCES

1. H. P. Gregor, in "Zinc-Silver Oxide Batteries," A. Fleischer and J. J. Lander, Editors, p. 219, John Wiley & Sons, Inc., New York (1971).
2. V. D'Agostino (RAI Corporation), Private communications to D. N. Bennion (UCLA) (1975).
3. K. W. Choi, D. N. Bennion, and J. Newman, *This Journal*, **123**, 1616 (1976).
4. D. N. Bennion and B. W. Rhee, *I EC Fundam.*, **8**, 36 (1969).
5. D. N. Bennion, Dissertation, University of California, Berkeley (1964).
6. K. W. Choi, D. Hamby, D. N. Bennion, and J. Newman, *This Journal*, **123**, 1628 (1976).
7. H. S. Carslaw and J. C. Jaeger, "Conduction of Heat in Solids," p. 103, Oxford Clarendon Press, Oxford (1959).
8. M. Sinha, Dissertation, University of California, Los Angeles (1977).

An Electrochemical Study of Chromium in Molten $NaCl\text{-}AlCl_3$

C. L. Hussey,* L. A. King,* and J. K. Erbacher

The Frank J. Seiler Research Laboratory (AFSC), United States Air Force Academy, Colorado 80840

ABSTRACT

Chromium, introduced into NaCl-saturated $AlCl_3$ melt ($N_{AlCl_3} = 0.498$) as $CrCl_3$, underwent two reduction steps at a glassy carbon disk electrode. For the first reduction wave, $n = 1$ and $E_{1/2} = 1.09V$ *vs.* a reference electrode of aluminum in NaCl-saturated $AlCl_3$ at 175°C. The stationary electrode voltammetric response indicated that a reversible chemical step preceded electron transfer. A second reduction wave, $E_p{}^c$ *ca.* 0.1-0.2V, was attributed to the deposition of Cr(O). The chronoamperometric response for this wave was similar in form to that observed for nucleation rate-controlled depositions. Reoxidation of the Cr(O) deposit on the surface of a glassy carbon rotating disk electrode indicated that the oxidation product of this deposit, most likely a Cr(II) species, was adsorbed on the electrode surface. The adsorption of this species could be eliminated by employing either increased scan rates or higher temperatures. No chromium species other than Cr(III), Cr(II), and Cr(O) could be generated within the anodic limit of the NaCl-saturated $AlCl_3$ melt, *viz.*, 2.2V, in the temperature range of this study.

Chromium compounds are of considerable interest as cathodes for thermally activated molten salt reserve batteries, particularly batteries with LiCl-KCl eutectic electrolytes (1). Recent work in our laboratory has indicated that chromium compounds may also be used as cathodes for thermal batteries containing $NaCl\text{-}AlCl_3$ fused salt electrolytes (2). The discharge be-

* Electrochemical Society Active Member.
Key words: cyclic voltammetry, rotating disk electrode voltammetry, chronoamperometry, chromium (III) chloride, molten salt.

havior of these battery systems is dependent in part on the electrode kinetic behavior of the cathode material. In order to realize the maximum efficiency of NaCl-$AlCl_3$ batteries which utilize chromium compounds as cathodes, knowledge of the electrode kinetic behavior of chromium compounds in the NaCl-$AlCl_3$ melt is required.

Previous electrochemical studies of chromium have been confined largely to the fused LiCl-KCl eutectic. Most of these examinations concerned the CrO_4^{-2} species. Unfortunately Cr(VI) compounds do not appear stable in alkali chloride-aluminum chloride melts (3, 4). Lower oxidation states of chromium have also been examined in the LiCl-KCl melt (5-7). In a recent cyclic voltammetric study, Levy and Reinhardt (7) determined the reduction mechanism of Cr(III) in LiCl-KCl to proceed via a two-step process to the metal. The intermediate species in this process, Cr(II), reacted with solvent chloride ions and precipitated as $CrCl_2$.

More limited electrochemical investigations of chromium compounds have been undertaken in alkali chloride-aluminum chloride fused salts (3, 8). Marshall and Yntema (3) found $CrCl_3$ to be insoluble in 14-20-66 mole percent (m/o) KCl-NaCl-$AlCl_3$ while $CrCl_2$ was soluble and could be decomposed to chromium metal at 0.16V *vs.* aluminum. Topol *et al.* (8) found similar behavior for $CrCl_3$ and $CrCl_2$ in 39-61 m/o NaCl-$AlCl_3$[1] and in addition obtained Cr(III) as an electrode surface film which could be reduced at 0.95V *vs.* aluminum.

This paper details an investigation of the electrode kinetic behavior of $CrCl_3$ in NaCl-saturated $AlCl_3$ melt, which was undertaken using stationary and rotating disk electrode cyclic voltammetry, chronoamperometry, and controlled potential coulometry.

Experimental

Apparatus.—Experiments were conducted in a nitrogen-filled glove box (Vacuum/Atmospheres Company, Model HE-53-6 DRI LAB). The moisture content was determined with a calibrated probe (Panametrics Company, Model 1000) and was maintained below 2 ppm.

For experiments with stationary and rotating disk electrode voltammetry, chronoamperometry, and controlled potential coulometry, a Princeton Applied Research Corporation Model 173 potentiostat/galvanostat, Model 179 digital coulometer, and Model 175 universal programmer were employed in combination. A Pine Instrument Company ASR-2 electrode rotator provided controlled electrode rotation. Data was recorded on a Houston Model 2077 X-Y recorder equipped with a time base.

The electrochemical cell used for stationary and rotating disk electrode voltammetry and chronoamperometry consisted of a Pyrex cup with a Teflon lid. Reference and counterelectrodes consisted of aluminum wire spirals (Alfa Ventron m5N purity) immersed in the same melt but isolated in tubes by fine porosity frits. The tubes were inserted into the melt through holes in the Teflon lid. A glassy carbon disk working electrode (9), geometrical area = 0.22 cm^2, was inserted into the melt in a similar fashion except that the hole in the Teflon lid was made large enough to allow free rotation of the electrode. For controlled potential coulometric determination of n values, a glassy carbon crucible was used as the working electrode. The resistance between the working and reference electrodes was determined to be 18-20Ω and was measured with a Beckman Instrument Company, Model RC-18A conductivity bridge.

Cell temperature was maintained to ±0.5°C with a platinum resistance element controlled furnace. The furnace consisted of an insulated aluminum block equipped with a cartridge heater. Regulated current to power the furnace was furnished by a Leeds and Northrup Electromax III controller.

Reagents.—Anhydrous $CrCl_3$ (Alfa-Ventron, 98% purity) was used as obtained. NaCl-saturated $AlCl_3$ was prepared by mixing $AlCl_3$ (Fluka, A.G., iron free) with excess NaCl (Baker, AR grade) and fusing at 175°C. The melt was purified utilizing a constant current electrolysis procedure (10). It was colorless after 14 days electrolysis with aluminum electrodes at 0.5 mA cm^{-2}. The composition of NaCl-saturated $AlCl_3$ melt was determined with the titration procedure of Boxall *et al.* (11) to be 49.75 m/o $AlCl_3$ (pCl = 1.03) at 175°C. This procedure was also used to change the $AlCl_3$ content of the melt as desired.

Results and Discussion

Chromium was introduced into NaCl-saturated $AlCl_3$ melt as $CrCl_3$. The material dissolved slowly to give a magenta solution and exhibited a solubility of 6.2 mmoles at 175°C. Adjustment of the chloride concentration of a melt 3.68 mmoles in Cr(III) from 89 mmoles (49.75 m/o $AlCl_3$) to 50 mmoles (49.86 m/o $AlCl_3$) induced precipitation of $CrCl_3$. This precluded detailed investigation of the electrochemical behavior of Cr(III) with changes in melt acidity. $CrCl_2$ was insoluble in the NaCl-saturated melt.

Figure 1 shows a stationary electrode cyclic voltammogram of Cr(III) in NaCl-saturated $AlCl_3$ melt. All potentials are referred to the Al(III)/Al couple in the same melt. Cathodic peaks are evident at 1.06V (A) and 0.19V (B) as are anodic peaks at 0.55V (C), 0.61V (D), 1.26V (E), and 1.15V (E'). Peak E' is obtained by reversing the scan immediately after the response at A is observed. Peaks C, D, and E are obtained by reversing the scan after the reduction process, B. Peaks *A* and *E'* were attributed to the apparently reversible Cr(III)/Cr(II) couple. The 0.10V anodic shift in the peak potential of E with respect to E' and the increased symmetry of E over E' indicates that the Cr(II) produced as a result of an A-B-C-D-E scan is absorbed on the electrode (12).

Peak B in Fig. 1 appears at a potential close to that observed by Marshall and Yntema (3) and Topol *et al.* (8) for the deposition of chromium metal. The B-C-D process is attributed to the deposition and stripping of Cr(O). A more detailed discussion of this electrode reaction is presented in a later section.

The cyclic volammograms shown in Fig. 2 were obtained with a rotating disk electrode. The reduction peak, A, in Fig. 1 appears as a rotation rate-dependent wave in Fig. 2a. The wave for B is not clearly defined due to the high background current but is approximately twice the height of the preceding wave for A.

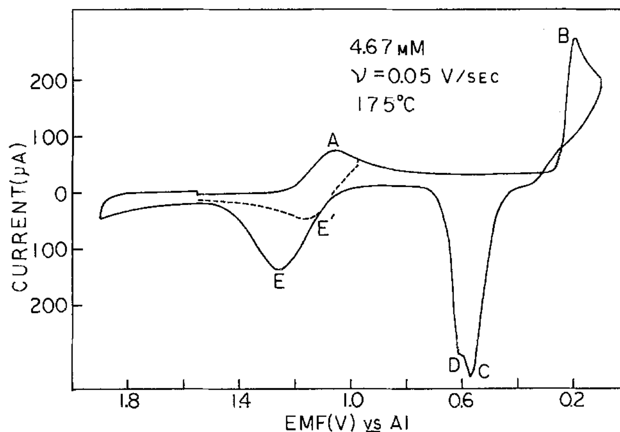

Fig. 1. Stationary electrode cyclic voltammogram of Cr(III). Dashed line shows response obtained by reversing scan after Cr(III) to Cr(II) reduction. Initial potential = 1.55V.

[1] Hereafter only the composition of the NaCl will be indicated. For example, 39 m/o NaCl-$AlCl_3$ will imply the presence of 61 m/o $AlCl_3$.

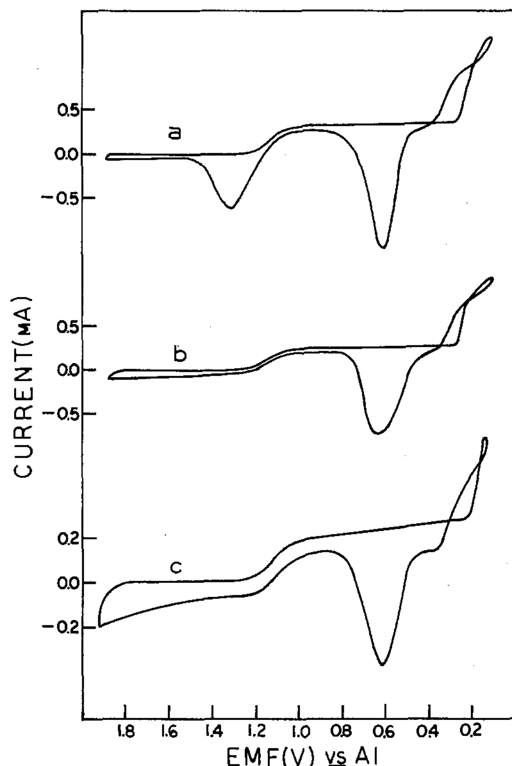

Fig. 2. Rotating disk electrode cyclic voltammograms of Cr(III) in 49.75 m/o $AlCl_3$. Initial potential = 1.55V. Rotation rate = 26.1 rad sec^{-1}. a, Cr(III) concentration = 4.67mmoles, ν = 0.05V sec^{-1}, 175°C; b, Cr(III) concentration = 2.73 mmoles, ν = 0.05V sec^{-1}, 225°C; c, Cr(III) concentration = 2.80 mmoles, ν = 0.20V sec^{-1}, 175°C.

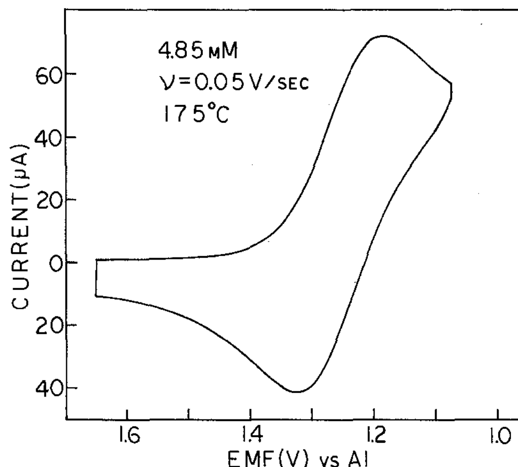

Fig. 3. Stationary electrode cyclic voltammogram of Cr(III) in NaCl saturated $AlCl_3$. Potential scan 1.700 to 1.075 to 1.700V.

The anodic process, E, in Fig. 1 also appears as a symmetrical peak in Fig. 2a. Peaklike responses obtained with rotating disk electrodes are due to reactions occurring on the electrode surface (13).

Transition of the surface response to a diffusional response can be brought about by simultaneously decreasing the Cr(III) concentration and increasing the temperature. The conversion becomes complete with 2.73 mmoles Cr(III) at 225°C as shown in Fig. 2b. Similar results can be induced at 175°C by increasing the sweep rate (Fig. 2c).

Characterization of the Cr(III) reduction.—A cyclic voltammogram represented by peaks A and E' in Fig. 1 is shown in more detail in Fig. 3. Using stationary electrode cyclic voltammetry, this couple was investigated as a function of sweep rate and concentration in NaCl-saturated $AlCl_3$ at 175°C. Data resulting from this investigation comprise Table I. Zero scan rate values of $i_p^c/\nu^{1/2}$ were obtained at 2.87 and 4.85 mmoles by constructing $i_p^c/\nu^{1/2}$ *vs.* $\nu^{1/2}$ plots from the data in Table I. The ratio of these intercepts was 1.66. In agreement with this, the ratio of Cr(III) concentrations for these two experiments was 1.69. The behavior of i_p^a/i_p^c [calculated using the empirical method of Nicholson (14)] with increasing scan rate indicates that a chemical step preceded the reduction wave (15). At slow scan rates E_p^a-E_p^c, E_p^c-$E_{1/2}$, and $E_{p/2}$-$E_{1/2}$ approach theoretical values of 0.089, −0.043, and 0.042V, respectively, expected for a one-electron reversible process at 175°C. A cathodic shift of E_p^c and an increase in the potential separations with increasing scan rate are also evident in Table I. A chemical reaction preceding Cr(III) reduction alone would be expected to cause an anodic shift in E_p^c with increasing scan rate (15). A cathodic shift resulting from *iR* effects would amount to only 5 mV maximum for the cell used in this study. Thus, the deviation of E_p^c from the expected behavior may indicate that either an additional reversible chemical step follows the reduction of Cr(III) or the Cr(III)/Cr(II) charge transfer process exhibits quasi-reversible behavior at fast scan rates.

Nicholson and Shain (15) showed the behavior of $i_p^c/\nu^{1/2}$ and i_p^a/i_p^c with increasing scan rate for reversible preceding and following chemical steps to be of an opposite nature. A reversible following chemical step with an equilibrium constant of sufficient magnitude to cause a 60 mV cathodic shift in E_p^c with a tenfold increase in scan rate as observed in this study certainly would be expected to cause the behavior of i_p^a/i_p^c to be more complex than observed. Thus, a reversible following chemical reaction seems unlikely.

A quasi-reversible charge transfer, which typically exhibits a cathodic potential shift, would account for the over-all cathodic shift in E_p^c with increasing scan rate (16). However, rate data for this process cannot be measured without some ambiguity since many of the effects observed with increasing scan rate, *e.g.*, the increase in potential separations also may be attributed to the preceding chemical step (15).

Table I. Cyclic voltammetric results for Cr(III) reduction

ν (V sec^{-1})	E_p^c (V)	$E_p^a - E_p^c$ (V)	$E_p^c - E_{1/2}$ (V)	$E_{p/2} - E_{1/2}$ (V)	$i_p^c/\nu^{1/2}$ (μA $V^{-1/2}$ $sec^{1/2}$)	i_p^a/i_p^c
			Concentration = 2.87 mmoles			
0.020	1.025	0.140	−0.050	0.050	192	1.04
0.050	1.020	0.150	−0.053	0.051	189	1.11
0.100	1.005	0.173	−0.058	0.056	186	1.14
0.200	0.980	0.210	−0.064	0.059	175	1.20
0.500	0.950	0.255	−0.079	0.066	171	1.33
1.000	0.900	0.320	−0.089	0.077	149	1.57
			Concentration = 4.85 mmoles			
0.020	1.041	0.125	−0.053	0.046	323	0.99
0.050	1.035	0.138	−0.052	0.049	311	1.09
0.100	1.026	0.154	−0.056	0.050	304	1.14
0.200	1.008	0.185	−0.063	0.053	295	1.19
0.500	0.990	0.210	−0.063	0.060	271	1.31
1.000	0.949	0.267	−0.085	0.068	243	1.47

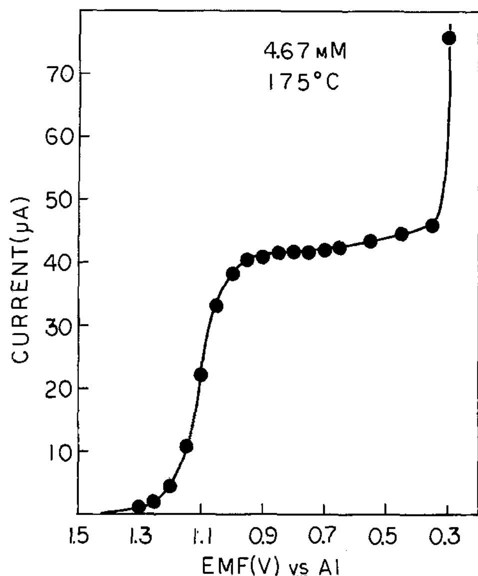

Fig. 4. Polarogram for the reduction of Cr(III) to Cr(II). Constructed from current-time data at 5 sec.

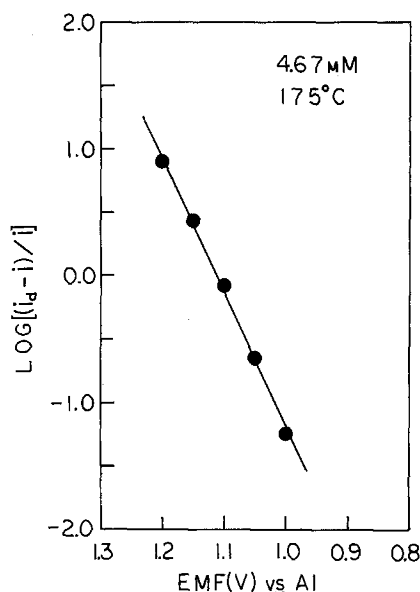

Fig. 5. Log $[i_d - i)/i]$ *vs.* potential for the polarogram in Fig. 4

A polarogram for the Cr(III)/Cr(II) reduction wave, constructed from current-time curves (17), is shown in Fig. 4. A plot of E *vs.* log $[(i_d - i)/i]$ for the polarographic wave (Fig. 5) was approximately linear over the region 0.11-0.95 i_d and exhibited a slope consistent with a one-electron reversible process. This information indicates that the Cr(III)/Cr(II) reduction process was nearly reversible for time intervals of 5 sec or longer. Table II summarizes polarographic data taken at different Cr(III) concentrations.

Cr(III) diffusion coefficient.—Provided that the Cr(III)/Cr(II) charge transfer process is sufficiently rapid at slow scan rates to be considered diffusion controlled, a diffusion coefficient for the Cr(III) species can be estimated by using techniques which allow extrapolation of the data to regimes in which diffusion control predominates over the preceding chemical step. Values of the voltammetric current function, $i_p^c/\nu^{1/2}$, approach the diffusion-controlled value at slow scan rates (15). Chronoamperometric currents approach diffusion-controlled values at sufficiently long times (18). Diffusion coefficients can be calculated from the zero current intercepts of $i_L/\omega^{1/2}$ *vs.* i_L plots which are constructed from limiting current data obtained at a rotating disk electrode (19).

At 175°C the Cr(III) diffusion coefficient was determined from the average values of the zero scan rate intercepts of $i_p^c/\nu^{1/2}$ *vs.* $\nu^{1/2}$ plots at different concentrations to be 2.2×10^{-6} cm² sec⁻¹, while the intercepts of chronoamperometric $it^{1/2}$ *vs.* $t^{1/2}$ plots yielded 2.4×10^{-6} cm^2 sec^{-1}. Viscosity values from Tørklep and Øye (20) density data from Fannin *et al.* (21) were used to calculate a value of 2.2×10^{-6} cm^2 sec^{-1} from the $i_L/\omega^{1/2}$ *vs.* i_L plot shown in Fig. 6.

The values obtained using the different methods are reasonably consistent. It is interesting to compare values obtained for other metal ions in NaCl-$AlCl_3$ melts. Boxall *et al.* (16) measured a value of 8.8×10^{-6} cm^2 sec^{-1} for Fe(III) in 50 m/o NaCl-$AlCl_3$ at 175°C. Gilbert *et al.* (22) determined a value of 7×10^{-6} cm^2 sec^{-1} for Zr(IV) in 48-49 m/o NaCl-$AlCl_3$ at 175°C. For Nb(V) in NaCl-saturated $AlCl_3$ at 180°C, Ting *et al.* (23) found a diffusion coefficient of $4.5\text{-}4.9 \times 10^{-6}$ cm^2 sec^{-1}. Recently, Phillips and Osteryoung (24) determined a value of 3.2×10^{-6} cm^2 sec^{-1} for Mo(V) in NaCl-saturated $AlCl_3$ at 175°C. The diffusion coefficient for Cr(III) appears considerably smaller than that measured for other metal ions in NaCl-$AlCl_3$ melts. Since it is not possible to assess how much the postulated quasi-reversibility of the charge transfer decreases this value, the average Cr(III) diffusion coefficient at 175°C, 2.3×10^{-6} cm^2 sec^{-1}, must be considered only approximate.

Characterization of the Cr(II) reduction.—Exhaustive coulometry of a melt 4.15 mmoles in Cr(III) at a potential of 0.10V resulted in a metallic deposit on the surface of the glassy carbon cell. A value of 2.1 was estimated for n for the Cr(II)/Cr(O) reduction after correction for the background current resulting from the proximity of aluminum deposition. The latter data were obtained in a melt containing no $CrCl_3$; the background current amounted to approximately 30% of the total current observed.

Table II. Polarographic data for Cr(III) reduction

Cr(III) concentration (mmoles)	$E_{1/2}$ (V)	i_d (μA)	Slope of E vs. log[$(i_d - i)/i$] (V)
2.87	1.09	25.0	0.093
4.67	1.10	40.5	0.093
6.23*	1.11	54.0	0.088

* Value estimated polarographically for a melt saturated with $CrCl_3$ at 175°C.

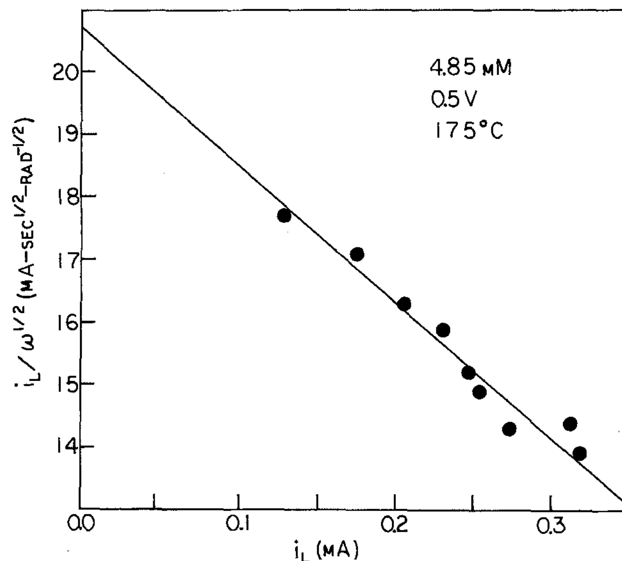

Fig. 6. Limiting current function *vs.* the limiting current for reduction of Cr(III) to Cr(II).

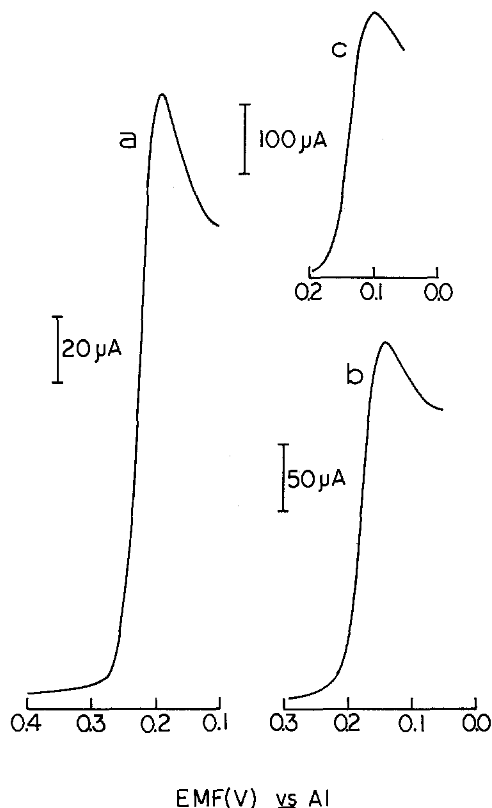

Fig. 7. Voltammetric peaks for the Cr(II) to Cr(O) reduction obtained during a cyclic voltammetric scan from 1.55 to 0.10 to 1.55V. Cr(III) concentration = 4.67 mmoles. a, ν = 0.05 V sec^{-1}, b, ν = 0.10 V sec^{-1}, c, ν = 0.20 V sec^{-1}.

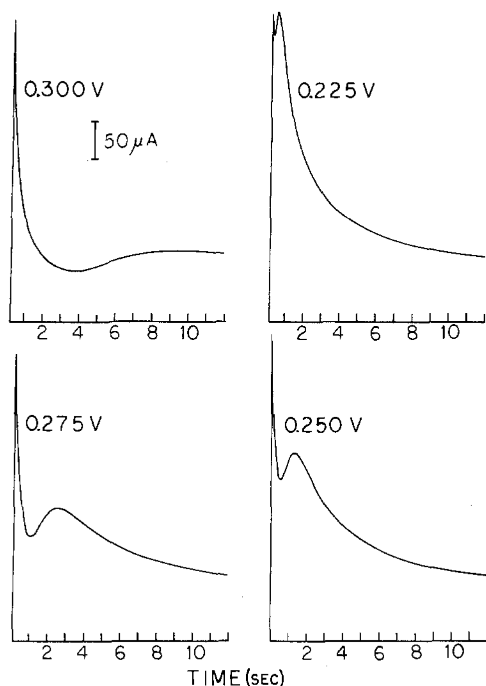

Fig. 8. Chronoamperometric response for the reduction of Cr(II) to Cr(O) at 175°C. Cr(III) concentration = 2.67 mmoles. Initial potential = 1.70V.

Voltammetric peaks for the Cr(II)/Cr(O) reduction are shown in Fig. 7. The cathodic shift in the voltammetric peak potential with increasing scan rate and the shape of chronoamperometric current-time curves (Fig. 8) indicate that reduction of Cr(II) is controlled by rate of nucleation in the initial phase of deposit formation (25). Similar behavior recently has been observed in NaCl-$AlCl_3$ melts for the deposition of insoluble $ZrCl_3$ and iron (22) and for the deposition of aluminum at a glassy carbon electrode (26).

When the deposit was reoxidized during stationary electrode voltammetry, it gave rise to two closely spaced peaks (Fig. 1) rather than the single stripping peak expected. Behavior closely resembling this was observed during reoxidation of iron deposited on a tungsten electrode in the 50 m/o NaCl-$AlCl_3$ melt (27) and was explained in that instance by considering that Fe(II) produced during anodization first depleted melt chloride in vicinity of the electrode and then diffused out into the bulk melt. This process may also be taking place during the oxidation of chromium in our study. Further, more detailed studies of this phenomena are needed to fully characterize the Cr(II)/Cr(O) deposition-stripping process.

Conclusion

The electrochemical reduction scheme of Cr(III) at a glassy carbon electrode at 175°C was shown to include the following reactions

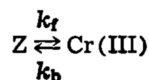

$$\mathrm{Z} \underset{k_b}{\overset{k_f}{\rightleftarrows}} \mathrm{Cr(III)}$$

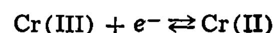

$$\mathrm{Cr(III)} + e^- \rightleftarrows \mathrm{Cr(II)}$$

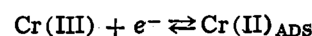

$$\mathrm{Cr(III)} + e^- \rightleftarrows \mathrm{Cr(II)_{ADS}}$$

$$\mathrm{Cr(II)} + 2e^- \rightleftarrows \mathrm{Cr(O)}$$

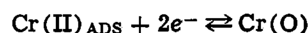

$$\mathrm{Cr(II)_{ADS}} + 2e^- \rightleftarrows \mathrm{Cr(O)}$$

Determination of the nature of the electroinactive form of Cr(III), Z, was hampered by the insolubility of $CrCl_3$ in melts less than 50 mmoles in chloride ion. Thus, the identity of the preceding chemical reaction was not established. The Cr(III)/Cr(II) electron transfer exhibited quasi-reversible behavior at fast scan rates, and the Cr(II)/Cr(O) reduction exhibited behavior consistent with a nucleation rate-controlled reduction. The formation of Cr(II) electrode surface species was shown to depend on the following parameters: $CrCl_3$ concentration, temperature, and sweep rate. No oxidation states of chromium above Cr(III) could be obtained voltammetrically in NaCl-saturated $AlCl_3$ within the anodic limit of the melt.

Acknowledgment

We wish to express our appreciation to Professor Robert A. Osteryoung, Colorado State University, for many helpful discussions concerning this work.

Manuscript submitted May 23, 1977; revised manuscript received Nov. 18, 1977.

Any discussion of this paper will appear in a Discussion Section to be published in the December 1978 JOURNAL. All discussions for the December 1978 Discussion Section should be submitted by Aug. 1, 1978.

Publication costs of this article were assisted by the United States Air Force Academy.

LIST OF SYMBOLS

$E_{1/2}$	polarographic half-wave potential (V)
$E_{p/2}$	half-peak potential (V)
$E_p{}^a$, $E_p{}^c$	anodic and cathodic peak potentials (V)
i	current (A)
i_d	current for a diffusion-controlled process (A)
i_L	rotating electrode limiting current (A)
$i_p{}^a$, $i_p{}^c$	anodic and cathodic peak currents (A)
k_b, k_f	rate constants for reverse and forward reactions
n	number of electrons in the charge transfer step
t	time (sec)
Z	electroinactive form of Cr(III)
ν	sweep rate (V sec^{-1})
ω	rotation rate (rad sec^{-1})

REFERENCES

1. D. M. Bush, Sandia Laboratories, Albuquerque, N.Mex., Technical Report SC-RR-69-497A (1972).

2. C. L. Hussey, J. K. Erbacher, and L. A. King, F. J. Seiler Research Laboratory (AFSC), USAF Academy, Colo., Technical Report SRL-76-0003 (1976).
3. E. E. Marshall and L. F. Yntema, *J. Phys. Chem.*, **46**, 353 (1942).
4. R. S. Drago and K. W. Whitten, *Inorg. Chem.*, **5**, 677 (1966).
5. I. I. Naryshkin, V. P. Yurkinskii, and P. T. Stangrit, *Elektrokhimiya*, **5**, 1043 (1969).
6. K. Cho and T. Kuroda, *Denki Kagaku*, **39**, 206 (1971).
7. S. C. Levy and F. W. Reinhardt, *This Journal*, **122**, 200 (1975).
8. L. E. Topol, W. A. McCollum, Jr., and S. J. Yosim, North American Rockwell Corp., Canoga Park, Calif., Technical Report NASA-CR-72791 (1970).
9. J. Phillips, R. J. Gale, R. G. Wier, and R. A. Osteryoung, *Anal. Chem.*, **48**, 1266 (1976).
10. R. J. Gale and R. A. Osteryoung, *This Journal*, **121**, 983 (1974).
11. L. G. Boxall, H. L. Jones, and R. A. Osteryoung, *ibid.*, **120**, 223 (1973).
12. R. H. Wopschall and I. Shain, *Anal. Chem.*, **39**, 1514 (1967).
13. D. C. Johnson and S. Bruckenstein, *This Journal*, **117**, 460 (1970).
14. R. S. Nicholson, *Anal. Chem.*, **38**, 1406 (1966).
15. R. S. Nicholson and I. Shain, *ibid.*, **36**, 706 (1964).
16. R. S. Nicholson, *ibid.*, **37**, 1351 (1965).
17. K. W. Fung and G. Mamantov, in "Comprehensive Analytical Chemistry," Vol. III, G. Svehla, Editor, pp. 326-327, Elsevier Scientific Publishing Co., New York (1975).
18. R. W. Murray, in "Techniques of Chemistry," Vol. I, "Physical Methods of Chemistry, Part IIA, Electrochemical Methods," A. Weissberger and B. W. Rossiter, Editors, p. 604, John Wiley & Sons, Inc., New York (1971).
19. S. Piekarski and R. N. Adams, in *ibid.*, p. 572.
20. K. Tørklep and H. A. Øye, Personal communication.
21. A. A. Fannin, Jr., F. C. Kibler, Jr., L. A. King, and D. W. Seegmiller, *J. Chem. Eng. Data*, **19**, 266 (1974).
22. B. Gilbert, G. Mamantov, and K. W. Fung, *Inorg. Chem.*, **14**, 1802 (1975).
23. G. Ting, K. W. Fung, and G. Mamantov, *This Journal*, **123**, 624 (1976).
24. J. Phillips and R. A. Osteryoung, *ibid.*, **124**, 1465 (1977).
25. G. J. Hills, D. J. Schiffrin, and J. Thompson, *Electrochim. Acta*, **19**, 657 (1974).
26. P. Roland and G. Mamantov, *This Journal*, **123**, 1299 (1976).
27. L. G. Boxall, H. L. Jones, and R. A. Osteryoung, *ibid.*, **121**, 212 (1974).

Cathodic Deposition of CdTe from Aqueous Electrolytes

M. P. R. Panicker, M. Knaster,* and F. A. Kroger*

Department of Materials Science, University of Southern California, Los Angeles, California 90007

ABSTRACT

CdTe of well-defined composition has been deposited cathodically from an aqueous solution of $CdSO_4$ and TeO_2. Films with a rest potential of $< -0.3V$ *vs.* SCE are n-type, those with a rest potential $> -0.3V$ *vs.* SCE are p-type semiconductors. The rate of deposition increases with stirring rate; it is proportional to the TeO_2 concentration but independent of the $CdSO_4$ concentration. Films deposited at room temperature are amorphous, those deposited at higher temperatures are partly crystalline, the degree of crystallinity increasing with deposition temperature. Grain sizes are in the range 500-1000Å. Annealing at 350°C causes the crystallite size to increase to ≥ 0.5 μm.

Fabrication of large area solar cells on CdTe basis requires an economical process for the formation of thin films of n- and p-type CdTe on a conducting base. For front wall cells the base may be a metal; for back-wall cells the base must be transparent. Glass covered with semiconducting SnO_2:Sb or In_2O_3:Sn has been recommended.

So far, films of semiconducting II-VI compounds were usually made by deposition from the vapor phase. It seems attractive to investigate the possibility of using an electrochemical method. In principle both anodic and cathodic deposition can be used. CdS has been made by anodic deposition of sulfur from a solution containing S^{2-} ions on a cadmium anode (1) and a similar method should be possible for CdTe. On the other hand, both Cd and Te can be deposited cathodically; Cd from an aqueous solution of $CdSO_4$, Te from a solution of TeO_2 in H_2SO_4 and/or HF (2) or water (3). Therefore it may be possible to deposit CdTe cathodically.

The anodic method has the disadvantage that the stoichiometry of the deposit cannot be easily regulated. Therefore, we concentrate our efforts on cathodic deposition.

* Electrochemical Society Active Member.
Key words: overpotential, amorphous deposit, crystalline deposit, Pourbaix diagram.

Cathodic deposition can occur either by deposition of the individual components in the required ratio, or by deposition resulting from discharge and decomposition of a complex containing the two components. The former mechanism has been proposed for formation of CdSe and Ag_2Se (4), the latter mechanism was proposed for the cathodic deposition of Ni_3S_2 from a Ni thiosulfate solution, the proposed cathodic reaction being (5)

$$Ni_3(S_2O_3)_3 + 6e^- \rightarrow Ni_3S_2 + S_2O_3^{=} + 2SO_3^{=}$$

In the latter case the stoichiometry of the deposit can only be varied if individual deposition of Ni or S atoms also occurs.

A choice between the two different cathodic deposition mechanisms can be made by a study of the current efficiency of deposition and of the secondary products formed in the solution (6).

In this paper it will be shown that cathodic deposition of CdTe is possible, that it occurs by the deposition of the components individually, and that CdTe with a required deviation from stoichiometry can be deposited.

Theoretical; CdTe Deposition

Table I shows electrode reactions and the corresponding equilibrium electrode potentials for Cd or

Table I. Electrode reactions and the corresponding potentials vs. the normal hydrogen electrode according to Pourbaix (3)

Activity of ions refer to species in solution (moles per kg H_2O); activities of atoms refer to components of the deposited solid (equal to one for the pure component)

	Reactions	*E vs.* NHE (V)
a.	$Cd(s) = Cd^{2+} + 2e^-$	$E^\circ_{Cd} + \frac{RT}{2F}\ln(a_{Cd^{2+}}/a_{Cd}) = -0.403 + 0.0295\log(a_{Cd^{2+}}/a_{Cd})$
b.	$Te(s) = Te^{2-} - 2e^-$ (pH > 11) (7)	$E^\circ_{Te(b)} + \frac{RT}{2F}\ln(a_{Te^{2-}}/a_{Te}) = -0.94 + 0.0295\log(a_{Te^{2-}}/a_{Te})$
c.	$Te(s) = Te^{4+} + 4e^-$ (pH < −0.5)	$E^\circ_{Te(c)} + \frac{RT}{4F}\ln(a_{Te^{4+}}/a_{Te}) = 0.568 + 0.0148\log(a_{Te^{4+}}/a_{Te})$
d.	$Te(s) + 2H_2O = HTeO_2^+ + 3H^+ + 4e^-$ (0 < pH < 5)	$E^\circ_{Te(d)} + \frac{RT}{4F}\ln(a_{HTeO_2^+}/a_{Te}) + \frac{3RT}{4F}\ln c_{H^+} = 0.551 + 0.0148\log(a_{HTeO_2^+}/a_{Te}) - 0.0443\ pH$
e.	$In(s) = In^{3+} + 3e^-$	$E^\circ_{In} + \frac{RT}{3F}\ln(a_{In^{3+}}/a_{In}) = -0.342 + 0.0197\log(a_{In^{3+}}/a_{In})$
f.	$Ga(s) = Ga^{3+} + 3e^-$	$E^\circ_{Ga} + \frac{RT}{3F}\ln(a_{Ga^{3+}}/a_{Ga}) = -0.529 + 0.0197\log(a_{Ga^{3+}}/a_{Ga})$
g.	$As(s) + 2H_2O = HAsO_2 + 3H^+ + 3e^-$ (−1 < pH < 8)	$E^\circ_{As} + \frac{RT}{3F}\ln(a_{HAsO_2}/a_{As}) + \frac{RT}{F}\ln c_{H^+} = 0.248 + 0.0197\log(a_{HAsO_2}/a_{As}) - 0.0591\ pH$
h.	$Sb(s) + 2H_2O = HSbO_2 + 3H^+ + 3e^-$	$E^\circ_{Sb} + \frac{RT}{3F}\ln(a_{HSbO_2}/a_{Sb}) + \frac{RT}{F}\ln c_{H^+} = 0.23 + 0.0197\log(a_{HSbO_2}/a_{Sb}) - 0.0591\ pH$
i.	$Cu(s) = Cu^{2+} + 2e^-$	$E^\circ_{Cu} + \frac{RT}{2F}\ln(a_{Cu^{2+}}/a_{Cu}) = 0.337 + 0.0295\log(a_{Cu^{2+}}/a_{Cu})$
j.	$Ag(s) = Ag^+ + e^-$	$E^\circ_{Ag} + \frac{RT}{2F}\ln(a_{Ag^+}/a_{Ag}) = 0.799 + 0.0591\log(a_{Ag^+}/a_{Ag})$

Te according to Pourbaix (3). All potentials depend on the activities of ions in solution and on the activity of the component in the deposit. The potential of reaction d in addition depends on *p*H. For the formation of CdTe, in particular reactions a and d are important.

In a companion paper by one of us (8), cathodic deposition of compounds was classined under two classes, I and II, depending on whether the difference in equilibrium potentials of the pure components is larger or smaller than the shift in potentials due to variation of the component activity in the deposit resulting from compound formation. The activities of Cd and Te in CdTe depend on the stoichiometric composition of the compound, the two being related through the reaction

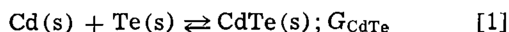

$$Cd(s) + Te(s) \rightleftarrows CdTe(s); G_{CdTe} \quad [1]$$

giving

$$\frac{a_{CdTe}}{a_{Cd}a_{Te}} = \exp(-G_{CdTe}/RT) \quad [2]$$

or for $a_{CdTe} = 1$

$$a_{Cd}a_{Te} = \exp(G_{CdTe}/RT) \quad [3]$$

At temperatures at which deposition is to take place, CdTe has an existence range stretching from CdTe in equilibrium with Cd to CdTe in equilibrium with Te. Thus the Cd activity varies from $a_{Cd} = 1$ at the CdTe/Cd boundary to $a_{Cd} = \exp(G_{CdTe}/RT)$ at the CdTe/Te boundary where $a_{Te} = 1$, with an opposite variation of a_{Te}. It is this variation of a_{Cd} and a_{Te} which causes the shift in the Cd and Te potentials.

For reactions a and d $\Delta E^\circ = E^\circ_{Te(d)} - E^\circ_{Cd} = 0.551 + 0.403 = 0.954V$. The free enthalpy of formation of CdTe from Cd and Te, $(G_{CdTe})_{298} = -24.5 - 2.4T = -25.5$ kcal/mole (9). Compound formation causes a shift of the Cd potential from the standard value (−0.403V) at the CdTe/Cd phase boundary to $-0.403 + (G_{CdTe})_{298}/2\mathbf{F} = -0.403 + 0.546 = 0.143V$ at the CdTe/Te phase boundary. The Te potential shifts similarly from 0.551V at the CdTe/Te phase boundary to $0.551 + (G_{CdTe})_{298}/4\mathbf{F} = 0.551 + 0.273 = 0.824V$ at the CdTe/Cd boundary (8).

It is seen that $\Delta E^\circ > (G_{CdTe})_{298}/2\mathbf{F}$. Therefore, CdTe has to be classified under class I, with Cd the potential-determining species under all conditions (8). The potentials at which CdTe can be deposited extend from $V_{dep} = -0.403 + 0.295 \log a_{Cd^{2+}} - \Delta V$ (the CdTe/Cd phase boundary) to $V_{dep} = 0.143 + 0.295 \log a_{Cd^{2+}} - \Delta V$ (the CdTe/Te phase boundary). Here ΔV is the overpotential; it is equal to

$$\Delta V = \eta + iR \quad [4]$$

where η is the discharge overpotential, i the current density, and R the resistance per square centimeter of electrode of the circuit between the cathode contact and the calomel electrode used to measure the cathode voltage. It contains contributions from the conducting layer of the cathode and from the deposited film. The former is appreciable for deposition on SnO_2:Sb or In_2O_3:Sn but would be negligible for deposition on a metallic cathode. The resistance of the deposit is expected to be proportional to the film thickness (d) and equal to ρd, ρ being the specific resistance of the deposit. Measurement of ΔV as $f(d)$ for deposition on a metallic cathode should make it possible to determine ρ.

In order to be able to deposit Cd and Te in almost equal quantities it is necessary to use an electrolyte with a high concentration of the less noble component, Cd, and a low concentration of the noble component, Te. During deposition the concentration of $HTeO_2^+$ in the electrolyte at the electrode-electrolyte interface is reduced to practically zero. The rate of Te deposition is therefore diffusion controlled. The larger $CdSO_4$ concentration, however, will not be appreciably changed during deposition. CdTe deposition occurs at a potential that is more positive than required for deposition of Cd as a separate phase, Cd required for CdTe formation only being deposited as a result of the free energy gain in forming CdTe and occurs only after Te has been deposited. Therefore, the rate of CdTe deposition should be limited by Te deposition and, since the latter is diffusion controlled, should increase with increased stirring and be proportional to the concentration of $HTeO_2^+$ in the electrolyte (10). It should be independent of the $CdSO_4$ concentration in the electrolyte.

It is to be expected that deposition at low current density (corresponding to a potential at the positive end of the deposition range) favors Te deposition and gives rise to Te-rich CdTe (a_{Te} is large); deposition at a large current density (corresponding to a potential

at the negative end of the deposition range) should give rise to Cd-rich CdTe (a_{Cd} large). For pure CdTe this should lead to formation of p-type CdTe at low current densities and to n-type CdTe at high current densities, with a gradual shift from one to the other with changing current density (11).

During deposition of CdTe, the concentrations of both Cd^{2+} and $HTeO_2^+$ in the solution tend to diminish. This is not a serious effect for Cd^{2+} which is present at a relatively large concentration. Periodic addition of Cd-salt to the solution may keep the concentration practically constant. On the other hand, both the low solubility of H_2TeO_3 and the need to limit the concentration of $HTeO_2^+$ in the electrolyte in order to be able to deposit Cd and Te in equal amounts restricts the $HTeO_2^+$ concentration to a relatively low value. This in turn makes it necessary to take special steps to keep this concentration constant. There are two ways in which this can be achieved. The first follows a proposal by Gobrecht *et al.* (4) to use two anodes. One of these is inert, consisting of platinum or graphite; the other one is active and consists of the noble component to be deposited, in our case, Te. Current passed through the Te anode injects $HTeO_2^+$ into the solution. By making $i_{Te}/(i_{Te} + i_{inert}) = 4/6$, the ratio of the numbers of electrons involved in the deposition of Te (4*e*) and CdTe (6*e*), or $i_{Te}/i_{inert} = 2$, just as much Te is injected into the solution as is deposited on the cathode, and the $HTeO_2^+$ concentration in the electrolyte remains constant.

In a second method the $HTeO_2^+$ concentration is kept constant by keeping the electrolyte saturated with TeO_2 by having TeO_2 present as a second phase. Either one or two anodes may be used: inert, the other (if used) consisting of Cd. Now maintenance of a ratio $i_{inert}/i_{Cd} = 2$ keeps the concentrations of both Cd and Te in the electrolyte constant.

Doped crystals can also be grown. For donor doping indium or gallium can be used. As seen in Table I, reactions e and f, the deposition potential of In is so close to that of Cd that addition of a small amount of indium salt to the solution should lead to codeposition of Cd and In in about the same ratio as they are in the electrolyte. As acceptors, Cu, Ag and Au or As and Sb can be used. Since these are relatively noble, the best results are to be expected with the addition of these elements in a small concentration to the electrolyte combined with the use of a Te-dopant alloy as active anode.

Experimental

Cathodic deposits were made from an aqueous solution of $CdSO_4$ (1 mole/liter) at a *p*H of 2.5-3. The $CdSO_4$ was analytical grade containing as impurities 100 ppm Cu and 50 ppm As. Two sets of experiments were done. In one the $CdSO_4$ solution was used without purification. In the other, the $CdSO_4$ solution was first purified by electrolysis with inert electrodes at a cathode potential of $-(0.6 + \Delta V)$V *vs.* SCE, just below the potential required for Cd deposition, which is $-(0.66 + \Delta V)$V *vs.* SCE. An initial current density of 0.1 mA/cm^2 decreased gradually, falling to a constant value of 0.02 mA/cm^2 after 12 hr. The current drop is due to removal of the impurities from the solution, the small rest current being due to evolution of H_2 and/or reduction of O_2.

TeO_2 was added to both the pure and nonpurified solution, either 10^{-5}-10^{-3} mole/liter to give an unsaturated solution, or excess amount to give a saturated solution. For deposition of CdTe from the unsaturated solution two anodes were used, one a rod of graphite (3 mm diam, 5 cm long), the other a rod of Te (5 mm diam, 5 cm long). As cathodes were used either nickel plates of $\approx$ 6 cm^2 submerged area, or glass plates covered with semiconducting SnO_2:Sb with a resistance of 10-20 Ω/□. The latter were put at our disposal by R. L. Rod and W. Penick of Monosolar Corporation, Santa Monica.

Currents through the two anodes with a ratio $i_{Te}/i_{inert} \approx 2$ were established by dividing a regulated current with the aid of a potentiometer. For deposition from a solution saturated with TeO_2 one inert anode was used. Experiments at constant cathode voltage were carried out with the aid of a potentiostat, Princeton Applied Research Model 173, using the potential difference between the cathode and a saturated calomel electrode as its input. Current-voltage and voltage-time curves were measured with the aid of a Moseley Autograf X-Y recorder, Model 7030A. The experiments were carried out from 25° to 100°C. The bath was stirred with a magnetic stirrer of variable rotation speed. The current efficiency of the deposition process was determined by comparing the weight of the deposit deposited in a certain time with the weight calculated from the number of coulombs passed through the circuitry, assuming a certain deposition mechanism and the corresponding number of electrons required per molecule of CdTe. With Cd requiring 2 and Te 4 electrons (reaction a and d of Table I), 6 electrons are required for CdTe.

The crystal structure of the deposition products was analyzed by x-ray diffraction and by low angle electron diffraction. The microstructure of the deposit was determined with the aid of the scanning electron microscope. The chemical composition was determined by the energy dispersive microanalytic unit of the scanning electron microscope. Conductivity type was determined by a hot probe thermoelectric power measurement, an initial positive voltage of the hot probe placed on the deposit indicating n-type, a negative voltage indicating p-type conductivity.

Results

Deposition conditions.—A plot of current density *vs.* cathode voltage (measured relative to a saturated calomel electrode, SCE) for deposition from a 1.2 mole purified $CdSO_4$ solution saturated with TeO_2 at 85°C, *p*H = 3.4 is shown in Fig. 1. The current increases rapidly at $-V_{dep} > 0.8$V. For various deposition voltages, the rest potential of the cathode covered with product was determined by measuring cathode voltage as a function of time after interruption of the current. Figure 2 shows the result for deposition under slightly different conditions (0.5 mole $CdSO_4$, unsaturated TeO_2 solution, *p*H = 1.45, *T* = 90°C). The potential drops instantaneously to a lower value (a → b) corresponding to $E_{rest} = V_{dep} + \Delta V$, then (in most of the cases) gradually drifts to a less negative value, E_{final}. E_{rest} is the rest potential of the product in equilibrium with the electrolyte of the composition which it has at the cathode/electrolyte interface during deposition, with $c_{HTeO_2^+} \approx 0$. E_{rest} shifts to more negative

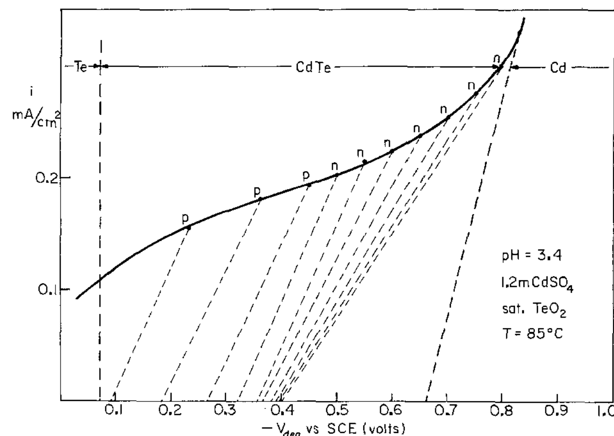

Fig. 1. Current density *vs.* cathode voltage for deposition at 85°C from a 1.2 moles $CdSO_4$ solution saturated with TeO_2; *p*H = 3.4, stirring rate 160 rpm.

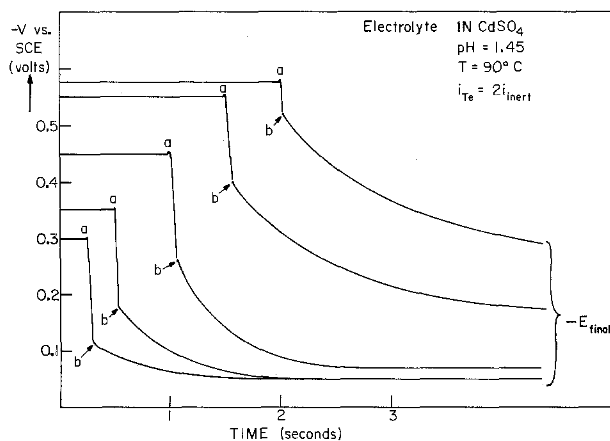

Fig. 2. Cathodic voltage *vs.* time during deposition from 0.5 mole $CdSO_4$, unsaturated TeO_2 solution, *p*H = 1.45, *T* = 90°C at different current densities (curves up to points a) and after interruption of the current.

values when the deposition voltage becomes more negative, *i.e.*, at larger current densities.

Figure 1 shows values of E_{rest} linked to the corresponding V_{dep} values by dashed lines. All except one are in the potential range expected for CdTe. The values of E_{final} are almost constant and correspond to the potential of the CdTe/Te phase boundary. E_{final} corresponds to the equilibrium potential of the deposit in equilibrium with electrolyte at its surface after this electrolyte has regained its normal bulk composition. Establishment of E_{final} involves electroless exchange of Cd from the product surface (ps) with Te from the electrolyte according to

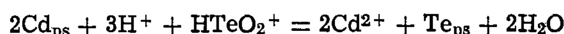

$$2Cd_{ps} + 3H^+ + HTeO_2^+ = 2Cd^{2+} + Te_{ps} + 2H_2O$$

(a combination of reactions a and d of Table I). Since the bulk concentration of $HTeO_2^+$ in the electrolyte is far from zero, this leads to a surface consisting almost exclusively of Te, yet with sufficient Cd to have its potential determined by that species, thus establishing the potential of the CdTe/Te phase boundary.

For deposits made at $-V_{dep} > 0.8V$, E_{rest} remains for a long time constant at $E_{rest} = -0.66V$ *vs.* SCE, indicating that pure Cd has been deposited. Only when all the Cd has been transformed to CdTe by exchange of half of the Cd with Te does the potential shift to more positive values, reaching the same final value as found for the other deposits. These results suggest that the product layers having rest potentials $\geqq -0.66V$ *vs.* SCE consist of CdTe, layers deposited at more negative values consisting of Cd. For the prevailing conditions, formation of a Te product layer is expected at $V < (-0.66 + 0.546) \approx -0.11V$ *vs.* SCE, *i.e.*, at negative values of the current in Fig. 1. Deposition of pure Te is possible if the TeO_2 concentration in the electrolyte is increased to 10^{-3} which can be done if the *p*H is decreased to 2 (3). On the other hand, deposition on SnO_2:Sb of CdTe films with $E_{rest} < -0.5V$ *vs.* SCE requires that the *p*H is raised to 3 or 3.5. If this is not done, the SnO_2 layer dissolves, as would be expected from its electrochemical properties (3).

Figure 3 shows i-V_{dep} characteristics for different stirring rates, showing the increase in i with increasing stirring rate. Figure 4 shows i-V_{dep} characteristics for deposition from solutions with a fixed TeO_2 concentration of 7×10^{-3} and normal but different $CdSO_4$ concentrations. The current density and thus the deposition rate is independent of Cd^{2+} concentration, as expected.

Figure 5 shows the dependence of the current density on the TeO_2 concentration. The current density (and thus the deposition rate) is proportional to the TeO_2 concentration as expected for a process limited by Te diffusion. The shift in the V_{dep} of Cd to more

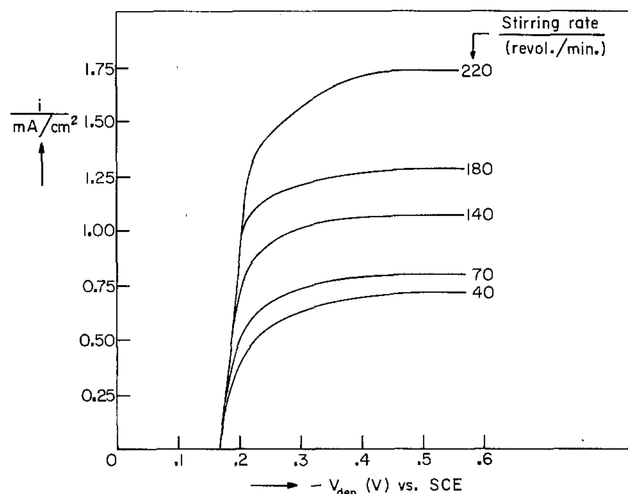

Fig. 3. Current density *vs.* cathode voltage for deposition at 75°C from an electrolyte 0.5 mole $CdSO_4$, low TeO_2 concentration, *p*H = 2.25 at different stirring rates (two anodes, $i_{Te} = 2i_{inert}$).

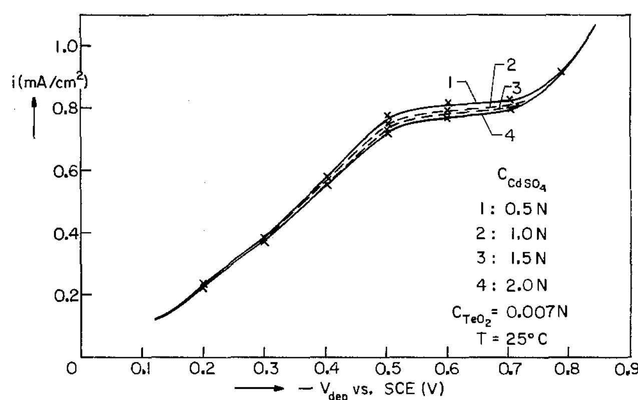

Fig. 4. Current density *vs.* cathode voltage for deposition at 25°C from an aqueous solution of 7×10^{-3} n-TeO_2 and different $CdSO_4$ concentrations varying from 0.5 to 2 normal.

negative values with increasing TeO_2 concentration is caused by the increase of ΔV resulting from a larger thickness of the product layer with increasing current density.

As mentioned earlier, $\Delta V = E_{rest} - V_{dep} = \eta + iR$. For deposition on a metallic cathode $R \approx \rho d$ and thus $\Delta V = \eta + i\rho d$. Figure 6 shows plots of ΔV *vs.* film thickness for deposition at different temperatures on

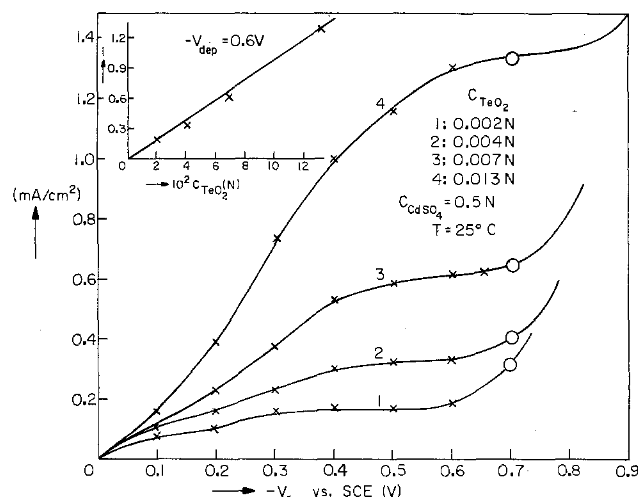

Fig. 5. Current density *vs.* cathode voltage for deposition at 25°C from an aqueous 0.5 n-$CdSO_4$ solution containing different amounts of TeO_2; *p*H = 0.5. Inset: *i* *vs.* c_{TeO_2} at $V_{dep} = -0.6V$ *vs.* SCE.

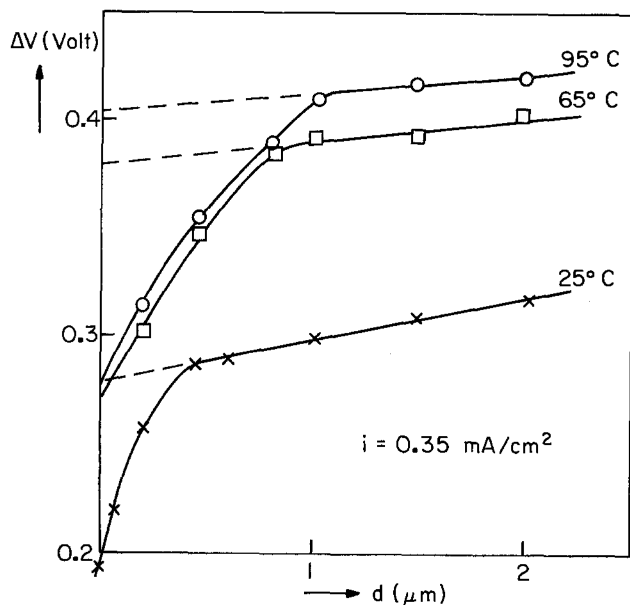

Fig. 6. $\Delta V = E_{rest} - V_{dep}$ as function of thickness of deposit, d, for deposits on nickel made at different temperatures from an aqueous solution of 1 mole $CdSO_4$/l saturated with TeO_2 at pH = 1.2, i = 0.35 mA/cm^2, different stirring rates.

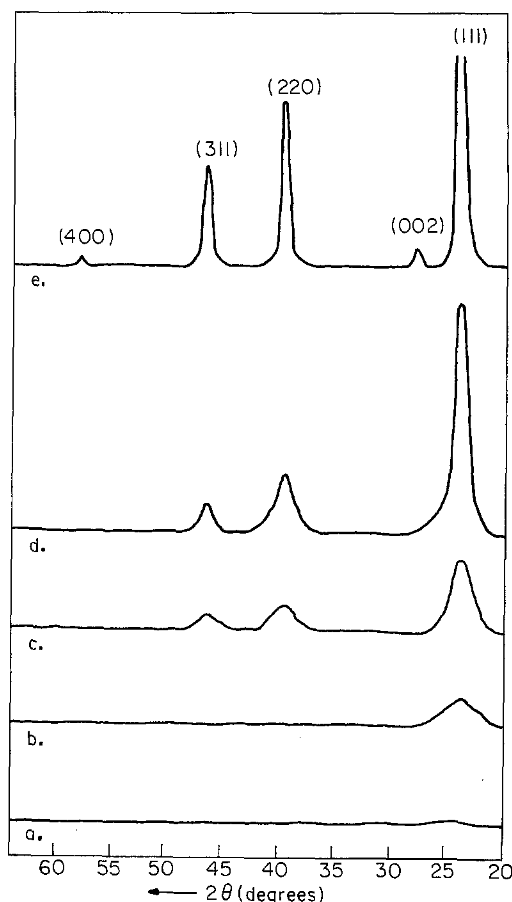

Fig. 7. X-ray diffraction patterns of films deposited on SnO_2-covered glass from a solution of 1 mole $CdSO_4$, saturated with TeO_2, pH ≈ 2.7, with current density 0.5 mA/cm^2 (E_{rest} = 0.18V) at 22°C (a), 35°C (b), 65°C (c), and 90°C (d), and the pattern (e) of film (a) after annealing for 3.5 hr at 350°C in an argon atmosphere.

a nickel cathode. The plots are nonlinear near the origin, indicating healing of the film, but are linear at thicknesses ≧ 1 μm. The slopes of the linear sections indicate resistivity values of 5.2 × 10^5 Ω cm for deposition at 25°C and of 2.9 × 10^5 Ω cm for deposition at 65° and 95°C. The discharge overvoltage η is 280 mV at 25°C, 380 mV at 65°C, and 404 mV at 95°C.

The deposition current efficiency calculated for formation of CdTe by deposition of Cd and Te individually, requiring 6 electrons per molecule CdTe, was found to be 87.5 ± 2.5% indicating that the assumed deposition mechanism is indeed operative. The small fraction of the current not used for CdTe formation must be due to evolution of H_2 or reduction of O_2.

Microstructure and composition determination.—The conclusions arrived at in the previous section are supported by results of determinations of chemical composition and crystal structure. Using the energy dispersive microanalyzer unit in the scanning electron microscope, layers with rest potentials between −0.6 and −0.2V *vs.* SCE were found to consist of 46.3 ± 4 atom percent (a/o) Cd and 53.3 ± 4 a/o Te. Layers with E_{rest} = −0.66V *vs.* SCE consist of Cd only.

Figure 7 shows x-ray diffraction patterns for deposits with E_{rest} between −0.2 and −0.6V *vs.* SCE made at differnt temperatures. Deposits made at 25°C show only the weakest indication of one diffraction peak at 2θ = 25°; these deposits are largely amorphous. Deposits made at higher temperatures show diffraction lines of the blende structure with a lattice constant of 6.48Å as characteristic for CdTe. The diffraction lines increase in intensity with increasing deposition temperature. The width of the diffraction lines does not change appreciably with deposition temperatures between 35° and 90°C, indicating a constant crystallite size in the range 500 to 1000Å.

Annealing in an inert atmosphere for 3.5 hr at 350°C produces a film with the diffraction pattern shown in Fig. 7e; now the lines are sharp, indicating that the crystallite size has increased to ≧0.5 μm. The intensity ratio of different lines is not always the same in all CdTe patterns, indicating a certain amount of orientation in some of the films. Low angle electron diffraction of the films gives again the pattern of the blende structure with the lattice constant of CdTe.

Inspection of the films under the scanning electron microscope shows that films deposited at 25°C are amorphous. Figure 8a shows a top view, Fig. 8b shows a view of a fracture surface, and Fig. 9 shows a top view of a film deposited at 90°C. Films deposited under these conditions show a coarse structure, but it is difficult to determine the crystallite size with certainty.

Semiconductor properties.—Measurement of the voltage difference between a hot and a cold contact as a function of the time starting with the moment that the hot probe made contact with the film gave signals as depicted in Fig. 10. For one group of deposits the initial potential difference is negative, changing to positive after a few seconds. For another group the potential difference is positive at all times. It is believed that the former behavior indicates p-type, the latter n-type semiconductivity, the change in sign in the former group occurring as a result of a contribution of the n-type SnO_2:Sb base to the thermoelectric power. Attempts to make the method quantitative for carrier density determinations have failed. The type of semiconductivity determined in this manner for samples deposited at various voltages is indicated in Fig. 1. It is seen that films with $E_{rest} \leqq -0.3 \pm -0.05$V *vs.* SCE are n-type, those with $E_{rest} \geqq -0.3 \pm -0.05$V *vs.* SCE are p-type. Extrapolation to 85°C of de Nobel's data for the cadmium pressure at the p ⇄ n transition point of CdTe cooled after equilibrium at 700°-1000°C (11) gives $(a_{Cd})_{p,n} = 5.9 \times 10^{-14}$, corresponding to a potential $E_{rest} = -0.66 + 0.39 = -0.27$V *vs.* SCE, close to the observed value of 0.3 ± 0.05V.

The current density required to produce exactly stoichiometric CdTe with a rest potential equal to that of the p-n transition increases with increasing TeO_2 concentration in the electrolyte or, for deposition from a saturated TeO_2 solution, with decreasing pH (the

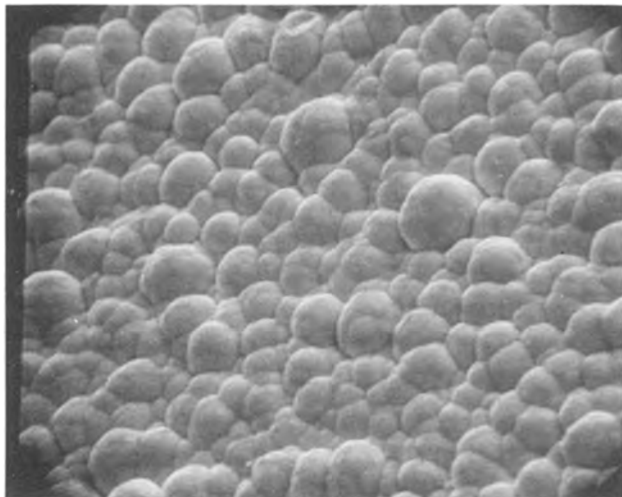

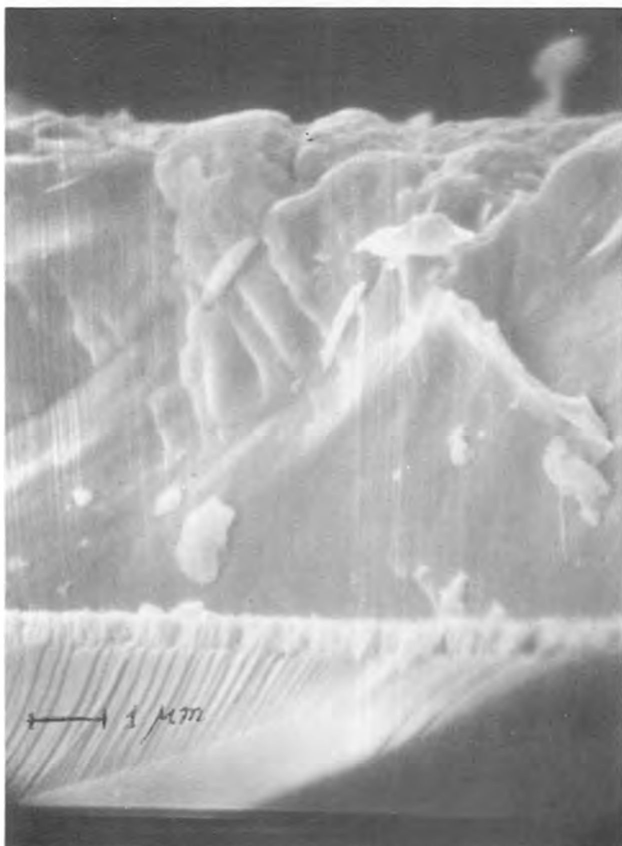

Fig. 8. Scanning electron microscope picture of a film deposited at 25°C on glass covered with SnO_2:Sb. (a, upper) Top view (magnification 5000×); (b, lower) fracture surface (magnification 10,000×) (the thin intermediate layer is the SnO_2).

TeO_2 solubility increases with decreasing *p*H at *p*H < 5); at given TeO_2 concentration, it increases with the rate of stirring. These effects result from the fact that the Te content of the deposit depends critically on the saturation current of the Te deposition which is proportional to TeO_2 concentration and the rate of stirring. The larger the saturation current, the more Te is deposited and the larger the current density has to be to deposit enough Cd to make the material stoichiometric.

N-type material was obtained at all deposition potentials by deposition from an electrolyte to which $10^{-2}\%$ $In_2(SO_4)_3$ had been added. P-type material was obtained at all deposition potentials by deposition from unpurified $CdSO_4$ solution (which contained Cu and

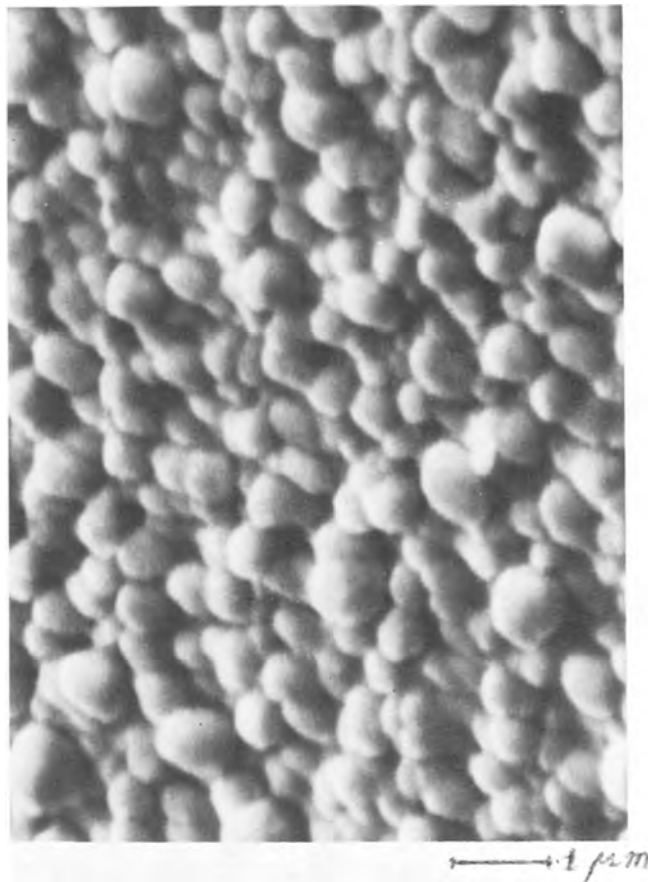

Fig. 9. Scanning electron microscope picture (magnification 10,000×) of a film deposited at 90°C (top view).

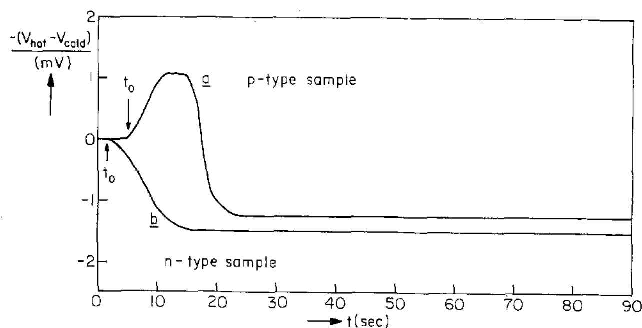

Fig. 10. ($V_{hot} - V_{cold}$) as *f*(time) for samples with different E_{rest} (prepared at different V_{dep}). a, n-type sample; b, p-type sample; t_0 = time at which hot point makes contact with the sample.

As) or from purified $CdSO_4$ solutions to which $10^{-2}\%$ $CuSO_4$ had been added.

The Pourbaix diagram of CdTe.—Recently Ohashi (12) constructed potential-*p*H diagrams for CdTe and ZnTe. The upper boundary of the CdTe field is in fair agreement with our results. However, the lower phase boundary (-1.1V *vs.* NHE at *p*H $= 0$) calculated from the reaction

$$2H^+ + 2e^- + CdTe = Cd + H_2Te$$

is much more negative than the potential at which in our experiments CdTe in equilibrium with Cd is formed: the equilibrium potential of Cd (-0.41V *vs.* NHE). The lower phase boundary is not determined by H_2Te formation, but by dissolution of cadmium present in excess over the stoichiometric ratio according to

$$Cd_{1+\delta}Te = \Delta Cd^{2+} + 2\Delta e^- + Cd_{1+\delta-\Delta}Te$$

with, at the phase boundary CdTe/Cd, $a_{Cd} = 1$. CdTe + Cd is not stable in a solution containing appreciable amounts of Te, Cd exchanging with Te with formation of CdTe. As long as free Cd is present and accessible, however, the potential remains determined and equal to the Cd potential. When all the Cd is used up or has become inaccessible by being covered with CdTe, Cd from the CdTe surface exchanges with Te with formation of a Te-rich surface, and the potential drifts to that of the CdTe/Te phase boundary. A corrected Pourbaix diagram for standard activities of the potential-determining species in the electrolyte is shown in Fig. 11. Formation of $HCdO_2^-$ will limit the CdTe field only at low concentrations and high pH.

Summary

Films made by cathodic deposition from an aqueous solution of $CdSO_4$ and TeO_2, having $0.2V < -E_{rest} < 0.6V$ *vs.* SCE, are identified as CdTe. The deposit is amorphous when deposited at room temperature, semicrystalline with grain size 500-1000Å when deposited in the range 35°-90°C. Annealing at 350°C in argon increases the crystalline size to ≥5000Å. The material is n-type when deposited to have $-E_{rest} > 0.3V$ *vs.* SCE p-type when having $-E_{rest} < 0.3V$ *vs.* SCE. Films doped with donors (In) or acceptors (Cu) grown from electrolytes containing these species are n- respectively p-type for all deposition conditions.

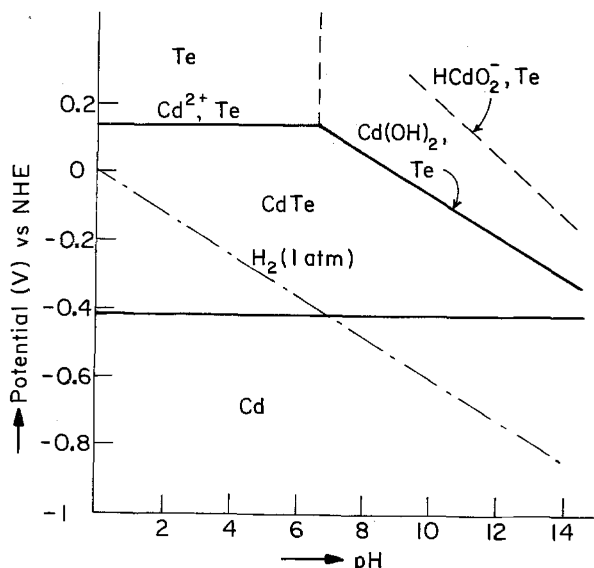

Fig. 11. Pourbaix diagram for CdTe calculated for standard concentrations of the potential-determining species.

Acknowledgment

This work was done for the Division of Solar Energy, United States Energy Research and Development Administration, Award No. E(49-18)2457 under a subcontract from Monosolar, Incorporated, a division of Monogram Industries, Incorporated.

Manuscript submitted June 1, 1977; revised manuscript received Dec. 1, 1977.

Any discussion of this paper will appear in a Discussion Section to be published in the December 1978 JOURNAL. All discussions for the December 1978 Discussion Section should be submitted by Aug. 1, 1978.

REFERENCES

1. W. McNeill, U.S. Pat. 3,573,177 (1971).
2. F. C. Mathers and H. L. Turner, *Trans. Am. Electrochem. Soc.*, **54**, 293 (1928).
3. M. Pourbaix, "Atlas d'Equilibres Electrochimiques," Gauthiers-Villars et Cie, Paris (1963).
4. H. Gobrecht, H. D. Liess, and A. Tausend, *Ber. Dtsch. Bunsenges. Phys. Chem.*, **67**, 930 (1973).
5. D. C. Gernes, G. A. Lorenz, and G. H. Montillon, *Trans. Electrochem. Soc.*, **77**, 177 (1940); D. C. Gernes and G. H. Montillon, *ibid.*, **81**, 231 (1942).
6. A. Brenner, "Electrodeposition of Alloys," Vol. 2, p. 611, Academic Press, New York (1963).
7. A. J. Panson, *J. Phys. Chem.*, **67**, 2177 (1963); *ibid.*, **68**, 1721 (1964).
8. F. A. Kröger, Paper submitted to *This Journal*.
9. O. Kubaschewski and E. Ll. Evans, "Metallurgical Thermochemistry," Table A, Pergamon Press, London (1955).
10. T. Erdey-Gruz, "Kinetics of Electrode Processes," p. 101, Wiley-Interscience, New York, London (1972); A. Brenner, "Electrodeposition of Alloys," Vol. 1, p. 319, Academic Press, New York (1963).
11. D. de Nobel, *Philips Res. Rep.*, **14**, 361 (1959).
12. T. Ohashi, J. O'M. Bockris, and K. Uosaki, *This Journal*, **124**, 1348 (1977).

Technical Notes

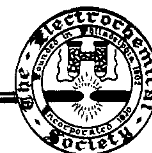

The Standard Free Energy of Formation of Liquid Na_2SO_4 1160°-1220°K

Winston W. Liang*

Department of Materials Engineering, University of Illinois-Chicago Circle, Chicago, Illinois 60680

and John F. Elliott*

Department of Materials Science and Engineering, Massachusetts Institute of Technology, Cambridge, Massachusetts 02139

With the use of the sodium reference electrode employing β-alumina as a solid electrolyte that has been described earlier (1-3), it has been possible to investigate the properties of liquid sodium sulfate in the temperature range 1160°-1220°K. This communication is a brief description of the results of the work. The

* Electrochemical Society Active Member.
Key words: sodium sulfate, emf measurements, free energy.

cell is the same as that employed earlier (2)

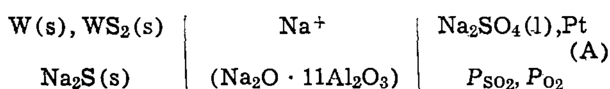

$$\begin{array}{c|c|c} W(s), WS_2(s) & Na^+ & Na_2SO_4(l), Pt \quad (A) \\ Na_2S(s) & (Na_2O \cdot 11Al_2O_3) & P_{SO_2}, P_{O_2} \end{array}$$

The over-all cell reaction is

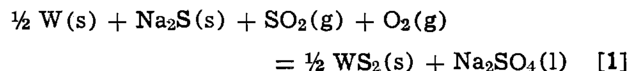

$$\tfrac{1}{2} W(s) + Na_2S(s) + SO_2(g) + O_2(g) = \tfrac{1}{2} WS_2(s) + Na_2SO_4(l) \quad [1]$$

The cathode liquid consisted of reagent-grade anhydrous granular sodium sulfate which was purified further by drying it in a vacuum chamber at 600°-650°C for at least two days. The cell arrangement and the experimental procedure have been given in detail elsewhere (2). The gas compositions at the cathode employed in this study are given in Table I.

With equilibrium among the compounds in the anode chamber, and equilibrium between the gases and liquid Na_2SO_4 at the cathode

$$\Delta G^\circ_1 = -2\mathbf{F}E + RT \ln P_{SO_2} + RT \ln P_{O_2} \quad [1a]$$

The potential of the cell is E and $\mathbf{F}$ is Faraday's constant. Equation [1a] can be rewritten

$$-2\mathbf{F}E = \Delta G^\circ_f(Na_2SO_4) + \tfrac{1}{2} G^\circ_f(WS_2) - \Delta G^\circ(Na_2S) - \Delta G^\circ(SO_2) - RT \ln P_{SO_2} - RT \ln P_{O_2} \quad [2]$$

It is to be noted that the experimental cell potential must be corrected for the thermoelectric effect of the Pt-W junction to obtain the value of E for Eq. [1a] and [2]. The correction is 20-30 mV in the range of temperature of this work.

The cell (A) was used to measure the activity of sodium oxide in liquid sodium sulfate over a range of partial pressures of oxygen ($10^{-6} < P_{O_2}$, atm < 0.5) and sulfur dioxide ($10^{-6} < P_{SO_2}$, atm < 0.5) with a total pressure of 1 atm. With this cell it is possible to monitor the change in activity of sodium oxide in sodium sulfate arising from additions of Na_2O and SO_3 (SO_2 and O_2) to the sulfate. Sulfur trioxide, alumina/beta-alumina and platinum react to neutralize the sodium oxide added to the sodium sulfate melt depending on the selected experimental conditions. The neutralization of Na_2O by platinum is important when $a_{Na_2O} > 10^{-6}$; by alumina/beta alumina when $10^{-6} < a_{Na_2O} < 10^{-12}$ and by $SO_3(g)$ when the composition of the gas mixture employed has $P_{SO_3} > 10^{-5}$ atm.

The standard free energy of formation of liquid sodium sulfate by the reaction

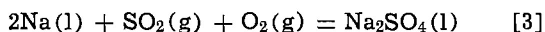

$$2Na(l) + SO_2(g) + O_2(g) = Na_2SO_4(l) \quad [3]$$

can be obtained from the experimental results and data in Table II using Eq. [2] as follows

Table I. Composition of gas mixtures in volume percent

Gas mixture	Volume percent SO_2	O_2	N_2	Ar
A	50	50	—	—
B	50	10.5	bal.	—
C	50	2.5	—	bal.
E	0.45	50	bal.	—

Table II. Thermodynamic data

Compound	$\Delta G^\circ = \Delta H^\circ - T\Delta S^\circ$ (J/mole)	Reference
$\tfrac{1}{2}WS_2(s)$	$-168,200 + 78.24T$	4
$Na_2S(s)$	$-435,550 + 124.3T$	5
$Na_2O(l)$	$-353,550 + 88.91T$	5
$SO_2(g)$	$-361,920 + 72.89T$	5
$Na_2SO_4(l)$	$-1,383,900 + 410.3T$	5

Standard states; W(s), $S_2(g)$, Na(l), $O_2(g)$, all at 1 atm pressure.

$$\Delta G^\circ_3 = -2\mathbf{F}E + RT \ln P_{SO_2} + RT \ln P_{O_2} - 267,400 + 46.06T, \text{(J)} \quad [3a]$$

Alternatively for the reaction

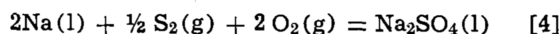

$$2Na(l) + \tfrac{1}{2} S_2(g) + 2\,O_2(g) = Na_2SO_4(l) \quad [4]$$

and

$$\Delta G^\circ_4 = -2\mathbf{F}E + RT \ln P_{SO_2} + RT \ln P_{O_2} - 629,300 + 118.95T, \text{(J)} \quad [4a]$$

Thus, with the cell it is possible to determine the standard free energy of formation of liquid sodium sulfate.

The experimental measurements are shown in Table III and the results in terms of ΔG°_1 are shown in Fig. 1. The full line through the data is the least-squares line for all points; its equation is

$$\Delta G^\circ_1 = -637,800 + 178.62T, \text{(J)} \quad [1b]$$

with uncertainties of approximately ±2500 J/mole in free energy, ±5000 J/mole in enthalpy, and ±4 J/mole °K in entropy. There appeared to be no systematic variation of the cell potential with the gas compositions. Inserting these results into Eq. [3a]

$$\Delta G^\circ_3 = -905,200 + 224.68T, \text{(J)} \quad [3b]$$

and into Eq. [4a] gives

$$\Delta G^\circ_f(Na_2SO_4) = -1,267,000 + 297.6T, \text{(J)} \quad [4b]$$

for the liquid with estimated uncertainties of ±15,000 J/mole in free energy, ±18,000 J/mole in enthalpy, and ±10 J/mole °K in entropy. It is to be recognized that the temperature interval over which the measurements were obtained is relatively small so that the un-

Table III. Experimental measurements

Cell No.	Gas mixture	Temp. (°K)	Cell EMF* (volts)	$\log a_{Na_2O}$
15	A	1178	2.134	−16.84
15	A	1221	2.092	−15.98
39	A	1203	2.107	−16.31
41	A	1204	2.109	−16.31
46	A	1202	2.104	−16.30
47	A	1206	2.106	−16.27
47	A	1200	2.114	−16.40
47	A	1205	2.108	−16.29
47	A	1162	2.151	−17.21
48	A	1201	2.114	−16.39
51	A	1202	2.108	−16.33
51	A	1177	2.134	−16.85
20	B	1172	2.046	−16.53
20	B	1199	2.021	−16.00
23	B	1199	2.028	−16.06
23	B	1213	2.015	−15.79
23	B	1193	2.036	−16.19
23	B	1182	2.054	−16.48
23	B	1165	2.080	−16.91
23	B	1187	2.056	−16.43
15	C	1218	1.948	−15.83
15	C	1177	1.982	−16.29
15	C	1220	1.934	−15.40
16	C	1215	1.938	−15.49
16	C	1812	1.963	−16.07
17	C	1168	1.982	−16.40
39	C	1207	1.938	−15.57
39	C	1213	1.934	−15.47
39	C	1190	1.954	−15.90
39	C	1173	1.963	−16.17
39	C	1164	1.978	−16.41
39	C	1185	1.970	−16.09
39	C	1218	1.933	−15.41
36	E	1213	1.852	−14.07
36	E	1162	1.913	−15.11
36	E	1193	1.882	−14.52
36	E	1217	1.849	−14.00
36	E	1202	1.862	−14.26
36	E	1193	1.870	−14.41
36	E	1177	1.889	−14.74
36	E	1164	1.909	−15.05
46	E	1175	1.895	−14.81
46	E	1160	1.915	−15.15
46	E	1181	1.893	−14.73
46	E	1201	1.872	−14.35
46	E	1213	1.858	−14.12
46	E	1202	1.865	−14.28

* Corrected for Pt-W thermoelectric effect.

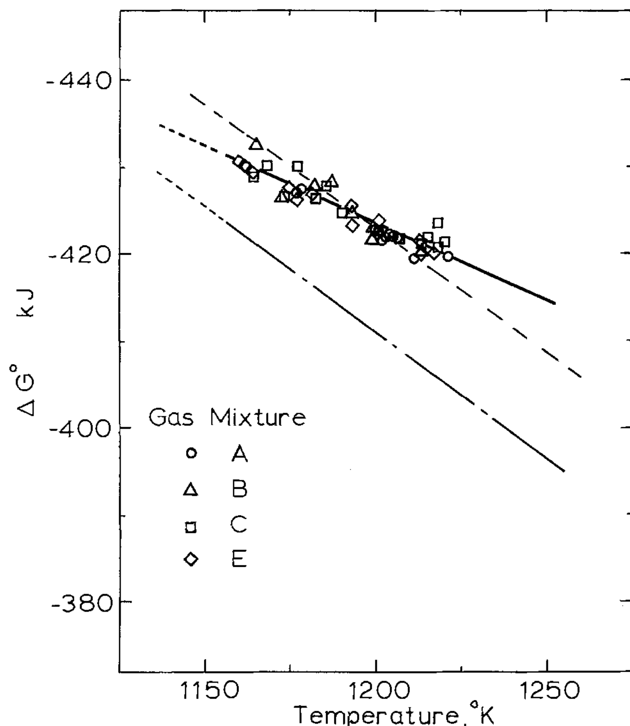

Fig. 1. The standard free energy of reaction [1]. ——— Least-squares line through experimental data; – – – line based on data in literature (4, 5); —·—·— line through data with slope from thermochemical data (4, 5).

certainties in the enthalpy and entropy terms may be very large even though the precision of the value of the free energy may be relatively good. The experimental result (Eq. [4b]) at 1200°K is approximately 12,000J (3000 cal) below the value given in the JANAF tables (5). The data on sodium sulfate in those tables were calculated from measurements of the enthalpy of sodium sulfate by Coughlin (6). Considering the nature of the two sets of data the agreement in the values for the free energy is considered to be reasonably good. On the other hand, however, the thermodynamic properties of sodium sulfide which are used in obtaining Eq. [3a] and [4b] are somewhat uncertain (5).

Because of the large uncertainty in the slope of the experimental line in Fig. 1, it may be better to fit a line to the data based on the standard entropy of formation that has been obtained from thermal data, *i.e.*, −291.35 J/mole °C. Use of this slope with the experimental value of ΔG°_1 at 1200°K gives a value for ΔH°_1 of −773,000 J/mole as compared to −760,600 J/mole from the JANAF tables. With these data and with the data on Na_2S, SO_2, and WS_2 from Table II, the following is obtained for the standard free energy of formation of Na_2SO_4 [*e.g.*, (4)]

$$G^\circ_4 = -1{,}402{,}300 + 410.3T, \text{ (J)}$$

It is to be seen that this modified experimental result is in reasonable agreement with the published results (5), the enthalpy of formation of liquid sodium sulfate from Na(l), S_2(g), and O_2(g) being 12 kJ (3000 cal) more negative than the published value.

Acknowledgment

The authors wish to acknowledge financial support by the Energy Research and Development Administration [Contract No. E(49-18)2215] of the work reported here.

Manuscript submitted June 10, 1977; revised manuscript received Nov. 10, 1977.

Any discussion of this paper will appear in a Discussion Section to be published in the December 1978 JOURNAL. All discussions for the December 1978 Discussion Section should be submitted by Aug. 1, 1978.

Publication costs of this article were assisted by the Massachusetts Institute of Technology.

REFERENCES

1. W. W. Liang, H. K. Bowen, and J. F. Elliott, "Metal-Slag-Gas Reactions and Processes," Z. A. Foroulis and W. W. Smeltzer, Editors, pp. 608-624, The Electrochemical Society Softbound Symposium Series, Princeton, N.J. (1975).
2. W. W. Liang and J. F. Elliott, *This Journal*, **123**, 617 (1976).
3. W. W. Liang and J. F. Elliott, "Properties of High Temperature Alloys," Z. A. Foroulis and F. S. Pettit, Editors, The Electrochemical Society Softbound Symposium Series, Princeton, N.J. (1976).
4. J. P. Hager and J. F. Elliott, *Trans. AIME*, **239**, 513 (1967).
5. JANAF Thermochemical Tables, 2nd ed., NBS **37**, U.S. Department of Commerce (1970).
6. J. P. Coughlin, *J. Am. Chem. Soc.*, **77**, p. 868 (1955).

Transient Pitting during Film Growth on Aluminum at 1000 mV vs. SCE

J. Zahavi,[1] I. D. Ward, and M. Metzger*

Department of Metallurgy and Mining Engineering and Materials Research Laboratory, University of Illinois at Urbana-Champaign, Urbana, Illinois 61801

Electronmicroscopic evidence of transient pitting during growth of a porous anodic film on 99.999% Al in 2.4M H_2SO_4 even without Cl^- has been presented by Zahavi and Metzger (1). Anodizing was at 5 mA/cm² yielding a cell voltage ~7V with respect to a Pt cathode; some supplementary observations were made at 25 mA/cm² (~16V). It is of interest to know whether transient pitting phenomena also occur at lower potentials. A gravimetric study of film growth at +1000 mV_{SCE} in 2.4M H_2SO_4 without or with Cl^- additions had been made by Smaga and Metzger (2) with the material and specimen preparation (Electropolish A) employed previously (1). Electronmicroscopic examination of films grown under these conditions in acid without Cl^- is described in this note. Previously, the lowest potentials for which anodic film structure had been examined in any investigation were those of Ref. (1).

At 1000 mV_{SCE} it was found that after 2640 sec the film reached constant weight (2), as expected for a porous film when the pores have grown to a length at

* Electrochemical Society Active Member.
[1] Present address: Israel Institute of Metals, Technion, Haifa, Israel.
Key words: film growth, pitting, aluminum.

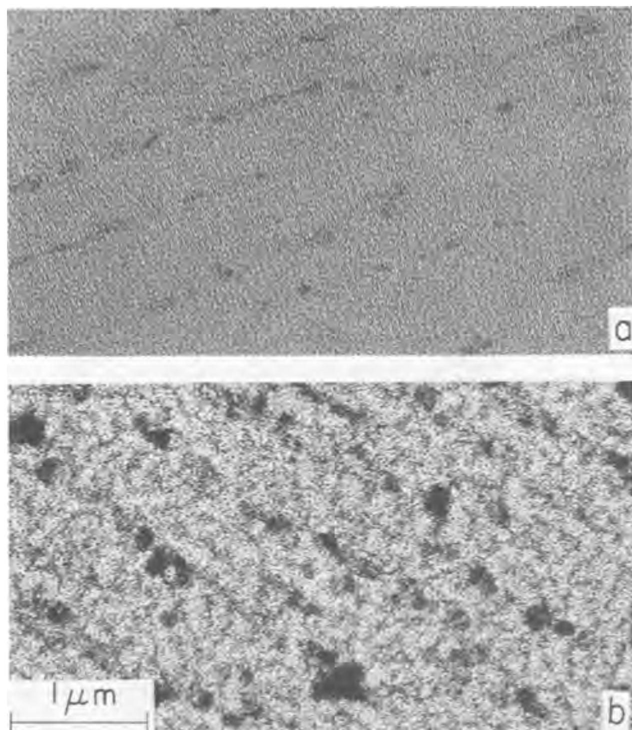

Fig. 1. Transmission electron micrographs of films detached after a) 1080 sec; b) 3000 sec anodizing at +1000 mV_{SCE}.

which the rate of chemical dissolution of their walls equals the rate of growth at the film base (3). From the tapered-pore model and limiting thickness was estimated as ~½ μm (2). Films for electronmicroscopic examination were formed for 600, 1080, and 3000 sec; over this period, the cell current, after its initial fall, was rising slowly from 0.6 to 0.8 mA/cm^2.

In transmission micrographs of detached films, Fig. 1a and b, the films were seen to be porous, and breakdown-pitting repair (BPR) "events" were visible as dark patches, usually elongated. The veining visible in the background of Fig. 1b originated in the surface topography produced by the $HClO_4$ electropolishing bath ("granular structure"), as discussed in Ref. (1). The appearance of the events was remarkably similar to that noted earlier (1) at a potential ~6V higher. The contrast at an event is the result of the extra mass thickness provided by the repair film beneath the main film and/or the local perturbation of the pore structure, as described previously (1).

Examination of films at much higher magnifications showed that pore diameters were small (<10 nm), but a precise determination could not be made. The pores apparently were far from being straight cylinders since they did not image as separated sharp round silhouettes of uniform size. The factors responsible for this would be (*i*) the pores were tapered by chemical dissolution of their walls; (*ii*) they were jogged or had sloping segments resulting from the BPR processes which had interrupted their growth (thus images of adjacent pores could overlap). Microscopic measurements of pore and cell diameters of anodic films are usually made on much coarser structures produced in various acids at "forming voltages" well over 10V and sometimes over 100V (3, 4, 5). If the figure for pore diameter of approximately 1.0 nm/V obtained in these studies (4, 5) is applied to the present case, and if the "forming voltage" in the present experiments is taken as the overpotential above the Al/Al_2O_3 reversible potential, the pore diameter predicted would be ~3 nm, which is not inconsistent with the observations.

Figure 2 shows an underside-replica micrograph of the 600 sec film. Evidence that this structure did not represent artifacts was (*i*) two sets of such replicas

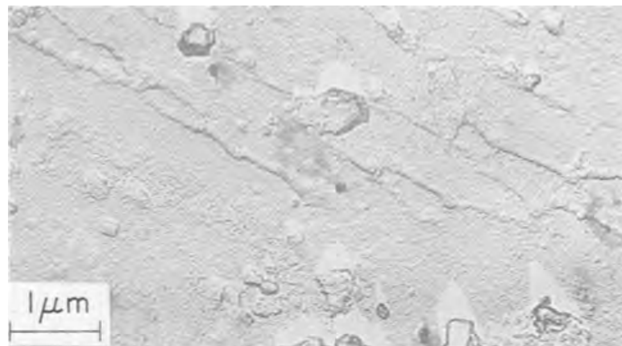

Fig. 2. Replica of underside of 600 sec film. Shadowed with Pt-C at $\tan^{-1}$ ¼.

from the 600 sec film and one from the 1080 sec film prepared with close attention to and some variation in details of procedure all gave consistent structures; (*ii*) the structures were basically similar to those obtained in an extended study of films formed at 5 mA/cm^2. Visible in Fig. 2 are irregular strings of very fine repaired pits and on them or elsewhere some larger repaired pits which are thought to have formed subsequently. The latter are the "events" visible in transmission as dark patches. It was deduced that the strings of fine pits gave by themselves little or no visible contrast in transmission and that the tendency toward elongation of the events seen in transmission was the result of the tendency for events to nucleate on the strings and sometimes a tendency for the events themselves to be elongated. The evolution of structures of this type and their relation to substrate orientation has been studied in some detail for anodizing $\lesssim$ 100 sec at 5 mA/cm^2 and is reported separately. Although anodizing times were much longer in the present work, the mass thicknesses of the films examined were in the same range, and the similarity of the transient-pitting structures in the two cases is taken to mean that the stages through which film structure passes depend more on mass-thickness than on potential in the range studied. This conclusion had been drawn earlier from observations on films formed at 5 mA/cm^2 at reduced cell voltages in acid containing Cl^- (1).

The significance of the transient pitting accompanying film growth for the understanding of several phenomena has recently been discussed elsewhere (6).

Acknowledgments

This work was supported by the Department of Energy Contract DOE-76-C-02-1198 through the Materials Research Laboratory and by the U.S. Army Research Office.

Manuscript submitted Dec. 15, 1977.

Any discussion of this paper will appear in a Discussion Section to be published in the December 1978 JOURNAL. All discussions for the December 1978 Discussion Section should be submitted by Aug. 1, 1978.

Publication costs of this article were assisted by the University of Illinois at Urbana-Champaign.

REFERENCES

1. J. Zahavi and M. Metzger, *This Journal*, **121**, 268 (1974).
2. J. A. Smaga and M. Metzger, Abstract 65, p. 163, The Electrochemical Society Extended Abstracts Fall Meeting, New York, New York, October 13-17, 1974.
3. M. Nagayama, K. Tamura, and H. Takahashi, *Corr. Sci.*, **10**, 617 (1970).
4. G. C. Wood and J. P. O'Sullivan, *Electrochim. Acta*, **15**, 1865 (1970).
5. J. P. O'Sullivan and G. C. Wood, *Proc. Roy. Soc. (London)*, **A317**, 511 (1970).
6. M. Metzger and J. Zahavi, To be published in Proceedings of the Fourth International Symposium on Passivity, The Electrochemical Society, Inc., Princeton, N.J.

SOLID-STATE SCIENCE
—AND TECHNOLOGY

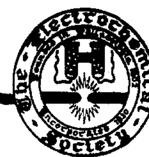

APRIL
1978

Thermal Oxidation Kinetics of Silicon in Pyrogenic H_2O and 5% HCl/H_2O Mixtures

Bruce E. Deal*

Fairchild Camera and Instrument Corporation, Research and Development Laboratory, Palo Alto, California 94304

ABSTRACT

The kinetics of the thermal oxidation of silicon in H_2O and in 5 volume percent (v/o) HCl in H_2O using a pyrogenic system have been investigated over the temperature range 900°-1100°C. Oxide thickness-oxidation time data, rate constants, and activation energies have been obtained for (111) and (100) oriented, 1×10^{15} cm^{-3}, n-type silicon. Results obtained for oxidation in H_2O are very similar to those reported previously for water bubbler systems. The addition of HCl to H_2O does not increase the silicon oxidation rate as with dry O_2, but the rate actually decreases apparently because of the reduced H_2O vapor pressure. The HCl also appears to reduce impurity contributions from the oxidation system.

Recent investigations concerning the oxidation kinetics of silicon in dry oxygen containing small additions of HCl or Cl_2 have been reported (1-4). These and other studies have indicated that such chlorine additions provide certain benefits to the resulting device structures, such as alkali ion passivation, higher and more uniform oxide dielectric strength, and improved junction properties due to lower leakage (5-8). Coincidentally increased oxidation rates have been observed with increasing chlorine concentration in the oxygen ambient (1-4). The reported improvements in device properties are probably due in part to actual incorporation of a chlorine species in the silicon oxide and reaction of this species with impurities (8, 9). It has been proposed that the increased oxidation rates are due either to the reaction products (such as H_2O and Cl_2 from O_2 plus HCl) or the effect of the chlorine species itself on the oxide growth mechanism, or both (1-4).

Less information is available concerning the oxidation of silicon in H_2O which contains small amounts of chlorine. There are indications, however, that chlorine is not incorporated in the oxide and that oxidation rates are not increased by the addition of HCl and other chlorine species to the water ambient (10).

Water or water-containing ambients have been used for the thermal oxidation of silicon since silicon dioxide was first employed for masking dopants during diffusion of silicon devices (11-13). Silicon oxidation kinetics in H_2O have been reported by several authors (14-16) for various process conditions. Most of these results were for wet O_2 (oxygen bubbled through H_2O) or steam (H_2O vapor boiled from a flask). More recently oxidation in a water ambient has been carried out by the pyrogenic reaction of H_2 and O_2 (17). This process is reported to be cleaner and easier to control in production environments.

The purpose of this investigation was to establish oxidation kinetics for the thermal oxidation of silicon in H_2O, to determine the effect of small HCl additions to the ambient on oxidation kinetics, and to compare the results of pyrogenic H_2O oxidation to those previously obtained with wet O_2 or steam introduced into the furnace from a quartz flask (hereafter referred to as a "bubbler" system). Data are reported for 1×10^{15} cm^{-3} n-type silicon with (111) and (100) orientations over the temperature range 900°-1100°C. A brief comparison with dry O_2 oxidation results is also included.

* Electrochemical Society Active Member.
Key words: oxidation, water, kinetics.

Experimental

Experimental conditions and procedures were the same as those reported previously (4). Silicon wafers used for this investigation were n-type 4-6 Ω-cm, with (111) and (100) orientations. Introduction of H_2O into the furnace was acomplished using a pyrogenic oxidation system involving water generation in the end of the furnace tube by the direct reaction of H_2 and O_2. The system, Model D-101, was manufactured by Corso-Gray Instruments, Sunnyvale, California. HCl of 99.99% purity was also introduced through this system. Concentrations of O_2, H_2, and HCl were controlled by calibrated flowmeters. Oxidations at selected ratios of H_2 to O_2 were carried out at temperatures of 900°, 950°, 1000°, 1050°, and 1100°C. Oxidation temperatures for the H_2O/HCl mixture were 900°, 1000°, and 1100°C. For the H_2O oxidations, wafers were pushed into the furnace with the water ambient flowing at 2 liters/min (44 cm/min). At the end of the oxidation time, the wafers were pulled rapidly from the furnace. For the addition of 5% HCl, the HCl flow was started after the wafers were in the furnace; at the end of the oxidation time, an N_2 flow was started, the HCl, H_2, and O_2 flows were stopped, and the system was purged with N_2 for 15 min before the wafers were pulled. Oxidation times in general ranged from 9 min to 8 hr.

Oxide thicknesses were measured using a Rudolph Model 436-200-E ellipsometer with a helium-neon source, with measurement reproducibility of ±3%. Mobile ion concentrations, Q_o/q, and fixed oxide charge, Q_{ss}/q, were determined by conventional capacitance-voltage techniques.

Oxidation kinetic data were analyzed in terms of the oxidation general relationship (15)

$$x_o^2 + Ax_o = Bt \quad [1]$$

where x_o is oxide thickness, t is oxidation time, and B and A are constants. [For H_2O oxidation, the constant

τ normally included in Eq. [1] has been found to be approximately zero (15).] The parabolic rate constants, B, and the linear rate constants, B/A, were calculated using the conventional procedure (15). These constants were then used to determine activation energies by means of Arrhenius-type plots.

Results

System calibration.—The first procedure in conjunction with this program was to calibrate the pyrogenic oxidation system. An attempt was made to generate 100% H_2O (760 Torr) by using exactly 2 parts H_2 to 1 part O_2. Oxidations were carried out at a particular temperature (1000°C) for specific times (15 and 60 min), and oxide thicknesses were compared with those reported previously for atmospheric steam (14-16). Unfortunately, some disagreement exists among the previous works because steam obtained from a boiling flask is difficult to control and reproduce. Even so, the results obtained in the pyrogenic system indicated lower thicknesses than most of those reported for the boiling flask method.[1] It was therefore decided to duplicate the oxidation rate obtained using O_2 bubbled through 95°C water (15). A series of oxidations with varying ratios of H_2 to O_2 indicated that 2.0 liters/min of H_2 plus 1.175 liters/min O_2 did duplicate reasonably well the O_2 through 95°C H_2O data over the temperature range investigated. This ratio was used for the H_2O oxidations reported here. In both cases, the ambient will contain a small excess of O_2 but its contribution to the over-all oxidation process is calculated to be less than 1%. It is also of interest to note that these results are identical to those reported in Ref. (17) for 1 atm H_2O oxidation of (111) silicon in a pyrogenic system.

H_2O oxidation data.—The data for the oxidation of (111) and (100) oriented silicon in pyrogenic H_2O over the temperature range 900°-1100°C are plotted in Fig. 1. The plots are in the form of log oxide thickness *vs.* log oxidation time. Also included are previous bubbler results for 1200°C (15), at which temperature differences between orientations are assumed to be negligible. The plots follow the general oxidation relationship (Eq. [1]) where at higher temperatures and for thicker oxides the reaction is generally parabolic (diffusion controlled) and at lower temperatures and for thinner oxides it is linear (surface controlled).

[1] Conversations with other investigators indicate the pyrogenic reaction of H_2 and O_2 is not 100% efficient.

Table I. Rate constants for the thermal oxidation of n-type, 4-6 Ω-cm, (111) and (100) oriented silicon in water

(2.0 liters/min H_2 + 1.175 liters/min O_2)

Oxidation temp. (°C)	Silicon orient.	A (μm)	B (μm²/hr)	B/A (μm/hr)	B/A ratios (111)/(100)
900	(100)	0.95	0.143	0.150	
	(111)	0.60	0.151	0.252	1.68
950	(100)	0.74	0.231	0.311	
	(111)	0.44	0.231	0.524	1.68
1000	(100)	0.48	0.314	0.664	
	(111)	0.27	0.314	1.163	1.75
1050	(100)	0.295	0.413	1.400	
	(111)	0.18	0.415	2.307	1.65
1100	(100)	0.175	0.521	2.977	
	(111)	0.105	0.517	4.926	1.65
					Avg. 1.68 ± 0.03

Rate constants were determined and are tabulated in Table I. Included in the table are the ratios of linear rate constant (B/A) values between (111) and (100) orientations. The ratios are quite consistent and the average is 1.68 ± 0.03 over the temperature range investigated.

Figure 2 is an Arrhenius-type plot of log B *vs.* $1/T$ from which an activation energy may be determined. The data are for both (111) and (100) orientations since B is not a function of orientation. Also included in the figure are previous data for dry O_2 oxidation (4, 15). The parabolic activation energy value of 0.78 eV for the pyrogenic system is similar to that previously reported (0.71 eV) for the bubbler process (15). It is not known if the falloff of B at 900°C is real or due to experimental error. A similar plot for the linear rate constant B/A is shown in Fig. 3. Here, the differences for the two silicon orientations are

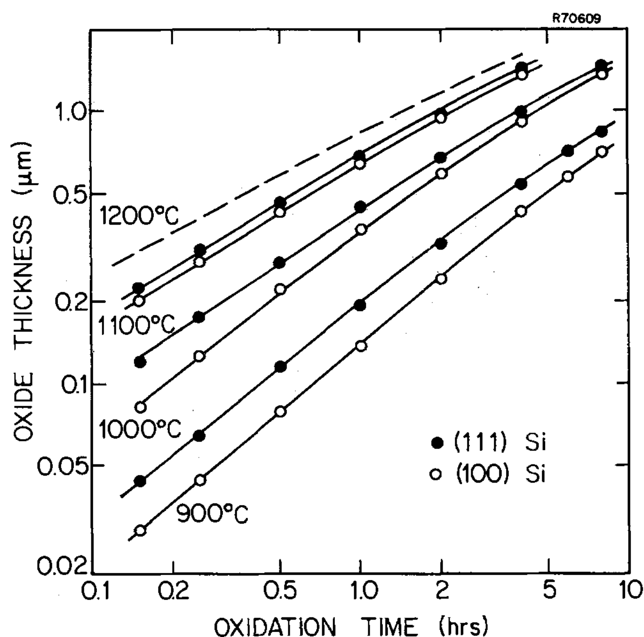

Fig. 1. Oxide thickness *vs.* oxidation time for silicon oxidation in H_2O (640 Torr).

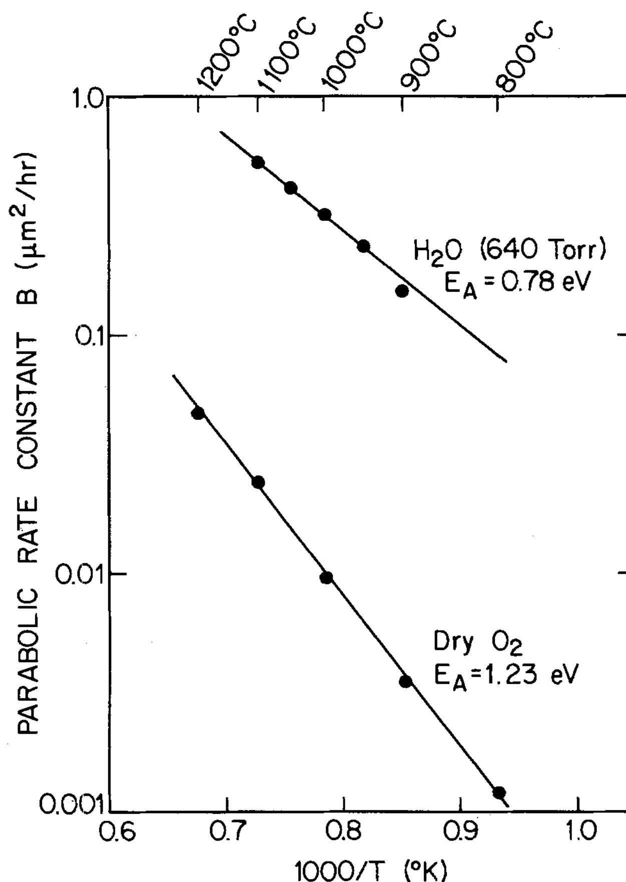

Fig. 2. Dependence of parabolic rate constant B on temperature for the thermal oxidation of silicon in pyrogenic H_2O (640 Torr) or dry O_2.

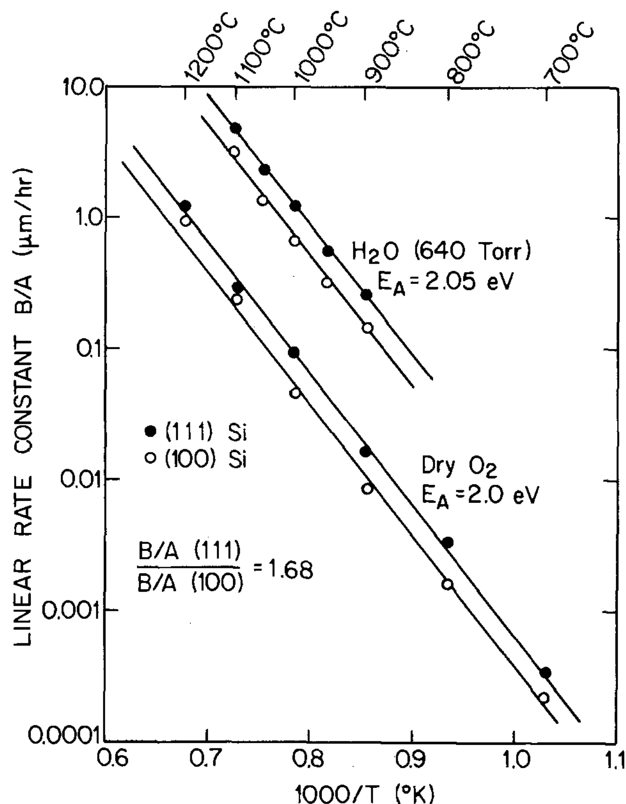

Fig. 3. Dependence of linear rate constant B/A on temperature for the thermal oxidation of silicon in pyrogenic H_2O (640 Torr) or dry O_2.

reflected by the two different but parallel plots. The activation energies for both are 2.05 eV, very similar to the previous bubbler results (15). Again, dry O_2 B/A values are included for comparison. However, in the latter case it is assumed that the activation energies for (111) and (100) silicon should be equal and the ratios of the B/A values should be the same as for H_2O. Thus, the line drawn through the (100) data points is drawn following this assumption. It can be noted that this constant ratio assumption for dry O_2 provides a reasonable fit for the (100) data, which was not possible previously because of its nonlinear nature (4).

If Arrhenius-type expressions of the form $B = C_1 e^{-E_1/RT}$ and $B/A = C_2 e^{-E_2/kT}$ are assumed, then values for the constants C_1 and C_2 may be calculated. These values, along with activation energies E_1 and E_2, are tabulated in Table II for both pyrogenic H_2O and dry O_2 silicon oxidation.

H_2O/HCl results.—Oxidations were carried out at 900°, 1000°, and 1100°C in a pyrogenic H_2O ambient with a 5% HCl addition. When oxide thickness-oxidation time data were compared with the H_2O results of Fig. 1, not only did the HCl addition provide no increase in oxidation rate, but an actual decrease was observed. Coincidentally, this decrease appeared to be about 5%; the amount of HCl added. Rate constants were determined and these are tabulated in Table III, along with B/A ratios for the two orientations. The latter average value of 1.72 was quite similar to the 1.68 value for H_2O.

If the values of B, the parabolic rate constant, for 5% HCl additions are compared with those for H_2O, an average ratio of 0.934 is obtained. This is reasonably close to 0.95 which would be expected for a straight dilution by the HCl. A similar reduction ratio between HCl and no HCl is obtained for the linear rate constant B/A, probably through the partial pressure reduction effect on B.

Special oxidations were carried out at 1000°C in which 5% N_2 was added to H_2O. Oxidation rates were approximately the same as those obtained with 5% HCl additions. This tends to confirm that the reduced oxidation rate for the HCl/H_2O mixture is due to a dilution of the H_2O by the HCl addition.

Table II. Dependence of rate constants on temperature using Arrhenius relationship

Parabolic	$B = C_1 e^{-E_1/kT}$
Linear	$B/A = C_2 e^{-E_2/kT}$
(111) Silicon	
Dry O_2	$C_1 = 7.72 \times 10^2$ μm²/hr
	$C_2 = 6.23 \times 10^6$ μm/hr
	$E_1 = 1.23$ eV
	$E_2 = 2.0$ eV
H_2O (Pyrogenic)	$C_1 = 3.86 \times 10^2$ μm²/hr
	$C_2 = 1.63 \times 10^8$ μm/hr
	$E_1 = 0.78$ eV
	$E_2 = 2.05$ eV
(100) Silicon	
	C_2 (100) = C_2 (111)/1.68

Table III. Rate constants for the thermal oxidation of n-type 4-6 Ω-cm, (111) and (100) oriented silicon in 5 v/o HCl/H_2O mixtures

(1.9 liters/min H_2, 1.115 liters/min O_2, 0.1 liters/min HCl)*

Oxidation temp. (°C)	Silicon orient.	A (μm)	B (μm²/hr)	B/A (μm/hr)	B/A ratios (111)/(100)
900	(100)	0.90	0.133	0.148	
	(111)	0.505	0.133	0.263	1.78
1000	(100)	0.46	0.294	0.639	
	(111)	0.26	0.294	1.131	1.77
1100	(100)	0.175	0.500	2.860	
	(111)	0.11	0.509	4.630	1.62
					Avg. 1.72 ± 0.07

* Actual v/o HCl = 4.6%.

Oxide properties.—Some mention should be made concerning various physical and electrical properties of the oxides prepared in 5% HCl/H_2O ambients. First, the apparent thickness uniformity and appearance of these oxides were considerably better than corresponding H_2O oxides. Very few defects or color variations were observed. This is probably related to the fact that ionic contamination in the HCl/H_2O oxides was also low, as evidenced by Q_o/q values of less than 2×10^{10} cm^{-2} over the entire temperature range. These may be compared with Q_o/q values for the regular H_2O oxides of $<2 \times 10^{10}$ cm^{-2} at 900°C but ranging up to 3×10^{11} cm^{-2} at 1100°C. This trend of increasing contamination with oxidation temperature is believed to be due to increased reaction of the water with ionic impurities in the quartz tube at the higher temperatures. Apparently the HCl serves to complex these impurities in the apparatus.

Preliminary measurements of Q_{ss}/q indicated somewhat lower values at a given temperature than previously obtained for 95°C H_2O oxidations. This may be due to an effect of free hydrogen in the pyrogenic oxidation ambient.

Summary

Kinetic data for the oxidation of (111) and (100) oriented silicon in H_2O over the temperature range 900°-1100°C have been presented. The water was generated by the direct reaction of H_2 and O_2 in a pyrogenic system. Since it is apparently not possible to generate 100% water in this system, flow rates of the gases were selected to provide oxidation rates equal to those previously obtained for O_2 bubbled through 95°C H_2O, *i.e.*, ~0.85 partial pressure of H_2O.

Rate constants for the general oxidation relationship were determined, and values for (111) silicon agree quite well with those previously obtained for a 95°C H_2O bubbler system. As predicted by theory, the parabolic rate constants, B, exhibit no orientation de-

pendence. Linear rate constants, B/A, for (111) silicon are 1.68 times the (100) silicon values. Activation energies are 0.78 and 2.05 eV for the parabolic and linear rate constants, respectively. Again, these values correspond favorably with wet O_2 bubbler results. The 1.68 ratio between (111) and (100) linear rate constants was applied to the dry oxygen data recently obtained, and the line drawn for (100) silicon provides a reasonable fit for the Arrhenius-plot data points.

Oxidation kinetics were also determined for mixtures of 5 volume percent (v/o) HCl in H_2O using the pyrogenic system. Other process conditions were the same as indicated above for H_2O oxidations. It was found that the only change in the oxidation process due to the HCl addition is a decrease in rate constants approximately equal to the HCl concentration in the oxidation ambient. Apparently no chlorine species is incorporated in the oxide during H_2O/HCl oxidations (10). This fact plus the probability that HCl does not react with the H_2O would indicate that the HCl species itself does not enter into the reaction directly in either H_2O/HCl oxidations or in the O_2/HCl oxidations discussed previously (4, 18). If this is true, the previous proposal that the reaction products H_2O and Cl_2 are the primary species affecting O_2/HCl oxidation kinetics (18) is corroborated.

The results of this investigation also indicate that small HCl additions to H_2O oxidation ambients provide beneficial effects because of the gettering or complexing of alkali impurities in the quartz system. In addition, more uniform oxides with fewer defects are produced. The question of possible effects on the oxide charges due to free hydrogen in the pyrogenic system must yet be resolved.

Acknowledgments

The author wishes to thank Drs. J. M. Early and R. M. Das for critically reviewing this manuscript. Helpful discussions and suggestions regarding this work were provided by Dr. D. W. Hess, Mr. C. P. Ho, and Dr. J. D. Plummer. Mrs. J. H. Bien conducted much of the experimental part of the program. A portion of this work was supported by ARPA Contract No. DAABO7-77-C-2684.

Manuscript submitted Sept. 15, 1977; revised manuscript received Dec. 7, 1977.

Any discussion of this paper will appear in a Discussion Section to be published in the December 1978 JOURNAL. All discussions for the December 1978 Discussion Section should be submitted by Aug. 1, 1978.

Publication costs of this article were assisted by Fairchild Camera and Instrument Corporation.

REFERENCES

1. R. J. Kriegler, Y. G. Cheng, and D. R. Colton, *This Journal*, **119**, 388 (1972).
2. K. Hirabayashi and J. Iwamura, *ibid.*, **120**, 1595 (1973).
3. Y. J. van der Meulen and J. G. Cahill, *J. Electron. Mater.*, **3**, 371 (1974).
4. D. W. Hess and B. E. Deal, *This Journal*, **124**, 735 (1977).
5. R. S. Ronen and P. H. Robinson, *ibid.*, **119**, 747 (1972).
6. R. J. Kriegler, *Denki Kagaku*, **41**, 466 (1973).
7. Y. J. van der Meulen, C. M. Osburn, and J. F. Ziegler, *This Journal*, **122**, 284 (1975).
8. R. L. Meek, *ibid.*, **120**, 308 (1973).
9. A. Rohatgi, S. R. Butler, F. J. Feigl, H. W. Kraner, and K. W. Jones, *Appl. Phys. Lett.*, **30**, 104 (1977).
10. R. J. Kriegler, "Semiconductor Silicon," H. R. Huff and R. R. Burgess, Editors, p. 363, The Electrochemical Society Softbound Symposium Series, Princeton, N.J. (1973).
11. C. J. Frosch and L. Derick, *This Journal*, **104**, 547 (1957).
12. M. M. Atalla, E. Tannenbaum, and E. J. Scheibner, *Bell Syst. Tech. J.*, **38**, 749 (1959).
13. J. R. Ligenza and W. G. Spitzer, *Phys. Chem. Solids*, **14**, 131 (1960).
14. H. C. Evitts, H. W. Cooper, and S. S. Flaschen, *This Journal*, **111**, 688 (1964).
15. B. E. Deal and A. S. Grove, *J. Appl. Phys.*, **36**, 3770 (1965).
16. W. A. Pliskin, *IBM J. Res.*, **10**, 198 (1966).
17. R. M. McLouski, Paper No. 177 presented at the Fall Meeting of the Electrochemical Society, Chicago, Ill., Oct. 15-20, 1967.
18. B. E. Deal, D. W. Hess, J. D. Plummer, and C. P. Ho, *This Journal*, **125**, 339 (1978).

Thermal Oxidation of GaAs in Arsenic Trioxide Vapor

Hiromitsu Takagi, Gota Kano, and Iwao Teramoto*

Matsushita Electronics Corporation, Research Laboratory, Takatsuki, Osaka, Japan

ABSTRACT

A new technique for thermal oxidation of GaAs is proposed. The native oxide films composed of As_2O_3 are plus β-Ga_2O_3 thermally grown under controlled vapor pressures of arsenic trioxide. The breakdown strength of the films is found to be as high as 5-7 $\times$ 10^6 V/cm, which is comparable with the highest value ever obtained for anodic oxide films. The leakage current is also on such a low level that it is of the order of 10^{-8} A/cm^2 per 1000Å at an applied voltage of 10V. The chemical properties evaluated in terms of etching rates for various etchants exhibit satisfactorily stable and favorable characteristics for GaAs planar processes.

Increasing interest is being shown in the growth of native oxide films on GaAs with the required properties for device applications. However, two previous procedures for the oxidation, thermal (1, 2) and anodic (3-8), have not proved consistently successful in obtaining chemically stable films with satisfactory physical properties.

It empirically appeared to be plausible that the poor electrical characteristics inherent in thermal oxide films, though much more stable than anodic oxide films, might be due to the chemical composition lacking arsenic trioxide (As_2O_3).

On the basis of these considerations we propose a new technique for thermal oxidation of GaAs in the As_2O_3 vapor phase. The native oxide films grown under controlled vapor pressure of As_2O_3 have shown excel-

* Electrochemical Society Active Member.
Key words semiconductor, integrated circuits, etching, oxidation.

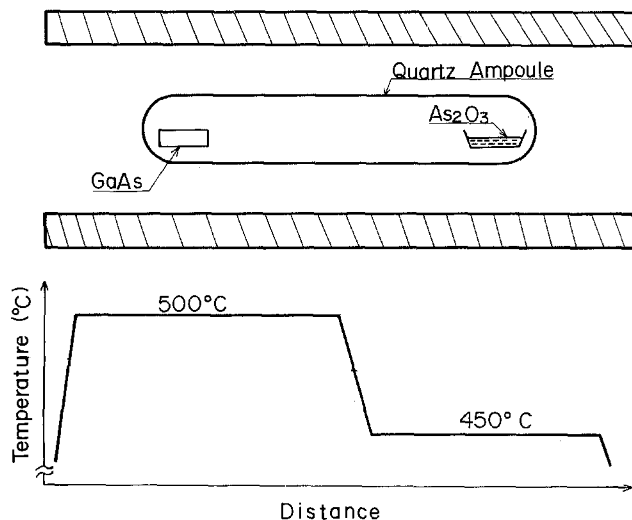

Fig. 1. Experimental setup for thermal oxidation in As_2O_3 vapor

lent properties in electrical characteristics as well as chemical stability.

Experimental Procedures

Figure 1 shows an experimental setup for the oxidation of GaAs crystals. A GaAs wafer to be oxidized is placed at one end of a quartz tube and high purity powder of As_2O_3 put into a platinum boat is placed at the other end. The quartz tube is then evacuated and placed into a double furnace which is regulated so that the GaAs wafer is maintained at an oxidation temperature (T_{OX}) while the As_2O_3 powder is at a lower temperature (T_{AO}) determining the vapor pressure in the system. The thermal equilibrium will be reached within 1 min. After the oxidation time the quartz ampul is quenched in water avoiding the As_2O_3 deposition on the oxide film. Wafers of Zn-doped p-type GaAs with a carrier concentration of 5 $\times$ 10^{16} cm^{-3} were used in the experiments. The (100) surfaces of the wafers to be oxidized were mechanochemically polished in an aqueous solution of NaOCl followed by chemical etching in a H_2SO_4:H_2O_2:H_2O (3:1:1) solution at 60°C for 10 min. The thermal oxidation was carried out at 500°C under an As_2O_3 vapor pressure of 700 mm Hg being in equilibrium with liquid As_2O_3 at 450°C.

Results and Discussions

In Fig. 2 an experimental result is shown of the relation between the oxide film thickness and the oxidation time. From the linearity observed up to about 1 μm thickness the oxidation rate is estimated to be

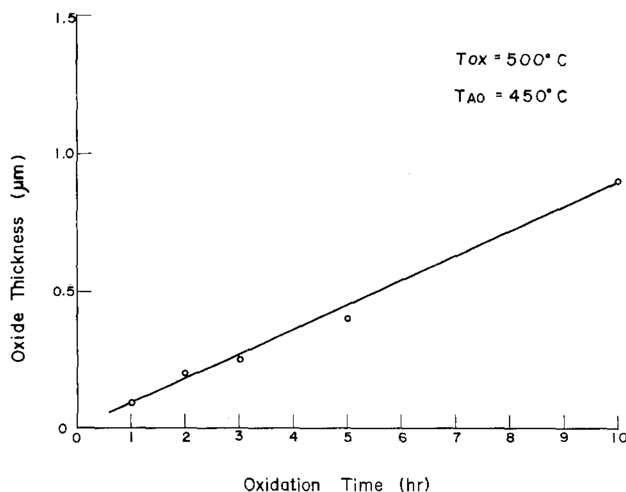

Fig. 2. Oxide film thickness vs. oxidation time

Fig. 3. Electron beam diffraction pattern of an oxide film. Film thickness is 3000Å.

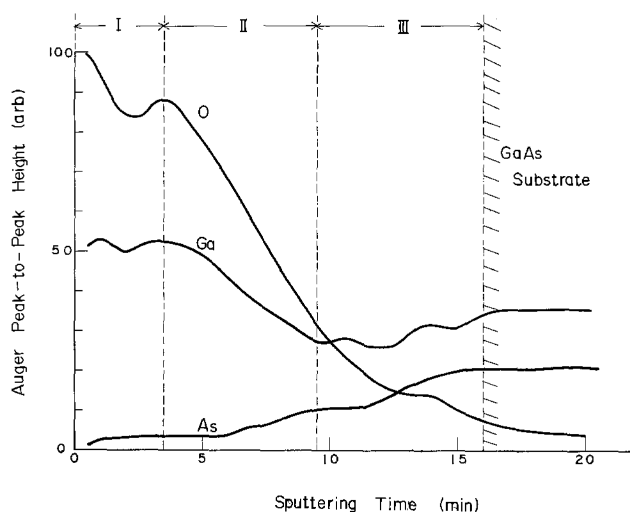

Fig. 4. Auger peak-to-peak height vs. sputtering time. Film thickness is 3000Å.

approximately 15 Å/min for T_{OX} = 500°C and T_{AO} = 450°C.

Figures 3 and 4 show an electron-beam diffraction pattern and a depth profile of the Auger peak-to-peak height, respectively, of an oxide film grown to a thickness of 3000Å. These figures apparently show that the dominant constituents of the film grown in the As_2O_3 vapor are represented by a quasibinary solid system As_2O_3-β-Ga_2O_3.

The composition profile along the film depth may be divided into three regions, I, II and III, as shown in Fig. 4. Within the top surface region I and the bottom interface region III, which are about 800 and 1200Å thick, respectively, the composition ratios of As_2O_3 to β-Ga_2O_3 can be regarded constant. The ratio in the intermediate region II which is about 1000Å thick, however, gradually decreases towards the substrate. This composition profile suggests that the oxidation process is diffusion limited in the solid oxide phase.

Electrical characteristics of the oxide films grown by the present technique were evaluated in terms of the breakdown strength and the leakage current. The aluminum evaporated dots with a 50 μm diameter were used for these measurements. In Fig. 5 the breakdown voltage and the breakdown strength are plotted as a function of the film thickness. The breakdown strength is as high as 5-7 $\times$ 10^6 V/cm, being comparable with the highest value ever obtained for the anodic oxide films. The leakage currents measured are of the order of 10^{-8} A/cm^2 per 1000Å thickness at an applied voltage of 10V.

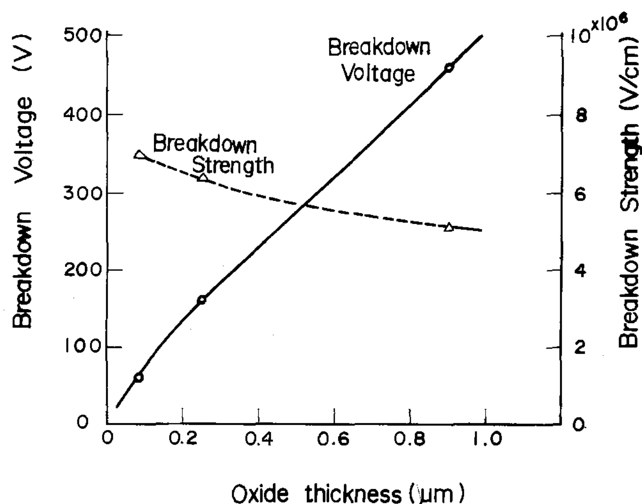

Fig. 5. Breakdown voltage and breakdown strength vs. oxide film thickness. Solid line and dashed line show breakdown voltage and breakdown strength, respectively.

The chemical properties of the films were also examined by measuring the etching rate for various etchants. In view of the results shown in Table I, it is expected that the conventional chemical technology for the silicon planar process is applicable to GaAs devices by using the present native oxide films.

Table I. Etching rates for various etchants (25°C)

Etchant	Etching rate (Å/min)
HCl (35%)	506
HCl (35%):H_2O = 1:1	227
HCl (35%):H_2O = 1:3	90
HF (46.5%)	179
HF (46.5%):H_2O = 1:1	108
HF (46.5%): H_2O = 1:5	52
H_3PO_4 (85%)	24

Summary

It has been shown that the GaAs native oxide films grown by the new thermal oxidation technique in the As_2O_3 vapor are composed of As_2O_3 and β-Ga_2O_3. Striking improvements in electrical and chemical characteristics of the films have been achieved. The present technology will be useful for the surface passivation and the planar integration of GaAs devices. Realization of GaAs MOSFET's is also expected.

Acknowledgments

The authors are grateful to Prof. J. Nakai of Osaka University and Dr. H. Mizuno of our research laboratory for valuable discussions and encouragements. Thanks are also due to Mr. S. Ichikawa of our research laboratory and Mr. M. Nakajima of the central research laboratory of Matsushita Electric Industrial Co., Ltd. for the electron beam diffractometry and the Auger spectroscopy, respectively.

Manuscript submitted Aug. 11, 1977; revised manuscript received Nov. 2, 1977.

Any discussion of this paper will appear in a Discussion Section to be published in the December 1978 JOURNAL. All discussions for the December 1978 Discussion Section should be submitted by Aug. 1, 1978.

Publication costs of this article were assisted by Matsushita Electronics Corporation.

REFERENCES

1. S. P. Murarka, *Appl. Phys. Lett.*, **26**, 180 (1975).
2. F. Koshiga and T. Sugano, "Digest of Technical Papers," The 8th Conference on Solid State Devices, Tokyo (1976).
3. S. M. Spitzer, B. Schwartz, and G. D. Weigle, *This Journal*, **122**, 397 (1975).
4. H. Hasegawa and H. L. Hartnagel, *ibid.*, **123**, 713 (1976).
5. H. Hasegawa, K. E. Forword, and H. L. Hartnagel, *Electron. Lett.*, **11**, 53 (1975).
6. H. Hasegawa, K. E. Forword, and H. L. Hartnagel, *Appl. Phys. Lett.*, **26**, 567 (1975).
7. D. L. Lile, A. R. Clawson, and D. A. Collins, *ibid.* **29**, 207 (1976).
8. A. Shimano, A. Moritani, and J. Nakai, Private communication.

Electroluminescence in an Epoxy Resin

R. Coïsson, C. Paracchini, and G. Schianchi

Istituto di Fisica dell'Università, Parma, Italy

ABSTRACT

Electroluminescence—which can be used as a probe for studying breakdown mechanisms—is studied in one type of epoxy resin at room temperature. The electroluminescence spectrum is compared with x-ray and ultraviolet radiation stimulated emissions. The behavior of luminescence bands with increasing applied voltage suggests that charge injection takes place and that the electroluminescence mechanism is that of impact ionization.

Several insulators with high dielectric strength exhibit a persistent electroluminescent emission at alternating fields some orders of magnitude lower than breakdown value. Such an effect has been observed both in crystalline (1) and amorphous materials (2). The emission appears localized near the metal-insulator interface, and it is probably caused by the same mechanisms that at higher fields trigger the breakdown (3). Under this point of view, electroluminescence can be used as a probe for studying the breakdown mechanisms and the effects intimately related to it.

In this work some results obtained from the study of the electroluminescence of one type of epoxy resin are reported. The interest in this kind of polymers in electrical applications has grown in the last years, mostly in view of their insulation properties (4). Nevertheless, it seems that the little knowledge of the phenomena leading to breakdown corresponds to the widespread electrical applications. Electroluminescence may give information on this subject (5).

The samples are thin foils (about 0.1 mm) of diglycidyl ether of bisphenol A (EPON 828, Shell), cured with triethylene tetramine (13 parts in weight every

100 parts of resin), prepared by a standard method in our laboratory. The measurements are performed at room temperature, under vacuum to avoid possible discharges in air. The electroluminescent effect appears with any alternating electric field of the order of 10^5 V/cm. Usually the samples are excited with square waves at a frequency of about 200 Hz. Electroluminescence spectra are recorded by measuring the signal, through a Hilger-Watts D.330 monochromator, with a trialkali photomultiplier (E.M.I. 9558 QA) and improving the signal-noise ratio by means of a Boxcar Integrator (PAR 160). The samples have on one side a contact indium or silver paint metal electrode, the other being insulated by means of a thin Teflon foil. In this way the possibilities of breakdown are greatly reduced without a great reduction of the applied field. For comparison, photoluminescence measurements at room temperature are also performed, exciting the emission either with soft x-rays (40 kV, 30 mA) or with u.v. radiation (60W deuterium lamp). The absorption spectrum of the resin is also recorded, by means of a Cary 15 spectrophotometer.

Figure 1 shows the luminescence spectra of the resin samples obtained with x-ray, electric, and u.v. stimulation (curves A, B, and C, respectively); the absorption spectrum (dotted curve) is also reported. The observed emission under x-ray excitation extends from ~500 to ~300 nm, with a maximum at about 325 nm; at shorter wavelengths, where the luminescence drops abruptly, the steep absorption edge is observed. If the luminescence is excited by electric field, the band extends approximately in the same spectral region, but its maximum is at about 340 nm. If the two spectra are normalized at 350 nm, the low energy sides of the two emissions nearly coincide. The same features are obtained with the spectrum of the luminescence excited by u.v. radiation; in this case the maximum intensity is at about 400 nm. The results reported in Fig. 1 suggest that the observed luminescence spectra are envelopes of several close bands, which are subsequently excited when the energy of the exciting source is increased. Moreover, it is also probable that the emission spectrum extends, at sufficient excitation energies, in the u.v. region beyond 300 nm, and that the self-absorption of the material is responsible for the drop on the short wavelength side.

Electroluminescence effects observed in high resistivity materials are usually attributed either to the alternate injection of carriers of opposite sign from the electrodes into the insulator (double injection) or to the impact excitation processes generated by one single type of carriers injected into the dielectric and accelerated by the high field region near the metal-insulator interface. If, in our case, different radiative recombinations are possible, each one excited at slightly different energy, one should expect, in the case of the impact excitation mechanism, a progressive shift of the spectrum toward the shorter wavelengths while the carrier energy, that is, the applied voltage, increases. On the contrary, it would be difficult to justify such a shift of the spectrum in the case of double injection mechanism, as an increase in the applied voltage would influence only the density of injected carriers, without affecting appreciably the recombination features.

On account of the low emitted light intensity, it would be difficult to notice this shift by directly comparing the spectra obtained under different voltage stimulation; it is easier to find the possible differences by comparing filtered emissions, as shown in Fig. 2. The light responses obtained simultaneously from two photomultipliers (say, A and B) are reported in arbitrary units, while the applied voltage is increased up to 2000V. In the case of curve 1 both photomultipliers receive the unfiltered emitted light: The straight line assures that their responses are proportional. In the case of curve 2 the light detected by the phototube B is filtered by a 400 nm cutoff filter: In this case the responses are no longer proportional, the signal of phototube B being progressively reduced with respect to the unfiltered situation. This result suggests that the electroluminescence emission is shifted toward shorter wavelengths when the applied voltage is increased and provides indirect evidence of an impact excitation mechanism. According to this model, Fig. 1 suggests that the energy of the accelerated injected carrier is intermediate between that of the u.v. and the X photons.

The above results suggest: (*i*) The luminescence of the resin is formed by several close bands extending from about 550 nm to the u.v. region; (*ii*) in the u.v. the emission is cut off due to self-absorption; (*iii*) by applying an electric field it is possible to inject carriers (presumably electrons) into the material; and (*iv*) the electric field generates impact excitation processes near the metal insulator interface, giving rise to luminescence.

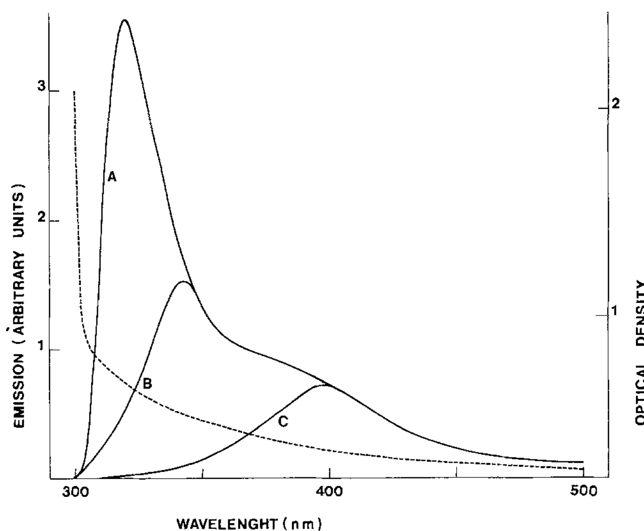

Fig. 1. Luminescence (full line) and absorption (dotted line) spectra at room temperature of a sample of diglycidyl ether of bisphenol A cured with triethylene tetramine. The three luminescence spectra indicated with A, B, and C refer to the light emissions obtained with x-rays, electric field, and u.v. stimulation, respectively.

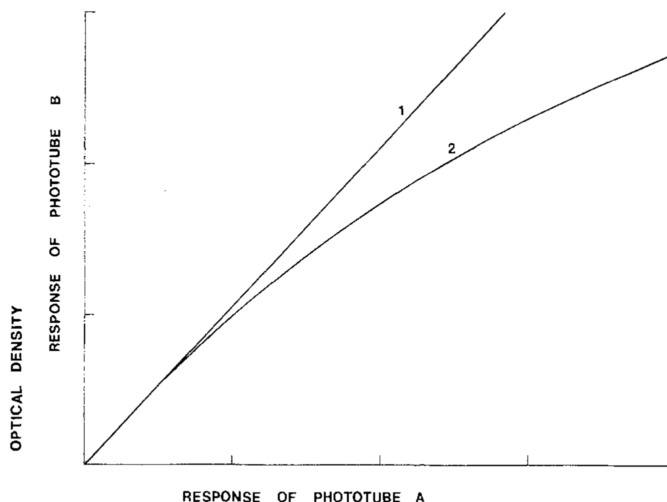

Fig. 2. The simultaneous responses of two phototubes (A and B) detecting luminescence are plotted one against the other. In the case of curve 1 both phototubes are unfiltered and their responses, when the applied voltage is increased, are proportional. In the case of curve 2 the light arriving at the phototube B is filtered through a filter cutting off at about 400 nm. On increasing the voltage, the signal of phototube B is progressively reduced with respect to that of A..

Acknowledgments

The authors are grateful to the Camattini Company (Parma, Italy) for having kindly supplied the material, to Dr. A. Sansoni for helpful discussions, and to Mr. C. Mora for technical collaboration. The "Gruppo Nazionale di Struttura della Materia," of C.N.R., Roma (Italy) has given financial support.

Manuscript submitted Sept. 26, 1977; revised manuscript received Nov. 16, 1977.

Any discussion of this paper will appear in a Discussion Section to be published in the December 1978 JOURNAL. All discussions for the December 1978 Discussion Section should be submitted by Aug. 1, 1978.

Publication costs of this article were assisted by the Università Degli Studi di Parma.

REFERENCES

1. C. Paracchini, *Phys. Rev.*, **B8**, 848 (1973); C. Paracchini and G. Schianchi, *Solid State Commun.*, **21**, 1107 (1977).
2. K. Kaneto, K. Yoshino, K. Kao, and Y. Inushi, *Jpn. J. Appl. Phys.*, **13**, 1023 (1974); W. A. Hartman and H. L. Armstrong, *J. Appl. Phys.*, **38**, 2393 (1967); H. Baessler, G. Vambel, K. Rasskopf, and K. Reinke, *Z. Naturforsch.*, **A26**, 814 (1971).
3. J. J. O'Dwyer, "The Theory of Electrical Conduction and Breakdown in Solid Dielectrics," pp. 234-235, Clarendon Press (1973).
4. T. W. Dakin, *IEEE Trans. Electrical Insulation*, **ei-9**, 121 (1974).
5. R. Lovell, *ibid.*, **ei-11**, 110 (1976).

Studies of X-Ray Image Intensifier Output Screens

J. S. Prener* and R. K. Swank

General Electric Corporate Research and Development, Schenectady, New York 12301

ABSTRACT

The performance of an x-ray image intensifier is governed by the properties of its four components: input phosphor screen, photocathode, electron optics, and output screen. P-20 output phosphor screens of various thicknesses were prepared by centrifugal settling and by electrophoretic deposition. In addition to the determination of screen density, we measured, as a function of accelerating voltage, screen brightness, MTF, and spatial noise due to screen graininess. Although there are claims in the literature regarding the superiority of electrophoretic screens, we found them to be no better than carefully deposited centrifugal screens.

An x-ray image intensifier (XRII) is a device for converting an incident x-ray pattern (as in medical radiology) to a visible light image. The brightness of the light image is considerably higher than that obtained with a simple fluoroscopic screen (1). The performance of an XRII is governed largely by the properties of its four major components (Fig. 1): the input phosphor screen, the photocathode, the electron optical system, and the output phosphor screen. For example, the resolution capability of an XRII is determined by the product of the modulation transfer functions (MTF's) of its components and the brightness of the visible image at a given x-ray flux, and operating voltage is determined by the conversion efficiencies of the input and output phosphor screens and the photocathode.

In XRII tubes the area of the light image is about one-hundredth that of the incident x-ray pattern in order that the image be transferred to a suitable receptor (eye, video pickup, cine film, etc) via optical lenses. Because of the reduced size of the optical image, the output screen must be capable of high resolution.

Various techniques have appeared in the literature for the preparation of output phosphor screens, each claiming to produce higher quality screens than those made by other methods.[1] In particular, claims have been made for the production of dense, fine-grained phosphor screens by electrophoresis having superior resolution, greater smoothness, and more uniform thickness and coverage when compared with screens made by the more common method of centrifugal or gravity settling of a phosphor (2-5). However, we could find in the same literature very little quantitative data relating screen density, MTF, and spatial noise (arising from screen graininess and thickness irregularities) to screen weight, electron accelerating potential, and methods of screen deposition. We describe in this paper our work on output phosphor screens in which we measured the density, MTF, and spatial noise of output screens of various weights per unit area, prepared by centrifugal settling and by electrophoresis as described by Varma and Ghosh (2).

Preparation of Screens

Centrifugal settling.—The screens were made using a fine-grained P-20 phosphor of 2.2μ median particle diameter.[2] A suitable weight of phosphor was suspended in 200 ml of a dilute aqueous solution of sodium bicarbonate and dispersed ultrasonically. It was then poured into a settling tank, shown in Fig. 2. During the settling, larger particles and agglomerates were

[2] Phosphor obtained from the General Electric Company, Chemical Products, Cleveland, Ohio.

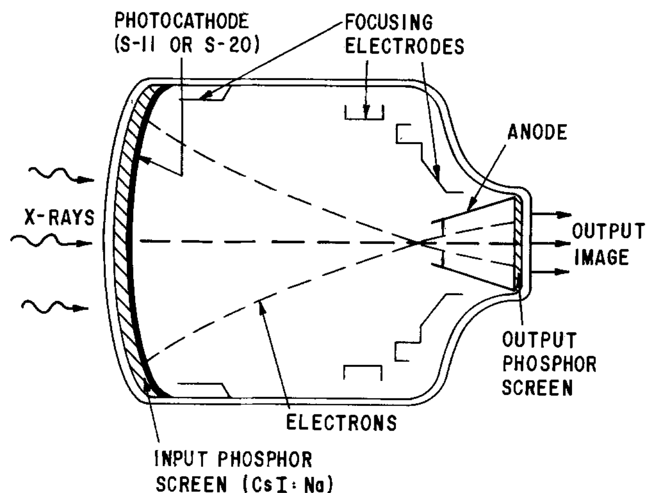

Fig. 1. X-ray image intensifier

* Electrochemical Society Active Member.

Key words: spatial noise, resolution, modulation transfer, phosphors.

[1] For a description of the various methods, see Ref. (1).

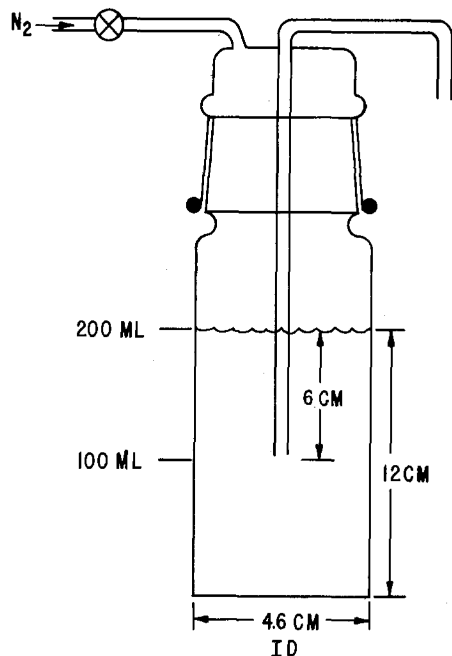

Fig. 2. Settling tank used in preparing phosphor suspensions for centrifugal deposition of screens.

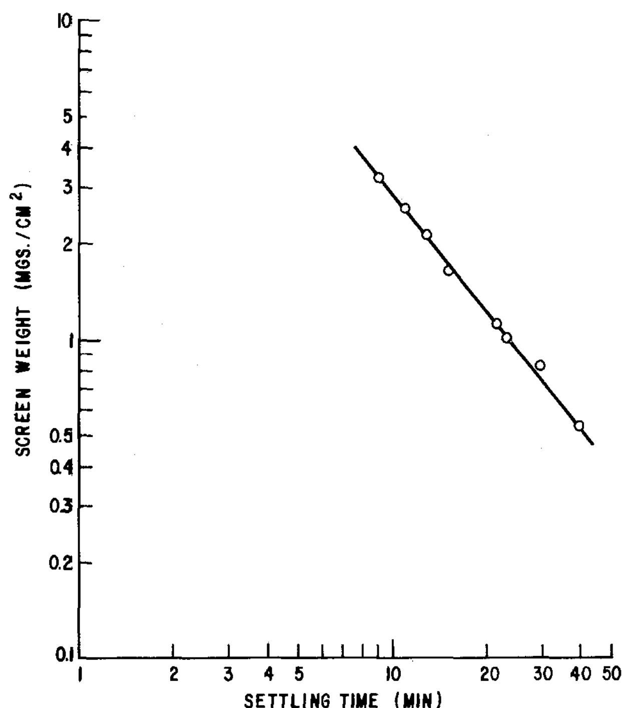

Fig. 3. Screen weight per unit area plotted as a function of settling time of phosphor suspension.

removed from the suspension. The final screen weight was determined by the settling time as indicated in Fig. 3. The top 100 ml were withdrawn after the required time, the potassium silicate binder added, and the suspension poured into two stainless steel cups containing the glass substrates. The phosphor was deposited by centrifuging for 15 min at 1000 rpm.

Electrophoretic deposition.—The method described by McGee *et al* (4) was used with the same P-20 phosphor. The system is shown in Fig. 4. The screen weight could be controlled by the time during which the potential was applied. Electrophoretic screens were found to be highly adherent, contrary to the statement made by Diakides (6). The good adherence is due to the increase in pH in the vicinity of the cathode and the consequent deposition of lanthanum and aluminum hydroxides at the cathode along with the

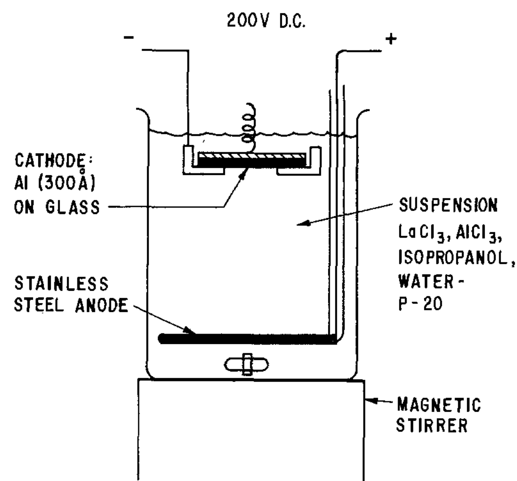

Fig. 4. Electrophoretic deposition system

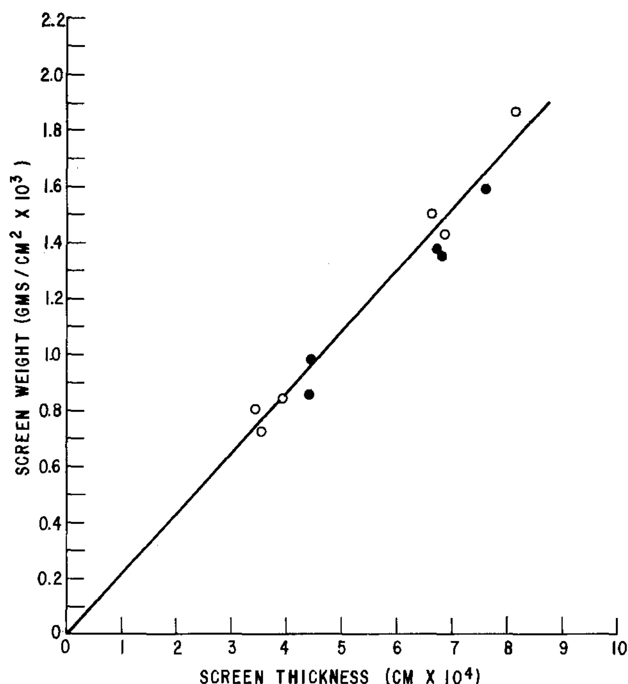

Fig. 5. Screen weight plotted against mean screen thickness. The slope of the line gives the screen density in g/cm^3. ○ Centrifugally deposited screens, ● electrophoretically deposited screens.

electrophoretically deposited phosphor. These hydroxides apparently act as cementing agents for the phosphor particle.[3] We did note, however, that there were pinholes in the phosphor screen which could be traced to pinholes in the evaporated aluminum layer.

Measurements and Results

Screen density.—The screen weight per unit area was determined by weighing. The screens were then covered with about 1000Å of Al and the mean thickness determined using a Sloan Dektak surface profilimeter. The thick Al coating prevented damage to the phosphor surface by the profilimeter probe. The results are given in Fig. 5. There appears to be no significant difference in density between our centrifugally deposited screens and those prepared by electrophoresis. The least squares fit to the data points yields a screen density of 2.17 g/cm^3, which is one-half the density of the P-20 phosphor crystals. This value of 50% in packing density is typical of phosphor screens.

Modulation transfer function.—Spatial resolution of imaging systems is usually described by the modulation transfer function. This function gives the relative

[3] See also Ref. (4) for a similar effect with magnesium salts.

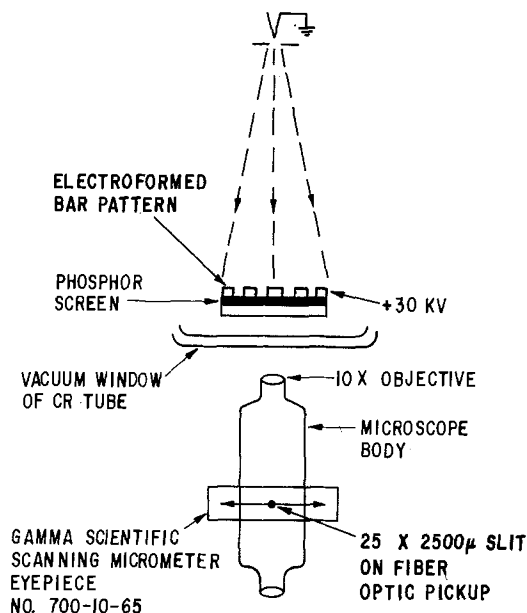

Fig. 6. Experimental arrangement used for measuring MTF

frequency response of the system to a sinusoidal spatially modulated input pattern. The limiting resolution of a system is commonly taken to occur at an MTF value of 0.05. The ideal output screen should have a high MTF value at a spatial frequency corresponding to the resolution of the XRII tube. Since this is typically near four line-pairs per millimeter at the input plane of the system, the 10-fold reduction in image diameter at the output phosphor required that we measure MTF at spatial frequencies to at least 40 line-pairs per millimeter (lp/mm).

The method used for the MTF measurements under cathode-ray excitation is illustrated in Fig. 6. An electroformed square wave nickel bar pattern was placed to within 25 μm of the phosphor surface.[4] The bar pattern consisted of seven line-pairs (*i.e.*, bar and space) each at spatial frequencies of 10, 20, and 40 lp/mm. In actual fact, what we label MTF in this paper is determined from the square wave response. The sine wave response would yield somewhat lower values but our data do not extend to high frequencies so as to permit the conversion. For purposes of comparison between screens the square wave response suffices. The emitted light from the phosphor was detected by scanning with a 25 μm wide slit on a fiber optic pickup located in the image plane of a 10-power objective.[5] A typical emitted light pattern as recorded on an X-Y recorder is shown in Fig. 7.[6] The MTF at any of the three frequencies was calculated from

$$\mathrm{MTF}_{(\text{output screen})} = \frac{1}{\mathrm{MTF}_{(\text{optical system})}} \times \frac{(S_{\max} - S_{\min})}{(S_{\max} + S_{\min})}$$

where $S_{\max}$ and $S_{\min}$ are the average of the five central maximum and minimum signals. The MTF of the optical system was determined by putting a piece of opal glass illuminated by a tungsten lamp in contact with the back side of the bar pattern. The microscope was then focused on the bar pattern and the square wave response recorded as above. The MTF of the optical system was found to be 0.899, 0.895, and 0.837 at

[4] To avoid charging under electron excitation the phosphors were coated in the standard manner with a thin nitrocellulose film and then with 800Å of Al. The organic film was then removed by baking in air at 350°C.

[5] The scanning microscope eyepiece was a Gamma Scientific Model No. 700-10-65 which has a 25 × 2500 μm slit. It was used with a Gamma Scientific Photometric Microscope System which consisted of a photomultiplier and photometer. The output signal was recorded on an X-Y recorder.

[6] The spacing variation particularly obvious at 10 lp/mm is not due to the bar pattern but arises from the nonlinearity of the scanning eyepiece output voltage with sweep distance. The variation is of no consequence as far as MTF measurements are concerned.

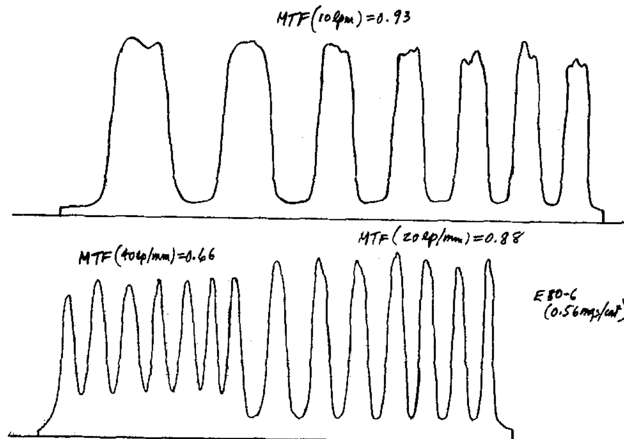

Fig. 7. Recorder trace of emitted light pattern in MTF measurement. Centrifugally deposited screen (0.56 mg/cm²); 30 kV.

the three frequencies. The results as obtained with a number of screens are shown in Fig. 8. For the range of screen weights investigated, the MTF decreases linearly with screen weight. Again we found no difference between the electrophoretic and settled screens.

The accelerating voltage dependence of the MTF is illustrated in Fig. 9. At lower voltages the MTF improves somewhat for thinner screens. The effect may be due to the decreasing range of the scattered electrons with decreasing electron energy. For the thick

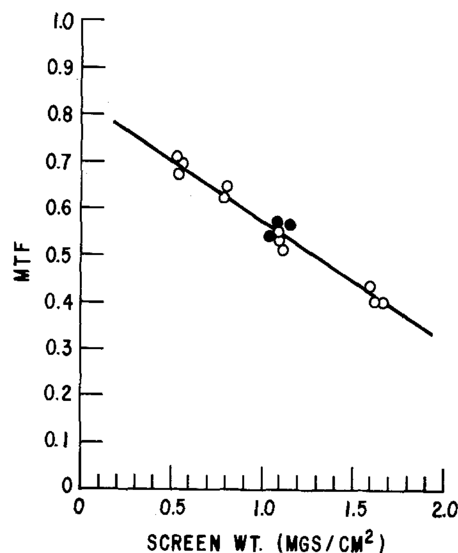

Fig. 8. MTF (at 40 lp/mm) plotted against screen weight. Accelerating potential 30 kV. ○ Centrifugally deposited screens, ● electrophoretically deposited screens.

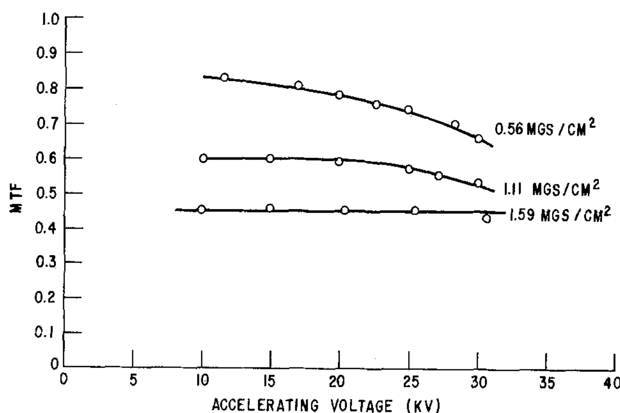

Fig. 9. Accelerating voltage dependence of MTF at 40 lp/mm. Centrifugally deposited screens.

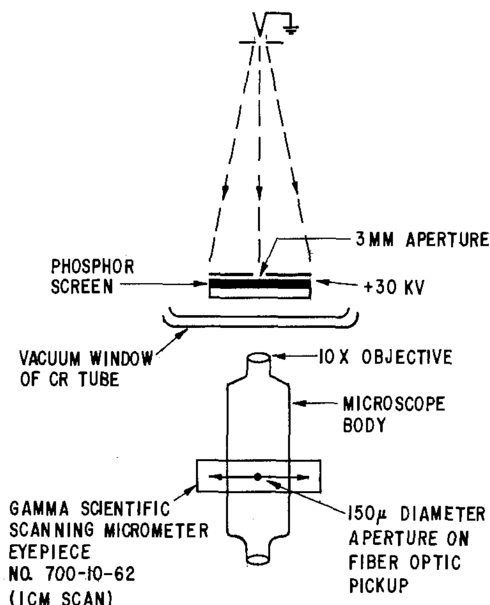

Fig. 10. Experimental arrangement for measuring spatial noise

screens no such dependence is seen since the low MTF value is determined primarily by light-scattering effects.

Spatial noise.—Spatial noise in the light image arises from the granular nature of the screen and from irregularities in thickness of screens so that electron penetration can take place at the thin spots. Presumably the "smoother" electrophoretic screens reported in the literature would have less spatial noise. The measurements were carried out as indicated in Fig. 10. The equipment was similar to that used in the MTF measurements. The bar pattern was replaced by a 3 mm aperture and the slit on the fiber optic pickup replaced by a 150μ diameter hole.[7] The Al-coated output screens were flooded by electrons and we scanned four separate 0.8 mm long sections of each screen. The 150μ aperture located at the image plane of a 10× objective corresponds to 67 lp/mm at the output screen. A typical trace of the emitted light is shown in Fig. 11. The ratio of the rms to the d-c value of the emitted light was taken as a measure of the spatial noise of a screen. The illumination of the screen by the electron beam was not perfectly uniform over the measured surface. As seen in Fig. 11 the light level is generally lower on the right than on the left and there is some bowing of the curves in the middle. It was, therefore, necessary to perform a Fourier analysis of the emitted waveforms in order to remove the very low spatial frequency components of the emitted light before determining the rms/d-c ratio.

Each trace as shown in Fig. 11 was sampled and digitized at 160 points. The result was attenuated by a half-sine wave over the initial and final 16 points so that the end points were brought smoothly to zero. This is necessary in order to reduce spurious high frequencies introduced when periodic boundary conditions are brought about by the discrete Fourier transform. The number of data points was increased to 256 by adding zeros, in order that a fast Fourier transform program could be utilized. After transformation, the spectrum was filtered by a sharp-cut filter to remove frequencies corresponding to less than about four full waves across the scans shown in Fig. 11. The spectrum was then retransformed, so that the filtered waveform could be compared to the original. When laid one over the other, the only difference visible to the eye was the removal of the base line tilt and curvature and the end attenuation referred to above. The rms noise value was

[7] Gamma Scientific scanning microscope eyepiece, Model No. 700-10-62. The output voltage of this eyepiece was linear with sweep distance.

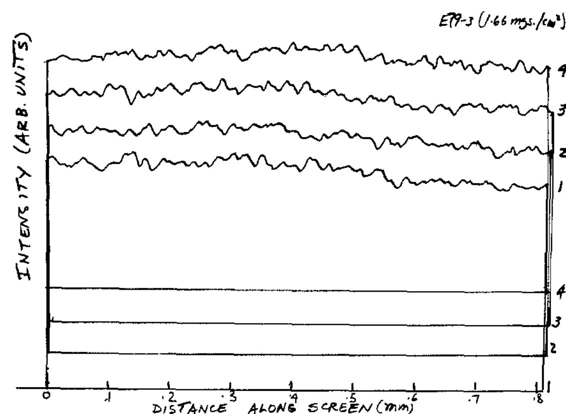

Fig. 11. Recorder trace of emitted light pattern in noise measurement. Centrifugally deposited screen (1.66 mg/cm^2); 30 kV.

computed from the area under a plot of the square of the filtered Fourier spectrum (Wiener spectrum). The results of four independent traces were measured and averaged for each observation point.

The results of our spatial noise measurements at 30 kV are given in Fig. 12. The spatial noise is seen to decrease linearly with increasing screen weight up to about 1.2 mg/cm^2. At 1.6 mg/cm^2 the spatial noise was not much lower. The reason for the knee in the curve is seen from the data on the dependence of emission intensity with accelerating voltage, as shown in Fig. 13. Screens with thicknesses of 1.6 mg/cm^2 were sufficiently thick so that electron penetration did not occur whereas thinner screens exhibited such penetration below 30 kV. Thus the noise in thin screens appears to arise primarily from electron penetration due to local variations in screen thickness. For thicker screens the spatial noise arises from light-scattering effects due to the granular structure of the screen. We also note that there is no significant difference between settled and electrophoretic screens. It appears that electrophoretic screens are not "smoother" than settled screens.

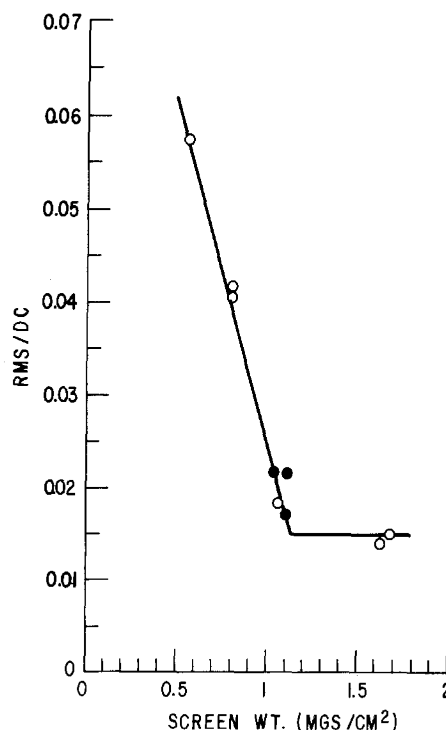

Fig. 12. RMS/D-C values of spatial noise plotted against screen weight. Accelerating potential 30 kV. ○ Centrifugally deposited screens, ● electrophoretically deposited screens.

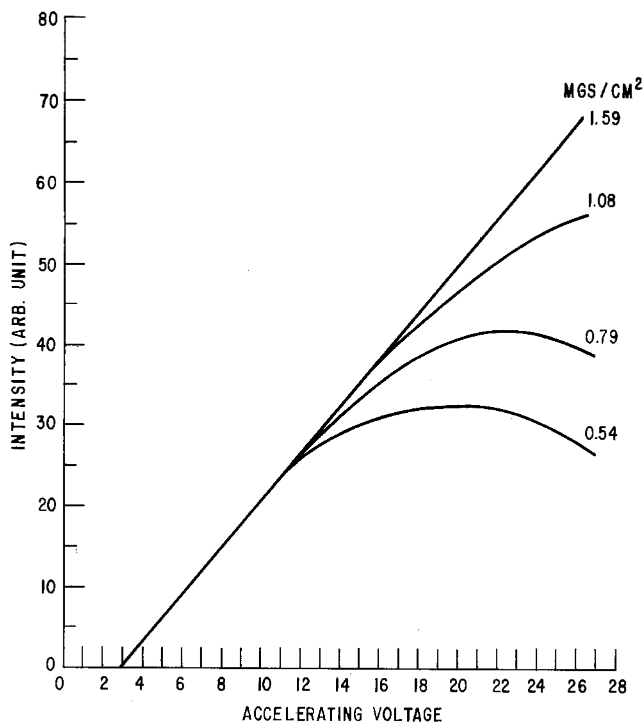

Fig. 13. Light emission plotted as a function of accelerating potential for various screen weights. Centrifugally deposited phosphors.

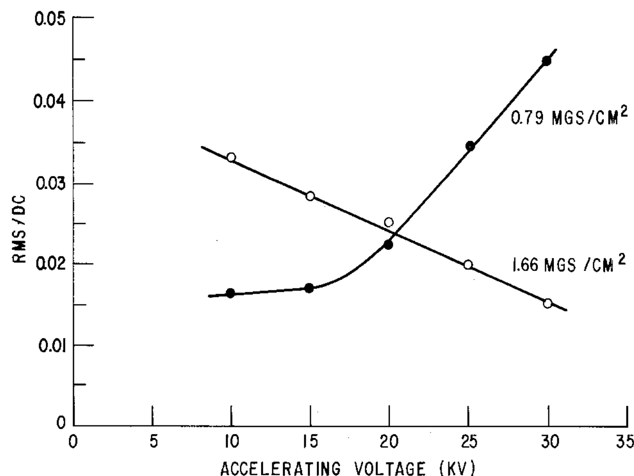

Fig. 14. Accelerating voltage dependence of spatial noise for two different centrifugally deposited screens.

The voltage dependence of spatial noise is shown in Fig. 14 for a thick and a thin screen. With decreasing electron energy the noise of the thin screen decreases since there are fewer thin regions available for electron penetration. At 10 kV the spatial noise of the thin screen is about as low as that of the thick screen at 30 kV. For the thick screen, however, we see that the noise increases with decreasing electron energy. We do not understand this result but it must be related to complex light-scattering effects arising from the fact that electron excitation occurs in thinner sections of the screen at low accelerating potentials.

Summary

Electrophoretically deposited screens appear to have the same density, MTF, and spatial noise as carefully prepared centrifugally deposited screens. Since electrophoretic deposition presents certain difficulties with regard to pinholes, there seems to be no advantage in this method of deposition.

P-20 screens of about 1.1 mg/cm² have high gain, low noise, and MTF values near 0.55 at 40 lp/mm. Higher MTF values can be achieved with thinner screens if the decreased brightness and increased spatial noise do not lead to objectionable image quality.

Manuscript submitted Oct. 3, 1977; revised manuscript received Nov. 7, 1977. This was Paper 147 presented at the Philadelphia, Pennsylvania, Meeting of the Society, May 8-13, 1977.

Any discussion of this paper will appear in a Discussion Section to be published in the December 1978 JOURNAL. All discussions for the December 1978 Discussion Section should be submitted by Aug. 1, 1978.

Publication costs of this article were assisted by General Electric Corporate Research and Development.

REFERENCES

1. K. G. Vosburgh, R. K. Swank, and J. M. Houston, *Adv. Electron. Electron Phys.*, **43**, 205 (1977).
2. B. P. Varma and G. Ghosh, *Indian J. Pure Appl. Phys.*, **12**, 670 (1974).
3. P. F. Grosso, R. E. Rutherford, Jr., and D. E. Sargent, *This Journal*, **117**, 1456 (1970).
4. J. D. McGee, R. W. Airy, and M. Aslam, *Adv. Electron. Electron Phys.*, **22A**, 571 (1966).
5. K. Franz, G. Kochmann, and R. Lohmann, *ibid.*, **33A**, 483 (1972).
6. N. A. Diakides, *Proc. Soc. Photo-Opt. Instrum. Eng.*, **42**, 82 (1974).

Ce^{3+} Luminescence in Hexagonal Aluminates Containing Large Divalent or Trivalent Cations

A. L. N. Stevels

Philips Research Laboratories, Eindhoven, The Netherlands

ABSTRACT

By analogy with earlier studies on Eu^{2+} phosphors the luminescence of the Ce^{3+}-doped hexagonal aluminates, containing large divalent or trivalent cations, was also studied in relation to the crystal structure of the host lattices. The u.v. band ascribed to the luminescence of Ce^{3+} ions is found at a relatively short wavelength in the magnetoplumbites Ca-, Sr-, and CaMg aluminate: Ce and at a relatively long wavelength in the β-aluminas Ba- and BaMg aluminate. The distorted magnetoplumbites which include La- and LaMg aluminate and Ce- and CeMg aluminates themselves occupy an intermediate position in between the above-mentioned groups. The existence of various types of host lattices is also reflected in the shape and position of the excitation spectra of the Ce^{3+} luminescence. Differences in bond strength between Ce^{3+} ions and its surrounding oxygen ions, however, complicate the discussion of the position of the excited 5d levels of the Ce^{3+} ion. Apart from the u.v. band, a blue luminescence band was found in several Ce-activated aluminates. This band occurs in phosphors where oxygen ions are thought to have partially replaced the large cations of the host lattice and is ascribed to Ce-O associates. Next to direct excitation of these centers, the u.v.-emitting Ce^{3+} ions transfer part of their energy of the associates. If Mg^{2+} ions are present in the lattice, the oxygen ions at large cation sites seem to be "screened" and no blue luminescence is found. The quantum efficiency of most Ce-activated aluminate phosphors is 50-70%. Due to ineffective mutual energy transfer between u.v. emitting Ce^{3+} ions and between Ce-O associates no concentration quenching occurs in the systems considered. For the same reason the influence of the preparation method on the luminescence properties is generally less drastic than that of the corresponding Eu^{2+} phosphors.

The hexagonal aluminates can be divided into three groups with different, but closely related, crystal structures (1). The compounds $MeAl_{12}O_{19}$ (Me = Ca, Sr, Eu) have the magnetoplumbite-type structure (Fig. 1A). To this group also belong Mg-substituted Ca aluminates. Phases with the β-alumina structure (Fig. 1B) include $MeMgAl_{10}O_{17}$ (Me = Sr, Ba, Eu) types and also Ba aluminate itself.

$LaMgA_{11}O_{19}$ and $CeMgAl_{11}O_{19}$ belong to the group of distorted magnetoplumbites. The essential difference from magnetoplumbites is that in the distorted type part of the La(Ce) ions are thought to be replaced by oxygen ions (2). We designate such ions as O_{Me}. In β-aluminas the presence of O_{Me} has been established by an x-ray diffraction study on single crystals (1). Up to now we were not successful in obtaining single crystals from distorted magnetoplumbite-type materials. However, their nonstoichiometry and the occurrence of red Mn luminescence (2) strongly suggest the presence of O_{Me}. In La(Ce) aluminate itself 10-15% of the trivalent ions seems to be replaced by oxygen ions; in Mg-containing phases the percentage O_{Me} is between 5 and 10. As is shown in Fig. 1C the positioning of oxygen ions at La(Ce) sites would also involve a local rearrangement of Al^{3+} ions.

The Eu^{2+} luminescence in hexagonal aluminates containing large di- or trivalent cations has been studied extensively (1-7). Since the Ce^{3+} luminescence in these lattices has many aspects similar to the Eu^{2+} case, we give here a short survey of the properties of Eu^{2+} phosphors as far as these are relevant for the discussion of the Ce^{3+} luminescence.

In magnetoplumbite host lattices the Eu^{2+} luminescence is at a relatively short wavelength, that is in the blue and near u.v. In β-aluminas we find this band at a relatively long wavelength, namely in the blue or blue-green. The La(Mg) aluminates doped with Eu^{2+} take up an intermediate position in this respect. The existence of various types of host lattice is also reflected in the shape and the position of the excitation spectra of the Eu^{2+} luminescence (1). The quantum efficiency of the Eu^{2+} phosphors was found in most cases to be high. However, in magnetoplumbites the luminescence is quenched by substitution of small amounts of Mg^{2+} for Al^{3+} ions (6). Most probably oxygen vacancies are involved in the quenching processes. In distorted magnetoplumbites and β-aluminas the replacement of Al^{3+} by Mg^{2+} rather increases than decreases the efficiency of the phosphor (2, 7).

It was found that in β-aluminas the oxygen ions occurring at large cation sites can form associates with Eu ions, resulting in green-emitting centers. This green luminescence is strong in β-aluminas containing no Mg, that is in Ba aluminates (7). It can be argued that Mg^{2+} ions screen the Eu and O_{Me} ions from each other and thus prevent the formation of green-emitting centers.

Let us now consider the organization of the present paper on the Ce^{3+}-luminescence. First, the Ce^{3+} luminescence in the magnetoplumbites Ca-CaMg and Sr-aluminates is discussed. This group of phosphors shows features similar to the Eu^{2+} luminescence in these systems. To some extent this also holds for Ce^{3+} luminescence in β-aluminas. In the last named phases the solubility of Ce is only limited due to a preference of Ce^{3+} ions for magnetoplumbite surroundings. This hampers detailed studies, especially of the luminescence of Ce-O_{Me} complexes.

A further subject is the luminescence of the $(La,Ce)_{0.86}Al_{11.90}O_{19.14}$ series. These show a basic difference from the comparable La, Eu system since the u.v.-emitting Ce^{3+} ions can transfer effectively their excitation energy to the Ce-O_{Me} associates, whereas such a transfer from the "blue" Eu^{2+} ion to the "green" Eu-O_{Me} complex has only a low probability.

In the Ce aluminate/CeMg aluminate system it is demonstrated how the introduction of Mg^{2+} ions reduces the intensity of the blue band ascribed to the Ce-O_{Me} associates.

Key words: hexagonal aluminates, Ce^{3+} luminescence, energy transfer.

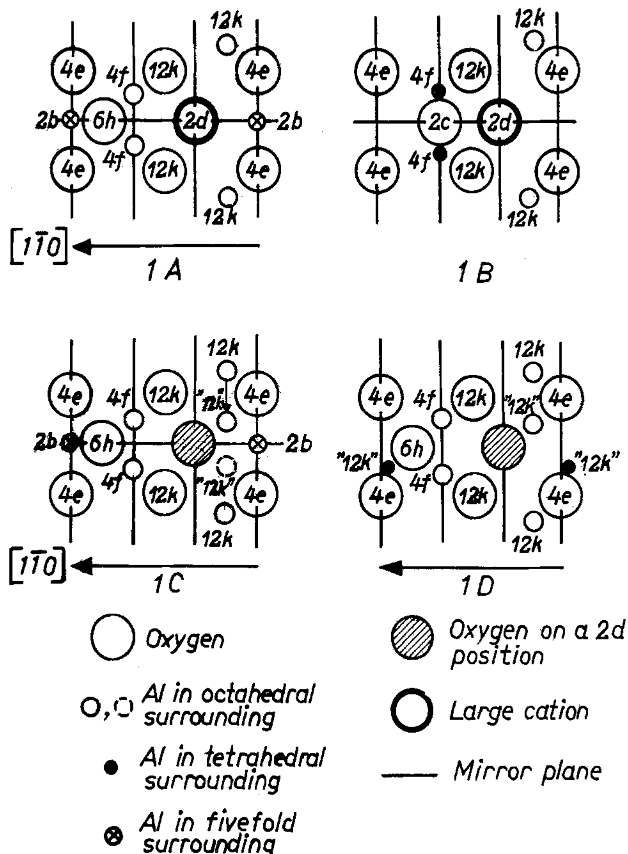

Fig. 1. Part of the unit cells of hexagonal aluminates. Only atoms in the [1$\bar{1}$0] plane have been drawn. A, the magnetoplumbite configuration; B, the β-alumina-type configuration; C, the configuration around oxygen ions replacing the large cation in the A type. The arrow indicates the shift of Al ions to one of the octahedral "12k" sites near the oxygen ion in the 2d position. The dashed "12k" site is available for excess Al^{3+} ions (see text); D, the configuration around oxygen ions replacing the large cation in magnetoplumbites (A type) containing small divalent cations (Mg^{2+}, Mn^{2+}). For the Al ions originating from the 2b site only half of octahedral "12k" sites near the oxygen ion are available. The divalent ions are located at tetrahedral "12k" sites.

The excitation spectra of the luminescence of Ce^{3+} ions are discussed in this paper. They show three (and sometimes more) bands between 220 and 320 nm. In contradistinction to the corresponding Eu^{2+} phosphors, the position of the center of gravity of the excited 5d levels is dependent on the host lattice. This can be correlated with the Stokes shift between the lowest excitation band and the emission band.

Our last subject is the discussion of the quantum efficiencies of Ce^{3+}-activated aluminates. Recent estimates (8) indicate that the energy transfer between Ce^{3+} ions is ineffective; the absence of concentration quenching in the systems considered confirms this opinion. The ineffective energy transfer in the Ce^{3+}-activated phosphors has the effect that in such materials the quenching of the luminescence by unintentionally introduced defects is generally less drastic than in the corresponding Eu^{2+} phosphors in which the Eu^{2+}-Eu^{2+} transfer efficiency was observed to be high.

Experimental

The samples were prepared by standard ceramic techniques (firing temperatures between 1200° and 1600°) from highly reactive γ-Al_2O_3, $MeCO_3$ (Me = Ca,Sr,Ba), or La_2O_3. The Ce ions were introduced in the form of CeO_2; by heating in N_2 containing a few percent H_2 these are reduced to their trivalent state. X-ray diffraction showed that only samples heated above 1400°-1450°C were free of $CeAlO_3$. The luminescence measurements were carried out as described in Ref. (9).

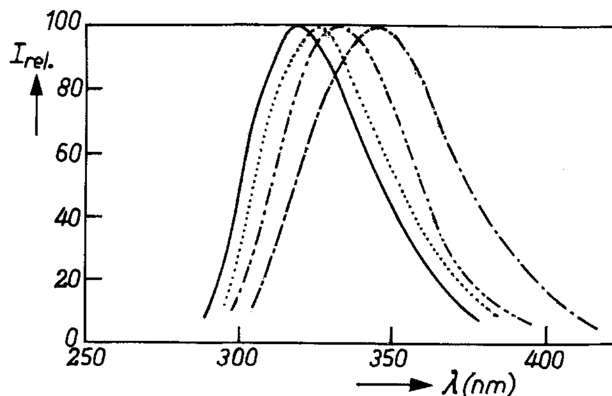

Fig. 2. Luminescence spectrum at 300°K (under 250-270 nm excitation) of the magnetoplumbites $SrAl_{12}O_{19}$: $0.14Ce^{3+}$ (———); $CaAl_{12}O_{19}$:$0.14Ce^{3+}$ (.....); $CaMgAl_{11.33}O_{19}$:$0.14Ce^{3+}$ (··—··—··—); and $La_{0.92}MgAl_{11.13}O_{19.08}$:$0.14 Ce^{3+}$ (—·—·—·).

Results and Discussion

Luminescence spectra.—Ce^{3+}-doped magnetoplumbites.—In Fig. 2 we show the luminescence spectra at 300°K of Ce^{3+}-doped magnetoplumbites and of the distorted magnetoplumbite $LaMgAl_{11}O_{19}$:Ce. The wavelengths of the maxima of the band are summarized in Table I where the maxima of the corresponding Eu^{2+} phosphors, see Ref. (1), have also been given. The curves in Fig. 2 and the data in Table I refer to samples containing 0.14 Ce. The well-known "two-band" character of the Ce band, due to the splitting of the ground state, is not clearly observed at these activator contents. In samples containing 0.02 Ce the two components of the luminescence band are better resolved.

On inspection of Table I it is seen that a striking analogy exists between Ce^{3+} and Eu^{2+}-activated aluminate phosphors. In the u.v.-emitting Ce^{3+} phosphors, $SrAl_{12}O_{19}$:Ce peaks at the shortest wavelength, 320 nm. Similarly $SrAl_{12}O_{19}$:Eu is the nearest u.v. one of the blue-emitting Eu^{2+} phosphors. Its maximum is at 395 nm. The order of peak wavelengths in the other Ce^{3+}-activated phosphors is the same as in the Eu^{2+}-activated materials. For sake of clarity, the spectrum of La aluminate has been omitted in Fig. 2. As is described later, this phosphor also has a strong luminescence band in the blue. However this band is not ascribed to the luminescence of "normal" Ce^{3+} ions but to the luminescence of Ce ion at a very short distance from oxygen ions. In $SrAl_{12}O_{19}$:Ce this blue band was observed to be present only in samples prepared with excess Al_2O_3 (see Fig. 3). If we consider, for instance, the phosphor $Sr_{0.85}Ce_{0.15}Al_{11.95}O_{19}$, O_{Sr} ions can be thought to be formed in the following

Table I. Maximum of the luminescence band, λ_{max} and quantum efficiency q.e. of aluminate:Ce^{3+} phosphors at 300°K. Within brackets the data are given for the corresponding phosphors activated with 2% Eu^{2+}

	λ_{max} (nm)	q.e. (250-270 nm excitation) %
Magnetoplumbites		
$CaAl_{12}O_{19}$:0.14Ce	325 (410)	50 (50)
$SrAl_{12}O_{19}$:0.14Ce	320 (395)	70 (55)
$CaMgAl_{11.33}O_{19}$:0.14Ce	330 (425)	50 (40)
β-aluminas		
$BaAl_{10\ 2/3}O_{17}$:0.14Ce	350 (440)	50 (70)
$BaMgAl_{10}O_{17}$:0.14Ce	365 (450)	60 (70)
Distorted magnetoplumbites		
$Ce_{0.86}Al_{11.90}O_{19.14}$	430 (—)	60 (—)
$La_{0.86}Al_{11.90}O_{19.14}$:0.14Ce	330 (435)	55 (50)
$Ce_{0.92}MgAl_{11.13}O_{19.08}$	340 (—)	60 (—)
$La_{0.92}MgAl_{11.13}O_{19.08}$:0.14Ce	345 (450)	60 (60)

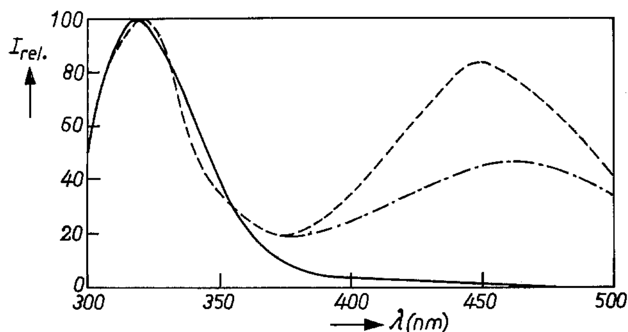

Fig. 3. Luminescence spectrum at 300°K (under 250-270 nm excitation) of $Sr_{0.85}Ce_{0.15}Al_{11.95}O_{19}$ (———); $Sr_{0.72}Al_{12.75}O_{19.14}$ (— — —); and $Sr_{0.64}Ce_{0.11}Al_{12.30}O_{19.25}$ (—·—·—·).

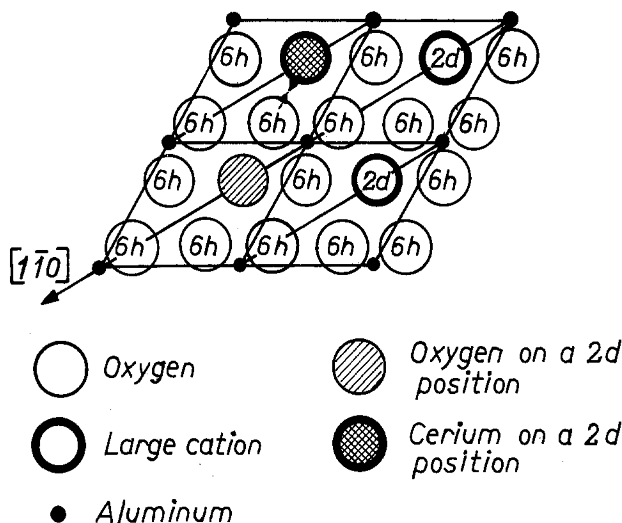

Fig. 4. xy plane at $z = \frac{1}{4}$ of the magnetoplumbite structure. Four unit cells are shown. In the lower left-hand cell an oxygen ion has replaced the large cation at the 2d site. The arrow indicates the interaction of an oxygen atom at a 6h site with an activator ion.

way

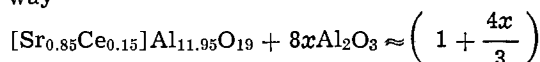

$$[Sr_{0.85}Ce_{0.15}]Al_{11.95}O_{19} + 8xAl_2O_3 \approx \left(1 + \frac{4x}{3}\right)$$

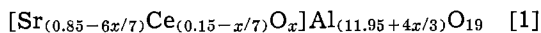

$$[Sr_{(0.85-6x/7)}Ce_{(0.15-x/7)}O_x]Al_{(11.95+4x/3)}O_{19} \quad [1]$$

(approximate formulas are given).

It was found that up to $x \approx 0.15$ the percentage of blue emission increases with x (that is the number of oxygen ions at Sr sites) so that it is most probable that the extra luminescence band is due to strong interaction of O_{Sr} with Ce ions.

As is seen in Fig. 4, this interaction is thought to proceed in an "indirect" way in the case of magnetoplumbites like Sr-aluminate. In fact, the presence of oxygen ions at 2d sites is supposed to induce a shift of one of its nearby oxygen (6h) ions toward a Ce^{3+} ion[1] in a neighboring unit cell, see also Fig. 1A.

Returning now to Eq. [1] and Fig. 3 we see that above $x \approx 0.15$ the relative intensity of the blue band decreases again, see Fig. 3, dash-dot line. In order to explain this observation, we note that in order to stabilize O-Ce complexes in "ideal" magnetoplumbites like $SrAl_{12}O_{19}$, Al ions at octahedral 12k sites in the crystal structure are supposed to shift to octahedral "12k" sites near O_{Sr}, see arrow in Fig. 1C and also Ref. (7). The Al^{3+} ions in excess of the "ideal" number of 12 per unit cell are most probably located at the 12k positions which are emptied by such a shift. With help of formula [1] it can be seen that above $x \approx 0.15$ the number of excess Al^{3+} ions ($=4x/3 - 0.05$) exceeds the number of shifted octahedral Al^{3+} ions ($=x$). This has the result that part of these excess ions will be located at "12k" sites as well, for instance, at the one indicated by the dashed circle in Fig. 1C. Apparently the presence of two Al^{3+} ions near O_{Me} screens the interaction with Ce ions so that a lower number of O-Ce associates results.

In Ce-activated Ca and CaMg aluminates no blue luminescence was observed in samples with excess Al_2O_3. This corroborates our earlier observation that in these compounds no O_{Ca} can be formed (2), or that the O_{Ca} formed are effectively screened from activator ions.

β-Alumina-type:Ce phosphors.—Figure 5 shows the luminescence spectra at 300°K of the Ce-doped β-aluminas $BaAl_{10\,2/3}O_{17}$, $BaMgAl_{11}O_{17}$, and $KAl_{11}O_{17}$. In all cases, very broad bands around 350 nm were found. The "two-band" character due to splitting of the Ce^{3+} ground state is clearly recognized. From Table I it is concluded that the maxima of the bands are situated at longer wavelengths than for magnetoplumbite:Ce phosphors. On comparing the emission maxima with those of Eu^{2+} phosphors we see, as in the magnetoplumbites, a parallel change of the peak positions on going from one host lattice to another.

The solubility of Ce^{3+} in β-aluminas was found to be only limited. Apparently Ce^{3+} ions prefer to enter magnetoplumbite surroundings rather than a β-alumina one. This is rather obvious in view of the fact that both Ce and CeMg aluminate have (distorted) magnetoplumbite crystal structures. The limited solubility especially refers to $SrMgAl_{10}O_{17}$-based phosphors, where we did not succeed in preparing single-phase samples. With x-ray diffraction it was established that $SrMgAl_{10}O_{17}$:Ce compositions decompose into a Ce-rich Sr aluminate and $SrMgAl_{10}O_{17}$. It could not be established whether the additional short-wavelength bands occurring in many Ba and BaMg aluminates were due to separation of a Ce-containing magnetoplumbite phase or to the existence of Ce-containing local Al_2O_3-rich deviations of the over-all composition in the β-alumina phase itself, see also Ref. (6).

We tried also in vain to prepare homogeneous Ba-aluminate:Ce phosphors with a blue luminescence band due to O-Ce complexes. In the compositions for which in the Eu-analog a strong green luminescence is found due to O-Eu associates (7), only a weak blue luminescence of O-Ce complexes was observed. The last named samples turned out to lie outside the homogeneity range of the β-alumina:Ce phase. In the x-ray diagram of such materials a number of lines were found which could not be identified as one of the forms of Al_2O_3, or as $CeAlO_3$. Attempts to prepare a homogeneous sample of the unknown phase, possibly a Al_2O_3-rich Ba-Ce aluminate, were not successful.

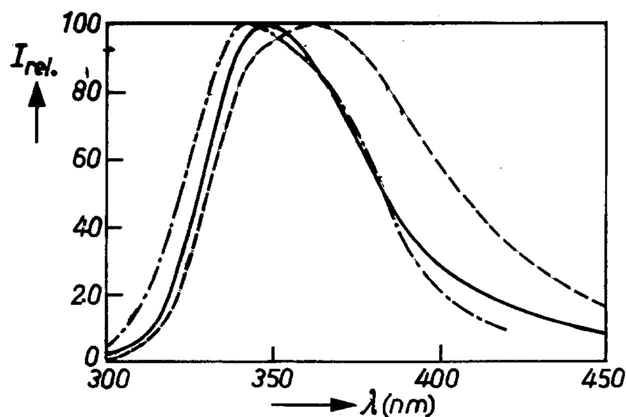

Fig. 5. Luminescence spectrum at 300°K (under 250-270 nm excitation) of $BaAl_{10\,2/3}O_{17}$:0.14Ce (———); $BaMgAl_{10}O_{17}$:0.14Ce (— — — —); and $KAl_{11}O_{17}$:0.14Ce (—·—·—).

[1] For simplicity reasons we call this "association;" the blue emitting centers are called O-Ce associates.

The La-aluminate/Ce-aluminate system.—It was reported before (1, 2) that the compounds La-aluminate and Ce-aluminate have a narrow homogeneity range. Homogeneous phases were obtained for the starting compositions $La_{0.86}Al_{11.90}O_{19.14}$ and $Ce_{0.86}Al_{11.90}O_{19.14}$ after firing at 1400°-1500°C. These formulas suggest that 14% of the large cation sites is occupied by oxygen ions. If these O_{Me} form associates with Ce ions, we expect to find two luminescence bands in $(La_{1-x}Ce_x)_{0.86}Al_{11.90}O_{19.14}$ phosphors, namely one due to the luminescence of single Ce^{3+} ions and one of the Ce-O associates.

In Fig. 6 a number of luminescence spectra at 300°K of phosphors of the (La,Ce)-aluminate series are shown (excitation 250-270 nm). Indeed two bands are observed, one having a maximum in the 330-350 nm region and the other with a maximum in the 410-430 nm region. With increasing Ce content x, the relative intensity of the longwave band increases. Since the quantum efficiency of the phosphors considered is 50-60% in the whole system, and the absorption of the 250-270 nm excitation energy is about 90% in all cases, it is concluded that the intensity of the blue band grows at the cost of the u.v. one. In Fig. 7 the percentage of quanta emitted in the blue has been plotted against the Ce content x. For x near 0 we see a percentage of the blue of about 16. If the O-Ce associates are formed in a random way, that is, if there is no preference of oxygen ions for association with La or Ce ions, the percentage of O-Ce associates is calculated, independent of the Ce content, to be equal to the figure observed in phosphors with low Ce content, namely $0.14/0.86 \times 100\% = 16\%$. In addition to the existence of a similar band in Al_2O_3-rich $SrAl_{12}O_{19}$: Ce, the agreement between the observed and the calculated amount of blue near $x = 0$ may be another piece of evidence for ascribing the blue luminescence band to the luminescence of O-Ce associates. Since the number of Al^{3+} ions per formula unit is lower than 12 it is concluded that as in $SrAl_{12}O_{19}$:Ce with $O_{Sr} < 0.15$ no Al^{3+} ions are present which would partially block Ce-O association.

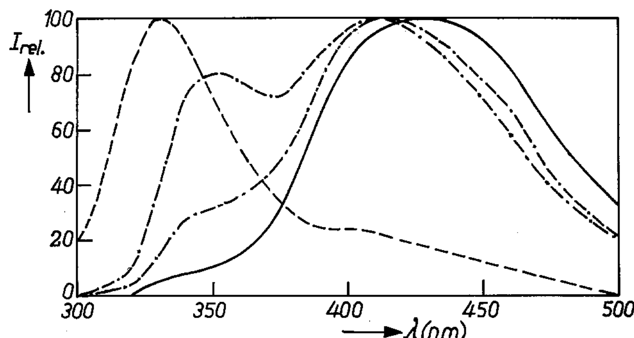

Fig. 6. Luminescence spectra at 300°K (under 250-270 nm excitation) in the $(La_{1-x}Ce_x)_{0.86}Al_{11.90}O_{19.14}$ system — — — —, $x = 0.02$; —·—·—, $x = 0.5$; — —·— —, $x = 0.14$; ———, $x = 1.0$.

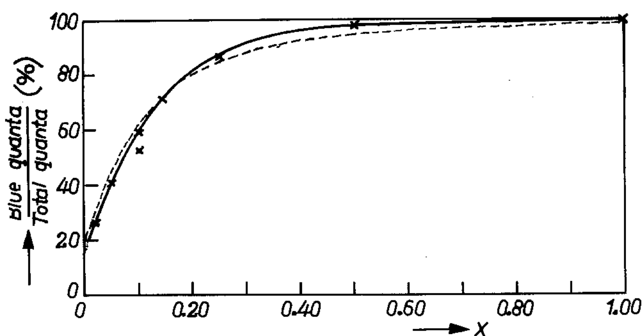

Fig. 7. Percentage of quanta emitted in the blue as a function of x in $(La_{1-x}Ce_x)_{0.86}Al_{11.90}O_{19.14}$ phosphors. The crosses represent measurements at 300°K, 250-270 nm excitation. The drawn line represents a calculated curve according to the Perrin model (12), $y_o = 0.13$, the dashed line that to the Förster model (13), $y_o = 0.20$, $R_c = 25Å$.

Let us now discuss why the relative intensity of the blue band increases strongly with the Ce content in $(La_{1-x}Ce_x)_{0.86}Al_{11.90}O_{19.14}$. Figure 8 shows that the excitation spectrum of the blue emission-drawn line, strongly overlaps the u.v. luminescence band, dashed line, of the "free" Ce^{3+} ions. The normalized overlap integral was estimated to be 0.6 eV^{-1}, which is considerably higher than for the overlap between excitation and emission spectra of free Ce^{3+} or Eu^{2+} ions (10).

If we assume that a dipole-dipole mechanism is operative we can write for the probability of energy transfer from free Ce^{3+} ions to Ce-O associates

$$P_{tr} = 3 \cdot 10^{12} \cdot \frac{P_{Ce}}{R^6 \tau_{Ce}} \cdot \frac{1}{E^4} \int f_{Ce}(E) \mathbf{F}_{Ce\text{-}O}(E) dE \quad [2]$$

where P_{Ce} = the oscillator strength of the $4f \rightarrow 5d$ transition in the Ce^{3+} ion; R = the distance between the free Ce^{3+} ion and the Ce-O associate (Å); τ_{Ce} = the decay time of the Ce^{3+} luminescence (sec); E = the energy transferred (eV); and $\int f_{Ce}(E)\mathbf{F}_{Ce\text{-}O}(E)dE$ = the normalized overlap integral. For $P_{Ce} = 0.01$ [a usual figure for this transition, (10)], $R = 5.6Å$ (the distance for nearest neighbors), 20 nsec for τ_{Ce} (11) and $E = 3.5$ eV, we find $P_{transfer}$ to be $2 \cdot 10^{11}$ sec^{-1} for nearest neighbors. This figure is about 4000 times higher than the radiative probability of the Ce ion $P_{rad,Ce}$ which is $\tau^{-1} = 5 \cdot 10^7$ sec^{-1}. We conclude that energy transfer between nearest neighbor Ce^{3+} and Ce-O associates will be very effective.

If the Ce^{3+} ions and the Ce-O associates are farther apart, the ratio $P_{transfer}$ drops with the sixth power of the distance R. It can be derived from Eq. [2] that at $R_c = 22Å$, $P_{transfer} \approx P_{rad}$. For comparison we note that for the effective Eu^{2+}-Eu^{2+} energy transfer in hexagonal aluminates R_c has a rather similar value, namely 18Å (1).

Now we will try to find a more quantitative description of the increase of the blue emission as a function of the Ce content x. Measurements of excitation spectra showed that the light output in the blue, on excitation at 330-380 nm, is essentially independent of the Ce content x, that is always about 45% of that on excitation in the 250-270 nm region. Since the efficiency is also independent of the energy transfer from Ce^{3+} ions to Ce-O associates—the quantum efficiency of the (u.v. + blue) luminescence is 50-60% in the whole system—we can apply models given by Perrin (12) and Förster (13) for sensitizer (the free Ce^{3+} ion)-activator (the Ce-O associates) systems where

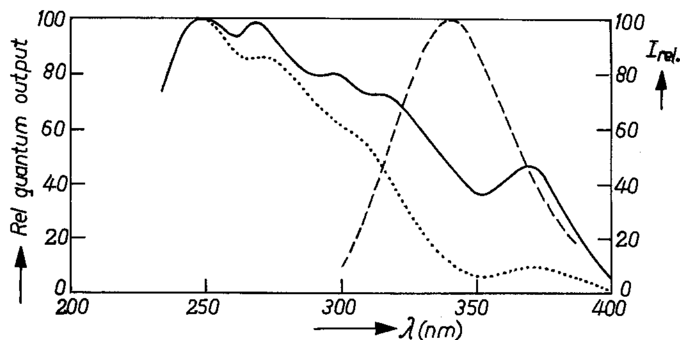

Fig. 8. Excitation spectra of the blue luminescence in $(La_{1-x}Ce_x)_{0.86}Al_{11.90}O_{19.14}$ phosphors (———); and of $Ce_{0.91}Mg_{0.25}Al_{11.65}O_{19.09}$ (. . . . . .). The dashed line represents the u.v. luminescence band in $(La_{0.98}Ce_{0.02})_{0.86}Al_{11.90}O_{19.14}$.

the sensitizer to sensitizer transfer is absent. As regards the last named point we note, see Ref. (8), that the probability of energy transfer between nearest neighbor Ce^{3+} ions in aluminate host lattices is very low, namely $\approx 4 \cdot 10^5$ sec^{-1}.

In the Perrin model (12) each sensitizer ion has an "active" sphere with radius R_o, in which energy transfer has an infinite rate and outside of which there is no energy transfer at all. Using the Perrin formula we can write for the percentage p of quanta emitted in the blue

$$p_{\text{blue}} = q + (100 - q)(1 - e^{-y/y_o}) \quad [3]$$

where q = the percentage of Ce ions associated with oxygen (= 16% in the La/Ce system); y = the effective Ce^{3+} content (in mole/m^3); y_o = the "critical" concentration. This parameter is related to R_o by $y_o = 3/(4\pi R_o^3)$. We note that R_o in the Perrin approach cannot be compared directly with critical distance R_c mentioned above.

The drawn curve in Fig. 7 has been calculated for $y_o = 0.13$. It is seen that with this value a very good agreement is found with the observed figures.

On using the same figure for y_o it is calculated that in Al_2O_3-rich $SrAl_{12}O_{19}$:Ce phosphors the maximum percentage of blue, found at a composition $Sr_{0.73}Ce_{0.13}Al_{12.15}$, would be 73%. A figure of 67% is observed (see Fig. 3), so that a satisfactory agreement exists between observed and calculated data.

The model of Förster (13) uses the fact that for dipole-dipole interaction P_{tr} is proportional to $1/R^6$. In our case his formula reads

$$p_{\text{blue}} = q + (100 - q)\left[\sqrt{\pi}\frac{y}{y_o}e^{(y/y_o)^2}(1 - \text{erf}\, y/y_o)\right] \quad [4]$$

where q and y are defined in the same way as in Eq. [3]. y_o is now related to the critical distance R_c by the (similar) expression $y_o = 3/(4\pi R_c^3)$. The dashed line in Fig. 7 shows that for a critical concentration y_o = 0.20 a reasonable agreement is obtained between observed and calculated figures of p_{blue}. The systematic discrepancies may indicate that y_o is slightly dependent on y. For $y > 0.20$, y_o would be <0.20 and vice versa. This is related to the fact that the Förster theory was derived for diluted and spherically symmetrical systems. In our case we deal with high activator contents which are concentrated in certain crystal planes. In view of these arguments a figure of 25Å for the critical distance R_c (estimated from y_o by formula 19 in Ref. (13), note that $y_o = 6\frac{1}{4}\,C_o$) is in reasonable agreement with the 22Å estimated for R_c with help of formula [3].

From the considerations given above we conclude that the simple Perrin model gives a good description of the observations. For the Förster approach several prerequisites are not fulfilled. However the agreement between calculated and observed figures is reasonably good. A better agreement is likely to be obtained if we calculate $P_{\text{tr to Ce-O}}/P_{\text{rad, Ce}}$ for discrete distances relevant in the aluminate lattice and apply the appropriate statistics.

The Ce-aluminate/CeMg-aluminate system.—In Eu^{2+}-activated β aluminas the oxygen ions at large cation sites were observed to be effectively screened from the activator by Mg^{2+} ions (2). In such a system no O-Eu associates were found to occur. In order to study such screening effects in Ce^{3+}-activated phosphors, the Ce-aluminate/CeMg-aluminate was chosen since it was found that the Ce-aluminate luminescence is almost completely blue, whereas CeMg aluminate shows a very strong u.v. emission band, see, for instance, Fig. 9. As is seen in Fig. 9, the compositions in between Ce- and CeMg aluminate, as those containing ½ Mg or ¼ Mg atom per formula unit, show both a blue and a u.v. luminescence band. Apart from changes

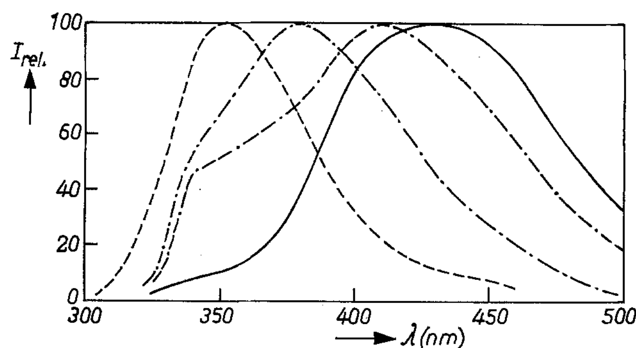

Fig. 9. Luminescence spectrum at 300°K (under 250-270 nm excitation) in the Ce/CeMg aluminate system. ———, $Ce_{0.86}Al_{11.90}O_{19.14}$; —·—·—, $Ce_{0.91}Mg_{0.25}Al_{11.65}O_{19.09}$; —·—·—, $Ce_{0.92}Mg_{0.5}Al_{11.47}O_{19.08}$; — — — —, $Ce_{0.92}MgAl_{11.13}O_{19.08}$.

in the position of the blue band we see that the amount of u.v. increases with increasing Mg content so that we conclude that O_{Ce} and Ce ions are screened from each other as in Eu^{2+}-phosphors.

Due to the fact that Mg^{2+} ions prefer to enter tetrahedral surroundings in the type of host lattice discussed here (15) it is assumed that the screening Mg^{2+} ions are located at tetrahedral "12k" positions as indicated in Fig. 1D. Three of such positions occur near one O_{Ce}; they can be considered to arise by shifting atoms in fivefold oxygen surrounding, position 2b in Fig. 1A, off the hexagonal axes which are indicated by drawn vertical lines

In order to discuss the screening effect of Mg^{2+} ions more quantitatively, we must first say a few words about the number of O_{Ce} as a function of the Mg content. The homogeneity of CeMg-aluminate was found experimentally to be narrow and to be around $Ce_{0.92}MgAl_{11.13}O_{19.08}$ in samples slowly cooled from 1500°C. For LaMg-aluminate a similar composition is found so that in both cases about 8.5% of the large cation sites is occupied by oxygen ions which is lower than in Ce- and La-aluminates where this percentage is 14%, see above. For the compositions in between Ce aluminate and for CeMg aluminate and corresponding La-compositions, the number of oxygen cations has not been established. However, it seems reasonable to assume that the number of $O_{Ce}(O_{La})$ decreases linearly with increasing Mg content, see drawn line in Fig. 10.

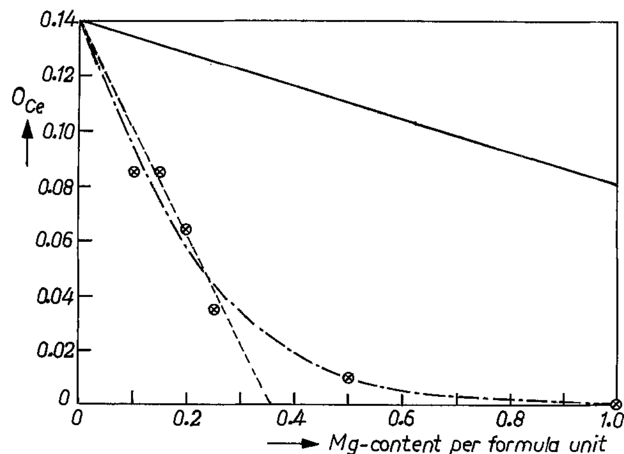

Fig. 10. Number of oxygen ions at Ce sites (O_{Ce}) in the CeMg-aluminate system. The drawn line represents the number of O_{Ce} assumed to be present. The crosses represent the number of O_{Ce} ions which are not screened by Mg^{2+} ions. This number was derived from luminescence spectra with the help of Eq. [3]. Through the crosses the dash-dot curve has been fitted. The dashed line represents the number of nonscreened atoms assuming that 3 Mg^{2+}-ions are needed to achieve complete screening of O_{Ce} from Ce.

If it is assumed that $3Mg^{2+}$ ions are needed completely to screen the O_{Ce} ions [see above and also Ref. (2)], the number of O ions which form complexes with Ce is represented by the dashed line in Fig. 10. The number of such ions derived with the help of formula [3] from the observed luminescence spectra, y_o, is taken to be 0.13, as given by the dash-dot line. It is seen that at very low Mg contents all Mg^{2+} ions seem indeed to be located near O_{Ce} in a ratio of 3:1. At higher Mg contents, Mg^{2+} ions also substitute on other sites of the lattice, giving rise to higher percentages of blue luminescence than expected from our considerations.

The number of ions involved in complex formation can also be estimated from excitation spectra in the 330-380 nm region. For the composition $Ce_{0.91}Mg_{0.25}Al_{11.65}O_{19.09}$ it is estimated that in this wavelength region the number of "active" O_{Ce} is about ¼ of that in $Ce_{0.86}Al_{11.90}O_{19.14}$, see dotted and drawn line in Fig. 8, so that q in formula [3] is equal to 4. Taking $y_o = 0.13$, it is then estimated that 85% of the emitted quanta would then be in the blue. The observed figure of 87% is in good agreement with the calculated one.

Excitation spectra.—In this section we restrict ourselves to the excitation spectra of the u.v. Ce luminescence in aluminates containing large di- or trivalent ions. The excitation spectra of the blue luminescence bands have essentially the same form and the same peak positions in the wavelength region below 300 nm, compare for instance Fig. 8 and 13, and are not discussed separately.

In Fig. 11-13 we show excitation spectra at 300°K of the maxima of the shortwave luminescence bands presented in Fig. 2, 5, 6, and 9. In all cases broad bands are seen which are rather superimposed. The D_{3h} local symmetry of the Ce^{3+} ions at the 2b sites, see Fig. 1A and 1B, leads us to expect that the excited 5d levels of Ce^{3+} are split into three (A′, E′, and E″) sublevels. Indeed three main bands can be recognized in the excitation spectra, although, especially in La-

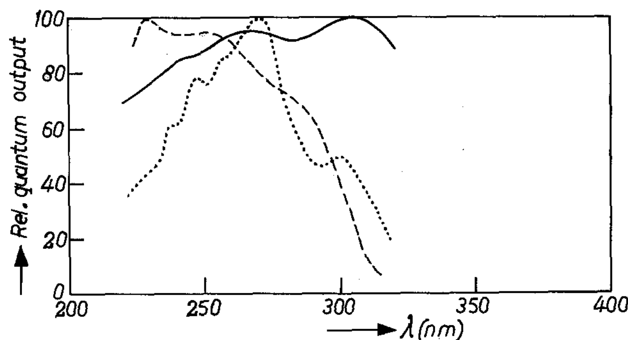

Fig. 11. Excitation spectra at 300°K of the u.v. luminescence in $Ce_{0.86}Al_{11.90}O_{19.14}$ (———); $Ce_{0.92}MgAl_{11.13}O_{19.08}$ (– – –); and $La_{0.86}Al_{11.90}O_{19.14}$:0.14Ce (......).

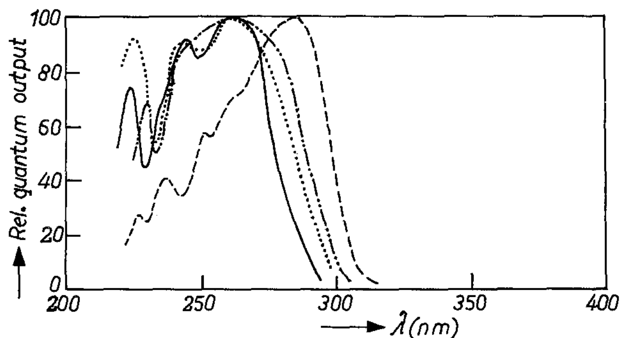

Fig. 12. Excitation spectra at 300°K of the u.v. luminescence in $SrAl_{12}O_{19}$:0.14Ce (———); $CaAl_{12}O_{19}$:0.14Ce (......); $CaMgAl_{11.33}O_{19}$ (—··—··—); and $La_{0.92}MgAl_{11.13}O_{19.08}$ (– – –).

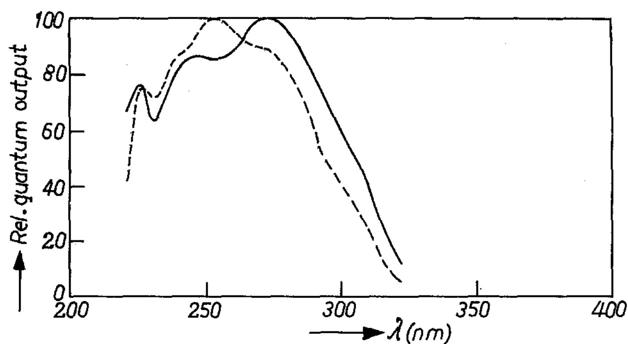

Fig. 13. Excitation spectra at 300°K of the u.v. luminescence in $BaAl_{10\,2/3}O_{17}$:0.14Ce (———) and $BaMgAl_{10}O_{17}$:0.14Ce (– – – –).

and LaMg-aluminate: Ce and the β-aluminas: Ce, further splittings of these bands occur

In order to facilitate the discussion of the excitation spectra, a number of data are summarized in Table II. It is seen that in contradistinction to Eu^{2+}-doped aluminates (1), the center of gravity of the excited 5d levels of Ce^{3+} ions varies as a function of the aluminate host lattice between 36,800 and 41,300 cm^{-1}. Since the crystal field parameter Dq cannot be derived directly from energy level data; in the D_{3h} symmetry the energy difference between the highest and the lowest excited levels is used as a yardstick for the strength of the crystal field. It is seen in the second column of Table II that this field is the strongest in the β-aluminas, followed by the distorted magnetoplumbites containing Ce^{3+} or La^{3+} ions. Relatively weak fields are found in Ca, Sr, and CaMg-aluminate: Ce. In last-named phosphors a large Stokes shift between the lowest lying excitation band and the luminescence band is found. For CeMg aluminate and LaMg aluminate: Ce this shift is also large, whereas in β-aluminas and Ce aluminate or La aluminate: Ce much lower shifts are found.

In the corresponding Eu^{2+} phosphors the β-aluminas were also found to have a stronger crystal field and a lower Stokes shift than the magnetoplumbites (1). It was concluded that this is due to the fact that in the last-named lattice the bond strength [the rigidity of the lattice, see Ref. (16) and (17)] is higher and that the activator ion is very close to one of the surrounding oxygen ions. Since Ce^{3+} has a formal positive charge in aluminates containing large divalent ions a more detailed comparison with Eu^{2+} ions is hardly feasible. This also holds for the distorted magnetoplumbites where the Eu^{2+} ions have a formal negative charge.

As regards a qualitative explanation of the data in Table II the position of the center of gravity of the 5d levels seems to play a key role. It is seen that in Ce aluminate it is situated at the lowest energy, so that

Table II. Some data derived from the excitation spectra of aluminate:Ce^{3+} phosphors

	Center of gravity of excited 5d levels (10^3 cm^{-1})	Energy difference between highest and lowest excited 5d levels (10^3 cm^{-1})	Stokes shift (cm^{-1})
Magnetoplumbites			
$CaAl_{12}O_{19}$:0.14Ce	41.3	6.3	7400
$SrAl_{12}O_{19}$:0.14Ce	41.3	6.3	6700
$CaMgAl_{11.33}O_{19}$:0.14Ce	40.7	7.0	7000
β-aluminas			
$BaAl_{10\,2/3}O_{17}$:0.14Ce	39.1	11.6	4100
$BaMgAl_{10}O_{17}$:0.14Ce	39.0	11.6	5100
Distorted magnetoplumbites			
$Ce_{0.86}Al_{11.90}O_{19.14}$	36.8	9.3	3000
$La_{0.86}Al_{11.90}O_{19.14}$:0.14Ce	37.9	9.0	3200
$Ce_{0.92}MgAl_{11.13}O_{19.08}$	38.9	9.1	5900
$La_{0.92}MgAl_{11.13}O_{19.08}$:0.14Ce	39.9	8.9	6000

the contraction with respect to the free-ion level [at 51,000 cm^{-1}, see Ref. (17)] is very large. This contraction is ascribed to the reduction of interelectronic repulsion by a more covalent character of the bonds. If these bands are relatively strong the lattice can be considered to be "rigid." In that case, the Stokes shift between excitation and emission is relatively small due to the fact that the excited Ce^{3+} state cannot contract appreciably (16). In CeMg aluminate and LaMg aluminate: Ce the center of gravity of the 5d levels has shifted $\approx$2000 cm^{-1} toward higher energy. Apparently this lattice is "weaker," which results in a larger Stokes shift. A further increase of the Stokes shift is expected if we change from CeMg (or LaMg aluminate) to Ca, Sr, and CaMg aluminate: Ce phosphors. The observed shift is, however, much less than expected on the basis of the difference between Ce and CeMg aluminate or between the corresponding La-phosphors. We ascribe this to the formal positive charge on the Ce^{3+} ion when it replaces Ca or Sr. This charge causes a contraction of the ground state of the Ce^{3+} ion (17), resulting in a reduction of the crystal field and a moderation of the increase of the Stokes shift.

The formal charge on the Ce^{3+} ion also plays a role in considering the β-alumina: Ce^{3+} phosphors. Since, for instance, CeMg-aluminate has 5d levels centered at the same energy, we expect the β-alumina phosphors to have a weaker crystal field and a lower Stokes shift compared to this compound. The difference in crystal structure (see above) predicts, however, a stronger crystal field. This is indeed observed, so that we conclude that this difference is more decisive than the "charge effect."

Quantum efficiency of the luminescence.—In Table I, typical quantum efficiencies at 300°K of aluminate: Ce phosphors are given. The excitation used was at 250-270 nm. From the excitation spectra in Fig. 11-13 and from reflection spectra it is concluded that most of the phosphors listed are at about 90% from their maximum efficiency on excitation in this wavelength region. The only exception in this respect is LaMg aluminate: Ce where the maximum efficiency is about 80-85% against 60% at 250-270 nm excitation. The efficiencies of the phosphors containing 2% Eu^{2+} as activators are given within brackets (1). It is concluded that the Ce^{3+}-doped magnetoplumbites have slightly higher efficiencies than the Eu^{2+} ones; in the distorted magnetoplumbites the efficiencies are equal, whereas in β-aluminas the Eu^{2+}-doped phosphors are more efficient. The consideration of the "maximum" efficiencies does not change this picture substantially; except that for La-aluminate: Eu^{2+} the maximum efficiency is slightly higher than that of the Ce^{3+}-doped phosphor.

It was shown (8) that energy transfer between Ce^{3+} ions in aluminates has a low probability compared to radiative decay, so that concentration quenching phenomena are unlikely to occur. This is also evident from Table I since the quantum efficiency of the Ce- and CeMg-aluminate phosphors is only slightly lower than that of the La-diluted materials. A further illustration is that in aluminates containing large divalent cations the efficiencies of samples with high Ce content, for instance 0.14 per formula unit, see Table I, are higher than those with 0.02 Ce. This is in contradistinction, for instance, to the Eu^{2+}-doped Ca, Sr, and Ba aluminates (7). In the last-named phosphors energy transfer is very efficient compared to radiative decay.

The luminescence of magnetoplumbites doped with Eu^{2+} ions was reported (6) to be very susceptible to quenching by defects; energy transfer between the activator ions was found to play a crucial role in such quenching processes. Although the preparative conditions of the present materials were chosen in such a way that quenching by defects is avoided as much as possible, the susceptibility to quenching of the Eu^{2+} phosphors may be the reason why the efficiency of Ce^{3+}-doped magnetoplumbites is still slightly higher.

The lower efficiency of the Ce^{3+}-doped β-aluminas may be explained by the fact that in these phosphors a large number of large cation vacancies are present which quench the luminescence. In Eu^{2+}-activated β-aluminas these vacancies were found (2) to occur in concentrations up to 0.01 per formula unit. The efficiency of the Eu^{2+} luminescence was reported to decrease almost linearly below Eu^{2+} concentrations of 1%. We have not checked such relationships extensively in Ba-aluminate: Ce^{3+}, but in view of the fact that Ba aluminate 0.02 Ce ($q = 25\%$) already has a lower efficiency than of Ba aluminate: 0.14 Ce ($q = 50\%$) it is likely that in such phosphors even more Ba vacancies are formed than in the Eu^{2+} case. This may be related to the fact that, since Ce^{3+} is trivalent, not only may the "substitution reaction" of the type $Ba^{2+}{}_{Me} + Ce^{3+} \rightarrow Ce^{3+}{}_{Me} + Ba^{2+}$ occur, but also $3Ba^{2+}{}_{Me} + 2Ce^{3+} \rightarrow 2Ce^{3+}{}_{Me} + \square_{Me} + 3Ba$. Large cation vacancies may also be responsible for the low efficiency of Ca- and Sr-aluminates with low Ce content.

Acknowledgments

The author is indebted to Mrs. A. D. M. Schrama-de Pauw and Mrs. R. B. Engelen for their experimental work and to Dr. A. T. Vink for discussion of the manuscript. Dr. P. B. Braun and his research group are thanked for their x-ray diffraction studies.

Manuscript submitted Aug. 5, 1977; revised manuscript received Nov. 21, 1977.

Any discussion of this paper will appear in a Discussion Section to be published in the December 1978 JOURNAL. All discussions for the December 1978 Discussion Section should be submitted by Aug. 1, 1978.

Publication costs of this article were assisted by Philips Research Laboratories.

REFERENCES

1. A. L. N. Stevels and A. D. M. Schrama-de Pauw, *This Journal*, **123**, 691 (1976).
2. A. L. N. Stevels, Submitted to *J. Lumin.*
3. G. Blasse and A. Bril, *Philips Res. Rep.*, **23**, 201 (1968).
4. J. M. P. J. Verstegen and A. L. N. Stevels, *J. Lumin.*, **9**, 406 (1974).
5. J. M. P. J. Verstegen, *This Journal*, **121**, 1623 (1974).
6. A. L. N. Stevels and A. D. M. Schrama de Pauw, *J. Lumin.*, **14**, 147, 153 (1976).
7. A. L. N. Stevels, Submitted to *J. Lumin.*
8. J. L. Sommerdijk, J. A. W. van der Does de Bye, and P. H. J. M. Verberne, *ibid.*, **14**, 91 (1976).
9. A. Bril and W. L. Wanmaker, *This Journal*, **111**, 1363 (1964).
10. G. Blasse, *Philips Res. Rep.*, **24**, 131 (1969).
11. J. A. W. van der Does de Bye, Unpublished results.
12. F. Perrin, *Compt. Rend.*, **178**, 1978 (1924).
13. Th. Förster, *Z. Naturforsch., Teil A*, **4**, 321 (1949).
14. A. L. N. Stevels and J. M. P. J. Verstegen, *J. Lumin.*, **14**, 207 (1976).
15. J. Antoine, D. Vivien, J. Livage, J. Thery, and R. Collonques, *Mater. Res. Bull.*, **10**, 865 (1975).
16. G. Blasse and A. Bril, *Philips Tech. Rev.*, **31**, 304 (1971).
17. G. Blasse, *J. Solid State Chem.*, **9**, 147 (1974).
18. E. Loh, *Phys. Rev.*, **154**, 270 (1967).

Solar Cells from Zone-Refined Metallurgical Silicon

T. L. Chu,* Shirley S. Chu,* and R. W. Kelm, Jr.
Southern Methodist University, Dallas, Texas 75275

and G. W. Wakefield*
Texas Instruments Incorporated, Dallas, Texas 75222

ABSTRACT

Metallurgical-grade silicon has been purified by the Czochralski pulling and floating-zone techniques. The purified material was used as substrates for the preparation of solar cells by diffusion and chemical vapor deposition techniques. The structure and electrical characteristics of purified metallurgical silicon and solar cells have been investigated.

Metallurgical grade silicon with a purity of about 98% is the most economical form of silicon available. It contains aluminum (up to about 0.75% by weight) and iron (up to about 0.5%) as the major impurities; other impurities include boron, chromium, copper, magnesium, manganese, nickel, titanium, and vanadium at concentrations up to several hundred parts per million. Because of its high impurity content, metallurgical silicon is unsuitable for device purposes. Since most metallic impurities have relatively low segregation coefficients (10^{-7}-10^{-3}) at the melting point of silicon, the zone refining of metallurgical silicon could provide silicon of sufficient purity for certain device applications where the purity requirements are not stringent.

In this work, silicon ingots were prepared from the metallurgical-grade material by the Czochralski pulling technique and were further purified by the floating-zone technique. Both Czochralski and float-zoned metallurgical silicon were used for the fabrication of solar cells. The electrical characteristics and conversion efficiencies of solar cells were measured. The experimental procedures and results are summarized below.

Experimental

Metallurgical silicon supplied by the Ferroalloy Division of Union Carbide Corporation was used as the starting material. A typical emission spectrographic analysis of metallurgical silicon is shown in Table I. Silicon ingots of about 2.7 cm diam were pulled from metallurgical silicon in a fused silica crucible by the Czochralski technique, and 60-70% of the charge was consumed. Because of the high concentration of impurities and particulate matter in the melt, the resulting ingots were polycrystalline and were further purified by floating-zone refining in a helium atmosphere for two passes at a rate of about 2.5 cm/hr. Both the Czochralski-pulled and zone-refined materials were sliced and used for the fabrications of solar cells. The structural defects in silicon slices were revealed by the Sirtl etch (2).

Silicon slices produced by both Czochralski and zone-refining techniques were all p-type with electrical resistivities in the range of 0.02-0.06 Ω-cm. They were used for the fabrication of solar cells by the diffusion and chemical vapor deposition techniques. The phosphorus diffusion was carried out at 950°C in the conventional manner using phosphorus oxytrichloride as the source material. The duration of diffusion was adjusted to yield a junction depth of 0.3-0.4 μm, and the sheet resistance of the diffused layer was in the range of 25-50 Ω/□. The grid contact to the diffused surface, 3 lines per centimeter, and the ohmic contact to the back surface were made by evaporating successively 1000Å of titanium and 2-3 μm of silver through metal masks, followed by annealing at 550°C in a hydrogen atmosphere.

In the chemical vapor deposition technique, the thermal reduction of trichlorosilane with hydrogen containing diborane or phosphine was used for the deposition of the active region on purified metallurgical silicon substrates (3). Typically, 5-20 μm of 0.05-1 Ω-cm p-type silicon and 0.4-0.6 μm of 0.003-0.006 Ω-cm n-type silicon were deposited successively on the substrate at 1150°-1200°C. The trichlorosilane content in the reactant mixture was adjusted to yield a deposition rate of about 1 μm/min for the p layer and of about 0.1 μm/min for the n^+ layer. The contacts to the epitaxial cells were also applied by evaporation as in the diffused cells. No antireflection coatings were applied.

The solar cells were characterized by measuring their current voltage characteristics in the dark and under illumination. The dark current-voltage characteristics of the p-n junction is directly related to the performance of the solar cell, and the data were fitted by the least squares method to the following two-exponential model (4)

$$I = I_{01}[\exp(qV/A_1kT) - 1] + I_{02}[\exp(qV/A_2kT) - 1] + \frac{V}{R_{sh}}$$

Where the first two terms represent the diffusion and the recombination currents, and the third term is the contribution from shunting. The illumination was carried out with an AMO solar simulator or a quartz-halogen lamp calibrated to AMO conditions, *i.e.*, the short-circuit current of a standard cell measured with the quartz-halogen lamp is the same as that measured with the solar simulator.

Results and Discussion

Czochralski ingot from metallurgical silicon.—Silicon ingots prepared from metallurgical silicon by the Czochralski technique were polycrystalline with large crystallites. Figure 1 shows the chemically etched surface of a slice cut perpendicular to the pulling direction; the center region is essentially single crystalline,

Table I. Impurity content (ppm by weight) in silicon

Element	Metallurgical silicon	First section of Czochralski ingot	Upper third of two zone-pass material
B	10-100	10-100	1-10
Al	>>3000	1-10	<1
Fe	>>3000	1-10	1-10
V	100-1000	<1	N.D.
Cu	10-100	<1	<0.1
Ti	30-300	<0.1	N.D.
Mn	30-300	<0.1	N.D.
Mg	10-100	<1	0.1-1
Cr	30-300	<2	N.D.
Ni	10-100	<1	N.D.

* Electrochemical Society Active Member.

Key words: p-n junctions, diffusion, vapor deposition.

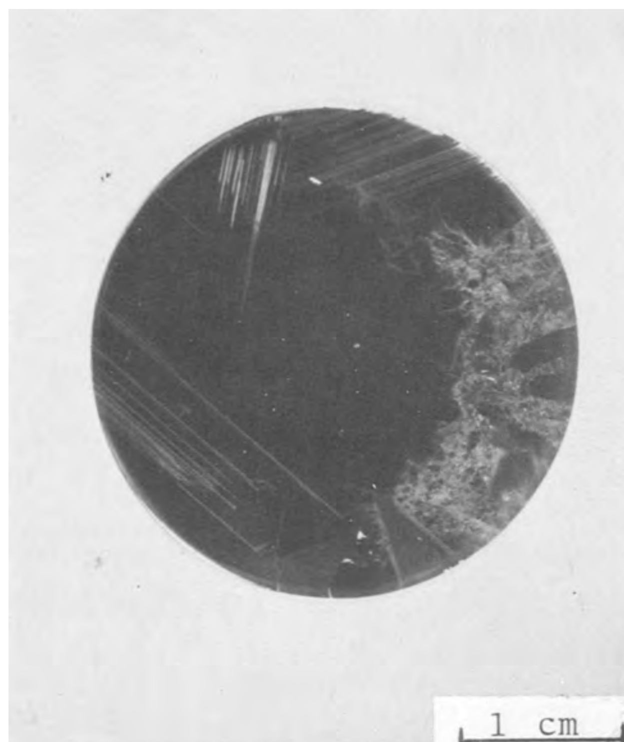

Fig. 1. Chemically etched surface of a silicon slice cut from a Czochralski metallurgical silicon ingot.

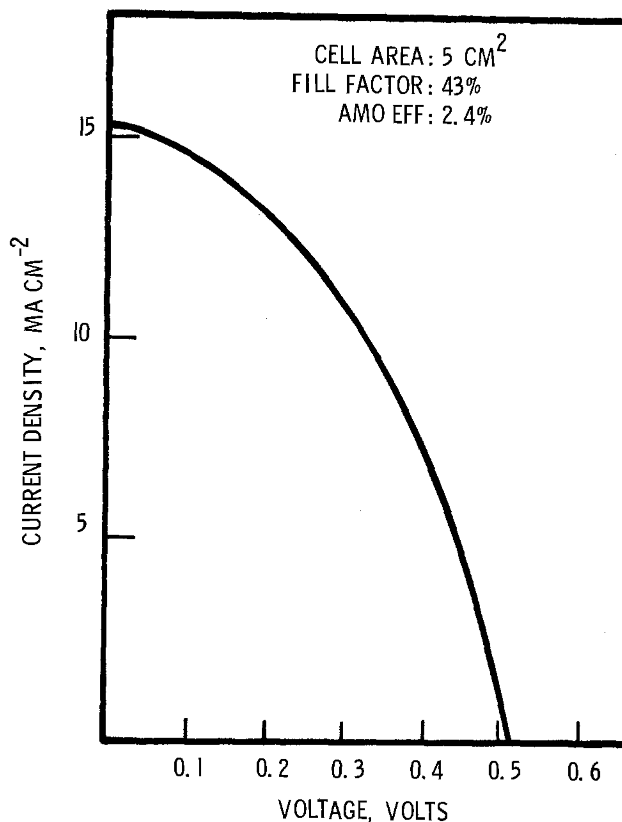

Fig. 2. Current-voltage characteristics of a solar cell fabricated from polycrystalline Czochralski metallurgical silicon by diffusion under illumination with a quartz-halogen lamp equivalent to AMO conditions.

and the periphery area has many grain boundaries. The emission spectrographic analysis of the first section of a Czochralski ingot is shown in Table I. It is apparent that considerable purification of metallurgical silicon has been achieved because of the low segregation coefficients of metallic impurities in silicon.

Solar cells fabricated from Czochralski-pulled metallurgical silicon had poor characteristics. Figure 2 shows the current-voltage characteristics of a typical cell of about 5 cm^2 area under illumination with a quartz-halogen lamp equivalent to AMO conditions, and the solar cell parameters are summarized in Table II. Its low conversion efficiency, 2.4%, is due at least to two factors: carrier recombinations at grain boundaries and poor chemical perfection in the starting material. Attempts to fit the dark current-voltage characteristics of several cells into the two exponential model have produced no meaningful results due presumably to the large contributions of grain boundaries to the current flow.

Solar cells prepared on Czochralski-pulled metallurgical silicon by the thermal reduction of trichlorosilane showed better characteristics. The parameters of a solar cell of about 5 cm^2 area under AMO conditions are also summarized in Table II. Its conversion efficiency, 4%, is considerably higher than that of the diffused cell, indicating that the deposited silicon p-n junction structures are of considerably better chemical and structural perfection than the p-n junctions produced in metallurgical silicon by diffusion.

Table II. Properties of solar cells (5 cm^2 area without AR coatings) under AMO conditions

Starting material	Fabrication technique	V_{OC} (volts)	I_{SC} (mA/cm^2)	Fill factor (%)	Conversion effect (%)
Czochralski met. Si	Diffusion	0.5	15	32	2.4
Czochralski met. Si	CVD	0.57	15	63	4
Zone-refined met. Si	Diffusion	0.57	17	60	4.3
Zone-refined met. Si	CVD	0.58	17	70	5.1

Float-zone refined metallurgical silicon.—The concentration of metallic impurities in Czochralski ingots pulled from metallurgical silicon was further reduced by the float-zone process. After two-zone passes, emission spectrographic analysis has shown that in the upper one-third of the crystal, boron, aluminum, and iron at 1-10 ppm are the major impurities (Table I). The resulting ingot was essentially single crystalline, however, the density of defects (mainly dislocations) was relatively high, 10^5-10^6/cm^2.

The typical characteristics of solar cells fabricated from float-zoned metallurgical silicon by diffusion are shown in Fig. 3 and 4. Figure 3 shows the dark current-voltage characteristics of a solar cell of about 5 cm^2 area. Two distinct regions are apparent in the forward direction: carrier recombination dominates at low voltages, and normal injection occurs at higher voltages. The least squares fitting of this relation yielded the following data: $I_{01} = 1.5 \times 10^{-13}$ A/cm^2, $I_{02} = 1.9 \times 10^{-8}$ A/cm^2, and $A_2 = 1.79$. These characteristics are similar to the diode parameters reported in the literature (4). Figure 4 shows the current-voltage characteristics of this cell under illumination with a quartz-halogen lamp calibrated to AMO conditions, and the solar cell parameters are summarized in Table II. Its characteristics are considerably improved over those shown in Fig. 2, due to better structural perfection and higher purity in the zone-refined material.

The chemical vapor deposition technique was also used for the fabrication of solar cells on metallurgical silicon substrates purified by two floating-zone passes. Solar cells of both n^+/p/substrate and n^+/p^+/substrate configurations were prepared, and the latter showed somewhat better characteristics. The dark characteristics of a solar cell of about 5 cm^2 area prepared by depositing successively a 15 μm 0.1 Ω-cm p layer and a 0.4-0.5 μm 0.005 Ω-cm n layer on a substrate were analyzed on the basis of the two-exponential model. The I_{01}, I_{02}, and A_2 values at room tempera-

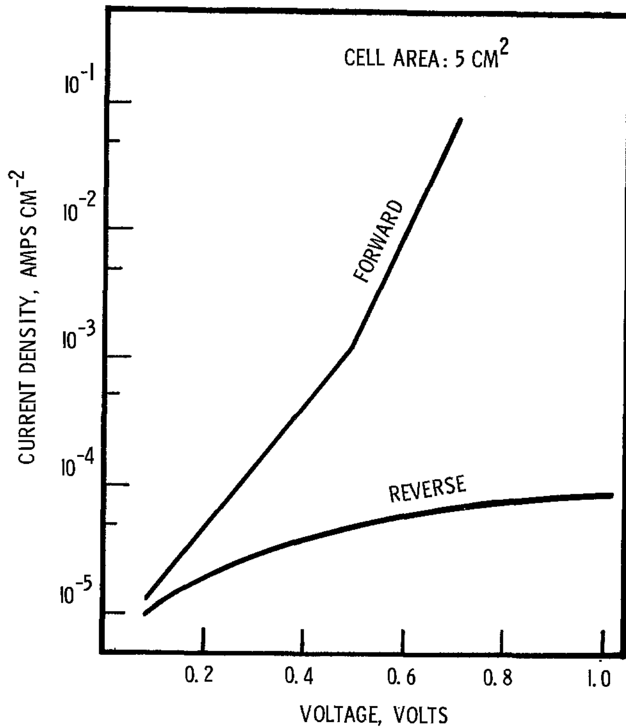

Fig. 3. Dark current-voltage characteristics of a solar cell fabricated from two zone-pass metallurgical silicon by diffusion.

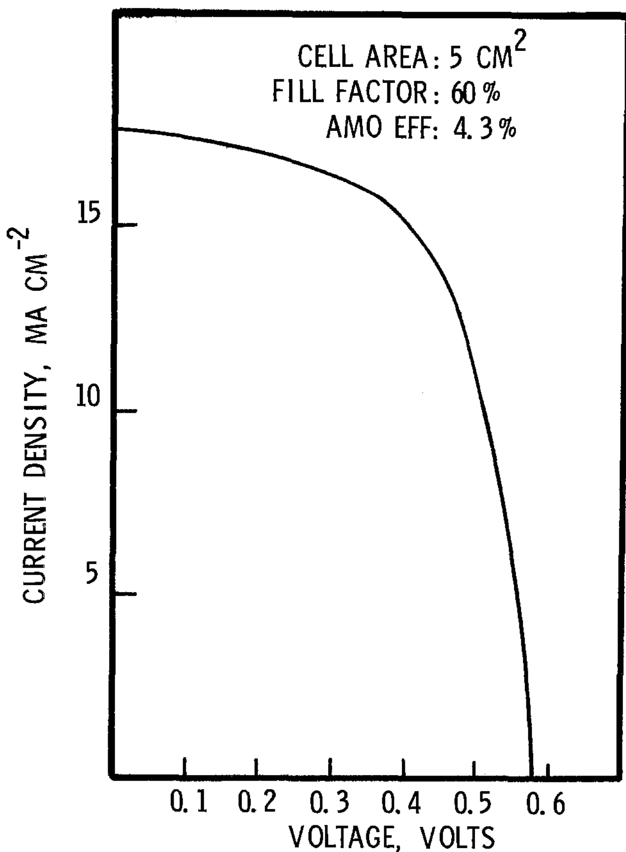

Fig. 4. Current-voltage characteristics of a solar cell fabricated from two zone-pass metallurgical silicon by diffusion under illumination with a quartz-halogen lamp under AMO conditions.

ture are 6.8×10^{-13} A/cm^2, 2.2×10^{-8} A/cm^2, and 1.76, respectively, again similar to the parameters reported in the literature. Figure 5 shows the characteristics of this cell under illumination equivalent to AMO conditions, and the cell parameters are summarized in Table II. These results again indicate that the deposited silicon p-n junction structures are of better chemical and structural perfection than those produced by diffusion.

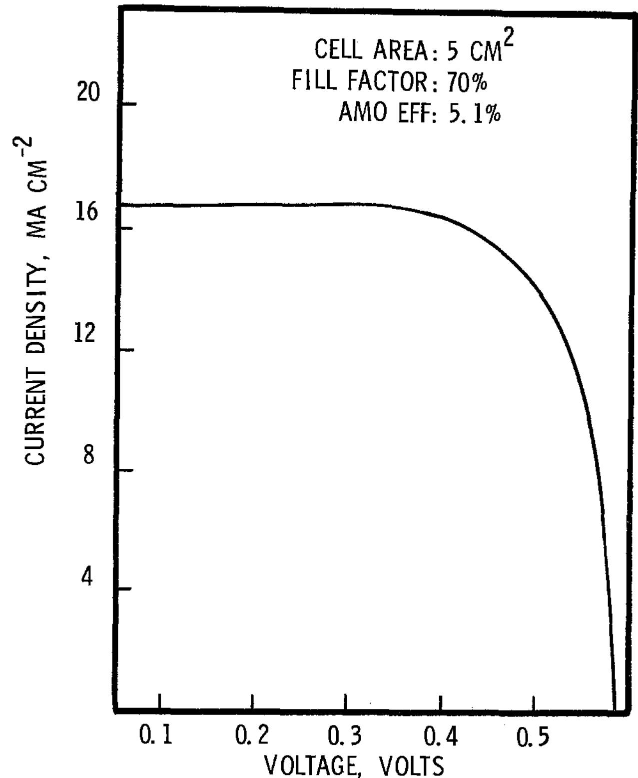

Fig. 5. Current-voltage characteristics of a n^+-silicon/p-silicon/metallurgical silicon (two zone-pass) solar cell under illumination with a quartz-halogen lamp equivalent to AMO conditions.

Summary

Metallic impurities in metallurgical-grade silicon can be removed substantially by zone refining because of their low segregation coefficients in silicon. Solar cells prepared from the metallurgical silicon purified by two zone-pass refining, though somewhat inferior to those from semiconductor grade silicon, have reasonable conversion efficiencies.

Acknowledgments

Supported by the National Science Foundation under Grant AER 73-07843 and the Division of Solar Energy of the Energy Research and Development Administration under Contract E(04-3)-1285.

Manuscript submitted July 29, 1977; revised manuscript received Nov. 30, 1977. This was Paper 217 presented at the Toronto, Canada, Meeting of the Society, May 11-16, 1975.

Any discussion of this paper will appear in a Discussion Section to be published in the December 1978 JOURNAL. All discussions for the December 1978 Discussion Section should be submitted by Aug. 1, 1978.

Publication costs of this article were assisted by Southern Methodist University.

REFERENCES

1. F. A. Trumbore, *Bell Syst. Tech. J.*, **39**, 205 (1960).
2. E. Sirtl and A. Adler, *Z. Metallk.*, **52**, 529 (1961).
3. T. L. Chu, H. C. Mollenkopf, and S. S. Chu, *This Journal*, **123**, 106 (1976).
4. R. J. Stirn, Conference Record of the 9th IEEE Photovoltaic Specialists Conference, p. 72 (1972).

Isothermal Silicon Liquid Phase Epitaxy from Supersaturated Tin

B. Jayant Baliga*

General Electric Company, Corporate Research and Development Center, Schenectady, New York 12301

ABSTRACT

It is demonstrated that liquid phase epitaxial layers of silicon can be grown under isothermal conditions by using a supersaturated tin melt. This technique produces superior surface morphologies as compared to epitaxial growth using slow cooling of the melt. The epitaxial layer thickness has been found to vary linearly with supersaturation and as the square root of the growth time in agreement with the theory by Ghez and Giess.

Liquid phase epitaxial growth of III-V and other compound semiconductors has been extensively studied and used for many applications. In contrast, very little has been reported on the epitaxial growth of silicon from the liquid phase. D'Asora *et al.* (1) have reported on the growth of silicon layers by the undercooling of a tin melt with the objective of obtaining a low density of surface defects. Kim (2) has applied this technique to the growth of silicon contact pedestals. More recently, Girault *et al.* (3) have reported the growth of silicon layers by undercooling Ga-Al alloys. However, no attempts at isothermal silicon epitaxial growth have been reported in the literature. The use of isothermal conditions for the liquid phase epitaxial growth of gallium arsenide layers and magnetic garnet films has been reported to produce good results (4, 5). This growth process, consequently, merits investigation for the growth of silicon layers.

The kinetics of the epitaxial growth of silicon by the undercooling of a tin melt was examined in detail in an earlier paper (6). The surface morphology of such layers was also examined and has been reported (7). In these papers, it was demonstrated that at slow cooling rates, the growth is mass transport controlled and at fast cooling rates the growth becomes kinetically limited. Under fast cooling rates, terraced epitaxial layer surfaces were observed, and increasingly smoother surfaces were obtained by decreasing the cooling rate. In all these experiments no initial melt supersaturation was used. The above results indicate that growth under isothermal conditions should produce the smoothest surface morphologies. This growth can only be achieved of course, with initial melt supersaturation. This paper examines the kinetics and the morphology of silicon epitaxial layers grown under such isothermal conditions with melt supersaturations ranging up to 30°C. It is demonstrated that this growth technique can be used for the growth of thin epitaxial layers with ripple-free, specular surfaces.

Experimental Procedure

Apparatus.—All the epitaxial growth reported in this paper was performed using tin as the solvent. The experiments were conducted using the dipping technique with a vertical substrate geometry. The epitaxial reactor used in this study has been described in detail in Ref. (6), and only a brief description is given here. A 100-g tin melt was heated to the saturation temperature in a ¾ in. diam quartz crucible within a hydrogen ambient. The temperature of the melt was maintained to within ±0.5°C using a controller with a Pt/Pt-Rd thermocouple to control the power fed to the furnace elements. The temperature of the melt was monitored by using another Pt/Pt-Rd thermocouple placed outside the quartz tube and positioned at the center of the crucible. The emf of this external monitor thermocouple was calibrated to the melt temperature by inserting a Pt/Pt-Rd thermocouple (within a quartz tube) into the melt and maintaining the melt at various temperatures. In order to obtain uniform epitaxial growth over the substrate, the melt temperature was vertically profiled from the bottom of the crucible to the top, and the crucible position in the furnace was adjusted until this profile was uniform to within ±0.5°C.

Growth procedure.—The melt was saturated at the saturation temperature using 0.01 Ω cm, boron-doped silicon wafers. The saturation was conducted with stirring until no further loss in weight of the saturation wafer could be detected. Typical saturation times were 45 min long. After saturation, the melt temperature was lowered to the growth temperature. Throughout this study, the growth temperature was maintained at 949°C, and in order to obtain layers of uniform radial thickness no rotation of the substrate was performed during epitaxial growth (6).

The epitaxial layers were grown on (111) oriented (±1°), 25-35 Ω-cm, phosphorus-doped silicon substrates. The growths were conducted on the polished surface of the wafers as received from the vendor. The wafers were degreased, boiled in nitric acid, and given a dip in hydrofluoric acid just before loading into the reactor. The substrate temperature was brought up to the melt temperature by holding the wafer above the melt for 10 min. The wafer was then inserted into the melt for the growth duration. After the growth period, the substrate was quickly withdrawn from the melt and spun to minimize the adherence of tin droplets on the wafer. Some tin was usually found to be present at the bottom edge of the wafer and was removed by etching in aqua regia. The bottom and edges of the wafer have been excluded during the analysis of layer thickness and morphology.

The layers grown in this study were observed to be of p-type conductivity because the melt was saturated with boron-doped substrates. Since the growth was conducted on n-type substrates, the epitaxial layer could be defined by angle lapping and delineating the junction with copper sulfate solution. The epitaxial layer thickness was then measured using an interferometer to within ±0.2 μm. The epitaxial layer thickness was found to be independent of substrate size.

Experimental Results

Morphology.—Under isothermal growth conditions, a significant improvement in surface morphology, as compared to that achieved with slow cooling, was immediately apparent. The surfaces of layers grown with slow cooling have been previously demonstrated to exhibit surface ripples (7). Under isothermal growth these ripples were absent for all the layers grown under the range of supersaturation (up to 30°C) and

* Electrochemical Society Active Member.

Key words: liquid phase epitaxy, epitaxial growth, supersaturation.

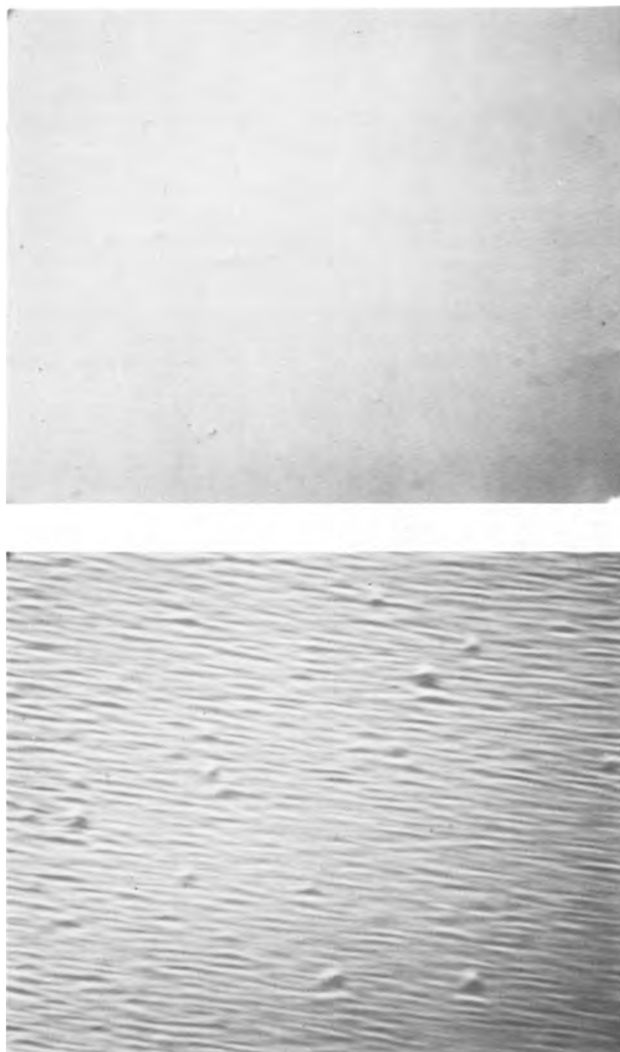

Fig. 1. Photomicrographs of wafers grown under (upper) isothermal growth conditions with a supersaturation of 21°C for 200 min (layer thickness of 4 μm), and (lower) a slow cooling rate of 0.2°C/min for 25 min (layer thickness of 5 μm). The shorter edge of each photograph represents 1 mm on the wafer surface.

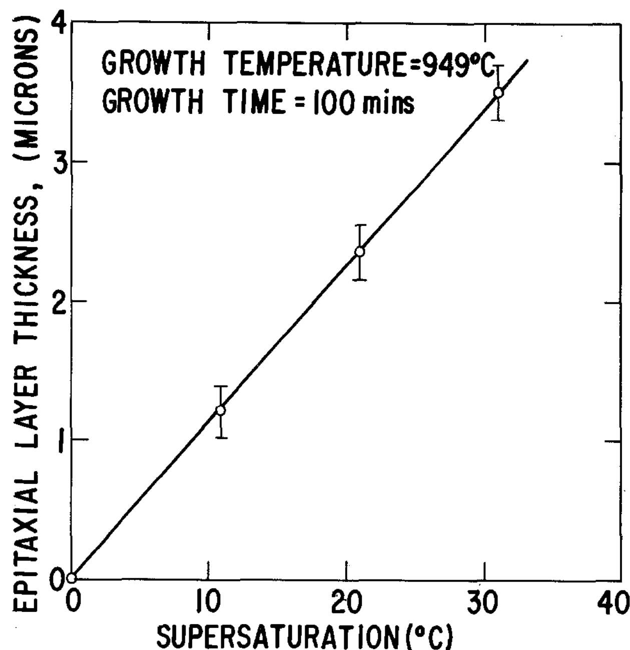

Fig. 2. Variation in epitaxial layer thickness with melt supersaturation.

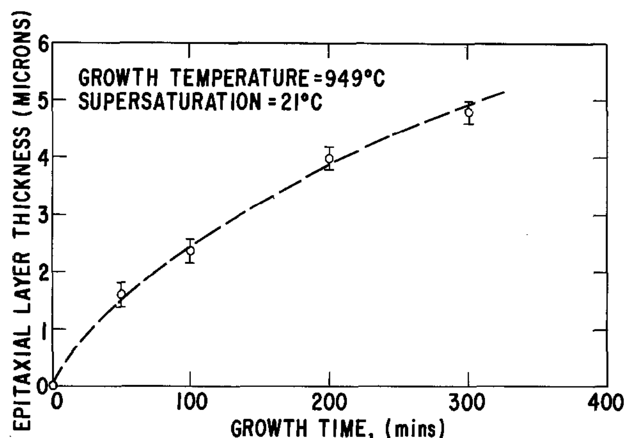

Fig. 3. Variation in epitaxial layer thickness with growth time at a fixed supersaturation.

epitaxial layer thickness (up to 10 μm) studied here. For purposes of comparison, Nomarski interference contrast photomicrographs of the surfaces of wafers grown under isothermal conditions and under slow cooling conditions are shown in Fig. 1. The significant improvement in surface morphology is apparent from these photographs.

Thickness.—The epitaxial layer thickness was measured as a function of both supersaturation and growth time. The variation in the layer thickness with supersaturation is shown in Fig. 2 for a growth time of 100 min. In this figure, the supersaturation has been given as the temperature difference between the melt saturation temperature and the growth temperature because the solubility of silicon in tin increases linearly in this small temperature range (8), and consequently the temperature difference directly represents the supersaturation. It is observed that the epitaxial layer thickness increases linearly with increasing supersaturation.

The change in epitaxial layer thickness as a function of growth time is shown in Fig. 3 for a supersaturation of 21°C. It is observed that the growth rate (slope of dashed line) is decreasing with increasing growth time. This type of behavior has also been observed during the epitaxial growth of GaAs under isothermal conditions (9). The nature of this increase in thickness with time, at a decreasing growth rate, is discussed in the next section.

Discussion

The kinetics of the epitaxial growth of thin films under isothermal growth conditions has been analyzed by Ghez and Giess (5). Although their paper discusses the growth of magnetic garnet films, the theoretical analysis can be applied to the data obtained in the growth of silicon layers in this study. The theory is based upon the assumption of a stagnant boundary layer through which growth units (silicon atoms here) can diffuse and the incorporation of these units into the epitaxial layer by a first-order reaction at the interface between the epitaxial layer and the melt. Further, a fixed concentration, C_L, is assumed beyond the boundary layer. Under these assumptions, the epitaxial layer thickness is predicted to increase linearly with the square root of the growth time and with supersaturation as long as the layer density is much larger than the solute concentration in the melt and as long as the growth rate is low (since the moving-phase boundary was neglected during the analysis). It can then be shown (5) that a plot of epitaxial layer thickness *vs.* square root of time will have a slope given by

$$\text{Slope} = \frac{2(C_L - C_e)}{\rho} \cdot \sqrt{\frac{D}{\pi}} \quad [1]$$

and a negative y-axis intercept given by

$$\text{Intercept} = -\frac{D(C_L - C_e)}{\rho k} \quad [2]$$

where C_e is the equilibrium concentration, ρ is the epitaxial layer density, D is the diffusion coefficient for the growth units in the melt, and k is the surface reaction constant.

It has been shown that the epitaxial growth of silicon in the present system is mass transport controlled at the lower cooling rates (6). Thus, under a zero cooling rate (isothermal growth) mass transport controlled growth by diffusion through a boundary layer can also be expected to occur. The other assumptions of the above theory are also satisfied here because the density of silicon (2.4 g/cm^3) is much larger than the silicon concentration in the melt (a maximum value of 0.045 g/cm^3 for a saturation temperature of 980°C), and the growth rates are extremely small (less than 0.05 μm per minute). This theory can, therefore, be used to analyze the data given in the previous section.

The data shown in Fig. 3 has been replotted in Fig. 4 in accordance with the above theory. It is observed that the layer thickness indeed increases linearly with the square root of time and has a negative intercept on the y-axis. By using this data and Eq. [1] and [2] for the slope and intercept, the diffusion coefficient (D) for silicon in tin at 949°C is calculated to be 6.4×10^{-5} cm/sec by using a supersaturation ($C_L - C_e$) of 0.37 atomic percent silicon in the tin (8). These values indicate that both reaction rate at the interface and the diffusion rate through the boundary layer play a role in controlling the growth rate.

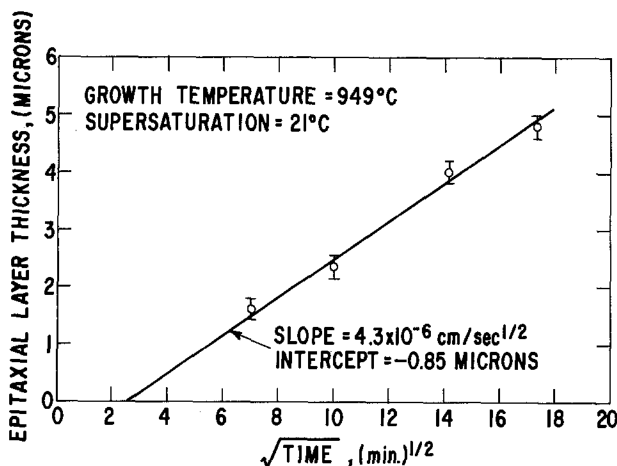

Fig. 4. Epitaxial layer thickness as a function of the square root of the growth duration under fixed supersaturation.

Conclusions

It has been demonstrated that the epitaxial growth of silicon can be achieved under isothermal growth conditions by using a supersaturated tin melt. It is observed that with this growth technique the epitaxial layer thickness increases linearly with supersaturation and as the square root of growth time. It is found that the epitaxial layers grown under isothermal conditions have superior surface morphologies as compared to those grown with slow cooling of the melt. However, the isothermal growth technique is primarily suitable for the growth of thin epitaxial layers. Since the silicon concentration in the melt depletes during growth, the growth rate decreases rapidly as film thickness increases. The application of the isothermal growth technique for thick epitaxial layers is, consequently, limited by the need for extremely large growth durations, as well as by the advent of bulk precipitation in the melt at high supersaturations.

Manuscript submitted Sept. 26, 1977; revised manuscript received Nov. 14, 1977.

Any discussion of this paper will appear in a Discussion Section to be published in the December 1978 JOURNAL. All discussions for the December 1978 Discussion Section should be submitted by Aug. 1, 1978.

Publication costs of this article were assisted by General Electric Company.

REFERENCES

1. L. A. D'Asaro, R. W. Landorf, and R. A. Furnanage, in "Semiconductor Silicon," R. R. Haberecht and E. L. Kern, Editors, p. 233, The Electrochemical Society Softbound Symposium Series, Princeton, N.J. (1969).
2. H. J. Kim, *This Journal*, **119**, 1394 (1972).
3. B. Girault, F. Chevrier, A. Joullie, and G. Bougot, *J. Cryst. Growth*, **37**, 169 (1977)
4. J. J. Hsieh, *ibid.*, **27**, 49 (1974).
5. R. Ghez and E. A. Giess, *Mater. Res. Bull.*, **8**, 31 (1973).
6. B. J. Baliga, *This Journal*, **124**, 1627 (1977).
7. B. J. Baliga, *J. Cryst. Growth*, **41**, 199 (1977).
8. C. D. Thurmond and M. Kowalchick, *Bell Syst. Tech. J.*, **39**, 169 (1960).
9. M. G. Astles, J. C. H. Birbeck, C. J. Laversuch, and M. C. Rowland, *J. Cryst. Growth*, **34**, 24 (1976).

Reactive Plasma Deposited Si-N Films for MOS-LSI Passivation

A. K. Sinha,* H. J. Levinstein, T. E. Smith, G. Quintana, and S. E. Haszko

Bell Laboratories, Murray Hill, New Jersey 07974

ABSTRACT

Amorphous Si-N films have been synthesized from SiH_4 and NH_3 by reactive plasma deposition at 275°C in an improved radial flow reactor. With appropriate control of machine and process variables, films have been made with Si/N ratio of 0.75-1.5, density of 2.8-2.2g cm^{-3}, refractive index of 1.9-2.3, stress of 2×10^9 dynes cm^{-2} compressive to 5×10^9 dynes cm^{-2} tensile, and electrical resistivity at 2×10^6 V/cm of 10^{20}-10^4 Ω-cm. The process is MOS compatible and it produces relatively thick (1 μm) crack-resistant Si-N films (at 450°-500°C) having excellent step coverage and good adhesion to both Au and Al metallization. This paper describes the deposition technique, effect of deposition parameters on various film properties, and the advantages these films offer in silicon integrated circuit technology.

In MOS-LSI technology, it is recognized that the effectiveness of the final passivation layer will, to a large extent, determine the ultimate reliability of the packaged device. The passivation layer is intended to protect sensitive areas of the device from outside contamination by, *e.g.*, Na^+ and moisture, and also to provide scratch protection for the Al metallization.

A potentially attractive material for this purpose is silicon nitride which provides an inert barrier (1, 2) to Na and H_2O as opposed to phosphosilicate glass (3) which acts as a "getter" for Na as well as moisture. However, the use of Si_3N_4 has been restricted because of the high temperatures ($\gtrsim$700°C) required for chemical vapor deposition of Si_3N_4 films (4) and because of high tensile stresses which limit the usable film thickness to ~2000Å (5).

Several investigations have been made concerning deposition of silicon nitride films at lower temperatures (<450°C) using an rf plasma to provide some of the activation energy needed for the reaction between SiH_4 and NH_3 or N_2 (6-10). The earlier systems utilized a quartz tube, an inductively coupled plasma, and gases flowing at a pressure of ~100 mTorr. These techniques generally lead to poor uniformity from wafer to wafer and inadequate step coverage. Reinberg (11) developed a radial flow reactor for Si-N deposition. He utilized a capacitively coupled rf discharge in a gas mixture consisting of SiH_4, NH_3, N_2, and Ar at relatively high pressures (0.5-1 Torr) and low powers (~50 W), in order to achieve good thickness uniformity and good step coverage. Rosler *et al.* (12) recently described a CVD process which also utilizes a radially symmetrical gas flow but in a direction opposite to that used by Reinberg; the capacitive discharge operates at a higher power (500W) and a relatively low frequency (50 kHz). Detailed data on the resulting $Si_xN_yH_z$ film composition ($0.8 \leq y/x \leq 1.0$), density (2.5-2.8 g cm^{-3}), resistivity (10^{15} Ω-cm), stress (1×10^9 dynes cm^{-2} compressive) etc., were reported by Kern and Rosler (13) for films deposited at 300°C.

We have devised certain improvements in the Reinberg radial flow reactor design which allows use of a wider range of deposition conditions and, consequently, a high degree of flexibility in tailoring the film properties (14). The main improvement consisted of a gas-flow discharge limiting shield which confines the plasma to a region above the substrates. It thereby enables use of higher rf powers without the adverse effects of a premature reaction between SiH_4 and NH_3 underneath the substrate table. This paper describes the deposition technique, effect of deposition parameters on various film properties, and the advantages these films offer in silicon integrated circuit technology.

Deposition Technique

Apparatus.—Figure 1 schematically shows the deposition apparatus consisting of a reactor, associated pumping systems, gas lines, and an rf power source.

The deposition reactor was a metal bell jar with a nominal diameter of 18 in. The cathode (16 in. diam) and the substrate table were made of Al and separated from each other by about 1 in. Heating was accomplished by means of quartz lamps mounted underneath the substrate table. A glow-discharge limiting shield was provided concentric with the heater and separated from it by ~¼ in. The gases were admitted underneath the heater, directed by the shield to flow radially inward over the surface of the substrate table and then exit to the pump through the center of the substrate table/heater assembly. Use of the gas flow discharge limiting shield eliminated premature decomposition of silane at higher rf powers since the gases were not exposed to the plasma until they were flowing over the substrates.

The pumping system was compatible with a high gas flow (>2 liters/min) at 1 Torr pressure. It consisted of a 150 cfm Leybold-Hereaus roots blower backed by two 17 cfm mechanical pumps running in parallel. The gas pressure was controlled by a throttle valve located in the roots blower line. The pressure was monitored

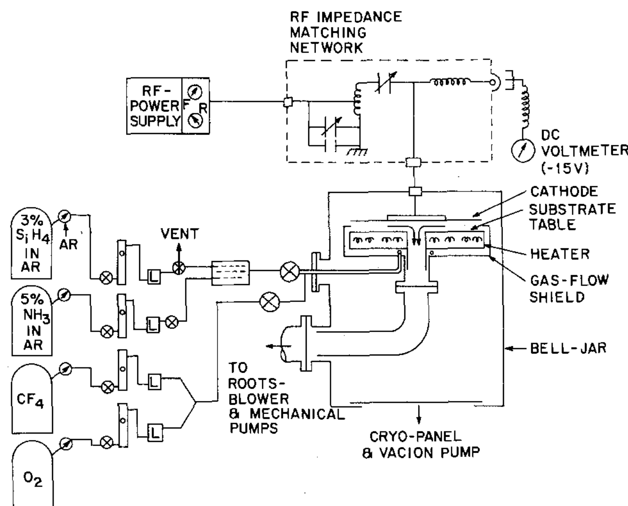

Fig. 1. Schematic of the apparatus used for deposition of RPD Si-N films.

* Electrochemical Society Active Member.

Key words: plasma-enhanced CVD, silicon nitride, thin films.

using a capacitance manometer (MKS Baratron) which provides measurements independent of the nature of the gas (and its conductivity). Facility was also provided to pump the system initially down to a base pressure of $\lesssim 10^{-6}$ mm with a cryopanel and a 400 liters/sec sputter-ion pump.

The reacting gases were 3% SiH_4 in Ar and 5% NH_3 in Ar. The delivery pressure was kept at 15 psig. The gases were led through rotameters to leak valves, L, and then on to a mixing chamber and finally to the deposition system. Special care was taken to keep these lines leak-tight. Similar but separate lines were provided for CF_4 and O_2 and an appropriate mixture of these two gases was used for plasma-etch cleaning of the station.

The rf power to the cathode was supplied by a Varian (13.56 MHz) power supply and an impedance-matching network of the conventional L-C type to which was added a fixed capacitor (Jennings, 220 pF) in parallel with the tunable load capacitor. This enabled satisfactory tuning with less than 10W reflected power at ~1 Torr pressure. The cathode d-c self-bias could be measured with a d-c voltmeter attached to the cathode power line via rf chokes.

Procedure.—The wafers (2 in. diam) were loaded in two concentric circles the bell jar was closed, and the system pumped down to $\sim 10^{-6}$ Torr using successively the mechanical pumps (to ~1 Torr), the roots blower (to ~3 mTorr), and the cryopanel and the sputter-ion pump (to $\sim 10^{-6}$ Torr). The final stage of the pumping added only 2-5 min to the total pumpdown time (~20 min). Next, the sputter-ion pump isolation valve was closed, the gases were admitted into the reactor, and the roots blower valve was opened again. A dynamic pressure (~600 mTorr) was established in the system with the gases flowing at the desired flow rates. Thereafter the roots blower valve was throttled to the desired pressure.

The rf plasma was excited to the desired power level. The plasma initiated and sustained the reaction between SiH_4 and NH_3 on the surface of the heated substrates. Typically, depositions were carried out for 1 hr to give Si-N films 1.1(±0.1)μm thick. The total turnaround time was <2 hr.

After every three runs, the system was cleaned *in situ* for 1-2 hr in a plasma (1000W) containing CF_4 + 8% O_2 at a flow of ~250 cm^3/min and a pressure of ~1000 mTorr with the substrate heater on. Subsequent to the cleaning operation a predeposition run (~15 min) was made with SiH_4 and NH_3 at the desired flows and pressure.

Film Evaluation Techniques

The film stress was deduced from change in curvature of the Si substrate due to the Si-N layer. For evaluation of 1 μm thick films, use was made of an optically levered laser beam to determine the substrate curvature (15). A more sensitive method was used for measurements on thinner films (~200Å); namely, the ABAC (automatic Bragg angle control) x-ray technique (16).

The refractive index was measured using an ellipsometer (5461Å). For film thickness and etch rate measurements, a step was etched in the film with 7:1 buffered HF (BHF) and the resulting step height was measured with the Talystep.

Rutherford backscattering analysis was used to determine the film composition and its density (17). Thinner films (~2000Å) on (111) Si were employed so as to get "clean" spectra and to reduce the background due to Si substrate by channeling along the [110] direction.

The density measured by Rutherford backscattering analysis was always within 10% and generally smaller than that determined from weight gain measurements on certain thicker films deposited under identical conditions (*e.g.*, conditions A and B of Table I).

The growth morphology of the film and its step coverage for various device topologies were determined using scanning electron microscopy on cleaved sections. The film structure was established using transmission electron microscopy in conjunction with selected area transmission electron diffraction.

The crack resistance of these films on various device structures was ascertained by heating them up to 450°-550°C (½ hr periods, air ambient), after which the films were examined in an optical microscope under interference contrast and/or polarized light. Usually when cracking occurred, it was gross and easily revealed. Further confirmation of the film integrity was provided by exposing the device structures to a metallization etch for 15 min followed by examination in the optical microscope.

Effect of Deposition Parameters

Five main process variables were investigated: (*i*) gas composition, (*ii*) total gas flow, (*iii*) pressure, (*iv*) substrate temperature, and (*v*) rf power to the plasma. Table I contains a summary of two "standard" processes (A and B) and the resulting film properties. Studies of variables (*i*) through (*iv*) were carried out in conjunction with process A, *i.e.*, at an rf power of 250W and with the remaining three parameters at the values given for process A.

Most of the data points, except those pertaining to "standard" processes A and B (Table I), represent averages of a limited number of measurements on 3-6 2 in. diam Si wafers located in the main outer row of the substrate table. In the worst cases, *i.e.*, at conditions farthest away from optimum, variations in some properties such as film thickness and etch rate could be as much as ±15%, but the uniformity improved to well within ±10% as the conditions approached optimum values.

Table I. Reactive plasma deposition conditions and resulting Si-N film properties for standard processes A and B

		Process A		Process B
A.	Reacting gases		$SiH_4/NH_3/Ar$	
B.	SiH_4 concentration (% flow)	1.70		1.78
	SiH_4/NH_3	0.71		0.79
C.	Total gas flow (sccm)		2320	
D.	Pressure (mTorr)		950	
E.	Substrate temperature (°C)		275	
F.	RF power (fwd/rev., W)	250/0		300/0
1.	Typical thickness (μm)		1.1 (±0.1)	
2.	Stress (10^9 dynes cm^{-2})	1-5, T		1, C
3.	BHF etch rate (Å/min)	100-200		75-150
4.	Refractive index	2.05 (±0.1)		1.95 (±0.1)
5.	Density (g cm^{-3})	2.55 (±0.05)		2.75 (±0.05)
6.	Composition (Si/N)	1.05 (±0.05)		0.8
7.	Cracking resistance (°C)	450		550
8.	Adhesion		Good	
9.	Step coverage		Excellent	
10.	Scratch resistance		Good	
11.	Dielectric constant	6.4		6.8
12.	Breakdown strength (10^6 V/cm)	3.9		5.0
13.	Resistivity at 2 × 10^6 V/cm (Ω-cm)	4 × 10^{13}		3 × 10^{15}

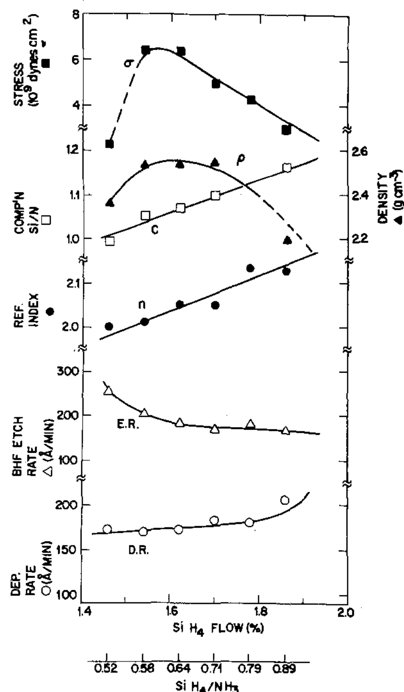

Fig. 2. Effect of SiH_4 concentration and SiH_4/NH_3 ratio on the properties of RPD Si-N films. (Other parameters kept constant at the values given for process A).

Gas composition.—Figure 2 shows the effect of increasing SiH_4 concentration ($1.4 \leq$ % $SiH_4 \leq 1.9$; $0.5 \leq SiH_4/NH_3 \leq 0.9$) on film properties for total flow of 2.3 std liters min^{-1}.

Increasing the SiH_4 concentration in the gas led to a corresponding linear increase in the Si/N ratio in the film (from ~1.0 to ~1.2) and a linear increase in the refractive index (from ~1.9 to ~2.2). With increasing SiH_4/NH_3 ratio, the film density ρ showed a broad peak ($\rho \approx 2.55$ g cm^{-3}) for $0.58 \leq SiH_4/NH_3 \leq 0.79$. The ρ decreased again at SiH_4/NH_3 ~0.9; however, this was not accompanied by a corresponding increase in the BHF etch rate, presumably because the films now had a much higher Si content (Si/N ~1.2). The film stress, σ, always tensile, showed a peak at SiH_4/NH_3 ~0.6, which is located at a slightly lower SiH_4 concentration than that for the peak in ρ. The choice of SiH_4/NH_3 ~0.7 for process A was selected on the basis of data on σ and ρ; one of the goals being to achieve a low σ in conjunction with high ρ (see section on Crack resistance, below).

Gas flow.—The total gas flow was varied in the range 1.0-2.5 liters min^{-1}, with the SiH_4/NH_3 ratio constant at 0.71 (Fig. 3) (% SiH_4 = 1.70). Under these conditions, the Si/N ratio in the film varied from 0.8 to 1.05; for this composition range, the film density seems to have a dominant effect on the BHF etch rate; a broad maximum in ρ corresponds to a broad minimum in the etch rate. The tensile stress decreases with increasing flow; this is probably the result of a higher film purity (with respect to possible N_2 contamination, see below) as the flow is increased.

Pressure.—The total pressure during deposition was varied from ~700 to 1000 (±25) mTorr. As shown in Fig. 4, increasing the pressure led to a higher deposition rate, whereas the density or the BHF etch rate did not change much. The refractive index decreased linearly. This generally (*i.e.*, for pressures $\gtrsim$ 750 mTorr) correlates with a decrease in the Si/N ratio in the film. The stress remains nearly constant in the range 700-950 mTorr.

Substrate temperature.—The range of substrate temperatures studied was $200 \leq T_S \leq 300°C$ (Fig. 5).

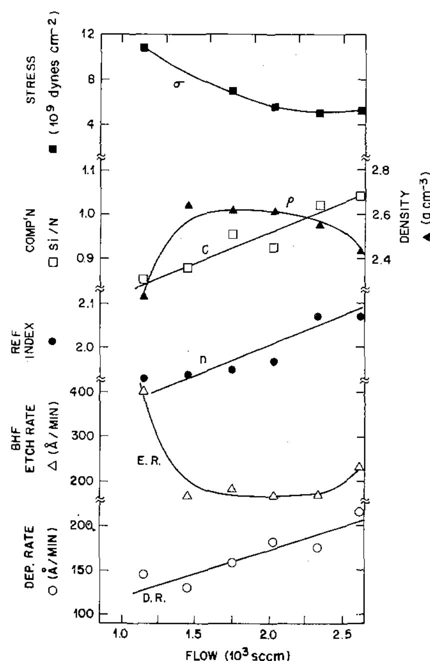

Fig. 3. Effect of gas flow on the properties of RPD Si-N films

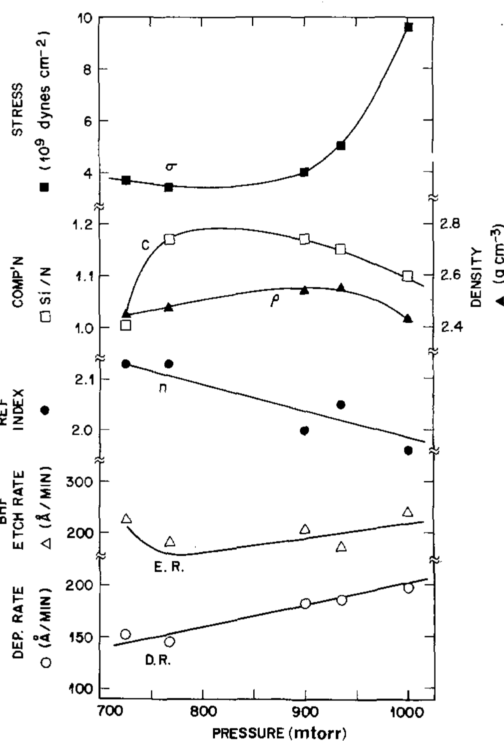

Fig. 4. Effect of gas pressure on the properties of RPD Si-N films

Higher temperatures were not investigated because the nitride films were intended for use on Ti/Pd/Au as well as Al metallization. As shown in Fig. 5, T_S has a pronounced effect on the BHF etch rate, which decreases almost exponentially with increasing T_S. The decrease in BHF etch rate is associated with a linear increase in the film density, ρ, and in the refractive index, n. Thus, for films deposited at 200°C, the BHF etch rate was 700 Å/min, the density was ~2.3 g cm^{-3}, and the refractive index was ~1.85. Interestingly, these films also had a rather large Si/N ratio (~1.2) and a high tensile stress (7×10^9 dynes cm^{-2}). With increasing T_S, both σ and Si/N ratio in the film displayed a shallow minimum at ~250°C; however, a higher T_S of 275°C was preferred because it led to films with yet larger density (2.55 g cm^{-3}) and somewhat lower etch rate without an excessive increase in σ.

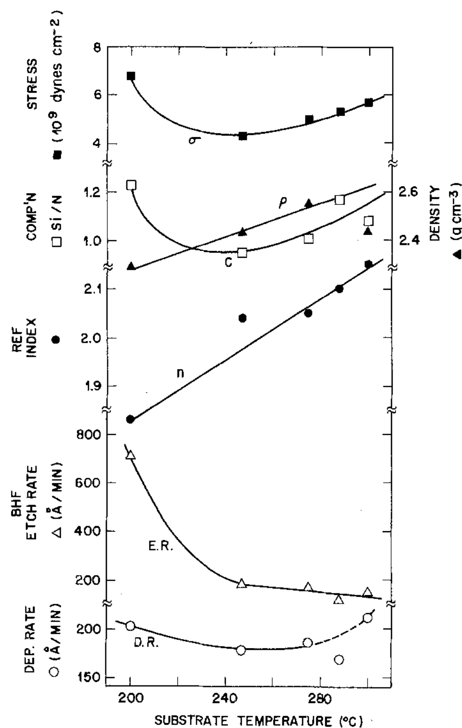

Fig. 5. Effect of substrate temperature on the properties of RPD Si-N films.

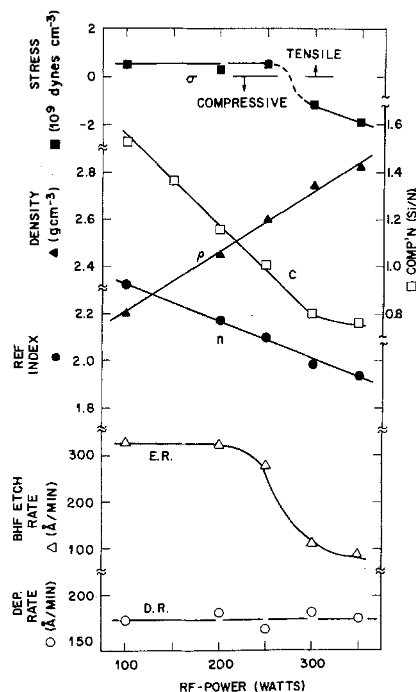

Fig. 6. Effect of rf power on the properties of RPD Si-N films. (Other parameters kept constant at values given for process B).

Rf power.—Tuned rf powers were investigated in the range 100-350W nominal, which were read off meters located at the power supply (Fig. 6). For this series of experiments, the SiH_4/NH_3 ratio was kept constant at 0.8 and % SiH_4 at 1.8. With increasing rf power, there is a rapid and linear increase in the film P (weight-gain measurements, using 1 μm thick films) from 2.2 g cm^{-3} at 100W to 2.8 g cm^{-3} at 350W. Films (1 μm) with Si/N >> 1 and lower density had a yellowish tinge when deposited on Al-metallized devices whereas those with Si/N $\lesssim$ 1 and densities $\gtrsim$ 2.4 g cm^{-3} appeared to be grayish and more transparent. Both the film σ and BHF etch rate showed a bimodal behavior at ~ 275W. Below this power level the stresses were very low tensile (~0.5 × 10^9 dynes cm^{-2}) and the etch rates were relatively high (275-325 Å/min). At rf powers $\gtrsim$ 300W, the stresses were compressive (1-2 × 10^9 dynes cm^{-2}) and the BHF etch rates were relatively low (~100 Å/min). Significantly, the refractive index decreased with increasing rf power, as did the Si/N ratio in the film. The latter, however, tended to level off at the stoichiometric value (Si/N ~ 0.75) for rf power > 300W.

The rf power readings quoted above are specific to the present system and its capacitive and inductive losses. It was found that the d-c (negative) voltage measured from cathode to ground was very small (1-10V). Peak-to-peak rf voltages were not measured, but since the cathode d-c voltages are small relative to gas ionization potentials [*e.g.*, 15.7 eV for Ar (18)], it is expected that the (positive) plasma potential with respect to ground must be quite high. This effect may be related to the system geometry, which consists of large electrodes (16 in. diam) in a relatively small volume (1 in. interelectrode spacing), and to the relatively large pressure (~ 1 Torr) of the discharge. These voltage characteristics may be contrasted with those present in typical rf sputtering systems (19), where the discharge operates at 5-10 mTorr pressure. The rf sputtering systems are associated with a very large cathode d-c self-bias of ~ 1 kV (19), which is nearly half the peak-to-peak or electron accelerating voltage. In such systems, the plasma is only slightly positive with respect to the ground.

Effect of N_2 and O_2 Additions to the Preferred Gas Mixture

Small amounts of air-leaks into the system, or substituting the NH_3 with N_2 as the source of N_2, were found to severely degrade the crack resistance. This was an unexpected observation since the literature contains examples of reactive plasma and reactive sputtering processes where preference is expressed for either N_2 (9) or NH_3 (6). Therefore, mixtures of NH_3 and N_2 were not suspect.

Figures 7 and 8 show the effect of N_2 addition on Si-N film properties. The control sample had a low tensile stress of 5 × 10^8 dynes cm^{-2}, an etch rate of 75 Å/min, and a refractive index of 1.92. Addition of small amounts of N_2 (up to 2%) caused a steep increase in tensile stress (up to 6 × 10^9 dynes cm^{-2}) as well as

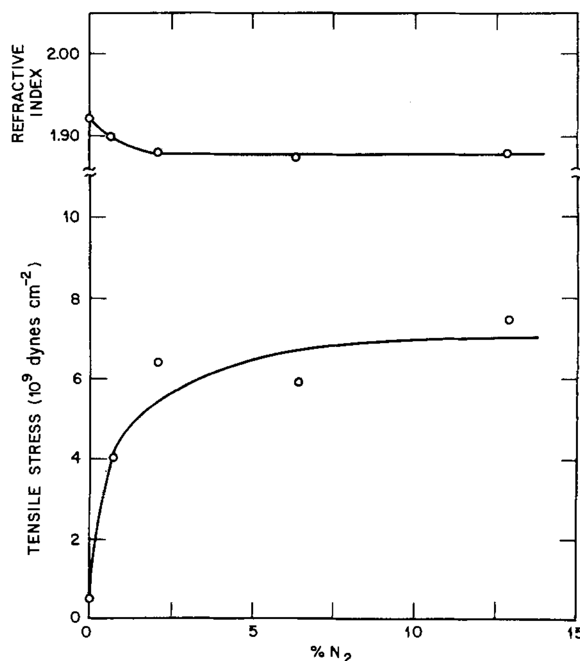

Fig. 7. Effect of N_2 additions to the reactant gas mixture (process A) on the tensile stress and refractive index of RPD Si-N films.

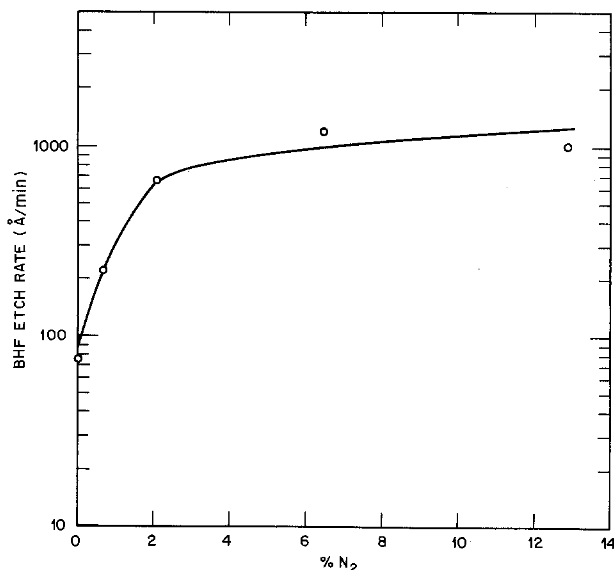

Fig. 8. Effect of N_2 addition to the reactant gas mixture on the etch rate in BHF of RPD Si-N films.

in the BHF etch rate (up to 700 Å/min) and a small decrease in the refractive index. At higher N_2 concentration in the gas stream, all of these film properties tend to level off. The high etch rate implies that these films have a lower density; the combination of low density and high tensile stress has been found to correlate with poor crack resistance of Si-N films at temperatures $\gtrsim$ 450°C (14, 15).

The addition of small amounts of O_2 to the reactant gas mixture had an even greater effect on BHF etch rate. As shown in Fig. 9, the etch rate continues to increase exponentially to ~3000 Å/min for 0.65% O_2, showing no sign of saturation. The effect on refractive index, n, is also quite severe (Fig. 10); n decreases from ~1.9 to ~1.6 for 0.65% O_2. The effect on film stress, σ, is relatively small. The σ initially increases to ~3×10^9 dynes cm^{-2} and then it decreases to almost zero for 0.65% O_2. It appears that some of the O_2 added to the gas stream gets incorporated into the film, leading to an oxynitride; hence the low n, very high etch rate, and the apparent stress-compensation effect (20).

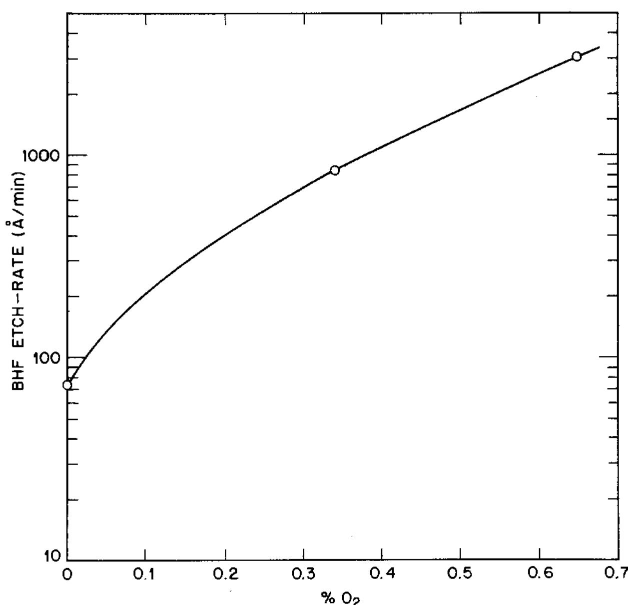

Fig. 9. Effect of O_2 addition to the reactant gas mixture on the BHF etch rate of RPD Si-N films.

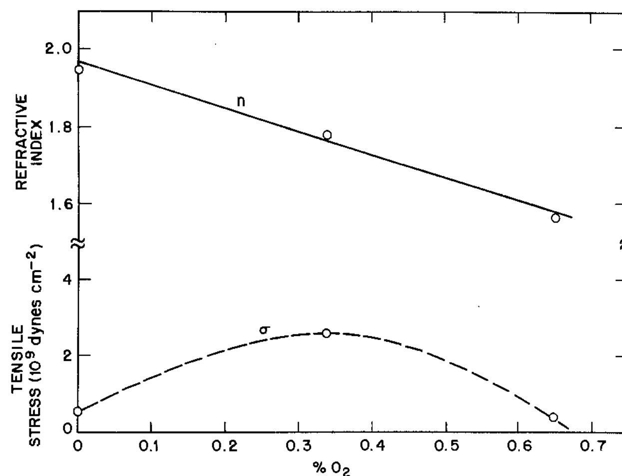

Fig. 10. Effect of O_2 addition to the reactant gas mixture on the tensile stress and refractive index of RPD Si-N films.

Discussion of Film Properties

Crack resistance.—Thick Si-N films (1 μm) on Al-metallized wafers cracked on heating to 450°C if the film stresses were too high ($\gtrsim 8 \times 10^9$ dynes cm^{-2}) or if the densities and deposition temperatures were too low ($\lesssim$2.2 g cm^{-3} and <<275°C, respectively). An example of extensive nitride cracking over both Al metallization and dielectric areas is shown in Fig. 11 for a Si-N film made at 250°C with a density of ~2.2 g cm^{-3} and a tensile stress of ~0.5×10^9 dynes cm^2. In contrast, films made using process A withstood 450°C, ½ hr treatments and those using process B did not show any cracking even at 550°C, ½ hr when the underlying Al was properly stabilized and it did not form large hillocks that punched through the Si-N film. Thermal stresses in Al, which form the driving force for hillock formation, have been shown to be a sensitive function of the film thickness and the initial microstructure (21). Most of our studies involved Al metallization (1-2 μm) evaporated at ~300°C and H_2 baked at 450°C prior to Si-N deposition.

It was recently proposed (14, 15) that the cracking resistance, CR, of a thick Si-N film at a given temperature T is functionally related to its density, ρ, intrinsic stress, σ_i, thermal mismatch, $\Delta\alpha$, with Si, and the deposition temperature, T_s, through the following equation (14)

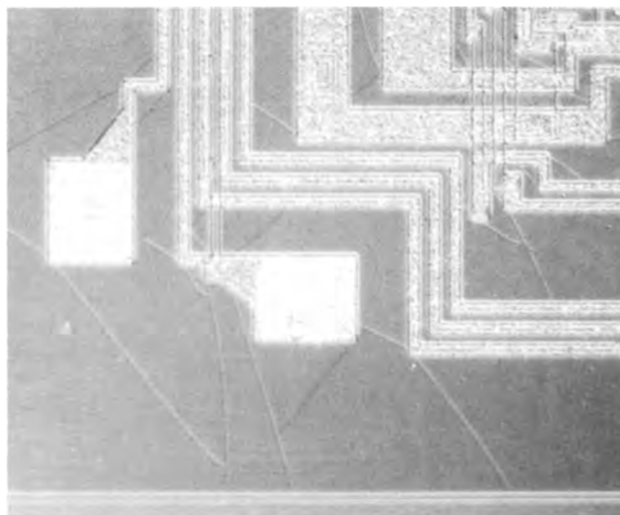

Fig. 11. Effect of a 450°C, ½ hr, air heat-treatment on the integrity of RPD Si-N film over Al-metallized Si wafer (film made at 250°C with a density of ~ 2.2 g cm^{-3} and a stress of ~ 0.5 $\times$ 10^9 dynes cm^{-2}).

$$\mathrm{CR} \approx \frac{\rho}{\rho_0} \cdot \sigma_u - \sigma_i - \frac{E'}{1-\nu'} \int_{T_s}^{T} \Delta\alpha \cdot dT$$

Where, σ_u is the ultimate tensile stress of a structurally "perfect" Si_3N_4 film with density ρ_0, and E' and ν' are the Young's modules and Poisson's ratio for the film. This equation correctly predicts that CR will be improved if ρ is increased, σ_i and $\Delta\alpha$ are made small, and T_s is made high relative to the test temperature. A quantitative application of the above equation, including thermal stress measurements, for various Si-N films is described in Ref. (15).

Thickness uniformity.—The radial symmetry of gas flow and of plasma electron density inherent in the reactor design provides a useful means of attaining good thickness uniformity on wafers arranged in concentric circles. There still remains the problem of uniformity as a function of radius of the circle in which the wafers are placed. Here, two opposing effects may be involved (11): (*i*) the reactant gas concentration, which gets depleted as the gases flow inward; high gas flow will prevent such depletion, which is also countered by increased velocity as the gases approach the center of the substrate table, and (*ii*) the electron density which depends on the rf power and increases on going toward the center of the substrate table. Therefore, in principle, uniformity can be optimized by adjusting the gas flow for a particular rf power or vice versa.

For the preferred processes (A and B of Table I), we employed both a relatively high throughput of the reactants (2.3 liters/min) and a high rf power (250 or 300W); conditions which are compatible with a fair degree of uniformity. The uniformity was better than $\pm 10\%$ from wafer-to-wafer (arranged in two circles containing 14 and 8, 2 in. diam wafers, respectively) and from one deposition run to the other. The best thickness uniformity was observed at the lowest powers investigated (100W at $T_s = 275°C$), but these films were unacceptable because of a tendency toward cracking at 400°C. At the higher rf powers ($\geq$ 350W), the thickness uniformity got much worse and $\pm 10\%$ uniformity could be achieved only over wafers in the outer circle.

Structure and growth morphology.—The amorphous nature of the present Si-N films was established by transmission electron microscopy. No contrast effects due to crystallites or voids could be seen in the bright- or dark-field mode, and electron diffraction patterns showed broad, diffuse halos characteristic of amorphous structure. Further insight into the nature of these films has been obtained by Lorentz-Lorenz correlation of the data on the film density, composition, and refractive index (17). The resulting magnitudes of electronic polarizabilities (α) suggest that the effective size of "Si" in plasma Si-N is quite high and probably corresponds to that of a Si-H complex. The α_{Si} increases with Si/N ratio indicating that Si-H complexes assume an increasing role in Si-rich Si-N films.

The growth morphology, as revealed by SEM examination, was always found to be smooth (layered) on the various surfaces investigated (Si, SiO_2, Al_2O_3, Si_3N_4, Al, Pd, Au) provided these surfaces were clean. However, in certain cases, we observed sporadic incidence of nodular growth, or hillocks; an extreme case is shown in Fig. 12(a). The device area in Fig. 12(b) shows nodules only in the dielectric areas, and with adequate cleaning, the situation corresponded to that of Fig. 12(c) where only a layered growth was observed.

We have correlated the occurrence of nodular growth with surface contamination (from baked-on residues of photoresist and intentionally introduced Sn and Pb at monolayer levels) and/or particulate matter. The presence of such contamination apparently triggers a vapor-liquid-solid growth (22) and/or gas

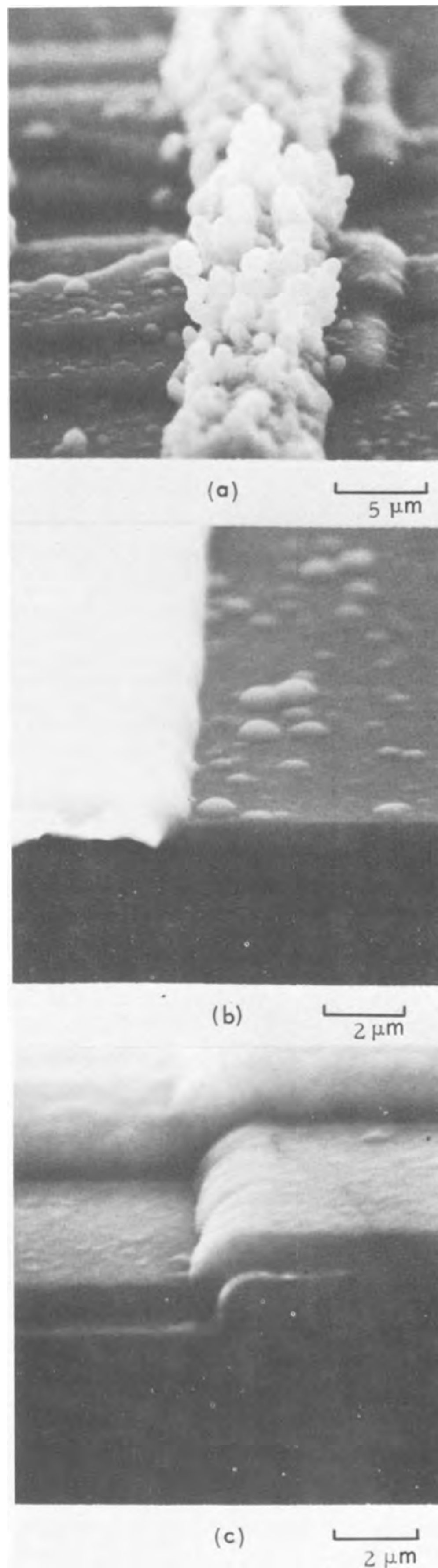

Fig. 12. Growth morphology of RPD Si-N films showing: (a) and (b) sporadic nodular growth (hillocks) on contaminated areas of device wafers, namely, Au lines and dielectric areas, respectively, and (c) layered growth on properly cleaned device wafers.

phase reaction (13) in the vicinity of the contaminated area. Such reactions in response to surface contamination were found to be more likely to occur under conditions of higher temperatures and larger flows, which also lead to "superior" crack-resistant films. Proper cleaning of the metallized wafers to remove any particulates and surface chemical contamination prior to H_2 bake was found to be desirable. One effective cleaning process involved scrubbing both sides of the wafer in Triton X (Rohm & Haas, Philadelphia, Pennsylvania) (1:20,000 dilution), followed by boiling in a mixture of 90% water and 10% H_2O_2 (high purity) for 10 min, followed by a cold deionized water rinse for $\geqq$ 15 min.

Step coverage.—Use of high pressures (relative to sputtering) during deposition and a surface-activated film growth process leads to excellent step coverage as illustrated in Fig. 13 and 14 for Ti/Pd/Au beam leads and Al metallization, respectively. As shown in Fig. 14(c), the Si-N layer conforms well to the underlying topology even where the walls are vertical or they have a slight negative slope. Particularly important is the absence of any reentrant angles at the bottom of the steps. Further evidence of excellent step coverage was obtained by immersing the coated device wafers for $\geqq$15 min in an appropriate metallization etch, such as hot H_3PO_4-CH_3COOH-H_2O for Al and KI-I_2 for Au, and then finding no attack on the underlying metal.

Si-gate MOS device compatibility.—MOS measurements were made on Si-gate MOS devices processed through second-level metallization and then subjected to the Si-N reactive plasma deposition, plasma etching of Si-N, and O_2 plasma stripping of the resist. The gate oxide capacitors showed no measurable increases in the oxide fixed charge or the surface-state density at midgap nor any radiation-induced bias-temperature instability. The absence of radiation-damage in above structures where the gate oxide is protected against soft radiation damage by the poly-Si appears to be due mainly to the use of relatively high pressures in the plasma and low levels of cathode d-c bias, as compared to rf or d-c sputtering processes.

Electrical properties of the present films were found to be a function of the film composition and its structures (23). The electrical resistivities (at 2×10^6 V/cm) for films with Si/N of 1.8, 1.0, and 0.75 were 4×10^4, 4×10^{13}, and 5×10^{19} Ω-cm, respectively. The dielectric strength similarly increased from $0.8 \rightarrow 3.9 \rightarrow 8.1$ MV/cm. The thermal activation energy for conduction was ~0.3 eV. The dielectric constant (1 MHz) ranged from 6 to 8.

The Si-N films have been successfully utilized to form structures containing Ti/Pt/Au beam leads on Al (Fig. 15); the device is effectively sealed by the combination of Au-beam leads and plasma SiN. Si-gate PMOS and CMOS logic devices have been fabricated with the above structure in plastic packages; the latter devices showed an extrapolated median time to failure of > 40,000 hr under bias-humidity-temperature (85°C/85% RH) aging with intentional ionic contamination present. No cases were encountered of any cathodic corrosion of Al after 10^6 device-hours of 85/85 aging.

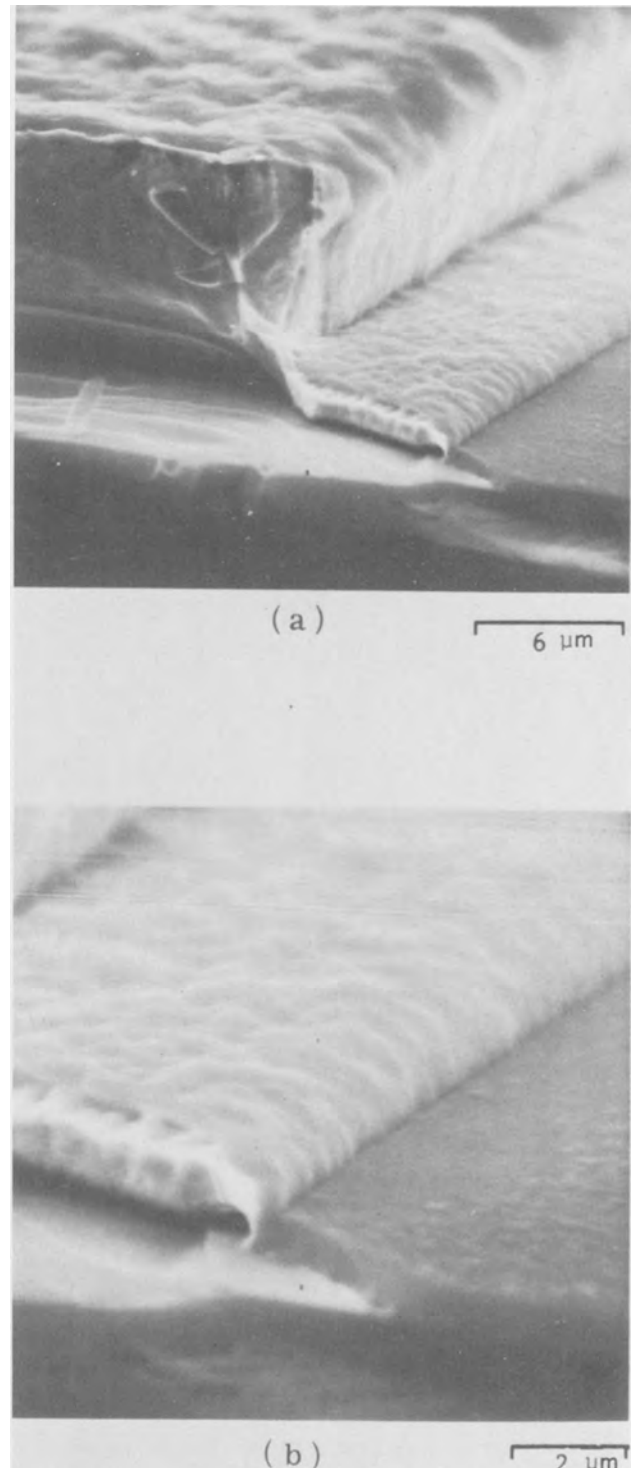

Fig. 13. SEM photographs of step coverage by 1 µm thick Si-N film on Au beams: (a) thick (12 µm) Au on Au (1 µm)/Pd/Ti metallization, (b) detail of base of the Au beam.

Conclusions

Certain plasma deposited Si-N films may compare favorably with PSG passivation layers and even with CVD Si_3N_4. Thus, these Si-N films provide an inert barrier to Na and H_2O, unlike heavily doped, low temperature CVD (LTCVD) P-glass which is hygroscopic and can react with H_2O to form corrosive H_3PO_4 (24). Si-N films have excellent step coverage whereas LTCVD often leads to films with a dog-bone type of feature on top and reentrant angles on the bottom of the steps. Si-N films provide a suitable surface for subsequent deposiiton of Ti/Pt/Au films whereas the surfaces of undensified P-glass are such that it is difficult to deposit adherent films on it. The electrical resistivity and the density of plasma Si_3N_4 films are comparable with those of CVD Si_3N_4, but the former can have much lower and compressive stresses which allows a higher usable thickness of 1 µm.

In conclusion, plasma-enhanced CVD provides an attractive deposition technique for Si-N films for final passivation. Its advantages are: manufacturability, low temperature operation, good step coverage/uniformity, compatibility with Si-gate MOS devices, and great flexibility with regard to control of stresses, film composition, density, and cracking resistance. The dis-

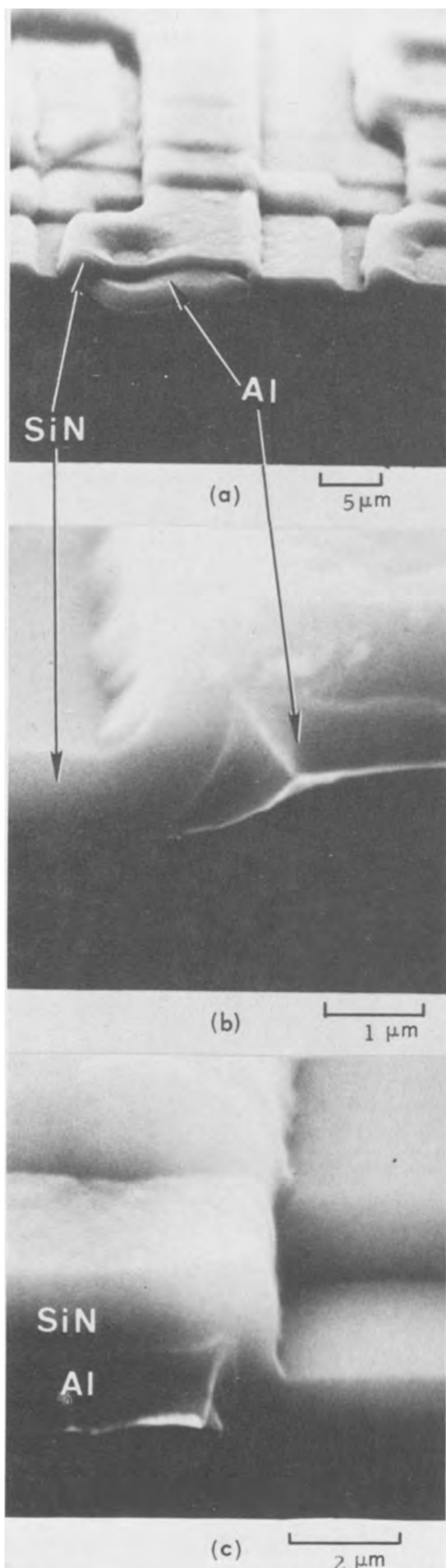

Fig. 14. Step coverage by RPD Si-N films on an Al-metallized LSI device: (a) section showing contact areas and Al runners, (b) detail of Si-N on Al with tapered edges, (c) Si-N on Al runner with nearly vertical edges.

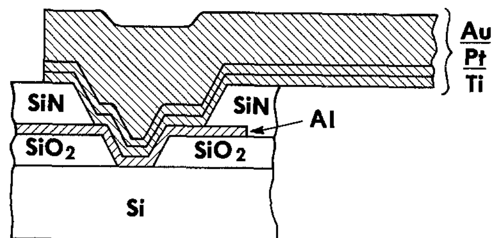

Fig. 15. Ti/Pt/Au beam leads to Al metallization passivated with RPD Si-N (Si/N = 1).

advantages are: a relatively complex reactor and process (many variables) and a sensitive growth morphology under certain conditions.

Acknowledgments

The authors would like to thank P. D. Cruzan and J. V. Dalton for experimental assistance, J. M. Dishman for MOS evaluations, J. M. Poate and E. Lugujjo for Rutherford backscattering analysis, T. T. Sheng for transmission electron microscopy, and R. S. Wagner for many useful discussions.

Manuscript submitted Oct. 19, 1977; revised manuscript received Dec. 1, 1977.

Any discussion of this paper will appear in a Discussion Section to be published in the December 1978 JOURNAL. All discussions for the December 1978 Discussion Section should be submitted by Aug. 1, 1978.

Publication costs of this article were assisted by Bell Laboratories.

REFERENCES

1. J. V. Dalton and J. Drobek, *This Journal*, **115**, 865 (1969).
2. M. T. Duffy and W. Kern, *RCA Rev.*, **31**, 742 (1970).
3. D. R. Kerr, J. S. Logan, P. J. Burkhardt, and W. A. Pliskin, *IBM J. Res. Dev.*, **8**, 376 (1964).
4. V. Y. Doo, D. R. Kerr, and D. R. Nichols, *This Journal*, **115**, 61 (1968).
5. W. A. Kohler, *Trans. AIME*, **246**, 735 (1970).
6. R. C. G. Swann, R. R. Mehta, and T. P. Cage, *This Journal*, **114**, 713 (1969).
7. H. F. Sterling and R. C. G. Swann, *Solid-State Electron.*, **8**, 653 (1965).
8. Y. Kuwano, *Jpn. J. Appl. Phys.*, **7**, 88 (1968).
9. R. Gereth and W. Scherber, *This Journal*, **119**, 1248 (1972).
10. O. Meyer and W. Scherber, *J. Phys. Chem. Solids*, **32**, 1909 (1971).
11. A. R. Reinberg, Abstract 6, p. 19, The Electrochemical Society Extended Abstracts, Spring Meeting, San Francisco, California, May 12-17, 1974; U. S. Pat. 3,757,733.
12. R. S. Rosler, W. C. Benzing, and J. Baldo, *Solid-State Technol.*, **19**, 45 (1976).
13. W. Kern and R. S. Rosler, *J. Vac. Sci. Technol.*, **14**, 1082 (1977).
14. A. K. Sinha, Abstracts 242, 244, pp. 625, 626, 629, 630, The Electrochemical Society Extended Abstracts, Fall Meeting, Las Vegas, Nevada, Oct. 17-22, 1976.
15. A. K. Sinha, H. J. Levinstein, and T. E. Smith, To be published in *J. Appl. Phys.*
16. G. A. Rozgonyi and T. Ciesielka, *Rev. Sci. Instrum.*, **44**, 1053 (1973).
17. A. K. Sinha and E. Lugujjo, *This Journal*, **123**, 189C (1976); *Appl. Phys. Lett.*, **32**, 245 (1978).
18. E. U. Condon and H. Odishaw, "Handbook of Physics," pp. 7-35, McGraw-Hill Book Co., New York (1967).
19. J. L. Vossen and J. J. O'Neill, *RCA Rev.*, **29**, 149 (1968).
20. C. M. Drum and M. J. Rand, *This Journal*, **115**, 194C (1968).
21. A. K. Sinha and T. T. Sheng, *Thin Solid Films*, **48**, 117 (1978).
22. R. S. Wagner and W. C. Ellis, *Trans. AIME*, **223**, 1053 (1965).
23. A. K. Sinha, *J. Electron. Mater.* **5**, 441 (1976); A. K. Sinha and T. E. Smith, To be published in *J. Appl. Phys.*
24. N. Nagasima, H. Suzuki, K. Tanaka, and S. Nishida, *This Journal*, **121**, 434 (1974).

Boron Predeposition in Silicon Using BBr_3

P. Negrini, A. Ravaglia,[1] and S. Solmi

C.N.R.-LAMEL Laboratory Via Castagnoli, 1-40126 Bologna, Italy

ABSTRACT

The process of boron predeposition in silicon using a BBr_3 source is investigated for different times, temperatures, and doping gas compositions. The experimental conditions leading to the formation on the silicon surface of the boron-rich layer are determined. It is shown that the boron surface concentration in silicon, in equilibrium with the boron-rich layer, is higher than the solubility value and depends on doping gas composition. Different surface concentrations corresponding to different boron-rich layer compositions can explain the "anomalous" decrease of the amount of boron entering the silicon, which is observed in particular experimental conditions. In this evaluation both the strong concentration dependence of the boron diffusion coefficient and the translation of the BRL-Si interface have also been taken into account. Finally the rate-determining steps of the transfer of boron into silicon are discussed.

Boron is the p-type dopant most often used in silicon planar technology. The predeposition process, in spite of the many investigations carried out (1-12), still presents several important features not completely explained and interpreted.

It is well known (3-8) that in the usual working conditions a boron-rich layer (BRL), insoluble in HF, grows at the interface between boron silicate glass (BSG) and silicon. Notwithstanding the poor knowledge of the composition of the BRL, it has frequently been reported in the literature that the boron surface concentration in silicon, in the presence of this phase, is the solubility one (2-5, 12, 13).

Recently Armigliato *et al.* (14), by x-ray analysis performed on BRL specimens, clearly demonstrated the presence of SiB_6 as well as some additional interplanar spacings which may be attributed to B_4Si and B_6O. They conclude that the BRL consists of a mixture of phases and show that the boron surface concentration in silicon is markedly higher than the solubility value.

In this work we study the predeposition of boron in silicon for different times, temperatures, and doping gas partial pressures. The experimental conditions leading at the formation of the BRL are determined and the rate-determining steps of the doping process are discussed.

Experimental Procedure

Dislocation-free (111) oriented, phosphorus-doped, Czochralski-pulled silicon of nominally 1 Ω-cm has been used in our experiments. Slices were about 300 μm thick and mirror finished on one side.

Predepositions have been carried out at 900°, 1000°, 1050°, and 1100°C using a BBr_3 source kept at 24°C. High purity nitrogen was bubbled through the liquid boron tribromide source, and then, before entering the furnace, it was mixed with the main carrier gas which consisted of a mixture of variable amounts of nitrogen and oxygen. The apparatus and the procedures are described in a previous paper (15).

The predeposition cycle consisted of a 5 min preheating (N_2 plus O_2 flowing) followed by deposition for a given time, t_d, (BBr_3, N_2, and O_2 flowing), and by a final 3 min flush (N_2 plus O_2 flowing). A set of predepositions has been performed changing the partial pressure of oxygen, and another set changing that of the boron tribromide. In all cases the total gas flow was kept constant (2500 ml/min) by adjusting the main nitrogen flow.

The thicknesses of BSG and BRL formed during the predeposition cycles were accurately measured by a Talystep by making at least ten determinations for each specimen.

After predeposition, the BSG was etched with dilute HF, while the BRL was removed by boiling the slices in nitric acid or by anodic oxidation. The last technique makes possible a selective etching of the BRL to form the step necessary for the thickness measurement. The anodic oxidation was carried out at a constant current value and using as electrolyte a solution of 900 ml of ethylene glycol, 100 ml of H_2O, and 5g of KNO_3. Typical behavior of the experimental voltage *vs.* oxidation time relationship for samples with and without the BRL is shown in Fig. 1. When no BRL is present, the voltage drop across the growing SiO_2 layer is added to the voltage drop V_o due to the resistance of the electrolyte and of the silicon slice. In the presence of the BRL, this layer is first oxidized with formation of a compound soluble in the electrolyte, so that no increase of the voltage drop takes place during this time. The sudden growth of the voltage indicates the entire removal of the BRL and the beginning of the oxidation of the silicon below.

Sheet resistance, ρ_s, was measured by the four-point probe technique; five distinct determinations were made on each specimen.

Boron doping profiles were determined by successive anodic oxide stripping followed by Hall and resistivity measurements, using a Van der Pauw geometry. The total amount, Q, of boron entered into the

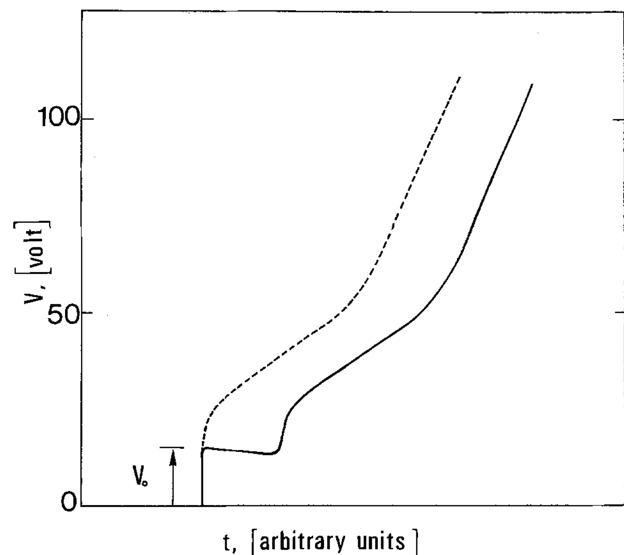

Fig. 1. Experimental voltage vs. time relationship during anodic oxidation. Continuous line refers to a sample with BRL.

[1] Present address: SGS-ATES, Agrate B. (Milano) Italy.

Key words: silicon, boron tribromide, boron predeposition, boron-rich layer.

silicon has been accurately determined in some cases by integration of the doping profiles. However, as this method is tedious and time consuming, a sufficiently accurate Q value can also be obtained more easily from the measured sheet resistance by the relationship

$$Q = \frac{1}{e \cdot \mu_{eff} \cdot \rho_s} \quad [1]$$

where e is the electronic charge and μ_{eff} the "effective mobility" of the boron-doped layer defined in Ref. (15). In all the measured predeposition profiles values of μ_{eff} very close together ($\mu_{eff} = 43.8 \pm 1.6$ cm^2/V·sec) have been ascertained. Therefore, a linear relationship between Q and $1/\rho_s$, with accuracy better than 4%, could be established for a broad range of values. A similar result has also been obtained by Allen (16).

Finally the predeposited specimens have been examined by transmission electron microscopy (TEM) in order to verify the eventual presence of boron precipitates.

Experimental Results and Discussion

Doping dependence on gas composition.—The amount of boron, Q, introduced into silicon during predepositions performed at 900°, 1000°, 1050°, and 1100°C is reported in Fig. 2 and 3 as a function of oxygen concentration. Boron tribromide partial pressure (0.04%) and predeposition cycle (5 + 20 + 3 min) were kept constant.

At 900°C, for the gas composition range considered, Q is quite insensitive to the oxygen percentage. At this temperature we have low oxidation rate and large deposition of B_2O_3, since its vapor pressure increases greatly with temperature (17). Thus the BSG consists largely of B_2O_3 and it is, in fact, partially dissolvable in H_2O. All the samples were covered with a thin BRL detectable by the hydrophilic behavior of the surface.

Conversely, Q is a sensitive function of the oxygen content at 1000°C; in particular, when the oxygen concentration is higher than about 8%, no BRL

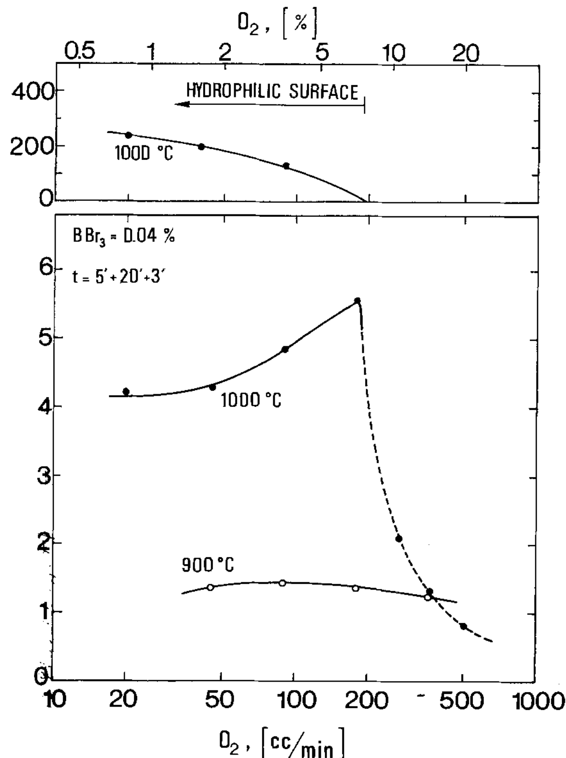

Fig. 2. Amount of boron, Q, and BRL thickness, X_{BRL}, vs. oxygen concentration for predepositions performed at 900° and 1000°C. BBr_3 concentration (0.04%) and deposition time (20 min) are kept constant. Dotted line means lack of BRL.

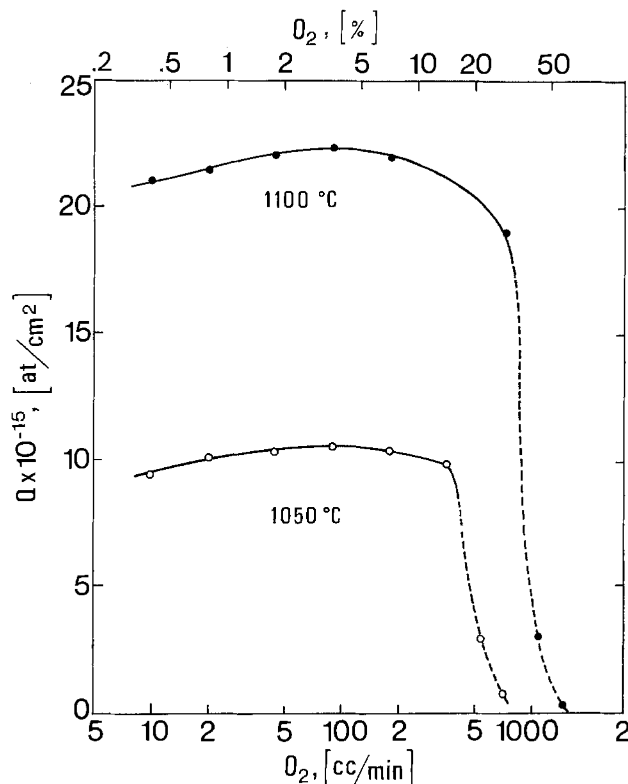

Fig. 3. Amount of boron, Q, vs. oxygen concentration for predepositions carried out at 1050° and 1100°C. BBr_3 concentration (0.04%) and deposition time (20 min) are kept constant. Dotted line means lack of BRL.

grows: In these conditions the doping, which is limited by B_2O_3 diffusion through the boron glass (5), considerably decreases when the oxygen concentration increases. For oxygen concentrations lower than about 8% we observe the formation of the BRL with thickness which increases as the oxygen concentration decreases. In spite of the presence of the BRL, Q is not a constant, but decreases with the increase of the BRL thickness.

The same qualitative behavior is obtained at temperatures of 1050° and 1100°C. For oxygen concentration higher than 14 and 29%, respectively, no BRL forms and Q greatly decreases when the O_2 percent increases. At lower oxygen partial pressures the BRL grows on the silicon surface reducing the dependence of Q on the gas composition. However we can again observe that Q is not kept constant by the presence of the BRL.

At temperature of 1000°C, where this phenomenon is more marked, the dependence of Q and of the BRL thickness, X_{BRL}, on boron tribromide concentration has also been studied. Figure 4 shows these results for predeposition carried out with a cycle of 5 + 20 + 3 min for two different oxygen concentrations (7.2 and 1.8%). With higher oxygen content Q increases with the BBr_3 concentration until the BRL starts to grow on the sample surface; then a further increase in the doping gas leads to an increase in X_{BRL} and to a decrease in Q. With lower oxygen concentration the BRL forms on all the specimens and its thickness greatly increases with BBr_3 percent while Q decreases.

Also in this case the presence on the silicon surface of the BRL does not provide a constant value of Q. A similar behavior has been reported in the literature (5, 12), but it has not been clearly explained.

Finally, as has been previously observed by other authors (3, 6), we have found that predepositions carried out in the conditions which give rise to the formation of the BRL, are more reproducible. From several experiments we have deduced that the fractional standard deviation

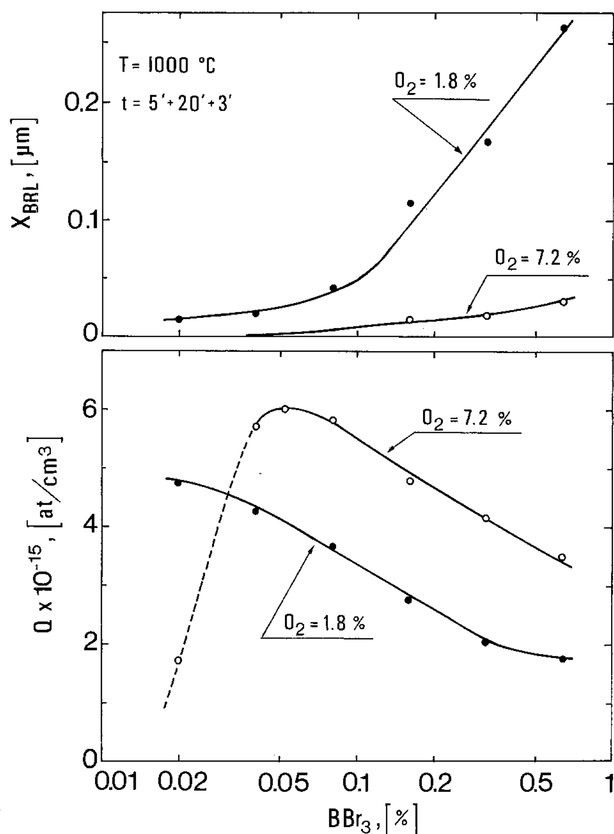

Fig. 4. Amount of boron, Q, and BRL thickness, X_{BRL}, vs. BBr_3 concentration for 20 min predepositions at 1000°C.

$$\sigma = \frac{1}{\overline{X}} \sqrt{\frac{\sum_{i\ j}^{n} (\overline{X} - X_j)^2}{n - 1}}$$

for different predepositions, carried out in the same conditions, was about 4% when the BRL grows and higher than 10% when the BRL is not present.

Doping dependence on predeposition time.—Figure 5 shows the value of Q as a function of predeposition time, t ($t = t_d + 3$ min; *i.e.*, deposition time plus 3 min flush time) for processes performed at

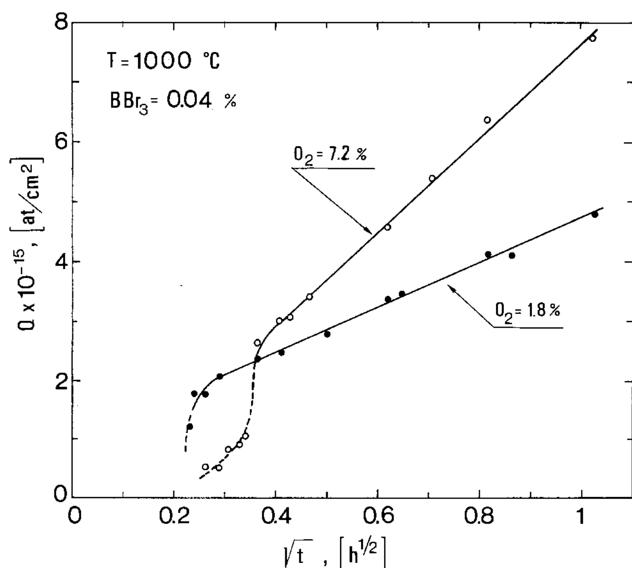

Fig. 5. Amount of boron, Q, vs. time (deposition time plus 3 min flush time) for predepositions carried out at 1000°C with 0.04% BBr_3. Dotted line means lack of BRL.

1000°C with 0.04% BBr_3 and two different oxygen concentrations, 1.8 and 7.2%, respectively. In both cases, after an initial transient, Q grows linearly with the square root of time.

A simple analysis of these data suggests that the surface concentration of boron in silicon, notwithstanding the presence of the BRL, is different for the two oxygen concentrations. In fact, the solution of the diffusion equation, considering the BRL as an infinite source, is (18)

$$Q = C_s \frac{2}{\sqrt{\pi}} \sqrt{Dt} \qquad [2]$$

where C_s is the surface concentration and D is the boron diffusion coefficient, both assumed to be constant.

Equation [2] gives a linear behavior of Q with $\sqrt{t}$, and the slope is proportional to the surface concentration.

The initial transient of Q is related to the presence of the BRL. In fact, if during the deposition time a layer of this phase forms on the slice surface, boron also keeps entering into the silicon during the 3 min flushing time. With an oxygen concentration of 1.8%, the BRL forms in a very short time (~0.5 min), while, with an oxygen concentration of 7.2%, the BRL formation is delayed (~3.5 min) by the silicon oxide grown during the preheating time and by the faster oxidation process occurring during predeposition.

Boron surface concentration.—Results presented in Fig. 2 and 4 show a decrease of Q when increasing X_{BRL} for predepositions carried out in the same conditions of time and temperature. Stach and Turley (9) ascribe this behavior to the displacement of the interface BRL-Si toward the bulk, as a consequence of the silicon consumption resulting from the formation of the surface phase. The contribution of this phenomenon, surely present, can be evaluated by solving the diffusion equation in a semi-infinite medium with a moving boundary. The solution in this case yields (19)

$$C(x) = (C_s/2) \left[\text{erfc} \left(\frac{x + \alpha \cdot X_{BRL}}{2\sqrt{Dt}} \right) + \exp \left(- \frac{\alpha \cdot X_{BRL} \cdot x}{Dt} \right) \cdot \text{erfc} \left(\frac{x - \alpha \cdot X_{BRL}}{2\sqrt{Dt}} \right) \right] \qquad [3]$$

where $\alpha \cdot X_{BRL}$ is the fraction of silicon consumed by the formation of a thickness X_{BRL} of the surface phase. By numerical integration of Eq. [3] the total amount of boron in silicon as a function of X_{BRL} is obtained. These results, together with the experimental behavior obtained from the data reported in Fig. 4, are shown in Fig. 6. The calculations have been performed with the hypothesis that the BRL consists of SiB_6 ($\alpha = 0.31$) and with the limiting case in which the consumed silicon is equal to the thickness of the BRL ($\alpha = 1$). From the plot it appears that this phenomenon aids in diminishing Q, but it cannot explain our experimental results.

Brown and Kennicott (12) observed the same phenomenon using a low temperature CVD deposited BSG as a source. They interpreted this behavior by assuming that a sudden lowering in the boron diffusivity takes place when the surface concentration reaches the solubility value. This effect was associated with a change of BSG properties which causes a reduction of the stress induced in the silicon crystal. This hypothesis, however, does not explain the results of Fig. 5 (Q *vs.* $\sqrt{t}$), where a different behavior for the samples processed at different O_2 partial pressures is also observed after the BRL formation.

We believe that in our case the phenomenon can be ascribed to the different value assumed bv the boron surface concentration in contact with a BRL of different composition.

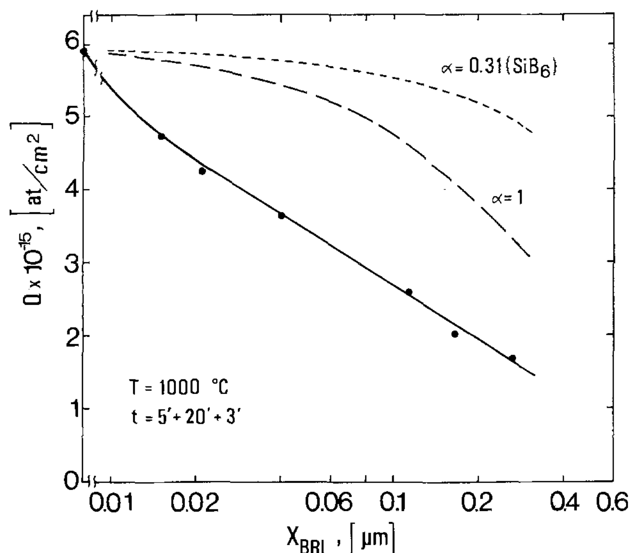

Fig. 6. Amount of boron, Q, vs. BRL thickness, X_{BRL}, for predepositions carried out at 1000°C for 20 min. The theoretical curves (dotted and broken line) are obtained by numerical integration of Eq. [3] with $\alpha = 0.31$ and $\alpha = 1$, respectively. Experimental data are obtainable from Fig. 4.

Accurate analysis of the chemical composition of the BRL carried out by Rutherford backscattering (20) and x-ray microanalysis (21) on samples processed at 1000°C with different doping gas compositions (the same conditions as Fig. 4) have clearly shown the presence of three elements: boron, silicon, and oxygen. The atomic percent of these elements is a function of the process conditions: In all the examined cases the percentage of boron is the prevailing one and is greater than 70 atom percent (a/o); this value increases up to about 80 a/o as the BBr_3 partial pressure increases. Oxygen and silicon range from 4 to 15 a/o and from 14 to 20 a/o, respectively. These analyses, together with the x-ray diffraction observations (14), lead to the conclusion that the BRL is formed by a mixture of several compounds and not by the conjugate phase of the Si-B system (B_4Si). Consequently, the boron concentration at the silicon surface is not the one corresponding to solid solubility and may change with the BRL composition.

In order to verify hypotheses, in Fig. 7 are reported the measured doping profiles of specimens processed at 1000°C for 20 min with different doping gas and, consequently, different BRL compositions. Profiles (a) and (c) refer to situations of high Q with thin BRL and low Q with thick BRL, respectively, while (b) represents an intermediate case. It appears from these results that there is an appreciable difference in the boron surface concentrations certainly higher than the uncertainty which affects the measurements ($C_s(a) = 2.7 \times 10^{20}$ cm^{-3}; $C_s(b) = 2.5 \times 10^{20}$ cm^{-3}, and $C_s(c) = 1.85 \times 10^{20}$ cm^{-3}).

We notice that in all cases the surface concentration is higher than solubility value [1.2×10^{20} atoms/cm^3 at this temperature (14)]. This is due to the presence of SiB_6 in the BRL; in fact the chemical potential of the solute associated with the second intermediate phase (SiB_6) must be higher than that corresponding to the equilibrium between the primary solid solution and its conjugate phase (B_4Si); therefore boron concentration in silicon is increased above the solubility value.

Studies on the kinetics of nucleation and precipitation of boron in silicon confirm that in the conditions of time, temperature, and oversaturation typical of a predeposition process, the nucleation of the conjugate phase B_4Si is hindered (14). Moreover, lack of precipitation has been confirmed by TEM observations on samples treated in the same experimental conditions as the one of Fig. 7.

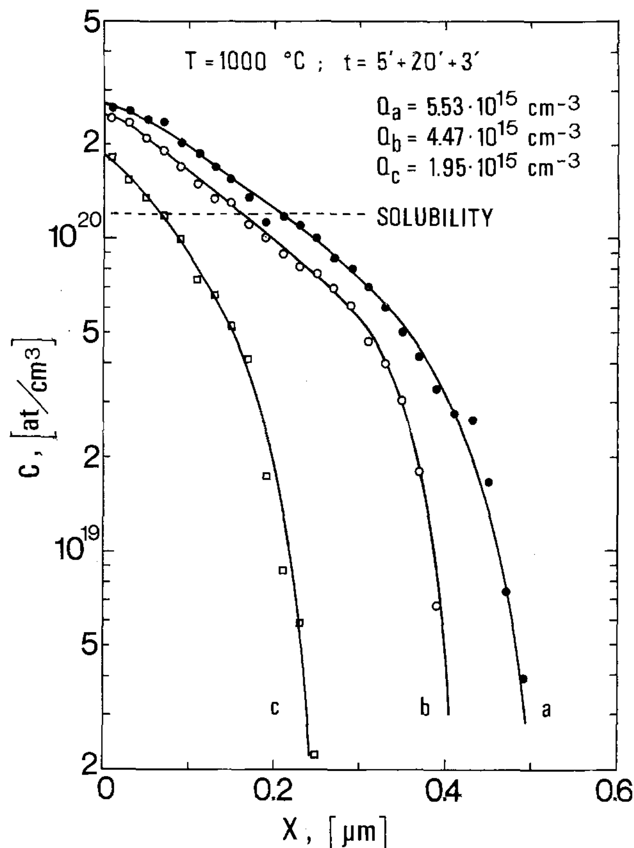

Fig. 7. Boron concentration profiles in silicon predeposited at 1000°C for 20 min. Gas composition: (a) 7.2% oxygen, 0.04% BBr_3, $X_{BRL} \leq 50$Å; (b) 1.8% oxygen, 0.04% BBr_3, $X_{BRL} = 210$Å; (c) 1.8% oxygen, 0.32% BBr_3, $X_{BRL} = 1600$Å. Solubility value is also reported in Ref. (14).

The observed differences in the surface concentration can explain the different values of Q provided that the dependence of boron diffusion coefficient on concentration is taken into account.

With reference to profiles (a) and (c), and assuming a linear dependence of D on concentration, as proposed by Fair (22), it can be shown that

$$\frac{Q(c)}{Q(a)} = \left[\frac{C_s(c)}{C_s(a)}\right]^{3/2} = 0.57 \quad [4]$$

If one assumes the concentration dependence of D proposed by Thai (23) and subsequently modified by Jain and Overstraeten (24), a ratio $Q(c)/Q(a) \simeq 0.47$ is obtained. Adding to this effect the further decrease of Q due to the displacement of the BRL-Si interface we can explain the experimental ratio $Q(c)/Q(a) = 0.36$, resulting from the profiles reported in Fig. 7.

Finally we point out that changes of boron surface concentration in presence of BRL are very small with respect to the ones observed when the surface phase is not present: In fact, in order to have a reduction of 30% in C_s it has been necessary to increase by an order of magnitude the BBr_3 concentration.

Summary and Conclusions

This work presents the results of an experimental investigation of the boron predeposition in silicon carried out for different times, temperatures, and gas composition.

The formation of the BRL on silicon samples is favored by the decrease of the oxygen and/or the increase of the BBr_3 partial pressure.

The rate-determining step of the boron predeposition process may be summarized as follows:

(*i*) *BRL not present.*—The amount of boron available at the BSG-Si interface completely penetrates

into the silicon and the rate-determining step is the diffusion of B_2O_3 through the boron glass (5). Reproducibility and uniformity of the process depend largely on the oxygen and boron tribromide concentrations in the furnace.

(*ii*) *BRL present.*—Q is limited by the diffusivity of boron in silicon and by its surface concentration. This concentration, which is not the solubility one, changes with the composition of the BRL. However the process is repeatable since the changes of C_s with doping gas composition are small.

The different values of Q obtained by predeposition carried out with the same time and temperature can be quantitatively explained by the change in C_s, if the large concentration dependence of the boron diffusion coefficient and the translation of the BRL-Si interface are considered.

Manuscript submitted June 20, 1977; revised manuscript received Nov. 22, 1977.

Any discussion of this paper will appear in a Discussion Section to be published in the December 1978 JOURNAL. All discussions for the December 1978 Discussion Section should be submitted by Aug. 1, 1978.

Publication costs of this article were assisted by C.N.R.-LAMEL.

REFERENCES

1. P. C. Parekh and D. R. Goldestein, *Proc. IEEE*, **57**, 1507 (1969).
2. M. C. Duffy, D. W. Foy, and W. J. Armstrong, *This Journal*, **114**, 29 (1967).
3. G. M. Oleszek and W. M. Whittemore, in "Semiconductor Silicon," R. R. Haberecht and E. L. Kern, Editors, p. 490, The Electrochemical Society Softbound Symposium Series, New York (1969).
4. M. S. R. Heynes, *Electrochem. Technol.*, **5** 25 (1967).
5. E. Arai, H. Nakamura, and Y. Terunuma, *This Journal*, **120**, 980 (1973).
6. K. M. Busen, W. A. FitzGibbons, and W. K. Tsang, *ibid.*, **115**, 291 (1968).
7. W. A. FitzGibbons, T. Kloffensteins, and K. M. Busen, *ibid.*, **117**, 272 (1970).
8. K. M. Busen, W. A. FitzGibbons, and T. Kloffensteins, *Electrochem. Technol.*, **6**, 256 (1968).
9. J. Stach and A. Turley, *This Journal*, **121**, 722 (1974).
10. D. Rupprecht and J. Stach, *ibid.*, **120**, 1266 (1973).
11. K. M. Whittle and G. L. Vick, *ibid.*, **116**, 645 (1969).
12. D. M. Brown and P. R. Kennicott, *ibid.*, **118**, 293 (1971).
13. G. L. Vich and K. M. Whittle, *ibid.*, **116**, 1142 (1969).
14. A. Armigliato, D. Nobili, P. Ostoja, M. Servidori, and S. Solmi, in "Semiconductor Silicon 1977," H. R. Huff and E. Sirtl, Editors, p. 638, The Electrochemical Society Softbound Symposium Series, Princeton, N.J. (1977).
15. P. Negrini, D. Nobili, and S. Solmi, *This Journal*, **122**, 1254 (1975).
16. W. G. Allen, *Solid-State Electron.*, **16**, 709 (1973).
17. J. Stach and J. Kruest, *Solid State Technol.*, **19**, 60 (1976).
18. B. I. Boltaks, "Diffusion in Semiconductors," p. 106, Goldsmid, London (1963).
19. H. S. Carslaw and J. C. Jaeger, "Conduction of Heat in Solids," p. 388, Oxford University Press (1959).
20. A. Armingliato, G. G. Bentini, G. Ruffini, G. Della Mea, and A. Drigo, 3rd International Symposium on Ion Beams in Solids, Washington, June 27-July 1, 1977.
21. A. Armigliato, G. G. Bentini, A. Desalvo, R. Rinaldi, R. Rosa, and G. Ruffini, XII National Conference of Microbeam Analysis Society, Boston, Aug. 18-24, 1977.
22. R. B. Fair, *This Journal*, **122**, 800 (1975).
23. N. D. Thai, *Solid-State Electron.*, **13**, 165 (1970).
24. R. K. Jain and R. Van Overstraeten, *J. Appl. Phys.*, **44**, 2437 (1973).

On the Electrical Properties of Cuprous Iodide

T. Jow* and J. Bruce Wagner, Jr.*,[1]

Materials Research Center and Department of Materials Science and Engineering, Northwestern Universtiy, Evanston, Illinois 60201

ABSTRACT

The electrical properties of single and polycrystalline CuI have been studied using the a-c method for CuI equilibrated with copper and C. Wagner's d-c polarization cell. Values for the total conductivity, electron hole conductivity, transference number for Cu^+ and electron holes, the diffusivity of electron holes, and double layer capacitance at the CuI-graphite interface were obtained.

The electrical conductivity of cuprous iodide has been measured by various authors (1-6). Cuprous iodide is a predominantly ionic conductor at temperatures above 300°C (2). Its conductivity greatly depends on the small deviation from the ideal metal-to-nonmetal ratio (2, 5). The excess conductivity is due to hole conduction induced by the excess iodine (1, 4-5).

Hebb (7) first pointed out that it is possible to suppress either the ionic or the electronic transport in galvanic cells by an appropriate choice of the electrodes and to deduce the partial conductivity of the migrating particles from the quotient of the current density and the potential gradient. C. Wagner (8) established the d-c asymmetric cell (or d-c polarization cell) measurement for the determination of the partial electronic conductivity in a predominantly ionic conductor by evaluating the steady-state current-voltage relation. This method has been utilized on cuprous halides (9, 10), silver halides (11-13), lead halides (14-16), calcia stabilized zirconia (17), etc.

In addition to steady-state polarization cell measurements, unsteady-state or transient polarization cell measurements have been used to study the kinetic properties of the electrode (18-20), the electrolyte (10, 21), and the interfacial phenomena (21, 22) between the electrolyte and the electrode. In the present study, an ion-blocking electrode (graphite) was used as the electrode. Because of virtually no solubility of copper in the graphite electrode, the kinetics of copper ion diffusion into the graphite electrode are not considered.

Raleigh (22, 23) first used the potentiostatic technique on a polarization cell to study the double layer

* Electrochemical Society Active Member.
[1] Present address: Center for Solid State Science, Arizona State University, Tempe, Arizona 85281.
Key words: electrical conductivity, transference number, double layer capacitance, electron hole diffusivity.

capacitance of AgBr against the blocking electrode. Weiss (21) measured the voltage relaxation in a polarization cell to obtain the diffusivity of the electrons in AgBr. Joshi and Wagner (10) combined the d-c steady-state and the aforementioned unsteady-state measurement methods of the polarization cell to obtain the partial conductivity, mobility, and concentration of electron holes in cuprous chloride.

The purpose of the present study on cuprous iodide is to use d-c steady-state measurements to obtain the partial electronic conductivity of cuprous iodide and transient measurements to obtain the diffusivity of the electronic carriers in cuprous iodide, and the double layer capacitance at the interface between the cuprous iodide and the blocking electrode.

Theory

Steady-state polarization cell measurements.—Wagner's polarization cell (8) of the following configuration

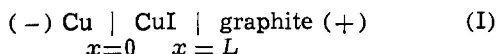

$$(-)\ \mathrm{Cu}\ |\ \mathrm{CuI}\ |\ \mathrm{graphite}\ (+) \qquad \text{(I)}$$
$$x=0 \quad x=L$$

was used to measure the electronic conductivity of the mixed conductor, CuI.

The steady-state current passed through cell (I) with a positive d-c potential, E, which is smaller than the decomposition potential of CuI, applied on the graphite electrode consists of only electronic current. The equation for this current as a function of the applied potential has been derived by C. Wagner (8). When $\sigma_\oplus >> \sigma_\ominus$ and $EF/RT >> 1$, Wagner's equation may be expressed by (9, 10)

$$I_e = I_\oplus = (ART/L\mathbf{F})\ \sigma_\oplus{}^\circ \exp\left(\frac{E\mathbf{F}}{RT}\right) \qquad [1]$$

where I_e = electronic current at steady state; $I_\oplus$ = electronic current due to electron holes; A = cross-sectional area of the electrolyte (assumed constant and the same as the interface area of the electrodes); $\sigma_\oplus{}^\circ$ = electronic conductivity due to electron holes in CuX equilibrated with Cu; and the other terms have their usual significance. $\sigma_\oplus{}^\circ$ can thus be determined from a plot of log I_e *vs.* the polarization potential E. Equation [1] was derived under several assumptions which are discussed in Ref. (8). In the derivation of Eq. [1], the band bending and any interfacial effects are neglected.

Unsteady-state or transient polarization cell measurements.—When a potential E_1 is applied to the polarization cell (I) with the positive potential on the graphite electrode, the activity of copper partial pressure of iodine at the blocking electrode ($x = L$) are fixed electrochemically by the potential. They are given by

$$a_{\mathrm{Cu}} = \exp(-E_1\mathbf{F}/RT) \qquad [2]$$

$$P_{\mathrm{I_2}} = \exp[-2(E_d - E_1)\mathbf{F}/RT] \qquad [3]$$

where E_d is the decomposition potential of CuX. Since copper halides are p-type conductors (9, 24), the electron hole concentration at the blocking electrode ($x = L$) can be expressed as follows (8)

$$c_\oplus{}^1 = c_\oplus{}^\circ \exp(E_1\mathbf{F}/RT) \qquad [4]$$

where the superscript 1 denotes "under potential E_1," and $c_\oplus{}^\circ$ is the electron hole concentration in cuprous iodide coexisting with copper. The steady-state electron hole distribution at E_1 can be expressed as

$$c_\oplus(x) = c_\oplus{}^\circ + (c_\oplus{}^1 - c_\oplus{}^\circ)x/L, \quad 0 \leq x \leq L \qquad [5]$$

A transient response or the unsteady state of the polarization cell is achieved either by the "potentiostatic method" (22, 23), *i.e.*, the applied voltage is changed abruptly from E_1 to E_2 where E_2 is a new value of the applied potential and observing the change of current with time, or by the "voltage relaxation method" (21) in which the polarized potential E_1 is switched off suddenly and the change of the open-circuit potential of the cell with time is observed.

The phenomena of these two methods have been discussed rather extensively in Ref. (10). The main results are mentioned in the following sections.

Potentiostatic method.—When there is an abrupt change in applied potential on cell (I) from E_1 to E_2, a transient current flows corresponding to kinetic processes which are required to repolarize the cell at the newly fixed potential. The reasons (10, 25-27) for the occurrence of this unsteady-state current may consist of: the solid electrolyte-solid electrode interfacial double layer capacitance existing at CuX and graphite interface; redistribution of electrons and electron holes inside the electrolyte; or copper diffusion into the graphite electrode.

A typical transient current-time profile for a potential step from E_1 to E_2 is shown schematically as in Fig. 1 $I_\oplus(E_1)$ and $I_\oplus(E_2)$ are the initial and final currents at steady states under potentials E_1 and E_2, respectively. I_0 is the initial peak current. (In the present study, the current due to copper diffusion into the graphite electrode is too small to be considered.)

For a pure capacitance, the decay of the charging current should obey

$$I(t) = I_0 e^{-t/RC} \qquad [6]$$

where I_0 is the initial peak current, R is the total resistance, and C is the capacitance. Raleigh (22, 23, 28) has studied double layer capacitance in silver halide polarization cells rather extensively. He attributed double layer capacitance as an intrinsic property existing between solid ionic and solid electronic conductors. He found that the decay of the double layer capacitance charging current generally does not show one single decay constant (29).

The current-time relation due to redistribution of electron holes for a potential step changing from E_1 to E_2 can be obtained by solving Fick's second law

$$\frac{\partial c_\oplus}{\partial t} = \tilde{D}_\oplus \frac{\partial^2 c_\oplus}{\partial x^2} \qquad [7]$$

with the following initial and boundary conditions

$$c_\oplus(x) = c_\oplus{}^\circ + (c_\oplus{}^1 - c_\oplus{}^\circ)x/L \quad t = 0, \quad 0 \leq x \leq L \qquad [8]$$

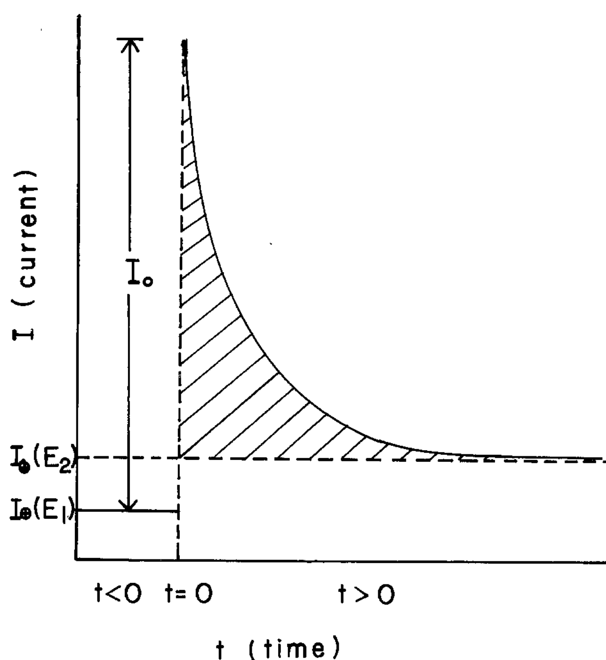

Fig. 1. Schematic current-time profile for a potential step from E_1 to E_2 in a (—)Cu|CuI|Graphite(+) polarization cell.

$$c_{\oplus} = c_{\oplus}^{\circ} \quad \text{at} \quad x = 0, \quad t \geq 0 \qquad [9]$$

$$c_{\oplus} = c_{\oplus}^{2} \quad \text{at} \quad x = L, \quad t \geq 0 \qquad [10]$$

where $c_{\oplus}^1$ and $c_{\oplus}^2$ can be obtained by using Eq. [4] and the superscripts 1 and 2 refer to the concentrations of electron holes in CuI at the blocking electrode under E_1 and E_2, respectively.

The current due to electron holes at $x = L$ for the semi-infinite rod, or the short-time solution (30) has the following form

$$I(t)|_{x=L} = \frac{A}{\sqrt{\pi \tilde{D}_{\oplus}}} (RT/\mathbf{F}) \sigma_{\oplus}^{\circ} t^{-1/2} (e^{E_2\mathbf{F}/RT} - e^{E_1\mathbf{F}/RT}) + I_{\oplus}(E_2) \qquad [11]$$

where $\sigma_{\oplus}^{\circ} = \mu_{\oplus} e c_{\oplus}^{\circ}$ and $\tilde{D}_{\oplus} = \mu_{\oplus} RT/\mathbf{F}$ were used.

But the current for the finite length L (31) can be expressed as follows for $x = L$

$$I(t)|_{x=L} = I_{\oplus}(E_2) + 2[I_{\oplus}(E_2) - I_{\oplus}(E_1)] \sum_{1}^{\infty} e^{-\tilde{D}_{\oplus} n^2 \pi^2 t/L^2} \qquad [12]$$

and the current at $x = 0$ is

$$I(t)|_{x=0} = I_{\oplus}(E_2) + 2[I_{\oplus}(E_2) - I_{\oplus}(E_1)] \sum_{1}^{\infty} (-1)^n e^{-\tilde{D}_{\oplus} n^2 \pi^2 t/L^2} \qquad [13]$$

From the semi-infinite rod solution Eq. [11], the slope of $I(t)$ *vs.* t plot is independent of the thickness of the electrolyte but depends on the initial and final potentials, E_1 and E_2.

Equations [12] and [13] can be approximated by retaining the first term of the infinite series if $t > L^2/\tilde{D}_{\oplus}\pi^2$. Thus

$$I(t)|_{x=L} \cong I_{\oplus}(E_2) + 2[I_{\oplus}(E_2) - I_{\oplus}(E_1)] e^{-\tilde{D}_{\oplus} \pi^2 t/L^2} \qquad [14]$$

$$I(t)|_{x=0} \cong I_{\oplus}(E_2) - 2[I_{\oplus}(E_2) - I_{\oplus}(E_1)] e^{-\tilde{D}_{\oplus} \pi^2 t/L^2} \qquad [15]$$

Accordingly, the unsteady current due to redistribution of electron holes at $x = L$ changes from a value higher than steady state to that at steady state. At $x = 0$, it changes from a value lower than steady state to that of the steady state.

Voltage relaxation method (10, 21, 30).—Consider the polarization cell (I) under a potential E_1 at steady state. When the potential is removed from the cell, the open-circuit potential $\Delta V(t)$ of the cell will change with time according to the equation

$$\Delta V(t) = \frac{RT}{\mathbf{F}} \ln \left[\frac{c_{\oplus}(t)}{c_{\oplus}^{\circ}} \right] \qquad [16]$$

where $c_{\oplus}(t)$ is the concentration of holes at the CuI|graphite interface which decreases with time because of the diffusion process inside the electrolyte (the double layer capacitance existing at the CuI|graphite interface is assumed negligible).

By substituting $c_{\oplus}(t)$ which can be obtained by solving Fick's second law with proper boundary conditions into Eq. [16], a relation of $\Delta V(t)$ with t is obtained as follows (30)

$$\tilde{D}_{\oplus} t = -\frac{4L^2}{\pi^2} \ln \left\{ \frac{\pi^2}{4} \frac{\exp\left(\frac{\Delta V(t)\mathbf{F}}{RT}\right) - 1}{\exp\left(\frac{E\mathbf{F}}{RT}\right) - 1} \right\} \qquad [17]$$

Therefore, if $t > 4L^2/\pi^2\tilde{D}_{\oplus}$ a plot of log [exp $(\Delta V(t)\mathbf{F}/RT) - 1$] *vs.* t should yield a straight line. This method can be used to test the significance of any interference from the double layer capacitance at the CuI|graphite interface by using electrolytes with different thicknesses since the rate of the voltage relaxation is inversely proportional to the square of the thickness of the electrolyte.

Experimental

A single crystal pellet of CuI was obtained from Professor C. Schwab of the Universite de Strasbourg. It was sectioned, polished, and washed successively in acetone, dilute HCl, and acetone. The Cu|CuI|graphite cell was then assembled in a spring-compressed mounting.

The two different length pellets (0.17 and 0.53 cm) used in voltage relaxation measurements were prepared by pressing the CuI powder at 75,000 psi in a 5/16 in. steel die. Alfa ultrapure anhydrous CuI powder (99.998%) was used without further purification. The freshly pressed pellets were then mounted in a double polarization cell (25, 30). The double cell was then heated at 440°C for one day under 1 atm of purified flowing argon. Table I shows the spark source mass spectrometric analysis of the crystal and of the powder samples.

The density of the pressed pellets was about 95% of theoretical as determined by measuring the dimensions and weighing. Copper (99.999%) rod from American Smelting and Refining Company was used as the reversible electrode. Pyrolytic graphite from Union Carbide was used as the blocking electrode. A resistance furnace was used in a horizontal position, the cell temperature was controlled by a Research Incorporated Model TC 5192 thermac controller and AMBAC Brute II d.c. power supply. A Chromel-Alumel thermocouple which was calibrated by the phase transitions of CuI was used to monitor the cell temperature. The principle of the circuit for applying the voltage steps to the cells is the same as that of Joshi and Wagner (10).

Table I. Mass spectrometric analysis of impurity concentrations in cuprous iodide (in parts per million by weight)

Element[a]	Detection limit[b]	Single crystal	Powder pressed pellet
B	0.007	N.D.	0.007
C	0.03	0.29	10
F	0.01	0.019	0.066
Na	0.01	1.4	3.6
Mg	0.05	0.59	1.0
Al	0.03	0.18	3.1
Si	0.05	0.50	38
P	0.05	0.091	0.062
S	0.07	0.11	6.4
Cl	0.07	0.12	290
K	0.01	7.4	12
Ca	0.05	0.20	1.3
Ti	0.05	0.37	2.4
V	0.05	0.091	0.091
Cr	0.05	2.4	1.1
Mn	0.05	0.098	0.23
Fe	0.1	2.6	10
Ni[c]	0.1	0.58	0.62
Ga[c]	0.1	5.0	3.7
As[c]	0.05	0.53	1.5
Se	0.1	1.2	1.6
Br	0.1	0.18	0.53
Nb	0.1	0.56	0.82
Ag	0.2	15	17
Cd	0.5	5.0	6.2
In	0.1	0.25	0.24
Ba	0.2	0.23	0.36
La	0.07	0.11	0.69
Ce	0.1	0.1	1.3
Pr	0.1	0.1	0.76
Tl	0.3	0.3	4.7
Pb	0.3	1.6	3.3
Bi	0.3	N.D.	6.1

[a] No determination was made for hydrogen. Determinations of tantalum and gold were not made since tantalum slits are used in the mass spectrometer and the samples were sparked against high purity gold counterelectrodes. Residuals in the mass spectrometer interfere with the determinations of O, Te, and Hg. Background lines interfere with the detection of N. Other impurities not listed were undetected and have concentrations less than 0.1 ppm atomic except for zinc. Because of interfering background lines, the detection limit for zinc is 2 ppm by weight.

[b] Determined for 3×10^{-7}C exposure.

[c] May be due to residuals in the mass spectrometer.

N.D., not detected.

The d-c input potentials were supplied by Keithley 260 Nanovolt Source. The cell current in response to a voltage step was monitored across various standard resistors using a Tektronic Model 564B storage oscilloscope with a Type 2A63 differential amplifier and Type 3B3 time base for short time periods of 10 sec or less, and an analog-to-digital converter in Data General's Nova 1220 computer for longer time periods. The computer data taking time interval can be 10 msec or integer multiples of it. The applied polarization potential and steady-state cell current were measured by a Doric Model DS-100 digital voltmeter.

The total conductivity of the single and polycrystalline CuI pellets was measured by an impedance bridge (General Radio 1650A) at 1000 Hz on a Cu|CuI|Cu cell. For the voltage relaxation measurements, the open-circuit potentials of the cell were recorded by an X-Y recorder (Ominographic 2000).

Results and Discussion

Steady-state polarization measurements.—The total conductivity σ_{tot} and partial electronic hole conductivity $\sigma_{\oplus}^{o}$ of CuI are shown in Fig. 2. The Arrhenius plot of the total conductivity in γ-phase cannot be fitted into a straight line. This curvature has been discussed by Matsui and J. B. Wagner (32). The electron hole conductivity obtained from C. Wagner's polarization method gradually approaches the total conductivity below 250°C. These samples of CuI exhibited predominantly electronic conduction below 220°C The total conductivity agrees very well with the data of Biermann and Oel (6) and of J. B. Wagner and C. Wagner (9). The activation energies in the three phases inferred from the Arrhenius plot of the logarithms of the total conductivities *vs.* $1/T$ are shown in Table II. The activation energy in γ-phase is calculated from the temperature range of 330°-360°C. The dependence of electronic hole conductivity on temperature of cuprous iodide in the γ-phase can be expressed as

Table II. Activation energies for total conduction in cuprous iodide

Phase	Transition temp. (°C)	Temperature range (°C)	Activation energy (eV)
α	TM 605	402-440	0.09
β	Tr. 405	372-400	0.90
γ	Tr. 369	330-369	2.03

$$\sigma_{\oplus}^{o}(\gamma\text{-CuI}) = 16 \exp\left(\frac{0.44\text{ eV}}{kT}\right) \quad [18]$$

The transference number t_j of a mixed conductor is defined as the ratio of the partial conductivity σ_j to the total conductivity σ_{tot} where j denotes an ionic or an electronic carrier. The transference numbers of cuprous iodide of this study are compared with Tubandt's results (2) in Fig. 3. The larger electronic transference numbers obtained by Tubandt at low temperatures may possibly result from electrolyte surface leakage effects and impurities in his samples.

Plots of log $I_{\oplus}$ *vs.* the applied polarization potential E of cell (I) used to obtain the electronic conductivity, are shown in Fig. 4 and 5. These plots yield a theoretical slope of $\mathbf{F}/2.303\,RT$ in accord with the Wagner's

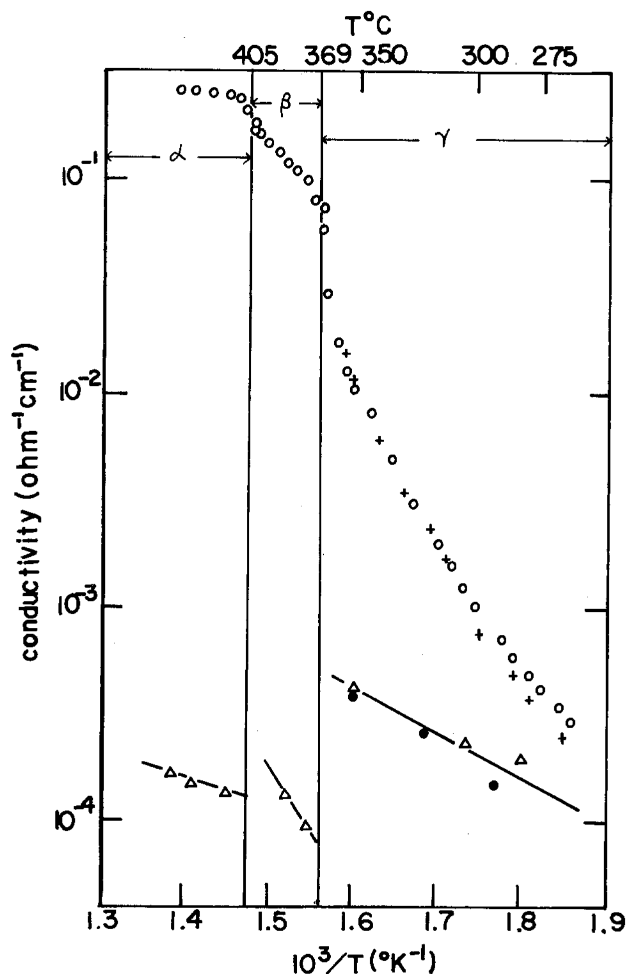

Fig. 2. Log of total and electronic conductivity vs. $1/T$ plot for CuI coexisting with copper. ○ and + denote total conductivity of poly and single crystal, respectively. △ and ● denote electron hole conductivity of poly and single crystal, respectively.

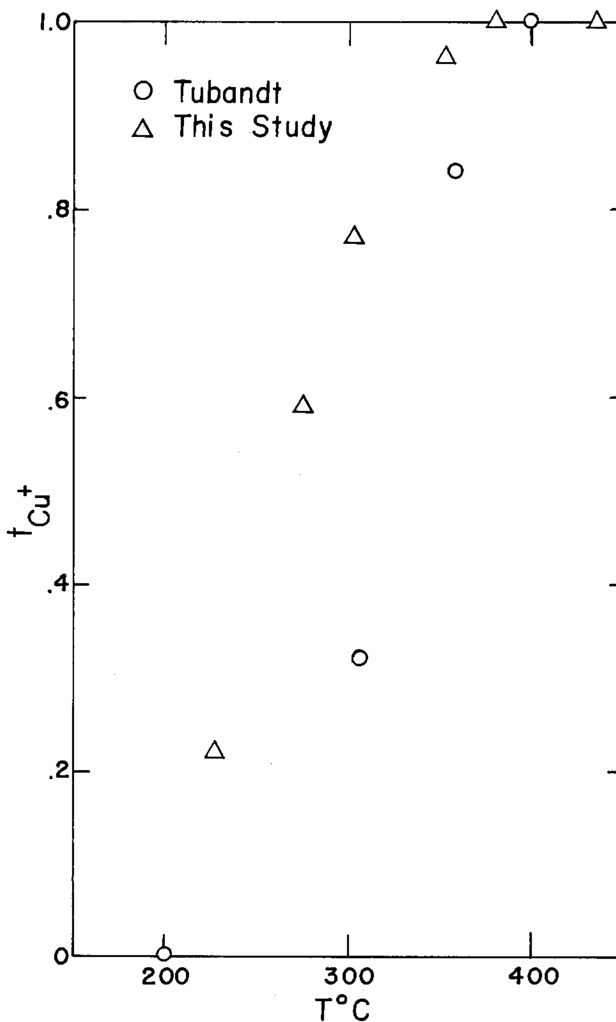

Fig. 3. Transference number of Cu^+ vs. T for CuI coexisting with copper.

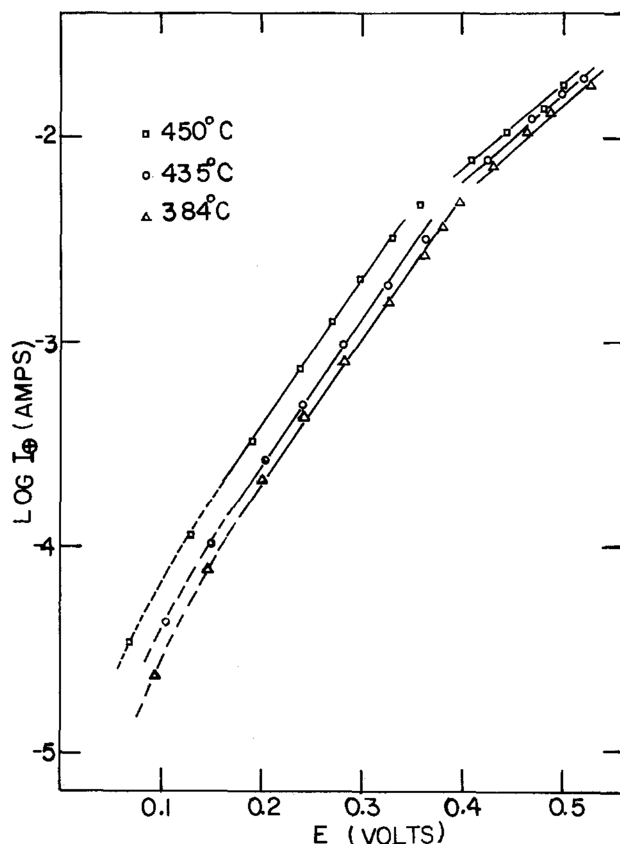

Fig. 4. Plot of log I vs. E for single crystalline CuI (0.51 cm thick by 0.78 cm diam) at temperatures 450°, 435°, and 384°C.

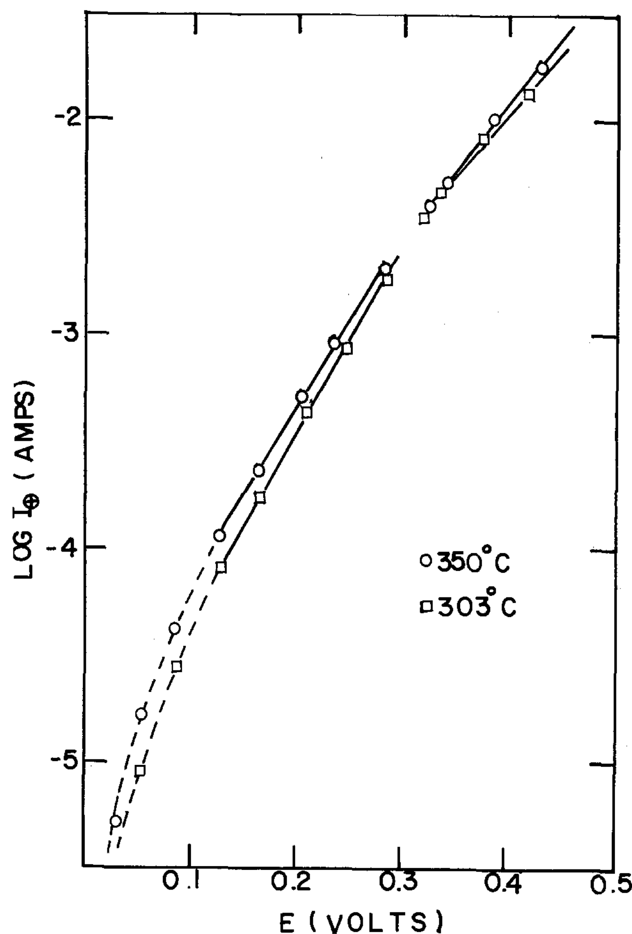

Fig. 5. Plot of log I vs E for single crystalline (0.51 cm thick by 0.78 cm diam) CuI at temperatures 350° and 303°C.

equation below a certain potential E_o. These slopes deviate from the theoretical values when $E > E_o$. The linear region which exhibits the theoretical slope becomes narrower as temperature decreases for the γ-phase.

Joshi and Liang (16) have proposed a critical potential E_c, where the Wagner equation is only valid when $E < E_e$. They defined E_c by following equation

$$E_c \equiv -\frac{2.303\,RT}{\mathbf{F}}\log\left[\frac{\sigma_\oplus{}^o}{\sigma_{ion}}\right] \qquad [19]$$

The above equation is obtained by equating the electronic hole conductivity at the blocking electrode $\sigma_\oplus{}^o \exp(E\mathbf{F}/RT)$ to the ionic conductivity of the electrolyte σ_{ion}, that is to say that Wagner's equation is valid when $\sigma_\oplus{}^o \exp(E\mathbf{F}/RT) << \sigma_{ion}$. For PbF_2, which was studied by Joshi and Liang (16), the applied polarization potentials that satisfy the Wagner's equation range from 30 to 80% of the critical potential E_c calculated from Eq. [19]. For CuI, the experimentally determined potential E_o (E_o is the highest potential that still satisfies Wagner's equation, *i.e.*, where the slope of log $I_\oplus$ *vs.* E amounts to $\mathbf{F}/2.303\,RT$) is smaller or approximately equal to the critical potential E_c in α- and β-phases. However, in γ-phase, when $E > E_c$, a plot of log $I_\oplus$ *vs.* E still exhibits Wagner's theoretical slope. The comparisons of E_o with E_c for CuI are shown in Table III. These results indicate that Joshi and Liang's criterion is too restrictive for CuI.

The reason for the changed slope of log $I_\oplus$ *vs.* E when $E > E_o$ may be explained as follows. The increasing applied potential on the polarization cell increases the hole concentration at the CuI-graphite interface exponentially with the applied potential (see Eq. [4]). In the derivation of Eq. [4]. Boltzmann statistics (or ideal solution law) is used for the electron holes. But when the hole concentration starts to become comparable to the density of states at the bandedge, Fermi-Dirac statistics instead of Boltzmann statistics should be used. Therefore, the hole concentration no longer increases exponentially with voltage at the previous rate.

Using the value of the hole concentration of CuI equilibrated with copper obtained in this study (see Eq. [11]), the hole concentration at the CuI-graphite interface can be calculated. For example, at 384°C, $c_\oplus{}^o = 5 \times 10^{16}$ cm^{-3}, when $E = 0.38$V, the hole concentration $c_\oplus$ at the CuI-graphite interface is 4×10^{19} cm^{-3}, at $T = 352$°C, $c_\oplus{}^o = 1.2 \times 10^{17}$, when $E = 0.24$V, $c_\oplus$ at the CuI-graphite interface is 1×10^{19} cm^{-3}. However, if we assume that the effective mass of holes in CuI is the mass of electron, the density states of holes can be estimated (33) to be about 8.1×10^{19} cm^{-3} at 384°C; 7.5×10^{19} cm^{-1} at 352°C. Since the calculated hole concentrations at the CuI-graphite interface and the estimated density of states at the bandedge are of the same order of magnitude, we conclude that the failure of the Boltzmann statistics is responsible for the change of the slope at the higher potentials.

The reason that Joshi and Liang's criterion is too restrictive for CuI is because there is a regime in which the hole concentration at the CuI-graphite interface is not large enough to invalidate Boltzmann statistics but large enough such that σ_{ion} is not very much larger than $\sigma_\oplus{}^o \exp(E\mathbf{F}/RT)$.

Table III. Comparisons of E_o with E_c for cuprous iodide

T°C	σ_{tot} $(\Omega\text{-cm})^{-1}$	$\sigma_\oplus{}^o$ $(\Omega\text{-cm})^{-1}$	E_c (V)	E_o (V)	E_o/E_c
450	2.57×10^{-1}	1.73×10^{-4}	0.45	0.35	0.78
435	2.53×10^{-1}	1.54×10^{-4}	0.45	0.35	0.78
384	1.20×10^{-1}	1.38×10^{-4}	0.38	0.38	1.0
352	1.07×10^{-2}	4.02×10^{-4}	0.17	0.24	1.4
320	2.4×10^{-3}	2.67×10^{-4}	0.11	0.24	2.2
303	1.15×10^{-3}	2.63×10^{-4}	0.07	0.24	3.4

Unsteady-state polarization cell measurements.—Current-time relation during the transient state.—A schematic current-time profile for a potential step from E_1 to E_2 was shown in Fig. 1. The peak current I_o represents the total current of the electrolyte. The corresponding initial resistance, R_o, from the potential step $\Delta E = E_2 - E_1$ is the total resistance of the electrolyte. Since the d-c electronic resistance, R_e, is much greater than ionic resistance, R_i, in a predominantly ionic conductor R_o is approximated by R_i. A linear relation is obtained by plotting I_o *vs.* potential step $\Delta E = E_2 - E_1$ with $E_2 > E_1$ and the value of E_1 fixed.

The transient current-time relation plotted as log $[I(t) - I_{\oplus}(E_2)]$ *vs.* t and $[I(t) - I_{\oplus}(E_2)]$ *vs.* $t^{-1/2}$ at $T = 375°C$ are shown in Fig. 6 and 7, respectively. From Fig. 6 one sees that the current decay exhibits multiple relaxation processes rather than one single decay constant. The residual decay current even lasts for a few minutes. The charge transfer contributed by this residual current decay consists of about 50% of the total. This has also been observed by Raleigh (22,

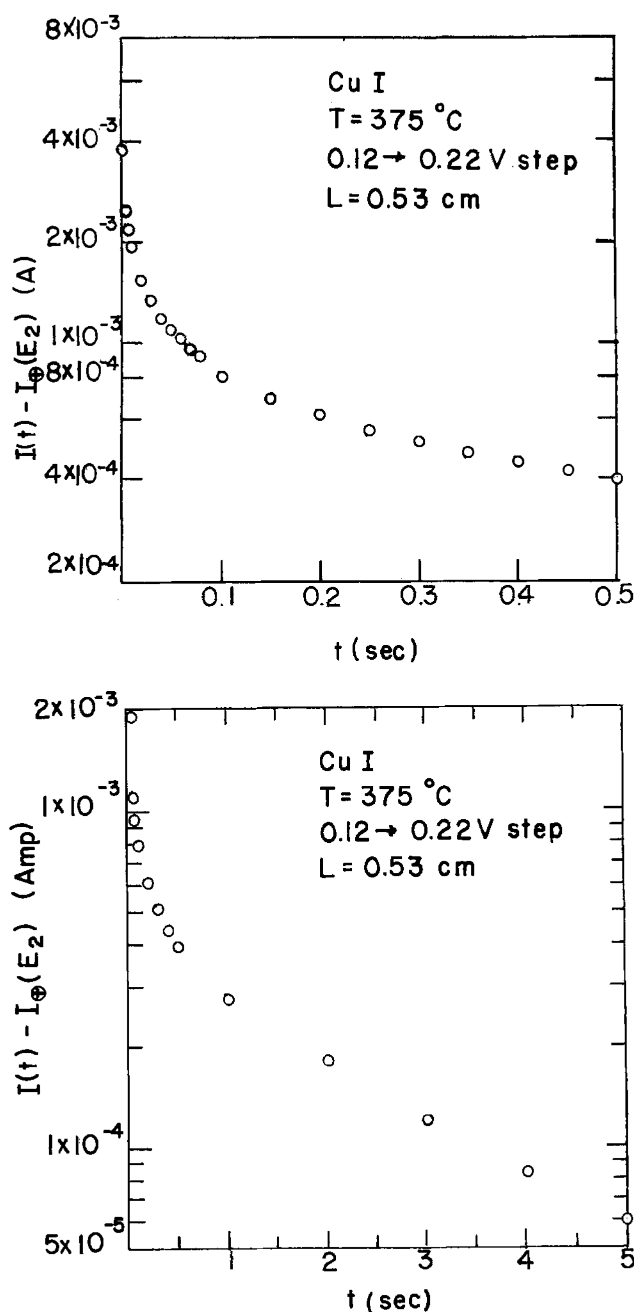

Fig. 6. Plots of log $[I(t) - I_{\oplus}(E_2)]$ vs. t for a potential step from 0.12 to 0.22V for polycrystalline CuI of $L = 0.53$ cm at 375°C.

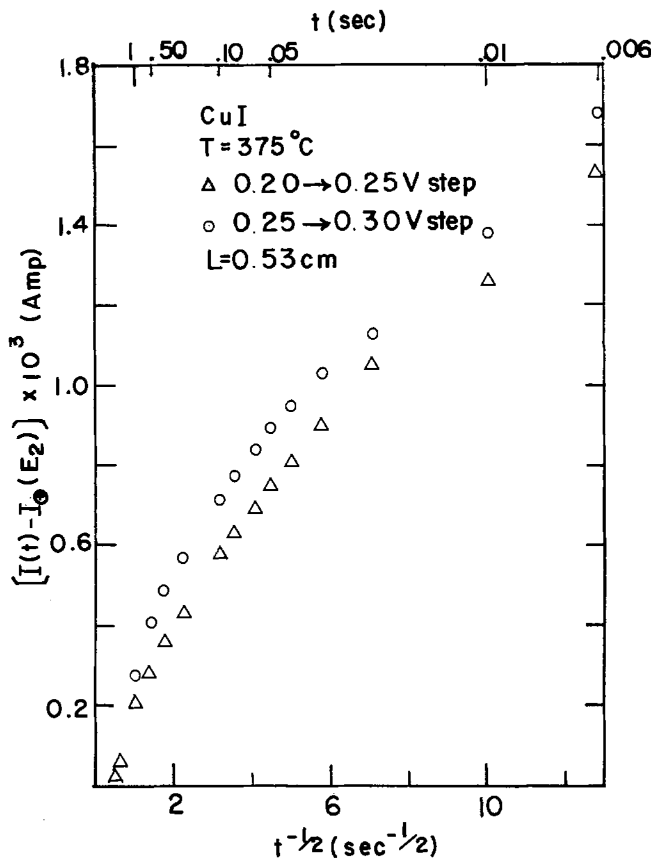

Fig. 7. Plots of $[I(t) - I_{\oplus}(E_2)]$ vs. $t^{-1/2}$ for polycrystalline CuI

23) on the double layer capacitance studies on AgBr polarization cells.

According to Eq. [11], the slope of a plot of the transient current due to redistribution of electron holes *vs.* $t^{-1/2}$ is proportional to $[\exp(E_2\mathbf{F}/RT) - \exp(E_1\mathbf{F}/RT)]$. However, from Fig. 7, the slopes at 0.20-0.25V and 0.25-0.30V voltage steps do not show the relation indicated, since at $T = 375°C$ the slope ratio should be $[\exp(0.30\ \mathbf{F}/RT) - \exp(0.25\ \mathbf{F}/RT)]/[\exp(0.25\ \mathbf{F}/RT) - \exp(0.20\ \mathbf{F}/RT)] \cong 127/52 = 2.4$ according to Eq. [11]. The nonapplicability of the semi-infinite rod solution may be a result from an inevitable interference of the double layer charging current in the short time range and/or the predominant ionic conduction assumption for the solution is no longer satisfied within this voltage range.

In the γ-phase, the electronic conductivity which contributes to the total conductivity is appreciable (see Fig. 2). When the applied potential jumps to a higher value but lower than the decomposition potential E_d, the current-time profile is different from that shown in Fig. 1. This is shown schematically in Fig. 8. The current decays first and then goes up.

The physical situation can be understood as follows. When the d-c potential on a γ-CuI cell is stepped upwards, $E_2 - E_1$ appears across the resistance part of the cell where the cuprous iodide is of the initial stoichiometry which is fixed by E_1. The step current (peak current I_o) corresponds to this voltage step. But because of the capacitive charging effect which is a short-time process, the current will decay as $I_o e^{-t/RC}$. Simultaneously, the current due to the redistribution of electron holes occurs. At short times, the graphite electrode will inject holes into CuI at a rate according to Eq. [11] or [12]. That is also a decaying current. The current at the copper-cuprous iodide interface during transient increases from the initial steady state to the final steady state (see Eq. [13] or [15]). When $\sigma_{\oplus}°$ is appreciable and E is high, the conduction at the cuprous iodide-graphite interface is predominantly electronic. Therefore, the slower upgoing transient

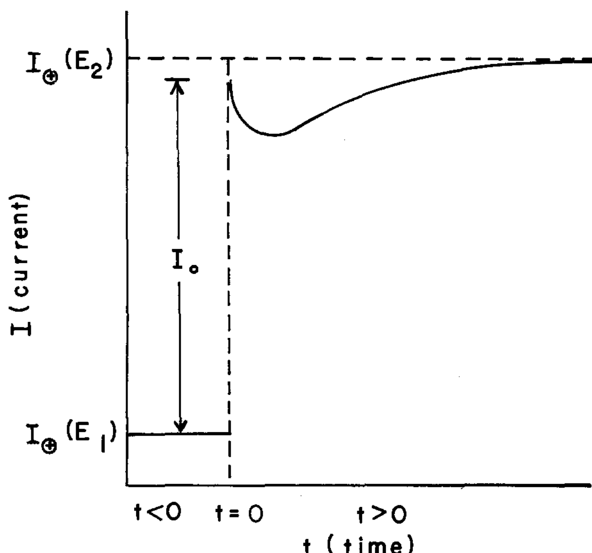

Fig. 8. Schematic current-time profile for a potential step from E_1 to E_2 when E_2 is high for polycrystalline CuI in the γ-phase.

response at the copper-cuprous iodide interface is shown.

Voltage relaxation measurements.—The voltage relaxation $\Delta V(t)$ was recorded after the polarized voltage, 0.2V, was switched off from the cell. Figure 9 shows log [exp $(V(t)\mathbf{F}/RT) - 1$] *vs.* t for the β-phase of CuI. The effective diffusivities of holes, $\tilde{D}_\oplus$'s, were obtained from the slope using Eq. [17]. By the same method, $\tilde{D}_\oplus$'s in a temperature range of 324°-362°C were also obtained. These values are plotted against $10^3/T$°K in Fig. 10.

According to Eq. [17], the ratio of the slopes of log [exp $(\Delta V(t)\mathbf{F}/RT) - 1$] *vs.* t of a long specimen to that of a short specimen is $L^2(\text{short})/L^2(\text{long})$. The slope ratio of samples at 403°C with lengths of 0.53 cm to those of 0.17 cm was calculated as 1/9.2 from Fig. 9 (straight line portion of the curves). The inverse ratio of the square of the thickness of these two specimens is 1/9.7. The agreement between these two ratios is very good. This indicates that the voltage relaxation is a diffusion-controlled process and the interference from the double layer capacitance is negligible.

By using the Einstein relation, $\mu_\oplus = D_\oplus/kT$ and $\sigma_\oplus{}^o = e\mu_\oplus c_\oplus{}^o$, the hole concentration in CuI equilibrated with copper is calculated and is shown in Fig. 11.

Double layer capacitance.—The double layer capacitance was measured at 347°C by applying a voltage step in a very low voltage range (from 10 to 50 mV) to the thin single crystalline sample (0.12 cm). The transient current due to redistribution of holes is minimized and double layer capacitance becomes dominant. The charge was obtained by graphically integrating the current with respect to time from oscillographic pictures. The capacitance was obtained from the slope of the charge transfer Q *vs.* E plot (see Fig. 12). The value was found to be 357 μF/cm^2.

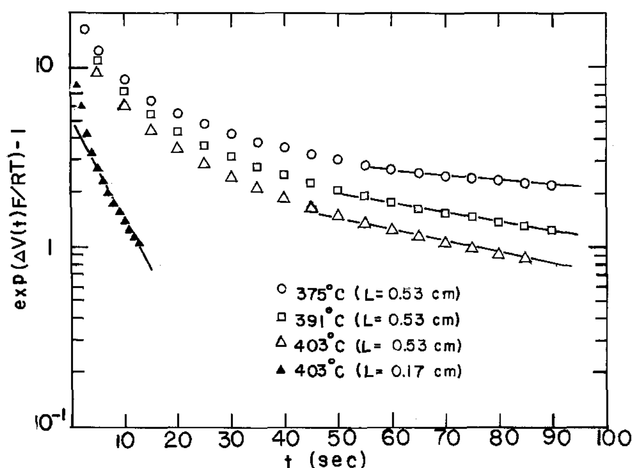

Fig. 9. Plot of log {exp($\Delta V(t)F/RT$) — 1} vs t for the long (0.53 cm) and short (0.17 cm) samples of polycrystalline CuI.

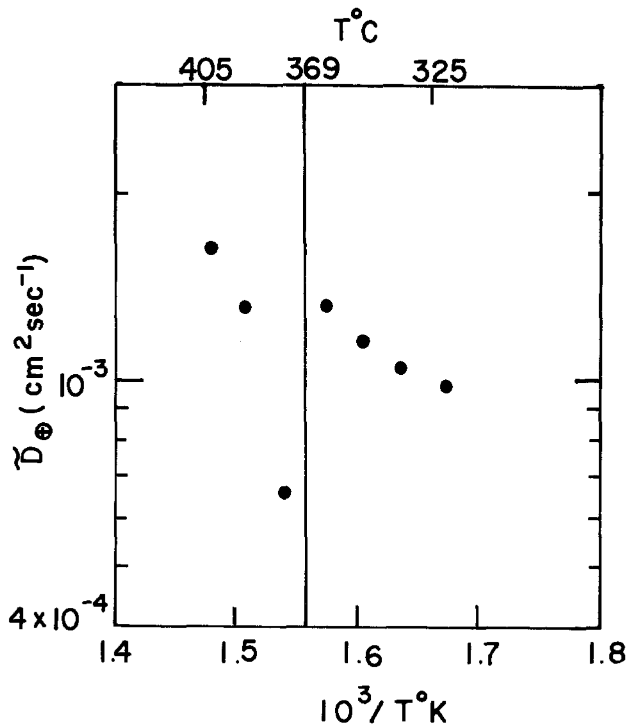

Fig. 10. Plot of log $D_\oplus$ vs. $1/T$ for polycrystalline CuI

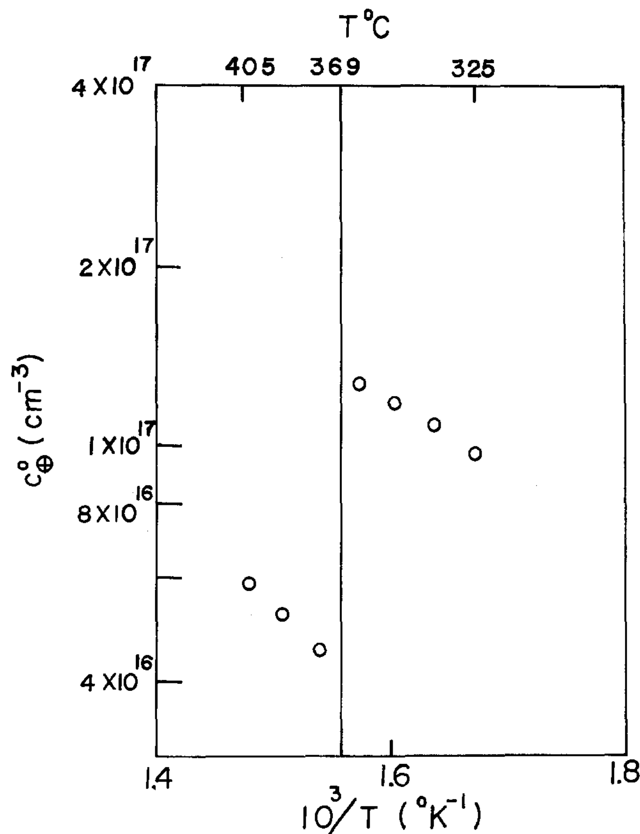

Fig. 11. Plot of log $c_\oplus{}^o$ vs. $1/T$ for polycrystalline CuI

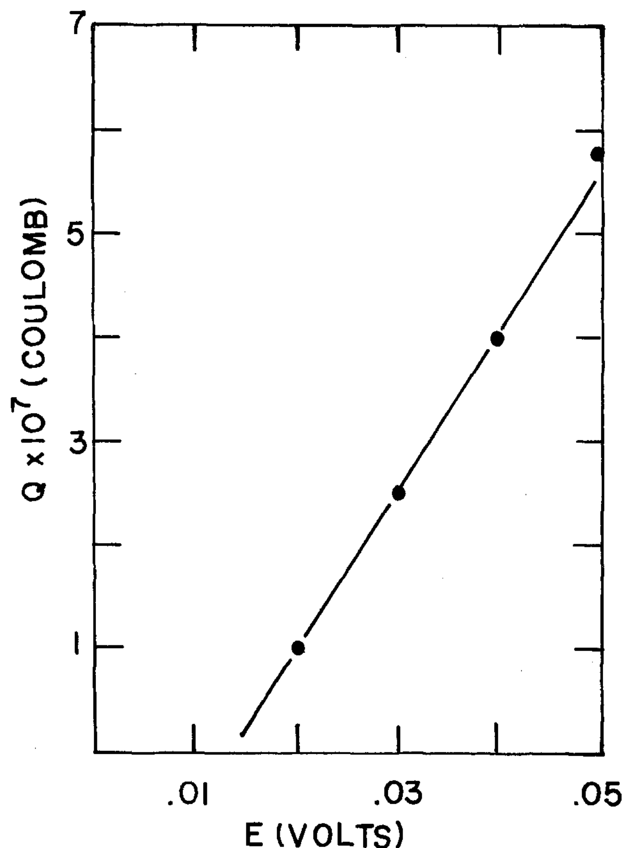

Fig. 12. Plot of charge transfer Q vs. potential E for single crystalline CuI of 0.12 cm thickness by 0.21 × 0.21 cm at 346°C.

Conclusions

From the steady-state measurements cuprous iodide was shown to be a predominantly ionic conductor in the α- and β-phases and it gradually becomes a predominantly electronic conductor as the temperature decreases in the γ-phase. The log $I_\oplus$ *vs.* E plots satisfied the Wagner theoretical slope for low values of applied potentials. This indicated that the electronic conductivity of cuprous iodide is proportional to the square root of the partial pressure of iodine. At higher applied voltages, the log $I_\oplus$ *vs.* E plots deviate from the Wagner theoretical slope because of the nonideality of the electron holes at high concentrations large applied potential).

The unsteady current-time relation was too complicated to be analyzed by the pure capacitance model and the current due to redistribution of electron holes. Comparing the voltage relaxations of different cuprous iodide sample lengths, the voltage relaxation method has good applicability, and the diffusivities of electron holes at various temperatures were calculated by this method. The double layer capacitance was obtained by measuring the charge transfer in the low voltage range. Its value is about 357 μF/cm² at 346°C.

Acknowledgments

The authors are especially grateful to Professor C. Schwab of the University of Strasbourg for providing the single crystal of CuI and to D. O. Raleigh for helpful discussions. This work was supported by the Advanced Research Projects Agency of the Department of Defense under Grant No. DAHC 15-73-G-19. It was monitored by the Office of Naval Research through the Materials Research Center of Northwestern University.

This paper was taken in part from the Ph.D. Thesis of T. Jow, Northwestern University, 1977.

Manuscript submitted April 18, 1977; revised manuscript received Nov. 3, 1977.

Any discussion of this paper will appear in a Discussion Section to be published in the December 1978 JOURNAL. All discussions for the December 1978 Discussion Section should be submitted by Aug. 1, 1978.

Publication costs of this article were assisted by Northwestern University.

REFERENCES

1. K. Baedeker, *Ann. Phys. (Leipsig)*, **29**, 566 (1909).
2. C. Tubandt, *Handb. Exp. Phys.*, **XII**, No. 1, 414 (1932); C. Tubandt, R. Rindtorff, and W. Jost, *Z. Anorg. Allg. Chem.*, **165**, 195 (1927); A. B. Lidiard, "Encyclopedia of Physics," Vol. XX, S. Flügge, Editor, p. 246, Springer, Berlin (1956).
3. K. Nagel and C. Wagner, *Z. Phys. Chem.*, **(B)25**, 71 (1934).
4. R. J. Maurer, *J. Chem. Phys.*, **13**, 321 (1945).
5. B. H. Vine and R. J. Maurer, *Z. Phys. Chem.*, **19**, 147 (1951).
6. W. Biermann and H. J. Oel, *ibid.*, **(NF)17, 163** (1958).
7. M. H. Hebb, *J. Chem. Phys.*, **20**, 185 (1952).
8. C. Wagner, in "Proceedings of the Seventh Meeting C.I.T.C.E. Lindau (1955)," p. 361, Butterworths Publications, London (1957).
9. J. B. Wagner, Jr. and C. Wagner, *J. Chem. Phys.*, **26**, 1597 (1957).
10. A. V. Joshi and J. B. Wagner, Jr., *This Journal*, **122**, 1071 (1975).
11. B. Ilschner, *J. Chem. Phys.*, **28**, 1109 (1958).
12. D. O. Raleigh, *J. Phys. Chem. Solids*, **26**, 329 (1965).
13. Y. J. Van der Meulen and F. A. Kröger, *This Journal*, **117**, 69 (1970).
14. J. B. Wagner, Jr. and C. Wagner, *ibid.*, **104**, 500 (1957).
15. J. Schoonman and A. J. H. Macke, *J. Solid State Chem.*, **5**, 105 (1972).
16. A. V. Joshi and C. C. Liang, *J. Phys. Chem. Solids*, **36**, 927 (1975).
17. J. W. Patterson, E. C. Bogren, and R. A. Rapp, *This Journal*, **114**, 752 (1967).
18. R. A. Rapp and D. A. Shores, in "Techniques in Metal Research," Vol. IV, Part 2, R. A. Rapp, Editor, p. 123, Interscience, New York (1970).
19. H. Rickert, in "EMF Measurements in High Temperature Systems," C. B. Alcock, Editor, p. 59, Inst. Mining Metallurgy, London (1968).
20. B. C. H. Steele, in "Heterogeneous Kinetics at Elevated Temperatures," G. R. Belton and W. L. Worrell, Editors, p. 135, Plenum Publishing Corp., New York (1970).
21. K. Weiss, *Z. Phys. Chem. (NF)*, **59**, 242 (1968).
22. D. O. Raleigh, *J. Phys. Chem.*, **70**, 689 (1966).
23. D. O. Raleigh, *ibid.*, **71**, 1785 (1967).
24. V. W. Hsueh and R. W. Christy, *J. Chem. Phys.*, **39**, 3519 (1963).
25. A. V. Joshi, in "Fast Ion Transport in Solids," W. van Gool, Editor, p. 173, North Holland Publishing Co., Amsterdam (1973).
26. J. B. Wagner, Jr., *ibid.*, p. 489.
27. J. B. Wagner, Jr., in "Electrode Processes in Solid State Ionics," M. Kleitz and J. Dupuy, Editors, p. 185, D. Reidel Publishing Co., Dordrecht-Holland, (1976).
28. D. O. Raleigh, in "Electronanalytical Chemistry," Vol. 6, A. J. Bard, Editor, p. 81, Marcel Dekker, New York (1973).
29. D. O. Raleigh, *This Journal*, **121**, 632 (1974).
30. A. J. Joshi, Ph.D. Thesis, Northwestern University (1972).
31. J. Crank, "The Mathematics of Diffusion," 2nd ed., p. 47, Clarendon Press, Oxford (1975).
32. T. Matsui and J. B. Wagner, Jr., *This Journal*, **124**, 303 (1977).
33. "Semiconductors," N. B. Hannay, Editor, pp. 28-29, Reinhold Publishing Co., New York (1959).

The Detection of Structural Defects in GaAs by Electrochemical Etching

M. M. Faktor and J. L. Stevenson

Post Office Research Centre, Martlesham Heath, Ipswich, Suffolk, IP5 7RE England

ABSTRACT

Two methods of anodically etching n-GaAs have been investigated. Subsequently they have been used to detect crystallographic defects present in bulk-grown, single crystal material. The first method provides topographical featuring of the semiconductor anode. The selective discrimination of defects achieved via this controlled electrochemical technique is superior to that obtainable from standard chemical etchants. The second dissolution regime, in which an interfacial oxide layer is continuously present, permits smooth, featureless removal of material. Thus a simple two-stage anodization procedure has allowed the damage characteristic of the Beilby layer to be probed. Thereafter, a total, smooth removal of this damaged surface layer permits identification of bulk crystallographic defects—dislocation structures well known in GaAs require the dissolution of only 0.5 μm. Analysis of the semiconductor electrode condition in the electrolytes used for etching has yielded model results. Such analyses have enabled the relationship between the electrical properties of the defected GaAs and the individual topography of the defects as etched to be explored.

The electrochemical characteristics of gallium arsenide and other III-V semiconductors have recently attracted increasing interest. As well as providing a route for an automated electrical assessment of both epitaxial and substrate quality material (1, 2), anodic oxide films have been intensively studied (3, 4), mostly in connection with MOS device applications utilizing GaAs.

The studies reported here have some relation to both of these topics, but are differently aimed overall. It has become increasingly clear in the production of liquid-phase epitaxial GaAs and $Ga_xAl_{1-x}As$ for optoelectronic devices that routine evaluation of the material should center on the crystallographic defect content of the epilayers (5). Some defects act as nonradiative, enhanced recombination centers, which reduce the efficiency of photoabsorptive devices (solar cells) and which degrade and may terminate the efficiency of photoemissive units (lasers) (6). Chemical etching would appear to provide the technically easiest means of defect identification once the etchant has been calibrated (7). However, the current state of the art is inadequate for the purpose indicated. Optical resolution of etch pits in single $Ga_xAl_{1-x}As$ layers has recently been reported by Komiya *et al.* (8) as possible only after the dissolution of 4 μm in a H_2O_2/HF solution. For $GaAs/Ga_xAl_{1-x}As$ double heterostructure material, where all five epilayers together occupy about this very thickness (9), a ten-fold improvement in the resolution achieved per unit depth probed would be the minimum desired. Although defect detection in heterostructures has been displayed (5) via the use of the AB etchant (10) in a modified form, an extra thickness of epitaxial growth was necessitated in order to accommodate the lack of etch discrimination.

Both Ambridge *et al.* (1) and Niehaus and Schwartz (3) were able to report in the work already cited that electrolytic etching of GaAs produced features at the electrode surface. These were presumed related to the defects in the sample. Kuhn-Kuhnenfeld (11) used a chemical etchant of standard composition for GaAs under conditions where the photovoltaic properties of the semiconductor provided effective electrolytic control. Although the procedure was not subjected to a critical calibration, various features became well resolved after 2 μm of etching. Several appeared "dislocation like." Later Saitoh *et al.* (12) used the same scheme of photoassistance together with the AB etch composition and were able to gain a good delineation of defects with the removal of less than 1 μm of material.

We report here on the development of two complementary techniques of anodic dissolution of n-GaAs; one to yield a topographically featured surface, and the second to allow continuous, smooth etching. The electrode polarization studies which preceded the design of each technique are detailed in an Appendix. Correlation of the morphological detail displayed via the first etching mode has been carried out with the use of double crystal x-ray reflection topographs. The selective resolution of defects such as dislocations by our electrochemical technique is shown to be superior to that obtained from other currently advocated etching techniques (7). Minimal dissolution is required (0.5 μm or less) close to the target set.

In this instance, our attention is given to bulk-grown n-GaAs alone. Therefore we are describing the trial of these methods on substrate quality material. However, as a specific example of the resolution capability and to illustrate how the procedures can be used to profile the defect content of a GaAs slice in depth with high accuracy the differentiation of surface damage and bulk defects close to the surface of a substrate are described.

Experimental

Much of the apparatus used in this work has been described previously by Ambridge *et al.* (1, 2). A major difference here, however, concerned the cell construction, where an all-glass unit was designed. This was basically a small spectrophotometer cell with a PVC sample mounting ring (2) mounted directly onto one face which had been predrilled as appropriate. There were, as before, inlet/outlet ports for electrolyte flow and limbs for the insertion of a saturated calomel reference electrode and a carbon cathode. A platinum wire electrode for capacitance measurements was inserted directly through the side of the PVC ring. Both the sealing of the GaAs sample onto the ring and the provision of electrical contact to it were achieved via sprung probes of tin-coated gold wire (2).

By mounting the cell directly onto a microscope stage plate and using an inverted metallurgical microscope, observation of the whole exposed GaAs electrode surface (~7 mm^2) was possible at a magnifica-

Key words: gallium arsenide, electroetching, oxide films, dislocations, striations.

tion of 30× (at the eyepiece). Examination of fine topographical details developed during anodization such as etch pits, areas of nondissolution, and surface film nucleation sites was very straightforward. Illumination of the electrode was direct via the microscope optics and since all of the polarization behavior reported here involves illumination, a continuous visual observation of the electrode was possible. The optical source was a 250W high pressure mercury arc lamp set to provide Koehler irradiance of the sample.

Measurement of electrode potential was obtained through a high impedance digital voltmeter (Solartron LM 1604). An autobalance capacitance bridge (Wayne Kerr B641), operating at 1.592 kHz, was used for measurement of interfacial capacity. Polarization of the illuminated electrode was attained by use of the potentiostat designed by Bremner *et al.* (13). Cell current was monitored using an electrometer (Keithley Model 602) with its output facility linked to a digital integrator (Time Electronics TS100A). Two electrolytes new to GaAs electrochemistry were used throughout this work. They were: as stock solutions, 0.5M Tiron (1,2 dihydroxybenzene-3,5 disulfonic acid disodium salt) which had a pH = 3.45; and 0.3M sodium dihydrogen orthophosphate pH = 4.32. The GaAs used had been boat grown and cut into slices in a {100} orientation (Mining and Chemical Products Limited and Monsanto Chemicals Limited). All were silicon doped.

Electrochemical Characteristics and Technique

Electrode capacitance.—Reproducible Mott-Schottky characteristics were obtained from unilluminated n-GaAs ($N_d = 2.0 \times 10^{17}$ cm^{-3}) electrodes (14) using both of the electrolytes chosen for use here. The flatband and open-circuit potentials are plotted in Fig. 1 together with previously published data.

Electrode polarization.—Illumination of the same electrode samples yielded sizable photopotentials (~ −450 mV) and, in the usual manner, allowed stable anodic polarization (reverse-biasing of the Mott-Schottky barrier) curves to be obtained (Fig. 2). Current/voltage behavior was also examined using various solutions formed by mixing the two basic electrolytes.

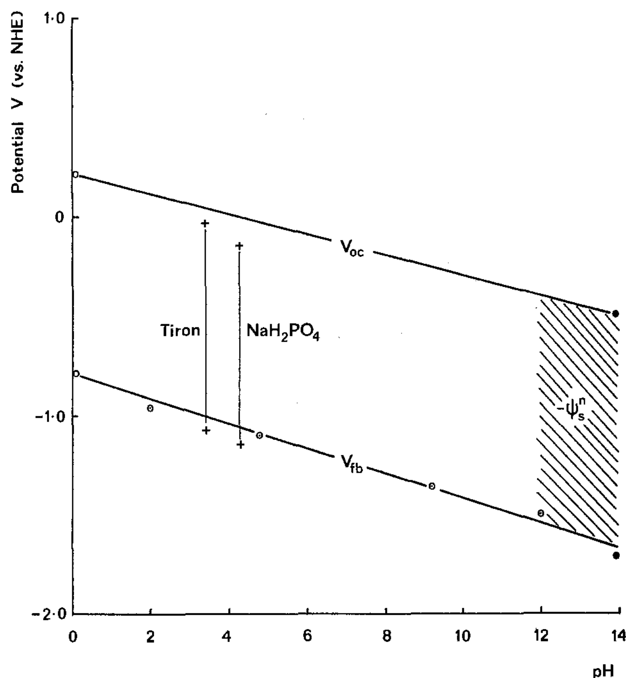

Fig. 1. Collation of data concerning the variation in band bending at the unilluminated n-GaAs electrode with electrolyte pH. Values for the flatband potential (V_{FB}) and the open-circuit (rest) potential (V_{oc}) are taken as follows: ○ Benard and Handler (29); ⊙ LaFlere *et al.* (41); ● Ambridge and Faktor (14).

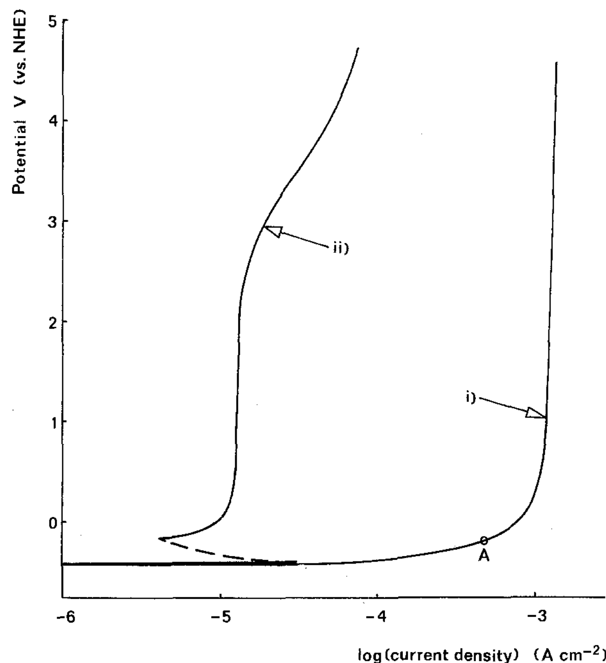

Fig. 2. Current-voltage behavior of an illuminated n-GaAs electrode (same sample as Fig. 1) in: i. 0.5M Tiron; and ii. 0.3M NaH_2PO_4. The point A marks the experimental condition for step 2, Fig. 5.

For example, it was found that only small proportions of Tiron (10% v/v) were required in the electrolyte to yield current characteristics identical to Fig. 2i. In this case, the reverse-bias breakdown behavior of a lower doped n-GaAs electrode was examined—again with illumination—and found to be as plotted in Fig. 3.

Electrode morphology.—Since all of the curves such as shown in Fig. 2 and 3 were gained with an experimental arrangement which allowed direct visual inspection of the electrode, the surface morphology developed was very easily relatable to particular polarization conditions. The photographs in Fig. 4 are representative of etching under steady-state conditions at the points marked A in Fig. 2i and B in Fig. 3.

The result of the single etching experiment shown as Fig. 4i bears no similarity to morphologies found either by Kuhn-Kuhnenfeld (11) or Saitoh *et al.* (12)

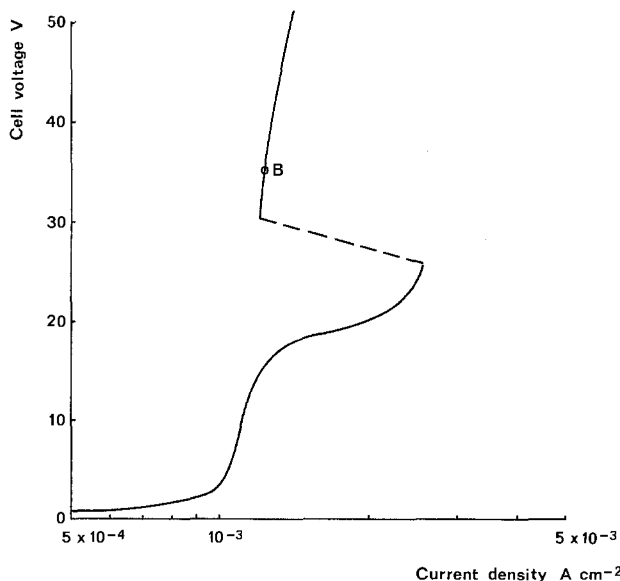

Fig. 3. Extended current-voltage plot for an illuminated n-GaAs electrode (2.6 × 10^{16} donors per cm^3) in a mixed electrolyte (10% 0.5M Tiron/90% 0.3M NaH_2PO_4). The point B marks the experimental condition for step 1, Fig. 5.

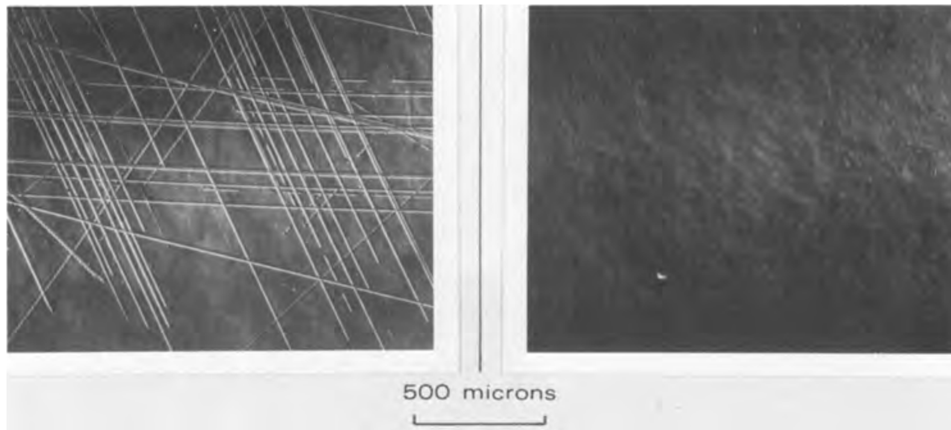

Fig. 4. Photomicrographs (Nomarski interferometry) showing surface morphologies developed after electrochemical etching of two separate samples: i. at point A in Fig. 2i, 0.2 μm removed; and ii. at point B in Fig. 3, 5.2 μm removed.

in those studies of the photoassisted chemical dissolution of n-GaAs which we judge to be closest to our fully controlled electrochemical conditions. In our case, the sample used had been mechanochemically polished using a standard bromine/methanol routine immediately prior to anodization. It appeared, therefore, that the low overpotential etching in Tiron solution had revealed features representing imperfections introduced during the sample preparation. This supposition was confirmed by subjecting similarly finished slices to a sequential etching experiment as indicated in Fig. 5. Step 1 was accomplished by use of the defect-independent etching conditions (point B in Fig. 3) leaving a surface typically as that shown in Fig. 4ii. Then after a simple replacement of electrolyte, step 2 was initiated and the surface topography monitored through its duration using the microscope. Both d_1 and d_2—the successive etch depths— were easily calculable via the integrated current density (for details, see the Appendix). As an example, the two etched surfaces pictured in Fig. 6i and 6iv were obtained with material removals of $d_1 = 2.0$ μm and $d_2 = 0.57$ μm. The minimum value of d_1 found necessary in order to avoid the appearance of etch features caused by polishing damage was 0.5 μm for the mechanochemically polished slices.

Crystallographic Defect Studies

We shall begin here with comments concerning the polishing damage encountered during the single etch experiments. Clearly no information concerning the bulk defect structure of n-GaAs substrate wafers can be obtained definitively without the removal of the damaged surface layer.

In fact, the appearance of prepolished surfaces after a single step 2 etch changed quite sharply with prior alteration of the polishing rate (this made principally by varying the bromine content of the polishing solution). Where low rates had been used, the surface took on a continuously disturbed form, with all of the linear features as per Fig. 4i in close coalescence. Thus a form of Beilby layer (15) was present. Its characteristic depth was, however, no different from that exhibited by the discretely scratched surface. The damage itself might arise from particles of abrasive material or even GaAs which have remained attached to the slice after any mechanical treatment, or, more probably, have become trapped on the polishing pad at any time since its manufacture. We note that in spite of warnings to the contrary (7), mechanochemically prepared GaAs slices are still taken to be damage free (16). Our ability here to reveal minor work damage, such as that caused by mechanochemical polishing, and to profile its region of confinement near the surface at submicron levels, illustrates nicely the fine resolution of defective material attainable with the electrochemical etching methods.

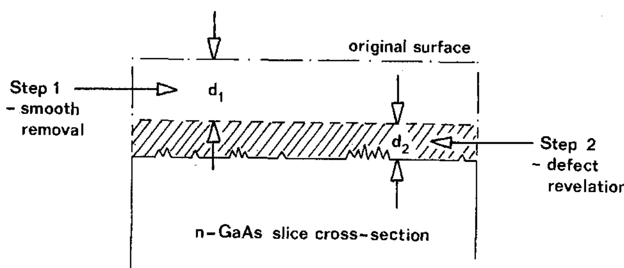

Fig. 5. Schematic representation of the sequential electrochemical etching experiment. The cross-hatched region marks the "layer" probed for defect content.

With regard to the crystallographic imperfections of the bulk, the etched slice photographed in Fig. 6i is only one of a number which have been subjected to a cross correlation with structural defect analysis by x-ray methods. Double crystal x-ray reflection topography was chosen—it has the advantage of probing a near surface layer alone (17, 18). More generally the two techniques used over-all then have independent origins, particularly so, as we shall show later, with the etching performed electrolytically. The x-ray topography was used first to map as fully as possible the defect content of the sample. Since not all possible dislocation Burgers' vectors will yield contrast at a single reflection, only a superposition of two x-ray topographs will provide a complete map of the dislocation distribution. Figures 6ii and 6iii are micrographs of the photographic plates on which the two x-ray exposures covering the same area were recorded, but the superposition is made difficult because the topographs are unavoidably distorted geometrically with their foreshortened axes perpendicular. Attempts at reaching a graphical correspondence between all three topographs, that is including the detail available after the sequential etching of the same sample area (Fig. 6i), are further hindered by a significant disparity in the depth resolution of the techniques. The morphology of Fig. 6i resulted from a dissolution in the topographical etching mode (d_2) of 0.57 μm, while the surface layer thickness imaged by the x-ray technique was ~18 μm (17, 18). Hence there is involved here a sampling discrepancy factor of more than thirty.

In view of these problems, the over-all correlation is judged fairly satisfactory. Note first that the pronounced linear feature present at the left-hand edge of all three topographs is the result of a deliberate scratch mark made as a geographical reference point. Thereafter, particular correspondences can be seen between the linear array of features extending along the line of the arrow marked A in Fig. 6i and 6ii, and also between a group of features at B in both Fig. 6i and 6iii. The line of detail labeled A in Fig. 6ii contains several linear images (one is arrowed at a) which do not appear in the complementary x-ray topograph. Analysis

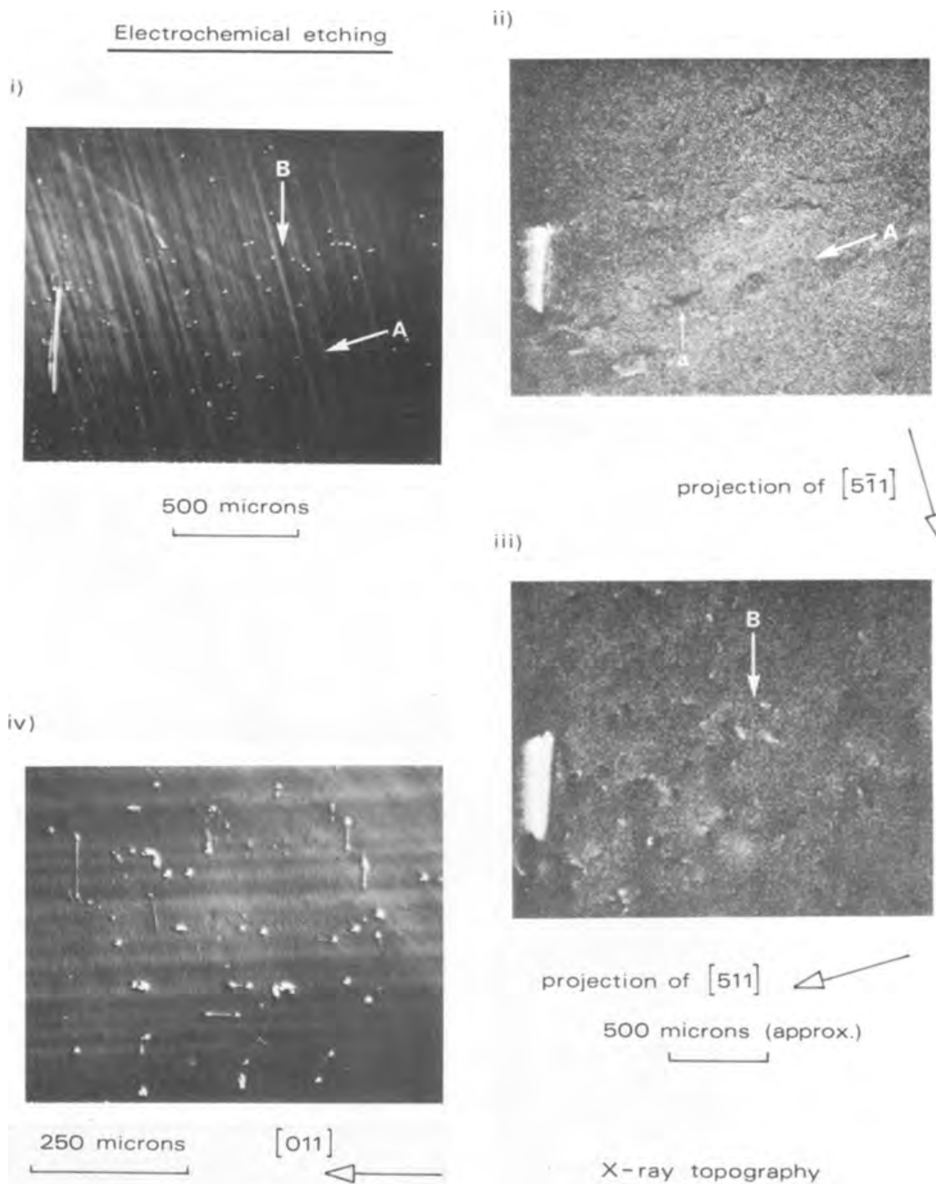

Fig. 6. Results of the etching calibration. i. Sample surface-morphology after electrochemical etching as indicated in Fig. 5, with d_2 0.57 μm; ii. and iii. double crystal x-ray reflection topographs recorded for the sample prior to etching, using the 5$\bar{1}$1 and 511 reflections from GaAs, respectively; and iv. features resulting from sequential electrochemical etching at an adjacent area to that shown as i. (n-GaAs sample, Si-doped, 8.6 $\times$ 10^{17} donors per cm^{-3}).

of the diffraction conditions show this to be a dislocation with a high (probably complete) edge component. Clearly it lies in a [011] direction. The absence of a comparable linear feature from the etched surface is probably attributable to the difference in depths probed, as described already. On a neighboring area of the same sample (which was not clearly imaged by the x-ray method due to slice curvature) the electrochemical etching did produce linear features arrayed along both the [011] and the [0$\bar{1}$1] directions (see Fig. 6iv, which has an increase in magnification and a sample rotation relative to Fig. 6i). Thus an ability to reveal both dislocation outcrops (for dislocations inclined to the surface plane) and dislocation lines (lying in the surface plane) is indicated. In this connection, note that the linear features present in Fig. 6iv are all terminated by a roundel, similar to those which, individually, represent dislocation outcrops. This indicates a segmentation of the dislocation into, presumably, the <110> directions and therefore at these points it either enters the bulk or was originally attached to the slice surface. Electron microscopy of bulk-grown GaAs has indicated previously that this dislocation type is often dominant (19).

The type and scale of defect discrimination demonstrated here is simply not attainable with many of the chemical etchants reported in the literature as suitable for defect analysis in GaAs (7), though the best characterized of these, the AB etch (10), may, under conditions of dilution (5, 20) and together with photoassistance (12), yield a comparable detection.

Some significant information concerning the mechanism by which defects are revealed in the step 2 electrolytic etching case can be gained by consideration of the data contained in Fig. 1 and 2i. (Note that an account of the characteristics contained in Fig. 1-3, together with their relation to previous work on the electrochemistry of GaAs, is given in the Appendix.) First, by using the surface barrier potential ($\psi_s{}^n$) shown for Tiron in Fig. 1, a band diagram for the appropriate semiconductor/electrolyte contact (at open-circuit, and unilluminated) can be constructed. This is shown as Fig. 7i. With subsequent illumination, the electron hole pairs photogenerated within the electrode produce a decrease in the barrier height while any anodic overpotential applied thereafter acts in the reverse-bias sense, assisting the diffusion of holes toward the interface. Under these circumstances, the photocurrent shown as Fig. 2i is produced. The diagram ii in Fig. 7 is a schematic representation of the electrode condition at point A on the polarization curve 2i where the anodic overpotential is +250 mV. If applied potentials in excess of 250 mV are used, a photocurrent saturation is attained and the electrode subjected to normal reverse-bias conditions, the depletion width increasing with voltage. Finally, on any further increase in potential, breakdown conditions will be approached.

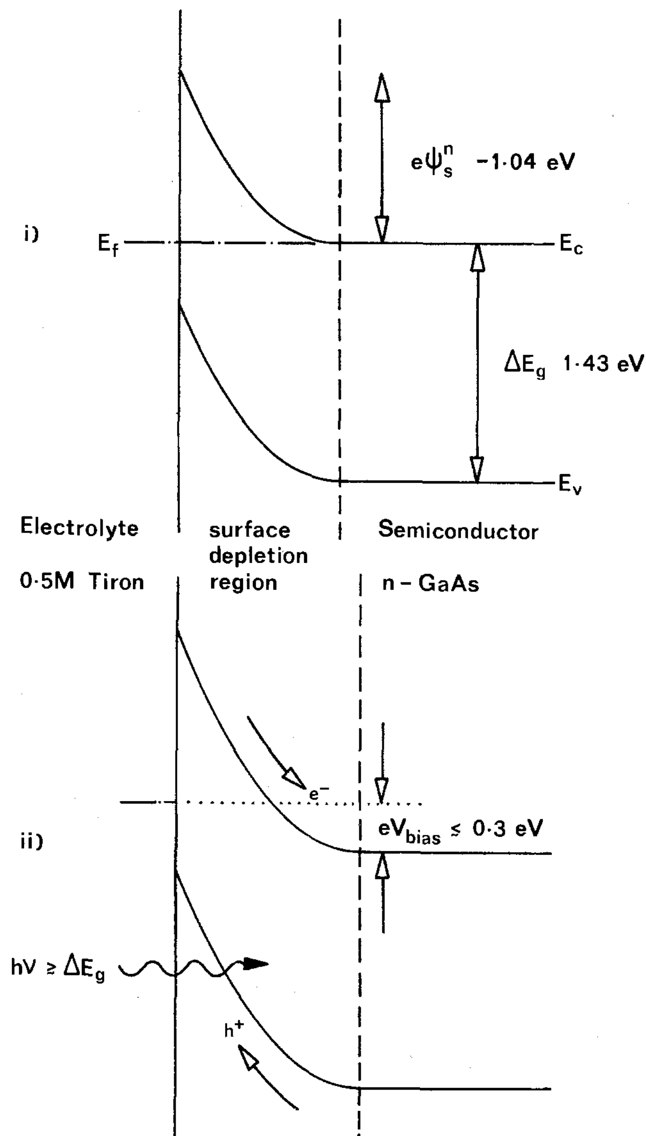

Fig. 7. Band diagrams representing: i. quantitatively, the n-GaAs electrode (unilluminated, and at the open-circuit condition) in contact with 0.5M Tiron electrolyte; and ii. schematically, the n-GaAs/0.5M Tiron half-cell under conditions represented by point A in Fig. 2i.

Any interband state acting as an electron-hole recombination center within the depletion width marked in Fig. 7ii will then introduce two localized perturbations to the over-all polarization behavior near the rest condition. First, there is a reduction in the open-circuit photopotential, and second, a stifling of the hole current which supplies the anodic dissolution reaction. Clearly the operation of the latter will produce points of low etching rate at the sites where nonradiative recombination processes are facile. It has long been well-known that dislocations can act as efficient nonradiative centers in most of the III-V compound semiconductors (21).

We have found that all of the discrete features etched on samples such as shown in Fig. 6i (where all of the defects are supposed characteristic of the bulk material) and Fig. 4i (where the defects arise from polishing operations) are indeed elevated in profile. This was ascertained by use of a Talysurf instrument on some heavily etched samples. The surface features produced on n-GaAs samples in both of the photoassisted chemical etching studies already referred to (11, 12) exhibited a similar cross-sectional geometry. Although Kuhn-Kuhnenfeld (11) recorded negative photopotentials—as happened here—and attempted an explanation of the etching action via his data, no ascription of a mechanism for defect delineation can be realistically made on the basis of such singular observations. This is because the overpotential available for the dissolution remains largely chemical in origin. Only by the addition of a full electrochemical control, as that obtained by our fixing of the electrode potential of the semiconductor sample, can the over-all mechanism depicted semiquantitatively in Fig. 7ii be justifiably proposed.

This contention is open to experimental test. Although at low overpotentials the localized recombination processes are responsible for impeding the dissolution, an increase in applied bias should lead to a reduction in defect resolution. This follows because the increased field strength imposed in the depletion region during the traversal of the photosaturation is responsible for a decrease in the probability of minority carrier trapping at the imperfection (22). There is an intrinsic mechanism involved (that is a field effect on the capture cross section of the trap) and probably also a contribution resulting from the increased energy imparted to the carrier (23). Thus the experiment consists of comparing the resolution of defects at different anodic potentials. The photomicrographs of Fig. 8 display the results obtained from such a study.

Two separate Si-doped samples were involved, labeled D and S, and clearly have very different defect morphologies. Each was examined at three adjacent areas. The micrographs Di and Si show the surface morphology obtained after "standard" sequential electrochemical etching, as per Fig. 5, with a step 2 overpotential of ≤ 300 mV and with $d_2 = 0.57$ μm and 0.40 μm, respectively. There is a significant discrepancy between the resolution attained for Di and that yielded by the sample shown in Fig. 6i and 6iv, even though the etching conditions were the same in each case. Their dissimilar behavior might be taken to indicate that a different degree or type of dislocation decoration was specific to each. The wafers had almost identical carrier concentrations, but originated from different manufacturers. This marked discrepancy in etch behavior was observed consistently through a whole range of samples obtained from these two suppliers. The topography shown by the sample S has, in the equivalent case (Si) two basic elements. The striations present in the left-hand portion of the micrograph were originally supposed to derive from a known facet effect often incurred during the bulk solidification of GaAs (24). Clearly some extensive microfaceting would be required to produce the features as observed. However, the same defected area gave a strongly imaged, banded contrast on an x-ray topograph. This is probably inconsistent with simple variations in dopant concentration alone (7). The common severity with which these features were resolved by both techniques leads us to suspect that they have a basic crystallographic origin, possibly linked to lamellar twinning (7). (Note that there are also striations present in Fig. 6i, but they are very much weaker than those of Si. Also the accompanying x-ray topographs there (6ii and 6iii) have no image matching the striae. Our conclusion is that these etch features do correlate with simple variations in dopant concentration, and hence carrier mobility, and that the periodic distribution arose there from thermal cycling occurring during solidification.) Also present for Si, and covering the whole area of the micrograph, is an array of small nodular features at a density of $\sim 2 \times 10^6$ cm^{-2}. Their origin is as yet uncertain. However, considering the carrier concentration of the sample ($N_d = 2.4 \times 10^{18}$ cm^{-3}), dopant precipitation would appear to be a strong possibility. Some attempts were made to check the comparative behavior of this wafer on use of the AB chemical etchant (10), both in a standard form and also with dilution and photoassistance together (12). Only in the latter case was a clear resolution of the same nodular topography attained. The concentrated etchant produced only a marginal featuring of the

surface, certainly not as clear a morphology as that observed for GaAs doped with Se and Te at the same concentration levels (25). For these materials, Stirland (25) has observed good correlation between etch pit features (at localized densities of between 10^6 and 10^8 cm^{-2}) and small defects allied to dopant precipitates. The evidence for the presence of similar imperfections in silicon-doped material is certainly much less clear and our result can only be advanced as an additional preliminary indication of similar precipitation effects.

The changes in the etch morphologies developed at different electrode potentials are shown in sections ii and iii of Fig. 8. The central pair of micrographs (Dii and Sii) illustrate the results gained after using an overpotential of 1.25V. (This is sufficient to double the possible voltage drop across the depletion region and therefore to increase the field strength relative to that of the first etching experiment by a factor of $\sqrt{2}$.) Interestingly, the resolution of each defect type is affected differently. The striated features (in Sii), the origin of which we have been unable to identify with complete confidence, remain as well resolved as in the initial case Si. In Dii, only those dislocations resolved most severely in the first instance have now produced a local perturbation of the anodic current, while the distinctive nodular features present in Si are no longer revealed at all in the second case. The material removal was held constant for each sample ($d_2 = 0.57$ and 0.40 μm were the average removals for D and S, respectively). At this stage we can conclude that the qualitative model dealing with the selective resolution of imperfections has been amply verified by the experi-

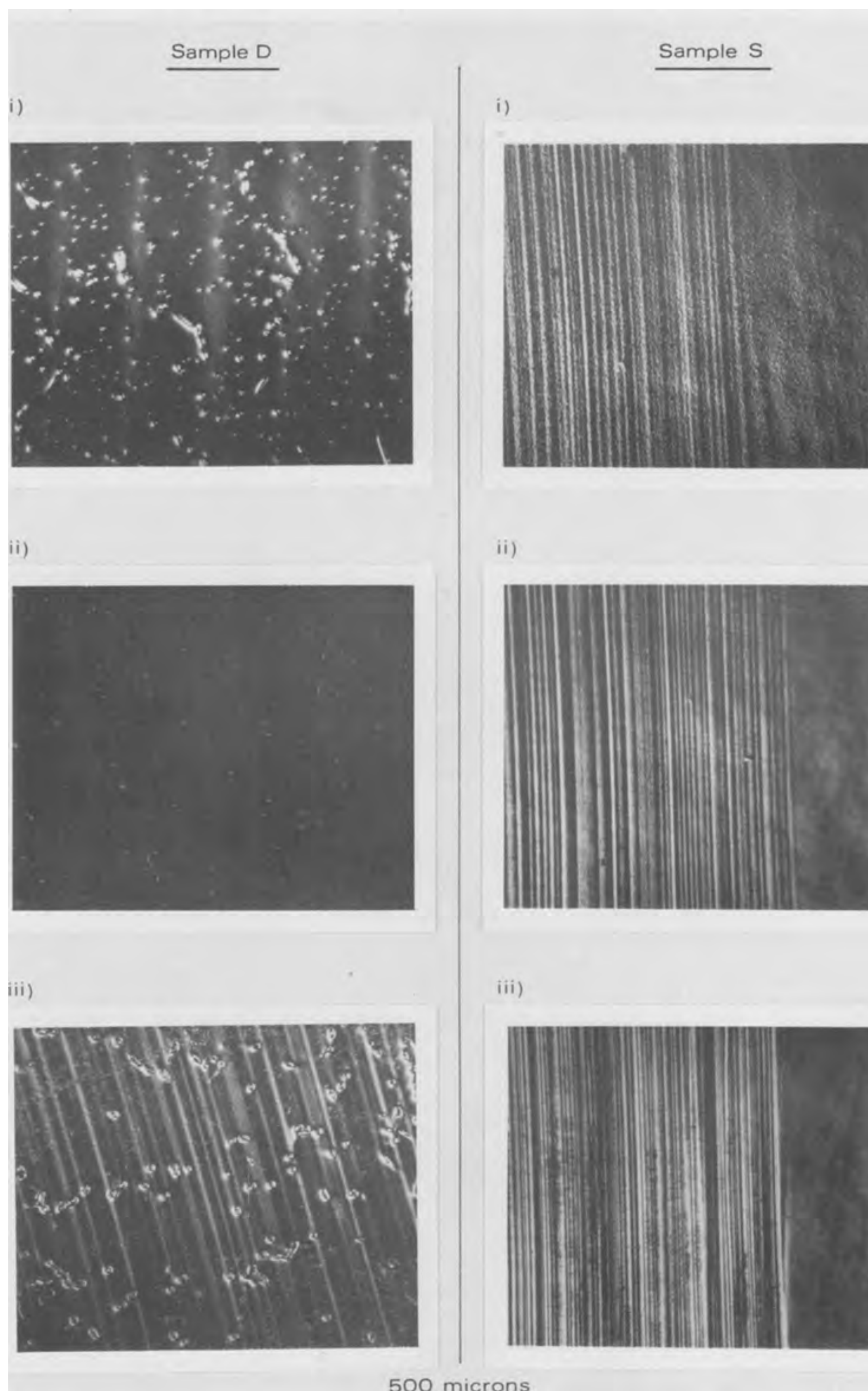

Fig. 8. Nomarski interference micrographs showing the etch morphologies developed during the defect revelation procedure at different anodic electrode potentials; i. overpotential ~250 mV; ii. overpotential 1.25V; iii. overpotential ≥ 1.75V. (n-GaAs samples: D, Si-doped, 7.8 × 10^{17} donors per cm^3; S, Si-doped, 2.4 × 10^{18} donors per cm^3).

mental results. Additionally, there appears to be available some semiquantitative information concerning the minority carrier lifetime at different defect centers.

In connection with this last statement, the results gained at current densities exceeding the photosaturation are of interest (Diii and Siii). The defects which were acting primarily as recombination centers in the low overpotential etching, should, under the necessarily higher overpotential conditions now required, participate as localized breakdown sites. The use of this etching regime is known from previous experiments to result in a discretely pitted surface (26, 27). Thus an inversion of the etch morphology is possible on traversing the whole anodic potential range. This is shown separately here in Fig. 9 by the comparative display of Talysurf traces for the two sample areas photographed as Di and Diii in Fig. 8. Because the electrochemical etching was confined to a well-defined circular area, the boundary etch step could be used for calibration of the vertical axis. These steps are positioned in line on the left-hand side of Fig. 9. The etch profile is then clearly resolved in both cases, consisting of elevated (ridged) features for Di and depressed (pitted) features for Diii. The edge step was also used to calibrate optical microinterferometers of the standard Michelson type and also a Nomarski differential interference contrast objective and use of these techniques confirmed that an inversion of etch topography was indeed gained on increasing the anodic potential. Finally, sample S was also subjected to etching at current densities > 1.5 mA cm^{-2}. In this case, (Siii), the dissolution is largely confined to the heavily striated material and the imperfections responsible for the nodular features in Si do not contribute individually to the reverse-bias breakdown of the sample area probed. The generation/recombination characteristics of each type of defect are clearly quite different.

Summary and Discussion

Our aim in this work was to procure a technically simple method for the resolution of crystallographic defects in GaAs, preferably with a resolution such that reproducible results could be gained with the removal of ≤ 0.5 μm of material. Of necessity, two previously untried methods of anodic dissolution have been investigated. The technique thus developed consists of:

(*i*) A defect-insensitive etch (step 1 in Fig. 5) which can be used for the removal of damaged material from as-polished surfaces, or to accurately section the slice to any predetermined depth. The anodic dissolution here is carried out continuously with an oxide film present at the interface to preserve the initial topography.

(*ii*) A defect-revealing etch for n-GaAs which has a high sensitivity related directly to the electronic characteristics of the imperfection (step 2 in Fig. 5).

Used in sequence, these two dissolution regimes allow: (*i*) the depth characteristic of polishing damage to be gauged quantitatively for any method of slice preparation; and (*ii*) the defect content of the bulk material (n-GaAs substrate) to be determined with a resolution not attainable with any of the standard chemical etchants used previously for GaAs.

One distinctive element of the technique described here has cardinal importance. The adoption of fully electrochemical etching conditions, in which chemical reaction between the etchant and semiconductor has been deliberately excluded, leaves the dissolution totally dominated by the optoelectronic properties of the sample. That is, etching only occurs at locations on the surface where the anodic current is either uninhibited or, alternatively, enhanced. Therefore the correlation of morphological features produced against defects identified by an independent crystallographic technique (as per Fig. 6) comprises a relation between the structural origin of the imperfection and its electronic consequence. Thus our experimental method corresponds quite closely to those adopted for detailed studies of structural defects and their nonradiative recombination characteristics in n-GaP (23, 28), except that in this case the etching and the optoelectronic probe are done neatly in combination.

Furthermore, the manner in which the semiconductor properties of GaAs dominate its electrode behavior indicates an easy extension of the method into analyses of epitaxial GaAs and probably also other III-V compounds. Working, for example, with the epitaxial structure of most interest at this time [the five-layer GaAs/$Ga_xAl_{1-x}As$ sequence grown for injection laser fabrication (9)], we have been able to probe the n-GaAs buffer material and its homoepitaxial interface with the substrate, and also, separately, the succeeding n-$Ga_{0.65}Al_{0.35}As$ layer. Results from this and other areas of similar material assessment will be described in a subsequent publication.

Note

During the period while this paper was under review, a publication on the same topic (42) has appeared in the literature. We have carried out anodic etching experiments on n^+-GaAs exactly as described by

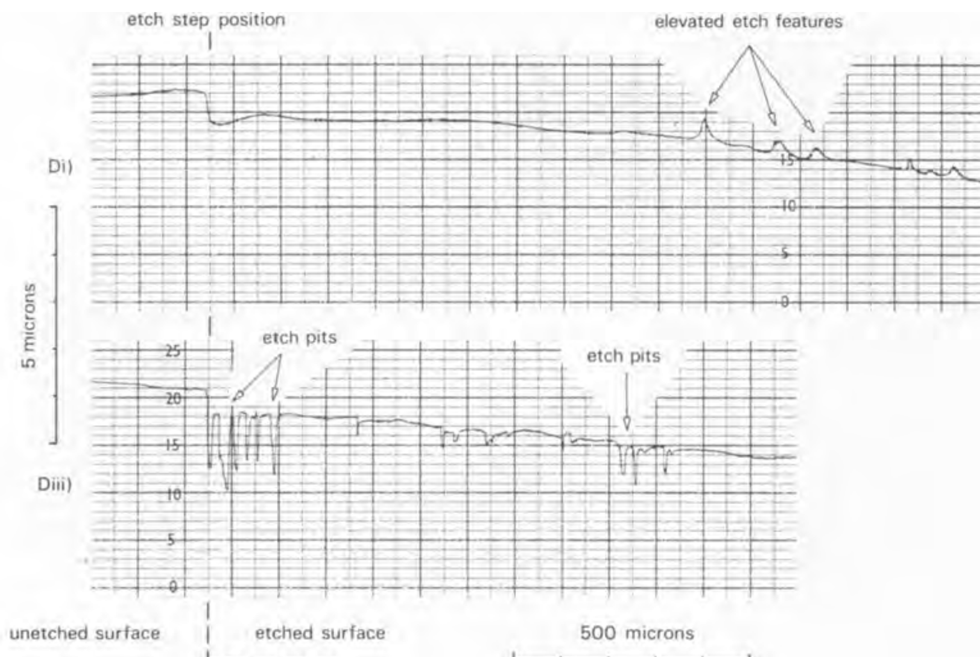

Fig. 9. "Talysurf" profiles of the etched surfaces photographed as Di and Diii in Fig. 8.

Greene in an attempt to classify the defect revealing conditions according to our Fig. 8. The most important distinction is that no deliberate illumination is included in Greene's experimentation. Thus, automatically, the rather "heavy-weight" conditions imposed (maximum current density 2 mA cm^{-2} and cell voltage 10V) lead to a defect resolution of types ii and iii in Fig. 8, depending somewhat on the level of ambient illumination. These are not the most sensitive conditions. For example, only the prephotosaturation current density etching of sample S in Fig. 8 (Si) resolves the high density of nodular features which we suspect are related to impurity precipitation defects in Si-doped n^+-GaAs.

Acknowledgments

We are grateful to Mrs. M. A. G. Halliwell for pursuing the x-ray topographic study referred to in this paper, and for many useful discussions concerning this aspect of the work. Further experimental design and assistance was given by R. M. Redstall, M. C. Case, and J. C. Regnault. We are also indebted to Dr. T. Ambridge and Dr. R. Heckingbottom for their interest and advice.

This paper is published by permission of the Director of Research of the British Post Office.

Manuscript submitted March 21, 1977; revised manuscript received Oct. 31, 1977.

Any discussion of this paper will appear in a Discussion Section to be published in the December 1978 JOURNAL. All discussions for the December 1978 Discussion Section should be submitted by Aug. 1, 1978.

Publication costs of this article were assisted by the Post Office Research Centre.

APPENDIX

Use has been made in these studies of the anodic capacitance and polarization characteristics of n-GaAs.

Electrode capacitance.—The only systematic examination of the depletion characteristics of GaAs/electrolyte contacts is that due to Benard and Handler (29), who determined specifically the semiconductor surface potentials but used only strongly acidic media. The collection of data assembled in Fig. 1 includes that measured for the electrolytes used here, and confirms that the n-type semiconductor surface is in substantial depletion under open-circuit conditions. One noteworthy aspect is that the band-bending ($|\psi_s^n|$) for the electrolytic contact appears to exceed almost everywhere in the pH range the values measured for n-GaAs/metal junctions ($-0.80V \geqq \psi_s^n \geqq -0.95V$) by Mead (30). There is also present a systematic variation of ψ_s^n with pH, and this produces a differential resolution of the crystallographic defects in step 2 etching conditions, just as that obtained by variation of the bias voltage and pictured in Fig. 8. The highest etch discrimination is procured therefore with acidic media, where the field strength in the depletion layer is lower. Note that Fig. 1 will not apply to electrolytes containing strong oxidizing agents (31).

Electrode dissolution and passivation.—It is well known that the anodic dissolution of the wide bandgap semiconductors requires the participation of holes. Pleskov (32) first confirmed that this was the case for GaAs, having investigated the anodic currents gained using both acidic and alkaline electrolytes. The curve shown as Fig. 2i here, where use has been made of the complexant electrolyte Tiron, is of the same classical form (33, 34) and yields, over-all, two important advantages in the topographical etching studies. First, the anodic reaction has a strict six-electron equivalence (35), which allows the integrated current density to be converted automatically to the average dissolution depth. Second, it allows the electroetching to occur without interference from insoluble products at the electrode surface, in contrast to, say, sulfuric acid solutions which leave precipitated arsenious oxide (26). Importantly also, the electrolyte is acidic (see a, above).

Conversely, the anodic polarization curve obtained using the phosphate electrolyte (Fig. 2ii) shows passivation characteristics similar to those observed for various GaAs electrodes by Harvey (36, 37). Since curves 2i and 2ii were recorded under identical illumination conditions, it is clear that the straightforward photosaturation limitation present in the first instance has been replaced in 2ii by a kinetic restraint due to product insolubility.

From Fig. 3 it is apparent that a mixture of the two electrolytes allows both of these individual characteristics to appear in succession. Specifically, the addition of the complexant (Tiron) to the barrier oxide forming electrolyte (NaH_2PO_4) has led to a large increase in the steady-state current density achievable in the presence of a uniform anodic oxide film (compare point B in Fig. 3 with the original passivation curve 2ii). As yet we have been unable to clearly resolve the individual roles of photoinjection and Schottky barrier breakdown in the supply of holes for the over-all dissolution reaction. A six-electron equivalence is maintained however, with a 1 mA cm^{-2} current density corresponding to a continuous removal rate of 1.7 μm per hour. Some experimental observations concerned with the effect of aqueous electrolyte composition on the outcome of GaAs anodization have been published by Schwartz *et al.* (38). In comparison, the specific complexant action of Tiron, as set out above for the mixed electrolyte, is rather better defined than the anion-type dependencies noted by Schwartz *et al.* Also, the use of an electrochemical regime where oxide dissolution is uniformly enhanced for the machining of GaAs (see step 1 in Fig. 5) was not dealt with. In fact, one particularly important application (the precise thickness trimming of epitaxial layers) has generally been subjected to a noncontinuous method, where, in separate steps, the oxide is first grown and then removed under open-circuit dissolution conditions (3, 39, 40). Clearly this multiple-stage processing may lead to some cumulative inaccuracy in assessing the over-all material removal.

REFERENCES

1. T. Ambridge, C. R. Elliott, and M. M. Faktor, *J. Appl. Electrochem.*, **3**, 1 (1973).
2. T. Ambridge and M. M. Faktor, *ibid.*, **5**, 319 (1975).
3. W. C. Niehaus and B. Schwartz, *Solid-State Electron.*, **19**, 175 (1976).
4. H. Hasegawa and H. L. Hartnagel, *This Journal*, **123**, 713 (1976).
5. G. R. Woolhouse, A. E. Blakeslee, and K. K. Shih, *J. Appl. Phys.*, **47**, 4349 (1976).
6. J. I. Pankove, "Optical Processes in Semiconductors," Prentice-Hall, Inc., Englewood Cliffs, N.J. (1971)
7. D. J. Stirland and B. W. Straughan, *Thin Solid Films*, **31**, 139 (1976).
8. S. Komiya, K. Akita, Y. Nishitani, S. Isozumi, and T. Kotani, *J. Appl. Phys.*, **47**, 3367 (1976).
9. H. Kressel, in "Fundamentals of Fibre Optic Communication," M. K. Barnoski, Editor, p. 109, Academic Press, New York (1976).
10. M. S. Abrahams and C. J. Buiocchi, *J. Appl. Phys.*, **36**, 2855 (1965).
11. F. Kuhn-Kuhnenfeld, *This Journal*, **119**, 1063 (1972).
12. T. Saitoh, S. Matsubara, and S. Minagawa, *This Journal*, **122**, 670 (1975).
13. E. G. Bremner, T. Ambridge, and C. R. Elliott, *J. Phys. E*, **6**, 326 (1973).
14. T. Ambridge and M. M. Faktor, *J. Appl. Electrochem.*, **4**, 135 (1974).
15. G. Beilby, "Aggregation and Flow of Solids," Macmillan Publishing Co., Inc., London (1921).
16. R. T. Holm, J. W. Gibson, and E. D. Palik, *J. Appl. Phys.*, **48**, 212 (1977).
17. M. A. G. Halliwell, J. B. Childs, and S. O'Hara, *Inst. Phys. Conf. Ser.*, **17**, 98 (1973).
18. G. A. Rozgonyi and D. C. Miller, *Thin Solid Films*, **31**, 185 (1976).
19. D. Laister and G. M. Jenkins, *J. Mater. Sci.*, **8**, 1218 (1973).
20. K. K. Shih, G. R. Woolhouse, A. E. Blakeslee, and J. M. Blum, *Inst. Phys. Conf. Ser.*, **24**, 165 (1975).
21. G. B. Stringfellow and P. E. Greene, *J. Appl. Phys.*, **40**, 502 (1969).
22. A. G. Milnes, "Deep Impurities in Semiconductors," p. 103, Wiley-Interscience, New York (1973).
23. A. R. Peaker, B. Hamilton, D. R. Wight, I. D. Blenkinsop, W. Harding, and R. Gibb, *Inst. Phys. Conf. Ser.*, **33a**, 326 (1977).
24. C. LeMay, *J. Appl. Phys.*, **34**, 439 (1963).

25. D. J. Stirland, *Inst. Phys. Conf. Ser.*, **33a**, 150 (1977).
26. J. P. Krumme and M. E. Straumanis, *Trans. Met. Soc. AIME*, **239**, 395 (1967).
27. M. M. Faktor, D. G. Fiddyment, and M. R. Taylor, *This Journal*, **122**, 1566 (1975).
28. T. J. Hayes, A. Rasul, and S. M. Davidson, *J. Electron. Mater.*, **5**, 100 (1976).
29. D. J. Benard and P. Handler, *Surf. Sci.*, **40**, 141 (1973).
30. C. A. Mead, *Solid-State Electron.*, **2**, 1023 (1966).
31. H. Gerischer, *Surf. Sci.*, **18**, 97 (1969).
32. Yu. V. Pleskov, *Doklady Akad. Nauk SSSR*, **143**, 1399 (1962).
33. W. H. Brattain and C. G. B. Garrett, *Bell Syst. Tech. J.*, **34**, 129 (1955).
34. W. W. Gartner, *Phys. Rev.*, **116**, 84 (1959).
35. H. Gerischer, *Ber. Bunsenges.*, **69**, 578 (1965).
36. W. W. Harvey, *This Journal*, **114**, 472 (1967).
37. W. W. Harvey and J. Kruger, *Electrochim. Acta*, **16**, 2017 (1971).
38. B. Schwartz, F. Ermanis, and M. H. Brastad, *This Journal*, **123**, 1089 (1976).
39. D. L. Rode, B. Schwartz, and G. D. Weigle, *Solid-State Electron.*, **17**, 1119 (1974).
40. H. Muller, F. H. Eisen, and J. W. Mayer, *This Journal*, **122**, 651 (1975).
41. W. H. LaFlere, F. Cardon, and W. P. Gomes, *Surf. Sci.*, **44**, 541 (1974).
42. L. I. Greene, *J. Appl. Phys.*, **48**, 3739 (1977).

On the Nature of Fixed Oxide Charge

S. I. Raider[*,1] **and A. Berman**

IBM System Products Division, East Fishkill Facility, Hopewell Junction, New York 12533

ABSTRACT

An oxidation-induced fixed oxide charge Q_{ss} is known to be generated in the SiO_2-Si interfacial region. In the light of recent determinations of the composition and width of this interfacial transition region, a reexamination of the nature of this charge is undertaken. A model, consistent with known transition region composition, is proposed in which a positively charged silicon-oxygen complex is formed as an intermediate reaction product of the oxidation process. This intermediate may be trapped within the transition region when the oxidation reaction is terminated by quenching in the oxidizing ambient. The concentration of this complex is proportional both to the excess oxygen concentration and to the nonoxidized Si-Si bond density in the transition region. The model is also consistent with the dependence of Q_{ss} on such factors as oxidant pressure, oxidation temperature, inert-gas annealing, and substrate orientation.

Electrically active sites such as fixed oxide charge, Q_{ss} form in the oxide film at or near the SiO_2-Si interface (1) during the oxidation reaction. Their formation occurs within the same region in which Si is incompletely oxidized and within which the oxidation process takes place (2, 3). The number of nonoxidized Si atoms present within this transition region cannot be identified with Q_{ss}. The density of these charge sites after oxidation (10^{12} cm^{-2}) (1, 4) is significantly lower than the nonoxidized Si-Si bond density (10^{15} cm^{-2}) within the transition region. Q_{ss} is reduced further (to 10^{10}-10^{11} cm^{-2}) by postoxidation annealing treatments (1, 4). The magnitude of Q_{ss} depends intimately upon the thermal oxidation process (1). Despite numerous studies, the relationship between thermal oxidation and Q_{ss}, as well as the chemical nature of Q_{ss} is not well understood. Control of fixed oxide charge densities, which are of technological importance, remains largely empirical.

Recently, the composition and width of the SiO_2-Si interface, formed by thermal oxidation of <100> and <111> oriented Si surfaces were characterized by analysis of x-ray photoelectron spectroscopy (XPS) data (5-8). Changes in Si chemical bonding at this interfacial region were derived from XPS spectra (5, 8). Although the detection limit of x-ray photoelectron spectroscopy is approximately 10^{13} cm^{-2} and does not provide a means for direct observation of the sites responsible for Q_{ss}, the XPS findings do provide a new picture of the transition region within which these electrical instabilities must be understood. We have therefore reconsidered the thermal oxidation process and the related chemistry that occurs at an SiO_2-Si transition region and that may influence the oxide charge densities.

[*] Electrochemical Society Active Member.
[1] Present address: Thomas J. Watson Research Center, Yorktown Heights, New York 10598.

Key words: silicon, oxidation, SiO_2-Si interface, electrical instabilities, surface states.

Fixed Oxide Charge

The properties of fixed oxide charge have been summarized in several papers (1, 4) and review articles (9-12) and are only briefly described here. These charges form a positive space charge in the oxide film during the thermal oxidation process and induce a negative image charge in the Si substrate. Fixed oxide charges are stable under moderate temperature-bias conditions and are unaffected by changes in surface potential. Densities are dependent upon substrate orientation with Q_{ss}<111> > Q_{ss}<100>. Chemical etching (1) and internal photoemission experiments (13, 14), as well as the dependence of Q_{ss} upon substrate orientation, indicate that Q_{ss} is near to the substrate. For example, results of internal photoemission experiments suggest that most of the charge is located at less than 20Å from the substrate and is spatially distributed within the SiO_2-Si transition region.

Factors that influence Q_{ss} include oxidation and annealing ambients and the oxidation temperature. Charge densities reflect the final oxidation or annealing conditions. The formation or reduction of Q_{ss} is reversible provided that steady-state conditions are achieved. In a reactive dry oxygen ambient, Q_{ss} increases with decrease in oxidation temperature. An example taken from the earlier literature (1) shows that Q_{ss} is about 4.2×10^{11} cm^{-2} after 2000Å thick films have been annealed to minimize Q_{ss} and subsequently oxidized at 550°C. After oxidation of Si at 1200°C, Q_{ss} is 2×10^{10} cm^{-2}. Varying the rate at which a sample is pulled from a hot zone in an oxidation furnace is equivalent to adjusting the final effective oxidation temperature at which the oxidation reaction is quenched, thereby altering Q_{ss}. High temperature an-

nealing in an inert ambient, such as Ar gas, minimizes Q_{ss}. N_2 gas, which is often used as an annealing ambient to reduce charge densities, is not chemically inert. Under certain conditions, annealing in N_2 will result in an interaction between N_2 and Si and will increase the density of electrically active sites (15-18).

The relationships between oxidation temperature, inert gas annealing, and Q_{ss} are summarized in Fig. 1 by the well-known Deal oxidation triangle (1, 11). The cross sections in Fig. 1 show a clear relationship between Q_{ss} and the concentration of excess oxygen, C_i, at the transition region. For instance, at high temperatures (cross section a), C_i is low because the oxidation rate is high compared with the rate of supply of in-diffusing oxygen. At low temperatures (cross section b), C_i is high because the diffusion rate is large compared with the greatly reduced oxidation rate. Finally, an inert-gas anneal (cross section c) will both consume and out-diffuse the excess oxygen.

When an annealed SiO_2-Si structure with low Q_{ss} is subjected to further oxidation, the rate at which the new value of Q_{ss} is reached is proportional to the oxide film thickness (4). This rate is associated with the rate of oxygen transport through the oxide film and thus with the attainment of the steady-state value of C_i. Pautrak and Pfister (19) obtained a direct relationship between Q_{ss} and oxygen pressure by annealing 2500Å thick films, grown at 1240°C, in oxygen at various oxygen pressures, p, and anneal temperatures. Q_{ss} increased linearly with $p^{1/2}$ to some saturation pressure (determined by the given anneal temperature) once a steady-state concentration of oxygen oxidant at the transition region had been reached.

Other workers have observed that Q_{ss} is a monotonic function of the excess oxygen within the transition region, C_i (4, 20, 21). As early as 1967, Kubo and Ichinohe (21) suggested that electrical instabilities, such as Q_{ss}, caused flatband voltage shifts in capacitance-

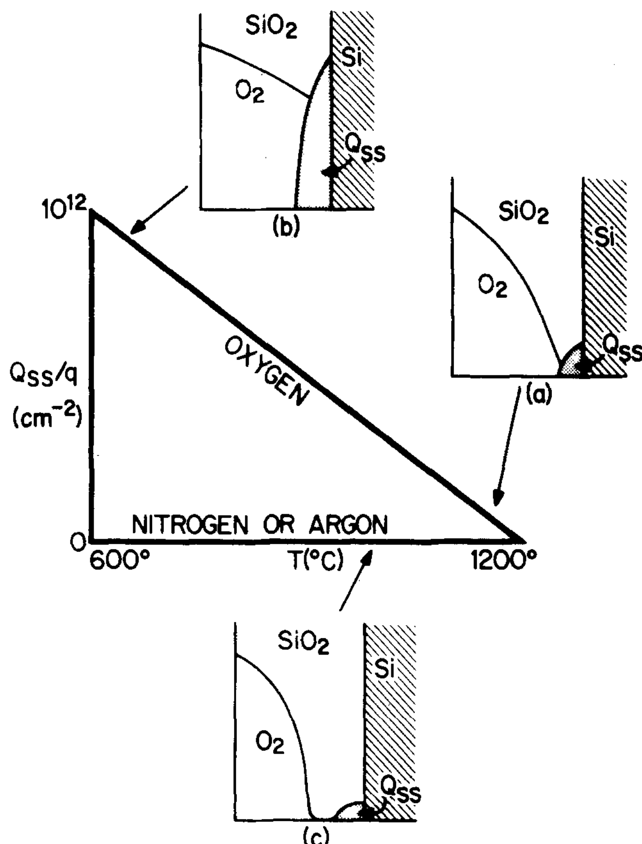

Fig. 1. The dependence of Q_{ss} on final oxidation temperature and ambient as represented by Deal's Q_{ss}-oxygen triangle. The sketches of the thermal oxide cross sections indicate the proposed relationship between Q_{ss} and the oxidation conditions.

voltage curves and were related to dissolved oxygen in SiO_2 near the interface. The solubility of oxygen in 10Å transition region layers should range from 6×10^9 to 2×10^{11} cm^{-2} based on oxygen solubilities in SiO_2 (3) and in crystalline Si (22, 23). These appear somewhat low to account for maximum Q_{ss} values of about 2×10^{12} cm^{-2}.

In addition to the relationship between Q_{ss} and C_i, Q_{ss} is also associated with the fast surface-state density, N_{ss}. For example, Arnold *et al.* (20) have observed that Q_{ss} and fast surface-state density, N_{ss}, are initially proportional to each other after Si oxidation in O_2 and that their densities exhibit the same dependence upon orientation. Although both are formed during oxidation, the fact that these instabilities have different annealing properties demonstrates that they are not manifestations of a single chemical entity. The chemical processes that affect N_{ss} and the ability of these states to act either as donors or as acceptors are consistent with the model in which a surface state corresponds to a chemically unsaturated silicon atom, $\equiv$Si· (24). No single microscopic model is accepted that accounts for the reported variations in Q_{ss} with changes in processing.

SiO_2-Si Transition Region (6, 7, 9)

Several compositional changes occur at an SiO_2-Si interface. The total Si atom concentration per unit volume decreases by a factor of 2.2 when Si is oxidized to form SiO_2. Crystalline Si surfaces with <100> and <111> orientations possess 6.78×10^{14} and 7.85×10^{14} Si atoms cm^{-2}, respectively. As a consequence of the directionality of the bonds in the Si substrate, the number of Si-Si bonds accessible to an oxidant at a <111> oriented surface is 11.76×10^{14} cm^{-2}; on a <100> oriented surface, the corresponding number of bonds is 6.78×10^{14} cm^{-2} (25). Based upon the XPS detectability limit, the number of nonoxidized Si-Si bonds in thermally grown, amorphous SiO_2 was found to be less than 10^{13} cm^{-2} (6).

A nonstoichiometric interfacial transition region, 7-10Å thick, is formed between single crystal Si substrates and thermally grown SiO_2 films. It is graded in composition and increases in chemically bonded oxygen content with distance from the substrate. This gradation is nonlinear. The Si is more than 50% oxidized in the first 2.5Å beyond the substrate. For example, the average composition of the first 2.5Å of oxide film is $SiO_{1.4}$ on a <100> oriented substrate and is $SiO_{1.2}$ on a <111> oriented substrate (6b). Both Si-Si bonds and Si-O-Si groups are present within the transition region, but not as a mixture of Si and SiO_2. Instead, x-ray photoelectron spectroscopy data indicate that Si tetrahedra, Si-$(O)_x(Si)_{4-x}$, are formed, in which x varies from 0 to 4 in going from the substrate to the stoichiometric SiO_2 film. Within the sensitivity limits of x-ray photoelectron spectroscopy, no evidence of the formation of an intermediate, such as Si^+, whose binding energy should be greater than that of Si 2p in SiO_2, is detected. The width and composition of this region remain invariant with change in oxidation temperature (25°-1050°C), in oxidant [O_2, O_2/N_2, H_2O, HNO_3, H_2O_2(30%)], or in oxide film thickness (20-1000Å). Postoxidation annealing at 1000°C in N_2 for 30 min does not alter the transition region.

The composition and width of the transition region are altered only with change in substrate orientation (7, 9). Oxides formed on <111> oriented substrates have transition regions that are 10Å thick and that possess 1.4×10^{15} nonoxidized Si-Si bonds cm^{-2}, whereas transition regions on <100> oriented substrates are 7.5Å thick and possess 0.8×10^{15} Si-Si bonds cm^{-2} (6b). The nonoxidized Si bonds within the transition regions are proportional to the accessible Si-Si bonds (25) at a substrate surface.

Transition region nonstoichiometry, which is often suggested as the origin of Q_{ss} (1), does not contribute

directly to the density of electrically active sites. As previously indicated, transition region composition is unaffected by several of those factors or processes that alter Q_{ss}. Changes in Q_{ss} are directly related only to changes in transition region composition associated with a change in substrate orientation. However, the number of nonoxidized Si-Si bonds within these transition regions is significantly greater than the change in the density of electrically active sites.

Thermal Oxidation of Si

During the thermal oxidation process, crystalline Si substrate surfaces are converted into amorphous SiO_2 films. This conversion involves an interfacial chemical reaction in which the oxidant is first transported through an oxide film and is absorbed in the transition region. Oxidant transported to this region is assumed to be neutral (26) and composed either of O_2 molecules, which subsequently dissociate, or of (O) atoms. The nature of the oxygen adsorption and dissociation processes within the transition region is not known although several models for the initial oxidation steps have been proposed (27-30). When an oxidation reaction does occur, considerable strain should arise at an SiO_2-Si interface as a result of direct insertion of oxygen atoms between Si-Si bonds. A transition region between a single-crystal Si surface and an amorphous, stoichiometric SiO_2 film presumably forms in order that oxygen atoms be accommodated by the substrate with a minimum of internal strain. The formation of different transition regions on <111> and on <100> Si substrates is then associated with differences in the internal strains that would otherwise accompany oxidation of these oriented surface layers. Bond distances change from 2.3Å for a Si-Si bond in the substrate, to 3.0Å, for a Si-O-Si group in an oxide film. Incorporation of oxygen into the Si substrate lattice to form an oxide film while still retaining a predominantly 3 dimensional structure requires displacement of Si atoms from their original lattice sites. These displacements are consistent with the decrease in Si atom concentration of more than 50% when crystalline Si is oxidized to form SiO_2 within the transition region. The tetrahedral bonding of the nonoxidized Si surface atoms to the substrate acts as a constraint upon this oxidation process. Changes at the substrate surface are facilitated if the oxidation reaction occurs via a multistep process. The consequences of a multistep oxidation process are considered below.

Model

The oxidation reaction occurs at accessible nonoxidized Si atoms within the transition region. However, fixed oxide charges, which are associated with the oxidation process, form at only a small subset of these reaction sites. This can be rationalized when considering the observed correlations between the excess oxidant concentration and Q_{ss} and by assuming that electrically active sites are intermediates formed during an oxidation reaction. A two-step oxidation reaction is proposed that involves Si-Si bond breaking and siloxane (Si-O-Si) group formation. The Si-Si bonds within the transition region are under tension. Oxygen molecules or atoms, both of which contain unpaired electrons, interact with accessible nonoxidized Si-Si bonds. This initial oxidation reaction in which Si-Si bonds are broken is only weakly thermally activated with an activation energy, E_a, near zero. For a given substrate orientation, the extent of this interaction is determined by C_i. Oxygen solubility is presumably enhanced by complex formation with nonoxidized Si. A reaction occurs with formation of two different electrically active intermediates such as are shown in Eq. [1]

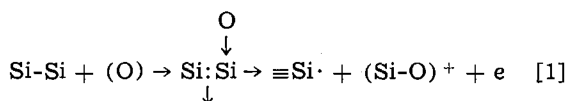

$$\text{Si-Si} + (\text{O}) \rightarrow \text{Si:Si} \rightarrow \equiv\text{Si}\cdot + (\text{Si-O})^+ + e \quad [1]$$

The dangling bond, $\equiv Si\cdot$, corresponds to fast surface states, and the positive Si-oxygen complex, $(Si\text{-}O)^+$, corresponds to fixed oxide charge. This positive complex represents a possible configuration for Q_{ss} consistent with the known composition of the transition region and with the properties of Q_{ss} (31). Little is known of positive Si-oxygen complexes, although Brosious (32) has recently proposed that an ESR signal from oxygen dissolved in crystalline Si can be associated with a positively charged vacancy-oxygen defect.

Reaction [1] implies that the fixed oxide charge density and the fast state density are equal and consistent with the proportionality observed by Arnold (20). Differences detected between the magnitudes of the oxide charge and the fast state densities can indicate that additional chemical reactions are occurring. Alternatively, they may signify that the stabilities of the two intermediates formed in reaction [1] at elevated temperatures during an oxidation reaction are significantly different when brought to room temperature, perhaps because of different effective quench temperatures.

Reaction [1] involves neutral reactants. An electron must be transferred to the substrate to obtain a positive charge within the transition region. This positive oxide charge is localized within the transition region by formation of the oxygen complex, whereas the transferred electron is delocalized in the substrate. A double layer exists as a consequence of this first step in the oxidation reaction at the SiO_2-Si interface. This double layer, rather than the transport of charged oxygen species through the oxide film to the transition region, may account for changes in oxidation kinetics observed by Jorgenson (2) when a bias is applied across an oxide film during the thermal oxidation reaction (33).

Formation of intermediates at a transition region during a Si oxidation reaction presumably occurs with other oxidants, such as H_2O, HCl, and Cl_2. In contrast to reaction with O_2, these reactants form nonbridging, or terminally bonded, intermediates during the Si-Si bond breaking reaction as is shown below

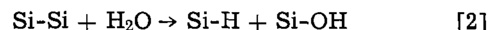

$$\text{Si-Si} + H_2O \rightarrow \text{Si-H} + \text{Si-OH} \quad [2]$$

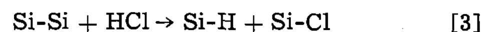

$$\text{Si-Si} + \text{HCl} \rightarrow \text{Si-H} + \text{Si-Cl} \quad [3]$$

$$\text{Si-Si} + Cl_2 \rightarrow 2\text{Si-Cl} \quad [4]$$

The parabolic and linear rate constants both increase when Si is oxidized with these oxidants which form terminally bonded groups (1, 34-36). A higher steady-state broken-bond density is obtained both within the oxide film and within the transition region. Oxidant diffusion rates are increased. Oxidation kinetics are also enhanced at the SiO_2-Si interface (37). Intermediates such as Si-Cl, which have bond energies only 0.7 eV less than Si-O (4.7 eV), are detected within the first 200Å of the oxide film (38).

The second oxidation reaction step involving oxygen as oxidant is the thermally activated reaction in which siloxane groups are formed as is shown in [5]

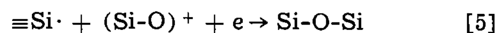

$$\equiv\text{Si}\cdot + (\text{Si-O})^+ + e \rightarrow \text{Si-O-Si} \quad [5]$$

In reaction [5], $(Si\text{-}O)^+$ complexes react at typical oxidation temperatures with incompletely oxidized Si atoms such as $\equiv Si\cdot$, as shown above, or with Si-Si bonds. Reaction [5] therefore decreases both Q_{ss} and N_{ss}. This reaction is exothermic and leads to a stable siloxane structure. The reactants are covalently bonded to the 3 dimensional transition region structure and therefore require local reorientation for reaction [5] to occur. Restructuring, or the displacement of Si atoms from their original lattice sites during this thermal oxidation reaction, can occur at three levels: at the substrate surface, within the transition region, and within the oxide film where bond angles are modified to accommodate newly formed oxide film (38). This restructuring is presumably a thermally activated

process that, in part, determines the rate of oxide film formation.

Electrically active intermediates are formed in reaction [1] and are consumed in reaction [5]. The temperature dependence of the O_2 oxidation reaction on Q_{ss} formation is readily understood by considering these reactions. As oxidation temperatures decrease, reaction [1], with $E_a = 0$, dominates and is limited only by the availability of oxidant at the transition region. The concentration of intermediates in the transition region increases during the Si-Si bond-breaking reaction. This results in a maximum Q_{ss} at low oxidation temperatures. As oxidation temperatures are increased, reaction [5] competes with reaction [1]. Intermediates formed in the Si-Si bond breaking reaction at the higher oxidation temperatures react during the siloxane formation reaction yielding a low steady-state concentration of these intermediates. This results in a low fixed oxide charge density.

Annealing in an inert ambient involves only reaction [5]. Intermediates formed in reaction [1] react to form siloxane groups by annealing in inert ambients at elevated temperatures. As the transition region is depleted of excess oxygen, the density of $(Si\text{-}O)^+$ complexes is reduced. This proceeds until the $(Si\text{-}O)^+$ density is minimized and results in a minimum Q_{ss}.

Other chemical reactions can occur during high temperature annealing that yields electrically active intermediates. For example, minimization of oxidant at the transition region by annealing at elevated temperatures in vacuum or in inert gases free of oxidant can cause SiO to form. Decomposition of the unstable SiO species will presumably generate electrically active sites. Vacuum annealing SiO_2(1000Å)-Si structures at greater than 1000°C for about 2 hr has been reported to increase N_{ss} and cause oxide shorts (4, 40). Oxide films, 150Å thick, have been evaporated from Si surfaces while annealing in high purity Ar at 1100°C for about 16 hr (41). At present, it is not known whether this formation of SiO occurs uniformly at an SiO_2-Si interface or at local defect sites (42). An additional reaction, the interaction of N_2 gas with Si at elevated temperatures, mentioned above, also generates electrically active instabilities in the absence of oxidant.

The concentration of nonoxidized Si-Si bonds in the transition region, as well as C_i, determine the concentration of complexes formed during the oxidation reaction and, therefore, the fixed charge density. Differences in densities of fixed oxide charge associated with substrate orientation can be associated with different Si-Si bond concentrations at the oriented substrate interface. More Si-Si bonds are present at <111> interfaces. More complexes are formed in the <111> transition region during the oxidation process. The capability of minimizing Q_{ss} and N_{ss} in transition regions on <111> and <100> oriented substrates is determined by the ability to drive the oxidation reaction to completion at these interfacial regions.

The stability of Q_{ss} is determined by the stability of the Si-oxygen complex formed within the transition region as an intermediate during the thermal oxidation process. This positively charged complex is localized, or fixed, as a result of complex formation with oxygen. Charge densities are minimized under conditions at which an oxidation reaction is driven to completion and siloxane groups are formed. Positive charge may also be introduced into the oxide film by other means. These include biasing at electric field strengths of about 1 MV/cm and at temperatures > 300°C (1) and ionizing radiation. However, it is not expected that these positive charges are chemically equivalent to fixed oxide charge formed during an oxidation reaction or that they will possess similar stabilities.

Summary

It has been conjectured in the past that fixed oxide charge is a reflection of excess unoxidized Si bonds, or sometimes of an oxygen deficiency, in the oxide. Recent studies show that the density of excess Si bonds in the SiO_2-Si transition region is of the order of the surface density of atoms in Si, *i.e.*, far greater than observed values of Q_{ss}/q. Furthermore, the stoichiometry and width of the transition region are unaffected by those parameters that can drastically influence the magnitude of Q_{ss}.

The chemical origin of oxidation-induced fixed charge and fast surface states is proposed to be the intermediate complexes generated during the formation of the SiO_2-Si transition region. These electrical instabilities are formed during the oxidation reaction

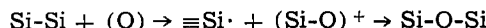

$$\text{Si-Si} + (\text{O}) \rightarrow \equiv\text{Si}\cdot + (\text{Si-O})^+ \rightarrow \text{Si-O-Si}$$

where the dangling bonds, $\equiv Si\cdot$, are identified with fast states and the $(Si\text{-}O)^+$ complexes are identified with fixed charge. This transition region has a steady-state gross stoichiometry and width, but is being continuously reformed at a rate that is necessarily that of the oxidation reactions. The density of the intermediates depends upon the concentration of nonoxidized Si bonds (orientation-dependent) as well as the concentration of excess (probably dissolved) oxygen. The values of Q_{ss} and N_{ss} will reflect this density at the time the reaction is quenched.

The electrically active intermediate sites are attached to the 3 dimensional solid structure. Elimination of these sites requires completion of the above oxidation reaction. This is accomplished as a consequence of postoxidation inert-gas annealing. The model proposed here is consistent with the known properties of oxide charge and fast surface-state generation and anneal as well as with the properties of the SiO_2-Si transition region.

Manuscript submitted May 16, 1977; revised manuscript received Jan 12, 1978. This was Paper 137 presented at the Washington, D.C., Meeting of the Society, May 2-7, 1976.

Any discussion of this paper will appear in a Discussion Section to be published in the December 1978 JOURNAL. All discussions for the December 1978 Discussion Section should be submitted by Aug. 1, 1978.

Publication costs of this article were assisted by IBM Corporation.

REFERENCES

1. B. E. Deal, M. Sklar, A. S. Grove, and E. H. Snow, *This Journal*, **114**, 266 (1967).
2. P. J. Jorgenson, *J. Chem. Phys.*, **37**, 874 (1962).
3. B. E. Deal and A. S. Grove, *J. Appl. Phys.*, **36**, 3770 (1965).
4. F. Montillo and P. Balk, *This Journal*, **118**, 1463 (1971).
5. S. I. Raider and R. Flitsch, *J. Vac. Sci. Technol.*, **13**, 58 (1976).
6. a) R. Flitsch and S. I. Raider, *ibid.*, **12**, 305 (1975); b) *IBM J. Res. Dev.*, **22** (1978).
7. R. A. Clarke, R. L. Tapping, M. A. Hopper, and L. Young, *This Journal*, **122**, 1216 (1975).
8. S. I. Raider, R. Flitsch, and R. Rosenberg, Paper 136 presented at The Electrochemical Society Meeting, Washington, D.C., May 2-7, 1976.
9. D. R. Lamb, *Thin Solid Films*, **5**, 247 (1970).
10. B. E. Deal, *This Journal*, **121**, 198C (1974).
11. A. Goetzberger, E. Klausmann, and M. J. Schulz, *Crit. Rev. Solid State Sci.*, **6**, 1 (1976).
12. B. E. Deal, "Semiconductor Silicon 77," H. Huff and E. Sirtl, Editors, The Electrochemical Society Softbound Symposium Series, Princeton, N.J. (1977).
13. R. J. Powell, *IEEE Trans. Nucl. Sci.*, **ns-17**(6), 41 (1970).
14. R. J. Powell and C. N. Berglund, *J. Appl. Phys.*, **42**, 4390 (1971).
15. S. I. Raider, R. A. Gdula, and J. R. Petrak, *Appl. Phys. Lett.*, **27**, 150 (1975).
16. J. K. Howard, S. I. Raider, and R. Flitsch, *J. Vac. Sci. Technol.*, **14** (1977).
17. D. W. Hess and B. E. Deal, *This Journal*, **122**, 1123 (1975).
18. M. Revitz, S. I. Raider, and R. A. Gdula, Unpub-

lished results.
19. J. L. Pautrak and J. C. Pfister, *Phys. Status Solidi A*, **11**, 669 (1972).
20. E. Arnold, J. Ladell, and G. Abowitz, *Appl. Phys. Lett.*, **13**, 413 (1968).
21. S. Kubo and E. Inchinohe, *Jpn. J. Appl. Phys.*, **6**, 1072 (1967).
22. W. J. Patrick, "Silicon Device Processing," C. P. Marsden, Editor, p. 442, N.B.S. Special Publication 337 (1970).
23. P. E. Freeland, K. A. Jackson, C. W. Lowe, and J. R. Patel, *Appl. Phys. Lett.*, **30**, 31 (1977).
24. P. Balk, Paper 109 presented at The Electrochemical Society Meeting, San Francisco, California, May 9-13, 1965.
25. J. R. Ligenza, *J. Phys. Chem.*, **65**, 2011 (1961).
26. R. H. Doremus, *ibid.*, **80**, 1773 (1976).
27. R. Ludeke and A. Koma, *Phys. Rev. Lett.*, **34**, 1170 (1975).
28. H. Ibach and J. E. Rowe, *Phys. Rev.*, **B10**, 710 (1974).
29. W. A. Goddard III, A. Redondo, and T. C. McGill, *Solid State Comm.*, **18**, 981 (1976).
30. J. E. Rowe, G. Margaritondo, H. Ibach, and H. Froitzheim, *ibid.*, **20**, 277 (1976).
31. C. T. Sah, *IEEE Trans. Nucl. Sci.*, **NS-23**, 1563 (1976).
32. P. R. Brosious, *Appl. Phys. Lett.*, **29**, 265 (1976).
33. D. O. Raleigh, *This Journal*, **113**, 782 (1966).
34. Y. J. van der Meulen and J. G. Cahill, *J. Electron. Mater.*, **3**, 371 (1974).
35. W. A. Pliskin, *IBM J. Res. Dev.*, **10**, 198 (1966).
36. E. A. Irene and R. Ghez, *This Journal*, **124**, 1757 (1977).
37. K. Hirabayashi and J. Iwamura, *ibid.*, **120**, 1595 (1973).
38. A. Rohatgi, S. R. Butler, F. J. Feigl, H. W. Kraner, and K. W. Jones, *Appl. Phys. Lett.*, **30**, 104 (1977).
39. J. W. Matthew, Private communication.
40. D. M. Brown and P. V. Gray, *This Journal*, **115**, 760 (1968).
41. S. I. Raider and R. A. Gdula, Unpublished results.
42. T. W. Hickmott, *J. Vac. Sci. Technol.*, **9**, 311 (1972).

Diffusion Layers Formed in Si Substrates during the Epitaxial Growth of BP and Application to Devices

Takao Takenaka, Mitsuharu Takigawa, and Katsufusa Shohno*

Faculty of Science and Technology, Sophia University, Kioicho 7, Chiyoda-ku, Tokyo 102, Japan

ABSTRACT

Either n-type (phosphorus) or p-type (boron) diffused layers are formed on Si substrates during the epitaxial growth of n- or p-type boron monophosphide (BP) on Si substrates by using a B_2H_6-PH_3-H_2 system. At an early growth stage of BP on Si substrates a very small amount of boron and phosphorus covers the substrate surface, which will be a diffusion source. The properties of the diffused layers thus formed are dependent on substrate temperatures and reactant gas flow rates. BP layers then grown on the substrate do not act as a diffusion source. So we can realize many types of BP-Si heterojunctions. Of these combinations, a wide gap window solar cell (η = 8.3%) and a wide gap emitter transistor (β = 16) are fabricated and their characteristics are investigated.

Since Chu *et al.* (1) succeeded in epitaxial growth of boron monophosphide (BP) on a SiC substrate in 1971, several attempts have been made to grow BP epitaxially on Si substrates (2-4). We found that p-type (boron) or n-type (phosphorus) diffused layers are formed on Si substrates during the epitaxial growth of n- or p-type BP on Si substrates by using a B_2H_6-PH_3-H_2 system. In this paper, properties of p-type (boron) or n-type (phosphorus) diffused layers thus formed on Si substrates are studied. Conduction types of a grown BP film and a diffused layer can be controlled easily, so it is possible to fabricate many combinations of BP-Si heterostructures. Here a window solar cell and a wide gap emitter transistor are fabricated and their characteristics are investigated.

Epitaxial Growth of BP on Si

The apparatus for the epitaxial growth of BP on Si substrates using a B_2H_6-PH_3-H_2 system was described previously (3, 4). The upper part of a quartz reaction chamber having inner dimensions of 25 × 40 × 400 mm^3 was water-cooled. Mirror-finished Si substrates had a plane 2° off-oriented from the (100) face in the direction of a (110) plane. They were placed on a SiC-coated graphite susceptor and heated externally by an rf generator (5). The substrate temperature was measured with an optical pyrometer calibrated by a platinum-platinum-rhodium thermocouple beforehand.

* Electrochemical Society Active Member.

Key words: diffusion, BP, epitaxy, solar cell, transistor.

Reactant gases were diborane (B_2H_6) and phosphine (PH_3) diluted to 1 and 5% in hydrogen, respectively. The carrier gas was high purity hydrogen and the flow rate was 2500 cm^3/min. The diluted B_2H_6 gas of 20 cm^3/min and the diluted PH_3 gas from 50 ~ 1000 cm^3/min were mixed with the main carrier gas. Particular attention was paid to the control of the amount and time of introduction of reactant gases. The flow rate of B_2H_6-H_2 gas is extremely important to obtain BP layers of high crystal perfection. On the other hand the flow rate of the PH_3-H_2 gas does not change the perfection of a grown crystal.

The substrate temperature was 950°C for growing n-type BP and 1050°C for p-type BP, independent of the flow rate of PH_3-H_2 gas. The results are shown in Fig. 1. The main impurity in grown BP layers was autodoped Si ($\simeq 10^{19}$ cm^{-3}) which is known as an amphoteric impurity. That is, both types of BP are grown without any additional doping gas.

Diffusion Layers Formed in Si Substrates

We found that the diffusion of P and/or B onto a Si substrate takes place during the growth of BP. Diffusion layers thus formed on Si substrates of n-type with 3 ~ 5 Ω-cm and of p-type with 10 Ω-cm were investigated.

BP layers were removed electrolytically from the substrates and a thin SiO_2 layer on the Si surface was etched with HF-NH_4F solution. The conduction type of a diffused layer was determined from its thermoelectric

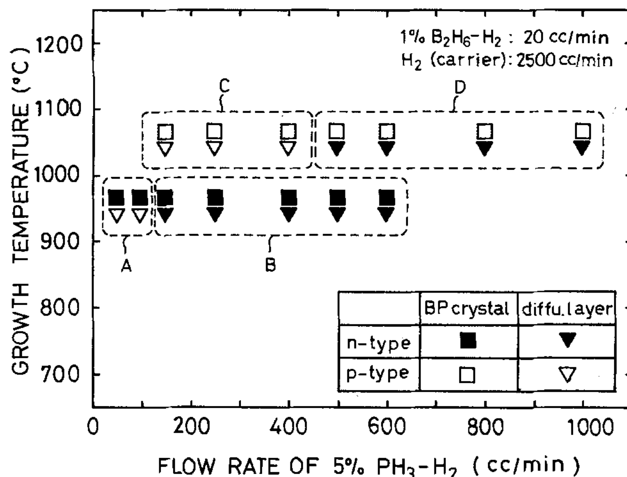

Fig. 1. Conduction type of BP and diffusion layer depending on flow rate of 5% PH_3 and substrate temperature.

power. The surface resistance was measured by the conventional four-point probe method and the diffusion depth by spherical drilling (6) and staining. The surface concentration of diffused impurities was determined by assuming an error function as the impurity profile.

It is possible to realize easily both conduction types of the diffused layers on Si substrates as well as of the BP layers by varying the flow rate of the PH_3-H_2 gas or the substrate temperature. The results are summarized in Fig. 1 for the flow rate of the 5% PH_3-H_2 gas. The conduction type of diffused layers on Si substrates is determined mainly by the flow rate of the PH_3-H_2 gas when the substrate is kept at a constant temperature: n-type (phosphorus) diffused layers are obtained for a flow rate larger than 150 cm^3/min at 950°C and 450 cm^3/min at 1050°C while p-type diffused layers are formed for a flow rate smaller than 100 cm^3/min at 950°C and 400 cm^3/min at 1050°C.

The surface concentration of n-type diffused layers increases with increasing flow rate of the PH_3-H_2 gas at 950°C as shown in Fig. 2. The growth time was 20 min and the B_2H_6-H_2 flow rate was strictly kept at 20 cm^3/min. On the other hand the surface concentration of p-type diffused layers decreases by increasing the flow rate of the PH_3-H_2 gas at 1050°C. The flow rate of the B_2H_6-H_2 gas has to be controlled very carefully because it determines the growth of BP and influences its crystal perfection: BP films of best quality are obtained when the growth rate is 700 Å/min. If the crystal perfection is so poor as to have twins, planar defects, and so on, the surface concentration of the diffused layers cannot be reproduced. The surface concentration and the diffusion depths of n-type diffused layers are given as a function of their growth time in Fig. 3. The surface concentration decreases inversely proportional to the square root of the growth time but the diffusion depth increases. This suggests that a very thin diffusion source, which does not crystallize to BP, is formed at an early growth stage. The amount of diffused phosphorus is calculated from the figure to be $Q = 5 \times 10^{13}$ cm^{-2}. Similar results were obtained for BP samples which were grown epitaxially and then heat-treated.

Next, diffusion experiments were performed by using B_2H_6-H_2 gas (20 cm^3/min) and PH_3-H_2 gas (250 cm^3/min) independently. The surface concentration of boron and phosphorus is shown in Fig. 4 as a function of diffusion temperature. The values for boron at temperatures higher than 1100°C are almost the same as the value of its solid solubility in Si (7), but the values for phosphorus are far less than that for boron. The curves for boron and phosphorus cross at

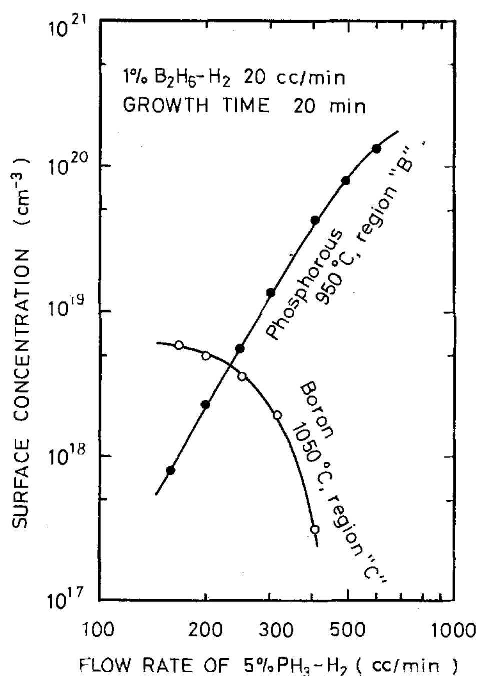

Fig. 2. Phosphorus and boron surface concentration as a function of flow rate of 5% PH_3.

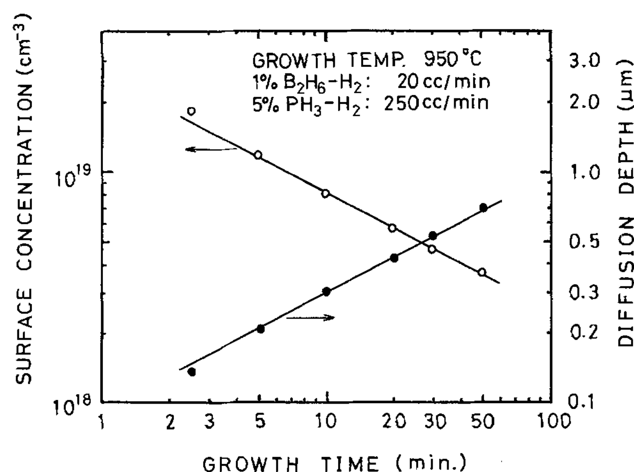

Fig. 3. Phosphorus surface concentration and diffusion depth as a function of growth time.

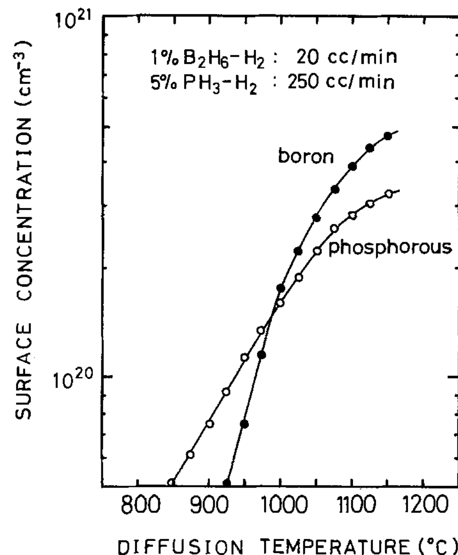

Fig. 4. Phosphorus and boron surface concentration as a function of diffusion temperature using individual reactant gas of 5% PH_3 and 1% B_2H_6.

about 1000°C. This indicates that n-type diffused layers will be formed at 950°C and p-type diffused layers at 1050°C. It is expected from the surface concentration of phosphorus, $N = 1.2 \times 10^{20}$ cm^{-3}, calculated from Fig. 4 and the total amount of diffused-in phosphorus $Q = 5 \times 10^{13}$ cm^{-2}, that the diffusion source should be formed within 5 sec in the very early growth stage of the BP. That is, only a small amount of boron or phosphorus covers the Si surface first and the BP layer then grown protects this diffusion source and the grown BP crystal does not act as a diffusion source.

Figure 4 also indicates that the compensation of boron and phosphorus occurs on the substrate under BP layers: Thus the concentration of boron or phosphorus determined experimentally is only a net value estimated from concentration in Fig. 2.

Application to Devices

By combining the conduction types of grown layer BP, diffused layer, and Si substrate, eight different junctions are realized as shown in Table I. The combination in groups A and B includes a wide gap window solar cell (8) and a wide gap emitter transistor (9, 10).

Wide gap window solar cell.—BP is a semiconductor with an indirect forbidden energy gap of 2.0 eV, low resistivity ($10^{-3} \sim 10^{-4}$ Ω-cm) (11-14), low reflectivity (10% in visible light) (11), and large hardness (4700 kg/mm²) (15). So the thin BP layer is useful for a window of Si solar cells and is also effective in reducing the radiation degradation. Furthermore it reduces the series resistance and reflection loss.

The nBP-pSi heterostructures were obtained in the growth region A on a p-type Si substrate of 0.1 Ω-cm. The acceptor concentration is larger than the p-type (boron) diffused layer of 4×10^{17} cm^{-3}. The grown n-type BP layer has a thickness of 0.75 μm and a carrier concentration of about 10^{19} cm^{-3}. The BP layer was removed from the Si substrate selectively by the usual photolithographic process and comb-shaped Al electrodes were evaporated. The size of the cell thus fabricated was 2×2 mm². The current-voltage characteristic suggests the existence of interface states in the BP-Si heterojunction: The forward current has a region proportional to exp (eV/nkT) with $n = 6 \pm 2$. The backward current is large and does not saturate.

Spectral photocurrents excited with monochromatic light (Shimadzu Spectronic 20) were measured at room temperature. The results are shown in Fig. 5. Apparently the spectrum broadens towards the short wavelength region compared with the spectrum of a Si cell. This is attributed to BP having the wider forbidden energy gap than Si. The conversion efficiency of the cell is fairly low. There would be many recombination states in the BP-Si interface due to the differences in lattice constants ($a_{Si} = 5.43$Å, $a_{BP} = 4.53$Å) and thermal expansion coefficients ($\alpha_{Si} = 2.6 \times 10^{-6}$ deg^{-1}, $\alpha_{BP} = 4.8 \times 10^{-6}$ deg^{-1}).

Table I. Eight junctions realized by combining conduction type of BP, diffusion layer, and Si substrate

REGION	BP CRYSTAL	DIFFU. LAYER	Si SUB.	ENERGY BAND STRUCTURE (BP / Si)	DEVICE
A	n	p	n		TRANSISTOR
			p		DIODE
B	n	n	n		OHMIC
			p		DIODE
C	p	p	n		DIODE
			p		OHMIC
D	p	n	n		DIODE
			p		TRANSISTOR

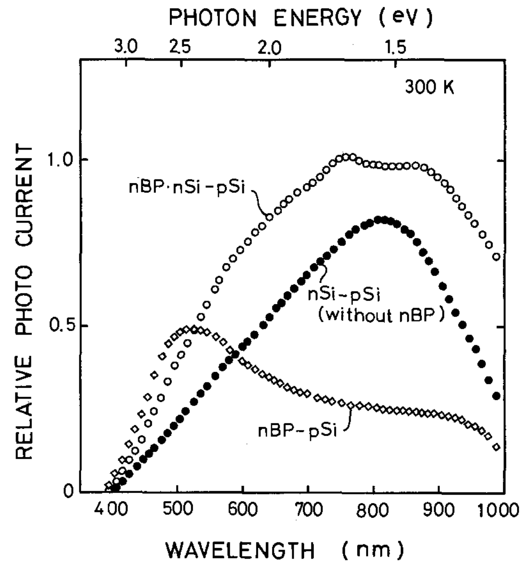

Fig. 5. Spectral photocurrent of wide gap window solar cells with nBP-pSi and nBP·nSi-pSi structure. That of nSi-pSi cell after removing nBP layer from nBP·nSi-pSi cell is shown for comparison.

The nBP · nSi-pSi cell was fabricated by growing BP epitaxial layer on a p-type (100) Si substrate (5-8 Ω-cm) in the region B of Fig. 1. The carrier concentration of the n-type BP layer was about 10^{19} cm^{-3} and the thickness was about 0.75 μm. The surface concentration of the n-type diffused layer was 8×10^{18} cm^{-3} and the diffusion depth was 0.3 μm. The forward current has two regions proportional to exp (eV/nkT) with $n = 1.9$ and 1.5. The dark current-voltage characteristics are almost the same as those of a Si p-n junction cell.

The spectral photocurrents of nSi-pSi cells, made by removing the nBP layer electrolytically from the nBP · nSi-pSi cell are shown in Fig. 5 for comparison. The short-circuit current with an nBP layer is apparently larger than that without an nBP layer, due to a difference in reflectivity of BP and Si. The conversion efficiency of the solar cell with an nBP layer and without an nBP layer is $\eta = 8.3\%$ and $\eta = 6.5\%$, respectively. These values are estimated roughly by using a commercially available solar cell of p-n Si structure with antireflection coating of SiO and a conversion efficiency of 12% as a standard.

Wide gap emitter transistor.—The electrical properties of the BP-Si interface will be evaluated by the injection efficiency at an emitter junction. Two types of wide gap emitter transitors were prepared: One is nBP-pSi-nSi and the other is nBP · nSi-pSi-nSi structure having a cascade junction nBP · nSi-pSi emitter, whose electronic band structures are shown in Fig. 6.

The fabrication process is shown in Fig. 7. After the p-type base was diffused for n-type Si, nBP was epitaxially grown. At the same time, the n-type diffused layer for cascade junction was formed. Fabrication processes are as follows: Remove the nBP layer selectively mesa-etch by masking the nBP emitter then evaporate Al and delineate contact areas, and again mesa-etch the collector junction. A photograph of a chip is shown in Fig. 8.

The forward current of the emitter heterojunction for the nBP-pSi-nSi transistor has a region proportional to exp (eV/nkT) with $n = 6.0$. The backward current is large and does not saturate. The common emitter current gains of these transistors are $0.6 \sim 0.8$. These characteristics are strongly affected by recombination states located at the interface between BP and Si.

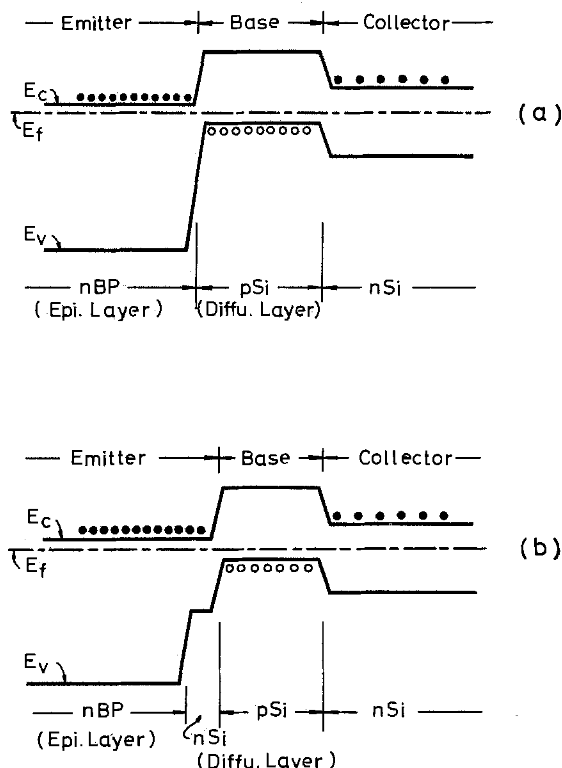

Fig. 6. Energy band diagram of wide gap emitter transistors with nBP-pSi-nSi (a) and nBP·nSi-pSi-nSi (b) structure.

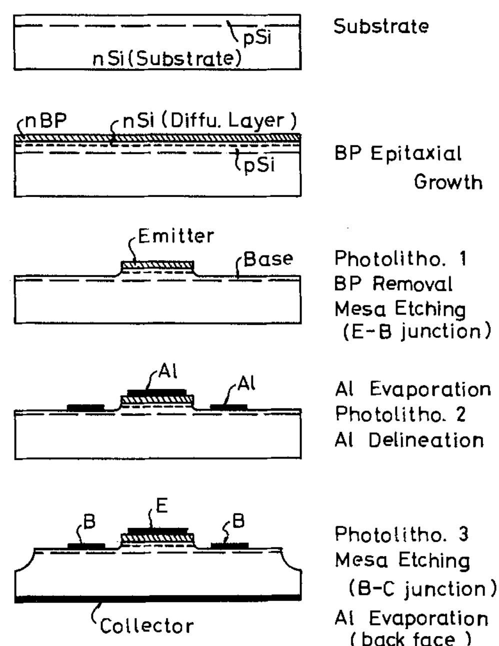

Fig. 7. Fabrication process of wide gap emitter transistor with nBP·nSi-pSi-nSi structure.

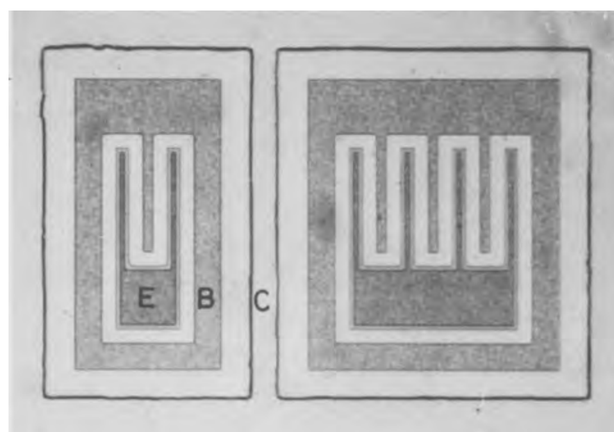

Fig. 8. Photograph of wide gap emitter transistor with nBP·nSi-pSi-nSi structure (E, emitter; B, base; C, collector).

Typical current-voltage characteristics for the nBP nSi-pSi-nSi transistor are shown in Fig. 9. The common emitter current gain β is about 16 and the injection efficiency of the emitter heterojunction is about 0.94 if the other gain factors are assumed to be unity. The forward current of the emitter junction has two regions proportional to exp (eV/nkT) with $n = 2.6$ and 1.6. The backward current of the junction does not saturate, similar to that of a Si p-n junction. The breakdown voltage of the collector junction was about 250V.

Conclusions

The epitaxy of BP on Si substrates using a B_2H_6-PH_3-H_2 system can be controlled to form either n-type (phosphorus) or p-type (boron) diffusion layer on the Si substrates. At an early growth stage within the first few seconds, a small amount of boron and phosphorus was supplied as a diffusion source, and BP layers grown subsequently do not act as diffusion sources. Several types of BP-Si junctions were realized out of possible combinations of BP layer, diffused layer, and Si substrate. A wide gap window solar cell ($\eta = 8.3\%$) of nBP · nSi-pSi structure and a wide gap emitter transistor ($\beta = 16$) of nBP · nSi-pSi-nSi structure demonstrated applicability to devices.

Manuscript submitted Aug. 29, 1977; revised manuscript received Nov. 14, 1977.

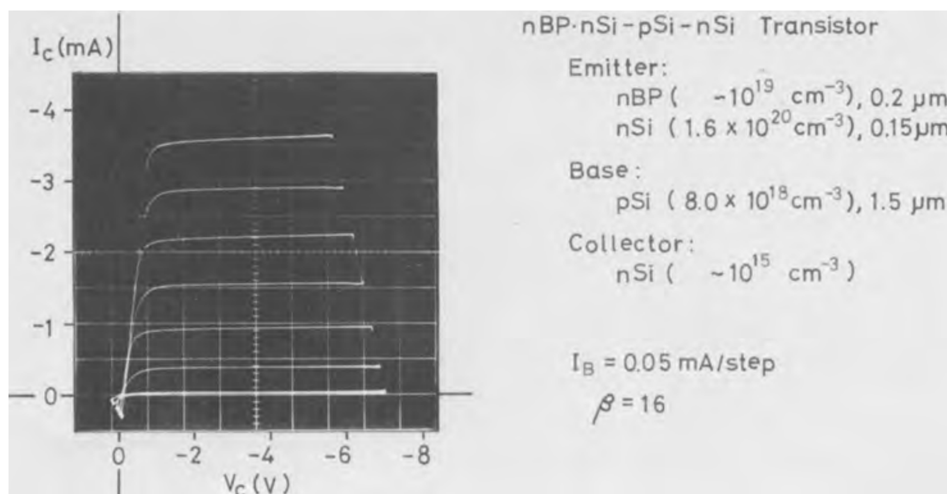

Fig. 9. Common emitter current-voltage characteristics of wide gap emitter transistor with nBP·nSi-pSi-nSi structure.

Any discussion of this paper will appear in a Discussion Section to be published in the December 1978 JOURNAL. All discussions for the December 1978 Discussion Section should be submitted by Aug. 1, 1978.

Publication costs of this article were assisted by Sophia University.

REFERENCES

1. T. L. Chu, J. M. Jackson, A. R. Hyslop, and S. C. Chu, *J. Appl. Phys.*, **42**, 420 (1971).
2. T. Nishinaga, H. Ogawa, H. Watanabe, and T. Arizumi, *J. Cryst. Growth*, **13/14**, 346 (1972).
3. M. Takigawa, M. Hirayama, and K. Shohno, *Jpn. J. Appl. Phys.*, **13**, 411 (1974).
4. K. Shohno, M. Takigawa, and T. Nakada, *J. Cryst. Growth*, **24/25**, 193 (1974).
5. Y. Hirai and K. Shohno, *ibid.*, **41**, 124 (1977).
6. T. Kinoshita and K. Shohno, *Oyo Buturi*, **37**, 788 (1970) (in Japanese).
7. G. L. Vick and K. M. Whittle, *This Journal*, **116**, 1142 (1969).
8. H. J. Hovel and J. M. Woodall, *ibid.*, **120**, 1246 (1973).
9. H. Kroemer, *Proc. IRE*, **45**, 1535 (1957).
10. M. Konagai and K. Takahashi, *J. Appl. Phys.* **46** 2120 (1975).
11. K. Shohno, T. Takenaka, and M. Takigawa, Proceedings of 12th International Conference on the Physics of Semiconductor, Stuttgart, p. 286 (1974).
12. T. Takenaka, M. Takigawa, and K. Shohno, *Jpn. J. Appl. Phys.*, **14**, 579 (1975).
13. M. Takigawa, T. Satoh, and K. Shohno, *This Journal*, **122**, 824 (1975).
14. T. Mizutani, J. Ohsawa, T. Nishinaga, and S. Uchiyama, *Jpn. J. Appl. Phys.*, **15** 1305 (1976).
15. T. Takenaka, M. Takigawa, and K. Shohno, *ibid.*, **15**, 2235 (1976).

Kinetics of Silicon Growth under Low Hydrogen Pressure

M. Jean-Pascal Duchemin, M. Michel Bonnet, M. François Koelsch

Thomson CSF, Département Microélectronique Hyperfréquence, Domaine de Corbeville, 91401 Orsay, France

ABSTRACT

The kinetics of silicon deposition have been studied in a reactor working under reduced hydrogen pressure between 10 Torr and atmospheric pressure (760 Torr) for the following silicon sources: SiH_4, SiH_2Cl_2, $SiHCl_3$, and $SiCl_4$. In every case, the kinetics are controlled by the surface at low hydrogen pressure whereas at higher pressure the mass transfer becomes slower. When the kinetics are controlled by the surface, the deposition rate is inversely proportional to the square root of the hydrogen pressure and is activated. In the opposite case the deposition rate is inversely proportional to the hydrogen pressure and does not depend on the temperature. This result, and the fact that the depositions are monocrystalline even at low temperature when the pressure is lower than 70 Torr, show that the hydrogen is strongly adsorbed on the silicon surface. The deposition made at low pressure and low temperature have abrupt impurity profiles which allow us to realize good quality microwave components.

Over the past few years there has been a demand for submicron monocrystalline silicon layers. These structures are grown, for instance, in order to make IMPATT diodes working over 50 GHz (such a structure for use at 90 GHz has 3 layers whose total thickness is 7000Å) microwave Schottky diodes (for X and Ku bands) or rapid integrated circuits.

In every case these layers must be grown upon very heavily doped substrates ($\rho \leq 0.001\ \Omega \cdot cm$) or upon substrates containing buried layers having this resistivity. It is essential for the active layer to be clearly defined and the substrate-layer or layer-layer transitions to be as steep as possible (some hundred angstroms). Further, it is necessary to reduce solid-state diffusion of impurities of the substrates toward the active layer to minimize the autodoping of the active layer by the impurities of the substrate, and finally, to eliminate the transient mechanisms which take place at the beginning and end of growth. One can act on diffusion by lowering the growth temperature. For that reason silicon sources with a fast kinetics of decomposition such as SiH_4, SiH_2Cl_2, or even $SiHCl_3$ are used. Typical growth temperatures are 1000°C.

Some years ago, Chiang (1, 2) reported that with a helium carrier gas it is possible to grow defect-free silicon at temperatures lower than 900°C. However the absence of the reducing effect limits the possibility of using this process. More recently, Townsend (3) has shown that one can reduce the quantity of hydrogen adsorbed on the silicon surface and grow excellent quality layers at a lower temperature by using a low hydrogen pressure. This technique has the added advantage of reducing autodoping because the impurities which escape from the substrate diffuse faster through the stagnant layer. In addition, purging and the transient mechanisms at the beginning and end of the epitaxial process are accelerated at reduced pressure. For all these reasons, this technique is expected to be a significant development. However, little is known up to now about the kinetics of epitaxial growth at a low hydrogen pressure. The purpose of this work is to study some features of the growth kinetics as a function of pressure and to compare low pressure and atmospheric pressure growth mechanisms.

Key words: silicon growth, reduced pressure, autodoping.

Experimental Procedure

For this study we used a horizontal reactor heated by induction at low frequency (50 kHz) and with air-cooled walls.

The control gas panel is classical and is like the panels which are on conventional systems working at atmospheric pressure. It is equipped with four source lines of silicon ($SiCl_4$, $SiHCl_3$, SiH_2Cl_2, SiH_4) and four doping lines (one line N, another P, another N^+, and finally a line P^+); the N doping is obtained with arsine and the P doping with diborane.

Pressure control is carried out by means of a mechanical gauge, and temperatures are measured by an optical pyrometer using Allen's corrections so as to take into account the emissivity peculiar to silicon. It should be noted here that there is a great difference in temperature between the substrate and the susceptor when working at low pressure; this difference is as much as 140°C at 10 Torr. The reason for this is the re-

duction of the thermal conductivity of the gas layer between the substrate and the susceptor.

A rotary pump of 100 m^3/hr is used to maintain the pressure of the gases which flow in the reactor at a level lower than atmospheric pressure.

A molecular sieve serves to prevent the back diffusion of oil toward the reactor; a liquid nitrogen trap is used during hermiticity trials but this is ineffective when working at several Torr because the mean free path is then much lower than the trap dimensions. An adjusting valve is used to control the internal pressure of the reactor independently from the rate of reactant gas flow, this being done by limiting the pumping rate.

The graphite susceptor, coated by a thin layer of silicon carbide (SiC) can contain three substrates, 40 mm in diameter. In all the experiments described below, the hydrogen flow is kept constant at the rate of 18 liters/min, measured under standard conditions of pressure and temperature. A rough diagram of this equipment is given in Fig. 1.

Results

The kinetics of growth of the silicon have been studied as a function of the following parameters: nature and partial pressure of the silicon source, hydrogen pressure, and temperature. Let us start by defining these parameters:

p_{source} and p_{H_2}—partial pressures of the source species and of the hydrogen inside the reactor and

x_{source}—molar fraction of the source in the hydrogen

$$x_{source} = \frac{\text{number of source molecules}}{\text{number of source molecules} + \text{number of hydrogen molecules}}$$

In the case where the number of molecules of the source species is far lower than that of hydrogen (100 times smaller), $p_{total} \simeq p_{H_2}$

$$p_{source} = x_{source} \times p_{H_2}$$

It is to be noted that the partial pressure of the source can be changed in two different ways: (*i*) either by maintaining the molar fraction constant and modifying the total pressure; or (*ii*) by maintaining the total pressure constant and varying the molar fraction of the source

Order related to the source molar fraction.—For the 10-500 Torr pressure range, we have observed that the growth rate is linearly proportional to the source molar fraction when the source is silane, as can be seen in Fig. 2a and 2b. In the case of the chlorosilanes, the growth rate is not strictly a linear function of the source molar fraction as can be seen for trichlorosilane in Fig. 2c.

Order related to the hydrogen pressure.—Experiments made with a constant source molar fraction.—The variation of the growth rate as a function of the hydrogen pressure in the reactor was studied by maintaining constant the following parameters: the hydrogen flow measured at atmospheric pressure; the source molar fraction; and the surface temperature. Under these conditions, three growth rate variation ranges can be observed for silane: (*i*) for low hydrogen pressures, the growth rate increases proportionally to the square root of hydrogen pressure; (*ii*) within a second pressure range, the growth rate becomes almost independent of the pressure; and (*iii*) at higher H_2 pressures, the growth rate decreases following a function which is more abrupt than a linear function. These results are given in Fig. 3a. Figures 3b-d show similar data for the other sources SiH_2Cl_2 $SiHCl_3$, and $SiCl_4$. The same three variation ranges are again observed. However, the growth rate at low H_2 pressures is strictly proportional to the square root of the hydrogen pressure only in the case of silane.

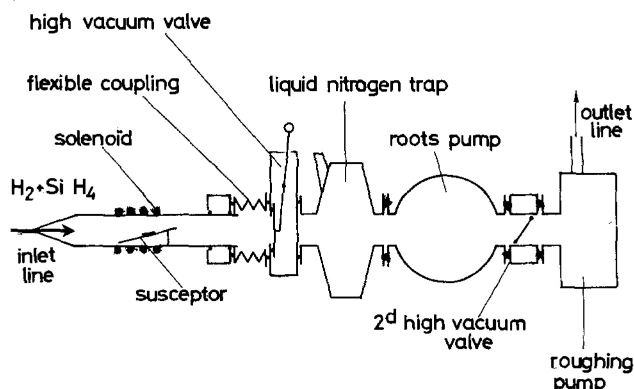

Fig. 1. Diagram illustrating the principle of the system used to study growth process at low pressure.

Expression of these results for a constant partial pressure of the source.—In order to understand the growth mechanisms it is easier to use as a fixed parameter the partial pressure of the source at various total pressures in the reactor. It is, however, difficult to do this experimentally. It would require one to vary at one and the same time the hydrogen pressure and the source molar fraction so as to keep product $x_{source} \cdot p_{H_2}$ constant. On the other hand, one can readily recalculate the growth rates as a function of the hydrogen pressure for a fixed partial pressure of the silane. This can be done using the preceding results (Fig. 2b) in the case of silane by employing the linear relation between the growth rate and the source molar fraction for a fixed hydrogen pressure. Thus, the new value of the growth rate for a partial pressure of silane (P silane) different from the experimental partial pressure is

$$\left(\frac{dx}{dt}\right)_{calculated} = \left(\frac{dx}{dt}\right)_{\substack{experimental \\ at\ p_{source}\ (experimental)}} \times \left[\frac{p_{source}}{p_{source}}\right]_{experimental}^{selected}$$

Thus in the case of silane, three variation ranges are observed in the calculated diagrams: (*i*) The growth rate varies proportionally to $(p_{H_2})^{-1/2}$ within a first range; (*ii*) the growth rate is proportional to $(p_{H_2})^{-1}$ within a second range; and (*iii*) the growth rate decreases more rapidly than $(p_{H_2})^{-1}$ beyond a certain value of the pressure. These results can be seen in Fig. 4a. Figures 4b-d give the results for the compounds SiH_2Cl_2, $SiHCl_3$, and $SiCl_4$. The same variation ranges are observed for the chlorosilanes although strictly speaking the transformation is not exact since the growth rate is not completely proportional to the partial pressure for these compounds.

Influence of the temperature.—The temperature has a very different action on the two variation ranges of the growth rate. It can thus be seen in Fig. 5a, which corresponds to experiments made in function of the pressure for a constant initial molar fraction of silane, that a rise in temperature increases the growth rate in the first (low pressure) range while the temperature is without effect on the same growth rate beyond a certain value of the hydrogen pressure. This same effect can also be seen in Fig. 5b which gives the same experimental results calculated for a constant partial pressure of the silane source.

The results of a more complete study of temperature as a variable parameter are given in Fig. 6a-c in the

Fig. 2. (a) Growth rate as a function of SiH_4 molar fraction, the pressure is 20 Torr, and temperature 900°C; (b) Growth rate as a function of SiH_4 molar fraction for different hydrogen pressures; temperature 930°C; (c) Growth rate as a function of $SiHCl_3$ molar fraction for different hydrogen pressures; temperature 990°C.

case of silane for an initial molar fraction of this source of 2.1×10^{-3} and different hydrogen pressures: 10, 70, and 500 Torr. Figure 6d gives these same results recalculated to a partial pressure of silane of 2.1×10^{-2} in all cases.

Influence of hydrogen pressure on crystalline perfection.—We have observed that the temperature limit at which the deposited layer becomes polycrystalline is lowered when working under reduced pressure. This result has been mentioned by Townsend (3). We studied this phenomenon by keeping constant the hydrogen flow at 18 liters/min and the silane molar fraction at 10^{-3} in all cases. The results obtained are given in Table I and correspond to an averaged estimation made over a large number of depositions.

Thus for example, at 910°C for a hydrogen pressure of 10 Torr and a growth rate of 0.18 μm/min, the surface finish remains perfectly polished and only a few stacking faults are to be seen on the edge of the substrate in the case where this latter has been cleaned in the reactor by an HCl etching for a few moments at atmospheric pressure before putting the system under vacuum.

Under our experimental conditions, the surface finishes obtained with the different chlorosilanes are satisfactory when the pressure is greater than 250 Torr. At a lower pressure the surface finish is rough. However, the layers are monocrystalline. This can be explained by the effects of the silicon transport by HCl between the susceptor which is very hot and the substrate which is much colder. (This difference in temperature is due to the difficulty of substrate heating by contact in a system under vacuum.) This silicon transport is made easier under low pressure by the fact that the diffusion coefficients of all the compounds contained in the gas phase are higher at low pressure than at atmospheric pressure.

Kinetics of doping.—We studied the epitaxial layer doping with arsenic using arsine as a doping source. The experiments were made at 930°C for a silane molar fraction of 2.1×10^{-3}. In Fig. 7 we can see the variation of the level of the free carriers as a function of the hydrogen pressure when the arsine molar fraction is kept constant. When the hydrogen pressure varies, the level of the free carriers follows the same variation function as the growth rate. At the lowest pressures, the dopant carrier concentration is proportional to $(p_{H_2})^{+1/2}$. Beyond a certain higher value of the hydrogen pressure it becomes insensible to the pressure.

In the same way as before for the growth rate, the evolution of the level of the free carriers can be cal-

Table I

Hydrogen pressure (Torr)	1050°C	1000°C	950°C	900°C	850°C	800°C
760	mono	mono	poly	poly	poly	poly
250	mono	mono	poly	poly	poly	poly
70	mono	mono	mono	poly	poly	poly
30	mono	mono	mono	mono	mono	poly
10	mono	mono	mono	mono	mono	mono

Fig. 3. Growth rate as a function of H_2 pressure for a given source molar fraction: (a) in the case of SiH_4; (b) in the case of SiH_2Cl_2; (c) in the case of $SiHCl_3$; and (d) in the case of $SiCl_4$.

culated for a constant value of the partial pressure of arsine. These results are given in Fig. 7 curve II. Two ranges can be seen: At low pressure, the level of free carriers is proportional to $[p_{H_2}]^{-1/2}$; and beyond a certain value of the pressure the level of free carriers is proportional to $[p_{H_2}]^{-1}$.

Discussion.—All the experimental results which have been described can be easily explained by using a model of heterogeneous catalysis recently used by Seto (4) in the case of polycrystalline silicon deposition under nitrogen atmosphere at atmospheric pressure. In this model, Seto makes the following assumptions: (*i*) growth rate is proportional to the number of adsorbed species; (*ii*) the absorption of all species takes place on crystalline sites of the silicon surface which are of the same type. Under these conditions, the different heteroequilibrium are functions of the values of the partial pressures and equilibrium coefficients. These equilibriums can be represented by the following chemical equations

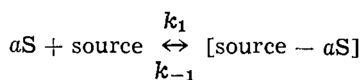

$$aS + \text{source} \underset{k_{-1}}{\overset{k_1}{\leftrightarrow}} [\text{source} - aS]$$

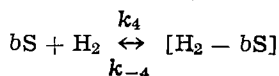

$$bS + H_2 \underset{k_{-4}}{\overset{k_4}{\leftrightarrow}} [H_2 - bS]$$

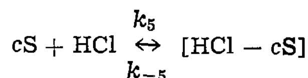

$$cS + HCl \underset{k_{-5}}{\overset{k_5}{\leftrightarrow}} [HCl - cS]$$

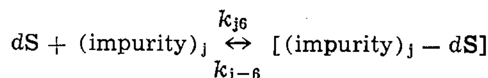

$$dS + (\text{impurity})_j \underset{k_{j-6}}{\overset{k_{j6}}{\leftrightarrow}} [(\text{impurity})_j - dS]$$

Where: a is the number of sites fixing a molecule of the source; b is the number of sites fixing a molecule of H_2; c is the number of sites fixing a molecule of HCl; d_j is the number of sites fixing a molecule of impurity j; S represents one silicon surface site; and k_1, k_4, k_5, k_6 and k_{-1}, k_{-4}, k_{-5}, k_{-6}, are, respectively, the adsorption and desorption coefficients. In the case of the hydrogen, $b = 2$ can mean that the adsorption of a H_2 molecule takes place on two crystalline sites or that two hydrogen atoms are adsorbed on two adjoining sites.

Let us introduce the covering ratio of the silicon surface, called θ, defined as the ratio of the number of crystalline sites of the surface occupied by a particular type of adsorbed atoms, to the total number of sites. These covering ratios are thus θ_{source}, θ_{H_2}, θ_{HCl}, θ_{impurity}. The covering ratio of the surface by an impurity can be calculated if we assume that the surface remains in equilibrium with the gas phase; that is to say that the adsorption and desorption rates are high

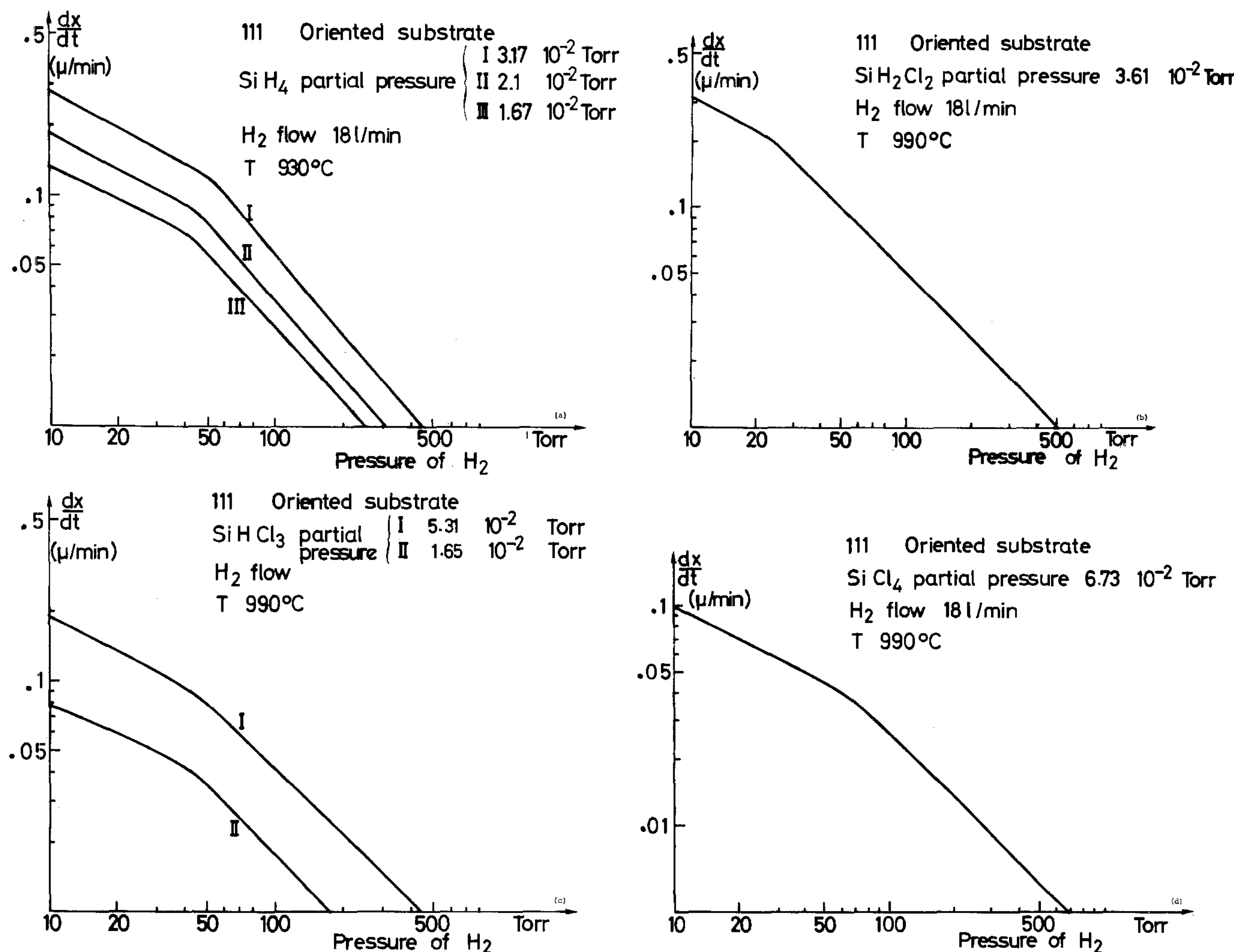

Fig. 4. Growth rate recalculated from the data of Fig. 3 for a given source partial pressure: (a) in the case of SiH_4; (b) in the case of SiH_3Cl_2; (c) in the case of $SiHCl_3$; and (d) in the case of $SiCl_4$.

in comparison with the decomposition rate of the silane. In this case, we can just say that the adsorption rate is equal to the desorption rate. The adsorption rate of a specie is proportional to its partial pressure, to the number of sites available to fix one molecule, and to the adsorption constant

$$v = p_{SiH_4} k_1 [1 - \theta_{SiH_4} - \theta_{H_2} - \theta_{impuritiesj}]^a$$

The desorption rate is proportional to the quantity of sites occupied by the concerned species

$$v = k_{-1} [\theta_{SiH_4}]^a$$

If we suppose that the growth rate is proportional to the number of sites occupied by a source molecule (of silane, for example)

$$\frac{dx}{dt} N = \frac{m_{Si} k_2}{d_{Si}} \times \frac{[K_1 \, p_{source}]^{1/a}}{1 + [K_1 \, p_{source}]^{1/a} + [K_4 \, p_{H_2}]^{1/b} + \ldots}$$

K_1, K_4, K_5, and K_6 represent in this equation the different coefficients of equilibrium

$$K_1 = \frac{k_1}{k-1} \quad K_4 = \frac{k_4}{k-4}$$

The other parameters being defined as: dx/dt is the growth rate; N is the number of silicon atoms per cm^3; m_{Si} is the mass of a silicon atom; and k_2 is the true coefficient of the chemical reaction on the surface.

The molar fraction of the HCl source compounds is small in comparison to H_2, typically $\leq 10^{-3}$. That of the doping impurities is about 10^{-5}-10^{-9} in most cases. There are therefore good reasons to think that

$$[k_4 \, p_{H_2}]^{1/b} >> [K_1 \, p_{source}]^{1/a} + [K_5 \, p_{HCl}]^{1/C} + \ldots$$

We can therefore pose the problem of whether the adsorption of hydrogen is strong or not, that is to say whether it plays a physical role or not. These two hypotheses are given by the inequalities

$$K_4 \, p_{H_2} >> 1 \quad \text{or} \quad K_4 \, p_{H_2} << 1$$

In the first case the hydrogen pressure is an active parameter on the growth rate; in the second case, this pressure is without effect. However the experimental results have shown that the growth rate was influenced by this parameter, it is therefore necessary to admit that $K_4 \, p_{H_2} >> 1$. The growth rate can therefore be represented by the relation

$$\frac{dx}{dt} = \frac{m_{Si} \, k_2 [K_1 \, p_{source}]^{1/a}}{N \, d_{Si} [K_4 \, p_{H_2}]^{1/b}}$$

Thus the apparent coefficient of the decomposition rate is in fact a function of the true coefficient of the reaction rate k_2 and of the equilibrium coefficients K_1 and K_4.

The constant k_2 can be studied while working under a low pressure of a pure silicon source, silane for example, or in an atmosphere of a rare gas which is very little adsorbed on the surface. Thus Joyce and Bradley (5) have shown the results observed while working with pure silane under low pressure; Seto has recently published results obtained with silane in argon, while Richman and Chiang (6) had published the same results in a helium atmosphere.

The experiments undertaken during this study were made under different pressures with the view to explaining the role of this gas on the surface of the silicon during growth. Thus when the pressure is fairly

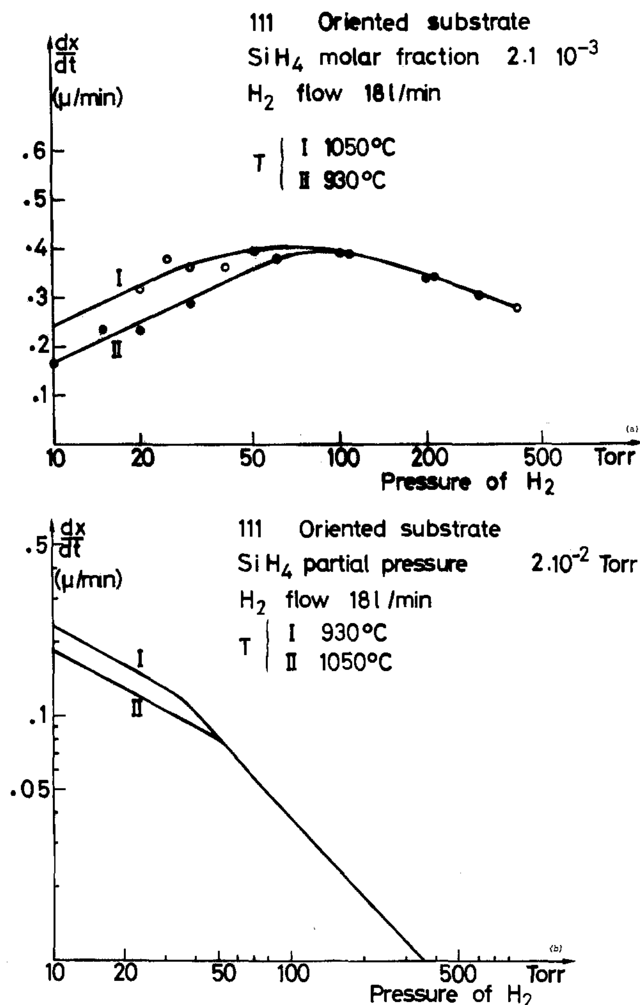

Fig. 5. (a) Growth rate as a function of H_2 pressure for a given SiH_4 molar fraction and two different temperatures; (b) Growth rate as a function of H_2 pressure for a given SiH_4 partial pressure and two different temperatures.

low, the gas diffusion coefficients and the mass transfer coefficients are higher than at atmospheric pressure, the concentrations of the different species are therefore the same on the surface of the layer and in the gas phase. Moreover, the efficiency of the reactor is so weak ($\eta \simeq 5\%$) that it can be considered that the concentration of the source is at any point in the reactor very close to that of the gases that have been introduced. All the experimental results can be explained simply with the model thus defined.

In the first variation range, represented for example in Fig. 5b or 4a, in the case of silane for pressures lower than 40 Torr, the mass transfer is fast and the film growth rate can be considered to be controlled by the rate of surface reaction. Seto's model shows that if the rate is proportional to $[p_{H_2}]^{-1/2}$ the adsorption of the hydrogen molecule is on two silicon sites, while a direct proportion between growth rate and the partial pressure of the silane would indicate an adsorption of silane on a single silicon site. We should note that Seto came to this conclusion as far as the adsorption of the silane on silicon is concerned. In contrast, Joyce and Bradley thought that they had shown the adsorption of the silane molecule on two silicon sites. However it is possible that their system was not well defined or there were, perhaps, important depositions on the sides of the reactor. Chabert and Peyrelavigne also concluded that silane is adsorbed on two silicon sites in the preparation of SiO_2.

In the first pressure range, for which the growth rate is controlled by the pressure, the reaction is controlled by the rate of the surface reaction. An activation energy of 15 [kcal][mole]$^{-1}$ can be deduced from the curve of Fig. 6a where the logarithm of the growth rate is plotted as a function of the inverse of the absolute temperature.

The second variation range of the growth rate, observed at pressures greater than 40-50 Torr corresponds to a limitation of the rate by gaseous diffusion. The growth rate is proportional to the diffusion rate of the source. It is therefore inversely proportional to the total pressure and relatively independent of temperature.

At very low pressure, 10 Torr for example, we are in a region controlled by the surface. At higher pressure, that is 70 Torr, the growth rate can be either controlled by the surface or by the mass transfer according to the temperature; under $T = 850°C$ the reaction is activated. Finally above 500 Torr, the mass transfer is low compared to the surface reaction and growth rate is insensitive to temperature.

Seto's model of heterogeneous catalysis can also explain the influence of the total pressure on the incorporation process of arsenic. Silane, the usual source, is not the only specie in competition with hydrogen on the surface, all the species present in the gas phase share the silicon surface. It is therefore the same for the molecules of the impurities which are also in competition with the hydrogen. In this way

$$N_d = \frac{\text{Constant}[K_{j6}\, p_{(\text{impurity})j}]^{1/d}}{K_4\, p_{H_2}{}^{1/2}}$$

The model thus defined therefore explains the fact that the doping level is proportional to $[p_{H_2}]^{-1/2}$ for low hydrogen pressures, when the partial arsine pressure is constant. The doping level then becomes proportional to $[p_{H_2}]^{-1}$ for higher pressures when the mass transfer has become sufficiently small.

The results given here concerning the quality of the crystal should be compared with those of Bloem (8). This author observed, at atmospheric pressure, that the limit of growth rate for which the layer becomes polycrystalline increases when the growth rate increases. Bloem showed that when we plot the curve which represents this growth rate as a function of the inverse of the absolute temperature, we obtain a straight line whose slope allows the calculation of an activation enery of 115 kcal/mole. Bloem then suggests that this energy is similar to that of silicon diffusion in silicon. He indicates that the slow stage in the monocrystalline growth of silicon is therefore the diffusion of free silicon which is looking for a crystalline site on the surface. The coefficient of self-diffusion of silicon in silicon has an activation energy of 110 kcal.

There is no real disagreement between our results and those of Bloem. However, there is matter for discussion since he does not take into account the role of hydrogen on the growth surface, an effect which becomes clear when the hydrogen pressure decreases. We must then admit, as shown by Townsend, that the adsorbed hydrogen molecules on the surface as well as all the species present there, hinder the crystalline arrangement of the growth.

Application of epitaxial growths obtained at low pressure.—P-n junctions.—Very abrupt junctions have been obtained by growing boron doped p^+ layers at low pressure under the following conditions: temperature, 930°C; pressure, 10 Torr; $dx/dt = 0.2$ μm/min; and hydrogen flow, 18 liters/min, measured at 760 Torr. Levels of free carriers of $7 \cdot 10^{19}$ acceptors per cm^3 were obtained. When the p^+ layer is grown immediately after a type n layer of a level close to 10^{17} carriers per cm^3, in a same growth process, the transition between the n layer and the p^+ layer is less than 300Å.

Impurity profile between the substrate and the epilayer.—The autodoping of epitaxial layers grown at atmospheric pressure is great when the substrates are heavily doped with phosphorus ($\rho \lesssim 10^{-3}$ Ω·cm). We

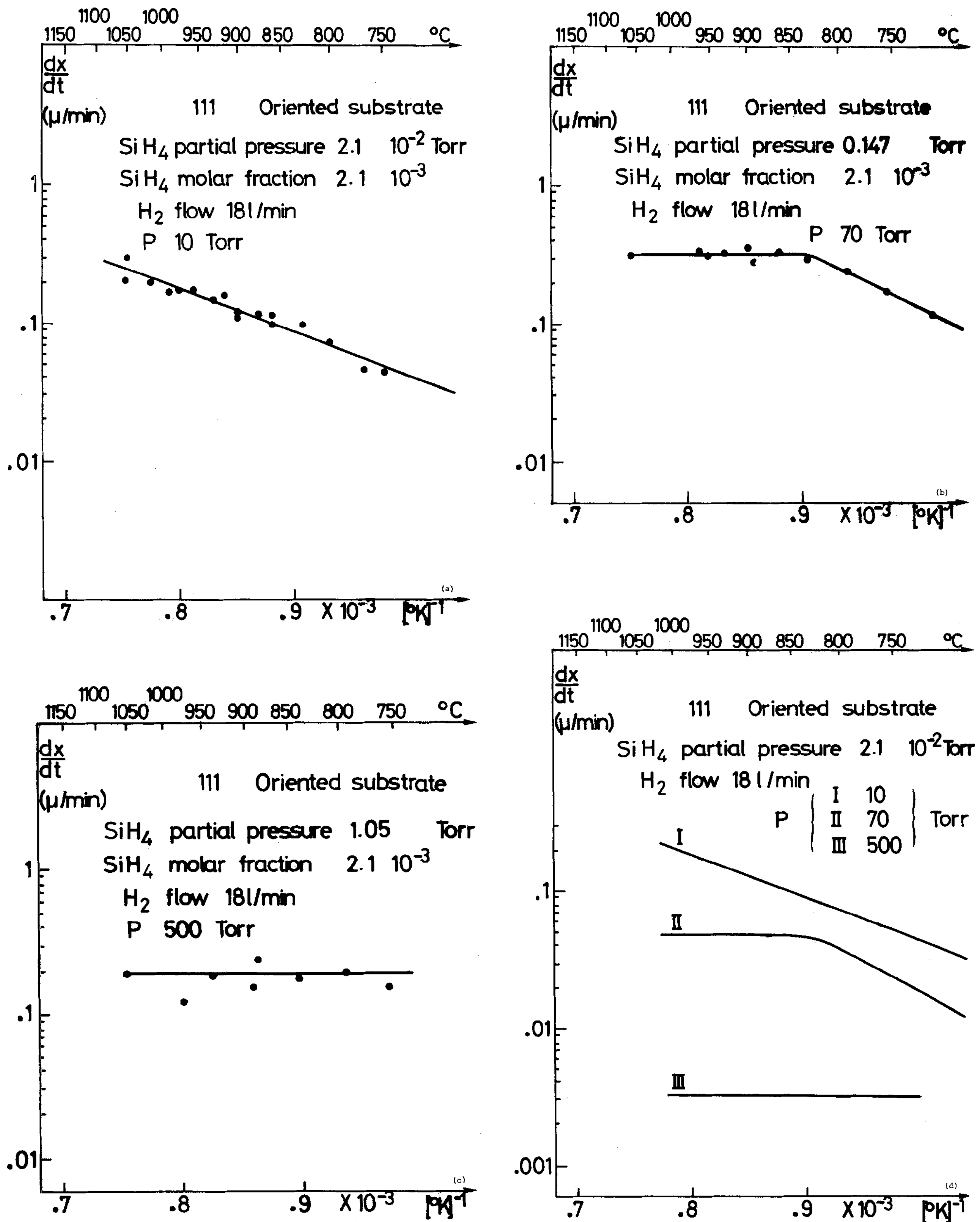

Fig. 6. Growth rate as a function of temperature in the case of silane for a given SiH_4 molar fraction: (a) H_2 pressure is 10 Torr; (b) H_2 pressure is 70 Torr; (c) H_2 pressure is 500 Torr; and (d) the same results recalculated for a given SiH_4 partial pressure.

have made similar layers on such substrates when operating at a hydrogen pressure of 10 Torr. As can be seen in Fig. 8, the effect due to autodoping is suppressed and the transitions are very abrupt. The exact profile of the impurities is more abrupt than the profile measured by the capacity-voltage method because of the Debye length. The actual profiles are then in agreement with Fick's laws. The abrupt transitions and the rapid purges obtained at low pressure allow the growth of layers of several thousand angstroms with a precision of ± 300Å. The reduction in autodoping due to the contamination by impurities which have escaped from the back side of the substrate can also be explained by Seto's model. For this, let us suppose that the evaporation rate of the impurities from the the back side of the substrate is constant. The partial pressure of the residual impurities in the reactor is

$$p_{\text{impurities}} = x_{\text{impurities}} \times p_{H_2}$$

which gives for the residual level of free carriers

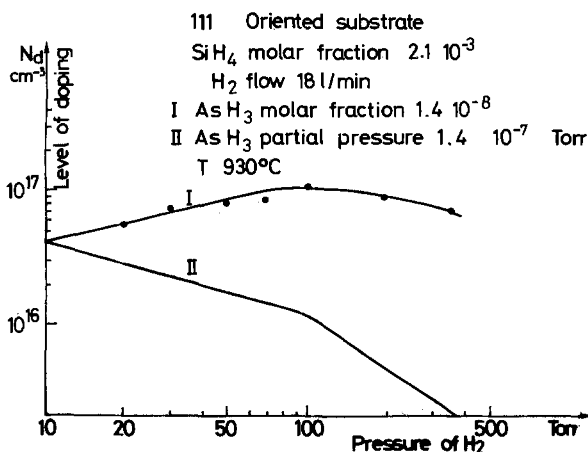

Fig. 7. Level of doping as a function of H_2 pressure: I, for a given AsH_3 molar fraction; II, for a given AsH_3 partial pressure.

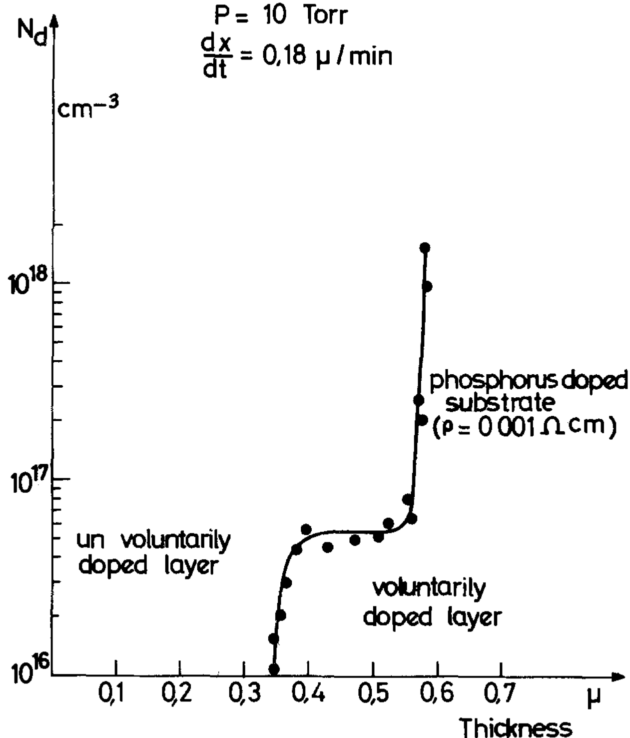

Fig. 8. Impurity profile obtained between a very heavily doped substrate and an epilayer by using a low temperature process.

$$N_{d_{\text{residual}}} = \frac{\text{constant } K_6 \, x_{\text{impurities}} [p_{H_2}]^{1/2}}{[K_4]^{1/2}}$$

The observations made of this phenomenon are in agreement with the preceding expression. Thus when the working pressure is 10 Torr, the residual level due to the escaped impurities of the substrate is reduced by a factor between 5 and 10.

Realization of microwave devices.—Schottky diodes working at 10 GHz have been made by using epitaxial structures grown under low pressure. The characteristics of the layer, the growth conditions, and the electrical performances of these diodes are summarized below.

For the epitaxial layer we used 111 oriented substrates, doped with phosphorus, of 10^{-3} Ω·cm resistivity. The metallurgical thickness of the layer was 0.17 μm, the electrical thickness 0.14 μm, the level of free carriers $1 \cdot 10^{17}$ atoms/cm³.

The layers were deposited at an actual temperature of the substrate of 930°C and a pressure of 10 Torr. The growth rate was 0.2 μm/min.

The geometrical characteristics of the diodes are the following: contact, Cr-Au; diameter of the diodes, 8 μm. The electrical characteristics of the diodes were then: 0V junction capacity, $C_{jo} = 0.12$ pF; breakdown voltage, 3V; noise factor, 4.7 dB when the input power of the local oscillator was 2 mW.

Conclusions

The experiments of silicon crystal growth carried out at a low hydrogen pressure have underlined the important role of hydrogen on the silicon surface during growth. By growing between 10 and 100 Torr for a constant partial pressure of each of the compounds SiH_4, SiH_2Cl_2, $SiHCl_3$, and $SiCl_4$, the growth rate presents following variation rate ranges: (*i*) At low pressure, the rate of film growth is proportional to $[p_{H_2}]^{-1/2}$ and is activated by temperature. Growth is controlled by surface hydrogen in competition with different source species (or doping species) on the surface. Layers are defect free even for temperatures lower than 900°C; (*ii*) At higher pressure, growth rate is proportional to $[p_{H_2}]^{-1}$. It is not a function of temperature; it is mass transfer limited.

Growth at low temperature and at low pressure allows us to obtain very steep impurity profiles between a very heavily doped substrate and the epilayer because both solid-state diffusion of impurities and autodoping are reduced. Less autodoping is obtained because the rate of gaseous diffusion of impurities which escape from the substrate is accelerated further, transitions between layers differently doped are more abrupt because purges are accelerated, and transient mechanisms are suppressed. For all these reasons the low pressure growth process is a great improvement in the fabrication of microwave devices.

Acknowledgments

This work has been sponsored by the French Ministry of Defense D.R.M.E., Semiconductors and Components Department.

The authors would like to thank C. Raffet, M. Dupre, D. Huyghe, and D. Le Guen for their excellent technical assistance and maintenance of the experimental apparatus. Frequent and very useful discussions with Professor Deschanvres of the University of Caen are gratefully acknowledged.

Manuscript submitted Nov. 16, 1976; revised manuscript received Oct. 7, 1977.

Any discussion of this paper will appear in a Discussion Section to be published in the December 1978 JOURNAL. All discussions for the December 1978 Discussion Section should be submitted by Feb. 1, 1978.

Publication costs of this article were assisted by Thomson-CSF.

REFERENCES

1. Y. S. Chiang, in "Semiconductor Silicon 1973," H. R. Huff and R. R. Burgess, Editors, p. 285-291, The Electrochemical Society Softbound Symposium Series, Princeton, N.J. (1973).
2. Y. S. Chiang and G. W. Looney, *This Journal*, **120**, 550 (1973).
3. W. G. Townsend and M. E. Uddin, *Solid State Electron.*, **16**, 39 (1973).
4. J. Y. W. Seto, *This Journal*, **122**, 701 (1975).
5. B. A. Joyce and R. R. Bradley, *ibid.*, **110**, 1235 (1963).
6. D. Richman, Y. S. Chiang, and P. H. Robinson, *RCA Rev.*, **31**, 613 (1970).
7. F. M. Chabert and M. Peyrelavigne, Ph.D. Thesis, University of Marseilles, Marseilles (1975).
8. J. Bloem, *J. Cryst. Growth*, **20**, 70 (1973).

An Experimental Study of Various Cross Sheet Resistor Test Structures

Martin G. Buehler* and W. Robert Thurber

National Bureau of Standards, Electronic Technology Division, Washington, D.C. 20234

ABSTRACT

Newly designed cross sheet resistors are shown to give the same (within 0.5%) measured sheet resistance as conventional van der Pauw structures. Diffused boron and phosphorus layers with sheet resistances near 200 Ω/□ were studied with the sampled areas varying from a square 6.4 μm (0.25 mil) on a side to a circle 762 μm (30.0 mils) in diameter. An increase in measured sheet resistance values was observed due to surface leakage currents, and an equivalent circuit model was developed to explain the results. The effect of joule heating on measured sheet resistance values was observed in both large and small cross structures.

In the microelectronics industry the sheet resistance of conducting layers is frequently measured with a four-terminal resistor in the shape of a bridge (1) or a van der Pauw (2) test structure. More recently, it was shown mathematically that the sheet resistance can be determined from the van der Pauw formula if the resistor has the shape of a Greek cross provided the arm length of the cross is greater than the arm width (3). Since the cross sheet resistor can be made as small as allowed by lithographic processes, the structure permits the study of electrical conduction effects in inhomogeneous materials where the nonuniform regions are of the order of the dimensions of the heart of the cross. Such effects have been observed in silicon on sapphire by Ham (4) and are anticipated in deposited layers such as aluminum and polycrystalline silicon. In this study the previous theoretical work is verified experimentally by comparing measurements on the new Greek-cross structures with conventional van der Pauw structures where the region of interest is contacted by four contacts which approximate points. Effects such as surface leakage currents and joule heating are discussed in terms of their influence on sheet resistance values. It was found that leakage currents due to surface channels can cause an apparent increase in the measured sheet resistance.

Equivalent Circuit Model

Experimental studies of various sheet resistor test structures were undertaken to verify that the sheet resistance can be properly calculated from the van der Pauw formula when interferences are negligible. In these studies, the six different test structures shown in Fig. 1 were fabricated by a planar silicon technology where the diffusions were made through oxide openings and contacted by evaporated metal layers. These structures appear on test pattern NBS-4 which includes many structures previously studied on test pattern NBS-3 (5). The structures are listed in Table I where various critical dimensions are cited. Structure 4.11 is a circular gated van der Pauw sheet resistor with a field plate extending from the periphery of the diffused layer to a channel stop diffusion which is the same conductivity type as the substrate. The offset quadrate cross, represented by structure 4.26, was studied experimentally by Perloff and co-workers (6) and found to be a viable test structure.

An equivalent circuit model for these junction-defined sheet resistors is shown in Fig. 2 where the sheet resistor terminals are labeled A, B, C, and D. In the model, the four resistors labeled R_1 represent the resistance of the region of interest, R_2 is the arm resistance, and R_3 is the surface shunt resistance between contact pads. In one test structure, the peripheral surface resistance R_3 can be controlled by a gate labeled G. The surface resistance between one of the contact pads and a nearby diffused area labeled

* Electrochemical Society Active Member.

Key words: cross structure, diffused layer, sheet resistance, silicon, van der Pauw structure.

Table I. Test structures

Number	Type	Critical dimension μm (mil)*
4.11	Circular gated van der Pauw	D = 431.8 (17.00)
4.22	Greek cross (small)	S = 6.4 (0.25)
4.24	Greek cross (large)	S = 38.1 (1.50)
4.25	Greek cross (large)	S = 38.1 (1.50)
4.26	Offset quadrate cross	S = 38.1 (1.50) D_2 = 6 4 (0.25)
4.35	Circular van der Pauw	D = 762.0 (30.00)

* D = diameter, S = width of cross, D_2 = width of tap.

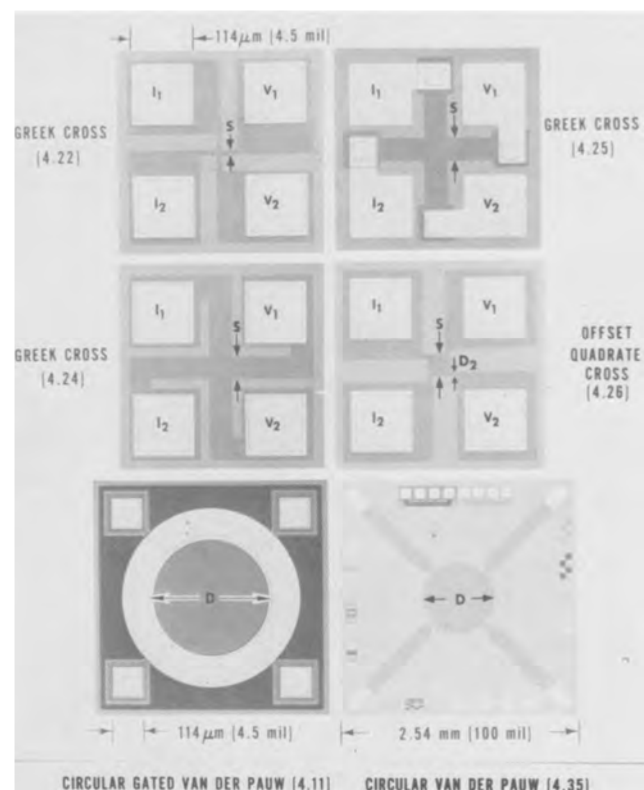

Fig. 1. Sheet resistor test structures. See Table I for explanation of symbols. The structures at the periphery of the square containing structure 4.35 are not a part of this structure.

E is shown as R_3^*. The entire structure is isolated by a junction from the substrate which is contacted at S. The model assumes that contact resistance at the probe pads is negligible and that pinhole shorting from the probe pads to the substrate is absent. In addition, current in the oxide is assumed to be negligible, and the substrate is assumed to have negligible resistance.

The computation of the sheet resistance and other factors follows from the measurement of resistance. The notation used for these resistances follows from the observation that the contact pads A, B, C, and D are arranged in a square as shown in Fig. 2. Two measurement positions are designated as the zero- and ninety-degree positions. In the zero position forward current $I_{AB}(+I)$ is passed into A and out of B and the voltage $V_{DC}(+I)$ is measured at D with respect to C. For reverse current, the current $I_{AB}(-I)$ is passed into B and out of A and the voltage is measured at D with respect to C. Both $I_{AB}(-I)$ and $V_{DC}(-I)$ are negative quantities. The static resistances, determined for the zero-degree position for both forward $(+I)$ and reverse $(-I)$ currents, are

$$R_0(+I) = V_{DC}(+I)/I_{AB}(+I) \quad [1a]$$

$$R_0(-I) = V_{DC}(-I)/I_{AB}(-I) \quad [1b]$$

In the ninety-degree position the current terminals are D and A and the voltage terminals are B and C. The static resistances are

$$R_{90}(+I) = V_{CB}(+I)/I_{DA}(+I) \quad [2a]$$

$$R_{90}(-I) = V_{CB}(-I)/I_{DA}(-I) \quad [2b]$$

The incremental resistance for both forward $(+I)$ and reverse $(-I)$ currents determined from measurements at the zero-degree position is

$$R'_0(\pm I) = \frac{[V_{DC}(+I) - V_{DC}(-I)]}{[I_{AB}(+I) - I_{AB}(-I)]} \quad [3]$$

and at the ninety-degree position is

$$R'_{90}(\pm I) = \frac{[V_{CB}(+I) - V_{CB}(-I)]}{[I_{DA}(+I) - I_{DA}(-I)]} \quad [4]$$

Note that $V_{DC}(-I)$, $I_{AB}(-I)$, $V_{CB}(-I)$, and $I_{DA}(-I)$ are all negative quantities. The average resistance determined from measurements at the zero- and ninety-degree positions for currents $\pm I$ is

$$R(\pm I) = [R'_0(\pm I) + R'_{90}(\pm I)]/2 \quad [5]$$

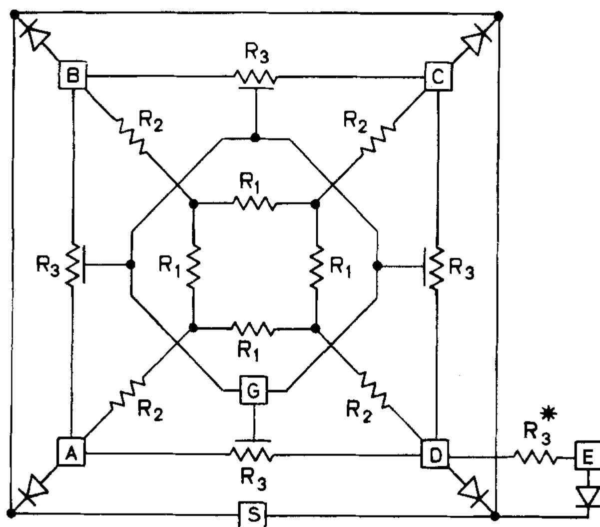

Fig. 2. Seven-terminal equivalent circuit model used to explain the effect of surface leakage currents on sheet resistance values. This circuit models a symmetrical, peripherally gated, junction-defined sheet resistor with a substrate and isolated junction contacts.

The sheet resistance is determined from the van der Pauw formula (2)

$$R_s = f[\pi R(\pm I)/\ln 2] \quad [6]$$

where f is a correction factor related to the geometrical asymmetry of the sheet resistor; see the Appendix. The value of f is related to the asymmetry factor, F_A, which is given by

$$F_A = [R'_0(\pm I) - R'_{90}(\pm I)]/R(\pm I) \quad [7]$$

As indicated in the Appendix, f is within 0.1% of unity for $F_A \leq 10.74\%$. The value of F_A is used in the experimental studies to quantify the degree of asymmetry encountered in the various sheet resistors. Since the sheet resistors in this study have a high degree of symmetry ($F_A \leq 3\%$), f was taken as unity in the computation of the sheet resistance.

The measurement of the sheet resistance assumes that offset voltages encountered in the measurement system can be eliminated by taking the difference in voltages at both forward and reverse currents. The zero offset factor, F_0, is calculated from

$$F_0 = \frac{(|R_0(+I) - R_0(-I)| + |R_{90}(+I) - R_{90}(-I)|)}{2R(\pm I)} \quad [8]$$

where taking the absolute value of the quantities leads to a worse case estimate. Small values of F_0 indicate that the measurement system is adequate.

In the measurement of the sheet resistance, it is assumed that the conduction mechanism is ohmic. To quantify the linearity of the current voltage characteristics, a linearity factor, F_L, is calculated by determining the average resistance at two different current levels. For currents at $\pm I$ and $\pm nI$, F_L is given by

$$F_L = [R(\pm nI) - R(\pm I)]/R(\pm I) \quad [9]$$

One might be tempted to try to quantify the linearity of a layer by measuring additional resistance values at the 180- and 270-degree positions. For layers with linear resistivity, the reciprocity theorem indicates that such resistances determined at 180 and 270 degrees are equivalent to resistances determined from the zero- and ninety-degree position, respectively (2). If the resistivity of the layer is linear, reciprocity holds. However, the converse—that if reciprocity is obeyed, the resistivity is linear—may not be true. Layers with nonlinear resistivity are better identified by the linearity factor, F_L.

Test Structure Intercomparison

The test structures listed in Table I were fabricated in both n- and p-type silicon wafers. Sheet resistance variations across typical wafers are shown in Fig. 3 and 4. The values shown in Fig. 3 were obtained from a p-type layer formed by a boron nitride diffusion at 965°C for 45 min with a junction depth of 1.6 μm in a (111)-oriented, phosphorus-doped 59 Ω·cm silicon wafer. The sheet resistance values in Fig. 4 were obtained from an n-type layer formed by a solid silicon pyrophosphate diffusion at 950°C for 20 min with a junction depth of 1.1 μm in a (111)-oriented, boron-doped 3 Ω·cm silicon wafer. On test pattern NBS-4 all the sheet resistors are in close proximity except for structure 4.35. The sheet resistance values shown for this structure are an average of two values measured at sites on either side of the one where the other structures are clustered. This procedure reduces the effect of sheet resistance gradients on the comparison of sheet resistance values from structure 4.35 with those from the other structures.

In these studies measurements were made in the dark. The current from a constant current source was either determined from the voltage drop across a standard resistor or assumed to be within the stated accuracy. Current reversal was achieved by switching the current through a mechanical switch or relay rather than reversing the current source. For the

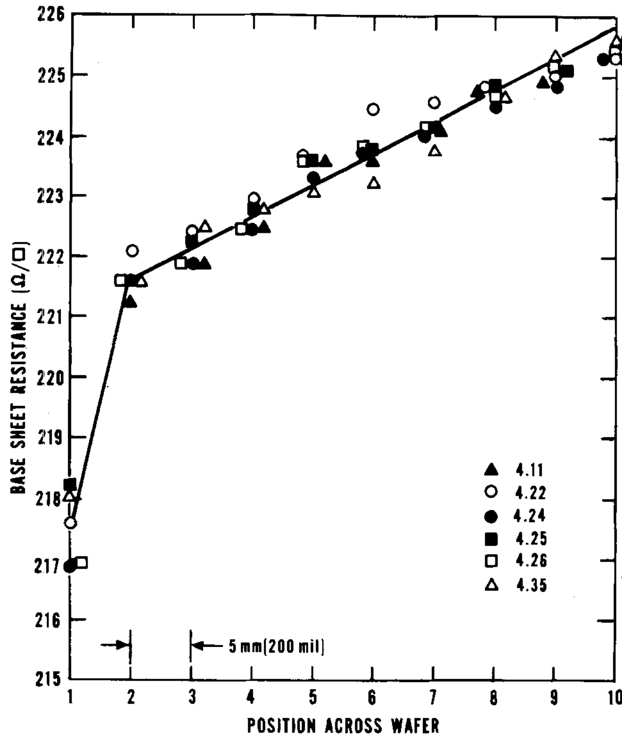

Fig. 3. The p-type sheet resistance variation as measured by various test structures across an n-type 59 Ω·cm wafer (B59Ph-1).

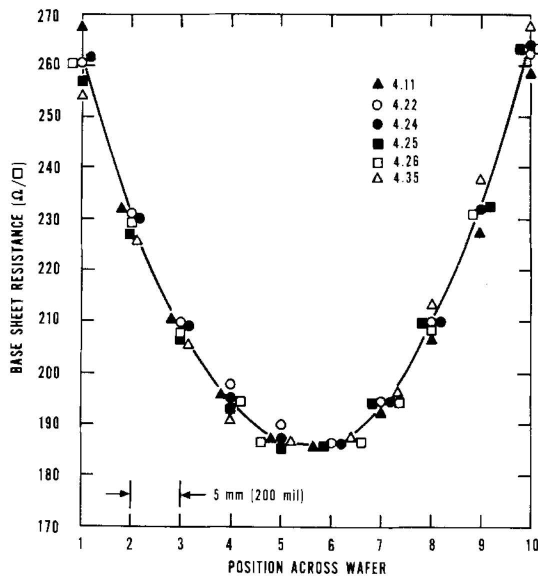

Fig. 4. The n-type sheet resistance variation as measured by various test structures across a p-type 3 Ω·cm wafer (B3.0B-3).

resistive structures studied here this procedure ensures that the magnitude of the reverse current equals that of the forward current. Voltages were measured with a digital voltmeter with a resolution of 1 μV. The measurement current was chosen so that the measured voltage was between 0.5 and 10 mV. The sheet resistance was calculated from Eq. [6] where the currents used in the computation were approximately 100 μA. The substrate was allowed to float electrically during these measurements.

Figure 3 reveals that the measured sheet resistance values for the various test structures are typically within 0.5% of each other in spite of the fact that the region being sampled is as small as a square 6.4 μm on a side (structure 4.22) or as large as a circle 762 μm in diameter (structure 4.35). This is a ratio of over 10^4 in area. The excellent agreement of these values confirms experimentally the conclusion drawn from a theoretical analysis (3) that the Greek crosses in Fig. 1 are valid van der Pauw sheet resistors. The ratio of arm length to arm width varies from 2.2 for structure 4.25 to 5.0 for structure 4.22. It is anticipated that structures with ratios as low as unity would also give results consistent with theory.

Interferences

In the measurement of the sheet resistance various interferences can lead to erroneous values. Some of these are listed in Table II and are discussed in this section.

The effect of surface leakage currents on sheet resistance values measured on wafer B92B-2 is dramatically shown in Fig. 5. This wafer was fabricated along with the wafer shown in Fig. 4 except that near the end of the process the oxide was removed and a new thin wet oxide (120 nm thick) was regrown at 925°C for 50 min. As shown in Fig. 5, sheet resistance values vary by as much as a factor of 4 from the corrected value obtained on the gated van der Pauw structure, 4.11. To quickly verify that surface leakage currents were excessive, the two-terminal resistance between two adjacent junction-isolated sheet resistors was measured on each of the wafers used in this study. These resistances are shown in Table III as R_3* values. The surface leakage current problem is clearly indicated by the fact that R_3* for wafer B92B-2 is at least 500 times lower than other values.

The equivalent circuit model, shown in Fig. 2, was used to explain the effect of surface leakage currents on the sheet resistance values shown in Fig. 5. (In the following development the diodes, R_3*, and the gate shown in Fig. 2 were ignored.) When measuring the sheet resistance, the current, I, is passed between adjacent terminals (*e.g.*, A, B) and the voltage difference, V, is measured between the other two terminals (*e.g.*, C, D). The desired situation is one in which the value of R_3 is infinite and the value of R_2 is zero. In this case, $R = V/I = R_1/4$. By setting R_1 equal to the sheet resistance, R_s, then $R = R_s/4$. For this simple model, $R = R_s/4$ is a sufficient approximation to the van der Pauw expression, $R = R_s(\ln 2/\pi) = R_s/4.53$.

The network shown in Fig. 2 was solved for $R = V/I$ with the use of the indefinite admittance matrix ap-

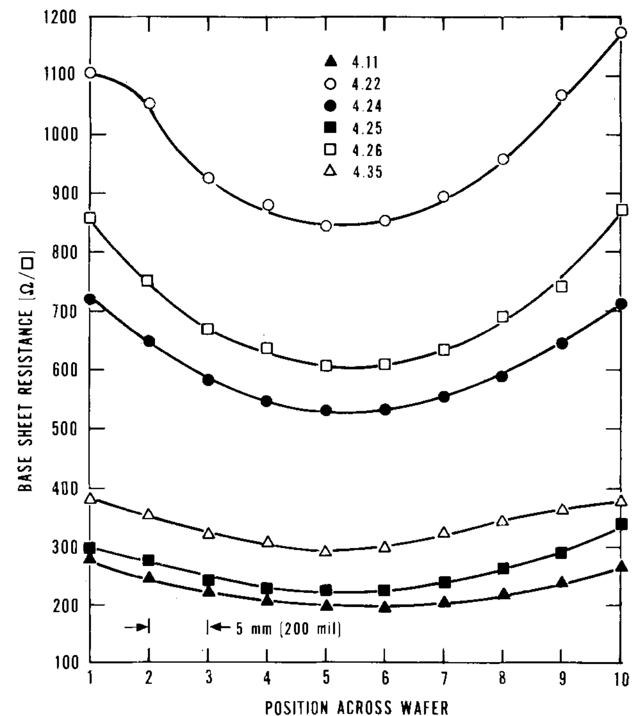

Fig. 5. The n-type sheet resistance variation as measured by various test structures across a p-type 92 Ω·cm wafer (B92B-2). This data shows that surface leakage currents can dramatically affect measured sheet resistance values.

Table II. Effect of interferences on various quantities determined from junction-defined, cross sheet resistors

Effect	Interference	Possible cause
Asymmetry factor large	Nonuniform sheet resistance across structure	Nonuniform lateral doping and/or junction depth variations
	Nonuniform structure boundaries	Poor photomasks and/or poor wafer fabrication
	Bulk leakage current	Low junction breakdown voltage
Zero offset factor large	Photovoltaic effect	Too much light
	Thermoelectric effect	Thermal voltages at relays and/or probe contacts
	DVM zero offset	Instrumentation problem
Linearity factor large	Joule heating	Excessive current. Poor design (structure too narrow)
	Nonlinear resistivity	Grain boundaries and/or junctions
	Oxide-silicon interface currents	Oxide charge causes channels
Sheet resistance value incorrect	Part of structure missing	Poor fabrication and/or structure near edge of wafer
	High contact resistance	Poor fabrication
	Metal-to-substrate shorts	Pinholes in oxide
	Surface currents across oxide	Incomplete metal removal
	Oxide-silicon interface currents through inversion layer	Excessive oxide charge and/or interface states
	Poor junction isolation	Low breakdown voltage or too much light

Table III. Parameters for wafers used in this study

Wafer number	Type	Resistivity ($\Omega \cdot$ cm)	R_3* (Ω)	BV (V) at 10 μA
B92B-2	p	92	3000	6
B3.0B-3	p	3.0	1.5 M	60
B59Ph-1	n	59	>100 M	220

proach (7). The solution requires the reduction of both 7 by 7 and 5 by 5 matrices. The result is

$$R = \frac{V}{I} = (8G_1^3G_2G_3 + 16G_1^3G_3^2 + G_1^2G_2^3 + 8G_1^2G_2^2G_3 + 20G_1^2G_2G_3^2 + 2G_1G_2^3G_3 + 8G_1G_2^2G_3^2 + G_2^3G_3^2) \div (4G_1^3G_2^3 + 32G_1^3G_2^2G_3 + 80G_1^3G_2G_3^2 + 64G_1^3G_3^3 + 12G_1^2G_2^3G_3 + 64G_1^2G_2^2G_3^2 + 80G_1^2G_2G_3^3 + 12G_1G_2^3G_3^2 + 32G_1G_2^2G_3^3 + 4G_2^3G_3^3) \quad [10]$$

where $G_1 = R_1^{-1}$, $G_2 = R_2^{-1}$, and $G_3 = R_3^{-1}$.

An evaluation of this expression normalized by $R_1/4$ is shown in Fig. 6. It shows that, when the surface leakage currents are negligible ($R_3 >> R_1$), the region of interest is measured ($4R/R_1$ approaches 1) provided that the resistance, R_2, in the arms is not too large. It also shows that, when surface leakage currents are large ($R_3 \lesssim R_1$), surface conduction completely dominates the measured R value and R is smaller than the desired $R_1/4$ value. Finally, when surface leakage currents are modest ($R_3 > R_1$), the curves show that the surface conduction causes R to be much larger than the desired $R_1/4$ value when the arm resistance is large ($R_2 > R_1$).

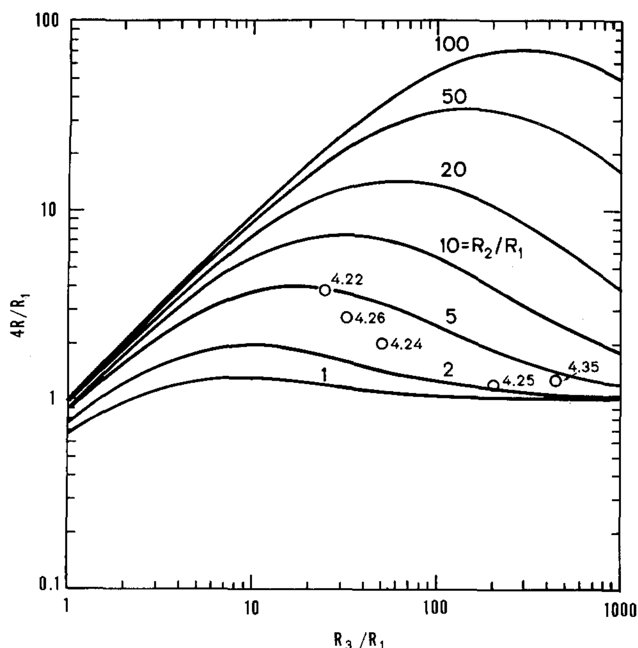

Fig. 6. An evaluation of the equivalent circuit model shown in Fig. 1. The data points are values from wafer B92B-2; see Table IV.

For each structure used to obtain the results shown in Fig. 5, R_1, R_2, and R_3 values were determined. In this analysis the sheet resistance of the phosphorus layer was taken as 200 $\Omega/\square$. Thus, R_1 is 200Ω and R_2 is 200Ω times a geometry factor for the arm. From circular MOSFET measurements [structure 4.15 which is identical to structure 3.15 (5)] the surface channel sheet resistance on wafer B92B-2 was found to be 20,000 $\Omega/\square$ at zero gate voltage. Thus, R_3 is 20,000Ω times a geometry factor representing surface conduction between adjacent arms. From the R_2/R_1 and R_3/R_1 ratios, the $4R/R_1$ values were determined from Fig. 6; the results are listed in Table IV. Also listed in Table IV are the sheet resistance values from Fig. 5 taken at position 5 and normalized to $R_{so} = 199\ \Omega/\square$. As seen in Table IV, the correlation between the R_s/R_{so} ratio taken from Fig. 5 is close to the $4R/R_1$ ratio calculated from the equivalent circuit model. This confirms the effect of surface leakage current on sheet resistance values.

Geometrical asymmetry of test structures is reflected in the asymmetry factor F_A. For the structures studied, F_A was always small (less than 3%) so that in evaluating the sheet resistance from Eq. [6], little error is introduced in assuming $f = 1$. The F_A values are interpreted in the following way. For the n-type wafers the results in Table V indicate that the cross structures 4.22, 4.24, and 4.25 have a higher degree of symmetry than the other structures in that their mean F_A values are low. The higher mean F_A values for structures 4.11, 4.26, and 4.35 are attributed to human errors introduced in the hand preparation of the 100× photomask artwork. The F_A values measured from the p-type wafer do not have a trend identical to the n-type wafers, and this is thought to be due to small surface channel currents. The exact interpretation of F_A values is still under study, but

Table IV. Sheet resistance values compared with equivalent circuit model (wafer B92B-2 position 5)

Structure number	R_s ($\Omega/\square$)	R_s/R_{so}	$4R/R_1$
4.22	844	4.24	3.8
4.26	606	3.05	2.7*
4.24	529	2.66	2.0
4.35	290	1.46	1.3
4.25	224	1.13	1.2
4.11	R_{so} = 199	1	1

* Including constriction resistance at the arms.

Table V. The mean and standard deviation of various sheet resistor factors (in percent)

Structure number*	F_0 n-type	F_0 p-type	F_L n-type	F_L p-type	F_A n-type	F_A p-type
4.11	0.063 ± 0.022	0.086 ± 0.036	+0.007 ± 0.060	+0.035 ± 0.039	−1.05 ± 0.91	−0.03 ± 0.54
4.22	0.040 ± 0.012	0.148 ± 0.153	−0.059 ± 0.074	−0.147 ± 0.052	+0.52 ± 1.17	+1.20 ± 1.19
4.24	0.051 ± 0.015	0.088 ± 0.041	−0.028 ± 0.049	−0.045 ± 0.040	−0.29 ± 0.82	+0.22 ± 0.42
4.25	0.059 ± 0.052	0.045 ± 0.015	−0.047 ± 0.082	+0.002 ± 0.016	−0.17 ± 1.01	+0.18 ± 0.45
4.26	0.050 ± 0.015	0.085 ± 0.050	−0.022 ± 0.061	−0.016 ± 0.037	+1.54 ± 1.06	+2.91 ± 1.01
4.35	0.078 ± 0.053	0.106 ± 0.052	−0.024 ± 0.127	+0.022 ± 0.018	−1.73 ± 0.62	−0.34 ±0.60

* The structures 4.11-4.35 were fabricated in wafer B59Ph-1 (n-type) and B3.0B-3 (p-type).

geometrical asymmetry introduced by photomask fabrication, photolithography and etch processes, and nonuniform conductivity must be contributing factors. The asymmetry factor, F_A, is also expected to be useful in detecting structural boundary anomalies and in identifying those structures which have a high degree of symmetry.

To ensure that zero offset and nonlinearities have a minimal effect on the sheet resistance values, the factors F_0 and F_L were evaluated using Eq. [8] and [9] with $I = 100$ μA and $n = 2$. Results determined from measurements on at least 10 sheet resistors on two wafers are listed in Table V. The offset factors, F_0, are generally below 0.2% which means that photovoltaic, thermoelectric, and DVM zero offset effects can be neglected. The linearity factors, F_L, are generally much less than 0.2% which means that the conducting layers are being measured in the ohmic range.

Bulk leakage current problems can be identified by monitoring the breakdown voltage from the structure to the substrate. Breakdown voltage values for the wafers used in this study are listed in Table III. The breakdown voltage current of 10 μA was chosen to be one-tenth of the current used to measure the sheet resistance. As seen in Table III, wafer B92B-2 has a breakdown voltage of only 6V. However, this breakdown voltage is large enough to allow the sheet resistance to be determined since the compliance voltage at the current source did not exceed 1V at 100 μA.

The effect of joule heating on sheet resistance values is shown in Fig. 7 for structures 4.22 and 4.24 found on wafers B59Ph-1 and B3.0B-3. These measurements were taken at a fixed time after the current was switched to the next higher value. As seen in the figure, the structure with the larger arms (4.24) can carry more current before overheating. The ratio of arm widths for the two structures is six to one. This

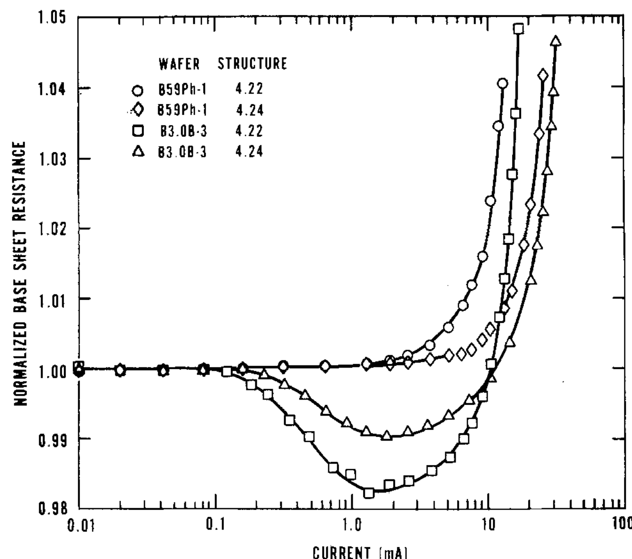

Fig. 7. The effect of joule heating on the sheet resistance of p-type and n-type layers fabricated with the use of a small cross (4.22) 6.4 μm wide and a large cross (4.24) 38.1 μm wide.

leads to an expected current ratio of $\sqrt{6} = 2.45$ for equal power dissipation. As seen in the figure, the observed current ratio of about two is slightly less than anticipated. The dip in the curves of Fig. 7 for wafer B3.0B-3 is attributed to the saturation of a small surface channel current. The increase in the resistance at high currents is consistent with the positive temperature coefficient of resistivity for moderately doped silicon layers. The heating effect was confirmed by an increase in the temperature of the wafer chuck as monitored by a thermocouple imbedded in the chuck. Junction breakdown effects can be ruled out since the compliance voltage at the current source was always less than the junction breakdown voltage.

Design Considerations

It is important that interference-free test structures be designed so that a minimum of tests is needed to ensure correct sheet resistance values. With proper design and proper measurement procedures most of the above interferences can be minimized and those that remain can be detected and faulty data identified. To minimize the effect of surface leakage current the curves in Fig. 6 indicate that the cross arms should be as short as possible. This is confirmed in Fig. 5 where structure 4.25 is clearly superior to structure 4.22. However, the arm length should not be less than the arm width or a correction factor must be used in evaluating the sheet resistance (3). In addition the surface resistance should be as large as possible. One way to accomplish this is by making the current path between contact points as long as possible. This is difficult if large diffused probe pad areas are needed for probing the layer prior to metallization, but if a channel stop diffusion is used, the surface resistance can be made large. The ultimate in control is achieved with a channel stop and a peripheral gate biased so as to shut off surface currents. If channel stops or gates are not feasible, then surface currents can be detected by measuring the resistance to a nearby diffused region which is physically separated from the sheet resistor but is the same type of diffusion.

A minimum of six probe pads is needed to ensure that a junction-defined sheet resistor is fully testable and that interferences are identifiable. The six pads should include the four sheet resistor contacts, a substrate contact, and either a gate or a separately diffused region. The substrate contact allows the effect of bulk junction leakage currents to be evaluated. Excessive bulk leakage can be expected when the junction has a soft reverse breakdown. Of course, no measurement is possible when the compliance voltage at the current source exceeds the junction breakdown voltage. When the sixth contact is a separately diffused region, surface leakage current problems can be identified but accurate sheet resistance values may not be obtainable. When the sixth contact is a gate and if a channel stop is used (such as in structure 4.11), problems due to surface leakage currents can be eliminated as interferences on the sheet resistance values.

The cross and van der Pauw test structures present a measurement problem because the measured voltages are much lower than those measured on bridge-type

structures. In some cases large currents must be forced through the cross structure in order to obtain a detectable voltage. This is particularly true for low sheet resistance layers formed by emitter diffusion or metal deposition. If a voltmeter with limited sensitivity is used, then the arm width of the cross structure should be as large as possible to allow measurements at high currents with minimum joule heating. If a voltmeter with adequate resolution is used, then a minimum line width cross can be measured with currents small enough to avoid joule heating.

Conclusion

Experimentally it was demonstrated that sheet resistance values derived from cross sheet resistors can be correctly calculated from the van der Pauw formula. Conventional van der Pauw sheet resistors as large as 762 μm (30.0 mils) in diameter agree within 0.5% with cross structures as small as 6.4 μm (0.25 mil) in width. The geometrical asymmetry of all structures studied was no worse than 3% so that the sheet resistance can be evaluated from the van der Pauw equation with $f = 1$. The effect of interferences such as surface leakage current and joule heating on sheet resistance values was observed experimentally and design suggestions are given to minimize these effects.

Acknowledgment

The authors are indebted to Y. M. Liu for developing the various diffusion processes used to fabricate the wafers. This work was conducted as part of the Semiconductor Technology Program at NBS. Portions of this work were sponsored by the Defense Advanced Research Projects Agency (Order No. 2397, Program Code 7D10) and the Defense Nuclear Agency (IACRO 77-809).

Manuscript submitted Aug. 3, 1977; revised manuscript received Nov. 28, 1977.

Any discussion of this paper will appear in a Discussion Section to be published in the December 1978 JOURNAL. All discussions for the December 1978 Discussion Section should be submitted by Aug. 1, 1978.

Publication costs of this aticle were assisted by the National Bureau of Standards.

Table VI. The relationship between the geometrical asymmetry, F_A, and the correction factor, f

F_A (%)	$1 - f$ (%)	r
2	0.0035	1.020
4	0.0139	1.041
6	0.0312	1.062
8	0.0555	1.083
10	0.0867	1.105
12	0.1249	1.128
14	0.1700	1.151

APPENDIX

The van der Pauw factor f shown in Eq. [6] is related to the resistances measured at the zero- and ninety-degree positions through (2)

$$\cosh\left(\frac{r-1}{r+1}\frac{\ln 2}{f}\right) = \frac{1}{2}\exp\left(\frac{\ln 2}{f}\right)$$

where

$$r = R'_0(\pm I)/R'_{90}(\pm I)$$

The asymmetry factor, F_A, given in Eq. [7] and expressed in terms of r, is

$$F_A = 2(r-1)/(r+1).$$

Values for r, F_A, and $1 - f$ are listed in Table VI. They indicate that F_A values can be quite large before f is significant. Calculations from the above equations reveal that for $F_A \leq 10.74\%$, $1 - f$ is less than 0.1%.

REFERENCES

1. ASTM Designation F 76, "Annual Book of ASTM Standards," Part 43 (November 1977).
2. L. J. van der Pauw, *Philips Tech. Rev.*, **20**, 220 (1958); L. J. van der Pauw, *Philips Res. Rep.*, **13**, 1 (1958).
3. J. M. David and M. G. Buehler, *Solid-State Electron.*, **20**, 539 (1977).
4. W. E. Ham, Private communication.
5. M. G. Buehler, *Semiconductor Measurement Technol.*, NBS Special Publication 400-22 (May 1976). Requests for releasing the NBS-4 mask set (or the earlier NBS-3 set) from a commercial mask-making company should be made directly to M. G. Buehler, National Bureau of Standards, Washington, D.C. 20234. The cost of a set is about $200.
6. D. S. Perloff, F. E. Wahl, and J. Conragan, *This Journal*, **124**, 582 (1977).
7. G. S. Moschytz, "Linear Integrated Networks," pp. 116-136, van Nostrand-Reinhold Co., New York (1974).

Bridge and van der Pauw Sheet Resistors for Characterizing the Line Width of Conducting Layers

M. G. Buehler,* S. D. Grant, and W. R. Thurber

National Bureau of Standards, Electronic Technology Division, Washington, D.C. 20234

ABSTRACT

It is shown that the line width of conducting layers can be computed from simple d-c electrical measurements made on bridge and van der Pauw shaped test structures. A compact six-contact, cross-bridge sheet resistor test structure was developed to make this measurement directly. Line widths measured on boron nitride diffused layers indicate that the method is sensitive to width variations of the order of ±0.1 μm (±4 μin.)

The measurement of line widths in the microelectronic industry is needed for the process control and design of integrated circuit components. For process control, line-width measurements are useful in monitoring the many etching processes which define the width of oxide windows and conducting layers. In circuit design, the value of diffused or implanted resistors is determined in part by the line width of the conducting layer.

Conventional methods for measuring the line width include both optical (1) and electrical techniques.

* Electrochemical Society Active Member.
Key words: cross-bridge structure, diffused layer, line width, process control, sheet resistance.

The electrical techniques commonly employ the double-bridge method (2) which requires the fabrication of two bridge structures of different width. Since this measurement technique is a differential-type method, it suffers from errors in taking the difference of large numbers.

An alternative to these methods is the determination of line widths using a bridge structure (3) in combination with a van der Pauw test structure (4). The width of the bridge structure is calculated from measurements of its resistance along with knowledge of the length between the voltage taps and the sheet resistance value obtained from the van der Pauw structure. The advantage of these vehicles is that they can be combined into one compact structure with the same line width, which means that the conductivity of the composite is more uniform than would generally be true for separate structures. In addition, the computation of the line width does not depend on the difference of large numbers; however, the analysis of the van der Pauw structure requires the measurement of low voltages, usually in the range from 1 to 10 mV. This is not a problem for laboratory-based instrumentation but precludes the use of those integrated circuit testers which do not measure these low voltages.

Test Structure Design and Fabrication

Line drawings of the test structures used in this study are shown in Fig. 1-4. Metallized contact to diffused regions is shown by the crosshatched areas. Structures 3.22 and 3.28 were fabricated as a part of test pattern NBS-3 (5) and the structures 7.18 and 7.23 were fabricated as a part of test pattern NBS-7 (6). The dimensions for these structures are listed in Table I.

The bridge test structure shown in Fig. 1 was designed in accordance with the ASTM standard (3) which requires that $W_m \geqq 3D_m$ and $B_m \geqq 2W_m$. In addition the lateral diffusion and overetch effects were minimized by requiring that $A_m \geqq 5X_j$ and $C_m \geqq 5X_j$, where X_j is the junction depth. The subscript m indicates a parameter referred to photomask dimensions.

The offset quadrate-cross test structure shown in Fig. 2 was designed to eliminate the contact shorting

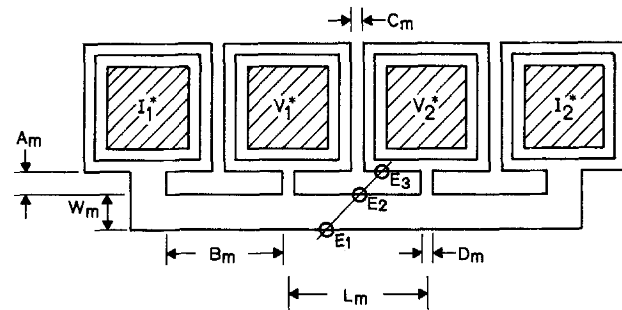

Fig. 1. Bridge sheet resistor test structure (3.28). The edges E_1, E_2, and E_3 are used to determine the width from optical photomicroscopic measurements.

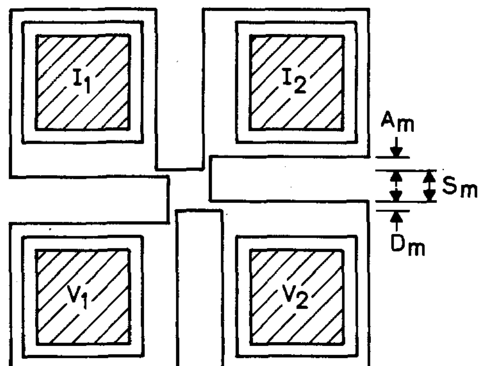

Fig. 2. Offset quadrate-cross test structure (3.22)

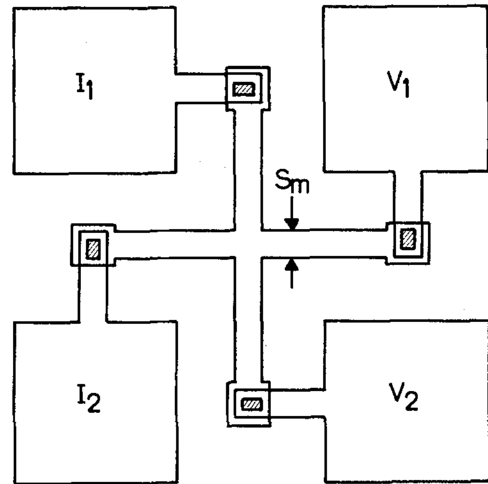

Fig. 3. Greek-cross sheet resistor test structure (7.18)

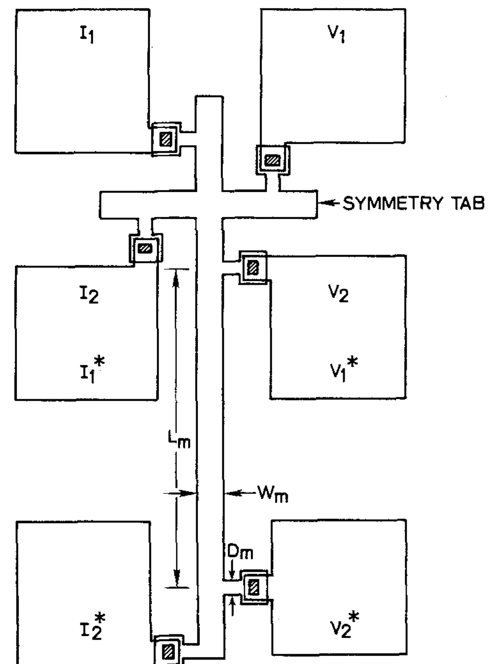

Fig. 4. Cross-bridge sheet resistor test structure (7.23)

correction factor (7) associated with the van der Pauw equation. For this structure where $A/S = 0.33$ and $D/S = 0.17$, the correction factor is much less than 0.1% and may be neglected. Likewise, the Greek-cross test structure shown in Fig. 3 was designed so that the arm length is greater than the arm width which means that the contact shorting correction factor associated with this structure also can be neglected (7).

The cross-bridge structure shown in Fig. 4 is a combination of the bridge structure shown in Fig. 1 and

Table I. Test structures

Number	Figure	Type	Photomask dimensions μm (mil)
3.28	1	Bridge	A_m = 25.4 (1.00) B_m = 127.0 (5.00) C_m = 12.7 (0.50) D_m = 12.7 (0.50) L_m = 139.7 (5.50) W_m = 38.1 (1.50)
3.22	2	Offset quadrate cross	A_m = 25.4 (1.00) D_m = 6.4 (0.25) S_m = 38.1 (1.50)
7.18	3	Greek cross	S_m = 14.0 (0.55)
7.22	4	Cross bridge	D_m = 8.0 (0.31) L_m = 200.0 (7.87) W_m = 16.0 (0.63)

the Greek-cross structure shown in Fig. 3. The bridge part was designed in accordance with the ASTM standard (3) except that $W_m = 2D_m$. The cross part was designed to eliminate the contact shorting correction factor (7). In order to preserve the symmetry of the cross, symmetry tabs were introduced at the ends of the arms denoted I_1, I_2, and V_1. These tabs are intended to compensate for the extension of the structure along the arm denoted V_2.

The test structures shown in Fig. 1-4 were fabricated by photolithographic processes using contact printing and an n-p-n transistor process. Both emitter and base sheet resistors were fabricated. The base sheet resistors, which were used to obtain the results reported in this study, were fabricated on n-type, (111)-oriented silicon substrates on which a 300 nm thick oxide was grown in steam at 1100°C. Diffusion windows were etched in the oxide. The boron nitride predeposition diffusion was at 965°C in dry nitrogen for about 30 min. After a deglaze in 10% hydrofluoric acid solution, the base was diffused at 1100°C for 18 min in wet oxygen, followed by 40 min in dry oxygen, followed by 15 min in dry nitrogen. This creates over the base regions a 350 nm thick oxide that masks the subsequent emitter diffusion. The final high temperature steps occurred at 1025°C for 20 min and at 925°C for 45 min. The structures were complete after opening the contact windows and patterning the aluminum metallization. The base sheet resistance was nominally 200 Ω/□. Test structures 3.22 and 3.28 were fabricated in wafers numbered 28, 29, and 30; the junction depth was 2.1 μm. Structures 7.18 and 7.23 were fabricated in a 9 Ω-cm wafer, D8.8 Ph-1; the junction depth was 1.6 μm.

Electrical Measurements

The electrical measurements utilized the d-c four-probe method where current was forced between two contacts to the resistor and the voltage was measured between two additional contacts. The current from a constant current source was determined either from the voltage drop across a standard resistor or was assumed to be within the stated accuracy. Current reversal was achieved by switching the current through a mechanical switch or relay to ensure that the magnitude of the reverse current equals that of the forward current. The magnitude of the current was chosen so that the measured voltage was between 0.5 and 10 mV. The substrate was allowed to float electrically during these measurements.

The line width is determined from measurements on the bridge structure in combination with measurements on the van der Pauw structure. The sheet resistance is determined from the van der Pauw structure by utilizing probe pads labeled I_1, I_2, V_1, and V_2 shown in Fig. 2, 3, or 4 and is calculated from the van der Pauw formula (4)

$$R_s = \pi R(\pm I)/\ln 2 \quad [1]$$

where $R(\pm I)$ is the incremental resistance determined from the current and voltage measurements for both directions of current and both contact orientations; see preceding paper (8). The parameter f which appears in the complete form of the van der Pauw formula is assumed to be unity in this study since the asymmetry factor, F_A, was much less than 10% (8).

The line (or window) width is determined by utilizing probe pads labeled I_1^*, I_2^*, V_1^*, and V_2^* shown in Fig. 1 and 4. The effective width, W_e, of the current-carrying channel is calculated from

$$W_e = R_s L_m / R^*(\pm I) \quad [2]$$

where R_s is determined from Eq [1] and L_m is the distance between voltage taps as determined from the photomask. The incremental resistance determined from measurement for both forward $(+I)$ and reverse $(-I)$ currents is given by

$$R^*(\pm I) = [V^*(+I) - V^*(-I)]/[I^*(+I) - I^*(-I)] \quad [3]$$

For measurements made in the forward current mode, the current $I^*(+I)$ is passed into I_1^* and out of I_2^* where both $I^*(+I)$ and $V^*(+I) = V_1^*(+I) - V_2^*(+I)$ are positive quantities. For measurements made in the reverse current mode, both $I^*(-I)$ and $V^*(-I)$ are negative quantities. The above expressions assume that the voltage taps do not significantly perturb the current flow in the current-carrying channel.

If the test structure is a diffused layer then the effective width is

$$W_e = W_m + \alpha X_j + W_{oe} \quad [4]$$

where W_m is the width determined from the photomask, W_{oe} is the incremental change in the width due to photolithographic effects and overetching, and αX_j is the effective incremental change in the width due to lateral diffusion where X_j is the junction depth and α is the lateral diffusion factor (9). Since the lateral diffusion cannot be observed from the top surface of the structure, the optically observable line width is

$$W = W_e - \alpha X_j = W_m + W_{oe} \quad [5]$$

These quantities are shown in detail in Fig. 5.[1]

Line-Width Measurements

Line widths for the bridge structure shown in Fig. 1 were measured as a function of position across a wafer by both electrical and optical techniques. In order to compare the two techniques, the factor αX_j, with α assumed to have the value 0.3 (9) and $X_j = 2.1$ μm for wafers 28, 29, and 30, was subtracted from the effective line width, W_e, which was evaluated from the electrical measurements with the use of Eq. [2]. In Fig. 6 the sensitivity of the method to etch time is illustrated by an experiment where the base diffusion

[1] If the test structure is a deposited layer, the effective width, which is the same as the optically observable width, W, is $W_e = W_m - W_{oe}$.

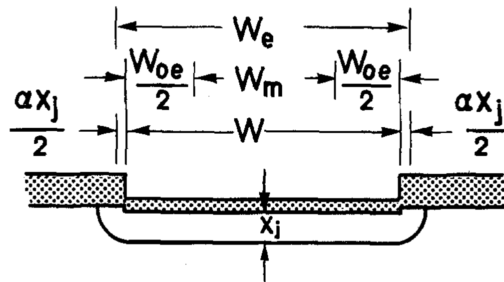

Fig. 5. Cross-sectional view of a diffused region showing various dimensions. To account for lateral diffusion effects, the width of the conducting channel is increased by an amount αX_j where the conductivity in this region is the same as in the main channel.

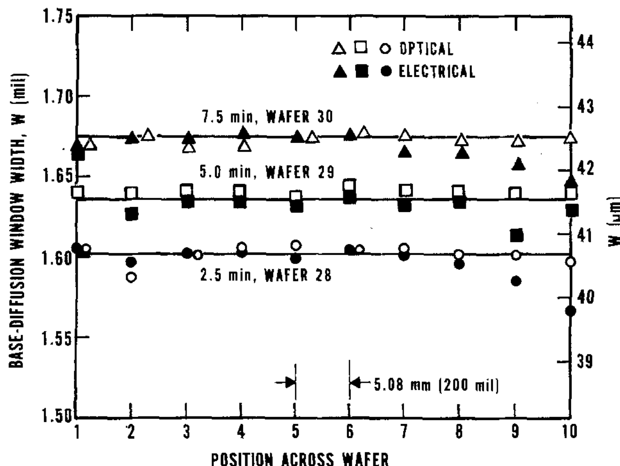

Fig. 6. Width of the base diffusion window as measured electrically and from photomicrographs along the diameter of wafers etched for different times.

window was etched for a different time on each of three wafers. The measurements demonstrate the effect of increased etch time on the window width.

The optical measurements were made directly on photomicrographs of various bridge test structures. An optical microscope with a 40× objective was operated in the dark field mode to obtain photomicrographs. The magnification as measured on the photomicrograph was 585×. The method used to determine the line width is illustrated by the points labeled E_1, E_2, and E_3 shown in Fig. 1. The distance between edges E_1 and E_3 is assumed to be unaffected by the photolithographic processes or the etch times. This distance was taken from the nominal photomask dimension and for structure 3.28 is 63.5 ± 1.3 μm (2.50 ± 0.05 mils). The distance between edges E_1 and E_2 corresponds to the optically observable width. In measuring this width a scale was placed on the photomicrograph at a convenient angle such that the distance between E_1 and E_3 was a convenient multiple of the actual dimension. The distance between edges E_1 was read directly from the scale. The estimated repeatability of both the electrical and optical line-width measurements was ±0.05 μm (±2 μin.).

The results obtained from the photomicrographs and shown in Fig. 6 compare favorably with the values obtained from the electrical measurements and in all cases the values are larger than the measured photomask width, $W_m = 39.2 \pm 0.3$ μm (1.545 ± 0.01 mils). Sheet resistance values are typically more uniform in the center of a wafer than at the periphery. The fact that the bridge and van der Pauw resistors are located about 50 mils apart on the test pattern would affect the agreement between the electrical and optical measurements more at the edge of the wafer. The results from the center of the wafer illustrate that the electrical width measurements are sensitive to width changes of the order of ±0.1 μm (±4 μin.).

Line widths were also measured with the use of the cross-bridge test structure shown in Fig. 4. Before computing the line width it is necessary to verify that the sheet resistance is correctly determined from the cross-bridge structure. This demonstration is shown in Fig. 7 where the sheet resistance from adjacent Greek-cross (7.18) and cross-bridge structures are compared. The results shown in Fig. 7 were analyzed by the least squares method where the slope of the line is 0.98 and the intercept is 2.9 Ω/□. The standard deviation for these measurements is 0.7% which means that sheet

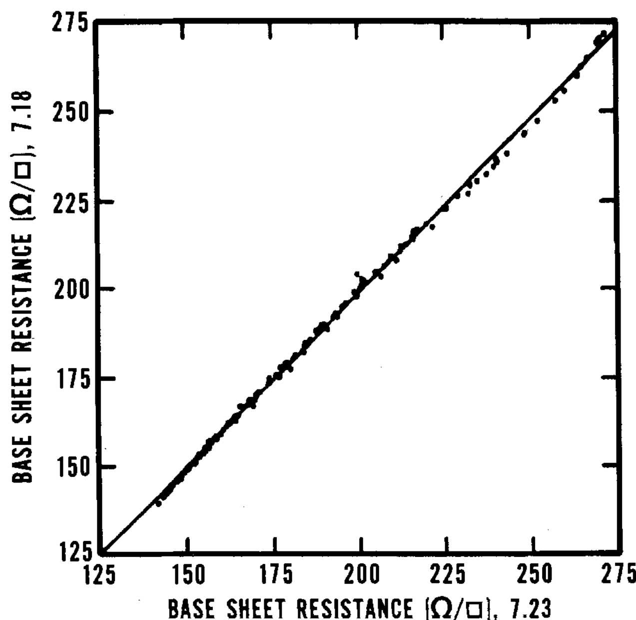

Fig. 7. Comparison of sheet resistance results from the Greek-cross (7.18) and cross-bridge (7.23) test structures.

Table II. The mean and standard deviation of various sheet resistor factors (in percent)

Structure number	F_0	F_L	F_A
7.18	0.133 ± 0.050	−0.011 ± 0.031	−0.55 ± 0.65
7.18*	1.39 ± 0.39	−0.005 ± 0.007	+0.13 ± 1.38
7.23	0.141 ± 0.050	−0.011 ± 0.010	−1.48 ± 0.72
7.23*	0.59 ± 0.11	−0.019 ± 0.006	−1.00 ± 1.21

* Data on structures designated by an * were obtained with an automated data acquisition system.

resistance values can be adequately determined from the cross-bridge test structure.

Other comparisons between the Greek-cross (7.18) and the cross-bridge (7.23) test structures are listed in Table II. The factors F_0, F_L, and F_A listed in Table II are defined in the preceding paper (8). The offset factors, F_0, measured with an automated data acquisition system are significantly larger, because of thermal voltages in the relay scanners, than those measured on a system where the digital voltmeter was connected directly to the voltage contacts. The linearity factors, F_L, are quite small being less than 0.02% which indicates that the conduction mechanism in these test structures is ohmic. As expected, the asymmetry factors, F_A, indicate that the Greek cross (7.18) is more symmetrical than the cross bridge (7.23); however, since F_A << 10%, the van der Pauw formula can be used without correction to compute the sheet resistance.

As an example of how electrical line width measurements can be utilized in process control, wafer maps of sheet resistance and effective line width W_e from Eq. [2] as determined from measurements on the cross bridge (7.23) are shown in Fig. 8. Each wafer map is divided into five increments indicated by symbols given in the key. The numbers listed in the left-hand column are measured parametric values. The numbers in the right-hand column are the number of devices

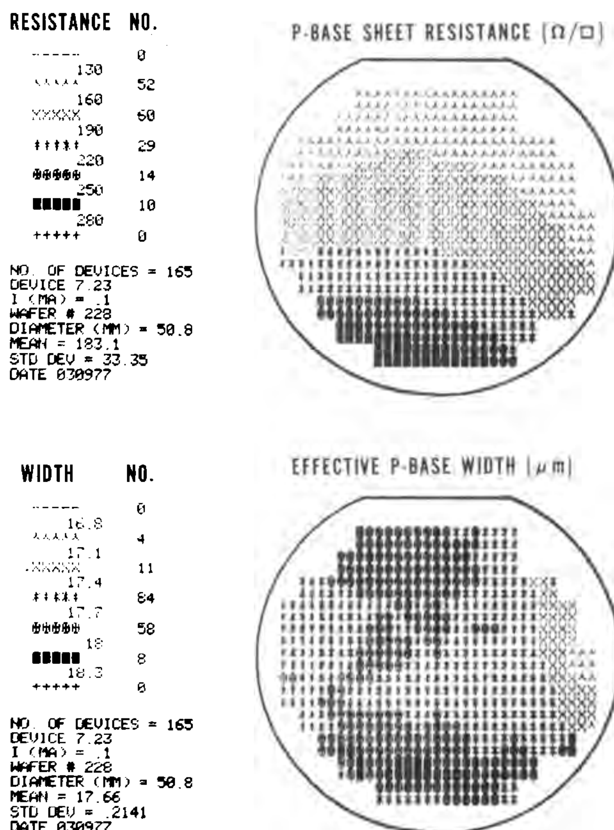

Fig. 8. Wafer maps of a p-type base diffusion into a 9 Ω·cm n-type substrate as analyzed by the cross-bridge test structure (7.23).

measured in each increment. Every other symbol shown in the wafer map represents a measured point; from these values the remaining symbols were obtained by interpolation. The sheet resistance shows a rather large top to bottom variation which is indicative of a diffusion problem; however, the effective line width shows a reasonably flat profile which is indicative of good etch control. Similar wafer maps have been reported elsewhere (6) for both the base and emitter sheet resistors using separate cross and bridge structures.

The use of the cross-bridge method in evaluating the width of very narrow diffused (or implanted) layers should be viewed with caution. This situation occurs when the incremental lateral diffusion width αX_j is comparable with the over-all width. In fact, the caution applies to any layer in which strong lateral resistivity gradients exist. In such cases the effective sheet resistance determined at the cross may not be the correct value for use in the computation of the effective width from Eq. [2]. The method described here has also been applied to the measurement of the line width of phosphorus emitter diffusions with a sheet resistance of about 1 Ω/□ (5, 6). In addition, the width of aluminum metallization with a sheet resistance of about 0.03 Ω/□ has been measured.

Conclusion

It was demonstrated that effective line width can be determined from electrical measurements on diffused bridge and van der Pauw sheet resistors and that these electrical measurements agree with those determined from optical photomicrographs of the sheet resistors. The method is sensitive to width changes of the order of ± 0.1 μm (± 4 μin.). A new cross-bridge sheet resistor was developed; wafer maps of the sheet resistance and line width illustrate the utility of this structure for process control.

The advantage of electrical line-width measurements is that they can be made quickly and at low cost using automatic data acquisition equipment with sufficient voltage resolution. Thus these measurements are important because of their potential use as process control and design vehicles in the manufacture of semiconductor devices.

Acknowledgment

The authors are indebted to Y. M. Liu for developing the various diffusion processes used to fabricate the NBS-3 and NBS-7 test pattern wafers, to R. L. Mattis for the wafer maps shown in Fig. 8, and to C. A. Cannon for making the photomicrographs. This work was conducted as part of the Semiconductor Technology Program at NBS. Portions of this work were supported by the Defense Advanced Research Projects Agency (Order No. 2397, Program Code 7D10) and the Defense Nuclear Agency (IACRO 77-809).

Manuscript submitted Aug. 3, 1977; revised manuscript received Nov. 28, 1977.

Any discussion of this paper will appear in a Discussion Section to be published in the December 1978 JOURNAL. All discussions for the December 1978 Discussion Section should be submitted by Aug. 1, 1978.

Publication costs of this article were assisted by the National Bureau of Standards.

REFERENCES

1. D. A. Swyt, *Solid State Technol.*, **19**, 55 (April 1976).
2. W. E. Ham, *Semiconductor Measurement Technol.* NBS Special Publication 400-15, p. 30 (January 1976).
3. ASTM Designation F 76, "Annual Book of ASTM Standards," Part 43 (November 1977).
4. L. J. van der Pauw, *Philips Tech. Rev.*, **20**, 220 (1958); L. J. van der Pauw *Philips Res. Rep.*, **13**, 1 (1958).
5. M. G. Buehler, *Semiconductor Measurement Technol.*, NBS Special Publication 400-22 (May 1976). Requests for releasing the NBS-4 mask set (or the earlier NBS-3 set) from a commercial mask-making company should be made directly to M. G. Buehler, National Bureau of Standards, Washington, D.C. 20234. The cost of a set is about $200.
6. M. G. Buehler and D. E. Sawyer, *Circuits Manufacturing*, **17**, 46 (February 1977).
7. J. M. David and M. G. Buehler, *Solid-State Electron.*, **20**, 539 (1977).
8. M. G. Buehler and W. R. Thurber, *This Journal*, **125**, 645 (1978).
9. W. M. Penney and L. Lau, Editors, "MOS Integrated Circuits," p. 80, van Nostrand Co., New York (1972).

Boron Determination in Silicon by the Nuclear Track Technique

W. Robert Thurber

National Bureau of Standards, Electronic Technology Division, Washington, D.C. 20234

and B. Stephen Carpenter

National Bureau of Standards, Analytical Chemistry Division, Washington, D.C. 20234

ABSTRACT

The nuclear track technique was used for the determination of the boron dopant density in silicon. It was found that boron in the range of 10^{15}-10^{20} atoms/cm^3 could be detected. The resistivity of the silicon specimens as a function of the boron density determined by the nuclear track technique compares well with the work of Wagner relating resistivity to boron density. The results obtained by the nuclear track technique show some scatter, but in general agree with those determined by the junction capacitance-voltage method.

Boron is the most common dopant used in the preparation of p-type silicon single crystals for the microelectronics industry. The resistivity of the silicon is a function of the amount of boron present as a dopant in the crystal. It is desirable to have a chemical technique which can determine the boron density

Key words: alpha track, boron, dopant density, nuclear track technique, silicon.

for comparison with that obtained from electrical methods. Neutron activation analysis, a useful technique for many other impurities in silicon, is not suitable for the analysis of boron. Other methods have been cited in the literature including electron microprobe, nuclear backscattering, microchemistry, and alpha spectroscopy. However, of these methods only alpha spectroscopy (1-5) is able to measure the boron dopant density in the 10^{15} cm^{-3} range. This paper describes the use of the nuclear track technique (NTT) (6-9) as a new way of determining the boron density in silicon. The NTT is based on the same nuclear reaction as α spectroscopy, but a different method of detection is used. Silicon crystals containing boron densities[1] between 10^{15} and 10^{20} cm^{-3} were analyzed by the technique and the results are compared with junction capacitance-voltage measurements and the work of Wagner (10).

In brief the NTT is based on the number of radiation-damaged areas produced in a dielectric material in contact with the silicon. These radiation-damaged areas are a result of α particles and ^7Li recoil particles (9) that are produced during thermal neutron bombardment of the boron by the nuclear reaction $^{10}B(n,\alpha)^7Li$. The latent radiation damaged areas or tracks are made visible in the dielectric material by chemically etching that material. Then the number of α tracks per unit area in the detector is determined and assumed proportional to the boron density (atoms/cm^3) in the silicon. The path length of the α particle [with a primary energy of 1.44 MeV (11)] in silicon is ~2.5 μm and that length times the area yields the volume sampled.

Experimental

Sample preparation.—Specimens for analysis were obtained from boron-doped silicon crystals grown by the Czochralski process with a <111> growth axis. Some of the specimens were prepared from wafers supplied by commercial vendors and others from wafers cut and polished at NBS. Prior to scribing or cutting into sections for analysis, four-probe resistivity measurements were made on the back side of the wafers following the standard procedure (12).

For most of the specimens, the uniformity of the resistivity across the wafer was measured. For other specimens the uniformity had been previously checked by one of the following measurements on a companion wafer cut from the same crystal: four-probe measurements at center and half-radius positions or spreading resistance measurements along a diameter. All wafers showed resistivity variations of less than 5% between center and half-radius positions and no fine structure was observed in the spreading resistance.

Analytical procedure.—In the analytical procedure, a square specimen, typically 7.5 mm on a side and 0.3 mm thick was sandwiched between two pieces of the detecting material, a cellulose acetate butyrate plastic (250 μm thick), vacuum heat sealed in polyethylene and irradiated in the thermal neutron pneumatic facilities of the NBS Research Reactor (13). The irradiation time and position in the reactor were dependent on the anticipated boron density. Time in the reactor ranged from 1 sec to 10 min for a typical thermal neutron flux of 1.33×10^{13} $n \cdot cm^{-2}$ sec^{-1}. Following irradiation, the detectors were separated from the silicon specimens and chemically etched in 6.5N NaOH for 5 min at 72°C. The etched detectors were then rinsed with distilled water and air dried. The detectors were mounted on microscope slides and the visible α tracks, as seen in Fig. 1, were counted wtih the aid of an optical transmission light microscope. The area for counting was 1500 μm^2; usually several such areas on the detector were counted and averaged to compute the boron density for the specimen.

[1] In the chemical literature, concentration (*i.e.*, μg/g) is the commonly used term, but herein density is used in referring to atoms/cm^3.

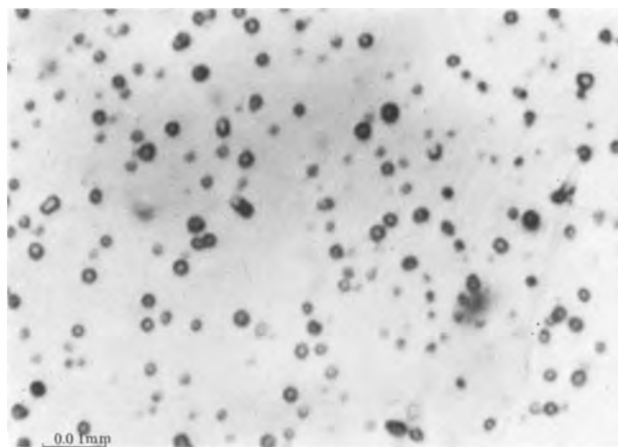

Fig. 1. Photomicrograph of α particle tracks in an etched cellulose acetate butyrate detector which was in contact with boron-doped silicon during neutron irradiation.

Standard reference materials, SRM 619 Trace Element Glass Standards, containing known densities of boron in glass (7) were simultaneously irradiated with the silicon samples. The boron density in the silicon was obtained by comparing the track count from the silicon with that from the boron in the SRM 619 Standards with a correction for the range difference of the α particle in the dissimilar matrixes (14). The correction is simply the ratio of the density of silicon (2.33 g/cm^3) to that of glass (2.5 g/cm^3). In later irradiations, a silicon sample previously analyzed with respect to the SRM's was used as a secondary standard.

Discussion of Results

In Fig. 2, the boron density by the nuclear track technique is plotted against specimen resistivity as determined by four-probe measurements. Also shown is the resistivity-dopant density relationship of Wagner (10) which was derived from measurements on silicon implanted with boron. The amount of boron retained in the silicon was determined by integration of data obtained from incremental sheet resistance and

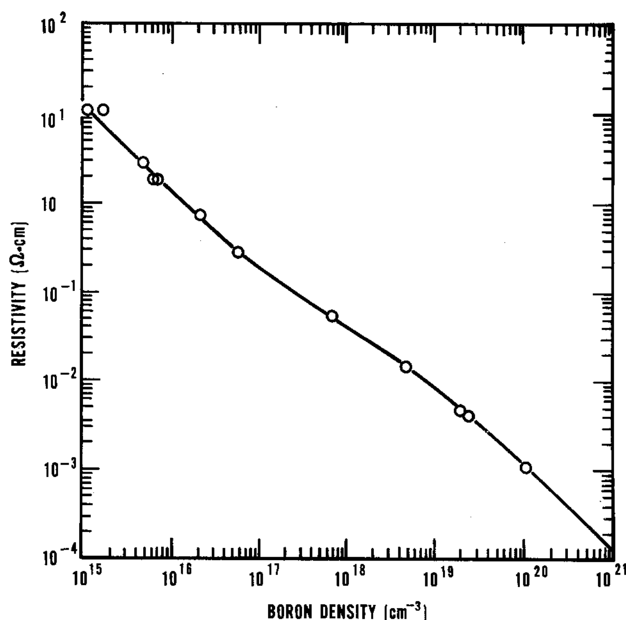

Fig. 2. Resistivity of p-type silicon at room temperature as a function of boron density determined by the nuclear track technique. Also shown is the resistivity-dopant density curve of Wagner. The error bars (1 std. dev.) associated with these data points lie within the symbols shown.

Hall effect measurements on layers which were sectioned by anodic oxidation. A mobility value as a function of boron density was derived which made the integrated dose equal to the implanted dose. The mobility expression was then used to calculate the curve shown in Fig. 2.

A boron density of about 10^{15} cm^{-3} (~8 ppb by weight) appears to be the lower limit of measurements by the nuclear track technique based on results obtained on a 135 ± 5 Ω · cm silicon sample. The Wagner curve predicts a boron density of 9×10^{13} cm^{-3} for this specimen compared to a value of 4.5×10^{14} cm^{-3} from the NTT measurements. The discrepancy at this point is due to interference from detector background. The interference is due to the α particle which originates in the oxygen present in the cellulose acetate butyrate *i.e.*, $^{17}O(n,\alpha)^{14}C$. Lithium and oxygen in the silicon also produce interfering α tracks during neutron irradiation, but these impurities do not interfere significantly until their concentrations are high, *i.e.*, ≥200 μg/g for lithium and ≥10 mg/g for oxygen. Since the maximum solubility of oxygen in silicon is 20 μg/g (3×10^{18} atoms/cm^3), oxygen in the silicon is not a factor in determining the lower limit of detection.

The accuracy and precision of the present results are illustrated by a graph of $1/\rho N$ as a function of boron density where ρ is the measured resistivity and N is the boron density determined by the nuclear track technique. The values are plotted in Fig. 3 along with others obtained from resistivity measurements (15) and junction capacitance-voltage (*C-V*) measurements (16) for boron density on wafers fabricated with the NBS-3 (17) and NBS-4 test patterns. The nuclear track technique data scatter somewhat at low boron densities but the general agreement with the junction *C-V* values and the Wagner mobility curve is apparent. One source of scatter is the fact that the lateral homogeneity of the boron was observed to vary as much as ±10% within the counting area.

The boron density by the track technique was compared with that obtained from the junction *C-V* method for companion slices from three of the silicon crystals for which data are shown in Fig. 3. The results are shown in Table I. The good agreement suggests that compensation by n-type impurities is probably not significant as the track technique measures total boron density whereas the junction *C-V* method measures the difference between the p- and n-type dopant densities.

Conclusions

The nuclear track technique has been shown to be a useful method for the determination of boron in silicon for boron densities in the range 10^{15}-10^{20} cm^{-3}. A plot of the resistivity of the silicon specimens as a function of the boron density determined by the track technique agrees with the trend of the Wagner curve relating resistivity to boron dopant density. Values of boron density from the track technique agree well with those obtained by the junction *C-V* method on companion slices from the same silicon crystals.

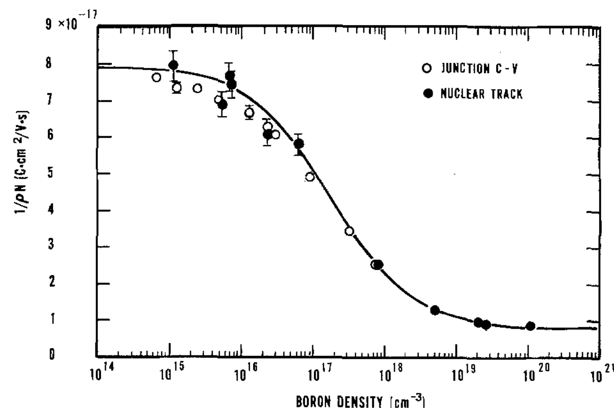

Fig. 3. Values of $1/\rho N$ (ρ = resistivity, N = boron density) at 300°K as a function of boron density obtained from nuclear track or junction *C-V* measurements. The solid curve is from the Wagner relationship between resistivity and dopant density. Error bars not shown in the ordinate direction are less than the size of the symbol. All error bars in the abscissa direction for boron density lie within the symbols.

Table I. Comparison of boron density by nuclear track and junction *C-V*

Crystal No.	Resistivity of NTT specimen (Ω · cm)	Boron density by NTT (cm^{-3})	Resistivity of j. C-V wafer (Ω · cm)	Boron density by j. C-V (cm^{-3})
521-22	2.91	5.01×10^{15}	3.06	4.67×10^{15}
521-53	0.73	2.26×10^{16}	0.72	2.22×10^{16}
521-62	0.054	7.30×10^{17}	0.055	7.15×10^{17}

Acknowledgment

The authors are indebted to D. R. Ricks for four-probe resistivity measurements, to R. L. Mattis for junction *C-V* measurements, to Y. M. Liu for wafer fabrication, and to M. G. Buehler for helpful comments on the manuscript.

This work was conducted as part of the Semiconductor Technology Program at NBS. Portions of this work were supported by the Defense Advanced Research Projects Agency (Order No. 2397, Program Code 7D10) and the NBS Office of Standard Reference Materials.

Manuscript submitted July 28, 1977; revised manuscript received Nov. 17, 1977.

Any discussion of this paper will appear in a Discussion Section to be published in the December 1978 JOURNAL. All discussions for the December 1978 Discussion Section should be submitted by Aug. 1, 1978.

Publication costs of this article were assisted by the National Bureau of Standards.

REFERENCES

1. K. Müller, R. Henkelmann, and H. Boroffka, *Nucl. Instrum. Methods*, **129**, 557 (1975).
2. J. F. Ziegler, B. L. Crowder, G. W. Cole, J. E. E. Baglin, and B. J. Masters, *Appl. Phys. Lett.*, **21**, 16 (1972).
3. J. F. Ziegler, G. W. Cole, and J. E. E. Baglin, *J. Appl. Phys.*, **43**, 3809 (1972).
4. G. Mezey, Z. Szökefalvi-Nagy, and Cs. Badinka, *Thin Solid Films*, **19**, 173 (1973).
5. H. Ryssel, H. Kranz, K. Müller, R. A. Henkelmann, and J. Biersack, *Appl. Phys. Lett.*, **30**, 399 (1977).
6. C. P. Bean, R. L. Fleischer, P. S. Swartz, and H. R. Hart, Jr., *J. Appl. Phys.*, **37**, 2218 (1966).
7. B. S. Carpenter, *Anal. Chem.*, **44**, 600 (1972).
8. R. L. Fleischer, P. B. Price, and R. M. Walker, "Nuclear Tracks in Solids: Principles and Applications," University of California Press, Berkeley, Calif. (1975).
9. J. S. Armijo and H. S. Rosenbaum, *J. Appl. Phys.*, **38**, 2064 (1967).
10. S. Wagner, *This Journal*, **119**, 1570 (1972).
11. K. H. Beckurts and K. Wirtz, "Neutron. Physics," p. 14, Springer-Verlag, Berlin (1964); This particular alpha particle energy is produced from the predominant (93.9%) branching of the $^{10}B(n_{th}, \alpha)^7Li$ reaction.
12. ASTM Designation F 84, "Annual Book of ASTM Standards," Part 43, American Society for Testing and Materials, Philadelphia (1977).
13. "Activation Analysis Section: Summary of Activities," P. D. LaFleur and D. A. Becker, Editors, NBS Tech Note 548, pp. 5, 88 (1970).
14. B. S. Carpenter and G. M. Reimer, Conference on Accuracy in Trace Analysis: Sampling, Sample Handling, and Analyses, Gaithersburg, Md., 1974, NBS Spec. Publ. 422, p. 457 (1976).
15. M. G. Buehler and W. R. Thurber, *IEEE Trans.*

Electron Devices, ed-23, 968 (1976).
16. R. L. Mattis and M. G. Buehler, This Journal, 124, 1918 (1977).
17. M. G. Buehler, "Semiconductor Measurement Technology," Microelectronic Test Pattern NBS-3 for Evaluating the Resistivity-Dopant Density Relationship of Silicon, NBS Spec. Publ. 400-22 (1976).

Solidus Isotherms and Isoconcentration Lines in the System Ga-In-Sb

Michel F. Gratton and John C. Woolley

Physics Department, University of Ottawa, Ottawa, Ontario Canada K1N 6N5

ABSTRACT

Solidus isotherms and isoconcentration lines have been experimentally determined for the Ga-In-Sb ternary diagram by means of the technique of annealing samples in the two-phase liquid-solid field and quenching, a method shown previously to give good results for the pseudobinary section. The results are compared with data predicted by the simple solution model. In this analysis, the linear temperature dependence of the interaction parameters $\alpha_{Ga\text{-}Sb}$, $\alpha_{In\text{-}Sb}$, $\alpha_{Ga\text{-}In}$, and $\alpha_{GaSb\text{-}InSb}$ has been examined and also the effect on the predicted data of variation in the values of these parameters. It is shown that while the model can give values of liquidus isotherms in good agreement with the available experimental data, the predicted solidus isotherms and isoconcentration lines are very different from the experimental data. No reasonable variation of the α parameters can eliminate this latter discrepancy and it is seen that in the case of this particular ternary system the simple solution model is of no value for prediction of solidus data.

Because of the possibility of using ternary III-V alloys in various technological applications, considerable interest has been focused during the last few years on the investigation and prediction of the relevant ternary phase diagrams. Following the model developed by Guggenheim (1), a number of workers (2-8) have made calculations for various parts of the general ternary diagrams. Much of the work has been concentrated on the form of the pseudobinary sections $A_xB_{1-x}C$ since these contain all of the solid phases of interest technologically and for which there exists a considerable amount of experimental data (9-10) for comparison with theoretically predicted values. Most of the remaining work has been concerned with the prediction of liquidus sheets and with solidus isoconcentration lines (*i.e.*, a line giving the composition values of points on the liquidus sheet which are in equilibrium with a solid phase of given composition), data which are of importance in the liquid phase epitaxy technique.

In the present work, the Ga-In-Sb diagram has been considered and experimental measurements made to determine the isoconcentration lines. These, together with liquidus isotherms previously determined (5, 8, 11), are compared with theoretical values obtained from the simple solution type of analysis carried out previously (5, 7, 8). The values of the input parameters have been carefully considered to see if any over-all agreement between experiment and theory is possible in this particular case.

Theory

For all of these types of ternary diagram, the data are calculated from the conditions for equilibrium between a general ternary liquid solution A-B-C (Ga-In-Sb in this case) and a pseudobinary solid solution AC-BC (GaSb-InSb here). The theory has been presented by various workers (2-8) and hence only the necessary final equations are given here

$$\ln \gamma_{AC} = \ln \frac{\gamma_A \gamma_C}{\gamma_A^{sl} \gamma_C^{sl}} + \ln 4 \frac{N_A N_C}{x} + \frac{\Delta S^F_{AC}}{RT} (T^F_{AC} - T) \quad [1a]$$

$$\ln \gamma_{BC} = \ln \frac{\gamma_B \gamma_C}{\gamma_B^{sl} \gamma_C^{sl}} + \ln 4 \frac{N_B N_C}{1 - x} + \frac{\Delta S^F_{BC}}{RT} (T^F_{BC} - T) \quad [1b]$$

$$RT \ln \gamma_{AC} = \alpha_{AC\text{-}BC} (1 - x)^2 \quad [2a]$$

$$RT \ln \gamma_{BC} = \alpha_{AC\text{-}BC} x^2 \quad [2b]$$

$$RT \ln \gamma_A = \alpha_{AB} N_B^2 + \alpha_{AC} N_C^2 + (\alpha_{AB} + \alpha_{AC} - \alpha_{BC}) N_B N_C \quad [3a]$$

$$RT \ln \gamma_B = \alpha_{AB} N_A^2 + \alpha_{BC} N_C^2 + (\alpha_{AB} + \alpha_{BC} - \alpha_{AC}) N_A N_C \quad [3b]$$

$$RT \ln \gamma_C = \alpha_{AC} N_A^2 + \alpha_{BC} N_B^2 + (\alpha_{AC} + \alpha_{BC} - \alpha_{AB}) N_A N_B \quad [3c]$$

where the γ's are activity coefficients, the α's interaction parameters, N_A, N_B, and N_C concentrations of the three elements, x the mole fraction of AC in the solid phase, and ΔS^F_j and T^F_j the entropy of fusion and melting temperature of the compound j.

Calculations

Vieland (12) has given the relation for the liquidus curve of a binary system A-C with a line compound AC as

$$\alpha_{AC} = -\frac{RT}{2(0.5 - c)^2} \left[\ln 4c(1 - c) + \frac{\Delta S^F_{AC}}{RT} (T^F_{AC} - T) \right] \quad [4]$$

where c is the atomic fraction of C. From this, Thur-

Key words: ternary phase diagram, simple solution model, solidus isotherms, solidus isoconcentration lines.

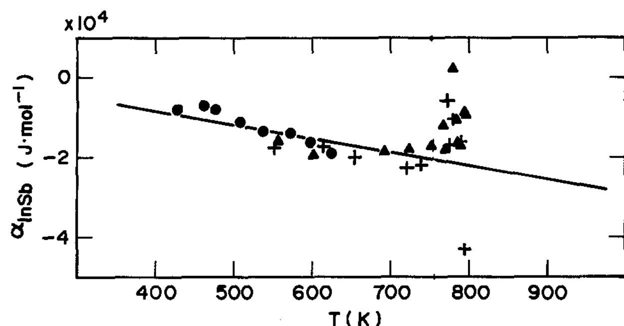

Fig. 1. InSb. The interaction parameter $\alpha_{In\text{-}Sb}$ as a function of temperature. The line shows the least squares fit. ● Hall (17), ▲ Liu and Peretti (16), + Pogodin and Dubinsky (18).

mond (14) has shown empirically that for Ga-As, α has a linear dependence on temperature and has suggested that the same form applies for α in other III-V systems if only in the range where the saturated liquid phase is dilute, *i.e.*, well away from the compound AC. Ilegems and Panish (15) have indicated that this linear behavior is due to the liquid phase being effectively a simple solution and they give evidence that the binary liquid III-V systems are effectively simple over a large concentration range.

Here, the binary phase diagram data of Liu and Peretti (16), Hall (17), and Pogodin and Dubinsky (18) for the In-Sb system have been analyzed using Eq. [4] with T^F_{AC} and ΔS^F_{AC} equal to 798°K and 59.91 J·mole⁻¹·°K⁻¹, respectively (19). To produce consistent data, the resutls of Pogodin and Dubinsky were corrected by −8°K to take into account the accepted melting point value of InSb. The variation of α_{InSb} with T for the composition range from pure In to the eutectic point (32 atomic percent In) is shown in Fig. 1. The data in the temperature range 400°-770°K have been fitted by a least squares method to the relation $\alpha = p + qT$ and the values obtained are given in Table I. Above $T = 770$°K, the data clearly deviate from linear behavior and this may be explained by the suggestion that linearity applies only in dilute solutions. However, the values of $\alpha_{In\text{-}Sb}$ are quite sensitive to small variations in experimental values in this range, and it was found by varying T by ±5°K or c by ±0.02 that for values somewhere in these ranges the value of $\alpha_{In\text{-}Sb}$ was brought back to the linear form indicated above. Thus it is possible that the apparent deviation from linear form at concentrations close to InSb is due to small experimental errors in the observed values.

A similar analysis of the available data for the Ga-Sb system (17, 20-22) has been carried out using $T^F_{AC} = 985$°K and $\Delta S^F_{AC} = 66.11$ J·mol⁻¹·°K⁻¹ (19). Similar results were obtained and the resulting value of $\alpha_{Ga\text{-}Sb}$ is given in Table I.

Values are needed also for the parameters $\alpha_{Ga\text{-}In}$ and $\alpha_{GaSb\text{-}InSb}$. In previous work, the binary diagram data of Bros *et al.* (23) and Macur *et al.* (24) are usually quoted for the evaluation of $\alpha_{Ga\text{-}In}$ while the value of $\alpha_{GaSb\text{-}InSb}$ is usually obtained by a fit to the pseudobinary liquidus and solidus data (9) or from the calculations of Foster and Woods (25). In all cases the parameter values have been assumed independent of T. Joullié *et al.* (8) determined both $\alpha_{Ga\text{-}In}$ and $\alpha_{GaSb\text{-}InSb}$ from the pseudobinary data by solving equations equivalent to the present Eq. [1], [2], and [3] for composition values from the liquidus and solidus curve. However, they used the data for one temperature only and again assumed that $\alpha_{Ga\text{-}In}$ and $\alpha_{GaSb\text{-}InSb}$ were independent of temperature.

Here, the pseudobinary liquidus and solidus data have been used to determine both $\alpha_{Ga\text{-}In}$ and $\alpha_{GaSb\text{-}InSb}$ as a function of temperature over the range between the melting points of the two compounds. At each temperature, appropriate composition values from the liquidus and solidus curves (9) were inserted in Eq. [1], [2], and [3] and values of $\alpha_{Ga\text{-}In}$ and $\alpha_{GaSb\text{-}InSb}$ determined. There was appreciable scatter in the graphs of α *vs.* T for each case, as the α values were very sensitive to the values of x used in the calculations. However, it was found that in each case the value of α could be written as a linear function of T and the values determined by least squares fit are given in Table I.

For comparison purposes, Table I gives the expressions for $\alpha_{Ga\text{-}Sb}$, $\alpha_{In\text{-}Sb}$, $\alpha_{Ga\text{-}In}$, and $\alpha_{GaSb\text{-}InSb}$ determined here and also those used by Blom and Plaskett (5), Panish and Ilegems (7), and Joullié *et al.* (8). For ease of comparison, values are given for each α at 650° and 900°K.

Using the values of the various α's derived above, Eq. [1], [2], and [3] were solved with sets of values of N_{Ga}, N_{In}, and N_{Sb} over the whole ternary diagram to yield values of T and x. The values were then appropriately interpolated to give liquidus and solidus isotherms and solidus isoconcentration lines for the Ga-In-Sb system and the curves so obtained are shown in Fig. 2 and 5. The liquidus isotherms are found over most of the composition range to be in fairly good agreement with those determined previously (5, 8), even though, as is seen from Table I, the α values used were in some cases rather different. It appears that the predicted isotherms are not in general very sensitive to the values of α's used. The main discrepancies between the present results and those of Blom and Plaskett (5) and Joullié *et al.* (8) are at points close to the pseudobinary section. The present results are tied to the measured pseudobinary data by the method used for determining $\alpha_{Ga\text{-}In}$ and $\alpha_{GaSb\text{-}InSb}$ and hence will be in better agreement with those experimental data. This is discussed further below.

Experimental Methods and Results

Experimental results for the liquidus isotherms are already available (5, 8, 11) and are shown in Fig. 2. It is seen that there is reasonably good agreement between the available experimental data and the present theoretical values. The experimental points of Blom and Plaskett (5) for 600°C do not fit well with the present curves but neither are they in good agreement with the values in the pseudobinary section (9, 26, 27).

The present experimental work has been the determination of solidus isotherms and hence isoconcentra-

Table I. Interaction parameters for the ternary system Ga-In-Sb and typical values at two temperatures, 650° and 900°K

Source	$\alpha_{Ga\text{-}Sb}$ (J · mol⁻¹)	$\alpha_{In\text{-}Sb}$ (J · mol⁻¹)	$\alpha_{Ga\text{-}In}$ (J · mol⁻¹)	$\alpha_{GaSb\text{-}InSb}$ (J · mol⁻¹)
This study	23,824 − 32.38T	4,895 − 33.72T	12,000 − 12.97T	−2,816 + 11.42T
650°K	2,774	−17,025	3,569	4,610
900°K	−5,322	−25,455	326.4	7,466
Joullié *et al.* (8)	25,062 − 34.43T	33,472 − 83.68T	8,368	6,694
650°K	2,680	−20,920	8,368	6,694
900°K	−5,929	−41,840	8,368	6,694
Panish and Ilegems (7)	19,665 − 25.10T	14,225 − 50.21T	4,435	7,950
650°K	3,347	−18,410	4,435	7,950
900°K	−2,929	−30,962	4,435	7,950
Blom and Plaskett (5)	26,024 − 33.93T	33,472 − 69.79T	4,460	6,276
650°K	3,969	−11,891	4,460	6,276
900°K	−4,515	−29,338	4,460	6,276

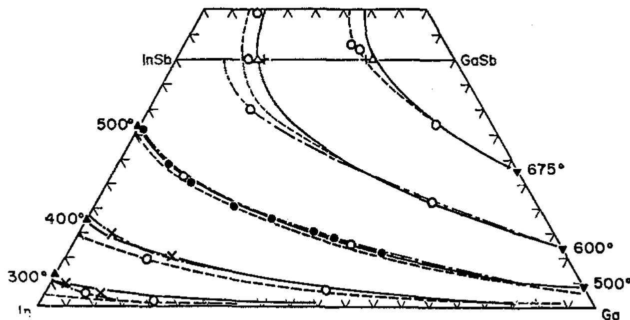

Fig. 2. Liquidus isotherms in the Ga-In-Sb ternary phase-diagram. (Temperatures in °C). Theoretical calculations: —— this study, ------ Blom and Plaskett (5), — — — Joullié *et al.* (8). Experimental determination: ○ Blom and Plaskett (5), ● Antypas (11), × Joullié *et al.* (8), ▲ Liu and Peretti (16), △ Wooley and Lees (9), + Koster and Thoma (26), ▼ Koster and Thoma (21).

tion lines in the region of the diagram between the pseudobinary section and the Ga-In binary (*i.e.*, $0 \leq N_{Sb} \leq 0.5$) The technique used was that described previously for the determination of the solidus curve of the pseudobinary section and which was found to give good agreement with standard DTA measurements (9) and also with data from "first-to-freeze" analysis of stoichiometric melt growth samples (27). Samples of various compositions were weighed out, sealed under a reduced pressure of argon in quartz ampuls, and melted by holding for 1 or 2 hr at a temperature above the melting point of the compounds (usually 800°C). The temperature of each sample was then reduced to the required values and the sample annealed to equilibrium. In the two-phase liquid-solid field below the liquidus sheet, because the solid phase is very finely dispersed throughout the liquid phase, annealing for 24 hr was quite sufficient to attain this equilibrium condition. A small number of samples were annealed for times up to 20 days but showed no change from the condition observed after 24 hr annealing. Over the anneal period the temperature was kept constant at ±2°C, and its mean value determined to ±2°C by means of a calibrated Pt-Pt 13% Rh thermocouple. At the end of the anneal, the sample was rapidly quenched by plunging into an oil bath so that the equilibrium solid phase was frozen in and no solid diffusion occurred. The lines of this solid phase were easily determined in an x-ray powder photograph. The homogeneity of this solid phase was clearly demonstrated by the sharpness of the x-ray lines, the K_α doublet being clearly resolved, and by the fact that no variation could be observed in different x-ray specimens taken from the same quenched sample. The lattice parameter of the equilibrium solid phase and hence its composition were thus determined (9). The position of the phase on the pseudobinary section plus the composition of the initial sample clearly define the position of the tie-line on the phase diagram. To check further the consistency of the results, in one or two cases further samples were investigated, which lay on the tie-lines so determined. In each case, the solid composition found was in good agreement with the previous value, confirming that a two-phase tie-line had been obtained. To determine the liquid end of the tie-line, knowledge of the liquidus sheet is required. Since, as indicated above, the predicted liquidus isotherms are in good agreement with the available experimental data, these have been used here to determine the composition of the equilibrium liquid phase, being the point of intersection of the tie-line and the corresponding liquidus isotherm. A typical set of tie-lines, for $T = 525$°C, is shown in Fig. 3, while the data for the other temperatures investigated are given in Table II.

From these data, solidus isotherms can be drawn, and examples plotting composition of solid phase (x)

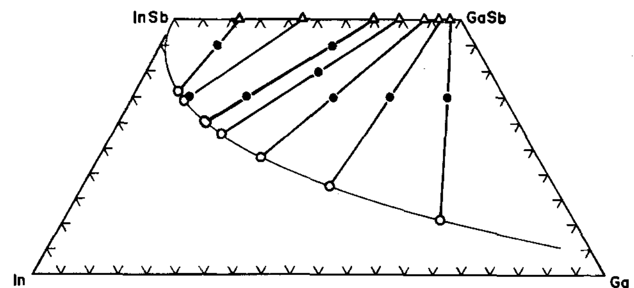

Fig. 3. The 525°C liquidus isotherm and tie-lines of the Ga-In-Sb system. ● Initial composition, △ solidus composition, ○ liquidus composition.

vs. gallium concentration of equilibrium liquid phase (N_{Ga}) at fixed temperature are shown in Fig. 4, both experimental values from the above data and predicted values from the theoretical analysis being shown. Finally, from these solidus isotherms, solidus isoconcentration lines have been constructed and are shown in Fig. 5, again both experimental and theoretical values being given.

Discussion

The input data for the calculated phase diagram results are mainly in the four α parameters. Here, each has been assumed to vary linearly with temperature and its value obtained from the known data of an appropriate binary or pseudobinary section. Although previously it had been suggested that these

Table II. Compositions of samples annealed in liquid-solid two-phase field at temperature T and of resulting equilibrium solid and liquid phases. Values give tie-lines and points on solidus isotherms

	Initial composition			Solidus composition			Liquidus composition		
T (°C)	N_{Ga}	N_{In}	N_{Sb}	N_{Ga}	N_{In}	N_{Sb}	N_{Ga}	N_{In}	N_{Sb}
380	0.050	0.550	0.400	0.050	0.450	0.500	0.05	0.82	0.13
	0.100	0.550	0.350	0.135	0.365	0.500	0.05	0.82	0.13
	0.200	0.450	0.350	0.255	0.245	0.500	0.11	0.79	0.10
	0.300	0.300	0.400	0.355	0.145	0.500	0.14	0.77	0.09
	0.350	0.300	0.350	0.435	0.065	0.500	0.19	0.73	0.08
	0.550	0.100	0.350	0.485	0.015	0.500	0.70	0.29	0.01
430	0.050	0.550	0.400	0.050	0.450	0.500	0.05	0.76	0.19
	0.100	0.550	0.350	0.150	0.350	0.500	0.05	0.76	0.19
	0.200	0.450	0.350	0.295	0.205	0.500	0.09	0.74	0.17
	0.150	0.650	0.200	0.360	0.140	0.500	0.12	0.72	0.16
	0.195	0.550	0.255	0.365	0.135	0.500	0.13	0.72	0.15
	0.300	0.300	0.400	0.370	0.130	0.500	0.13	0.72	0.15
	0.200	0.550	0.250	0.380	0.120	0.500	0.14	0.71	0.15
	0.350	0.300	0.350	0.435	0.065	0.500	0.22	0.66	0.12
	0.450	0.200	0.350	0.470	0.030	0.500	0.42	0.51	0.07
	0.550	0.100	0.350	0.470	0.030	0.500	0.71	0.26	0.03
475	0.050	0.550	0.400	0.065	0.435	0.500	0.03	0.70	0.27
	0.100	0.550	0.350	0.165	0.335	0.500	0.06	0.69	0.25
	0.200	0.450	0.350	0.310	0.190	0.500	0.11	0.66	0.23
	0.300	0.300	0.400	0.380	0.120	0.500	0.15	0.64	0.21
	0.350	0.300	0.350	0.435	0.065	0.500	0.25	0.58	0.17
	0.450	0.200	0.350	0.465	0.035	0.500	0.42	0.46	0.12
	0.550	0.100	0.350	0.480	0.020	0.500	0.68	0.26	0.06
525	0.100	0.450	0.450	0.115	0.385	0.500	0.07	0.57	0.36
	0.100	0.550	0.350	0.225	0.275	0.500	0.09	0.57	0.34
	0.200	0.450	0.350	0.350	0.150	0.500	0.15	0.55	0.30
	0.300	0.250	0.450	0.350	0.150	0.500	0.15	0.55	0.30
	0.300	0.300	0.400	0.395	0.105	0.500	0.19	0.53	0.28
	0.350	0.300	0.350	0.440	0.060	0.500	0.28	0.49	0.23
	0.450	0.200	0.350	0.465	0.035	0.500	0.43	0.40	0.17
	0.550	0.100	0.350	0.485	0.015	0.500	0.66	0.23	0.11
550	0.200	0.450	0.350	0.390	0.110	0.500	0.18	0.49	0.33
	0.300	0.300	0.400	0.400	0.100	0.500	0.21	0.48	0.31
	0.350	0.300	0.350	0.450	0.050	0.500	0.29	0.44	0.27
	0.400	0.200	0.400	0.450	0.050	0.500	0.33	0.42	0.25
	0.450	0.200	0.350	0.495	0.005	0.500	0.41	0.37	0.22
	0.550	0.100	0.350	0.495	0.005	0.500	0.63	0.23	0.14
	0.650	0.050	0.300	0.500	0.000	0.500	0.81	0.10	0.09
600	0.250	0.350	0.400	0.425	0.075	0.500	0.24	0.36	0.40
	0.300	0.300	0.400	0.435	0.065	0.500	0.27	0.35	0.38
	0.350	0.300	0.350	0.450	0.050	0.500	0.34	0.33	0.33
	0.400	0.200	0.400	0.460	0.040	0.500	0.35	0.33	0.32
	0.450	0.200	0.350	0.480	0.020	0.500	0.44	0.28	0.28
	0.550	0.100	0.350	0.495	0.005	0.500	0.60	0.19	0.21
	0.650	0.050	0.300	0.495	0.005	0.500	0.76	0.08	0.16
650	0.380	0.170	0.450	0.465	0.035	0.500	0.35	0.22	0.43
	0.400	0.200	0.400	0.470	0.030	0.500	0.40	0.20	0.40
	0.450	0.100	0.450	0.470	0.030	0.500	0.42	0.20	0.38
	0.490	0.110	0.400	0.495	0.005	0.500	0.49	0.17	0.34
	0.550	0.100	0.350	0.495	0.005	0.500	0.57	0.13	0.30
	0.650	0.050	0.300	0.500	0.000	0.500	0.69	0.06	0.25

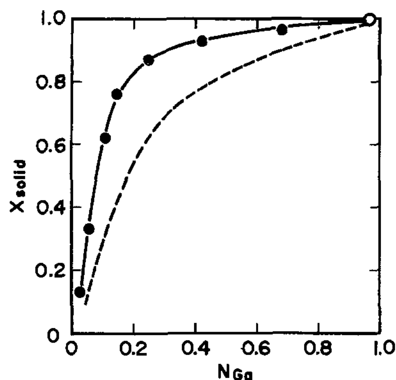

Fig. 4. The 475°C solidus isotherm of the Ga-In-Sb system. —●— Present experimental data, ○ Koster and Thoma (21), ------ present theoretical calculation.

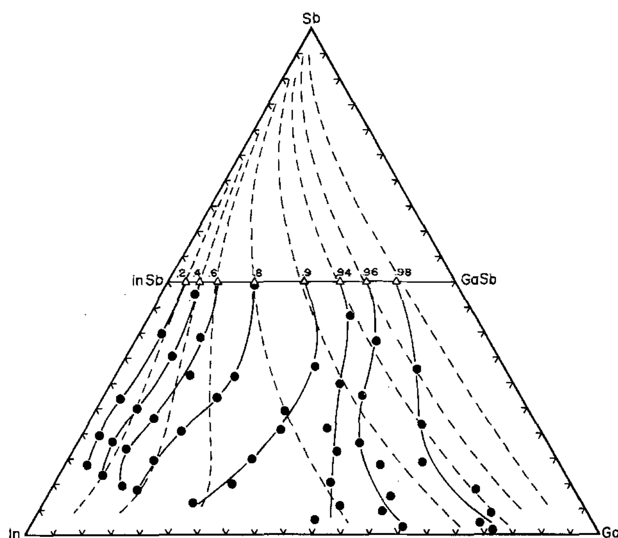

Fig. 5. Solidus isoconcentration lines in the Ga-In-Sb ternary phase diagram. —●— Present experimental data, ------ present theoretical calculation.

α values could be obtained from ranges of dilute solution only, it appears that consistent values of α can probably be obtained over a very wide range of composition of the relevant section as indicated by Ilegems and Panish (15). Comparison of the predicted data obtained with the present values of α and those of previous workers (5, 7, 8) indicates that the form of the liquidus isotherms is not very sensitive to the exact value of α.

In the present work, the method of determining $\alpha_{\text{Ga-In}}$ and $\alpha_{\text{GaSb-InSb}}$ ensures that a good fit to the data of the pseudobinary section is obtained, which was not the case in some of the previous work. In all cases, the fit to the liquidus isotherms in the range 350°-500°C is good. However, the present choice of α values gives a slightly worse fit to the 300°C liquidus isotherm data than that of Blom and Plaskett (5) and Joullié *et al.* (8). Thus even for the liquidus isotherms, it appears that no single set of α values gives an excellent fit over the whole range of composition considered here, but that reasonable agreement with experiment can be obtained with a careful choice of α values.

One factor which may influence the fit to experimental data in this particular case is the value of the ΔC_p term in Vieland's equation for chemical potential, *i.e.*

$$\mu_{AC}^{so} = \mu_A^{sl} + \mu_C^{sl} - \Delta S^F_{AC}(T^F_{AC} - 1)$$

$$+ \Delta C_P \left[T^F_{AC} - T - \ln\left(\frac{T^F_{AC}}{T}\right)\right] \quad [5]$$

Throughout the analysis the ΔC_p term has been assumed to be negligible. While this is true in most cases, calculation shows that for the case of In-Sb the ΔC_p term can at low temperatures become a nonnegligible part of the right-hand side of Eq. [5], (*e.g.* 6% at 500°K). Thus neglecting this term could have some effect on the value of $\alpha_{\text{In-Sb}}$ calculated and on the predicted form of the low temperature liquidus isotherms.

In the case of the solidus isotherms and isoconcentration lines, as previously suggested by Panish and Ilegems (4) and by Antypas (11), there is very little agreement between measured and predicted values (Fig. 5). Varying the input values of the α parameters over the range given in Table I changed the predicted curves to a small extent but in no case could agreement with experiment be obtained, since the differences between experimental and theoretical values were always very large. While the experimentally determined values of the solidus isotherms and isoconcentration lines required a knowledge of the liquidus isotherms, as indicated above, the predicted values in that case are sufficiently close to the experimental values that little error is to be expected in the results quoted here. No reasonable set of liquidus isotherms can be designed which would cause the experimental solidus results to agree with the predicted values.

Thus it is clear that for the Ga-In-Sb ternary system the simple solution model has serious limits on its usefulness. It can be used to give reasonable values of liquidus isotherms, but solidus data predicted by this method in the temperature range 300° to 712°C are of no practical value.

In a review by Panish and Ilegems (7) of a number of these alloy systems, it is indicated that fair agreement between predicted and experimental values of the solidus parameters can be obtained for the ternary alloys involving phosphorus and possibly aluminum but that the agreement is poor for the heavier systems such as $Ga_xIn_{1-x}As$ and $InAs_ySb_{1-y}$. Clearly the use of the simple solution model to predict solidus data is only of value if one can predict the cases for which the model gives valid results. One possible factor in this consideration is the temperature, since it would appear that the lower the range of temperature concerned the worse is the agreement. Thus one possible reason for the discrepancy between prediction and experiment is the ΔC_p term and the associated Vieland equation. But as indicated above the ΔC_p term is significant only below 600°K and hence should have little effect even in the upper temperature range of the solid phase of the $Ga_xIn_{1-x}Sb$ alloys. However, Jordan and Weiner (28) have shown that Vieland's equation is exact only if α is a linear function of temperature and as has been seen above, this may not be the case here.

A second possible factor in this temperature range is that association in the liquid phase may become important (29). However Jordan has indicated that this effect is mainly of importance when the liquidus curve of the appropriate binary system shows a cusp around the line compound (*e.g.*, Zn-Te, Cd-Te) and should not be important for systems showing the smooth "convex" liquidus curves typical of most III-V combinations.

Manuscript submitted July 11, 1977; revised manuscript received Nov. 22, 1977.

Any discussion of this paper will appear in a Discussion Section to be published in the December 1978 JOURNAL. All discussions for the December 1978 Discussion Section should be submitted by Aug. 1, 1978.

Publication costs of this article were assisted by the University of Ottawa.

REFERENCES

1. E. A. Guggenheim, "Mixtures," Oxford University Press, Oxford (1952).

2. G. B. Stringfellow and P. E. Greene, *J. Phys. Chem. Solids*, **30**, 1779 (1969).
3. G. A. Antypas and L. W. James, *J. Appl. Phys.*, **41**, 2165 (1970).
4. M. B. Panish and M. Ilegems, "Proceedings of 1970 Symposium on GaAs," p. 67, The Institute of Physics and The Physical Society, London (1971).
5. G. M. Blom and T. S. Plaskett, *This Journal*, **118**, 1831 (1971).
6. T. Y. Wu and G. L. Pearson, *J. Phys. Chem. Solids*, **33**, 409 (1972).
7. M. B. Panish and M. Ilegems, in "Progress in Solid State Chemistry," Vol. 7, H. Reiss and J. O. McCaldin, Editors, p. 39, Pergamon Press, Oxford (1972).
8. A. Joullié, R. Dedies, J. Chevrier, and G. Bougnot, *Rev. Phys. Appl.*, **9**, 455 (1974).
9. J. C. Woolley, in "Compound Semiconductors," Vol. 1, R. K. Willardson and H. L. Goering, Editors, p. 3, Reinhold Publishing Corp., New York (1962).
10. G. B. Stringfellow, *J. Phys. Chem. Solids*, **33**, 665 (1972).
11. G. A. Antypas, *J. Cryst. Growth*, **16**, 181 (1972).
12. L. J. Vieland, *Acta Met.*, **11**, 137 (1963).
13. I. Prigogine and R. Defay, "Chemical Thermodynamics," Longmans, Green and Co., London (1954).
14. C. D. Thurmond, *J. Phys. Chem. Solids*, **26**, 785 (1965).
15. M. Ilegems and M. B. Panish, *ibid.*, **35**, 409 (1974).
16. T. S. Liu and E. A. Peretti, *Trans. Am. Soc. Metals*, **44**, 539 (1952).
17. R. N. Hall, *This Journal*, **110**, 385 (1963).
18. S. A. Pogodin and S. A. Dubinsky, *Izv. Sektora. Fiz.-Khim. Anal.*, **17**, 204 (1949).
19. B. D. Lichter and P. Sommelet, *Trans. AIME*, **245**, 99 (1969).
20. I. G. Greenfield and R. L. Smith, *J. Metals*, **7**, 351 (1955).
21. W. Koster and B. Thoma, *Z. Metallk.*, **46**, 291 (1955).
22. A. G. Kalyuzhnaya, I. K. Polushina, and D. N. Tret'yakov, *Russ. J. Inorg. Chem.*, **9**, 813 (1964).
23. J. P. Bros, R. Castanet, and M. Lafitte, *Compt. Rend., Serie C*, **264**, 1804 (1967).
24. G. J. Macur, R. K. Edwards, and P. G. Wahlbeck, *J. Phys. Chem.*, **72**, 1047 (1968).
25. L. M. Foster and J. F. Woods, *This Journal*, **118**, 1175 (1971).
26. W. Koster and B. Thoma, *Z. Metallk.*, **46**, 293 (1955).
27. F. A. Trumbore, P. E. Freeland, and A. D. Mills, *This Journal*, **109**, 1 (1962).
28. A. S. Jordan and M. E. Weiner, *J. Phys. Chem. Solids*, **36**, 1335 (1975).
29. A. S. Jordan, *Met. Trans.*, **1**, 239 (1970).

Purification and Characterization of Metallurgical Silicon

T. L. Chu,* G. A. van der Leeden, and H. I. Yoo

Southern Methodist University, Dallas, Texas 75275

ABSTRACT

Metallurgical-grade silicon is a convenient starting material for the preparation of solar cell-grade silicon. The purification of metallurgical silicon by the treatment of its melt with gaseous reagents and in some cases followed by unidirectional solidification, has been investigated. The purified material was analyzed for major impurities by the atomic absorption technique. Single crystals have been prepared from purified metallurgical silicon by the Czochralski technique, and their electrical properties, such as electrical resistivity, carrier mobility, and diffusion length, were measured.

At present, silicon solar cells are manufactured from semiconductor-grade single crystalline silicon, doped to a carrier concentration of about 10^{16} cm^{-3}, by the diffusion technique. Semiconductor-grade silicon is produced from the metallurgical-grade material (about 98% purity) by (*i*) the conversion of silicon into trichlorosilane, (*ii*) the purification of trichlorosilane, and (*iii*) the thermal reduction of trichlorosilane with hydrogen. This sequence of processing is tedious and expensive, and the cost of silicon is increased from $1/kg to $60/kg. The use of semiconductor-grade silicon is a major factor contributing to the high cost of solar cells. It is generally recognized that the purity of silicon required for solar cells is considerably less than the purity of semiconductor-grade silicon. The development of solar cell-grade silicon at a cost significantly below that of semiconductor-grade silicon is essential for the terrestrial utilization of solar energy.

Metallurgical silicon is a convenient starting material for the preparation of solar cell-grade silicon. It contains aluminum (up to about 0.75% by weight) and iron (up to about 0.5%) as the major impurities; other impurities include boron, chromium, copper, magnesium, manganese, nickel, titanium, and vanadium at concentrations of up to several hundred parts per million. Most metallic impurities have deep levels in silicon and act as traps or recombination centers with large cross sections for capture of minority and majority carriers. These impurities reduce the minority carrier lifetime and must be removed as completely as possible.

To overcome the high cost of purification of metallurgical silicon via the halide intermediates, several direct purification techniques were attempted during the fifties. For example, the treatment of pulverized metallurgical silicon with aqua regia, sulfuric acid, hydrofluoric acid, etc., has been claimed to produce silicon suitable for microwave diodes (1). The gettering of molten metallurgical silicon with fused silicates has been reported to reduce the concentrations of iron and aluminum from 4.4 and 1.8% to 1.2 and 0.8%, respectively (2). Also, the treatment of molten metallurgical silicon with an equimolar mixture of oxygen and hydrogen chloride has been found to increase the purity from 98 to 99.99% (3).

During the past few years, there have been renewed interests in the direct purification of metallurgical silicon for solar cell purposes. For example, the zone-refining, crystal pulling, and other unidirectional solidification techniques have been shown to be effective in removing substantially the metallic impurities because of their low segregation coefficients in silicon (4-7). The chemical treatment of molten metallurgical silicon has also been reexamined (8-9). Although single crystals have been grown from purified metallurgical silicon to fabricate solar cells, their electrical properties, such as carrier mobility and diffusion length, have not been characterized.

* Electrochemical Society Active Member.

Key words: chemical treatment, diffusion length, Hall mobility, unidirectional solidification.

In this work, the purification of metallurgical silicon by the treatment of the melt with chlorine, a chlorine oxygen mixture, hydrogen chloride, and hydrogen fluoride has been further investigated, and the results compared with the earlier work. Also, in some experiments, the chemical treatment of the melt was followed immediately by unidirectional solidification in a one-step process. Furthermore, single crystals have been grown from purified metallurgical silicon, and their electrical properties, such as Hall mobility-temperature relation and diffusion length, were measured.

Thermochemical Considerations

The chemical treatment technique is based on the reactivity of the impurities in molten metallurgical silicon toward halogens or hydrogen halides to form volatile halides. The available information on the free energy of formation, in kilocalories/mole, of the halides of silicon and the major impurities in metallurgical silicon at 1700 °K is summarized in Table I (10-12). Since all chlorides have negative and relatively large free energies of formation and are volatile at the melting point of silicon, the treatment of molten metallurgical silicon with chlorine should result in considerable purification. Also, chemical equilibrium is presumably established during the chemical treatment due to the high temperature used. Thus the reaction between aluminum and chlorine is thermochemically more favorable than that between silicon and chlorine, while the reaction between iron and chlorine is less favorable than that between silicon and chlorine.

Hydrogen chloride or hydrogen fluoride also reacts with silicon and major impurities in metallurgical silicon, such as aluminum and iron, to form chlorides or fluorides. The standard free energy changes of these reactions, in kilocalories/mole, at 1700°K are summarized in Table II. The data indicate that aluminum can be preferentially removed and that iron is essentially inert under these conditions. However, the formation of volatile iron trichloride becomes more favorable by using a mixture of oxygen and hydrogen chloride according to the equation

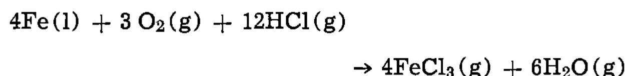

$$4Fe(l) + 3\,O_2(g) + 12HCl(g) \rightarrow 4FeCl_3(g) + 6H_2O(g)$$

The standard free energy change of this reaction at 1700°K is −30.5 kcal/mole of iron. On the other hand, silicon and boron will compete for oxygen since the free energies of formation of silicon dioxide (s), silicon monoxide (g), and boron oxide (g) at 1700°K are −146, −60, and −183 kcal/mole, respectively. The preferential removal of boron from molten silicon by water vapor or oxygen has been demonstrated (13).

Experimental and Results

Apparatus and chemical analysis.—The apparatus used for the chemical treatment of molten metallurgical silicon and the unidirectional solidification of the resulting melt is shown schematically in Fig. 1. It consisted of a fused silica tube of 69 mm ID containing a silica crucible in a graphite susceptor, and gas inlet tubes were provided to flow argon through the fused silica tube and to introduce the gaseous reagent into the melt. To carry out the purification process, metallurgical silicon was placed in the fused silica crucible, and with argon flowing through the silica tube, the graphite susceptor was heated externally with an rf generator. After the silicon became molten, the reagent was bubbled through the melt until about 10% of the silicon had been reacted and volatilized. When unidirectional solidification of the melt was desirable, the graphite susceptor was slowly lowered out of the rf coil so that the melt solidified from the bottom of the charge in the upward direction.

Table I. Free energy of formation, kilocalories/mole, of halides of aluminum, boron, iron, and silicon at 1700°K

Fluorides		Chlorides		Bromides		Iodides	
AlF_3	−261.8	$AlCl_3$	−116.4	$AlBr_3$	−91.6	AlI_3	−45.2
BF_3	−246.3	BCl_3	−75.7	BBr_3	−40.0	BI_3	13.4
FeF_2	−105.6	$FeCl_2$	−49.2	$FeBr_2$	−40.4	FeI_2	−15.7
FeF_3	−181.4	$FeCl_3$	−50.9	$FeBr_3$	—	FeI_3	—
SiF_4	−327.3	$SiCl_4$	−104.2	$SiBr_4$	—	SiI_4	—

Table II. Free energy change, kilocalories/mole, of the reaction $M\ (l) + nHX\ (g) \rightarrow MX_n\ (g) + n/2\ H_2\ (g)$ at 1700°K

M	n	X = F	X = Cl
Al	3	−60.7	−41.1
B	3	−45.2	−0.4
Fe	3	19.7	24.4
Si	4	−59.2	−3.9

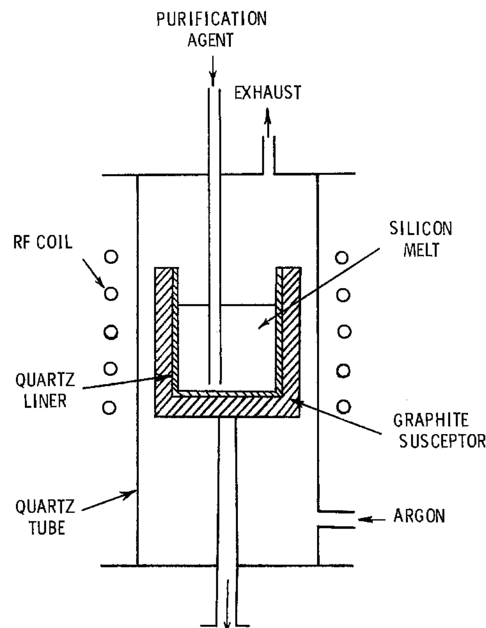

Fig. 1. Schematic diagram of the apparatus for the purification of metallurgical silicon.

The sampling of chemically treated metallurgical silicon for analysis is important in order to obtain meaningful results. Since a small amount of silicon (<1g) is generally used for analysis and the solidified material after chemical treatment is highly inhomogeneous due to the small segregation coefficients of impurities in silicon, improper sampling could result in a considerable error. To overcome this problem, a relatively small amount of metallurgical silicon, 20-25g, was used in the chemical treatment experiments, and the entire charge was dissolved in a nitric acid-hydrofluoric acid mixture. Aliquots of these solutions were analyzed for aluminum and iron, the major impurities in metallurgical silicon, by the atomic absorption technique. Some results on the effectiveness of oxygen, chlorine, a chlorine-oxygen mixture, and hydrogen fluoride for the purification of metallurgical silicon are shown in Table III. It appears that chlorine and chlorine-oxygen mixtures are similarly effective in reducing substantially the concentration of aluminum in metallurgical silicon, in agreement with the results of Dosaj *et al.* (9). However, no appreciable change in the concentration of iron was observed in all

Table III. Impurity concentration, parts per million by weight, in chemically treated metallurgical silicon

	Metal silicon	O_2 treat.	Cl_2 treat.	$Cl_2 + O_2$ treat.	HF treat.
Al	3000	590	<50	<50	100
Fe	3400	2900	2300	2500	2700

cases. These results may be related to the thermochemical data discussed previously. Since aluminum is chemically more reactive than silicon, chemical treatment of the melt is effective for the preferential removal of aluminum from metallurgical silicon. The chemical treatment technique cannot reduce the concentration of iron in silicon to any appreciable extent due to the stronger reactivity of silicon. The ineffectiveness of chemical treatment for the removal of iron has been reported by Hunt *et al.* (6); however, considerably lower iron content in chemically treated metallurgical silicon has been reported by others (3, 9) due presumably to improper sampling techniques.

When the purification of metallurgical silicon was carried out by a combination of chemical treatment and unidirectional solidification, the resulting material was cut into wafers perpendicular to the direction of solidification. Wafers from four different positions (bottom, 1/3 from the bottom, 2/3 from the bottom, and the top) were used for analysis by the atomic absorption technique. The results of analysis of chlorine-treated and unidirectionally solidified metallurgical silicon are shown in Table IV; it is noted that the concentration of iron in the bottom half of the charge has been reduced substantially due to its low segregation coefficient (14). The emission analysis of two sections of a chlorine-treated and unidirectionally solidified sample is shown in Table V, together with the impurity content in metallurgical silicon. These results are in qualitative agreement with the results reported by other investigators (9).

Czochralski crystals from purified metallurgical silicon.—To further evaluate the usefulness of chemical treatment for the purification of metallurgical silicon, single crystals of about 2.5 cm diam were grown from chlorine-treated, chlorine-oxygen treated, and chlorine-treated plus unidirectionally solidified (lower 2/3 of the ingot only) metallurgical silicon by the Czochralski technique at a rate of about 10 cm/hr. Approximately 75-90% of the charge was pulled. The ingots were sliced, and the upper, middle, and lower sections of each ingot were analyzed for aluminum and iron content by the atomic absorption technique. The results are shown in Table VI. The crystals pulled from the chlorine-treated and chlorine-oxygen treated metallurgical silicon have very similar distribution of aluminum and iron. The concentration of iron is significantly lower than that in the starting material due to the low segregation coefficient of iron in silicon. However, the concentration of iron increased rapidly along the length of the crystal indicating that the diffusion of iron from the melt at the solidifying interface was a slow process. The concentrations of aluminum and iron in the crystal pulled from the chlorine-treated and unidirectionally solidified metallurgical silicon are below the detection limit of the atomic absorption technique.

Table VI. Impurity concentration, parts per million by weight, in Czochralski crystals pulled from purified metallurgical silicon

	Cl_2 treated		Cl_2-O_2 treated		Cl_2 treated and unidirectionally solidified	
	Al	Fe	Al	Fe	Al	Fe
Top section	<100	<10	<100	<10	<100	<10
Middle section	<100	700	<100	480	<100	<10
Bottom section	150	11,700	<100	21,300	<100	<10

The slices from the upper section of the ingots were chemically etched with a nitric acid-hydrofluoric acid mixture to remove the mechanical damage. They were all p-type. The resistivities and Hall mobilities in these slices were measured at room temperature by the van der Pauw technique (15). The ohmic contacts to the specimen were made by evaporating titanium-silver to the surface through a metal mask, followed by annealing in a hydrogen atmosphere at 550°C. The room temperature resistivities are approximately 0.32, 0.26, and 0.14 Ω-cm for chlorine-treated, chlorine and oxygen-treated, and chlorine-treated plus unidirectional solidified material, respectively. The differences in resistivities are presumably related to the differences in the extent of compensation. Their Hall mobility-temperature relations in the temperature range 81°-350°K are shown in Fig. 2. In this temperature range, the crystal from chlorine-treated plus unidirectionally solidified metallurgical silicon have higher mobilities than those from chlorine-treated and chlorine and oxygen-treated metallurgical silicon. Thus, the incorporation of unidirectional solidification into chemical treatment provides a more efficient way for the purification of metallurgical silicon than chemical treatment alone. However, the room temperature mobilities in all crystals (81, 108, and 127 cm^2/V-sec for chlorine-treated, chlorine and oxygen-treated, and chlorine-treated plus unidirectionally solidified materials, respectively) are

Table IV. Atomic absorption analysis of metallurgical silicon purified by chlorine treatment and unidirectional solidification, parts per million by weight

Element	Bottom	1/3 from the bottom	2/3 from the bottom	Top
Fe	<10	<10	680	27,800
Al	<100	<100	<100	<100

Table V. Emission analysis of metallurgical silicon purified by chlorine treatment and unidirectional solidification, parts per million by weight

Element	Metallurgical silicon	Purified material: Bottom section	Purified material: 2/3 from bottom
Al	>>1000	<10	<10
B	10-100	N.D.	N.D.
Ca	—	<10	<10
Cr	30-300	N.D.	10-100
Cu	10-100	<10	<10
Fe	>>1000	<10	10-100
Mg	10-100	<10	<10
Mn	30-300	N.D.	<10
Ni	10-100	N.D.	N.D.
Pb	—	<10	<10
Ti	30-300	N.D.	<10
V	100-1000	N.D.	10-100
Ag	—	<10	10-100

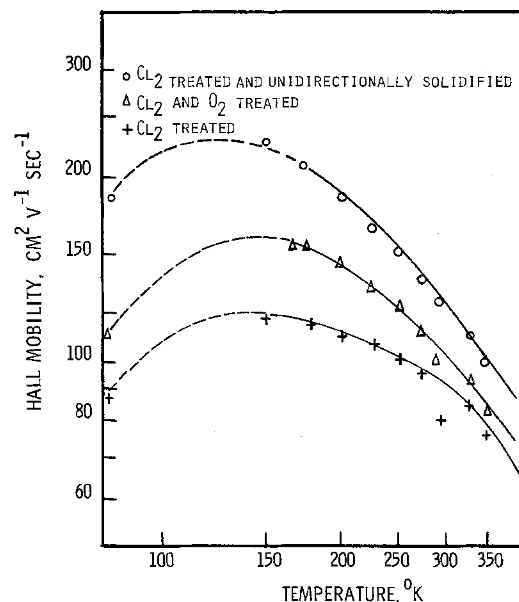

Fig. 2. Hall mobilities of holes in the upper section of silicon crystals pulled from metallurgical silicon purified by chlorine treatment, chlorine and oxygen treatment, and chlorine treatment plus unidirectional solidification.

significantly lower than those in semiconductor grade silicon of similar carrier concentrations [higher than 200 cm^2/V-sec (16)]. Furthermore, the mobility-temperature relations peak at temperatures considerably higher than those observed in semiconductor grade silicon of similar carrier concentrations. These results indicate compensation in crystals pulled from purified metallurgical silicon.

Figure 3 shows the plots of $\sigma/\mu_H q$ *vs.* $1/T$ for all three crystals, where $\sigma/\mu_H q$ is directly proportional to the net carrier concentration. These relations are linear with a slope of $-E_I/2k$, where E_I is the ionization energy of the dopant. The ionization energy deduced in this manner is 0.044-0.052 eV, suggesting boron as the acceptor impurity. Furthermore, the relatively slow change in Hall mobility with temperature (μ_H in the chlorine-treated plus unidirectionally solidified material varies approximately with T^{-1} in the temperature range 150°-350°K) indicates that the donors have similar ionization energies as the acceptor.

The minority carrier diffusion length in silicon slices was measured by the steady-state surface photovoltage method at room temperature (17). In this method, the surface of a semiconductor is illuminated with chopped monochromatic radiation with energy slightly higher than the energy gap of the semiconductor. When $t << L$, $d >> L$, $\alpha t << 1$, $\alpha d >> 1$ (where t is the depletion layer thickness at the surface, d is the specimen thickness, L is the diffusion length, and α is the optical absorption coefficient), and the carrier injection is at a low level, then the incident light intensity at various wavelengths required to produce a given surface photovoltage is a linear function of the reciprocal absorption coefficient for each wavelength. Thus, the extrapolation of the incident light intensity *vs.* the reciprocal absorption coefficient plot to zero intensity yields "diffusion length" as the negative intercept. Figure 4 shows the diffusion length data for a silicon slice from chlorine-treated plus unidirectionally solidified metallurgical silicon, where the optical absorption data of stress-relieved silicon were used. A least squares fit of the data yields a diffusion length of 25 ± 2 μm. As a comparison, silicon slices from chlorine-treated and

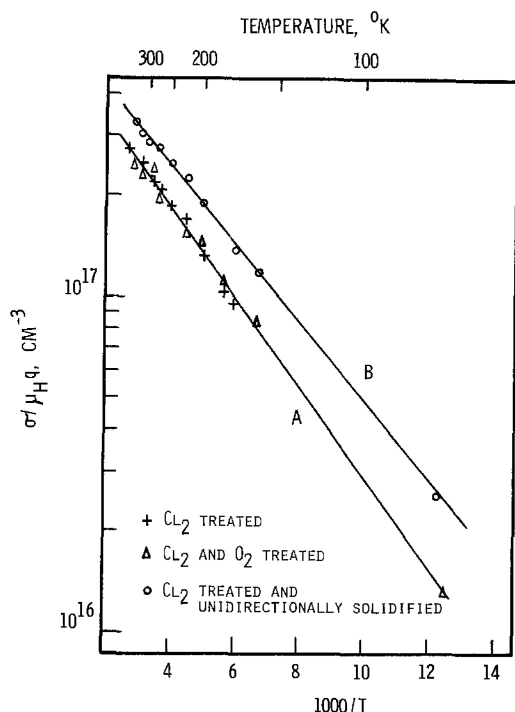

Fig. 3. Relations between $\sigma/\mu_H q$ and reciprocal temperature for the upper section of silicon crystals pulled from metallurgical silicon purified by chlorine treatment, chlorine-oxygen treatment, and chlorine treatment plus unidirectional solidification.

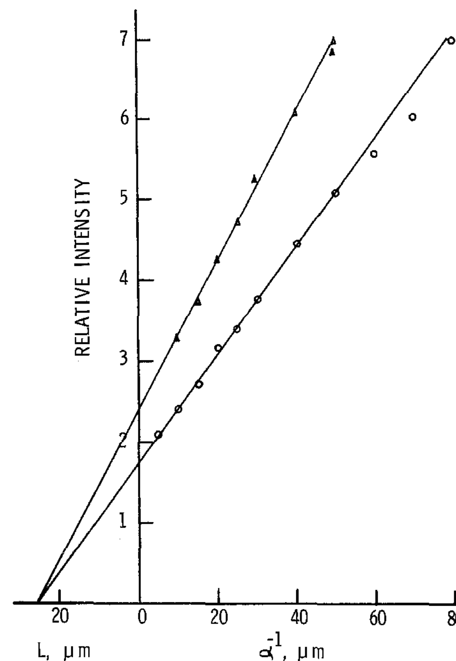

Fig. 4. Diffusion length data for a single crystalline silicon slice, prepared from chlorine-treated plus unidirectionally solidified metallurgical silicon, at two illumination levels.

chlorine-oxygen treated metallurgical silicon had diffusion lengths of (4-5) ± 1 μm, again indicating the effectiveness of unidirectional solidification.

Summary and Conclusions

The purification of metallurgical silicon has been carried out by the chemical treatment and, in some cases, followed by unidirectional solidification. The treatment of molten metallurgical silicon with chlorine or a chlorine-oxygen mixture has been found to be effective for reducing substantially the concentration of aluminum in silicon. However, the concentration of iron was not appreciably lowered by the treatment of molten metallurgical silicon with chlorine, oxygen, a chlorine-oxygen mixture, or hydrogen fluoride. Because of the low segregation coefficients of most metals in silicon, the use of unidirectional solidification following chemical treatment provides an efficient technique for the purification of metallurgical silicon. The extent of purification is in qualitative agreement with that obtained by similar methods reported by other investigators.

Acknowledgment

This work was supported by the National Science Foundation under Grant AER 73-07843 and the Division of Solar Energy of the U.S. Energy Research and Development Administration under Contract E(04-3)-1285.

Manuscript submitted July 25, 1977; revised manuscript received Dec. 1, 1977.

Any discussion of this paper will appear in a Discussion Section to be published in the December 1978 JOURNAL. All discussions for the December 1978 Discussion Section should be submitted by Aug. 1, 1978.

Publication costs of this article were assisted by Southern Methodist University.

REFERENCES

1. W. Voos, U. S. Pat. 2,972,521 (1961).
2. C. J. Brockbank, U. S. Pat. 1,180,968 (1916).
3. E. Enk and J. Nickl, German Pat. 1,098,931, *C. A.*, **56**, 5633 (1960).
4. T. L. Chu, T. K. Powell, H. J. Wu, and G. F. Wakefield, Abstract 217, p. 507, The Electrochemical Society Extended Abstracts, Spring Meeting, Toronto, Canada, May 11-16, 1975.
5. J. R. McCormick, L. D. Crossman, and A. Ranch-

holz, Conference Record of the 11th IEEE Photovoltaic Specialists Conference, May 1975, p. 270.
6. L. P. Hunt, V. D. Dosaj, J. R. McCormick, and L. D. Crossman, Conference Record of the 12th IEEE Photovoltaic Specialists Conference, November 1976, p. 125.
7. T. L. Chu, S. S. Chu, R. W. Kelm, Jr., and G. W. Wakefield, *This Journal*, in press.
8. T. L. Chu, R. W. Kelm, Jr., and G. F. Wakefield, Abstract 174, p. 455, The Electrochemical Society Extended Abstracts, Fall Meeting, Dallas, Texas, Oct. 5-9, 1975.
9. V. D. Dosaj, L. P. Hunt, and L. D. Crossman, Conference Record of the 11th IEEE Photovoltaic Specialists Conference, May 1975, p. 275.
10. D. R. Stull and H. Prophet, JANAF Thermochemical Tables, 2nd ed. National Bureau of Standards, NSRDS—NBS 37, Washington, D.C. (1971).
11. M. W. Chase, J. L. Curnutt, A. T. Hu, H. Prophet, A. N. Syverud, and L. C. Walker, *J. Phys. Chem. Ref. Data*, **3**, 311 (1974).
12. M. W. Chase, J. L. Curnutt, H. Prophet, R. A. McDonald, and A. N. Syverud, *ibid.*, **4**, 1 (1975).
13. H. C. Theuerer, *J. Met.*, **6**, 1316 (1956).
14. F. A. Trumbore, *Bell Syst. Tech. J.*, **39**, 205 (1960).
15. L. J. van der Pauw, *Philips Res. Rep.*, **13**, 1 (1958).
16. F. J. Morin and J. P. Maita, *Phys. Rev.*, **96**, 28 (1954).
17. A. M. Goodman, *J. Appl. Phys.*, **32**, 2550 (1961).

Thermal Oxidation of Heavily Phosphorus-Doped Silicon

C. P. Ho,* J. D. Plummer, and J. D. Meindl****

Integrated Circuits Laboratory, Stanford University, Stanford, California 94305

and B. E. Deal†

Fairchild Camera and Instrument Corporation, Research and Development Laboratory, Palo Alto, California 94304

ABSTRACT

The effects of high substrate phosphorus impurity levels on the kinetics of thermal oxidation of <111> oriented silicon have been studied for a dry oxygen ambient in the temperature range 800°-1100°C. The observed enhanced oxidation rates with phosphorus doping levels $\gtrsim 10^{19}/cm^3$ are found to be consistent with a simplified interpretation of the linear-parabolic oxidation model together with phosphorus redistribution effects. The linear rate constant B/A increases substantially at all temperatures, implying significant change in the $Si\text{-}SiO_2$ interface reaction rate, though apparently with only slight effect on the associated activation energy. The parabolic rate constant B increases somewhat at lower temperatures, indicating a finite change in oxidant diffusion through the oxide, possibly via an additional diffusion mechanism at high phosphorus concentrations, with reduced activation energy. Reasonable closed-form approximations to these phosphorus concentration dependencies of the oxidation rate constants are described.

Thermal oxidation of silicon remains an essential part of integrated circuit technologies, both bipolar and MOS, being used for such diverse purposes as masking against dopant diffusion, passivation of active device regions and junctions, insulating "field regions" between active devices, and, in the gate dielectric, as an actual component of active MOS devices. Often encountered is the growth of thermal oxide over silicon that is heavily doped with donor or acceptor levels not infrequently approaching the solid solubility limit of the impurity in silicon. Typical examples are bipolar emitter regions and MOSFET source and drain regions. This situation, together with the demonstration that oxide growth rates over silicon with impurity levels $\gtrsim 10^{18}$ cm^{-3} are significantly greater than rates over lightly doped silicon (1, 2), has prompted a continuing investigation of the effects of dopant impurity levels on oxidation rates and mechanisms. Part of this investigation has been a quantitative study of thermal oxidation of heavily phosphorus-doped, <111> oriented silicon in a dry oxygen ambient. The results of this study are presented here.

General Theory

A brief review of general oxidation theory indicates qualitatively what may be expected in the case of heavily doped substrates or diffused regions. The macroscopic model of Deal and Grove (3) for silicon oxidation by water or dry oxygen involves the diffusion of the oxidizing species from the ambient through an existing oxide to react with silicon at the Si/SiO_2 interface. Analysis based on requiring continuity of steady-state flux of the oxidant through the ambient/oxide/interface structure yields the familiar linear-parabolic growth relationship (3)

$$\frac{x_o^2}{B} + \frac{x_o}{B/A} = t + \tau \qquad [1]$$

where x_o = oxide thickness, B = parabolic rate constant, B/A = linear rate constant, t = oxidation time, and τ = correction factor which accounts for an initial oxide thickness x_i, or effective x_i due to an observed initial accelerated growth rate in dry oxygen.

For thick oxides and oxidation times long relative to a characteristic time $A^2/4B$, the first term on the left-hand side of Eq. [1] dominates, resulting in parabolic, diffusion-limited growth. Under these conditions, B is the dominant rate constant and is given by

$$B = 2D_{eff}C^*/N_1 \qquad [2]$$

where D_{eff} = effective diffusion coefficient of the oxidant in the oxide, C^* = equilibrium concentration of the oxidant in the oxide, and N_1 = number of oxidant molecules incorporated per unit volume of oxide grown. B exhibits an Arrhenius temperature dependence with activation energies of 1.2 eV for dry O_2 and 0.71 eV for H_2O, apparently reflecting the activation energies for the diffusivity of O_2 and H_2O, respectively, in SiO_2 (3).

For thin oxides and oxidation times short relative to $A^2/4B$, the second term on the left-hand side of

* Electrochemical Society Student Member.
** Electrochemical Society Active Member.
Key words: oxidation kinetics, rate constants, silicon, phosphorus.

Eq. [1] dominates, resulting in linear interface reaction-limited growth. B/A is the governing rate constant under these conditions and is given by

$$\frac{B}{A} = \frac{kh}{k+h}\frac{C^*}{N_1} \simeq k\frac{C^*}{N_1} \quad [3]$$

where h = gas phase transport coefficient for the oxidizing species from the ambient to the outer oxide surface and k = Si/SiO_2 interface reaction rate constant. An activation of energy of 2 eV is observed for B/A for both dry O_2 and H_2O ambients, apparently determined by the energy required to break a Si-Si bond (3, 4).

In an idealized interpretation, then, factors likely to influence the interface reaction rate should alter B/A, while those affecting oxidant diffusion will change B. Sufficiently high impurity levels in the substrate should be expected to modify the interface reaction. Similarly, high impurity content in the oxide may affect diffusivity of the oxidizing species. The relative magnitudes of such effects should depend on the particular impurity involved and its behavior during oxidation.

Specifically, phosphorus, as with the other commonly used donor impurities arsenic and antimony, diffuses more slowly in the oxide than in the silicon and tends to segregate at the interface in favor of greater phosphorus levels on the silicon side. As a result, a pile-up of phosphorus at the interface to levels greater than bulk concentrations in the silicon may occur during oxidation, with relatively much lower levels in the oxide. In addition, the pile-up should be more substantial for H_2O than for dry O_2 oxidation due to even slower diffusion relative to oxide growth rates (5).

Therefore, oxidation regimes dominated by the linear rate constant should exhibit greater dependence on heavy phosphorus doping level than should regimes dominated by the parabolic rate constant. Shorter oxidations which are interface reaction rate limited should show greater variation with heavy phosphorus doping than should longer oxidations which are diffusion limited. The influence of heavy phosphorus doping via large B/A variations should also diminish or saturate with increasing oxidation temperature, since diffusion-limited oxidation dominates at shorter oxidation times with increasing temperature.

Over-all, then, this qualitative model indicates that greater influence of heavy doping levels of phosphorus (and also arsenic and antimony) should be seen at shorter oxidation times and lower oxidation temperatures, and that these effects should be greater for H_2O than for dry oxygen oxidations. The validity of this simple model for the enhanced oxidation rates observed over N^+ regions will now be considered quantitatively.

Experimental Procedures

Substrate preparation.—Because silicon wafers with phosphorus impurity levels $\geq 10^{19}$ cm^{-3} are not readily available, heavily doped samples were prepared by diffusion of phosphorus using a standard $POCl_3$ source into lightly phosphorus-doped, 10-15 Ω-cm <111> oriented substrates. Predeposition and drive-in schedules were chosen to produce diffused phosphorus profiles that were flat, within 10% over at least the first 2μ into the silicon. Drive-ins were done in an N_2 ambient to minimize oxidation and hence redistribution of the phosphorus during preparation of the samples.

Five types of heavily doped samples were prepared with target impurity levels ranging from $\sim 5 \times 10^{19}$ cm^{-3} to essentially solid solubility (at standard furnace temperatures). The resulting diffused impurity profiles were measured for electrically active phosphorus concentration using both spreading resistance and incremental sheet resistance via anodic oxidation. Agreement between the two measurement techniques was excellent, giving the values in Table I. Reproducibility of diffused phosphorus impurity levels from run to run of sample preparation was checked using the electrical measurement techniques and found to be very good. Total chemical phosphorus concentrations and hence the percentage of the species electrically active in the diffused samples were studied with both sputtering Auger[1] and SIMS techniques, also with generally good agreement, as shown in Table I. The relation between chemical and electrical values found is consistent with published results (6). Both electrical and chemical phosphorus profiles appeared sufficiently flat to allow treating the samples as effectively initially uniformly doped at the measured surface concentrations for purposes of first-order analyses of results from oxidations of the prepared samples.

Table I. Electrically active C_{BE} and chemical C_{BC} dopant concentrations in heavily phosphorus-doped samples

Sample	C_{BE}	C_{BC} SIMS	C_{BC} AES
A	$(\sim 10^{15})$	—	—
B	5.1×10^{19}	5.5×10^{19}	5.2×10^{19}
C	7.2×10^{19}	1.5×10^{20}	8.2×10^{19}
D	1.8×10^{20}	2.4×10^{20}	2.8×10^{20}
E	2.8×10^{20}	4.5×10^{20}	5.0×10^{20}
F	3.2×10^{20}	7.0×10^{20}	6.8×10^{20}

Oxidation and measurement procedures.—Samples of each of the five selected heavy substrate doping levels, together with a control wafer of the lightly doped substrate from which the heavily doped samples were prepared, were next oxidized together at various times and temperatures. In each case, the samples were subjected to standard cleaning procedures and then placed horizontally on a quartz boat in order of increasing substrate doping level, with the lightly doped control farthest upstream and the most heavily doped sample farthest downstream relative to gas flow in the oxidation furnace, such that possible effects of out-diffusion of phosphorus into the ambient from the more heavily doped wafers might be minimized. The wafers were then pushed rapidly directly into the oxidizing ambient in the furnace for the desired oxidation time, or, for times of 1 hr or less, pushed into nitrogen and allowed 5 min to come to temperature before the oxidizing ambient was initiated. With completion of the desired oxidation time, the samples were fast-pulled directly from the oxidizing ambient.

Resulting oxide thicknesses were measured using multiple-beam interferometric techniques to avoid uncertainties of possible effects on the optical properties of the samples due to high phosphorus impurity levels in the silicon and the oxide. With these experimental methods, reproducibility of oxide thickness was found to be well within the accuracy of the interferometric measurement technique (±25Å).

Data evaluation.—A quantitative measure of the increase of oxidation rate with heavy phosphorus doping may be obtained via extraction of effective rate constants from the data using the macroscopic linear-parabolic oxidation model. Conventionally, extraction is achieved using the alternative form of the general growth relationship (3)

$$x_o = B\left(\frac{t+\tau}{x_o}\right) - A \quad [4]$$

Thus, a plot of x_o *vs.* $(t+\tau)/x_o$ yields B as the slope and $-A$ as the intercept. However, τ itself is a function of B, B/A, and x_i. At a given oxidation temperature, the value of τ will decrease with heavy substrate doping and becomes very difficult to determine directly by extrapolating a curve fit to the experimental x_o *vs.* t data. This is especially true in view

[1] Auger measurements were done by J. S. Johannessen, C. R. Helms, and W. E. Spicer of Solid State Laboratory, Electrical Engineering Department, Stanford University.

of the nonlinear nature of the fitted lines when growth is most rapid, and the possible scatter inherent in data points for very short oxidation times.

It will be shown, though, that the apparent initial thickness x_i varies relatively only slightly with heavy phosphorus doping about the value of $x_i \simeq 200$Å typically seen for dry oxygen oxidation. That is, the initial rapid growth mechanism responsible for the apparent nonzero x_i for dry O_2 oxidation seems relatively unaffected by heavy phosphorus doping. To first order, then, assumption of a constant $x_i \simeq 200$Å appears reasonable, and analysis may proceed employing another alternative form of the general relationship

$$(x_o + x_i) = B\left(\frac{t}{x_o - x_i}\right) - A \quad [5]$$

A linear plot of $(x_o + x_i)$ *vs.* $t/(x_o - x_i)$ produces, as before, B as the slope and $-A$ as the intercept.

Experimental Results

An extensive series of oxidations were done in a dry O_2 ambient at temperatures of 800°, 900°, 1000°, and 1100°C. The data produced are shown in Fig. 1 and 2 as oxide thickness *vs.* oxidation time curves for each of the five heavily doped sample types and the lightly doped control. At each temperature, the bottom curve represents the lightly doped control and agrees well with published data for <111> substrates, while the additional curves represent the heavily doped samples, in order of increasing substrate doping. Specific doping levels are indicated in Table I.

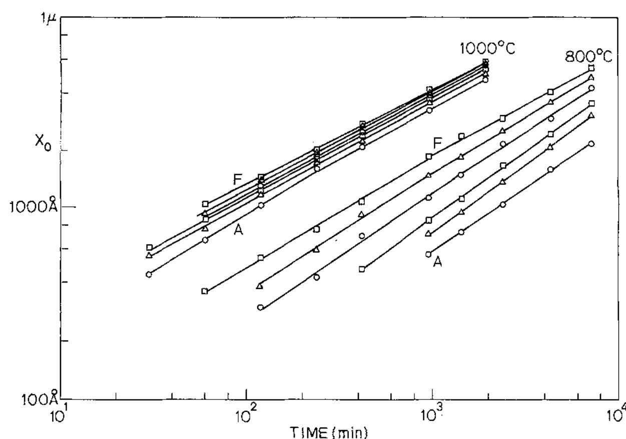

Fig. 1. Oxide thickness *vs.* oxidation time for <111> oriented silicon in dry O_2 ambient with substrate phosphorus doping level as parameter, at 800° and 1000°C.

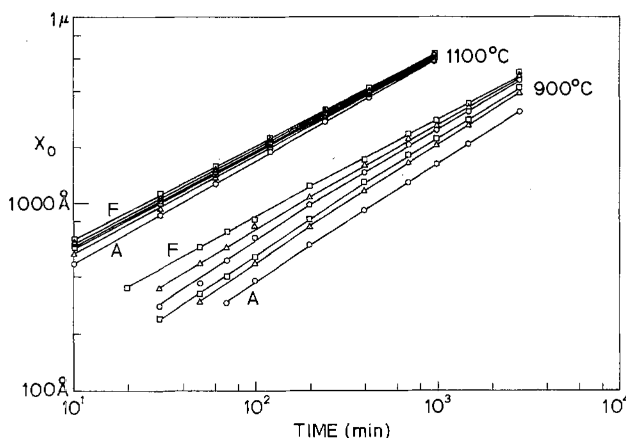

Fig. 2. Oxide thickness *vs.* oxidation time for <111> oriented silicon in dry O_2 ambient with substrate phosphorus doping level as parameter, at 900° and 1100°C.

The data in Fig. 1 and 2 already lend qualitative support to the predictions based on the simple interpretations of doping effects presented earlier. Clearly the greatest relative variations of oxide thickness occur at the shorter times and lower temperatures, the regions in which the interface reaction and hence B/A are expected to dominate, indicating that the increasing substrate phosphorus level has a very strong effect on the interface reaction. At the longer times and higher temperatures, in the diffusion-limited regime, substantially less variation of thickness with doping is seen, implying that oxidant diffusion and the parabolic rate constant are influenced to a much smaller extent by the increasing substrate phosphorus levels. Indeed, a few selected oxidations at 1200°C, when the characteristic time $A^2/4B$ for lightly doped substrate oxidations is only about 0.5 min and therefore oxidation is effectively entirely B dominated, produced essentially no variation of oxide thickness with increasing phosphorus doping that could be resolved within the limits of interferometer accuracy.

Extrapolation on linear scales of thickness *vs.* time to the effective initial oxide thickness x_i attributable to the initial rapid growth mechanism shows only slight variation around 200Å as the substrate changes from lightly to heavily phosphorus doped. Thus, to first order a constant $x_i \simeq 200$Å may be assumed, as described above.

Discussion

The variation of the effective B/A and B values with increasing initial substrate total chemical phosphorus concentration, representatively illustrated in Fig. 3 for 900°C dry O_2 oxidation, exhibits dramatically the expected behavior. B/A, reflecting interface reaction-limited oxidation, increases sharply by more than an order of magnitude as the phosphorus level rises toward solid solubility. On the other hand, B, which represents the diffusion-limited regime, is affected only slightly by the increasing substrate phosphorus doping. Clearly, the predictions of the simplified interpretations presented have been convincingly confirmed. We now consider the effects on B/A and B in detail.

Linear rate constant.—The temperature dependence of B/A is shown in Fig. 4, where log (B/A) is plotted against $1/T$ with substrate doping level as a parameter. The lowest points are the values found for the lightly doped control samples, while the higher points correspond, respectively, to the increasingly heavily phosphorus-doped substrate types used. To a reasonable approximation, Arrhenius temperature dependence may be assumed for the effective B/A values

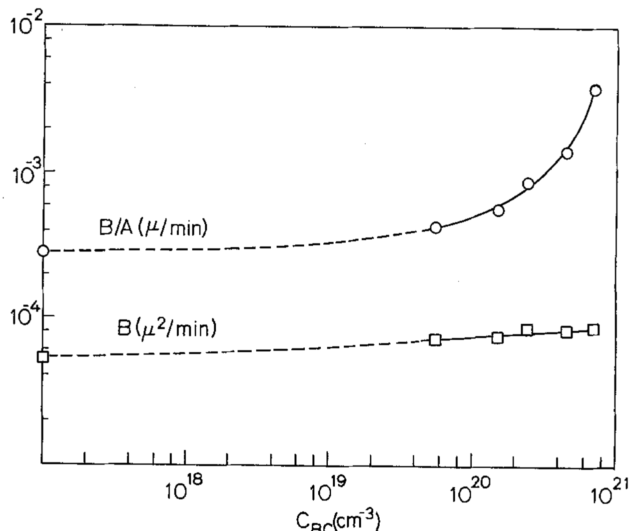

Fig. 3. Oxidation rate constants *vs.* initial substrate chemical phosphorus doping level at 900°C.

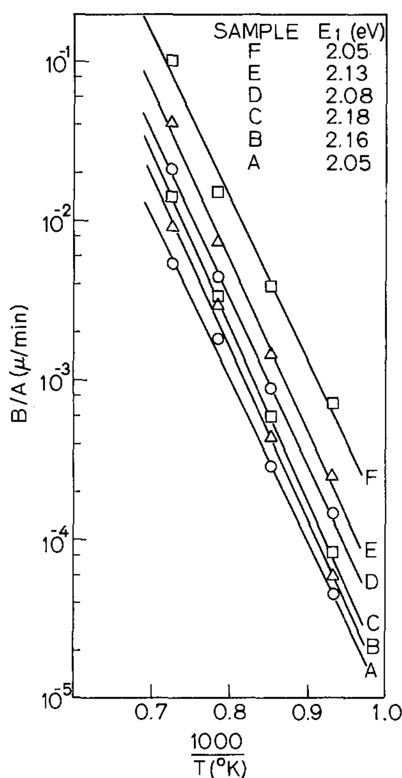

Fig. 4. Linear rate constant temperature dependence and effective activation energies with substrate phosphorus doping level as parameter.

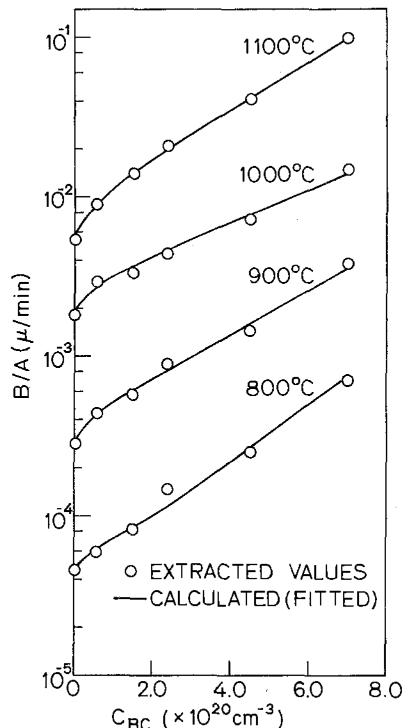

Fig. 5. Linear rate constant vs. initial substrate chemical phosphorus doping level with oxidation temperature as parameter.

corresponding to each substrate doping level, leading to the least squares fitted lines and apparent activation energies of the figure.

High impurity levels may produce the large increases of effective B/A by altering the activation energy and/or the preexponential factor. Apparently the basic limiting activation energy of approximately 2 eV associated with the interface reaction is not substantially altered by the high phosphorus levels, while significant dependence on dopant concentration may be found in the preexponential factor.

Some indication of the nature of this dependence may be gained via examination of the variation of B/A with concentration at a given temperature, as was done in Fig. 3 for 900°C. The sharp increase of the linear rate constant suggests an exponential dependence of C_{BC}, the initial chemical substrate phosphorus concentration, a possibility that is tested further by investigating the variation of log (B/A) with C_{BC} in Fig. 5. Evidently log (B/A) eventually exhibits roughly a linear dependence on C_{BC}, and hence B/A an exponential dependence on C_{BC}, at each given temperature, but only after a stronger initial increase. There may be a slight temperature dependence in the magnitude of this initial increase, but to a large extent the substrate background phosphorus concentration dependence is very similar at all temperatures.

Clearly, many closed-form relationships for this C_{BC} dependence may be used to approximate this data to varying degrees of complexity, in the absence of an accurate physical model for that dependence. A fairly simple form, producing a reasonable first-order approximation, might be

$$\frac{(B/A)}{C_0 e^{-E_1/kT}} \equiv (B/A)' = 1 + k_1 C_{BC}^{n_1} e^{k_2 C_{BC}} \quad [6]$$

where $C_0 e^{-E_1/kT}$ is the published temperature dependence of the linear rate constant for lightly doped substrates with $E_1 \simeq 2$ eV (3). Thus, the exponential eventually dominates, but the power law dependence produces the stronger initial increase. Optimal k_1 and k_2 values may be found by rewriting Eq. [6] in the alternative form

$$\log\left[\frac{(B/A)' - 1}{C_{BC}^{n_1}}\right] = \log k_1 + k_2 C_{BC} \quad [7]$$

Plotting $\log\left[\frac{(B/A)' - 1}{C_{BC}^{n_1}}\right]$ *vs.* C_{BC} should therefore produce a linear dependence with intercept log k_1 and slope k_2, for an appropriate value of n_1. Such analysis indicates that a value of $n_1 \simeq 0.5$-1.0 should be used, with $n_1 \simeq 0.5$ giving particularly consistent linear dependences. Thus, the curves plotted together with the experimental B/A values in Fig. 5 have been calculated using $n_1 = 0.5$ and the resulting appropriate k_1 and k_2 values. Agreement appears very reasonable. The fitted k_1 and k_2 values are presented *vs.* $1/T$ in Fig. 6, confirming that the temperature dependence is relatively slight when compared with the over-all dependence of B/A. In fact, appropriate constant values of k_1 and k_2 independent of T conceivably could be used for all temperatures. While agreement not surprisingly is not as good, using values of $k_1 = 5.9 \times 10^{-11}$ $cm^{3/2}$ and $k_2 = 3.0 \times 10^{-21}$ cm^3 gives reasonable agreement with the experimental results over the entire temperature range investigated.

Parabolic rate constant.—B has been found to be a much weaker function of high phosphorus concentrations. Nevertheless, it does appear to increase somewhat with concentration, as seen in Fig. 7, where log B is plotted *vs.* $1/T$ with substrate doping as a parameter. At each temperature, the lowest point represents the lightly doped control while the higher points correspond to the heavily doped samples. It is apparent that, unlike the case for B/A, the concentration dependence of B varies significantly with temperature. Dopant level has a greater effect at lower temperatures and virtually no effect at 1100°C. Also, for a given doping level, the net temperature dependence is not readily reconcilable with a single activation energy Arrhenius relation, implying changes in activation energy and a temperature-dependent preexponential factor, or addition of a new, phosphorus-related term with different activation energy. Figure 8, presenting log B *vs.* C_{BC} with temperature as parameter, empha-

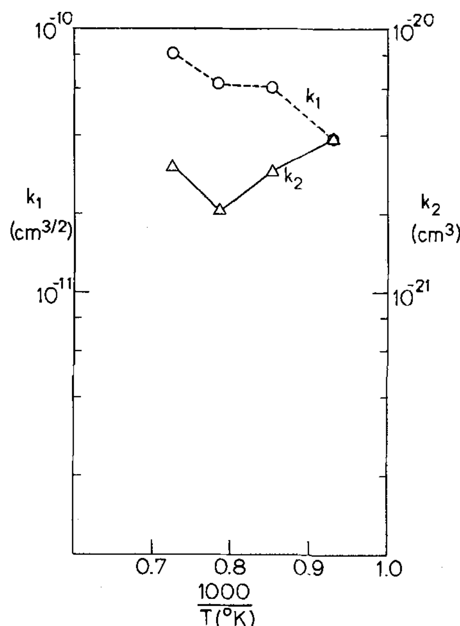

Fig. 6. Fitted parameters vs. $1/T$ for linear rate constant dependence on initial substrate chemical phosphorus doping level.

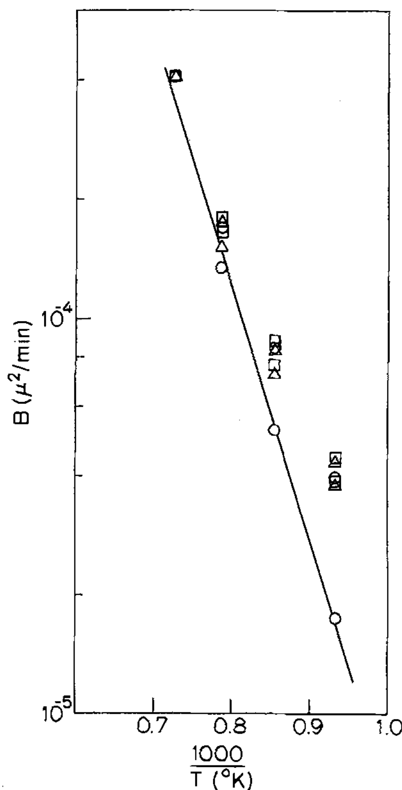

Fig. 7. Parabolic rate constant temperature dependence with substrate phosphorus doping level as parameter.

sizes this additional temperature dependence. Further, the dopant concentration effects at a given temperature become evident. As substrate doping level increases (and consequently the lower phosphorus level in the oxide also rises), B first increases rapidly and then begins to "saturate," increasing only very slowly, if at all.

As with B/A, a convenient closed-form approximation of the B variations may be made. For convenience, no new explicit T dependence is included, but the fitted "constants" should then reflect any dependence thus hidden. The initial rapid rise and subsequent sluggishness suggest a possible power law dependence on dop-

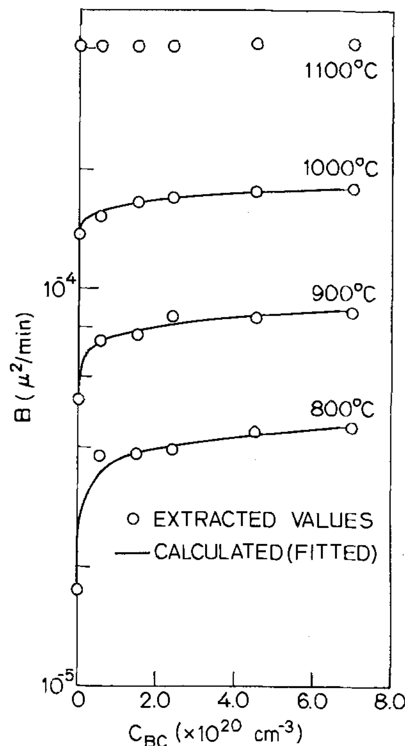

Fig. 8. Parabolic rate constant vs. initial substrate chemical phosphorus doping level with oxidation temperature as parameter.

ant levels. Initial substrate phosphorus level is used as the variable for this analysis, though actual levels in the oxide should be more directly relevant. (This factor will be discussed below.)

$$\frac{B}{B_0 e^{-E_2/kT}} \equiv B' = 1 + k_3 C_{BC}^{n_2} \quad [8]$$

where $B_0 e^{-E_2/kT}$ is the published temperature dependence of the parabolic rate constant for lightly doped substrates with $E_2 \simeq 1.2$ eV for dry O_2 (3).

Appropriate k_3 and n_2 values may be extracted in a manner analogous to Eq. [7]. This approach was used with the extracted B values for 800°, 900°, and 1000°C, with surprisingly good linear relations found. The calculated curves in Fig. 8 illustrate the very reasonable fit to the extracted B values produced by the above relation with the k_3 and n_2 values shown vs. $1/T$ in Fig. 9. The expected additional T dependence is clearly evident in k_3 and possibly, to a lesser extent, in n_2. A new additional activation energy is strongly suggested, and this will be explored.

Factors affecting data interpretation.—Analysis to this point has been based on C_{BC}, the initial substrate chemical phosphorus level prior to oxidation. However, as mentioned previously, all common dopants redistribute during oxidation, with phosphorus "snowplowing" in the silicon to produce an increased interface concentration $C_{SC} > C_{BC}$, and reduced effective levels in the oxide $C_{ox} < C_{BC}$. Further, the relative magnitudes of the pile-up and oxide phosphorus levels increase as dopant diffusivity decreases relative to oxidation rate (5); that is, for H_2O rather than O_2 oxidation, for lower temperature oxidation, or for lower initial phosphorus concentration (7).

Thus, for analysis of the effects on B/A or the interface reaction, the actual doping parameter realistically should be C_{SC} rather than C_{BC}. The effective B/A values found will correspond to higher C_{SC} values, tending to shift the B/A data points to higher values along a dopant concentration axis. And, since the relative amount of pile-up decreases as C_{BC} increases and as temperature increases, these shifts may be greater for the lower concentration points at lower temperatures.

A time-dependent effect may further complicate consideration of dopant redistribution. The first-order

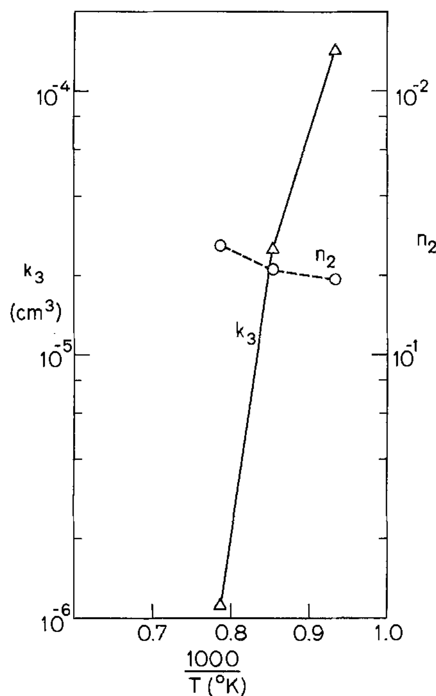

Fig. 9. Fitted parameters vs. 1/T for parabolic rate constant dependence on initial substrate chemical phosphorus doping level.

theory mentioned (5) assumes parabolic oxidation, or the same $t^{1/2}$ dependence as for dopant diffusion, to find a "steady-state" time-independent dopant redistribution. Yet, oxidation must proceed through a linear growth period before achieving parabolic growth, and consequently redistribution should be subject to a finite time-dependent transient period before achieving a steady-state value. Onset of essentially parabolic oxidation may be reasonably taken as achievement of steady-state pile-up conditions. Therefore, the characteristic time $A^2/4B$ is useful as a measure of the duration of the transient period. In any event, since B/A is most relevant in this linear growth transient period, the effective B/A value found may actually be an averaged value corresponding to a time-averaged C_{SC} value presumably less than the steady-state phosphorus C_{SC}. Evidently, then, time dependence may offset somewhat the shifts along the concentration axis from the initial C_{BC} value toward the greater C_{SC} values.

Nevertheless, redistribution and pile-up of phosphorus should produce a net "forward" shift of the heavily doped substrate points in a plot of extracted B/A *vs.* dopant level such as that of Fig. 5, reducing the apparent initially rapid increase of B/A with heavy substrate doping, to produce possibly a solely exponential dependence on C_{SC}, of the form

$$B/A \simeq C_0 e^{-E_l/kT} e^{k'C_{SC}} \quad [9]$$

There may also be uncertainty of B/A values due to the method of analysis (8). Since changes in B are relatively slight, the "source" of the large B/A increase seen is the significantly reduced A value or the intercept in the $(x_o + x_i)$ *vs.* $t/(x_o - x_i)$ plot of the data. As temperature and high dopant level rise, this intercept moves increasingly toward a value of 0, or an infinite B/A. Possible error due to data scatter produces much greater error in extracted B/A value as T and C_{BC} increase. So, particularly for the heaviest phosphorus-doped substrate types, the 1100°C B/A values, for example, may contain significant error which, while not important in calculating actual oxide growth because of increased B dominance, may alter apparent activation energies for B/A.

Extraction of B as the slope of $(x_o + x_i)$ *vs.* $t/(x_o - x_i)$ should, on the other hand, produce comparable errors for all the conditions studied, and such potential errors should not be as significant in consideration of B. Transient effects should be less significant as well, since B does not really become meaningful until parabolic oxidation is approached, precisely the time at which, presumably, redistribution approaches its steady-state value. Redistribution itself and its temperature dependence must be considered, however. The actual dopant level of importance in B or oxidant diffusion should be C_{ox} rather than the C_{BC} used in the analysis. Also, the effective B values for a given heavily doped substrate type may then correspond to different C_{ox} values as the magnitude of redistribution varies with temperature.

It is apparent that accurate measure of C_{SC} and C_{ox}, and their possible time dependence, for a given C_{BC} and oxidation condition would be highly desirable in furthering realistic and meaningful analysis and interpretation. Such efforts are being pursued currently using sputtering Auger and ion microprobe techniques and will be reported in a future publication.

Possible mechanisms.—Some indication of possible physical mechanisms for the effects of heavy substrate phosphorus doping on oxidation may be drawn from the present data. Intuitively, the enhanced oxidation rates observed in this study may be related to chemical, electrical, or even mechanical effects of the heavy doping.

For example, the very high phosphorus levels enhanced by redistribution pile-up at the interface may, by size mismatch relative to Si of substitutional phosphorus or by "interstitial" cluttering or precipitates (9, 10), create lattice strain and, therefore, alter the Si-Si bond strength that has been linked to the limiting activation energy of the interface oxidation reaction. Further, the preexponential factor of the interface reaction may include such components as the number of interfacial Si atoms or the number of "available" interfacial Si bonds that have been suggested as the source of differences in oxidation rates for various Si wafer orientations (11). Possibly, the high interfacial dopant levels could affect such factors to produce increased oxide growth rates as well.

In fact, the analysis of the temperature dependence of B/A with C_{BC} as the parameter suggested strongly that the primary effect of heavy phosphorus levels is on the preexponential factor. So, as simple an effect as an increased interface "roughness," leading to higher numbers of available Si bonds and attributable to phosphorus atoms, clusters, or precipitates, could explain the enhanced interface reaction.

These dopant-related effects on B/A may not be purely mechanically induced. The thermodynamics of the interfacial oxidation reaction may well be affected, such that the Gibbs free energy change driving force for the reaction would be altered significantly. Also, the position of the Si Fermi level will be altered by such high dopant levels, even at the high temperatures of thermal oxidation, to create electrical effects on the interface reaction rate.

Heavy phosphorus effects on B or diffusion of the oxidizing species in the oxide are relatively smaller, but they do exist. If B were unaffected, then at long t the oxide thicknesses resulting from the various heavy doping levels and enhanced B/A values should approach that of the lightly doped control. This behavior is not apparent in the data, especially at low temperatures.

These real effects on B should be related to the phosphorus level found in the oxide. The trends observed appear to agree at least qualitatively with redistribution theory (5). That is, pile-up and C_{ox} should increase as T decreases such that the effect on B for a given initial C_{BC} is greater at lower temperatures. The relative amount of C_{ox}/C_{BC} decreases at the highest substrate phosphorus levels, resulting in C_{ox} levels varying less than C_{BC} levels. Consequently, the B increase, or enhanced oxidant diffusion, tends to "saturate" quickly at the high C_{BC} values.

The analysis above suggests that oxidant diffusion in the oxides grown on heavily doped substrates may be subject to a phosphorus-related term, with different activation energy, in addition to the diffusivity term governing diffusion in "pure" oxides. Quite reasonably, diffusion in a phosphorus-rich region of the oxide would present a different, presumably reduced activation energy. So, this new diffusivity, multiplied by a phosphorus concentration factor related to the "richness" and/or the extent relative to the total oxide of the phosphorus region of the oxide, might combine with the diffusivity remaining in effect in the rest of the oxide. Since C_{BC} rather than C_{ox} has been used in this concentration factor, the apparent slightly T dependent power law form of the factor might reflect the tendencies of redistribution of C_{BC} to produce C_{ox}. The greater temperature dependencies of the two activation energies, in any event, would produce the over-all nonlinear $1/T$ dependence observed for log B in oxidation of heavily doped substrates.

Much additional information is obviously needed to resolve fully the possible mechanisms suggested or implied by the present data. Work being performed currently, including effects of heavy arsenic, antimony, and boron doping, combined effects of substrate orientation and heavy doping levels, H_2O oxidation of heavily doped substrates, and other aspects of heavy doping effects on oxide and the $Si\text{-}SiO_2$ interface, may produce some of the additional clues and information needed.

Conclusions

Enhanced thermal oxidation effects in the heavily phosphorus-doped silicon regions commonly seen in integrated circuits have been studied, producing some indication of possible physical mechanisms explaining the greatly increased B/A and somewhat enhanced B macroscopic model rate constants. In the absence of more complete quantitative physical models, closed-form relations have been presented, giving good approximation to the effects which have been shown to be most substantial at lower temperatures. As the trend in technology is toward lower temperature processing in view of the larger wafers being used, these heavy phosphorus-enhanced oxidation effects appear very likely to impact integrated circuit technology. In addition, careful design of processing schedules can make use of these enhanced oxidation effects to, for example, reduce gate-to-source and gate-to-drain capacitance in MOS transistors.

Acknowledgment

The authors gratefully acknowledge support of the work described in this paper by the Defense Advanced Projects Agency under Contract No. DAA-B07-75-C-1344. One of the authors (C.P.H.) also received support from a National Science Foundation Fellowship. In addition, the authors would like to thank their colleagues for many useful discussions during the course of this work, particularly H. Massoud, S. Combs, H. Jerman, and T. Nunn, of the Stanford Integrated Circuits Laboratory, and D. Hess, of the Fairchild Camera and Instrument Corporation Research and Development Laboratory.

Manuscript submitted Aug. 26, 1977; revised manuscript received Nov. 28, 1977.

Any discussion of this paper will appear in a Discussion Section to be published in the December 1978 JOURNAL. All discussions for the December 1978 Discussion Section should be submitted by Aug. 1, 1978.

REFERENCES

1. B. E. Deal and M. Sklar, *This Journal*, **112**, 430 (1965).
2. W. A. Pliskin, *IBM J. Res. Develop.*, **10**, 198 (1966).
3. B. E. Deal and A. S. Grove, *J. Appl. Phys.*, **36**, 3770 (1965).
4. L. Pauling, "The Nature of the Chemical Bond," 3rd ed., p. 85, Cornell University Press, Ithaca, N.Y. (1960).
5. A. S. Grove, O. Leistiko, Jr., and C. T. Sah, *J. Appl. Phys.*, **35**, 2695 (1964).
6. R. B. Fair and J. C. C. Tsai, *This Journal*, **124**, 1107 (1977).
7. S. K. Ghandi, "The Theory and Practice of Microelectronics," chap. 4, John Wiley & Sons, Inc., New York (1968).
8. D. W. Hess and B. E. Deal, *This Journal*, **122**, 579 (1975).
9. A. Armigliato, D. Nobili, M. Servidori, and S. Solmi, *J. Appl. Phys.*, **47**, 5489 (1976).
10. T. H. DiStefano, NBS Special Publication 400-23, ARPA/NBS Workshop IV, Surface Analysis for Silicon Devices, Gaithersburg, Md, April 23-24, 1975 (issued March 1976).
11. J. R. Ligenza, *J. Phys. Chem.*, **65**, 2011 (1961).

Brief Communication

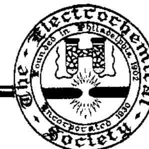

Disclosure of Dislocation Loops and Dislocation Dipoles in GaP by Chemical Etching

C. Werkhoven

Philips Research Laboratories, Eindhoven, The Netherlands

Since chemical etching is fast and in principle nondestructive, this technique is, at least for III-V single crystals, widely used for the assessment of defects. An analysis of the microscopic structure of extended defects and the identification of microdefects as can be performed by TEM is difficult to obtain with the etching technique, however.

It is shown in this paper that on the conditions of an optimized etching time and the use of high magnification optical microscopy techniques, information about the submicron structure of defects in GaP single crystals can be obtained. For this purpose the $R\text{-}C$ etchant (1) was used because it requires short etching times at a moderate bath temperature, *viz.* 65°C, and because it is a preferential etchant for the {111} P growth plane leading to faceted, triangular-shaped etch pits which have a distinct apex at the emergence point(s) of the defect.

The etched surfaces were examined with a Zeiss interference contrast Photomicroscope II. On 9 × 13 cm^2 prints a final linear magnification of 2600X was obtained using the 100X objective with oil immersion. The high optical quality of the microscope allowed even further enlargements of the negatives.

The observations presented apply to LEC-pulled substrate wafers and layers grown by LPE on these wafers. Prior to etching, the {111} P surfaces were chemically polished in a Cl_2-saturated methanol bath to avoid etch pits due to damage. The appearance, the growth, and also, in the case of small microdefects, the disappearance of the etch pits was followed by choosing the appropriate etching steps. Finally, the etching features of the substrate crystals and the layers are compared in order to establish possible correlations.

In GaP substrate material etch pits due to extended dislocations [D pits (2, 3)] and to unidentified microdefects [S pits (2, 3)] have been observed previously. The new etching phenomenon reported here can unambiguously be assigned to small dislocation loops. These loops give rise to etch-pit pairs (DL pits) when they are intersected by the surface. A typical property of the DL pits was that they disappeared upon continued etching, *i.e.*, the pairs grew together and finally one shallow etch pit without apex (like the S pits) was left. At the same time new pairs became visible at other sites on the surface. This behavior established the localized nature of the corresponding defect. The change from a structured etch-pit pair to a nonfaceted shallow pit took place within 1 min etching time. This is shown in Fig. 1.

The distance between the apexes, which equals approximately the diameter of the loop, varied from crystal to crystal but was always found to be 0.5-2 μm. In some pairs the apexes were connected by a ridge, similar to that found for large stacking faults. It is therefore concluded that the latter loops are faulted loops such as observed by TEM (4, 5).

The highest density of dislocation loops was found in macroscopically "dislocation-free" crystals, *viz.*, 5×10^5 cm^{-2}. In highly dislocated (D-pit density $\sim 10^5$ cm^{-2}) crystals the density was lower and occasionally even zero dislocation-loop densities were observed. The latter phenomenon might be due to variations in as yet unknown growth parameters.

The number of shallow pits left behind by dislocation loops increases rapidly as the etching process proceeds (the etching rate for an unstirred solution is about 0.2 μm/min). It will be obvious then that, at the above-mentioned density of dislocation loops, short etching times are required to avoid an accumulation of etch pits.

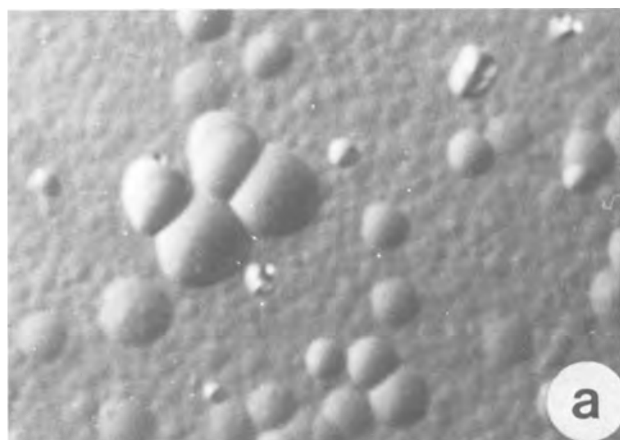

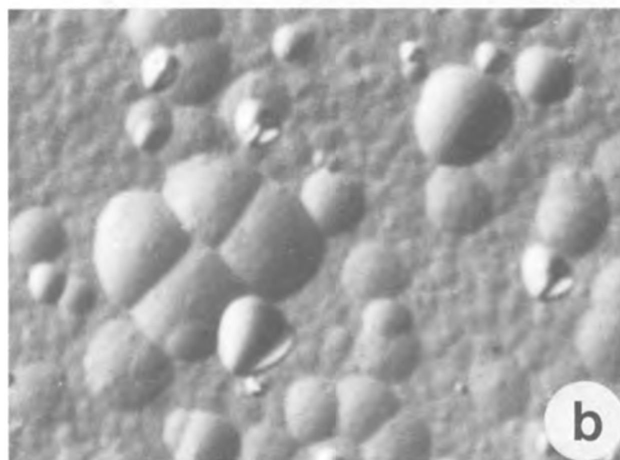

Fig. 1. Etch pits in the same area of a "dislocation-free" GaP substrate after: (a) 1½ min; (b) 2½ min etching time. The change to shallow pits and the appearance of new etch-pit pairs indicate that they correspond to small dislocation loops (DL pits).

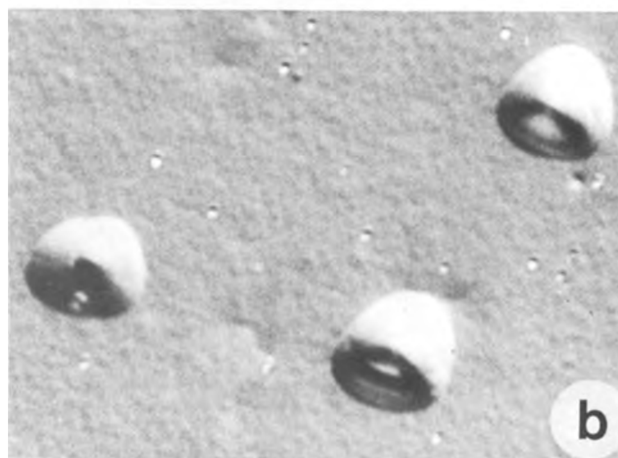

Fig. 2. Etch pits due to dislocation dipoles (DD pits) in an LPE layer grown on a "dislocation-free" substrate. The separate dislocations of the three dipoles in this area are spatially resolved after: (a) ¾ min etching time; but (b) have grown together after 3 min etching time. The other features in the photographs are due to surface irregularities.

Like for the substrate material both single and paired etch pits were observed in LPE material. The etch-pit pairs could only be resolved at high magnifications and using very short etching times, *i.e.*, ~ 3/4 min. In contrast with the etch-pit pairs in the substrate material, however, prolonged etching did not change them into shallow pits; only faceted single pits were left after 3-5 min etching time, as is shown in Fig. 2. In that stage of etching the originally paired pits were therefore hard to distinguish from the single pits. These findings indicate that both the single [D pits (3)] and the paired etch pits correspond to extended defects.

Upon correlating the surface density of the substrate defects and those of the epitaxial layer we observed that (*i*) the density of etch-pit pairs in the layer was about equal to that of its substrate for growth on "dislocation-free" substrates, and (*ii*) in layers grown on substrates without dislocation loops no etch-pit pairs were revealed. In the latter case the density of single pits in the layer was equal to that of its substrate. We therefore assign all etch-pit pairs in the layer to dislocation dipoles (DD pits) which originate from interfacial dislocation loops in the substrate. A feature like this was already observed by Petroff *et al.* (6) by means of TEM. The single pits in the layer are dislocations of the substrate which propagate into the layer.

Summarizing, it is demonstrated that the assessment of defects on a submicron scale in GaP is possible using high magnification optical microscopy techniques and properly etched surfaces. Using these techniques a correlation is established between the defect structure of epitactically grown layers and their substrates.

Acknowledgments

The author wishes to thank A. J. R. de Kock for helpful discussions and J. M. Nieuwenhuizen for assistance with the microscopy work.

Manuscript submitted July 26, 1977; revised manuscript received Nov. 7, 1977.

Any discussion of this paper will appear in a Discussion Section to be published in the December 1978 JOURNAL. All discussions for the December 1978 Discussion Section should be submitted by Aug. 1, 1978.

Publication costs of this article were assisted by Philips Research Laboratories.

REFERENCES

1. R. H. Saul, *This Journal,* **115,** 1184 (1968).
2. T. Iizuka, *ibid.,* **118,** 1090 (1971).
3. G. A. Rozgonyi and T. Iizuka, *ibid.,* **120,** 673 (1973).
4. M. Dupuy and D. Lafeuille, *J. Cryst. Growth,* **31,** 244 (1975).
5. A. J. R. de Kock, W. M. v. d. Wijgert, P. J. Roksnoer, and J. M. P. L. Huijbregts, *J. Cryst. Growth,* **41,** 13 (1977).
6. P. M. Petroff, P. G. Lorimor, and J. M. Ralston, *J. Appl. Phys.,* **47,** 1583 (1976).

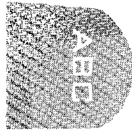

On the Thermal Analysis of Li/$SOCl_2$ Batteries

P. Bro

P. R. Mallory & Company, Incorporated, Burlington, Massachusetts 01803

The Li/$SOCl_2$ system provides a higher energy density primary battery than does any other system, 1.24 whr/cm^3 and 612 whr/kg (1), and it is of interest for many applications, some of which involve capacities in excess of 10,000 ampere-hours. For high capacity batteries, the thermal design factors may become quite important, and a requirement exists for data on the magnitude and the rate of heat generation associated with the discharge of such batteries.

An examination of the generally accepted primary discharge reaction (2,3):

$$2\ Li + SOCl_2 \longrightarrow 2\ LiCl + SO^*$$

shows that an unstable species, SO*, is formed that may be expected to react further (4) with the evolution of heat in excess of that calculated from the cell overvoltage and the cell current. Furthermore, since the SO* reactions appear to be slow, the excess heat effect may be expected to depend on the temperature, the discharge regime, and the cell design, and it would be expected to continue beyond the termination of the discharge per se.

We have found that the excess heat may be a significant quantity that needs to be taken into account in the design of high capacity Li/$SOCl_2$ batteries. This may be illustrated by some of the data from our laboratory, Table I. The data were obtained with "D" cells discharged at 25.0°C under low rate conditions. They show that the excess heat may be comparable to that calculated from the cell current and the overvoltage. There is no simple relationship between the excess heat and the discharge conditions. The total heat effect increases with the current, as expected, but the ratio of the total heat effect to the electrochemical heat effect increases at first and then decreases as the current increases from 5 ma to 20 ma. This dependency may be explained in terms of a reduction of the unstable species at the cathode.

The purpose of this brief note is to emphasize that the analysis of the heat transfer in high capacity Li/$SOCl_2$ batteries must allow for the excess heat attributable to the non-electrochemical reactions associated with the discharge process. We expect to discuss the heat generation in Li/$SOCl_2$ cells in more detail in a forthcoming paper.

Table I. The Excess Heat Evolution in Li/$SOCl_2$ "D" Cells at 25.0°C

Discharged Capacity coul.	Excess Heat Effect*, Joules Discharge Current 5 ma	10 ma	20 ma
0.5	0.099	0.156	0.188
	(0.047)	(0.059)	(0.103)
1.0	0.224	0.359	0.403
	(0.094)	(0.118)	(0.224)
2.0	0.493	0.715	0.846
	(0.186)	(0.230)	(0.442)

*The electrochemical heat effect in parenthesis. The sum of the two associated numbers is the total heat effect.

REFERENCES

1. A. N. Dey and P. Bro, Paper No. 32, Proceedings International Power Sources Symposium. Brighton, October 1976.

2. A. N. Dey, J. Electrochem. Soc. 123, 1263 (1976).

3. C. Schlaikjer, F. Goebel, and N. Marincic, Paper presented at Atlanta, GA, Electrochemical Society Fall Meeting, October 1977.

4. A. N. Dey, Thin Solid Films, 43, 131 (1977).

Key words: calorimetry, discharge reactions, heat effect, lithium cells, primary batteries

Manuscript submitted Oct. 31, 1977; revised manuscript received Nov. 16, 1977.

Publication costs of this article were assisted by P. R. Mallory & Company, Incorporated.

Annealing of GaAs Solar Cells Damaged by Electron Irradiation

Gilbert H. Walker* and Edmund J. Conway

NASA Langley Research Center, Hampton, Virginia 23665

The object of this communication is to report measurements illustrating thermal annealing of radiation damage in GaAℓAs/GaAs solar cells and to give the approximate magnitude of the short-circuit current recovery.

GaAℓAs/GaAs solar cells are of interest for space applications such as the Solar Power Satellite and near-Sun missions. With the achievement of 18.5 percent AMO efficiencies in the laboratory (1), research is being focused on the radiation damage properties of GaAℓAs/GaAs solar cells. Initially, the effect of 200°C annealing on the short-circuit current of 1 MeV electron irradiated GaAℓAs/GaAs solar cells has been studied. GaAℓAs/GaAs solar cells were grown by the etch-back epitaxy process (1). The cells had very deep junctions (approximately 4 μm) with a GaAℓAs layer thickness of 0.3 to 0.5 μm. The substrates were n-type, Si doped GaAs with a carrier concentration of 2×10^{17} carriers/cm^3. The p-type, Zn doped layer had a carrier concentration of 8×10^{18} carriers/cm^3. Back contacts were Sn-Ag and front contacts were Pd-Ag.

These deep junction cells were irradiated with 1 MeV electrons at NASA Lewis Research Center. A total of 20 cells were exposed, five at each of four fluences (10^{13}, 10^{14}, 10^{15}, and 10^{16} electrons/cm^2). A fluence of 10^{16} electrons/cm^2 is equivalent to the

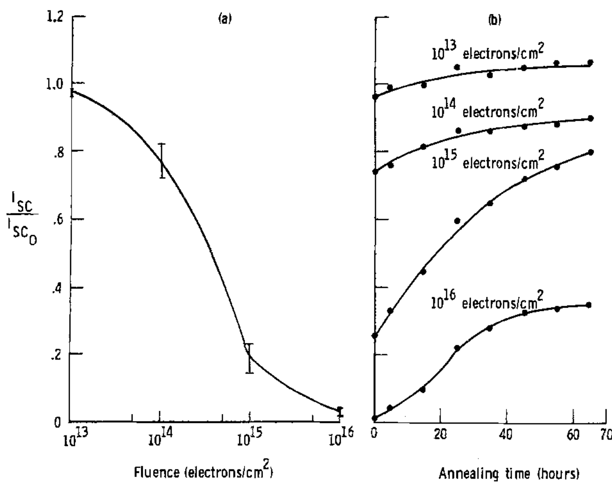

Figure 1.- Ratio of final short-circuit current to initial short-circuit current as a function of (a) 1 MeV electron fluence, and (b) annealing time at 200°C for deep junction GaAℓAs/GaAs cells.

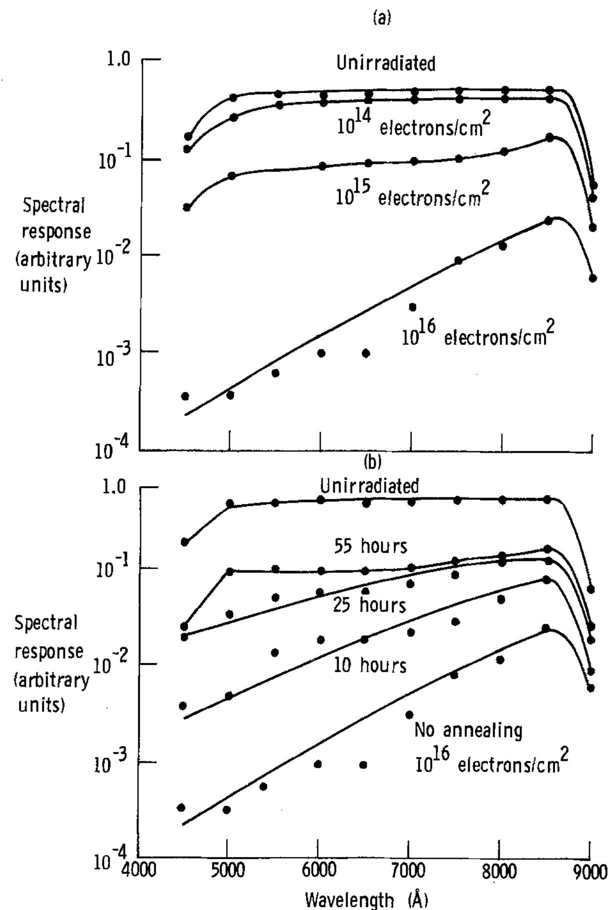

Figure 2.- Spectral response of deep junction GaAℓAs/GaAs cells: (a) unirradiated and for fluences of 10^{14}, 10^{15}, and 10^{16} electrons/cm^2, and (b) unirradiated and at 10^{16} electrons/cm^2 for various annealing times at 200°C

*Electrochemical Society Active Member
Key Words: Solar Cells, Radiation Damage, Annealing, Gallium Arsenide

electron exposure a solar cell with a 50 μm cover glass would encounter after 30 years in geosynchronous orbit. Flux levels were held such that the cells remained at ambient temperature during irradiation.

The short-circuit current under simulated AMO illumination and relative spectral response of each cell was measured both before and after irradiation. Figure 1(a) shows the ratio of the short-circuit current after irradiation to the short-circuit current before irradiation for the four fluence levels. As expected, these deep junction cells show severe degradation of short-circuit current and thus provide good vehicles for studying radiation damage in GaAℓAs/GaAs solar cells.

Figure 2(a) shows typical relative spectral response curves for unirradiated cells and cells irradiated at 10^{16}, 10^{15}, and 10^{14} electrons/cm^2. Irradiation produces a large decrease in the spectral response of the cells. Note especially the large decrease in the short wavelength response for the heavily damaged cells. This decrease in response is indicative of degradation in minority carrier diffusion length in the p-region.

A method that has been used for healing ion damage in semiconductors (2) and for healing radiation damage in semiconductors is annealing. In order to investigate the effect of annealing on the short-circuit current of 1-MeV electron-damaged cells, a representative cell at each fluence was annealed in vacuum of 10^{-5} Torr at 200°C. Measurements of short-circuit current and relative spectral response were obtained at intervals during the annealing.

Figure 1(b) shows the ratio of short-circuit currents as a function of annealing time at 200°C. The cell irradiated at 10^{13} electrons/cm^2 recovers all of its lost short-circuit current after annealing at 200°C for 15 hours. Additional annealing produces short-circuit currents slightly higher than the undamaged cell current. This is probably caused by either additional contact annealing or an increase in minority carrier diffusion length. The short-circuit current ratio of the cell irradiated at 10^{14} electrons/cm^2 recovers from 0.75 to 0.88 after annealing at 200° C for 65 hours. The short-circuit current of the cell irradiated at 10^{15} electrons/cm^2 was degraded to 0.25 by irradiation; however, after annealing at 200°C the degradation is reduced to only 0.74. The short-circuit current ratio of the cell irradiated at 10^{16} electrons/cm^2 was only 0.03; however, after annealing at 200°C the short-circuit current ratio recovered to 0.34.

Figure 2(b) shows the spectral response of the cell irradiated at 10^{16} electrons/cm^2 after different annealing times. While the entire spectral response recovers with annealing, there is significantly more recovery at the short wavelengths. This is indicative of minority carrier diffusion length increase with annealing time.

The short-circuit current recovery of 1 MeV electron damaged solar cells is significant for space applications. Assuming that the same type of annealing recovery occurs for cells irradiated with electrons of different energies and for cells irradiated with protons, it may be possible to periodically anneal GaAℓAs/GaAs solar cells while in space thus significantly prolonging the life of GaAℓAs/GaAs solar cells in space. Also, GaAℓAs/GaAs solar cells operated at high temperatures (200°C) may continually anneal radiation damage and never be degraded to any significant extent.

REFERENCES

(1) J. M. Woodall and H. J. Hovel, Appl. Phys. Lett. 30, 492 (1977).
(2) R. G. Hunsperger and O. J. Marsh, Metall. Trans. 1, 603 (1970).

ACKNOWLEDGMENT

The authors would like to thank Dr. Stanley J. Marsik of NASA Lewis Research Center for providing the irradiation facility used in these studies.

Manuscript submitted Nov. 17, 1977; revised manuscript received Jan. 24, 1978.

Publication costs of this article were assisted by NASA Langley Research Center.

Increase of the Rest Potential of Nonstoichiometric Lead Sulfide in 0.1M Borax with its p-Semiconducting Character

Claudio Gutiérrez and M. C. López

Instituto de Química Física Rocasolano, Madrid-6, Spain

We report here what we believe is the first experimental proof of the influence of the semiconducting character of a sulfide on its electrode potential. The system under study was lead sulfide in 0.1 M borax, both in air and under N_2.

EXPERIMENTAL DETAILS

The synthesis of PbS and conditioning of its semiconducting character have been described elsewhere (1). PbS was obtained by a wet method and vacuum dried. Cylindrical pellets were made in a hydraulic press. The pellets were conditioned in an evacuated Pyrex cell for not less than a week at 500°C in a system of two furnaces; the temperature of the other end of the cell, which contained a small amount of sulfur, could be varied from 50 to 200°C. The p-character of the PbS increases with its sulfur content, and this, in turn, increases with increasing temperature of the sulfur furnace (t_S).

The cylindrical pellets of PbS were joined to the end of a glass tube with Araldite; electrical contact was made with mercury. Three kinds of previous treatment were used: the "polished" electrodes were rubbed with No.400 sandpaper; for the "washed" electrodes this treatment was followed by immersion for a few minutes in 0.1 M Na_2S; and, finally, the "aged" electrodes were "washed" ones which, after having been used for electrochemical measurements, had been rubbed with No.400 sandpaper.

The Pyrex electrochemical cell was conventional. A saturated calomel electrode was connected to the cell with a double salt bridge; all the potentials are given with reference to this electrode. The solutions were 0.1 M borax, pH 9.2. When necessary nitrogen (N 47 from S.E.O., purity ≥99.997%) was bubbled through the solution; the residual oxygen concentration, measured with an Oxygen Analizer, Model 2010, from Delta Scientific, was 0.2 mg/l.

Key words: rest potential, non-stoicheiometry, lead sulfide, semiconducting character.

RESULTS

Semiconducting character of conditioned PbS.--The thermoelectric potential and Hall coefficient measurements of conditioned PbS are given in Table I. The transition from n to p semiconducting character corresponded to a sulfur temperature of about 110°C, which is in fair agreement with the value of 104°C found by Brebrick and Scanlon (2). Contrary to the expected behaviour, the value of the Hall coefficient for the n samples did not increase monotonically in absolute value with sulfur temperature up to the transition temperature; this lack of a monotonical decrease of the concentration of conduction electrodes could be due to the presence of impurities. On the other hand, the p samples showed the expected behaviour: the Hall coefficient decreased monotonically in absolute value with increasing

Table I. Thermoelectric potential and Hall coefficient of conditioned PbS pellets.

t_S/°C	Thermoelectric power/mV/°C	Hall coeff. cm^3/C
53	-0.25	-23.8
58	-0.26	- 6.2˙
60	-0.27	-29.2
66	-0.29	-16.9
101	-0.24	-10.6
108	-0.23	-11.1
115	+0.34	+ 9.3
132	+0.29	+ 8.5
195	+0.26	+ 8.0

sulfur temperature, which corresponds to a monotonical increase in the concentration of holes, these being produced by the ionization of an increasing excess of sulfur atoms.

Potential of PbS in borax.--The potential of PbS came to a steady value after a time from 10 to 40 minutes. The final rest potentials are given in Table II. For the three kinds of previous treatment, and both in air and under N_2, the rest potential increased with increasing temperature of the sulfur furnace t_S, i.e. with increasing *p*-character of the PbS, the largest potential difference being that of 320 mV for "polished" electrodes under N_2. This difference is nearly as high as the energy gap of PbS, which is of 0.41 eV (3).

Table II. Rest potentials, E, of PbS electrodes in 0.1 M borax (mV vs. SCE)

Electrodes	t_S/°C	E in N	E in air
"Aged"	145	-140	-140
"	125	-150	-150
"	66	-190	-190
"	58	-200	-200
"Polished"	145	-110	-110
"	125	-150	-150
"	66	-420	-320
"	58	-430	-340
"Washed"	145	-350	-210
"	125	-360	-230
"	66	-410	-260
"	58	-425	-280

The potential of PbS under our experimental conditions is certainly a mixed (corrosion) potential in which an anodic reaction (oxidation of PbS) and a cathodic reaction (probably reduction of O_2, as in germanium (4)) take place at the same rate on the surface. The increase of the final potential of PbS with its *p*-character could be due to a change of the exchange current i_0 for one or both of the processes with the variation of the semiconducting character of PbS. An increase of i_0 for the cathodic reaction with increasing *p*-character of germanium was postulated by Lovreček and Bockris (5) to explain their finding that the rest potential of *p*-Ge was 5 mV more positive that of *n*-Ge.

ACKNOWLEDGEMENTS

The authors wish to thank Dr.J.A. Pajares for the Hall effect measurements, and Dr.F. Colom and Dr.M. Sánchez for their valuable help. One of us (M.C.L.) is indebted to the Ministerio de Educación y Ciencia for a P.F.P.I. scholarship during three years.

REFERENCES

1. J.M.Gamboa, C.Gutiérrez, and J. Llopis, An.Real Soc.Esp.Fís.Quím., B64, 679 (1968).
2. R.F.Brebrick, and W.W.Scanlon, Phys. Rev., 96, 598 (1954).
3. R.Dalven, Solid State Phys., 28, 179 (1973).
4. W.W.Harvey, and H.C.Gatos, THIS JOURNAL, 105, 660 (1958).
5. B.Lovreček, and J.O'M.Bockris, J. Phys. Chem., 63, 1368 (1959).

Manuscript submitted Oct. 20, 1977; revised manuscript received Nov. 8, 1977.

Publication costs of this article were assisted by the Instituto de Quimica Fisica Rocasolano.

Simple Method of Fabricating and Passivating High Power Pin Diodes

A. Rosen, G. A. Swartz, F. C. Duigon, and A. M. Gombar

RCA Laboratories, Princeton, New Jersey 08540

In this paper we describe the fabrication of a moat configuration deep-diffused PIN diode which is used as a switch in a microwave circuit.

A PIN diode is composed of an undoped I-region bounded by a heavily-doped P-type layer on one side and by an N-type layer on the other. When the diode is reverse-biased, the I-region is swept free of mobile charge carriers so that the diode approximates a low-loss capacitor. During forward biasing, holes and electrons are injected into the I-region from the P and N layers, forming a dense plasma of electrical charges, which ultimately converts the previous high-resistivity I-region into a conducting medium. In this stage, the PIN diode acts like a fixed resistor.

The moat configuration device, Fig. 1, has been developed in order to eliminate shadowing of the diode junction by the metal overhang during deposition of a sputtered passivation layer. The evaluation of PIN diodes passivated by rf bias sputtered SiO_2 and Si_3N_4[1,2] and having film thicknesses of 2250Å and 2500Å respectively utilizing this technique has included a temperature bias test (blocking test) in addition to the moisture resistance, temperature cycling, and thermal shock tests (MIL-STD-883A). In this test, diodes were reverse-biased up to 400 V at temperatures of up to 175°C without any failure.

PIN diodes which have a 150 μm thick mesa structure with a metal overhang (Fig. 2) in contrast to the moat configuration which is only partially etched, have been passivated with SiO_2 and Si_3N_4 using the sputtering technique. These diodes have shown excess current leakage, and under severe reverse bias tests eventually burned at 130°C. By contrast, diodes from the same batch which were passivated by the use of plasma-deposited silicon nitride layers have survived the blocking test up to the required temperature of 175°C. The sputtering technique was found to be inadequate due to metallization shadowing of the junction (overhang), which prevent uniform coverage. The passivation by plasma deposition was more uniform. The moat configuration, which eliminates the overhang, permits the utilization of either sputtering or plasma techniques, and is an attractive way of processing high-power PIN diodes.

The silicon wafer, with an n^+ contact layer on one surface and a p^+ contact layer on the opposite surface, is metallized on both sides, Fig. 3. Metallization contacts are defined on the p-side by utilizing photoresist techniques, after which moats are etched to produce a mesa structure. The moat diameter, which is 5 mils larger than the metallization diameter, is defined also by photoresist and the silicon is etched to a depth of 25 μm. This procedure eliminates metal overhang (Fig. 3.). A spreading resistance plot of the p^+n^- and n^+n^- structure made by probing the conductivity of an angle-lapped wafer section is shown in Figs. 4 and 5.

The moat configuration diode, having multilayer passivation with SiO_2 and Si_3N_4 by the sputtering technique, withstood all tests in accordance with military specifications MIL-STD-883A. A reverse bias test of 400 V (blocking test) was performed at temperatures up to 175°C for 160 hours without any failure.

Diodes fabricated by this simple method

have also demonstrated good uniformity and high yield. The electrical characteristics of the moat configuration PIN diodes are similar to those described before with the exception of breakdown voltage (V_{BD}). V_{BD} obtained with the negative level mesa is 800 V as contrasted with 1000 V PIN diodes previously described.[4,5]

Acknowledgement

The authors wish to thank J. Murr and E. Mykietyn for their technical assistance; J. Zelez and L. Penticolas for their aid in diode passivation. We also wish to thank L. Napoli, R. D'Aiello, and J. Vossen, for their helpful advice.

REFERENCES

1. J. L. Vossen, "Control of Film Properties by rf-Sputtering Techniques," J. Vac.-Sci. Technologies, 8, p. 512 (1971).

2. A. W. Stephens, J. L. Vossen & W. Kern, "The Effect of Substrate Bias on Reactively Sputtered Silicon Nitride," J. Electrochem. Soc., 123, p. 303 (1976).

3. R. S. Rosler, W. C. Benzing, J. Baldo, "A Production Reactor for Low-Temperature Plasma-Enhanced Silicon Nitride Deposition," Solid State Technology, June 1976, p. 45-50.

4. P. T. Ho, G. A. Swartz & A. Schwarzmann, "Low Loss PIN Diode for High Power MIC Phase Shifter," 1977 IEEE ISSCC, Vol. XX, p. 82.

5. G. A. Swartz, A. Rosen, P. T. Ho, and A. Schwarzmann, "Low-Loss PIN Diode for High Power MIC Phase Shifter," to be published.

Manuscript submitted Jan. 2, 1978; revised manuscript recieved Jan. 24, 1978.

Publication costs of this article were assisted by RCA Laboratories.

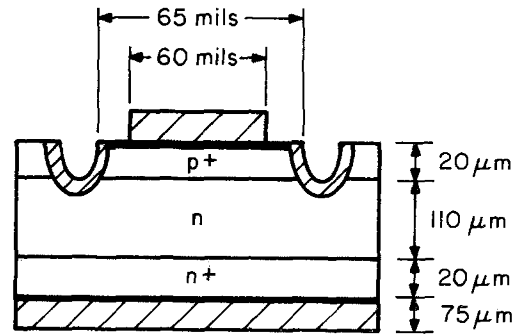

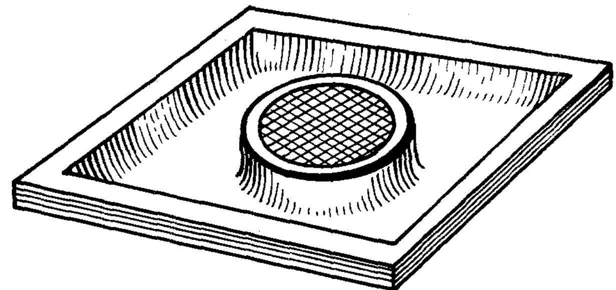

Fig. 1. Moat configuration PIN diode with SiO_2 and Si_3N_4 Passivation.

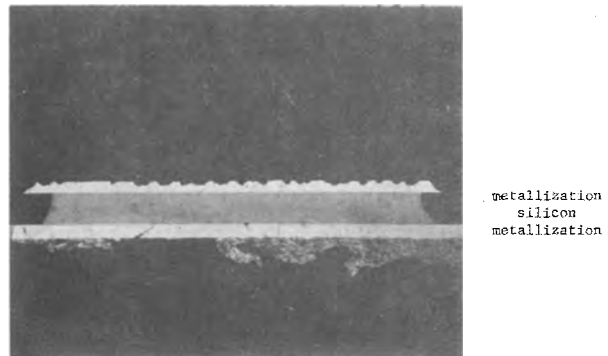

Fig. 2. Mesa structure PIN diode.

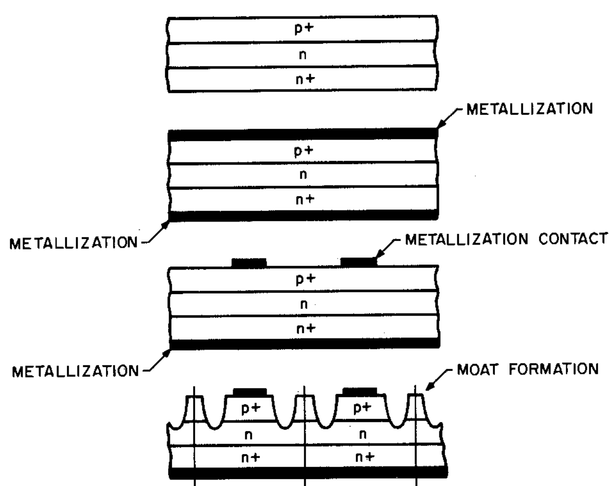

Fig. 3. Moat configuration processing steps.

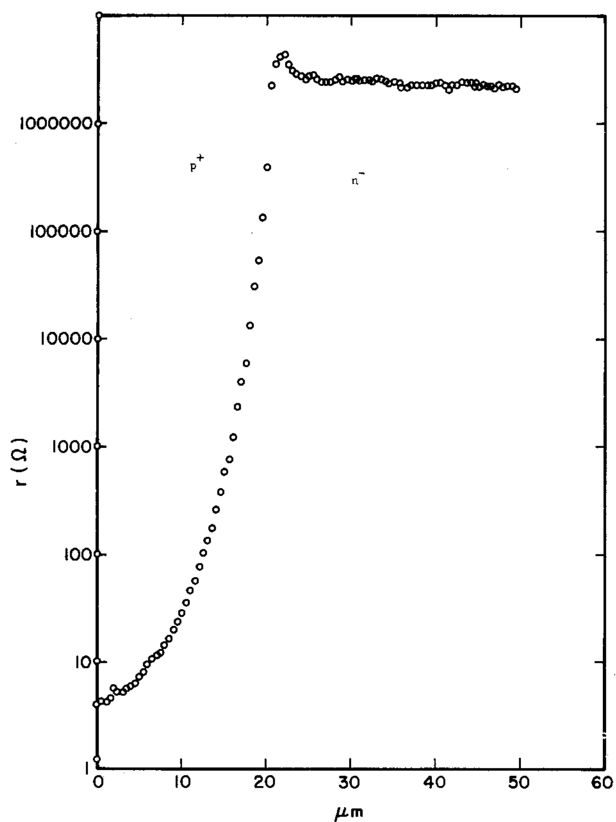

Fig. 4. Spreading resistance as a function of distance across p^+-n junction.

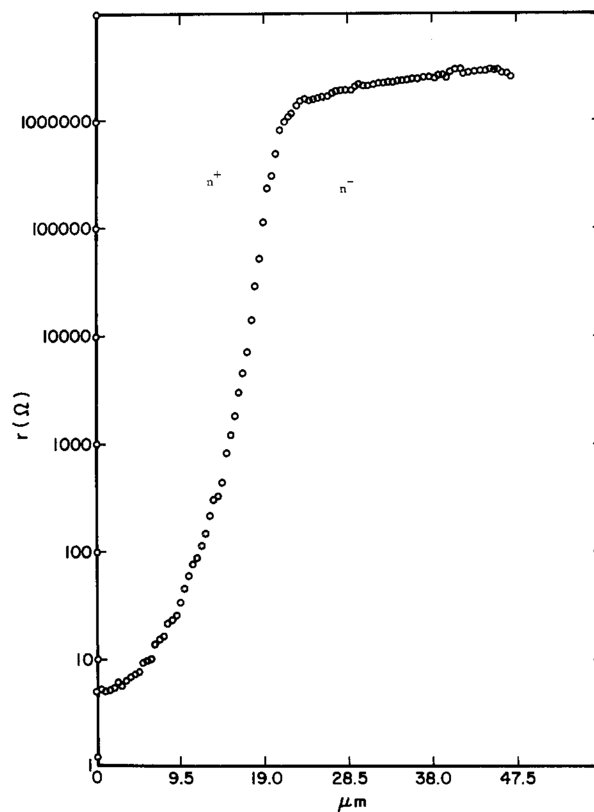

Fig. 5. Spreading resistance as a function of distance across n^+-n junction.

JOURNAL OF THE ELECTROCHEMICAL SOCIETY

REVIEWS AND NEWS

JANUARY 1978

Report of the Electrolytic Industries for the Year 1976[1]

F. B. Leitz*

U.S. Department of the Interior, Bureau of Reclamation, Denver, Colorado 80225

and C. J. Harke*

Hoooker Chemicals Canada Limited, North Vancouver, British Columbia, Canada V7H 1S4

RN

Chlorine—Caustic Soda

I. Production and capacity.—Total chlorine production in the United States and Canada for 1976 was 11,374,000 tons. This was an increase of 12.7% over the 1975 figure but 4.8% below the record high of 11,942,000 tons in 1974. Breakdown of chlorine and caustic production figures are as follows (1, 2, 57):

Chlorine production	United States	Canada
First half of 1976	5,077,000 tons	486,000 tons
Second half of 1976	5,290,000 tons	521,000 tons
Total in 1976	10,367,000 tons	1,007,000 tons

Caustic production (liquid and solid)	United States	Canada
1976 (100% NaOH basis)	10,147,000 tons	922,000 tons

Although production for the year was up considerably, the industry was still below the traditional rates of capacity use. Both the United States and Canada had increases in the capacity use rate; in the United States this increased from 72% in 1975 to 80% in 1976, while in Canada the rate went up from 68% to 75%.

During 1976, new or expanded facilities started up at seven locations in the United States. One new facility went on stream in Mexico, none in Canada. Production capacity will be increased considerably over the next 2 years. A number of large expansions and new plants are in various stages of engineering and construction. (See Table 1A and 1B)

There has been no appreciable change in chlorine capacity by production method, viz (9):

	United States	Canada
Diaphragm and membrane cells	73.7%	68.0%
Mercury cells	21.4%	32.0%
Other	4.9%	None

II. Prices and markets.—Chlorine production increased considerably during the year but, over-all, the industry did not fully recover from the recession in 1975. Production dropped in several chlorinated hydrocarbons, and there were no indications that this trend will be reversed. Chlorine producers were faced with higher energy prices and other operating costs. Chlorine prices in the United States were relatively stable in 1976. Late in the fourth quarter, Gulf Coast prices were raised $10 to $135 per ton. Prices in other regions, which ranged from $135 to $150, remained unchanged (10).

There were no major changes in markets or usage of chlorine, *e.g.*, vinyl chloride, propylene oxide, solvents, inorganic chemicals, pulp and paper, and water and wastewater treatment. Significant increases in chlorine demand growth will be required over the next 2 years to balance present unused production capacity plus the large increments of new capacity. The impact of new air emission standards on the plastic industry is unknown. Fluoro-chlorocarbon producers may experience further declines in demand. Chlorine used in pulp bleaching, which accounts for about 13% of chlorine production in the United States, has had a growth rate of only 3.5% during the last few years. This could drop to 2% if changes in bleaching are accepted (11).

The demand for caustic during the year was weaker than for chlorine, and producers in many locations were faced with high inventories. An economic slump in the aluminum industry followed by a slow recovery affected the chlorine-caustic balance in 1976. Although aluminum metal production is up considerably, there was a lag in caustic demand as the aluminum industry was gradually reducing high inventories of alumina. Caustic prices in the United States fluctuated downwards slightly and at year end were in the $140-$160 per ton range. Imported bulk caustic in the Gulf Coast regions was running considerably below published prices. The situation in Europe was similar as producers were faced with extremely high inventories due to below normal activity in alumina production (12, 13).

The pattern of caustic consumptions remained essentially unchanged and main markets were in the following areas: organic chemicals, pulp and paper, inorganic chemicals, soaps and detergent, alumina, petroleum, rayon, and cellulose. Approximately 10% of caustic production was exported. Growth of aluminum demand in automobiles, containers, etc., and amount of recycle will have a bearing on caustic demand. Another unknown is in the pulp and paper industry where competition from soda ash is possible. Increasing the recycle of pulping chemicals will reduce usage of caustic. Demand for certain agricultural chemicals is high (7, 14).

There were no changes in chlorine or caustic markets in Canada where the industry is highly dependent on the pulp and paper economy. Over 50% of the total chlorine production is consumed in pulp bleaching. Second largest usage of chlorine is vinyl chloride. Caustic imports accounted for 12% of the total 1,042,000 tons consumed in 1976. Breakdown of the caustic usage pattern in Canada for the year was as follows:

[1] This report is sponsored by the Industrial Electrolytic Division of The Electrochemical Society. It presents a summary of published information on production and developments in the chlor-alkali and related industries and on other electrolytic industries. The material presented herein has been gathered from many sources, as noted in the reference list, and does not necessarily represent the opinions of the authors.

* Electrochemical Society Active Member.

Table 1A. Changes in current chlorine operations (3-6, 8, 9)

	Producer and location	Cell type/change	Capacity, tons/ day chlorine	Completion date
1.	Vulcan Materials Co. Geismar, La.	Diamond MDC-55 (diaphragm)	600	November 1976
2.	Diamond Shamrock Corp. Painesville, Ohio	Shutdown of facility (diaphragm)	250	September 1976
3.	Kaiser Aluminum and Chemical Corp. Gramercy, La.	Hooker (diaphragm) Expansion	37	May 1976
4.	Stauffer Chemical Co. Henderson, Nev.	Modernization, Diamond MDC-29 (diaphragm)	320 (unchanged)	November 1976
5.	General Electric Co. Mt. Vernon, Ind.	Hooker H-2A (diaphragm)	—	November 1976
6.	Mobay Chemical Co. Baytown, Texas	Uhde (HCl) Expansion	100	March 1976
7.	Dow Chemical Company Plaquemine, La.	Dow (diaphragm) Expansion	500	1976
8.	Georgia Pacific Corp. Bellingham, Wash.	DeNora (mercury) 20% expansion	—	1976
9.	Pennwalt del Pacifico Guadalajara, Jalisco, Mexico	Diamond DS45 (diaphragm)	—	May 1976
10.	Alcan Smelters and Chemicals Jonquiere, Que., Canada	Shutdown (mercury)	—	June 1976

Table 1B. New or expanded chlorine plants planned or under construction (7, 9)

	Produced and location	Cell type	Capacity, tons/ day chlorine	Status	Completion date
1.	Olin Corp. McIntosh, Ala.	Hooker H-4 (diaphragm)	1,000	Engineering	1st Quarter 1978
2.	BASF Wyandotte Corp. Geismar, La.	Diamond (diaphragm) Modest expansion	—	Underway	2nd Quarter 1977
3.	BASF Wyandotte Corp. Port Edward, Wis.	DeNora (mercury) Modest expansion	—	Underway	2nd Quarter 1977
4.	PPG Industries, Inc. Lake Charles, La.	Glanor® 1144 (diaphragm)	750	Underway	3rd Quarter 1977
5.	Hooker Chemicals and Plastics Corp. Niagara Falls, N.Y.	Hooker H-4 (diaphragm)	450	Engineering	1st Quarter 1978
6.	Hooker Chemicals and Plastics Corp. Tacoma, Wash.	Expansion	400-675	Engineering	Mid 1979
7.	Pennwalt Corp. Portland, Ore.	Diamond (diaphragm) Expansion	200	Building	1st Quarter 1977
8.	E. I. du Pont de Nemours Corpus Christi, Texas	Diamond MDC 55 (diaphragm)	1,000	Underway	2nd Quarter 1977
9.	Dow Chemical Co. Freeport, Texas	Dow (diaphragm) Expansion	500	Underway	1977
10.	Dow Chemical Co. Freeport, Texas	Dow (diaphragm) Expansion	500	—	1978
11.	Dow Chemical Co. Freeport, Texas	Dow (diaphragm) Expansion	1,000	—	1979
12.	Dow Chemical Co. Plaquemine, La.	Dow (diaphragm) Expansion	500	—	1977
13.	Dow Chemical of Canada Fort Saskatchewan, Alta., Canada	Dow (diaphragm) Expansion	900	Approved	3rd Quarter 1977
14.	Cloro de Tehuantepec SA Pajaritos, Veracruz, Mexico	Glanor® 1144 (diaphragm)	500	Underway	1st Quarter 1977
15.	Industrias Quimicos de Istomo SA Parjaritos, Veracruz, Mexico	Diamond MDC 55 (diaphragm)	—	Engineering	2nd Quarter 1977

Pulp and paper	62%
Propylene oxide	10%
Alumina	7%
Soaps and cleaners	6%
Inorganics	5%
Rayon, cellulose	2%
Other uses	8%

Caustic demand was depressed due to a slowdown in pulp and paper production and a prolonged strike in the aluminum industry. Expansions planned in the plastic industry will alter the use pattern of both chemicals and chlorine-caustic balance. Although imports will drop, Canada is expected to remain a net importer of caustic (2, 15).

Steady growth of 5% annually through 1985 was predicted for chlorine and caustic by one major United States producer. This was based on adequate energy and a balanced demand for both products. Vinyl chloride which is also the largest outlet was stated as the strongest market for chlorine whereas pulp and paper was the weakest. For caustic, organic chemicals were predicted as having strong markets and alumina a weak market during this period (7).

Changes in demand for both chemicals and lower growth rates were predicted for the next decade, according to a United States market consultant. Uncertainties in future demand for chlorine in chlorinated compounds, increasing cost and availability of energy, and environmental-related costs were given as factors that could affect future growth (16).

III. Membrane cells.—Worldwide interest and effort in the development of ion-exchange membranes and commercial testing of cell systems is continuing at a high level of activity. Major incentives for chlorine-caustic producers to test new membranes and evaluate membrane cell technology are: lower over-all energy consumption, high purity products, replacement for asbestos, mercury cell conversions.

Commercial operation of a membrane plant, rated at 40,000 metric tons per year of caustic soda, was announced by Asahi Chemical Industry Company of Japan. This plant has been in operation since April 1975, at Nobeoka on Kyushu Island. Initially, commercial testing was done with du Pont's Nafion® membranes but more recently a perfluorocarboxylic acid membrane developed by Asahi Chemical is being substituted for the du Pont membranes. The major advantage claimed with their own membrane is better current efficiency which is over 90% for caustic concentrations up to 40%. Electrolyzers are large and a single unit is capable of producing 10,000 metric tons per year of caustic soda. Along with the membrane cell, Asahi Chemical designed a special heat-recovery evaporator (17).

Another Japanese firm, Asahi Glass, reported producing 200 metric tons per month of caustic soda since

September 1975, at Osaka City. Performance disclosed after 6 months of testing was 90-92% current efficiency with 40-41% caustic, power consumption of 3300 kW-hr per metric ton of caustic soda. The type of membrane is not known (18).

More recently, Tokuyama Soda announced startup by January 1977, of a 1,000 metric tons per month of caustic soda pilot plant at Tokuyama City. Both du Pont's and their own membrane will be tested in the commercial size cells (19).

Diamond Shamrock Corporation announced startup of a membrane cell circuit at its Muscle Shoals plant in Alabama. The cells will replace mercury cells now operated at this location. The membrane used will be Diamond's modification of du Pont's Nafion®. Production of 30-40% caustic at 85% current efficiency was stated (20).

Toyo Soda plans to construct a new 2,000 metric tons per month caustic soda plant at its Sakata factory with provision for 50% expansion. Hooker MX® membrane cells will be used (21).

Asahi Chemical has licensed its membrane cell technology to Denki Kagaku Kogyo for a 40,000 metric tons per year caustic soda plant at Omi (22).

The first membrane cell plant in Europe will be at Uddeholms pulp and paper complex in Skoghall, Sweden. Cells used will be Diamond Shamrocks' new membrane cell. The plant, rated at 20,000 metric tons per year of chlorine, is scheduled to start up by the end of 1977 (23).

du Pont is proceeding with engineering for a plant to manufacture Nafion® or perfluorosulfonic acid products. No date has been set for start of commercial production (24).

Maruzen Oil Company in Japan will start regular production of its new ion-exchange membrane in the fall of 1976. Unlike du Pont's and other membranes of the fluorine type, Maruzen's membrane is suitable for use in "three-cell" type of electrolyzers (25).

IV. Developments.—The Bureau of Mines is studying the feasibility of recovering chlorine and iron oxide from ferric chloride. During a test with low density ferric chloride, the chlorine product reached a concentration of 92% with the balance being oxygen. Economics were not discussed but the process indicates feasibility of producing chlorine from recycle (26).

The Japan Soda Industry Association is sponsoring development work at Kyoto University on fused salt electrolysis using the β-alumina diaphragm method. Current efficiency on laboratory scale tests was almost 100%. Cell voltage at 50 A/dm^2 was given as 3.18V (27, 28).

Asahi Glass Company has developed a method for removing salt from the diaphragm cell caustic process. This method is capable of reducing salt to less than 0.1% in 50% caustic, and costs were given as one-third of those for existing methods. The company is working on technology which will reduce the salt content to less than 0.02% in 50% caustic (29).

Diamond Shamrock Corporation has acquired research facilities, patents, and other assets in the field of industrial electrochemistry previously owned by Electronor Corporation (31).

Supported by the National Science Foundation, the University of North Carolina is developing chemical modification techniques for electrodes. Reactive molecules were covalently bonded to the surface of an electrode. Such molecules did not interfere with the electrochemical effectiveness of the electrode but can be used to perform reactions in tandem with the electrochemical ones at the electrode. They can provide a more favorable environment for the electrochemical reactions or participate themselves as intermediates in electrochemical reactions occurring at the surface of the electrode. Research workers are searching for a reversible electroactive surface molecule which could be bound selectively to electrodes to assist the electrochemical reaction (32).

Researchers at Pennsylvania State University claim that iodine may replace chlorine as a swimming pool disinfectant. Iodine is more effective against organic matter, does not irritate the eyes, and is easier to monitor. One drawback is its ineffectiveness against algae (33).

New developments in ozone generators for sewage and water treatment have resulted in significant reductions in the cost of producing ozone. Ozonation as a replacement for chlorination is gaining in interest. The city of St. Johns, Newfoundland, is installing Union Carbide's ozonator for treatment of their 11 million-gal/day potable water supply. A joint development by Accelerators, Incorporated, Austin, Texas, and R. P. Industries, Incorporated, Hudson, Massachusetts, has produced a generator which can produce ozone at energy-consumption cost of less than 10 cents per pound. This new approach produces ozone from untreated air in an electron beam generator. A prototype system is being installed at Marlboro, Massachusetts, to treat 1 million gal/day of water discharged from a sewage plant (34).

V. Mercury Cells.—There were no new mercury cell plants in the planning or construction stage in the United States or Canada during 1976. The 80 tons per day chlorine plant, Prince Albert Pulp Company, Saskatoon, Saskatchewan, will be converted from mercury cells to membrane cells supplied by Asahi Chemical Industry, Osaka City. Diamond Shamrock at their Muscle Shoals, Alabama, site announced conversion of mercury cells to membrane cells of their own design. Capacity was not reported (20, 35).

Conversion from mercury cells to other types of cells in Japan has been further delayed. At the end of September 1975, the original goal of 64.6% conversion set by the Japanese Ministry of International Trade and Industry (MITI) was not reached as only 34.5% was converted to mercury-free methods. The March 1978 date for completion of the second-phase conversion program is also seriously lagging, and the goals will have to be revised. By April 1976, only 59.3% was converted. Delays were attributed to the severe recession, difficulties in raising capital, equipment deliveries, uncertainties with respect to diaphragm cell *vs.* membrane cell technology and low rate of capacity utilization (36, 37).

Efforts are continuing toward further reduction in the level of mercury discharge from plants. Osaka Soda and Okayama Chemical carried out investigations and process modifications at their plants and reported achieving less than 1.5g mercury per ton of NaOH in a new plant and less than 2.5g in an older type plant (38). A closed mercury cell process developed by Kashima Chlorine and Alkali will be used by Diamond Shamrock in their United States plants. Requirements of 1g mercury per ton of chlorine were reported. (39).

New ion-exchange resins, ImacTMR®, developed by Akzo Chemie, Netherlands, are reported to be more selective than other resins in mercury removal from effluent streams. Levels in chlor-alkali plant effluent have been reduced to 5 ppb mercury with the new resins, compared to 0.1-1 ppm for other resins and methods (40).

United States production of primary mercury in 1976 totaled 20,000 flasks (76 lb). This was produced in four mines, three in California and one in Nevada which was starting to supply a larger share of the market. Secondary production dropped 53% below that produced in 1975. The General Services Administration established a new strategic stockpile goal of 54,004 flasks and at year end the stock pile contained 191,407 flasks. Stocks of 28,500 flasks held by producers, consumers, and dealers at year end were only slightly below 1975 year-end stocks (41).

Consumption of mercury for 1976 was estimated at 65,000 flasks, a 25% increase over the previous year. Usage by chlorine-caustic producers was essentially unchanged from the reported 15,200 flasks in 1975 (41).

World production of mercury dropped about 3% to 242,300 flasks in 1976. Producers in Mexico and Italy reduced or completely shutdown mercury mining operations. Canadian mining operations which closed down in 1975, because of the poor economy, did not reopen in 1976. There were reports that producers in Spain, Italy, and U.S.S.R. dropped out of international marketing of mercury (41).

EGAM, a mercury producer in Italy, shut down in October for 3 1/2 years to upgrade facilities and improve operating economics (42).

VI. Health and environment.—There is an increasing tendency to equate chemicals, particularly chlorinated organics, with carcinogens. However, there is no agreement on how to establish safe levels of exposure or on what constitutes an acceptable risk. Methods in use today provide only qualitative indications in many instances and test results are difficult to express on a quantitative basis. More long-term testing is believed to be necessary, and it will be some time in the future before test results can be translated into "meaningful and practical regulations" (43-45).

A spokesman for the Synthetic Organic Chemical Manufacturers Association predicts carcinogens as a long-term problem for the chemical industry. The science of toxicology, already complex, is further complicated by a number of governmental agencies with different philosophies. The Occupational Safety and Health Administration (OSHA) is expected to announce new standards for chemical carcinogens in 1977 or early 1978. The new regulations and sequence of testing for carcinogens can have far-reaching implications (46).

Two chlorinated organics, trichlorethylene and chloroform, have been singled out by the National Cancer institute as probable causes of cancer in humans. Based on animal tests, the findings were considered definitive for animals, but the extent of risk in humans cannot be predicted. However, it can serve as a warning on possible carcinogenicity in humans (47).

The Toxic Substance Control Bill is expected to become law on January 1, 1977. All chemical producers will be subject to terms of this bill. The main feature of this legislation is that manufacturers will not be able to commercialize new chemicals without notifying the Government. Producers of chemicals which have been linked with health hazards such as chlorinated organics can expect closer scrutiny. The U.S. Environmental Protection Agency (EPA), under this bill, will require 90 days notice before manufacture and distribution of chemicals that may be considered as risks in public health or to the environment (48).

Tighter controls are being imposed on the plastics industry, as in-plant control of vinyl chloride monomer (VCM) emission was extended to cover the industrial community. With authority under the Clean Air Act, the EPA has declared VCM as a hazardous air pollutant. Air emission standards proposed would reduce VCM entering the air within a 5 mile radius of the plant by more than 90% when compared to emission standards in 1974. These new standards, announced October 21, allow plants only 90 days to comply with the regulations. Vinyl chloride, ethylene dichloride, and polyvinyl chloride producers are presently seeking extensions of up to 2 years in order to install control equipment. Higher PVC prices are anticipated as a result of additional control equipment and higher operating costs (49, 50).

Environment Canada is proposing to reduce atmospheric emissions of mercury to 5.3g per day for each 1000 kg of chlorine production. Total atmospheric release from mercury cell plants is expected to drop from the current 12 tons to 2 tons mercury per year. Some plants, particularly older facilities, will require further capital expenditures (51).

Recognition of the potential dangers from airborne asbestos emissions is increasing. The proposed regulation under discussion would reduce the limit to 0.5 fiber per cubic centimeter in a time weighted 8 hr average. Establishment of a dose-response level has been difficult. Medical surveillance and studies on workers exposed to asbestos emissions are continuing in many countries. OSHA has emphasized the complexity of the regulatory process which results in a long lapse of time from issuing a proposed standard to publication of a regulation. Against a background of strict emission limitations, Johns-Manville indicated that the supply is lagging the demand and the industry is 2-3 years away from starting new asbestos mines (52).

The National Institute for Occupational Safety and Health (NIOSH) has recommended to OSHA that exposure of workers to chlorine be reduced. NIOSH proposed an exposure limit of 0.5 ppm for periods of not more than 15 min. The present standard is 1 ppm for a time-weighted average 8 hr per day (53).

The Food and Drug Administration (FDA) is asking for information on the safety and use of chlorine in food processing. The exposure of a wide variety of foods to chlorine when used as processing aids is coming under closer scrutiny. Safety data to justify such uses will be reviewed by the FDA and general guidelines covering the safe use of chlorine in food processing will eventually be published (54).

Burning of PVC plastics can release significant amounts of methyl chloride which is capable of dissociating into chlorine atoms and destroying the ozone layer in the stratosphere. The two main sources of man-made methyl chloride were cited as combustion of PVC plastics in wastes and fires in buildings containing PVC materials of construction. Unless combustion of PVC is rigidly controlled, release of methyl chloride is expected to rise as a result of greater use of PVC materials (55).

The EPA is urging a worldwide approach to the control of fluorocarbon emissions in the air by regulating emissions and conducting atmospheric research. EPA is preparing a 10 yr research budget for stratospheric research (56).

Other Alkaline or Chlorine Compounds

I. Caustic potash.—Production of caustic potash in 1976 was 226,800 tons as 88-92% liquid. This is an increase of 6% over the previous year (57).

The caustic potash market improved somewhat during the year but production plants were still running well below capacity. Total United States production capacity of 335,000 tons per year is made up from six producers. viz. (59):

IMC	95,000
Diamond Shamrock	87,000
Monsanto	55,000
Hooker	53,000
Pennwalt	25,000
PPG	20,000

The price of caustic potash remained at $7.50 per 100 lb, 45% basis, throughout 1976. In November, a new price of $8.00 was announced and this will become effective January 1, 1977 (59).

United States production of marketable potassium salts dropped slightly from 2.5 million in 1975, to 2.4 million tons in 1976, expressed as K_2O equivalent. About 2 million tons or 82% of the production came from New Mexico with the balance from Utah and California. Potassium muriate from Canada constituted nearly 3.8 million tons as K_2O equivalent or 96% of total imports (58).

The price of standard bulk potassium muriate from Canada and New Mexico dropped to 55-70 cents per unit of K_2O (20 lb of K_2O) during the June through August period. Prices for the fall season (September through January) were quoted at 70-75 cents per unit. Prices for the spring season (February through May) of 1977 are expected to increase by 5 cents per unit (60, 61).

During the second half of 1976, there were indications that the potash market was slowly improving as inventories dropped and shipments increased. Based on reports from the first World Fertilizer Conference, growth in potash can be expected as increased consumption of fertilizers will be necessary to assist in meeting the world's food production requirements. A world potash demand of 31 million tons was predicted by 1980 (62, 63).

A degree of uncertainty with respect to raw materials exists as the result of the Saskatchewan government's first move to nationalize the potash industry. Duval Corporation's 1.5 million tons per year plant was purchased by Potash Corporation of Saskatchewan, a Crown company. The $128.5 million purchase price was short of the $150 million price sought by Duval. Engineering is proceeding with a 25% expansion of the mine. Negotiations are in progress for the purchase of two more potash companies. The Government is planning to buy a 51% interest in the potash industry and only use expropriation if purchase agreements cannot be negotiated. Although the Government has given assurance of unrestricted supplies with no manipulation of prices, there is some skepticism in the United States by government and industry. About 70% of the Saskatchewan potash is marketed in the United States (63-65).

International Minerals and Chemical Corporation (Canada) is engaged in a potash exploration project in the Salt Springs region of New Brunswick. The company is encouraged by core data which are showing potash averaging 28-32% K_2O. It is too early to determine the economic feasibility of the project. Core testing is expected to continue for 1 to 1 1/2 years. The company is also engaged in exploration of potash deposits in Northern Ontario. First-phase drilling tests indicated yields of about 24 million tons of recoverable potash. However, commercial development of the deposit cannot be justified under current economic conditions (66, 67).

II. Soda ash.—Domestic production of soda ash increased 7.6% from 7.13 million tons in 1975 to 7.6 million tons in 1976 (68). Natural soda ash (trona) increased from 4.33 to 5.19 million tons (69), while synthetic (Solvay process) soda ash decreased from 2.80 to 2.42 million tons.

Expansion in capacity for natural soda ash continues. Total capacity was estimated to be 7.3 million tons per year at the end of 1976 and is expected to be 8.8 million tons per year by the end of 1977.

Most natural soda ash is mined in Wyoming. FMC Corporation's 0.75 million tons per year expansion of the Green River, Wyoming, soda ash plant will make it the world's largest at 2.5 million tons per year (70). Texasgulf, Incorporated, joined other Wyoming producers when a 1 million tons per year plant started production in October; this plant is expandable to twice its present production capacity (71, 72). About 1.8 tons of ore were mined for each ton of soda ash produced. Stauffer Chemical Company was adding 0.2 million tons per year to the company's existing 1.35 million tons per year capacity. Allied Chemical Corporation has 2.2 million tons per year capacity. Numerous other companies held trona leases in the Green River area. The Green River formation contains an estimated reserve of 50 billion tons of ore (73).

Natural soda ash is also produced at Searles Lake, California, by carbonation of lake brines. This process has produced about 400,000 tons per year for the past several years. Kerr-McGee is expanding their facility from 0.145 to 1.3 million tons per year at a cost of $175 million, the expansion to be completed in 1977 (74).

The number of synthetic plants decreased from four to three with a total capacity slightly greater than 2 million tons (75, 76). Diamond Shamrock shut down its 800,000 tons per year Painesville, Ohio, plant at year end. Reasons cited for closing the plant, started up in 1912, were the plant's age, stringent pollution-control standards, escalating energy costs, and competition from natural soda ash. The remaining synthetic producers are Allied at Syracuse, New York, BASF Wyandotte at Wyandotte, Michigan, and PPG Industries at Corpus Christi, Texas.

Consumption in the United States was estimated to be 7.0 million tons in 1976, an increase of approximately 7% over 1975 (68). Approximately one-half is used in glass making, another quarter is used in formulation of detergents, and the rest in miscellaneous uses.

Exports and imports are a small component of the soda ash market. Exports, primarily of refined material, increased to an estimated 502,000 tons, 7.6% of production. Imports for consumption were negligible at 1,000 tons.

Average prices of soda ash in 1976 were up 19% from the previous year (77). List prices on December 31, 1976, ranged from $57 to $71 per ton. In general, synthetic soda ash is $15 to $20 per ton more expensive, f.o.b. plant, than the natural product.

III. Sodium chlorate.—Sodium chlorate production in the United States for 1976 was a record 196,400 tons. This represents a 17% increase over the 1975 total of 167,700 tons (57).

Production capacity in the United States is 253,500 tons per year with facilities at 12 locations. In Canada, sodium chlorate is produced in 11 facilities for a total capacity of 226,000 tons per year (78, 79).

Demand for sodium chlorate remained strong throughout the year with tight supply situations occurring on the west coast. By midyear, chlorate capacity in North America was sold. Pulp bleaching remains the principal market for sodium chlorate. More chlorine dioxide, derived from sodium chlorate, probably will be required as pulp mills increase chemical recycle. Pulp and paper producers are forecasting the possibility of continuing short supply situations in 1977 (80, 81).

Effective July 1976, the price of bulk sodium chlorate was raised from $250 to $280 per ton. In December, further increases brought the price of bulk up to $300-$310 per ton. Similar price increases were experienced in Canada where end of year prices for bulk sodium chlorate were $250-$256 per ton (82-85).

The ERCO Industries division of Albright and Wilson, Limited, will expand chlorate output at several locations. At Buckingham, Quebec, a 12,000 ton per year expansion is scheduled for April 1977. An additional 15,000 tons per year is slated for the first quarter of 1978. This will bring ERCO's capacity at this location to nearly 77,000 tons per year. At the Vancouver location, modifications to electrical equipment and electrolyzers are expected to add 6,000 to 10,000 tons per year. The company's total capacity in Canada should reach 125,000 tons per year in 1978. A 50,000 ton per year sodium chlorate plant on the Gulf Coast was announced by ERCO. The first phase of 20,000 tons is scheduled for the first quarter of 1979 (86, 87).

More recently ERCO Industries, Limited, announced plans to build a new chlorate plant at Thunder Bay, Ontario. Initial capacity of 25,000 tons per year will consist of 15,000 in the first stage for early 1979 completion and 10,000 in the second stage (88).

In November, Dow Chemicals canceled its planned facility at Thunder Bay. The plant was to have an initial capacity of 30,000 tons per year and was scheduled to go onstream in 1977 (89).

Pennwalt Corporation will construct a new sodium chlorate plant at its Tacoma plant site. Capacity was not disclosed. First phase is expected to go onstream in early 1978 (90).

The Electrochemical Division of International Minerals and Chemical Corporation plans to build a 40,000 ton per year sodium chlorate plant at its Orrington, Maine, plant site. Start up is scheduled for mid-1978 (91).

Olin announced construction of a 6,000 tons per year plant at its chlor-alkali plantsite in Niagara Falls, New York. Start up is scheduled for late 1977, with two-thirds of production going to captive use (92).

Table 2. Summary of new or expanded sodium chlorate plants

Producer	Capacity, tons per year	Completion
1. ERCO Industries		
Buckingham, Que. Canada	Expansion — 12,000	April 1977
Buckingham, Que., Canada	Expansion — 15,000	1st Quarter 1978
North Vancouver, B. C. Canada	Expansion — 6,000-10,000	1977
Thunder Bay, Ont., Canada	New — 1st phase — 15,000	1st Quarter 1979
	2nd phase — 10,000	—
Gulf Coast, U.S.	New — 1st phase — 20,000	1st Quarter 1979
	2nd phase — 30,000	—
2. Pennwalt Corp. Tacoma, Wash.	New — 1st phase — —	1st Quarter 1978
3. International Minerals and Chemical Corp. Orrington, Me.	New — 40,000	Mid 1978
4. Olin Corp. Niagara Falls, N.Y.	New — 6,000	4th Quarter 1977

Stanchem, Beauharnois, Quebec, increased production to 33,000 tons per year, a 10% increase, by installing metal anodes developed by Kema-Nord and PPG Industries (78).

New or future expansions of sodium chlorate plants in the United States and Canada are summarized in Table 2.

Metals

I. Aluminum.—United States production of primary aluminum was 4,240,000 tons in 1976. Although this represents a 9.3% increase over the 1975 figure, production for 1976 was still 13.5% below the record year of 1974. Total aluminum supply for 1976, was 6,370,000 tons which was a 14% increase over the previous year but still well below the 7.3 million total for 1974. Secondary recovery of aluminum for 1975, totaled 1,451,000 tons. This was a 23% increase over the previous year (93). Recovery from the 1975 recession in the aluminum industry was slow. At the start of 1976, primary aluminum producers were operating at a 75% rate and by mid-March the rate was still only 76%. However, production gradually improved to 85% by midyear and by year end had climbed further to 94% of capacity. Canadian producers operated at 80% at the beginning of the year, dropped to 42% during the strike, and by year end were at 71% (94, 95).

With prospects for improvements in aluminum demand and due to lower inventories, idle capacity was restarted at various locations (96-98). Another reason for bringing on idle capacity was the Alcan strike in Canada. The 5 month strike crippled nearly 600,000 tons per year capacity and full production will be delayed another 3 months due to damaged potlines (99, 100).

Imports of crude, semicrude, and scrap aluminum were up by about 55% over the previous year. Exports of crude and semicrude increased by 20% compared to 1975. Total metal inventories of aluminum decreased gradually by about 10% during the year (101).

United States aluminum producers raised the price of primary ingot from 41 to 44 cents per pound in April. A further increase to 48 cents went into effect in August (102, 103). Tight supplies in early 1977 were predicted by economists, and this could result in further escalations in price (104).

The slow economic recovery in the aluminum industry resulted in postponement or cancellation of a number of new alumina projects, viz. (105-108):

1. The 880,000 tons per year refinery in Ireland proposed by Alcan and two partners.
2. West Pacific Alumina's 800,000 metric tons per year refinery on Mindanao in the Philippines.
3. A 400,000 metric tons per year refinery planned for Bintan Island in Indonesia by Sumitomo Chemical, Showa Denko, and Nippon Light Metal.
4. Pacminex's option to build a 1.2 million metric tons per year refinery in West Australia.
5. Comalco's 320,000 metric tons per year at Gladstone, Australia.
6. Alcan's 200,000 tons per year smelter in Quebec.

New projects in different stages of planning or construction were announced, viz. (101, 109-113):

1. A 1 million metric tons per year plant, built by a consortium including France's PUK, will be located on the Black Sea in Russia.
2. Russia will assist Indonesia with a 600,000 metric tons per year refinery on Bintan Island.
3. Reynolds Metals and partners are planning a 1 million tons per year refinery in Wagerup, Australia.
4. An aluminum project agreement between Brazil and Japan will include a 320,000 metric tons per year smelter at Belem.
5. Completion of a second 70,000 tons per year potline at New Madrid, Missouri, was announced by Noranda.
6. The feasibility of adding an additional potline at Alcoa, Texas, is being studied by Alcoa.

The U.S. Bureau of Mines expects the United States demand for aluminum to grow about 6% per year until 1985, and then relax to a growth of 4.5% per year over the next 15 years. A major uncertainty is usage of aluminum in the automobile industry. Recycled aluminum is expected to show steady growth. By 1989, 40% of the United States requirements could be met by secondary aluminum (114, 115).

Aluminum producers in the Pacific Northwest, who have a 31% capacity of United States total, may be faced with a power crisis in the mid-1980's. Bonneville Power may not be able to renew their power contracts which are based on cheap hydroelectric power. Power from other sources will be more expensive (116).

A trend towards more aluminum in automotive use in order to improve fuel economy is predicted. Present usage of 87 lb per car is estimated to increase up to 9[illegible]-100 lb for 1977. Forecast figures are 150-300 lb for 1980, and by 1985, this is expected to rise to 200-425 lb per car. Another reason for increased use in automobiles is Aloca's development of new sheet alloys which offer scrap compatability and other improved characteristics (117-120). A new aluminum radiator was developed by Union Carbide (121).

The industry's goal of reducing energy consumption by 10% from 1972 to 1980 appears to be possible. Since 1972, the industry has achieved a 6.5% reduction (122).

Bauxite production in the United States, an increase of about 11%, was 2 million tons in 1976. Imports of dried and calcined bauxite were about 13 million tons, up slightly from 1975, but below 1974 imports. Jamaica, Guinea, and Surinam remained the main sources of bauxite. Alumina imports, which largely came from Australia, were about the same as 1975 (101).

Alcoa and the Jamaican Government reached an 8 year agreement on levies and a 40 year agreement on ownership of Jamaica's bauxite mining and refining facilities (123). Separate settlements between Jamaica and Reynolds and Kaiser were reported to be very close to final agreements (124). Disputes between Revere and Jamaica over the government's bauxite production levy have not been resolved (125).

Present distribution of known bauxite reserves is estimated as follows (126):

Africa	38%
Australia	25%
America	22%
Europe	8%
Asia	7%

The Jamaican Bauxite Institute's latest estimate of Jamaican reserves is 2 billion tons (127).

A major milestone in new process technology was achieved when Alcoa energized cells in late May at its new smelter at Palestine, Texas. Initially rated at 15,000 tons per year, the plant will eventually be increased to 300,000 tons per year. This process cuts 30% off the most efficient power requirement for a net of 4.2 kW-hr/lb. Instead of electrolyzing alumina directly, chlorine is used to produce aluminum chloride, which is then electrolyzed. The chlorine is recycled. In addition to the energy saving, the process is free of fluoride emissions, the working environment is improved, and power interruptions can be tolerated (128, 129).

The Energy and Mineral Resources Research Institute at Iowa State University is working on two different processes to obtain alumina or aluminum chloride from flyash which has an average alumina content of 22% (130). The Bureau of Mines is coordinating a cost-sharing program with nine companies to develop processes for recovering alumina from domestic nonbauxite materials. Kaolinitic clay was tested in the first two processes (101).

According to a Russian foreign trade journal, the U.S.S.R. has developed techniques for the production of alumina from nepheline, alunites, kaolin, shale, ash, and other alkali-free alumo-silicates. Southwire Company of Carrollton, Georgia, has licensed a U.S.S.R. alumina-aluminum process. An 8,700 tons per year pilot plant at Golden, Colorado, will produce alumina from alunite. The process yields alumina and potassium sulfate (131, 132).

The United States EPA has set pollution control standards for new and modified smelters. Removal of 95% of the fluoride emissions from the air before discharge will be required (133).

II. Beryllium.—Data on production of beryllium metal and products are not published. However, production is believed to have increased from depressed 1975 levels (134).

Brush Wellman, Incorporated, and Kawecki Berylco Industries, Incorporated (KBI) are the only substantial producers of beryllium in the free world. Brush extracts beryllium from bertrandite ores ($Be_4Si_2O_7(OH)_2$), mined in Millard County, Utah, while KBI relies on imported beryl ores (135). Brush Wellman announced a planned expansion of the extraction facilities at Delta, Utah. The expanded facilities will also have the capability of processing beryl ore. When completed this will represent about 90% of the extraction capability in the free world (134).

Metal consumption in 1976 was thought to be equal to or slightly less than in previous years, which was estimated to have been 260 tons. The market breakdown based on contained beryllium was estimated to be: 70-80% beryllium-copper alloys, 15-20% beryllium metal, and 4-8% beryllium oxide. This represents an increase in usage of the alloys and a decrease in the use of the metal.

Alloys with copper containing 0.5-2.0% beryllium have greater strength and resistance to fatigue and corrosion than copper, and are used for a wide variety of specialty products. Beryllium metal is used in aerospace and nuclear applications. The oxide is employed as a refractory and in electronic devices.

Prices for beryllium metal, quoted as 5 in. rod, remained unchanged at approximately $155 per lb during 1976 (136, 137). The price of imported beryl ore (10-12 BeO) rose from $30 to $42 per short ton.

The over-all production and consumption of beryllium ores in 1976 was about the same as in 1975 (135). In the first 10 months of 1976, 815 tons of beryl were imported. This can be compared to 1,550 tons in 1975, and to the peak importation of 6,422 tons in 1969. The major source of the imports was Brazil followed by France, India, Australia, and other countries.

Exports of beryllium metal, alloys, waste, and scrap totaled 163 tons in the first 11 months of 1976, compared to 17 tons for the similar period in 1975. The major importers were the United Kingdom and Japan (134).

As of November 30, 1976, government stockpiles of beryllium contained 229 tons of beryllium metal, 7,387 tons of Be-Cu master alloy (4% Be) and 17,986 of beryl. These were unchanged from year end 1974. During 1976, the General Services Administration announced new stockpile objectives: for beryllium metal, 895 tons, an increase from 88 tons, and for the master alloy, 16,710 tons, an increase from zero. The stockpile objective for beryl remains at zero (135).

III. Chromium.—Although the demand for chromium was higher in 1976 than in 1975, it did not reach the record demands established in 1973-1974. Total chromite consumption was 1,040,000 tons and all three consuming industries reported increases in consumption, viz.

Metallurgical	20% higher
Refractory	10% higher
Chemical	10% higher

Consumption of chromium alloys was 22% higher than the previous year due to increased production of stainless steel (138).

Imports of chromite which totaled 1,350,000 tons is only slightly higher than in 1975. Shipments were higher from South Africa, Finland, and Turkey but lower from U.S.S.R., Rhodesia, and Philippines. Shipping problems and political disputes plagued the Rhodesian and South African chrome industry. Due to delays in shipments from some countries, India was offering chrome for export (138-140).

Imports of ferrochromium, although down 16% from the previous year, are still at a high level, and this has resulted in higher inventories at producer and consumer locations. The 1976 total was estimated at 270,000 tons. Depressed demands for ferrochrome alloys are expected to continue in 1977. Inventories remain high and there was an oversupply of imported alloys. The situation is not expected to improve until stocks of steel products diminish (138, 141).

Despite opposition from domestic ferrochrome producers, it appears likely that the Byrd Amendment of 1972 would be repealed and embargoes on Rhodesian chrome would be reimposed. Dependence on Rhodesian chrome has been dropping steadily. Countries such as Brazil and Turkey have made substantial expansions in chrome mining and smelting. If the embargo is imposed, activity in domestic production will increase. Mine owners reported production capacity of mines in Del Norte County, California, at 120,000 tons per year (147).

On October 1, the Federal Preparedness Agency established new government stockpile goals for chromium materials. Inventories in government stockpiles of refractory and chemical grade chromite were below the new goals at year end (138).

Foote Mineral discontinued its chrome alloy business (142).

There was essentially no change in published chromite prices from those of 1975. High-chromium chromite also remained at the same price. Year-end prices were:

High-chromium Russian	- $136 per ton
High-chromium Turkish	- $120-129 per ton
High-iron South African	- $35-$42 per ton

Chromium alloys dropped in price. United States charge chromium decreased from 50 cents per pound to 43 cents by year end. Low-carbon ferrochromium dropped from $1 per pound to $0.85 during the year. Chromium metal increased from $2.44 per pound to $2.63 (138).

The 120,000 tons per year Tubatse Ferrochrome plant at Steelport, South Africa, a joint venture of Union Carbide and General Mining, is not expected to start up until 1977. Union Carbide will discontinue charge chrome production in the United States when ship-

ments of charge chrome start flowing from this plant. The Turkish state-owned plant, Etibank, with a capacity of 50,000 metric tons per year is behind schedule and probably will not start until 1977. Johannesburg Consolidated Investments and Showa Denko plan to start up a $50 million ferrochrome plant at Lydenburg in early 1977. The impact of large power increases in South Africa is not clear. Power rates increased 15% in April, 13% in September, and 25% is expected in January 1977 (143, 144).

Three Japanese companies, Nippon Kokan, Itoh and Company, and Kokan Mining, are studying a chromo ore venture in Kenya (145). The Sudanese government plans to double chromite production from 25,000 to 50,000 metric tons per year over the next 2 years (146).

Increased interest and activity in domestic production of chromite was evident during the year. A firm in California rehabilitated a mine and plant that had been idle since the 1950's. Mining of chromite was last reported in 1961. Mining interest in northern California and southern Oregon reactivated the Cal-Ore Chrome Producers Association and construction of a mill is under discussion (138).

Research is continuing by the Bureau of Mines to recover chromium from laterites and low-grade domestic resources. Successful development could extend world resources of chromium and provide a broader geographical supply base. Research on recovery of chromium from waste material is also continuing (138).

IV. Copper.—Production from primary materials at refineries in 1976 was 1,537,188 tons, 6.5% above 1,443,378 tons in 1975. Smelter production from primary materials was 1,534,622 tons, up 6% over 1,447,128 tons in 1975. Production of refined copper from scrap was 374,480 tons, up 8.7% from 344,480 tons in 1975. Stocks at year end were 189,500 tons of refined copper, 312,000 tons of blister, and 137,913 tons of scrap, essentially unchanged from year end 1975 (148).

Asarco dedicated its new Amarillo facility in June 1976. The plant, which actually came on stream in late 1975, has a capacity of 420,000 tons per year of copper at a cost of $190 million. Copper reaches the plant in three forms: anodes from smelters in El Paso, Texas, and Hayden, Arizona, blister copper from both foreign and domestic smelters, and No. 2 grade scrap. Copper from Amarillo will be available in all shapes used by industry: cathodes, wirebars, cakes, billets, and continuous cast rod (149).

The new solvent-extraction-electrowinning plant of Cities Service Company in Miami, Arizona, went on stream. The plant has a design capacity of 15 tons per day of cathode copper (150).

Anaconda announced plans to reopen its Arbiter plant in Anaconda, Montana, in July (151).

Asarco scheduled closing of the 188,000 tons per year refinery at Perth Amboy, New Jersey (152).

Consumption of primary refined copper (apparent consumption) was 1,825,000 tons, up 39% from 1,310,000 tons. Total consumption (including secondary recovery materials) increased 27.7% from 1,534,505 to 1,960,075 tons (148).

The Federal Preparedness Agency set a stockpile goal of 1.299 million tons of copper. Since the previous stockpile goal was zero, the 20,261 tons from the previous stockpile that remained unsold was transferred into the new stockpile. The new goal is thought to be excessive by many industry observers who note that domestic production is adequate for present national needs (153, 154). Pending congressional action, the government may become a substantial copper consumer.

Mine production, expressed as recoverable copper, increased 19% from 1,413,366 to 1,611,341 tons. Production occurred predominantly in Arizona (63%) followed by Utah (12%), New Mexico (11%), and others (148).

Production start-up at Hecta Mining Company's Lakeshore mine near Casa Grande, Arizona, was delayed by slippage in the construction schedule. Full production was expected in the second quarter of 1976 (155).

After investing more than $30 million in land acquisition and drilling, Continental Oil Company has indefinitely postponed plans for development of its 800 million tons orebody near Florence, Arizona. This decision was attributed to marketing uncertainties (156).

A major copper find south of Crandon, Wisconsin, was announced by Exxon Corporation (157).

Amax has stepped up exploration of the Minnamax copper-nickel prospect in Minnesota (158).

Eisenhower Mining Company will develop a 27,000 tons per year open pit copper mine to work the Palo Verde copper deposit south of Tucson, Arizona. The deposit contains an estimated 125 million tons of ore grading 0.6% copper (159).

Homestake Copper Company has reported finding a new copper deposit in the Keweenaw Peninsula in upper Michigan (160).

Some production cost guidelines were provided by industry spokesmen. According to Arthur Reef, Vice President of Amax Incorporated, the cost of developing a new mining complex in the western U.S. from mine through refinery has risen from $3,500 per annual ton in 1970 to at least $6,500 per annual ton at the end of 1976. By 1980, the cost is expected to be $7,500 in 1976 dollars (161). U.S. copper producers would need a price of 80-85 cents per pound to expand capacity at existing facilities and higher prices to justify construction of a new operation according to Phelps Dodge President, George B. Munroe (162). These remarks were confirmed by J. C. Agarwal, Director of Kennecott Copper Corporation's Ledgemont Research Center, who was quoted as saying that the investment for copper has reached from $6,000 to $6,500 per annual ton and that it would take a price of $1.25-$1.50 per lb to support such an outlay (163).

The price per pound of U.S. producer electrolytic copper (delivered) as quoted by Metals Week opened the year at 63.6 cents just below the average for 1975. It increased to 70.6 cents in May and again to 74.6 cents in July. Strength held through September when the slide, some said "crash", began, which left the December price at 65.8 cents. A general explanation of this behavior was widespread speculation supported by a general anticipation that an over-all economic recovery had set in (148, 164).

Imports exceeded exports but the difference was a small factor in the total domestic market picture. Imports of refined copper were 384,002 tons up 162% over 146,809 in 1975. Exports of refined copper, alloyed scrap and unalloyed scrap were down 28% from 316,641 to 227,000 tons (48).

Free world production of refined copper was 7,362,000 tons, up 6.68% from 6,901,000 tons in 1975, but down 3.9% from 7,660,000 tons in 1974. Each year the United States was the largest producer followed by Japan and Zambia. Free world mine production was 6,431,000 tons of copper, up 1.8% from 6,317,000 tons in 1975, but down 5% from 6,769,000 tons in 1974. The largest producers were the United States, Chile, and Canada (164).

Granby Mining Corporation planned to end operations at the Phoenix copper mine near Grand Forks, British Columbia, because of exhaustion of ore reserves. Production recently had been running 1 million tons per year (165).

Production at the Thierry copper mine near Pickle Lake, Ontario, was started in August after expenditure of about $100 million by Union Miniere Explorations and Mining Corporation. The mine has a 4,000 tons per day mill and concentrator. Reserves are estimated at 15 million tons containing 1.63% copper (166, 167).

The Mexican La Carida copper project is scheduled for startup in 1978. This includes a mine at Nacozari with an initial production rate of 79,000 tons per day of ore and a 500 tons per day smelter at Empaline. Costs are approximately $400 million for the mine and $240 million for the smelter (168).

Devaluation of the peso may permit reactivation of the LaVerde Project, at Michoacan, Mexico. The project was slated to produce 38,500 tons per year of electrolytic copper after an investment of $96 million (169).

Agreements were signed between Texasgulf and the Panamanian government concerning development of the Cerro Colorado copper deposit, perhaps the largest known undeveloped copper deposit in the world. According to current estimates an open-pit mine could produce 33 million tons of ore for at least 70 years. The project is estimated to cost $800 million (170-172).

The Cuajone Project in Southern Peru came on-stream at a completion cost of $655.7 million. When in full production the project will produce 170,000 tons per year of blister copper (173).

Androcollo, in Central Chile, with estimated ore reserves of 330 million tons of 0.7% copper will become a joint venture of Noranda and the Chilean government. Three other large copper properties are still being offered by the Chilean government to foreign investors (174).

Codelco, the state-run copper corporation, predicted that being Chile's largest copper exporting company, it would produce an average of 800,000 tons per year between 1976 and 1980 (175).

A large scale expansion of its Ertsbert copper mine at Tembagapura, Indonesia, is being considered by Freeport Indonesia. In 1975, the mine produced 225,000 tons of copper concentrate (176).

Construction of a 92,900 tons per year copper smelter, the first smelter in the Philippines is expected to start in 1977, with first production in 1978. The smelter using Outokumpu Oy's flash process is estimated to cost $250 million (177).

A 66,000 ton expansion of the tankhouse at Hoboken-Overpelt's Olen (Belgium) electrolytic copper refinery was commissioned in 1975, increasing capacity to 363,000 tons per year (178).

A copper smelter and refinery complex is planned for Onsan, South Korea. The complex will have a capacity of 88,000 tons of cathode copper per year and be readily expandable to 110,000 tons. The complex to cost $180 million is scheduled to start in 1979 (179).

Watching wildflowers may pay off. The Swedish state-owned mining company LKAB has announced discovery of an estimated 22 million tons of 1.0-1.5% copper ore in Viscarra Field, Sweden. The deposit was discovered when a geologist observed that the alpine carnation, a plant which survives in earth having a high copper content, grew in abundance in the area (180).

Deposits of ore rich in copper have been located in Kauria, Bihar, India. These are believed to be the largest known deposits in India (181).

Western Selcast and Mount Isa Mines announced a rich find of copper, silver, and zinc in the Teutonic Bore area northwest of Leonara, Western Australia (182).

A feasibility study of the Ok Tedi copper prospect in Papua-New Guinea has confirmed the existence of at least 275 million tons of copper ore. The government indicated that an operation of about 50,000 tons per day seems certain to go ahead (183).

Deposits roughly estimated at 200 million tons have been found in the Chagai district in Baluchsstan, Pakistan (184).

Low copper prices affected operations at several locations. The Israeli government closed the Timna copper mines (185). The 97 year old mine at Mt. Morgan in Central Queensland, Australia, faced closure by the end of 1976. The work force was reduced and an associated mill was closed in February (186). Plans to double copper production and exports by opening new mines at Quansimi and Tazalaght, Morocco, have been seriously affected (187). Broken Hill South has decided to wind down all operations at the Kanmantoo mine in South Australia, only 4 years after its launching because of continuing losses (188). Mt. Lyell Mining and Railway Company, Limited, is closing down two mines in Queenstown, Tasmania, but keeping its main mine open (189). Plans to build a 132,000 tons per year electrolytic refinery in Cape Province, South Africa, have been shelved by O'Okiep Copper Company, Limited and Tsumeb Corporation. Cost of the project was initially estimated at $44 million (190).

The giant Tenke Fungurume copper project in Zaire was suspended in January because of soaring costs which produced nearly insurmountable financing problems. Later in the year members of the consortium were conducting independent studies on the feasibility of smaller plants (191, 192).

The Polish government announced plans to increase copper output by 70% to 468,000 tons per year for the period 1976-1980. This encompasses enlarging mines at Ubin, Polkovice, and Rudna, opening a new mine at Sieroszowice, expanding smelters at Legnica and Glogow I, and building new smelting complexes at Gedynia and Glogow II (193).

A newly developed copper deposit at Reosk, Hungary, will raise annual ore production to 8-9 million tons. This will eliminate that country's needs for copper imports (194).

The Soviet Union is exploring the possibilities of western involvement in development of the massive Udokan copper mine northeast of Lake Baikal. The deposit is estimated to contain some 2 billion tons of ore averaging 1.3-1.5% copper. Initial construction would be a plant with a capacity of 400,000 tons per year. Cost including mine development, a smelter, and a refinery is estimated at $1 billion (195, 196).

Domestic industry continues to have environmental difficulties. An Arizona decision on water rights may affect massive mining and processing operations south of Tucson (197). Proposed sulfur dioxide regulations for Arizona smelters are not as harsh as expected but they may affect the Phelps Dodge Douglas smelter on which $20 million had been spent to meet state standards when Federal standards were not known (198, 199). Asarco received a 5 year variance for its Tacoma, Washington, smelter on arsenic and sulfur dioxide emission levels after agreeing to spend $4.7 million during that period on emission controls (200). The Environmental Protection Agency and Kennecott Copper Corporation are still at odds over means of meeting sulfur dioxide emission standards at the smelter at McGill, Nevada. The plant has been closed since August 1 (201).

V. Lithium.—The United States continues to remain as the world's major producer and consumer of lithium. Exports, primarily to Western Europe and Japan, amount to about 20% of production. Imports, exports, and domestic consumption increased by about 11% over 1975.

United States and world usage is mostly in the form of chemicals, primarily lithium carbonate; the balance is mostly lithium hydroxide monohydrate. Amount of lithium metal marketed is comparatively small. The pattern of usage is unchanged (203).

Foote Mineral Company and Lithium Corporation of America, with mining and processing facilities in North Carolina, continued as major suppliers. Late in the year, a new processing unit went on stream at Foote's Kings Mountain, North Carolina, plant and added 12 million lb per year of lithium carbonate. Other sources of lithium carbonate were derived from subsurface and lacustrine brines at Searles Lake, California, and Silver Peak, Nevada (202, 203).

Surplus lithium hydroxide was available and for sale by the General Services Administration and by year end about 400,000 pounds had been sold. Stockpile remaining was about 3.1 million pounds (203).

Prices for lithium and various types of lithium compounds increased during 1976, and prices going into 1977 were (204-206):

Lithium carbonate	$0.84 per lb
Lithium hydroxide (monohydrate)	$1.46 per lb

Lithium chloride	\$1.75 per lb
Lithium metal ingots	\$11.60 per lb

Energy developments in two major fields could place a strong demand on lithium reserves. Although commercial development of nuclear fusion is not expected to be completed until the early decades of the 21st century, large quantities of lithium would be required if the breeder-coolant design concept were utilized. Secondly, in the not too distant future, lithium-type batteries could put a strain on supplies of lithium. According to Argonne National Laboratory, commercial introduction of electric cars is anticipated in 1985. Based on design life of 10 years and 25% annual growth rate, batteries for electric vehicles would require 70 million lb of new lithium annually. One of Argonne's high energy primary batteries, a lithium-iron sulfide type, is expected to have a cell energy-density ratio of 80-85 W-hr per lb. The high operating temperature of 380°-450°C has caused design problems with corrosion and materials of construction (207).

Matsushita Electric Industrial Company, Osaka, has developed a lithium-polycarbon monofluoride type of battery which is reported as having the world's highest density. A license has been granted to Eagle-Picher to manufacture and sell the battery in the United States (208).

A lithium-metal sulfide battery similar to Argonne's is being developed by General Motors. Exxon Enterprises has revealed research on a lithium battery that operates at room temperature but has an energy density in the 50-60 W-hr per lb range. These and other researchers of advanced battery systems probably will be encouraged by the Electric Vehicle Development and Demonstration Act which was passed in September. Ultimately, the nonmarine subsurface brines may become a greater source of lithium (207).

VI. Magnesium.—Figures on domestic production of magnesium are not published, but it appears that production was limited by available plant capacity. Dow Chemical, the major producer, has a 111,000 metric tons per year plant at Freeport, Texas. American Magnesium Company at Snyder, Texas, increased production from 4,000 to 5,500 metric tons per year. Northwest Alloys at Addy, Washington, brought its 22,000 metric tons per year plant into production (209, 210).

The NL Industries plant at Rowley, Utah, was essentially out of service for all of 1976. The \$110 million complex completed in 1972 was to produce 40,000 metric tons per year. A series of problems prevented production from exceeding 12,000 metric tons per year. Following an analysis by Norsk Hydro, Norwegian magnesium manufacturer, and a successful series of tests, NL Industries plans to go ahead with a \$30 million modification program and expects to operate at 25,000 tons per year in 1977 (211-213).

United States consumption of magnesium was estimated at 125,000 short tons (214). The largest single market for magnesium is in alloys with aluminum. This accounts for about 50% of the magnesium consumed in the United States. Other uses which are expected to increase in importance are steel desulfurization, die castings, and various applications in the automotive industry.

Prices of magnesium rose during 1976. Beginning at values which had held for all of 1975, 82 cents per lb for ingot and 85 cents per lb for die casting alloy, magnesium prices were increased in steps to 92 cents per lb for ingot and 94 cents per lb for alloy at year end (215-217).

For the first time the United States became a net importer of magnesium in 1976. Total imports were 19,800 tons with the following breakdown: metallic and scrap, 12,968 tons; magnesium content of alloys, 1,820 tons; and sheet, tubing, and other, 20 tons. Exports were 13,441 tons of which 12,279 tons were metal and alloys in crude form and 1,162 tons were semifabricated. Exports were 58.8% below those of 1975 (218).

Outside the United States, Chromasco in Canada has a capacity of 5,000 metric tons per year and Norway produces about 45,000-50,000 metric tons per year. Total production by members of the International Magnesium Association in 1976 was 178,115 metric tons, a slight increase over the 173,597 metric tons produced in 1975 (209). This association does not include producers in the U.S.S.R. who are believed to turn out about 50,000 metric tons per year.

Norsk Hydro has announced plans for a complex at Mongstad, Norway, to include production of 100,000 metric tons of magnesium and simultaneous production of chlorine to feed an ethylene dichloride plant. If tests being conducted at Heroya, Norway, are successful, the company will install an initial increment of 30,000 metric tons per year. Over-all costs are expected to reach \$200 million (209).

VII. Manganese.—There was no production of manganese ore, concentrate, or nodules containing 35% or more manganese in the United States during 1976. Manganiferous ores of lower grade continued to be produced and shipped from New Mexico and Minnesota.

Production of ferromanganese dropped in the latter part of the year but the total consumption of manganese increased. Ferromanganese imports for 1976 surpassed those of the previous record year. Main suppliers of ferromanganese and manganese ore were:

Ferromanganese:	South Africa	35%
	Japan	20%
	France	18%
Manganese Ore:	Gabon	41%
	Brazil	25%
	Australia	17%

New stockpile goals for the various grades of ore and types of manganese were established by the General Services Administration on October 1. Releases from stockpiles continued to be very high and consisted mostly of ore (220).

Price of standard high carbon ferromanganese (minimum 78% Mn) was reduced in early January from \$440 to \$425 per long ton and it remained at this price for the remainder of the year. Prices of imported alloy of the same grade dropped about 12% during the year and by mid-November the price range was \$345-370 per long ton. Prices declined even further in the lower grades of alloy. The price of standard electrolytic manganese metal increased 4 cents per lb to 58 cents per lb. Price declines and uncertainties during 1976 were linked to heavy inventories and a poor economy in the steel industry (220, 221).

Groote Eylandt Mining Company, Australia, completed its planned expansion to 2 million metric tons per year of high grade ore. Further expansion is possible if market conditions are favorable (222).

Anglo-American Corporation is planning to develop an underground manganese mine at Middelplaats, South Africa, with production scheduled to start in 1979. Ore deposits are running 38% manganese (223).

Large manganese deposits have been discovered in Brazil's Carajas Range. Amazonia Mining, a joint venture of U.S. Steel and state-controlled Vale do Rio Doce, will mine the deposits (224).

Minera Autlan at Tamos, Mexico, has started a new facility which will be capable of producing 120,000 metric tons per year of manganese alloys. Plans are to increase output to 800,000 metric tons per year over the next 2 years. There is a growing trend toward location of alloy facilities in countries where ore is produced (225).

United States ocean miners have completed extensive prospecting and are approaching final phases of development. Major technological problems are reported as being resolved and sea testing of prototype mining systems is planned. If production plans mate-

rialize, manganese imports could fall by 40%, nickel by 50%, and copper by 33%. Unfortunately, since these deposits are in the oxidized form in contrast to sulfide deposits, extraction by low cost physical means is not possible. The future is, however, clouded by international legal and political interest. The concept that all nations have a right of access to resources in the seabed is not being universally endorsed (226, 227).

The Panel on Manganese Recovery Technology, National Academy of Sciences, has completed assessment of existing technology for manganese production from domestic resources. The Cuyuna deposits in Minnesota and Aroostook deposits in Maine were considered as the best land-based domestic resources for further development. Deep-sea nodule deposits, particularly some in the Pacific Ocean, have high potential as a manganese source. The lower grade deposits of the Blake Plateau in the Atlantic Ocean may be considered as a domestic resource. The ammonium carbamate process and the sulfur dioxide-roast process were considered as the best processes for manganese recovery. However, neither process has been fully developed (220).

VIII. Nickel.—High inventories of nickel at consumers dropped during the year and there was a general recovery in the demand for nickel. Domestic nickel consumption rose 11% when compared with that of 1975. Primary nickel consumption for 1976 was estimated at 162,000 tons.

The distribution of nickel consumption was essentially the same as previous years: 44% in steels, 21% in nickel and nickel alloys, and 16% in electroplating. Ferronickel increased its share of the domestic nickel market in 1976, whereas pure unwrought nickel lost an equivalent share of the market. This situation was reversed in 1975. An estimated 74,000 tons of nickel was recovered from scrap (228).

Although nickel inventories in the world were high and recovery from poor economic conditions in 1975 was slow, prices moved upwards for most materials. Domestic ferronickel remained fairly steady at $2.16 per lb until October 1, when the price was raised to $2.34. Later in the year, an allowance of 8 cents per lb was announced on all firm orders for delivery in early 1977. The price of pure nickel was quoted as $2.41 per lb, effective October 1, but the old price of $2.20 was expected to prevail until 1977, for major consumers of nickel. The price of imported ferronickel ranged from $2.35 to $2.39 per lb of nickel content, an increase of 9% over 1975 prices (228, 229).

On the domestic scene, Amax Incorporated's nickel refinery in Louisiana is expected to reach its rated capacity of 40,000 tons of nickel during 1977. The one domestic mine in Oregon produced 17,000 tons of nickel from laterite ore and the associated smelter produced 13,000 tons of nickel in ferronickel (228).

United States imports of nickel in 1976 are expected to total 178,000 tons, an increase of 10% over 1975, but well below the record import of 221,000 tons in 1974. Supply sources were (228):

Canada	58%
Norway	8%
Botswana	7%
New Caledonia	5%
Philippines	5%
Dominican Republic	5%
South Africa	4%
Other countries	8%

Production of nickel in Canada was 263,000 tons in 1976, a decrease of 1% from the previous year (242).

Adequate supplies of nickel were available throughout the world during 1976, and new capacity or expansion at various locations appears to be more than adequate towards meeting demands for nickel in the immediate future.

INCO's Indonesian project, scheduled for completion by the end of 1976, will produce 18,000 tons per year of nickel matte. In 1977, INCO will start up the 14,000 tons per year Guatemalan lateritic nickel project (234, 240).

The Agnew nickel project in West Australia, scheduled for production startup in late 1978 of 10,000 metric tons per year of nickel in concentrate, is virtually assured of going ahead. Reserves were reported at 2 million tons with ore containing 3.5-5% nickel. Shimura Chemical will build a 10,000 metric tons per year of electrolytic nickel in Japan. Completion is expected by 1978. Greece's Larco nickel mining company is proceeding with expansion plans at Larymna which will increase nickel capacity by 40,000 metric tons per year (230-232).

An agreement has been reached between the Netherlands based Patino NV and Bureau de Recherches Geologiques et Minieres for development of a nickel project in northern New Caledonia. Production of 30,000-40,000 metric tons per year from garnierite nickel deposits is planned (233).

International Nickel, a subsidiary of INCO, will build a nickel reclamation facility which will have a capacity to process 40,000 tons per year of wastes. Completion is scheduled for mid-1978 (235).

Due to declining levels of nickel ore, Falconbridge Nickel Mines, Manibridge, Manitoba, expects to close its nickel mine by mid-1977. About 185,000 tons per year of ore were produced (241).

The Federal Preparedness Agency on October 1 set the stockpile goal for nickel at 204,335 tons (228).

At present, 70% of world consumption comes from sulfide ores and 30% from oxide ores. A greater shift to oxide-ore deposits is predicted due to rising demands and consumption which is doubling every 10 years. Estimates of world nickel ore reserves are as follows (236):

Sulfide ores—		
14.8% of world reserves	Canada	9.3%
	U.S.S.R.	3.8%
Oxide Ores—		
85.2% of world reserves	New Caledonia	43.0%
	U.S.S.R.	15.5%
	Philippines	7.5%
	Cuba	4.8%

Development work is continuing by a number of countries in recovery of nickel from ocean mining. Nodules contain from 0.2 to 2% nickel. No large scale ocean mining operations are expected for another 15 years due to economic, legal, and political problems associated with seabed mining. United States and Canada are studying proposals to limit seabed mining with output tied to growth projection for nickel consumption (237, 238).

Soc. Metallurgique Le Nickel (SLN) has developed a proprietary electrowinning method referred to as "Resin Ion Exchange and Electrolytic Process," for producing high purity nickel. Initial production will come from a 15,000 metric ton per year refinery at Sandouville. SLN expects to start selling pure nickel in the United States in 1979. Arrangements will be made with Nippon Nickel to produce pure nickel in Japan, probably before 1980. (239).

Interest and development of nickel-copper deposits in the Duluth gabbro continued during the year. Although INCO suspended activity on their project near Ely, Amax is proceeding with a 5,000 ton ore sample for metallurgical testing from their 1700 ft mining shaft near Babbitt. Research by the Bureau of Mines is continuing on a number of projects: recovery of nickel and cobalt from low-grade domestic laterites, production of ferronickel from oxide ores, recovery of nickel and other metals from ocean nodules, and recovery of nickel and copper from ores in the Duluth gabbro complex (228).

Sodium.—Sodium metal production is in a long-term downtrend. According to the Bureau of Mines, produc-

tion in 1976 was essentially unchanged from a total of 144,000 tons the previous year (243).

The total U.S. capacity is 189,000 tons per year, relatively evenly divided among five plants.

The predominant use for sodium metal has been for antiknock compounds. As much as 80% of sodium consumption has been for production of compounds like tetraethyl lead. However, in June of 1976, the Supreme Court refused to hear a petition which would halt the phasedown of lead in gasoline proposed by the Environmental Protection Agency. Because new cars require lead-free fuel, the demand for leaded gas will decrease in any case (244).

Average prices for sodium metal in 1976 were reported by the Bureau of Mines to be 20% higher than in 1975 (243). The 1975 price was reported as 22-22.5 cents per pound.

X. Titanium.—The two domestic producers of sponge, Titanium Metals Corporation of America and R.M.I., Incorporated, have a total capacity of approximately 18,500 tons per year. Consumption and imports for consumption of sponge in 1976 were 13,315 and 1,778 tons, respectively, down from 17,626 and 4,192 tons in 1975 (245). Sponge inventory had reached 1975 levels by year end being 3,633 tons down from 6,300 tons in February 1976. Consequently one can see that production of sponge was well below capacity and well below last year's. The Bureau of Mines notes that production of sponge was 43% less than in 1975 (246).

Imports for consumption of sponge, by source, extrapolated from the first 10 months were Japan, 1,400 tons; U.S.S.R., 275 tons; and UK, 55 tons. Japanese supplies to the U.S. were the lowest since 1964. The two Japanese sponge producers operated at 50% of capacity (247).

Oregon Metallurgical Corporation in Albany, Oregon, announced that it was reactivating its sponge plant in January 1977. The plant, which operated only for a short time, has a reported capacity of 2,500 tons per year (247).

The price of domestic sponge remained constant at $2.70 to $2.75 per pound through the year. Japanese sponge was quoted at $2.65 to $2.70 per pound at the beginning of the year. Both it and Russian sponge dropped to $2.45 in February. Late in the year one Japanese supplier announced a restoration of prices to previous levels, but Japanese sponge was still quoted at $2.45 to $2.50 at year end (247).

Consumption of titanium scrap was 9,211 tons in 1976 compared to 8,317 tons in 1975. Stocks at year end were 5,764 tons (245).

Titanium Fabrication Corporation is negotiating with several Brazilian mining firms concerning the possibility of a joint-venture titanium sponge plant using Ti-Fab's extraction technology (248).

Titanium ingot production in 1976 was 21,614 tons, down from 25,562 tons in 1975. Consumption was 21,004 tons, down from 24,485 tons. (245). During the first 6 months of 1976 smelters were operating at 50% capacity. By November they had increased to 66% with some increase in backlog.

Despite efforts of titanium producers to develop industrial markets, the industry is still dominated by aerospace demands. A modest resurgence in commercial airplane orders supported the market. The distribution of titanium mill products in 1976 was approximately as follows: forging and extrusion billet, 6,500 tons; sheet, strip, and plate, 3,626 tons; pipe and tube, 2,821 tons; rod and bar, 1,260 tons; castings, 239 tons; and wire, 200 tons. Pipe and casting were the only categories where production exceeded that of 1975 (247).

The Federal Preparedness Agency recommended that the Government stockpile goals be increased to 131,503 tons of sponge and 173,928 tons of rutile. At that time the stockpile contained 32,329 tons of sponge and 39,186 tons of rutile (246).

Mine production of titanium minerals, principally ilmenite, decreased to 652,404 tons, 9% below the 1975 level. Imports of ilmenite, mostly from Australia, were 168,622 tons, an increase of 18%. Imports of slag from Canada are estimated at 188,431 tons, slightly less than in 1975. Natural rutile imports, mostly from Australia, were 196,035 tons, an increase of 11%. Synthetic rutile imports were 83,421 tons, an increase of almost 50% (245).

Titanium mineral deposits were reported in southwestern Colorado (251), in upstate New York (252), in southern Tanzania (253), and in the seas around Ratnagiri, India (254). The Australian Government prohibited export of mineral sand concentrates from Frazer Island, Queensland, for environmental reasons. Lost to industry are 793,000 metric tons of rutile and smaller quantities of ilmenite and other minerals (245).

Published prices for ilmenite ore and slag remained constant at $55 and $60 per long ton, respectively. Rutile dropped from $710 to $510 per short ton at year end (249, 250).

Demand for titanium dioxide pigment increased. Domestic production was about 735,000 tons, an increase of 22 from 1975. Pigment exports increased to 20,000 tons and imports increased to 70,000 tons. The latter was attributed to a shortfall caused by a strike at the Sayreville, New Jersey plant of NL Industries (246). du Pont has authorized an additional $20 million of an expected total of $150 million for its 150,000 ton per year plant at DeLisle, Mississippi. Completion is now set for 1979 (255).

XI. Zinc.—Domestic smelter production of slab zinc in 1976, was 535,856 tons, 8% above the 495,937 tons produced in 1975. Producer and consumer stocks at year end, had increased to 199,706 tons, an increase of 9% over 1975 (256).

Ground was broken in Clarksville, Tennessee, for a 90,000 tons per year refinery. The complex, a joint venture of New Jersey Zinc Company and Union Miniere of Belgium, is estimated to cost $100 million. Production techniques to be used are self-contained chemical and electrolytic processes, which permit excellent pollution control. Completion is expected in 1979. Associated with the complex are three mines near Carthage, Tennessee, which are to supply concentrates for the Clarksville refinery. Mine development is now estimated to cost $90 million (257).

National Zinc Company's electrolytic zinc refinery was completed in August but a 3-month strike delayed start-up until year end. The 50,000 tons per year refinery replaces the horizontal retort plant at a cost of $40 million (258-260).

Consumption of slab zinc was 1,127,078 tons, an increase of 22% from 925,330 tons in 1975. Total zinc consumption including ores for other than slab zinc, zinc content of alloys, and scrap, increased 16% to 1,420,002 from 1,231,815 tons. Of the slab zinc, 38% was used for galvanizing, 37% for zinc-based casting alloys, 15% for brass and bronze, 3.6% for zinc oxide, 2.8% for rolled zinc, and 3.6% for other uses (256). A significant factor in the market for zinc is the increase in activity in the automotive market.

It appears that the General Services Administration is out of the zinc sales business. The Federal Preparedness Association set a new stockpile objective of 1,313,000 tons. Previously the stockpile objective had been 202,700 tons with 172,130 tons of surplus available for disposal (261, 262).

Mine production in 1976 was 477,369 tons of recoverable zinc up 17% from 469,355 tons in 1975 (256). Tennessee, Missouri, New York, and Colorado accounted for 60% of the output (260).

Imports for consumption of zinc as block, pig, or slab totaled 695,131 tons, up 85% from 1975. Countries supplying imports included Canada (45%), Mexico (8%), and West Germany (7%). Exports of slab, scrap, and dross were 12,459 tons, up 4%. Imports of ores and concentrates were 155,803 tons of zinc content, down 63%. Chief sources were Canada (80%), Honduras (8%), and Mexico (6%) (256).

Early in January the price per pound of zinc was cut from 39 to 37 cents by Asarco with the rest of the industry quickly following (263). In August, the price was raised to 39 or 40 cents (264). This price hike was rescinded, in October. Some producers made the price reduction retroactive (265). The year closed with average prices at 37 cents per pound (266). On the London Metal Exchange, zinc prices had been quoted in U.S. dollars since late 1975. In June, the Lead-Zinc Producers Association filed a protest with the U.S. Treasury against the 12% rebate offered U.S. buyers of Spanish zinc (267). In December, the U.S. Treasury found that the Spanish government was granting an illegal rebate, but no penalty tariff was ordered pending a final decision on the case (266).

World slab production was 4,247,000 tons, up 2% from 1975, and mine production was essentially unchanged at 4,900,000 tons. Slab consumption increased from 3,829,000 to 4,557,000 tons. World producer inventories were reduced during the year from 700,000 to 500,000 tons, a quantity which is considered large enough to affect the zinc market for some time (257).

Feasibility studies are being made of a smelter with a capacity of more than 110,000 tons per year in New Brunswick, Canada. The cost would be in the area of $200 million with possible production in 1980 or 1981 (268).

An expansion of the electrolytic refinery at LaOroya, Peru, is planned which would increase capacity from 70,000 to 90,000 tons per year and increase recovery of zinc in concentrates from 79 to 84%. Cost is estimated at $65 million (269).

Forty firms were invited for discussions concerning construction of a lead-zinc smelter to process ore from two mines near Navan, Ireland. The smelter will process 100,000 to 150,000 tons of ore per year making it the largest smelter in Europe (270, 271).

Metallgesellschaft's electrolytic zinc plant at Datteln, Germany, operating at reduced capacity to permit installation of new equipment, is increasing production. The $2 million refurbishing program has increased capacity from 110,000 to 140,000 tons per year (272).

Australia's largest zinc refinery, Electrolytic Zinc Industries' Risdon works in Tasmania, was reported as operating at 75% of capacity with decreasing stocks in March as against 60% a few months before (273).

Sheritt Gordon Mines reported that zinc resources in its Ruttan mine in Manitoba may extend further than anticipated. Ruttan reserves at the end of 1975 were placed at 10.9 million tons of open pit ore grading 2.31% and 32.7 million tons of underground ore grading 1.17% zinc (274).

Texasgulf reported excellent results from drilling at Izok Lake in the Northwest Territories. The central zone contains 7 million tons of ore averaging 14.8% zinc plus other minerals. Two other zones have not been delineated (275).

Sabina Industries has released results which indicate an "important discovery" of zinc, lead, and silver in Bathurst-Newcastle area of New Brunswick, Canada (276).

Asarco is presently building a 350 tons per day sulfuric acid plant in Corpus Christi, Texas, to handle SO_2 off-gases from the company's zinc roasting process. Completion was scheduled for late 1976 (277).

New regulations to control emissions from new or modified primary zinc smelters passed by the Environmental Protection Agency were published in the January 15, 1976 Federal Register. These limit discharge of particulate matter and capacity of emissions from sintering machines and emission of sulfur dioxide from roasters. The regulations also require monitoring and recording of emissions (278).

The Electrical Industry

The year 1976 acted very much like a year of economic recovery. Production and consumption of almost everything were up. In particular, consumption of energy was up in all sectors; industrial consumption was up dramatically (279). The electrical industry predicted steadily increasing kilowatt hour sales for the foreseeable future at a rate of about 5% per year (280). By 1995, sales are forecast to be almost three times as great as now. The benefits of a constantly increasing supply of electrical energy are unquestionable (281).

The question, "Where is all of this energy going to come from?" is very important, but it is hard to answer. Oil is an unlikely source (282) as is natural gas (283). There are large reserves of coal, but conversion of equipment to coal-firing is expensive and in some cases not possible, and conversion of coal itself has technical, environmental, and economic problems. Further, there is a question of whether we can develop the capability to get that much coal out of the ground.

The growth of nuclear power is surrounded by uncertainties. There is a major question of public acceptance. Problems of waste disposal can be considered solved only on a limited and temporary basis. At present, construction of new plants is logjammed by increasing regulation and decreasing investment attractiveness. Even the supply of nuclear fuel is not limitless.

What about other sources? Both the present supply and the potential supply of hydroelectric power are significant but limited (284). Geothermal, solar, wind, and tidal power all seem to be dark horses.

We are forced to the conclusion that some present trend will change in the near future. Some possibilities are: lower energy availability, probably at greatly increased price; a dramatic increase in conservation and efficiency of energy utilization; increased use of nuclear energy despite its present hazards; or successful development of one of the dark horses. The most likely future course appears to be some mixture of the above. The mixture will be determined by the decisions which are made, or not made, by industry, by the government, and by the people.

I. United States power generation.—Tables 3-7 summarize the production, installed generating capacity, fuel consumption, sales to ultimate consumers, cost, and average usage of electrical energy for the period January to December 1976. The figures are preliminary and in some cases partially estimated. For comparison, revised final figures are given for 1975, except for Table 5 where a longer time span is examined.

The production of electrical energy from all sources increased by more than 7% from 1975. This included a

Table 3. Production of electrical energy* (285)
(billions of kilowatt-hours)

Electrical utility	1975	1976	% change
Coal fired	852.8	942.4	+10.51
Oil fired	288.8	319.2	+10.53
Gas fired	299.7	294.4	−1.77
Nuclear	172.1	190.7	+10.81
Other**	3.4	3.8	+11.76
Total generated by consumable fuels	1616.8	1750.5	+8.27
Hydroelectric***	268.2	276.8	+3.21
Total	1885.0	2027.3	+7.55

* Excluding generation of approximately 100 billion kW-hr by private industry.
** Includes production from geothermal sources, wood, and waste.
*** Estimated.

Table 4. Installed generating capacity by fuel type (285, 286)
(millions of kilowatts)

Fuel type	1975	1976	% change
Conventional hydro	55.8	57.6	+3.23
Pumped storage	9.7	10.2	+5.15
Fossil fuel	351.2	366.5	+4.36
Nuclear	38.9	42.4	+9.00
Internal combustion	5.0	5.3	+6.00
Combustion turbine	43.5	45.7	+5.06
Total	504.1	527.7	+4.68

Table 5. Fuel consumption by electric utilities (285)

Fuel	1975	1976	% change
Coal, millions of tons	406.0	447.4	+10.20
Oil, millions of barrels	507.1	557.2	+9.88
Gas, billions of cubic feet	3,146.9	3,066.8	−2.55
Coal equivalent, millions of tons*	769.7	831.0	+7.96

* Includes equivalent for oil, gas, nuclear, geothermal, wood, and waste.

Table 6. Electric utility sales to ultimate consumers (285)
(billions of kilowatt-hours)

Consumer	1975	1976	% change
Residential	586.1	610.6	+4.18
Commercial	418.1	442.0	+5.72
Industrial	661.6	722.0	+9.13
Other	67.2	71.1	+5.80
Total	1,733.0	1,845.7	+6.50

Table 7. Cost and average usage of electrical energy (285)

Consumer	1966	1969	1976
	(cost in cents per kilowatt-hour)		
Residential	2.20	2.09	3.47
Commercial	2.06	1.99	3.45
Industrial	0.89	0.91	2.07
	(average usage in kilowatt-hours per year)		
Residential	5,265	6,571	8,326
Commercial	30,133	36,950	50,905
Industrial	1,486,552	1,633,362	1,709,693

decrease in the use of gas and an increase in all other sources including oil.

The distribution of installed capacity shows an increase in every category.

The data on fuel consumption show an increase in use of all types of consumable fuel, except for gas where a continued decrease is observed.

Oil consumption increased more than it had decreased the previous year so that consumption of oil in 1976 was greater than in 1974. Contrary to the established trend, a small increase in the efficiency of fuel utilization was reported. The coal rate per kilowatt-hour was 0.949 for 1976 compared to 0.952 for 1975 and 0.869 in 1966.

The data on sales to ultimate consumers show that, while all categories increased consumption in 1976, the increase in industrial usage was by far the greatest. This suggests that the decrease in industrial usage observed last year was due more to depressed business conditions than to any other reason.

The data on costs reflect an increase of 4.0 to 6.7 percent with the smaller consumers paying the greater increase.

II. Energy from fossil fuels.—As shown in Table 5, consumption of both coal and oil increased between 1975 and 1976. Domestic resources of both oil and gas continue to dwindle. Industry spokesmen feel that current federal policies remove incentives for development of new domestic supplies (287).

The supply of technical manpower for fossil energy research and development was considered inadequate for the present and apt to be seriously short in the near future (288).

The Federal Energy Administration planned to issue orders prohibiting burning of fuel oil to about 10 chemical plants as part of its nationwide program to force conversion from oil to coal wherever possible. A number of utilities have already received such orders (289).

Suspension of the Coalcon coal-to-fuels project is under consideration. ERDA expressed concern about the marginal economics of the process and technical problems with the fluidized-bed carbonizer (290, 291).

On other fronts positive steps were being taken to convert coal into liquid and gaseous fuels. Early in the year, ERDA was pushing for a program providing incentives to develop a synthetic fuels industry equivalent to 350,000 barrels of oil per day in 1985 (292). ERDA selected Conoco Coal Development Company and the Illinois Coal Gasification Group from five firms submitting proposals for plant design on a high BTU-coal gasification project (293, 294). A combined-cycle coal-conversion plant, cosponsored through ERDA is targeted for operation in 1978 at Commonwealth Edison Company's Powerton station at Pekin, Illinois. The plant will use Lurgi technology to convert 24 tons of high sulfur coal per hour into gas to be used in a 25-MW gas turbine (295). Hydrocarbon Research, Incorporated is ready to demonstrate the H-coal process. The demonstration plant at Catlettsburg, Kentucky, costing $80 million is scheduled for completion in 1978 (296). The $60 million coal-to-gas plant located near Flower City, Pennsylvania, using the Bi-gas process of Bituminous Coal Research, Incorporated, was dedicated September 14 (297).

Government actions which failed to provide financing for oil-shale developments and which decreased the price of domestic crude have caused most developers to reconsider development plans even though the results in some cases have been quite encouraging (298). However, Occidental Petroleum was preparing to have a 5,000 barrels per day underground retort in operation by the end of 1976. The company estimates the cost of its *in situ* retorting operation at $250 million and total cost of oil at $5-6 per barrel (299).

A new program aimed at tapping the estimated 500 quadrillion cubic feet of natural gas trapped in shale underlying parts of the eastern United States is being launched by ERDA. Funding in fiscal year 1976 was $10 million for resource evaluation and technology development (300).

Of the $9.5 billion to be spent by United States business in 1976, the electric utilities' share was estimated to be $2.467 billion. Of this, $1.725 billion was for control of air pollution, $602 million was for water, and $140 million was for solid waste (301). An 825-MW unit due online in 1979 at the Bruce Mansfield station in Shippingport, Pennsylvania, will be the first commercial user of Pullman-Kellogg's flue gas desulfurization system. The installation, costing more than $50 million erected, will remove more than 90% of the sulfur from 3.3 million ft^3/min of flue gas from coal containing 4.75% sulfur (302). Initial agreements toward a 2,000 tons per day plant for solvent refining of coal was announced by Wheelabrator-Frye, Incorporated. Southern Company, an electric utility, is expected to consume most of the plant's output (303). Catalytic, Incorporated has been awarded a 3 year contract by the United States Environmental Protection Agency to make a rigorous on-site evaluation of all commercial processes for desulfurizing residual fuel oil (304).

III. Energy From Nuclear Sources.—The very modest increase in nuclear capacity and in nuclear generation demonstrates the difficulties presently dominating the nuclear picture. Four plants were reported as completed in 1976: Bear Valley 1, Pittsburgh, Pennsylvania (852 MW); St. Lucie 1, Fort Pierce, Florida (810 MW); Indian Point 3, Buchanan, New York (965 MW); and Salem 1, Salem, New Jersey (1090 MW) (305).

The number of nuclear power plants scheduled to start up between 1977 and 1986 is 128 with a total capacity of 138,354 MW. The total number of committed nuclear plants is 211 with a capacity of 207,983 MW. This list stretches to 1992 with nine plants listed as indefinite with respect to completion dates. Three plants with a total capacity of 3440 MW were committed in 1976. By comparison in the previous decade an average of 19 plants were committed each year (305).

A freeze on nuclear-power plant construction and a stoppage of new operating permits was ordered by the

Nuclear Regulatory Commission in August pending completion of a study on environmental effects of reprocessing and handling spent fuels. The moratorium was lifted in November (306, 307). The NRC found the risks of siting twin 1150 MW reactors 2.8 miles off the New Jersey coast acceptable (305). However, it remained on the fence on the idea of clustering nuclear plants. Building 15-20 plants could produce a reduction in construction costs of as much as 12% (309).

Factors inhibiting reactor investments by domestic utilities are concern over reactor safety, increasing regulation, which diminishes the utilities control over its own destiny, uncertainties as to future fuel supply, and mounting costs of investment per kilowatt hour.

Six states carried referendum questions on the ballots in November which would make nuclear projects subject to legislative approval. In all six states the proposals were defeated (310).

The disposal of nuclear wastes is the most frequently mentioned aspect of reactor safety. Nuclear wastes exist whether we have nuclear plants or not and the disposal of such wastes is an international problem (311). Sir John Hill of the United Kingdom Atomic Energy Authority expressed the opinion that present techniques for storage of wastes are adequate to allow for a well-researched determination of the best of the possible alternatives (312). A salient concern is that some wastes have half-lives which are much longer than the lives of most social institutions (313). A $900,000 waste treatment facility was completed at the Los Alamos Scientific Laboratory (314).

There is a serious question whether the fuel supply will continue to be adequate. The uncertainty of future power plant construction has limited enthusiasm for construction of plants to supply enriched fuel for the reactors, even if sufficient supplies of uranium ore were available. Government guarantees appear to be required to limit the risk by private industry (315-317).

Sixty percent of the research and development budget of ERDA is earmarked for nuclear work. This includes large outlays for fission reactor development, fusion power development, and nuclear fuel cycle and safeguards (318).

Controversy still rages over the breeder reactor. Professional opinion is expressed on both sides of the question whether adequate safeguards including safeguards against theft of plutonium or sabotage can be built into breeder plants (319-321). The Joint Committee on Atomic Energy concluded that a high-priority effort for developing the breeder reactor is essential for the United State's energy future (322). The Clinch River reactor is now scheduled to begin operating in 1982 (323).

Eighteen countries outside the U.S. are producing electricity with nuclear power. The top three countries were Switzerland with 1006 MW capacity enough to produce 15% of its electricity; West Germany with 7300 MW, 15%; and Sweden with 3180 MW, 13%. Commitments outside the United States include 454 plants with a capacity of 342,355 MW. The list includes 41 countries committed to nuclear power. The most recent are Indonesia, Poland, and Turkey (324).

IV. Other energy sources.—The data in Table 4 indicate a modest increase in primary hydroelectric capacity. It is estimated that one-third of the total possible energy is currently being obtained from such sources. However, development of new sites is limited by economic and environmental factors.

The first national assessment of geothermal sources, published by the United States Geological Survey, concluded that geothermal energy could be a significant factor in the regions in which such resources occur (325). The Northern California Power Agency proposes to build a 165 MW power plant driven by steam from The Geysers geothermal field. Estimated cost of the project is $30 million (326). The first volcanic geothermal well was drilled south of Pahoa on the island of Hawaii. The well, which has a temperature measured at 617°F, was estimated to be capable of generating 10 MW of electrical power (327). The "slim hole" drilling concept using a 4 in. diameter well may significantly reduce the cost of geothermal exploration (328). Geothermal research has reached the stage where some of the real-world problems are beginning to be appreciated. These include the fact that it is hard to come by, expensive, and not as clean as once believed. Even in this context it is a resource which cannot be ignored (329).

Conversion of biomass to fuels and chemical feed stocks by a variety of processes is under consideration. One decisive asset is the sales appeal to the public (330). Weyerhauser indicates that short-rotation forestry using the wood for fuel may be on the verge of viability (331). Battelle Columbus Laboratories have demonstrated conversion of municipal solid wastes to methane on a 0.2 ton per day basis (332). Gas wells are being drilled in a San Francisco trash dump in an effort funded by the Environmental Protection Agency and Pacific Gas and Electric Company to show that methane gas formed by decomposition of municipal refuse can be recovered economically as fuel (333).

The 32 kW of energy produced at ERDA's Sandia Laboratories represent the first significant production of electric power from a solar driven turbogenerator (334). SES, Incorporated, plans to begin commercial manufacture of thin-film cadmium sulfide solar cells by early 1977 (335). ERDA unveiled plans for a modest Solar Energy Research Institute. The first year SERI will have a budget of $6 to $12 million and a staff of 50-75 persons (336).

A large step is being taken in demonstrating fuel cell technology. A 4.8 MW unit, costing $42 million, is being built under joint sponsorship of ERDA, the Electric Power Research Institute, and United Technologies Corporation. (337).

ERDA awarded a $2 million, 38 month contract to General Electric Company for further research work into magneto-hydrodynamics. Under this contract General Electric will investigate the feasibility of closed-cycle MHD power generation using a coal-fired heat exchanger (338).

Under the impetus of increased energy prices the potential of a variety of ocean energy sources is being probed. These include both thermal and tidal energies (339,340).

Under ERDA contracts power generation by windmills will be tested at four sites. The first site, Clayton, New Mexico, will have 200 kW wind-turbine generator in late 1977. Other sites, not yet selected, will be used for testing another 200 kW unit and two 1.5 MW units (341, 342).

Perhaps it is appropriate to close on news of a process which, if not precisely an energy source, is an electrochemical process. Four advanced battery systems are currently being developed on multimillion dollar contracts from ERDA and EPRI. These are to be used in banks with sufficient capacity for load-leveling of generation or consumption cycles. General Electric Company and Ford Motor Company have contracts for sodium-sulfur batteries, ESB, Incorporated for sodium-antimony chloride, Argonne National Laboratory and Atomics International for lithium-iron sulfide or other metal sulfide, and Energy Development Associates for zinc-chloride batteries (343).

REFERENCES

1. *Chemical Marketing Reporter*, p. 4, Feb. 7, 1977.
2. CPI Management, p. 5, March 7, 1977.
3. *Chemical Marketing Reporter*, p. 3, June 14, 1976.
4. *Ibid.*, p. 4, Nov. 29, 1976.
5. *Ibid.*, p. 3, May 31, 1976.
6. *Electrochemical Progress*, p. 7, Feb. 1976.
7. *Chemical and Engineering News*, p. 11, May 17, 1976.
8. *Chemical Week*, p. 26, March 2, 1977.
9. North American Chlor-Alkali Industry Plants and Production Data Book, Chlorine Institute Pamphlet 10, January 1977.
10. *Chemical Marketing Reporter*, p. 53, Dec. 13, 1976.
11. *Chemical Week*, p. 32, March 24, 1976.

12. *Chemical Marketing Reporter*, p. 28, Oct. 11, 1976.
13. *Ibid.*, p. 30, Nov. 1, 1976.
14. *Chemical and Engineering News*, p. 14, Feb. 21, 1977.
15. *Canadian Chemical Processing*, p. 12, Jan. 1977.
16. *European Chemical News*, p. 38, June 11, 1976.
17. *Chemical Engineering*, p. 86, June 21, 1976.
18. *Chemical Week*, p. 39, April 7, 1976.
19. *Ibid.*, p. 61, Nov. 10, 1976.
20. *Chemical Engineering*, p. 61, March 29, 1976.
21. *Chemical Marketing Reporter*, p. 3, June 21, 1976.
22. *Chemical Week*, p. 21, July 14, 1976.
23. *Chemical Engineering*, p. 67, May 10, 1976.
24. *Ibid.*, p. 80, March 29, 1976.
25. *Japan Chemicals*, p. 1, Aug. 26, 1976.
26. *Chemical Engineering*, p. 119, Feb. 16, 1976.
27. *Japan Chemicals*, p. 1, Sept. 16, 1976.
28. *Chemical Economy and Engineering Review*, p. 34, June 1976.
29. *Japan Chemicals*, p. 5, Feb. 5, 1976.
30. *Chemical Age*, p. 3, Oct. 15, 1976.
31. *Chemical Marketing Reporter*, p. 4, Aug. 23, 1976.
32. *Chemical and Engineering News*, p. 23, July 19, 1976.
33. *Ibid.*, p. 23, May 17, 1976.
34. CPI Management Service, p. 1, Dec. 6, 1976.
35. *Chemical Week*, p. 47, Feb. 23, 1977.
36. *Japan Chemicals*, p. 7, April 27, 1976.
37. *Chemical Economy and Engineering Review*, p. 38, June 1976.
38. *International Chemical Engineering*, p. 1, Jan. 1977.
39. *Chemical Marketing Reporter*, p. 7, Nov. 1, 1976.
40. *Chemical Week*, p. 39, May 14, 1975.
41. Mercury in 1976, Mineral Industry Surveys, Bureau of Mines, U.S. Dept. of the Interior, December 21, 1976.
42. *Metals Week*, p. 9, Sept. 13, 1976.
43. *Chemical Marketing Reporter*, p. 4, Dec. 6, 1976.
44. *Chemical Week*, p. 29, Sept. 22, 1976.
45. *Ibid.*, p. 47, Sept. 15, 1976.
46. *Chemical Marketing Reporter*, p. 3, Feb. 7, 1977.
47. *Ibid.*, p. 4, June 14, 1976.
48. *Ibid.*, p. 3, Oct. 4, 1976.
49. *Ibid.*, p. 4, Dec. 13, 1976.
50. *Chemical Week*, p. 40, Jan. 19, 1977.
51. *European Chemical News*, p. 20, Aug. 9, 1976.
52. *Engineering and Mining Journal*, p. 37, Oct. 1976.
53. *Chemical Marketing Reporter*, p. 3, Aug. 2, 1976.
54. *Ibid.*, p. 4, July 12, 1976.
55. *Chemical Week*, p. 43, Sept. 15, 1976.
56. *Chemical Engineering*, p. 68, Oct. 25, 1976.
57. Current Industrial Reports, Inorganic Chemicals, Jan. 1976 to Dec. 1976, Bureau of the Census, U.S. Dept. of Commerce, Feb. 1977.
58. Potash in Crop Year 1976, Mineral Industry Surveys, Bureau of Mines, U.S. Dept. of the Interior, Sept. 1976.
59. *Chemical Marketing Reporter*, p. 30, Nov. 1, 1976.
60. *Ibid.*, p. 33, May 31, 1976.
61. *Ibid.*, p. 30, Sept. 6, 1976.
62. *Chemical and Engineering News*, p. 9, Sept. 27, 1976.
63. *Chemical Week*, p. 26, Sept. 29, 1976.
64. *Ibid.*, p. 17, June 23, 1976.
65. *Ibid.*, p. 57, Nov. 10, 1976.
66. *Engineering and Mining Journal*, p. 17, May 1976.
67. *Chemical Marketing Reporter*, p. 5, Feb. 28, 1977.
68. *Engineering and Mining Journal*, pp. 141-142, March 1977.
69. Sodium Compounds in December 1976, Sodium Compounds Monthly, Mineral Industries Surveys, Bureau of Mines, U.S. Dept. of the Interior, Feb. 1, 1977.
70. *Chemical Engineering*, **83**, No. 8, p. 65, 1976.
71. *Engineering and Mining Journal*, pp. 70-73, Dec. 1976.
72. *Chemical and Engineering News*, p. 10, Oct. 11, 1976.
73. *Engineering and Mining Journal*, pp. 67-76, April 1976.
74. *Ibid.*, pp. 73-86, Jan. 1976.
75. *Chemical and Engineering News*, p. 10, June 14, 1976.
76. *Chemical Engineering*, **83**, No. 13, p. 68, 1976.
77. Sodium Compounds in 1976, Annual Preliminary, Mineral Industries Surveys, Bureau of Mines, U.S. Dept. of the Interior, Dec. 28, 1976.
78. *Chemical Marketing Reporter*, April 1, 1976.
79. *Canadian Chemical Processing*, p. 42, Dec. 1976.
80. *Paper Trade Journal*, p. 28, Aug. 1, 1976.
81. *Canadian Chemical Processing*, p. 42, Dec. 1976.
82. *Chemical Marketing Reporter*, p. 33, May 31, 1976.
83. *Ibid.*, p. 16, Nov. 29, 1976.
84. *Ibid.*, p. 20, Dec. 6, 1976.
85. CPI Management Service, p. 4, Jan. 10, 1977.
86. *Chemical Marketing Reporter*, p. 7, Nov. 15, 1976.
87. *Chemical Age*, p. 1, Aug. 13, 1976.
88. Wall Street Journal, p. 4, Feb. 18, 1977.
89. *Canadian Chemical Processing*, p. 10, Nov. 1976.
90. *Chemical Week*, p. 19, Nov. 10, 1976.
91. *Chemical Marketing Reporter*, Jan. 24, 1976.
92. *Chemical and Engineering News*, p. 13, Dec. 6, 1976.
93. Aluminum Industry in 1976, Mineral Industry Surveys, Bureau of Mines, U.S. Dept. of the Interior, Feb. 2, 1977.
94. *Metals Week*, p. 3, July 5, 1976.
95. *Ibid.*, p. 9, Dec. 20, 1976.
96. *Chemical Marketing Reporter*, p. 52, July 5, 1976.
97. *Ibid.*, p. 55, Sept. 6, 1976.
98. *Metals Week*, p. 3, March 15, 1976.
99. *Ibid.*, p. 3, July 5, 1976.
100. *Ibid.*, p. 3, Nov. 22, 1976.
101. Aluminum and Bauxite in 1976, Mineral Industry Surveys, Bureau of Mines, U.S. Dept. of the Interior, Dec. 21, 1976.
102. *Metals Week*, p. 3, April 26, 1976.
103. *Ibid.*, p. 3, Aug. 9, 1976.
104. *Ibid.*, p. 9, May 17, 1976.
105. *Ibid.*, p. 2, Jan. 5, 1976.
106. *Engineering and Mining Journal*, p. 9, Feb. 1976.
107. *Metals Week*, p. 3, April 26, 1976.
108. *Ibid.*, p. 3, April 5, 1976.
109. *Chemical and Engineering News*, p. 7, May 10, 1976.
110. *Metals Week*, p. 3, May 31, 1976.
111. *Ibid.*, p. 3, Dec. 13, 1976.
112. *Ibid.*, p. 7, Sept. 27, 1976.
113. *Ibid.*, p. 10, May 17, 1976.
114. *Chemical Marketing Reporter*, p. 7, Sept. 20, 1976.
115. *Chemical Week*, p. 60, Dec. 8, 1976.
116. *Metals Week*, p. 1, May 24, 1976.
117. *Chemical Week*, p. 12, Aug. 18, 1976.
118. *Metals Week*, p. 1, April 12, 1976.
119. *Ibid.*, p. 3, Oct. 18, 1976.
120. *Ibid.*, p. 6, Oct. 15, 1976.
121. *Chemical and Engineering News*, p. 13, March 1, 1976.
122. *Metals Week*, p. 9, Dec. 20, 1976.
123. *Ibid.*, p. 3, Oct. 11, 1976.
124. *Ibid.*, p. 6, Nov. 15, 1976.
125. *Ibid*, p. 3, April 26, 1976.
126. *Mining Magazine*, p. 331, April 1976.
127. *Metals Week*, p. 3, Aug. 9, 1976.
128. *Chemical Engineering*, p. 63, June 7, 1976.
129. *Metals Week*, p. 1, May 24, 1976.
130. *Chemical Engineering*, p. 69, July 19, 1976.
131. *Engineering and Mining Journal*, p. 35, June 1976.
132. *Metals Week*, p. 3, Feb. 2, 1976.
133. *Electrochemical Progress*, p. 4, March 1976.
134. *Engineering and Mining Journal*, pp. 169-170, March 1977.
135. Beryllium in 1976, Annual Preliminary, Mineral Industry Surveys, Bureau of Mines, U.S. Dept. of the Interior, Dec. 17, 1976.
136. *Engineering and Mining Journal*, pp. 49-64, Jan. 1976.
137. *Ibid.*, pp. 48-97, Jan. 1977.
138. Chromium in 1976, Metal Industry Surveys, Bureau of Mines, U.S. Dept. of the Interior, Dec. 31, 1976.
139. *Metals Week*, p. 9, Feb. 16, 1976.
140. *Ibid.*, p. 3, July 5, 1976.
141. *Ibid.*, p. 2, Oct. 25, 1976.
142. *Ibid.*, p. 7, March 29, 1976.
143. *Ibid.*, p. 2, Aug. 23, 1976.
144. *Ibid.*, p. 6, Sept. 20, 1976.
145. *Mining Magazine*, p. 59, July 1976.
146. *Ibid.*, p. 473, Nov. 1976.
147. *Chemical Week*, p. 24, Feb. 23, 1977.
148. Copper Industry in December, Mineral Industry Surveys, Bureau of Mines, U.S. Dept. of the Interior, March 10, 1977.
149. *Engineering and Mining Journal*, pp. 23-27, Aug. 1976.
150. *Ibid.*, p. 128, Aug. 1976.

151. *Ibid.*, p. 264, March 1976.
152. *Ibid.*, p. 266, March 1976.
153. *Ibid.*, pp. 40-41, Nov. 1976.
154. Copper in 1976, Annual Preliminary, Mineral Industry Surveys, Bureau of Mines, U.S. Dept. of the Interior, Dec. 21, 1976.
155. *Engineering and Mining Journal*, p. 151, Jan. 1976.
156. *Ibid.*, p. 9, Dec. 1976.
157. *Ibid.*, p. 17, June 1976.
158. *Ibid.*, pp. 17-138, Feb. 1976.
159. *Ibid.*, p. 9, Sept. 1976.
160. *Ibid.*, p. 167, Jan. 1976.
161. *Ibid.*, p. 128, Dec. 1976.
162. *Ibid.*, p. 9, June 1976.
163. *Ibid.*, p. 9, April 1976.
164. *Ibid.*, pp. 73-76, March 1977.
165. *Ibid.*, p. 131, Dec. 1976.
166. *Ibid.*, p. 155, June 1976.
167. *Ibid.*, p. 136, Oct. 1976.
168. *Ibid.*, p. 128, July 1976.
169. *Ibid.*, p. 134, Dec. 1976.
170. *Ibid.*, p. 131, Feb. 1976.
171. *Ibid.*, p. 23, April 1976.
172. *Ibid.*, p. 32, Oct. 1976.
173. *Ibid.*, pp. 157-159, Jan. 1976.
174. *Ibid.*, p. 9, Feb. 1976.
175. *Ibid.*, p. 138, Oct. 1976.
176. *Ibid.*, p. 313, Sept. 1976.
177. *Ibid.*, p. 314, Sept. 1976.
178. *Ibid.*, p. 326, June 1976.
179. *Ibid.*, p. 140, Dec. 1976.
180. *Ibid.*, p. 279, March 1976.
181. *Ibid.*, p. 338, June 1976.
182. *Ibid.*, p. 17, Dec. 1976.
183. *Ibid.*, p. 181, Sept. 1976.
184. *Ibid.*, p. 140, Feb. 1976.
185. *Ibid.*, p. 132, Feb. 1976.
186. *Ibid.*, p. 26, Feb. 1976.
187. *Ibid.*, p. 160, Jan. 1976.
188. *Ibid.*, p. 165, April 1976.
189. *Ibid.*, p. 139, Dec. 1976.
190. *Ibid.*, p. 131, July 1976.
191. *Ibid.*, p. 32, March 1976.
192. *Ibid.*, p. 9, Aug. 1976.
193. *Ibid.*, p. 153, April 1976.
194. *Ibid.*, pp. 129-130, July 1976.
195. *Ibid.*, p. 23, Feb. 1976.
196. *Ibid.*, p. 141, Aug. 1976.
197. *Ibid.*, pp. 31-33, Dec. 1976.
198. *Ibid.*, pp. 31-37, Jan. 1976.
199. *Ibid.*, p. 32, Feb. 1976.
200. *Chemical Engineering*, **83**, No. 6, p. 51, 1976.
201. *Engineering and Mining Journal*, p. 27, Nov. 1976.
202. *Ibid.*, p. 83, Jan. 1976.
203. Lithium in 1976, Mineral Industry Surveys, Bureau of Mines, U.S. Dept. of the Interior, Jan. 4, 1977.
204. *Chemical Marketing Reporter*, p. 24, Dec. 20, 1976.
205. *Ibid.*, p. 32, Oct. 4, 1976.
206. *Metals Week*, p. 4, Dec. 20, 1976.
207. *Chemical Week*, p. 31, Dec. 1, 1976.
208. *Chemical Marketing Reporter*, p. 5, Dec. 6, 1976.
209. *Engineering and Mining Journal*, pp. 165-166, March 1977.
210. *Ibid.*, pp. 160-162, March 1976.
211. *Chemical and Engineering News*, p. 9, Jan. 26, 1976.
212. *Engineering and Mining Journal*, p. 9, June 1976.
213. *Chemical and Engineering News*, p. 15, May 17, 1976.
214. Magnesium and Magnesium Compounds, Annual Preliminary, Mineral Industry Surveys, Bureau of Mines, U.S. Dept. of the Interior, Dec. 17, 1976.
215. *Engineering and Mining Journal*, pp. 52-69, Jan. 1976.
216. *Ibid.*, p. 56, July 1976.
217. *Ibid.*, pp. 48-97, Jan. 1977.
218. Primary Magnesium in the Fourth Quarter, Mineral Industry Surveys, Bureau of Mines, U.S. Dept. of the Interior, Feb. 23, 1977.
219. *Chemical Engineering*, p. 83, Dec. 6, 1976.
220. Manganese in 1976, Mineral Industry Surveys, Bureau of Mines, U.S. Dept. of the Interior, Dec. 30, 1976.
221. *Metals Week*, p. 1, Nov. 1, 1976.
222. *Engineering and Mining Journal*, p. 81, Jan. 1976.
223. *Mining Magazine*, p. 59, July 1976.
224. *Metals Week*, p. 3, Sept. 13, 1976.
225. *Ibid.*, p. 7, Nov. 8, 1976.
226. *Engineering and Mining Journal*, p. 37, Feb. 1976.
227. *Mining Magazine*, p. 175, Aug. 1976.
228. Nickel in 1976, Mineral Industry Surveys, Bureau of Mines, U.S. Dept. of the Interior, Dec. 30, 1976.
229. *Chemical Marketing Reporter*, p. 56, Sept. 27, 1976.
230. *Metals Week*, p. 3, Oct. 18, 1976.
231. *Metal Bulletin*, p. 23, April 13, 1976.
232. *Mining Magazine*, p. 163, March 1976.
233. *Ibid.*, p. 59, June 1976.
234. *Metals Week*, p. 10, April 26, 1976
235. *Chemical Marketing Reporter*, p. 63, July 12, 1976.
236. *Mining Magazine*, p. 177, Aug. 1976.
237. *Metals Week*, p. 3, May 17, 1976.
238. *Mining Magazine*, p. 177, Aug. 1976.
239. *Metals Week*, p. 6, May 17, 1976.
240. *Engineering and Mining Journal*, p. 81, Jan. 1976.
241. Wall Street Journal, p. 25, March 8, 1977.
242. Copper and Nickel Production, January 1977, Statistics Canada, March 1977.
243. Sodium compounds in 1976, Annual Preliminary, Mineral Industries Surveys, Bureau of Mines, U.S. Dept. of the Interior, Dec. 20, 1976.
244. *Engineering and Mining Journal*, p. 55, July 1976.
245. Titanium in the Fourth Quarter 1976, Mineral Industry Surveys, Bureau of Mines, U.S. Dept. of the Interior, March 3, 1977.
246. Titanium in 1976, Annual Preliminary, Mineral Industry Surveys, Bureau of Mines, U.S. Dept. of the Interior, Dec. 23, 1976.
247. *Engineering and Mining Journal*, pp. 160-165, March 1977.
248. *Ibid.*, p. 322, June 1976.
249. *Ibid.*, pp. 52-64, Jan. 1976.
250. *Ibid.*, pp. 48-97, Jan. 1977.
251. *Ibid.*, p. 17, April 1976.
252. *Ibid.*, p. 338, June 1976.
253. *Ibid.*, p. 175, April 1976.
254. *Ibid.*, p. 17, March 1976.
255. *Chemical and Engineering News*, p. 12, July 12, 1976.
256. Zinc Industry in December 1976, Mineral Industry Surveys, Bureau of Mines, U.S. Dept. of the Interior, March 9, 1977.
257. *Engineering and Mining Journal*, p. 211, Sept. 1976.
258. *Ibid.*, p. 315, June 1976.
259. *Ibid.*, pp. 77-79, March 1977.
260. Zinc in 1976, Annual Preliminary, Mineral Industry Surveys, Bureau of Mines, U.S. Dept. of the Interior, Dec. 21, 1976.
261. *Engineering and Mining Journal*, p. 40, Nov. 1976.
262. *Ibid.*, p. 53, Aug. 1976.
263. *Ibid.*, p. 49, Feb. 1976.
264. *Ibid.*, p. 44, Oct. 1976.
265. *Ibid.*, p. 51, Nov. 1976.
266. *Ibid.*, pp. 47-97, Jan. 1977.
267. *Ibid.*, p. 55, July 1976.
268. *Ibid.*, p. 279, Sept. 1976.
269. *Ibid.*, p. 326, June 1976.
270. *Ibid.*, p. 153, April 1976.
271. *Ibid.*, pp. 23-26, Feb. 1976.
272. *Ibid.*, p. 272, March 1976.
272. *Ibid.*, p. 272, March 1976.
273. *Ibid.*, p. 274, March 1976.
274. *Ibid.*, p. 317, June 1976.
275. *Ibid.*, p. 168, Jan. 1976.
276. *Ibid.*, p. 170, April 1976.
277. *Ibid.*, p. 153, Jan. 1976.
278. *Ibid.*, p. 37, March 1976.
279. *Electrical World*, p. 59, March 15, 1977.
280. *Ibid.*, p. 49, Sept. 1, 1976.
281. *Ibid.*, pp. 58-59, Dec. 15, 1976.
282. *Science*, **194**, 681 (1976).
283. *Chemical Engineering*, **83**, No. 9, p. 49, 1976.
284. Federal Power Commission, Annual Report 1975, p. 79.
285. *Electrical World*, pp. 35-61, March 13, 1977.
286. *Ibid.*, pp. 39-70, March 15, 1976.
287. *Chemical and Engineering News*, p. 14, April 12, 1976.
288. *Ibid.*, p. 8, March 29, 1976.
289. *Chemical Engineering*, **83**, No. 14, pp. 35-36, 1976.
290. *Chemical and Engineering News*, p. 30, Dec. 13, 1976.
291. *Ibid.*, p. 8, Dec. 20, 1976.
292. *Ibid.*, pp. 16-18, Feb. 16, 1976.
293. *Chemical Engineering*, **83**, No. 15, p. 72, 1976.

294. *Chemical and Engineering News*, p. 31, Feb. 16, 1976.
295. *Chemical Engineering*, **83**, No. 14, p. 39, 1976.
296. *Chemical and Engineering News*, p. 8, March 22, 1976.
297. *Electrical World*, p. 27, Oct. 15, 1976.
298. *Engineering and Mining Journal*, p. 81, Aug. 1976.
299. *Ibid.*, pp. 101-103, Sept. 1976.
300. *Chemical and Engineering News*, p. 23, Feb. 1976.
301. *Chemical Engineering*, **83**, No. 12, p. 78, 1976.
302. *Ibid.*, **83**, No. 11, p. 73, 1976.
303. *Ibid.*, **83**, No. 18, p. 49, 1976.
304. *Ibid.*, **83**, No. 18, p. 55, 1976.
305. *Electrical World*, pp. 35-44, Jan. 15, 1977.
306. *Chemical Engineering*, **83**, No. 18, p. 52, 1976.
307. *Electrical World*, p. 30, Dec. 1, 1976.
308. *Chemical Engineering*, **83**, No. 10, p. 67, 1976.
309. *Chemical and Engineering News*, p. 14, Feb. 9, 1976.
310. *Engineering and Mining Journal*, p. 27, Dec. 1976.
311. *Electrical World*, p. 30, Aug. 15, 1976.
312. *Chemical and Engineering News*, pp. 21-23, Aug. 2, 1976.
313. *Ibid.*, p. 15, Aug. 9, 1976.
314. *Chemical Engineering*, **83**, No. 18, p. 55, 1976.
315. *Chemical and Engineering News*, p. 10, July 12, 1976.
316. *Ibid.*, p. 6, July 19, 1976.
317. *Chemical Engineering*, **83**, No. 16, p. 38, 1976.
318. *Chemical and Engineering News*, p. 16, Feb. 2, 1976.
319. *Ibid.*, p. 41, Oct. 18, 1976.
320. *Electrical World*, pp. 39-41, Dec. 1, 1976.
321. *Chemical and Engineering News*, p. 13, Sept. 13, 1976.
322. *Ibid.*, p. 9, Feb. 23, 1976.
323. *Ibid.*, p. 7, May 3, 1976.
324. *Electrical World*, pp. 13-14, July 1, 1976.
325. *Engineering and Mining Journal*, p. 9, July 1976.
326. *Ibid.*, p. 310, June 1976.
327. *Ibid.*, p. 186, Sept. 1976.
328. *Ibid.*, p. 138, Feb. 1976.
329. *Chemical and Engineering News*, pp. 27-28, Oct. 1976.
330. *Ibid.*, pp. 24-26, Feb. 23, 1976.
331. *Ibid.*, pp. 35-36, Dec. 13, 1976.
332. *Chemical Engineering*, **83**, No. 10, p. 72, 1976.
333. *Chemical and Engineering News*, p. 26, June 21, 1976.
334. *Engineering and Mining Journal*, p. 217, Sept. 1976.
335. *Chemical Engineering*, p. 79, Nov. 22, 1976.
336. *Chemical and Engineering News*, p. 8, March 22, 1976.
337. *Electrical World*, p. 15, Sept. 1, 1976.
338. *Chemical and Engineering News*, p. 16, June 28, 1976.
339. *Ibid*, p. 26, Feb. 23, 1976.
340. *Ibid.*, p. 19, Feb. 9, 1976.
341. *Chemical Engineering*, **83**, No. 18, p. 50, 1976.
342. *Electrical World*, p. 13, Jan. 1, 1977.
343. *Ibid.*, pp. 21-22, Jan. 1, 1977.

75th Anniversary Review Series

Advances in Electrolytic Production of Industrial Chemicals from 1952 to 1977

William C. Gardiner*

Stratford, Connecticut 06497

Industrial chemicals that are produced electrochemically include sodium hypochlorite, caustic soda, sodium methylate, caustic potash, chlorine, sodium chlorate, sodium perchlorate, ammonium peroxydisulfate, hydrogen peroxide, fluorine, and manganese dioxide. Chlorine and caustic soda, or caustic potash, are coproducts of diaphragm and mercury cells, but chlorine is also made by electrolysis of by-product hydrochloric acid. Fused salt cells making sodium and magnesium also produce chlorine; the chlorine is recycled in some magnesium plants. Sodium methylate is made in decomposers of mercury cells by feeding in methanol instead of water.

Twenty-five years ago mercury arc rectifiers were being used at circuit voltages of 500-800V, giving conversion efficiencies of about 90%. They have been replaced by silicon rectifiers which give conversion efficiencies of around 97% at half the circuit voltage. This lower voltage has resulted in much safer operations and the development of cells using currents up to 500 kA. Thyristor control has improved regulation of rectifiers, and vacuum tap changers have quadrupled the life of switch contacts.

Coated titanium anodes are replacing graphite anodes for producing many industrial chemicals. Mr. Henri B. Beer and Dr. J. Cotton, almost simultaneously, discovered that a coating of platinum on a titanium base was resistant when anodic in a sodium chloride solution. Improvements of coated titanium anodes such as those incorporating ruthenium and other metal oxides or mixtures, and improved methods of application followed. The Beer patents were acquired by Oronzio de Nora, Italy, and commercialized around the world under the trademark DSA, dimensionally stable anodes. Electrode Corporation first introduced DSA's in the United States in 1968. Cotton's work was commercialized by Marsten Excelsior Limited, Wolverhampton, England.

Plastics such as Teflon, fiberglass-reinforced polyester (FRP), and improved hard rubber linings for steel are now widely used in all construction.

* Electrochemical Society Emeritus Member.

Electrolytic Sodium Hypochlorite

Most hypochlorite is made by chlorination of caustic soda or lime, but in some circumstances electrolysis is used. For instance, power plants on the seacoast using seawater in their condensers are generating sodium hypochlorite by electrolysis of the seawater for control of algae. Special small cells for chlorinating swimming pools are on the market. Ionics and du Pont are offering a sodium hypochlorite generating system for destroying cyanide-containing wastes in the plating industry. The cells use Nafion (R) membranes.

The Chlor-Alkali Industry

Advances in Alkali-Chlorine Production

Chlorine production in the U.S. has increased about 6-fold in the last 25 years, as shown in Table I. Production capacity was slightly under 7000 short tons per day in the early 1950's; now it is around 41,000 short tons per day. Production in 1976 was 10,267,000 short tons (1). In Canada, the increase in production capacity was from around 500 to 3700 short tons per day now. Mercury cells increased in popularity in the United

Table I. Production of chlorine

	United States		Canada	
	1952 (2)	1976 (1)	1952 (2)	1976 (1)
Capacity (short tons/day)	6800	41,000	400-500	3735
Capacity, diaphragm cells (%)	80	73.7	43*	68.0
Capacity, mercury cells (%)	12	21.4	57*	32.0
Capacity, other (%)	8	4.9	—	—
Diaphragm, cell size (kA)	30	150	30	150.0
Mercury cell size (kA)	30	300-500	30	300-500.0
No. of plants	63	69	—	19
Diaphragm cell plants	?	32	—	8
Mercury cell plants	?	22	—	10
Mercury and diaphragm plants	?	5	—	—
Fused salt plants	?	4	0	—
HCl electric plants	0	1	0	0
Diaphragm and fused salt	1	1	0	0
Diaphragm and magnesium	1	1	0	0
Membrane cell		1	0	1
Nonelectrolytic		2	0	0
Size of new plants (tons/day)	100-300	500-1500	100-300	500-1500

* 1962.

States until 1970, when the mercury scare occurred. No new mercury cell plants have been built since then in the United States, although some small expansions of existing plants occurred. Production in diaphragm cells decreased from 80 to 73.7% of the total during the period. In Canada, in the early 1950's, 14% more chlorine was produced in mercury cells than in diaphragm cells, but this has reversed to 36% more in diaphragm cells now. Several mercury cell plants were shut down.

More than 50% of the world's chlorine is now produced with metal anodes with substantial energy saving. They have also stimulated new cell designs that are larger and more economical. The number of chlorine plants has increased from 63 to 69 in the United States, and to 19 in Canada. The size of new installations has increased from 100 to 300 tons per day capacity to ones for 500-1500 tons per day. Chlorine is being made by electrolysis of by-product hydrochloric acid in one plant in the United States using technology from Germany, where there are several plants using the technique. Markets for chlorine have changed in the past 25 years, primarily due to the growth of vinyl chloride, which has increased to the point where it comprises 20% of the total chlorine market, as shown in Table II.

Various health and environmental agencies have discovered dangerous effects from some chlorinated organic products. The potential of carcinogenesis by such compounds as vinyl chloride monomer, chloroform, trichlorethylene, chlorinated biphenyls, and various insecticides has been publicized. Industry is meeting, or preparing to meet OSHA standards for workers and EPA requirements for vinyl chloride monomer emissions to a level of 10 ppm in all exhaust gases, except for emergency relief valve discharges.

The use of chloroform in drug products has been stopped by FDA regulation. Chlorination of city water supplies containing organic matter results in some chloroform in the water. Other means of sterilizing public water systems are being studied. Chlorine dioxide can be substituted for chlorine without formation of chloroform. Removal of organics by adsorption on activated carbon before chlorination is another approach.

The Federal Task Force on Inadvertent Modification of the Stratosphere due to the use of fluorocarbons in aerosols recommended that fluorocarbons in aerosols be banned. The State of Oregon has already banned their use. They are used as refrigerants in most chlorine liquification systems, and, of course, chlorine is used in their production.

Caustic Soda and Caustic Potash

The production of caustic soda has grown from 3,000,000 short tons in 1952 (3) to 11,000,000 short tons as 100% NaOH in 1976 (4). Caustic soda is all produced electrolytically now, whereas in 1952, 17% was made in lime-soda plants, which have since been shut down. The capacity has increased from 4,000,000 to 14,000,000 short tons per year. The trend in uses of caustic soda is shown in Table III. The major change is due to the reduced percentage used by the declining rayon industry.

Six of the 22 mercury cell plants and none of the diaphragm cell plants produced 226,800 short tons of caustic potash, as 88-92% KOH in 1976 (1). Nippon Soda Company Limited established an ion-exchange membrane process for caustic potash using du Pont's Nafion (R) membranes (7).

Developments—Mercury Cells

Through the 1960's there was very active development of mercury cells by Olin-Mathieson, Solvay, de Nora, Hoechst-Uhde, Krebs-BASF, and other companies in Europe and Japan. All of these companies designed mercury cells that were installed in America. The demand for larger plants and development of silicon rectifiers resulted in mercury cell designs up to 500 kA in capacity. Advances included anode designs for improved gas release, adjustable anodes, reduction in use of mercury, reduction in slope of the volt-ampere curve, which permitted higher current densities, operation at higher temperature due to the improved resistance of new rubber linings, improved packing for decomposers, and condensers on individual cells to cool hydrogen so that water and mercury return to the decomposer. Also, advances were made in improved cell layout to reduce the quantity of bus bar material and substitution of aluminum for copper bus bars and development of aluminum-to-steel connections, and optimization procedures using computer programs for cell and plant design. Anode adjustment progressed from individual anode adjustment to group adjustment, to remote adjustment, and finally to remote computerized control with overriding short-

Table II. Trend in uses of chlorine in the United States

	1950's (%)	1976 (%)
Vinyl chloride	—	20
Other chlorinated organics	64	30
Inorganic chemicals	10	11
Pulp and paper	15	15
Miscellaneous	10	17

Table III. Trend in uses of NaOH

	1950 (3) (%)	1976 (4) (%)
General chemicals	43	50
Pulp and paper	7	15
Alumina	2	10
Rayon and cellulosics	24	5
Other industries	13	5
Miscellaneous and exports	13	—

circuit protection. The thickness of the mercury cathode changes with time, sometimes rather quickly, so that danger of touching the anode occurs. This was not serious with graphite anodes, but can melt and destroy metal anodes. Metal anodes have to be kept at a comparatively great distance from the cathode for safety unless short-circuit protection is provided. Fortunately, conditions for a short-circuit build up gradually. If changes in current distribution to groups of anodes are monitored, an impending short circuit can be corrected before a short circuit occurs by raising the anodes. Metal anodes have reduced the amount of cell cleaning required, the anode maintenance, mercury loss due to less "thick mercury," and brine treatment sludge. Cell voltages are less, so that energy efficiency is increased.

The Mercury Problem (6, 7)

Early in 1970, mercury loss from mercury cell plants was recognized in America as a serious hazard to the environment. The Chlorine Institute organized an ad hoc Mercury Committee of representatives of mercury cell operators in Canada and the United States. Effluent plant wastes were dammed up in most plants until methods for reducing and treating them could be developed and put in effect.

In a typical mercury cell plant, the sources of mercury loss were *(i)* brine treatment, *(ii)* drainage, *(iii)* thick mercury treatment, *(iv)* emissions from the cell room area and *(v)* entrainment with caustic and hydrogen. It was necessary to separate sewer and collecting systems for mercury-containing from mercury-free liquids Some systems could be recycled. The mercury-carrying liquids could be reduced and filtered or oxidized with hypochlorite and filtered. Reduced mercury is recovered by roasting the filtered solids and condensing the mercury vapor formed. Oxidized mercury is present as the soluble complex, the $HgCl_4^{=}$ ion, and can be absorbed on one of several proprietary resins, from which it is later recovered. Waste water can also be treated with sodium sulfide under carefully controlled *p*H and excess sulfide conditions, then settled and/or filtered before discharge to remove precipitated mercury sulfide (8).

Brine-treating sludge can be handled by several processes: hypochlorite and chlorine oxidation; electrolytic oxidation with brine; roasting; and acid digesting followed by roasting (8). A multiple-hearth furnace produced lower mercury sludge than an indirectly fired rotary calciner. "Thick mercury" is treated by distillation along with plant solids. Emissions from the cell room area may include effluents from end boxes, mercury pumps, and collection tanks, and ventilation air from the cell room and maintenance areas. A collection system under a slight vacuum is connected to the many vents. Vent gas is cooled and scrubbed with chlorinated brine, which can return dissolved or entrained mercury to the brine system. One proposal is to add a trace of chlorine to vent gas after cooling so as to form calomel, Hg_2Cl_2, which is caught on a suitable filtering material before releasing to the atmosphere. Special mercury adsorbent resins are also available for adsorbing mercury from the vent gas before releasing (7, 9).

Cell room ventilation air is the most difficult problem. Mercury gets into cell room air by evaporation of mercury spilled on the floor and cell parts, and from open cells during maintenance. Mercury exposure to workers was reduced by improving the surface of floors to improve efficiency of prompt cleanup of spills and instituting new procedures in cell maintenance, such as cooling a cell before removing its cover, and replacing it with a temporary cover while the regular cover was removed to a maintenance room. The maintenance room is connected to the vent system for mercury recovery. A multipoint mercury-in-air analyzer-recorder monitors the air exhausted from the cell room. Metal anodes became available about the same time as the mercury problem was recognized. Their use has reduced the frequency of opening cells for cleaning as compared to graphite anode practice, so this helped reduce mercury exposure. A reduction from 0.03-0.04 mg/m^3 to 0.002-0.004 mg/m^3 mercury in cell room air is reported by one operator (7). The current OSHA TLV for worker exposure is 0.05 mg/m^3, and, according to EPA emission standards, mercury emissions are not to exceed 2300g per 24 hr (10).

Both caustic soda and hydrogen contain mercury as they leave the cells. It probably is in chlorine also as entrained chloride, but this is removed in cooling and drying operations, and the chlorine water condensate is returned to the brine circuit. Mercury is removed from hydrogen by cooling and demisting. Then traces can be removed by several methods, such as adsorption on special resins (7, 9), and molecular sieves (11) or activated resin impregnated with KI or silver salts. Some adsorbents can be reactivated, while others are sent to the mercury calciner with other solids. In another process, trace of chlorine is added after cooling, calomel is adsorbed in a filter, and then the hydrogen is scrubbed with caustic soda before use. The calomel can be removed from the carrier by leaching with chlorinated brine, and is then reused. It can also be removed by calcining.

Mercury cell caustic was normally collected, settled, and filtered using diatomaceous earth or alpha-cellulose filter aids. The addition of a layer of activated carbon insured removal of mercury well below the Codex specification of 1 ppm on 100% NaOH basis (12).

Between July 1970 and end of August 1970, the total industrial discharge of mercury was cut from 287 to 40 lb/day. It is now estimated that, through recycling mercury waste, mercury discharges have been reduced at least 95% since early 1970 (13). A closed mercury cell process by Kashima Chlorine and Alkali Company will be used by Diamond Shamrock. Loss of only 1g of mercury per ton of chlorine has been reported (14).

Several mercury cell chlorine plants have been shut down in the United States and Canada. A new chlorine capacity has been built using diaphragm cells rather than mercury cells. In Japan, the government ordered conversion to diaphragm or membrane cells by March 1978. As of December 1976, 42% of Japan's 42 million metric tons per year of caustic soda was still made in mercury cells. The deadline may be extended because synthetic fiber makers will not accept the diaphragm cell caustic soda because of its high NaCl content. The program may even be scrapped because the mercury cell operators have reduced their emissions (1).

An excellent textbook on the manufacture of chlorine and its products has been published. The theory of both mercury cells and diaphragm cells is included (15).

Developments—Diaphragm Cells

Coated titanium anodes have been a great advantage to diaphragm cells. With graphite anodes, the anode-cathode gap increased as the graphite wore away. This increase in electrode gap increased cell voltage and heat evolution, and shortened the life of the diaphragm due to clogging the pores with graphite particles and chlorinated organics. First designs were substituted for metal anodes with similar dimensions to the graphite ones. This was improved upon by adding an adjustable feature (16).

A protected metal bottom supporting the metal anodes has replaced lead and mastic. Cell covers are now made of fiberglass-reinforced polyester. Teflon gaskets are used between cell parts. Asbestos diaphragms swell and become more porous due to loss of fine particles of asbestos. A thermoplastic material has been added to the asbestos to prolong the life of the diaphragm.

Ion-permeable membranes have been tested for diaphragms for many years, but failed to withstand

conditions in the cell. However, du Pont's Nafion (R) membrane material has changed this. Cells are in commercial operation producing up to 20% NaOH with low chloride, using Nafion (R) membranes. They are economical where dilute caustic soda can be used, as in paper mills. Asaki Chemical, in Japan, developed their own membrane material, a perfluorocarboxylic acid, that can produce a more concentrated caustic soda, 20-30%. They utilize hot caustic soda from the cell to supply part of the heat for evaporating the caustic soda to 50%.

Improved diaphragms and membranes as well as new cell designs are under active development here and abroad at such companies as Diamond Shamrock Corporation, Hooker Chemicals and Plastics Corporation, and PPG Industries, Incorporated in the United States, and Asahi Chemical Industry, Limited, Asahi Glass Company, and Tokuyama Soda Company in Japan.

Diamond Shamrock diaphragm cells (16).—Diamond Shamrock Corporation has been experimenting with DSA (R) electrodes since 1966, and they are distributed now by a subsidiary, Electrode Corporation. Cell components have been optimized including an improved current distribution system, assured parallel anode orientation, improved base design, expandable anode, FRP cover, and modified asbestos diaphragm. A comparison of two types of Diamond Shamrock cells is shown in Table IV. These cells can produce 360% more chlorine at 2.5% less power per ton on one-half of the original floor space. The modified asbestos diaphragm retains the good qualities of asbestos, and troublesome properties are reduced. It provides easier hydrogen evolution, prevents swelling, and has longer life, improved uniformity, and improved flow properties, is easy to remove, and can be stored up to 5 months before use. The modified asbestos diaphragm decreased power consumption 6.7%, and their expandable anode decreased it another 7.1%.

Diamond Shamrock has been working with du Pont on application of the Nafion (R) membrane and announced start-up of membrane cells to replace mercury cells at their Muscle Shoals, Alabama, plant. Production of 30-40% NaOH at 85% current efficiency is claimed (17). The first membrane cell installation with D-S membrane cells in Europe at Uddeholm's paper mill complex in Skogall, Sweden, for 20,000 metric tons per year of chlorine, has been announced for startup at the end of 1977 (18).

Hooker diaphragm cells.—Hooker Chemicals and Plastics Corporation has developed a number of diaphragm and membrane cells. Diaphragm cells include the H-2 (80 kA), HU-80, and H-4 (150 kA); the MX cell is a bipolar cell with Nafion (R) membranes. H-2 and H-4 are similar to previous Hooker cell designs, but are much larger in physical size and production capacity. These monopolar cells have a cubic shape with a plastic top, multifingered steel cathodes, and metal anodes. They have thinner, resin-bonded asbestos, [HAPP (R)] diaphragms, closer anode-cathode spacing, and improved electrical conductors. Cathode fingers go all the way across the cell, and are perforated steel plate instead of wire mesh. Current density has been increased from 1.0 A/in.^{2} (1.6 kA/m^2) to 1.5 A/in.^{2} (2.4 kA/m^2). Voltage has been improved, as shown in Table V (19).

Table IV. Performance of two types of Diamond Shamrock cells

Anode	DS-85	D-3, graphite
Anode area (m^2)	54.8	26.5
Operating range (kA)	75-150	20-42
A selected operating current (kA)	110	30
Voltage at selected point (volts)	3.66	3.75
Current density at rated conditions (kA/m^2)	2.0	1.13
D-c power at selected point (kW-hr/mt)	1876	1949
Cl_2 (mt/day)	3.35	0.92
Floor space per daily mt Cl_2 (m^2)	5.6	11.7

Table V. Analysis of voltage improvements at 1 A/m^2 in Hooker cells

	H-4, 1976	S-3, 1960
Decomposition, anode	1.32	1.32
Decomposition, cathode	0.93	0.93
Overvoltage, anode	0.03	0.33
Overvoltage, cathode	0.27	0.27
Brine gap	0.27	0.49
Hardware	0.17	0.36
Diaphragm	0.16	0.30
	3.15	4.00

The HU-80 cell was designed together with Friedrich Uhde GmbH with geometry similar to a mercury cell, i.e., a long narrow cell shape, made for installation on columns or an elevated floor, with a jumper under the cells, close coupling of adjacent cells, minimum use of copper, and a rubber-lined cover. A prototype was tested from 50 to 100 kA (15.5-25 A/dm^2) to optimize asbestos and HAPP (R) diaphragms and all cell components. Operation showed a saving of 100 mV in the hardware at 25 A/dm^2 over H-2 cells. A commercial plant is being built, or is in operation, in Sweden.

The MX cell is the result of many years of experimentation with ion-permeable membranes. The promise of success came with metal anodes and du Pont's Nafion (R) membrane. Du Pont cooperated with Hooker in supplying various types of membrane material. Cells with Nafion membranes have been installed at its Tacoma, Washington, plant, and are in commercial operation at Reed Paper Limited, Dryden, Ontario, producing 45 tons per day of chlorine and 9-10% NaOH. Another installation of 73 tons of chlorine per day has been announced for construction at Toyo Soda.

The Dryden plant has 18 cell stacks, each stack operating at 3000A and 14V. Feed and product headers are part of individual plastic cell frames. A stack can be removed to a maintenance area for repair, but some work can be done in place, such as replacing a membrane in 2 hr. New designs operate in the range of 10-15 kA. Latest membranes will produce 30-40% NaOH, with 50 ppm NaCl impurity, on a 50% NaOH basis. Energy consumption is 2806 kW-hr/metric ton NaOH. Cell voltage is close to 4V, compared to 3.5V with diaphragm cells. Extra care in brine purification is required for membrane cells, and solid salt is required as raw material.

PPG-de Nora Glanor (R) electrolyzers (20, 21).—PPG Industries, Incorporated joined with Oronzio de Nora Impianti Elettrochimici in a development called the Glanor (R) Vertical Type 1144 Electrolyzer. It is an 11-cell bipolar electrolyzer, equipped with dimensionally stable metal anodes and cathodes of standard steel wire mesh. The first generation of commercial electrolyzers use deposited asbestos diaphragms, but PPG is actively working on improved diaphragm material and ion-permeable membranes, and has designed the cell to be adaptable to their use.

The anolyte compartment of each cell is connected to an independent FRP brine feed tank by flanged connections. Chlorine escapes from each cell through the brine feed tank. Hydrogen leaves the top of the cathode compartment of each cell, and cell liquor is discharged from a conventional inverted-U pipe system. A gasket of special elastomer insulates one cell from another, and the whole assembly is clamped together with tie rods to form a tight, essentially leak-proof unit. The electrolyzer rests on a steel frame supported on porcelain insulators. Each electrolyzer has a brine level alarm to monitor the level of all cells in the unit.

The bipolar electrode consists of a steel plate to which anode fingers are connected on one side and cathode fingers on the other. This bipolar electrode is set into an 18 in. wide steel channel frame, lined with titanium surrounding the anodes. The electrical connection between anodic and cathodic sections is said to

have a low voltage drop and low fabrication cost. The design is claimed to simplify maintenance including diaphragm depositing, assembly, disassembly, cathode washing, and inspection of electrodes. It is difficult to misalign the electrodes or damage the diaphragms because of features built into the unit and the use of simple assembly jigs and fixtures. A unit with conventional asbestos diaphragms operated 32 months with characteristics shown in Table VI. There were numerous shutdowns for external reasons, which the unit took easily. The unit is 17 ft long × 11 ft wide × 12 ft high over-all. It weighs 85,000 lb empty and 150,000 lb in operation. Conventional asbestos diaphragms have a life of 12-24 months. An automatic cathode washer was developed. The anodes are expected to last 4-5 yr before recoating. The titanium base should withstand a number of recoating cycles. An installation could consist of 8-20 electrolyzers in series, but 14 in 2 rows is suggested. They are placed end to end, 3-5 ft apart. The cell room would be 160 ft long × 80 ft wide. This cell room would produce approximately 415 tons per day of chlorine, so that floor space requirement is 31 ft^2/ton per day of chlorine (2.83 m^2/t/d). Electrolyzers can be elevated or on ground level depending on the transportation system preferred. An electrolyzer is short-circuited with a portable switch without interrupting the circuit. Interconnecting bus bar plates are removed, and the cell transported to a maintenance area. There are 4 plants in Japan and 1 in United States producing 200-500 tons per day in 76 electrolyzers totaling 2000 tons of chlorine per day, and 2500 tons per day are under construction or under contract.

Asahi Chemical's bipolar electrolyzer (22, 23).— In April 1975 Asahi Chemical Industry Company, Limited started operating a plant which put out 40,000 metric tons per year of caustic soda, using a bipolar cell with the du Pont Nafion 315 membrane and coated titanium anodes. Since then they have changed to their own membrane of perfluorocarboxylic acid. They licensed Denki Kagaku Kogyo Company, Limited, and that plant (putting out 60,000 metric tons per year of caustic soda) started in September 1976.

Asahi Chemical found that the maximum concentration of caustic soda obtained by the Nafion (R) membrane cell was 17.6%, at a current efficiency of 80%. Their own perfluorocarboxylic acid membrane can produce up to 40% caustic soda at high current efficiency, but optimum concentration is 21.6%. The membrane has a low electrical resistance. Voltage is less than 4V per cell at current densities of 40-60 A/dm^2 and current efficiency of at least 90%. Cells operate at 90°-120°C for optimum voltage. The membrane has sufficient mechanical strength and toughness so that it can be made in 4 × 8 ft sheets and used in their electrolyzer having a capacity of 10,000 metric tons of caustic soda per year.

Asahi Chemical also developed their own anode coating of a 3 component solid solution, which is over 50% ruthenium oxide plus oxides of titanium and another metal. This coating has a low anode potential and high alkali resistance. Anode and cathode compartments are separated by a partition of explosively bonded titanium and steel. The anode compartment is lined with titanium and the cathode compartment is steel. Vertical plates welded at right angles to the partition plate carry current to electrode surfaces; titanium on the anode side, and steel on the cathode side. Several holes in these vertical conductor plates permit electrolyte circulation. Expanded metal electrodes are welded to the vertical plates and to the channel, forming the rectangular frame around the unit. The voltage drop between adjacent electrodes is about 3 mV at 50 A/dm^2. The effective area of a single electrode is 270 dm^2, and the 32 ft^2 (297 dm^2) membrane is clamped between units using Teflon gaskets. The anode-cathode gap is 2-3 mm. Chlorine and hydrogen are released to the rear portion of electrodes and rise up in compartments behind the electrodes, so that the claim is made that voltage is not influenced by gas generation on electrodes. One electrolyzer has 80 bipolar cells clamped together, and has a voltage of about 300V at 10.8 kA.

Pure brine is fed into the bottom at one end of a unit, and depleted brine and chlorine leave through a pipe at the opposite top corner of the unit, and are then delivered to a collecting main above the electrolyzer. Circulating catholyte (dilute caustic soda) is fed into the bottom of the cathode compartment at the opposite end to the brine inlet. Catholyte and hydrogen leave through a pipe in the top at the other end and discharge into a collecting main, also above the electrolyzer. The collecting mains drain to anolyte and catholyte tanks where the gases and liquids separate. A part of the effluent brine is sent to the salt dissolving tank, and the rest is returned to the anode compartment. The amount of brine sent back for reconcentration is adjusted to maintain salt utilization at about 70%. Reconcentrated brine is conventionally purified, and then passed through a bed of ion-exchange resin for further removal of traces of calcium, magnesium, iron, and aluminum ions. Pure brine is added to the anolyte tank.

Caustic soda solution is recirculated between the cathode compartment and catholyte tank. Water is added to the catholyte stream to maintain the desired concentration. The optimum concentration of catholyte is 20-30% NaOH. Above 25% NaOH the membrane resistance increases sharply. A part of the catholyte is sent to the first stage of the flash evaporator, part of which is returned to the catholyte tank and part of which goes on to the second stage as product, which is heated by steam from the first stage. The final concentration of caustic soda is adjusted by using steam in a final, single effect vacuum evaporator. Considering steam and electric power combined, the optimum catholyte concentration is 21.6% NaOH. This heat recovery evaporator system uses 0.7 metric ton of steam to concentrate 21.6% NaOH to 48-50% on the basis of 1 metric ton of 100% NaOH, and 0.4 metric ton of steam to concentrate from 25% NaOH to 50%. Operating results for the 80 cell electrolyzer are given in Table VII.

Asahi Glass Company (no relation to Asahi Chemical Industries) and Tokuyama Soda Company are both working on membrane cells using membranes of their own development. The Asahi Glass Company cell (24), with their newly developed cation exchange membrane, has operated on a commercial scale since August 1976. It is a monopolar, filter press-type electrolyzer rated at 3000 metric tons of caustic soda per year. The membrane is 1.2 × 2.2m in size, with an anode-cathode gap of 2-3 mm. Membranes had a life of 2 yr on a pilot cell. It produces 40% NaOH containing 0.0009% NaCl. Extra pure brine is required. Pennwalt is de-

Table VI. Characteristics of Glanor (R) vertical-type 1144 electrolyzer

Current (kA)	71-73
Volts per cell	3.43-3.67
Current efficiency (%)	95.3-96.7
Energy consumption, d.c. (kW-hr/short ton Cl_2)	2450-2580
Cell gas (% Cl_2)	96.6-98.2
Cell gas (% O_2)	1.4-2.2
Cell gas (% H_2)	0.02-0.20
NaOH in cell liquor (g/liter)	125-140
$NaClO_3$ in cell liquor (%A.B.)	0.03-0.20

Brine feed: 320-325 g/liter NaCl, at 160°-165°F, at pH 10.0-11.4

Table VII. Characteristics of Asahi Chemical bipolar electrolyzer

Current (kA)	10.8
Cell voltage	3.75
Electrolyzer voltage	300
Current efficiency (%)	93
Current density (A/dm^2)	40
Average power consumption, d.c. (kW-hr metric ton NaOH and 0.89 metric ton Cl_2*)	2703

* 0.06 metric ton Cl_2 is converted to HCl and required for pH control of anolyte. 48% NaOH contains 44 ppm NaCl. Cell gas is 99.27% Cl_2 and 0.14% O_2.

veloping a membrane cell system (25) which involves coating the anode in a mixture of asbestos and Kynar (R). In commercial use at one of Pennwalt's plants, the system gives 90% efficiency.

The Japan Soda Industry Association is sponsoring development work at Kyoto University on fused $NaCl$-$ZnCl_2$ electrolysis using a β-alumina diaphragm (25). Current efficiency on laboratory scale tests was almost 100%. Cell voltage at 50 A/dm^2 was 3.18V.

Electrolysis of Hydrochloric Acid

Chlorine is being recovered from byproduct hydrogen chloride with Hoechst-Uhde (27) electrolyzers at 4 plants in Germany and now one at Mobay Chemical, Baytown, Texas, which is increasing its capacity. The Hoechst-Uhde electrolyzer has 30-45 bipolar cells working at current densities of 4-5 kA/m^2. A cell consists of a frame of phenol or cresol formaldehyde plastic containing ducts for products and for inlet and outlet hydrochloric acid. Graphite plates are cemented into the frame to form bipolar electrodes. They have vertical slots on both sides to carry away gases. They rise to the top of the electrodes and pass through openings into proper ducts in the frame. Chlorine together with anolyte passes to one end of the assembly, and hydrogen together with catholyte goes to the other end. A diaphragm of PVC fabric is fixed to the sides of the frame. Rubber-lined steel plates clamp the cells together with tie rods. Electrical connections to the graphite plates in each end frame are made with graphite nipples through stuffing boxes. The electrodes have an effective area of 2.5m^2 and can use current up to 12 kA. An electrolyzer with 30 cells is approximately 3.5m long $\times$ 2.2m wide $\times$ 2.2m high.

The anolyte and catholyte operate in separate cycles, but each has a head tank, a run-down tank, circulating pump, heat exchangers, and filter. The filters remove abrasive particles and precipitates. The electrolytes are maintained at 20-22% HCl and 75°C for optimum results. Part of the 20% HCl from the catholyte cycle is sent to the absorption unit for enrichment to about 30% and returned to the two cycles as required. The two gases are first cooled, and condensed 8-12% HCl is then returned to the catholyte or anolyte cycle. After cooling, chlorine is treated as in alkali-chlorine plants. Hydrogen is scrubbed with caustic soda solution. The chlorine contains less than 0.1% hydrogen with new diaphragms, but they deteriorate after 2 or 3 yr and are replaced when hydrogen rises to 0.5% in the chlorine. Graphite anodes are not attacked in this service. For all practical purposes, any hydrogen chloride can be processed for use in the electrolyzer. Organic impurities have two kinds of effect. They may affect quality of products, or they may clog diaphragms and form deposits on electrodes. Some processing, followed by absorption on activated carbon, may be required. Inorganic impurities containing multivalent ions will reduce current efficiency. Sulfates may attack the anodes. The original article should be consulted for further details.

Chlorine Handling

There have been advances in practically every step of conveying, cooling, drying, compressing, condensing, and shipping chlorine. Chlorine-resistant plastics and titanium have been responsible for many improvements. Automatic analyzers for impurities in cell gas and moisture have improved safety in operation. The use of coated metal anodes has reduced organics in liquid chlorine.

Chlorine is collected from the cells under a slight vacuum in hard rubber-lined steel pipe or FRP plastic pipe. Cell gas is cooled in 2 stages, first with plant water, and then with chilled water, to about 15°C. Plastic or plastic-lined steel towers with ceramic packing may be used for countercurrent, direct-contact cooling with water circulated by plastic or titanium pumps through titanium heat exchangers. Efficient demisters between cooling and drying operations have reduced sulfuric acid consumption.

Drying is still done with 2 or 3 drying towers in series using countercurrent flow of sulfuric acid, starting with 93-98% H_2SO_4 and discarding about 70% H_2SO_4 at the bottom of the first tower to meet wet chlorine. Acid is cooled and recirculated through each tower. Teflon acid coolers and high alloy pumps are available for this service. Demisters are important after drying, particularly if centrifugal compressors are used.

Centrifugal compressors handling up to 600 tons of chlorine per day at 10 atmospheres pressure have superseded nonlubricated reciprocating and acid-sealed compressors. Designers have a choice between high chlorine pressure and relatively warm condensing temperature or lower chlorine pressure and lower condensing temperature. Freon refrigeration systems provide adequate choice. Noncondensible gas or "blow-off gas" is absorbed in caustic soda or milk of lime for bleach, or the chlorine can be absorbed in a chlorinated solvent system and regenerated. Liquid chlorine is distributed in cylinders up to 150 lb in 1 ton containers on flat-bed multiunit railroad cars of 15 tons total capacity, or in railroad tank cars of 16, 20, 55, 85, and 90 tons capacity or in barges up to 1200 tons. For short hauls, there are 16 ton tank trucks. Nearby consumers can get gas or liquid by pipeline. The two largest railroad cars and tank trucks are the most recently approved equipment. All cars, containers, valves, and safety devices used in transportation of chlorine are built to very rigid specifications, developed in cooperation with government agencies and chlorine producers through the Chlorine Institute.

Chlorates

In the past 25 years production has increased from 40,000 to 196,400 short tons per year in the United States. The production capacity is now 254,000 short tons and is increasing. There were 12 U.S. plants in 1976. In Canada, there were 11 plants with a total capacity of 226,000 short tons per year.

The trend in consumption is shown in Table VIII. Sodium chlorate's largest use is in combination with sulfuric acid and a reducing agent such as sulfur dioxide, methanol, or sodium chloride to make chlorine dioxide for bleaching pulp. Other chlorates are made from sodium chlorate by double decomposition and crystallization. Potassium chlorate is used in the manufacture of matches and pyrotechnics. Sodium chlorate is raw material for producing perchlorates. Sodium chlorate is used in weed control, but is being displaced by newer and more selective materials. Miscellaneous uses include textile bleaching, ore processing, and chemical processing.

The application of coated titanium anodes has stimulated new cell designs, permitted higher operating temperatures, and increased cell output. For example, Stanchem, the Canadian Division of PPG Industries, increased capacity 10% by installing metal electrodes developed jointly by Kema-Nord of Sweden and PPG.

Huron Chemicals Limited and Electrode Corporation have developed the EH 120 Multipolar Chlorate Cell Unit (28) (Table IX). With metal anodes, claims are made for improved energy efficiency, increased chlorate concentration ranges, elimination of filtration, and reduction in evaporation. Physical size has been reduced to 1/3 that of old graphite cells of equal

Table VIII. Trend in consumption of $NaClO_3$

	1955 (thousands of short tons/yr)	1974
Pulp and paper bleaching	14	173
Other chlorates and perchlorates	6	27
Herbicides	18	11
Miscellaneous	11	11
	49	222

Table IX. Operating characteristics of the EH120 cell unit

Current (kA)	10
Bipolar cells per unit	12
Volts per cell, depending on concentration	3.2-3.6
Total voltage (V/unit)	39-43
Current efficiency (%)	91-96
Dimensions: 3.0m high × 2.4m wide × 4.0m long	
Weight: 8600 lb (3900 kg) empty; 63,800 lb (29,000 kg) full	
Energy: C.E. 93.5%, a.c.-d.c. 3% loss, 600 g/liter $NaClO_3$, 100 g/liter NaCl, large plant with more than 3 units, 10 kA—5020 kW-hr/short ton	
Daily capacity for $NaClO_3$ production	3930 lb (1783 kg)

capacity. Units are now offered for 2, 3, and 4 tons nominal capacity of sodium chlorate per day. Two or more bipolar units operate in series electrically and chemically.

Brine with 300 g/liter NaCl and 350-400 ppm $Na_2Cr_2O_7$ is fed into the first unit, and product from the last unit contains up to 600 g/liter $NaClO_3$ and 100 g/liter NaCl. The pH of each unit is individually controlled between 6.5 and 7.5 by addition of hydrochloric acid. Temperature is controlled at 60°-65°C by water-cooled coils in each cell tank.

Several other new cell designs making use of metal anodes and new materials are undoubtedly available.

The electrochemistry and technology of chlorates and perchlorates up to 1969 was reviewed by J. C. Schumacher (29).

Perchlorates

Table VIII indicates that approximately 6000 short tons of $NaClO_3$ were used for perchlorates in 1955 and 27,000 short tons were used in 1974. The major use of perchlorates is as an oxidizer in solid propellants. Potassium perchlorate was used at first, but was superseded by ammonium perchlorate, which is now the most important. Lithium perchlorate has the highest percent oxygen, and has been tested as an oxidizer in propellants, but has not been accepted.

Sodium perchlorate is the principal raw material for the manufacture of perchloric acid and perchlorate salts. Because of the high solubility of sodium perchlorate, it need not be isolated from finished cell solution and can be purified for conversion by double decomposition to other salts. Perchlorate cells consist of steel tanks with cooling coils, which act as the cathode, and bright platinum anodes suspended from the cover.

A typical electrolyte feed is 400 g/liter $NaClO_3$, 400 g/liter $NaClO_4$ and 5 g/liter $Na_2Cr_2O_7$. Feed to the cells may be in parallel or series cascade. If in parallel, the electrolyte is circulated from a feed tank through the cells, is returned to the feed tank until the desired concentration is reached, and then a new tank is started. In series operation, the feed enters the first cell and then cascades from one cell to another, leaving the last cell at the desired concentration. The series system has the advantage that individual cells can be regulated with respect to temperature and current density for most economical production.

Most commercial cells use platinum anodes. Some cells use platinum-covered tantalum or copper. One manufacturer is reported to use lead dioxide anodes. The cells must then be made of nickel or stainless steel because chromate poisons lead dioxide anodes. Typical operating data are shown in Table X. The optimum operating temperature is a compromise. An increase in temperature lowers energy consumption but increases platinum loss.

Table X. Typical data for perchlorate cells (30)

Temperature	35°-45°C
Minimum feed rate	6 liter/min
pH	6.0-6.8
Cathode current density	30 A/dm
Voltage	6.5-7.0
Energy consumption	1.36-1.60 kW-hr d.c./lb
Sodium dichromate	2.5-5 g/liter
Calcium and magnesium	As low as possible
Final sodium perchlorate	As high as purification permits

Hydrogen Peroxide and Persulfates

In the manufacture of electrolytic hydrogen peroxide, ammonium bisulfate is electrolyzed with formation of ammonium peroxydisulfate, $(NH_4)_2S_2O_8$ (also known as ammonium persulfate). This solution can be used either for hydrolysis to hydrogen peroxide or for crystallization of the ammonium peroxydisulfate. Electrolytic hydrogen peroxide is now largely displaced by the chemical anthraquinone (AQ) or isopropyl alcohol processes (IPA). Of the eight plants in the United States making hydrogen peroxide in 1970, only three used electrolysis to make approximately 20% of the 164 million lb per year as 100% H_2O_2. Economics favor the AQ process in general. Ammonium peroxydisulfate must be made by the electrolytic process. No production data were found for the peroxydisulfate, so it may be included in the hydrogen peroxide figure.

Hydrogen peroxide is used for bleaching cotton textiles and some wool. It is also preferred for bleaching ground wood pulp over hypochlorite because it gives high yields of pulp. The uses in 1969 were distributed as follows: textile bleaching, 30%; pulp and paper bleaching, 8%; plasticizers and other chemicals, 26%; glycerine, 15%; miscellaneous, 21%. Other peroxydisulfates can be made by reacting the carbonate or hydroxide to replace the ammonium ion, which is evaporated as ammonia. Potassium, sodium, barium, and lithium peroxydisulfates have been produced in this way. Peroxydisulfates are used for polymerization catalysts, dye fixing, detergent additives, modification of starches, and desizing of textiles. Ammonium peroxydisulfate is used for etching printed circuits. The persulfates are shipped in multiwall paper bags and fiber drums (31).

Fluorine

Fluorine is used in the separation of U-235 from U-238 via UF_6 in the nuclear electric-power industry. It is also used in the manufacture of SF_6, a gaseous insulator for electrical and electronic equipment, and of Freon refrigerants. ClF_3 is used for chemical cutting of oil well casings. ClF_3 and OF_2 are rocket fuel oxidizers. Production of fluorine in 1974 was reported to be 137,000 tons and consumption was 689,000 tons. The annual growth rate of production was reported as 2 and 4% of consumption (32). No explanation was found for the difference between production and consumption in these figures. Plants are operated by Allied Chemical Company at Metropolis, Illinois, and Union Carbide Nuclear Corporation at Oak Ridge, Tennessee, and Paducah, Kentucky (33).

Potassium fluoride containing 40-42% HF is electrolyzed between carbon anodes and steel cathodes. Cells are jacketed and may have internal cooling pipes to maintain 95°C. Cooling water at 58°C is used to prevent crystallization of bifluoride on cooling surfaces. A metal skirt extends down from the cover to keep the H_2 separated from the F_2. A 6 mesh screen below the skirt prevents broken anodes from short-circuiting a cell. It was found that this screen also improved current efficiency. Anodes are 2 × 8 × 20-5/8 in. carbon blades bolted to AISI-4140 steel bars using bolts of the same steel and copper pressure plates. Each anode bar has three 1-1/8 in. copper conductor posts extending through insulating packing glands in the cover. This connection has been a source of trouble, but anode life has been improved to 20 million A-hr. Typical data for a Union Carbide cell are shown in Table XI.

Table XI. Typical operating data of the fluorine cell

Current (kA)	4	6
Operating voltage	8-12	9-12
Temperature (°C)	90-105	90-105
HF in electrolyte (%)	40-42	40-42
Anode area (dm²)	390	390
Current density (A/dm²)	10.3	15.4
Anodes (no.)	32	32
Life of anodes (A-hr)	16×10^6	15.5×10^6

HF and CF_4 are removed from liquid fluorine to less than a total of 0.2% by refrigeration to −140°C. HF can also be removed by passing through NaF in a scrubbing tower. The fluorine is liquified under pressure and low temperature.

Handling fluorine

Nickel, Monel, aluminum, magnesium, copper, brass, stainless steel, and carbon steel are used for handling dry fluorine. All except carbon steel are good down to −190°C. Nickel and Monel are good up to 550°C. aluminium to 450°, magnesium to 400°, stainless steel and carbon steel up to 250°C. Tetrafluoroethylene (Allied's Halon TFE and du Pont's Teflon) are resistant to gas under static conditions.

Equipment must be thoroughly cleaned, such as by flushing with trichlorethylene and then purging with nitrogen. The surface must be passivated by flushing out the nitrogen with fluorine. After 2 hr the equipment surfaces will be passivated. Carbon steel is used for fluorine gas and stainless steel for liquid fluorine. Soft copper or aluminum gaskets are used for flanged connections that have to be broken. Liquid fluorine can be transferred by pressurizing with helium. Nitrogen is unsatisfactory because it is soluble in liquid fluorine.

Fluorine gas is shipped under 400 psi in 6 and 4-1/2 lb steel cylinders. Special liquid nitrogen-cooled Dewar steel tank trucks for 5000 lb of sealed liquid fluorine are approved for use under carefully controlled conditions.

Manganese Dioxide (33)

World production was estimated to be 83,000 tons of synthetic manganese dioxide in 1976, of which Japan produced 40,000 tons and the United States produced 25,000 tons (34). Electrolytic manganese dioxide is used in high capacity batteries where weight and size are of great importance.

Reduced oxide ore is leached with spent electrolyte containing 50g $MnSO_4$ and 67g H_2SO_4 per liter at 90°C. After purification, the solution containing 150g $MnSO_4$ per liter is mixed with an equal volume of spent electrolyte and is fed to electrolytic cells at such a rate that outlet electrolyte is 50g $MnSO_4$ and 67g H_2SO_4.

American cells are graphite lined with graphite cathodes and graphite or titanium anodes, spaced 1 in. apart. The dioxide builds up as a dense, coherent, 6 mm thick or more black coat on the anodes before it is stripped. Cells are covered and maintained at 90°C. Current density is 6-10 A/ft^2 (0.6-1.1 A/dm^2), and current efficiency is normally 80-90%. Stripped oxide is crushed, neutralized with ammonia, soda ash or caustic soda. It is dried cautiously so as not to remove combined water, which would decrease depolarizing activity of the manganese dioxide.

Summary

Advances over the past 25 years in production of sodium hypochlorite, caustic soda, sodium methylate, caustic potash, chlorine, sodium chlorate and perchlorate, ammonium peroxydisulfate and hydrogen peroxide, fluorine, and manganese dioxide are covered. Electrolytic hydrogen peroxide has mostly been displaced by chemical processes during the time period reviewed. Coated titanium anodes in chlor-alkali and chlorate cells are replacing graphite, thus decreasing energy use and cell size. Concern about the effects of mercury and asbestos in the environment has resulted in a shift to modified asbestos diaphragms and membrane cells for chlor-alkali. Silicon rectifiers, centrifugal compressors, titanium, corrosion resistant alloys and plastics have all contributed to advances.

REFERENCES

1. *This Journal*, preceding paper.
2. "The Chlorine Institute Pamphlet 10," North American Chlor-Alkali Industry Plants and Production Data Book, The Chlorine Institute, Inc., New York (1976).
3. W. C. Gardiner, Paper presented at a meeting of the Chemical Market Research Assoc., Niagara Falls, N.Y. (1954).
4. *Chem. Eng. News*, **55**, Feb. 21, 14 (1977).
5. *Jpn. Chem. Week*, **15**, Nov. 21, 6 (1974).
6. W. C. Gardiner, in "Electrochemical Contributions to Environmental Protection," T. R. Beck, O. B. Cecil, C. G. Enke, J. McCallum, and S. T. Wlodek, Editors, p. 16, The Electrochemical Society Softbound Symposium Series, Princeton, N.J. (1972).
7. F. Hine, N. Yokota, and T. Takasaki, *Int. Chem. Eng.*, **17**, 1 (1977).
8. R. A. Perry, in "Chlorine Bicentennial Symposium," T. C. Jeffrey, P. A. Danna, and H. S. Holden, Editors, p. 131, The Electrochemical Society Softbound Symposium Series, Princeton, N.J. (1974).
9. C. J. N. Rekers, Paper presented at the Chlorine Institute Plant Managers Seminar, Houston, Texas (1973).
10. *Chem. Eng. (N.Y.)* **80**, April 16, 60 (1973).
11. *Chem. Eng. News*, **50**, Feb. 21, 17 (1972).
12. 4th Supplement to the Food Chemical Codex, 1st ed., Publication 1406D, National Academy of Science, National Research Council, Washington, D.C. 20418, 1971.
13. Chamber of Commerce of U.S., Community and Regional Development Group, Pollution Facts, Mercury.
14. *Chem. Mark. Rep.*, **207**, 7 (1976).
15. J. S. Sconce, *ACS Monogr.*, **154**, 81, 1962.
16. V. H. Thomas and K. J. O'Leary, in "Chlorine Bicentennial Symposium," T. C. Jeffrey, P. A. Danna, and H. S. Holden, Editors, p. 218, The Electrochemical Society Softbound Symposium Series, Princeton, N.J. (1974).
17. *Chem. Eng.* (*N.Y.*), **83**, March 29, 61 (1976).
18. *ibid.*, **83**, May 19, 67 (1976).
19. Hooker Chemicals & Plastics Corp., Communication (1976).
20. P. J. Kienholz, in "Chlorine Bicentennial Symposium," T. C. Jeffrey, P. A. Danna, and H. S. Holden, Editors, p. 198, The Electrochemical Society Softbound Symposium Series, Princeton, N.J. (1974).
21. T. C. Jeffery and R. J. Scott, Paper presented at The Society of Chemical Industry Symposium on Diaphragm Cells to Make Chlorine, London, England, June 17, 1976.
22. M. Seko, Paper presented at the Chlorine Institute Plant Managers Seminar, New Orleans, February 9, 1977.
23. N. R. Iammartino, *Chem. Eng.* (*N.Y.*), **83**, June 21, 86 (1976).
24. H. Ukihashi and T. Asawa, Paper 247 presented at The Electrochemical Society Meeting, Philadelphia, Pennsylvania, May 8-13, 1977.
25. *This Journal*, preceding paper.
26. *ibid.*
27. S. Payer and W. Strewe, in "Chlorine Bicentennial Symposium," T. C. Jeffrey, P. A. Danna, and H. S. Holden, Editors, p. 257, The Electrochemical Society Softbound Symposium Series, Princeton, N.J. (1974).
28. Huron Chemicals, Private communication, Kingston, Ontario, Canada.
29. J. C. Schumacher, *This Journal*, **116**, 68C (1969).
30. T. W. Clapper, in "The Encyclopedia of Electrochemistry," C. A. Hampel, Editor, p. 887, Reinhold Publishing Company, New York (1964).
31. *ibid*, p. 898.
32. "Mineral Trends and Forecasts," Bureau of Mines, U.S. Dept. of the Interior (1976).
33. H. R. Neumark and J. M. Siegmond, in Kirk-Othmer Encyclopedia of Chemical Technlogy, 2nd ed., Interscience Publishers, New York (1967).
34. A. Kozawa, T. Takamura, and T. Ishikawa, in "Selected Topics in the History of the Electrochemical Society," G. Dubpernell and J. H. Westbrook, Editors, The Electrochemical Society Softbound Symposium Series, Princeton, N.J., To be published.

JOURNAL OF THE ELECTROCHEMICAL SOCIETY

REVIEWS AND NEWS

FEBRUARY
1978

Twenty-Five Years' Progress in Electrowinning and Electrorefining of Metals

G. M. Cook*

Kennecott Copper Corporation, Ledgemont Laboratory, Lexington, Massachusetts 02173

During 1952, the fiftieth anniversary of The Electrochemical Society, several reviews of electrowinning and electrorefining processes were presented in the **Journal.** H. N. Gilbert (1) discussed the history of electrolytic sodium production, J. D. Edwards (2) examined 50 years of development in the Aluminum Industry, W. S. Loose (3) reviewed the 36 years of industrial magnesium production, and A. C. Loonam (4) wrote about the progress that occurred in the electrolytic production of other metals over the 50 year period. By 1952, the electrolytic production of metals was a mature industry. Mantell (5) gives a good description of the commercial electrolytic plants operating at that time. Since then only a few metals such as antimony, zirconium, and titanium have been added, even to the list of those obtained at pilot scale. ASARCO has recently completed a plant for the production of antimony (6). AMAX and Titanium Metals Corporation of America (TIMET) have both produced zirconium at pilot scale (7); and TIMET (6) and New Jersey Zinc (8) have both demonstrated titanium sponge production. The results obtained at TIMET (9) indicate that an electrolytic titanium process is competitive with the Kroll process. In an effort to improve product quality, Alcoa and Moly Corporation, together piloted a Bureau of Mines method for the pilot scale electrolytic production of pure rare earth metals (10). For the most part, the final commercialization of these processes is waiting for an increased demand to require the construction of new facilities.

Process and equipment developments (11-16), on the other hand, have resulted in numerous improvements in the electrowinning and electrorefining of the commodity metals: aluminum, magnesium, sodium, copper, nickel, and zinc. Several improvements have been made in electrolytic plants in general. The following items summarize these improvements and are considered further in the discussion of particular metals.

(*i*) Silicon rectifiers have been used to obtain improved reliability and energy conversion efficiencies on the order of 97% compared with about 94% for mercury arc rectifiers.

(*ii*) Larger cells or increased cell throughput have resulted in increased energy efficiency and improved materials handling.

(*iii*) Increased automation has improved the reliability of electrolytic processes and reduced operating costs.

(*iv*) Improved methods for feed material purification have reduced operating costs and increased yields.

(*v*) Modifications of cells have permitted the use of higher current densities in conventional tankhouses or extraction from low metals content electrolytes in plants of novel design.

(*vi*) Changes in electrodes have been used to increase anode life or metal purity.

* Present address: Argonne National Laboratory, Argonne, Illinois 60439.

Background

The primary emphasis in this review is on the impact of developments in electrolytic metal production upon technology in the United States. As a result of the various technical and economic developments over the past 25 years, there has been a great change in the relative importance of the major electrolytically produced metals. This is reflected in the growth of capacity and consumption for the commodity metals (6, 7, 17). Table I shows the change in the electrolytic plant capacities over the past 25 years. Figure 1 shows the variation in the quantities of the electrolytic metals consumed over the past 50 years. There are basically two categories of metals; the high growth metals which have increased at roughly 9% per year and the low growth metals which have increased at only about 1-2% per year. Magnesium production growth has been rapid and very erratic primarily due to variable military and space requirements. Though aluminum production has grown rapidly, it has been affected to a lesser degree by military requirements. Copper, zinc, and sodium, the low growth metals, have been minimally affected by noncommercial needs.

Much of the economic impact of the metals produced electrolytically in the United States arises in the fabrication steps. In order to put the several metal industries into perspective, it is instructive to examine the statistics for electrolytic metal production in the United States during 1974-1975. This comparison is given in Table II. From these data, it is seen that even though the value of these metals as a group is only about 4/10 of 1% of the gross national product, the impact on the electrical energy consumption is an order of magnitude greater, at over 4%. The increasing cost of this energy has a direct impact on the operating costs of these processes. It is particularly important to aluminum, magnesium, and sodium, which consume large amounts of energy in their electrolytic pro-

Table I. Approximate U.S. capacities

(In thousands of short tons)

	1952		1975-1976	
	Electrolytic	% of total	Eectrolytic	% of total
Zn	375	40	350	80
Al	1300	80	5000	80
Mg	110	90	200	90
Cu	2000	85	2750	85
Na	130	100	190	100

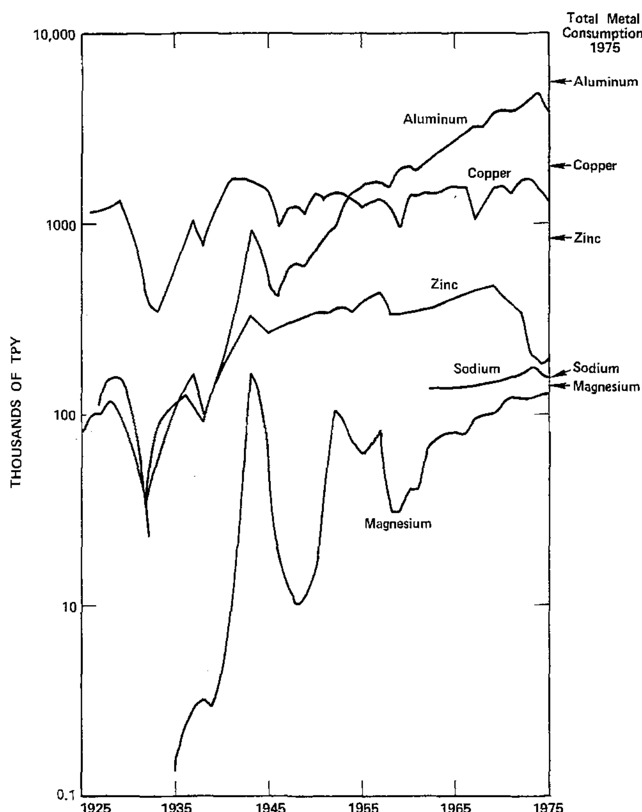

Fig. 1. U.S. total consumption and historical U.S.-production of several electrolytic-based commodity metals.

duction. Indirectly, the capital investment costs also increase with energy costs. This cost factor is more important to the metals which consume proportionately less energy in the electrolytic step.

In addition to energy, environmental concerns have had an impact on both operating and capital costs by imposing lower emission requirements on production plants. These new requirements have resulted in the need for new processing methods which reduce the emissions to an acceptable level. This has caused the shutdown of outmoded plants on the one hand, and the construction of new electrolytic plants on the other.

Also in the area of environmental concern, both industrial and environmental groups have become aware of the need to increase the extent of recycling of metals to reduce the amount of metal discarded. However, the statistics for the electrolytically important metals, except nickel, do not show a significant increase in the percent of metals recycled over the past ten years. Table III is based upon total scrap recycle. Kellogg (18) indicates that the total scrap recycle includes new or industrial scrap, with nearly 100% recovery, and old or product scrap with a

Table II. Electrolytic metal production, value, and energy consumption

Metal	Production (short tons $\times 10^{-3}$)	Approx. price (¢/lb)	Total ($ $\times 10^{-9}$)	Energy used* (kW-hr $\times 10^{-9}$)	Average energy* consumption (kW-hr/lb)
Al	4900	47	4.60	73.4	7.5
Cu	1600	69	2.20	0.4	0.13
Zn	240	37	0.18	0.7	1.5
Na	170	22	0.07	1.7	5.0
Mg	130	71	0.18	2.2	8.5
			GNP	U.S. Total	
			1400	2000	

* This is the energy used in the electrolytic step only.

Table III. Percent of metals recycled (6)

(Secondary consumption)

Metal	1971-1975	1961-1965
Nickel	36.9	29.7
Tin	28.6	28.4
Lead	44.0	43.6
Zinc	21.2	19.6
Copper	42.1	41.7
Aluminum	23.5	21.3
Cobalt	1.6	1.6
Magnesium	14.2	19.5

highly variable recovery. Typically, old scrap represents 20-25% of metals recycled. (Since year-to-year variations are considerable, Table III gives the 5 year averages for the two time periods.) A great deal of effort is likely to be required to change these percentages drastically. In the case of aluminum, many of the more recent applications have resulted in greater dispersion of the metal (*e.g.*, beer cans). Very recently, industrial efforts have increased the efficiency of collection of used cans to the point where over 25% recycle is obtained.

Fused Salt Systems

The commercial electrolytically recovered metals fall naturally into two categories: (*i*) those obtained from fused salt electrolytes at a high energy cost and (*ii*) those obtained from aqueous solutions at a relatively low energy cost. The fundamental differences between these two categories lead to differences in the technological innovations that are required to improve the recovery processes. On the one hand, operating costs are minimized with fused salt electrolysis, while on the other hand, capital costs are reduced when aqueous systems are used.

The metals produced in large quantities by fused salt electrolysis are aluminum, magnesium (19), and sodium. Much smaller quantities of beryllium (20), calcium, lithium, mischmetal,[1] and uranium are electrowon (21, 22), and pilot scale processes (7) have been used to win hafnium, individual rare earth metals, titanium, and zirconium. Of all these metals, only aluminum is not produced primarily from a chloride-based electrolyte. However, a fused chloride electrolyte is now being used in commercial production even for aluminum.

In recent years the emphasis in the area of electrowinning from fused salts has been in the development of anhydrous chloride electrolytes to reduce energy consumption. In such electrolytes, it is possible to use permanent, chlorine-producing electrodes. This is in contrast to the older processes in which consumable carbon anodes were used to produce CO and CO_2 from the oxygen-containing feed materials. In addition to the savings in carbon, there has been significant reduction in the electrical power consumed for electrowinning.

Aluminum.—During the past twenty-five years, the production of primary aluminum in the United States rose from less than 1,000,000 short tons to nearly 5,000,000 short tons in 1974. In the past two years, the general lessening of economic activity has resulted in significant decreases in the production of all metals. In the case of aluminum, it dropped to below 4,000,000 tons per year in 1975. In spite of this recently reduced demand, the average annual growth rate in the aluminum industry has remained very high at approximately 9%. At the same time, the process has remained essentially unchanged from that invented by Charles Martin Hall in 1886. Modifications in cell design and anodes, and the use of LiF additions (23) to the electrolyte have been important in reducing the energy consumption. The most important modification was simply increasing the size of the individual cells in order to approach adiabatic operation more closely,

[1] Mixed rare earth metals.

thereby reducing the heat losses. During the past 25 years, nearly 95% of the reduction in energy consumption can be attributed to this change. In 1952 the consumption was about 8.5 d-c kW-hr/lb, whereas in 1977, it is estimated to be about 6.5 d-c kW-hr/lb in the better plants. If the Alcoa chloride process lives up to its promise, the power could be reduced even further, to about 4.5 d-c kW-hr/lb. This reduction in the energy consumption is essential to the aluminum industry because aluminum, more than other metals, has been produced in the past using very low cost power. As such a user, it is likely to see higher than average increases in power cost.

A great deal of research and development effort has been directed to the reduction of energy consumption. The conventional aluminum process has been modified and new processes developed. The basic technology of the Bayer-Hall-Heroult aluminum production process has been extremely successful. However, it has shortcomings in addition to its low energy efficiency. The BHH process itself is somewhat capital intensive and the installation of newly required pollution control equipment in existing plants is expensive.

A number of modifications are being made to improve the BHH process (9). These are currently in pilot test by Kaiser Aluminum and Chemical Corporation and in production by Sumitomo Chemical Company. The newly designed plants will include: prebaked anodes; increased anode area; graphite linings on electrodes; computer control of electrode spacing (24); increased control of electromagnetic effects; minimized heat losses; and improved hooding. These factors are expected to lead to an energy consumption of less than 6 d-c kW-hr/lb, a greater on-line time, and a lower labor requirement. Further improvements might be possible by using permanent cathodes such as TiB_2 operating with only a thin layer of liquid aluminum which would permit the use of smaller interelectrode distances. The thick aluminum layer, used in conventional cells, is subject to erratic oscillations by the magnetic fields related to changes in current density.

In spite of these improvements in the BHH process, other competitive processes are on the horizon (25). These other processes use $AlCl_3$ in various steps. Three of these are not electrolytic. The Alcan process (a 5000 TPY pilot plant was operated in 1968) and a "monochloride process" (laboratory scale) proposed by Peacey and Grimshaw both depend upon the high temperature (1300°-1800°C) stability of AlCl and its relative instability at 700°C according to the equilibrium.

$$2Al(l) + AlCl_3 \rightleftarrows 3AlCl$$

The third proposed process (26) for the production of aluminum is the Toth process which depends upon the reduction of liquid aluminum chloride with manganese metal. This process is likely to be costly and to have difficulty meeting purity specifications.

The most promising chloride process is the Alcoa smelting process in which a fused salt mixture, possibly NaCl-LiCl-$AlCl_3$, is electrolyzed in a cell of novel design. This cell reportedly uses bipolar electrodes, thus increasing the number of electrodes per unit volume and thereby reducing plant space requirements and energy consumption. This novel process, as does the BHH process, starts with alumina. However, the alumina is first reacted with coke and chlorine obtained from the electrolysis cell to produce $AlCl_3$. The $AlCl_3$ is sent to the electrowinning cell to produce aluminum and chlorine. A side benefit of the process is a greater tolerance to interruptions of the power to the system, and thus it might be amenable for use as a method for load leveling for a utility facing periodic high demands for power.

Magnesium.—Magnesium consumption has also grown rapidly during the past twenty-five years. Its growth as an export metal has been even more explosive. In 1952, the exported metal amounted to less than 3% of the United States consumption. By 1975, it had reached 35% of internal consumption. Thus while internal consumption and imports grew by a factor of 3, exports grew by a factor of 30. The continued rapid growth of magnesium can be expected as new facilities operate with lower production costs and the demand increases for strong, light-weight aluminum alloys in automotive applications.

A problem which has been associated with magnesium production since it was first produced is that of the presence of water or oxide. The Dow Chemical Company used $MgCl_2 \cdot 1\frac{1}{4}\ H_2O$ to $\cdot\ 1\frac{3}{4}\ H_2O$, as feed to the electrolytic cells. This resulted in the production of mixed gases at a consumable anode. Continuing efforts are being expended to work with anhydrous $MgCl_2$ which permits the use of permanent anodes and produces Cl_2 as a by-product. Under the proper conditions, the additional cost of producing the anhydrous $MgCl_2$ feed is more than offset by lower operating costs. Manpower requirements are reduced since the electrodes are not consumed, thereby requiring less systems work. Electric power consumption is reduced by about 40% since the electrodes are closely spaced. In addition, a credit of 2-9% of the magnesium cost is obtained from the chlorine. The details of the production of magnesium are highly confidential, but general processing descriptions (27, 28) indicate that the trend of future production plants is, indeed, toward the use of anhydrous $MgCl_2$. If a low cost process for producing this metal is to be found, the energy consumption for magnesium production must be greatly reduced.

Sodium.—The production of sodium continues to be carried out primarily by the Downs process. The United States growth rate has been only about 1.5% per year. A depressing feature has been a reduction in the demand for tetraethyl lead, the production of which is the primary user of sodium metal. On the other hand, world consumption has been growing. As a result of this growth, the Tekkosha Company developed a staged aqueous/fused salt electrolysis process which reduces energy consumption, labor requirements, and corrosion problems (29). The first commercial plant went on stream in 1971.

The three stages of this process are: (*i*) Brine electrowinning of sodium to form a mercury amalgam; (*ii*) 240°C fused slag, NaOH-NaI-NaCN, electrorefining of the amalgam to produce a crude sodium; and (*iii*) purification steps to remove mercury and calcium. The low temperature operation improves the system operability and the operating environmental conditions. At the same time, a 20% reduction in energy is obtained. In addition, it appears that this process could be adapted for use with conventional chlorine-mercury cells to produce sodium metal instead of NaOH. If possible, this would lead to an improved flexibility in the productive capacity for sodium.

Rare earth metals.—Mischmetal is the only rare earth metal product produced in large quantities. The growing demand for rare earth-cobalt magnets, ductile iron (15% increase per year in 1973) and high strength low alloy steel (50% increase in 1973) is expected to provide a large increase in the demand for rare earths (7). A pilot scale joint venture of Aluminum Company of America and Molycorp evaluated the United States Bureau of Mines developed process (10) for the production of pure rare earth metals. The electrolyte used consists of a lanthanide suboxide (Ln_2O_3) plus fluoride dissolved in a mixture of BaF_2 and LiF. The 99.9% purity metal (cerium or lanthanum) was obtained at 75-95% current efficiency compared with the 45-50% typically obtained from the conventional chloride-based electrolyte. To date, the market for rare earth metals has not increased to the point where further development of this new approach is economically justified.

Titanium.—In 1952 a question was raised concerning the possibility that titanium and other "rare" metals might be electrowon from fused salt electrolytes. Since that time, the domestic production of titanium sponge has grown from a few hundred tons annually to roughly 21,000 TPY in 1974, or about 19% per year. Commercial production still is carried out by the Kroll process. However, electrolytic pilot plants have been operated by the New Jersey Zinc Company (8), Howmet Corporation, and Titanium Metals Corporation of America (TIMET) (9). The TIMET Division itself has produced several tons of electrolytic sponge. The process (30) offers lower energy and simple pollution control. A small bleed stream of valuable by-products is treated for secondary recovery. As the market improves, it is quite likely that some of the new capacity will be electrolytic.

Aqueous Systems

No new metals have been produced by the commercial electrowinning and refining of metals using aqueous solutions. New processes have been developed; and many processes, some of which were developed over 75 years ago, have been modified only slightly to build the aqueous electrolytic metals industry that exists today. The following examines the changes that have occurred and those that are on the horizon for introduction into commercial plants in the coming years (11-16).

With aqueous electrowinning and electrorefining, the major development efforts have been directed toward obtaining metal: at higher than conventional current densities (31), by using new cell designs (32-38); from new sources such as dilute solutions (39-43), sulfide anodes (44-46), and so forth; and with less manpower, by automation (46).

Many of the developments have a rather general applicability. For example, high surface area packed or fluidized bed cathodes (32-34) have been studied by several investigators. Pilot plant results indicate that these cathodes are economical for obtaining copper, gold, nickel, and cobalt from solutions containing less than 10 g/liter of metal. The metals are removed at relatively high rates and with low power consumption.

The metal content of dilute solutions has been recovered in two ways: (*i*) high surface area electrodes have been used when the solution contains only a single electrorecoverable species (40); and (*ii*) liquid ion exchange is used to separate and concentrate recoverable species (39, 41-43). The concentrated solutions are then amenable to conventional electrowinning.

Ore concentrates have been used as anode material. The first commercialization of such a process was the use of high metal-content nickel sulfide anodes (44) by INCO to produce a cathode grade nickel. Cymet (45) and Envirotech (46) have examined "pulp" anodes which use sulfide ore concentrates. The importance of this approach, rather than a simple leach-electrowin process, is that the rate of metal dissolution is synergetically enhanced so that the leach time can be significantly reduced.

Another factor of major impact is the use of various automated procedures to reduce manpower requirements. A high level of automation has been achieved at Mitsubishi's Naoshima Copper refinery (47) where no personnel are required to work within the operating tankhouse. This may be an example of tankhouses of the future. The first applications of automation that have appeared in more conventional copper and zinc tankhouses are for stripping cathode blanks, electrical short inspection, and loading and unloading cells. A more detailed review of developments follows with the discussion of the production of various electrolytic metals. It is important to realize, when reading these paragraphs, that much of the equipment has broad application even though it is discussed with emphasis on a particular metal.

Copper.—Since 1952 the actual cathode production has increased only slightly in the United States. At the same time, however, the electrolytic copper refinery capacity has increased by 66%. The changes in the methods for electrorefining copper have been minor until the past 10-15 years (48-52). These recent improvements in commercial plants include the following: The changeover to silicon rectifiers for d.c. power is nearly complete. The use of automatic stripping of blanks is progressing rapidly. Automated short detection is obtained in a few plants by infrared scanning of the cells or by computer analysis of cell electrical parameters. Titanium blanks are increasingly specified for starter sheet production and have also been used to produce full term (80-120 lb) deposits. Higher electrolyte circulation rates with careful filtration have permitted some producers to use current densities as high as 325-375 A/m^2. Periodic current reversal has also been used with current densities of 325-375 A/m^2. This technique has reduced the incidence effect of dendritic shorting. The deposit which results has an acceptable, though rough, surface. Other modifications include half cylinder rather than triangular electrical contact bars, plastic instead of lead liners for tanks, plastic capping boards to replace the wooden ones, and aluminum bus bars when the cost of copper was especially highly priced.

Electrowinning is becoming increasingly important since purification and concentration of dilute copper-containing solutions have become possible by using a liquid ion exchange (LIX) step. This process has required significant development efforts to improve cathode quality. Since this copper has not generally been considered to be of "cathode quality," it has not been included in production statistics. The basic failure to meet this standard is the almost invariably high lead content of the copper which has been electrowon. Only recently has Cyprus Mines Corporation been able to sell electrowon copper from two production plants as cathode.

The presence of the high acid electrolytes used in the LIX-electrowon process and the other operating conditions (typically 200 A/m^2 and 40°C) generally produce a product which is contaminated with lead slimes to the extent of about 6-12 ppm lead. The quality is generally high with respect to other impurities. Two approaches have been taken to alleviate this problem: (*i*) reduce the amount of lead in the suspended slimes, and (*ii*) substitute other anodes for the commonly used lead.

Two successful approaches have been taken to reduce the amount or effectiveness of lead in the suspended slimes. In the first approach calcium-lead anodes have been used to replace those of antimonial-lead. The lower corrosion rate in some electrolytes and the improved morphology of the PbO_2 formed on the surface have resulted in lower lead contamination of the copper product. The second approach is the addition of cobalt to the electrolyte, at the rate of 60 mg/liter-2 g/liter. It also improves the PbO_2 morphology.

Efforts have also been made to eliminate the lead substrate by using anodes of titanium with a precious metal catalyzed surface. These are similar to the dimensionally stable anodes used in the chlorine industry. At the present cost, it would be very difficult to justify the use of such anodes for the winning of common metals. As a result, MnO_2 and PbO_2 surfaces have been developed with some success. The remaining major deterrents to the use of these anodes are the brittleness of the deposits, the solubility of MnO_2, and the higher cost of titanium. However, if the use of calcium-lead anodes and cobalt additions to the electrolyte is found not to produce a satisfactory low lead content in a particular copper product, the development of titanium anodes may offer an alternative.

In addition to the preceding developments, which have been applied to improve the performance of existing electrolytic copper production plants, pilot scale

and laboratory work have been carried out to improve future plant performance even more. Much of this developmental work is directed toward the recovery of copper by other means. These include: several techniques to use high current densities with conventional electrolytes; particulate cathodes to permit copper recovery from dilute solutions at reasonable current densities; direct concentrate electrorefining to cathode copper; electroforming during refining (53), and series electrowinning and electrorefining. In addition, laboratory investigations are continuing in the areas of univalent copper electrodeposition by Duval, tapered-profile anodes by INCO and SO_2 depolarized anodes by Conoco. It is reasonable to expect some of these pilot plant and laboratory developments to become part of commercial practice in the next twenty-five years.

At the present time, conventional copper electrodeposition plants are not operating at the optimum current density. Several authors (34, 36) have estimated the optimum range to be 700-1000 A/m^2 rather than the present 200-250 A/m^2. In order to operate at such high current levels, it is necessary to improve the mass transport at the electrode surface. Several approaches have been tried (31). Channel cells with very high fluid flow which require very close electrode spacing, ultrasonic agitation which requires a high energy input and mechanical stirring which requires oversized cells have not been demonstrated to have commercial application. The commercial use of direct flow in the CCS (or SEC) process developed by Continental Copper and Steel Industries, Incorporated, has produced smooth dense deposits at 500 A/m^2. Air sparging on the other hand has been revived by INCO, Kennecott Copper Corporation, and the National Institute for Metallurgy in South Africa. In all cases, it is suggested that operation at 1000 A/m^2 produces high quality copper and is economically attractive. It is anticipated that air sparging will be used commercially in a few years. If such a technique should become commercial on a large scale, it is conceivable that new tankhouses would be built only because of location, or obsolescence, not because of need for increased productive capacity.

Particulate bed cathodes are another area of very active development. In such electrodes, the deposition occurs over some finite bed depth rather than solely in a plane, as in conventional electrodeposition. Therefore, the true electrode area is many times the cross-sectional area. In this manner, the copper contained in dilute solutions can be directly electrowon. A pilot scale fluidized bed electrode has been evaluated by Constructors, John Brown Limited. It has achieved low power consumption with solutions containing 0.5-3 g/liter copper at current densities of several thousand amperes per square meter. However, below 0.5 g/liter the energy consumption rises as side reactions become more important. Kennecott Copper Corporation has been evaluating a pilot scale, packed-coke, bed electrode. It is capable of recovering, with relatively low power consumption, greater than 95% of the copper from solutions containing 0.5-1 g/liter copper in a single pass through the bed. At concentrations below about 0.6-2 g/liter, it appears to be economically competitive with LIX electrowinning.

A final area of development is the use of sulfide concentrates or matte as anodes. These efforts, by many workers, have intensified somewhat since the INCO success using nickel matte anodes in 1961. Two pilot scale cells have been operated by Cyprus Mines Corporation (Cymet Process) and Envirotech Corporation (Electroslurry Process). Precious metal (DSA) anode collectors have been used in both systems with current densities in the range of 800-2200 A/m^2. The copper is not of electrorefined cathode quality. The economics of the process may be reasonable for small production plants using chalcocite concentrates. Further work is needed to evaluate the effect of using other minerals and that of minerals with other impurity contents.

Zinc.—The United States capacity for electrolytic zinc production is almost exactly the same now as it was twenty-five years ago (54), with a corresponding increase in the dependence upon imports. According to "Metal Statistics" (6) the capacity for electrolytic zinc production peaked eight years ago at a level about 50% higher than that of the present. However, the indications are that there will be a rapid rise in the United States electrolytic zinc capacity over the next ten years.

At the present time, the pollution problems associated with pyrometallurgical treatment of zinc and zinc concentrates puts it at an economical disadvantage. As a result, during the past eight years a new generation of electrolytic zinc plants has come on stream (55-60). While capacity in the United States dropped, worldwide over 1½ million short tons per year of capacity has been added. This capacity in foreign countries and the general economic doldrums have combined to slow the recovery in the United States.

Much of the improvement in the new generation zinc plants is in the concentrate preparation and hydrometallurgy (61, 62) rather than in electrowinning. Concentrate preparation consists of several steps. Preleaching is sometimes used to remove magnesium. This is followed by fluid bed roasting with sulfur emissions control. A new development is the use of zinc oxide slurry in the SO_2 scrubbers. For the electrowinning plant, the zinc-rich solution is obtained in two stages. The conventional neutral leach is followed by a hot acid leach. The hot acid leach was developed in the late 1960's to obtain the zinc which was previously lost as zinc ferrite. The iron in this leachate is removed as the sodium or ammonium jarosite or as Goethite while the acid solution is returned to the neutral leach step. In this way, zinc recovery can be increased by several percent.

As already mentioned, the changes in the tankhouse have been relatively minor. For example, even though current densities in excess of 800 A/m^2 are used in some plants, the average current density remains at about the same levels as the mid-1950's, about 400 A/m^2. Operational and electrolyte purity improvements have resulted in longer stripping cycle times. In the 1950's it was on the order of 24 hr, whereas 48 hr is more common at the present time. The existence of this short cycle time has encouraged the development of automatic cathode handling and stripping equipment.

Nickel.—Electrolytic nickel production is presently of negligible economic importance in the United States, with less than 200 tons per year produced. However, the hydrometallurgical techniques for nickel recovery from lateritic and manganese nodule sources are being rapidly developed. It is very likely that nickel will be obtained from LIX treated solutions and that electrowinning of the metal will be carried out on a significant fraction of this solution.

On a world-wide basis, the methods for electrorefining nickel metal have changed little in the past twenty-five years (46). The major innovations have been in electrowinning. Three electrowinning processes are operating to produce nickel on a commercial scale.

In 1961 INCO's electrolytic refinery at Thompson, Manitoba began operation. The novelty of this plant is its use of nickel sulfide anodes. The 20% sulfur, 76% nickel matte is cast directly from the converters. Even with careful cooling the anodes are somewhat fragile. These anodes are placed in bags to collect the voluminous sulfur sludge. The cathodes are placed in cathode boxes into which the purified electrolyte is directed. Electrolysis is carried out at about 220 A/m^2. The cell voltage which initially is roughly 2.8V, climbs as the anode sludge builds up. By the end of the anode life the voltage is nearly 4V.

The Outokumpu process has been used since 1960 to electrowin nickel in cells using insoluble anodes. In

this process the high grade, 65% nickel 28% copper, matte is leached, purified primarily by controlling the process chemistry and electrowon. During electrowinning, the nickel content of the solution is reduced from 75 to 50 g/liter. Consequently, the acid content of the effluent from the cell is about 50 g/liter. This requires that the electrolyte composition at the cathode be controlled. It is accomplished by placing the cathodes into tightly woven bags into which the feed electrolyte is introduced. The result is about 94% current efficiency at 190 A/m^2 with the production of very pure nickel.

In 1971 SEC Corporation became the only commercial producer of electrowon nickel in the United States (37). The small plant produces about ½ ton per day from a refinery waste stream. There are two novel approaches used in the plant. First, the pure nickel electrolyte is obtained by using a liquid ion exchange process to extract the nickel from the waste stream followed by stripping into a nickel electrowinning solution. Secondly, the electrowinning cells are modified to use directed solution flow, which permits operation at 380 A/m^2. By using a 3 g/liter drop in nickel content, there is a very slight increase in acid content. Therefore, the SEC approach eliminates bagging of the cathodes.

The developments in nickel recovery have been significant over the past twenty-five years. It is also likely that the use of new sources of nickel and the use of new technologies, such as that of SEC Corporation, will result in further development over the next twenty-five years.

Other metals.—The United States production of other metals by electrodeposition from aqueous solutions has changed little since 1952. Improvements and other changes in the related area of electroplating are discussed in a separate review. The following three items conclude this review. Two are processes which are speculative or at least not reported upon; the other is a description of a modified and expanded production plant.

Cobalt electrodeposition has not been greatly developed since cobalt generally occurs as a by-product in nickel or copper. The metal is often obtained by hydrogen reduction of solution. In addition, the oxide is frequently an acceptable source of cobalt. Generally, one thinks of cobalt electrodeposition as being similar to that of nickel. However, the deposit is usually brittle and difficult to handle. For this reason, it can be expected that deposition in a fluidized cathode cell might prove to be a most satisfactory method for cobalt metal recovery.

A reportedly new aqueous electrolytic process has been developed for the production of antimony. ASARCO is currently starting up a small plant, based on this process, in Texas. A description of the process is likely to be publicly disclosed in early 1978. The capacity is presumed to be about 2000 tons per year.

In 1963, the Texas City Tin Smelter, now Gulf Chemical and Metallurgical Company, installed an electrolytic tin refining plant with a capacity on the order of 5000 tons per year. Recently, the tankhouse size was increased. This increased tankage and operation at higher current densities has approximately doubled the electrorefining capacity. Except for a higher current density of about 150-185 A/m^2, the electrolytic process (63) is much like that described by Mantell.

In summary, there have been significant research and development efforts carried out since 1952 to improve the electrorefining and electrowinning of metals. Some new processes have been developed and many improvements on existing processes have been made. In the past ten years the state of commercial practice has developed rapidly. In aqueous based processes, the metal recovery and throughput is improving; while in fused salt processes, the energy consumption is decreasing. During the next few years, economic conditions will likely limit changes in present operations to process and efficiency improvements. By the centennial of The Electrochemical Society, it is quite likely that there will be further significant innovations in the commercial electrochemical processes being used to obtain metals.

REFERENCES

1. H. N. Gilbert, *This Journal*, **99**, 305C (1952).
2. J. D. Edwards, *ibid.*, **99**, 298C (1952).
3. W. S. Loose, *ibid.*, **99**, 304C (1952).
4. A. C. Loonam, *ibid.*, **99**, 295C (1952).
5. C. L. Mantell, "Electrochemical Engineering," McGraw-Hill Book Co., New York (1960).
6. 69th Annual "Metal Statistics," Fairchild Publications, Inc., New York (1976).
7. "Minerals Yearbook Vol. I, Metals, Minerals and Fuels," U.S. Dept. of The Interior, Washington, D.C. (1973).
8. A. J. Myhren, E. H. Kelton, R. L. Johnson, G. E. Snow, L. D. Grady, E. W. Andrews, L. J. Reimert, and C. E. Barnet, *J. Met.*, **20**, No. 5, 38 (1968).
9. M. D. Rosenzweig, *Chem. Eng. (N.Y.)* **82**, No. 15 62 (1975).
10. I. S. Hirschhorn, *J. Met.*, **20**, No. 3, 19 (1968).
11. P. Duby, *ibid.*, **29**, No. 3, 13 (1977).
12. P. Duby, *ibid.*, **28**, No. 3, 8 (1976).
13. M. R. Edwards and D. G. Lovering, *Inter. Metall. Rev.*, **21**, No. 10, 123 (1976).
14. J. Mackowiak, *Met. Rev.*, **5**, No. 3 (1971).
15. "Non-Ferrous Extractive Metallurgy in The United Kingdom," W. Ryan, Editor, The Institute of Mining and Metallurgy, London (1968).
16. J. S. Jacobi, Institution of Chemical Engineers Symposium Series No. 42, "Hydrometallurgy," 25.1 (1975).
17. "Minerals and Materials," Monthly Survey U.S. Bureau of Mines.
18. H. H. Kellogg, *J. Met.*, **28**, No. 12, 29 (1976).
19. E. F. Emley, "Principles of Magnesium Technology," pp. 9-69, Pergamon Press, New York (1966).
20. "Beryllium, Its Metallurgy and Properties," H. H. Hausner, Editor, University of California Press, Berkeley, Calif. (1965).
21. D. Schlain, in "Techniques of Materials Preparation and Handling," Vol. 1, Part 2, R. F. Bunshah, Editor, pp. 493-548, Interscience Pub., New York (1968).
22. F. Habashi, "Principles of Extractive Metallurgy," pp. 327-395, Gordon and Breach Science Publishers, Inc., New York (1970).
23. G. Wendt, TMS Paper No. A70-39, p. 20, Metallurgical Society AIME, New York (1970).
24. D. W. Dow and J. B. Todd, TMS Paper No. A70-24, p. 12, Metallurgical Society AIME, New York (1970).
25. J. G. Peacey and W. G. Davenport, *J. Met.*, **26**, No. 7, 25 (1974).
26. K. Grjotheim, C. Krohn, and H. A. Øye, *Aluminum (Duesseldorf)*, **51**, 697 (1975).
27. N. Hoy-Petersen, *J. Met.*, **21**, No. 4, 43 (1969).
28. S. Fougner, TMS Paper No. A74-51, p. 19, Metallurgical Society AIME, New York (1974).
29. T. Nakamara and Y. Fakuchi, *J. Met.*, **24**, No. 8, 25 (1972).
30. M. Hoch, in "Titanium Science and Technology," Vol. I, R. I. Jaffee and H. M. Barte, Editors, pp. 205-331, Plenum Press, New York (1973).
31. G. M. Cook, Paper 92d presented at the 69th Annual Meeting of the American Institute of Chemical Engineers, Chicago, Illinois (1976).
32. J. A. E. Wilkinson, R. S. E. Leslie, D. M. Glinden, K. P. Haines, and K. Baker, U.S. Pat. 3,956,086 (1976).
33. M. Fleischmann and R. E. W. Jansson, Institution of Chemical Engineers Symposium Series No. 42, "Hydrometallurgy," 1.1 (1975).
34. "Cell Design in Electrowinning and Electrorefining," Joint Meeting of Electrochemical Technology Group, Society of Chemical Industry and Electrochemistry Group, Chemical Society at Southampton University. 1974. Part I, Chem. and Ind., No. 8,326-336 (1975); Part II, Chem. and Ind., No. 9,370-391 (1975).
35. T. Kitamura, I. Kawakita, Y. Sakoh, and K. Sasaki, "Extractive Metallurgy of Copper, Vol. I, Pyro-

metallurgy and Electrorefining," pp. 525-538, Metallurgical Society AIME, New York (1976).
36. W. W. Harvey, M. R. Randlett, and K. L. Bangerskis, Trans./Sect. C Inst. of Min. and Met., **84**, 210 (1975).
37. R. D. Eliasen and E. Edmunds, *CIM*, **67**, No. 742, 82 (1974).
38. A. S. Gendron, B. V. K. S. R. A. Tilak, and V. A. Ettel, U.S. Pat. 3,928,153 (1975).
39. W. R. Hopkins and A. J. Lynch, E/MJ, **178**, No. 2, 56 (1977).
40. P. R. Ammann, G. M. Cook, C. Portal, and W. E. Sonstelie, "Extractive Metallurgy of Copper, Vol. II. Hydrometallurgy and Electrowinning, Metallurgical Society," pp. 994-1008, AIME, New York (1976).
41. M. E. Wadsworth, *J. Met.*, **29**, No. 3, 8 (1977).
42. M. E. Wadsworth, *J. Met.*, **28**, No. 3, 4 (1976).
43. A. R. Burkin, *Proc. R. Soc. Lond. Ser. A.*, **338**, 419 (1974).
44. J. R. Boldt, "The Winning of Nickel," pp. 336-386, D. Van Nostrand Co., Inc., New York (1967).
45. P. R. Kruesi, E. S. Allen, and J. L. Lake, *CIM*, **66**, No. 734, 81 (1973).
46. R. C. Emmett, F. A. Baczek, and B. C. Wojcik, "The Electro Slurry Process in Direct Electrowinning of Copper from Concentrate," p. 31, SME-AIME Denver (1976).
47. H. Ikeda and Y. Matsubara, "Extractive Metallurgy of Copper, Vol. I. Pyrometallurgy and Electrorefining," pp. 588-608, Metallurgical Society AIME, New York (1976).
48. C. W. Eichrodt and J. H. Schloen, in "Copper," A. Butts, Editor, pp. 165-222, Hafner Pub. Co., Inc., New York (1970).
49. "Extractive Metallurgy of Copper, Nickel, and Cobalt," P. Queneau, Editor, pp. 401-633, Interscience Publishers (1961).
50. J. D. McIver, "Copper Metallurgy," pp. 260-274, Metallurgical Society AIME, New York (1970).
51. I. S. Blair and L. R. Verney, *ibid.*, pp. 275-313 (1970).
52. K. J. Richards, *J. Met.*, **29**, No. 3, 19 (1977).
53. N. J. Finch and A. Cibula, "Electrodeposition of Copper for Direct Coldworking," pp. 755-802; "Mineral Processing and Extractive Metallurgy," Vol. 3, The Institute of Mining and Metallurgy, London (1970).
54. F. S. Weimer, G. T. Wever, and R. J. Lapee, in "Zinc," C. H. Mathewson, Editor, pp. 174-224, Hafner Pub. Co., Inc., New York (1970).
55. "Lead and Zinc, Vol. 2, Extractive Metallurgy of Lead and Zinc," C. H. Cotterill and J. M. Cigan, Editors, The Metallurgical Society AIME, New York (1970).
56. G. M. Meisel, *J. Met.*, **26**, No. 8, 25 (1974).
57. P. Tarassoff, *ibid.*, **28**, No. 3, 11 (1976).
58. T. R. A. Davey, *ibid.*, **28**, No. 3, 16 (1976).
59. T. R. A. Davey, *ibid.*, **29**, No. 3, 24 (1977).
60. H. L. Montague, TMS Paper No. A71-74, p. 52, Metallurgical Society AIME, New York (1971).
61. G. Steintveit, Institution of Chemical Engineers Symposium Series No. 42 "Hydrometallurgy," 8.1 (1975).
62. A. R. Gordon and R. W. Pickering, *Met. Trans. B*, **6B**, 53 (1975).
63. T. S. Mackey, *J. Met.*, **21**, No. 6, 32 (1969).

Diffusion of Chromium in Magnetite as a Function of Oxygen Partial Pressure

James D. Hodge

Institut für Physikalische und Elektrochemie, Technische Universität Hannover, 3 Hannover, Germany

Recently, a great deal of data has been published concerning the diffusion characteristics of magnetite. While all of this data are reliable and in fairly good agreement, many questions still remain concerning the defect structure and transport properties of magnetite. One of these questions concerns the behavior of impurities in magnetite. To date, no reliable data exist in the literature concerning the diffusion of impurities in magnetite. The purpose of this paper is to describe experiments and report results of a study of the diffusivity of chromium in magnetite.

A number of studies have, to date, looked at the tracer diffusivity of iron in magnetite. So far, the most complete set of data for self-diffusion in magnetite is that compiled by Dieckmann and Schmalzried (1). These workers used Fe-59 to obtain tracer diffusion coefficients at various temperatures and oxygen partial pressures. Their results show that a change of mechanism occurs in the middle of the magnetite phase field, *i.e.*, a plot of log $D_{Fe}{}^*$ *vs.* log P_{O_2} shows that at high oxygen partial pressures the slope of the observed curve is always found to be 2/3, while at low oxygen partial pressures the slope is always $-2/3$. A similar $+2/3$ to $-2/3$ oxygen partial pressure dependence was also observed by Halloran (2) in his studies of magnetite at 1380°C. These results are interpreted as meaning that cation vacancies are the predominant defect at high oxygen partial pressures and that cation interstitials are the predominant defect at low oxygen partial pressures. Dieckmann and Schmalzried give the appropriate defect reactions as being

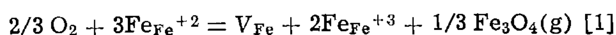

$$2/3\, O_2 + 3Fe_{Fe}{}^{+2} = V_{Fe} + 2Fe_{Fe}{}^{+3} + 1/3\, Fe_3O_4(g) \quad [1]$$

$$Fe_{Fe}{}^{+2} = V_{Fe} + Fe_i{}^{+2} \quad [2]$$

where Eq. [1] is the reaction for the formation of cation vacancies through the dissolution of oxygen in the magnetite lattice and Eq. [2] is the reaction for the formation of cation interstitials via a Frenkel mechanism. The law of mass action, when applied to these equations, yields

$$[V_{Fe}] = KP_{O_2}{}^{2/3} \quad [3]$$

$$[Fe_i{}^{+2}] = K'P_{O_2}{}^{-2/3} \quad [4]$$

(Note: An equation similar to Eq. [4] can also be written for $[Fe_i{}^{+3}]$.)

The excellent agreement between this simple defect model and the observed experimental results indicates that point defects in magnetite behave as an ideal solution, *i.e.*, no complexing or vacancy-vacancy interactions, despite their relatively high concentrations (up to 0.01 cation site fraction). It is assumed that this ideality stems from the presence of large concentrations of Fe^{+2} and Fe^{+3} cations present in the magnetite lattice which can shield vacancies from feeling the effects of any long range coulombic interactions between vacancies.

From the results outlined briefly above, Dieckmann and Schmalzried draw two important conclusions concerning the defect structure of magnetite: (*i*) Thermal disorder in magnetite is of the Frenkel type; and (*ii*) point defects exhibit ideal solution behavior even at high concentrations of defects.

With these results in mind, experiments were performed to determine the diffusivity of chromium in

magnetite in order to study the behavior of impurities in the magnetite lattice and compare this behavior with that observed for self-diffusion. Chromium is an interesting impurity because (*i*) it is a major alloying agent in many steels and should therefore be present in significant amounts in the oxide layers of these steels where a knowledge of its diffusive properties would be useful to steel manufacturers and users, and (*ii*) the Cr^{+3} ion has an almost identical ionic radius as Fe^{+3}, but unlike iron, at these partial pressures of oxygen it exists as a fixed trivalent ion.

Experimental Procedure

Samples were prepared from a Fe_2O_3 starting material which was melted in a controlled argon-air (70:30) atmosphere to reduce it to Fe_3O_4. Once it was melted and reduced, the magnetite sample was slowly cooled from its melting temperature until the sample was solidified. This slow cooling was accomplished by slowly lowering the sample, which was contained in a Pt-30% Rh crucible to reduce the loss of iron due to its high solubility in platinum, out of the hot zone of a vertical carbon element furnace. After solidification, the magnetite sample was quenched to room temperature. Disks of 0.2 cm were cut from the sample with a diamond saw and ground round to a diameter of 0.8 cm with a diamond wheel. These resulting samples contained anywhere from 2 to 10 grains without any visible cracks or pores.

Prior to a diffusion experiment, the magnetite samples were equilibrated at the appropriate oxygen partial pressure. To do this, an experimental apparatus similar to that shown in Fig. 1 was used. The oxygen pressure, which was fixed during the test by using an appropriate CO_2/CO mixture, and the temperature near the sample were determined simultaneously through the use of a solid-state stabilized zirconia electrolyte galvanic cell and a platinum-rhodium thermocouple. The temperature of the sample was measured independently with a second thermocouple. Samples could be brought in and out of the hot zone with the help of an electromagnet as is shown in Fig. 1. After the pre-equilibration anneal, the samples were treated in the following manner: First, they were ground parallel and then polished on one side using a 3 μm diamond wheel. Cr-51 in the form of aqueous chromate solution was placed on the polished surface with a microsyringe and the sample was then dried at about 100°C. After drying, the samples were sandwiched together to reduce evaporation of tracer from the surface of the sample during the test, held under a slight pressure between alumina rods, and then placed in the same furnace at the same temperature and oxygen partial pressure as was used in the pre-equilibration run.

After a diffusion run, which typically lasted from 2 to 5 days, thin layers of the magnetite sample were removed with a 3 μm diamond wheel and the rest activity of Cr-51 was determined. The depth of the diffusion profiles obtained in this manner ranged from 20 to 100 μm. During the grinding operation, the sample surfaces remained parallel to within 1 μm. Between 10 and 25 cuts were performed on each sample. Every diffusion coefficient was determined with two samples.

Usually, in analyzing tracer diffusion data, absorption of emitted gamma rays by the sample is neglected. However, since the energy of the gamma radiation emitted by Cr-51 is relatively low (0.32 MeV), self-absorption of gamma radiation by the magnetite sample cannot be immediately ignored when analyzing data collected in this study. For situations where self-absorption is significant, Frischat and Oel (3) have derived the following expression for the rest activity

$$A(x,t) = A(o,t) \exp(yx) \frac{1 - \text{erf}\left(\frac{x}{2\sqrt{Dt}} + y\sqrt{Dt}\right)}{1 - \text{erf}(y\sqrt{Dt})} \quad [5]$$

where y is the absorption coefficient. It should be noted that to obtain a diffusion coefficient from this equation numerical methods must be used since D cannot be solved for explicitly.

Therefore, to see if this correction for self-absorption would be needed, the absorption coefficient of magnetite was determined by measuring the drop in Cr-51 gamma radiation intensity across samples of various thicknesses. The value obtained in this manner (0.058 mm^{-1}) was sufficiently small and the average depth of the experimental diffusion profiles was sufficiently shallow that self-absorption could be ignored at the experimental temperature used (1200°C) and the more conventional equation for rest activity

$$A(x,t) = A(o,t) \left[1 - \text{erf}\left(\frac{x}{2\sqrt{Dt}}\right)\right] \quad [6]$$

could be used. However, at higher temperatures, where diffusion profiles will be deeper, this correction may have to be made.

Using Eq. [6], the precision of the determination of $D_{Cr}{}^*$ was never worse than ±10%. A determination from a typical experiment is shown in Fig. 2.

Results and Discussion

As was stated previously, all experiments in this study were performed at 1200°C. The results of all experiments done at this temperature are presented in Fig. 3 along with previously measured values for iron self-diffusion (1). From the figure, it can be seen that chromium diffusion exhibits the same oxygen partial pressure dependencies as iron diffusion, *i.e.*, the slope of the log $D_{Cr}{}^*$ *vs.* log P_{O_2} curve is −2/3 at low oxygen partial pressures and +2/3 at high oxygen partial pressures. Two important observations can be

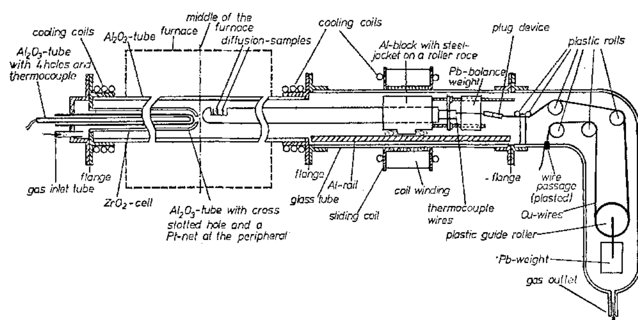

Fig. 1. Schematic of apparatus used for diffusion experiments

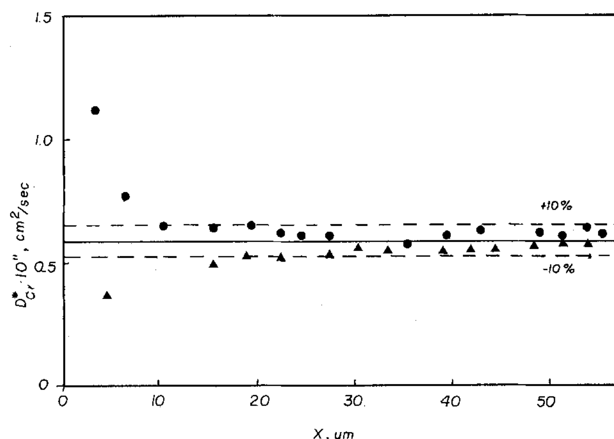

Fig. 2. Typical result of a diffusion experiment. T = 1200°C, $P_{O_2} = 2.95 \times 10^{-5}$ atm.

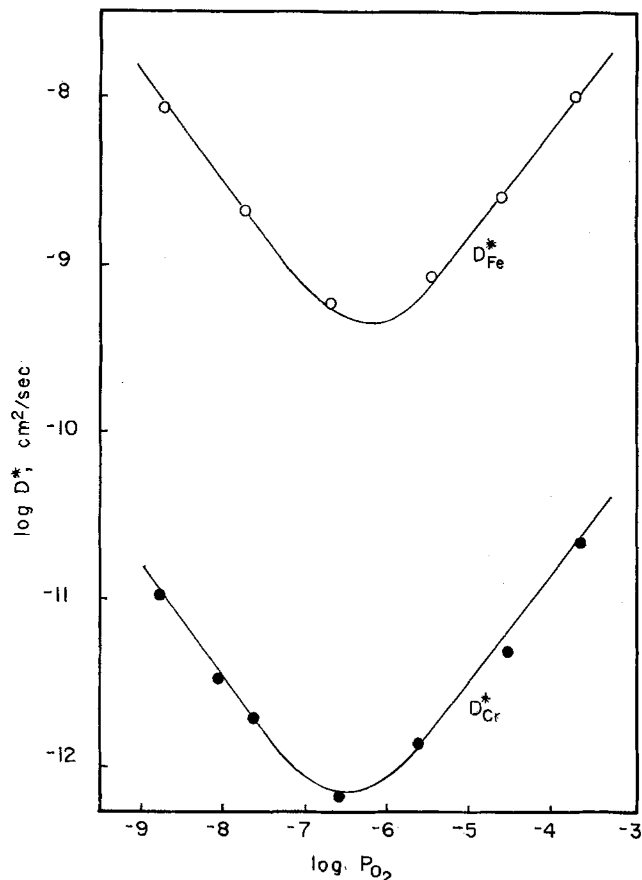

Fig. 3. Chromium tracer diffusion coefficients, D_{Cr}* compared with iron tracer diffusion coefficients, D_{Fe}*, as a function of P_{O_2} at 1200°C.

made from this figure. The first is that the absolute magnitude of Cr tracer diffusion is 2.5 orders of magnitude slower than that of Fe tracer diffusion. This is in qualitative agreement with the Al tracer diffusion estimates made by Petuskey (4). The second observation, which is not in agreement with Petuskey's calculations, is that the minimum in the log D^* *vs.* log P_{O_2} curves occurs at very nearly the same oxygen partial pressure in both Fe and Cr tracer diffusion.

Since the concentration of defects is set by fixing the oxygen partial pressure, it is unlikely that Cr tracer diffusion is low because of a difference in defect concentration between chromium and iron diffusion. Therefore, the reason for chromium's low diffusivity probably stems from a lower jump frequency than iron. Since the ionic radius of chromium is essentially the same as that of trivalent iron, this lower jump frequency is probably not related to a size effect. However, two other possibilities do exist. The first possibility is that in magnetite, because of coulombic interactions with surrounding oxygen anions, a jump by a trivalent cation could be more difficult than a jump by a divalent cation. Since the very high mobility of electrons in magnetite at these temperatures makes it impossible to distinquish between a divalent iron cation jump and a trivalent iron cation jump, this effect would not be noticed in iron self-diffusion experiments. However, at these oxygen partial pressures, chromium exists as a fixed valence +3 ion. Therefore, this effect, if real, should cause a lower chromium diffusivity in magnetite. The second possibility is that the trivalent chromium ion is not as easily deformed as an iron cation and it, therefore requires more energy to jump through its coordinating sphere of oxygen anions. An estimate of this effect can be made by comparing the electronic polarizabilities of the chromium and the iron ions since the electronic polarizability is a measure of how easily an ion's electron cloud can be deformed with respect to its nucleus. A comparison of these values shows that the polarizability of Cr^{+3} is approximately a factor of three lower than that of Fe^{+2} ($1.45\ 10^{-25}$ cm^3 for chromium *vs.* $5.69\ 10^{-25}$ cm^3 for iron) (5). Therefore, this effect could also contribute to chromium's low diffusivity.

In regard to the second observation, namely, the coincidence of the Fe and Cr minima, it should be noted that this indicates that the ratio of vacancy jump frequency to interstitial jump frequency is the same for both iron and chromium diffusion. Why this should necessarily be so is not immediately obvious. However, if it is assumed that the empty octahedral and/or tetrahedral sites in the magnetite lattice are the interstitial positions, intuitively it would seem that a jump from a normal site to an interstitial position and a jump from one interstitial position to another would be energetically similar to a normal vacancy jump and, therefore, the jump frequency ratios mentioned above would be approximately equal if it is assumed that chromium is relatively indistinguishable from iron in the magnetite lattice.

It is also possible that the coincidence of the two minima is merely fortuitous and that experiments at other temperatures will reveal that the minima are not always coincident. Such experiments are presently being performed and the results of these tests will be published along with other impurity diffusion data in a later paper of the series on magnetite by Dieckmann and Schmalzreid.

Summary

Tracer diffusion experiments using Cr-51 as a tracer were performed in order to determine the diffusivity of chromium in magnetite. The results of these experiments were compared with previously obtained values for iron self-diffusion. This comparison showed that although chromium diffusion exhibited the same oxygen partial pressure dependencies, indicating that it diffused via the same mechanisms as iron, the absolute magnitude of chromium diffusivity was several orders of magnitude slower than that of iron. Two possible reasons for this slow diffusivity were advanced, both of which could cause chromium to have a lower jump frequency than iron. The first is related to the fact that chromium has a fixed +3 valence state while iron has a variable valence of either +2 or +3 at these oxygen partial pressures. The second is related to the relative polarizabilities of the iron and the chromium ions. It was also noted that the minimum in the log D^* *vs.* log P_{O_2} curve occurs at the same oxygen partial pressure for both iron and chromium tracer diffusion. The reason for this coincidence is not clear at this time and awaits further experimentation at other temperatures. Such experimentation is currently in progress.

REFERENCES

1. R. Dieckmann and H. Schmalzried, *Z. Phys. Chem. N. F.*, **96**, 331 (1975); *Ber. Bunsenges. Phys. Chem.*, **81**, 344 (1977); *ibid.*, **81**, 414 (1977).
2. J. W. Halloran, Ph.D. dissertation, M.I.T. (1977).
3. Frischat and Oel, *Z. Angew. Phys.*, **20**, 195 (1966).
4. W. T. Petuskey, Sc.D. dissertation, M.I.T. (1977).
5. C. Kittel, "Introduction to Solid State Physics," 5th ed., p. 410, Wiley (1976).

Advances in Corrosion over the Past 25 Years

Herbert H. Uhlig

Department of Materials Science and Engineering,
Massachusetts Institute of Technology, Cambridge, Massachusetts 02139

There is little doubt that the factor of corrosion in present materials problems has gained greater recognition than in any time previous. Advances in corrosion control during the past quarter century have noticeably accelerated. Reference to the author's survey in 1952 (1) of some accomplishments in corrosion over the previous 50 years and a glance at the large size of the present corrosion literature here and abroad confirm this trend. Some indication of the magnitude of the latter may be had from Table I which, although by no means complete, presents some representative additions to the secondary and tertiary literature on corrosion appearing during the past 25 years. There are several reasons why this increased recognition and attention to the corrosion problem should have occurred in addition to the usually cited economic factors, the need for greater safety of equipment and structures, and the justified arguments on conservation. For one thing, metals have moved to higher levels of strength and of chemical resistance to uniform corrosion making them unfortunately vulnerable to various unsuspected types of environmental damage and sensitively dependent on stress and on features of design. Environments in turn have become more aggressive and of higher temperatures; even the air in some cities has become polluted to an extent causing metal failures—of, for example, telephone relay springs—in epidemic proportions. On the whole, reported corrosion failures observed as pits, cracks, and intolerable rates of surface attack have proliferated markedly over the recent past.

Advances in corrosion control have served to reduce much of the presently experienced damage, but it is fair to acknowledge that engineering information on the influence of environment on properties of materials continues to lag behind that which is urgently needed. More distressing is the frequent neglect by engineers and architects to use and apply what is already known about corrosion control in their designs of modern structures, machines, and buildings. There are both research and educational gaps that require closing up.

Notwithstanding that much more remains to be done, there has been significant progress made recently in both corrosion theory and practice indicative of the information that should be made available in greater measure. The electrochemical theory of corrosion, still being debated 75 years ago, has received perhaps its most important support through the derivation published in 1957 by Stern and Geary (2) of a simple equation relating electrochemical polarization parameters to uniform corrosion rates. This approach to reaction rate measurements at high or low temperatures, applicable to all structural metals, has been used in many metal-environment systems including the monitoring of metallic (prosthetic) devices for intended use in the human body. Mansfeld (3) has recently provided a general treatment of the theory and limitations underlying this approach to corrosion-rate measurements. Electrochemical techniques in general over recent years have assumed greater importance in all types of corrosion measurements (4).

The elusive subject of the structure and composition of the passive film on metals and alloys, vigorously debated for the past 140 years, has been scrutinized by scientific discussions held at three international symposia (1957 in Germany, 1962 in Canada, 1970 in England) sponsored prominently by this Society among other groups. A fourth symposium was held in Arlie, Virginia, October 17-21, 1977. A joint seminar by American and Japanese scientists active in research on passivity was held in Honolulu in 1975 (5). Many of the contributors to these several symposia have continued to advocate a diffusion-barrier oxide model. But to others, including the present author, the results of coulometry and recently developed surface analyses stress the greater probability of an adsorbed oxygen and nonstoichiometric oxide composition for the passive films on metals like iron, nickel, stainless steels, aluminum, and similar metals (6). One of the ongoing challenges, accordingly, is to relate metal-proton-oxygen ratios in the passive film to observed chemical stability of the film in various electrolytes and at various temperatures, and to outline the factors that cause transformation of the film to stoichiometric oxides having lesser protective properties.

The concept of a critical potential above which the passive film breaks down leading to localized corrosion or pitting has been discussed qualitatively for many years. The quantitative treatment of this subject including the effects of alloying and extraneous anions has more recently received a larger measure of attention (7-11). This information has led to a practical understanding of how best to cathodically protect metals, such as the stainless steels, against pitting attack in sea water and other environments, and also to a better understanding of the proper choice and adequate concentration of inhibiting salts effective for avoiding pitting. These studies help to explain why the 5000 and 6000 series of Al alloys with corrosion potentials active to their critical potentials have generally shown better resistance to pitting in sea water than those alloys of more noble corrosion potentials (12).

Crevice corrosion which initiates in passive metals largely independent of the critical potential has been minimized by choosing alloys whose passivity is relatively stable in acidic halide solutions or in aqueous media within a crevice low in dissolved oxygen. For example the Ti alloys containing a few tenths percent Pd, or the Mo-bearing type 316 austenitic stainless steels are in this category. More alloys possessing this kind of stable passivity are needed to help the engineer design structures where crevices are unavoidable and hence where crevice corrosion poses a threat.

Within the past years, the problem of stress corrosion cracking (SCC) has loomed as especially critical in the design and operation of chemical, oil, and nuclear plants including high pressure gas lines. A detailed mechanism of environmental cracking applying to specific metals and plastics or to materials in general has not yet received over-all acceptance despite the considerable attention focused on the problem. A handicap in this respect is the continuing tendency in some circles to confuse SCC always requiring a tensile stress with intergranular corrosion which does not, even though intergranular corrosion may sometimes result in cracking. The two mechanisms of failure are probably quite different. There is also current confusion resulting from the overlapping of SCC with hydrogen cracking, the latter depending on interstitial hydrogen in the metal. High strength steels, according to Asphahani and Uhlig (13), may fail from either cause depending on the potential range natural to or imposed on the steels. Hence to successfully avoid failure by cracking in a given environment may require knowledge about the cause before applying the remedy. It would seem that SCC in

Table I. A partial list of new secondary and tertiary literature since 1952

Review Series (frequently containing reviews on corrosion)
- Annual Reviews of Materals Science 1971 —
- Metallurgical Reviews 1956 —
- Modern Aspects of Electrochemistry 1954 —
- Adv. in Corrosion Science and Technology 1970 —

New Journals
- *British Corrosion Journal* 1966 —
- *Corrosion Science*, J. C. Scully, Editor, Pergamon Press 1961 —
- *Corrosion Prevention and Control*, London 1954 —
- *Corrosion et Anti-Corrosion* (French) Paris 1953—
- *Zashchta Metalloy* (Russian) 1965 —
  (also in English as) *Protection of Metals* 1965 —
- *Australian Corrosion Engineering*, Vol. 1 — North Sidney: W. Meagher 1957
- *Corrosion Reporter*, Vol. 1 — New York: International Nickel Co., Inc. 1953 —
- *Corrosion Technology*, Vol. 1 — London: Leonard Hill Technical Group 1954 —
- *Materials Protection*, Vol. 1 — Houston, Texas: National Association of Corrosion Engineers, Inc. 1962 —

Abstract Series
- Corrosion Control Abstracts 1966 –
- Corrosion Abstracts 1962 —

Conferences
- The International Conferences on Metallic Corrosion
  - London 1961, New York 1963, Moscow 1966, Amsterdam 1969, Tokyo 1972, Sydney 1975, Brazil 1978.
- The NACE Research Conferences on Corrosion
  - Fundamental Aspects of Stress Corrosion Cracking 1967
  - Corrosion Fatigue 1971
  - Localized Corrosion 1971
  - High Temperature High Pressure Electrochemistry in Aqueous Solutions 1973
  - Stress Corrosion Cracking and Hydrogen Embrittlement of Iron Base Alloys 1973 (in press)
- Metallurgical Society Conferences
  - Physical Metallurgy of Stress Corrosion Fracture, T. N. Rhodin, Editor, Vol. 4, Wiley Interscience New York 1959 408 pages

Data Compilations
- "Guide to Corrosion Resistance I," Polar 1961
- "Korrosionstabellen Metallischer Werkstoffe," F. Ritter, Springer Verlag, Vienna, 4th ed. 1958
- "Corrosion Resistant Materials Handbook," I Mellan, Noyes Dev. Corp., 1966
- Corrosion Guide, E. Rabald, 2nd ed. Elsevier 1968
- D. J. DePaul, "Corrosion and Wear Handbook," McGraw-Hill, New York (for Atomic Energy Commission) 1957, 293 pages
- G. A. Nelson, Corrosion Data Survey," 5th ed., Shell Development Co., Emeryville, Calif. 1974
- "Taschenbuch des Metallschutzes: Activer und Passiver Korrosionsschutz der Metalle," W. Wiederholt and J. Elze, Wisenschaft Verlag, Stuttgart 1960

Important Treatises and Monographs
- "Corrosion," 2 Vols., 2nd ed. L. L. Shreir, Editor Butterworths (1977).
- U. R. Evans, "The Corrosion and Oxidation of Metals: Scientific Principles and Practical Applications," St. Martin's Press, 1960, 1094 pages and 2 supplemental volumes.
- F. L. LaQue and H. R. Copson, "Corrosion Resistance of Metals and Alloys," 2nd ed., ACS Monograph 58, Reinhold, New York 1963 736 pages
- F. A. Champion, "Corrosion Testing Procedures," J. Wiley, New York 1964
- H. Kaesche, "Die Korrosion der Metalle: physikalische — chemische Prinzipien und actuelle Problem," Springer, Berlin 1966, 374 pages
- H. J. Engell and D. Behrens, "Werkstoffe und Korrosion," Verlag Chemie, Weinheim/Bergstrasse, West Germany
- ECS Corrosion Monograph Series
  - H. P. Godard, W. B. Jeppson, M. R. Bothwell, and R. L. Kane, "Corrosion of Light Metals" 1967
  - H. L. Logan, "The Stress Corrosion of Metals" 1966
  - H. Leidheiser, "The Corrosion of Copper, Tin, and Their Alloys" 1971
  - W. E. Berry, "Corrosion in Nuclear Applications," 1971
  - W. H. Ailor, "Handbook on Corrosion Testing and Evaluation" 1971
  - F. L. LaQue, "Marine Corrosion" 1975
- ASTM STP Series
  - STP 516 "Localized Corrosion — Cause of Metal Failure" 1972
  - STP 518 "Stress Corrosion Cracking of Metals —A State of Art" 1972
  - STP 576 "Galvanic and Pitting Corrosion — Field and Laboratory Studies" 1976
  - STP 610 "Stress Corrosion — New Approaches" 1976

Literature Guides
- R. B. Diegle, and W. K. Boyd, "Critical Surveys of Data Sources: Corrosion of Metals," NBS Spec. Publication 396-3 1976
- K. Boodson, "Nonferrous Metals — A Bibliographic Guide," section in Chemical Properties: Corrosion, pp. 219-250 1972

most metal systems operates by a mechanism unrelated to that of hydrogen cracking, although this matter is still being debated. In any event, protecting against SCC involves choosing the proper alloys, avoiding specifically damaging anions, selecting optimum rolling direction for some cold-rolled materials, *e.g.*, Al alloys, cathodically protecting below the critical potential for SCC in the given environment, and adding inhibiting salts which shift the critical potential to more noble values. Reducing tensile stresses, residual or applied, may increase life but does not generally avoid failure.

Incidence of hydrogen cracking for some metals, *e.g.*, 10% Ni-Fe alloys may also be sensitive to rolling direction, and potentials must be avoided at or below which hydrogen ions discharge at the metal surface, especially in the presence of catalyst poisons like H_2S which favor absorption of hydrogen by the metal. Laboratory and service data show that the face-centered cubic metals, *e.g.*, the austenitic stainless steels, are more resistant than body-centered cubic metals, *e.g.*, the ferritic and martensitic stainless steels, a property that is made use of to avoid hydrogen cracking of ship propellors made of stainless steel, pipe-line hardware, and fasteners for aluminum structures. However, face-centered cubic alloys of compositions that allow heat-treatment to high strength levels are not necessarily resistant to environments notorious for their hydrogen cracking tendencies. Some high strength alloys may also fail by SCC in the presence of moist air. Hydrogen embrittlement (loss of ductility) of Ta can be avoided by applying a thin, not necessarily pore-free, coating of Pt to the surface which acts as a catalyst favoring hydrogen evolution rather than absorption of the gas by the metal (14). A similar catalytic coating applied to high strength steel has been shown in the laboratory to be analogously effective (15).

Failures by SCC are probably much more common in practice than the usual diagnoses of metal failures would indicate, a situation which is still more acute in cases of corrosion fatigue. It has been known for a long time that engineering structures subject to variable stress fail by fatigue, but what is not generally recognized is the magnitude to which the environment contributes to such failures. A well-defined minimum stress (fatigue limit) below which fatigue failures do not occur in any length of time is established for steels in air; no such limit is observed in sea water or fresh waters. Failures in corrosive electrolytes occur at any level of stress given a sufficient number of stress cycles. The traditional explanation of corrosion fatigue has involved the formation of pits by the corrosion process, the pits in turn serving as stress raisers and as nuclei for fatigue cracks. Recently (16, 17), it has been proposed that the environment accelerates plastic deformation of metals at a given stress level independent of pits, thereby favoring the formation of extrusions and intrusions in the metal accompanying the fatigue process. Correspondingly, surface dissolution of polycrystalline brass, copper, and steel has been shown to accelerate slow plastic deformation (creep) of these metals subject to constant stress (18-20). Practical measures to avoid or minimize corrosion fatigue include proper alloy selection for optimum corrosion resistance, cathodic protection to the same approximate potential effective for avoiding uniform corrosion, addition of corrosion inhibitors to the environment, deaeration of aqueous environments (*e.g.*, steels in sea water), surface peening to reduce high surface stresses, and the use of various coatings.

Relatively new organic coatings for metal protection made up of various synthetic vehicles continue to be offered on the market. Such coatings usually but not always provide improved protection to the underlying metal compared to the older standard available paints. In general, all organic coatings, new or old, are permeable in some degree to water and oxygen; in addition their deterioration is affected to a variable degree, depending on the vehicle, whenever they become exposed to temperatures near the boiling point of water. Caution should be exercised in the use of some coatings

and plastics in a confined space; they may exude slight amounts of volatile acids which accelerate corrosion of Zn, Mg, Cd, Al, Cu, and steels. One commercial plastic which exuded trace amounts of amines was found by the present author to cause SCC of brass fixtures exposed to air contaminated by the plastic. Substantial advances in protective organic coatings for use in corrosive environments are limited despite the impressive commercial importance of the field; new ideas are few and far between. As E. L. Koehler (21) expressed it: "(organic coatings) would seem to be an area where basic corrosion research has largely been lagging, with only a handful of investigators giving sporadic attention."

The dezincification of brass has for some time been explained in two differing ways with supporting evidence for either proposed mechanism. The alloy is assumed to corrode with redeposition of Cu in spongy or porous form, or instead the zinc is assumed to corrode preferentially leaving behind a porous residue of Cu or a Cu-rich alloy. Convincing support of the latter mechanism was presented by Pickering and Wagner (22), who proposed that surface divacancies are formed by the corrosion process; these readily diffuse at room temperature into the bulk of the alloy and become filled preferentially with Zn atoms. The Zn then migrates along available diffusion paths to the metal surface and reacts with the corrosive environment. A similar preferential corrosion of Cu in Cu-Au alloys was explained by them along the same lines; here contrary to brass the initial general corrosion of the alloy followed by redeposition of Au is not an equal possibility. Gold does not enter into solution at any time. The formation of divacancies and their interaction with dislocations (dislocation climb) was proposed by Revie and Uhlig (19) to explain the accelerated creep of brass (and other metals) that they observed during anodic dissolution. Correspondingly, divacancies also enter the over-all explanation of corrosion fatigue dependent on environmentally induced plastic deformation, as described earlier.

Direct logarithmic kinetics and two-stage logarithmic kinetics for thin film oxidation of metals have been explained by electron transfer control at the oxide-metal interface (23). Inverse logarithmic kinetics has been explained by high electric field-induced ion migration through the oxide film (24). Differentiation of the two models is made difficult by the limited time over which thin film kinetics is observed; most, although not all, available data for which a differentiation can be made obey the direct logarithmic equation. Pretreatment of clean metal surfaces, *e.g.*, Cu or Fe, with H_2 or N_2 has been found to cause surface faceting with a correspondingly large effect (depending on the gas) on subsequent thin film oxidation rates (25-26). This effect can account for some of the wide discrepancies in reported thin-film oxidation rates.

The introduction of rare earth elements, which mainly improves spalling properties of the metal oxides, has been made use of to improve practical oxidation-resistant alloys, *e.g.*, yttrium added to 25% Cr-Fe alloys. One of the important continuing problems is the adequate protection of Ni-base alloys employed for gas-turbine blades exposed to high temperature air containing small amounts of sulfates in suspension. Various protective coatings are in use, including Ni-Al alloys (27) which on oxidizing form adherent coatings of Al_2O_3.

Among recent practical advances is the increasing use of special low alloy steels called weathering steels for construction of buildings, bridges, and other structures. Painting is not required throughout the life of the structure. The detailed mechanism accounting for the protective, adherent rust-scales forming naturally on such steels is still under study.

The economic application of cathodic protection in media like sea water has been advanced by the recent availability of remarkably corrosion-resistant platinized Ti or platinized Nb electrodes (28). Their long life at relatively high current densities, convenient size, and good mechanical properties under stress and strain give them a marked advantage over the usual electrodes available heretofore for applied current protection. Corrosion resistant titanium anodes coated with ruthenium oxide have found important application in the alkali-chlorine industry (29). Sacrificial anodes of the Zn or Mg variety are now supplemented by Al alloy electrodes containing a small percentage of Sn and sometimes additional Zn and Hg. In chloride solutions, they exhibit a continuing active potential compared to pure Al and account for a large tonnage of Al consumed annually for cathodic protection purposes (30).

Improved bright metal trim for autos has recently been made available consisting of a bimetal strip with stainless steel on the exterior and aluminum in contact with the auto body (31). The aluminum cathodically protects the steel body and its paint coating against otherwise damaging galvanic effects when stainless steel is in direct contact with it. The introduction some years ago of microcracked chromium deposited over bright electrodeposited Ni continues to afford maximum protection against tarnish of the Ni coating (*e.g.*, on auto bumpers) as well as delaying rusting of the underlying steel at pores in the coating.

Continuing urgent needs in the corrosion field include more efficient, nontoxic and inexpensive inhibitors for use in recycled cooling waters. Inexpensive, metallically bright, passive alloys are needed that depend on elements other than chromium for atmospheric corrosion resistance—not an easy goal. As mentioned before, corrosion-protective organic coatings containing reliable and longer lasting corrosion inhibiting pigments and which withstand higher temperatures would be welcome. Alloys with improved resistance to SCC in chemical environments and also resistant to hydrogen cracking (such as in sour gas wells) are urgently in demand. There is also a need for better methods and materials to reduce the little-known fretting type of corrosion which often causes the initiation of fatigue in air or corrosion fatigue in presence of an electrolyte. Fretting corrosion results from the slight oscillatory sliding of one metal surface over another surface, metal or nonmetal, resulting in wear and pitting. A recent book by Waterhouse is available which summarizes the known facts of fretting corrosion (32).

Since 1952 some of the requirements for educating engineers in corrosion prevention have been met by various short courses arranged at several universities and also by the National Association of Corrosion Engineers. The time is perhaps overdue when all students of engineering and architecture will be required to take courses on environmental effects on properties of materials comparable to standard courses now available on mechanical properties. Furthermore, more attention in support of research in corrosion science should be provided in order to supply a basis for improved engineering information. The design of modern structures and machines will continue to suffer without such research. The Electrochemical Society through its Corrosion Division has been prominent in encouraging the type of information that is needed, and in promoting its availability to those who can best apply it to practical situations.

REFERENCES

1. H. H. Uhlig, *This Journal*, **99**, 275C (1952).
2. M. Stern and A. Geary, *ibid.*, **104**, 56 (1957).
3. F. Mansfeld, *Adv. Corros. Sci. Technol.*, **6**, 163 (1976).
4. "Electrochemical Techniques for Corrosion," R. Baboian, Editor, National Association of Corrosion Engineers, Houston (1977).
5. "Passivity and its Breakdown on Iron and Iron-Base Alloys," R. Staehle and H. Okada, Editors, National Association of Corrosion Engineers,

Houston (1976).
6. H. H. Uhlig, *Corros. Sci.*, **7**, 325 (1967); "Corrosion and Corrosion Control," p. 74, Wiley & Sons, New York (1971).
7. Y. Kolotyrkin, *Corrosion (Houston)*, **19**, 261t (1963).
8. H. Kaesche, *Z. Phys. Chem. Frankfurt am Main*, **34**, 87 (1962).
9. H. Leckie and H. Uhlig, *This Journal*, **113**, 1262 (1966).
10. J. Horvath and H. Uhlig, *ibid.*, **115**, 791 (1968).
11. H. Böhni and H. Uhlig, *ibid.*, **116**, 906 (1969).
12. R. Groover, T. Lennox, Jr., and M. Peterson, *Mater. Prot.*, **8**, No. 11, 25 (1969).
13. A. Asphahani and H. Uhlig, *This Journal*, **122**, 174 (1975).
14. C. Bishop and M. Stern, *Corrosion (Houston)*, **17**, 379t (1961).
15. I. Matsushima and H. Uhlig, *This Journal*, **113**, 555 (1966).
16. D. Duquette and H. Uhlig, *Am. Soc. Met. Trans. Q.*, **61**, No. 9, 449 (1968).
17. H. Lee and H. Uhlig, *Met. Trans.*, **3**, 2949 (1972).
18. R. W. Revie and H. H. Uhlig, *Corros. Sci.*, **12**, 669 (1972).
19. R. W. Revie and H. H. Uhlig, *Acta Metall.*, **22**, 619 (1974).
20. H. H. Uhlig, *This Journal*, **123**, 1699 (1976).
21. E. L. Koehler in "Localized Corrosion," Roger Staehle, Editor, p. 117, Nat. Assoc. Corros. Engineers, Houston (1974).
22. H. Pickering and C. Wagner, *This Journal*, **114**, 698 (1967); H. Pickering, *ibid.*, **115**, 143 (1968).
23. H. H. Uhlig, *Acta Metall.*, **4**, 541 (1956).
24. N. Cabrera and N. Mott, *Rep. Prog. Phys.*, **12**, 163 (1949).
25. W. Bradley and H. H. Uhlig, *This Journal*, **114**, 669 (1967).
26. A. Swanson and H. H. Uhlig, *ibid.*, **118**, 1325 (1971); **121**, 1551 (1974).
27. J. Elliott, Private communication.
28. R. Baboian, *Mater. Perform.*, **16**, No. 3, 20 (1977).
29. A. Kuhn and C. Mortimer, *This Journal*, **120**, 231 (1973).
30. H. H. Uhlig, "Corrosion and Corrosion Control," p. 217, Wiley & Sons, New York (1971).
31. R. Baboian, Paper No. 770110 presented at the meeting of the Society of Automotive Engineers, February 1977.
32. R. B. Waterhouse, "Fretting Corrosion," Pergamon Press, New York (1973).

JOURNAL OF THE ELECTROCHEMICAL SOCIETY

REVIEWS AND NEWS

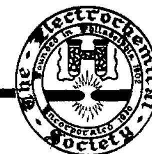

MARCH 1978

25 Years of Fuel Cell Development (1951-1976)

K. V. Kordesch[1]

Union Carbide Corporation, Battery Products Division, Parma, Ohio

"A fuel cell is an electrochemical cell which can continuously change the chemical energy of a fuel and oxidant to electrical energy by a process involving an essentially invariant electrode-electrolyte system" (1). For good reason, this definition is placed ahead of this review of the past 25 years of "Fuel Cell History" because this time period covers the third cycle in periodic attempts to realize what W. Ostwald (2) envisioned in 1894 as an electrochemical element more efficient than the heat engine which, being based on random energy, is limited by Carnot's law. The practical experiment of W. R. Grove (3) (usually called the first electrolysis fuel cell discovery) was, in its time, just a laboratory curiosity. However, around the turn of the century such eminent physicochemists as Nernst and Haber devoted much effort to direct carbon-oxidizing fuel cells. Their expectations failed due mainly to operating difficulties and material problems; that ended the first period. After World War I, new activities started the second cycle, still aimed at direct coal-oxidizing cells. The final statement by E. Baur (4) in his 1933 summary paper gave the best chance for success to the galvanic element which operated at room temperature in alkaline electrolyte with hydrogen as the fuel. After 1933 followed the "quiet years" before the start of the third cycle which was to progress on an international, worldwide basis.

Bischoff, Justi, and Spengler (1956) were probably the last ones to consider a direct coal-burning fuel cell (with Cu/CuO air cathodes). The findings of the Russian O. K. Davtyan (5) published in 1946 can be considered the start of a new period of development. Davtyan's work and the "Nernst mass" [a solid electrolyte based on ZrO_2 (85%) and Y_2O_3 (15%)] were the starting points for G. H. Broers, working for the Dutch organization T.N.O., together with J. A. A. Ketelaar in the early 1950's laying the groundwork for successful high temperature molten carbonate cells operating on H_2 and CO (6). Broers supplied the gases through porous layers and thus established a steady interface between the electrode structure and an electrolyte-containing solid matrix (of MgO).

Figure 1 shows the construction of this high temperature cell. Early work on high temperature cells paralleling the efforts at T.N.O. was also done at the Sondes Place Research Institute in England by H. H. Chambers and A. D. S. Tantram (7). F. T. Bacon (8) worked on high pressure hydrogen-oxygen fuel cells at Marshall's Flying School, Limited, in Cambridge, England, for 10 years until he was successful with porous nickel gas-diffusion electrodes containing a dual-porosity structure which served to keep the reaction zone gas/liquid/solid stable through gas pressure action and balancing capillary forces.

Figure 2 shows a photograph of Bacon's dual-porosity electrode. His fuel cell was later to become the basis of the NASA-Apollo fuel cell program. Under contract, United Aircraft Corporation, Pratt & Whitney Division, developed the fuel cells which resulted in the most spectacular success for "Fuel Cell Power Systems" achieved to date. Figure 3 shows the schematic diagram of their cell.

A third type of fuel cell emerged in the 1950's, based on the results of studies on carbon electrode activation by K. V. Kordesch and A. Marko (9) at the University of Vienna. Fuel cells with hydrophobic porous carbon electrodes catalyzed with spinels on the air side and Pt on the hydrogen side were operated at high current densities in alkaline electrolytes without pressure at room temperature (E. Baur's prediction of

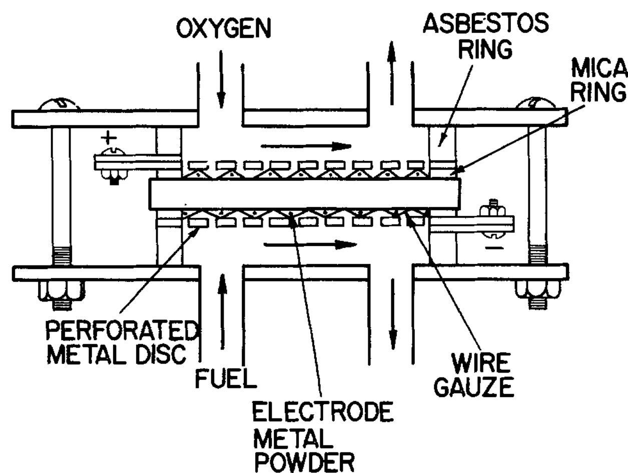

Fig. 1. The high temperature fuel cell of Broers

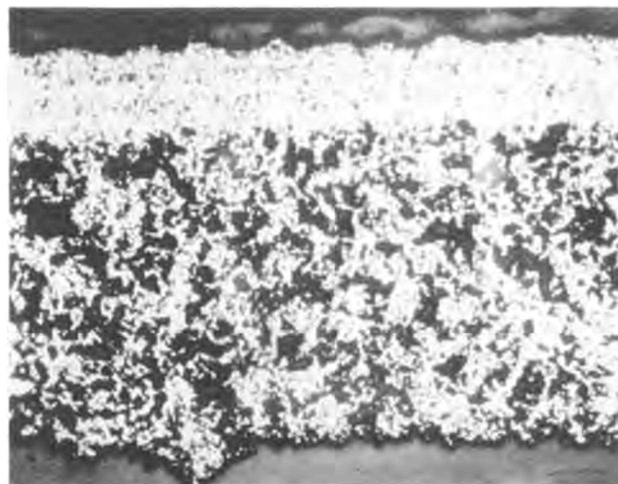

Fig. 2. Microsection showing coarse and fine pore layers of an oxygen electrode (38X).

[1] Present address: Institute of Inorganic Chemical Technology, Technical University of Graz, Graz, Austria.

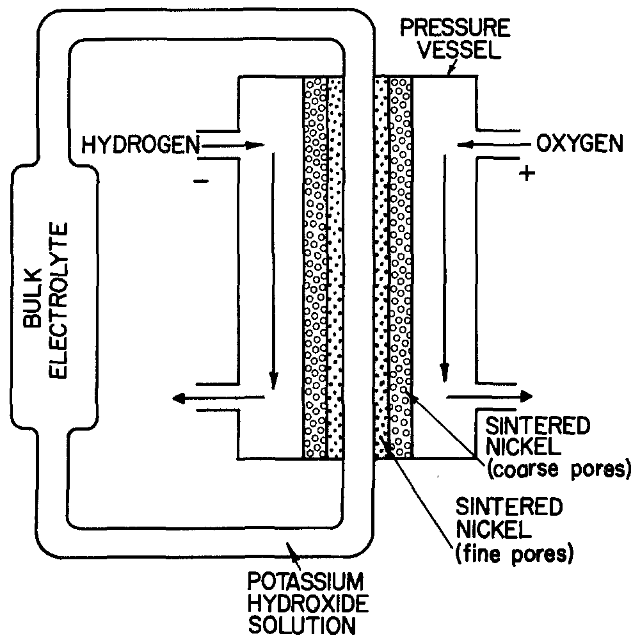

Fig. 3. Principle design of the Bacon fuel cell system

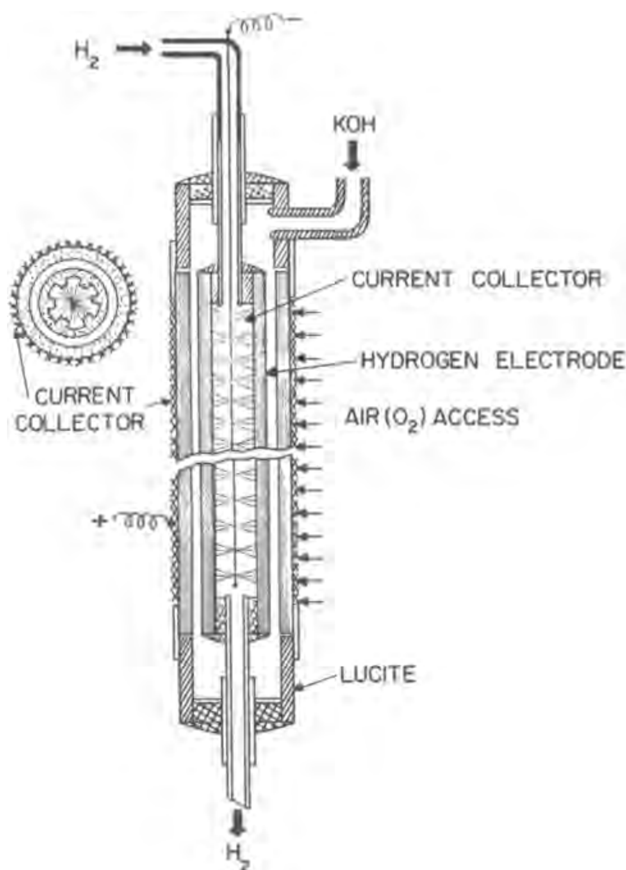

Fig. 4. Concentric hydrogen-air fuel cell

1933 come true). Such electrodes became the basis of the fuel cell systems built by Union Carbide Corporation, first in the tubular shape, and then later as thin composite electrodes using a porous metal and carbon in a layer design. A picture of the early concentric hydrogen-air fuel cell is shown in Fig. 4.

Another significant development of the 1950's was the work of E. Justi's group at the Technical University in Braunschweig, Germany (10). Justi succeeded in producing porous metal electrodes (single pore size and dual-porosity structures) which operated at room temperature without noble metal catalyst. He used Raney structures. Later technical developments at Siemens, A.G. and at Varta, A.G. in Germany were based on the work of Justi's group.

Considering now the significance and the common features of those inventions which materialized in the 1950's (the beginning of our 25-year historic survey), it can be stated that it was the recognition of the need for a stable, large interface between electrode and electrolyte which caused the sudden "breakthrough" in technology. Different designs led to the same result, but all were realized through the following: a porous electrode structure; inert, conductive substrates (*i.e.*, carbon, nickel, metal oxides); catalysts, or pressure, or high temperature for a high reaction rate; wetproofing or gas pressure balance for stability; gases (later also liquids) as a replacement for carbon as fuel; recognizing the fuel cell as a "system" (*i.e.*, as a primary cell with continuously supplied chemicals); learning that success depended on the functioning of the auxiliary components as much as on the electrochemical reactions.

Beginning in the 1950's, electrochemical knowledge had also made tremendous steps forward, not the least of which was due to the fact that fuel cells made excellent electrochemical vehicles to experiment with, but also because they included nearly all of the conceivable principles of physical chemistry and thus were equally challenging to engineers, designers, and theoretical minds alike. Electrode kinetics became known as an important field, superseding the thermodynamic considerations which gave no answers beyond the principle of feasibility.

The porous electrode structure was subjected to rigorous analysis, and models were constructed to explain the behavior of the electrodes under load conditions. The role of the all-encompassing Nernst equation was scrutinized, and it was widely agreed that the overpotential was not the result of but the reason for the changing current flow. Still, the mechanism of the charge transfer at an electrode surface was not clear, and complicated models competed for acclamation.

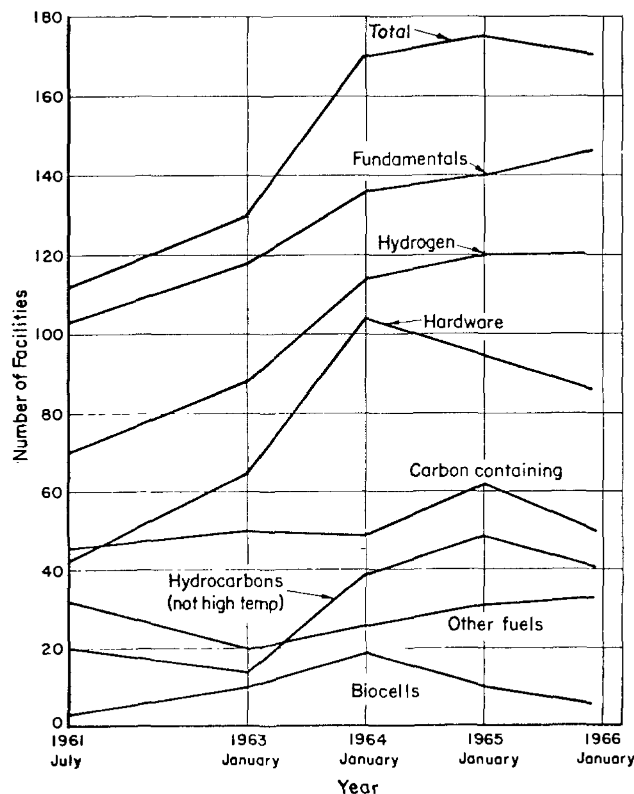

Fig. 5. General topical areas of fuel cell research

Table I. Government-sponsored contracts on fuel cells*

Estimated value of contracts, million dollars							
Totals	Hydrogen	Hydrocarbon	HTFC	Biocells	Other fuels	Publications	Totals
1963	10.82	2.61	0.89	0.93	0.60	—	15.85
1964	11.75	2.45	0.43	0.20	0.74	0.03	15.60
1965	9.44	3.17	0.22	0.20	0.43	0.03	13.49

Estimated value of contracts, million dollars, by government agency								
Totals	Army	Navy	Air Force	NASA	Department of Interior	AEC	ARPA	Totals
1961	1.3	1.8	2.4	0.1	—	—	—	5.6
1962	2.7	0.7	1.5	8.9	1.0	—	0.8	15.6
1963	4.0	1.5	1.0	8.5	0.5	0.2	0.2	15.9
1964	1.6	0.2	0.4	9.6	0.5	—	3.3	15.6
1965	1.6	0.4	0.3	7.8	—	—	3.3	13.5

* Based on project briefs from the power information center, University of Pennsylvania, as referenced by Battelle Memorial Institute of Columbus, Ohio.

Catalysts were developed empirically (without much benefit from theory at the time) and, coupled with hindsight, systems were designed by trial and error. In spite of this, the 25-year history of fuel cells is an honorable period for electrochemistry during which time it was applied to seemingly unsurmountable tasks such as providing the electrical power for a space capsule on a trip to the moon.

With the decline of space programs in the 1970's, fuel cell technology also stopped growing. So, within this 25-year period we also see the decline of fuel cell-related arts and sciences. However, within recent years a revival has started concerning uses and applications for the general public right here on earth for power production on large and small scales.

Before presenting a chronological survey of fuel cell technology, Fig. 5 depicts a representation of the distribution of worldwide fuel cell efforts concerning the various government agencies, industry, and universities. Table I lists the government expenditures for fuel cells (excluding classified programs). Figure 5 and Table I are based on a survey conducted by Battelle Memorial Institute (11) and cover the five peak years of fuel cell work.

Figure 6 lists the number of Chemical Abstract fuel cell citations over the years 1958-1972 (12). A selected bibliography listing the major books on fuel cells and related subjects has also been provided to help in finding more detailed information.

Chronological Survey of Fuel Cell Systems

High temperature cells.—Molten carbonate cells.— Pittsburgh Consolidation Coal Company, under contract to the U.S. Army, continued work on high temperature fuel cells for use with water-gas mixtures (H_2, CO, CO_2, and H_2O) as fuel and air as oxidant (13). Cracking occurred in initial laboratory cell disks made of a solid electrolyte against which porous metal electrodes (3 mm thick stainless steel) were pressed. Later, molten sodium carbonate (soaked in MgO) disks were used, but the disks still cracked and the molten phase leaked from the disks. It was discovered that CO_2 in the air supply stream was necessary to maintain cell operation (with transfer of oxygen across the electrolyte). Further developments produced cells with porous nickel (on the fuel side) electrodes using equimolar sodium-lithium carbonate melts. For improvement of air electrode quality, some lithiated nickel electrodes and silver-pasted cathodes were prepared. At 750°C, these cells produced 75 mA/cm^2 at 0.70V using hydrogen. In the final report (14), cracking of disks and flooding of the electrodes were still mentioned as failure modes.

Work at Central Technical Institute T.N.O. on a U.S. Government contract (15) in Holland continued beyond Broer's research cited in Ref. (6). Their H_2 electrodes used platinum as the catalyst and silver for the cathodes. The principal aim was to lower the matrix resistance by designing the cell in tubular form, whereby the porous metal tube was coated on the outside with metal powder soaked with MgO-$LiNaCO_3$, followed by another layer of metal powder. The inside of the tube constituted one gas chamber and the outside was the other chamber. The fuel electrode limited the output to 15 mA/cm^2 at 0.6V, and the lowest operating temperature was 400°C (Li-Na-K-carbonate-eutectic). As work on this system continued (16), considerable improvements were achieved; current densities up to 200 mA/cm^2 (100 mA/cm^2 for 700 hr at 0.8V) with H_2-CO_2 (1:1) mixtures. In 1969, the superiority of the Li-Na-K-carbonate/aluminate system over that of the MgO-paste systems was established (17).

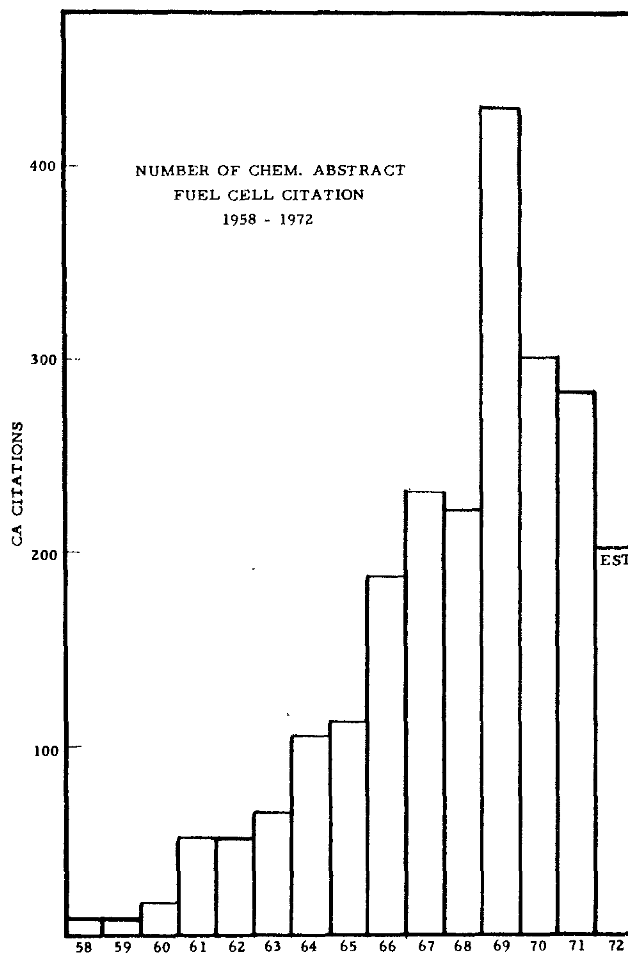

Fig. 6. Number of Chemical Abstracts' fuel cell citations dating from 1958 through 1972.

Texas Instruments, Incorporated, had a molten-carbonate fuel battery program during 1963-1965, with the purpose of producing a 400W unit which would operate on gas from reformed liquid hydrocarbons (18). Porous metal electrodes (of silver) were bonded to the electrolyte disk to prevent leakage; the electrolyte was $LiNaCO_3$ in a refractory MgO disk. The operating temperature was 600°C. Power densities were approximately 0.1 W/cm^2; lifetimes in the 1000 hr range. I. Trachtenberg (19) was the main investigator of these "slurried molten-carbonate cells," in which there was no requirement for structural integrity on the electrolyte component. Interactions of electrolyte stability, silver corrosion, and current density are discussed in Ref. (20).

At the Institute of Gas Technology in Chicago, B. S. Baker and coworkers (21) avoided the use of noble metal catalysts (needed for stability at high temperatures, not really for catalytic purposes). Eutectic mixtures (such as Broer's) allowed operation between 500° and 700°C. Silver fiber cathodes and porous fiber-nickel anodes were used, with reformed natural gas as the fuel. Cost/performance figures of $20/kW-$45/kW were quoted already in 1965.

At General Electric Company, some early work was done by D. L. Douglas (22) on molten-alkali carbonate cells with gas diffusion electrodes, mainly with a ternary electrolyte system.

At Union Carbide Corporation, M. L. Kronenberg evaluated high temperature fuel cells using an impregnated ceramic matrix. The tapered tubular cell construction (which made series cell connections easy and was later used extensively in solid-state cells) was invented at that time (23).

In Great Britain at Energy Conversion, Limited, A. D. S. Tantram originally worked on many different high temperature cell designs (24). Later, most of his work was devoted to Pd-Ag foil anodes (25).

In France at Gaz de France, A. Salvadori developed semi-industrial fuel cell elements of tubular design. Palladium on graphite was the catalyst used, and it consisted of a layer of refractory oxides deposited by flame spraying to establish a matrix. A silver-based thin film was used at the cathode (26). At Electricité de France, molten-carbonate cells were studied by a larger group of investigators (27). A collection citing French fuel cell work can be found in Ref. (28).

In Germany, work on molten-carbonate electrolytes was neglected in favor of the upcoming, and at that time more promising, solid-state high temperature cell systems.

The state of art found in 1969 did not change during the next five years. Because material problems were blamed for lifetime limitations, technology shifted to phosphoric acid fuel cells which could operate also as well on reformed natural gas. Only very recently, however, has the molten carbonate work at the Institute of Gas Technology obtained new importance. United Technologies, ERDA (through the Argonne National Laboratory), and EPRI have sponsored new studies. Performances of over 1000 hr have been quoted. This system is now considered as the "second generation" of fuel cells for power plants (29). Operation at 600°-750°C (without noble metal catalyst) for 40,000 hr (with multistack units) is considered a near-term goal (about 1980). Coal gasification will be an integral part of the system.

Solid electrolyte cells.—In 1960, J. Weissbart and R. Ruka established that cells with electrolytes of the type $(ZrO_2)_{1-x}(Y_2O_3)_x$ could be operated as solid-state high temperature cells. In principle, an O_2 concentration cell of that nature could use any fuel which reacts with oxygen (30). The oxygen-ion transport requirements limited the number of suitable oxides to those of mixed oxides with an imperfect structure. Nernst had already observed such ionic conduction in 1899. The early experimental cells produced accurate emf measurements of the H_2/H_2O, Pt-mixed oxides-Pt, O_2 cell at 1015°C. Current densities of 10 mA/cm^2 could be sustained for two months at that temperature.

Under the sponsorship of the USAF Aero Propulsion Laboratory (31), this system was investigated during 1962-1963, and the Westinghouse hollow cylinder bell-and-spigot design with electrodes applied to the inner and outer surfaces of the solid electrolyte was developed.

Current densities of 150 mA/cm^2 were reported by Archer and co-workers in 1965 (32). Cells measured 1.2 cm diam and were 0.9 cm in length. It was estimated that a 500W unit would weigh 12-20 kg. The platinum coating was 0.7 mm thick at the seals, covered with 1.5 mm of gold. Electrodes in series arrangement were brazed together with a Ni-Au shim. The first contract had the purpose of developing a 100W unit to burn gasified coal.

In 1962 the Office of Coal Research (33) sponsored work to provide design data for a 100 kW unit. To avoid expensive yttrium, electrolytes of the Zr, Ca, and Mg types were tested, with partial replacement of platinum with nickel. Promising results were obtained with perovskite systems such as $LaCoO_3$-$SrCoO_3$. A 100W unit was built from 20 tubes containing 20 cells each. Area per cell was only 2 cm^2. The O.C.V. was 200V. Performance with hydrogen and air was as expected (0.15 W/cm^2). CO was unsatisfactory as a fuel, therefore a catalytic shift reactor was incorporated. The 100 kW design was, most certainly, overambitious considering that cell details had not yet been thoroughly worked out. Doubts appeared concerning the claims that the solid-state high temperature cell was truly an O_2-concentration cell. The inability to operate on CO without a preceding water-gas shift is a major disadvantage and tends to disprove the original theory. Use of hydrogen-oxygen cells for space application was also studied but later abandoned.

The application of tin oxide and indium oxide films to zirconium electrolytes (by vapor deposition) resulted in very low polarization losses during air operation, and in 1967 E. V. Sverdrup and co-workers (34) claimed current densities up to 1000 mA/cm^2 at 1000°C, with operating life of around 1000 hr. The oxide films, however, flaked off with passing time. In 1969 it was estimated that there was enough applicable technology available to construct a fuel cell system which would use coal for central station power generation of 150 kW/m^3 at a cost of $30/kW (35).

Brown, Boveri Research Laboratories at Heidelberg (Germany) designed high temperature solid-state cells. The oxide powders were pressed with ammonium bicarbonate into disks 0.3 mm thick and 40 mm in diameter. Sintering was done with aluminum oxide additives. The active electrode materials were deposited by means of a plasma-spray process. With silver on the oxygen side and nickel or cobalt-iron on the fuel side, the cell was stable up to 850°C (36). Figure 7 shows a drawing of their 10-cell battery. Current densities of 100 mA/cm^2 were achieved, with reported lifetimes in the hundreds of hours.

At the Battelle Institute research laboratories at Frankfurt M (Germany) (37) and at Geneva (Switzerland) (38), solid-state electrolytes of the zirconium type were studied extensively.

In France, extensive studies of solid electrolytes were pursued until 1967 at the University of Grenoble by C. Deportes and co-workers (39). Platinum electrodes were used for studying the various mixed oxide systems.

In Japan, solid electrolytes were studied at the University of Nagoya. The emphasis was on replacement of noble metals with powder-metal sinters on the anode side and ZnO and Al_2O_3-containing electrodes on the cathode side (40).

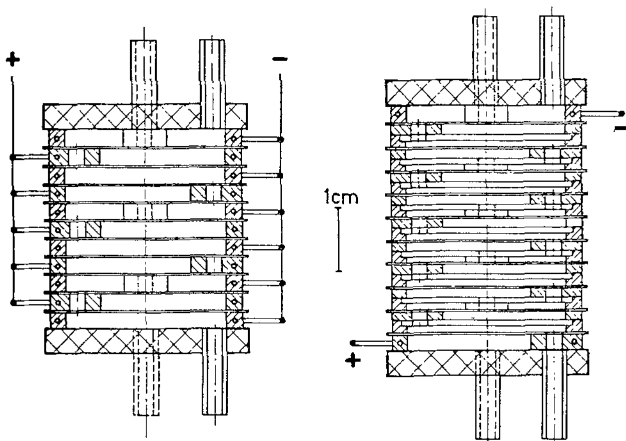

Fig. 7. Ten-cell battery; parallel connection on the left, series connection on the right. ("Solid-state battery.")

In Russia, at the Ural Institute of The Academy of Sciences, such systems as Zr, Ce, and Ca oxides which showed considerable conductivities have been studied since 1960 (41).

At the General Electric Company, W. E. Tragert (42) studied a system containing stabilized ZrO_2 as electrolyte in which was used a silver cathode in liquid form at 800°-1100°C, deviating from the "solid" electrolyte concept, but using to his advantage the high solubility of O_2 in silver.

A hydrogen-fueled power system based on the Westinghouse/Office of Coal Research high temperature solid electrolyte fuel cell has been recently suggested (43). Such cells would be used with pure hydrogen and oxygen (from an electrolyzer), with pure hydrogen (stored) and air, or with hydrogen from a gasifier or reformer and air. Utility use is contemplated, depending on cost, efficiency, and lifetime. Time scale for this application is about 1990.

Medium temperature fuel cells.—Modifications of the Bacon cell.—The hydrogen-oxygen cell developed by F. T. Bacon operated at 200°-240°C with 45% KOH. To prevent boiling of the electrolyte, a pressure of 40-55 atm was required. In this environment, the porous nickel electrodes tended to oxidize and to form a high resistance coating. The heavy and expensive construction was its major drawback. Further developments of the system for the space program were carried on under U.S. Government sponsorship.

At Patterson-Moos Research, Division of Leesona Corporation, the contract with the U.S. Air Force (44) calling for construction and testing of a 1.5 kW Bacon cell was started in 1957. Lithiated cathodes which could withstand oxidation were the first improvement. Although the performance of the finished stack declined within hours, a few of the cells lasted for as long as 2000 hr at 150 mA/cm², thus indicating, in principle at least, that the system could work.

Pratt & Whitney Aircraft, Division of United Aircraft Corporation, started their development of the Bacon cell in 1961. Their first goal was to produce a 250W H_2/O_2 fuel cell unit to demonstrate feasibility for space application. The operating parameters were changed to 260°C with 85% KOH (solid at room temperature) and operation at essentially atmospheric pressure. The current density was 150 mA/cm² at 0.87V (45). Some cells worked for 5000 hr; even the entire module reached 690 hr without failure.

The Apollo project.—Details of the design for the Apollo fuel cell projects have not as yet been fully published. However, principle descriptions are available (46). The Pratt & Whitney power plant, PC3A-2, is characterized in Table II.

Figure 8 shows a picture of the PC3A power plant. Three such units were mounted in the service compartments adjacent to the command modules of the space capsules in all Apollo missions. The moon flight, Apollo 8, lasted for 440 hr; during that time, 291.7 kW-hr of electricity were produced together with more than 100 liters of water. No further units were produced after the Apollo program ended. No exact cost estimates are available for the fuel cell power part of this program; a conservative estimate is $100 million, and perhaps up to $150 million.

Table II. Apollo fuel cell system, Pratt & Whitney PC3A-2 power plant

Number of cells	31
Cell pressure	50 psia
Nominal temperature	400°F (204°C)
Reactant gas pressure	10 psi above cell pressure
Heat and water removal	By hydrogen circulation
Voltage	27-31V
Power	563-1420W
Duration	400 hr
Maximum power	2295W at 20.5V
W-hr/lb reactants	1220 (at 1420W)
Weight	220 lb

During follow-up work planned for future space missions (space shuttle), Pratt & Whitney Aircraft Company developed an advanced 7 kW fuel cell system (1973 model) which improved the specific weight and volume figures nearly a magnitude over the Apollo system. (Fuel Cell Technology Program, Johnson Space Center, NASA, Houston, Texas.)

Low temperature fuel cells.—With carbon electrodes.—The early Union Carbide hydrogen-oxygen (air) fuel cells with liquid KOH electrolyte used baked carbon tubes (20 mm OD, 12 or 14 mm ID) in arrangements of 4 or 9 tube bundles, or (with air)

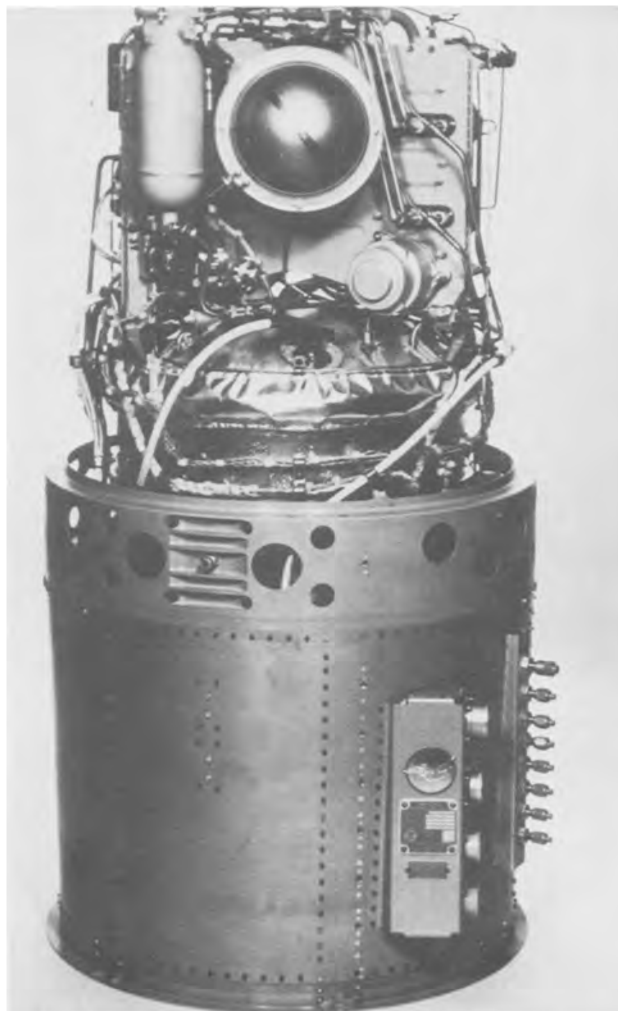

Fig. 8. PC3A power plant for Apollo project

in concentric cell designs with the outer (air) electrode having a 24 mm ID and 30 mm OD (47).

After 1960, the parallel-plate design prevailed; 3 or 6 mm thick carbon plates were surface-activated in the presence of spinels in a stream of carbon dioxide-containing gas atmosphere and subsequently catalyzed with silver or noble metals in the amount of 1 mg/cm^2 of geometric surface (48).

Hydrogen-oxygen batteries (up to multikilowatt output) were built from baked carbon plates during government-sponsored contracts (49-51). The largest electrodes had dimensions of 30 × 30 × 0.6 cm; the largest battery produced 30 kW output.

In 1964, thin composite porous metal/carbon electrodes started to replace the previous heavy voluminous carbon plates (52). These new thin plates were only 1-1.5 mm thick and used the "fixed-zone" principle, thus locking the reaction zone into the confines of the interface between the porous nickel backing (gas side) and the catalyzed carbon layer (electrolyte side). Figure 9 shows a cut through the thin, fixed-zone electrode.

These thin electrodes were used in compact hydrogen-air batteries studied under a government contract (53). Complete systems and accessories were developed (54) and, in an arrangement with General Motors Corporation, a van was equipped with a 32 kW hydrogen-oxygen battery (55). The system could be overloaded up to 150 kW for short periods to provide peak power for the vehicle. The current densities on oxygen were 350 mA/cm^2 at terminal voltages above 0.80V. With air as oxidant, the limiting current densities were 150 mA/cm^2 at atmospheric pressure; 250 mA/cm^2 at 10 atm (absolute). The system operated in water equilibrium conditions at 65°C in 9*N* KOH at 100 mA/cm^2. Most of the water which was produced transpired through the anodes into the hydrogen circulation system.

An experimental electric car was used to test the concept of a "hybrid vehicle" powered by a 6 kW hydrogen-air fuel cell battery in parallel with a lead-acid battery (56). The vehicle had a range of 200 miles with six lightweight hydrogen fuel tanks. Refilling was done within minutes from a high pressure hydrogen supply.

A further significant improvement of the fixed-zone electrode concept was in the change to a double-porosity nickel structure on the electrolyte side to assure proper wetting of the interface and to prevent gas bubble breakthrough at higher gas pressures. The active carbon layer (PTFE bonded) is on the gas side of the electrode, this being a reverse arrangement with respect to the previous design shown in Fig. 9. The improved electrode thereby combined the features of the Bacon electrode with the hydrophobic carbon electrode to improve performance and prolong life (57). Limiting current densities were 500 mA/cm^2 on oxygen, and 250 mA/cm^2 on air. Lifetimes reached 5000 hr. These thin electrodes can be used in rechargeable nickel-hydrogen cells employing existing nickel-cadmium technology (58).

Fig. 9. Fuel cell-lead acid battery automobile

Fuel cells with platinum black "Teflon" electrodes.—American Cyanamid Company produced high performance electrodes for use in alkaline and acidic systems using liquid and matrix electrolytes. The basic principle for manufacture of these types of electrodes is to make a mixture of platinum black (with or without carbon) and "Teflon" [*e.g.*, 3:1 weight percent (w/o)] and apply it to a screen support. For alkaline systems the carrier material is gold-plated nickel screen; for acidic systems a tantalum screen is used (59). The matrix used was asbestos filled with 5*N* KOH, or glass-fiber paper filled with 5*N* H_2SO_4. The Type A electrodes used no extender with the platinum black, and loadings varied from 9 to 40 mg/cm^2; Type B electrodes used graphite as diluent for the platinum black, making it possible to reduce the Pt level to 2.5 mg/cm^2 and still achieve current densities of 100 mA/cm^2 at 0.75V in KOH at 30°C. Operating life at 70°C had been over 1500 hr when 9.5 mg Pt/cm^2 were used. High performance lightweight fuel cell electrodes were especially investigated by American Cyanamid Company for NASA (60).

The General Electric Company's "Teflon"-bonded platinum electrodes consisted, typically, of a Pt screen embedded with a mixture of "Teflon" and catalyst, with a thin porous film of "Teflon" on the gas side. An aluminum foil was used as a backup material to press the mixture into the screen (it was later stripped from the electrode). Loading with the noble metal catalyst was on the order of 30 mg Pt/cm^3. Electrode sizes up to 50 × 25 cm were suggested to be optimal for the U.S. Navy for use in fuel cells for submarine propulsion (61). Electrode structures of this type (62) finally progressed to spaceworthy components and were incorporated in the Gemini space power source.

Similar electrodes were used in fuel cells operating on hydrocarbon fuels. Studies to reduce the amount of platinum led to a loading of 1-2 mg Pt/cm^2 for hydrogen electrodes; using oxygen and hydrocarbons, there was shown to be a direct relationship between platinum loading and performance. Tungsten or tantalum powders as well as boron carbide were tried successfully as diluents. In liquid 6*N* KOH, current densities up to 400 mA/cm^2 at 0.7V were achieved with 35 mg Pt/cm^2. In 5*N* H_2SO_4 at the same catalyst level, a hydrogen-air cell could produce 400 mA/cm^2 at 0.4V. With electrolyte circulating between the electrodes, internal heating produced temperatures up to 70°C at high current densities. Local "hot spot" temperatures were probably far higher, sometimes leading to electrode failure by gas cross-leakage.

Engelhard Industries produced platinum and platinum alloys (especially Pt-Ru) catalysts which were designed for acidic matrix-type electrodes (63). A mixture of the noble metal catalyst and carbon was bonded with "Teflon" to form a thin electrode on a metal screen structure. These electrodes were utilized in phosphoric acid cells operating with alcohols and dissociated ammonia as fuel and air as the oxidant.

Fuel cells with porous metal electrodes.—Gas diffusion electrodes based on a double-skeleton-catalyst (DSK) design had been studied by E. Justi's group at the Technical University Braunschweig in Germany since the early 1950's (64). The principle of these electrodes was first described in early German patents (65). A homeoporous metal structure (to balance the capillary action with gas pressure in an optimal way) is combined with a highly active nonnoble metal catalyst by mixing size-controlled carbonyl nickel powder and Raney alloy powder. Pressing and sintering results in a strong electrode with a "double structure," part of it serving as a coarse skeleton for good conductivity and part acting as a catalyst.

The Raney catalysts were, basically, Al-Ni alloys for hydrogen electrodes and Al-Ag alloys for oxygen electrodes. The aluminum was leached out with caustic solutions. Later special activators and pyro-

phoric inhibitors were added to facilitate production. The German companies, Ruhrchemie A.G. and Steinkohlen Elektrizitäts A.G., financed the early work.

Varta A.G. continued the development work up to kilowatt sizes (66). A special development, the "Eloflux" electrode (67), was unique in its design of electrolyte flow (perpendicular to the electrode surface) and manifolding of multiple cell units. One hundred units of that type were built in small quantities until 1972.

Siemens A.G. followed another path in the further development of the Raney catalyst electrodes to produce the so-called "Schüttelektrode" in which the particles of active materials were sedimented on asbestos without any additional binder. The electrodes were held in place by other layers of porous nonconductive materials (68). These electrodes were used to construct hydrogen-oxygen fuel cell batteries up to kilowatt sizes. Even the powering of automobiles (in hybrid fashion) was suggested (69).

A 7 kW hydrogen-oxygen battery was built by Siemens A.G. around 1976. Development work at Siemens did not stop when most other fuel cell efforts in the United States and elsewhere folded or were reduced to laboratory levels. Work was continued in the direction of lower cost units and air operation (70). The air electrode was based on an ammonia-treated carbon material and the electrode design was comprised of three layers: a hydrophobic cover layer, a hydrophobic working layer, and a porous PTFE cover on the gas side. This electrode is also suitable for rechargeable air cells (71).

Allis-Chalmers Manufacturing Company built hydrogen-oxygen fuel cells based on an electrode consisting of a porous nickel plaque catalyzed with noble metals facing a porous asbestos sheet in which the electrolyte is retained by capillary action. The early cell construction used direct evaporation of the formed water (at the H_2 electrode) as a means for keeping the electrolyte concentration constant in the asbestos matrix (72). As an early demonstration project, a tractor was fitted with a 15 kW hydrogen-oxygen battery in 1959. With a working voltage of 750V, the current of 20A represented a current density of 20 mA/cm^2. Battery weight was 917 kg.

During the years from 1961 to 1965, several large units were constructed under government contracts (73-75). The first was a 1.5 kW unit operating at about 65°C and 5 psig. A 400W unit was built with bipolar plates and the operating temperature was increased to 90°C. It worked for 700 hr.

In order to adapt the Allis-Chalmers cell to space operations, the so-called "static water vapor control method" was invented (76). In essence, a moisture-removal membrane supported by a porous support plaque was added behind the hydrogen cavity. With this principle, the auxiliary controls became simpler, and a 2 kW space fuel cell battery was built for the G. C. Marshall Space Flight Center, Huntsville, Alabama.

This type of fuel cell operated so successfully that this system was visualized as a follow-up system after Apollo to replace it in future space ventures (which were later cancelled). The noble metal catalyst level was high (partly replaced by gold), but the reliability and power/weight requirements of space missions warranted this approach. Testing of such a system continued even after Allis-Chalmers closed down their fuel cell work in 1969. Through the use of nickel boride, their Research Division developed a hydrogen catalyst free of noble metal (77). A very active catalyst for the oxygen electrode was prepared from silver oxalate (78).

Allis-Chalmers also manufactured a 5 kW hydrocarbon-air fuel cell system which employed their 1965 fuel cell technology to produce the hydrogen in a steam reformer unit (79). The biggest problem in this system was reliability of the auxiliary components. However it provided experience for procuring H_2 producers, air scrubbers, and inverters on an engineering scale. A weight breakdown shows for instance, that the fuel cell module weighed only 22% of the unit (150 kg), the reformer weight was 240 kg, and the inverters and auxiliaries together weighed over 300 kg for a total of over 700 kg to achieve only 5 kW net power output (gross fuel cell power: 7.3 kW). Allis-Chalmers also built hydrazine and methanol batteries.

The fuel cell system of ASEA, Sweden, used layer electrodes which consisted of an inactive, coarse, porous layer of nickel, an active intermediate layer of porous nickel with nickel boride, and a fine layer of porous nickel (on the electrolyte side). The propulsion of submarines was a considered application, and a very sizable effort was expended in Sweden to build suitable systems (80). However, accidents prevented the success of the project and it was abandoned. Still, the progress made during this technological phase was considerable and much was learned about the behavior of different electrode designs (81). Some of the results with oxygen electrodes were later applied to rechargeable iron-air systems.

The Electric Storage Battery Company produced microporous metal electrodes for hydrogen-oxygen cells as early as 1960. Larger tubes (2.5 cm diam) or plates made from tiny tubes were fabricated and tested (82). Current densities up to 200 mA/cm^2 and lifetimes of 3000-5000 hr were reported, especially in NaOH. The oxygen electrodes were heterogeneous alloys of 50-90% Ag and 10-50% Ni.

Compagnie Général d'Electricité in France, at the Laboratories in Marcousis, experimented with alkaline fuel cell batteries in sizes up to 2 kW. Oxygen electrodes were based on carbon-silver structures; hydrogen electrodes used porous nickel electrodes of adjusted pore sizes carrying nonnoble metal oxides as catalysts (83).

AEG-Telefunken in Germany developed tungsten carbide catalysts for fuel cell anodes (hydrogen and reformer fuels) in acidic electrolytes (84). Thin electrodes (0.75 mm) reached current densities of 50 mA/cm^2.

At the Battelle Institut in Frankfurt, Germany, tungsten carbide was also studied as an anode catalyst in acidic electrolytes (85). In sulfuric acid at 70°C, the polarization at 50 mA/cm^2 was 0.2V. Such electrodes were also used in phosphoric acid and with different fuels such as formic acid, hydrazine, etc.

Ion-exchange membrane cells.—General Electric Company's fuel cell program was mainly military and space oriented. The electrodes previously described were used in combination with ion-exchange membranes (IEM's) serving as the electrolyte member of the cell. Phenol-sulfonic IEM's were the first types used in a 24V, 200W Navy battery design (1959) which aimed for a weight of 16 kg, including one day's fuel supply. The operating mode desired was 14 hr/day for seven days on hydrogen and air (86).

The life of the IEM's was short if the membranes dried out; therefore, water was retained by wicks on the oxygen side. The ribbed titanium contact plate provided space for it next to the air supply and cooling channels. The cells operated at 15 mA/cm^2 at 0.6V for over 500 hr. One failure mode was the flaking off of the Pt-Pd catalyst (50 mg/cm^2) from the membrane on which it was deposited. The fuel canister and the hydrogen generator (Na-borohydride and acid) of the earlier model was subsequently replaced by a bottle of compressed hydrogen. During the following development work, the cell resistances were reduced by higher contact pressure.

In the HOPE fuel cell program (USAF), the performance of IEM cells under orbital flight conditions was studied. Improvements in heat removal (copper-

plated condensors with radiators) and membrane compositions resulted. Sulfonated (polymer "A") polystyrene resins made it possible to achieve current densities of 100 mA/cm^2 above 0.6V. However, pressure imbalances leading to cross-leaks and drying out of membranes were still troublesome. In view of the Gemini Project (General Electric/NASA) which was showing faster progress in the state of the art, Project HOPE was abandoned in 1962.

A program under Navy sponsorship (87), using "Series D" sulfonated polystyrene membranes, produced large-size electrodes (50 $\times$ 25 cm) which had a "Teflon" coating for improved repellency and a special coolant chamber built into the cells between the anode and cathode (bipolar). Operation at elevated temperatures or on open circuit decreased membrane life. However, some cells survived 4000 hr testing. Extensive studies (88) of airflow management and a new design for electrode collectors increased limiting current densities to nearly 300 mA/cm^2 in 1963.

The Gemini fuel cell system (89) consisted of three modules (32 cells each) in a cylindrical container. This Gemini system used two batteries, each of which could produce 1 kW at 26.5-23.3V. Each battery, including accessories, weighed 31 kg. A description of the long history of the General Electric IEM from the early testing stages to the space flights of Gemini 4 and 5 is provided in Ref. (90). One production battery repeated more than three successive two-week Gemini missions.

In a post-Gemini development at General Electric, new polymer electrolytes have been found which are extremely resistant to chemical oxidation and temperature variations. Cells containing such materials survived 5000 hr of testing. In 1973, high current densities (100 mA/cm^2) and long life expectancies were reported at the end of the NASA acid electrolyte fuel cell program (91) using IEM's. In 1975, the use of IEM hydrogen-oxygen (air) fuel cells was suggested for large power installations for energy storage and peak-load sharing (29, 92).

Matrix (phosphoric acid) fuel cells.—The phosphoric acid-matrix cell has been late in receiving attention as being a type of cell which could be suitable for system development, most probably because that particular acid is a poor conductor and is extremely corrosive, and also because a noble metal catalyst must be used. However, earlier disappointments with hydrocarbon-converted fuel systems using alkaline electrolytes prepared the way for the use of the acidic-matrix cell. O. J. Adlhart (93) at Engelhard Industries, Incorporated, pioneered the use of plastic-bonded electrolytes for acidic systems with the intention of using them for direct methanol or propane cells. The application in phosphoric acid-matrix cells proved to be much more successful, and by 1970 Adlhart's company had built a 1 kW hydrogen-air power system for the U.S. Army (MERDEC) which had a lifetime of 2500 hr at 180 mA/cm^2 (94). The catalyst cost was estimated at \$300/kW. The degradation rates of the catalyst were given as 3 mV per 100 hr at 100 mA/cm^2 and 150 C for hydrogen-fueled cells. The problems with steam reformates were the reduced H_2 utilization and the catalyst-activity reduction by CO, reasons to switch to catalytically cracked ammonia in later systems.

At Pratt & Whitney Aircraft Division W. Vogel, J. Lundquist, and A. Bradford (95) studied the reduction of oxygen on Pt-black electrodes and concluded that a layer of catalyst in contact with a porous "Teflon" layer should give very high current densities even at low Pt loadings providing the Pt agglomerates were interconnected (*e.g.*, with gold). With about 1 mg of Pt-black/cm^2 the voltage drop between open circuit and 100 mA/cm^2 was 0.30V if air was used, and only 0.25V using pure oxygen (measured in 85% H_3PO_4 at 120°C). Using only 0.05 mg Pt/cm^2 (and gold), they measured a drop of 0.3V (with O_2). In a later paper (96) with P. Stonehart, the performance of hydrogen electrodes in phosphoric acid was reported with respect to the CO poisoning effect on Pt. The effect was reduced by increasing the temperature of cell operation to 180°C.

Thin electrodes were studied using carbon paper as substrate and a "Teflon"-bonded carbon layer as catalyst carrier by R. F. Scarr and K. V. Kordesch (97) of Union Carbide with a goal of producing lower cost air electrodes for phosphoric acid cells. The quantity of Pt was held low by impregnating carbon with Pt salts. A tantala cloth soaked with phosphoric acid was used as the electrolyte matrix. Up to 7000 hr operating time were achieved (98). The operation of hydrogen electrodes in acid media is well understood (96, 99). All investigations of declining performance of acidic cells point to recrystallization (increase in agglomerate size) of platinum. This is still an unsolved problem today.

Not much is reported concerning the composition and manufacturing of the "matrix." In earlier experiments, a certain specially prepared type of asbestos was used, and later "gels" consisting of "Teflon"-phosphoric acid mixtures were prepared and further immobilized by fillers of a proprietary nature.

The technical development of the phosphoric acid-matrix cell was carried out with the financial support of a group of gas utility companies in the TARGET[2] program (100). Work at Pratt & Whitney Aircraft Division (now United Technologies Corporation, Power Systems Division) led to the design of 15 kW systems for local power production. Originally, natural gas was considered the preferred fuel which would be steam converted to a hydrogen-rich fuel. The objectives were to develop a competitive system used by utility companies as a load-leveling device and distribution aid which would ultimately lead to a gas-line-supplied electric home or small industrial complex. Today, this goal is even more important because of the present need to shift electric energy production from oil to coal. Hydrogen is really the fuel to be employed with fuel cells, since it can be provided through nuclear power use by electrolysis. Therefore, it is not surprising that plans are presently being made for the development of phosphoric acid electrolyte fuel cell power plants for both on-site and dispersed-power generation. Prototypes of 40 kW units have operated on pipeline gas at 40% over-all efficiency for more than 5000 hr. A 1 MW power plant is scheduled to run on naphtha and air (FCG-1 program). The benefits of fuel cell power plants were recently outlined in an ERDA publication (101). However, there are still problems, and their ultimate economy will be determined by the usual trade-offs between catalyst cost, power density, and projected life.

Other systems—Other fuels.—Acidic methanol cells. —In the period 1960-1963, Esso Research and Engineering (102) studied the oxidation of methanol on platinum black electrodes (8 mg/cm^2) in acids; a complete conversion to water and CO_2 was obtained. At 83°C with 4% methanol in 30% sulfuric acid, the air cell produced 0.4V at 50 mA/cm^2. Nitric acid air electrodes were initially used as cathodes (with membranes); platinum black-screen cathodes were later employed. Lifetimes up to 1000 hr were achieved. A 10 cell stack was built which operated at 20 mA/cm^2 at an efficiency of about 40%.

Engelhard Industries (103) used anodes with "Teflon"-bonded catalysts of the type 60 Pt:20 Ta at 20 mA/cm^2. E. J. Cairns at General Electric operated a medium-temperature (130°C) cell with methanol vapor. With $CsCO_3$ electrolyte, the current density was also 20 mA/cm^2 (104).

[2] Team to Advance Research for Gas Energy Transformation, Incorporated.

In general, acidic methanol-air cells suffered from high catalyst costs and low output figures. Since fuel reacted on both electrodes, either a membrane had to be used or the fuel concentration had to be limited to low levels (0.1-0.5%). In 1964 at Shell Research, Limited, K. R. Williams, D. P. Gregory, and co-workers (105, 106) succeeded in building a 40 cell battery which delivered 300W at 12V at 60°C. They used microporous PVC as the substrate for the air and methanol electrodes, with the space between being used to feed the 1M methanol solution in 6N H_2SO_4. Operational parameters were a compromise in temperature, alcohol level, and cell resistance (separator). The performance of this battery was only 0.55V at 20 mA/cm², and the side products of methanol oxidation were also disturbing.

The kinetics of anodic oxidation of methanol in acidic electrolytes has been studied by S. Gilman and M. W. Breiter (107), and they proposed the reaction to a methoxyl radical and hydrogen as the first step.

Alkaline cells with methanol or methanol-derived fuels.—The anodic oxidation in caustic solution has been investigated by W. Vielstich (108). He used Pt-metal catalysts and found that formaldehyde and formic acid are reaction products which, by themselves, can be used as fuels, finally giving CO_2. The current densities are on the same order (2-5 mA/cm²) as were observed in earlier cells operating with Raney nickel catalysts (109). A large (60W) methanol-air battery for sea buoys was built by Brown, Boveri, and Cie on the basis of Vielstich's studies and was field tested for several months. In later cells, the use of formates and glycols was preferred, mainly because of the far higher current densities and the reduced interaction between the fuel and the carbon cathode with Ag catalyst (110).

Formate-air primary cells and fuel cells have been given very recent attention as high capacity, low cost cells with reversible electrolyte (111). At Allis-Chalmers, methanol-oxygen batteries were built as early as 1962 (80 cells, 500W output). The use of bipolar electrodes with a solid foil as the separator also allowed the operation of small methanol-peroxide systems (112). The larger systems used sandwich-type cells in which grooved, folded stainless steel endplates allowed the flow of the fuel-electrolyte mixture and oxygen. Asbestos was used as a separator-spacer between the electrodes (113). During the development of the Allis-Chalmers batteries, the move to formate ion/oxygen cells was made at a later date (114). The superior current density figures were the main reason for the change.

At Gould-National Batteries, Incorporated, R. E. Biddick and D. L. Douglas (115) constructed a 24 cell methanol-air battery with thin membranes as separators. It was operated in parallel with a sealed Ni-Cd battery as a hybrid power source.

A comparison between direct fuel utilization and separate steam reforming or "internal reforming" of the methanol was made in the design studies of two 6 kW systems at Leesona-Moos Laboratories (116). The availability of thin hydrogen-permeable Pd-Ag membranes necessary for the production of pure hydrogen turned out to be the key factor for cost reduction and high current operation over a long time period.

Considering the difficulties encountered with carbonate removal from the electrolyte (a necessary evil of dissolved methanol fuel cells), it is not surprising that there was a strong shift of emphasis to hydrazine fuel cells as the best representative system for dissolved fuel systems.

Hydrazine cells.—Hydrazine (N_2H_4) can be considered as a liquid "hydrogen fuel," since it decomposes easily into hydrogen and nitrogen at the electrode (catalyst) surface. For this reason the voltage observed is only that of a hydrogen cell and not that of a true hydrazine cell (theoretically, about 0.3V higher). In most systems the hydrazine is added to the caustic electrolyte and measures are taken to minimize interaction with the air or oxygen cathode through the use of a low hydrazine concentration or cathode catalyst with low sensitivity to hydrazine or through the insertion of a membrane.

Hydrazine-air fuel cells in the 1930's were already operating at the Union Carbide and Carbon Research Laboratories (117) in Long Island City, New York. However, since no commercial application could be visualized at that time, the project was abandoned without even reaching patent status. Work on the hydrazine-air system was not resumed at Union Carbide Corporation until 1961 (likewise in other companies), and publications concerning complete systems started to appear in 1962. M. Eisenberg (118) demonstrated a 30W hydrazine-oxygen system and proposed a 300W unit for space application. M. I. Gillibrand and G. R. Lomax (119) in England at the Electric Power Storage, Limited, produced a system intended for lift truck operation, while Allis-Chalmers Manufacturing Company showed a 3 kW hydrazine battery propelling a golf cart using cathodically compressed oxygen stored in a high pressure cylinder (113).

Air electrodes were not used in these early systems because of their poor performance in hydrazine-containing electrolyte unless a membrane was used. Improvements in anode catalysts decreased parasitic losses and subsequently also made it possible to operate with low N_2H_4 concentrations. R. Jasinski (120) replaced noble metal catalysts with nickel boride for H_2 and N_2H_4 anodes. At Monsanto Corporation (121), development of a 60W portable power source was achieved, and a 5 kW battery for a ¾-ton truck was demonstrated for the U.S. Army (122). Originally, eight of these units were planned, but only four were finally installed and those were used in parallel with a lead-acid battery. Asbestos layers were used to prevent hydrazine access to the cathodes, despite the use of only 6% N_2H_4 concentration.

At Union Carbide Corporation a 300W hydrazine-air battery, the "Silent Power Source," was also developed for the U.S. Army (122). Highly active anode catalysts allowed lowering the hydrazine concentration to 1 or 2%, precluding the need for the asbestos sheet for cathode protection, and thus preventing the resistance troubles caused by gas bubbles lodged in the separator. This battery was later improved by the use of "reversed" composite electrodes which protected the carbon from the hydrazine by an inactive porous nickel structure and a very accurate hydrazine-concentration/voltage-sensing system (123). Its power output reached 600W in 1969 (124). At Monsanto Research Corporation a special fuel-feed system based on electrolysis current sensing was developed (125). Efforts at the U.S. Army Electronics Command (126), Fort Monmouth, focused on ultimate simplicity of hydrazine-air cells, trying to avoid the use of mechanical accessories.

During this "high time" of hydrazine-air fuel cells, practically every electrochemically oriented research laboratory worked on hydrazine batteries. A demonstration of a hydrazine-powered motorcycle was given by K. V. Kordesch (127) in 1967. The development of hydrazine-air batteries reached its peak in 1970 after the 5 year evolution of various ideas and technologies at different companies. An excellent summary is given by several authors in the *Proceedings of the 24th Power Sources Symposium* (128) at Atlantic City. After that period, development stopped abruptly with drying up of Government funding, and work has not been resumed to date.

Overseas a similar course of events took place. Interest in hydrazine fuel cell systems was high in England, leading to well-developed batteries (119).

In Germany work centered in academic laboratories where modern methods and techniques were studied (129-132). In Russia hydrazine cells were built at the Moscow Power Institute (133). In France the concept of the dissolved-liquid fuel cell was applied to hydrazine (and methanol) cells by Alsthom as well as in a combined effort with Exxon. This two-phase system was developed by B. Warszawski (134) and actively pursued until just recently. In Japan a comprehensive study of dissolved liquid fuels was made (135) and catalyst work proceeded well. However, except for some research studies, work on hydrazine fuel cells stopped just as abruptly on the international basis after 1970 as it did in the United States.

Ammonia as fuel.—Using ammonia as fuel, the direct oxidation of NH_3 to N_2 and H_2O occurs on selected noble metal catalyst, but to date no technologically viable system has been built. Research efforts at Allis-Chalmers (136) were expanded in the 1960's. M. Eisenberg also operated direct ammonia cells between 180° and 300°C in 1964, and a basic study was reported from the University of Bonn, Germany as late as 1971 (137).

Sodium amalgam cells.—Expectations were quite high in the 1960's when the sodium-amalgam system was transferred from research to the development level. E. Yeager (138) from the (then) Western Reserve University, and the M. W. Kellogg Company investigated this system for proposed use for submarine propulsion (139). A design was prepared for a 1000 kW unit specified by the U.S. Navy, and it represented a system energy density of 30 kW/m^3. Actually, 8 kW units were constructed and tested. The amalgam inlet manifold was designed as a "shower head" to prevent between-cell shorts. The anodes were steel plates, and the cathodes were proprietary porous silver electrodes with a porous plastic surface barrier developed by the Electric Storage Battery Company. After 1963, this system was studied only occasionally (*e.g.*, in Japan), and no commercial application was found for the sodium cell. Figure 10 shows the sodium cell.

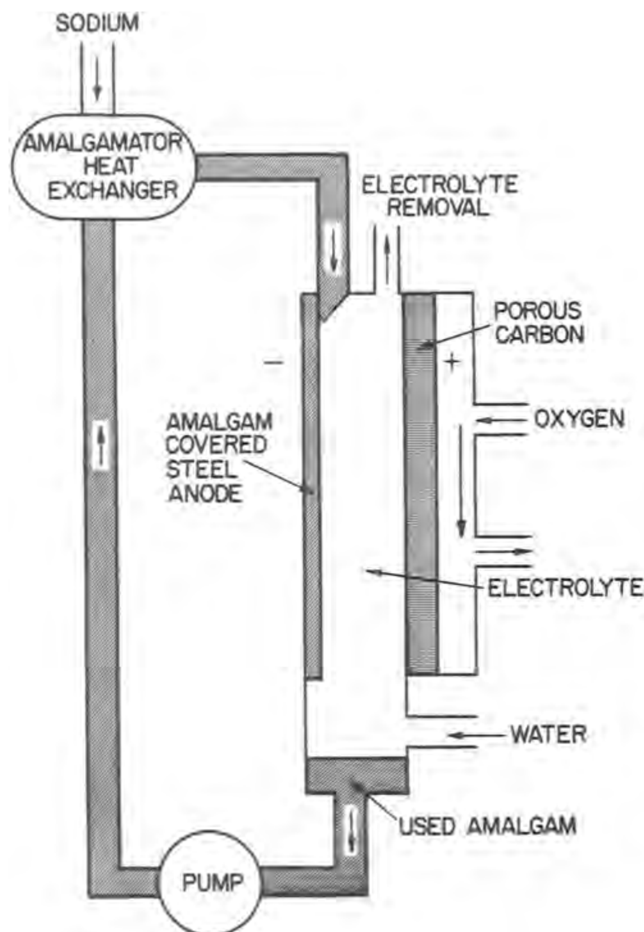

Fig. 10. Principle of the sodium amalgam cell

Regenerative H_2-O_2 fuel cell systems.—Pratt & Whitney Aircraft investigated a storage system whose intended primary source of energy would be secured from solar energy in space (140). In 1960, the fuel cell choice was the "hydrox cell" combined with a zero gravity electrolytic cell.

General Electric Company proposed its 50W ion-exchange fuel cell system (141) for cyclic operation. Single sealed units which contained the produced gases within the cell housing itself were built by Xerox Corporation (142) for NASA. One unit consisted of 34 cells and produced 500W. The good features of the rechargeable H_2-O_2 fuel cells were soon overshadowed by a negative one: the self-discharge by gas recombination could not be prevented, even by the very sophisticated separator designs (initially, asbestos soaked with electrolyte used for that purpose in alkaline cells). It is interesting to note that the difficulties with this system led to the development of the recently very successful nickel oxide-hydrogen systems.

A further enhancement of the early electrolysis electrodes by E. Justi (143) (*i.e.*, the "valve electrodes") was never developed beyond basic principles. Some day, however, these electrodes (at least in principle) may become useful in modern power storage units.

Thermally regenerative systems.—MSA Corporation proposed a lithium-hydrogen cell for cycling between 570° and 1000°C with a Carnot efficiency of 42% (144). It is interesting to note that hydrogen picks up an electron to become a negative-charged ion in this cell. Figure 11 is a diagram showing the cell reactions.

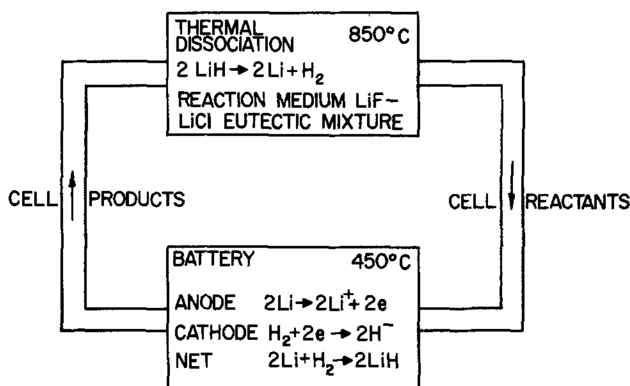

Fig. 11. A thermally regenerative system

Photochemically regenerative cells.—A cell based on the properties of the proflavine-ascorbic acid system was proposed by a research group at Lockheed Aircraft Corporation (145). A survey of photogalvanic systems, including the silver halides was made at the Philco Corporation (146).

Radioactive regenerative fuel cells.—At Union Carbide Corporation, the radiolytic regenerable redox system (cobalt^{60}/H_2SO_4, H_2/Fe^{3+}) was found to be feasible (147). Yielding 5W at 3% efficiency, it could be a way of utilizing radioactive waste material in remote locations. The conversion of oxygen to ozone by γ or ultraviolet radiation was frequently proposed, but conventional oxygen electrodes did not improve with O_3.

Chemical redox systems.—A cell design using continuous chemical regeneration of the two electrolyte solutions was worked on by General Electric Company (148) in the late 1950's. The idea was to produce hydrogen from a gasification plant and to reduce

Ti(IV) to Ti(III), similarly as A. M. Posner in England reduced the stannic/stannous couple in coal in the early 1950's (149). The Br/Br^- couple was used as the (air) oxygen transfer means on the cathode, aided by nitric acid to ease the reoxidation. A 100W system was actually built which consisted of seven cells in series (open-circuit voltage: 0.95V each). Continuing efforts were not successful, however, and the redox systems were forgotten for many years until just recently (150) when their application as large storage devices for electric utilities was considered promising (151).

The nitric acid-oxygen redox electrode.—The electrochemical reduction of oxygen in acidic electrolytes is usually far slower than in alkaline solutions and it requires expensive metal catalysts. It is not surprising, therefore, that efforts were made to use a chemical redox system to attain high current performance. This seemed an especially suitable way to utilize air as an oxidant in direct hydrocarbon fuel cells.

In the HNO_3/HNO_2 systems made by Esso Research and Engineering Company (152), the electrolyte used was H_2SO_4 with only 0.2M HNO_3. The carbon-based electrodes (with Pt catalyst) produced current densities of 75-100 mA/cm^2. Their disadvantage was that for each kW-hr of actual fuel cell operation on air 45g of nitric acid were needed, thus indicating that regeneration was incomplete. Attempts to use the Ce(IV)/Ce(III) redox couple rather than nitric acid were also unsuccessful (153).

Biochemical cells.—The term "bio-electrode" is used to describe an electrode where a microorganism is grown in, or in the immediate vicinity of, the electrode structure. A typical bioanode, for example, could use glucose as feed stock which would then be converted by enzymes (via several intermediate compounds) to ethanol. In the biofuel cell, alcohol is then directly oxidized to CO_2 and H_2O. The cathode may also be a biocathode where, for example, CO_2 can be converted to methane by a methanobacillus. Cells using biological waste products (H_2S, NH_3, alcohols) are called indirect biofuel cells; the electrochemical mechanism is separate from the biological metabolism.

Large efforts were made in the mid-1960's to construct fuel cells along biological principles or in the conventional ways but using waste products. The U.S. Army sponsored contracts with Electric Autolite Company, Magna Corporation, Melpar, Incorporated, Philco Corporation, and the Marquart Corporation over several years (154, 155), wherein final emphasis was placed on indirect systems using fermentation systems as fuel sources. The use of photosynthesis in algae as an oxygen producer is described by Vielstich (156). A magnesium/sulfate biocell was actually built by the Magna Corporation for the U.S. Navy (157). However, difficulties arose due to the low current densities (~1 mA/cm^2) and the side products which, with time, damaged the electrodes.

The use of solar energy for production of biomass may some day bring fuel cell conversion schemes back into the technology.

Direct hydrocarbon cells.—Unfortunately, hydrocarbon fuels are relatively inactive on anodes when compared with hydrogen, hydrazine, or alcohols. M. J. Schlatter at California Research Corporation (158) found early in 1960 that some small current could be drawn from a platinized porous carbon electrode when it was exposed to ethylene or propane and that complete oxidation to CO_2 occurred. Similar reports appeared at that time from other laboratories; W. T. Grubb at General Electric Company (159) and C. E. Heath and co-workers at Esso Research and Engineering (160) oxidized saturated hydrocarbons at platinum electrodes. These findings caused a high number of publications and resulted in a rush to study and develop low temperature hydrocarbon electrodes. Many U.S. Government contracts were initiated and efforts were made to eliminate, or at least reduce, the noble metal catalyst requirements (161).

Space permits only a very few significant contributions to the literature to be named. M. W. Breiter and S. Gilman (162) studied the adsorption of methanol, carbon monoxide, and hydrogen extensively, and new techniques for the study of electrodes by pulsing methods were developed. Electrochemical processes were treated from the standpoint of theoretical electrochemistry (163). H. Binder and co-workers (164) at the Battelle Institut, Frankfurt/M, concentrated on the behavior of noble metal (Raney) catalysts and compared performances in acidic and alkaline electrolytes, Robert Bosch, GmbH in Germany sponsored this work over many years.

An extensive study of hydrocarbon oxidation by-products, especially of the olefins, was published by M. J. Schlatter in 1965. Poisoning of the paraffin electrodes by air or oxygen was reported (165). Still, a hopeful note was taken by H. A. Liebhafsky in his book (B-6) in 1968, expressing the findings that, indeed, CO_2 and water were the only reaction products. However, short lifetimes were the rule with hydrocarbon cells operating at low temperatures (90°C). Raising the temperature to 140°C and using phosphoric acid as the electrolyte improved the current density (0.6V, 50 mA/cm^2), but the problems with irreversible adsorption of oxidized species remained. S. B. Brummer and co-workers at Tyco Laboratories (166) and J. Giner (167) studied octane of extraordinary purity in this respect and used special circuits for potential-step pretreatments of the electrodes.

The platinum-"Teflon" electrodes used were essentially those of W. T. Grubb and L. W. Niedrach (168) and contained platinum blacks. Supported noble metal catalysts and special reduction treatments with borohydride were introduced by the researchers at American Cyanamid Company (169). E. J. Cairns (170) at General Electric experimented with CsF-HF-H_2O electrolytes and obtained up to 200 mA/cm^2 at 150°C with propane. Very thin cells using inorganic membranes (171) as catalyst carriers were also tested for hydrocarbon operation with the hope of achieving better life by reducing cross-leakage.

Indirect hydrocarbon cells.—The use of steam reforming for hydrogen production to supply the anodes of H_2-air (or oxygen) fuel cells became the only way to use hydrocarbons with the expectation of achieving long life for the fuel cell; this was dictated by the high cost of noble metal-rich electrodes. The military contracted for several models of reformers: small portable units using oxidative cracking (172-174) and a multitude of larger units for multikilowatt batteries (175). Figure 12 is a schematic diagram of such a converter/fuel cell system.

Alkaline cells need careful CO_2 scrubbing, while acidic cells needed more platinum as catalyst. Work

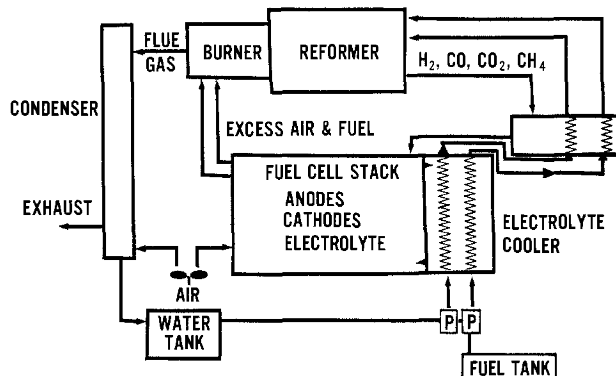

Fig. 12. Schematic diagram of a converter/fuel cell system

on hydrogen generator designs was carried on quite extensively at the Institute of Gas Technology (176, 177). Pratt & Whitney Aircraft designed a 500W hydrocarbon system (178) and Allis-Chalmers delivered a 5 kW hydrocarbon-air system for the U.S. Army (179). Both systems used alkaline electrolytes, and they were the last ones of this type; in a later 1.5 kW system, immobilized phosphoric acid was used exclusively as the electrolyte (180). Esso Research and Engineering (181) studied an acidic indirect system for the U.S. Army, with the goal to utilize octane and JP-4 fuel; 50 mg Pt was used per cm^2 of electrodes! In England, Shell Research, Limited extended the methanol-reformer work to hydrocarbon systems; exceptionally long lifetimes (15,000 hr) were reported (182). The fuel electrodes were hydrogen electrodes and operated in sulfuric acid.

The long lifetimes achieved with pure hydrogen led many researchers to use the Pd-diffusion membranes as a separation means (183). In the article "Internal Reforming Cells," the Pd-Ag membrane was a part of the electrode (184). Very recent work centered on the use of special electrolytes (replacing the phosphoric acid) to accelerate the hydrocarbon reaction. Promising results were obtained with trifluoromethyl sulfonic acid (185) as electrolyte. However, the consensus of opinion of the catalyst specialists is that direct hydrocarbon oxidation is far from practical utilization. The methanol oxidation in acidic or alkaline cells seems to be a far easier way to use the energy stored in coal (186).

It may be significant that the U.S. Army resumed the study of the feasibility of using Kipp-type generators as the hydrogen supply means; at least for small units (30W), the use of metal hydrides seems to be advantageous (187).

Outlook for the Next 25 Years

On the basis of past historic development of fuel cells, it could be predicted that a new wave of fuel cell developments would be starting today. The papers at The Electrochemical Society meetings, Fall 1975 and Spring 1977, and the special session on fuel cells for Fall 1977, show this renewed interest.

The key question is economy. Stationary fuel cell power plants have a better chance of succeeding than mobile vehicular fuel cell batteries, simply on the basis of the maximum dollars per kW which can be spent by the consumer, be it a utility company or the motorist driving an electric car. However, the bigger impact on society would be the fuel cell-operated vehicle with a conversion efficiency of probably 40%.

The technology of fuel cells has not been supported by basic scientific studies to the extent that we can explain catalyst action or even predict ways to improve electrode kinetics beyond the routine methods of engineering and design optimization; *i.e.* making electrodes more conductive, thinner, more repellent, reducing pressure differentials, etc. Hopefully this will change and, with better understanding of the principles, unpredicted improvements may take place, perhaps paralleling the progress of solid-state science over the last decades. This is partly a matter of attracting enthusiastic young scientists to the field—an obligation to be shared by the educational system and industry alike. With growing interest in efficient energy conversion, fuel cells should be the center of attention.

BIBLIOGRAPHY

1. "Fuel Cells," G. T. Young, Editor, Rheinhold Publishing, New York. Vol. 1: Symposium of Am. Chem. Soc., 1959 (1960); Vol. 2: Symposium of Am. Chem. Soc., 1961 (1963).
2. "Fuel Cells," W. Mitchell, Jr., Editor, Academic Press, New York (1963).
3. "Handbook of Fuel Cell Technology," C. Berger, Editor, Prentice-Hall, Englewood Cliffs, New Jersey (1968).
4. E. W. Justi and A. W. Winsel, "Kalte Verbrennung-Fuel Cells," Franz Steiner Verlag, Wiesbaden (1962); English Translation, Pergamon, New York (1965).
5. W. Vielstich, "Brennstoffelemente-Fuel Cells," Verlag Chemie, Weinheim/Bergstr. (1965); English translation, John Wiley & Sons, London (1970).
6. H. A. Liebhafsky and E. J. Cairns, "Fuel Cells and Fuel Batteries," John Wiley & Sons, New York, (1968).
7. "Hydrocarbon Fuel Cell Technology," B. S. Baker, Editor, Academic Press, New York (1965).
8. "Fuel Cell Systems," R. F. Gould, Editor, Advances in Chemistry Series 47, Am. Chem. Soc., Washington (1965).
9. "Fuel Cell. Systems II," R. F. Gould, Editor, Advances in Chemistry Series 90, Am. Chem. Soc., Washington (1969).
10. J. O'M. Bockris and S. Srinivasan, "Fuel Cells, Their Electrochemistry," McGraw-Hill, New York (1969).
11. L. G. Austin, "Fuel Cells, A Review of Government-Sponsored Research, 1950-1964," NASA SP-120, Office of Technology Utilization, Washington (1967).
12. A. B. Hart and G. J. Womak, "Fuel Cells," Chapman & Hall, London (1967).
13. "Les Piles à Combustible, O. Block, Editor, Publications de l'Institut Francais du Petrole, Collection No. 6, Editions Technip. Paris (1965).
14. United States Army Electronics Laboratory, Washington, D.C., "Status Reports on Fuel Cells," 1st, by B. R. Stein (1959); 2nd, by B. R. Stein and E. M. Cohen (1960); 3rd, by H. F. Hunger *et al.* (1962); 4th, by F. R. Franke and H. F. Hunger (1962); 5th, by S. J. Bartosh *et al.* (1965); 6th, by G. R. Frysinger *et al.*, Final, (1967). (Reports 3-6 were published by the U.S. Army Electronics Command, Fort Monmouth, N.J.)
15. "From Electrocatalysis to Fuel Cells," G. Sandstede, Editor, Battelle Seattle Research Center, Univ. of Washington Press, Seattle (1972).
16. United States Army, Proceedings, 1956-1976; 10th-12th Annual, Research & Development Conferences, Signal Corps Engineering Laboratories (1956-1958); 13th-22nd Annual Power Sources Conference, U.S. Army Signal Research & Development Laboratories, Ft. Monmouth, N.J., (1959-1968); 23rd Power Sources Conference (1969) and 24th Power Sources Symposium (1970), PSC Publication Committee, Red Bank, N.J.; 25th-27th Biennial Power Sources Symposium, PSC Publication Committee, Red Bank, N.J. (1972, 1974, 1976).
17. D. H. Collins, Editor, Biennial Proceedings, 1962-1976, Joint Services of the Electrical Power Sources Committee; "Batteries," 3rd Symposium Bournemouth (1962), Pergamon, New York (1963); "Batteries II," 4th Symposium Brighton (1964), Pergamon, New York (1965); "Power Sources 1," Brighton (1966), Pergamon, New York (1967); "Power Sources 2," Brighton (1968) Pergamon, New York (1969); "Power Sources 3," Brighton (1970), Oriel, New Castle upon Tyne, (1971); "Power Sources 4," Brighton (1972), Oriel, New Castle upon Tyne (1973); Power Sources 5," Brighton (1974), Academic, New York (1975); "Power Sources 6," Brighton (1976) Academic, New York (1977).
18. ECS Fuel Cell Symposia, Extended Abstracts, Electrochemical Society Battery Division, October 1961, Detroit; October 1962, Boston; October 1963. New York; October 1964, Washington, D.C.; October 1966, Philadelphia; October 1968, Montreal; October 1970, Atlantic City.
19. I.E.C.E.C., Proceedings of Intersociety Energy Conversion Engineering Conferences (published by the host organization of the particular year: 1st, Los Angeles, Calif. (1966); 2nd, Miami Beach, Fla. (1967); 3rd, Boulder, Colo. (1968); 4th, Washington, D.C., 1969 (Index 66-69); 5th, Las Vegas, Nev. (1970); 6th, Boston, Mass. (1971); 7th, San Diego (1972); 8th, Philadelphia, Pa. (1973); 9th, San Francisco (1974); 10th, Newark, Del. (1975); 11th, State Line, Nev., Vol. I and II (1976).
20. C.I.T.C.E. Proceedings of the Comité International de Thermodynamique et de Cinétique Electrochimiques [named I.S.E. (International Society

for Electrochemistry) from 1971 on]: 1959 (11th) Vienna, 1960 (no meeting), 1961 (12th) Brüssels, 1962 (13th) Rome, 1963 (14th) Moscow, 1964 (15th) London-Cambridge, 1965 (16th) Budapest, 1966 (17th) Tokyo, 1967 (18th) Schloss Elmau (no Fuel Cells), 1968 (19th) Detroit, 1969 (20th) Strasbourg, 1970 (21st) Prague, 1971 (22nd) Dubrovnik (no Fuel Cells), (23rd) Stockholm, 1972 (24th) Munich, 1973; (25th), Brighton, 1974; (26th) Hague, 1975; (27th) Zurich, 1976; (28th) Varna, 1977.
21. Proceedings of the Battery Technology Symposia of the Southern California-Nevada Section of the Electrochemical Society; 1st, 1965; continued annually; 6th Symposium, 1970.
22. Société d'Etude de recherches et d'applications (S.E.R.A.I.) and COMASCI, International Symposia on Fuel Cells, Brussels, June 1965; June 1967; June 1969. Proceedings (1969) published by Presses Academiques Europeennes, Bruxelles, Belgium (1969).
23. K. V. Kordesch, in "Modern Aspects of Electrochemistry," Vol. 10, J. O'M. Bockris and B. E. Conway, Editor, pp. 339-443, Plenum Press, New York (1975).
24. M. W. Breiter, "Electrochemical Processes in Fuel Cells," Springer Verlag, New York (1969).
25. "Electrode Processes," E. Yeager, Editor, 1st Conference (1959), 2nd Conference (1966), Electrochemical Society Publications.
26. "Toplivne Elementy," (Fuel Cells), V. S. Bagotskii and Yu B. Vasil'ev Editors, Academy of Sciences of the USSR, Moscow (1964). English Translation, Consultants Bureau, New York (1966).
27. "Proceedings of the International Fuel Symposium, K. Schwabe and E. Winkler, Editors, Dresden (1967); Vol. 49, Abh. d. Sächs. Akad. d. Wiss., Leipsiz, Academic Verlag, Berlin (1968).
28. "Brennstoffelemente," Vol. 6, H. H. v. Döhren and K. J. Euler, Editors, Varta Fachbuchreihe, VDI Verlag, Düsseldorf (1961).
29. K. R. Williams, "An Introduction to Fuel Cells," Elsevier Publ., Amsterdam (1966).
30. National Fuel Cell Seminar Abstracts, June 21-23, 1977, Boston, Dynatrend Inc. (1977).
31. "Fuel Cells, a Bibliography," TID-3359, U.S. Energy Research & Dev. Adm. (1977).
32. Proceedings of the Symposium on "Power Systems for Electric Vehicles," U.S. Dept. of Health, Education, and Welfare, Columbia University and Polytechnic, Inst. of Brooklyn, April 1967, in Public Health Service Publication No. 999-AP-37 (1967).
33. Proceedings of the Fuel Cell Symposia, New Orleans, La., March 1963 and in Buffalo, N.Y., May 1963, American Inst. of Chemical Engineers, in CEP-Manual: "Fuel Cells," by AIChE, New York (1963).

REFERENCES[3]

1. NEMA Standard, Publ. No. CV 1-1968, National Electrical Mfgs. Assoc., New York (1968).
2. W. Ostwald, *Z. Elektrochem.*, **1**, 122 (1894).
3. W. R. Grove, *Philos. Mag.*, No. 3, **14**, 127 (1839).
4. E. Baur and J. Tobler, *Z. Elektrochem.*, **36**, 169 (1933).
5. O. K. Davtyan, *Bull. Acad. Sci. USSR, Sci. Technol.*, **107**, 125 (1946).
6. G. H. J. Broers, Ph. D. Thesis, University of Amsterdam, Netherlands (1958).
7. H. H. Chambers and A. D. S. Tantram, in B-1, Vol. 1, pp. 94-108.
8. F. T. Bacon, *BEAMA J.*, **6**, 61 (1954).
9. K. Kordesch and A. Marko, *Oesterr. Chem. Ztg.*, **52**, 125 (1951).
10. K. Bishoff and E. Justi, *Jahrb. Akad. Wiss. Lit. (Mainz)*, 250 (1955).
11. Battelle Memorial Institute, Final Report to the Fuel Cell Research Group, Columbus Laboratories (1965).
12. K. V. Kordesch, Paper presented at the 23rd Meeting, Internat. Soc. of Electrochem., Stockholm, Sweden (1972).
13. E. Gorin and H. L. Recht, in B-1, pp. 109-128.
14. Pittsburgh Consolidation Coal Co., Contract DA-36-039-63090, USAERDL, New Jersey (1954-1957); Final Report, No. 12 (1957).
15. Central Technical Institute, Contract DA-91-591-EUC-1023, USDA/ERO (1/59-12/59); M. Schenke, Contract DA-91-591-EUC-1398, USDA/ERO (11/60-1/61), The Hague, Netherlands.
16. G. H. J. Broers and M. Schenke, in B-7, pp. 225-250.
17. G. H. J. Broers and H. J. J. Van Ballegay, B-22 pp. 77-86 (1969).
18. Texas Instruments, Inc., Contract DA-44-009-AMC-54(T), USAERDL/Va. 2/63-2/64.
19. I. Trachtenberg, in B-7, pp. 251-265.
20. I. Trachtenberg and D. F. Cole, in B9, pp. 269-280.
21. B. S. Baker, L. G. Marianowski, J. Zimmer, and G. Price, in B-7, pp. 293-307.
22. D. L. Douglas, in B-1, Vol. I, pp. 129-149.
23. M. L. Kronenberg, *This Journal*, **109**, 753 (1962).
24. A. D. S. Tantram, in B-7, pp. 187-212.
25. A. D. S. Tantram, in B-18, pp. 332-339 (1967).
26. A. Salvadori, in B-7, pp. 267-283.
27. J. Millet and R. Buvet, *ibid.*, pp. 285-292.
28. B-13
29. A. Fickett, *EPRI J.*, No. 4, 14 (1976).
30. J. Weissbart and R. Ruka, in B-1, Vol. 2, pp. 37-49.
31. Westinghouse Electric Corp., Contract AF33(657)-8251 (2/62-3/63), USAF/WP, Final Report ADS TDR-63-448 (7/63).
32. D. H. Archer, R. L. Zahradnik, E. F. Sverdrup, W. A. English, L. Elikan, and J. J. Allen, in B-16, pp. 36-40 (1964).
33. R. L. Zahradnik, L. Elikan, and D. H. Archer, in B-8, pp. 343-355.
34. E. F. Sverdrup, D. H. Archer, and A. D. Glasser, in B-9, pp. 301-314.
35. E. F. Sverdrup, C. J. Warde, and A. D. Glasser, in B-15, pp. 255-277.
36. H. T. Böhme and F. J. Rohr, in B-22, pp. 120-124 (1969); H. Eysel and H. Kleinschmager, *ibid.*, pp. 92-96 (1969).
37. W. Baukal, in B-15, pp. 247-254.
38. H. Tannenberger and H. Siegert, in B-9, pp. 281-300.
39. C. Deportes and J. Bessen, B-22, pp. 354, 368, 411 (1967).
40. T. Takahashi, H. Iwahara, and Y. Suzuki, pp. 113-119 (1969).
41. S. F. Pal'guev *et al.*, *Doklady Akad. Nauk, USSR*, **134**, 1138 (1960).
42. W. E. Tragert, U.S. Pat. 3,310,433 (1967).
43. C. J. Warde, R. J. Ruka, and A. O. Isenberg, NASA-N76-23703, Westinghouse Phase I Final Report, Vol. XII-Fuel Cells, pp. 13, 74, 86 (1976).
44. Leesona Corp., Contract AF33(600)-34709 (2/57-2/62), USAF/WPAFB.
45. Pratt & Whitney Aircraft, B-11, pp. 113-116.
46. C. C. Morrill, B-16, pp. 38-41 (1965).
47. K. Kordesch, in B-1, Vol. 1, pp. 11-22.
48. K. V. Kordesch, in B-2, pp. 329-370.
49. Union Carbide Corp., Contract DA-36-039-SC-78367 (7/60-8/63), USAERDL/N. J.
50. Union Carbide Corp., Contract NObs-78633 (6/60-3/64), USN/BuShips.
51. Union Carbide Corp., Contract AF33(616)-7256, SA/5, USAF/WP, (4/61-2/63).
52. K. V. Kordesch, in B-3, pp. 361-421.
53. Union Carbide Corp., Contract DA-36-039-AMC-02314 (E), USAERDL/N.J., (5/63-5/66).
54. L. M. Litz and K. V. Kordesch, in B-8, pp. 166-187.
55. The "Electrovan," Society of Automotive Engineers, Paper No. 670176, 670181, and 670182, presented at the SAE Congress, Detroit (1967).
56. K. V. Kordesch, *This Journal*, **118**, 815 (1971).
57. R. J. Elbert, U.S. Pat. 3,556,856 (1971).
58. K. V. Kordesch and S. J. Cieszewski, in B-17, pp. 249-258 (1977).
59. R. G. Haldeman, W. P. Colman, S. H. Langer, and W. A. Barber, in B-8, pp. 106-115.
60. American Cyanamid Co., Contract NAS3-2786, NASA/Lewis, (from 10/1963 onward).
61. General Electric Co. Contract NObs-86380, USN/BuShips, (11/61-9/63).
62. H. A. Liebhafsky, E. J. Cairns, W. T. Grubb, and L. W. Niedrach, in B-8, pp. 116-140.
63. Engelhard Industries, Contract DA-36-039-SC-85043, (6/60-6/62) USAERDL/N.J. (1962).
64. E. Justi and A. Winsel, B-4 (1962).
65. E. Justi, A. Winsel, and W. Scheibe, DBP 1019361 (1954).

[3] **Note: The letter "B" stands for Bibliography.**

66. H. H. von Döhren and K. J. Euler, Varta Fachbuchreihe, Bd. 6, Brennstoff-elemente, VDI-Verlag, Düsseldorf (1971).
67. R. Wendtland and A. Winsel, *Chem. Ing. Technik*, **39**, 756 (1967).
68. H. Cnobloch, M. Marchetto, H. Nischik, G. Richter, and F. v. Sturm, in B-18, pp. 203-209 (1969).
69. A. Michel and W. Frie, Paper No. 7452 presented at the Third International Electric Vehicle Symposium, Washington, D.C. (1974).
70. H. Cnobloch, G. Siemsen, and V. v. Sturm, in B-17, pp. 311-325 (1972).
71. H. Cnobloch, D. Gröppee, D. Kühl, W. Nippe, and G. Siemsen, in B-17, pp. 261-282 (1974).
72. R. A. Wynveen, in B-2, pp. 389-431.
73. Allis-Chalmers Manuf. Co., Contract DA-49-186-502-ORD-1057, HDL, (12/61-8/64).
74. Allis-Chalmers Manuf. Co., Contract NAS8-2696 (5/62-3/65), NASA/Marshall.
75. Allis-Chalmers Manuf. Co., Contracts AF33(657)-8970 (3/62-3/64) and AF33(615)-1185 (11/63-1/65), USAF/WPAFB.
76. J. L. Platner, D. Ghere, and P. Heiss, in B-16, pp. 32-35 (1965).
77. R. T. Jasinski, in B-8, pp. 95-105.
78. J. E. Shroeder, D. Pouli, and H. J. Seim, in B-9, pp. 93-101.
79. T. G. Kirkland and W. G. Smoke Jr., in B-16, pp. 26-37 (1965).
80. W. Vielstich, B-5, p. 373.
81. O. Lindström, in B-9, pp. 24-40.
82. P. Ruetschi *et al.*, in B-17 (1963); also in B-4, pp. 374-383.
83. J. Jacquelin and J. P. Pompon, in B-18, pp. 47-52 (1969); see also B-13.
84. F. A. Pohl and H. Böhm, in B-18 pp. 180-186 (1969).
85. K. v. Benda, H. Binder, A. Köhling, and G. Sundstede, in B-15, pp. 87-100.
86. General Electric Co. Contract NObsr-77620 (5/59-6/61), USN/BuShips.
87. B-6, pp. 587-619.
88. General Electric Co., Contract DA-36-039-AMC-00095 (E) (10/62-11/64), USAERDL/Belvoir.
89. J. H. Russel, in B-16, pp. 35-38 (1963).
90. H. A. Liebhafsky and E. J. Cairns, B-6.
91. General Electric Co., Contract NAS-9-12332, SPR-113, Lyndon B. Johnson Space Center, R&D Branch, Houston (1973).
92. Assessment Study of Devices for the Generation of Electricity from Stored Hydrogen, Final Report, Aug. 1975; Chem. Engr. Div., Argonne National Lab., Argonne, Ill. 60439.
93. O. J. Adlhart and A. J. Hartner, in B-16, pp. 4-6 (1967).
94. O. J. Adlhart, in B-16, pp. 182-185 (1970).
95. W. Vogel, J. Lundquist, and A. Bradford, *Electrochim. Acta*, **17**, 1735 (1972).
96. W. Vogel, J. Lundquist, P. Ross, and P. Stonehart, *ibid.*, **20**, 79 (1975).
97. K. V. Kordesch and R. F. Scarr, in B-19, pp. 12-19 (1972).
98. Contract DAAK02-71-C-0297, U.S. Army Mobility Equip. R&D Center, Ft. Belvoir, 4th and Final Report (1973).
99. P. N. Ross and P. Stonehart, *J. Res. Inst. Catalysis, Hokkaido Univ.*, **22**, **1** (1974).
100. M. V. Burlingame, in B-9, pp. 377-832.
101. ERDA-76-4, National Benefits Associated with Commercial Application of Fuel Cell Power Plants, United Technologies Corp., Power Systems Div. (1976).
102. Esso Research and Engineering Co. Contracts DA-36-039-SC-89156 (1/62-12/61) and AMC-00134 (E) (1/63-12/63), USAERDL/N.J.; see also B-16, pp. 41-43 (1965).
103. A. J. Adlhart, DA-36-039-SC-90691 (6/62-4/63), USAERDL/N.J. (1963).
104. E. J. Cairns and D. C. Bartosik, *This Journal*, **111**, 1205 (1964).
105. K. R. Williams, M. R. Andrew, and F. Jones, in B-7, pp. 143-149.
106. K. R. Williams and D. P. Gregory, *This Journal*, **110**, 209 (1963).
107. S. Gilman and M. H. Breiter, *ibid.*, **109**, 622, 1099 (1962).
108. W. Vielstich, *Chem.-Ing.-Tech.*, **35**, 362 (1963).
109. E. W. Justi and A. Winsel, B-4, pp. 240-245 (1962).
110. W. Vielstich and U. Vogel, in B-9, pp. 341-353.
111. C. H. Haman and P. Schmode, in B-16, pp. 175-177 (1975).
112. E. W. Justi and A. Winsel, B-4, pp. 370-372 (1962).
113. S. S. Tompter and A. P. Anthony, in "Fuel Cells," CEP Tech. Manual, A.I.Ch.E., New York (1963).
114. P. G. Grimes and H. H. Spengler, in B-7, pp. 121-130.
115. R. R. Biddick and D. L. Douglas, in B-7, pp. 131-142.
116. N. I. Palmer, B. Lieberman, and M. A. Vertes, in B-7, pp. 151-167.
117. E. G. Doying and A. Ray, Union Carbide and Carbon Res. Labs., Inc., selected archive data (12 24/30-2/28/31), Long Island City, N.Y. (1931).
118. M. Eisenberg, in B-16, pp. 97-98 (1963).
119. M. I. Gillibrand and G. R. Lomax, in B-17, p. 221 (1963).
120. R. J. Jasinski, *Electrochem. Technol.*, **3**, 129 (1965).
121. Monsanto Research Corp. Contract DA-28-043-AMC-01460(E), USAECOM, Fort Monmouth; B-16, pp. 39-41 (1966).
122. E. A. Gillis, in B-16, pp. 41-45 (1966).
123. G. E. Evans, in B-16, pp. 1-6 (1968).
124. G. G. Fee and E. Storto, in B-16, pp. 8-10 (1969).
125. R. E. Salathe, R. L. Sampson, W. A. Holmes, J. P. Gallagher, J. O. Smith, P. Dantowitz, D. Whitehouse, and J. Kozloff, in B-16, pp. 6-10 (1968).
126. J. Perry, Jr., in B-16, pp. 10-12 (1968).
127. K. V. Kordesch, in "Modern Aspects of Electrochemistry," Vol. 10, J. O'M. Bockris and B. E. Conway, Editors, p. 398, Plenum Press, New York (1975).
128. B-16; Papers by: F. G. Perkins, U.S. Army, pp. 202-204; R. E. Salathe, Whitley Hydraulics, Inc., pp. 204-207; K. V. Kordesch and M. B. Clark, Union Carbide Corp., pp. 207-210; L. C. Hymes, J. E. Ward, and G. L. Reed, Allis Chalmers, pp. 210-213 (1970).
129. W. Vielstich, *Angew. Chem., Int. Ed. Engl.*, **13**, 683 (1974).
130. J. Jindra, M. Svata, and J. Mrha, in B-17, pp. 505-519 (1968).
131. K. Schwabe and E. Wiedner, in B-22, pp. 292-295 (1967).
132. W. Wiesener, in B-22, pp. 215-219 (1969).
133. N. V. Korovin, A. G. Kitcheev, and N. S. Lidorenko, in B-18, pp. 73-76 (1969).
134. B. Warszawski, in B-22, pp. 109-117 (1967).
135. M. Yamano and H. Ikeda, in B-7, pp. 169-184.
136. R. A. Wynveen, in B-1, Vol. 2, pp. 153-167.
137. W. Vielstich and U. Vogel, *Chem.-Ing.-Technol.*, **43**, 195 (1971).
138. E. Yeager, in B-2, pp. 300-328.
139. M. W. Kellogg Co. Contract NObs-78461, USN/BuShips (12/58-6/63) (1963).
140. W. H. Podolny, in B-16, pp. 64-67 (1960).
141. J. S. Bone, S. Gilman, L. W. Niedrach, and M. D. Read, in B-16, pp. 47-50 (1961).
142. E. Findl and M. Klein, in B-16, pp. 49-52 (1966).
143. E. Justi and A. Winsel, B-4, pp. 253-259 (1962).
144. R. C. Werner, R. E. Shearer, and T. A. Ciarlariello, in B-16, pp. 122-124 (1959).
145. H. Silverman, W. R. Momyer, and M. Eisenberg, in B-16, pp. 53-58 (1961).
146. M. E. Lasser, S. Zaromb, and F. Kalhammer, in B-16, pp. 66-68 (1960).
147. J. F. Yeager, R. J. Bennett, and D. R. Allenson, in B-16, p. 39 (1962).
148. W. N. Carson, Jr. and M. L. Feldman, in B-16, pp. 111-113 (1959).
149. A. M. Posner, *Fuel*, **34**, 330 (1955).
150. L. H. Thaller, 9th Intersociety Energy Convention Engineering Conference, New York, Am. Soc. of Mech. Engr., p. 924 (1974).
151. M. A. Reid and R. F. Gahn, Paper 357 presented at The Electrochemical Society Meeting, Philadelphia, Pennsylvania, May 8-13, 1977.
152. J. A. Shropshire and B. A. Tarmy, in B-8, pp. 153-165.
153. B. R. Stein, in B-14, pp. 60-62 (1959).
154. B-16, Session on Biochemical Fuel Cells, pp. 53-64 (1963).
155. J. Perry, Jr. and J. Cristopulos, B-16, pp. 19-23 (1965).
156. W. Vielstich, B-5, p. 279.
157. G. H. Rohrback, W. R. Scott, and J. M. Canfield, in B-16, p. 16 (1962).
158. M. J. Schlatter, in B-1, Vol. 2, pp. 190-215.
159. W. T. Grubb, in B-16, pp. 69-72 (1963).

160. C. E. Heath and C. H. Worsham, in B-1, Vol. 2, pp. 182-189.
161. General Electric Co., Contracts DA-44-009-ENG-4853 (1/61-11/62); ENG-4909 (1/62-6/64); DA-44-009-AMC-479 (T) (6/64-12/66), USAER-DL/Va.
162. M. W. Breiter and S. Gilman, *This Journal,* **109**, 662 (1962).
163. B-20.
164. H. Binder, A. Köhling, H. Krupp, K. Richter, and G. Sandstede, in B-15, pp. 269-282, 283-291.
165. M. J. Schlatter, in B-8, pp. 292-317 (1965).
166. S. B. Brummer, in B-9, pp. 223-230.
167. J. Giner, *This Journal*, **111**, 376 (1964).
168. W. G. Grubb and L. W. Niedrach, *ibid.*, **110**, 1086 (1963).
169. J. D. Voorhies, J. S. Mayell, and H. P. Landi, in B-7, pp. 455-461.
170. E. J. Cairns, in B-7, pp. 465-484.
171. C. Berger and M. P. Strier, in B-7, pp. 485-494.
172. J. E. Rothfleisch and L. M. Litz, B-16, pp. 28-30 (1966).
173. M. A. Callahan and E. G. Starkowich, B-16, pp. 169-172 (1972).
174. R. E. Engdahl, E. S. Tillman, and J. S. Johnstone, B-16, pp. 165-169 (1972).
175. G. R. Frysinger, in B-7, pp. 9-15.
176. J. Meek, B. S. Baker, and A. C. Allen, in B-7, pp. 25-37.
177. J. Meek and B. S. Baker, in B-8, pp. 221-231.
178. S. J. Bartosh, B-16, pp. 31-35 (1966).
179. T. G. Kirkland, B-16, pp. 35-39 (1966).
180. E. A. Gillis, B-16, pp. 159-162 (1972).
181. E. H. Okrent and C. E. Heath, in B-9, pp. 328-340.
182 K. R. Williams and A. G. Dixon, in B-9, pp. 336-376.
183. D. P. Gregory and H. Heilbronner, in B-7, pp. 509-523.
184. W. R. Alcorn and H. G. Oswin, in B-9, pp. 41-59.
185. A. A. Adams, R. T. Foley, R. V. Lawson, and G. W. Walker, Paper 49 presented at The Electrochemical Society Meeting, Dallas, Texas, October 5-9, 1975.
186. S. Brummer, in Proceedings of the Fuel Cell Catalysis Workshop, Electric Power Research Inst., pp. 131-134 (1975).
187. M. Onischak and B. S. Baker, B-16, pp. 178-181 (1974).

JOURNAL OF THE ELECTROCHEMICAL SOCIETY

ELECTROCHEMICAL SCIENCE
—AND TECHNOLOGY

MAY
1978

The Electrical Conductivity of β-PbF_2

Wei-Chou Fang*,[1] **and Robert A. Rapp****

Department of Metallurgical Engineering, The Ohio State University, Columbus, Ohio 43210

ABSTRACT

The electrolytic properties of pure β-PbF_2 were studied by a-c conductivity measurements and Hebb-Wagner d-c polarization experiments as a function of fluorine pressure and temperature. The partial ionic and electronic conductivities of β-PbF_2 were determined over a range of fluorine pressure and temperature. Because of the introduction of p-type electronic conduction, the electrolytic domain of β-PbF_2 is truncated at high values of P_{F_2}, with $P_{F_2} = 10^{-21}$ atm at 492°C. At low P_{F_2}, predominant ionic conduction extends to P_{F_2} for the coexistence of Pb and PbF_2.

The electrolytic properties of nominally pure and doped β-PbF_2 and α-PbF_2 have been extensively investigated recently (1-16). Bonne and Schoonman (13) calculated the temperature dependences of the concentrations and mobilities of the interstitial fluoride ions and anion vacancies based on their a-c conductivity measurements of pure and doped β-PbF_2 and existing literature data. Their results indicated that interstitial fluoride ions are the principal mobile species in pure β-PbF_2 for temperatures greater than 300°C. Hebb-Wagner polarization experiments have also been conducted by many authors to elucidate the electronic conductivity in PbF_2. Kennedy *et al.* (4) reported that the electronic conductivity of pure β-PbF_2 at 150°C was p-type. At 25°C Kennedy and Miles (12) could not specify whether the electronic current in β-PbF_2 was carried by electrons or holes. Benz (10) found that pure β-PbF_2 was essentially an n-type conductor from 400° to 600°C. Schoonman *et al.* (8) also found an n-type conductor for pure β-PbF_2 single crystal from 52° to 137°C. Joshi and Liang (9) reported that α-PbF_2 is a p-type conductor.

Both α-PbF_2 and β-PbF_2 are known to be predominant ionic conductors. To elucidate the ionic domain (17, 18) of PbF_2, the determination of the range of log P_{F_2} beyond which electronic conduction becomes appreciable is studied here. Previous studies did not include several well-defined fluorine activities in conductivity studies on PbF_2. The present study consists of measurements of the total a-c conductivity, together with the measurements of the partial conductivity for electrons and electron holes as a function of fluorine activity. These results define the limits for the electrolytic domain for PbF_2. Hebb-Wagner polarization studies of β-PbF_2 also clarify the controversial results regarding n-type conduction as the predominant electronic conduction mode.

D-C Polarization Study

The Hebb-Wagner d-c polarization experiment (19) was adopted for the present study of β-PbF_2. Consider the d-c polarization cell

inert electrode | PbF_2 | reversible (Me/MeF_2) electrode [I]

* Electrochemical Society Student Member.
** Electrochemical Society Active Member.
[1] Present address: General Electric Research and Development Center, Schenectady, New York 12391.
Key words: solid electrolytes, conduction, electrolytic domain.

A reversible electrode consisting of a more noble metal (Me) coexisting with its fluoride (MeF_2) provides a fixed and known P_{F_2} on one side of the cell. On the other side, a pure noble metal with low solubility for fluorine serves as an inert blocking electrode. The cell is subjected to various d-c potentials below the decomposition potential of PbF_2. If the right-hand reversible electrode is made negative, under the steady-state condition the ionic current is blocked and the steady-state polarization current i_∞ is then carried exclusively by electrons and electron holes according to the equation

$$i_\infty = i_\oplus + i_\ominus = \frac{RT}{FL}\{\sigma_\oplus{}^\circ [\exp(u) - 1] + \sigma_\ominus{}^\circ [1 - \exp(-u)]\} \quad [1]$$

where L is the cell constant (thickness/area), $\sigma_\oplus{}^\circ$ and $\sigma_\ominus{}^\circ$ are, respectively, the partial electron hole and electronic conductivities at the equilibrium fluorine activity of the reversible electrode and $u = EF/RT$, where E is the applied voltage, **F** is Faraday's constant, and R and T have their usual meaning. The details of the theory have been given elsewhere (19-21).

If the polarity of the applied voltage for cell (I) is reversed (positive reversible electrode), an equation similar to Eq. [1] can also be derived. The usual approach in polarization experiments by all the authors, except Patterson *et al.* (21), has been to assume the validity of Eq. [1] and then evaluate either $\sigma_\oplus{}^\circ$ or $\sigma_\ominus{}^\circ$ according to limiting cases given by Wagner (19, 20).

If the electrolyte is a predominant p-type electronic conductor, and $\exp(u) >> 1$, the equation for the current reduces to

$$i_\infty = i_\oplus = \frac{RT}{FL}\sigma_\oplus{}^\circ \exp(u) \quad [2]$$

An exponentially increasing current will be observed with increasing potential in a plot of i_∞ *vs.* E, while a linear relationship will be observed in a plot of log $(FL/RT)i_\infty$ *vs.* E. The value for the electron hole conductivity $\sigma_\oplus$ can then be calculated from the intercept of the latter plot.

If the electrolyte exhibits predominant n-type electronic conduction, Eq. [1] reduces to

$$i_\infty = i_\ominus = \frac{RT}{FL}\sigma_\ominus{}^\circ [1 - \exp(-u)] \quad [3]$$

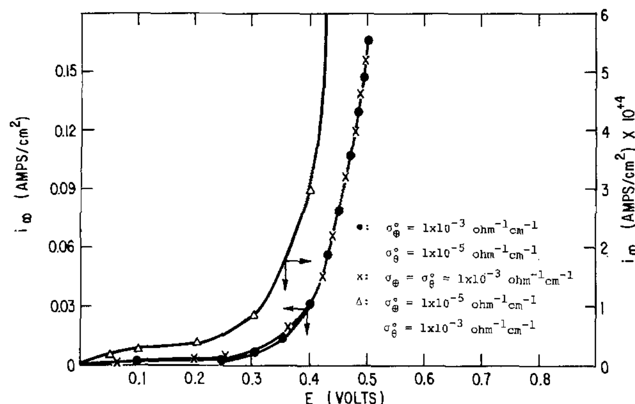

Fig. 1. Calculated i-E curves according to Eq. [1]. $L = 0.2\ cm^{-1}$, $T = 400°C$.

In plots of i_∞ vs. E, with increasing voltage, the current increases and tends to the saturation value. From the plot of log $(\mathbf{F}L/RT)i_\infty$ vs. E, the electronic conductivity can be calculated from the plateau current value which is $\sigma_\ominus°$.

Under certain conditions, the analysis of limiting cases can result in an erroneous conclusion. Figure 1 illustrates i-E plots for the complete Eq. [1] for three limiting cases. Each plot exhibits an apparent exponential curve when the applied voltage is above some value. Obviously, the decision between p- or n-type behavior based on the shape of the experimental plot is not reliable. An improved technique for analyzing polarization data was presented by Patterson *et al.* (21). Both sides of Eq. [1] may be divided by $[1 - \exp(-u)]$ or by $[\exp(u) - 1]$ to obtain

$$i_\infty/[1 - \exp(-u)] = \frac{RT}{\mathbf{F}L}[\sigma_\oplus° \exp(u) + \sigma_\ominus°] \quad [4]$$

or

$$i_\infty/[\exp(u) - 1] = \frac{RT}{\mathbf{F}L}[\sigma_\oplus° + \sigma_\ominus° \exp(-u)] \quad [5]$$

According to Eq. [5], a plot of $i_\infty/[\exp(u) - 1]$ vs. $\exp(-u)$ should give a straight line of slope $\frac{RT}{\mathbf{F}L}\sigma_\ominus°$ and intercept $\frac{RT}{\mathbf{F}L}\sigma_\oplus°$. Analogous equations can be obtained for a positive reversible electrode. Thus the values of both $\sigma_\oplus°$ and $\sigma_\ominus°$ can be simultaneously obtained from a single experimental run. The d-c polarization data in the present study were treated according to this method.

Experimental materials and procedures.—Cubic β-PbF_2 was made by heating the orthorhombic α-PbF_2 (99.99% pure) to over 500°C prior to each experimental run.

A-c conductivity measurements.—The various fluorine activities for a-c conductivity measurements were established through the double cell electrochemical arrangement shown in Fig. 2. The cell was comprised of two symmetrical cells with perforated platinum foils as fluorine gas electrodes contacting PbF_2. Reference electrodes were prepared from nickel-nickel fluoride-calcium fluoride mixtures in a volume ratio of approximately 6:2.5:2 and pressed in a 1.3 cm diam steel die. The calcium fluoride was added to eliminate electrode polarization. The electrolyte CaF_2 was prepared from pressed ultrapure calcium fluoride powder. The fluorine activity P_{F_2} at the platinum foils was fixed by the applied voltage E according to the relation

$$P_{F_2} = P_{F_2}° \ (Ni/NiF_2) \exp\frac{2E\mathbf{F}}{RT} \quad [6]$$

where $P_{F_2}°$ is the equilibrium fluorine pressure of the

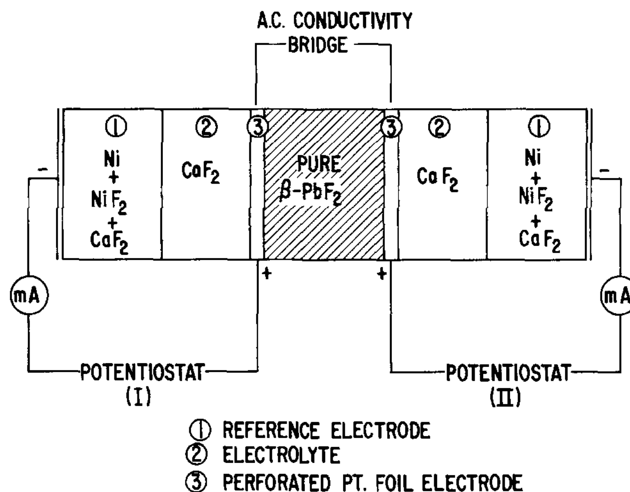

Fig. 2. Experimental cell to study the electrical conductivity of PbF_2.

reference electrode. Preliminary experiments showed that the actual P_{F_2} at the platinum electrodes was a linear function of the current through the cells which was monitored by a Keithley 153 microammeter. The current indicated the existence of a small steady-state fluorine ion discharge at the Pt/CaF_2 interface. This discharge resulted from fluorine escape through the bond between the CaF_2 electrolyte and the platinum foil. Because of the linear relation between the actual P_{F_2} and the cell current, a knowledge of the actual P_{F_2} at the platinum foils was possible. The applied voltages were provided from two potentiostats which were separately supplied with power to avoid an electrical ground loop between the two instruments. Measurements of the a-c conductivity at a frequency of 1592 Hz were made by the Wayne-Kerr Low Universal Bridge B211 which balances the sample conductance and capacitance against standards. When the conductance of a specimen was higher than 0.1 $\Omega^{-1}\ cm^{-1}$ a Wayne-Kerr Low Impedance Adaptor Q211 was used in conjunction with the bridge.

Hebb-Wagner d-c polarization measurements.—Figure 3 shows the cell arrangement for d-c polarization measurements. The reversible electrodes used for this cell were prepared from two-phase equilibrium mixtures of Cu/CuF_2 and Ni/NiF_2. Again, some CaF_2 was added to these mixtures to prevent polarization of the reversible electrode. The blocking electrode consisted of a Pt foil about 0.003 cm thick pressed against a vapor-deposited Au layer.

When Cu/CuF_2 mixtures were used as reversible electrodes at positive polarity, the applied voltages were kept below 640 mV (the difference in the standard Gibbs energies of formation for β-PbF_2 and CuF_2) to avoid the decomposition of PbF_2. On the other hand, for positive polarity at the blocking electrode, the applied voltage could be any value which would avoid excessive F_2 vapor generation (about 2.0V).

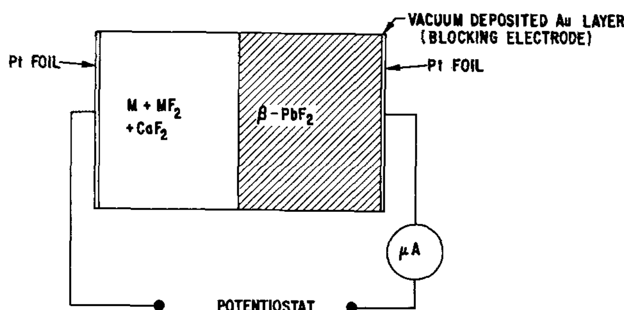

Fig. 3. Cell arrangement for d-c polarization studies of β-PbF_2

If Ni/NiF_2 electrodes are used at positive polarity, the permissible experimental voltage range is too small. Therefore, negative Ni/NiF_2 electrodes are preferred to allow a large applied voltage range (about 2.4V). The steady-state polarization currents were independent of the argon flow rate in the system and were stable over long periods of time.

Results and Discussion

A-c conductivity measurements.—The results of a-c total conductivity measurements are plotted in Fig. 4 as a function of fluorine pressure at various temperatures. By careful examination, there is a very small positive slope for each line. But essentially, the a-c conductivity of β-PbF_2 is independent of fluorine pressure, indicating that β-PbF_2 is a predominant ionic conductor over a wide range of fluorine activity.

D-c polarization measurements.—The converted plot of data for the cell

$$\ominus Ni/NiF_2 \mid PbF_2 \mid Au\oplus \quad [II]$$

according to Eq. [5] is shown in Fig. 5. The values for $\sigma_\ominus^\circ$ and $\sigma_\oplus^\circ$ were obtained from the slope and intercept of the plot, respectively, as already discussed.

The curve shown in Fig. 5 is not a perfectly straight line as was expected, but exhibits an increasing slope with the increasing voltage. Taking the maximum and the minimum values of slope gives

$$\sigma_\ominus^\circ = 3.12\text{-}4.15 \times 10^{-6}\,\Omega^{-1}\,cm^{-1}$$

correspondingly

$$\sigma_\oplus^\circ = 2.14\text{-}1.04 \times 10^{-8}\,\Omega^{-1}\,cm^{-1}$$

for $P_{F_2}{}^\circ$ for coexistence of Ni and NiF_2. This result indicates that $\sigma_\ominus^\circ >> \sigma_\oplus^\circ$; in other words, pure β-PbF_2 is an n-type conductor at the equilibrium fluorine activity for Ni/NiF_2.

To obtain the polarization data for β-PbF_2 at the equilibrium fluorine activity of Cu/CuF_2, cell [III] was used. Positive polarity was applied at the blocking electrode

$$\ominus Cu/CuF_2 \mid PbF_2 \mid Au\oplus \quad [III]$$

Unfortunately, some difficulties arose with this cell. Nonreproducible currents of the order of 1 μA were observed at applied voltages below 0.4V. Further, this cell required 1-1.5 days to reach a steady-state current. As a result, cell [III] with reverse polarity was used. As mentioned earlier, the maximum voltage for cell [III] with opposite polarity is only 640 mV, since higher voltages threaten the decomposition of the lead fluoride. On the other hand, potentials below 0.4V result in very small nonreproducible currents. Because of these two limitations, the voltage range between 0.4 and 0.6V was investigated. A converted plot of data for two such runs is shown in Fig. 6. The analysis yields for run No. 1

$$\sigma_\ominus^\circ = 1.89\text{-}3.81 \times 10^{-9}\,\Omega^{-1}\,cm^{-1}$$

$$\sigma_\oplus^\circ = 4.33\text{-}3.72 \times 10^{-5}\,\Omega^{-1}\,cm^{-1}$$

and for run No. 2

$$\sigma_\ominus^\circ = 6.39\text{-}6.61 \times 10^{-9}\,\Omega^{-1}\,cm^{-1}$$

$$\sigma_\oplus^\circ = 6.93\text{-}6.84 \times 10^{-5}\,\Omega^{-1}\,cm^{-1}$$

The values of $\sigma_\ominus^\circ$ and $\sigma_\oplus^\circ$ show that β-PbF_2 is a p-type conductor in equilibrium with Cu/CuF_2. Therefore, the fluorine activity at which the transition of p-type to n-type takes place falls between $P_{F_2}{}^\circ$ (Ni/NiF_2) and $P_{F_2}{}^\circ$ (Cu/CuF_2).

Figure 7 is a plot of log σ *vs.* log P_{F_2} for pure β-PbF_2; the slopes of log $\sigma_\oplus^\circ$ and log $\sigma_\ominus^\circ$ *vs.* log P_{F_2} approach, respectively, 0.5 and -0.5 at 492°C. These are the slopes expected from a Kroger-Vink diagram for F_i' and $V_F^{\cdot}$ defects in absolutely pure PbF_2, as well as in a doped crystal where an impurity fixes the defect concentration. Since $\sigma_\oplus^\circ$ and $\sigma_\ominus^\circ$ are negligible compared to σ_{ionic}, the total a-c conductivity is essentially equal to σ_{ionic}. Combining the results for $\sigma_\oplus^\circ$, $\sigma_\ominus^\circ$, and σ_{ionic} allows an estimation of the fluorine partial pressure $P_\oplus$ and $P_\ominus$ at which $\sigma_\oplus = \sigma_{ionic}$ and $\sigma_\ominus = \sigma_{ionic}$ at the temperature 492°C. For the condition $\sigma_\oplus = \sigma_{ionic}$, $P_\oplus$ equals 1.0×10^{-21} atm. The P_{F_2} for the condition where $\sigma_\ominus = \sigma_{ionic}$ is far below the P_{F_2} for PbF_2 decomposition and is therefore of no physical significance.

Only two different reference electrodes with differing values of P_{F_2} were used to determine the slopes in

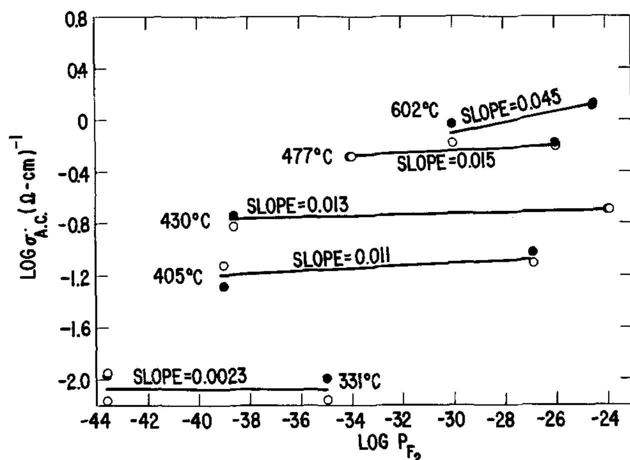

Fig. 4. Fluorine pressure dependence of total conductivity for β-PbF_2 at 330°-600°C. Open and closed circles represent duplicated runs.

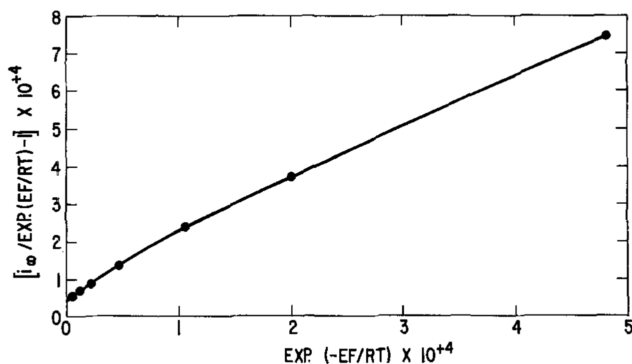

Fig. 5. Converted data plot for d-c polarization measurements with the cell $\ominus$ Ni/NiF_2 | β-PbF_2 | Au$\oplus$ at 492°C.

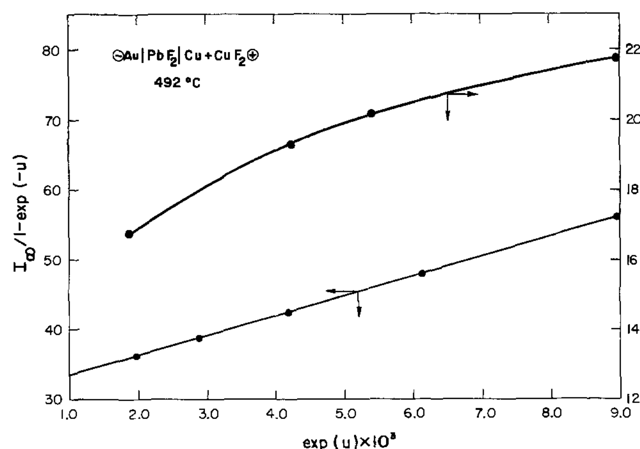

Fig. 6. Converted data for d-c polarization measurements with the cell $\ominus$ Au | PbF_2 | Cu/CuF_2 $\oplus$ at 492°C.

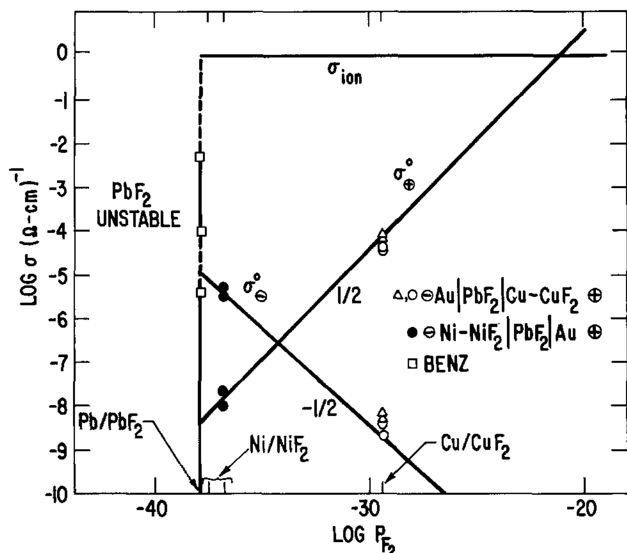

Fig. 7. Plot of log $\sigma_{a\text{-}c}$, log $\sigma_{\oplus}$, and log $\sigma_{\ominus}$ for the polarization and a-c conductivity study of β-PbF_2 at 492°C.

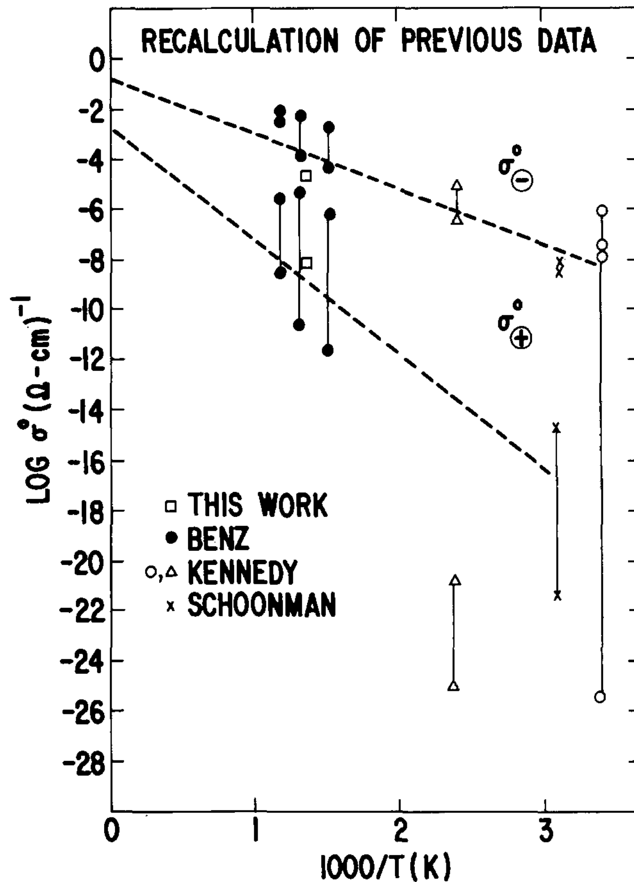

Fig. 8. Plot of log $\sigma_{\oplus}$° and log $\sigma_{\ominus}$° in equilibrium with lead as a function of temperature for β-PbF_2.

the plot of log σ *vs.* log P_{F_2}. These two seem to be the only available fluorides which are solid, have low vapor pressures at relatively high temperature, but yet are less stable than PbF_2.

As mentioned earlier, controversial results of d-c polarization of PbF_2 exist between various authors (4, 8-10, 12). Recalculation of the experimental data of previous studies according to Eq. [4] and [5] becomes necessary and interesting. Data for $\sigma_{\oplus}$° and $\sigma_{\ominus}$° and β-PbF_2 in equilibrium with Pb from these recalculations (4, 8, 10, 12) are plotted as a function of temperature in Fig. 8, extrapolation of the present experimental results for $\sigma_{\oplus}$° and $\sigma_{\ominus}$° from Fig. 7 are also shown on the same plot. Figure 8 shows reasonable agreement among different authors and the present study. Data for $\sigma_{\oplus}$° and $\sigma_{\ominus}$° from Joshi and Liang (9) are not included in Fig. 8 because their results were for α-PbF_2. Figure 8 shows that β-PbF_2 is an n-type conductor in equilibrium with Pb over the temperature range 25°-600°C. This conclusion incorporates the controversial results on polarization experiments from various authors. The improved method for interpreting converted d-c polarization data of Patterson *et al.* was useful in determining both $\sigma_{\oplus}$° and $\sigma_{\ominus}$° in this study. Comparison of electronic conductivities is shown in Table I. The set of values with an asterisk represents the values of $\sigma_{\ominus}$° and $\sigma_{\oplus}$° that fit best in Eq. [4] or [5].

Obviously, opposite conclusions are then sometimes obtained from the simple limiting graphical interpretation and from the improved, converted interpretation of Patterson *et al.*

Conclusions

The a-c conductivity of pure β-PbF_2 has been found to be essentially independent of P_{F_2}. This pressure independence indicates that β-PbF_2 is an ionic conductor over the experimental ranges of P_{F_2} and temperature.

The measurements of electronic conduction of pure β-PbF_2 in the d-c polarization experiment indicates a $P_{F_2}{}^{-1/2}$ dependence for $\sigma_{\oplus}$, and a $P_{F_2}{}^{-1/2}$ dependence for $\sigma_{\ominus}$, in accordance with a simple Kroger-Vink diagram for β-PbF_2. Recalculation of data from previous

Table I. Review of the literature data and present results for Pb halide conductivity in equilibrium with Pb

Material	(C) Temperature	Proposed by orig. authors	$\sigma_{\oplus}$° $(\Omega\text{-1 cm})^{-1}$	$\sigma_{\ominus}$° $(\Omega\text{-cm})^{-1}$	Present calculation	$\sigma_{\oplus}$° $(\Omega\text{-cm})^{-1}$	$\sigma_{\ominus}$° $(\Omega\text{-cm})^{-1}$	Ref.
β-PbF_2	25	—	—	—	n-type	2.05×10^{-16}* $\sim 3.76 \times 10^{-28}$	3.75×10^{-10}* $\sim 1 \times 10^{-8}$	12
β-PbF_2	150	p-type	3.3×10^{-11}	—	n-type	1.85×10^{-21}* $\sim 1.39 \times 10^{-25}$*	4.89×10^{-7}* $\sim 9.96 \times 10^{-6}$*	4
β-PbF_2	400	n-type	—	2.1×10^{-8}	n-type	7.37×10^{-7} $\sim 2.15 \times 10^{-12}$*	3.84×10^{-5} $\sim 1.93 \times 10^{-3}$*	10
	500	n-type	—	5.5×10^{-8}	n-type	4.8×10^{-6} $\sim 2.0 \times 10^{-11}$*	1.19×10^{-4} $\sim 4.97 \times 10^{-3}$*	10
	600	n-type	—	7.7×10^{-8}	n-type	1.7×10^{-5} $\sim 2.62 \times 10^{-9}$*	4.70×10^{-4} $\sim 7.92 \times 10^{-8}$*	10
α-PbF_2	127	p-type	1.72×10^{-20}	—	n-type	1.43×10^{-20} $\sim 1.4 \times 10^{-22}$*	5.5×10^{-10} $\sim 1.5 \times 10^{-8}$*	9
	259	p-type	1.82×10^{-11}	—	n-type	4.06×10^{-12} $\sim 1.71 \times 10^{-13}$*	1.22×10^{-8} $\sim 5.2 \times 10^{-8}$*	9
	287	p-type	8.60×10^{-11}	—	n-type	1.76×10^{-10} $\sim 8.12 \times 10^{-12}$*	1.13×10^{-9} $\sim 4.43 \times 10^{-8}$*	9
Pure β-PbF_2	492	(present estimates)			n-type	$\sim 2.5 \times 10^{-9}$*	2.86×10^{-5}*	
Pure β-PbF_2	52	n-type	—	4.7×10^{-9}	n-type	3.6×10^{-9} $\sim 4.7 \times 10^{-9}$*	2.2×10^{-15} $\sim 6.1 \times 10^{-22}$*	8

* Values of $\sigma_{\oplus}$° and $\sigma_{\ominus}$° best fitted to Eq. [4] and [5].

d-c polarization measurements for α-PbF_2 and β-PbF_2 from various authors, along with the $\sigma_{\oplus}$ and $\sigma_{\ominus}$ from the present study, gives the following conclusion: α-PbF_2 and β-PbF_2 are n-type conductors in equilibrium with Pb. P-type electronic conduction becomes important at high P_{F_2}, with $P_{\oplus} \approx 1.0 \times 10^{-21}$ atm at 492°C. The Patterson method was also applied to recalculate d-c polarization data existing in the literature for $PbBr_2$ and $PbCl_2$. The results indicate that both $PbCl_2$ and $PbBr_2$ are n-type conductors in equilibrium with Pb.

Acknowledgments

This work was supported by the Materials Science Program, Division of Physical Research, U.S. Energy Research and Development Administration, under contract E(11-1)-2671.

Manuscript submitted June 1, 1977; revised manuscript received Dec. 22, 1977.

Any discussion of this paper will appear in a Discussion Section to be published in the December 1978 JOURNAL. All discussions for the December 1978 Discussion Section should be submitted by Aug. 1, 1978.

Publication costs of this article were assisted by The Ohio State University.

REFERENCES

1. R. W. Bonne and J. Schoonman, *Solid State Commun.*, **18**, 1005 (1976).
2. J. Schoonman, G. J. Dirksen, and G. Blasse, *J. Solid State Chem.*, **7**, 245 (1973).
3. C. E. Derrington and M. O'Keeffe, *Nature (London), Phys. Sci.*, **246**, 44 (1973).
4. J. H. Kennedy, R. C. Miles, and J. Hunter, *This Journal*, **120**, 1441 (1973).
5. J. C. Gianduzzo and J. Pistre, *Electrocomp. Sci. Techn.*, **2**, 55 (1977).
6. J. M. Reau, J. Claverie, G. Campet, C. Deportes, D. Ravaine, J. L. Souquet, and A. Hammou, *C. R. Acad. Sci., Ser. C*, **280**, 225 (1975).
7. J. Schoonman, L. B. Ebert, C. H. Hsieh, and R. A. Huggins, *J. Appl. Phys.*, **46**, 2873 (1975).
8. J. Schoonman, G. A. Korteweg, and R. W. Bonne, *Solid State Commun.*, **16**, 9 (1975).
9. A. V. Joshi and C. C. Liang, *J. Phys. Chem. Solids*, **36**, 927 (1975).
10. R. Benz, *Z. Phys. Chem. N.F.*, **95**, 25 (1975).
11. C. C. Liang and A. V. Joshi, *This Journal*, **122**, 466 (1975).
12. J. H. Kennedy and R. C. Miles, *ibid.*, **123**, 47 (1976).
13. R. W. Bonne and J. Schoonman *ibid.*, **124**, 28 (1977).
14. J. Schoonman, *ibid.*, **123**, 1772 (1976).
15. J. H. Kennedy and J. C. Hunter, *ibid.*, **123**, 11 (1976).
16. A. V. Joshi and C. C. Liang, *ibid.*, **124**, 1253 (1977).
17. J. W. Patterson, *ibid.*, **118**, 1033 (1971).
18. J. W. Patterson, in "The Physics of Electronic Ceramics," L. L. Hench and D. B. Dove, Editors, p. 131, Marcel Dekker Inc., New York (1971).
19. C. Wagner, "International Committee of Electrochemical Thermodynamics and Kinetics," Proceedings 7th meeting, Butterworth Publications, London (1957).
20. C. Wagner, *Z. Elektrochem.*, **60**, 4 (1956).
21. J. W. Patterson, E. C. Bogren, and R. A. Rapp, *This Journal*, **114**, 752 (1967).

Lithium Dimethyl Sulfite Graphite Cell

Sanjay L. Deshpande*,[1] and Douglas N. Bennion*

Chemical, Nuclear, and Thermal Engineering Department, University of California, Los Angeles, California 90024

ABSTRACT

Reactions occurring at the positive and negative electrodes and in the solution phase of cells of the type Li/$LiClO_4$, DMSU/graphite have been studied. Discharge capability of 36 hr at a current density of 2 mA/cm^2 has been achieved. Discharge potential was about 3.00V measured *vs.* a lithium wire reference electrode. Coulombic efficiency was 100% at 2 mA/cm^2 but dropped rapidly at higher current densities. Charging potentials increased and discharge potentials decreased at higher current densities. Performance of the cell was poor when propylene carbonate was substituted for dimethylsulfite (DMSU) and $LiBF_4$. Changes in the positive electrode materials did not alter performance very much as long as graphite was present.

Lithium is attractive as a possible negative battery electrode because of its strong reducing potential and low equivalent weight. As a secondary or rechargeable electrode, lithium must operate in an aprotic solution. A major problem in developing room temperature, lithium storage batteries has been finding a suitable positive electrode which is compatible with the lithium negative electrode and the aprotic, electrolytic solution. A summary of various lithium battery systems has been presented elsewhere (1).

A possible battery system using a lithium negative electrode, $LiClO_4$-dimethylsulfite (DMSU) electrolytic solution, and a graphite positive electrode has been reported on previously (2-4). It was proposed (2) that a lamellar compound of graphite formed at the positive electrode as a product of the charge storage mechanism

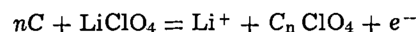

$$nC + LiClO_4 = Li^+ + C_n\,ClO_4 + e^-$$

Some later results (4) suggested that the above reaction is not the dominant reaction and that the solvent, DMSU, is involved more directly in the electrochemical reaction. This paper is intended to determine more clearly the positive electrode reaction and the limits of operating capability when used in a Li/$LiClO_4$, DMSU/C secondary battery system.

Experimental

The electrolytic solutions were prepared by vacuum distilling the solvents and vacuum drying the salts. Further drying was achieved by stirring solvents and solutions with lithium chips followed by filtering. Lithium chips were covered with a white deposit as a result of the drying. The stir-and-filter operation

* Electrochemical Society Active Member.

[1] Present address: Honeywell Power Sources Center, Horsham, Pennsylvania 19044.

Key words: nonaqueous solvents, dimethyl sulfite, lithium perchlorate, intercalation, radical cations.

was repeated to expose fresh lithium to the water in the solvent and the solution. Water content was determined using the Karl Fischer technique. Only solutions containing an upper limit of 50 ppm water were used. Graphite powder (99.95% pure, 0.8 μm in size) was used to fabricate the positive electrode. It is a natural graphite originating from Madagascar. Teflon molding powder and Union Carbide National C-34 glue were used as binders. Carbon cloth and titanium foil were used as current collector backing plates.

All experiments were performed in an argon atmosphere dry box. The test cells were glass H-cells as shown in Fig. 1. The two compartments were separated by a fine-size glass frit. Polyethylene stoppers were used to minimize solvent losses by evaporation. Electrode leads came out the top between the polyethylene stopper and the glass wall. The two electrodes, one graphite the other lithium, were held flat to the bottom of their respective compartments by glass sleeves 2 cm inside diam and 1.25 cm high. The sleeves were short enough so they did not block the connecting limb. The liquid level was just above the connecting limb. Each compartment contained about 10 cm^3 of solution. The electrical circuit is shown in Fig. 2. A Perkin Elmer chromatograph, Model 880, with a hot wire detector was used to analyze the electrolytic solution before and after cell operation. Further details of the experimental procedure, sources of material and equipment, and purification techniques can be obtained elsewhere (1).

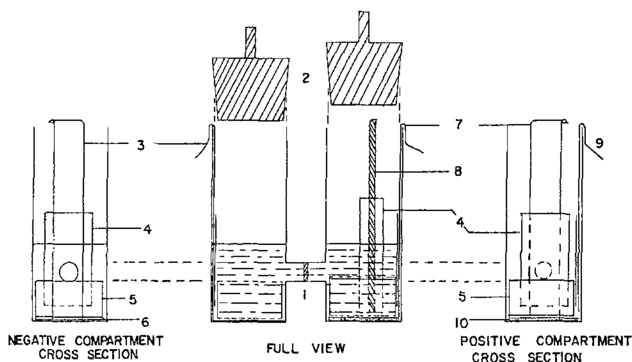

Fig. 1. The H-cell used in all experiments. 1. Glass frit; 2. polyethylene stoppers; 3. negative lead; 4. polypropylene masks for the three electrodes; 5. glass sleeve; 6. negative electrode; 7. positive lead; 8. reference electrode; 9. reference lead; 10. positive electrode.

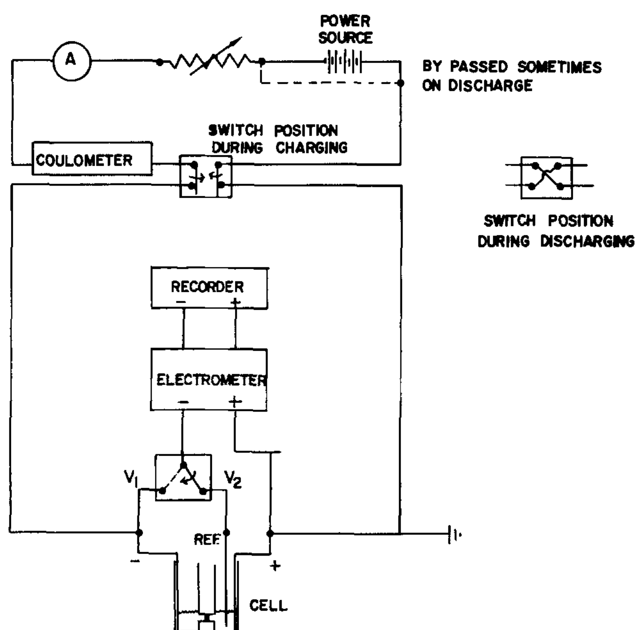

Fig. 2. Electrical circuit diagram for charging and discharging

Both pyrolized and cloth positive electrodes were used. In one case a plain platinum sheet was used. The pyrolized electrodes were made by mixing graphite glue with twice its weight of graphite powder. In one case just the glue was used. The paste was spread on carbon cloth and pressed between two steel plates to form a disk 1.00 mm or less thick. The disk was fired in an argon atmosphere at 800°C for about 6 hr. The result was a brittle, porous disk which adhered well to the cloth. The disk separated easily from the steel plates. The resistance across the cloth disks was about 5Ω. Cloth electrodes were the carbon cloth alone. Prior to use, the carbon electrodes were dried at 50 μm of Hg and 120°C for 6 hr.

In assembling the cells, gas bubbles trapped under the electrodes were shaken free. A thin strip of lithium was placed in the positive compartment as a reference electrode. Strips of polypropylene were placed over electrode leads and the reference electrode wire to prevent a direct current path to them.

The potential between the positive electrode and the lithium wire reference electrode was measured as a function of time while the cell operated at constant charging or discharging current. During one set of measurements, propylene carbonate was used in place of DMSU and $LiBF_4$ in place of $LiClO_4$.

The variables measured were: V_o, the open-ciruit potential right after assembly or a 30 sec interruption in current of the positive electrode *vs.* the reference electrode; V_o', the open-circuit potential after an interruption of a few hours in current of the positive electrode *vs.* the reference electrode; V_1 the operating potential of the complete cell, the positive *vs.* the negative electrode; V_2, the operating potential of the positive electrode *vs.* the reference electrode; V_f, cut-off potential, V_2, when discharging was stopped; Q_{in}, the charge put into the cell during charging; Q_{4V} the charge recovered from the cell with V_2 above 4.0V; Q_{Vf} the charge recovered from the cell with V_2 above V_f.

Potential measurements were made with the positive electrode grounded. Measured values were multiplied by −1 and then reported so that the reported values would conform to the usual sign convention.

Results

Demonstration of reversible electrical storage capacity.—The electrode weighed 0.7245g of which 0.3735g was carbon cloth, 0.2318g graphite powder, and the rest pyrolized graphite glue. Initial thickness was 1 mm and diam 2.0 cm. The electrolytic solution was 1.04 moles $LiClO_4$ per 1000 cm^3 of solution. The initial open-circuit potential, V_o, right after filling was 2.70V. The cell was cycled four times with progressively larger charge in (Q_{in}). Results are shown in Fig. 3, 4, 5, and 6. Charging and discharging was at 3.2 mA (1.0 mA/cm^2) on the first cycle and 6.3 mA (2.0 mA/cm^2) on cycles 2, 3, and 4. On cycle 2, current was increased to 10 mA for short intervals. The curves in Fig. 3, 4, 5, and 6 are typical of many tens of runs.

On the first cycle, two discharge plateaus were observed, one with $V_2 > 4.0V$ and the other with V_2 between 3.0 and 2.8V. Typically, the higher plateau was not observed after the first one or two cycles and following a prolonged (several hours) stand after charging but before discharging. The cutoff voltage, V_f, was 2.5V. The coulombic efficiency on the first cycle exceeded 100%. The excess charge is attributed to reactive impurities initially present in the positive electrode.

On both charging and discharging the potential on prolonged open circuit drifted to $V_o' = 3.75V$. The charge and discharge curves were not significantly affected by long interruptions at open circuit. The sustained discharge for 36 hr at 2 mA/cm^2 demon-

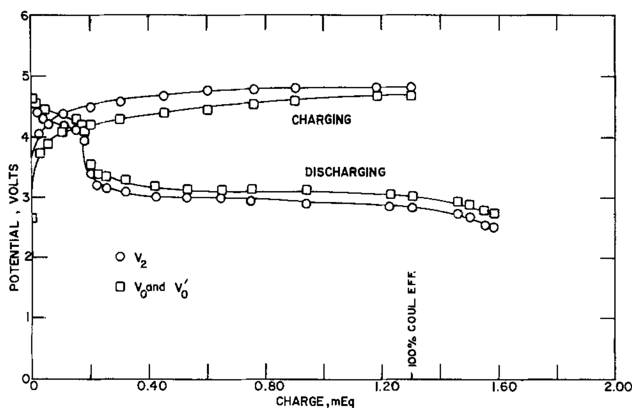

Fig. 3. Galvanostatic charge-discharge curves for the cell Li/$LiClO_4$, DMSU (1.0M)/graphite + graphite glue on carbon cloth. Cycle No. 1. I = 3.20 mA; Q_{in} = 1.30 mequiv.; coulombic eff. = 121.5% above V_f = 2.50V; discharge begun after 0 hr of wet stand on charge; positive electrode weight = 0.7245g; graphite = 0.2318g; carbon cloth = 0.3735g; initial thickness of carbon disk = 0.1 cm; top surface area = 3.14 cm^2; resistance = 1.0Ω.

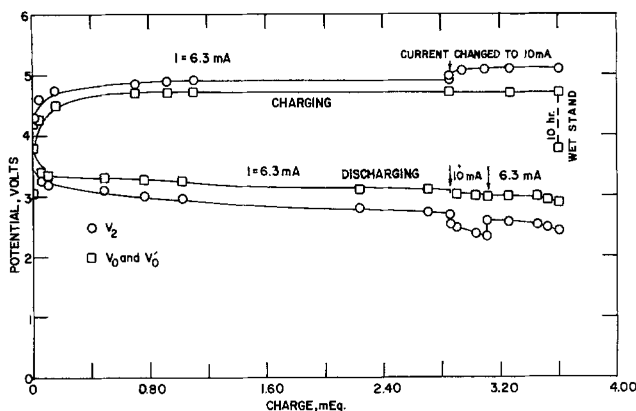

Fig. 4. Galvanostatic charge-discharge curves for the cell Li/$LiClO_4$, DMSU (1.0M)/graphite + graphite glue on carbon cloth. Cycle No. 2. I = 6.30 mA; Q_{in} = 3.60 mequiv.; coulombic eff. = 100.0% above V_f = 2.50V; discharge begun after 10 hr of wet stand on charge; positive electrode weight = 0.7245g; graphite = 0.2318g; carbon cloth = 0.3735g; initial thickness of carbon disk = 0.1 cm; top surface area = 3.14 cm^2; resistance = 1.0Ω.

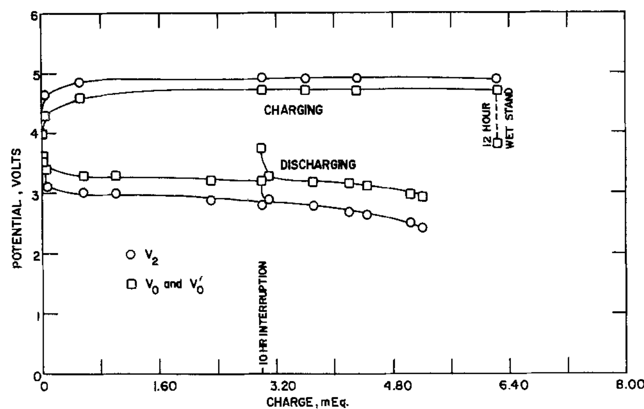

Fig. 5. Galvanostatic charge-discharge curves for the cell Li/$LiClO_4$, DMSU (1.0M)/graphite glue on carbon cloth. Cycle No. 3. I = 6.3 mA; Q_{in} = 6.23 mequiv.; coulombic eff. = 83.4% above V_f = 2.50V; discharge begun after 12 hr of wet stand on charge; positive electrode weight = 0.7245g; graphite = 0.2318g; carbon cloth = 0.3735g; initial thickness of carbon disk = 0.1 cm; top surface area = 3.14 cm^2; resistance = 1.0Ω.

strates a much larger energy storage than the capacity of 1 hr at 2 mA/cm^2 reported by Dunning *et al.* (2). However, Dunning *et al.* looked primarily at the higher, 4.2V plateau; while in this work the lower 2.9V plateau was examined.

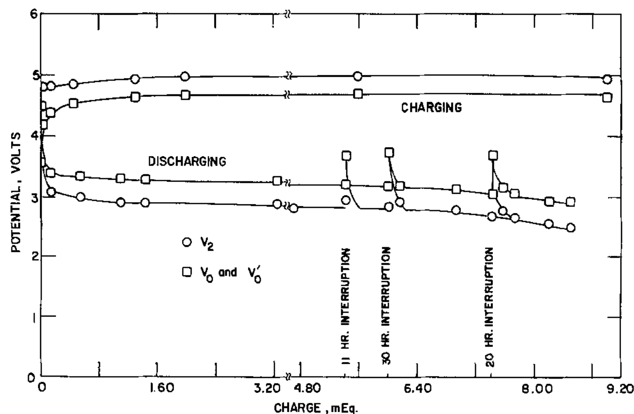

Fig. 6. Galvanostatic charge-discharge curves for the cell Li/$LiClO_4$, DMSU (1.0M)/graphite + graphite glue on carbon cloth. Cycle No. 4. I = 6.3 mA; Q_{in} = 8.92 mequiv.; coulombic eff. = 95.3% above V_f = 2.50V; discharge begun after 0 hr of wet stand on charge; positive electrode weight = 0.7245g; graphite = 0.2318g; carbon cloth = 0.3735g; initial thickness of carbon disk = 0.1 cm; top surface area = 3.14 cm^2; resistance = 1.0Ω.

This comparison is intended to highlight the importance of the lower discharge plateau. Dunning *et al.* used a positive electrode made out of reinforced pyrolytic graphite that weighed 1.4535g and had a cross-sectional area of 8.5 cm^2 (active area was 17 cm^2). About 4 cm^3 of electrolyte solution was used in that test. In comparison, the positive electrode (total weight 0.7245g) reported herein consisted of graphite powder (0.2318g) and graphite glue (0.1192g) and had a cross-sectional area of 3.14 cm^2. About 10 cm^3 of electrolytic solution were present in each half-cell. Table I compares the energy available at the two plateaus. By any criterion, energy available at the lower plateau is higher.

The positive electrode disk swelled from 1 mm thick initially to 5 mm thick after the fourth cycle. The swelling was rapid in the first two cycles, but it swelled little on the last two cycles. The disk remained rigid and adhered to the carbon cloth backing. Final disk resistance was about 3Ω. The surface of the electrode was covered with a thin white deposit. During the charging run of the first cycle, the solution in the positive half-cell gradually turned dark brown. When Anderson Physics Lab ultrapure $LiClO_4$ was used in place of K and K Labs $LiClO_4$, the brown substance did not appear.

The deposit on the negative electrode was dendritic and adhered weakly to the lithium substrate. A white, gelatinous floc appeared at the surface of the lithium. On long cycles a small but steady bubbling appeared on the lithium electrode. The appearance of a white floc agrees with observations of Selim and Bro (5).

Bubbles appeared on the lithium wire reference electrode occasionally during long charging periods, and twice during the 36 hr discharging run it corroded badly enough so that replacement was necessary.

To study the effect of operating current on cell performance, cells of the type just described were operated at varying currents. The results are shown in Fig. 7. Above 2 mA/cm^2 the coulombic efficiency drops rapidly. The current voltage curves are shown in Fig. 8 for charging and discharging. The potentials are average values of the plateau regions. After the high current operation, a cycle was carried out at

Table I. Comparison of upper and lower voltage discharge plateaus

	Upper plus lower plateaus (This paper)	Upper plateau only [Dunning *et al.* (2)]
Energy Stored-W-hr	0.6560	0.1428
W-hr/g electrode	0.9054	0.0982
W-hr/cm^2	0.2088	0.0084
W-hr/cc solution	0.0656	0.0357

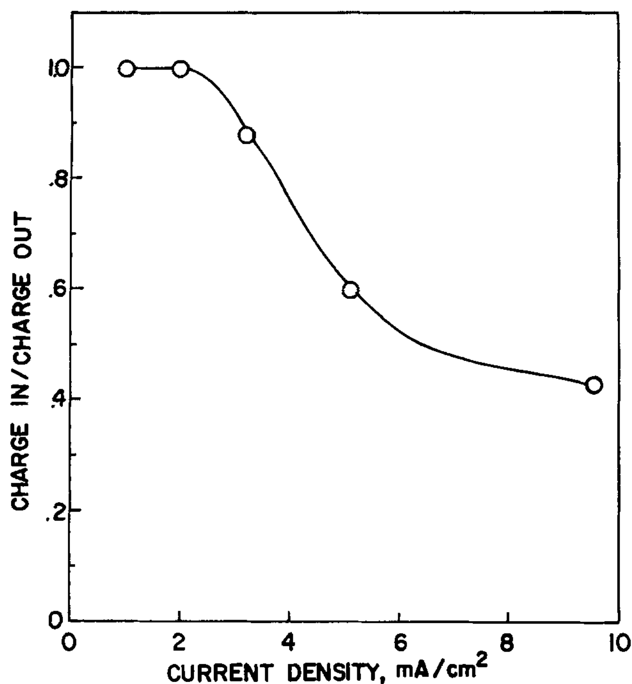

Fig. 7. Effect of operating current density on coulombic efficiency (based on a cutoff potential of $V_f = 2.0V$).

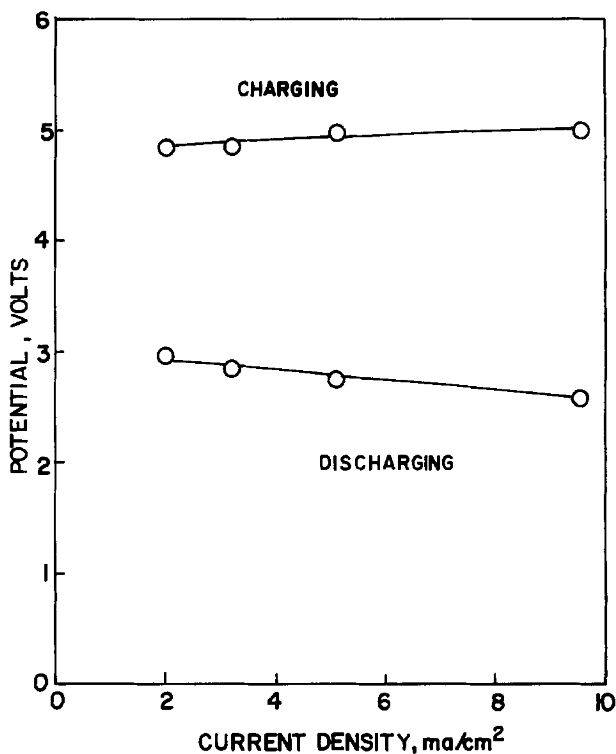

Fig. 8. Effect of operating current density on the potential of the positive electrode vs. the lithium wire reference electrode, V_2, during the charging and discharging runs.

6.3 mA (2 mA/cm²) and coulombic efficiency returned to 100%.

In order to check for involvement of electrolytic solution species in the electrode reactions, propylene carbonate (PC) was substituted for DMSU and $LiBF_4$ for $LiClO_4$. The results are shown in Fig. 9, 10, and 11. A comparison of results is shown in Table II. The results imply that DMSU is a necessary part of the positive electrode reaction process and that $LiClO_4$ gives better performance than $LiBF_4$.

The effect of different materials in the positive electrode on cell performance was examined. Results

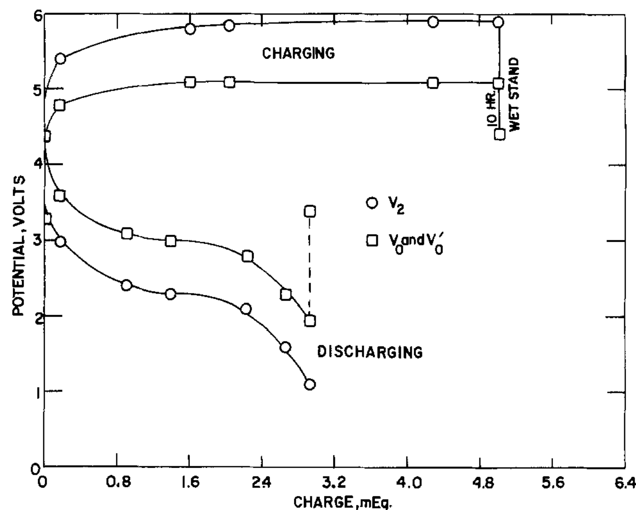

Fig. 9. Galvanostatic charge-discharge curves for the cell Li/ $LiClO_4$, PC (0.89M)/graphite + graphite glue on carbon cloth. Cycle No. 5. $I = 6.3$ mA; $Q_{in} = 5.0$ mequiv.; coulombic eff. = 45.6% above $V_f = 2.0V$; positive electrode weight = 0.6260g; graphite = 0.1980g; carbon cloth = 0.3262g; initial thickness of carbon disk = 0.10 cm; top surface area = 3.14 cm²; resistance = 1.0Ω.

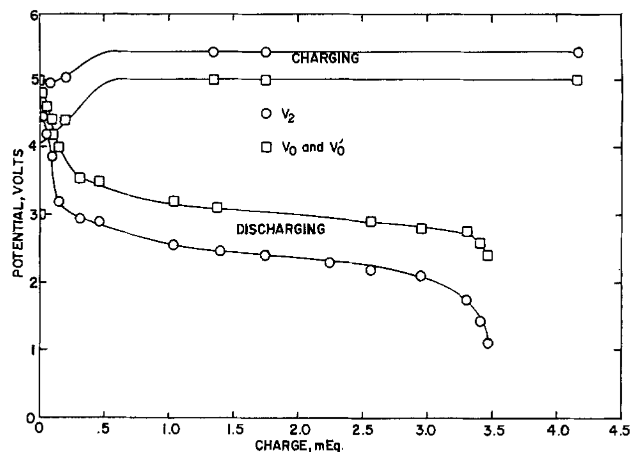

Fig. 10. Galvanostatic charge-discharge curves for the cell Li/ $LiBF_4$, DMSU (1.03M)/graphite + graphite glue on carbon cloth. Cycle No. 3. $I = 6.3$ mA; $Q_{in} = 4.16$ mequiv.; coulombic eff. = 72.3% above $V_f = 2.0V$; positive electrode weight = 0.2218g; graphite = 0.0448g; carbon cloth = 0.1540g; initial thickness of carbon disk = 0.04 cm; top surface area = 3.14 cm²; resistance = 3.0Ω.

with bare platinum as the positive showed a fairly flat charging plateau at 5.6V, but no discharge plateau was observed. Pyrolized glue on carbon cloth (no graphite powder) gave typically observed results as shown in Fig. 12. Results using only carbon cloth are shown in Fig. 13. The charging runs were flat at 5.2V and not shown. The coulombic efficiency increased with increased cycling. During run 4, 41% of the 8.52 Mequiv. had been recovered when discharging was stopped because the reference electrode had dissolved away and cell resistance had increased from 1.0 to 2.8 kΩ. However, V_0 was steady at 3.2V. There was bubbling at the lithium counterelectrode and the reference electrode. Although all the carbon

Table II. Comparison of performance for four electrolytic solutions

	$LiClO_4$-DMSU	$LiClO_4$-PC	$LiBF_4$-DMSU	$LiBF_4$-PC
Charge recovered, m equiv.	8.50	2.26	3.00	1.10
Coulombic efficiency	95.3	42.2	72.3	50.0
Cutoff potential, V_f	2.5	2.0	2.0	1.25

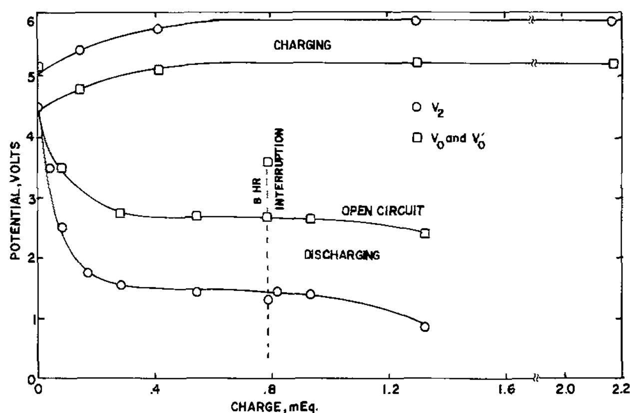

Fig. 11. Galvanostatic charge-discharge curves for the cell Li/$LiBF_4$, PC (1.55M)/graphite + graphite glue + carbon cloth. Cycle No. 3. I = 6.3 mA; Q_{in} = 2.17 mequiv.; coulombic eff. = 50.0% above V_f = 1.25V; positive electrode weight = 0.1709g; graphite = 0.0300g; carbon cloth = 0.1200g; initial thickness of carbon disk = 0.04 cm; top surface area = 3.14 cm^2; resistance = 3.0Ω.

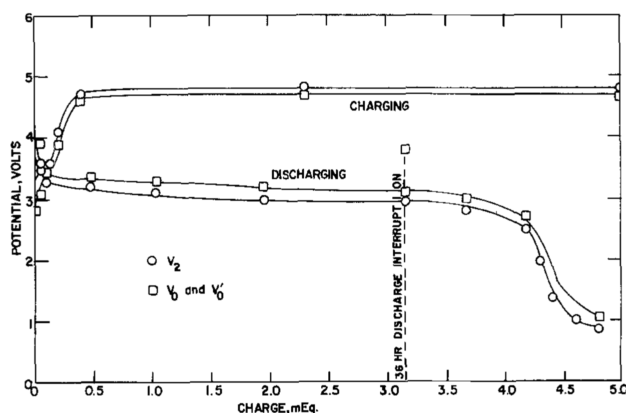

Fig. 12. Typical galvanostatic charge-discharge curves for the cell Li/$LiClO_4$, DMSU (1.53M)/graphite glue on carbon cloth. Cycle No. 2. I = 6.3 mA; Q_{in} = 5.0 mequiv.; coulombic eff. = 64.0% above V_f = 2.50V; positive electrode weight = 0.7258g; carbon cloth = 0.5053g; initial thickness of carbon disk = 0.07 cm; top surface area = 3.14 cm^2; resistance = 4.0Ω.

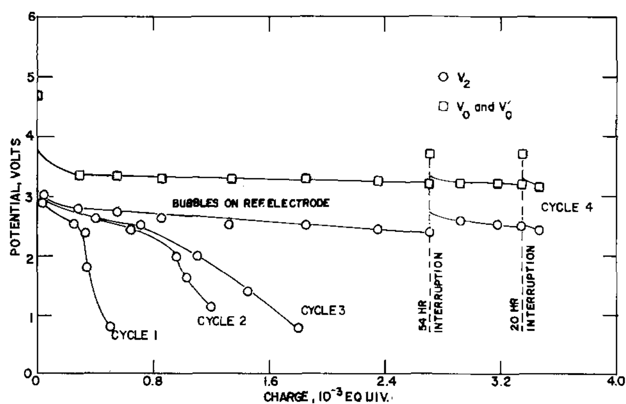

Fig. 13. Galvanostatic discharge curves for the cell Li/$LiClO_4$, (2.13M) DMSU/carbon cloth. V_2 (charging) = 5.15V. I = 6.30 mA; weight of carbon cloth electrode = 0.1273g; thickness = 0.02 cm; exposed area = 3.14 cm^2; V_0 (charging) = 4.70V.

	Cycle 1	Cycle 2	Cycle 3	Cycle 4
Charge in, 10^{-3} equiv.	1.25	2.28	3.13	8.52
Coulombic eff. above V_f = 2.50V	20.32	27.81	22.36	40.63

electrodes gave appreciable charge storage, the high surface area electrodes gave the greatest charge retention.

Gas chromatographic analysis was carried out on the electrolytic solution of the positive half-cell at various stages of charge and discharge. A new peak was observed at the end of charging which was not present at the end of discharging. This implies that the oxidizing agent formed on charging is at least partially soluble, and it is consumed on discharging.

X-ray powder diffraction data ($Cu_{K\alpha}$ radiation) on cycled positive electrodes in cells containing DMSU showed a number of diffraction lines that could not be assigned to a known compound. The most intense of these lines had a d value of 4.42Å followed in intensity by the line with d = 7.76Å. Thus, there is evidence for some intercalation of graphite. On samples of positive electrodes from cells using PC as solvent, however, there were only two unassigned peaks with d values of 2.39 and 1.80Å, the latter being more intense. Thus, intercalation of graphite (characteristic d = 3.38Å) in PC solutions is not significant.

Discussion

The need for carbon as natural graphite, carbonized graphite glue, or carbon cloth for charge storage in the positive electrode has been demonstrated by substantial charge storage in the carbon positive electrodes and the inability of a bare platinum electrode to demonstrate charge storage. Graphite or carbon appears to be a suitable catalyst and possibly a participant in the charge storage reactions at the positive electrode. The high storage of the graphite powder-graphite glue compared to carbon cloth alone is attributed to better adsorption properties of the powder plus glue.

The initial swelling of the pyrolized graphite-glue electrodes is attributed to formation of intercalation compounds, possibly intercalation of perchlorate anions and/or the solvent molecules. However, substantial charge storage was achieved with carbon cloth alone, which did not swell. This implies that the intercalation reactions are side reactions which do not contribute significantly to charge storage but help to increase the carbon surface area available for storage of the oxidizing agent produced during charging.

The attack on the lithium wire reference electrode and the new peak observed by gas chromatography of samples taken after charging imply that the oxidizing agent formed during charging is at least partially soluble. It is not expected that intercalation compounds would be soluble. Since the perchlorate ion is already highly oxidized and no chlorine or oxygen gas evolution was observed, it appears that DMSU is the principal reactant. This conclusion is further strengthened by the observations that, when DMSU was replaced by PC, the charge storage capability of the positive electrode, the coulombic efficiency, and the value of the discharge potential all dropped substantially (Table I).

DMSU molecules contain sulfur in the valence state 4. Valence states 5 and 6 are known for sulfur. Thus it is reasonable to expect DMSU to be oxidized during charging

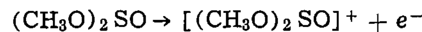

$$(CH_3O)_2SO \rightarrow [(CH_3O)_2SO]^+ + e^-$$

or

$$(CH_3O)_2SO \rightarrow [(CH_3O)_2SO]^{+2} + 2e^-$$

During charging, it appears possible that the initial reaction product, presumably a radical cation, may rearrange or react further. The radical cation is expected to be reduced back to DMSU which would complete the reversible cycle. However, charged species resulting from subsequent rearrangement may form final products other than DMSU during discharge. Since there was a large excess of DMSU in all of the experiments run in this investigation, it has not been established whether or not subsequent cycles complete a reversible cycle or whether fresh DMSU

is oxidized each charge cycle implying that a storage battery type cycle does not exist for this system.

At the negative electrode dendritic lithium deposits were observed to change during discharging into a white floc which could be $LiClO_4$. If that is the case, it is implied that during discharging a local supersaturation of $LiClO_4$ occurs near the negative electrode. This behavior would be expected if the ClO_4^- mobility is much larger than the Li^+ mobility. Since the Li^+ is probably highly solvated, it is reasonable to expect the ClO_4^- ion to have a higher mobility. Preliminary x-ray analysis indicated the white precipitate was $LiClO_4$, but the results were not conclusive.

Acknowledgments

Financial support for this work has been provided by the U.S. Navy, Office of Naval Research.

Manuscript submitted April 13, 1977; revised manuscript received Dec. 19, 1977.

Any discussion of this paper will appear in a Discussion Section to be published in the December 1978 JOURNAL. All discussions for the December 1978 Discussion Section should be submitted by Aug. 1, 1978.

Publication costs of this article were assisted by the University of California.

REFERENCES

1. S. L. Deshpande, M.S. Thesis, School of Engineering and Applied Science, University of California, Los Angeles, California (1976).
2. J. S. Dunning, W. H. Tiedemann, L. Hsueh, and D. N. Bennion, *This Journal*, **118**, 1886 (1971).
3. Z. I. Mirza, M.S. Thesis, School of Engineering and Applied Science, University of California, Los Angeles, California (1971).
4. R. K. Hebbar, M.S. Thesis, School of Engineering and Applied Science, University of California, Los Angeles, California (1974).
5. R. Selim and P. Bro, *This Journal*, **121**, 1457 (1974).

Activities and Surface Tension of Liquid AgCl-KCl Solutions

Z. Moser,* M. Kucharski, and K. Rzyman

Institute for Metal Research, Polish Academy of Sciences, Kraków, Reymonta 25, Poland

ABSTRACT

Thermodynamic properties of liquid AgCl-KCl solutions were investigated at concentrations of $X_{AgCl} = 0.43\text{-}1.00$ at temperatures of 860°-1000°K by the method of formation cells with chlorine electrode. The partial thermodynamic data of AgCl were interpreted by Krupkowski's method and the relations of activity coefficients of both AgCl and KCl were obtained. Simultaneously, the surface tension measurements of pure AgCl, KCl, and AgCl-KCl liquid solutions were carried out using the maximum bubble pressure method at temperatures of 734°-1220°K dependent on the composition of investigated solutions and the melting points of pure salts. Using the thermodynamic data of bulk AgCl-KCl solutions, results of surface tension, and the calculations of the composition of the surface phase of the thickness 4.29×10^{-8} cm, the activity coefficients of AgCl in this phase were obtained.

Experimental methods dealing with the determination of thermodynamic properties of liquid solutions do not take into account the surface phenomenon, *i.e.*, the adsorption of the surface. On the other hand, the case of equilibrium between the surface phase and the bulk may be considered in order to explain surface properties. In this case, however, it is possible to determine the thermodynamic properties of both phases mentioned above despite the fact that the surface phase is not a separate one. To investigate these problems, thermodynamic properties of the bulk phase were determined by the emf method for the AgCl-KCl liquid solutions, while surface tension measurements of pure AgCl, KCl, and AgCl-KCl solutions made it possible to follow the change of activities in the solution in the surface layer.

Thermodynamic Properties of Liquid AgCl-KCl Solutions

Experimental investigations on AgCl-KCl liquid solutions form part of the studies on ternary salt solutions including AgCl-LiCl-KCl. The aim of these studies is to show the possibility of applying Krupkowski's formalism (1) to salt systems with single charge ions and to verify the similarities between liquid salt and metallic systems. It was shown by Moser and Fitzner (2) when analyzing available experimental data from the literature for the AgCl-LiCl-KCl system on plot $(\ln \gamma_{AgCl})_{X_{AgCl}=0}$ *vs.* X_{LiCl} that, as in the case of liquid metal solutions (3), the deviation from linear dependence forms the term connected with the binary system KCl-LiCl.

Applying the method of formation cells with a chlorine electrode of the following type

$$Ag(s)/AgCl\text{-}KCl(l)/Cl_2(g), \text{graphite} \quad [1]$$

the thermodynamic properties of liquid AgCl-KCl solutions were investigated at concentrations of $X_{AgCl} = 0.43\text{-}1.00$ and at temperatures of 860°-1000°K. The scheme of the cell is shown in Fig. 1. A crucible, 2, made of silica and containing liquid salts, 6, was placed in an alumina crucible, 1. The following were immersed in liquid salts:

A. A high melting glass tube, 13, closed at one end with the orifice enabling contact with liquid salts, in the bottom of which was placed a silver electrode, 3. A silver electrode in the form of a sheet was connected with an alumina tube, 14, by alundum cement. The upper part of the silver sheet was connected with Pt wire, 4, passing through a rubber stopper, 5.

B. Pt-PtRh10 thermocouple, 11, was inserted into a silica tube enabling temperature measurements to ±2°C.

C. An asbestos diaphragm, 7, sealed in a silica tube, 8, separates the two electrode compartments and forms the bottom part of the chlorine electrode. The

* Electrochemical Society Active Member.

Key words: activity coefficient, fused salts, thermodynamics, solvents.

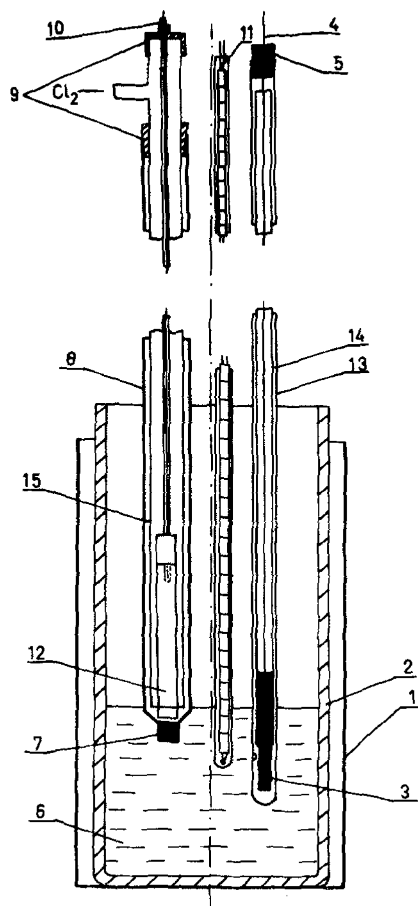

Fig. 1. Scheme of the experimental cell

chlorine electrode consists of a graphite rode, 12, connected with a high melting glass tube, 15, and a Pt wire. Seals, 9, were made of Teflon.

The results of emf measurements obtained for increasing temperatures (open circles) and decreasing (solid circles) are shown in Fig. 2. As these plots show the linear dependence of emf *vs.* temperature, the least squares method was used for averaging the data.

From the resulting linear equations presented in Table I, the emf values at the chosen temperatures of 873°-973°K were calculated each 20°. These emf data were used for calculations of silver chloride activities employing the Nernst equation with $P_{Cl_2} = 1$ atm and with the activity of silver taken as unity. The activity coefficients of silver chloride are calculated from the following relation

$$E_{AgCl} - E^{\circ}_{AgCl} = -\frac{RT}{n\mathbf{F}} \ln \gamma_{AgCl} - \frac{RT}{n\mathbf{F}} \ln X_{AgCl} \quad [2]$$

where E°_{AgCl} is the standard cell potential obtained with pure AgCl (bottom line in Fig. 2) and E_{AgCl} is the emf value of the formation cell.

The obtained experimental values of $\ln \gamma_{AgCl}$ were described by Krupkowski's relation

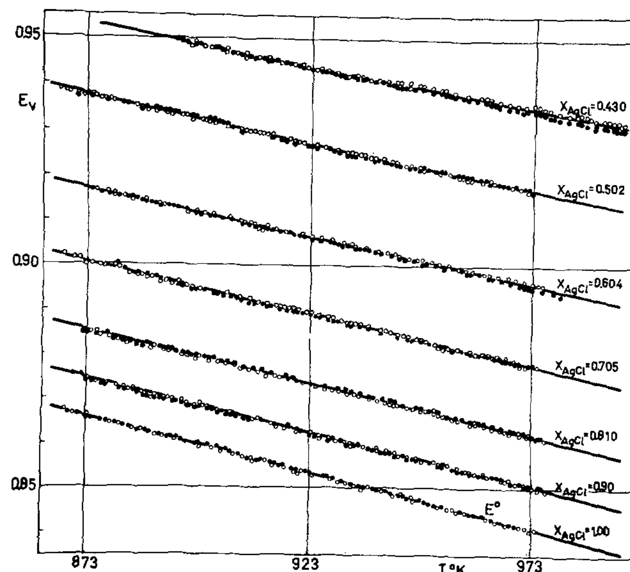

Fig. 2. EMF_{volts} vs. temperature in the system AgCl-KCl

$$\ln \gamma_{AgCl} = \omega(T)(1 - X_{AgCl})^m \quad [3]$$

The value of m ($m = 1.72$) was obtained from the plot $\log|\ln \gamma_{AgCl}|$ *vs.* $\log(1 - X_{AgCl})$ as the slope, and $\omega(T)$ as intercept. Next, the relation of $\omega(T)$ *vs.* temperature [$\omega(T) = -863/T + 0.1468$] were calculated. In this manner the following relations for $\ln \gamma_{AgCl}$ and $\ln \gamma_{KCl}$ were obtained in the form

$$\ln \gamma_{AgCl} = \left(-\frac{863}{T} + 0.1468\right)(1 - X_{AgCl})^{1.72} \quad [4]$$

$$\ln \gamma_{KCl} = \left(-\frac{863}{T} + 0.1468\right)[(1 - X_{AgCl})^{1.72} - 2.389(1 - X_{AgCl})^{0.72} + 1.389] \quad [5]$$

The form of $\omega(T)$ with $\alpha = -863$ and $\beta = 0.1468$ results in equations for partial ($\Delta\overline{H}_{AgCl}$) and integral enthalpy ($\Delta H'$) of the following form

$$\Delta\overline{H}_{AgCl} = -RT^2\left(\frac{\partial \ln \gamma_{AgCl}}{\partial T}\right) = R\alpha(1 - X_{AgCl})^{1.72} = -1714(1 - X_{AgCl})^{1.72} \quad [6]$$

$$\Delta H' = R\alpha \frac{1}{m-1}[1 - (1 - X_{AgCl})^{0.72}]X_{KCl} = -2381[1 - (1 - X_{AgCl})^{0.72}]X_{KCl} \quad [7]$$

The experimental data and those calculated from Eq. [4]-[7] as well as thermodynamic data at 973°K presented by Pelton and Flengas (4) are compared in Table I. Besides the partial thermodynamic properties of AgCl there also exists a good agreement of integral enthalpy when compared with Hersh and Kleppa's (5) calorimetric data (at $X_{AgCl} = 0.5$; $\Delta H' = -550$ cal/mole).

In addition it should be mentioned that similar parameters of $\omega(T)$ and m in Eq. [4] and [5] were

Table I. Experimental and calculated data in AgCl-KCl liquid solutions at 973°K

Experimental data			Calculated from Eq. [4]-[7]				Experimental data of Pelton and Flengas	
X_{AgCl}	$E_{volts} = a - b\,T°K$	γ_{AgCl}	γ_{AgCl}	γ_{KCl}	$-\Delta\overline{H}_{AgCl}$ (cal/mole)	$-\Delta H'$ (cal/mole)	X_{AgCl}	γ_{AgCl}
0.430	$E = 1.11102 - 1.8061 \cdot 10^{-4}T$	0.752	0.755	0.878	651	452	0.3497	0.699
0.502	$E = 1.11245 - 2.0075 \cdot 10^{-4}T$	0.800	0.800	0.835	517	468	0.4994	0.800
0.604	$E = 1.10670 - 2.1697 \cdot 10^{-4}T$	0.860	0.860	0.763	348	459	0.6392	0.907
0.705	$E = 1.10124 - 2.2999 \cdot 10^{-4}T$	0.914	0.913	0.681	210	411	0.8505	0.976
0.810	$E = 1.08831 - 2.3307 \cdot 10^{-4}T$	0.963	0.958	0.585	99	315		
0.900	$E = 1.08326 - 2.3937 \cdot 10^{-4}T$	0.990	0.986	0.530	33	193		
1.000	$E =$ 1.0[illegible]025 $- 2.5648 \cdot 10^{-4}T$	1.000						

obtained when Krupkowski's method was applied to the data of Pelton and Flengas (4): $\omega(T) = -863/T + 0.054$; $m = 1.80$ as shown previously by Moser and Fitzner (2). The same method was also used by Ptak and Szczygiel (6) for interpretation of emf data of concentration cells applied to AgCl-KCl liquid solutions. The obtained values of $\omega(T) = -917/T$ and $m = 1.87$ also lead to data similar to those presented in Table I.

Surface Tension Measurements of Liquid AgCl, KCl, and AgCl-KCl Solutions

Measurements of surface tension have been carried out by the maximum bubble pressure method. Experimental arrangements were similar to those for liquid metals (7), but some modifications were introduced to limit the vapor transport effect. This limitation is an important factor as it was shown that measurements of surface tension of liquids with significant vapor pressure may result in erroneous data, in the case when the equilibrium of the gaseous with the liquid phase is not attained (8, 9). This phenomenon has been proved in the present investigations as liquid KCl and solutions AgCl-KCl rich in KCl have, in experimental conditions, sufficiently high pressure to influence the surface tension measurements, especially those carried out with free evaporation.

To limit this evaporation a crucible with tested salt was placed in special graphite vessel, 4, with a screwed cover in which an orifice for capillary introduction had been made. The other parts of experimental arrangements are presented in Fig. 3. They consist of a manometer filled with dibutylphalate, 1, a gas train for the purification of argon, 2, a quartz capillary, 3, a crucible vessel with the salt sample, 4, Pt-PtRh10 thermocouple, 5, a resistance furnace, 6, an arrangement to move the crucible with the salt up and down, 7, and a micrometer screw, 8. A quartz capillary with a diameter of 0.7-1 m/m was used. It was initially wetted in liquid salt which improves the reproducibility of results. First, a sample of the investigated salt was placed in the furnace which was then closed. In the meantime the gas train system was open and argon passed through this closed system for a minimum of 24 hr. Next, the furnace was switched on until the first desired temperature was attained. Then, the surface tension measurements were initiated after immersing the capillary at one or two chosen depths. The maximum pressure required for forming and detaching several bubbles was measured. The average value of this measurement was taken for the first approach of surface tension calculations using the relation

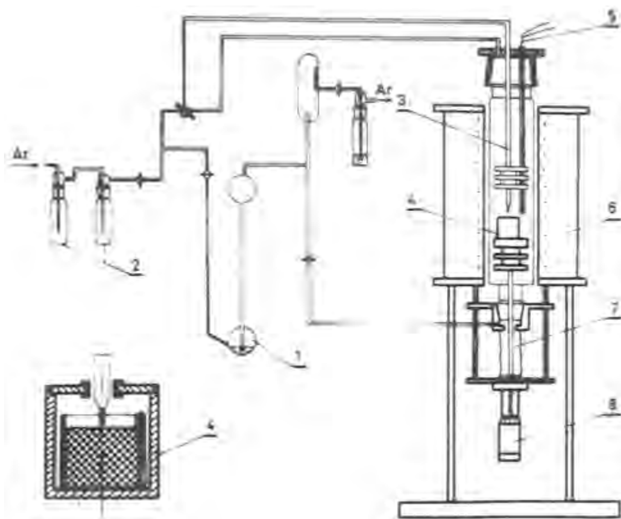

Fig. 3. Scheme of the experimental arrangements for the surface tension measurements.

$$P = \frac{1}{2} r P_{\max} \quad [8]$$

where P is the surface tension in dynes per centimeter, r the capillary radius, and $P_{\max}$ the maximum pressure required for forming and detaching bubble.

The real values of surface tension were obtained using Sudgen's correction method (10). For measurements, AgCl and KCl of high purity were used. Salts were stored in the heater at a temperature of 150°C for about 24 hr and, next, after transferring to the furnace, melted in a stream of gaseous dry HCl. HCl passed through the melt for about 0.5 hr. To obtain a homogeneous mixture of AgCl + KCl the weighed amounts of purified salts were also melted together in a stream of purified HCl and next cast in a quartz form, quickly cooled, and stored in a dessicator. The preparations of the salts for formation cells in the first part was analogical.

The results of surface tension measurements of pure AgCl *vs.* temperature are plottted in Fig. 4. The surface tension decreases linearly with the increase of temperature, also the obtained results are in good agreement with data from monograph (11) and are slightly different in comparison with Ref. (12). It should be added that the results for the different runs from this paper were averaged together by the least squares method as shown by the thick continuous line. The results for pure KCl shown in Fig. 5 were averaged in a similar way and the surface tension also changes linearly *vs.* temperature. Figure 5 presents the results obtained in this investigation for both limited evaporation (solid line) and free evaporation (dashed line). Differences appear between both sets, as at the investigated temperatures KCl has clearly noticeable pressure and the apparatus used enabled measurements in conditions approaching equilibrium between the liquid and gaseous phases. Our results for free evaporation are in good agreement with Ref. (13-15) as shown in Fig. 6.

As in the case of surface tension measurements of pure liquid KCl, our results with limited transport effect for AgCl-KCl mixtures show divergences in

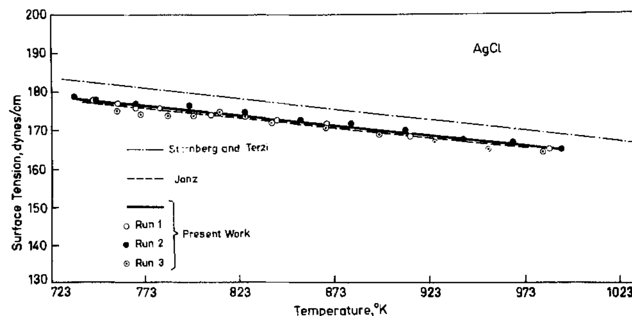

Fig. 4. The surface tension of AgCl *vs.* T°K

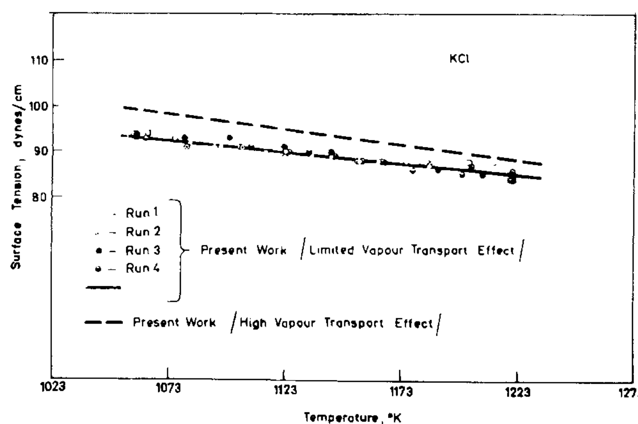

Fig. 5. The surface tension of KCl *vs.* T°K for limited and free evaporation.

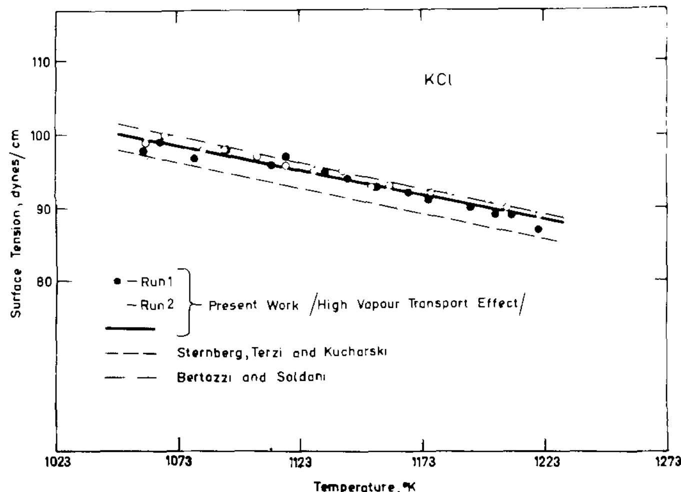

Fig. 6. The surface tension of KCl vs. T°K for free evaporation compared with the data from different sources.

comparison with literature data (13) for AgCl-KCl. Our data also decrease linearly with the increase of temperature. For both pure salts and AgCl-KCl solutions the relations of surface tension *vs.* temperature were described by linear dependences $\sigma = a - bt$°C, where a is the intercept and b the slope of the line. The values of both parameters for pure salts and mixtures, respectively, are summarized in Table II with the standard error of estimate and the temperature range of measurements.

On analyzing the maximum bubble pressure method it appears that it is less precise in comparison, for instance, with the pin method and, taking into account the standard error of estimate, errors in surface tension measurements are of the order of $\pm$2-3 dynes. These errors, however, and the different influence of limitation of evaporation in respect to the composition of investigated salt compositions were sufficient to introduce in linear equations of surface tension *vs.* temperature (Table II) the lack of fluid change in slopes from pure AgCl to KCl.

Using the linear equation from Table II, surface tension was calculated at 973°K and a relation of σ *vs.* X_{AgCl} was plotted in Fig. 7 as shown by circles. The continuous line on this plot refers to Eberhart's relation (16). Eberhart has presented an equation for the surface tension of binary liquid mixtures based on the assumption that the surface tension is a linear function of the surface layer mole fraction. The condition for equilibrium between the surface layer and the bulk liquid phase gives a relationship between the surface and the bulk compositions and results in the following equation

$$\sigma = \frac{X_{AgCl}\sigma_{AgCl} + SX_{KCl}\sigma_{KCl}}{X_{AgCl} + SX_{KCl}} \qquad [9]$$

where σ_{AgCl} and σ_{KCl} are the surface tensions of the pure salts, and S is the coefficient dependent on temperature which gives the extent of surface layer enrichment of the component of lower surface tension. For results of surface tension at 973°K the value of the coefficient $S = 6.21$ was determined according to the procedure presented in Ref. (16).

Table II. Experimental data of surface tension for AgCl, KCl, and AgCl-KCl liquid solutions

X_{AgCl}	$\sigma = a - bt$°C	Standard error of estimate $s(\hat{y})$	$\sigma_{700°C}$	Range of temperature (°C)
1.0	$\sigma = 202\ 54 - 0.0527t$	1.07	165.65	461-720
0.9	$\sigma = 167.50 - 0.0457t$	1.36	135.51	458-722
0.7	$\sigma = 173.40 - 0.0838t$	0.69	114.74	360-718
0.5	$\sigma = 149.70 - 0.0578t$	1.11	109.24	518-725
0.3	$\sigma = 161.30 - 0.0843t$	0.66	102.29	650-751
0.1	$\sigma = 138\ 40 - 0.0546t$	0.38	100.18	745-846
0.0	$\sigma = 133.10 - 0.0506t$	0.82	97.68	785-947
0.0	$\sigma = 151.70 - 0.0665t$	0.93	105.15	785-947*

* Data for pure KCl obtained with free evaporation.

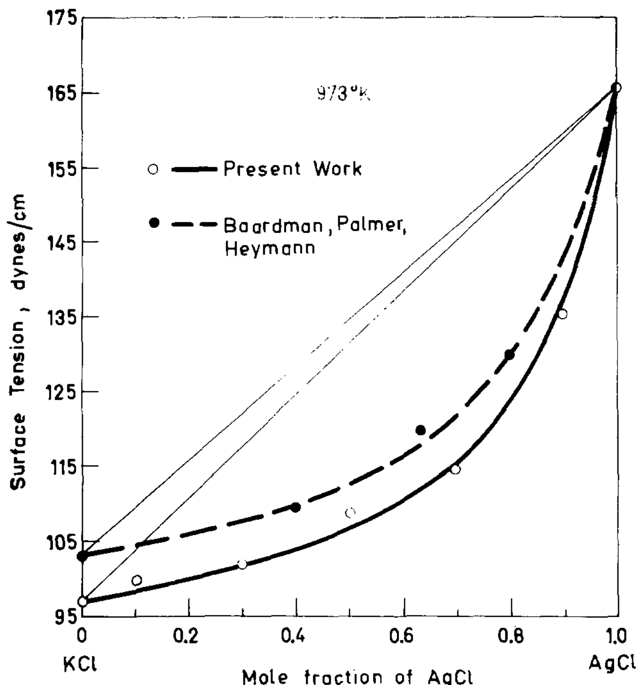

Fig. 7. The surface tension of the AgCl-KCl liquid solutions vs. X_{AgCl} at 973°K.

Composition of the Surface and the Relation Between the Thermodynamic Properties of the Bulk and Surface Phase

The basic relation which combines the surface tension with the activities of components in the surface layer and in the bulk phase according to (17) takes the form

$$RT \ln a_{AgCl^{\bar{\omega}}} = RT \ln a_{AgCl} + \frac{\overline{V}_{AgCl^{\bar{\omega}}}}{\tau}(\sigma - \sigma_{AgCl}) \qquad [10]$$

where $a_{AgCl^{\bar{\omega}}}$ and a_{AgCl} are the activities in the surface layer and in the bulk phase, respectively, τ is the assumed thickness of the surface layer, $\overline{V}_{AgCl^{\bar{\omega}}}$ is the partial molar volume of AgCl in the surface phase assumed to be equal molar volume V_{AgCl}, σ_{AgCl} is the surface tension of pure AgCl, and σ is the surface tension of AgCl-KCl solutions.

To obtain results of $\gamma_{AgCl^{\bar{\omega}}}$ in the surface phase a knowledge of the composition of the surface phase is necessary for interpretation by Krupkowski's method as in the case of the bulk. Various procedures for the computation of concentrations of both AgCl and KCl in the surface phase are presented below. On the basis of the assumption of the existence of the surface phase (18) it is possible to calculate the relative adsorption $\Gamma_{AgCl(KCl)}$ by the following relation

$$\Gamma_{AgCl(KCl)} = \Gamma_{AgCl} - \frac{X_{AgCl}}{X_{KCl}}\Gamma_{KCl} = -\frac{d\sigma}{d\mu_{AgCl}} \qquad [11]$$

where Γ_{AgCl} and Γ_{KCl} are the number of moles of AgCl and KCl, respectively, in the surface phase per unit area, μ_{AgCl} is the chemical potential of AgCl in the bulk phase, σ is the surface tension, and X_{AgCl} and X_{KCl} are the mole fractions of AgCl and KCl in the bulk phase.

The value of $\Gamma_{AgCl(KCl)}$ is independent of the arbitrarily assumed areas which separate from the solu-

tion the surface area to which we ascribe the properties of the phase. The only limitation is that the adsorption area must be contained between these two areas. The values of Γ_{AgCl} and Γ_{KCl} may be calculated if certain additional assumptions are made concerning the structure of the surface layer. One such assumption (9) may be represented by the equation

$$\Gamma_{AgCl}\overline{V}_{AgCl^{\bar{\omega}}} + \Gamma_{KCl}\overline{V}_{KCl^{\bar{\omega}}} = \tau \qquad [12]$$

where $\overline{V}_{AgCl^{\bar{\omega}}}$ and $\overline{V}_{KCl^{\bar{\omega}}}$ are the partial molar volumes of AgCl and KCl in the surface phase and τ is the thickness of the surface layer.

Basing on Eq. [10] and [12] values of adsorption Γ_{AgCl}, Γ_{KCl} may be calculated as follows

$$\Gamma_{AgCl} = \frac{X_{AgCl}\tau - X_{KCl}\overline{V}_{KCl^{\bar{\omega}}}\dfrac{d\sigma}{d\mu_{AgCl}}}{X_{KCl}\overline{V}_{KCl^{\bar{\omega}}} + X_{AgCl}\overline{V}_{AgCl^{\bar{\omega}}}} \qquad [13]$$

and

$$\Gamma_{KCl} = \frac{X_{KCl}\left(\tau + \overline{V}_{AgCl^{\bar{\omega}}}\dfrac{d\sigma}{d\mu_{AgCl}}\right)}{X_{KCl}\overline{V}_{KCl^{\bar{\omega}}} + X_{AgCl}\overline{V}_{AgCl^{\bar{\omega}}}} \qquad [14]$$

Considering Eq. [11], [12], [13], and [14], thermodynamic properties of AgCl-KCl solutions (Eq. [4]), and the results of surface tension measurements, the relative adsorption as well as adsorption of respective components were calculated assuming that $\overline{V}_{AgCl^{\bar{\omega}}} = V_{AgCl}$ and $\overline{V}_{KCl^{\bar{\omega}}} = V_{KCl}$. The molar volumes of AgCl and KCl were computed from densities of these salts, taken from monograph (11). Calculations were carried out for thicknesses of the surface phase, namely $\tau = 4.29 \times 10^{-8}$ cm and $\tau = 8.58 \times 10^{-8}$ cm. They are equal to a single and double diameter of a KCl molecule. Then the concentrations of AgCl and KCl in the surface phase were calculated from the relations

$$X_{AgCl^{\bar{\omega}}} = \frac{\Gamma_{AgCl}}{\Gamma_{AgCl} + \Gamma_{KCl}}$$

and

$$X_{KCl^{\bar{\omega}}} = \frac{\Gamma_{KCl}}{\Gamma_{AgCl} + \Gamma_{KCl}} \qquad [15]$$

When analyzing the results of the calculations, adding to the calculated number of moles of the respective components in the first layer of molecules of the thickness $\tau = 4.29 \times 10^{-8}$ cm the number of moles of the second layer of the same thickness but of bulk composition, the values of the AgCl concentration obtained were identical to those in calculations when it was assumed that $\tau = 8.58 \times 10^{-8}$ cm. This proves that the adsorption refers only to the first layer of molecules. The results of the calculations for the monomolecular layer are shown in Fig. 8.

The composition of the surface phase in the case of weak adsorption may also be calculated by the procedure assuming that the differences between the composition of surface and bulk phase take place only in the first layer of atoms. In such a case (18) the following relation is valid

$$\Gamma_{AgCl}A_{AgCl} + \Gamma_{KCl}A_{KCl} = 1 \qquad [16]$$

where A_{AgCl} and A_{KCl} are the partial molar areas of AgCl and KCl in the surface monomolecular layer, respectively. Using Eq. [16] and [11] the composition of AgCl in the surface layer was calculated and is also presented in Fig. 8.

In addition, the composition of the surface phase may be calculated as proposed by Eberhart (16) given the coefficient S and considering relations

$$S = \frac{X_{AgCl^{\bar{\omega}}}}{X_{KCl^{\bar{\omega}}}} \cdot \frac{X_{KCl}}{X_{AgCl}} \qquad [17]$$

and

$$X_{AgCl^{\bar{\omega}}} + X_{KCl^{\bar{\omega}}} = 1 \qquad [18]$$

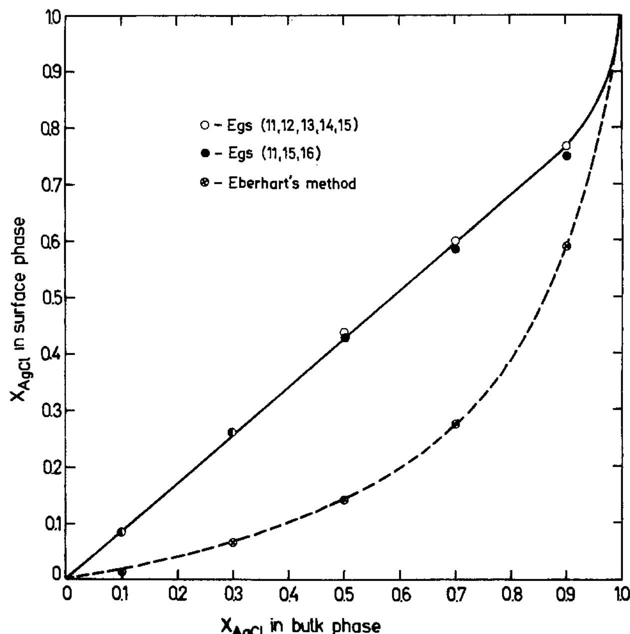

Fig. 8. Computed concentrations of AgCl in the surface phase vs. X_{AgCl} in the bulk phase.

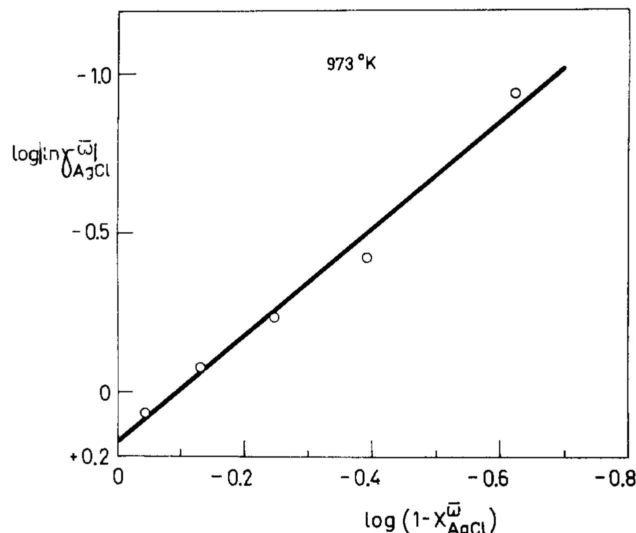

Fig. 9. The relation of log (ln $\gamma_{AgCl^{\bar{\omega}}}$) vs. log (1 − $X_{AgCl^{\bar{\omega}}}$) for the surface phase of the AgCl-KCl liquid solutions at 973°K.

Using Eq. [10] with the activities of the bulk calculated by Eq. [3] assuming that $\overline{V}_{AgCl^{\bar{\omega}}} = V_{AgCl}$ and $\tau = 4.29 \times 10^{-8}$ and taking into account $X_{AgCl^{\bar{\omega}}}$ (Eq. [15]), activity coefficients of the surface monomolecular layer were computed. The obtained results were described as for the bulk by Eq. [3]. Figure 9 shows a fit of calculated values of activity coefficients ln $\gamma_{AgCl^{\bar{\omega}}}$ to Eq. [3] as log (ln $\gamma_{AgCl^{\bar{\omega}}}$) vs. log (1 − $X_{AgCl^{\bar{\omega}}}$).

In this procedure at 973°K, the following values were obtained: m = 1.67 and $\bar{\omega}(T)$ = −1.44. By comparison with similar values of the bulk phase, m = 1.72 and $\omega(T)$ = −0.74 it is concluded that the asymmetry of thermodynamic properties connected with parameter m is almost similar, and the main significant difference in the thermodynamic properties of the surface and bulk phase appear in the values of function $\omega(T)$.

The same conclusion may be reached using different values for surface tension obtained experimentally by Sternberg and Terzi (12). The calculated parameters m and $\omega(T)$ for the surface phase are equal to 1.87 and −1.32 at 973°K, respectively.

Conclusions

The results of surface tension measurements obtained with limited evaporation giving conditions approaching equilibrium between the liquid and gaseous phase are lower for KCl and liquid AgCl-KCl solutions in comparison with Ref. (12) and (19). The main reason for these differences lies in the fact that the experiments in Ref. (12) and (19) were not carried out in equilibrium between the liquid and gaseous phases. This is confirmed by the fact that the results of our measurements performed in conditions of free evaporation are close to literature data.

A similar influence of experimental conditions has been observed in surface tension measurements for liquid metals with high vapor pressures (8, 9).

In view of these facts it is desirable to conduct further research in order to elaborate the experimental method for surface tension measurements ensuring full equilibrium between liquid and vapor. Calculated values of the logarithm of the activity coefficients of AgCl in the surface phase interpreted by Krupkowski's method show that the thermodynamic asymmetry of this phase and the bulk phase of AgCl-KCl solutions is the same within the range of experimental errors, but the differences in the values of the $\omega(T)$ function of both phases suggest in the case of the surface phase much higher deviations from ideality than in the bulk phase. Differences in partial enthalpy and excess entropies of components in both phases may also be suggested.

Manuscript submitted Aug. 17, 1977; revised manuscript received Jan. 3, 1978.

Any discussion of this paper will appear in a Discussion Section to be published in the December 1978 JOURNAL. All discussions for the December 1978 Discussion Section should be submitted by Aug. 1, 1978.

REFERENCES

1. A. Krupkowski, *Bull. Acad. Pol. Sci., Ser. A*, **1**, 15 (1950); *This Journal*, **122**, 132 (1975); *ibid.*, **122**, 691 (1975); *Met. Trans.*, **6B**, 457 (1975); *ibid.*, **6B**, 653 (1975).
2. Z. Moser and K. Fitzner, *Rev. Roumaine Chim.*, **19**, 1573 (1974).
3. Z. Moser, *Metall. Trans.*, **6B**, 103 (1975).
4. A. D. Pelton and S. N. Flengas, *This Journal*, **118**, 1307 (1971).
5. L. S. Hersh and O. J. Kleppa, *J. Chem. Phys.*, **42**, 1309 (1965).
6. W. Ptak and Z. Szczygiel, *Arch. Hutn.*, **12**, 265 (1967).
7. W. Ptak and M. Kucharski, *ibid.*, **19**, 301 (1974).
8. D. W. G. White, *Trans. Metall. Soc. AIME*, **236**, 796 (1966).
9. M. Kucharski, *Zeszyty Naukowe AGH*, **3**, 329 (1977).
10. S. Sugden, *J. Chem. Soc.*, **121**, 858 (1922).
11. G. J. Janz, "Molten Salts Handbook," Academic Press, New York (1967).
12. S. Sternberg and M. Terzi, *Rev. Roumaine Chim.*, **15**, 527 (1970).
13. G. Bertozzi and G. Soldani, *J. Phys. Chem.*, **70**, 1536 (1966).
14. R. B. Ellis and A. C. Freeman, *ibid.*, **69**, 1943 (1965).
15. S. Sternberg, M. Terzi, and M. Kucharski, *Arch. Hutn.*, **22**, 169 (1977).
16. J. G. Eberhart, *J. Phys. Chem.*, **70**, 1183 (1966).
17. J. E. B. Randles and B. Behr, *J. Electroanal. Chem.*, **35**, 389 (1972).
18. E. A. Guggenheim, "Mixtures," Clarendon Press, Oxford (1952).
19. N. K. Boardman, A. R. Palmer, and E. Heymann, *Trans. Faraday Soc.*, **15**, 277 (1955).

Design of an Electrocoating Cell for Constant Current Density Operation

A Fourier-Transform Method of Solution of the Laplace Equation

Rodney L. LeRoy*

Noranda Research Centre, Pointe Claire, Quebec H9R 1G5, Canada

ABSTRACT

Continuous electrocoating is normally carried out by passage of a foil, strip, or wire substrate between parallel electrodes in a coating cell. It has been shown that improved unformity of deposition in such a cell, and thus improved dielectric properties of the product, can be achieved using a converging electrode geometry. A method is described for deriving the optimal electrode geometry based on solution of the Laplace equation in the electrolyte region. A semianalytical solution is used, with boundary conditions on the converging cathode being applied by a novel Fourier-transform method. For the electrocoating cell the resulting optimal geometry is well approximated by a simple result which assumes that current flow is perpendicular to the moving substrate.

Commercial application of electrodeposition of organic coatings has expanded rapidly over the last 15 years, first in the automotive industry and more recently in applying coatings to the products of the electrical, heating and cooling, furniture, aluminum extrusion, and other industries (1). The electrocoating process is particularly suited to application of thin, nonporous organic coatings to continuous foil, strip, or wire (2-4). In some applications, production speeds of 300-500 cm/sec have been achieved with uniform coating thicknesses of 2.5-5 μm.

* Electrochemical Society Active Member.

The electrodeposition process is characterized by simultaneous occurrence of electrophoresis, electrolysis, and electroendosmosis (5, 6). All practical resin systems developed to date have been anaphoretic, involving deposition of the organic coating on a stationary or moving anode. The basic resin types used have thus been acidic and include carboxylated drying oils, alkyds and epoxy esters of high acid value, carboxyl-bearing acrylic copolymers, phenolics and triazine condensates. Typical coating baths consist of approximately 80-85% deionized water, 2-3% co-solvent, and 1% solubilizing base, with the balance being the anionic

polymer. The potential applied to the electrocoating cell is typically 100-250V.

When potential is applied to the electrodes of the coating cell, the negatively charged polymer ions migrate toward the anode under the influence of the electrical field by the processes of ionic migration and electrophoresis. In the immediate vicinity of the anode several reactions can occur. For polycarboxylic acid polymers as were used in this work, direct decarboxylation can occur by the Kolbe reaction

$$2RCOO^- \rightarrow R{-}R + 2CO_2 + 2e \quad [1]$$

This reaction, however, is believed to be relatively unimportant, with the majority of the applied current being consumed by anodic dissolution of the anode substrate

$$M \rightarrow M^{z+} + ze \quad [2]$$

and by the anodic decomposition of water to give hydrogen ions and oxygen gas

$$2H_2O \rightarrow O_2 + 4H^+ + 4e \quad [3]$$

Some polymeric carboxylate ions are precipitated or coagulated in the vicinity of the anode by reaction with the ions of the substrate metal which are produced by reaction [2]. However, the principal anodic process is believed to be reaction [3], with polymer coagulation occurring by reaction with hydrogen ions in the low pH region in the immediate vicinity of the electrode. The local pH near the anode can drop to about 2, while most resins used for electrocoating will coagulate at pH values between 4 and 5 (7).

Thus anodic resin deposition occurs concurrently with vigorous evolution of oxygen gas. When an anode substrate is moved continuously through a coating cell between parallel cathode plates, a highly nonuniform current density distribution is established along the substrate in the coating cell. Deposition is rapid when the uninsulated substrate first enters the cell, but falls off as electrical insulation of the substrate by the deposited resin increases the resistance to the flow of current. These effects result in less than optimal coating properties. Resin deposition occurs at a very high rate at the entrance to the cell with simultaneous evolution of oxygen, resulting in a less homogeneous coating on the final product than would be achievable under more controlled conditions.

The final process occurring in the coating cell is electroendosmosis. This is the phenomenon by which much of the water in the film deposited on the anode substrate migrates in the direction of the cathode under the influence of the applied potential, resulting in water contents as low as 5-15%. On emergence from the cell, the electrocoated film is normally baked at between 150° and 200°C to promote further drying and, in many cases, oxidative cross-linking.

It has been found that use of a converging electrode geometry in an electrocoating cell can result in improved deposit properties by enabling a relatively constant current density on the anode substrate throughout the cell. The purpose of this paper is to describe a method of designing an electrode to achieve this constant current density objective. The method is based on solution of the Laplace equation within the electrolyte.

Basis of the Method

No calculations to derive optimal cathode geometries are possible until the boundary conditions in the electrocoating cell are defined. The cathode presents no problem in this regard, as the reaction here is simply hydrogen evolution. For typical substrates (*e.g.*, stainless steel) the overvoltage for this reaction will always be less than 1V in the range of current densities which are used. This is small compared with the potential applied to the cell, which is normally greater than 100V. Thus the cathode-electrolyte interface can be treated as being at the same potential as the cathode itself. The oxygen overvoltage on the anode and the reversible potential for the water decomposition reaction (totaling less than 1.6V) can be similarly neglected.

However, the potential on the anode-electrolyte interface varies strongly with position in the cell due to the deposition of the insulating polymer. In a parallel-electrode electrocoating cell, it would be difficult to deduce this anode interface potential as a function of position in the cell. For the converging electrode geometry, if it is assumed that a constant anode current density can be achieved, the problem becomes more amenable to solution. In this case, the constant electrocoating current density is under the control of the operator, so the variation of the anode film-electrolyte interface potential with time can be determined in a static experiment for the resin which is being used.

A typical result is illustrated in Fig. 1 for an aluminum substrate. The resin used was BASF Lewipal No. E-33, a mixed acrylate ester/acrylic acid resin solubilized with polyamines. The operating current density was 9.3 mA/cm^2. The film voltages measured in the static cell were obtained as a function of deposition time, but this result is readily translated into film voltage as a function of position in the continuous electrocoating cell as has been done in Fig. 1. This method is valid if the mass-transfer limiting current density is appreciably larger than the value selected. Provided this condition is satisfied, such static experiments allow translation of a desired constant current density of operation into a film voltage profile as a function of position in the electrocoating cell.

The conductivity of the resin-containing electrolyte must also be determined for use in the calculations described below. The conductivity of the BASF E-33 resin solution was 0.00056 Ω^{-1} cm^{-1}.

Derivation of the Cathode Geometry

A first approximation.—If it is assumed that current flows directly across the cell, perpendicular to the anode, the electrode geometry can be approximated using the equation

$$\text{total resistance } (R_t) = \text{solution resistance } (R_s) + \text{film resistance } (R_f) \quad [4]$$

Consider a small segment of the anode substrate, the length of which is $1/N$th of the total cell length L. Assuming that the current density is constant along the anode, the total resistance between this segment of the substrate and the corresponding segment of the cathode (on one side) is

$$R_t = U/(I/2N) \quad [5]$$

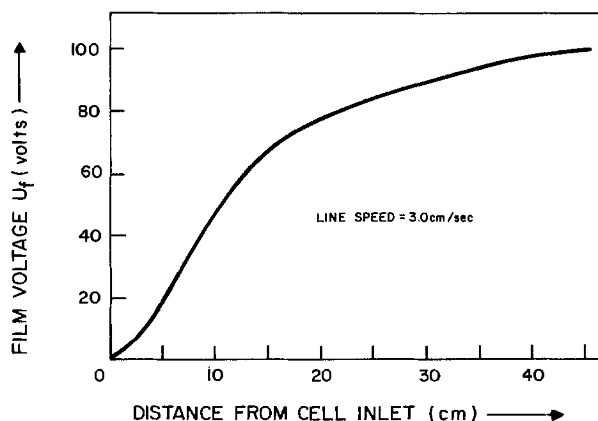

Fig. 1. Film voltage as a function of distance from the inlet of the continuous electrocoating cell. Data is translated from a static experiment assuming a constant current density in the cell of 9.3 mA/cm^2. The resin used was BASF E-33 of conductivity 0.00056 Ω^{-1} cm^{-1}.

where U is the total voltage applied to the cell, and I is the total current. By a similar argument, the film resistance on the segment of the anode being considered is

$$R_f = U_f/(I/2N) \quad [6]$$

where U_f (cf. Fig. 1) is the film voltage determined from static measurements. By definition the solution resistance is

$$R_s = \frac{d}{\kappa \left[\frac{W_a + W_c}{2}\right] \frac{L}{N}} \quad [7]$$

where d is the desired anode-cathode separation, κ is the solution conductivity, and W_a and W_c are, respectively, the widths of the anode and the cathode.

Substitution of the resistance factors from Eq. [5] to [7] into Eq. [4] gives the desired result for the anode-cathode separation as a function of position in the cell

$$d = \frac{\kappa L(W_a + W_c)}{I}(U - U_f) \quad [8]$$

The electrode configuration calculated from the film-voltage data of Fig. 1 using Eq. [8] is sketched as a broken curve in Fig. 2. Cell dimensions were $L = 45.7$ cm, $W_c = 10.2$ cm, and $W_a = 3.2$ cm, and the total current for a constant current density of 9.3 mA/cm^2 was set at $I = 2.7A$. An applied cell voltage of $U = 135V$ was assumed. However, polarization effects and the reversible potential for the over-all cell reaction have been ignored, so in practice it would be necessary to adjust the applied potential until the required current density was achieved.

Solution of the Laplace equation.—Introduction.— The electrode geometry calculated using Eq. [8] is an approximation, because current does not flow directly across the cell perpendicular to the anode substrate. The current flowing at any point in the electrolyte is sensitive to the potentials at all points on the enclosing electrodes.

This problem is solved as follows. Assuming that the current is not significantly limited by mass-transfer effects, the potential $\phi(x, y)$ can be accurately represented by the Laplace equation in the region between the anode and the cathode (8, 9). This is

$$\frac{\partial^2\phi(x, y)}{\partial x^2} + \frac{\partial^2\phi(x, y)}{\partial y^2} = 0 \quad [9]$$

Rectangular coordinates are used for the cell geometry being considered here, with the x and y directions defined in Fig. 3 for an arbitrary, converging electrode geometry.

Laplacian problems are commonly encountered in aerodynamics, hydrodynamics, heat transfer, electrostatics, and many other physical problems as well as in electrochemical applications, so considerable effort has been devoted to their solution. One approach is to use experimentally based analogical or graphical methods (10, 11). However, such methods are time consuming to use and are not well adapted to iterative determination of an optimal electrode design. Also, with the availability of high-speed digital computers, numerical solutions of Eq. [9] can be obtained. Such brute force solutions depend on a process of iteration (12) and for a complex geometry, such as that of Fig. 3, solution can require several minutes of computer time and thus a substantial cost.

Analytical solutions are, therefore, to be preferred in many instances, even if they entail major approximations. Examples of such solutions abound (9, 13-15).

Once the potential distribution has been established, the current density J normal to the anode can be calculated directly from the gradient of the potential perpendicular to the substrate, from the Ohm's law expression

$$J = -\kappa \frac{\partial\phi(x, y)}{\partial x}\bigg|_{x\to 0} \quad [10]$$

The process of determination of an optimal cathode geometry is as follows. A particular geometry is selected, Eq. [9] is solved for the potential in the electrocoating solution, and current density values along the anode substrate are calculated from Eq. [10]. If these values differ significantly from constancy, appropriate modifications are made in the electrode geometry and the process is repeated until relatively constant current density is achieved.

A suitable general form of the solution to Eq. [9] is

$$\phi(x, y) = \sum_{m=0}^{\infty} (A'_{1m}e^{ax} + A'_{2m}e^{-ax}) (B_{1m}\sin(ay) + B_{2m}\cos(ay)) \quad [11]$$

where the infinite set of constants A'_{1m}, A'_{2m}, B_{1m}, B_{2m} and a must be determined from the boundary conditions. Thus, on the cathode, whatever its geometry, $\phi(x,y)$ must reduce to the value of the applied potential U, while on the anode substrate at $x = 0$ it must reduce to the film voltage U_f (cf. Fig. 1). In the method of solution which has been selected here, these boundary conditions are applied by identifying Eq.

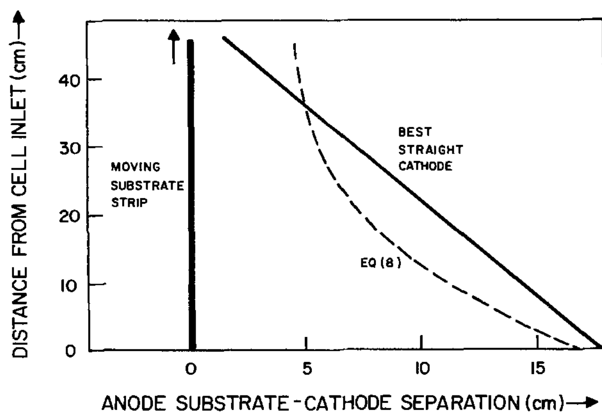

Fig. 2. Representative converging electrode geometries in the electrocoating cell. The broken curve is the cathode whose geometry is calculated from Eq. [8], based on the variation of film voltage with position in the cell which is given in Fig. 1. For the same film-voltage variation, the solid line is the linear electrode giving closest to constant current density.

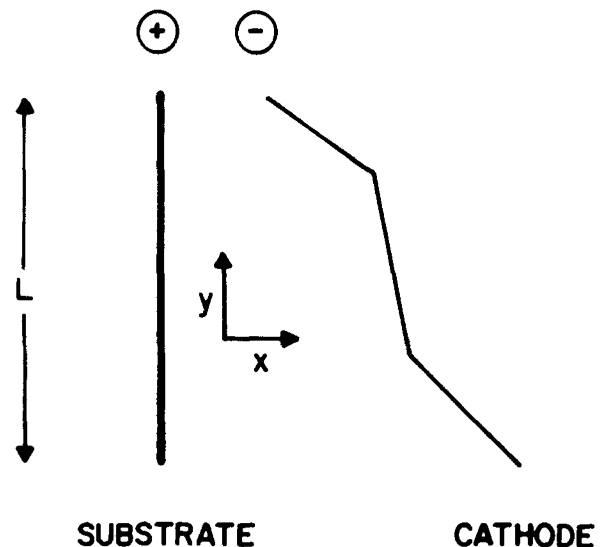

Fig. 3. A typical converging electrode geometry, with the cathode consisting of 3 straight-line segments.

[11] with Fourier expansions of the known potential on each of the two electrodes.

A third boundary condition applies at $y = 0$ and $y = L$. These are the insulating walls of the cell, and the lines of equipotential must be perpendicular to them. This condition may be expressed as (12, 15)

$$\left.\frac{\partial\phi(x,y)}{\partial y}\right|_{y=0,L} = 0 \qquad [12]$$

Examination of Eq. [11] reveals that Eq. [12] would be satisfied if all of the constants B_{1m} were 0, and the period of the function were L, *i.e.*, if $a = m\pi/L$. In this case, $\phi(x, y)$ would reduce to

$$\phi(x,y) = \sum_{m=0}^{\infty}\left[A_{1m}e^{\frac{m\pi x}{L}} + A_{2m}e^{-\frac{m\pi x}{L}}\right]\cos\frac{m\pi y}{L} \qquad [13]$$

The two series of constants A_{1m} and A_{2m} would then be determined by application of the boundary conditions on the electrodes.

It was found that Eq. [13] would not converge to a sufficient degree of accuracy with a reasonable number of terms in the series. This was because the identification of the boundary conditions using Fourier series resulted in sharp discontinuities at $y = 0$ and $y = L$.

An approximate solution was, therefore, used. Boundary conditions were applied for a cell which was twice as long as the actual cell (Fig. 4). The anode potential outside the "true" cell was taken to be a constant at each end, equal to the value just inside the cell. The cathode potential was set equal to its constant value U over its entire length. In this way the potential lines were forced to be approximately perpendicular to the insulating walls at $y = L/2$ and $y = 3L/2$, even though $\partial\phi/\partial y$ was not analytically equal to zero at these points.

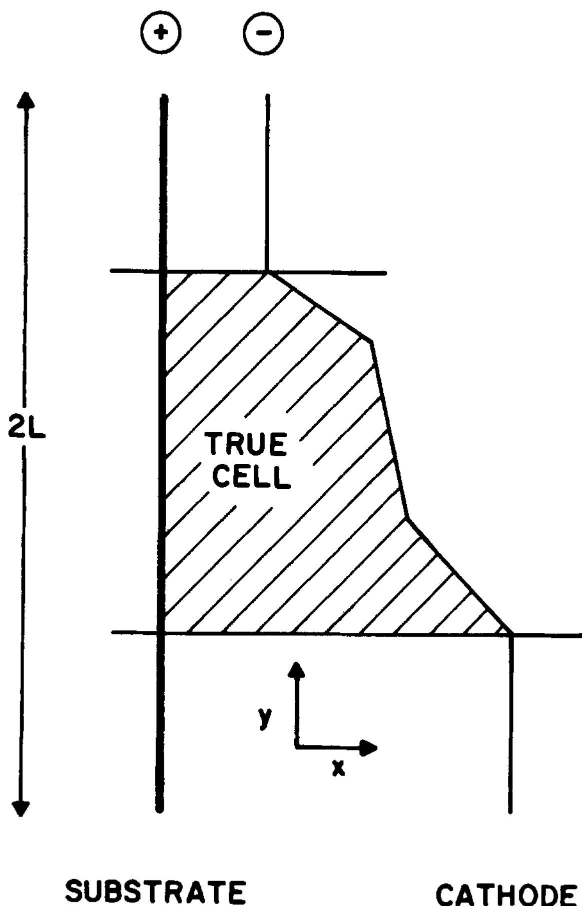

Fig. 4. Schematic representation of the geometry assumed in applying the boundary conditions to Eq. [14].

With this expanded cell geometry, the sine series of Eq. [11] was used as an approximation to the potential $\phi(x, y)$

$$\phi(x,y) = \sum_{m=1}^{\infty}\left[A_{1m}e^{\frac{m\pi x}{2L}} + A_{2m}e^{-\frac{m\pi x}{2L}}\right]\sin\frac{m\pi y}{2L} \qquad [14]$$

Boundary condition on the anode substrate.—The variation of film voltage U_f with position in the cell, exemplified by the result in Fig. 1, can be accurately approximated by a quadratic equation of the general form

$$U_f(y) = c_1y + c_2y^2 + c_3y^3 \qquad [15]$$

The parameters c_i are determined for the particular resin composition being used by least squares fitting of the data from the static experiment by Eq. [15]. For the data of Fig. 1, these constants are $c_1 = 5.799$ V cm^{-1}, $c_2 = 0.1180$ V cm^{-2}, and $c_3 = 0.000847$ V cm^{-3}.

The general expression for the potential (Eq. [14]) reduces on the anode substrate to

$$\phi(x = 0, y) = \sum_{m=1}^{\infty}(A_{1m} + A_{2m})\sin\frac{m\pi y}{2L} \qquad [16]$$

The potential on the anode is already known to be

$$\begin{aligned} U_f(y) &= 0, && 0 < y < L/2 \\ &= c_1\left(y - \frac{L}{2}\right) + c_2\left(y - \frac{L}{2}\right)^2 + c_3\left(y - \frac{L}{2}\right)^3 && L/2 < y < 3L/2 \\ &= c_1L + c_2L^2 + c_3L^3 && 3L/2 < y < 2L \end{aligned} \qquad [17]$$

Equations [16] and [17] are equated by expanding Eq. [17] as a Fourier series in $\sin(m\pi y/2L)$. The result, when identified with the series of Eq. [16], gives a general expression for $T_{1m} = A_{1m} + A_{2m}$

$$T_{1m} = \frac{1}{L}\int_0^{2L} U_f(y)\sin\frac{m\pi y}{2L}\,dy \qquad [18]$$

The integral of Eq. [18] is recorded in Eq. [A-1] of Appendix A. Although somewhat formidable in appearance, the result depends only on the parameters c_1, c_2, and c_3 of the film voltage U_f. The expression is readily evaluated by computer and has a single value for each term of the Fourier series.

Boundary condition on the cathode.—Although the cathode geometry is not assumed at this time to be known, it can be defined in general terms by writing the anode-cathode distance d as a function of y, $d = T(y)$. Thus, the Laplace solution on the cathode may be written as

$$\phi(x = T(y), y) = \sum_{m=1}^{\infty}\left[T_{1m}e^{\frac{m\pi T(y)}{2L}} - A_{2m}\left(e^{\frac{m\pi T(y)}{2L}} - e^{-\frac{m\pi T(y)}{2L}}\right)\right]\sin\frac{m\pi y}{2L} \qquad [19]$$

where A_{1m} has been eliminated by writing it in terms of A_{2m} and the known parameter (Eq. [A-1]) T_{1m}.

The infinite series of constants A_{2m} are the only remaining unknowns in Eq. [19]. These constants are evaluated by equating Eq. [19] to the known value of the potential on the cathode, U. This constant potential is readily expanded in a Fourier sine series

$$U = \sum_{n=1}^{\infty} T_{2n} \sin \frac{n\pi y}{2L} \quad [20]$$

where

$$T_{2n} = \frac{1}{L}\int_0^{2L} U \sin \frac{n\pi y}{2L} dy$$

$$= \frac{2U}{n\pi}(1 - \cos n\pi) \quad [21]$$

At first glance it would appear that the parameters A_{2m} could be immediately calculated by identifying the coefficients of the sine terms in Eq. [19] and [20]. In the general case where $T(y)$ is not a constant this is not possible because the coefficient in Eq. [19] is itself a function of y. This difficulty is circumvented by expanding the summation of Eq. [19] itself as a sine series. Although the result appears cumbersome, it can be efficiently used in a digital machine for solution of the boundary condition and, thus, for calculation of the current density distribution from Eq. [10].

The general term of the Fourier expansion of the right-hand side of Eq. [19] may be written as follows, and equated to T_{2n}

$$\frac{1}{L}\int_0^{2L} \left\{ \sum_{m=1}^{\infty} \left[T_{1m} e^{\frac{m\pi T(y)}{2L}} - A_{2m} \left[e^{\frac{m\pi T(y)}{2L}} - e^{-\frac{m\pi T(y)}{2L}} \right] \right] \sin \frac{m\pi y}{2L} \right\} \sin \frac{n\pi y}{2L} dy = T_{2n} \quad [22]$$

This result can be rewritten as an infinite set of linear equations in the parameters A_{2m}

$$\sum_{m=1}^{\infty} K_{1m} A_{2m} = K_{2n} - L\,T_{2n} \quad [23]$$

where

$$K_{1m} = \int_0^{2L} \left\{ e^{\frac{m\pi T(y)}{2L}} - e^{-\frac{m\pi T(y)}{2L}} \right\} \sin \frac{m\pi y}{2L} \sin \frac{n\pi y}{2L} dy \quad [24]$$

and

$$K_{2n} = \int_0^{2L} \left\{ \sum_{m=1}^{\infty} T_{1m} e^{\frac{m\pi T(y)}{2L}} \sin \frac{m\pi y}{2L} \right\} \sin \frac{n\pi y}{2L} dy \quad [25]$$

The procedure used for solution of Eq. [23] is to truncate the summations (Eq. [23] and [25]) at a finite number of terms, for example 20. The parameters K_{1m} and K_{2m} are then evaluated for values of m from 1 to the cut-off value of m. Using these values, and the known values of T_{2n} (Eq. [21]), the linear Eq. [23] are solved for the parameters A_{2m}.

The Laplace solution.—Using the results of the preceding sections for T_{1m} and A_{2m}, the potential may be calculated at any point in the electrocoating solution

$$\phi(x, y) = \sum_{m=1}^{m'} \left[T_{1m} e^{\frac{m\pi x}{2L}} - A_{2m} \left[e^{\frac{m\pi x}{2L}} - e^{-\frac{m\pi x}{2L}} \right] \right] \sin \frac{m\pi y}{2L} \quad [26]$$

where m' is the cut-off value selected for truncating the series.

The current density perpendicular to the anode, at a distance x from it, can be written directly from this result and Eq. [10]

$$J = -\kappa \sum_{m=1}^{m'} \left(\frac{m\pi}{2L}\right) \left[T_{1m} e^{\frac{m\pi x}{2L}} - A_{2m} \left[e^{\frac{m\pi x}{2L}} + e^{-\frac{m\pi x}{2L}} \right] \right] \sin \frac{m\pi y}{2L} \quad [27]$$

It would theoretically be possible to evaluate the current density on the anode substrate by setting $x = 0$ in Eq. [27]. However, it has been found that better accuracy is achieved for reasonable values of the truncation parameter m' when J is evaluated for a small positive value of x, for example, between 0.2 and 0.5 cm. A similar effect has been noted by Waber for a related problem (16).

Definition of the cathode geometry.—The method of solution of the Laplace equation which has been developed here is most efficiently carried out if the parameters K_{1m} and K_{2m} can be expressed in analytical form. This is possible if the arbitrary cathode geometry being considered, $d = T(y)$, is expressed as a series of straight lines.

The cathode geometry is defined as follows in the computer program written to carry out this analysis. The number of straight line segments to be used, l, is entered first followed by the defining parameters of each segment as they are given in Fig. 5. The two parameters for each junction point are f_i, the fraction of the substrate length from the cell entrance, and d_i, the anode-cathode separation at this point. With the cathode defined in this way, Eq. [24] and [25] can be written in analytical form, the parameters A_{2m} and T_{1m} can be evaluated, and the current density distribution calculated from Eq. [27]. The analytical results for K_{1m} and K_{2n} are recorded in Appendix B.

Results and Discussion

Parallel electrodes.—The Laplace solution is simplified substantially when the anode-cathode separation is a constant, d. In this case the coefficients of sin $(m\pi y/2L)$ in Eq. [19] and [20] can be equated giving the following result for A_{2m}

$$A_{2m} = \frac{T_{1m} e^{\frac{m\pi d}{2L}} - T_{2m}}{e^{\frac{m\pi d}{2L}} - e^{-\frac{m\pi d}{2L}}} \quad [28]$$

Figure 6 records a typical potential distribution obtained for a cell having a parallel electrode configuration. In this case, the applied potential was $U = 100$V, and the film voltage U_f was assumed to increase linearly from 0 at the cell inlet ($y = L/2$) to 50V at the outlet ($y = 3L/2$).

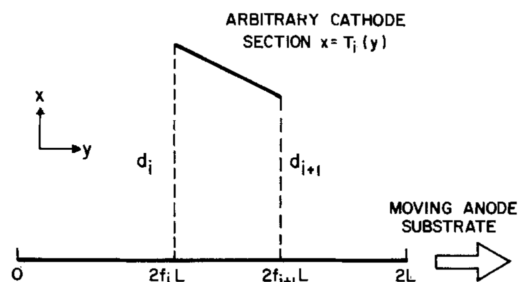

Fig. 5. Definition of the parameters used in representing a cathode of arbitrary geometry as a series of straight-line segments.

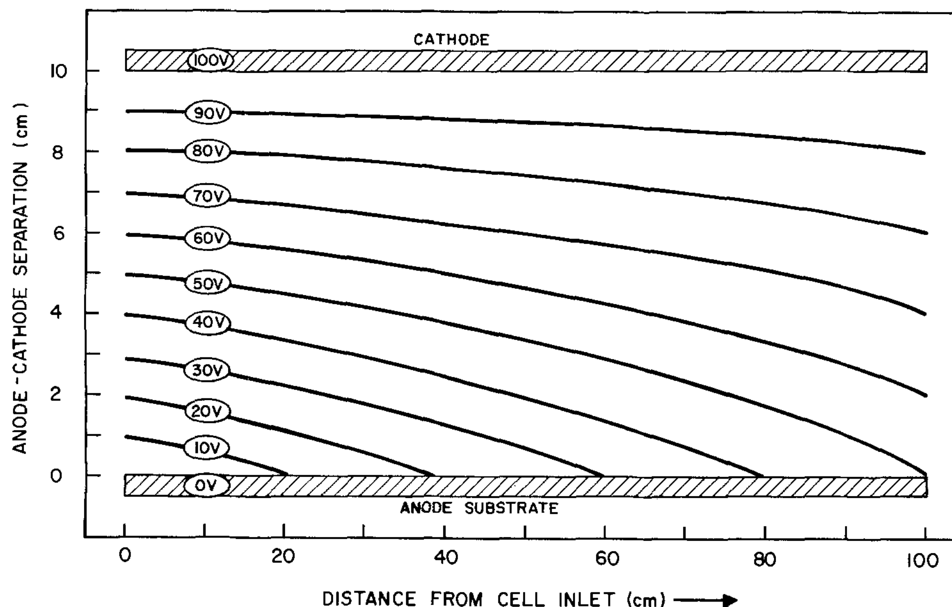

Fig. 6. Equipotential lines in an electrocoating cell between parallel electrodes, for an applied potential of 100V. The film voltage is assumed to rise linearly from zero volt at the cell inlet to 50V at the outlet. Anode-cathode separation is 10 cm, while the cell length is 100 cm.

Solution of the boundary condition on the substrate is simplified for such a linear film-voltage variation. In general, if the film voltage rises from 0 at the inlet to a fraction F of the total applied potential U at the outlet, Eq. [A-1] reduces to ($c_1 = FU/L$; $c_2 = c_3 = 0$)

$$T_{1m} = \frac{2FU}{m\pi}\left\{\frac{2}{m\pi}\left(\sin\frac{3m\pi}{4} - \sin\frac{m\pi}{4}\right) - \cos m\pi\right\} \quad [29]$$

For the example of Fig. 6, $FU = 50\text{V}$.

The potential distribution of Fig. 6 indicates that the current flow is strongly concentrated on the end of the anode at the cell entrance for the parallel electrode configuration. In fact, the current density at the entrance in this example is twice as great as it is at the exit.

Converging, straight electrodes.—An obvious "first guess" at a cathode geometry which would give more constant current density on the anode than a parallel configuration is a single straight converging element. This is illustrated, for example, by the solid lines of Fig. 2.

Several examples were worked out to delineate the qualitative effects of such a converging structure on the current density distribution. Results are summarized in Fig. 7. A total cell voltage of 100V was assumed, with the film voltage increasing linearly from zero at the cell entrance to 50V at the cell exit. Because of this assumed linearity in the film voltage, the result of Eq. [29] could be used, but the nonparallel structure of the electrodes necessitated the use of the full solution of Eq. [23] for A_{2m}. Current densities were calculated from Eq. [27] for $x = 0.5$ cm. Initial calculations were carried out with the potential (Eq. [14] and subsequent results) truncated at $m' = 20$ and 40 terms. Essentially identical results were obtained for both series lengths, so $m' = 20$ terms were used in all subsequent calculations.

The assumed cell length was 100 cm. The calculated current densities are expressed divided by the conductivity, so as not to introduce an extraneous arbitrary factor to these illustrative results.

In Fig. 7a the anode-cathode separation at the cell exit was set equal to 10 cm, and the current-density variation was calculated for electrode separations at the entrance of 10, 15, 20, and 40 cm. The parallel configuration ($d_1 = 10$ cm) gave a strong variation of current density with position in the cell, as was anticipated from Fig. 6. Increasing the entrance separation to 20 cm improved the constancy of the current density, while increasing it to 40 cm resulted in a

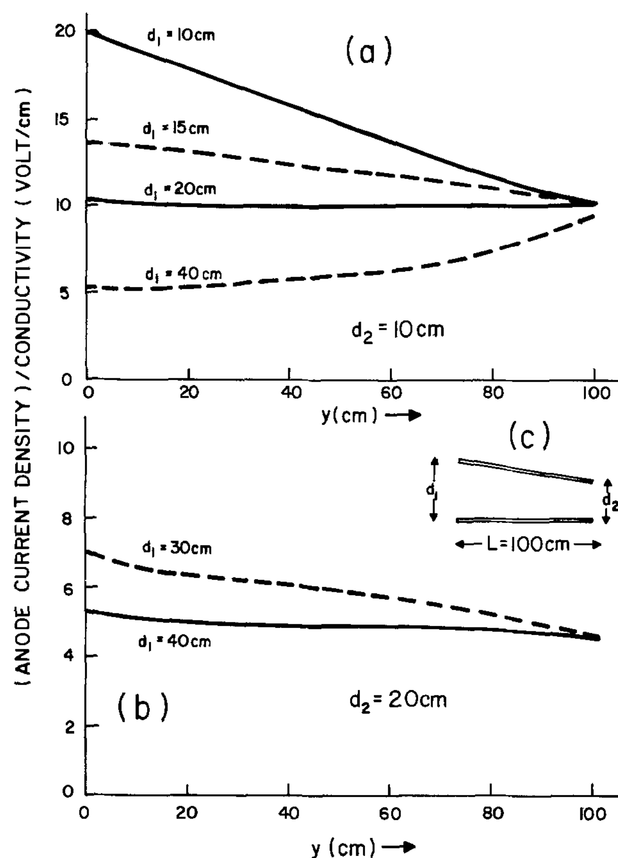

Fig. 7. Variation of anode current density with position in an electrocoating cell having converging, straight electrodes. An applied potential of $U = 100\text{V}$ is assumed. Cell length is 100 cm, with the anode-cathode separation as defined in Fig. 7c. Results in Fig. 7a were computed for an electrode separation of 10 cm at the cell exit, while those in Fig. 7b assumed an electrode separation at the exit of 20 cm.

relatively high current density at the cell exit. Similar results are recorded in Fig. 7b for an anode-cathode separation of 20 cm at the cell exit. Solution for each configuration required approximately 1.4 sec (core) on the McGill University IBM 360 computer.

Further calculations were carried out using the experimental film voltage data of Fig. 1. This necessitated use of the full results of Eq. [A-1] for application of the boundary condition on the anode substrate. The nonlinearity of the film voltage variation resulted in

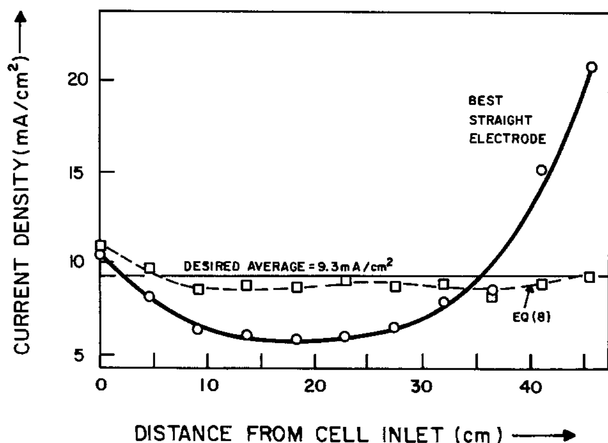

Fig. 8. Variation of current density with position in the electrocoating cell, for the variation of film voltage with position in the cell which is recorded in Fig. 1, and the electrode geometries drawn in Fig. 2. Both curves correspond to an applied potential of 135V. The broken curve is derived for the electrode geometry of Eq. [8], while the solid curve is for the "best" converging, straight electrodes (solid lines, Fig. 2).

relatively higher current densities near the cell entrance, and relatively lower current densities near its exit. The converging solid electrode drawn in Fig. 2 was derived in an iterative program which minimized the sum of the squares of the deviations of the current density from the desired average value. The corresponding current-density variation is plotted as a solid curve in Fig. 8. Clearly a single straight electrode can only very approximately compensate for the film voltage variation as it occurs in the practical cell.

In spite of the imperfect establishment of constant current density within the cell, use of the converging configuration of Fig. 2 resulted in substantially improved properties of electrocoated strip. Table I records a comparison of the properties of strips prepared in a continuous electrocoating cell with conventional, parallel electrodes (substrate-cathode separation 3.3 cm) and with the converging straight-line electrodes of Fig. 2. The continuous strip was 3.2 cm wide × 0.005 cm thick aluminum, run at a line speed of 3.3 cm/sec with the BASF E-33 resin. Both sets of electrodes were 10.2 cm wide, and the cell length was 45.7 cm. The current to each cell was kept constant at 2.7A, or 9.3 mA/cm² of substrate area.

The average build was 12% greater for the converging electrodes compared to the parallel electrodes, for the same average applied voltage. More important, the electrocoated deposits on the strips treated in the converging cell were of superior quality, containing fewer gas bubbles.

Table I. Comparison of parallel and converging electrode electrocoating cells

Electrode configuration	Run number	Applied voltage (V)	Coating thickness* (10^{-3} cm)
Converging**	1	131	3.81
	2	121	4.06
	3	125	3.81
	4	120	4.19
	Average	124	3.97
Parallel†	1	128	3.56
	2	126	3.56
	3	122	3.56
	4	121	3.56
	Average	124	3.56

* Measured after drying and curing.
** Linear cathode. Anode-cathode separation 17.8 cm at the entrance and 1.5 cm at the exit (Fig. 2).
† Anode-cathode separation was 3.3 cm.

Curvilinear cathode geometry.—No experiments were performed using a curvilinear cathode geometry. However, a calculation was made to test how closely a cathode designed according to the approximate Eq. [8] gives a constant current density through the cell.

Using the parameters for the BASF E-33 resin, Eq. [27] was solved by the method of this paper for the electrode defined by Eq. [8]. This electrode (the broken curve of Fig. 2) was approximated by 10 straight-line segments when applying the boundary condition on the cathode as described in Appendix B.

The resulting current-density variation in the cell for an applied potential of $U = 135$V is plotted as a broken curve in Fig. 8. The corresponding potential distribution in the electrocoating solution is sketched in Fig. 9. It is apparent that the calculation of Eq. [8] gives a good approximation to the desired electrode geometry. It is likely that converging cathode geometries derived using this equation could give further improvements in the properties of continuously electrocoated products.

Acknowledgments

I am indebted to Dr. M. A. Dudley for suggesting that improved electrocoating quality could be achievable using a converging electrode geometry. Mr. G. Bersolami carried out the experiments reported in Table I and Fig. 1. This work was supported by Canada Wire and Cable Limited. The work described in this paper is the subject of U.S. Patent No. 3,933,611 and equivalent patents granted or pending in other countries.

Manuscript submitted July 12, 1977; revised manuscript received Jan. 9, 1978.

Any discussion of this paper will appear in a Discussion Section to be published in the December 1978

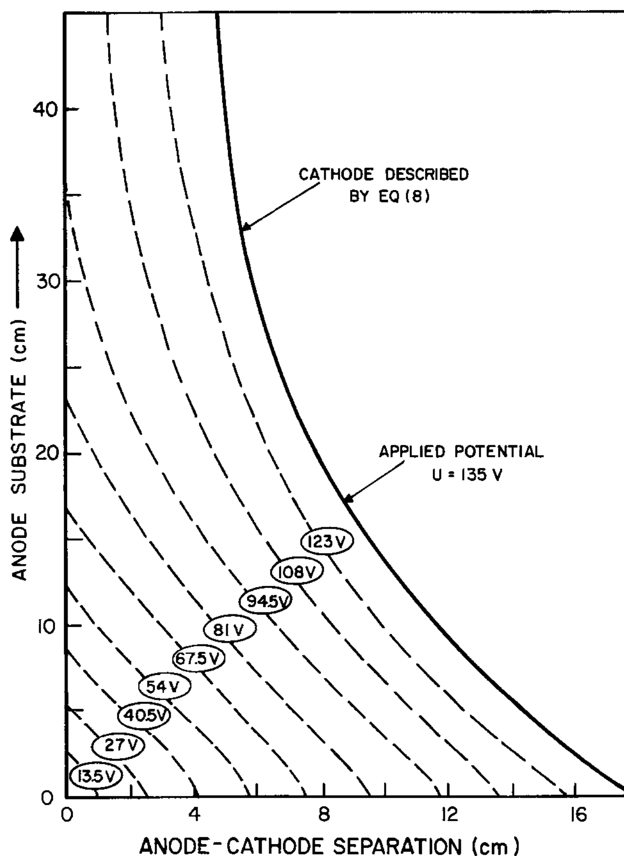

Fig. 9. Equipotential lines in the electrocoating solution for the cathode geometry defined by Eq. [8]. The film-voltage variation with position on the anode substrate is taken from Fig. 1.

JOURNAL. All discussions for the December 1978 Discussion Section should be submitted by Aug. 1, 1978.

APPENDIX A

Evaluation of the General Term in the Fourier Expansion of the Potential on the Substrate

The general term (Eq. [18]) is

$$T_{1m} = \frac{1}{L}\int_0^{2L} U_f(y)\sin\frac{m\pi y}{2L}\,dy \qquad [18]$$

Substituting for the substrate potential $U_f(y)$ from Eq. [17] and integrating yields the result

$$\begin{aligned}
T_{1m} = {} & \frac{2}{m\pi}(c_1L + c_2L^2 + c_3L^3)\left(\cos\frac{3m\pi}{4} - \cos m\pi\right) \\
& + \frac{2}{m\pi}\left(-\frac{c_1L}{2} + \frac{c_2L^2}{4} - \frac{c_3L^3}{8}\right)\left(\cos\frac{m\pi}{4} - \cos\frac{3m\pi}{4}\right) \\
& + \frac{2}{m\pi}\left(\frac{2L}{m\pi}\right)\left(c_1 - c_2L + \frac{3c_3L^2}{4}\right)\left(\sin\frac{3m\pi}{4} - \sin\frac{m\pi}{4} - \frac{3m\pi}{4}\cos\frac{3m\pi}{4} + \frac{m\pi}{4}\cos\frac{m\pi}{4}\right) \\
& + \frac{2}{m\pi}\left(\frac{2L}{m\pi}\right)^2\left(c_2 - \frac{3c_3L}{2}\right)\left(\frac{3m\pi}{2}\sin\frac{3m\pi}{4} - \frac{m\pi}{2}\sin\frac{m\pi}{4} - \left[\left\{\frac{3m\pi}{4}\right\}^2 - 2\right]\cos\frac{3m\pi}{4} + \left[\left\{\frac{m\pi}{4}\right\}^2 - 2\right]\cos\frac{m\pi}{4}\right) + \frac{2}{m\pi}c_3\left(\frac{2L}{m\pi}\right)^3 \\
& \left(\left[3\left\{\frac{3m\pi}{4}\right\}^2 - 6\right]\sin\frac{3m\pi}{4} - \left[3\left\{\frac{m\pi}{4}\right\}^2 - 6\right]\sin\frac{m\pi}{4} - \left[\left\{\frac{3m\pi}{4}\right\}^3 - 6\left\{\frac{3m\pi}{4}\right\}\right]\cos\frac{3m\pi}{4} \right. \\
& \left. + \left[\left\{\frac{m\pi}{4}\right\}^3 - 6\left\{\frac{m\pi}{4}\right\}\right]\cos\frac{m\pi}{4}\right) \qquad [A\text{-}1]
\end{aligned}$$

APPENDIX B

Evaluation of the Cathode Boundary Condition for an Arbitrary Cathode

The equation of the straight line segment of Fig. 5 is

$$T_i(y) = a_i - b_i y \qquad [B\text{-}1]$$

where

$$a_i = d_i + \frac{d_i - d_{i+1}}{f_{i+1} - f_i} f_i \qquad [B\text{-}2]$$

and

$$b_i = \frac{1}{2L}\,\frac{d_i - d_{i+1}}{f_{i+1} - f_i} \qquad [B\text{-}3]$$

Substituting this expression for $T_i(y)$ in Eq. [24] gives the general result for K_{1m}

$$\begin{aligned}
K_{1m} = {} & \sum_{k=1}^{l}\left\{ e^{\frac{m\pi a_k}{2L}} \int_{2f_kL}^{2f_{k+1}L} e^{-\frac{m\pi b_k y}{2L}} \sin\frac{m\pi y}{2L}\sin\frac{n\pi y}{2L}\,dy \right. \\
& \left. + e^{-\frac{m\pi a_k}{2L}} \int_{2f_kL}^{2f_{k+1}L} e^{\frac{m\pi b_k y}{2L}} \sin\frac{m\pi y}{2L}\sin\frac{n\pi y}{2L}\,dy \right\} \\
= {} & \sum_{k=1}^{l}\left\{ e^{\frac{m\pi a_k}{2L}} I_1(k,m,n) - e^{-\frac{m\pi a_k}{2L}} I_2(k,m,n) \right\} \qquad [B\text{-}4]
\end{aligned}$$

where the two integrals $I_z (z = 1, 2)$ are defined by the second equality. A similar result can be written for K_{2n}

$$\begin{aligned}
K_{2n} = {} & \sum_{m=1}^{m'} T_{1m}\left\{ \sum_{k=1}^{l} e^{\frac{m\pi a_k}{2L}} \int_{2f_kL}^{2f_{k+1}L} e^{-\frac{m\pi b_k y}{2L}} \sin\frac{m\pi y}{2L}\sin\frac{n\pi y}{2L}\,dy \right\} = \sum_{m=1}^{m'} T_{1m} \\
& \left\{ \sum_{k=1}^{l} e^{\frac{m\pi a_k}{2L}} I_1(k,m,n) \right\} \qquad [B\text{-}5]
\end{aligned}$$

where $I_1(k, m, n)$ has the same value as in Eq. [B-4].

Evaluation of K_{1m} and K_{2n} in this general case is completed by recording the value of the integral $I_z(k, m, n)$

$$I_z(k, m, n) = \xi(2f_{k+1}L) - \xi(2f_kL) \qquad [B\text{-}6]$$

where

$$\xi(y) = \frac{e^{\alpha y}}{2}\left\{ \frac{\beta\sin\beta y + \alpha\cos\beta y}{\alpha^2 + \beta^2} - \frac{\gamma\sin\gamma y + \alpha\cos\gamma y}{\alpha^2 + \gamma^2} \right\} \qquad [B\text{-}7]$$

α, β, and γ are defined by

$$\alpha = (-1)^z\frac{m\pi b_k}{2L} \qquad [B\text{-}8]$$

$$\beta = \frac{(m-n)\pi}{2L} \qquad [B\text{-}9]$$

$$\gamma = \frac{(m+n)\pi}{2L} \qquad [B\text{-}10]$$

REFERENCES

1. C. O. Hutchinson, Paper presented at Electrocoat 71, (The National Paint, Varnish, and Lacquer Association), Chicago, Illinois, April 27-28, 1971.
2. Anon, "Coil Coating by Electrodeposition," *Can. Paint Finishing*, 30 (February 1971).
3. M. A. Dudley and R. L. LeRoy, Paper presented at The Electrochemical Society Meeting, Ontario-Quebec Section, Toronto, February 1973.
4. M. A. Dudley and P. L. Claessens, *Can Pat.* 984,331 (1976).
5. L. R. LeBras, *J. Paint Technol.*, **38**, 85 (1966).
6. A. R. H. Tawn, *Paint, Oil Colour J.*, 821 (Nov. 21, 1969).
7. F. Beck, *Farbe Lack*, **72**, 218 (1966).
8. J. Newman, in "Advances in Electrochemistry and Electrochemical Engineering," Vol. 5, C. W. Tobias, Editor, p. 87, Interscience, New York (1967).
9. E. McCafferty, Naval Research Laboratories Report 7835 (Jan. 31, 1975).
10. R. H. Rousselot, *Metal Finishing*, 56 (October 1959).
11. R. H. Rousselot, "Repartition du Potential et du Courant dans les Electrolytes," Dunod, Paris (1959).
12. J. A. Klingert, S. Lynn, and C. W. Tobias, *Electrochim. Acta*, **9**, 297 (1964).
13. H. E. Haring and W. Blum, *Trans. Electrochem. Soc.*, **44**, 313 (1923).
14. C. Kasper, *ibid.*, **77**, 353, 365 (1940); *ibid.*, **78**, 131, 147 (1940); *ibid.*, **82**, 153 (1942).
15. C. Wagner, *This Journal*, **98**, 116 (1951).
16. J. T. Waber, *ibid.*, **101**, 271 (1954).

The Influence of Carbon Matrix Characteristics on the Performance of Sulfur Electrodes for Sodium-Sulfur Cells

M. P. J. Brennan

Chloride Silent Power Limited, Astmoor, Runcorn, England

ABSTRACT

Sodium-sulfur cells of the central sulfur configuration, though free from the problems of case corrosion, can still exhibit capacity losses of up to 50% over 100 cycles of operation. This is mainly due to a failure to recharge fully in the two-phase regime of the operating cycle. This paper describes an investigation of the relationship between rechargeability and the surface properties of the carbon matrix employed as the current-collecting member in the sulfur electrode. The influence of cell constructional variants is also considered.

The earliest sodium-sulfur cells tested by Chloride Silent Power were of the tubular central sodium type, incorporating a beta-alumina tube of 13 mm diam. With these cells, sulfur utilization was found to diminish with time and cycling, typical values being 56% utilization after 300 cycles (100% being defined as conversion of the sulfur charge to Na_2S_3). At the time, a major contributory factor to the decline in utilization was recognized to be corrosion of the cell case by the molten sulfur and sodium polysulfide reactant contained within it. This could affect utilization both by tying up sulfur in the form of metal sulfides, and by breaking the electronic contact between the case and the carbon felt matrix dispersed within the sulfur electrode, leading to premature polarization on both charge and discharge. With the development of larger electrolyte shapes, it was possible to change the cell configuration, locating the sulfur electrode reactant within the beta-alumina tube, so that the cell case came into contact only with sodium. Current collection from the sulfur electrode was achieved by a carbon or graphite pole, located co-axially within the ceramic electrolyte.

With these central sulfur cells, it was found that despite the elimination of case corrosion, the utilization of sulfur still showed a declining trend with cycling, with effective capacity losses of up to 50% over 100 cycles being not uncommon. This was found to be mainly due to failure of the cells to recharge fully in the two-phase region of the operating cycle.

One theory advanced to explain the poor rechargeabilities linked this phenomenon to the relative wetting propensities of sulfur and sodium polysulfides on carbon surfaces. It was suggested that sulfur wets carbon more effectively than does molten sodium polysulfide, so that sulfur formed during recharging has a tendency to spread out over the carbon fibers as a continuous insulating film. As the proportion of occluded surface will be expected to increase as charging proceeds, this phenomenon should manifest itself as a rising cell resistance, which could lead to the cell failing to fully recharge either within a time limit (constant voltage charging) or voltage limit (constant current charging).

Chemical modification of the wettability of carbon fibers is a process well known in the fiber-reinforced composites industry (1, 2). It is generally found that the wetting of carbon fibers by epoxy resins is enhanced by subjecting the fibers to a preoxidation procedure. This can be either a wet oxidation, using nitric acid, permanganates, dichromates, etc. (2-4), or a dry oxidation in air, oxygen, or ozone (2, 5).

Were such treatments to preferentially enhance the wetting of carbon fibers by the predominantly ionic component of a two-phase sulfur/sodium polysulfide melt, then the performance of cells with modified matrices should be significantly improved. Conversely, if the pretreatment promoted wetting by the sulfur-rich phase, then a deterioration in cell performance could be expected.

It is an unresolved question as to whether the improvement in wetting observed with epoxy resins is due principally to changes in surface chemistry, or whether the roughening of the fiber surfaces which accompanies the oxidation process is the major factor. For this reason two pretreatments were employed in this section of the work. One, (oxidation with $Na_2Cr_2O_7/H_2SO_4$) is known to oxidatively etch carbon, whereas the other (neutralization with aqueous NaOH) was expected to change only the surface chemistry.

Another pretreatment investigated in this work involved subjecting carbon felt for cells to exposure to reagents known to intercalate in well-ordered graphite. There are many such reagents, falling into two broad groups, the electron donors, such as the alkali metals, and the electron acceptors. The latter group is more numerous, and includes some of the halogens, interhalogens, and transition metal chlorides. The formation of an intercalation compound is accompanied by a change in the electronic band structure of the graphite to produce a more metallic material (6) as evidenced by changes in electrical conductivity (7), and Hall effect coefficient (8). Surface properties are also altered (9). Full conversion of a graphite sample to an intercalation compound is possible only with highly ordered graphites, containing a minimum of lattice defects. Carbon fibers do not fall in this category, however lattice resolution studies with the electron microscope have shown the surfaces of the fibers to be more ordered than the interior (10), and lattice parameters close to those of pure graphite have been obtained by electron diffraction studies of fiber edges (11). Since the aim was to produce changes in the surface wetting characteristics of the fibers, restriction of the intercalation reaction to the surface layers was acceptable.

For a permanent effect on cell performance it was necessary that the intercalated felt be stable in the cell environment. This requirement at once ruled out the use of n-type lamellar compounds, based on alkali metal insertion, because in these the inserted species can usually be totally desorbed by the application of heat. Complete desorption of the inserted material in p-type compounds is usually impossible, and a certain amount remains forming the so-called residue compound. In particular chromyl chloride is capable of extensive fixation to form a permanent lamellar compound (12) and this reagent was chosen for this work. Also selected was antimony pentachloride, for its ease

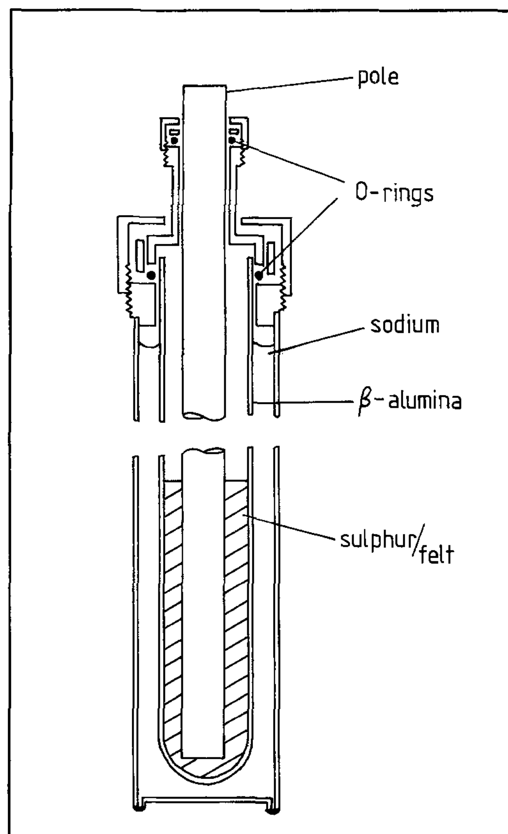

Fig. 1. Schematic diagram of the sodium-sulfur cell design used in this work.

of handling (like chromyl chloride it is a liquid), for its reported high reactivity (13), and because the intercalation reaction of $SbCl_5$ has been extensively studied (14).

Experimental

The cell design used in this work is shown in Fig. 1. It is a central sulfur cell based on an electrolyte tube of diameter 26 mm. The felt in the sulfur electrode was introduced in the form of rings surrounding the central graphite rod pole. RVC 4000 (Le Carbone) was the felt material, and the rings were held under an axial compression of 2:1. The cell operated in a temperature gradient, so that the electrodes could be sealed with silicon rubber O-rings; however, the 10 cm working length of the electrolyte was held at a temperature of 340° ± 15°C throughout. For the cells incorporating intercalated felt the graphite pole was drilled and tapped at the top end to accept a stainless steel (316) insert, upon which the upper O-ring seal was made. This produced a hermetic seal. In the other cells, the upper seal was made to the graphite rod and was not as leak-tight.

The felt variants were prepared as follows. (*i*) Oxidation: The felt rings were refluxed in an aqueous solution of sodium dichromate (0.3M) and sulfuric acid (2.0M) for 24 hr. They were then thoroughly washed with deionized water until the washings had a pH of 7. (*ii*) Neutralization: The felt rings were refluxed for 24 hr in an aqueous solution of sodium hydroxide (0.4M), then washed with deionized water as above. (*iii*) $SbCl_5$: The felt was predried for 2 days at 110°C and then refluxed with antimony pentachloride at 80°C for 12 hr. The felt was then washed with constant boiling point hydrochloric acid in a soxhlet extractor for 2 days, followed by extraction with deionized water until the washings had a pH of 7. (*iv*) CrO_2Cl_2: The felt was predried as above, then refluxed with chromyl chloride at 100°C for 2 hr. The washing procedure was the same as for antimony pentachloride. (*v*) Control: Because the cell design differed slightly for the two groups of pretreatments, control cells were made up to each design. In both cases the felt was refluxed with deionized water for 12 hr, then extracted with deionized water as above.

Samples of the oxidized felt were analyzed to obtain a quantitative estimate of the degree of surface oxidation induced. The method employed was that recommended by Ludtke (15) for the determination of carboxylate functions in oxycelluloses and adapted by Donnet *et al.* (16) for the determination of the same functions on carbon blacks. The method consists of refluxing the carbon material with an aqueous solution of calcium acetate, which effects an ion-exchange reaction liberating acetic acid, which is then estimated by titration. It was found that as-received felt did not liberate sufficient acetic acid for estimation by this technique, however the oxidized material was found to have an acidity of 0.45 mequiv. g^{-1}, slightly less than the figures reported by Donnet *et al* (16) for oxidized carbon blacks (0.62-1.2 mequiv. g^{-1}).

Two cells of each variant were constructed and cycled to the following regime at a temperature of 340° ± 15°C. (*i*) Discharge—via a fixed resistor arranged to give a discharge rate of approximately 0.3-0.2C (current density 40-60 mA-cm^2) and (*ii*) Recharge—via a series resistor for the remainder of the 24 hr cycle, with a cell voltage limit of 2.6V. Recharge was essentialy complete in 11 hr at an average current density of 20 mA-cm^{-2}.

For some cycles the cells were controlled by a computer, the discharge being terminated when the instantaneous open-circuit voltage fell to 1.76V. When not under computer control discharge was terminated at a load voltage of 1.35V.

Two cell characteristics were recorded for analysis; first the discharge capacity to 1.76V, and second the cell resistance at an open-circuit voltage of 2.00V on the discharge half-cycle. It was found that the resistance of a cell did not vary much from this value except at extremes of charge and discharge.

Cell Performances

Oxidized and neutralized felt.—The sulfur utilization for these cells was measured over a period of approximately 3000 hr ≡ 100 cycles. The data was analyzed for the following periods: 0-1000 hr, 1000-2000 hr, 2000-3000 hr. Table I lists the mean values recorded for each cell during each period, as a percentage of theoretical capacity. These figures suggest that the cells can be ranked in order of merit with respect to sulfur utilization as follows: control>neutralized> oxidized. The significance of this trend was determined by subjecting the data to variance analysis. Table II lists the values of the *F*-statistic and corresponding

Table I. Mean sulfur utilization

		0-1000 hr		1000-2000 hr		2000-3000 hr	
Cell	Type	Mean	SD	Mean	SD	Mean	SD
395	Control	76.9	4.3	72.2	4.4	62.8	9.0
398*	Control	77.3	2.9	76.1	1.3	See note*	
394	Neutralized	72.2	4.5	58.2	4.8	42.1	4.7
397	Neutralized	71.3	3.0	66.1	4.4	57.8	2.6
393	Oxidized	69.1	6.5	54.0	4.2	46.9	5.2
396	Oxidized	63.2	8.6	58.7	3.9	49.4	5.1

* This cell failed after 1944 hr on test.

Table II. Variance analysis

Time period (hr)	*F*	Significance level (%)
0-1000	10.05	95.3
1000-2000	9.92	95.2
2000-3000	1.22	55.0

significance level for each time period. Table III lists two-tailed probabilities derived from the t-test for the comparison of mean performance and shows that the ranking of felt treatments is significant in the early cycles, but the distinction becomes less clear at longer times.

The cell resistances were treated in the same way. Table IV lists the summary data. The resistances are quoted in the Ω-cm^2 form, derived by multiplying the total cell resistance by the area of beta-alumina carrying the current.

Although the trend is apparent in the early period that the cells can be ranked control<neutralized<oxidized in terms of resistance, variance analysis of the data indicated a significance of not greater than 82% at any time. A correlation between utilization and resistance is indicated, particularly in the first period, and this was evaluated by a least squares fit analysis of data. Table V gives the parameters in the linear regression equation $U = aR + b$, where U = utilization, R = resistance. "r" is the correlation coefficient for the regression which is seen to diminish with increasing time. The data is also shown graphically in Fig. 2.

Intercalated felt.—These cells were tested over a similar time period, but owing to experimental difficulties a limited amount of information was gathered during the period 1000-2000 hr. For this reason the data for these cells is grouped into only two periods for analysis, 0-1000 hr and 1000-3000 hr. Table VI lists the summary data for mean utilization, as a percentage of theoretical capacity. Only one cell of the $SbCl_5$ variant is quoted, the other having been recorded as an early failure. The data do not appear to indicate any correlation between cell type and performance, a conclusion borne out by the analysis of variance, which indicated less than 50% significance for either period. The resistance data also lacked any discernable trend, as shown in Table VII. Significant correlation with utilization was absent, the regression coefficients for a least squares fit being 0.2 and 0.4 for 0-1000 hr and 1000-3000 hr, respectively.

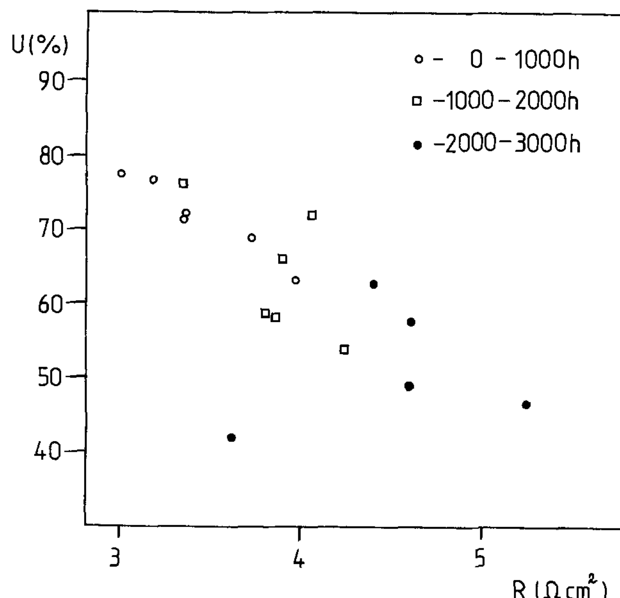

Fig. 2. A plot of mean percentage utilization (U) vs. mean resistance (R) for cells containing felt subjected to oxidative and neutralizing pretreatments. Control cell data is also included.

Table III. Comparison between treatments

Hypothesis	0-1000 hr	1000-2000 hr	2000-3000 hr
Control = Neutr.	1%	11%	N/A
Control = Oxid.	7%	3%	N/A
Neutr. = Oxid.	20%	33%	84%

Table IV. Mean resistances

Cell	Type	0-1000 hr Mean	0-1000 hr SD	1000-2000 hr Mean	1000-2000 hr SD	2000-3000 hr Mean	2000-3000 hr SD
395	Control	3.18	0.35	4.06	0.12	4.40	0.08
398	Control	3.00	0.08	3.32	0.15	See note*	
394	Neutralized	3.66	0.40	3.86	0.37	3.62	0.26
397	Neutralized	3.35	0.41	3.90	0.48	4.61	0.14
393	Oxidized	3.73	0.13	4.25	0.17	5.25	0.51
396	Oxidized	3.97	0.51	3.31	0.74	4.60	0.15

* This cell failed after 1944 hr on test.

Table V. Utilization-resistance correlation

Period	a	b	r
0-1000 hr	−14.2	120.3	0.96
0-2000 hr	−16.1	126.6	0.80
0-3000 hr	−12.7	112.9	0.69

Table VI. Mean sulfur utilization

Cell	Type	0-1000 hr Mean	0-1000 hr SD	1000-3000 hr Mean	1000-3000 hr SD
574	Control	84.5	1.43	85.1	0.59
575	Control	81.6	1.44	81.2	0.55
576	$SbCl_5$	82.6	5.44	83.4	1.33
577	CrO_2Cl_2	97.8	24.3	81.3	2.10
581	CrO_2Cl_2	77.9	4.58	77.4	3.18

Discussion

For the first group of cells, the control cells gave consistently better performances than either of the pretreated variants. The differences between the groups were significant up to 2000 hr, but thereafter the confidence level diminished considerably. Considering these results in terms of the differential wetting hypothesis, one would conclude that the pretreatments enhance the preferential wetting of felt by sulfur, a result not unexpected. However there is an alternative interpretation which does not involve wetting effects. Sulfur is known to react with carbon surfaces at temperatures as low as 350°C (17, 18), giving rise to carbon-sulfur complexes of high stability, and accompanied by the evolution of small quantities of hydrogen sulfide and carbon disulfide. This chemical fixation of sulfur is hindered by the presence of oxygen (18, 19), suggesting some degree of competition for similar sites. It is highly likely, therefore, that a carbon surface saturated with oxygen functions will experience partial displacement of the oxygen on immersion in sulfur at 350°C, and the oxygen displaced therefrom will most likely be converted to sulfur dioxide. Mechanisms exist therefore whereby a sulfur electrode may contain vapor species which under the conditions of liquid flow set up during charging and discharging may combine to form macroscopic bubbles, as shown in Fig. 3. The presence of such bubbles will have a deleterious effect on sulfur utilization, by isolating reactive materials in pockets, as shown. Substantive evidence for this hypothesis may exist in the cell resistance data, for clearly any bubble large enough to isolate reactive material will also, by virtue of the "shadow" cast on the

Table VII. Mean resistances

Cell	Type	0-1000 hr Mean	0-1000 hr SD	1000-3000 hr Mean	1000-3000 hr SD
574	Control	2.39	0.05	2.43	0.04
575	Control	5.01	0.36	4.81	0.32
576	$SbCl_5$	3.29	0.23	3.02	0.12
577	CrO_2Cl_2	3.57	0.19	5.35	0.83
581	CrO_2Cl_2	2.85	0.12	3.57	0.63

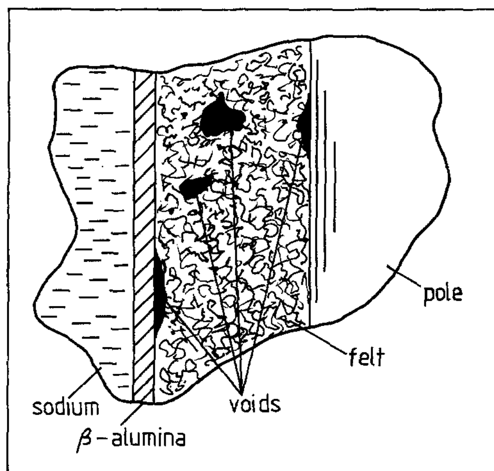

Fig. 3. Representation of the disposition of voids within the sulfur electrode.

electrolyte and pole, reduce the over-all conductance of the sulfur electrode. It is interesting, therefore, to note the correlation between utilization and resistance shown in Fig. 2 and tabulated in Table V. At short times the correlation is good, but becomes less clear over a longer period of test, as does the distinction between cell types, which indicates a common deterioration mechanism.

The cells which incorporated felts treated with intercalating agents did not appear to be distinguishable on the basis of utilization over 3000 hr. Neither did there appear to be the same relationship between utilization and resistance. The conclusion is drawn, therefore, that the variation in resistances for this group of cells must arise from a different cause to that proposed above. A likely cause of the variation is the contact resistance between the carbon pole and steel insert used in these cells, an enlarged detail of which is shown in Fig. 4. Carbon thread was compressed between the pole and the shoulder of the insert. The effectiveness of this arrangement in producing a reproducibly good contact between the two components was doubtful, and while it is not possible to state definitely that here was the cause of the variation in resistances, nevertheless it is a strong possibility.

One clear picture which emerged when the data for the oxidized/neutralized cells were compared with that for the intercalated cells was that superimposed on the performance variations within the two groups was a significant difference between them. In order to analyze this difference the data for the oxidized/neutralized cells were rearranged to cover the same time

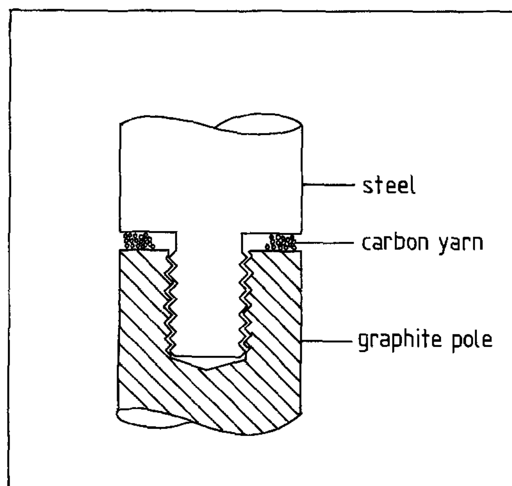

Fig. 4. The steel-to-carbon joint used on the current collectors of the later cells.

Table VIII. Mean utilization

Cell	Type	0-1000 hr Mean	SD	1000-3000 hr Mean	SD
395	Control	76.9	4.3	67.8	8.31
398	Control	77.3	2.9	76.1	1.30
394	Neutralized	72.2	4.5	51.8	9.40
397	Neutralized	71.3	3.0	62.9	5.60
393	Oxidized	69.1	6.5	51.2	5.73
396	Oxidized	63.2	8.6	54.7	6.40
574	Control	84.5	1.43	85.1	0.59
575	Control	81.6	1.44	81.2	0.55
576	$SbCl_5$	82.6	5.44	83.4	1.33
577	CrO_2Cl_2	97.8	24.3	81.8	2.10
581	CrO_2Cl_2	77.9	4.58	77.4	3.18

periods as the intercalated cells, viz., 0-1000 hr and 1000-3000 hr. Mean utilization data are summarized in Table VIII.

Comparison of the two groups by the Student's t-test revealed that the differences between groups were significant at the 99.3% level for the period 0-1000 hr, and at the 99.9% level for the period 1000-3000 hr. The superiority of the latter group at longer periods is shown also in Fig. 5, where utilization data for this group are given over 5000 hr of cycling. The same conclusion is reached if only the control cells in each group are compared, indicating that the differentiating factor is unrelated to the felt characteristics. It is most likely that the cause of the improved capacity retention in the second group of cells is the much better quality of the sulfur electrode seal which resulted from compressing the sealing O-ring against a smooth steel member in these cells, rather than against a graphite rod as in the first group. It is clear, therefore, that efforts directed at improving sulfur electrode performance should not be undertaken in poorly sealed cells even when the experimental period is limited to 1000 hr of cycling.

Insofar as utilization is concerned, none of the felt pretreatments resulted in an improvement in this parameter, and two of them were found to have an adverse effect. However in the case of the second group of cells, it is hardly surprising that the control cells were not surpassed in view of the remarkably good performances they exhibited. When one bears in mind the fact that the cells were cycled to an instantaneous open-circuit voltage value of 1.76V, the 20% utilization loss which most of these cells incurred is not an unreasonable amount to ascribe simply to polarization at the 5 hr rate. We believe that the sustained high utili-

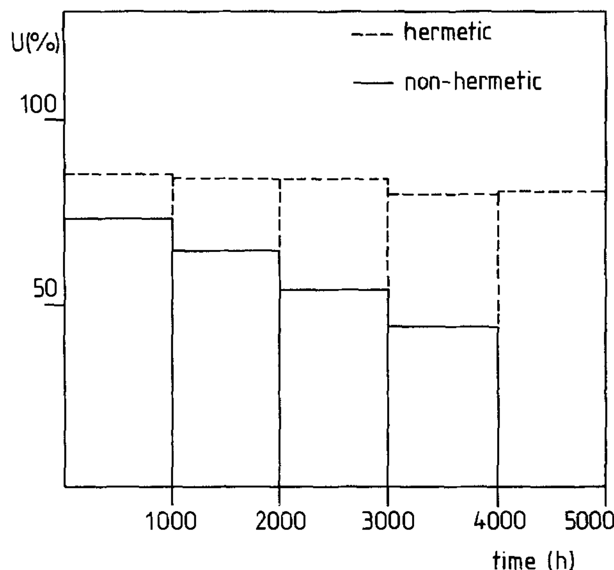

Fig. 5. A bar chart showing the mean percentage utilization (U) as a function of cell life for the hermetically sealed and non-hermetically sealed cells.

zation rates which these cells have operated at for more than a year now is a significant advance on the sulfur electrode position of 12 months ago, and gives tremendous encouragement for the further development of the sodium-sulfur battery to a commercially viable product.

Acknowledgment

I am indebted to my colleague Graham Robinson who initiated most of the early work leading up to this study and who contributed by helpful discussions throughout.

Manuscript submitted July 22, 1977; revised manuscript received Dec. 5, 1977. This was Paper 398 presented at the Philadelphia, Pennsylvania, Meeting of the Society, May 8-13, 1977.

Any discussion of this paper will appear in a Discussion Section to be published in the December 1978 JOURNAL. All discussions for the December 1978 Discussion Section should be submitted by Aug. 1, 1978.

Publication costs of this article were assisted by Chloride Silent Power Limited.

REFERENCES

1. R. J. Bobka and L. P. Lowell, AFML TR66-310, Part 1, U.S.A.F. Materials Laboratory (October 1966).
2. D. W. McKee and V. J. Mimeault, *Chem. Phys. Carbon*, **8**, 151 (1973).
3. M. Yamamoto, S. Yamada, Y. Sakatani, M. Taguchi, and Y. Yamaguchi, Paper 21, International Conference on Carbon Fibres—Their Composites and Applications, Plastic Institute, London (1971).
4. J. W. Herrick, 23rd Annual Technical Conference, S.P.I., Reinforced Plastics/Composites Division, Section 16A (February 1968).
5. J. C. Goan and S. P. Prosen, in "Interfaces in Composites," ASTM Special Tech. Pub. No. 452, pp. 3-26 (1969).
6. F. R. McDonnel, R. C. Pink, and A. R. Ubbelohde, *J. Chem. Soc.*, **1951**, 151.
7. G. R. Hennig, *J. Chem. Phys.*, **19**, 922 (1951).
8. G. R. Hennig, *ibid.*, **20**, 1443 (1952).
9. M. C. Robert, M. Oberlin, and J. Mering, *Chem. Phys. Carbon*, **10**, 141 (1973).
10. D. J. Johnson, D. Crawford, and B. F. Jones, *J. Mater. Sci.*, **8**, 286 (1973).
11. M. P. J. Brennan, Unpublished work.
12. J. G. Hooley, *Chem. Phys. Carbon*, **5**, 321 (1969).
13. R. C. Croft, *Aust. J. Chem.*, **9**, 184 (1956).
14. J. Melin and A. Herold, *C.R. Acad Sci. Paris, Ser. C.*, **269**, 877 (1969).
15. M. Ludtke, *Biochem. Z.*, **268**, 372 (1954).
16. J. B. Donnet, F. Hueber, C. Reitzer, J. Oddoux, and G. Riess, *Bull. Soc Chim. France*, **1962**, 1727.
17. R. Juza and W. Blanke, *Z. Anorg. Allgem. Chem.*, **210**, 81 (1933).
18. M. L. Studebaker and L. G. Nabors, *Rubber Age*, **80**, 661 (1957).
19. B. R. Puri, *Chem. Phys. Carbon*, **6**, 191 (1970).

Photooxidation of Water at α-Fe_2O_3 Electrodes

John H. Kennedy* and Karl W. Frese, Jr.

Department of Chemistry, University of California, Santa Barbara, California 93106

ABSTRACT

Photoelectrochemical properties of high purity α-Fe_2O_3 and TiO_2-doped α-Fe_2O_3 were investigated. Photocurrent efficiencies were measured in various electrolytes and found to depend on the electrolyte used. Direct measurement of spectrophotometric absorption coefficients showed them to be significantly higher than those deduced from i-V curves indicating that only a fraction of the light absorbed resulted in electrochemically reactive holes. When the lower absorption coefficients were employed the current-potential curves could be fit within $\pm 1\%$ to the depletion layer theory of Gärtner.

Recent interest in the photoelectrochemistry of semiconductor electrodes has led to the discovery of new materials capable of sustaining the photoelectrolysis of water (see for example Ref. (1-3) and references contained therein). Among these materials is α-Fe_2O_3 with a sufficiently low bandgap to be of practical interest and first reported on as CVD films by Hardee and Bard (3, 4). Later, Quinn *et al.* (5) reported on the properties of the flux-grown single crystal α-Fe_2O_3. However, a detailed study of the photoelectrochemical properties of polycrystalline ceramic α-Fe_2O_3 has been lacking, and therefore a study of ultrapure and TiO_2-doped α-Fe_2O_3 was undertaken.

We report here: (*i*) the effects of electrolyte on measured photocurrent efficiencies; (*ii*) quantitative comparison of absorption coefficients from spectral and photoelectrochemical methods; (*iii*) the effects of donor density on photocurrent efficiency; and (*iv*) a fit of the i-V characteristics to the depletion layer theory of Gärtner (6). Flatband potentials and donor densities for the polycrystalline α-Fe_2O_3 electrodes in this study have been previously reported (7). These polycrystalline electrodes appear to behave in a similar fashion to single crystal electrodes including photocurrent efficiencies and flatband potentials.

* Electrochemical Society Active Member.

Key words: absorption coefficient, α-Fe_2O_3, TiO_2-doped α-Fe_2O_3, photooxidation, water.

Experimental

Electrode preparation.—The details of the preparation of high purity (99.999%) and TiO_2-doped reagent α-Fe_2O_3 electrodes are given elsewhere (7).

Illumination.—The procedures used for monochromatic light intensity measurements are given elsewhere (2). Polychromatic light intensities, $300 \leq \lambda \leq 540$ nm $= E_g$, were determined with the Reinecke salt actinometer (8) for which the quantum yield ($\sim$0.30) is practically independent of wavelength. The equivalent photon current for the system including the 150W Xe lamp, infrared filter, and quartz lens was found to be 49.6 mA (300-540 nm) at the electrode surface. Lower light intensities were obtained using neutral density screens.

Electrical measurements.—The general cell arrangement, measurement of i-V curves, and calculation of photocurrent efficiencies were described previously (2).

Optical measurements.—The spectrophotometric absorption coefficient of polycrystalline α-Fe_2O_3 was measured using a KBr pellet technique (9-12). Pellets containing up to 500 ppm w/w α-Fe_2O_3 were made and had dimensions $\sim$0.03 cm thick $\times$ 1.29 cm diam. Absorbance measurements were made with a Beckman Model B spectrophotometer with a spectral slit width of $\leq$5 nm. Samples were run *vs.* a KBr blank

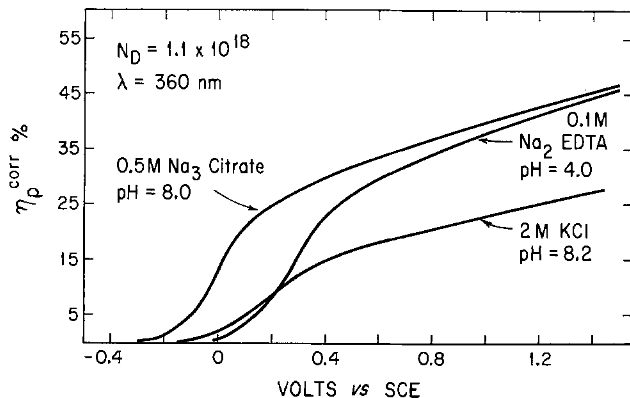

Fig. 1. Current-potential curves in various electrolytes. Polycrystalline α-Fe_2O_3; 23°C.

of comparable thickness utilizing a sample in-sample out technique. Suitable corrections for bulk scattering by α-Fe_2O_3 particles were applied and are discussed later.

Results

Photocurrent efficiency, η_p, curves obtained in 2*M* KCl, 0.1*M* Na_2 EDTA, and 0.5*M* Na_3 citrate are shown in Fig. 1. These efficiencies have been corrected for light reflection at the Fe_2O_3-solution interface according to well-known procedures (13). This correction amounted to 15-20%.

A significant enhancement of the efficiency was found for the chelating-type electrolytes. Comparison of the curves for citrate and EDTA solutions shows that the photocurrent efficiency is practically identical when compared at the same overvoltage. The rate of change of the potential at zero efficiency, V_o*, was −60 mV/*p*H. This potential (turn-on voltage) for the 2*M* KCl solution was 100 mV more anodic than the citrate solution at about the same *p*H (8.0 *vs.* 8.2), and the efficiencies at any given overvoltage in EDTA and citrate solutions were considerably higher than in KCl solution. Efficiencies comparable to those for KCl solutions were found in 0.5*M* Na_2SO_4 and 0.5*M* sodium acetate, and somewhat lower values in 0.5*M* KNO_3. The enhanced efficiency in the presence of citrate may be due to the interaction of these anions with the α-Fe_2O_3 electrodes and is discussed below.

The effect of the bulk citrate concentration on the increase in efficiency was investigated for three different electrodes resulting in qualitatively similar results as shown in Fig. 2. The effect had a threshold at 10^{-6}-10^{-5}M. The increase in efficiency was initially proportional to log[citrate]; with increasing concentration a saturation effect was observed. For all electrodes, both citrate and EDTA had no effect on the dark current at all concentrations studied. Finally, no effect was found with TiO_2 and $SrTiO_3$ polycrystalline electrodes, materials for which the valence bands are 0.7-0.8 eV below the valence band of α-Fe_2O_3.

Photocurrent efficiency curves at various wavelengths are shown in Fig. 3 for 0.5M citrate solution.

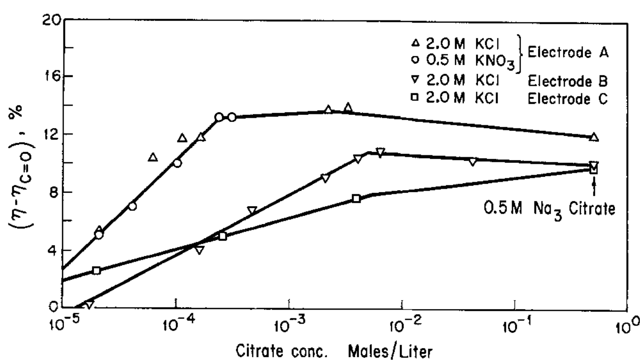

Fig. 2. Effect of bulk citrate concentration on photocurrent efficiency. 1.0V overvoltage; 23°C; 360 nm.

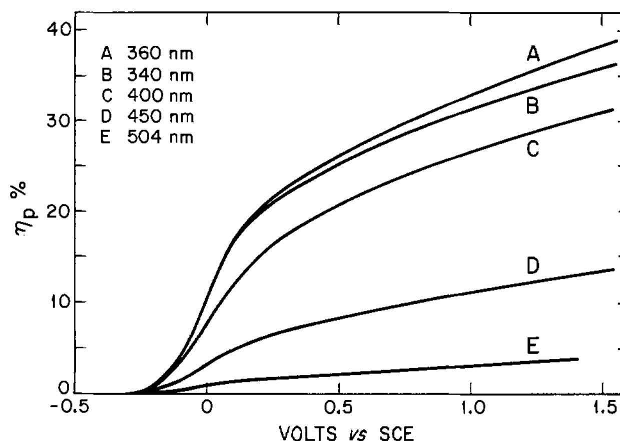

Fig. 3. Effect of wavelength on photocurrent efficiency. Polycrystalline α-Fe_2O_3; 0.5M Na_3 citrate; *p*H 8.0.

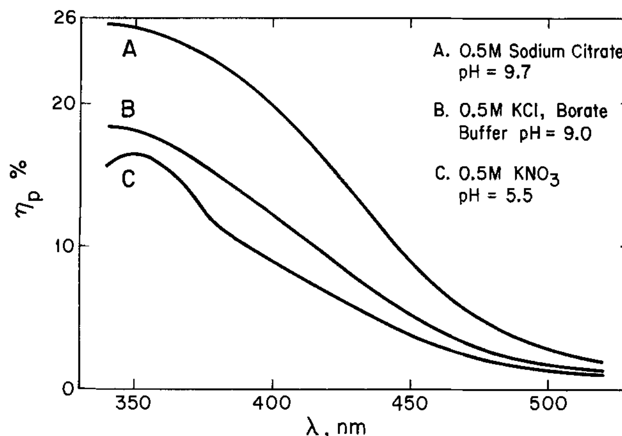

Fig. 4. Effect of electrolyte on photocurrent spectrum. 1.0V overvoltage; polycrystalline α-Fe_2O_3.

The photocurrent spectra in three different electrolytes are shown in Fig. 4. The relative efficiency in each electrolyte appears to follow the order of extent of surface adsorption (14) expected on the basis of chemical consideration. That is, the extent of complexing of the anions with Fe^{3+} should be in the order citrate > Cl^- > NO_3^-. A maximum in the photocurrent spectrum at ~350 nm is evident from Fig. 3 and 4. Light absorption by KNO_3 may be responsible for the more pronounced maximum for curve C in Fig. 4. Efficiencies observed in citrate and EDTA solutions agreed well with published (5) photocurrent efficiencies at single crystal α-Fe_2O_3 electrodes.

Photocurrent efficiencies for polychromatic light (300-540 nm) are shown in Fig. 5 at various *p*H

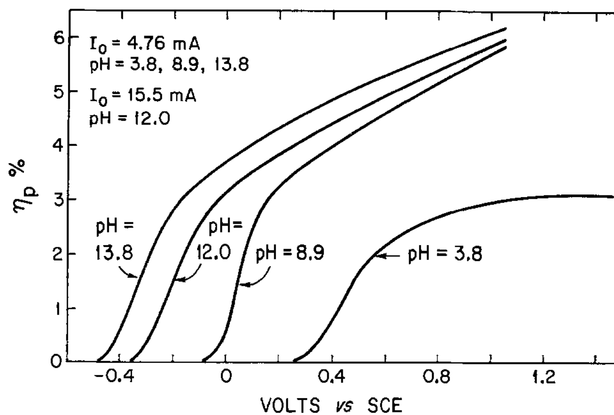

Fig. 5. Effect of *p*H on photocurrent efficiency for polychromatic light. Polycrystalline α-Fe_2O_3; 23°C.

values. In basic solutions the i-V characteristics were nearly identical showing a lack of saturation and comparable efficiencies at the same overvoltage. At pH 3.8, on the other hand, the efficiency was considerably lower and tended toward a saturation value. This could reflect a change in the rate-limiting step at high light intensities from solid-state process control (diffusion and/or conduction) to electron transfer control at the semiconductor-electrolyte interface. This change in mechanism could occur because of a reduced concentration of oxidizable species (*e.g.*, OH^-) either at the electrode surface or at the outer Helmholtz plane. It should be noted that the polychromatic light intensity of 4.76 mA in Fig. 5 was about 60 times the monochromatic intensity at 400 nm in Fig. 3 and 4.

Some experiments were carried out at higher light intensities utilizing the complete photosensitive range of α-Fe_2O_3. The variation of photocurrent with light intensity at 1.0V overvoltage is shown in Fig. 6. For both low intensity monochromatic light (lower line) and for high intensity polychromatic light (upper line) the photocurrent was proportional to the first power of light intensity within experimental error. This result shows that one photogenerated hole is involved in the rate-limiting step of the over-all electrode process.

Data for α-Fe_2O_3 highly doped with TiO_2 are shown in Fig 7 in which photocurrent efficiency at $(V - V_{fb}) = 1.25V$ is compared with doping level. The points for $N_d > 10^{19}$ cc^{-1} correspond to TiO_2 levels of 0.05-2.0% (Ti/Fe). The donor densities calculated from doping stoichiometry agreed well with N_d calculated from Mott-Schottky plots reported previously (7). The i-V curves for these samples were characterized by a sudden onset of a large dark current similar to those observed by Hardee and Bard (4). It was observed that lower doped samples exhibited less dark current under similar conditions. After subtraction of the dark current, normal-shaped i-V curves were obtained except that the turn-on voltage was shifted several tenths of a volt anodic, the shift increasing with TiO_2 concentration. This effect was probably due to the narrow-space charge layer at low overvoltages, resulting in photocurrents too small to be measured until sufficient space charge depth was established. However, an anodic shift of the flatband potential with the high level doping cannot be ruled out.

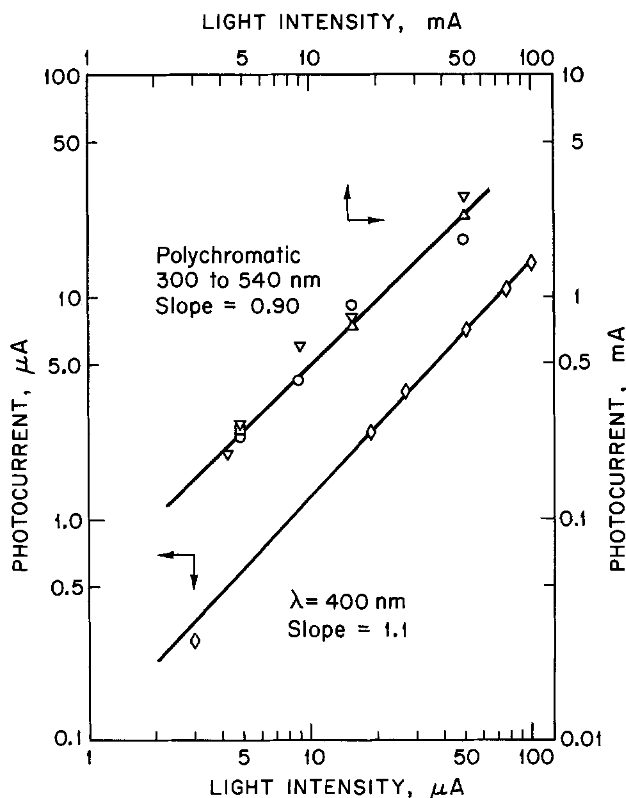

Fig. 6. Effect of light intensity on photocurrent. 1.0V overvoltage

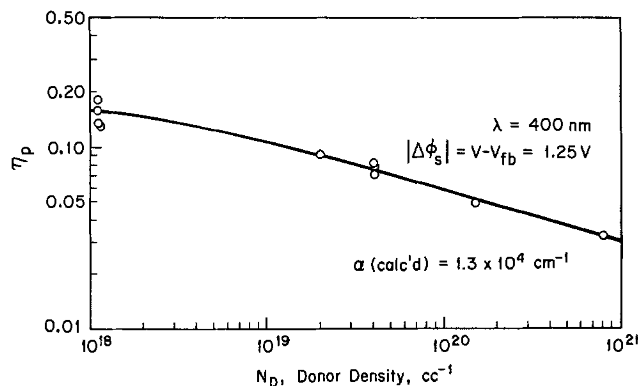

Fig. 7. Effect of donor density on photocurrent efficiency. Polycrystalline α-Fe_2O_3.

Absorption coefficients obtained directly from spectrophotometric data are shown in Fig. 8 (curve A) and compared with apparent absorption coefficients (Fig. 8, curve B) obtained by fitting the current-potential curves to the depletion layer theory of Gärtner (6). The spectrophotometric data are in good agreement with published data (15, 16) for polycrystalline α-Fe_2O_3 films. Correction for bulk scattering was made by assuming the validity of the equation

$$I = I_0 \exp - (St_1 + \alpha t_2) \quad [1]$$

where I and I_0 are the transmitted and incident light intensities, S is the coefficient of scattering, α is the absorption coefficient, t_1 is the KBr pellet thickness, and t_2 is the apparent thickness of the α-Fe_2O_3 (volume of Fe_2O_3 in pellet/pellet area).

The scattering coefficient is related to scattering particle properties through the relation (17)

$$S = \pi a^2 N Q_S \quad [2]$$

where a is the particle radius (assumed spherical), N is the particle density, cc^{-1}, and Q_S is the dimensionless efficiency factor for scattering. The efficiency factor represents the ratio of the effective surface area of a sphere which is available for light scattering to the cross-sectional area (18). In the limit of geometrical optics $Q_S \rightarrow 2$. Calculation of Q_S from the Mie scattering theory (17) is an involved but straightforward procedure. However, La Mer *et al.* (19) dis-

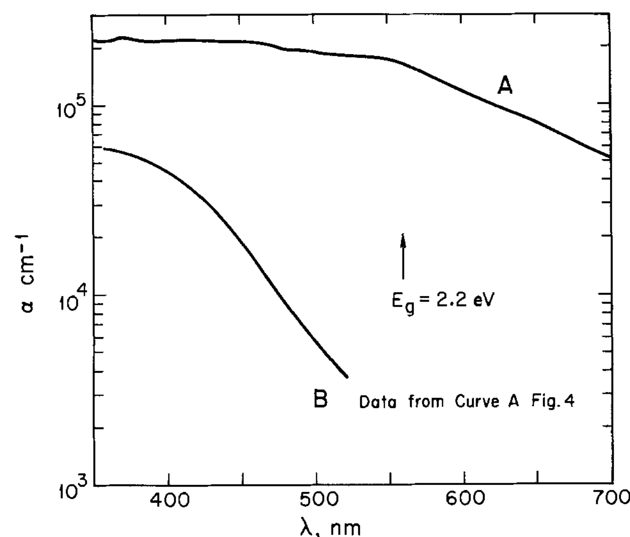

Fig. 8. Comparison of absorption coefficients calculated from spectral data and current-potential curves. Polycrystalline α-Fe_2O_3; 23°C. (A) Absorption coefficient from direct measurement. (B) Absorption coefficient calculated from photocurrent.

covered that both Mie calculations and their experimental values of Q_S could be plotted on one curve forming a universal scattering curve. The curve (18, 19) shows Q_S (K_S their notation) plotted *vs.* the dimensionless parameter, $[n_1 d/\lambda (m^2 - 1)/(m^2 + 2)]$, where m is the relative refractive index, n_2/n_1; n_1 is the refractive index of the medium; n_2 is the refractive index of the scattering particle; and d/λ is the ratio of scattering particle diameter to the wavelength of light. The iron oxide particles were found by microscopic examination to have a diameter of 2.0 ± 0.5 μm. With $m = 3.0/1.56 = 1.9$, Q_S becomes a constant value of 2.0 for the wavelengths studied.

It is seen from Fig. 8 that in the case of α-Fe_2O_3 the absorption coefficient from optical measurements does not correspond to the absorption coefficient for the excitation process giving rise to the photocurrent. Further discussion of this point is given later.

Discussion

The mechanism by which complexing ions such as citrate and EDTA enhance the photocurrent at α-Fe_2O_3 electrodes is not known. However, the effect of citrate concentration on the increase in photocurrent followed a Temkin isotherm relationship. For intermediate coverage, $0.2 < \theta < 0.8$, the isotherm is usually written as (20)

$$r\theta = -q\Delta\phi + kT \ln K + kT \ln c \quad [3]$$

where r is an interaction energy parameter, θ is the surface coverage, $\Delta\phi$ is the potential difference between the electrode surface and the solution, K is the equilibrium constant for adsorption in the absence of interaction between the adsorbing particles, and c is the bulk concentration of adsorbate. If it may be assumed that the increase in photocurrent efficiency is proportional to surface coverage, then $\eta - \eta_{c=0} \propto \ln$ [citrate] and Eq. [3] accounts for the linear portions of the curves in Fig. 2. The saturation effect is of course a property of the Langmuir isotherm which applies as $\theta \rightarrow 1$. The results did vary for different electrodes as can be seen in Fig. 2 even when compared in the same electrolyte, and they probably reflect the different surface conditions present. Consideration of these observations makes specific adsorption of citrate and EDTA on α-Fe_2O_3 a reasonable conclusion especially in view of the very high stability constants for these ions with Fe^{3+} in aqueous solution.

It would be expected that specific adsorption of strong complexing anions might shift the turn-on voltage and thereby cause an increase in photoefficiency. In actual fact, the flatband potentials and turn-on voltages did not shift sufficiently (<100 mV) to cause the observed change in efficiency. In addition, the efficiencies were measured at a given overvoltage so that any change in turn-on voltage would not be included. However, because the higher energy level of the valence bandedge of α-Fe_2O_3 compared to TiO_2 or $SrTiO_3$ may result in better energy overlap, photooxidation of citrate and EDTA by photogenerated holes at the α-Fe_2O_3 surface cannot be ruled out without evidence of the reaction products distribution in the various electrolytes. The additional possibility of "current doubling" also exists. In this mechanism (21, 22) photooxidation by a hole in the valence band leads to a radical species which then injects an electron into the conduction band in a chemical step. Thus two current carriers are produced for a single photon leading to the term "current doubling." This reaction is well known on other semiconductors with reactants containing the carboxylate group. This mechanism would lead to decomposition of the citrate or EDTA solute and probably not enhance the oxidation of water. Again, detection of decomposition products is needed and will be investigated in the future.

The η_p-V curves (*e.g.*, Fig. 1 and 3) were fit to the depletion layer theory of Gärtner (6) which leads to the following equation for the photocurrent efficiency

$$\eta_p = 1 - \exp(-\alpha L)/(1 + \alpha Lp) \quad [4]$$

In a previous (2) the application of this equation to i-V-λ data for polycrystalline $BaTiO_3$ electrodes was discussed and it was shown how Lp and N_d could be calculated using the following equation

$$\ln(1 - \eta_p^{corr}) = -\alpha \left(\frac{2\epsilon\epsilon_0}{qN_d}\right)^{1/2} (V - V_o^*)^{1/2} - \ln(1 + \alpha Lp) \quad [5]$$

A similar approach was taken with α-Fe_2O_3 data except that V_o^* has now been taken as a best fit parameter for the plots of $\ln(1 - \eta_p^{corr})$ *vs.* $(V - V_o^*)^{1/2}$, and values of N_d from Mott-Schottky plots (7) were used to calculate α, the absorption coefficient for the process giving rise to active holes. Equation [5] was applied for $(V - V_o^*) \gtrsim 250$ mV.

In order to obtain a good fit at low overvoltages (<250 mV) Eq. [4] was used with the value of L calculated from the parallel plate capacitor Eq. [23]

$$L = \frac{\epsilon\epsilon_0}{C} \quad [6]$$

where C is given by the more general equation of Dewald (24)

$$C = \left(\frac{q^2 N_d \epsilon\epsilon_0}{2kT}\right)^{1/2} \frac{|e^y - 1|}{(e^y - y - 1)^{1/2}} \quad [7]$$

The term y measures the space charge overvoltage, *i.e.*, $y = q\Delta\phi_S/kT$ and is negative for anodic bias. It was assumed that

$$V - V_o^* = |\Delta\phi_S| \quad [8]$$

Equations [6] and [7] give the more familiar $|\Delta\phi_S|^{1/2}$ dependence for L under sufficient anodic bias corresponding to the Mott-Schottky regime. Typical calculated curves are compared with experimental points in Fig. 9. The experimental data correspond to those in Fig. 3 and have been corrected for reflection. The fit is seen to be usually ±1% even at low overvoltages. The values for the various quantities determined from the data are summarized in Table I. An important point not yet fully understood is that V_o^* from best fit did not correspond to the flatband potential or the turn-on voltage for the photocurrent but was several tenths of a volt more anodic. This may be due in part to the fact that the Gärtner model implies an irreversible photocurrent. That is, no account is taken of possible cathodic current either in the valence band or conduction band. These effects would become more important at electrode potentials near the point of zero photocurrent.

It was also found that the theory could be fit to data with polychromatic light even though the theory was derived for monochromatic light. From this fit the calculated absorption coefficient was 1×10^4 cm^{-1} as would be expected if α represented some sort of

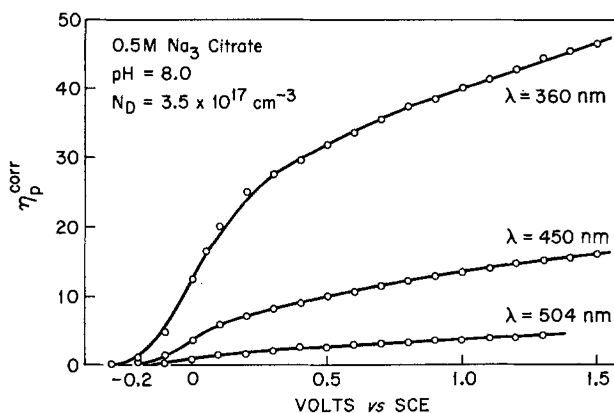

Fig. 9. Comparison of observed and calculated photocurrent efficiency. Polycrystalline α-Fe_2O_3; electrode no. 2.

Table I. Summary of values obtained from current-potential curves (99.999% α-Fe_2O_3)

Electrolyte	pH	V_o* (SCE)	α(calc.), cm^{-1}	Lp, cm
0.1M Na_2 EDTA	4.0	+0.20	5.9×10^4 (360 nm)	3×10^{-7}
0.5M Na_3 citrate	8.0	−0.10	3.1×10^4 (360 nm)	2×10^{-7}
0.5M Na_3 citrate	8.0	−0.10	9.3×10^3 (450 nm)	—
0.5M Na_3 citrate	8.0	−0.10	2.6×10^3 (504 (nm)	—
0.5M KCl	8.9	+0.17	2.3×10^4 (400 nm)	10×10^{-7}
2.0M NaOH	13.8	−0.48	1.0×10^4*	4×10^{-7}

* Polychromatic light (300-540 nm), intensity 4.76 mA.

average value over the 300-540 nm spectral range. The diffusion lengths found for α-Fe_2O_3 were 2-4 $\times$ 10^{-7} cm and were considerably lower than values found for TiO_2 (1×10^{-5} cm) and the barium and strontium titrates ($3\text{-}6 \times 10^{-6}$ cm) (25). Possible reasons for these differences will be discussed in a future publication.

The absorption coefficients calculated from the data in Fig. 8 curve A using Eq. [5] and Lp data from Table I and Mott-Schottky values for N_d are compared with spectrophotometric α in Fig. 8. It is seen that the absorption coefficient from optical measurements did not correspond to the absorption coefficient for the excitation process giving rise to the photocurrent. It is reasonable to presume that the absorption coefficient derived from i-V characteristics corresponds to the ligand to metal-charge transfer ($O^{2-} \rightarrow Fe^{3+}$), yielding reactive holes on the oxygen sites (valence band). The spectrophotometric measurements show that another process with comparable absorption is occurring, *i.e.*, there is an overlap of at least two absorption bands. The large absorption coefficient indicated for this overlapping process may mean that another type of charge transfer is occurring—possibly metal to metal, which can be envisaged as

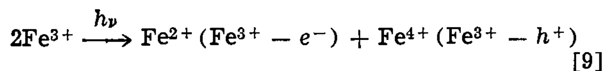

$$2Fe^{3+} \xrightarrow{h\nu} Fe^{2+}(Fe^{3+} - e^-) + Fe^{4+}(Fe^{3+} - h^+) \quad [9]$$

This process would give rise to a second type of hole, now on an iron site with a different energy level than the hole in the oxygen valence band. Indeed it has been suggested (27, 28) that this process is responsible for the intrinsic conductivity in α-Fe_2O_3 with $E_g \sim 1.7\text{-}2.0$ eV. The Fe^{4+} hole may no longer be capable of evolving oxygen from water while at the same time the electron trapped on iron (Fe^{2+}) may not be free to conduct and therefore would yield no photocurrent.

The validity of using absorption coefficients determined from i-V curves is supported by the plot shown in Fig. 10 calculated from data in curve B, Fig. 8. It is well known that for semiconductors the dependence of α on energy near the absorption edge usually follows the form (28)

$$\alpha h\nu = A(h\nu - E_g)^{n/2} \quad [10]$$

where A is a constant and n depends on the nature of the transition ($n = 1$ for a direct transition and $n = 4$ for an indirect transition). The slope in Fig. 10 is 2.07 giving $n = 4.1$, indicating an indirect transition requiring phonon support.

A further test of the plausibility of the absorption coefficient found for α-Fe_2O_3 was made by plotting the data in Fig. 7 in the form

$$\ln(1 - \eta_p^{corr}) = -\alpha\left(\frac{2\epsilon\epsilon_0\Delta\phi_S}{q}\right)^{1/2} \Big/ N_d^{1/2} - \ln(1 + \alpha Lp) \quad [11]$$

For $\lambda = 400$ nm, α was found to be 1.3×10^4 cm^{-1} in reasonable agreement with the value of 4.4×10^4 cm^{-1} from Fig. 8. This result supports the conclusion stated earlier that α for the charge transfer process

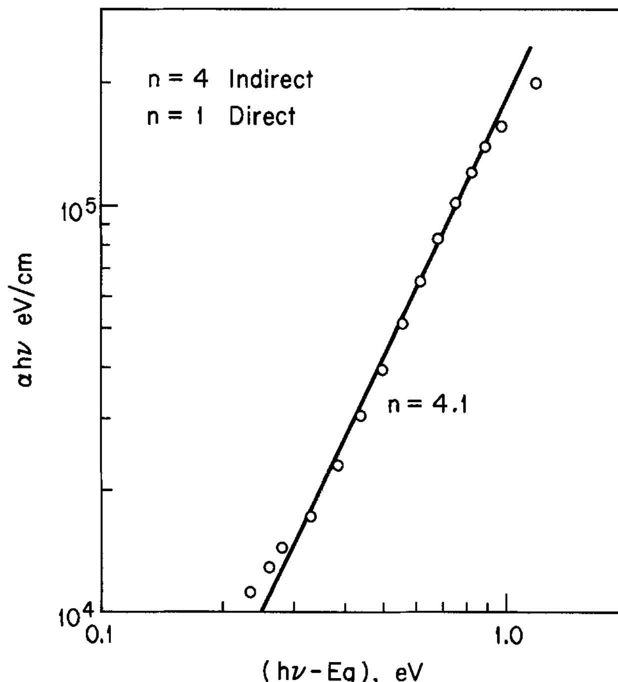

Fig. 10. Test for nature of electronic transition on absorption edge. Polycrystalline α-Fe_2O_3.

leading to photocurrent is considerably smaller than the spectrophotometric value.

Acknowledgments

The authors acknowledge partial financial support of this project by the National Science Foundation, Grant No. DMR 73-07507 AO2 and by the Committee on Research, University of California.

Manuscript submitted Oct. 11, 1977; revised manuscript received Dec. 12, 1977. This was Paper 328 presented at the Philadelphia, Pennsylvania, Meeting of the Society, May 8-13, 1977.

Any discussion of this paper will appear in a Discussion Section to be published in the December 1978 JOURNAL. All discussions for the December 1978 Discussion Section should be submitted by Aug. 1, 1978.

Publication costs of this article were assisted by the University of California.

REFERENCES

1. J. M. Bolts and M. S. Wrighton, *J. Phys. Chem.*, **80**, 2641 (1976).
2. J. H. Kennedy and K. W. Frese, Jr., *This Journal*, **123**, 1683 (1976).
3. K. L. Hardee and A. J. Bard, *ibid.*, **124**, 215 (1977).
4. K. L. Hardee and A. J. Bard, *ibid.*, **123**, 1024 (1976).
5. R. K. Quinn, R. D. Nasby, and R. J. Baugham, *Mater. Res. Bull.*, **11**, 1011 (1976).
6. W. W. Gärtner, *Phys. Rev.*, **116**, 84 (1959).
7. J. H. Kennedy and K. W. Frese, Jr., *This Journal*, **125**, 723 (1978).
8. E. Wegner and A. Adamson, *J. Am. Chem. Soc.*, **88**, 394 (1966).
9. M. M. Stimson and M. J. O'Donnell, *ibid.*, **74**, 1805 (1952).
10. G. M. Wyman, *J. Opt. Soc. Ann.*, **45**, 965 (1955).
11. M. J. S. Dewar and A. R. Lepley, *J. Am. Chem. Soc.*, **83**, 4560 (1961).
12. B. L. Van Duren and C. E. Bardi, *Anal. Chem.*, **35**, 2198 (1963).
13. F. A. Jenkins and H. E. White "Fundamentals of Optics," 3rd ed., Chap. 25, McGraw-Hill, New York (1957).
14. S. M. Ahmed and D. Maksimov, *Can. J. Chem.*, **46**, 3841 (1968).
15. R. F. G. Gardner, F. Swett, and D. W. Tanner, *J. Phys. Chem. Solids*, **24**, 1183 (1963).
16. D. Lewis and W. Westwood, *Can. J. Phys.*, **42**, 2367 (1964).
17. H. C. Van de Hulst, "Light Scattering by Small

Particles," p. 415, John Wiley & Sons, New York (1957).
18. R. H. Harding, B. Golding, and R. A. Morgen, *J. Opt. Soc. Am.*, **50**, 446 (1960).
19. V. K. LaMer, OSRD Rept. 4904, PB 32208, U.S. Dept. of Commerce (1944).
20. J. O'M. Bockris and S. Srinivasan, "Fuel Cells," pp. 97-102, McGraw Hill, New York (1969).
21. W. P. Gomes, T. Freund, and S. R. Morrison, *This Journal*, **115**, 818 (1968).
22. T. Freund and W. P. Gomes, *Catal. Rev.*, **3**, 1 (1969).
23. F. Möllers, H. J. Tolle, and R. Memming, *This Journal*, **121**, 1160 (1974).
24. J. F. Dewald, *Bell Syst. Tech. J.*, **39**, 615 (1960).
25. K. W. Frese, Jr., Ph.D. Thesis, University of California, Santa Barbara (1977).
26. F. J. Morin, *Phys. Rev.*, **93**, 1195 (1954).
27. J. B. Goodenough, in "Advances in Solid State Chemistry," H. Reiss, Editor, Chap. 4, McMillan, New York (1964).
28. E. J. Johnson, in "Semiconductors and Semimetals," Vol. 3, R. K. Willardson and A. C. Beer, Editors, Chap. 6, Academic Press, New York (1967).

Coulometric Study of the Reduction of Dinitroaniline Compounds

Csaba P. Keszthelyi,*[,1] Barbara A. Kenney, and Paul J. Buras

Department of Chemistry, Louisiana State University, Baton Rouge, Louisiana 70803

and Lloyd M. Southwick and Guye H. Willis

United States Department of Agriculture, Agricultural Research Service, Baton Rouge, Louisiana 70893

ABSTRACT

The authors' d.c.-polarographic study [*Anal. Chim. Acta.* **82**, 29 (1976)] has been extended to include a coulometric investigation of the cathodic reduction of six substituted dinitroanilines: 4-(trifluoromethyl)-2,6-dinitro-*N*,*N*-dipropylaniline (I) was measured in 40% aqueous ethanol buffered at four *p*H values (1.5, 5.1, 7.4, 9.2), and *N*-butyl-*N*-ethyl-4-(trifluoromethyl)-2,6-dinitroaniline (II), 2,6-dinitro-4-isopropyl-*N*,*N*-dipropylaniline (III), N^1,N^1-diethyl-4-(trifluoromethyl)-2,6-dinitro-*m*-phenylenediamine (IV), 4-(methylsulfonyl)-2,6-dinitro-*N*,*N*-dipropylaniline (V), and 3,5-dinitro-N^4,N^4-dipropylsulfanilamide (VI) were measured in 40% aqueous ethanol buffered at one *p*H value (1.5). Preparative scale runs and product analyses indicate that the electroreduction mechanism is *p*H dependent, as evidenced by substantial benzimidazole formation at 1.5 *p*H and little production of this compound at 7.4 *p*H.

Controlled potential coulometry (1-4) utilizes the modern instrumental capabilities of potentiostats and is a powerful electroanalytical technique that makes possible the elucidation of certain chemical reaction paths by allowing direct measurement of the number of Faradays taken up by a given amount of a compound (5-7). Similar information has been obtained on occasion from d-c polarograms (8-10); whereas in favorable circumstances, it is possible to arrive at the correct number of electrons involved (n), examination of the Ilkovic equation

$$i_d = kncD^{1/2}m^{2/3}t^{1/6}$$

reveals that n can be expressed only in terms of several constants or parameters whose cumulative uncertainty affects n. Indeed, it is customary to use the Ilkovic equation to find the diffusion coefficient D—a procedure which in turn assumes that n is known. An alternative procedure that uses the slope of a polarogram to find n is not applicable to quasireversible systems, and hence to many systems, including the substituted dinitroanilines of our study.

Coulometry in nonaqueous media often employs electrodes fabricated from the platinum metal family (5), but in aqueous solvents the problem of hydrogen discharge curtails their utility and mercury becomes the common choice, as was discussed in the report of our previous polarographic study (11). It should be mentioned that there are specific problems associated with controlled potential coulometry and large mercury pool cathodes; these are discussed later on in the paper.

* Electrochemical Society Active Member.
[1] Present address: Visiting Exchange Scientist, U.S. National Academy of Sciences—Hungarian Academy of Sciences, Szeged, Hungary.

Key words: cathodic reduction, controlled potential coulometry, mercury pool, substituted dinitroaniline.

Experimental

The general instrumental link-up in the coulometric experiments is presented in a simplified manner in Fig. 1. A buffered ethanol:water solution (40%:60% by vol.) similar to the polarographic solutions discussed previously (11), containing 50.0 μmoles of solute in the 150 ml total volume used in the "working" compartment of the coulometry cell (Fig. 2), was thoroughly

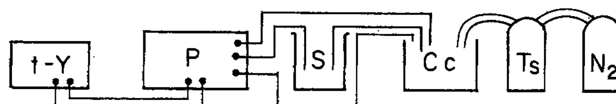

Fig. 1. Simplified block diagram of instrumental layout. Legend: *t-Y:* time-base X-Y recorder; P: potentiostat; S: silver coulometer; Cc: coulometry cell; Ts: bubbler-tower containing ethanol:water; N_2: purging gas tank.

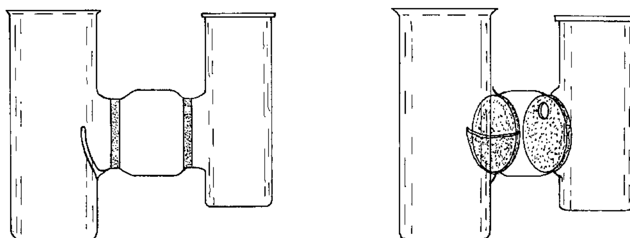

Fig. 2. Coulometry cell

purged with nitrogen, followed by applying a potential selected as appropriate from known $E_{1/2}$ values (11) in the three-electron mode. The actual mercury pool cathode (working electrode)-platinum coil anode (auxiliary electrode) voltage, reflecting IR losses due to the two medium porosity frits as well as solution resistance, was intermittently monitored with a Hewlett-Packard[2] 34703A/34740A DCV/DCA/Ω measurement system (the maximum voltage recorded was ~20V, far short for causing troublesome voltage-limiting conditions with the GBE Wenking 61-R potentiostat). In a number of experiments, the current output of the potentiostat was recorded on a Hewlett-Packard 7044-A X-Y recorder equipped with a time-base accessory. Because of the full-current output feature of the Wenking 61-R, measuring resistors and multipole switches were selected with special care. Product analysis for compound (I) at pH 1.5 and 7.4 was performed using a Perkin-Elmer 621 spectrophotometer and Varian HA-100 NMR spectrometer.

The coulometry cell (Fig. 2) containing the alcohol: water mixtures was preceded by a saturation tower containing a similar alcohol: water mixture, so that the purging nitrogen gas would not significantly alter the composition of the mixed solvent. A special feature of the coulometry cell was the glass lip protruding from the frit toward the center of the cathodic compartment; its purpose was to reduce the voltage drop along the surface of the mercury pool as a function of distance from the frit.

In a typical experiment, the 100 ml solution (60 ml aq. buffer + 40 ml ethanol) to be used in the auxiliary compartment and the 145 ml solution (90 ml aq. buffer + 55 ml ethanol) to be used in the working compartment were deaerated for 1 hr in separatory funnels placed above the coulometry cell; simultaneously, the coulometry cell itself was purged with N_2. After deaeration, the solutions were introduced and the background current was measured under the chosen conditions of stirring rate and applied potential; values ranged between 40 and 70 μA, with an observable slight decrease with time. Addition of 5 ml of alcohol containing the 50.0 μmoles of solute produced initial currents of less than 20 mA; electrolysis was continued past the 99% completion stage to background. Total time for an experiment was 12-15 hr, with the exception of silver coulometry and preparative scale (100 mg solute) runs which required up to 24 hr.

Silver coulometry was done using a 250 ml beaker containing 150 ml solution, 1M in $AgNO_3$ and 5M in $NaNO_3$ (alternately, 1M $AgNO_3$ and 2M KCN). The outside of the beaker was taped with black PVC tape to prevent photochemical decomposition and the top was also shielded from direct light. The electrodes (Ag wire or Ag foil) were suspended from a ⅛ in. diam glass rod that had an elongated W shape, and fit reasonably snugly on the spout and beaker rim. (Ideally the least number of sharp surfaces should produce best results, and the foil is preferable to the coiled wire.)

[2] Mention of tradenames is for the convenience of the reader and does not constitute any preferential endorsement by the U.S. Department of Agriculture over similar products available.

Only about 2/3 of the electrode was immersed in the solution to protect the contacts; voltage drop across the system, connected in series onto the auxiliary electrode, was about 2V. In silver coulometry weight is measured before the experiment, and after the experiment the electrodes are removed with Teflon-tipped forceps, washed thoroughly and gently in a stream of distilled water followed by acetone, then dried for 15 min at 50°C before weighing again. For reuse the electrodes were soaked in 1M KCN for over an hour, and the gaining electrode was polished with a piece of fine sandpaper (00) to remove loosely adhering silver. The losing electrode will eventually need replacement—for best results the two electrodes should never be interchanged. By measuring both the loss and gain values of the electrodes, a precision better than 0.5 mg was routinely observed, and with special care 0.1 mg can be expected according to our results. In case of higher discrepancy the loss figure was regarded as the more accurate because the gaining electrode often acquires crystalline deposition which may not adhere.

The present report is based on 56 coulometric determinations, with 36 runs on 4-(trifluoromethyl)-2,6-dinitro-N,N-dipropylaniline (I). Nine out of the 36 runs were preparative scale, including isolation and identification of product. Additional information concerning experiments is given in Table I and the following section.

Results and Discussion

Appropriate voltages for use in controlled potential coulometry can be selected from polarographic or sweep voltammetric information. Our polarographic study (11) gave the following $E_{1/2}$ values (−mV *vs.* SCE) at pH 1.5, 5.1, 7.4, and 9.2, respectively: (I) 190, 430, 700, 810; (II) 190, 430, 700, 810; (III) 170, 360, 720, 810; (IV) 230, 510, 720, 1010; (V) 160, 480, 710, 790; (VI) 160, 530, 680, 810. These values correspond to the second polarographic wave when it was distinguishable; at pH = 1.5 all compounds displayed a single wave whose height closely corresponded to the sum of the two wave heights for the compound observed at the higher pH's. A salient feature of the polarograms was the similarity in which pH affected all six compounds; for this reason, we felt that the essential coulometric information could be obtained by investigating all compounds at one pH and, in addition, one compound at all four pH's. The results are given in Table I.

The difference between our combined average value of ne^- ($7.53 \pm 0.16_6$) and the $8e^-$ required ideally to reach the dihydroxylamine stage was large enough that we interpret the difference as an indication of some kinetic perturbation rather than as an instrumental artifact. The assignment of two $4e^-$ reduction steps (11) on the basis of simple d-c polarography is, therefore, seen in the perspective of coulometry as a close approximation rather than an ultimate conclusion.

The chemistry of nitroaromatics is known to be complex. Peltier and his co-workers (12-14) have extensively studied the controlled potential electroreduction of a large number of substituted mono- and dinitro

Table I. Summary of coulometric experiments

Compound	E(V *vs.* SCE)	pH	ne^-
4-(trifluoromethyl)-2,6-dinitro-N,N-dipropylaniline (I)*	−0.600	1.5	7.45
	−0.700	5.1	7.74
	−0.900	7.4	7.46
	−1.00	9.2	7.95
N-butyl-N-ethyl-4-(trifluoromethyl)-2,6-dinitroaniline (II)	−0.600	1.5	6.69
2,6-dinitro-4-isopropyl-N,N-dipropylaniline (III)	−0.600	1.5	6.93
N^1,N^1-diethyl-4-(trifluoromethyl)-2,6-dinitro-*m*-phenylenediamine (IV)	−0.600	1.5	8.75
4-(methylsulfonyl)-2,6-dinitro-N,N-dipropylaniline (V)	−0.600	1.5	7.80
3,5-dinitro-N^4,N^4-dipropylsulfanilamide (VI)	−0.600	1.5	7.23
All samples	—	—	$7.53 \pm 0.16_6$**

* Preparative scale runs gave ne^- value estimates that compare favorably: pH 1.5: 7.43 (5 runs); pH 7.4: 7.68 (3 runs).
** Standard deviation of the mean.

compounds. Their investigations, which included product identification, give evidence of the stepwise reduction of nitroaromatics. Their work also reveals complicating factors; n-values less than the theoretical seem to be characteristic of the nitroanilines.

Further insight into the electrochemistry of nitroaromatics is provided by the classical example of the reduction of picric acid in HCl; Lingane (2) found that 34 electrons are involved in the production of the primary product bis-(3,5-diamino-4-hydroxyphenyl) hydrazine, but subsequently Bergman and James (15), as well as Meites and Meites (16), demonstrated that ne^- is a function of both the initial picric acid concentration and the hydrochloric acid concentration.

In order to analyze the products of the pH 1.5 reduction, the pH of the reaction solution was adjusted to 7, the ethanol removed with a nitrogen stream, and the aqueous residue extracted with ether. Drying the extract with sodium sulfate and evaporation to dryness with nitrogen yielded an oily-solid red-brown residue. Thin layer chromatography (silica gel GF-254, benzene: ethyl acetate, 2:1) of the residue showed several u.v.-absorbing (254 nm) spots along the length of the plate and a single major spot ($R_f = 0.14$) which exhibited bright blue fluorescence under u.v. light. The residue gave the following spectroscopic data: infrared (film) 1620 cm^{-1}; NMR ($CDCl_3$) δ 7.50 (*s*, 1, ArH), 6.72 (*s*, 1, ArH), 4.20 (*t*, 2, CH_2), 3.75 (broad, 2, NH_2), 2.85 (quadruplet, 2, CH_2), 1.87 (*m*, 2, CH_2), 1.44 (*t*, 3, CH_3), and 0.99 ppm (*t*, 3, CH_3). These peaks in the NMR spectrum were observed almost to the exclusion of other absorptions and are similar to those reported for 2-ethyl-7-nitro-1-propyl-5-trifluoromethylbenzimidazole by Leitis and Crosby (17), who identified the benzimidazole as a product of the photochemical degradation of compound I.

Preparative thin layer chromatography of the residue on silica gel by developing three times with benzene: ethyl acetate, 2:1, afforded a chromatogram with the blue fluorescent spot at R_f 0.31-0.44. From this area a pale yellow solid was isolated which gave the following mass spectrum, m/e (%); 272 (15), 271 (100, M+), 256 (22), 252 (11), 243 (14), 242 (92), 229 (74), 228 (44), 227 (18), 214 (31), (212 (12), 159 (10).

We conclude from these spectroscopic data that the major product of the pH 1.5 reduction is 7-amino-2-ethyl-1-propyl-5-trifluoromethylbenzimidazole, compound VII

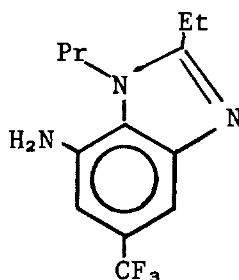

VII

Identification of a benzimidazole in our work at low pH is consistent with the studies of Peltier and co-workers (12c, 14), who observed benzimidazole formation in the electrochemical reduction of N,N-disubstituted-o-nitroanilines in 1N sulfuric acid: ethanol, 1:1.

The pH 7.4 reaction was worked up in a similar manner except without adjustment of the pH before ether extraction. Thin layer chromatography of the residue showed several u.v.-absorbing spots and a small fluorescent blue spot at $R_f = 0.14$. In addition to benzimidazole peaks, which were usually minor, the NMR spectrum ($CDCl_3$) of the resulting residue showed the following singlets in the aromatic region: δ7.68, 7.45, 7.14, 6.99, 6.73, 6.68, and 6.56 ppm. From one reaction to another the relative sizes of these peaks varied. We are continuing our study of the products of the pH 7.4 reduction. With regard to our NMR work, we plan to look into temperature-δ relationships for additional analytical capability.

Although the compounds of the present study are amenable to photodecomposition (17, 18), we found no evidence that exclusion of roomlight altered the polarographic or coulometric results at any of the four pH values. To our knowledge a converse study, involving the electrochemical investigation of photolysis products of these compounds (I-VI), has not been reported.

Conclusion

The present coulometric study of the number of electrons involved in the cathodic reduction of the substituted dinitroanilines, 4-(trifluoromethyl)-2,6-dinitro-*N,N*-dipropylaniline; *N*-butyl-*N*-ethyl-4-(trifluoromethyl)-2,6-dinitroaniline; 2,6-dinitro-4-isopropyl-*N,N*-dipropylaniline; N^1,N^1-diethyl-4-(trifluoromethyl)-2,6-dinitro-*m*-phenylenediamine; 4-(methylsulfonyl)-2,6-dinitro-*N,N*-dipropylaniline; and 3,5-dinitro-N^4 N^4-dipropylsulfanilamide in aqueous ethanol gave n values in close agreement with those previously estimated from polarographic measurements. The slight deviation of the experimentally obtained n value ([7.53 ± 0.16$_6$] e^-) from the number of electrons ideally required to reach the dihydroxylamine form (8e^-) is considered to be of chemical rather than artifactual origin and is not unexpected in view of the known complex chemistry of the species involved. The coulometric results necessitate a refinement of the previous mechanistic interpretation (11) based on d.c. polarography. Although there is only a relatively slight change in n values as a function of pH, preparative scale runs and product analyses reveal that the apparent merging of the two polarographic waves at low pH in effect involves a change in the reduction mechanism. Results of a separate study planned to provide information on this detail with the aid of additional electroanalytical techniques (5) will be presented subsequently.

Acknowledgment

We thank S. Swinney, P. Dasgupta, L. McGee, C. Lee, and M. Bertucci for contributions to this project.

Manuscript submitted Nov. 12, 1976; revised manuscript received Dec. 16, 1977.

Any discussion of this paper will appear in a Discussion Section to be published in the December 1978 JOURNAL. All discussions for the December 1978 Discussion Section should be submitted by Aug. 1, 1978.

Publication costs of this article were assisted by the U.S. Department of Agriculture.

REFERENCES

1. A. Hickling, *Trans. Faraday Soc.*, **38**, 27 (1942).
2. J. J. Lingane, *J. Am. Chem. Soc.*, **67**, 1916 (1945).
3. J. J. Lingane, *Anal. Chim. Acta.* **2**, 584 (1948).
4. A. J. Bard and K. S. V. Santhanam, *Electroanal. Chem.*, **4**, 215 (1970).
5. W. V. Childs, J. T. Maloy, C. P. Keszthelyi, and A. J. Bard, *This Journal*, **118**, 874 (1971).
6. E. J. Rudd, M. Finkelstein, and S. D. Ross, *J. Org. Chem.*, **37**, 1763 (1972).
7. H. Satonaka, Z. Saito, and T. Shimura, *Kanagawa-ken Kogyo Shikensho Kenkyu Hokoku*, **40**, 29 (1974).
8. O. H. Müller, *J. Biol. Chem.*, **145**, 425 (1942).
9. E. Friedheim and L. Michaelis, *ibid.*, **91**, 355 (1931).
10. R. Elema, *Rec. Trav. Chim.*, **50**, 807 (1931).
11. L. M. Southwick, G. H. Willis, P. K. Dasgupta, and C. P. Keszthelyi, *Anal. Chim. Acta*, **82**, 29 (1976).
12. M. Le Guyader, (a) *Bull. Soc. Chim. (France)*, **1966**, 1848; (b) *ibid.*, **1966**, 1858; (c) *ibid.*, **1966**, 1867.
13. A. Tallec, (a) *Ann. Chim.*, **3**, 155 (1968); (b) *ibid.*, **3**, 347 (1968); (c) *ibid.*, **4**, 67 (1969).
14. (a) M. Le Guyader and D. Peltier, *Bull. Soc. Chim. (France)*, **1966**, 2695; (b) A. Darchen and D. Pel-

tier, *ibid.*, 1974, 673.
15. I. Bergman and J. C. James, *Trans. Faraday Soc.*, **50**, 60 (1954).
16. L. Meites and T. Meites, *Anal. Chem.*, **28**, 103 (1956).
17. E. Leites and D. G. Crosby, *J. Agr. Food Chem.*, **22**, 842 (1974).
18. C. S. Helling, *J. Environ. Qual.*, **5**, 1 (1976).

Kinetics of the Electrochemical Reduction of Dicyanoaurate

E. T. Eisenmann

Bell Laboratories, Columbus, Ohio 43213

ABSTRACT

The mechanism of the electrochemical reduction of dicyanoaurate was studied by means of steady-state and relaxation methods in combination with a rotating disk electrode. The deposition of soft gold, lead-doped soft gold and cobalt-hardened gold was found to proceed via one common mechanism that involves adsorption equilibria preceding and following the electron transfer step. Special effects, such as epitaxy and preferred orientation of soft gold, the small-grained texture of hard gold, and the lead-induced depolarization of soft gold plating are explained in terms of the energetic states of the adsorbed, oxidized, and reduced gold species. The effect of lead is to lower the activation energy of the electron transfer, which results in the accelerated establishment of a preferred orientation. Cobalt increases the activation energy of the electron transfer and gives rise to a high nucleation rate. The proposed mechanism is shown to explain equally well the anodic behavior of gold in alkaline cyanide electrolyte.

The importance of gold plating in electronic device technology has led to greatly diversified, usually proprietary plating formulations. Yet apart from the description of particular bath features, there is a definite scarcity of the documentation of fundamental processes involved in the electrodeposition of gold. Cheh and Sard (1) used galvanostatic techniques to study the morphology of gold deposits on a rotating-disk electrode from various electrolytes. Harrison and Thompson (2) employed voltammetric techniques and postulate a reaction mechanism that involves AuCN as reacting species. Recently, McIntyre and Peck (3) reported with considerable detail on the depolarization of the deposition of soft gold through heavy metal ions. Numerous publications are available on the effects of codeposited impurities on the physical properties of gold plates (4-6). The review of the literature indicates that kinetic studies have been practically limited to soft gold systems. Although soft gold as well as hard gold is almost universally deposited from electrolytes containing dicyanoaurate, there is no indication that a unifying kinetic study of the two types of gold baths was ever attempted. Recent work on the deposition of gold on the reeds of sealed contacts (7) suggested such a unifying study. Using predominantly potentiostatic, steady-state, and relaxation techniques in combination with a rotating-disk electrode various aspects of the electrode kinetics were investigated.

Experimental

The following solutions were used in the present study: (*i*) Commercial hard gold baths (Selrex CI and Technic Orosene 999), operated at pH = 4 and 30°C; (*ii*) Soft gold bath, containing 0.1M $KAu(CN)_2$, 0.3M potassium phosphate, and no or 2 ppm Pb, operated at pH = 7 and 30°C or 65°C. Polarization measurements were carried out in these electrolytes either with Pt rods of 0.5 cm^2 area (under constant convection) or with a rotating Pt disk of 0.32 cm^2.

It was assumed that the gold deposition would usually proceed with less than 100% current efficiency. The gold partial currents were, therefore, determined by means of a coulometric analysis of the gold deposit. This approach was, evidently, quite time consuming and precluded current or voltage scanning techniques. It is believed, however, that superior accuracy of the data was achieved in this manner.

Key words: electrocrystallization, electrode adsorption processes, epitaxy, lead-induced depolarization.

Potentiostatic Polarization

A Pt disk electrode was polarized under constant potential conditions for various lengths of time in the electrolytes described above. The gold partial currents were evaluated from plots of the (coulometrically determined) electrical equivalents of the gold deposits *vs.* the plating time. For the hard gold baths, these plots were found to yield straight lines, indicating that the gold partial current at constant potential is independent of the plating time. In contrast to this behavior, the same kind of plots for soft gold deposition were curved, corresponding to an acceleration of the rate of deposition with time.

The slopes of the straight lines obtained for one of the hard gold baths and the limiting slopes of the curves at short plating times obtained for the soft gold baths were plotted semilogarithmically *vs.* the deposition potential, Fig. 1. The straight portions of these curves have slopes of $-4.4V^{-1}$ at 30°C and $-3.6V^{-1}$ at 65°C, the difference being accountable by the thermal energy difference. The shift in the deposition potential at equal current density for soft gold at 65° and 30°C is explained by the increased solubility of HCN at the lower temperature, which results in a decrease of the equilibrium potential. The similar shift observed for hard gold *vs.* soft gold at 30°C may be due to any of several differences in the makeup of the baths. However, because of the very striking difference in the grain size of the two types of gold deposits, it is postulated that the cobalt content in the hard gold bath increases the activation energy of the electron transfer, and consequently the nucleation rate of the gold deposition.

Time Dependence of the Deposition Rate

The observed increase of the deposition rate of soft gold with time at constant potential corresponds to the "depolarization effect" studied by various authors (8, 9) under galvanostatic conditions. Since it was unknown to what extent the soft gold bath was contaminated with heavy metal ions, which are capable of inducing the depolarization, an addition of 2 ppm lead

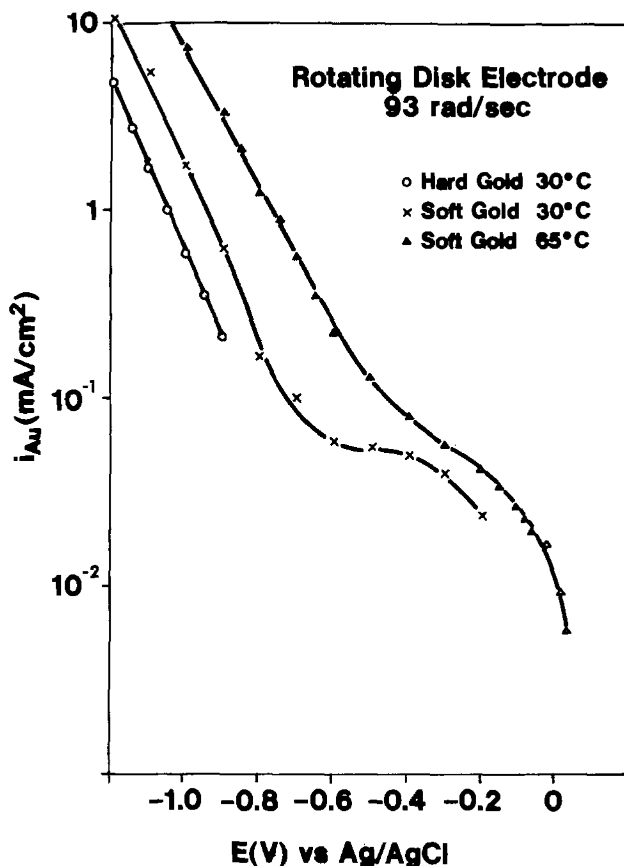

Fig. 1. Current density-potential curves at short polarization times.

was made to the plating solution. With this modified bath, gold was deposited potentiostatically for various lengths of time. Figure 2 shows the coulometric equivalents of the gold deposits in dependence of the deposition time. It is seen that at all potentials the gold deposit grows initially in proportion to t^2 and later in proportion to t, where t is the deposition time. Basically, the same behavior is also obtained for a soft gold bath without the intentional lead addition. However, the deposits grow for an extended period proportional to t^x, where $1 < x < 2$. Figure 2 indicates that in the case of lead-doped gold the time required for the current density to stabilize is practically independent of the deposition potential. Also, the steady-state condition is achieved at increasingly thicker deposits as the deposition potential assumes more negative values.

Generation of Polarization Curves under Steady-State Conditions

According to Fig. 2, steady-state conditions of the deposition of lead-doped gold are attained within about 5 min. Polarization curves were, therefore, derived from the slope of current density-time product *vs.* t curves for various potentials, at $t = 1000$ sec. A similar procedure was employed for the deposition of lead-free gold, measuring the slope between the plating times $t = 3$ and $t = 5$ hr. The results are given in Fig. 3. A considerable difference in the deposition potential between the two curves is noted at the center of the graph, which decreases, however, at very high and very low values of the deposition potential.

Both curves seem to approach the slope of the curves in Fig. 1 at extreme negative potentials, suggesting that the same mechanism is operative. The steep sections at the center of the graph are tentatively identified as the result of the proximity to the equilibrium potential, which is controlled by the concentration of cyanide at the electrode surface. In order to confirm this assumption it is necessary to explain the plateau which is evident at the right of the steep portions.

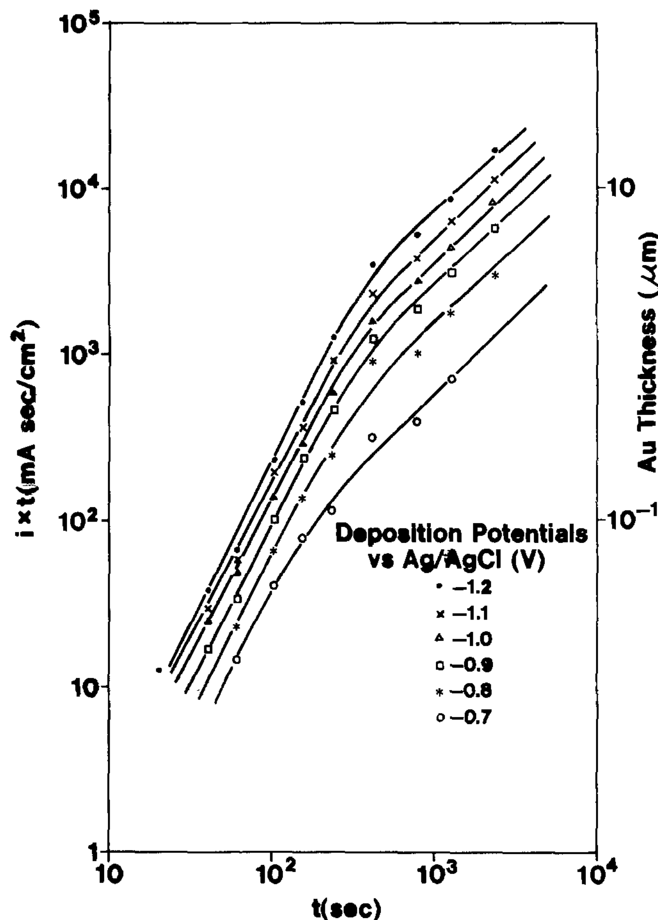

Fig. 2. The growth of Pb-doped soft gold

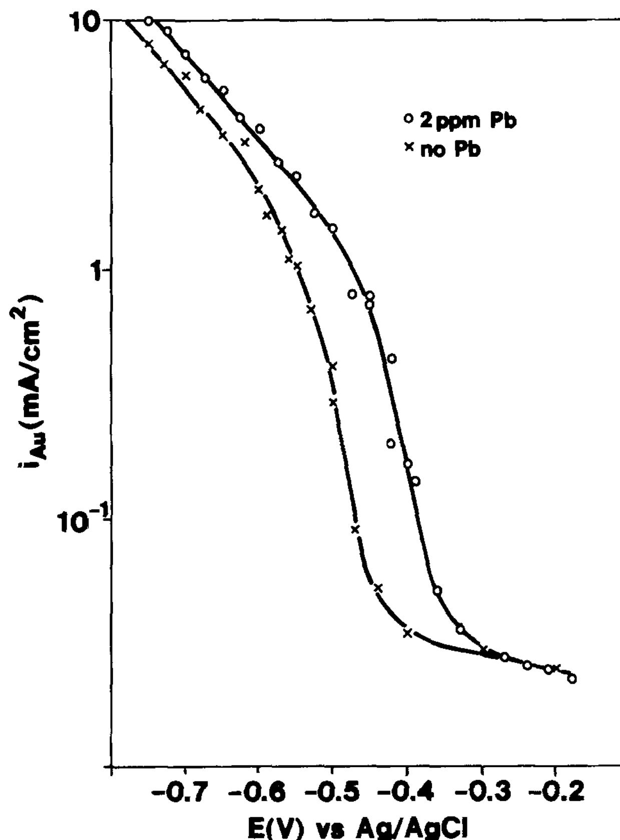

Fig. 3. Current density-potential curves for soft gold at long polarization times.

Evidence of Mixed Potential and Electroless Deposition at the $Au/Au(CN)_2^-$ Electrode

Rotating-disk experiments were designed to explain the plateau section in Fig. 1 and 3. In order to minimize the effect that may result from the accumulation of cyanide during plating, a large volume of electrolyte (2.5 liters) was circulated through the plating cell.

Under open-circuit conditions, a Pt disk electrode assumed a potential of +0.043V *vs.* Ag/AgCl at 65°C at a rotation velocity of 94 rad/sec. The potential increased with increasing rotation velocity. After prolonged exposure, the Pt disk was coated with gold. The rate of gold deposition appeared to be strongly dependent on the history of the bath (*e.g.*, previous use), but was constant within a given test series over many hours. This result proves that the open-circuit potential of the gold electrode corresponds to a mixed potential.

Discussion and Additional Results

Electroless deposition of gold.—The electron donor that causes the reduction of the $Au(CN)_2^-$ ions is hypothesized to be the cyanide ion, according to

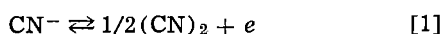

$$CN^- \rightleftarrows 1/2(CN)_2 + e \quad [1]$$

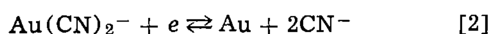

$$Au(CN)_2^- + e \rightleftarrows Au + 2CN^- \quad [2]$$

or after adding Eq. [1] and [2]

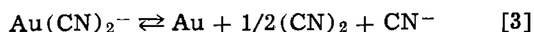

$$Au(CN)_2^- \rightleftarrows Au + 1/2(CN)_2 + CN^- \quad [3]$$

It is seen that the cyanide ion has the dual role of promoting reaction [1] and retarding reaction [2]. The kinetics of the over-all reaction [3] is, therefore, strongly dependent on the cyanide concentration. The oxidation potentials of reactions [1] and [2] can be expressed by the Nernst equation (brackets indicate activities or, approximately, concentrations)

$$E_{(CN)2} = E^\circ_{(CN)2} - \frac{RT}{\mathbf{F}} \ln [CN^-] + \frac{RT}{2\mathbf{F}} \ln [(CN)_2] \quad [4]$$

$$E_{Au} = E^\circ_{Au} - 2\frac{RT}{\mathbf{F}} \ln [CN^-] + \frac{RT}{\mathbf{F}} \ln [Au(CN)_2^-] \quad [5]$$

where

$E^\circ_{Au} = -0.84V$ *vs.* Ag/AgCl[10]

$E^\circ_{(CN)2} = -0.46V$ *vs.* Ag/AgCl[10]

Reaction [3] is at equilibrium if

$$E_{Au} = E_{(CN)2} \quad [6]$$

From Eq. [4] and [5] it follows that equilibrium is achieved in a soft gold bath at room temperature if

$$\ln [CN^-][(CN)_2]^{1/2} = -16.8$$

i.e., if the cyanide and cyanogen concentrations are about 10^{-5} moles/liter.

Under equilibrium conditions, the mass balance of reaction [3] is shifted to the right as the concentration of cyanide decreases. Continuous removal of CN^- and $(CN)_2$ species from the reaction surface, *e.g.*, under the conditions of a rotating-disk electrode, allows continued deposition of gold. Favorable conditions for the reaction were generated in the experiments by continued degassing of the electrolyte. At pH = 7, the cyanide ion is protonated to form HCN, which along with cyanogen tends to escape into the gas phase. A large surface to volume ratio and agitation of the solution were used to promote this transition.

For the system under consideration, the deposition rate of gold i_{Au}, is equal to the mass fluxes of $Au(CN)_2^-$, CN^-, and $(CN)_2$

$$i_{Au} = \frac{k_1}{\delta}\Delta[Au(CN)_2^-] = -\frac{k_2}{\delta}\Delta[CN^-] = -\frac{k_3}{\delta}\Delta[(CN)_2] \quad [7]$$

The Δ's indicate the difference between bulk and surface concentrations; k_1, k_2, and k_3 are constants and δ represents the diffusion layer thickness. At a rotating-disk electrode, the velocity of rotation, w, influences the diffusion layer thickness δ in the inverse proportion to $\sqrt{w}$ (11)

$$\delta = 1.61 \frac{D^{1/3}}{\nu} \frac{\nu}{w} \quad [8]$$

(D = diffusion coefficient, ν = kinematic viscosity).

Concerning the concentration differences, $\Delta[CN^-]$ and $\Delta[(CN)_2]$, the following inequalities may be both true, both false, or either of them true.

$$[CN^-] \text{ (bulk)} << [CN^-] \text{ (surface)} \quad [9]$$

$$[(CN)_2] \text{ (bulk)} <<](CN)_2[\text{ (surface)} \quad [10]$$

If both are true then

$$\Delta[CN^-] = [CN^-] \text{ (surface)} \quad [11]$$

$$\Delta[(CN)_2] = [(CN)_2] \text{ (surface)} \quad [12]$$

From Eq. [7] together with Eq. [8], [11], and [12] (dropping the specific reference to the surface in Eq. [11] and [12]) it follows that

$$\frac{d \log i_{Au}}{d \log w} = \frac{d \log[CN^-]}{d \log w} + \frac{1}{2} \quad [13]$$

$$\frac{d \log i_{Au}}{d \log w} = \frac{d \log[(CN)_2]}{d \log w} + \frac{1}{2} \quad [14]$$

The concentration terms in Eq. [13] and [14] are expected to deviate from zero for the conditions of the electroless gold deposition.

In a carefully executed experiment at two velocities of the rotating-disk electrode, the rate of gold deposition was found to vary proportionally to $w^{1/4}$. This result indicates that the concentration terms in Eq. [13] and [14] are $-1/4$. Correlated with the variation of the deposition rate, the electrode potential was measured to increase by 0.032V per decade increase in rotation velocity. The combination of this information with the derivatives of Eq. [4] and [5] yields for 65°C (assuming that Eq. [9] and [10] are both true)

$$\frac{d E_{Au}}{d \log w} = -0.134 \frac{d \log[CN^-]}{d \log w} = 0.033V \quad [15]$$

$$\frac{d E_{(CN)2}}{d \log w} = -0.067 \frac{d \log[CN^-]}{d \log w} + 0.033 \frac{d \log[(CN)_2]}{d \log w} = 0.0084V \quad [16]$$

Comparing Eq. [15] and [16] with the observed value of 0.032V per decade increase in rotation velocity it is evident that only Eq. [15] and, therefore, Eq. [9] and [13] are consistent with the experimental results. Hence E_{Au} is the controlling potential and reaction [2] is closer to its equilibrium than the electron donor reaction [1]. At potentials corresponding to the plateau section of Fig. 3 the deposition rate of gold was also found to follow the $w^{1/4}$ dependence as demonstrated in Fig. 4. It is noted that Eq. [7]-[9] may be insufficient to account for the observed transport process because the rate of cyanide removal from the reaction surface is most certainly enhanced by the protonation reaction

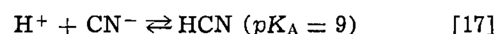

$$H^+ + CN^- \rightleftarrows HCN \ (pK_A = 9) \quad [17]$$

Assuming either extreme or minimal deviation from the equilibrium of reaction [17], the concentration of free cyanide at the surface of the rotating-disk electrode was calculated by means of Eq. [7] and [8]. Inserting the results into Eq. [5] yields the equilibrium potential for each polarization condition.

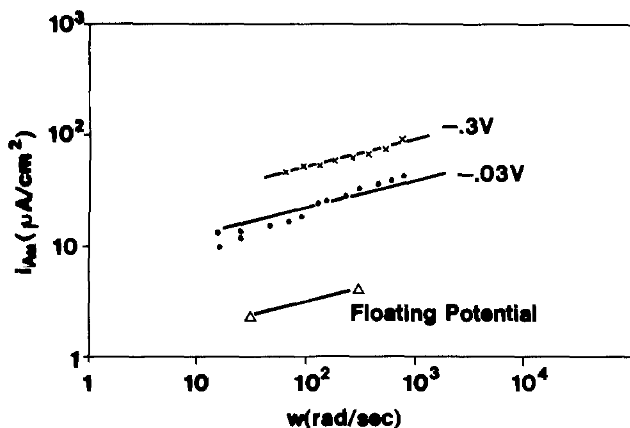

Fig. 4. Dependence of the Au deposition rate in the plateau range on convection.

The following is concluded from the comparison of the calculated with the applied electrode potentials. Under electroless and mildly polarized conditions at 65°C between 0.043 and −0.02V *vs.* Ag/AgCl, reaction [17] and electrode reaction [2] are practically at equilibrium. At current densities within the linear portion of the polarization curve, between −0.5 and −0.9V *vs.* Ag/AgCl, reaction [17] is far from its equilibrium and the difference between the calculated and the applied potential exceeds 0.1V, *i.e.*, the deposition of gold is activation controlled. The plateau section of the polarization curve is identified, therefore, as the result of the influence of the cyanide protonation on the equilibrium electrode potential.

Deposition of gold under activation control.—The equation describing the rate of a cathodic electrode process that proceeds under activation control at potentials far from the equilibrium potential in the absence of the double layer effect has the general form (12)

$$i = i_o \exp\left[-\alpha n \frac{\mathbf{F}}{RT}(E - E^e)\right] \quad [18]$$

with

$$i_o = n\mathbf{F}k^\circ \, a_{ox}^{(1-\alpha)} \, a_R^{\alpha} \quad [19]$$

where α = transfer coefficient; n = number of electrons exchanged; E = electrode potential; E^e = equilibrium electrode potential; a_{ox} = activity of the oxidized species; a_R = activity of the reduced species; and k° = apparent standard rate constant.

This equation may be used to correlate the slope of the polarization curves in Fig. 1 and 3 with specific reactions involved in the electrode process. From Eq. [18] and [19] it follows

$$\frac{d \ln i}{d E} = \frac{d \ln i_o}{d E} - \alpha n \frac{\mathbf{F}}{RT} + \alpha n \frac{\mathbf{F}}{RT}\frac{d E^e}{d E} \quad [20]$$

$$\frac{d \ln i_o}{d E} = (1-\alpha)\frac{d \ln a_{ox}}{d E} + \alpha \frac{d \ln a_R}{d E} \quad [21]$$

In the present application, E^e is identical with E_{Au} of Eq. [5]. For constant hydrodynamic conditions the cyanide concentration at the electrode surface is proportional to the gold partial current, i_{Au}. Therefore, with Eq. [5], at constant convection

$$d E_{Au} = -2\frac{RT}{\mathbf{F}} d \ln [CN^-] = -2\frac{RT}{\mathbf{F}} d \ln i_{Au} \quad [22]$$

Combining Eq. [20]-[22] yields for the deposition of gold (converting to the common logarithm)

$$\frac{d \log i_{Au}}{d E} = \frac{0.434}{1+2\alpha}\left[(1-\alpha)\frac{d \log a_{ox}}{d E} + \alpha \frac{d \log a_R}{d E} - \alpha \frac{\mathbf{F}}{RT}\right] \quad [23]$$

In many metal deposition reactions, α is found to be approximately 0.5. Accordingly, the slopes of log i *vs.* E curves usually show a slope that is equal to a simple fraction of $S = 0.434\mathbf{F}/2RT$. This is also observed in Fig. 1 and 3 for strong cathodic polarization, where the slopes amount to $-4.4V^{-1}$ at 30°C and $-3.6V^{-1}$ at 65°C. Considering the precision of the measurements, these slopes agree well with the assumption of $\alpha = 0.5$ and with

$$\frac{d \log i_{Au}}{d E} = -\frac{0.434\mathbf{F}}{4RT} \quad [24]$$

By comparison with Eq. [23] it is concluded that

$$\frac{d \log a_{ox}}{d E} = -\frac{d \log a_R}{d E} \quad [25]$$

Two distinct reaction paths can be visualized, which both conform with Eq. [25]:

The electron transfer proceeds without prechemical adsorption of the oxidized species ($Au(CN)_2^-$), to form Au atoms whose energetic state is not significantly different from that of their final lattice site. In this case

$$d \log a_{ox} = -d \log a_R = 0 \quad [26]$$

The electron transfer is preceded by the chemisorption of the oxidized species and followed by the dissociation of the reduced species in the adsorption layer, according to the following sequence:

Prechemical adsorption equilibrium

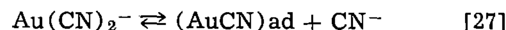

$$Au(CN)_2^- \rightleftarrows (AuCN)ad + CN^- \quad [27]$$

Electron transfer step (rate limiting)

$$(AuCN)ad + e \rightleftarrows (Au^\circ CN)^- ad \quad [28]$$

Postchemical desorption and crystallization

$$(Au^\circ CN)^- ad \rightleftarrows Au(lattice) + CN^- \quad [29]$$

Equilibria [27] and [29] may be dependent on the crystal orientation of the substrate as well as on various solution properties, *e.g.*, the presence of cobalt or lead. All modifications of equilibria [27] and [29] may result in a modification of the electron transfer probability. For each energetic condition, however, Eq. [25] is applicable. If the electrode is saturated with the adsorbates, then a_{ox} and a_R are independent of concentration variations in the aqueous phase and

$$d \log a_{ox} = -d \log a_R = 0 \quad [26a]$$

Observations relating to effects of adsorption.—The effect of adsorption on the crystal size and preferred orientation of electrodeposits is, qualitatively, well known, as evidenced by the commercial use of addition agents and brighteners. Certain features of the gold-plating system are also indicative of adsorption processes and are discussed here.

The structure of soft gold is commonly referred to as "columnar," because etched cross sections show longish crystallites whose length axes coincide with the growth direction of the deposit. The nucleation rate is, evidently, small, and the tendency toward preferred growth orientation is large. If soft gold is deposited on the polished surface of a polycrystalline, annealed fcc metal, a strong epitaxial effect is observed. Substrate grains with the "right" orientation produce well-formed gold crystals at a substantially higher rate than adjoining grains, which do not have the "right" orientation, as shown in Fig. 5. Hard gold deposits, in contrast, have a grain size in the submicron range and exhibit, intrinsically, featureless surfaces. The nucleation rate during hard gold deposition is many orders of magnitude higher than during soft gold deposition.

It is noted that the principal difference between soft gold and hard gold lies in the crystallization behavior, while the electron transfer step is activation controlled in both cases. The role of adsorbed species is, therefore, that of either increasing or decreasing the activation

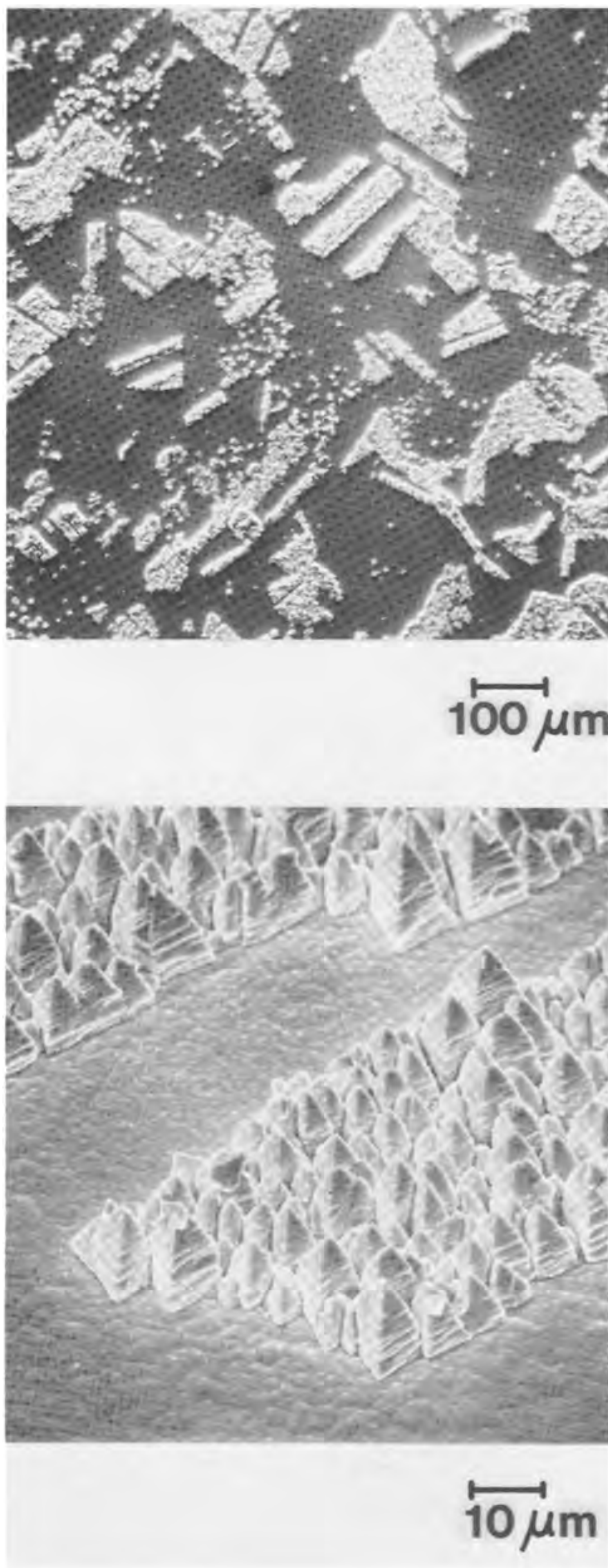

Fig. 5. Epitaxial growth of Au crystals on the surface of an annealed fcc metal.

energy of the electron transfer step. In terms of electrode processes, each crystal orientation has, at constant potential, a typical crystallization current density $i\{a, b, c\}$ (13), where for example

$$i\{100\} \neq i\{110\} \neq i\{111\} \quad [30]$$

Dependent on the relative magnitude of the crystallization current densities, more or less pronounced preferential orientation of the gold deposit results. The experimental current density, i_{Au}, is equal to the average of the various crystallization current densities. If the crystallization process is initiated on randomly oriented nuclei, preferential deposition tends to generate more surface area of equivalent orientation and an increase in i_{Au} results. This is observed during the deposition of regular and lead-doped soft gold. If the differentiation between the crystallization current densities is enhanced, *e.g.*, under the condition that coadsorbed lead lowers the activation energy of the electron transfer, Eq. [28], then one crystallization current density may become dominant. With negligible growth in all but one orientation, the increase in reactive surface area, and as a result the increase of i_{Au}, is proportional to the deposition time. This condition of extreme differentiation between the crystallization current densities is observed in Fig. 2 ($it \propto t^2$).

The deposition of hard gold proceeds without noticeable variation in i_{Au}. This result is consistent with the size of the crystallites formed, whose growth period is limited to a few seconds. In terms of Eq. [28], and in contrast to the effect of lead, the coadsorption of cobalt provides for an increase in the activation energy of the electron transfer. Under this condition, the differentiation between the crystallization current densities may be minimized, but more importantly, the nucleation rate is increased, thus explaining the texture of hard gold deposits.

Perturbation of the adsorption layer.—The transient behavior of the gold-cyanoaurate electrode has, to some extent, been described earlier (7). Additional experiments were deemed necessary to clarify the common and contrasting features of the deposition of soft gold, lead-doped soft gold, and hard gold. The potential transients of a rotating-disk electrode, after prepolarization at constant potential, were recorded, therefore, for a variety of conditions.

Regardless of the specific experimental conditions the potential transients were always found to follow the same pattern. After the interruption of the cathodic (*i.e.*, negative) polarization, the potential was found to increase in at least three distinctly different modes. The initial, fastest variation of the potential has been identified with double layer charging effects. The subsequent, slower variation was recognized to depend on the potential and the duration of the prepolarization period, as well as on the rotation velocity of the electrode. The third mode of potential variation proceeded at constant rate, dependent only on the temperature; however, the range over which the variation occurred was also dependent on other variables. Figure 6 shows the transients for hard gold, prepolarized for 3 min at potentials ranging from -1.1 to -0.4V *vs.* SCE in 0.1V steps. On the time scale used, the double layer charging effect is not discernible (regime 1).

The potential transients are strong indication that the electrochemical reduction of $Au(CN)_2^-$ proceeds via chemisorbed species (14, 15). Details of the curves

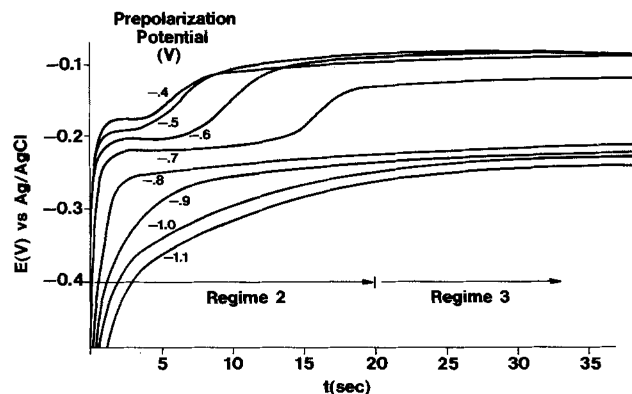

Fig. 6. Potential transients of the $Au/Au(CN)_2$-system (hard gold) after prepolarization.

shown in Fig. 6 are interpreted in terms of the sequence of reactions [27]-[29] as follows:

During the prepolarization period, reactions [27] and [29] are at equilibrium, while reaction [28] is not. At the instant of the current interruption, reaction [28] starts to approach equilibrium at a rate limited only by the recharging of the double layer. Once equilibrium is achieved, reactions [27] and [29], which were previously independent, are now coupled through reaction [28] in correspondence with Eq. [2]. Thermodynamic equilibrium with respect to the bulk of the electrolyte is, however, not achieved yet, mostly because the surface concentrations of CN^-, (AuCN)ad, and $(Au^\circ CN)ad^-$ are higher than when in equilibrium with the bulk. Removal of CN^- tends to shift both equilibria, reactions [27] and [29], to the right. (AuCN)ad remains constant, therefore, while $(Au^\circ CN)ad^-$ decomposes. This occurs within the range of regime 2 of Fig. 5. The process appears to be diffusion controlled, as evidenced by the strong dependence of the potential decay upon the rotation velocity of the disk electrode. At all times, the potential is controlled by the ratio of (AuCN)ad: $(Au^\circ CN)ad^-$. Predictably, $(Au^\circ CN)ad^-$ as source of cyanide will be depleted after some time. Due to the lack of CN^-, the excess amount of (AuCN)ad cannot revert to its origin, $Au(CN)_2^-$. The removal of (AuCN)ad has to proceed via the electron transfer reaction [28], which seems impossible without a source of electrons. An electron source is available, however, as evidenced by the electroless deposition of gold. In preference to reaction [3] the process may be formulated as

$$(AuCN)ad \rightarrow Au(lattice) + \tfrac{1}{2}(CN)_2 \qquad [31]$$

It has been discussed earlier that the electron donor reaction [1] is not at equilibrium. Reaction [31] is, therefore, not at equilibrium either and the removal of (AuCN)ad from the surface should be a first-order reaction. This is confirmed by the observation that the potential decay in regime 3 shows a close to linear dependence on time.

Addressing the potential variation in regime 3 of Fig. 6, it is noted that for prepolarization potentials $< -0.8V$ the curves nearly coincide, while for potentials $> -0.8V$ substantially deviating curves are obtained. This dispersion signifies the change of the surface concentration of the adsorbate from a saturated to a less-than-saturated state. The corresponding behavior, obtained with the other electrolytes, leads to the conclusion that the electrodeposition of gold proceeds, in practice, under surface saturation with (AuCN). It is assumed that surface saturation means a nearly complete monolayer of the adsorbate, regardless of the type of electrolyte. From the potential level, at which the desorption of (AuCN)ad starts in the three different electrolytes, it follows with equilibrium [28] that the surface concentration of $(Au^\circ CN)ad^-$ is greatest for regular soft gold and about equal for lead-doped soft gold and hard gold. It should be mentioned that these results were obtained under prepolarization conditions where the deposition of lead-doped soft gold was far better equilibrated ("depolarized") than that of regular soft gold. In view of the crystallization phenomena discussed earlier, it is concluded that the establishment of a preferred crystal orientation is accompanied by a shift of equilibrium [29] from left to right. Concerning the behavior of the hard gold system, it is concluded that equilibrium [28] is shifted to the left relative to the conditions of soft gold deposition.

Reversibility of the electrode processes.—The electrochemical oxidation of gold in cyanide solution should, doubtlessly, follow the sequence of reactions [27]-[29] in reverse. An experiment was carried out accordingly in which a gold disk electrode was polarized anodically in 0.5M KCN solution at 55°C and two rotation velocities. Figure 7 shows the results which are interpreted as follows. Near the equilibrium potential at about $-0.9V$ *vs.* Ag/AgCl the anodic current

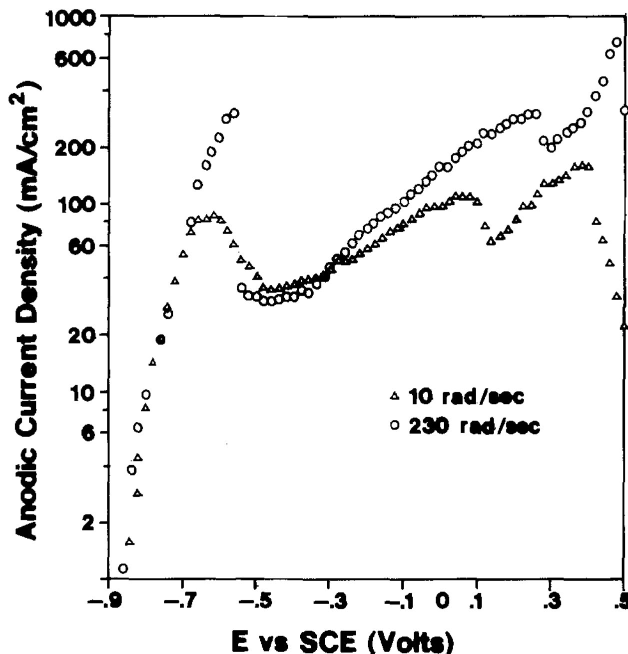

Fig. 7. Anodic dissolution of gold in 0.5M KCN at 55°C

density rises, as expected, very steeply. With increasing potential three maxima and minima are passed. The maxima at $-0.6V$ and 0-0.2V are caused by diffusion limitation of the cyanide ions. As the surface concentration of CN^- approaches zero, the concentration of $(Au^\circ CN)ad^-$ also approaches zero, which results in a rapid drop of the current density. Thereafter, even though the surface concentration of CN^- is not zero anymore, the dissolution rate at $-0.5V$ is controlled by the formation of $(Au^\circ CN)ad^-$. Over the potential range, where in previous experiments the surface concentration of (AuCN)ad was found to deviate from saturation, the current density rises again. The decrease in coverage with AuCN promotes, necessarily, the reaction of gold in lattice sites with cyanide, and hence the rate of dissolution. At the point where once again the concentration of CN^- at the electrode surface drops to zero a change in mechanism occurs. At 0.1-0.2V it appears that trivalent gold is formed, as the current density at 225 rad/sec reaches 1.5 times the value observed at the other maxima. The minimum at 0.5V was positively identified with the onset of passivation since at still higher potentials no dissolution of gold was observed.

The features of the anodic dissolution of gold in cyanide solution are evidently compatible with the existence and the controlling nature of chemisorbed layers postulated for the cathodic reduction of dicyanoaurate.

Summary and Conclusions

The mechanism of the electrochemical reduction of dicyanoaurate was studied by means of steady-state and relaxation methods combined with rotating-disk electrode techniques. The experimental results permit the following statements:

1. The deposition of soft gold, lead-doped soft gold, and cobalt-hardened gold proceeds via one common mechanism that involves adsorption equilibria preceding and following the electron transfer step.

2. Special effects such as the epitaxy and preferred orientation of soft gold deposits, the small grained texture of hard gold, and the lead-induced depolarization effect during soft gold deposition can be explained in terms of the energetic states of the adsorbed, oxidized, and reduced gold species. These are influenced by the crystal orientation of the deposition site and by the coadsorption of cobalt and lead ions, respectively.

3. The proposed mechanism explains readily the features of the anodic dissolution of gold in alkaline cyanide electrolyte.

Acknowledgments

Thanks are due to P. C. Milner and P. W. Renaut for stimulating discussions, and to N. H. Winquist for preparing the electron micrographs.

Manuscript submitted May 19, 1977; revised manuscript received Nov. 14, 1977.

Any discussion of this paper will appear in a Discussion Section to be published in the December 1978 JOURNAL. All discussions for the December 1978 Discussion Section should be submitted by Aug. 1, 1978.

Publication costs of this article were assisted by Bell Laboratories.

REFERENCES

1. H. Y. Cheh and R. Sard, *This Journal*, **118**, 1737 (1971).
2. J. A. Harrison and J. Thompson, *J. Electroanal. Chem.*, **40**, 113 (1972).
3. J. D. E. McIntyre and W. F. Peck, Jr., *This Journal*, **123**, 1800 (1976).
4. R. L. Cohen, K. W. West, and M. Antler, *ibid.*, **124**, 342 (1977).
5. G. B. Munier, *Plating (East Orange, N.J.)*, **56**, 1151 (1969).
6. Ch. J. Raub, A. Knoedler, and J. Lendvay, *ibid.*, **64**, 35 (1976).
7. E. T. Eisenmann, "The Effect of Current Modulation on the Porosity of Gold-Cobalt Electrodeposits," to be published.
8. H. A. Reinheimer, U.S. Pat. 3,833,487 (1974).
9. J. D. E. McIntyre and W. F. Peck, Jr., *This Journal*, **123**, 1800 (1976).
10. NBS Technical Note 270-3, 4, U.S. Department of Commerce (1968).
11. V. G. Levich, "Physical Hydrodynamics," p. 69, Prentice-Hall, Inc., Englewood Cliffs, N.J. (1962).
12. P. Delahay, "Double Layer and Electrode Kinetics," p. 153, John Wiley & Sons Inc., New York (1965).
13. W. E. Tragert and W. D. Robertson, *This Journal*, **182**, 86 (1955).
14. M. Maja, *Atti Accad. Sci. Torino Cl. Sci. Fis. Mat. Nat.*, **99**, 1111 (1965).
15. D. M. MacArthur, *This Journal*, **119**, 672 (1972).

Flatband Potentials and Donor Densities of Polycrystalline α-Fe_2O_3 Determined from Mott-Schottky Plots

John H. Kennedy* and Karl W. Frese, Jr.**

Department of Chemistry, University of California, Santa Barbara, California 93106

ABSTRACT

Capacitance and conductivity measurements were made on high purity α-Fe_2O_3 and TiO_2-doped α-Fe_2O_3 in liquid junction cells. Flatband potentials and donor densities were determined from Mott-Schottky plots and evidence for deep and shallow donors is presented. Potentials of zero photocurrent were determined using chopped light and were in excellent agreement in basic solution with flatband potentials calculated from 1 kHz capacitance measurements.

Detailed studies of flatband potentials and their correlation with photoeffects have been carried out to date largely on single crystal samples. Also, it is not clear that space charge layer capacitance theories would apply to polycrystalline electrodes in electrochemical cells and that photoeffects could be obtained from polycrystalline samples comparable to single crystal samples. To help answer these questions we report here on capacitance data for the α-Fe_2O_3-electrolyte junction. Current-potential characteristics of these polycrystalline samples will be published separately. In a previous paper (1) we reported on the flatband potential (and photocurrents of) polycrystalline sintered $BaTiO_3$ electrodes with results which agreed well with published data for single crystal samples (2). The techniques used for the studies of $BaTiO_3$ have now been extended to the studies of other metal oxides, in particular, α-Fe_2O_3.

Experimental

Electrode preparation.—Alpha-iron(III) oxide n-type semiconductor electrodes were prepared from either high purity, 99.999% (Apache Chemical Company) or analytical reagent-grade (Mallinckrodt) material. The ultrapure material was pressed and sintered in air at various temperatures from 1050° to 1320°C for 4 hr and then quenched in room temperature air. This treatment resulted in electrodes with apparent densities of 75-85% of theoretical and conductivities ranging from 8×10^{-6} to 2×10^{-4} Ω^{-1} cm^{-1}. Attempts to make semiconducting electrodes from the reagent-grade material by air quenching always resulted in nonconductive material even for sintering temperatures of up to 1300°C. This was probably due to the presence of Cu^{2+}, Zn^{2+}, and Mg^{2+} impurities which would tend to compensate the n-type conductivity. However, the reagent-grade material could be made highly conductive ($\sigma \sim 1$ Ω^{-1} cm^{-1}) by heating in a stream of N_2 for temperatures $\gtrsim$ 1100°C. The conductivities were difficult to control, and therefore TiO_2 doping was used to obtain highly doped samples. Also, the N_2 reduced samples showed virtually no photoeffect, probably due to the very thin space charge layer. The reagent-grade material doped with TiO_2 was sintered at 1150°-1200°C in air for 14 hr and quenched in room temperature air. Densities were 95-99% of theoretical. The TiO_2 doping level was varied from 0.05% to 2% (Ti/Fe). No further treatment was given the electrodes after sintering.

A copper wire electrode lead was attached to the semiconductor electrodes by applying Ag epoxy (Epoxy Technology). The electrode and wire were then sealed in a glass tube with epoxy resin.

Capacitance measurements.—Capacitance measurements of the cell, α-Fe_2O_3/electrolyte/Pt, were made

* Electrochemical Society Active Member.
** Electrochemical Society Student Member.
Key words: semiconductor, photo conductivity, capacitance.

using a General Radio 1650-A impedance bridge operated at 1 kHz. Electrode potential measurements were made (*vs.* SCE) with a Keithley 610-C electrometer.

Dielectric constant measurements.—Dielectric constant measurements of high density, insulating α-Fe_2O_3 were made at various frequencies in the range 1-50 kHz. The dielectric cell was a parallel plate type with the area of one plate much larger (~150X) than the other. The cell was connected to the GR 1650-A impedance bridge and the capacitance measured with and without the α-Fe_2O_3 disk. Electrodes of conducting Ag epoxy were applied to each face of the α-Fe_2O_3 disks. A sine wave a-c voltage (10 mV amplitude) was applied to the bridge using a Hewlett-Packard Function Generator, Model 3311A.

Pulsed photocurrent.—Pulsed photocurrent measurements were made by using polychromatic light from a 300W tungsten source and a rotating-disk chopper. The chopping frequency was 40-60 Hz. The photocurrent was measured as the voltage drop across a precision 5 kΩ resistor with a Tektronix Model 564B storage oscilloscope with a Type 3A6 dual trace amplifier and Type 3B3 time base. The α-Fe_2O_3 electrode was biased cathodically until the voltage amplitude decreased to zero. The minimum photocurrent pulse which could be detected was $\lesssim 0.1\ \mu A$.

Resistance measurements.—The resistance of the cell α-Fe_2O_3/electrolyte/Pt was measured under zero applied voltage with the impedance bridge at 1 kHz. The resistance was predominantly due to the α-Fe_2O_3 electrode since the contributions to the cell resistance from the Pt electrode and the electrolyte were negligible.

Results

Flatband potentials.—Mott-Schottky plots (3) were constructed from capacitance *vs.* electrode potential measurements at 1 kHz and are shown in Fig. 1 and 2 for undoped α-Fe_2O_3. The flatband potentials were obtained from the intercepts of $1/C^2$ *vs.* V by subtracting $kT/q = 0.025$V from the intercept. The flatband potentials and donor densities calculated from these plots are given in Table I.

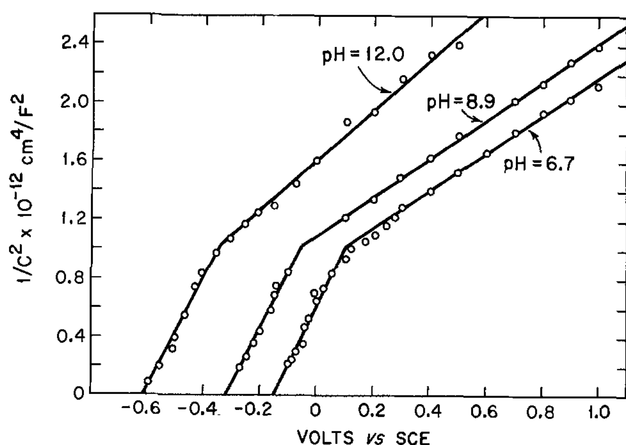

Fig. 1. Mott-Schottky plots for polycrystalline α-Fe_2O_3. Electrode No. 5. In dark, $t = 23°C$.

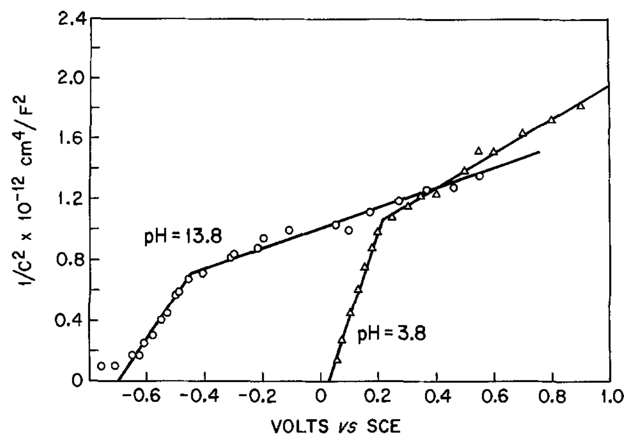

Fig. 2. Mott-Schottky plots for polycrystalline α-Fe_2O_3. Electrode No. 4. In dark, $t = 23°C$.

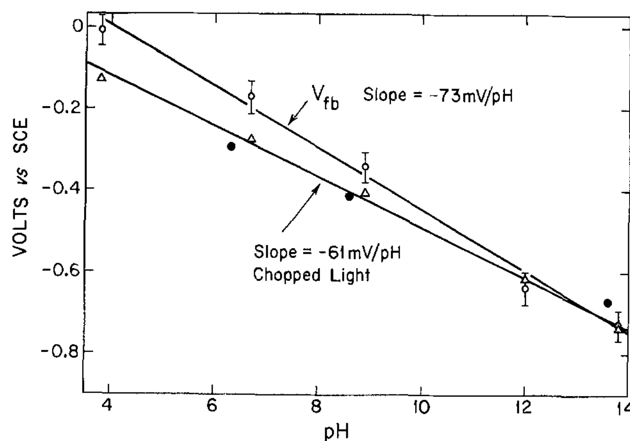

Fig. 3. Flatband potential and zero photocurrent potential of polycrystalline α-Fe_2O_3 *vs.* pH, $t = 23°C$. Solid circles from Ref. (4).

The flatband data are in remarkably good agreement with the data reported by Quinn *et al.* (4) for single crystal α-Fe_2O_3 differing by less than 0.1V. However, these authors did not correlate their data with *p*H. Flatband potentials for our polycrystalline samples at various *p*H values are shown in Fig. 3 together with the single crystal data (solid circles) given in Ref. (4). It is not clear whether or not the deviation of the *p*H dependence of the flatband potential from −59 mV/*p*H was significant. The deviation appears to increase in more acidic solutions indicating that electrode instability may be a factor. Another possible reason could be specific adsorption of chloride ions.

A striking feature of the Mott-Schottky plots is the sharp break at about +0.3V *vs.* flatband. Values

Table I. Shallow (N_1) and deep (N_2) donor densities obtained from Mott-Schottky plots (99.999% α-Fe_2O_3)

Electrolyte	*p*H	V_{fb} (SCE)	V_C (SCE)	$N_1 + N_2$, cm^{-3}	N_1, cm^{-3}	N_2, cm^{-3}
0.5M KCl*	3.8	0.00	0.21	1.5×10^{18}	3.1×10^{17}	12×10^{17}
0.5M KCl**	6.7	−0.17	0.10	1.3×10^{18}	4.1×10^{17}	9×10^{17}
0.5M KCl***	8.9	−0.34	−0.05	1.3×10^{18}	4.5×10^{17}	9×10^{17}
0.1M NaOH	12.2	−0.64	−0.35	1.0×10^{18}	4.6×10^{17}	5×10^{17}
2.0M NaOH	13.8	−0.73	−0.45	2.6×10^{18}	6.3×10^{17}	20×10^{17}

* Phthalate buffer.
** Phosphate buffer.
*** Borate buffer.

of the critical potential (V_C) for the break are given in Table I. The break was observed for three different samples at *p*H values from 3.8 to 13.8 in both KCl and NaOH solutions. This interesting feature can be explained by assuming the existence of two kinds of donors, one very close to the conduction band and the other at about 0.6V below the conduction band, and will be discussed in detail.

The potential of zero photocurrent was measured with pulsed illumination (nearly full output of 300W tungsten lamp) for the samples used in the capacitance measurements and the points shown in Fig. 3 represent averages at each *p*H. These potentials varied regularly with *p*H at a rate of -61 mV/*p*H. In the more basic solutions (*p*H $=$ 12.2-13.8) the net current at zero photocurrent was cathodic whereas in more acidic solutions (*p*H 3.8-8.9) the net current was anodic.

Typical Mott-Schottky plots for TiO_2-doped α-Fe_2O_3 are shown in Fig. 4, and Table II summarizes the data for the total donor densities, N, TiO_2 stoichiometry, the bulk ionized donor densities, N^+, calculated from conductivity data, and the apparent fraction of ionized donors.

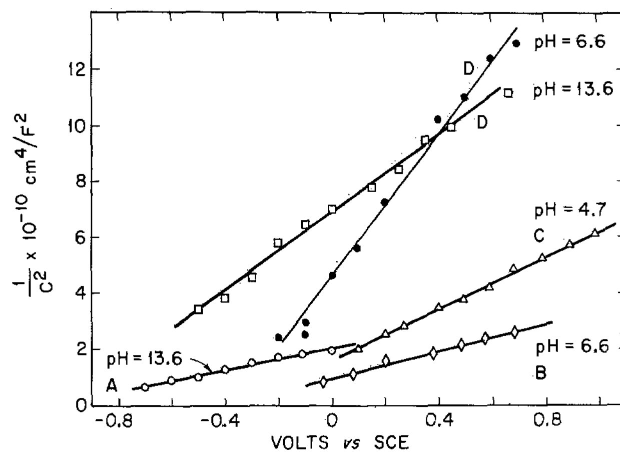

Fig. 4. Mott-Schottky plots for polycrystalline α-Fe_2O_3 at various TiO_2 doping levels and *p*H values. A, B, C, D refer to different TiO_2 doping levels as shown in Table II.

Dielectric constant.—The dielectric constant, ϵ, was calculated from capacitance data according to the following equation

$$\epsilon = 9.0 \times 10^{11} \frac{4\pi t}{A} \Delta C \qquad [1]$$

where t and A are the disk thickness and area and ΔC is the difference in the capacitance with and without the sample. A dielectric constant value of 80 was obtained. Quinn *et al.* (4) reported a value of 120 for the dielectric contact for α-Fe_2O_3 for an unspecified single crystal face.

Discussion

The two slopes for each of the plots in Fig. 1 and 2 suggest that the Mott-Schottky slope may be written (5) as

$$s_1 = \frac{2}{\epsilon\epsilon_0 q N_1} \quad \text{for} \quad V < V_C \qquad [2]$$

and

$$s_2 = \frac{2}{\epsilon\epsilon_{0}q (N_1 + N_2)} \quad \text{for} \quad V > V_C \qquad [3]$$

where N_1 and N_2 are the densities of the shallow and deep donors, respectively, and V_C is a critical voltage for ionization of the deep donors in the space-charge layer. The existence of a critical voltage can be traced to the nature of the Fermi-Dirac distribution function governing the number of ionized donors. The relation (3)

$$N^+(x) = N_2 \left[\frac{1}{1 + g_e\,(E_F - E_D + e\Delta\phi(x)/kT)} \right] \qquad [4]$$

gives the number of ionized donors as a function of position, total deep donor density, donor energy level, and the space-charge potential drop. The degeneracy factor, g, is usually assumed to be two, however, for transition metal ion donors it could be larger due to spin-orbit coupling. It is characteristic of the Fermi-Dirac distribution function that a large change in occupancy is realized over a narrow voltage range, in fact according to Eq. [4] the fraction ionized changes from 0.1 to 0.9 within a $\sim$100 mV change in $\Delta\phi(x)$. If V_C is arbitrarily identified with $N^+/N_2 = 0.5$ then

$$e(V_C - V_{fb}) \cong E_F - E_{D_2} \qquad [5]$$

within $\sim$50 mV. The data show that the deep donor is located about 0.3V below E_F. Flatband data can give the position of the Fermi level relative to the bottom of the conduction band (E_C) provided the density of states in the conduction band, N_C, is known (5)

$$E_C - E_F = kT \ln \frac{N_C}{N_1} \qquad [6]$$

assuming each shallow donor donates one electron to the conduction band. For iron oxide N_C has been assumed to be 4×10^{22} cm^{-3} (6), the number of cations in the lattice. This is consistent with the model of phonon-assisted hopping for the conductivity mode in narrow *d*-band semiconductors. The Fermi level is calculated to be 0.3V (for $N_1 = 4 \times 10^{17}$ from Table I) below the conduction band. The position of the deep donor level is then 0.6V below the conduction band.

The conductivity and spectroscopic studies of Morin (7) were consistent with a deep donor at 0.6-0.8 eV below the conduction band. Gardner *et al.* (8) also found their low temperature conductivity data gave an activation energy of 0.7 eV that could be associated with the energy for carrier formation. A summary of the energy level data is shown in Fig. 5. It should be noted that since the chemical or physical identity

Table II. Total donor density (N) and ionized donor density (N^+) for TiO_2-doped α-Fe_2O_3

Electrolyte	V_{fb}	*p*H	N^+, cm^{-3}	N (Mott-Schottky), cm^{-3}	TiO_2, a/o	N^+/N
				Sample A $\sigma = 1.1 \times 10^{-3}$ (Ω-cm)$^{-1}$		
0.5M Acetate/HOAc	-0.23	4.7	3.2×10^{17}	8.8×10^{19}	1.0	4×10^{-3}
0.5M KCl	-0.43	6.6	3.2×10^{17}	8.3×10^{19}	1.0	4×10^{-3}
1M NaOH	-1.06	13.6	3.2×10^{17}	7.3×10^{19}	1.0	4×10^{-3}
				Sample B $\sigma = 4.5 \times 10^{-4}$ (Ω-cm^{-1})		
0.5M KCl	-0.42	6.6	1.3×10^{17}	7.0×10^{19}	0.5	2×10^{-3}
				Sample C $\sigma = 1.9 \times 10^{-3}$ (Ω-cm)$^{-1}$		
0.5M Acetate/HOAc	-0.38	4.7	5.6×10^{17}	3.8×10^{19}	0.25	2×10^{-2}
				Sample D $\sigma = 4.4 \times 10^{-4}$ (Ω-cm)$^{-1}$		
0.5M KCl	-0.39	6.6	1.3×10^{17}	1.2×10^{19}	0.1	1×10^{-2}
0.5M KCl	-0.74	9.0	1.3×10^{17}	2.5×10^{19}	0.1	5×10^{-3}
1M NaOH	-1.00	13.6	1.3×10^{17}	1.4×10^{19}	0.1	9×10^{-3}

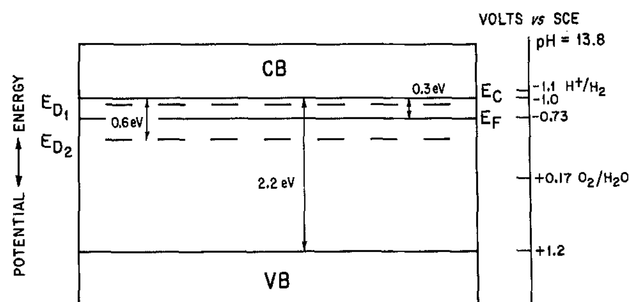

Fig. 5. Energy level diagram. Polycrystalline α-Fe_2O_3

of the donor level at E_2 is not known at present, it may not be an intrinsic property of α-Fe_2O_3 reduced to the level, $N_D \approx 10^{18}$ cm^{-1}. The indirect evidence presented, however, supports the assignment of the deep donor level as being Fe^{2+}.

Evidence for incompletely ionized donors and thus a deep donor level was also found for the TiO_2-doped α-Fe_2O_3 samples. The evidence was gained by comparing ionized donor densities calculated from conductivity and mobility data with donor densities calculated from Mott-Schottky slopes.

Advantage was taken of the fact that the bulk-ionized donor density, N^+, can be calculated from the standard conductivity equation

$$\sigma = N^+ q \mu_n \qquad [7]$$

and that electron mobility (μ_n) remains relatively constant with the doping level (9).

The value of electron mobility to be used in Eq. [7] was calculated by measuring the conductivity of three samples of thermally doped n-type α-Fe_2O_3 (99.999%) at room temperature. The values were 2.35×10^{-4}, 2.95×10^{-4}, and 5.62×10^{-5} $(\Omega\text{-cm})^{-1}$. These three samples showed two distinct Mott-Schottky slopes and the higher slope together with an assumed roughness factor of 2 were used to calculate N^+ for the thermally doped samples. From these values the mobility was calculated. The results for μ_n were 0.012, 0.017, and 0.034 cm^2/V sec for $t = 23°C$ and ionized donor densities of 4×10^{16} to 2×10^{17} cc^{-1}. The average value of 0.021 cm^2/V sec was adopted.

Measurement of the conductivity activation energy for these polycrystalline samples gave values of 0.05-0.10 eV (23°-100°C). Both the mobility and activation energies are in good agreement with the electron mobility equation suggested by Gardner *et al.* (10)

$$\mu_n = \frac{232}{T} e^{-0.1(\text{eV})/kT} \qquad [8]$$

This equation gives a room temperature mobility of 0.016 cm^2/V sec for TiO_2-doped samples.

The value of μ_n could now be used along with conductivity measurements on TiO_2-doped samples (Table II) to calculate N^+, the concentration of ionized donors from Eq. [7]. The values are given in Table II.

The total donor density, N, was calculated from the Mott-Schottky slope according to

$$S = \frac{2}{\epsilon\epsilon_0 q N} \qquad [9]$$

using slopes shown in Fig. 4. As can be seen from Table II the fraction of ionized donors, $N^+/N \sim 5 \times 10^{-3}$. We take this value as strong evidence for a deep donor in TiO_2-doped α-Fe_2O_3. The deep donor level was estimated to be 0.4 eV below the conduction band by using an equilibrium constant approach and the concentrations of ionized and total donors given in Table II.

The flatband potentials extrapolated from the plots in Fig. 4 are about 0.2V more cathodic than those shown in Table I. Two factors could account for this difference. One is that the flatband potential is known (11) to depend on donor density increasing more cathodic by 60 mV per order of magnitude of donor density. This effect amounts to ~0.1V from comparison of the donor densities in Tables I and II. The second effect, pointed out by De Gryse *et al.* (12) is that the extrapolation of $1/c^2$ *vs.* V plots leads to a voltage, V_o, given by

$$V_o = V_{fb} + \frac{kT}{q} - \frac{\epsilon\epsilon_0 q N_D}{2C_H^2} \qquad [10]$$

where C_H is the Helmholtz layer capacitance ~10^{-5} F/cm^2. This effect is magnified by high donor densities such as in our TiO_2-doped samples. The estimated shift in V_{fb} for the samples shown in Fig. 3 is 0.1V. Thus, the observed shift of ~0.2V is adequately accounted for by the theory.

We conclude that flatband potential data can be obtained from sintered polycrystalline α-Fe_2O_3 which are consistent with single crystal results, and that donor densities accurate to within a factor of four or less may be obtained without surface roughness corrections.

Acknowledgments

The authors acknowledge partial financial support of this project by the National Science Foundation, Grant No. DMR73-07507 AO2, and by the Committee on Research, University of California.

Manuscript submitted June 30, 1977; revised manuscript received Dec. 12, 1977.

Any discussion of this paper will appear in a Discussion Section to be published in the December 1978 JOURNAL. All discussions for the December 1978 Discussion Section should be submitted by Aug. 1, 1978.

Publication costs of this article were assisted by the University of California.

REFERENCES

1. J. H. Kennedy and K. W. Frese, Jr., *This Journal*, **123**, 1683 (1976).
2. R. D. Nasby and R. K. Quinn, *Mater. Res. Bull.*, **11**, 985 (1976).
3. H. Gerisher, in "Physical Chemistry," Vol. IXA, H. Eyring, D. Henderson, and W. Jost, Editors, chap. 5, Academic Press, New York (1970).
4. R. K. Quinn, R. D. Nasby, and R. J. Baugham, *Mater. Res. Bull.*, **11**, 1011 (1976).
5. V. A. Myamlin and Y. V. Pleskov, "Electrochemistry of Semiconductors," chap. 3, Plenum Press, New York (1967).
6. F. J. Morin, *Phys. Rev.*, **93**, 1195 (1954).
7. F. J. Morin, *ibid.*, **83**, 1005 (1951).
8. R. F. G. Gardner, F. Swett, and D. W. Tanner, *J. Phys. Chem. Solids*, **24**, 1183 (1963).
9. A. J. Bosman and J. H. Van Daal, *Adv. Phys.*, **19**, 1 (1970).
10. R. F. G. Gardner, F. Swett, and D. W. Tanner, *J. Phys. Chem. Solids*, **24**, 1175 (1963).
11. J. F. Dewald, *Bell Syst. Tech. J.*, **39**, 615 (1960).
12. R. De Gryse, W. P. Gomes, F. Cardon, and J. Vennik, *This Journal*, **122**, 711 (1975).

Technical Notes

Structure and Cyclic Discharge Behavior of LiAl Electrodes

C. A. Melendres* and C. C. Sy

Argonne National Laboratory, Chemical Engineering Division, Argonne, Illinois 60439

Considerable interest exists in the use of lithium-aluminum alloys as negative electrodes in molten salt secondary batteries (1). A number of recent investigations have dealt with the electrochemical characterization of this binary alloy system. Equilibrium potentials as a function of alloy composition were measured by Yao *et al.* (2) and by Selman and co-workers (3). L'vov *et al.* (4) determined the diffusion coefficient of Li in LiAl at 450°C to be $\sim 10^{-6}$ cm^2/sec from measurements of transition times during discharge. Similarly, James (5) has obtained a value of 5×10^{-5} cm^2/sec at 450°C from discharge curves. In a study of the kinetics of the electrochemical incorporation of lithium into aluminum (6), we obtained a value for the Li diffusivity in LiAl on the order of 10^{-8} cm^2/sec from galvanostatic charging curves. Values obtained on discharging the electrochemically formed LiAl electrodes were one to two orders of magnitude higher than on charging and were poorly reproducible. Realizing that this discrepancy may be due to changes in electrode morphology which accompany the incorporation or extraction of Li, we have conducted the present investigation on the structure of LiAl electrodes. We also hoped to obtain information on the role of electrode structure in determining the cycle life of LiAl electrodes in engineering prototype cells.

Experimental

The electrochemical measurements were carried out inside a glovebox under high purity helium atmosphere. The cell consisted of a 5.5 cm diam alumina crucible with three electrodes (Fig. 1): an Al or LiAl wire working electrode, a LiAl coil counterelectrode, and a reference electrode consisting of a cast Li-Al alloy [40 atomic percent (a/o) Li] that is 0.5 cm diam $\times$ 1.2 cm long. The composition of the latter is in the $\alpha + \beta$ region of the phase diagram (7); its potential at 450°C is about 290 mV anodic of Li/Li^+. The counterelectrode was prepared by electrochemically charging a 0.318 cm diam Al rod (previously formed into a coil) with Li to the $\alpha + \beta$ composition range. The Al working electrode was a 1.6 mm diam wire of 99.99% purity (Marz grade material purchased from Materials Research Corporation, Orangeburg, New York). The LiCl-KCl eutectic electrolyte was polarographic grade and was obtained from Anderson Physics Laboratories (Champaign, Illinois). The electrochemical and associated instruments that were used consisted of a Princeton Applied Research (PAR) Model 173 Potentiostat/Galvanostat, a PAR Model 179 Digital Coulometer, a Hewlett-Packard Model 7040A X-Y Recorder, and an R5103N Oscilloscope. Charged and discharged electrodes were mounted on plastic and examined using standard metallographic techniques. The mounted samples were ground successively through silicon carbide paper of grit sizes 120-C, 180-C, 240-A, 400-A, and 600-A, respectively. Polishing was done with alumina powder of 0.3 and 0.05 μm particle size. The last two operations were

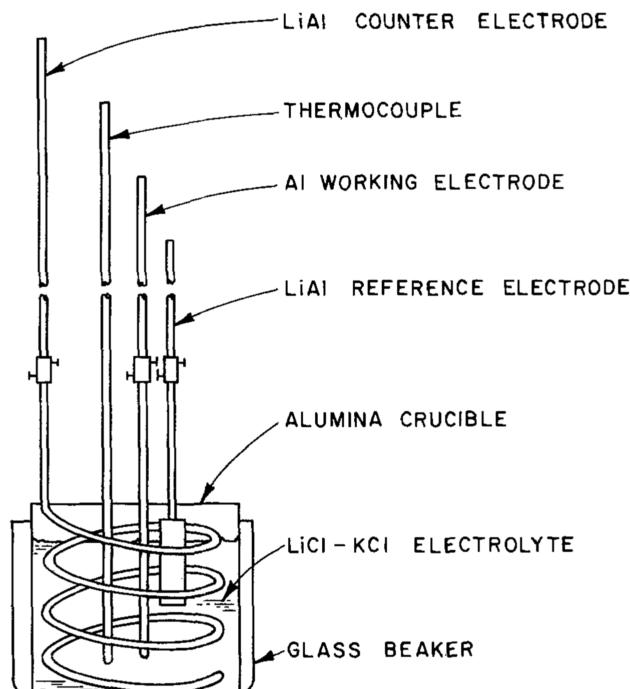

Fig. 1. Experimental apparatus

both done under oil using a Dow Corning 200 fluid (a dimethylpolysiloxane). Samples for electron microprobe analysis were ground with silicon carbide paper using HYPRES OS lubricant (Engis Equipment Company, Morton Grove, Illinois), polished with dia-

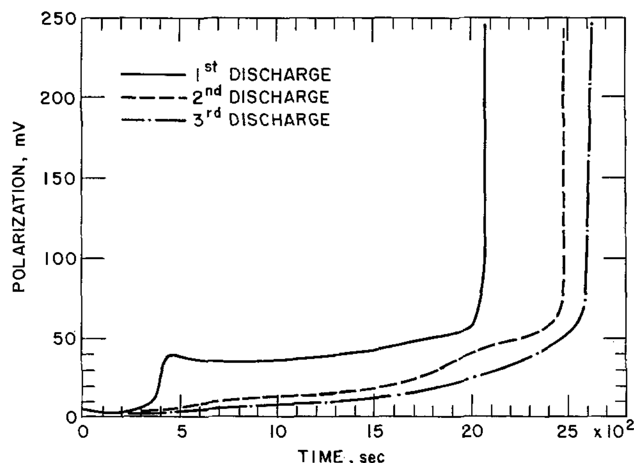

Fig. 2. Anodic polarization curves for successive discharge of LiAl wire electrodes (current density = 107 mA/cm^2 based on wetted area of original wire, T = 450°C).

* Electrochemical Society Active Member.

Key words: LiAl electrode, molten salt electrolyte, LiAl structure and morphology, anodic discharge behavior.

mond paste, and then ultrasonically washed with Freon-113 (Matheson Gas Products).

Results and Discussion

Cyclic discharge behavior of LiAl wire electrodes.— Figure 2 shows typical polarization behavior on cyclic discharge of LiAl wire electrodes that have been initially charged to the β-phase (48 a/o Li). As can be seen from this figure the anodic overpotential remains flat for some time and then increases rapidly. On subsequent discharges (following replacement of the Li removed by recharging at the same current density as initially used), a decrease in anodic polarization and an increase in transition time is observed. Coulometric determination of the charge passed at the transition point shows that the Li extracted anodically is 66, 78, and 81% of the initial loading for the first, second, and third cycles, respectively. The occurrence of a transi-

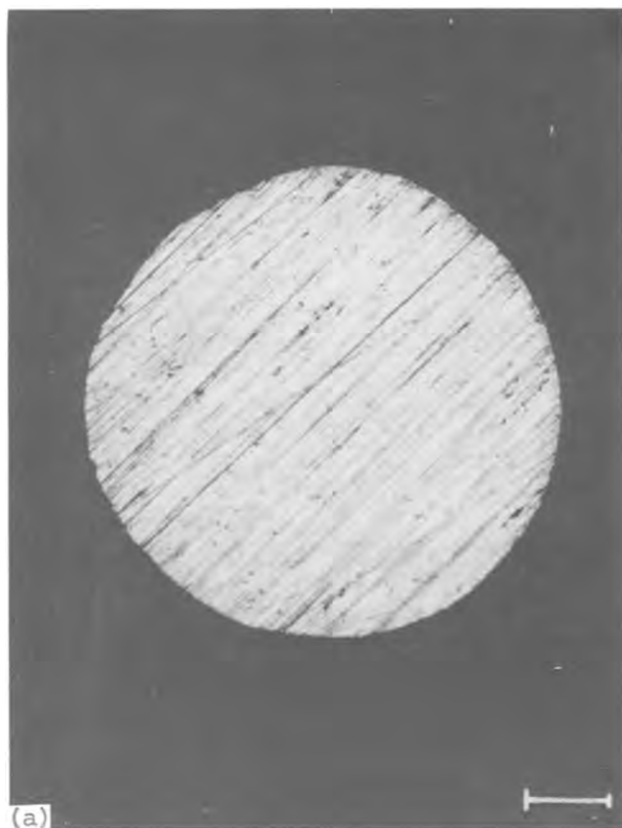

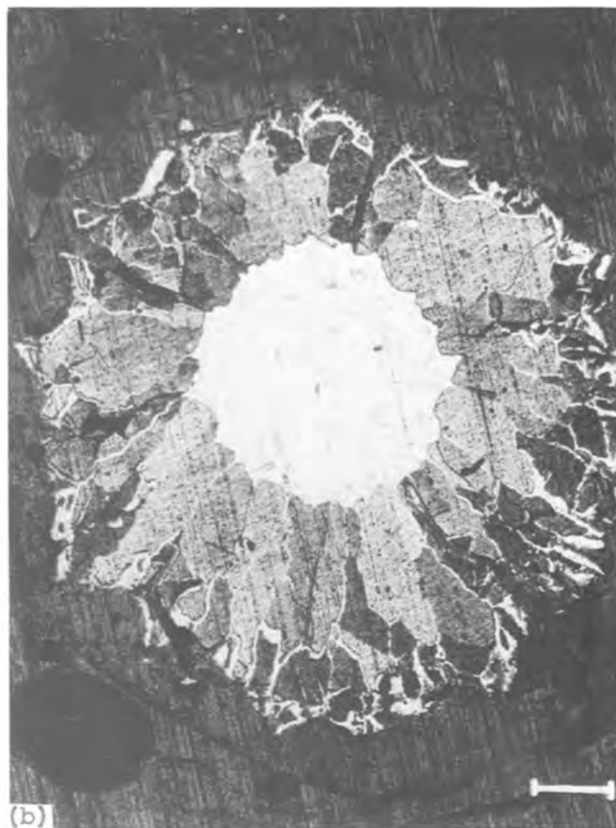

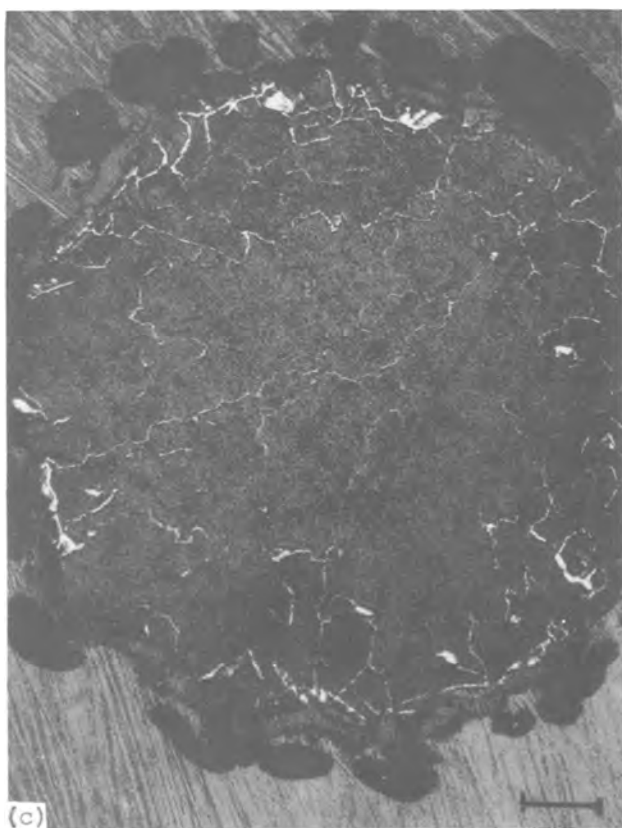

Fig. 3. (a) Photomicrograph of original Al wire (marker = 0.025 cm); (b) photomicrograph of partially charged wire, i = 80 mA/cm^2 (marker = 0.025 cm); (c) photomicrograph of fully charged wire, i = 105 mA/cm^2 (marker = 0.025 cm).

tion time in the discharge curves has been attributed by L'vov (4) and James (5) to diffusional limitation in the solid state. The increase in transition time with cycling indicates an apparent increase in Li diffusivity. Using Sand's equation (8) the values calculated for the curves shown correspond to 1.6×10^{-6}, 1.9×10^{-6}, and 2.02×10^{-6} cm²/sec, respectively. This "development" of the electrode during cycling is presumably associated with structural changes in the electrode or the creation of defects. Difficulty in obtaining reproducible results was encountered in our attempts to carry out further cycling. In addition the electrode would not maintain its physical integrity. A slight decrease in the cathodic overpotential is also observed with cycling, but is not as pronounced as that on discharge.

Microstructure of charged electrodes.—Figure 3b shows a metallographically polished cross section of an aluminum wire partially charged with Li to 70% of capacity (based on conversion of the wire to β-LiAl, *i.e.*, 48 a/o Li). For comparison, a section of the original Al wire (0.145 cm diam) is shown in Fig. 3a. The light central core of Fig. 3b represents the unreacted portion of the wire (Al), whereas the annular region corresponds to that portion which converted to the β-phase (LiAl). A difference in optical reflectivity of some areas in the latter region is apparent. The presence of a "vein-like" structure emanating from the core is particularly striking. Such "veins" appear to persist even in the fully charged electrode (Fig. 3c). Electron microprobe analysis showed that areas of different optical reflectivity vary in aluminum content, *i.e.*, lighter areas are richer in Al (lower Li) than darker ones. This is illustrated by the Al K_α x-ray map (Fig. 4b) of area X in Fig. 4a. The intensity of white dots in the x-ray picture is proportional to the amount of Al present. Therefore, during charging, the incorporation of Li does not appear uniform throughout the electrode. Even in the fully charged state, Al-rich areas represented by the "veins" are present. Two other features worth pointing out here are: the presence of cracks on charged electrodes and the increase in diameter from 0.145 cm for the original Al wire to 0.213 cm for the fully charged LiAl electrode. This latter exemplifies the lattice expansion that accompanies the transition from pure Al or α-phase (lattice constant = 4.05Å) to β-LiAl (lattice parameter = 6.36Å). The cracks observed in the photomicrographs may be due to the mechanical stresses set up during the volumetric expansion.

Discharged electrodes.—Figures 5a and 5b show the structure of partially and nearly fully discharged electrodes, respectively. The breakdown of electrode structure is evident, and is obviously more prominent on discharge than on charge. The α-phase on the near surface layers of Fig. 5a (light areas) was confirmed by microprobe analysis. A β-LiAl core remains in the electrode of Fig. 5b as shown in the enlarged picture of Fig. 5c. It appears that, on anodic extraction of Li, the Al structure is not able to reform to the original and does so only in patches resulting in the broken-up appearance shown. The effect of depth of discharge on structural breakdown is also brought to light in these pictures. It appears in Fig. 5b that the β-phase holds the radial structure together. Presumably if the discharge can be carried to completion (*i.e.*, 100% Li recovery), the structure would fall into pieces. The progressive increase in electrode area on discharge probably counteracts the increasing anodic polarization with time giving rise to the relatively flat portion of the discharge curve.

Structure after cycling.—Figure 6 shows the microstructure of a LiAl electrode after three charge-discharge cycles. The anodic polarization curves for this electrode are the ones shown in Fig. 2. It is obvious that the observed decrease in electrode polarization with cycling must be due to comminution of the electrode. The presence of unutilized Li is shown by the β-core (center) in the picture.

Effect of current density and potential on structure.—In order to examine the effect of charging potential and current density on electrode structure, Al wires were charged completely to β-LiAl composition

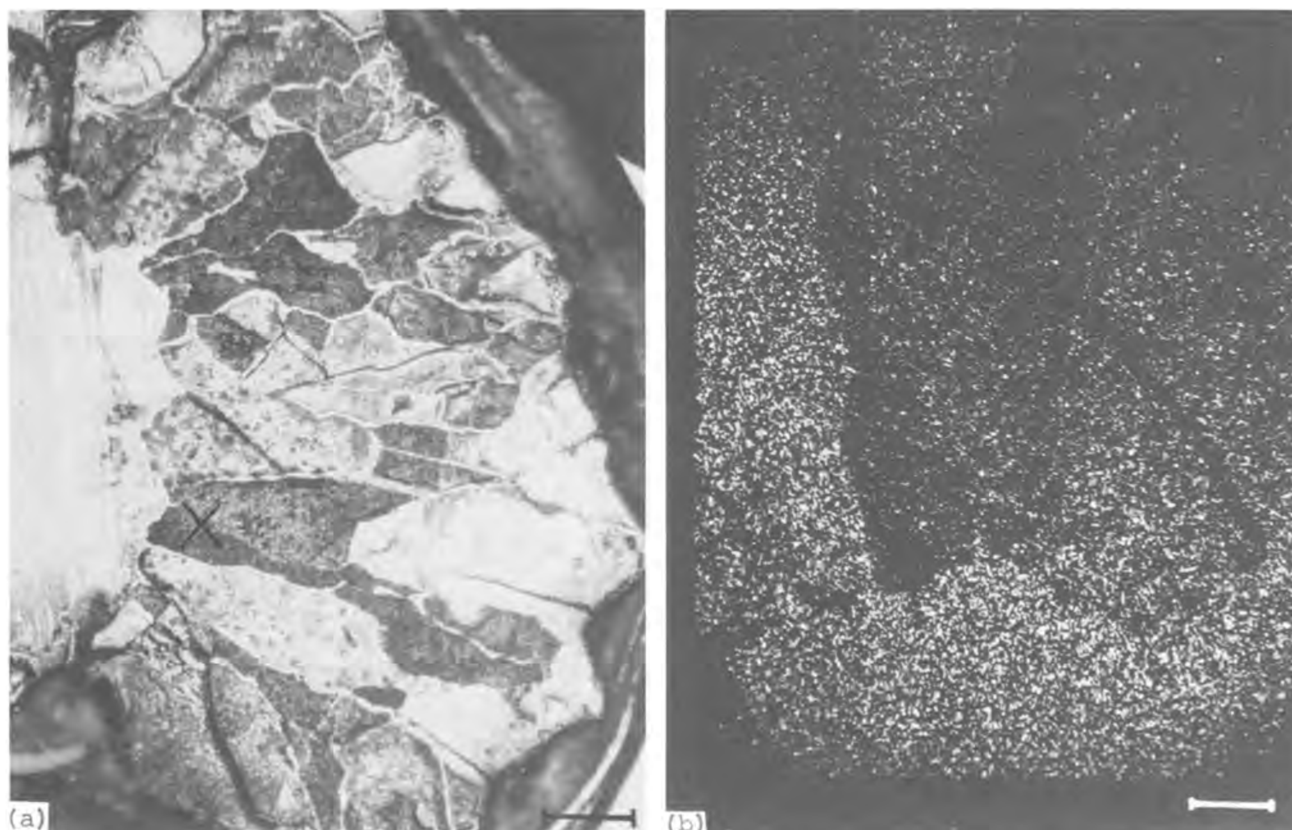

Fig. 4. (a) Enlarged area of portion of Fig. 3b (marker = 0.0125 cm); (b) aluminum K_α x-ray map of area "X" in 4a

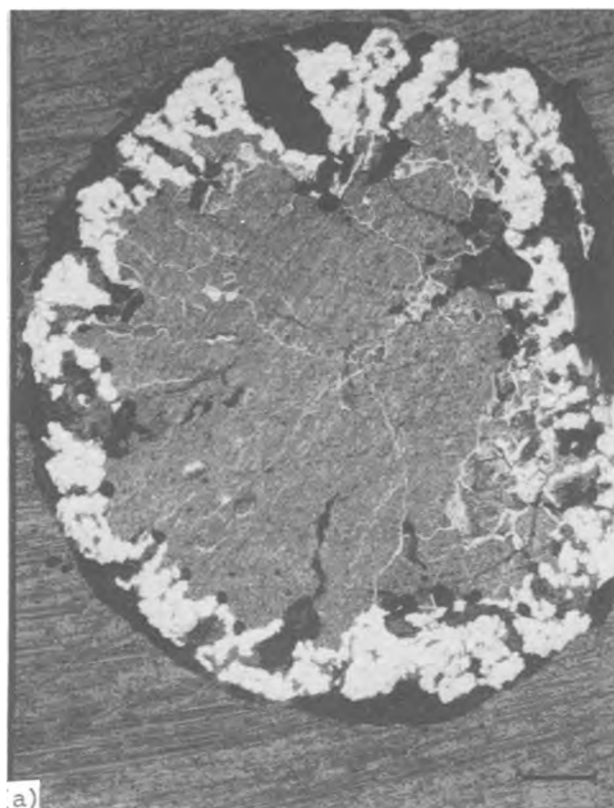

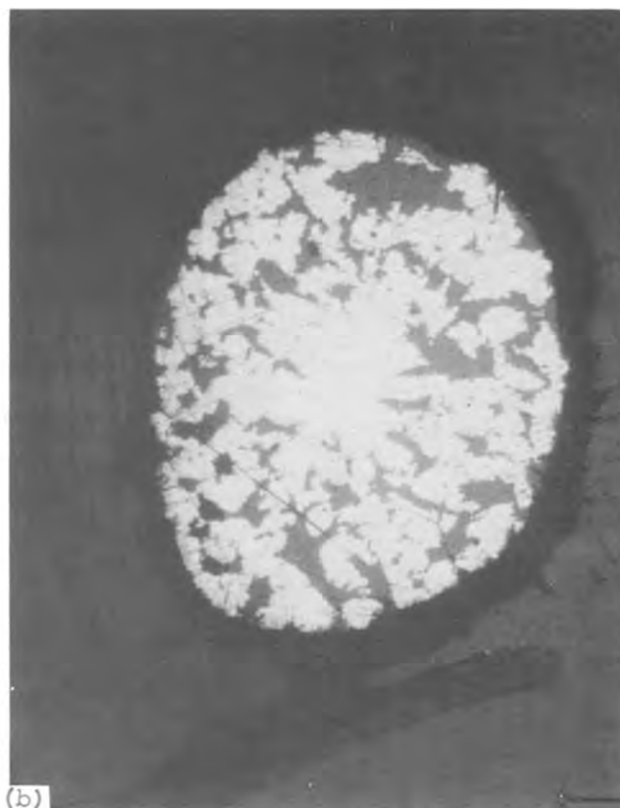

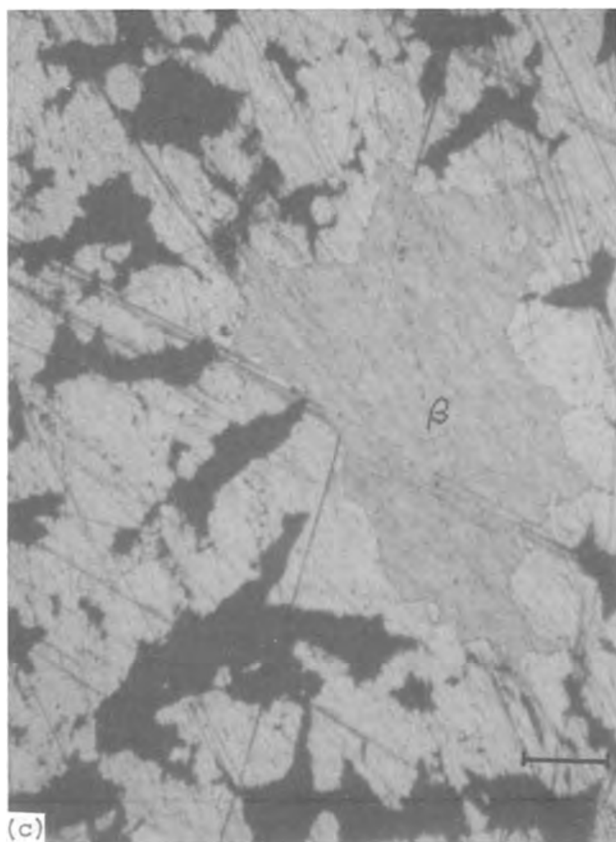

Fig. 5. (a) Photomicrograph of partially discharged LiAl electrode, $i = 380$ mA/cm^2 (marker = 0.025 cm); (b) photomicrograph of nearly fully discharged LiAl electrode, $i = 70$ mA/cm^2 (marker = 0.03125 cm); (c) photomicrograph of β-LiAl core portion of 5b (marker = 0.01 cm).

at constant potentials of −10, −20, −30, −40, −50, and −80 mV *vs.* LiAl and at current densities of 25, 50, 100, 150, 200, 300, and 500 mA/cm^2, respectively. The charged electrodes were mounted in plastic, then ground and polished metallographically. While a difference in structure among the electrodes is observed, we were unable to obtain any systematic correlation between the extent of structural breakdown and the charging potential or current density. Samples were also charged at a constant current density of 100 mA/cm^2, then discharged at current densities of 50, 100, 150, 200, and 300 mA/cm^2. A progressive decrease in the thickness of the outer α-phase layer (cf., Fig. 5a) is observed with increasing current density due to the shorter transition times and progressively lower utilization. The effect on structure is roughly the same as that observed with varying the depth of discharge at constant current.

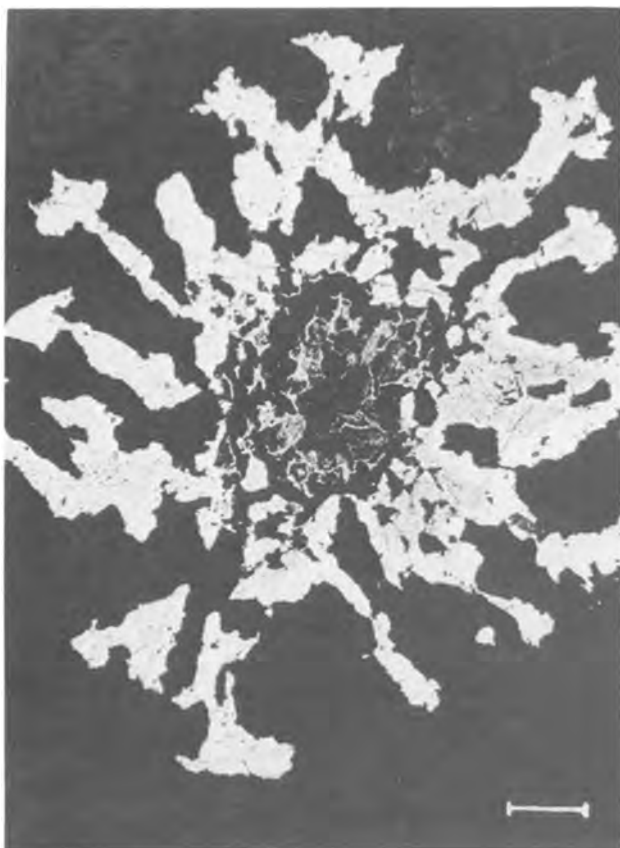

Fig. 6. Photomicrograph of discharged LiAl electrode after three cycles, $i = 107$ mA/cm^2 (marker = 0.025 cm).

Summary

A study of the anodic polarization behavior of LiAl wire electrodes shows a decrease in overpotential and an increase in transition time for Li extraction on successive discharge cycles. This appears to correlate with changes in the electrode structure as examined by metallographic techniques. The degree of electrode breakdown was found to be more pronounced on discharge than on charge and to depend mainly on the depth of discharge. Li distribution in wire electrodes during charging appears to be nonuniform. The results obtained show the need to consider structural changes in the interpretation of measurements of transport properties in solid alloy electrodes. Electrode comminution can lead to current collection problems and loss of active material in engineering-type cells; these can be important factors in determining the cycle life of such cells.

Acknowledgments

The authors are grateful to Dr. F. A. Cafasso for his continued interest and support of this work. We are indebted to Dr. A. Martin and F. Mrazek for assistance in metallography and to W. Shinn for the electron microprobe analysis. Valuable discussions were held with Dr. S. Siegel. This work was done under sponsorship of the U.S. Energy Research and Development Administration, Division of Physical Research.

Manuscript submitted Oct. 21, 1977, revised manuscript received Jan. 10, 1978.

Any discussion of this paper will appear in a Discussion Section to be published in the December 1978 JOURNAL. All discussions for the December 1978 Discussion Section should be submitted by Aug. 1, 1978.

Publication costs of this article were assisted by Argonne National Laboratory.

REFERENCES

1. W. J. Walsh, J. .W Allen, J. D. Arntzen, L. G. Bartholme, H. Shimotake, H. C. Tsai, and N. P. Yao in, "Proceedings of the 9th IECEC," San Francisco, Calif. p. 911 (1974).
2. N. P. Yao, L. A. Heredy, and R. C. Saunders, *This Journal*, **118**, 1039 (1971).
3. J. R. Selman, D. K. DeNuccio, C. C. Sy, and R. K. Steunenberg, *ibid.*, **124**, 1160 (1977).
4. A. L. L'vov, A. A. Gnilomedov, A. P. Selemenov, and E. N. Protasov, *Elektrokhim.*, **11**, 1322 (1975).
5. S. D. James, *Electrochim. Acta*, **21**, 157 (1976).
6. C. A. Melendres, *This Journal*, **124**, 650 (1976).
7. M. Hansen and K. Anderko, "Constitution of Binary Alloys," McGraw-Hill Book Co., New York (1969).
8. P. Delahay, "New Instrumental Methods in Electrochemistry," Interscience, New York (1954).

Propagation of Pitting on Aluminum Alloys

Steven Dallek*,[1] and R. T. Foley*

Department of Chemistry, The American University, Washington, D.C. 20016

Previous reports from this laboratory have dealt with the effect of anions on the pitting of aluminum (1, 2). The technique employed was based on a derived relationship between the pitting induction time, t_i, and the concentration of the halide ion and it yielded a stoichiometric number, n, the number of halide ions associated with an aluminum reaction site during the primary pitting process. This number for several aluminum alloys varied between one and four, dependent on the halide and the pH of the solution. The current-time curve obtained from the experiment also allows an observation with respect to the kinetics of the propagation of the pit which, with microscopic examination, produces some understanding of the influence of anions in promoting pitting. This is the subject of the present note.

* Electrochemical Society Active Member.
[1] Present address: Naval Surface Weapons Center, White Oak Laboratory, Silver Spring, Maryland 20910.
Key words: pitting corrosion, anion effects, halide effects, corrosion kinetics, pit geometry.

Experimental

The method of investigation (2) involves holding the metal sample potentiostatically in the passive anodic range in an appropriate electrolyte, rapidly injecting into the cell a specific concentration of halide solution, and then measuring the resulting current flowing at the electrode as a function of time. Following an induction period, t_i, which is a measure of the rate of pit initiation, the anodic current increases exponentially coinciding with the onset of visible pitting. The resulting current-time curve is a measure of the faradaic reactions associated with the growth of pits on the electrode surface. Furthermore, the shape of the curve can provide information on the morphology of the resulting pits, as discussed below. Experiments were conducted with aluminum alloys 1199 (99.997% Al) and 7075 (Zn, 5.1-6.1; Mg, 2.1-2.9; Cu, 1.2-2.0; Cr, 0.18-0.40; Fe, 0.7; Si, 0.5, Mn, 0.3; remainder Al) at pH's of about 1 and 6. The halides injected into the $1N$ H_2SO_4 solution were solutions of NaF, NaCl, NaBr,

and NaI. Experiments were conducted over the temperature range of 15°-60°C.

Results and Discussion

Microscopic observations of the pits formed on aluminum alloy 7075 in halide solutions, excluding fluoride solutions, showed that the pits were predominantly hemispherical. The rate of propagation expressed as current as a function of time took the form

$$i - i_p = a\,(t - t_i)^b$$

where i = the dissolution current; i_p = the passive current; t = time; t_i = induction time; a = a constant dependent on the halide; and b = a constant dependent on the geometry of the pit. In Fig. 1 the current-time curve for pitting initiation and propagation by Br^- ion in $1N$ H_2SO_4 is presented as a typical curve. A plot of log $(i - i_p)$ *vs.* log $(t - t_i)$ the slope of which is "b", is given in Fig. 2. An equation similar to the above was obtained experimentally and derived theoretically by Engell and Stolica (3) for the pitting of iron by chloride solution. In their derivation they assumed that the pitting sites are hemispherical, that the dissolution current density is much greater than the passive dissolution current density and is proportional to the sum of the pit cross sectional areas, and that the rate of development of new pits is linearly dependent on time. According to the derivation, when the number of pits is constant with time, b is 2; when the number of pits is proportional to time, b is 3. The data plotted for the aluminum alloy in Fig. 2 apparently meet or approximate these specifications, as the data fit the cubic equation quite well.

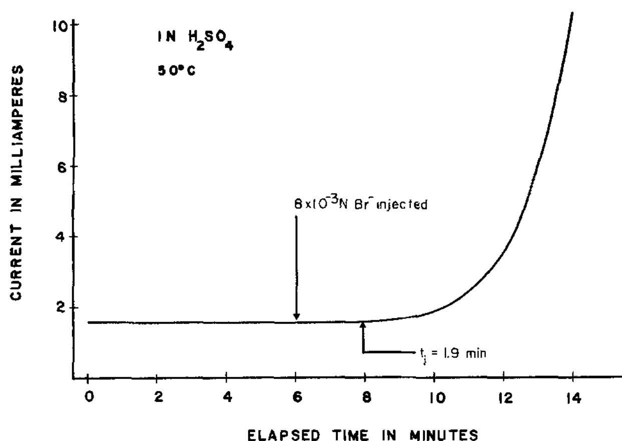

Fig. 1. A typical pitting initiation and propagation curve

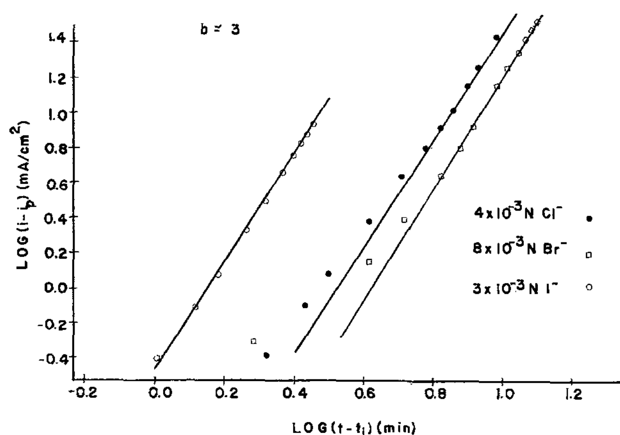

Fig. 2. Determination of "b" in pit growth equation. ●, Chloride solution, □, bromide solution, ○, iodide solution.

The data plotted in Fig. 2 follow the equations

for $3 \times 10^{-2}N\ I^-$ $(i - i_p) = 0.073\ (t - t_i)^3$
for $4 \times 10^{-3}N\ Cl^-$ $(i - i_p) = 0.0051\ (t - t_i)^3$
for $8 \times 10^{-3}N\ Br^-$ $(i - i_p) = 0.00195\ (t - t_i)^3$

It is important to recognize that the behavior of aluminum alloys described here probably represents a special case insofar as the curves experimentally yield a $b = 3$ or exhibit cubic behavior. Tousek (4, 5) investigating the pitting corrosion of iron and nickel, developed equations for different current-time dependencies and then used the equations to describe the dimensions of the active pits. For iron, a value of $b = 3$ was obtained, but for a Cr-Ni-Fe alloy we obtained a value of $b = 2$. Stolica (6), investigating a number of Cr-Fe alloys, found that $b = 3$ for a 5.6% Cr-Fe alloy and a 14.9% Cr-Fe alloy, but for several others the current-time curves were too irregular to yield consistent exponents. The literature on the kinetics of pitting has been extensively reviewed by Szklarska-Smialowska (7, 8) and she has concluded that the Engell-Stolica treatment is oversimplified to apply in a general way to all cases of pitting. Rather, the pits should be placed in one of the three categories (8): (*i*) Case I: The pits are hemispherical and the radius of the pit approximates the pit depth; (*ii*) Case II: The pit is nonhemispherical, the radius is greater than the depth; (*iii*) Case III: The pit has a cylindrical shape with the radius less than the height of the cylinder. For this reason, experimentally, b values varying from 0.5 to greater than 5 have been obtained. Moreover, in the pitting of Ni in solutions containing various concentrations of $SO_4^=$ and Cl^- the b value changes with the ratio of the two ions (9). From the foregoing, it is concluded that a value of $b = 3$ conforms with hemispherical pits growing in cross section linearly with time with the number of pits also increasing linearly with time.

It is generally accepted that the morphology of the pits bears directly on the kinetics of pit growth. From the present study it is possible to record some qualitative trends from microscopic examination of the pitting specimens. The hemisphericity of pits propagated in chloride solution was always greater than those formed in bromide or iodide solution. In fluoride solution, pitting corrosion did not occur, but rather uniform surface corrosion resulting in the formation of an insoluble fluoride compound on the surface. Hemisphericity was also enhanced by going from near-neutral solution (pH = 5.8) to an acidic medium (pH = 0.3). The greatest deviations from hemisphericity were always observed in pits developed in bromide solution.

In addition to aluminum alloy Type 7075, experiments were performed with chloride and bromide on alloy Type 1199 to test the effect of alloy composition on pit morphology. The pits produced in chloride solution became almost perfectly hemispherical, although the most striking change occurred in bromide solution where the pit morphology also became hemispherical as compared with some iregularly shaped figures observed on alloy Type 7075.

There has been very little reported in the literature regarding the morphology of the pit as affected by the nature of the aggressive anion. Politycki and Fischer (10) described the different etching patterns formed on high purity aluminum by attack in HCl, HBr, HI, and HF. Cubic cavities were formed in HCl and HBr solutions, cubooctahedral cavities in HI, and no well-defined etch figures in HF solution. These patterns were explained in terms of steric relationships that derive from the direct contact between halide ions of a given radius with surface aluminum atoms separated by a given distance in the metallic lattice.

Tokuda and Ives (11) studied the pitting corrosion on nickel by chloride ion in sulfuric acid solution and analyzed the pit morphologies by simulation of dis-

solution, based on the assumption that a metal atom which has fewer nearest neighbors, and hence fewer bonds, is removed preferentially. However, this simple model failed to adequately account for the observed pit morphologies, and the authors thus incorporated into their model the concept of dissolution based on the accessibility of aggressive ions, a concept which correctly predicted the pit morphologies.

Conclusions

Pit propagation on aluminum alloys in chloride, bromide, and iodide solutions follows a cubic time expression due to the approximate hemisphericity of the pits. This is considered to be a special case in the general pitting of metals. The different pit morphologies obtained on aluminum depend on both the nature of the agressive anion in solution and on the composition of the metal sample.

Acknowledgment

The support of the Office of Naval Research under Contract N 00014-75-C-0799, NR 036-106 is gratefully acknowledged.

Manuscript submitted Sept. 22, 1977; revised manuscript received Jan. 19, 1978.

Any discussion of this paper will appear in a Discussion Section to be published in the December 1978 JOURNAL. All discussions for the December 1978 Discussion Section should be submitted by Aug. 1, 1978.

Publication costs of this article were assisted by The American University.

REFERENCES

1. F. D. Bogar and R. T. Foley, *This Journal*, **119**, 462 (1972).
2. S. Dallek and R. T. Foley, *ibid.*, **123**, 1775 (1976).
3. H. J. Engell and N. D. Stolica, *Z. Physik. Chem.*, **N.F. 20**, 113 (1959).
4. J. Tousek, *Corros. Sci.*, **12**, 1 (1972).
5. J. Tousek, *Collect. Czech. Chem. Commun.*, **33**, 1009 (1968).
6. N. Stolica, *Corros. Sci.*, **9**, 455 (1969).
7. Z. Szklarska-Smialowska, *Corrosion (Houston)*, **27**, 223 (1971).
8. Z. Szklarska-Smialowska, *Werkst. Korros.*, **22**, 780 (1971).
9. Z. Szklarska-Smialowska, *Corros. Sci.*, **12**, 527 (1972).
10. A. Politycki and H. Fischer, *Z. Elektrochem.*, **57**, 393 (1953).
11. T. Tokuda and M. B. Ives, *This Journal*, **118**, 1404 (1971).

JOURNAL OF THE ELECTROCHEMICAL SOCIETY

SOLID-STATE SCIENCE
AND TECHNOLOGY

MAY 1978

An Instrumental Gravimetric Method for Indexing Materials, Contaminants, and Corrosion Products According to Their Hygroscopicity

J. D. Sinclair*

Bell Laboratories, Holmdel, New Jersey 07733

ABSTRACT

The moisture pickup characteristics of selected dusts, contaminants, corrosion products, and aged insulation and substrate materials have been determined in a dynamic humid environment by instrumental gravimetric analysis. These are compared with pure salts and other standard materials to categorize their relative hygroscopicities during the initial adsorption stage and subsequent stages of moisure pickup. In addition, the minimum relative humidities at which some pure salts and a variety of other substances will pick up moisture are reported.

Humidity has long been recognized as a dominant factor in the rate of deterioration of electronic devices. Degradation may occur as a result of inappropriate choice and design of materials, or because of in-service contamination or corrosion problems. In spite of the importance to the electronics industry of knowledge about the moisture pickup characteristics of components, contaminants, and corrosion products, the "hygroscopicity" of most substances is generally not known. This is due in part to the lack of a uniform concept of hygroscopicity. There are nearly as many definitions of the term as there are papers on the subject.

Since Vernon's (1) recognition nearly 50 years ago that significant corrosion of most materials will only occur above a "critical relative humidity" (CRH), attempts to predict the effects of humidity on devices have usually been based on knowledge or an estimate of this number. In many cases, Vernon's CRH relates to the thermodynamic CRH of the surface components. For composite materials, contaminants, and some corrosion products, it is generally not appropriate to apply the thermodynamic concept of the CRH because of the insoluble nature of the substances. In this work, the term will usually be used broadly to describe an effective relative humidity (RH) at which a surge in moisture pickup occurs.

Some information is available on the over-all moisture pickup at elevated humidity of substances often encountered in the electronics industry. In some early work, Mulder (2) found that $CaCl_2$ on exposure to water-saturated air at 16°-20°C increased its weight by 712% in an unspecified period. A 0.6% weight increase is documented by Mellor (3) for sodium chloride exposed to air, but the RH and exposure time were not specified.

Preston and Sanyal (4) reported that $CaCl_2$ and NaCl showed weight increases of 625 and 314%, respectively, during exposure to an atmosphere maintained at 97% RH (at room temperature) for 14 days. Lindsay (5) has studied the moisture content at intervals from 0 to 100% RH of fibrous materials used for electrical insulation, including manila paper, press board, leatheroid paper, silk, empire cloth, and asbestos paper. Excess water content ranged from 1 to 6% by weight at 30% RH and from 4 to 18% at 90% RH. Asbestos paper was the least hygroscopic material examined.

Alkali halides have been recently studied by Kanazawa *et al.* (6). The "hygroscopicity" of powdered NaCl, KBr, and KI, prepared by recrystallization from ethanol, was studied by comparing the surface conductivity of the salts with their water adsorption isotherms. Water molecules which were adsorbed to a thickness of less than two monolayers were stated to be physisorbed. Water films thicker than two monolayers were thought to dissolve salt and form mobile hydrated ions. The vapor pressures at which the adsorbed water molecules were said to form hydrated ions at 30°C were 33, 36, and 27%, respectively. Hara *et al.* (7) studied the effects of crystal structure and surface energy on the hygroscopicity of $NaClO_3$ and found that increasing strain within the crystal was coincident with an increase in hygroscopicity.

A number of workers have studied the moisture pickup of ammonium salt formulations used for fertilizers and explosives. Pawlikowski *et al.* (8) have studied the effect of grain size on "the velocity of water sorption" of ammonium nitrate fertilizers. Vakhrusev and Gradinar (9) have found that the "hygroscopic point" of ammonium nitrate fertilizers decreases from 63.3% RH for granulated material to 55.6% RH for fine grained material. Further, he finds the "hygroscopic point" decreases with increasing urea concentration by as much as 20% from 65% RH. On the other hand, Trzesniowski (10) found by gravimetric methods that granule size, mole ratio, and phosphoric acid content had no effect on the CRH of N-P fertilizers, though the CRH increased somewhat with increasing ammonium sulfate content. Shokin and Solov'eva (11) determined that coating ammonium bicarbonate ferti-

* Electrochemical Society Active Member.
Key words: moisture pickup, deliquescence, critical relative humidity, device deterioration.

lizers with petroleum products was very effective in reducing the rate of moisture "absorption." Runge (12) has developed equations based on percent weight changes for calculating the moisture pickup capacity of similar fertilizers based on the initial moisture and composition. Yee (13) has studied the CRH of water soluble fertilizers by measuring the RH over saturated salt solutions with an electric hygrometer.

Puri and Bhushan (14) have examined the moisture pickup capacity by percent weight gain of zinc, nickel, chromium, and cobalt oxides prepared in a variety of ways. At 50% RH, moisture pickup for zinc oxide ranged from 0.5 to 2.4%, for nickel oxide from 2.7 to 10.3%, for chromium trioxide from 0.9 to 4.8%, and for cobalt oxide from 0.2 to 2.5%. At 99% RH, the moisture pickup for zinc oxide ranged from 0.7 to 9.1%, for nickel oxide from 5.9 to 32.5%, for chromium trioxide from 3.8 to 15.2%, and for cobalt oxide from 3.2 to 30.0%. These wide variations indicate that the hygroscopicity of many substances cannot generally be estimated from a single physical measurement.

Kearsley and Birch (15) recently measured the hygroscopicity of glucose syrup fractions as percent weight gain at saturation (approximately 14 days at 75% RH) and found that the moisture content increased from 14 to 34% as the glucose fraction increased from 0.3 to 61.6%. The method of drying was found to affect the initial rate of moisture pickup but not the final moisture content of the sample. The presence of inorganic contaminants was determined to increase the rate of pickup and the capacity. Whittier and Gould (16) used vapor pressure meaurements for saturated solutions as the basis for comparing "hygroscopic tendencies" and determined the equilibrium humidities for sucrose, glucose, galactose, and lactose to be 77, 81, 81, and 93% RH, respectively.

Grebennikova *et al.* (17), Twomey (18), and Bakhanova and Ivanchenko (19) have investigated the growth of hygroscopic dust particles and droplets in moisturized air streams by *in situ* microscopic examination. Unkown dust particles were often identified by the relative humidity at which visible moisture collected on their surfaces.

Markowitz and Boryta (20) have determined "hygroscopicity potentials," for saturated salt solutions at various temperatures. These authors defined the hygroscopicity potential (HP) as being $RT \ln (p_{H_2O,\,pure}/p_{H_2O,\,system})$. By this procedure the thermodynamic imbalance in chemical potential between ambient water and system water is emphasized. Pawlikowski *et al.* (21) prefer a "hygroscopic value" $\Delta p = pn\text{-}pr$, where pn is the vapor pressure of the saturated salt solution and pr is the ambient water vapor pressure.

Modrzejewski and Pokora-Bartyzel (22) have defined the "hygroscopic point" of pulverized pharmaceutical substances as the RH at which the material takes on 1% moisture in 24 hr. They state that the value is somewhat lower than the CRH of saturated solutions but that it is constant and characteristic of each substance. Moisture pickup was monitored gravimetrically for samples stored in 10 chambers maintained at uniformly distributed RH's between 10 and 100%. The "hygroscopic point" was determined from a percent moisture *vs.* relative humidity plot.

Shen and Springer (23) presented expressions for moisture content as a function of time for homogeneous and composite materials exposed to humid air or water. Test data for graphite T-300 Fiberite 1034 composites supported the mathematical analysis. The method requires knowledge of the maximum moisture content and the moisture diffusivity and unfortunately is readily applicable only if the initial moisture concentration inside the material is uniform and the temperature and moisture content of the environment is constant. Balarev *et al.* (24) have recently tabulated 140 inorganic salts according to their increasing hygroscopicity. The rankings were based on the equilibrium vapor pressures of saturated salt solutions. Phipps and Rice (25) have described an extremely sensitive gravimetric method employing a quartz crystal oscillator to detect monolayers of water on thin metal films. Unfortunately, the technique is readily useful only under vacuum conditions and consequently is not directly applicable to the measurement of moisture pickup rates and capacities of contaminants, corrosion products, and many electronic materials. Very recently Foster and Arbach (26) used a recording microbalance to measure the moisture pickup characteristics of β''-sodium gallate as a function of particle size at 50% RH and found finely divided powder picked up approximately one mole of water for each gram-atom of sodium whereas monocrystals showed no measureable water pickup.

Mansfeld and Kenkel (27), Sereda (28), and Gutman (29) have developed atmospheric corrosion monitors which measure the "time-of-wetness" which local environmental contaminants produce under extended exposure to atmospheric humidity. The time-of-wetness is an experimental determination of the summation of time intervals during which the CRH of the surface contaminants is exceeded. Berukshtis and Klark (30) have attempted to correlate time-of-wetness and pollutant concentrations with corrosion rates of steel, aluminum, zinc, cadmium, and copper for several urban environments.

In ranking substances according to their experimental hygroscopicities, a number of factors should be considered, including the magnitude and rate of moisture pickup in a selected time interval and the temperature, RH, and flow characteristics of the test atmosphere. In this work the moisture pickup parameters for several pure salts were examined in a static moisture-saturated environment to gain further understanding of the factors which have, in the past, led to classifying pure substances as hygroscopic or nonhygroscopic. From this data and the work of the authors already described, gravimetric measures were recognized as being best suited to estimating moisture pickup characteristics. Subsequently, an instrumental gravimetric method was developed for rapidly measuring the CRH and moisture pickup rates for samples of electronic materials, corrosion products, dusts, and other contaminants. Through this information an indexing method evolved for ranking substances according to their hygroscopicities and, thereby, for assessing corrosion or device failure hazards.

Experimental

Static atmospheres.—Measurement of the moisture pickup of pure salts in a static environment was accomplished with small bell jars sealed through ground glass joints with Apiezon N. A beaker of distilled water and a beaker containing 1.0g of a reagent grade anhydrous salt were placed in each bell jar. The RH was presumed to equilibrate at 100% in a time frame which was negligibly small relative to the interval between measurements. The salts analyzed were $CaCl_2$, $ZnCl_2$, $CuCl_2$, $FeCl_2$, and NaCl. The bell jars were periodically opened and the water pickup by the salts was monitored gravimetrically. The time required for complete dissolution of each salt was noted.

Flowing atmospheres.—Rapid determination of the moisture pickup characteristics of pure salts, composite materials, contaminants, and corrosion products was accomplished with a du Pont 951 thermogravimetric analyzer coupled to a 990 thermal analyzer. Continuous moisture pickup rates for the various materials at nearly 100% RH at 23°C were determined by passing a stream of air, which had been moisturized by bubbling it through distilled water, through the microbalance sample tube (2.5 cm diam × 12 cm long). It was found that flow rate strongly affected the moisture pickup rate. Commercial "Arizona Road Dust" (AC

Fine prepared by the AC Spark Plug Division of General Motors Corporation) was analyzed at flow rates of 10, 100, and 1000 ml/min and was found to increase its weight by 1.0% after 570, 55, and 18 min, respectively. The substantial acceleration possible at rapid flow rates was offset by the reduced sensitivity and resolution caused, in part, by increased turbulence in the balance housing. A flow rate of 10 ml/min provided sufficient acceleration for the work anticipated for this study. Relative to flow rates found in buildings housing electronic equipment, a flow rate of 10 ml/min, when translated to linear dimensions, is about an order of magnitude lower than those typically encountered. The apparatus is capable of handling samples weighing from 0.1 to 110 mg and, if the atmosphere and sample are properly equilibrated prior to loading, the minimum detectable weight change is approximately 10 μg/hr.

Weight was recorded graphically as a function of time, and each run was allowed to proceed until the rate of weight gain approached zero or reached an extended steady state. It is impractical to provide weight *vs.* time profiles for every sample examined, but the general characteristics of each sample can usually be sufficiently described through knowledge of the initial, final, and average percent weight gain rates along with sample weight and total exposure time or total weight gain. Field samples were generally equilibrated for several days or weeks with the laboratory atmosphere (RH approximately 30%) before they were analyzed in the microbalance. Weight increase with time at 23°C was initially recorded for 19 pure chemicals whose hygroscopicities spanned a wide range. Sample weight for the laboratory samples varied from 25 to 107 mg with only two samples weighing less than 50 mg. The amount of water vapor passing through the sample chamber was in very large excess of the amount of water picked up by the samples. Therefore, the sample size effect is probably minimal except perhaps for the smaller samples. The texture and crystallinity of the samples were variable and probably contribute to the results.

CRH measurements were made using the same balance with a modified air stream apparatus. A minimum RH in the balance housing (maintained at 23°C) of 22% was achieved by passing a stream of dry air through a dispersion frit submerged in distilled water cooled to 0°C. By allowing the water to warm from 0°C to nearly 23°C under ambient control, the RH increased from 22% to nearly 100%.

The RH *vs.* time profile is shown in Fig. 1. Flow rates ranging from 10 to 5000 ml/min were examined. The lag time in establishing in the balance housing the specific RH created at the humidity source was substantial at the slower flow rates, but the faster flow rates caused severe turbulence. A flow rate of 1500 ml/min was found to be rapid enough to insure rapid response in the sample chamber to humidity variations without producing a severe loss of sensitivity or resolution because of turbulence. The unloaded apparatus including the sample pan registered a weight increase of 0.02 mg on increasing the RH from the minimum to the maximum level, which is a negligible correction for most of the samples encountered. A recording of weight *vs.* time was translated to weight (normalized to 20 mg) *vs.* RH using hand recorded data of water temperature *vs.* time. The relative humidity at which an onset in weight gain occurred was taken to be the CRH. For the pure salts examined, the moisture pickup process was reversible and the measured CRH remained constant.

Discussion

At least three different stages of moisture pickup, each of which should have a characteristic rate behavior, can be considered in evaluating the hygroscopicity of a pure dry salt which becomes exposed to a humid atmosphere. Initially, presuming the water vapor pressure in the atmosphere is greater than that of adsorbed water or water of hydration, water will be chemisorbed and physisorbed on the surface. The surface area and surface energetics of the salt will be dominating rate factors at this stage. Included in this phase will be the formation of possible hydrates. Secondly, as the hydration layers continue to physisorb, a thin continuous film of water will form on the surface. At this stage the thin continuous film will be a saturated salt solution and the water pickup rate will be a function of the difference between the vapor pressure of the saturated salt solution and the vapor pressure of the atmosphere. Eventually the salt will completely dissolve and the solution will begin to dilute. The rate of moisture pickup will then decrease as the solution dilutes and its vapor pressure increases. These stages are denoted phase one, phase two, and phase three in the following discussion.

Hygroscopicity of pure salts in a static environment.—The rate of moisture pickup of a substance will depend in part on its initial state, which will generally be either a phase one or phase two condition. It will also depend on the temperature, the humidity, and the moisture transport processes taking place at the surface. Moisture transfer in a static environment will be diffusion controlled but in an environment where convective transport processes occur, the air flow rate over the surface will be important.

The acquisition of moisture by 1.0g samples of 5 salts at 100% RH was monitored for 133 days. These results are shown in Fig. 2. The amount of moisture pickup registered for $CaCl_2$ or NaCl after 14 days is about one-third of that found by Preston and Sanyal (4). This discrepancy is probably caused by differences

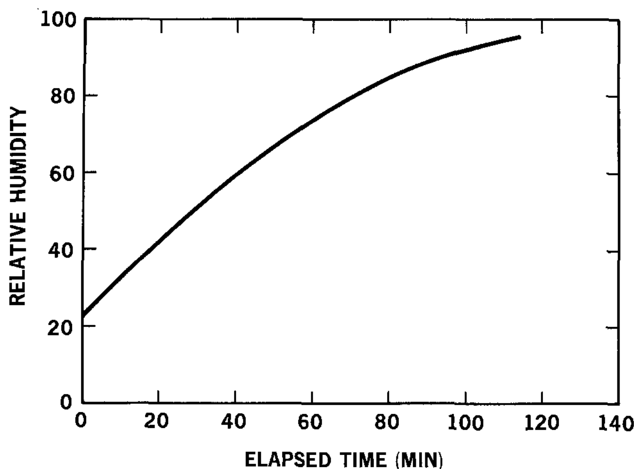

Fig. 1. Relative humidity program

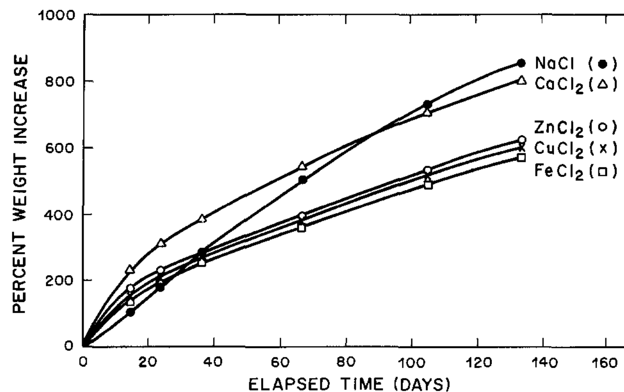

Fig. 2. Hygroscopicity of 1g samples of selected salts at 100% RH as measured by the percent weight increase.

in the experimental configurations. In both experiments $CaCl_2$ picked up twice as much moisture as NaCl in 14 days. $ZnCl_2$ and $CaCl_2$ picked up a sufficient amount of moisture to completely dissolve in 3 and 6 days, respectively, while $CuCl_2$, NaCl, and $FeCl_2$ dissolved in 20, 34, and 46 days, respectively. These observations are consistent with the usual expectation that $ZnCl_2$ and $CaCl_2$ are very hygroscopic materials while the other salts are moderately hygroscopic. Once a film of water has collected on the dry salt, a saturated salt solution will form. A saturated $ZnCl_2$ solution (CRH approximately 10% and vapor pressure approximately 2.4 mm Hg at 25°C) and a saturated $CaCl_2$ solution (CRH 31% and vapor pressure 7.3 mm Hg at 25°C) are expected to exhibit a stronger tendency to pick up water from a water-saturated atmosphere than a saturated NaCl solution (CRH 75.7% and vapor pressure 18.0 mm Hg at 25°C). The initial quantitative weight gains, as indicated by the percent weight increases, reflect this expectation but also indicate that the differences in solubility of these salts are partially responsible for the hygroscopicities commonly ascribed to them. The solubilities of $ZnCl_2$, $CaCl_2$, and NaCl are 4320, 819, and 350g solute/1000g water. If NaCl were as soluble as $ZnCl_2$ it can be very roughly estimated from the solubilities and the dissolution times that NaCl would have required about the same amount of time as $ZnCl_2$ to dissolve. Similarly, the dissolution time for NaCl, if it were as soluble as $CaCl_2$, would have been only two or three times that of $CaCl_2$. Dry NaCl, then, gains weight at a rate which is initially somewhat slower than $ZnCl_2$ and $CaCl_2$, but not nearly as slowly as the usual recognition of its hygroscopicity implies.

After dissolution of all the salt has occurred, the ionic molality of the solution is expected to determine the rate of moisture pickup more or less independently of the salt involved. If the magnitude of the water pickup is calculated in terms of the reciprocal of the ionic molality, which is a measure of the water pickup potential per ion present in solution, then the time required to attain a selected minimum value of this reciprocal may also be a useful method of expressing hygroscopicity. The reciprocal of the ionic molality is specified as a function of time in Fig. 3. The nonuniform behavior found for NaCl using pure percent weight gain information is no longer apparent. If the selected value for the reciprocal is arbitrarily chosen to be 0.20, the hygroscopicity is found to decrease in the order $CaCl_2 > ZnCl_2 > CuCl_2 > NaCl > FeCl_2$. For salts of only moderate solubility a higher minimum for the selected reciprocal value would be required to permit comparisons. The data suggest that selection of moderately higher values will lead to only minor variations in the relative order. For all the salt solutions the rate at which water vapor is condensed in the beakers decreases in a uniform manner consistent with a uniform increase in the vapor pressure of the solution as the salt concentration decreases.

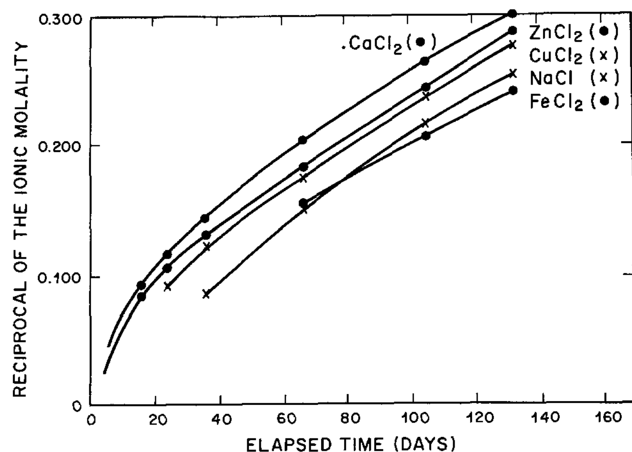

Fig. 3. Hygroscopicity of saturated solutions of selected salts at 100% RH as measured by the reciprocal of the ionic molality.

Interpretations based on solution concentrations are probably most useful and informative in analyzing laboratory data for pure salts, but the total capacity to pick up moisture in specific time intervals may be more useful in analyzing field samples, including dust, silt, and corrosion salts, since the amount of hygroscopic material in the sample may be very small. In this case, the extent to which the nonhygroscopic constituents can be dissolved and dispersed by the total amount of water present may be the dominant factor in terms of corrosion potential and other deleterious effects. It is apparent from the percent weight increase data given in Fig. 2 that once dissolution of the salts occurs, a beaker containing 1g of NaCl will pick up more water than a beaker containing 1g of $ZnCl_2$. This trend is expected to continue indefinitely. Similarly, a beaker containing 1g of NaCl will gain more weight than a beaker containing 1g of $CaCl_2$ for exposures to water-saturated air in a static environment of over 90 days. For some humid field environments, this suggests that contaminants and corrosion products containing NaCl in an otherwise nonhygroscopic matrix could be more hazardous than samples containing comparable amounts of $ZnCl_2$ or $CaCl_2$.

Table I summarizes some data for various procedures which could be used to estimate the hygroscopicity of pure salts. All the rankings, except those based on the CRH and solubility, were experimentally determined in this work.

The rank orders based on percent weight gain after 10, 40, and 100 day exposures are identical except for the position of NaCl, which ranges from the least to the most hygroscopic salt. It is surprising that $ZnCl_2$ appears somewhat less hygroscopic than $CaCl_2$ by either the percent-weight-gain or reciprocal-of-the-ionic-molality methods in that, because of its low CRH, dry $ZnCl_2$ becomes wet in all but the very driest of atmospheres, whereas $CaCl_2$ remains dry at RH's less than about 30%. Similarly, nonuniform characteristics are found for the set $FeCl_2$, $CuCl_2$, and NaCl. Their CRH's are 40, 69, and 75%, respectively, but the rank order of their hygroscopicities based on the reciprocal of the ionic molality is $CuCl_2 > NaCl > FeCl_2$. In a humid atmosphere, the CRH of a substance is apparently not always a satisfactory indicator of its hygroscopicity, but weight gain data by themselves, particularly if only one measurement period is examined, are not sufficient either. The length of the exposure affects the relative ranking and will be important in estimating moisture hazards with electronic devices. Whether a macroscopic method should be chosen or one which implicitly includes the effects of each ion in solution will depend on the circumstances and rather arbitrary preferences.

For most substances of interest to the electronic devices field, methods requiring measurements in solution will not be applicable. Modern instrumental gravimetric procedures readily provide a precise recording of weight change information which can be used

Table I. Relative hygroscopicities

Criteria for estimation	Rank order
1. Dissolution time	$ZnCl_2 > CaCl_2 > CuCl_2 > NaCl > FeCl_2$
2. Solubility (g solute/1000g water)	$ZnCl_2 > CaCl_2 > CuCl_2 > FeCl_2 > NaCl$
3. Percent weight gain after 10 days	$CaCl_2 > ZnCl_2 > CuCl_2 > FeCl_2 > NaCl$
4. Percent weight gain after 40 days	$CaCl_2 > NaCl > ZnCl_2 > CuCl_2 > FeCl_2$
5. Percent weight gain after 100 days	$NaCl > CaCl_2 > ZnCl_2 > CuCl_2 > FeCl_2$
6. Reciprocal of the ionic molality	$CaCl_2 > ZnCl_2 > CuCl_2 > NaCl > FeCl_2$
7. Critical RH	$ZnCl_2 > CaCl_2 > FeCl_2 > CuCl_2 > NaCl$

for ranking substances according to their hygroscopicity. The remainder of this paper describes such a procedure. By employing a flowing atmosphere, variable accelerations are feasible. Measurement of an effective CRH can be accomplished with RH programming of the flow system.

Critical relative humidities of pure salts and field samples.—Corrosion products and other contaminants contain varying amounts of hygroscopic materials, and consequently their moisture pickup characteristics are less predictable than those of pure salts. The surface area of the nonhygroscopic substances in the contaminant mixture, particularly if these substances are of low solubility, may be sufficient to chemisorb and physisorb most of the hygroscopic substances and all the moisture picked up by these substances, effectively stopping the moisture pickup process before a thin continuous film of water forms. For this and other reasons one of the most important moisture-related factors in considering corrosion and contamination problems with electronic devices is the rate at which a substance collects moisture in the first few hours of exposure to humidity levels above its CRH. Initial experimentation established that a significant weight change in a salt could be produced at the CRH starting with either a dry sample and increasing the RH or starting with a moist sample and decreasing the RH. For pure salts which were stable to moisture and did not react significantly with the aluminum sample pan, reproducible minima and maxima were recorded at the same RH for repetitive scans of the same sample. However, for corrosion products, dusts, and some materials the weight *vs.* RH plots were often complex and repetitive scans were not always reproducible. Generally, this behavior was caused by chemical or physical changes associated with the moisture pickup which were irreversible at reasonable conditions. For these reasons, the usual procedure for most samples was to equilibrate the sample at 22% RH and then to record a single run from low (22%) to high (nearly 100%) RH.

The results for four pure salts are shown in Fig. 4. The literature values for the CRH of KCNS and $NaNO_2$ (31) are 47 and 66%, respectively, at 20°C. The onset of weight gain for these salts in this work (23°C) occurred at 46 and 66%, respectively, establishing that the method is sufficiently sensitive and accurate to measure the CRH of many substances. The onset of weight gain for NaCl occurred at 84%, which is somewhat higher than the literature value of 76% (31), but NaCl was later found, as is discussed below, to pick up moisture at a slower rate during the initial adsorption phase than during the later stages controlled by the solution vapor pressure. It is anticipated that if the RH programming had proceeded at a slower rate the observed critical RH would be lower for this salt. This measurement requires development of more sophisticated humidity control equipment which is in progress. Moisture pickup for CrO_3 is initiated at 29% RH, which is somewhat below the literature value of 35% (31). This discrepancy may be due in part to the procedure used to determine the RH of the system. The vapor pressure of water in the air stream was assumed to be identical to the vapor pressure of the distilled water bath. The vapor pressure of the bath was estimated from its temperature. The temperature differential between the input air stream and the water bath for the low humidity readings was substantial and could lead to significant warming of the water at the surface of the air bubbles, thereby increasing the vapor pressure and the corresponding RH. The determined RH would be low consistent with the observation for CrO_3. An improved apparatus which will eliminate this uncertainty is under construction.

The results for several field samples are shown in Fig. 5-8. The electrolytic corrosion product samples No. 1 and 2, shown in Fig. 5, each exhibited two weight gain onsets but are otherwise very different. The electrolytic corrosion products from sample No. 2 were produced with relatively clean water and consisted primarily of copper and nickel oxides and carbonates with minor amounts of chloride salts. The weight onset at approximately 27% RH is probably associated with dust that was unavoidably collected with the corrosion products. The second onset at about 50% RH could be due to chloride salts. The concentration of such salts must be low, however, since the weight gain rapidly approaches saturation at approximately 65% RH. Corrosion product No. 1 was the result of water contamination from a water line serving an air conditioning system. The water contained chromate salts and possibly other additives for rust inhibition. The initial onset at 23% RH saturated at about 32%. The identity of this contaminant was not clear. The second onset is somewhat obscured but appears to occur at roughly 30% RH. This onset appears to be caused by a major hygroscopic component in the corrosion product as there is no indication that saturation is approached during the remainder of the run. The identity of this product was ascertained from chemical analysis

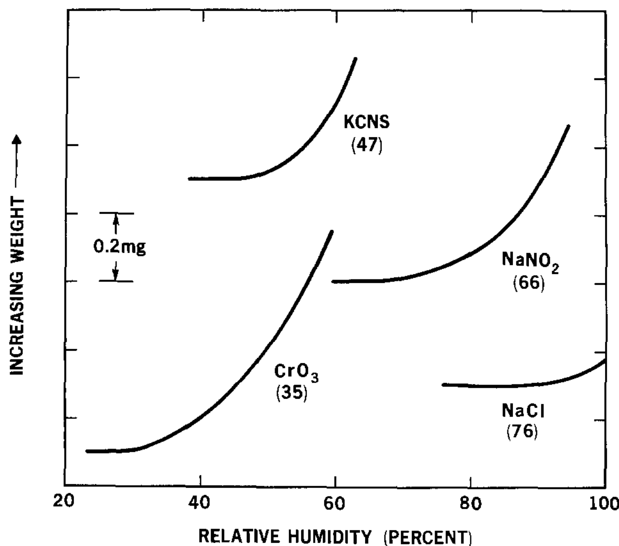

Fig. 4. Moisture pickup onset for selected salts on exposure to increasing RH.

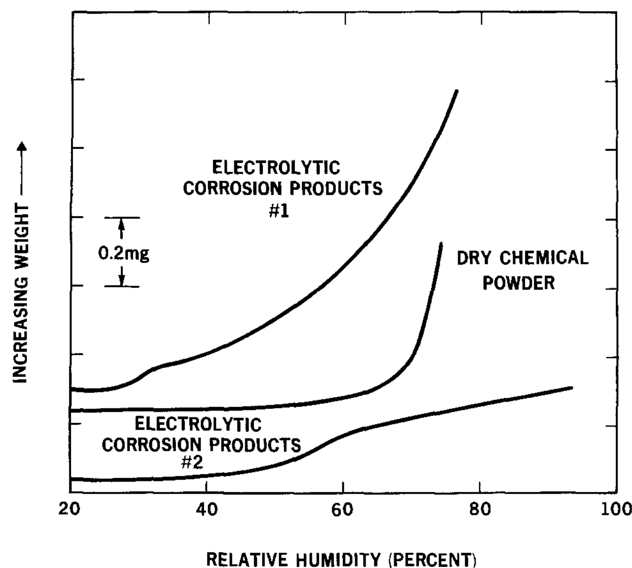

Fig. 5. Moisture pickup onset for corrosive contaminants on exposure to increasing RH.

to be a combination of copper, zinc, and calcium chromates.

The data for a contaminant found on an electromechanical switching device after a nearby battery fire had been extinguished with "dry chemical powder" are also shown in Fig. 5. Again, two onsets occur. The first onset at 27% RH is probably due to adsorption on dust present before the fire and on soot and dry chemical powder. The second onset at 55% RH can be attributed to the formation of a thin aqueous film on the dry chemical powder and the subsequent initiation of rapid moisture pickup. The dry chemical powder was primarily sodium bicarbonate.

The results for dust samples from Holmdel (No. 1) and two locations in New York City (No. 2 and 3) are shown in Fig. 6. The samples exhibited similar characteristics with initial moisture pickup occurring at about 26% RH. These dusts are not known to have caused significant moisture-induced problems on electromechanical switching equipment except at elevated humidity levels, suggesting that moisture pickup is primarily limited to an adsorption process. The large surface area and complex composition typical of dusts permit a significant weight increase to occur before appreciable thin films of aqueous salt solutions are created.

The information summarized in Fig. 7 and 8 demonstrates the utility of this method in ascertaining the quality of materials for electronic devices and assessing contamination or corrosion problems. Data for insulating materials used as substrates and for other purposes are shown in Fig. 7. A number of phenol fiber samples were examined and they exhibited widely variable behavior. The data for a typical sample are shown. An alumina ceramic material exhibited a moderate tendency to pick up moisture at very high RH. The epoxy glass sample was only slightly susceptible to moisture pickup at high RH. Aged textile insulation materials removed from copper wire from two locations in New York City are compared in Fig. 8 with recently manufactured product. Sample No. 1 is from a location which experienced contamination from hydrochloric acid. The onset point at 26% is substantially more pronounced than that of sample No. 2 (which was of similar vintage) or that of the new material. This difference is attributable to the presence of chloride salts in sample No. 1.

Hygroscopicity of substances in a dynamic environment.—Information on the moisture pickup characteristics of substances at high RH is useful for assessing contamination and corrosion hazards and for engineering equipment specifications and building environments. In this study these measurements were accomplished rapidly for a wide variety of substances using a 10 ml/min flow of air nearly saturated with water vapor to simulate typical indoor environments in an accelerated time frame. The substances are ordered on a time-averaged weight-percent basis in Tables II and III according to the increasing tendency of the various materials to gain weight through pickup of water from the nearly saturated air stream. The samples span a broad range of hygroscopicities and are arbitrarily categorized as strongly, moderately, or weakly hygroscopic according to whether their average weight gain rate is greater than 0.110, 0.011-0.110, or less than 0.011 %/min, respectively.

While ordering the samples on this basis seems generally most appropriate, examination of the data indicates this arrangement disguises some factors. For instance, $FeCl_3$ was determined to undergo an average percent weight gain of 0.421 %/min, but the rate decreased over the 94 min exposure period from 0.58 to 0.19 %/min. On the other hand, $CuCl_2 \cdot 2H_2O$ gained weight at an average rate of 0.087 %/min throughout a 324 min exposure period, and the weight gain rate for $FeCl_2 \cdot 4H_2O$ and NaCl actually increased slightly over the duration of the experiments. While it is pos-

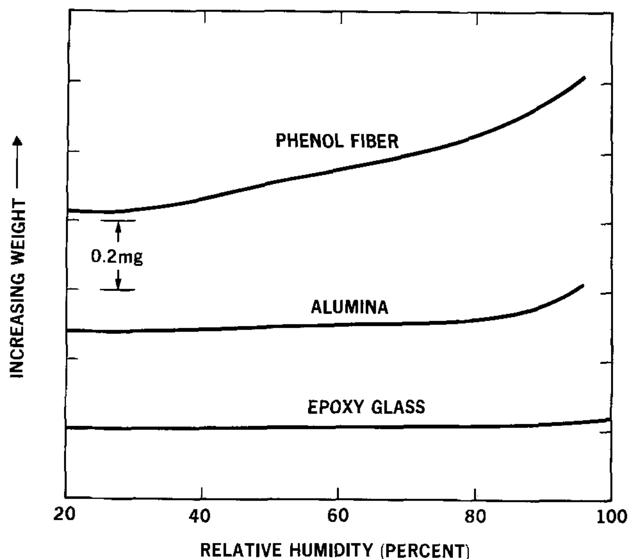

Fig. 7. Moisture pickup onset for insulation and substrate materials on exposure to increasing RH.

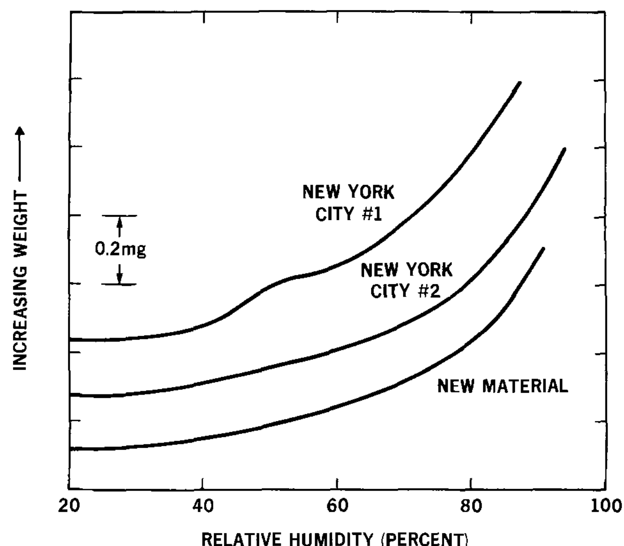

Fig. 8. Moisture pickup onset for textile insulation materials on exposure to increasing RH.

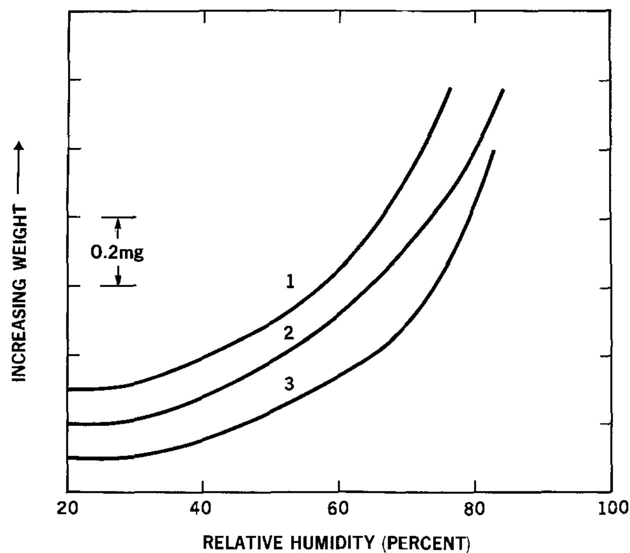

Fig. 6. Moisture pickup onset for dusts on exposure to increasing RH.

Table II. Hygroscopicity studies

Material	Initial rate of weight gain* (%/min)	Weight gain rate at termination† (%/min)	Total weight gain at termination (%)	Total exposure time (min)	Average weight gain rate throughout run (%/min)	Initial sample weight (mg)
A. Substances of very low hygroscopicity						
Phenol fiber insulation No. 3 (extended urban exposure)	<0.01	<0.01	0.27	1,350	0.0002	62
Epoxy glass (shredded)	<0.01	<<0.01	0.68	2,295	0.0003	67
Alumina ceramic (chips)	<0.01	0	0.18	600	0.0003	106
$PbCO_3$ (powder)	<0.01	0	0.03	68	0.0004	84
CuO (chopped wire)	<0.01	0.00	0.1	165	0.0006	58
Bakelite (chunks)	0.02	<<0.01	2.1	2,640	0.0008	66
Phenol fiber insulation No. 2 (freshly manufactured)	0.02	<<0.01	3.4	4,305	0.0008	57
Arizona Standard Dust	0.02	<<0.01	1.1	1,050	0.001	64
Phenol fiber insulation No. 4 (extended urban exposure)	0.02	<<0.01	2.7	1,380	0.002	35
Talc (hydrous magnesium silicate)	0.03	<<0.01	0.5	165	0.003	54
$NaHCO_3$ (powder)	0.01	<0.01	0.6	135	0.004	87
Textile insulation No. 1 (extended urban exposure)	0.08	0	4.1	825	0.005	58
Textile insulation No. 3 (freshly manufactured)	0.09	0	4.3	860	0.005	43
Textile insulation No. 2 (extended urban exposure)	0.09	0	6.0	1,200	0.005	45
Soot and fire extinguisher powder (White Plains)	0.05	<0.01	78.7	11,250	0.007	60
$CuSO_4 \cdot 5H_2O$ (crystalline)	0.06	<<0.01	0.8	107	0.007	69
$ZnCO_3$ (powder)	0.06	0.00	1.1	128	0.009	25
Phenol fiber insulation No. 1 (freshly manufactured)	0.03	0.01	1.1	113	0.010	73
B. Moderately hygroscopic substances						
Dust (New York, 30th Street)	0.10	0.01	36.0	3,000	0.012	20
Electrolytic corrosion (Philadelphia)	0.11	<0.01	16.2	1,350	0.012	13
Dirt (Red Bank)	0.06	0.00	1.1	84	0.013	69
$CuCO_3$ (powder)	0.05	<<0.01	2.1	167	0.013	102
Dust (New York, 36th Street)	0.06	0.01	21.6	1,545	0.014	31
Dust (New York, Second Ave.)	0.30	<0.01	12.9	860	0.015	21
Electrolytic corrosion (New York)	0.34	<0.01	33.4	1,760	0.019	19
KCl (crystalline)	0.02	0.02	2.2	90	0.024	50
Ag_2S (granules)	0.03	0.03	2.0	75	0.027	80
Electrolytic corrosion (Belle Harbour)	0.14	0.00	2.7	100	0.027	12
Cotton	0.36	0.00	1.7	60	0.028	22
Dust (Holmdel)	0.32	0.01	38.8	1,295	0.030	18
NaCl (crystalline)	0.03	0.04	3.8	110	0.035	87
$SnCl_2 \cdot 2H_2O$ (crystals)	0.05	0.03	6.9	145	0.048	57
$FeCl_2 \cdot 4H_2O$ (crystals)	0.05	0.06	8.9	175	0.051	80
$NiCO_3$ (powder)	0.13	0.03	8.8	143	0.062	45
$CuCl_2 \cdot 2H_2O$ (crystals)	0.09	0.09	28.2	324	0.087	66
C. Very hygroscopic substances						
Electrolytic corrosion (Albuquerque)	0.30	0.00	39.5	323	0.122	7
Drierite (calcium sulfate)	0.17	0.07	4.9	40	0.123	107
Silica gel	0.15	0.11	3.5	26	0.135	87
$ZnCl_2$	0.28	0.19	8.7	34	0.256	102
$CaCl_2$	0.34	0.34	8.1	24	0.338	53
$FeCl_3$	0.58	0.19	39.6	94	0.421	52

* Averaged for the first 2 min.
† Averaged for the last 2 min.

sible to measure or, in principal, calculate the percent weight increase of an initially dry sample maintained at a specific relative humidity until equilibrium is attained, the hazards of estimating corrosion rates of contaminated surfaces solely from such determinations are apparent. Thus, NaCl exposed to 95% RH has a theoretical potential to increase its weight to 1136% of its dry weight (see Table II), while $ZnCl_2$ will increase to only 610% of its dry weight. In a practical sense, however, a surface contaminated with NaCl gaining weight at the rate of 0.035 %/min at 100% RH would require about 48 hr to gain its own weight in water, while a similar amount of $ZnCl_2$ picking up moisture at the rate of 0.19 %/min (the experimental rate at termination of the experiment) would achieve the same weight gain in less than 6 hr. At these rates a 100 mg sample of $ZnCl_2$ (solubility 4320g/1000g H_2O) would completely dissolve in about 90 min, while a 100 mg sample of NaCl (solubility 350g/1000g H_2O) would require about 140 hr to completely dissolve.

A number of samples of corrosion products and contaminants, as well as materials used by the electronics industry, are ranked in Tables II and III with the pure chemicals. The manner in which the data can be used for assessing corrosion and contamination problems can be illustrated with a few examples.

Electrolytic corrosion products which contaminated equipment in an Albuquerque switching center that had been flooded are seen by this ranking procedure to be more hygroscopic than $CuCl_2 \cdot 2H_2O$ and of similar hygroscopicity to Drierite and silica gel. SEM/x-ray analysis of the contaminants indicated that a major component, in addition to sandy soil, was copper chloride or oxychloride. The data indicate the contamination on the Albuquerque equipment could produce serious consequences in the event a high humidity condition occurs. Caution must obviously be exercised, however, to avoid drawing unjustified conclusions based only on the average weight gain rates. For instance, the Albuquerque sample initially picks up moisture at a rate of 0.30 %/min but the rate decreases to essentially zero after 323 min. $CuCl_2 \cdot 2H_2O$ was found, though, to gain weight at a constant rate of 0.09 %/min throughout a 320 min run. Although the average weight gain rate is significantly higher for the Albuquerque sample, it would be inappropriate to predict, on this basis alone, that the Albuquerque sample would pose a greater hazard than contamination by pure $CuCl_2 \cdot 2H_2O$. In a humid environment the $CuCl_2 \cdot 2H_2O$ would eventually pick up moisture equivalent to several times its initial dry weight, while the Albuquerque sample would pick up a maximum of 39.5% of its initial weight. The sandy soil and other insoluble components present in the Albuquerque sample adsorb the cupric chloride and disperse the moisture picked up by the cupric chloride very effectively. Exposure to humidity levels above the calculated CRH for cupric chloride of 69% is rare for heated indoor environments in Albuquerque, so that the hazard posed by this contaminant was estimated to be minimal. Several years of successful operation of most of the equipment since the flood occurred indicates that this is indeed the case.

The electrolytic corrosion sample from the Belle Harbour (New York) equipment, in contrast to that from Albuquerque, contains only traces of chloride salts and is substantially less hygroscopic than the Albuquerque sample. On this basis, only minimal problems were anticipated if exposure to high humidity could be eliminated. The Belle Harbour switching

Table III. Hygroscopicity studies

Material	Average weight gain rate throughout run (%/min)	Solubility (g solute/1000g water)*	Maximum theoretical uptake of water at 95% relative humidity (percent of dry weight)*	Critical relative humidity	
				From this work	Literature or calculated values
A. Substances of very low hygroscopicity					
Phenol fiber insulation No. 3 (extended urban exposure)	0.0002			<22	
Epoxy glass (shredded)	0.0003			Nondiscrete	
Alumina ceramic (chips)	0.0003			Nondiscrete	
$PbCO_3$ (powder)	0.0004	0.0014 (20°C)[L]			
CuO (chopped wire)	0.0006				
Bakelite (chunks)	0.0008			Nondiscrete	
Phenol fiber insulation No. 2 (freshly manufactured)	0.0008			27	
Arizona Standard Dust	0.001				
Phenol fiber insulation No. 4 (extended urban exposure)	0.002			25	
Talc (hydrous magnesium silicate)	0.003				
$NaHCO_3$ (powder)	0.004	69 (0°)[CRC]			
Textile insulation No. 1 (extended urban exposure)	0.005			26, 50	
Textile insulation No. 3 (freshly manufactured)	0.005			27, 55	
Textile insulation No. 2 (extended urban exposure)	0.005			23, 47, 69	
Soot and fire extinguisher powder (White Plains)	0.007			27, 50	
$CuSO_4 \cdot 5H_2O$ (crystalline)	0.007	255 (30°C)[ST]			98[CRC]
$ZnCO_3$ (powder)	0.009	0.206 (25°C)[L]			
Phenol fiber insulation No. 1 (freshly manufactured)	0.010				
B. Moderately hygroscopic substances					
Dust (New York, 30th Street)	0.10			27	
Electrolytic corrosion (Philadelphia)	0.012			23, 30	
Dirt (Red Bank)	0.012				
$CuCO_3$ (powder)	0.013	<0.03 (18°C)[L]			
Dust (New York, 36th Street)	0.06			26	
Dust (New York, Second Avenue)	0.015			25	
Electrolytic corrosion (New York)	0.019			27, 50	
KCl (crystalline)	0.024	373 (30°C)[ST]			
Ag_2S (granules)	0.027	9×10^{-15} (18°C)[CRC]			
Electrolytic corrosion (Belle Harbour)	0.027				
Cotton	0.028				
Dust (Holmdel)	0.030			26	
NaCl (crystalline)	0.035	350 (25°C)[ICT]	1136[PM]	84	75.7[CRC]
$SnCl_2 \cdot 2H_2O$ (crystals)	0.048	839 (0°C)[CRC]			
$FeCl_2 \cdot 4H_2O$ (crystals)	0.051	684 (25°C)[ICT]	855[PM]		40[PM]
$NiCO_3$ (powder)	0.062	0.8 (15°C)[L]			
$CuCl_2 \cdot 2H_2O$ (crystals)	0.087	770 (25°C)[ICT]	735[PM]		69[PM]
C. Very hygroscopic materials					
Electrolytic corrosion (Albuquerque)	0.122				
Drierite (calcium sulfate)	0.123	0.67 (20°C)[L]			
Silica gel	0.135	0.12 (25°C)[L]			
$ZnCl_2$	0.256	4320 (25°C)[ICT]	610[PM]		10[LG]
$CaCl_2$	0.338	819 (25°C)[ICT]	971[PM]		31[CRC]
$FeCl_3$	0.421	918 (20°C)[L]			

* L, W. F. Linke, Editor, "Solubility of Inorganic and Metal Organic Compounds," 4th ed (1965). CRC, "Handbook of Chemistry and Physics," 56th ed. (1975). ST, "Smithsonian Tables," 9th ed. ITC, "International Critical Tables," Vol. 4 (1929). PM, From calculations by P. C. Milner, LG, "Lange's Handbook of Chemistry and Theoretical Chemistry," 11th ed.

center is located in a very humid environment one block from the Atlantic Ocean, but, unfortunately, at the time this water damage occurred, the method described above for determining the CRH was not available and it was not feasible to estimate the CRH by other means. Consequently, specific recommendations concerning the maximum tolerable humidity were not possible.

Recently an electronic switching center in Philadelphia was contaminated with water containing a rust inhibitor. The equipment was powered and electrolytic corrosion occurred. The CRH of the primary contaminant was found to be about 30%, which suggests a serious problem could exist, since the local humidity would nearly always exceed that value. However, the over-all hygroscopicity based on average weight gain rate and total moisture pickup after 1350 hr (16%) was low. This information, coupled with the successful operation of most of the equipment for several weeks after the flood indicated that the restored equipment would continue to operate normally without the need for extensive modifications to the building humidity control.

The equipment installation in White Plains (New York), which suffered the small battery fire described earlier, was analyzed for moisture pickup by this procedure. The contaminant was found to be less hygroscopic than the Philadelphia sample in terms of the average weight gain rate, but this average was based on roughly 10 times the sampling period. The total pickup before an extended steady state was reached was 78.7%. This result, coupled with the dramatic increase in moisture pickup observed above 50% RH, shown in Fig. 5 and discussed above, indicated that cleaning or replacement of the equipment was necessary.

The dust samples from the New York City locations and from Holmdel behave similarly, though the dust from the rural Holmdel environment is, surprisingly, somewhat more hygroscopic. None of these dusts has caused particular problems with electronic equipment. The large surface area of the dusts permits relatively large amounts of moisture adsorption to occur without creating thin films of water. The texture of the Arizona Standard Dust sample was much finer and less fibrous than the dust found in New York City and Holmdel, suggesting the surface area per unit weight is probably greater. The hygroscopicity of the Arizona Dust is, however, about an order of magnitude lower than the other dusts. As more locations are sampled, it is anticipated that unusual dusts bearing localized hygroscopic components will be distinguishable from "ordinary" dusts.

All of the insulation and substrate materials examined fit into the category of substances of low hygroscopicity. Obviously, only nonhygroscopic substances are reasonable candidates for such uses. Within this category, however, a range of moisture pickup rates was found, even for similar materials. For instance, phenol fiber No. 3 picked up moisture at an average of 0.0002 %/min, while phenol fiber samples No. 2 and 4 exhibited rates of 0.0008 and 0.002 %/min, respectively. There appears to be no correlation between age and hygroscopicity, and apparently the dif-

ferences are manufacturing in origin for these samples. Except for one phenol fiber sample, the least hygroscopic substrate materials are the epoxy glass and the alumina ceramic. More data would be needed to draw firm conclusions about the relative hygroscopcity of these substrate materials, and these results should not be extrapolated to all epoxy glass, alumina, and phenol fiber substrates available. Wide variability is likely to exist for different manufacturers and in some cases for different lots. These data demonstrate, however, that instrumental gravimetric methods can be effectively employed in distinguishing the hygroscopic characteristics of a variety of substrate materials that might be considered for device applications.

The behavior of three textile material samples from insulated wire was very similar at the high humidity level at which these experiments were run. Samples 1 and 2 had been exposed approximately 35 years to an urban environment. Sample 2 is of particular interest, as mentioned earlier, because of its unique exposure to hydrochloric acid fumes. Textile insulation typically performs poorly at high humidity levels in terms of insulation resistance. Normally, these humidity levels are not encountered at indoor installations. Unfortunately, the present apparatus is not readily suited to monitoring weight gain characteristics at an intermediate RH, where the effects of contamination on sample 2 would be pronounced. It would also be interesting to know if the freshly manufactured sample would be distinguishable from sample 1 at an intermediate RH.

Conclusion

This work was carried out to determine whether instrumental gravimetric analysis is suited to readily measure the moisture pickup characteristics of materials and substances important to the electronics industry. It was found that many substances initiate moisture pickup processes that are detectable at discrete relative humidities. Furthermore, it was found that moisture pickup characteristics measured gravimetrically at high humidity levels can be used to rank substances in a manner which is useful for assessing hygroscopicity and corrosion hazards. Unknown mixtures of materials weighing only a few tenths of a milligram can be readily analyzed. Moderately to strongly hygroscopic materials can probably be analyzed with even smaller samples. The rate of hygroscopicity change was found, in some cases, to be a signature of the material analyzed, which may prove useful when analyzing samples of unknown composition. The information gathered here clearly demonstrates the need for and the usefulness of an expanded system capable of precise relative humidity programming. Such a system is now under development. Further experiments will include the effects of pollutant gases introduced into the air stream on the measured CRH and moisture pickup rates of substances.

Manuscript submitted Aug. 4, 1977; revised manuscript received Nov. 29, 1977. This was Paper 21 presented at the Philadelphia, Pennsylvania, Meeting of the Society, May 8-13, 1977.

Any discussion of this paper will appear in a Discussion Section to be published in the December 1978 JOURNAL. All discussions for the December 1978 Discussion Section should be submitted by Aug. 1, 1978.

Publication costs of this article were assisted by Bell Laboratories.

REFERENCES

1. W. H. J. Vernon, *Trans. Faraday Soc.*, **27**, 265 (1931); *ibid.*, **31**, 1668 (1935).
2. G. J. Mulder, in "A Comprehensive Treatise on Inorganic and Theoretical Chemistry," Vol. III, J. W. Mellor, Editor, p. 707 (1956).
3. J. W. Mellor, "A Comprehensive Treatise on Inorganic and Theoretical Chemistry," Vol. II, p. 552 (1956).
4. R. St. J. Preston and B. Sanyal, *J. Appl. Chem.*, **6**, 26 (1956).
5. D. C. Lindsay, "International Critical Tables," Vol. 2, pp. 321-325 (1927).
6. T. Kanazawa, M. Chikazawa, M. Kaiho, and T. Fujimaki, *Nippon Kagaku Kaishi*, **9**, 1669 (1973).
7. Y. Hara, S. Okimoto, and H. Osada, *Kogyo Kayaku Kyokai-sh*, **30**, 25 (1969).
8. S. Pawlikowski, S. Szymonik, and A. Chomiakow, *Chem. Stosowana*, **4**, 243 (1960).
9. Yu. A. Vakhrushev and Yu. B. Gradinar, *App. Chem. (USSR)*, **47** (3), 627 (1974).
10. W. Trzesniowski, *Przem. Chem.*, **53**, 225 (1974).
11. I. N. Shokin and A. S. Solov'eva, *Tr. Mosk. Khim.-Technol. Inst.*, **35**, 43 (1961).
12. P. Runge, *Chem. Tech. (Leipzig)*, **27** (6), 359 (1975).
13. J. Yee, *Ind. Eng. Chem.*, **16**, 367 (1944).
14. B. R. Puri and V. Bhushan, *J. Sci. Industr. Res.*, **11B**, 504 (1952).
15. M. W. Kearsely and G. G. Birch, *J. Fd. Technol.*, **10**, 625 (1975).
16. E. O. Whittier and S. P. Gould, *Ind. Eng. Chem.*, **22**, 77 (1930).
17. A. P. Grebennikova, O. M. Todes, and V. A. Fedoseev, *Colloid J.*, **24**, 352 (1962).
18. S. Twomey, *J. Appl. Phys.*, **24**, 1099 (1953).
19. R. A. Bakhanova and L. V. Ivanchenko, *Tr. Ukr. Nauchno-Issled. Gidrometeorol. Inst.*, **133**, 110 (1974).
20. M. M. Markowitz and D. A. Boryta, *J. Chem. Eng. Data*, **6**, 16 (1961).
21. S. Pawlikawski, S. Szymonik, and A. Chomiakow, *Przemysl Chemiczny*, **38**, 598 (1959).
22. F. Modrzejewski and O. Pokora-Bartyzel, *Acta Pol. Pharm.*, **5**, 480 (1966).
23. C-H. Shen and G. S. Springer, *J. Composite Mat.*, **10**, 2 (1976).
24. Kh. Balarev, Kh. Stoeva, and Kh. Stoev, *God. Vissh. Khim.-Tekhnol. Inst., Burgas, Bulg.*, **10**, (10), 623 (1973).
25. (a) P. B. P. Phipps, "The Role of Water in Atmospheric Corrosion," New York Chapter American Vacuum Society Symposium on Corrosion in Thin Films, Princeton, New Jersey, November 17, 1967.
    (b) D. W. Rice, P. B. P. Phipps, and R. Tremoureux, "Atmospheric Corrosion of Nickel Thin Films and Foils," Symposium on Deterioration of Electronic Devices, Electrochemical Society Meeting, Philadelphia, May 8-13, 1977.
26. L. M. Foster and G. V. Arbach, *This Journal*, **124**, 164 (1977).
27. F. Mansfeld and J. V. Kenkel, *Corrosion*, **33**, 13, (1977); *Corros. Sci.*, **16**, 111 (1976).
28. P. J. Sereda, ASTM Bull. No. 246, 47 (1960).
29. H. Gutman, Metal Corrosion in the Atmosphere, ASTM STP 435, 223 (1968).
30. G. K. Berukshtis and G. B. Klark, "Corrosion of Metals and Alloys," Collection, NLL Boston Spa., 379 (1964).
31. "CRC Handbook of Chemistry and Physics," 52nd ed., R. C. Weast, Editor (1971-1972).

Kinetics of the Slow-Trapping Instability at the Si/SiO_2 Interface

A. K. Sinha* and T. E. Smith

Bell Laboratories, Murray Hill, New Jersey 07974

ABSTRACT

The slow-trapping instability can be a potentially major threat to reliability of p-channel enhancement-mode IGFET's. We have determined the kinetics of slow trapping for Al-gate MOS structures on (111) n-Si and evaluated the role of surface states, N_{SS}, for n- and p-type Si of (111) and (100) orientation. Slow trapping, as revealed by negative bias-temperature aging, generates a characteristic distribution of N_{SS} with a peak near the midgap. This effect is responsible for the fact that for n-Si, the threshold shift, $\Delta V_T >> \Delta V_{FB}$, the flatband shift, and for p-Si, $\Delta V_T < \Delta V_{FB}$. In the regime where ΔV_{FB} is less than the saturation value, our data on slow-trapping kinetics can be represented by the factorial relationship

$$\Delta V_{FB} \sim A|V_B|^n t^{0.2} \exp\left(-\frac{\epsilon_a}{kT}\right)$$

where V_B is the applied negative bias (10-40V), t is the time (10-10^3 min), T is the temperature (373°-573°K), k is the Boltzmann constant, $n = 4.76 - 5.3 \times 10^{-3}T$, $A \sim 1.6 \times 10^3$, and ϵ_a is the thermal activation energy ($\sim$0.64 eV). This equation emphasizes the strong field dependence of ΔV_{FB} at lower temperatures.

The so-called slow-trapping instability [instability No. VI of XVII compiled by Deal (1)] can be a potentially major threat to reliability of p-channel enhancement mode IGFET devices (1-4). This instability is revealed by a negative bias-temperature aging test which causes a negative shift in the flatband voltage and hence in the threshold voltage of the device. The exact mechanism of slow trapping has not been established. But it is known that slow trapping is more pronounced for MOS structures with a high fixed charge, Q_{SS} (4). Slow-trapping instability can be also aggravated by radiation damage (5) and by a low temperature post Al-metallization H_2 anneal (6).

Accelerated aging tests are commonly used to compare the slow-trapping characteristics of different MOS structures and also to evaluate the effectivity of various processing improvements [such as high temperature H_2 annealing (6)] aimed at reducing the slow trapping. However, a knowledge of kinetics is also obviously necessary in order to estimate the lifetime under device operating conditions and to stimulate work on understanding of slow-trapping phenomena.

The objective of the present work is twofold. First, the role of surface states, N_{SS}, was investigated in the slow-trapping phenomena. It is shown that a characteristic distribution of N_{SS} is generated as a result of slow trapping, and depending upon whether the Si is n- or p-type, the flatband shift ΔV_{FB} can be less than or greater than ΔV_T. Second, detailed kinetics measurements were made of slow trapping in $Al/SiO_2/$(111) n-Si capacitors. The effect of applied bias (for a given time and at lower temperatures) is found to be more severe than previously believed.

Experimental

Slow-trapping measurements were made on both n- and p-type Si wafers [(111 and 100) orientation, 2 in. diam, $N_{D,A} \sim 10^{15}$ cm^{-3}]. The wafers were cleaned and then oxidized to 1000Å thickness at 1100°C in a dry oxygen ambient in an HCl-cleaned quartz tube. The oxidized wafers received an *in situ* Ar-anneal at 1100 C for ½ hr. An array of MOS capacitors was fabricated by filament evaporating Al-field plates (20 mil diam) through a mechanical shadow mask. The SiO_2 was etched off from the back side and an Al back contact was formed also by filament evaporation. The samples were then H_2-baked at 450°C, ½ hr.

MOS measurements were made in a test facility consisting of an electroglas 910 prober equipped with a Temptronix TP 35 thermochuck and enclosed in a dry N_2 glove box (7). High frequency (1 MHz) C-V measurements were made at a sweep rate of 100 mV/sec. Quasistatic measurements were made at 20 mV/sec using the slow-ramp technique (8). The data were analyzed in the usual manner to give the Si-doping level (9), the flatband capacitance and voltage, the oxide fixed charge Q_{SS}, and the surface-state density as a function of the relative surface potential, ψ_S. The surface-state density was obtained from the high-low frequency capacitance technique (10) and ψ_S found as a function of bias using the Berglund techniques (11).

The extent of slow trapping was evaluated through measurements of negative shift in the flatband voltage, ΔV_{FB}, following bias-temperature aging at various temperatures in the range 100°-300°C, with applied negative bias of 10-40V, and for times of 10 min-16 hr.

Results and Discussion

Positive bias-temperature aging under conditions (10^5 V/cm, 200°C, 30 min) where slow trapping is very small caused little or no negative shift (<0.1V) in the C-V curves, signifying that the mobile charge contamination levels were below 2×10^{10} cm^{-2}.

Representative C-V curves.—Figure 1 shows typical C-V curves for a MOS structure on (111) n-Si in the as-received condition and after B-T aging at -23.5V, 250°C, for 15 min. The as-received sample had a Q_{ss} of 2×10^{11} cm^{-2} and a midgap N_{SS} of $\sim 5 \times 10^{10}$ cm^{-2} eV^{-1}. Upon negative B-T aging, the slow trapping is revealed in three ways: (*i*) the high frequency C-V curve is shifted to more negative values reflecting an increase in the apparent Q_{SS} and a ΔV_{FB} of -0.8V; (*ii*) the initially single minimum in the quasistatic C-V curve is split into two minima which now occur at significantly higher C/C_{ox}; this higher C/C_{ox} is the result of an order of magnitude increase in the N_{SS} which has a peak near the midgap, as shown in Fig. 2; (*iii*) there is an increase (by $\sim$1.5V) in the negative threshold voltage from V_{T1} to V_{T2}, as indicated by the vertical

* Electrochemical Society Active Member.
Key words: MOS devices, reliability, surface states.

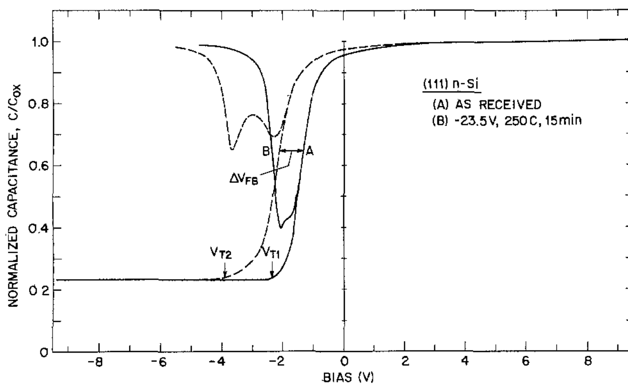

Fig. 1. *C-V* curves for $Al/SiO_2/n(111)Si$ capacitors: (A) as-received; (B) after −23.5V, 250°C, 15 min bias-temperature aging.

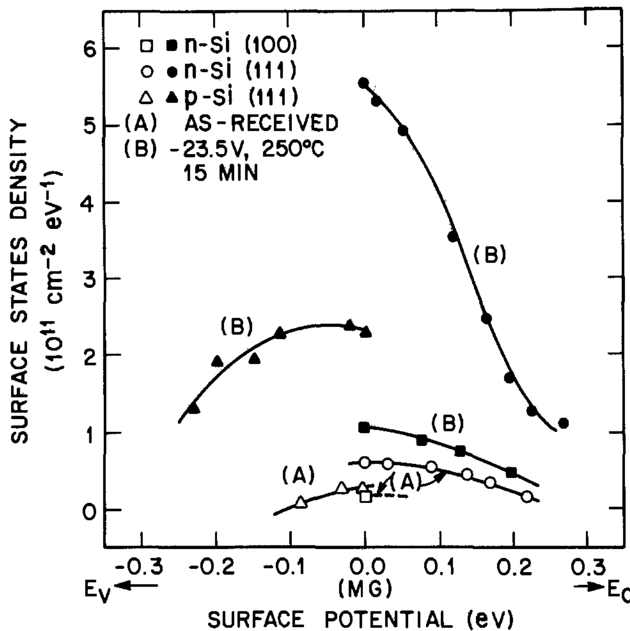

Fig. 2. Distribution of surface states in various $Al/SiO_2/Si$ structures: (A) as-received; (B) after −23.5V, 250°C, 15 min B-T aging.

arrows in Fig. 1, with $\Delta V_T >> \Delta V_{FB}$. This is due to the fact that increases in both Q_{SS} and N_{SS} due to slow trapping with n-Si cause threshold shifts in the same direction, which are therefore additive. Moreover, for n-Si, there are fewer occupied surface states at V_T than at flatband voltage. For p-Si, there are more occupied states at T than at flatbands.

Figure 3 shows the effects of slow trapping in an Al-gate MOS structure on (111) p-Si. Here too there is a negative shift in the flatband voltage, ΔV_{FB}, which is nearly equal in magnitude to that observed with (111) n-Si. There is also a significant increase in N_{SS} and a tendency toward splitting of the minimum in the quasistatic *C-V* curve. However, in this case, ΔV_T is much smaller than ΔV_{FB}, since the apparent ΔV_T components due to additional Q_{SS} and N_{SS} now are in opposite directions. The distribution of $N_{SS}(\psi_S)$ for the (111) p-Si sample before and after B-T aging is shown in Fig. 2 and is similar to that for (111) n-Si.

Figure 4 shows *C-V* data for (100) n-Si before and after B-T aging. The magnitudes of both ΔV_{FB} and ΔV_T are smaller by a factor of four than those for (111) n-Si. It should be also noted that the initial Q_{SS} ($\lesssim 10^{10}$ cm^{-2}) and N_{SS} at midgap ($\sim 10^9$ cm^{-2} eV^{-1}, see Fig. 2) for this sample were lower by an order of magnitude when compared with (111) n-Si.

This and other recent work support the conclusion that the initial Q_{SS} may be a major factor controlling the slow-trapping instability—a small Q_{SS} correlates with reduced slow trapping. For (111) n-Si samples, the Q_{SS} can be decreased to $\lesssim 1 \times 10^{11}$ cm^{-2} by a high temperature H_2 anneal (800°-900°C, ½-1 hr). These samples show a very small ΔV_{FB} of $\sim$0.2V after 250°C, −20V, 15 min aging. On the other hand, a low temperature H_2 anneal (450°C, ½ hr), which lowers the N_{SS}, tends to enhance the slow-trapping instability (6).

Kinetics data.—Kinetics measurements were made for (111) n-Si samples which had received the post-Al H_2-bake (450°C, ½ hr) but no high temperature H_2 anneal. The ΔV_{FB} was measured for various conditions of negative-bias temperature aging in which two of the three variables, namely, time, temperature, and bias, were kept constant and the third one was changed.

Figure 5 shows the effect of applied bias V_B on ΔV_{FB} induced by slow trapping. Results are shown for various temperatures (80°, 150°, 200°, 250°, and 300°C) for a fixed time of 15 min and for bias voltages ranging from −4 to −80V. [Although bias voltages are quoted in this paper, it should be understood that the field across the oxide and not the voltage is the parameter that determines ΔV_{FB} for various oxide thicknesses (4).] At a given temperature, ΔV_{FB} is a strong function of V_B, with

$$\frac{\partial \log (\Delta V_{FB})}{\partial \log |V_B|} \approx n \qquad [1]$$

where the exponent n ($1.5 < n < 3.2$) is an inverse function of the aging temperature T (°K), as shown in Fig. 6. According to this figure, n will approach unity around 400°C, at which temperature ΔV_{FB} will be a simple linear function of V_B. This is the form of ΔV_{FB} (V_B) relationship reported by Deal *et al.* (4) who plotted the maximum flatband shift measured at $\sim$400°C. At this temperature, saturation in ΔV_{FB} is reached in a relatively short time of few minutes. For the temperatures used in the present work, 15 min was too short a time to reach saturation or steady-state

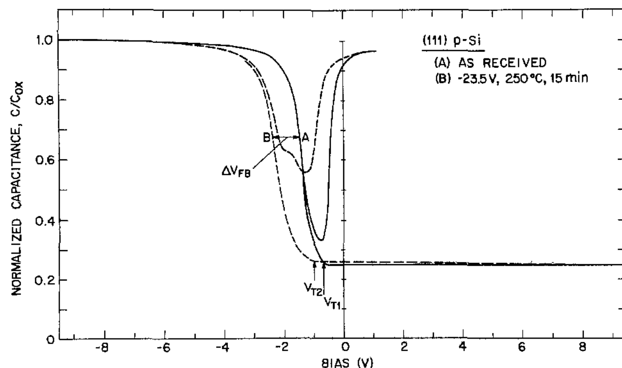

Fig. 3. *C-V* curves for $Al/SiO_2/p(111)Si$ capacitors: (A) as-received; (B) after −23.5V, 250°C, 15 min B-T aging.

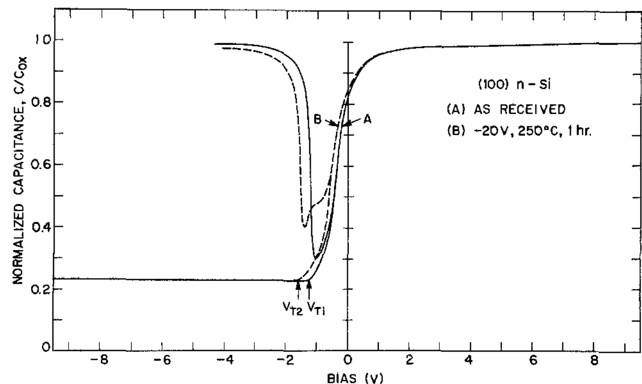

Fig. 4. *C-V* curves for $Al/SiO_2/n(100)Si$ capacitors: (A) as-received; (B) after −23.5V, 250°C, 15 min B-T aging.

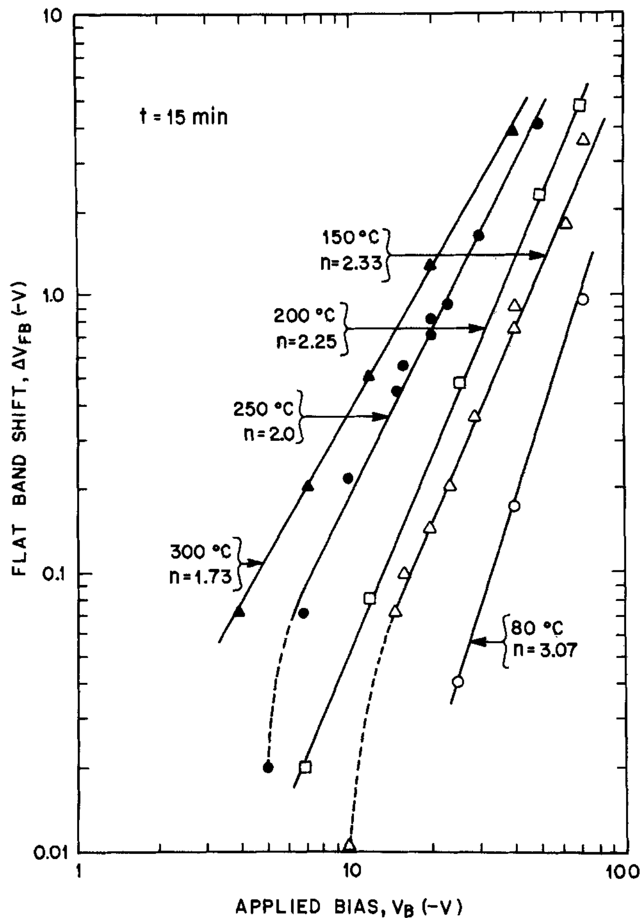

Fig. 5. Variation of slow-trapping induced flatband shift with applied bias at different temperatures, and for times of 15 min.

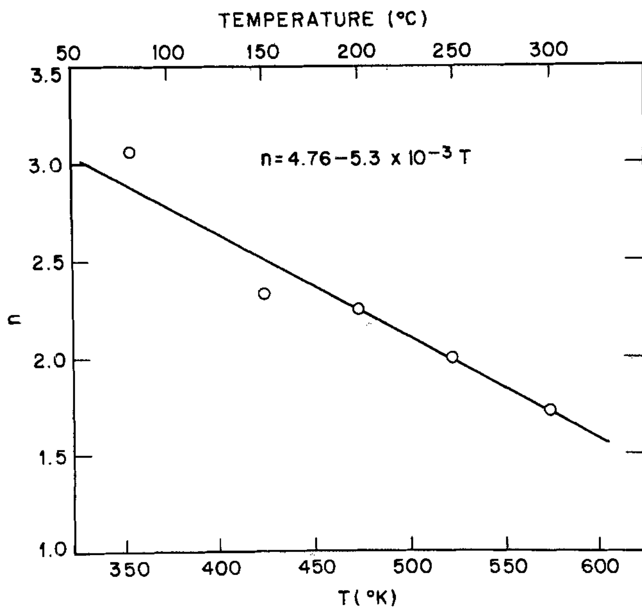

Fig. 6. Temperature dependence of exponent n in Fig. 5

conditions, yet it was adequate to reveal a ΔV_{FB} of 0.1-5V provided the bias fields were large enough.

The nonsteady-state conditions investigated in the present work were preferred because they were convenient and also because they correspond more closely to the device behavior during its operation. Thus, slow-trapping shifts usually cause the device threshold voltage to go out of specification long before the saturation value has been attained.

Figure 7 shows the variation with time of ΔV_{FB} at various temperatures, keeping V_B constant at −20V. It

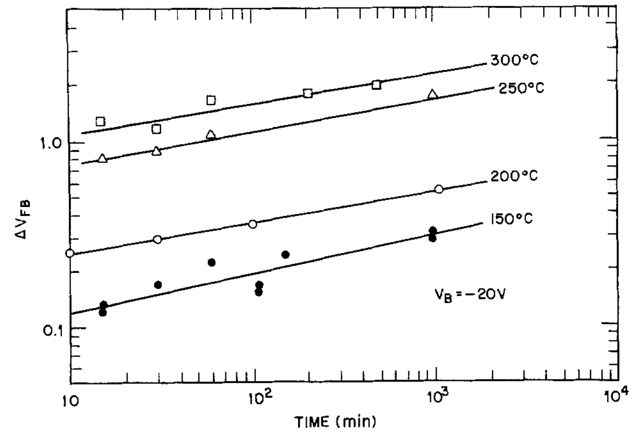

Fig. 7. Time dependence of flatband shift due to slow trapping at various temperatures and for an applied bias of −20V.

may be seen that a substantial portion of the slow trapping shift is revealed in 15 min; however, there continue to be additional shifts with increasing time. For the present samples, the time dependence ($t > 10$ min) was relatively weak, with

$$\frac{\partial \log \Delta V_{FB}}{\partial \log t} \approx 0.2 \quad [2]$$

This form of time dependence again relates to ΔV_{FB} data below the saturation value.

Figure 8 shows an Arrhenius plot in which ΔV_{FB} has been normalized with $|V_B|^n$ and $t^{0.2}$. A remarkably good fit is obtained for the present set of samples, giving an apparent thermal activation energy of ~0.64 eV. Also shown in Fig. 8 are certain results taken from the work by Broydo and Waggener (12). The combined data show a relatively large degree of scatter, indicating that the slow-trapping kinetics are also a sensitive function of the starting material and that

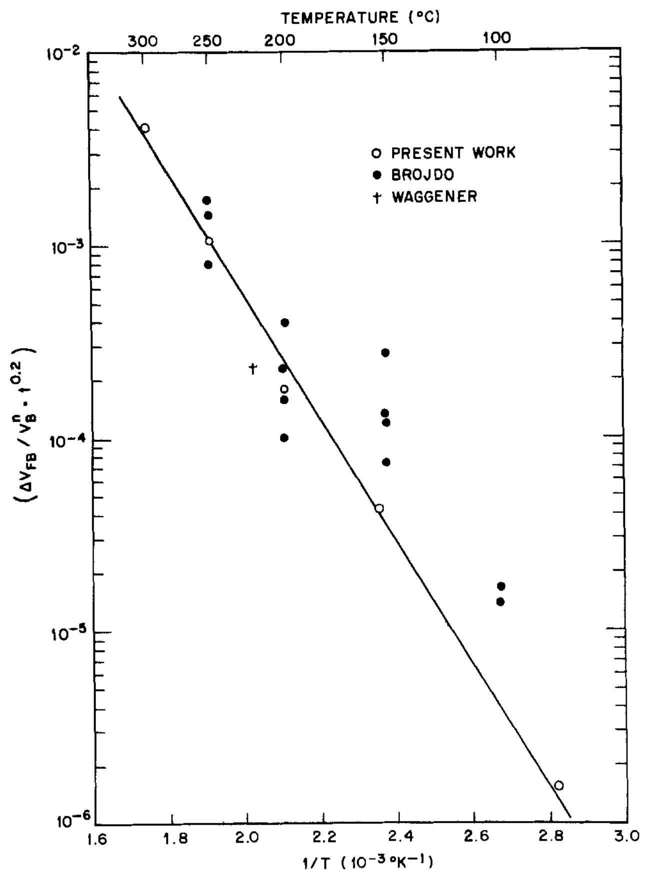

Fig. 8. Arrhenius plot of normalized ΔV_{FB} due to slow trapping

it may not yet be possible to provide a universal equation for ΔV_{FB}.

Results in Fig. 8 for the present samples (a single lot of six wafers) do indicate, however, that it is possible to rationalize over 30 measurements of ΔV_{FB} in terms of the following simple factorial relationship

$$\Delta V_{FB} = A|V_B|^{n(T)}t^{0.2} \exp\left(-\frac{\epsilon_a}{kT}\right) \quad [3]$$

where, $A = 1.576 \times 10^3$, $\epsilon_a = 0.64$ eV, $n = 4.76 - 5.3 \times 10^{-3}T$. Equation [3] contains only a single thermal activation energy term and it gives proper weight to the effects of applied bias and time. As noted earlier, the above functional dependence is valid only for ΔV_{FB} values prior to saturation.

The theoretical implications of Eq. [3] are not clear. We believe that the present results lend some support to the model of Deal (1), namely that slow trapping is caused by field-temperature induced structural rearrangements at the Si/SiO_2 interface. In Deal's model (1), a displaced oxygen atom which would otherwise bridge two Si atoms at the interface can simultaneously lead to a positive charge in the oxide and a surface state (dangling bond) in the Si. The ease of such a displacement would depend on the microstrain initially present in the Si-O bond at the interface. It is conceivable that the interfacial strain is related to the magnitude and screening distance of the fixed charge (excess Si atoms?) always present at the SiO_2/Si interface. It appears that this (compressive) strain also provides the driving force for slow trapping. The roles of temperature and applied field in causing dissociation of strained O-Si bonds appear to be complementary. Thus, as the temperature gets smaller, V_B tends to have a more pronounced effect on ΔV_{FB}.

Summary and Conclusions

The slow-trapping instability has been investigated for n- and p-type (111) Si and for n-type (100) Si.

1. For well-annealed MOS structures, negative bias-temperature aging causes a characteristic splitting of the quasistatic C-V curve; the resulting N_{SS} has a peak near the midgap. This N_{SS} effect is responsible for the fact that for n-Si, $\Delta V_T > \Delta V_{FB}$ whereas for p-Si, $\Delta V_T < \Delta V_{FB}$.
2. For a given time and temperature and ΔV_{FB} less than the saturation value, ΔV_{FB} increases with the applied field. The field dependence gets stronger at lower temperatures.
3. For a given field and temperature, and time greater than 10 min, there is a relatively slow variation ΔV_{FB} with time.
4. For a given set of identical samples, it is possible to normalize ΔV_{FB} with respect to the applied bias and time, the resulting temperature dependence yields a single-valued activation energy equal to 0.64 eV for the presently studied $Al/SiO_2/n(111)Si$ structures.

Acknowledgments

Thanks are due to J. V. Dalton and W. Sachs for their assistance with sample fabrication and to W. Bertram, H. J. Levinstein, and R. S. Wagner for helpful conversations.

Manuscript submitted June 23, 1977; revised manuscript received Nov. 7, 1977.

Any discussion of this paper will appear in a Discussion Section to be published in the December 1978 JOURNAL. All discussions for the December 1978 Discussion Section should be submitted by Aug. 1, 1978.

Publication costs of this article were assisted by Bell Laboratories.

REFERENCES

1. B. E. Deal, *This Journal*, **121**, 198C (1974).
2. E. H. Nicollian, "12th Annual IEEE Proceedings Rel. Phys.," p. 267 (1974).
3. S. R. Hofstein, *Solid-State Electron.*, **10**, 657 (1967).
4. B. E. Deal, M. Sklar, A. S. Grove, and E. H. Snow, *This Journal*, **114**, 266 (1967).
5. K. G. Aubuchon, E. Harari, and P. Chang, Ann. Rep. Contract No. N00014-72-C-0424, Dept. of Navy, Office of Naval Research, Arlington, Va., October 1974.
6. A. K. Sinha, H. J. Levinstein, L. P. Adda, E. N. Fuls, and E. I. Povilonis, To be published.
7. A. K. Sinha, *This Journal*, **123**, 65 (1976).
8. M. Kuhn, *Solid-State Electron.*, **13**, 873 (1970).
9. A. S. Grove, B. E. Deal, E. H. Snow, and C. T. Sah, *Solid State Electron.*, **8**, 145 (1965).
10. R. Castagne and A. Vapaille, *Surf. Sci.*, **28**, 157 (1971).
11. C. N. Berglund, *IEEE Trans. Electron. Devices*, **ed-13**, 701 (1966).
12. S. Broydo and T. Waggener, Private communication.

Two-Layer Model for Heat-Treated Anodic Tantalum Oxide

A. Climent, J. M. Martinez-Duarte and J. M. Albella[1]

Departamento de Física Aplicada e Instituto de Física del Estado Sólido (C.S.I.C.), Universidad Autónoma de Madrid, Cantoblanco, Madrid, Spain

ABSTRACT

The dielectric properties of Ta_2O_5 thin films, grown anodically in a phosphoric acid solution and subjected to heat-treatment, have been investigated as a function of frequency in the range 0.1-100 kHz and temperatures from $-100°$ to $300°C$. The experimental evolution of tan δ and series capacitance with the frequency and temperature is reproduced theoretically assuming that the anodic oxide has two layers with a different exponential conductivity gradient. The imaginary part of the dielectric constant shows a relaxation process of the Maxwell-Wagner type, which is also explained by the above model for the oxide.

In the manufacture of tantalum capacitors the anodic oxide is normally subjected to temperatures above 200°C in the process of the pyrolytic deposition of the manganese oxide solid electrolyte. The dielectric properties of the resulting oxide have been thoroughly investigated by Smyth *et al.* (1), who reached the conclusion that a gradient in the electrical conductivity

[1] Permanent address: Instituto de Optica Daza de Valdés (C.S.I.C.), Serrano, 121, Madrid-6, Spain.
Key words: dielectric properties, Maxwell-Wagner model, tantalum capacitors, heat-treatment in anodic oxides.

across the oxide is formed due to the migration of oxygen atoms which are partially dissolved in the tantalum substrate. Furthermore, the incorporation of phosphorus in the outer part of the oxide during anodization in the standard phosphoric acid electrolyte has been well established by several techniques such as radiotracer measurements (2), Auger electron spectroscopy (3, 4), and infrared reflectance spectroscopy (5). For these samples, the heat-treatment results in two layers in the oxide with different electrical conductivity gradients (1). The outer layer presents a steeper gradient and lower conductivity than the inner layer as a consequence of a smaller diffusion of the oxygen atoms due to the phosphorus incorporation.

Based on the previous work of Smyth *et al.* (1), the two-layer exponential gradient model has been quantitatively applied in this paper to tantalum oxide anodized in a phosphoric solution. From the experimental results obtained in this work, all the parameters which characterize the dielectric properties of each layer have been evaluated. Then, according to the model, the curves of the dependence of capacitance and loss factor with frequency and temperature are computed and compared to the experimental values, resulting in a good agreement. In addition, it has been mathematically shown in detail how a relative maximum in the dependence of the loss factor with frequency arises in the two-layer exponential gradient model.

Experimental

Tantalum foil from Reframet Hoboken with a thickness of 0.1 mm and 99.96% purity was anodized in a 0.01% H_3PO_4 electrolyte at a current density of about 10A m^{-2}. Previous to anodization, the samples were thoroughly degreased and chemically etched in a 5:2:2 mixture of sulfuric, nitric, and fluorhydric acids. Samples of 1.5 $\times$ 0.5 cm were cut and three gold counterelectrodes with a diameter of about 2 mm were evaporated along each of the samples. A thin copper wire was attached to the gold spot by means of a gold paint. Finally, the samples were subjected to a 350°C heat-treatment for 20 min under high vacuum.

The series capacitance, C_s, and the loss factor, tan δ, $\pi/2 - \delta$ being the angle between the current and the voltage, were measured with a General Radio 1620-A capacitance bridge in which the oscillator was substituted by a Hewlett Packard 3310-A sinusoidal generator in order to increase the frequency range to 100 kHz. All the measurements were performed with the samples inside a cryostat connected to a vacuum pump. The temperature was controlled by means of a Chromel-Chromel Alumel thermocouple.

Results and Theoretical Model

Figures 1-4 show the dependence of the capacitance and tan δ with temperature and frequency. These results suggest the existence of a conductivity profile (1) with two different exponential gradients. They also imply the existence of a critical level of conductivity σ_c such that the portion of the dielectric film with $\sigma > \sigma_c$ is short-circuited acting as part of the electrode. σ_c is given by

$$\sigma_c = \omega\epsilon\epsilon_0 \quad [1]$$

where ω is the angular frequency, ϵ the dielectric constant, and ϵ_0 the permittivity of vacuum. From Eq. [1] we can get an idea of the variation of the conductivity across the oxide by plotting the logarithm of frequency as a function of $1/C$, since $1/C$ is proportional to the effective thickness of the dielectric. Figure 5 shows such plots, obtained from Fig. 1, at different temperatures. It can be appreciated that for a temperature of 193°K and in the frequency range studied, σ_c should be above the value of σ at the $Ta-Ta_2O_5$ interface (conductivity profile at T_1 in Fig. 6a). As the temperature is raised to 303°K, the conductivity increases and the most conductive portion of the profile raises above σ_c (relative position as for the profile at T_2 in Fig. 6a). As the temperature is further increased to 383°K, the most resistive or outer layer of the film starts to appear and at 433°K

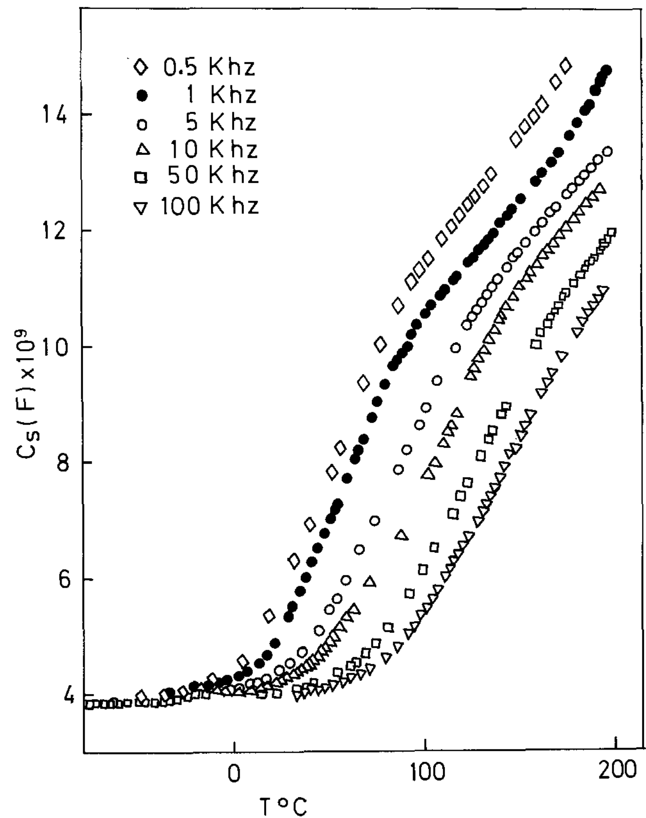

Fig. 1. Temperature dependence of capacitance at several frequencies. The sample was subjected to a heating of about 400°C during 20 min in vacuum. The formation voltage is 100V.

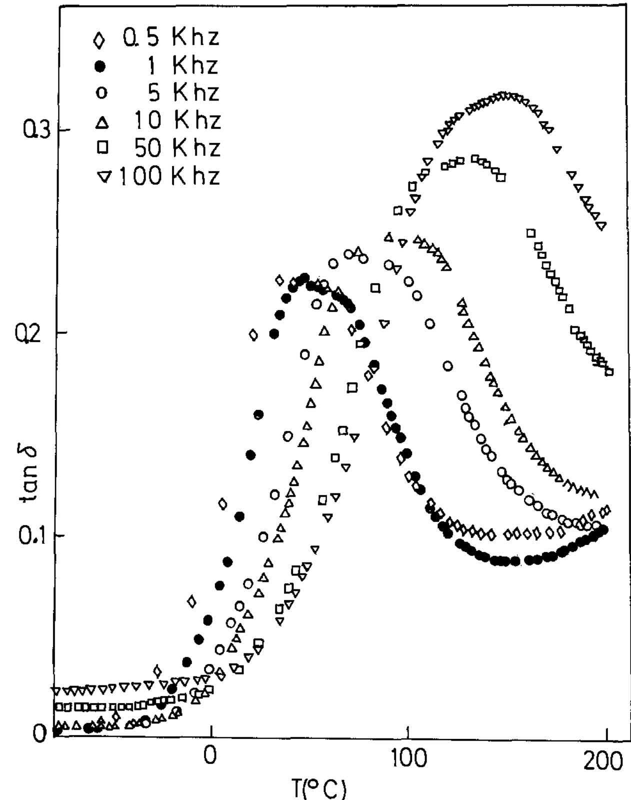

Fig. 2. Temperature dependence of tan δ for the sample of Fig. 1.

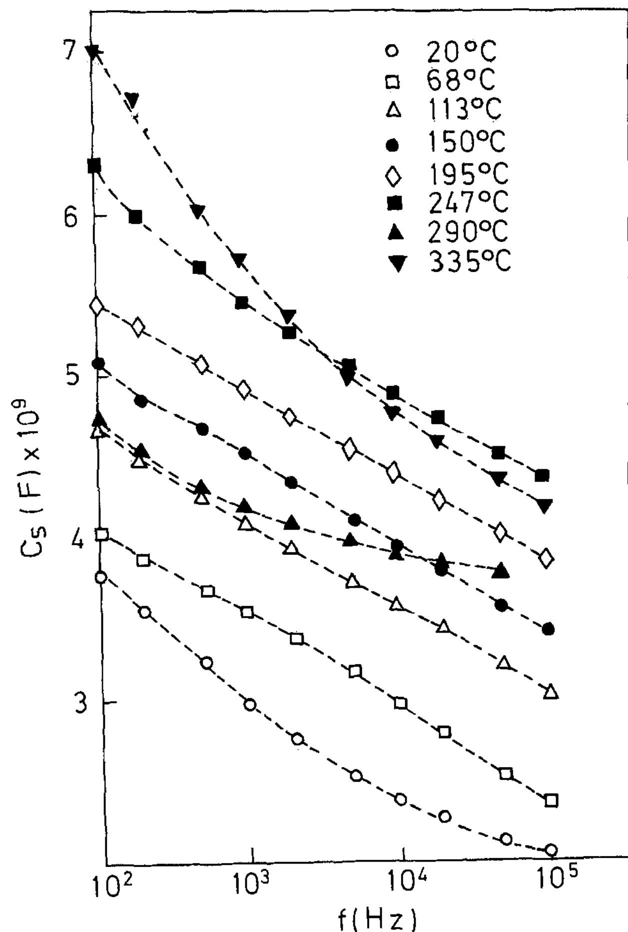

Fig. 3. Frequency dependence of capacitance at several temperatures. The sample was subjected to a heating of about 400°C during 20 min in air. The formation voltage is 120V.

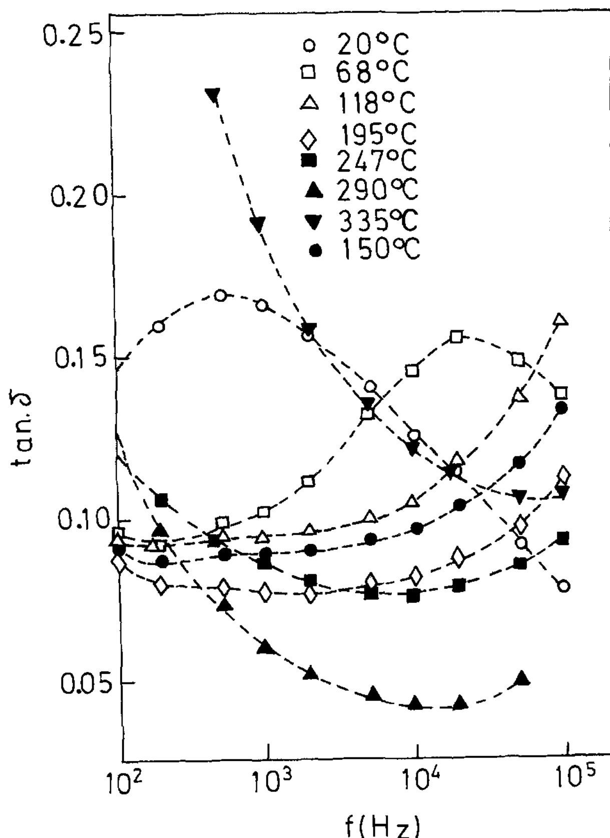

Fig. 4. Frequency dependence of tan δ at several temperatures for the sample of Fig. 3.

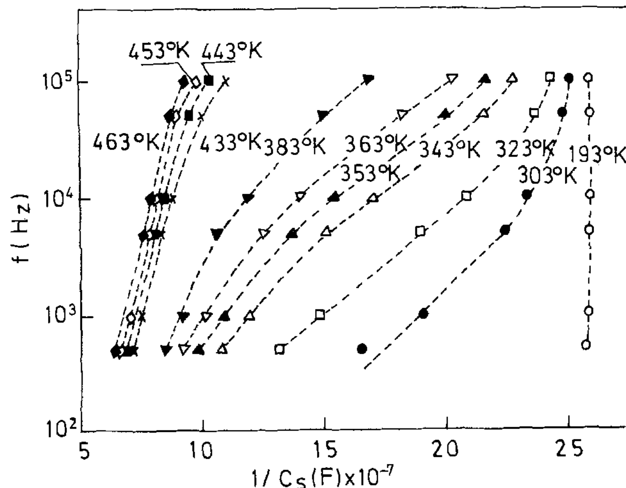

Fig. 5. log f vs. $1/C_s$ for the sample of Fig. 1

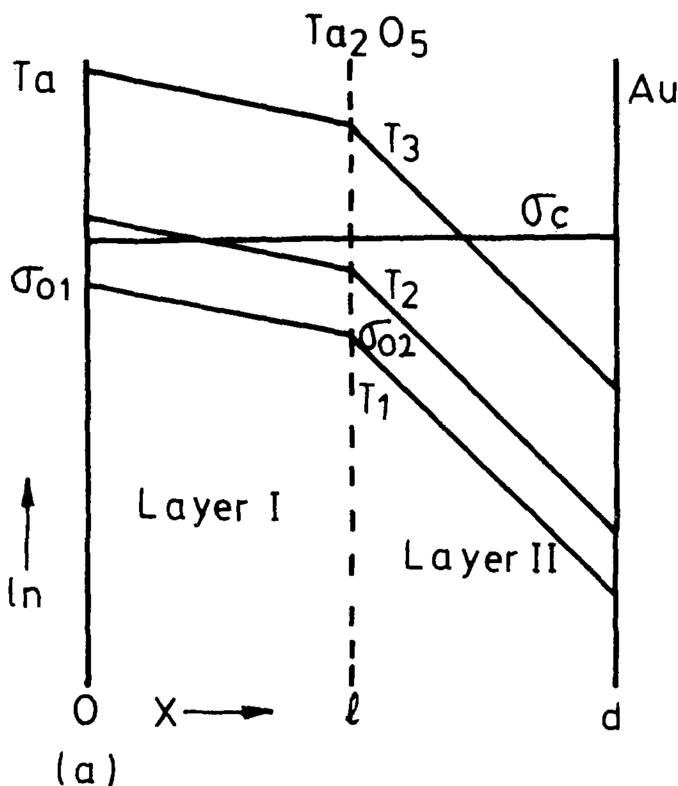

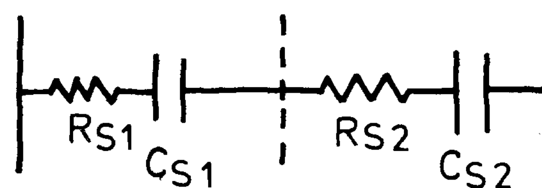

Fig. 6. (a) Double exponential gradient conductivity profile across the oxide for three temperatures $T_1 < T_2 < T_3$ and fixed frequency. (b) Equivalent circuit for the two-layer dielectric.

the conductivity of an important part of this layer is above σ_c (conductivity profile at T_3 in Fig. 6a).

The oxide's equivalent circuit chosen for our model is shown in Fig. 6b. It is formed by two capacitance-resistance series circuits, each representing one portion of the film, connected in series. Young (6) has obtained expressions for the series capacitance C_s and

the equivalent series resistance R_s of a dielectric with an exponential gradient conductivity profile of the form

$$\sigma = \sigma_0 \exp(-ax) \qquad [2]$$

These expressions are

$$R_s = \frac{1}{aA\omega\epsilon\epsilon_0}\left(\tan^{-1}\frac{\omega\epsilon\epsilon_0}{\sigma_0 e^{-ad}} - \tan^{-1}\frac{\omega\epsilon\epsilon_0}{\sigma_0}\right) \qquad [3]$$

$$\frac{1}{C_s} = \frac{1}{2aA\epsilon\epsilon_0}\log\left[\frac{1+\left(\frac{\omega\epsilon\epsilon_0}{\sigma_0 e^{-ad}}\right)^2}{1+\left(\frac{\omega\epsilon\epsilon_0}{\sigma_0}\right)^2}\right] \qquad [4]$$

where A is the electrode's area and d is the thickness of the dielectric. In this derivation ϵ is supposed to be a constant, that is, the influence exerted on the capacity as a consequence of the variation of ϵ with frequency will be neglected in comparison to the influence due to a change in the effective dielectric thickness when $\sigma > \sigma_c$. We will apply next Eq. [3] and [4] to each of the layers in the dielectric.

At a distance x from the Ta-Ta_2O_5 interface and at a temperature T, the conductivity of the oxide can be expressed as

$$\sigma_{x,T} = B\exp\left(-\frac{E_x}{kT}\right) \qquad [5]$$

where E_x, the activation energy of the conductivity (7), is given by

$$E_x = E_o + bx \qquad [6]$$

In this equation, E_o is the activation energy at the Ta-Ta_2O_5 interface and the value of the coefficient b depends on the value of the slope of the exponential gradient. We will also take into account the variation of the dielectric constant with temperature according to

$$\epsilon = \epsilon_c + \alpha T \qquad [7]$$

The values of ϵ_c and α can be deduced from the experimental values of Fig. 1 in the region of low temperatures where $\sigma_c > \sigma_{x=0}(T)$ and the decrease of the effective dielectric thickness has not occurred yet.

Taking into account the dependence of σ and ϵ with temperature by means of Eq. [5] and [7] and defining R_s and C_s for each layer of the dielectric by Eq. [3] and [4], we get

$$C_s(T,\omega) = \frac{C_{s1}(T,\omega)\cdot C_{s2}(T,\omega)}{C_{s1}(T,\omega) + C_{s2}(T,\omega)} \qquad [8]$$

$$R_s(T,\omega) = R_{s1}(T,\omega) + R_{s2}(T,\omega) \qquad [9]$$

$$\tan\delta(T,\omega) = R_s(T,\omega)C_s(T,\omega)\omega \qquad [10]$$

The theoretical results predicted by the double layer conductivity profile model are obtained from Eq. [8] and [10] and later on compared to the experimental results. The parameters $\sigma_{x=0}(T)$, $\sigma_{x=1}(T)$, $a_1(T)$, and $a_2(T)$ in Eq. [8]-[10] are obtained from the experimental values. The dependence of a_1 and a_2 on temperature can be derived from Eq. [2], [5], and [6]

$$a_1 = \frac{b_1}{kT}; \quad a_2 = \frac{b_2}{kT} \qquad [11]$$

The values of the electrical parameters shown in Table I have been obtained by the procedure just indicated from the results of Fig. 1 and 2. The position l within the oxide (see bottom of Table I), where the exponential conductivity gradient changes, is first obtained from the break in slope of the lines in Fig. 5 and further adjusted by fitting the curves obtained from Eq. [8] and [10] to the experimental values.

The dependence of the capacitance and tan δ with temperature, at several frequencies, which is given by Eq. [8] and [10], has been calculated by means of a computer and are compared in Fig. 7 and 8 with the experimental results.

Table I. Values of some significant parameters for the sample described in Fig. 1

Formation voltage V_f = 100V
$b_1 = 1.554 \times 10^{-4}$ eV Å^{-1} | $b_2 = 1.164 \times 10^{-3}$ eV Å^{-1}
a_1 (at 293°K) = 6.15×10^{-3}Å^{-1} | a_2 (at 293°K) = 4.61×10^{-2}Å^{-1}
a_1 (at 520°K) = 3.47×10^{-3}Å^{-1} | a_3 (at 520°K) = 2.60×10^{-2}Å^{-1}
At 293°K: $\sigma_o = 8.62 \times 10^{-8}\Omega^{-1}$cm^{-1}; $\sigma_l = 1.2 \times 10^{-10}\Omega^{-1}$cm^{-1}
σ_d(extrapolating) = $5.3 \times 10^{-24}\Omega^{-1}$cm^{-1}
At 520°K: $\sigma_o = 2.75 \times 10^{-3}\Omega^{-1}$cm^{-1}; $\sigma_l = 6.8 \times 10^{-5}\Omega^{-1}$cm^{-1}
σ_d(extrapolating) = $2.0 \times 10^{-12}\Omega^{-1}$cm^{-1}
Activation energy at interface Ta-Ta_2O_5: E_o = 0.60 eV
Activation energy at interface between layers I and II: E_l = 0.76 eV
$B = 1.79 \times 10^3\Omega^{-1}$cm^{-1}
$\epsilon = \epsilon_c + \alpha T$, where ϵ_c = 23.36 and $\alpha = 3.44 \times 10^{-3}$ K^{-1}
Thickness d = 1730Å [assuming an anodization constant of k = 17.3 Å/V (11)]
l (distance between the Ta-Ta_2O_5 interface and the layer I-layer II interface): 1063Å

Discussion

The agreement between the values deduced from the two-layer conductivity profile model and the experimental values is quite good as it can be appreciated from Fig. 7 and 8. The maxima in the tan δ *vs.* T curves are usually higher and more pronounced for the computed curves. This is attributed to the hypothesis that the dielectric is only formed by two layers, the exponential conductivity gradient being constant in each layer. In practice, at the two metal-oxide junctions as well as at the junction between the two layers in the dielectric, the conductivity might have values quite different from the assumed ones. One refinement, therefore, could be to assume that the dielectric is divided into three zones, with one intermediate in which the exponential gradient has a slope with a value between a_1 and a_2.

The evolution with frequency of some of the parameters characterizing each of the two layers is represented in Fig. 9. From Eq. [8] and [9], tan δ can be written as

$$\tan\delta = \omega(R_{s1} + R_{s2})\frac{C_{s1}C_{s2}}{C_{s1} + C_{s2}} \qquad [12a]$$

or

$$\tan\delta = \tan\delta_1\frac{C_{s2}}{C_{s1} + C_{s2}} + \tan\delta_2\frac{C_{s1}}{C_{s1} + C_{s2}} \qquad [12b]$$

where $\tan\delta_i = \omega R_{si}C_{si}$, $(i = 1, 2)$.

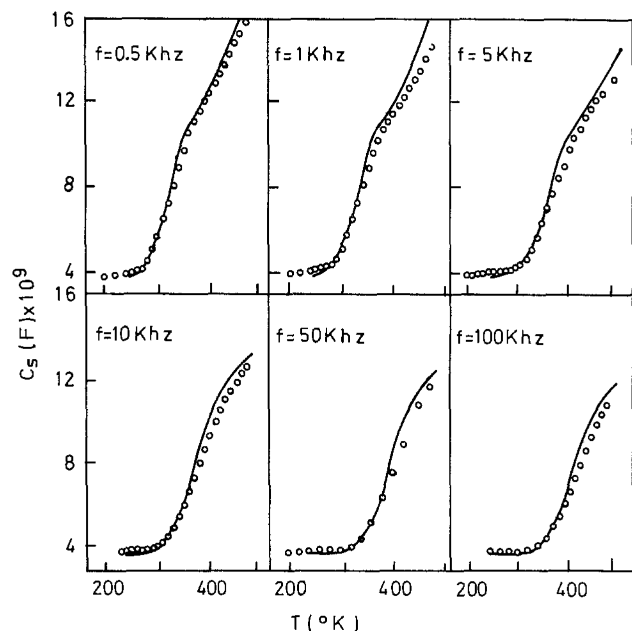

Fig. 7. Temperature dependence of capacitance for the sample of Fig. 1. The dots represent the experimental values and the lines represent the values computed from Eq. [8].

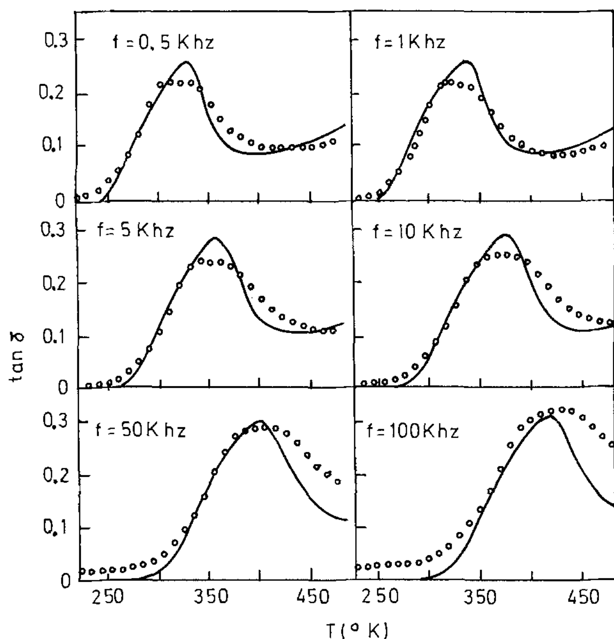

Fig. 8. Temperature dependence of tan δ for the sample of Fig. 1 (The symbols as in Fig. 7).

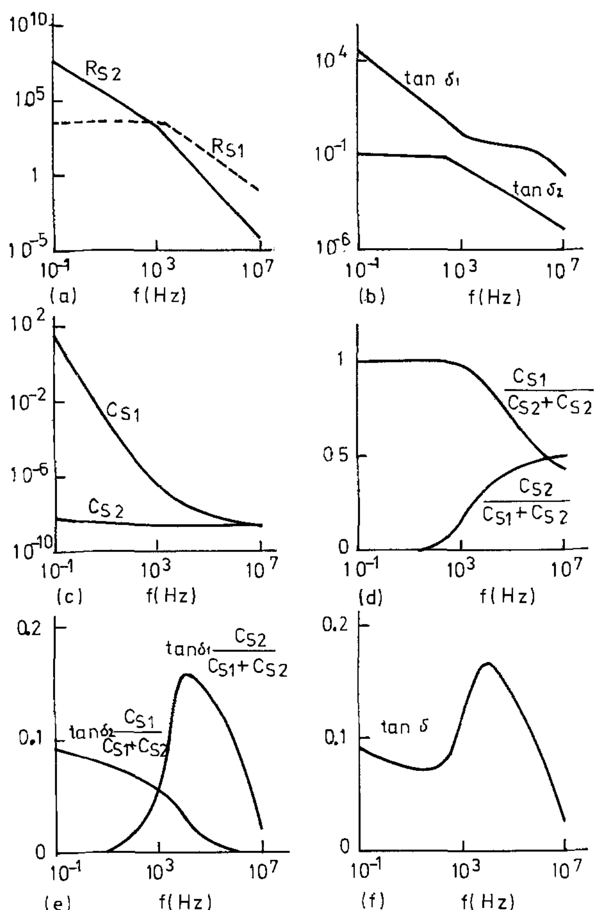

Fig. 9. Frequency dependence at $T = 68°C$ of several parameters computed from the double layer model for the dielectric (same sample as in Fig. 3).

At low frequencies (much lower than the frequency at which log σ changes its slope, about 1 kHz in this particular case), it can be observed in Fig. 9a that $R_{s2} >> R_{s1}$, and according to Eq. [12a]

$$\tan\delta \simeq \tan\delta_2 \frac{C_{s1}}{C_{s1} + C_{s2}} \quad [13]$$

In addition, for these frequencies, $C_{s1} >> C_{s2}$ (Fig. 9c) and therefore

$$\tan\delta \simeq \tan\delta_2 \quad [14]$$

For frequencies much higher than the frequency at which $R_{s1} = R_{s2}$ in Fig. 9b, we have $R_{s1} >> R_{s2}$ and

$$\tan\delta \simeq \tan\delta_1 \frac{C_{s2}}{C_{s1} + C_{s2}} \quad [15]$$

In this case, as the frequency gets higher, $C_{s2}/(C_{s1} + C_{s2})$ increases much slower than tan δ_1 decreases and as a result of this tan δ given by Eq. [15] presents a maximum (Fig. 9f).

As the frequency increases, C_{s1} decreases and becomes comparable to C_{s2} (Fig. 9c), thus having a more important contribution to the total capacitance. All of this is in agreement with the existence of a critical level of conductivity σ_c as proposed by Smyth *et al.* (1). It is also interesting to notice that the graph of tan δ *vs.* log f is the specular image of the graph of tan δ *vs.* T as it should be expected from the conductivity profile model and has been experimentally checked (Fig. 4 and 8).

Figure 10 represents log f as a function of the value of $1/T$ for the occurrence of the maxima of tan δ in Fig. 8. From the slope of this line, an activation energy $E_\delta = 0.726$ eV can be gotten by assuming the following expression for the angular frequency

$$\omega = \omega_0 \exp\left(-\frac{E_\delta}{kT}\right) \quad [16]$$

It can be easily shown that E_δ is the activation energy of the conductivity at the point in which the conductivity profile corresponding to the temperature for the occurrence of the maximum intersects the line $\sigma = \sigma_c = \omega\epsilon\epsilon_0$ and that the distance from this point to the Ta-Ta_2O_5 interface is the same for every temperature. Accordingly, it is not surprising that the value found for E_δ is of the same magnitude as the value reported for E_1 in Table I since the appearance of the maximum is related to the point where the exponential conductivity gradient changes its slope from a_1 to a_2. Similarly, a value for ω_0 equal to 8.6×10^{14} sec^{-1} is obtained from Eq. [16], which multiplied by $\epsilon\epsilon_0$ yields a value of the constant B which is very close to the one reported in Table I.

It can be concluded from this work that the two-layer exponential gradient conductivity profile model predicts, in the case of thermally treated Ta_2O_5 films anodized in phosphoric acid solutions, a dependence with frequency and temperature of the electrical parameters which is in satisfactory agreement with

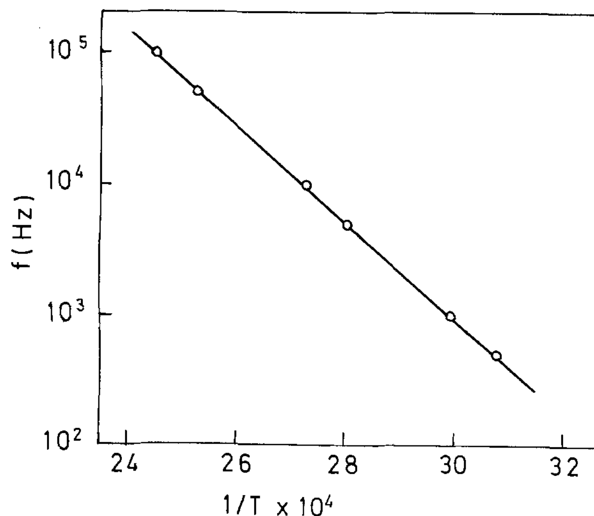

Fig. 10. Log f vs. $1/T$ for the occurrence of the maxima of tan δ in Fig. 8.

the experimental results. The agreement could still be improved by introducing some additional zones in the dielectric, the computations still being straightforward. The two-layer model can be assimilated to a generalized Maxwell-Wagner model (8) with a distribution of resistivity values and just one value for the dielectric constant. The behavior of tan δ with frequency found in this work is similar to the one predicted by the Maxwell-Wagner model.

As far as the value found for l in the present work (Table I), which implies that the boundary between the two layers in the oxide is closer to the oxide-counterelectrode interface, it is in qualitative agreement with the conclusions reached by Smyth *et al.* (1) for anodization in a low concentration phosphoric acid electrolyte. Applying the infrared reflectance spectroscopy technique, Kihara-Morishita (5) measured the relative thicknesses of the phosphorus-free and phosphorus-contaminated layers and found that, for Ta_2O_5 films of the thickness employed in this work, the boundary between the two layers is around the location computed in this paper. The conditions of anodization, *i.e.*, the concentration of the electrolyte and the current density, influence the amount of phosphorus incorporated, which in our case might be estimated as 0.03 moles of phosphorus per mole of Ta^{5+} (2).

Young (6) applied the one-layer exponential conductivity gradient to explain the behavior of R_s and C_s with frequency and obtained a straight line for the plot of $1/C_s$ as a function of log f. Winkel and Groot (9), advocating the multiple distribution of relaxation times model of Gevers and du Pré (10), emphasize that in some experimental results a curvature of the $1/C_s$ plots is observed at frequencies above 1 kHz, thus deviating from Young's simple model. In this context, it is interesting to observe that the curvature in the $1/C_s$ curves can also be explained by assuming a conductivity exponential gradient with two or more different slopes as proposed by Smyth *et al.* (1). In addition, it can be concluded from this work that the double-layer conductivity profile model can quantitatively account for the values of the dielectric properties of anodic tantalum oxide thermally treated. However, we do not believe that this model will substitute in every case the more general model of multiple relaxation times.

Manuscript submitted Sept. 21, 1977; revised manuscript received Dec. 5, 1977.

Any discussion of this paper will appear in a Discussion Section to be published in the December 1978 JOURNAL. All discussions for the December 1978 Discussion Section should be submitted by Aug. 1, 1978.

Publication costs of this article were assisted by the Universidad Autonoma de Madrid.

REFERENCES

1. D. M. Smyth, G. A. Shirn, and T. B. Tripp, *This Journal*, **110**, 1264 (1963); *ibid.*, **111**, 1331 (1964); *ibid.*, **113**, 100 (1966).
2. J. J. Randall, W. J. Bernard, and R. R. Wilkinson, *Electrochim. Acta*, **10**, 183 (1965).
3. M. Romand, G. Bouyssoux, J. S. Solomon, and W. L. Baun, *J. Electron Spectrosc.*, **9**, 41 (1976).
4. J. M. Martínez-Duart, C. Palacio, and J. M. Sanz, Paper presented at the Third International Conference on Solid Surfaces, Vienna, Sept. 12-16, 1977.
5. H. Kihara-Morishita, *Thin Solid Films*, **29**, 211 (1975).
6. L. Young, "Anodic Oxide Films," pp. 161-162, Academic Press, New York (1961).
7. D. M. Smyth, in, "Oxides and Oxide Films," Vol. II, J. W. Diggle, Editor, p. 95, Marcel Dekker, New York (1973).
8. J. Volger, in, "Progress in Semiconductors," Vol. IV, A. F. Gibson and R. E. Burgess, Editors, p. 206, Temple Press Books, Ltd. (1960).
9. P. Winkel and D. G. de Groot, *Philips Res. Rep.*, **13**, 489 (1958).
10. M. Gevers, *ibid.*, **1**, 298 (1946).
11. J. M. Albella, J. M. Martínez-Duart, and F. Rueda, *Opt. Acta*, **22**, 973 (1975).

Direct Determination of the Electrical Conductivity-Nonstoichiometry Relationship in Ionically Conducting Metallic Oxides

J. Fouletier and M. Kleitz*

E.N.S. d'Electrochimie et d'Electrométallurgie de Grenoble, Domaine Universitaire, 38401 St Martin d'Hères, France

ABSTRACT

The small quantities of oxygen driven off zirconia solid solutions by solid-state electrolysis were accurately measured and the relevant departure from stoichiometry determined by using oxygen gauges and pumps. The variations in the electronic conductivity and in the ionic transport number were determined as functions of temperature and deviation from stoichiometry. By measuring the rate of oxygen release during the first stage of the electrolysis of prereduced and homogenized samples, the ionic transport number was also determined according to another independent method. The two sets of results compared quite favorably. These methods of measurement offer the possibility of investigating nonstoichiometric oxides, especially in experiments involving small departures from stoichiometry and very reducing conditions.

In solid-state electrochemistry, an oxide is traditionally characterized by the variation of its conductivity as a function of equilibrium oxygen pressure and temperature $\sigma(p_{O_2}, T)$. Recently, Blumenthal and Hofmaier (1) proposed a technique of measuring the variation of conductivity with temperature at fixed values of the stoichiometric ratio.

A sound demonstration of a point defect model further requires another independent set of data, for

* Electrochemical Society Active Member.
Key words: electrical conductivity, ionic transport number, nonstoichiometry, zirconia.

example, the variation of the stoichiometric ratio as a function of the same parameters $x(p_{O_2}, T)$ (2). This can be determined by using a thermobalance when the corresponding weight changes are sufficiently large (3-5).

In this paper we propose a method of measurement which allows us to directly determine the variation of conductivity as a function of the stoichiometry ratio and temperature $\sigma(x, T)$. We also report on experimental observations which could lead to a second, complementary method of measurement of the ionic transport number employing the same parameters $t_i(x, T)$.

These methods, which are based on the utilization of solid-state oxygen pumps and gauges, can now be applied because of the recent improvements (6-7) in the performances and reliability of these devices. For example, a 10 ppm variation of the oxygen content in an inert gas stream can be measured within 5%. A straightforward calculation shows that such a variation occurring over a period of 5 min in a gas streaming at 5 liters·hr^{-1} flow rate corresponds to an extraction (or addition) of only 6 μg of oxygen. If this change results from oxygen pickup by a 100g sample, the measured variation corresponds to a relative change in its weight of 6×10^{-8}. This simple calculation indicates how attractive the use of these devices can be.

Experimental Setup

The experimental setup is essentially composed of a gas circuit (Fig. 1) involving a gas cylinder, an oxygen electrochemical pump, the experimental vessel, an oxygen gauge, and an accurate flowmeter connected in series. The oxygen content in the inert gas is established by the electrochemical pump and measured with the oxygen gauge on bypassing the experimental vessel. It is also measured by the gauge after the gas passes over the sample. Argon was used as the carrier gas. The flow rate ranged from 5 to 20 liters·hr^{-1} which corresponds to average linear velocities of 8-31 cm·sec^{-1}. All the details regarding the pump and gauge characteristics have been given in previous papers (6-11).

The oxygen gauge was composed of a laboratory-made closed-ended electrolyte tube of composition $(ZrO_2)_{0.91}(Y_2O_3)_{0.09}$. The electrodes were obtained by painting with platinum the outer and inner surfaces of its flat bottom. Air in contact with the outer electrode was used as a reference gas. The temperature of the cell was 650°C. The oxygen pressure in the working gas which circulates inside the tube was deduced from the voltage, E, measured between the electrodes by application of the Nernst law, the numerical expression of which was

$$E(\text{mV}) = 19.89 \times \ln \frac{p(\text{atm})}{0.201} \quad [1]$$

The oxygen pump was formed of a simple tube of the same composition as the gauge. The electrodes coated on the inner and outer surfaces were also of porous platinum. Its operating temperature was 750°C. The working gas was circulated inside the tube. The amount of oxygen added or extracted from it per second was simply correlated to the current passing through the pump by the Faraday law

$$q(\text{l}_{\text{NTP}} \cdot \text{sec}^{-1}) = 5.803 \times 10^{-8} \times I(\text{mA}) \quad [2]$$

The time lag of the gauge voltage after a rapid variation in oxygen concentration became significantly longer than 1 min with oxygen contents lower than 10 ppm. This could have greatly limited the methods we proposed. To avoid this difficulty, the experimental conditions were selected so that the oxygen content was either very low (purified argon) or higher than 10 ppm, apart from short transitions between these two states.

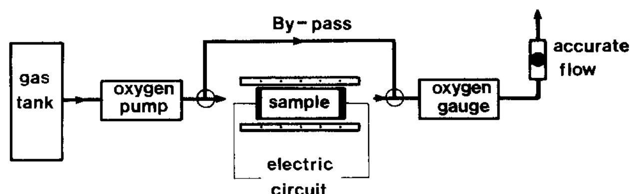

Fig. 1. Experimental setup

The sample was a small cylinder 2.2 cm long and 1.1 cm in diameter with porous platinum electrodes at both ends. These electrodes were connected either to an impedance meter for measuring the sample resistance or to a direct current source for electrolyzing the sample. Its composition was $(ZrO_2)_{0.87}(Y_2O_3)_{0.12}(CeO_2)_{0.01}$ or $(ZrYCe)O_{1.893}$. It was prepared by dry mixing of the oxide powders (ZrO_2, Merck, purity 99.9%; Y_2O_3, Pechiney; CeO_2, Pechiney), pressing at 1.5 tons·cm^{-2} and sintering at 2000°C for 2 hr.

For oxygen pressures higher than 10^{-7} atm, the electronic transport number of this material has been evaluated to a few percent (12). It was neglected in the following derivations.

Nonstoichiometry Measurement and Control

The intentional modifications of the stoichiometry and the corresponding measurements of the stoichiometric ratio variation were performed as follows.

The argon carrier gas flowing around the sample was purified by applying a suitable voltage of about −1.5V to the pump (13). Thus, all traces of free oxygen in the gas were eliminated and the traces of water vapor and carbon oxides partly reduced. The oxygen gauge exhibited a voltage around −0.9V. Then, a suitable constant current, I, was passed through the sample for a time, δ_e. The applied voltage (which included the ohmic drop in the sample and the decomposition voltage) greatly depended on the temperature. In the experiments reported below, it varied between a few volts and 200V. It was applied in such a way that oxygen evolved from the downstream side of the sample (positive electrode on this side). After a certain delay, which corresponded to the flow rate of the gas, the gauge indicated an enrichment in oxygen which lasted for a time, δ_e, and then sharply decreased (Fig. 2). From the plot of the gauge voltage *vs.* time, the determination of the amount of oxygen released by the sample during the electrolysis was calculated. The oxygen flux released at a given time was obtained by multiplying the gas flow rate, D ($\text{l}_{\text{NTP}} \cdot \text{hr}^{-1}$), by the ratio of the measured oxygen pressure p to the total pressure, p_{total}, in the gauge. The total amount of oxygen, Q, is simply determined by integration according to the equation

$$Q(\text{mole}) = \frac{D}{22.4} \cdot \int_0^{\delta_e} \frac{p}{p_{\text{total}}} \cdot dt \quad [3]$$

It is straightforward to deduce from Q the induced deviation from stoichiometry x. Accordingly the formula of the reduced sample was written $(ZrYCe)_{1.893-x}$.

This technique constitutes an easy means to control the stoichiometric ratio by appropriately selecting the parameters I and δ_e. The sensitivity in the adjustment of these parameters is obviously far greater than the sensitivity in the stoichiometric ratio measurements and does not limit the performance of the method.

Initially we verified the validity of the method of measurement. The point to be checked concerned the possible errors due to measurement of oxygen pressure during transient periods. For that purpose we also measured the amount of oxygen picked up by the sample during its reoxidation. The sample was initially kept under pure argon. The experimental vessel was bypassed and the oxygen content in the gas fixed at a value in the range 10-100 ppm. Then the gas was passed through the experimental vessel and the gauge voltage recorded. The amount of oxygen absorbed by the sample was determined as for the reduction proc-

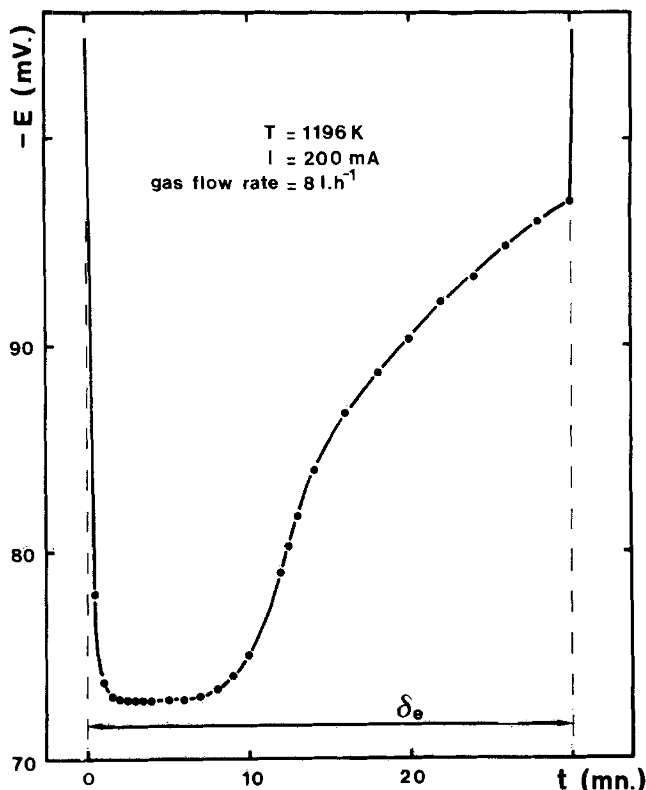

Fig. 2. Typical curve of the gauge voltage vs. time recorded during electrolysis of the sample.

ess. Some reoxidation runs were performed in several partial steps: purified argon, enriched argon, purified argon, enriched argon, etc., in order to increase the number of transient periods and to determine their effects as a possible source of error. Such experiments were carried out many times and have been reported in a previous paper dealing with an oxygen getter (10). For oxygen concentrations in the oxidizing gas higher than 10 ppm, the calculated amounts of oxygen lost during electrolysis and dissolved during reoxidation were always within 5%.

One of the assumptions of this measurement technique is that the sample exchanges no significant amount of oxygen when it is kept under pure argon, *i.e.*, its over-all stoichiometric ratio is fixed. This assumption which has also been made by Blumenthal and Hofmaier (1) was clearly confirmed by the fact that the equality mentioned above was also verified for delays of several days between the electrolysis and reoxidation runs.

Experimental Results: $\sigma(x,T)$ Relationship

After electrolysis, the sample resistance was measured in purified argon using the so-called impedance diagram method (14). In the experiments reported, several measurements were made after each electrolysis. The first measurements indicated a variation due to the homogenization of the sample. After a certain time (always less than a few hours in the runs reported), the results were stable. An example of the dependence of the resistance of the homogenized sample on the deviation from stoichiometry x is given in Fig. 3.

With the sample investigated, we could further derive the following. In all the experiments reported, the concentrations of the vacancies created by the reduction (less than 3×10^{20} cm^{-3}) remained small compared to the initial concentration (6.3×10^{21} cm^{-3}) which resulted from the cationic composition of the material. So, we could reasonably assume that the reduction process did not alter the ionic conductivity. If this assumption is correct, the variations of the measured resistance $R(x)$ concerned only the electronic

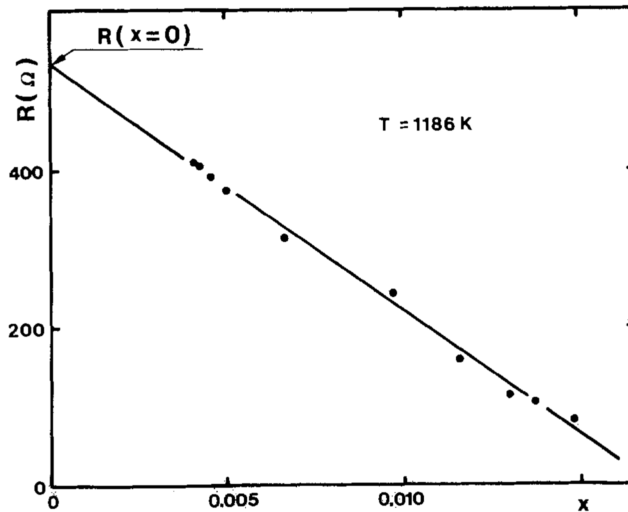

Fig. 3. Resistance variation as a function of the deviation from stoichiometry x.

conductivity. Consequently, the electronic resistance $R_e(x)$ of the sample at a given deviation from stoichiometry can be approximately calculated from

$$1/R(x) = 1/R_e(x) + 1/R_{\text{ionic}}(x) \quad [4]$$

or with our assumption

$$1/R(x) = 1/R_e(x) + 1/R(x = 0) \quad [5]$$

The deduced variations of the electronic resistance as functions of temperature are shown in Fig. 4. A similar trend toward lower activation energies as the departure from stoichiometry increases has been observed by Casselton (15). Figure 5 shows the variations of the ionic transport number $t_i(x)$ calculated from the data in Fig. 3 using the equation

$$t_i = 1 - R(x)/R_e(x) \quad [6]$$

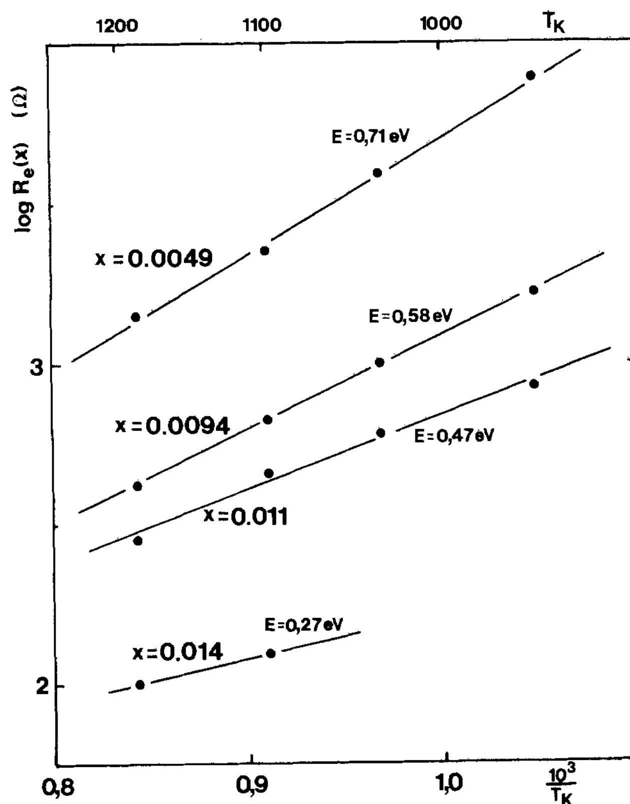

Fig. 4. Arrhenius plot of the electronic resistance of the sample for various deviations from stoichiometry x.

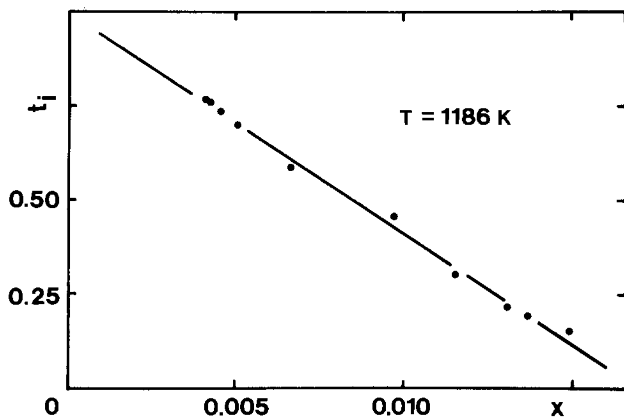

Fig. 5. Variation of the ionic transport number as a function of deviation from stoichiometry.

Direct Determination of $t_i(x,T)$ Relationship

This determination is based on a measurement of the rate that oxygen is driven off the reduced sample during its electrolysis.

When a solid oxide electrolyte is a pure anionic conductor, the quantity of oxygen carried by the ions and the relevant oxygen flow, J, released at the anode of the cell obeys Faraday's law

$$J = I/4\mathbf{F} \quad [7]$$

where I is the current. This has been accurately checked with oxygen pumps (8).

The results reported above, on electrolysis experiments, also obeyed Faraday's law under appropriate conditions. This is consistent with the observations (16-18) that, during a certain lapse of time, no electrochemical coloration occurs on the anodic side. The ionic transport number remains locally equal to 1 (the small electronic transport number induced by the presence of 1% ceria in the zirconia solid solution is neglected). An example of the oxygen flow released from the sample, at a constant current, is given in Fig. 6 ($x = 0$). In a certain interval, the plot exhibits a plateau, the ordinate of which obeys formula [6]. After longer times the reduced zone had reached the anode, the local value of the ionic transference number markedly decreased

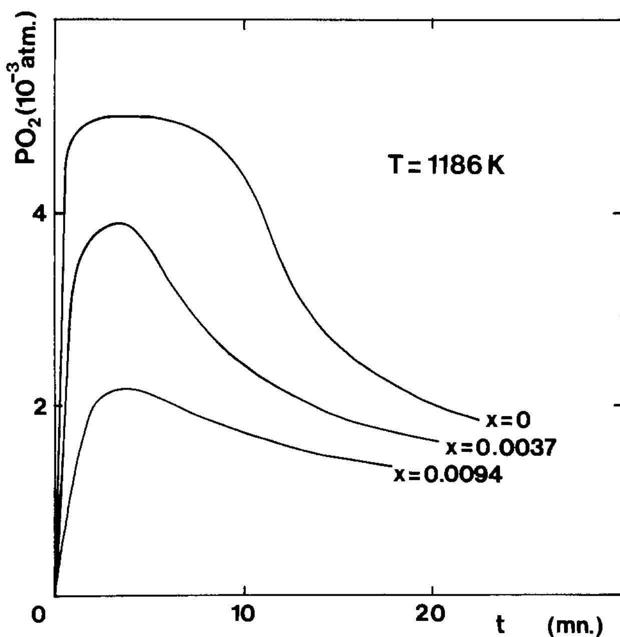

Fig. 6. Oxygen flow released from the sample during the electrolysis, for various initial deviations from stoichiometry.

Table I. Comparison of the ionic transport numbers deduced from Eq. [6] and [8] as functions of the deviation from stoichiometry x of the sample at 1186°K

x	t_i (resistance)	t_i (electrolysis)
0.0048	0.71	0.71
0.0094	0.44	0.42
0.014	0.16	0.13

and consequently so did the oxygen flow. This behavior also explains the shape of Fig. 2.

A simplistic approach to the general problem for a mixed conductor would allow us to conclude that the rate of oxygen evolution from the anode is given by

$$J = J_{th} \cdot t_i \quad [8]$$

where t_i is the ionic transport number in the close vicinity of the anode and J_{th} the theoretical value corresponding to Faraday's law.

In order to see whether Eq. [8] was indeed obeyed, we carried out the following experiment. After the reduction of the sample to a certain degree (curve $x = 0$ in Fig. 6), the sample was maintained for a while in pure argon under open-circuit condition to let it homogenize. Then a new electrolysis experiment was performed, according to the same procedure, on this prereduced sample. Instead of a plateau, the oxygen flow *vs.* time plot exhibited a simple maximum located at lower oxygen pressure (Fig. 6). From the value of this maximum, which was assumed to represent the initial rate of oxygen evolution, we calculated an ionic transport number t_i (electrolysis) according to formula [8].

To verify the validity of Eq. [8], we compared such values of the ionic transport number to the values deduced from the resistance measurements reported above: t_i (resistance). Three results obtained for various degrees of prereduction are reported in Table I; there is good agreement. This suggests that the material was homogeneous up to the electrode surfaces before the electrolysis voltage was applied and the evolution of oxygen obeyed formula [8].

If this result is confirmed by further experimental results obtained under more appropriately defined conditions, such measurements could lead to a convenient estimation of ionic transport numbers. It would be especially appropriate for average ionic transport numbers for which the traditional emf method is frequently questionable (17, 19). It would also have the advantage of complementing the first type of measurement as the emf method complements conventional conductivity measurements.

It is emphasized that both types of measurement proposed can be performed however reducing the system may be. That is a great advantage over the gas-equilibration technique which is limited on the low oxygen pressure side, and over the use of metal-oxide electrodes which requires tedious manipulations. An obvious deficiency, however, is the lack of information they can provide about equilibrium oxygen pressures.

Manuscript submitted Nov. 1, 1977; revised manuscript received Jan. 3, 1978. This was Paper 78 presented, in part, at the Washington, D.C. Meeting of the Society, May 2-7, 1976.

Any discussion of this paper will appear in a Discussion Section to be published in the December 1978 JOURNAL. All discussions for the December 1978 Discussion Section should be submitted by Aug. 1, 1978.

Publication costs of this article were assisted by the Laboratoire d'Energétique Electrochimique (Institut Polytechnique de Grenoble).

REFERENCES

1. R. N. Blumenthal and R. L. Hofmaier, *This Journal*, **121**, 126 (1974).
2. R. N. Blumenthal and R. K. Sharma, *J. Solid State Chem.*, **13**, 360 (1975).
3. R. J. Panlener, R. N. Blumenthal, and J. E. Garnier, *J. Phys. Chem. Solids*, **36**, 1213 (1975).

4. J. E. Garnier, R. N. Blumenthal, R. J. Panlener, and R. K. Sharma, *ibid.*, **37**, 369 (1976).
5. O. Toft Sorensen, *J. Solid State Chem.*, **18**, 217 (1976).
6. J. Fouletier, H. Seinera, and M. Kleitz, *J. Appl. Electrochem.*, **5**, 177 (1975).
7. J. Fouletier, P. Fabry, and M. Kleitz, *This Journal*, **123**, 204 (1976).
8. J. Fouletier, G. Vitter, and M. Kleitz, *J. Appl. Electrochem.*, **5**, 111 (1975).
9. M. Kleitz and J. Fouletier, in "Measurement of Oxygen," H. Degn, I. Balslev, and R. Brook, Editors, Elsevier Scientific Publishing Co., Amsterdam (1976).
10. J. Fouletier and M. Kleitz, *Vacuum*, **25**, 307 (1975).
11. J. Fouletier, H. Seinera, and M. Kleitz, *J. Appl. Electrochem.*, **4**, 305 (1974).
12. C. Deportes, G. Robert, and M. Forestier, *Electrochim. Acta*, **16**, 1003 (1971).
13. M. Kleitz, Thesis, Grenoble, 1968.
14. E. Schouler, M. Kleitz, and C. Deportes, *J. Chim. Phys.*, **70**, 923 (1973).
15. R. E. W. Casselton, *J. Appl. Electrochem.*, **4**, 25 (1974).
16. P. Fabry, C. Deportes, and M. Kleitz, *J. Solid State Chem.*, **6**, 230 (1973).
17. P. Fabry, Thesis, Grenoble, 1976.
18. J. Fouletier, Thesis, Grenoble, 1976.
19. P. Fabry, C. Deportes, and M. Kleitz, *J. Solid State Chem.*, **5**, 1 (1972).

Electronic Conductivity in Solid CaF_2 at High Temperature

J. Delcet, R. J. Heus, and J. J. Egan

Brookhaven National Laboratory, Upton, New York 11973

ABSTRACT

Polarization measurements have been made on CaF_2 using cells of the type

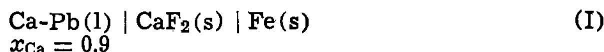
Ca-Pb(l) | CaF_2(s) | Fe(s) (I)
$x_{Ca} = 0.9$

and

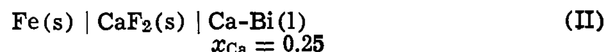
Fe(s) | CaF_2(s) | Ca-Bi(l) (II)
$x_{Ca} = 0.25$

Steady-state values of the currents at various applied voltages yielded the electronic conductivity in CaF_2 as a function of calcium activity. Results are presented between 800° and 950°C. The experimental arrangement is described and appropriate equations are presented. Values of the transference number of ions are given as a function of temperature and the activity of Ca in CaF_2.

Calcium fluoride has proven to be a useful solid electrolyte for high temperature emf studies (1-20). A review has been given by Tretyakov and Kaul (21). It remains an ionic conductor under very reducing conditions and is useful for measurements with electropositive metals such as U, Th, and Mg in contrast to solid oxide electrolytes.

The problem of electronic conduction in CaF_2 has previously been studied by Wagner (22) and by Hinze and Patterson (23). Using the measurements of Mollwo (24) on the number of color centers in CaF_2 and their mobility, Wagner has calculated the transference number of electrons as a function of calcium activity. Hinze and Patterson have measured the total electrical conductivity as a function of the partial pressure of fluorine. They have concluded that CaF_2 exhibits negligible electronic conductivity even when equilibrated with Ca metal. Baukal (25) has measured the electronic conduction in CaF_2 doped with NaF at temperatures between 490° and 550°C.

In this study the electronic conductivity of pure CaF_2 is measured directly using a polarization technique developed by Wagner (26, 27). This technique has previously been used to study copper halides (28-32), silver halides (33-36), thallium bromide (37), doped oxides of zirconium, thorium, and hafnium (38-41), and lead fluoride (42).

General Approach

The general ideas and detailed equations for the polarization technique to measure electronic conductivity in ionic crystals are discussed in detail in Ref. (27). Cells are employed having a reversible reference electrode and an inert electrode. Ionic conductivity is suppressed by operating at potentials below the onset of ionic currents.

To study CaF_2 the following cell was employed

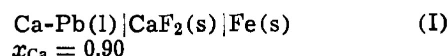
Ca-Pb(l) | CaF_2(s) | Fe(s) (I)
$x_{Ca} = 0.90$

where the reference electrode is the Ca-Pb alloy. The current at various applied voltages, where the Ca-Pb alloy is negative, is given by the expression

$$i = \frac{RT}{FG}\left\{ \sigma_e' \left[1 - \exp\left(-\frac{EF}{RT}\right)\right] + \sigma_h' \left[\exp\left(\frac{EF}{RT}\right) - 1\right]\right\} \quad [1]$$

Here G is the cell constant (thickness of CaF_2 crystal divided by the area of the electrodes), σ_e' and σ_h' are the electron and electron hole conductivities of CaF_2 equilibrated with the reference electrode and E is the potential applied to Cell (I). A Ca-Pb alloy was used instead of pure Ca metal for experimental reasons. Ca-Pb (x_{Ca} = 0.90) is liquid at 800° and could be contained in iron cups which fit closely onto the CaF_2 crystals. Electrodes of solid Ca formed a conducting film on the CaF_2 surface and interfered with the measurements. The activity of Ca in the Ca-Pb alloy was calculated from the heat of fusion of Ca and the Ca-Pb diagram.

If the electron hole conductivity is very small under highly reducing conditions and the voltage applied to Cell (I) is small compared to the potential at which FeF_2 forms, Eq. [1] reduces to

$$i = \frac{RT}{FG}\sigma_e'\left[1 - \exp\left(-\frac{EF}{RT}\right)\right] \quad [2]$$

* Electrochemical Society Active Member.

Key words: electrical conductivity, transport properties, solid electrolyte, electrolyte, mass transport.

Results of current-potential curves on Cell (I) yield the value of σ_e'. To obtain the electronic conductivity at other activities of Ca one may use the equation

$$\sigma_e = \sigma_e' \left(\frac{a_{Ca}}{a_{Ca}'} \right)^{1/2} \quad [3]$$

Polarization experiments on cells of type (II) where the inert iron electrode is made negative also yield electronic conductivity

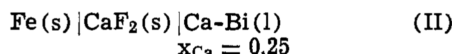

$$Fe(s)|CaF_2(s)|Ca\text{-}Bi(l) \quad (II)$$
$$x_{Ca} = 0.25$$

Under reducing conditions, the steady-state current of Cell (II) at various applied voltages is given by

$$i = \frac{RT}{FG} \sigma_e'' \left[\exp\left(\frac{EF}{RT}\right) - 1 \right] \quad [4]$$

where σ_e'' is the electronic conductivity of CaF_2 whose Ca activity is the same as that for Ca-Bi($x_{Ca} = 0.25$). The activity of Ca in the Ca-Bi alloy is obtained from emf measurements on the auxiliary cell

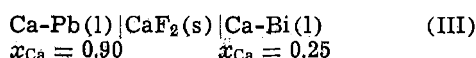

$$Ca\text{-}Pb(l)|CaF_2(s)|Ca\text{-}Bi(l) \quad (III)$$
$$x_{Ca} = 0.90 \qquad x_{Ca} = 0.25$$

The emf of Cell (III) is given by the expression (43)

$$E = \frac{1}{2F} \int_{\mu_{Ca}''}^{\mu_{Ca}'} t_{ion} d\mu_{Ca} \quad [5]$$

where

$$t_{ion} = \frac{\sigma_{ion}}{\sigma_e + \sigma_{ion}} = \frac{\sigma_{ion}}{\sigma_e^o a_{Ca}^{1/2} + \sigma_{ion}} \quad [6]$$

Here σ_e^o is the electronic conductivity of CaF_2 with $a_{Ca} = 1$. Equation [5] may then be expressed as

$$E = \frac{RT}{2F} \int_{a_{Ca}''}^{a_{Ca}'} \frac{\sigma_{ion}}{a_{Ca}(\sigma_e^o a_{Ca}^{1/2} + \sigma_{ion})} da_{Ca} \quad [7]$$

$$E = \frac{RT}{2F} \ln \frac{a_{Ca}'}{a_{Ca}''} + \frac{RT}{F} \ln \frac{\sigma_e'' + \sigma_{ion}}{\sigma_e' + \sigma_{ion}} \quad [8]$$

where

$$\sigma_e' = \sigma_e'' \left(\frac{a_{Ca}'}{a_{Ca}''} \right)^{1/2} \quad [9]$$

This equation can be solved for a_{Ca}'' or the activity of Ca in the Ca-Bi alloy if one determines σ_e'' from steady-state measurements on Cell (II), knowing the activity a_{Ca}' from the phase diagram. The activity a_{Ca}'' is given by the expression

$$a_{Ca}''^{1/2} = \frac{\exp\left(-\frac{\eta F}{RT}\right) - \sigma_e'' a_{Ca}'^{1/2}}{\sigma_{ion}} \quad [10]$$

where

$$\eta = E - \frac{RT}{2F} \ln a_{Ca}' - \frac{RT}{2F} \ln (\sigma_{ion} + \sigma_e'') \quad [11]$$

Polarization cells of type (II) were found very useful for the measurements above 800°C. After determining a_{Ca}'' the electronic conductivity may be calculated at any activity by use of the equation

$$\sigma_e = \sigma_e'' \left(\frac{a_{Ca}}{a_{Ca}''} \right)^{1/2} \quad [12]$$

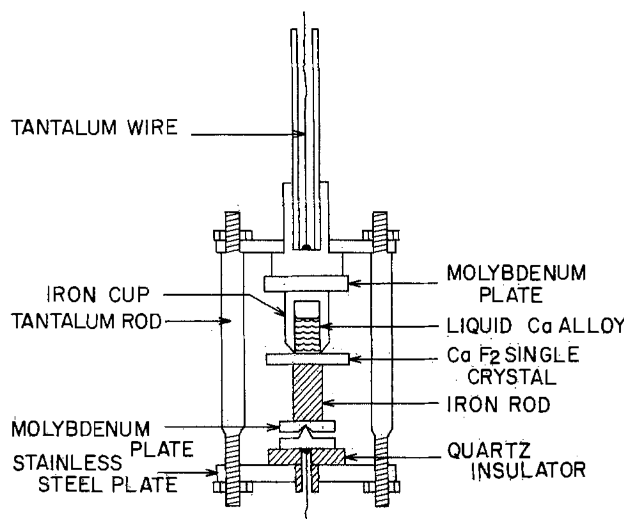

Fig. 1. Experimental arrangement for polarization cells

Experimental Details

The experimental setup for both Cell (I) and (II) is shown in Fig. 1. The iron cup is filled with either a Ca-Pb alloy or a Ca-Bi alloy. The open end of the cup is machined to a sharp edge so that it digs into the CaF_2 single crystal under pressure. CaF_2 softens somewhat around 600°C. The pressure arises from the cell arrangement, since the iron rod and cup expand more than the holder made of tantalum rods. The CaF_2 crystals were generally between 0.1 and 0.2 cm thick. The diameter of the inert iron electrode is 1.0 cm for Cell (I) and 1.6 cm for Cell (II). In order to minimize the edge effect caused by the CaF_2 diameter being larger than the iron electrode diameter, the ratio of the crystal thickness to the electrode area was kept small in accordance with Barrer, Barrie, and Rogers (44). Cell (III) used essentially the same arrangement as shown in Fig. 1 except that two iron cups were used and the cell operated in a horizontal position. The entire cell arrangement was contained in a vacuum-tight Vycor tube filled with purified argon.

Results and Discussion

Steady-state currents obtained at various applied voltages for Cell (I) operated at 800°C are shown in Table I. Steady values were obtained only after several days of cell operation at a given voltage. Values of σ_e' were calculated from Eq. [2] and values of σ_e^o from Eq. [3] with $a_{Ca} = 1$. Only currents measured on the plateau of the current voltage curve yielded consistent values of t_{ion}.

Attempts to operate Cell (I) at voltages lower than 0.300V proved unsuccessful. It is believed that the

Table I. Results from cells of type (I)

E	i (μa)	G	σ_e'	σ_e^o	t_{ion}^o	a_{Ca}'
1.000	250	0.302	8.17×10^{-4}	8.6×10^{-4}	0.635	0.90
0.500	242	0.302	7.94×10^{-4}	8.4×10^{-4}	0.641	0.90
0.300	183	0 302				
1.000	344	3.222	8.27×10^{-4}	8.7×10^{-4}	0.633	0.90
0.500	330	0.222	7.95×10^{-4}	8.4×10^{-4}	0.641	0.90
0.300	283	0.222				

Table II. Results from experiments on cells of type (II) and (III)

T°C	E_{III} (volts)	σ_{ion}	σ_e''	a_{Ca}''	σ_e^o	a_{Ca}'
800	0.7436	1.5×10^{-3}	1.72×10^{-7}	3.89×10^{-8}	8.72×10^{-4}	0.632
825	0.7391	2.45×10^{-3}	3.55×10^{-7}	5.95×10^{-8}	1.46×10^{-3}	0.627
850	0.7345	4.0×10^{-3}	7.1×10^{-7}	9.47×10^{-8}	2.31×10^{-3}	0.634
875	0.7300	6.1×10^{-3}	1.36×10^{-6}	1.42×10^{-7}	3.61×10^{-3}	0.628
900	0.7256	9.3×10^{-3}	2.5×10^{-6}	2.16×10^{-7}	5.38×10^{-3}	0.634
950	(0.7164)	2.1×10^{-2}	8.4×10^{-6}	4.59×10^{-7}	1.24×10^{-2}	0.629

greater solubility of Ca in the crystal at lower voltages caused a density change in CaF_2 which breaks the seal formed between the cup holding the alloy and the CaF_2 crystal.

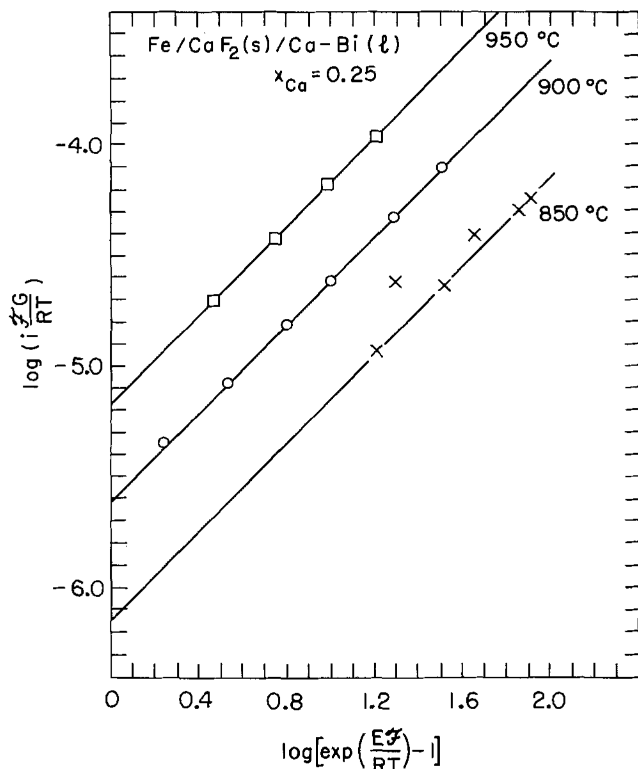

Fig. 2. Results of polarization measurements on Cell (II)

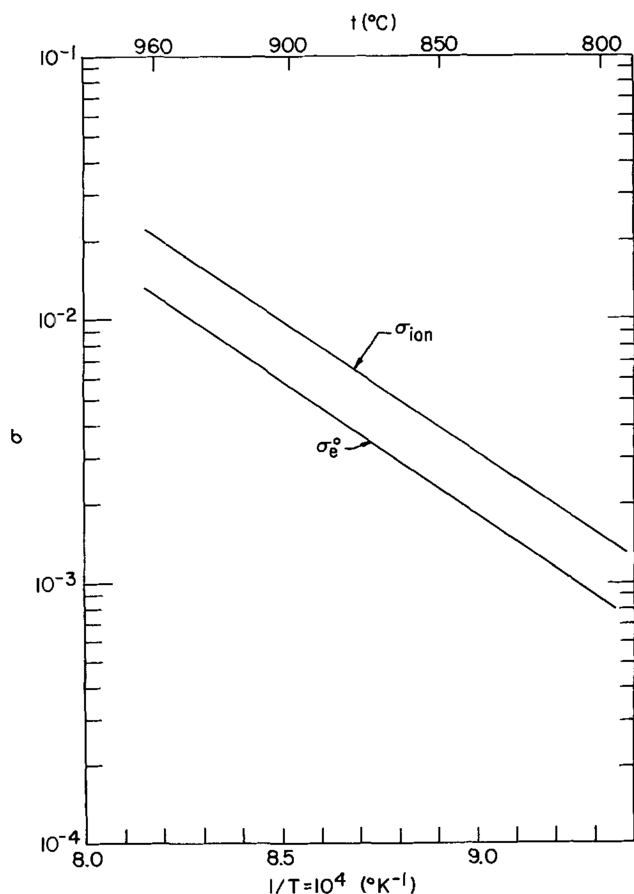

Fig. 3. Ionic and electronic ($\alpha_{Ca} = 1$) conductivity of CaF_2 at various temperatures.

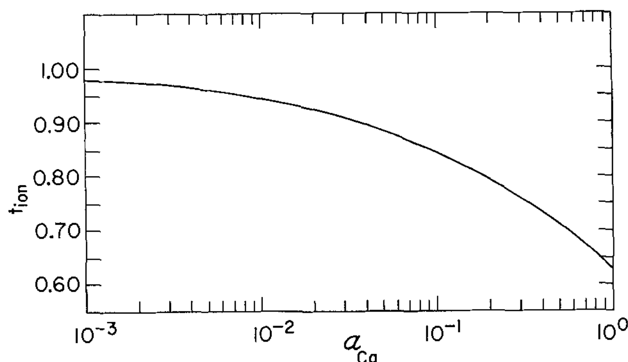

Fig. 4. The transference number of ions in CaF_2 at various Ca activities.

Results from Cells (II) and (III) are shown in Table II at temperatures between 800° and 950°C. Steady-state currents from Cell (II) are shown graphically in Fig. 2. One expects a slope of one for this plot and experiments showed this to be true. Cell (III) was operated between 800° and 900°C, the value of 950°C being an extrapolation.

Values of $t_{ion}°$ were calculated in all cases with Eq. [6], using the results of Ure (45) for the ionic conductivity of CaF_2. The values of the electronic and ionic conductivity in CaF_2 are plotted in Fig. 3, the electronic conductivity being for CaF_2 equilibrated with Ca metal. Figure 4 shows the transference number of ions in CaF_2 at various activities of Ca.

Acknowledgment

The authors would like to thank Prof. Carl Wagner for many helpful comments during the course of this work.

Manuscript submitted Nov. 5, 1975; revised manuscript received Dec. 19, 1977. This was Paper 193 presented at the San Francisco, California, Meeting of the Society, May 12-17, 1974.

Any discussion of this paper will appear in a Discussion Section to be published in the December 1978 JOURNAL. All discussions for the December 1978 Discussion Section should be submitted by Aug. 1, 1978.

Publication costs of this article were assisted by Brookhaven National Laboratory.

REFERENCES

1. R. Benz and C. Wagner, *J. Phys. Chem.*, **65**, 1308 (1961).
2. J. J. Egan, *ibid.*, **68**, 978 (1964).
3. S. Aronson, "Compounds of Interest in Nuclear Reactor Technology," p. 247, AIME (1964).
4. S. Aronson and J. Sadofsky, *J. Inorg. Nucl. Chem.*, **27**, 1769 (1965).
5. S. Aronson and A. Auskern, in "Thermodynamics," Vol. 1, p. 165, IAEA, Vienna (1966).
6. K. Gingerich and S. Aronson, *J. Phys. Chem.*, **70**, 2517 (1966).
7. W. K. Behl and J. J. Egan, *This Journal*, **113**, 378 (1966).
8. R. J. Heus and J. J. Egan, *Z. Phys. Chem. (Frankfurt am Main)*, **49**, 38 (1966).
9. R. Bones, J. Markin, and V. Wheeler, *Proc. Brit. Ceram. Soc.*, **8**, 51 (1967).
10. F. Moattar and J. S. Anderson, *Trans. Faraday Soc.*, **67**, 2303 (1971).
11. R. J. Heus and J. J. Egan, *Z. Phys. Chem. (Frankfurt am Main)*, **74**, 108 (1971).
12. H. Kleykamp, *Ber. Bunsenges. Phys. Chem.*, **73**, 354 (1969).
13. T. N. Rezukhina and B. S. Pokarev, *J. Chem. Therm.*, **3**, 369 (1971).
14. W. H. Skelton, N. J. Magnani, and J. F. Smith, *Met. Trans.*, **2**, 473 (1971).
15. W. H. Skelton, N. J. Magnani, and J. F. Smith, *ibid.*, **1**, 1833 (1970).
16. H. Holleck and H. Kleykamp, *J. Nucl. Mater.*, **35**, 158 (1970).

17. W. H. Skelton and J. W. Patterson, *J. Less-Common Metals*, **31**, 47 (1973).
18. W. H. Skelton, N. J. Magnani, and J. F. Smith, *Met. Trans.*, **4**, 917 (1973).
19. M. Kanno, *J. Nucl. Mater.*, **51**, 24 (1974).
20. R. J. Heus and J. J. Egan, *ibid.*, **51**, 30 (1974).
21. Y. D. Tretyakov and A. R. Kaul, in "Physics of Electrolytes," Vol. 2, p. 623, Academic Press, New York (1972).
22. C. Wagner, *This Journal*, **115**, 933 (1968).
23. J. W. Hinze and J. W. Patterson, *ibid.*, **120**, 96 (1973).
24. E. Mollwo, *Nachr. Gesellsch. Wissenack. Gottingen Math. Physik. Kl. N.F.*, **6**, 79 (1934).
25. W. Baukal, *Ber. Bunsenges. Phys. Chem.*, **79**, 1148 (1975).
26. C. Wagner, *Z. Electrochem.*, **60**, 4 (1956).
27. C. Wagner, *Proc. CITCE*, **7**, 361 (1957).
28. J. B. Wagner and C. Wagner, *J. Chem. Phys.*, **26**, 1597 (1957).
29. A. V. Joshi and J. B. Wagner, Jr., *J. Phys. Chem. Solids*, **33**, 205 (1972).
30. A. V. Joshi, in "Fast Ion Transport in Solids," North Holland Publishing Co., Amsterdam (1973).
31. A. V. Joshi and J. B. Wagner, Jr., *This Journal*, **122**, 1071 (1975).
32. J. Goldman and J. B. Wagner, Jr., *ibid.*, **121**, 1318 (1974).
33. B. Ilschner, *J. Chem. Phys.*, **28**, 1109 (1958).
34. D. Raleigh, *J. Phys. Chem. Solids*, **26**, 329 (1965).
35. K. Weiss, *Electrochim. Acta*, **16**, 201 (1971).
36. Y. J. van der Meulen and F. A. Kröger, *This Journal*, **117**, 69 (1970).
37. A. Morkel and H. Schmalzried, *J. Chem. Phys.*, **36**, 3101 (1962).
38. J. Patterson, E. Bogren, and R. Rapp, *This Journal*, **114**, 752 (1967).
39. L. D. Burke, H. Rickert, and R. Steiner, *Z. Phys. Chem. (Frankfurt am Main)*, **74**, 146 (1971).
40. J. D. Schieltz, J. W. Patterson, and D. R. Wilder, *This Journal*, **118**, 1257 (1971).
41. R. Hartung, *Z. Phys. Chem. (Leipzig)*, **254**, 393 (1973).
42. R. Benz, *Z. Phys. Chem. (Frankfurt am Main)*, **95**, 25 (1975).
43. C. Wagner, *Z. Phys. Chem.*, **B21**, 25 (1933).
44. R. M. Barrer, J. A. Barrie, and M. G. Rogers, *Trans. Faraday Soc.*, **58**, 2473 (1962).
45. R. W. Ure, Jr., *J. Chem. Phys.*, **26**, 1363 (1957).

Some Studies on a Solid-State Sulfur Probe for Coal Gasification Systems

K. T. Jacob[1]

Department of Mechanical Engineering, University of California, Berkeley, California 94720

and D. Bhogeswara Rao[2] **and Howard G. Nelson**

Ames Research Center, NASA, Moffett Field, California 94035

ABSTRACT

Measurements on the solid electrolyte cell

$$(Ar + H_2 + H_2S/CaS + CaF_2 + (Pt)//CaF_2//(Pt) + CaF_2 + CaS/H_2S + H_2 + Ar)$$

show that the emf of the cell is directly related through the Nernst equation to the difference in sulfur potentials established at the two $Ar + H_2 + H_2S/$ electrode interfaces. The electrodes are designed to convert the sulfur potential gradient across the calcium fluoride electrolyte into an equivalent fluorine potential gradient with the aid of the reaction, $CaF_2(s) + \frac{1}{2} S_2(g) \rightarrow CaS(s) + F_2(g)$. The response time of the probe varies from approximately 9 hr at 990°K to 2.5 hr at 1225°K. The conversion of calcium sulfide and/or calcium fluoride into calcium oxide should not be a problem in anticipated commercial coal gasification systems. Suggestions are presented for improving the cell for such commercial applications.

The ability to continuously monitor the sulfur potential in coal gasification reactors is of crucial importance for efficient gasifier operation and for accurate life prediction of corroding construction materials. From an engineering point of view, *in situ* solid-state sensors that directly measure the sulfur potential are preferable to devices that employ liquid electrolytes or involve sampling of gases for low temperature analytical procedures. Despite the concerted efforts of many laboratories during the last decade to find suitable sulfide electrolytes, analogous to $CaO\text{-}ZrO_2$ or $Y_2O_3\text{-}ThO_2$ for oxygen potential measurements, no acceptable material has been identified in which the ionic transport number is higher than 0.99 over a large range of sulfur potentials and temperatures.

[1] Permanent address: Department of Metallurgy and Materials Science, University of Toronto, Canada, M5S 1A4.
[2] Also from: Materials and Molecular Research Division, Lawrence Berkeley Laboratory, Berkeley, California 94720.

Key words: sulfur probe, calcium fluoride sensor for sulfur, galvanic cell, solid electrolyte cell, coal gasification-sulfur control.

The prospect of designing a suitable sulfide electrolyte does not appear promising in the near future because the bandgaps in the sulfides are generally narrower than in the corresponding oxides (1). An alternate approach may be to use calcium fluoride (CaF_2) as the electrolyte in a solid-state cell, in which the electrodes are designed to convert the sulfur potential in the gas into an equivalent fluorine potential.

Calcium fluoride has been found to be a suitable electrolyte at high temperatures and over a large range of fluorine potentials (2-7). Colorless, pure CaF_2 contains virtually equal concentrations of interstitial anions and anion vacancies. The fluoride ions are the mobile species, and they migrate as interstitials and vacancies. At very low fluorine potentials or in the presence of calcium vapor, an excess of calcium dissolves in CaF_2 according to the reaction

$$Ca(g) + 2F_F{}^x \rightarrow CaF_2 + 2e_F{}^x \quad [1]$$

where $F_F{}^x$ is a fluoride ion on a regular anion site,

and e_Fx is an electron substituted for an anion, producing a color (F) center. Wagner (8) has given an analysis of the onset of electronic conduction in CaF_2 due to the dissolution of calcium metal. Patterson (9) has also discussed the electrolytic conduction domain for CaF_2 at high temperatures. Because of the extreme electronegativity difference between Ca^{2+} and F^- ions and the correspondingly large forbidden bandgap for CaF_2, positive hole conduction will not be significant until the fluorine pressure is increased to several atmospheres. The open-circuit emf (E) across the electrolyte is a direct measure of the chemical potential difference, provided the fluorine pressures at the electrodes and the temperatures of operation lie within the electrolytic conduction domain (that is, the transport number of electrons or holes is less than 0.01).

An advantage of the solid electrolyte sensors is that the output is an electric potential that can readily be used to actuate a control circuit. It was, therefore, decided to study the efficiency of the solid electrolyte cell

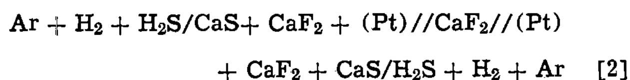

$$Ar + H_2 + H_2S/CaS + CaF_2 + (Pt)//CaF_2//(Pt) + CaF_2 + CaS/H_2S + H_2 + Ar \quad [2]$$

as a part of our program on the development of a sulfur probe. The experimental results, the limitations of this technique to coal gasification systems, as well as anticipated improvements are presented in this paper.

Experimental

Materials.—High purity $Ar + H_2 + H_2S$ gas mixtures and their analyses were obtained from Matheson. A slight decrease in the H_2S concentration of the gases was observed over extended periods of storage, presumably due to the reaction of H_2S with the storage tank. Correction factors for gas ratios were obtained by periodically observing the ion intensity ratios of H_2S to H_2 in a mass spectrometer. For the electrolyte, optical grade single crystals of CaF_2, in the form of disks of 1.5 cm in diameter and 0.2 cm thick, were obtained from Harshaw Chemical Company. Ultra pure anhydrous CaF_2 (99.999%)[3] and CaS (99.99%) powders were supplied by Apache Chemical Company and Ventron Corporation. Fine platinum powder and porous platinum sheet with porosity of 29% were obtained from Johnson-Matthey Company. The electrode pellets were made by double end compression of an intimate mixture of −200 mesh size powders of CaF_2, CaS, and Pt in the molar ratio 1.5 : 1 : 0.2. The pellets were sintered in evacuated silica capsules at 1225°K for 12 hr.

Apparatus.—A schematic diagram of the apparatus is shown in Fig. 1. A disk of CaF_2 electrolyte was spring loaded against an alumina tube with a gold O-ring between them to obtain a gastight joint. The alumina tube was held firmly in a water-cooled brass head, to which the springs were attached. Since gold softens at the high temperatures used in these experiments, low tension springs were sufficient to produce a gastight joint. Thus, the ceramic components of the assembly were not subjected to high applied stresses. Electrode pellets containing CaF_2 + CaS + Pt were spring loaded on either side of the electrolyte, with a thin porous platinum sheet sandwiched between the pellet and the electrolyte. Platinum leads, flame sprayed with alumina, were spot-welded to the porous platinum sheets. At the low sulfur potentials used in the experiments, no chemical attack on the platinum was observed in the hot zone of the furnace. At the cooler end, however, there was some evidence of reaction between platinum and H_2S gas. Therefore, in this region, the platinum leads were protected by an alumina sheath closed on both ends by alumina cement.

[3] CaF_2 contained the following elements in parts per million level: 0.5 Pb, 0.5 Ni, 0.5 Cd, 0.5 Mn, 500 Sr, 100 Ba, 5 Li, 10 Sn, and 5 K.

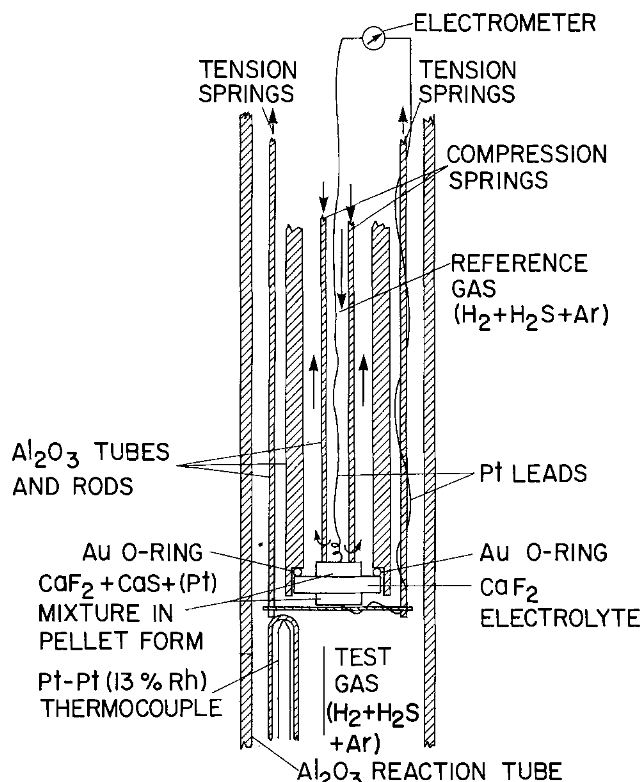

Fig. 1. Schematic diagram of the apparatus used for testing the CaF_2 electrolyte-based sulfur probe.

The cell was designed to provide two separate gastight compartments around the two electrode pellets. Separate gas streams with differing sulfur potentials were passed through these compartments. The test gas was admitted to the system at the lower end of the reaction tube and flowed past the outer electrode pellet at a rate of 250 ml min^{-1}. The reference gas was passed around the inner electrode at a flow rate of 100 ml min^{-1}. The two gas streams were isolated in the reaction tube and escaped through different ports in the brass head. The escaping gases were bubbled through two 25 cm high columns of NaOH solution to remove H_2S and HF. The exit gases were further scrubbed before being pumped through the fume exhaust system.

The entire cell assembly, attached to the brass head, was lowered into a vertical alumina reaction tube. The cell was electrically shielded by connecting a platinum foil, wrapped around the reaction tube, to ground. The reaction tube was heated by a Kanthal resistance furnace. Temperatures of the furnace and of the cell were measured by two separate Pt-Pt (13% Rh) thermocouples. The furnace temperature was controlled to ±1°K by use of a stepless current-compensating controller.

Procedure.—The test cell was assembled as shown in Fig. 1, and the reaction tube was evacuated by a mechanical pump to a pressure of 0.5 Nm^{-2} and then backfilled with purified argon. The argon purification train consisted of magnesium perchlorate (to absorb the residual moisture) and copper turnings at 700°K and titanium turnings at 1100°K (to remove residual oxygen). The cell was heated to 500°K, evacuated, and refilled with argon. The temperature of the cell was then raised to 1225°K. The reference gas was introduced into the inner gas compartment of the cell, while argon flow was maintained through the outer reaction tube. Gastightness of the O-ring seal was checked by analyzing the argon stream exiting from the reaction tube for traces of H_2S. After ensuring that the test cell was leaktight and the two gas streams were isolated, the test gas was introduced into the reaction tube. Cell voltage was monitored using a Keithley digital voltmeter with an internal impedance

of $10^{12}\Omega$. After the start of the experiment, approximately 5 hr were required to obtain a steady emf.

Two procedures were followed during the investigations: (*i*) During isothermal runs, cell temperature was kept constant at 1073° or 1173°K and the steady, reversible emf corresponding to different test gases was measured, and (*ii*) for two selected test gases, the temperature dependence of the steady, reversible emf was measured.

Results

Response time.—Composition of the test gases and the reference gas and the emf obtained at 1073° and 1173°K are shown in Table I. Generally, the response time of the cell at 1225°K, after a small change in temperature or gas composition, was 2.5 hr, while at a lower temperature of 990°K the response time was approximately 9 hr. The cell emf was insensitive to moderate increase in the flow rate of the test gas and/or the reference gas. However, when the flow rate of one of the streams was increased by factors greater than two, while keeping the flow rate of the other stream constant, significant changes in the emf were noted: about 20 mV during the transient period and about 15 mV during the steady-state period. The changes were, however, not always reproducible. When the flow rates of both streams were changed simultaneously by the same amount, the cell emf remained virtually constant. It is likely that a substantial increase in the flow of gas through one stream may have resulted in differential cooling, thus creating a thermal gradient across the electrolyte. Changes in emf resulting from the presence of a steady-state thermal gradient are quantitatively related to the partial entropy of fluorine in the gas phase, as discussed by Fitzner, Jacob, and Alcock (10).

Reversibility of the emf was checked by passing small currents (5 μA) through the cell in either direction for 2 min. It was found that the emf returned to the steady value before the titration in approximately 30 min. After several days of use, the electrode pellets became fragile and fractured easily.

Calculation of sulfur potentials.—Experimental emf's obtained at 1073° and 1173°K for different test gases are compared in Fig. 2 with known values calculated from the difference in sulfur potential between the test gas and the reference gas. The emf developed across a CaF_2 electrolyte can be related through the Nernst equation to the partial pressure of fluorine (fluorine potential) across the electrolyte, provided the ionic transport number is close to unity

$$E = \frac{\Delta\mu_{F_2}{}^R - \Delta\mu_{F_2}{}^T}{n\mathbf{F}} = \frac{RT}{n\mathbf{F}} \ln \frac{p_{F_2}{}^R}{p_{F_2}{}^T} \quad [3]$$

where E is the emf, $\Delta\mu_{F_2}{}^R$ and $\Delta\mu_{F_2}{}^T$ are the fluorine potential at the reference and the test electrodes, $\mathbf{F}$ is the Faraday constant, n is the number of electrons ($= 2$) involved in the transfer of one molecule of F_2 gas between the two electrodes, R is the gas constant, T is the absolute temperature, and p_{F_2} is the fluorine partial pressure. The gas phase containing Ar + H_2 + H_2S establishes a partial pressure of sulfur (sulfur potential) over the electrode, depending on the ratio of H_2 to H_2S, by virtue of the reaction

Table I. Composition of the test gas mixtures and the corresponding cell emf's

Test gas	Composition (vol. %)			EMF (mV)	
Number	H_2	H_2S	Ar	1073°K	1173°K
1	40.6	8.3	51.1	−32	−34
2	50.4	2.05	47.55	43	47
3	54.0	0.79	45.21	87	96
4	55.1	0.18	44.72	160	174
5*	25.2	2.52	72.28	—	—

* Reference gas.

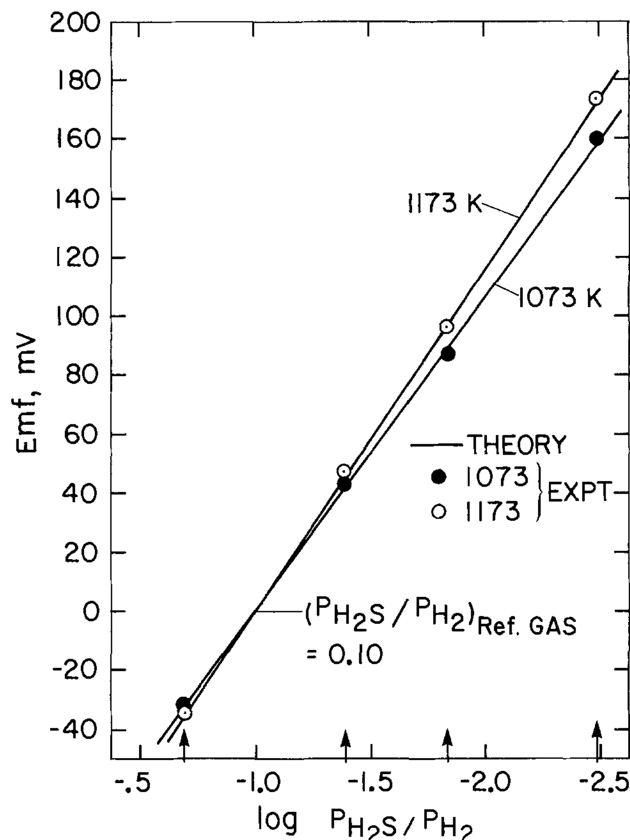

Fig. 2. Variations of the emf with H_2S/H_2 ratio of the test gas at 1073° and 1173°K; — theoretical values Eq. [9].

$$H_2(g) + \tfrac{1}{2} S_2(g) \rightarrow H_2S(g) \quad [4]$$

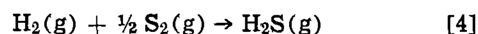

$$\tfrac{1}{2}\,\Delta\mu_{S_2} = RT \ln p_{S_2}{}^{1/2} = \Delta G°_4 + RT \ln (p_{H_2S}/p_{H_2}) \quad [5]$$

where $\Delta G°_4$ is the standard Gibbs' free energy change for reaction [4] (11). The sulfur potential established by the gas phase, when in contact with the electrode pellet consisting of CaS and CaF_2, fixes a fluorine potential through the reaction

$$CaF_2(s) + \tfrac{1}{2} S_2(g) \rightarrow CaS(s) + F_2(g) \quad [6]$$

$$\Delta\mu_{F_2} = \tfrac{1}{2}\,\Delta\mu_{S_2} - \Delta G°_6 \quad [7]$$

where $\Delta G°_6$ is the standard Gibbs' free energy change for reaction [6]. The platinum in the electrode pellet acts as a catalyst for the reaction. Since there is neither a ternary compound nor significant solid solubility in the CaF_2-CaS system, the condensed phases in the electrode pellets are present at unit activity. Combining Eq. [3] and [7], an expression is obtained relating the emf to the difference in the sulfur potential between the electrodes

$$E = \frac{\Delta\mu_{S_2}{}^R - \Delta\mu_{S_2}{}^T}{2n\mathbf{F}} = \frac{RT}{2n\mathbf{F}} \ln \frac{p_{S_2}{}^R}{p_{S_2}{}^T} \quad [8]$$

Equation [8] may also be expressed in terms of the ratio of H_2S to H_2 in the gas phase over the two electrodes

$$E = \frac{RT}{n\mathbf{F}} \ln \frac{(p_{H_2S}/p_{H_2})^R}{(p_{H_2S}/p_{H_2})^T} \quad [9]$$

The measured emf's as shown in Fig. 2, do not deviate by more than 2.5 mV from that calculated using Eq. [9]. Deviations from theoretical values have the same sign at different temperatures for each test gas. Thus, it is likely that these deviations arise from small errors in gas analysis.

The variation of the emf of the cell with temperature and with two test gases (3 and 4 in Table I) is shown

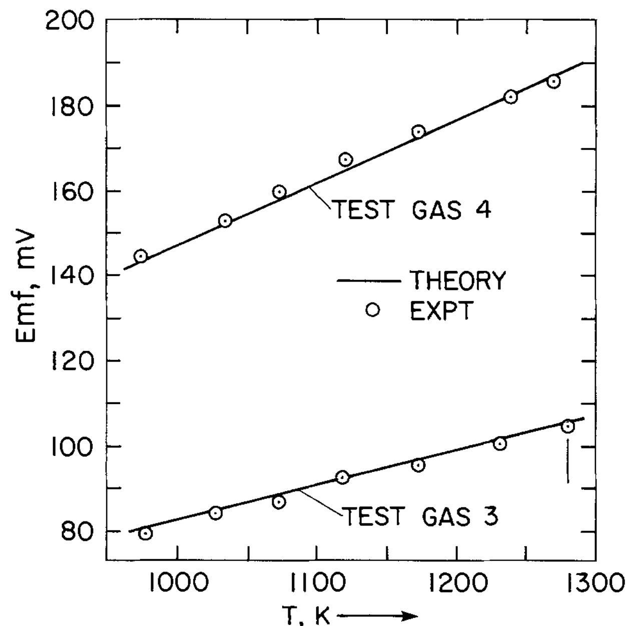

Fig. 3. The temperature dependence of the reversible emf with test gases 3 and 4 passing through the cell; — theoretical values Eq. [10].

in Fig. 3. Again, measured temperature dependence is in agreement with the theoretical value given by the derivative of Eq. [9] with respect to temperature

$$\frac{dE}{dT} = \frac{R}{n\mathbf{F}} \ln \frac{(p_{H_2S}/p_{H_2})^{R}}{(p_{H_2S}/p_{H_2})^{T}} \qquad [10]$$

Discussion

The activity of calcium at the electrodes, during the present investigation, can be evaluated by considering the reaction

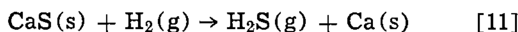

$$CaS(s) + H_2(g) \rightarrow H_2S(g) + Ca(s) \qquad [11]$$

The activity of calcium, a_{Ca}, is given by

$$a_{Ca} = (p_{H_2}/p_{H_2S}) \exp(-\Delta G^\circ_{11}/RT) \qquad [12]$$

where ΔG°_{11} is the standard Gibbs' free energy change for reaction [11] (11). It can readily be shown from known thermodynamic data that the activity of calcium varies from 9.5×10^{-19} to 6.0×10^{-17} at 1113°K over the range of test gas composition (gases 1 and 4, respectively, Table I). Wagner (8) has suggested that the electronic transport number of CaF_2 is 10^{-2} when the activity of calcium is 6×10^{-6} at 1113°K. It is apparent, therefore, that the electronic transport number is much less than 10^{-2} and contributes very little to the results of the present study.

The exact factors affecting the slow response time of galvanic cells based on a CaF_2 electrolyte have not yet been determined. The length of the electrolyte may influence the response time. In the present investigation the dimensions of the electrolyte were unaltered and a further study is necessary to relate the response time with electrolyte length. The more important are that the kinetics of the electrode reaction [6] may be rate controlling, or the transport of ions in CaF_2 may be slow, such that the composition gradient across the electrolyte cannot readjust rapidly after a perturbation in the chemical potential at the electrode. Additionally, since the fluorine potentials are low ($p_{F_2} \simeq 10^{-24}$ to 10^{-28} Nm^{-2}), gas phase polarization at the electrolyte-electrode interface may be the rate-limiting step. This latter possibility seems rather improbable, however, because sufficient concentration of HF gas should be created by the reaction of H_2S with CaF_2 to transport the fluorine potential to the electrolyte surface.

Electrical current techniques, such as voltage recording after a galvanostatic pulse or impedance measurement at low frequencies, can be used to determine whether the kinetics of the electrode reaction is responsible for the slow response of the cell (13). Heyne and Engelson (14) have recently suggested that for oxygen probes containing calcia-stabilized zirconia as the electrolyte, the uptake or release of oxygen by the electrolyte, when the partial pressure of oxygen in the ambient atmosphere is altered, is the main reason for the sluggishness in response and variation with time of the emf developed. If a similar mechanism is valid for CaF_2, a reduction in the thickness of the electrolyte or doping, to increase the effective diffusion coefficient, may accelerate the response of the probe to changes in sulfur potential. Another alternative is to use β-alumina as the electrolyte (15). β-alumina has much higher conductivity than CaF_2, especially at lower temperatures. Further, the electrodes would be redesigned to convert the sulfur potential gradient into an equivalent sodium potential gradient.

Although systematic studies on the catalytic behavior of platinum or other materials have not been undertaken, it was found in preliminary experiments that approximately 0.2 moles of platinum per mole of CaS is the optimum amount of catalyst in the electrode pellets. To use the cell for sulfur potentials higher than those studied in this investigation, a more suitable catalyst than platinum is needed. Platinum readily forms sulfides at higher sulfur potentials (12). Transition metal sulfides that do not react with CaS and in which cations exist in multivalent states may prove to be good catalysts.

Typical compositions of the raw gases in some coal gasification processes are shown in Table II. It can readily be shown that under the conditions of coal gasification, the conversion of CaS to CaO, according to the scheme

$$CaS(s) + H_2O(g) \rightarrow CaO(s) + H_2S(g) \qquad [13]$$

is not thermodynamically favorable. However, the reaction of $H_2S(g)$ with CaF_2

$$CaF_2(s) + H_2S(g) \rightarrow CaS(s) + 2HF(g) \qquad [14]$$

will result in a partial pressure of HF in the immediate neighborhood of the electrode that can vary from 2.8×10^2 to 80 Nm^{-2}. Since all the gas passing through the probe is not saturated in HF, the average HF concentration in the exit gas is estimated to be approximately 200 ppm and, therefore, must be scrubbed for the removal of HF. Additionally, for commercial application, the probe must be designed in such a way as to prevent particulate material in the gas from depositing on the electrodes of the sensor.

Conclusion

The theory, design, and operation of a solid-state sulfur probe based on CaF_2 electrolyte has been demonstrated. The cell responds to changes in sulfur potential in a manner predicted by the Nernst equation. Further research is needed to determine the main reason for the slow response of the cell. The rate-limiting steps may be either the kinetics of electrode reactions or the

Table II. Composition of raw gases in various coal gasification processes (16)

	Battelle-Union Carbide agglomerate ash process	BCR-Bi-gas process	Bureau of Mines synthane process	IGT Hygas process
H_2	48.8	15	19	19
H_2O	14	52	36	20
CO	26	12	9	17
CO_2	5	13	21	16
H_2S	0.3	0.53	1.1	0.78
N_2	0.5	—	—	—
NH_3	0.002	0.25	0.6	0.4
CH_4	6	7	12	13

Compositions are given in volume percent.

rate of transport through the electrolyte. If the reaction kinetics is rate controlling, suitable catalysts may be developed to overcome the problem. If the slow transport of ions in the electrolyte is the reason for the sluggish response, a cell based on β-alumina electrolyte may be more suitable.

Acknowledgments

The authors thank Dr. Ian Finnie, University of California, Berkeley, and Mr. A. V. Levy, Lawrence Berkeley Laboratory, for their support and encouragement.

Manuscript submitted Sept. 28, 1977; revised manuscript received Dec. 15, 1977.

Any discussion of this paper will appear in a Discussion Section to be published in the December 1978 JOURNAL. All discussions for the December 1978 Discussion Section should be submitted by Aug. 1, 1978.

Publication costs of this article were assisted by the Ames Research Center.

REFERENCES

1. C. N. R. Rao and K. P. R. Pisharody, *Prog. Solid State Chem.*, **10**, 207 (1976).
2. R. Benz and C. Wagner, *J. Phys. Chem.*, **65**, 1308 (1961).
3. J. J. Egan, *ibid.*, **68**, 978 (1964).
4. W. K. Behl and J. J. Egan, *This Journal*, **113**, 378 (1966).
5. W. J. Heus and J. J. Egan, *Z. Phys. Chem. N.F.*, **49**, 38 (1966).
6. S. Aronson and A. Auskern, in "Thermodynamics," Proceedings of Symposium, Vienna, 1965, Vol. 1, p. 165, International Atomic Energy Agency, Vienna (1966).
7. N. L. Lofgren and E. H. McIver, "Thermodynamic Properties of Some Fluoride Systems," U.K.A.-E.A. Rep., 5169 (1966).
8. C. Wagner, *This Journal*, **115**, 933 (1968).
9. J. W. Patterson, *ibid.*, **118**, 1033 (1971).
10. K. Fitzner, K. T. Jacob, and C. B. Alcock, *J. Chem. Thermodyn.*, In press (1977).
11. D. R. Stull and H. Prophet *et al.*, JANAF Thermochemical Tables, pp. 760, 761, NSRDS-NBS 37, U.S. Department of Commerce, Washington, D.C. (1971).
12. W. Biltz and R. Juza, *Z. Anorg. Chem.*, **190**, 166 (1920).
13. J. E. Bauerle, *J. Phys. Chem., Solids*, **30**, 2657 (1969).
14. L. Heyne and D. den Engelson, *This Journal*, **124**, 727 (1977).
15. J. T. Kummer, *Prog. Solid State Chem.*, **7**, 141 (1972).
16. A. J. McNab, "Materials Problems and Research Opportunities in Coal Conversion," NSF-OCR Workshop Proceedings, Table II, Ohio State University, p. 33 (April 1974).

Reduction of Excess Phosphorus and Elimination of Defects in Phosphorus Emitter Diffusions

B. L. Morris and L. E. Katz*

Bell Laboratories, Allentown, Pennsylvania 18103

ABSTRACT

The successful production of LSI bipolar circuits requires that a high level of transistor junction yield be maintained. One of the chief causes of junction degradation is the defects induced by the high concentration of phosphorus normally used in the emitter diffusion of bipolar transistors. This diffusion results in a total phosphorus concentration that is greater than the electrically active phosphorus; precipitates and other defects result from this excess phosphorus. These defects can cause crystal damage which in turn can degrade junction integrity, and in the worst case lead to emitter-collector shorts. The purpose of this work was to find processing parameters which may be used to minimize the excess phosphorus in an emitter diffusion. We have studied the effect of bubble rate, the amount of preheat time, thickness of preformed barrier oxide, percent oxygen in the gas stream, and percent time that the bubbler is on for a 1000°C phosphorus diffusion using PBr_3. The diffusions were characterized by sheet resistance, junction depth, total surface concentration (as measured by an electron microprobe), and Sirtl etching. It is shown that the proper choice of diffusion processing parameters minimizes the excess phosphorus, eliminates etching defects, improves transistor junction yield, and results in only a small increase in final sheet resistance. This occurs when the total phosphorus concentration, averaged over 0.34 μm from the surface, is kept below 4.0 to 4.5 $\times$ 10^{20} cm^{-3}.

The most common n-type dopant used in silicon integrated circuit (SIC) processing is phosphorus, and the two most widely used phosphorus diffusion sources are $POCl_3$ and PBr_3. A considerable amount of work exists (1-4) on the relationship between the electrical properties of these diffusions and the process parameters. It is well known that for high concentrations of phosphorus ($C_{atomic} \geqq 10^{20}/cm^3$) the amount of electrically active phosphorus is less than the total amount introduced during diffusion (5). The explanation given in the literature for this difference is that the excess phosphorus forms precipitates which are not electrically active (6-9). Although a large amount of work has been done on the relationship between the electrical properties of phosphorus diffusions and processing parameters, very little work has been reported on how to minimize this excess phosphorus (8).

The work presented here was undertaken to determine the processing parameters which would result in a minimum amount of excess phosphorus for the typical emitter diffusions used in bipolar digital SIC's. This is important since the excess phosphorus can cause crystal damage resulting in the creation of recombination-generation centers (9-11) in the region of the emitter-base junction, and/or emitter collector shorts. At the same time, the electrically active con-

* Electrochemical Society Active Member.
Key words: phosphorus diffusion, defects in silicon, bipolar transistors.

centration should be as high as possible since in many cases the emitter diffusion is used as a diffused cross-under and a sheet resistance as low as possible is desired to minimize parasitic voltage drops. For circuits operated at low current levels such as injection logic and low power transistor-transistor logic, an increase in the sheet resistance of approximately 50% or less should not have any effect on the noise immunity of the circuits.

All of the work described in this paper was done on 3 in. diam slices using standard bipolar processing. The goal was to determine processing which can reduce the electrically inactive phosphorus concentration without appreciably changing the sheet resistance (*i.e.*, the electrically active phosphorus concentration).

Experimental

The diffusion system used for PBr_3 predepositions is shown schematically in Fig. 1. The bubble rate is the amount of nitrogen that is bubbled through a flask of liquid PBr_3. The oxygen is needed to form a phosphorus-doped glass on the silicon surface. It is this glass which acts as the diffusion source. The main N_2 is adjusted if bubble rate or O_2 content is changed, so that the total gas flow is always 8.0 liters/min. This flow has been found sufficient to assure uniformity and eliminate backstreaming.

The processing variables which control the total amount of phosphorus are: diffusion temperature; total diffusion time; bubble rate (nitrogen flow: liters/min); percent oxygen in gas stream; percent time bubbler is on; temperature of PBr_3 source; preheat time (time elapsed before bubbler is turned on). In a typical bipolar process, the desired emitter junction depth is ≈ 1.2 μm. Typical total diffusion time and temperature to achieve this junction depth are 35-40 min at 1000°C. To first order, all of the other parameters listed above have a secondary effect on this junction depth, and hence on the active base width of the transistor. Although it has been shown that higher phosphorus diffusion temperatures can result in a smaller amount of excess phosphorus than lower temperatures (8), due to the higher phosphorus solubility at higher temperatures, use of higher temperatures is ruled out due to the very short, and hence poorly controllable, total diffusion times.

Two approaches were initially taken to reduce the electrically inactive phosphorus concentration. The first of these involved lowering the amount of phosphorus in the gas stream by varying the bubble rate, percent time that the bubbler is on, and percent of oxygen. The second approach was to grow a thin layer of thermal oxide on the silicon just prior to the phosphorus diffusion. This may be done in a separate oxidation furnace or *in situ* in the phosphorus diffusion furnace by using a relatively long preheat time and a high O_2 level.

All diffusions except those used in junction yield studies were into p-type bulk wafers with a <111> orientation and a resistivity in the range of 0.5-1.0 Ω-cm. The diffusions were performed at 1000°C for total times of 36 or 60 min which correspond to emitter junction depths of 1.2 and 1.6 μm, respectively. The nitrogen bubble rate was varied from 0.5 to 2.0 liters/min. The oxygen flow was varied from 0 to 20% of the total gas flow. Bubbler time was varied from 16 to 92% of the total diffusion time.

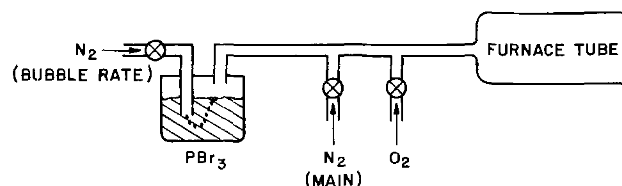

Fig. 1. Diffusion system used for PBr_3 predepositions

Three lots of 24 n-type epitaxial wafers each (0.5 Ω-cm, 5-6 μm thick, <111> oriented) were run to observe the effect of the emitter diffusion on transistor junction yield, which we define as the percent of transistors with $BV_{CEO} \geqq 5V$ at 10 μa. The first lot was split four ways; two different low phosphorus methods, a "worst case" high phosphorus diffusion, and an intermediate phosphorus diffusion which is the standard currently used in production. The second and third lots were split two ways; standard diffusion and low phosphorus diffusion. Twenty large transistors, emitter area 270 mil^2, were measured on each wafer. The transistor junction yield, the base pinch sheet resistance (the sheet resistance of the base under the emitter), and final (*i.e.* reoxidized) emitter sheet resistance were also measured.

Results and Discussion

Sirtl etching of wafers following the phosphorus diffusions was used to reveal dislocation size and density for the different diffusion conditions. Since defect analysis is performed at high magnification (200×), the statistical variation from sample to sample for these wafers was considerable, hence large areas from each of the wafers within a particular run must be examined. Typical defects from such an examination using Normarski interference contrast microcopy are shown in Fig. 2 and 3. The diffusion conditions of the various samples will be discussed later. It is possible to prepare samples with no defects (Fig. 2a), with small defects (Fig. 2b and 2c), and with large defects (Fig. 2d and Fig. 3a-3d). These defects, as mentioned earlier, are dislocations arrays. Their sizes, as revealed by etching, range from ~3-5 μm for the small defects to 50-60 μm for the large ones. Because of the range in size and position of these defects, no quantitative estimate of their density has been attempted. All results are presented in a qualitative and comparative manner.

Table I shows the effect of the total phosphorus concentration on the defects produced by the emitter diffusion as observed by Sirtl etching. The phosphorus concentration was varied by varying the percent of time the bubbler is on, the bubble rate, and the percentage of oxygen in the gas flow.

This table indicates that a reduction of the phosphorus concentration below 4.0 to 4.5 × $10^{20}/cm^3$ (averaged over the first 0.34 μm) by appropriate choice of diffusion parameters is sufficient to produce defect-free emitters.

The second approach used to reduce the phosphorus induced defects involves growing a thin oxide prior to the phosphorus diffusion. Table II shows the results for a separate oxidation, and once again it is found

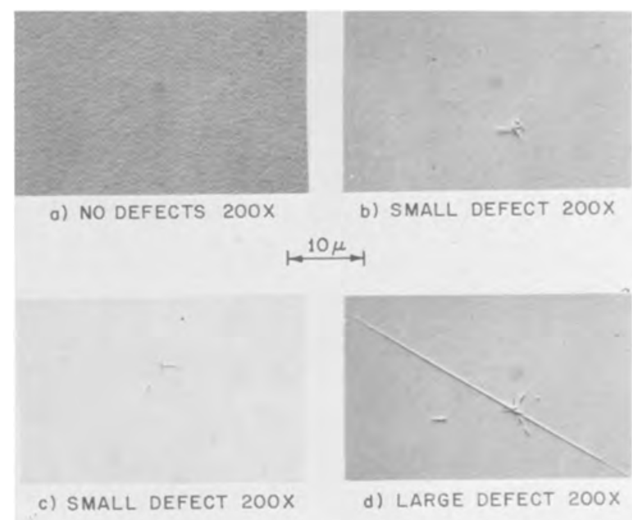

Fig. 2. Defects produced by phosphorus predeposition (1000°C)

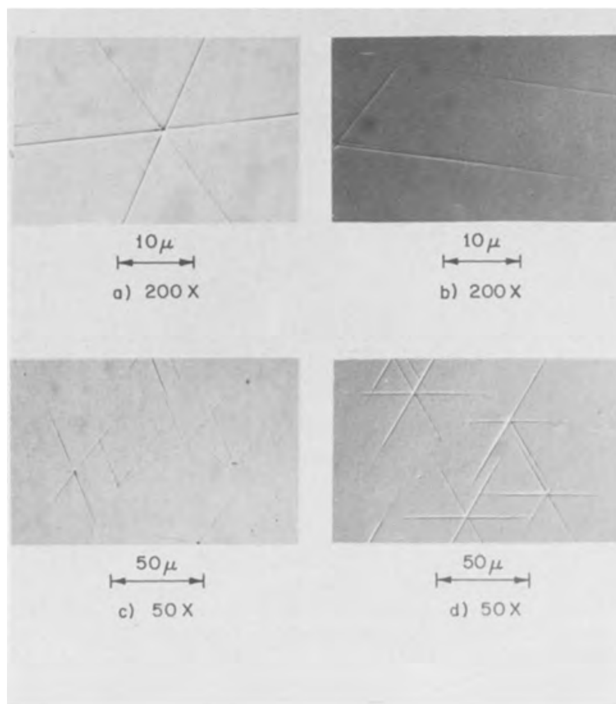

Fig. 3. Large defects produced by phosphorus predeposition (1000°C).

that reducing the phosphorus concentration below 4.0 to 4.5 × $10^{20}/cm^3$ (averaged over 0.34 μm) results in the elimination of phosphorus-induced defects. Table III shows results for thin, $\lesssim$ 110Å, oxides grown *in situ* in the phosphorus diffusion furnace in dry O_2. In this case the number of defects decreases as the oxide thickness increases, but there is no apparent decrease in the total phosphorus concentration. This apparent contradiction of the previous correlations may be understood by recalling that: (*i*) the electron microprobe measurement gives an average concentration

Table I. Effect of total phosphorus concentration on defects

(Total diffusion time 60 min)

Sheet resistance Rs (Ω/□)	Total phos. conc.* per cm³	Etching results (refer to Fig. 2 and 3)
5.6	3.3 × 10^{20}	No defects
4.4	4.5 × 10^{20}	Small defects at center, large defects at edge
4.2	5.4 × 10^{20}	Small and large defects at center, large defects at edge
4.2	6.1 × 10^{20}	Small and large defects at center, large defects at edge
4.0	7.5 × 10^{20}	Small and large defects at center, large defects at edge

* Averaged over 0.34 μm depth (electron microprobe results).

Table II. Diffusion through previously formed thin oxide

(Total diffusion time 60 min)

Barrier oxide thickness (A)	Sheet resistance Rs (Ω/□)	Total phos. conc.*	Etching results (refer to Fig. 2 and 3)
0	3.9	5.9 × 10^{20}	Large defects throughout
165.0	4.2	5.4 × 10^{20}	Large defects but lower density than above
290.0	4.6	4.9 × 10^{20}	Small defects
450.0	5.4	4.3 × 10^{20}	None
700.0	8.3	2.9 × 10^{20}	None
1000.0	17.8	$<1 \times 10^{20}$	None

* Averaged over 0.34 μm.

Table III. Diffusion through an *in situ* oxide

(Total diffusion time 60 min)

Oxide formed (A)	Sheet resistance Rs (Ω/□)	Total phos. conc.* (cm^{-3})	Etching results (refer to Fig. 2 and 3)
50	4.5	4.8 × 10^{20}	Low density of small defects
66	4.5	4.4 × 10^{20}	Low density of small defects
110	4.2	4.7 × 10^{20}	Very few, small defects

* Averaged over 0.34 μm depth.

over ≈0.34 μm from the surface; and (*ii*) it is the maximum phosphorus concentration which occurs at the surface that is the cause of the SiP precipitates and dislocation networks. It appears, therefore, that even a thin oxide ($\lesssim$110Å) over the silicon acts to decrease the surface phosphorus concentration and "flatten out" the profile, with very little effect on the total amount of phosphorus that is diffused into the silicon.

The *in situ* oxidation method has a number of advantages over a preformed oxide layer; it eliminates the need for an additional process step, it eliminates the possibility of accidental removal of the thin oxide during a reclean, and it results in a reproducibly thin oxide (≈100Å) which decreases the defect density while resulting in a minimal increase in the sheet resistance.

The results of combining these two approaches (lowering the amount of phosphorus in the ambient and growing an SiO_2 layer prior to diffusion) are shown in Table IV. In three "low phos" examples, the phosphorus glass thickness is not appreciably different from the "standard" condition for any of these cases. After the emitter reoxidation, 900°C for 60 min in steam, the final sheet resistance of low phos III is slightly greater than standard, while the other two cases have appreciably larger values. The amount of oxide grown over the emitter, which is known to depend on the phosphorus concentration, is also shown in the table.

Table IV. Some characteristics of "optimum" emitter diffusion

(Total diffusion time 36 min)

	Diffusion conditions		After predep			After reox			
Emitter diffusion	Oxygen (%)	Bubble rate (l/min)	Glass thickness (Å)	Rs (Ω/□)	Total phos conc.*	Rs (Ω/□)	Total phos conc.*	Oxide thickness (Å)	Etching results
Low phos I	10	0.5	670	11.4	2.4 × 10^{20}	16.5	1.7 × 10^{20}	3450	No defects
Low phos II	10	0.75	715	8.8	3.1 × 10^{20}	12.7	2.7 × 10^{20}	3700	No defects
Low phos III	10	1.0	720	7.7	3.4 × 10^{20}	11.0	3.5 × 10^{20}	3860	Some small defects
Standard	3	1.0	600	6.2	4.3 × 10^{20}	9.0	4.6 × 10^{20}	4020	Small defects at center, large defects near edges

* Averaged over 0.34 μm depth.

Table V. Effect of emitter diffusions on transistor junction yield

(Total diffusion time 36 min)

Diffusion emitter	Diffusion conditions		Junction yield (% BV_{CEO} > 5^v at 10 μA)	Base pinch sheet res. (kΩ/□)	Final emitter sheet res. (Ω/□)	Total phosphorus concentration* (cm^{-3})
	Bubble rate (l/min)	Oxygen (%)				
Lot No. 1						
Low phos I	0.5	10	90%	4.1	13	2.9×10^{20}
Low phos III	1.0	10	83%	5.0	10	4.1×10^{20}
Standard	1.0	3	52%	5.3	9.2	4.4×10^{20}
High phos	2.0	3	52%	5.0	7.0	1.1×10^{21}
Lot No. 2						
Low phos I	0.5	10	69%	5.7	14.0	2.6×10^{20}
Standard	1.0	3	43%	5.8	9.4	4.6×10^{20}
Lot No. 3						
Low phos III	1.0	10	83%	3.3	9.8	Not measured
Standard	1.0	3	67%	3.7	8.5	Not measured

* Averaged over 0.34 μm from surface.

The results of the transistor junction yield experiments previously described are shown in Table V. For Lot 1 the low phos I results may be too optimistic due to the wide basewidth of this part of the split lot (as indicated by the low base pinch sheet resistance). However the results of low phos III *vs.* standard clearly show a real improvement.

Conclusion

To increase transistor junction yield the amount of excess, electrically inactive, phosphorus in the emitter diffusion must be kept to a minimum. Two approaches to this are: (*i*) minimize the amount of phosphorus in the gas stream; and (*ii*) grow a thin layer of thermal oxide over the silicon prior to the diffusion. These two approaches have been combined into "optimum" diffusion schedules which produce total phosphorus concentrations (averaged over 0.34 μm from the surface as measured by electron microprobe) less than or equal to approximately 4.0 to 4.5 $\times 10^{20}$ cm^{-3}. As a result, defect-free surfaces are obtained and transistor junction yield is significantly increased (up to ~80%) as compared to higher concentration phosphorus diffusions.

Acknowledgments

The help of David Wonsidler in making the electron microprobe measurements is gratefully acknowledged.

Manuscript submitted Oct. 3, 1977; revised manuscript received Dec. 28. 1977.

Any discussion of this paper will appear in a Discussion Section to be published in the December 1978 JOURNAL. All discussions for the December 1978 Discussion Section should be submitted by Aug. 1, 1978.

Publication costs of this article were assisted by Bell Laboratories.

REFERENCES

1. J. C. C. Tsai, *Proc. IEEE*, **57**, 1499 (1969).
2. P. C. Parekh, *This Journal*, **119**, 173 (1972).
3. M. S. R. Heynes and P. G. G. van Loon, *ibid.*, **116**, 890 (1969).
4. J. S. Kesperis, *ibid.*, **117**, 554 (1970).
5. E. Tannenbaum, *Solid-State Electron*, **2**, 123 (1961).
6. R. J. Jaccodine, *J. Appl. Phys.*, **39**, 3105 (1968).
7. M. L. Joshi and S. Dash, *IBM J.*, **11**, 271 (1967).
8. P. Negrini, D. Nobili, and S. Solmi, *This Journal*, **122**, 1254 (1975).
9. C. Donolato, P. G. Merli, and I. Vecchi, *ibid.*, **124**, 473 (1977).
10. F. Barson, M. S. Hess, and M. M. Roy, *ibid.*, **116**, 304 (1969).
11. F. Barson, S. P. Klepner, and D. K. Seto, Paper 144 presented at the Toronto, Canada, Meeting of the Society, May 11-16, 1975.

Formation and Properties of Thin Tunnelable SiO_2 Films Using a Vaporized O_2 Source at Liquid N_2 Temperature

Masatada Horiuchi, Yoshiaki Kamigaki, and Takaaki Hagiwara

Hitachi, Limited, Central Research Laboratory, Kokubunji, Tokyo 185, Japan

ABSTRACT

A high temperature (700°-1100°C) oxidation process for the formation of thin tunnelable SiO_2 (20-70Å) is described. This oxidation process uses liquid O_2 at liquid N_2 temperature as a source of oxidant and oxygen is vaporized just before the furnace tube to supply a water-free oxidant ambient. The activation energy (20.2 kcal/mole) of oxidation rate differs from that previous (43.9 kcal/mole) which has been evaluated for thin oxide growth using the O_2/N_2 partial pressure method. By the use of this technique we can control thickness to ±0.5Å accuracy. The rate of oxidation has been found to be governed by the inverse-logarithmic growth law, *i.e.*, Mott-Cabrera's field-assisted diffusion law. Electrical characteristics, such as dynamic conductance, capacitance, and tunnel current, are measured and discussed. The increment of the oxidation temperature is found to result in the decrease of surface-state density at the Si-SiO_2 interface. The process described enables the way for wider application of thin oxide devices.

There has been a good deal of recent interest in thin oxide nonvolatile memory devices such as metal-nitride-oxide silicon (MNOS) devices. This is because of the proposed use of MNOS devices in electrically alterable read-only memories as well as for various other applications (1). In these devices, a thin tunnelable oxide plays a very important role in governing several properties of the memory actions, such as switching speed, retention characteristics, and degradation phenomena. Although there is a considerable amount of information available about the kinetics and electrical properties of relatively thick (0.02-1 μm) SiO_2 layers (2-4), there has been comparatively little published on thin (<200Å) SiO_2 films (5-7). Most importantly, there is little information on the reproducibility of the formation and quality control of thin tunnelable oxides.

This paper presents a study of the growth of thin tunnelable oxides (20-80Å) on freshly etched Si at 700°-1100°C in dry oxygen. It describes the successful development of a technique for reproducibly fabricating thin tunnelable SiO_2 films (on Si) and for improving the Si-SiO_2 interface properties.

Experimental Procedures

Sample preparation.—Most of the single crystal silicon wafers in this study were 8-12 Ω-cm p-type with a chemmechanically polished (100) face. Conductance measurements were carried out using sample wafers of 0.002 Ω-cm p^{++}-type or 0.009 Ω-cm n^{++}-type (111) face. The wafers were cleaned by a standard ammoniacal peroxide process as a preoxidation wafer treatment after the field oxide was etched off to expose the gate region. Wafers for studying the rate of formation of thin tunnelable SiO_2 films did not have a field oxide, so only the cleaning sequence was carried out.

All thickness measurements were made ellipsometrically. The films formed in air during 7-10 min measurement time on freshly etched Si wafers were measured to be about 6.0Å (assuming that the films were SiO_2 films). In this study, the refractive indexes of $n_{SiO_2} = 1.47$ and $n_{Si} = 4.08\text{-}0.028i$ were assumed.

The oxidation was carried out in a resistance-heated 3 zone oxidation furnace tube with a specially prepared oxygen source for the desired amount of oxidation time. The oxidation apparatus for formation of thin tunnelable SiO_2 is shown in Fig. 1. In this oxidation process, the oxygen source is liquid O_2 vaporized at the temperature of liquid N_2 and carried into a conventional oxidation furnace with purified N_2 gas. N_2 gas does not bubble through liquid O_2 but simply passes over liquid O_2 face. The oxygen vaporization just before the furnace tube inherently decreases impurity content in the oxidant ambient. Oxidation was carried out at 700°-1100°C.

After oxide growth samples to be used for measurement of the electrical properties were placed in a vacuum system. Aluminum was evaporated with a resistive heater and gate electrodes were formed by photoetching. Contact with the back side of the structure was accomplished by N^+ diffusion before formation of the thin SiO_2 films.

Measuring procedure.—Dynamic conductance and capacitance measurements are made by properly adjusting the phase shifter of the lock-in amplifier (8). A ramp voltage supply provides d-c voltage to the sample, thereby enabling data to be plotted automatically. Signal frequency is about 19.2 Hz and peak-to-peak voltage is about 5 mV. The absolute measurement of conductance or capacitance is made by a substitution technique in which the system is first calibrated to give a certain deflection for a known conductance or capacitance. After calibration the sample is switched into the circuit. This system can verify conductance values of more than 2×10^{-8} mho.

Results and Discussion

Thickness evaluation.—The vapor pressure of oxygen does not stabilize for about two days after liquefaction at liquid N_2 temperature. The fluctuation of the formed oxide thickness under these conditions is plotted

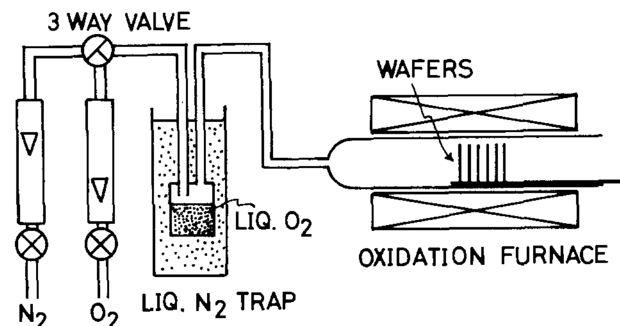

Fig. 1. Oxidation apparatus for formation of thin tunnelable SiO_2 with liquid O_2 source vaporized at liquid N_2 temperature.

Key words: high temperature oxidation, excellent accuracy, inverse-logarithmic growth law, surface-state density decrease.

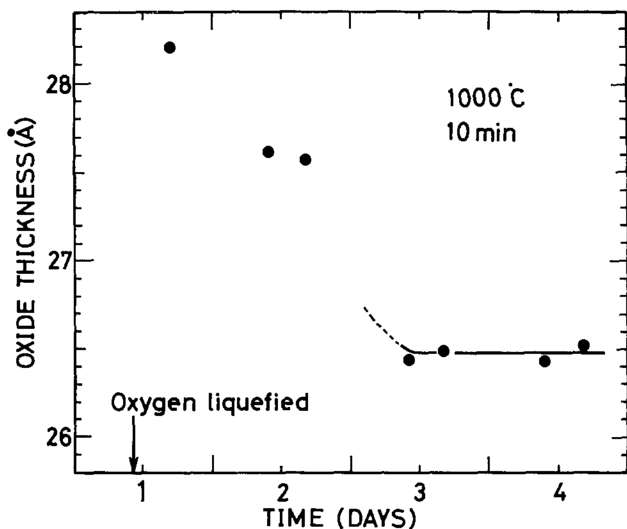

Fig. 2. Fluctuation of the oxide thickness under the same conditions (1000°C, 10 min). Oxide thickness is reproducible within ±0.5Å accuracy after three days from oxygen liquefaction.

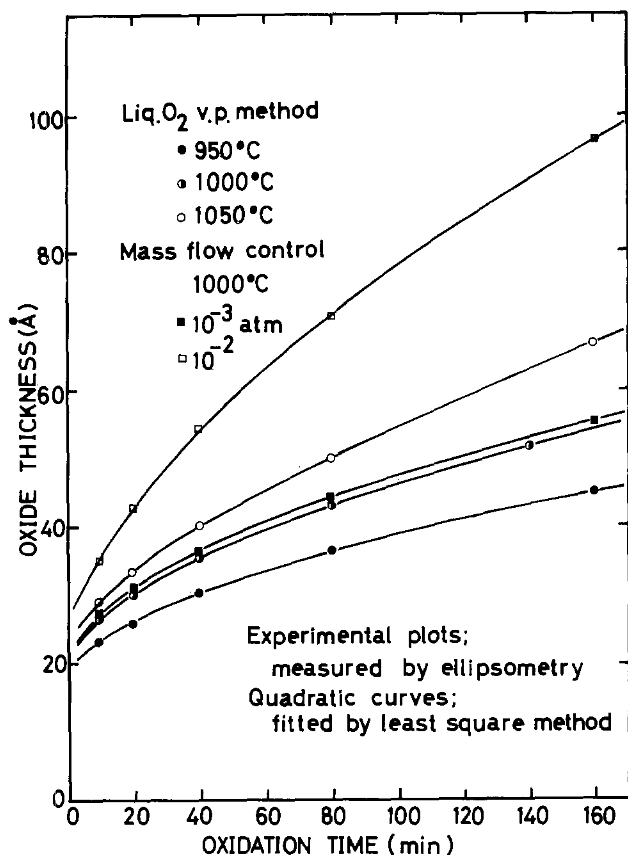

Fig. 3. Rate of formation of thin tunnelable SiO_2 films using a liquid O_2 source vaporized at liquid N_2 temperature. The results of the O_2-N_2 mixture method varying oxygen concentration at 1 atm total pressure by mass-flow controller are shown for comparison.

against time after liquefaction in Fig. 2. After three days, the oxygen vapor pressure reaches a steady-state condition and good reproducibility can be obtained within ±0.5Å accuracy.

The rate of formation of thin tunnelable SiO_2 films using liquid O_2 oxidant source is shown in Fig. 3. The results of the O_2-N_2 mixture method (varying oxygen concentration at 1 atm total pressure by mass flow controller) are shown in this figure for comparison. By comparison with the O_2-N_2 mixture method, partial pressure of O_2 is verified as being nearly equal to 10^{-3} atm for the liquid O_2 vapor pressure method.

In this figure, the Deal-Grove linear parabolic relationship, $X^2 + AX = B(t + \tau)$ is not applied as an analytical procedure, but the second-order regression curves $t = a_0 + a_1X + a_2X^2$ are fitted to the experimental data plots using the least squares method. This is because the Deal-Grove relationship cannot actually be applied in the case of thin oxide growth involving field and space charges within the oxide layer thinner than oxide-Debye length (9, 10).

It has been reported in the previous paper (10) that the thin oxide growth under low oxygen partial pressure is governed by the inverse-logarithmic growth law $dX/dt = u \exp (X_1/X)$, *i.e.*, one case ($X_1 >> X$) of the Mott-Cabrera's field-assisted diffusion law $dX/dt = 2u \sinh (X_1/X)$, where $u \propto \exp(-W/kT)$ and X_1 are the characteristic velocity and distance, respectively (11).

The results of the experimental and analytical data at 950° and 1000°C oxidation temperature are presented in detail in Table I. Average relative error $\overline{dX/X}$ is as small as 0.34%. Average thickness error $\overline{dX}$ is remarkably small, *i.e.*, 0.11Å. The Deal-Grove's rate constants can easily be calculated from Table I. The resulting rate constant A has negative values in our experimental range. This means that the Deal-Grove linear parabolic relationship cannot be accepted in our experimental range. The relation between oxidation velocity and oxide thickness is also given in Table I. The log $(d\overline{X}/dt)$ *vs.* $1/X$ plots at 950°, 1000°, and 1050°C are shown in Fig. 4. It is clear that a strictly linear relation can be obtained in this figure. The values u and X_1 can be obtained from Fig. 4, *i.e.*, u by extrapolating the straight line back to $1/\overline{X} = 0$. The gradient of this line gives X_1. The good linear relationship, as is seen in Fig. 4, proves that the oxide growth using liquid O_2 vapor pressure method is also governed by the inverse-logarithmic law, *i.e.*, Mott-Cabrera's field-assisted diffusion growth law.

All values obtained for u can be plotted as a function of oxidation temperature. Activation energy (W) in the Arrhenius expression is about 20.2 kcal/mole.

This value is smaller than 43.9 kcal/mole, that of previous study (10) where O_2-N_2 partial pressure method was used as a thin oxide formation. However, it may be compared with 25.8 kcal/mole for the thicker oxide formation as referred to by Revesz and Evans (3). They obtained this value by rf heating oxidation with dry O_2 containing less than 0.1 ppm of water. According to them, the water and sodium content in the oxidizing ambient greatly affects the rate constant and its activation energy. The activation energy increases with the increment of sodium and water content. In their study or in the previous studies (2, 12), 43.3-44.0 kcal/mole were presented as the largest values of activation energy.

In our experiment liquid O_2 is vaporized just before the furnace tube, and water vapor in the oxidant

Table I. Data analysis for the oxidation of silicon with the liquid O_2 vapor pressure method

	950°C				1000°C			
t	X	$\overline{X}$	dX	dX/dt	X	$\overline{X}$	dX	dX/dt
10	23.03	22.98	0.05	0.3326	26.44	26.29	0.15	0.4507
20	25.74	25.85	−0.11	0 24[illegible]6	30.05	30.12	−0.07	0.3283
40	30.18	30.09	0 09	0.1824	35.51	35.65	−0.14	0.2358
80	36.19	36.22	−0.03	0.1313	43.66	43.54	0.12	0.1682
160	45.01	45.01	0.00	0.0937	52.26*	52.29	−0.03	0.1276
$\overline{dX}$	0.07Å				0.11Å			
$\overline{dX/X}$	0.26%				0.34%			
a_0	3.31×10				2.66×10			
a_1	−4.99				−3.46			
a_2	1.74×10^{-1}				1.08×10^{-1}			
u	2.55×10^{-2}				3.54×10^{-2}			
X_1	59.0Å				67.3Å			

t = min, X = Å, a_0 = min, a_1 = min/Å, a_2 = min/Å^2.
* Oxidation time is 140 min.

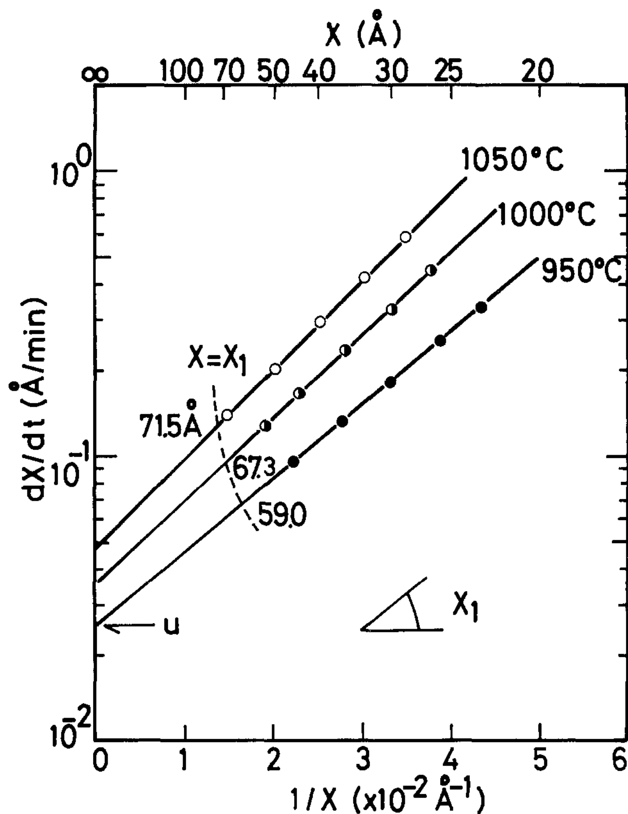

Fig. 4. Relation between log($d\overline{X}/dt$) and $1/\overline{X}$ at 950°, 1000°, and 1050°C. This figure utilizes the values from Table I. The values of u and X_1 are given by extrapolating the straight line back to $1/X_1$ and by the slope of this line, respectively.

source at liquid N_2 temperature is less than 2×10^{-26} atm, *i.e.*, water-free oxidant source. According to this, the liquid O_2 vapor pressure method may apparently be distinguished from other thin oxide formation methods for impurity content in the formed oxide.

Electrical properties.—A typical capacitance *vs.* voltage characteristic measured by a lock-in amplifier with 100 kHz superposed frequency is shown in Fig. 5. Thickness of this film measured by ellipsometry is 57.2Å. Maserjian *et al.* (13) provided a method to evaluate the value of the density of states-effective

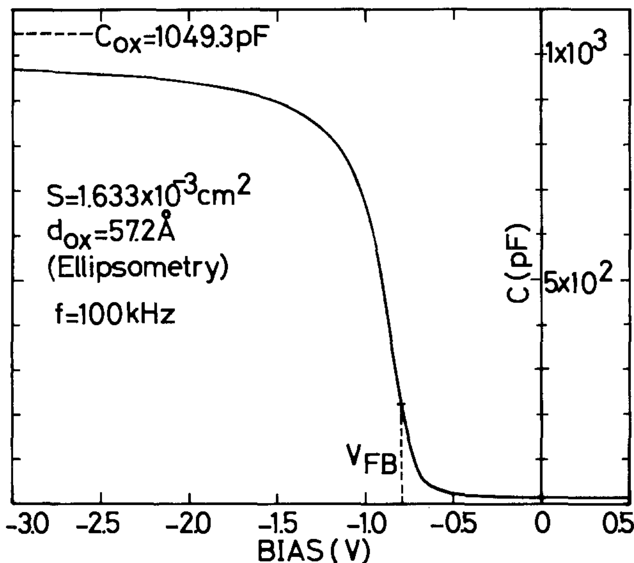

Fig. 5. A typical capacitance *vs.* voltage characteristic. Oxide thickness measured by ellipsometry is 57.2Å. Capacitance fails to saturate at the oxide capacitance C_{ox}. Thus, the C_{ox} value is estimated after Ref. (13) exactly.

mass m_D for the valence band. According to their method, m_D is evaluated as 0.296 m_o. The value of m_D obtained from this method differs considerably from the bulk density of states mass which is $m_D = 0.55\ m_o$ for the valence band. Maserjian *et al.* suggested that one possible reason for this is surface quantization effects. They calculated $m_D = 0.29\ m_o$ for the valence band of the (100) surface assuming the triangular potential approximation for a strongly accumulated semiconductor surface. Quite good agreement can be seen between the value found from surface quantization and our calculated value in spite of measurement at room temperature.

The flatband voltage value is nearly −0.8V and discrepancy from the Al-Si work function difference (14) is less than 0.05V. No hump caused by the interface state density distribution (15, 16) can be observed in this capacitance curve. These facts prove the quality of the thin oxide films described in this paper.

Tunnel current is measured in a "transistor structure" with a N^+-diffused region instead of the usual diode structure. The use of the transistor permits the estimation of the amount of charge transfer between the Si substrate and trap sites in thin oxide nonvolatile memory devices. A cross-sectional view of this transistor is shown in Fig. 6. In this figure, the current between the Si surface inversion layer and counter-electrode can be distinguished from the conventional MOS diode tunnel current.

Typical current density *vs.* voltage (*J-V*) curves for various oxide thicknesses are shown in Fig. 6 for two different current paths. The broken lines show the *J-V* characteristics between Al electrode and Si substrate (N^+-diffused region is electrically in floating condition). The dotted lines show the *J-V* characteristics between the Al electrode and N^+-

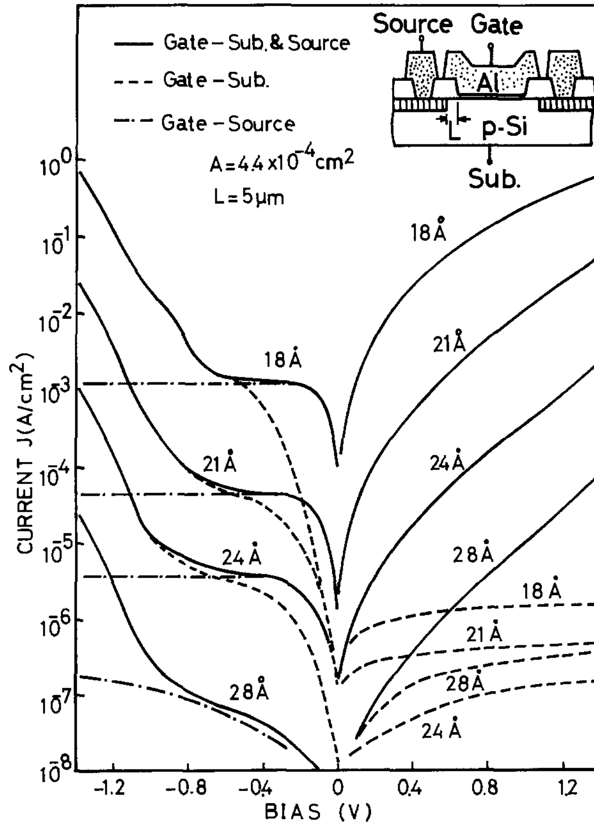

Fig. 6. Typical current density J *vs.* voltage V curves with various oxide thickness. Oxide films are formed at 1000°C. Broken lines show the *J-V* curves between Al and Si substrate. Dotted lines show the *J-V* curves between the Al and N^+ diffused region through the surface inversion layer. Solid curves indicate the *J-V* curves between Al and Si substrate by shorting the N^+-diffused region and substrate.

diffused region through the surface inversion layer (the substrate is electrically in floating condition). The solid lines indicate data summarizing the above two curves (current densities are measured between the Al electrode and substrate by shorting the N^+ region and substrate). The dotted lines in the positive voltage regime coincide exactly with the solid curves.

When the oxide is moderately thin (<40Å) and the electron supplement source is the only generation current in the depletion layer, electrons can more easily transit from the Si surface to the metal electrode than maintain the inversion layer at the Si surface (Si surface is strongly depleted). The broken lines in the positive direction show this generation-limited current. This current density is independent of the applied voltage and oxide thickness. Furthermore coincidence of the dotted curves with the solid one in the positive direction indicates that most electrons are supplied from the N^+-diffused regions. The current in the positive direction may be limited by the length L of the offset region and the conductance value at this regime or by the tunnel transition probability. These currents are functions of the oxide thickness and applied voltage. The solid curves correspond to the real behavior of tunnel transitions for the switching actions in thin oxide nonvolatile memory devices.

To improve switching speed, especially in the case of electron injection from the substrate to trap sites, it is desirable that devices adopt thinner tunnelable oxide, if possible, without any fatal demerit to other device properties. Another recommendation is decrementation of the offset length, L, *i.e.*, providing a large conductance value without leakage or degradation of thin oxide films over the N^+-diffused regions.

To evaluate another feature of thin tunnelable oxide prepared by the liquid O_2 vapor pressure method, a-c conductance of MOS diode is measured with 30-22Å thick oxide over p^{++}- or n^{++}-degenerate substrates. The electrode is a mask-evaporated 1 mm diam Al dot. A typical a-c conductance dI/dV *vs.* applied voltage V curves with 30Å thick oxide over p^{++}-degenerate substrates are shown in Fig. 7. As an experimental parameter, oxidation temperature is varied from 700° to 1100°C. Conductance values for the low temperature (700°C) oxidized sample increase rapidly with increment of applied voltage in the negative direction. For a sample oxidized at 900°C, a little hump in the conductance curve can be observed for the negative bias regime corresponding to the forbidden band. For the higher temperature (1100°C) oxidized sample, only an abrupt conductance increment corresponding to the electron injection from the metal electrode to the lower edge of the conduction band can be observed. The discrepancy for positive-biased conductance curves may be caused by the fact that the heavy degeneration effect and the valence bandedge become obscure in p^{++} substrates with over 10^{19} impurities/cm^3 (17).

The frequency dependence of a-c conductance for p^{++} substrates with 22Å thick tunnelable oxide is shown in Fig. 8. The tunnelable oxide is formed at 900°C. The significant properties of these humps in the conductance curves are that (*i*) the location of the humps along the voltage axis is independent of frequency over the range 19.2 Hz-19.2 kHz; and (*ii*) the magnitude of the hump increases a little with increasing frequency. Because of property (*i*), this hump cannot due to inversion layer coupling (18). It must be due either to tunneling to interface states or to charge exchange between the interface states and the majority carriers at the valence band.

In case of a MOS tunnel diode with p^{++} substrate and thin (20-40Å) oxide film, metal carriers tunnel through the oxide into interface states and then rapidly recombine with the majority carrier at the valence band for bias corresponding to the forbidden bandgap. Thus, the current through the interface states is tunneling controlled ($\tau_{tunnel} >> \tau_{recombine}$) (19). Then the humps in Fig. 8 may be due to tunneling to interface states.

Frequency response of a-c conductance characteristic depends on the transition probability of an elec-

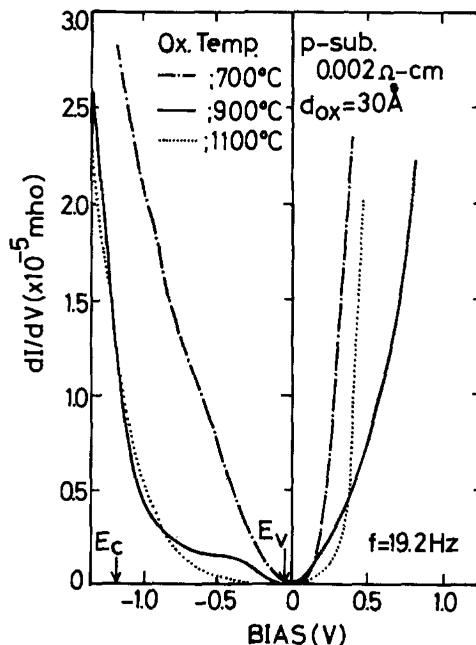

Fig. 7. A typical a-c conductance vs. applied voltage curves with 30Å thick oxide over p^{++} substrates.

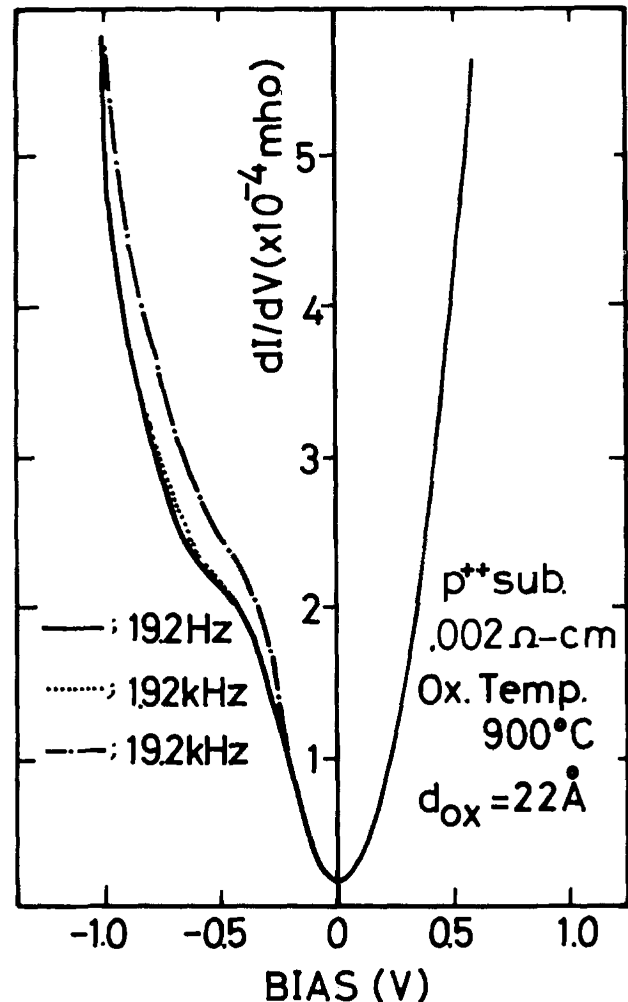

Fig. 8. Frequency dependence of a-c conductance for p^{++} substrates with 22Å thick oxide. The oxide is formed at 900°C.

tron from the metal into the interface states. The characteristic frequency depends linearly on the density of interface states (18). Thus, little frequency dependence indicates that there are few interface states in that sample.

D-c and a-c conductance distinctly reflect the effect of the semiconductor band structure and the density of interface states. Freeman and Dahlke provided a theoretical analysis (19) to evaluate the d-c and low frequency a-c conductance characteristics assuming various energy distributions of interface states. In the case of degenerate substrate, surface potential is usually a negligible correction and the variable range of surface potential at maximum is less than 3×10^{-3}V for p^{++} substrates with the applied voltage range in Fig. 7. According to this fact and Freeman's theoretical evaluation, tunneling conductance is approximately proportional to the density of interface states. This indicates that humps or increments in conductance curves shown in Fig. 7 correspond to the distribution map of interface state density. An energy band diagram and distribution map of interface state density derived from Fig. 7 is shown in Fig. 9. In this figure, the vertical axis is expressed in arbitrary units. This is because the magnitude of experimental results does not coincide with the calculated one. This discrepancy may be caused by the misestimation of values such as capture cross section of interface state or average attenuation constant at the interface.

The a-c conductance curves for a sample having an n^{++} degenerate (0.009 Ω-cm) substrate with a 22Å thick oxide is shown in Fig. 10.

The tunnelable oxide is formed at 900°C. The approximate voltages corresponding to bandedges are also shown in this figure as E_v and E_c. As can be seen in Fig. 10, conductance values increase simply as a result of increment in the positive and negative applied voltage.

For n^{++} substrate, the effective oxide barrier is expected to be smaller than for those of p^{++} sample (14). For a negative bias on the gate electrode, electrons tunnel from the gate to empty states of the semiconductor conduction band, resulting in a large, rapidly increasing current. A small positive bias on the gate produces increased electron tunneling from the semiconductor conduction band into the gate electrode. In addition to this current component, electron tunneling from the interface states into the metal gate is generated by a further increase in bias. This second component (19) is due to the decrease in effective oxide barrier.

For larger voltage additional tunneling from the valence band to the gate electrode occurs. However, this tunneling has a comparatively small influence on the total conductance characteristic on account of the high oxide barrier, *i.e.*, p^{++} sample. This is why

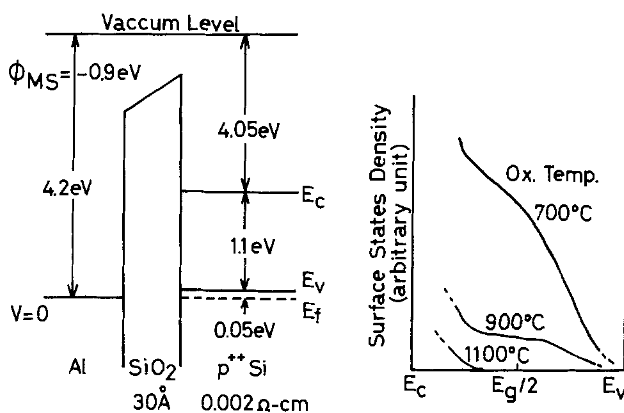

Fig. 9. Energy band diagram of MOS tunnel diode with 30Å thick oxide over p^{++} substrates and a distribution map of $Si\text{-}SiO_2$ surface state density evaluated from Fig. 7.

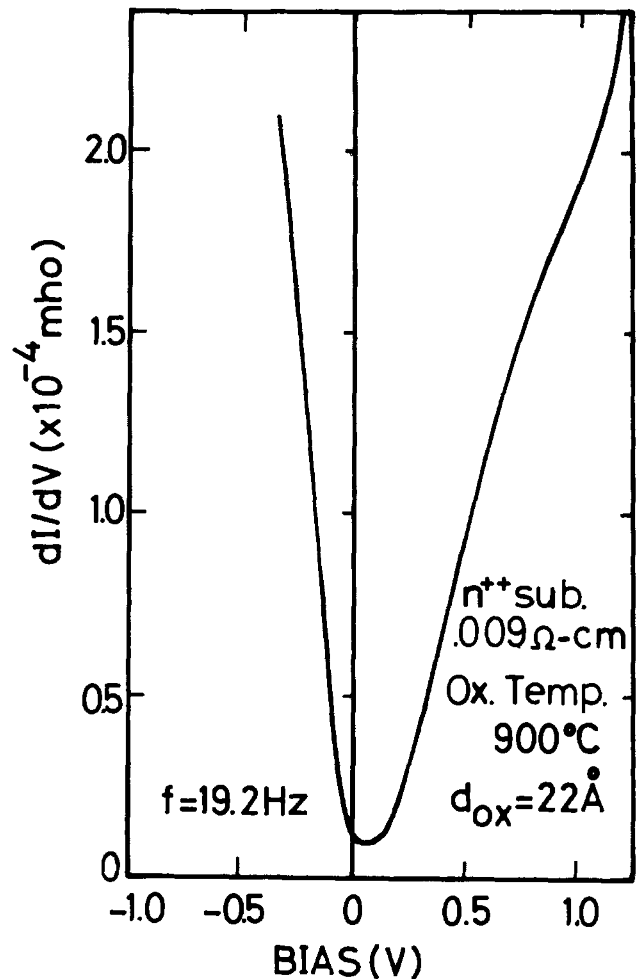

Fig. 10. Typical a-c conductance curve for a sample with an n^{++} substrate under 22Å thick oxide which is formed at 900°C. The band structure of Si has a much smaller influence on the conductance characteristics compared to p^{++} samples.

the Si band structure has a much smaller influence on the conductance characteristics of the n^{++} sample (Fig. 10) compared to the p^{++} one (Fig. 7 and 8).

Conclusion

Thin tunnelable oxides (20-80Å) are formed by a high temperature (up to 1100°C) oxidation method within ±0.5Å accuracy. This oxidation process uses liquid O_2 as an oxidant source at liquid N_2 temperature. The partial pressure of vaporized O_2 in steady-state conditions is verified as being nearly equal to 1×10^{-3} atm. The oxidation kinetics in our experimental range are governed by the inverse-logarithmic relation which is caused by the field-assisted diffusion law.

The activation energy of oxidation rate is evaluated as 20.2 kcal/mole and this value is smaller than previous data. The smaller value of the activation energy may suggest that the described process is distinguished from other formation methods of thin oxide films for impurity content in the oxide films.

Electrical properties such as effective mass in the valence band and $Si\text{-}SiO_2$ interface state density are evaluated and discussed by capacitance and a-c conductance measurements. Results obtained are; $m_D = 0.296\ m_o$ and interface state density decreases with increasing oxidation temperature. No hump can be observed in the capacitance curve for the sample oxidized at higher temperature. This indicates that less interface state is originated by the oxidation process described. Interface state density for p^{++} substrate increases as the energy level approaches the lower edge of the conduction band within the forbidden

band for samples oxidized at low temperature. However, for n^{++} substrate, interface state density cannot be estimated because interface states are filled with conduction electrons due to recombination.

To estimate the real behavior of charge transition in the thin oxide nonvolatile memory devices, tunnel currents are measured in an actual transistor structure. This permits the current between the Si surface inversion layer and the counterelectrode to be distinguished from the conventional MOS diode tunnel current. As a result, it is predicted that channel conductance near the source region may play an important role in governing the electron injection rate into the trap sites.

The thin tunnelable oxide layers described have been and are being used in FTMIS (floating silicon gate tunnel injection metal-insulator-silicon) memory devices. They are tunnel-mode type nonvolatile memory devices (20, 21). In the thin oxide memory devices, memory characteristics such as fatigue phenomena depend strongly on the properties of the thin oxide and most devices have degradated after 10^6-10^8 cycles of operation (1). However, FTMIS memory devices with thin tunnelable oxide described can operate without any fatigue phenomena after 2×10^{12} cycles endurance operation (21). Thus, this oxidation process is best fit for fabrication of various kinds of thin oxide devices.

Acknowledgment

The authors wish to express their appreciation to Dr. Ruji Kondo, Sigeru Nishimatsu, Hisao Katto, and Yokichi Itoh for their valuable advice and technical discussion throughout the course of this study.

Manuscript submitted April 19, 1977; revised manuscript received Nov. 15, 1977.

Any discussion of this paper will appear in a Discussion Section to be published in the December 1978 JOURNAL. All discussions for the December 1978 Discussion Section should be submitted by Aug. 1, 1978.

Publication costs of this article were assisted by Hitachi, Limited.

REFERENCES

1. J. J. Chung, *Proc. IEEE*, **64**, 1039 (1976).
2. B. E. Deal and A. S. Grove, *J. Appl. Phys.*, **36**, 3770 (1965).
3. A. G. Revesz and R. J. Evans, *J. Phys. Chem. Solids*, **30**, 551 (1969).
4. B. E. Deal, M. Shlar, A. S. Grove, and E. H. Snow, *This Journal*, **114**, 266 (1967).
5. J. A. Aboaf, *ibid.*, **118**, 1370 (1971).
6. Y. J. van der Meulen, *ibid.*, **119**, 530 (1972).
7. T. Smith and A. J. Carlen, *J. Appl. Phys.*, **43**, 2455 (1972).
8. J. Shewchun and A. Waxman, *Rev. Sci. Instr.*, **37**, 1195 (1966).
9. D. W. Hess and B. E. Deal, *This Journal*, **122**, 579 (1975).
10. Y. Kamigaki and Y. Itoh, *J. Appl. Phys.*, **48**, 2891 (1977).
11. N. Cabrera and N. F. Mott, *Rep. Prog. Phys.*, **12**, 163 (1948).
12. J. T. Law, *J. Phys. Chem.*, **61**, 1200 (1957).
13. J. Macerjian, G. Petersson, and C. Svensson, *Solid-State Electron.*, **17**, 335 (1974).
14. B. E. Deal, E. H. Snow, and C. A. Mead, *J. Phys. Chem. Solids*, **27**, 1873 (1956).
15. W. R. Hunter, D. H. Eaton, and C. T. Sah, *Appl. Phys. Lett.*, **17**, 211 (1970).
16. S. Karr and W. E. Dahlke, *ibid.*, **18**, 401 (1971).
17. P. V. Gray, *Phys. Rev.*, **140**, No. 1A, 179 (1965).
18. J. Shewchun, A. Waxman, and G. Warfield, *Solid-State Electron.*, **10**, 1165 (1967).
19. L. B. Freeman and W. E. Dahlke, *ibid.*, **13**, 1483 (1970).
20. M. Horiuchi, Paper presented at the IEEE International Electron Devices Meeting, Washington, D.C., 1972.
21. M. Horiuchi and Y. Itoh, *IEEE Trans. Electron Devices.*, **ed-24**, 587 (1977).

The Effect of Chloride Etching on GaAs Epitaxy Using TMG and AsH$_3$

Rajaram Bhat*,[1] and Sorab K. Ghandhi*

Electrical and Systems Engineering Department, Rensselaer Polytechnic Institute, Troy, New York 12181

ABSTRACT

A study has been made of the effect of *in situ* etching of (100) Cr-doped semi-insulating and Te-doped n$^+$-GaAs substrates on epitaxial layers, grown by the reaction of trimethylgallium and arsine. It is shown that *in situ* etching enables the growth rate to be increased by a factor of two while retaining a specular surface. In addition, the Hall mobility is higher in epitaxial layers grown on *in situ* etched substrates than on unetched ones. Epitaxial films on both $AsCl_3$ and HCl gas-etched substrates had a room temperature mobility that decreased from $\simeq$6100 cm^2/V-sec in 5.5 μm layers to $\simeq$5100 cm^2/V-sec in 1 μm layers. However, for layers grown on substrates which were not *in situ* etched, the mobility decreased from $\simeq$5800 to $\simeq$3800 cm^2/V-sec for layer thicknesses from 5.5 to 1 μm, respectively. Further it is shown that the carrier concentration profile is more abrupt near the epitaxial layer/Te-doped GaAs substrate interface when the substrates were *in situ* etched. Finally, experiments with chloride etching during growth were disappointing because it was not possible to obtain simultaneously good surface morphology, low carrier concentration, and high mobility for any given set of reactor conditions.

The growth of epitaxial layers of III-V semiconductors using organometallic compounds as sources of the group III element and hydrides as sources of the group V element was first reported by Manasevit (1). Since that time, the inherent simplicity of organometallic systems has been exploited in the growth of many other materials. One of their many advantages is that the

* Electrochemical Society Active Member.
[1] Present address: General Electric Company, Semiconductor Products Department, Syracuse, New York.

metal alkyl-hydride reaction is an irreversible one, so that etching and autodoping effects are notably absent. Unfortunately, however, this feature necessitates the use of an *in situ* etch step prior to epitaxial growth, which has been recognized by many workers as an essential step in the growth sequence to improve the quality of the epitaxial deposit (2, 3, 4). In GaAs epitaxial growth systems using trimethylgallium (5), this necessitates the use of etchants such as HCl gas or $AsCl_3$ vapor to incorporate this capability. The experimental conditions under which vapor-phase etching and polishing of GaAs substrates can be achieved have been established earlier (6, 7). In this paper, we report the effects of *in situ* etching on the properties of the subsequently deposited GaAs layer. It is demonstrated that *in situ* etching enables an increase in the growth rate while still retaining a specular surface. In addition, it is shown that this etching step results in an improvement in the electrical properties of the epitaxial layers, especially when they are thin (1-2 μm). Hall measurements, in conjunction with layer-by-layer stripping, were used to characterize epitaxial layers deposited on semiinsulating Cr-doped substrates. *C-V* and *dC/dV-V* measurements on Au-GaAs Schottky barrier diodes were used to obtain the free carrier concentration profiles in epitaxial layers grown on n^+ Te-doped GaAs.

Finally, we report on the results of GaAs epitaxy involving the reaction of TMG and AsH_3 in the presence of HCl gas or $AsCl_3$ vapor. The experimental results were disappointing, however, since we found that it was not possible to achieve simultaneously good morphology, low carrier concentration, and high mobility for any given set of reactor conditions.

Experimental Conditions

Apparatus.—*In situ* etching and epitaxial growth were carried out in a conventional rf heated, cold-wall reactor whose schematic is shown in Fig. 1. The reactants were introduced into a 50 mm ID, 37 cm long, horizontally positioned quartz reaction chamber containing a pyrolytic graphite-coated graphite susceptor. A baffle (not shown) was used to mix the reactants prior to their entry into the hot zone. The temperature was monitored using a Pt/Pt-13% Rh thermocouple enclosed in a quartz sheath and inserted into the susceptor, and verified by infrared pyrometric measurements. Gases were delivered to the reaction chamber through stainless steel tubing, except in the case of HCl gas and $AsCl_3$ vapor where Monel and Teflon, respectively, were used to minimize contamination.

Reactants.—Technical grade hydrogen (99.95% purity) was successively passed through an oxygen-removing catalyst,[2] a molecular sieve,[2] a palladium purifier,[2] and a cold trap at 77°K to obtain the carrier gas used in this investigation. This carrier gas was passed through a stainless steel bubbler containing electronic grade trimethylgallium[3] at 0°C. The arsine gas used was a 10% mixture of electronic grade arsine (99.998% purity) in six nines hydrogen.[4] The etchants used were either a 1% mixture of electronic grade HCl gas (99.995% purity) in six nines hydrogen[3] or vapors of $AsCl_3$[5] (99.9999% purity) produced by passing hydrogen through a Pyrex bubbler, containing the liquid at room temperature.

Substrates.—Experiments were carried out on chromium-doped semi-insulating and tellurium-doped n^+-GaAs substrates, with 2° off (100) towards (110) orientation. The wafers were obtained with one side chemimechanically polished by the vendors.[6] These were degreased in hot methanol, boiled in hydrochloric

[2] Matheson Gas Products, East Rutherford, New Jersey 07073.
[3] Alfa Products Division, Beverly, Massachusetts 01915.
[4] Precision Gas Products, Incorporated, Rahway, New Jersey 07065.
[5] Metal Specialties, Fairfield, Connecticut 06430.
[6] Laser Diode Laboratories, Incorporated, Metuchen, New Jersey.

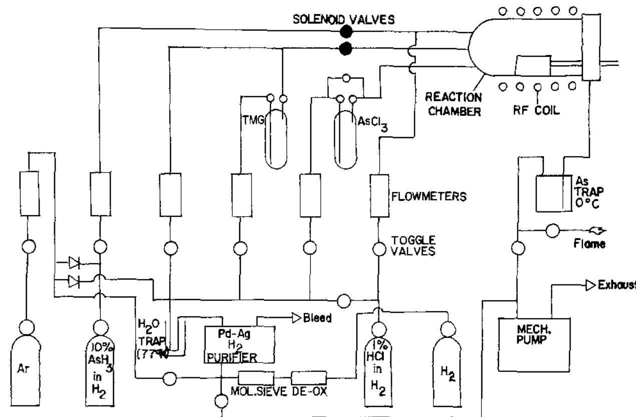

Fig. 1. Schematic of the epitaxial reactor

acid for 2 min, rinsed in methanol, and blown dry in filtered nitrogen. They were then etched in Caro's etch [$10H_2SO_4$ (97%):$1H_2O_2$ (30%):$1H_2O$] at 60°C for 30 sec, rinsed in DI water, rinsed in methanol, and blown dry in filtered nitrogen.

Procedure.—Substrates measuring 5 × 10 mm were placed on the susceptor such that they were nearly perpendicular to the direction of gas flow. The system was evacuated with a mechanical pump before establishing a flow of hydrogen (5 liters/min). The susceptor was then heated to 900°C (in those cases where an *in situ* etch was performed), after introducing the required amount[7] of arsine (30 ml/min) to prevent decomposition of the GaAs substrates. The etching was performed using either a flow of 4.2 ml/min of HCl gas or a hydrogen flow of 80 ml/min through the $AsCl_3$ bubbler. These processes removed a 4.5 μm thick layer from the substrate surface at a rate of 2.25 μm/min. The temperature was then stabilized at 700°C before commencing epitaxial growth. Subsequent GaAs epitaxial layers were deposited using a total hydrogen flow of 5 liters/min, an arsine flow of 15 ml/min, and a hydrogen flow through the TMG bubbler of up to 12 ml/min. The growth rate was determined by cleaving and staining.

In a second series of experiments GaAs layers were also grown on *in situ* etched substrates in the presence of HCl gas or $AsCl_3$ vapor. The introduction of HCl gas during deposition resulted in an increase in the free electron concentration by at least an order of magnitude. This was attributed to the impure nature of the gas, and all further experiments were restricted to the use of high purity $AsCl_3$ vapors during the growth. In these experiments, GaAs was deposited on (100) Cr-doped substrates at 700°C, using a hydrogen flow of 5 liters/min, a hydrogen flow through the TMG bubbler of 10 ml/min, and arsine flow of 15 ml/min. The hydrogen flow through the $AsCl_3$ bubbler was varied between zero and 80 ml/min.

Surface Morphology and Growth Rates

Effect of in situ etching on surface morphology.—Epitaxial layers were deposited on both *in situ* etched and unetched substrates. Layers on unetched substrates exhibited specular surfaces at low growth rates ($\leq$ 0.25 μm/min), corresponding to a H_2 flow through the TMG bubbler of $\leq$ 5 ml/min. With *in situ* etching, however, mirror-like surfaces could be achieved for growth rates as high as 0.5 μm/min. This is shown in the Nomarski interference micrographs of Fig. 2 for layers grown at 0.4 μm/min, both with and without *in situ* etching. Furthermore, differences in surface quality of layers deposited on HCl gas and $AsCl_3$ etched GaAs substrates were very slight, as shown in this figure.

[7] In this paper, flow rates for AsH_3 and HCl gas are all quoted in terms of the actual arsine and hydrogen chloride gas content of the diluted gas.

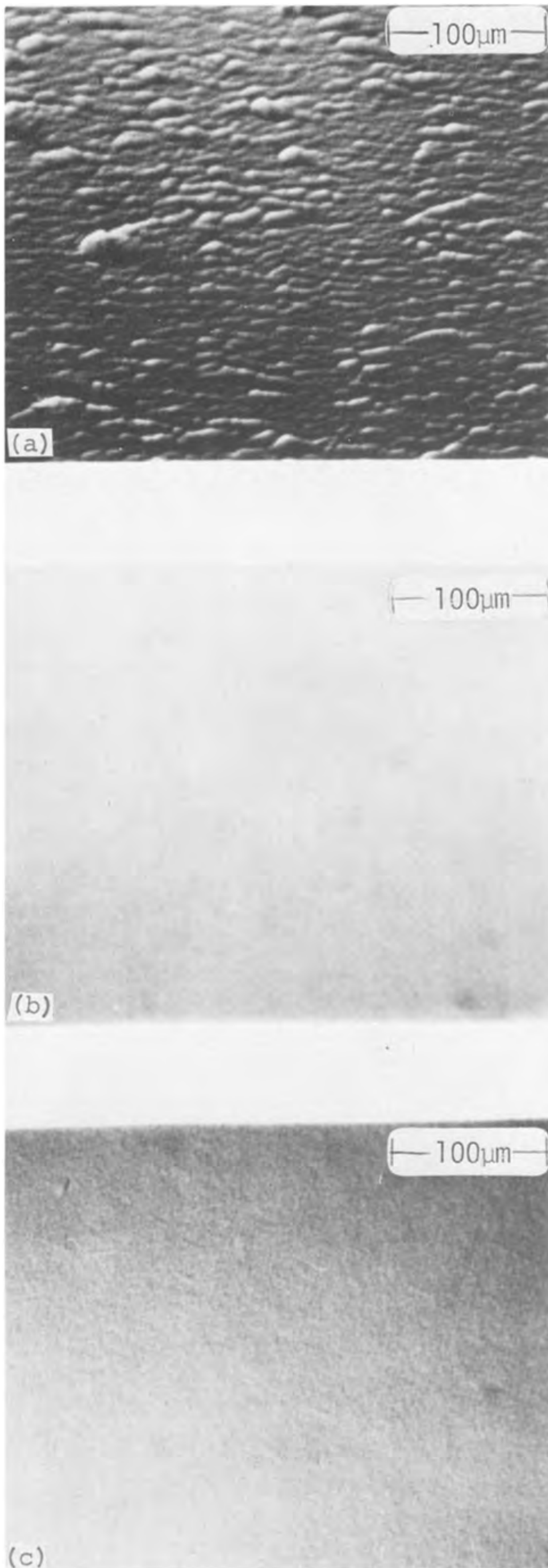

Fig. 2. Typical Nomarski interference photomicrographs showing the effect of *in situ* etching of GaAs substrates on the surface morphology of epitaxial layers (a) no *in situ* etch; (b) HCl gas etch; and (c) $AsCl_3$ etch (growth rate: 0.4 μm/min).

Effect of introducing $AsCl_3$ vapor during epitaxy.—The growth rate of layers deposited at 700°C in the presence of $AsCl_3$ fell linearly with increasing hydrogen flow through the $AsCl_3$ bubbler, varying from 0.4 μm/min for no $AsCl_3$ to 0.2 μm/min for a hydrogen flow of 80 ml/min. There was considerable scatter in the data, however, accompanied by a deterioration in surface morphology at low growth rates. Better surfaces were obtained for layers deposited at 900°C. However, this temperature is far from the optimum for growth using TMG and AsH_3, and resulted in layers with low mobility and high compensation.

Electrical Properties

Epitaxial layers on Cr-doped substrates.—Epitaxial layers were deposited at 700°C on unetched and on *in situ* etched (100) Cr-doped semi-insulating substrates. A total hydrogen flow of 5 liters/min, an arsine flow of 15 ml/min, and a hydrogen flow of 10 ml/min through the TMG bubbler were used to obtain a growth rate of 0.4 μm/min. Tables I and II list[8] the carrier concentration and mobility of epitaxial layers of varying thickness, as obtained by Hall measurements on successively etched layers. Room temperature values of mobility ranged from 6150 cm^2/V-sec for thick (5.5 μm) layers for substrate etching with $AsCl_3$, to 3800 cm^2/V-sec for thin (1 μm) layers with no substrate etching. Results at liquid nitrogen temperature showed a similar trend.

Hall measurements were also made on 5 μm thick GaAs layers, grown at 700°C in the presence of $AsCl_3$ vapor. As expected, the increase of hydrogen flow through the $AsCl_3$ resulted in a fall in carrier concentration, as shown in Fig. 3. However, this fall in elec-

[8] Error limits on this data are ±10% on thickness, ±5% on mobility, and ±15% on carrier concentration. Layer thickness variations over the surface of the Hall samples were undetectable.

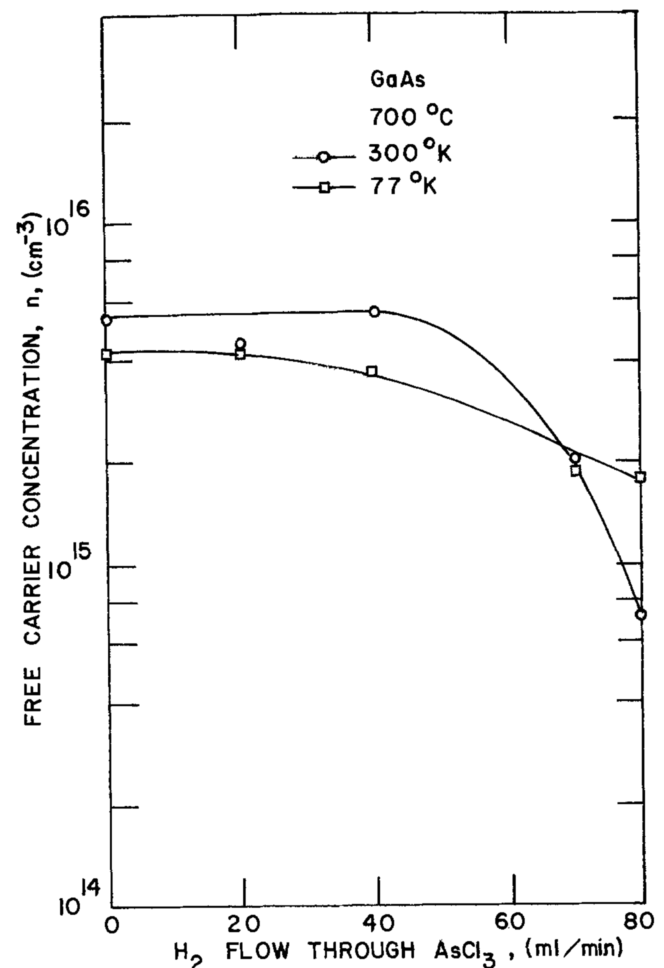

Fig. 3. Carrier concentration vs. hydrogen flow rate through the $AsCl_3$ bubbler during epitaxy.

Table I. Carrier concentration and mobility at room temperature for epitaxial layers of different thickness

Thickness, μm	No etch: Carrier concentration, per cm^3	No etch: Mobility, cm^2/V-sec	HCl gas etch: Carrier concentration, per cm^3	HCl gas etch: Mobility, cm^2/V-sec	$AsCl_3$ etch: Carrier concentration, per cm^3	$AsCl_3$ etch: Mobility, cm^2/V-sec
5.5	8.3×10^{16}	5780	8.4×10^{15}	6100	5.7×10^{15}	6150
4	8.6×10^{15}	5550	9.1×10^{15}	6020	5.7×10^{15}	6070
2	8.74×10^{15}	5240	1.13×10^{16}	5710	6.1×10^{15}	5770
1	1.6×10^{16}	3800	1.4×10^{16}	5010	3.4×10^{16}	5090

Table II. Carrier concentration and mobility at liquid nitrogen temperature for epitaxial layers of different thickness

Thickness, μm	No etch: Carrier concentration, per cm^3	No etch: Mobility, cm^2/V-sec	HCl gas etch: Carrier concentration, per cm^3	HCl gas etch: Mobility, cm^2/V-sec	$AsCl_3$ etch: Carrier concentration, per cm^3	$AsCl_3$ etch: Mobility, cm^2/V-sec
5.5	6.2×10^{15}	13,800	6.4×10^{15}	14,400	4.5×10^{15}	15,300
4	6.83×10^{15}	12,700	6.8×10^{15}	13,900	4.75×10^{15}	15,000
2	8.1×10^{15}	11,100	8.7×10^{15}	13,700	5.6×10^{15}	14,000
1	4.8×10^{15}	7,000	1.2×10^{16}	12,000	5.7×10^{15}	12,500

tron concentration was accompanied by increasing compensation in the films, as evidenced by the disparity in the 300° and 77°K data. Figure 4 shows that the compensation ratio (8) changed from below 0.5 for no $AsCl_3$ to as high as 0.95 for 80 ml/min hydrogen flow through the $AsCl_3$ bubbler.

Experiments with films grown at 900°C showed a similar trend. Consequently, the quest for making films of improved quality (lower carrier concentration, lower compensation ratio, and higher mobility) by epitaxy in the presence of $AsCl_3$ vapor was abandoned.

Epitaxial layers on Te-doped substrates.—GaAs epitaxial layers were deposited on unetched and *in situ* etched Te-doped (100) substrates, the deposition and *in situ* etching being performed simultaneously with those on Cr-doped substrates used for obtaining the Hall measurement data presented earlier. The layers were chemically thinned to approximately 1 μm to allow carrier concentration profiling of the epitaxial layer-substrate interface using Au-GaAs Schottky barriers. The free carrier concentration profiles were obtained from C-V and dC/dV-V data using the relation

$$n(x) = \frac{C^3}{q\epsilon_r\epsilon_0 A^2 (dC/dV)}$$

where $n(x)$ is the free carrier concentration at a depth x below the surface, C is the capacitance of the Schottky barrier, of area A, ϵ_0, ϵ_r are the permittivity of free space and relative permittivity of GaAs, respectively, q is the electronic charge, and V is the reverse voltage applied across the Schottky barrier.

Figure 5 shows normalized plots of the free carrier concentration profiles obtained [any effect due to the presence of traps (9) has been ignored]. The carrier concentration in these layers was approximately 5×10^{15} per cm^3. Doping profiles obtained for *in situ* etched substrates are seen to be far more abrupt than for the case with no substrate etching.

Discussion

Epitaxial layers on Cr-doped substrates.—A number of observations can be made from a study of the data of Tables I and II. Thus:

(*i*) The mobility was higher in those layers deposited on substrates which were vapor etched than

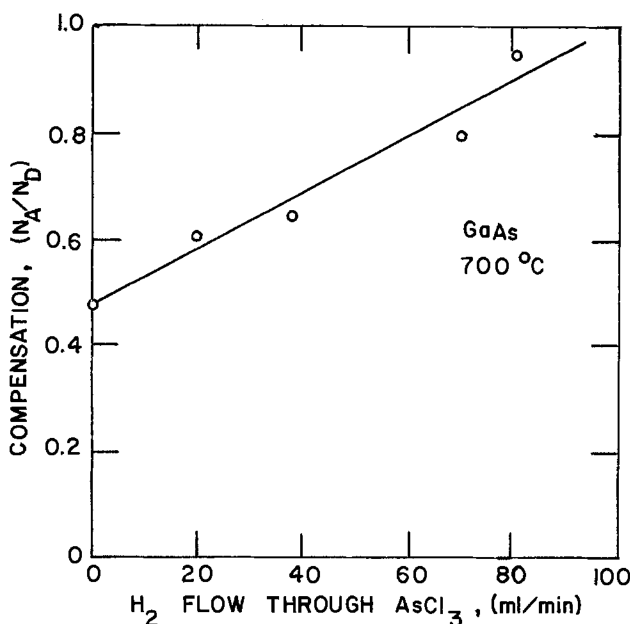

Fig. 4. Compensation ratio vs. hydrogen flow rate through the $AsCl_3$ bubbler during epitaxy.

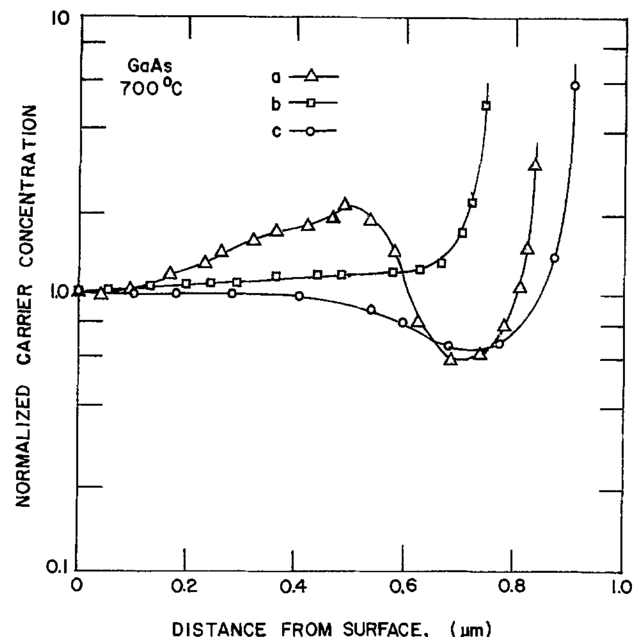

Fig. 5. Normalized carrier concentration profiles of epitaxial layers on (100)Te-doped GaAs substrates (a) unetched substrates; (b) HCl gas etched substrates; and (c) $AsCl_3$ etched substrates.

in those which were not vapor etched. *In situ* etching of substrates, therefore, enables the growth of epitaxial layers of superior crystalline quality. The room temperature mobility was comparable for epitaxial layers on $AsCl_3$ and HCl etched substrates. The slightly higher 77°K mobility obtained for layers on $AsCl_3$ etched substrates is due to the lower carrier concentration in these layers.

(*ii*) The mobility in all cases decreased with epitaxial layer thickness, the decrease being most rapid for layers grown on unetched substrates. A decrease in mobility with epitaxial layer thickness has also been observed by other investigators (10-12), and has been attributed to the increasingly important role of space-charge scattering effects at the epitaxial layer-substrate interface. The results obtained in this study indicate that *in situ* etching of substrates prior to growth results in a cleaner surface and thus reduces, but does not eliminate, the space charge centers due to defects created in the epitaxial layers. It should be noted that growth instabilities exist even when ideally clean and perfect GaAs substrate surfaces are used. These will set a lower limit to the density of space charge centers, and are inherent to the growth process. The decrease in mobility with epitaxial layer thickness can also be due to increasing compensation, and hence ionized impurity concentration, with decreasing thickness. However, the relative contributions of ionized impurity and space charge scattering in thin layers cannot be estimated from the available data.

(*iii*) The free carrier concentration is highest in layers grown on HCl etched substrates, particularly in thin layers. This is probably due to contamination of the substrate surface by n-type impurities present in the HCl gas. In contrast, the $AsCl_3$ used for this study was better than six nines purity, so contamination of the substrate surfaces by this etchant is not expected. This is borne out by the fact that the lowest carrier concentrations are observed in layers grown on $AsCl_3$ etched substrates (except for the 1 μm layers, where strong compensation effects are present, as described below).

(*iv*) The carrier concentration decreased with decreasing layer thickness for both unetched and $AsCl_3$ etched substrates. This effect was, however, significantly more rapid for layers grown on unetched substrates. Acceptor-type defects introduced in the early stages of growth are believed to be responsible for this behavior, since substantially more defects are expected to occur in epitaxial layers grown on unetched than on etched substrates. With HCl gas etching, contamination of the substrate surface masks the compensation due to these acceptor-type defects, and results in an increase in carrier concentration at the epitaxial layer-substrate interface.

Epitaxial layers on Te-doped substrates.—It is seen from Fig. 5 that the carrier concentration for layers on HCl gas etched substrates increased monotonically as the epitaxial layer-substrate interface was approached. However, a slight fall in carrier concentration was noted near the interface for epitaxial layers on $AsCl_3$ etched substrates. These observations can be explained by noting that instabilities during the early stages of growth cause acceptor-type defects to be created. The effect of these acceptor-type defects is not observed in the case of epitaxial layers on HCl gas etched substrates because of the n-type contaminants introduced by this etchant in the interface region. However, substrates etched with $AsCl_3$ were not contaminated since this etchant was ultrapure. As a result, epitaxial layers on these substrates showed a decrease in carrier concentration near the interface because of these acceptor-type defects. In contrast, the carrier concentration profile exhibited a pronounced undulation near the interface for layers grown on unetched substrates. A possible explanation for this behavior can be based on the fact that a large concentration of acceptorlike defects can be expected to occur for this case. In addition, the unetched surface of GaAs is highly reactive, and probably has a large concentration of adsorbed sulfur (an n-type impurity) on its surface because of the Caro's etch prior to growth (13). The competing decay of these impurities with distance may, in this situation, lead to the observed undulation in the impurity profile.

Epitaxial layers deposited in the presence of $AsCl_3$ vapor.—There are a number of possible explanations for the increase in the compensation of epitaxial layers from TMG and AsH_3 in the presence of $AsCl_3$ vapor. Of these, the most plausible is that the $AsCl_3$ removes donor impurities faster than acceptor impurities from the source materials. The major acceptor impurity in GaAs grown from TMG and AsH_3 is carbon, whereas the major donor impurity is silicon (14, 15). The change in Gibbs free energy for the reaction of these impurities with the etchant species (HCl) is negative for silicon, so that only silicon chlorides are stable at growth temperatures. Consequently, silicon is selectively removed during epitaxy in the presence of $AsCl_3$ vapor, resulting in an increase in the compensation ratio. In marked contrast, the principal impurities in the halide transport system are silicon and zinc, both of which have stable chlorides at deposition temperatures. Consequently, increasing the $AsCl_3$ concentration in halide transport systems is a highly successful technique for reducing the free electron concentration with no increase in the compensation ratio (16).

Conclusions

In summary, *in situ* etching of GaAs substrates prior to epitaxy enables the growth of epitaxial layers with specular surfaces at higher growth rates than are otherwise possible. The mobility, particularly in thin ($\simeq$ 1 μm) layers, was higher for layers on substrates which were *in situ* etched. The carrier concentration profiles for epitaxial layers on Te-doped substrates were more abrupt at the interface for layers on substrates which were vapor etched than on those which were not. Epitaxial layers on $AsCl_3$ and HCl gas-etched substrates had comparable mobility. Further, the carrier concentration, particularly in thin layers, was higher in epitaxial layers on HCl gas-etched substrates due to n-type contaminants introduced by this etchant. Finally, experiments with epitaxial growth in the presence of $AsCl_3$ showed that it was possible to obtain a reduction in the free electron concentration by this technique. However, this was accompanied by an increase in the compensation ratio and a general deterioration in the crystal quality. This result is in marked contrast to that obtained by workers with halide transport systems.

Acknowledgments

This work was partly supported by Grant No. DAAG29-76-G-0127 from the U.S. Army Research Office, Durham, North Carolina. One of the authors (R. Bhat) wishes to acknowledge Fellowship support from the IBM Research Foundation. The authors are also indebted to Ms. R. C. Rafun for assistance in manuscript preparation.

Manuscript submitted June 20, 1977; revised manuscript received Dec. 19, 1977.

Any discussion of this paper will appear in a Discussion Section to be published in the December 1978 JOURNAL. All discussions for the December 1978 Discussion Section should be submitted by Aug. 1, 1978.

Publication costs of this article were assisted by Rensselaer Polytechnic Institute.

REFERENCES

1. H. M. Manasevit, *Appl. Phys. Lett.*, **12**, 156 (1968).
2. C. M. Wolfe, A. G. Foyt, and W. T. Lindley, *Electrochem. Tech. J.*, **6**, 208 (1968).
3. R. D. Fairman and R. Solomon, *This Journal*, **120**, 541 (1973).

4. T. Nozaki and T. Saito, *Jpn. J. Appl. Phys.*, **11**, 110 (1972).
5. H. M. Manasevit and W. I. Simpson, *This Journal*, **116**, 1725 (1969).
6. R. Bhat, B. J. Baliga, and S. K. Ghandhi, *ibid.*, **122**, 1378 (1975).
7. R. Bhat and S. K. Ghandhi, *ibid.*, **124**, 1447 (1977).
8. C. M. Wolfe, G. E. Stillman, and W. T. Lindley, *J. Appl. Phys.*, **41**, 3088 (1970).
9. L. C. Kimerling, *ibid.*, **45**, 1839 (1974).
10. B. J. Baliga and S. K. Ghandhi, *This Journal*, **121**, 1646 (1974).
11. Y. Nakayama, S. Ohkawa, H. Hashimoto, and H. Ishikawa, *ibid.*, **123**, 1227 (1976).
12. A. Shibatomi, N. Yokoyama, H. Ishikawa, K. Dazai, and O. Ryuzan, *J. Cryst. Growth*, **31**, 240 (1975).
13. D. J. Stirland and B. W. Straughan, *Thin Solid Films*, **31**, 139 (1976).
14. S. J. Bass, *J. Cryst. Growth*, **31**, 172 (1975).
15. S. Ito, T. Shinokara, and Y. Seki, *This Journal*, **120**, 1419 (1973).
16. J. V. DiLorenzo, *J. Cryst. Growth*, **17**, 189 (1972).

Effect of Proton Damage on Optical Modulation Spectra of Gallium Arsenide

Moshe Oren,[1] A. R. Quinton, and Claude M. Penchina

Department of Physics and Astronomy, University of Massachusetts, Amherst, Massachusetts 01003

ABSTRACT

We studied the effect of proton bombardment on the electroreflectance (ER), electroabsorption (EA), and transmission (T) spectra of high resistivity Cr-doped single crystal GaAs. The high resolution of ER and EA and their sensitivity to crystalline order make it possible to study shift, broadening, and gradual distortion of the spectral peaks as disorder increases with successive irradiations. The sample is bombarded with 150 keV protons. We have measured ER and EA at the absorption edge E_0, ER at the E_1 critical point, and d-c optical absorption. All these measurements are sensitive to proton irradiation of the sample; the most sensitive one is ER at E_0. In the range of 3×10^{14} to 5×10^{15} protons/cm^2, optical absorption just below the energy gap increases sublinearly with proton dose; the peak-to-peak amplitudes of ER at E_0 and E_1 vary linearly with the logarithm of the dose and hence can be used to measure the degree of damage in the sample. The EA signal at E_0 develops a tail toward the low energy side of the spectrum. The ER at E_0 has a peak shift of $\approx$4 meV to higher energy while the peak of the ER signal at E_1 shifts by about 15 meV to lower energy. Broadening is evident in the ER signals at E_0 and E_1. Annealing at 300°C for up to 2 hr only partially recovers the unbombarded state. A model based on the gradual amorphization of the sample by an increasing number of proton damaged, amorphous islands with well-defined boundaries can partially explain the experimental results.

Lattice damage in single crystals plays a major role in device applications. Lattice damage caused by ion implantation received special attention in recent years following the introduction of ion implantation as a method for doping semiconductor materials. There are several experimental techniques that can be applied to study radiation damage in semiconductors, among others: optical (1), electrical (2), Rutherford back scattering (3), and electron paramagnetic resonance (4).

The optical absorption and reflection of GaAs were found to be sensitive to ion bombardment damage but the sensitivity of such measurements (reflectivity in particular) is low, and quantitative results are difficult to obtain.

In the present work we use electromodulation (EM) spectroscopy to study the effect of proton bombardment on single crystal, semi-insulating GaAs. In electromodulation one measures the change in reflectance (ΔR) or transmittance (ΔT) when an external electric field is applied to the sample (5). The EM response is spectrally concentrated around the critical points in the band structure. A phase sensitive detection system tuned to the frequency and phase of the external field greatly enhances the sensitivity of the measurement to critical points in the spectrum. These critical points are a manifestation of the long range order in the crystal; a change in the EM signal on successive bombardment would indicate, therefore, the gradual relaxation in this long range order. This relation allows a semi-quantitative measure of lattice damage to be made.

EM has been applied to date primarily to problems of intrinsic band-structure analysis (5), but as a powerful spectroscopic method it is now finding new areas of applications. Jonath *et al.*, (6) studied electroabsorption (EA) of oxygen impurities in GaAs. Bauer (7) used EA to study the symmetry properties of defect states in nitrogen-doped GaP and their interaction with the host band structure. Gavrilenko *et al.* studied the influence of low energy argon ion bombardment on the electroreflectance (ER) and photoluminescence spectra of n-type $Al_xGa_{1-x}As$ solid solution (8) and Si (9). Anderson *et al.* (10) used ER to detect shallow impurity levels in GaAs doped with Si, Te, Zn, or Cd impurities. A disadvantage of this method is that different types of lattice damage cannot be distinguished.

Experimental

High resistivity, n-type GaAs:Cr single crystal was used in this experiment. The sample had $\approx 10^8$ Ω-cm room temperature resistivity. For radiation damage experiments it is preferable to have the sample front surface free of any evaporated electrode or insulating layer. For that reason, the sample geometry used in the ER and the EA measurements is based on the transverse configuration (11). Slices were cut from the GaAs crystal, lapped, polished with 0.3μ alumina powder, and then etch polished with Monsanto Syton solution. For contacts, two Au films were evaporated on the

[1] Present address: Spire Corporation, Bedford, Massachusetts 01730.

Key words: electroreflectance, electroabsorption, GaAs-Cr, amorphous GaAs, ion implantation.

polished sample surface forming a gap 1 mm wide (see insert in Fig. 1). The current voltage characteristics up to 900V show good ohmic behavior. The light beam was incident in the [111] crystal direction. The magnitude of the ER signal is a function of surface potential. Therefore, it varies from sample to sample due to slight changes in surface preparation, which may alter considerably the surface potential. To avoid this complexity, only half of the gap between the field electrodes was bombarded and the other half was used as a reference for all successive measurements. The gap height is more than twice the height of the incident light beam in order that the light will not overlap the bombarded and nonbombarded regions.

The system used for the ER and EA measurement is shown in Fig. 1. It includes the following components: 250W tungsten halogen lamp, monochromator, optics, dewars, and detectors. All measurements were made at LN_2 temperature. Two photomultipliers (PM) were permanently mounted in the sample chamber, 1P28 PM to measure ER at E_1 critical point and 7102 PM for ER at the E_0 critical point. A removable front surface aluminum mirror directs the reflected beam into the PM in use. A PbS detector was used for the EA and transmission measurements. The two PM's were wired such that higher voltage was impressed between the last dynode and the anode than on the intermediate stage of the voltage divider. This allows greater linear swing of the anode voltage, which is desirable when a small a-c signal, superimposed on a large d-c signal, is to be measured. The voltage applied to the sample was 1 kHz, 2000V peak-to-peak sine wave superimposed on 1000V d-c. For the ER measurement a d-c photon flux was used, a lock-in amplifier measured the a-c signal ($I_o \cdot \Delta R$) and an electrometer measured the d-c reflection ($I_o \cdot R$). For the transmission (T) and EA measurements the incident light beam was chopped at 147 Hz; two lock-in amplifiers tuned at 1 kHz and 147 Hz measured the ΔT and T signal, respectively.

Sample bombardment was done with a 150 keV proton beam. The sample was mounted on a water-cooled holder. An in-line cold trap was used to remove oil vapor that may otherwise be carried along with the proton beam to contaminate the sample surface. In addition when a high dose was used ($\gtrsim 5 \times 10^{15}$ p/cm^2), a thin carbon film (≈ 20 μm) was inserted in front of the sample, to further prevent possible oil contamination.

Isothermal annealing of the sample was done at 300°C in an oil-free vacuum system ($\approx 5 \times 10^{-7}$ Torr).

Results

Transmission.—The sample transmission in the range of the fundamental absorption edge was measured at LN_2 temperature for various bombardment doses. In order to determine more conveniently the effect of proton damage on the sample transmission, the ratio of the transmitted intensity from the bombarded (T_b) and nonbombarded (T_o) regions was determined at one wavelength. Such a graph is shown in Fig. 2 (insert). Taking into account reflection losses, R, from the sample front and back surfaces, one can write

$$T_o = (1 - R)^2 \exp(-\alpha_o d_o) \quad [1]$$

α_o and d_o are the sample absorption coefficient and thickness, respectively (multiple internal reflections are neglected). The transmission through the bombarded region is

$$T_b = (1 - R')(1 - R) \exp(-\alpha_o d_o - \alpha_b d_b) \quad [2]$$

where R' is the reflectivity coefficient from the front surface of the bombarded region, α_b is the average value of the change in absorption coefficient over the bombarded layer thickness d_b. Measurement of $I_o \cdot R$ (when R is the reflectivity and I_o is the incident intensity) in the vicinity of the absorption edge shows a change of less than 5% due to proton bombardment. Similarly, Kalma (12) found no change in reflectivity in the vicinity of the absorption edge of GaAs following a 1 MeV electron irradiation; Sell and MacRae (1b), found a change of $\sim 3\%$ in reflectivity at 2.5 eV in argon-implanted GaAs. We assume therefore $R \approx R'$. Then

$$\ln(T_o/T_b) = \alpha_b d_b \quad [3]$$

α_b can be related to the number, N, of the optically active defects produced in the bombarded layer (13)

$$\alpha_b = N\sigma_b \quad [4]$$

where σ_b is the cross section for optical absorption by these defects. The best straight line fit to the data in the log-log plot of Fig. 2 (insert) provides the relation

$$T_o/T_b = \gamma\phi^\beta \quad [3a]$$

with $\ln \gamma = -16.9$ and $\beta = 0.48$. Therefore, from Eq. [3], [3a], and [4]

$$d_b N\sigma_b = d_b\alpha_b = \ln \gamma + \beta \ln \phi \quad [5]$$

The production rate of defects is sublinear in dose. This is due to damaged regions overlapping and possible room temperature annealing (14, 15).

If we approximate the damaged layer thickness, d_b, by the projected range (16) ($\approx 1.5\mu$) of the proton beam, the wavelength dependence of the added absorption due to bombardment can be expressed using Eq. [3]. Such a graph is presented in Fig. 2. The featureless increase in absorption indicates that the bombardment generates a continuous distribution of energy levels right below the bandgap with no evidence of discrete levels in this range. Kalma (12) studied electron irradiated GaAs, Si, Ge, InSb, and PbTe and

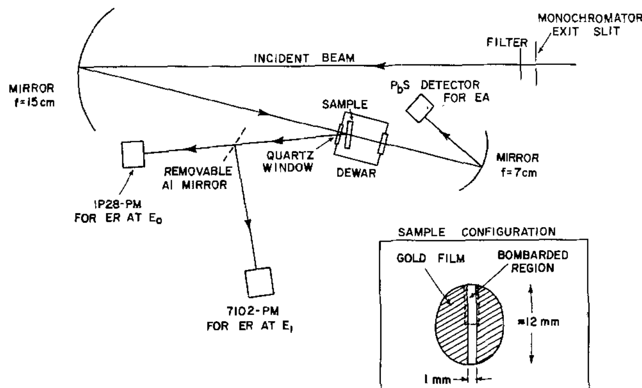

Fig. 1. Optical system used for the ER and EA measurements

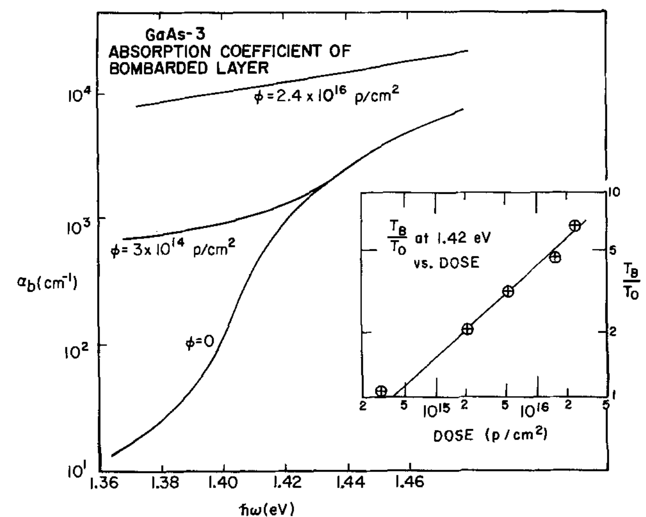

Fig. 2. Absorption coefficient of bombarded and not-bombarded regions.

suggested that increased absorption near the bandedge observed in GaAs can be attributed to tailing of the density of states into the bandgap. Note that the range of α_b ($\approx 10^4$ cm^{-1}) is about two orders of magnitude higher than the absorption coefficient observed in neutron damaged GaAs (17).

Theoretical Model

A simple picture of gradual amorphization of the sample by the incident radiation was used by a number of workers (3, 18) to describe the process in which long-range order in the bombarded layer is destroyed. In such a picture each incident proton produces a highly disordered region along its track in the sample. Assuming these regions have well-defined boundaries, at low dose they are separated from each other except for random overlapping. As the dose increases the overlapping increases until a completely amorphous layer is formed. The added absorption coefficient in this picture will be due to the introduction of amorphous islands with higher absorption

$$\alpha_b = \frac{A}{A_o}(\alpha_a - \alpha_c) \quad [6]$$

where A is the area of the amorphous regions, A_o is the total sample area exposed to the beam, and subscripts a, b, and c correspond to amorphous, bombarded, and crystalline, respectively.

Based on this description we can define a quantity $\sigma(\phi)$ which is the cross section for added amorphization per proton which hits a previously undamaged area. The probability that an additional incident proton will not hit the amorphous region A is $1 - (A/A_o)$. In terms of this cross section, the change in A per incident proton, dA/dP will be therefore

$$\frac{dA}{dP} = \frac{A}{A_o}\frac{dA}{d\phi} = \left(1 - \frac{A}{A_o}\right)\sigma(\phi) \quad [7]$$

and after integration

$$1 - \frac{A}{A_o} = \exp[-\int\sigma(\phi)\,d\phi] \quad [7a]$$

Using Eq. [6] and [7a]

$$\exp[-\int\sigma(\phi)\,d\phi] = 1 - \frac{A}{A_o} = 1 - \frac{\alpha_b}{\alpha_a - \alpha_c} \quad [8]$$

Using the experimental data for α_b as expressed in Eq. [5] and taking the logarithmic derivative of Eq. [8], we get

$$\sigma_{TR}(\phi) = \frac{1}{\phi(K_2 - \ln\phi)} \quad [9]$$

with

$$K_2 = \frac{d(\alpha_a - \alpha_c)}{\beta} - \frac{1}{\beta}\ln\gamma \quad [10]$$

For $h\nu = 1.42$ eV, $\alpha_a H >> \alpha_c$, thus α_a approximated by α_b at high dose (where $A \rightarrow A_o$)

$$\alpha_a(1.42\text{ eV}) \cong \alpha_b(1.42\text{ eV}, \phi = 2.4 \times 10^{16}\text{ p/cm}^2) = 1.24 \times 10^4\text{ cm}^{-1} \quad [11]$$

this gives

$$K_2 = 38.9 \quad [10a]$$

This same picture will be applied for the ER data, and the result compared with the results above.

ER at E_o and E_1 Critical Points

Figure 3 shows the ER at the absorption edge E_o and Fig. 4 shows the ER response at the E_1 critical point. The most obvious feature of the bombarded spectrum is the reduction in signal intensity in both cases compared to the unbombarded spectrum. To better evaluate this effect, the peak-to-peak amplitude (PPA), Δ_b, of the bombarded region, normalized to the

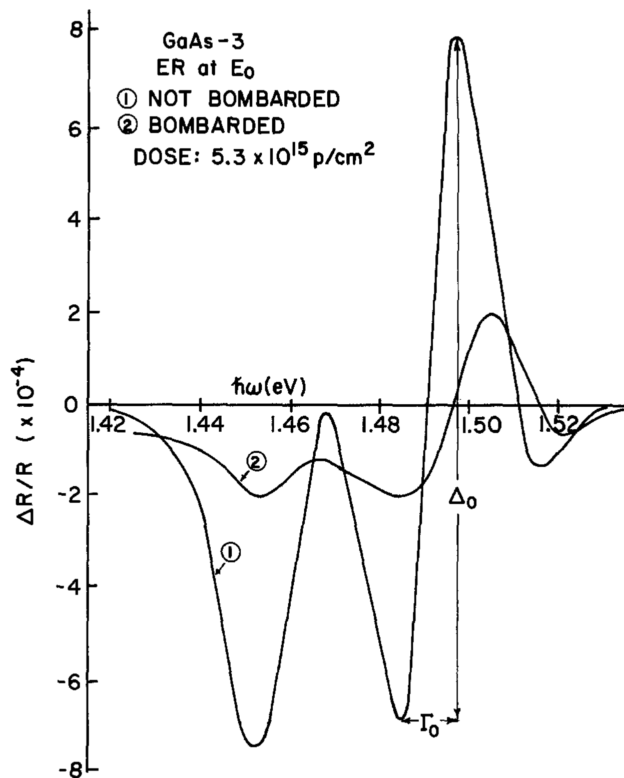

Fig. 3. ER at E_o from the bombarded and not-bombarded regions

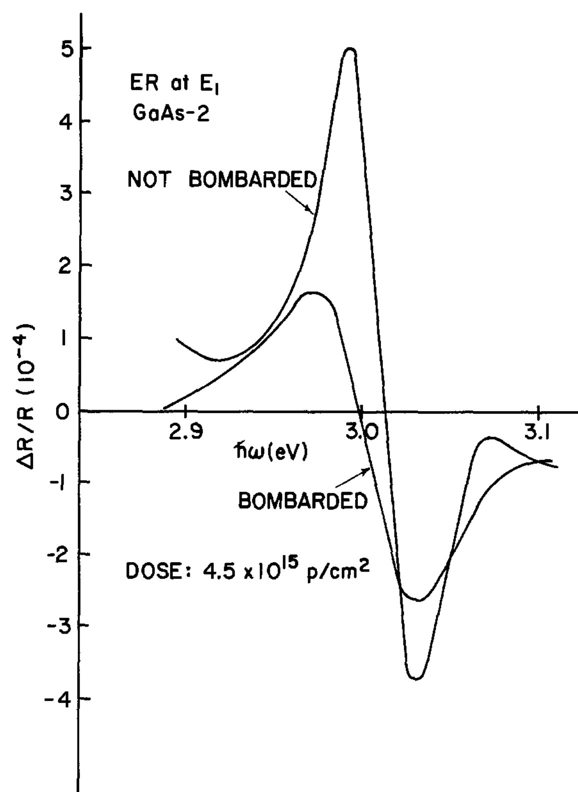

Fig. 4. ER at E_1 from the bombarded and not-bombarded regions

PPA from the nonbombarded region, Δ_o, is plotted *vs.* dose in Fig. 5 for both E_o and E_1 critical points.

It is apparent that the attenuation of Δ for a given dose is larger at E_o than at E_1. This can be explained qualitatively by the higher penetration depth of the light beam at E_o. At the bandgap transition, the penetration depth of the light is of the same order as that of the proton beam range, $\approx 1.5\mu$ (19), where the induced crystalline damage is mostly concentrated. At the E_1 transition the light penetration depth is only

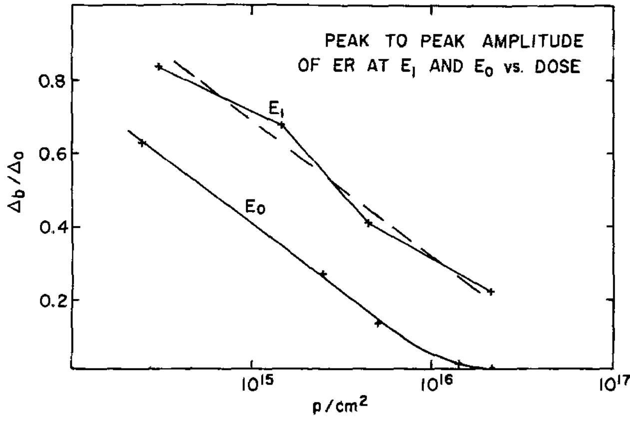

Fig. 5. Peak-to-peak amplitude (PPA) of the ER at E_1 and E_0 normalized to the PPA from the not-bombarded region.

0.017μ (19). The ER signal at E_0 is reduced to below the detection limit ($\approx 10^{-6}$) for dose $\gtrsim 2.4 \times 10^{16}$. This increased sensitivity of ER at E_0 to irradiation damage can be a useful tool for damage detection. The PPA will be used to give a semi-quantitative value for the amount of damage introduced into the sample, averaged over the damaged layer thickness. The ER will not distinguish, though, between the various types of damage in the sample. It is of interest to note that the linear fits of Eq. [3] to both E_0 and E_1 data are parallel, although the data at the E_1 critical point are more scattered. Between 2.5×10^{14} p/cm² and 5×10^{15} p/cm² the decrease in Δ_b/Δ_o for E_0 is linear in the logarithm of the dose ϕ

$$\Delta_b/\Delta_o = a \ln(\phi/\phi_o) \qquad [12]$$

with: $a = -0.16$ and $\ln \phi_o = 36.9$. For the E_1 critical point we get

$$\Delta_b/\Delta_o = a' \ln(\phi/\phi_o') \qquad [13]$$

with: $a = a' = -0.16$, $\ln \phi_o' = 38.0$.

Proton bombardment resulted in a small shift of about 15 meV toward the low energy in the ER peak at E_1, and 4 meV shift toward higher energy in the ER peak at E_0. A contribution to the shift at E_0 may come from the uneven attenuation of the ER peak due to strong variation in the penetration depth of the light beam near the absorption edge combined with the fact that the damaged layer peaks about 1.5μ below the surface.

Gavrilenko *et al.* (9) found that bombardment of Si with 1 keV He^+ ions causes a shift in the E_1 ER peak to higher energy; 1 keV Ar^+ bombardment of $Al_xGa_{1-x}As$ solution shifts the ER peak at E_1 to lower energy (8). Figure 6 shows the increased broadening in the E_1 and E_0 ER peaks *vs.* bombardment dose. Here too, note the higher values obtained for E_0 compared to E_1. Various sources can contribute to broadening of the ER signal, among others, temperature effect, local random electric field, and microstress due to defects. In our case a local electric field can be created by the proton doping of the damaged crystal.

The ER signal disappears at high dose. Based on the gradual amorphization model, the ER peak-to-peak amplitude, Δ_b, at a given dose, will be proportional to the area fraction which is still in the crystalline state

$$\Delta_b = \Delta_o\left(1 - \frac{A}{A_o}\right) \qquad [14]$$

Thus from Eq. [7a], [12], and [14]

$$\exp[-\int\sigma(\phi)\, d\phi] = 1 - \frac{A}{A_o} = \frac{\Delta_b}{\Delta_o} = a \ln(\phi/\phi_o) \qquad [15]$$

Taking the logarithmic derivative on both sides

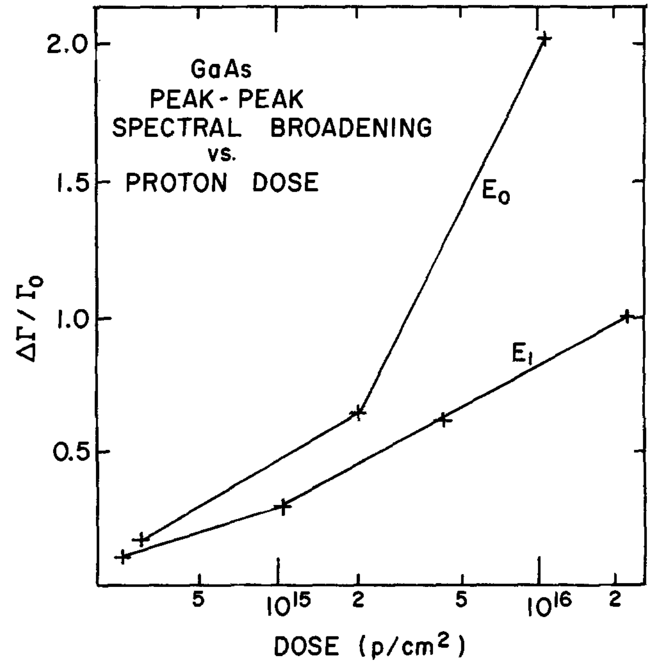

Fig. 6. Spectral broadening vs. proton dose of the ER signals at E_0 and E_1.

$$\sigma_{ER} = \frac{1}{\phi(K_o - \ln \phi)} \qquad [16]$$

where $K_o = \ln \phi_o$.

We previously found (Eq. [12]) that

$$K_o = \ln \phi_o = 36.9 \qquad [17]$$

Thus, from electroreflectance at E_0, at a dose of $\phi = 10^{15}$ p/cm² we get (Eq. [12], [16], and [17])

$$\sigma_{ER}\ (\phi = 10^{15}\ \text{p/cm}^2) = 4 \times 10^{-16}\ \text{cm}^2$$

Similarly, from transmission measurements, at this same dose we get (Eq. [9] and [10a]

$$\sigma_{TR}(\phi = 10^{15}\ \text{p/cm}^2 = 2 \times 10^{-16}\ \text{cm}^2$$

The relatively small discrepancy between the values obtained for σ_{ER} and σ_{TR} indicates that the simple picture used to describe the amorphization process is essentially correct in the first approximation. The result $\sigma_{ER} > \sigma_{TR}$ is to be expected because the ER is more sensitive to bombardment; partially damaged regions, neglected in the simple model, will affect the ER more than the transmission. It was suggested (20) that such partially damaged regions are caused by diffusion of defects from the outer portion of the ion track, into the undamaged bulk.

EA at the Absorption Edge E_o

The effect of proton bombardment on the band-to-band electroabsorption (EA), $\Delta T/T$, of the sample is shown in Fig. 7. Just below the bandgap, $\Delta T/T$ is negative, corresponding to a red shift of the absorption edge on application of the electric field as expected from the Franz Keldysh theory (5). Due to the high value of αd ($\sim 10^2$-10^3) the expected (5) oscillations in $\Delta T/T$ above the bandgap, have not been observed. Such oscillations have been seen previously by workers studying EA in thin films of GaAs (21).

The peak in the $\Delta T/T$ spectrum around 1.45 eV gradually disappears with increasing proton bombardment dose; ΔT also develops a tail toward the low energy side which is also seen in the $\Delta T/T$ spectrum below 1.45 eV. This newly created tail in the EA spectrum suggests the creation of a tail in the joint-density of states of the conduction and valence bands. This assumption is also in agreement with the results for α_b, the added absorption coefficient of the bombarded layer.

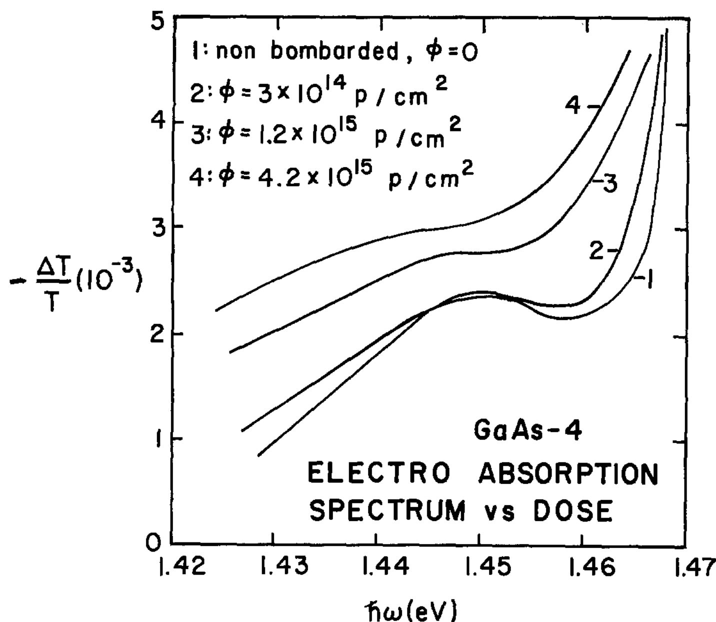

Fig. 7. EA vs. dose of bombarded and not-bombarded regions

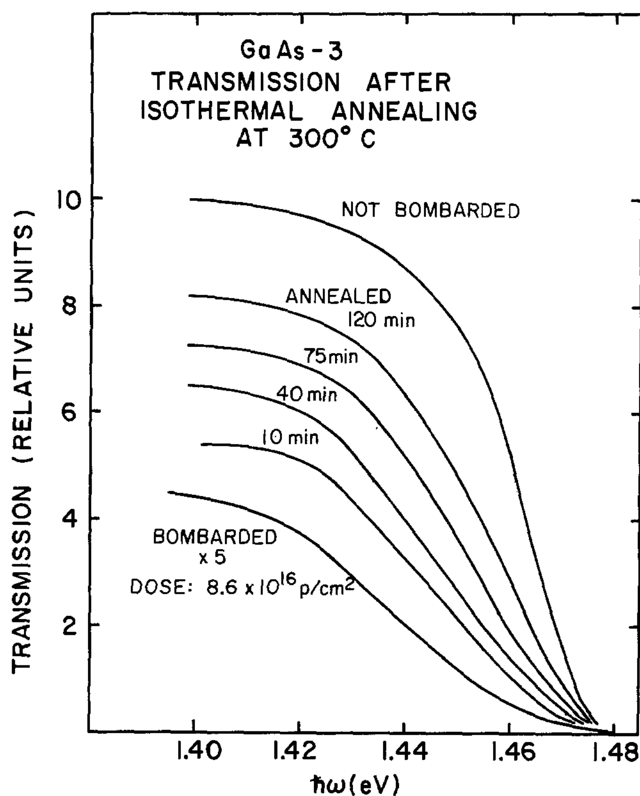

Fig. 8. Transmission from the bombarded region after isothermal annealing at 300°C.

Annealing

The effect of heat-treatment on the sample transmission in the vicinity of the E_0 critical point is shown in Fig. 8.

The sample was subjected to a bombardment dose of 8.6×10^{16} p/cm^2 (which completely eliminated its ER signals) and then isothermally annealed in vacuum at 300°C for up to 2 hr. The heat-treatment only partially recovers the transmission (Fig. 8) and ER signals before bombardment. For a given annealing time, the recovery of the ER signal is smaller than the recovery of the transmission; this is in agreement with our previous finding that the ER at E_0 is more sensitive to crystalline damage than the transmission and does not necessarily indicate that different types of defects are involved.

Dyment *et al.* (22) showed that the optical absorption of proton bombarded GaAs can be annealed more easily than the resistivity. They concluded that there must be at least two types of defects involved in the bombardment process.

Summary and Conclusions

All electromodulation signals decrease in intensity following proton bombardment of the sample. Due to better overlap of the incident light beam and the damaged region, the ER at E_0 is the most sensitive to proton bombardment. The added absorption just below the energy gap increases sublinearly with dose in the dose interval between 3×10^{14} and 5×10^{15} p/cm^2. In the same dose interval, the peak-to-peak spectral amplitude, Δ, of the ER at E_0 and E_1 critical points both vary linearly with the logarithm of the dose and thus can be used as a measure for the degree of the sample amorphicity.

The EA at E_0 develops a tail toward the low energy side of the spectrum. The ER at E_0 has a shift of ≈ 4 meV to higher energy while the peak of the ER signal at E_1 shifts by ≈ 15 meV to lower energy. The origins of these shifts are not yet clear.

Annealing at 300°C for up to 2 hr only partially recovers the unbombarded state. The recovery is not linear in time.

A model based on the gradual amphorization of the sample by an increasing number of proton-damaged amorphous islands with well-defined boundaries was considered. The change in absorption coefficient, α_b, or the change in the ER signal, in this model, depends on the volume fraction, A/A_0, made amorphous by the bombardment. Assuming a layer of average thickness d_b to be damaged, the number of unit cells made amorphous per incident proton will be

$$N = d_b \cdot \frac{dA}{dP}/a_0^3 = d_b\left(1 - \frac{A}{A_0}\right)\sigma(\phi)/a_0^3 \quad [18]$$

where a_0 is the lattice constant for GaAs (5.65Å).

Using Eq. [12] and [15]-[18], we find from the E_0 ER data

$$N = -\frac{\alpha d_b}{\phi a_0^3} = \frac{1.3 \times 10^{17}/\text{cm}^2}{\phi}$$

which corresponds to 26 unit cells amorphized per incident proton for $\Phi = 5 \times 10^{15}$ p/cm^2. Wempe *et al.* (3) found that in a 300 keV proton bombardment of GaP a similar number of unit cells was made amorphous per incident proton: *i.e.*, 10 for a dose of 10^{15} or 10^{16} protons/cm^2. The ER signal at E_0 is reduced below the detection limit ($\Delta R/R \sim 10^{-6}$) at $\phi \sim 2.5 \times 10^{16}$ p/cm^2 while the ER at E_1 is reduced to that level only at $\phi \sim 10^{17}$ p/cm^2. According to our model this implies that a dose of about 10^{17} p/cm^2 amorphizes the sample throughout the damaged layer of thickness ~ 1.5 μm, whereas 2.5×10^{16} p/cm^2 amorphizes it only in the region near 1.5 μm away from the surface.

The electronic band structure of a tetrahedrally bonded amorphous material is expected to have tails in the density of states which extend from the valence and conduction bands into the bandgap (23, 24). The tail in the EA signal at E_0 is tentatively attributed to transitions between these tails of the density of states.

Acknowledgment

This work was supported in part by the Office of Naval Research under Contract N00014-76-C-0890.

Manuscript submitted June 23, 1977; revised manuscript received Oct. 20, 1977.

Any discussion of this paper will appear in a Discussion Section to be published in the December 1978 JOURNAL. All discussions for the December 1978 Discussion Section should be submitted by Aug. 1, 1978.

REFERENCES

1. (a) T. Pankey, Jr. and J. E. Davey, *J. Appl. Phys.*, **41**, 697 (1970). (b) D. D. Sell and A. V. MacRae, *ibid.*, **41**, 4929 (1970).
2. B. R. Prumax, J. C. North, and G. L. Miller in, "Second International Conference on Ion Implantation in Semiconductors," I. Ruge and J. Graul, Editors, p. 212. Springer-Verlag, New York (1971).
3. S. H. Wemple, J. C. North, and J. M. Dishman, *J. Appl. Phys.*, **45**, 1578 (1974).
4. B. L. Crowder, R. S. Title, H. H. Brodsky, and G. D. Pettit, *Appl. Phys. Lett.*, **16**, 205 (1970).
5. For general reference on modulation spectroscopy see: (a) M. Cardona, "Solid State Physics," Suppl. 11, Academic Press, New York (1969); (b) "Semiconductors and Semimetals," Vol. 9, R. K. Willardson and A. C. Beer, Editors, Academic Press, New York (1972).
6. A. D. Jonath, E. Voronkov, and R. H. Bube, *J. Appl. Phys.*, **46**, 1754 (1975).
7. R. S. Bauer, *J. Electron. Mater.*, **4**, 1067 (1975).
8. V. I. Gavrilenko, A. V. Drazhan, V. A. Zuev, D. V. Korbutyak, and V. G. Litovchenko, *Sov. Phys. Semicond.*, **10**, 185 (1976).
9. V. I. Gavrilenko, A. P. Dubchak, V. A. Zuev, V. G. Litovchenko, and V. S. Lysenko, *ibid.*, **9**, 460 (1975).
10. W. J. Anderson, C. A. Douglass III, and Y. S. Park, *J. Appl. Phys.*, **46**, 3875 (1975).
11. V. Rehn and D. S. Kysen, *Phys. Rev. Lett.*, **18**, 848 (1967).
12. A. H. Kalma, *IEEE Trans. Nucl. Sci.*, **ns-19**, 209 (1972); also see Ref. 1(a).
13. S. M. Spitzer and J. C. North, *J. Appl. Phys.*, **44**, 214 (1973).
14. B. L. Gregory and H. H. Sander, *Proc. IEEE*, **58**, 1328 (1970).
15. A. W. Tinsley, *Radiat. Eff.*, **23**, 165 (1974).
16. J. F. Gibbons, W. S. Johnson, and S. W. Myroie, "Projected Range Statistics," 2nd ed., Halsted Press, New York (1975).
17. A. A. Gutkin, D. N. Nasledov, and F. E. Faradzhev, *Sov. Phys. Semicond.*, **8**, 298 (1974).
18. B. O. Seraphin and H. G. Bennett, in "Semiconductors and Semimetals," Vol. 3, R. K. Willardson and A. C. Beer, Editors Academic Press, New York (1967).
19. F. F. Morhead and B. L. Crowder, *Radiat. Eff.*, **6**, 27 (1970).
20. J. C. Dyment, J. C. North, and L. A. D'Asaro, *J. Appl. Phys.*, **44**, 207 (1973).
21. L. W. Aukerman, P. W. Davis, R. D. Graft, and T. S. Shilliday, *This Journal*, **34**, 3590 (1963).
22. E. W. Mitchell and C. Norris, *J. Phys. Soc. Jpn.*, **21**, 656 (1967).
23. B. A. Bobylev, A. F. Kravchenko, and A. S. Terekhov, *Sov. Phys. Semicond.*, **7**, 1381 (1974).
24. W. J. Anderson and Y. S. Park., *J. Appl. Phys.*, **47**, 3094 (1976).

Surface Electrical Properties of the Wustite Phase

J. Nowotny and I. Sikora

Research Laboratories of Catalysis and Surface Chemistry, Polish Academy of Sciences, ul. Niezapominajek, 30-239 Kraków, Poland

ABSTRACT

The iron-oxygen system has been studied using work function measurements between 675° and 950°C, the stability range of the wustite phase. The work function of wustite *vs.* nonstoichiometry indicates a decrease of the Fermi energy below 850°C while for the temperatures between 900° and 950°C an initial decrease is followed by the final increase. The measured work function data depend only on the temperature and oxygen partial pressure. This indicates that the system is well equilibrated. The values of the partial pressures of oxygen corresponding to the wustite phase equilibria with iron and with magnetite determined in this work agree well with the reported literature data. A short equilibration time favors the work function method as a convenient one for investigating phase diagrams of oxide systems. The experimental data do not confirm the p- to n-type transition postulated for $Fe_{1-y}O$ on the basis of earlier measurements of the Seebeck coefficient.

Electrical properties of wustite have been the subject of several papers dealing mainly with the Seebeck coefficient and electrical conductivity measurements (1-11). Several essential questions, however, concerning electrical data as well as their correlation with structural properties of this phase have not been sufficiently explained. There are still essential contradictions concerning the conductivity mechanism within the wustite phase field and its defect structure *vs.* nonstoichiometry. Moreover, there is a general lack of thermodynamic data for temperatures below 900°C at which the system wustite-oxygen requires considerably longer times to achieve its equilibrium state. On the other hand, the rare experimental data available for the phase diagram of the iron-oxygen system below 900°C show many discrepancies.

One of the most extensively studied problems of the wustite phase concerns its defect structure. As is known, wustite exhibits a very large nonstoichiometry varying from 5 atom percent (a/o) at the iron-wustite boundary up to about 15 a/o at the wustite-magnetite phase boundary. This nonstoichiometry may simply be related to the concentration of cation vacancies. Taking into account, however, interactions between these simple defects leading to the formation of Roth's complexes ($V_{Fe}Fe_iV_{Fe}$) (12), clusters n ($V_{Fe}Fe_iV_{Fe}$) (13, 14), and even structural domains (15-19), the real concentration of defects involving both cation vacancies and interstitial cations may reach 30 a/o. This significant value implies a complex picture of the defect structure of wustite, especially at its higher nonstoichiometry.

Numerous works concerning the defect structure of the wustite phase are based mainly on either gravimetric investigations, leading directly to deviations from stoichiometry, or electrical conductivity, giving information about the concentration and mobility of

Key words: work function, ferrous oxide, surface potential, Fermi energy, nonstoichiometry.

electron carriers as well as about the degree of ionization of ionic defects.

Bransky and Tannhauser (7) have found that electrical conductivity of wustite above 1000°C, for lower nonstoichiometry is proportional to the sixth root of the oxygen partial pressure. Such dependence fits the simple model involving formation of doubly ionized cation vacancies when oxygen is incorporated into the wustite lattice

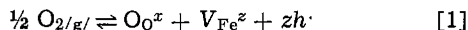

$$\tfrac{1}{2}\, O_{2/g/} \rightleftharpoons O_O{}^x + V_{Fe}{}^z + zh^{\cdot} \quad [1]$$

where according to the Kroger-Vinck notation $O_O{}^x$ denotes the oxygen in the anion sublattice, $V_{Fe}{}^z$ the cation vacancy, z the degree of ionization, and $h^{\cdot}$ the electron hole.

Applying the mass action law and assuming that interactions among defects may be neglected as well as supposing appropriate electroneutrality conditions of the lattice, the deviation from stoichiometric composition may be expressed as the following function of temperature

$$y = V_{Fe}{}^z = \text{const}\, p_{O_2}{}^{1/n} \exp\left[-\frac{\frac{1}{z+1}\Delta H_f}{RT}\right] \quad [2]$$

where $1/n$ is the parameter depending on the ionization degree of cation vacancies and ΔH_f is the enthalpy of formation of the vacancies. The parameter $1/n$ may thus be determined by measuring directly the changes of the deviation from stoichiometry, or any parameter that can be correlated with the concentration of cation vacancies (*e.g.*, electrical conductivity) as a function of oxygen partial pressure p_{O_2}

$$\frac{1}{n} = \frac{\partial \ln y}{\partial \ln p_{O_2}} = \frac{\partial \ln \sigma}{\partial \ln p_{O_2}} \quad [3]$$

Equation [3] is valid only when the mobility of electron carriers is independent of their concentration.

The simple model illustrated by Eq. [1] has been supported by the gravimetric studies of Hauffe and Pfeiffer (20). Also Smyth (21) postulated doubly ionized cation vacancies as predominant defects. More detailed investigations of this phase, however, have shown that the parameter $1/n$, determined both gravimetrically and by electrical conductivity (22, 23), changes from 1/4, for the smallest deviation from stoichiometry, to 1/6, or even below, with increasing y, thus indicating that the effective charge of defects *vs.* y changes continuously. According to the present knowledge of the defect structure of wustite this phenomenon can be attributed to association (12) and clustering (13) of defects. Vallet and Raccah (15), Kleman (16), and Fender and Riley (17) postulate the existence of three separate "phases" or structural domains within the wustite phase field; however, they do not give a defect structure for these domains. Moreover, numerous investigations of several structure-sensitive properties of wustite (*e.g.*, electrical conductivity) *vs.* oxygen partial pressure do not indicate a drastic change of defect structure at compositions corresponding to the postulated domain boundaries (24). Thus the existence of the domains still remains an open question.

Bransky and Tannhauser (7) have found a change of sign of the Seebeck coefficient of wustite for the composition O/Fe = 1.09. The authors suggest that this effect, observed above 900°C, can be attributed to the transition of the conductivity from p-type at low stoichiometry to n-type at high oxygen content. The change of sign of the Seebeck coefficient above 900°C has been confirmed by Wagner and co-workers (5, 6) for both poly- and single-crystalline samples of wustite. This effect has also been observed by Meussner, Richards, and Fujii at 1000°C (4), but at much higher oxygen content than that observed by Bransky and Tannhauser or by Wagner and co-workers (5). Nevertheless the supposition concerning p- to n-type transition is in strong contradiction to electrical conductivity data which show no minimum in the whole range of the wustite homogeneity range *vs.* oxygen content. This would indicate that only one type of electron carriers (electrons or holes) predominate throughout the whole wustite field. Recently, the p-type conductivity of the wustite phase has been confirmed by Bowen, Adler, and Auker (11). Seltzer and Hed (9) have proposed an original interpretation of these apparently conflicting data. The authors involved a "negative term" describing the temperature dependence of the scattering mechanism in the transport of charge carriers through the crystal lattice. Their calculation based on this assumption gives good agreement with the literature data of the electrical conductivity and Seebeck coefficient reported for the wustite phase.

Statement of the Problem

The discussion of the literature data shows that the electronic properties of the wustite phase still remain the subject of dispute and require additional investigation for an explanation of the electronic phenomena as well as the correlation between structural and electronic data for this highly defect crystal. The purpose of the present work is to apply the work function technique which may supply direct information about the chemical potential of electrons (Fermi energy level) for the surface layer of investigated oxide sample.

The work function technique has been widely used for investigations of adsorption properties of oxides and metals. The measurements have generally been carried out in the range of low and moderate temperatures. However, under these conditions most of the oxides are in a "quenched" state. Thus the measured work function data gave information concerning the surface oxide layer, which because of kinetic reasons was not equilibrated with either the crystalline bulk or the gaseous phase. Under these conditions, the nonstoichiometry of the surface layer is in a continuous change as the oxide crystal tends toward an equilibrium state (25). Thus the measured work function values depend essentially on the experimental procedure applied and the sample history.

It should be emphasized that the absolute value of the work function of metal oxides, as well as of most of the binary compounds, has no physical meaning when measured at temperatures where the compounds are not equilibrated with the gas phase. In these cases the state of the surface depends on many uncontrolled factors, such as surface coverage by adsorbed impurities, surface topography, and nonstoichiometry of the layer near the surface. Each of these factors has a strong influence on the measured value of the work function. Relative work function changes may be used for monitoring some surface processes, *e.g.*, chemisorption of gases. Then the measured electronic effect accompanying chemisorption represents the chemical affinity between the investigated surface and the adsorbate. In this kind of study, the absolute value of the work function may be used as a monitor for adjusting the standardized procedure to a reproducible surface state, or for following the kinetics of any surface process accompanied by electronic transitions. As the temperature increases, however, the whole crystalline grain is being brought into thermodynamic equilibrium with the coexistent gas atmosphere. Under these, conditions the surface state, and thus the work function, are independent of the experimental procedure applied before the measurement and are determined by the parameters of the experiment, such as temperature and gas composition.

The work function measurements commonly reported for studies of the surface electrical properties of metal oxides are based on the dynamic condenser

method. This method, proposed by Kelvin (26) and improved by Zisman (27) and numerous other investigators (28-39), is the most convenient one for studying oxides under a controlled gaseous atmosphere. The dynamic condenser method described in the literature operates in a temperature range up to about 400°C; however, this range is too low for such transition metal oxides as NiO, CoO, MnO, or FeO. Thus the purpose of the present work was to perform the work function measurements at a sufficiently high temperature that the investigated crystal could be equilibrated with oxygen. The relatively well-known ferrous oxide (wustite) seemed to be a very interesting system for the present studies because this oxide phase shows the largest nonstoichiometry among the other transition metal oxides of the series exhibiting the NaCl-type structures as NiO, CoO, or MnO. It was also expected that the work function data of the wustite phase might supply interesting material for comparison with other available electrical data involving the electrical conductivity and the Seebeck coefficient. In the present studies the work functions of the iron-oxygen system were measured *vs.* the oxygen activity in the gaseous phase. Experimental conditions were adjusted in order to cross the wustite phase field from metallic iron to the magnetite phase.

Experimental

Apparatus.—The dynamic condenser method was used for the work function measurements (40, 41). It is illustrated schematically by the block diagram in Fig. 1. The method is based on the measurement of the constant potential difference (CPD) existing between the plates forming the condenser, 3, whose capacity varies with time. The vibration of the condenser generates an a-c voltage across the resistance, 4. The value of this voltage is proportional to CPD. The a-c voltage is then amplified, 5, and monitored, 6. When CPD is compensated by an external d-c voltage, $V_{d.c.}$, 2, from the compensator, 1, a minimum in the signal is observed on the monitor

$$V_{CPC} - V_{d.c.} = 0 \quad [4]$$

Thus the CPD is equal to the value of $V_{d.c.}$ with the opposite sign. The plates of the dynamic condenser are the sample being investigated, 1, and the reference electrode, 2. The CPD is equal to the difference in the work function of the plates of the dynamic condenser

$$V_{CPD} = \frac{\Phi_1 - \Phi_2}{e} \quad [5]$$

Hence an increase of the CPD corresponds to an increase in the work function of the oxide. The measurement of changes in the work function of the oxide sample *vs.* oxygen pressure are possible only when the surface potential of the reference electrode is known or is constant in the experimental conditions applied

$$\Delta\Phi_1 = e(\Delta V_{CPD}) + \Delta\Phi_2 \quad [6]$$

A platinum plate was used as the reference electrode. Changes in the work function of the platinum plate for high temperatures may be calculated as for the oxygen electrode

$$\Delta V_{Pt} = \frac{\Delta\Phi_2}{e} = \frac{RT}{4F} \ln \frac{p_{O_2}^{(1)}}{p_{O_2}^{(2)}} \quad [7]$$

where values $p_{O_2}^{(1)}$ and $p_{O_2}^{(2)}$ correspond to the extreme oxygen pressures of the experimental conditions.

The oxygen partial pressure in the reaction chamber is controlled by the ratio of the CO-CO_2 gas mixture at a total pressure of 1 atm. The experimental compositions of the CO_2-CO gas mixture are indicated in Fig. 2 by the dividing spots on the isothermal (dotted) lines. The lowest oxygen activity is determined here by pure carbon monoxide limiting investigations of the iron-oxygen system to the right side from line 1 in Fig. 1. Thus at temperatures below 750°C the experiments concern only the phase boundary wustite-magnetite.

Figure 3 shows the experimental setup including both the gas flow system for adjusting required composition of CO_2-CO mixture and the schematic of the dynamic condenser. The details of the construction

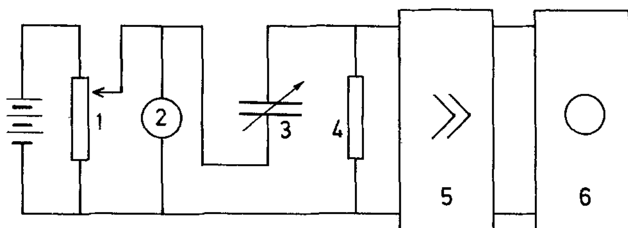

Fig. 1. Schematic drawing of the electrical circuit for the work function measurements: 1, compensator; 2, voltmeter; 3, dynamic condenser; 4, high impedance; 5, amplifier; 6, monitor.

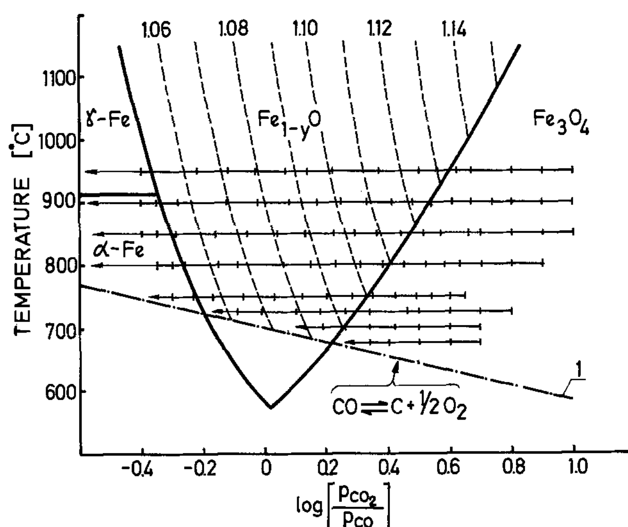

Fig. 2. Wustite phase field according to Darken and Gurry (29) in temperature *vs.* logarithm of the CO_2/CO ratio. Dashed curves indicate constant composition O/Fe. Curve 1 represents the decomposition line of CO. Spots on the isothermal lines correspond to the experimental conditions applied in this work.

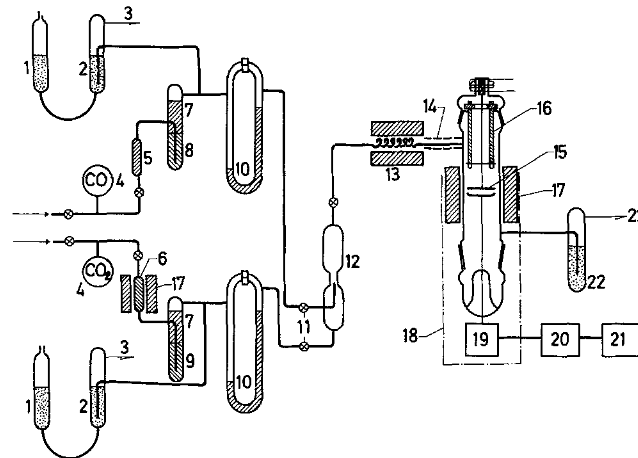

Fig. 3. Experimental setup: 1, chamber with dibuthyl-phtalate for fixing overbubbling pressure; 2, overbubbler of manostat; 3, overflow gas outlet; 4, gas chambers; 5, ascarite; 6, copper turnings; 7, silicagel; 8, molecular sieves Type 4A; 9, molecular sieves Type 3A; 10, flowmeter; 11, stopcock; 12, gas mixer; 13, preheater of the reaction gas mixture; 14, thermal isolation; 15, dynamic condenser; 16, vibrator of the dynamic condenser; 17, heating element; 18, electrical screening; 19, preamplifier; 20, amplifier and compensator; 21, monitor; 22, gas flow controller; 23, reaction gas outlet.

of the dynamic condenser were described previously (42). The powdered, spectroscopically pure iron sample (prepared by Johnson-Matthey) was spread over the lower stainless steel electrode. The sample formed a layer about 0.5 mm thick. The gas mixture entered the upper part of the chamber of the dynamic condenser, passed down over the sample, and was exhausted near the bottom. The gas flow velocity was about 0.9 cm/sec as recommended by Darken and Gurry (43) to prevent the formation of a concentration gradient in the experimental gas mixture. Oxygen partial pressures corresponding to the appropriate compositions of the CO_2-CO mixture were calculated using the data of Jacobi (44)

$$\frac{p_{CO}}{p_{CO_2}} = [p_{O_2} \exp (68,100T^{-1} - 20.9)]^{-0.5} \qquad [8]$$

The reading accuracy of the CPD was about 0.05V.

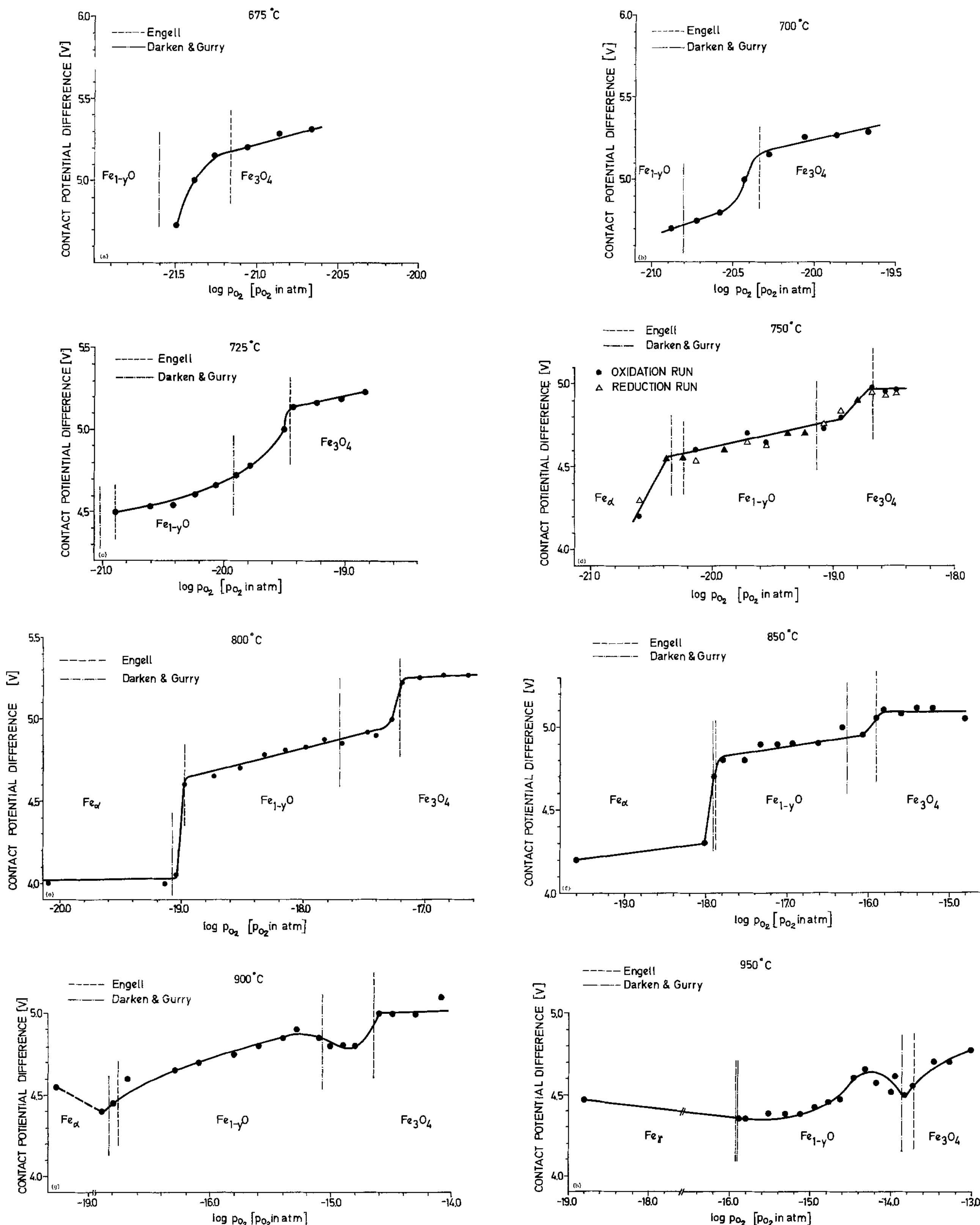

Fig. 4. Contact potential difference CPD for the iron-oxygen system measured at different temperatures vs. gas composition corresponding to the stability range of the wustite phase for temperatures: a, 675°C; b, 700°C; c, 725°C; d, 750°C; e, 800°C; f, 850°C; g, 900°C; h, 950°C. Oxygen partial pressures corresponding to equilibria at the phase boundaries Fe-$Fe_{1-y}O$ and FeO-Fe_3O_4 are indicated after Engell (3) and Darken and Gurry (29).

Procedure

The reaction system was heated to the required temperature in the gas mixture corresponding to the magnetite phase. Then the gas composition was gradually changed toward decreasing oxygen activity as illustrated by the dotted lines in Fig. 2. Experiments for which oxygen activity decreased or increased in successive readings were termed reduction or oxidation runs, respectively. The CPD was measured when a constant value was reached, *i.e.*, in 5-10 min after the new ratio of the CO_2-CO mixture was fixed on the new level. The experimental values of the CPD were taken from two to three independent readings. The data are reproducible within 0.1V.

Results and Discussion

Figures 4a-h illustrate the measured values of CPD as the function of oxygen partial pressure for a series of the temperatures between 675° and 950°C within the phase field of wustite as indicated in Fig. 2. The experimental data were found to be the same for both oxidation and reduction runs, as can be seen in Fig. 4d for 750°C. For other temperatures the CPD data for the oxidation runs are given. The dotted, vertical lines indicate the literature values of equilibrium oxygen partial pressures corresponding to the phase boundaries iron-wustite and wustite-magnetite, according to Engell (31) and Darken and Gurry (29). The observed sharp CPD changes fit the literature data well, thus indicating that the work function is a parameter very sensitive to the crystalline structure.

The change in the surface potential of the platinum reference electrode, calculated according to Eq. [7] for extreme oxygen pressures corresponding to Fe/FeO and FeO/Fe_3O_4 phase boundaries, was equal to about 0.05V. According to Eq. [7], these changes are linear in the coordinates used for plotting the experimental data in Fig. 4a-h. According to Eq. [6], the work function changes of the investigated sample are the sum of the measured CPD changes and $\Delta\Phi_2$. Because of the very small $\Delta\Phi_2$ values, however, the CPD changes are practically equal to $\Delta\Phi_1$.

As seen in Fig. 4c-f, the work function increases almost linearly within the wustite phase *vs.* oxygen partial pressure between 725° and 850°C. This is in accordance with the reported defect structure of wustite showing cation vacancies forming acceptor centers in the energetic model of wustite according to Eq. [1]. An increase in their concentration shifts the Fermi level downward. Since the energetic model of the wustite phase is not sufficiently developed it is difficult to indicate the form of the defects and their acceptor "activity." These may be both doubly and singly ionized cation vacancies as well as complexes. The observed increase of the work function indicates that the p-type conductivity should dominate within the whole wustite range if p-type is assumed at the lowest nonstoichiometry. This effect is in contradiction to the data of Bransky and Tannhauser (7) as well as of Wagner and co-workers (5) who reported a monotonous decrease of Seebeck coefficient (referring to the increase of the Fermi level) *vs.* increase of nonstoichiometry.

Figures 4g and 4h refer to 900° and 950°C, respectively. For 900°C and at low nonstoichiometry, the CPD changes linearly with oxygen pressure as was found for the experimental runs below 900°C. A slight decrease of the work function is observed at higher nonstoichiometry. This effect is even more pronounced at 950°C. In both cases, however, the final work function value is still higher than the initial one. Thus the postulated change of the conductivity type from p-type, at low nonstoichiometry, to n-type, at higher oxygen content (3-6) cannot be confirmed in the present investigations. The maxima of the work function observed at 900° and 950°C for higher nonstoichiometry may correspond to the change of sign of the Seebeck coefficient which was found by Bransky and Tannhauser (7) as well as Geiger, Levin, and Wagner (5). Both work function and Seebeck coefficient indicate an increase of the Fermi level *vs.* oxygen pressure at higher O/Fe ratios than those referring to the maxima. The discrepancy in the results of the Seebeck effect and the work function observed at lower nonstoichiometry, however, requires additional investigation involving the simultaneous measurement of the electrical parameters. It should be emphasized, however, that a good qualitative agreement between the work function and the electrical conductivity data was found for lower defect concentrations (both parameters indicating decrease of the Fermi energy *vs.* oxygen content), although the maxima of the work function *vs.* oxygen pressure was not confirmed.

Over the temperature range studied in this work, no effect was observed that could be ascribed to structural "regions" which have been postulated by Vallet and Raccah (15), Kleman (16), and Fender and Riley (17).

All of the experimental studies of CPD *vs.* log p_{O_2} show, more or less, sharp changes of the work function. These changes occur at values of oxygen partial pressures corresponding to the expected phase transformations of wustite into the metallic iron phase, on one hand, and into the magnetite phase, Fe_3O_4, on the other. The parameters of temperature and oxygen partial pressure determined in the present studies for the appropriate phase equilibria are plotted in Fig. 5 and compared with other literature data. The equilibrium data of oxygen partial pressure obtained from the work function measurements were recalculated after Engell (45) into corresponding values of nonstoichiometry y in order to compare the presently obtained results with the literature data reported in this measure (Fig. 6). As seen the data obtained from the work function agree very well with the data obtained by Engell (31), Marion (46), Vallet and Raccah (15), and other investigators (47). The results obtained here may be helpful in more precise determinations of the wustite phase boundary especially at lower temperatures (between 575° and 800°C) for which great discrepancies are observed among the available data.

Conclusions

1. The work function values of the iron-oxygen system measured at temperatures above 675°C were determined from the temperature and oxygen partial pressure and are independent of the experimental procedure applied. This indicates that the sample was equilibrated, and the work function data is characteristic of the studied materials.

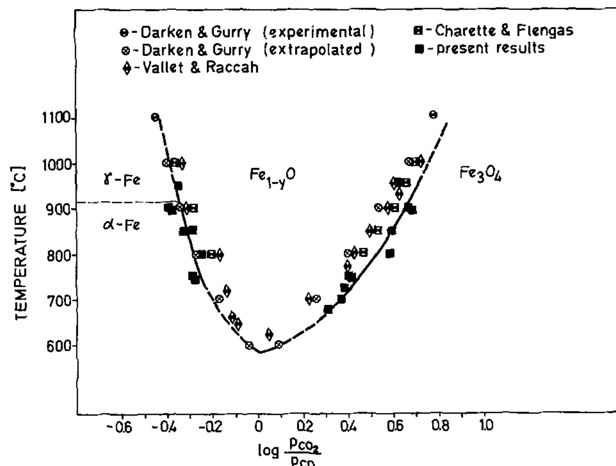

Fig. 5. Experimental data for the wustite phase diagram plotted in temperature *vs.* logarithm of the CO_2/CO ratio.

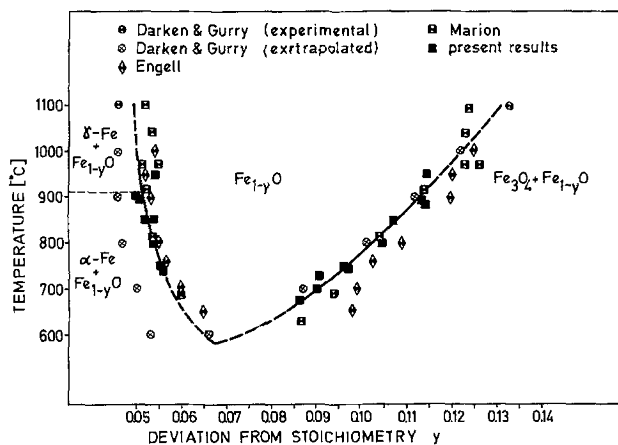

Fig. 6. Experimental data for the wustite phase diagram plotted in temperature vs. oxide composition.

2. The work function data do not confirm the earlier postulated p- to n-type transition for the wustite phase (3-6).

3. The work function is very sensitive to crystalline structure and thus may be used to determine the partial pressure of oxygen corresponding to the thermodynamic equilibrium state between the two phases. A surprising agreement between the presently obtained data from the work function measurements and the literature data concerning phase boundaries of the wustite phase indicates that this typical surface sensitive method is capable of giving information relevant to the bulk when the investigated system is well equilibrated.

4. The phase boundaries of the wustite phase determined from the work function measurements agree well with other literature data (31-33).

5. The hypothesis of Vallet and Raccah (15), Kleman (16), and Fender and Riley (17) concerning different structural domains in the wustite phase was not confirmed in the present investigations.

Acknowledgments

This work has been done with the financial support of the Metallurgical Institute, Academy of Mining and Metallurgy, Kraków, under contract MR-19-1.6.5. This support is gratefully acknowledged.

Manuscript submitted May 4, 1977; revised manuscript received ca. Dec. 19, 1977.

Any discussion of this paper will appear in a Discussion Section to be published in the December 1978 JOURNAL. All discussions for the December 1978 Discussion Section should be submitted by Aug. 1, 1978.

REFERENCES

1. C. Wagner and E. Koch, *Z. Phys. Chem., B*, **32**, 439 (1936).
2. F. Marion, Thesé d'Etat, Université de Nancy (1955).
3. D. S. Tannhauser, *J. Phys. Chem. Solids*, **23**, 25 (1962).
4. R. A. Meussner, L. E. Richards, and C. T. Fujii, Rep. NPL Progr., p. 26 (December 1965).
5. G. H. Geiger, R. L. Levin, and J. B. Wagner, Jr., *J. Phys. Solids*, **27**, 947 (1966).
6. W. J. Hillegas, Jr. and J. B. Wagner, Jr., *Phys. Lett.*, **25A**, 742 (1967).
7. I. Bransky and D. S. Tannhauser, *Trans. AIME*, **239**, 75 (1967).
8. W. J. Hillegas, Jr., Ph.D. Thesis, Northwestern University (1968).
9. M. S. Seltzer and A. Z. Hed, *This Journal*, **117**, 815 (1970).
10. D. Neuschutz and N. Towhidi, *Arch. Eisenhuttenwes.*, **41**, 303 (1970).
11. H. K. Bowen, D. Adler, and B. H. Auker, *J. Solid State Chem.*, **12**, 355 (1975).
12. W. L. Roth, *Acta Crystallogr.*, **13**, 140 (1960).
13. F. Koch and J. B. Cohen, *ibid., Sect. B*, **25**, 275 (1969).
14. Chyong Rkhi Khing, A. D. Romanov, Ya. L. Shaiovich, and R. A. Zvinchuk, *Vestn. Leningr. Gosudarstvennogo Univ.* (News of the Leningrad National University, in Russian), **4**, 144 (1973).
15. P. Vallet and P. Raccah, *Mem. Sci. Rev. Metall.*, **62**, 1 (1965).
16. M. Kleman, *ibid.*, **62**, 457 (1965).
17. B. E. F. Fender and F. D. Riley, *J. Phys. Chem. Solids*, **30**, 793 (1969).
18. J. S. Anderson, *Bull. Soc. Chim. Fr.*, No. 7, 2203 (1969).
19. J. S. Anderson, NBS Spec. Publ. 364, p. 295, Solid State Chemistry Proceedings, 5th Materials Research Symposium, July 1972.
20. K. Hauffe and H. Pfeiffer, *Z. Metallk.*, **44**, 27 (1953).
21. D. M. Smyth, *J. Phys. Chem. Solids*, **19**, 167 (1961).
22. I. Bransky and A. Z. Hed, *J. Am. Ceram. Soc.*, **51**, 231 (1968).
23. B. Swaroop and J. B. Wagner, Jr., *Trans. Metall. Soc. AIME*, **239**, 1215 (1967).
24. S. Bialas, J. Nowotny, and I. Sikora, In preparation.
25. J. Nowotny, *Bull. Acad. Pol. Sci., Ser. Sci. Chim.*, **21**, 413 (1973).
26. Lord Kelvin, *Phil. Mag.*, **46**, 82 (1898).
27. W. A. Zisman, *Rev. Sci. Instrum.*, **3**, 367 (1932).
28. R. Gunn, *Phys. Rev.*, **40**, 307 (1932).
29. W. E. Meyerhof and P. H. Miller, *Rev. Sci. Instrum.*, **17**, 15 (1946).
30. J. C. P. Mignolet, *Discuss. Faraday Soc.*, **8**, 326 (1950).
31. J. C. Devins and S. I. Reynolds, *Rev. Sci. Instrum.*, **28**, 11 (1957).
32. V. F. Bogoliubov, *Radiotekh. Elektron.*, **2**, 323 (1957).
33. P. H. Burshtein and L. A. Larin, *Zh. Fiz. Khim.*, **32**, 194 (1958).
34. J. F. Rybkin, N. F. Schevtschenko, and N. A Izmailov, *ibid.*, **35**, 220 (1961).
35. A. A. Zhukhovitski and A. A. Andreev, *Dokl. Akad. Nauk SSSR*, **142**, 1319 (1962).
36. S. M. Kotshergin and G. A. Golikov, *Zh. Fiz. Khim.*, **37**, 1116 (1963).
37. O. M. Artamonov and P. J. Berlaga, *Prib. Tekh. Eksp.*, **2**, 151 (1963).
38. T. Delchar, A. Eberhagen, and F. C. Tompkins, *J. Sci. Instrum.*, **40**, 179 (1963).
39. H. Pauly, H. W. Petmecky, and C. Schmidt, *Z. Angew. Phys.*, **91**, 207 (1965).
40. J. Nowotny and I. Sikora, *Bull. Acad. Pol. Sci., Ser. Sci. Chim.*, **23**, 1045 (1975).
41. R. Chruściel, J. Dereń, and J. Nowotny, *Exp. Techn. Phys.*, **14**, 127 (1966).
42. J. Nowotny and I. Sikora, *Z. Phys. Chem. N. F.*, In print.
43. L. S. Darken and R. W. Gurry, *J. Am. Chem. Soc.*, **67**, 1398 (1945).
44. H. Jacobi, Ph. D. Thesis, Technische Universität Clausthal (1965).
45. H. J. Engell, *Arch. Eisenhuettenwes.*, **28**, 109 (1957).
46. F. Marion, *Doc. Metall.*, No. 24, 5 (1955).
47. G. G. Charette and S. N. Flengas, *This Journal*, **115**, 796 (1968).

Aluminum Oxidation in Water

C. C. Chang, D. B. Fraser, M. J. Grieco, T. T. Sheng, S. E. Haszko,
R. E. Kerwin, R. B. Marcus, and A. K. Sinha*

Bell Laboratories, Murray Hill, New Jersey 07974

ABSTRACT

Water rinse of aluminum metallized integrated circuits must be carefully monitored because the Al can oxidize rapidly under certain conditions. Al oxidation in 10 MΩ deionized water was therefore studied using Auger spectroscopy, and transmission and scanning electron microscopies, to investigate the oxide growth as a function of water temperature and rinse time, use of photolithography, and Cu-doping of the Al. Al oxide thicknesses were 20-30Å before any treatment and were 35, 70, and ≅3000Å after 5 min rinses in 40°, 60°, and 80°C water, respectively. Photolithography and Cu doping induced no large effects. In 40°C water, little oxidation occurred for 20 min and rapid oxidation began after 40 min, especially at nucleation sites with C and Si contamination. The oxide grown in water has a porous structure, is nearly amorphous, and contains gamma-alumina and hydrated oxides. Near 80°C, several thousand angstroms of oxide can grow in minutes.

Oxidation of Al metallization in integrated circuits (IC's) can significantly affect device yield by increasing the contact resistance. This is especially true with beam leaded (1) devices to which contacts are established without any physical means of breaking the oxide barrier over the Al. Even with wire bonded devices, excessive oxide growth is obviously undesirable. Because deionized (DI) water rinsing of Al is an integral part of IC processing, the growth of Al oxide in DI water was investigated in this work.

Experimental

Sample preparation.—The samples studied are listed in Table I together with the relevant final treatments. Abbreviated descriptions of the processing steps are given in Table II; the water rinse step, No. 4, is the critical operation of interest here. The Cu-doped Al films of Table I were 1.5 μm thick, with 0.5 atom percent (a/o) Cu deposited at either ≅40°C or at 300°C by e-gun evaporation, and the undoped films were similarly deposited at 40°C. The column labeled "EG-BHF" refers to a 30 sec dip in 1:1:1 ethyleneglycol:buffered-HF:H_2O etch, and "450°C anneal" refers to a 30 min anneal in 1 atm H_2. The EG-BHF treatment removes Al oxide as well as some Si-nitride and SiO_2, with only a minimal attack of the Al and therefore its value as a cleaning etch for the entire Al metallized IC wafer was examined. In Table I, all "Testers" are full-surface Al films (on oxidized Si) unless photolithography is indicated. The device samples 18 to 21 were pulled from device lots, after the processing steps indicated; these steps are listed in Table II. The DI water entering the overflow rinse bath had a resistivity over 10 MΩ and was heated in a stainless steel tube just prior to admission into the bath.

Analysis methods.—Instances of extensive Al oxidation could be detected under the optical microscope, by a halo type of feature along the edges of patterned Al. After 450°C anneal, the oxide layer sometimes developed cracks and the oxide could be removed with adhesive tape, as demonstrated in Fig. 1. A scanning electron microscope (SEM) was used in this work for rapidly evaluating the effect of a particular water rinse and to scan many different areas of a chip. Typical SEM micrographs are displayed in Fig. 2. Surface oxide films >100Å thick appeared to quickly degrade the SEM spatial resolution. Auger electron spectroscopy (AES) was used for chemical analysis and for measuring oxide thicknesses <100Å. Details of this technique, which utilizes the chemically shifted Auger peak of Al in the oxide, is described in Ref. (2); the technique requires no ion milling and has high rela-

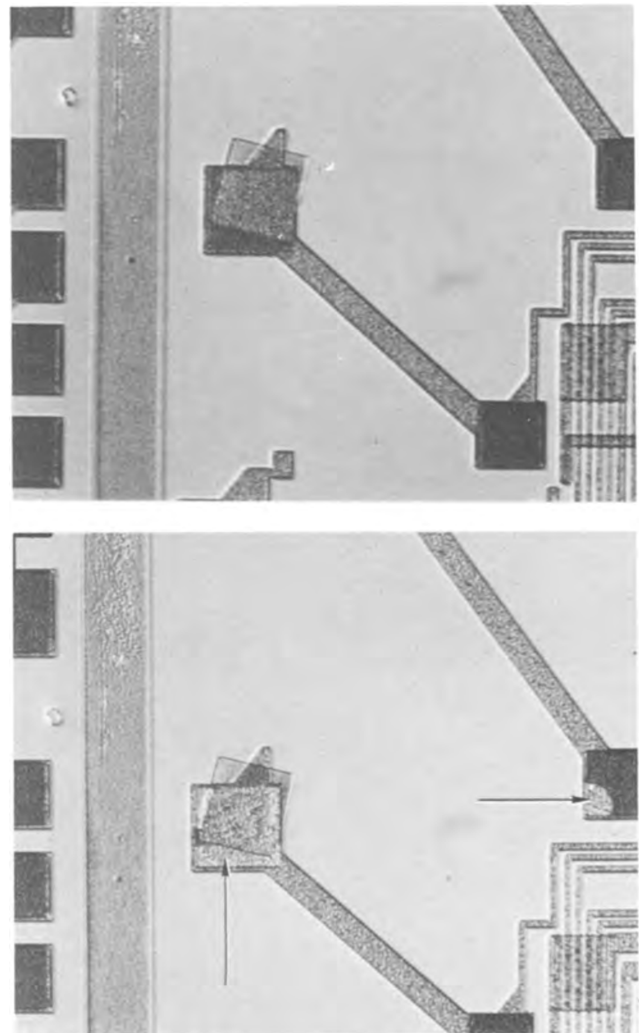

Fig. 1. Optical micrographs of films in contact windows to Al; after step 10 of Table II, sample 20. (Top) a wafer that was rinsed in 80°C DI water. (Bottom) after adhesive tape was applied to above sample and removed; the two arrows point to areas of missing Ti-Pt. The displaced square near center is a sheet of Al oxide which became detached and moved, probably just prior to Si-nitride deposition.

* Electrochemical Society Active Member.

Key words: integrated circuits, dielectric, oxidation, insulator.

Table I. Al oxide thickness vs. treatment

	Cu-doped	Photolithog.	DI water (°C)	EG-BHF	450°C anneal	Oxide thickness (A)
Testers samples						
1	Yes	—	None			32
2	Yes	—	40			35
3	Yes	Yes	40			35
4	Yes	—	40, 10 min			33
5	Yes	—	40, 20 min			31.2 ± 0.4
6	—	Yes	40	—	—	38
7	Yes	Yes	40	Yes	—	42
8	Yes	Yes	40	Yes	Yes	65
9	Yes	Yes	50	—	—	62
10	Yes	—	60	—	—	61
11	—	Yes	60		—	70
12	Yes	—	80		—	3000
13	Yes	Yes	80		Yes	2900
14	—	Yes	80		—	3300
15	Yes	Yes	80		—	Thick
16A	Yes		None			29
16B	Yes		40, 20 min			29
16C	Yes		40, 40 min			33
16D	Yes		40, 60 min			46
17A			None			19
17B			40, 20 min			38
17C			40, 40 min			55
17D			40, 60 min			87
Devices						
18, step 7	Yes	Yes	80	Yes	Yes	>>100
19, step 4	Yes	Yes	80	—	—	>6000
20, step 10	Yes	Yes	80	Yes	Yes	1600
21, step 4	Yes	Yes	40	—	—	43

Notes: Unless otherwise specified, DI water rinse time is 1 min, then 5 min, at indicated temperature, then 5 min in 20°C water, utilizing a separate bath for each rinse; nonstandard times at temperature following the first 1 min are indicated.

Table II. Abbreviated summary of process sequence

1. Al deposition.
2. Photolithography (HR100*), Al etch (H_3PO_4-based etchant).
3. Photoresist strip (A30**, 110°C, 10 min).
4. Overflow DI water rinse.
5. EG-BHF clean, 30 sec.
6. 450°C, H_2 anneal, 1 atm, 30 min.
7. EG-BHF clean, 30 sec.
8. Si-nitride (passivation layer) deposition.
9. Contact window photolithography and etch.
10. Ti and Pt deposition in preparation for beam leads.

Notes: EG-BHF = 1:1:1 mixture of ethylene glycol, buffered HF, and water. Although water is not a necessary component, it enhances the cleaning ability by increasing the rate of Al attack; however, water also increases the residual oxide thickness by hydration.

* HR100: photoresist (Phillip Hunt).

** A30: photoresist stripping solution (Allied Chemical).

tive accuracy (several angstroms) and spatial resolution (<10 μm). Thicknesses >100Å were estimated approximately using the ion-mill Auger technique, assuming the ion milling rate for SiO_2. This estimate is obviously inaccurate and was used only to demonstrate that the oxide grown was very thick. Final detailed information was obtained using the transmission electron microscope (TEM) by examining thin cross sections of the regions of interest. This last technique has been described elsewhere (3).

Results

Preliminary identification of Al oxidation problem.—An optically visible film formed on Al by rinsing in 80°C water (device sample 18) was determined by AES to be essentially pure Al oxide. On this sample, a halo visible optically and by the SEM on SiO_2 areas more than 20 μm away from patterned Al was also found by AES to be Al oxide; evidently, this oxide spreads beyond Al areas. Optical examination after Al etch and before photoresist strip had revealed no Al on these SiO_2 areas so that this oxide is not formed from unetched Al residues. These initial results clearly established the importance of Al oxidation during device processing.

Auger studies.—Testers 1-17 of Table I were then prepared and AES experiments were performed to answer four questions:

1. What are typical Al-oxide thicknesses after various treatments?
2. What is the critical DI water temperature below which oxidation rate becomes negligible?
3. Does oxidation depend on Cu doping?
4. Does oxidation proceed in pure water, free of photoresist and/or A30 carry-over?

Results are as follows: Samples 1, 16A, and 17A established the typical air-formed oxide thickness (20-30Å) on as-deposited Al (Cu doped and undoped). We have not compared the initial oxide growth rates of Cu doped and undoped Al in detail. Typically, oxide thicknesses were about 20Å within 2 hr after deposition, about 30Å after several weeks, and about 35Å after several months of air exposure for both types of Al. Samples 1-15 were taken from many different deposition runs and received varying times of air exposure prior to experimental treatments and analyses. Therefore, their initial surface oxides varied somewhat and these variations may have masked the smaller effects; the experiments using these samples were intended to reveal only the stronger effects. This defect is rectified for samples 16A-17D, as explained below.

Samples 2, 4, and 5 showed that the surface oxide thickness does not increase appreciably up to 20 min at 40°C (35Å maximum). The statistical accuracy of the Auger data is demonstrated with sample 5, for which the average oxide thickness and standard deviation of one measurement each from five different areas within about 3 mm of each other were 31.2 ±0.4Å. Thus in principle, measured differences between samples of 3% (1Å at 30Å) could be significant; in practice, it has been demonstrated (2) that differences of 10% (3Å) are meaningful.

Samples 3 and 6 showed that photolithography does not affect the oxide thickness after 40°C rinse for Cu doped and undoped Al, respectively.

Sample 7 showed that the EG-BHF etch leaves a surface oxide of about 42Å.

Sample 8 revealed that the H_2 anneal, preceded by the EG-BHF treatment, increases the oxide thickness by about 30Å, to about 65Å. It might appear surprising at first that oxide growth occurs in a reducing (H_2) ambient. However, we have reproduced this result many times (not listed in Table I) and it is in fact consistent with the following two observations. (*i*) H_2 anneal has not been found to decrease the oxide thick-

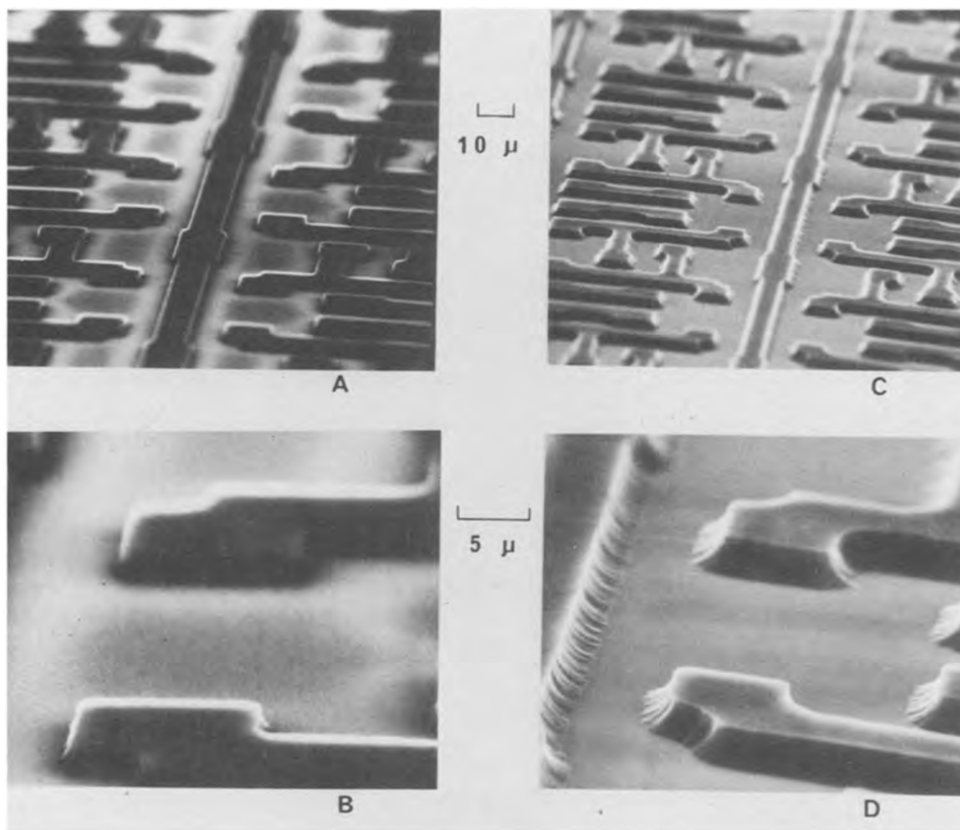

Fig. 2. SEM micrographs of the halo feature due to thick oxide growth. (A), (B) taken at two magnifications using sample 15 with thick surface film. The halo is the light contrast surrounding Al features; note the poor spatial resolution caused by the presence of an insulating film. (C), (D) from sample 3 with thin oxide (35Å); there is no halo, and spatial resolution is greatly improved.

ness in any of the present experiments, and (*ii*) it is obviously not possible to remove all contaminants during the anneal. We propose that small amounts of contaminants, either from the furnace or the wafers themselves, cause the Al to oxidize; once formed, the oxide is apparently stable in H_2 at 450°C.

Samples 9, 10, and 11 demonstrated that the oxide thickness begins to increase at 50°-60°C, to 60-70Å. Photolithography and Cu doping did not produce large effects.

Samples 12-15 showed the rapid oxide growth (to approximately 3000Å) at 80°C, which is fairly independent of photolithography and Cu doping. The 3000Å estimate does not take into account the porosity factor; for example, if the porosity factor (defined as the percentage of total film thickness occupied by pore space) is 75%, the actual oxide thickness could be 1.2 µm. The oxide thickness on sample 15 was estimated

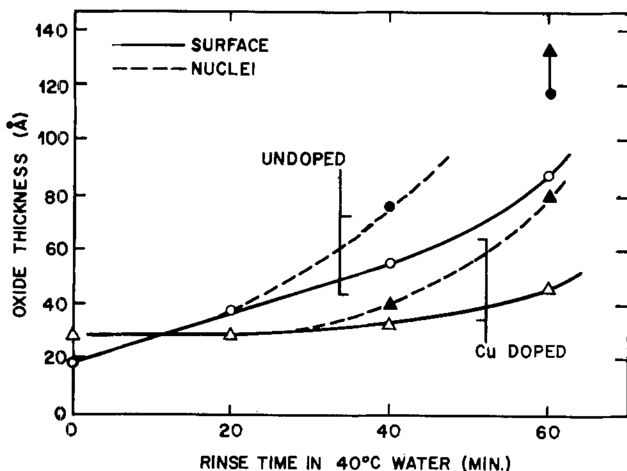

Fig. 3. Oxidation rate of Cu-doped (triangles) and undoped (circles) Al in 40°C water, samples 16 and 17. Filled points are data from the contaminated nucleation centers. The arrow on the filled circle at 116Å indicates that the oxide was thicker than 116Å.

from SEM photographs of cleaved specimens to be at least several thousand angstroms.

For samples 1-15, wafers from several Al deposition runs were used, so that the initial oxide thickness before treatment probably varied from wafer to wafer. To ensure identical starting conditions, samples 16 and 17 (Cu doped and undoped, respectively) were cleaved into 4 quarters each. These were then treated in 40°C water for 0, 20, 40, and 60 min, and the resultant surface oxide thicknesses were measured and are shown in Fig. 3. When viewed in the SEM mode of the Auger apparatus, the untreated surfaces 16A and 17A appeared featureless, and the Auger spectra revealed only slight C and S contamination. The inability to detect Si indicated that the cleaving operation for separating each wafer into samples A-D resulted in no serious Si contamination. After 20 min rinse, a faint, uneven texture was visible on both samples 16B and 17B, when viewed in the SEM mode of the Auger apparatus. After 40 min treatment, these features appeared clearly as nucleation centers that were sufficiently large (>10 µm) for Auger analysis. They were found to be oxide nuclei which grew even larger after 60 min treatment; the Auger data from these areas are also included in Fig. 3. The arrow on the data point at 116Å indicates that the oxide was >116Å thick.

No Si was detectable (<0.1%) on 16A and 17A, but about 2% Si was found on all B, C, and D samples. Since similar amounts of Si were found on surfaces of unbroken wafers after 40°C rinse, this contaminant was not unique to these cleaved samples. Although the significance of this surface Si is not clear, the nucleation centers contained higher Si and C contamination, suggesting that the more rapid oxidation at these centers is related to the contaminants. Possible sources of these contaminants are the wafer itself for Si and the original C contamination on the Al surface. This result points out the importance of removing all photoresist residues during IC processing. The data of Fig. 3 lead to the following conclusions (applies to 40°C rinse):

1. Cu-doped Al oxidized more slowly than undoped Al. However, it is not known whether the slower oxi-

dation rate of the doped film was due to its thicker initial passivating oxide, or to a difference in some other property of films deposited in different machines.

2. Oxidation rate is slow for the first approximately 20 min and becomes rapid after about 40 min.

3. Oxidation is more rapid at nucleation sites. These sites were more contaminated with C and Si than the rest of the surface.

For sample 18, a device wafer after 80°C rinse, the total oxide thickness was not measured, but was determined by Auger analysis to be >>100Å, in agreement with the above.

For sample 19, the oxide growth caused by 80°C rinse was measured following the processing to step 4 of Table II. The oxide thickness was estimated from TEM micrographs to be 6000-9000Å.

Sample 20 was processed to step 10 and the oxide thickness was estimated using Auger analysis by ion milling through the Ti-Pt layer and into the Al at a contact window. The oxide thicknesses of $\lesssim$ 6000 and 1600Å for samples 19 and 20, respectively, verify the rapid oxide growth for a device configuration, and comparison of samples 19 and 20 suggests that large amounts of oxide are removed by the brief EG-BHF etch.

Finally, sample 21 demonstrated that devices can be processed using 40°C water rinse with oxide growth limited to 43Å. This oxide thickness, which further increases upon H_2 anneal, is uncomfortably close to the limit of 55Å beyond which electrical contact problems after subsequent Ti deposition are expected, as established in a separate report (4); this point is further amplified in the Discussion.

AES indicated that after photolithography and 40°C water rinse, the amount of surface C was <0.5 atom layer (<1Å) and the Al surface is therefore sufficiently clean for the next processing step. The only other contaminants detected were about 0.05 atom layer of Si and S and much smaller quantities of Cl and F, and the dopant Cu in Cu-doped Al.

Attempts were made in this work to check the Auger measurements, d(Auger), of Al-oxide thickness by comparison with ellipsometric measurements, d(ellip.), for the full surface testers. Values of d(ellip.) were usually in reasonable agreement with d(Auger) but they sometimes differed by over a factor of 3, with d(ellip.) always larger. When the electrical breakdown voltages of these oxides were measured, the breakdown voltage was linear with d(Auger) but not related in any obvious manner to some of the d(ellip.) values (4). Therefore, we conclude that ellipsometric measurements may be sensitive to the contaminants and precise structure of the oxide and cannot be used except under certain controlled conditions. Values of d(Auger) have also been checked using a gravimetric method (in which the oxide film is weighed) and were in agreement with the resulting d(grav.) (4). Thus in addition to a fairly sound theoretical basis (2), there is experimental evidence that the Auger method of oxide thickness measurement gives probably the most reliable results available at present.

TEM analyses.—TEM of cleaved edges of sample 12 revealed the oxide to be about 5000Å thick and to have a porous, filamentary structure; typical micrographs are exhibited in Fig. 4. The oxide thickness estimates from TEM are often over a factor of two larger than from ion-mill Auger analysis. This disagreement is due at least in part to the film porosity. Cleaved samples were investigated in addition to sectioned samples (following paragraph) because of the avoidance of sectioning and ion-milling artifacts (sectioned samples are ion milled during the final stages of preparation). Avoidance of these artifacts is particularly important for obtaining reliable diffraction patterns (discussed below). Although the cleavage method is simple and fast, the cleavage geometry is not precisely known for the oxide, and details of the Al film are difficult to study because of the uneven cleavage geometry and because the Al probably deforms during breakage. Therefore, some samples were also sectioned and examined.

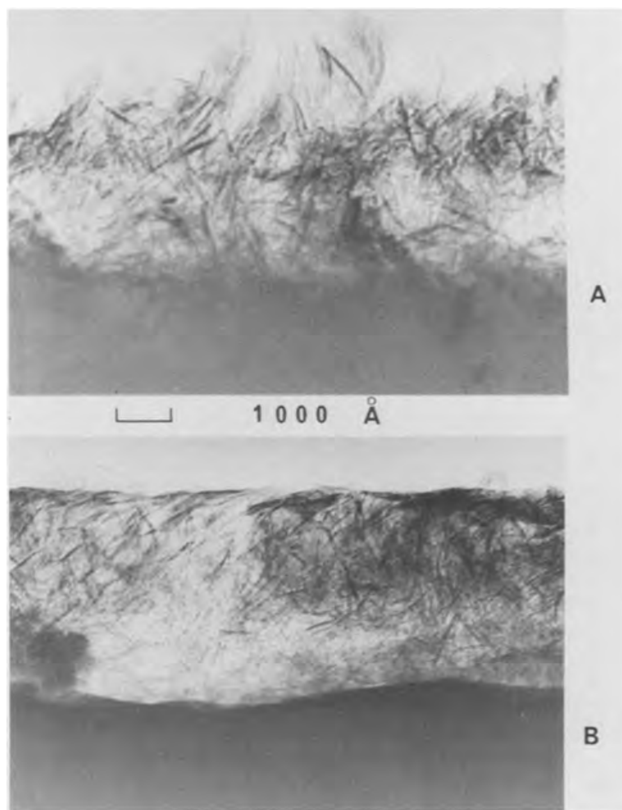

Fig. 4. TEM micrographs from a cleaved edge of sample 12, (80°C water rinse), taken from two areas. The filamentary material is Al oxide; the featureless region below the oxide is Al. The plane of the Al surface is tilted about 45°C from the electron beam axis.

TEM micrographs of cross sections of device wafer 19 are shown in Fig. 5 and 6. The appearance of the Al oxide is similar to that of sample 12 in Fig. 4, although the method of sample preparation for TEM was entirely different (simple cleaving *vs.* sectioning). In Fig. 5, a "hairline crack" can be seen running the entire width of the photograph from left to right just above the oxide-Al interface. This crack may be responsible for the lifting of the oxide as seen in Fig. 1. There is no preferential oxidation of the Al grain boundaries. Figure 6 was taken from an area tens of microns away from an Al runner that was found to the far right, out of the photograph. The horizontal line running across the photograph near center is the surface of the substrate Si, and the wavy features below this surface are mostly diffraction contrast from ion milling artifacts such as thickness variations. The cantilevered object entering from the left is a poly-Si gate (left edge) which ascends the (45°) tapered field oxide to a poly-Si runner (center). Material surrounding the poly-Si is SiO_2; close scrutiny reveals faint outlines of the various layers of thermal and deposited SiO_2. The Al oxide (filamentary material) is seen to migrate onto the SiO_2 surface and its thickness decreases toward the left, away from the Al source to the right (out of the picture).

Electron diffraction analysis of sample 12 indicated a nearly amorphous phase of gamma-alumina; the electron diffraction data are presented in Table III, under the "Measured" column, and compared to the expected values for gamma-alumina, boehmite, and bayerite. Relative intensities (x-ray) are also given in parentheses. The best match is with gamma-alumina; there is a possible presence of the monohydrate, boehmite, and no indication of the presence of the trihydrate, bayerite. This does not mean that bayerite is absent, as it may be in a more amorphous state

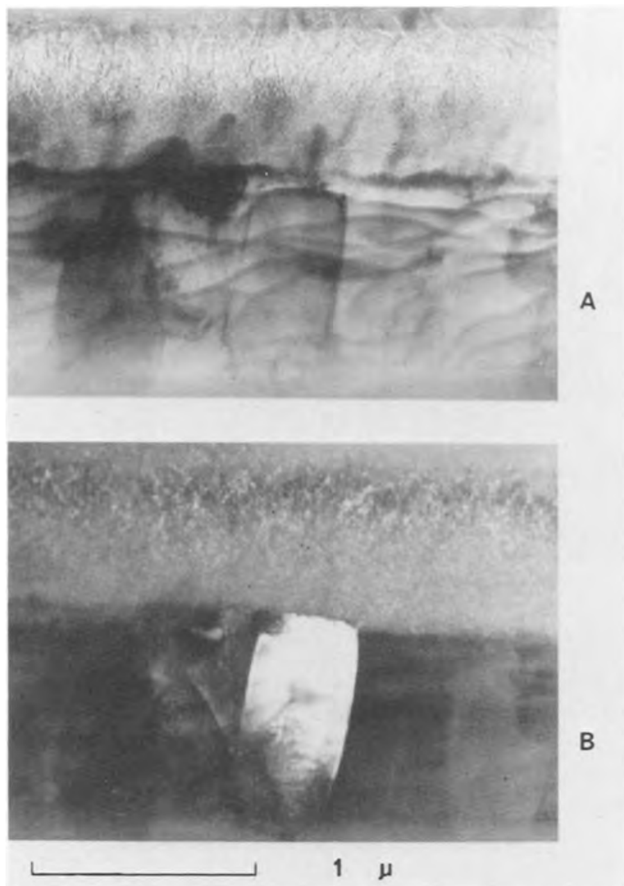

Fig. 5. TEM of thin cross sections of sample 19 taken perpendicular to the plane of the chip; the Al surface normal points up in the photograph. (A) Bright field picture showing the Al oxide (upper half) and the polycrystalline Al (lower half of photograph). (B) Dark field picture of the same area; revealing the precise location of the oxide-Al interface and the presence of small crystallites in the oxide.

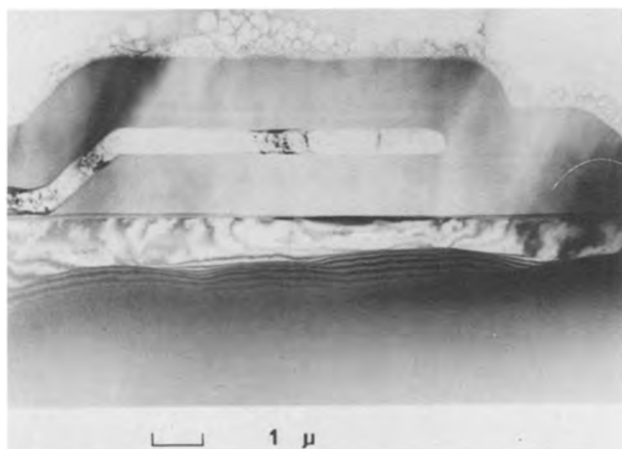

Fig. 6. SiO_2 area of sample 19, tens of microns away from an Al runner located to the far right (out of the picture). The identity of each feature is explained in the text. The filamentary material on the SiO_2 surface is Al oxide. The bubbles seen above the Al oxide are artifacts in the epoxy used to embed the specimen to facilitate handling. The Al oxide is thinner toward the left, away from the Al runner, suggesting that the runner is the source of the oxide.

than the others. All three compounds have been previously identified in diffraction patterns from Al oxidized in hot water (5, 6) (to a much greater extent than attempted here). The absence of the strong lines at d = 4.56, 2.80, 2.28, and 1.52Å for gamma-alumina and 6.11Å for boehmite in our diffraction data might

Table III. Crystallographic d-spacings (Å) of oxide on sample 12

Measured	Gamma-alumina	Boehmite	Bayerite
		6.11 (100)	4.71 (90)
	4.56 (40)		4.35 (70)
3.16 (weak)		3.16 (65)	3.20 (30)
	2.80 (20)		
2.41 (medium)	2.39 (80)	2.35 (55)	2.36 (4)
	2.28 (50)		2.22 (100)
1.96 (strong)	1.98 (100)	1.98 (6)	1.98 (4)
		1.86 (30)	
		1.85 (25)	
			1.72 (40)
		1.66 (14)	1.60 (10)
	1.52 (30)	1.53 (6)	1.55 (8)
		1.45 (16)	1.46 (12)
		1.43 (10)	1.45 (8)
1.39 (strong)	1.40 (100)	1.38 (6)	1.39 (6)
		1.31 (16)	1.33 (18)
1.13 (weak)	1.14 (20)	1.16 (4)	1.17 (6)
0.966 (v. weak)	0.989 (10)		
0.877 (v. weak)	0.886 (10)		
0.790 (v. weak)	0.806 (20)		

Note: From JCPDS Tables (formerly ASTM); x-ray intensities are given in parentheses and all lines with intensities totaling >(10) are listed. "Measured" results are electron diffraction data, 200 keV.

be due to the difference in atomic scattering factor between x-ray and electron diffraction, and to diffraction effects from extremely small crystallites with anisotropic growth habits.

The relatively thick oxide film on sample 12 (3000Å) could not be detected using x-ray diffraction and we attribute this result to its nearly amorphous nature. In agreement with this conclusion, no individual crystallites could be resolved with TEM. For the more extensively oxidized device wafer of Fig. 5 with an oxide 6000-9000Å thick, small particles, about 50Å in diameter, were visible in the dark field micrographs (Fig. 5B).

Discussion

The most significant new results of this work are the accurate quantitative measurements of the first <100Å of oxide growth in 10 MΩ DI water, under conditions actually experienced in IC processing. The fact that Al oxidizes in hot water is well documented (5-11). Our results are in qualitative agreement with literature; namely, that oxidation becomes rapid above 60°C and that the initial thin oxide is essentially amorphous. Although alloying of the Al and contaminants in the water certainly produce large effects (5, 9, 12) all the workers agree that the purest Al in the purest water available to them has resulted in oxidation (5-12).

The mechanism of Al oxidation in water has been described in some detail (6, 8). Oxidation proceeds in two major steps. In the first, Al and water react and release hydrogen, forming gamma-alumina. In the second, this oxide is hydrated and also redeposited. Thus the role played by any initial passivating oxide in delaying the onset of this oxidation is obviously important.

More generally, Al corrosion occurs in polar liquids, such as water and methanol (12). It is in polar liquids that nonneutral *p*H is readily attained, and the dependence on *p*H of the oxidation rate of Al in hot water has been clearly demonstrated (6, 8). This means, for example, that replacement of water with nonaqueous solutions will not necessarily eliminate the oxidation problem, since many nonaqueous solutions, such as methanol, are polar. Our finding that a low level of Cu doping retards oxidation slightly is of interest because, at high levels (≅4%), Cu has been reported to increase the corrosion activity (5, 9). However, our result is in qualitative agreement with the fact that anodization rate decreases with Cu doping (10). Investigation of Si-doped Al may also be interesting, because it has been reported (7) that Si doping retards Al oxidation in water. This last point is

interesting because Si is always present in Si IC processing and Si was one of the contaminants found on the Al in this work.

The usefulness of the above results to IC processing is obvious. Although DI water rinse is most effective at higher temperatures, we have established that above 50°C, oxide growth rate becomes too fast and the allowed thickness limit (4) of about 55Å can be exceeded in a matter of minutes. This limit is the sum of the amount of oxide that is effectively nullified by subsequent Ti deposition (45Å) and the electron tunneling distance (12Å), as determined by electrical breakdown measurements. The EG-BHF etch was shown here to be very effective for removing thick Al oxide. However, it leaves a relatively thick residual oxide (about 40Å) which further increases in thickness upon H_2 anneal (to about 65Å). A different etch based on a mixture of CrO_3 and H_3PO_4 has been shown (4) to leave a much thinner residual oxide (about 30Å) and may be preferable for reducing oxide thickness.

The rapid oxidation property of Al is not always undesirable and can be exploited to useful purpose. For example, even a mild treatment in hot water may be sufficient to passivate exposed Al areas of an IC chip. If an entire device is coated with Al, a passivating layer can be grown by completely oxidizing the Al. It should be kept in mind, however, that during oxidation, hydrated oxides will migrate and redeposit on adjacent areas that are tens of microns away from the Al. Since many materials are stable in hot water, they can be used as mask material for selective oxidation of thin Al films.

Conclusions

1. 40°C is a "safe" temperature for DI water rinse of Al (up to about 20 min); 50°-60°C is the "danger point" beyond which excessive oxidation will occur. The Al surface is quite clean (<1Å of C) after a 5 min, 40°C rinse following photolithography.
2. Al-oxide growth occurs in pure water; (HR100) photolithography, (H_3PO_4-based) Al etch, (A30) resist stripping, and Cu doping ($\cong$0.5 a/o), do not significantly affect the oxidation rate.
3. This oxide is porous and contains nearly amorphous gamma-alumina and probably some hydrated oxides.
4. The Al oxide is able to spread >20 μm from the Al to adjacent areas; this probably occurs by dissolution of gamma-alumina and redeposition of the hydrated oxides (6, 8).
5. This oxide is loosely adherent to Al, especially after 450°C H_2 anneal, and causes poor adhesion of subsequent metals deposited over the Al.

Acknowledgment

The authors are grateful to M. H. Read for x-ray diffraction analysis.

Manuscript submitted Sept. 29, 1977; revised manuscript received Jan. 3, 1978.

Any discussion of this paper will appear in a Discussion Section to be published in the December 1978 JOURNAL. All discussions for the December 1978 Discussion Section should be submitted by Aug. 1, 1978.

Publication costs of this article were assisted by Bell Laboratories.

REFERENCES

1. M. P. Lepselter, *Bell Syst. Tech. J.*, **45**, 233 (1966).
2. C. C. Chang and D. M. Boulin, *Surf. Sci.*, **69**, 385 (1977).
3. T. T. Sheng and C. C. Chang, *IEEE Trans. Electron Devices*, **ed-23**, 531 (1976).
4. T. A. Shankoff, C. C. Chang, and S. E. Haszko, *This Journal*, **125**, 467 (1978).
5. R. K. Hart, *Trans. Faraday Soc.*, **53**, 1020 (1957).
6. M. Pourbaix, in "Atlas of Electrochemical Equilibria in Aqueous Solutions," p. 168, Pergamon Press (1966).
7. J. M. Bryan, *J. Soc. Chem. Ind.*, **69**, 169 (1950).
8. W. Vedder and D. A. Vermilyea, *Trans. Faraday Soc.*, **65**, 561 (1969).
9. R. S. Alwitt and L. C. Archibald, *Corros. Sci.*, **13**, 687 (1973).
10. G. C. Schwartz, Abstract 80, Electrochemical Society Symposium, Toronto, Canada, May 11-16, 1975.
11. K. A. Phatak, S. S. Tamhankar, and K. Sathianandan, *Thin Solid Films*, **41**, 137 (1977).
12. P. A. Totta, Abstract A-3, American Vacuum Society Symposium, Philadelphia, October 1975.

Silicon-on-Sapphire Crystalline Perfection and MOS Transistor Mobility

C. E. Weitzel* and R. T. Smith

RCA Corporation, RCA Laboratories, Princeton, New Jesrey 08540

ABSTRACT

Experimental data show that there is a correlation between the crystalline perfection of a (100) silicon-on-sapphire epitaxial film and the magnitude and direction of misorientation of the sapphire substrate from the $\{1\bar{1}02\}$ normal. The perfection is ascertained by measuring the half-width of Si {400} θ:2θ x-ray diffraction profiles. Data obtained from SOS/MOS transistors show a direct relationship between epitaxial perfection and FET mobility. Other factors which influence the perfection of the SOS film are growth temperature and film thickness.

For many years considerable effort has been expended in optimizing the quality of the epitaxial silicon films grown on sapphire substrates. In the earliest work (1-3), the optimization was achieved by selecting the appropriate Al_2O_3 planes which allow single crystal silicon growth and by using silane rather than silicon tetrachloride as the source gas. To achieve higher quality SOS films later workers (4-11) found it necessary to optimize other parameters: type of sapphire, substrate polishing and cleaning, predeposition firing, growth rate and temperature, and postdeposition annealing. Additional work (12-18) was directed toward understanding and optimizing changes in the SOS films which resulted from MOS transistor fabrication. More recently a vast array of sophisti-

* Electrochemical Society Active Member.
Key words: x-ray diffractometry, θ:2θ half-width, FET mobility, growth temperature, Czochralski sapphire.

cated analysis techniques have been used by numerous workers (19-35) whose goal is to understand and optimize the Si-Al_2O_3 system.

Despite all of this work on optimizing (100) SOS films, there is no mention of the possible dependence of SOS film quality on the sapphire substrate misorientation from the {1$\bar{1}$02} plane. Recently we presented data (36) that were obtained from wafers cut from EFG (edge defined film fed growth) sapphire ribbons that were polished using techniques that subsequently have been improved. These data indicate that small misorientations of the substrate away from the {$\bar{1}$102} affect the SOS film perfection, and as a result the transistor mobility. More importantly the data show that the most perfect (100) SOS films are not obtained on the {$\bar{1}$102} sapphire plane but rather off this plane. The data presented here are corroborating observations obtained using state-of-the-art Czochralski substrates. The relative crystalline perfection of SOS films is determined by x-ray diffraction profiles and is shown to correlate with SOS/MOS transistor mobility. The data from the Czochralski substrates also indicate that the most perfect SOS films are grown on substrates which are off the {1$\bar{1}$02} plane. Since the same results were obtained for both sources of sapphire and both polishing techniques we must conclude that the optimum substrate orientation is independent of these parameters. The transistor mobility and film perfection are also shown to be directly related for SOS films grown at different temperatures and of different thicknesses.

Experimental Techniques

The 1½ in. diam sapphire substrates used in this investigation were cut from Czochralski sapphire boules and polished by Union Carbide using state-of-the-art techniques. Since a systematic investigation of substrate misorientation was planned, the misorientation of a large number of substrates was measured using x-ray Laue and diffractometry techniques. Each wafer had a fiducial flat ground at 45° to an Al_2O_3 "a" axis lying in the plane of the wafer face. The projection of the Al_2O_3 "c" axis in the polished side of the wafer was determined relative to the ground fiducial flat by the back-reflection Laue method. Components of misorientation of the face of the wafers from the {1$\bar{1}$02} were thus measured in orthogonal directions perpendicular and parallel to the projection of the "c" axis. The orthogonal components of misorientation were measured on a Siemens diffractometer equipped with a Siemans single crystal orienter and using a Cu $K\alpha_1$ {1$\bar{1}$02} reflection. Components of misorientation were read directly to an accuracy of ±0.02°.

From this pool of substrates four groups of five substrates were selected to be processed together. In selecting the substrates for each group, care was taken to select substrates with widely varying misorientation so that any difference in transistor parameters would be obvious. Figure 1 shows the misorientation components of 20 of the substrates which were studied. A perfectly oriented wafer would be located at the origin of this graph. Figure 1 also shows how the wafers are divided into four processing lots and the processing lot number. At the time the wafers were purchased, the orientation specification was 2.0° in any direction from {1$\bar{1}$02}. Only three of the 20 wafers were outside of this specification.

After the components of misorientation of the substrates were measured, the substrates were fired in H_2 at 1200°C for 30 min. The epitaxial silicon films were grown on five substrates at a time in a five-sided barrel reactor by the pyrolysis of SiH_4 at 970°C pyrometer. The films were doped 1 × $10^{15}/cm^3$ n-type during growth. Nominally 0.6 μm films were grown in 20 sec. Following epitaxial silicon growth, diffraction profiles were obtained from both the Al_2O_3 {2$\bar{2}$04} and Si {400} in the rocking curve (ω-scan) and θ:2θ

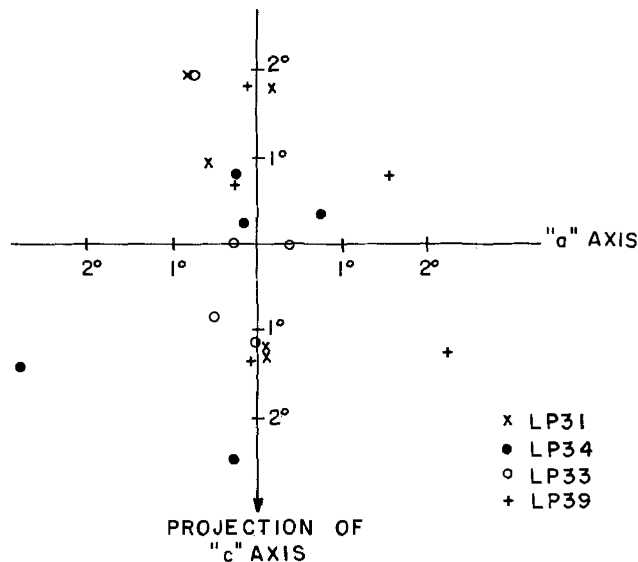

Fig. 1. Misorientation components of 20 Czochralski {1102} sapphire substrates.

modes. These diffraction profiles were obtained from a rectangular area about 1 cm × 1 mm near the center of each wafer. A Siemans ω-drive diffractometer with Cu Kα radiation was used to record the peak profiles. The smallest entrance and receiving slits (0.125 and 0.05 mm, respectively) were used to minimize the instrumental broadening. Scanning speeds were 1/8°/min in the θ:2θ mode and 1/4°/min in the ω-mode. The crystal scanning-chart speed coupling gave a strip chart recording sensitivity of 0.03125°/cm and 0.0625°/cm in the θ:2θ and ω-modes, respectively. In the θ:2θ mode, one samples only from a set of parallel planes, and the broadening over instrumental may be caused by a crystalline defect causing nonuniformity in the d-spacing of these planes or small crystallite size effects or both. In the ω-mode the detector is set at a fixed position centered within an angular range of 0.02° about the maximum diffracted intensity setting; hence any plane having a d-spacing characteristic of the angular setting of the detector may be sampled as the crystal alone is rotated through its diffracting range. Broadening in this mode may be caused by relative misorientation of crystallites or sample curvature or both. Each sample was oriented such that its diffraction normal was in the plane of the diffractometer. This was accomplished by incrementally rotating the sample about its face normal and successively readjusting the crystal ω setting and detector 2θ setting to maximize the diffracted intensity. The correct setting is attained when ω reaches a maximum or minimum value.

Following characterization of the epitaxial silicon film, SOS/MOS transistors were fabricated using the P+ polysilicon gate deep depletion process (37). Briefly the processing steps are: silicon island definition and etching, growth of 1200Å of channel oxide, polysilicon deposition, doping and etching, channel oxide self-aligned etch, doping of sources and drains from doped oxides, contacts, metallization and overcoat. The process results in the fabrication of an n-channel deep depletion transistor and a p-channel enhancement mode transistor. The average FET mobility for a wafer is determined by averaging the mobilities measured at five points on each wafer, one point at the center of the wafer and four points equally spaced around the perimeter of the wafer within ¼ in. of the wafer edge. The mobility of each point is arrived at by plotting the drain current *vs.* gate voltage with V_D = 0.1V. The transconductance is determined from the linear part of this curve where the g_m is maximum. The FET mobility is then calculated using the physical dimensions of the transistor (38).

Experimental Results

Substrate misorientation and silicon epitaxial perfection.—Of the four diffraction profiles obtained from each sample, the Si $\theta:2\theta$ half-widths were found to have the greatest correlation to device performance. The Si ω-scan half-widths paralleled those of the $\theta:2\theta$ with some exceptions. It is thought that these exceptions are due to the dependence of the ω-scan half-width on the direction of scan. Since each crystal was oriented so that it was scanned in the direction of misorientation and the orientation of each was different, a common scanning direction did not exist. Since the $\theta:2\theta$ half-widths are a valid qualitative comparison of relative crystalline quality or perfection, we have chosen to compare device performance characteristics with the crystalline quality as obtained from $\theta:2\theta$ scan half-widths.

The half-widths obtained from $\{2\bar{2}04\}$ $\theta:2\theta$ scans of all the Al_2O_3 substrates were found to have a mean value of 0.0413° ± 0.0029°. Although the Al_2O_3 half-widths showed very little variation, the {400} $\theta:2\theta$ half-widths of Si deposited on these substrates ranged from 0.117° to 0.157° as shown in Table I. The half-width of a {400} Cu $K\alpha_1$ reflection of bulk Si obtained with the same instrumental conditions was found to be 0.0500°. Thus it appears that the method was insensitive to any variations in the quality of the Al_2O_3 substrate, if present; while, the $\theta:2\theta$ half-widths of the epi Si were from 2.3 to 3.1 times as large as those of bulk Si. Repeated half-width measurements of the same SOS sample indicated that the measured half-widths are reproducible to within ±3.0%. The diffraction profiles of the {400} Si reflection were similar to those reported earlier (36).

The half-widths obtained from each of the 20 wafers are shown in Table I. The wafers in each processing lot are listed in order of increasing $\theta:2\theta$ half-width. Therefore, the SOS film having the smallest half-width is listed first in each group of five wafers, and the one with the largest half-width is listed last. An examination of the components of misorientation of each wafer revealed a correlation between the component of misorientation parallel to the mirror plane and the $\theta:2\theta$ half-width as shown in Table I. The wafers, whose component of misorientation parallel to the mirror plane is positive, have the smallest half-widths; whereas, the wafers whose component of misorientation is negative have the largest. Therefore, wafers misoriented in the top half plane of Fig. 1 consistently have smaller half-widths than those in the bottom half plane. This correlation is obvious for all of the lots except LP33. Possible causes of this lack of correlation in lot LP33 are discussed later. No correlation was found between the components of misorientation parallel to the "a" axis and the $\theta:2\theta$ half-widths. This is not surprising since most of the wafers are only slightly displaced from the mirror plane, Fig. 1.

Table I. $\theta:2\theta$ X-ray half-widths of SOS films, sapphire substrate component of misorientation parallel to mirror plane and SOS/MOS transistor mobility

Processing lot	Sapphire substrate component of misorientation parallel to mirror plane (degrees)	Silicon $\theta:2\theta$ half-width (degrees)	SOS/MOS transistor mobility (cm^2/V sec) n-channel Max	n-channel Avg	n-channel Min	p-channel Max	p-channel Avg	p-channel Min
LP31	+1.80	0.117	457	447	440	218	214	209
	+1.92	0.123	460	424	402	207	204	197
	+0.92	0.134	356	353	344	177	170	163
	−1.22	0.138	350	343	320	176	174	169
	−1.28	0.142	336	320	300	171	165	155
LP33	+1.94	0.125	453	447	445	161	159	158
	−0.03	0.126	491	483	477	186	182	180
	−1.13	0.129	506	483	431	168	164	153
	0.00	0.134	575	542	518	189	186	176
	−0.84	0.145	432	416	399	153	150	146
LP34	+0.82	0.118	458	432	415	164	162	159
	+0.35	0.122	451	426	409	169	161	154
	+0.25	0.128	347	337	330	143	141	139
	−1.41	0.133	320	314	305	136	131	128
	−2.50	0.141	295	268	236	130	114	109
LP39	+0.69	0.130	509	497	487	202	197	194
	+0.81	0.134	535	530	523	225	218	212
	+1.85	0.142	483	456	419	191	188	179
	−1.34	0.150	420	410	405	193	185	169
	−1.26	0.157	Wafer broke					

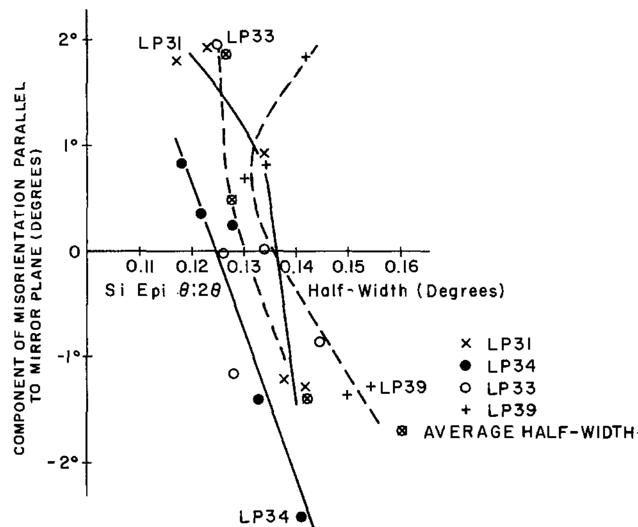

Fig. 2. Silicon {400} $\theta:2\theta$ half-widths vs. component of misorientation parallel to the mirror plane.

The data from the first two columns of Table I are shown graphically in Fig. 2. The ordinate in Fig. 2 is the component of misorientation parallel to the mirror plane and the abscissa is the $\theta:2\theta$ half-width. The lines are drawn to approximately fit the experimental data points. Three of the lines show a monotonic decrease in $\theta:2\theta$ half-width as the component of misorientation changes from negative to positive; whereas, the fourth line, for processing lot LP39, shows a decrease followed by an increase for the most positive component of misorientation. The 20 points plotted in Fig. 2 could be gathered together into three groups: those with components of misorientation parallel to the mirror plane of about −1°, those with components between 0° and +1°, and those with components around +2°. The average half-widths of these three groups are 0.140°, 0.128°, and 0.127°, respectively. These averages also reflect the correlation with substrate orientation. The average half-width and misorientation component of these three groups is plotted in Fig. 2 by the circled X.

Silicon $\theta:2\theta$ half-width and SOS/MOS transistor mobility.—Since the $\theta:2\theta$ diffraction profile is a measure of the quality of the epitaxial film, such a parameter should also correlate with the electrical properties of the film that are also affected by film quality. Since the mobility of charge carriers is limited by scattering events, the mobility of carriers in a more highly defected material would necessarily have to be smaller than in a more defect-free material. This correlation is shown by the transistor mobility data in Table I. The maximum, minimum, and average mobilities of both n-channel and p-channel transistors on each wafer are shown. With the exception of data for lot LP33, the average mobility decreases as the $\theta:2\theta$ half-width increases. The maximum and minimum mobilities for each wafer also show this trend. For most of the wafers the maximum and minimum mobilities differ from the average mobility by less than 5%. For a few wafers, however, the difference is as great as 10%.

This correlation between crystalline perfection and FET mobility is shown graphically in Fig. 3. The FET mobility for n-channel deep depletion transistors and p-channel enhancement transistors from lot LP34 is plotted *vs.* the $\theta:2\theta$ half-width of the silicon epitaxial film. The spread in mobility above and below

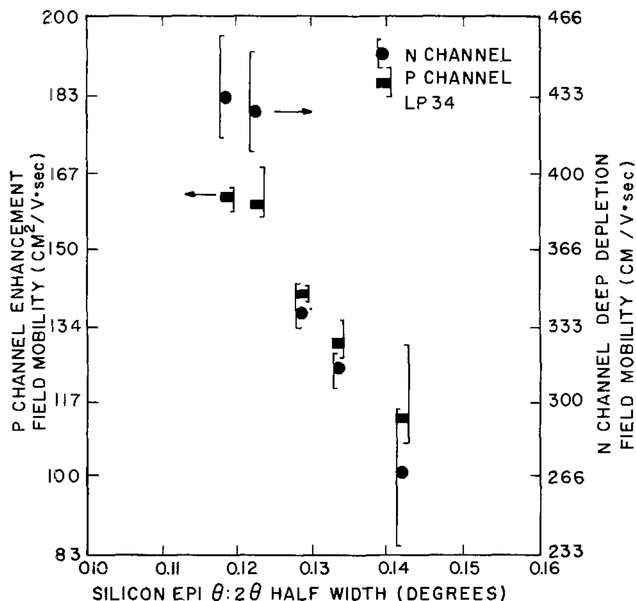

Fig. 3. FET mobility of n-channel deep depletion and p-channel enhancement transistors vs. θ:2θ half-width of silicon epitaxial film for wafers in lot LP34.

the average is shown by the vertical bar. The data show that the mobility in the accumulation layer of the n-channel device is reduced from 432 cm^2/V sec for a half-width of 0.118° to 268 cm^2/V sec for a half-width of 0.141°. The average mobility in the inversion layer of the p-channel device decreases from 162 to 114 cm^2/V sec. For a 3.32° change in substrate orientation, the mobility is reduced to 70% of its maximum value. The average mobilities for the devices on wafers in the three groups previously discussed in reference to Fig. 2 also show the same effect. The average n-channel mobility for the three groups is 380, 450, and 443 cm^2/V sec, respectively, and the average p-channel mobility for the groups is 164, 183, and 197 cm^2/V sec, respectively.

Since the crystalline perfection correlates with misorientation direction and also with the FET mobility, the mobility must also correlate with misorientation direction. This correlation is shown in Fig. 4 for processing lot LP31. In Fig. 4 the misorientation components for each substrate are plotted on a graph similar to Fig. 1. Next to each point is given the average n-channel and p-channel FET mobility. Devices fabricated on substrates which are above the origin, which in Fig. 2 have been shown to have lower

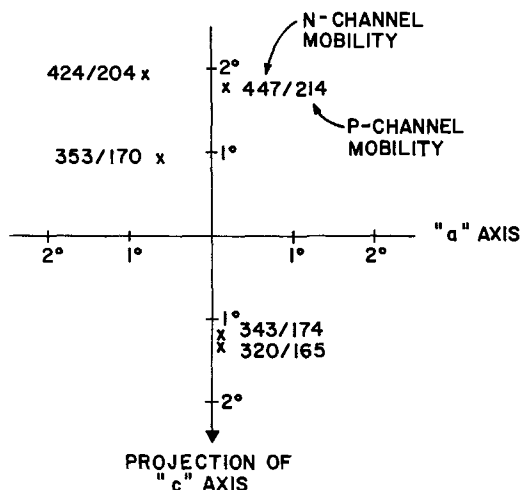

Fig. 4. FET mobility of n-channel deep depletion and p-channel enhancement transistors vs. components of substrate misorientation for wafers in lot LP31.

defect concentrations, have higher FET mobilities than devices fabricated on substrates which are located below the origin which have been shown to have higher defect concentrations.

Other parameters affecting SOS epitaxial perfection.—The correlation between substrate misorientation, silicon θ:2θ half-width, and SOS/MOS transistor mobility is quite obvious when the data from the five wafers which were processed together are compared. However, the correlation becomes less obvious when all 20 wafers are grouped together for analysis. In addition, the lack of correlation for the data from lot LP33 is unexpected in light of the data from the other lots. These facts indicate that, in addition to substrate misorientation, there are other factors which affect SOS epitaxial quality. If other parameters were not important, all of the lines connecting the data points in Fig. 2 would cross the zero degree axis at the same point. Instead, there is a 0.0115° variation in half-width on this axis. This variation exists in spite of the fact that the wafers were processed as identically as is presently possible.

The factors that are not totally controlled are probably those that affect the substrate polishing and cleaning and the silicon growth. Until recently no technique for quantitatively measuring the perfection of a polished sapphire surface has been available. The infrared work by Duffy and Zanzucchi (31) is a step in this direction. An important factor to control with regard to the silicon growth is the temperature. This is usually done with an optical pyrometer. Since the pyrometer measures the temperature through the wall of the growth reactor any deposit that accumulates on the inside wall of the reactor will cause an error in the temperature at which the film is grown. The sensitivity of the quality of the SOS film to growth temperature is shown by the data in Fig. 5. To eliminate the effect of the accumulating deposit the bell jar was thoroughly cleaned prior to growing the SOS films for this experiment. In addition after each deposition run the bell jar was cleaned again. These precautions were taken so that the susceptor temperature could be measured accurately. The FET mobility of n-channel deep depletion transistors is plotted on the ordinate and the growth temperature, as measured by an optical pyrometer, is plotted on the abscissa. The vertical bars indicate the spread in mobility across each 1½ in. diam wafer. The misorientation components of all of the wafers are the same to within 0.100°. As the deposition temperature is increased from 930° to 1000°C, the average FET mobility increases from 260 cm^2/V sec to a high of 445 cm^2/V sec and back down to 258 cm^2/V sec. The spread in mobility across a wafer is smallest for films grown near the optimum temperature. The films grown at 930° and 1000°C had

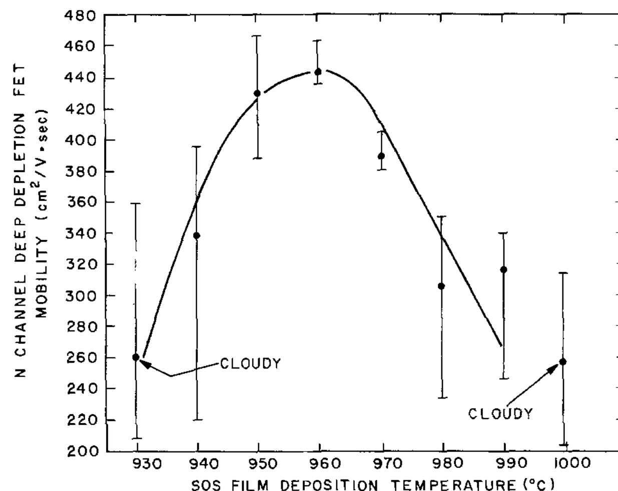

Fig. 5. N-channel FET mobility vs. SOS film growth temperature

a cloudy or milky appearance when viewed with intense low-angle lighting. In all probability there are degrees of cloudiness not discernible to the human eye for some of the other lower mobility wafers. The crystalline structure of the cloudy films is presently being studied. The θ:2θ half-width of cloudy films is larger than that of noncloudy films for identically oriented wafers. The data indicate that temperature control to within ±5.0° of the optimum temperature is desirable. However, it is still not that simple, because the temperature across the surface of the growth susceptor varies. In addition, the temperature variation across a warped wafer will be different from that across a flat wafer.

Talysurf measurements indicate that occasionally the films on one or more wafers in a deposition run are thicker or thinner than expected. Again as with temperature, this can have a measurable effect on FET mobility and θ:2θ half-width, as shown in Fig. 6. The misorientation components of all of the wafers are the same within 0.100°. The mobility for n-channel deep depletion transistors is plotted on the left-hand ordinate, and θ:2θ half-width is plotted on the right-hand ordinate. Again the vertical bar indicates the spread in mobility across the wafer. The preprocessed film thickness is plotted on the abscissa. Approximately 700Å of silicon is consumed during oxidation in the process. As the film thickness decreases the mobility first decreases slowly and then rapidly below 3000Å. This mobility decrease is mirrored by an increase in θ:2θ half-widths. These mobility data are consistent with those of other workers (39-41). These data indicate that the defect density of an SOS film increases as the Si-Al_2O_3 interface is approached. Cross-section transmission electron micrographs also show this dependence of defect density on film thickness (24).

The high temperature processing steps that the film undergoes during the fabrication of MOS devices also have a significant effect on the defect density of the SOS epitaxial film, as shown by the data in Fig. 7. These data were taken by measuring the θ:2θ half-width of as grown 0.6μ thick films. Then a thermal SiO_2 layer is grown in HCl steam on each of the films, as would be done in normal processing. A different oxidation temperature and time was used for the two films. Normally the SiO_2 is used as an etch mask for the silicon film. However, in this experiment the oxide is merely removed before the θ:2θ half-widths are re-measured. The results are shown in Fig. 7. It is interesting to note that the film with the larger half-width that was oxidized at the higher temperature for the longer time had the smaller half-width following the oxidation. Next the films were oxidized as if the channel oxide were being grown. The oxide was removed, and the half-widths remeasured. This process was repeated after each of the anneals at 1050°C

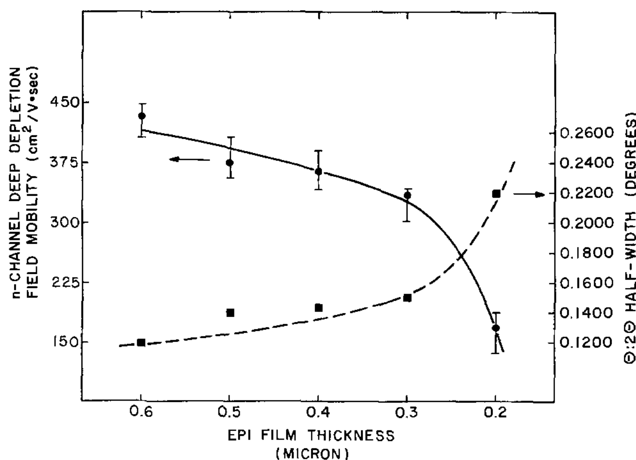

Fig. 6. N-channel FET mobility and θ:2θ half-width vs. SOS film thickness.

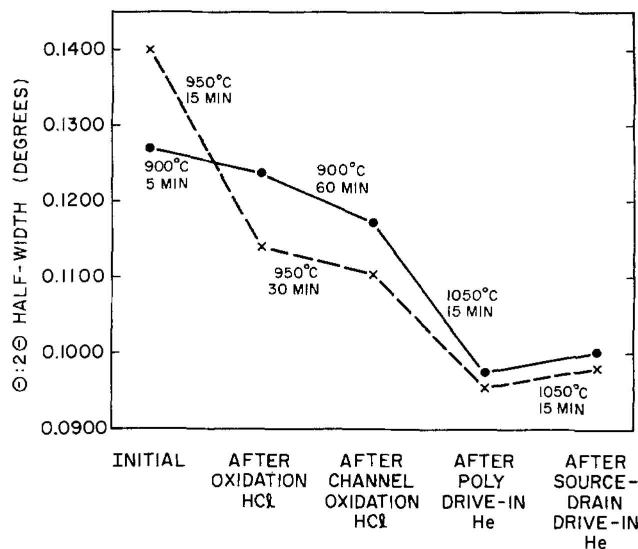

Fig. 7. Effect of high temperature processing steps on silicon {400} θ:2θ half-widths.

in helium for 15 min. The data clearly show that the high temperature processing steps cause a decrease in the θ:2θ half-width. This is indicative of an annealing out of some of the defects in the SOS film. That the more defective film had less defects at the end of the processing shows the importance of the time and temperature for improving the perfection of the film. Finally the data show that continued annealing does not reduce the SOS, θ:2θ half-width to that observed for bulk silicon, 0.0500 degrees. Rather the half-width decrease saturates at a value between 0.0900 and 0.1000 degrees. These results were confirmed by other experiments in which SOS films were annealed in inert ambients for periods of hours or days. In all cases the half-widths decreased; and in many cases following saturation, the half-widths increased with further annealing, as did the data in Fig. 7. The smallest half-width measured for an annealed 0.6μ SOS film was 0.0844 degrees, and only one other film out of about 30 had a measured half-width of below 0.0900 degrees.

Discussion

The experimental data presented here is additional evidence for the correlation between sapphire substrate misorientation, silicon θ:2θ half-width, and SOS/MOS transistor mobility. In the earlier work (36) this correlation was found using wafers cut from EFG sapphire ribbons that were polished using techniques that have subsequently been improved. As a result there was concern that the source of the sapphire and polishing techniques might have contributed to the effect. The present observations, however, were obtained using substrates cut from Czochralski boules. These wafers were fabricated using state-of-the-art techniques which included a final polish using colloidal-silica type polishing agents. Since the same behavior was found for both sources of sapphire and both polishing techniques, we must conclude that one factor that determines the qualtity of the SOS film is the substrate misorientation. In addition the data show that the highest quality SOS films are not grown on the {1$\bar{1}$02} plane, as was formerly supposed, but rather off this plane by an, as yet, undetermined amount. This optimum orientation is presently being sought.

Although most of the experimental data clearly shows the correlation between substrate misorientation, SOS film perfection, and FET mobility, anomalous results are occasionally found. In this work the data from lot LP33 is clearly anomalous when compared with the data from the other lots. In addition the wafer with the component of misorientation parallel to the mirror plane of +1.85 degrees in lot LP39 is

also somewhat anomalous. One possible explanation of this behavior is that factors other than substrate misorientation are affecting the film quality. The data in Fig. 5 and 6 show that growth temperature and film thickness are two other factors which affect film perfection. The growth temperature could be different for wafers in the same deposition run if the faces of the susceptor are at different temperatures or if there is poor thermal contact between the wafer and susceptor which could be caused by wafer warpage. The data in Fig. 5 clearly show that a deviation of only 10°C from the optimum growth temperature can cause a signficant decrease in transistor mobility. A limited study of film thickness variation for wafers grown at identical conditions revealed that although the thickness of 90% of the films was within ±10% of the average thickness of all the SOS films, the thickness of the films on the other 10% of the wafers differed by as much as ±25%. This translates to a film thickness variation of ±1500Å. The data in Fig. 6 show that a variation in thickness of this magnitude would also have a significant effect on $\theta:2\theta$ half-width and transistor mobility.

The data in Table I show that for the anomalous wafer in lot LP39 not only is the mobility lower than expected, but the half-width is also greater than would be expected for a wafer with this misorientation. Therefore, the correlation between mobility and half-width still holds; whereas the correlation with misorientation is violated. This type of behavior would be expected if the film were too thin or if the growth temperature were not optimum.

In light of the correlation between misorientation, half-width, and mobility for the data from the other three lots, the data for lot LP33 is most disconcerting. The data for lot LP33 in Table I show very little correlation between any of the measured parameters. If the half-width data correlated with the mobility data, but not the misorientation the arguments used for the wafer in lot LP39 with regard to growth temperature and film thickness could be applied here. However, the data for LP33 in Table I do not show this correlation. Therefore, the only explanation for the lack of correlation is that either the wafers became mixed up or that there are other factors which can affect the film mobility but not the half-width.

The data which show the decrease in half-width following various processing steps points out an important fact about SOS films. The fundamental properties of SOS films are not unaffected by the processing steps required for transistor fabrication. On the contrary SOS films are very sensitive to processing parameters. These x-ray diffraction techniques are merely another tool that can be used to acquire a better understanding of the dynamics of the $Si-Al_2O_3$ system. The ultimate goal of all this work is the optimization of SOS transistor performance.

Summary

Experimental data obtained from state-of-the-art Czochralski sapphire substrates were presented which show a correlation between substrate misorientation, SOS film perfection, as measured by x-ray diffraction techniques, and SOS/MOS transistor mobility. The correlation is identical to that obtained in earlier work (36) in which EFG ribbon wafers were used. The data indicate that the optimum substrate orientation is not the $\{1\bar{1}02\}$ plane but rather off this plane. Growth temperature and film thickness are also shown to have a large effect on film perfection and transistor performance.

Acknowledgments

The authors are indebted to D. Capewell and T. Pawlicki for their technical assistance.

Manuscript submitted June 8, 1977; revised manuscript received Nov. 9, 1977. This was Paper 177 presented at the Las Vegas, Nevada, Meeting of the Society, Oct. 17-22, 1976.

Any discussion of this paper will appear in a Discussion Section to be published in the December 1978 JOURNAL. All discussions for the December 1978 Discussion Section should be submitted by Aug. 1, 1978.

Publication costs of this article were assisted by the RCA Corporation.

REFERENCES

1. H. M. Manasevit and W. I. Simpson, *J. Appl. Phys.*, **35**, 1349 (1964).
2. H. M. Manasevit, A. Miller, F. L. Morritz, and R. Nolder, *Trans. Metall. Soc. AIME*, **233**, 540 (1965).
3. R. Nolder and I. Cadoff, *ibid.*, **233**, 549 (1965).
4. C. W. Mueller and P. H. Robinson, *Proc. IEEE*. **52**, 1487 (1964).
5. P. H. Robinson and C. W. Mueller, *Trans. Metall. Soc. AIME*, **236**, 268 (1966).
6. D. J. Dumin and P. H. Robinson, *This Journal*, **113**, 469 (1966).
7. D. J. Dumin, *J. Appl. Phys.*, **38**, 1909 (1967).
8. J. F. Allison, D. J. Dumin, F. P. Heiman, C. W Mueller, and P. H. Robinson, *Proc IEEE*, **57**, 1490 (1969).
9. D. J. Dumin and E. C. Ross, *J. Appl. Phys.*, **41**, 3139 (1970).
10. D. J. Dumin, *Solid-State Electron.*, **13**, 415 (1970).
11. D. J. Dumin, P. H. Robinson, G. W. Cullen, and G. E. Gottlieb, *RCA Rev.*, **31**, 620 (1970).
12. D. J. Dumin and P. H. Robinson, *J. Appl. Phys.*, **39**, 2759 (1968).
13. E. C. Ross and G. Warfield, *ibid.*, **40**, 2339 (1969).
14. G. W. Cullen, G. E. Gottlieb, and C. C. Wang, *RCA Rev.*, **31**, 355 (1970).
15. J. H. Scott and J. R. Burns, Abstract 138, p. 355, The Electrochemical Society Extended Abstracts, Spring Meeting, Los Angeles, Calif., May 10-15, 1970.
16. D. J. Dumin, *J. Vac. Sci. Technol.*, **8**, 235 (1971).
17. G. E. Gottlieb, J. F. Corboy, G. W. Cullen, and J. H. Scott, *Metall. Trans.*, **2**, 653 (1971).
18. G. W. Cullen, *J. Cryst. Growth*, **9**, 107 (1971).
19. C. C. Chang, *J. Vac. Sci. Technol.*, **8**, 500 (1971).
20. P. T. Picroux and G. J. Thomas, *J. Appl. Phys.*, **44**, 594 (1973).
21. M. Druminski, C. Kühl, E. Preuss, F. Schwidefsky, and J. Tihanyi, Abstract 139, p. 329, The Electrochemical Society Extended Abstracts, Vol. 74-2, Fall Meeting, New York, N.Y., Oct. 13-17, 1974.
22. P. Rai-Choudhury and D. K. Schroder, Abstract 143, p. 339, The Electrochemical Society Extended Abstracts, Vol. 74-2, Fall Meeting, New York, N.Y., Oct. 13-17, 1974.
23. C. Lee and K. Hu, Abstract 177, p. 417, The Electrochemical Society Extended Abstracts, Vol. 75-1, Spring Meeting, Toronto, Canada, May 11-16, 1975.
24. M. S. Abrahams and C. J. Buiocchi, *Appl. Phys. Lett.*, **27**, 325 (1975).
25. A. M. Goodman, *IEEE Trans. Electron Devices*, **ed-22**, 63 (1975).
26. G. W. Cullen, J. F. Corboy, and R. T. Smith, *J. Cryst. Growth*, **31**, 274 (1975).
27. C. Kühl, H. Schlötterer, and F. Schwidefsky, *This Journal*, **123**, 97 (1976).
28. M. S. Abrahams, C. J. Buiocchi, R. T. Smith, J. F. Corboy, J. Blanc, and G. W. Cullen, *J. Appl. Phys.*, **47**, 5139 (1976).
29. J. Blanc and M. S. Abrahams, *ibid.*, **47**, 5151 (1976).
30. M. S. Abrahams, C. J. Buiocchi, G. W. Cullen, and J. F. Coroby, *Appl. Phys. Lett.*, **28**, 275 (1976).
31. M. T. Duffy and P. J. Zanzucchi, Abstract 171, p. 460, The Electrochemical Society Extended Abstracts, Vol. 76-2, Fall Meeting, Las Vegas, Nevada, Oct. 17-22, 1976.
32. E. Preuss, Abstract 173, p. 465, The Electrochemical Society Extended Abstracts, Vol. 76-2, Fall Meeting, Las Vegas, Nevada, Oct. 17-22, 1976.
33. E. Preuss and H. Schlötterer, Abstract 178, p. 476, The Electrochemical Society Extended Abstracts, Vol. 76-2, Fall Meeting, Las Vegas, Nevada, Oct. 17-22, 1976.
34. M. Druminski, Abstract 183, p. 490, The Electrochemical Society Extended Abstracts, Vol. 76-2, Fall Meeting, Las Vegas, Nevada, Oct. 17-22, 1976.
35. A. M. Goodman and C. E. Weitzel, *IEEE Trans. Electron Devices*, **ed-24**, 215 (1977).

36. C. E. Weitzel and R. T. Smith, *This Journal*, **124**, 1080 (1977).
37. A. C. Ipri and J. C. Sarace, *IEEE J. Solid-State Circuits*, **sc-11**, 325 (1975).
38. A. S. Grove, "Physics and Technology of Semiconductor Devices," p. 326, J. Wiley and Sons Inc. New York (1967).
39. A. C. Ipri, *J. Appl. Phys.*, **43**, 2770 (1972).
40. S. T. Hsu and J. H. Scott, *RCA Rev.*, **36**, 240 (1975).
41. K. Lehovec and S. Lin, *J. Appl. Phys.*, **47**, 2088 (1976).

Optical Monitoring of the Etching of SiO_2 and Si_3N_4 on Si by the Use of Grating Test Patterns

H. P. Kleinknecht and H. Meier

Laboratories RCA Limited, CH-8048 Zurich, Switzerland

ABSTRACT

An optical technique is described which monitors both the etch depth and the amount of lateral underetching during the etching process. This technique applies to wet chemical etching as well as to plasma etching. For this purpose a test pattern containing one or more diffraction gratings is included on the mask, which is used to define the particular etching step. During the etching process a laser beam is aimed at this test pattern on the Si wafer and the reflected first-order diffraction intensities are monitored. As the etching progresses and the grating profile deepens, the diffracted intensity goes through oscillations which give an in-process indication of etch depth and etch rate. In the wet process the complete underetching underneath the photoresist bars of the grating is signaled by a drastic drop in the diffraction intensity. The simultaneous monitoring of a number of gratings with different bar widths permits one to follow the underetching in fine steps.

In silicon devices and integrated circuits fabrication many processing steps involve etching of SiO_2 and Si_3N_4 layers on Si through photoresist patterns. The lateral dimensions and the profiles of the patterns etched into the layers depend to some degree on the amount of underetching or undercutting in lateral direction underneath the photoresist mask. In many cases this undercutting is undesirable because it reduces the edge definition. In other cases a certain amount of undercutting is desirable for a sloped, rounded edge of the layer which is required in order to ensure continuity of the metallization stripes at the edge. In any case it is necessary to have control over the amount of underetching, and it is desirable to have in-process control over this parameter.

One technique, which reduces undercutting, is plasma etching (1). Unfortunately, in contrast to wet etching, the plasma-etching process does not stop completely when the SiO_2 has been removed, but it continues to etch into the silicon. This problem has been addressed by Heinecke (2), who has obtained a ratio of etch rates of 10:1 in favor of SiO_2. However, with etch rates being very much dependent on rf power, temperature, flow rate, and pressure (3, 4), one still would like to monitor the etch depth *in situ*.

Poulsen and Smith (5) have described an endpoint detection system which operates on the change of the spectral emission from the plasma during the plasma etching process. Konnerth and Dill (6) have used a computed-controlled spectrophotometer for measuring the thickness of glass and SiO_2 layers during etching and of photoresist during development. Van der Meulen and Hien (7) have constructed an automated ellipsometer for *in situ* measurement of dielectric layers at high temperature.

This paper describes a technique for in-process monitoring of the etching which is probably cheaper and more flexible than the systems quoted above and which has been shown to work for wet chemical etching as well as for plasma etching of SiO_2 and Si_3N_4 layers on Si wafers. In addition to the etch depth, this technique also monitors the amount of underetching which, to the knowledge of the authors, has not been done before. The new method uses test patterns in the form of diffraction gratings which can be arranged in a "knock-out" area on the normal photomask used for the delineation of the particular etching step to be controlled. Such gratings can be monitored during the etching process by reflection of a laser beam which results in a diffraction pattern. The intensities of the diffraction orders can give information about the profile of the grating, in particular on the etch depth, etch rate, and undercutting.

Figure 1 shows in a schematic way what can be expected to happen if, for instance, a SiO_2 layer is etched in HF through a fine photoresist grating pattern: As the etching progresses, the thickness, h, of the SiO_2 layer will decrease. This will cause the phase difference of the light reflected from the photoresist bars and from the SiO_2 to change. As a result the diffracted intensity will oscillate. This oscillation will stop when the etch has reached the SiO_2-Si interface. At the same time the etching will progress laterally. As soon as this lateral underetching has gone as far as half the width of the photoresist bars ($u \geq a/2$), the grating bars will start to shift and finally fall off. This will destroy the periodicity of the grating, and as a consequence the diffraction pattern, *e.g.*, the first order, will decrease in intensity.

Exploratory Tests with Wet Etching

In order to test this, a number of polished silicon wafers were covered with a SiO_2 layer of 0.94 μm thickness (as measured by ellipsometry), coated with photoresist and exposed through a mask containing 1.5×3 mm^2 areas with a grating-like parallel bar pattern of a periodicity of 10.2 μm and a width of the bars of $a = 3.0$ μm.

Key words: wet etching, plasma etching, etch depth, etch rate, underetching.

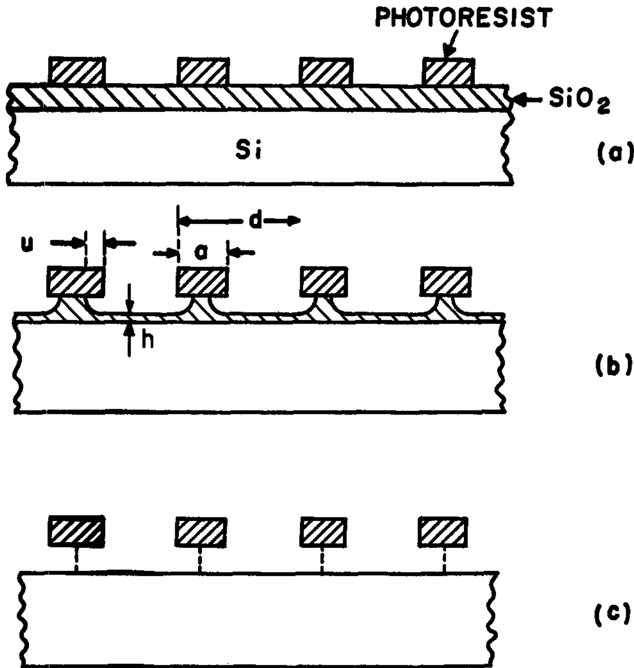

Fig. 1. Etching of a grating test pattern

Samples cleaved from these wafers were mounted on a Teflon holder which could be immersed into a Teflon etch container provided with a window of transparent acrylic sheet. The optical setup is described in Fig. 2. The beam of a He-Ne laser ($\lambda = 6328$Å) is chopped and aimed approximately perpendicular at the grating area of the sample. During the etching, which was done in buffered HF, the intensity, I_1, of the first-order diffraction beam was measured with a silicon PIN diode and a lock-in amplifier.

Figure 3 shows the recorder curves for three consecutive experiments. One observes the expected oscillations which stop after 5.5 min, indicating that the etching has reached the $Si\text{-}SiO_2$ interface. After about 7 min there is the sharp decrease which indicates an undercutting of $u = a/2 = 1.5$ μm. This interpretation was confirmed by microscopic inspection of the samples after the etching cycle.

Analysis of the Diffraction Intensity

For a quantitative interpretation of the oscillations of the diffracted intensity *vs.* time one has to use diffraction theory, which is relatively simple for the Fraunhofer regime only. The diffracted intensities of the 10 μm grating were measured for up to 12 orders with the incident beam polarized parallel and perpendicular to the grating lines. No significant difference was observed, which was taken as a justification to use the Fraunhofer integral (8). One can write the diffracted amplitude, U, for the case of a square aperture as

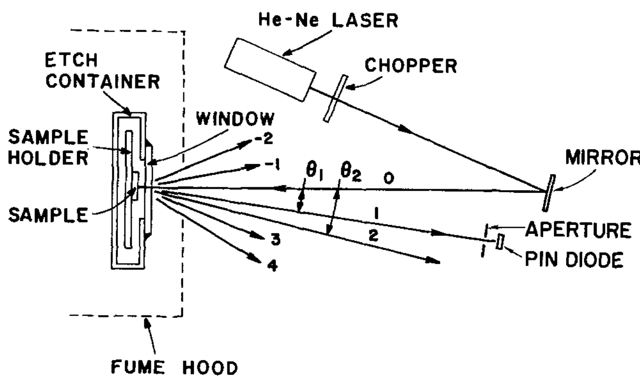

Fig. 2. First experimental set-up

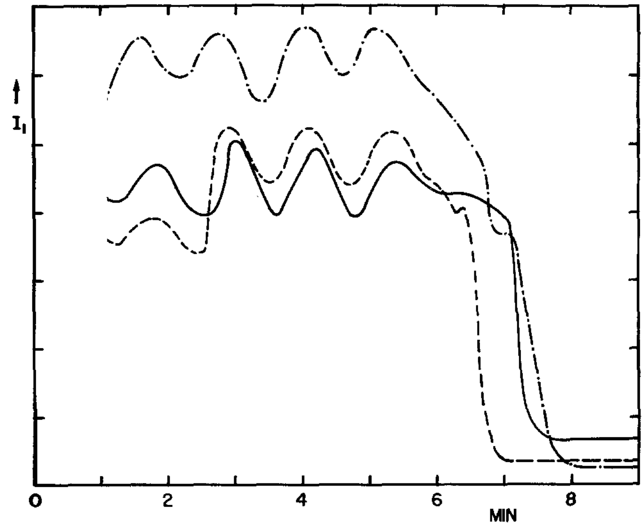

Fig. 3. First-order intensities vs. time of three samples with 10 μm gratings measured during wet etching.

$$U(\zeta) \propto \frac{e^{i\zeta N} - 1}{e^{i\zeta} - 1} \int_0^d r(x) e^{-i\zeta \frac{x}{d}} dx \quad [1]$$

Here N is the total number of grating lines, d the grating constant, and

$$\zeta \equiv \frac{2\pi}{\lambda} d \sin \theta \quad [2]$$

θ is the angle of diffraction (see Fig. 2). $r(x)$ is the complex reflectivity as a function of the coordinate x running perpendicular to the grating bars in the plane of the grating. The analysis will be restricted to a rectangular grating profile as shown in Fig. 4. Fortunately, as will be shown below, this will be good enough for our purpose. For this case the reflectivity, $r(x)$, can be taken to be constant across the grating bars ($= r_a$) and across the spaces in between ($= r_b$). If ϕ is the phase difference between the two reflectivities, one has

$$r(x) = \begin{cases} r_a \equiv |r_a| & i(o < x < a) \\ r_b \equiv |r_b| \exp(i\phi); & (a < x < d) \end{cases} \quad [3]$$

where $|r_a|$, $|r_b|$ and ϕ are independent of x.

On inserting Eq. [3] into Eq. [1] the intensity $I(\zeta) = |U|^2$ can be calculated. $I(\zeta)$ is large for $\zeta = m \cdot 2\pi$ only, *i.e.*, for the directions of the diffraction orders (order number m), namely

$$I(m) \propto \frac{\sin^2\left(m\pi \frac{a}{d}\right)}{m^2} [|r_a|^2 + |r_b|^2 - 2|r_a||r_b| \cos \phi] \quad [4]$$

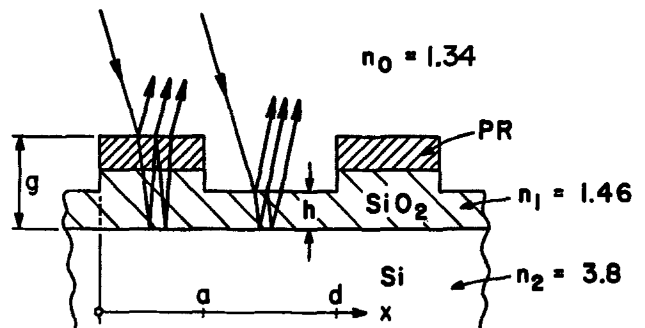

Fig. 4. Rectangular grating profile used for calculating diffraction intensities.

Note that the bracket does not contain the order number, m. In order to test the validity of the rectangular profile approximation, the intensities of the first 10 diffraction orders were measured quantitatively on several samples and plotted as a function of the order number, m. Figure 5 gives such a plot. The curve is a computer fit to the measured points according to Eq. [4]. As can be seen, the rectangular approximation is justified for the first three orders which is good enough for the present work since only the first-order intensities are used.

The reflectivities r_a and r_b in Eq. [4] depend on the refractive indexes and the thicknesses of the four media: etching solution, photoresist, SiO_2, and Si. For monitoring the SiO_2 thickness, h, in the region $a < x < d$ during etching, one only needs an expression for r as a function of h. Since in the practical case the photoresist is not etched, r_a can be considered to be constant. Using, for instance, Ref. (9) one gets for normal incidence

$$r_b = \frac{r_1 + r_2 \exp(i2\beta)}{1 + r_1 r_2 \exp(i2\beta)} \exp(i2\gamma) \qquad [5]$$

with

$$r_1 = \frac{n_0 - n_1}{n_0 + n_1}; \quad r_2 = \frac{n_1 - n_2}{n_1 + n_2} \qquad [6]$$

and

$$\beta = \frac{2\pi}{\lambda} n_1 h; \quad \gamma = \frac{2\pi}{\lambda} n_0 (g - h) \qquad [7]$$

n_0 is the refractive index of the etching solution (buffered HF), which we measured to be 1.34; $n_1 = 1.46$ for SiO_2; $n_2 = 3.8$ for Si at $\lambda = 6328Å$. The factor $\exp(i2\gamma)$ in Eq. [5] is due to profile depth, $g - h$ (see Fig. 4). From this one can calculate $|r_b|$, ϕ, and the bracket of Eq. [4], which is proportional to the intensity. The result is plotted in Fig. 6 for three photoresist thicknesses, *i.e.*, three different values of r_a. As can be seen, the main oscillations are the same for all three curves, having a period of about $\Delta h = 0.22$ μm.

Knowing this period, one can by comparison of Fig. 3 and 6 assign to each point in time an oxide thickness, h. We notice that within 5.5 min we go through a total of 4.5 periods of 0.22 μm each, which gives a layer thickness of 0.99 μm in good agreement with the ellipsometric value of 0.94 μm and an etch rate of 0.18 μm/min.

Plasma Etching of SiO_2 Layers

The technique of monitoring the etch depth and the etch rate described above was also tried out with plasma etching. The etching apparatus used was a commercial system: Model "PDE/PDS-301" built by the LFE Corporation. The etching chamber of this system has a plane front window which is suitable for the optical tests. The samples and the optical equipment were the same as described above.

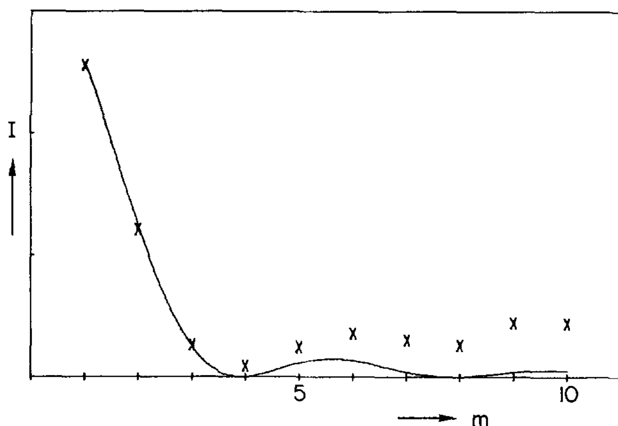

Fig. 5. Intensity vs. order number of a sample containing a 10 μm photoresist grating on Si + SiO_2. The curve is a fit to Eq. [4].

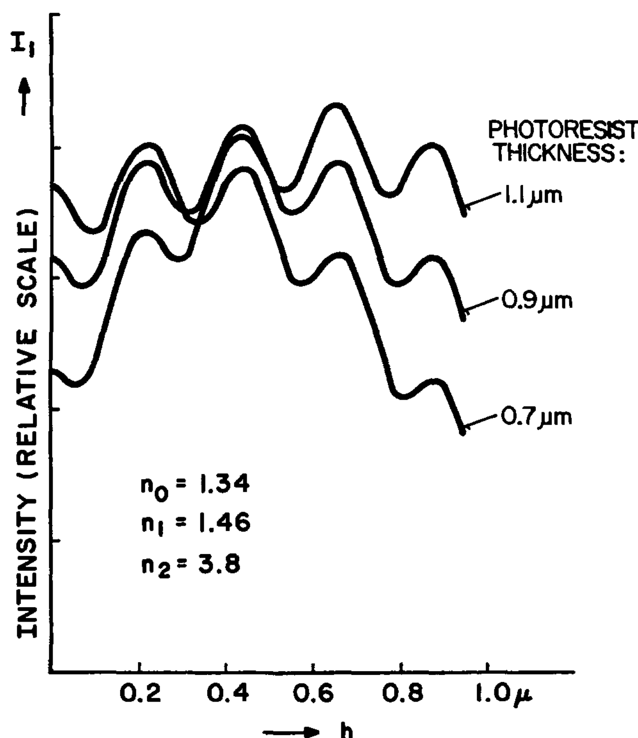

Fig. 6. Calculated first-order intensity as a function of the SiO_2 thickness, h, for three different photoresist thicknesses.

Figure 7 gives recordings of the first-order intensities for three runs with different flow rates of the reactive gas. Aside from the shoulders and small maxima in the top curve, which are very likely due to sputter abrasion of the photoresist, one can see that the spacing of the maxima decreases, *i.e.*, the etch rate increases, with increasing gas flow. In addition, the spacing of the maxima decreases, as the etching goes on; very likely an increase of etch rate due to heating (3).

It has to be pointed out that similar reflectivity oscillations can be obtained by interference in specular

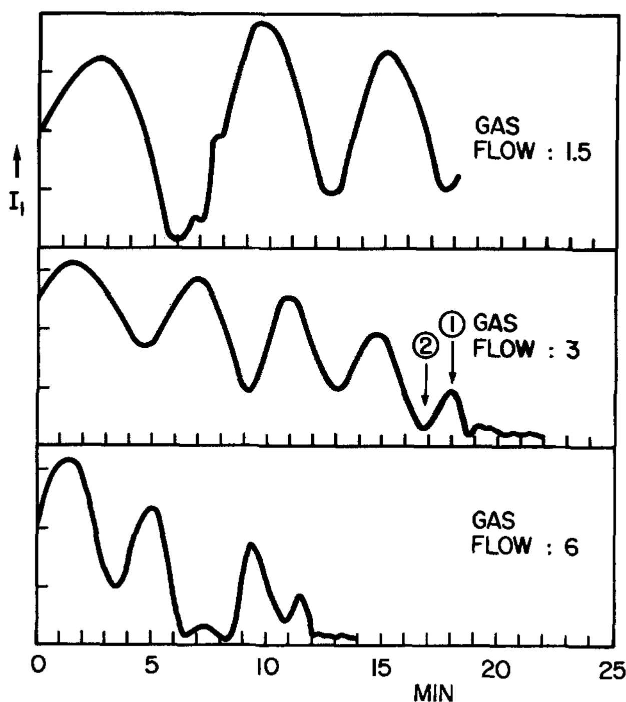

Fig. 7. First-order intensities vs. time of three samples measured during plasma etching.

reflection on uniform SiO_2 layers without gratings. However, the practical disadvantage of the specular reflection for monitoring IC processing is that it requires a uniform area on the sample which is as large as the laser beam. If a large part of the beam is reflected from other areas of the structure containing photoresist, other oxides, etc., this reflection will largely go in the same specular direction and distort or bury the wanted signal. The grating gives the possibility to use test areas on the wafer, which can be smaller than the laser beam. The detector properly positioned as in Fig. 2 will receive nearly no other signal but the one coming from the grating. All light reflected, diffracted, and scattered from other structures on the wafer will go mostly in other directions.

For a quantitative evaluation one again has to go through the analysis which was indicated above for wet etching with the only difference that now the refractive index of the surrounding medium is $n_0 = 1$ instead of 1.34. The results of these calculations are strong oscillations in I_1 with a period of 0.217 μm.

The middle and bottom curves in Fig. 7 show 5 maxima. The last maximum occurs after 4.4 periods giving a total oxide thickness of $4.4 \times 0.217 = 0.95$ μm in good agreement with the ellipsometric thickness measurement. After the 5th maximum the intensity drops to a low constant value. Microscopic inspection after that showed that the spaces not covered by photoresist were heavily pitted and showed a mat silvery gray color characteristic of bare Si.

In several etching experiments the process was interrupted at the top of the 5th maximum (arrow 1 in Fig. 7). The microscope then showed that the Si was bare and very little pitting was present. For other samples etching was stopped at the 4th minimum (arrow 2 in Fig. 7) leaving a residual SiO_2 layer of uniform blue color indicating a thickness of 700-800Å. These experiments prove that satisfactory control can be achieved by the monitoring process with the possibility to stop the etching at a given etch depth regardless of the etch rate, *i.e.*, independent of the particular conditions.

Nevertheless, this technique permits very rapid and simple measurement of the etch rates as the process goes on. As a demonstration of this we summarize in Fig. 8 these preliminary plasma etch data in terms of the etch rates in SiO_2 as a function of gas flow for two rf power levels. The etch rate at the beginning of the process (initial) is lower than the final value because of heating.

Plasma Etching of Si_3N_4 and SiO_2

The problem of defining patterns and etching windows into Si_3N_4-SiO_2 double layers is particularly suited for plasma etching. In this case wet chemical etching is rather complicated and troublesome. Therefore the optical monitoring technique was tried out for this case too, using samples with 1000Å of Si_3N_4 on top of 1 μm of SiO_2. Figure 9 gives one of the I_1 *vs* t curves taken during the process. In the first 5 min a rather irregular pattern is seen which is interpreted as the etching through Si_3N_4 indicating an etch rate of 200 Å/min. After that the curve looks similar to the other SiO_2 etching curves. The etch rates obtained from the curve fit quite well with the other SiO_2 etch rate data. They are included in Fig. 8 with the points marked "N".

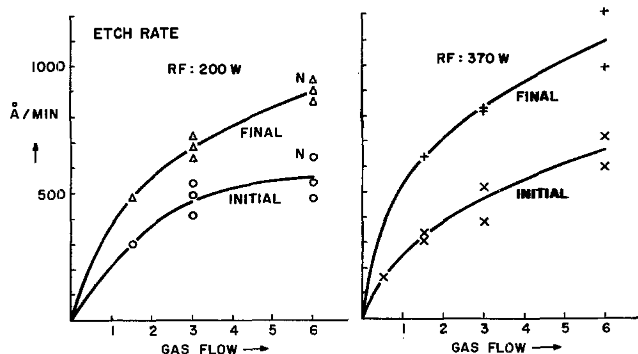

Fig. 8. Etch rates vs. gas flow in plasma etching

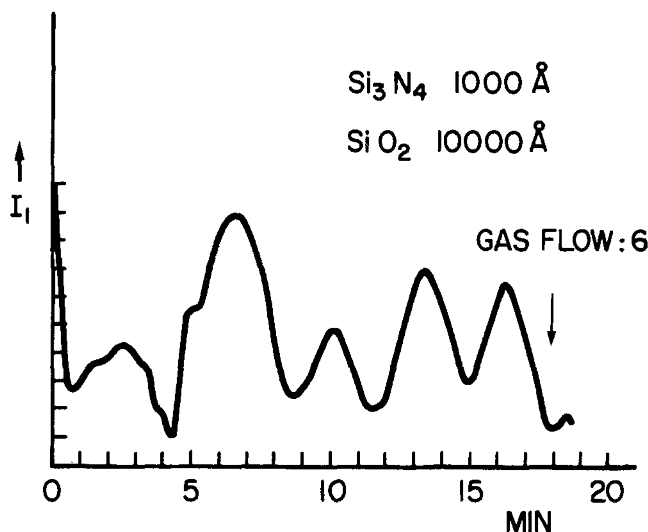

Fig. 9. First-order intensity vs. time during plasma etching of a Si_3N_4-SiO_2 double layer.

With the particular sample in Fig. 9 the etching was terminated after the 5th oxide maximum as shown. The microscope showed bare Si and pitting. In another run with a similar sample the etching was interrupted at the 4th minimum (arrow in Fig. 9). This left a blue, uniform 700Å thick SiO_2 layer. This thin SiO_2 layer can now easily be removed with dilute HF without the danger of undercutting.

Refinement of the Technique for Wet Etching

Encouraged by these exploratory experiments, we have proceeded to refine the technique to bring it closer to usefulness in the factory. In order to obtain a finer measure for the degree of underetching a test pattern containing 4 gratings with 4 different periodicities, $d = 10$, 6, 4, and 3 μm, and bar width $a \sim d/2$, was designed, which is sketched at the top of Fig. 10. The dimension, 1×1 mm, is small enough to fit into a "knock-out" area of the wafer. The four gratings are rotated by 45° with respect to one another. This results in 4 diffraction patterns which also are rotated by 45°, making the separation of the 4 signals easier. The bottom part of Fig. 10 shows the diffraction reflexes as they appear on a screen if the laser beam strikes the test pattern with normal incidence.

By positioning four Si detectors at the locations of the four first orders, one can simultaneously monitor the underetching of the 4 gratings. With $a = d/2$ one will expect the fall-off of the 4 signals for a lateral underetching, u, equal to 0.75, 1.0, 1.5, and 2.5 μm, respectively.

Figure 11 gives the traces of the signal from 3 of those 4 gratings recorded simultaneously during one etch run. One sees the oscillations, simultaneous in all 3 traces, and the fall-off successively for the 3, 4, and 6 μm gratings.

A large number of etching runs in buffered hydrofluoric acid were made. No special care was taken to keep the etch rate constant by temperature control or by always using fresh solutions, etc. This was not done, because the objective of the optical test is to obtain the right amount of etching in the presence of changing etch rates. In spite of these changes the characteristic behavior of the four first-order diffraction intensities of the 10, 6, 4, and 3 μm gratings as shown on the recorder were always the same. Another example of

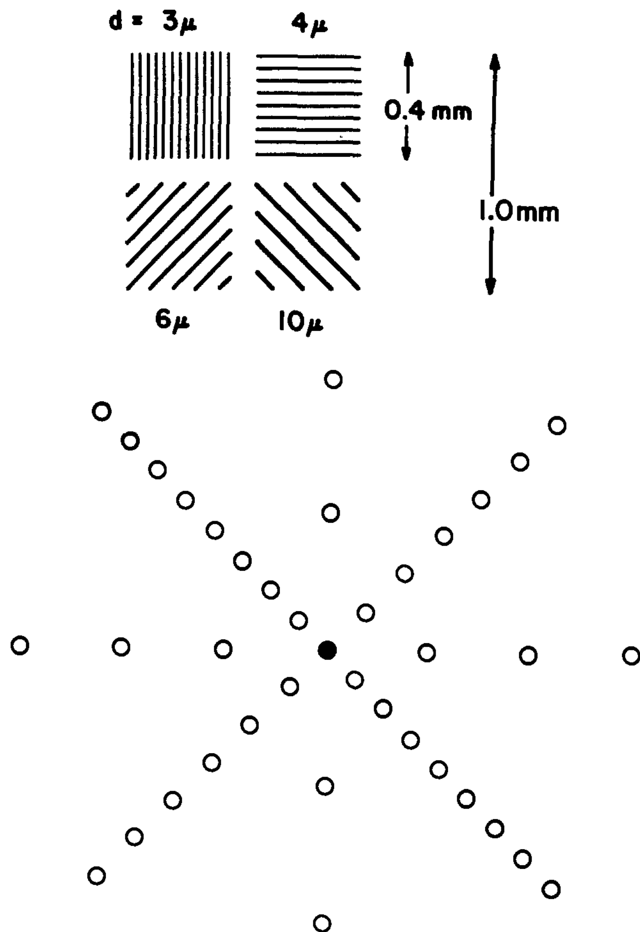

Fig. 10. Schematic drawing of the 4 grating test pattern (top) and the corresponding diffraction pattern.

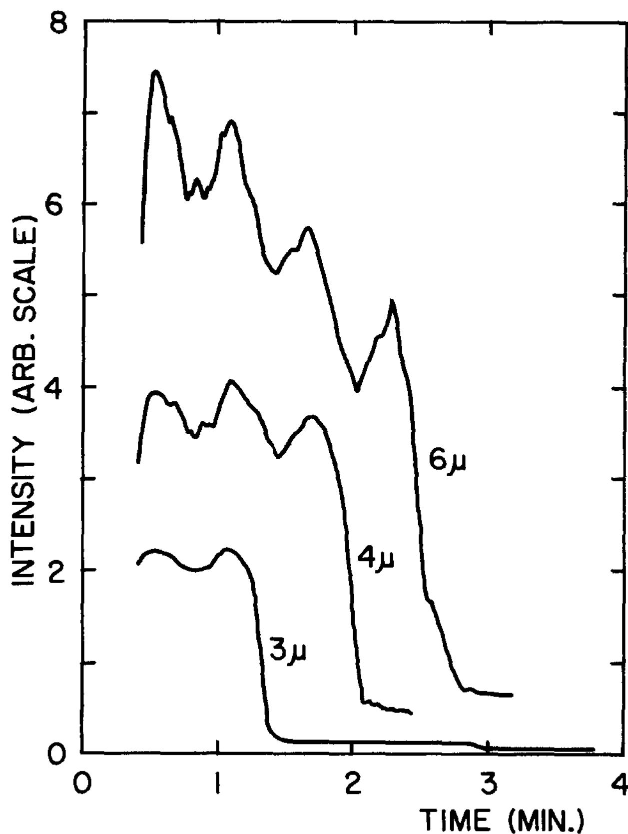

Fig. 11. Recorder trace of an etch run with first-order intensities for 3 gratings simultaneously.

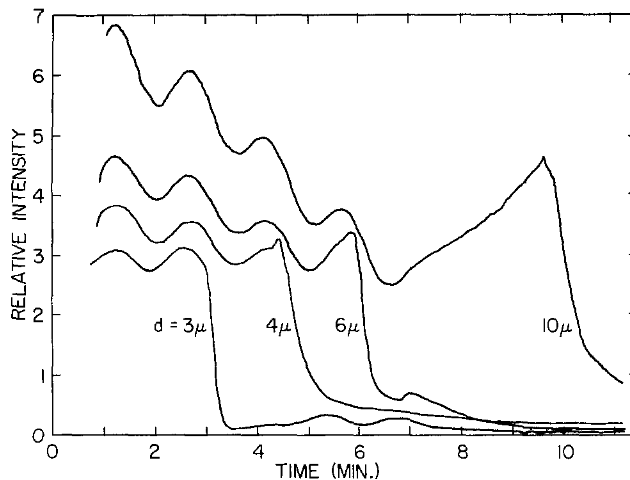

Fig. 12. Recorder trace of a typical etch run: first-order intensities of the four gratings (d = 3, 4, 6, and 10 µm) vs. time.

such a recorder trace for all 4 gratings is shown in Fig. 12. Again, all four signals oscillate in synchronism, each period corresponding to a decrease in h of about 0.22 µm. After about 2.2 periods, *i.e.*, after 0.48 µm of normal etching, the 3 µm grating starts to fall off. This indicates that in this case lateral undercutting has penetrated somewhat faster (0.75 µm) than the normal etching. After 3.3 periods (0.7 µm of normal etching) the 4 µm grating starts to fall off, indicating an undercutting of 1.0 µm, and after 4.1 periods (0.9 µm) the fall-off of the 6 µm grating starts, signaling an undercutting of 1.5 µm. The oscillations of the signal from the 10 µm grating stop after about 5 periods corresponding to the SiO_2 thickness of 1.1 µm. From then on the 10 µm signal rises smoothly until it shows a fall-off after 16 min, at which point the lateral etching has reached about 2.5 µm.

As can be seen from this plot, the normal etch rate is rather uniformly 0.16 µm/min and the lateral undercutting is about 1.5 times as fast as the normal etching for all four gratings. These figures may be different for other etch conditions. However, in any case a recording of the type of Fig. 12 gives the etch rate, and most important, signals the exact time at which the lateral underetching has reached a certain extent, namely, for the test pattern used here, 0.75, 1.0, 1.5, and 2.5 µm.

Finally Fig. 13 shows the equipment used for these last experiments. The test sample, T, is placed in a suitable etch container in the fume hood, H. This sample can be the end wafer of a whole lot of wafers being etched together. The beam of the laser, L, (λ = 0.6328 µm, 1 mW) goes through the chopper, C, and is di-

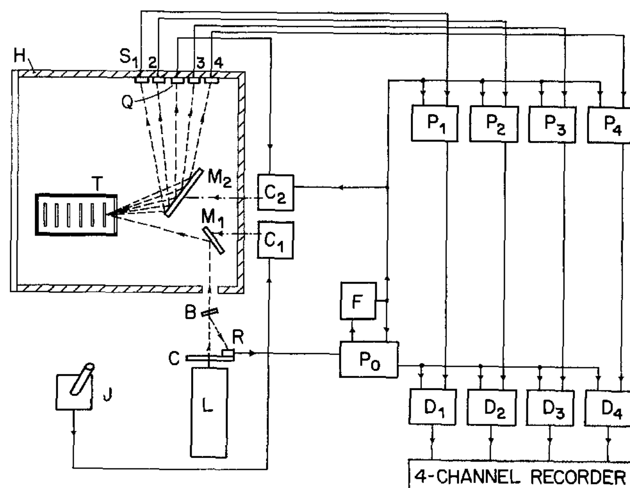

Fig. 13. Block diagram of the test set

rected by the mirror, M_1, at the test pattern on the sample. The mirror, M_2, directs the reflected diffraction pattern at the four silicon solar cells, S_1, S_2, S_3, and S_4, which are connected to the four phase-sensitive amplifiers P_1, P_2, P_3, and P_4. The signal coming from the reference detector, R, is amplified in P_0 and processed in F to be used as a frequency reference. The amplifiers P_1-P_4 are sample-and-hold type operational amplifiers, which make the system insensitive to room light. In order to be independent of any changes in the incident laser intensity, the reference signal is fed together with the signals from P_1 to P_4 into the divider circuits D_1, D_2, D_3, and D_4.

During the first experiments it was recognized that it was desirable to adjust the mirror, M_1, very quickly and conveniently in order to "find" the test pattern on the wafer during a few seconds after immersion into the etch bath. For this reason, the mirror, M_1, was equipped with servo motors for remote control of the two tilt angles, which are operated from the joy stick, J, via the servo circuit, C_1.

The mirror, M_2, is equipped with a similar servo system in order to make sure that, regardless of the orientation of M_1 and of the sample, the diffraction pattern always strikes the solar cells S_1-S_4. This servo system is controlled by the signal of a quadrant sensor, Q, which senses the position of zero-order diffracted beam.

Conclusion

Test patterns in the form of diffraction gratings offer a simple technique for the in-process control of the etching of patterns into SiO_2 through photoresist masks both for wet etching as well as for plasma etching. In the case of the wet etching the time at which the undercutting has reached a given amount can be determined by a pronounced drop of the diffraction signal. A test pattern containing several gratings of different line widths appears to be promising for the tailoring of a desired amount of undercutting. In plasma etching the grating technique gives reliable control of the etch depth even if the SiO_2 is covered with a Si_3N_4 layer.

The theory of this process as well as detailed information about the equipment has been given.

Acknowledgments

The authors would like to thank J. Gaylord of Somerville, New Jersey and N. Goldsmith and W. Schneider of Princeton, New Jersey for help and stimulation in the early part of the work, and A. Oberholzer for experimental assistance.

Manuscript submitted Nov. 14, 1977; revised manuscript received Dec. 28, 1977.

Any discussion of this paper will appear in a Discussion Section to be published in the December 1978 JOURNAL. All discussions for the December 1978 Discussion Section should be submitted by Aug. 1, 1978.

Publication costs of this article were assisted by Laboratories RCA Limited.

LIST OF SYMBOLS

a	width of grating lines
d	grating constant
ζ	see Eq. [2]
ϕ	phase of reflectivity r_b
g	see Fig. 4
h	thickness of SiO_2
I	intensity
I_1	intensity of first order
λ	laser wavelength
m	order number
$n_{0,1,2}$	refractive indexes
N	total number of grating lines
$r(x)$, $r_{a,b}$, r_1, r_2	reflectivities
θ	diffraction angle
u	width of underetching
U	diffracted amplitude
x	coordinate in grating plane perpendicular to the grating lines

REFERENCES

1. R. G. Poulsen, *J. Vac. Sci. Technol.*, **14**, 266 (1977).
2. R. A. H. Heinecke, *Solid-State Electron.*, **19**, 1039 (1976).
3. R. G. Poulsen and M. Brochu, "Etching," H. G. Hughes and M. J. Rand, Editors, p. 111, The Electrochemical Society Softbound Symposium Series, Princeton, N.J. (1976).
4. R. Kumar, C. Ladas, and G. Hudson, *Solid State Technol.*, **19**, 54 (1976).
5. R. G. Poulsen and G. M. Smith in, "Semiconductor Silicon 1977," H. R. Huff and E. Sirtl, Editors, p. 1058, The Electrochemical Society Softbound Symposium Series, Princeton, N.J. (1977).
6. K. L. Konnerth and F. H. Dill, *IEEE Trans.*, **ed-22**, 452 (1975).
7. Y. J. van der Meulen and N. C. Hien, *J. Opt. Soc. Am.*, **64**, 804 (1974).
8. M. Born and E. Wolf "Principles of Optics," p. 401-403, Pergamon Press, Inc., Elmsford, N.Y. (1965).
9. M. Born and E. Wolf, *ibid.*, pp. 61 and 62 (1965).

Oxidation of Copper in CO_2 at 800°-1000°C

W. J. Tomlinson and J. Yates[1]

Department of Applied Sciences, Lanchester Polytechnic, Eastlands, Rugby, United Kingdom

ABSTRACT

The oxidation of spectrographically pure copper in carbon dioxide has been studied at 800°-1000°C. An initial linear oxidation rate changed gradually to a second, lower, linear oxidation rate. During the first linear stage the surface was covered with a feathery pattern of small dendrites of unknown structure which were replaced progressively with more massive crystallites of Cu_2O associated with the second linear stage. The thickness of the Cu_2O layer at 1000°C when the surface was fully covered was 14 μm. Surface finish, preannealing, and gas flow rate in the range 0.1-2.0 cm sec^{-1} had no effect on the reaction. It is reasoned that the rate-controlling process was the decomposition of CO_2 to form chemisorbed oxygen which was influenced by a change of catalytic activity on the surfaces of the structures associated with the two linear kinetic curves.

Oxidation is a multistep process. The early stages involve oxygen dissolution in the metal and nucleation and growth of the oxide. Once the surface is covered with a continuous layer of oxide, for oxidation to continue the following steps for the reactants must occur: (*i*) transport within the gas, (*ii*) reaction at the gas/

[1] Chester Education Department, Chester, United Kingdom.
Key words: linear kinetics, nucleation, Cu_2O.

oxide interface, (*iii*) transport within the oxide, and (*iv*) reaction at the metal/oxide interface. One step is usually rate controlling, and the reaction is reflected in the kinetics. Parabolic oxidation kinetics typically indicates that diffusion within the oxide layer is rate controlling. Linear kinetics are relatively uncommon and imply that the slow step is a phase boundary reaction; provided the reaction products form a uniform dense layer they frequently change to a parabolic form as the amount of oxidation increases.

Linear oxidation in CO_2 or CO_2-CO mixtures has been observed with Fe by Hauffe and Pfeiffer (1) and other workers (2-5), with Co (6), Mn (7), Ni (8), and with Cu (9, 10). Hauffe and Pfeiffer found that the linear oxidation rate of Fe in CO_2/CO mixtures is proportional to $(P_{CO_2}/P_{CO})^{2/3}$, and the rate depended solely on the decomposition of CO_2 to form chemisorbed oxygen. Smeltzer (2) interpreted his linear oxidation rates of Fe in CO_2 as incorporation of chemisorbed oxygen into FeO at temperatures below 910°C and both dissociation of CO_2 and incorporation into FeO above 910°C. C. Wagner (11) derived a formula which indicated that the linear oxidation rate should depend not only on the CO_2/CO ratio but also on the sum of the partial pressures of CO_2 and CO. This was confirmed by Pettit *et al.* (4). Swaroop and J. B. Wagner studied the oxidation of Cu in CO_2/CO mixtures at 1000°C (10). Two linear curves were observed with a distinct change occurring at an oxide thickness of 0.4-0.6 μm. From the pressure dependence of the first linear rate constant, it was inferred that the reaction mechanism did not involve chemisorption.

The present work investigates the oxidation of Cu in CO_2 at 800°-1000°C. The equilibrium pressures of oxygen with CO_2, Cu_2O, and CuO are shown in Table I. From these data CuO is not expected to form on Cu oxidized in CO_2, and it is seen that the P_{O_2} from dissociation of CO_2 is only slightly greater than that from dissociation of Cu_2O. However, these data are for bulk substances at equilibrium, and during oxidation the interfacial energies and dynamic flow conditions will alter the thermodynamic data and possibly the catalytic effects due to the electronic/atomic defect equilibria being altered. The early stages of oxidation are usually very sensitive to surface structure and cleanliness, and so the purity of the Cu and CO_2, and the surface finish are important. Transport in the gas may also have an influence because of the low pressure of oxygen in CO_2.

Experimental

The Cu was spectrographically pure with maximum impurities (ppm): Ag 10, Pb 2, Si 1, Ca < 1, Mg < 1, Fe < 1. It was supplied by Johnson Matthey and Company Limited as 0.25 mm thick cold-worked sheet and cut into coupons about 4 cm² surface area with a hole for a Pt suspension wire. Four surface finishes were used. In the as-received condition the specimen was simply degreased in acetone before exposure. Mechanical polishing consisted of polishing to 6/0 grade paper then washing in turn with distilled water and acetone. The bath used for chemical polishing (12) consisted of 55 v/o HNO_3 (density 1.75), 25 v/o glacial acetic acid, and 20 v/o H_3PO_4 (density 1.40), and the specimen was immersed for 1-2 min at 55°C and then washed as above. The bath for electrochemical polishing was 33 cm³ HNO_3 and 67 cm³ CH_3OH cooled to 0°C and operated at 3V and 1 A cm^{-2} for 30 sec. After polishing the specimen was washed as above.

The quartz-spring thermobalance was similar to one used previously (13). The main difference was a magnetic winch which allowed insertion and removal of a specimen to and from the hot zone while under vacuum or CO_2. Temperature control was within ± 2°C and the weight gain could be measured to within ± 0.03 mg cm^{-2}. The operating procedure was as used previously (13), but in addition the oxidized specimen could be quickly quenched in cool CO_2.

Special analytical grade CO_2 supplied by Distillers Company Limited was used. It had maximum impurities : residual gases (non-KOH soluble) < 25 ppm (by volume), water < 50 ppm (by weight), and other gases < 5 ppm (by volume). The water content was further reduced by passing through silica gel and then phosphorus pentoxide. Gas flow was measured by a rotameter. Gas pressure was 1 atm.

Standard x-ray diffraction techniques were used to examine the surface products.

Table I. Equilibrium pressures of oxygen at 1000°C [Ref. (10)]

Reaction	P_{O_2} (atm)
$CO_2 = CO + \frac{1}{2} O_2$	1.2×10^{-6}
$Cu_2O = 2Cu + \frac{1}{2} O_2$	5.6×10^{-7}
$2CuO = Cu_2O + \frac{1}{2} O_2$	1.4×10^{-1}

Results

Figure 1 shows the rate curves for the oxidation of chemically polished Cu in CO_2 flowing at 0.2 cm sec^{-1}. At 900° and 1000°C there were two linear curves with the gradient of the first curve greater than that of the second, and an intermediate region which is shown dashed. At 800°C there was only one linear curve. The amount of oxidation was small, and in such cases surface finish, gas speed, and preannealing might be particularly important so oxidation data were obtained under the following conditions: (*i*) Cu chemically, mechanically, and electrolytically polished, and in the as-received condition, was oxidized at 800°-1000° in CO_2 flowing at 0.2 cm sec^{-1}; (*ii*) chemically polished Cu was oxidized at 1000°C in CO_2 flowing at 0.1-2.0 cm sec^{-1}; and (*iii*) Cu was preannealed at 1000°C and 10^{-5} mm Hg, chemically or electrolytically polished, then oxidized at 1000°C in CO_2 flowing at 0.2 cm sec^{-1}. In all cases the results were of the same form as Fig. 1. All these data are summarized in Tables II, III, and IV.

In Fig. 1 the points in the dashed region could belong to either curve. This represents a gradual transition from the first linear curve to that of the second. The extrapolated intersection coordinates of the lines were used to characterize the change, and these are reported with the other kinetic data in Tables II, III, and IV. It is seen that at 900° and 1000°C the transition

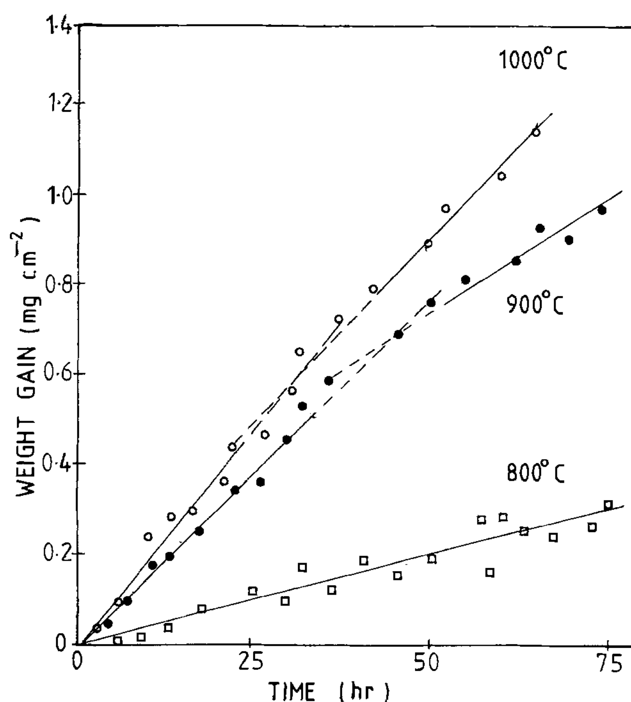

Fig. 1. The oxidation of chemically polished Cu in CO_2. Gas speed 0.2 cm sec.

Table II. Linear rate constants and transition coordinates for Cu with various surface finishes oxidized in CO_2 at various temperatures. Gas speed 0.2 cm sec^{-1}.

Surface finish	Temperature (°C)	Rate constants (g cm^{-2} sec^{-1} × 10^{-9}) K_{L_1}	K_{L_2}	Transition coordinates Wt. gain (mg cm^{-2})	Time (hr)
Chemical	1000	5.33	4.72	0.6	31
Chemical	1000	6.11	4.53	0.8	36
Chemical	900	4.32	2.89	0.7	45
Chemical	900	4.39	3.19	0.7	44
Chemical	800	1.11	—	—	—
Mechanical	1000	6.83	4.53	0.8	33
Mechanical	1000	6.28	4.67	0.7	31
Mechanical	900	4.00	3.31	0.6	42
Mechanical	900	4.31	3.33	0.6	39
Mechanical	800	0.94	—	—	—
Electrochemical	1000	5.31	4.03	0.6	31
Electrochemical	1000	5.28	4.06	0.7	37
Electrochemical	900	3.28	2.78	0.6	51
Electrochemical	900	3.61	2.94	0.6	46
Electrochemical	800	0.75	—	—	—
As-received	1000	6.33	4.03	0.70	31
As-received	1000	6.08	4.50	0.70	32
As-received	900	4.58	3.89	0.60	36
As-received	900	4.39	3.44	0.60	38
As-received	800	1.00	—	—	—

Table III. The effect of gas speed on chemically polished Cu oxidized in CO_2 at 1000°C

Gas speed (cm sec^{-1})	Rate constants (g cm^{-2} sec^{-1} × 10^{-9}) K_{L_1}	K_{L_2}	Transition coordinates Wt. gain (mg cm^{-2})	Time (hr)
0.1	5.31	4.64	0.7	37
0.5	5.00	4.42	0.6	33
1.0	5.33	4.50	0.7	36
2.0	5.06	3.86	0.6	33

Table IV. The effect of preannealing 12 hr at 10^{-5} Torr before oxidation in CO_2 at 1000°C. Gas speed 0.2 cm sec^{-1}.

Surface finish	Rate constants (g cm^{-2} sec^{-1} × 10^{-9}) K_{L_1}	K_{L_2}	Transition coordinates Wt. gain (mg cm^{-2})	Time (hr)
Chemical	5.28	3.89	0.7	37
Electrochemical	5.83	3.33	0.6	38

Table V. Average linear rate constants for Cu oxidized in CO_2

Temperature (°C)	K_{L_1} (g cm^{-2} sec^{-1} × 10^{-9}) Mean	Std. dev.	Coef. variation	K_{L_2} (g cm^{-2} sec^{-1} × 10^{-9}) Mean	Std. dev.	Coef. variation
1000	5.67	0.57	10.05	4.19	0.44	10.50
900	4.11	0.45	10.95	3.22	0.36	11.18
800	0.95	0.15	15.79	—	—	—

occurs at a critical weight gain of 0.6-0.7 mg cm^{-2} but at 800°C the total amount of oxidation was only 0.3 mg cm^{-2} so the transition was absent. An unexpected feature of the kinetic data is its insensitivity to changes in surface finish, preannealing, and gas speed in the range 0.1-0.2 cm sec^{-1}. Because of this insensitivity, all the data have been analyzed together, and the results are reported in Table V. The Arrhenius function of the first linear curve is shown in Fig. 2.

Specimens oxidized 72 hr at 900° and 1000°C were examined by x-ray diffraction powder techniques, and in back reflection after 40 and 72 hr at 1000 C and 72 hr at 800° and 900°C. The amount of reaction product at 800°C was too small to be detected. Cu_2O was observed in all other cases but no CuO was detected.

The surface was examined after oxidation at various times at 800°, 900°, and 1000°C. Figure 3 shows typical oxidized surfaces. There were two types of surface structures, one small, feathery, and acicular, and the other much larger, thicker, and more rounded. For convenience in this paper they will be called dendrites and crystallites, respectively. The crystallites were identified as Cu_2O, but the structure of the dendrites is uncertain. The formation of the surface products always followed the sequence: dendrites were nucleated

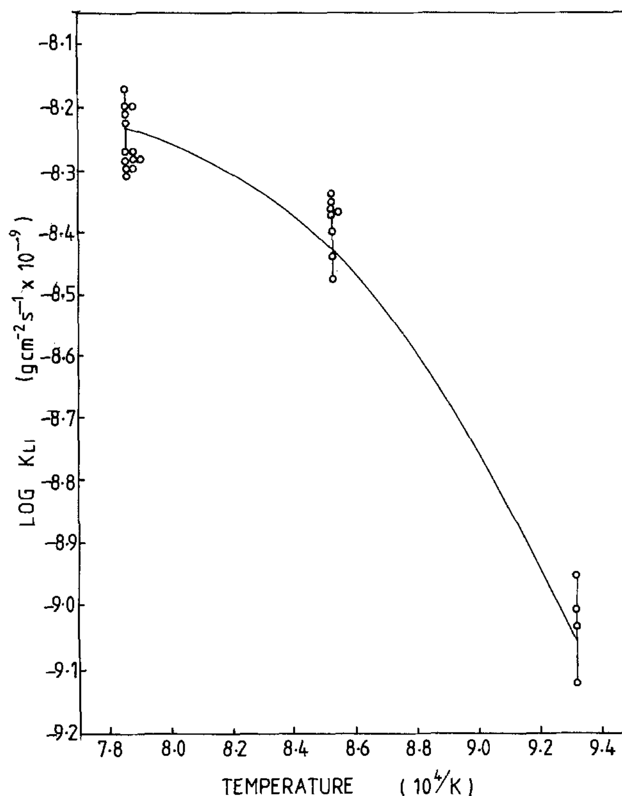

Fig. 2. The Arrhenius function of the first linear rate constant

(Fig. 3a) and spread rapidly over the whole surface (Fig. 3b), crystallites then nucleated on the dendrites, and further oxidation resulted in the growth of the crystallites (Fig. 3c) until the whole surface was covered (Fig. 3d). In Fig. 3 note that (a) is for oxidation at 800°C and the others for specimens oxidized at 1000°C. The reaction at 1000°C was so fast that it was not possible to record at 1000°C the stage shown in Fig. 3a for oxidation at 800°C. The times the structures appeared at each temperature are shown in Table VI where it is seen that the structures always appeared in the same sequence, but after longer times as the temperature was lowered. No detailed topographical studies were carried out but the crystal heights were estimated using the depth-of-focus of a microscope. Using a fine adjustment with a drum calibrated in micrometers, under oil immersion it was observed that for a given oxidation the crystallites were approximately the same height, and that at 1000°C their height was nearly the same for crystallites on specimens oxidized for 20 and 40 hr. The height of the dendrites was always very much less than the height of the crystallites. Figure 4 shows the cross section of the dendrites and crystallites formed on a specimen oxidized for 24 hr at 1000°C. The concave Cu surface clearly reflects the Cu used in the nucleation and growth of the oxide. The maximum thickness of the dendrites and crystallites shown are about 1-2 and 10 μm, respectively. Cu_2O has a density of 6.0 g cm^{-3} (14), so at 1000°C the Cu_2O film was about 14 μm thick when the surface was covered.

Discussion

The kinetic data summarized in Table V indicates good reproducibility for the rate constants in the two linear kinetic stages over the temperature range 800°-1000°C. Swaroop and Wagner (10) also observed at 1000°C two linear curves and the first one had rate constants in the range 6.1 to 8.93 × 10^{-9} g cm^{-2} sec^{-1}. This agrees well with the present, lower, values of 5.00-6.83 × 10^{-9} g cm^{-2} sec.$^{-1}$. However, the two linear curves of Swaroop and Wagner appear to make a sharp transition whereas in the present work the change was gradual over a large weight gain range.

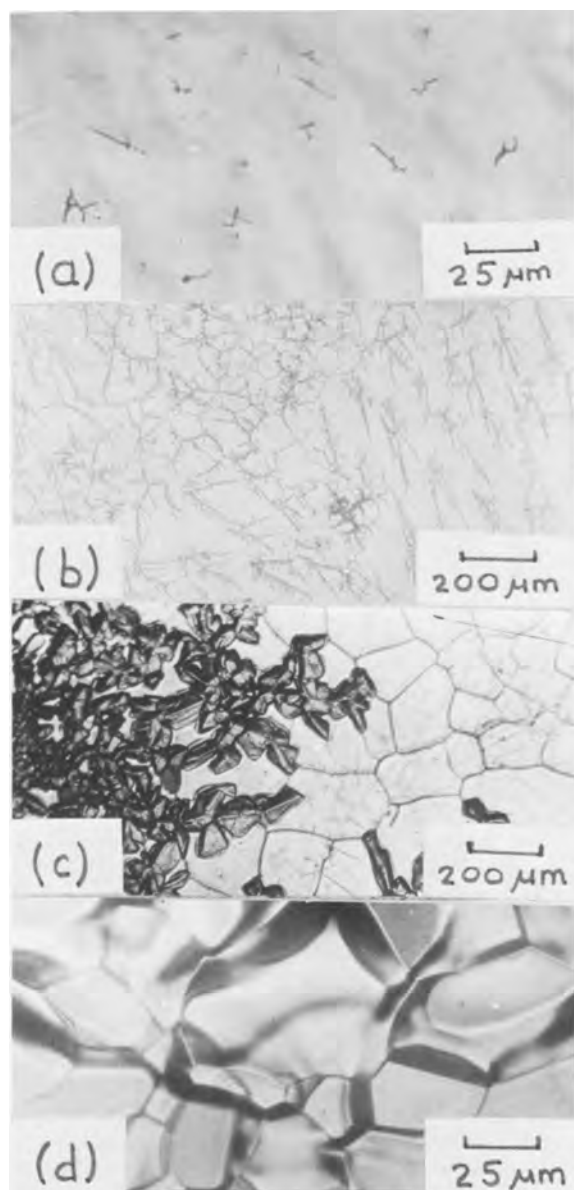

Fig. 3. Surface morphology of chemically polished Cu oxidized in CO_2. (a) 800°C, 72 hr; dendrites nucleated. (b) 1000°C, 10 min; dendrites cover the surface, a crystallite nucleating. (c) 1000°C, 20 hr; dendrites and crystallites. (d) 1000°C, 72 hr; surface covered with crystallites.

There is a direct relation between the kinetics and surface morphology. The kinetic transition co-ordinates are shown in Tables II, III, and IV, where it is seen that the change occurs at a critical amount of oxidation of 0.6-0.7 mg cm^{-2}, and in the time range 30-38 hr at 1000°C and 36-51 hr at 900°C. When compared with the surface morphologies, it is seen that the first linear kinetic curve occurs when mainly den-

Table VI. The surface morphology of chemically polished Cu oxidized in CO_2 flowing at 0.2 cm sec^{-1}

	Time oxidized (hr)			
°C	0.17	20	40	72
1000	D	DC	DC	C
900	D	DC	DC	DC
800	—	—	—	D

D = dendrites only.
DC = crystallites and dendrites present.
C = surface covered with crystallites.

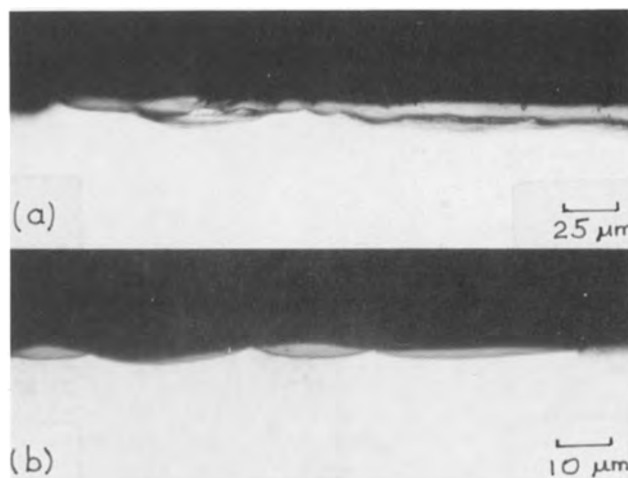

Fig. 4. Chemically polished Cu oxidized in CO_2 for 24 hr at 1000°C. Unetched. Cu at bottom. (a) Cross section of a crystallite about 10 μm thick. Note the concave Cu surface due to removal of Cu into the preexisting dendrites and separate crystallites before lateral growth formed the uniformly thick massive crystallite. (b) Cross section of dendrites in the intercrystalline regions. Note the concave Cu surface containing the oxide dendrites with a maximum thickness of 1-2 μm.

drites cover the surface, and the second linear curve is associated with the crystallites, and the gradual change in kinetics reflects the change in structure as the crystallites grow to cover the surface. Because the two gradients are so close, scatter in the data tends to mask the transition and so the change in kinetics cannot be defined precisely. A more appropriate equation describing the apparent dependence of the rate constant on surface features would be

$$\text{rate} = K_{L1}(1 - f) + K_{L2}f$$

where f is the fraction of the surface that is covered with crystallites.

Linear oxidation kinetics reflect a phase boundary reaction, or a constant rate of supply of gas from the interior of the gas across a boundary layer of constant thickness. In the present case gas supply is not the rate-controlling process since the thickness of the boundary layer, and so the flux of gas reaching the surface, is a function of gas speed, and no effect of gas speed on the oxidation rate was detected. Moreover, if the gas supply was rate controlling, then there would be only one linear reaction rate corresponding to the gas supply, whereas two linear kinetic curves were observed. The insensitivity of the kinetics to surface finish and preannealing indicates that the rate-controlling process is also not at the metal/oxide interface. It appears from these considerations that reaction control is at the oxide/gas interface where the possible reactions are chemisorption and incorporation represented by the equations

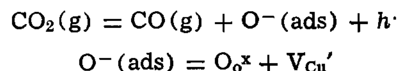

$$CO_2(g) = CO(g) + O^-(ads) + h^{\cdot}$$

$$O^-(ads) = O_o^x + V_{Cu}'$$

with similar equations for O(ads) and O^{2-}(ads). Here the defect chemistry notation of Kröger and Vink (15) is used. The average activation energies of the first linear curve (Fig. 2) are of the order $E_{800\text{-}900} = 170$ kJ mol^{-1} and $E_{900\text{-}1000} = 50$ kJ mol^{-1} and while these have no detailed diagnostic value it is clear that they are within those typical of adsorption processes, and also they become less as the temperature is increased. Hauffe and Pfeiffer (1) have shown that the rate-controlling process during the oxidation of Fe in CO_2/CO mixtures is the decomposition of CO_2 on the surface to form chemisorbed O^-. Also Kobayashi and Wagner

have shown (16) that the catalytic activity of a surface depends not only on the composition of the gas phase, but also on the composition of the solid phase, in particular the concentration of electronic defects.

During the second linear stage the catalytic surface is clearly Cu_2O crystallites but during the first linear stage the surface structure is uncertain. While spread over the whole surface, the dendrites represent only a small fraction of the area. The Cu atoms in Cu_2O form a fcc lattice with oxygen atoms occupying one quarter of the tetrahedral sites (17). The linear misfit in the Cu_2O/Cu system is 18% (18), and it is probable that the dendrites are a distorted epitaxial form of Cu_2O. Considerable effort has been made in nucleation studies to identify the surface structures in between the nuclei but its nature is still largely conjectural. Rhead (19) assumed on the basis of known data that a thin layer exists which is intermediate between a chemisorbed layer and an oxide layer which is formed by place exchange, and the mixed character of such an adsorbed layer has been shown by recent emission microscopical research where molecules made up of a nucleus of three or four metal atoms around an oxygen atom have been identified (20).

With Cu_2O the equation of nonstoichiometry is

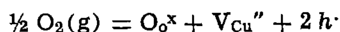

$$\frac{1}{2}\, O_2(g) = O_o^x + V_{Cu}'' + 2\, h^{\cdot}$$

and there is a relation between the concentrations of atomic and electronic defects. Since the energies of the intermediate layer/metastable Cu_2O and Cu_2O are different they will have different concentrations of atomic defects and so by the above, different concentrations of $h^{\cdot}$, *i.e.*, the two surfaces will have similar but slightly different catalytic activities. The two linear rate constants are similar in magnitude and so could reflect the different rates of catalytic decomposition of CO_2 to form adsorbed oxygen on the two similar surfaces. Moreover, the higher linear rate constant is associated with the intermediate surface structures which would be expected to have a higher catalytic activity. Also a nonlinear activation energy as observed for the first linear rate (Fig. 2) is not inconsistent with these ideas. Dissociation of defect complexes and/or ionization of defects may occur (21, 22) as the temperature is raised, and these would alter the concentrations of atomic and electronic defects and so affect the catalytic activity of the surface. A complication with oxidation in CO_2 is that there will be additional oxygen at higher temperatures owing to the greater degree of dissociation of CO_2. However, in the present case there is a lower than expected oxidation rate at higher temperatures and this would indicate that the rate of oxidation is less sensitive to the extra oxygen present than it is to the reduced catalytic activity of the surface. A possible cause of such a reduced catalytic activity as the temperature is raised is that the intermediate structure of the catalytic surface may move towards a lower energy and so less active structure. A similar mechanism to decomposition of CO_2 has been observed with the decomposition of N_2O on Cu_2O and the simultaneous oxidation of Cu, where the catalytic decomposition depended on the concentration of $h^{\cdot}$ (23).

Swaroop and Wagner (10) found that the first linear rate constant for Cu oxidized in CO_2/Ar mixtures obeyed an empirical equation of the form

$$K_{L1} = CP^{n}_{CO_2}$$

where C and n are constants, and found values of $n =$ 1.3 and 1.5. For oxidation of Ni in CO_2/CO mixtures $n = 1$ and for Fe in CO_2/CO mixtures $n = 0.33$ while Fe in low pressure oxygen $n = 0.7$ (10). It is stated (10) that for $n > 1$ the oxidation mechanism is not due to chemisorption but the basis of this statement is not clear. Moreover, Swaroop and Wagner have taken their surface oxide in the first linear stage to be Cu_2O and have assumed it forms a uniform layer, whereas in the present work the first linear kinetics is associated with an intermediate surface structure whose area is changing, and it may be that the cause of the unusual (if indeed they are) n values for Cu is the changing areas during nucleation and growth available for a catalytic chemisorption reaction.

Conclusions

Copper oxidized in CO_2 at 800°-1000°C follows an initial linear kinetic law which changes gradually to a second, lower, linear law. At any temperature small feathery-patterned unstable dendrites formed. Later crystallites of Cu_2O formed on the dendrites and grew to cover the whole surface. The first linear curve was associated with a surface covered with dendrites and the second linear curve with the Cu_2O crystallites. Surface finish, preannealing, and gas flow rate in the range 0.1-2.0 cm sec^{-1} have no effect on the oxidation rate. It is considered that the rate-controlling process is the catalytic decomposition of CO_2 on the surface to form chemisorbed oxygen.

Manuscript submitted Oct. 27, 1976; revised manuscript received Nov. 18, 1977.

Any discussion of this paper will appear in a Discussion Section to be published in the December 1978 JOURNAL. All discussions for the December 1978 Discussion Section should be submitted by Aug. 1, 1978.

REFERENCES

1. K. Hauffe and H. Pfeiffer, *Z. Metallk.*, **44**, 27 (1953).
2. W. W. Smeltzer, *Acta Metall.*, **8**, 377 (1960).
3. W. W. Smeltzer, *Trans. Metall. Soc. AIME.*, **218**, 674 (1960).
4. F. Pettit, R. Yinger, and J. B. Wagner, Jr., *Acta Metall.*, **8**, 617 (1960).
5. F. Pettit and J. B. Wagner, Jr., *ibid.*, **12**, 35 (1964).
6. F. Pettit and J. B. Wagner, Jr., *ibid.*, **12**, 41 (1964).
7. K. Fueki and J. B. Wagner, Jr., *This Journal*, **112**, 970 (1965).
8. K. Fueki and J. B. Wagner, Jr., *ibid.*, **112**, 1079 (1965).
9. I. G. Murgulescu and D. Cismaru, *Acad. Repub. Pop. Rom. Stud. Cercet. Chim.*, **7**, 197 (1959).
10. B. Swaroop and J. B. Wagner, Jr., *This Journal*, **114**, 685 (1967).
11. C. Wagner, Mimeographed notes, Course 3.23, Kinetics in Metallurgy, Massachusetts Institute of Technology (Spring, 1955).
12. H. A. H. Pray, I. Igelstrud, and G. L. Simund, U.S. Pat. 2,446,060 (1948).
13. I. A. Menzies and W. J. Tomlinson, *J. Iron Steel Inst. (London)*, **204**, 1239 (1966).
14. L. H. Van Vlack, "Physical Ceramics for Engineers", Addison-Wesley, Reading, Massachusetts (1964).
15. F. A. Kröger and H. J. Vink, in "Solid State Physics" Vol. 3, F. Seitz and D. Turnbull, Editors, pp. 431-435, Academic Press, London (1955).
16. H. Kobayashi and C. Wagner, *J. Chem. Phys.*, **26**, 1609 (1957).
17. R. W. G. Wyckoff, "Crystal Structures," Vol. 1, p. 331, Wiley-Interscience, New York (1963).
18. D. A. Goulden, *Phil. Mag.*, **33**, 393 (1976).
19. G. E. Rhead, *Trans. Faraday Soc.*, **61**, 787 (1965).
20. J. Oudar, "Physics and Chemistry of Surfaces," p. 92, Blackie and Sons Ltd., Glasgow (1975).
21. J. Oudar, *ibid.*, p. 109.
22. P. Kofstad, "Nonstoichiometry, Diffusion and Electrical Conductivity in Binary Metal Oxides," p. 331, Wiley-Interscience, New York (1972).
23. R. M. Dell, F. S. Stone, and P. F. Tiley, *Trans. Faraday Soc.*, **49**, 201 (1953).

Thermodynamic Properties of Metal-Water Systems at Elevated Temperatures

Dale F. Taylor

General Electric Corporate Research and Development, Schenectady, New York 12301

ABSTRACT

The advent of commercial nuclear power generation has created an increased need for thermodynamic data on metal-water systems at temperatures up to 350°C. The entropy correspondence principle discovered by Criss and Cobble [*J. Am. Chem. Soc.*, **86**, 5385 and 5391 (1964)] provides an excellent means of estimating high-temperature partial molar ionic entropies and hence high-temperature heat capacities, from entropy values at 25°C. It is therefore often possible to calculate both equilibrium constants and standard electrode potentials with surprising accuracy for elevated temperatures. Unfortunately, different conventions have been used by several authors in publishing calculated numerical data. One purpose of the present paper is to clarify these differences. In addition, a means of simplifying the calculations is described. This new approach permits rapid modification or augmentation of existing values when more accurate data become available, or when information at other temperatures is required. Values of K_w, the ionization product of water, and $E^\circ_{AgX/Ag}$, the standard electrode potentials of silver-silver halide electrodes, are calculated as examples for temperatures up to 300°C, and these values are compared with available experimental data.

The advent of commercial nuclear power generation has created an increased need for thermodynamic data on metal-water systems at temperatures up to 350°C. An understanding of the corrosion processes which can facilitate the transport of radioactive contaminants or cause cracking of structural materials is particularly important, and with faster reaction rates at higher temperatures, thermodynamic properties play an increasingly important role in controlling the chemistry of dissolved species.

Unfortunately the entropy, heat capacity, and volume data required for calculating the relevant values of ΔG°, and hence the equilibrium constants and standard cell potentials, for conditions other than 25°C and 1 atm pressure are not presently available for many species of interest. However, the entropy correspondence principle discovered by Criss and Cobble (1) provides an excellent means of estimating high-temperature partial molar ionic entropies, and hence high-temperature heat capacities, from entropy values at 25°C. It is therefore often possible to calculate both equilibrium constants and standard electrode potentials with surprising accuracy for elevated temperatures. For example, at temperatures up to 250°C, most predicted values of K_w, the ionization product of water, and $E^\circ_{AgX/Ag}$, the standard electrode potentials of silver-silver halide electrodes, agree with available measured values within the quoted experimental uncertainty. Beyond 250°C, the contribution of pressure to changes in free energy starts to become important, and systematic deviations occur. Calculations involving temperatures above 300°C are probably only semiquantitatively correct.

Robins *et al.* (2), Townsend (3), Cowan and Staehle (4), MacDonald *et al.* (5-7), and Cobble and Murray (8) among others, have used this approach to predict the thermodynamic behavior of several elements and their oxidation products in high-temperature aqueous systems. Some confusion may arise, however, because different conventions have been used in listing numerical data. One purpose of the present paper is to clarify these differences.

In addition, a means of simplifying the calculations is described. This new approach permits rapid modification or augmentation of existing values when more accurate data become available, or when information at other temperatures is required.

Key words: electrolyte, chemical potential, heat capacity, entropy, equilibrium constant, standard hydrogen electrode (SHE), electrode potential.

Free Energy Changes at Elevated Temperatures

For a reaction which goes to completion at temperature T and pressure P, the change in free energy is given by

$$\Delta G = \sum_p \alpha_p \mu_p - \sum_r \alpha_r \mu_r \qquad [1]$$

where α_p and α_r are the stoichiometric coefficients of the products and reactants, respectively, and $\mu(T, P)$ is the chemical potential: the molar free energy for pure substances and the partial molar free energy for species in solution.

Since the activity of system component i, a_i, is defined by

$$\mu_i(T, P) = \mu_i^\circ + RT \ln a_i \qquad [2]$$

where μ_i° is the chemical potential of component i in some conveniently specified standard state at temperature T, the value of μ_i° depends on the units chosen to express a_i, and on the choice of standard state. The standard state for gases is the hypothetical pure ideal gas at unit pressure, usually 1 atm. The standard chemical potential μ°_{gas} thus depends only on temperature. The standard state for a liquid or solid element or compound is its stable state of aggregation as a pure substance at equilibrium, and therefore μ°_{solid} and μ°_{liquid} depend on both the temperature and pressure. This is the usual choice of standard state for the solvent in an electrolyte solution, but it is not convenient for the solute. The standard state for electrolyte solutions is that of a hypothetical ideal solution at unit concentration, most often unit molality to avoid complications from density changes, and μ°_{solute} is dependent on both temperature and pressure.

If the chemical potential of any component in its standard state is known at 25°C, 1 atm (298.15°K, 1.01325×10^5 Pa), integration of the relationships

$$\left(\frac{\partial \mu_i}{\partial T}\right)_P = -\bar{S}_i, \quad \left(\frac{\partial \mu_i}{\partial P}\right)_T = \bar{V}_i \qquad [3]$$

with the definition

$$\left(\frac{\partial \bar{S}_i}{\partial T}\right)_P \equiv \frac{\bar{C}_{P_i}}{T} \qquad [4]$$

yields the chemical potential of this component in its

standard state at any temperature (or pressure for condensed phases and electrolyte solutions)

$$\mu_i^\circ(T,P) = \mu_i^\circ(25^\circ C, 1\ \text{atm}) + \int_{1\ \text{atm}}^{P} \overline{V}_i^\circ dP'$$
$$+ \int_{298.15}^{T} \overline{C}_{Pi}^\circ dT' - T\int_{298.15}^{T} \overline{C}_{Pi}^\circ d\ln T'$$
$$- (T - 298.15)\overline{S}_i^\circ(25^\circ C, 1\ \text{atm}) \quad [5]$$

where the superscript ° denotes the standard state and unit activity, V, S, and C_P have their usual thermodynamic meanings, and the superscript $^-$ denotes $(\partial/\partial n_i)_{P,T,n_j}$: the molar value for pure substances and the partial molar value for components in solution.

$\Delta\mu_i^\circ$ is independent of the integration path, but since $\overline{V}_i^\circ$ and $\overline{C}_{Pi}^\circ$ are each functions of both T and P, the order of integration is important. $\overline{C}_{Pi}^\circ$ is generally available as a function of temperature for a pressure of 1 atm. $\overline{V}_i^\circ$ is then required as a function of P at temperature T.

$\mu_i^\circ(25^\circ C, 1\ \text{atm})$ for ions in solution and pure compounds is defined as the molar Gibbs free energy of formation by Eq. [1] and the convention which assigns a chemical potential of zero to H^+_{aq} and the elements in their standard states at the arbitrary reference point of 25°C and 1 atm. Thus the values of $\mu_i^\circ(T, P)$ calculated from [5] are not correct on an absolute scale, but the value of $\Delta G^\circ(T,P)$ calculated from [1] for any reaction is correct because a change is being evaluated and the arbitrary zero cancels out. This approach to calculating $\Delta G^\circ(T,P)$ is particularly convenient when a number of reactions with several common reactants and products are being considered. MacDonald was the first to adopt the procedure, but added an unnecessary complication by extending the Gibbs energy of formation terminology to temperatures and pressures other than 25°C and 1 atm (5, 9, 10).[1]

Cobble anticipated minor effects from changes in partial molar volumes at temperatures up to 300°C, and suggested that the pressure term could be ignored, especially since very little is known about the partial molar volumes of ions (11). It will be shown that this approximation is a good one.

Accurate molar heat capacity data is available for many pure substances in a readily integrable power series of the form (12, 13)

$$\overline{C}_{Pi}^\circ(T) = A_i + B_iT + C_iT^{-2} \quad [6]$$

but ionic partial molar heat capacities are generally not available.

Criss and Cobble (1) developed a technique for evaluating $\overline{S}_i^\circ(T)$ for ions, and their results suggest a very simple new approach to calculating $\overline{C}_{Pi}^\circ$, one which is both more accurate at higher temperatures than the average value they proposed, and conveniently consistent with [6].

[1] Cobble and Murray (8) have chosen to list values of the free energy function (FEF) based on a reference temperature of 25°C

$$\text{FEF}_i(T) \equiv \frac{\mu_i^\circ(T) - \overline{H}_i^\circ(25^\circ C)}{T} = \frac{\overline{H}_i^\circ(T) - \overline{H}_i^\circ(25^\circ C)}{T} - \overline{S}_i^\circ(T)$$

Thus, since

$$\text{FEF}_i(T) = \frac{1}{T}\int_{298.15}^{T} \overline{C}_{P_i}^\circ(T')dT' - \int_{298.15}^{T} \overline{C}_{P_i}^\circ(T')d\ln T' - \overline{S}_i^\circ(25^\circ C)$$

$$\mu_i^\circ(T) = \mu_i^\circ(25^\circ C) + T[\text{FEF}_i(T)] - 298.15[\text{FEF}_i(25^\circ C)]$$

This modification of the direct approach requires separate specification of μ_i° (25°C) values and some additional computation. However, the value of $\overline{S}_i^\circ$ (25°C) is immediately available as—FEF_i (25°C), and the slow variation of the free energy function with temperature permits interpolation between calculated values.

Criss and Cobble observed that "a standard state can be chosen at every temperature such that the partial molar entropies of one class of ions at that temperature are linearly related to the corresponding entropies at some reference temperature." The zero for ionic entropies at each temperature was defined by the value of $\overline{\overline{S}}{}^\circ_{H^+}(T)$, the partial molar ionic entropy of the hydrogen ion which resulted in the best linear fit of experimental data. The reference temperature was chosen to be 25°C. Thus for a given class of ion (simple cations, simple anions, oxy-anions, acid oxy-anions)

$$\overline{\overline{S}}{}_i^\circ(T) = a(T) + b(T)\overline{\overline{S}}{}_i^\circ(25^\circ C) \quad [7]$$

where $\overline{\overline{S}}$ denotes a partial molar entropy not referred to the conventional scale which sets $\overline{S}^\circ_{H^+}(T) \equiv 0$.

In fact, the $\overline{\overline{S}}{}_i^\circ$ values defined in this manner appear to be absolute or "third law" entropies. $\overline{\overline{S}}{}^\circ_{H^+}$ (25°C) is −5.0 calories mole^{-1} degree^{-1}, in relatively good agreement with the value of −4.48 calories mole^{-1} degree^{-1} deduced by deBethune *et al.* for the standard ionic entropy of electrochemical transport of hydrogen ions at 25°C (14), and the value of −5.5 calories mole^{-1} degree^{-1} obtained by Laidler and Pegis for the standard entropy of hydration of hydrogen ions (15).

Entropies on the conventional scale are related to the absolute scale at any temperature by the equation

$$\overline{\overline{S}}{}_i^\circ(T) = \overline{S}_i^\circ(T) + z\overline{\overline{S}}{}^\circ_{H^+}(T) \quad [8]$$

where z is the charge on the ion (with sign). At 25°C, this becomes

$$\overline{\overline{S}}{}_i^\circ(25^\circ C) = \overline{S}_i^\circ(25^\circ C) - 5.0z \quad [9]$$

Criss and Cobble noted that up to 150°C the parameters $a(T)$ and $b(T)$ in Eq. [7] varied approximately linearly with temperature, with most of the deviation occurring near 60°C. On this basis they extrapolated their results to 300°C. Thus for a given class of ion, the tabulated values can be reproduced quite accurately by relationships of the form

$$a = a_1 + a_2T, \quad b = b_1 + b_2T \quad [10]$$

and by substituting from Eq. [7] and [10] into [4]

$$\overline{C}_{Pi}^\circ(T) = [a_2 + b_2\overline{\overline{S}}{}_i^\circ(25^\circ C)]T \equiv B_iT \quad [11]$$

Equation [11] will be referred to as the linear ionic heat capacity approximation (LIHCA). This relationship makes computer or calculator programs based on Eq. [5] and [6] directly applicable to ionic species with $A_i = C_i = 0$, and μ_i° can be calculated in one step for any temperature in the range where the constant pressure approximation is valid. Note that the choice of $\overline{S}_i^\circ(25^\circ C)$ or $\overline{\overline{S}}{}_i^\circ(25C^\circ)$ in Eq. [5] does not affect the value of ΔG° obtained from [3] provided that the same choice is made for calculations of all μ_i°. Since absolute values must be used in [11], there is less confusion if they are used throughout. In either case, the choice of convention must be clearly stated.

The apparent linearity of partial molar ionic heat capacities with temperature was noted first in studies of weak acids (16, 17), and the work of Criss and Cobble (1) seems to confirm its generality. Naumov *et al.* (18) also list partial molar ionic heat capacities in this form. A reasonable estimate of high-temperature partial molar ionic heat capacities can thus be obtained easily when the values at 25°C are available.

Electrode Potentials at Elevated Temperatures

The change in free energy for the generalized reduction in an aqueous system

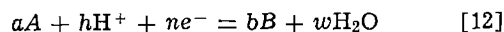

$$aA + hH^+ + ne^- = bB + wH_2O \quad [12]$$

is not experimentally accessible, but the tendency for any such reduction to occur can be measured relative

to a standard reduction, usually chosen to be the standard hydrogen electrode (SHE) reaction

$$H^+(a_{H^+} = 1) + e^- = 1/2\, H_2(a_{H_2} = 1) \quad [13]$$

in aqueous systems. Thus for constant n, the values of $\Delta G°_{A/B}$ at any temperature for the complete reactions represented by

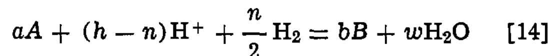

$$aA + (h - n)H^+ + \frac{n}{2} H_2 = bB + wH_2O \quad [14]$$

are one basis for comparing the relative tendencies of the reductions represented by [12] to occur at that temperature.

Since

$$\Delta G = - n\mathbf{F}E \quad [15]$$

where E is a measurable cell potential and $\mathbf{F}$ is the Faraday, it is logical to define a "standard electrode potential" for [12]

$$E°_{A/B} \equiv -\Delta G°_{A/B}/n\mathbf{F} \quad [16]$$

The standard electrode potential for [12] at any temperature can therefore be obtained by determining $\Delta G°_{A/B}$ through Eq. [1] and [5]. It follows as a natural consequence of [16] that

$$E°_{H^+/H_2} = 0 \quad [17]$$

at all temperatures since $\Delta G°_{A/B}$ is identically zero when Eq. [12] represents the SHE reaction.

The definition of the standard electrode potential can be generalized to include activities other than unity for the reactants and products in [12] through Eq. [1] and [2]. Since the activities of H_2 and H^+ contributed from [13] are unity by definition

$$E_{A/B} = E°_{A/B} - \frac{RT}{n\mathbf{F}} \ln \left[\frac{a_B{}^b a_{H_2O}{}^w}{a_A{}^a a_{H^+}{}^h} \right] \quad [18]$$

The electrode potential, or "potential *vs.* SHE at the same temperature" provides a very convenient basis for comparison among all the reactions which are possible in the system at a given temperature.

The concept of the electrode potential is by definition independent of the convention which sets $\mu°_{H_2}$ and $\mu°_{H^+}$ equal to 0 at 25°C, and does not require, as suggested by Van Rysselberghe (19), that

$$\tfrac{1}{2}\mu°_{H_2} = \mu°_{H^+} \quad [19]$$

This relationship is true only at the temperature for which $\mu°_{H_2}$ and $\mu°_{H^+}$ are defined to be zero.

The variation of $E_{A/B}$ with temperature defines the "isothermal" temperature coefficient of the electrode potential since $E_{A/B}$ is referred to the SHE at the same temperature. Another alternative for describing the effect of temperature on reaction [12] is to measure the tendency for this reaction to occur at temperature T relative to the same reaction at a fixed reference temperature, normally 25°C. This is satisfying from an experimental point of view since any two identical electrodes at different temperatures in the same cell will develop a potential difference which is independent of metallic thermocouple effects and the thermal liquid junction potential (14).

For two hydrogen electrodes, this thermal cell reaction is

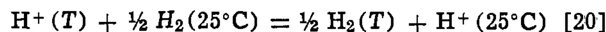

$$H^+(T) + \tfrac{1}{2} H_2(25°C) = \tfrac{1}{2} H_2(T) + H^+(25°C) \quad [20]$$

and

$$\Delta G°^*_{H^+/H_2}(T) = \tfrac{1}{2}\mu°_{H_2}(T) - \mu°_{H^+}(T) \quad [21]$$

where * denotes the 25°C "thermal" convention. In a manner analogous to that used in defining $E°$, a standard "thermal" electrode potential can be defined for the SHE

$$E°^*_{H^+/H_2}(T) = - \Delta G°^*_{H^+/H_2}(T)/\mathbf{F} \quad [22]$$

It is important to note that absolute ionic entropies must be used in Eq. [5] to obtain standard thermal electrode potentials. The use of absolute entropies for all calculations therefore seems advisable.

Comparison of the Linear Ionic Heat Capacity Approximation with Experimental Data

Very accurate values for the ionic dissociation constant of water, K_w (20), and the standard electrode potentials (*vs.* SHE at the same temperature) of the silver/silver halide electrodes (21-23) are available for comparison with predicted values over a wide temperature range. Both comparisons have been made previously on a limited or graphical basis using the multiparameter Criss-Cobble approximation (4, 6, 11). These studies provide an excellent source of calculated data. In addition, the measurements of Fales and Mudge (24) are available for verifying predictions of thermal hydrogen electrode potentials up to 60°C.

Table I contains the thermodynamic data used in all the calculations of $\mu_i°$ values. The parameters for water are not included since $\mu°_{H_2O}$ values were taken directly from the data of Helgeson and Kirkham (25) and these are listed in Table II. $\mu°_{OH^-}(25°C)$ was calculated by [1] using the value of $\Delta G°_w(25°C)$ determined by Sweeton, Mesmer, and Baes (20)

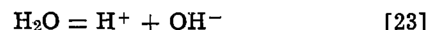

$$H_2O = H^+ + OH^- \quad [23]$$

$$\Delta G°_w = - RT \ln K_w = \mu°_{H^+} + \mu°_{OH^-} - \mu°_{H_2O} \quad [24]$$

B_i values (for $\overline{C}_{Pi}°$) were calculated from Eq. [4] for H^+ and Eq. [11] for the other ions. A linear fit of the Criss-Cobble entropy parameters to 300°C, excluding the values at 60°C, resulted in the following values for H^+, and simple anions

$$(\partial \overline{\overline{S}}°_{H^+}/\partial T)_P = 9.35 \times 10^{-2} \text{ cal mole}^{-1} \text{ deg}^{-2}$$
$$a_2 = -1.77 \times 10^{-1} \text{ cal mole}^{-1} \text{ deg}^{-2}$$
$$b_2 = -1.12 \times 10^{-4} \text{ deg}^{-1}$$

Table II summarizes the results from calculations of $\Delta G°_w$ and pK_w using the linear ionic heat capacity approximation (LIHCA). The number of significant figures is not warranted by the accuracy of the original

Table I. Thermodynamic data

	$\mu°$ (25°C) (26, 27) (calories mole^{-1})	$\overline{\overline{S}}°$ (25° C) (26, 27) (calories mole^{-1} degree^{-1})	$\overline{C}_P° = A + BT + CT^{-2}$ (12, 13) (calories mole^{-1} degree^{-1})		
			A	B	C
H^+	0	−5.0	0	9.35×10^{-2}†	0
OH^-	−37596	2.43*	0	-1.77×10^{-1}†	0
Cl^-	−31372	18.5	0	-1.79×10^{-1}†	0
Br^-	−24850	24.7	0	-1.80×10^{-1}†	0
I^-	−12330	31.6	0	-1.80×10^{-1}†	0
H_2	0	31.208	6.52	0.78×10^{-3}	0.12×10^5
Ag	0	10.17	5.09	2.04×10^{-3}	0.36×10^5
AgCl	−26244	23.0	14.88	1.00×10^{-3}	-2.70×10^5
AgBr	−23160	25.6	7.93	15.40×10^{-3}	0
AgI	−15820	27.6	5.82	24.10×10^{-3}	0

† Calculated using the linear ionic heat capacity approximation (LIHCA).
* Consistent with $\Delta S°_w$ (25°C) and $\overline{S}°_{H_2O}$ (25°C) from (20) and (25).

Table II. Thermodynamic parameters for the ionic dissociation of water—comparison of experimental values with those calculated using the linear ionic heat capacity approximation (LIHCA)

Temp. (°C)	$\mu°_{H_2O}$ (25) (cal mole^{-1})	$\mu°_{H^+}$ (LIHCA) (cal mole^{-1})	$\mu°_{OH^-}$ (LIHCA) (cal mole^{-1})	$\Delta G°_w$ (LIHCA) (calories)	$\Delta G°_w$ (20) (calories)	pK_w (LIHCA)	pK_w (20)
25	−56686	0	−37596	19090	19090 ± 9	13.994	13.993 ± 0.009
50	−57122	96	−37601	19617	19624 ± 12	13.268	13.272 ± 0.006
75	−57593	133	−37496	20230	20245 ± 12	12.700	12.709 ± 0.006
100	−58096	112	−37280	20928	20939 ± 12	12.258	12.264 ± 0.009
125	−58630	32	−36953	21709	21704 ± 18	11.917	11.914 ± 0.009
150	−59191	−106	−36516	22569	22541 ± 21	11.657	11.642 ± 0.012
175	−59779	−302	−35968	23509	23460 ± 24	11.465	11.441 ± 0.012
200	−60392	−557	−35309	24526	24468 ± 24	11.329	11.302 ± 0.012
225	−61029	−870	−34539	25620	25578 ± 27	11.241	11.222 ± 0.012
250	−61688	−1242	−33659	26787	26801 ± 36	11.191	11.196 ± 0.015
275	−62369	−1672	−32668	28029	28151 ± 69	11.176	11.224 ± 0.027
300	−63069	−2161	−31566	29342	29638 ± 117	11.189	11.301 ± 0.045

data, but all $\mu_i°$ and $\Delta G°$ values were calculated to the nearest calorie for direct comparison with the results published by other authors. Six of the calculated pK_w values are within ±0.1% of the experimental values, and all ten of the values up to 250°C deviate less than ±0.25%. The deviation at 275°C is −0.43%, and at 300°C, −1%.

This systematic error escalation above 250°C probably results from contributions to $\Delta G°$ by the rapidly increasing vapor pressure of water. Sweeton *et al.* indicated that the effects of density changes on the partial molar volumes of ions are not well understood in this temperature region (20). Extrapolation of the constant pressure approximation to temperatures above 300°C is a questionable procedure, especially since no experimental data are available for comparison.

The accuracy below 300°C is quite remarkable. MacDonald and Butler (6, 9) assumed all discrepancies in K_w were the result of inaccuracies in $\mu°_{H^+}$ and recalculated "corrected" values of this parameter for application to other systems. However, since Criss and Cobble obtained $\bar{\bar{S}}°_{H^+}$ by fitting all available ionic entropy data (1), $\mu°_{H^+}$ is probably more accurate than the other calculated values, and further comparison with experimental observations seems to bear this out.

Table III lists the results from calculations of $\mu_i°$ for components of the hydrogen and silver-silver halide electrodes, again using the linear ionic heat capacity approximation.

Corresponding standard potentials (*vs.* SHE at the same temperature) appear in Table IV, along with values calculated from MacDonald and Butler's results (6) and observed values (21-23). Equation [14] takes the form

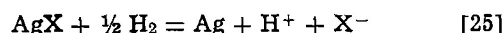

$$AgX + \tfrac{1}{2} H_2 = Ag + H^+ + X^- \quad [25]$$

and hence

$$E°_{AgX/Ag} = (\mu°_{AgX} + \tfrac{1}{2}\mu°_{H_2} - \mu°_{Ag} - \mu°_{H^+} - \mu°_{X^-})/\mathbf{F} \quad [26]$$

A value of 23060.9 calories V^{-1} equivalent^{-1} was used for **F**.

Once again, the calculated results are quite accurate. The agreement for Ag/AgCl is almost perfect. The very systematic error of ~+4 mV for Ag/AgBr can be eliminated by a change of +90 cal in the $\mu°_{Br^-}$(25°C) value. The Ag/AgI results do not agree nearly as well, and no simple adjustment of parameters can bring them more closely into line. However, the linear ionic heat capacity approximation with no special adjustment of parameters duplicates the MacDonald-Butler results at lower temperatures, and yields consistently better results at higher temperatures.

The excellent agreement with experimental results obtained for K_w and the silver-silver chloride and

Table III. Standard chemical potentials for components of the hydrogen and silver-silver halide electrodes calculated using the linear ionic heat capacity approximation (LIHCA)

Temperature (°C)	(calories mole^{-1})								
	H^+	H_2	Ag	AgCl	AgBr	AgI	Cl^-	Br^-	I^-
25	0	0	0	−26244	−23160	−15820	−31372	−24850	−12330
60	118	−1106	−368	−27073	−24081	−16812	−31910	−25604	−13325
90	127	−2074	−701	−27822	−24909	−17703	−32196	−26076	−14003
100	112	−2401	−816	−28079	−25193	−18009	−32256	−26197	−14193
125	32	−3225	−1109	−28736	−25917	−18789	−32327	−26422	−14588
150	−106	−4061	−1413	−29415	−26664	−19593	−32287	−26534	−14871
175	−302	−4906	−1725	−30115	−27432	−20421	−32134	−26534	−15040
200	−557	−5761	−2046	−30833	−28221	−21272	−31869	−26422	−15097
225	−870	−6626	−2375	−31571	−29030	−22146	−31493	−26197	−15042
250	−1242	−7499	−2711	−32326	−29858	−23042	−31005	−25860	−14873
275	−1672	−8380	−3056	−33099	−30706	−23961	−30405	−25411	−14592
300	−2161	−9270	−3407	−33888	−31572	−24901	−29693	−24850	−14198

Table IV. Standard potentials for the silver-silver halide electrodes (mV)

Temp. (°C)	AgCl/Ag				AgBr/Ag				AgI/Ag			
	LIHCA	(21)[1]	(21)[2]	(6)	LIHCA	(22)[1]	(22)[2]	(6)	LIHCA	(23)[1]	(23)[2]	(6)
25	222	222	222	222	73	72 ± 1	71	73	−151	−152	−152	−151
60	197	197	197	196	53	50 ± 1	50	53	−164	−166	−167	−165
90	170	170	170		31	25 ± 1	27		−181		−185	
100	160		160	160	22		18	22	−187	−193 ± 1	−192	−187
125	132	133	133		−1	−5 ± 1	−5		−205	−213 ± 1	−213	
150	102	103	103	103	−29	−31 ± 1	−32	−27	−227	−238 ± 1	−238	−226
175	69	71	71		−57	−61 ± 1	−62		−252	−270 ± 1	−271	
200	33	35	35	40	−90	−95 ± 1	−94	−84	−280	−309 ± 1	−307	−273
225	−6	−5	−4		−126		−130		−311		−346	
250	−48	−54 ± 2	−45	−34	−165		−169	−150	−345		−390	−331
275	−93	−90 ± 5	−90		−206		−210		−383		−437	
300	−141		−138	−124	−251		−255	−233	−424		−488	−406

[1] Experimental.
[2] Smoothed/extrapolated.

bromide standard potentials undoubtedly reflects the fact that these or similar experimental results were used to determine values for the parameters of the correspondence principle in the first place. This in no way detracts from the demonstrated general internal consistency of the approach, but suggests that the silver-silver iodide results may be a better indication of the accuracy to be expected. It should also be noted, however, that silver iodide undergoes a phase transition at 144.6°C (23), and it is possible that at least part of the discrepancy arises from the failure to account for this in the calculations.

The value of a_2 for simple anions used in these calculations was obtained from the parameters of the linear correspondence principle as they appeared in Criss and Cobble's original publication (1). The value of a_2 calculated after correcting for an apparent typographical error which was first noticed by Tremaine *et al.* (a for simple anions at 300°C should be -47.2 instead of -49.2) (28) is -1.72×10^{-1} calories mole^{-1} degree^{-2}. This "corrected" value actually causes a slight deterioration in the agreement between all calculated and observed values, with the original value fortuitously producing a fit which does not benefit significantly from optimization.

Even at 60°C, where the linear ionic heat capacity approximation should be least accurate, it compares well with experimental data from thermal electrode measurements. From [21] and [22], and the data in Table III,

$$E^{\circ *}_{H^+/H_2}(60^\circ C, \text{LIHCA}) = 0.029\text{V} \quad [27]$$

From the data of Fales and Mudge (24), deBethune *et al.* calculated an expression for the thermal potential of the hydrogen electrode (Pt/H_2 ($f = 1$), 0.1M HCl/sat'd KCl) which gives $E^*_{H^+(0.1m)/H_2}(60^\circ C)$ as 0.022V (14). The standard thermal potential at 60°C can be calculated from [28], an equation obtained by generalizing Eq. [21] and [22] to include activities other than unity

$$E^{\circ *}_{H^+/H_2}(60^\circ C) = E^*_{H^+(0.1m)/H_2}(60^\circ C) + \left[\frac{RT}{\mathbf{F}} \ln a_{H^+}\right]_{25^\circ C} - \left[\frac{RT}{\mathbf{F}} \ln a_{H^+}\right]_{60^\circ C} \quad [28]$$

where $a_{H^+} = 0.1\ \gamma_\pm(\text{HCl})$. The values obtained by Greeley *et al.* (29) for $\gamma_\pm(\text{HCl}, 0.1m)$, 0.7972 at 25°C and 0.776 at 60°C, yield

$$E^{\circ *}_{H^+/H_2}(60^\circ C, \text{OBS.}) = 0.030\text{V} \quad [29]$$

It is interesting to note that [22] predicts that the temperature coefficient of the thermal SHE potential, $\partial E^{\circ *}_{H^+/H_2}/\partial T$, decreases significantly as the temperature increases, contrary to the behavior first assumed by MacDonald (9). Using the values in Tables I and III, the temperature coefficient is 0.893 mV deg^{-1} at 25°C, passing through zero and changing sign at a temperature of about 265°C. This result differs slightly from MacDonald's later calculation (10) because of his "corrected" $\mu^\circ_{H^+}$ values.

Conclusions

1. The Criss-Cobble entropy correspondence principle makes possible surprisingly accurate predictions of thermodynamic properties in aqueous systems at temperatures up to *ca.* 300°C.

2. The linear ionic heat capacity approximation (LIHCA) reduces the number of parameters required, simplifies the calculations, and makes possible a one-step computation while improving over-all accuracy.

3. Extrapolation of the constant pressure approximation to temperatures above 300°C may involve considerable error.

4. It is important to state the $\mu_i^\circ(25^\circ C)$ and $\overline{S}_i^\circ(25^\circ C)$ values used in calculations on any system. Separate $\mu_i^\circ(T)$ values are the most useful parameters for subsequent applications of the data.

Manuscript submitted Sept. 23, 1977; revised manuscript received Jan. 3, 1978.

Any discussion of this paper will appear in a Discussion Section to be published in the December 1978 JOURNAL. All discussions for the December 1978 Discussion Section should be submitted by Aug. 1, 1978.

Publication costs of this article were assisted by the General Electric Company.

REFERENCES

1. C. M. Criss and J. W. Cobble, *J. Am. Chem. Soc.*, **86**, 5385 and 5391 (1964).
2. R. J. Biernat and R. G. Robins, *Electrochim. Acta*, **14**, 809 (1969); B. W. Edenborough and R. G. Robins, *ibid.*, **14**, 1285 (1969).
3. H. E. Townsend, Jr., *Corrosion Sci.*, **10**, 343 (1970).
4. R. L. Cowan and R. W. Staehle, *This Journal*, **118**, 557 (1971).
5. D. D. MacDonald, G. R. Shierman, and P. Butler, Atomic Energy of Canada Ltd., AECL-4136, 4137, 4138, 4139 (1972).
6. D. D. MacDonald and P. Butler, *Corrosion Sci.*, **13**, 259 (1973).
7. D. D. MacDonald, *ibid.*, **16**, 461 (1976).
8. J. W. Cobble and R. C. Murray, Jr., in the Annual Report for EPRI Contract No. RP 311-2, San Diego State University Foundation, March 1977.
9. D. D. MacDonald, in "Modern Aspects of Electrochemistry, Vol. 11, J. O'M. Bockris and B. E. Conway, Editors, pp. 141-197, Plenum Press, New York (1975).
10. D. D. MacDonald, Paper No. 146, NACE Corrosion/77, San Francisco, March 1977.
11. J. W. Cobble, *J. Am. Chem. Soc.*, **86**, 5394 (1964).
12. K. K. Kelley, Bulletin 584, Bureau of Mines, U.S. Government Printing Office, Washington (1960).
13. C. E. Wicks and F. E. Block, Bulletin 605, Bureau of Mines, U.S. Government Printing Office, Washington (1963).
14. A. J. deBethune, T. S. Licht, and N. Swendeman, *This Journal*, **106**, 616 (1959).
15. K. J. Laidler and C. Pegis, *Proc. Roy. Soc. (London)*, **A241**, 80 (1957).
16. H. S. Harned and R. A. Robinson, *Trans. Faraday Soc.*, **36**, 973 (1940).
17. R. A. Robinson and R. H. Stokes, "Electrolyte Solutions," Second Edition (Revised), p. 357, Butterworths, London (1965).
18. G. B. Naumov, B. N. Ryzhenko, and I. L. Khodakovsky," Handbook of Thermodynamic Data," Transl. from Russian by the U.S. Geological Survey, Report No. USGS-WRD-73-001 (1974).
19. P. VanRysselberghe, Introduction to "Atlas of Electrochemical Equilibria in Aqueous Solutions" by M. Pourbaix, Pergamon Press, Oxford (1966).
20. F. H. Sweeton, R. E. Mesmer, and C. F. Baes, Jr., *J. Solution Chem.*, **3**, 191 (1974).
21. R. S. Greeley, W. T. Smith, Jr., R. W. Stoughton, and M. H. Lietzke, *J. Phys. Chem.*, **64**, 652 (1960).
22. M. B. Towns, R. S. Greeley, and M. H. Lietzke, *ibid.*, **64**, 1861 (1960).
23. G. Kortüm and W. Häussermann, *Ber. Bunsenges. Physik. Chem.*, **69**, 594 (1965).
24. H. A. Fales and W. A. Mudge, *J. Am. Chem. Soc.*, **42**, 2434 (1920).
25. H. C. Helgeson and D. H. Kirkham, *Am. J. Sci.*, **274**, 1089 (1974).
26. N. B. S. Technical Note 270-3 (1968).
27. N. B. S. Technical Note 270-4 (1969).
28. P. R. Tremaine, R. VonMassow, and G. R. Shierman, *Thermochimica Acta*, **19**, 287 (1977).
29. R. S. Greeley, W. T. Smith, Jr., M. H. Lietzke, and R. W. Stoughton, *J. Phys. Chem.*, **64**, 1445 (1960).

Boron in Near-Intrinsic $\langle 100 \rangle$ and $\langle 111 \rangle$ Silicon under Inert and Oxidizing Ambients—Diffusion and Segregation

Dimitri A. Antoniadis,* Adalberto G. Gonzalez, and Robert W. Dutton

Stanford Electronics Laboratories, Stanford University, Stanford, California 94305

ABSTRACT

The diffusivity of boron in <100> and <111> silicon is experimentally determined under both inert and oxidizing (dry O_2) ambient conditions in the range of temperatures 850°-1200°C. The boron is implanted at moderate dose (1.3×10^{14} cm^{-2}) and energy (70 keV) and subsequently activated by a moderate temperature anneal. The resulting profile ensures near-intrinsic silicon at the processing temperatures and serves as initial condition for subsequent processing. Diffusivities and segregation coefficients are calculated as fitting parameters in numerical solution of the experiments. A systematic fitting procedure is used and the target experimental parameters are sheet resistances and junction depths. Inert ambient diffusivities agree well with previous measurements, thus demonstrating the integrity of newly published mobility data used in the simulations. Diffusivities in oxidizing ambient are enhanced, more so in <100> than in <111> silicon. The enhancement increases with decreasing temperature, being about 10 for <100> at 850°C. It is demonstrated that there is good agreement between the observed diffusivity enhancement and growth of oxidation stacking faults if an interstitialcy mechanism is invoked to explain both phenomena. Observed segregation coefficients are different for the two silicon orientations but they obey the same activation energy over the temperature range.

Boron is the dominant p-type dopant for silicon technology. For this reason a great amount of effort has been expended during the last two decades for the determination of physical properties of boron in silicon at fabrication conditions. Since the device electrical characteristics depend strongly on the final impurity distributions, a detailed understanding of boron impurity diffusivity in silicon and its partition (segregation) in the silicon-silicon oxide interface is essential.

It is presently established that boron diffuses at least partly by means of charged-defect interactions (1, 2). For this reason the diffusivity of boron is affected by substitutional impurities in silicon present at sufficient levels to cause the crystal to become extrinsic at the fabrication temperatures. The terms intrinsic and extrinsic in this paper refer to the condition of the silicon at the process temperature. Boron diffusivity in absence of oxidation is uniform, *i.e.*, independent of impurity concentration provided this concentration is lower than that of intrinsic carriers at the process temperature. We refer to this as "intrinsic boron diffusivity." Boron diffusivity under extrinsic conditions becomes a function of Fermi level position increasing as the Fermi level approaches the valence band and decreasing as the Fermi level approaches the conduction band. The results of this effect are to a large degree responsible for the abundance of conflicting values of boron diffusion coefficients. Reviews on this matter have been presented by Kendall and DeVries (4) and Fair (5).

It has also been established that the diffusivity of boron in silicon is enhanced by the growth of silicon dioxide at the surface (6-9). The degree of enhancement is greater in <100> crystal orientation than in <111>. Again a number of mostly conflicting diffusion coefficients have been reported mainly because of the coexistence, in most experiments, of high concentration effects, oxidation effects, and redistribution of boron at the moving silicon-silicon oxide boundary (10).

The redistribution of boron during oxidation is, to a large degree, controlled by the segregation (or partition) process at the moving silicon-oxide interface (3). This physical process gives rise to a nonunity segregation coefficient defined as $m = C_{si}/C_{ox}$, where C_{si} and C_{ox} are the impurity concentrations at the two sides of the interface. The only direct measurements of the ratio m for boron as a function of temperature and crystal orientation have been presented by Colby and Katz (11). Most of the other values appearing in the literature have been indirectly calculated from redistribution models under various degrees of approximations and thus do not present a consistent picture of the physical process (10).

In the present paper we report the results of a study of boron diffusivity in near intrinsic <100> and <111> silicon under inert (N_2) and oxidizing (dry O_2) ambients at various temperatures. For the oxidation cases we also calculate the effective segregation coefficients, which we define as the constant ratios, m_{eff}, that best fit the experimental data over the entire time of each experiment.

The initial distribution of boron for all experiments was established by means of an ion-implantation and annealing process that insures the complete boron electrical activation and the intrinsic silicon requirements at the temperatures of the experiments. Diffusivities and segregation coefficients have been calculated using a new IC process simulator (12) together with an automatic optimizer program that seeks the best-fit parameters compatible with the measured data. For the determination of diffusivities in inert atmosphere the only measured data were the initial and final sheet resistance for each experiment. For the simultaneous determination of diffusivity and segregation coefficients in the oxidation experiments, the additional information of junction depths was used. Recently reported hole mobilities were used (13, 14) for the calculation of sheet resistances resulting from the simulation. The reliability of the technique and the integrity of the mobility data is demonstrated by the excellent fit of the diffusivity in inert ambient by a single activation energy and the agreement with other reliable data (15).

In dry O_2, diffusivity enhancement has been observed, more so in <100> than in <111>. This is in

* Electrochemical Society Active Member.

Key words: boron, oxidation, diffusivity, enhancement, segregation.

qualitative agreement with previously reported data (9, 11). For both orientations the observed enhancement increases as the temperature is decreased and the results cannot be characterized by a single activation energy. We demonstrate that this behavior is predicted by the self-interstitial supersaturation model proposed by Hu (16) to explain the growth of stacking faults and the diffusivity enhancement during silicon oxidation. In this context we show that the diffusivity data obtained here are compatible with the stacking fault growth data obtained by Hu (17, 18).

The segregation coefficients determined here are generally higher than those measured by Colby and Katz.[1] Also in all cases the calculated segregation coefficient is higher in <100> than in <111> silicon, but their difference is not as large as that reported by the above workers.

Experiment

The substrate materials used were low dislocation density ($\leq 100/cm^2$), Czochralski-grown, phosphorus-doped, <111> and <100> crystal orientation silicon wafers, with an initial resistivity of 5-10 Ω-cm. Clean wafers were oxidized at 1000°C for 60 min in dry oxygen, growing about 510Å of SiO_2 for <100> material and about 615Å of SiO_2 for <111> material. Subsequently the wafers were implanted with B^{11+} at a dose of 1.33×10^{14} atoms/cm², at an energy of 70 keV, and at 7° misalignment to minimize channeling. The oxide layer was used to minimize silicon damage at the surface during implantation and to prevent evaporation of impurities during subsequent nitrogen drive-ins. Such a static oxide film does not affect the diffusion of boron (6). Although it is possible to have oxygen knock-ons into the silicon during implantation (19), it was assumed that the amount of oxygen present in the lattice would not seriously affect the diffusion of boron (less than 10^{12} atoms/cm² get knocked on to a maximum depth of 1000Å in the worst case). After implantation, the wafers were annealed in an N_2 atmosphere at 900°C for 35 min. The implantation and the annealing conditions were chosen in order to give the initial distribution of substitutional boron that has been experimentally determined by Hofker *et al.* (20), using secondary ion mass spectroscopy (SIMS) and electrical profiling techniques. This distribution is shown in Fig. 1. The only difference between the present process and that of Hofker *et al.* was the presence of the thin capping oxide, in which a maximum of 6% of the implanted dose is retained. The importance of excluding the implant annealing phase from the diffusion experiments cannot be overemphasized. Transient diffusion phenomena (20, 21) occurring during the electrical activation of the implant can easily lead to overestimation of the normal (thermal) diffusivity, particularly at the lower temperatures (20). Also, since initial sheet resistances are needed with our method, the implant had to be fully electrically activated prior to subsequent processing. Each as-annealed wafer was cut into quarters and one quarter was retained as a reference, while the other three were used for experiments at the same temperature and ambient. Since the peak concentration of the as-annealed boron profile was below 4×10^{18} atoms/cm³ and the intrinsic carrier concentration even at the lowest temperature considered here (850°C) is about 5×10^{18} carriers/cm³ (22), the silicon substrate was near intrinsic under all conditions of our experiments and thus extrinsic diffusivity effects have been avoided.

For inert ambient experiments, <100> and <111> quarter wafers were subjected to nitrogen atmosphere drive-ins for different times and temperatures. For oxidizing ambient experiments, the quarter wafers were previously stripped of capping dioxide in 5:1 H_2O/HF solution until hydrophobic, and then subjected to 100% dry O_2 atmosphere drive-ins for different times and temperatures. In most cases diffusion of <100> and <111> wafers was performed simultaneously in the same furnace to guarantee the same processing conditions.

After processing, junction depths were measured using angle lapping and electrical probing with a high precision spreading resistance two-point probe (23). The mechanical reliability of the probe yields junction depths with a resolution of ± 500Å for deep junctions (2-5 μm), and ± 250Å for shallow ones (0.5-2 μm). Some of the deeper junction depths were verified using groove and stain techniques and a sodium light dual-beam interferometer. Sheet resistances were measured using a light (45g) and a heavy pressure (180g) linear four-point probe array. Agreement between the measured values had a relative deviation no greater than 3%. Oxide thicknesses were measured with an ellipsometer at various points on the wafer, observing a fluctuation no greater than 2%. Good agreement was observed between the experimental thicknesses and those reported recently (24), except for the experiments at 900°C where thicknesses were consistently lower.

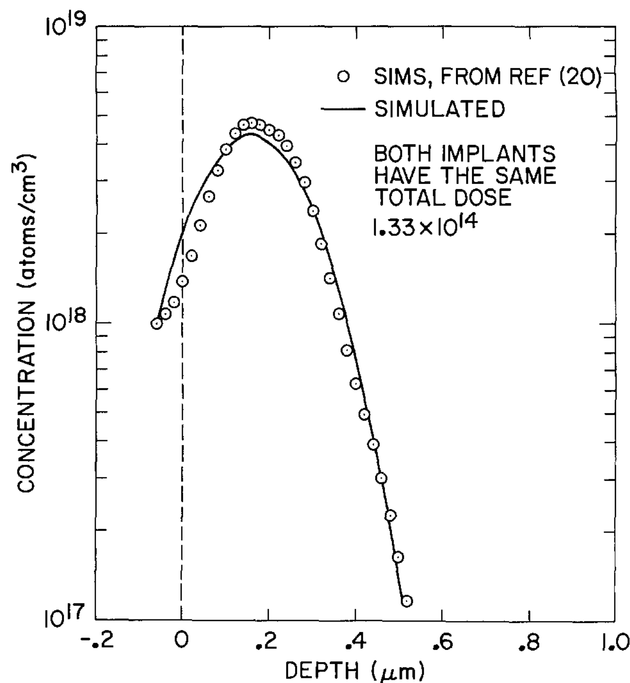

Fig. 1. Boron implant, 1.33×10^{14} ions/cm² dose, 70 keV, annealed at 900°C for 35 min.

Analysis

The process simulator SUPREM (12) was used to model the impurity distribution of boron, on a computer, for every one of the different experimental processing schedules. In each case, the simulated profile characteristics were matched to the corresponding measured values. The diffusion and segregation coefficients were thus obtained as a result of the fitting process. In the simulation of oxidation, minor adjustments were made to the linear and parabolic oxide growth rates (25) in order to simulate the proper experimental oxide thicknesses.

The simulated junction depths and sheet resistances were compared with the corresponding measurements of these quantities. In each case, the initial estimates of diffusion and segregation coefficients were iteratively adjusted until agreement (within less than 1%) between measured and simulated values was established. The iterative adjustment was carried out by the built-in SUPREM optimizer (26). The optimizer

[1] The definition of the segregation coefficient here follows that of Grove *et al.* (19), and is the inverse of the one used by Colby and Katz. Since boron generally prefers the oxide, "higher" segregation coefficient, in this paper, means a smaller boron concentration in the oxide side of the interface for a given concentration in silicon.

is operated as a nonlinear equation solver in which the unknown diffusion coefficient in the case of inert ambient drive-ins is found by fitting the measured sheet resistance. In the case of oxidizing ambient drive-ins the diffusion and segregation coefficients are found by fitting both the measured sheet resistances and junction depths.

Optimized parameter extraction is a systematic way of obtaining model-dependent parameters from measured data, even under conditions where parameters interact strongly. This method proves most useful when two or more parameters are to be fitted simultaneously as in the case of oxidizing ambient diffusion, where the boron diffusivity tends to increase the junction depth and lower sheet resistance, whereas segregation and the moving boundary tend to raise sheet resistance and decrease junction depth. It is important to note that in this work both diffusion and segregation coefficients were extracted simultaneously.

The simulated sheet resistance computed by SUPREM is a strong function of the hole mobility. Recently available information (13, 14) has been used to achieve substantially better agreement with actual measured values than was possible using older references (27, 28). The new mobility data as well as a smooth function fitted to them are shown in Fig. 2. Details on the fitting function are given in the Appendix. In order to minimize the effect of small process variations and measuring equipment condition in the observed values of sheet resistance, a constant ratio technique was employed. Each time sheet resistance was measured on a processed wafer, the corresponding control wafer was also monitored. Thus the goal of the fitting process was to match the observed and simulated ratios of processed-to-unprocessed sheet resistances rather than exact absolute values. Since the control wafers reflect the state of the common initial impurity distributions, small variations in the process up to this step tend to cancel out. Also, by measuring process and control wafers at the same time, probe conditioning variations tend to cancel out.

Results and Discussion

Diffusion.—Figure 3 is an Arrhenius plot of boron diffusivity obtained in inert ambients. An activation energy of 3.42 eV with an intercept factor of 0.55 cm^2/sec (often called preexponential factor), is found to describe boron diffusivity in <111> and <100> crystal orientation silicon, in the range of 900°-1200°C. For comparison, the diffusivity obtained by Kurtz and Yee under near intrinsic conditions (15) is also plotted. The agreement of our results with those generally accepted data supports the reliability of our fitting approach, namely, using only sheet resistance data. As a further confirmation we also performed junction depth measurements in selected nonoxidized samples, and the agreement with simulation was found to be satisfactory.

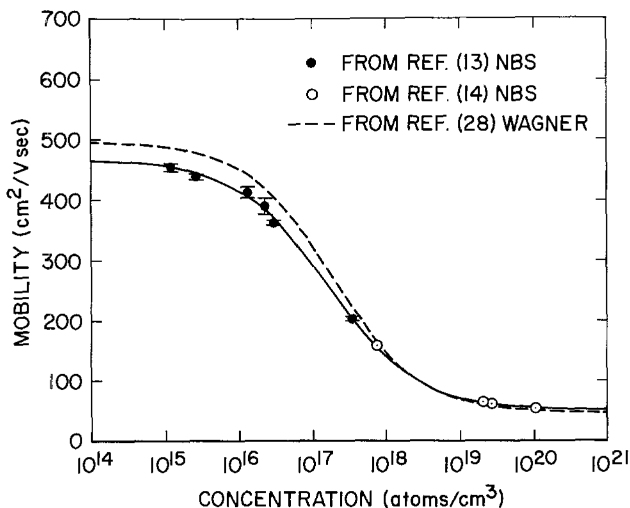

Fig. 2. Hole mobility in boron-doped silicon

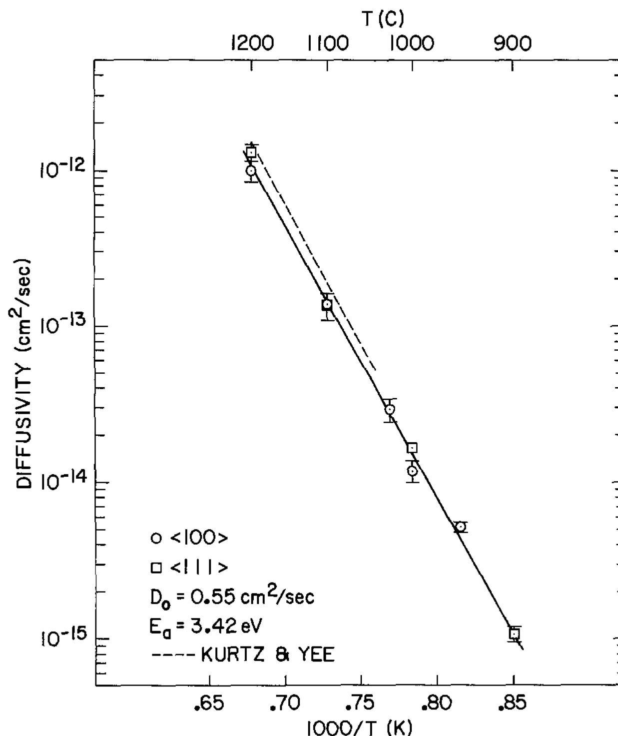

Fig. 3. Boron diffusivity in intrinsic silicon in nonoxidizing ambient

Having established the integrity of the sheet resistance approach we have been able to confidently use the additional information of junction depth for the simultaneous determination of diffusivity and effective segregation coefficient in the oxidation experiments. The results are shown in Fig. 4. As a reference, the inert ambient diffusivity is also plotted. Diffusivity enhancement has been obtained for the <100> orientations in practically all temperatures investigated. However, for the <111> orientation, enhancement was observed only at 900° and 850°C. Although other investigators have also reported absence of enhancement (6, 7) or reduced <111> enhancement (9) at the higher temperatures, we do recognize the fact that our data may be slightly underestimating the diffusivity because the spreading resistance method often tends to underestimate junction depth.

A remarkable feature of the data presented here is the multifold increase of boron diffusivity at the lower temperatures. For <100> silicon there exist enhancements of order 2, 5, and 10 at 1000°, 900°, and 850°C, respectively. For <111> silicon the enhancement order is 2 at 900°C and 5 at 850°C. It is clear that for both orientations the enhancement increases with decreasing temperature. An attempt to fit the data by a single activation energy over the entire range of the present experiments would be misleading.

An extensive set of boron diffusivities in <100>, <110>, and <111> silicon has recently been published by Masetti *et al.* (9). However, since they have used chemical predeposition the silicon was not intrinsic at least for part of the process duration. Furthermore, their numerical scheme cannot take concentration dependence into account. For dry O_2 in the range from 950° to 1200°C they have reported data fitted by single activation energies. Enhancement for <111> is small (about 1.2 over the whole range), but larger for <100>, increasing with decreasing temperature. Qualitatively these data are similar to ours but there is significant quantitative disagreement in the <100> case, particularly at 1000-1100°C. In general it

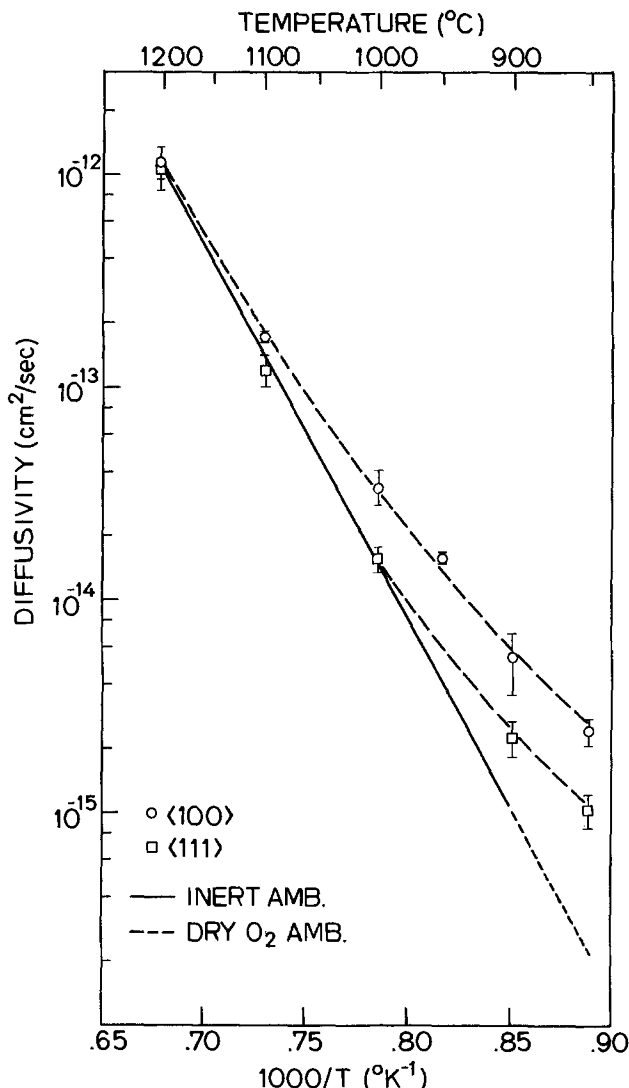

Fig. 4. Boron diffusivity in silicon in an oxidizing ambient

is difficult to compare our oxidation results to previously published data mainly because of differences in experimental conditions and in some instances, methods of data analysis. For this reason we will not pursue a comparative survey of the literature at this point.

Concentrating on the data presented in this paper, an explanation of the temperature-dependent behavior of the diffusivity enhancement will now be presented based on the model proposed by Hu (16) to explain the formation of stacking faults and enhanced diffusion during oxidation of silicon. Briefly, this model envisages a supersaturation of the silicon lattice by excess self-interstitials at concentrations dependent on the oxide growth rate and silicon orientation. These interstitials are thus responsible for the growth of stacking faults and, by invoking a dominant interstitialcy diffusion mechanism for boron, also responsible for diffusion enhancement. Assuming a fractional interstitialcy mechanism, f_A, it is straightforward to show that the effective diffusivity $<D>$ of boron in an oxidation process of duration t, is given by

$$<D> = \frac{1}{t}\int_0^t D dt$$

$$= D^* + \frac{D^*}{tC_i^*} f_A \int_0^t (C_i - C_i^*) dt \quad [1]$$

where D^* is the intrinsic diffusivity of boron and C_i^* and C_i the intrinsic and the extrinsic concentrations of silicon self-interstitials, respectively. Using Hu's theory (16), the above equation allows one to relate the effective diffusivity to the size of oxidation stacking faults. Indeed, from Eq. [13] of Ref. (16) the length, r, of stacking faults as a function of the process duration, t, can be expressed as

$$r = \pi\alpha_0^2 D_i \int_0^t (C_i - C_i^*) dt \quad [2]$$

where α_0 is the capture distance of interstitials by the faults and D_i the silicon interstitial diffusivity. Thus the ratio $<D>/D^*$ can be expressed by

$$\frac{<D>}{D^*} = 1 + f_A \frac{r}{\pi\alpha_0^2 D_i C_i^* t} \quad [3]$$

Assuming further that the diffusivity of silicon is partly due to an interstitialcy mechanism (29, 30), we may write

$$D_i C_i^* = f_s D_s C_s \quad [4]$$

where f_s is the fractional interstitialcy mechanism, and D_s and C_s the intrinsic diffusivity and lattice concentration of silicon. Thus Eq. [3] becomes

$$\frac{<D>}{D^*} - 1 = \frac{f_A}{f_s} \frac{r}{\pi\alpha_0^2 D_s C_s t} \quad [5]$$

Recently Hu (17, 18), published an empirical relationship for r based on his experiments

$$r = (Ae^{-Q_f/kT}) t^{0.8} \quad [6]$$

where T is the absolute temperature, k is Boltzmann's constant, and for both wet and dry oxygen $Q_f = 2.3$ eV while the values of A for dry oxygen are $A = 326$ cm sec$^{-0.8}$ for $<100>$, and $A = 156$ sec$^{-0.8}$ for $<111>$ silicon. Finally, it is well known that at least within limited temperature ranges the self-diffusivity of silicon can be expressed in terms of a single activation energy, Q_s (4, 5, 31)

$$D_s = D_{os} \exp\left(-\frac{Q_s}{kT}\right) \quad [7]$$

Hence using Eq. [6] and [7] in Eq. [5] we have

$$\left(\frac{<D>}{D^*} - 1\right) t^{0.2} = \frac{f_A}{f_s} \frac{A}{\pi\alpha_0^2 D_{os} C_s} \exp\left(\frac{Q_s - Q_f}{kT}\right) \quad [8]$$

In the above expression all factors are experimentally determinable with the exception of the ratio f_A/f_s.

Figure 5 is a plot of the quantity $(<D>/D^* - 1)t^{0.2}$ obtained from our $<100>$ experiments. It can be seen that this quantity exhibits a negative activation energy of -1.8 eV at the temperatures below 1000°C while over-all an activation energy of about -2 eV may be fitted. Assuming the experimentally determined values $Q_f = 2.3$ eV (17, 18) and $Q_s = 4.4$ eV (an average of values in literature for the low temperature end), the activation energy expected from Eq. [8] is -2.1 eV. Thus, there is at least good qualitative agreement between theory and experiments. This agreement is even better if the value $Q_s = 4.1$ eV recently obtained by Sanders and Dobson (31), near the lower temperatures of our experiments is used.

A quantitative comparison between theory and experiments is not directly feasible. The reason is mainly the presence of the term f_A/f_s. Accepting the Sanders and Dobson data (31), as representative of lower temperatures (5), and $\alpha_0 = 3.85 \times 10^{-8}$ cm, we obtain the following relationship from Eq. [8]

$$\frac{f_s}{f_A}\left(\frac{<D>}{D^*} - 1\right) t^{0.2} = B \exp(1.8/kT) \quad [9]$$

where $B = 2.4 \times 10^{-7}$ for boron in $<100>$ silicon and $B = 1.1 \times 10^{-7}$ for boron in $<111>$ silicon. Table I summarizes the observed $(<D>/D^* - 1)t^{0.2}$ results

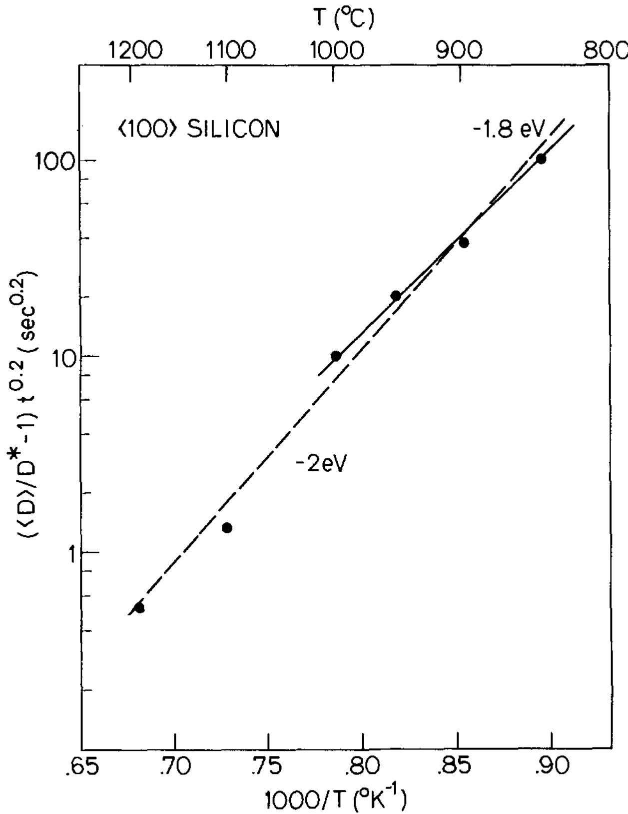

Fig. 5. The boron diffusivity enhancement factor in <100> silicon as a function of temperature.

and the calculated values of f_A/f_S from Eq. [9]. It is clear that a value of about 3 would be expected from the presented theory. The meaning of this is that the fractional interstitialcy mechanism for boron diffusion in silicon is about three times larger than that for silicon self-diffusion. Although this conclusion cannot be supported from independent data we do feel that it is quite plausible.

It is clear from Eq. [8] that the presented theory together with the experimentally determined growth of stacking faults predict a slight inverse time dependence ($\sim t^{-0.2}$) of the diffusivity enhancement. Due to the magnitude of experimental errors we have not attempted to accurately establish this time dependence. However, we have indeed observed a consistent time dependence suggesting at t^{-a} relation and although the exact value of "a" is not clear, there is conclusive evidence that it is smaller than 0.5.

In conclusion it should be mentioned that an inherent assumption in the present theory is that the concentration of excess silicon interstitials is not affected by the density of stacking faults. This assumption is quite valid since only a small fraction of the excess interstitials is expected to participate in the fault growth. Thus, although the density of oxidation stacking faults may vary significantly in accordance to the density of available nucleation sites that, in turn, depends on sample preparation, the length of the faults is only dependent on oxidation conditions and surface orientation (16, 7, 32). Thus, we do not expect that the introduction of boron by ion implantation

Table I. f_A/f_S from data and theory

T (°C)	From experiments ($\langle D\rangle/D^* - 1$) $t^{0.2}$ (sec.$^{0.2}$)		f_A/f_s	
	<100>	<111>	<100>	<111>
850	104	42	3.6	3.2
900	38	14	2.9	2.3
950	21	—	3.3	—
1000	10	—	3.1	—

(which increases strain sites) may have affected the diffusion enhancement mechanism. In addition, transient phenomena such as excess point defect concentration due to the ion implantation do not affect our results because, as already mentioned, all samples received annealing prior to the diffusion experiments.

Segregation.—Under conditions of thermal equilibrium the chemical potential as seen by an impurity species such as B, As, or P must be continuous across the Si/SiO_2 boundary. Thus, generally the concentration of impurities across the boundary are not equal, giving rise to a nonunity equilibrium segregation coefficient, m_{eq}. Theoretical calculations only bracket the value of m_{eq} within several orders of magnitude. It is not clear whether during thermal oxidation of silicon the segregation process is actually in equilibrium. It thus follows that the actual impurity ratio may not be either equal to m_{eq} or even constant throughout an oxidation process step. In the present work we have assumed that at a given temperature, the segregation process can be characterized by a constant (effective) segregation coefficient. The segregation coefficients thus obtained are plotted as a function of temperature and silicon orientation in Fig. 6. For comparison, the data presented by Colby and Katz (11), Prince and Schwettmann (33), and Murarka (34) are also shown. As can be seen, our data can be fitted by a single activation energy over the entire range of temperature of the experiments. However, there is a disagreement with the other three sets of data. Although no explanation can be given at present, the difference in experimental methods between the various works needs to be outlined. (*i*) Colby and Katz have obtained their data by direct measurement of boron concentrations across the interface using SIMS. As in the present work they have used dry O_2 oxidation. However, unlike our case the silicon crystal was not intrinsic, but rather it was uniformly doped at relatively high concentration (2×10^{19} cm^{-3}). (*ii*) Prince and Schwettmann have obtained their data by a fitting technique similar to ours. However, their oxidation process was performed in steam ambient. (*iii*) Finally, Murarka (34) has also used a fitting technique similar to ours and in addition his experiments were at low dose and in dry O_2 ambient. Thus, the experimental and fitting procedures

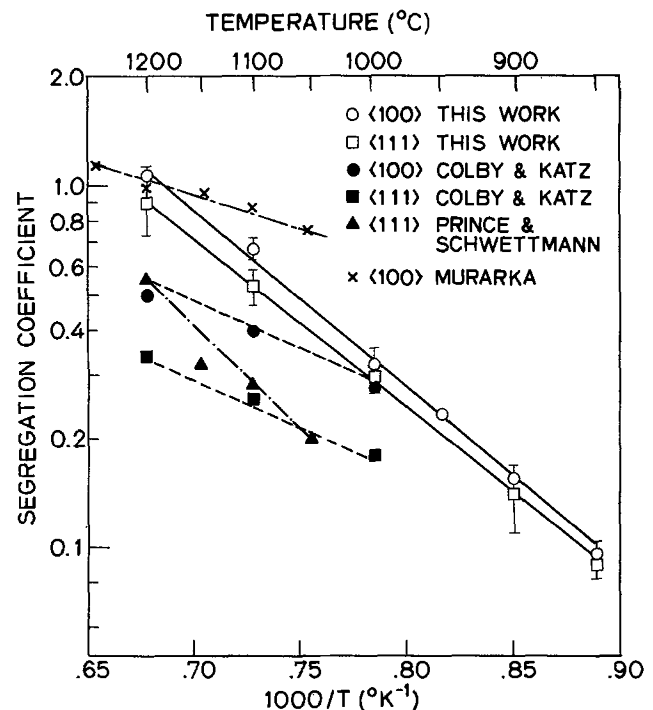

Fig. 6. Boron effective segregation coefficient in <100> and <111> silicon.

are similar with only two but possibly important differences. First, Murarka's samples were not annealed prior to the oxidation experiments, and second the mobility data he used was after Caughey and Thomas (27). If a fast-transient diffusivity exists at the beginning of the oxidation, the effect would be to preserve more boron in the silicon, thus appearing as a lower effective segregation coefficient. This effect would be more pronounced at lower temperatures (29), with a resulting decrease in the activation energy of the segregation coefficient.

Conclusions

The diffusivity of ion-implanted boron in <100> and <111> near-intrinsic silicon has been studied experimentally under inert (N_2) and oxidizing ambients (dry O_2). The method has consisted of fitting computer-simulated process results to observations by means of an automatic zero-in algorithm. As-annealed rather than as-implanted initial profiles were used to avoid the regime of transient diffusion during initial annealing and to ensure full implant activation. The initial profile was assumed similar to that experimentally determined (by SIMS) in another work (20) under almost identical conditions. For inert ambient experiments the only measured data were the initial and final sheet resistance. The determined intrinsic diffusivity agrees well with previously reported data (15) and thus it may be concluded that the recent mobility data used in the present simulation are quite realistic. Previously accepted mobility data (27, 28) would give different results.

In the oxidation experiments both sheet resistance and junction depth were measured. The fitting process has thus yielded the effective segregation and diffusion coefficients. Diffusivity enhancement has been observed in both orientations. In qualitative agreement with previous works more enhancement was observed in <100> than in <111>. Also this enhancement was found to increase with decreasing temperature. Quantitative differences do exist between this and the only comparable published work (9), which, however, was carried out using chemical deposition.

The determined effective segregation coefficients are in the general range of previously reported ones and obey a single activation energy. There is, however, a small difference between <100> and <111> orientations. Such an effect has been previously observed (11).

We have demonstrated that there is reasonable agreement between experimentally determined oxidation enhanced diffusion and growth of stacking faults, if one accepts the interstitialcy oversaturation model proposed by Hu (16). Within the context of this model it is necessary to assume at least a fractional interstitialcy diffusion mechanism for boron. Also, in order to bring the two sets of data to quantitative agreement, a fractional interstitial self-diffusion mechanism must be assumed for silicon, approximately three times smaller than for boron. The model readily predicts the observed increase of enhancement with decreasing temperature. It also predicts a slight time dependence of the diffusivity enhancement. At present the experimental errors of our method have not allowed verification of this dependence.

Acknowledgment

This research has been supported by ARO Contract DAAG-29-77-C-006.

Manuscript submitted Oct. 19, 1977; revised manuscript received Dec. 28, 1977.

Any discussion of this paper will appear in a Discussion Section to be published in the December 1978 JOURNAL. All discussions for the December 1978 Discussion Section should be submitted by Aug. 1, 1978.

Publication costs of this article were assisted by Stanford University.

APPENDIX

From the work of Caughey and Thomas (27), mobility can be expressed in the following functional form

$$\mu(C) = \mu_{min} + \frac{(\mu_{max} - \mu_{min})}{1 + (C/C_{ref})^{\beta}} \quad [A-1]$$

where μ_{min} and μ_{max} are the minimum and maximum mobility values expected, C_{ref} a reference concentration value, and β an exponential factor that controls the slope around $C = C_{ref}$. From Ref. (13) and (14), the following values were obtained for this work

p-type	μ_{min}	μ_{max}	C_{ref}	β
Ref. (26)	47.7	495	6.3 E16	0.76
Ref. (27)	47.7	495	1.9 E17	0.76
This work	49.705	467.729	1.606 E17	0.700

n-type	μ_{min}	μ_{max}	C_{ref}	β
Ref. (26)	65	1330	8.5 E16	0.72
This work	55.24	1388.157	1.072 E17	0.733

The use of these new mobility function values resulted in excellent fit between measured and simulated sheet resistance values.

REFERENCES

1. B. L. Crowder, J. F. Ziegler, F. F. Morehead, and G. W. Cole, in "Ion Implantation in Semiconductors and Other Materials," B. L. Crowder, Editor, p. 267, Plenum Press, New York, (1973).
2. R. B. Fair, *This Journal*, **122**, 800 (1975).
3. A. S. Grove, D. Leistiko, Jr., and C. T. Sah, *J. Appl. Phys.*, **35**, 2695 (1964).
4. D. C. Kendall and D. B. DeVries, in "Semiconductor Silicon 1969," R. R. Haberecht and E. L. Kern, Editors, pp. 358-421, The Electrochemical Society Softbound Symposium Series, New York (1969).
5. R. B. Fair, in "Proceedings of the Third International Symposium on Silicon Materials Science and Technology," p. 968, The Electrochemical Society (1977).
6. W. G. Allen, *Solid-State Electron.*, **16**, 709 (1973).
7. W. G. Allen and K. V. Anand, *Solid-State Electron*, **14**, 397 (1971).
8. G. Masetti, P. Negrini, and S. Solmi, in "Redistribution and Anisotropic Diffusion of Boron in <100> and <111> Orientation Silicon," Alta Frequenza, Vol. 42, No. 11, pp. 626-630, (1973).
9. G. Masetti, S. Solmi, and G. Soncini, *Solid-State Electron.*, **19**, 545 (1976).
10. W. G. Allen and C. Atkinson, *ibid.*, **16**, 1283 (1973).
11. J. W. Colby and L. E. Katz, *This Journal*, **123**, 409 (1976).
12. D. A. Antoniadis, S. E. Hansen, R. W. Dutton, and A. G. Gonzales," Stanford Electronics Lab. Tech. Rep. No. 5019-1, May 1977.
13. NBS Special Pub. 400-29, W. M. Bullis, Editor, p. 16 (1977).
14. W. R. Thurber, Private communication.
15. A. D. Kurtz and R. Yee, *J. Appl. Phys.*, **31**, 303 (1960).
16. S. M. Hu, *ibid.*, **45**, 1567 (1974).
17. S. M. Hu, *ibid.*, **27**, 165 (1975).
18. S. M. Hu, *J. Vac. Sci. Technol.*, **14**, 17 (1977).
19. H. S. Rupprecht, in "NATO Advanced Study Institute on Process and Device Modeling for Integrated Circuit Design," Univ. Catholique de Louvain, France, July 19-29, 1977.
20. W. K. Hofker, H. W. Werner, D. P. Oosthoek, and H. A. M. deGrefte, *J. Appl. Phys.*, **2**, 265 (1973).
21. A. Chu and J. F. Gibbons, in "Proceedings of Fifth International Conference on Ion Implantation in Semiconductors and Other Materials," Plenum Press, New York (1976).
22. F. J. Morin and J. P. Maita, *Phys. Rev.*, **96**, (1954).
23. R. G. Mazur and D. H. Dickey, *This Journal*, **113**, 255 (1966).
24. R. W. Dutton, D. A. Antoniadis, J. D. Meindl, T. I. Kamins, K. C. Saraswat, B. E. Deal, and J. D. Plummer, Stanford Electronics Labs., Tech. Rep. No. 5021-1, Sect. 3.3 and Fig. 18 (1977).
25. B. E. Deal and A. S. Grove, *J. Appl. Phys.*, No. 36, (1965).
26. R. W. Dutton, A. G. Gonzalez, R. D. Rung, D. A.

Antoniadis, in "Semiconductor Silicon 1977," H. R. Huff and E. Sirtl., Editors, pp. 910-922, The Electrochemical Society Softbound Symposium Series, Princeton, N.J. (1977).
27. D. M. Caughey and R. E. Thomas, *Proc. IEEE*, **55**, 2192 (1967).
28. S. Wagner, *This Journal*, **119**, 1570 (1972).
29. A. Seeger and K. P. Chik, *Phys. Status Solidi*, **29**, 455 (1968).
30. S. M. Hu, "Atomic Diffusion in Semiconductors," D. Shaw, Editor, Chap. 5, Plenum Press, New York (1973).
31. I. R. Sanders and P. S. Dobson, *J. Mater Sci.*, **9**, 1987 (1974).
32. C. L. Clacys, E. E. Laes, G. J. Declerck, and R. J. van Overtraeten, in "Proceedings of Third International Symposium on Silicon Materials Science and Technology," p. 773, The Electrochemical Society, Princeton, N.J., May 1977.
33. J. L. Prince and F. N. Schwettmann, *This Journal*, **12**, 705 (1974).
34. S. P. Murarka, *Phys. Rev. B.*, **12**, 2502 (1975).

Preparation and Some Properties of Chemically Vapor-Deposited Si-Rich SiO_2 and Si_3N_4 Films

D. Dong,* E. A. Irene,* and D. R. Young

IBM Thomas J. Watson Research Center, Yorktown Heights, New York 10598

ABSTRACT

Films of SiO_2 and Si_3N_4 containing excess Si were prepared by chemical vapor deposition at 700°C by the reaction of gaseous SiH_4 and N_2O for the Si-rich SiO_2 and NH_3 for the Si-rich Si_3N_4. By adjusting the gas-phase ratio of the reactants it was possible to vary the amount of Si in the films. Transmission electron microscopy studies revealed that the films contain two amorphous phases. One phase is amorphous Si while the other is SiO_2 or Si_3N_4. The Si content of the films was measured by electron microprobe analysis. Ellipsometry measurements on the films were made at several angles of incidence in order to measure the film absorption coefficients which were found to increase with increasing Si content. The d-c conduction characteristic for the Si-rich films was found to be nonohmic. The resistivity at any given field was found to decrease with an increase of the Si content.

Films of silicon dioxide (SiO_2) and silicon nitride (Si_3N_4) prepared by chemical vapor deposition (CVD) have received considerable study. These films are used as gate dielectrics and for a variety of masking procedures within the MOS technology. Typically, the films are prepared in an open-tube CVD reactor at temperatures greater than 500°C by the reaction of a volatile silicon compound such as SiH_4 with a gaseous oxidant such as O_2, CO_2, H_2O, N_2O, etc. for SiO_2 films and SiH_4 with NH_3 for Si_3N_4 films. The films are usually amorphous and if the SiH_4 is maintained at about 10% or less of the reactive gas mixture, the film compositions are stoichiometric SiO_2 or Si_3N_4. It has been reported (1-4) that the Si content of Si_3N_4 films can be increased for CVD films. In these previous studies, the Si content of the films was inferred from refractive index changes, etch rate measurements, and electrical behavior. For Si-rich SiO_2 films, several articles (5-8) demonstrate the preparation of these films by sputtering, glow discharge, and evaporation techniques except for a recent paper (9), in which Si-rich SiO_2 was prepared by CVD using a SiH_4-N_2O-N_2 mixture. The Si-rich films exhibited higher conductivity (3, 4, 9) than the stoichiometric analogs, and the conductivity increased with Si content. Use was made of this variable conductivity property to controllably limit reverse current for a pn-junction diode (9).

The goals of the present study were to determine the CVD parameters which yield Si-rich SiO_2 and Si_3N_4 with a desired amount of Si; to identify the relationships between gas phase mixtures, solid phase composition, resistivity, and refractive index; and to determine whether the films are homogeneous or phase separated. Presently, there exists controversy (5, 7) whether Si-rich SiO_2 is composed of a mixture of Si-Si_4 and Si-SiO_4 tetrahedra or simply separate Si and SiO_2 phases. Therefore, transmission electron microscopy (TEM) was performed on the films prepared in this study to elucidate the morphology.

* Electrochemical Society Active Member.
Key words: dielectric films, variable conductivity, excess Si.

Experimental Procedures

CVD.—The CVD apparatus was the same resistance-heated system previously described (10). The Si-rich films were deposited on cleaned <100> oriented, chem-mechanically polished, 2 Ω-cm p-type Si wafers (3.2 cm diam). The cleaning procedure for the Si substrates was also previously reported (11). A temperature of 700°C was used for all depositions. This temperature was chosen to be low enough to preclude extensive decomposition of the SiH_4 prior to injection into the reaction zone of the furnace. Although higher temperatures can be used to prepare Si-rich films, the amount of SiH_4 used for the preparations becomes excessively large.

The Si-rich SiO_2 films were prepared by the reaction of gaseous N_2O and SiH_4; for Si-rich Si_3N_4, NH_3 and SiH_4 were the reactants. In both cases the reactants were diluted with a N_2 carrier. The total flow into the CVD reactor (at 20°C, 1 atm) was maintained at 15 liters/min (~13 cm/sec linear gas stream velocity) of which the reactant gases were always less than 0.5 liters/min. In order to alter the Si content of the films, the gas phase reactant ratios, R_O (N_2O/SiH_4), for Si-rich SiO_2 and R_N (NH_3/SiH_4) for Si-rich Si_3N_4 was varied.

The elemental composition of the films was obtained from electron microprobe analyses on films several thousands of angstroms thick. Film thickness, index of refraction, and optical adsorption were measured by ellipsometry. Electrodes for electrical measurements

were evaporated Al dots (0.8 mm diam) on the film side of the samples and gallium-indium paste was used for the Si side electrical contact.

Ellipsometry.—Excess Si in the films causes optical absorption. The absorption needs to be characterized in order to perform accurate ellipsometric measurements of the film thickness. For this purpose, a special procedure was used (12) in which ellipsometry was performed at multiple angles of incidence. The procedure is outlined as follows: (*i*) Two zone ellipsometric measurements were made on a particular sample at constant wavelength (5461Å) but at several angles of incidence, ϕ, ranging between 60° and 80° in 5° intervals. (*ii*) A range of values for adsorption, κ, was arbitrarily chosen. The film thickness, D, and the real part of the film refractive index, N, were calculated for each κ and at each ϕ. The relationship between κ, N in the complex refractive index, N is given by the equation

$$\overline{N} = N(1 - i\kappa)$$

(*iii*) For each value of ϕ a line in κ, N, and D space was obtained. The sets of lines for various ϕ were plotted together on a three coordinate axes graph. In principle, all the lines should intersect yielding one value for N, κ, and D. However, due to experimental uncertainties (12), a zone of convergence is realized. From the zone of convergence, an average value for N, κ, and D can be obtained. An example of the convergence is given in Fig. 1a. Figure 1b shows a cut of Fig. 1a showing the κ and N planes. Such projections were used to obtain the numerical values reported later.

Electrical measurements.—The resistivity, ρ, was measured with the 2 Ω-cm p-type silicon substrates in accumulation. Heavily doped substrates were not used in order to preclude possible dopant effects in the films. Capacitance-voltage measurements at 1 MHz were made to determine whether the films stored charge or whether they lost the injected charge as anticipated by considering the measured values of ρ.

In order to compare the results for films with different Si content, films of approximately the same thickness (700 ± 100Å) were measured. The applied voltage ramp speed and amplitude were kept constant and the films were ramped first from depletion to accumulation, and then in reverse. The hysteresis in the C-V curve measured on the voltage near flatband (called ΔV) is proportional to the amount of charge, assumed to be near the Si surface, stored by the films.

Transmission electron microscopy (TEM).—The samples for TEM studies were prepared as previously described (13). Starting with films ~500Å on an Si substrate, the substrate was etched with HF-HNO_3 mixtures. The etch mixtures vigorously attacked the Si-rich SiO_2 and stoichiometric SiO_2 films. The etchant moderately attacked Si-rich Si_3N_4 films and only slightly attacked stoichiometric Si_3N_4 films. The qualitative difference in the etch rates observed and the resultant morphologies lead to the results to be reported.

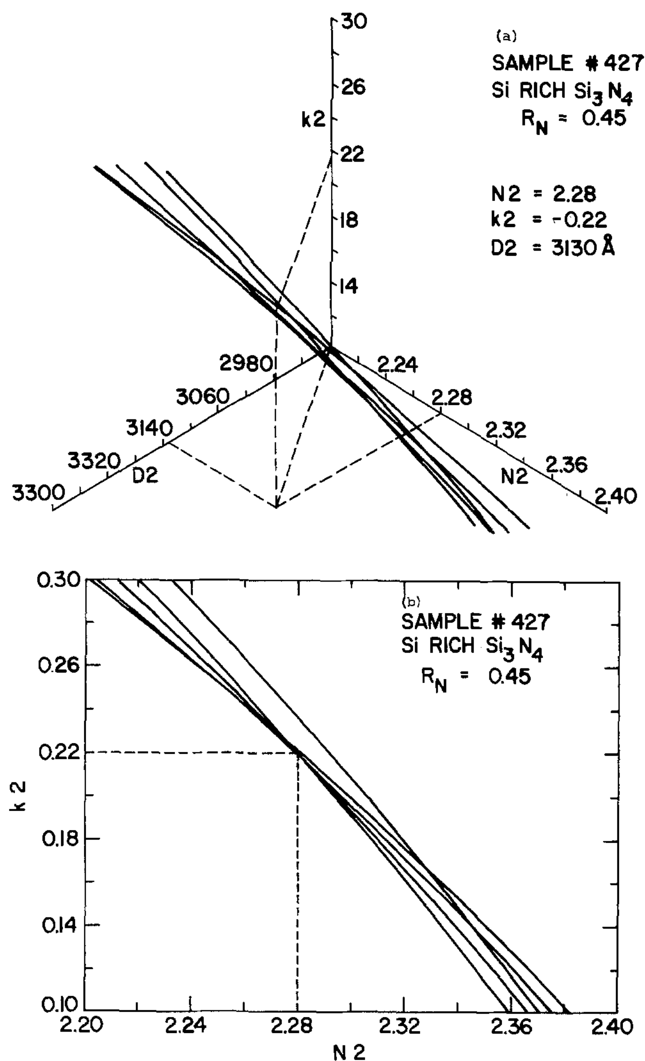

Fig. 1. a, A plot of the zone of intersection of the lines representing various angles of incidence, ϕ, on the axes of absorption coefficient, *K2*, real part of the refractive index, *N2*, and film thickness, *D2*; b, a cut of Fig. 1a showing the *K2*, *N2* plane.

Results

Film composition.—The solid-phase compositions as a function of gas phase reactant ratios, R_O and R_N, are shown in Fig. 2a for Si-SiO_2 films and in Fig. 2b for Si-Si_3N_4 films. For the higher gas phase ratios, the films approach stoichiometric SiO_2 and Si_3N_4. For R_O < 50 and R_N < 25, there is Si enrichment of the oxide

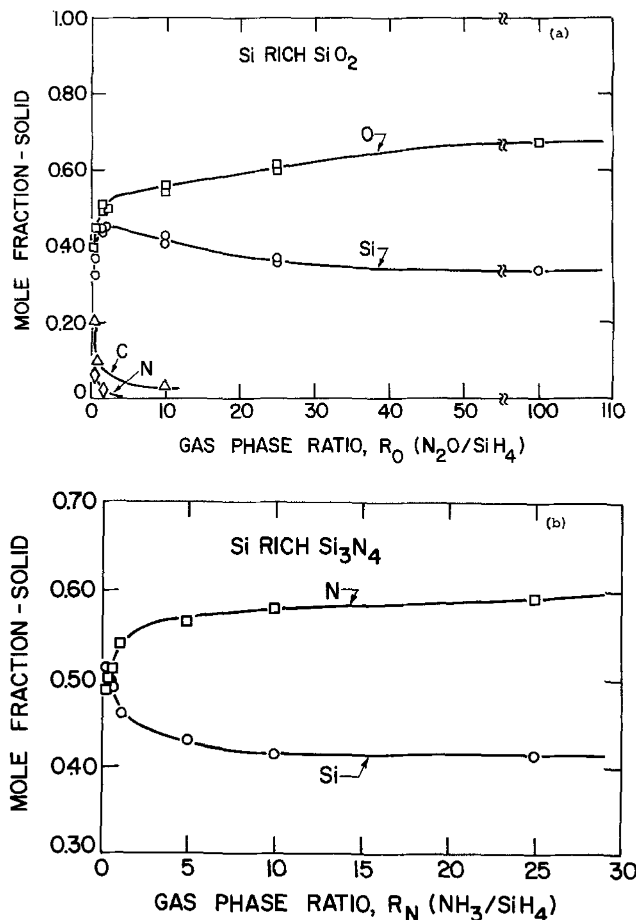

Fig. 2. a, Electron microprobe analyses of Si-rich SiO_2 vs. the gas-phase ratio; b, the same relationship for Si-rich Si_3N_4.

and nitride films. For the Si-rich Si_3N_4 films, the Si content increases smoothly with decreasing R_N for the entire range studied ($0.6 < R_N < 25$), and the Si content varies from 42 to 51% in this R_N range. Similarly, for R_O values between 100 and ~ 3, the Si content for the oxide films varies from 33 to 45%. However, for $R_O < 3$, both the Si and O content drop sharply while significant amounts of N and C appear. Later-reported resistivity values are also sensitive to this anomalous drop in Si content. Although not experimentally verified in this study, we believe that silicon oxynitride and/or oxycarbide type compounds were formed due to carbon impurities in the N_2O and the large amount of N_2 that was present.

Refractive index.—The optical absorption of these Si-rich films was characterized by the previously outlined ellipsometry procedures. The measured absorption coefficient values are shown in Fig. 3. The values of κ are seen to be small for the Si range studied, and if κ is assumed to be zero, less than 10% error in thickness is made for film thicknesses in the first ellipsometric period. Figure 3a shows that the absorption increases nearly linearly with Si content. Figure 3b shows that Si content for Si-rich SiO_2 films does not increase smoothly for low R_O values. In fact, as observed in Fig. 2a, the Si content drops for low R_O values while N and C levels increase. Therefore, κ is a sensitive measure of the Si content for these films.

Electrical measurements.—Figure 4 summarizes the resistivity measurements. The d-c behavior is seen to be nonohmic and ρ decreases as the Si content increases. Therefore, from Fig. 4a and 4b, films with desired values of ρ can be grown if the value for the operating field, E, across the film is specified. As mentioned previously for the Si-rich SiO_2 films at low values of R_O, the Si content drops anomalously. As seen in Fig. 4a, the curve for $R_O = 1$ shows larger values for ρ at any field studied than for the $R_O = 3$ curve. Therefore, the ρ value for a specified E is also

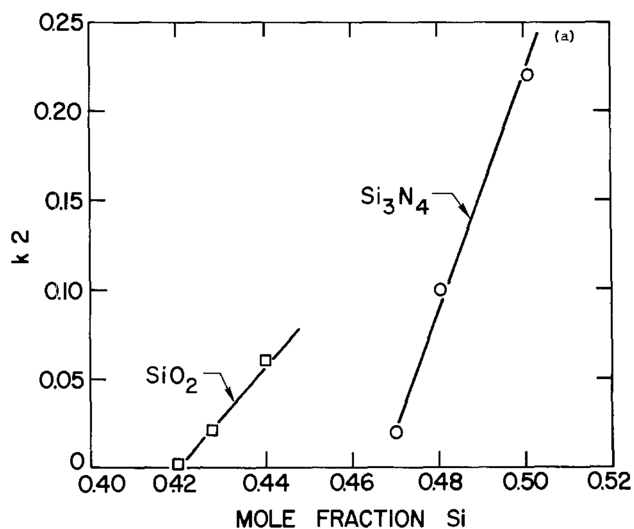

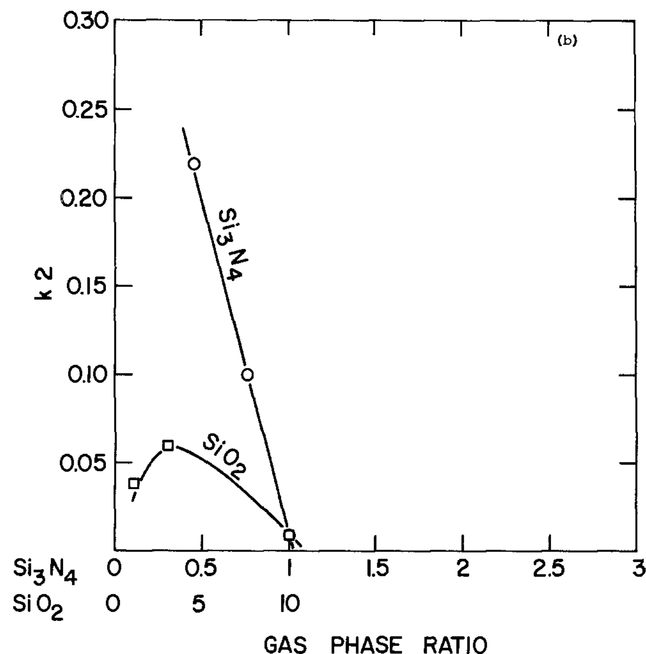

Fig. 3. a, The absorption coefficient, $K2$, vs. the Si content for both Si-rich SiO_2 and Si_3N_4 films; b, $K2$ vs. the gas-phase ratios R_O and R_N.

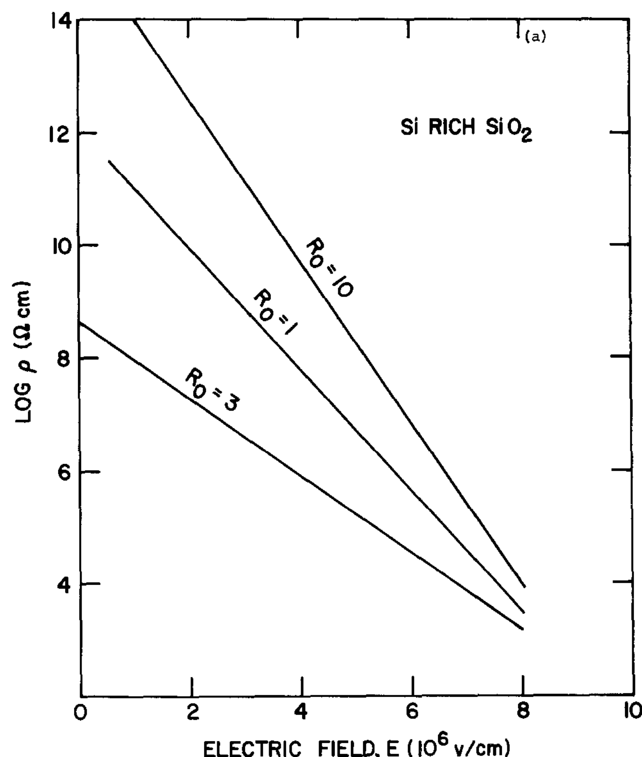

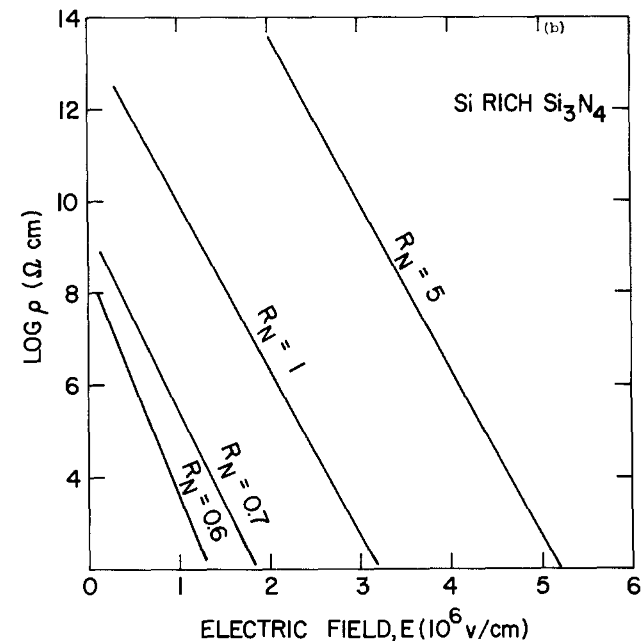

Fig. 4. a, The plot of $\log_{10} \rho$ vs. the applied electric field, E, for Si-SiO_2 with various gas phase ratios, R_O; b, the same as Fig. 4a for Si-Si_3N_4 for various R_N.

a sensitive indicator of the Si content of the film. For the Si-rich Si_3N_4 film, the Si content increased smoothly with decreasing R_N in the range studied, and the ρ values decreased for decreasing R_N.

The capacitance-voltage, *C-V* measurements are summarized in Fig. 5. Figure 5a shows that for Si-Si_3N_4 films the amount of stored charge, as measured by the hysteresis in the *C-V* curves, decreases with increasing Si content. This is to be expected inasmuch as with decreasing ρ the time constant for the storage of charge should also decrease. However, Fig. 5b for Si-SiO_2 shows an enhancement of charge storage with increasing Si content. This may be due to a thin thermal oxide being formed at the Si surface in the ambient containing N_2O. When the thin thermal oxide is coated with the Si-rich SiO_2, a metal, insulator, SiO_2, silicon (MIOS), charge storage structure is formed.

Transmission electron microscopy.—The TEM results are summarized by Fig. 6. The photographs are interpreted by remembering that the etchant used to prepare the samples attacks Si very vigorously, SiO_2 vigorously, and only very mildly attacks Si_3N_4. Figure 6a shows the TEM results for stoichiometric Si_3N_4. With the exception of some particulate in the films, the micrographs are featureless indicating uniform etching. Figure 6b, however, shows the result from the etchant attacking the Si-rich Si_3N_4. The bright areas are regions where Si has been preferentially attacked by etchant. Both photographs show only diffuse diffraction halos indicative of amorphous material. The Si-rich material shows randomly distributed Si areas having a rather connective appearance. Figure 6c and 6d show a comparison for stoichiometric and Si-rich SiO_2 films. Although the effect is not as definitive as for the Si_3N_4 films, it is clear that some regions of the

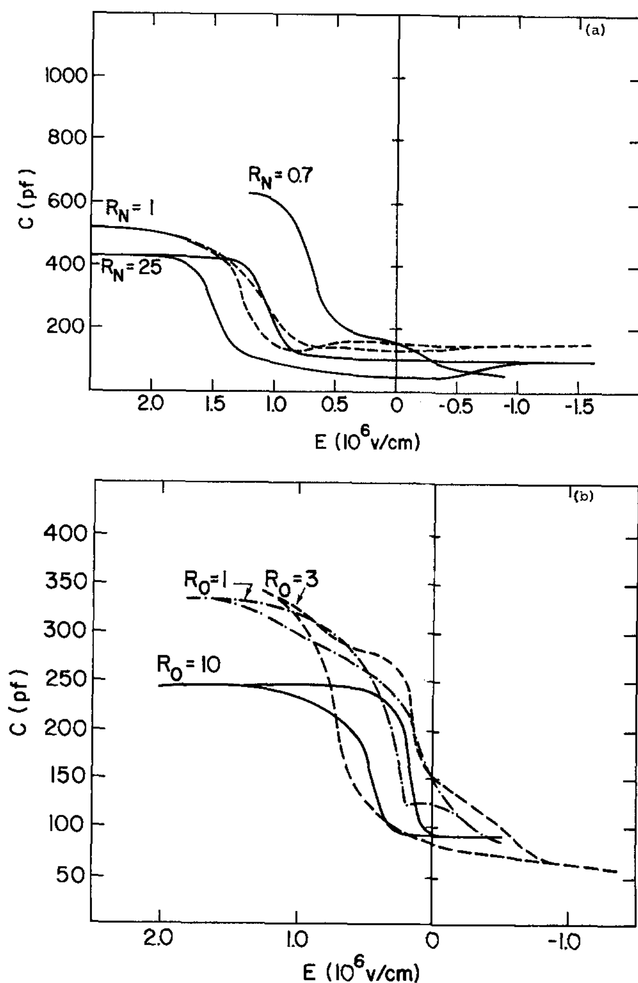

Fig. 5. a, *C-V* curves for Si-Si_3N_4 with various R_N; b, *C-V* curves for Si-SiO_2 with various R_O.

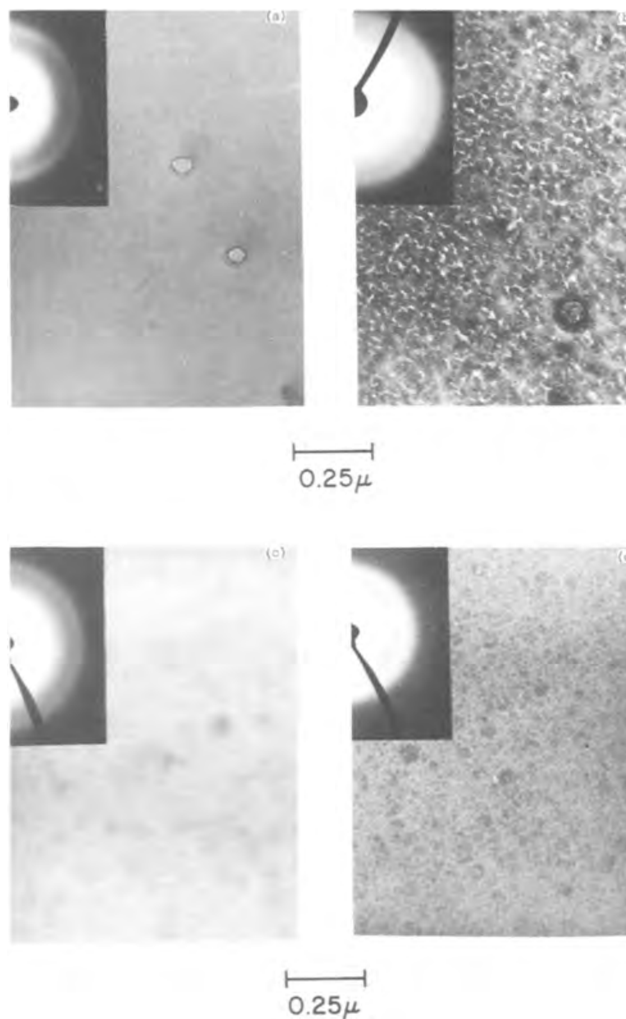

Fig. 6. TEM micrographs and diffraction patterns for stoichiometric and Si-rich Si_3N_4 and SiO_2. a, stoichiometric Si_3N_4, $R_N = 25$; b, Si-rich Si_3N_4, $R_N = 0.5$; c, stoichiometric SiO_2, $R_O = 100$; d, Si-rich SiO_2, $R_O = 1$.

Si-rich SiO_2 shown in Fig. 6d are attacked more vigorously than others while by comparison Fig. 6c shows uniform etching characteristics. Since SiO_2 and Si are attacked by the etchant, this result for Si-rich SiO_2 is expected. Both 6b and 6d reveal that the etched phase is connective rather than spherical.

Based on the morphologies discovered by TEM, it is concluded that these Si-rich materials are composed of two amorphous phases: a silicon phase and either a SiO_2 or Si_3N_4 phase.

Summary

It has been shown that films of SiO_2 and Si_3N_4 can be prepared with a controllable excess of Si by chemical vapor deposition by adjusting the gas phase reactant ratios. The excess Si forms a rather connective secondary phase under the conditions of the present study. The resistivity and optical absorption are both sensitive to the Si content of the films. The d-c conductive behavior for the Si-rich films is nonohmic but for any given field the resistivity decreases with increasing Si content.

Acknowledgment

The authors gratefully acknowledge the electron microprobe work by S. Ellmann and R. Schad and critical reviews of this manuscript by Drs. A. B. Fowler and J. A. VanVechten.

Manuscript submitted Nov. 3, 1977; revised manuscript received Dec. 20, 1977. This was Paper 268 pre-

sented at the Atlanta, Georgia, Meeting of the Society, Oct. 9-14, 1977.

Any discussion of this paper will appear in a Discussion Section to be published in the December 1978 JOURNAL. All discussions for the December 1978 Discussion Section should be submitted by Aug. 1, 1978.

Publication costs of this article were assisted by IBM Corporation.

REFERENCES

1. W. A. Kohler, *Metall. Trans.*, **1**, 735 (1970).
2. J. R. Yeargan and H. L. Taylor, *This Journal*, **115**, 273 (1968).
3. V. Y. Doo, D. R. Kerr, and D. R. Nichols, *ibid.*, **115**, 61 (1968).
4. K. Tanabashi and K. Kobayashi, *Jpn. J. Appl. Phys.*, **12**, 641 (1973).
5. H. R. Philipp, *J. Phys. Chem. Solids*, **32**, 1935 (1971).
6. M. V. Coleman and D. J. D. Thomas, *Phys. Status Solidi.*, **22**, 593 (1967).
7. B. J. Joyce, H. F. Sterling, and J. H. Alexander, *Thin Solid Films*, **1**, 481 (1967/1968).
8. J. S. Johannessen and W. E. Spicer, *J. Appl. Phys. Lett.*, **27** (1975).
9. T. Aoki, T. Matsushita, H. Yamoto, H. Hayashi, M. Okayama, and Y. Kawara, Paper 148 presented at the Toronto, Canada, Meeting of the Society, May 11-16, 1975.
10. V. J. Silvestri, E. A. Irene, S. Zirinsky, and J. D. Kuptsis, *J. Electron. Mater.*, **4**, 429 (1975).
11. E. A. Irene, *This Journal*, **121**, 1613 (1974).
12. S. S. So and K. Vedam, *J. Opt. Soc. Am.*, **62**, 16 (1971); S. S. So, IBM Tech. Rep. TR 55034 (1975); S. S. So, Private communication.
13. E. A. Irene, V. J. Silvestri, and G. R. Woolhouse, *J. Electron. Mater.*, **4**, 409 (1975).

Technical Notes

Protective Glassy Layers Passivating Copper at 500°C

B. J. Mulder

Philips Research Laboratories, Eindhoven, Netherlands

Copper objects of complicated shape have been coated with a protective glassy layer consisting mainly of SiO_2 with a thickness of a few tenths of a micron. The coating offers protection against oxidation in air at temperatures up to 500°C. The coating is applied by chemical vapor deposition in sealed ampuls using a technique worked out by Chu and Gruber (1) for coating semiconductor materials. The reactive gases (HF and H_2O) were not, however, introduced as such, but generated *in situ* from copper difluoridehydrate (2). Glass is transported from the walls of the ampul in a cooler zone onto the copper in a hotter zone.

The arrangement for the coating reaction is shown in Fig. 1. Ampuls were made of borosilicate glass. Larger ampuls were sprung open at A for loading. The ampuls contained: (*i*) Copper difluoridehydrate, preferably in a separate glass container with the powder not in direct sight of the copper substrate. The water content of the fluoride[1] was apparently not critical: the mono and the dihydrate served equally well. Normally a technical-grade monohydrate was used in amounts corresponding to 1-2 mg per milliliter of ampul volume; (*ii*) The carefully cleaned and degreased copper objects. The copper was normally pretreated with a polishing etch; (*iii*) A glass heat shield, protecting the copper against oxidation when the ampul was repaired (in a vertical position) at A. The ampul was pumped with a rotary pump and sealed at B. It was then heated without delay in a furnace with two temperature zones, one at 550°C (just below the softening point of the glass) where the copper was placed, and one at 500°C for the fluoride. Heating up took about 5-10 min; after another 30 min the ampul was taken out of the furnace and cooled. We froze the bottom end of the ampul in liquid nitrogen to prevent reverse transport reactions and also to avoid condensation of vapor on the copper.

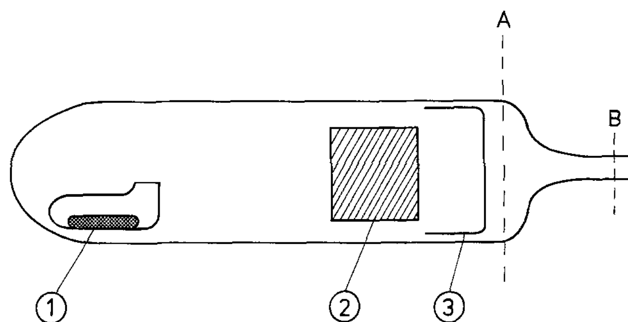

Fig. 1. Arrangement for chemical vapor deposition of glass onto copper in sealed borosilicate ampuls. Ampuls were used with diameters ranging from 10 to 60 mm and a length of about 250 mm.

The layers had a very uniform and smooth appearance, which was preserved when the copper was heated in air up to temperatures of 500°C. This suggests that the layers are essentially pinhole free.

The thickness of the layers was determined from measurements of their x-ray fluorescence.[2] With 500°C for the temperature of the source region and 550°C for the substrate the layers attained their final thickness of a few tenths of a micron in about 30 min. The thickness increased with the amount of copper di-

Key words: chemical vapor deposition, copper, passivation, SiO_2, glass.

[1] The water content of a hydrate was determined by slowly heating in air to 600°C and weighing the residue of CuO.

[2] The intensity of the characteristic fluorescence of silicon was referred to standard layers prepared by bias sputtering fused quartz on copper foil. The intensity was almost proportional to the thickness of the standards up to 0.4 μm. Since the sample layers consisted almost entirely of SiO_2, intensities were converted into thickness using data for fused quartz.

fluoride weighed into the ampul: for a tenfold increase in copper-difluoride (from 0.7 to 7 mg per ml volume of the ampul) the thickness approximately doubled from 0.15 to 0.3 μm SiO_2. The composition of the layer was studied qualitatively by secondary ion mass spectrometry (SIMS), revealing F, B, and OH as minor contaminants of the SiO_2. The F/Si ratio was determined quantitatively by electron-excited x-ray spectrometry[3] and was found to correspond to $x = 0.005$ in the composition formula $SiO_{2-x}F_{2x}$. Heating in air for 16 hr at 450°C approximately halved the fluorine content of the layers without affecting their integrity.

[3] Thin standard layers with a known Si/F ratio were prepared by mixing polyvinylidenefluoride, $[(-CH_2CF_2)_n]$ dissolved in hot cyclohexanone, and heavy silicone oil $[(-Si(CH_3)_2O)_n]$ dissolved in hot toluene, spraying the hot mixture onto warm copper foil and evaporating the solvents. The correction required for the difference between the mass absorption coefficients of standards and samples turned out to be quite small.

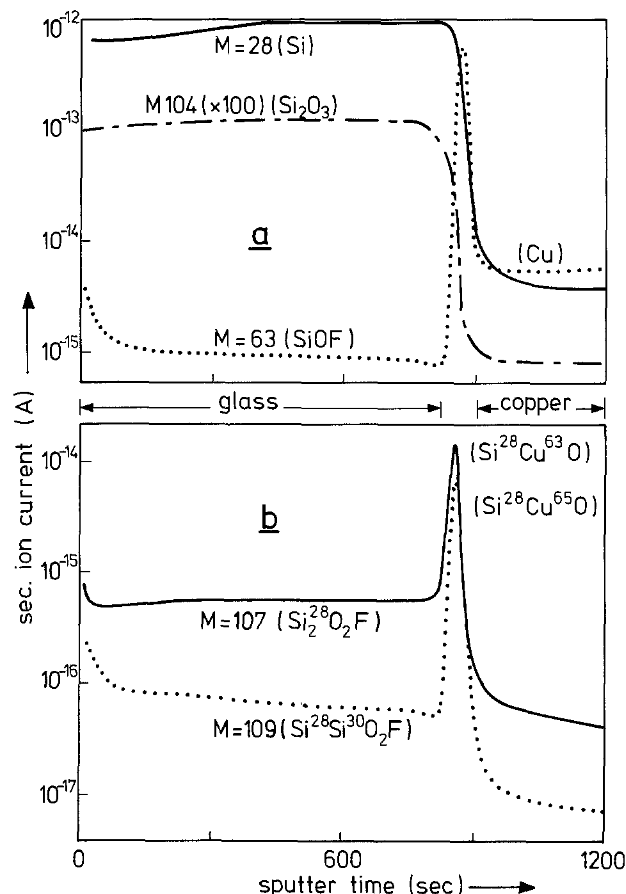

Fig. 2. Depth profiles obtained by SIMS for a 2000Å thick glass coating on copper.

An in-depth analysis with SIMS revealed the existence of an interlayer between glass and copper, characterized by the production of CuSiO clusters. Depth profiles of a typical coating are shown in Fig. 2. The curves were traced while scanning an area of 1 mm^2 with a primary beam of oxygen ions. Positive ions with a fixed mass and originating from the central 50 × 50 μm^2 region of the erosion crater were detected. The presence of an interlayer of ~ 200Å thick is evident from the peak in the curves traced for mass numbers 107 and 109 (Fig. 2b). In the peak the intensity ratio for the two mass numbers is equal to the abundance ratio of Cu^{63} and Cu^{65} (2.23), showing the peak to be associated with the production of CuSiO clusters. "Mixed" clusters (Cu and Si) are not observed in SIMS when scanning an abrupt junction (3) and are therefore indicative of the presence of an interlayer. To the left of the peak the intensity ratio in Fig. 2b is close to the ratio expected for Si^{28} and Si^{30} containing clusters (~14). Other noticeable features of the curves are the very efficient production of copper ions (see curve for M = 63) from the interlayer and the relatively high production of fluorine containing clusters from the surface region of the coating.

The interlayer may arise from the diffusion of copper into the defective SiO_2 at the temperature of the coating reaction. An in-depth inhomogeneity was also suggested by measurements of the electrically insulating properties of the layers, using a mercury drop as one of the electrodes. Layers thicker than about 0.1 μm behaved normally in that they withstood voltages corresponding to field strengths of several times 10^6 V/cm, whereas thinner layers usually broke down at voltages corresponding to only 10^4-10^5 V/cm.

Acknowledgments

The x-ray radiation of the layers was measured by E. W. J. M. van Meijl. SIMS was performed by H. A. M. de Grefte.

Manuscript submitted Sept. 23, 1977; revised manuscript received Jan. 5, 1978.

Any discussion of this paper will appear in a Discussion Section to be published in the December 1978 JOURNAL. All discussions for the December 1978 Discussion Section should be submitted by Aug. 1, 1978.

Publication costs of this article were assisted by Philips Research Laboratories.

REFERENCES

1. T. L. Chu and G. A. Gruber, *Trans. Metall. Soc. AIME*, 233, 568 (1965).
2. Le Van My, G. Perinet, and P. Bianco, *J. Chim. Phys.*, 63, 719 (1966).
3. H. A. M. de Grefte, Private communication.

Anodization of Layered Semiconductors: A Method to Count the Number of Layers

A. Moritani, H. Kubo, and J. Nakai

Department of Electronics, Faculty of Engineering, Osaka University, Suita, Osaka, 565, Japan

In the anodization process of metals and semiconductors, it has been known that there exist nonpassive (or active) states and passive states, depending on the surface potential of the anode materials. We define the nonpassive state as the state in which the anodic dissolution is in process or a nonpassive film is growing with little increase of the anode potential on the surface of the anode material when anodization is performed under constant current condition. In this paper we demonstrate that anodization provides a new and simple method to count the number of layers

Key words: semiconductor, anode, ellipsometry, passivity.

in some layered semiconductors by utilizing the property of the nonpassive-passive transition which has been widely observed in the fundamental anodic process in metals and semiconductors (1, 2).

The layered semiconductors have been a recent topic in both experimental and theoretical studies (3). The micalike layer structures are characterized by strong covalent bonds within each layer and by weak van der Waals forces between layers, so that there exist high and fairly wide potential barriers and the crystals are easily cleaved at the layer boundary which we may consider to be another surface. Therefore, it is reasonable to expect that if a layered semiconductor is anodized in the direction normal to the cleaved surface, the nonpassive-passive transition will repeat at the nth layer boundary (n = 1, 2, 3, . . .). Thus, a periodically varying structure reflecting the layered structure with the monolayer thickness of ~10Å is expected to be observed in the cell voltage *vs.* time (V_c-*vs.*-t) characteristic curve when anodization is performed under a proper constant current condition with the use of a proper electrolyte. These observations will enable us to count the number of layers in the layered semiconductors: we can count the number of layers by this method after some experiments with the layered semiconductor of interest are over.

The electrolytic cell-system used in this study consists of a platinum cathode, the semiconductor anode, a simple quartz beaker, a magnetic stirrer, and a solution of sodium borate in ethylene glycol as the electrolyte. The cell voltage is measured and recorded through a buffer amplifier with high input impedance. The second derivatives of the V_c-*vs.*-t characteristics are recorded simultaneously in order to clarify the periodic structure and make it easier to count the number. P-type Bi_2Te_3 and p-type GaTe with carrier concentrations of 1-5 $\times$ 10^{19} cm^{-3} and 0.5-2 $\times$ 10^{16} cm^{-3} at room temperature were used as the semiconductor samples. The samples were cleaved in laboratory air, and edges and ohmic contact of the samples were covered for insulation by an epoxy paint.

Periodically increasing cell voltages are observed in Fig. 1 and 2 for Bi_2Te_3 and GaTe, respectively, as expected. It is seen in these figures that these periodic structures are formed by repetition of the unit-line-shape shown in the insert of Fig. 1, where τ_n represents the duration time of the nonpassive state and V_{cn} represents the cell voltage increase in the passive state for the nth layer.

For the purpose of confirming that the unit line-shape really results from anodization of the monolayer, we have performed ellipsometric measurements on the anodic films grown by anodization of more than 20 layers and obtained the anodized film thickness of 16 ± 1Å for monolayer anodization. The ratio of this value to the monolayer thickness of Bi_2Te_3, *i.e.*, 10.16Å (4) is 1.57 which is in close agreement with the theoretically expected value.[1]

Another experiment was done as in what follows to confirm that the region indicated by τ_n in the unit lineshape is really in the nonpassive state. The experimental result of τ_n *vs.* current density J_d (τ_n-*vs.*-J_d) characteristics are shown in Fig. 3 where the solid and broken curves were obtained with the use of the electrolytes which were prepared by dissolving 100 and 200g of sodium borate in one liter of ethylene glycol, respectively. It is observed in Fig. 3 that τ_n increases as J_d decreases and is dependent upon the electrolyte: the slope of the τ_n-*vs.*-J_d characteristic lines in log-log plot is found in the range of −1−−2, depending upon the electrolyte. These observations may be sufficient for the verification that the region indicated by τ_n is in the nonpassive state.

[1] The theoretical ratio of the oxide thickness to the monolayer thickness of Bi_2Te_3 (so-called Pilling-Bedworth ratio) was evaluated to be 1.54 ± 0.02 under the assumption that the growth film consists of trioxides, *i.e.*, Bi_2O_3 and TeO_3 which seem to be the most probable products of oxides from Bi_2Te_3; see Ref. (10).

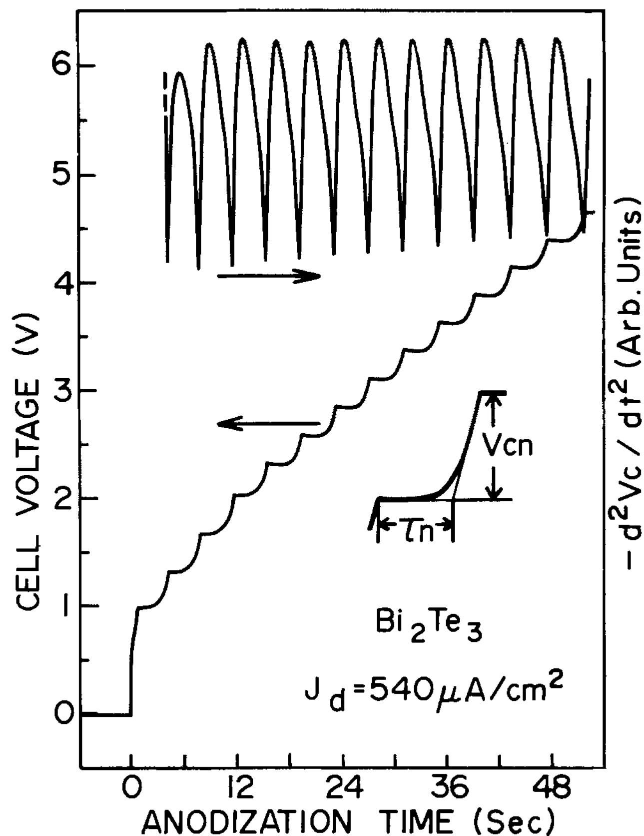

Fig. 1. The V_c-*vs.*-t characteristic and the second derivative of the V_c-*vs.*-t characteristic in Bi_2Te_3. Anodization was performed under constant current density J_d = 540 $\mu A/cm^2$. The initial voltage drop induces large transient output in the second derivative circuit, so that the initial part of the second derivative is not recorded in this figure. The inserted figure shows the unit line-shape from which the V_c-*vs.*-t characteristic curve is constructed.

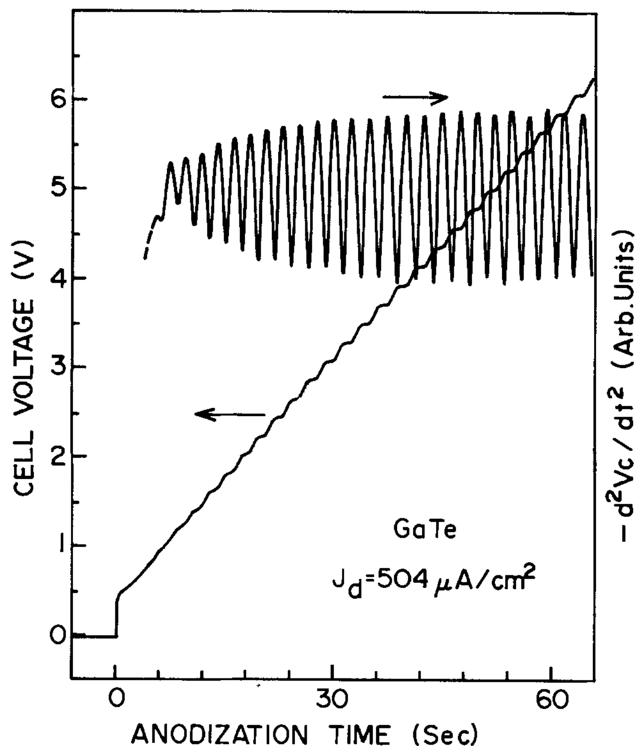

Fig. 2. The V_c-*vs.*-t characteristic and the second derivative of the V_c-*vs.*-t characteristic in GaTe. Anodization was performed with constant current density J_d = 504 $\mu A/cm^2$. The initial voltage drop induces large transient output in the second derivative circuit, so that the initial part of the second derivative is not recorded in this figure.

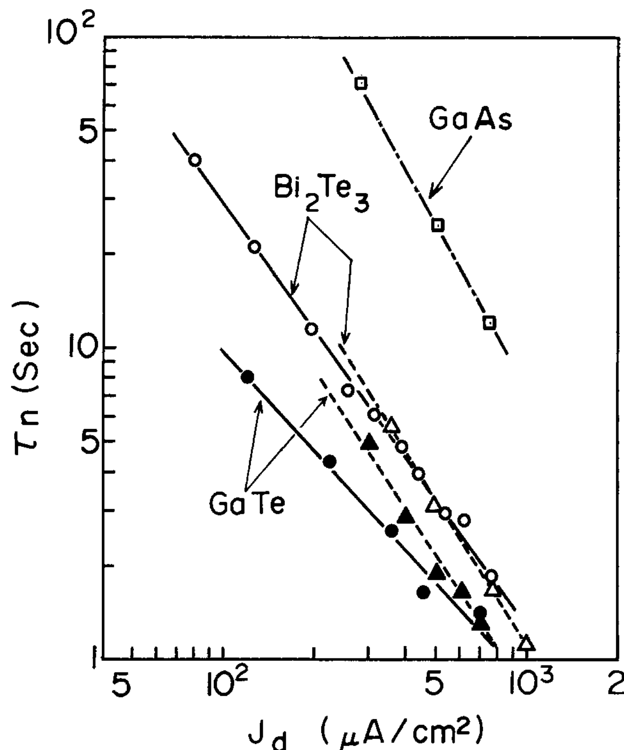

Fig. 3. The τ_n-vs.-J_d characteristics. The solid and broken lines were obtained with the use of electrolytes of sodium borate in ethylene glycol (100 g/liter) and (200 g/liter), respectively. The τ-vs.-t characteristic obtained in GaAs is shown for reference.

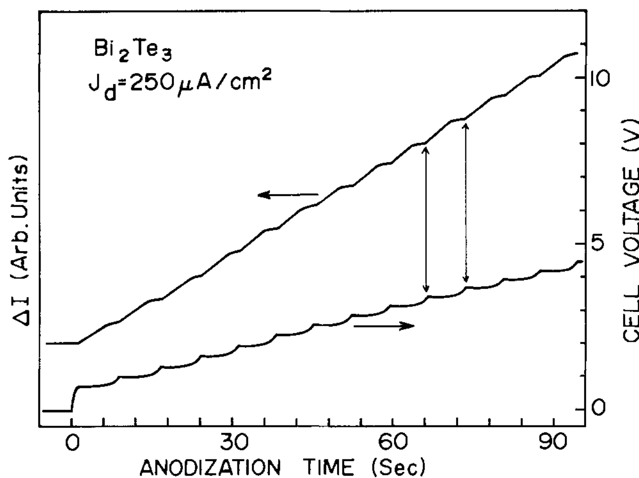

Fig. 4. The off-null signal of *in situ* ellipsometry (ΔI) and the corresponding V_c-vs.-t characteristic during constant current anodization with $J_d = 250\ \mu A/cm^2$ in Bi_2Te_3.

For reference, the τ-*vs.*-t characteristic observed in GaAs (5) is shown in Fig. 3, where τ is the duration time in the nonpassive region.

We have observed the periodic structure optically too in *in situ* ellipsometric measurements.[2] In Fig. 4, the *in situ* ellipsometry signal with initial null setting is shown together with V_c-*vs.*-t characteristic for Bi_2Te_3. ΔI is the increase of photomultiplier intensity due to the anodic film growth which causes the offset from the null setting. It is noted that ΔI shows rapid increase in the nonpassive region and little increase in the passive region. This observation strongly suggests that a conductive nonpassive film grows in the nonpassive state and transforms into a passive film in the passive state. These phenomena have been found in the anodic processes of iron and indium (6):[3] the initial film on iron in slightly alkaline solution at potentials $V < V_p$ is $Fe(OH)_2$, which transforms completely into Fe_2O_3 at higher potentials $V > V_p$, where V_p is a critical anode potential.

Thus, we have come to the stage that the unit lineshape represents anodization of the monolayer and it is possible to count the number of layers with extremely thin monolayer, *i.e.*, 7.45Å in GaTe (7) and 10.16Å in Bi_2Te_3 (4). In Fig. 1 and 2 are shown the second derivatives of the V_c-*vs.*-t characteristics which enable us to count more clearly the number, especially of the initial several layers in GaTe. We have counted the number up to 115 for Bi_2Te_3 and 95 $\pm$ 2 for GaTe in one anodization procedure.[4]

It should be noted that the nonpassive region for the first layer of Bi_2Te_3 was not observed in many cases, in other words, $\tau_1 \approx 0$. This experimental result for the first layer in Bi_2Te_3 may be corresponding to the observation in the anodization of GaAs by Harvey and Kruger (8). They have shown that, in the nonpassive region, no change in ellipsometric parameters attributable to a film forming on an initially clean anode was observed, but nonpassive anodic film was grown with virtually no change in potential when a vestige of a previously formed passive film presumably remained. In the present case, it is reasonable to consider that the passive film of the first layer can possibly be the nucleus for the nonpassive film growth of the second layer and this process repeats in the nth layer ($n \geqq 2$).

It should be also noted that in Bi_2Te_3 the steady state in the anodization process is built up in the region $n \leqq 5$ in many cases

$$V_{cn} \gtrsim V_{c(n+1)}; \quad (n = 1, 2, 3, 4),$$

$$V_{cn} = V_{c(n+1)}; \quad (n \geqq 5)$$

On the other hand, a quite different feature from Bi_2Te_3 is observed before the steady state in anodization of GaTe: not little increase of cell voltage in the nonpassive (?) regions is observed in Fig. 2, which causes uncertainty in counting the number of initial few layers, and more layer numbers are required to realize the steady-state anodization than in Bi_2Te_3. The electrochemical mechanism which induces different values of V_{cn} or amplitude of the second derivative between, before, and under the steady state in both cases is not understood at present. However, it is a realistic idea that materials with different quality will be produced in different situations: one anodization proceeds adjacent to the electrolyte and the other at a distance from the electrolyte through the buffer layer of previously anodized film.

We have obtained very similar results in Bi_2Se_3 and GaSe to those in Bi_2Te_3 and GaTe. The anodized films of these semiconductors are easily removed by most acids and alkalis, so that successive anodization and removal of the films will enable us to count the number in thick semiconductor samples.

It is of great interest to investigate the structure and electrical property of the anodized films or to apply the present method to the intercalation study in the layered transition metal dichalcogenides (9).

Acknowledgments

The authors would like to thank Prof. C. Hamaguchi and Dr. T. Shirakawa for kindly providing the second derivative circuit and for useful discussions. They would also like to thank Professor H. Yoneyama for helpful and stimulating discussions. This work is partially supported by the Grant-in-Aid for Scientific Re-

[2] The details of the present experimental setup will be reported elsewhere. The readers should refer to Ref. (8) for details in the *in situ* ellipsometry.

[3] We have also obtained the experimental results which suggests the formation of the nonpassive film on GaAs which probably transforms into the passive film; see Ref. (5).

[4] The error limit is due to the uncertainty in counting the number of initial few anodized-layers of GaTe; it does not include miscount which would result if atomic layers of more than those contained within the monolayer are consumed in the anodic dissolution process before the onset of passivation in the initial stage of anodization.

search on "Surface Electronics" from the Ministry of Education of Japan.

Manuscript received June 1, 1977.

Any discussion of this paper will appear in a Discussion Section to be published in the December 1978 JOURNAL. All discussions for the December 1978 Discussion Section should be submitted by Aug. 1, 1978.

Publication costs of this article were assisted by Osaka University.

REFERENCES

1. T. P. Hoar, in "Modern Aspects of Electrochemistry," No. 2, J. O. M. Bockris, Editor, Butterworths Scientific Publications, London (1959).
2. H. Hasegawa and H. L. Hartnagel, *This Journal*, **123**, 713 (1976).
3. See, for instance, "Proceedings of International Conference on Layered Semiconductors and Metals," Bari, Italy, (1976); *Il Nuovo Ciment*, **38B**, (1977).
4. J. O. Jenkins, J. A. Rayne, and R. W. Ure, Jr., *Phys. Rev.*, **B5**, 3171 (1972).
5. A. Moritani, H. Kubo, and J. Nakai, *J. Appl. Phys.*, **48**, 2638 (1977).
6. V. Brusic "The Anodic Behavior of Metals and Semiconductors Series," J. W. Diggle, Editor, Marcel Dekker, Inc., New York (1972).
7. C. Tatsuyama, Ph.D. Thesis, Osaka University (1971).
8. W. W. Harvey and J. Kruger, *Electrochim. Acta*, **16**, 2017 (1971).
9. J. A. Wilson, F. J. Di Salvo, and S. Makajan, *Advances in Phys.*, **24**, 117 (1975).
10. "Handbook of Chemistry and Physics," R. C. Weast, Editor, Chemical Rubber Publishing Co., Cleveland, Ohio (1975).

Etching Characteristics of Phosphorus Containing Polycrystalline Silicon in a CF_4 Plasma

Kiyokatsu Jinno,[1] Hiroshi Kinoshita,[1] and Yasuo Matsumoto[1]

Tokyo Shibaura Electric Company, Limited, Toshiba Research and Development Center, Kawasaki 210, Japan

The use of a rf-generated plasma for the etching of dielectric and other films and for the removal of photoresists has become a viable alternative to the conventional wet chemical etching used in the fabrication of semiconductor devices since the plasma process is simpler and more economical (1-9). Using a CF_4 plasma for poly-Si etching eliminates the additional oxidation and associated process steps since photoresists can be used as a masking material in the plasma.

From a device fabrication viewpoint, it is important to investigate the plasma etching of phosphorus containing poly-Si which is widely used to reduce the resistivity of the interconnections and gate electrodes in MOS LSI's. In our experiments, phosphorus was introduced into the poly-Si films by two methods; doping with PH_3 during the chemical vapor deposition of the poly-Si films at 550°C in an Ar ambient (doped poly-Si method) and diffusion from a phosphosilicate glass (PSG) film after the deposition of an undoped poly-Si film by the decomposition of SiH_4 at 800°C in an N_2 ambient (diffused poly-Si method). The films were about 5000Å thick. Plasma etching was carried out in the IPC 2005-1813SC plasma etcher with an 8 in. diam quartz reactor with aluminum shield. The etching gas was a CF_4, the gas pressure was maintained at 0.6 Torr, and the rf power was kept at 150W. Film thicknesses were measured by using a Talystep.

The phosphorus concentration of the poly-Si films was varied by changing the flow rate ratio of PH_3 to SiH_4 and keeping the diffusion time at 1000°C. It was estimated by the Auger electron analysis.

In Fig. 1, the relative etch rates (defined as the etch rate of the doped poly-Si film to that of the undoped poly-Si film) of the poly-Si film formed by the two doping methods are shown as a function of phosphorus concentration. The two methods give almost the same results. It is apparent that the etch rate of phosphorus containing poly-Si films in a CF_4 plasma is independent of the doping methods and only depends on the phosphorus concentration in those films. This fact is clearly seen in Fig. 2 which shows the scanning electron micrographs of the cross section of a 4 μm wide line. The etch rate is high

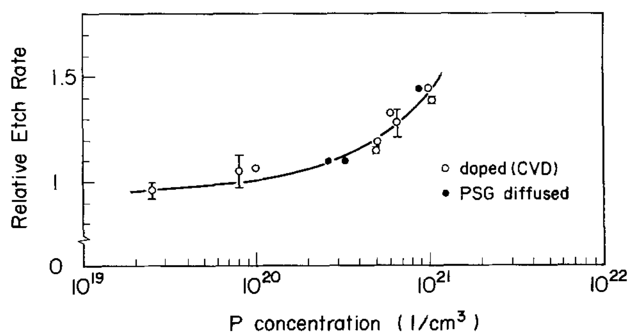

Fig. 1. Relative etch rate of the poly-Si films vs. phosphorus concentration.

at the surface of the diffused poly-Si film due to the high phosphorus concentration measured by the Auger electron analysis. From Auger electron analysis data, high phosphorus concentration regions exist to 800Å in depth from the diffused poly-Si film surface, whereas below the regions the phosphorus concentration takes a constant value and increases with increasing diffusion time. Meanwhile, the phosphorus-doped poly-Si film has an isotropical edge due to the uniform concentration of phosphorus measured by the Auger electron analysis. The etched profile of an undoped poly-Si film has also isotropical edge and is shown in Fig. 2 for a comparison.

In a CF_4 plasma etching, a gas plasma is generated in the reaction chamber by the rf power and silicon compound films begin to react with an activated fluorine species. A large plasma etch rate is obtained for elements which produce fluorides with high volatility. Therefore, phosphorus doping effect in a CF_4 plasma etching can be interpreted by high volatility of PH_3 (bp = 101.5°C at 760 mm Hg) compared to SiF_4 (bp = 94.8°C at 760 mm Hg) (10).

As a conclusion, the plasma etch rate of phosphorus containing poly-Si films is dependent on the phosphorus concentration, and the etched profile of those films depends on the phosphorus concentration distribution in depth direction.

Acknowledgment

The authors express their sincere thanks to Drs. Y. Nishi and S. Horiuchi for their useful discussions. They

[1] Present address: NEC-Toshiba Information Systems Incorporated, Kawasaki 210, Japan.

Key words: plasma etching, phosphorus effect, polycrystalline silicon.

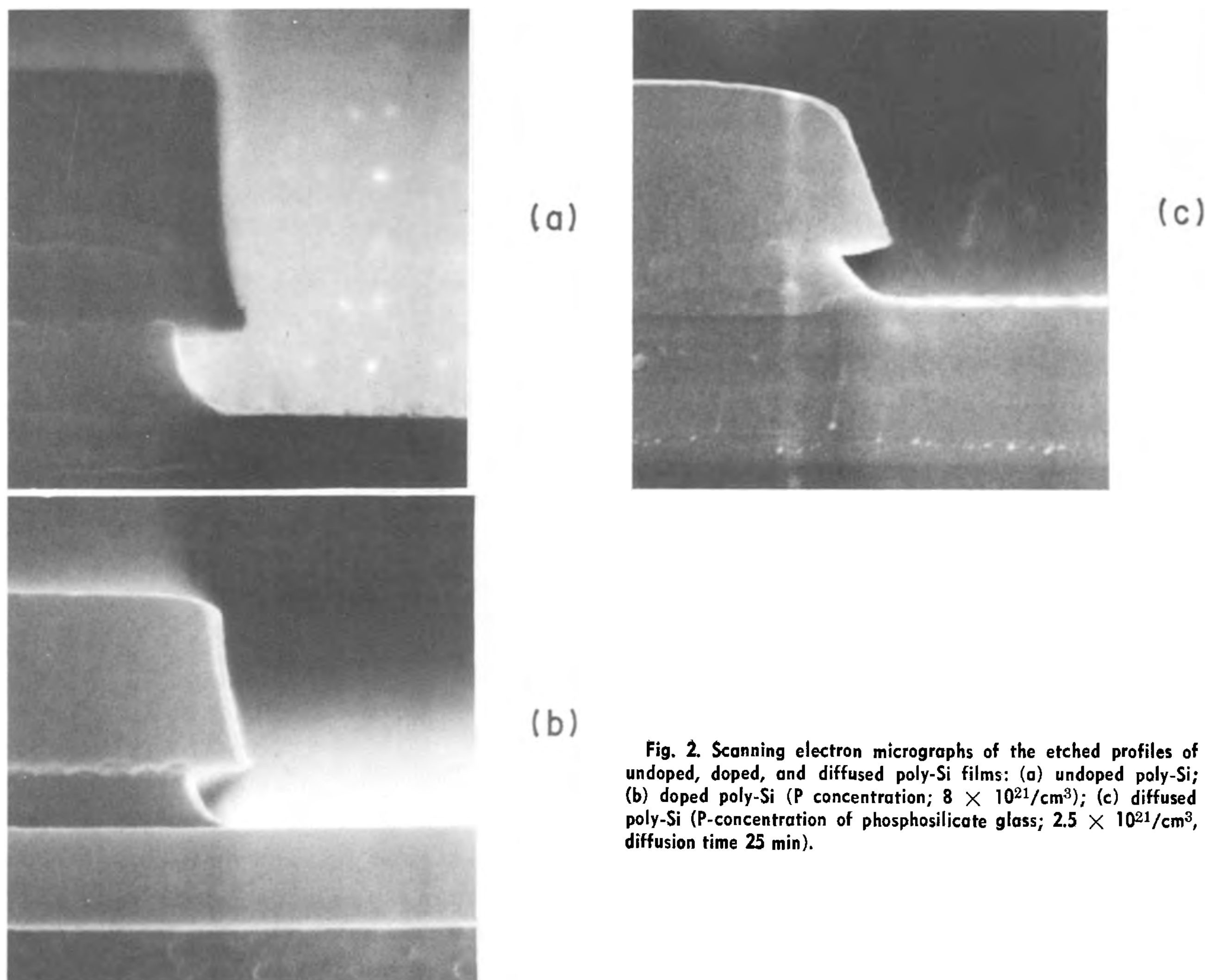

Fig. 2. Scanning electron micrographs of the etched profiles of undoped, doped, and diffused poly-Si films: (a) undoped poly-Si; (b) doped poly-Si (P concentration; $8 \times 10^{21}/cm^3$); (c) diffused poly-Si (P-concentration of phosphosilicate glass; $2.5 \times 10^{21}/cm^3$, diffusion time 25 min).

are also grateful to T. Matsuo, T. Moriya, and M. Yamanaka for their valuable support in the sample preparation and to T. Inoue for the Auger electron analysis.

Manuscript submitted May 11, 1977; revised manuscript received Nov. 10, 1977.

Any discussion of this paper will appear in a Discussion Section to be published in the December 1978 JOURNAL. All discussions for the December 1978 Discussion Section should be submitted by Aug. 1, 1978.

Publication costs of this article were assisted by Tokyo Shibaura Electric Company, Limited.

REFERENCES

1. H. Abe, in, "Proceedings of the 6th Conference on Solid State Devices," Tokyo (1974); O. Buturi, *J. Jpn. Soc. Appl. Phys.*, **44**, Suppl. 287 (1975).
2. R. A. H. Heinecke, *Solid-State Electron.*, **18**, 1146 (1975).
3. Y. Horiike and M. Shibagaki, in "Proceedings of the 7th Conference on Solid State Devices," Tokyo (1975); Suppl. to *J. Jpn. Appl. Phys.*, **15**, 13 (1976).
4. K. Jinno, Y. Matsumoto, and S. Inomata, *J. Electrochem. Soc. Jpn.*, **44**, 204 (1976).
5. L. Zielinski and G. C. Schwarz, Paper 53 presented at The Electrochemical Society Meeting, Toronto, Canada, May 11-16, 1975.
6. H. A. Clark, Paper 54 presented at The Electrochemical Society Meeting, Toronto, Canada, May 11-16, 1975.
7. A. R. Reinberg, Paper 50 presented at The Electrochemical Society Meeting, Washington, D.C., May 2-7, 1976.
8. M. Brochu and R. G. Poulson, Paper 51 presented at The Electrochemical Society Meeting, Washington, D.C., May 2-7, 1976.
9. A. Jacob, *Solid State Technol.*, Sept., p. 70 (1976).
10. "Handbook of Chemistry and Physics," WEAST 56th, CRC Press (1975-1976).

JOURNAL OF THE ELECTROCHEMICAL SOCIETY

ACCELERATED

BRIEF COMMUNICATIONS

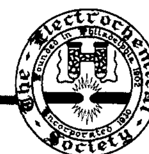

MAY

1978

End Point Determination of Aluminum CCl_4 Plasma Etching by Optical Emission Spectroscopy

B. J. Curtis and H. J. Brunner

Laboratories RCA Limited, Zurich, Switzerland

The use of optical emission spectra for end point detection has been reported for the CF_4 plasma etching of Si (1, 2) and for the O_2 plasma stripping of photoresist (3, 5). This note reports the application of the method to the CCl_4 plasma etching of aluminium

Etching experiments were carried out in a parallel plate reactor consisting of a pyrex glass cylinder 30 cm in diameter and 35 cm high with ports to accommodate a silica window and a quadrupole mass-spectrometer; the end plates were made of stainless steel. The water-cooled electrodes, made of polished nickel-plated copper, were 20 cm in diameter and, for these experiments, were spaced 40 mm apart. CCl_4 was introduced through the centre of the upper electrode which was connected to a 13.56 MHz rf generator. The substrates were placed on the lower, grounded electrode. Optical emission spectra were taken on a Heathkit EUE-700 Monochromator using an RCA photomultiplier type IP28, a Keithley 601 electrometer as an amplifier and a chart recorder. The distance between the monochromator entrance slit and the plasma was 30 cm; the emission was viewed through the silica window without focussing.

Fig. 1 (upper) shows the spectrum of a CCl_4 plasma at a pressure of 7 Pa and 500 Watts power; the CCl_4 flowrate was 20 scc per minute. An unequivocal assignment (4) of all of the peaks has so far not been possible, even though the species present in the gas phase are known from mass-spectrometric measurements. However, bands due to CCl can be identified with maxima at 255.8 nm, 277.7 nm, 278.6 nm, 305.5 nm and 460 nm. Free chlorine is known to be present in the system and bands at 257.0 nm and 307.0 nm overlap with those due to CCl. The peaks at 199.1 nm, 297.2 nm and 312.7 nm are also probably due to reactive, chlorine containing species since during etching, their intensity is very much reduced (see Fig. 1 (lower)). The peaks at

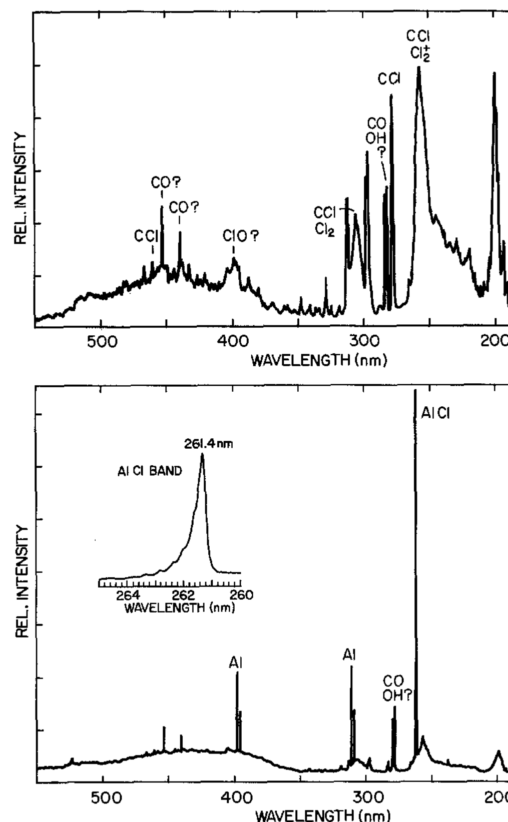

Fig. 1 (upper) Emission spectrum of CCl_4 plasma and 500 Watts, 7 Pa and 20 scc per minute flow rate. Scan rate 30 nm per minute. (Lower) Emission spectrum during CCl_4 plasma etching of aluminium under the same conditions as (upper). Spectrometer sensitivity one third of that used in (upper).

282.3 nm and 282.8 nm probably result from CO and OH; their intensity is unchanged during etching (Fig. 1 (lower)). The assignment of the peaks at 398.2 nm (possibly ClO) and at 438.7 nm and 452.8 nm (both possibly CO) is not certain.

Fig. 1 (lower) shows the spectrum obtained during the etching of an aluminium

plate of the same size as the grounded electrode. It should be noted that due to the high intensity of the peak at 261.4 nm, the sensitivity of the detection system was reduced by a factor of three compared to Fig. 1 (upper). The intensity of the CCl and Cl_2 lines is drastically reduced together with those at 199.1 nm, 297.2 nm and 312.7 nm which indicates that these too are probably due to a reactive chlorine containing species. A number of new peaks appear which can be identified as being due to AlCl (261.4 nm) and atomic Al (308.2 nm, 309.3 nm, 394.4 nm and 396.2 nm). In the inset, the AlCl band is shown at higher resolution.

For end point detection purposes, the AlCl band at 261.4 nm is more sensitive than the atomic Al lines which are not always detected from a small area substrate. Fig. 2 shows the course of etching a 3x3 cm substrate consisting of a 1300 nm thick Al layer evaporated onto a glass substrate. A photoresist grating with lines 200 um wide and a spacing of 200 um was defined on the Al layer. The CCl_4 plasma was ignited (500 Watts, 7 Pa, flow rate 20 scc per minute) and after an induction period of several minutes, etching began as indicated by the rapid build-up of the intensity of the 261.4 nm band. The decay of intensity at the end of etching was not so rapid but could possibly be influenced by geometrical factors. In this instance the etch rate was 185 nm per minute.

Etching can also be followed by the intensity of the lines resulting from CCl and/or Cl_2. For instance, the intensities of the peaks at 199.1 nm, 297.2 nm, 305.5 nm and 312.7 nm all decrease when etching begins and increase again at the end point.

In conclusion it can be said that the 261.4 nm emission band of AlCl is a sensitive indicator of aluminium etching in a CCl_4 plasma and should prove to be useful in further studies on this system and other halogen containing species. Furthermore, the CCl and/or Cl_2 peaks at 199.1 nm, 297.2 nm, 305.5 nm and 312.7 nm are also very effective end point indicators and merit further study.

Acknowledgement

The authors would like to thank H.W. Lehmann for useful discussions.

References

1. R.G. Poulsen and G.M. Smith, Semiconductor Silicon (1977), p. 1058-1070.
2. W.R. Harshbarger, R.A. Porter, T.A. Miller and P. Norton, Applied Spectroscopy 31 (3) p. 201-207 (1977)
3. J.E. Griffiths and E.O. Degenkolb, Applied Spectroscopy 31 (2), p. 134-137 (1977).
4. The spectra were identified with the aid of the book: "The Identification of Molecular Spectra", R.W.B. Pearse, A.G. Gaydon (Chapman & Hall 1976).
5. B.B. Stafford and G.J. Gorin, Solid State Technology 20 (9) 51-55 (1977).

Key words: Plasma etching, aluminium, emission spectroscopy

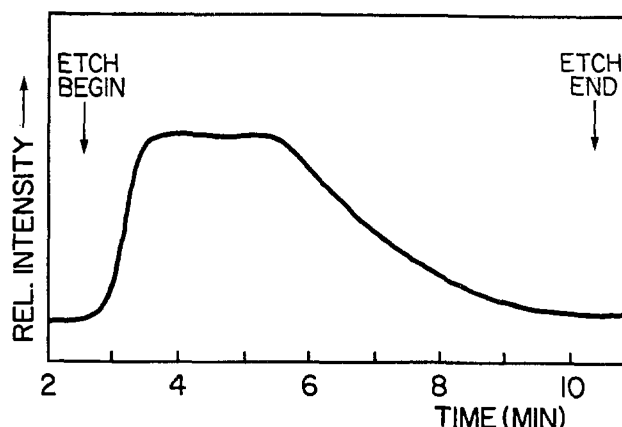

Fig. 2. CCl_4 plasma etching of a grating into an evaporated Al layer as followed by the intensity of the 261.4 AlCl band.

*Electrochemical Society Active Member.

Manuscript submitted Dec. 27, 1978; revised manuscript received March 23, 1978.

Publication costs of this article were assisted by Laboratories RCA Limited.

$CuInS_2$ Liquid Junction Solar Cells

M. Robbins, K. J. Bachmann,* V. G. Lambrecht, F. A. Thiel, J. Thomson, Jr., R. G. Vadimsky, S. Menezes, A. Heller,* and B. Miller*

Bell Laboratories, Murray Hill, New Jersey 07974

We report that single crystal and pressure sintered polycrystalline electrodes of n-$CuInS_2$ in the cells n-$CuInS_2$/1-2 F Na_2S, 1-3 F S°, 0-2 F NaOH/C exhibit good quantum efficiency under short circuit and respectable voltage at open circuit with irradiation at and above solar intensities. The output stability of the system at steady illumination appears particularly promising.

Samples of single crystal $CuInS_2$ were grown by the gradient freeze technique and were annealed in cadmium vapor at 700°C for 100 hours in sealed, evacuated silica tubes to convert the material into n-type of low resistivity. Polycrystalline $CuInS_2$ was prepared from ultrapure CuO and In_2O_3 (Alfa Research Chemicals). Appropriate mixtures of the oxides were heated in flowing H_2S at 800°C for 4 hours and cooled. The resulting $CuInS_2$ powder was pressure sintered at 700°C and 10,000 psi for 2 hrs. to yield pellets with 99.5 to 99.9% of single crystal density. The pellets were annealed in Cd vapor as above.

The experimental techniques for current-voltage curves, photospectra, and stability measurement have been earlier described (1,2). Studies of the temperature dependence of the current-voltage behavior were made with a jacketed cell equipped with a bottom optical flat and a semiconductor electrode of an approximately circular slice, indium back-contacted, and mounted on a steel shaft in a rotating disk configuration. A sequence of a 30 sec. immersion in 4:1 HCl-HNO_3, H_2O rinse, 30 sec 10% KCN immersion, and H_2O rinse was used to etch the semiconductor surface.

Current-voltage curves for n-$CuInS_2$ crystal electrodes in the jacketed cell exposed to constant tungsten-halogen illumination as a function of temperature are shown in Figure 1. The maximum power output vs. temperature is presented in the figure insert. At 60-75 mw/cm^2 insolation levels, cells with different n-$CuInS_2$ specimens delivered, at ambient temperatures, maximum power outputs corresponding to power conversion efficiencies of 3.5 - 4.3%. The temperature data at light intensities equivalent to up to three times AM2 show a 50% increase from 26 to 70°C. The corresponding fill factor improves from 0.23 to 0.31. Fill factors up to 0.45 have been measured at lower current density in 2F Na_2S - 3F S solution. The low fill factor reflects poor behavior at the foot of the voltammetric curve. Correcting the short circuit current to AM2 insolation (75 mw/cm^2) in the sunlight experiments, the quantum efficiency, calculated using the 21 ma/cm^2 theoretical value (3) for a 1.53 e.v. band gap (4), ranges from 50-60%.

Extended runs of $CuInS_2$ photoanodes (to 2 x 10^4 coul/cm^2 charge passage) produce no detectable weight loss or visible alteration in these cells, i.e. no evidence of photocorrosion. Additionally, the current output at short circuit or resistive load has been essentially constant for this same level of charge passage throughout test periods approximating 1.5 months of 8 hr./day sun.

*Electrochemical Society Active Member.

The n-$CuInS_2$ electrode is so far notable for its stability in operation in its anion-element redox couple. It resembles, in this respect, n-CdS which has a 2.4 e.v. band gap and thus a poorer overlap with the solar spectrum. Common anion cells avoid the ion exchange problem. Even for the weight-stable photoanode of n-CdSe in sulfide-polysulfide cells (2) such surface exchange processes appear implicated in output stability deterioration (5).

In view of the close to optimum band gap (6) for solar conversion of $CuInS_2$, these photoelectrochemical cells have considerable possibility for improvement in efficiency. If the fill factor can be increased to take advantage of the good limiting open circuit and short circuit parameters, the n-$CuInS_2$ based cell may be a useful entrant in the field of liquid junction solar cell systems.

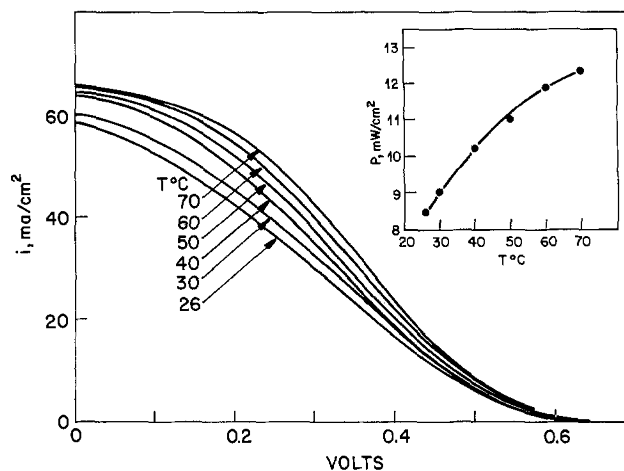

Fig. 1 Current-voltage curves for the cell n-$CuInS_2$/2F Na_2S, 3F S, 2F NaOH/C with constant tungsten-halogen illumination at different cell temperatures without stirring. The insert shows the maximum power plotted vs. temperature.

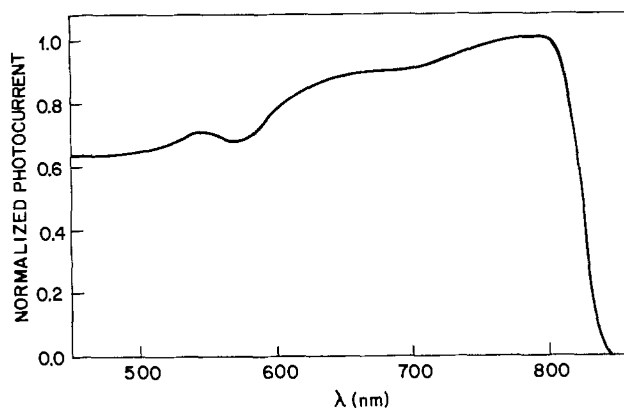

Fig. 2 Photocurrent spectrum at short circuit to a carbon electrode of a n-$CuInS_2$ electrode in 1F Na_2S-1F NaOH.

REFERENCES

1. A. Heller, K. C. Chang, and B. Miller, J. Electrochem. Soc. 124, 697 (1977).
2. B. Miller, A. Heller, M. Robbins, S. Menezes, K. C. Chang, and J. Thomson, Jr., J. Electrochem. Soc. 124, 1019 (1977).
3. H. J. Hovel, "Semiconductors and Semimentals, Vol. 11, Solar Cells", Academic Press, N. Y. (1975), p.38.
4. B. Tell, J. L. Shay, and H. M. Kasper, Phys. Rev. B 4, 2463, (1971).
5. A. Heller, G. P. Schwartz, R. G. Vadimsky, S. Menezes and B. Miller, to be published.
6. Ref. 3, p. 75.

Manuscript submitted Dec. 21, 1977; revised manuscript received Feb. 24, 1978.

Publication costs of this article were assisted by Bell Laboratories.

JOURNAL OF THE ELECTROCHEMICAL SOCIETY

ELECTROCHEMICAL SCIENCE
AND TECHNOLOGY

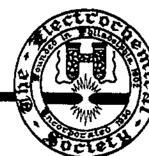

JUNE
1978

EST

Resin-Bonded Cellulose Separators: An Overview with Prognoses

James R. Dafler*,[1]

ESB Incorporated Technology Center, Yardley, Pennsylvania 19067

ABSTRACT

Resin-bonded cellulose separators are very widely used in the starting, lighting, and ignition battery industry. Since their appearance and maturity, they have undergone systematic improvements, but their basic shortcomings have remained. Separator development is reviewed here, and the pertinent structure and chemistry of the cellulose substrate is discussed. The current literature, which indicates that improvements in substrate character and acid resistance can be made, is also reviewed.

In 1917, almost the beginning of the modern starting, lighting, and ignition battery industry, Brooks pointed out the lead-accumulator was unexcelled in portable service applications (1). Separators at that time were wood veneer and were superior to anything in use despite the stringent requirements of their manufacture. At that time, only treated wood possessed good wicking action and reasonable conductivity and held active material in place against vibration and the eroding action of hydrogen generated on overcharge. Other materials had been tried, but until the microporous hard rubber separator appeared, wood veneers and combinations of wood and other materials dominated separator practice. Eyanson developed an unglazed porcelain membrane with incorporated lead spacers (2), but this product undoubtedly gave a cell of high internal resistance. Sperry developed a perforated, corrugated, hard rubber sheet that was really a simple, open spacer (3). The earliest hard rubber separators, used as adjuncts to wood, were approximately 30% porous. Batteries in which they were used were poor for cranking purposes (4).

Hardy and Hungerbuhler (5) experimented with artificial stone for making separator membranes. They compressed and then baked silicates, feldspars, bone, and lime to form refractory porous sheets. Rodman (6, 7) experimented with techniques to make porous glass separators, developing membranes of sand or fine glass powder fritted together.

In 1910, Flanders described an untreated wood veneer separator using a well-defined rib structure (8), and after this a number of wood/hard rubber combinations were developed. Carpenter (9) coated thin wood sheets with vulcanized rubber, and Chamberlain described a process to produce wood veneers machined so that the ribs were integral to the separator structure (10). Gould's patent, describing the use of hard rubber and wood laminated together, appeared in 1916 (11).

Many battery researchers applied themselves to the separator problem between Brooks's time and the period during which the resin-bonded paper separator appeared, then matured. One of the more interesting inventions was Bliss's (12) ingenious attempt to make a porous phenol-formaldehyde sheet. He mixed asbestos and zinc with resin, polymerized it, and removed the zinc with acid. A number of other inventions included a separator of chopped bird feathers and sodium sulfite (13), bitumen-impregnated felts (14), roofing felt with extruded hard rubber ribs (15), and Willard's novel combination of fiber cables and wood strips bonded into sheets with a latex (16).

The search for the correct material to allow ionic transport and still provide a useful, robust separator later followed several newer lines of inquiry. Ekisler described a separator made of layers of drawn glass fibers and bound with rubber latex or a phenolic resin (17), and Lunn used rubber cements to fix flexible rubber separators directly to plates (18). Slayter made a separator of crossed felts and wools (19) to realize a gradient of pore sizes normal to the separator; he also developed a braided fiberglass structure for tubular lead-acid batteries (20). The Chloride Electrical Storage Company, Limited patented a separator formulation that used diatomaceous earths or other fillers with rubber latexes or thermoplastic resins (21). Fuller and Sudlow anticipated the envelope separator concept as early as 1939 in their patent describing an electrolyte-retaining separator matrix (22).

In 1943, Slayter patented a process for making porous, fibrous glass sheets (23), and Vinal later (1950) experimented with complex laminates of glass wool and thermoplastics such as polystyrene (24). He developed pores in the plastic by using leachable salts such as potassium sulfate or magnesium sulfate. During this period, Szper developed an electrolyte-retaining separator matrix by mixing kieselguhr, sulfur, soluble alginates, and rubber, then pasting the slurry onto glass wool sheets (25). This was followed by several attempts to use diatomaceous earths and various resins. Walker (26) used neoprene and diatomaceous earth, while Phillips (27) used glass fibers matted with diatomaceous earth and styrene-butadiene copolymer laminated to phenolic-bonded glass mat. With this technique, he hoped to realize a selected, one-sided microporosity.

Wood separator technology was pioneered much earlier and by 1917 was relatively mature, represent-

* Electrochemical Society Active Member.
[1] Present address: Institute of Gas Technology, Chicago, Illinois 60616.
Key words: cellulose, hydrolysis, heterogeneous, lead acid battery, polymerization.

ing a large patent and process-patent literature. The 1911 patents of Dodge (28) and Taylor (29) describe processes to manufacture separators using complex, serial treatments of the wood veneers in acids and alkali. Skinner (30) used hot sulfite solutions (100°-175°C) and pressurized washing and drying to make separator sheets, while Morrison (31) cooked wood sheets in hot paraffins to remove the volatile matter. The finished product was produced by solvent extraction. Later, Skinner (32) boiled his wood veneers in solutions of sodium sulfide or, more simply, plain water, but retained pressurized drying and washing.

Wright (33) used a process he referred to as electrical osmosis in his process for making separators of bass and cherrywood. Morrison attempted to alleviate lead-tree formation by precipitating barium sulfate or strontium sulfate in the pores of his wooden matrixes (34). The 1916 Shimazu patents describe a complex procedure for making thin wood separators (35). Shimazu specified acid sulfite treatment, alkali carbonate washes, and even alkali peroxide treatments in his processes.

After 1917, wood technology continued to be elaborated as shown by Lunn's development of integral grooves and ribs (36), Norris's combination of wood, hard rubber, and celluloid (37), and several combinations of wood with glass-matt (38) and other spacers and protectors (39-41). The bulk of wood used was treated by one or another complex aqueous treatments (28-35). The most novel preparation of wood veneers seems to be that of Steerup (42), who opened the pores by steaming, followed by treatment with ammonia. The ammonia and ammoniacal compounds were then volatilized with steam at 125°-130°C.

The drain on the supply of Port Orford Cedar, the wood separator of choice up to that time, led to definitive research and development on other coniferous woods. The paper by Peakes, Lloyd, Barnes, Berry, and Ritter (43) represents the most complete study of wood preparation in the nonpatent literature. It was a seminal effort that came, unfortunately, at the end of the period of dominance by wood in separator practice.

Schidrowitz and Goldsbrough were, apparently, the first developers of porous, spongy rubber sheet materials (44). Their original patent of 1914 (45) used a rubber latex, sulfur, and substances that decomposed during the cure to develop porosity during vulcanization.

Willard appears the first to use hard rubber in a battery separator development (46). His development consisted of cloth fibers and other filaments embedded in hardened or vulcanized rubber. Separators were made by cutting thin sheets of the composite normal to the direction of the embedded filaments. Willard's later patents were also embodiments, albeit different ones, of the same general idea (47).

By the mid-1930's, hard rubber separators were made commercially by a number of different techniques such as Beckmann's molded latex sheet with ribs (48) and Martindell's hard rubber separator with specially positioned ribs (49). In 1937, Greenup and Olcott (50, 51) demonstrated the over-all chemical stability of vulcanized natural latex separators. By that time, hard rubber separators gave long life and improved cranking performance (in automotive applications).

Hard rubber separators are widely used for industrial batteries (forklift truck, telephone substations, etc.) and a lesser extent for the manufacture of automotive and truck cranking batteries. However, as Palmer (52) points out, resin-bonded paper is the basic separator in use today in the starting, lighting, and ignition (SLI) battery industry. It appears, historically, as a natural follow-up to cedar and other wood veneer separator materials. The good-to-excellent resistivity and integrity of wood veneers suggest that impregnated cellulose (as in wood cell-wall coverings) should make a good, porous matrix suitable for SLI applications. Resin-bonded paper and wood veneer separators have similar total porosities, quite different pore size distributions (53), and different chemical stabilities in the acid environment of SLI batteries. Like wood, resin-bonded paper separators have good stiffness and burst strength properties (53, 54).

Cellulosic separators—evolution.—Resin-bonded paper separators entered the SLI battery field with considerable impact in the 1950's. Commercial manufacture by paper and fiber specialties manufacturing firms has resulted in a separator that possesses a considerable cost-effective advantage over hard rubber and other polymer materials and currently occupies a dominant position in SLI battery assembly (52).

Cellulose appeared as early as 1922 when Wood and Smith brought out a complex matrix of hard rubber, wool, and cotton fibers (55). This was to be a separator that developed increased pore volume as the cotton linters were digested in the acidic medium. The future use of paper separators may have been forecast by Benner *et al.* in their 1930 development, a matrix which consisted of cellulose fibers and tough, noncorroding spacers bonded into a composite sheet (56).

Dillehay developed a paper polymerized with furfuryl alcohol (57) that consisted of approximately 85% cellulose. Later, Lehmberg processed a felt of Vinyon (a vinyl acetate-polyvinyl chloride copolymer) and cotton (58), asserting that hydrolysis of the cotton, by increasing the porosity, relieved "leading-through."

Uber's 1951 patent (59) represents the modern resin-bonded cellulose (RBC) separator. His matrix was impregnated with phenolic resins and is still used in present-day separator practice. There was a rush to develop similar matrixes but with refinements and minor improvements. Wilson patented (60) phenolic-impregnated papers, sometimes with complex refinements, as was the patent awarded Merrill in 1954 (61). Uhlig *et al.* (62) embellished the basic concept by adding pinewood resins—for reasons not clear to this reader. Merrill and Mears pulped glass fibers with the basic cellulose slurry. In Merrill's development (63) furfural- and urea-formaldehyde resins were used as impregnating agents. Mear's use of glass fibers (64) was more complex: he hoped to develop a matrix so that the separator was rich in glass fibers on one side and rich in cellulose content on the other.

During this period a number of patents appeared dealing with standard phenolic-impregnated matrixes reinforced with sprays or coatings of other additional resins. Raphael and Schweitzer (65) and Beckvold and Hartman (66) treated regular RBC-separators with sprays of other thermosetting resins. Raphael and Schweitzer endorsed the use of suspended, acid-resistant fibrous material in the sprays; they suggested polyvinyl chloride, polyethylene, polystyrene, butadiene-styrene copolymers, and many others, including polymers and copolymers of isobutylene.

Dowse and his colleagues (67) developed rather complex cellulose separators employing special folds at the edges of grids and plates, and Stickel (68) brought out a simple two-faced die used to crimp a permanent rib into partially cured phenolic-impregnated paper. Later, Little (69) and Hall (70) made simple improvements in the rib used on typical paper separators.

After this period of activity, most new developments in these separator areas appear to be more visionary than practical. Mills's (71) and Vedovelli's (72) developments are rather complicated, involving special impregnations or various kinds of duplex laminates of plastics bonded to paper. Zenczak's development (73), a separator using phenolics as impregnates but starting with a lignocellulose paper base, is rather interesting in view of the frequent and profitable use of lignins in expander technology.

Antimonial alloy grids—A complication.—Several authors have pointed out the strengths and weaknesses of RBC separators. For automotive end use, Lander (74) has indicated, given current element design, that economics or cost effectiveness is the principal factor considered for separator selection. Sundberg (75) showed an increasing awareness of the role that pores play in the failure of SLI batteries related, apparently, to antimony migration and diffusion.

Antimony transfer from the positive grid alloy to the negative grid has been recognized as a major system problem for some time (76). Crennell and Milligan (77) investigated the hydrogen overpotential of aged cells with antimonial positive grids to explain the steady, irreversible sulfation of negative electrodes. Antimony migration and its effects—self-discharge of the negative on stand, reduced charging efficiency and sulfation of the negative, and stibine evolution on overcharge (78)—remain a complex problem. The lowering of end-of-charge voltage (ECV) may be the result of extensive antimony transfer or the result of high resistance short circuits built up in the separator by deposition, solution, and crystallization of lead dioxide or other semiconducting lead salts (perforation failure).

Some investigators believe lead trees are responsible for failures similar to short circuits, and there remains in separator practice a "leading through" measurement to test a separator's resistance to lead "dendrite" growth. Wranglen has demonstrated which conditions are necessary for well-characterized lead dendrite growth in electrocrystallization systems (79). Unfortunately, he reported no work in sulfuric acid media.

Lead dendrites are propagated from asperities in high current-density environments and represent a diffusion-controlled phenomenon. In low current density environments, nondendritic growth layers may form on exposed planes. This mode is quite slow, compared with dendritic growth, resulting in plates and mosaics. In the transition region of current density, layered growth can also occur at surface asperities.

The isolation of separator failure effects in batteries having antimony-lead alloys is a complex problem that can be settled only by direct physical examination of suspect elements. The charge history of deeply discharged automotive batteries will show gradual lowering of the ECV due, no doubt, to antimony transfer. This may be the cause of element failure if there is no direct evidence of short-circuit failure. In the presence of very low ECV's and physical evidence of shorting, then the latter must be assumed the preponderant cause of failure.

Resin-Bonded Cellulose Separators

Corrosion in SLI battery electrolyte.—In mineral acids, cellulose is highly reactive and hydrolyzes rapidly. For RBC separators to be useful in sulfuric acid (H_2SO_4) media ranging from 3.3*N* (sp gr approximately 1.1) to 10.7*N* (sp gr approximately 1.3), they must resist their native tendency to hydrolyze. The currently used impregnation, a two-stage, water-borne phenolic resin, accomplishes considerable protection, but RBC separators lose up to 15% of their weight if stored in battery grade acid (approximately 9.2*N* H_2SO_4) at 52°C. In actual battery practice, the loss has been seen to be greater (52).

Straightforward corrosion experiments were done in this laboratory. A very large number of carefully cut and preweighed pieces of RBC separator were placed in 9.18*N* H_2SO_4 (1.256 sp gr) and stored at 52°C for an extensive period. Samples taken over periods up to 2400 hr suffered considerable weight loss and continuous darkening of the materials, as shown in Fig. 1. These are two separate but related phenomena. When we applied regression analysis to our isothermal corrosion data, we found that weight loss, based on the percent cellulose in the composite, fit a logarithmic relationship

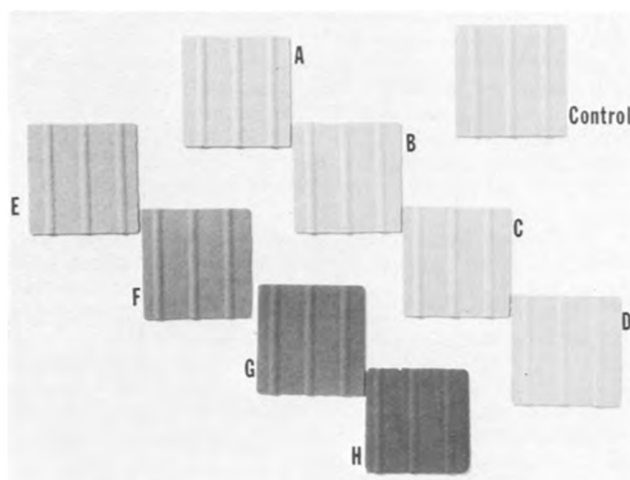

Fig. 1. Color change in sulfuric-acid treated RBC separators. Separator pieces were stored in 9.2*N* H_2SO_4, at 52°C for: A, 19 hr; B, 43 hr; C, 230 hr; D, 530 hr; E, 840 hr; F, 1200 hr; G, 1500 hr; and H, 2400 hr.

$$P(\%\ \text{wt loss in } 9.18N\ H_2SO_4) = 2.058 \log_{10}{}^2 t + 0.30176 \quad [1]$$

where t is expressed in hours.

The degradation of cellulose by mineral acids has been studied in very great detail since 1844 (80). De Carolles found a spectrum of what he called "wood sulfuric acids" when wood cellulose was treated with strong H_2SO_4. Addition compounds were found (81) when very concentrated H_2SO_4 was used. These compounds were of the form $(C_6H_{10}O_5 \cdot 4H_2O \cdot H_2SO_4)_n$.

Freudenberg and colleagues (82) studied the degradation of cellulose in 51% H_2SO_4 at 18°C. They presumed the H_2SO_4 to be instrumental in the reaction—the process was not ordinary hydrogen ion catalyzed hydrolysis. Freudenberg assumed the hydrolysis unimolecular, with the velocity constant a function of the fraction of reacted glucose linkages.

The cellulose in RBC separators is significantly protected, but is not protected well enough, and separators taken from very old cells or from batteries cycled for very long periods are usually extremely frangible. They seem, almost, a lacy network of phenolics unsupported by the original cellulose. This is not the case, however, and weight measurements show that, even in this brittle condition, much of the original cellulose remains.

The probable key to better RBC separators, with respect to hydrolysis, lies in a better resin impregnation technique. Other resins have been used (57, 58, 63, 66), but the phenolic impregnation scheme remains the most common current practice. For the relatively undemanding applications in SLI batteries, RBC separators are the most cost effective (74).

Phenolics of the same kind used in RBC separators are used in other kinds of lead-acid battery systems. In tubular plate cells which are used for industrial and stationary applications, the tubes are frequently braided fiberglass bundles with a phenolic binder. After considerable cycle life, the resin bonding on the fiberglass tubes is found to be completely eroded. The tubes then lose their rigidity, and considerable active material loss is possible, with an associated loss of battery performance.

The phenolics associated with RBC separators are known to discolor and react in battery electrolyte after extensive exposure (Fig. 1). They do not, however, erode completely, indicating that their long life is, in part, due to the association with the cellulose substrate.

An obvious conclusion is that the cellulose and phenolic resin binders copolymerize to form a matrix that resists corrosion in this environment. The evidence for copolymerization is quite strong: a combination of structural evidence of inter- and intramolecular hydrogen bonds (83), labile hydroxyl groups (84, 85), and differences seen in the ability of dry alpha cellulose to reorganize in the presence of water vapor (86). Much of the evidence has been assembled in a recent paper (87).

It is essentially the corrosion of the substrate cellulose that brings about the degradation of RBC separators. The currently used phenolic impregnation system is effective in delaying the loss of material, but not as well as battery manufacturers could wish for. The hope for better RBC separators, therefore, lies in improving the current process of impregnation, or in a new or modified process that will produce a more corrosion-resistant matrix that still retains most of the desired cost effectiveness of paper.

A note on cellulose structure.—Cellulose, derived from whatever source, is a highly crystalline material that yields definite x-ray diffraction patterns. This was, apparently, first discovered by Nishikawa and Ono (88). X-ray investigation was intensified, and several cellulose modifications were determined (Cellulose I, II, III, and IV). Alpha cellulose, the main raw material from cotton and many woods, is principally Cellulose I, referred to as native cellulose. A monoclinic unit cell structure possessing two screw axes was proffered by Meyer and Misch (89) and has retained its essential usefulness for several decades, in spite of many modifications. The Meyer and Misch unit cell is a refinement of earlier predictions (90) and has withstood a fairly steady current of refinement.

Considered to be made up of crystalline regions imbedded in an amorphous matrix, cellulose structure was for a long period described as two phased, or micellar, a description that culminated in the fringed-micelle model (91-94) now questioned by many investigators. Cellulose is a polymer of beta-cellobiose, and its structure is determined, in extension, by the nature of the monomer and the character of the chain linkages (95, 96). Beta-cellobiose is a Beta-linked dimer of glucose and in Haworth's (97) nomenclature is represented by the structure shown in Fig. 2.

The unit cell for cellulose is still not generally determined to everyone's satisfaction, but many reasonably satisfactory models exist (89, 90, 98). It is generally agreed that the pyranose rings assume the less-strained *trans*- or chair-form. Transitions to the *cis*-form which occur in excess energy environments are suggested by Reeves (99) as a possible cause for differences in physical structure and reactivity. This suggestion has been supported by work done by Bjornhaug, Ellefsen, and Tonnesen (100).

The cellulose structural element attains a rod-like stiffness due to stability imparted by intermolecular and intramolecular hydrogen bonding. Liang and Marchessault, in a series of infrared spectroscopic analyses, obtained extensive evidence for the existence of these bonds (83). The hydrogen bonds restrict the anhydroglucose units to a limited region of movement about the acetal linkage. The net result of hydrogen bonding is a spectrum of activity for the hydroxyls associated with the ring carbons. Recently, Røwland, Roberts, and Bose (84) measured the relative reactivities of the carbons associated with intramolecular hydrogen bonds and with intermolecular bonds. Using a hydrocellulose, they found the C-2 hydroxyl (Fig. 2) to be stable, with the C-6 and C-3 hydroxyls approximately 54% and 29%, respectively, as available for reaction. For fibrous cotton, the relative availabilities were approximately 77 and 32%, respectively, the difference being due, presumably, to the greater relative order and crystallinity of the regenerated cellulose (hydrocellulose).

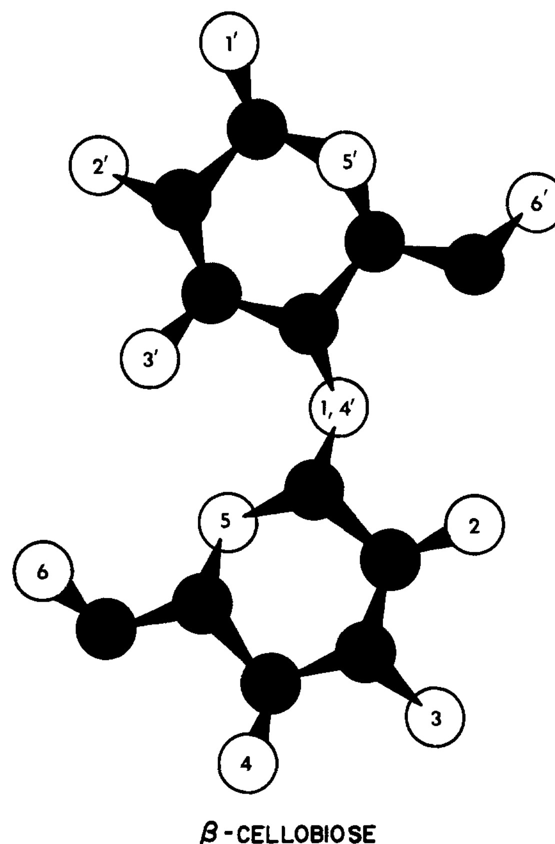

Fig. 2. The structure of α cellobiose. Open circles are oxygen, closed circles carbon. The associated hydrogens are not shown.

St. John Manley argues that we should consider cellulose from the molecular point of view, and he shows how the reactivity and puzzling retention of apparent crystallinity can be explained using his protofibril model (101). The protofibril model explains how the index of crystallinity of hydrocellulose and cotton fibers appears the same, in spite of the great difference in their physical properties. It also obviates the group-theoretical work of Jones (102), who was unable to correlate the x-ray intensities and derived structure factors for cellulose I and II to any conventional space group.

The St. J. Manley model says, essentially, that the protofibril is completely crystalline and the properties and reactivity of cellulose may best be understood by studying the processes into which protofibrils enter. Accessibility and the properties of other cellulose structures are, in this construction, only reflections of the manner in which the protofibrils form larger superstructures (Cellulose I, Cellulose II, etc.).

The protofibril model, incorporating as it does an orderly pleating and folding of supermolecular structures, uses a natural, flattened helix and encompasses the persistently proffered hypothesis of screw dislocations and spiral structures first adumbrated by Balls in 1923 (103). The small but finite regions that are essentially the physical zones between ribbons and folds give rise to the amorphous halo of typical Debye-Scherrer x-ray diffraction patterns.

The spirally wound protofibril model is not uniquely St. John Manley's. R. Mark *et al.*, to explain the high elastic modulus of cellulose, formulated an extended (nonfolded) chain model that is very like a coiled bedspring (104).

Later structure investigation by electron diffraction and newer calculations on existing x-ray diffraction data still lead to diverging hypotheses. Kulshreshthwa

and Dweltz (105) give reasons for abandoning the notion of degree of crystallinity entirely, and they discredit the fringed-micelle (two-phase) model, pointing out that crystallinity as currently understood indicates only a difference between the molecular order of a sample and that of a crystalline standard. Hebert and Muller (106), using electron diffraction, have partially substantiated Jones's conclusions (102) about the unit cell and its space group. The Meyer-Misch unit cell requires it to be of space-group symmetry $P2_1$, which requires the absence of x-ray or electron diffraction lines, corresponding to [0*k*0] indexing (*k* an odd integer, only). Because these lines are present in both x-ray and electron diffraction, the Meyer-Misch unit cell clearly fails to correlate all the available data.

X-ray diffraction experiments have long been a primary means to investigate the structure and the chemical stability of cellulose (107). It has been used in a limited way to study the corrosion of RBC separators in battery grade acids (108). The x-ray diffraction spectrum of RBC separators is a characteristic that is sensitive to the condition of the matrix (87, 108) and can be used, in conjunction with density and weight-loss measurements, to index the quality of the retained cellulose in samples that have been hydrolyzed.

The impregnation of cellulose with phenolics in the paper-making and polymer-curing processes leads to an x-ray diffraction spectrum only qualitatively different from the spectrum of alpha cellulose as shown in Fig. 3. However, the reaction of RBC separator matrixes to water is quite different, and water vapor actually lowers the order of the separator matrix while having a definite ordering effect on untreated alpha cellulose (86, 87, 109, 110).

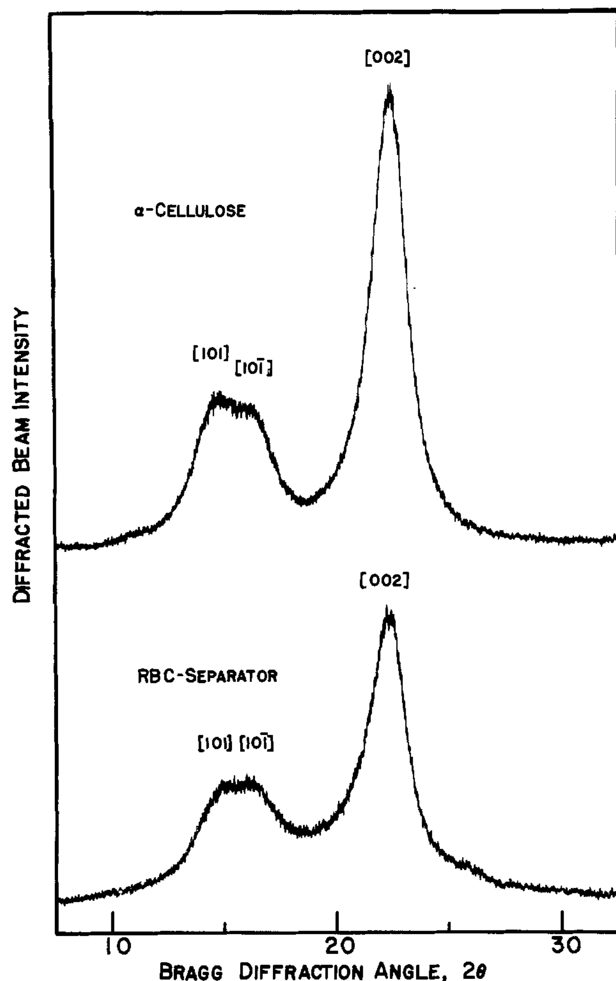

Fig. 3. The x-ray diffraction spectra of α cellulose compared to RBC separator. Conditions of the analysis (field and beam current) were unchanged.

It should be noted that cellulose, as in all highly crystalline materials, can be decrystallized physically (107c) and chemically (111), but it can also be reordered or annealed by heat-treatment (112) and a water-plasticization process (109, 113). The structure and properties of this matrix, alpha cellulose with a reactive polymer impregnate is still not fully understood and characterized. Enough, however, is known to make careful, qualified prognoses on the future of this matrix for separator applications. This writer, unlike Palmer (52), is convinced cellulose can be the primary substrate for a much improved SLI-separator matrix.

Some relevant chemistry.—The two-phase hypothetical description of cellulose—the amorphous/crystalline model (fringed micelle)—was very useful for correlating data from a great number of early studies on hydrolysis in acid media. Meller (114) investigated the acid hydrolysis of what he called the "easily accessible fraction" in two papers published in 1949 and 1953. He measured activation energies for hydrolysis that indicated the rate of weight loss to be controlled by an "activated diffusion" process. Meller suggested that reactivity could be used to measure the crystalline/amorphous ratio.

Nickerson and Haberle had already assumed that the attainment of a constant reaction rate meant much the same thing for the retained crystalline fraction in hydrolyzing cellulose (115). They also assumed the crystalline/amorphous ratio could be determined by hydrolysis measurements. Sharples (116) demonstrated that certain linkages were more acid sensitive than others in the cellulose chains of Egyptian cotton. Sharples, however, did this work on chemically modified cotton samples, and it is not clear whether the chemical preparation altered the reactivity, because Sharples found differences in acid-sensitive linkages in regenerated cottons from different sources.

Ant-Wuorinen and Visapaa concluded from extensive hydrolysis experiments, coupled with x-ray diffraction measurements, that changes in the "index of crystallinity" indicated little about amorphous/crystalline ratios but indicated, rather, the degree of lateral order (117). These workers used the crystalline/amorphous concept to deal with hydrolysis data, assuming that the micellar, crystalline bodies are fundamentally more stable to hydrolysis. The difficulty with their lateral order hypothesis is pronounced for extensively hydrolyzed cellulose such as Nickerson's hydrocellulose (115). These are materials without extensive lateral order (in a micro sense) but with very high indexes of crystallinity.

In this laboratory, alpha cellulose (Cellulose I) was hydrolyzed in 1.40 sp gr H_2SO_4 for 36 hr at 52°C. The liquor was black to dark brown and the cellulose slabs completely degraded. The solid particulate matter was washed in distilled water until free of $(SO_4^{=})$. The resulting material was white and formed a viscous dispersion in water. A small hand sheet was made by filtration and dried in vacuo; the result, a brittle horny material, was analyzed by x-ray diffraction. The x-ray spectrum was compared directly with the spectrum of raw material cellulose (87). The spectra are almost identical, and the crystallinity indexes, in the sense of Segal (107b) or Hermans and Weidinger (107a), are virtually the same. This indicates that the crystallinity index is dependent, mainly, on structural elements much smaller than regular fiber bodies (118a). The degree of polymerization of alpha cellulose is on the order of 10^3-10^4, while that of extensively treated hydrocellulose is approximately 10^2 (118b).

As pointed out, the crystallinity of separators is somewhat lower for finished separators than for native cellulose (87, 108), however, the crystallinity index is not greatly decreased by storage in battery electro-

lytes. Physical examination of separator pieces stored for hundreds of hours in SLI electrolyte indicated corroded edges and other signs of weight loss, but x-ray examination indicated a practically unchanged degree of crystallinity (87).

The discoloration of the separators (Fig. 1) during long periods of acid storage and cycling is not easy to explain. Many battery researchers assume that it is a charlike, darkened, hydrolyzed product of cellulose or glucose degradation. For this explanation to hold, we must assume these dark species are labile, reacted parts of the fibrous network, and somehow bound by the polymer resins used to protect the cellulose; however, hydrocelluloses made by acid hydrolysis are clean and white (115). The dark products, being water- or acid-soluble, are not trapped in the fiber matrix that remains after hydrolysis and cannot account for the darkening.

The possibility that the darkening is due to degradation of the phenolformaldehyde resins must be examined. Resins of this type are cured at temperatures on the order of 195°C (119). The resins used in separator manufacture are treated at approximately 210°C in a continuous process, and the "cure" may be incomplete; thus there are likely to be labile moeities in the finished separators. It is known that sulfonation of phenol-formaldehyde resins has been used to produce ion-exchange resins (120), generally reddish-brown in color. Though the acid medium in batteries is dilute compared with sulfonation media, exposure is extensive, and the presence of partially cured resins may make this speculation palatable.

The dark color taken on by H_2SO_4-treated separators may also be the result of acidic oxidation of labile phenol moeities and of acid-catalyzed formation of phenolic and aldehydic condensation products. The acid undoubtedly catalyzes a certain amount of "curing" in the resins present, but prolonged H_2SO_4 exposure will certainly catalyze condensation reactions, which are known to be pH sensitive. Phenol alcohols condense rapidly on contact with sulfuric acid (121).

The bulk of experimentation concerned with the hydrolysis of cellulose itself has been done in hydrochloric acid (HCl) media (114-116, 118b, 122-125), and weight changes in HCl are used to define the character of alpha cellulose used as a raw material in various polymer processes (126). An extensive and continuous research into the properties of cellulose in H_2SO_4 media has been done in Finland by Ant-Wuorinen and colleagues (117, 127-130) at the State Institute for Technical Research at Helsinki.

Ant-Wuorinen's hydrolysis data (130) for bleached sulfite pulp is shown plotted in Fig. 4. Bleached sulfite pulp is the basic raw material of RBC separators, and to the present, these are some of the best developed H_2SO_4-hydrolysis data available. In this scheme, the investigators were interested, mainly, in reaction velocity (as a function of H_2SO_4 concentration) and the

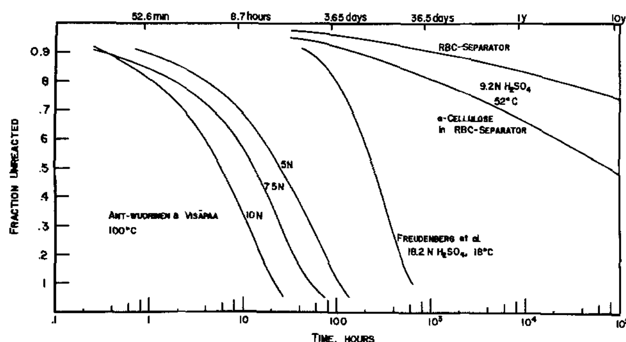

Fig. 4. Hydrolysis data for cellulose I. The data of several investigators are compared here, with all data plotted as the normalized unreacted fraction vs. time of hydrolysis.

reaction half-lives. Also plotted in Fig. 4 are data generated by regression analysis of RBC separator weight loss (Fig. 1). We have also plotted the Freudenberg *et al.* data (82) to indicate the complex relationship that exists between acid concentration, temperature, and time (131, 132). What is clear is that the cellulose in RBC separators reacts almost typically with sulfuric acid, though at a much lower rate. Inherent in this is the obvious suggestion that better impregnation can be performed or that an improved resin (more sulfuric-acid-resistant) will yield a separator capable of longer life in a typical battery environment.

Prognoses: Toward a Better Separator

Phenolic-bonded cellulose matrixes are the most widely used kind of separators in the SLI industry (52) for reasons of cost effectiveness (74), but a cursory perusal of the patent and the specialized literature clearly shows that this very mature product has not been significantly improved in years. Its dominance in the automotive battery industry, that most numerous and profit stimulating of lead-acid batteries, has inadvertently placed it in a limbo from which it promises never to come forth. Recent work in separator technology (87, 133) indicates that the problem of RBC separator failure is a complex problem associated with the fundamental paper matrix and with the nature of the impregnation.

The paper matrix—Pore size distribution.—Palmer (52), Sundberg (75), and others (133) argue effectively that pore size distribution in the separator is the principal variable in considering failure, whether due to antimony transfer or so-called perforation failure. It has been shown (133) that large pore separators most frequently fail by the perforation mechanism and offer an excellent matrix for capture and growth of suspended and dissolved lead species, and Sundberg (75) has argued that large pore matrixes permit greater transport of antimony from the positive grid to the negative, placing the blame on antimony diffusion. Diffusive transfer should be practically the same whatever the separator or barrier; however, the electrolyte in a cycling cell is subject to a great deal of stirring during charge and overcharge. The transfer is in part convective, but it ought to be noted the pores in RBC separators are so large that convective mixing can take place within them (134), so that transport of antimony through these separators is more likely than through microporous separators (135).

A water-laid paper (fourdrinier) can be made so that the pore size distribution is much smaller. Filter paper manufacturers have sold papers with pore sizes in the 1-5μ range for many years (136). Figure 5 shows the pore size distribution (PSD) of three matrixes: wood, fine filter paper, and coarse filter paper (137). The PSD of the coarse filter is very similar to the PSD found for RBC separators (75, 133). Wood veneer is known to be a superior separator for lead-acid applications, so these data suggest that an impregnated fine-pore paper matrix will approach wood in performance. As Sundberg has shown (75), such a matrix would slow the transfer of antimony and yield a lower hydrogen evolution test datum than a typical RBC separator.

In manufacturing a paper matrix with smaller pores and a PSD shifted to smaller values, there would, undoubtedly, be a premium to pay. The paper could be made with knife-milled fibers to produce a more dense, less porous matrix. It would also be possible to formulate with microcrystalline cellulose to selectively fill pores and reduce net porosity and average pore size. Formulation of a new, small-pore matrix should result in (*i*) higher density, (*ii*) lowered wettability, and (*iii*) increased frangibility. There will be a resistivity penalty to pay, and the use of additional synthetic fibers may be necessary to retain required breaking strength. Such a matrix, however, should be lighter by

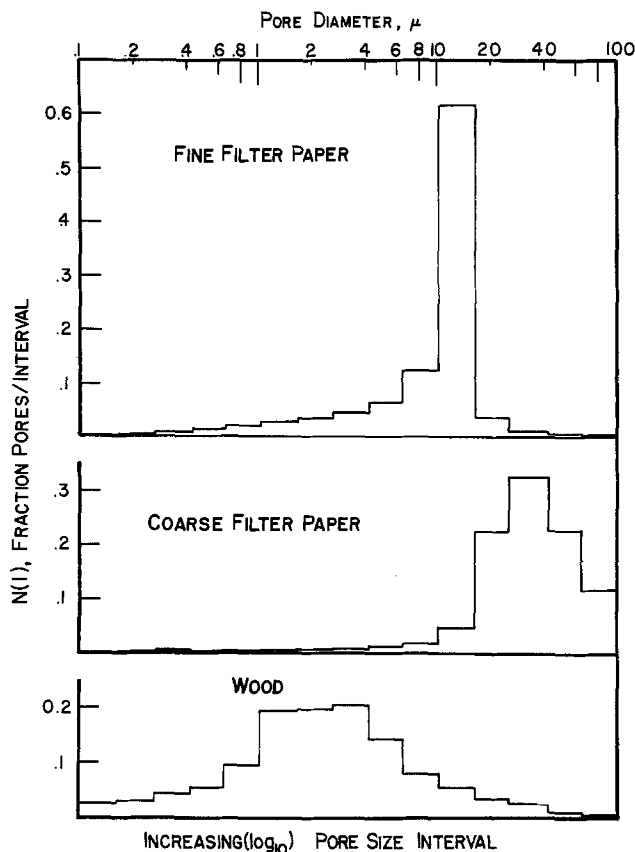

Fig. 5. Pore size distributions for paper and wood matrixes compared. Data from Ref. (137).

virtue of requiring a thinner back-web. There will be increased expense due to the use of processed cellulose, but this will be minimized by thinner separators and longer life.

There should be considerable incentive for developing such a matrix. The RBC separator now holds an almost 2:1 price advantage over the widely used microporous separator matrixes. The dollar incentive therefore is great, and the clear-cut attractiveness of a better RBC separator and its probable penetration into deep-cycling lead-acid battery markets is indisputable.

Impregnation—Key to stability.—The RBC separator using phenolic resin impregnation has proved to be reasonably stable in H_2SO_4 media, but clearly the labile hydroxyls and acetal linkages in the substrate are not completely involved in the curing scheme which gives acid resistance to the matrix. Whether the paper matrix can be made receptive to more complete sorption and penetration of the uncured resin is a complex question. Thode, Swanson, and Becker (138) measured the BET specific surface area of swelled alpha cellulose and found a high value (100 sq m/g). They showed that beating increases the BET area and the cumulative pore volume in the range of 44-800Å.

Ruzicka and Kudlacek (139) used argon and did very careful solvent-exchange drying to develop a more detailed picture of the surface area and pore volume dependence on fiber treatment. For native cellulose, they found a specific area of about 30 sq m/g but showed that chemical treatment tended to produce "swelled" fibers with areas of approximately 225 sq m/g, and the swelled condition was maintained if azeotropic drying was used to prepare the sample.

The sorption by cellulose of polymeric materials was shown by Luce and Robertson to depend strongly on the degree of swelling (140) that took place, either prior to or during polymer sorption. The equilibrium sorption of polyvinyl alcohol (with a molecular weight of about 10^5) was very strongly affected by the nature of the polymer carrier. If a "swelling" carrier such as water is used, the sorbed quantity is far greater than if a "non-swelling" solvent is used. Preswelled fibers also took up greater quantities of PVA, in direct proportion to the degree of swelling produced by the swelling agent. Luce and Robertson also found that more polymer was sorbed if the temperature rose, with the higher molecular weight fractions of polymer being sorbed more strongly.

These sorption data point to the necessity of optimizing the resin treatment procedures currently used to make separators. We know, for example, that there is a great degree of swelling that takes place during the original pulping of the alpha cellulose, the subsequent beating, and the blending with synthetic fibers. The basic matrix is then made by typical paper-forming techniques. Currently, the absorption of protective resins is a continuous process, indicating that a real equilibrium among the fiber matrix, the polymer, and the swelling agent is not likely to be reached.

In SEM examination of resin-bonded separators, globules are found. These can only be explained as excesses of resin that cured in place before they could be evaporated. Other effects that we have interpreted as due to an excess of liquid-phase resins on the fiber surfaces have been seen in SEM photos: dimplelike surface artifacts. These are shown in Fig. 6, which also shows the globules of excess resin that are sometimes seen.

Both phenomena indicate that RBC separators are frequently formulated with a large excess of resin. In one case, the excess is so large that liquid (midcure) resins coalesce into relatively large globules (Fig. 6a and 6b). In the other case, the liquid excess is confined to fiber surfaces but does not effectively penetrate. As the resin cures and the liquid layer contracts, it undergoes normal surface-free energy minimization (141), resulting in the circular dimples seen in Fig. 6c and 6d.

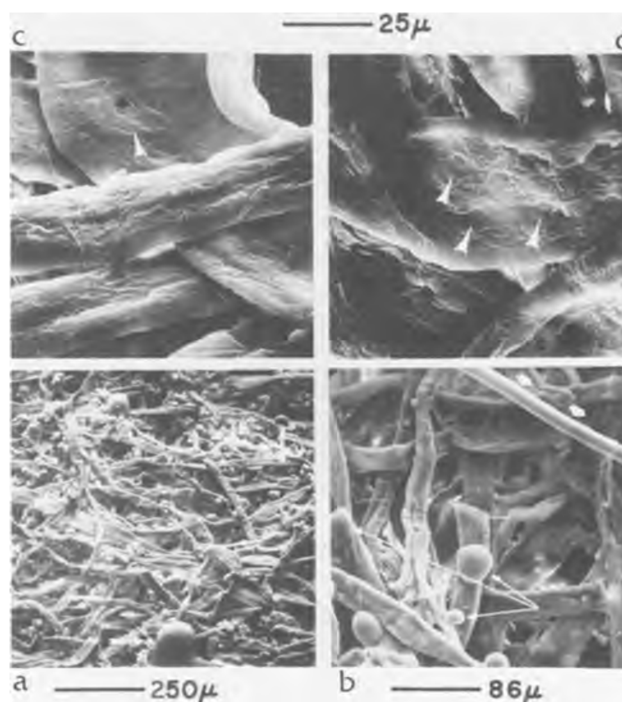

Fig. 6. Scanning electron micrographs of RBC separator matrixes. The evidence for nonequilibrated sorption is indicated. a and b show large liquid excesses of impregnate, as indicated by the globules (narrow arrows). The broad arrows (b) indicate the synthetic resins used to give breaking strength to the sheets. c and d indicate zones where normal surface free energy minimization has created dimplelike structures in the curing liquid film on the fiber surface.

The specific reactivities of the —OH present on the cellulose chains are different, and the accessibility of the sites is different, some being distant from the reactive interface (84) and requiring, therefore, special swelling techniques to allow more complete access to the reactive sites. The spectrum of accessibilities is associated with the highly structured nature of alpha cellulose, and the annealing work of Attala and Nagel (112) and Basch and Lewin (113) shows that the basic structural units can be opened to reactive and reorganizing influences. Morosoff's work on rewetting and drying indicates much the same conclusions (109).

Another interesting suggestion is that of formulating the substrate paper with mechanically decrystallized cellulose. Amorphous cellulose is more reactive than crystalline material, and a paper formulated of a large proportion of this more reactive species should absorb the impregnating resins more fully and therefore be better protected. In-process methods of decrystallization may also be possible. Tsuji, Hirai, and Hosono (142) decrystallized fabrics chemically, using a sodium hydroxide/acrylonitrile treatment, and realized very high accessibilities with only small changes in fabric properties. Using a wide variety of pretreatments, they produced highly decrystallized cellulose with very high specific reactivities. Treatments such as these may be the key to providing a more completely prereacted (impregnated) separator matrix. The usefulness of simple mechanical decrystallization is reduced by the tendency of amorphous cellulose to recrystallize when immersed in water (143).

Graft copolymerization—A new fiber.—A second development route to a new, more efficient separator matrix may lie in generating what is basically a new fiber. This can be done by graft copolymerization of newer or better impregnates onto the cellulosic backbone. Mino and Kaizermann (144) found that ceric ion redox systems gave high yields of copolymer, because the free-radical sites were generated mainly on the trunk polymer. Richards described, in 1961, several interesting approaches to grafting, using the ceric ion (145) and also diazonium cellulose derivatives (146) as initiators. He was able to graft acrylonitrile onto cellulose in this way. Similarly, styrene-cellulose copolymers have been made, using hydroxyl radicals (147) as initiators or catalysts. Irradiation from gamma sources has been successfully used to graft ethyl acrylate onto cellulose (148). Other energetic radiation schemes are expected to be efficient as initiating methods.

The number of monomers studied to date has been large (149), and the dominant initiator technique has utilized ceric salts or other strong oxidizers (150) to create reactive sites on the cellulose backbone. This technique has been popular because it has resulted in low yields of homopolymer, apparently because (144) initiation (free-radical production) is restricted to the trunk molecule. Ide and Takayama found low yields of polymethyl-methacrylate (PMMA) when grafting MMA onto cellulose, using $Ce(NO_3)_3 \cdot 2NH_4NO_3$ as initiator (151). When he grafted vinyl acetates onto cellulose (152), Ide found somewhat higher homopolymer yields, indicating that initiation also takes place on the monomer in this case. Ide also found the homopolymer yield higher with acrylonitrile (153). Ogiwara and Kubota (154) found that the yield of homopolymer, in the case of MMA/cellulose grafts, might depend on the order of addition of initiator (in this case, ceric ion). They found grafting more efficient if ceric-ion initiator was added to an aqueous suspension of cellulose and MMA, but in this scheme, the homopolymer yield folowed graft efficiency.

The graft copolymerization of monomers onto cellulose has been pursued most actively using methyl methacrylates and related monomers (126, 148, 150, 151, 153-155). Styrene has been studied (146, 156), as has vinylpyridine (157) and methylvinylpyridine (158). The latter is a very interesting prospect for separator applications, because Kryazhev and Rogovin found large ion exchange capacities (3-4 mequiv. HCl/g) for the cellulose-methylvinylpyridine copolymer (158).

Most grafts decrease the hydrophilic character of the copolymer, though Hui and Lepoutre made copolymers with quite enhanced water absorbency (159). They used a cationic monomer of poly(2-dimethylaminoethyl-methacrylate). These water absorbency properties should appear very interesting to those working in the lead-acid battery industry. Lepoutre *et al.* studied the effect of grafted vinyl monomer on the water sorption kinetics of alpha cellulose (160). Grafted styrene was studied, in particular, and it was found that the degree of swelling during grafting played a large part in determining final properties. They found that nonpolar grafts decreased equilibrium water content but increased the diffusivity of water. Polar monomers, such as ethyl acrylate, acrylonitrile, and acrylic acid had the opposite effect, showing that side-chain configuration was instrumental in determining properties.

Grigoryan and Rogovin grafted poly(2,3-dichlorobutadiene) onto cellulose and found decreased hydrophilic character and increased resistance to mineral acids (161). It is expected that resistance to mineral acids will be dependent on the acid resistance of the grafted monomer.

Ogiwara, Kubota, Murayama, and Sakamoto studied the physical and chemical stability of papers made from copolymers of MMA, acrylonitrile, vinyl acetate, and styrene (162). They found the papers generally weak, with dimensional stability a function of water retention, becoming lower as water content increased. The papers were all made from grafted material, indicating the feasibility of such processes. Goynes and Harris (163) studied the character of cotton onto which acrylonitrile or butyl methacrylate was grafted. Up to grafts of approximately 60%, the fiber surfaces appeared almost normal. Higher fractions of graft caused flaking and shredding. Abrasion testing and flex abrasion tests indicated the resistance to tearing, and abrasion decreased as the fraction of graft increased. In cross-sectional microscopic analyses, the fibers were seen to be grafted throughout their bodies, with apparent uniformity a direct function of graft percentage.

Manuscript submitted Aug. 8, 1977; revised manuscript received Dec. 29, 1977.

Any discussion of this paper will appear in a Discussion Section to be published in the December 1978 JOURNAL. All discussions for the December 1978 Discussion Section should be submitted by Aug. 1, 1978.

Publication costs of this article were assisted by ESB Incorporated.

REFERENCES

1. W. C. Brooks, *Trans. Electrochem. Soc.*, **33**, 311 (1917).
2. G. T. Eyanson, U.S. Pat. 688,077 (1901).
3. E. A. Sperry, U.S. Pat. 729,100 (1903).
4. H. E. Pratt, U.S. Pat. 1,056,299 (1913).
5. W. F. Hardy and E. H. Hungerbuhler, Ger. Pat. 256,401 (1912).
6. H. Rodman, U.S. Pat. 1,051,637 (1913).
7. H. Rodman, U.S. Pat. 1,051,638 (1913)
8. L. H. Flanders, U.S. Pat. 963,216 (1910).
9. C. C. Carpenter, U.S. Pat. 1,087,637 (1914).
10. R. N. Chamberlain, U.S. Pat. 1,185,058 (1916).
11. W. S. Gould, U.S. Pat. 1,195,924 (1916).
12. W. L. Bliss, U.S. Pat. 1,203,983 (1917).
13. W. H. Wood, U.S. Pat. 1,502,455 (1924).
14. P. E. Norris, U.S. Pat. 1,589,419 (1926).
15. P. E. Norris, U.S. Pat. 1,665,604 (1928).
16. T. A. Willard, U.S. Pat. 1,500,353 (1924).
17. J. Ekisler, U.S. Pat. 2,015,006 (1935).
18. E. G. Lunn, U.S. Pat. 2,014,390 (1935).
19. G. Slayter, U.S. Pat. 2,117,371 (1938).
20. G. Slayter, U.S. Pat. 2,168,366 (1939).
21. The Chloride Electrical Storage Co., Ltd., Brit.

Pat. 479,390 (1938).
22. L. Fuller and E. W. Sudlow, Brit. Pat. 506,062 (1939).
23. G. Slayter, U.S. Pat. 2,306,347 (1943).
24. G. W. Vinal, U.S. Pat. 2,511,887 (1950).
25. J. A. Szper, U.S. Pat. 2,526,591 (1950).
26. H. E. Walker, U.S. Pat. 2,607,810 (1952).
27. T. E. Phillips, U.S. Pat. 2,653,985 (1953).
28. N. Dodge, U.S. Pat. 1,000,350 (1911).
29. W. Taylor, Brit. Pat. 28,858; 28,859 (1911).
30. J. M. Skinner, U.S. Pat. 1,052,851 (1913).
31. W. Morrison, U.S. Pat. 1,058,779 (1913).
32. J. M. Skinner, U.S. Pat. 1,098,357 (1914); 1,130,640 (1915).
33. F. Wright, U.S. Pat. 1,200,682 (1916).
34. W. Morrison, U.S. Pat. 1,228,368; 1,228,369 (1916).
35. G. Shimazu, Jpn. Pat. 30,445; 30,446; 30,447 (1916).
36. E. Lunn, U.S. Pat. 1,529,839 (1925).
37. P. E. Norris, U.S. Pat. 1,492,260 (1924).
38. H. J. Hampton, U.S. Pat. 1,674,594 (1928).
39. J. P. Wilburn, U.S. Pat. 1,607,496 (1926).
40. E. W. Shepherd, U.S. Pat. 1,496,495 (1924).
41. E. W. Smith, U.S. Pat. 1,800,364 (1931).
42. G. Steerup, U.S. Pat. 1,370,064 (1921).
43. L. V. Peakes, Jr., R. A. Lloyd, V. S. Barnes, J. H. Berry, and J. G. Ritter, *Ind. Eng. Chem.*, **38**, 780 (1946).
44. P. Schidrowitz and H. A. Goldsbrough, *India Rubber J.*, **44**, 1147 (1913).
45. P. Schidrowitz and H. A. Goldsbrough, Ger. Pat. 321,092 (1914); Fr. Pat. 478,369 (1915).
46. T. A. Willard, Ger. Pat. 293,700 (1915).
47. T. A. Willard, Canad. Pat. 171,821 (1916); U.S. Pat. 1,243,368-1,243,371 (1918); U.S. Pat. 1,295,-660 (1919); U.S. Pat. 1,375,763 (1921).
48. H. Beckmann, U.S. Pat. 1,831,406 (1931).
49. M. H. Martindell, U.S. Pat. 2,007,093 (1935).
50. H. W. Greenup, U.S. Pat. 1,959,160 (1934).
51. H. W. Greenup and L. E. Olcott, *Ind. Eng. Chem.*, **29**, 193 (1937).
52. N. I. Palmer, Paper presented to the BCI Convention, Mexico City, Mexico (1975).
53. J. A. Orsino and E. J. Dunn, Jr., SAE International Congress, Detroit, Michigan, January 1961.
54. J. A. Orsino and E. J. Dunn, Jr., Paper presented at the Electrical Insulator Conference, Washington, D.C., February 1962.
55. W.H. Wood and H. E. Smith, U.S. Pat. 1,432,938 (1922).
56. R. C. Benner and N. K. Chaney, U.S. Pat. 1,786,328 (1930).
57. E. R. Dillehay and R. D. Schuetz, U.S. Pat. 2,531,-504 (1950).
58. W. H. Lehmberg, U.S. Pat. 2,579,589 (1951).
59. J. J. Uber, U.S Pat. 2,543,137 (1951).
60. H. D. Wilson, U.S. Pat. 2,591,754 (1952); H. D. Wilson, U.S. Pat. 2,591,755 (1952).
61. E. W. Merrill, U.S. Pat. 2,687,446 (1954).
62. E. C. Uhlig and A. Defusco, U.S. Pat. 2,678,961 (1954).
63. E. W. Merrill, U.S. Pat. 2,687,445 (1954).
64. E. L. Mears, U.S. Pat. 2.273,095 (1956).
65. T. Raphael and R. W. Schweitzer, U.S. Pat. 2,810,-775 (1957).
66. O. E. Beckvold and P. Hartman, U.S. Pat. 2,873,-497 (1959).
67. J. Dowse and F. Booth, U.S. Pat. 2 837,592 (1958).
68. W. N. Stickel, U.S. Pat. 2,850,559 (1958).
69. J. F. Little, U.S. Pat. 3,228 803 (1966).
70. G. E. Hall, U.S. Pat. 3,205,098 (1965).
71. C. L. Mills, U.S. Pat. 2,980,750 (1961).
72. M. Vedovelli, U.S. Pat. 3,037,899 (1962).
73. P. Zenczak, U.S. Pat. 3,272.657 (1966).
74. J. J. Lander, in "Proceedings of the Symposium on Battery Separators," p. 4, Columbus, Ohio, February 1970.
75. E. Sundberg, *ibid.*, p. 32.
76. S. Parr, *J. Inst. Elec. Eng.*, **36**, 406 (1905).
77. J. T. Crennell and A. G. Milligan, *Trans. Faraday Soc.*, **27**, 103 (1931).
78. H. E. Haring and K. G. Compton, *Trans. Electrochem. Soc.*, **68**, 283 (1935).
79. G. Wranglen, *Electrochim. Acta*, **2**, 130 (1960).
80. B. de Carolles, *J. Prakt. Chem.*, **32**, 427 (1844).
81. A. Ekenstam, *Berichte*, **69D**, 549 (1936).
82. K. Freudenberg *et al.*, *Ber. Dtsch. Chem. Ges.*, **63**, 1510 (1930); **63**, 484 (1932); **68**, 2070 (1934).
83. C. Y. Liang and R. H. Marchessault, *J. Polymer Sci.*, **35**, 529 (1959); **39**, 269 (1959).
84. S. P. Rowland, E. J. Roberts, and J. L. Bose, *ibid.*, **9A1**, 1431 (1971).
85. I. Rusznak and I. Tanczos, *ibid.*, **C42**, 1475 (1973).
86. S. Seitsonen and I. Mikkonen, *ibid.*, **A2-10**, 1743 (1972).
87. J. R. Dafler, *J. Appl. Polymer Sci.*, **21**, 2551 (1977).
88. S. Nishikawa and S. Ono, *Proc. Tokyo Math.-Physic Soc.*, **7**, 131 (1913).
89. K. H. Meyer and L. Misch, *Helv. Chem. Acta*, **20**, 232 (1937).
90. G. Clark, *Ind. Eng. Chem.*, **22**, 474 (1930).
91. W. O. Statton, *J. Polymer Sci.*, **C-18**, 33 (1967).
92. S. Kovesh and J. M. Schultz, *Polymer Eng. Sci.*, **9**, 452 (1969).
93. H. D. Smith, *Ind. Eng. Chem.*, **29**, 1081 (1937).
94. M. M. Y. Chang, *J. Polymer Sci.*, **A1-12**, 1349 (1974).
95. R. A. Jacobson, J. A. Wunderlich, and W. N. Lipscomb, *Acta Cryst*, **14**, 598 (1961).
96. C. J. Brown, *J. Chem. Soc.*, **1966A**, 927 (1966).
97. W. N. Haworth, "The Constitution of Sugars," Arnold, London (1929).
98. A. Sarko and R. Muggli, *Macromolecules*, **7**, 486 (1974).
99. R. E. Reeves, *J. Am. Chem. Soc.*, **71**, 215 (1949).
100. A. Bjornhaug, O. Ellefson, and B. A. Tonneson, *Nor. Skogind.*, **7**, 171 (1953).
101. R. St. John Manley, *J. Polymer Sci.*, **A2-9**, 1025 (1971).
102. D. W. Jones, *ibid.*, **42**, 173 (1960).
103. W. L. Balls, *Proc. Roy. Soc.*, **B95**, 72 (1923).
104. R. E. Mark, P. N. Kaloni, R. C. Tang, and P. P. Gilbis, *Science*, **164**, 72 (1969).
105. A. K. Kulshreshthwa and N. E. Dweltz, *J. Polymer Sci.*, **A2-11**, 487 (1973).
106. T. J. Hebert and L. L. Muller, *J. Appl. Polymer Sci.*, **18**, 3373 (1974).
107. (a) P. H. Hermans and A. Weidinger, *J. Appl. Phys.*, **19**, 491 (1948); (b) L. Segal, M. L. Nelson, and C. M. Conrad, *J. Phys. Colloid Chem.*, **55**, 325 (1951); (c) L. Segal, J. J. Creely, A. E. Martin Jr., and C. M. Conrad, *Textile Research J.*, **29**, 786 (1959).
108. B. A. Campbell and J. R. Dafler, *This Journal*, **122**, 1084 (1975).
109. N. Morosoff, *J. Appl. Polymer Sci.*, **18**, 1837 (1974).
110. M. F. Froix and R. Nelson, *Macromol.*, **8**, 726 (1975).
111. A. Venkataswaran and J. A. Van den Akker, *J. Appl. Polymer Sci.*, **9**, 1167 (1965).
112. R. H. Attala and S. C. Nagel, *J. Polymer Sci., Lett.*, **12**, 565 (1974).
113. A. Basch and M. Lewin, *ibid.*, **13**, 493 (1975).
114. A. Meller, *J. Polymer Sci.*, **4**, 619 (1949); **10**, 213 (1953).
115. R. F. Nickerson and J. A. Haberle, *Ind. Eng. Chem.*, **37**, 1115 (1945); **38**, 299 (1946); **39**, 1507 (1947).
116. A. Sharples, *J. Polymer Sci.*, **13**, 393 (1954); **14**, 95 (1954).
117. O. Ant-Wuorinen and A. Visapaa, *Paperi Puu*, **38**, 523 (1956).
118. (a) R. G. Ranby, *Acta Chem. Scand.*, **3**, 649 (1949). (b) O. A. Battista, *Anal. Chem.* **16**, 351 (1944).
119. F. Raschig. *Kuntstoffe*, **27**, 51 (1937).
120. C. L. Moyle and P. A. Wolfe, U.S. Pat. 2,630,458 (1953).
121. F. D. Chattaway and A. A. Morris, *J. Chem. Soc.*, 2031 (1927).
122. R. F. Nickerson, *Ind. Eng. Chem.*, **34**, 85 (1942).
123. O. A. Battista, *ibid.*, **42**, 502 (1950).
124. M. A. Millet, W. E. Moore, and J. F. Saeman, *ibid.*, **43**, 1493 (1954).
125. M. Chang, T. C. Pound, and R. St. John Manley, *J. Polymer Sci.*, **A2-11**, 399 (1973).
126. H. Kurosu and K. Horuke, *Mokuzai Gakkaishi*, **22**, 92 (1976).
127. O. Ant-Wuorinen, *Paperi Puu*, **38**, 583 (1958).
128. O. Ant-Wuorinen and A. Visapaa, *ibid.*, **39**, 151 (1957).
129. O. Ant-Wuorinen and A. Visapaa, *ibid.*, **39**, 229 (1957).
130. O. Ant-Wuorinen and A. Visapaa, *ibid.*, **51**, 107, 617, 737, 756 (1969-1970).
131. O. Ant-Wuorinen, *ibid.*, **27**, 307, 322 (1939).
132. J. F. Saeman, *Ind. Eng. Chem.*, **37**, 43 (1945).
133. J. R. Dafler, A. A. Garwood, F. W. Wentzel, B. Cambell, and D. L. K. Chu, *This Journal*, **123**, 780 (1976).

134. W. V. R. Malkus, *Proc. Roy. Soc.*, **A225**, 185 (1954).
135. E. Zehender, W. Herrman, and H. Leibssle, *Electrochim. Acta*, **9**, 55 (1964).
136. Whatman Laboratory Products, p. 1-19, Clifton, N.J. (1976).
137. Aminco-Winslow Porosimeter Bulletin, typical percent undersize curves supplied with instrument, Aminco-Winslow, Yellow Springs, Maryland.
138. E. F. Thode, J. W. Swanson, and J. J. Becker, *J. Phys. Chem.*, **62**, 1036 (1958).
139. J. Ruzicka and L. Kudlacek, *Vysokomol. Soyed.*, **6**, 577 (1964).
140. J. E. Luce and A. A. Robertson, *J. Polymer. Sci.*, **51**, 317 (1961).
141. D. Taylor, "Gases, Liquids and Solids," p. 212ff, Penguin Press, Baltimore, Maryland (1969).
142. W. Tsuji, A. Hirai, and H. Hosono, *J. Appl. Polym. Sci.*, **20**, 2837 (1976).
143. P. Hermans and A. Weidinger, *J. Am. Chem. Soc.*, **68**, 2547 (1946).
144. G. Mino and S. Kaizerman, *J. Polym. Sci.*, **31**, 242 (1958).
145. G. N. Richards, *J. Appl. Polym. Sci.*, **5**, 539 (1961).
146. G. N. Richards, *ibid.*, **5**, 553 (1961).
147. G. Landells and C. S. Whewell, *J. Soc. Dyers Colourists*, **67**, 338 (1951); **71**, 171 (1955).
148. Y. Nakamura, O. Hinojosa, and A. C. Jett, Jr., *J. Appl. Polym. Sci.*, **14**, 789 (1970).
149. R. M. Livshits and Z. A. Rogovin, *Progr. Polim. Khum.*, 158, (1968); *Chem. Abstr.*, **47**, 3627e.
150. Y. Ogiwara and H. Kubota, *J. Appl. Polym. Sci.*, **14**, 817 (1970).
151. F. Ide and Y. Takayama, *Kogyo Kagaku Zasshi*, **64**, 2B (1961); *Chem. Abstr.*, **47**, 3627e.
152. F. Ide, *ibid.*, **64**, 925 (1961); *Chem. Abstr.*, **47**, 4862c.
153. F. Ide, *ibid.*, **65**, 82 (1962); *Chem. Abstr.*, **47**, 10030c.
154. Y. Ogiwara and H. Kubota, *J. Appl. Polym. Sci.*, **14**, 1049 (1970).
155. M. Rebek, *Holzforschung*, **21**, 58 (1967).
156. F. Ide, *Kogyo Kagaku Zasshi*, **65**, 88 (1962); *Chem. Abstr.*, **47**, 10030e.
157. M. U. Sadykov, U. Azizov, Kh. Usmanov, and I. M. Mirkamilov, *Vysokomol. Soedin*, **A10**, 322 (1968).
158. Y. G. Kryazhev and Z. A. Rogovin, *ibid.*, **A-3**, 1847 (1961).
159. S. H. Hui and P. Lepoutre, *J. Appl. Polym. Sci.*, **19**, 1771 (1975).
160. P. F. Lepoutre, H. B. Hoffenberg, and V. Stannett, *J. Polym. Sci.*, **C-37**, 309 (1972).
161. R. G. Grigoryan and Z. A. Rogovin, *Izv. Vyssh. Ucheb. Saved. Teknol. Tekst. Prom.*, p. 90 (1967).
162. Y. Ogiwara, H. Kubota, H. Murayama, and A. Sakomoto, *Tappi*, **53**, 1685 (1970).
163. W. R. Goynes and J. A. Harris, *J. Polym. Sci.*, **C-37**, 277 (1972).

The Characterization of Internal Power Losses in Pacemaker Batteries by Calorimetry

L. D. Hansen

Thermochemical Institute and Department of Chemistry, Brigham Young University, Provo, Utah 84602

and R. M. Hart

Tronac, Incorporated, Orem, Utah 84057

ABSTRACT

A calorimeter for measuring heat output from batteries is described. The calorimeter has a peak-to-peak noise level of 0.3 μW. A thermodynamic analysis of battery processes is given and a method of using the calorimetric data to study and define parasitic processes is illustrated with data on several batteries.

One of the limits on the operational life of pacemakers is the battery which is used as a power source. All batteries are subject to internal self-discharge which, in turn, limits or shortens the life of the batteries. This self-discharge can result from three processes: (*i*) migration and direct chemical combination of anode or cathode substances; (*ii*) spontaneous decomposition of the anode or cathode; and (*iii*) reaction of the anode or cathode with contaminant gases or some battery component that was supposedly inert. The rates of these self-discharge processes can be dependent on or independent of the current being drawn from the battery. Since self-discharge is essentially a chemical reaction occurring inside the battery, it can be measured and studied by determining the rate of heat production of the battery in a calorimeter (1-5). The possibility also exists for developing the calorimetric method into a nondestructive quality control test to eliminate batteries with abnormally high self-discharge rates.

The purposes of this paper are: (*i*) to describe a calorimeter which was designed specifically for studying pacemaker batteries; (*ii*) to give a thermodynamic basis for determining the dependence of the rate of self-discharge on electrical current in the battery; and (*iii*) to present some of the results which have been obtained on various types of batteries.

Key words: thermodynamics, lithium, silver, mercury, zinc.

Calorimeter

The calorimeter used in this study is commercially available and is a twin-cell differential heat flow instrument as shown in Fig. 1. The calorimeter has a peak-to-peak noise level of less than 0.3 μW and a precision better than 1 μW on a battery measurement.

The calorimeter consists of an aluminum block 15 cm wide, 17 cm high, and 30 cm long with a tapered channel 10 cm wide, 10 cm deep, and 25 cm long cut into it, four wedges of 2.5 cm thick aluminum which were placed in the channel, and four thermoelectric measuring devices (Cambion Model 1052) which are mounted on the aluminum wedges together with two battery holders made of thin aluminum. The large aluminum block assembly was suspended by four 0.25 in. bolts in the center of a watertight box which was then submerged in a Tronac Model 405 water bath controlled to

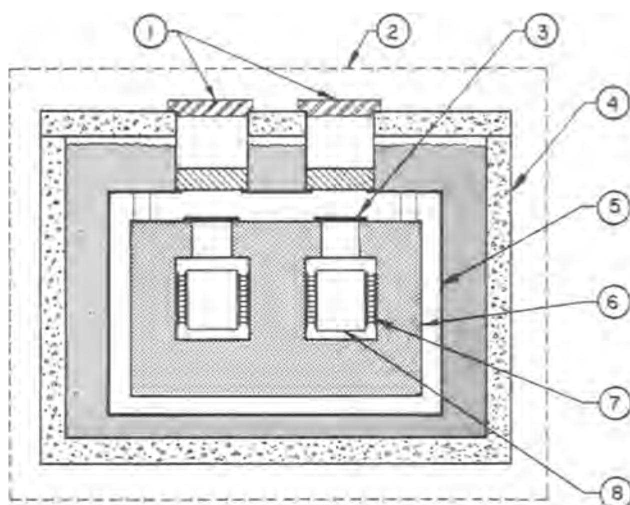

Fig. 1. Schematic of Tronac battery calorimeter. 1, access tubes and covers; 2, temperature-controlled air bath with electronics inside; 3, covers on block compartments; 4, temperature-controlled water bath; 5, water-tight stainless steel box; 6, aluminum heat sink block; 7, thermoelectric sensors; 8, battery holder.

$\pm$ 0.0002°C. Two pipes, sealed around holes in the box cover, give access through the water bath to the battery holders. During a measurement, the holes in the box cover and the battery holders are covered with aluminum plates to prevent heat transfer by air currents.

The outputs from the two sets of thermoelectric devices were connected with opposing polarities so that the effects of any temperature fluctuations in the block would be canceled in the output. The difference in the output voltages of the two compartments, which is proportional to the difference in the rates of heat production in the two compartments, was filtered with a simple R-C filter (time constant = 6 min), amplified by a Keithley Model 150B amplifier, and recorded on a strip chart recorder. Typically the recorder was run at 5 cm/hr and 100 mV full scale and the amplifier at a gain of 3×10^4. A 5½-digit digital voltmeter and printer were connected in parallel with the recorder for some runs in which the recorder dead band was a significant limitation. Peak-to-peak baseline noise was found to be about ± 0.1 μW if the heat capacity of the compartment used as a reference was carefully adjusted by an aluminum block to be the same as the compartment containing a battery.

Calibrations were done in two ways. In most cases, a 1 kΩ resistor mounted in the battery holder was used to provide a known rate of heat to the cell. In one case, a 1 kΩ resistor was mounted directly on a battery. There was no significant difference in the results. Calibrations were done at heater powers of 20, 27, 137, and 184 μW. Again, there was no significant difference in the output voltage/μW of heat input. The calibration constant is believed to be accurate to ~2% on the lowest heater power and to ~1% on the higher ones. A Tronac 450EC board was used to supply power to the heater. Heater and standard resistor voltages were measured with a Data Precision Model 3500, 5½ digit DVM. The results from a sample set of calibration runs are given in Table I.

Measurements of open-circuit heat dissipation of batteries were made by equilibrating the batteries for 8-12 hr in the space above the measurement compartment, placing a battery in a compartment, waiting until any heat stored in the battery because of a temperature difference was dissipated totally as shown by a flat baseline (usually about 1 hr) and then removing the battery. The difference in the measured rate of heat output from a given compartment before and after removal of the battery is then the heat output of the battery. Tests using an aluminum block in place of

Table I. Sample calibration runs

Displacement from baseline in μV*

	Heater power = 19.77 μW Left side	Heater power = 19.81 μW Right side
	3408	
	3399	3149
	3410	3153
	3402	3139
	3404	3140
	3405	3144
Average	3405 $\pm$ 2**	3145 $\pm$ 3**

* Corrected to sensor outputs. Data in this table were collected digitally with a DVM.
** Standard deviation with respect to the mean.

a battery showed that the reproducibility of this procedure was better than $\pm$ 1 μW.

Measurements of heat dissipation in batteries under discharge were made by electrically connecting the battery to a resistor outside the calorimeter with two No. 40AWG wires. The wires were placed in good thermal contact with the calorimeter block to prevent thermal leakage from outside the calorimeter. All measurements were made at 37°C.

Theory

For an experiment on an ideal battery where the battery is in a calorimeter and connected electrically to a load resistor outside the calorimeter

$$Q = \text{heat produced in the calorimeter} \quad [1]$$

$$W = I^2Rt = \text{electrical energy dissipated in the resistor if the battery is sealed so that } \Delta PV \text{ work is zero} \quad [2]$$

and

$$W = I^2Rt + P\Delta V \text{ if the battery is open to the atmosphere} \quad [3]$$

The first law of thermodynamics states that

$$\Delta E = Q - W \quad [4]$$

Substituting Eq. [2] into Eq. [4] and taking the derivative with respect to time, we have Eq. [5]

$$\frac{d\Delta E_1}{dt} = \frac{I\Delta E_1}{\mathbf{F}} = q - I^2R \quad [5]$$

where I is the current in the resistor, $\mathbf{F}$ is the Faraday, ΔE_1 is the total energy change per equivalent of current producing reaction under the conditions extant in the battery, q is the rate of heat production in the battery, and R is the load resistance value. For a real battery with more than one reaction occurring and less than 100% current producing efficiency of the main reaction, it is necessary to add a term to the left side of Eq. [5] for each extra reaction and for that part of the main reaction that does not produce current.

$$\frac{I\Delta E_1}{\mathbf{F}} + \frac{d\Delta E_2}{dt} + \frac{d\Delta E_3}{dt} + \ldots = q - I^2R \quad [6]$$

Equation [6] applies exactly only if the battery is sealed so that ΔPV work is zero. If the battery is open to the atmosphere so that P is constant

$$\Delta E = \Delta H - P\Delta V \quad [7]$$

and [8] can be obtained by substituting [7] and [3] into [4], taking the time derivative, and adding the terms for the extra reactions

$$\frac{I\Delta H_1}{\mathbf{F}} + \frac{d\Delta H_2}{dt} + \frac{d\Delta H_3}{dt} + \ldots = q - I^2R \quad [8]$$

Since the extended life batteries studied here were sealed, Eq. [6] will be used in the remainder of this paper although it should be obvious that H may be substituted for E in any of the following equations.

Rearranging Eq. [6] so that all known terms are on the right side gives Eq. [9], where P_{internal} is the sum of the unknown derivative terms. The

$$P_{\text{internal}} = q - I^2R - \frac{I\Delta E_1}{\mathbf{F}} \quad [9]$$

behavior of P_{internal} as a function of the current can tell much about the nature of the unknown processes in a battery as is shown in the discussion.

Results and Discussion

Table II gives the results obtained for a series of open-circuit ($I = 0$) heat dissipation measurements on batteries of various kinds, shapes, and sizes. These results clearly show the capabilities of the calorimeter as well as the reproducibility of open-circuit heat dissipation in a set of supposedly identical batteries.

Calorimetric measurements of open-circuit heat dissipation of batteries may not accurately reflect that a primary chemical reaction is occurring in the battery with a consequent loss in amp-hours available. Any process, such as crystal growth, evaporation of liquids, curing of plastics and cements, and mechanical strain release can produce a change in the total energy content of the battery and, hence, an output signal to the calorimeter. These changes are usually not significant in determining battery life, although they can lead to mechanical failure of some battery component. Calorimetric experiments can be done to determine the magnitude and source of most of these effects by measuring the heat output of each of the battery components separately. Open-circuit heat dissipation is also typically a function of age as shown in Fig. 2, and this must be taken into account in interpreting these kinds of data.

Table III gives representative results of measurements of heat dissipation for three different types of batteries under discharge. The data from Table III were used to calculate values of P_{internal} (Eq. [9]) which were then plotted as shown in Fig. 3.

Since P_{internal} represents the chemical or stored energy dissipated as heat by all reactions that do not produce current, a line with a slope equal to zero, as in the Li/I_2 system, shows that all such processes are independent of the current. The slope of zero also proves that all of the current producing reactions have been accounted for properly by the one assumed reaction with a current efficiency of 100% in the Li/I_2 battery. The nonzero intercept is thus probably due to processes as mentioned above which do not cause a loss in total available current.

The AgO/Zn battery becomes slightly more efficient in the use of total stored energy as the current increases while the HgO/Zn battery apparently rapidly loses energy efficiency as the current increases (Fig. 3). Both of the latter effects are probably due to changes in current producing reactions since intermediate oxidation states are possible for the Hg and Ag. Further evidence that more than one current producing reaction is involved in the AgO/Zn battery was observed in the calorimetric data produced during the transient from zero to 156 μA of discharge as shown in Fig. 4. The shoulder on the curve clearly shows that an additional reaction occurs at the higher current after depletion of some intermediate component.

The linearity of the curve for the HgO/Zn battery at the higher currents suggests that either the ΔE_1 value is in error by about 4%, which is unreasonable for these substances, or that we have not fully accounted for the battery reactions which produce current.

In summary, data plotted as shown in Fig. 3 can be used to show that all current dependent battery proc-

Table II. Open-circuit battery measurements

Battery type	Amp hours	Volts	Power,* μW	No. in sample
Mercury, HgO/Zn, pacemaker Set I	1	1.4	4.1 ± 0.1	2
Mercury, HgO/Zn, pacemaker Set II	1	1.4	7.5 ± 0.3	2
Alkaline, MnO_2/Zn, penlight	2	1.5	46 ± 2	2
Mercury, HgO/Zn, penlight	2	1.4	68 ± 5	2
Carbon-Zn, penlight	1	1.5	15	1
AgO/Zn watch battery set I	0.16	1.5	7 ± 1	8
AgO/Zn watch battery set II	0.16	1.5	10.2 ± 0.4	3
AgO/Zn watch battery set III	0.16	1.5	13 ± 1	5
Lithium-iodine pacemaker set I	1.2	2.7	5 ± 1	2
Lithium-iodine pacemaker set II	1.5	2.7	30 ± 5	2
Lithium-iodine pacemaker set III	3.0	2.7	6 ± 2	2

* Deviations are the standard deviation with respect to the mean between batteries.

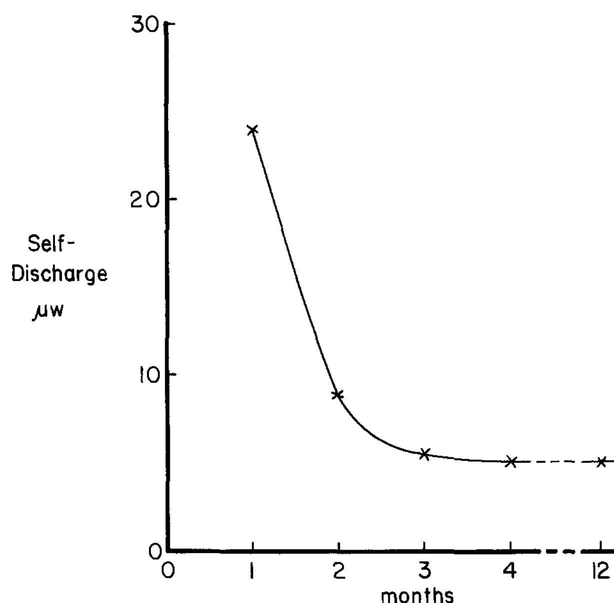

Fig. 2. Effect of aging on open-circuit heat dissipation from Li/I_2 batteries.

Table III. Heat dissipation from batteries under discharge

Voltage	Current, μA	Load resistor, kΩ	Rate of heat production,* μW
Li/I_2: Li + ½I_2 = LiI ΔE = −272 kJ/equiv.			
2.8093	—	Open circuit	—
2.7955	4.9	566	−1.25
2.7816	10.2	273	−0.63
2.7526	21.3	129	1.25
2.7056	39.8	68.04	2.50
2.6344	67.4	39.10	11.3
2.5682	94.4	27.20	24.0
2.4615	137	17.97	46.0
2.3196	195	11.92	86.6**
AgO/Zn: AgO + Zn = Ag + ZnO ΔE = −168 kJ/equiv.			
1.5810	—	Open circuit	—
1.5614	78	20.0	9.5
1.5610	156	10.01	24.3
1.5580	311	5.01	51.6
HgO/Zn: HgO + Zn = Hg + ZnO ΔE = −129 kJ/equiv.			
1.3996	—	Open circuit	—
1.3960	5.1	273	7.2
1.3896	20.4	68.04	7.9
1.3780	50.7	27.20	11.6
1.3701	114.9	11.92	13.5
1.3629	197	6.93	18.5
1.3578	407	3.34	28.5
1.3533	752	1.80	43.5

* Values given in this column are the actual measured differences between the rate of heat production with the external load resistor circuit closed and open. To get the total heat production rate for calculation of P_{internal}, 5, 7, or 6 μW from the independent measurement of the open-circuit heat-production rate without wires attached to the battery must be added for the Li/I_2, AgO/Zn, and HgO/Zn battery, respectively.

** This value is significantly in doubt because the battery did not reach a steady-state heat production rate for several hours and the return to the baseline after opening the circuit was also extremely slow.

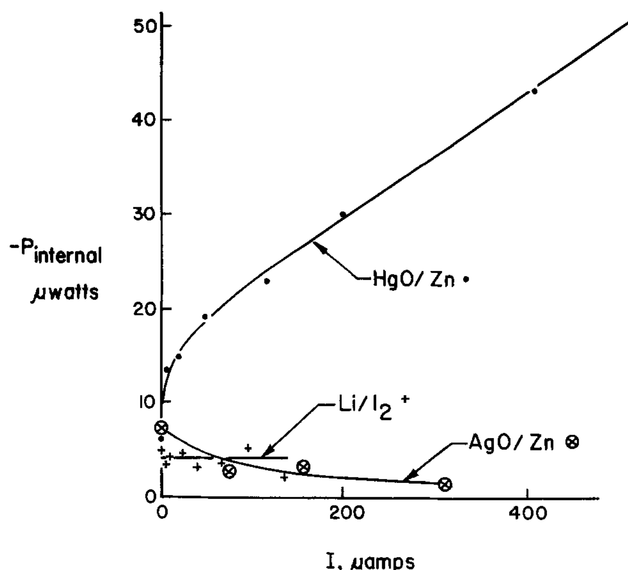

Fig. 3. Plots of $P_{internal}$ against current being drawn from the battery. (See text Eq. [9].)

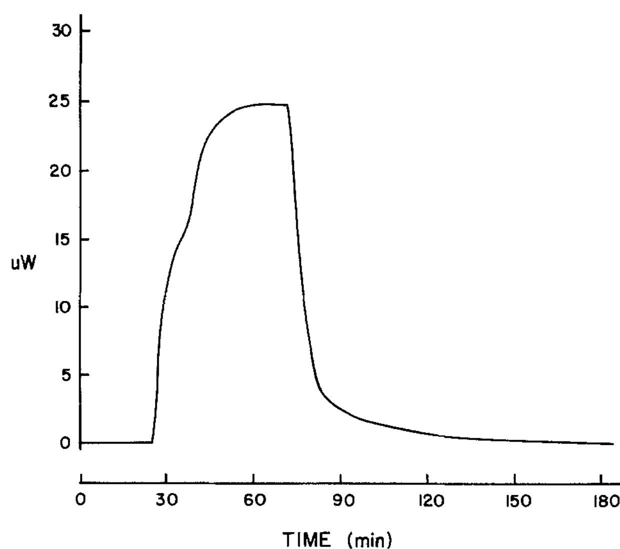

Fig. 4. Actual calorimeter output for a AgO/Zn battery. From 0 to 28 min the battery circuit was open. At 28 min a 10 kΩ resistor was connected across the battery. The circuit was opened at 70 min. Power dissipation is relative to the baseline with the battery in the calorimeter with wires attached but with the circuit open.

esses have been correctly described (slope = zero) or that they have not. In the latter case, the form of the curve suggests the nature of the remaining processes.

Manuscript submitted Sept. 29, 1977; revised manuscript received Jan. 23, 1978.

Any discussion of this paper will appear in a Discussion Section to be published in the December 1978 JOURNAL. All discussions for the December 1978 Discussion Section should be submitted by Aug. 1, 1978.

Publication costs of this article were assisted by Tronac, Incorporated.

REFERENCES

1. E. J. Prosen and J. C. Colbert, NBS Special Pub. 400-42, August, 1977.
2. A. Thorin and A. Lodin, Siemens-Elema AB, S-17194 Solna, Sweden, Paper presented at Tokyo in March, 1976, Personal communication.
3. "Evaluation of Pacemaker Battery Parameters by Microcalorimetry," report issued by Wilson Greatbatch Ltd., Clarence, N.Y. (1977).
4. D. F. Untereker and B. B. Owens, Personal communication Medtronics, Inc.
5. H. F. Gibbard, Paper submitted to *This Journal.*

Anodic Behavior of Lithium in Aqueous Electrolytes

III. Influence of Flow Velocity, Contact Pressure, and Concentration

E. L. Littauer,* K. C. Tsai,* and R. P. Hollandsworth

Lockheed Palo Alto Research Laboratory, Palo Alto, California 94304

ABSTRACT

The influence of electrolyte flow velocity, concentration, and contact pressure on the anodic behavior of lithium at constant temperatures in LiOH was studied. The experimental results reveal that, under constant load polarization, a steady-state *i-E* curve is obtained consisting of resistance and concentration polarization components. A method to accurately determine the film thickness was devised. It was found that the oxide film at the anode surface is quite thick, *ca.* 10^{-2} cm, and its thickness remained constant irrespective of polarization level at constant electrolyte concentration, flow rate, and anode-cathode contact pressure. The effective diffusion layer at the Li active surface is thin, *ca.* 10^{-3} cm. The fraction of active surface area was found to change significantly with LiOH concentration (ranging from 0.05 in 4.84M to 0.39 in 2.96M), but it was virtually independent of flow velocity and contact pressure. Likewise, electrolyte concentration has far greater influence on film resistance than flow rate or contact pressure. Electrolyte flow velocity variation is, however, an effective means to alter power output from the cell.

The oxide/hydroxide film which forms on Li anodes in aqueous, strongly alkaline electrolytes has some unusual properties. For example, even though it is fairly thick (*ca.* 5×10^{-2} cm) it will support high flux rates with very low polarization and yet have sufficient strength to tolerate the counterelectrode being pressed against it without shorting at pressures up to 30×10^4 Pa. In high rate Li-H_2O cells, the counterelectrode comprises a ribbed backplate overlaid by a metallic mesh screen active surface. It is the

* Electrochemical Society Active Member.

Key words: lithium, lithium hydroxide, concentration polarization, limiting current, diffusion layer.

screen which presses against the anode surface and the electrolyte passes behind and around the mesh.

The performance of the cell is controlled by the nature of the anodic film. This film moderates the normally rapid corrosion reaction of the metal with aqueous electrolytes and, provided the OH^- concentration is sufficient, the Li will discharge with good coulombic efficiency if it is polarized by about 300 mV from its OCV ($E_o' = -2.78V$ *vs.* NHE). In other words, the direct corrosion reaction of Li with H_2O (the parasitic reaction) can be effectively inhibited. An unexpected phenomenon is observed with Li, namely, a highly characteristic transient passivation which occurs at $-2.66V$ *vs.* NHE. This phenomenon was examined in detail in a previous paper (1), where specifics of the cell and its operational features were also described.

It has been found that the rates of the electrochemical and parasitic reactions respond very reproducibly to the following factors: (*i*) anode-cathode contact pressure, (*ii*) velocity of electrolyte flow across the anode surface, (*iii*) electrolyte temperature, and (*iv*) OH^- concentration. Increasing contact pressure and flow result in enhanced cell power output without decrement in faradaic efficiency. Significant temperature increase (to $< 40°C$) or decrease of OH^- concentration ($<$ 3M LiOH) increase cell power substantially but generally at some sacrifice in efficiency.

The above-listed factors *i-iv* influence the properties of the LiOH protective layer and these properties control the functioning of the cell. In normal operation the film is in a state of quasi-equilibrium dissolving at the film/electrolyte interface at the same rate as the metal is oxidized. The higher the hydroxyl ion concentration over the range 2-5M, the slower is the dissolution rate and the more protective is the film. This paper examines quantitatively and diagnostically the influence of electrolyte flow velocity, concentration, and anode-cathode contact pressure on the anodic behavior of Li in LiOH solution at constant temperature. Polarization behavior and *in situ* film thickness measurements are reported.

Experimental

Polarization experiments.—The test arrangements and procedures have been detailed previously (1). The *i-E* curves were obtained using the constant load (resistive) polarization technique. A custom electronic load capable of maintaining $\pm$ 0.01V was employed. Electrolyte concentrations ranged from 2.96 to 4.84M and the temperature was maintained at 298° $\pm$ 0.1°K. In the electrolyte flow velocity study, the anode-cathode contact pressure was held at 6.2×10^4 Pa (630 g/cm^2). The solution flow velocity which refers to the average inlet velocity was controlled to within 5%. The velocities studied ranged from 0.064 to 0.42 m/sec. The experimental conditions used in this investigation correlated with actual Li-H_2O battery operation. Generally, a steady-state *i-E* reading was achieved within 1 sec for a given load at any flow velocity. Fresh 99.9% Li anodes were used for each run. In the contact pressure study, a single flow rate of 0.18 m/sec was used. Experiments were performed with the anode-cathode contact pressure controlled to within 5% of 4.1, 6.2, 10.3, and 20.7×10^4 Pa by using an air pressure cylinder linked to the anode push rod. Hydraulic pressure on the electrode which would normally be created by the circulating solution was eliminated by a thrust balance cylinder connected to the inlet and outlet lines of the cell. Polarization runs were performed in triplicate. Reproducibility was such that the experimental curves could be exactly superimposed.

Film thickness determinations.—For these experiments a modified test cell was used. Alterations were made to the cathode compartment to equip it with a solenoid-actuated needlepoint penetrometer. The needle was platinum-plated 4130 steel. The probe was positioned so that on activation it could pass through the cathode matrix and subsequently penetrate the anode surface. Details of the assembly are given in Fig. 1. A Hewlett-Packard 4815A rf impedance meter set at 500 kHz was connected to the anode and to the needle probe. The distance traveled by the probe was monitored by a G. L. Collins Corporation linear motion transducer which had a voltage output directly proportional to position. The outputs of the impedance meter and the linear motion transducer were recorded with a Honeywell Model 1858 CRT visicorder. The probe position could be measured with an accuracy of about 10^{-3} cm. To confirm the sensitivity of the technique, a penetrometer test was performed in a dry room on a lightly oxidized Li specimen. The film thickness result was then compared with precise microscopic measurements of cross sections of the same specimen. The penetrometer gave an average thickness of 6.1×10^{-3} cm and by microscope measurement it was found to be 5.3×10^{-3} cm.

Film thickness was determined as a function of solution flow rate at 0.10, 0.16, 0.23, 0.32, and 0.39 m/sec in 3.2 to 4.7M LiOH. The measurements were taken at six polarization points from OCV to $E_H = -1.0V$. Similarly, film thickness was determined at five anode-cathode contact pressures; 3.5, 7.0, 14.0, 21.0, and 28.0×10^4 Pa over the same polarization range in 4M LiOH. A typical visicorder plot is shown in Fig. 2. Here curve Z represents the impedance between the probe and the anode. It was observed that the resistance within the film was slightly higher than within the electrolyte. After activation, the penetrometer probe plunged through the electrolyte at *ca.* 0.7 m/sec contacted the film, slowed down, and contin-

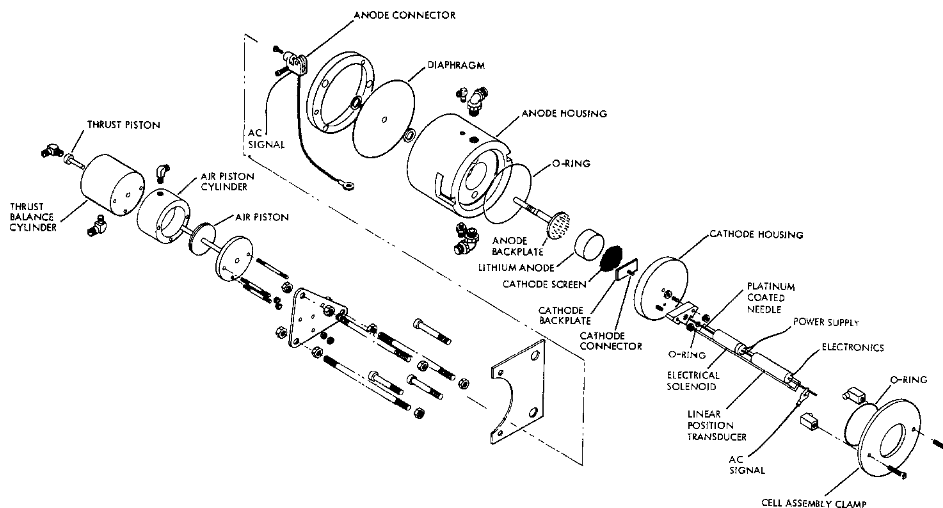

Fig. 1. Exploded view of 1.14 $\times$ 10^{-3} m^2 lithium test cell for film thickness measurement.

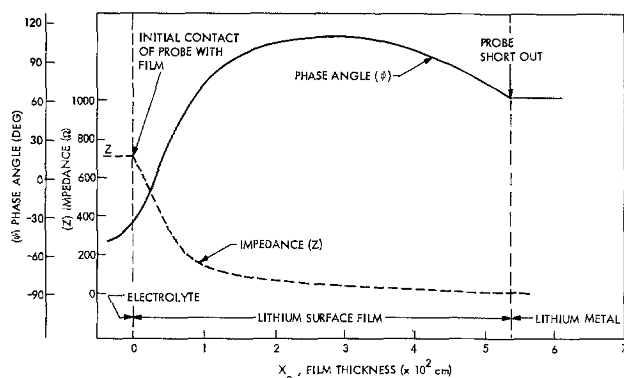

Fig. 2. Visicorder trace of film thickness measurement

ued through the film into the underlying Li. The total time spent by the probe in the film was about 2 sec. The initial point of this measurement was obtained from the instance of film-probe contact where an abrupt change in impedance (curve Z) was observed. The end point of this film thickness measurement was obtained when the probe made direct contact with the Li and the circuit shorted. But, because the measuring system possessed a residual impedance, the exact location of the end point was difficult to determine. It was found that if, in addition to the impedance measurement, the phase angle was also recorded the end point was more clearly indicated. Curve ψ depicts a trace of phase angle output between the probe and the anode from $-45°$ to $+110°$. A change in slope of the phase angle scan at short-out was clearly indicated in all the experiments.

Potential decay experiment.—The thickness of the diffusion layer at the limiting current is an important factor in the development of the theoretical model. To determine its value under typical test conditions at the polarization level characteristic of the limiting current [which has been arbitrarily selected as $\eta = 2.87V$, $E_H = 0(V)$], a potential decay experiment was designed. Knowing the time of the potential decay transient, the diffusion layer thickness may be calculated. For this experiment, a special cell was constructed. It was identical to the 1.14×10^{-3} m^2 unit used for the polarization experiments except that it accommodated a smaller 1×10^{-4} m^2 anode. With this reduced surface area, a Princeton Applied Research Model 173 potentiostat/galvanostat could be utilized and this in conjunction with a Tektronix Model 549 storage oscilloscope provided the necessary instrumentation. The Li was polarized potentiostatically to $E_H = 0(V)$ in 4M LiOH at a flow rate of 0.2 m/sec and a contact pressure of 6.2×10^4 Pa. A Hg/HgO reference electrode was used. When the current was interrupted, the potential decay was measured as the anode reverted to its OCV. The experiment was run in triplicate, reproducibility was to within 10%.

Results

Flow velocity experiments.—Figure 3 shows the effect of flow velocity, v, on the anodic polarization in 4M LiOH at 25°C. The polarization curves possess two distinct regions. The initial portion of the curve depicted as a-c is linear. It represents *IR* across an essentially invariant protective layer. The curved, highly polarized portion c-l, has a configuration which is often characterized by a limiting current situation. [It should be noted here that the transient passivation phenomenon described previously (1) was observed at low flow rates. Since it does not occur at the higher rates and is not significant to the present investigation, it has not been shown in Fig. 3.]

In the region a-c it is assumed that the anodic film formation rate is balanced by the film dissolution rate. At constant anode-cathode contact pressure, in-

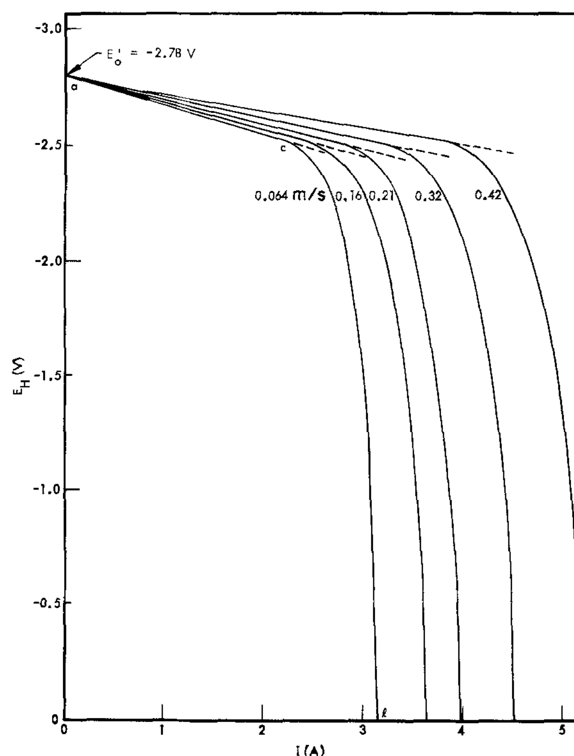

Fig. 3. Effect of flow velocity on the anodic polarization of lithium in 4M LiOH at 298°K. Anode-cathode contact pressure = 6.2×10^4 Pa, $A = 1.14 \times 10^{-3}$ m^2.

crease in flow velocity decreases the film's resistance. It is also observed that the maximum current density depicted as i_l increases substantially with increasing flow.

From the slopes of the resistive polarization sections of the curves in Fig. 3, a plot may be drawn of film resistance *vs.* velocity. This is shown in Fig. 4, as curve A. In Fig. 5 is shown the relationship between film thickness and polarization level at fixed anode-cathode contact pressure and flow velocity. It will be observed that the thickness remains virtually constant under the polarization conditions studied in this work. For comparison purposes, the results of the film thickness *vs.* flow velocity experiments are also plotted in Fig. 4. These appear as curve B.

Anode-cathode contact pressure experiments.—Figure 6 shows a filmed Li anode after operation at a contact pressure of 7×10^4 Pa in 4M LiOH at 2.3

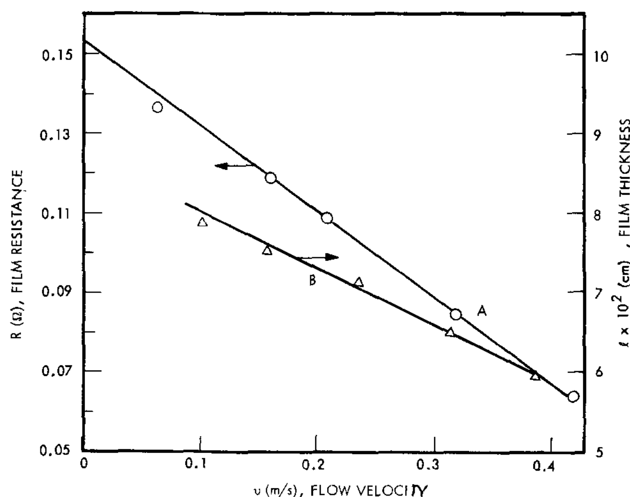

Fig. 4. Effect of flow velocity on anode film resistance and film thickness in 4M LiOH at $P = 6.2 \times 10^4$ Pa, $T = 298°$K.

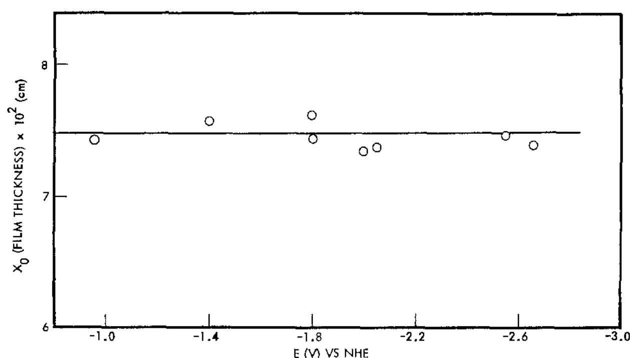

Fig. 5. Invariant dependence of film thickness on anodic polarization at $v = 0.16$ m/sec, $P = 6.2 \times 10^4$ Pa in 4M LiOH.

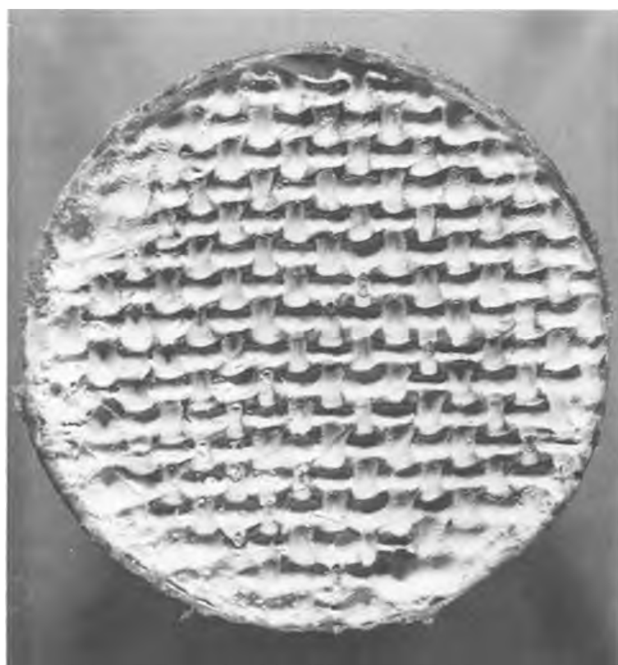

Fig. 6. Imprint of cathode screen on the anode surface

kA/m^2. The imprint of the cathode screen due to electrolyte flow is clearly evidenced. It was found that at up to 28×10^4 Pa (the limit of the experimental apparatus) no short-circuiting occurred. This remarkable property of the anode film is of course the key to the successul operation of the cell without the need for a separator.

The influence of contact pressure on the anodic polarization is shown in Fig. 7. The slope of the ohmic polarization region a-c is plotted against contact pressure in Fig. 8. Curve A represents the derived film resistance and curve B represents the measured film thickness as a function of contact pressure.

The influence of electrolyte concentration on anode film resistance and film thickness is given in Fig. 9. Unlike the situation with contact pressure and electrolyte flow velocity, the film resistance is not linearly related to electrolyte concentration.

Table I lists the limiting current (I_l), the critical current (I_c), film thickness (x_o), and film resistance (R) values obtained in the experiments where the flow rate was 0.16 m/sec at a contact pressure of 6.2×10^4 Pa. Also included in this table are literature data for LiOH mean activity $a_\pm$, conductivity k, and LiOH mean diffusion coefficient D_o.

Potential decay experiment.—The average value measured for the potential decay transient τ at the limiting current I_l in 4M LiOH was 3.5×10^{-3} sec. It has been shown (2) that when a metal is potentio-

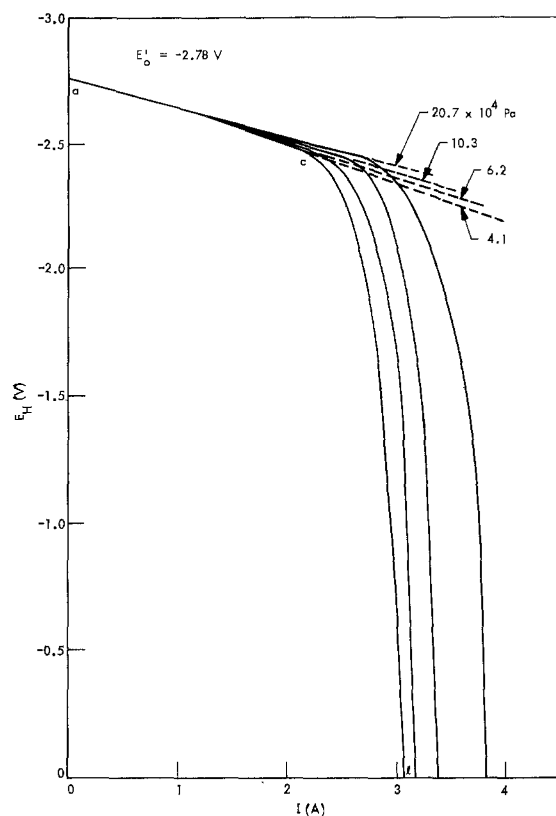

Fig. 7. Effect of contact pressure on the anodic polarization of Li in 4M LiOH at 298°K, $v = 0.064$ m/sec, $A = 1.14 \times 10^{-3}$ m^2.

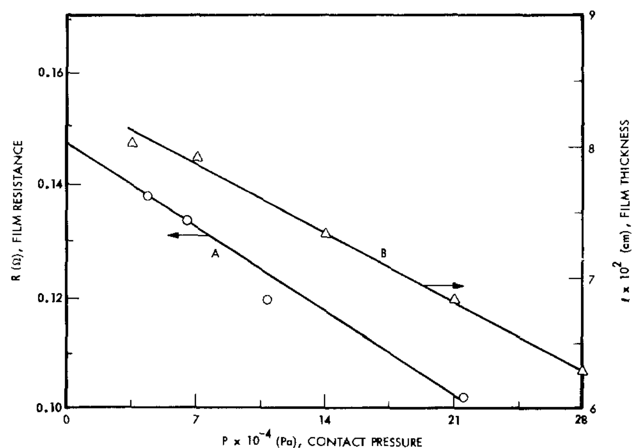

Fig. 8. Effect of contact pressure on anode film resistance and film thickness at 298°K, $v = 0.064$ m/sec.

statically polarized, the diffusion layer thickness may be calculated using the equation

$$\delta = \sqrt{\pi D \tau} \quad [1]$$

where D is the diffusion coefficient of the current limiting species. In this system where LiOH is the only electrolyte solute, it is appropriate to use the mean diffusion coefficient rather than the coefficient for the hydroxyl ion (3). D_o for 4M LiOH is 5.3×10^{-6} cm^2 sec^{-1} and thus δ computes to 2.4×10^{-4} cm.

Discussion

The dissolution of Li in strongly alkaline solutions appears either as an electron-producing electrochemical reaction, or as a direct corrosion (parasitic) reaction.

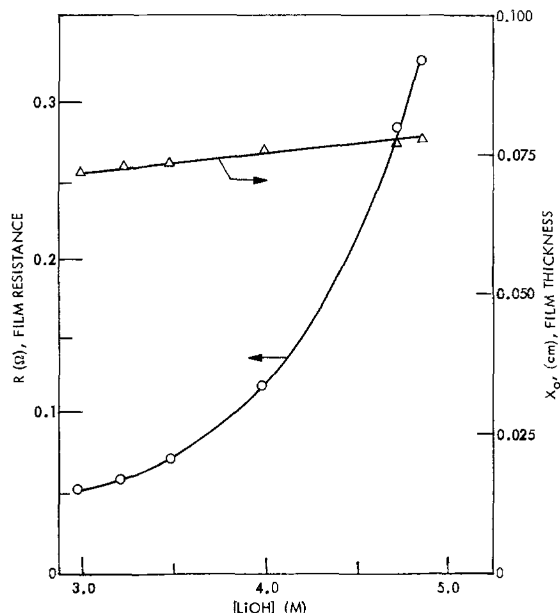

Fig. 9. Influence of electrolyte concentration on anode film resistance and film thickness at 298°K, $P = 6.2 \times 10^4$ Pa, $v = 0.16$ m/sec.

In the electron-producing reaction, a number of steps presumably occur in the process of producing a Li^+ aquocation. However, it is generally accepted that in an anodic oxidation such as this the resulting charge transfer reaction may be expressed (4)

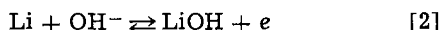

$$Li + OH^- \rightleftarrows LiOH + e \quad [2]$$

(Then, by dissociation $LiOH \rightleftarrows Li^+ + OH^-$) .

The corrosion reaction on the other hand is simply represented by the over-all reaction

$$Li + H_2O \rightleftarrows LiOH + 1/2\, H_2 \quad [3]$$

(The over-all corrosion reaction [3] is of course a coupling of [2] with the cathodic reduction of H_2O at adjacent sites on the corroding surface.)

In situ stereozoom microscope observation of the anode surface indicates that the Li is always evenly covered by an oxide layer, and SEM examination of a filmed anode reveals a porous structure. The significance of this observation must be taken with caution because the observed porosity could have resulted from reaction of electrolyte with the Li after removal of the specimen from the electrolyte.

However, even though pores in the film have not actually been seen during polarization experiments (the highest magnification available with the existing experimental setup is only 80×), there exists sufficient diagnostic data to support the hypothesis that the protective film is, in fact, porous (5).

The anodic polarization curves, Fig. 3 and 7, can be described in terms of an active resistive polarization region depicted as a-c and a highly polarized region shown as c-l. As will be indicated subsequently, the electrochemical controlling mechanisms are different in these two regions so, for convenience, this discussion considers each separately.

Polarization region a-c.—Over the span of the active polarization region, steady-state conditions are observed. It is believed that in this region a quasi-equilibrium state exists between active and inactive sites. The slope of the curve dE/Adi represents the effective resistance across the film. This resistance R may be tied to the tortuosity of the film by the relationship (5)

$$R = \frac{Tx_o}{kA\,(1 - \theta_o)} \quad [4]$$

where x_o is the film thickness, k is the average specific conductivity of electrolyte permeating the film, A is the projected surface area, T is the tortuosity, and θ_o is the surface coverage by the oxide film.

Inspection of Fig. 9 shows that x_o/R and therefore θ_o change significantly with concentration, especially above 4M LiOH, whereas from Fig. 4 and 8 it can be seen that, in the cases of the other variables, *i.e.*, flow rate and contact pressure, the ratio of x_o/R and therefore θ_o do not change greatly over the ranges studied. This effect serves to explain why the anodic polarization of Li is very strongly influenced by OH^- concentration especially at high molarities, and electrolyte flow rate and contact pressure have been observed to be of secondary importance in cell operation.

Accurate assessment of the surface coverage requires knowledge of the tortuosity factor but this cannot be measured directly. For the present discussion, T is assumed to be 1. Errors arising from this if T is in fact somewhat greater than 1 will be reflected in an incorrect value of $1 - \theta_o$. However, of importance in this paper is not the absolute magnitude of the surface coverage, but merely a knowledge of significant changes in surface coverage as the experimental conditions are varied. From the film thickness *vs.* film resistance data of Fig. 9, $1 - \theta_o$ may be determined as a function of electrolyte concentration. Values of the surface coverage (assuming $T = 1$) are given in Table II and are plotted in Fig. 10. Inspection of this figure shows how sensitive the surface coverage is to varying electrolyte concentrations. In Li-H_2O battery operation, the LiOH concentration is maintained between 3.5 and 5M if good coulombic efficiency is to be expected. It will also be seen that over the range 3.5-5M LiOH the active surface area decreases from *ca.*

Table II. Some calculated parameters of the Li-H_2O system*

[LiOH] (M)	$1 - \theta_o$	$\delta \times 10^4$ (cm)	i_l (kA/m²)
2.96	0.34	5.0	24.5
3.20	0.30	5.7	22.1
3.44	0.24	6.4	21.3
4.00	0.15	7.8	19.6
4.70	0.06	9.9	16.7
4.84	0.05	11.3	14.0

* Data obtained at $v = 0.16$ m/sec, $P = 6.2 \times 10^4$ Pa, and $T = 298°K$.

Table I. Some basic parameters of the Li-H_2O system

[LiOH] (M)	$a_\pm \times 10^3$ (mole cm⁻³)*	k (Ω⁻¹ cm⁻¹)	I_l (A)**	I_c (A)**	x_o (cm)**	R (Ω)**	$D_o \times 10^5$ (cm² sec⁻¹)†
2.96	1.45	0.350	10.9	5.3	0.072	0.053	0.77
3.20	1.57	0.360	8.3	4.6	0.073	0.060	0.67
3.44	1.70	0.369	6.4	3.9	0.074	0.072	0.61
4.00	1.92	0.375	3.6	2.6	0.075	0.119	0.53
4.70	2.20	0.383	1.2	1.07	0.076	0.281	0.44
4.84	2.23	0.390	0.8	0.75	0.077	0.321	0.43

* H. S. Harned and B. B. Owens, "The Physical Chemistry of Electrolytic Solutions," 3rd ed., p. 498, Reinhold Publishing Corp., New York (1963). Data beyond 4M are obtained by extrapolation.
** Data obtained at $v = 0.16$ m/sec, $P = 6.2 \times 10^4$ Pa, and $T = 298°K$.
† R. V. Homsy, Report No. UCID-17159, Lawrence Livermore Laboratory, Univ. of Calif., Livermore, Calif. (1976).

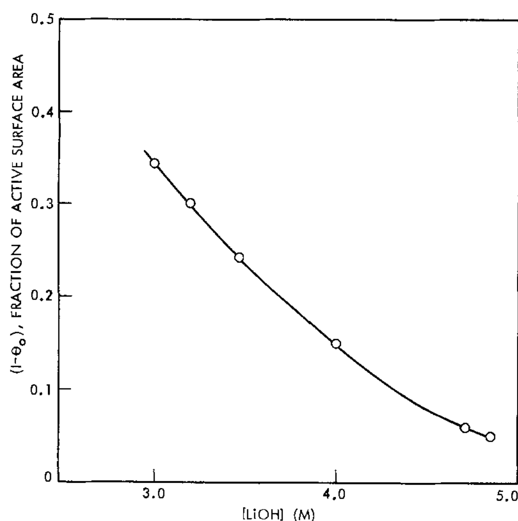

Fig. 10. Influence of electrolyte concentration on the active surface area.

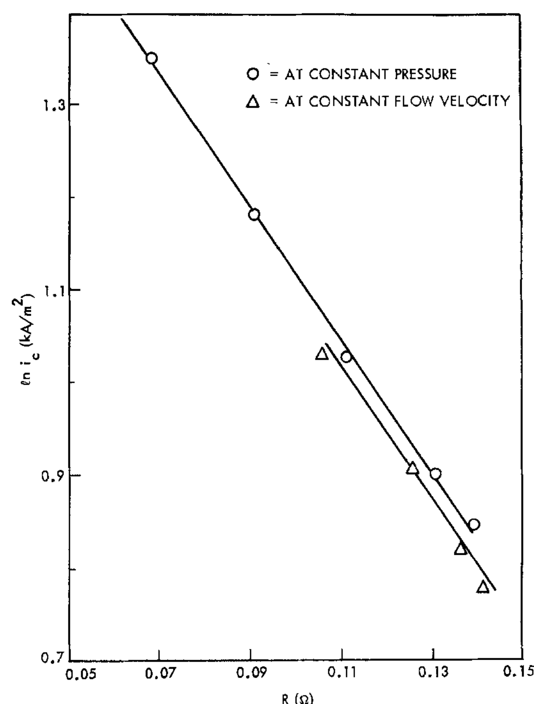

Fig. 11. Variation of critical current density as a function of film resistance.

25 to 8%, and, in the active polarization region, the coverage is almost independent of flow rate, contact pressure, and polarization potential. In this region a steady-state polarization is established almost immediately; it may be assumed that the concentration of Li^+ at the active surface equals the initial concentration. The rate of removal of Li^+ by diffusion is equal to the total Li^+ flux and no concentration buildup occurs at the surface. It has been established [Ref. (6), Eq. 12] that the current density, i_c, defined by polarization point c, may be expressed by the equation

$$i_c = (n\mathbf{F}D_o\rho)C_o \qquad [5]$$

where C_o is the Li^+ or OH^- concentration at the Li surface at OCV. **F** is the Faraday and n is the equivalents per mole. It has also been shown [Ref. (6), Eq. 6] that the concentration C_o is related to the bulk concentration C_b by the relationship

$$C_b = C_o \exp(-\rho\delta) \qquad [6]$$

where ρ is a constant.

As will be shown later, δ and x_o are each related linearly to flow rate and therefore x_o may be expressed in terms of δ, viz., $x_o = \rho/\rho'\ \delta$ where ρ' is also a constant. Then Eq. [6] becomes

$$C_b = C_o \exp(-\rho' x_o) \qquad [7]$$

The magnitude of i_c is strongly influenced by flow velocity and by contact pressure. Of interest is the relationship between i_c and film resistance or film thickness. This can be obtained theoretically from Eq. [4], [5], and [7] viz.

$$\ln i_c = K + \gamma R \qquad [8]$$

where K and γ are constants at any given electrolyte concentration and temperature. Here

$$K = \ln(n\mathbf{F}D_o\rho)C_b \qquad [9]$$

and

$$\gamma = \rho' kA(1-\theta_o)T \qquad [10]$$

Figure 11 displays a plot of film resistance R *vs.* ln i_c. The data to construct this plot were obtained from Fig. 3 and 7 (i_c values) and Fig. 4 and 8 (R values). It is consistent with Eq. [8] and, at the same time, it shows how diffusion of Li^+ away from the active surface or OH^- to the active surface through the oxide film are the key processes governing the inner working of the Li-H_2O cell.

Determination of the current density depicted as i_c is critical to the operation of the cell. It is at this point that the Li anode can be discharged with high current efficiency (*i.e.,* 90%) (7). Also the concentration gradient within the diffusion layer remains constant. This is important and it indicates that to maximize cell efficiency at a specified operating point, the bulk concentration must be held constant.

Transition potential c.—Though contact pressure and electrolyte flow velocity significantly influence the magnitude of i_c they have very small effect on the observed polarization potential $\eta_c = E_c - E_o'$. Over the experimental conditions reported here, η_c was found to range from 240 to 300 mV.

Polarization η_c can be expressed in terms of the resistance across the film R and the transition current $I_c^\dagger$ at electrode potential E_c, *i.e.*, $\eta_c = I_c^\dagger R$. η_c may be calculated from a relationship which combines Eq. [4], [5], and [7]

$$\eta_c = m\frac{x_o}{\exp(\rho' x_o)} \qquad [11]$$

Since $\rho' x_o = \rho\delta$, and $m = [n\mathbf{F}D_o\rho TC_b]/[k(1-\theta_o)]$, then by selecting an η_c from Fig. 3 and a corresponding x_o (film thickness) from Fig. 4, and the other parameters from Tables I and II, the constants ρ and ρ' may be obtained.

In the resistance polarization region (a-c) in Fig. 3 and 7, $C_b \simeq C_o$ and it then follows from Eq. [7] that $\rho' x_o << 1$. Thus Eq. [11] can be approximated

$$\eta_c^o \simeq m\frac{x_o^o}{\exp(\rho' x_o^o)} \qquad [12]$$

where x_o^o is the film thickness at $v = 0$ and $P = 0$ and η_c^o is the maximum polarization at point c. Extrapolation of the curves of Fig. 4 and 8, *i.e.*, film thickness as a function of electrolyte flow or contact pressure shows that in 4M LiOH at 298°K, x_o^o is 8.8 $\times 10^{-2}$ cm. Calculation from this makes $\eta_c^o = 300$ mV. In actual practice, increasing flow velocity or contact pressure reduces this polarization slightly but increases i_c significantly.

It has been found that η_c's calculated using Eq. [11] are very close to the polarization levels observed in actual Li-H_2O battery discharges. As has been mentioned previously and is repeated here for emphasis, the knowledge of η_c's under various experimental conditions is important for optimizing control of the Li-H_2O battery.

Polarization region c-l.—At first inspection, the rapid polarization in this region seems to be due to a passivation phenomena. In the Li-H_2O system, mechanical passivation is indeed observed especially under forced flux, *i.e.*, under galvanostatic polarization (6). In a subsequent paper which is in preparation, we show that under constant load polarization, characteristic anodic passivation curves are observed when the OH^- concentration is significantly greater than 5M (accomplished by adding KOH or NaOH to the electrolyte). By characteristic passivation curves, we mean the response observed as the potential becomes more noble and the current increases until it passes through an initial maximum. Subsequently the current decreases to a greater or lesser extent reflecting surface blockage. At even more noble potentials the current increases again as transpassivity occurs. This passivation in strong $[OH^-]$ takes place when the overvoltage is *ca.* 400 mV. The point we wish to make here is the fact that under constant load polarization in the LiOH solutions of the present work, no decrease in current is observed; not even when the electrode is polarized by as much as 2.8-3V. Further, we have observed in studies in strong $[OH^-]$ solution that once the anode has passivated, it requires a minimum of half a minute for the potential to revert to OCV when the load is removed. This is to be expected since dissolution of pore plugging crystallites to reestablish a specific equilibrium point generally requires considerable time for consummation. The delay accounts for the hysteresis usually observed when metals are passivated by thick films. In the work reported in this paper, OCV was reattained within milliseconds of removing the load. In the light of these factors, it was decided that a passivation phenomenon could not satisfactorily explain the configuration of the polarization curves or the extremely rapid potential recovery on removing the load. It is proposed that a better explanation is tied to a solution mass transport phenomenon in which concentration polarization becomes dominant.

Concentration polarization.—Under constant load (resistance polarization), the Li^+ surface concentration remains constant at any specific polarization level and passivation does therefore not occur because the surface concentration of LiOH does not normally exceed saturation in this electrolyte. Under galvanostatic polarization, on the other hand, at potentials more noble than point c of Fig. 3 and 7, there is a subtle but important difference in the mass transport. Here, the Li^+ flux is held constant and supersaturation of LiOH and precipitation of crystallites occurs in pores and interstices in the LiOH film (6). The behavior of Li in LiOH solution is in certain ways analogous to electropolishing. In studies of this topic (8), it has been shown that the change from concentration polarization to passivation polarization is due mainly to whether the reaction products can be dissolved and transported away from the interface fast enough to prevent precipitation of the products on the surface. To better understand the processes occurring at a Li anode under resistance polarization, it should be realized that neither the flux at the interface, *i.e.*, $(\partial C/\partial x)_{x\to o}$, nor the surface concentration C_o are held constant. Figure 12 has been constructed to show schematically the concentration gradient for Li^+, or OH^- within the effective diffusion layer, δ. In the schematic it is assumed that a linear diffusion model holds. Electroneutrality requires that, in this 1.1 binary electrolyte, the concentration of Li^+ always equals that of OH^-. Thus, the slope of each curve represents the flux of LiOH (or Li^+) diffusing away from the active metal surface which has a LiOH surface concentration, C_o. At I_l, C_o attains its maximum, *i.e.*, $C_o = C_s$.

In the context of concentration polarization, it is of interest to note that the effective diffusion layer thickness, δ, calculated from the potential decay experi-

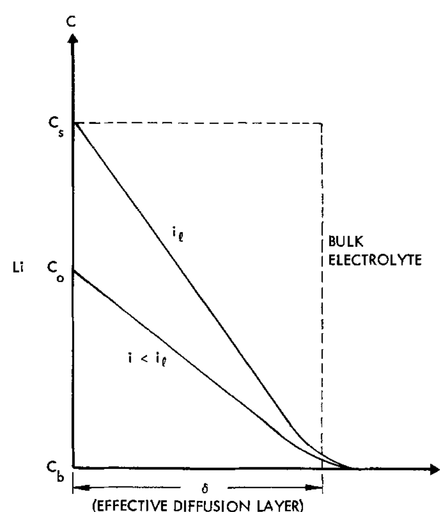

Fig. 12. Concentration distribution within the effective diffusion layer of thickness δ (idealized). C_b = bulk LiOH concentration, C_s = saturated concentration, C_o = LiOH concentration at the active surface where the flux $i < i_l$ (limiting current density).

ment, *i.e.*, 2.4×10^{-4} cm, is of the same order as the value 7.8×10^{-4} cm obtained from the limiting current and film thickness experimental results. Details of this calculation are given in the next section under limiting current.

Limiting current.—From the previous discussion, the concentration polarization region c-l should be dealt with as a resistance polarization due to the current-dependent resistance of the diffusion layer within the porous lithium electrode (9). In this case, the removal of the reaction product, Li^+, is rate determining when current flows. Under steady-state condition, the surface concentration, C_o, at any polarization point beyond c is constant but is greater than C_b. At c no concentration polarization is observed, but only ohmic polarization. At l concentration polarization is predominant whereby the surface concentration of the reaction product reaches its saturation, *e.g.*, $C_o = C_s$. It is obvious that when the concentration at the electrode surface gets closer to saturation, it is more difficult to remove the reaction product via diffusion and thus a higher overpotential is observed. It has been shown previously (6) that the limiting current flowing at the electrode surface is related to its surface concentration by

$$i_l - i_c = \frac{n\mathbf{F}D_o}{\delta}(C_s - C_b) = \frac{I_l - I_c}{A(1-\theta_o)} \quad [13]$$

Eq. [4] and [13] yield

$$I_l - I_c = \frac{n\mathbf{F}D_o T x_o}{\delta k R}(C_s - C_b) \quad [14]$$

Figure 13 which has been obtained from Fig. 3 shows that a linear relationship exists in this system between I_l and v. This relationship, which presumably comes about because of the unusual mass transport occurring across the anode film when the cathode screen is pressed against it, is quite different from the classical flat plate approximations of Lévéque (10) where $I_l \alpha v^{1/3}$. Taking experimental I_l's and the parameters of Table I, the effective diffusion layer δ can be obtained from Eq. [14]. The results of this calculation are plotted in Fig. 14. The δ's so calculated are smaller than would normally be expected. Generally in the case of a tranquil solution, $\delta = 3 \times 10^{-2}$ cm, or at a flat plate under laminar flow $\delta = 10^{-2}$ cm or less. It seems therefore that the cathode

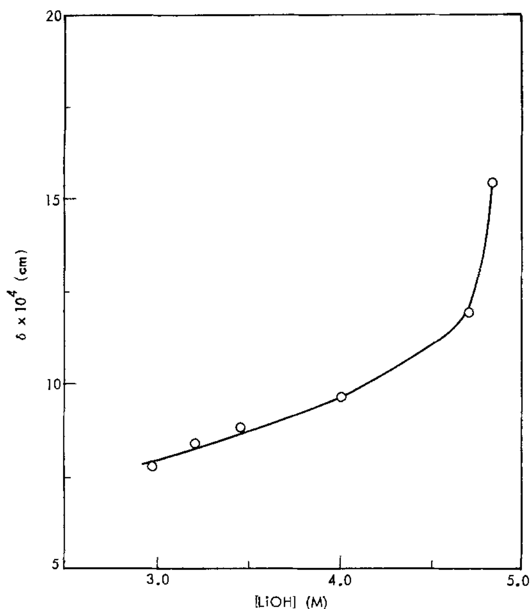

Fig. 13. Influence of electrolyte flow velocity on limiting current in 4M LiOH at 298°K, $P = 6.2 \times 10^4$ Pa, $A = 1.14 \times 10^{-3}$ m^2.

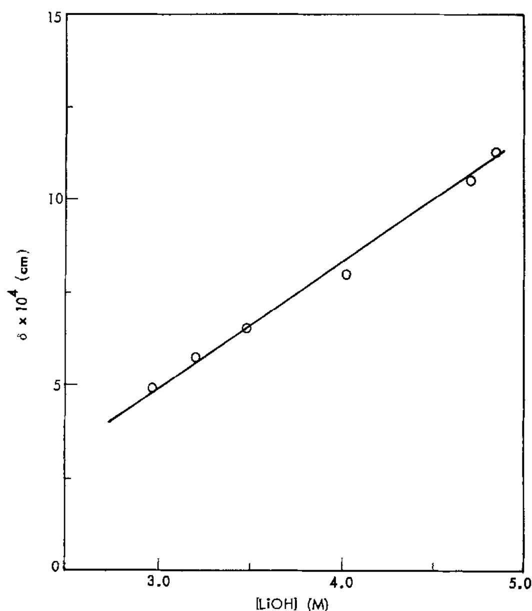

Fig. 14. Concentration dependence of the effective diffusion layer in LiOH.

screen geometry has a major impact on the hydrodynamics within the interelectrode flow channel. The reduced dimensions of δ can be explained by the existence of a substantial electrolyte flow component perpendicular to the anode surface. This component arises from the fluid passing around the metal screen elements.

Finally, the actual limiting current density based on the true active surface area, *i.e.*, $A(1 - \theta_o)$ rather than the projected surface area A can be calculated from Eq. [13], Table I, and Fig. 13 and the results are given in Table II. It is of interest to note that the limiting current densities obtained here are generally high (*i.e.*, > 10 kA/m^2) in this highly alkaline solution. An unusual situation is observed in this system, namely, as is seen in column 4 of Table II, the limiting current density decreases with increasing concentration. This anomaly is readily understood by further inspection of Eq. [13]; when C_b increases D_o and $C_s - C_b$ decrease while δ increases. The end result of these interdependent factors is the reverse trend of the limiting currents.

Conclusions

This study has confirmed that a Li anode in LiOH electrolyte is almost completely covered with a protective film. The active surface area amounts to a small percentage of the projected area and at a fixed LiOH concentration it does not change over a polarization span of ~ 3V from OCV. Also of significance is the fact that the film thickness changes only slightly with electrolyte concentration, polarization level, anode-cathode contact pressure, and electrolyte flow velocity. The paper has shown how electrolyte concentration because of its effect on surface coverage has such major impact on the operation of the cell. Variations in electrolyte flow rate have a nominal influence on the transition current density, which corresponds to the polarization level at which the cell operates most efficiently, and thus changing the flow rate is a convenient way to adjust cell power while maintaining good efficiency. Electrolyte concentration remains, however, the critical control parameter.

Of interest is the observation that the diffusion layer thickness is about 1/50 the thickness of the anodic oxide film and is far thinner than that normally observed on metals at which an electrochemical reaction is proceeding. This suggests that a major electrolyte flow component must exist perpendicular to the electrode surface. It confirms the important role which the cathode screen element plays and shows how vital it is to place this element very close to or have it touching the anode surface. By doing this the electrolyte flow is presumably perturbed into the desired direction. Quantitatively, this concept has not been resolved as yet. Work is proceeding at this time to model the mass transport in the interelectrode cavity. A convective component term on the same coordinate as the diffusion direction now appears to the authors to be a significant factor.

Acknowledgment

The authors wish to thank Professor E. Gileadi, of Tel Aviv University, for many stimulating discussions concerning this paper. This work was supported in its entirety by Lockheed Missiles & Space Company, Incorporated.

Manuscript submitted July 13, 1977; revised manuscript received Jan. 23, 1978.

Any discussion of this paper will appear in a Discussion Section to be published in the December 1978 JOURNAL. All discussions for the December 1978 Discussion Section should be submitted by Aug. 1, 1978.

Publication costs of this article were assisted by Lockheed Palo Alto Research Laboratory.

REFERENCES

1. E. L. Littauer and K. C. Tsai, *This Journal*, **123**, 771 (1976).
2. J. O'M. Bockris and A. K. N. Reddy, "Modern Electrochemistry," Vol. II, pp. 1055-1059, Plenum Press, New York (1970).
3. K. S. Spiegler, *Desalination*, **9**, 367 (1971).
4. K. J. Vetter, "Electrochemical Kinetics," pp. 644-664, Academic Press, New York (1967).
5. E. L. Littauer and K. C. Tsai, *This Journal*, **124**, 850 (1977).
6. E. L. Littauer and K. C. Tsai, *ibid.*, **123**, 964 (1976).
7. E. L. Littauer, W. R. Momyer, and K. C. Tsai, *J. Power Sources*, **2**, 163 (1977/1978).
8. J. M. West, "Electrodeposition and Corrosion Processes," pp. 104-108, D. Van Nostrand, London (1965).
9. K. J. Vetter, op. cit., pp. 387-392.
10. J. S. Newman, "Electrochemical Systems," pp. 316-320. Prentice-Hall, Inc., Englewood Cliffs, N.J. (1973).

Electrodissolution Kinetics of Iron in Chloride Solutions

VI. Concentrated Acidic Solutions

H. C. Kuo and Ken Nobe*

School of Engineering and Applied Science, University of California, Los Angeles, California 90024

ABSTRACT

Anodic iron dissolution in acidic chloride solutions (constant ionic strength of 4.5M) over a wide range of H^+ and Cl^- concentrations has been investigated. Anodic dissolution in low $[H^+]$-concentrated chloride solutions is accelerated by both Cl^- and OH^- with Tafel slopes of 0.075 V/decade at low polarization and accelerated by only OH^- with Tafel slopes of 0.04 V/decade at high polarization. On the other hand, anodic dissolution in highly acidic-concentrated chloride solutions is accelerated by both H^+ and Cl^- with Tafel slopes of 0.11 V/decade and first-order dependence on both H^+ and Cl^-. For low Cl^- concentrations in either dilute or concentrated acidic solutions, anodic dissolution is inhibited by Cl^-. The experimental results indicate that anodic iron dissolution in acidic chloride solutions proceeds by simultaneous parallel reactions. Mechanisms which are consistent with the empirical rate expressions have been developed.

The OH^--accelerated mechanisms of anodic iron dissolution in acidic solutions proposed by Heusler (1) and Bockris *et al.* (2) have stimulated considerable activity in fundamental metal electrodissolution kinetic studies. There is a voluminous literature on iron studies alone confirming the acceleration of its anodic dissolution by hydroxyl ions in acidic solutions.

Recently, McCafferty and Hackerman (3) reported that in highly acidic and concentrated chloride solutions, anodic dissolution of iron is accelerated by both hydrogen and chloride ions. Shortly thereafter, Lorenz and co-workers (4) also reported such phenomena. On the other hand, both groups found that at lower acid concentrations, the rate of iron electrodissolution is decreased by increases in both Cl^- and H^+ concentrations. There were significant differences in some of the kinetic parameters (anodic Tafel slopes and reaction orders) reported by the two groups. At about the same time, Chin (5) reported that in acidic solutions of $[Cl^-] \leq 1.9M$ and $[H^+] \leq 1M$ anodic dissolution of iron is accelerated by both chloride and hydroxyl ions. This result appears to contradict the chloride-inhibited results of McCafferty and Hackerman (3) and Lorenz (4) at low acid concentrations. All three papers provide reviews of the literature on anodic dissolution of iron in acidic chloride solutions.

The purpose of the present work is to determine more precisely the conditions under which iron electrodissolution occurs by either an OH^- or H^+-accelerated mechanism and by either a chloride-accelerated or chloride-inhibited mechanism. The kinetics of the anodic dissolution of iron in acidic solutions is investigated by the rotating-disk electrode technique over a wide range of chloride and hydrogen ion concentrations with all solutions maintained at a constant ionic strength of 4.5M.

Experimental

The description of the rotating-disk electrode apparatus and instrumentation, the electrochemical cell, and the experimental procedure are given elsewhere (6).

The test electrodes were made from a 1.27 cm (½ in.) diam rod of Ferrovac E iron. The rod was first turned down and polished on a lathe to a diameter of 1.257 cm. It was then cut into 1.27 cm lengths using an Al_2O_3 abrasive wheel. During the cutting process, water was used to cool the iron rod. Both faces of the electrodes were polished with waterproof alumina paper of various grit (No. 240, No. 400, and No. 600). After polishing, the electrodes were washed and rinsed in distilled water, degreased with hot benzene in a Soxhlet column for 4 hr, and then annealed under vacuum ($<10^{-4}$ mm Hg) at 700°C for 1 hr and cooled down slowly to room temperature.

The reference electrode was a saturated calomel electrode (SCE). All potentials reported in this study were referred to this electrode. The reference electrode was housed in a small glass reservoir and connected to the Luggin capillary through a glass tube. In those experiments in which perchlorate ions were present in the electrolyte, a fiber junction salt bridge (double junction) was inserted between the saturated calomel electrode and electrolyte to preclude precipitation of potassium perchlorate within the fiber junction of the calomel electrode. This bridge was filled with 4.2M NaCl solution.

A dual-function Princeton Applied Research potentiostat/galvanostat (Model 173) with a current-voltage converter plug in (PAR Model 176) was used to control the potential between the test and reference electrode (potentiostat mode) or to supply constant current through the electrochemical cell (galvanostat mode). The potential of the test electrode was measured with a Keithley electrometer (Model 602 B). The current through the cell was measured either by the built-in panel meter on the potentiostat/galvanostat or by a Simpson ammeter (Model 269) connected to the circuit. A dual-channel Moseley strip chart recorder (Model 1700A) was used to monitor the potential and current. An Exact function generator (Model 255) was connected to the potentiostat in order to supply the triggering pulse to switch the applied potential/current from one setting to another during polarization. In the pulse polarization or transient studies the current transients were recorded on a Tektronix storage oscilloscope (Type 564).

All solutions were prepared from Analytical Reagent Grade chemicals and deionized water which was subsequently distilled. The electrolyte was continuously deoxygenated with prepurified nitrogen gas which was first passed through a heated (480°C) copper column to remove the residual oxygen. The electrode was immersed in the electrolyte about 12 hr after the deoxygenation was started. Before immersion the electrode was activated in 5N HCl solution for 20 min, fol-

* Electrochemical Society Active Member.

Key words: anodic, corrosion, dissolution, mechanisms.

lowed by thorough rinsing in a stream of distilled water. The corrosion potential of the working electrode was continuously monitored and recorded after immersion in the electrolyte. The corrosion potential usually attained a steady-state value within 2 hr. Polarization was started after about 3 hr immersion. In all of the polarization experiments, the rotation rate was fixed at 1000 rpm; however, a few experiments were performed by varying the rotation rate to check for mass transfer effects.

The H^+ effects were studied in (*i*) xNaCl + yHCl ($x + y = 4.5M$) solutions. The Cl^- effects were studied in (*ii*) solutions of pH = 1.1, xNaCl + $y$$NaClO_4$ + 0.01M $HClO_4$ ($x + y = 4.49M$), and (*iii*) solutions of 4.5M H^+, xHCl + $y$$HClO_4$ ($x + y = 4.5M$). In the last two series, the concentration of chloride ions was varied from 0 to 4.5M. The solutions were maintained at room temperature ($\approx$ 23°C).

All the potential values have been corrected for the ohmic overpotentials. The potential values have also been corrected for the liquid junction potentials which have been estimated by calculations given elsewhere (6).

Results

Effect of H^+ in 4.5M Cl^- (xNaCl + yHCl, $x + y = 4.5M$).—Table I presents the corrosion potentials at various H^+ concentrations. Anodic Tafel plots for $[H^+] \leq 0.5M$ solutions are shown in Fig. 1. With the exception of the $[H^+] = 0.5M$ plot, 2 linear Tafel regions are observed (*i.e.*, for $[H^+] \leq 0.1M$ plots). Slopes of correlating anodic Tafel lines are as follows

at low polarization, $b_a = 0.075$ V/decade, $[H^+] \leq 0.1M$

and

at high polarization, $b_a = 0.040$ V/decade, $[H^+] \leq 0.1M$

Only the higher Tafel slope is obtained for $[H^+] = 0.5M$ over the potential range shown in Fig. 1.

For both Tafel regions, the rate of anodic dissolution increases with decrease in H^+ concentrations. Electrochemical reaction order plots are presented in Fig. 2 and shows that

for the low polarization region,

$$\left(\frac{\partial \log i_a}{\partial pH}\right)_{\phi_a = -0.50V} = 0.6, \quad [H^+] \leq 0.1M$$

and

for the high polarization region,

$$\left(\frac{\partial \log i_a}{\partial pH}\right)_{\phi_a = -0.40V} = 1.1, \quad [H^+] \leq 0.1M$$

The low polarization data are in accord with the results of Chin (5), while the high polarization data with the OH^--accelerated mechanism proposed by Bockris *et al.* (2).

Figure 3 shows the results for more highly acidic solutions ($[H^+] \geq 1M$) with the data for $[H^+] = 0.5M$ included for comparison. For solutions of $1M \leq [H^+] \leq 4.5M$ the corelating anodic Tafel line of slope

Table I. Iron in 4.5M Cl^- and variable H^+ solutions

Electrolyte	pH	ϕ_{corr} (mV *vs.* SCE)	i_{corr} (mA/cm^2)
4.5M NaCl − HCl	4.25	−739 ± 5	0.026
4.5M NaCl − HCl	2.65	−635 ± 7	0.045
4.5M NaCl − HCl	2.00	−600 ± 5	0.044
4.5M NaCl − HCl	1.22	−565 ± 10	0.055
4.45M NaCl + 0.05M HCl	0.50	−515 ± 7	0.090
4.40M NaCl + 0.1M HCl	0.24	−500 ± 5	0.058
4.0M NaCl + 0.5M HCl		−430 ± 5	0.20
3.5M NaCl + 1.0M HCl		−425 ± 8	1.3
2.5M NaCl + 2.0M HCl		−395 ± 4	4.5
1.5M NaCl + 3.0M HCl		−391 ± 5	6.6
4.5M HCl		−397 ± 4	10.1

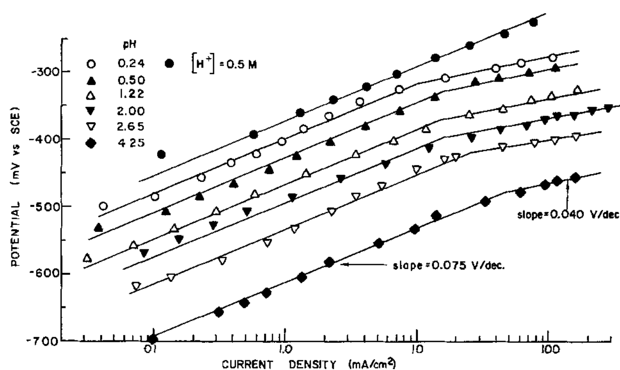

Fig. 1. Effect of pH on anodic iron dissolution in xNaCl + yHCl ($x + y = 4.5M$). $[H^+] \leq 0.5M$.

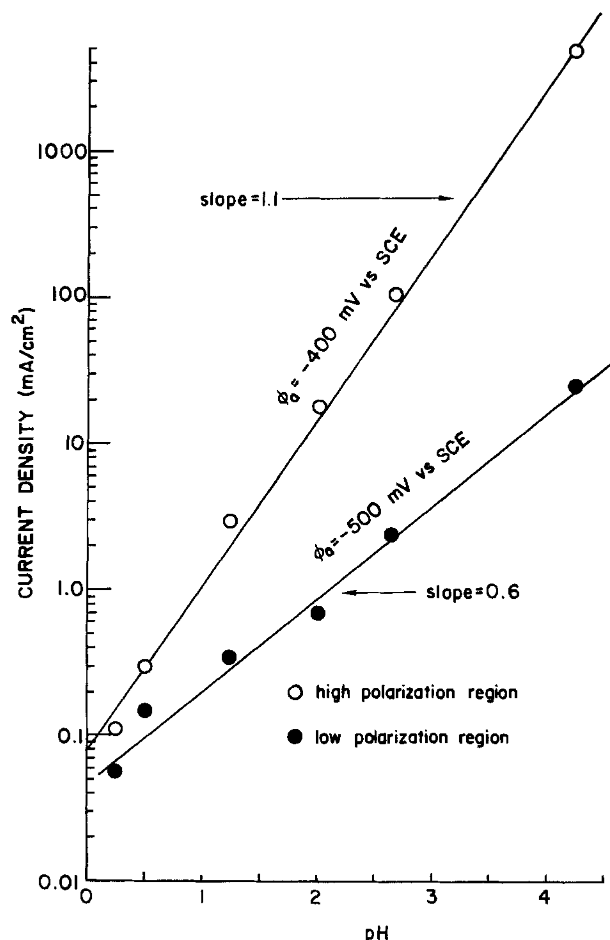

Fig. 2. Reaction order plots of anodic iron dissolution in xNaCl + yHCl ($x + y = 4.5M$) with respect to pH.

$$b_a = 0.110 \text{ V/decade}, \quad [H^+] \geq 1M$$

The results in Fig. 3 show that for 4.5M Cl^- solutions in which $[H^+] \geq 1M$, the rate of anodic dissolution increases with increase in H^+ concentrations, which is directly opposite to that observed at lower acidic solutions ($[H^+] \leq 0.5M$). These results confirm those reported previously by McCafferty and Hackerman (3), and Lorenz and co-workers (4) that H^+ accelerates the anodic dissolution of iron in highly acidic, concentrated chloride solutions.

Figure 4 gives the reaction order plot for $[H^+] \geq 1M$ and shows that

$$\left(\frac{\partial \log i_a}{\partial \log [H^+]}\right)_{\phi_a = -0.30V} = 1.0, \quad [H^+] \geq 1M$$

The first-order dependence on $[H^+]$ is in accord with

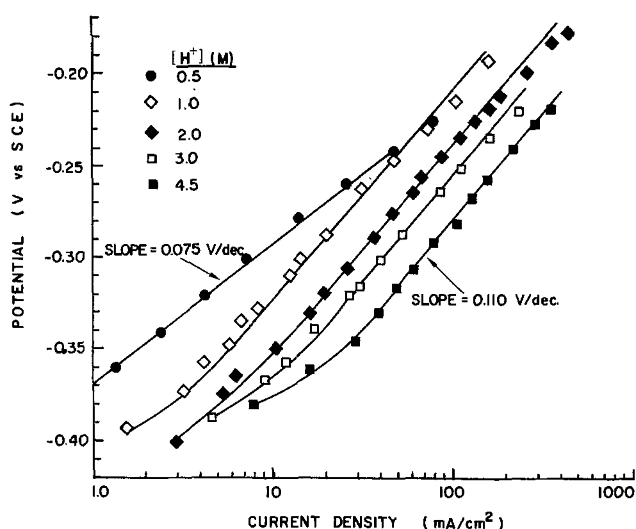

Fig. 3. Effect of H^+ on anodic iron dissolution in xNaCl + yHCl ($x + y = 4.5$M). $[H^+] \geqq 0.5$M.

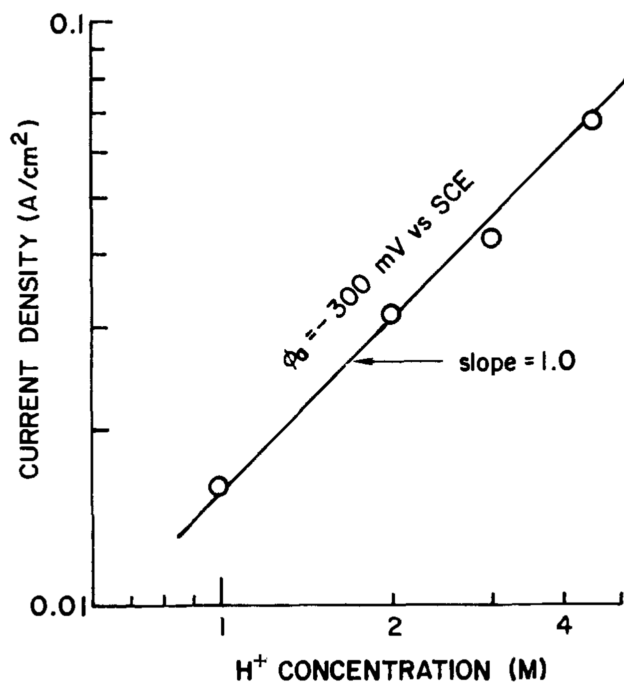

Fig. 4. Reaction order plot of anodic iron dissolution in xNaCl + yHCl ($x + y = 4.5$M) with respect to H^+. $[H^+] \geqq 1$M.

the work of Lorenz and co-workers (4), but not with the results of McCafferty and Hackerman (3) who reported a second-order dependence on $[H^+]$.

Effect of Cl^- in pH = 1.1 solutions (0.01M $HClO_4$- + xNaCl + yNaClO$_4$, $x + y = 4.49$M).—Table II gives the corrosion potentials at various Cl^- concentrations.

Table II. Iron in pH = 1.1 and variable Cl^- solutions

Electrolyte	ϕ_{corr} (mV vs. SCE)	i_{corr} (mA/cm^2)
4.49M NaClO$_4$ + 0.01M HClO$_4$	-498 ± 2	0.520
4.49M NaClO$_4$ + 0.01M HClO$_4$ + 0.001M NaCl	-501 ± 3	0.140
4.49M NaClO$_4$ + 0.01M HClO$_4$ + 0.005M NaCl	-514 ± 4	0.026
4.48M NaClO$_4$ + 0.01M HClO$_4$ + 0.01M NaCl	-516 ± 8	0.017
4.47M NaClO$_4$ + 0.01M HClO$_4$ + 0.02M NaCl	-518 ± 5	0.014
4.44M NaClO$_4$ + 0.01M HClO$_4$ + 0.05M NaCl	-523 ± 4	0.017
4.39M NaClO$_4$ + 0.01M HClO$_4$ + 0.10M NaCl	-530 ± 7	0.018
4.29M NaClO$_4$ + 0.01M HClO$_4$ + 0.20M NaCl	-533 ± 6	0.019
3.99M NaClO$_4$ + 0.01M HClO$_4$ + 0.50M NaCl	-535 ± 6	0.026
3.49M NaClO$_4$ + 0.01M HClO$_4$ + 1.00M NaCl	-547 ± 8	0.024
2.49M NaClO$_4$ + 0.01M HClO$_4$ + 2.00M NaCl	-564 ± 8	0.017
0.49M NaClO$_4$ + 0.01M HClO$_4$ + 4.00M NaCl	-573 ± 8	0.020

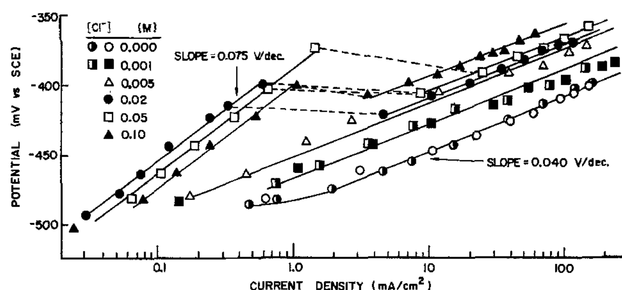

Fig. 5. Effect of Cl^- on anodic iron dissolution in 0.01M $HClO_4$ + xNaCl + yNaClO$_4$ ($x + y = 4.49$M). pH = 1.1 and $[Cl^-] \leqq 0.10$. Half-filled points represent galvanostatic data. Open and closed points represent potentiostatic data.

Anodic Tafel plots for $[Cl^-] \leqq 0.1$M are shown in Fig. 5. Linear Tafel lines of slope = 0.04 V/decade are obtained for $[Cl^-] \leqq 0.005$M. In this range, anodic dissolution of iron is inhibited by chloride ions. For $[Cl^-] > 0.005$M, anodic Tafel slopes are 0.075 V/decade at low polarization. In this region, Cl^- accelerates anodic dissolution. Above -0.425V, pseudosteady-state currents, which followed the Tafel lines with the higher slope, are observed but subsequently increase to much higher steady-state values (dashed lines). These latter values followed the Tafel lines with the lower slope. Since potentiostatic control is maintained throughout the transition period, the corrected potential of the iron electrode is decreased as the current is increased in the shift from the higher Tafel slope region to the lower Tafel slope region. This is due to the larger *IR* drop correction for the potential at the higher current value.

A typical current transient ($[Cl^-] = 0.01$M), which exhibits the above phenomenon is shown in Fig. 6. For $\phi_a = -0.48$V (Fig. 6a) the current quickly reaches steady state (A) in about 2 sec. The actual transient was followed for about 10 min with no discernible change in this steady-state value. For $\phi_a = -0.40$V (Fig. 6b), the current remains steady (A) for the time period between 2-12 sec. After about 12 sec, the current increases and, at about 40 sec, attains a new much higher steady-state value (B). For $\phi_a = -0.38$V (Fig. 6c) and above the current quickly reaches a minimum (A) and then rapidly increases to the final steady value (B). The duration of the pseudosteady state (A) decreases rapidly with increase in the applied potential. The time rate of increase of the current transient from the pseudosteady state (A) to the final steady state (B) increases rapidly with increasing applied potential. For applied potentials higher than -0.37V, the final steady state (B) is attained within a few milliseconds.

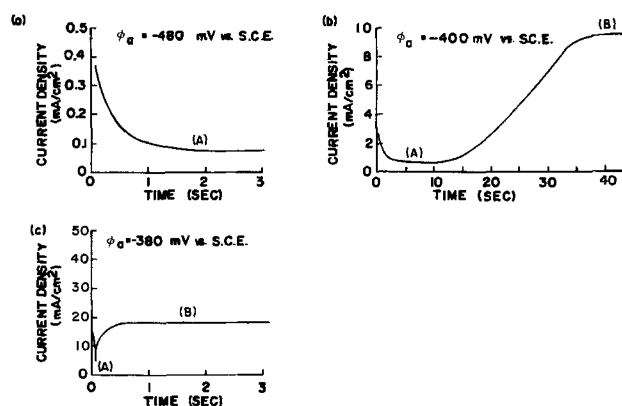

Fig. 6. Current transient during anodic potential pulse polarization of iron in 0.01M $HClO_4$ + 0.01M NaCl + 4.48M NaClO$_4$. pH = 1.1.

Table III. Iron in 4.5M H^+ and variable Cl^- solutions

Electrolytes	ϕ_{corr} (mV *vs.* SCE)	Anodic Tafel slope (mV/decade)	i_{corr} (mA/cm²)
4.500M $HClO_4$	−353 ± 5	44	0.50
4.500M $HClO_4$ + 0.001M HCl	−364 ± 7	60	0.24
4.500M $HClO_4$ + 0.003M HCl	−357 ± 5	75	0.33
4.490M $HClO_4$ + 0.01M HCl	−351 ± 6	80	0.35
4.473M $HClO_4$ + 0.027M HCl	−353 ± 5	90	0.30
4.45M $HClO_4$ + 0.05M HCl	−364 ± 6	95	0.14
4.4M $HClO_4$ + 0.1M HCl	−375 ± 6	95	0.09
4.3M $HClO_4$ + 0.2M HCl	−387 ± 6	95	0.14
4.1M $HClO_4$ + 0.4M HCl	−390 ± 10	105	0.31
3.5M $HClO_4$ + 1.0M HCl	−381 ± 5	105	1.4
2.5M $HClO_4$ + 2.0M HCl	−375 ± 6	105	3.0
1.5M $HClO_4$ + 3.0M HCl	−382 ± 10	105	4.7
0.5M $HClO_4$ + 4.0M HCl	−390 ± 9	105	5.3

The above transient behavior occurs in the intermediate potential region of the Tafel plots for $0.01 \leq [Cl^-] \leq 0.1M$. Current values (A) fall on the Tafel lines with slope of 0.075 V/decade and current values (B) fall on the Tafel lines with slope of 0.04 V/decade. In addition to significantly different anodic Tafel slopes, the effect of Cl^- on anodic dissolution is directly opposite in the two cases. Anodic dissolution of iron represented by Tafel lines with the higher slope is accelerated by Cl^- while anodic dissolution is inhibited by Cl^- for the other case.

For $[Cl^-] \geq 0.2M$, Tafel lines of slope = 0.075 V/decade are obtained at low polarization and anodic dissolution is accelerated by chloride ions (Fig. 7). At higher polarization, the Tafel lines have slope of 0.04 V/decade and appear independent of Cl^-. That is

at high polarization,

$$\left(\frac{\partial \log i_a}{\partial \log [Cl^-]}\right)_{\phi=-0.33V} = 0, \quad [Cl^-] \geq 0.2M$$

On the other hand, Fig. 8 shows that

at low polarization,

$$\left(\frac{\partial \log i_a}{\partial \log [Cl^-]}\right)_{\phi=-0.45V} = 0.4, \quad [Cl^-] \geq 0.2M$$

Effect of Cl^- in 4.5M H^+ ($xHCl + yHClO_4$, $x + y$ = 4.5M).—For $[Cl^-] \leq 0.05M$, anodic Tafel plots are given in Fig. 9. In pure perchloric acid, an anodic Tafel slope of 0.044 V/decade is observed. With increasing chloride concentration up to 0.05M, the anodic Tafel slope monotonically increases to about 0.095 V/decade. It is observed that Cl^- inhibited the anodic dissolution of iron in this concentration region.

For $[Cl^-] \geq 0.1M$, Fig. 10 shows that Cl^- accelerates anodic dissolution and, except for 0.1 and 0.2M Cl^-, which had anodic Tafel slopes of 0.095 V/decade, slopes of 0.11 V/decade are obtained for the correlating Tafel lines ($[Cl^-] \geq 0.4M$).

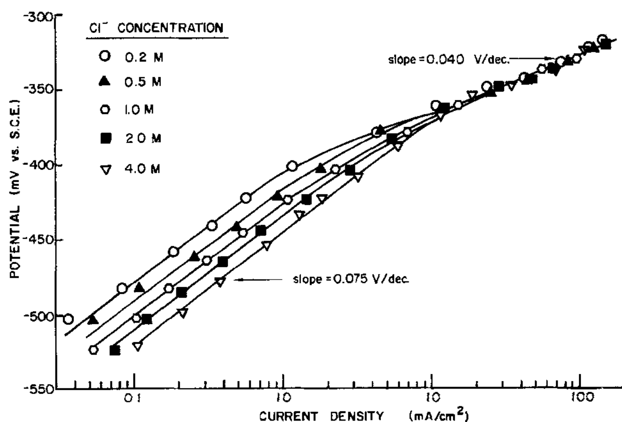

Fig. 7. Effect of Cl^- on anodic iron dissolution in 0.01M $HClO_4$ + $xNaCl$ + $yNaClO_4$ ($x + y$ = 4.49M). pH = 1.1 and 0.2M ≤ $[Cl^-]$ ≤ 4.0M.

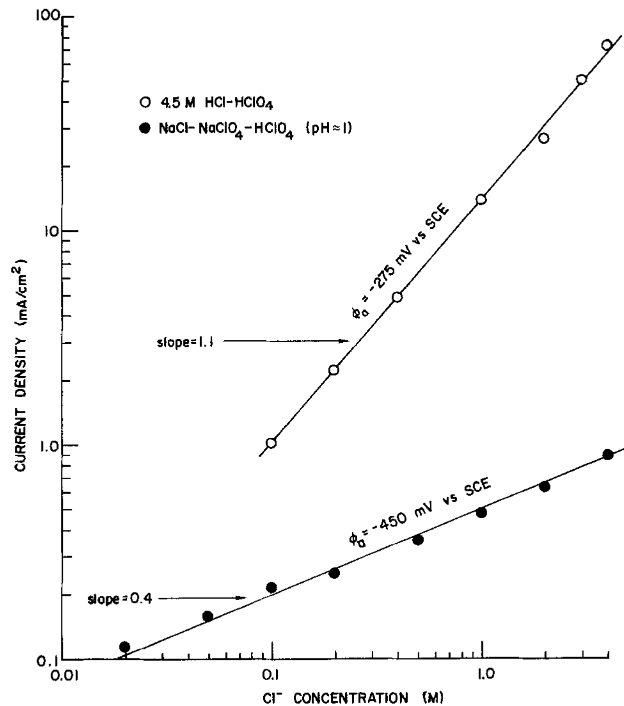

Fig. 8. Chloride reaction order plots of anodic iron dissolution. pH = 1.1 and $[H^+]$ = 4.5M solutions.

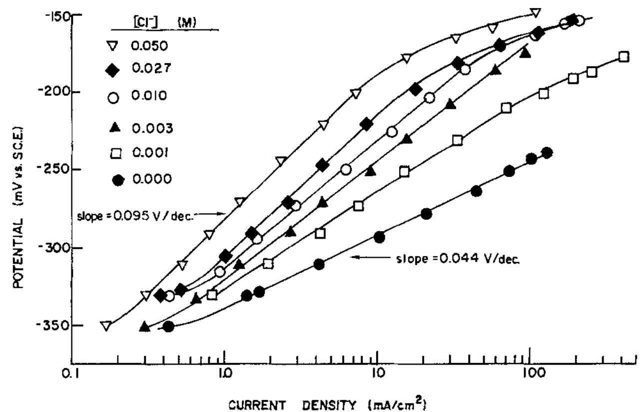

Fig. 9. Effect of Cl^- on anodic iron dissolution in $xHCl$ + $yHClO_4$ ($x + y$ = 4.5M). $[H^+]$ = 4.5M and 0 ≤ $[Cl^-]$ ≤ 0.050M.

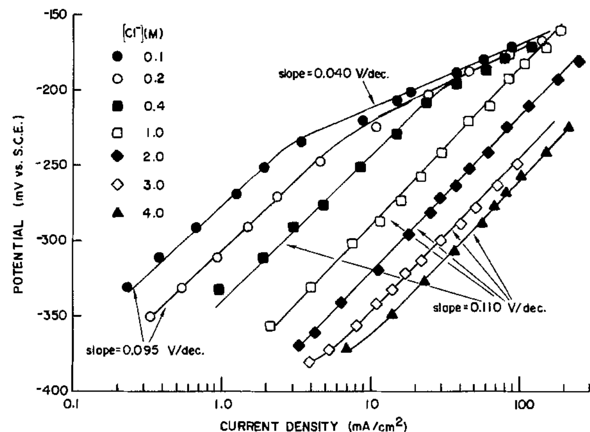

Fig. 10. Effect of Cl^- on anodic iron dissolution in $xHCl$ + $yHClO_4$ ($x + y$ = 4.5M). $[H^+]$ = 4.5M and 0.1M ≤ $[Cl^-]$ ≤ 4.0M.

The reaction order plot of the data obtained in Fig. 8, show that

$$\left(\frac{\partial \log i_a}{\partial \log [Cl^-]}\right)_{\phi_a=-0.275V} = 1.1, \ [Cl^-] \geq 0.1M$$

Empirical rate expressions for anodic dissolution of iron.—On the basis of the experimental polarization data, the kinetics of iron electrodissolution in acidic chloride solutions, ionic strength of 4.5M, can be expressed as follows

For low $[H^+]$, concentrated Cl^-

$$i_a = k_a[Cl^-]^{0.4}[OH^-]^{0.6} \exp\left(\frac{4}{5}\frac{F\phi}{RT}\right), \quad \text{at low polarization} \quad [1]$$

$$i'_a = k'_a[OH^-] \exp\left(\frac{3}{2}\frac{F\phi}{RT}\right), \text{ at high polarization} \quad [2]$$

For high $[H^+]$, concentrated Cl^-

$$i_a = k''_a [H^+][Cl^-]^{1.1} \exp\left(\frac{F\phi}{2RT}\right) \quad [3]$$

Equation [1] is in accord with the previous results, at lower chloride concentrations, of Chin (5). Equations [1] and [2] indicate, as suggested earlier by Chin (5), that the electrodissolution of iron in dilute acidic chloride solutions proceeds by two coupled parallel reactions as represented by the Cl^--accelerated mechanism (5) and the OH^--accelerated mechanism (2). In a series of papers, Bech-Nielsen [*e.g.*, see Ref. (7-9)] has discussed the idea of 2 distinctly different parallel anodic dissolution processes of iron in acidic solutions.

Plots of the potential (ϕ_t) and current (i_t) coordinates of the intersection of the two Tafel lines, as shown in Fig. 1, *vs.* pH are presented in Fig. 11. Equations [1] and [2] give the pH dependence of these intersection coordinates as

$$\frac{\partial \phi_t}{\partial pH} = -34 \text{ mV}/pH \quad [4]$$

and

$$\frac{\partial \log i_t}{\partial pH} = 0.14 \quad [5]$$

These values compare well with the experimental plots in Fig. 11 which give −40 mV/pH and 0.15, respectively.

Equation [3], which represents anodic iron dissolution in highly acidic concentrated chloride solutions, is in accord with the work of Lorenz and co-workers (4) except for the chloride reaction order which they report as 0.6. On the other hand McCafferty and Hackerman (3) reported a much lower anodic Tafel slope of about 60 mV/decade, an H^+ reaction order of 2 compared to first order in this work and a chloride reaction order between the first order obtained in the work and the value reported by Lorenz (4).

Discussion

Low H^+ concentrations.—In low $[H^+]$ and concentrated chloride solutions the results of anodic iron dissolution of this work are compared with those of McCafferty and Hackerman (3) and Lorenz and co-workers (4, 10) below:

In this work

$$i_a = k_a[Cl^-]^{0.4}[OH^-]^{0.6} \exp\left(\frac{4}{5}\frac{F\phi}{RT}\right), \quad \text{at low polarization} \quad [1]$$

and

$$i'_a = k'_a[OH^-] \exp\left(\frac{3}{2}\frac{F\phi}{RT}\right), \text{ at high polarization} \quad [2]$$

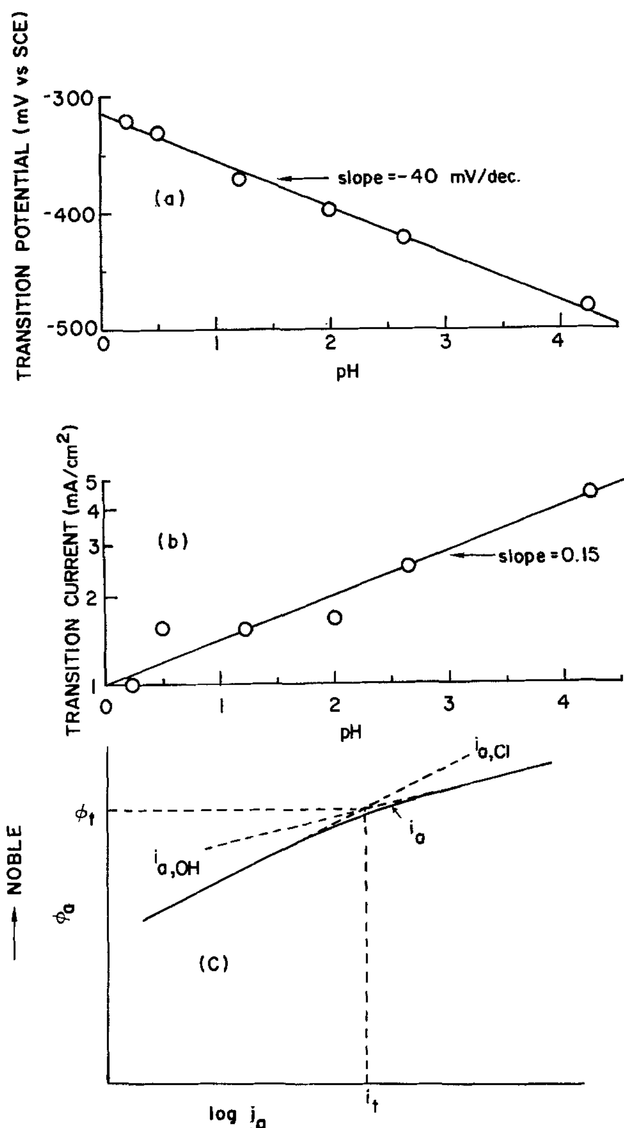

Fig. 11. (a) Transition potential (ϕ_t) *vs.* pH; (b) Transition current (i_t) *vs.* pH; (c) Schematic diagram of coupled, parallel OH^--accelerated and Cl^--accelerated anodic iron dissolution in acidic chloride solution.

McCafferty and Hackerman (3) found

$$i_a = k_a[Cl^-]^{-0.9}[OH^-]^{0.9} \exp\left(\frac{4}{5}\frac{F\phi}{RT}\right) \quad [1a]$$

and Lorenz and co-workers (4, 10) obtained

$$i_a = k_a[Cl^-]^{-0.7}[OH^-]^{0.7} \exp\left(\frac{F\phi}{RT}\right) \quad [1b]$$

The results of the latter two groups indicate that at low $[H^+]$, chloride ions inhibit anodic iron dissolution in contrast to Chin's (5) and this work which show that chloride ions accelerate anodic dissolution.

The experimental results of this work can be interpreted in terms of coupled parallel reactions as represented by the Cl^--accelerated mechanism (5) and the OH^--accelerated mechanism (2, 11) given below:

Cl^--accelerated mechanism

$$Fe \cdot H_2O + Cl^- = FeClOH^-_{ads} + H^+ + e \quad [a]$$

$$FeClOH^-_{ads} \xrightarrow{\text{rds}} FeClOH + e \quad [b]$$

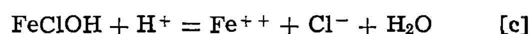

$$FeClOH + H^+ = Fe^{++} + Cl^- + H_2O \quad [c]$$

OH^--accelerated mechanism

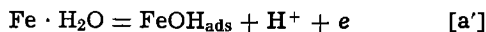
$$Fe \cdot H_2O = FeOH_{ads} + H^+ + e \qquad [a']$$

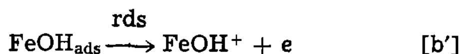
$$FeOH_{ads} \xrightarrow{rds} FeOH^+ + e \qquad [b']$$

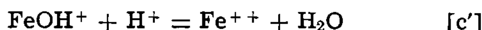
$$FeOH^+ + H^+ = Fe^{++} + H_2O \qquad [c']$$

The surface coverage of $FeClOH^-$ is assumed to range between 0.2 -0.8 and to follow Temkin adsorption behavior. On the other hand, the surface coverage of FeOH is assumed to be very small, *i.e.*, $\theta_{FeOH} \rightarrow 0$. By following the derivation given previously (5), the anodic iron dissolution rate equation for the Cl^- accelerated mechanism can be obtained

$$i_{a,Cl} = k_{a,Cl} [Cl^-]^{0.5} [OH^-]^{0.5} \exp\left(\frac{\mathbf{F}\phi}{RT}\right) \qquad [6]$$

The charge-transfer (β) and adsorption (γ) symmetry factors are assumed to be 0.5, *i.e.*, $\beta = \gamma = 0.5$.

Since $\theta_{FeOH} \rightarrow 0$ and the standard free energy of adsorption of FeOH should be much larger than that of $FeClOH^-$, ΔG°_{FeOH} should remain essentially constant and FeOH should follow Langmuir adsorption behavior. The rate equation for the OH^--accelerated mechanism can be derived as

$$i_{a,OH} = k_{a,OH} [OH^-] \exp\left(\frac{3}{2}\frac{\mathbf{F}}{RT}\right) \qquad [7]$$

Both Eq. [6] and [7] are in good agreement with the empirical relationships, Eq. [1] and [2], respectively. By considering the two equations as representing parallel anodic dissolution reactions, the total rate of anodic iron dissolution in solutions of low $[H^+]$ and concentrated Cl^- can be expressed as

$$i_{a,total} = i_{a,Cl} + i_{a,OH} \qquad [8]$$

At lower anodic potentials,

$$i_{a,Cl} >> i_{a,OH}$$

and

$$i_{a,total} \approx i_{a,Cl} \qquad [8a]$$

At higher anodic potentials,

$$i_{a,Cl} << i_{a,OH}$$

and

$$i_{a,total} \approx i_{a,OH} \qquad [8b]$$

A schematic diagram of Eq. [8], the continuous line, and Eq. [8a] and [8b] is shown in Fig. 11c. At the transition point (ϕ_t, i_t)

$$i_t = i_{a,Cl} = i_{a,OH} \qquad [9]$$

As discussed above, Eq. [4] and [5] give the *p*H dependence of the transition coordinates and compares well with the experimental results shown in Fig. 11.

For low $[H^+]$ (*p*H = 1.1) and $[Cl^-] \leq 0.005M$ (Fig. 5), the surface area accessible for anodic iron dissolution by the OH^--accelerated mechanism is decreased with increase in Cl^- concentrations due to increases in both θ_{FeOHCl^-} (for low $[Cl^-]$, $\theta_{FeOHCl^-} << 1$), and surface adsorption of Cl^-. This leads to the apparent inhibition effect of Cl^- on anodic iron dissolution.

For low $[H^+]$ (*p*H = 1.1) and $0.01M \leq [Cl^-] \leq 0.10M$, $FeOHCl^-$ attains intermediate surface coverage and, at low polarization, anodic iron dissolution proceeds by the Cl^- accelerated mechanism. At higher potentials, the OH^--accelerated mechanism becomes dominant. In the Cl^- concentration range, 0.01M-0.10M, adsorption of Cl^- and the surface coverage of $FeOHCl^-$ continues to increase with increase in Cl^- concentration. The consequent decrease in accessible surface area for OH^--accelerated anodic dissolution leads to further decreases in the apparent rate, $i_{a,OH}$. For $[Cl^-] \geq 0.2M$, and low $[H^+]$ (*p*H = 1.1), the surface area accessible for OH^--accelerated anodic dissolution remains essentially constant, and the total anodic dissolution rate, at high polarization, is independent of further increases in Cl^- concentration.

High H^+ concentrations.—In highly acidic and concentrated chloride solutions, anodic iron dissolution is accelerated by both chloride and hydrogen ions and follows the rate expression

$$i_{a,H} = k_{a,H} [H^+][Cl^-]^{1.1} \exp\left(\frac{\mathbf{F}\phi}{2RT}\right) \qquad [10]$$

This empirical rate expression is consistent with the following H^+-accelerated mechanism

$$Fe \cdot H_2O + Cl^- = FeCl_{ads} + H_2O + e \qquad [a'']$$

$$FeCl_{ads} + H^+ = FeClH^+ \qquad [b'']$$

$$FeClH^+ + Cl^- \xrightarrow{rds} FeCl_2 + H^+ + e \qquad [c'']$$

$$FeCl_2 = Fe^{++} + 2Cl^- \qquad [d'']$$

It is assumed that $\theta_{FeCl} \rightarrow 1$ and $\theta_{FeClH^+} \rightarrow 0$ so that both adsorbed species follow Langmuir adsorption behavior. The rate of step [c''] is expressed as

$$i_{[c'']} = k_{a,[c'']} \theta_{FeClH^+} [Cl^-] \exp\left(\frac{\beta_{[c'']}\mathbf{F}\phi}{RT}\right) \qquad [11]$$

If step [b''] is assumed to be in quasiequilibrium

$$\theta_{FeClH^+} = K_{[b'']} \theta_{FeCl} [H^+] \qquad [12]$$

$$= K_{[b'']} [H^+], \text{ since } \theta_{FeCl} \rightarrow 1 \qquad [13]$$

Equations [11] and [13], then, give

$$i_{[c'']} = k_{a,[c'']} K_{[b'']} [H^+][Cl^-] \exp\left(\frac{\beta\mathbf{F}\phi}{RT}\right) \qquad [14]$$

If $\beta = 0.5$, the rate of anodic dissolution is

$$i_{a,H} = k_{a,H} [H^+][Cl^-] \exp\left(\frac{\mathbf{F}\phi}{2RT}\right) \qquad [15]$$

Equation [15], which is derived from the proposed mechanism, is in accord with Eq. [10] which is a representation of the experimental results.

Steps [a'']-[d''] are a modification of the steps proposed by Lorenz and co-workers (4). However, in the mechanism proposed by the latter group, Temkin adsorption behavior of the adsorbed species, FeCl, was assumed in contrast to Langmuirian behavior of FeCl and $FeClH^+$ as proposed in the mechanism in this work.

Figure 10 shows that for $[Cl^-]$ = 0.1, 0.2, and 0.4M, the anodic Tafel lines (with slopes of approximately 0.1 V/decade), which shifted to higher anodic dissolution rates with the increase in Cl^- concentration, changed to an anodic Tafel line with a slope of 0.04 V/decade at high polarization. Anodic dissolution, in the latter region, appeared to be independent of Cl^- concentration. This observation suggests, although the experimental data is not, by any means, extensive, that anodic iron dissolution in highly acidic and concentrated chloride solutions may also occur by parallel reactions as represented by the H^+-accelerated mechanism and the OH^--accelerated mechanism, *i.e.*

$$i_{a,total} = i_{a,H} + i_{a,OH} \qquad [16]$$

The former ($i_{a,H}$) is dominant at lower polarization and the latter ($i_{a,OH}$) at higher polarization. More extensive anodic polarization studies at higher potentials than those examined in this work are required to verify this point. At much higher potentials, limiting diffusion currents have recently been observed in studies of high anodic iron dissolution rates in concentrated acidic and neutral chloride solutions (12, 13).

The results in Fig. 10 for Cl^- concentrations of 0.1, 0.2, and 0.4M at higher polarization also suggest that

anodic iron dissolution in chloride-free concentrated perchloric acid follows the OH^--accelerated mechanism even at low polarization. Some preliminary results of anodic iron dissolution in chloride-free acidic perchlorate solutions ($x HClO_4 + y NaClO_4$, $x + y =$ 6M), as shown in Fig. 12, indicate that anodic dissolution is, indeed, decreased with increase in H^+ concentration over the entire potential range examined.

In highly acidic ($[H^+] = 4.5M$) and dilute chloride ($[Cl^-] \leq 0.05M$) solutions, the anodic dissolution rate is decreased and the anodic Tafel slope is increased with increase in concentration of chloride ions. The increase in anodic Tafel slope from 0.04 to 0.095 V/decade, when Cl^- is increased from 0.000 to 0.050M indicates that the mechanism of anodic iron dissolution is changing in this concentration range. On the other hand, at low H^+ (pH = 1.1) and low Cl^- concentrations, as discussed above, Cl^- also inhibits anodic dissolution, but the anodic Tafel slope (0.04 V/decade) remains constant, indicating no change in the mechanism.

The OH^--accelerated mechanism is dominant for highly acidic and very dilute chloride solutions. If $\theta_{FeCl} \rightarrow 0$ and $\theta_{FeCl} >> \theta_{FeOH} + \theta_{FeClH^+}$ (exclusive of adsorbed water molecules), the rate of anodic iron dissolution can be expressed as

$$i_a = k_{a,OH}(1 - \theta_{FeCl})[OH^-] \exp\left(\frac{3}{2}\frac{\mathbf{F}\phi}{RT}\right) \quad [17]$$

For Langmuir adsorption and step [a″] in quasiequilibrium

$$k_{[a'']}[Cl^-](1 - \theta_{FeCl}) \exp\frac{\beta \mathbf{F}\phi}{RT} = k_{-[a'']}\theta_{FeCl} \exp - \frac{(1-\beta)\mathbf{F}\phi}{RT} \quad [18]$$

An expression for θ_{FeCl} in terms of the potential and Cl^- concentration is obtained from Eq. [18]

$$\theta_{FeCl} = \frac{k_{[a'']}[Cl^-]\exp\left(\frac{\mathbf{F}\phi}{RT}\right)}{k_{[a'']}[Cl^-]\exp\left(\frac{\mathbf{F}\phi}{RT}\right) + k_{[-a'']}} \quad [19]$$

Also

$$(1 - \theta_{FeCl}) = \frac{1}{K_{[a'']}[Cl^-]\exp\left(\frac{\mathbf{F}\phi}{RT}\right) + 1} \quad [20]$$

where

$$K_{[a']} = \frac{k_{[a'']}}{k_{[-a'']}}$$

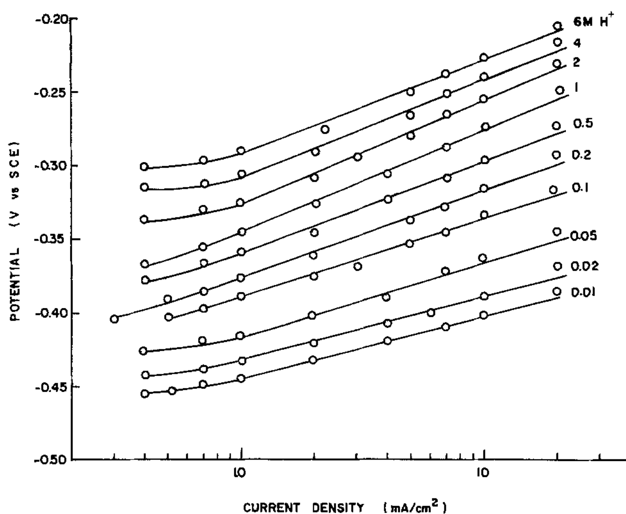

Fig. 12. Effect of H^+ on anodic iron dissolution in chloride-free acidic perchlorate solutions ($xHClO_4 + yNaClO_4$, $x + y = 6M$).

With the expression for $(1 - \theta_{FeCl})$ given in Eq. [20], Eq. [17] becomes

$$i_a = k_{a,OH}[OH^-] \frac{\exp\left(\frac{3}{2}\frac{\mathbf{F}\phi}{RT}\right)}{K_{[a'']}[Cl^-]\exp\left(\frac{\mathbf{F}\phi}{RT}\right) + 1} \quad [21]$$

For chloride-free solutions, Eq. [21] becomes

$$i_a = k_{a,OH}[OH^-] \exp\left(\frac{3}{2}\frac{\mathbf{F}\phi}{RT}\right)$$

which is the rate expression for the OH^--accelerated mechanism. For dilute concentrations of Cl^- in which $K_{[a'']}[Cl^-] \exp(\mathbf{F}\phi/RT) >> 1$, Eq. [21] gives

$$i_a = k_{a,OH}K^{-1}_{[a'']}[Cl^-]^{-1}[OH^-] \exp\left(\frac{\mathbf{F}\phi}{2RT}\right) \quad [22]$$

For the dilute concentrations, $[Cl^-] \leq 0.05M$, the rate expression for anodic dissolution is assumed to be between the latter two limiting cases, and Eq. [20] is given a power law form

$$(1 - \theta_{FeCl}) \approx K_{[a'']}^{-\delta}[Cl^-]^{-\delta} \exp\left(-\frac{\delta \mathbf{F}\phi}{RT}\right) \quad [23]$$

where $0 \leq \delta \leq 1$. δ changes from 0 to 1 with increase in $[Cl^-]$. Then Eq. [23] and [17] give

$$i_a \approx k_{a,OH}K_{[a'']}^{-\delta}[Cl^-]^{-\delta}[OH^-] \exp\left[\frac{\left(\frac{3}{2} - \delta\right)\mathbf{F}\phi}{RT}\right] \quad [24]$$

As δ increases from zero to values approaching one as $[Cl^-]$ increases from zero to some finite dilute concentration of Cl^-, Eq. [24] shows the inhibition effect of Cl^- and the increase in the anodic Tafel slope from 0.04 V/decade to values approaching 0.12 V/decade with increase in Cl^- concentration. Therefore, Eq. [24] predicts anodic iron dissolution behavior for $[H^+] =$ 4.5M and $0.000M \leq [Cl^-] \leq 0.050M$ as shown in Fig. 9. For $[Cl^-] \geq 0.1M$ and $H^+ = 4.5M$, the anodic behavior follows the H^+ and Cl^--accelerated mechanism.

General comments.—The results obtained in this work indicate that anodic iron dissolution behavior in acidic chloride solutions depends strongly on both the H^+ and Cl^- concentrations. Electrodissolution appears to proceed by parallel anodic reactions in both dilute and concentrated acidic chloride solutions. Proposed mechanisms which have been developed to interpret the experimental electrode kinetic data, involve several chloro-iron complexes as adsorbed reaction intermediates. Similar complexes have also been proposed in other mechanisms (*e.g.*, see Ref. (3, 4, 10, 14, 15). A good review of work indicating the importance of halo-iron complexes in iron corrosion is given by Foley (16, 17).

Hysteresis effects in the anodic polarization of iron in HCl have been ascribed by Foroulis (18) to complexation. The results shown in Fig. 5 and 6 of this work are not only consistent with this speculation, but, in addition, provide the further information which indicates that this phenomenon is due to the simultaneous occurrence of two parallel anodic dissolution reactions, one involving a chloro-iron complex and the other which does not.

The relevance of these parallel anodic dissolution reactions (depending on both H^+ and Cl^- concentrations) to localized corrosion and to the efficiency and efficacy of electrochemical machining processes is indicated since both of the latter are are so strongly dependent on the type of anions present in the electrolyte. However, much more detailed kinetic studies

on the effect of anions on anodic metal dissolution in both the active and transpassive regions are required for a fuller understanding. The importance of such further work to the prevention or control of localized corrosion and to optimization of electrochemical machining is evident.

Acknowledgment

This work was supported by the Metallurgy Program, Office of Naval Research Grant No. N0014-69-A-200-4029. The polarization measurements shown in Fig. 12 were performed by M. Yasuda.

Manuscript submitted Sept. 23, 1977; revised manuscript received Jan. 3, 1978.

Any discussion of this paper will appear in a Discussion Section to be published in the December 1978 JOURNAL. All discussions for the December 1978 Discussion Section should be submitted by Aug. 1, 1978.

Publication costs of this article were assisted by the University of California at Los Angeles.

REFERENCES

1. K. E. Heusler, Z. *Elektrochem.*, **62**, 582 (1958).
2. J. O'M. Bockris, D. Drazic, and R. Despic, *Electrochim. Acta*, **4**, 325 (1961).
3. E. McCafferty and N. Hackerman, *This Journal*, **119**, 999 (1972).
4. N. A. Darwish, F. Hilbert, W. J. Lorenz, and H. Rosswag, *Electrochim. Acta*, **18**, 421 (1973).
5. R. J. Chin and K. Nobe, *This Journal*, **119**, 1457 (1972).
6. H. C. Kuo, Ph.D. dissertation, UCLA (1975).
7. H. Nord and G. Bech-Nielsen, *Electrochim. Acta*, **16**, 849 (1971).
8. G. Bech-Nielsen, *ibid.*, **18**, 671 (1973).
9. G. Bech-Nielsen, *ibid.*, **21**, 627 (1976).
10. W. J. Lorenz, *Corr. Sci.*, **5**, 121 (1965).
11. E. J. Kelly, *This Journal*, **112**, 124 (1965).
12. H. C. Kuo and D. Landolt, *Electrochim. Acta*, **20**, 393 (1975).
13. H. C. Kuo and D. Landolt, *Corr. Sci.*, **16**, 915 (1976).
14. S. Asakura and K. Nobe, *This Journal*, **118**, 13 (1971).
15. S. Asakura and K. Nobe, *ibid.*, **118**, 19 (1971).
16. R. T. Foley, *Corrosion*, **26**, 58 (1970).
17. R. T. Foley, *This Journal*, **122**, 1493 (1975).
18. Z. A. Foroulis, *ibid.*, **113**, 532 (1966).

Electrochemical Aspects of the Beveling of Sputtered Permalloy Films

J. J. Kelly and G. J. Koel

Philips Research Laboratories, Eindhoven, The Netherlands

ABSTRACT

For the production of thin film magnetic heads, beveled steps in sputtered Permalloy films have been made using a duplex layer chemical etching technique. In this work, special attention was paid to galvanic interaction between the Permalloy base layer and the top layer metal, titanium. By changing the HF concentration of the $H_2SO_4/H_2O_2/HF$ etchant, the beveling angle α could be varied between 6° and 40°. The fact that (*i*) the rest potential of the bimetallic system lies in a region of the anodic polarization curve for titanium, in which the metal dissolution rate is almost completely independent of potential but strongly dependent on HF concentration, and (*ii*) the etch rate of Permalloy is insensitive to HF concentration, is important in this application. Values of α calculated on the basis of electrochemical measurements agree favorably with values found in chemical etching experiments. Factors that influence the beveling process when, as in the present case, a metal is used as the top layer to etch another metal are discussed.

In two recent reviews (1, 2) attention has been drawn to the fact that, while chemical etching of metals is widely used for pattern definition in semiconductor technology, relatively little study has been devoted to the specific electrochemistry of practical etching systems. In many cases a purely empirical approach is adopted when choosing an etchant for a particular application. In some recent publications (3-6) it has been shown that certain problems relating to metal etching for device fabrication could be solved by making use of the insight gained from electrochemical measurements.

In this paper we report on an electrochemical study of the bevel-etching of sputtered Permalloy, which is used in thin film magnetic heads. Figure 1 shows a SEM photograph of such a head, containing 6 turns. The lay-out and fabrication process have been described elsewhere (7, 8). One of the main problems in making this head was failure due to open metallization; electrical breaks were found in conductors crossing silica-covered steps in the Permalloy pattern. This results from incomplete coverage of the sharp Permalloy profiles normally obtained by chemical etching. Similar effects have been observed in integrated circuit technology (9). The problem can be avoided by beveling the steps using a duplex layer chemical etching technique (2, 10, 11). In the present paper we focus attention on the specific electrochemical problems involved when a metal or alloy, such as Permalloy, is bevel-etched in this way.

Key words: metal, transducer, polarization, etching.

Beveling of Metal Films

In previous publications (10, 11) it was shown that, by using a duplex layer chemical etching technique, beveling of thin films could be achieved. The method depends on the fact that, while both layers dissolve in the chemical etchant, the etch rate of the top layer is greater than that of the underlying layer (Fig. 2). The beveling angle α is given by the equation (10)[1]

$$\sin \alpha = \frac{\text{etch rate base layer}}{\text{etch rate top layer}} \quad [1]$$

[1] In Ref. (10), sin α is given by the ratio of the base layer and lateral etch rates, u_B and u_L, respectively. However, $u_L = u_T$, the etch rate of the top layer, if $u_T t >> d$, where t is the etching time for the system and d is the top layer thickness. This can easily be shown to hold in the present case.

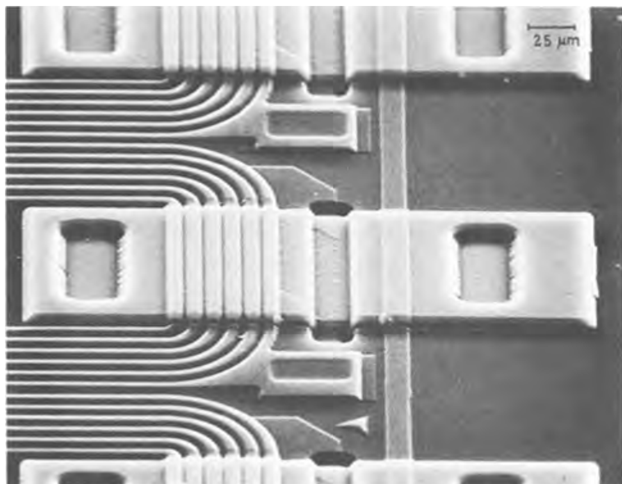

Fig. 1. SEM photograph of a six-turn thin-film magnetic head. Various crossovers and feed-through hole steps are obvious.

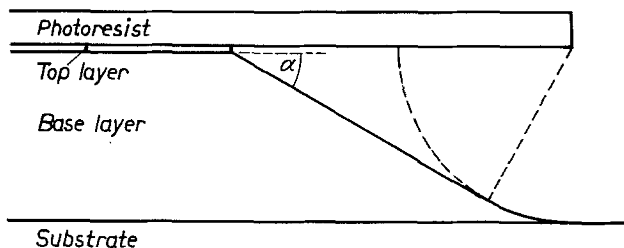

Fig. 2. Theoretical undercutting profile in a base layer with a faster etching top layer. The circular dashed line shows the etch profile expected for isotropic dissolution of the base layer when the top layer is not present.

Good agreement between experimental and theoretical values of α has been obtained for sputtered silica layers (12).

Difficulties may be encountered when a metal is used as top layer in order to bevel-etch another metal. As a result of the electrical contact between the two metals in the etching electrolyte, a galvanic element is formed; a potential is established which may be different from the rest potentials of the individual metals in the etchant. This means that the chemical etch rate of each metal of the bimetallic system may be modified. The direction and magnitude of these changes in etch rate depend on the current density-potential characteristics of the metals in the particular etchant and on the relative surface areas of the metals exposed to the etching solution (2, 3).

During bevel-etching, the exposed area of the top layer is much smaller than that of the base layer and the potential of the bimetallic system is essentially determined by the underlying metal. The resulting potential shift experienced by the top layer metal will be in the anodic direction if this metal is less noble than the underlying metal, and in the cathodic direction if it is more noble. In many cases the etch rate of a metal depends exponentially on its potential (1). The potential shift resulting from the bimetallic contact may therefore lead to a considerable increase or decrease in the etch rate of the top layer (2, 3).

In order to prevent extreme acceleration or deceleration of this etch rate, careful consideration must be given to the choice of top layer metal and etchant. In an attempt to avoid such problems, we used a metal which was less noble than the underlying metal but which had a potential-independent anodic partial current in the region of the rest potential of the bimetallic system (3, 13).

The electrochemical concept involved will be illustrated in this paper for the bevel-etching of sputtered Permalloy, using a sputtered titanium film as top layer. Titanium can be passivated in sulfuric acid solution (14). A characteristic active/passive peak is observed, followed by a potential region in which the anodic current (passive current) is very low and constant. Addition of fluoride ions to the solution increases the current both in the peak and in the passive regions (15, 16). Permalloy can be readily dissolved in a H_2SO_4/HF solution containing a suitable oxidizing agent. In the present study, hydrogen peroxide was mainly used. Some experiments were also carried out with other oxidizing agents.

The experimental results are presented in three sections. The first section describes beveling of Permalloy using various H_2SO_4/HF etchants and Ti as top layer. In the two subsequent sections electrochemical results for titanium and Permalloy are given. Finally the relevance of these results to the bevel-etching of Permalloy is discussed.

In order to avoid galvanic effects during dissolution of Permalloy films it is also possible to use an insulating top layer instead of a metal. In this way beveled steps in Permalloy films can be made by applying a sputtered silica top layer. However, our experience has shown that the etch rates of such oxide layers depend strongly on their composition, *i.e.*, on sputtering conditions such as oxygen pressure and rf power density. On the other hand, the results obtained with Ti layers were much less sensitive to such factors and reproducible steps of varying angle could be easily achieved.

Experimental

Beveling experiments.—Permalloy films, containing 79 weight percent (w/o) Ni, 16 w/o Fe, and 5 w/o Mo, were deposited on oxidized silicon slices by sputtering bulk alloy at an argon pressure of 5-10 mTorr, an rf power density of 0.6-1.2 W/cm^2, and a substrate temperature of 320°C. The deposition rate, which depended on the sputtering conditions, was between 0.6 and 0.8 μm/hr. Titanium films were sputtered at an rf power density of 0.6 W/cm^2 and an argon pressure of 10 mTorr. The deposition rate was approximately 100 Å/min. For beveling experiments, 0.05-0.10 μm thick Ti layers were deposited on 3 μm thick Permalloy layers.

Shipley AZ 1350H photoresist was applied on the Ti top layer by spinning at 3000 rpm. The photoresist was exposed for 20-25 sec in a Kulica Soffa exposure unit and developed for 1 min in an AZ 1350H developer. The resist was then baked out at 140°C for 1 hr. The metal was etched through the windows of the pattern.

When a 2 μm thick Ti film was etched using a photoresist pattern, applied as described above, beveling of the Ti film was not observed. This indicates that photoresist lift from the Ti top layer does not play a role in the Permalloy beveling process.

Beveling angles were calculated from the thickness of the Permalloy layer and the length of the beveled slope. The layer thickness was determined by using a Talystep or a Leitz interferometer. The length of the slope was measured by normal optical microscopy. These results were checked against beveling angles found using SEM photos.

Electrochemical measurements.—Because it was inconvenient to sputter very thick films and because thin film electrodes could only be used for a rather limited period, electrochemical measurements were also made with bulk metal electrodes. For these experiments the metal, in the form of a cylinder with a face area of between 0.5 and 1.0 cm^2, was tightly imbedded in a Teflon holder. Electrode surfaces were mechanically polished before use. For Ti electrodes, 99.95% pure metal, supplied by Imperial Metal Industries, England, in the form of 10 mm diam rods was used. Permalloy electrodes were machined from pellets which were made by casting the melt obtained using an argon arc onto a water-cooled copper surface. The composition of the bulk alloy was nominally the same

as that of the thin films. In both cases 99.99% pure Ni, Fe, and Mo were used for making the Permalloy.

Film electrodes were made by sputtering approximately 5 μm of the metal or alloy onto the respective bulk electrode under conditions similar to those described above. The substrate was first sputter-etched in order to remove surface oxide.

For certain experiments the electrodes were rotated in order to investigate the influence of stirring on the dissolution reaction. The experimental arrangement has been previously described (3).

Steady-state polarization curves were measured using a Wenking 70 TS 1 potentiostat controlled by a Wenking stepping-motor potentiometer, Model SMP 72. A glass-free cell and measuring system was used with either a saturated calomel electrode (SCE) or a mercury/mercury sulfate electrode as reference. All potentials are given with respect to SCE. Polarization curves were reproducible to within 5%.

Other experimental conditions.—The temperature of the beveling and electrochemical experiments was 23° ± 2°C. All chemicals used were of reagent grade, supplied by Merck. The fluoride concentration of the solutions was measured using an Orion fluoride electrode Type 96-09.

Results

Beveling of Permalloy films.—The hydrogen peroxide etchant used to bevel sputtered Permalloy films with Ti as top layer contained 3.9M H_2SO_4, 1.12M H_2O_2, and a variable HF concentration of between 0.4 and 4.0M. Gas evolution was observed during etching. In Fig. 3 a SEM photo of a beveled step is shown. The beveling angle α could be varied between 6° and 40° by changing the HF concentration, as shown in Fig. 4.

Beveled steps in Permalloy films were also made using H_2SO_4/HF etchants in which hydrogen peroxide was replaced by other oxidizing agents, *e.g.*, ferric ammonium sulfate or potassium dichromate. Gas evolution was not observed in these cases. The dissolution rates of the metals, and consequently the beveling angles, were found to be dependent on the hydrodynamic conditions maintained during etching.

Electrochemical results for titanium.—Previous work (15-17) on the influence of fluoride ions on the anodic behavior of Ti in H_2SO_4 solution has been confined to lower concentrations (≤0.1M NaF or HF). In order to achieve practicable etch rates it was necessary to increase the fluoride concentration considerably.

Figure 5 shows the steady-state anodic polarization curve for a Ti rotating disk electrode (RDE) in a solution containing 0.75M HF, 3.9M H_2SO_4 at 23°C and 500 rpm. The general form of this curve is similar to that observed for lower fluoride concentrations (15, 16), but in the present case the current in both the active and passive regions is much larger. The rest potential of Ti in this solution is approximately −0.9V. For potentials higher than 0V, the current is almost completely independent of potential. In this region the current changes by less than 10% when the H_2SO_4 concentration is reduced by a factor of 2. The passive current increases markedly, however, with increasing HF concentration, as is clear from Fig. 5.

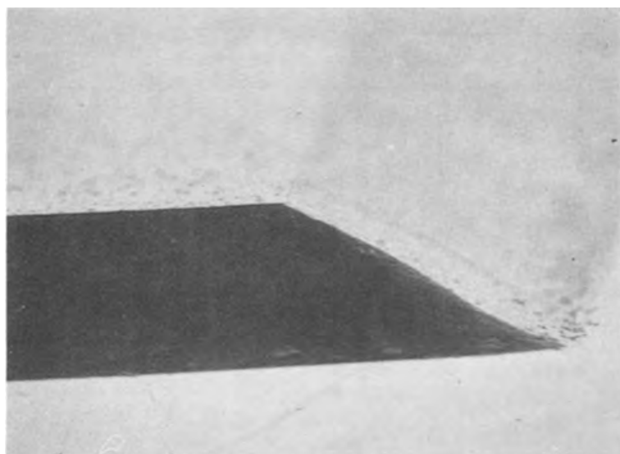

Fig. 3. SEM photograph showing a beveled step in a 3 μm thick Permalloy layer obtained using a titanium top layer. The photoresist film has been removed.

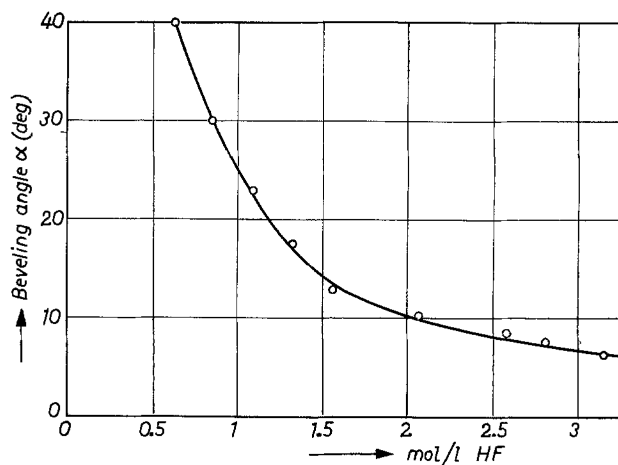

Fig. 4. Dependence of the beveling angle α on the HF concentration of the H_2SO_4 (3.9M)/H_2O_2 (1.12M)/HF etchant.

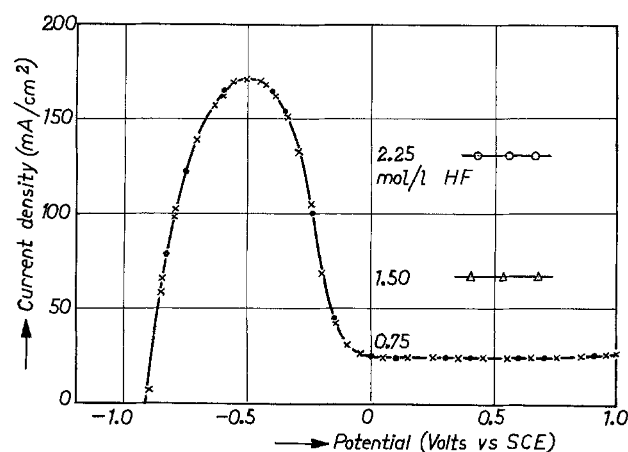

Fig. 5. Anodic polarization curve for a Ti RDE in 3.9M H_2SO_4, 0.75M HF at 23°C and 500 rpm. Passive current densities are also shown for 1.50 and 2.25M HF.

Similar results were found for sputtered Ti film electrodes. In the peak region, the curves differed somewhat from those measured with bulk metal electrodes. The passive current, however, was the same for both cases. This agrees with the observations of Caprani (16) who showed that for low fluoride concentrations the polarization behavior in the rising part of the peak depended on the origin of the Ti samples. On the other hand, in the descending part of the peak and in the passive region the curves were practically independent of the sample.

The passive current depends on the rotation rate ω of the electrode as shown in Fig. 6. Between 0 and 150 rpm the current is almost doubled. At higher rotation rates the current increases more slowly and practically levels off.

Reduction of H_2O_2 on Ti is negligible in the passive region, as can be seen from curve b of Fig. 7. Curve a was measured using the same HF/H_2SO_4 solution but without H_2O_2. A measurable contribution from H_2O_2 reduction is only found for potentials in the peak region (<0V). On the other hand, considerable reduc-

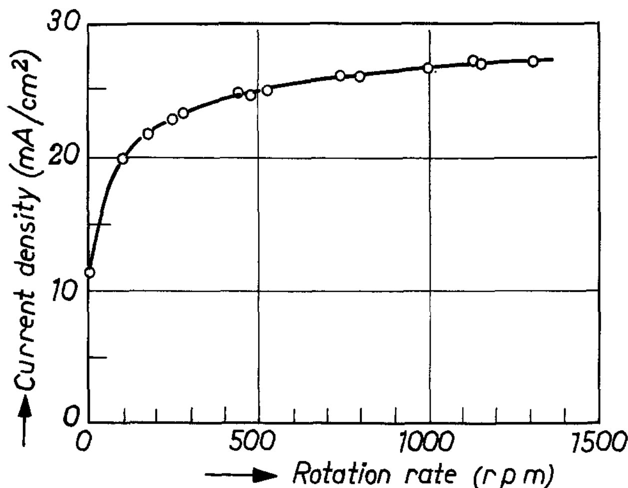

Fig. 6. The influence of the rotation rate on the passive current density of a Ti RDE at 23°C in 3.9M H_2SO_4, 0.75M HF.

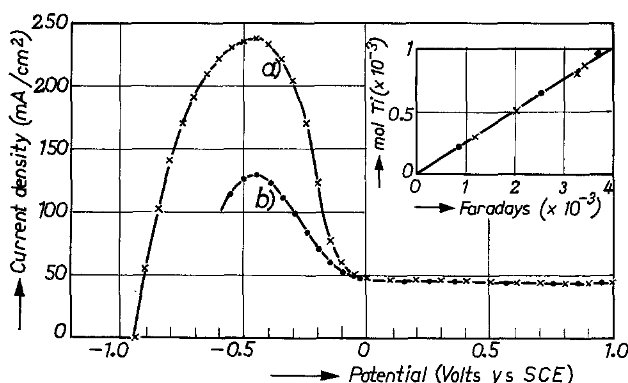

Fig. 7. Anodic polarization curves for a Ti RDE at 23°C, 500 rpm in a 3.9M H_2SO_4, 1.0M HF solution: curve a without H_2O_2, curve b with 1.12M H_2O_2. The insert shows the number of moles of Ti dissolved as a function of the charge passed at 0.40V (SCE) for the conditions used to measure curves a and b.

tion of H_2O_2 on Pt is observed at much higher potentials in this solution. Other oxidizing agents such as ferric salts show a similar behavior, being appreciably reduced only at lower potentials. Oxygen evolution is not observed for potentials up to 3V.

From weight-loss experiments it was shown that, in the passive region, Ti dissolves in the tetravalent state. An example of results is shown in the insert of Fig. 7. It is clear that four faradays are required to dissolve 1 mole Ti and this result is not affected by the presence of H_2O_2 in the electrolyte.

Dissolution of Ti in the passive region is partly controlled by mass transport in the solution. At higher rotation rates the current becomes almost independent of ω and a value close to that expected for $\omega = \infty$ is found. In this case, steady-state, potential step, and impedance measurements have indicated (17) that dissolution of Ti is primarily determined by ionic transport through a surface film on the metal. Since the film thickness is directly proportional to the applied potential, dissolution of the metal occurs under the influence of an almost constant electric field across the surface film. This accounts for the potential-independent anodic current. The steady-state film thickness decreases with increasing fluoride concentration; the electric field across the film increases and consequently the anodic current increases. That the reduction of oxidizing agents present in the solution is negligible in the passive region can be ascribed to the poor electronic conductivity of the passivating layer (18).

Electrochemical results for Permalloy.—The chemical etch rate of sputtered Permalloy films in 3.9M H_2SO_4, 1.12M H_2O_2 solution is practically independent of the HF concentration in the range 0.2-4.0M, as shown in Fig. 8. A similar result was found for the bulk alloy. The presence of a small quantity of HF in the etchant is necessary to ensure dissolution.

Figure 9 shows the influence of HF concentraion on the polarization curves for Permalloy in this solution. In each case a straight line is observed over a region of approximately 50 mV on either side of the rest potential. A slight shift in rest potential is found for increasing HF concentrations. This amounts to 35 mV for an increase from 0.25 to 1.25M. The slope of all curves is the same. It is not clear why the polarization curves for Permalloy in this electrolyte are linear over a potential range of approximately 100 mV. It is also strange that, while the rest potential of Permalloy in the solution changes as a function of the HF concentration, the chemical dissolution rate of the alloy remains constant. The anodic behavior of alloys can, of course, be quite complex (19) and, in Fig. 9, we are considering the dissolution of a three-component alloy together with the reduction of hydrogen peroxide.

Passive behavior is observed if HF is not present in the electrolyte: At potentials noble to the rest potential (approximately 0.5V), a very small anodic current is observed; at more cathodic potentials H_2O_2 reduction occurs.

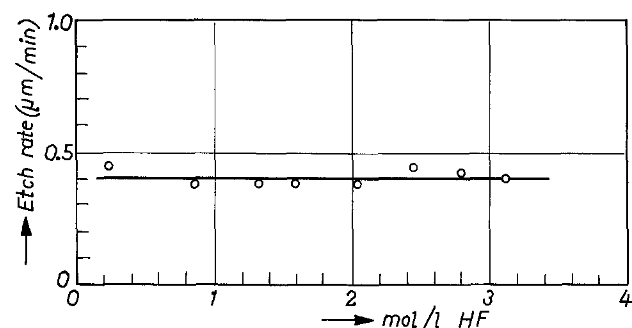

Fig. 8. The chemical etch rate of sputtered Permalloy films as a function of the HF concentration of the chemical etchant.

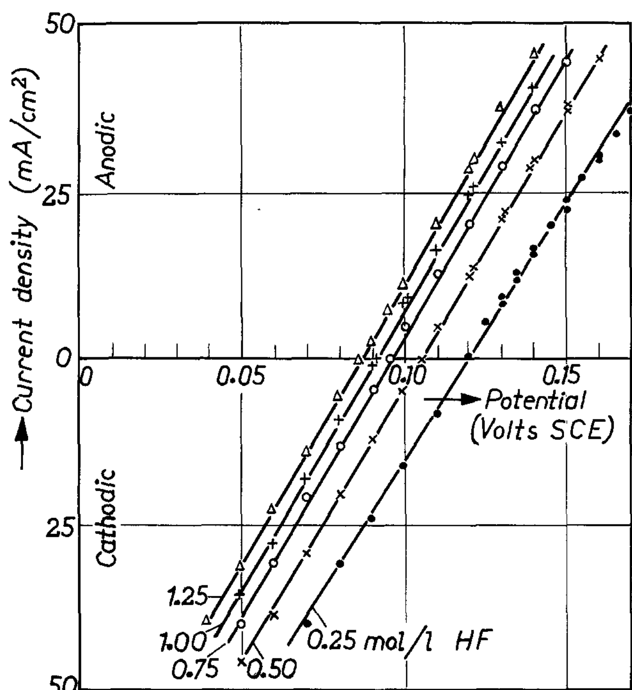

Fig. 9. Polarization curves for a Permalloy RDE at 24°C, 500 rpm in 3.9M H_2SO_4, 1.12M H_2O_2, and HF concentrations as indicated on the curves.

Considerable oxygen evolution is observed at the surface of the Permalloy during its chemical dissolution in this $H_2SO_4/H_2O_2/HF$ medium. Electrochemical oxidation of H_2O_2 on the alloy seems unlikely at the low value of the rest potential. Oxygen evolution may be due to catalytic decomposition of H_2O_2.

Figure 10 shows the steady-state polarization curve for a stationary Permalloy electrode in 2.0M H_2SO_4, 0.9M HF solution, containing 0.5M $NH_4Fe(SO_4)_2$. At potentials lower than the rest potential a cathodic current plateau is observed, and this results from diffusion-controlled reduction of ferric ions. As expected, the current density in this region depends on the ferric concentration and on the stirring conditions at the electrode.

Discussion

As was shown in Fig. 4, the beveling angle α can be varied between 6° and 40° by changing the HF concentration of the etchant. The chemical etch rate of sputtered Permalloy films does not depend significantly on this concentration (Fig. 8). This indicates that the beveling process is controlled by the Ti dissolution rate, which in turn is determined by the HF concentration of the etchant. Using the data for beveled steps given in Fig. 4, an experimental etch rate for Ti can be obtained from Eq. [1]. Results are shown as circles in Fig. 11.

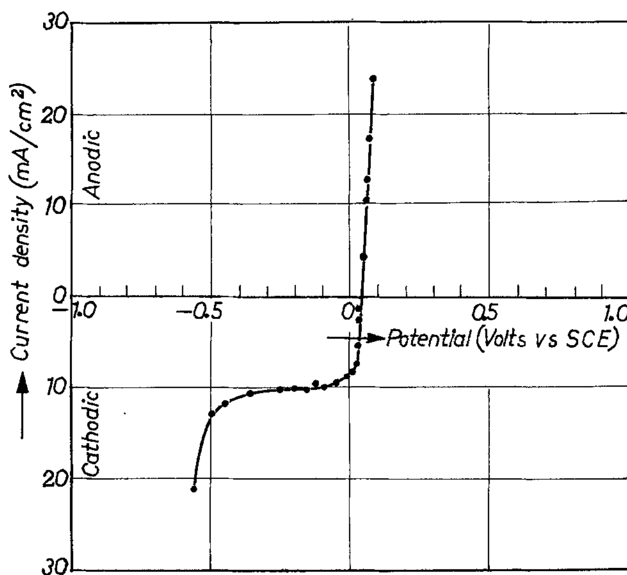

Fig. 10. Polarization curve for a stationary Permalloy electrode at 24°C in 2.0M H_2SO_4, 0.9M HF, and 0.5M $NH_4Fe(SO_4)_2$ solution.

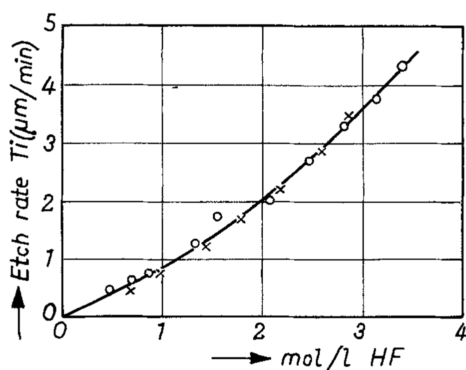

Fig. 11. The etch rate of Ti as a function of the HF concentration of the etchant: ○, values calculated from Eq. [1] and Fig. 4; ×, values calculated from the current density at the rest potential of the bimetallic system.

The electrochemical measurements have shown that the rest potential of the bimetallic system, determined by the Permalloy, lies in the constant current region for Ti (compare Fig. 5 and 9). In this region the dissolution rate of Ti is not sensitive to shifts in potential of up to 100 mV. It is therefore not affected by the change in rest potential caused by the increase in HF content of the etchant (Fig. 9). The etch rate of Ti can, however, be varied over orders of magnitude by changing the HF concentration of the solution. If these electrochemical results reflect the conditions which exist for the bimetallic system during beveling, then the current in the plateau region of the polarization curve for Ti should be a measure of the etch rate of this metal. Since considerable gas evolution occurs during dissolution of Permalloy in this $H_2SO_4/H_2O_2/HF$ medium, stirring conditions are created at the dissolving Ti surface. The effect of stirring can be simulated by the rotating disk experiments. We have arbitrarily assumed that gas evolution is equivalent to a rotation rate of 500 rpm. A decrease of this value to 200 rpm or an increase to 1500 rpm gives a change of less than 12% in the passive current (Fig. 6). Values for the etch rate of Ti, calculated from the passive current at 500 rpm and assuming that the metal dissolves as tetravalent ions, are shown as crosses in Fig. 11. The agreement between the etch rates of Ti as obtained from the beveling experiments and the results calculated from the electrochemical measurements is reasonably good (Fig. 11). This suggests that the proposed electrochemical approach to bevel-etching in bimetallic systems is justified.

Chemical dissolution of Permalloy in H_2SO_4/HF solution containing $NH_4Fe(SO_4)_2$ is determined by the diffusion-controlled cathodic reaction (Fig. 10). This means that the dissolution rate of the alloy depends on the concentration of the oxidizing agent and on the hydrodynamic conditions at the electrode. This is probably also the case for the dichromate solutions. The absence of gas evolution during etching with ferric or dichromate etchants may be an advantage for certain applications since gas bubbles, adhering to the metal surface, may locally inhibit dissolution (2). However, beveling systems based on the above etchants are sensitive to changes in the stirring conditions during etching. Reproducibility can be ensured by rotating the substrates at a fixed rate.

A peculiarity of this particular beveling system is the fact that Ti is dissolved at a potential (approximately 0.1V in the case of the H_2O_2 etchant) at which chemical dissolution of the metal itself should not be possible since reduction of the oxidizing agent of the etchant does not occur, to any appreciable extent, at potentials in the passive region. The metal dissolves because it is in galvanic contact with Permalloy, and the cathodic reaction, *e.g.*, reduction of H_2O_2, occurs exclusively on the alloy.

Conclusions

When a metal is employed as top layer in order to bevel-etch another metal using the duplex layer chemical etching technique, certain precautions are essential. Under unfavorable conditions, quite disastrous undercutting can occur as a result of galvanic effects (2, 3).

In the present study involving sputtered Permalloy, satisfactory results were obtained by using a suitable combination of top layer metal and etchant. These results suggest that, for a reliable etching process, the anodic partial current-potential curve of the top layer metal in the etchant should be relatively flat in the region of the rest potential of the bimetallic couple, *i.e.*, the metal should show passivating or polishing behavior.

Manuscript submitted Feb. 22, 1977; revised manuscript received Sept. 30, 1977. This was Paper 82 presented in part at the San Francisco, California, Meeting of the Society, May 12-17, 1974.

Any discussion of this paper will appear in a Discussion Section to be published in the December 1978 JOURNAL. All discussions for the December 1978 Discussion Section should be submitted by Aug. 1, 1978.

Publication costs of this article were assisted by Philips Research Laboratories.

REFERENCES

1. D. Mac Arthur, in "Etching," H. G. Hughes and M. J. Rand, Editors, p. 76, The Electrochemical Society Softbound Symposium Series, Princeton, N.J. (1976).
2. L. T. Romankiw, *ibid.*, p. 161.
3. J. J. Kelly and C. H. de Minjer, *This Journal,* **122,** 931 (1975).
4. D. M. Mac Arthur, Paper 220 presented at The Electrochemical Society Meeting, New York, Oct. 13-17, 1974.
5. W. Kern and J. M. Shaw, *This Journal,* **118,** 1699 (1972).
6. R. P. Frankenthal and D. H. Eaton, *ibid.,* **123,** 703 (1976).
7. J. C. v. Lier, G. J. Koel, W. J. v. Gestel, L. Postma, J. T. Gerkema, F. W. Gorter, and W. F. Druyvesteyn, *IEEE Trans. Magn.,* **mag 12,** 716 (1976).
8. G. J. Koel, L. Postma, J. T. Gerkema, and J. T. Snijders, Paper 145 presented at The Electrochemical Society Meeting, Washington, D.C., May 2-7, 1976.
9. J. L. Vossen, G. L. Schnable, and W. Kern, *J. Vac. Sci. Technol.,* **11,** 60 (1974).
10. T. Yanagawa and I. Tekekoshi, *IEEE Trans. Electron Devices,* **ed-17,** 964 (1970).
11. G. J. Koel and T. C. J. Bertens, Paper 82 presented at The Electrochemical Society Meeting, San Francisco, California, May 12-17, 1974.
12. G. J. Koel, Unpublished results.
13. P. V. Shchigolev, "Electrolytic and Chemical Polishing of Metals," p. 6, Freund Publishing House, Holon, Israel. (1970).
14. N. T. Thomas and Ken Nobe, *This Journal,* **119,** 1450 (1972).
15. M. J. Mandry and G. Rosenblatt, *ibid.,* **119,** 29 (1972).
16. A. Caprani, *J. Chim. Phys.,* **72,** 171 (1975).
17. J. J. Kelly, Extended Abstract No. 134, 27th Meeting ISE, Zürich, Sept. 6-11, 1976.
18. K. J. Vetter, "Electrochemical Kinetics, Theoretical and Experimental Aspects," p. 765, Academic Press, London (1967).
19. Y. Hori, M. Ikawa, and T. Mukaibo, *Electrochim. Acta,* **19,** 569 (1974).

Unsteady Mass Transfer in the Boundary Layer on a Continuous Moving Sheet Electrode

Rama Subba Reddy Gorla

Department of Mechanical Engineering, Cleveland State University, Cleveland, Ohio 44115

ABSTRACT

An analysis is presented to investigate the transient mass transfer in the boundary layer on a continuous moving sheet electrode. The unsteady mass flux and details of the concentration field are obtained and have been presented graphically. The asymptotic approach of the transient surface mass flux toward the final steady state has been described. The range of Schmidt numbers investigated was from 0.01 to 1000.

The study of mass transfer on a continuous flat surface moving at high speed is of considerable practical interest. Such systems are used in the electrotinning of steel sheets and copper wires, paper drying, glass sheet and steel plate cooling, etc.

Sakiadis (1) was probably the first to examine the laminar and turbulent boundary layers on a continuous moving belt. The corresponding problem involving cylindrical surfaces has been studied by Koldenhof (2). Tsou *et al.* (3) developed a method for creating the continuous surface, using a rotating drum of large diameter. The heat-transfer coefficients and data related to transition from laminar to turbulent flow have been obtained by them experimentally. References (4-6) include numerical solutions and experimental data related to the study of heat transfer from a continuous moving belt. More recently, Chin (7) presented an asymptotic solution valid for large Schmidt numbers for mass transfer to a continuous moving flat sheet under laminar conditions.

The present work is undertaken in order to study the unsteady mass transfer to a continuous moving sheet electrode. The transient surface response behavior and the details of the transient concentration fields for the case of a step change in surface concentration are obtained for various Schmidt numbers. The step function result serves as a fundamental solution, since by a superposition technique it can be generalized to apply for arbitrary time variations in the wall concentration.

Key words: mass transport, transients, electrodeposition.

Analysis

Let us consider a continuous flat-sheet electrode moving with a constant velocity U_w through a stationary electrochemical cell. The sheet enters the cell through a slot at one end of the cell and leaves the cell at the opposite side through another slot. A model of the flow with the coordinate system has been shown in Fig. 1. We assume the flow to be steady and the bulk concentration of the diffusing ion to be constant at C_∞. Initially the concentration of the diffusing ion at the electrode surface is C_∞ and at time $t = 0$ a step change in surface concentration is applied.

The appropriate governing equations within boundary layer approximation may be written as

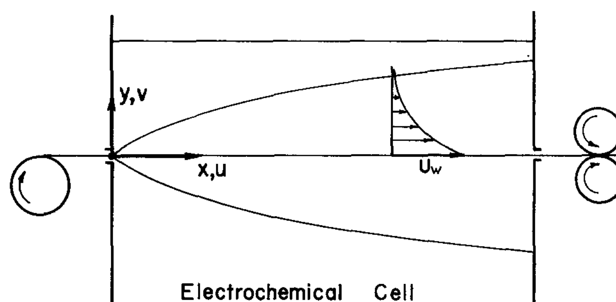

Fig. 1. Coordinate system and flow development

Mass

$$\frac{\partial u}{\partial x} + \frac{\partial v}{\partial y} = 0 \quad [1]$$

Momentum

$$u\frac{\partial u}{\partial x} + v\frac{\partial u}{\partial y} = \nu \cdot \frac{\partial^2 u}{\partial y^2} \quad [2]$$

Diffusion

$$\frac{\partial C}{\partial t} + u\frac{\partial C}{\partial x} + v\frac{\partial C}{\partial y} = D \cdot \frac{\partial^2 C}{\partial y^2} \quad [3]$$

The boundary conditions for the velocity field are

$$u(x,0) = U_w,\ v(x,0) = 0, \text{ and } u(x,\infty) = 0 \quad [4]$$

The initial and boundary conditions for the concentration field are

$$C(x,y,0) = C_\infty,\ C(x,0,t) = C_\infty + (C_w - C_\infty)\cdot 1(t), \text{ and } C(x,\infty,t) = C_\infty \quad [5]$$

Proceeding with the analysis, we define

$$\eta = y\sqrt{\frac{U_w}{\nu x}}$$

$$u = U_w \cdot f'(\eta)$$

$$v = \frac{1}{2}\sqrt{\frac{\nu U_w}{x}}\,[\eta f'(\eta) - f(\eta)] \quad [6]$$

The primes above designate differentiation with respect to η only. It may be verified that the continuity equation is automatically satisfied and the momentum equation becomes

$$f''' + \frac{ff''}{2} = 0 \quad [7]$$

The transformed boundary conditions for the velocity field are

$$f'(0) = 1,\ f(0) = 0, \text{ and } f'(\infty) = 0 \quad [8]$$

A numerical solution of Eq. [7] and [8] yields the velocity profile.

To transform the diffusion equation, we define

$$\theta = \frac{C - C_\infty}{C_w - C_\infty}$$

$$\tau = \frac{U_w t}{x} \quad [9]$$

Equation [3] then becomes

$$\mathrm{Sc}\{1 - f'\tau\}\frac{\delta\theta}{\delta\tau} = \frac{\delta^2\theta}{\delta\eta^2} + \frac{Scf}{2}\cdot\frac{\delta\theta}{\delta\eta} \quad [10]$$

with initial and boundary conditions

$$\theta(\eta,0) = 0,\ \theta(0,\tau) = 1(\tau), \text{ and } \theta(\infty,\tau) = 0 \quad [11]$$

Defining the Laplace transform of θ as

$$\bar\theta(\eta,p) = \int_0^\infty e^{-p\tau}\cdot\theta(\eta,\tau)\,d\tau$$

and applying the Laplace transformation to Eq. [10] and [11], we have

$$\bar\theta'' + \frac{\mathrm{Sc}f}{2}\bar\theta' = \mathrm{Sc}\left\{p\bar\theta + f'\frac{\delta p\bar\theta}{\delta p}\right\} \quad [12]$$

with boundary conditions

$$\bar\theta(0) = \frac{1}{p} \text{ and } \bar\theta(\infty) = 0 \quad [13]$$

We now seek a series solution of the form

$$\bar\theta(\eta,p) = \frac{1}{p}\cdot\exp\left\{-\frac{\mathrm{Sc}I}{2} - [\mathrm{Sc}(p+\lambda)]^{1/2}\eta + \frac{\mathrm{Sc}\eta f}{4}\right\}\cdot\sum_{n=0}^{\infty} u_n(\eta)\cdot[\mathrm{Sc}(p+\lambda)]^{-n/2} \quad [14]$$

where

$$I = \int_0^\eta f\,d\eta \quad [15]$$

and λ is a function of η which is still unknown.

From an inspection of Eq. [14] we see that $\theta(\infty) = 0$ is satisfied. Substituting Eq. [14] into [12] and equating the coefficients of similar powers of $(p + \lambda)$, there results a set of second-order ordinary differential equations from which one can deduce

$$u_0(\eta) = 1$$

$$u_1(\eta) = \frac{\mathrm{Sc}\cdot\lambda\eta}{2} + \frac{\mathrm{Sc}}{8}(\eta f' - f) + \frac{\mathrm{Sc}^2}{32}\int_0^\eta[(\eta f')^2 - f^2]\,d\eta$$

$$u_2(\eta) = \frac{\mathrm{Sc}^2}{8}\eta^2\lambda^2 + \frac{\mathrm{Sc}\eta\lambda}{2}\chi_1 + \chi_2$$

where

$$\chi_1 = \frac{\mathrm{Sc}}{8}(\eta f' - f) + \frac{\mathrm{Sc}^2}{32}\int_0^\eta[(\eta f')^2 - f^2]\,d\eta$$

$$\chi_2 = \frac{1}{2}(\chi_1^2 + \chi_1') + \frac{\mathrm{Sc}}{4}\left[f\chi_1 + \int_0^\eta(\eta f' - f)\chi_1'\,d\eta\right]$$

etc.

It has been found that first five terms in the series provide satisfactory convergence.

Taking the inverse of Eq. [14], we obtain an expression for the concentration field as

$$\theta(\eta,\tau) = \exp\left\{-\frac{\mathrm{Sc}}{2}\left(I - \frac{\eta f}{2}\right) - (\mathrm{Sc}\lambda)^{1/2}\eta\right\}\cdot\sum_{n=0}^{\infty}u_n(\eta)\,(\mathrm{Sc}\lambda)^{-n/2}\cdot H_n \quad [16]$$

where

$$H_0 = h_1 + h_2$$

$$H_1 = h_1 - h_2$$

$$H_2 = H_0 - h_3$$

$$H_3 = H_1 + (\mathrm{Sc}\lambda)^{1/2}\eta h_3 - h_4$$

$$H_4 = H_0 - \left(1 + \lambda\tau + \frac{\mathrm{Sc}\lambda\eta^2}{2}\right)h_3 + \frac{1}{2}(\mathrm{Sc}\lambda)^{1/2}\cdot\eta h_4$$

etc.

and

$$h_1 = \frac{1}{2}\,\mathrm{erfc}\,[\mathrm{Sc}^{1/2}(4\tau)^{-1/2}\eta - (\lambda\tau)^{1/2}]$$

$$h_2 = \frac{1}{2}\exp[2(\mathrm{Sc}\lambda)^{1/2}\eta]\cdot\mathrm{erfc}\,[\mathrm{Sc}^{1/2}(4\tau)^{-1/2}\eta + (\lambda\tau)^{1/2}]$$

$$h_3 = \exp[(\mathrm{Sc}\lambda)^{1/2}\eta - \lambda\tau]\cdot\mathrm{erfc}\,[\mathrm{Sc}^{1/2}(4\tau)^{-1/2}\eta]$$

$$h_4 = 2\pi^{-1/2}(\lambda\tau)^{1/2}\exp - [\mathrm{Sc}^{1/2}(4\tau)^{-1/2}\eta - (\lambda\tau)^{1/2}]^2 \quad [17]$$

One can notice that H_n varies from 0 to 1 as τ varies from 0 to ∞ and also as η varies from 0 to ∞. For all values of η, as $\tau \to \infty$, $H_n \to 1$.

The steady-state temperature distribution is obtained by letting $\tau \to \infty$ in Eq. [16]. For steady state, we have

$$\theta_S(\eta) = \exp\left\{-\frac{Sc}{2}\left(I - \frac{\eta f}{2}\right) - (Sc\lambda)^{1/2}\eta\right\} \cdot \sum_{n=0}^{\infty} u_n(\eta) \cdot (Sc\lambda)^{-n/2} \quad [18]$$

Differentiating Eq. [18] with respect to η and setting $\eta = 0$, one obtains for the steady-state value for the wall concentration gradient

$$\theta_S'(0) = -(Sc\lambda_w)^{1/2} + \sum_{n=1}^{\infty} u_n'(0)\,[Sc\lambda_w]^{-n/2} \quad [19]$$

To evaluate λ, it becomes necessary to find the steady-state solution. θ_S satisfies the second-order differential equation

$$\theta_S'' + \left(\frac{Scf}{2}\right)\theta_S' = 0 \quad [20]$$

with boundary conditions

$$\theta_S(0) = 1 \text{ and } \theta_S(\infty) = 0$$

Equation [20] is solved by using a fourth-order Runge Kutta method of numerical integration. Since the value of $\theta_S(0)$ is known, a search for $\theta_S(0)$ was made so that the resulting solution yields $\theta_S(\infty) = 0$. This was accomplished numerically by means of an iterative computer program. The present results for $\theta_S'(0)$ are shown in Table I and a comparison with the results reported in literature reveals a good agreement for the whole range of Schmidt numbers. The numerical solution thus generated for $\theta_S(\eta)$ was used to determine $\lambda(\eta)$ from Eq. [18]. For $\eta = 0$, the series in Eq. [18] becomes identically unity and so use of Eq. [20] was made to evaluate λ_w. An iterative computer program was devised to evaluate $\lambda(\eta)$ numerically. Figure 2 shows the distribution of λ for Sc ranging from 0.01 to 1000. The numerical results for λ_w are tabulated in Table II for the same range of Schmidt numbers.

After obtaining the numerical results for $\lambda(\eta)$, it is now possible to evaluate the transient concentration distribution and the mass flux at the electrode surface. Equation [16] was used to get the former. Equations [16] and [19] were used to evaluate $\theta'(0,\tau)/\theta_S'(0)$ which is same as the ratio of the instantaneous to steady-state Sherwood numbers. Figures 3, 4, and 5 illustrate the growth of the concentration layer with time, for Sc = 0.01, 1, and 1000, respectively. For the sake of brevity, data for other Schmidt numbers are not included.

The local mass flux at the electrode surface is related to the concentration gradient by

Table I. Values of $-\frac{d\theta_S(0)}{d\eta}$ for constant wall concentration

Sc	Present results	Ref. (7)
1000	17.74612	
100	5.54471	5.545
10	1.68063	
1	0.44474	0.4430
0.7	0.35015	
0.1	0.073003	
0.01	0.0081344	

Table II. λw vs. Sc

Sc	λw
1000	0.00043695
100	0.0042764
10	0.040611
1	0.37597
0.7	0.53040
0.1	3.13084
0.01	18.05501

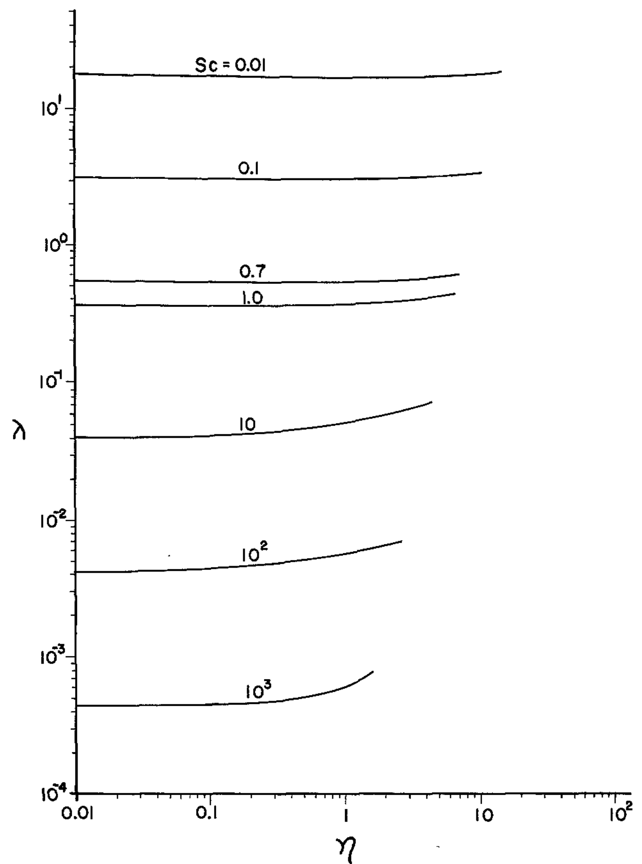

Fig. 2. Distribution of λ for various Schmidt numbers

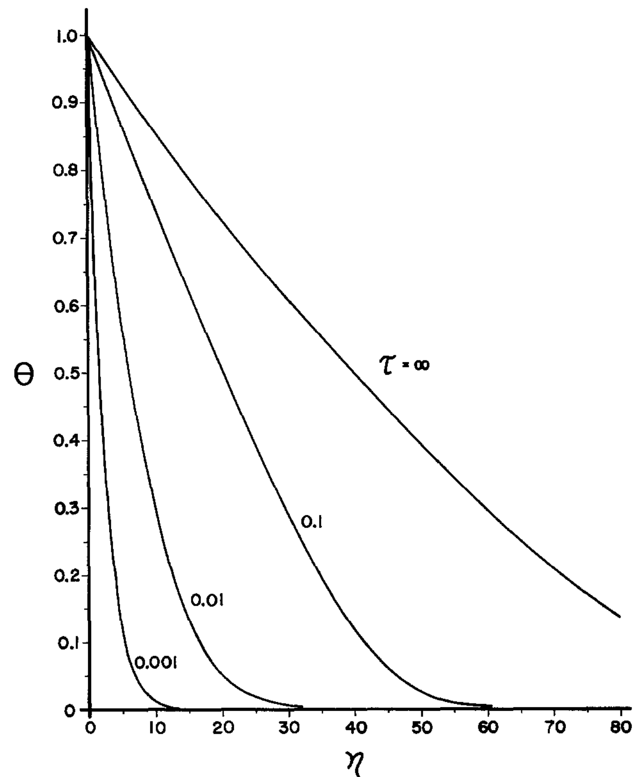

Fig. 3. Transient concentration profiles for Sc = 0.01

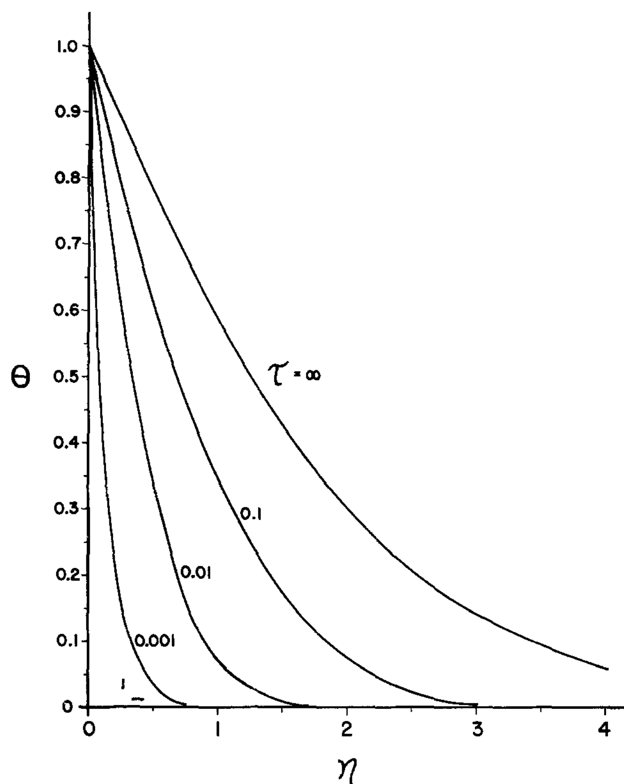

Fig. 4. Transient concentration profiles for Sc = 1

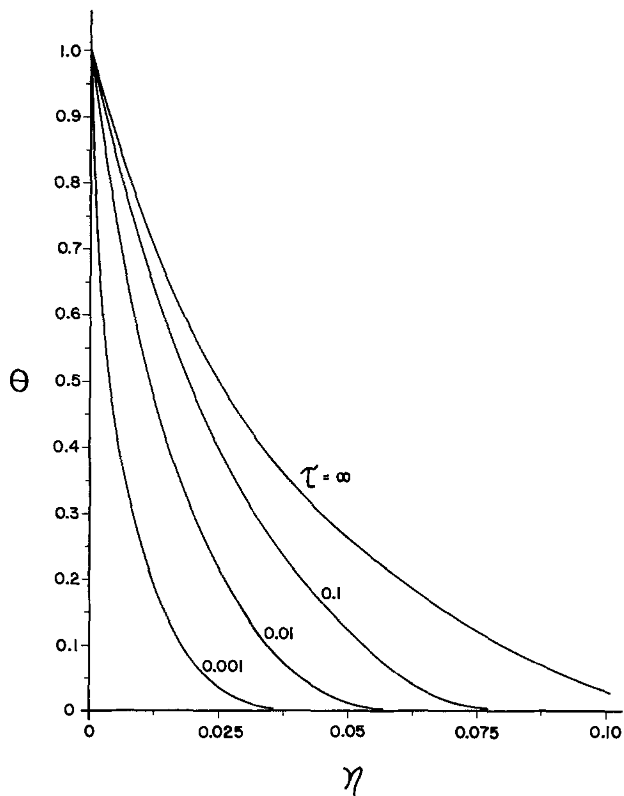

Fig. 5. Transient concentration profiles for Sc = 1000

$$j_w = -D\left(\frac{\partial C}{\partial y}\right)_{y=0} = k(C_w - C_\infty) \quad [21]$$

where k is the local mass transfer coefficient. The local Sherwood number Sh_x can be written as

$$Sh_x = \frac{kx}{D} = -Re_x^{1/2} \cdot \theta'(0,\tau) \quad [22]$$

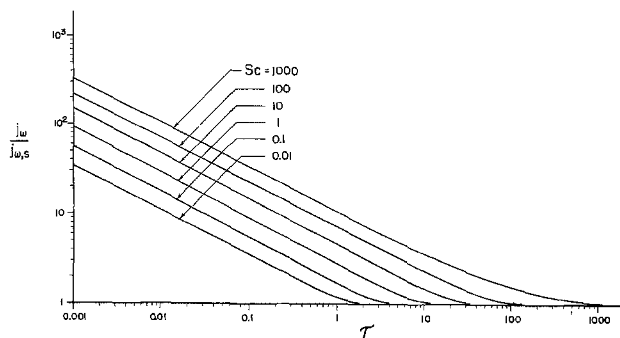

Fig. 6. $(j_w/j_{w,s})$ vs. τ for Sc = 0.01-1000

A quantity of practical interest is the ratio of the instantaneous to steady-state values of the mass flux rates. We have then

$$\frac{j_w}{j_{ws}} = \frac{Sh}{Sh_s} = \frac{\theta'(0,\tau)}{\theta_s'(0)} \quad [23]$$

The above can be deduced from Eq. [16] and [19] for any value of time and Schmidt number. Figure 6 shows such results for Sc ranging from 0.01 to 1000. It may be observed that the surface mass transfer approaches the steady-state conditions asymptotically.

Concluding Remarks

The problem of transient mass transfer in the boundary layer on a continuous sheet electrode has been solved analytically for the case of step change in surface concentration. The results for the case of arbitrary surface concentration variation can be deduced from the present results by numerical superposition methods. The problem corresponding to the step change in surface mass flux is presently under investigation and these results will be reported at a later date.

Acknowledgments

The author wishes to thank Dr. Vincent Larson, Professor and Chairman of the Department of Mechanical Engineering at Cleveland State University, for his support and encouragement.

Manuscript submitted Dec. 20, 1977; revised manuscript received Feb. 1, 1978.

Any discussion of this paper will appear in a Discussion Section to be published in the December 1978 JOURNAL. All discussions for the December 1978 Discussion Section should be submitted by Aug. 1, 1978.

Publication costs of this article were assisted by Cleveland State University.

LIST OF SYMBOLS

- C concentration of the diffusing ion (g mole/cm³)
- D diffusivity of the diffusing ion (cm²/sec)
- f nondimensional stream function
- j_w local rate of mass flux at the surface of the electrode (g mole/cm² sec)
- k local mass transfer coefficient (cm/sec)
- K average mass transfer coefficient (cm/sec)
- L length of the moving sheet (cm)
- p parameter in Laplace transform
- Re Reynolds number (U_wL/ν)
- Re_x local Reynolds number (U_wx/ν)
- Sc Schmidt number (ν/D)
- Sh average Sherwood number (KL/D)
- Sh_x local Sherwood number (kx/D)
- t time
- u velocity component in x-direction (cm/sec)
- U_w velocity of the continuous sheet moving through the electrolyte (cm/sec)
- v velocity component in y-direction (cm/sec)
- x coordinate along the moving sheet (cm)
- y coordinate normal to the wall (cm)

$\Gamma(n)$ Gamma function $= \int_0^\infty \alpha^{n-1} \cdot e^{-\alpha} d\alpha$

$\Gamma_x(n)$ incomplete Gamma function $= \int_0^x \alpha^{n-1} e^{-\alpha} d\alpha$

η nondimensional coordinate
θ nondimensional concentration
ρ density
τ nondimensional time

Subscripts

s steady state
w conditions at the wall
∞ conditions at very large distances away from the wall

REFERENCES

1. B. C. Sakiadis, *AIChE J.*, **7**, 26 (1961).
2. E. A. Koldenhof, *AIChE J.*, **9**, 411 (1963).
3. F. K. Tsou, E. M. Sparrow, and R. J. Goldstein, *Int. J. Heat Mass Transfer*, **10**, 219 (1967).
4. C. A. Rhodes and H. Kaminer, *AIAA J.*, **10**, 331 (1972).
5. J. F. Griffin and J. L. Throne, *AIChE J.*, **13**, 1210 (1967).
6. L. E. Erickson, L. C. Cha, and L. T. Fan, *Chem. Eng. Prog.*, **62**, 157 (1966).
7. D. T. Chin, *This Journal*, **122**, 643 (1975).
8. R. S. R. Gorla, *Int. J. Eng. Sci.*, **11**, 841 (1973).
9. D. R. Jeng and R. S. R. Gorla, *Trans. ASME, J. Heat Transfer*, 419 (1973).

Electrochemical Parametric Pumping

Y. Oren and A. Soffer*

Atomic Energy Commission, Nuclear Research Centre-Negev, Beer-Sheva, Israel

ABSTRACT

An electrochemical column consisting of two high surface porous carbon electrodes and a thin separator, was operated in four-action electrochemical parametric pumping cycles at the double layer potential range. A significant concentration profile was built up along the column indicating that several theoretical plates were attained. The separative properties of a single theoretical plate was derived. The method seems promising for industrial water processing.

Many solid-fluid phase systems could adequately serve in multistage separation columns, as they exhibit a high separation factor α, where $\alpha = K_A/K_B$, where K_A and K_B are, respectively, the partition coefficients of the two constituents to be separated, A and B. However, if the solid phase is used as stationary packing, the concentration profile will escape from the column, as in the case of chromatography. This renders chromatography unsuitable for large scale separation, although its analytical value is of no doubt.

Various separation modes have been suggested, which engage the entire active solid phase of the column length. For example, a chromatographic column can be fed by several pulses prior to elution of the first pulse (1) or the solid phase can be mobilized in order to imitate the fluid-fluid countercurrent process (2). The disadvantages of this last mode are mechanical problems associated with the solid mobilization.

Another approach (3) is cyclic variations of the intensive variable which rule the partition coefficients, while the fluid in the column is moved according to a predetermined routine. The thermodynamic intensive variables employed experimentally were pressure (4), concentration (5), temperature (6-8), and electrical potential (9). Pressure change does not allow multistage operation of the column, because the expansion due to pressure reduction would cause appreciable mixing of the column contents. The concentration parameter can be varied either by dilution or by addition of a competing material. Both these modes do not allow efficient multistage operation.

Unlike the other variables, temperature changes can be applied more easily and independent of the axial flow. On the other hand, the temperature parameter involves considerable energy dissipation because part of the heat is transferred to the bulk of the column contents.

The electrical potential as a variable intensive parameter can be immediately and speedily applied to the system without disturbing the axial flow. Also the associated energy per cycle is close to the heat of adsorption. This implies that, unlike heat transfer, electrical energy is transferred as a whole to the solution-electrode interface, thereby influencing the material transfer from the solid electrode phase to the solution.

Single cycles of electrodeposition and dissolution of heavy metal ions were used by several authors for batch separations (10-12). These processes are noncontinuous and can be classified with chromatographic concepts rather than with the continuously operated cyclic system. They, however, all differ from ordinary electrochemical cells by the very high material hold-up of the electrode.

Among the cyclic modes applied to stationary solid adsorbent columns, parametric pumping received major consideration. Parametric pumping was introduced in 1966 (6) and is still studied (7). The striking feature of this method is its multistage separation property, *i.e.*, very large concentration differences can be formed along the column (8).

The Electrochemical Parametric Pumping Concept

The present work demonstrates the experimental and few of the theoretical aspects of the electrochemical parametric pump which combines the high separation capability of the parametric pumping method and the electrochemical properties of high surface porous carbon electrodes. We use the separation of NaCl from water (desalination) as a process model for introducing this concept. Blair and Murphy (13) and Johonson and Newman (14) discussed extensively the use of a two high surface porous carbon electrodes set up for desalting water by means of electroadsorption and electrodesorption cycles in a batch process. It was shown by Johonson and Newman and by Soffer and Folman (15) that ionic adsorption in the double layer (dl) region of these electrodes was the actual mechanism of the desalination process. This adsorption is quantitative due to the high charging capacity caused by the high specific surface area of the carbon electrodes.

* Electrochemical Society Active Member.

Key words: porous carbon electrodes, parametric pumping, separation, desalination.

It is, however, possible to predict the properties of such a cell by the study of a single porous carbon electrode being the working electrode in the usual three electrode system (working, auxiliary, and reference) (15, 16). Relying on the experimental results of the porous carbon-Ag/AgCl cell, it was shown (16) that anion and cation adsorption efficiencies[1] as high as 83 and 85%, respectively, can be achieved when the carbon electrode is in the potential ranges 0.2-0.4V and −0.2 to −0.4V *vs.* SCE. Adsorption efficiency was also discussed by Johonson and Newman (14) who used the terms "cation and anion responsive electrodes" for the more negative and the more positive electrodes, respectively.

The electrochemical parametric pumping column for the separation of NaCl from water consist in principle of two identical high surface carbon electrodes separated by an inert separator and filled with the appropriate solution. Each electrochemical parametric pumping cycle consists of four consecutive operations (Fig. 1): A. Adsorption, which, in a generalized sense is a step of transfer of g moles of the material to be separated from the solution to the electrode phase. This transfer is induced by changing the potential difference (as the intensive parameter) across the electrodes. F. Forward axial pumping of the solution during which the g moles which are bound to the solid electrode, remain stationary. D. Desorption, which is also an electrically induced step and causes a back transfer of the g moles from the electrode to the solution phase. B. Backward axial pumping of the solution where the g moles are free to move.

The separation capability of the electrochemical parapump can be readily understood through the fact that the component to be separated is differently adsorbed by the electrode (say, component "a" is preferred). Averaging on a cycle, a stream moving forward (F) is poorer, and a stream moving backward (B) is richer in component "a." This resembles the countercurrent separation processes, while the F and B streams are in complete analogy with the two fluid phases.

Experimental

The experimental setup was composed of the electrochemical column and its accessories. They included a control system for automatic parametric pumping operation, electrochemical instrumentation, pumping equipment, an air thermostat, and a solution deaeration arrangement. The assembly operated almost fully automatically.

The electrochemical column.—The electrode material was Carbopack B, supplied by Supelco Incorporated. This is a graphitized carbon black, similar to that referred to as "Graphon." According to the manufacturers specifications, it has a specific surface area of 100 m^2/g. This was verified by us by BET measurements. Like other blacks, it should be composed of almost spherical particles of average diameter 25 μm. The particles are stacked as granules of 60/80 mesh. A bed of such material should therefore exhibit two distinct pore ranges: the interparticle range of 20-30 mμ (mesopores) and the 10^5 fold intergranular range of 0.1-0.3 mm (macropores). The column design is shown in Fig. 2. Each carbon electrode bed is 1 mm thick, 10 mm wide, and 96 cm long. The separator thickness is 0.35 mm. It was made of three layers in order to prevent electrode particles making short circuits between the electrodes along the column. The weight of each carbon electrode was 3.1g and the free volume of the column was 16.1 cm^3.

The pumping equipment.—The pumping flow diagram is shown in Fig. 3. Forward and backward pumping cycles at total reflux are induced by the ΔV pump. When the product is withdrawn, valve V_2 is open and the σ pump and the solenoid valve are operated parallel to the ΔV pump in synchronous cycles. The product may be either returned to the inlet vessel or sampled through valve V_1. As the volume of the solution in the inlet vessel was very large (4 liters), compared to the free column volume, its concentration remained prac-

[1] Adsorption efficiency is determined as $F(\partial\Gamma_+/\partial q)_\mu$ for cations and $F(\partial\Gamma_-/\partial q)_\mu$ for anions. F is the Faraday number, q is the dl charge, μ is the salt chemical potential, and Γ is the amount of ions adsorbed.

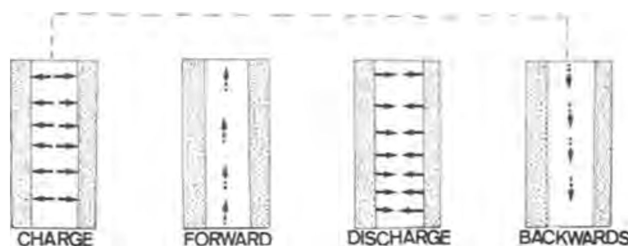

Fig. 1. The four basic stages of the electrochemical parametric pump: ——→ ionic movement, - - - -→ solution movement.

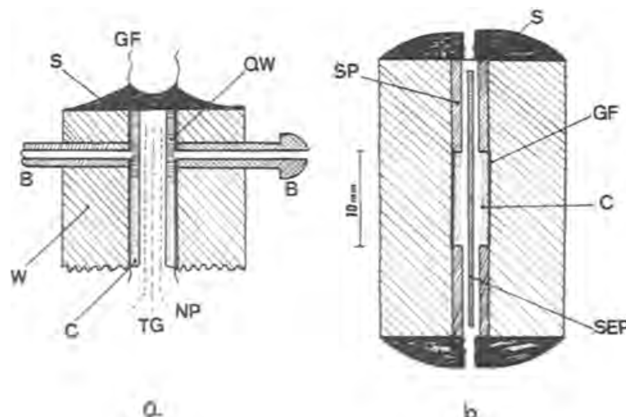

Fig. 2. a. Central longitudinal cross section of the column edge. b. Transversal cross section. B, Inlet or outlet glass bell joint; C, carbon electrode bed; GF, gold foil current collector; NP, nonwoven polypropylene separator; QW, quartz wool plug; S, seal; SP, spacers (1 mm thick); SEP, separator stack; TG, Teflon glass separator; W, column wall.

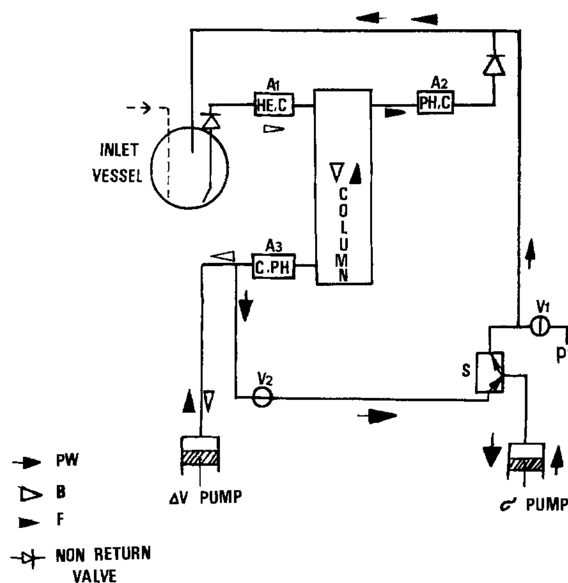

Fig. 3. Flow diagram of the electrochemical parametric pump. F, Forward pumping; B, backward pumping; PS, product sampling; PW, product withdrawal; S, solenoid valve; V, stopcocks; A, on-line accessory which may contain a conductivity cell (C), pH, electrode (PH), or heat exchanger (HE).

tically constant during each run. The volume of the lower head consists mainly of the connecting lines. This volume was minimized to 3.3 cm^3 to shorten the time of approach to steady state.

For cyclic pumping of the solution we used Metrohm EA 412 Microdosimat automatic titrators, remote controlled and modified for parametric pumping operation. They were equipped with upper and lower limit switches for the piston displacement, and an output of 1000 volumetric pulses for the full interchangeable piston stroke. Their original relay control systems were modified to enable forward or backward piston movement or arrest, after accepting suitable pulses from the control system.

The control system (Fig. 4).—This system consisted of six self-contained units for controlling electrochemical parapump functions: charge, discharge, forward ΔV pumping, backward ΔV pumping, product sampling, and withdrawal. Each function is started by an input signal applied to the control unit and terminates after an internal preset reference is reached.

Termination is followed by an output signal which can activate any other control unit. The termination reference potentials of the charge and discharge functions are preset by two voltage comparators, CVC and DVC, and compared with the column electrode potentials. Termination of the forward movement and product withdrawal functions is induced by upper limit switches of the ΔV and the product pumps. For backward movement and product sampling, the termination reference is preset on a counter, which is fed by the output pulses of the pumps. Charging and discharging are performed at constant current.

The temperature controlling system.—Temperature control was necessary to prevent solution conductivity variations due to temperature changes. An air thermostat was preferred because of the large dimensions of the setup. A fast response proportional controller (local production) enabled thermostating at 25° ± 0.1°C.

Conductivity, pH, and voltage measurements.—The conductivity was measured with a Wayne Kerr autobalance universal bridge, Model B 642. The pH in the lower and upper heads of the column was recorded continuously during each run; usually it was 6-8, indicating the conductance is due solely to NaCl. The two types of potential differences recorded were: (*i*) the potential difference between the electrodes, E, for continuous information about electrode capacity and *IR* drop; and (*ii*) the potential drop along the electrodes, e_1 and e_2, to verify the homogeneity of column packing.

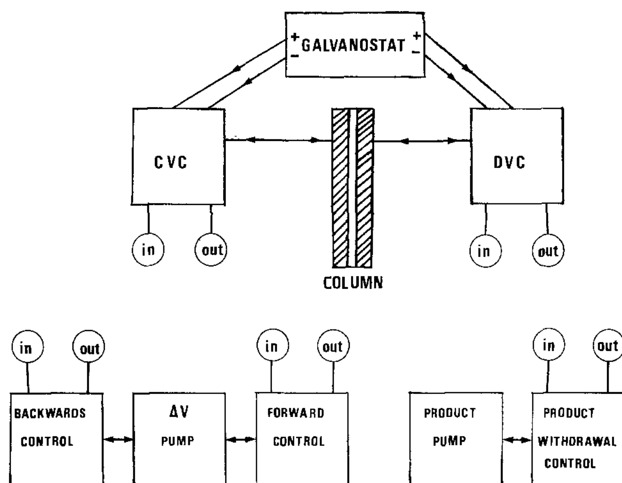

Fig. 4. Control system with pulse signal connections for electrochemical parametric pumping.

For solution deaeration, an inert gas was bubbled through the solution in the inlet vessel before and during each experiment. The gas was purified from O_2 by passing it over a copper bed at 450°C, then prewetted by bubbling through water to prevent evaporation of the solution. All experiments were carried out with 0.01*N* NaCl at the upper head.

Results and Discussion

The differential capacitance of the electrode material.—The dl capacity and charging rate of the electrode material were determined before packing the column. These two properties rule the column performance regarding the amount of salt holdup, *m*, moles per gram carbon, and cycle time. The transient behavior of the macropore (diameter > 100 μm) (17) was insufficient for evaluating the cycle time, since there was strong evidence that the solution conductivity within the interparticle mesopores is considerably lower than the corresponding free solution (18) or the solution in the macropores. A cyclic voltamogram of the Carbopack carbon is given in Fig. 5. The differential capacitance, *Cd*, can be calculated according to

$$Cd = \frac{i}{dv/dt} \qquad [1]$$

which corresponds to an equilibrated dl (19) and has the value of 4.3 $\mu F/cm^2$ at zero potential difference. The slow current reversal after the inversion of the voltage sweep gives the characteristic charging time of 15 sec for Carbopack. The charge and discharge times of the column were chosen considerably larger than this characteristic time.

Analysis of the chronopotentiogram.—A typical experimental plot of a single parametric pumping cycle is given in Fig. 6. The plot is composed of three main components repeated several times during the cycle: a vertical *IR* drop section, V_{IR}, a curved transient section, V_T, and a linear part. This behavior is readily understood considering the equivalent electrical circuit of a cross section of the electrode, sketched in Fig. 7. This is a serial combination of two equivalent circuits, each corresponding to the cell: porous electrode dl |solution| reference electrode. A detailed analysis for a galvanostatic charging mode is given in a previous report (17). The *IR* drop is due to the solution within the separator, the transient is due to the R.C. character of the porous electrode and the linear

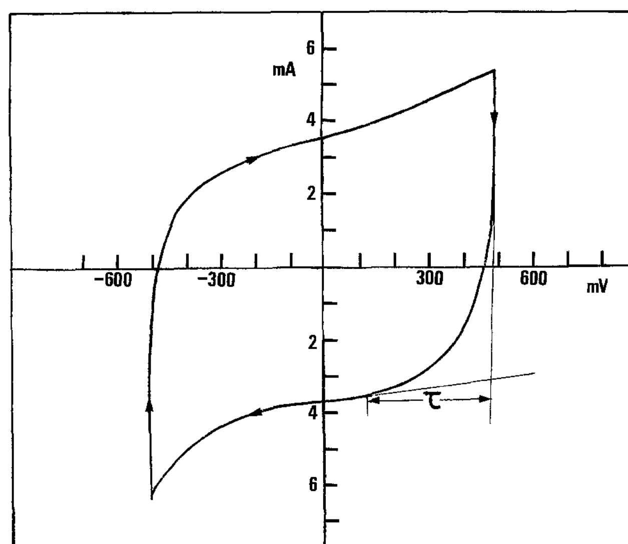

Fig. 5. A cyclic voltamogram of Carbopack Carbon in 0.01*N* NaCl solution. Potentials are against an Ag/AgCl reference electrode, *dV/dt* = 20 mV/sec. τ is the characteristic charging time.

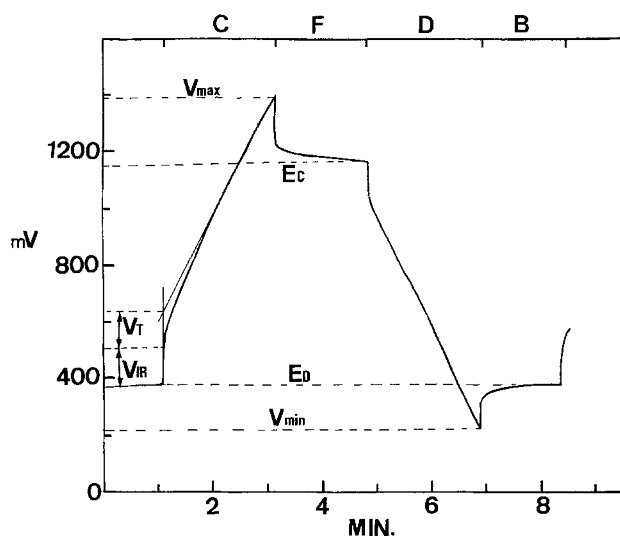

Fig. 6. A typical chronopotentiogram recorded during parametric pumping cycle. Charging current $i = 50$ mA. C, Charging; F, forward solution pumping; D, discharging; B, backward solution pumping.

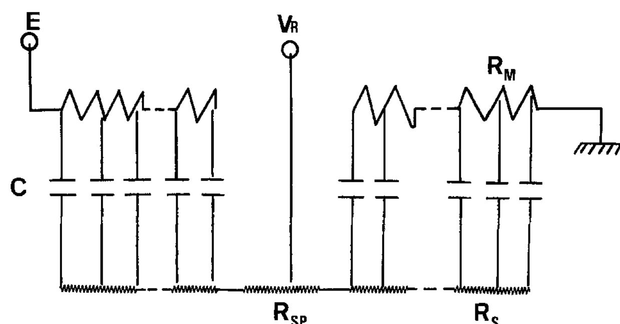

Fig. 7. The cross-sectional equivalent circuit of a unit length of the column for two identical electrodes. R_M, Electronic resistance; C, dl capacity; E, electrode potential; R_S, solution resistance; V_R, reference electrode potential [see Fig. 2 of Ref. (17)]; R_{SP}, separator resistance.

part is practically the charge *vs.* potential curve which emerges after the decay of the transient. The equilibrium value of the average integral dl capacity for two identical electrodes is evaluated by

$$C = \frac{2i\Delta t}{(E_C - E_D)GS} \qquad [2]$$

where Δt is the charging or discharging time (seconds), G is the mass of a single electrode (grams), S is the specific BET surface area (square centimeter/gram), and i is the charging or discharging current. E_C and E_D are shown in Fig. 6.

The value obtained for Fig. 6 is 4.1 μF/cm^2 and is within the values of the differential capacity obtained for the single electrode voltamogram of Fig. 5.

The following restrictions are made in order to obtain optimal operating conditions for the electrochemical parametric pump: the potential difference $V_{max} - (V_{min} + V_{IR})$ is limited to slightly less than 1.23V to prevent gas evolution; V_{min} is chosen to be within the potential difference range which causes a charge efficiency slightly higher than zero (see discussion below). The pumping time during steps F and B (Fig. 6) was long enough to enable a sufficient decay of the transient.

Charge distribution along the column.—The longitudinal equivalent circuit of the column is given in Fig. 8 together with two modes of the power supply connections and the voltage difference along the electrodes. Since these modes are virtually identical, the same e *vs.* time plots should be obtained. However, differences may arise if the column packing is longitudinally inhomogeneous, or a concentration gradient develops. Typical e plots are given in Fig. 9 for a case where no concentration gradient exists. The initial in-

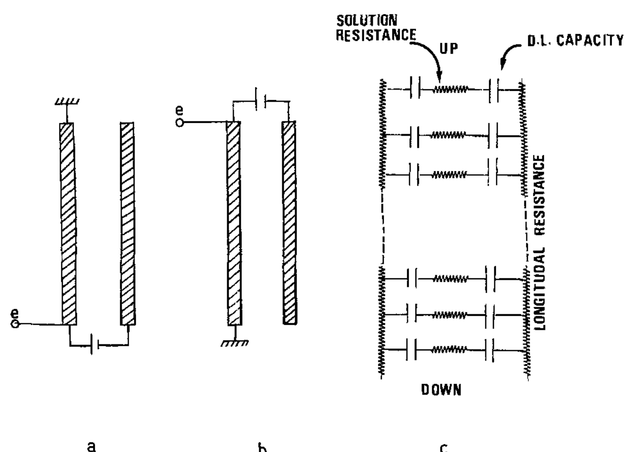

Fig. 8. a. Lower mode of power supply connection. b. Upper mode of power supply connection. c. Longitudinal equivalent circuit of column packing.

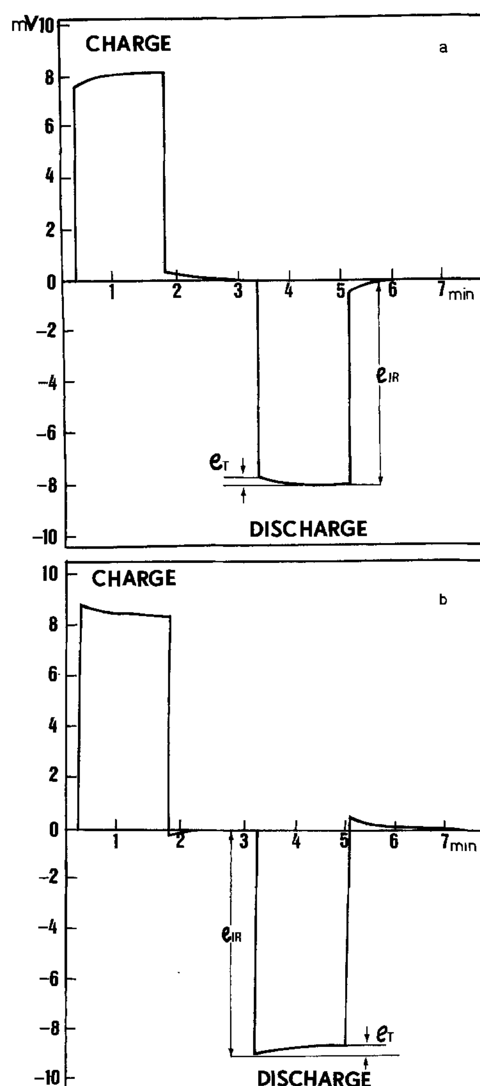

Fig. 9. The variation of the longitudinal potential during a cycle. a. With lower mode of power supply connection. b. With upper mode of power supply connection.

crease, e_{IR}, is immediate since no potential gradient is applied on the capacitors (Fig. 8) at $t = 0$. The (distributed) capacitors close to the current source are charged faster, as they encounter nonlongitudinal electrode resistivity. The initial longitudinal current path is therefore shorter and extends afterward to charge the farther capacitors. This results in an increasing transient, e_t, as shown in Fig. 9a. The decreasing transient of Fig. 9 contradicts, therefore, the expected trend and shows that the lower capacitors are preferentially charged. This clearly indicates that the lower part of the column is more densely packed, *i.e.*, the distributed capacitance is larger. The noticeable decrease of the transient, e_t, in the presence of a concentration profile confirms these arguments, since in this case the lower solution resistivity enables faster dl charging at the lower parts of the column.

Column separation capacity and charge efficiency.—The column separation capacity is defined as the net number of moles adsorbed per carbon weight unit. It can be calculated according to

$$C_p = \frac{(C_o - C_{\Delta E}) V_o}{G} \quad [3]$$

where C_o and $C_{\Delta E}$ are, respectively, solution concentration before and after charging the electrodes, V_o is the solution free volume in the column, and G is the total weight of carbon in the column.

The separation capacity is a function of the potential difference between the two carbon electrodes and, as expected (16), it increases as the potential difference increases (Fig. 10a). Figure 10b shows the differential charge efficiency of the column as a function of the potential difference. The differential charge efficiency at any potential difference is determined from the slope of separation capacity *vs.* electrode charge curve. It is clear from Fig. 10b that over a wide range at high potential differences there are no side reactions (water decomposition) at the dl and almost all the charge investment is directed to change NaCl concentration in the column. It is expected that the differential charge efficiency will decrease on going to higher potential differences as a result of a marked effect of side reactions.

The two curves described in addition to the electrochemical properties already discussed, give a complete description of the basic characteristics of the column.

Concentration profile buildup.—Figure 11 gives the results of an electrochemical parametric pumping run which was accomplished according to the mode shown in Fig. 3 (F and B pathways). It is, in principle, a total reflux mode because no product is withdrawn from the system. However, it differs from the common total reflux mode in that in each cycle, the top of the column is being washed with a solution volume equal to the displacement volume and having the initial concentration.

According to the operation scheme shown in Fig. 1, one should expect an increase of the concentration in the bottom of the column until reaching steady-state value. As shown in Fig. 11, the approach to steady state is faster and the steady-state concentration is lower when the displacement volume ratio is larger.

The unit batch process and the theoretical plate.—The equivalent height of a theoretical plate (EHTP) of a separation column is a fundamental property defining the length of the column required for accomplishing the basic and maximum separation. By knowing the separation power and the length of the theoretical plate of a given column, one could predict the separation properties of the whole column of steady state. We propose, in this section, a simple model by which it is possible to estimate the properties of the theoretical plate of an electrochemical parametric

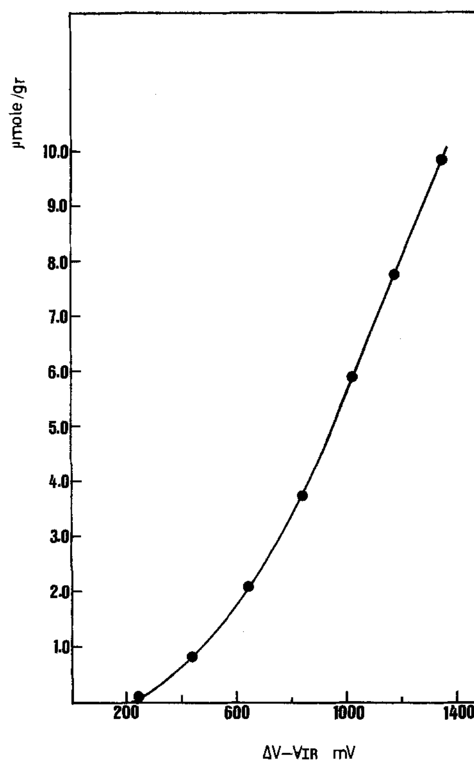

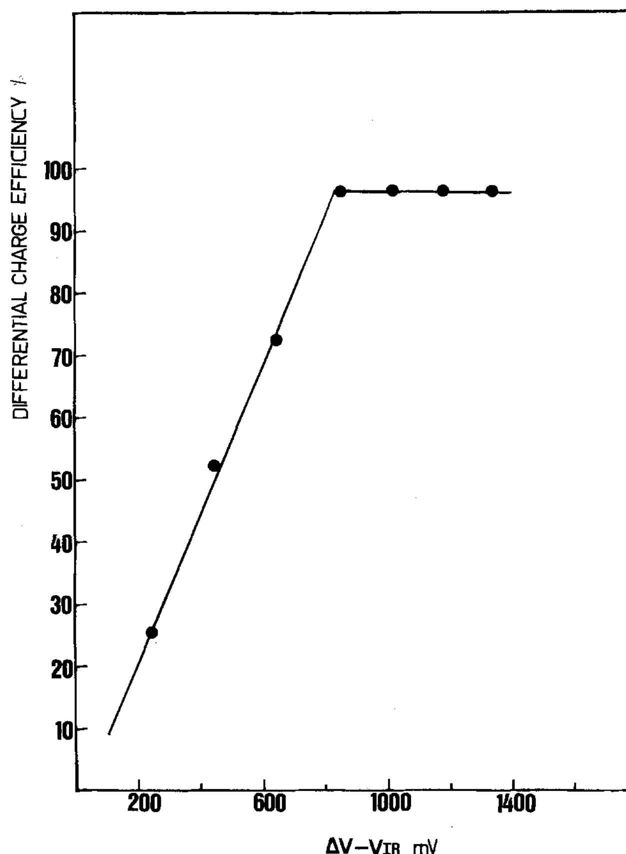

Fig. 10. a (top). Separation capacity of the column *vs.* potential difference. b (bottom). Differential charge efficiency of the column *vs.* potential difference. $C_o = 0.01N$, $I = 50$ mA.

pumping column. According to the model, the theoretical plate is assumed to be a batch unit active cell composed of two carbon electrodes of G grams total weight and solution free volume, V_t. The cell is connected to an upper and a lower imaginary reservoir, each with a total volume at least equal to the displacement volume, ΔV (Fig. 12).

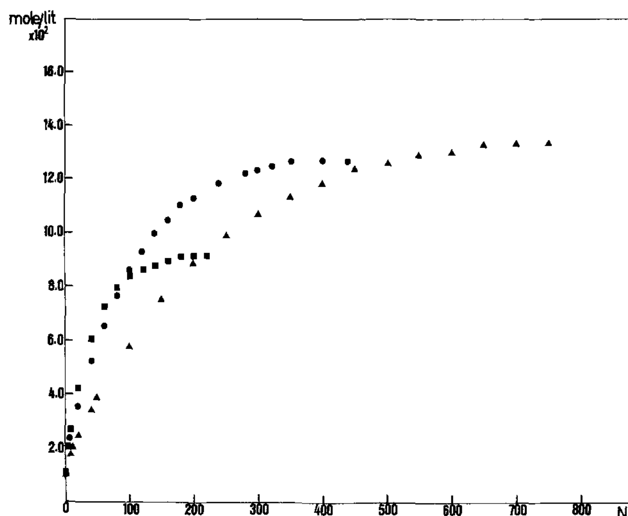

Fig. 11. Concentration at total reflux in the bottom head of the column vs. cycle number. The concentration in the upper head is kept constant. E_D = 360 mV, E_C = 1280 mV, C_o = 0.01N, I = 50 mA. Constant pumping rate. $\Delta V/V_t$: 0.5, ■; 0.25, ●; 0.125, ▲.

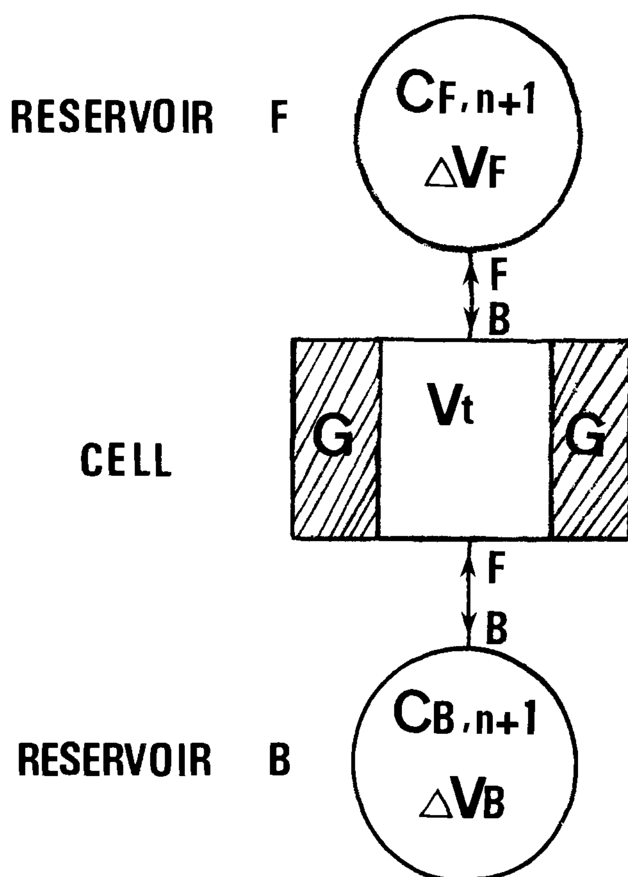

Fig. 12. Diagram of a unit batch process

The composition of the solutions in the reservoirs does not change after steady state has been reached. In this sense, it is equivalent to the steady-state behavior of any three adjacent theoretical plates in the column.

A second assumption of the model is the existence of a stationary fraction, f, of the solution volume, V_t, of the active unit cell. This stationary fraction may exist, since the plane of shear is located in the solution far from the interface. In the present case, the stationary solution may include the mesopore volume of the carbon granules. The displacement volume ΔV is therefore

$$\Delta V = (1 - f)V_t \qquad [4]$$

Each cycle n terminates with the backward step which empties the upper reservoir. In the following we give the material balance equations of the four steps: C, F, D, and B, of the subsequent cycle $n + 1$. Let C_Fn C_Bn, and C_Cn be, respectively, the concentration of the upper and lower reservoirs and of the active cell. For the charge step

$$V_tC^C_{C,n+1} = V_tC^B_{C,n} - mG \qquad [5]$$

The superscripts C and B stand for the charge and the backward steps, respectively. The amount of salt absorbed at the charge step is m moles per gram of carbon and G is the carbon electrode weight.

For the forward step, in the upper reservoir

$$C_{F,n+1} = C^C_{C,n+1} \qquad [6]$$

Forward step in active unit

$$V_tC^F_{C,n+1} = V_tfC^C_{C,n+1} + V_t(1-f)C_{B,n} \qquad [7]$$

For the discharge step in the active unit

$$V_tC^D_{C,n+1} = V_tC^F_{C,n+1} + mG \qquad [8]$$

Backward step in the lower reservoir

$$C_{B,n+1} = C^D_{C,n+1} \qquad [9]$$

Backward step in the active unit

$$V_tC^B_{C,n+1} = V_tfC^D_{C,n+1} + V_t(1-f)C_{F,n+1} \qquad [10]$$

At steady state, the concentration does not change with the cycle number, therefore

$$C^B_{C,n} = C^B_{C,n+1} \qquad [11]$$

and

$$C_{B,n} = C_{B,n+1} \qquad [12]$$

From these two conditions, together with the material balance equations, Eq. [5]-[10], the expression

$$C_{B,n+1} - C_{F,n+1} = \frac{mG}{fV_t} = \frac{\Delta C}{f} \qquad [13]$$

is obtained as a basic property of the theoretical plate.

The second equality is obtained using Eq. [5] and recognizing that ΔC is

$$\Delta C = C^B_{C,n} - C^C_{C,n+1} \qquad [14]$$

Thus a single batch unit is able to multiply the basic concentration difference, C, by the ultimate factor $1/f$ ($f < 1$).

The number of theoretical plates, N, in the column can be expressed in several ways

$$N = \frac{L}{\Delta 1} = \frac{C_f - C_o}{C_{B,n+1} - C_{F,n+1}} = \frac{V_o}{V_t} \qquad [15a]$$

$$\frac{L}{\Delta 1} = \frac{f(C_f - C_o)}{\Delta C} = \frac{V_o(1-f)}{\Delta V} \qquad [15b]$$

where L is the length of the column, V_o its total solution volume (free volume), C_f and C_o the steady-state concentrations at the lower and upper heads of the column, respectively, and $\Delta 1$ is the EHTP.

In order to obtain Eq. [15b], Eq. [14] and [13] were used. The last expression is arranged to obtain the stationary volume fraction as

$$f = \frac{V_o\Delta C}{\Delta V(C_f - C_o) + V_o\Delta C} \qquad [16]$$

Substituting in Eq. [13]

$$C_{B,n+1} - C_{F,n+1} = 1/V_o[\Delta V(C_f - C_o) + V_o\Delta C] \qquad [17]$$

The EHTP is given, using Eq. [15] and [16], by

$$\Delta 1 = \frac{L[\Delta V(C_f - C_o) + V_o\Delta C]}{(C_f - C_o)V_o} \qquad [18]$$

Since the theoretical plate multiplies the effect, ΔC, another theoretical plate length Δz may be defined

$$\Delta z = \frac{L \Delta C}{C_f - C_o} \qquad [19]$$

The magnitudes of some of the parameters in Eq. [16]-[19] are summarized in Table I for the parametric pumping experiments which approach steady state (Fig. 11).

Conclusion

The electrochemical parametric pump enables the use of the selectivity of electrode processes for multistage separating columns. The electrical energy acts only on the electrode/solution interface, *i.e.*, on the active part of the separating column. This is unlike thermal parametric pumping where heat is acquired by the passive matter, such as the bulk of the adsorbent, the solution, and the column walls. The separative power of the unit batch process at steady state exceeds the single cycle effect by $1/f$ and can thus attain very high values.

It seems, therefore, that electrochemical parametric pumping operated in multistage columns will have a high separation power for desalination. This seems promising for industrial water processing.

Table I. Experimental and theoretical results from two electrochemical parapump runs

Calculated Δl (cm)	f	$C_f \times 10^4$ (mole/liter)	$C_o \times 10^4$ (mole/liter)	$\Delta C \times 10^4$ (mole/liter)	$\Delta V/V_o$
52	0.074	953.9	108.2	33.7	0.5
27	0.103	1356.5	112.0	35.6	0.25
17	0.15	1529.8	109.5	31.4	0.125

Manuscript submitted Jan. 12, 1977; revised manuscript received Nov. 15, 1977.

Any discussion of this paper will appear in a Discussion Section to be published in the December 1978 JOURNAL. All discussions for the December 1978 Discussion Section should be submitted by Aug. 1, 1978.

REFERENCES

1. "Preparative Gas Chromatography," A. Slakis and V. Pretorius, Editors, John Wiley & Sons, Inc., New York (1971).
2. P. E. Barker, in "Progress in Separation and Purification," Vol. 4, E. S. Perry and C. J. Van Oss, Editors, pp. 325-406, John Wiley & Sons, Inc., New York (1971).
3. P. C. Wankat, *Sep. Sci.*, **9**(2), 85 (1974).
4. C. W. Skarstrom, *Ann. N.Y. Acad. Sci.*, **72**, 75 (1959).
5. J. E. Sabadell and N. N. Sweed, *Sep. Sci.*, **5**, 171 (1970).
6. R. H. Wilhelm, A. W. Rice, and A. R. Bendelius, *Ind. Eng. Chem.*, **5**, 141 (1966).
7. A. A. Camero and N. H. Sweed, *AIChE J.*, **22**(2), 369 (1976).
8. R. H. Wilhelm, A. W. Rice, D. W. Rolke, and N. H. Sweed, *Ind. Eng. Chem.*, **7**, 337 (1968).
9. D. W. Thompson and D. Bass, *Can. J. Chem. Eng.*, **52**, 345 (1974).
10. J. W. Blair and G. W. Murphy, *Adv. Chem. Ser.*, **27**, 206 (1960).
11. T. Fujinaga, *Pure Appl. Chem.*, **25**(4), 709 (1971).
12. D. K. Roe, *Anal. Chem.*, **36**, 2371 (1964).
13. W. J. Blaedel and J. H. Strohl, *ibid.*, **36**, 1245 (1964).
14. A. M. Johonson and J. Newman, *This Journal*, **118**, 510 (1971).
15. A Soffer and M. Folman, *J. Electroanal. Chem. Interfacial Electrochem.*, **38**, 25 (1972).
16. A. Soffer, Electroadsorption of Ions on High Surface Porous Electrodes, Ph.D. Thesis (1969).
17. M. Yaniv and A. Soffer, *This Journal*, **123**, 506 (1976).
18. H. Tobias and A. Soffer, Unpublished results.
19. J. Koresh and A. Soffer, To be published.

The Standard Potential of the Mercury-Mercuric Iodate Electrode

Charles P. Nash

Department of Chemistry, University of California, Davis, California 95616

ABSTRACT

Electrochemical cells of the type $Hg(l)|Hg_2(IO_3)_2(s)|KIO_3(aq,M)$-$|Hg(IO_3)_2(s)|Hg(l)$ have been used to determine the standard potential of the half-reaction $Hg(IO_3)_2(s) + 2e = Hg(l) + 2IO_3^-(aq)$ to be $\mathcal{E}^\circ = 0.4601 \pm 0.0007V$ at 298.2°K. For mercuric iodate $\Delta G^\circ_f = -167.2 \pm 0.3$ kJ · mole^{-1} at 298.2°K, and around room temperature $S^\circ \approx 159$ J · mole^{-1} · K^{-1}. The entropy of mercuric iodate is anomalously small, so that for the reaction $Hg(l) + Hg(IO_3)_2(s) = Hg_2(IO_3)_2(s)$ near room temperature $\Delta S^\circ \approx +33$ J · mole^{-1} · K^{-1}.

In the course of a brief survey aimed at comparing the reported thermodynamic properties of solid mercuric and mercurous compounds, it was found that the literature concerning mercuric iodate is confusing. Latimer (1) cited identical standard potentials of +0.394V for the two-electron reductions of both mercuric and mercurous iodates, but he also tabulated Gibbs energies of formation for these two compounds that imply that the mercurous salt is stable with respect to disproportionation by some 23.4 kJ·mole^{-1}. Milazzo (2) also lists the mercurous iodate potential as 0.394V and he reports the mercuric iodate potential to be 0.40V, but no basis is given for this figure.

Key words: thermodynamics, entropy, cell, metals.

There is no doubt that mercurous iodate is thermodynamically stable. The detailed studies of Haring and Zapponi (3) have established that the mercury-mercurous iodate electrode is both reproducible and reversible. Hills and Ives (4) have revised the value of the standard potential reported by Haring and Zapponi to account for subsequent changes in the accepted value of the potential of the calomel electrode, and for the half-reaction $Hg_2(IO_3)_2(s) + 2e = 2Hg(l) + 2IO_3^-(aq)$ cite $\mathcal{E}^\circ_{Hg_2(IO_3)_2} = 0.3944 \pm 0.0004V$ at

298.2°K. Haring and Zapponi (3) also mentioned that they made an approximate determination of the potential of the mercuric iodate electrode, and found it to be "5 to 6 centivolts higher than that of the mercurous iodate electrode."

The present paper reports measurements of the potentials of the cells of the type

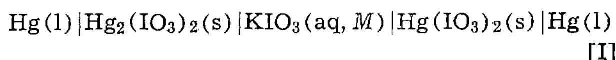

Experimental

Preliminary experiments established that at room temperature type [I] cells exhibited stable potentials for about three days. At about the same time that the cell potentials became erratic, the solid phase in the mercuric iodate electrode compartment turned distinctly gray in color, and a positive test for mercurous ion resulted when the gray solid was treated with concentrated ammonia. The general behavior of an old type [I] cell was similar to that of a cell that contained deliberately premixed mercuric and mercurous iodates (*vide infra*).

Deionized water was used throughout. All chemicals were Mallinckrodt Analytical Reagent Grade except for the mercury, which was Ballard's C. P. Triple Distilled, supplied by Quicksilver Products, Incorporated.

Mercurous iodate was prepared by adding 20 ml of $0.1M$ mercurous nitrate in $0.01M$ nitric acid to 20 ml of $0.2M$ potassium iodate over a 2 hr period with continuous stirring. Stirring was continued for 1 hr; then the precipitate was allowed to settle and the supernatant liquid was decanted. The precipitate was washed with vigorous stirring; five times with water, then five times with the potassium iodate solution that was to be used as the electrolyte in the cell of interest. The washed precipitate was also stored under the appropriate potassium iodate solution. Mercuric iodate was prepared in the same fashion by mixing stoichiometric amounts of mercuric nitrate and potassium iodate solutions, and similar washing and storage methods were also employed.

The cell was constructed by inserting the vertical side-arms of three single electrode half-cells (of local construction but similar to Sargent No. 30505) into a rubber stopper. The stopper was then sealed with wax into a 32 mm ID filter tube (Corning No. 9840). Moist mercurous iodate paste and mercury were placed in one half-cell, mercuric iodate paste alone was placed in the second, and a commercial saturated calomel electrode (Sargent No. 30490 or Beckman No. 39170) inserted in a rubber stopper was sealed into the third. The iodate electrode compartments were fitted with homemade platinum point electrodes held in place with rubber stoppers.

The potassium iodate electrolyte solution was sucked into each half-cell compartment through the filter tube, at the end of which operation the filled filter tube was capped with a dropper top. The assembled cell was equilibrated for at least 12 hr at the temperature of interest, either 25.00° ± 0.05°C or 0.00° ± 0.01°C. Then thermostated mercury was injected into the mercuric iodate electrode compartment, and the potentials of the three possible cell combinations were determined over a period of two days. At the end of each series of measurements at both temperatures the potential of the calomel working electrode was compared to that of a thermodynamic saturated calomel electrode prepared by the method of Hills and Ives (5). All cell potentials were measured with a Beckman Research pH meter.

Results and Discussion

The results of these experiments are summarized in Table I. The type [I] cell has already been diagrammed. Cell type [II] is

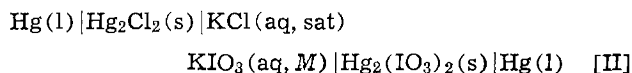

Table I. Measured cell potentials

Cell type	Temp (°C)	M	E_{obs} (volts)
I	25	0.05	0.0658 ± 0.0006
II	25	0.05	0.2357 ± 0.0006*
III	25	0.05	0.3015 ± 0.0006*
I	25	0.1	0.0656 ± 0.0005
II	25	0.1	0.2200 ± 0.0005*
III	25	0.1	0.2856 ± 0.0005*
I	25	0.2	0.0656 ± 0.0005
II	25	0.2	0.2056 ± 0.0005*
III	25	0.2	0.2712 ± 0.0005*
I	0	0.1	0.0615 ± 0.0003
II	0	0.1	0.1997 ± 0.0003*
III	0	0.1	0.2612 ± 0.0004*

* Referenced to a Hills and Ives type saturated calomel electrode (5) at the temperature of interest.

and cell type [III] is

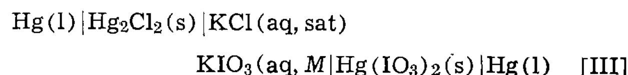

Each entry in Table I is a result of twenty determinations. Two cell assemblies were constructed for each concentration of the electrolyte, and ten sets of measurements were made on each assembly.

We note first that the measured potentials at 25°C of the three type [I] cells having different concentrations of potassium iodate electrolyte are in excellent agreement with each other. In every instance the cell potential stabilized within the first hour, and during its useful lifetime the cell was quite insensitive to mechanical vibration. This behavior is in marked contrast to that of a similar cell in which the solid phase in the right-hand electrode compartment was a mixture of 85% mercuric ioodate with 15% mercurous iodate, and the electrolyte was $0.05M$ potassium iodate. Here the potential of the undisturbed cell fluctuated erratically for the first 4 hr, but a relatively constant value of 58 mV was finally achieved. In the subsequent two-day period during which observations were made, the slightest tapping of the mixed-solid cell compartment caused the measured potential of the cell to vary unsystematically between the limits of 52 and 59 mV. On the basis of these observations it is highly probable that only a single solid phase is present in the mercuric iodate compartments of our stable type [I] or type [III] cells.

We find also that in the two instances where comparisons can be made, the measured potentials of the type [II] cells at 25°C are in reasonable agreement with the values that would be expected for them on the basis of the accepted potentials of the saturated calomel and mercurous iodate electrodes.

The emf of a type [II] cell is given by

$$\mathcal{E}_{II} = \mathcal{E}^{\circ}_{Hg_2(IO_3)_2} - \mathcal{E}_{sat.\ cal.} - \frac{RT}{2F} \ln (M_{KIO_3}\gamma_{\pm KIO_3})^2 + \mathcal{E}_{LJ} \quad [1]$$

where $\mathcal{E}_{LJ}$ is the liquid junction potential. When we use the values $\mathcal{E}^{\circ}_{Hg_2(IO_3)_2} = 0.3944V$ (4), $\mathcal{E}_{sat.\ cal.} = 0.2412V$ (6), and mean ion activity coefficients of 0.765 and 0.692 for 0.05 and $0.1M$ potassium iodate solutions (7), respectively, we calculate that in the absence of a liquid junction potential one should observe emf's for the type [II] cells at 25°C of 0.2369V for the cell containing $0.05M$ electrolyte and 0.2217V for the cell containing $0.1M$ electrolyte. According to the Henderson equation (8), the sign of the liquid junction potential in a type [II] cell is negative, and it is slightly more negative for the cell containing the more concentrated potassium iodate solution.

The emf of a type [I] cell is given by

$$\mathcal{E}^{\circ}_{I} = \mathcal{E}^{\circ}_{Hg(IO_3)_2} - \mathcal{E}^{\circ}_{Hg_2(IO_3)_2} \quad [2]$$

where $\mathcal{E}^{\circ}_{Hg(IO_3)_2}$ symbolizes the standard potential for

the half-reaction $Hg(IO_3)_2(s) + 2e = Hg(l) + 2IO_3^-(aq)$. We find $\mathcal{E}^\circ_{Hg(IO_3)_2} = 0.4601 \pm 0.0007V$ at 298.2°K. We also find that in the neighborhood of room temperature

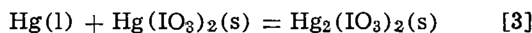

$$\left(\frac{\partial \mathcal{E}^\circ_I}{\partial T}\right)_P \approx \left(\frac{\Delta \mathcal{E}^\circ_I}{\Delta T}\right)_P = (1.7 \pm 0.2) \times 10^{-4}\,V \cdot K^{-1}$$

The chemical reaction consistent with a type [I] cell is

$$Hg(l) + Hg(IO_3)_2(s) = Hg_2(IO_3)_2(s) \quad [3]$$

for which $\Delta G^\circ_{298} = -2\mathbf{F}\mathcal{E}^\circ_I = -12{,}700 \pm 100$ J·mole^{-1}, and $\Delta S^\circ = 2\mathbf{F}(\partial \mathcal{E}^\circ_I/\partial T)_P \approx 33 \pm 4$ J·mole^{-1}·K^{-1}.

When the value for $\mathcal{E}^\circ_{Hg(IO_3)_2}$ is combined with the standard Gibbs energy of formation for $IO_3^-(aq)$ of -128.0 kJ·mole^{-1} given by Wagman *et al.* (9), we find $\Delta G^\circ_{f,Hg(IO_3)_2} = -167.2 \pm 0.3$ kJ·mole^{-1} at 298.2°K.

It is a remarkable finding that reaction [3] is accompanied by an increase in entropy. According to the data compiled by Wagman *et al.* (10), the corresponding reactions involving the mercurous and mercuric chlorides, bromides, and iodides all proceed with entropy decreases. The present results can be used to estimate the entropies of both mercurous and mercuric iodate, and thus find the origin of this unusual result.

If one takes the temperature derivative of Eq. [1], ignoring the temperature dependence of the activity coefficient of KIO_3, and also uses the experimental temperature dependence of what Hills and Ives (6) have termed $\mathcal{E}''$ to represent the behavior of the saturated calomel electrode together with the liquid junction potential, he obtains

$$\left(\frac{\partial \mathcal{E}^\circ_{Hg_2(IO_3)_2}}{\partial T}\right)_P \approx \frac{\Delta \mathcal{E}^\circ_{Hg_2(IO_3)_2}}{\Delta T} \approx \frac{\Delta \mathcal{E}_{II}}{\Delta T} + \frac{\Delta \mathcal{E}''}{\Delta T} + \frac{\mathbf{R}}{\mathbf{F}} \ln (M_{KIO_3}\gamma_{\pm KIO_3})$$

$$\frac{\Delta \mathcal{E}^\circ_{Hg_2(IO_3)_2}}{\Delta T} \approx (8.1 \pm 0.2) \times 10^{-4} - 6.3 \times 10^{-4} - 2.3 \times 10^{-4} = (-5 \pm 2) \times 10^{-5}\,V \cdot K^{-1} \quad [4]$$

Hence, for the reaction

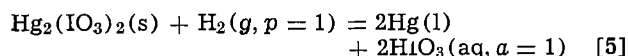

$$Hg_2(IO_3)_2(s) + H_2(g, p = 1) = 2Hg(l) + 2HIO_3(aq, a = 1) \quad [5]$$

$\Delta S^\circ \approx -10 \pm 4$ J·mole^{-1}·K^{-1} around room temperature. From this result and the known entropies of the other species at 298°K, namely, $S^\circ_{H_2} = 130$, $S^\circ_{HIO_3} = S^\circ_{IO_3^-} = 118$, $S^\circ_{Hg} = 76$ J·mole^{-1}·K^{-1} (9, 10), we find $S^\circ_{Hg_2(IO_3)_2} \approx 268$ J·mole^{-1}·K^{-1}. Since ΔS° for reaction [3] is about 33 J·mole^{-1}·K^{-1}, we then conclude that the standard entropy of mercuric iodate is approximately 159 J·mole^{-1}·K^{-1}.

Latimer (11) has published a tabular summary of ionic entropy contributions that suggests that, as an estimate, the entropy of the iodate salt of a divalent cation should exceed that of the corresponding chloride salt by about 117 J·mole^{-1}·K^{-1}. Given that the entropies of mercurous chloride and mercuric chloride are 192 J·mole^{-1}·K^{-1} and 146 J·mole^{-1}·K^{-1}, respectively, it is obvious that while both the iodates have entropies that are smaller than Latimer's group contributions would predict, the discrepancy is strikingly large for mercuric iodate.

At present, the crystal structures of the mercuric and mercurous iodates are both unknown. From the infrared spectra of the two solids, however, Dasent and Waddington (12) have concluded that in each case there is covalent bonding between the cation and the iodate ion. Moreover, the work of Belcher and Goulden (13), who measured the solubilities of mercuric and mercurous iodates in water, may be combined with the present results to provide some evidence that the mercuric ion interacts more strongly with iodate than does the mercurous ion.

Belcher and Goulden (13) found total iodate concentrations in saturated solutions of the mercuric and mercurous iodates of 1.6×10^{-4} and $6.4 \times 10^{-5}M$, respectively. The standard electrode potentials for these compounds lead to solubility products of 5.6×10^{-14} for mercuric iodate and 2.7×10^{-14} for mercurous iodate, from which it follows that the free iodate-ion concentrations in the corresponding saturated solutions are 4.8×10^{-5} and $3.8 \times 10^{-5}M$. If the difference between our calculated iodate ion concentrations and the measured total iodate content of the saturated solutions is attributed to the formation of aggregates in solution, it is apparent that of the two cations the mercuric ion has the greater iodate binding capacity. It is, of course, impossible to determine either the stoichiometries of the aggregates or their formation constants from the limited data available.

Conclusions

The mercury-mercuric iodate electrode is reproducible and reversible, provided that measurements are made before the spontaneous reaction between the electrode components has produced significant amounts of mercurous iodate. The standard potential of the half-reaction $Hg(IO_3)_2(s) + 2e = Hg(l) + 2IO_3^-(aq)$ is $\mathcal{E}^\circ = 0.4601 \pm 0.0007V$ at 298.2°K. For mercuric iodate at 298.2°K, $\Delta G^\circ_f = -167.2 \pm 0.3$ kJ·mole^{-1}, and around room temperature $S^\circ \approx 159$ J·mole^{-1}·K^{-1}. For mercurous iodate around room temperature $S^\circ \approx 268$ J·mole^{-1}·K^{-1}. The entropy of mercuric iodate is so small that the reaction $Hg(l) + Hg(IO_3)_2(s) = Hg_2(IO_3)_2(s)$ proceeds with an entropy increase of 33 J·mole^{-1}·K^{-1}.

Acknowledgment

The author gratefully acknowledges the advice and assistance of his colleague P. A. Rock.

Manuscript submitted Aug. 26, 1977; revised manuscript received Jan. 27, 1978.

Any discussion of this paper will appear in a Discussion Section to be published in the December 1978 JOURNAL. All discussions for the December 1978 Discussion Section should be submitted by Aug. 1, 1978.

Publication costs of this article were assisted by the University of California.

REFERENCES

1. W. M. Latimer, "Oxidation Potentials," 2nd ed., pp. 176, 178, 182, Prentice Hall, Inc., Englewood Cliffs, N.J. (1952).
2. G. Milazzo, "Electrochemistry," p. 165, Elsevier Publishing Co., New York (1963).
3. M. M. Haring and P. P. Zapponi, *Trans. Electrochem. Soc.*, **80**, 203 (1941).
4. G. J. Hills and D. J. G. Ives, in "Reference Electrodes," D. J. G. Ives and G. J. Janz, Editors, p. 171, Academic Press, New York (1961).
5. G. J. Hills and D. J. G. Ives, *J. Chem. Soc.*, **1951**, 311.
6. G. J. Hills and D. J. G. Ives, in "Reference Electrodes," D. J. G. Ives and G. J. Janz, Editors, pp. 160-161, Academic Press, New York (1961).
7. G. N. Lewis and M. Randall, "Thermodynamics," 1st ed., p. 362, McGraw-Hill, New York (1923).
8. D. A. Mac Innes, "The Principles of Electrochemistry," Chap. 13, Dover Publications, Inc., New York (1961).
9. D. D. Wagman, W. H. Evans, V. B. Parker, I. Halow, S. M. Bailey, and R. H. Schumm, NBS Tech. Note 270-3, U.S. Government Printing Office, Washington, D.C. (1968).
10. D. D. Wagman, W. H. Evans, V. B. Parker, I. Halow, S. M. Bailey, and R. H. Schumm, NBS Tech. Note 270-4, U.S. Government Printing Office, Washington, D.C. (1969).
11. W. M. Latimer. "Oxidation Potentials," 2nd ed., p. 363, Prentice Hall, Inc., Englewood Cliffs, N.J. (1952).
12. .W E. Dasent and T. C. Waddington, *J. Chem. Soc.*, **1960**, 2429.
13. R. Belcher and R. Goulden, *Mikrochim. Acta*, **1953**, 290.

The Reduction of Oxygen on Teflon-Bonded Perovskite Oxide Electrodes

K. L. K. Yeung* and A. C. C. Tseung*

Department of Chemistry, The City University, London, England

ABSTRACT

The electrochemical reduction of oxygen on Teflon-bonded $Nd_{0.5}Sr_{0.5}CoO_3$ electrodes in 45% KOH was studied as a function of temperature and oxygen partial pressure. The activation energy was 10.75 kcal/mole and the relationship between i and P_{O_2} obeys the relationship $d \ln i / d \ln P_{O_2} = ½$, suggesting that the rate of oxygen chemisorption is the rate-controlling step, Galvanostatic oxygen stripping showed that the surface coverage of oxygen was only 1% for both Sr-doped $LaCoO_3$ and $NdCoO_3$, and that the coverage was independent of temperature in the range 25°-80°C.

Earlier work by Tseung and Bevan (1) shows that Sr-doped $LaCoO_3$ exhibits reversible behavior toward oxygen reduction in 45% KOH solution at room temperature. The performance at room temperature is low ~2 mA/cm², 500 mV *vs.* DHE (Dynamic Hydrogen Electrode) but it increases linearly with temperature and surpasses that of platinum black at 170°C (250 mA/cm² as compared to 180 mA/cm² for Pt black, 75% KOH, 900 mV *vs.* DHE). It is suggested that the performance is controlled by the number of Co^{3+}/Co^{4+} couples free to interact with the oxygen molecule and that the numbers of such couples are low at 25°C but increase in number as the temperature rises. Studies by Kudo *et al.* (2, 3) on $La_{1-x}Sr_xCoO_3$ and $Nd_{1-x}Sr_xCoO_3$ ($x = 0.5$) suggest that the electrochemical reduction of O_2 on these oxides proceed via two parallel routes

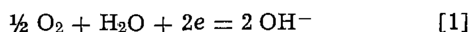

$$½\, O_2 + H_2O + 2e = 2\, OH^- \quad [1]$$

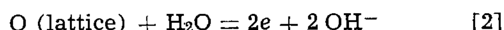

$$O\ (\text{lattice}) + H_2O = 2e + 2\, OH^- \quad [2]$$

They also suggest that the relatively low performance at room temperature is due to the slow rate of oxygen ion diffusion in the lattice. They reach this conclusion mainly from cyclic voltammetric studies on Teflon-bonded $La_{0.5}Sr_{0.5}CoO_3$ electrodes. When the potential is swept from an anodic potential more positive than the reversible oxygen electrode potential to the cathodic region, the cathodic current increases almost linearly with decreasing potential until an overvoltage of 400 mV is reached. Thereafter, the cathodic current decreases and in the reverse sweep the cathodic current is markedly lower. They claim that this shows that oxide is being reduced and that the limiting step is the rate of oxygen ion diffusion in the oxide lattice. This paper presents further cyclic voltammetric and pulse measuremnts on the reduction of oxygen on perovskite oxides.

Experimental

$La_{0.5}Sr_{0.5}CoO_3$ and $Nd_{0.5}Sr_{0.5}CoO_3$ were prepared by freeze drying of the mixed nitrate solutions (1), followed by vacuum decomposition at 250°C for 5 hr. The powders were then heated in air at 600°C for 5 hr. The formation of the perovskite phase was confirmed by x-ray powder diffraction, though it is not certain whether all the material had fully reacted since the lower limit for x-ray detection is only about 5%. The BET surface area for $La_{0.5}Sr_{0.5}CoO_3$ was 17 M²/g and $Nd_{0.5}Sr_{0.5}CoO_3$ was 20 M²/g. The powders were fabricated into Teflon-bonded electrodes on 100 mesh Pt screens (5). The catalyst: Teflon ratio was fixed at 10:3. The electrodes were tested in floating half-cells (6) using a dynamic hydrogen reference electrode (DHE). A piece of gold foil was used as the counter-electrode. The potential of the test electrode was controlled by a Chemical Electronics 3A Potentiostat. The KOH electrolyte solution was prepared by dissolving Analar grade KOH in distilled, deionized water. The impurities in the solution were preadsorbed (4) at 0.1V *vs.* RHE for 3 days. A Chemical Electronics Linear Sweep Generator was used in the cyclic voltammetric studies. Potentiostatic and galvanostatic pulse studies were performed with the aid of a Chemical Electronics pulse generator and the signals were recorded by a storage oscilloscope.

* Electrochemical Society Active Member.

Key words: surfaces, cell, charge, chemisorption.

Results and Discussion

Cyclic voltammetric studies.—Figure 1 shows the cyclic voltammograms of a "floating" Teflon-bonded $Nd_{0.5}Sr_{0.5}CoO_3$ electrode. The electrode was swept initially from the open-circuit potential to 1.5V. The subsequent cathodic current increases almost linearly with decreasing potential until 950 mV is reached.

Thereafter, the cathodic current decreases and on the reverse sweep, the cathodic current is markedly lower. The results are similar to those obtained by Kudo *et al.* (2). Kudo *et al.* suggest that this shows that the oxide ion is reduced and that the limiting step is the rate of oxygen ion diffusion in the oxide lattice. Their anomalous results, however, can be better explained by taking into account the presence of high pressure oxygen generated and stored inside the pores of the electrocatalyst (7). However, if the electrode is taken to 1.5V for 15 min and then purged with N_2 at the open-circuit potential for different periods of time, the anomalous behavior gradually disappears at longer

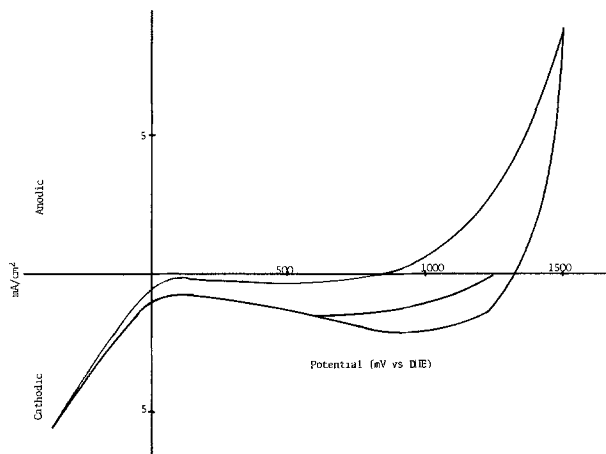

Fig. 1. The cyclic voltammogram of a Teflon-bonded $Nd_{0.5}Sr_{0.5}CoO_3$ electrode. 45% KOH, O_2, 25°C; catalyst loading = 17 mg; catalyst/Teflon = 10/3; scan rate 50 mV/sec.

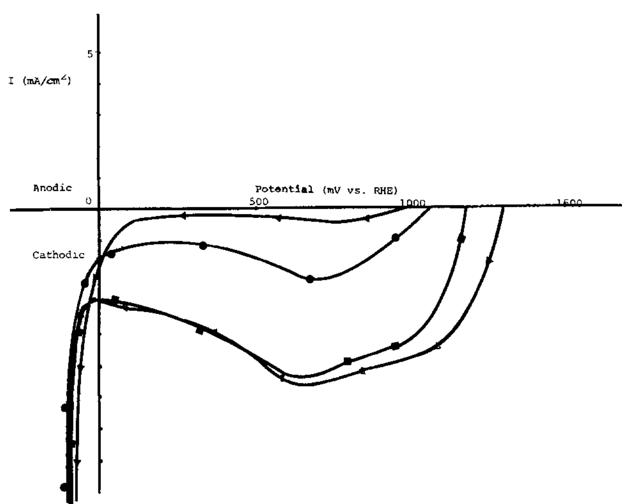

Fig. 2. The cathodic curves for a Teflon-bonded $Nd_{0.5}Sr_{0.5}CoO_3$ electrode after holding at 1.5V for 15 min and subsequently purged with N_2 for different time. Scan rate = 50 mV/sec; N purging time (min). △, 10; ■, 30; ●, 90; ▲, 240.

purging times, as shown in Fig. 2. When the electrode is swept from the open-circuit potential to more cathodic potentials under N_2, the current is very low; these results indicate that the anomalous behavior is associated with the high pressure oxygen inside the pores and not due to the reduction of the oxide.

Steady-state performance of $Nd_{0.5}Sr_{0.5}CoO_3$.—Figure 3 shows the performance of $Nd_{0.5}Sr_{0.5}CoO_3$ at 25°, 40°, 60°, and 80°C. The open-circuit voltage of the electrode at 25°C was 1.20V, very close to the oxygen electrode potential (1.22V *vs.* RHE at 25°C, 45% KOH). The attainment of reversible oxygen electrode potential suggests that oxygen is dissociatively chemisorbed (1). Therefore, for every oxygen molecule chemisorbed "side-on," there will be two electron-transfer sites. Thus the current should be directly proportional to the square root of O_2 partial pressure, *i.e.*

$$I = k(P_{O_2})^{0.5}$$

By plotting log I at constant electrode voltage *vs.* RHE against log P_{O_2}, the value of the index in the general relation $I = kP^n$ can be ascertained. Results for tests at different oxygen partial pressures and temperatures show that the value of n is between 0.45 and 0.53 (Fig. 4). A plot of $1/T$ *vs.* ln i (Fig. 5) shows that the performance increases linearly with temperature and the activation energy for the oxygen reduction is 10.75 kcal/mole.

Potentiostatic pulse studies.—In order to get more precise kinetic information on the oxygen reduction process on Teflon-bonded $Nd_{0.5}Sr_{0.5}CoO_3$, it is necessary to eliminate mass transfer effects as much as possible. In principle, the potentiostatic pulse method is ideally suited for this type of investigation (8, 9). The

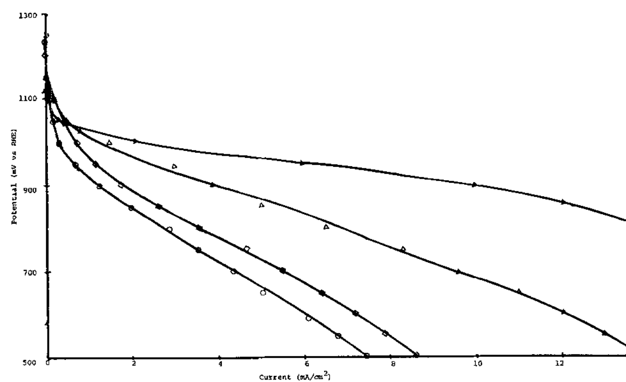

Fig. 3. *V-i* curves of a Teflon-bonded $Nd_{0.5}Sr_{0.5}CoO_3$ electrode at different temperatures. 45% KOH, O_2, *iR* corrected. Temperature (°C). ▲, 80; △, 60; □, 40; ○, 25.

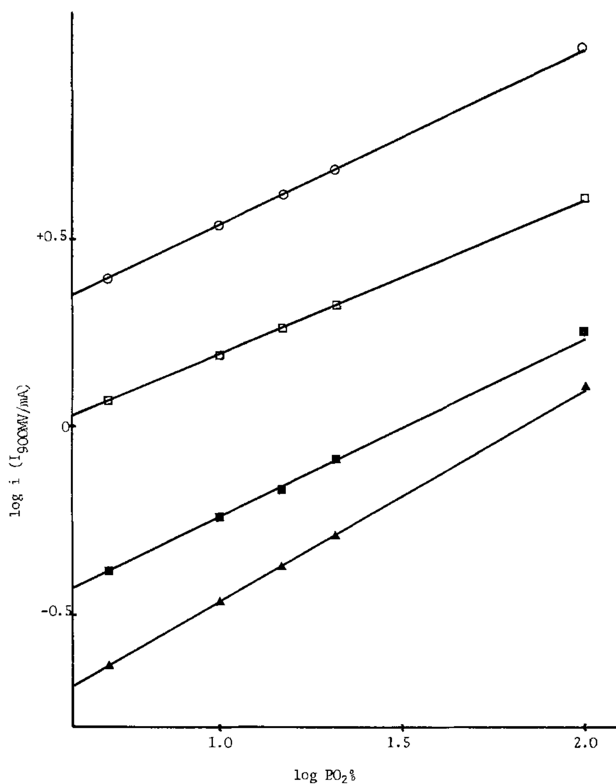

Fig. 4. Evaluation of index N for $Nd_{0.5}Sr_{0.5}CoO_3$ at different temperatures. Temperature (°C). ○, 80; □, 60; ■, 40; △, 25.

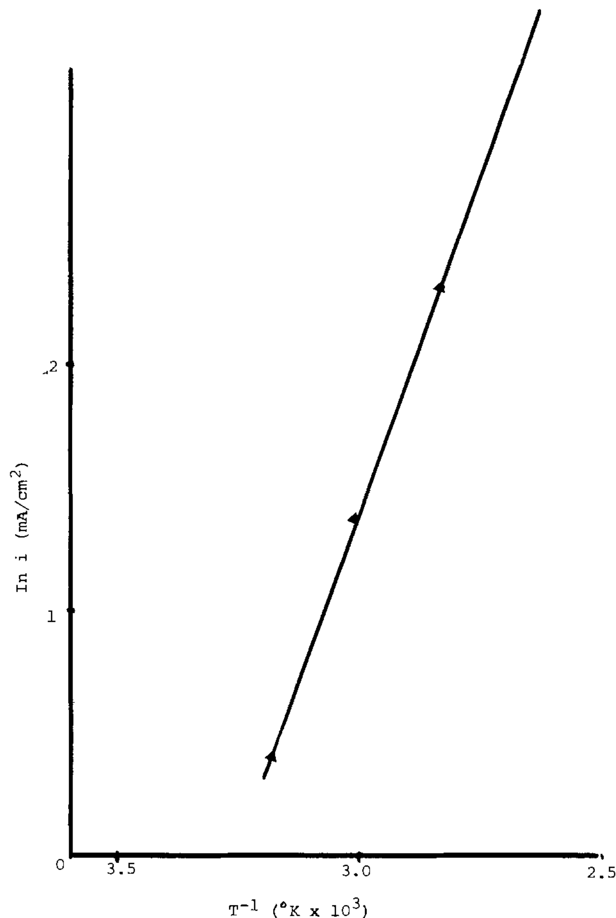

Fig. 5. ln *i* vs. $1/T$ plot for Teflon-bonded $Nd_{0.5}Sr_{0.5}CoO_3$ electrode (steady-state measurement).

transient behavior of an electrode under "mass transfer free" conditions at zero time can be displayed on an oscilloscope screen. However, it is not possible to make measurements at exactly zero time due to double layer charging effects; every electrode behaves as a "leaky" condenser and at the instant of applying a potential or current, a very short but finite time is required to charge the electrode. This time interval depends on the capacity of the electrode double layer and therefore the electrode surface area. An approximate method is to take measurements at the shortest time interval after which double layer charging is complete and accept a small amount of concentration polarization.

The double layer charging time can be measured from the potential transients in the absence of reactants. This approach was adopted in the present study.

Figure 6 compares the steady-state performance of a $Nd_{0.5}Sr_{0.5}CoO_3$ with its potentiostatic pulse performance (after 1 msec) at 25°C, 45% KOH. At 500 mV, the steady-state performance was only 7.5 mA/cm², whereas over 85 mA/cm² was obtained by potentiostatic pulse measurements. Since Teflon-bonded electrodes do not show appreciable mass transfer limitations except at very high current densities, the differences in performance could not be attributed to mass transfer limitations alone. Figure 7 shows that there is only a small difference between the steady-state and potentiostatic pulse performance for a Teflon-bonded Pt electrode operating under similar conditions.

As shown in Fig. 8 a plot of ln i (i, current density at 200 mV overpotential) against $1/T$ for the potentiostatic pulse results gave a straight plot, but the calculated activation energy was only 2.26 kcal/mole; significantly lower than the results obtained earlier from the steady-state results (10.75 kcal/mole). The very low activation energy for results obtained by

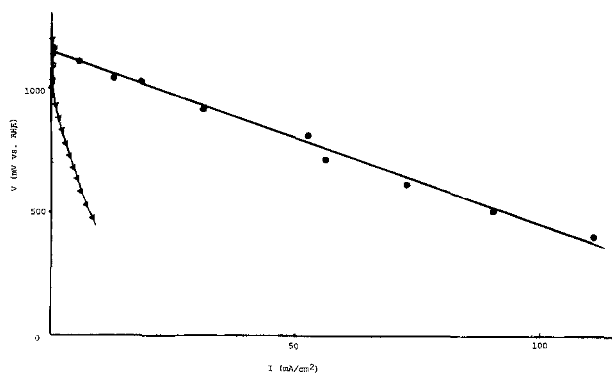

Fig. 6. The polarization curve of a Teflon-bonded $Nd_{0.5}Sr_{0.5}CoO_3$ electrode. 45% KOH, O_2, 25°C, iR corrected. ●, potentiostatic pulse; △, steady state.

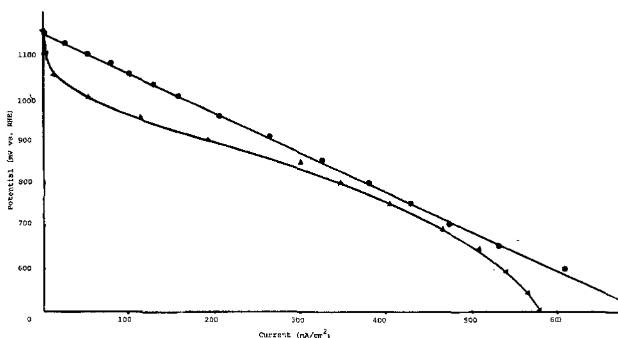

Fig. 7. The polarization curve of a Teflon-bonded Pt black electrode. 45% KOH, O_2, 25°C, iR corrected. Pt loading, 24.7 mg. ●, potentiostatic pulse; △, steady state.

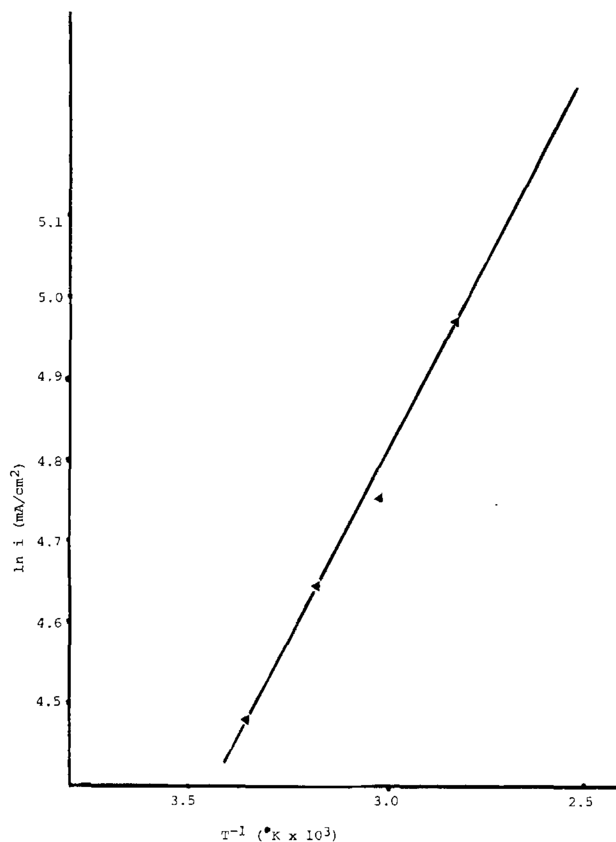

Fig. 8. ln i vs. $1/T$ for a Teflon-bonded $Nd_{0.5}Sr_{0.5}CoO_3$ electrode (potentiostatic pulse measurement).

potentiostatic pulse suggest that under transient conditions the rate of reaction is not controlled by the rate of oxygen chemisorption, since before each pulse the oxygen molecules have already been adsorbed on the electrode surface.

Measurement of oxygen coverage.—The galvanostatic "oxygen" stripping method (10) was used to determine the electrochemical surface area for oxygen reduction. Oxygen was bubbled through the test cell until a steady open-circuit voltage was reached. The electrode was then potentiostatically held at this potential and a stream of deoxygenated white spot N_2 was used to purge dissolved oxygen in the electrolyte for 15 min. A cathodic, galvanostatic pulse was then used to reduce the oxygen chemisorbed on the electrode surface. The potential was recorded on a storage oscilloscope. A mercury relay switching circuit was used to switch the potentiostatic circuit to the galvanostatic circuit. Figure 8 shows a typical potential time curve for a $Nd_{0.5}Sr_{0.5}CoO_3$ electrode. Most of the oxygen reduction reaction was completed within 900-400 mV. Table I gives the oxygen coverage on $Nd_{0.5}Sr_{0.5}CoO_3$ and $La_{0.5}Sr_{0.5}CoO_3$ as a function of temperature. The electrochemically active surface area was based on the galvanostatic results for oxygen reduction, assuming that the oxygen molecule to be chemisorbed "side-on" (cross section area of oxygen atom 1.72°A²). The total surface area of the electrode

Tablel I. O_2 surface coverage

$$\left(\frac{\text{electrochemical area}}{\text{BET area}}\right)$$

Temperature (°C)	Pt (%)	$Nd_{0.5}Sr_{0.5}CoO_3$ (%)	$La_{0.5}Sr_{0.5}CoO_3$ (%)
25	100	1.08	1.06
40	—	1.08	1.06
60	—	1.08	1.06
80	—	1.08	1.06

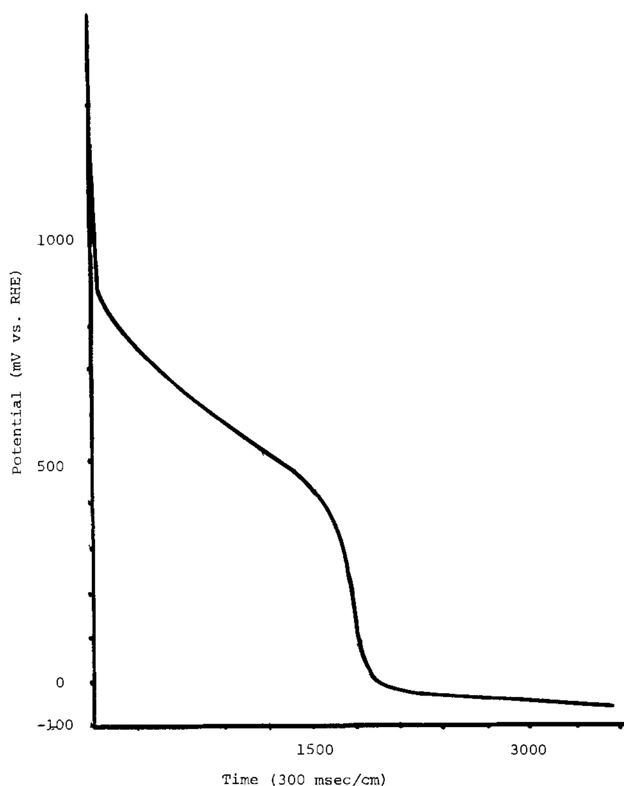

Fig. 9. The voltage-time relationship for O_2 stripping from a Teflon-bonded $Nd_{0.5}Sr_{0.5}CoO_3$ electrode at 45°C in 45% KOH.

was calculated from the catalyst loading and the BET surface area of the catalyst. The result for a Pt electrode is also included for reference.

The results show that the oxygen coverage is very low in both Sr-doped $NdCoO_3$ and $LaCoO_3$ electrodes, and the surface coverage is independent of temperature. The degree of surface coverage is almost the same in both cases. This is to be expected since Sr doping levels are the same in both cases. The fact that there is no change in surface coverage with temperature suggests that the improvement in performance with temperature is not due to the increase in the number of active sites as suggested previously by Tseung and Bevan (1).

General discussion.—Recent homomolecular studies by Hibbert and Tseung (11) have shown that the activation energy for the dissociative oxygen chemisorption on $La_{0.5}Sr_{0.5}CoO_3$ is 15 kcal/mole, similar to the activation energy for oxygen reduction under steady-state conditions, 13 kcal/mole, suggesting that the rate of dissociative oxygen chemisorption is the rate-limiting step. The present electrochemical studies are also in accord with the above findings.

If the rate of oxygen chemisorption is the rate-determining step, then we can derive the mathematical relationship between the current density and oxygen partial pressure. When O_2 is dissociative chemisorbed, the reaction mechanism can be expressed as

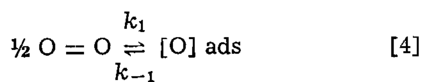

$$\tfrac{1}{2}\,O = O \underset{k_{-1}}{\overset{k_1}{\rightleftharpoons}} [O] \text{ ads} \qquad [4]$$

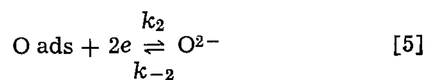

$$O \text{ ads} + 2e \underset{k_{-2}}{\overset{k_2}{\rightleftharpoons}} O^{2-} \qquad [5]$$

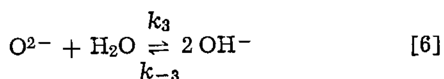

$$O^{2-} + H_2O \underset{k_{-3}}{\overset{k_3}{\rightleftharpoons}} 2\,OH^- \qquad [6]$$

Let p be the partial pressure of O_2 in contact with the electrode and θ be the fraction of energetically and geometrically suitable sites covered by [O] ads at given current i. At steady state, this fraction remains constant. The fraction of the surface covered at p is then found by setting $d\theta/dt$ equal to zero, since the surface coverage is low (1%), the Langmuir adsorption equation can be applied to this case

$$\frac{d\theta}{dt} = k_1 p^{1/2}(1-\theta) - k_{-1}\theta - k_2\theta = 0 \qquad [7]$$

$$\therefore\ \theta = \frac{k_1 p^{1/2}}{k_{-1} + k_2 + k_1 p^{1/2}} \qquad [8]$$

If the chemisorption is the rds, then the current i is given by $2\mathbf{F}k_2\theta$, thus

$$i = \frac{2\mathbf{F}k_1 k_2 p^{1/2}}{k_{-1} + k_2 + k_1 p^{1/2}} \qquad [9]$$

However, the rate constant (k_2) for the ionization [O] ads is dependent on the electrode potential

$$k_2 = k \exp\left[(1-\alpha)\mathbf{F}\eta/RT\right] \qquad [10]$$

Substitute Eq. [10] into Eq. [9]

$$i = \frac{2\mathbf{F}k_1 k p^{1/2} \exp\left[(1-\alpha)\mathbf{F}\eta/RT\right]}{k_{-1} + k\exp\left[(1-\alpha)\mathbf{F}\eta/RT\right] + k_1 p^{1/2}} \qquad [11]$$

If the reaction is controlled by the rate of chemisorption, k_1 and $k_1 p^{1/2}$ should be small. Under heavy cathodic polarization, the denominator of Eq. [11] is determined mainly by the exponential term. Hence the current is given approximately by

$$i = \frac{K p^{1/2} \exp\left[(1-\alpha)\mathbf{F}\eta/RT\right]}{k_{-1} + k\exp\left[(1-\alpha)\mathbf{F}\eta/RT\right]} \qquad [12]$$

where $K = 2\mathbf{F}k_1 k$.

Taking logarithms on both sides, we have

$$\ln i = \ln A + \tfrac{1}{2}\ln P \qquad [13]$$

where

$$A = \frac{K_2 \exp\left[(1-\alpha)\mathbf{F}\eta/RT\right]}{k_{-1} + k\exp\left[(1-\alpha)\mathbf{F}\eta/RT\right]}$$

therefore

$$\frac{d\ln i}{d\ln p} = \frac{1}{2} \qquad [14]$$

Since both $La_{0.5}Sr_{0.5}CoO_3$ (1) and $Nd_{0.5}Sr_{0.5}CoO_3$ obey Eq. [14], it is suggested that the rate-limiting process is the rate of dissociative oxygen chemisorption on the electrode surface.

Acknowledgment

This study was supported by the Science Research Council.

Manuscript submitted May 2, 1977; revised manuscript received Feb. 1, 1978. This was Paper 297 presented at the Philadelphia, Pennsylvania, Meeting of the Society, May 8-13, 1978.

Any discussion of this paper will appear in a Discussion Section to be published in the December 1978 JOURNAL. All discussions for the December 1978 Discussion Section should be submitted by Aug. 1, 1978.

REFERENCES

1. A. C. C. Tseung and H. L. Bevan, *Electroanal. Chem. Interf. Electrochem.*, **45**, 429 (1973).
2. T. Kudo, H. Obayashi, and M. Yoshida, *This Journal*, **124**, 321 (1977).
3. T. Kudo, H. Obayashi, and T. Jejo, *ibid.*, **122**, 159 (1975).
4. J. Giner, G. Holleck, and P. A. Malachasky, Rep. Contract NA5313234, NASACR-7299, p. 8 (1971).
5. A. D. S. Tantram and A. C. C. Tseung, *Nature (London)*, **221**, 167 (1969).
6. J. Giner, J. M. Parry, S. Smith, and M. Turchan, *This Journal*, **116**, 1692 (1969).
7. K. L. K. Yeung, M.Sc. dissertation, The City University, London (1975).

8. B. S. Hobbs, P. R. Vassie, and A. C. C. Tseung, Electrochemical Engineering Symposium, Newcastle, J. D. Thornton, Editor, Vol. 1, p. 123 (1972).
9. E. Gileadi, E. Kirowa-Eisner, and J. Penciner, "Interfacial Electrochemistry," p. 359, Addison-Wesley Publishing Company, Inc., Reading, Mass. (1975).
10. A. C. C. Tseung and S. C. Dhara, *Electrochim. Acta*, **19**, 845 (1974).
11. D. B. Hibbert and A. C. C. Tseung, *This Journal*, **125**, 74 (1978).

Technical Note

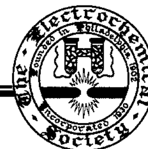

Epitaxial Layers of Cu_2S Grown from Liquid Solution and Investigated by RHEED

O. J. Cain
IBM General Technology Division, Essex Junction, Vermont 05452

and R. W. Vook
Department of Chemical Engineering and Material Science, Syracuse University, Syracuse, New York 13210

A study of epitaxial overgrowths of Cu_2S obtained by reacting copper films with sulfur vapor was reported earlier (1). Similar reaction overgrowths can be accomplished in liquid solutions; however, the solvent must not react with the metal, and the solubility of the solute (reactive species) should be low so the growth proceeds slowly. Methanol was found to work well as a solvent with sulfur. The purpose of this work was to determine if sulfide layers formed by a liquid solution technique would grow epitaxially, to study the overgrowth structure and morphology, and to compare it with similar overgrowths formed by a vapor-growth technique.

Experimental Approach

Single crystal copper film substrates were prepared by evaporating copper onto muscovite at 400°C to a thickness of 1200Å. Details of the substrate preparation were discussed earlier (1). The copper/mica sample was mounted on a RHEED specimen mount with silver paint and the oxide on the copper was removed by a 1-3 sec etch in dilute nitric acid (3:1, H_2O:70% HNO_3). The specimens were then rinsed sequentially with deionized water and methanol and finally dried in a stream of nitrogen. Reflection high energy electron diffraction (RHEED) patterns from these etched copper films showed only copper lines (with a small amount of polycrystalline structure shown by the faint ring pattern) (see Fig. 1). Also, the shortened streaks show that the surface is now somewhat rougher than before the etch. The diffraction patterns exhibited oxide lines if the copper films were etched before and not after mounting. Nitric acid is a strong oxidant and may be expected to leave oxide on the copper film. However, RHEED and Transmission Electron Diffraction (TED) patterns did not reveal any oxide overgrowth. Nevertheless, a very thin oxide layer may be present and not detected. Although the RHEED pat-

Key words: RHEED investigation, Cu_2S epitaxial layers, liquid solution.

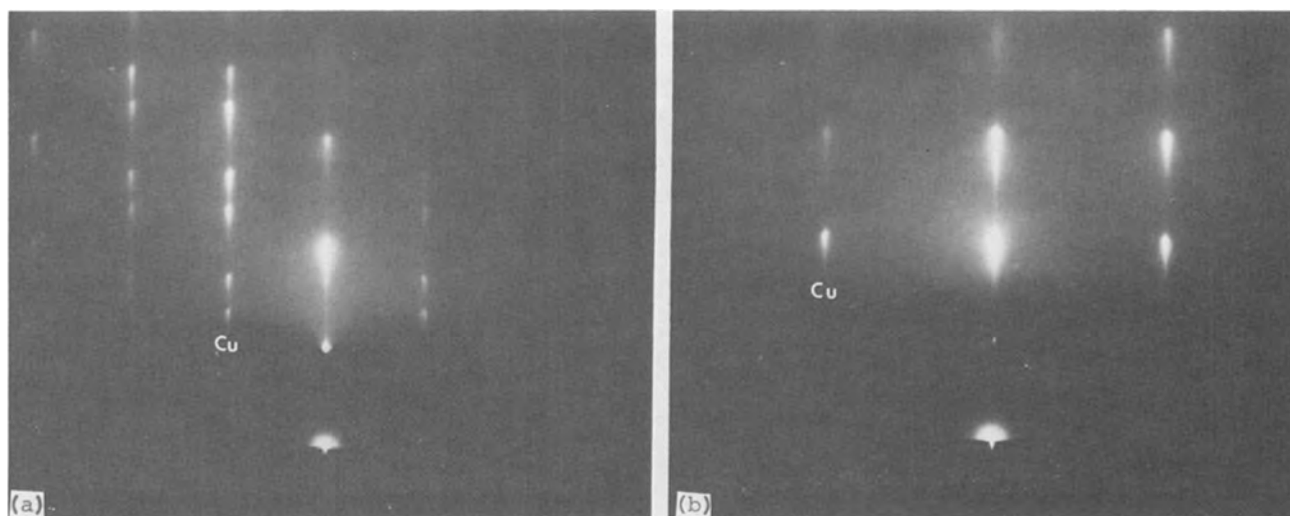

Fig. 1. RHEED patterns from (111) Cu etched in dilute nitric acid. (a) $[1\bar{1}0]$ azimuth; (b) $[2\bar{1}\bar{1}]$ azimuth

terns indicate some roughening, the surface was not grossly faceted by the acid etch as shown by the SEM prints in Fig. 2.

The sulfur/methanol solution was prepared by placing a small quantity of sulfur in the methanol and letting it stand for about 100 hr to reach saturation.

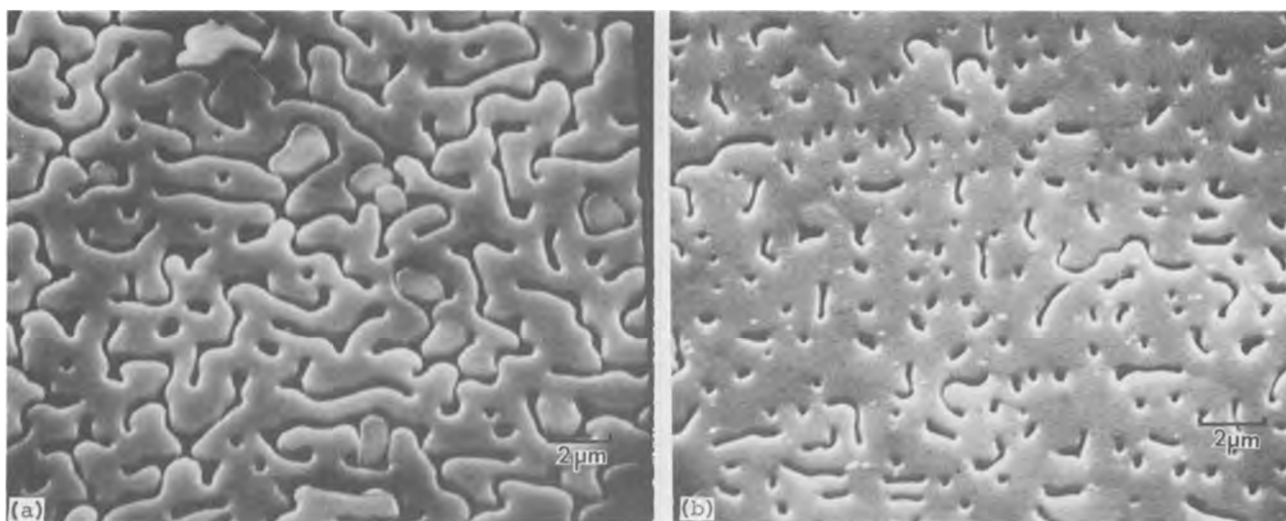

Fig. 2. Scanning electron micrographs of (111) Cu films. The films are in the channel-growth stage. Therefore, the black areas are holes in the film. (a) Before etching with HNO_3; (b) after etching with HNO_3.

Fig. 3. RHEED patterns (00.1) Cu_2S overgrowths on (111) Cu (a) [1$\bar{1}$0] Cu azimuth showing a weak [12.0] pattern from (00.1) Cu_2S; (b) [2$\bar{1}\bar{1}$] Cu azimuth showing a weak [10.0] pattern from (00.1) Cu_2S; (c) and (d) similar patterns as in (a) and (b), respectively, for overgrowths but only for Cu_2S. These patterns also contain orthorhombic and double diffraction effects.

The concentration of sulfur in saturated methanol was measured at 0.27 g/liter at room temperature. This concentration was determined by filtering the solution through filter paper to remove undissoved sulfur, sampling the solution to a specific volume of 4.5 cm^3 and placing thin, clean silver disks in the sampling solution serially until no tarnish was observed on the disks after a 2 day soak. The amount of sulfur on the disks was then measured electrometrically (2). The accuracy of the tarnish film thickness measurement under the present constraints is probably only within a factor of 2.

Copper films were immersed in the sulfur-saturated solution of methanol for various times immediately after the etch-rinse-dry sequence. The films were then studied by RHEED and SEM.

Results

The (111) copper films developed a visible tarnish after 1 sec of exposure in sulfur-saturated methanol at room temperature. The RHEED patterns indicate a hexagonal Cu_2S overgrowth in the earliest stages (*i.e.*, for a 1 sec exposure) and a progression to orthorhombic structures for the thicker films. There was no indication that the overgrowths started out as cubic Cu_2S as in the vapor-grown case (1).

The hexagonal overgrowths yielded RHEED patterns shown in Fig. 3. These patterns show that the orientation relation is {00.1} Cu_2S || {111} Cu with <10.0> Cu_2S || <211> of Cu. This epitaxial relationship shows the same 30° rotation between the sulfide and copper as the most prominent one produced in both the cubic and hexagonal vapor-grown sulfide layers reported elsewhere (1). The 30° rotation between the overgrowth and substrate reduces the misfit from 0.377 in the case of a "parallel" growth to 0.0796 for the rotated growth. The interfacial energy is then reduced significantly in the case of the rotated overgrowth.

Patterns from thicker overgrowths contained additional spots (Fig. 3c and 3d) identified as orthorhombic Cu_2S as well as some that can be explained by double diffraction between a "parallel" hexagonal growth and one rotated by 30°. When the thickness of the overgrowths prevented observation of the substrate diffraction pattern (Fig. 3c and 3d) the substrate azimuth could still be determined in RHEED by means of the strong Kikuchi bands from the copper showing on the projector screen. The Kikuchi bands seldom show up in the prints because short exposure times were used to get optimum spot resolution.

The RHEED patterns produced by the liquid solution-grown layers are not as sharp as those from vapor grown layers. The more diffused pattern indicates a lower quality epitaxial layer. Also, in the thicker overgrowths there is some arcing of the spots and even some rings in the patterns, indicating some polycrystalline growth. Poorer quality epitaxial growth obtained by the liquid solution method is not surprising, considering that the growth rates in this case were at least three orders of magnitude larger (based on the relative exposure times and size of the island growths) than for the vapor grown layers.

The morphology of growth in the liquid solution method is shown in the scanning electron micrograph in Fig. 4. The growth resulted in three-dimensional islands.

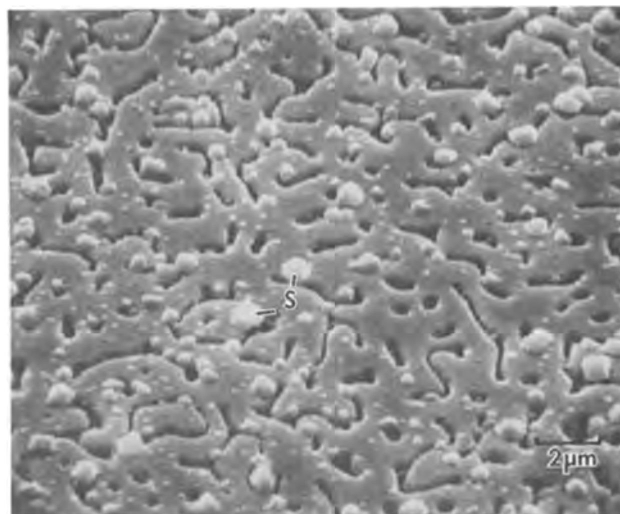

Fig. 4. Scanning electron micrograph print of Cu_2S growth, S, on noncontinuous film of (111) Cu.

Discussion

There is very little published work closely related to the present study. Two papers (3, 4) have dealt with tarnish layers produced by exposing copper to sulfur containing organic compounds. Wolynec (3) used 0.008 and 0.22M aqueous solutions of thiourea for exposure times of 210-360 min. The tarnish films consisted of an orthorhombic phase of Cu_2S or $Cu_{1.96}S$. The present study used solutions of approximately the same concentration of sulfur as Wolynec's (0.26 g/liter), but for much shorter exposure time. Wolynec's work with K poly S also showed orthorhombic Cu_2S for his shortest exposures. However, he also obtained other sulfur species together with oxides of copper. Labor (4) grew sulfide layers on copper in solutions of sulfur in organic solvents, CS_2 (high sulfur solubility), and C_6H_6 (low solubility). He found a quadratic metastable phase $Cu_{1.97}S$, orthorhombic and cubic $Cu_{(2-x)}S$, and eventually CuS.

The present work with low exposure levels resulted in thin epitaxial overgrowths of Cu_2S. No evidence for other sulfides or oxides was found from RHEED or TED results. The previous work (3, 4) involved high exposures that resulted in thick polycrystalline films and tended to produce sulfide phases containing more than 33 atom percent sulfur as well as oxides.

In summary, epitaxial overgrowths of hexagonal Cu_2S were produced on (111) copper substrates reacted with a solution of sulfur in methanol. The orthorhombic phase of Cu_2S was found in the thicker overgrowths. The orientation characteristics were similar to those of layers grown by the vapor technique (1).

Manuscript submitted Dec. 22, 1977; revised manuscript received Jan. 31, 1978.

Any discussion of this paper will appear in a Discussion Section to be published in the December 1978 JOURNAL. All discussions for the December 1978 Discussion Section should be submitted by Aug. 1, 1978.

Publication costs of this article were assisted by IBM Corporation.

REFERENCES

1. O. J. Cain and R. W. Vook, To be published.
2. T. P. Hoar and C. D. Stockbridge, *Electrochim. Acta*, **3**, 94 (1960).
3. S. Wolynec, Ph.D. Thesis, University of Sheffield (1970).
4. C. Labor, *Corros. Sci.*, **12**, 613 (1972).
5. *Powder Diffraction File*, published by Joint Committee on Powder Diffraction Standards, Swarthmore, Penn. (1974).

Brief Communications

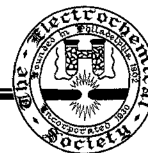

The Photogalvanic Effect in a Modified Iron Thionine System

H. Ti Tien and James M. Mountz

Department of Biophysics, Michigan State University, East Lansing, Michigan 48824

Photoelectrochemical cells have been proposed for the direct conversion of solar energy to electricity or chemical fuel (1). These cells, on the basis of two well-established photoeffects, can be classified as either photovoltaic or photogalvanic. The operation of a photovoltaic cell depends on the generation of an electromotive force as a result of the absorption of light, whereas the operation of a photogalvanic cell relies on the excitation by light of photoactive species in solution which induces a faradaic process at the electrode. The best-known example of photogalvanic cells is the iron-thionine system studied extensively by Rabinowitch (2) and others (3-7), in which the photoinduced reduction of thionine by ferrous ions takes place in the bulk solution.

In the course of our attempt in developing a new type of photoelectrochemical cell (8), the operation of which would be based on the combined principles of the two photoelectric effects, we have observed the photogalvanic effect in a modified thionine iron solution which should be of interest in the development of a practical photogalvanic device.

The usual photogalvanic effect is observed by immersing two identical platinum electrodes into the iron thionine solution and shielding one in the dark while the other is illuminated. The usual solution consists of 10^{-4}M thionine, 10^{-2}M $FeSO_4$, 4 × 10^{-4}M $(Fe)_2(SO_4)_3$, and 10^{-2}M H_2SO_4 (see Table I). This solution was prepared and placed in a glass chamber which was illuminated with a light intensity of 800 W/m^2 from a tungsten halogen projection lamp. A heat filter was installed and the system was shielded from spurious light. Upon illumination we observed a photoresponse of 112 mV as shown in Fig. 1(A). Using a 0.1M H_2SO_4 solution did not improve the photoresponse.

We found that by changing the electrolyte solution to 10^{-4}M thionine, 10^{-2}M $FeCl_2$, 10^{-4}M $FeCl_3$, and 0.1M sodium acetate at *p*H 4 a photoresponse of more than 200 mV could be observed in the identical experimental setup. This response is shown in Fig. 1(B). The magnitude of the response had an interesting dependence on the *p*H of the solution and thus was further investigated.

The results of our study of the effect of *p*H on the maximum light-induced potential are shown in Fig. 2. Below *p*H 3, the photopotential behaves in a complex manner. Above *p*H 3.5 the photopotential varies linearly with *p*H, with a slope of 60 mV following the Nernst equation. The maximum change is obtained at a *p*H equal to 3.4.

Following the suggestions by Rabinowitch (2) and others (9), we can write the following for the potential-determining reaction of the illuminated electrode

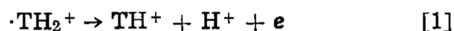

$$\cdot TH_2^+ \rightarrow TH^+ + H^+ + e \qquad [1]$$

Key words: photocell, solar energy, photoelectrochemical cell.

Table I. Photopotentials of some thionine-iron systems

Solution (M)	*p*H	Photopotential (mV)	Reference
Thionine (1.5×10^{-5}) Fe^{3+} (5×10^{-5}) Fe^{2+} (1×10^{-2})	2.5	185	(3)
Thionine (4×10^{-5}) Fe^{2+} (1×10^{-2})	2.5	111	(4)
Thionine (10^{-5}-10^{-3}) Fe^{3+} (10^{-5}-10^{-3}) Fe^{2+} (10^{-2})	1-2	200	(5)
Thionine (10^{-3}) Fe^{3+} (5×10^{-4}) Fe^{2+} (10^{-2}) H_2SO_4 (10^{-2}) in 5% acetonitrile	2	175	(6)
Thionine (10^{-4}) Fe^{3+} (10^{-4}) Fe^{2+} (10^{-2}) in 0.1M sodium acetate	3.4	230	This work

where $\cdot TH_2^+$ and TH^+ are the semiquinoid form and oxidized form of the dye thionine, respectively. The photopotential (E^*) can then be given by

$$E^* = E^\circ + \frac{RT}{\mathbf{F}} \ln \frac{[TH^+][H^+]}{[\cdot TH_2^+]} \qquad [2]$$

where E° denotes the standard redox potential for $\cdot TH_2^+$ to TH^+. Equation [2] predicts a decreasing photopotential for the cell with increasing *p*H. This has been found to be the case at *p*H higher than 3.5 (Fig. 2).

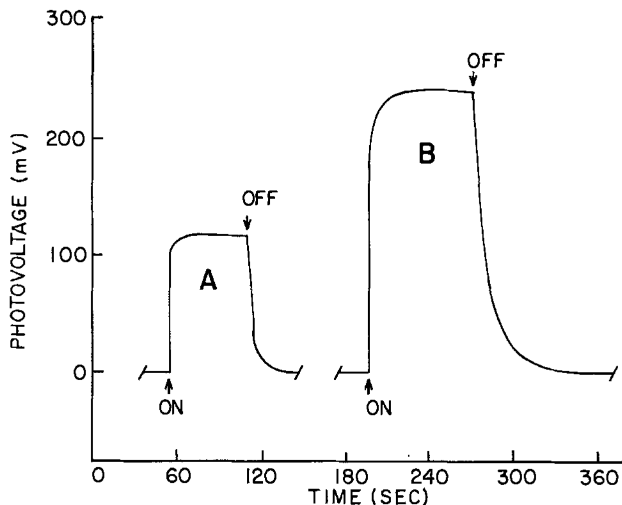

Fig. 1. Open-circuit photoresponses of the photogalvanic cell against time. The cell was illuminated by a 250W tungsten-halogen projector lamp (EHJ-Sylvania). ↑, light on; ↓, light off. A, the conventional iron-thionine solution; B, the modified iron-thionine solution described in this report.

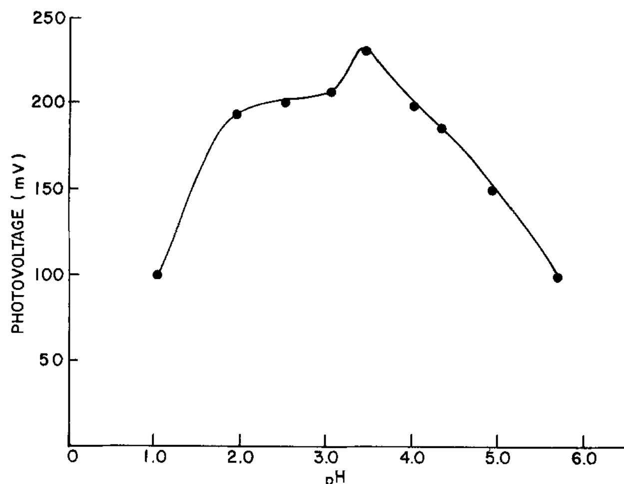

Fig. 2. The dependence of the photogalvanic response for the solution as a function of pH.

As to why the maximum photopotential should occur around pH 3.4, we have no ready answer, for this phenomenon has not been studied. However, it appears that, since the species $\cdot TH_2^+$ is generated by light, it is evident from Eq. [1] that the observed photopotential should depend on the stability of the entity at the electrode surface. Conceivably the acetate ion acting as a ligand can somehow either alter the redox potential of the system or increase the rate of interfacial electron transfer. Additional experiments using a variety of ligands are of obvious interest.

Summarizing, we have shown that the photoresponse of the conventional iron thionine system can be enhanced with a slight modification of the solution. In addition, an interesting pH dependence was observed. The finding presented here merits further exploration.

Acknowledgments

This work was supported, in part, by a postdoctoral energy-related fellowship to J. M. Mountz from the National Science Foundation and the College of Natural Sciences, Michigan State University.

Manuscript submitted Oct. 14, 1977; revised manuscript received Feb. 13, 1978.

Any discussion of this paper will appear in a Discussion Section to be published in the December 1978 JOURNAL. All discussions for the December 1978 Discussion Section should be submitted by Aug. 1, 1978.

Publication costs of this article were assisted by Michigan State University.

REFERENCES

1. G. Porter and M. D. Archer, *Interdiscip. Sci,. Rev.*, **1**, 119 (1976).
2. E. Rabinowitch, *J. Chem. Phys.*, **8**, 551, 560 (1940).
3. A. E. Potter, Jr. and L. H. Thaller, *Sol. Energy*, **3**, 1 (1959).
4. L. J. Miller, Tech. Ser. Rep., AD 282, 878, U.S. Dept. of Commerce Washington, D.C. (1962).
5. W. D. K. Clark and J. A. Eckert, *Sol. Energy*, **17**, 147 (1975).
6. D. E. Hall, J. A. Eckert, N. N. Lichtin, and P. D. Wildes, *This Journal*, **123**, 1705 (1976).
7. N. N. Lichtin, in "Photochemical Conversion and Storage of Solar Energy," J. R. Bolton, Editor, Academic Press, New York (1977).
8. J. M. Mountz and H. T. Tien, *Sol. Energy*, To be published.
9. R. Gomer, *Electrochim. Acta*, **20**, 13 (1975).

Electrochemical Oxidation and Reduction of Thin Films of Prussian Blue

Vernon D. Neff

Department of Chemistry, Kent State University, Kent, Ohio 44242

We would like to communicate some interesting preliminary results concerning the electrochemical behavior of thin films of Prussian blue. There are actually two well-characterized forms of Prussian blue (PB) which have the formulas $KFe^{III}Fe^{II}(CN)_6$ and $Fe^{III}_4[Fe^{II}(CN)_6]_3$ (1). The latter compound is prepared from a solution containing a large excess of ferric ion. In addition to PB itself, two additional, closely related compounds are of interest. These are Everitt's salt $K_2Fe^{II}Fe^{II}(CN)_6$, which is colorless, and Berlin Green $Fe^{III}Fe^{III}(CN)_6$ (2). All three compounds have the same basic cubic crystal structure consisting of iron ions bridged by the cyanide groups, although subtle structural modifications may occur, depending on the stoichiometry (3, 4). The physical and chemical properties of these compounds have been reviewed by Robin and Day (5).

We have discovered a method for preparing thin adherent films of PB on various metal and semiconductor substrates. The particular experiment we wish to discuss is concerned with a thin PB film on a platinum foil electrode. The film is obtained from a solution containing equimolar amounts of ferric chloride and potassium ferricyanide. A one-to-one complex between ferric ion and ferricyanide ions forms in such solutions (6). The solution must be freshly prepared because the complex will slowly polymerize and eventually a colloidal precipitate of insoluble Berlin green is formed (7).

Key words: electrochemical oxidation, electrochemical reduction, Prussian blue films.

A fresh solution 0.01M in reagent grade $FeCl_3 \cdot 6H_2O$ and 0.01M in reagent grade $K_3Fe(CN)_6$ was prepared in triply distilled water. A 1 cm^2 platinum foil electrode, with platinum lead encased in Teflon, was cathodized for 1 hr at 1 mA in a 1M HCl solution. The electrode was placed in the ferric ferricyanide solution and, after several minutes a blue film was formed on the surface. The electrode was removed from the solution and rinsed thoroughly with distilled water.

A cyclic voltammogram of the PB electrode in quiet 1M KCl solution is shown in Fig. 1. The voltammogram was obtained with a PAR Model 173 potentiostat equipped with a Model 175 voltage programmer. The interesting feature of this voltammogram is that on the anodic side of the sweep (0.6V *vs.* SCE) the electrode is bright blue, whereas on the cathodic side (0.0V *vs.* SCE) it is colorless. Furthermore it is possible to switch rapidly between the blue and colorless states with the selecting switch on the potentiostat. The electrode reaction evidently occurs in the film itself and corresponds to the ultimate reduction of PB to the colorless "Everitt's salt."

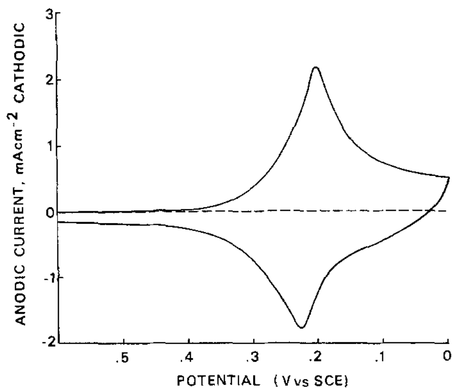

Fig. 1. Single sweep voltammogram of a thin film of Prussian blue on platinum foil in 0.1M KCl solution. The scan rate is 10 mV/sec.

A second observation is concerned with the oxidation of the PB film at more anodic potentials. At a potential of approximately 1.0V *vs.* SCE the film becomes green. In this case the film has apparently been oxidized to Berlin green. Again the color can be switched rapidly between blue and green but the film begins to deteriorate after several cycles presumably because of the simultaneous oxidation of chloride ion and the formation of surface oxide on the platinum.

The details of these electrochemical reactions are currently under investigation.

Manuscript submitted Sept. 29 1977; revised manuscript received Dec. 1, 1977.

Any discussion of this paper will appear in a Discussion Section to be published in the December 1978 JOURNAL. All discussions for the December 1978 Discussion Section should be submitted by Aug. 1, 1978.

Publication costs of this article were assisted by Kent State University.

REFERENCES

1. D. Davidson and L. A. Welo, *J. Phys. Chem.*, **32**, 1191 (1928).
2. J. F. Duncan and P. W. R. Wigley, *J. Chem. Soc.*, 1120 (1963).
3. J. F. Kegin and F. D. Miles, *Nature (London)*, **137**, 577 (1936).
4. A. Ludi and H. U. Gudel, *Struct. Bonding (Berlin)* **14**, 1 (1973).
5. M. B. Robin and P. Day, *Adv. Inorg. Chem. Radiochim.*, **10**, 247 (1967).
6. J. A. Ibers and N. Davidson, *J. Am. Chem. Soc.*, **73**, 476 (1961).
7. D. E. Knapp, Ph.D. dissertation, Kent State University, Kent, Ohio (1966).

DISCUSSION SECTION

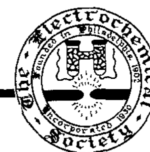

This Discussion Section includes discussion of papers appearing in the *Journal of The Electrochemical Society*, Vol. 124, No. 7, 9, and 12, July, September, and December 1977.

Fabricating Patterns in Tin Oxide Film by Electrochemical Reaction

B. J. Baliga and S. K. Ghandhi
(pp. 1059-1060, Vol. 124, No. 7)

I. F. Chang:[1] The technique of fabricating patterns of tin oxide films by electrochemiceal reaction has also been developed in our laboratory.[2] We have found that the over-all etching rate of tin oxide film is not significantly dependent on the concentration of HCl in water as shown by Baliga *et al.*[3] However, we would like to point out an important fact concerning the selection of a critical HCl concentration.

Since the over-all etching process consists of two consecutive steps: (*i*) electrochemical reduction of tin oxide to tin (the dark coloration of metal tin can be directly observed during the etching and analyzed by interrupting the etching process); and (*ii*) etching of tin by HCl, it is necesary to select the electrolyte composition such that the reduction rate of tin oxide (step *i*) is higher than the etching rate of tin metal (step *ii*). This selection guarantees that all the detail patterns to be etched are etched away with no electrically isolated oxide regions formed on the glass substrate. We have found that, for achieving best etching results, the concentration of HCl in water should be approximately 7%. An etched pattern with resolution on the order of 20 μm is shown in Fig. 1.

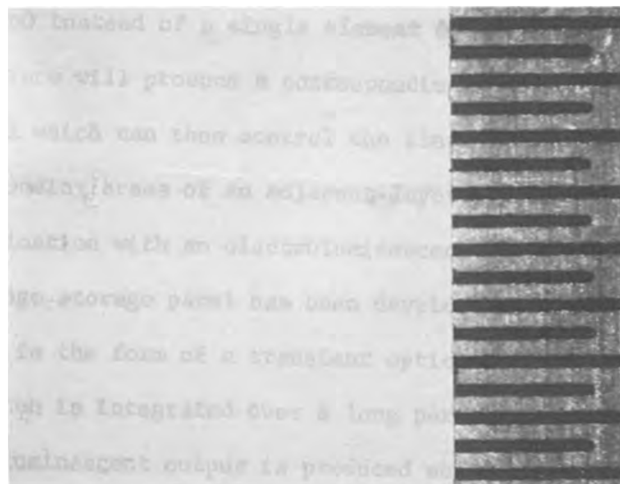

Fig. 1. Etched pattern in tin oxide film on glass substrate by electrochemical reaction technique (the ruler indicates 0.05 mm per division).

During the course of our work, we have also discovered some prior art in the patent literature[4,5] describing general metal oxide etching by electrochemical reaction.

B. J. Baliga and S. K. Ghandhi:[6] We agree with Chang that better etching can be achieved by ensuring

[1] IBM Thomas J. Watson Research Center, Yorktown Heights, New York 10598.
[2] I. F. Chang, W. P. Hornberger, and H. H. Taub, *IBM Tech. Disclosure Bull.*, **16**, 3463 (1974).
[3] B. J. Baliga and S. K. Ghandi, *This Journal*, **124**, 1059 (1977).
[4] R. F. Shaw, US Pat. 3,507,759 (1970).
[5] R. E. Szupillo, US Pat. 3,616,349 (1971).
[6] General Electric Corporate Research & Development, Schenectady, New York 12309.

that the reduction rate of the tin oxide is higher than the etching rate of tin metal. However, we disagree that it is necessary to select the electrolyte composition from this consideration. Our work has shown that the above requirement can instead be satisfied by controlling the current density, as was stated in the paper. We, therefore, prefer to choose the electrolyte composition in the range where the etch rate is independent of the HCl concentration (see Fig. 1) in order to obtain good control and reproducibility during etching. We also wish to point out that we have been able to achieve a pattern resolution of 6 μm, which is the limit of our present photolithographic equipment, and can expect even better results with this technique.

We apologize for not providing a reference to the authors prior publication. Unfortunately, we (and the reader) only have ready access to the professional literature in which we found no mention of this work.

The Hydrogen Electrode in Molten Carbonate

W. M. Vogel and C. D. Iacorangelo
(pp. 1305-1309, Vol. 124, No. 9)

A. Borucka:[7] This paper offers a comparison between experimental measurements of the "open-circuit" potentials and calculations of the theoretical equilibrium potential values based on consideration of four possible over-all electrochemical reactions, three of which, however, have not as yet been demonstrated to occur practically.

At this stage of progress of the scientific studies of the anodic gas reactions in molten carbonates, it is almost more important to point out the necessity of better design of the experimental apparatus than to question the assumptions upon which the calculations are based.

The apparatus presented by the authors (Fig. 1 in the paper under discussion) does not ensure accurate or stable melt composition because of the indicated purging with pure nitrogen (which may also have upset the accuracy of the gas compositions studied). Purging of an alkali carbonate melt at 650°C with any pure gas (other than CO_2) must, necessarily, lead to unstable and ill-defined melt and gas compositions, as was pointed out twenty years ago by Broers[7a] and later demonstrated experimentally by others.[9-11]

Of the many possible over-all electrochemical and chemical reactions at fuel gas electrodes in molten carbonates (as noted by Broers[7a]), only two were so far confirmed by accurate experimental evidence:[10]

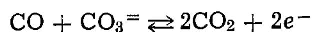

$$CO + CO_3^{=} \rightleftarrows 2CO_2 + 2e^-$$

and

$$2CO \rightleftarrows C + CO_2$$

On the other hand, the H_2/CO_2 gas electrode (which should be more properly regarded as a more complex $H_2/H_2O/CO_2/CO$ gas system) has not been to this date properly evaluated. Nevertheless, earlier studies[8,12] stress the presence of carbon monoxide even when only a dry H_2/CO_2 gas mixture is supplied to the carbonate electrolyte.

In view of the similarity of the theoretical equilibrium potentials (at 1000°K)[8] for the four reactions considered by the authors (*i.e.*, Eq. [7]-[10] in the paper under discussion) the analytical results of the Russian scientists,[12] and the prior work on dry CO/CO_2 gas anodes,[10] future more rigorous work on the $H_2/CO_2/CO_3^{=}$ system is indicated

[7] Borucka Research Company, Livingston, New Jersey 07039.
[7a] G. H. J. Broers, Ph.D. Thesis, Univ. of Amsterdam, Amsterdam (1958).
[8] J. Dubois, Ph.D. Thesis, Univ. of Paris, Paris (1965).
[9] A. Borucka, *Adv. Chem. Ser.*, 90, 242 (1969).
[10] A. Borucka, *This Journal*, 124, 972 (1977).
A. L. L'vov, *Elektrokhimya*, 5, 50 (1969).
[11] United Technologies Corporation, Power Systems Division, South Windsor, Connecticut 06074.
[12] Department of Chemistry, Rice University, Houston, Texas 77001.

W. M. Vogel and C. D. Iacorangelo:[11] The discussion by A. Borucka of our paper appears to center on two points, *i.e.*, which of the many reactions do actually take place at the H_2/H_2O electrode in molten carbonate, and the possibility that the melt used in this study was altered by purging with N_2.

In equilibrium all individual electrochemical reactions have the same potential. However it is not an easy task to supply the electrode with a gas which is in equilibrium under operating conditions. Ordinarily, one makes a gas mixture at room temperature. In the process of heating such a mixture to operating temperature the composition changes. The problem then is to determine the actual gas composition at the electrode from that of the feed gas. We have shown that, except under specified experimental conditions, the assumption of simultaneous shift and methane equilibria yields the observed OCP. It does not matter whether we use the Nernst equation for the H_2/H_2O, CO_2 reaction or some other reaction such as, *e.g.*, the CO/CO_2 electrode. The results are the same. The agreement of such values with the OCP does not allow one to make any statement about the rates of the various reactions, but it would appear to justify our conclusion that there are no unexplained differences between OCP and equilibrium potential as we find, *e.g.*, for the low temperature O_2 electrode.

It is somewhat misleading to say that the melt was purged with N_2. Only that melt which served as salt bridge between the various electrodes was purged with a slow stream of N_2 to keep air from entering. The working and reference electrodes were contained in individual compartments connected to the melt bridge via small holes. In addition, these electrode metals (wires) were immersed only a few mm in the melt. Because of these precautions only that melt was important, aside from possible liquid junction potentials, which surrounded the tips of these two electrodes, *i.e.*, essentially at the three-phase boundary melt/gas/electrode metal. Wiggling the electrode wires had no effect on the observed potentials as one should expect to see if there had been significant gradients of the $O^{=}$ concentration away from the three-phase boundary line.

The Pb/Pb^{2+} Exchange Reaction in Perchlorate Acidic Solutions

A. S. Gioda, M. C. Giordano, and V. A. Macagno
(pp. 1324-1329, Vol. 124, No. 9)

S. D. Kapusta:[12] The i *vs.* t relationship for a plane electrode having a large i_o and undergoing anodic dissolution at a constant potential is like that shown in Fig. 1.

The theoretical situation can be adequately described by solving the differential equations of semi-

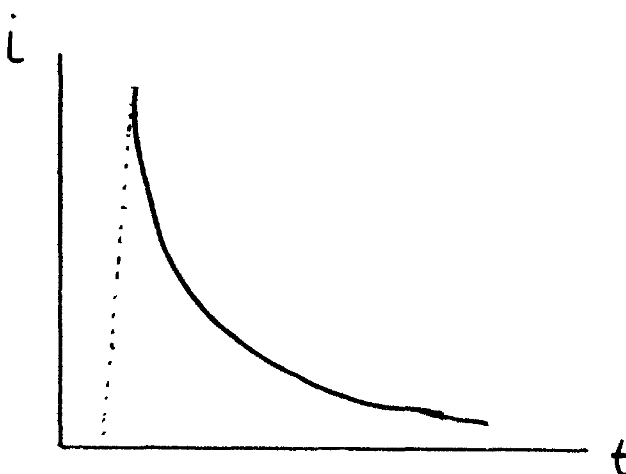

Fig. 1.

infinite lineal diffusion. Using the appropriate boundary conditions

$$i = n\mathbf{F}AC_r(D/\pi t)^{1/2}[1 - \exp(nf\eta)] \quad [1]$$

for long times or, for short times

$$i = i_a A \left(\frac{1 - 2\lambda t^{1/2}}{\pi^{1/2}} \right) \quad [2]$$

The symbols have their usual meaning. i_a is a current controlled only by activation.

Equation [1] represents an anodic current under diffusion control, while Eq. [2] represents one under mixed activated and diffusion control. Figures 2 and 3 describe these equations graphically.

Using a potential-step technique, we can obtain the current controlled only by activation by extrapolating the straight line of Fig. 3 to $t = 0$.

The authors used a potential-step technique for their steady-state polarization curve. Currents were read at a given time (*e.g.*, 1 min), so Eq. [1] holds. Under such circumstances, a Tafel-like behavior is obtained, with a slope

$$\partial\eta/\partial \ln i = 1/nf = 30 \text{ mV} \quad \text{since} \quad n = 2$$

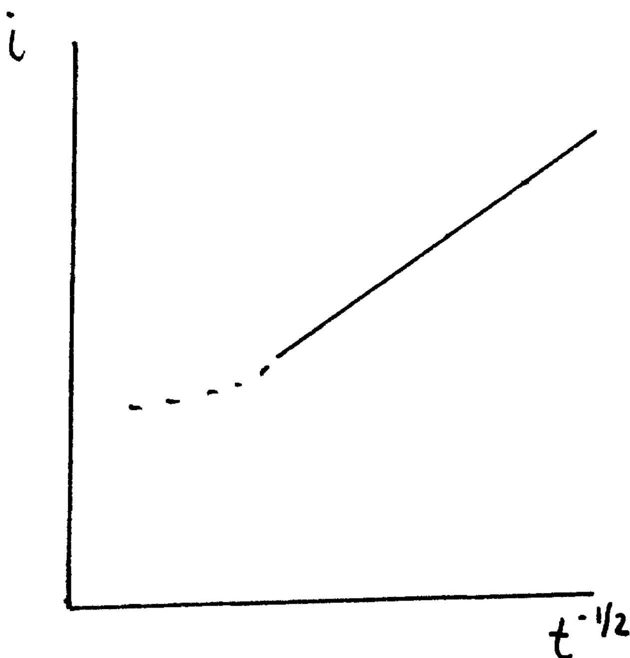

Fig. 2.

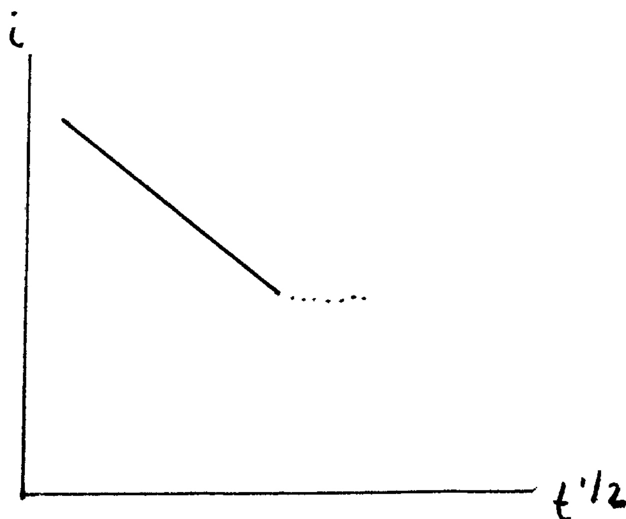

Fig. 3.

As is well known kinetic parameters cannot be obtained from diffusion data. Accordingly, the rate-determining step and the whole mechanism could be different, as previously proposed.[13]

A. S. Gioda, M. C. Giordano, and V. A. Macagno:[14] We thoroughly agree with the statement that kinetic parameters cannot be obtained from diffusion data.

The complete $I - \eta$ equation[15] for the potential-step method contains several terms to account for both charge transfer and diffusion control.

If there is not mass transfer polarization, I is a constant independent of t. Besides, as the correction term for mass transfer polarization becomes more pronounced with time, theoretically $I \to 0$ as $t \to \infty$ if diffusion is the sole mode of mass transfer.

The I *vs.* t curves under potentiostatic conditions performed by us[16] for the reaction under discussion show a constant current value within a few seconds following the potential step in unstirred solutions. The necessary time to reach a steady state becomes shorter (less than 1 sec) when the same experiment is performed at the rotating-disk electrode, but the value of the steady-state current is almost independent of the electrode rotation speed, w (see also the reference in footnote[17]).

This could be taken as an indication that the reaction is not under diffusion control. Moreover, the Tafel slope and reaction orders obtained by the potential-step method at $t = 0$ agree with our previous published values.

Furthermore, some experiments performed at low overpotentials[18] should indicate that "surface" diffusion could play an important role in the over-all process.

Standard Free Energy of Formation of Alumina

D. Ghosh and D. A. R. Kay
(pp. 1836-1845, Vol. 124, No. 12)

H. Byker and R. A. Howald:[19] Ten years ago the suggestion of Ghosh and Kay[20] that the accepted value for the standard heat of formation of corundum (-400.5 ± 0.3 kcal mole^{-1})[21] was in error by about 7 kcal mole^{-1} would have been welcomed, because at that time there was a serious discrepancy in the thermodynamic properties of Al(III) compounds between measured enthalpies and equilibrium measurements. Groups at the Geophysical Laboratory[22] and the Bureau of Mines[23] had extensive measurements on heats of solution in HF and NaOH solutions which provided good relative enthalpies for most Al(III) compounds, but corundum is not soluble to an appreciable extent at an appreciable rate in either of these solvents. However, with the introduction of high temperature oxide calorimetry by Kleppa *et al.*[24] there are good values for the enthalpies relative to corundum. Also in the meantime it has been clearly established that there had been errors in the heat of formation of

[13] S. B. Estevez and D. J. Schiffrin, "Disolucion Anodica del Plomo en Soluciones de Acido Perclorico," National Institute of Industrial Technology, Buenos Aires, Argentina (1975).
[14] Facultad de Ciencias Quimicas, Universidad Nacional de Cordoba, 5000 Cordoba, Argentiana.
[16] P. Delahay, in "Advances in Electrochemistry and Electrochemical Engineering," Vol. 1, P. Delahay, Editor, Interscience, New York (1961).
[16] A. S. Gioda, Doctoral thesis.
[17] A. N. Fleming and J. A. Harrison, *Electrochim. Acta*, **21**, 905 (1976).
[18] A. S. Gioda, M. C. Giordano, and V. A. Macagno, Unpublished results.
[19] Chemistry Department, Montana State University, Bozeman, Montana 59717.
[20] D. Ghosh and D. A. R. Kay, *This Journal*, **124**, 1836 (1977).
[21] D. R. Stull and H. Prophet, JANAF Thermochemical Tables, Nat. Stand. Ref. Data Ser. NSRDS-NBS37 (1971).
[22] F. C. Kracek *et al.*, Ann. Rept. Director of the Geophysical Laboratory, Geophysical Laboratory Paper 1215, pp. 69-75 (1953).
[23] K. K. Kelly, C. H. Shomate, F. E. Young, B. F. Naylor, A. E. Salo, and E. H. Huffman, U. S. Bur. Mines Tech. Paper, 688 (1946).
[24] J. L. Holm and O. J. Kleppa, *Am. Mineral.*, **51**, 1608 (1966); T. Yokokawa and O. J. Kleppa, *J. Phys. Chem.*, **68**, 3246 (1964).

secondary standards like gamma alumina,[24] gibbsite,[25] and aluminum chloride.[26] With new values for these enthalpies the discrepancies between enthalpy and equilibrium measurements have disappeared. If the enthalpy of corundum is to be adjusted now, the enthalpies of all Al(III) compounds will have to be shifted by an equivalent amount. The suggestion of Ghosh and Kay[20] does not conflict simply with oxygen bomb calorimetry of aluminum,[27-31] but also with careful determination of the heats of formation of AlF_3,[21,32] $Al(OH)_3$,[25] and $AlCl_3$.[21,26]

Even if one were comparing only the emf measurements with oxygen bomb calorimetry[27-31] the direction of the discrepancy suggests an error in the emf work. The most likely substantial errors in bomb calorimetry are incomplete combustion and unstable products, both of which lead to a less negative heat of formation. This kind of error easily accounts for the low values cited by Ghosh and Kay from the literature before 1940. In potentiometric work most errors will give a potential lower than the thermodynamic equilibrium value, and Ghosh and Kay have done very well to come within 50 mV of the calculated potential in this system. We suspect that the problem lies in the electronic conductance of solid Al_2O_3, which means that one is measuring in part oxygen or aluminum activities on both sides of an Al_2O_3 tube, or alternatively that a steady current is flowing through the Al_2O_3 in an attempt to bring the activities of Al and O_2 to equality on opposite sides of the tube.

We had hoped that data on the vaporization equilibria of corundum would settle the question decisively. The vaporization studies Drowart *et al.*,[33] and Rao and Motzfeldt[34] are in excellent agreement with the current JANAF[21] values for Al_2O_3 and $Al_2O(g)$, however the uncertainties are such that a heat of formation for Al_2O_3 of -393 kcal $mole^{-1}$ is not quite excluded. Similarly Farber *et al.*[35] report a heat of formation from vaporization to Al of -399 ± 10 in better agreement with the JANAF value but including -393 kcal $mole^{-1}$.

The difficulties with Knudsen cell materials at these temperatures are so serious that the best data are apparently those for free evaporation from a liquid surface[36] at the melting point. Burns[37] values for the pressures of Al and O over the liquid at the melting point give $P_{Al}P_O^{1.5} = 2.00 \times 10^{-15}$ $atm^{5/2}$, which can be compared to calculated equilibrium constants at the latest JANAF melting point[37] (2327°K) of 1.531×10^{-15} and 3.350×10^{-15} $atm^{5/2}$ for $H°_{298.15} = -400.5$ and -393.0 kcal $mole^{-1}$, respectively. If the liquid is actually 5° or 10° above the melting point due to its higher emissivity (and higher absorptivity), as suggested by the work of Paule,[38] the comparison will favor $H°_{298.15}$ (Al_2O_3, *c*, corundum) $= -400.5$ kcal $mole^{-1}$ even more.

D. Ghosh and D. A. R. Kay:[39] The contribution of Byker and Howald, which discusses our paper on the electrochemical determination of the high temperature standard free energy of formation of corundum in relation to mineralogical studies in aluminosilicate systems and mass spectrometric studies in the Al-O system, is most welcome.

In undertaking the high temperature electrochemical work it was hoped that a value of $\Delta G°_f(\alpha\text{-}Al_2O_3)$, which was consistent with related data in the literature, would be established unequivocally. Clearly, this is not the case.

The conflict between the values of $\Delta H°_{298}$ (α-Al_2O_3) as determined by oxygen bomb calorimetry and those derived from high temperature electrochemical measurements is well defined and there can be no argument with the comments of Byker and Howald on the direction of expected errors in both techniques. However, the authors have had difficulty in establishing incontrovertible evidence in support of either value, *i.e.*, a $\Delta H°_{298}$ (α-Al_2O_3) of -400.5 or -392.6 kcal/mole, from related work in the literature.

As implied in the discussion, the accuracy of studies in the Al-O system using Knudsen cell techniques is such that they could be consistent with either value, even when an alumina effusion cell is used.[40] The results of the surface evaporation studies of Burns[41] again cannot distinguish unambiguously between the two values when the effect of inaccuracies in the partial pressures are considered. An aluminum partial pressure of $1.25 \pm 0.25 \times 10^{-6}$ atm at 2318°K, for example, is quoted in this work.

The rationalization of a discrepancy between the thermodynamic properties of Al(III) compounds derived from thermochemical measurements and those derived from reversed hydrothermal equilibrium studies is much more complex. The suggestion of Zen,[42,43] who used the results of the high temperature oxide calorimetry of Holm and Kleppa[44] in his calculations, was that an error of about 7 kcal/mole in the presently accepted value of $\Delta H°_{298}$ (α-Al_2O_3) would eliminate the discrepancy, a suggestion consistent with the results of the electrochemical work. However, in 1974, Thompson[45] did recalculate the standard enthalpies of the aluminous minerals on the basis of a reported revised value for the standard enthalpy of formation of gibbsite. These recalculations resulted in a set of standard enthalpy and free-energy values for the aluminous minerals which were consistent with $\Delta H°_{298}$ (α-Al_2O_3) $= -400.5$ kcal/mole. Regressed Gibbs energy difference functions derived from reversed experimental equilibrium data were also used to generate a set of free-energy data for the aluminous minerals with a forced consistency with $\Delta H°_{298}$ (α-Al_2O_3) $=$ -400.5 kcal/mole.

The key question to be asked is whether the data used directly and indirectly by Thompson is his recalculations are now of sufficient accuracy to preclude a value of $\Delta H°_{298}$ (α-Al_2O_3) of -392.6 kcal/mole, bearing in mind the double-edged consideration that the maximum error quoted in all the work involving the determination of $\Delta H°_{298}$ (α-Al_2O_3) by oxygen bomb calorimetry is only $\pm$ 0.5 kcal/mole. If the answer is affirmative, then clearly there is a systematic error in the electrochemical work and the cells cannot be used to determine alumina activities in metallurgical slags, which was the original intention. If the answer is negative, then the problem has yet to be resolved.

Standard Free Energy of Formation of Alumina

D. Ghosh and D. A. R. Kay

(pp. 1836-1845, Vol. 124, No. 12)

O. F. Devereux:[46] This paper is an excellent example of the application of electrochemical techniques to high

[25] P. Gross, J. Christie, and C. Hayman, in A. B. Thompson, *Contrib. Mineral Petrol.*, **48**, 123 (1974).
[26] P. Gross and C. Hayman, *Trans. Faraday, Soc.*, **66**, 30 (1970); J. P. Coughlin, *J. Am. Chem. Soc.*, **78**, 5479 (1956).
[27] A. D. Mah, *J. Phys. Chem.*, **61**, 1572 (1957).
[28] P. E. Snyder and H. Selz, *J. Am. Chem. Soc.*, **67**, 683 (1945).
[29] C. E. Holley, Jr. and E. J. Huber, Jr., *ibid.*, **73**, 5577 (1951).
[30] A. Schneider and G. Gatlow, *Z. Anorg Allg. Chem.*, **277**, 41 (1954).
[31] W. A. Roth, U. Wolf, and O. Fritz, *Z. Elektrochem.*, **46**, 42 (1942).
[32] E. Rudzitis, H. M. Feder, and W. N. Hubbard, *Inorg. Chem.*, **6**, 1716 (1967); E. S. Domalski and G. T. Armstrong, *J. Res. Nat. Bur. Stand.*, **71A**, 105 (1967); *ibid.*, **69A**, 137 (1965).
[33] J. Drowart, G. DeMaria, R. P. Burns, and M. G. Ingraham, *J. Chem. Phys.*, **32**, 1366 (1960).
[34] D. B. Rao and K. Motzfeldt, *Acta Chem. Scand.*, **24**, 2796 (1970).
[35] M. Farber, R. D. Srivastava, and O. M. Uy, *J. Chem. Soc., Faraday Trans.*, **68**, 249 (1972).
[36] R. P. Burns, *J. Chem. Phys.*, **44**, 3307 (1966).
[37] JANAF Thermochemical Tables, 1974 Supplement, *J. Phys. Chem. Ref. Data*, **3**, 311 (1974).
[38] R. C. Paule, *High Temp. Sci.*, **8**, 257 (1976).
[39] Department of Metallurgy and Materials Science, McMaster University, Hamilton, Ontario, Canada L8S 4L7.

[40] M. Farber, R. D. Srivastava, and O. M. Uy, *J. Chem. Soc., Faraday Trans.*, **68**, 249 (1972).
[41] R. P. Burns, *J. Chem. Phys.*, **44**, 3307 (1966).
[42] E-anZen, *Am. Mineral.*, **54**, 1592 (1969).
[43] E-anZen, *ibid.*, **57**, 524 (1972).
[44] J. L. Holm and O. J. Kleppa, *Am. Mineral*, **51**, 1608 (1966).
[45] A. B. Thompson, *Contrib. Mineral Petrol.*, **48**, 123 (1974).
[46] Department of Metallurgy and Institute of Materials Science, University of Connecticut, Storrs, Connecticut 06268.

temperature thermochemistry. The significance of the conclusions notwithstanding, the clarity of presentation makes this a commendable study paper for research students. It is remiss, however, in two aspects.

First, the authors do not indicate that they determined the crystal structure of the Al_2O_3 participating in the cell reaction. Kubaschewski *et al.*[47] discuss this point in detail with reference to bomb calorimetry, citing the work of Schneider[48] as an example in which the reaction product, thought to be α-Al_2O_3, was in fact δ-Al_2O_3. The "Fisher Scientific, Certified" status of the authors' alumina documents only its purity and not its crystal structure. Clearly, the conclusions reached in this study would be strengthened if the authors established that the alumina used was, indeed, α-Al_2O_3.

Second, the authors' Fig. 1, purportedly a binary phase diagram, contains a thermodynamically impossible three-phase region. This point is clarified by Mitchel and Burel,[49] who note that "CaF_2" is actually CaF_2 + 1.5-2.0 w/o CaO. Figure 1 is, thus, a vertical section through a ternary phase diagram, a nontrivial distinction worthy of passing mention in the paper. Also on this point, it is pertinent to note that Mitchell and Burel attributed the difference between published binary phase diagrams for the (*i.e.*, "CaF_2"-Al_2O_3) system to variations in the Al_2O_3-$CaO \cdot (Al_2O_3)_6$ ratio, *i.e.*, to position along the CaO axis of the ternary diagram.

[47] O. Kubaschewski, E. L. Evans, and C. B. Alcock, "Metallurgical Thermo-Chemistry," 4th ed., Pergamon Press, Oxford (1967).
[48] A. Schneider and G. Gattow, *Z. Anorg. Allegem. Chem.*, **277**, 41 (1954).
[49] A. Mitchell and B. Burel, *J. Iron Steel Inst.*, London, **208**, 407 (1970).

D. Ghosh and D. A. R. Kay:[50] We would like to thank Professor Devereux for his interest and comments on our recent paper.

With regard to his first point, the room temperature crystallographic form of the alumina starting material is thought to be relatively unimportant in view of the presence of α-Al_2O_3 refractories in the high temperature slag system. However, routine x-ray powder diffraction analysis of "Fisher Scientific, Certified" alumina produced a pattern which matched that of ASTM No. 10-173 for α-Al_2O_3.

The second point regarding the "CaF_2"-Al_2O_3 phase diagram, is important in its own right and the fact that it is indeed a section of the CaF_2-CaO-Al_2O_3 ternary diagram was not emphasized in our paper. X-ray powder diffraction analysis of the "CaF_2"-Al_2O_3 electrolyte used in our experiments confirmed the presence of α-Al_2O_3, CaF_2, and $CaO \cdot (Al_2O_3)_6$ as determined originally by Mitchell and Burel. As indicated by these authors, the high temperature reactions

$$(CaF_2) + H_2O_{(g)} = 2HF_{(g)} + (CaO) \quad [1]$$

and

$$3(CaF_2) + (Al_2O_3) = 2AlF_{3(g)} + 3(CaO) \quad [2]$$

can lead to indeterminate quantities of CaO in high temperature "CaF_2"-Al_2O_3 slag systems. Whether or not the differences between published phase diagrams of the "CaF_2"-Al_2O_3 system can be attributed to the presence of varying amounts of CaO, must remain a matter for conjecture.

[50] Department of Metallurgy and Materials Science, McMaster University, Hamilton, Ontario, Canada L8S 4L7.

SOLID-STATE SCIENCE
AND TECHNOLOGY

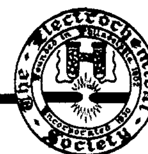

JUNE
1978

Thermal Oxidation of Phosphorus-Doped Polycrystalline Silicon in Wet Oxygen

Hideo Sunami

Hitachi Limited, Central Research Laboratory, Kokubunji, Tokyo 185, Japan

ABSTRACT

Oxidation characteristics of heavily phosphorus-doped polycrystalline silicon films and single crystal silicon substrates are investigated in a wet oxygen ambient over the temperature range 700°-850°C based on the linear-parabolic rate law. Polysilicon, undoped or uniformly doped with phosphorus of 1.1×10^{19}-2.2×10^{21} cm^{-3} by diffusion drive-in or ion implantation, is studied in comparison with lightly doped or heavily doped (100), (110), and (111) faces of silicon substrates. Phosphorus concentrations greater than 1×10^{20} cm^{-3} cause a significant increase in oxidation rates. Above 1×10^{21} cm^{-3}, however, oxidation rates tend to become saturated. A very rapid oxidation in the initial stage of oxidation is observed. This initial oxide does not fit the linear-parabolic rate law. The resistivity of the phosphorus-doped polysilicon is minimized at 5×10^{-4} Ω-cm for a phosphorus concentration of around 6×10^{20} cm^{-3}. The initial resistivity remains almost constant after reduction of the polysilicon thickness by oxidation. In addition, no evidence of enhanced oxidation along the grain boundaries is observed.

The thermal oxidation kinetics of silicon have been extensively investigated over the past twenty years. One result was the introduction of the linear-parabolic rate law (1) which successfully characterizes experimental results. The activation energies for the rate constants derived from the linear-parabolic model are found in the literature to vary between 0.4 and 2.3 eV (2). Discrepancies in activation energies have been validly attributed to the fact that thermal oxidation of silicon is highly influenced by sodium contamination (2) and/or water traces in the ambient (3, 4). In addition, thermal oxidation of silicon is also influenced by silicon dopant concentrations greater than 1×10^{20} cm^{-3} (5, 6). The dopant concentration dependence of rate constants was previously reported for dry oxidation (7). Although concentration dependent oxidation (CDO) is most pronounced in wet oxygen (5), the kinetics of CDO have not been thoroughly analyzed yet.

The use of polysilicon films has become increasingly important, since silicon gate technology is presently used for many MOS integrated circuits. Consequently several studies were reported on the thermal oxidation of polysilicon films particularly for the crystallinity effect (8) and some CDO effects (9). Recently, silicon dioxide films grown on polysilicon gates have been employed as intermediate insulators for double or higher level polysilicon devices for large scale charge coupled devices (10) and random access memories (11). The quality of the oxide grown on the polysilicon gates is expected to effect the reliability of these devices.

This work characterizes the thermal oxidation of polysilicon films in comparison with various silicon substrate faces with emphasis on heavy doping effects. Undoped polysilicon samples, phosphorus-diffused, and phosphorus-implanted films and single crystal silicon samples of both lightly doped crystals and phosphorus-diffused surfaces were examined. This work also discusses the resistivity of phosphorus-doped polysilicon films and the grain boundary effect on thermal oxidation of polysilicon films deposited on oxidized silicon substrates. Oxidation processes were carried out in wet oxygen (90°C H_2O) in the 700°-850°C range, and CDO was accomplished primarily at 750°C.

Key words: ion implantation, diffusion drive-in, resistivity, grain.

Experimental

In this study, polysilicon films were deposited on thermally oxidized silicon substrates by the thermal decomposition of silane at 625°C in the thickness range 350-500 nm. Grain size of as-deposited films was measured to be around 50 nm by transmission electron microscopy. Phosphorus doping was carried out by the conventional predeposition technique at 1000°C using $POCl_3$ source or ion implantation at 50 keV with doses of 1×10^{15}-1×10^{17} cm^{-2}. Subsequent annealing was realized in a dry oxygen ambient at 1000°C for 20 min in order to provide a uniform concentration across the film and to clean the surface for the implanted samples. Thin oxides formed on the film by the annealing in oxygen were removed with an HF aqueous solution prior to CDO. The annealing also gave rise to grain growth of the film, of which sizes were measured to be 80 and around 1000 nm for phosphorus concentrations of 1.1×10^{20} and 1.1×10^{21} cm^{-3}, respectively. Film resistivity was measured by four-point probe measurement after removal of the oxide.

Silicon substrates having (100), (110), and (111) faces were used in the form of circular slices, 76 mm in diameter, cut from Czochralski crystals, and mirror polished to 400 μm. Impurity concentrations of these substrates were 1×10^{15} cm^{-3} (boron), 1×10^{15} cm^{-3} (boron), and 3×10^{14} cm^{-3} (phosphorus), respectively. Phosphorus-doped surfaces on (100) substrates were obtained by the same predeposition mentioned above. Sheet resistivity and junction depth of the phosphorus-doped layer were 8.5 Ω/□ and about 1 μm, respectively. The carrier concentration of the surface was found to be 7×10^{20} cm^{-3} by incremental removal of the surface and subsequent four-point probe measurement.

A three-zone, resistance-heated furnace with a high purity alumina liner was used for this study. The oxidation chamber was a single wall, fused silica tube. The tube was thoroughly degreased and bathed in aqua regia and then bathed in a mixture of HF and H_2O and thoroughly rinsed in deionized water. Oxygen flow rate was 3 liters/min for this 11 cm ID tube. The resulting partial pressure of water vapor in oxygen was estimated to be 470 mm Hg. This value was obtained from the volume consumption of water supplied from a reservoir which kept the surface level of water in the bubbler constant. As vapor pressure is 524 mm Hg under equilibrium conditions at 90°C, the oxygen was almost completely saturated with water vapor in this experiment. Oxidation temperature was controlled to ± 1°C over the range of 700°-850°C. Cleaning procedures prior to CDO included rinses both in an organic solvent and aqua regia, and light etching of the surface layer, particularly for single crystal silicon with the exception of phosphorus-diffused surfaces.

Oxide thicknesses were determined using an ellipsometer for oxides on single crystal silicon or a Talystep meter for those on polysilicon films. Talystep measurements were calibrated by the ellipsometer for oxides on single crystal silicon, and both methods coincided to within 5%.

Results

Experimental oxidation data were taken to illustrate the following points:

1. The effect of phosphorus doping from 10^{19} to above 10^{21} cm^{-3} and rate constants and activation energies were calculated therefrom.
2. A comparison of the power law exponent (12), n, from the equation

$$x^n = kt$$

showing different behavior for an initial oxidation regime as compared with thicker oxides.

3. A comparison of polysilicon data with data taken on lightly doped single crystal silicon with (100), (110), and (111) faces.
4. The effect of oxidation on a resistivity change and a grain growth for the films.

Plots of the logarithm of oxide thickness *vs.* that of phosphorus chemical concentration for various oxidation times in the case of oxidation in wet oxygen (90°C H_2O) at 750°C are shown in Fig. 1. Oxidation rates increased sharply for concentrations greater than 1×10^{20} cm^{-3}. Almost the same concentration dependence was observed at both 700° and 800°C except absolute values of oxidation rates. These data in the form of the logarithm of oxide thickness *vs.* the logarithm of oxidation time at various concentrations are plotted in Fig. 2. Values indicated at the end of the curves correspond to the exponent n in the empirical power law dependence, $x^n = kt$, where x, k, and t are oxide thickness, rate constant, and oxidation time, respectively (12). Normally, n ranges from 1 for thinner oxides to 2 for thicker oxides. However, n exceeds 2 for two curves of 1.1×10^{21} and 2.2×10^{21} cm^{-3}. Their values of n are around 2.4. This anomalous phenomenon can be explained by the assumption that very rapid oxidation occurs at an early stage of oxidation resulting in an initial oxide which seems to exist analytically prior to CDO. This is discussed in detail in the next section.

Oxidation characteristics of heavily doped and non-doped polysilicon films are plotted in Fig. 3 for 700°, 750°, 800°, and 850°C. Phosphorus doping was accomplished by the conventional predeposition technique at 1000°C for 20 min. The resulting phosphorus concentration was indirectly estimated to be 3×10^{20} cm^{-3} by fitting the oxide thickness values in Fig. 3 to the plots in Fig. 1 for 750°C oxidation.

Similarly, the oxidation of heavily phosphorus-doped (100) surfaces and lightly doped substrates are shown in Fig. 4 for the same temperatures as in Fig. 3. Phosphorus doping of substrates was performed under the same conditions as described above. However, the phosphorus concentration was found to be 7×10^{20} cm^{-3} by incremental removal and four-point probe measurement in reference to Irvin's results (13). This difference between 3×10^{20} cm^{-3} for polysilicon and 7×10^{20} cm^{-3} for (100) silicon even with a simultaneous predeposition has not been explained yet.

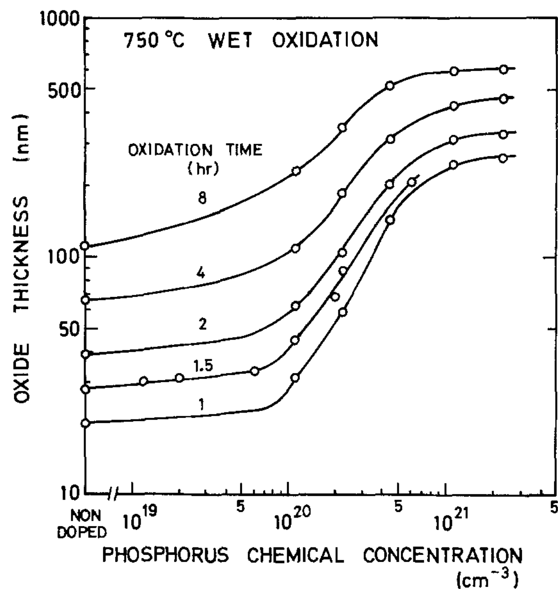

Fig. 1. Oxidation of heavily doped polysilicon films with phosphorus in wet oxygen (90°C H_2O). Polysilicon films were deposited on oxidized silicon substrates, 450-500 nm in thickness and doped through ion implantation. Annealing at 1000°C in dry oxygen was performed prior to oxidation.

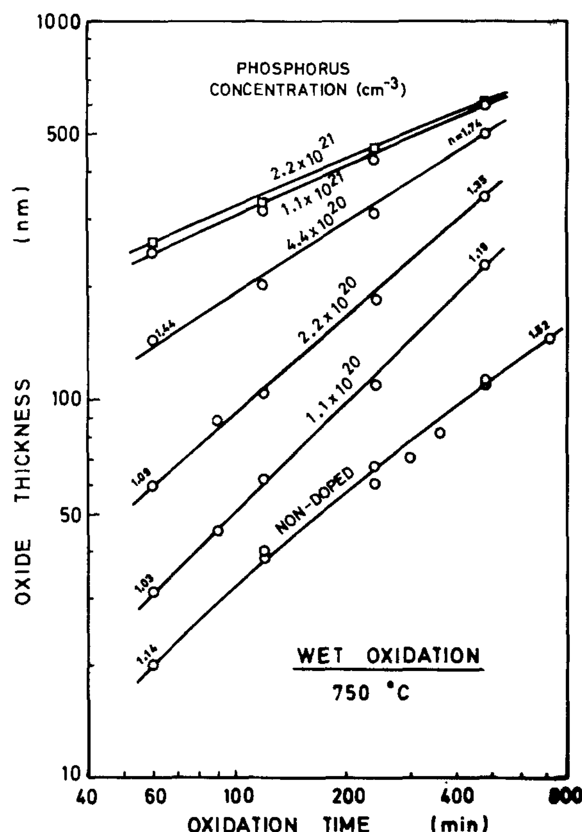

Fig. 2. Oxidation of heavily doped polysilicon films with phosphorus in wet oxygen (90°C H_2O). The plots employ the same data as shown in Fig. 1. Values indicated at the limit of each curve correspond to the exponent n in the power law dependence, $x^n = kt$.

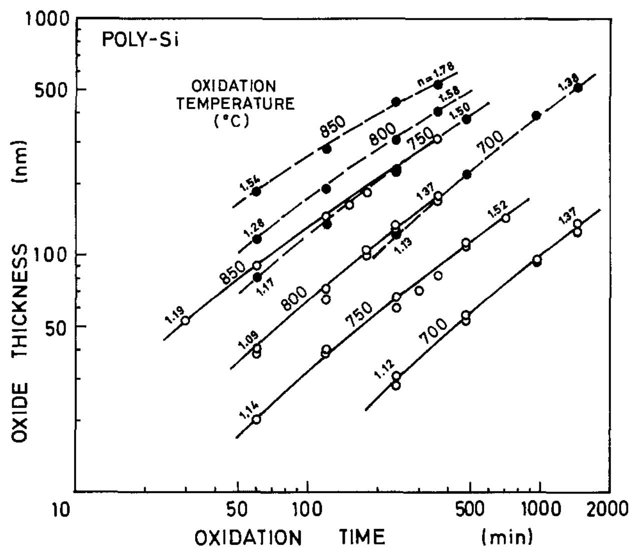

Fig. 3. Oxidation of phosphorus-doped and nondoped polysilicon films in wet oxygen (90°C H_2O): ●, phosphorus doped (3 × 10^{20} cm^{-3}); ○, nondoped.

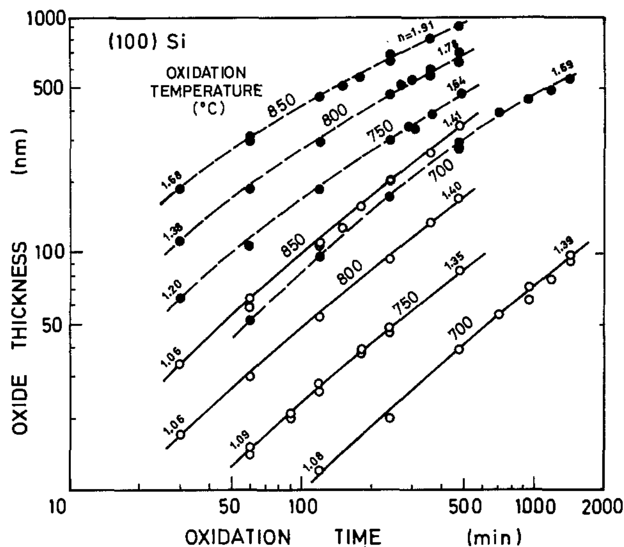

Fig. 4. Oxidation of phosphorus-doped (100) surfaces and lightly doped (100) substrates in wet oxygen (90°C H_2O): ●, phosphorus doped (7 × 10^{20} cm^{-3}); ○, uniformly boron doped (1 × 10^{15} cm^{-3}).

Wet oxidation of nondoped polysilicon in comparison with (100), (110), and (111) faces of single silicon substrates is shown in Fig. 5 for 700° and 750°C. It is seen that at both temperatures the polysilicon rate was between (110) and (111).

The resistivities obtained for phosphorus-doped polysilicon films are shown as a function of chemical concentration in Fig. 6. Resistivity was evaluated from the product of oxide thickness and sheet resistivity using four-point probe measurement. The existence of a resistivity minimum of 5 × 10^{-4} Ω-cm is clearly distinguished for a concentration of around 6 × 10^{20} cm^{-3}. As have been mentioned in the Experimental section, grain sizes of the films were found to be 80 and around 1000 nm for the concentrations of 1.1 × 10^{20} and 1.1 × 10^{21} cm^{-3}, respectively (14).

Resistivity changes in polysilicon films doped with phosphorus (3 × 10^{20} cm^{-3}) associated with wet oxidation are shown in Fig. 7. The abscissa denotes residual polysilicon thickness after oxidation. Solid symbols designate the initial values of resistivity and thickness. The resistivity of as-oxidized films increased to a great extent for 700°C because most phosphorus

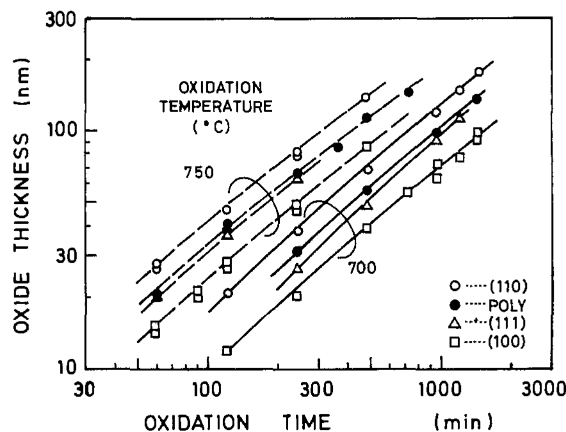

Fig. 5. Crystal orientation and crystallinity dependences of oxidation in wet oxygen (90°C H_2O) at 700° and 750°C. Impurity concentrations of (100), (110), and (111) faces are 1 × 10^{15} (boron), 1 × 10^{15} (boron), and 3 × 10^{14} cm^{-3} (phosphorus), respectively. The polysilicon films are not intentionally doped.

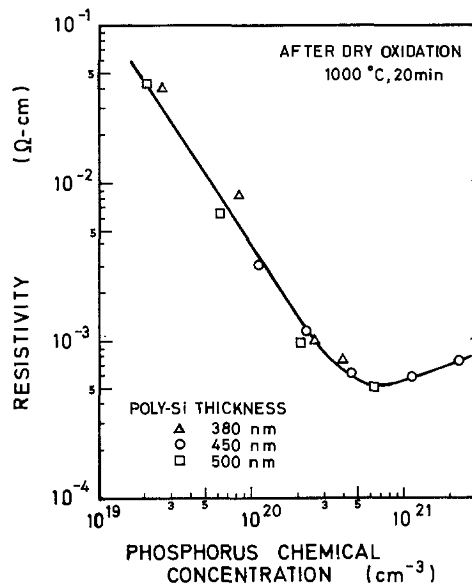

Fig. 6. Resistivity of phosphorus-implanted polysilicon films, 380-500 nm thick, deposited on oxidized silicon substrates. The films were annealed in dry oxygen at 1000°C for 20 min prior to resistivity measurements.

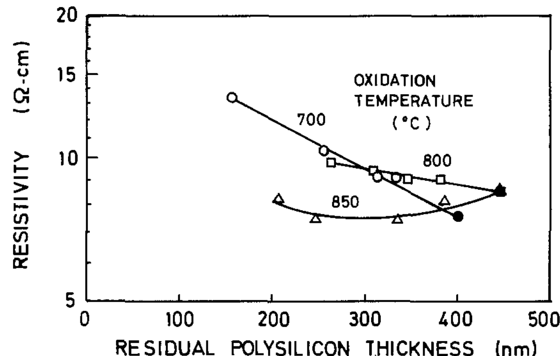

Fig. 7. Resistivity changes of polysilicon films doped with phosphorus (3 × 10^{20} cm^{-3}) associated with the wet oxidation (90°C H_2O). Solid symbols denote the initial conditions of polysilicon doped with phosphorus prior to the oxidation. Annealing at 1000°C for 5 min in nitrogen was added prior to resistivity measurement only in the case of 700°C.

atoms become segregated and electrically inactive. Therefore, annealing of 1000°C for 5 min in nitrogen ambient was introduced prior to resistivity measure-

ment in order to make the atoms electrically active, only in the case of 700°C.

Discussion

The effect of heavy doping on the initial oxide kinetics.—The linear rate constant B/A and the parabolic rate constant B were evaluated based on the general relationship for thermal oxidation of silicon (1). First, oxide thickness x was plotted *vs.* the value of oxidation time t divided by x. Then, the plots yielded a straight line with an intercept equal to $-A$, and slope equal to B by the least squares fitting technique. Two lines corresponding to phosphorus concentrations of 1.1×10^{21} and 2.2×10^{21} cm^{-3} yielded negative values of A contrary to the observations by Deal and Grove for wet oxidation (1). This result suggests the generation of an "initial oxide" which does not obey linear-parabolic kinetics for some cases of thermal oxidation with heavily doped silicon even for wet oxidation. The existence of an initial oxide gives rise to not only the negative values of A but also values of n greater than 2 previously mentioned.

To evaluate initial oxide thickness x_i, a plot of x^2 *vs.* t is made and shown in Fig. 8. The lines corresponding to phosphorus concentrations of 1.1×10^{21} and 2.2×10^{21} cm^{-3} show an almost true linear slope and yielded x_i^2 at $t = 0$ and initial oxidation time t_i at $x^2 = 0$. This initial oxidation regime was shown in Yeh's experimental data in the case of steam oxidation of phosphorus-doped (111) substrates (15). However, Deal and Sklar (5) concluded that this correspondence was attributed not to the concept of initial oxide but to an initial porous oxide present on the phosphorus-diffused surface. Values of x_i obtained are shown in Table I for the present work in comparison to Yeh's experiments.

The linear rate constant B/A and the parabolic rate constant B were evaluated for wet oxidation of phosphorus-doped polysilicon films at 750°C. These rate constants are shown in Fig. 8 considering initial oxidation regime for phosphorus concentrations of 1.1×10^{21} and 2.2×10^{21} cm^{-3}. With increasing phosphorus concentrations greater than 1×10^{20} cm^{-3}, B/A increases sharply. Besides, B increases only by a factor of 10 and then becomes saturated.

CDO can be divided into two regimes. One regime is derived from the enhancement of diffusion of oxidizing species due to phosphorus atoms incorporated in the oxide. The other is derived from the enhancement of surface reactions due to the catalytic behavior of phosphorus atoms. The results obtained shown in Fig. 9 indicate that the catalytic reaction becomes relatively

Table I. Initial oxide thicknesses, x_i evaluated from Yeh's (15) experiments and obtained in this work

Reference	Oxidation ambient	Oxidation temperature (°C)	Substrate	Phosphorus concentration (cm^{-3})	t_i (min)	x_i (nm)
Yeh (15)	H_2O	970	(111)	2.0×10^{21}	7*	162*
This work	O_2-H_2O	750	Polysilicon	2.2×10^{21}	32	156
				1.1×10^{21}	23	123

* Calculated from Yeh's (15) values of oxide thicknesses as a function of oxidation time.

dominant compared to the saturated parabolic rate constant especially in the region of higher phosphorus concentrations.

It is speculated that very rapid oxidation, giving rise to an initial oxide, may originate from the formation of P_2O_5 glass due to accelerated outward diffusion of phosphorus atoms in the very early stages of oxidation. Furthermore, an excess of phosphorus atoms implanted into polysilicon films greater than the solid solubility may take part in the P_2O_5 formation. Preliminary ion-probe microanalysis showed that the highest phosphorus concentration was located at the surface of the oxide exposed to the oxidation ambient and thus may support the above speculation. The "initial oxide," which forms during dry oxidation, has similar characteristics to initial oxide found in the present study, although they are derived from different mechanisms.

Effects of impurity redistribution and crystallinity.—It is well known that phosphorus atoms pile up at the silicon surface during thermal oxidation, resulting in higher surface concentrations. This "pile-up" is most pronounced in wet oxygen and/or at lower oxidation temperatures (15, 16). In wet oxidation of single crystal silicon at 750°C, the ratio of the phosphorus concentration in silicon near the oxide-silicon interface to the bulk concentration (C_s/C_B) is estimated to be greater than 10 assuming that the segregation coefficient and the diffusivity of phosphorus still hold. In addition, diffusivity increases significantly at higher concentrations and especially in polysilicon (17). Since the diffusivity of phosphorus in polysilicon is several times greater than that in single crystal silicon, the value of C_s/C_B for polysilicon is expected to be far less than that for single crystal silicon. The re-

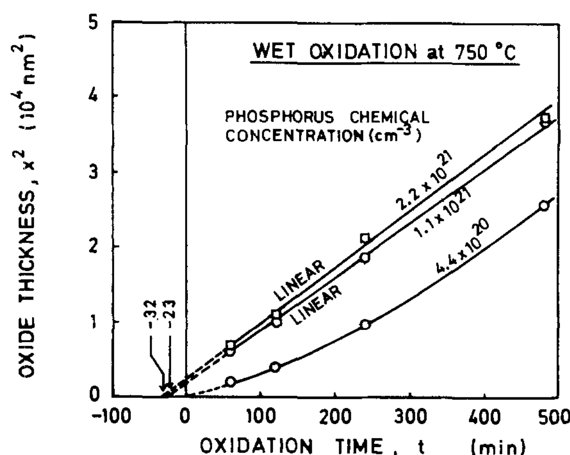

Fig. 8. Evaluation of initial oxide thickness x_i for thermal oxidation of phosphorus-doped polysilicon in wet oxygen (90°C H_2O) at 750°C. The lines for concentrations of 1.1×10^{21} and 2.2×10^{21} cm^{-3} show almost true linear slopes and yield values of x_i^2 at $t = 0$ and values of t_i at $x^2 = 0$.

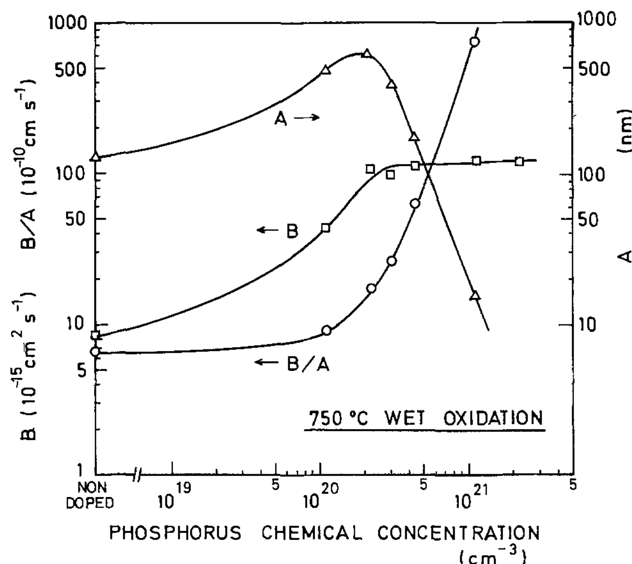

Fig. 9. Phosphorus concentration dependences of the linear rate constant B/A and the parabolic rate constant B for wet oxidation (90°C H_2O) of polysilicon films at 750°C.

sistivity changes obtained for phosphorus-doped polysilicon associated with the wet oxidation were very small as shown in Fig. 7. This was not expected from the value of C_S/C_B for single crystal silicon. Resistivity should decrease significantly following thickness reduction if the pile-up occurs for polysilicon similar to the predicted redistribution for single crystal silicon. Consequently the impurity redistribution in phosphorus-doped polysilicon associated with the wet oxidation may be relatively negligible compared to single crystal silicon.

Rate constants evaluated for different faces of single crystal silicon and polysilicon are shown in Table II for 750°C wet oxidation. The linear rate constant increases in the order (100), (111), polysilicon, and (110). The linear rate constant values obtained, shown in Table II, agree qualitatively with the relative order of the surface density of silicon bonds which are available to the water molecules (18, 19). Crystal orientation of the majority of grains in polysilicon films is highly affected by the film deposition technique (20). From transmission electron microscopy, the orientations of the majority of the grains were found to be <111> and <110>. This fact is consistent with the order of the rate constants for polysilicon and (111) and (110) faces of single crystal silicon.

The thermal oxidation of polysilicon in wet oxygen is similar to that of single crystal silicon considering that the resistivity changes of phosphorus-doped polysilicon and the crystal orientation effect on oxidation. In addition, neither penetration of oxide along grain boundaries nor grain growth were found associated with the wet oxidation with scanning electron microscope observations for cleaved surfaces of the film.

Oxide quality in this work.—Temperature dependence of the linear and the parabolic rate constants evaluated from the data plotted in Fig. 3 and 4 are shown in Fig. 10 and 11, respectively, over the temperature range from 700° to 850°C. Wet oxidation characteristics using a water bubbler in this work are compared with previous works (1, 2), particularly for a contamination effect. Concerning the contamination effect, Revesz and Evans (2) concluded that Na atoms increased the parabolic and linear preexponential factors and activation energies in the temperature range of 920°-1200°C (2, 21). The E_a of the parabolic rate constant B was observed to be 2.30 eV for lightly doped (100) silicon. This value is quite close to 2.29 eV for Na contaminated (111) silicon obtained in Ref. (2). Moreover, the E_a of the linear rate constant B/A for lightly doped (100) silicon was evaluated to be 1.52 eV, slightly less than the reported values of 1.92 eV (1) and 1.91 eV (2). Phosphorus atoms play the important role of Na-getters and presumably reduce the effect of Na on enhanced diffusion of oxidizing species, thus resulting in slower oxidation rates. In this sense it appears consistent that the E_a of B/A increases from 1.52 to 1.86 eV and E_a of B decreases from 2.30 to 1.03 eV due to phosphorus doping of 7×10^{20} cm^{-3}. From the above discussion, it is probable that these oxides in this study may be contaminated with Na to some extent. However, BT stress measurements gave mobile ion (almost Na) densities in the oxides of around 1×10^{11} cm^{-2} (10^{16} cm^{-3} for 100 nm thick oxide). This value obtained is far smaller than that of 10^{20}

Table II. Rate constants obtained for (110), polysilicon, (111), and (100) with 750°C wet oxidation

Face	B/A (10^{-10} cm/sec)	B/A value relative to (110)	B 10^{-14} cm^2/sec)
(110)	8.28	1.00	14.2
Polysilicon	6.70	0.81	8.58
(111)	6.32	0.76	8.89
(100)	4.38	0.53	6.68

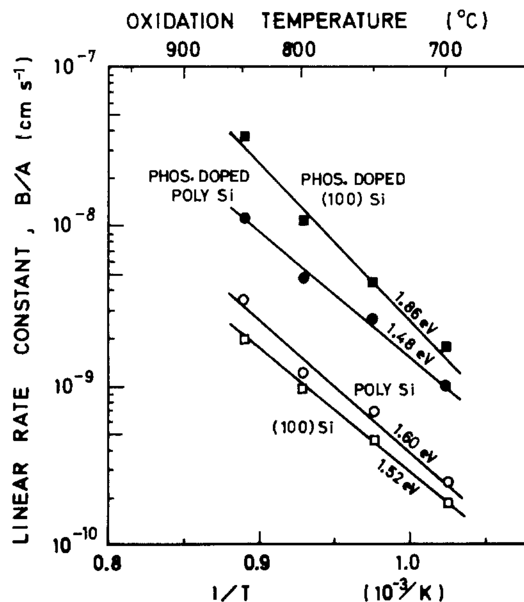

Fig. 10. Temperature dependence of the linear rate constants for wet oxidation: ■, phosphorus-doped (100) silicon (7×10^{20} cm^{-3}); ●, phosphorus-doped polysilicon (3×10^{20} cm^{-3}); ○, nondoped polysilicon; □, lightly boron-doped (100) silicon (1×10^{15} cm^{-3}).

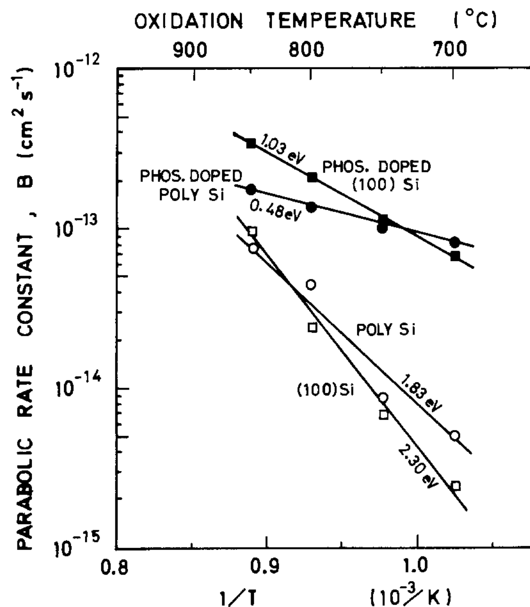

Fig. 11. Temperature dependence of the parabolic rate constants for wet oxidation (90°C H_2O). Others are the same as in Fig. 10.

cm^{-3} in the previous experiment where Na atoms were intentionally doped (2).

While most Na atoms incorporated into the oxide remain inactive (22), Na concentration of 10^{20} cm^{-3} (10^{15} cm^{-2} for 100 nm thick oxide) yielded such enhanced oxidation. As the BT stress measurement can detect only active ions, the result of BT stress measurement is not necessarily inconsistent with the previous results (2). Further investigation should be focused on this point.

Conclusions

It has been shown that thermal oxidation rates of heavily doped polysilicon films (phosphorus concentrations greater than 1×10^{20} cm^{-3}) in wet oxygen at 750°C depend on the phosphorus concentration in the film. The parabolic rate constant saturates at concentrations greater than 2×10^{20} cm^{-3}, while the linear rate constant increases are progressively accelerated.

Above phosphorus concentrations of 1×10^{21} cm^{-3}, very rapid oxidation takes place at the beginning of the oxidation period resulting in "initial oxide" formation. Thicknesses of the initial oxide are observed to be 123 and 156 nm for 1.1×10^{21} and 2.2×10^{21} cm^{-3}, respectively. It is speculated that the initial oxide may originate not from the space charge enhanced oxidation (1) but from growth of P_2O_5 glass which results from the phosphorus atoms exceeding solid solubility at the oxidation temperature.

The resistivity of phosphorus-implanted polysilicon films has a minimum value of 5×10^{-4} Ω-cm for doping concentrations of around 6×10^{20} cm^{-3} after annealing at 1000°C. After the annealing initial grain size of 50 nm was enlarged to 80 and around 1000 nm for concentrations of 1.1×10^{20} and 1.1×10^{21} cm^{-3}, respectively. After wet oxidation film resistivity remains fundamentally stable and neither penetration of oxide along grain boundaries nor additional grain growth were observed.

The oxidation rate of lightly doped silicon and nondoped polysilicon increases (100), (111), polysilicon, and (110), in this order. This is consistent with the observation that polysilicon films are oriented between <111> and <110> directions according to transmission electron microscopy.

The activation energies of linear and parabolic rate constants obtained for (100) silicon are 1.52 and 2.30 eV, respectively. The former increases and the latter decreases with phosphorus doping of 7×10^{20} cm^{-3}. These characteristics may lead to speculation that the wet oxidation in this work is possibly contaminated by Na atoms despite the fact that *BT* stress measurement, which can detect only active ions, gave mobile ion densities of around 1×10^{11} cm^{-2}.

Acknowledgments

The author is indebted to Y. Wada for valuable discussions regarding grain growth as well as to N. Hashimoto for his constant encouragement and discussions concerning ion microprobe analysis. The author also wishes to thank S. Nishimatsu and Y. Kamigaki for technical discussions generally concerning thermal oxidation of silicon and H. Usui for performing the ion implantation procedures used in this study.

Manuscript submitted July 29, 1977; revised manuscript received Jan. 3, 1978.

Any discussion of this paper will appear in a Discussion Section to be published in the December 1978 JOURNAL. All discussion for the December 1978 Discussion Section should be submitted by Aug. 1, 1978.

Publication costs of this article were assisted by Hitachi Limited.

REFERENCES

1. B. E. Deal and A. S. Grove, *J. Appl. Phys.*, **36**, 3770 (1965).
2. A. G. Revesz and R. J. Evans, *J. Phys. Chem. Solids*, **30**, 551 (1969).
3. E. A. Irene, *This Journal*, **121**, 1613 (1974).
4. T. Nakayama and F. C. Collins, *ibid.*, **113**, 706 (1966).
5. B. E. Deal and M. Sklar, *ibid.*, **112**, 430 (1965).
6. R. M. Burger and R. P. Donovan, "Fundamentals of Silicon Integrated Device Technology," Vol. 1, Prentice-Hall, Inc., Englewood Cliffs, N.J.
7. J. D. Plummer, Current Conference on Integrated Electronics Technology, American Physics Society Meeting, San Diego, March 1977, or C. P. Ho *et al.*, Future publications.
8. T. I. Kamins and E. L. MacKenna, *Metall. Trans.*, **2**, 2292 (1971).
9. Y. Yasuda, M. Yamakawa, T. Morita, and T. Yoshii, Paper 23 presented at The Electrochemical Society Spring Meeting, Houston, Texas, May 7-11, 1972.
10. C. H. Sequin, D. A. Sealer, W. J. Bertram, Jr., and R. R. Buckley, International Solid State Circuits Conference, Digest of Technical Papers, pp. 24-25, February 1974.
11. C. N. Ahlquist *et al.*, International Solid State Circuits Conference, Digest of Technical Papers, pp. 128-129, February 1976.
12. C. R. Fuller and F. J. Strieter, Paper 74 presented at The Electrochemical Society Spring Meeting, Toronto, Canada, May 3-7, 1964.
13. J. C. Irvin, *Bell Syst. Tech. J.*, **41**, 387 (1962).
14. Y. Wada and S. Nishimatsu, Submitted to *This Journal*.
15. T. H. Yeh, *J. Appl. Phys.*, **33**, 2849 (1962).
16. B. E. Deal, A. S. Grove, E. H. Snow, and C. T. Sah, *This Journal*, **112**, 308 (1965).
17. T. I. Kamins *et al.*, *J. Appl. Phys.*, **43**, 83 (1972).
18. J. R. Ligenza, *J. Phys. Chem.*, **65**, 2011 (1961).
19. R. J. Powell, J. R. Ligenza, and M. S. Schneider, *IEEE Trans. Electron Devices*, **ed-21**, 636 (1974).
20. T. I. Kamins and T. R. Cass, *Thin Solid Films*, **16**, 147 (1973).
21. A. G. Revesz, *Phys. Status Solidi*, **19**, 193 (1967).
22. D. R. Kerr, *IBM J. Res. Dev.*, **8**, 385 (1964).

Oxidation Kinetics of Cobalt Diffusing out of High Current Density (HCD) Plated Gold

J. H. Thomas, III[1]

Bell Telephone, Columbus, Ohio 43213

ABSTRACT

Auger electron spectroscopy and Auger depth profiling techniques have been used to study the growth kinetics of cobalt oxide films which form on thermally aged HCD-plated hard gold in dry laboratory air. Films were observed to grow according to parabolic growth kinetics. At temperatures of 150° and 180°C, a large amount of potassium is observed on the film surface and may be associated with the observed recrystallization in hard gold electroplates. Film growth appears to saturate at 180°C for times greater than 48 hr. A general model was developed for film growth on dilute two-component noble metal alloys exposed to a single reacting gas specie, assuming conservation of the reacting specie (flux continuity at the metal-film interface) and parabolic film growth. The conditions necessary for the film growth to be controlled by diffusion from the alloy are given in terms of the material constants. For this specific case, the general solution reduces to that of an infinite sink and the diffusion constant can simply be computed from the parabolic growth rate constant. The diffusion coefficients for Co in Au were calculated between 100° and 180°C. An activation energy of 1.83 eV was obtained for this process.

With the increased usage of high current density plated gold (HCD) in the electronics industry, it has become necessary to understand and characterize processes by which gold alloy electroplates thermally degrade (1). It has been shown that hard golds exhibit increases in contact resistance (2) presumably due to the diffusion and subsequent oxidation of cobalt (which is used as a hardener) on the gold surface (3). Thermal aging studies in dry air have shown cobalt to oxidize to what appears to be CoO (4). The diffusion coefficients for cobalt diffusing out of hard gold have been determined for HCD gold and LCD (low current density) gold using a model which requires that the controlling process for oxide growth is diffusion (3). The kinetics of oxide formation on noble metal alloys has been studied experimentally by a number of investigators [see Ref. (5) for references], and has been theoretically studied by Wagner (6).

In this paper, the kinetics of CoO growth on HCD-plated hard gold has been studied at temperatures ranging from 75°-180°C. Film growth kinetics have been analyzed using a model for film growth on a dilute noble metal alloy, and film growth rates and the diffusion coefficients for cobalt diffusion out of HCD hard gold have been computed using this model. As a result of model calculations, a more general method of computing corrosion rates due to reactions in a single component gas system and diffusion coefficients in a two component alloy from concentration profiles has been developed.

Experimental

Film thickness measurements and surface analysis of cobalt-hardened HCD gold were analyzed with a Physical Electronics Industries scanning Auger system. This system is equipped with a single pass cylindrical mirror analyzer (CMA), coaxial electron gun, and Varian rastered ion gun. Depth profiles reported in this paper were performed at a pressure of 5×10^{-5} Torr argon at a beam energy of 1 keV. The sputter rate of gold under these conditions was measured as 6.3 Å/min (7). All Auger spectra were obtained at a beam energy of 3 keV and an emission current of 1.8 mA.

Hard gold plating was performed in a production plater. All samples were processed by initially depositing a nickel layer (~2.5 μm) followed by a gold flash. Nominally, 7.3 μm of hard gold from a proprietary Engelhard phosphate plating bath was deposited at current densities of 150-225 mA/cm^2 (depending on sample geometry) on the gold flash. The cobalt concentration as determined by atomic absorption spectroscopy was found to be 0.25-0.26 weight percent (w/o) and was confirmed by quantitative AES. The gold plating thickness was measured by cross-sectioning techniques and was found to range from 6.6 to 8.2 μm. All samples were fabricated on CDA 725 rolled stock which was cleaned prior to electroplating. 1 × 1 in. samples were cut from the 1 in. wide continuous strip for study.

Prior to thermally aging the samples, all samples were cleaned in a trichloroethane vapor degreaser and subsequently in boiling 10% H_2O_2 solution for 3 min. Samples were then thoroughly rinsed in DI water and placed in chemically cleaned petri dishes to protect them from accidental contamination. Thermal treatments were performed for 50, 150, 250, 500, and 1000 hr at 75°, 100°, 125°, and 140°C, respectively, and 6, 24, 48, and 100 hr at 180°C. Samples were stored in a dessicator prior to performing AES measurements. One sample was measured at each time and temperature giving a total of 24 samples. Oven temperatures were stabilized to the desired set point and were found to vary within ±2°C of that set point. All aging was performed in laboratory air.

Results

Typical spectra for 75°/1000 hr, 140°/1000 hr, and 180°/100 hr are shown in Fig. 1 for comparison purposes. The primary contaminants which are characteristic of samples aged at temperatures less than 100°C for 1000 hr are carbon, oxygen, chlorine, and traces of copper and cobalt. The small amount of copper (at 75° and 100°C) may be due to the residue left from a reaction of the copper-based substrate material (CDA 725) with the peroxide cleaning solution. The largest signals are typically carbon and chlorine. During sputter depth profiling, these contaminants are removed within the first few minutes of sputtering. At higher temperatures, 140°C, the main signals observed are due to oxygen and cobalt with some carbon, chlorine, and a trace of potassium (in order of decreasing amplitude). Potassium is not observed at times and temperatures less than 140°C/1000

[1] Present address: RCA David Sarnoff Research Center, Princeton, New Jersey 08540.

Key words: alloy, diffusion, oxidation.

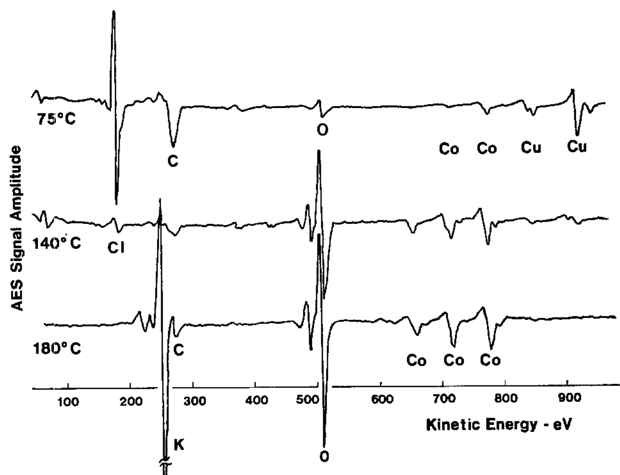

Fig. 1. Auger electron spectra are shown for HCD gold electroplate aged 75°C/1000 hr, 140°C/1000 hr. and 180°C/100 hr.

hr for these samples. With the exception of potassium and signal amplitude, this spectrum is similar to other spectra in the range 100°-140°C. At 180°C, potassium is the strongest Auger signal observed. Large oxygen and cobalt signals are also observed. Potassium is known to be incorporated in gold which is deposited from cyanide gold baths (8). The evolution of potassium from the gold deposit is characteristic of aging at higher temperatures (~140°C). Since Co and O appearing in the 100°-180°C temperature range are the primary surface species (except K at 180°C), the kinetics of CoO formation on the hard-gold surface have been studied in detail.

Figure 2 shows typical depth profiles for gold aged at 100°C and 140°C for 1000 hr and 180°C for 48 hr. At 100°C, contamination (film formation) appears to be limited to the surface region. However, Co is clearly observed. At times and temperatures less than this, cobalt is only observed in trace amounts. In the 140°C depth profile, cobalt and oxygen are observed to track in signal amplitude as has been observed by other investigators (3, 4). At 180°C, the potassium signal tracks the oxygen signal. Thus, it is likely that potassium is chemically involved in the film. Consequently, these films are not simply oxide films as observed from 100° to 140°C. At times less than 48 hr, at 180°C the films are similar to those in the range 100°-140°C. In all the data shown it is significant that the substrate materials (copper and nickel) are conspicuously absent. This indicates that for the times and temperatures studied, substrate diffusion is not an important mechanism.

To study film growth kinetics, the film thickness was measured as the sputtering time required for the cobalt Auger signal amplitude to reach ½ its peak signal amplitude. This method of film thickness determination was used consistently for each sample. Sputter times (at ½ the peak Co signal amplitude) were converted to film thickness by assuming the sputter rate for Co to apply to CoO. The sputter rate for Co relative to Au is 0.5 (9). Figure 3 summarizes the film thickness, determined in this way, for 100°, 125°, 140°, and 180°C data as a function of time. A CoO film is assumed for 180°C, 48 and 100 hr films. At 100°C, a marginally measurable CoO film is observed. Therefore, only one point is shown (5Å thickness at 1000 hr) and represents the detectability limits of the system. At 180°C, a scale change (2) is indicated. The CoO film thickness is observed to increase with time and temperature with what appears to be a parabolic dependence on time. At 180°C, after 48 hr, the film thickness (~200Å) does not appear to increase with time. If all the cobalt is assumed to diffuse to the gold surface and oxidize, a film thickness of ~750Å would be obtained (for 0.26 w/o Co). These data in-

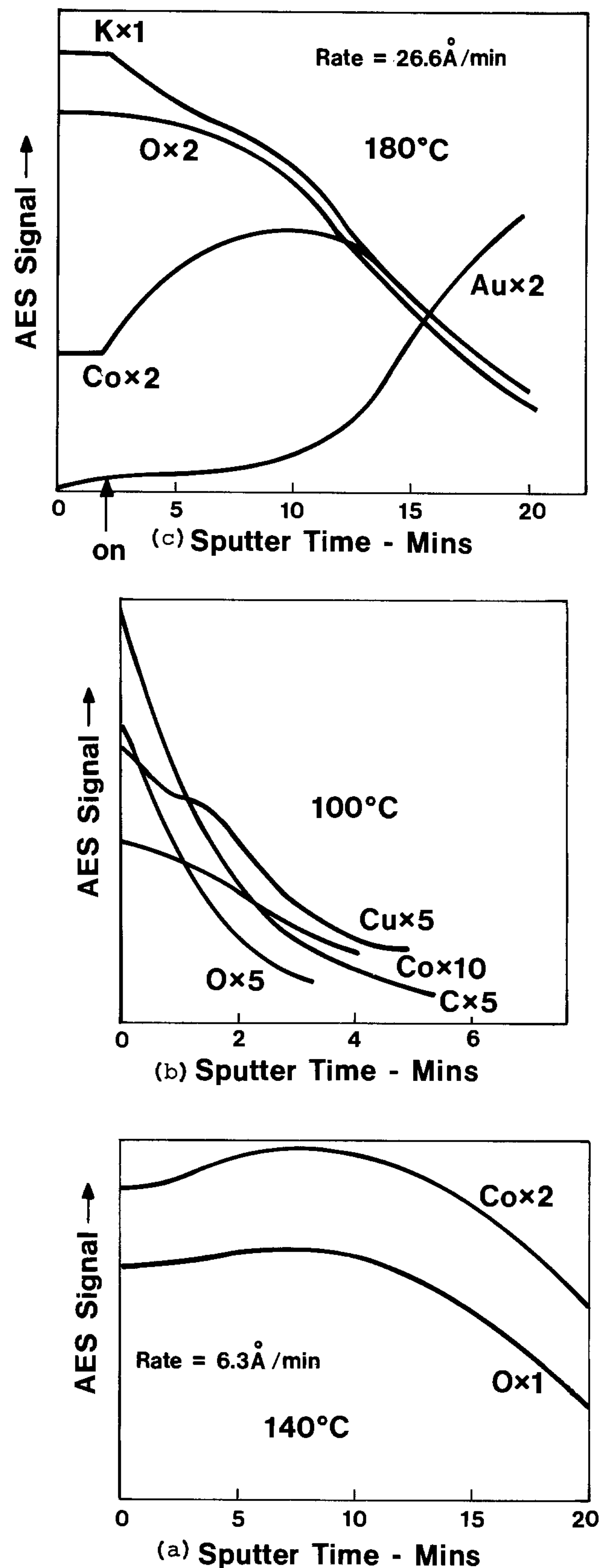

Fig. 2. Depth profiles are shown for 100°C/1000 hr, 140°C/1000 hr, and 180°C/100 hr. Auger signal amplitude is plotted as a function of film thickness using gold as a reference and correcting the rate to that of cobalt metal (as an approximation). (A) and (B) were sputtered at 6.3 Å/min. (C) was sputtered at 26.6 Å/min.

dicate that 27% of the total amount of cobalt has actually been oxidized. It is likely that the oxide observed on the gold surface is due to the oxidation of cobalt which diffuses to the surface easily (probably

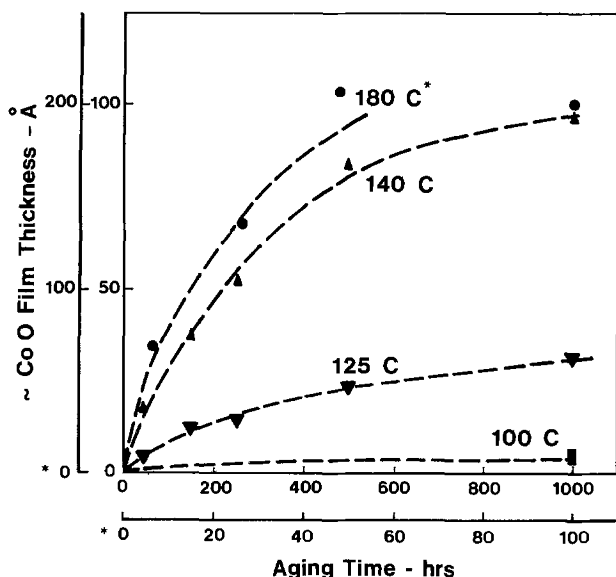

Fig. 3. Film thickness is plotted as a function of time with thermal aging temperature as a parameter. CoO thickness is determined from the sputter time required to reduce the Co signal to 1/2 its peak amplitude.

from grain boundaries). The remaining cobalt is probably in the gold metal lattice and thus would diffuse at a slower rate.

Model

To analyze the data presented in Fig. 3, a model has been developed for film growth on dilute noble metal alloys which incorporates the film growth rate of a reacting species (B) from the alloy. A sketch of the model is shown in Fig. 4 where the two-component alloy (A,B) is contained in the left-hand plane, that is, the alloy is assumed infinite in extent. The oxidized species concentration, $C(x,t)$, is shown as a function of x, the depth into the alloy. The alloy surface is assumed to be fixed at $x = 0$. After a time, t, an oxide $x_f(t)$ in thickness grows which contains C_o mole fraction of the oxidized species, B. C_o is assumed to be constant, that is, the oxide is assumed to grow stoichiometrically from $t = 0$. Fick's second law

$$D\frac{\partial^2 C(x,t)}{\partial x^2} = \frac{\partial C}{\partial t}, \quad x \leq 0 \qquad [1]$$

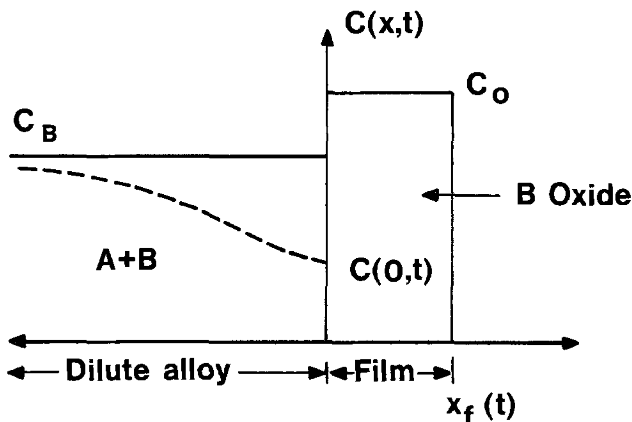

Fig. 4. A semi-infinite model is shown for noble metal alloy oxidation which contains a reactive specie. Fick's second law was solved using the boundary conditions as shown for the concentration of the reactive specie $C(x, t)$ for $x \leq 0$. C_B = bulk concentration of B in A; C_o = concentration of B in oxide (or film); x_f = film thickness. Solve Fick's second law with the initial condition that $C(x, 0) = C_B$ and the boundary conditions that $C(x, t) = C_B$, $x = -\infty$ and $D\, \partial C/\partial x_{x=0} = C_o\, dx/dt$.

is solved for the initial condition $C(x,0) = C_B$, where C_B is the bulk concentration of the oxidized species, D is the diffusion coefficient of the species in the alloy, and C is the concentration. One boundary condition is that at $x = -\infty$, $C(-\infty, t) = C_B$, that is, the concentration at $x = -\infty$ is fixed. The second boundary condition is derived from the conservation of the oxidized species [see Ref. (10)] for films which form according to parabolic growth kinetics (5), that is

$$x_f^2 = k_c t \qquad [2]$$

where k_c is the parabolic growth constant (cm²/sec). The boundary condition reduces to a condition relating the flux of B at the interface to the time dependence of the film growth on the surface (10)

$$D\frac{\partial C}{\partial x}\bigg|_{x=0^-} = C_o\frac{dx_f}{dt} = C_o\frac{k_c}{2x_f} \qquad [3]$$

Fick's second law for this problem is solvedThetaking the Laplace transform in time and applying the above initial condition and boundary conditions (11, 12). The solution in the Laplace variable, p, is

$$C(x,p) = -C_o\sqrt{\frac{p}{D}}\tilde{x}_f(p)\exp\left[x\sqrt{\frac{p}{D}}\right] + \frac{C_B}{p} \qquad [4]$$

where $\tilde{x}_f$ is the Laplace transform of $x_f(t)$. For the parabolic case of film growth, $x_f^2 = k_c t$, the Laplace transform is

$$\tilde{x}_f(p) = \sqrt{\frac{k_c \pi}{4}}\, p^{-3/2} \qquad [5]$$

The solution $C(x, t)$ is readily obtained by taking the inverse transform of Eq. [4] with Eq. [5] and is

$$C(x,t) = -C_o\sqrt{\frac{\pi k_c}{4D}}\,\mathrm{erfc}\left[-\frac{x}{2\sqrt{Dt}}\right] + C_B \quad x \leq 0 \qquad [6]$$

This solution is similar to Wagner's solution (6) for alloy oxidation when he assumes a nonmoving metal-oxide boundary.

Of particular interest is the concentration $C(0, t)$ at the alloy film interface. Equation [6] reduces, for $x = 0$, to

$$C(0,t) = C_B - C_o\sqrt{\frac{\pi k_c}{4D}} \qquad [7]$$

Thus, for a given set of material properties, k_c, D, C_o, and C_B the concentration, $C(0, t)$, is fixed. If $C(0, t)$ can be measured, since C_o and C_B are known, the ratio of k_c/D can be determined from Eq. [7]. Now consider two cases for Eq. [7]

$$C(0,t) > 0 \qquad [8]$$

and

$$C(0,t) \leq 0 \qquad [9]$$

When $C(0, t)$ is greater than zero, the concentration is dependent on both k and D. Therefore, the oxidation rate does, in part, control the film growth rate (simply the case of a finite sink). When $C(0, t)$ is less than zero, (which is physically impossible), the film should cease to grow until more material diffuses to the surface. Therefore, the limiting case for film growth is $C(0, t) = 0$. This is the case of the infinite sink (3), that is, all the material which diffuses out is immediately oxidized. In this situation, the concentration is solely dependent on the diffusion of specie B in the alloy. It can easily be shown that Eq. [6] reduces to a function of D only when $C(0, t) = 0$. C_B is then related to C_o, k_c, and D by Eq. (7). The film growth equation is then rewritten as

$$x_f^2 = \frac{4}{\pi}\left[\frac{C_B}{C_o}\right]^2 Dt \qquad [10]$$

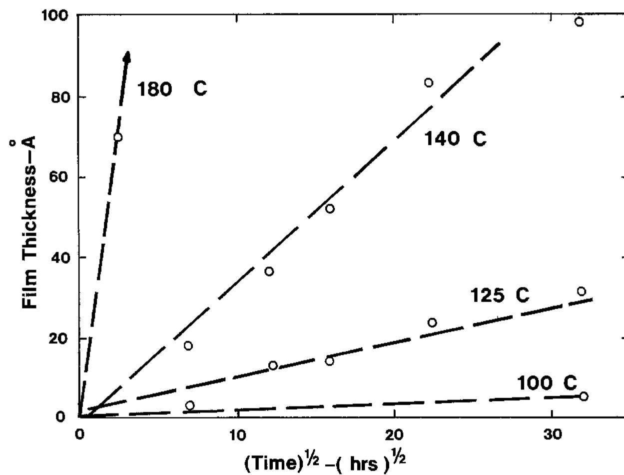

Fig. 5. Parabolic model $x = K_0 t$ data shown in Fig. 3 are replotted on x_f vs. $t^{1/2}$ coordinates, where x_f = film thickness and t = time.

x_f is simply a function of $\sqrt{Dt}$ for an infinite sink situation and k_c is $4/\pi \times (C_B/C_o)^2 D$. This model reduces to the case studied by Wagner (6) and more recently by Tompkins (3) in the limit of a diffusion-controlled process.

Analysis

The film thickness data shown in Fig. 3 can be used to compute both the corrosion rate constant, k_c, and the diffusion coefficient, D, for Co in Au as a function of temperature. If the film grows according to parabolic kinetics (Eq. [2]), the data should plot linearly on x_f vs. $t^{1/2}$ coordinates. Data of Fig. 3 are replotted in Fig. 5. Points have been least squares fitted to straight lines which are shown as dashed lines. Since the 100°C data consists of only one point, a line was drawn through this point. These data fit a straight line rather well. The slopes of the straight lines give directly the corrosion rate constant k_c as a function of temperature. This is summarized in Table I. Along with these data, Gulbransen and Andrew's (13) corrosion rates for cobalt metal, obtained by extrapolating their data to 100°C, have been included for comparison.

To obtain the diffusion coefficient for Co in Au from these data, k_c must be multiplied by the factor $\pi/4\ (C_o/C_B)^2$. This constant for 0.25-0.26 w/o Co in gold and CoO formation is 3500. An accurate determination of $C(0, t)$ was not performed in this study. However, experimentally $C(0, t)$ is observed to decrease, that is, the Co Auger signal decreases at what appears to be the film-alloy interface. It is assumed that this model for $C(0, t) = 0$ can be used to approximate the real system. In that case, D is directly obtained and is summarized in Table I.

To demonstrate the usefulness and validity of this model, D was also computed using Tompkins' model which was developed for an infinite sink assumption. Using his empirical relationship between film thickness and Dt, D was computed for each time and temperature. D was then arithmetically averaged at each temperature and is listed in Table I. Comparing D obtained from the corrosion rate constants or the slope of x_c vs. $t^{1/2}$ with values of D computed using Tompkins' empirical equation (3) shows excellent agreement. D ranges from 0.9×10^{-13} cm²/sec at 180°C to 2.4×10^{-18} cm²/sec at 100°C.

Finally, since D is activated, that is, $D \propto \exp(E_A/kT)$, the activation energy for the diffusion of cobalt out of HCD gold can be determined from an Arrhenius plot. Figure 6 shows D plotted as a function of $1/T$ (in °K)$^{-1}$. A straight line can be drawn through these points and the activation energy was computed from the slope of this line as 1.83 eV. This value is much higher than the value of 1.24 eV obtained by Tompkins (3) for LCD-plated cobalt-hardened gold. This determination is independent of an absolute measure of film thickness, that is, these values are only dependent on the slope of x_f vs. $t^{1/2}$.

Activation energy for diffusion can be computed accurately from a knowledge of the relative film thickness. Absolute values of D, however, require an accurate measurement of film thickness and when using Auger depth profiling for this purpose, an accurate measurement of the relative sputter rate of CoO with respect to gold is needed.

Table I

Temperature (°C)	Corrosion rate constant (k_c (cm²/sec))	Gulbransen-Andrew (k_c on Co)	Diffusion coefficient* (D_{Co-Au} (cm²/sec))	Diffusion coefficient** (Tompkins model) (cm²/sec)
100	7.0×10^{-22}	3.8×10^{-20}	2.4×10^{-18}	5.7×10^{-18}
125	5.4×10^{-20}	1.3×10^{-19}	1.9×10^{-16}	2.1×10^{-16}
140	3.2×10^{-19}	2.5×10^{-19}	1.1×10^{-15}	$2\ 3 \times 10^{-15}$
180	2.5×10^{-17}	2.0×10^{-18}	0.9×10^{-13}	1.9×10^{-13}

* From slopes.
** $F = 2.26\ \sqrt{Dt}/h^2$.

Conclusions

Auger electron spectroscopy has been employed to study thermally aged HCD hard-gold electrodeposits. At temperatures below 100°C, little film forms on the surface of the gold plate as measured by AES depth profiling. Typical surface contaminants observed by Auger are carbon, chlorine, oxygen, and traces of cobalt and copper. It is possible that small amounts of copper come from the H_2O_2 cleaning process. At 100°C/1000 hr and at higher temperatures cobalt and oxygen are observed to be the major surface species as observed in previous thermal aging studies. At 140°C/1000 hr and 180°C, potassium is observed to evolve.

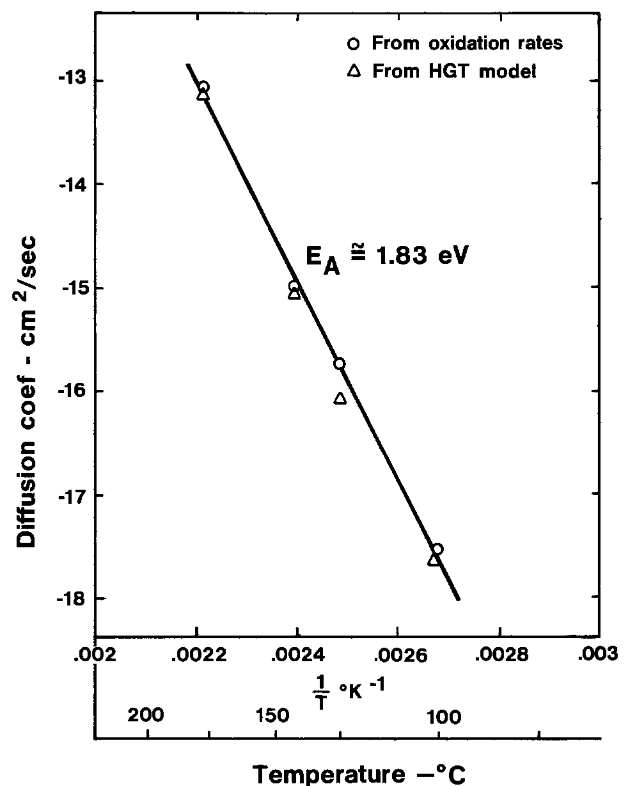

Fig. 6. The computed diffusion coefficient, D, for cobalt diffusion in hard gold is shown as a function of (temperature)$^{-1}$. From the slope of this data, the activation energy for D is 1.83 eV.

Kinetics of this process are presently being studied. It is likely that the potassium evolution which forms a substantial film with cobalt and oxygen, may be related to recrystallization around 150°C (14). It was also observed that only part of the available cobalt is oxidized at temperatures below 180°C. This is possibly due to the release and subsequent oxidation of an inter-granular cobalt species (14).

A model has been developed to analyze the kinetics of CoO film formation on the cobalt-hardened gold electroplate. Fick's second law was employed to derive a model for parabolic film growth on a dilute two-component noble metal alloy. Solutions of this equation show that the infinite sink model (that is, when all the oxidized species is oxidized as soon as it arrives at the surface or when $C = 0$ at the interface) is a special case of this more general model. In general, film growth is found to depend on both the diffusion of cobalt out of hard gold and the oxidation rate of cobalt. This model allows one to compute k_c/D if $C(0, t)$, C_B, and C_0 are known by experimental measurements.

Kinetic data for CoO formation on hard gold were analyzed using this model in the limit of $C = 0$ at the interface (infinite sink) for a parabolic film growth model. Data were shown to fit the parabolic growth model and, using this model, the diffusion coefficient of Co in Au was calculated. D ranges from $\sim 1 \times 10^{-13}$ to $\sim 3 \times 10^{-18}$ cm²/sec for 180° to 100°C, respectively. The activation energy for cobalt diffusion out of gold was calculated to be 1.83 eV. This calculation was made by using the slopes of the x_f *vs.* $t^{1/2}$ data, and hence, is independent of an absolute knowledge of film thickness. A finite model is presently being developed by S. P. Sharma and the author (15). D was also computed using Tompkin's empirical equation and was shown to agree closely with this model.

Acknowledgments

The author is indebted to Mr. G. Pigg for supplying the hard-gold samples used in this study. He also wishes to thank E. T. Ratliff, and especially L. L. Hines, for their technical assistance and F. E. Bader for his comments regarding this manuscript. The efforts of and numerous enlightening discussions with S. P. Sharma concerning the development of the model are most gratefully acknowledged.

Manuscript submitted Oct. 14, 1977; revised manuscript received Jan. 3, 1978.

Any discussion of this paper will appear in a Discussion Section to be published in the December 1978 JOURNAL. All discussions for the December 1978 Discussion Section should be submitted by Aug. 1, 1978.

Publication costs of this article were assisted by Bell Laboratories.

REFERENCES

1. R. P. Goel and F. E. Bader, *This Journal*, **123**, 1242 (1976).
2. M. Antler, Private communication.
3. H. G. Tompkins, *This Journal*, **122**, 983 (1975).
4. J. H. Thomas, *IEEE Trans Parts, Hybrids, Pack.*, **PHP-12**, 255 (1976).
5. K. Hauffe, "Oxidation of Metals," Plenum, New York (1965).
6. C. Wagner, *This Journal*, **99**, 369 (1952).
7. H. G. Tompkins, Private communication.
8. T. A. Davies and P. Watson, *Plating*, **60**, 1139 (1973).
9. N. Laegreid and G. K. Wehner, *J. Appl. Phys.*, **32**, 365 (1961).
10. A. S. Grove, "Physics and Technology of Semiconductor Devices," Chap 3, John Wiley & Sons, New York (1967).
11. J. Crank, "The Mathematics of Diffusion," Oxford University Press, London (1970).
12. H. S. Carslaw and J. C. Jaeger, "Conduction Of Heat In Solids," Oxford University Press, London (1959).
13. E. A. Gulbransen and K. F. Andrew, *This Journal*, **98**, 241 (1951).
14. Ch. J. Raub, H. R. Khan, and J. Lendvay, *Gold Bull.*, **9**, 123 (1976).
15. S. P. Sharma and J. H. Thomas, Paper submitted to *This Journal*.

Properties of Al_2O_3 Films Deposited from the $AlCl_3$, CO_2, and H_2 System

V. J. Silvestri,* C. M. Osburn,* and D. W. Ormond*

IBM Thomas J. Watson Research Center, Yorktown Heights, New York 10598

ABSTRACT

Films of aluminum oxide (Al_2O_3) have been deposited in a hot-walled chemical vapor deposition reactor using $AlCl_3$, CO_2, and H_2 gas. The deposition rate and film properties such as structure, composition, index of refraction, dielectric strength, and electrical conductivity were evaluated as a function of deposition temperature and gas input rates. Although the dielectric strength increased with decreasing grain size, the electrical conductivity was better correlated to deposition temperature than to grain size. Conditions were determined to optimize the dielectric strength of films grown in the temperature range 700°-900°C. Depending on the exact conditions, the deposition rate could be limited by either the $AlCl_3$ or the CO_2 input rate.

The initial use of gas phase hydrolysis of $SiCl_4$ with a mixture of H_2 and CO_2 gases to form SiO_2 was demonstrated by Steinmaier and Bloem (1) and Tung and Caffrey (2). Following this and using $AlCl_3$ instead of $SiCl_4$, polycrystalline films of Al_2O_3 have been deposited by a number of investigators (3-6). The most recent and extensive of these studies is that of Iida and Tsujide (6) and Kamoshida *et al.* (7-9) who studied films over a temperature range of 400°-1000°C. The dielectric properties of films using this process have also been reported (10-13). In general electrical properties were evaluated for films deposited using a fixed gas composition. This present study has made an effort to: (*i*) characterize deposition rates over a large range of system parameter changes (temperature, CO_2 and $AlCl_3$ input partial pressures); (*ii*) evaluate

* Electrochemical Society Active Member.
Key words: insulator, current, ellipsometry, CVD.

how these process variables can alter film properties such as structure, composition, index of refraction, dielectric strength, and electrical conductivity; and (*iii*) correlate the observed electrical properties with the structure of the films.

Experimental

The Al_2O_3 films were grown by chemical vapor deposition employing gas mixtures of $AlCl_3$, H_2, and CO_2 in a nitrogen carrier gas. The deposition took place in a resistance-heated, double-wall quartz tube. The inner tube was 100 cm in length and 5 cm in diameter. The $AlCl_3$-N_2 and H_2-CO_2-N_2 gas mixtures were introduced through separate lines into the reaction tube. There they could mix over a heated furnace length of 53.3 cm prior to the deposition zone. The Al_2O_3 was generally deposited on 2 Ω-cm, p-type Si wafers oriented in the <100>. Characteristically six 3.2 cm diam Si substrates were loaded horizontally along a holder for a film deposition. Details of the experimental systems have been reported elsewhere (14). In the present investigation the experimental parameters varied and their ranges were: substrate temperature (T_S), 730°-915°C; $AlCl_3$ input rate in moles per minute (n_{AlCl_3}/min) from 2.4×10^{-4} to 1.1×10^{-3}; and CO_2 input rate in moles per minute (n_{CO_2}/min) from 3.9×10^{-4} to 6.2×10^{-2}. The $AlCl_3$ input rates were varied by changing the temperature of the $AlCl_3$ evaporator over the range of 115°-130°C. The mole per minute input rate for CO_2 represents a range of flow of from 10-1500 cm^3/min. The nitrogen main carrier gas flow (f_{N_2}) was maintained at 15.2 liters/min for all experiments, and the flow of hydrogen (f_{H_2}) was kept at 3.8 liters/min. The average linear gas stream velocity for a typical flow rate of 21.5 liters/min corresponded to 18.3 cm/sec calculated at room temperature.

The deposition rate data were taken for a fixed substrate holder position and were monitored by ellipsometrically measuring thickness for a fixed set of conditions. The best thickness uniformity, for the six wafers along the substrate holder, was obtained when the temperature gradient was such that there was a 4°C increase from the center of the first wafer on the upstream side to the center of the last wafer, a distance of 15.2 cm. With such a gradient and a flow rate of 21.5 liters/min, film thicknesses could be kept to within ± 3% over 80% of the area of all six wafers. These results were reproducible to within ± 2% from run to run. If over a series of runs (40-50) the total change (decrease in growth rate) approached 8%, the $AlCl_3$ source was replenished.

Since the $AlCl_3$ source was not always at equilibrium at the carrier gas flows used here, separate experiments were carried out to determine the $AlCl_3$ output in moles per minute for the temperatures and evaporator flows most commonly used. The $AlCl_3$ output was gravimetrically measured by trapping the effluent $AlCl_3$ in a series of cold traps at Dry Ice temperatures for each flow and evaporator temperature of interest.

Several other samples were prepared in separate experiments by Zirinsky (15) of our laboratory using an $AlBr_3$ source with NO and H_2 to deposit films on substrates heated with an rf susceptor.

Film thickness and index of refraction were measured using ellipsometry (14, 16). Film structure was evaluated using transmission electron microscopy (TEM) and low angle x-ray diffraction as described earlier (17, 18). Composition data came from microprobe analysis (14).

The dielectric strength of the films was measured on aluminum-Al_2O_3-Si capacitor structures; typically the capacitor area was 5×10^{-3} cm^2. A linearly varying voltage ramp was applied to a capacitor and the current monitored with an electrometer. The breakdown voltage was recorded when the current jumped to a very high level signifying a shorted capacitor. Since defects (pinholes or particulate inclusions) can lower the breakdown voltage, many capacitors (typically 25) were broken down and the maximum breakdown voltage was taken to be the dielectric strength of a defect free film. Because this dielectric strength varies with the ramp rate, a uniform rate of 0.1 mV/cm-sec was chosen for all measurements.

Results and Discussion

Deposition rate.—Deposition rate was found to be independent of deposition time for all experimental conditions employed and was evaluated as a function of substrate temperature (Fig. 1), CO_2 input rate (Fig. 2), $AlCl_3$ input rate (Fig. 3), and CO_2/$AlCl_3$ ratio (Fig. 4). In Fig. 1 a logarithmic plot of the deposition rate *vs.* $10/T$ (°K) results in a straight line relationship. Also plotted are the data of Doo and Tsang (5) and Iida and Tsujide (6) showing higher deposition rates. Presumably the differences between the present system hot-wall furnace and nitrogen carrier gas and the systems used earlier (rf heated susceptors and hydrogen carrier gas) contribute to the observed growth rate differences. Nevertheless, the activation energy for deposition, −22.8 kcal/mole, is in good agreement with that found by Doo and Tsang (5). The growth rate dependence on temperature is not believed to be associated with a surface rate limitation. Deposition rate data (not included here) show that growth rate is a linear function of flow rate$^{1/2}$. This data supports a mass transport model.

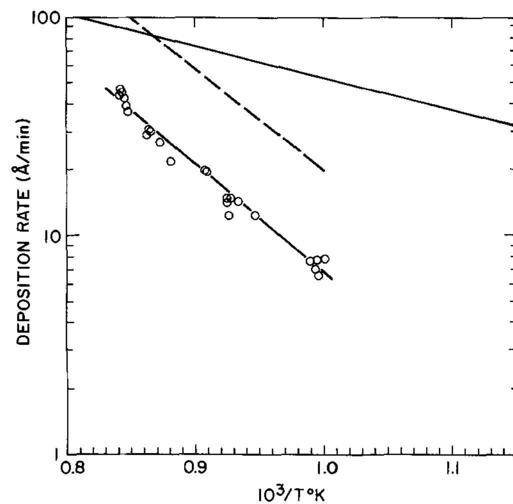

Fig. 1. Deposition rate as a function of substrate temperature, — Iida and Tsujide (6); -- Doo and Tsang (5); ○, present work, n_{AlCl_3}/min = 2.5×10^{-4}, n_{CO_2}/min = 3.85×10^{-3}, n_{H_2}/min = 0.17.

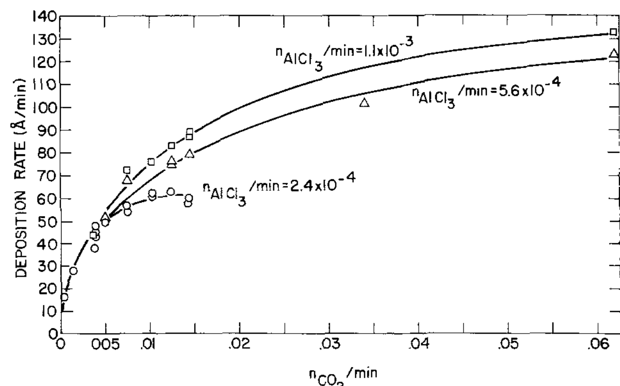

Fig. 2. Deposition rate at 914°C as a function of n_{CO_2} input rate (in moles per minute) for various n_{AlCl_3}/min rates.

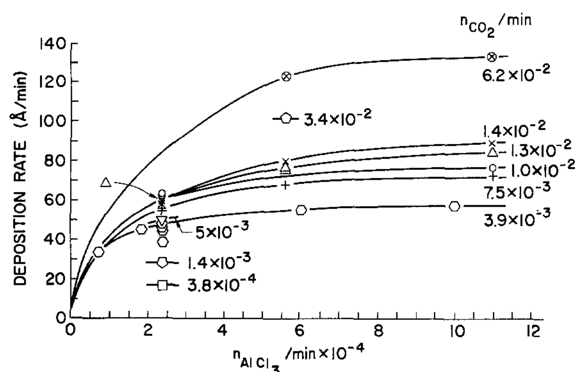

Fig. 3. Deposition rate at 914°C as a function of $AlCl_3$ input rate (in moles per minute) for various n_{CO_2}/min rates from the data taken from Fig. 2. Curve at $n_{CO_2} = 3.9 \times 10^{-3}$ is data obtained from experiments separate from Fig. 2.

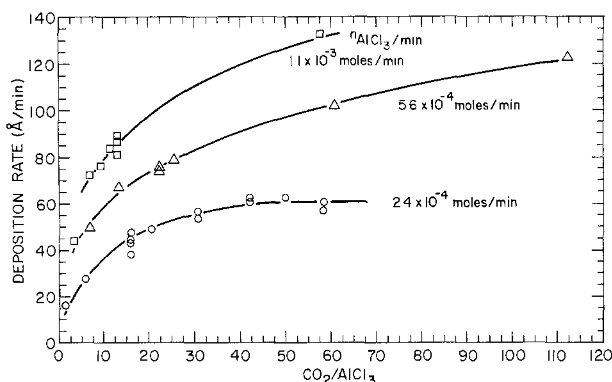

Fig. 4. Deposition rate vs. n_{CO_2}/n_{AlCl_3} ratio derived from Fig. 2

As plotted in Fig. 2 and 3 deposition rate at 914°C appears to be limited by either CO_2 or $AlCl_3$ input rates. In Fig. 2, the growth rate is independent of $AlCl_3$ input but increases steeply as the CO_2 input increases from 0-5 $\times$ 10^{-3} moles/min. When copious amounts of CO_2 are admitted, on the other hand, the deposition rate approaches a constant value determined by the $AlCl_3$ concentration. Similarly in Fig. 3 the data show that the growth rate increases steeply as $AlCl_3$ is admitted to the system but approaches a limit at high $AlCl_3$ flow rates. The data in Fig. 2 and 3 can also be plotted as a function of CO_2 and $AlCl_3$ mole fraction on log-log plots. Deposition rates for such plots show an increase as a function of increasing mole fraction on log-log plots. Deposition rates for $AlCl_3$, respectively. This would indicate a complex chemical system with more than a single rate-limiting step.

In a hot-wall system growth rate is very sensitive to position dependence and flow rate. It has been shown in previous work (14) that a characteristic decrease in growth rate is seen on substrates further

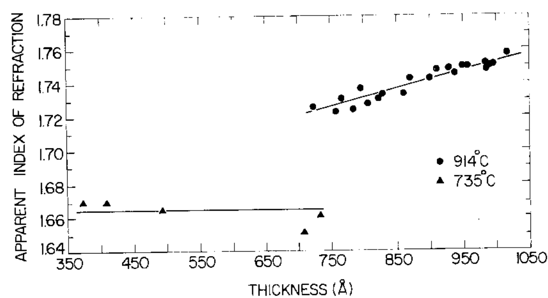

Fig. 5. Apparent index of refraction vs. thickness for films deposited at various temperatures.

downstream. The typical flow for the present experiments ~21.5 liters/min was chosen to keep this observed reduction in growth rate to a minimum over a considerable length (15.2 cm).

The reaction

$$H_2(g) + CO_2(g) = H_2O(g) + CO(g) \quad [1]$$

and the reaction.

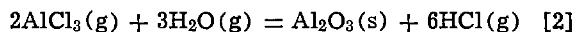

$$2AlCl_3(g) + 3H_2O(g) = Al_2O_3(s) + 6HCl(g) \quad [2]$$

are believed to be operative. From thermodynamic

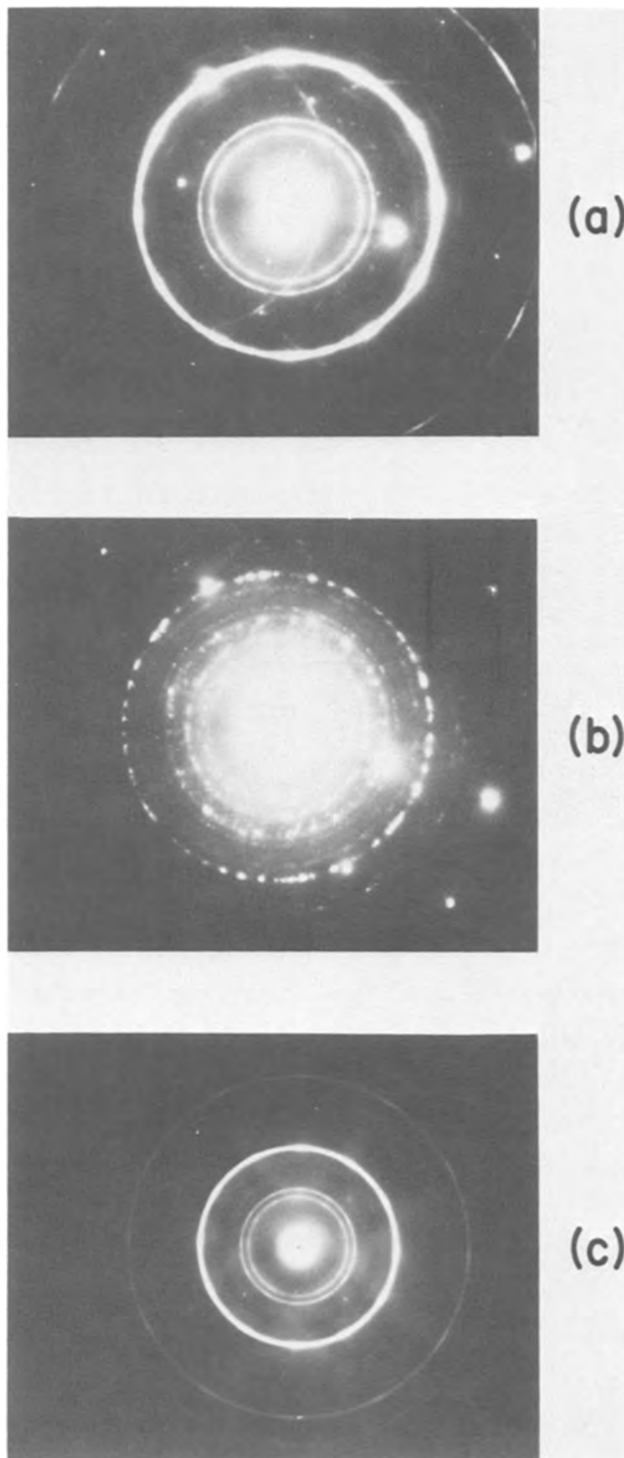

Fig. 6. Electron diffraction patterns: (a) film deposited at 915°C for conditions listed in Fig. 1; (b) film deposited at 808°C for conditions listed in Fig. 1; (c) film deposited at 914°C for n_{AlCl_3}/min $= 1 \times 10^{-3}$ and $CO_2/AlCl_3 = 10$ where maximum dielectric breakdown voltage was observed.

considerations alone, one can say that both reactions [1] and [2] would proceed to the right at 914°C. However, this argument would predict that the deposition rate at constant $AlCl_3$ input would saturate at CO_2/$AlCl_3$ ≈ 1.5. Considerably higher amounts of CO_2 are needed to saturate the reaction (see Fig. 4).

Index of refraction.—If the index of refraction was measured ellipsometrically assuming no absorption, the apparent index was observed to vary with film thickness at high substrate deposition temperatures (Fig 5). The films deposited at low temperature (~700°C) were transparent (*i.e.*, exhibited no haze when viewed with incident light and had an index of 1.665), whereas the high temperature films all exhibited haze to varying degrees and were most likely absorptive. Films grown at lower temperatures (735°C) have been shown to be amorphous by TEM (13) and low angle x-ray diffraction (14), while those grown at higher temperature (914°C) were polycrystalline. The apparent variations of index of refraction with thickness would thus appear to be associated with absorption of light by the polycrystalline films.

Composition.—An assessment of chlorine in films grown at temperatures from 730°-915°C was made using the electron microprobe. The chlorine content of films deposited at 805° and 732°C was 0.0015 and 0.008 weight fractions, respectively, and in agreement with earlier work (6). For films deposited above 900°C, the chlorine was below the detection limit of 0.0008 weight fraction. Carbon was not detected by microprobe analysis having a lower detection limit of 0.01 weight fraction.

Film structure.—The diffraction patterns for Al_2O_3 films grown under various conditions are shown in Fig. 6. Irene *et al.* (17) found the diffraction pattern to correspond most closely to the KI alumina phase described in Ref. (19, 20). Torkar and Krischner (20) attribute this phase to the presence of OH in the Al_2O_3 structure. Since these Al_2O_3 films are prepared in H_2O-rich ambients, the KI phase is most likely; however, it is not possible to unambiguously rule out α-alumina or γ-alumina. Using low angle diffraction techniques, Light *et al.* (18) characterized the films grown at 915°C as polycrystalline and probably γ-alumina having preferred orientation in the <111> direction when deposited on <100> Si surfaces.

Figure 7 shows the TEM grain structures of Al_2O_3 films deposited at different temperatures as well as under conditions giving the maximum dielectric breakdown voltage for the high temperature films. Films grown at low deposition temperatures (735°C) were found to be amorphous. The grain size of the film grown at 808°C appeared in general to be smaller that that found in the 915°C film, however, grain boundaries are not as clearly defined in the low temperature film. The grains in the 915°C film are in the range of 300-500Å.

Electrical properties.—The maximum dielectric strength of the Al_2O_3 films is given as a function of film deposition temperature in Fig. 8 where it can be seen that dielectric strength improves significantly with reduced temperature of growth. The data of Carnes and Duffy (21) and Zirinsky (15) are included for comparison. It is also of interest to note that the conductivity of the films varies with deposition temperature (Fig. 9). At a constant field, films grown at 735°C had 2-2.5 decades higher current density. Also shown in Fig. 8-9 are data from films deposited at 900°C by Zirinsky in a system employing an rf susceptor (cold-wall system) using H_2-NO-$AlBr_3$ gases. Even though the NO-$AlBr_3$, cold-wall sample had superior break-

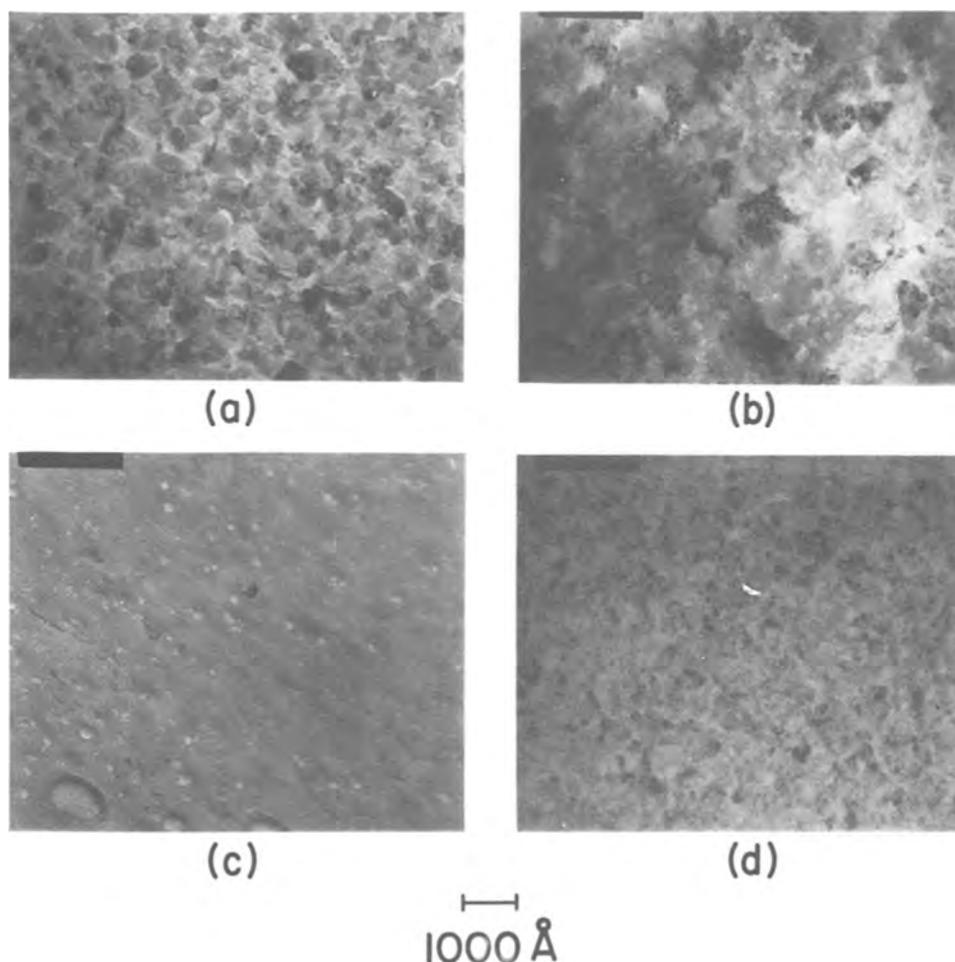

Fig. 7. Electron micrographs of Al_2O_3 films grown at various temperatures (T_S): (a) T_S = 915°C, film whose diffraction pattern is shown in Fig. 6a; (b) 808°C, film whose diffraction pattern is Fig. 6b; (c) 735°C; (d) 914°C, film whose diffraction pattern is shown in Fig. 6c.

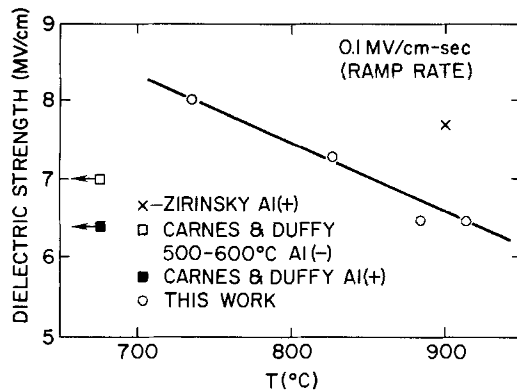

Fig. 8. Dielectric strength vs. deposition temperature for films grown under the conditions listed in Fig. 1.

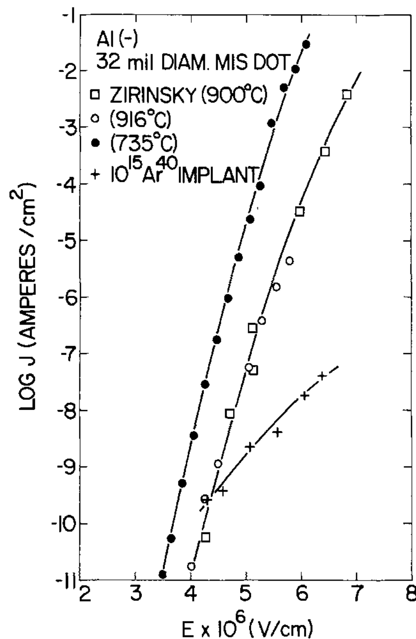

Fig. 9. Conductivity data for film grown under conditions in Fig. 1 compared to films grown using NO and $AlBr_3$, Zirinsky (15).

down strength (Fig. 8), it had the same conductivity. This improved breakdown for low temperature films could be related to the increased amorphous character of the films with reduced deposition temperature. Likewise, the improved breakdown observed for the 900°C sample grown using the NO-$AlBr_3$ process is believed to be related to reduced crystallite size since low angle x-ray techniques indicated that the NO grown films appear to have a similar grain size and more amorphous character than those films grown by the CO_2-$AlCl_3$ process at 808°C. For similar temperatures apparently, the cold-wall NO process tends to produce films having smaller grains and with more amorphous character in comparison to the hot-wall, CO_2 process.

The statistical distribution of breakdown voltage was found to be very dependent on wafer position on the susceptor (Fig. 10) and on the film thickness (Fig. 11). The second substrate in the series of six consistently had the highest breakdown strength (normalized to thickness) and tightest distribution of breakdown voltages. This same film was usually thicker than the preceding or following films. As Fig. 11 shows, thick films (>1000Å) had very tight distributions, while thin films (200Å) showed a bimodal breakdown distribution. While it could be speculated that this behavior is a result of breakdown at grain boundaries, direct substantiation is lacking.

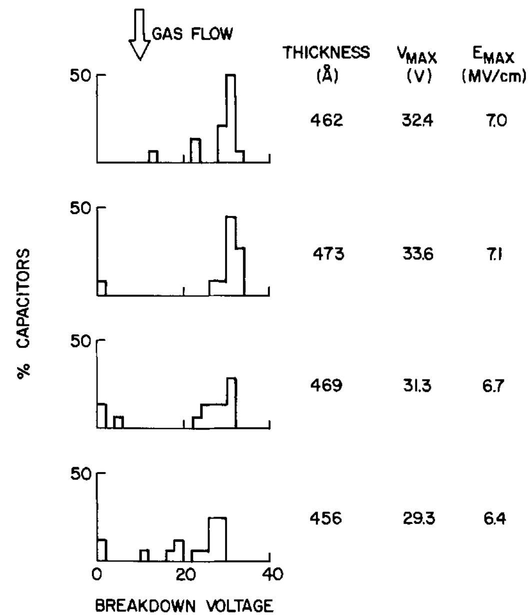

Fig. 10. Statistical distribution of breakdown voltage for different substrate positions in gas stream.

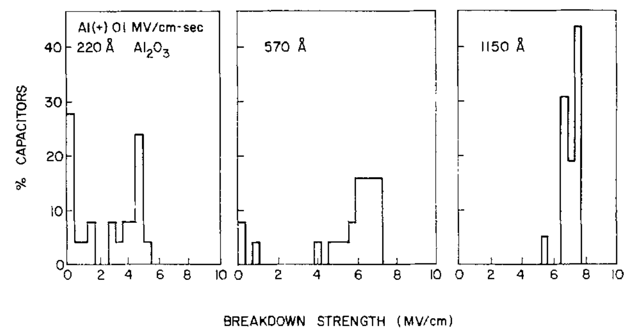

Fig. 11. Statistical distribution of breakdown voltage for different film thickness.

From Fig. 12 dielectric strength is found to be dependent on the ratio of CO_2 to $AlCl_3$ for each $AlCl_3$ source temperature. The optimization, however, does not relate to maximum growth rate (Fig. 4 and 13) but does occur at about 75 Å/min. Figures 7a and d compare the grain structure of two films grown at 915°C. The film in Fig. 7a was grown at $CO_2/AlCl_3$ = 16, had a 400Å grain size, and broke down at 6.5 mV/cm; the Fig. 7d film had 300Å grains, 7 mV/cm breakdown strength, and was deposited at 75 Å/min at $CO/AlCl_3$ of 10.

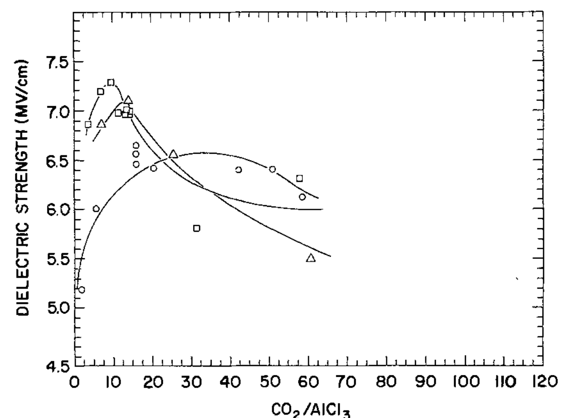

Fig. 12. Dielectric strength vs. $CO_2/AlCl_3$ for the films deposited under conditions in Fig. 2.

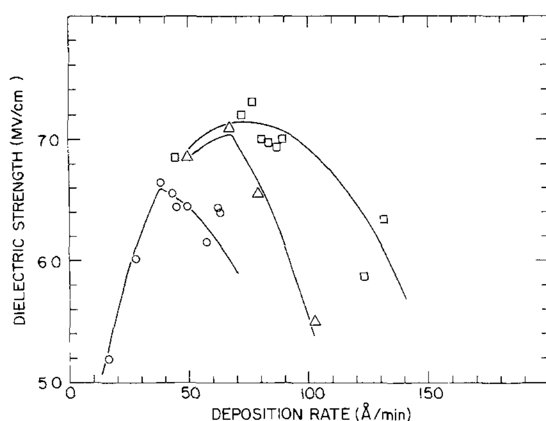

Fig. 13. Dielectric strength vs. deposition rate for the films in Fig. 2.

The general trend from the electrical-structure correlation studies is that films exhibit higher breakdown strengths with decreasing crystallite size. A comparison of these results with electrical properties and grain size observed for the AlN phase in the Al-O-N system (17) is also of interest. The data of Irene *et al.* (17) is summarized in Table I where it was also noted that dielectric breakdown increases with decrease in grain size. The maximum breakdown was observed at what was characterized as an amorphous film (<100Å grains). This finding is consistent with the present data found for Al_2O_3 (Fig. 8). The measured current density for the AlN case, however, decreases with decreasing grain size which is contrary to what is observed for Al_2O_3. It would appear that the conductivity of Al_2O_3 is more dependent on deposition temperature than on grain size possibly because of impurity content or stoichiometry.

In an attempt to make the structure more amorphous and thus improve the breakdown strength, Al_2O_3 films were implanted with argon or oxygen at 30 keV in doses 1-3 $\times$ $10^{15}/cm^2$. Although a profound decrease in conductivity resulted (Fig. 9), the breakdown voltage distribution was actually degraded.

Summary

A wide range of deposition conditions have been described for depositing Al_2O_3 films by the hydrolysis of $AlCl_3$ in the presence of CO_2 and H_2 using N_2 as a carrier gas. Deposition rate could be increased with increases of reactant partial pressures as well as temperature. Properties of the films such as index of refraction, impurity content, and crystallinity vary as these system parameters are changed. Films were decidedly polycrystalline at high deposition temperatures (~900°C) but were more amorphous with progressively lower deposition temperatures. Films deposited at lower temperature contained substantial Cl. Observed changes in electrical properties (dielectric breakdown and conductivity) have been correlated with both the gas composition used in depositing the films and the crystallinity of the films. The breakdown strength increased with decreasing grain size and deposition temperature but could be optimized at each temperature by proper choice of the deposition parameters.

Table I. Electrical properties and grain size for AlN phase (17)

Deposition temp (°C)	O content (atom %)	Grain size (A)	Dielectric breakdown (mV/cm)	Current (J) (A/cm^2) (2 mV/cm)
770	0	500	2.5	1×10^{-2}
770	8	250	3.2-6	1×10^{-6}
900	0	300	4.2	2×10^{-4}
900	20	<100*	8.0	1×10^{-8}

* Considered amorphous.

Acknowledgments

The authors gratefully acknowledge J. Eldridge, A. B. Fowler, and R. A. Ghez for helpful discussions, E. A. Irene for discussions of TEM studies, G. R. Woolhouse for TEM photographs, S. Zirinsky for special Al_2O_3 films, T. B. Light for low angle x-ray data, and J. D. Kuptsis for composition data.

Manuscript submitted Feb. 22, 1977; revised manuscript received Aug. 31, 1977.

Any discussion of this paper will appear in a Discussion Section to be published in the December 1978 JOURNAL. All discussions for the December 1978 Discussion Section should be submitted by Aug. 1, 1978.

Publication costs of this article were assisted by IBM Corporation.

REFERENCES

1. W. Steinmaier and J. Bloem, *This Journal*, **111**, 206 (1964).
2. S. K. Tung and R. E. Caffrey, *Trans. Metall. Soc. AIME*, **233**, 572 (1965).
3. P. S. Schaffer, *J. Am. Ceram. Soc.*, **48**, 508 (1965).
4. S. K. Tung and R. E. Caffrey, *This Journal*, **114**, 275C (1967).
5. V. Y. Doo and P. J. Tsang, *ibid.*, **116**, 116C (1969).
6. K. Iida and T. Tsujide, *Jpn. J. Appl. Phys.*, **11**, 840 (1972).
7. M. Kamoshida, I. V. Mitchell, and J. W. Mayer, *Appl. Phys. Lett.*, **18**, 292 (1971).
8. I. V. Mitchell, M. Kamoshida, and J. W. Mayer, *J. Appl. Phys.*, **42**, 4378 (1971).
9. M. Kamoshida, I. V. Mitchell, and J. W. Mayer, *ibid.*, **43-4**, 1717 (1972).
10. T. Tsujide, S. Nakanuma, and Y. Ikushima, *This Journal*, **117**, 703 (1970).
11. K. Iida, *Jpn. J. Appl. Phys. II.*, **3**, 288 (1972).
12. K. Iida, T. Tsujida, and M. Nakagiu, *ibid.*, **3**, 1153 (1972).
13. J. A. Aboaf, D. R. Kerr, and E. Bassous, *This Journal*, **102**, 1103 (1973).
14. V. J. Silvestri, E. A. Irene, S. Zirinsky, and J. D. Kuptsis, *J. Electron. Mater.*, **4**, 429 (1975).
15. S. Zirinsky, Private communication.
16. F. L. McCrackin, E. Passaglia, R. R. Stromberg, and L. Steinberg, *J. Res. Natl. Bur. Std., A. Phys. and Chem.*, **67** (No. 4), 363 (1973).
17. E. A. Irene, V. J. Silvestri, and G. R. Woolhouse, *J. Electron. Mater.*, **4**, 409 (1975).
18. T. Light, J. M. Eldridge, J. W. Matthews, and J. H. Greiner, *J. Appl. Phys.*, **46**, 1489 (1975).
19. ASTM Diffraction Card No. 16-435. American Society for Testing and Materials, Philadelphia, Pennsylvania.
20. K. Torkar and H. Krischner, *Monatsh. Chem.*, **91**, 659 (1960).
21. Carnes and Duffy, *J. Appl. Phys.*, **42**, 4350 (1971).

The Effect of Electrostriction on the Anodic Oxidation of Tungsten

J. L. Ord,* J. C. Clayton,[1] and K. Brudzewski[2]

Department of Physics, University of Waterloo, Waterloo, Ontario, Canada N2L 3G1

ABSTRACT

Ellipsometry is used to measure the strain induced in the oxide film by the electric field during the anodic oxidation of tungsten. The strain is found to vary as the 5/3 power of the field and to equal 1% at a field of 5.25×10^6 V/cm under galvanostatic oxidation at 200 μA/cm^2. Open-circuit transient analysis is used to determine the dependence of the current density and the dielectric constant on the field in the oxide film. The current is found to be limited by an effective field proportional to the product of the field and the dielectric constant. The dielectric constant is found to vary linearly with field, decreasing by 45% between zero field and the oxidation field. The Clausius-Mossotti relation is used to relate the variation in the dielectric constant to the strain in the film, and the results of the open-circuit transient analysis are found to be in very good agreement with the ellipsometric measurements of strain. It is concluded that field-induced strain in the oxide film has a strong effect on its dielectric constant, and through it on the effective field which controls the anodic oxidation process.

In a previous paper (1), we reported a field dependence of the dielectric constant during the anodic oxidation of tantalum, niobium, and tungsten, and used an effective-field model to relate it to the field dependence of the ionic current density. Ellipsometry was used to measure the strains induced in the oxide films by changes in field, and the associated changes in the low and high frequency dielectric constants were found to agree reasonably well with values predicted using the Clausius-Mossotti relation between dielectric constant and density. By assuming log (i) proportional to an effective field, we found that the field dependence of the dielectric constant could account fairly well for the curvature in the dependence of log (i) on E for the anodic oxidation of tantalum (2) and niobium (3). We were unable to test an effective field model for tungsten because no attempt had been made to measure log (i)-E curvature. We have now developed a technique for determining log (i)-E curvature from the analysis of open-circuit transients (4), and we apply this technique here to the anodic oxidation of tungsten.

More recently, Young and co-workers found that the field induces anisotropy in the anodic oxides of tantalum (5) and niobium (6), and carried out an anisotropic analysis of their optical data. Their values for the sign and magnitude of the strains and index changes agreed reasonably well with the results of our earlier work which used isotropic optical analysis. They varied the field over a wider range than we had used and found a quadratic field dependence instead of the linear dependence we had reported. More recent work in our laboratory (7) confirms the optical anisotropy of the anodic oxide of niobium, but not the quadratic field dependence, and concludes that relaxation processes complicate attempts to determine the field dependence. Studies on tantalum film capacitors (8, 9) found a complicated field dependence in that system also and reported a dependence of the results on the history of the sample, thus confirming the important role of relaxation processes.

Although tungsten oxide exhibits larger field-induced strains than do the oxides of tantalum and niobium, it is a more difficult system to study in sulfuric acid electrolyte because breakdown occurs at a relatively low potential, restricting the thickness range available for optical analysis, and film dissolution tends to mask field-induced thickness changes. In this study we use both sulfuric acid and the acetic acid electrolyte used by Keil and Salomon (10) to study the anodization of vanadium. Tungsten oxide does not dissolve in this electrolyte, and a wide range of film thickness can be studied, but one must be alert to the possibility of undesirable side effects. In some systems, organic electrolyte inclusions modify the dielectric properties of the outer portion of the oxide film, and effects of this type have been used (7, 11) as evidence to support an effective field model for ionic conduction in oxide films. In the case of tungsten oxide, the extensive work on electrochromism has shown the properties of the film to be highly sensitive to variations in its composition and structure (12). It has been claimed, on the basis of ellipsometric measurements (13), that even the anodic oxide formed on tungsten in dilute sulfuric acid is made up of two layers of approximately equal thickness but with refractive indexes which differ by 5%.

Experimental

The self-nulling ellipsometer used for the optical measurements has been described in detail elsewhere (14, 15). It uses a helium-neon laser for a light source, and the refractive index values we report here are for the helium-neon laser wavelength, 6328Å. In the configuration used for this study, the instrument has a resolution of 0.01°, and under favorable optical conditions its nulling time is less than 1 sec. A hollow equilateral glass prism is used as a cell and requires that the angle of incidence be set at 60°. The cell has standard-taper joints for mounting the electrode holder, a platinum counterelectrode, a mercurous sulfate reference electrode, and a gas dispersion tube used for saturating the electrolyte with argon. All measurements were made at room temperature, 22°C, and values given for the potential of the tungsten working electrode are relative to the reference electrode. In the experiments in acetic acid electrolyte, the mercurous sulfate reference electrode is replaced by a platinum wire. This has some effect on the potential values, but the resistance of the acetic acid electrolyte has a much greater effect. With our cell geometry, the correction for electrolyte resistance may be as large as 3V.

* Electrochemical Society Active Member.

[1] Present address: Marshall Space Flight Center, Huntsville, Alabama 35800.

[2] Permanent address: Institute of Physics, Technical University of Warsaw, Warsaw, Poland.

Key words: electrostriction, ellipsometry, tungsten, oxidation, oxide film, Tafel slope.

The tungsten working electrode is a cylindrical single crystal with a flat on one side for optical measurements. It is clamped between Teflon washers in the electrode holder and is mounted in the cell with its axis vertical, exposing an area of 1.25 cm^2 to the electrolyte. The optical surface is prepared by several stages of diamond polishing followed by an electropolish in sodium hydroxide. For all of the experiments reported here, the final surface preparation consists of immersion in dilute sodium hydroxide to dissolve the oxide film formed in a previous experiment. The sample is repolished only after oxidation to high potential in acetic acid electrolyte, and after polishing it is cycled several times before use in another experiment. The sulfuric acid electrolyte is 0.1M, and the acetic acid electrolyte is 2.0M in water, and 0.02M in sodium borate.

The circuitry used with the cell is operated by a HP 2114B minicomputer through D/A and A/D converters which enable currents to be set and potentials to be read under program control. At one second intervals the computer records time, potential, current density, and the null settings of the polarizer and analyzer prisms of the ellipsometer, and at 20 sec intervals it writes the accumulated data onto magnetic tape. In extended experiments, the time interval between readings is usually lengthened in order to reduce the total number of data points recorded. The computer can also apply and record open-circuit transients at specified intervals under program control. The way in which this is done is described in detail elsewhere (4).

Results

Ellipsometric measurements.—The first experiments were designed to see whether the range of oxide film thickness could be extended by using acetic acid electrolyte in place of sulfuric acid electrolyte. The results of one such experiment, performed at a current density of 200 $\mu A/cm^2$, are plotted in Fig. 1. Potential is plotted *vs.* time in the lower portion of the figure, and the null settings of the polarizer and analyzer prisms of the ellipsometer, *P* and *A*, are plotted one *vs.* the other in the upper portion of the figure. Initially potential rises linearly with time, and the optical data fall on the closed loop in the *P-A* plane. This result is similar to the result obtained in sulfuric acid, and the film grown in this region has the same refractive index as the film grown in sulfuric acid. At the end of the linear region, the film thickness is little different from the film thickness at breakdown in sulfuric acid.

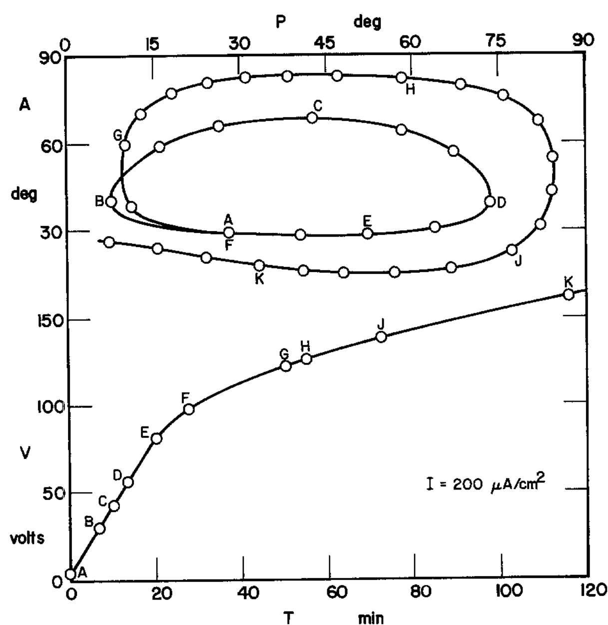

Fig. 1. Anodic oxidation of tungsten in acetic acid electrolyte at 200 $\mu A/cm^2$. Corresponding points are labeled A through K on the potential-time plot in the lower portion of the figure, and on the *P-A* plot of the optical data in the upper portion.

Under continued oxidation, the increase in potential becomes progressively slower, and the optical data begin to spiral outward in the *P-A* plane. In addition, the surface begins to scatter light diffusely as if it were roughening on a very fine scale, and the potential transients observed on changing the current density exhibit greatly enhanced overshoot. Scanning electron microscopy detects the formation of shallow pits on the order of 1 μm in diameter in this region, but Auger spectroscopy finds no sign of the electrolyte inclusion expected in a porous oxide or a duplex film. Clearly, both the film growth process and the structure of the film itself are different in this region, and hence optical measurements which extend into this region will be of no help in analyzing the anisotropy of the film grown in the initial region. We must, therefore, make an assumption about the degree of anisotropy of the oxide film in order to carry out our optical analysis. Wang (7) found that changes in the refractive index in the field direction were twice as large as those transverse to the field for niobium oxide, and we will assume that this is the case for tungsten oxide also.

Analysis of the first loop optical data in Fig. 1 using this assumption gives $n_z = 2.1144$ in the field direction, and $n_x = n_y = 2.1450$ transverse to the field with the oxidation field applied. At zero field the film is isotropic with a refractive index of $n = 2.1756$. The layer grows on a substrate of index $4.280 - 3.0781$ in a medium of index 1.375, and the initial film thickness is 16.5Å. Up to a potential of 65V, the field in the film at a current density of 200 $\mu A/cm^2$ is 5.25×10^6 V/cm, and when the first optical loop closes at point F, the oxide film is 1800Å thick. The results of this analysis differ little from the results of our earlier work which used isotropic analysis to calculate an index of 2.145 and a field of 5.2×10^6 V/cm at a current density of 200 $\mu A/cm^2$ in sulfuric acid electrolyte. Our results do not agree with the recent ellipsometric measurements of Sarakinos and Spyridelis performed at an angle of incidence of 60° and a wavelength of 5461Å in a medium of refractive index 1.333 (13). Under their optical conditions, they expect their first loop to close at a thickness of under 1500Å, but they find that their experimental data fall somewhat outside the loop at this point, then swing in toward the loop but do not cross it before breakdown. They analyze this behavior in detail and conclude that the anodic film is made up of two component layers of approximately equal thickness but with refractive indexes which differ by 5%. We often obtain optical data of this type as we condition a diamond-polished optical surface for electrochemical measurements by alternate anodic oxidation and oxide film dissolution. We follow the oxidation cycles optically and use closure of the first optical loop (at 1800Å under our conditions) as an indicator that the surface is ready for electrochemical measurements. We do not think that the suggestion that a duplex film forms on tungsten in sulfuric acid electrolyte merits serious consideration.

Although the useful range of oxide film thickness is no greater in acetic acid than in sulfuric acid, the oxide film does not dissolve in acetic acid, and this simplifies considerably the analysis of optical data in field-switching experiments. The results of a typical field-switching experiment performed in sulfuric acid electrolyte are plotted in Fig. 2, the potential-time plot in the lower portion of the figure and corresponding *P-A* plot in the upper portion. The algorithm which applies the transient reduces the overpotential at 60 sec intervals by 7/32nds of its initial value, and does this four times before reversing the stepping direction, then finally reapplying the original oxidation

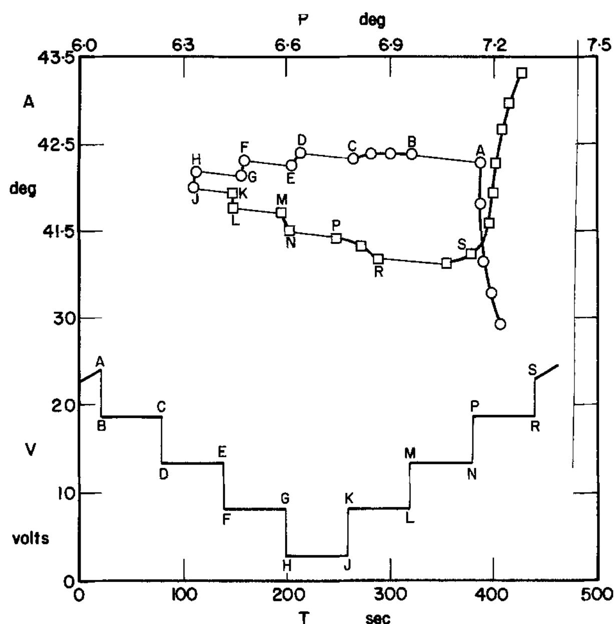

Fig. 2. Field switching experiment during the anodic oxidation of tungsten in sulfuric acid electrolyte at 200 $\mu A/cm^2$. The optical data fall in the region of point B in Fig. 1.

current density at point S. In sulfuric acid electrolyte this switching sequence provides optical data at the same set of electric field values independent of the initial potential or film thickness, but in acetic acid the resistive voltage drop in the electrolyte complicates matters somewhat. Ideally, one would like to perform this switching sequence at points B, C, and D based on the assumption that $\Delta n_z/\Delta n_x = 2$. The experiment plotted in Fig. 2 was performed in the region of point B in Fig. 1, and the scales used to plot the optical data in the upper portion of the figure are greatly expanded over the scales used in Fig. 1. The pattern traced out by the optical data, although somewhat complicated, shows up clearly in this figure because the layer dissolution which occurs in sulfuric acid displaces the data recorded on switching the field back up so that they do not overlap the data recorded on switching the field down. As the data recorded before and after the switching transient indicate, film growth at constant index displaces the optical data almost vertically upward in the figure, and the extent of film dissolution during the switching transient can be calculated from the amount that point S lies below point A. Interpretation of the lateral displacements in the optical data which occur when the potential is switched is more difficult because although vertical displacements are due to changes in film thickness only, lateral displacements involve changes both in film index and in film thickness. At the three lowest field values, the switching produces a sudden lateral shift which involves a change in film index and in film thickness, followed by a slow downward shift as the film dissolves at essentially zero applied current density. In regions BC and PR, a slow lateral shift continues after the rapid shift observed on changing the field. The lateral shifts from A to B and from R to S are consistent with what one would extrapolate from the rest of the data, but the additional lateral displacements from B to C and from P to R appear to be due to a relaxation process which requires charge transport. Regions BC and PR differ from the other constant potential regions in that they are the only ones during which there is appreciable current flow. It is likely that the relaxation process observed here is the same one which is responsible for the overshoot in the potential when the current density is changed suddenly from one value to another. Since our aim in this paper is to study field-dependent processes rather than relaxation processes, we base our analysis on data taken either at low current density or at times short compared to the relaxation time.

The data used in the quantitative optical analysis of the field dependence were obtained in acetic acid electrolyte by applying the field switching sequence from Fig. 2 at points B, C, and D at the extremes of the first optical loop in Fig. 1. The results obtained from the field-switching sequence applied at point C at the top of the optical loop are plotted in Fig. 3 using the same lettering scheme for the switching sequence as was used in Fig. 2. Theoretical curves for an anisotropic analysis based on a zero field isotropic index of 2.1756 and a $\Delta n_z/\Delta n_x$ ratio of 2 are superimposed on the data. Although the experiment was performed in a different optical region, the data exhibit the same general characteristics as the optical data in Fig. 2, except that there is no evidence of film dissolution, and the relaxation process appears more pronounced along BC and less so along PR than in Fig. 2. (The apparent difference in the relaxation process is largely due to an increase in the field in region BC in acetic acid due to a change in the resistive voltage drop in the electrolyte and to an increase in the field in region PR in sulfuric acid due to film dissolution.)

The data obtained as the field is switched down from C to H and back up from J to P fall on a single line on the P-A plot in Fig. 3. The fact that the line is inclined to both the constant index and constant thickness theoretical curves shows that both thickness and index change with field. The thickness change, a full 5Å, can be read directly in the figure. The constant index curves intermediate between the isotropic $n = 2.1756$ curve and the $n_z = 2.1154$ curve are fitted to the average of the down and up switching data at each field step, and correspond to n_z values of 2.1743, 2.1674, 2.1589, and 2.1548 reading from top to bottom in the figure. The form of the field dependence can be determined by plotting the change in n_z from its isotropic values as a function of field, and this is done in Fig. 4. The curve in the figure is a power law, E^p, fitted to the first four points. The best fit is obtained with this form of field dependence for $p = 1.67$. The deviation of the fifth point from the curve fitted to the first four is due to the optical shift associated with the relaxation process, and the fact that the field increment between the fourth and fifth points is smaller than the other increments is due to the voltage drop in the electrolyte at a current density of 200 $\mu A/cm^2$. The value used in Fig. 3 for the isotropic index at zero

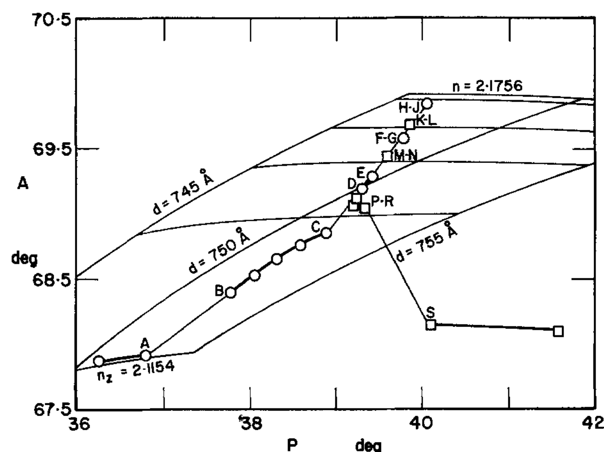

Fig. 3. Field switching experiment during the anodic oxidation of tungsten in acetic acid electrolyte at 200 $\mu A/cm^2$. The field-switching sequence from Fig. 2 was applied in the region of point C in Fig. 1. The theoretical thickness and index curves are for a film which is isotropic at zero field and whose index changes twice as much in the field direction as in the transverse direction when the field is applied.

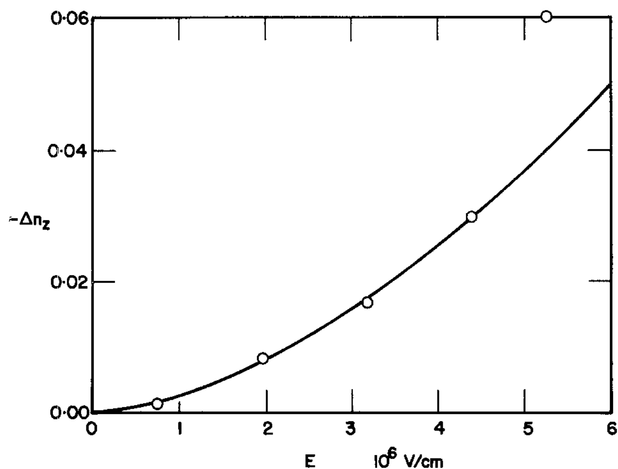

Fig. 4. The field dependence of Δn_z determined from the experiment plotted in Fig. 3. The plotted points correspond to the constant index curves in Fig. 3. The first 4 points fit a 5/3-power dependence on field, and the 5th point shows an offset due to a relaxation process (BC in Fig. 3).

field was obtained by extrapolating the field dependence plotted in Fig. 4 to zero field.

The optical analysis shown in Fig. 3 is consistent with the optical analysis of a switching experiment performed at point B in Fig. 1. When we say the analyses are consistent, we mean that all refractive index values agree and that thickness changes exhibit the proportionality to film thickness required to give a relation between field and strain which is independent of film thickness. The left end of the optical loop is probably the best place to perform field-switching experiments because the angle between constant-index curves and constant-thickness curves is greatest in this region, and although the over-all magnitude of the shift in the optical data is less than at the top of the loop, the null sensitivity is considerably better. At the right end of the first optical loop where the sensitivity to thickness and index changes is not as good, we do not get a consistent analysis, but we do not know whether this is due to the low sensitivity, or whether is is an early indication of breakdown.

Open-circuit transient measurements.—Open-circuit transients can be used to determine the dependence of current density on potential during anodic oxidation. We will only outline the steps involved in the analysis here, and we refer the reader elsewhere (4) for a detailed description of the experimental technique, methods of analysis, and effects of log (i)-E curvature. In the high overpotential region, the relation between current density and potential for an activation-controlled process can be written

$$i = i_o \exp((V - V^*)/V_o) \qquad [1]$$

where V^* is the zero of overpotential, i_o is the exchange current density, and V_o is the Tafel slope defined in terms of natural logarithms. If the applied current to the electrode is interrupted, the decay of overpotential across the oxide film will be governed by the relation

$$C\,dV/dt = -\,i_o \exp((V - V^*)/V_o) \qquad [2]$$

provided that the capacitance of the oxide film, C, is constant over the transient. This equation may be integrated under the condition that $i = i_1$ and $V = V_1$ when the circuit is opened at $t = 0$, to give

$$V = V_1 - V_o \ln(1 + t/T) \qquad [3]$$

where $T = CV_o/i_1$. Equation [3] can be fitted to V-t data by varying T to minimize the standard deviation in V given by least squares analysis. V_o and $1/C$ are determined directly by this analysis, and i_o and V^* can be determined from measurements at different film thicknesses if the current density is limited by the electric field in the oxide film.

The analysis of a transient produced by opening the circuit at a potential of 18V during the anodic oxidation of tungsten in sulfuric acid electrolyte at a current density of 200 μA/cm^2 is shown is shown in Fig. 5. In the lower portion of the figure the V-t data are plotted along with the least squares fitted line for $T = 4.3$ msec, the value which minimizes the standard deviation in V. The least squares analysis gives $V_o = 1.728$V and $1/C = 2.01$ cm^2/μF. In the upper portion of Fig. 5 we plot the deviation of the data from the fitted line on a 20 times expanded scale. This plot shows that the 33 mV standard deviation is systematic rather than random, and that the data exhibit very little real scatter.

Figure 6 shows the V_o and $1/C$ data obtained by analysis of sequences of open-circuit transients ap-

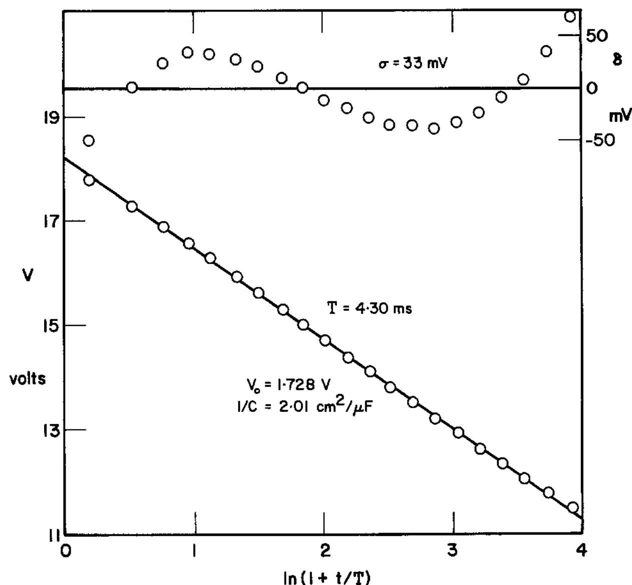

Fig. 5. Analysis of an open-circuit transient applied at a potential of 18V during the anodic oxidation of tungsten in sulfuric acid at a current density of 200 μA/cm^2. The deviation of the data from the least squares fitted line is shown on a 20-times expanded scale in the upper portion of the figure.

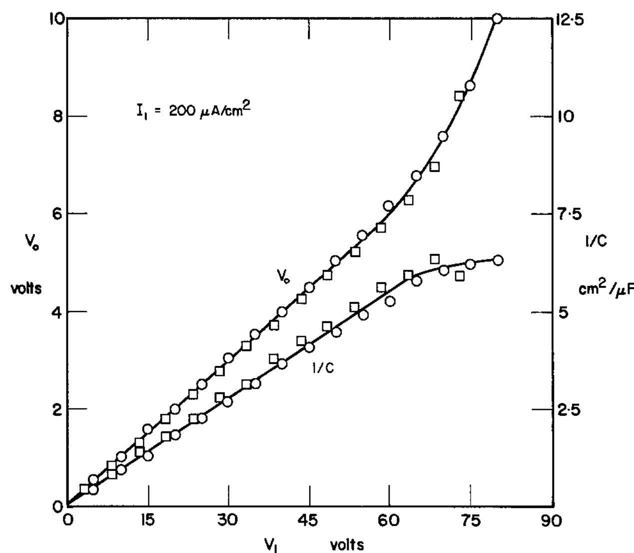

Fig. 6. Values of V_o and 1/C determined by the analysis of open-circuit transients applied at a sequence of potentials during the anodic oxidation of tungsten in acetic acid (squares) and sulfuric acid (circles) at a current density of 200 μA/cm^2.

plied during the anodic oxidation of tungsten at 200 $\mu A/cm^2$ in sulfuric and acetic acid electrolytes plotted as a function of V_1, the potential at which the transient was applied. In order to make the data obtained in the two electrolytes more readily comparable, the V_1 values in acetic acid were corrected for the iR drop in the electrolyte (approximately 2V), but not for the pH difference between the electrolytes. This plot can be used in many ways: It enables us to compare the electrochemical characteristics of oxide films formed in the two electrolytes, to determine whether or not the conduction process is controlled by the field in the film, to detect points at which the nature of the conduction process changes, and to determine the parameters i_o and V^* which cannot be determined by the analysis of a single transient.

There appears to be no significant difference in the electrochemical characteristics of the films formed in the two electrolytes. The small differences between $1/C$ values may be due to analysis problems associated with the iR correction in acetic acid, or, because capacitance is an area-dependent parameter, a difference in the roughness of the sample surface between the two runs. From the fact that the films have the same refractive index and the same electrochemical characteristics, we conclude that the same oxide film forms in the two electrolytes. The lower solubility of the oxide film in acetic acid makes it the preferred electrolyte for sensitive optical measurements, but the lower electrolyte resistance makes sulfuric acid the preferred electrolyte for second-order analysis of open-circuit transients.

The linear dependences of V_o and $1/C$ on V_1 below 60V are characteristic of a process controlled by the electric field in the oxide film. This could be demonstrated equally well by plotting V_o and $1/C$ *vs.* the oxide film thickness determined by ellipsometry, but the form of plot used in Fig. 6 has the advantage that V^*, the zero of overpotential, appears as a point on the graph, and the potential at which the conduction process begins to change can be read directly. For an ideal field-limited process, V^* is given by the common V_o and $1/C$ intercepts on the V_1 axis. For the sulfuric acid data in Fig. 6, the V_1 intercepts of least squares lines fitted to the V_o and $1/C$ data, -0.335 and -0.633V, respectively, are in close agreement. The curvature in the V_o and $1/C$ data above 60V in both electrolytes indicates a change in the conduction process, and we interpret this change as the earliest indicator of film breakdown. This result supports the conclusion we drew from the optical data that although the postbreakdown film-growth processes may differ, the film breaks down at the same potential in the two electrolytes. The restricted potential range available for study poses no problem for open-circuit transient measurements, so we restrict our second-order analysis to transients with V_1 values below 20V to be well clear of any breakdown effects.

The second-order analysis is based on three postulates: (*i*) The logarithm of the ionic current density is linearly dependent on the effective field in the oxide film, (*ii*) the effective field is proportional to the product of the applied field and the dielectric constant of the film, and (*iii*) the dielectric constant of the film depends on the electric field in the film. Under these postulates, the differential equation of a transient can be put into the same form as Eq. [2] by transforming to the variable U defined by

$$U = (V - V^*)K/K_1 \qquad [4]$$

where K is the dielectric constant of the oxide film, and K_1 is its value at the oxidation field, 5.25×10^6 V/cm. The differential equation of the transient is then

$$C_1\, dU/dt = -\, i_o \exp (U/V_o) \qquad [5]$$

where C_1 is the value of the capacitance at the oxidation field. The procedure for fitting a transient is similar to the first-order procedure except that an additional step is required to specify the field-dependence of the dielectric constant. In this study we assume a power-law dependence of K on E which, written in terms of potential, has the form

$$K = K_o(1 - \gamma_n((V - V^*)/(V_1 - V^*))^n) \qquad [6]$$

where K_o is the zero-field value of K, and γ_n is the fraction by which the dielectric constant decreases on going from zero field to the oxidation field. This form has the computational advantage that γ_n is dimensionless, but the value of γ_n does depend on the oxidation field. In fitting transients, we set n equal to 1 or 2, choose a value for γ_n, fit the transient by the first-order procedure, then repeat the process for other values of γ_n. We then test the effectiveness of the second-order analysis and find the best-fit value for γ_n by plotting σ, the standard deviation of the potential data from the fitted line, as a function of γ_n. This is done in Fig. 7 for second-order analysis of the transient plotted in Fig. 5. Standard deviation curves are shown for assumed linear and quadratic dependences of K on E, both of which intersect the σ-axis at the first-order value, 33 mV. The quadratic dependence gives a simple minimum at $\gamma_2 = 0.238$, but the linear dependence gives a relative minimum just below the very sharp absolute minimum at $\gamma_1 = 0.441$. At $\gamma_2 = 0.238$, σ is reduced by a factor of 6 from its first-order value, whereas at $\gamma_1 = 0.441$ the reduction factor is 25. The 1.3 mV standard deviation at $\gamma_1 = 0.441$ is really quite remarkable in view of the fact that the A/D converter has a least-significant bit of 5 mV. Our recording technique makes it theoretically possible to achieve such low values of σ provided the signal is noise-free, the A/D converter is highly linear, and the functional dependence of V on t is known precisely, but it is very unusual to meet all of these conditions in practice. When studying the anodic oxidation of tantalum (4) we did not achieve such low values of σ, and we were unable to discriminate between a linear and a quadratic dependence of K on E. Here we conclude that a linear dependence of dielectric constant on field fits the data very well across the field region spanned by the open-circuit transient.

The expressions determined by first- and second-order analysis for the dependence of the current density on the field are displayed graphically on a plot of log (i) *vs.* E in Fig. 8. The first-order expression is a line which intersects the i-axis at $i_o = 4.18 \times 10^{-3}$ $\mu A/cm^2$, and the second-order expression is a curve

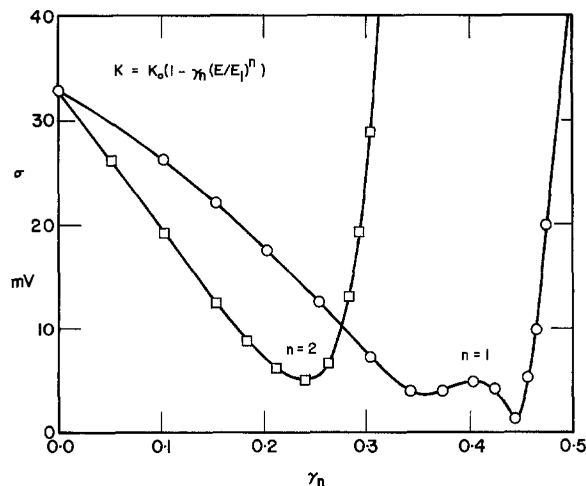

Fig. 7. Plot of σ, the standard deviation in V given by least squares analysis, as a function of γ_n, the field coefficient of the dielectric constant, for second-order analysis of the open-circuit transient from Fig. 5. At $\gamma_2 = 0.238$, $\sigma = 5.15$ mV, and at $\gamma_1 = 0.441$, $\sigma = 1.30$ mV.

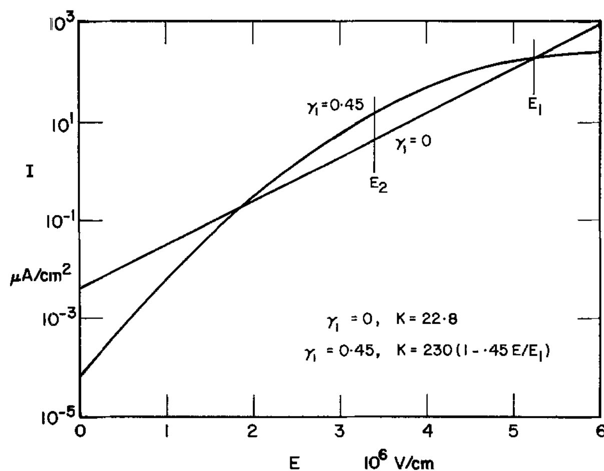

Fig. 8. Dependences of log (*i*) and *K* on field determined by first- and second-order open-circuit transient analysis. The expressions describe how log (*i*) and *K* respond as the field changes from an initial value of 5.25 × 10^6 V/cm under conditions where no relaxation takes place.

which intersects the i-axis at $i_o = 6.68 \times 10^{-5}$ μA/cm², and crosses the first-order line once at the oxidation field and again at lower field. (The value 0.45 for γ_1 comes from the analysis of a sequence of 10 transients, the final one of which is the transient with $\gamma_1 = 0.441$ plotted in Fig. 5.) The field region over which the open-circuit analysis was carried out is shown in the figure, and the plotted relations are seen to have substantially different average Tafel slopes across this region.

The first-order analysis gives a value of 22.8 for *K* independent of field, whereas the second-order analysis gives a value of 230 for *K* at zero field, decreasing to 127 at the oxidation field. The full order-of magnitude difference between the first- and second-order zero-field values for *K* may appear unreasonably large, but it is a direct consequence of the assumption that *K* depends on *E*. The capacitive discharge current involves two terms in second order

$$CdV/dt + (V - V^*)dC/dt = C_o(1 - 2\gamma_1)dV/dt \quad [7]$$

where C_o is the value of the capacitance at zero field. This equation predicts a value of $(1 - 2\gamma_1)$ for the ratio between the first- and second-order *K* values at zero field, and for $\gamma_1 = 0.45$ this is precisely an order of magnitude.

Discussion

The optical and open-circuit measurements give quite different results for the form and strength of the dependence of the dielectric constant on the field. Although the difference in the strength of the field dependence is not surprising in view of the difference in frequency, the difference in the form of the dependence does appear to be inconsistent. We can test the consistency of the two results if we assume that the changes in dielectric constant result from changes in density produced by field-induced strain in the film. This enables us to express the results of the two measurements in terms of a frequency-independent quantity, the strain in the film, but it does introduce one further assumption. In the case of the ellipsometric measurements, no assumption is needed to express the result in terms of strain: The analysis in Fig. 3 and 4 gives the field-dependence of the strain directly

$$\epsilon = 1.00 \times 10^{-2}(E/E_1)^{1.67} \quad [8]$$

where ϵ is the strain in the film and E_1 is the oxidation field, 5.25 × 10^6 V/cm.

The open-circuit result can be expressed in terms of strain if we use the Clausius-Mossotti relation to express the dependence of the dielectric constant on density

$$(K - 1)/(K + 2) = B\rho \quad [9]$$

where ρ is the density of the film and *B* is a constant. Although the applicability of the Clausius-Mossotti relation to anisotropic electrostrictive systems is certainly open to question, a recent series of papers suggests that Clausius-Mossotti theory can be extended to deal with the photoelastic behavior of anisotropic materials (16-19) If we attempt to test the applicability of the Clausius-Mossotti relation in our anisotropic optical analysis by using it to predict the change in refractive index which should result from the observed density change, we get a value which agrees well with the observed changes in n_x and n_y.

The Clausius-Mossotti relation predicts a much stronger effect of strain on the dielectric constant at low frequencies where the dielectric constant has a higher value. The form of the relation is such that the left side of Eq. [9] approaches a limiting value of 1 for large values of *K*. Near this limit, small variations in density can cause large fractional changes in *K*, and the relation between *K* and ϵ becomes nonlinear. It is this property of the Clausius-Mossotti relation which removes the apparent inconsistency between the results of the optical and open-circuit measurements. If we use the values $K_o = 230.67$ and $\gamma_1 = 0.4411$ which come from the second-order minimization plotted in Fig. 8, and use the Clausius-Mossotti relation to calculate the strain necessary to produce the field dependence of the dielectric constant, we obtain the relation

$$\epsilon = 5.71 \times 10^{-3}/(E_1/E - 0.437) \quad [10]$$

Equations [8] and [10] certainly use different functional forms to express the dependence of strain on field, but it must be remembered that the functional dependences are simply convenient ways of representing smooth curves through experimental results in a particular field region. Figure 9 shows a plot of the two functions *vs.* field. The optical data points are shown in the figure, as is the field region over which open-circuit transients are fitted.

The agreement between the two curves, particularly in the region where their fitting ranges overlap, is extraordinarily good; so good, in fact, that one hardly knows what to say about it. There are many steps involved in obtaining the curve in Fig. 9 from the initial table of 21 *V-t* values recorded during an open-circuit transient and it would be very easy to explain

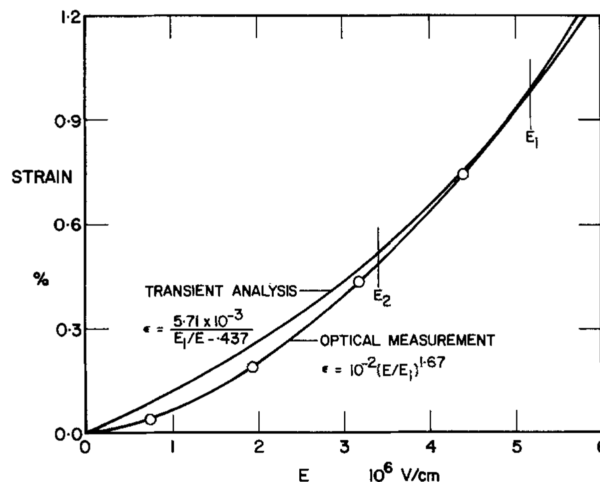

Fig. 9. The field dependence of the strain in the oxide film as determined by ellipsometry and as required by the Clausius-Mossotti relation to fit the dependence of *K* on *E* determined by second-order analysis of open-circuit transients. The curves become tangent near E_1 but do not cross.

away a discrepancy between the open-circuit and the optical results. The converse problem of what one can say about the many steps when there is no discrepancy in the final results is a challenging problem in inference. We regard Fig. 9 as a pivotal result which establishes the "physical" model as a quantitative theory which provides new insight into many of the phenomena associated with anodic oxidation. Fortunately the new insight suggests a wide variety of further experiments whose outcome will ultimately decide the fate of the theory.

There are two points which should be kept in mind when assessing the significance of Fig. 9. The first is the fact that the open-circuit analysis is primarily a technique for studying conductivity, not capacitance. This is true in second order as well as in first. Although the field dependence of the dielectric constant enters into both the capacitive discharge term on the left of Eq. [5] and the conductivity term on the right, the exponential dependence in the conductivity term dominates. Numerical integration of the equation shows that the capacitive term gives a second-order effect which is an order of magnitude smaller than that of the conductivity term and of the opposite sign. Hence the field dependence of the dielectric constant determined by the open-circuit measurements comes from the analysis of the conductivity, and the assumption that the conduction process is limited by an effective field KE is essential to the analysis.

It is also important to note that the curves in Fig. 9 describe the relation between field and strain in the absence of relaxation processes. The optical curve is fitted to data obtained at fields which are low enough that there is insufficient current to drive the relaxation process, and the open-circuit analysis is carried out over times short compared to the relaxation time. The plot of log (i) *vs.* E in Fig. 8 is subject to the same restriction: it describes the way log (i) responds when E is changed from an initial value of E_1 under conditions where no relaxation takes place. In the physical model, the relaxation process is a relaxation of stress in the film. Under steady growth at constant field, the continuous atomic rearrangement asociated with the ionic conduction and film growth processes makes it impossible for the film to support a shear stress. When the field is changed, stress is induced in the film, but this stress relaxes as the ionic current continues to flow. Unfortunately this mechanism does not allow for relaxation at zero field, and this greatly complicates the analysis of the system by the methods of continuum mechanics. It is our view that this is the reason we do not observe the quadratic dependence of strain on field predicted for electrostrictive systems in which the stress is zero at zero field.

Acknowledgment

This work received partial support from the National Research Council of Canada under Grant No. A-1151. Dr. Brudzewski would like to thank the Canada Council for their support during his stay in Canada.

Manuscript submitted Oct. 14, 1977; revised manuscript received Dec. 28, 1977.

Any discussion of this paper will appear in a Discussion Section to be published in the December 1978 JOURNAL. All discussions for the December 1978 Discussion Section should be submitted by Aug. 1, 1978.

Publication costs of this article were assisted by the University of Waterloo.

REFERENCES

1. J. L. Ord, M. A. Hopper, and W. P. Wang, *This Journal*, **119**, 439 (1972).
2. L. Young, *Proc. R. Soc. London, Ser. A*, **258**, 496 (1960).
3. L. Young and F. G. R. Zobel, *This Journal*, **113**, 277 (1966).
4. J. L. Ord, J. C. Clayton, and W. P. Wang, *ibid.*, **124**, 1671 (1977).
5. W. D. Cornish and L. Young, *Proc. R. Soc. London, Ser. A*, **335**, 39 (1973).
6. K. K. Yee and L. Young, *Appl. Opt.*, **14**, 1316 (1975).
7. W. P. Wang, Thesis, University of Waterloo (1975).
8. P. W. Wyatt, *This Journal*, **122**, 1660 (1975).
9. P. W. Wyatt, *ibid.*, **123**, 667 (1976).
10. R. G. Keil and R. E. Salomon, *ibid.*, **115**, 628 (1968).
11. J. J. Randall, *Electrochim. Acta*, **20**, 663 (1975).
12. B. W. Faughnan, R. S. Crandall, and P. M. Heyman, *RCA Rev.*, **36**, 177 (1975).
13. J. Sarakinos and J. Spyridelis, *Thin Solid Films*, **27**, 239 (1975).
14. J. L. Ord, *Surf. Sci.*, **16**, 155 (1969).
15. J. L. Ord, SPIE Proceedings, 112-07 (1977).
16. O. P. Sharma, H. P. Sharma, and J. Shanker, *Solid State Commun.*, **20**, 725 (1976).
17. J. Shanker, O. P. Sharma, and J. C. Sharma, *ibid.*, **22**, 355 (1977).
18. J. Shanker, H. P. Sharma, O. P. Sharma, and J. C. Sharma, *ibid.*, **22**, 401 (1977).
19. J. C. Sharma, H. P. Sharma, and J. Shanker, *Can. J. Phys.*, **55**, 1510 (1977).

Examination of Aluminum-Copper Films during the Galvanostatic Formation of Anodic Oxide

II. Rutherford Backscattering and Depth Profiling

H.-H. Strehblow,[1] C. M. Melliar-Smith,* and W. M. Augustyniak

Bell Laboratories, Murray Hill, New Jersey 07974

ABSTRACT

The anodization of evaporated aluminum/copper alloy films has been investigated using Rutherford backscattering. It has been shown that the copper, initially distributed uniformly through the aluminum film, is not incorporated in the anodic oxide but accumulated at the metal oxide interface. At high potentials this interface becomes rougher due to copper-rich inclusions which finally cause local film breakdown. An excess copper accumulation of about 1 atomic percent above average is distributed over 650Å of the metal phase and moves inward as the anodic oxide grows. This transport is explained by an enhanced diffusion of the copper through a disordered metal layer caused by the formation of the anodic oxide.

Rutherford backscattering is one of the best methods to obtain information about the elemental depth distribution near the surface of a material to a depth of about 1 μm. Studies have been made of anodic oxides on metals (1), the mobility of different implanted tracers in the high electric field of anodic films (2, 3), and their transfer from the metal to the oxide phase (4). This technique has been used to obtain additional information about the composition of vapor-deposited aluminum-copper films and their passivating oxides formed under galvanostatic conditions. The results have been used to explain some of the corrosion properties of these films.

Experimental

The anodization conditions and the electrochemical corrosion properties of the films have been already described in detail (5), and are only briefly described here. The aluminum/copper alloy films were deposited by electron beam evaporation and subsequently anodized in one of three buffer solutions: phthalate buffer, pH 5.0, 0.023M KHPhth + 0.027M K_2Phth; citrate buffer, pH 6.0, 0.1M; and borax buffer, pH 9.2, 0.1M. The as-deposited films showed a grain size of approximately 1000Å by transmission electron microscopy (5). Due to the small solid solubility of copper in aluminum (6), the copper is present as the θ-phase $CuAl_2$ and this phase could be detected by x-ray diffraction if the copper concentration exceeds 1 atomic percent (a/o) (7). The metal films were examined before and after galvanostatic anodization using Rutherford backscattering (8) from a 1.9 or 1.7 Me $_4He^+$ ion beam. The energy resolution of the detector was about 10 keV corresponding to an approximate 200Å depth resolution. The backscattered ions were collected by a solid-state detector at an angle of $\theta = 175°$ measured against the forward direction of the incident beam. Ion beam currents of 10 nA were used for the measurements.

Results

Figure 1 shows a spectrum for an Al-1.0% Cu (all copper concentrations are referred to as atomic percent) film on a quartz substrate before and after anodization in citrate buffer (pH = 6.0) with a current density of 1 mA/cm² to 100V. The parts of the spectra corresponding to scattering from the copper, aluminum, and oxygen in the film and oxygen in the quartz substrate are well resolved. The peaks at channel 160 for the anodized and at 180 for the original film are caused by the overlap of the energies of backscattered particles from the trailing edge of the aluminum film and the leading edge of the silicon in the quartz substrate. The overlap arises because the silicon atoms have only slightly higher mass than the aluminum atoms. This effect was not observed when sapphire was used as the substrate material. The position of the copper and aluminum high energy edges of the as-deposited films demonstrates that both metals are present at the surface. This was confirmed by taking the spectra of pure copper and pure aluminum specimens whose leading edges fall at these same energies.

The relative heights of the copper and aluminum plateaus in the spectra can be used to calculate values for the composition of the metal film. Taking the heights of the plateaus H_{Cu} and H_{Al} at the same energy separation from the leading edge one gets

$$\text{Cu}\ \% = \frac{H_{Cu}/(29)^2}{H_{Cu}/(29)^2 + H_{Al}/(13)^2} \qquad [1]$$

the relation containing a compensation for the fact that the Rutherford backscattering cross section of an element is approximately proportional to the square of its atomic number. In this work the plateau heights were measured 12 channels below the energy of the half-height at the leading edges at which point the rising portion of the leading edge is complete. The re-

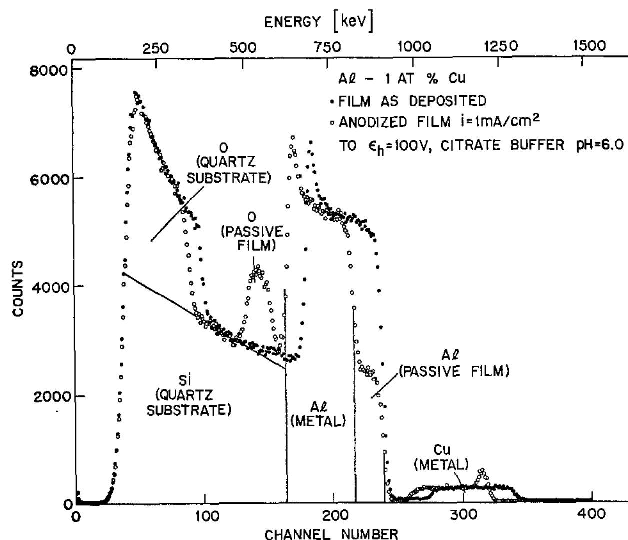

Fig. 1. Rutherford backscattering spectrum of an Al/1 a/o Cu film on quartz before and after anodization with $i = 1$ mA/cm² to $E_h = 100$V in 0.1M citrate buffer, pH = 6.0.

* Electrochemical Society Active Member.

[1] Present address: Free University Berlin Institute of Physical Chemistry, 1 Berlin 33, Germany.

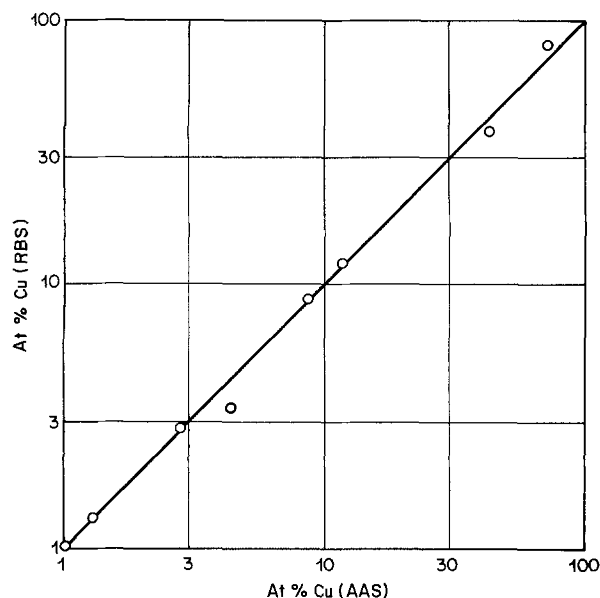

Fig. 2. Composition of vapor-deposited films determined by Rutherford backscattering and atomic absorption spectroscopy.

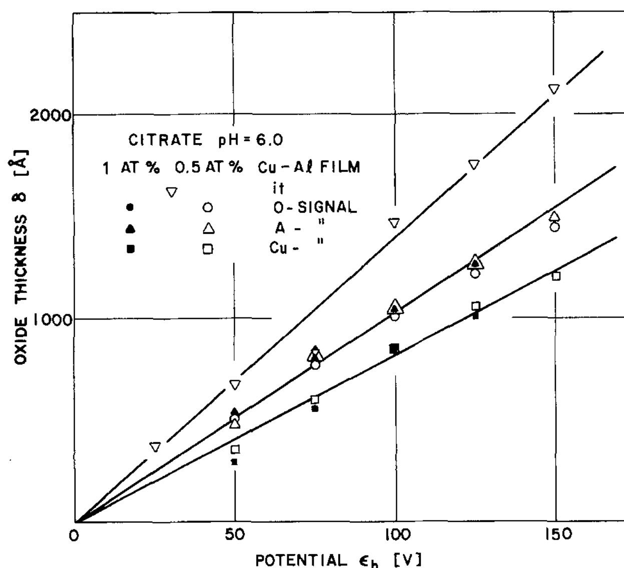

Fig. 3. Thickness of anodic oxide δ on Al/l a/o Cu films on sapphire formed with constant current to different potentials E_h, i = 1 mA/cm², 0.1M citrate, pH = 6.0, deduced from anodic charge and the changes of the O, Al, and Cu signals.

sults are shown in Fig. 2 as a function of the values for the averaged bulk composition obtained by atomic absorption spectroscopy. The films do not have any appreciable depth gradient of copper as can be seen by the nearly flat top of the copper plateau shown in Fig. 1 and 5. The small increase with decreasing energy E is due to the proportionality of the backscattering yield to E^{-2}. The copper concentration with depth is constant to about 2%.

The spectrum of the anodized film shows some significant changes. The leading edge of the copper signal is shifted by 22 channels. Similarly there is a step of 23 channels on the aluminum signal, although its leading edge has not changed position, and an oxygen peak with a width of 20 channels appears on top of the silicon signal of the substrate. These spectral changes are consistent with the formation of an anodic oxide on the surface of the metal film, with the shift in the leading edge of the copper peak showing that this constituent is not incorporated in the oxide, but rather lies beneath it.

The oxygen peak was integrated to determine the amount of oxide present. Background corrections were made for the contribution of the supporting material (Si or Al) by extrapolating their peaks to higher energies. The oxygen content of the passive film was found to increase linearly with the anodization charge and potential giving additional support that the passive oxide is nonporous and increases in thickness linearly with time at constant current. From the width of the step in the aluminum signal the oxide thickness was obtained.

The shift in the leading edge of the copper signal can also be used to calculate the amount of aluminum oxide on top of the copper. The layer thickness is obtained by the following relation (9)

$$'N = \Delta E[K^2(\epsilon(\text{in}) + |\sec\theta|\epsilon(\text{out}))]^{-1} \qquad [2]$$

$'N$ = at./cm², ΔE = energy width of plateau [keV between half-heights], θ = 175° (angle of detection), K^2 = backscattering kinematic factor, ϵ(in) = ^{4}He—stopping cross section [eV/10^{15} at./cm²] for E_o, ϵ(out) = for KE_o, and E_o = energy of incident ion beam (1.9 or 1.7 MeV). The stopping cross sections ϵ(in) and ϵ(out) for Al_2O_3 were calculated by applying Braggs rule from the values of the pure elements

$$\epsilon = 0.4\epsilon_{Al} + 0.6\epsilon_O$$

The values for ϵ were taken from Ref. (9). $'N$ was transformed into a thickness by dividing by the density of atoms in corundum. However, as the anodic film presumably has a somewhat lower density, this should be seen as a lower limit of the thickness.

Figure 3 shows the thickness (δ) of anodic oxides formed on Al/1% Cu and Al/0.5% Cu films to different potentials (citrate buffer, i = 1 mA/cm²). δ is calculated from the changes of the oxygen, aluminum, and copper signals in the Rutherford spectra.

The thickness values calculated from the oxygen peak and the aluminum peak, respectively, are very close to each other. The thickness calculated from the charge is significantly greater and it is apparent that some dissolution of the aluminum occurs during anodization, as previously observed by radioactive tracer methods (10). In contrast, the thickness calculated from the shift in the copper peak is somewhat less. This is probably due to a roughening of the metal/oxide interface or that some residual copper remains in the oxide close to the interface.

Within the major part of the oxide (~80%) no copper can be detected within the limits of detection (0.1%). Figure 4 shows a magnification of the copper signals of Fig. 1. Integration of the copper peak before and after the anodization shows no loss of this metal during anodization in either 0.1M borax (pH=9.2) or citrate (pH=6.0) solutions.

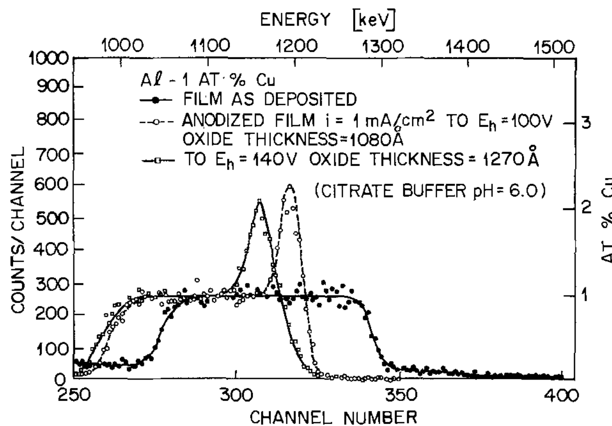

Fig. 4. Copper signals of an Al/l a/o Cu film as deposited and anodized to 100 and 140 V_H, in 0.1M citrate buffer, pH = 6.0, i = 1 mA/cm².

A pronounced enrichment of copper was detected at the metal oxide interface for aluminum films containing about 1% copper. The Rutherford spectrum shows that this enrichment is equivalent to an additional 1 a/o during anodization up to 80V, corresponding to about 800Å of oxide (Fig. 5a). This peak has a half-width of 33 keV corresponding to an enriched copper layer of about 650Å. The copper enrichment moves into the metal film thus retreating from the advancing, newly formed oxide, because it is not transferred into the oxide phase. Once the copper concentration rises above 2% no further enrichment occurs but rather the leading edge of the peak gets less steep (Fig. 4 and 5a). Galvanostatic anodization with 1 mA/cm² to 140V leads to an additional 400Å oxide (22 keV) surrounding local areas of copper-rich metal. Once the enrichment peak has reached its maximum height no change in the shape of its tailing edge can be detected even when the potential for local film damage is reached (Fig. 4 and 5a). This indicates that the transport mechanism of copper into the metal phase does not change during the different stages of oxide formation. Figure 5b shows the increasing accumulation of copper at the metal oxide interface for an Al/0.5% Cu film anodized to different potentials up to 150V, at which point a steady-state accumulation still has not been reached.

In some cases the specimen was tilted by 60° so that the beam was incident at 30° to the specimen's surface. Figure 6 demonstrates the change in the spectrum. The peaks of the surface atoms would not be expected to move; however, the remainder of the film will be broadened by the factor of $1/\cos \Delta\Phi = 2$. This broadening was observed for the copper peaks and demonstrates that the copper enrichment is distributed over a depth of several hundred angstroms and that the results were not caused by the depth resolution of the analytical technique. The broadening of the copper peak and its increase with sample tilting has been observed for specimens with 0.2-1.3% copper after anodization to different potentials. For $E_h < 75$V the effects of tilting are less marked as the accumulation of copper occurs over a small distance, approaching the depth resolution of the analysis. At $E_h = 25$V the copper enrichment is too small to be measured (Fig. 5b). The distribution of the copper enrichment was determined from the distance of the half-heights of the leading edge of the copper signal and the tailing edge of the copper enrichment peak. Applying relation [2], the copper accumulation layer is calculated to be 650Å thick.

Thin Al/1% Cu films of about 1500Å thickness have been anodized completely. In this case the copper moves to the substrate oxide interface as indicated by its peak shift equivalent to the 1400Å anodic oxide layer (Fig. 7). After this complete anodization the specimens are transparent. The interface is also

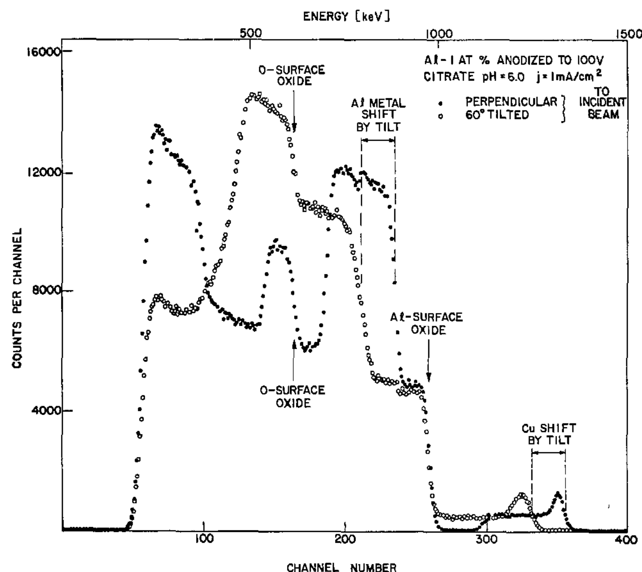

Fig. 6. Rutherford backscattering spectrum of an Al/1 a/o Cu film on sapphire anodized to 100 V_H with $i = 1$ mA/cm² in 0.1M citrate buffer, pH = 6.0. ●, He beam perpendicular to surface; ○, He beam incident at 30° to surface.

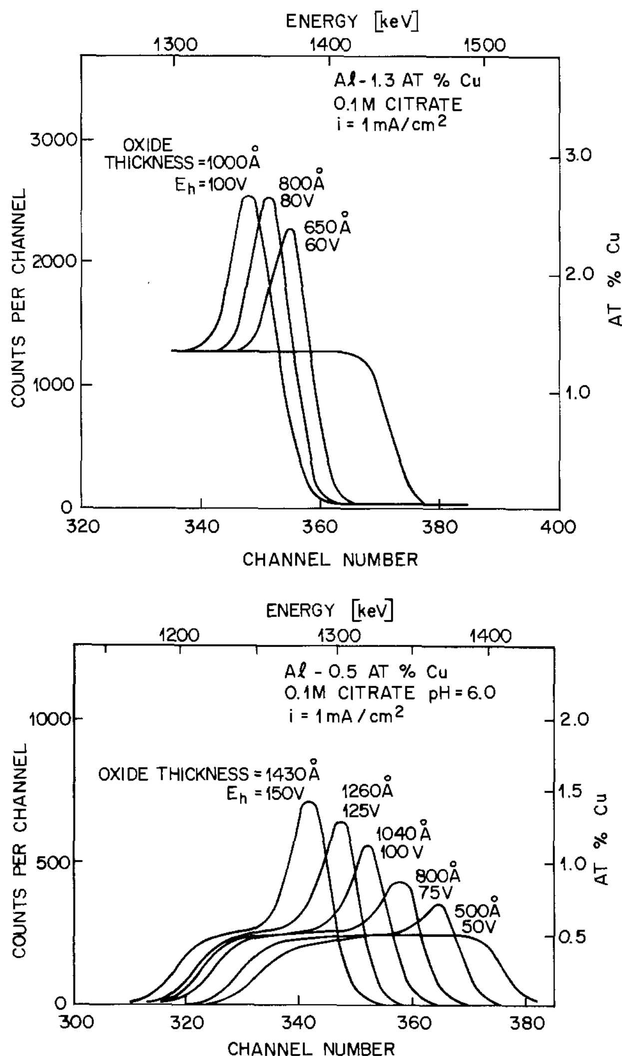

Fig. 5. Copper signal of an (a, upper) Al/1.3 a/o Cu and (b, lower) 0.5 a/o Cu film anodized to different potentials, $i = 1$ mA/cm², 0.1M citrate buffer, pH = 6.0.

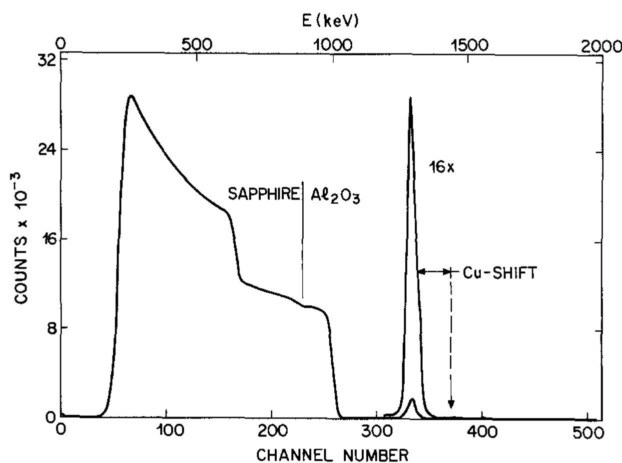

Fig. 7. Rutherford backscattering spectrum after complete oxidation of an Al/1 a/o Cu film on sapphire, $i = 5$ mA/cm², 0.1M citrate, pH = 6.0.

marked by a slight dip in the aluminum signal indicating the copper-rich layer at the aluminum oxide/sapphire interface. Films of higher copper content show less pronounced effects in the Rutherford spectrum as only thin oxides can be formed before oxide breakdown (5). In consequence relatively small copper enrichments are observed. For 2.9% Cu films, an enrichment by 1% is still observed after anodization to 70 V_H at $pH = 6.0$; whereas for 9% Cu, a quantitative result cannot be obtained due to the relatively small peak on a much larger signal. On metal films with copper concentrations higher than 10%, thick anodic oxides can no longer be formed and consequently the copper enrichment cannot be detected. Only a brittle, noncontinuous thick oxide is formed during long galvanostatic experiments (5).

Discussion

The results obtained from the Rutherford backscattering are in good agreement with the findings for aluminum and aluminum oxide implanted with copper (4). The implants show that copper has a higher mobility than aluminum in the oxide phase, and that it is not transferred from the metal to the oxide.

Starting with the native oxide of only a few angstroms a continuous film of aluminum oxide is formed during galvanostatic oxidation which does not contain copper. Rather the copper builds up at the metal/anodic oxide interface, its concentration increasing to approximately 1 a/o over the as-deposited uniform concentration. Once this critical enhanced concentration has been reached, further concentration increases do not occur, but rather the copper enhancement region becomes wider and the copper/oxide interface more diffuse. It is uncertain from the data whether this is due to the incorporation of a small concencentration of copper in the oxide near the interface or a roughening of the interface. This roughness could be caused by the formation of copper-rich inclusions of sufficient size, for example small crystals of the θ phase, that tend to restrict the growth of the anodic oxide in their vicinity. These inclusions are surrounded by the advancing oxide and remain in contact with the metal phase. This results in a roughening of the interface explaining the broadening of the leading edge of the copper signal. The potential distribution between the metal and the electrolyte across the anodic oxide is thus dependent on the microscopic location on the specimen surface. An increased field will occur at those parts of the anodic oxide where the copper-enriched metal intrudes into the oxide phase (Fig. 8). This could result in breakdown of the anodic film giving direct access of the electrolyte to the metal. As the metal inclusion is copper rich there is less tendency for repassivation and the increased corrosion at this point of the specimen will result in the complete perforation of the metal film. At this point the electrolyte comes into contact with the rear part of the metal film which loses adhesion to the supporting material and a bubble-like corrosion structure is observed (5).

The development of the copper enrichment peak under the anodic peak is the result of an anomalously high copper diffusion rate. This diffusion rate was measured by calculating the distance (ΔX) between the tailing edge of the copper plateau (which represents the metal film/ substrate interface) and the tailing edge of the copper enrichment peak. This distance decreases as the film is anodized and the copper enrichment peak moves into the film. The diffusion rate ($d\Delta X/dt$) was measured for Al/0.5% Cu and Al/1% Cu films and the results are shown in Fig. 9. The Al/0.5% Cu film shows constant anodization and copper diffusion rates up to 150V, the diffusion rate being measured at 3.5×10^{-8} cm/sec. In contrast the higher copper content film, while showing similar behavior at low anodization voltages, shows an increasing copper diffusion rate as the anodization voltage is increased above 80V. It can be postulated that this is due to the higher anodization rates which result from a roughening of the metal/anodic oxide interface.

Applying Einstein's relation ($D = x^{-2}/2t$) to the data for the Al/0.5% Cu film shown in Fig. 9, it is possible to obtain an approximate effective constant for this transport process, $D = 5.6 \times 10^{-15}$ cm²/sec. This estimated value is much higher than the value for volume diffusion for copper in aluminum, $D \approx 10^{-24}$ cm²/sec obtained by extrapolation to room temperature of the values measured in the range 433°-463°C (11). Room temperature grain boundary diffusion cannot be an explanation for this observation since the copper concentration profile was unchanged after several weeks of storage.

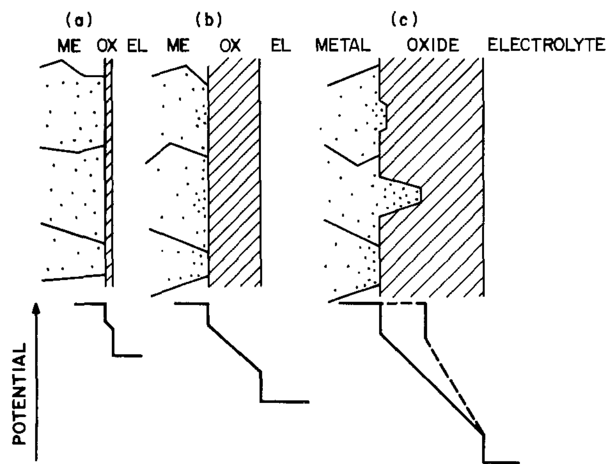

Fig. 8. Schematic representation of the different stages of oxide formation and the corresponding potential distribution (a) native oxide, (b) oxide with copper enrichment at the metal oxide interface, and (c) roughening of the interface leading to localized film damage.

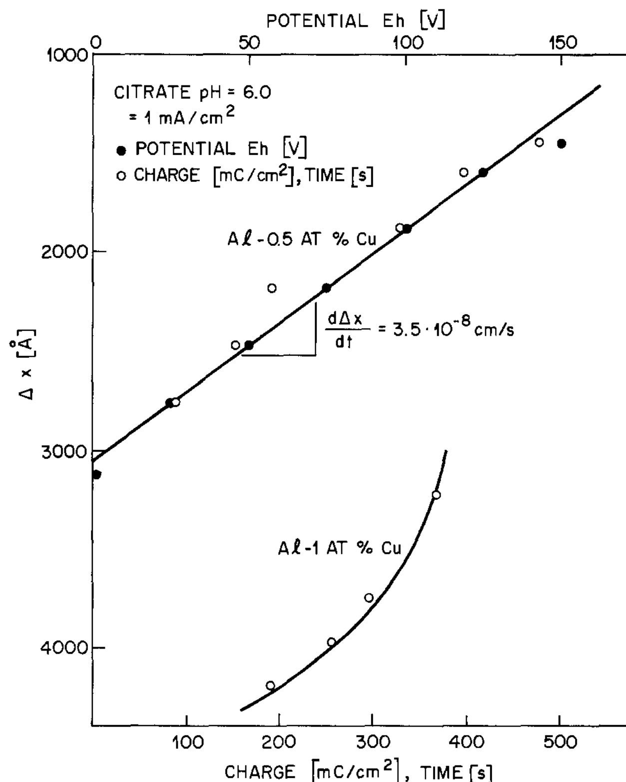

Fig. 9. In depth movement of the copper accumulation zone in the metal film during anodic oxide formation on Al/Cu films as a function of time and potential, $i = 1$ mA/cm², 0.1M citrate, pH = 6.0.

The comparatively fast transport of copper during anodization might be explained by diffusion over a highly disordered thin layer in the metal phase. The formation of an anodic oxide will produce stresses and vacancies at the metal/oxide interface. These vacancies will diffuse into the metal phase thus enhancing the transport of aluminum to the oxide phase and copper in the opposite direction. The breadth of the copper enrichment peak suggests that the vacancy-enhanced diffusion region extends over a depth of 650Å beneath the metal/oxide interface. A similar model has been postulated for the corrosion of binary alloys, involving a diffusion mechanism via divacancies to explain the observed fast transport (12).

The different behavior of the two components of the metal film are apparently a consequence of their differing standard potentials for oxide formation, as shown below (13):

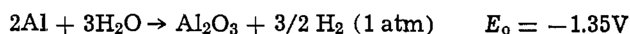

$$2Al + 3H_2O \rightarrow Al_2O_3 + 3/2\ H_2\ (1\ atm) \qquad E_o = -1.35V$$

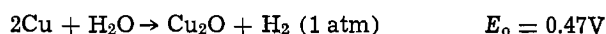

$$2Cu + H_2O \rightarrow Cu_2O + H_2\ (1\ atm) \qquad E_o = 0.47V$$

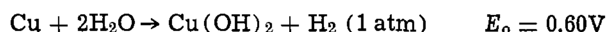

$$Cu + 2H_2O \rightarrow Cu(OH)_2 + H_2\ (1\ atm) \qquad E_o = 0.60V$$

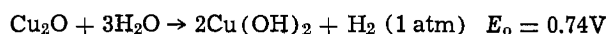

$$Cu_2O + 3H_2O \rightarrow 2Cu(OH)_2 + H_2\ (1\ atm) \qquad E_o = 0.74V$$

This shows clearly that only aluminum oxide is in thermodynamic equilibrium with an aluminum film containing a few percent of copper. During galvanostatic experiments the anodizing voltage is largely dropped across the anodic film (14, 15). This field is necessary to maintain the constant current condition and the corresponding migration of oxygen and aluminum ions within the oxide phase. As long as the potential drop and the activity of the metals are not changed appreciably at the metal/oxide interface the formation of a copper oxide phase is not possible. If, however, an increased copper concentration at some part of the metal film should occur, along with an increased potential drop at the interface, the difference in the potentials for oxide formation might be overcome leading to the formation of copper oxide. The necessary additional overvoltage may be caused by an increasing kinetic hindrance for the Al^{3+}-transfer reaction due to copper accumulation at the interface. Some indication for this is given by the steep increase in the electrode potential just before film damage is observed (5). Alternatively, the formation of copper oxide at sites in the metal film where copper has become enriched to a critical concentration, could be another cause for the localized breakdown.

Conclusion

The following results were obtained by the examination of anodized aluminum-copper films with Rutherford backscattering.

1. The anodic oxide formed under galvanostatic conditions on Al-1% Cu films grew nearly linearly with time and potential and does not contain copper.

2. For anodic voltages up to 80 V_H, copper accumulated at the oxide/metal interface to an excess 1 a/o. Further anodization caused no general increase of the copper concentration, but rather its extension over a greater depth into the metal film.

3. The breakdown of the anodic oxide and the development of characteristic corrosion structures are thought to be related to the copper accumulation, and the local formation of an increased field strength at these locations results in film damage.

4. The accumulated copper is distributed over a depth of about 650Å. The formation of the anodic oxide causes copper diffusion into the metal phase. This transport is presumably enhanced by a disordered layer containing internal stresses and excess vacancies. The corresponding diffusion constant is increased by about eight orders of magnitude compared to the value for volume diffusion.

5. Copper is not incorporated into the oxide phase unless the potential drop at the metal/oxide interface is increased by an additional overvoltage. This is due to the significant difference of the standard potentials for the formation of the corresponding oxides and hydroxides.

Acknowledgments

The authors are indebted to R. P. Frankenthal, J. M. Poate, K. L. Tai, and P. A. Turner for their most helpful advice and discussion, to C. J. Doherty for the preparation of the metal films, and to L. D. Blitzer for the analysis of films by atomic absorption spectroscopy.

Manuscript submitted May 11, 1977; revised manuscript received Jan. 6, 1978.

Any discussion of this paper will appear in a Discussion Section to be published in the December 1978 JOURNAL. All discussions for the December 1978 Discussion Section should be submitted by Aug. 1, 1978.

Publication costs of this article were assisted by Bell Laboratories.

REFERENCES

1. P. J. Silverman and N. Schwartz, *This Journal*, **121**, 550 (1974).
2. J. P. S. Pringle, *ibid.*, **120**, 398 (1973).
3. F. Brown and W. D. Mackintosh, *ibid.*, **120**, 1096 (1973).
4. W. D. Mackintosh, F. Brown, and H. H. Plattner, *ibid.*, **121**, 1281 (1974).
5. H.-H. Strehblow and C. J. Doherty, *ibid.*, **125**, 30 (1978).
6. M. Hansen and K. Anderko, "Constitution of Binary Alloys," p. 84, Metallurgy and Metallurgical Engineering Series, McGraw Hill Book Co., New York (1958).
7. R. Burbank, Private communication.
8. T. M. Buck, J. M. Poate, K. A. Pickar, and C. M. Hsieh, *Surf. Sci.*, **35**, 362 (1973).
9. J. F. Ziegler and W. K. Chu, *Atom. Data Nucl. Data Tables*, **13**, 463 (1974).
10. J. A. Davies, J. Friesen, and J. D. McIntyre, *Can. J. Chem.*, **38**, 1526 (1960).
11. M. Bishop and K. E. Fletcher, *Int. Metall. Rev.*, **17**, 203 (1972).
12. H. W. Pickering and C. Wagner, *This Journal*, **114**, 698 (1967).
13. "Handbook of Chemistry and Physics," 51, D111 (1971).
14. A. Güntherschultze and H. Beetz, *Z. Phys.*, **91**, 70 (1934); *ibid.*, **92**, 367 (1934).
15. K. J. Vetter, "Electrochemical Kinetics," p. 759, Academic Press, New York (1967).

Luminescence of Iron-Activated Lithium Meta Gallate

Jacob G. Rabatin*

General Electric Company, Advance Process Laboratory, Quartz and Chemical Products Department, Cleveland, Ohio 44110

ABSTRACT

$LiGaO_2$:Fe is an efficient phosphor under both ultraviolet and cathode-ray excitations, with peak emission at 742 nm in the near-infrared region. It is best prepared at about 1000°C with stoichiometric proportions of the host ingredients and 0.01 moles Fe_2O_3. At this optimum Fe^{3+} concentration, the relative quantum efficiency is about 80%. Potential use in fluorescent lamps is discussed in relation to plant growth applications for activation of the enzyme phytochrome.

The behavior of Fe^{3+} ions in various hosts has been studied extensively. In $LiAl_5O_8$ with a spinel-like structure (1), Fe^{3+} activator has a peak emission at about 680 nm under 254 nm excitation (2). On the other hand, Fe^{3+}-activated $LiAlO_2$ with a distorted tetragonal structure (3) emits at about 740 nm (4). In the search for efficient near-infrared emitting phosphors for special fluorescent lamp applications, the author examined several gallium-containing hosts for possible emission when activated with iron. $LiGaO_2$:Fe was found to be an efficient phosphor under both ultraviolet (u.v.) and cathode-ray (CR) excitation. This paper describes the preparation, luminescent properties, and performance of $LiGaO_2$:Fe in fluorescent lamps. Comparisons with $LiAlO_2$:Fe phosphors are also described. Some potential uses in fluorescent lamp applications are indicated.

Experimental

Phosphors were prepared from high purity Li_2CO_3, Al_2O_3, Fe_2O_3, and Ga_2O_3 starting materials. The desired formulations were intimately blended and fired twice in covered vessels at temperatures from 900° to about 1200°C and times of 2-4 hr. The final product was again ground finely and sifted through 325 mesh to remove oversize sintered aggregates of phosphor particles which generally were about 20% of the total weight.

The final phosphor powders were characterized by standard analytical methods for absolute density (pycnometer), particle size (Coulter Counter), surface area (BET), emission under 254 nm (Cary 14), refractive indexes (immersion oil method), and 254 nm absorption on plaques. Infrared emission was also measured on powder samples utilizing a RCA No. C31025C photomultiplier which has a flat energy response between 400 and 800 nm. The CR efficiency measurements were made on powder samples at 5 kV and 3 μA and were compared to Y_2O_3:Eu as a standard having 12% energy efficiency (5). The fluorescent lamp data were obtained on standard 40W lamps using organic based coating methods at 60% reflectance of visible light. The spectral emissions curves shown in Fig. 1 and 2 were performed on powder samples utilizing special apparatus designed by Dr. R. Bateman of GE Lighting Research Laboratory.

Results and Discussion

The preparations of $LiAlO_2$:Fe and $LiGaO_2$:Fe require similar conditions of firing temperatures and times with best results obtained by double firing procedures. Table I lists the effect of second fire temperatures on *IR* output of the phosphor. The optimum firing temperatures are 1000°C for $LiGaO_2$:Fe as compared to 1100°C for $LiAlO_2$:Fe. X-ray diffraction analyses indicate that $LiAlO_2$ and $LiGaO_2$, respectively, are the dominant phases. The resulting powders are well crystallized with some sintering occurring. The Coulter Counter particle size mediums are between 10 and 12 μm after the powders have been sifted through 325 mesh screens. The BET surface areas are between about 0.4 and 0.5 m^2/g. The data for absolute densities, refractive indexes, and crystal structure are listed in Table II. As expected $LiGaO_2$ has a higher absolute density and higher refractive index than $LiAlO_2$. It appears from x-ray diffraction data that both phases have tetragonal crystal structures.

The effect of compositional changes on the relative *IR* output of various Fe^{3+}-activated lithium aluminates are shown in Table III. The maximum *IR* output occurs at the stoichiometric *meta* aluminate composition. Small changes from this composition affect the *IR* output slightly. Similar results were also obtained for the lithium gallate phosphors. According to Palumbo (4), the differences in emission spectra of $LiAl_5O_8$:Fe at about 670 nm as compared to $LiAlO_2$:Fe at about 734 nm may be due to the Fe^{3+} ions having different site symmetries, namely, octahedral and tetrahedral, respectively.

The effects of Fe^{3+} activator concentrations on *IR* output are shown in Table IV for both $LiAlO_2$ and $LiGaO_2$ under 254 nm excitations. The optimum Fe^{3+} concentrations are 0.005 and 0.010 moles per mole of phosphor for $LiAlO_2$ and $LiGaO_2$, respectively. The percent absorptions are relatively large at 99%. Con-

Table I. Effect of firing temperatures on the relative *IR* output of $LiAlO_2$:0.005Fe and $LiGaO_2$:0.01Fe under 254 nm excitation

Firing temp (°C)	Relative *IR* output	
	$LiAlO_2$:0.005Fe	$LiGaO_2$:0.01Fe
900	—	92
1000	94	100
1100	100	83
1200	76	74

Table II. Physical characteristics of $LiAlO_2$ and $LiGaO_2$

	$LiAlO_2$	$LiGaO_2$
Crystal structure, distorted	Tetragonal	Tetragonal
Refractive indexes	1.60, 1.65	1.74
Absolute density	2.68	4.22

Table III. Effect of compositional changes on the relative *IR* output of various lithium aluminates under 254 nm excitation

Composition	Relative *IR* output (%)
$LiAl_5O_8$:0.005Fe	14
$Li_{0.9}AlO_{1.95}$:0.005Fe	88
$LiAlO_2$:0.005Fe	100
Li_5AlO_4:0.005Fe	53

* Electrochemical Society Active Member.

Key words: lithium metal gallate, infrared luminescence, preparation properties, iron activation.

Table IV. Effect of Fe^{3+} concentrations on *IR* output of $LiAlO_2$:Fe and $LiGaO_2$:Fe under 254 nm excitation

Fe^{3+} conc (mole)	$LiAlO_2$:Fe		$LiGaO_2$:Fe	
	Rel. *IR* output (%)	Abs., 254 nm (%)	Rel. *IR* output (%)	Abs., 254 nm (%)
0.003	81	81	74	72
0.005	100	92	90	95
0.010	93	96	100	98
0.050	59	99	76	99

centration quenching occurs at relatively high Fe^{3+} levels, especially in $LiGaO_2$.

Emission spectra under 254 nm excitation are shown in Fig. 1 for $LiAlO_2$:0.005Fe and in Fig. 2 for $LiGaO_2$:0.010Fe at 30° and 293°K, respectively. Both phosphors show zero phonon lines at about 710 nm at 30°K. Significant differences in crystal field splitting are observed at 30°K suggesting some differences in site symmetry between the two phosphors. At room temperature the spectra show single broad band emission peaks at 734 nm for $LiAlO_2$:Fe and at 742 nm for $LiGaO_2$:Fe.

The relative quantum efficiencies were measured and compared to a cool white calcium halophosphate at 92%. The results under 254 nm excitation are listed in Table V. Included also are the quantum efficiencies of iron-activated magnesium lithium aluminate and lithium gallium indate. Of more than 100 hosts examined only these four phosphors showed significant *IR* response. $LiGaO_2$:0.01Fe is somewhat more efficient than $LiAlO_2$:Fe.

The relative energy efficiencies of these phosphors were also measured under CR excitations at 5 kV and 3 μA based on the procedures suggested by Ludwig and Kingsley (5). Y_2O_3:Eu was used as the standard

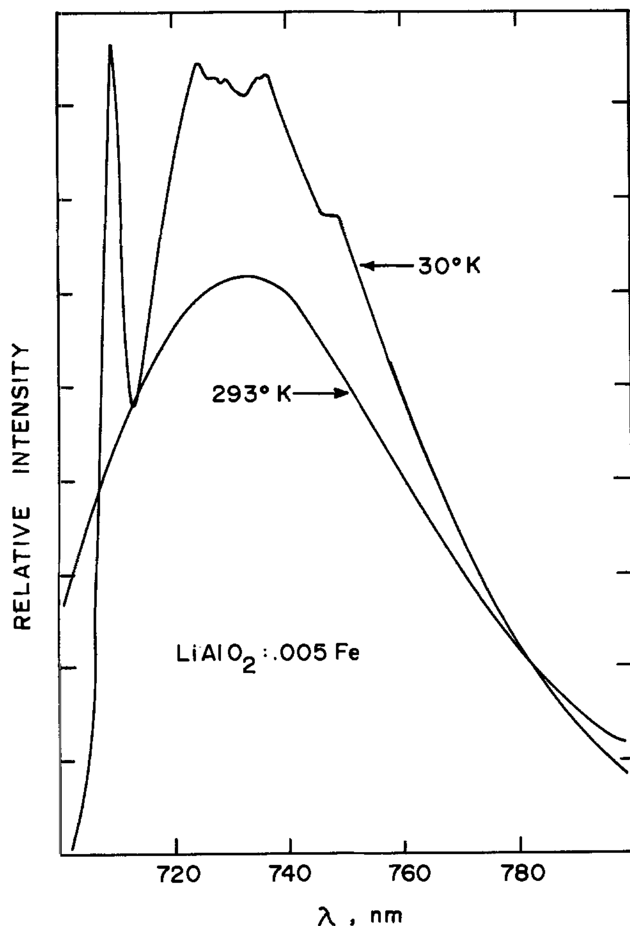

Fig. 1. Spectral emission curves for $LiAlO_2$:0.005Fe under 254 nm excitation.

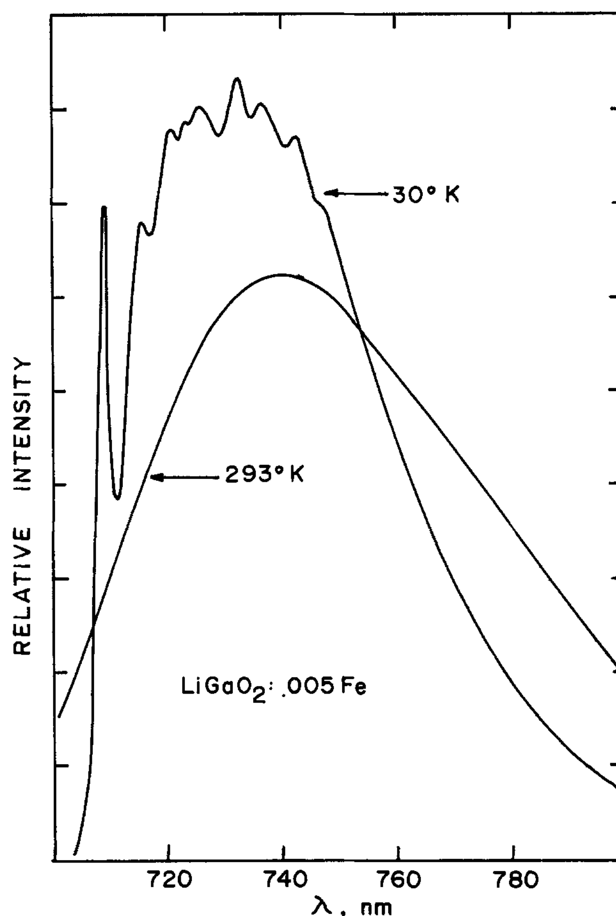

Fig. 2. Spectral emission curves for $LiGaO_2$:0.01Fe under 254 nm excitation.

at 12% energy efficiency. The results are presented in Table VI for the most efficient phosphor composition under CR excitations. Both phosphors are moderately efficient under CR excitations. The emission spectra are identical to those shown in Fig. 1 and 2. Under CR excitation, energy transfer from host to Fe^{3+} ions occurs with some nonradiative losses.

One of the more promising uses for a near *IR* emitting phosphor is in providing artificial illumination in plant growth applications (6). It has been shown that for balanced activation of the enzyme, phytochrome, which controls plant growth and flowering, light peaking at about 730 nm is needed (7, 8). Figure 3 shows the radiant power characteristics of $LiGaO_2$:0.01Fe in 40W fluorescent lamps. The fine narrow band emissions are due to the characteristic Hg emissions. The broad band peaking at about 740 nm is due to the Fe^{3+}

Table V. Relative quantum efficiencies of some *IR* phosphors under 254 nm excitations

Phosphor	Rel. Q E (%)
$LiAlO_2$:0.005Fe	75
$LiGaO_2$:0.010Fe	80
$MgLi_2Al_2O_8$:0.002Fe	22
$Li_4Ga_2In_2O_8$:0.004Fe	18

Table VI. Relative energy efficiencies under 5 kV 3 μA CR excitations

(Concentrations are optimum for CR excitation)

Phosphor	CR efficiency (%)
$LiAlO_2$:0.002Fe	4
$LiAlO_2$:0.001Fe	3.3
$LiGaO_2$:0.001Fe	4

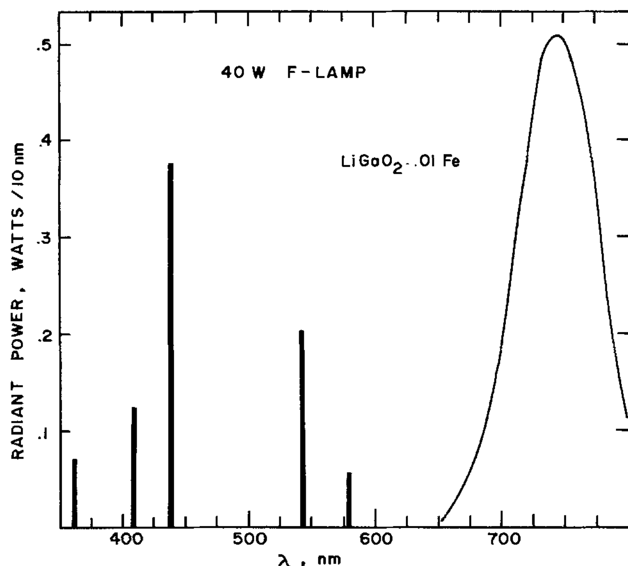

Fig. 3. Spectral emission curve for $LiGaO_2$:0.01Fe in a fluorescent lamp.

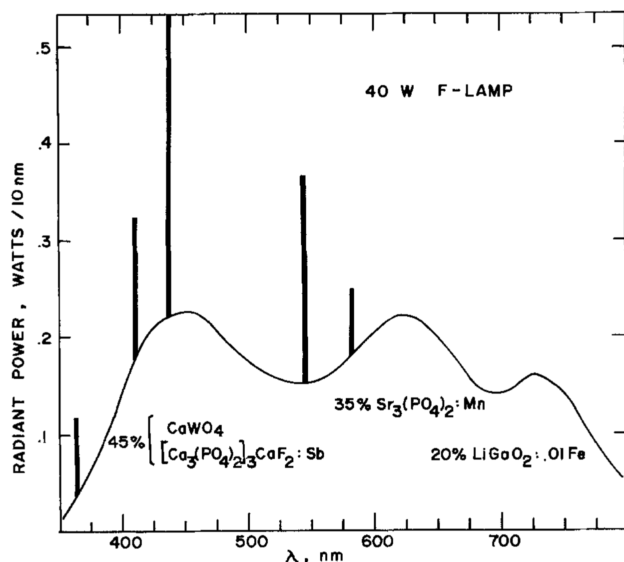

Fig. 4. Spectral emission curve for a four-component fluorescent lamp containing $LiGaO_2$:0.01Fe.

emission in $LiGaO_2$. Due to the Stokes shift at 740 nm, the radiant power output is only about 70% that for a emission peaking at 540 nm, for example. Similar results were also obtained for $LiAlO_2$:0.005Fe phosphors.

In Fig. 4, the radiant power characteristics are shown for a plant growth fluorescent lamp emission which approximates the chlorophyll action spectrum in the visible region and also contains about 20% output peaking at 740 nm due to $LiGaO_2$:Fe. Such fluorescent

Table VII. Depreciation data for 40W F-lamps containing *IR* emitting phosphors

Phosphor composition, weight	100 hr loss (%)	500 hr loss (%)
Cool White halophosphate (CW)	2.4	5.9
85% CW + 15% $LiAlO_2$:0.005Fe	4.5	8.8
80% CW + 20% $LiGaO_2$: 0.01Fe	3.0	6.6

lamp would be especially useful where maximum flowering conditions are desired.

The percent lumen depreciation data for various phosphor blend compositions are listed in Table VII. A standard Cool White (CW) calcium halophosphate lamp was used for comparison with the listed blends. The data indicate that $LiGaO_2$:Fe has better maintenance in blends with Cool White in fluorescent lamps as compared to $LiAlO_2$:Fe.

Summary

$LiGaO_2$:Fe is an efficient phosphor with peak emission at 742 nm under both u.v. and CR excitations. The physical properties are similar to those of $LiAlO_2$:Fe reported earlier.

The solid-state preparation of $LiGaO_2$ is best performed at about 1000°C with stoichiometric compositions of the host ingredients at optimum Fe^{3+} concentrations of 0.01 moles. The relative quantum efficiency is about 80% under 254 nm excitation somewhat more efficient than $LiAlO_2$:Fe. Possible uses of $LiGaO_2$:Fe in fluorescent lamps are in plant growth applications

Acknowledgments

The author wishes to thank Dr. J. Kingsley of Corporate Research and Development for many helpful comments, Dr. R. Bateman of the Lighting Research Laboratory for the emission spectra measurements, and R. Evans for many of the preparations and analyses.

Manuscript submitted Aug. 4, 1977; revised manuscript received Jan. 11, 1978. This was Paper 124 presented at the Philadelphia, Pennsylvania, Meeting of the Society, May 8-13, 1977.

Any discussion of this paper will appear in a Discussion Section to be published in the December 1978 JOURNAL. All discussions for the December 1978 Discussion Section should be submitted by Aug. 1, 1978.

Publication costs of this article were assisted by General Electric Company.

REFERENCES

1. H. Saalfeld, *Z. Anorg. Allgem. Chem.*, **291**, 117 (1958).
2. S. Jones, *This Journal*, **95**, 295 (1949).
3. M. Marezio, *Acta Crystallogr.*, **19**, 396 (1965).
4. D. T. Palumbo, *J. Lumin.*, **4**, 89 (1971).
5. G. W. Ludwig and J. D. Kingsley, *This Journal*, **117**, 348 (1970).
6. J. Van Broekhoven, IES Meeting, July 1, 1973.
7. M. W. Parker and H. A. Borthwick, *Plant Physiol.*, **24**, 345 (1949).
8. R. J. Downs, *ibid.*, **30**, 468 (1955).

Quantified Conditions for Emitter-Misfit Dislocation Formation in Silicon

Richard B. Fair*

Bell Laboratories, Reading, Pennsylvania 19604

ABSTRACT

The conditions under which misfit dislocations are generated during phosphorus diffusion in silicon are discussed. Van der Merwe's concept of critical misfit is used to determine the critical surface region depth for a given P surface concentration which causes spontaneous misfit dislocation formation. Using this model the times required to form misfit arrays are calculated as a function of temperature and surface concentration. The effect of misfit dislocation generation in an oxidizing ambient is also discussed.

High concentration P diffusions in Si can induce localized lattice strain which is often relieved through the formation of either hexagonal edge dislocation networks or arrays of concentric loops (1). The networks are usually confined within the diffused region at depths within ¼ to ½ of the P junction depth and at high densities ($>10^9$ dislocations/cm²) (2-5). However, dislocations at densities of 10^5-10^7/cm² have been observed (6, 7) deeper than the junction as a result of climb (for <111> Si) or glide (for <100> Si) processes. In <111> Si, electrically active dislocation loops have been found to extend to considerable distances (~100 μm) outside of the planar-diffused region since primary slip occurs in the (111) plane (2, 8, 9).

For <100> oriented Si glide is easiest for 60° dislocations in (111) planes. When suitably oriented glide dislocations meet, they form a stable network at some depth in the Si (10). External dislocations are generally not observed outside the diffused region in <100> Si (8).

The influence of dislocations on impurity diffusion and the electrical performance of Si devices has been reviewed extensively by Lawrence (11). Depending on the stability and electrical activity of induced dislocations and whether or not residual metal impurities and structural imperfections exist in the Si prior to emitter diffusion, the following effects have been correlated with misfit dislocations: (*i*) reduced transistor current gain (1, 2, 12, 13), (*ii*) emitter-collector shorts and excess leakage (1, 12, 14-19), (*iii*) high junction leakage currents (1, 11, 20-23), (*iv*) increased low frequency noise figure (21), and (*v*) variable temperature dependence of transistor current gain (21). Therefore, the detrimental effects of phosphorus emitter-induced misfit dislocations have been well documented.

There are also beneficial effects associated with dense dislocation networks. It has been shown that the onset of effective ion-damage gettering in Si occurs when damage-induced dislocations in densities greater than 2×10^8 cm^{-2} coalese to form networks (24). Similarly, Poponiak *et al.* (25) have shown that for the case of gettering with boron-diffused layers in Si, no metal gettering occurs unless dense misfit dislocations are induced. For n-type dopant gettering, donor impurities at high concentrations will getter metallic impurities via ion-pairing and solubility-enhancement effects (26). However, the formation of unstable misfit dislocations during diffusion will enhance the gettering efficiency of the diffused layer. Such gettering will be beneficial provided the accumulation of metal impurities is away from the active device region.

Regardless of whether one wants to avoid misfit dislocations in a P emitter diffusion or one seeks the effective gettering properties of misfit dislocations, it is important to know when they occur. It is the purpose of this paper to quantify the conditions under which misfit dislocations are generated during P diffusion.

Analysis: Conditions for Misfit Dislocation Generation

The critical misfit condition.—The conditions under which misfit dislocations are generated have been discussed by many workers (21, 28-36). According to Prussin's model (31) the maximum stress caused by the lattice misfit strain of the undersized P atoms is proportional only to the surface concentration of P. When the yield stress of Si is exceeded, dislocations appear. Several workers (21, 32, 33) have shown that the Prussin model is not adequate. The integrated concentration of atoms per square centimeter appears to be a better quantity to correlate with the threshold stress for dislocation generation (9). Watanabe *et al.* (21) have determined the critical total concentration for boron in Si to be $Q_B \simeq 1.5 \times 10^{16}$ cm^{-2}.

An attempt was made to establish the critical total concentration for P in Si using Czaja's theory (3, 36). However, it was found that a more rigorous theory was needed. Such a theory of interfacial misfit dislocations has been advanced by Van der Merwe (35) for epitaxy and the diffusion zone of a bicrystal system. For a small misfit, Van der Merwe derived an equation for a single crystal top layer relating the ratio h/a (the top layer thickness in units of lattice parameters) with δ_c, the critical misfit. This equation reduces to (36)

$$\ln \frac{2\pi e \delta_c}{(1-\gamma)} + \frac{4\pi(1-\gamma)^2 h \delta_c^2}{(1-2\gamma)a} = 0 \qquad [1]$$

for diffusion-induced strain in Si. When the top layer thickness exceeds a critical value, spontaneous generation of a dislocation network occurs. Assuming Poisson's ratio $\gamma = 0.29$, Eq. [1] becomes

$$\ln 24.06\, \delta_c + 15.08 \frac{h}{a} \delta_c = 0 \qquad [2]$$

Below critical misfit, the lattice in the diffused layer should adjust itself to the Si substrate lattice through elastic deformation. The critical misfit is defined as

$$\delta_c = \eta \frac{\Delta r}{r} = \eta \frac{(r_{Si} - r_I)}{r_{Si}} \qquad [3]$$

where η is the solute or impurity fraction and r_{Si} and r_I are the tetrahedral covalent radii of Si and the impurity, respectively. Using the Van Vechten and

* Electrochemical Society Active Member.

Phillips values (37) for Si and P yields the critical thickness h_c as

$$h_c = \frac{-4.94 \times 10^{15}}{C_{avg}} \ln (1.753 \times 10^{-23} C_{avg}) \quad [4]$$

C_{avg} is the average doping in atoms per cubic centimeter in the strained layer.

For the case of high concentration P diffusion in Si, a near-surface, highly doped "flat" region exists in the dopant profile as a result of the n^2 dependence of diffusivity on electron concentration (38). The width of this region, x_o, is taken as the depth at which the electron concentration falls to n_e (see Fig. 1). Below $n = n_e$, the n^2 dependence of P diffusivity disappears (38). At 1000°C, $n_e \simeq 1.3 \times 10^{20}$ cm^{-3}. Using the approximation that

$$C_{avg} = C_s/2$$

where C_s is the total P surface concentration, and assuming that the flat-region depth corresponds to the layer thickness, h, in Eq. [1], then

$$h_c = x_{oc} = \frac{-9.88 \times 10^{15}}{C_s} \ln (8.76 \times 10^{-24} C_s) \quad [5]$$

The width of the high concentration region, x_{oc}, at which misfit dislocations occur has been set equal to h_c. Equation [5] is plotted in Fig. 2. Also shown are the C_s and x_o coordinates of numerous P diffusions into both <111> and <100> Si. The occurrence of high densities of misfit dislocations in these diffused layers has been determined by x-ray topography, TEM, or careful Sirtl etching. The open circle data (○-data) indicate that dense misfit dislocations were observed, and the closed circle data (●-data) indicate that no dislocations were observed. Diffusions performed over the temperature range of 900°-1235°C are represented in Fig. 2 with the bulk of the data coming from the published literature (2, 4-6, 14, 21, 27, 36, 39-43). It can be seen that the calculated curve described by Eq. [5] is a good "line of demarcation" between the dense dislocated and nondislocated P diffusion data. Moreover, the $C_s \cdot x_{oc}$ product at $C_s = 2 \times 10^{21}$ cm^{-3} is 4×10^{16} cm^{-2}, whereas at $C_s = 1 \times 10^{20}$ cm^{-3} the product is 7×10^{16} cm^{-2}. However, if a constant $C_s \cdot x_{oc} = 4.6 \times 10^{16}$ cm^{-2} line is plotted on the figure, it too might serve as a good boundary. This fine point will be resolved in the next section.

Referring again to Fig. 2, it can be seen that data are also plotted (x-data) which indicate that isolated

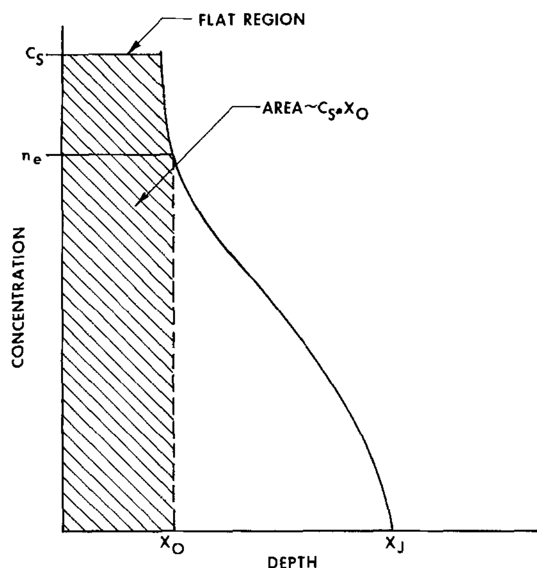

Fig. 1. Typical high concentration phosphorus diffusion profile in silicon. The surface region area is shown cross-hatched.

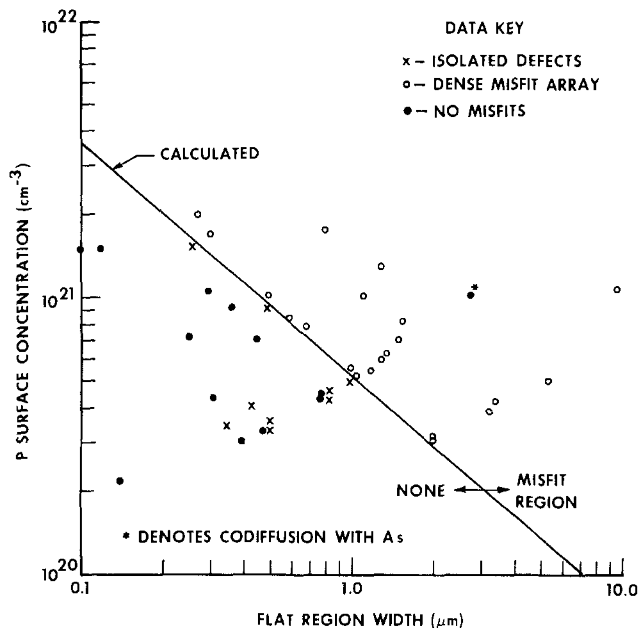

Fig. 2. Phosphorus surface concentration vs. the critical flat-region depth required for misfit dislocation formation.

defects (dislocations, stacking faults, etc.) occurred prior to the formation of dense misfit arrays. The increase of isolated defect density prior to "lattice collapse" has been recognized in the literature (3, 40, 43). The nucleation of these defects is dependent on the initial oxygen content and active dislocation density of the Si (21). Morris and Katz (14) have shown that even the existence of these isolated defects can affect junction yield.

The effect of codiffusing As with P is also indicated in Fig. 2. The effect of As is to inhibit dislocation formation since the As atoms are in interstitial sites in the Si. Thus, it has been proposed that the movement of Si atoms is obstructed by the interstitial As atoms making dislocation generation more difficult (44).

The effect of diffusion ambient on misfit dislocation generation.—Chemical source diffusions.—There have been various reports in the literature (2, 45) that the formation of misfit dislocations is dependent on the furnace ambient during drive-in of a predeposited P layer in Si. Duffy *et al.* (2) report the chemical predeposition of a P layer with an integrated concentration of ~2.5×10^{16} P atoms/cm^2 (970°C, 35 min in N_2 ambient with 2% O_2). No misfit dislocations were observed. However, misfits were observed after a 970°C drive-in cycle consisting of 5 min in dry O_2, 30 min in steam, and 40 min in dry O_2. At the end of this cycle the total P concentration was still ~2.5×10^{16} cm^{-2}. However, the $C_s \cdot x_o$ product had increased from ~3.5×10^{16} to ~4.6×10^{16} cm^{-2}. From the previous discussion of Fig. 2, a $C_s \cdot x_o$ product of ~4.6×10^{16} cm^{-2} is sufficient to create misfit networks. The effect of the oxidation drive-in cycle, then, has been to increase the amount of phosphorus in the "flat region" at the surface.

The effect can be understood by computer simulation of the P drive-in process. Duffy's P profile data for the predeposition step and the drive-in cycle are shown in Fig. 3. Also shown are the calculated profiles corresponding to computer simulations. Good agreement with the published data is obtained. Since the computer program prints out the P profile at the end of each drive-in step, a locus of points for the drive cycle can be generated to either the C_s *vs.* x_o plane or the C_{avg} *vs.* x plane. The locus for the oxidation cycle is shown in Fig. 4 where the average P doping in the surface layer was determined at each step. Point 1 cor-

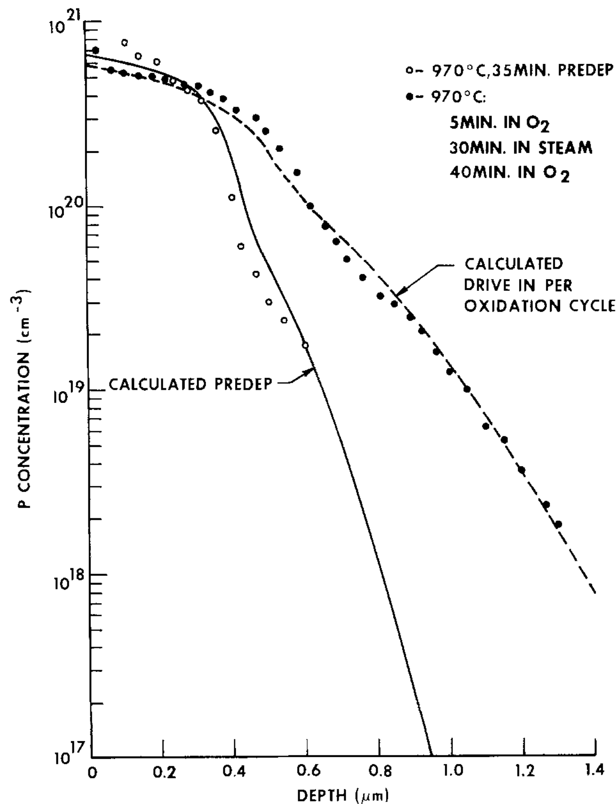

Fig. 3. Computer simulation of Duffy *et al.* phosphorus diffusion profiles.

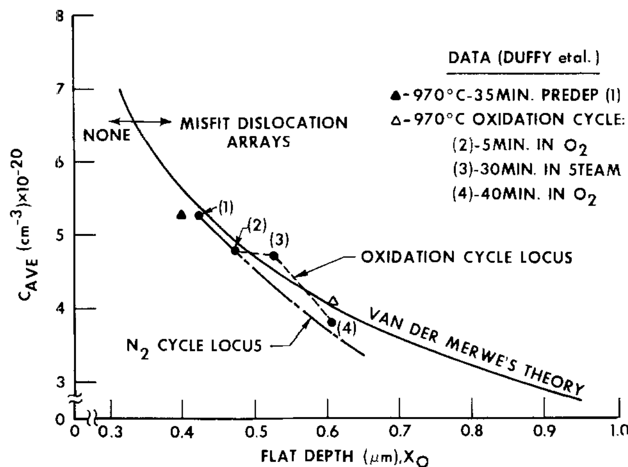

Fig. 4. Effect of drive-in ambient on the average phosphorus surface concentration vs. the flat region depth. Calculations and data are based upon Duffy *et al.* experiments.

responds to the profile after predeposition (▲-point is from Duffy's experimental data). Point 2 corresponds to a 5 min dry O_2 oxidation. Point 3 corresponds to the the 30 min steam oxidation. It can be seen that during the steam oxidation the average P doping in the surface only changed slightly, while the flat depth, x_o, increased. Therefore, during this step the locus crossed the no misfit/misfit line which is drawn on the figure according to Eq. [4] and Van der Merwe's theory. During the final dry O_2 step (40 min) the locus crossed the misfit line and terminated at point 4 (corresponds to the Δ-point from Duffy).

This same process has been simulated for the case where no oxidations were performed; all drive-ins were done in nitrogen for the same times and at 970°C. The resulting locus is also shown in Fig. 4. This locus does not cross the theoretical misfit line, and thus no misfit dislocation nets should be formed. This observation was verified by Fairfield and Schwuttke (8). Consequently, only the steam oxidation drive process which "snowplows" phosphorus has the potential ability to "push" the $C_{avg} \cdot x_o$ locus across the misfit line, if conditions for misfit formation have not already been incurred. Drive-ins in dry O_2 or neutral ambients will generate $C_{avg} \cdot x$ locii which tend to slope downward faster than the Van der Merwe curve in Fig. 4.

Diffusion of ion-implanted P layers.—For the case of ion-implanted phosphorus in silicon, Tamura, *et al.* (45) have shown that the dose required to generate misfit dislocations is 3×10^{15} cm^{-2} for drive-in in steam and 1×10^{16} cm^{-2} for drive-in in dry N_2. Implantation energies were 50-100 keV. It is clear that implantation-induced damage and stress make it very difficult to predict quantitatively when misfit dislocations will be formed. Because of the lower density of the amorphous Si layer created by high dose implantation, considerable expansion of the implanted layer occurs (46, 47). The disorder-induced stress can approach or even exceed the yield stress of Si ($\sim 4 \times 10^9$ dynes/cm^2). Since nonoxidizing atmosphere annealing results in the shrinkage of interstitial defects in Si and oxidation causes such defects to grow (48), higher doses of P are needed to generate dislocations during neutral ambient anneals.

For the case of ion-implanted As in Si, the critical dose for dislocation networks to form during steam drive-in is $\sim 2 \times 10^{16}$ cm^{-2} at 50 keV (45). Consequently, diffusion in a neutral ambient should occur first in order to anneal out damage and stress for a dislocation-free emitter process.

Phosphorus diffusion curves for misfit dislocation formation.—Curves of P surface concentration *vs.* diffusion time required to generate misfit dislocation arrays (MDA) are shown in Fig. 5. These curves are based on the time necessary for the critical flat region depth, x_{oc}, to be reached. The highest concentration point for each curve corresponds to the solid solubility at that temperature. For P concentrations above these limits, precipitation-induced stacking faults and dislocations will be formed in relatively short times (42). For a given C_s value the solid curves mark the boundaries beyond which in time dense misfit arrays will be formed.

Summary and Conclusions

A short review of the observed effects of emitter-misfit dislocations on Si device behavior has been presented. Generally, unstable dislocations created during high concentration P emitter diffusion are electrically active and have a high gettering efficiency for impurity atoms in Si. Thus, depending on the residual metal impurity concentrations and the densities of defects in the Si prior to emitter diffusion, misfit dislocations formed during emitter processing have been linked to

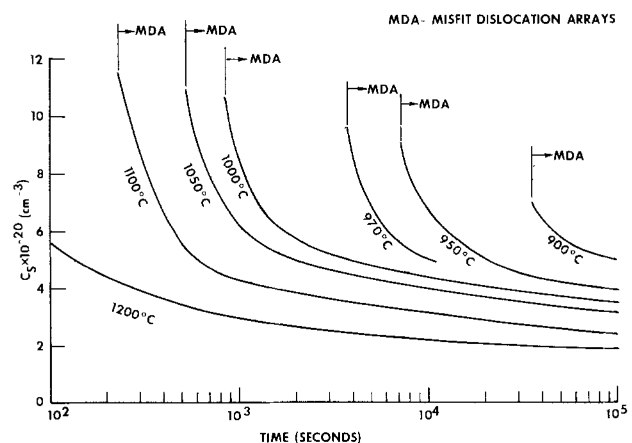

Fig. 5. Critical time to dislocation array formation for phosphorus diffusion in low oxygen ambients.

numerous transistor parameter nonuniformities and yield problems.

The conditions under which misfit dislocations are generated during P diffusion have been quantified using Van der Merwe's theory (35) of critical misfit. Curves have been generated which allow one to center P diffusion surface concentrations well into the dislocation-formation condition (for gettering) or well out of this condition.

Manuscript submitted Dec. 7, 1977; revised manuscript received Jan. 20, 1978.

Any discussion of this paper will appear in a Discussion Section to be published in the December 1978 JOURNAL. All discussions for the December 1978 Discussion Section should be submitted by Aug. 1, 1978.

Publication costs of this article were assisted by Bell Laboratories.

REFERENCES

1. J. E. Lawrence, *This Journal*, **115**, 860 (1968).
2. M. C. Duffy, F. Barson, J. M. Fairfield, and G. H. Schwuttke, *ibid.*, **115**, 84 (1968).
3. W. Czaja, *J. Appl. Phys.*, **37**, 3441 (1966).
4. M. L. Joshi and S. Dash, *IBM J. Res. Dev.*, **10**, 446 (1966).
5. M. L. Joshi and F. Wilhelm, *This Journal*, **112**, 185 (1965).
6. Y. Sato and H. Arata, *Jpn. J. Appl. Phys.*, **3**, 551 (1964).
7. M. Maeda and M. Tanimoto, *Phys. Status Solidi A*, **16**, 273 (1973).
8. J. M. Fairfield and G. H. Schwuttke, *This Journal*, **115**, 415 (1968).
9. J. E. Lawrence, *ibid.*, **113**, 819 (1966).
10. J. Washburn, G. Thomas, and H. J. Queisser, *J. Appl. Phys.*, **35**, 1909 (1964).
11. J. E. Lawrence, in "Semiconductor Silicon 1973," H. R. Huff and R. R. Burgess, Editors, p. 17, The Electrochemical Society Softbound Symposium Series, Princeton, N.J. (1973).
12. P. C. Parekh, *Solid State Electron.*, **14**, 273 (1971).
13. D. H. Lyon, Private communication.
14. B. L. Morris and L. E. Katz, Unpublished.
15. G. H. Plantinga, *IEEE Trans. Electron Devices*, **ed-16**, 394 (1969).
16. S. Dash, in "Semiconductor Silicon 1973," H. R. Huff and R. R. Burges, Editors, p. 626, The Electrochemical Society Softbound Symposium Series, Princeton, N.J. (1973).
17. W. K. Tice, R. C. Lange, and R. B. Shasteen, *ibid.*, p. 639.
18. F. Barson, M. S. Hess, and M. M. Roy, *This Journal*, **116**, 304 (1969).
19. E. M. Juleff, *Solid State Electron.*, **16**, 1173 (1973).
20. J. E. Lawrence, in "Semiconductor Silicon," R. R. Haberecht and E. L. Kern, Editors, p. 596, The Electrochemical Society Softbound Symposium Series, New York (1969).
21. M. Watanabe, H. Muraoka, and T. Yonezawa, Proceedings of the 6th Conference on Solid State Devices, Tokyo, 1974, in *Jpn. J. Appl. Phys.*, **44**, 269 (1975).
22. J. E. Iwersen, A. R. Bray, and J. J. Kleimack, *IRE Trans. Electron Devices*, **9**, 474 (1962).
23. A. E. Cosand and S. Prussian, Paper 109 presented at The Electrochemical Society Spring Meeting, Washington, D.C., May 2-7, 1976.
24. H. J. Geipel and W. K. Tice, *Appl. Phys. Lett.*, **30**, 325 (1977).
25. M. R. Poponiak, W. A. Keenan, and R. O. Schwenker, in "Semiconductor Silicon 1973," H. R. Huff and R. R. Burgess, Editors, p. 701, The Electrochemical Society Softbound Symposium Series, Princeton, N.J. (1973).
26. R. L. Meek, T. E. Seidel, and A. G. Cullis, *This Journal*, **122**, 786 (1975).
27. R. A. McDonald, G. G. Ehlenberger, and T. R. Huffman, *Solid-State Electron.*, **9**, 807 (1966).
28. S. K. Maksimov, V. D. Verner, and D. I. Piskunov, *Sov. Phys. Solid State*, **17**, 1387 (1976).
29. S. K. Maksimov and G. V. Akulova, *ibid.*, **15**, 2150 (1974).
30. H. J. Queisser, *J. Appl. Phys.*, **32**, 1776 (1961).
31. S. Prussin, *ibid.*, **32**, 1876 (1961).
32. A. Armigliato, M. Servidori, S. Solmi, and I. Vecchi, *ibid.*, **48**, 1806 (1977).
33. K. Yagi, N. Miyamoto, and J. Nishizawa, *Jpn. J. Appl. Phys.*, **9**, 246 (1970).
34. J. W. Matthews, *Philos. Mag.*, **6**, 1347 (1961).
35. J. H. Van der Merwe, "Single Crystal Films," pp. 139-163, MacMillan Co., New York (1964).
36. S. Dash and M. L. Joshi, in "Silicon Device Processing," C. P. Marsden, Editor, p. 202, Nat. Bur. of Standards Spec. Pub. 337, Gaithersburg, Md. (1970).
37. J. A. Van Vechten and J. C. Phillips, *Phys. Rev. B*, **2**, 2160 (1970).
38. R. B. Fair and J. C. C. Tsai, *This Journal*, **124**, 1107 (1977).
39. T. R. Huffman, Proceedings of the Semiconductor/IC Processing and Production Conference, Industrial and Scientific Conf. Manag., Inc., New York, June 1971, p. 25.
40. L. A. Koledov and R. B. Popova, *Sov. Phys. Semicond.*, **7**, 1568 (1974).
41. E. V. Dobrokhotov and P. V. Pavlov, *Sov. Phys. Solid State*, **18**, 1640 (1976).
42. A. Armigliato, D. Nobili, M. Servidori, and S. Solmi, *J. Appl. Phys.*, **47**, 5489 (1976).
43. D. G. Schimmel, Unpublished.
44. F. Fujimoto, K. Komaki, M. Watanabe, and T. Yonezawa, *Appl. Phys. Lett.*, **20**, 248 (1972).
45. M. Tamura, N. Yoshihiro, and T. Tokuyama, in "Semiconductor Silicon 1977," H. R. Huff and E. Sirtl, Editors, p. 726, The Electrochemical Society Softbound Symposium Series. Princeton, N.J. (1977).
46. R. E. Whan and G. W. Arnold, *Appl. Phys. Lett.*, **17**, 378 (1970).
47. U. Bonse, M. Hart, and G. W. Schwuttke, *Phys. Status Solidi*, **33**, 36 (1969).
48. I. R. Sanders and P. S. Dobson, *Philos. Mag.*, **20**, 881 (1969).

Structure and Stability of Low Pressure Chemically Vapor-Deposited Silicon Films

T. I. Kamins*

Hewlett-Packard Laboratories, Palo Alto, California 94304

and M. M. Mandurah and K. C. Saraswat*

Integrated Circuits Laboratories, Stanford University, Stanford, California 94305

ABSTRACT

The structure of silicon films deposited by low pressure, chemical vapor deposition in the 600°C temperature range has been investigated by x-ray diffraction and transmission electron microscopy. There is a critical temperature near 600°C, above which the deposited films are polycrystalline and below which amorphous films are obtained. This temperature is close to that used to deposit films for integrated circuit applications. When the films are polycrystalline, the <110> texture dominates. The polycrystalline films are reasonably stable upon annealing to temperatures up to approximately 1100°C. The initially amorphous films, however, easily crystallize. Crystallization has been observed to be well advanced after annealing at 800°C. Large stresses are built into the amorphous films, while the stresses in the polycrystalline films are lower.

In the past decade polycrystalline silicon has become important in several applications. Submicron films of polycrystalline silicon, especially, are of great commercial importance in silicon-gate MOS integrated circuits (1) and charge-coupled devices (2). Until recently, these films have generally been deposited in cold-wall reactors in which the silicon substrates lie flat on an externally heated susceptor. The low capacity and the high capital and operating costs of these reactors, however, may contribute significantly to the cost of the integrated circuit fabrication process.

Within the last two years, low pressure, chemical vapor deposition (LPCVD) systems for depositing polycrystalline silicon have been developed (3). The high capacity and lower costs of these systems have led to their rapid acceptance in high volume, integrated circuit manufacturing facilities. Since the deposition rate, temperature, and pressure in these reactors are markedly different from those conventionally employed, some characterization of the material deposited is needed to ensure that the characteristics and reliability of the integrated circuit in which it is used are not degraded. Because low pressure reactors are generally operated slightly above 600°C, a temperature close to the amorphous-crystalline transition temperature seen in silicon films deposited by chemical vapor deposition at atmospheric pressure (4, 5), the structure in the as-deposited film, and its stability upon further processing of the integrated circuit wafer are important topics to investigate.

The detailed properties of the polycrystalline silicon become especially important when it is used in critical applications, such as for high valued resistors in static memory circuits (6, 7). In image-sensing CCD's dependence of the optical transmission of the films on the structure will affect the device performance. Even in more conventional, silicon-gate applications, the stability of the structure may influence properties such as step coverage.

This paper reports the results of the first phase of a study being conducted at Stanford designed to investigate the properties of polycrystalline silicon deposited at low pressures. The crystal structure of the films is discussed and compared to that found in films deposited at atmospheric pressure, and the stability of the structure during further heat-treatment is reported.

* Electrochemical Society Active Member.

Key words: polycrystalline silicon, low pressure chemical vapor deposition, structure, annealing.

Film Preparation

Films were deposited in a Tempress (Unicorp) LPCVD reactor at several different temperatures and a pressure of approximately 0.35-0.5 Torr.[1] Silane was the deposition source gas, and no diluent was used. Although a temperature gradient is normally used along the length of an LPCVD reactor, for these depositions the temperature was adjusted to be uniform throughout the length of the deposition zone. A full load of 137, 3 in. diam silicon wafers was included in each deposition. Six of the wafers were sample wafers to be used in subsequent studies; the majority were dummy wafers included in order to avoid perturbing the gas flow with a different number of wafers in each deposition.

Films were deposited over the temperature range 580°-640°C. Samples of several different thicknesses were studied at the typically used, nominal deposition temperature of 620°C. The deposition temperatures, rates, and film thicknesses are summarized in Table I. The films were deposited on both <100>- and <111>-oriented, lightly doped silicon wafers which were covered with 1000Å of thermally grown silicon dioxide. The two different substrate orientations were used in order to allow investigation of the various crystallite orientations in the films without interference from the substrate.

Structure of As-Deposited Films

The films were investigated both by x-ray diffraction and by transmission electron microscopy. The x-ray

[1] The films were deposited by Intel Corporation.

Table I. Deposition conditions and x-ray texture

Deposition temperature (°C)	Film thickness (μm)	Deposition rate (A/min)	X-ray texture[a]			
			<111>	<110>	<311>	<331>
580	0.32	70	0	0	0	0
600	0.50	73	8	324	19	29
620	0.26	110	10	102	21	0
620	0.47	110	12	422	33	19
620	1.05	110	12	2000	56	221
640	0.45	99	11	259	21	19

[a] The magnitudes of the <111>, <220>, <311>, and <331> x-ray peak heights were divided by 1.00, 0.37, 0.18, and 0.054, respectively, (8-10) to obtain the x-ray texture.

texture (preferred orientation) was measured by observing the diffracted intensity at twice the angle of incidence of the x-ray beam in a Picker Model 3488K x-ray diffractometer with 20 keV copper radiation. The samples were tilted 2° to reduce substrate reflections. This tilt only slightly reduced the reflections from the polycrystalline films (Fig. 1). The intensity of the signal from the {220} planes in the 1.05 μm thick sample deposited at 620°C was reduced by a factor of approximately two for a 5° tilt, indicating a variation in the crystallite orientations of this magnitude. For comparison, a 2° tilt reduced the signal from the single crystal substrate by more than three orders of magnitude.

Resolvable reflections were observed from the {111}, {220}, {311}, and {331} planes in the thickest polycrystalline samples deposited at 620°C, but some of these peaks could not be observed in thinner samples or those deposited at lower temperatures. In no case was a signal corresponding to the {400} planes observed, indicating either the absence of grains with <100> orientation or the low sensitivity of the measuring technique to grains with this orientation.

After normalizing the measured peak heights by the signal expected from a randomly oriented sample, we obtain an indication of the relative importance of crystallites with various orientations (Table I). The standard normalization factors (8) for an infinitely thick sample have been modified (9) for this case where the samples are very much thinner than the reciprocal of the absorption coefficient [μ^{-1} = 71 μm (10)]. Table I shows that the <110> texture is dominant in all three of the films of different thicknesses deposited at 620°C. As the films become thicker, however, the amounts of <110> and <331> texture increase much more than linearly with film thickness, while the amounts of <111>- and <311>- oriented grains do not increase as significantly. The dramatic increase in <110> texture with increasing film thickness indicates that the preference for <110> texture is a growth phenomenon rather than nucleation behavior (11) and is similar to that seen in films deposited at atmospheric pressure (12). Table I also indicates that no texture could be resolved in films deposited at 580°C in two different depositions.

Samples were prepared for transmission electron microscopy by etching the supporting substrate and the oxide from the back of the polycrystalline film. The film was usually further thinned chemically from the back so that the electron beam could easily penetrate the film; in all cases, therefore, the results correspond to the portion of the film farthest from the substrate. After preparation the samples were examined in a Philips EM200 electron microscope with a 100 keV electron beam.

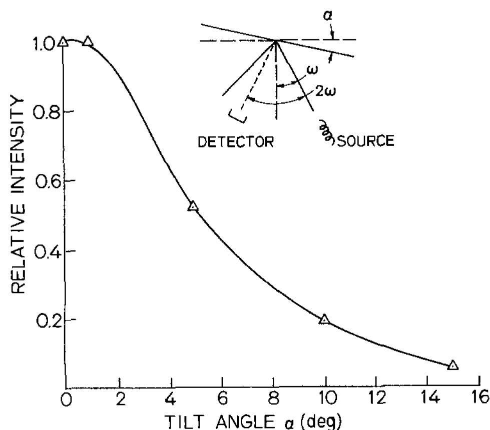

Fig. 1. Intensity of the diffracted x-ray signal intercepted from the <220> planes of the 1.05 μm, 620°C film as a function of the tilt angle α.

Typical micrographs are shown in Fig 2 for films deposited at 580° and 620°C, and the corresponding transmission electron diffraction (TED) patterns are shown below the micrographs. Films deposited at 600° and 640°C are similar to those deposited at 620°C. Films deposited at 600°C and above exhibit a more or less equiaxed, polycrystalline grain structure similar to that seen in films deposited at atmospheric pressure and somewhat higher temperatures in conventional CVD reactors (4, 12). Numerous twin lamella are seen within the grains. Films of different thicknesses deposited at 620°C appear to be qualitatively similar to each other, with the grain size near the top of the film increasing approximately linearly with increasing thickness. The grain size near the top of the film increases from about 0.05-0.1 μm in the 0.26 μm thick films to 0.15-0.2 μm in the 0.47 μm thick films, and to 0.3-0.4 μm in the thickest (1.05 μm) films. Transmission electron diffraction patterns (bottom of Fig. 2b) show the typical sharp rings and spots characteristic of polycrystalline material.

The films deposited at 580°C exhibit a different structure, although the results are not as consistent as in films deposited at higher temperatures. In some cases (Fig. 2a, top, left), a few crystallites appear to be embedded in a structureless background. In other cases some structure is seen (Fig. 2a, top, right), although the grains appear to be much smaller than those in the polycrystalline samples deposited at 600°-640°C. Variations in contrast as the sample is rotated a few degrees in the electron microscope indicate that there is crystalline character in at least some of these grains. However, no fine structure was observed within the grains. The less consistent results in the films deposited at 580°C suggest that this temperature is very close to the transition temperature between the deposition of amorphous silicon and polycrystalline silicon so that some regions of each are included in the deposited films.

The TED patterns of the films deposited at 580°C (bottom of Fig. 2a) appear qualitatively different from those of the films deposited at higher temperatures. Instead of sharp rings, only very diffuse halos are seen. Since these halos are suggestive of an amorphous structure (13), we will call these films "amorphous" in our discussion, although portions of the samples do show some crystalline character. Further evidence for classifying these films as amorphous is the absence of detectable x-ray texture in the as-deposited films and the dramatic change in the structure upon annealing, as considered in the next section.

From the results discussed above we may conclude that there is a transition between an amorphous and a polycrystalline structure at a deposition temperature very near 580°C. This temperature is somewhat lower than that at which a similar transition between amorphous and polycrystalline structure is seen in silicon films deposited by CVD at atmospheric pressure in a nitrogen ambient (4, 5).

The somewhat higher transition temperature in the latter case may be related to the reduction of the surface mobility of the depositing silicon atoms by adsorbed nitrogen or impurity atoms contained in the nitrogen (14). It may also be related to the higher deposition rates used at atmospheric pressure, rather than being directly related to the different pressures during deposition; deposition temperature and rate have been shown to be related over at least a limited range (15).

Structural Changes on Annealing

The presence of a transition from an amorphous to a polycrystalline structure for slight differences in deposition temperature and the use of markedly higher temperatures in subsequent IC fabrication steps lead to questions about the stability of the as-grown structure on further processing. To investigate the stability of the various structures, films grown at the different temperatures were annealed at 800°, 1000°, 1100°, and

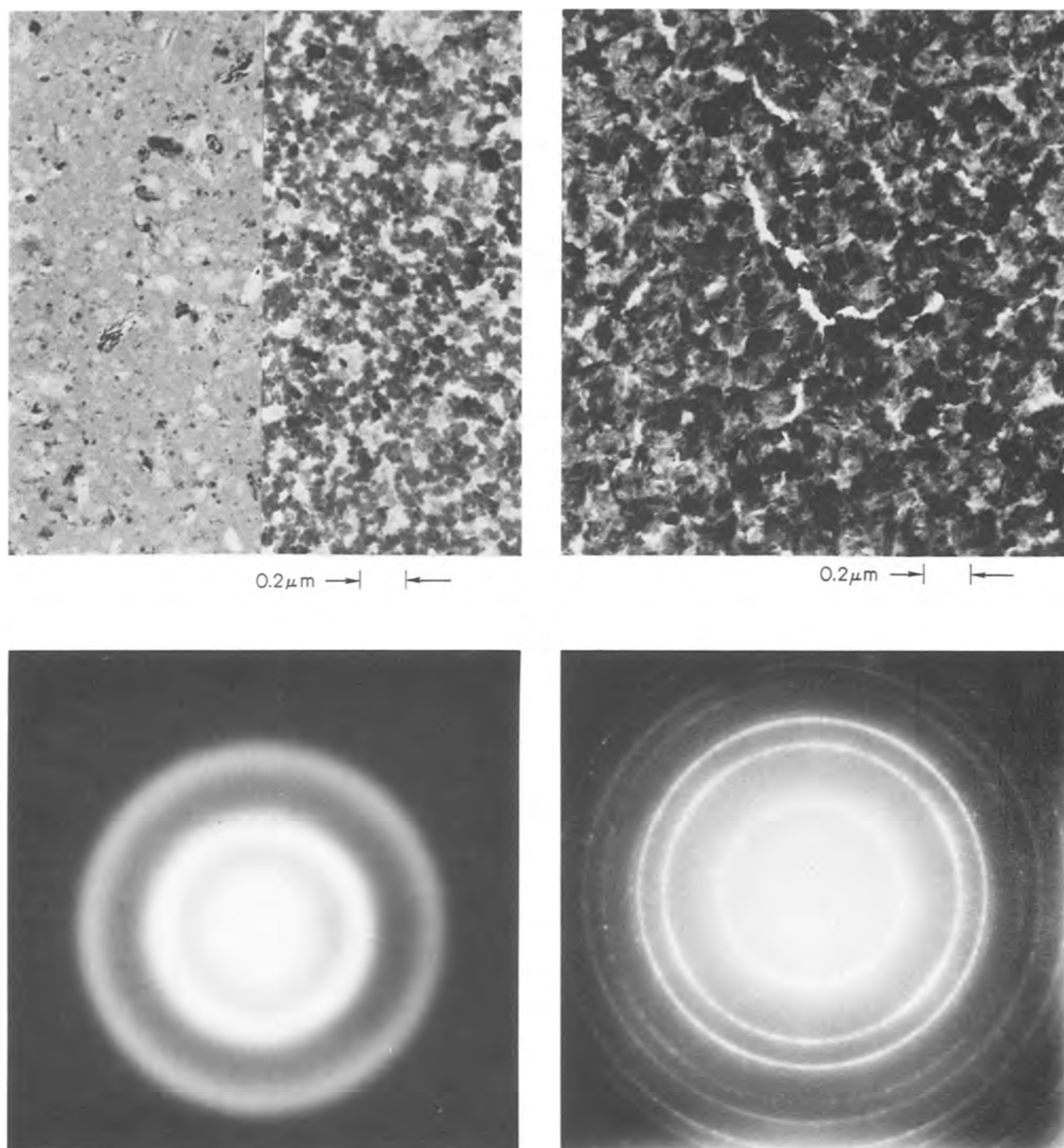

Fig. 2. Transmission electron micrographs of films deposited at (a, left) 580°C and (b, right) 620°C. The corresponding transmission electron diffraction patterns are shown below the micrographs.

1200°C for 1 hr in a nitrogen atmosphere in a standard diffusion furnace. A different piece of the film was used for each different annealing temperature, and the samples were rapidly inserted into the annealing furnace (within a few seconds). After annealing, the samples were investigated both by x-ray diffraction and by TEM, as before.

In some cases, especially at the higher annealing temperatures, the films were overcoated with a 0.5 μm thick layer of low temperature (480°C) deposited silicon dioxide before annealing in order to protect the silicon films from the furnace ambient. At the highest annealing temperature (1200°C) some deterioration of the optical quality of the films was observed after annealing when the films were not overcoated with oxide. However, no significant differences in the x-ray results were seen between bare and overcoated samples, indicating that the oxide cap does little to enhance or retard changes in structure during annealing.

The amorphous films deposited at 580°C were very unstable and showed marked changes in structure for all annealing temperatures. No structure was revealed by x-ray diffraction before annealing, while significant amounts were seen after annealing (Fig. 3a). The <311> texture appears to be dominant at intermediate annealing temperatures, while the <111> texture shows a tendency to increase at the highest annealing temperature employed. This preference for the growth of <311> and <111> textures on annealing is to be contrasted with the strong tendency of the <110> texture to develop during deposition and indicates that markedly different mechanisms may dominate during deposition and during annealing.

X-ray results taken after similar annealing are shown in Fig. 3b for the intermediate thickness film deposited at 620°C. Unlike the film deposited at 580°C, the higher temperature film, which is polycrystalline as deposited, is reasonably stable, showing

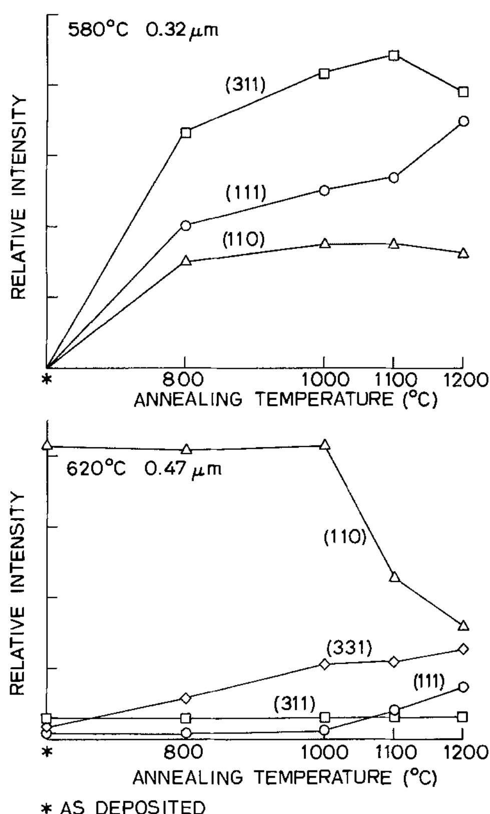

Fig. 3. Development of the x-ray texture after annealing at the indicated temperatures for films deposited at (a, top) 580°C and (b, bottom) 620°C.

little structural change for annealing temperatures up to 1000°C; only some tendency for growth of <331> texture is observed. At 1100°C and above, however, significant change is seen; the <110> texture decreases significantly, and the <111> and <331> textures increase slightly.

Films were also observed by TEM after annealing. The films deposited at 620°C showed little change after annealing at 800° or 1000°C, while they showed a significant increase in grain size after annealing at 1100° and 1200°C (Fig. 4), consistent with the x-ray results. The initially amorphous films deposited at 580°C showed more dramatic changes. After an 800°C anneal, definite structure was seen (Fig. 5a). The grain boundaries were not very well defined, but fine structure was easily visible within the grains. After higher temperature annealing, the films appeared more crystalline, with better defined, larger grains (Fig. 5b). The rapid change in structure can be seen from the TED pattern of the 580°C film annealed at 800°C (Fig. 6). The transition from a diffuse halo pattern (bottom of Fig. 2a) to a ring-spot pattern indicates the rapid growth of crystal structure.

Additional Discussion

Further evidence of a qualitative difference between films deposited at 580°C and those deposited at higher temperatures was seen during sample preparation for transmission electron microscopy. After the substrate and oxide were chemically etched and the samples were removed from the wax which protected the surface, the unannealed films deposited at 580°C curled, indicating large stresses built into these films. No tendency to curl was seen in films deposited at higher temperatures or in annealed films deposited at 580°C. Thus, large stresses appear to be present in the amorphous films, but not in polycrystalline samples.

The results of the present annealing experiments may be compared to results of similar studies of initially amorphous silicon films deposited by evaporation (4) or by atmospheric pressure CVD in a nitrogen ambient (16). In the evaporated films (4) a dendritic structure is seen after annealing at 650°C. After an 850°C anneal, an equiaxed grain structure is dominant, but some dendritic structure is still seen, indicating a competition between the two types of nucleation. Presumably, the details of the nucleation behavior are influenced by the rate of heating to the annealing temperature. After a 1040°C anneal, only the equiaxed structure appears. Nagasima and Kubota (16) also observe a needlelike grain structure after a 700°C anneal, while an 1100°C anneal produces an equiaxed structure.

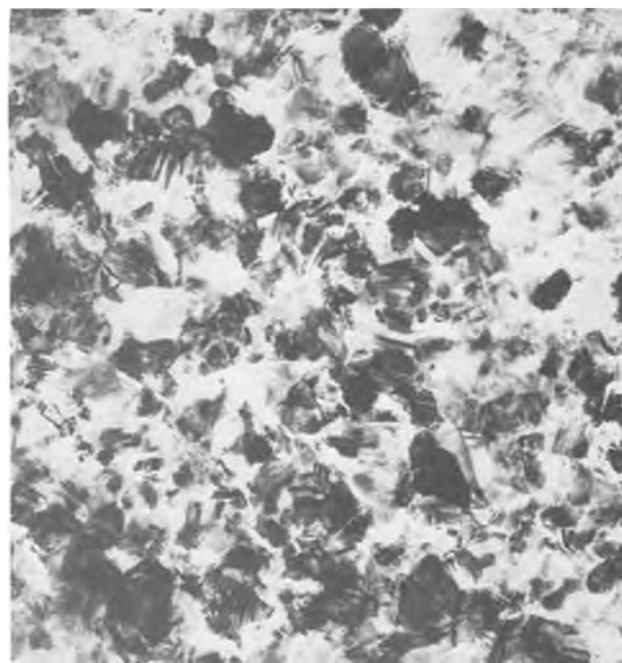

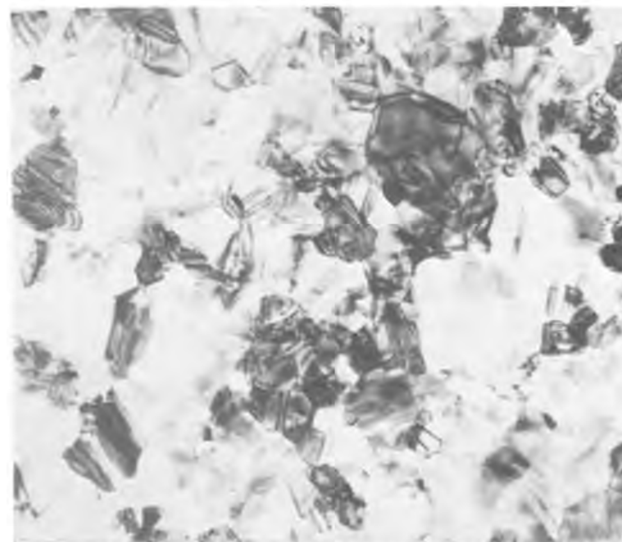

Fig. 4. Transmission electron micrographs of 0.47 μm thick films deposited at 620°C and annealed at (a, top) 1100°C and (b, bottom) 1200°C.

These observations are generally consistent with the results observed in the present investigation for the annealing of films deposited at 580°C. Both equiaxed grains and long, narrow structures are observed after

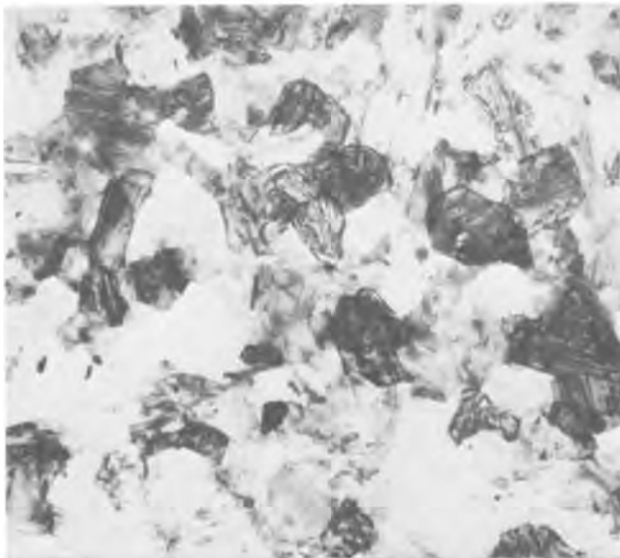

Fig. 5. Transmission electron micrographs of films deposited at 580°C and annealed at (a, top) 800°C and (b, bottom) 1200°C.

the 800°C anneal (Fig. 5a), while primarily a well-defined, equiaxed grain structure is seen after annealing at higher temperatures (Fig. 5b).

Anderson states (4) that stress in the as-deposited film provides the driving force for dendritic growth, while presumably the greater thermal energy at higher temperatures leads to the formation of the equiaxed structure. As we have seen, large stresses are present in the amorphous films considered in this study.

The structure which initially appears on crystallization of the amorphous films may possibly be related to the anomalous, dendritic structure seen in films deposited at atmospheric pressure and relatively low temperatures (12).

From this comparison, we see that the annealing behavior of amorphous silicon films deposited by several different techniques is qualitatively similar. However, residual impurities contained within the films

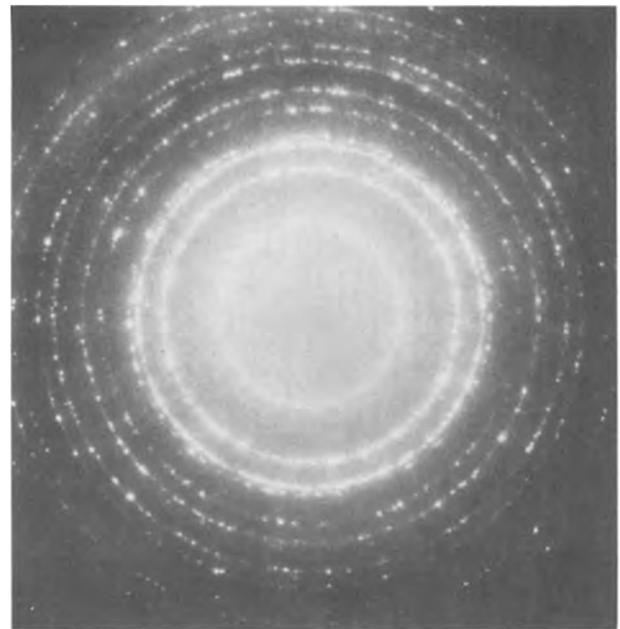

Fig. 6. Transmission electron diffraction pattern of film deposited at 580°C and annealed at 800°C.

may impede annealing, causing differing transition temperatures for the various types of films studied in the different investigations.

It should be emphasized that all of these results refer to annealing in an inert ambient. The presence of other gases or dopant sources during heat cycling may affect the structure of the film differently.

Conclusions

This study has shown that a critical transition temperature between amorphous and polycrystalline deposits exists for deposition temperatures close to those typically used to deposit films for integrated circuit applications. When the films are polycrystalline, the <110> texture is dominant, and this texture becomes of increasing importance in thicker films.

If silicon films deposited by low pressure CVD are initially polycrystalline, they should be reasonably stable and should not change markedly because of heat cycles normally seen in modern integrated circuit fabrication; however some changes may occur if temperatures above 1100°C are encountered. On the other hand, films deposited at slightly lower temperatures are initially amorphous and will crystallize during the thermal processing likely to be encountered. The implications of these changes on the electrical properties and reliability of integrated circuits incorporating these initially amorphous films must be considered further before the films can be used with confidence for device applications.

Acknowledgment

This work was performed at the Stanford Integrated Circuits Laboratories, Stanford University, and was supported by the Advanced Research Projects Agency of the Department of Defense under Grant No. DAAB07-77-C-2684. The authors would like to thank Dr. N. Ahlquist and S. Favre of Intel Corporation for depositing and supplying the films for this study.

Manuscript submitted Sept. 13, 1977; revised manuscript received Dec. 23, 1977.

Any discussion of this paper will appear in a Discussion Section to be published in the December 1978 JOURNAL. All discussions for the December 1978 Discussion Section should be submitted by Aug. 1, 1978.

Publication costs of this article were assisted by the Integrated Circuits Laboratories, Stanford University.

REFERENCES

1. F. Faggin and T. Klein, *Solid-State Electron.*, **13**, 1125 (1970).
2. D. F. Barbe, *Proc. IEEE.*, **63**, 38 (1975).
3. R. S. Rosler, *Solid State Technol.*, **20**, No. 4, 63 (1977).
4. R. M. Anderson, *This Journal*, **120**, 1540 (1973).
5. N. Nagasima and N. Kubota, *Jpn. J. Appl. Phys.*, **14**, 1105 (1975).
6. T. R. O'Connell *et al.*, IEEE International Solid State Circuits Conference, Philadelphia, Feb. 16-18, 1977, Paper WAM 1.2.
7. V. G. McKenny, *ibid.*, Paper WAM 1.3.
8. J. V. Smith, Editor, "X-Ray Powder Data File," Card 5-0565, American Society for Testing and Materials, Philadelphia (1960).
9. B. D. Cullity, "Elements of X-Ray Diffraction," p. 270, Eq. (9-4), Addison-Wesley, Reading, Mass. (1956).
10. B. D. Cullity, *ibid.*, p. 466.
11. E. Bauer, in "Single Crystal Films," M. H. Francombe and H. Sato, Editors, pp. 43-67, Pergamon Press, New York (1964).
12. T. I. Kamins and T. R. Cass, *Thin Solid Films*, **16**, 147 (1973).
13. M. H. Brodsky *et al.*, *Phys. Rev. B*, **1**, 2632 (1970).
14. T. I. Kamins, *This Journal*, **121**, 681 (1974).
15. T. I. Kamins, J. Manoliu, and R. N. Tucker, *J. Appl. Phys.*, **43**, 83 (1972).
16. N. Nagasima and N. Kubota, *J. Vac. Sci. Technol.*, **14**, 54 (1977).

Framed Recessed Oxide Scheme for Dislocation-Free Planar Si Structures

I. Magdo and A. Bohg

IBM System Products Division, East Fishkill, Hopewell Junction, New York 12533

ABSTRACT

Recessed oxide isolation is widely used to reduce defects and increase packing density in Si integrated circuits. Unfortunately, the use of SiO_2/Si_3N_4 layers to mask the Si during the formation of the recessed oxide creates an unevenness in the surface, known as bird's-head, and the lateral oxidation due to the SiO_2 under the Si_3N_4 layer creates bird's-beak. Bird's-head and bird's-beak limit packing density and performance. In the framed recessed oxide-isolation process presented in this paper, the Si_3N_4 is allowed to cover the Si surface in narrow stripes to define the recessed oxide boundary; thus both limitations are avoided. The samples were analyzed by Sirtl etch and TEM methods. For a Si_3N_4 layer 500Å thick, no induced crystal defects were present, probably because of partial stress relief within the narrow Si_3N_4 stripes. For a Si_3N_4 layer more than 1000Å thick, dislocations appeared along the edges. The dislocations, which are of the 60° type on (111) slip planes with alternate Burger's vectors, relieve part of the intrinsic tensile stress of the Si_3N_4.

Much work has been done in recent years to improve isolation schemes for integrated devices. Recessed oxide isolation (1) (ROI), along with the LOCOS (2-6) and Isoplanar (7) technologies, has been developed to overcome the limitation that junction isolation imposes on packing density. In ROI processing, the silicon surface is thermally oxidized and silicon nitride is deposited. The Si_3N_4/SiO_2 layer is etched outside the active device regions. The exposed silicon areas are etched and then thermally reoxidized. Since the thermal oxide underneath the Si_3N_4 is exposed at the periphery and does not block oxygen diffusion during the formation of the recessed oxide, "bird's-head" and "bird's-beak" are created. The bird's-head causes uneven surface topology, and the bird's-beak (slowly increasing oxide thickness at the lateral silicon interface) limits the packing density.

Double or triple oxidation reduces the bird's-head (8), but does not improve the beak itself. The longer oxidation time causes the shallow bipolar structures to suffer, for example, by an increased outdiffusion from the subcollector.

Surface planarity can also be improved by using a thick Si_3N_4 film on a very thin SiO_2 pad (9), typically 2000Å Si_3N_4 on 50Å SiO_2. Too thick a layer of Si_3N_4 or too thin a layer of SiO_2, however, will introduce crystal defects in the silicon because of the high intrinsic stress in the Si_3N_4.

The new method described here eliminates bird's-beak in recessed oxide structures. Si_3N_4 is deposited directly on the silicon only at the perimeter of the ROI regions to form a frame around them. With the proper oxide-nitride thickness, a dislocation-free structure can be obtained.

Key words: Si structures, recessed oxide scheme, recessed oxide boundary.

Structure and Experimental Procedure

A conventional recessed oxide structure is shown in Fig. 1. Thermally grown SiO_2, 1000Å thick, is formed on a 0.3 Ωcm n-type (001) silicon wafer, and a Si_3N_4 film 1000Å thick is deposited by SiH_4-NH_3 reaction at 800°C. Annular regions with edges aligned along <110> are etched in the Si_3N_4/SiO_2 layers through an auxiliary 1000Å film of pyrolytic SiO_2. The exposed silicon substrate is isotropically etched, in a 1:2:5 volume ratio solution of 49% HF, CH_3COOH, 76% HNO_3, diluted in a 1:20 ratio with 75% HNO_3 (etch rate about 800 Å/min), to a depth of about 3400Å. The wafer is reoxidized for 360 min at 1000°C in wet ambient; the resulting SiO_2 layer is about 10,000Å thick.

The new framed recessed oxide structure is shown in Fig. 2. The thermally oxidized wafer is photoetched in an annular shape to expose the silicon surface (Fig. 2). The recessed oxide boundary defining the device areas then forms within the annular region. Next the Si_3N_4 layer is deposited as in the conventional process, and is etched so that it extends over the underlying SiO_2 layer by about 2.0 μm in the device areas. The silicon is etched in the solution used for the conventional process and then reoxidized to a thickness of about 10,000Å. Since the lateral oxygen diffusion is blocked at the perimeter of the ROI, the beak is completely eliminated. The head is reduced from about

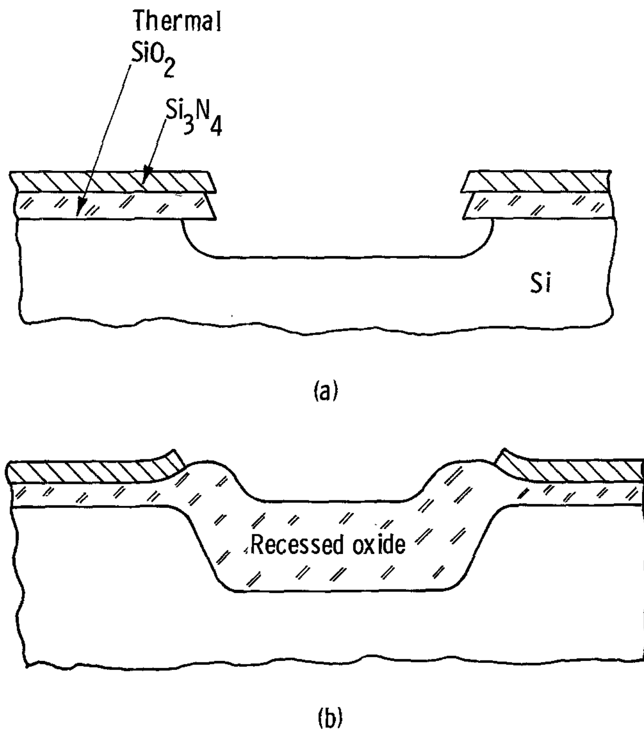

Fig. 1. Processing of conventional recessed oxide structure. (a) After silicon etching; (b) after recessed oxide formation.

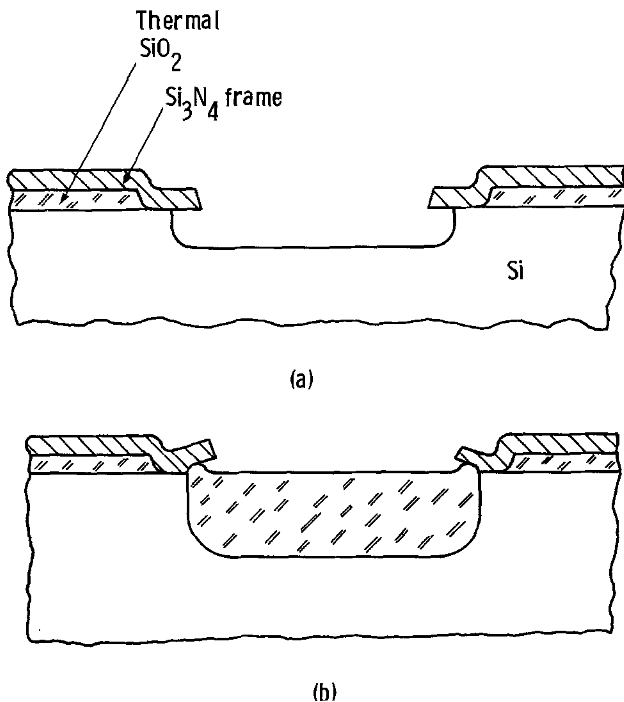

Fig. 2. Processing of framed recessed oxide structure. (a) After silicon etching; (b) after recessed oxide formation.

4500Å in structures made by the conventional process to less than 1000Å in the framed structure, as Fig. 2 shows. SEM micrographs of cross sections of both structures are shown in Fig. 3 for comparison.

The framed recessed oxide structure is usable only for geometries large enough to accommodate the thermally grown pad oxide, say $L > 2w$ (Fig. 4), where L is the width of the silicon island. For $L < 2w$, the Si_3N_4 is directly deposited on the silicon surface. In either case, the width of the Si_3N_4 stripes in direct contact with the silicon surface never exceeds $2w$ (4 μm in our case).

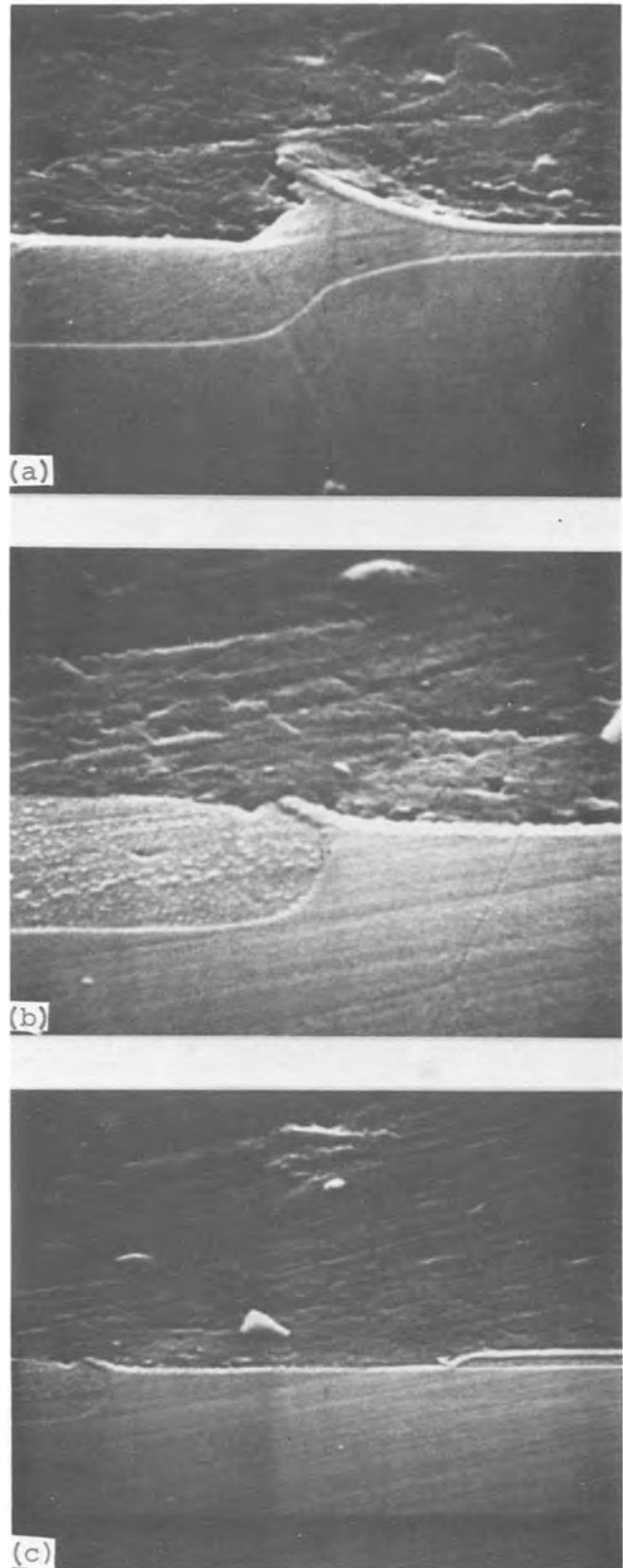

Fig. 3. SEM micrographs of 1 μm ROI. (a) Conventional ROI process; (b) framed ROI process; (c) framed ROI, depicting the lateral extent of the Si_3N_4/pad SiO_2.

As is well known, chemical vapor-deposited Si_3N_4 films exhibit a high intrinsic tensile stress [see Ref. (11) for a recent review] which may lead to crystal defects in the silicon. Therefore the effect of thermal SiO_2/Si_3N_4 layer thickness on crystal defects was investigated. Wafers were prepared by the framing process with three different combinations of thicknesses: 1000Å of SiO_2 on 1000Å of Si_3N_4; 500Å of SiO_2

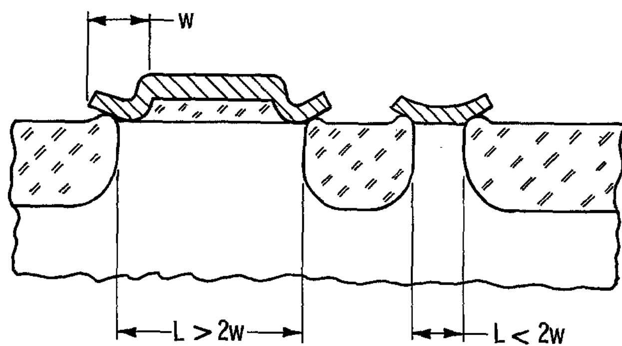

Fig. 4. Processing of silicon structures with $L > 2w$ (w is frame width) and $L < 2w$ with the framed recessed oxide scheme. The frame width used for this study was 2.5 μm. All edges are along <110>.

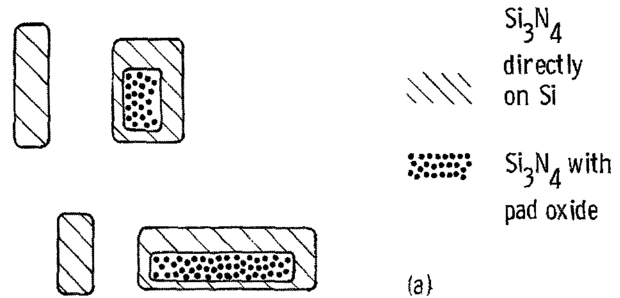

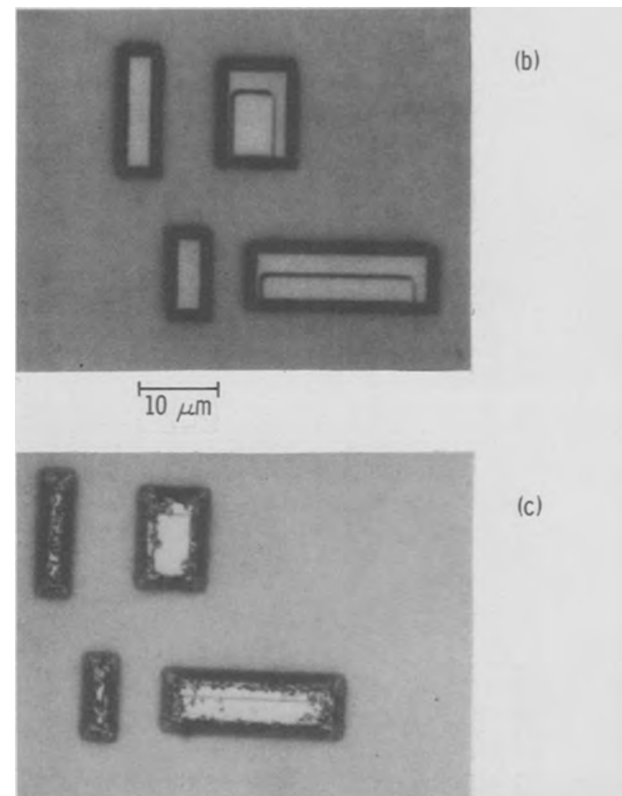

Fig. 5. Comparison of crystal perfection for Si_3N_4 thicknesses of 500 and 1000Å. (a) Layout of structures shown in (b) and in (c); the misalignment is intentional. (b) Sirtl-etched, 500Å Si_3N_4 on 500Å SiO_2, no dislocation. (c) Sirtl-etched, 1000Å Si_3N_4 on 500Å SiO_2, many dislocations.

on 500Å of Si_3N_4; and 1000Å of SiO_2 and 500Å of Si_3N_4. An experimental wafer with 1000Å of SiO_2 on 2000Å of Si_3N_4 was also processed. The general defect level was studied by Sirtl etching the wafer surface (after nitride stripping in hot phosphoric acid) and by Sirtl etching on vertical cleavage planes (110). Transmission electron microscopy (TEM) at 200 keV was used for detailed defect identification and Burger's vector analysis. The TEM samples were thinned by the combined ultrasonic dimpling/chemical etching method described in Ref. (14).

Crystal Defects in Silicon

The high intrinsic stress of the Si_3N_4 film generates crystal defects in the silicon substrate if the yield stress for silicon is locally exceeded during high temperature treatments. Using transmission electron microscopy, Tamura and Sunami (10) showed that straight dislocations of the 60° type form in the surface of a (100) silicon substrate as a result of nitride stress, if the wafer is completely covered with Si_3N_4. Westdorp and Schwuttke (14) had shown earlier that local stress concentrations near Si_3N_4 diffusion windows are preferred sites for dislocation generation, as was also reported for the recessed oxide structures investigated by Bassous, Yu, and Maniscalco (9). Calculations by Zeyfang (13) showed that the shear stress σ_{xz} near the edge of a stressed film window is about three times as high as the film stress σ_{xx} far away from the edge. The generation of dislocations is highly undesirable because these crystal defects may act as recombination centers or as gettering sites for impurities, and thus may cause artifacts to form during further processing. Therefore we have carefully checked the crystal perfection for all the thickness combinations, pad oxide on nitride, that we used.

In Table I, the perfection of the silicon crystal after framed recessed oxide processing is given for all the wafers studied, as concluded from Sirtl etching and confirmed by TEM. No dislocations were found along the recessed oxide edges on the wafers processed with 500Å of Si_3N_4 and 500 or 1000Å of pad oxide. Figure 5b shows the Sirtl-etched surface of a wafer processed with 500Å each of Si_3N_4 and of SiO_2. The absence of etch pits indicates that the substrate is free of dislocations; this finding was confirmed by TEM inspection. Increasing thickness of the Si_3N_4 to 1000Å, again for oxide thickness of 500Å, leads to dislocations in most of the structures (Table I). After Sirtl etching, the Si surface shows many etch pits along the former nitride edges (Fig. 5c). The in-depth distribution of the defects is revealed by Sirtl etching on a vertical (110) cleavage plane running through a device structure, which is shown in the series of light optical micrographs in Fig. 6a-6c. The etch pits start at the edges of the nitride islands and define V-shaped pairs of <211> directions, which are apparently the intersections of two {111} dislocation glide planes (normal to the plane of the micrograph) with the {110} cleavage plane (parallel to the plane of the paper). Dislocation generation on wafers with 1000Å Si_3N_4, however, was irregular. Many devices produced with the 500Å SiO_2/1000Å Si_3N_4 combination were entirely free of dislocations. For the 1000Å SiO_2/1000Å Si_3N_4 combination, only a few structures developed dislocations, and the rest remained dislocation-free, as was confirmed by TEM. Figure 7 shows the Sirtl-etched sili-

Table I. Crystal perfection after framed recessed oxide process for different combinations of nitride and pad oxide

The recessed oxide thickness in all cases is 10,000Å

Thickness of pad oxide (Å)	Thickness of Si_3N_4 film (Å)		
	500	1000	2000
500	No dislocations	Dislocations in most structures	—
1000	No dislocations	Dislocations in some structures	Dislocations in most structures

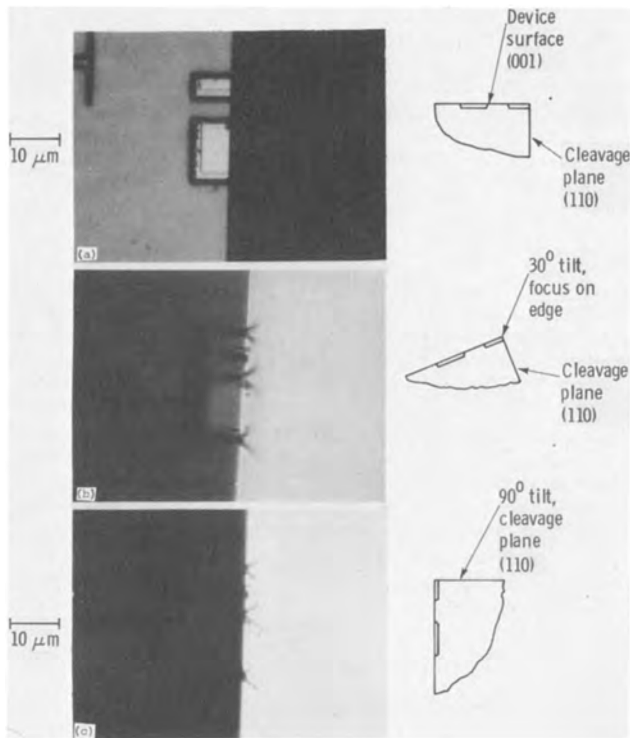

Fig. 6. In-depth distribution of dislocations (after Sirtl) for wafer with 1000Å Si_3N_4 on 500Å SiO_2.

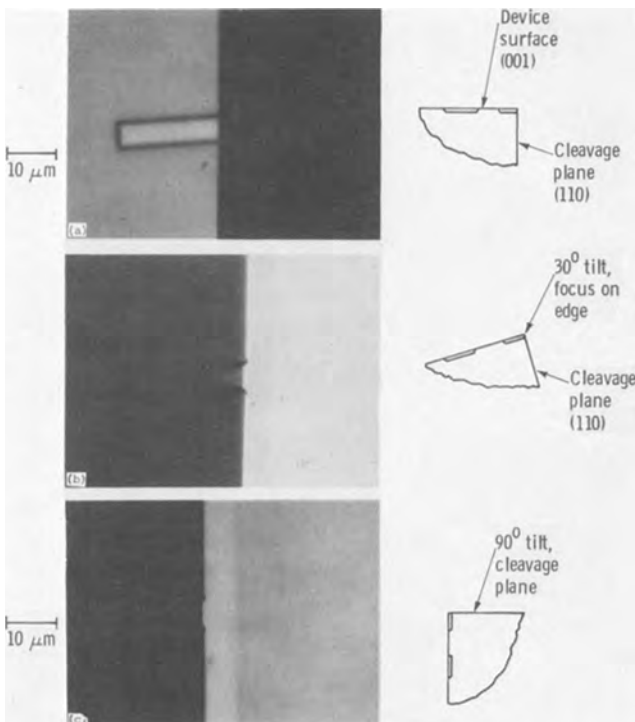

Fig. 7. Absence of dislocations on wafer with 1000Å Si_3N_4 on 1000Å SiO_2. Surface and cleavage plane Sirtl-etched as in Fig. 6.

con surface and cleavage plane of a typical device with 1000Å SiO_2/1000Å Si_3N_4: no dislocations are present. (The shallow notches visible at the device surface in Fig. 7c are caused by stress-induced preferential attack of the Sirtl etch solution at the recessed oxide edges.)

The defect structure introduced by thick ($\geqq$ 1000Å) Si_3N_4 along the edges was investigated by TEM. Figure 8 is a TEM micrograph of a recessed oxide structure produced with 1000Å Si_3N_4 on 500Å SiO_2. The nitride pattern was intentionally misaligned with respect to the pad oxide. For the TEM examination, the nitride and oxide were completely etched off for better electron transparency of the sample. The micrograph in Fig. 8 is composed of two contiguous prints of the same device obtained by different exposures of the same TEM negative in order to bridge the large contrast between the central silicon mesa region, about 1.5 μm thick, and the peripheral silicon, about 0.5 μm thick. Figure 8 shows that parallel to the former nitride edges many dislocations have been generated. At left, where the nitride edge was in direct contact with the silicon, the dislocation generation was the strongest. At right, where the nitride and the silicon were separated by an oxide pad 500Å thick, there are fewer dislocations. None at all were generated at the thin thermal SiO_2 step under the nitride (as is also apparent in Fig. 6); thus it seems that the thermal oxide alone is subjected to little stress during the formation of recessed oxide at 1000°C. The reduced number of crystal defects under the nitride edge with underlying pad oxide demonstrates that the oxide buffers the stress.

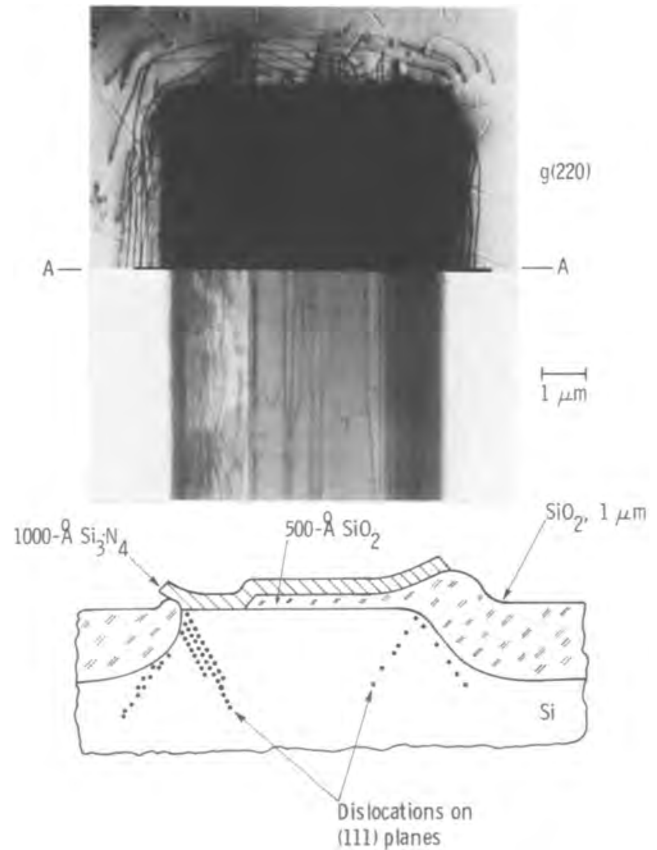

Fig. 8. TEM micrograph (top) and schematic cross section (bottom) along A-A through a structure with dislocations. For the TEM investigation, all Si_3N_4 and SiO_2 was etched off for better transparency. To bridge the large contrast range inside and outside the Si pedestal, the micrograph is composed of two contiguous prints with different exposures made from the same TEM micrograph. The misalignment between pad oxide and nitride was intended. Dislocation generation is strongest at left, where the Si_3N_4 and the silicon are in direct contact. Foil normal is $[00\bar{1}]$ with the nitride edges along <110>.

Figure 8 also gives a schematic cross section displaying the spatial arrangement of the dislocations, as deduced from stereo pairs of micrographs together with the Sirtl etching on the cleavage plane (Fig. 6). The dislocations emanate from the Si surface at the former position of the nitride edge and glide on the two {111}

planes, which contain the nitride edge as common intersection. Some dislocations are truncated by the advancing recessed oxide. Most of them are still within 1 μm from the edge, but some were able to glide as far as 5 μm under the influence of the edge stress and the repulsive force of neighboring dislocations.

The crystallographic nature of the dislocations was determined by using different diffraction vectors $\vec{g}$ and reversing the sense of $\vec{g}$. The results are explained with reference to Fig. 9, showing a section idealized by neglecting the occasionally observed dislocation reactions. The prominent dislocations are straight and parallel to the $[1\bar{1}0]$ nitride edge. They are all of the 60° type, with Burger's vectors inclined 45° towards the (001) Si surface. Outside the nitride edge, the dislocations occupy a common $(11\bar{1})$ slip plane. The Burger's vectors of this dislocation set lie within the $(11\bar{1})$ slip plane and alternate between the dislocations. Therefore the total silicon lattice displacement produced by the dislocations outside the nitride edge has only components normal to the nitride edge—none parallel to it. From the TEM analysis it was also established that the dislocations outside the nitride edge relieved a tensile strain near the silicon surface or a corresponding shear stress across the slip plane, as indicated by the ⊥ symbols in Fig. 9. A corresponding dislocation array exists on the $(\bar{1}\bar{1}\bar{1})$ plane extending beneath the nitride edge; again, the Burger's vectors alternate between the two <110> directions contained in the slip plane. From the shift of dislocation images upon reversal of the sense of $\vec{g}$, it follows that the dislocations under the nitride have relieved a compressive stress near the silicon surface, and thus a corresponding shear stress across the slip plane, as indicated by the T symbols in Fig. 9. On the average, the total deformation of the silicon under the nitride has only components normal to the nitride edge. To summarize these findings, 60° dislocations with four different Berger's vectors are found in the vicinity of the nitride edge, with most of the dislocations running parallel to the edges.

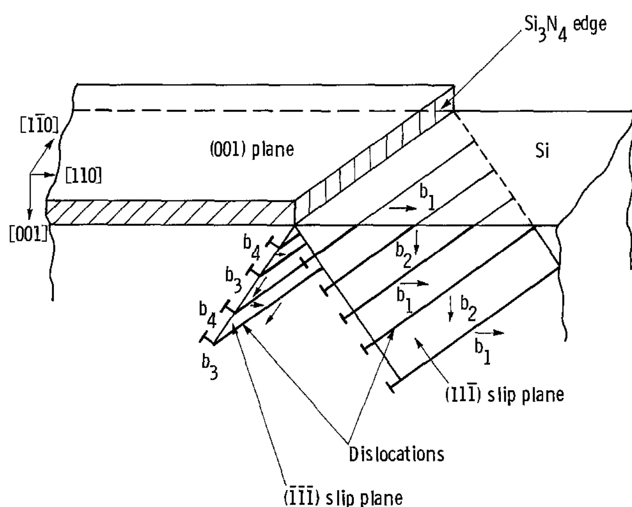

Fig. 9. Crystallography of dislocations along Si_3N_4 edges, idealized. The dislocations are parallel to the $[1\bar{1}0]$ nitride edge and glide on two {111} planes into the substrate. They are of the 60° type, with two alternating Burger's vectors. Outside the nitride-covered area, they have relieved a tensile strain in the silicon. Under the Si_3N_4 they have relieved a compressive strain in the silicon. The corresponding shear stresses are indicated by ⊥ and T.

Except for occasional deviations of dislocations from their ideal slip planes under the nitride and network formation by dislocation reactions, no other structural defects, such as stacking faults, were found.

Summary and Conclusions

The framed recessed oxide process described in this paper makes it possible to fabricate entirely beakless recessed oxide structures. No crystal defects were present for 500 or 1000Å thermal pad oxide, even under nitride patches which, because of their small lateral dimensions, had no central pad oxide. The structures prepared by the framed recessed oxide process showed no dislocations in spite of the direct contact of Si_3N_4 and silicon; this result is attributed to the fact that the nitride stripes in direct contact with the silicon are typically only 2.0 μm wide, and therefore allow a partial relief of the stress within the Si_3N_4.

Dislocation generation starts for nitride thickness of 1000Å and above. The dislocations are parallel to the (001) surface and glide on two symmetrical {111} planes that intersect at the <110> nitride edge. Each glide plane contains two sets of 60° dislocations with alternating Burger's vectors, relieving a tensile stress within the Si_3N_4 film (edge force points towards the nitride).

In our experiments, both the formation of a bird's-beak and the generation of dislocations were completely avoided for a nitride layer 500Å thick.

Acknowledgments

We would like to thank D. Cameron for SEM work and A. Dalay for sectioning.

Manuscript submitted Aug. 31, 1977; revised manuscript received Nov. 19, 1978.

Any discussion of this paper will appear in a Dissussion Section to be published in the December 1978 JOURNAL. All discussions for the December 1978 Discussion Section should be submitted by Aug. 1, 1978.

Publication costs of this article were assisted by IBM Corporation.

REFERENCES

1. I. Magdo, Ph.D. thesis, University of Budapest, Budapest, Hungary (1975).
2. J. A. Appels, E. Kooi, M. M. Paffen, J. J. H. Schatorge, and W. H. C. J. Verkuijlen, *Philips Res. Rep.*, **25**, 118 (1970).
3. J. A. Appels, H. Kalter, and E. Kooi, "Philips Technical Review," Vol. 7, 8, and 9, p. 225, Philips Research Center, The Netherlands (1970).
4. Anonymous, *ibid.*, **31**, 276 (1970).
5. J. A. Appels and M. M. Paffen, *Philips Res. Rep.*, **26**, 157 (1971).
6. E. Kooi, G. J. Van Lierop, W. H. C. J. Verkuijlen, and R. E. Werdt, *ibid.*, **26**, 116 (1971).
7. D. Peltzer and B. Herndon, *Electronics*, **44**, 52 (1971).
8. H. Sakai, T. Yoshimi, and K. Sugawara, *This Journal*, **124**, 318 (1977).
9. E. Bassous, H. N. Yu, and V. Maniscalco, *ibid.*, **123**, 1729 (1976).
10. M. Tamura and H. Sunami, *Jpn. J. Appl. Phys.*, **11**, 1097 (1972).
11. E. A. Irene, *J. Electron. Mater.*, **5**, 287 (1976).
12. R. Zeyfang, *Solid-State Electron.*, **14**, 1035 (1971).
13. W. A. Westdorp and G. H. Schwuttke, in "Thin Film Dielectrics," F. Vratny, Editor, p. 246, The Electrochemical Society Softbound Symposium Series, New York (1969).
14. A. Bohg, E. Mirbach, and L. Schneider, Paper submitted to *J. Phys. E.*

Photocharacteristics for Electrolyte-Semiconductor Junctions

Howard Reiss[1]

Bell Laboratories, Murray Hill, New Jersey 07974

ABSTRACT

The electrolyte-semiconductor junction has lately received considerable attention as a half-cell electrode to be used with or without illumination. In spite of the activity in this field very little has been done toward deriving the electrical photocharacteristics based on the transport of carriers and the quantitative treatment of junction potentials. In this paper we attempt to remedy the situation by setting down the logic underlying the problem and undertaking the derivation of the photocharacteristics, in terms of various phenomenological transport and kinetic coefficients, for a number of fairly realistic systems. Our purpose is not to be exhaustive but to illustrate the process of derivation so that the reader will be able to extend it to other particular systems of interest. When possible we show the relation of our results to previous analyses (in the few cases where they exist). This comparison identifies the condition under which some of the previous results are valid. We have tried to be as critical as possible. Among the effects included in our model are those due to Guoy layers, redox systems, overvoltage, surface recombination, and hole-electron transport and recombination in the bulk of the semiconductor.

In recent years, the semiconductor-electrolyte interface has attracted much attention (1, 2). This has been especially true where photoeffects have been concerned, since promising schemes for both photoelectrolysis (3, 4) and solar cells (5-9) exist, based on such an interface. At this writing, many experiments have been performed on such systems, and a variety of current-voltage characteristics have been determined, both in the dark and under illumination. It appears, however, that very little theory exists for the interpretation of these characteristics. Perhaps the most advanced in this respect are papers by Butler (10), Andersen (11), and Laser and Bard (12). A pioneering paper is due to Dewald (13).

This situation is not surprising since. in a sense, the field contains a "cultural" as well as "physical" interface. On one side we have the solid-state and semiconductor device physicist, while on the other side there is the modern but, nonetheless, canonical electrochemist. The electrochemist seems to have made a valiant, if incomplete effort to understand the language of the semiconductor physicist while an admittedly inaccurate estimate seems to indicate that the reverse has not been nearly as true. As a result, an optimum rate of progress has probably not been realized.

For example, in the early days of semiconductor devices, current-voltage characteristics for all manner of junctions were calculated at an almost explosive rate. Shockley's classic treatment (14) of the p,n-junction and the treatment of the famous Schottky barrier diode (15) are prominent examples. These papers provided a phenomenological treatment of the transport of holes and electrons in semiconductor structures and contained both macroscopic transport and kinetic coefficients (*e.g.*, mobilities, recombination velocities, lifetimes, etc.) which could be measured or derived from microscopic theory once the phenomenological framework was available. In contrast, most of the electrochemical treatments mentioned above involve a direct passage to the microscopic level and are frequently aimed at only one of the many relevant fundamental processes. In this connection Butler's paper (10) on the photoelectrolysis of water using a WO_3 electrode seems to have been the most free from this criticism, but even here, the study is limited to the case of substantial reverse bias under circumstances such that the redox reaction in the electrolyte solution exercises no control over rate. As a consequence, the treatment becomes, essentially, one of the photovoltaic behavior of a conventional Schottky diode, and limited to reverse bias at that. However, even for Schottky diodes, current-voltage characteristics under illumination do not seem to have been generally derived. Butler's calculation is to a large extent an adaptation of a theory proposed by Gärtner (16) for the treatment of such diodes.

Since most of the photoeffects at the semiconductor-electrolyte interface occur in the body of the semiconductor, the current voltage characteristic can be derived using many of the ideas conventional to ordinary semiconductor device physics. On the other hand, additional ideas conventional to the treatment of phenomena at electrode surfaces are necessary. Frequently the effects of the redox couple can be treated as boundary conditions on the semiconductor surface. It is therefore possible to make considerable progress in the analytical treatment of the semiconductor-electrolyte junction by focusing on hole-electron transport in the semiconductor alone. It is therefore surprising that so little has been done in this respect.

Undoubtedly part of the problem lies with the above-mentioned, only moderate interest of the semiconductor device physicist, but an important aspect has to do with the great variety of models which may have to be invoked to match the assortment of differing physical systems which are encountered. For example, there are systems in which rate control may be due to any of a number of processes, *e.g.*, (*i*) due to the transport of carriers in the semiconductor, (*ii*) due to processes in the Helmholtz layer, (*iii*) due to processes in the Gouy-Chapman layer (17) in the electrolyte, (*iv*) due to transport in the electrolyte solution, etc. Furthermore, it is necessary to consider various seats of control of the barrier layer potential. For example, (*i*) Are surface states important in fixing the band bending? (*ii*) Is the semiconductor doped uniformly, and is it homogeneous as regards chemical constitution, etc? (*iii*) What is the relation between the Fermi levels, relative to vacuum, of the semiconductor and electrolyte, respectively? In addition, it may be appropriate in deriving current-voltage characteristics, depending on the case, to use thermionic emission, diffusion theory, or a combination of both (18). If one uses diffusion theory it becomes necessary to decide whether carrier generation and recombination must be accounted for (and to what extent) in the

[1] Permanent address: Department of Chemistry, University of California at Los Angeles, Los Angeles, California 90024.
Key words: photoelectrode, band bending, recombination, overvoltage, depletion layer, diffusion theory.

depletion layer, at the interface, etc. If thermionic emission theory is used it may be necessary to assess the effects of image potentials (19), quantum tunneling, etc.

Last but not least it may be necessary to incorporate into the general development, the quantitative aspects of various decomposition and corrosion processes (11), inseparable from the operation of the diode (especially at high photon fluxes).

Each different model which may have to be treated may involve an algebraic tour de force in tedium, although possibly based on straightforward manipulation. It is therefore not surprising that only the most elementary, incomplete situations have received any algebraic attention at all. A general treatment of a model involving all possible physical features is out of the question. However, a method applicable to a wide variety of models is easily demonstrated by working out a few examples.

The goal of the present paper will be just this, *i.e.*, to derive the current-voltage and photovoltaic characteristics for a few important models, each complete enough to have a measure of reality against which some existing measurements may be checked, and with the hope that the method will be well enough demonstrated so that any reader will be able to apply it to particular situations in which he may have an interest. Before doing this however, it is appropriate to make some additional prefatory remarks concerning contact potentials, Fermi levels, redox potentials, and photovoltaic circuits.

Some Critical Remarks on Fermi Levels

When an electrolyte phase (or for that matter any phase) is placed in contact with a semiconductor, electrons will usually be transferred between the two phases such that a double layer potential, V_{DL}, will result, given by

$$V_{DL} = E_F^{(E)} - E_F^{(S)} \qquad [1]$$

in which $E_F^{(E)}$ and $E_F^{(S)}$ are the Fermi levels (measured from a common reference level) in the electrolyte and semiconductor, respectively. The definition in Eq. [1] is such that V_{DL} is positive when the semiconductor is at a higher electrical potential than the electrolyte. The common reference level is generally chosen such that the energy of the electron in vacuum is set equal to zero. This is called the "vacuum" level.

It is customary for solid-state physicists to both measure and work with Fermi levels defined relative to vacuum, and so reasonable values for $E_F^{(S)}$ relative to vacuum are frequently available. On the other hand, the same is not true for $E_F^{(E)}$ in the electrolyte. However, for electrolytes which can serve as redox couples, redox potentials, measured relative to the standard hydrogen electrode, are available. Gerischer (17) has set forth a formula relating this standard redox potential, U, to $E_F^{(E)}$ measured relative to vacuum. This formula is

$$E_F^{(E)} = -qU + E_F^{(H)} \qquad [2]$$

in which q is the absolute value of the charge on the electron and $E_F^{(H)}$ is the Fermi level, relative to vacuum, of the standard hydrogen couple

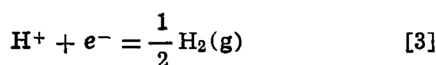

$$H^+ + e^- = \frac{1}{2} H_2(g) \qquad [3]$$

Some additional critical remarks concerning $E_F^{(E)}$ and $E_F^{(H)}$ are in order. If a half-cell (such as the reaction in Eq. [3] is set up only as a solution in contact with H_2 gas and not in contact with another phase (not in contact with a platinum electrode for example, and not even in contact with the walls of a containing vessel) it will have a definite Fermi level relative to vacuum. It is this Fermi level to which $E_F^{(H)}$ refers. (The same is true of $E_F^{(E)}$, it is the Fermi level in the redox solution out of contact with additional phases.) As soon as the solution contacts another phase, if the Fermi level of that phase differs from the level in the solution, electrons will be transferred between the two phases. As a consequence the electrical potential of one phase will increase, relative to vacuum, while the potential of the other will decrease.

Since the position of the Fermi level, relative to the spectrum of electron energy levels (relative to vacuum), must remain fixed in the bulk of each phase, this means that, in general, the Fermi level in each phase will change, relative to vacuum, although, at equilibrium with respect to the transfer of electrons, the Fermi levels in both phases will be identical, although, in both cases, changed from the levels prior to contact. In the case that one of the phases can support very little space charge (*e.g.*, a metal) its Fermi level will be only slightly changed on contact.

In the measurement of U the redox couple and the hydrogen electrode are connected to form a full cell and U is measured as the emf of this cell. However, the common Fermi level of this full cell (for the reasons just mentioned) will be neither $E_F^{(E)}$ nor $E_F^{(H)}$. Since in the thermodynamic expression for U, the common Fermi level of the full cell cancels out, this is of no consequence.

In Eq. [1] and [2], $E_F^{(E)}$ and $E_F^{(H)}$ refer to isolated phases. Gerischer (20) invoking a cycle due to Lohmann (21) sets $E_F^{(H)}$ equal to -4.5 eV. In accordance with the above, the net process in this cycle must involve a redox couple out of contact with additional phases. A key step in the cycle involves the free energy of solvation of the Ag^+ ion which Lohmann takes as 4.96 eV. This value involves quantities estimated theoretically as well as some determined by experiment. However, the estimate is old. A newer estimate has been set forth by Gomer (22), namely, 4.64 eV. If this estimate is used in Lohmann's cycle, $E_F^{(H)}$ is predicted to be -4.8 eV. Certain other evidence for which there is not room for discussion in this paper indicates that the -4.8 eV figure may be the more reliable.

Except for the quantitative value of $E_F^{(H)}$, Gerischer's formula in Eq. [2] can be shown to be correct. On the other hand, a reasonably careful derivation (for which we have no space here) is necessary, especially when ionic activities cannot be represented by concentrations. We reserve this task for a later paper.

Photo Characteristics for a Circuit

When a semiconductor-electrolyte junction is illuminated with light of the proper wavelength, V_{DL} will be changed from its equilibrium value, prescribed by Eq. [1], to a new value, $V_{DL} + V_f$, where V_f may be called the photovoltage. If the junction is part of a closed circuit, involving a reversible counterelectrode (1) and a load resistance then the current, I, flowing in the circuit will be

$$I = \frac{V_f}{R_{int} + R_{load}} \qquad [4]$$

where R_{int} and R_{load} are the internal and load resistances, respectively. If an external bias voltage, V_b, is present in the circuit, then Eq. [4] is replaced by

$$I = \frac{V_f + V_b}{R_{int} + R_{load}} \qquad [5]$$

Equations [4] and [5] represent the circuit characteristics. The photocharacteristic is obtained by computing the relation between I and V_f based on the properties of the junction alone. Insertion of this expression into Eq. [5] gives V_f or I as functions of $R_{int} + R_{load}$. The open-circuit characteristic is obtained by setting I, determined from the junction alone, equal to zero.

Organization of Derivations of Photocharacteristics

The computation of the photocharacteristics is dominated by the fact that the problem may be subdivided into a number of independent (or quasi-independent) analytical components which must eventually be interfaced with one another. It is simplified because the internal behavior of each component may be studied separately but complicated by the need to establish the interfaces and to arrange the calculation so that each such connection is dealt with properly. It is therefore convenient, at the outset, to perform a "systems analysis," the result of which will be a recipe showing how the final solution is assembled out of its components. Figure 1 is useful for this analysis.

In this figure the semiconductor lies to the right of the vertical, solid line which represents the interface between the semiconductor and the electrolyte solution to the left. We shall assume the semiconductor to be n-type (no greater difficulty is encountered in treating the p-type case) with the bands bending up from the bulk toward the interface so that a "depletion layer" (23) of thickness W develops. The potential across this depletion layer is V_s with zero taken in the bulk of the semiconductor, *i.e.*, the potential of the interface is V_s. Near the interface, on the electrolyte side, we consider an interphase region which may only be several molecular diameters thick in which hole or electron transfer, or both, between the semiconductor and the redox system in the electrolyte takes place. Normally, at equilibrium there will be a potential V_{Ie} (where the subscript e denotes "equilibrium") across the interphase layer. When a current is flowing there may be an additional voltage η across the layer so that the total voltage becomes

$$V_I = V_{Ie} + \eta \quad [6]$$

Clearly η vanishes at equilibrium. Finally, there is a diffuse space charge region in the electrolyte to the left of the charge transfer region [sometimes called the Gouy-Chapman layer (17)] across which there will be a further potential V_E.

When no current is flowing and the junction is at equilibrium V_{DL}, the potential across the junction, will be given by

$$V_{DL} = V_{Ee} + V_{Ie} + V_{Se} = E_F^{(E)} - E_F^{(S)} \quad [7]$$

where V_{Ee} and V_{Se} are the equilibrium values of V_E and V_S. When current is flowing, due to the presence of an external bias V_b and illumination which produces a photovoltage V_f, the potential across the junction will be given by

$$V_f + V_{DL} = V_f + E_F^{(E)} - E_F^{(S)} = V_E + V_I + V_S \quad [8]$$

Clearly from Eq. [7]

$$V_f = V_E + V_I + V_S + E_F^{(S)} - E_F^{(E)} \quad [9]$$

so that the determination of V_f requires the evaluation of V_E, V_I, and V_S, in their dependences on other system parameters.

The great advantage of depletion layer theory is that W can be determined as a function of V_S, and that the potential $V(x)$, where x denotes position in the depletion layer, can be determined as a function of V_S and W, independent of whether or not a current I is flowing (see next section) Thus W can always be eliminated from any formulas for the transport of holes and electrons, and $V(x)$ is available for use in such formulas.

In our treatment we eventually limit consideration to the case where $\eta = 0$. There is, however, no fundamental difficulty in treating the case, $\eta \neq 0$, provided a model (possibly phenomenological) for the generation of η is available.

We will assume that the diffuse layer in the electrolyte relaxes to equilibrium so quickly that the potential distribution within it, and V_E in particular, may be computed (see below) by assuming an equilibrium distribution even though a current I is flowing. In this way we find that

$$V_E = \Gamma(V_f, ---) \quad [10]$$

where the dashes again indicate dependence on various material parameters. Now from Eq. [6] and [8] we find

$$V_S = V_S(V_E, V_f, ---) \quad [11]$$

and substitution of Eq. [10] into Eq. [11] gives

$$V_S = \Lambda(V_f, ---) \quad [12]$$

Hole and electron currents flowing in the semiconductor can be computed (see below) as functions of V_S, V_E, and other parameters of both the material and of illumination. The external current I may be readily related to the hole and electron currents at the interface so that

$$I = I(V_S, V_E, ---) \quad [13]$$

Substitution of Eq. [10] followed by inversion of Eq. [13] then yields

$$V_S = \psi(I, V_f, ---) \quad [14]$$

This may also be expressed as

$$I = I(V_f, V_S, ---) \quad [15]$$

Then substitution of Eq. [11] and [14] into Eq. [9] with V_I expressed by Eq. [6] gives

$$V_f = \Gamma(V_f) + \psi(I, V_f) + V_{Ie} + E_F^{(S)} - E_F^{(E)} \quad [16]$$

This may be inverted to yield

$$V_f = \theta(I, ---) \quad [17]$$

which is the photocurrent-voltage characteristic. The open-circuit photovoltage is obtained by setting I to zero. Substitution of Eq. [17] into Eq. [5] yields

$$I = \frac{\theta(I) + V_b}{R_{int} + R_{load}} \quad [18]$$

This is the photocurrent characteristic. Elimination of I between Eq. [17] and [18] yields the photovoltaic characteristic.

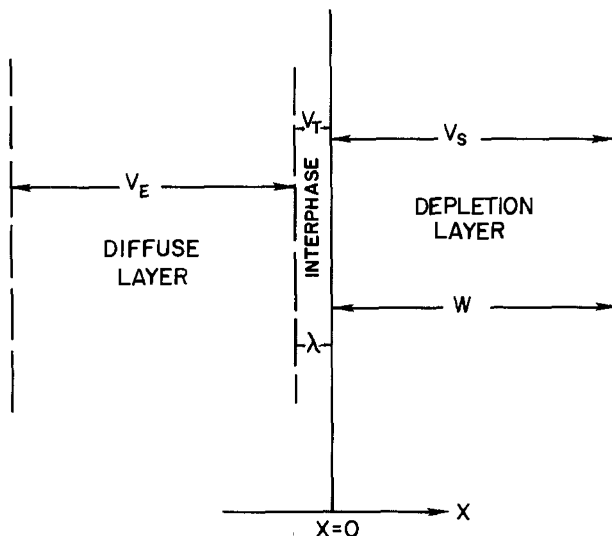

Fig. 1. Arrangement of the electrolyte-semiconductor junction, showing position of interface at $x = 0$, and the various layers, their potentials, and their widths. Note the total potential across the junction, $V_E + V_I + V_S$, equals the photovoltage V_f plus the difference in Fermi levels, $E_F^{(E)} - E_F^{(S)}$.

Potentials in the Various Layers

Equation [7] shows that the junction potential $V_f + V_b + V_{DL}$ consists of three components; one V_E,

across that part of the double layer in the electrolyte, V_I, across the charge interphase layer, and the other, V_S, extending across the portion of the double layer in the semiconductor.

Assume the junction to be plane parallel with the x direction normal to it. Furthermore let the semiconductor extend from $x = 0$ to $x = \infty$, while the electrolyte extends between $x = -\infty$, and $x = 0$. (We ignore the thickness, λ, of the interphase layer.) However the results we use can be shown to be the same as are obtained taking that layer into consideration so that the diffuse layer begins at $x = -\lambda$. For illustrative purposes we work out a simple example of the variation of potential within the junction double layer.

We assume V_{DL} to be negative, which according to Eq. [1] requires $E_F^{(E)} < E_F^{(S)}$. Furthermore, we assume the semiconductor to be doped uniformly n-type to the level N_D where N_D is the concentration of donor atoms. Furthermore we assume $N_D >> n_i$ where n_i is the intrinsic concentration of carriers in the semiconductor. Denoting the potential by V we set $V = 0$ in the bulk of the semiconductor. Invoking Schottky depletion layer theory (23) we have for Poisson's equation (using Gaussian units) in the depletion layer of the semiconductor

$$\frac{d^2V}{dx^2} = -\frac{4\pi q N_D}{\kappa_S}, \quad 0 < x \leq W \qquad [19]$$

where κ_S is the dielectric constant of the semiconductor, and W is the width of the depletion zone. The usual boundary conditions for depletion layer theory are

$$V(W) = 0 \qquad [20]$$

$$\left(\frac{dV}{dx}\right)_{x=W} = 0 \qquad [21]$$

$$V(0) = V_S \qquad [22]$$

The well-known parabolic solution to Eq. [19] subject to these boundary conditions is

$$V(x) = \frac{-2\pi q N_D}{\kappa_S}(x - W)^2, \quad 0 < x \leq W \qquad [23]$$

with

$$W = \left(\frac{-\kappa_S V_S}{2\pi_q N_D}\right)^{1/2} \qquad [24]$$

In approximating Poisson's equation by Eq. [19], *i.e.*, in invoking a depletion layer, we have implicitly assumed $V_S < 0$. This is in accordance with the assumption $V_{DL} < 0$, for the equilibrium situation. It may not, however, be accurate for a nonequilibrium case with sufficient forward bias. In any event, Eq. [21] and [22] show that $V(x)$ and the relation between V_S and W can be obtained independent of the flow of current.

On the electrolyte side we will first assume, for simplicity, that the diffuse space charge layer contains a uni-univalent electrolyte, ionizing as follows

$$MA = M^+ + A^-$$

and present in bulk concentration (at $x = -\infty$), c_0. Since $V(\infty) = V(W) = 0$ we must have

$$V(-\infty) = V_E + V_I + V_S \qquad [25]$$

Then, moving toward the Poisson-Boltzmann equation (24) we may write for $x < 0$

$$c_+ = c_0 \exp\left[-\frac{q}{kT}(V - V_E - V_I - V_S)\right] \qquad [26]$$

$$c_- = c_0 \exp\left[\frac{q}{kT}(V - V_E - V_I - V_S)\right] \qquad [27]$$

where k is the Boltzmann constant and T is temperature, and where c_+ and c_- are the local concentrations of cations and anions, respectively. Then the appropriate Poisson-Boltzmann equation (24) is

$$\frac{d^2V}{dx^2} = \frac{8\pi q c_0}{\kappa_E}\sinh\left\{\frac{q(V - V_E - V_I - V_S)}{kT}\right\} \qquad [28]$$

where κ_E is the dielectric constant in the electrolyte solution. This must be solved subject to the conditions

$$V(0) = V_S + V_I \qquad [29]$$

$$V(-\infty) = V_E + V_I + V_S \qquad [30]$$

$$\kappa_E\left(\frac{\partial V}{\partial x}\right)_{x=-0} = \kappa_S\left(\frac{\partial V}{\partial x}\right)_{x=+0} \qquad [31]$$

Equation [31] is an expression of the continuity of the electric induction at the interface and assumes the interphase layer to have no net charge. The solution of Eq. [28], subject to Eq. [29] and [30], can be carried out exactly (24). The result is

$$\ln\tanh\frac{q}{4kT}\{V - V_E - V_I - V_S\} - \ln\tanh\frac{q}{4kT}\{-V_E\} = x\sqrt{\frac{8\pi q^2 c_0}{\kappa_E kT}} \qquad [32]$$

Strictly speaking this equation applies to a diffuse layer in equilibrium; Eq. [26] and [29] are meant to hold at equilibrium. However, if the rate of adjustment (transport) in the layer is rapid enough, the layer will remain in quasi-equilibrium even though a current flows through it. Thus Eq. [32] may be adopted for a rapidly relaxing layer which, as indicated in the previous section, we assume. On the other hand, Eq. [23] and [24], incorporating the concept of a depletion zone, are in no way dependent on a differential equation based on the application of Boltzmann's law. Thus these equations hold for nonequilibrium situations quite generally.

Limiting our considerations to rapidly adjusting diffuse layers we may assume both Eq. [23] and [32] to apply to nonequilibrium situations. In these equations we then have two remaining unknown parameters, namely, V_E, and V_S. Equation [7] represents one relation which can be used for the determination of these parameters. Equation [31] is another which can be used for this purpose. Substituting Eq. [23] and [32] into Eq. [31] yields

$$[-2qN_D\kappa_S V_S]^{1/2} = -(8c_0\kappa_E kT)^{1/2}\sinh\frac{qV_E}{2kT} \qquad [33]$$

where we have used Eq. [24].

Substitution of Eq. [8] into Eq. [33] gives

$$[-2qN_D\kappa_S(E_F^{(E)} - E_F^{(S)} - V_f - V_E - V_I)]^{1/2} = -(8c_0\kappa_E kT)^{1/2}\sinh\frac{qV_E}{2kT} \qquad [34]$$

Equation [34] is the detailed version of Eq. [10], determining V_E as a function of V_f. Note that since we assume $\eta = 0$, $V_I = V_{Ie}$, where V_{Ie} is a fixed material parameter.

We have considered a uni-univalent electrolyte because in this case the Poisson-Boltzmann equation can be fully integrated to yield Eq. [32]. However redox couples do not usually consist of such symmetric electrolytes. Nonetheless the appropriate version of Eq. [10] can still be derived. We give an example.

To be definite, consider the case where the redox couple is

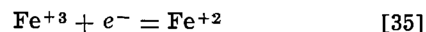

$$Fe^{+3} + e^- = Fe^{+2} \qquad [35]$$

Denote the concentrations of Fe^{+3} and Fe^{+2} at $x = -\infty$ by $c_3{}^0$ and $c_2{}^0$, respectively. The anion con-

centration which may consist, for example, of chloride ions will be denoted by c_1^0. These bulk concentrations will determine the redox potential U, and through Eq. [2], the Fermi level, $E_F^{(E)}$. The local concentrations of ions will be

$$c_3 = c_3^0 \exp\left[-\frac{3q}{kT}(V - V_E - V_I - V_S)\right] \quad [36]$$

$$c_2 = c_2^0 \exp\left[-\frac{2q}{kT}(V - V_E - V_I - V_S)\right] \quad [37]$$

$$c_1 = c_1^0 \exp\left[\frac{q}{kT}(V - V_E - V_I - V_S)\right] \quad [38]$$

Note that electroneutrality requires

$$3c_3^0 + 2c_2^0 = c_1^0 \quad [39]$$

The Poisson-Boltzmann equation now becomes

$$\frac{d^2V}{dx^2} = \frac{-4\pi q}{\kappa_E}\left\{3c_3^0 \exp\left[-\frac{3q}{kT}(V - V_E - V_I - V_S)\right] + 2c_2^0 \exp\left[-\frac{2q}{kT}(V - V_E - V_I - V_S)\right] - c_1^0 \exp\left[\frac{q}{kT}(V - V_E - V_I - V_S)\right]\right\} \quad [40]$$

This must be solved subject to the boundary conditions, Eq. [29] through [31]. It can be integrated once, immediately, subject to Eq. [30] and [31], with the result

$$\frac{dV}{dx} = \pm\left\{\frac{8\pi kT}{\kappa_E}\left[c_3^0\left\{\exp\left[-\frac{3q}{kT}(V - V_E - V_I - V_S)\right] - 1\right\} + c_2^0\left\{\exp\left[-\frac{2q}{kT}(V - V_E - V_I - V_S)\right] - 1\right\} + c_1^0\left\{\exp\left[\frac{q}{kT}(V - V_E - V_I - V_S)\right] - 1\right\}\right]\right\}^{1/2} \quad [41]$$

Equation [39] dictates the use of the positive sign in Eq.[41] if $(dV/dx) > 0$, and the negative sign for $(dV/dx) < 0$.

We choose the positive sign since in our examples $(dV/dx) < 0$. Then substitution of this equation and Eq. [29] into Eq. [31] yields

$$kT\kappa_E[c_3^0 e^{3qV_E/kT} + c_2^0 e^{2qV_E/kT} + c_1^0 e^{-qV_E/kT} - c_3^0 - c_2^0 - c_1^0]^{1/2} = -[-qN_D\kappa_S V_S]^{1/2} \quad [42]$$

Now we can again use Eq. [8] to eliminate V_S from Eq. [42] and determine V_E as a function of V_f, again giving the equivalent of Eq. [10].

It should, however, be indicated that large electrolyte concentrations (high ionic strengths) will cause V_E to approach zero, thereby eliminating the diffuse layer almost entirely. For example, in Eq. [34] a large c_0 coupled with the exponential dependence of the sinh function on V_E forces $V_E \to 0$. Since most junction measurements have involved such high ionic strengths, this has generally been the case. Thus the treatment of the diffuse space charge layer in the electrolyte may only represent an academic exercise and, in fact, in what follows we set $V_E = 0$. Incidentally rapid relaxation is facilitated by high electrolyte concentrations since small, mean ionic velocities may still correspond to large currents.

Modified Butler-Volmer Equation (25)

We need to determine a relation between the current in the interface layer and that in the semiconductor. Figure 2 illustrates the system we now deal with. In the figure the positive x-direction is horizontal and to the right. The interface lies at $x = 0$, marked in the figure. In the semiconductor, at positive values of x, the bands bend up to the left, a necessary consequence of the fact that it is doped n-type and that we are limiting consideration to cases where depletion layer theory is valid. Since electron energy is plotted in the figure, bands which bend up correspond to decreasing electrical potential. The negative of the potential is in fact shown as the dashed line designated by $-V(x)$. The width of the depletion zone is marked by W. The depletion zone necessarily contains positive space charge (marked by the word POSITIVE) due to ionized donors. Outside the space charge layer (marked by NEUTRAL) the semiconductor is neutral. The edges of the conduction and valence bands are respectively designated by E_c and E_v while the donor level is E_D. For equilibrium the common Fermi level is denoted by E_F. It is assumed that the collective energetics of the system is such that the donors are always fully ionized.

At the interface our model contains electronic traps all having level, E_T, shown in the figure. This trap will be capable of catalyzing the recombination of holes and electrons.

Outside of the semiconductor, in the electrolyte to the left of $x = 0$ we indicate the possible diffuse layer by DIFFUSE. Furthermore, the total decrease in potential, $V_E + V_I + V_S$, across the junction is shown as well as the components, $V_E + V_I$ and V_S.

At the interface itself holes, h^+, and electrons, e^-, can be transferred in the interphase layer to and from the redox system by the activated processes

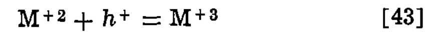

$$M^{+2} + h^+ = M^{+3} \quad [43]$$

and

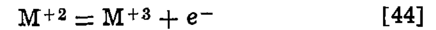

$$M^{+2} = M^{+3} + e^- \quad [44]$$

where for definiteness we assume that divalent and trivalent cations M^{+2} and M^{+3} are involved. The vertical bell-shaped curve with base along the interface represents a hypothetical density of electron states associated with M^{+2}. If this density of states is zero opposite both the conduction band and the valence band there can be essentially no coupling between the semiconductor and the redox process. If the density of states is zero opposite the conduction band, then

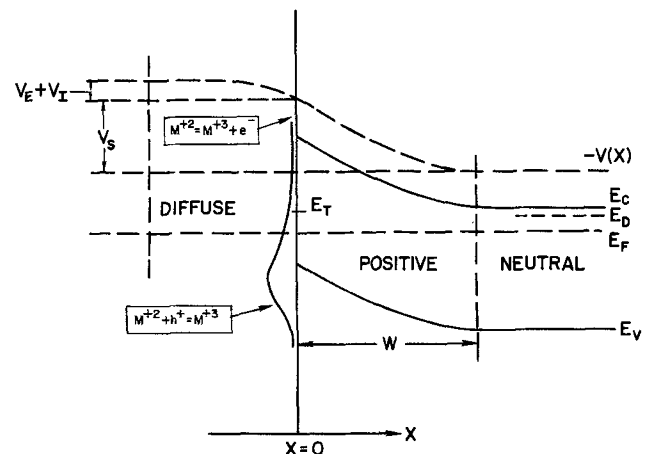

Fig. 2. Diagram of interface showing band bending, the various layers, and energy levels. The bell-shaped curve along the $x = 0$ ordinate is the redox system density of states. The interphase layer is not shown in order to avoid crowding.

only the process of Eq. [43], involving the valence band is possible. Equation [44] clearly applies to the conduction band.

In most situations the density of states will only be finite opposite one band, and, at the most, will have only a negligible tail opposite the other. We shall treat some examples in which the processes in both Eq. [43] and [44] are operative, but the more likely case, with n-type semiconductors and with bands bending up, is the situation in which only the process of Eq. [43] need be considered.

Consider Eq. [43] at equilibrium. We denote the forward rate, per square centimeter of interface by r_{fe}^+, where the subscript f stands for forward and subscript e for eqiulibrium. Then

$$r_{fe}^+ = \{k_f^+ e^{-E_f^+/kT}\} c_{2e}(0) p_e(0) \quad [45]$$

in which $c_{2e}(0)$ represents the equilibrium concentration of M^{+2} at $x = 0$ (at the interface), and

$$p_e(0) = \frac{n_i^2}{N_D} \exp(-qV_{Se}/kT) \quad [46]$$

where V_{Se}, the equilibrium value of V_S, represents the equilibrium (junction neither illuminated nor biased) concentration of holes in the valence band at $x = 0$. The product of these quantities appears in Eq. [45] in the normal chemical kinetic (mass action) sense. The quantity in curly brackets is the specific rate constant with k_f^+ the appropriate preexponential factor, and E_f^+, the activation energy. Similarly for the reverse process we may write

$$r_{re}^+ = \{k_r^+ e^{-E_r^+/kT}\} c_{3e}(0) n_v(0) \quad [47]$$

where the subscript r stands for reverse and where $c_{3e}(0)$ is the equilibrium concentration of M^{+3} at $x = 0$, and $n_v(0)$ is the essentially constant concentration of electrons in the valence band. At equilibrium the forward and reverse rates are equal, hence we define an exchange current

$$i_+ = r_{fe}^+ = r_{re}^+ = k_f^+ \exp(-E_f^+/kT) c_{2e}(0) p_e(0)$$
$$= k_r^+ \exp(-E_r^+/kT) c_{3e}(0) n_v(0) \quad [48]$$

When the junction is not at equilibrium, the transfer of a hole from the semiconductor to M^{+2} may occasion an "overvoltage" which adds, in the usual simple manner (26), to the activation energy. Denoting this overvoltage by η, the modified forward activation energy becomes

$$E_f^+ + \gamma_+ q\eta \quad [49]$$

where γ_+ is the transfer factor (possibly related to the position of the activated state along the reaction coordinate) (25) of the order of 1/2. Therefore, out of equilibrium, we may express the forward rate as

$$r_f^+ = \{k_f^+ e^{-(E_f^+ + \gamma_+ q\eta)/kT}\} c_2(0) p(0)$$
$$= i_+ \left\{ \frac{c_2(0) p(0)}{c_{2e}(0) p_e(0)} \right\} \exp(-\gamma_+ q\eta/kT) \quad [50]$$

where we have utilized Eq. [48] and $c_2(0)$ and $p(0)$ are the nonequilibrium concentrations of M_2^+ and holes.

For the reverse process we note that the transfer factor, γ_r, should be

$$\gamma_r = 1 - \gamma_+ \quad [51]$$

resulting in a nonequilibrium activation energy

$$E_r^+ - (1 - \gamma_+) q\eta \quad [52]$$

and the nonequilibrium rate

$$r_r^+ = \{k_r^+ e^{-[E_r^+ - (1-\gamma_+)q\eta]/kT}\} c_3(0) n_v(0)$$
$$= i_+ \left\{ \frac{c_3(0)}{c_{3e}(0)} \right\} \exp[(1 - \gamma_+) q\eta/kT] \quad [53]$$

The net nonequilibrium rate may now be expressed as

$$r_+ = i_+ \left\{ \left(\frac{p(0)}{p_e(0)} \right) \left(\frac{c_2(0)}{c_{2e}(0)} \right) \exp[-\gamma_+ q\eta/kT] - \left(\frac{c_3(0)}{c_{3e}(0)} \right) \exp[(1 - \gamma_+) q\eta/kT] \right\} \quad [54]$$

This is a modified Butler-Volmer equation (25).

An entirely parallel treatment yields, for the net rate corresponding to the process of Eq. [44]

$$r_- = i_- \left\{ \left(\frac{c_2(0)}{c_{2e}(0)} \right) \exp[-\gamma_- q\eta/kT] - \left(\frac{c_3(0)}{c_{3e}(0)} \right) \left(\frac{n(0)}{n_e(0)} \right) \exp[(1 - \gamma_-) q\eta/kT] \right\} \quad [55]$$

where the exchange current is

$$i_- = k_f^- \exp(-E_f^-/kT) c_{2e}(0) p_c(0)$$
$$= k_r^- \exp(-E_r^-/kT) c_{3e}(0) n_e(0) \quad [56]$$

The meaning of the symbols in Eq. [55] and [56] should be self-evident by comparing them with the corresponding symbols for the process of Eq. [43]. However, we will point out that $p_c(0)$ is the essentially constant concentration of holes in the conduction band, and

$$n_e(0) = N_D \exp(qV_{Se}/kT) \quad [57]$$

Equations [54] and [55] are the relations we wished to derive connecting the rates of charge transfer at the interface.

As we have mentioned several times, in this paper we shall limit consideration to cases where both V_E and η are zero. $V_E = 0$, is almost a rigorous practical requirement since electrolytes of high ionic strength are almost always involved, however cases in which $\eta \neq 0$ may occur and they must be treated by the introduction of some physically reasonable model for the generation of η. In any event, η, $V_E = 0$, has two immediate consequences for Eq. [54] and [55]. The first is the disappearance of the exponentials in these equations while the second, results in

$$c_{2e}(0) = c_2^0 \quad [58]$$

$$c_{3e}(0) = c_3^0 \quad [59]$$

where, as in the previous section, c_2^0 and c_3^0 are the concentrations of ions in the bulk of the electrolyte.

Transport in the Interphase

When $V_E = 0$, no field exists in the interphase region and transport from the bulk of the electrolyte to the semiconductor occurs by diffusion, possibly modified by convection. As a result the flux density of M^{+2} to the semiconductor is

$$J_2 = a_2[c_2^0 - c_2(0)] \quad [60]$$

while that for M^{+3} is

$$J_3 = a_3[c_3^0 - c_3(0)] \quad [61]$$

where a_2 and a_3 are phenomenological coefficients. Now the current, flowing externally, is given by

$$I = qAJ_2 = -qAJ_3 = qA(r_+ - r_-) \quad [62]$$

where A is the area of the interface. Combining Eq. [60] and [61] with Eq. [62] gives

$$c_2(0) = c_2^0 - \frac{I}{qAa_2} \quad [63]$$

$$c_3(0) = c_3^0 + \frac{I}{qAa_3} \quad [64]$$

so that, setting $\eta = 0$ and $c_e^0 = c^0$, we can write Eq.

[54] and [55] in the forms

$$r_+ = i_+ \left\{ \frac{p(0)}{p_e(0)} \left[1 - \frac{I}{qAa_2c_2^0} \right] - \left[1 + \frac{I}{qAa_3c_3^0} \right] \right\} \quad [65]$$

and

$$r_- = i_- \left\{ \left[1 - \frac{I}{qAa_2c_2^0} \right] - \frac{n(0)}{n_e(0)} \left[1 + \frac{I}{qAa_3c_3^0} \right] \right\} \quad [66]$$

Combining these equations with the last equation of Eq. [62] yields

$$I = qA \left\{ \frac{i_+ \left[\frac{p(0)}{p_e(0)} - 1 \right] + i_- \left[\frac{n(0)}{n_e(0)} - 1 \right]}{1 + i_+ \left[\frac{1}{a_2c_2^0} \frac{p(0)}{p_e(0)} - \frac{1}{a_3c_3^0} \right] - i_- \left[\frac{1}{a_3c_3^0} \frac{n(0)}{n_e(0)} + \frac{1}{a_2c_2^0} \right]} \right\} \quad [67]$$

Obviously the current can be determined once the ratios $p(0)/p_e(0)$ and $n(0)/n_e(0)$ are known.

Surface Recombination

Moving inward to the surface of the semiconductor, we next consider the recombination catalyzed by the surface trap whose energy levels are E_T and which are present at a specified surface density, σ_T. For this process we assume a simple Read-Shockley model (27). Then the rate of recombination (per square centimeter of surface) of holes and electrons will be given by (27)

$$\Omega = \frac{\xi\omega[p(0)n(0) - n_i^2]}{\xi[n(0) + n_1] + \omega[p(0) + p_1]} \quad [68]$$

where ξ and ω are constants (each of which is proportional to the surface density σ_T) and n_1 and p_1 are the concentrations of electrons and holes to be expected, respectively, in the conduction and valence bands when the Fermi level is at the trap level. Thus

$$n_1 = N_c e^{-(E_c - E_T)/kT} \quad [69]$$

$$p_1 = N_v e^{(E_v - E_T)/kT} \quad [70]$$

where N_c and N_v are the effective densities of states in the conduction and valence bands. In Eq. [68] n_i is the intrinsic concentration of carriers.

Formulation of the General Boundary Value Problem

We may denote the "particle" current densities, in the semiconductor, of holes and electrons, respectively, by $J_p(x)$ and $J_n(x)$. Then under steady-state conditions, particle conservation requires

$$J_p(0) = r^+ + \Omega \quad [71]$$

$$J_n(0) = r^- + \Omega \quad [72]$$

These represent two boundary conditions to be applied to the transport of holes and electrons at $x = 0$.

For $J_p(x)$ and $J_n(x)$ we employ diffusion theory (18) and use the standard expressions consisting of sums of diffusion and drift terms. Thus we have

$$J_p(x) = -D_p \left\{ \frac{\partial p}{\partial x} + \frac{q}{kT} \frac{\partial V}{\partial x} p \right\} \quad [73]$$

and

$$J_n(x) = -D_n \left\{ \frac{\partial n}{\partial x} - \frac{q}{kT} \frac{\partial V}{\partial x} n \right\} \quad [74]$$

where D_p and D_n are the diffusion coefficients of holes and electrons, respectively.

In our model we assume, like Gärtner (16) and Butler (10), that the semiconductor is illuminated by light of photon flux density ϕ_0 and optical absorption α so that the rate of photogeneration of hole-electron pairs, per cubic centimeter, is

$$g(x) = \phi_0 \alpha e^{-\alpha x} \quad [75]$$

The equations of continuity for holes and electrons, respectively, are then

$$-\frac{\partial J_p}{\partial x} + \phi_0 \alpha e^{-\alpha x} + \frac{p_0 - p}{\tau_p} = \frac{\partial p}{\partial t} \quad [76]$$

$$-\frac{\partial J_n}{\partial x} + \phi_0 \alpha e^{-\alpha x} + \frac{n_0 - n}{\tau_n} = \frac{\partial n}{\partial t} \quad [77]$$

In these equations t is time, and p_0 and n_0 are the unperturbed equilibrium concentrations of holes and electrons, respectively, while τ_p and τ_n are the thermal lifetimes of holes and electrons.

We shall neglect recombination in the depletion zone lying between $x = 0$ and $x = W$, hence in the depletion zone Eq. [76] and [77] may be written without the third terms (which specify the net rate of generation of holes and electrons per cubic centimeter) on the right of both equations. Thus we get

$$-\frac{\partial J_p^*}{\partial x} + \phi_0 \alpha e^{-\alpha x} = \frac{\partial p^*}{\partial t} \quad [78]$$

$$-\frac{\partial J_n^*}{\partial x} + \phi_0 \alpha e^{-\alpha x} = \frac{\partial n^*}{\partial t} \quad [79]$$

where the asterisk is used to denote quantities in the depletion zone.

Outside of the depletion zone, *i.e.*, for $x > W$, we take recombination into account, and hence retain Eq. [76] and [77], however, in this region $(\partial V/\partial x) = 0$ so that only diffusion currents need be considered for the minority carrier, *e.g.*, holes. At $x = W$, the majority electron concentration is only negligibly perturbed from the equilibrium value, N_D. Thus, as another boundary condition, this time at $x = W$, we have

$$n^*(W) = N_D \quad [80]$$

Because of Eq. [80], and because we shall evaluate the steady-state currents at $x = 0$, it proves possible to avoid the explicit study of the transport of electrons outside the depletion zone. However, it is still necessary to study hole transport. For this purpose we require additional boundary conditions. Clearly, outside the depletion zone at $x = \infty$, we have

$$p(\infty) = \frac{n_i^2}{N_D} \quad [81]$$

where the quantity on the right is the equilibrium concentration of holes in the bulk of the semiconductor. Furthermore at $x = W$, there are two conditions of continuity, namely

$$p^*(W) = p(W) \quad [82]$$

$$J_p^*(W) = J_p(W) \quad [83]$$

We now have enough differential equations and boundary conditions to constitute a determinative boundary value problem for the steady-state case in which all time derivatives are suppressed. For convenience we assemble these equations in one place

$$J_n^* = -D_n \left\{ \frac{\partial n^*}{\partial x} - \frac{q}{kT} \frac{\partial V}{\partial x} n^* \right\}, \quad 0 < x \leq W \quad [74']$$

$$-\frac{\partial J_n^*}{\partial x} + \phi_0\alpha e^{-\alpha x} = 0, \quad 0 < x \leq W \qquad [77']$$

$$J_n^*(0) = r^- + \Omega \qquad [72']$$

$$n^*(W) = N_D \qquad [80']$$

$$J_p^* = -D_p\left\{\frac{\partial p^*}{\partial x} + \frac{q}{kT}\frac{\partial V}{\partial x}p^*\right\}, \quad 0 < x \leq W \qquad [73']$$

$$-\frac{\partial J_p^*}{\partial x} + \phi_0\alpha e^{-\alpha x} = 0, \quad 0 < x \leq W \qquad [76']$$

$$J_p^*(0) = r^+ + \Omega \qquad [71']$$

$$p^*(W) = p(W) \qquad [82]$$

$$J_p^*(W) = J_p(W) \qquad [83]$$

$$J_p = -D_p\frac{\partial p}{\partial x}, \quad x > W \qquad [73'']$$

$$-\frac{\partial J_p}{\partial x} + \phi_0\alpha e^{-\alpha x} + \frac{\frac{n_i^2}{N_D} - p}{\tau_p} = 0, \quad x > W \qquad [76'']$$

$$p(\infty) = \frac{n_i^2}{N_D} \qquad [81]$$

Single and double primes on the equation numbers indicate that the equation was derived from an original equation having the number. Thus Eq. [74'], [72'], [80'], [73'], and [71'] are derived from the corresponding numbered equations by appending asterisks. Equations [76'] and [77'] are derived from Eq. [76] and [77] by appending asterisks and suppressing both time derivatives and terms corresponding to recombination. Equation [73''] is derived from Eq. [73] by setting $(\partial V/\partial x) = 0$, while Eq. [76''] is derived from Eq. [76] by replacing p_0 by n_i^2/N_D and suppressing the time derivative. The set of twelve equations [74'], [77'], [72'], [80'], [73'], [76'], [71'], [82], [83], [73''], [76''], and [81], constitute the complete steady-state boundary value problem. In the following sections we solve this problem for special limiting cases, and, eventually, generally.

Solutions for Infinite Interface Rate Constants

If either i_+ or i_- in Eq. [54] and [55], respectively, or ξ and ω in Eq. [68] are allowed to become infinite especially simple boundary value problems result.

If ξ and ω are infinite Ω may be very much larger than r^+ or r^-, and Eq. [71'] and [72'] will require

$$J_p^*(0) \approx \Omega \approx J_n^*(0) \qquad [84]$$

However, Ω will have to remain finite since $J_p^*(0)$ and $J_n^*(0)$ must be finite. Because of this the condition $\xi, \omega \to \infty$ requires, through Eq. [68], that

$$p(0)n(0) = n_i^2 \qquad [85]$$

Equation [84] indicates that photogenerated hole and electron currents "recombine" at the surface of the semiconductor so that essentially no external current flows under the stated conditions; the photovoltaic device will then deliver no power to be used externally. Obviously, an efficient device should avoid surface recombination as much as possible. The conditions to which Eq. [84] and [85] apply are therefore not very interesting. On the other hand, it is instructive to solve the boundary value problem for this case, and we now do this.

Substituting Eq. [74'] into Eq. [77'] and integrating twice with respect to x yields

$$n^*(x) = \exp[qV(x)/kT]\left\{K_2 + \frac{K_1}{D_n}I_1(x) + \frac{\phi_0}{D_n}I_2(x)\right\} \qquad [86]$$

where K_1 and K_2 are constants and where

$$I_1(x) = \int_0^x \exp[-qV(x)/kT]dx \qquad [87]$$

and

$$I_2(x) = \int_0^x \exp\{-[qV(x)/kT] - \alpha x\}dx \qquad [88]$$

A similar process based on the integration of Eq. [76'] together with Eq. [73'] yields

$$p^*(x) = \exp[-qV(x)/kT]\left\{M_2 + \frac{M_1}{D_p}S_1(x) + \frac{\phi_0}{D_p}S_2(x)\right\} \qquad [89]$$

where M_1 and M_2 are constants and where

$$S_1(x) = \int_0^x \exp[qV(x)/kT]dx \qquad [90]$$

and

$$S_2(x) = \int_0^x \exp\{[qV(x)/kT] - \alpha x\}dx \qquad [91]$$

Substituting Eq. [73''] into Eq. [76''] and integrating twice with respect to x, subject to the condition, Eq. [81] yields

$$p = \frac{n_i^2}{N_D} + M_3\exp(-x/L_p) - \frac{\alpha\phi_0 e^{-\alpha x}}{D_p\left(\alpha^2 - \frac{1}{L_p^2}\right)} \qquad [92]$$

where M_3 is still another constant and

$$L_p = \sqrt{D_p\tau_p} \qquad [93]$$

is the diffusion length for holes.

Using Eq. [86] in Eq. [74'] gives

$$J_n^*(x) = -K_1 - \phi_0 e^{-\alpha x} \qquad [94]$$

while Eq. [89] in Eq. [73'] gives

$$J_p^*(x) = -M_1 - \phi_0 e^{-\alpha x} \qquad [95]$$

and substitution of Eq. [94] and [95] into Eq. [84] gives

$$M_1 = K_1 \qquad [96]$$

Furthermore substitution of Eq. [86] and [89] into Eq. [85] gives

$$K_2M_2 = n_i^2 \qquad [97]$$

Equations [96] and [97] provide two relations on the five constants K_1, K_2, M_1, M_2, and M_3. Three more relations, making five in all, may be obtained from Eq. [80'], [82], and [83] into which we substitute Eq. [86], [89], [92], [94], and [95]. Solving these five equations for the five unknown constants gives, after some tedious, but straightforward, algebraic manipulation

$$M_1 = -\frac{B}{2} + \left(\frac{B^2}{4} - C\right)^{1/2} \qquad [98]$$

where

$$B = \frac{-D_nN_D}{I_1} - \frac{D_pn_i^2}{N_D(S_1 + L_p)} + \frac{\phi_0 I_2}{I_1} + \left(\frac{\phi_0}{S_1 + L_p}\right)\left[S_2 + \frac{e^{-\alpha W}}{\alpha + \frac{1}{L_p}}\right] \qquad [99]$$

and

$$C = \frac{\phi(\phi_0 I_2 - D_nN_D)(S_2 + \exp[-\alpha W/(\alpha + L_p^{-1})]N_D - \phi_0 I_2 D_p n_i^2}{N_D I_1(S_1 + L_p)} \qquad [100]$$

where I_1, I_2, S_1, and S_2 denote $I_1(W)$, $I_2(W)$, $S_1(W)$, and $S_2(W)$, respectively. Note that $C = 0$ when $\phi_0 = 0$, so that, according to Eq. [98], $M_1 = 0$. Then Eq. [96] requires $K_1 = 0$. From Eq. [94] and [95] we then have $J_n^* = J_p^* = 0$, which is just what is expected when the junction is not illuminated so that $\phi_0 = 0$.

With M_1 determined by Eq. [98] the other constants are determined by M_1 as follows

$$K_1 = M_1 \quad [101]$$

$$M_2 = \frac{n_i^2}{N_D - \frac{M_1 I_1}{D_n} - \frac{\phi_0 I_2}{D_n}} \quad [102]$$

$$K_2 = N_D - \frac{M_1 I_1}{D_n} - \frac{\phi_0 I_2}{D_n} \quad [103]$$

$$M_3 = \left\{ \frac{\phi_0 e^{-\alpha W}}{\alpha^2 L_p^2 - 1} - M_1 \right\} \frac{L_p}{D_p} \exp(W/L_p) \quad [104]$$

Thus the entire problem for the transport of holes and electrons in the semiconductor is solved.

As indicated earlier, however, the case of rapid surface recombination is of little interest since no external power is delivered, and therefore we have only solved it for illustrative purposes. We now consider a more useful case.

This is the case in which i_+ and i_- are infinite. Then since r^+ and r^- must remain finite Eq. [65] and [66] require

$$p(0) = p_e(0) \left\{ \frac{1 + (I/qAa_3c_3^0)}{1 - (I/qAa_2c_2^0)} \right\} \quad [105]$$

and

$$n(0) = n_e(0) \left\{ \frac{1 - (I/qAa_2c_2^0)}{1 + (I/qAa_3c_3^0)} \right\} \quad [106]$$

Equations [105] and [106] require

$$p(0)n(0) = p_e(0)n_e(0) = n_i^2 \quad [107]$$

so that if ξ and ω in Ω are finite, Eq. [68] demands

$$\Omega = 0 \quad [108]$$

Thus the problem we deal with now is the other face of the coin in which there is no surface recombination, and an external current flows, given by

$$I = qA(r^+ - r^-) \quad [109]$$

or, equivalently, by Eq. [67], where A is the area of the interface. Equations [72′] and [71′] substituted into Eq. [109] give

$$I = qA[J_p^*(0) - J_n^*(0)] \quad [110]$$

Furthermore since $\Omega = 0$, these same equations require

$$J_n^*(0) = r^- \quad [111]$$

and

$$J_p^*(0) = r^+ \quad [112]$$

Equations [105], [106], [80′], [82], [83], and [81] are to be used as new boundary conditions for the new boundary value problem.

In the present case Eq. [86], [89], and [92] still hold, and since

$$I_1(0) = I_2(0) = S_1(0) = S_2(0) = 0 \quad [113]$$

it follows from Eq. [86] and [89] that

$$K_2 = n(0) \exp(-qV_s/kT) \quad [114]$$

$$M_2 = p(0) \exp(qV_s/kT) \quad [115]$$

Furthermore Eq. [94] and [95] are still valid, and substitution of Eq. [92] into Eq. [73″] gives

$$J_p(x) = \frac{D_p M_3}{L_p} \exp(-x/L_p) - \frac{\alpha^2 \phi_0 e^{-\alpha x}}{\alpha^2 - \frac{1}{L_p^2}} \quad [116]$$

Once again we are confronted with the need to determine the five constants K_1, K_2, M_1, M_2, and M_3. For this purpose we can utilize Eq. [114], [115], [80′], [94], and [95], substituting Eq. [86], [89], [92], [94], [95], and [116]. With the constants determined in this manner, Eq. [94] and [95] yield

$$J_n^*(0) = -\frac{D_n N_D}{I_1} - \phi_0 \left[1 - \frac{I_2}{I_1}\right] + \frac{D_n}{I_1} n(0) e^{-qV_S/kT} \quad [117]$$

and

$$J_p^*(0) = \frac{-D_p n_i^2}{N_D(S + L_p)} - \phi_0 \left[1 - \frac{S_2}{S_1 + L_p}\right] + \frac{\phi_0 e^{-\alpha W}}{\left(\alpha + \frac{1}{L_p}\right)(S_1 + L_p)} + \frac{D_p p(0) e^{qV_S/kT}}{S_1 + L_p} \quad [118]$$

Substitution of these equations into Eq. [110] yields the current. The result is

$$I = qA \left\{ \frac{\phi_0 e^{-\alpha W}}{\left(\alpha + \frac{1}{L_p}\right)(S_1 + L_p)} + \frac{D_p p(0) \exp(qV_S/kT)}{S_1 + L_p} + \frac{\phi_0 S_2}{S_1 + L_p} - \frac{D_p n_i^2}{N_D(S_1 + L_p)} + \frac{D_n N_D}{I_1} - \frac{D_n n(0) \exp(-qV_S/kT)}{I_1} - \frac{\phi_0 I_2}{I_1} \right\} \quad [119]$$

where again I_1, I_2, S_1, and S_2 refer to the values of the respective functions at $x = W$.

In this equation $n(0)$ and $p(0)$ still need to be specified. For this purpose we make use of Eq. [105] and [106] as well as Eq. [46] and [57]. The results are

$$n(0) = N_D \left\{ \frac{1 - (I/qAa_2c_2^0)}{1 + (I/qAa_3c_3^0)} \right\} \exp(qV_{Se}/kT) \quad [120]$$

$$p(0) = \frac{n_i^2}{n_D} \left\{ \frac{1 + (I/qAa_3c_3^0)}{1 - (I/qAa_2c_2^0)} \right\} \exp(-qV_{Se}/kT) \quad [121]$$

Now substitution of Eq. [6], [7], and [8] with $\eta, V_E, V_{Ee} = 0$, into Eq. [120] and [121] yields

$$p(0) \exp(qV_S/kT) = \frac{n_i^2}{n_D} \left\{ \frac{1 + (I/qAa_3c_3^0)}{1 - (I/qAa_2c_2^0)} \right\} \exp(qV_f/kT \quad [122]$$

and

$$n(0) \exp(-qV_S/kT) = N_D \left\{ \frac{1 - (I/qAa_2c_2^0)}{1 + (I/qAa_3c_3^0)} \right\} \exp(-qV_f/kT) \quad [123]$$

Substitution of Eq. [122] and [123] into Eq. [119] yields

$$\frac{I}{qA} = \frac{D_p n_i^2}{N_D(S_1 + L_p)} \left[\left\{ \frac{1 + (I/qAa_3c_3^0)}{1 - (I/qAa_2c_2^0)} \right\} \exp(qV_f/kT) - 1 \right] + \frac{D_n N_D}{I_1} \left[1 - \left\{ \frac{1 - (I/qAa_2c_2^0)}{1 + (I/qAa_3c_3^0)} \right\} \exp(-qV_f/kT) \right] + \frac{\phi_0 S_2}{S_1 + L_p} - \frac{\phi_0 I_2}{I_2} + \frac{\phi_0 e^{-\alpha W}}{\left(\alpha + \frac{1}{L_p}\right)(S_1 + L_p)} \quad [124]$$

This is a cubic equation in I, relating I to V_f and V_S, the latter quantity appearing in W, I_1, I_2, S_1, and S_2 (see Eq. [23], [24], [87], [88], [90], and [91]). The proper root or roots of Eq. [124] can be inverted to furnish a detailed equivalent of Eq. [14]. Because V_E is zero in our case, $\Gamma(V_f)$ in Eq. [16] can be set to zero. The photocurrent-voltage characteristics then follow from Eq. [17], and the photocurrent characteristic, from Eq. [18].

The open-circuit photovoltage may be easily obtained from Eq. [124] by setting $I = 0$. This yields

$$\frac{D_p n_i^2}{N_D(S_1 + L_p)}[\exp(qV_f/kT) - 1] + \frac{D_n N_D}{I_2}[1 - \exp(-qV_f/kT)] + \frac{\phi_0 S_2}{S_1 + L_p} - \frac{\phi_0 I_2}{I_1} + \frac{\phi_0 e^{-\alpha W}}{\left(\alpha + \frac{1}{L_p}\right)(S_1 + L_p)} = 0 \quad [125]$$

However, W, I_1, I_2, S_1, and S_2 are still functions of V_S in this equation. V_S can be eliminated by using Eq. [9] which, in our case, specializes to

$$V_S = V_f + V_{Se} \quad [126]$$

Substitution of this equation into Eq. [125] yields a determinative relation for V_f. Under substantial reverse bias $\exp[qV(x)/kT]$ is very small and Eq. [90] and [91] indicate that $S_1(W)$ and $S_2(W)$ may be approximated by zero. Furthermore we note that because V_S is large and negative, under sufficient reverse bias, $\exp(-\alpha x)$ may be considered slowly varying with respect to $\exp[-qV(x)/kT]$. In Eq. [88] it may therefore be extracted from the integral and assigned its value where $\exp[-qV(x)/kT]$ has its largest value. This occurs at $x = 0$ so we get

$$I_2(W) \approx e^{-\alpha 0}\int_0^W \exp[-qV(x)/kT]dx = \int_0^W \exp[-qV(x)/kT]dx = I_1(W) \quad [127]$$

In semiconductors with bandgaps of approximately 3 eV, as in the case of WO_3 or TiO_2, we have at room temperature

$$n_i^2 \approx 10^{-80}$$

Assuming

$$N_D \approx 10^{15}\ \mathrm{cm}^{-3}$$

$$D_p \approx 1.0\ \mathrm{cm^2/sec}$$

$$L_p \approx 10^{-4}\ \mathrm{cm}$$

$$V_f \approx 1.5\mathrm{V}$$

possible reasonable values, we find

$$\frac{D_p n_i^2}{N_D L_p}\exp\left(\frac{qV_f}{kT}\right) \approx 10^{-31}\ \mathrm{cm^{-2}\,sec^{-1}}$$

By contrast the photon flux ϕ_0 will be orders of magnitude greater than unity, while $[e^{-\alpha W}/(\alpha + L_p^{-1})] - 1$ will be of order unity, implying that the last term in Eq. [125] will also be orders of magnitude greater than unity. Thus the first term can be neglected. Setting S_1 and S_2 equal to zero, and $I_1 = I_2$, in the remaining terms of Eq. [125] then gives

$$V_f = \frac{-kT}{q}\ln\left\{1 + \frac{\phi_0 I_1}{D_n N_D}\left[\frac{e^{-\alpha W}}{1 + \alpha L_p}\right]\right\} \quad [128]$$

This equation has been derived under the assumption of a reverse biased wide bandgap ($E_c - E_v \geqq 3.0$ eV) semiconductor. How well it can be used when these conditions do not prevail is uncertain. Furthermore although it appears to yield the usual logarithmic dependence of V_f on photon flux, ϕ_0, both I_1 and W depend on V_f; W less sensitively than I_1. In fact, we can approximate I_1 (see Eq. [87] and [126]) by

$$I_1 \approx K^* \exp(-qV_f/kT) \quad [129]$$

Substitution of Eq. [129] into Eq. [128] yields

$$W \approx \ln\frac{K^*\phi_0}{D_n N_D(1 + \alpha L_p)} \quad [130]$$

Then using Eq. [24] and [126] gives

$$V_f \approx -V_{Se} - \frac{2\pi q N_D}{\kappa_S}\left|\ln\frac{K^*\phi_0}{D_n N_D(1 + \alpha L_p)}\right|^2 \quad [131]$$

so that in this limit V_f depends on the square of the logarithm of ϕ_0. Furthermore V_f is maximized at $-V_{Se}$ (the flatband potential)[2] when ϕ_0 is such that the argument of the logarithm is unity.

Another simple limit of Eq. [124] occurs when a_2, $a_3 = \infty$, so that mass transport in the interphase layer exercises no rate control whatsoever. Then Eq. [124] becomes

$$\frac{I}{qA} = \frac{D_p n_i^2}{N_D(S_1 + L_p)}[\exp(qV_f/kT) - 1] + \frac{D_n N_D}{I_1}[1 - \exp(-qV_f/kT)] + \phi_0\left[\frac{S_2}{S_1 + L_p} - \frac{I_2}{I_1} + \frac{e^{-\alpha W}}{\left(\alpha + \frac{1}{L_p}\right)(S_1 + L_p)}\right] \quad [132]$$

If once again Eq. [126] is used to express W, I_1, I_2, S_1, and S_2 in terms of V_f, Eq. [132] again gives the photocurrent-voltage characteristic. Again the open-circuit voltage is obtained by setting $I = 0$.

Before leaving this case we should investigate under what conditions Eq. [132] reduces to the result obtained by Butler (10) who considered the special example of photocurrent in a junction under substantial reverse bias and such that the rate control did not reside in the redox process. This would certainly be the case when $i_+ = i_- = a_2 = a_3 = \infty$ so that Eq. [132] which incorporates this condition is relevant.

Butler's equation is

$$I = qA\phi_0\left\{\frac{e^{-\alpha W}}{1 + \alpha L_p} - 1\right\} \quad [133]$$

Under reverse bias we can set $S_1 = S_2 = 0$, and use Eq. [127] in Eq. [132] which then becomes

$$I = qA\phi_0\left\{\frac{e^{-\alpha W}}{\alpha + \frac{1}{L_p}} - 1\right\} + qA\left\{\frac{D_p n_i^2}{N_D L_p}(e^{qV_f/kT} - 1) - \frac{D_n N_D}{I_1}(e^{-qV_f/kT} - 1)\right\} \quad [134]$$

The first term on the right is Butler's result, however, we still have to contend with the second term. For this term to vanish would require $V_f = 0$, obviously impossible under conditions of illumination. Another explanation is therefore necessary. One possibility is the following.

If we assume $i_- = 0$ so that the redox process coupled to the conduction band does not occur (a perfectly reasonable and, in fact, probable circum-

[2] The fact that V_f decreases when the flatband potential is exceeded indicates, as mentioned earlier, that depletion layer theory fails beyond this point.

stance) while i_+, a_2, and a_3 continue to be infinite, and, in addition, we assume ξ, $\omega = 0$, so that there is no recombination at the interface (a possible situation) then we must still retain Eq. [105], but in place of Eq. [106] we must have

$$J_n^*(0) = -K_1 - \phi_0 = 0 \quad [135]$$

since both r_- and Ω are now zero. Carrying through the same manipulations, but using Eq. [135] instead of Eq. [106] we arrive at the result

$$I = qAr^+ = qAJ_p^*(0) = qA\phi_0 \left\{ \frac{e^{-\alpha W}}{\left(\alpha + \frac{1}{L_p}\right)(S_1 + L_p)} - 1 \right\} + qA \left\{ \frac{D_p n_i^2}{N_D(S_1 + L_p)} (e^{qV_f/kT} - 1) + \frac{\phi_0 S_2}{S_1 + L_p} \right\} \quad [136]$$

This is just Eq. [132] without the terms involving D_n, *i.e.*, without any current contribution from electron transport. If we now consider the case of sufficient reverse bias, we will once again have $S_1(W) \simeq S_2(W)$ 0, and $I_1(W) \simeq I_2(W)$. Then Eq. [136] becomes

$$I = qA\phi_0 \left\{ \frac{e^{-\alpha W}}{\left(\alpha + \frac{1}{L_p}\right)} - 1 \right\} + \frac{qAD_p n_i^2}{N_D L_p} (e^{qV_f/kT} - 1) \quad [137]$$

This equation would be identical with Butler's result if the last term could be ignored. Unfortunately V_f must be a forward voltage ($V_f > 0$) so that the last term cannot easily be suppressed unless the prefactor is quite small. Fortunately, for wide bandgap ($E_c - E_v > 3.0$ eV) semiconductors, the discussion between Eq. [127] and [128] assures us that this last term can be ignored and we do indeed recover Butler's result.

Finite Interface Rate Constants But No Recombination

If we assume no surface recombination, *i.e.*, $\Omega = 0$, then the boundary value problem posed at the end of the section on Surface Recombination can be solved even with i_+ and i_- finite. This is a fairly realistic situation and so we provide the solution in this section. The relevant problem now consists of Eq. [74'], [77'], [80'], [73'], [76'], [82], [83], [73''], [76''], and [81], together with Eq. [111] and [112] which now replace Eq. [72'] and [71']. The solution proceeds in essentially the same manner as in the preceding sections with Eq. [86], [89], [92], [94], [95], and [116] still valid. The constants in these equations are determined through the application of the various boundary conditions, (*e.g.*, Eq. [65], [66], [80'], [82], and [83]). Furthermore the current is specified by Eq. [110]. The final result, after considerable algebraic manipulation is

$$\frac{I}{qA} = \left\{ \frac{\frac{n_i^2}{N_D}\left\{ \frac{[1 + (I/qAa_3c_3^0) - (\phi_0/i_+)]\exp(qV_f/kT)}{[1 - (I/qAa_3c_3^0)]} - 1 \right\} + \frac{\phi_0}{D_p}\left\{ S_2 + \frac{e^{-\alpha W}}{\alpha + \frac{1}{L_p}} \right\}}{\frac{S_1 + L_p}{D_p} - \frac{n_i^2 \exp(qV_f/kT)}{N_D i_+ [1 - (I/qAa_2c_2^0)]}} \right\} + \left\{ \frac{i_- - \frac{\phi_0 \exp(-qV_f/kT) + i_-[1 - (I/qAa_2c_2^0)]\exp\left(\frac{-qV_f}{kT}\right)}{[1 + (I/qAa_3c_3^0)]} - \frac{\phi_0 i_- I_2}{D_n N_D}}{\frac{I_1 i_-}{D_n N_D} + \frac{\exp(-qV_f/kT)}{1 + (I/qAa_3c_3^0)}} \right\} \quad [138]$$

in which we have made use of Eq. [46], [57], and [126].

If we set i_+, $i_- = \infty$, then Eq. [138] reduces (as it should) to Eq. [124]. If on the other hand, we set i_+, a_2, $a_3 = \infty$, and $i_- = 0$, Eq. [138] reduces to Eq. [136] (as it should). However, Eq. [138] also applies to finite i_+ and i_- and is therefore valid for more general situations (in the absence of surface recombination). Equation [138] is a cubic in I, so to get the current-voltage characteristic the roots will have to be determined. The proper root can be inverted to furnish a detailed equivalent of Eq. [14], and with $\Gamma(V_f) = 0$, the photocurrent-voltage characteristic follows from Eq. [17], and the photocurrent characteristic from Eq. [18]. Again the open-circuit voltage is obtained by setting $I = 0$, in Eq. [138]. The result is

$$\left\{ \frac{\frac{n_i^2}{N_D}\{[1 - (\phi_0/i_+)]\exp(qV_f/kT) - 1\} + \frac{\phi_0}{D_p}\left\{ S_2 + \frac{e^{-\alpha W}}{\alpha + \frac{1}{L_p}} \right\}}{\frac{S_1 + L_p}{D_p} - \frac{n_i^2 \exp(qV_f/kT)}{N_D i_+}} \right\} + \left\{ \frac{i_-[1 - \exp(-qV_f/kT)] - \phi_0 \exp(-qV_f/kT) - \frac{\phi_0 i_- I_2}{D_n N_D}}{\frac{I_1 i_-}{D_n N_D} + \exp(-qV_f/kT)} \right\} = 0 \quad [139]$$

Expressing W, I_1, I_2, S_1, and S_2 as functions of V_S and then using Eq. [126] to express these quantities as functions of V_f, followed by substitution in Eq. [139] yields an equation on V_f whose root gives the open-circuit photovoltage.

If we let a_2, $a_3 = \infty$, in Eq. [138], so that there is no mass transport control in the interphase layer, the

cubic disappears and we obtain a relatively simple current voltage characteristic, namely, the equation obtained by replacing the zero on the right of Eq. [139] by I/qA.

Solution of the Full Problem

We now solve what is almost the full problem posed by Eq. [74'], [77'], [72'], [80'], [73'], [76'], [71'], [82'], [83'], [73"], [76"], and [81]. The only concession we make is to set r^- in Eq. [72'] equal to zero, thus replacing Eq. [72'] by

$$J_n^*(0) = \Omega \qquad [140]$$

It is in fact likely, in most real cases, that the overlap of the density of states of the redox couple with at least one of the bands will be negligible. The algebraic manipulation even with the modification contained in Eq. [140] is a tour de force in tedium (although straightforward) and it would be considerably more extensive if Eq. [72'] were retained. There is, however, no reason why it cannot be carried out for the full case if necessary.

Setting $r^- = 0$ in Eq. [109] eliminating Ω between Eq. [71'] and [140], and substituting r^+ from the result into Eq. [109] with $r^- = 0$ gives

$$I = qAr^+ = qA[J_p^*(0) - J_n^*(0)] \qquad [141]$$

Again Eq. [86], [89], [92], [94], [95], and [116] remain valid, and the constants must be determined by application of the various boundary conditions. Performing all of these operations and using Eq. [141] to evaluate the external current we obtain

$$\frac{I}{qA} = \frac{i_+(S_1+L_p)[1-(I/qAa_2c_2^0)]K_1}{i_+(S_1+L_p)[1-(I/qAa_2c_2^0)] - \dfrac{n_i^2D_p}{N_D}\exp(qV_f/kT)} + \frac{i_+\left\{[1-(I/qAa_2c_2^0)]\left[\dfrac{\phi_0 e^{-\alpha W}}{\alpha+\dfrac{1}{L_p}} - \dfrac{D_pn_i^2}{N_D} + \phi_0S_2\right] + D_p[1+(I/qAa_3c_3^0)]\dfrac{n_i^2}{N_D}\exp(qV_f/kT)\right\}}{i_+(S_1+L_p)[1-(I/qAa_2c_2^0)] - \dfrac{n_i^2D_p}{N_D}\exp(qV_f/kT} \qquad [142]$$

where, as usual, S_1 and S_2 refer to $S_1(W)$ and $S_2(W)$ and

$$K_1 = -\frac{Q_2}{2Q_1} + \left\{\left(\frac{Q_2}{2Q_1}\right) - \frac{Q_3}{Q_1}\right\}^{1/2} \qquad [143]$$

where

$$Q_1 = (S_1+L_p)\left\{\frac{\xi\omega I_1}{D_n} + \omega\exp(-qV_S/kT) + \frac{\xi I_1 i_+ N_D}{D_n n_i^2}[1-(I/qAa_2c_2^0)]\exp(qV_{Se}/kT)\right\} \frac{-D_p\xi I_1\exp(qV_S/kT)}{D_n} \qquad [144]$$

$$Q_2 = \left\{\xi\exp(qV_S/kT)\left(N_D - \frac{\phi_0I_2}{D_n}\right) - \frac{\xi\phi_0I_1e^{qV_f/kT}}{D_n} - \xi n_1 - \omega p_1\right\}\{D_p - i_+(S_1+L_p)[1 - (I/qAa_2c_2^0)]e^{-qV_f/kT}\} - \left\{\frac{\xi\omega I_1}{D_n} + \omega\exp(-qV_S/kT)\right\}$$
$$\left\{i_+(S_1+L_p)[1+(I/qAa_3c_3^0)] - \frac{D_pn_i^2}{N_D} + \phi_0S_2 - \frac{\phi_0e^{-\alpha W}}{\alpha+\dfrac{1}{L_p}}\right\} - (S_1+L_p)\left\{\xi\omega N_D - \frac{\xi\omega\phi_0I_2}{D_n} - \omega\phi_0\exp(-qV_S/kT)\right\} \qquad [145]$$

$$Q_3 = \left\{\xi\omega\left(N_D - \frac{\phi_0I_2}{D_n}\right) + \omega\phi_0\exp(-qV_S/kT)\right\}\left\{\frac{D_pn_i^2}{N_D} - \phi_0S_2 - \frac{\phi_0e^{-\alpha W}}{\left(\alpha+\dfrac{1}{L_p}\right)} - i_+(S_1+L_p)[1+(I/qAa_3c_3^0)]\right\} - \left\{\xi\omega n_i^2 - \phi_0\xi n_1 - \phi_0\omega p_1 - \xi\phi_0\exp(qV_S/kT)\left(N_D - \frac{\phi_0I_2}{D_n}\right)\right\}\left\{D_p - \frac{i_+N_De^{-qV_f/kT}}{n_i^2}(S_1+L_p)[1-(I/qAa_2c_2^0)]\right\} \qquad [146]$$

where I_1 and I_2 also refer to $I_1(W)$ and $I_2(W)$. In these equations I_1 I_2, S_1, S_2, and W can of course be expressed as functions of V_S and therefore of V_f by use of Eq. [124]. Although the equations are very complicated they can in principle be inverted to give the equivalent of Eq. [14] and then the characteristics can be derived by application of Eq. [16], [17], and [18]; $\Gamma(V_f)$ being set equal to zero, as usual.

As before, if we let a_2, $a_3 = \infty$ corresponding to no control by transport in the interphase layer, considerable simplifications result. Also, for the case $I = 0$, there is much simplification and the result can be used to obtain the open-circuit voltage.

A special case for which I should be zero occurs when $\phi_0 = 0$. In this case we note, setting I, ϕ_0, $V_f = 0$ in the quantity Q_3 that $Q_3 = 0$, and then, according to Eq. [143], $K_1 = 0$. Setting K_1, ϕ_0, $I = 0$ in Eq. [142] then yields $I = 0$, demonstrating the internal consistency of this complicated set of equations.

Concluding Remarks

In the foregoing sections we have derived photocharacteristics for fairly general electrolyte-semiconductor junctions. The resulting equations are sometimes complex but in certain limiting conditions exhibit considerable simplification.

We have confined our analysis to junctions where the diffuse Gouy-Chapman layer is, in essence, eliminated by high ionic strength, and where the density of surface traps is sufficiently low so as not to affect band bending. Furthermore, this density, as well as the density of states, is considered invariant. We have assumed that depletion layer theory can be applied to the semiconductor, and that recombination does not occur in this layer, although it may occur outside of it. The use of depletion layer theory compromises the accuracy of the derived characteristics under photon fluxes sufficient to flatten the bands. Insofar as the electrolyte is concerned we allow for possible rate control by mass transport in the interphase layer.

Even though many factors are included in the foregoing theory the resulting equations, already lengthy, are certainly not equal to the most general of situations. Unfortunately, there is no point in being more

general since an individual working on a specific experimental system should tailor the derivation to include those factors which seem to be important in his systems. For example, it is highly likely that surface states will play a dominant role in most cases, and we have hardly treated these adequately. However the same approach can be used for such cases.

Our development does illuminate some prior work. For example, the discussion surrounding Eq. [133] through [136] clearly shows the conditions necessarily underlying Butler's experiments and the theory which they fit.

A great deal of algebra has been performed to derive equations such as Eq. [140] through [146] and pains have been taken to eliminate all errors, typographical and otherwise. It is not likely that these full equations will ever have to be used but if they are they are at least available. They also demonstrate the level of complexity which may be necessary if too many factors are included simultaneously in the analysis. It is obviously necessary to be most judicious in this respect.

Although the "interphase" overpotential, η, has been set to zero in our analysis, in reality V_f, the photovoltage, is an overpotential because the band bending produces an additional "activation" energy for the transfer of electrons. What we really mean then is that the principal component of the overvoltage lies within the semiconductor rather than in the liquid.

In general our theory is based on macroscopic kinetic and transport coefficients. The calculation of these from a more microscopic theory represents still another task.

Acknowledgment

The author would like to express his appreciation to Drs. Adam Heller and Barry Miller, of Bell Laboratories, for many illuminating discussions during the conduct of the research reported in this paper.

Manuscript submitted Nov. 7, 1977; revised manuscript received Jan. 12, 1978.

Any discussion of this paper will appear in a Discussion Section to be published in the December 1978 JOURNAL. All discussions for the December 1978 Discussion Section should be submitted by Aug. 1, 1978.

Publication costs of this article were assisted by Bell Laboratories.

REFERENCES

1. H. Gerischer, in "Advances in Electrochemistry and Electrochemical Enginering," Vol. 1, P. Delahay, Editor, Interscience, New York (1961).
2. J. O'M. Bockris and A. K. N. Reddy, "Modern Electrochemistry," Plenum Press, New York (1970).
3. A. J. Nozik, *Nature,* **257,** 383 (1975).
4. J. Manassen, D. Cohen, and G. Hodes, *ibid.,* **263,** (1976).
5. M. D. Archer, *J. Appl. Electrochem.,* **5,** 17 (1975).
6. H. Gerischer, *This Journal,* **113,** 1174 (1966).
7. K. C. Chang, A. Heller, B. Schwartz, S. Menezes, and B. Miller, *Science,* **196,** 1097 (1977).
8. A. Heller, K. C. Chang, and B. Miller, *This Journal,* **124,** 697 (1977).
9. B. Miller, A. Heller, M. Robbins, S. Menezes, K. C. Chang, and J. Thomson, Jr., *ibid.,* **124,** 1019 (1977).
10. M. A. Butler, *J. Appl. Phys.,* **48,** 1914 (1977).
11. L. B. Andersen, in "Electrochemistry and Physics of Semiconductor-Liquid Interfaces under Illumination," Proceedings of a Topical Conference of the Electrochemical Society, A. Heller, Editor, Arlie, Virginia, May 1977.
12. D. Laser and A. J. Bard, *This Journal,* **123,** 1833 (1976).
13. J. F. Dewald, *Bell Syst. Tech. J.,* **39,** 615 (1960).
14. W. Shockley, *ibid.,* **28,** 435 (1949).
15. R. A. Smith, "Semiconductors," pp. 283-286, Cambridge University Press, New York (1959).
16. W. W. Gärtner, *Phys. Rev.,* **116,** 84 (1959).
17. E. J. W. Verwey and J. Th. G. Overbeek, "Theory of the Stability of Lypophobic Colloids," p. 41, Elsevier Publishing Co., New York (1948).
18. H. K. Henisch, "Rectifying Semiconductor Contacts," pp. 197-212, Cambridge University Press, New York (1957).
19. H. K. Henisch, *ibid.,* p. 209.
20. H. Gerischer, in "Photochemical Conversion and Storage of Solar Energy," Proceedings of an International Conference, London, Ontario, 1976.
21. S. Lohmann, *Z. Naturforsch.,* **224,** 843 (1967).
22. R. Gomer and G. Tryson, *J. Chem. Phys.,* To be published (1977).
23. A. S. Grove, "Physics and Technology of Semiconductor Devices," pp. 264-271, John Wiley & Sons, Inc., New York (1967).
24. E. J. W. Verwey and J. Th. G. Overbeek, "Theory of the Stability of Lyophobic Colloids," p. 24, Elsevier Publishing Co., New York (1948).
25. J. O'M. Bockris and A. K. N. Reddy, "Modern Electrochemistry," Vol. 2, pp. 862-880, Plenum Press, New York (1970).
26. J. O'M. Bockris and A. K. N. Reddy, *ibid.,* p. 871.
27. R. A. Smith, "Semiconductors," pp. 291-295, Cambridge University Press, New York (1959).

Some Properties of Palladium Photocathodes Used in the Electron Image Projection System (ELIPS)

W. Robert Sinclair,* L. H. Lin,[1] P. K. Gallagher, and R. A. Fastnacht

Bell Laboratories, Murray Hill, New Jersey 07974

ABSTRACT

Measurements of some properties of palladium photocathodes used in an electron image projection system (ELIPS) have been made to evaluate criticisms of their performance by Scott (1). It has been found that sputtered palladium films can be used successfully with 253.6 nm radiation, thus negating the claimed necessity of a tungsten impurity. It is suggested that the bulk impurity of H_2O [*ca.* 5 mole percent (m/o)] in the sputtered films found by evolved gas analysis is responsible for the necessary lowering of the work function of palladium. Surface contamination of the palladium is probably responsible for the observed lowering of the photocurrent and instabilities in the photocurrent, but is easily removed by heating externally with an infrared heater. It has been found that palladium-coated masks for ELIPS can be used for many exposures at 10^{-5} Torr by backfilling the chamber between exposures with tank nitrogen.

The electron image projection system (ELIPS) introduced by O'Keeffe *et al.* (2) has been investigated by others (1, 3) recently because it gives promise of rapid lithographic exposure of silicon wafers with better resolution than is possible with photolithography. As indicated in Fig. 1 the system uses a u.v. opaque mask (*e.g.,* chromium) on a quartz substrate with a semitransparent coating of an efficient photoelectron emitter over the mask and substrate. When the mask is illuminated as indicated in the figure, photoelectrons are emitted from the transparent areas and are accelerated to the anode under the combined influence of magnetic and electric fields. As a result a latent image of the mask is quickly produced in the electron resist-coated silicon slice (the anode).

Crucial for the practical use of this system are the properties of the photoelectron-emitting film. The photoemission must be sufficiently high that exposures are reasonable in length (*i.e.,* a few minutes or so), their output should be reasonably constant with time, and other properties such as susceptibility to contamination, adherence, etc., should be suitable.

Only two electron emitters, palladium and cesium iodide, have been described in the literature on ELIPS techniques. During the course of this study we have surveyed in a somewhat cursory fashion a variety of thin films: silver, gold, alloys in the silver-palladium system, tungsten, ruthenium, lead oxide, and indium oxide. None of these was found to be as intense an emitter under 253.6 nm radiation as palladium. Scott (4) has argued that palladium is inferior to cesium iodide for use in ELIPS. In particular, evaporated palladium films of reproducible photoemissivity are difficult to prepare. Scott also noted palladium's poor current stability, the requirement of a 10^{-7} Torr vacuum, and the poor stability of the films in air. We have not studied the performance of cesium iodide films. However, a disadvantage is the associated requirement for 184.9 nm radiation, which forces the use of extra high purity silica glass for the mask substrate and the vacuum window.

In this communication, we shall consider methods for improving the properties of palladium films for use in the ELIPS system.

Experimental Procedures and Results

All work was done in an apparatus essentially the same as that indicated in Fig. 1. In general, the pressure during exposures was about 2×10^{-5} Torr. We have found, however, that by rf sputtering palladium in argon, films can be made reproducibly which are active with 253.6 nm (4.89 eV) radiation despite the absence of tungsten, which Scott argues is necessary for lowering the work function. It is not certain why the work function of the sputtered palladium is lower than the ultrahigh vacuum value of 5.5 eV (5). Perhaps dissolved gases are the cause (6) (see below).

The other disadvantages claimed by Scott relate to poor current stability (up to 50% change during exposure), the necessity of working at 10^{-7} Torr, and instability in air. Each of these can be related to the mechanism of degradation of the palladium film activity. Livesay and Fritz (7) found that the main contaminants produced by the bombardment of the electron resist [poly-methyl-methacrylate (PMMA)] were oxygen and water. The dramatic effect of oxygen on the photocathode efficiency is shown in Fig. 2. In this experiment a bare silicon wafer or one coated with PMMA was bathed in photoelectrons for 2 min, a typical time for exposing an electron resist. Then the system was let down to atmospheric pressure in tank oxygen, air or tank nitrogen. It is evident that pure oxygen immediately impairs the usefulness of the photocathode and that the useful lifetime when exposed to nitrogen is much longer even when the lowest pressure encountered is only 2×10^{-5} Torr.

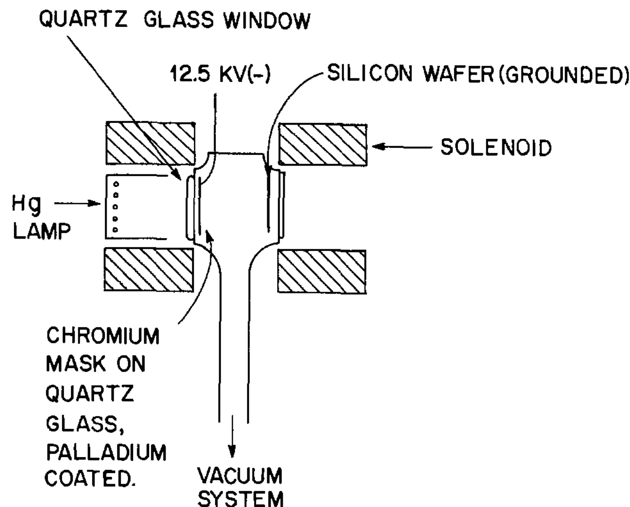

Fig. 1. Schematic diagram of ELIPS apparatus

* Electrochemical Society Active Member.

[1] Present address: RCA Laboratories, Princeton, New Jersey 08540.

Key words: photocathodes, palladium, electron image projection.

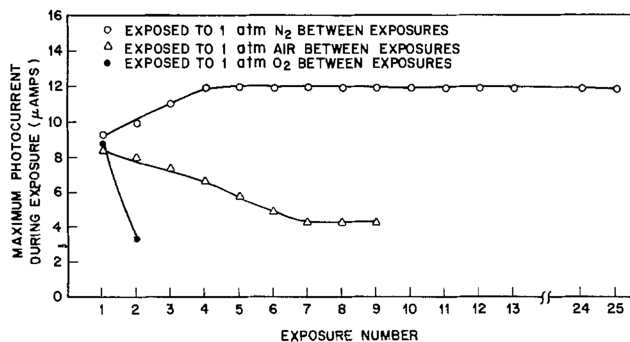

Fig. 2. Maximum photocurrent in 2 min exposure of palladium photocathode as a function of the number of exposures and as a function of the ambient (at 1 atm) that the photocathode was in contact with between exposures.

While irradiating a photocathode with 253.6 nm radiation one notes a continuous rise in the photocurrent as indicated in Fig. 3. This process of cleanup is inferior to that obtained by heating with 60W tungsten lamp, both in terms of ultimate photoemission and in terms of time required for cleanup. Livesay and Fritz (7) have also pointed out the cleanup effects of irradiation.

The lower curve of Fig. 4 shows the effects on the photocurrent of a series of 2 min irradiations at 2×10^{-5} Torr on a nonpreheated cathode followed by letting the system down to one atmosphere of nitrogen. In addition to the increased photoemission due to increased cleanup the current range during an exposure indicated by the height of the vertical bars at each data point decreases significantly as this clean up continues. As indicated by the upper curve of Fig. 4 the output of a film prebaked with a tungsten lamp in vacuum for 20 min varies about 10% when used in a 2 min exposure in a vacuum system at 2×10^{-5} Torr.

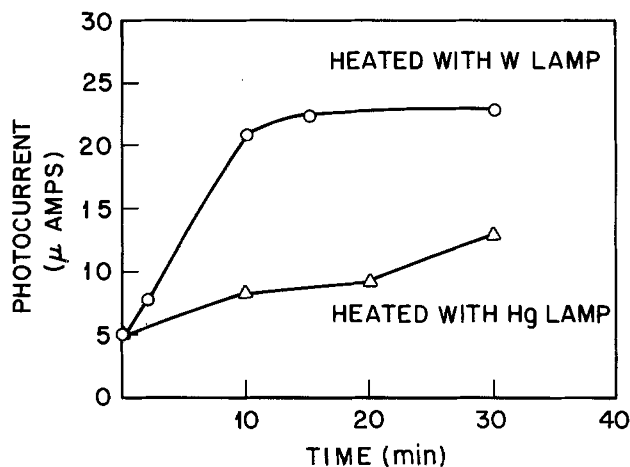

Fig. 3. Effect on photoemission of Pd films of long-term continuous irradiation by a 60W tungsten lamp or a mercury discharge lamp (253.6 nm). Pressure held at 2×10^{-5} Torr.

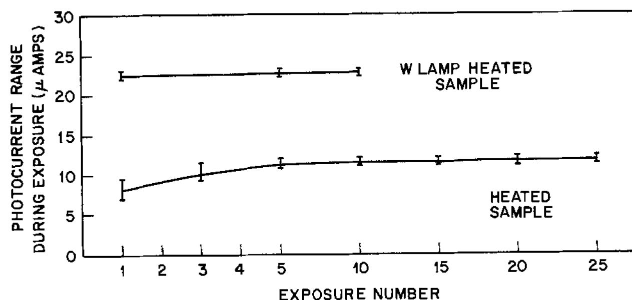

Fig. 4. Range of photocurrent in μA during 2 min exposure as a function of number of exposures. Samples let down to 1 atm of N_2 between exposures. One sample was precleaned by exposure to 60W tungsten lamp.

Using EGA techniques described by Gallagher (8) we studied palladium films on alumina substrates after aging in a room ambient. To minimize surface effects, films thicker than 4000Å were used for these measurements. The results show that the main impurity evolved is water. Figure 5 shows the intensity of the mass 18 line after subtraction of the normal background as a function of temperature at 10^{-7} Torr and at a heating rate of 10°C/min. A similar experiment on an alumina substrate treated identically but without a Pd film revealed no significant increase in mass 18 at temperatures beyond about 100°C. Clearly, a temperature of at least 400°C is necessary to drive off the main bulk of the water. Semiquantitative estimates indicate about 5 m/o of H_2O in the Pd. Auger analysis on a sample aged for several weeks in air at room temperature somewhat surprisingly shows very little oxygen or water (or anything else) on the palladium surface. To correlate these findings we suggest that surface oxygen or water is sufficiently lightly bound that it is easily desorbed by an electron beam and that this film accounts for the changes in photocurrent we have noted. The bulk impurity measured by EGA we suggest is responsible for the lowering of the work function of palladium. Such shifts of the photoelectric threshold with an oxygen impurity have been previously reported for other metals (6). It has already been shown by Sosniak (9) that rf sputtering in argon can lead to a considerable release of water from the sputtering chamber walls. The decreasing variation in photocurrent evidenced in Fig. 4 plus the results of EGA lead us to conclude that the main cause of photocurrent instability is due to contamination rather than changes in the intensity of the mercury line, as suggested by Scott. Of practical importance is the fact that masks stored at 150°C in an air ambient show excellent emission properties when inserted into the ELIPS apparatus reasonably quickly after removal from the oven.

Conclusions

In conclusion, we would like to make the following points: (*i*) Sputtered palladium films are efficient photoemitters using 253.6 radiation. (It is suggested that a bulk impurity of water in the film lowers the work function of palladium.) Thus, inclusion of tungsten from an evaporating coil is not required. (*ii*) Contamination is the prime source of current instability during irradiation of the film with mercury light. (*iii*) Heat-treatment with a 60W tungsten filament bulk leads to higher current output and relatively good (*ca.* 10%) current stability. (*iv*) It is suggested that palladium-coated masks be stored in an air heating oven kept at about 150°C.

Acknowledgment

The authors are grateful to H. Schreiber for Auger analysis performed.

Manuscript submitted Oct. 18, 1976; revised manuscript received Jan. 31, 1978.

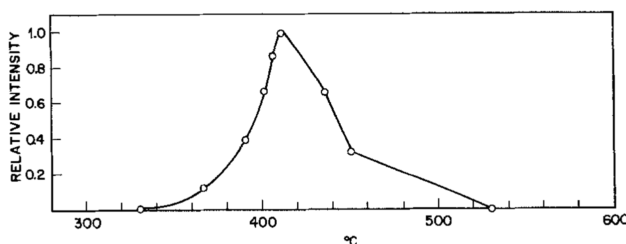

Fig. 5. Relative intensity of H_2O peak vs. temperature from EGA experiment on sputtered palladium film.

Any discussion of this paper will appear in a Discussion Section to be published in the December 1978 JOURNAL. All discussions for the December 1978 Discussion Section should be submitted by Aug. 1, 1978.

Publication costs of this article were assisted by Bell Laboratories.

REFERENCES

1. J. P. Scott, *J. Appl. Phys.*, **46**, 661 (1975).
2. T. W. O'Keefe, J. Vine, and R. M. Handy, *Solid State Electron.*, **12**, 841 (1969).
3. B. Fay, D. B. Ostrowsky, A. M. Roy, and J. Trotel, *Opt. Commun.*, **9**, 424 (1973).
4. J. P. Scott, *IEEE Trans. Electron. Devices*, **ed-22**, 409 (1975).
5. A. Y.-C. Yu and W. E. Spice, *R. Phys. Rev.*, **169**, 497 (1968).
6. H. C. Rentschler and D. E. Henry, *Trans. Electrochem. Soc.*, **87**, 289 (1945).
7. W. R. Livesay and R. B. Fritz, *IEEE Trans. Electron. Devices*, **ed-19**, 647 (1972).
8. P. K. Gallagher, *Thermochimica Acta*, (1978).
9. J. Sosniak, *J. Vac. Sci. Technol.*, **4**, 87 (1967).

Liquid Phase Epitaxy of II-IV-V_2 Chalcopyrite Compounds

S. M. Bedair[1] and M. A. Littlejohn

Department of Electrical Engineering, North Carolina State University, Raleigh, North Carolina 27607

and The Center for Synthesis and Study of Semiconducting Compounds, Research Triangle Institute, Durham, North Carolina 27703

ABSTRACT

Liquid phase epitaxial growth of single crystal chalcopyrite in an open tube system is reported for the first time. $ZnSnAs_2$ has been grown epitaxially on GaAs and InAs substrates from Sn solutions. Optical and electrical measurements have been made on these epilayers. The $ZnSnAs_2$/GaAs and the $ZnSnAs_2$/InAs heterojunctions were found to be abrupt and graded junctions, respectively.

Ternary II-IV-V_2 chalcopyrite crystals are currently of technological interest since they show promise for applications in such areas as visible and infrared light-emitting diodes, infrared detectors, and nonlinear optical devices (1). Despite such potential applications, these compounds are far less investigated than the III-V semiconductor compounds and information on them is still relatively scarce. Difficulties encountered in their preparations in the form of high quality single crystals have probably been responsible for this rather limited progress (2).

The present techniques for preparing single crystals of II-IV-V_2 compounds are either complicated or inadequate. For example, direct synthesis from constituent elements is usually not successful when incongruent melting or order-disorder transitions take place. With solution growth and chemical vapor deposition techniques, there is also very little control over crystal morphology and orientation, and platelet or needlelike crystals are often obtained (1). All these techniques are performed in closed tubes, thus limiting the flexibility during the growth process, and the possibility for explosion is usually present.

There have been very limited efforts devoted to the growth of epitaxial films of the chalcopyrite compounds, and most of these efforts have dealt with the growth on elemental or III-V compound substrates. For example, $ZnSiP_2$ has been grown on both Si and GaP single crystal substrates from Sn solutions (3), and by chemical vapor deposition (4). Also, several II-IV-V_2 layers of $CdSnAs_2$, $CdSnP_2$, $CdGe_xSn_{1-x}P_2$, and $ZnSn_xGe_{1-x}As_2$ have been deposited from Sn solutions on various substrates using different growth methods (3). However, the results show lack of epitaxy and the formation of polycrystalline layers. The liquid phase epitaxial growth (LPE) of $CdSnP_2$ on InP substrates from Sn solution seems to be the only such reported case which has been studied to date; but the growth was done in a closed-tube system with a tilting furnace.

Liquid phase epitaxial growth in an open tube system with a purified hydrogen environment is being extensively applied for the preparation of high quality layers of III-V semiconductor compounds. In principle this technique can also be applied for growth of the II-IV-V_2 chalcopyrites if the operating temperature is relatively low. This requirement is necessary to minimize the losses of the volatile components (mainly As and P) from the melt, and also to prevent any dissociations of the grown chalcopyrite layer (6). Such conditions can be met, with the proper choice of solvents, for most of the arsenide compounds and the low melting point phosphides. The open tube epitaxial technique is simple and flexible. Also, fundamental physical properties, such as photoluminescence, reflectance, mobility, and others can be readily performed on single crystal epilayers grown by this technique. Such measurements of material properties are greatly lacking and are presently being performed with crystals synthesized by the Bridgman technique.

We report for the first time the liquid phase epitaxial growth of single crystal chalcopyrite in an open tube system. $ZnSnAs_2$ has been synthesized epitaxially on GaAs and InAs substrates from Sn solutions. The optical and electrical properties of these grown layers have also been studied and are observed to be closely comparable to those obtained from material grown by other techniques.

Experimental

A vertical LPE dipping system was used (7). The essential components of the system are: a vertical tubular furnace, a quartz reaction tube through which a purified H_2 flow is maintained, a graphite crucible for the melt, and a substrate holder. The substrate can be dipped into the melt by a quartz tube, inside which a thermocouple is placed to measure the melt temperature directly. The starting materials consisted of 20g of 5*N* Sn and 6*N* $ZnAs_2$, and the $ZnSnAs_2$ concentration

[1] On leave from the Faculty of Engineering, Alexandria University, Alexandria, Egypt.

Key words: liquid phase epitaxy, chalcopyrite, zinc tin arsenide.

in the melt varied from 0.5-3 mole percent (m/o). The solution was homogenized for 1 hr at 550°C, and negligible vapor deposits were observed on the cold end of the growth tube.

The temperature at which the $ZnSnAs_2$ layer nucleates was determined in a set of experiments where (111) Si substrates were used. Si was chosen since it is not attacked by the Sn melt in the temperature range of interest (8). Cooling was accomplished at a linear rate of 10°C/hr, and the substrate was pulled from the melt after every cooling interval of 5°C for microscopic examination. Nuclei usually in the form of small triangular platelets of $ZnSnAs_2$ appeared, as shown in Fig. 1. Nucleations started at approximately 465°, 485°, and 505°C for $ZnSnAs_2$ of 1.4, 1.9, and 2.5 m/o in the melt. We realize that these are crude estimates; however, we found that these preliminary experiments were very useful when GaAs and InAs substrates were used. We were thus able to avoid dissolution of these substrates or growing low quality layers if the growth cycles were to start with an undersaturated or highly supersaturated melts, respectively. However, in some experiments additions of GaAs or InAs to the solution were made to prevent pitting of GaAs and InAs substrates, respectively.

Starting from slightly undersaturated solutions and cooling over an interval of 50°C resulted in continuous grown layers of approximately 40 μm thickness on (100) and (111)B oriented GaAs and on (111)B InAs substrates. While such thick layers were grown and used in these studies, there appear to be no limitations to the growth of thinner layers of a few microns in thickness. Future work with LPE of chalcopyrites will be directed toward thin layers more appropriate for some device applications. The Sn melt was found to adhere to some parts of the surfaces of the grown layers. This excess Sn was extracted with mercuric chloride (10.6g) in (50 ml) N-N dimethyl-formamide solution, followed by a chemical polish in a 1% solution of bromine in methanol. The surfaces of the grown layer that were not covered by Sn were shiny, whereas those parts revealed after Sn extraction were rough. For optical, electrical, and other measurements, we found that polishing with Al_2O_2 powder (0.05 μm) followed by etching in 10 HCl: 10 CH_3OOH: 1 HNO_3 was highly desirable.

We had also tried Ge substrates, however excessive dissolutions of Ge were observed.

Results and Discussion

In this section, results will be presented on composition profiles, orientation, crystal structure, electrical properties, and optical properties of the layers grown by open-tube LPE. Since the purpose of this paper is to demonstrate the technique of open tube growth of II-IV-V_2 chalcopyrite compounds, no attempt has been made to optimize or study in great detail the material properties with regard to device applications. It is intended to show that the measured material properties are comparable to those obtained from material grown by other techniques, and thus to conclude that the open tube LPE technique is a compatible materials growth technology for the II-IV-V_2 chalcopyrites. Future work in our laboratories will be directed toward refinements and improvements in material properties and oriented toward material for device applications.

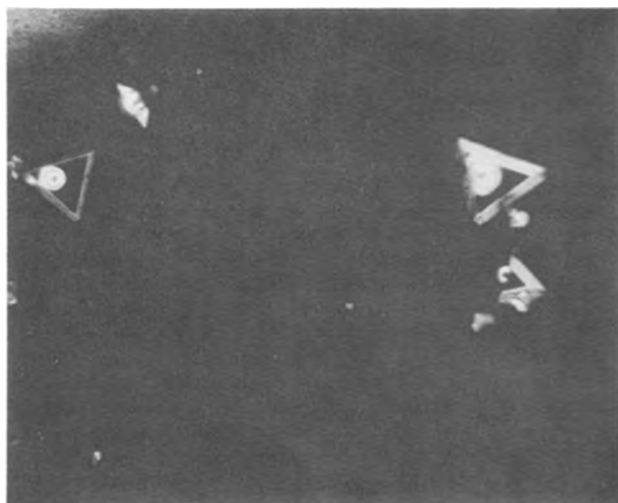

Fig. 1. The onset of nucleations of $ZnSnAs_2$ on Si (111) substrate (magnification 400×).

Composition of the grown layers.—The compositions of the grown layers were determined by electron microprobe (EMP) analysis. For dilute solutions of 0.5-3 m/o $ZnSnAs_2$, the grown layers had the stoichiometric composition of $ZnSnAs_2$. Scanning the grown layers surfaces indicated uniform composition (within the accuracy of the EMP technique). For more concentrated solutions of 10 m/o, precipitations of $ZnAs_2$ were observed with the EMP.

$ZnSnAs_2$ layers grown on GaAs substrates showed traces of Ga [less than 1 atomic percent (a/o)], where approximately 2-3 a/o of In was observed for layers grown on InAs substrates. The composition profile in the epilayers was studied on cleaved and angle-lapped sections of the samples. Scans across the heterojunction monitoring x-ray photons corresponding to Zn-Kα, Sn-Lα, and Ga-Kα or In-Lα are shown in Fig. 2. Figures 2a and b show that for layers grown on GaAs substrates, there are abrupt variations in composition at the junction. The scan across the angle-lapped junction, Fig. 2b, indicates that the first layers to be grown on GaAs are solid solutions having the composition $Ga_{2(1-x)}Zn_xSn_xAs_2$ with x approximately 10%. The value of x increases as the grown layer thickness increases and the epilayer is predominantly $ZnSnAs_2$ for spots greater than 30 μm off the junction. We believe that this is a result of partial dissolution of the GaAs substrate during the first stage of the cooling cycle followed by regrowth of $Ga_{2(1-x)}Zn_xSn_xAs_2$ layer. Similar observation had been reported for the dissolution and regrowth of GaAs from Sn solution (9). In order to examine the interface between the grown layer and the substrate, samples were mounted on glass slides and then the substrate was removed my mechanical polishing. Figure 3 shows an A-B etched (10) interface, where the process of dissolution and regrowth took place in symmetrical fashion. The triangular and rectangular structures indicate the corresponding symmetry for growth on the (111) and (100) GaAs substrates, respectively.

$ZnSnAs_2$ has a tetragonal structure (1) with a = 5.852Å and c/a = 2; thus a lattice mismatch of about 3.5% will be present with the GaAs substrate. However, the formation of the intermediate layer of $Ga_{(1-x)2}Zn_xSn_xAs_2$ will minimize the lattice misfit strain in the epilayer. The as-grown layer is shown in Fig. 4. The cross section of the cleaved junction is shown in Fig. 5 and the observed rough cleavage planes indicate that the epitaxial layer is still strained.

The situation is quite different for layers grown on InAs substrates. Graded junctions, with monotonic changes, from almost pure InAs to almost pure $ZnSnAs_2$ can be deduced from Fig. 2c. This result is consistent with the complete solid solubility previously observed for the InAs-$ZnSnAs_2$ system (11). The lattice mismatch between $ZnSnAs_2$ and InAs is also about 3.5%. The grading in the composition of the grown layer relieves the tension strains resulting from this lattice mismatch, thus avoiding cracking or even fracturing the grown $ZnSnAs_2$ epilayer.

Orientation and crystal structure.—In order to establish the epitaxial relationships, the x-ray diffraction and the back-Laue pattern methods were applied. For layers grown on (111) oriented substrates, the diffrac-

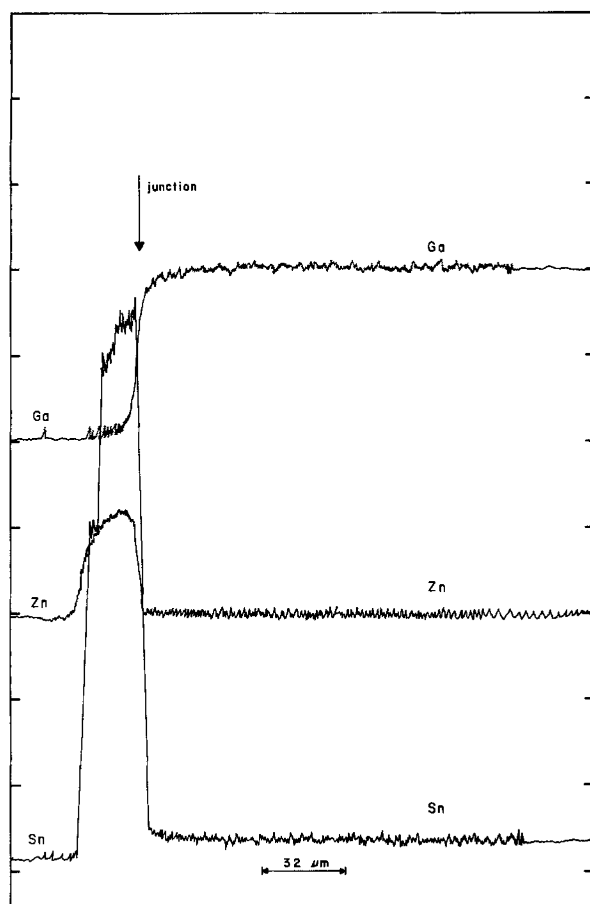

a. $ZnSnAs_2$/GaAs, cleaved

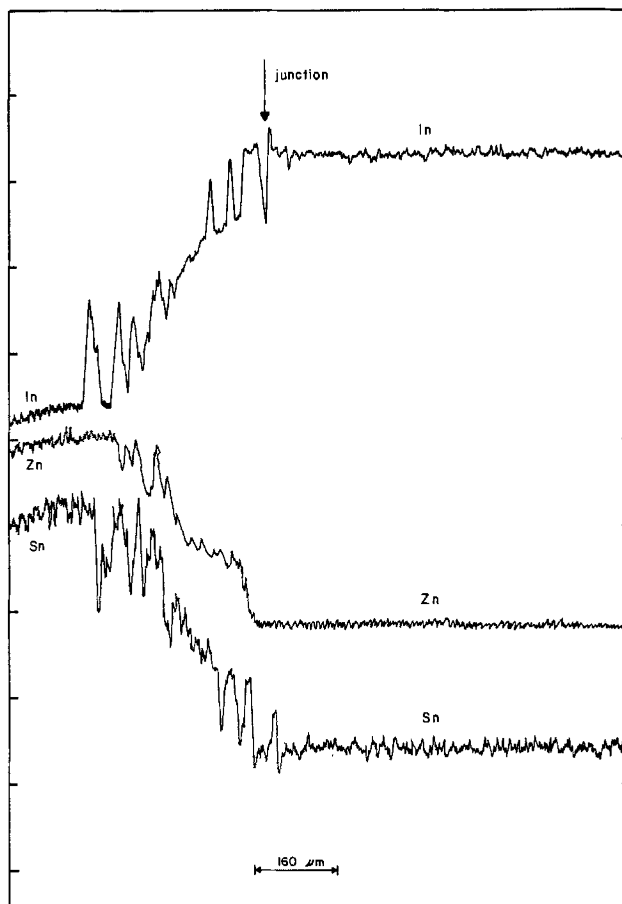

c. $ZnSnAs_2$/InAs, 2° angle lapped

Fig. 2. The composition profiles obtained by scanning across the heterojunction. Peaks appearing at the junction neighborhood are due to slight thickness nonuniformity at the interface and thus they show only for the angle lapped samples.

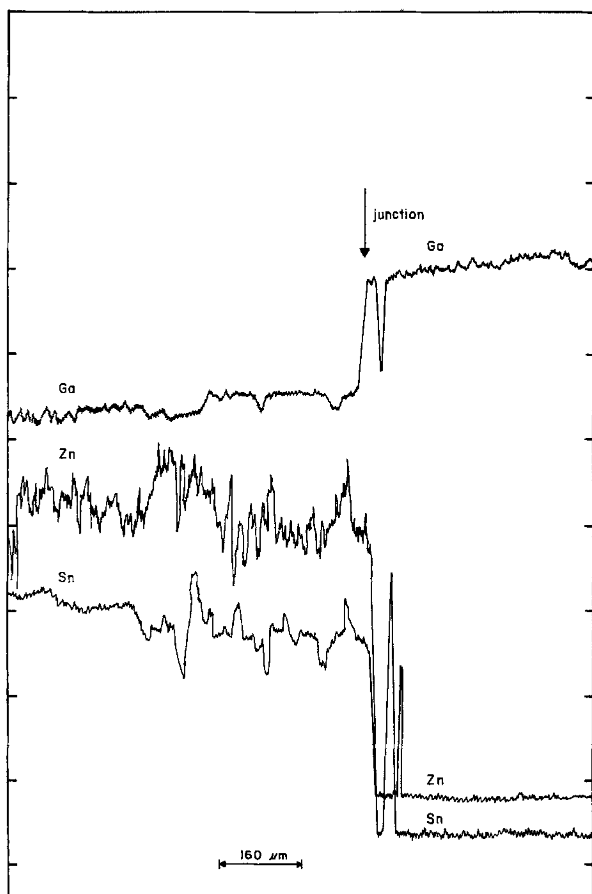

b. $ZnSnAs_2$/GaAs, 2° angle lapped

togram showed a single peak with an angle corresponding to the spacing of (112) $ZnSnAs_2$ having the chalcopyrite structure. Peaks corresponding to the (111) interplanar spacing of the substrates were also present with various heights depending on the thicknesses of the grown layers. For layers grown on (100) oriented substrates a single diffraction peak corresponding to either the (200) plane or the (004) plane was also observed. These two sets of planes have the same spacing in $ZnSnAs_2$, having a tetragonal structure with $c/a = 2$.

The back-Laue patterns showed the symmetry corresponding to the epitaxial growth on the (111) and (100) oriented substrates. Extra spots corresponding to the chalcopyrite structure were observed and no ring structures were detected. Careful examinations of these patterns show the presence of fourfold symmetry indicating that the epitaxial layers on (100) substrates has the (004) orientation. Such conclusions might be misleading since for $ZnSnAs_2$, $c/a = 2$, the intense reflection spots are either coincident or nearly coincident to those of the substrate. However, the Laue pattern for the grown layer alone was obtained and the results confirm the above conclusion of epitaxial growth over the entire substrate area of approximately 1 cm^2.

Electrical measurements.—Hall effect measurements were made on epitaxially grown $ZnSnAs_2$ on semi-insulating and n-type GaAs substrates. The results showed heavily doped p-type layers with carrier concentrations in the 10^{19} cm^{-3} range. A summary of the electrical properties measured at room temperature is shown in Table I. This low resistivity might be a result of arsenic deficiency accompanied by excess of Sn in the compound. Similar observations had been re-

a. (111) GaAs

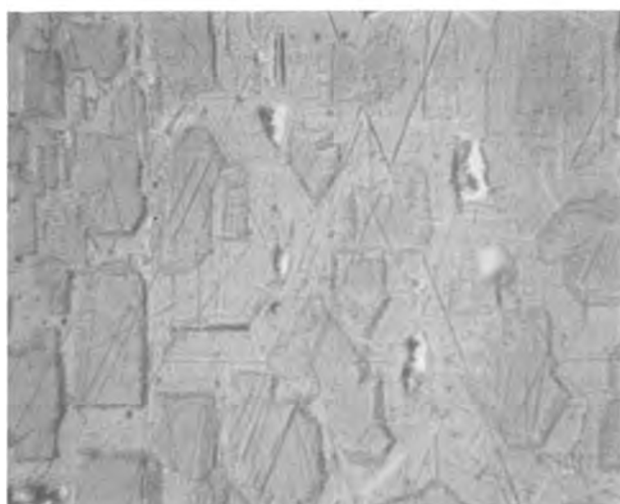

b. (100) GaAs

Fig. 3. The interface between the $ZnSnAs_2$ epilayer and the GaAs substrate. The substrate had been removed by lapping. The application of A-B etch resulted in the triangular and rectangular plateaus which are regions of GaAs (magnification 120×).

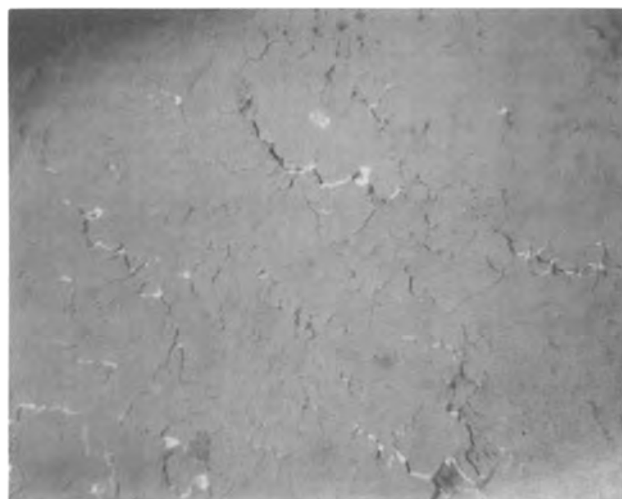

Fig. 4. The as-grown layer of $ZnSnAs_2$ on (111) GaAs substrate (magnification 80×).

ported for other solution-grown undoped chalcopyrites (13).

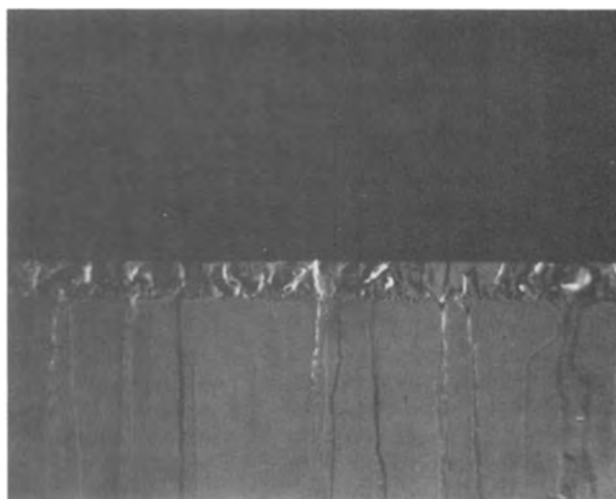

Fig. 5. Cross section of the cleaved $ZnSnAs_2$/GaAs heterojunction (magnification 120×).

It should be mentioned that for the same carrier concentrations, the mobility for these epilayers has the same value as for $ZnSnAs_2$ grown by Bridgman technique (12). Thus, even with the present relatively high lattice mismatch, this simple epitaxial growth technique does not at least degrade the carrier mobility. However, epitaxial $CdSnP_2$ grown on InP substrate in a closed tube system, shows a drastic decrease in the mobility and a value of 20 cm^2/V sec for carrier concentration of $\sim 5 \times 10^{18}$ cm^{-3} has been reported (14). The mobility in nominally pure ($n \simeq 10^{17}$ cm^{-3}) solution-grown $CdSnP_2$ is about 2000 cm^2/V sec.

Optical absorption.—Grown layers of $ZnSnAs_2$ mounted on separate glass (or quartz) slides were lapped until they became shiny, followed by chemical etching. The absorption measurement was done at room temperature with a Cary 14 double beam spectrometer. Sample areas were approximately 0.6 cm^2 having thicknesses in the range 10-20 μm. The absorption coefficient α was calculated after a correction had been made for the reflection coefficient (15), $R = 43\%$, and the results are shown in Fig. 6. The energy bandgap is related to the steep rise observed in the absorption spectrum. Extrapolation of the straight line portion in Fig. 5 gives a value of 0.63 eV for the energy gap at room temperature. This is in agreement with previous absorption edge measurements, where values of 0.6 (16), 0.66 (15), 0.67 (17), and 0.7 (18) eV have been reported for $ZnSnAs_2$. The reported carrier concentrations for both the absorption edge of 0.66 and 0.7 eV was 1.2×10^{18} cm^{-3} (15, 18). We believe the apparent shrinkage in the energy gap of our samples is a result of the present higher carrier concentrations in the 10^{19} cm^{-3} range. Similar observations had been reported for several heavily doped semiconductors (19).

Conclusions

Open tube liquid phase epitaxial growth of single crystals of $ZnSnAs_2$ on GaAs and InAs has been demonstrated for the first time. Optical and electrical measurements were made on these epilayers and found to

Table I. The electrical properties of $ZnSnAs_2$ epitaxially grown single crystals

Samples	Resistivity	Carrier concentrations (cm^{-3})	Mobility (cm^2/V sec)
Epitaxial on (111) GaAs	0.015	1.6×10^{19}	25
Epitaxial on (100) GaAs	0.012	2.7×10^{19}	34
Single crystal grown by Bridgman method Ref. (12)	0.03	10^{19}	30

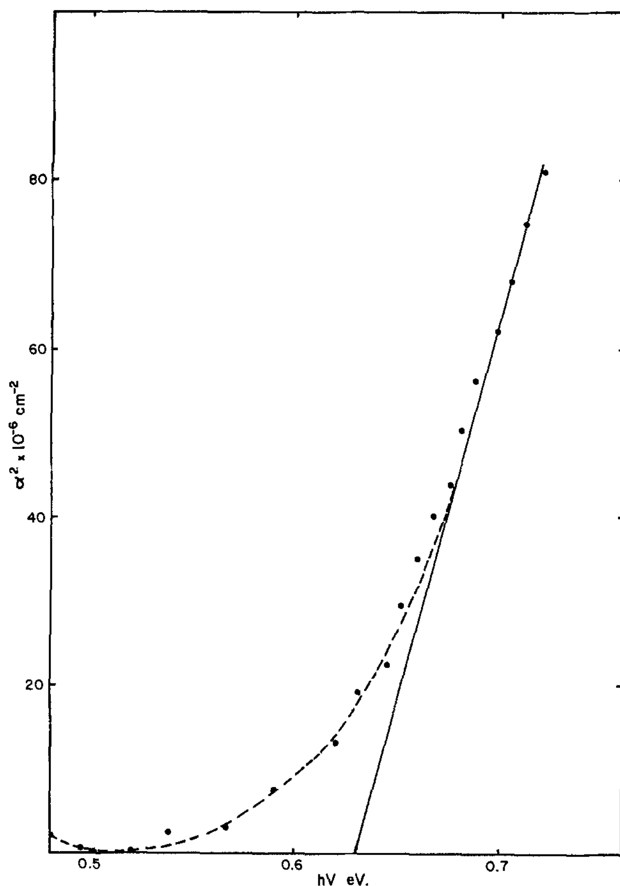

Fig. 6. Variation of the absorption coefficient of $ZnSnAs_2$ single crystal with photon energy.

be in agreement with those corresponding to $ZnSnAs_2$ crystals grown by Bridgman techniques. The composition profiles across the heterojunctions revealed that $ZnSnAs_2$-GaAs system has limited solid solubility where complete solid solubility is present in the $ZnSnAs_2$-InAs system.

We believe that such a simple growth technique can be applied with the proper choice of solvents and substrates to grow several other chalcopyrites. For example $ZnGeAs_2$, $CdGeAs_2$, and $CdGeP_2$ can be grown from bismuth solution, whereas $CdSnP_2$, $ZnSnP_2$, and $CdSnAs_2$ can be grown from tin solution.

Acknowledgments

The authors wish to thank H. H. Stadelmaier, J. R. Hauser, and A. F. Schreiner for their helpful discussions. They also thank J. W. Harrison and S. B. Phatak for their valuable assistances. This work was supported by ERDA Contract No. E(49-18)-2458.

Manuscript submitted Aug. 3, 1977; revised manuscript received Dec. 19, 1977.

Any discussion of this paper will appear in a Discussion Section to be published in the December 1978 JOURNAL. All discussions for the December 1978 Discussion Section should be submitted by Aug. 1, 1978.

Publication costs of this article were assisted by the North Carolina State University.

REFERENCES

1. J. L. Shay and L. H. Wernick, "Ternary Chalcopyrite Semiconductors: Growth, Electronic Properties and Applications," Pergamon Press, Inc., Elmsford, N.Y. (1975).
2. B. R. Pamplin, *J. Cryst. Growth*, **26**, 239 (1974).
3. Y. A. Valov, N. A. Goryunova, E. I. Leonov, and V. M. Orlov, *Acta Phys. Hung.*, **33**, 1 (1973).
4. B. L. Curtis and P. Wild, *Mater. Res. Bull.*, **5**, 69 (1970).
5. K. J. Backmann, E. Buehler, J. L. Shay, and G. W. Kammlott, *J. Electron. Mater.*, **3**, 451 (1974).
6. A. S. Borshchevskii, N. A. Goryunova, F. P. Kesamanly, and D. N. Nasledov, *Phys. Status Solidi*, **21**, 9 (1967).
7. L. R. Dawson and L. M. Whelan, *Bull. Am. Phys. Soc. Series 2*, **13**, 275 (1968).
8. C. D. Thurmond and M. Kowalchik, *Bell Syst. Tech. J.*, **39**, 169 (1960).
9. M. F. Millea and W. R. Wilcox, *This Journal*, **112**, 872 (1965).
10. M. S. Abrahams and C. J. Buiocchi, *J. Appl. Phys.*, **36**, 2855 (1965).
11. H. Borchers and R. G. Maier, *Metallurg.*, **8**, 775 (1963).
12. A. A. Vaipolin, F. P. Kesamanly, and Yu. V. Rud, *Izv. Akad. Nauk SSSR, Neorgan. Mater.*, **3**, 871 (1967).
13. S. A. Muchal, A. J. Payne, and B. Ray, *J. Mater. Sci.*, **4**, 895 (1969).
14. J. L. Shay, K. J. Bachmann, E. Buehler, and L. H. Wernich, *Appl. Phys. Lett.*, **23**, 226 (1973).
15. K. Masumoto and S. Isomura, *J. Phys. Chem. Solids*, **26**, 163 (1965).
16. G. C. Bhar and R. C. Smith, *Phys. Status Solidi A*, **13**, 157 (1972).
17. R. Bendorus, V. D. Prochukhan, and A. Sileika, *Phys. Status Solidi B*, **53**, 745 (1972).
18. Yu. V. Rud, V. V. Sobolev, and S. N. Shestatskii, *Sov. Phys. Semiconductors*, **2**, 745 (1968).
19. S. I. Pankove, "Optical Process in Semiconductors," Prentice-Hall, Englewood Cliffs, N.J. (1971).

Aluminum Diffusion into Silicon in an Open Tube High Vacuum System

Wojciech Rosnowski*

RCA Corporation, Materials and Processing Research Laboratory, Princeton, New Jersey 08540

ABSTRACT

A high vacuum, open tube method for aluminum diffusion into silicon has been described. This technique is simpler and more cost effective than the widely used sealed ampul diffusion. The process offers the possibility of aluminum doping with surface concentration from 10^{17}-10^{19} cm^{-3} and is suitable for high volume production. A simplified mass transport and diffusion model has been developed and used to evaluate the diffusion results. Aluminum diffusion coefficient into silicon has been determined to be: $D = 1.80 \exp(-3.2\ eV/kT)$ $cm^2\ sec^{-1}$ in the temperature range of 1025°-1175°C.

Aluminum diffusion into silicon is usually carried out in a sealed evacuated quartz tube (1-5). For large (2-in.) diameter wafers, the tube is backfilled with argon to prevent collapsing. The presence of argon decreases the aluminum partial pressure and, consequently, results in diffusions with low surface concentration (3, 5). The ampul process considerably limits the ability to widely control the surface concentration. Moreover, after each diffusion run, the quartz tube has to be discarded, thus increasing production costs. In this paper, an open tube, high vacuum method of aluminum diffusion into silicon is presented (6, 7). The process described uses a simple high vacuum setup and a reusable quartz diffusion chamber. The process offers the possibility of aluminum diffusions with surface concentrations from 10^{17} to 10^{19} cm^{-3} and is suitable for high volume production. Its cost per run compares favorably with the ampul technique.

Experimental

Figure 1 shows a sketch of the high vacuum, open tube system used for high volume diffusion. An aluminum disk with a diameter of 20 × 6 mm thick (99.999% purity) supported by an n-type silicon slab 20 × 20 × 5 mm is located on a flat 30 × 30 × 5 mm quartz block between the silicon wafers and at each end of the diffusion chamber of the quartz tube. A restrictor regulates, as illustrated, the aluminum vapor outflow rate during the process. The diffusion is carried out in a movable furnace having a thermal flat zone of better than ±1°C over the length of the diffusion chamber. Prior to diffusion, the quartz tube and boat must be passivated to eliminate the aluminum vapor interaction with the quartz. To accomplish this, two aluminum disks supported by silicon slabs of the same dimensions, as previously described, are located; one at the closed end of the tube and one at a distance of 10-12 in. from the closed end. The quartz boat and quartz blocks are inserted between the sources. The tube, without a restrictor, is then connected to the vacuum system. After evacuating, $<10^{-6}$ Torr for 1 hr, the furnace, set at 400°C, is moved over the tube. The temperature is raised at about 10°C/min to 1100°C. The furnace is heated for about 120 min at this temperature and then slow cooled at about 5°C/min to 400°C. During this process, vacuum is continuously maintained below 10^{-6} Torr. Under this condition, aluminum molecules easily evaporate from the aluminum vapor source since the aluminum partial pressure in the system is about three orders of magnitude higher than the pressure held in the vacuum system. The evaporated aluminum molecules hit the tube walls and react with the quartz: $3SiO_{2(g)} + 4Al_{(g)} \rightarrow 2Al_2O_{3(s)} + 3Si_{(s)}$. The product of this reaction next serves as a passivation layer during aluminum diffusion. The continuous pumping down during the passivation process eliminates the danger of poisoning the aluminum vapor source due to the oxidation by residues and moisture in the system. The development of an impervious skin on the aluminum vapor source surface, due to the reaction $2Al_{(g)} + 3/2\ O_{2(g)} \rightarrow Al_2O_{3(s)}$, is the main reason for diffusion runs which were unsuccessfully performed and so frequently observed in the sealed ampul technology. A thorough analysis of the thermodynamics of the Al-O-H-Si system has recently been presented elsewhere (8). When the passivation is complete, the furnace is slow cooled at 5°-7°C/min to 400°C. The furnace is then moved out over the tube. The tube is filled with nitrogen and disconnected from the vacuum system.

The diffusion process consists of (*i*) loading the cleaned wafers and aluminum-silicon assemblies into a previously passivated quartz tube; (*ii*) evacuating the system to $<10^{-6}$ Torr for about 1 hr and sliding the movable furnace over the tube. The temperature of the furnace when moved over the tube is set to 400°C; (*iii*) raising the temperature at about 10°-13°C/min to the desired deposition temperature and diffusing for the required time. This is usually between 1075° and 1175°C, since a higher temperature could cause the quartz tube to collapse; and (*iv*) cooling the furnace at about 5°C/min to 400°C, sliding the furnace back, filling the quartz tube with nitrogen, and disconnecting the tube from the pumping system and unloading. Wafers used in the experiment were n-type, 25-45 Ω cm resistivity, 2 in. diam float zoned silicon wafers cut to <111> surface orientation.

Mass Transport and Diffusion

The physical system considered in the present work consists of four components; aluminum diffusion source, wafers, tube walls, and gas phase.

During diffusion, the whole system is kept at a constant elevated temperature. Mass transport during

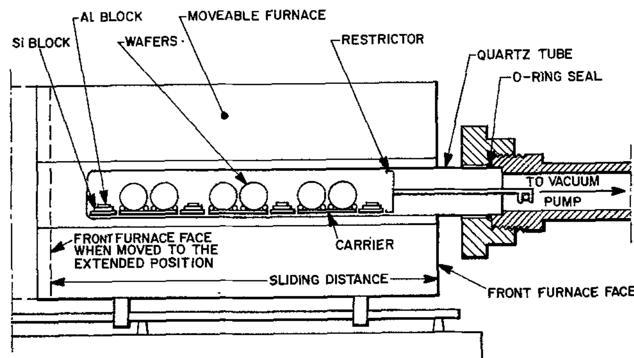

Fig. 1. Open tube, high vacuum aluminum diffusion system

* Electrochemical Society Active Member.

Key words: aluminum, diffusion, doping silicon, diffusion technique.

heating and cooling is not considered here, since it is negligible in comparison to that taking place in the over-all process. The diffusion into silicon and the transport of all material components in the diffusion chamber depend on (*i*) aluminum evaporation rate from the source, (*ii*) silicon evaporation from wafers, (*iii*) transport of the gaseous components, (*iv*) adsorption on the silicon wafers' surfaces, (*v*) adsorption on the tube walls and boat, (*vi*) diffusion into silicon, (*vii*) penetration into the tube walls and boat, and (*viii*) outflow of aluminum vapor from the diffusion chamber. The exact calculation of the contribution of each of these steps is either very difficult or impossible. Generally, adsorption effects at solid surfaces are rather complex and the material properties involved in most of the systems are not well known. Aluminum penetration through quartz proceeds through simultaneous diffusion and chemical reaction resulting in different by-products (4). Also, silicon vapor interacts with SiO_2 forming an SiO phase which evaporates rapidly (9, 10), therefore, the exact vapor composition in the diffusion chamber is difficult to establish. During the diffusion process, the system is connected to the vacuum pump and no equilibrium pressure of silicon and aluminum is maintained. However, by making some idealizations, the approximate mathematical calculations of the mass transport can be made:

1. During diffusion, aluminum evaporates from the surface of the Al-Si alloy. The particle current density of the evaporating atoms depends on the particle density and the activation energy of desorption via Arrhenius formula. In high vacuum, the evaporation per square centimeter·second can be obtained from kinetic theory as

$$\frac{\partial N}{\partial t} = \alpha (M/2\pi RT)^{1/2}\, p_{eq}$$

where P_{eq} denotes the aluminum partial pressure in equilibrium, M is the molecular weight, α is the evaporation coefficient, and R and T have generally accepted meanings. In the steady state, the evaporation per second from surface A is equal to

$$J_{evap} = \left(\frac{\partial N}{\partial t}\right)_{evap} = \alpha A (M/2\pi RT)^{1/2} (p_{eq} - p) \quad [1]$$

where p is the aluminum vapor pressure near the Al-Si alloy. We assume that the diffusing substance is emitted continuously from the source at a constant rate.

2. At the diffusion temperatures normally used, the silicon vapor pressure is about three orders of magnitude lower than that of aluminum (11) and, therefore, we assume that the transport mechanism in the gas phase is totally controlled by the aluminum vapor.

3. Due to the quartz tube passivation, aluminum-quartz reaction and aluminum penetration into quartz (tube walls and boat) are negligible. The reaction of aluminum with quartz results in a mixture of two solid products: Al_2O_3 and Si (passivation layer). The aluminum diffusion coefficient in Al_2O_3 is a few orders of magnitude lower than that of silicon. Therefore, we assume that the aluminum loss due to diffusion into Al_2O_3 can be omitted. The adsorption process inside the passivated quartz tube follows an exponential saturation characteristic (12)

$$S_W = S_{\infty W} \left\{ 1 - \exp\left(-\frac{t}{t_W} \right) \right\} \quad [2]$$

where the wall coverage S_W approaches the saturation value $S_{\infty W}$ with a time constant t_W. The absolute value of t_W depends on material properties and temperature. For silicon, the saturation time varies from minutes to seconds, between 1050° and 1200°C, respectively. For quartz, t_W is chosen to decrease with temperature with an absolute value somewhat higher than the saturation time for silicon (12, 13). Therefore, using a tube that has been previously passivated, we assume that wall coverage S_W approaches saturation value $S_{\infty W}$ in a very short time.

4. The outflow of aluminum vapor from the diffusion chamber can be represented by the "free molecular flow" through tubes and channels because of the very low pressure in the system. The mean free path of aluminum atoms is greater than the characteristic dimension of the tube. The rate flow is limited, not by collisions between molecules, but by collisions of molecules with the walls. For the tube of length L, cross section F, and perimeter B, the rate of the molecular outflow $J_{outflow}$ in the system is equal to (14)

$$J_{outflow} = \frac{\partial N}{\partial t_{outflow}} = \frac{4}{3} \frac{\bar{v}}{\int_0^L \frac{B}{F^2} dL} \Delta n = \frac{4}{3} \frac{\bar{v}}{\int_0^L \frac{B}{F^2} dL} \cdot n_2 \quad [3]$$

where $\bar{v} = (8RT/\pi M)^{1/2}$ is the mean molecular speed and Δn represents the difference between the number n_2 of molecules per cubic centimeter at pressure p_2 inside the diffusion chamber, and n_1 the number of molecules per cubic centimeter at pressure p_1 outside the diffusion chamber. We assume that $p_2 >> p_1$ and also $n_2 >> n_1$ and $\Delta n = n_2$.

In the open tube, high vacuum system, equilibrium is not reached and diffusion is carried out under a steady-state condition from the aluminum vapor continuously freed from the Al-Si alloy. In order to estimate the silicon surface concentration, we must know the arrangement of the wafers and the aluminum vapor source in the diffusion chamber. Figure 2a-d illustrates four different arrangements for which the surface concentration has been evaluated. Before the experiment began, we evaluated the evaporation flux using Eq. [1] and the outflow flux using Eq. [3] for different diffusion conditions. In those calculations, we assumed that evaporation coefficient α is equal to 1, $\alpha = 1$.

The computed results showed that for the designed physical conditions, the outflow flux of aluminum vapor

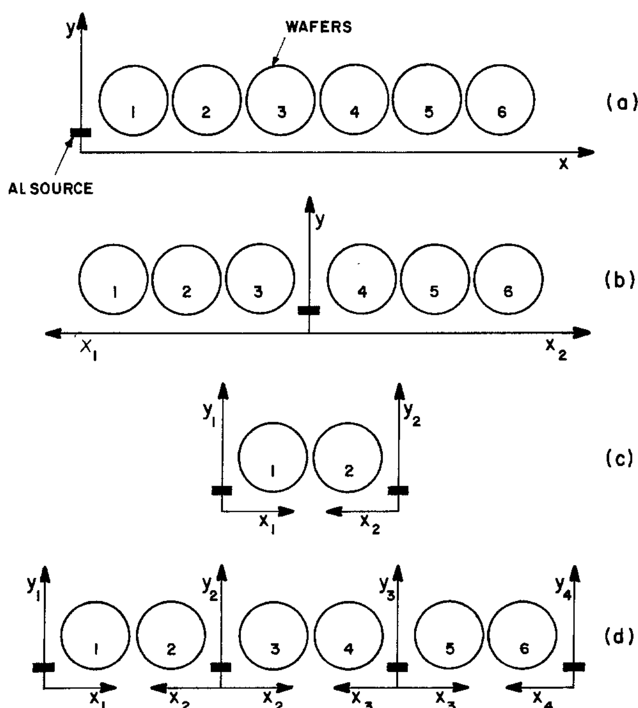

Fig. 2. Aluminum vapor source and wafers' arrangement in the diffusion chamber.

from the system is much smaller than the evaporation flux

$$J_{\text{evap}} >> J_{\text{outflow}} \quad [4]$$

so that

$$J_{\text{diff}} \simeq J_{\text{evap}} \quad [5]$$

The solution of Eq. [5] is

$$c = c_0\left[1 - \text{erf}\left\{\left(\left[\frac{\chi D}{hJ_{\text{evap}}}\right]x + y\right)\frac{1}{2\sqrt{Dt}}\right\}\right] \quad [6]$$

The details of the calculations are included in the Appendix. The relative decrease of C in the gas with increasing x is approximately

$$\frac{C(x,t)}{C_0} = \frac{c(x, y=0, t)}{c_0} \simeq 1 + x\left(\frac{\partial c}{\partial x}\right)_{x=0,y=0}$$

$$= 1 - \frac{2}{\pi}\frac{\chi D}{hJ_{\text{evap}}}\frac{x}{2\sqrt{Dt}} \quad [7]$$

Thus, the decrease in the gas phase is most marked for small values of t.

Equation [6] contains three unknown values, segregation coefficient χ, evaporation coefficient α, and $\Delta p = p_{eq} - p$, the segment in Eq. [1] for J_{evap}. Also h changes its value depending on the distance from the tube center. Introducing a new variable β

$$\frac{1}{\beta} = \frac{\chi}{\alpha \cdot \gamma (p_{eq} - p)} \quad [8]$$

where the γ-corection coefficient for h is defined as follows

$$\gamma = \frac{h}{H} \quad [9]$$

where H represents the inside tube diameter. By inserting Eq. [8] into Eq. [6] and combining with Eq. [1] for $y = 0$, we obtain

$$c = c_0\left[1 - \text{erf}\left\{\frac{1}{\beta}\frac{Dx}{2HA(M/2\pi RT)^{1/2}(Dt)^{1/2}}\right\}\right] \quad [10]$$

Equation [10] was used to evaluate the aluminum surface concentration as a function of distance x from the aluminum vapor source for the silicon wafers and aluminum vapor source arrangements illustrated in Fig. 2a and b. When the wafers and aluminum vapor source arrangements are represented as in Fig. 2c, doping will occur from two sources simultaneously. If the composition of these sources is identical, the second source only equalizes fluctuations between source 1 and source 2 without increasing the pressure over source 1. The surface concentration at any distance x from source 1 is equal to

$$c = c_1 + c_2 - c_{1(x=a)} \quad [11]$$

where a is the distance between two sources, and c_1, c_2 are the surface concentrations due to doping from source 1 and source 2, respectively. Combining Eq. [11] with Eq. [10] we obtain

$$c = c_{01}\left[1 - \text{erf}\left\{\frac{1}{\beta}\frac{Dx}{2HA(M/2\pi RT)^{1/2}(Dt)^{1/2}}\right\}\right] + c_{02}\left[1 - \text{erf}\left\{\frac{1}{\beta}\frac{D(a-x)}{2HA(M/2\pi RT)^{1/2}(Dt)^{1/2}}\right\}\right] - c_{1(x=a)} \quad [12]$$

Equation [12] was used for the calculation of the surface concentration *vs.* distance when the wafers and aluminum source arrangement was as shown in Fig. 2c and d. The computations were performed assuming different values for β. The results of the calculations are presented in the next section.

Results

Diffusion from the elemental aluminum vapor.—The purpose of this test was to investigate the possibility of the use of elemental aluminum as a vapor source. The silicon wafers and the elemental aluminum of 99.999% purity were placed in the diffusion chamber as illustrated in Fig. 2b. The quartz carrier contained only one wafer in every row. After evacuating the system for 1 hr, the furnace at 400°C was moved over the tube. The furnace was then heated to 1150°C. The total diffusion time was 180 min (incuding 47 min for heating from 400° to 1150°C). The results showed that the surface of the wafers placed nearest the aluminum source (wafers marked 3 and 4) in Fig. 2b were alloyed and contaminated with aluminum dots. The diameter of these dots varied depending on the distance from the source. The calculated surface concentration from Irvin's (15) curves using four-point probe data was close to the solubility limit (16) (2×10^{19} cm^{-3}). The enormous degradation observed on the silicon surface considerably limits the use of elemental aluminum as a vapor source for diffusion purposes without additional improvement in the pattern flow of the aluminum vapor.

Diffusion from the Al-Si alloy vapor.—For the next series of tests, the Al-Si alloy was used as an aluminum vapor source to avoid excessive alloying on the silicon surface. In the first tests, an Al-Si alloy was placed at the end of the diffusion chamber as illustrated in Fig. 2a. The Al-Si alloy was formed by fusing an elemental aluminum (99.999% purity) disk with an n-type silicon slab during the diffusion process when the temperature was raised to 1150°C. The purpose of this test was to investigate the variation in dopant concentration as a function of the distance from the Al-Si alloy. Results showed no surface alloying occurred on the wafers, even on those placed near the aluminum source. The surface concentration also decreased with distance from the aluminum vapor source. Figure 3 shows the experimental data and also the results of calculations based on Eq. [10]. The experimental data are best described when $\beta = 3 \times 10^{-3}$. When the wafers and aluminum vapor source arrangement is as illustrated in Fig. 2b, the aluminum vapor flow is symmetrical with respect to the y axis and, consequently, the aluminum surface concentration distribution is also symmetrical. The results of the experiment and the calculations based on Eq. [10] are shown in Fig. 4. All calculations were carried out for the following diffusion conditions: $T = 1150$°C, $t = 137$ min, $A = 12$ cm^2, $H = 3.5$ cm, and $D = 7.98 \times 10^{-12}$ cm^2 sec^{-1}. The value for D was calculated from the relation ob-

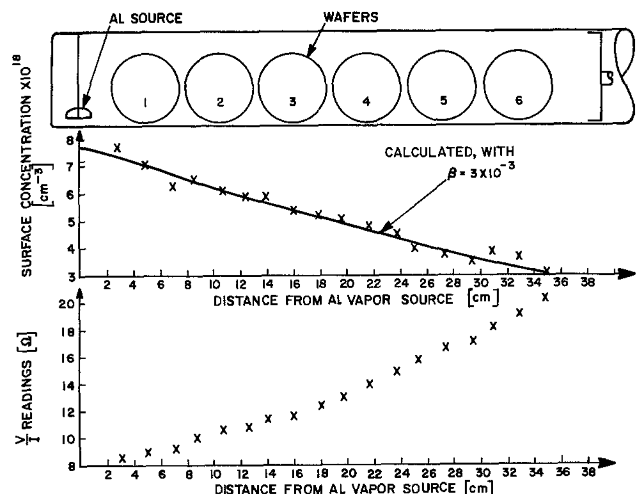

Fig. 3. Aluminum surface concentration *vs.* distance from Al vapor source (aluminum vapor source and wafers' arrangement as in Fig. 2a).

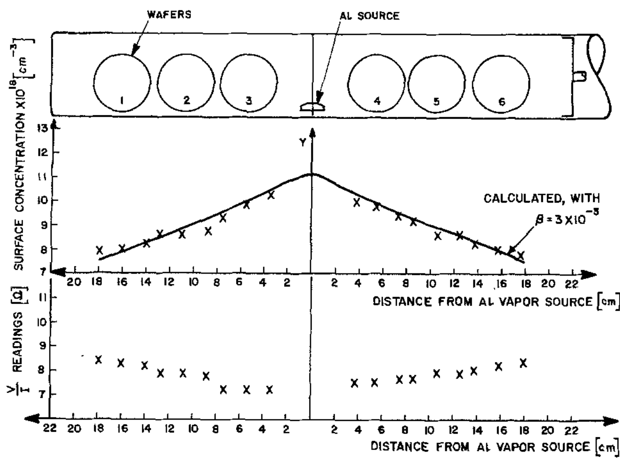

Fig. 4. Aluminum surface concentration vs. distance from Al vapor source.

tained from the experiments described in another section. If the wafers and aluminum source arrangement is as shown in Fig. 2c, the doping uniformity is significantly improved. The diffusion results presented in Fig. 5 show the changes in V/I readings and surface concentrations on two wafers, when two diffusion sources are used. The diffusion carried out for 66 wafers inserted in two rows in the boat for the same diffusion conditions resulted in almost the same V/I readings and surface concentration as obtained for 2 wafers/run. This is illustrated in Fig. 6. The results showed that the number of wafers does not influence the surface concentration. The calculations of the surface concentration based on Eq. [12] showed very good agreement with the experimental data. When the diffusion was carried out from a single aluminum vapor source, the calculations based on Eq. [10] showed less than a 2% discrepancy with experimental data. When the diffusion was performed for the wafers and aluminum vapor source arrangement represented in Fig. 2c and Fig. 1, the calculations based on Eq. [12] showed approximately a 5% discrepancy range with the experimental data.

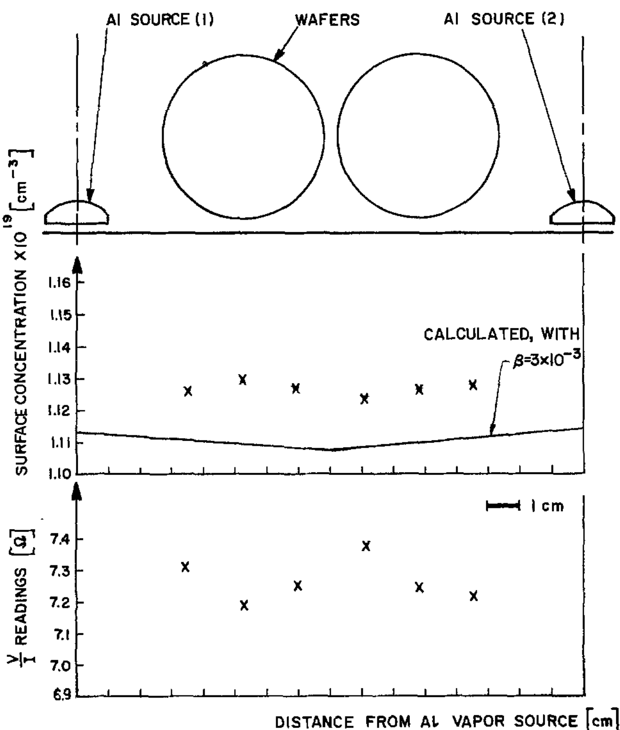

Fig. 5. Aluminum diffusion results for 2 wafers/run (one wafer placed in every row).

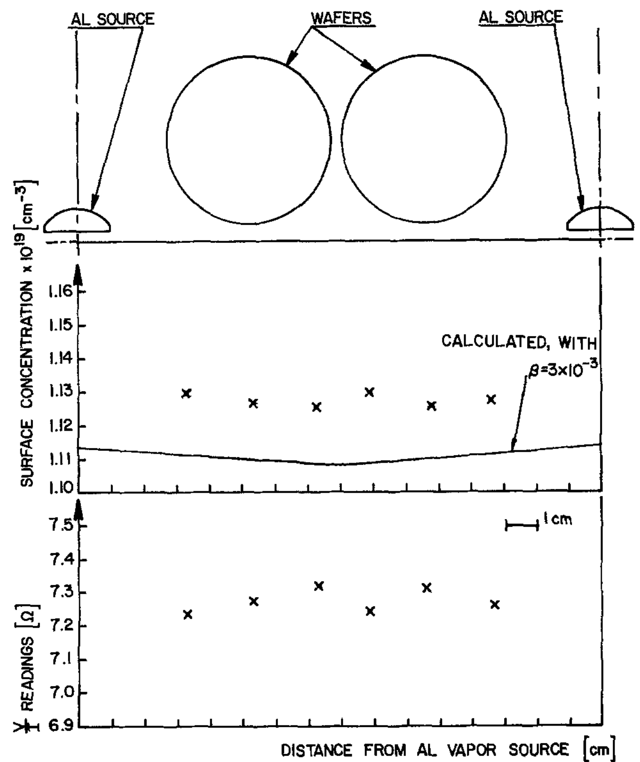

Fig. 6. Aluminum diffusion results for 66 wafers/run (33 wafers placed in every row).

High volume production process.—Several diffusion experiments were carried out for 198 wafers/run. The diffusion chamber was loaded as illustrated in Fig. 2d. It contained a triple wafer and aluminum source assembly as shown in Fig. 2c. The number of wafers diffused per run could be increased for a longer tube adding more sets of wafers and sources as shown in Fig. 2c. The next two figures represent the diffusion results obtained from the processing of 198 wafers/run. Figure 7 shows the spreading resistances obtained for

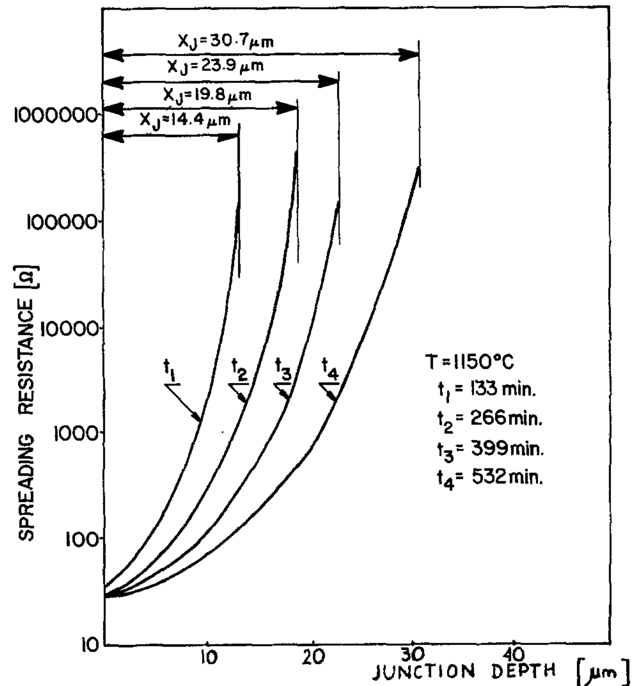

Fig. 7. Spreading resistance of aluminum diffused samples

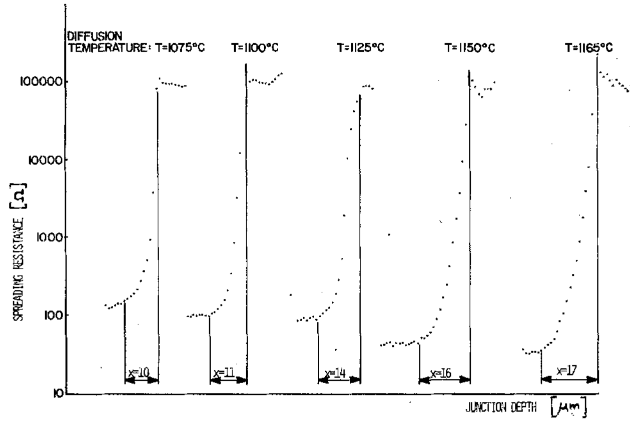

Fig. 8. Spreading resistance of aluminum diffused junctions vs. diffusion temperature.

aluminum diffusions carried out at 1150°C for $t = 133$, 266, 399, and 532 min. Assuming that the diffusions were performed under a steady-state condition, we should expect the surface concentration, as well as the spreading resistance, to be independent of diffusion time. Some differences obtained in spreading resistance measurements could be related to the error measurement introduced by the two-point probe method itself, since spreading resistance measurements tend to overestimate ρ_s more for shallower junctions than for deeper ones. Figure 8 illustrates the spreading resistance of aluminum diffused profiles obtained at different temperatures in the range of 1075°-1165°C. Several diffusion runs were also carried out to evaluate reproducibility of the process. The sheet resistances obtained varied from wafer to wafer and from run to run ±3%.

Temperature dependence of the diffusion coefficient.—Aluminum diffusion into silicon has been found to be a strong function of the way the dopant is transported to the silicon wafer and its surface activity. When the Al-Si alloy was first formed on the silicon surface by vacuum alloying and used (17) as a dopant source (solid-solid type diffusion), the calculated diffusion coefficient at 1200°C was about one order of magnitude higher than the one obtained for a diffusion carried out in a sealed evacuated ampul (2, 5) (vapor-solid type diffusion). On the other hand, when aluminum was incorporated (18) into the epitaxial layer by bubbling hydrogen through trimethyl aluminum, the diffusion coefficient was about one order of magnitude lower than that obtained in the ampul method. The calculations of the apparent activation energy and the diffusion constant were also performed from the diffusion results in an open tube, high vacuum system. Two-point probe spreading resistance data were used to determine junction depths and the surface concentrations. It was assumed that the impurity distribution followed a complementary error function. The relevant diffusion data obtained in this study, as well as data obtained by other researchers, are listed in Table I.

Discussion and Summary

In general, the relation between concentration and the distance from the diffusion source is seen in Eq. [10] and [12] depending on the wafers and the aluminum vapor source arrangement inside the diffusion chamber. In both of these equations, an artificial coefficient β appears which combines three coefficients with Eq. [8]: α, χ, and γ all of which have physical meanings. It appears that for a given experimental condition, those coefficients are constant. However, their values are difficult to evaluate theoretically.

In general, the aluminum evaporation coefficient strongly depends on the amount of moisture and oxygen in the system. The presence of either would cause the aluminum to react forming a stable Al_2O_3 skin on the diffusion source. A matte finish would be observed on those samples (8). The amount of evaporated molecules would also be insufficient to maintain the aluminum pressure resulting in doping with a high surface concentration. The reproducibility would also be inconsistent.

In this study, we found that after every diffusion run, the aluminum diffusion source showed a shiny surface. X-ray diffraction analysis performed has not revealed the presence of Al_2O_3 on those diffusion sources. The process has been reproducible, consistently resulting in doping with high surface concentration. We, therefore, concluded that the evaporation coefficient was constant during experiments performed with diffusion.

The value of the segregation coefficient χ on the aluminum vapor and silicon interface can clearly be read as a constant from Henry's law: $c = \chi \cdot p$, where c represents concentration on the silicon surface and p represents partial pressure of the doping element. It is well known that at low pressures Henry's law accurately describes experimental results. In an open tube, high vacuum system, we operate with low aluminum pressure and χ can be safely assumed to be a constant for a given experimental condition.

The correction coefficient γ depends on the characteristic tube dimensions only and is constant for a designed setup. Equation [8] also consists of segment $p_{eq} - p$ which expresses a deviation of the process from the equilibrium. For the isothermal and steady-state condition, this difference is constant due to the diffusion continuously proceeding and to the outflow of the vapor from the diffusion chamber. This difference is greater than zero: $p_{eq} - p > 0$. A theoretical calculation of all those coefficients: α, γ, and χ and $p_{eq} - p$ as well as β appears to be too complicated at this time.

In summary, the aluminum diffusion process has been described for high volume production. This process is different from the widely used sealed-ampul technology. It is less expensive, easier to control, and has more operational flexibility. Surface concentration and spreading resistance of aluminum-doped junctions were evaluated as a function of temperature and time. The process is described mathematically using an approximated mass-transport model. Equation [10] describes the aluminum surface concentration as a function of the distance from the vapor source. Equation [12] describes a similar relation for diffusion from two vapor sources. Equations [10] and [12] showed less than a 2% discrepancy and less than a 5% discrepancy range with the experimental data. The quality of the aluminum diffused junctions was tested on 224 × 224 mil square diodes, transistors, and thyristors. Reverse voltages measured were typically ~900V and 35 Ω cm

Table I. Aluminum diffusion data

Method	Author	Reference	D_o ($cm^2 sec^{1-}$)	E (eV)	$D_{1200°C}$ ($cm^2 sec^{-1}$)	Surface concentation (cm^{-3})
From Al-Si alloy (solid-solid)	Goldstein *et al.*	17	2800	3.9	1.28×10^{-10}	10^{16}-10^{17}
Epitaxy	Ghashtagore	18	1.385	3.41	3.00×10^{-12}	10^{18}-10^{19}
Open tube in argon ambient (vapor-solid)	Miller *et al.*	2	4.8	3.36	1.58×10^{-11}	10^{18}-10^{19}
Ampul in vacuum (vapor-solid)	Kao	5	0.5	3.0	2.74×10^{-11}	$\sim 10^{19}$
Ampul in vacuum (vapor-solid)	Fuller *et al.*	3	8	3.49	9.24×10^{-12}	10^{16}-10^{17}
Open tube, high vacuum (vapor-solid)	This author	This work	1.8	3.2	2.04×10^{-11}	10^{18}-10^{19}

silicon substrates and 1500V for 80 Ω cm substrates. In all cases, hard reverse characteristics were observed with excellent consistency.

Acknowledgments

The author wishes to thank G. Gilman for wafer processing, C. Sickles for help in setting up the vacuum facilities, and S. Ponczak for help with computer calculations. I am also indebted to Dr. A. Blicher, Dr. C. Nuese, and R. Denning for reviewing the manuscript.

Manuscript submitted June 9, 1977; revised manuscript received Dec. 12, 1977. This was Paper 85 presented at the Philadelphia, Pennsylvania, Meeting of the Society, May 8-13, 1977.

Any discussion of this paper will appear in a Discussion Section to be published in the December 1978 JOURNAL. All discussions for the December 1978 Discussion Section should be submitted by Aug. 1, 1978.

Publication costs of this article were assisted by RCA Corporation.

APPENDIX

If the arrangement of wafers and a single aluminum source is as shown in Fig. 2a, the distribution of the diffusant into the silicon wafer is a function of the space coordinates and time. Since, under the steady-state condition, the dopant is continuously liberated from the source, the diffusion is carried out from the aluminum vapor streaming continuously over the silicon surface as shown schematically in Fig. 9. The flow of vapor coincides with the x-direction. Assuming local equilibrium at the vapor-silicon interface, the ratio of concentrations in silicon c and vapor C is given by the segregation coefficient χ

$$\chi = \frac{c}{C} \qquad \text{[A-1]}$$

The flow of vapor into the silicon surface at point x is

$$-D\left(\frac{\partial c}{\partial y}\right)_{y=0} \qquad \text{[A-2]}$$

This must be equal to the decrease of the concentration of the vapor given by

$$-J_{\text{evap}}\, h\frac{\partial C}{\partial x} \qquad \text{[A-3]}$$

where h is the height of the vapor stream. Combining Eq. [A-1], [A-2], and [A-3] we obtain

$$\left(\frac{\partial c}{\partial y}\right)_{y=0} = \frac{J_{\text{evap}}\cdot h}{\chi D}\left(\frac{\partial c}{\partial x}\right)_{y=0} \qquad \text{[A-4]}$$

The vapor entering at $x = 0$ is of the concentration

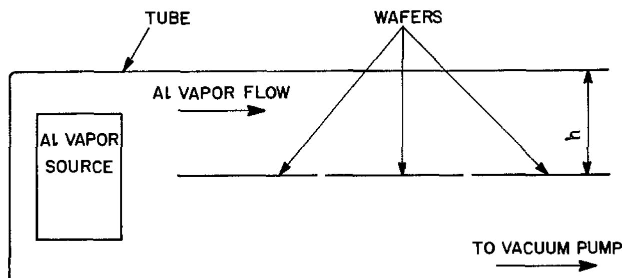

Fig. 9. Model for diffusion out of streaming vapor into Si wafers

C_0, thus $c_0 = \chi C_0$ at $x = 0$ and $y = 0$ for all $t > 0$. We further assume $c = 0$ at $t = 0$. We define the new variables as

$$\xi = (\chi D/hJ_{\text{evap}})\, x/2\sqrt{Dt}$$

and

$$\eta = y/2\sqrt{Dt} \qquad \text{[A-5]}$$

Fick's second law

$$\frac{\partial c}{\partial t} = D\frac{\partial^2 c}{\partial y^2} \qquad \text{[A-6]}$$

is transformed to

$$\frac{\partial^2 c}{\partial \eta^2} + 2\left(\xi\frac{\partial c}{\partial \xi} + \eta\frac{\partial c}{\partial \eta}\right) = 0 \qquad \text{[A-7]}$$

The boundary conditions in the new coordinates are

$$c = c_0 \text{ at } \xi = 0,\ \eta = 0;\quad c = 0 \text{ at } \xi = \infty,\ \eta = \infty$$

$$\frac{\partial c}{\partial \xi} = 2\sigma \text{ at } \eta = 0 \qquad \text{[A-8]}$$

A solution of Eq. [A-7] satisfying the boundary conditions of Eq. [A-8] may be obtained by assuming

$$c(\xi, \eta) = c(\sigma), \quad \sigma = \xi + \eta \qquad \text{[A-9]}$$

Substituting Eq. [A-9] into Eq. [A-4], we obtain the ordinary differential equation

$$\frac{d^2 c}{d\sigma^2} + 2\sigma\frac{dc}{d\sigma} = 0$$

The solution of this equation has been previously obtained (19) and is

$$c = c_0\left[1 - \text{erf}\left\{\left(\left[\frac{\chi D}{hJ_{\text{evap}}}\right]x + y\right)\frac{1}{2\sqrt{Dt}}\right\}\right] \qquad \text{[A-10]}$$

REFERENCES

1. P. Rai-Choudhury, Y. C. Dao, and G. G. Sweeney, *This Journal*, **121**, 1509 (1974).
2. R. C. Miller and A. Savage, *J. Appl. Phys.*, **17**, 1430 (1957).
3. C. S. Fuller and J. A. Ditzenberger, *ibid.*, **27**, 1288 (1956).
4. P. Rai-Choudhury and W. J. Takei, *This Journal*, **121**, 1288 (1974).
5. Y. C. Kao, *Electrochem. Technol.*, **5**, 90 (1967).
6. W. Rosnowski, U.S. Pat. 3,997,379 (1976).
7. W. Rosnowski, Paper 85, presented at the Electrochemical Society Spring Meeting, Philadelphia, May 8-13, 1977.
8. P. Rai-Choudhury, F. A. Selim, and W. J. Takei, *This Journal*, **124**, 762 (1977).
9. H. Schafer and R. Hornle, *Z. Anorg. Allgem. Chem.*, **263**, 261 (1950).
10. G. Grube and H. Speidel, *Z. Electrochem.*, **53**, 339 (1949).
11. R. E. Honig, *RCA Rev.*, **23**, 567 (1962).
12. A. Kostka, R. Gereth, and K. Kreuzer, *This Journal*, **120**, 971 (1973).
13. R. Gereth, A. Kostka, and K. Kreuzer, *ibid.*, **120**, 966 (1973).
14. S. Dushman, "Scientific Foundations of Vacuum Technique," p. 91, John Wiley & Son, Inc. New York (1966).
15. J. C. Irvin, *Bell Syst. Tech. J.*, **31**, 387 (1962).
16. F. A. Trumbore, *ibid.*, **29**, 205 (1960).
17. B. Goldstein, *Bull. Am. Phys. Soc. Ser. II*, **1**, 145 (1956).
18. R. N. Ghoshtagore, *Phys. Rev. B*, **3**, 2507 (1971).
19. C. Wagner, *Z. Physik. Chem. A*, **192**, 157 (1943).

Gettering of Gold and Copper in Silicon during Gallium Diffusion

N. Momma, H. Taniguchi, M. Ura, and T. Ogawa

Hitachi Limited, Hitachi Research Laboratory, Hitachi, Ibaraki, Japan

ABSTRACT

The gettering of Au and Cu during the sealed tube diffusion of Ga has been studied by using neutron activation analysis and the spreading resistance microprobe technique. It was found that Au in silicon was gettered during Ga diffusion regardless of the cooling conditions. Most of the Cu in the surface layer of silicon diffused out during Ga diffusion, while Cu in the bulk silicon was gettered during the slow cooling process after diffusion. Increases in the minority carrier lifetime in p^+n diodes prepared by Ga diffusion occurred with increasing the amount of Ga used as a source. It was ascertained that in Ga gettering the Ga metal sources played an important role as impurity sinks.

In silicon device processing, high temperature steps, such as oxidation and dopant diffusion, often result in the soft reverse characteristics of pn junctions. The origin of this high leakage current is believed to be the localized high electric field caused by the precipitates of metals, such as Au and Cu (1). These metals in silicon also lead to the degradation of minority carrier lifetime (2-4) which affects the forward voltage drop and other device parameters. These undesired metallic impurities can be removed by so called "gettering" processes. Up to now, various gettering techniques have been reported (5-14). Among them, gettering during diffusion of dopant impurities, such as phosphorus, boron, gallium, and so forth, is most important, because the dopant diffusion is the typical method for making pn junctions. The gettering by phosphorus and boron diffusion has been widely studied analytically and electrically (5-9), but only a few works have been reported concerning the gettering during Ga diffusion (14). Because of the relatively high diffusion coefficient of Ga in silicon, Ga diffusion is often used for the formation of p-type layers of silicon power devices. In these devices high lifetime values are often desirable. Therefore, the maintenance of a minimum lifetime during Ga diffusion is an outstanding problem in the power device processing. Lambert and Köhl (14) reported that metallic Ga layers painted on the silicon surface show pronounced gettering effect. However, the precise features of Ga gettering have not been offered yet. It is the purpose of this study to investigate analytically the behavior of Au and Cu in the sealed tube diffusion of Ga and to reveal the mechanism of the gettering during Ga diffusion.

Experimental

Sample preparation.—The starting materials used in this study were float-zone, n-type silicon wafers, 130-180 Ω-cm, with mechanically lapped surface. The wafers were intentionally contaminated with a moderate to a large amount of Au or Cu to obtain impurity levels above the background level. Au-contaminated samples were prepared by the following procedure. First, the wafers were etched by HF/HNO_3 solutions to remove the surface-damaged layer produced by mechanical lapping. Au films were deposited on one side of the silicon wafers by vacuum evaporation and then annealed at 900°C for 30 min in an argon atmosphere. The wafers were etched in order to remove the surface layers of high Au concentrations. By these processes, Au was almost uniformly distributed through the wafers in the concentration of about 1×10^{14} atoms/cm^3. For the study of the gettering effect by crystal imperfections introduced mechanically, the surface of the silicon wafers with uniform Au concentration were roughened by 12 μm garnet powder. Meanwhile, Cu-contaminated samples were prepared by sealed tube diffusion. The starting silicon wafers were cleaned by ultrasonic washing in hot alkaline solution and dipping in aqua regia. After cleaning, the wafers were encapsulated in a quartz tube under vacuum together with a high purity (99.999%) Cu metal piece put in a silicon boat. The capsule was then heated at 1150°C for 1 hr. The Cu-contaminated samples obtained by this method showed somewhat complicated Cu distribution as shown in Fig. 5 and elsewhere. The Cu concentration in silicon near the surface was extremely high, nearly 10^{20} atoms/cm^3, but in bulk silicon the concentration was the order of 10^{14}-10^{15} atoms/cm^3. The Cu-contaminated samples were used for the gettering experiments without removing the surface layer of high Cu concentration, because the level of the limiting concentration of the activation analysis for Cu (10^{14}-10^{15} atoms/cm^3) might not be low enough to clarify the gettering phenomena analytically.

Ga diffusion and heat-treatment.—After cleaning by alkaline solutions and aqua regia, the contaminated samples were encapsulated in quartz tubes in argon atmospheres together with high purity Ga(seven nine's) placed on silicon slices. Ga diffusion was carried out at 1250° or 1256°C. Two different kinds of cooling conditions were used; in one case, the capsules were air quenched after the diffusion (this process is hereafter designated "fast cooling"). In the other case, the capsules were cooled in the furnace at a rate of 40°C/hr from the diffusion temperature to 600°C and then removed from the furnace (this process is designated "slow cooling"). For comparison, sealed tube heat-treatments in argon atmospheres without Ga sources were also carried out under the same conditions as those of Ga diffusion.

Measuring methods.—The concentrations of Au, Cu, and Ga in silicon wafers were determined by the neutron activation analysis. The samples were irradiated with thermal neutrons of 2.1×10^{12} n/cm·sec for 10 hr in the Hitachi Training Reactor. After the activation the wafers were individually subjected to the following processes. First, metals present on the wafer surface were removed by rinsing in boiling aqua regia and the surface densities of the metals were determined. Then, thin layers were etched off from the surface of the samples successively by HF/HNO_3 solutions and the activities of the etching solutions were measured after each etching step. The neutron activation analysis was also used for determination of the concentrations of Au and Cu in Ga sources and quartz tubes. After the activation Ga sources and quartz tubes were dissolved in HCl and HF solutions, respectively. Au and Cu in the

Key words: sealed tube diffusion, minority carrier lifetime, impurity sink, neutron activation analysis, spreading resistance.

solutions were separated from the other elements using anion exchange resin columns and the activities were measured. The Cu concentrations in Ga sources and quartz tubes were also determined by atomic absorption spectrometry. Ga sources and quartz tubes were dissolved in HCl and HF solutions, respectively. The solutions were then subjected to evaporation to dryness. The residual was dissolved in HNO_3 solutions and the atomic absorptions were measured. The distributions of electrically active impurities in silicon wafers were estimated by the spreading resistance measurement (15). The minority carrier lifetimes of p^+n diodes prepared by Ga diffusion were measured by the microwave technique (16). The decreasing rate of the excess carriers, injected by a light pulse from a xenon lamp, was determined by measuring the reflection of microwave energy. The standard diode samples, whose lifetime values were calibrated by the method proposed by Lederhandler and Giacoletto (17), were used to convert the decreasing rates to lifetime values.

Results and Discussion

The gettering of Au.—Figure 1 shows the Au concentration in silicon before and after heat-treatment without a Ga source determined by neutron activation analysis. In this experiment, in order to examine the gettering effect of mechanically damaged layers on wafer surfaces, two kinds of samples, with lapped and etched surface, were used. It is clear from this figure that, in both samples, a fraction of Au in the bulk silicon was transferred to the regions near surfaces but that the total amount of Au remained almost unchanged after heat-treatment. This means that without a Ga source Au in silicon cannot be removed from the wafers at all and that the gettering effect of a surface-damaged layer is insignificant.

After Ga diffusion the densities of Au on silicon wafer surfaces were found to be less than $2\text{-}4 \times 10^{10}$ atoms/cm^2 in both cases of fast and slow cooling. This means that Au is not accumulated on the surface (or in a thin layer of Ga, if any) after the diffusion. Figure 2 shows the Au concentration profile in silicon before and after Ga diffusion. In this figure and other figures exhibited in this paper, dashed lines represent the levels of the limiting concentration of the activation analysis and indicate that impurities more than these levels

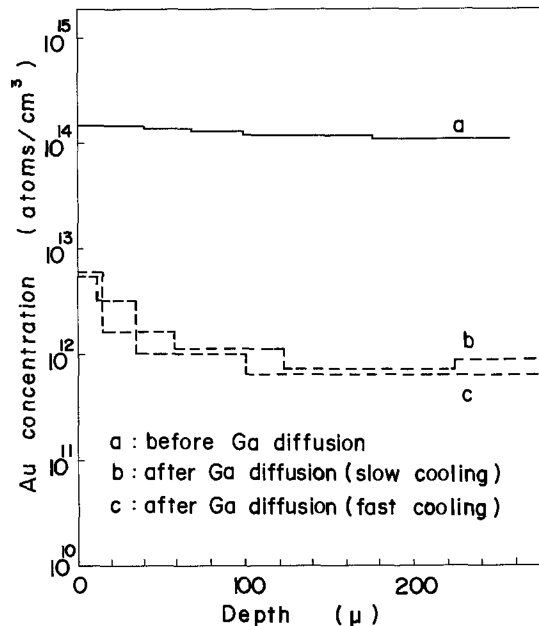

Fig. 2. Au concentration profiles after Ga diffusion (1256°C for 9.5 hr). Dashed lines indicate that no more Au than these levels can be detected.

could not be detected. The limiting concentration expressed in the unit of atoms/cm^3 varies from measurement to measurement, because it depends on the amount of sample (*i.e.* the thickness of the etched layer), the time interval between the activation and the activity measurement, the duration of the activity counting, and so on. It is clear from Fig. 2 that after Ga diffusion, the concentrations of Au decrease below the limiting concentration not only in the bulk silicon but also in the surface layer, whether the cooling is fast or slow. These results are also supported by the spreading resistance measurements as shown in Fig. 3. Before Au doping the level of spreading resistance lies around $3 \times 10^5\Omega$. On Au doping, the spreading resistance of n-type silicon increases to the order of $10^7\Omega$ due to the compensation by Au acceptors. After Ga diffusion, spreading resistance is restored to the same level as before Au doping, whether the cooling is fast or slow. These results suggest that both electrically

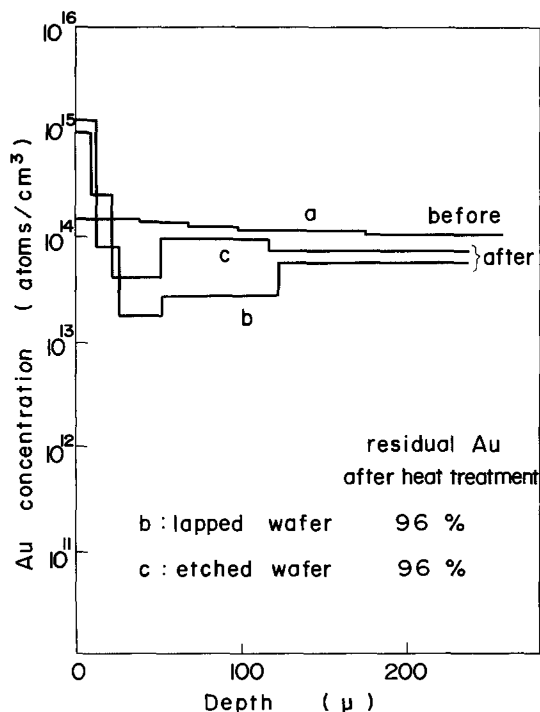

Fig. 1. Au concentration profiles after heat-treatment without Ga sources (1250°C for 10 hr).

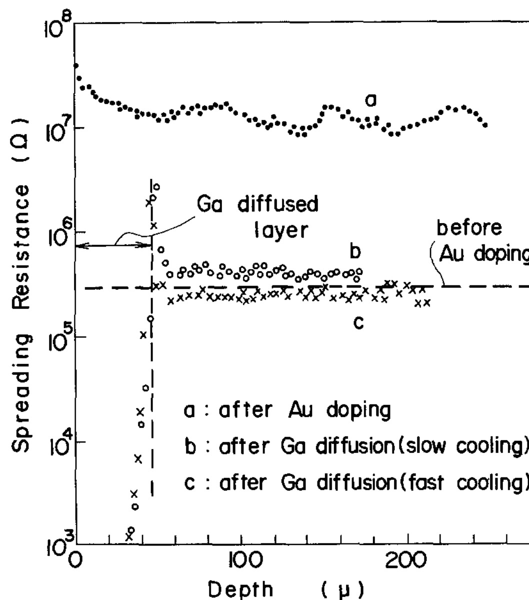

Fig. 3. The distribution of spreading resistance after Ga diffusion (1256°C for 9.5 hr).

Table I. The total amount of Au in silicon wafers and Ga sources before and after Ga diffusion (1256°C for 9.5 hr)

Cooling	Au in Si wafers (atoms)		Au in Ga sources (atoms)	
	Before	After	Before	After
Fast	1.1×10^{14}	$<1.5 \times 10^{12}$	5.0×10^{12}	8.4×10^{13}
Slow	1.1×10^{14}	$<1.6 \times 10^{12}$	3.7×10^{12}	4.7×10^{13}

active and inactive Au is removed from silicon wafers during Ga diffusion regardless of the cooling conditions.

In order to reveal the aspects of Au transfer in the diffusion system, Au contents in silicon wafers and Ga sources before and after the diffusion were measured. The results are shown in Table I. The total amount of Au in the sample wafers before diffusion is 1.1×10^{14} atoms, whereas it is less than $1.5\text{-}1.6 \times 10^{12}$ atoms after diffusion. On the other hand, the amount of Au in Ga metal sources increases more than one order of magnitude during Ga diffusion. This increment of Au in Ga sources corresponds to one-third to two-thirds of the total amount of Au contained in the silicon samples before diffusion. This means that Au that diffuses from the silicon samples accumulates not in the Ga-diffused layer but in the Ga metal sources, in other words, Ga sources play an important role as Au sinks.

In the course of this experiment, oxidation of silicon occurred unexpectedly in some diffusion lots due to the presence of oxygen which was accidentally introduced together with argon gas into the sealed tube. The effect of oxidation on the gettering of Au is shown in Fig. 4. When oxidation occurs during diffusion, the gettering effect of Ga was considerably reduced and after the diffusion nearly one-half of the total amount of Au remains in the silicon wafers. This result suggests that the diffusion of Au out of the wafers is interrupted by the presence of silicon dioxide layers on the sample surfaces.

The gettering of Cu.—Figure 5 shows the behavior Cu before and after heat-treatment followed by slow cooling. As shown in this figure, residual Cu in the whole silicon wafers after heat-treatment is only

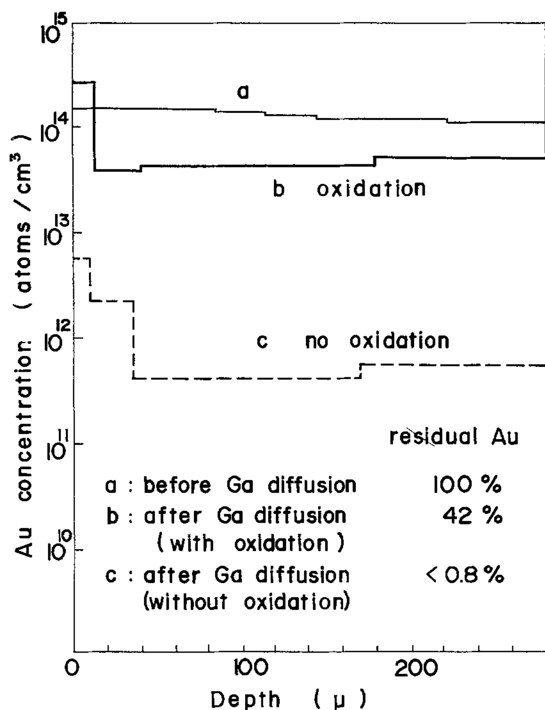

Fig. 4. The effect of oxidation on gettering of Au by Ga diffusion (1256°C for 8 hr). Dashed lines indicate that no more Au than these levels can be detected.

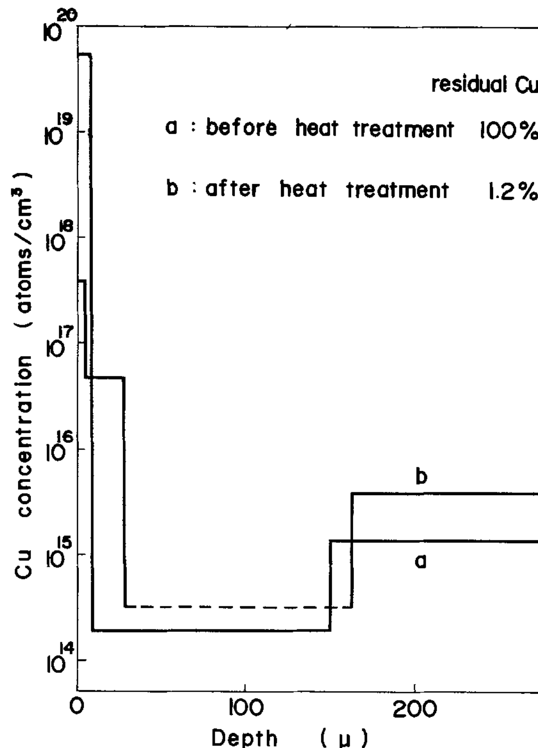

Fig. 5. Cu concentration profiles after heat-treatment (1256°C for 8 hr). Dashed line indicates that no more Cu than this level can be detected.

1.2%. This means that during the heat-treatment more than 98% of Cu diffused out from the samples. However, Cu in bulk silicon cannot be removed but rather increases as shown in this figure.

Figure 6 shows the concentration profiles of Cu before and after Ga diffusion. After Ga diffusion, and the following fast cooling, the percentage of residual Cu in silicon is 2.9%, that is, about 97% of the Cu diffuses out from the samples. But as shown in line b, Cu in bulk silicon, of the order of 10^{15} atoms/cm^3, remains. On the other hand, in the case of slow cooling, residual Cu is only 0.14-0.25% and the concentration of Cu in the bulk region decreases below the limiting

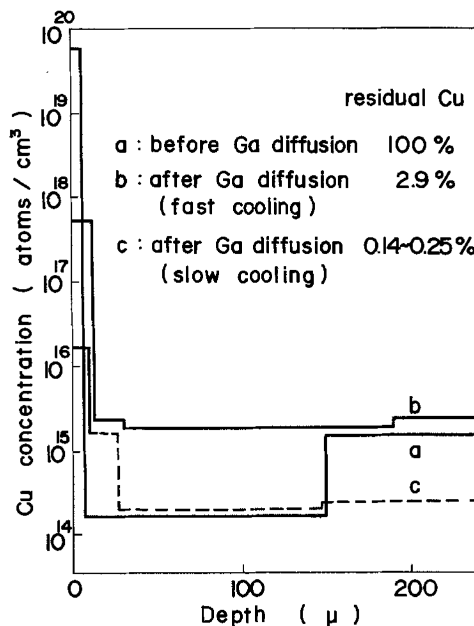

Fig. 6. Cu concentration profiles after Ga diffusion (1256°C for 8 hr). Dashed lines indicate that no more Cu than these levels can be detected.

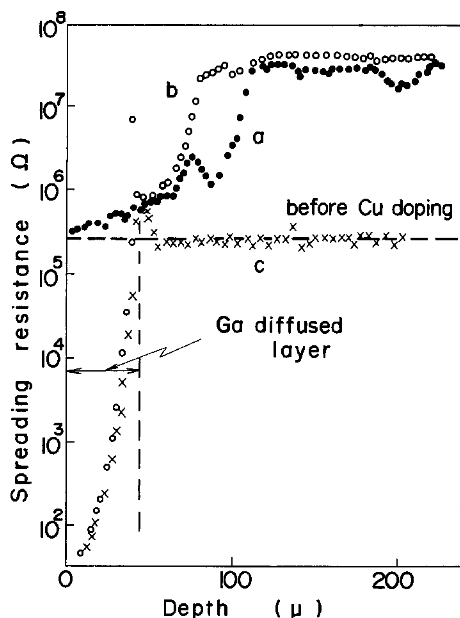

Fig. 7. Distribution of spreading resistance after Ga diffusion (1256°C for 8 hr): a, before Ga diffusion; b, after Ga diffusion (fast cooling); c, after Ga diffusion (slow cooling).

concentration, as shown in line c. These features of Ga diffusion are more clearly demonstrated by the results of the spreading resistance measurement as shown in Fig. 7. Spreading resistance before Cu doping is at the level of $3 \times 10^5 \Omega$. Curve a illustrates the distribution of the spreading resistance of a Cu-contaminated sample before Ga diffusion. As shown in curve b, in the case of fast cooling, the spreading resistance in the bulk silicon shows almost the same distribution as that of the Cu-contaminated sample before the diffusion. On the other hand, as shown in curve c, in the case of slow cooling, the spreading resistance is restored to the level it was at before Cu doping. From these results, it is considered that Cu diffuses out from the bulk silicon during the slow cooling process after diffusion.

The effect of oxidation on the gettering of Cu is shown in Fig. 8. Lines a and b are the concentration profiles of Cu after Ga diffusion followed by slow cooling with and without oxidation, respectively. In both cases, the concentration of Cu in the bulk silicon decreases below the limiting concentration. Moreover, the percentage of the total amount of Cu in the silicon wafer remaining after diffusion is almost the same in both cases. From these results, it is clear that the presence of a surface oxide layer does not affect the gettering of Cu. This is in marked contrast to the gettering of Au.

As stated before, the Ga sources play an important role in the gettering of Au. In order to know whether the same is true for the gettering of Cu, the behavior of Cu in the diffusion system was further examined analytically. Figures 9 and 10 show the Cu contents in the Ga source and in the quartz tubes before and after Ga diffusion, using silicon samples not intentionally contaminated with Cu. In these figures, open circles indicate the values obtained by the activation analysis and solid circles the values obtained by the atomic absorption spectrometry. The circles in parentheses represent the limiting concentration and indicate that no more Cu than this level could be detected. The Cu contents of the Ga source before diffusion are about 1.2×10^{15} atoms/g. After diffusion, even with uncontaminated samples, the Cu concentration increases to the order of 10^{17} atoms/g. On the contrary, it is revealed that the quartz tubes used in this experiment contain a considerable amount of Cu, 10^{14} to above 10^{15} atoms/g, before use. But after the diffusion, the Cu contents of the tubes decrease below 2×10^{13} atoms/g. It is clear that Cu that evaporates from the quartz tubes

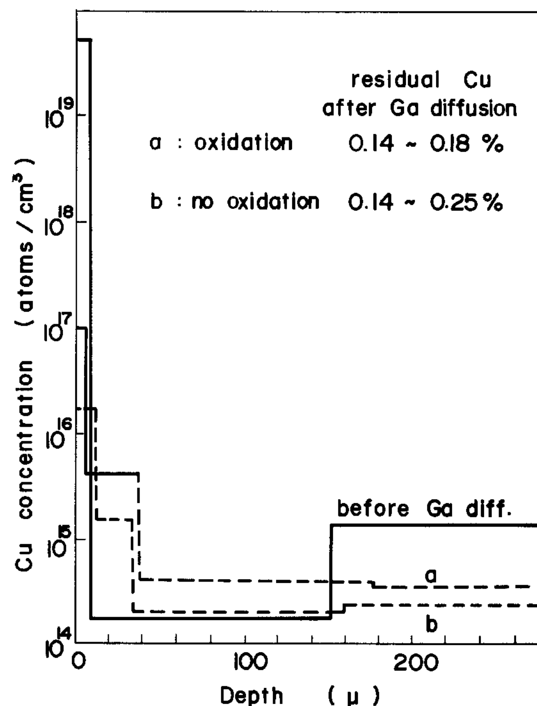

Fig. 8. The effect of oxidation on gettering of Cu by Ga diffusion (1256°C for 8 hr). Dashed lines indicate that no more Cu than these levels can be detected.

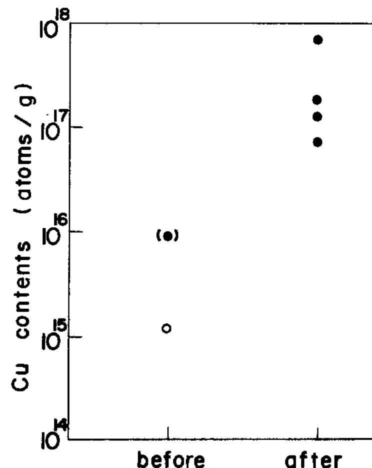

Fig. 9. Cu contents in Ga sources before and after Ga diffusion (1256°C for 86.5 hr): ○, activation analysis; ●, atomic absorption spectrometry. The circle in parenthesis indicates that no more Cu than this level can be detected.

accumulates in the Ga sources during the diffusion process. Considering the results mentioned above, it is suggested that during Ga diffusion, Cu is gettered mainly through out-diffusion and that Ga sources act as Cu sinks, in the same way that they act as Au sinks.

Minority carrier lifetimes of Ga-diffused wafers.—On the basis of the fact that Ga metal sources act as impurity sinks during Ga diffusion, it should be expected that the gettering would become more effective if the amount of Ga used as a source was increased. To confirm this view, the minority carrier lifetimes in the n-type layers of p^+n diodes prepared by Ga diffusion with different amounts of Ga used as sources were measured. In this experiment, in order to examine the gettering effect of Ga under conditions similar to those of the actual device fabrication, the sample wafers were not intentionally contaminated with impurities and Ga diffusion was carried out at 1256°C for 86.5 hr. The results are shown in Fig. 11. As was expected,

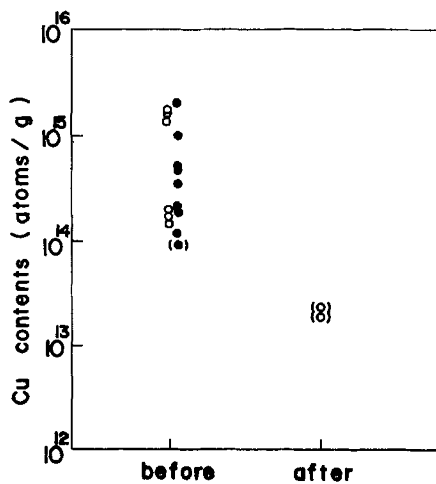

Fig. 10. Cu contents in quartz tubes before and after Ga diffusion (1256°C for 86.5 hr): ○, activation analysis; ●, atomic absorption spectrometry. The circles in parentheses indicate that no more Cu than these levels can be detected.

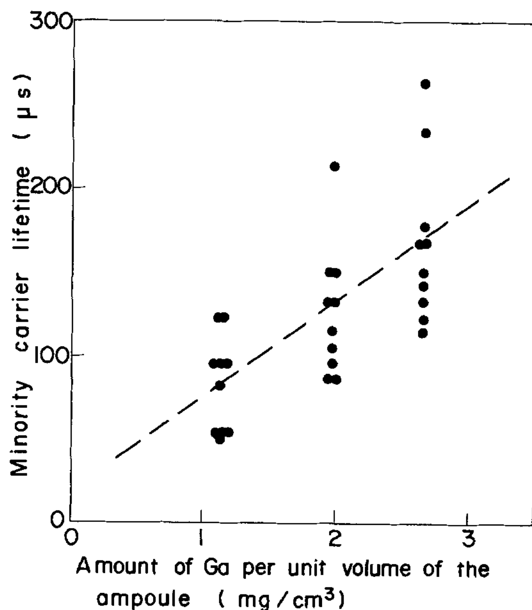

Fig. 11. The correlation between the minority carrier lifetime of p^+n diodes prepared by Ga diffusion (1256°C for 86.5 hr) and the amount of Ga used as a source.

lifetimes become longer when the amount of Ga used as a source is increased. Figure 12 shows the concentration profiles of electrically active Ga measured by the spreading resistance method. Figure 13 depicts the distribution of the total (active and inactive) Ga determined by the neutron activation analysis. It is clear from these figures that the concentration of Ga does not increase with increasing the amount of Ga used as a source. This means that there is no correlation between minority carrier lifetimes and Ga concentrations in p^+n diodes. In other words, the Ga layer on the surface of the silicon wafer does not play a significant role in Ga gettering but the Ga metal source itself plays an important role in the gettering. These features of Ga gettering are in striking contrast to phosphorus and boron diffusion gettering (5-9) in which the liquidus glass or high concentration diffused layers on silicon surfaces are important agents.

Summary

The gettering of Au and Cu during the sealed tube diffusion of Ga was studied by using neutron activation analysis and the spreading resistance microprobe technique. The results are summarized as follows;

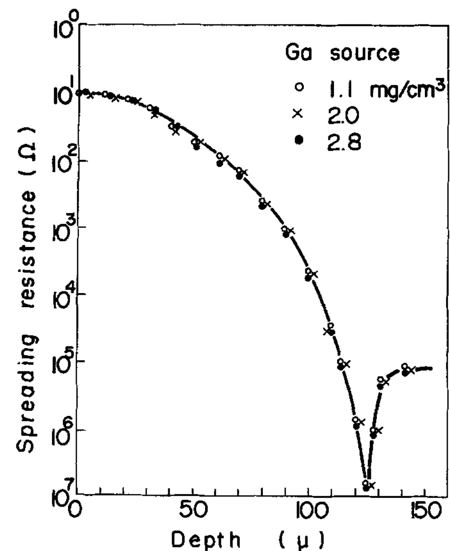

Fig. 12. Ga concentration profiles after Ga diffusion (1256°C for 86.5 hr) measured by spreading resistance microprobe technique.

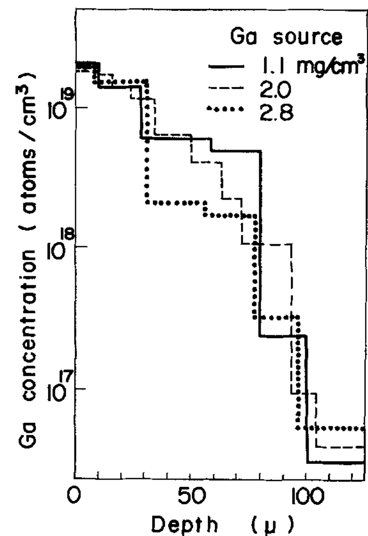

Fig. 13. Ga concentration profiles after Ga diffusion (1256°C for 86.5 hr) determined by activation analysis.

1. Au in silicon is gettered during Ga diffusion regardless of the cooling conditions.
2. Most of Cu in the surface layer of silicon diffuses out during Ga diffusion, while Cu in the bulk silicon is gettered during the slow cooling process after Ga diffusion.
3. The minority carrier lifetime in p^+n diodes prepared by Ga diffusion increases with increasing the amount of Ga used as a source.
4. In Ga gettering, Ga metal sources play an importatn role as impurity sinks.

Acknowledgments

The authors are greatly indebted to Drs. E. Kobayashi and M. Okamura and Messrs. K. Morita and S. Okano for their helpful suggestions and encouragement to this study. They also wish to express their thanks to Mr. N. Sakurai for the activation analysis.

Manuscript submitted Oct. 26, 1977; revised manuscript received Jan. 30, 1978. This was Paper 340 presented at the Las Vegas, Nevada, Meeting of the Society, Oct. 17-22, 1976.

Any discussion of this paper will appear in a Discussion Section to be published in the December 1978 JOURNAL. All discussions for the December 1978 Discussion Section should be submitted by Aug. 1, 1978.

Publication costs of this article were assisted by Hitachi Limited.

REFERENCES

1. A. Goetzberger and W. Shockley, *J. Appl. Phys.*, **31**, 1821 (1960).
2. J. M. Fairfield and B. V. Gokhale, *Solid-State Electron.*, **8**, 685 (1965).
3. G. Bemski and J. D. Struthers, *This Journal*, **105**, 588 (1958).
4. R. O. Carlson, *J. Appl. Phys.*, **29**, 1001 (1958).
5. R. L. Meek, T. E. Seidel, and A. G. Cullis, *This Journal*, **122**, 786 (1975).
6. M. Nakamura, T. Kato, and N. Oi, *Jpn. J. Appl. Phys.*, **7**, 512 (1968).
7. J. L. Lambert and M. Reese, *Solid-State Electron.*, **11**, 1055 (1968).
8. M. Waldner and L. Sivo, *This Journal*, **112**, 298 (1960).
9. S. W. Ing, R. E. Morrison, L. L. Alt, and R. W. Aldrich, *ibid.*, **110**, 533 (1963).
10. Y. Tokumaru, *Jpn. J. Appl. Phys.*, **2**, 542 (1963).
11. F. P. Heiman and P. H. Robinson, *This Journal*, **118**, 141 (1971).
12. R. S. Ronen and P. H. Robinson, *ibid.*, **119**, 747 (1972).
13. T. M. Buck, K. A. Picker, J. M. Poate, and C-M. Hsieh, *Appl. Phys. Lett.*, **21**, 485 (1972).
14. J. L. Lambert and G. Köhl, *Solid-State Electron.*, **14**, 430 (1971).
15. R. G. Mazur and P. H. Dickey, *This Journal*, **113**, 255 (1966).
16. Y. Terasawa, *IEEE Trans. Electron Devices*, **ed-20**, 714 (1973); Y. Terasawa, U.S. Pat. 3,939,415.
17. S. R. Lederhandler and L. J. Giacoletto, *Proc. IRE*, **43**, 477 (1955).

The Optical Constants of Silicon and Dry Oxygen Oxides of Silicon at 5461A

E. A. Taft*

General Electric Corporate Research and Development, Schenectady, New York 12301

ABSTRACT

The index of refraction of oxides grown on silicon in dry oxygen has been found to be a function of the growth temperature. There is an orientation effect for oxides grown at low temperatures. The index decreases with temperature, saturating above 1190°C at 1.4620, a value consistent with the index of fused quartz when stress corrections are made. The apparent density of oxide grown at 800°C is 3% greater than that grown above 1190°C. The complex index of refraction of silicon at 5461Å has been determined to be 4.086 − i0.031.

There is considerable variation in the literature of the reported values for the complex index of refraction of silicon and of the index of grown oxide at a wavelength of 5461Å. In 1972, papers on silicon (1) and on thermally grown silicon oxide (2) summarized some previous work and concluded with the best values for the index of silicon and of silicon oxide. The two values (two papers) for the complex index of refraction, n-*ik*, for silicon were 4.056 − i0.028 and 4.05 −i0.028. The index values obtained for thermally grown SiO_2 were 1.458 and 1.460. All results were measured at 5461Å. Except for the fact that both papers appear to explain away conflicting data, these ellipsometric studies agree quite closely in their results for both silicon and silicon dioxide. The value 1.458, however, does not agree with earlier results (3, 4) for SiO_2 which were obtained using different optical measurements. The earlier value for silicon oxide is 1.462. Moreover, more recent reports, again using ellipsometry (5, 6) have found still different results for the real part of the index of refraction of silicon and the index of the oxide. The new values advanced are 4.085 − i0.028 for silicon and 1.47 for the oxide.

In this paper we will present experimental results for the complex index of refraction of silicon; values of the index of oxide grown in dry oxygen on <111> and <100> silicon surfaces; and the variation of the index of silicon dioxide with growth temperature.

Experimental

Extinction coefficient of silicon.—As the ellipsometer is not well suited to the accurate measurement of small coefficients [van der Meulen (5) gives a short discussion as does Archer (7)], the extinction coefficient *k*, of silicon has been chosen by most workers from the available absorption data (8, 9). The original data of Dash and Newman (8), taken in this laboratory and available to me, actually gives *k* a value of 0.031, not 0.028, as often quoted. This still agrees with the published curve of Braunstein *et al.* (9).

The extinction coefficient is best established from absorption measurements in single crystal silicon; therefore, an independent check at 5461Å was made. Four wafers of 10 Ω-cm silicon crystal were chemically thinned so that reasonably uniform thickness was obtained. The thickness was determined from infrared interference measurements between 7.5 and 20 μm wavelengths where the index of refraction of silicon remains constant at 3.42 (10). A typical example is given in Fig. 1. The crystals were from 5 to 11 μm thick. The transmission of each of these crystals was measured using a prism monochromator with the 5461Å line from a mercury vapor lamp. The readings were corrected for background radiation and for silicon reflection to obtain an extinction coefficient for each sample. The values obtained are given in Table I. The average value of the extinction coefficient from the four determinations is $k = 0.031 \pm 5\%$; in excel-

Table I. Thickness, transmissivity, and extinction coefficient of single crystal silicon samples at λ 5461

Sample	Thickness (μm)	I/I_0	k
DE43	8.80	0.00219	0.03024
DE42	4.80	0.0278	0.03237
DE44	10.82	0.000384	0.03159
DE40	5.93	0.0180	0.02944
		Avg	0.03091

* Electrochemical Society Active Member.

Key words: ellipsometry, refractive index, silicon oxide, silicon, temperature dependence.

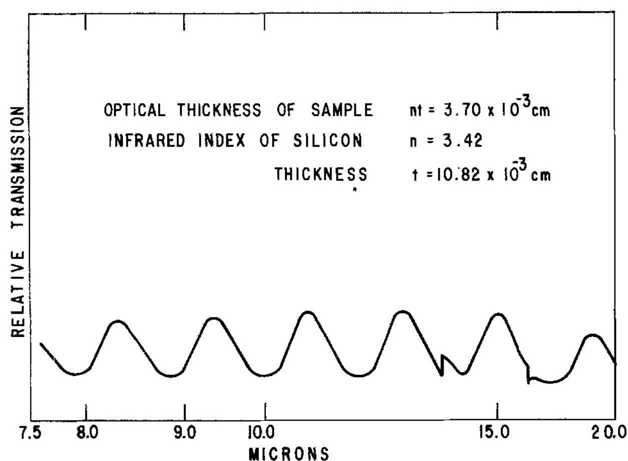

Fig. 1. Spectrophotometer data on infrared transmission through single crystal silicon.

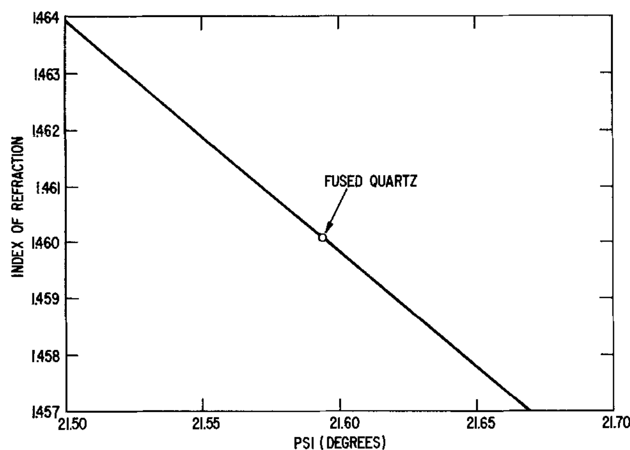

Fig. 3. Expanded plot of index of refraction of transparent material as a function of the analyzer angle, $A = -\Psi$.

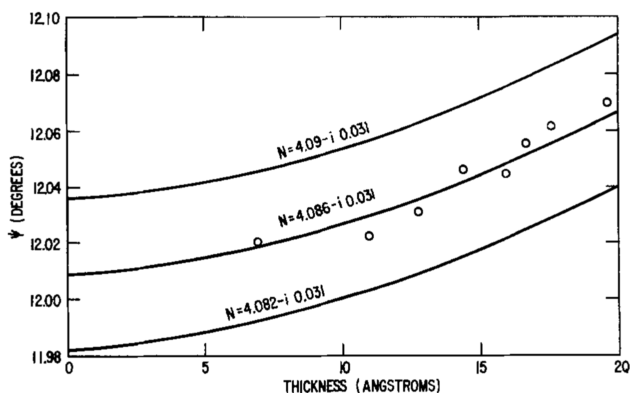

Fig. 4. Analyzer reading, $A = -\Psi$, for a thin transparent film on a slightly lossy substrate. The angle of incidence is 70° and λ is 5461Å.

lent agreement with Dash and Newman's earlier results.

Real part of index of refraction of silicon.—After careful alignment of a Gaertner L119 ellipsometer a measurement was made upon a clean optical quartz glass sample (G. E. Type 151) in order to check the instrument alignment and to verify the setting of the angle of incidence at 70°. Ψ calculated from two-quadrant measurements was 21.60° where $-\Psi$ is the analyzer reading.

Values of Ψ for transparent ($k = 0$) reflecting materials at a 70° angle of incidence are given in Fig. 2. They are obtained from usual ellipsometric formulas (11), the phase change, Δ, being 0° or 180° for a transparent material. Figure 3 is a highly expanded portion of this curve near the index for fused quartz of 1.4601 at 5461Å (12), Ψ should be 21.59°. This value is within the ± 0.01° precision of our instrument measurement.

Having verified, in this way, the ellipsometer calibration. we determined the real part of the index of refraction for Si. Ψ and Δ were observed for several hours on a freshly HF-etched and water-rinsed polished silicon wafer. Δ is used as the measure of thickness for very thin films. Ψ is plotted in Fig. 4 along with calculated curves of Ψ *vs.* film thickness on silicon. Ψ changes quite slowly as a film is formed on a clean Si surface. [van der Meulen (5) and Archer (7) also discuss this problem of a film-free surface.] The usual 6-8Å film on freshly HF-dipped and water-rinsed silicon gives a Ψ reading only 0.01° greater than a film-free sample. The index of the air-grown film is assumed to be 1.5 but any value up to 2.7 would change the measured thickness <20%. The Ψ value of 12.02° ± 0.01° obtained on numerous nearly film-free samples indicates that the real part of the index of refraction of silicon should be 4.086. Assuming that over-all errors, referred to a reading for Ψ, are ± 0.02°, this value for the index of silicon is correct to ± 0.003. No chemically etched silicon samples nor commercial chem-mechanically polished wafers have shown any appreciable deviation from this index.

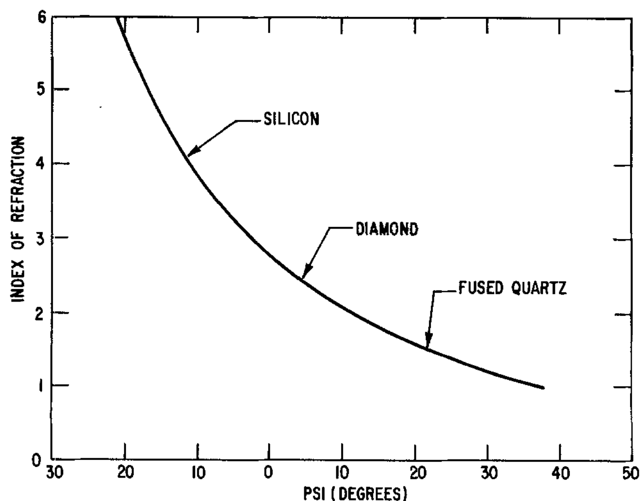

Fig. 2. Index of refraction of transparent materials as a function of the analyzer reading, $A = -\Psi$, of the ellipsometer. Angle of incidence is 70° and λ is 5461Å.

Thermally grown oxide films.—With the substrate index now assigned at 4.086 − i0.031, the index of thermally grown oxide films can be determined. Observers (1-5, 7) have found that the assumption of a constant index with changes in thickness of oxide did not disagree with their data. The same assumption is used here, although all of the films measured were in the small thickness range of 1000-1400Å. This range is the best for accurate determination of the film index and has been used by van der Meulen *et al.* (13) who also have shown a change of index when the growth temperature was changed.

For this study, chem-mechanically polished silicon wafers (<111>, p-type, 1 Ω-cm and <100>, n-type, 1 Ω-cm) were used. The wafers were usually scrubbed and solvent rinsed, but sometimes were given simply a buffered HF acid dip and water rinse. A quartz oxidation tube carying several cubic feet per minute of dry oxygen was used for growing the films. As a check of the furnace, a few oxides grown in other furnaces were also measured. The furnace was controlled to ±10°C after several hours of bake out at higher tem-

peratures. Oxidation times of the silicon in dry oxygen necessary to obtain 1000-1400Å of oxide at temperatures from 1290° to 750°C ranged from 2×10^1 to 1×10^4 min. The indexes of refraction of the oxide films grown at different temperatures are given in Fig. 5 and 6 for the two orientations. The bars show the estimated uncertainty in an oxide measurement.

Discussion

Preliminary data leading to this work were obtained on silicon of various orientation, resistivity,

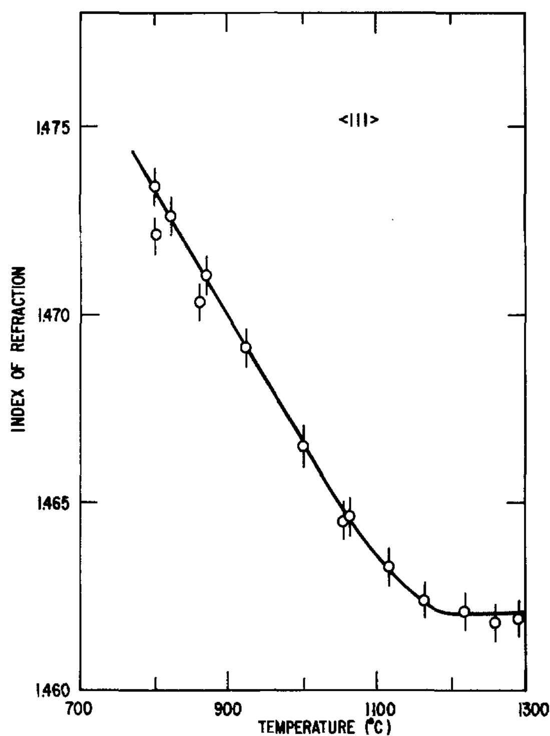

Fig. 5. Index of refraction of oxide grown on <111> silicon as a function of the growth temperature. $\lambda = 5461$Å.

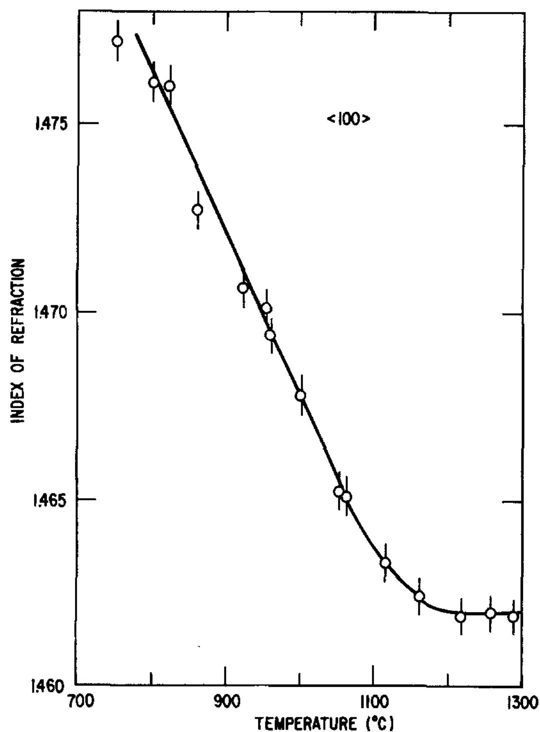

Fig. 6. Index of refraction of oxide grown on <100> silicon as a function of the growth temperature. $\lambda = 5461$Å.

and type. The oxidation temperatures were not always calibrated; precautions for holding a pure dry oxygen atmosphere were not rigorously observed. Despite these shortcomings, the ellipsometer data clearly indicated the refractive index-temperature variation. Some of these samples have been left in the data presentation and are always points below the line. (One exception was a very heavily doped n-type crystal.) The systematic study carried out as described above yielded the points which all fall on the curves to ± 0.0005 in the index value. The lower points, from the earlier, more casual oxidations, are most likely due to water vapor or other furnace contamination. No points above the curves have ever been observed using lightly doped silicon substrates.

The extrapolation of the straight line portion of these curves intersects the fused quartz index value of 1.4601 at 1190°C. At temperatures of 1190°C and above, the index appears to remain constant at the higher value of 1.4620. This high index suggested a film of higher density than fused quartz, while the constant value clearly indicated a stable material and the need for further analysis. If the two-dimensional compressive stresses on the film are considered (14), then we can calculate the volume decrease of the film $= 1 - 2\sigma/E\ (P_1 + P_2 + P_3)$ where σ is Poisson's ratio, E is Young's modulus, and P_1, P_2, P_3 are the orthogonal stresses.

The volume decrease in the film can also be estimated using the Lorentz-Lorenz relation (15) relating the volume, or density, ρ, of a transparent material to the index of refraction, n. This can be written $n^2 - 1/n^2 + 2\ (1/\rho) =$ a constant. Assuming that the oxide film is quartz glass with a normal index of 1.4601, an index of 1.4620 corresponds to a density increase of 0.0036. We may now calculate the stress on our oxide. If σ is 0.164 and $E = 0.76 \times 10^{12}$ dyne cm^{-2} (16), the compressive stresses in the plane of the film, $P_1 = P_2$ are found to be 2.1×10^9 dynes cm^{-2}. (As the film is not constrained in the third direction, $P_3 = 0$.) This value is considerably lower than the stresses of 3.1×10^9 dynes cm^{-2} reported by others (17-19). However, Primak and Post (16) find that fused quartz does not follow the Lorentz-Lorenz relation closely as their elasticity volume coefficient of refractive index of -0.34 is to be compared with the value from a Lorentz-Lorenz calculation of -0.53. Using their experimentally determined coefficient, the calculated stress on the high temperature film is then in good agreement with the reported values. The conclusion drawn here is that our measured value of the index of refraction for the higher temperature oxides is no different from that of pure fused quartz under compressive stress.

The strain in these high temperature silicon oxide films, therefore, using the above volume coefficient, causes a calculated density increase of 0.57% while the measured index of refraction increases by 0.0019. Jaccodine and Schlegel (17) show that the stress on grown oxides drops with growth temperature and appears to result from a simple thermal expansion difference. The refractive index increases of Fig. 5 and 6 would require (for an 800°C film) the equivalent of an isostatic pressure of >10 kbar on quartz glass (20).

Clearly the films grown at lower temperatures require a mechanism other than stress-strain for their high refractives indexes.

An assumption made here is that the films are stoichiometric SiO_2. The analysis of Deal and Grove (21) shows that oxides grown in dry oxygen actually contain about 5×10^{16} cm^{-3} of dissolved oxygen. The rapid appearance of large amounts of excess silcon in films grown at less than 1190°C in an excess oxygen environment seems improbable. Metastable high density quartz glass has been studied by Cohen and Roy (22), who discuss possible structural variations. Their

samples exhibited up to five times greater changes than have been observed here. Some grown-in structural change, which would be orientation sensitive, might be responsible for our results. (A quick look at the infrared absorption bands of some of these films with a Perkin Elmer 457 spectrophotometer yielded inconclusive results.)

The orientation effect of the silicon substrate on the oxide index is not apparent at the higher growth temperatures, but is pronounced at the lowest temperatures. If we look at the time required to grow a film of 1000-1400Å thickness on the <111> and <100> orientations at $>$1100°C, there is essentially no difference. At 1050°C, 20% more time is needed for the <100> film to get to the same thickness as the <111> silicon-based film. At 900°C, however, the difference has increased so that twice as much time is needed to grow the same oxide thickness on the <100> wafer.

It might be asked as to whether the long times involved in growing the oxide at the low temperature may be a factor. An 1150Å oxide was grown on <111> silicon at 1000°C in a nitrogen-oxygen atmosphere. It required the same total time to attain this thickness as is necessary for a growth temperature of ~775°C in pure oxygen. The index measured actually fell below the curve at 1000°C. As low readings have been noted before with oxide films grown in furnaces which have not been high temperature fired, I would assume some contamination, perhaps H_2O affected the 60 hr 1000°C oxidation. At least, the high index film associated with the usual dry oxygen oxidation at low temperatures was not observed. The actual formation temperature appears to be the dominant influence on the index.

Summary

It has been shown that there is growth temperature dependence of the index of refraction of oxide films grown on silicon in dry oxygen. At temperatures above 1190°C the index becomes constant at a slightly higher value than that for bulk fused quartz. This higher value can be accounted for entirely by the strain in the oxide, making the index at 5461Å the same as that of fused quartz. The lower temperature films have an orientation dependence. The index increase at low temperatures is over 1% with a calculated corresponding density increase of over 3%. The best value for the index of refraction of the silicon crystal substrate is 4.086 − *i*0.031.

Acknowledgments

P. V. Gray set up the initial computer program; modifications were made by L. F. Cordes. Ellipsometer alignment work was done with L. F. Cordes. The encouragement of M. Garfinkel is greatly appreciated.

Manuscript submitted Oct. 28, 1977; revised manuscript received Jan. 24, 1978.

Any discussion of this paper will appear in a Discussion Section to be published in the December 1978 JOURNAL. All discussions for the December 1978 Discussion Section should be submitted by Aug. 1, 1978.

Publication costs of this article were assisted by General Electric Company.

REFERENCES

1. S. S. So and K. Vedam, *J. Opt. Soc. Am.*, **62**, 596 (1972).
2. T. Smith and A. J. Carlan, *J. Appl. Phys.*, **43**, 2455 (1972).
3. W. A. Pliskin and R. P. Esch, *ibid.*, **36**, 2011 (1965).
4. I. Franz and W. Langheinreich, *Solid State Electron.*, **11**, 59 (1968).
5. Y. J. van der Meulen, *This Journal*, **119**, 530 (1972).
6. S. I. Raider, R. Flitsch, and M. J. Palmer, *ibid.*, **122**, 413 (1975).
7. R. J. Archer, *J. Opt. Soc. Am.*, **52**, 970 (1962).
8. W. C. Dash and R. Newman, *Phys. Rev.*, **99**, 1151 (1955).
9. R. Braunstein, A. R. Moore, and F. Herman, *ibid.*, **109**, 695 (1958).
10. C. D. Salzburg and J. J. Villa, *J. Opt. Soc. Am.*, **47**, 244 (1957).
11. J. A. Johnson and N. M. Bashara, *ibid.*, **60**, 221 (1970).
12. I. H. Malitson, *ibid.*, **55**, 1205 (1965).
13. Y. J. van der Meulen, C. M. Osburn, and J. F. Ziegler, *This Journal*, **122**, 284 (1975).
14. R. V. Southwell, "Theory of Elasticity," p. 119, Oxford University Press, New York (1941).
15. Slater and Frank, "Theoretical Physics," p. 280, McGraw-Hill Book Co. Inc., New York (1933).
16. W. Primak and D. Post, *J. Appl. Phys.*, **30**, 779 (1959).
17. R. J. Jaccodine and W. A. Schlegel, *ibid.*, **37**, 2429 (1966).
18. M. V. Whelan, A. H. Goemans, and L. M. C. Goossens, *Appl. Phys. Lett.*, **10**, 262 (1967).
19. R. A. Sigsbee and R. H. Wilson, *ibid.*, **23**, 541 (1973).
20. K. Vedam, E. D. D. Schmidt, and R. Roy, *J. Am. Ceram. Soc.*, **49**, 531 (1966).
21. B. E. Deal and A. S. Grove, *J. Appl. Phys.*, **36**, 3770 (1965).
22. H. M. Cohen and R. Roy, *Phys. Chem. Glasses*, **6**, 149 (1965).

Thermodynamics of Vaporization and High Temperature Enthalpy of Zirconium Tetraiodide

D. Cubicciotti* and K. H. Lau*

SRI International, Menlo Park, California 94025

and M. J. Ferrante

Albany Metallurgy Research Center, Bureau of Mines, Albany, Oregon 97321

ABSTRACT

The sublimation of ZrI_4 was studied by a torsion effusion-gravimetric technique in which the molecular weight of the effusing gas and its pressure in the effusion cell were measured simultaneously. The sublimation pressures of ZrI_4 were found to depend on the orifice size of the effusion cell. The measured pressures were extrapolated to zero orifice size to obtain the equilibrium vapor pressures, which could be represented by the equation

$$\log P(ZrI_4, \text{atm}) = 9.79 \pm 0.19 - \frac{6798 \pm 86}{T} \text{ (from 410° to 480°K)}$$

Enthalpies above room temperature, up to 703.1°K for solid zirconium tetraiodide were measured in a copper-block, drop calorimeter. The enthalpy increments above 298.15°K were expressed by the equation

$$H_T^\circ - H_{298}^\circ \text{ (kcal/mole)} = 29.498 \times 10^{-3}T + 1.906 \times 10^{-6}T^2 + 62.3 \cdot 10^2 T^{-1} - 9.173 \text{ (298°-772°K)}$$

The data were combined with literature vapor pressure data obtained at higher temperatures and a second law treatment used to derive the enthalpy and entropy of sublimation (31.88 kcal/mole and 46.9 cal/mole-degree, respectively, at 298°K). These values were used to evaluate the enthalpy of formation of gaseous ZrI_4 (−84.9 kcal/mole) and the absolute entropy of solid ZrI_4 (59.8 cal/mole-degree) at 298°K.

Zirconium and its alloys are susceptible to stress corrosion cracking in iodine vapor, and certain failures of nuclear reactor fuel rods have been ascribed to that cause (1). The mechanism of the iodine-induced stress cracking is not understood but it presumably involves the chemistry of the reactions of zirconium with iodine, and these reactions are themselves little understood. The present study of the vaporization of ZrI_4 is part of our program to investigate the chemistry of the zirconium-iodine system.

Zirconium forms several solid iodides and several gaseous iodides (2-5), of which tetraiodide is the highest oxidation state in both phases. Molecular constant and structural information for the gaseous molecule are available for calculation of the absolute entropy of the gas, and the enthalpy of formation of the solid has been measured. The vaporization thermodynamics interrelates these quantities between the equilibrium phases. We have supplemented vapor pressure data from the literature (6-8) with a torsion-effusion study and since the only available values for the heat capacity of the solid were estimated value, we have made measurements of the high temperature enthalpies. With those data we have derived values for the absolute entropy of the solid and the enthalpy of formation of the gas.

Experimental

Materials.—Zirconium tetraiodide was prepared directly from the reaction of high purity (99.9+%) zirconium powder (Ventron Corporation) and reagent grade iodine. A mixture of a 10% excess of zirconium with iodine was sealed under high vacuum in a 20 cm long and 1.6 cm diam thick-wall Pyrex tube. The sample tube was put in a tilted tube furnace and the temperature was then slowly raised to 485°C. After the tube was heated for 10 hr, the upper end was exposed to room temperature so that the zirconium tetraiodide condensed there. The reaction products were zirconium tetraiodide, which condensed in the upper end of the tube, and a small amount of black powder that contained the excess zirconium, presumably as a lower iodide in the lower end. The tube was carefully transferred to a dry box under an atmosphere of argon, purified over hot titanium sponge. The sample tube was cracked in the center, and a lump of reddish brown product was collected and stored in the dry box for the vapor pressure measurements. A part of the material was transferred to a glass bulb, sealed under vacuum and shipped to the Albany Metallurgical Research Center. Chemical analyses of the calorimetric sample gave 84.85% I by the AgI gravimetric method, and 15.15% Zr by an H_2SO_4-digested sample ignited to ZrO_2. Theoretical percentages for ZrI_4 are 84.77% I and 15.23% Zr. The stoichiometry of the sample was $ZrI_{4.026}$. Spectrographic analysis of a sample showed the total metallic impurities were less than 100 ppm, including Hf.

Vapor pressures.—All of the effusion measurements were made with graphite cells. Cell geometrical constants were measured with a traveling microscope and are given in Table I. Each cell had two sample chambers with essentially the same orifice size. The average constants were used since the orifice sizes were very similar. The constants of each cell were checked by measuring the torsion-effusion vapor pressure of KCl. The molecular weights were within 2% of KCl

Table I. Geometrical constants of effusion cells

Cell	Orifice diameter (cm)	Orifice length (cm)	$q_1 + q_2$ (cm)	$\Sigma Ca \times 10^2$ (cm^2)
A	0.0473	0.0964	1.107	0.1247
B	0.0803	0.0964	1.1734	0.4781
C	0.1335	0.0932	1.1294	1.7394
D	0.2077	0.1004	1.1173	4.602

* Electrochemical Society Active Member.

Key words: heat capacity, entropy, equilibrium, inorganic.

and the pressures within 5% of the data reported by Pugh and Barrow (9).

About 0.6g of the sample was loaded into each chamber of the cell in the dry box. The sample was protected from exposure to air during the transfer of the cell to the torsion apparatus as follows. The orifices were initially filled with naphthalene. When the apparatus was evacuated, the naphthalene sublimed from the orifices. The sample was then heated slowly to operating temperatures. Initially (while about 0.5% of the sample evaporated), the molecular weights were smaller than that of zirconium tetraiodide (599) due to the evolution of HI, but they soon reached a steady-state value close to 600. Measurements were recorded only after the molecular weight reached the steady-state value. Analysis of the residues left in one effusion cell, after a series of measurements that removed 30% of sample, gave 4.05 ± 0.02 for the I-to-Zr ratio, indicating congruent vaporization had occurred.

A schematic diagram of the torsion effusion-gravimetric apparatus is shown in Fig. 1. Details of this method have been described briefly in our previous publications (10-12). Recently it has been used successfully to study the decompositions of metal sulfates (13). In this arrangement, the torsion element and the effusion cell were suspended directly from the arm of a Cahn Model RH electrobalance and simultaneous measurements were made of the angular displacement and the total mass of the effusate. The cell region was heated by a Kanthal-wound electric furnace surrounding the 8.5 cm diam quartz vacuum enclosure. Temperatures were measured with a platinum 13% rhodium-platinum thermocouple made from wires calibrated at fixed points by the manufacturer (Sigmund Cohn Company) with the junction located adjacent to the effusion cell. Three layers of copper sheet were located between the aluminum damping disk and the molybdenum radiation shields to trap ZrI_4 vapor so as to avoid error in the mass loss measurements caused by the condensation of the effusate on the disk.

The torsion element was a 58.6 cm long Pt-10% Ni ribbon having a torsion constant of 0.07814 dyne cm/rad. Angular deflection of the cell was measured with a telescope by sighting a scale reflected in a mirror on the suspension system. Extraneous oscillations were damped magnetically, but the magnets were removed during the deflection measurements.

From the torque angle measurements the pressures, P, in the effusion cell can be calculated from the relation

$$P = \frac{2k\theta}{\Sigma afq} \quad [1]$$

where k is the torsion constant of the fiber, θ is the measured angular deflection, and a, f, and q are the area, force factor, and moment arm of each effusion orifice. When the rate of mass loss of the effusion cell is measured simultaneously with the angular deflection, the vapor molecular weights, M, can be calculated from the expression

$$M = 2\pi RT\{[\dot{W}(\Sigma afq)]/[2K\theta(\Sigma Ca)]\}^2 \quad [2]$$

where R is the gas constant, T is the absolute temperature, W is the total rate of mass loss, and C is the orifice Clausing factor.

High temperature enthalpies.—Enthalpies above 298.15°K were measured with a copper-block, drop calorimeter, essentially as described by Douglas and King (14). The calorimeter was modified by replacing the potentiometer and galvanometer with a more sensitive system (a six-dial microvolt potentiometer and electronic nanovolt null detector) which was capable of detecting a temperature change of ± 0.00005°K. Before and after the series of measurements on the ZrI_4 sample the calorimeter was calibrated electrically and the entire system was checked by measuring the enthalpy of MgO sealed in a Pt-10% Rh container. Measurements on MgO agreed with literature (15) values to less than 0.1%. Results of measurements are expressed in terms of thermochemical kilocalorie (1 kcal = 4184.0J). Temperatures refer to the International Practical Temperature Scale of 1968 (16). Weighings were corrected to vacuum.

The sample container was a silica glass capsule. After the capsule was filled with powdered sample in a dry box, it was transferred to a vacuum system without exposure to the air. The capsule was then evacuated and fusion sealed with a flame while the portion of the capsule containing the sample was immersed in ice water. The mass of ZrI_4 was 17.3459g. The mass of the silica was 4.2694g. The internal volume of the container was 6.21 cm^3, and the volume of the ZrI_4 was calculated to be 3.56 cm^3 based on the density (4.87 g/cm^3) calculated from the x-ray crystallographic data.

The temperature of the sample in the furnace was measured with a Pt-10% Rh-Pt thermocouple whose calibration was checked against the melting point of gold during this series of experiments. The mass of the sample and container was periodically checked for constancy during the series of measurements.

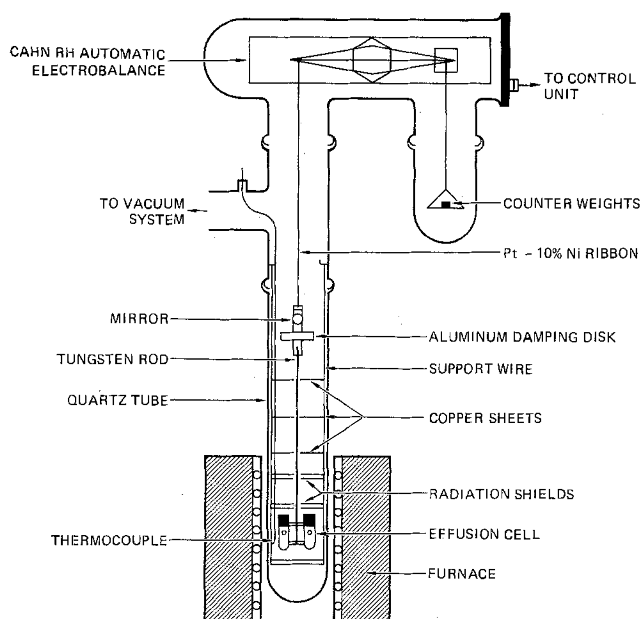

Fig. 1. Schematic diagram of the torsion effusion gravimetric apparatus.

Results

Vapor pressures.—The results of measurements on the four effusion cells with different orifice sizes are presented in Table II and Fig. 2. The equations given in the table represent the measured effusion pressures.

The measured pressures showed an orifice size dependence, which has frequently been observed in effusion studies. The pressures were treated by the Whitman-Motzfeld model for effusion, which relates the measured pressures (P) with equilibrium pressures (P_{eq}) by the equation

$$1/P = (1 + \beta Ca)/P_{eq} \quad [3]$$

In which a is the orifice area, C is the Clausing factor for the orifice, and β a parameter that depends on sample surface area and evaporation coefficient. A plot of $1/P$ against Ca should have a slope equal to β/P_{eq} and an intercept equal to $1/P_{eq}$. The data obtained with the four cells, extrapolated where necessary, are plotted in that way in Fig. 3. Straight lines were fit to the data at each temperature by the least squares method. The deviations of the points from the lines show some regularity, especially at the lower temperatures; the deviations were possibly due to differences in sample surface conditions for different loadings but were not

Table II. Observed vapor pressure (P), equilibrium vapor pressure (P_{eq}), and vapor molecular weights (M) for sublimation of ZrI_4

T (°K)	P × 10⁷ (atm)	P_{eq} × 10⁷ (atm)	M
Cell A			
451.9	58.6	61.5	
458.8	98.6	104	596
462.6	128	134	602
464.1	143	151	582
470.2	225	236	596
470.9	238	250	592
472.9	265	278	580
475.9	331	348	595
477.3	370	389	599

$$\log P(\text{atm}) = \frac{-(6710.9 \pm 45.9)}{T} + (9.74 \pm 0.10)$$

T (°K)	P × 10⁷ (atm)	P_{eq} × 10⁷ (atm)	M
Cell B			
431.6	8.88	10.6	592
439.9	18.0	21.5	589
441.3	18.7	22.7	—
442.4	21.8	26.0	585
447.5	31.7	37.8	587
450.0	40.9	48.8	589
451.6	41.9	50.0	586
455.1	60.0	71.6	584
456.4	61.6	73.5	569
457.9	66.8	79.7	592

$$\log P(\text{atm}) = \frac{-(6701.3 \pm 122.4)}{T} + (9.47 \pm 0.27)$$

T (°K)	P × 10⁷ (atm)	P_{eq} × 10⁷ (atm)	M
Cell C			
432.3	6.41	10.9	589
435.3	8.05	13.7	596
440.3	12.5	21.3	585
441.0	13.2	22.6	584
443.2	15.3	26.0	—
445.3	17.7	30.1	—
446.8	20.6	35.1	583
446.9	20.8	35.4	598
448.2	22.6	38.5	592
449.7	25.5	43.4	569

$$\log P(\text{atm}) = \frac{-(6710.9 \pm 69.9)}{T} + (9.33 \pm 0.16)$$

T (°K)	P × 10⁷ (atm)	P_{eq} × 10⁷ (atm)	M
Cell D			
413.4	0.835	2.39	
417.9	1.29	3.69	
423.3	2.04	5.83	
426.8	2.62	10.4	
431.2	4.04	11.6	
433.0	4.42	12.7	
438.1	6.63	19.0	
440.1	8.00	22.7	
443.7	10.5	30.0	

$$\log P(\text{atm}) = \frac{-(6603.7 \pm 59.0)}{T} + (8.90 \pm 0.14)$$

investigated further. Values of β calculated from the least squares slopes of the lines in Fig. 3 ranged from 38 to 42. An average value of 40 for β was selected to calculate equilibrium pressures by Eq. [3]. The calculated equilibrium pressures are given in Table II. They are well represented by the equation

$$\log P_{eq}(\text{atm}) = 9.79 \pm 0.19 - (6798 \pm 86)/T; \quad (\text{from } 410° \text{ to } 480°\text{K}) \quad [4]$$

which is shown as a dashed line in Fig. 2.

High temperature enthalpies.—The enthalpy of the ZrI_4 was obtained by subtracting the enthalpy due to the silica capsule, which was about 50% of the total, from the measured value. The enthalpy of the silica glass was determined as a function of temperature in a separate series of measurements. The measured values for the enthalpies of ZrI_4 above room temperature are given in Table III. A very small correction was made to the two highest temperature values for the enthalpy of vaporization of the ZrI_4 in the capsule, using the method of Ref. (14). For that correction, the vapor pressure and enthalpies of vaporization were derived from the results given later in this paper (Eq.

Table III. Measured values of the enthalpy of solid ZrI_4 above 298.15°K*

T (°K)	$H°_T - H°_{298}$ (kcal/mole)	T (°K)	$H°_T - H°_{298}$ (kcal/mole)
403.1	3.182	552.7	7.829
453.2	4.725	602.8	9.409
502.9	6.262	653.2	11.002**
503.0	6.259	703.1	12.592***
503.1	6.273		

* Calculated for 598.8g (one mole) of sample.
** Experimental value reduced by 0.09% for vaporization.
*** Experimental value reduced by 0.37% for vaporization.

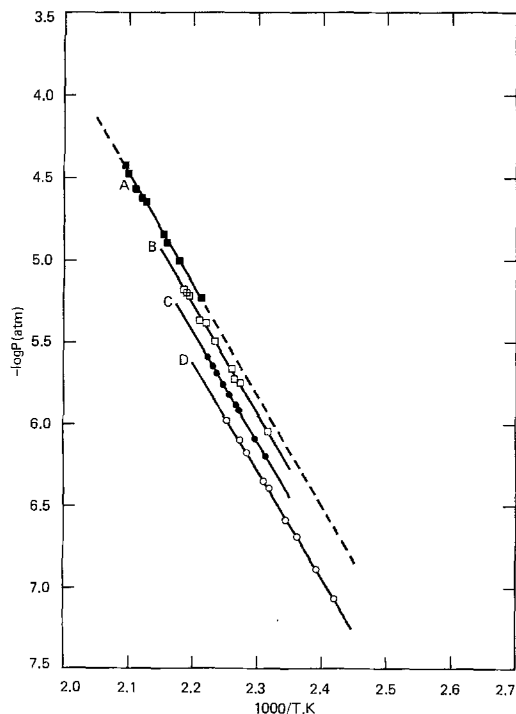

Fig. 2. Pressures measured by torsion effusion with four cells of different orifice size. Letters refer to cells described in Table II. The dashed line represents the equilibrium pressures.

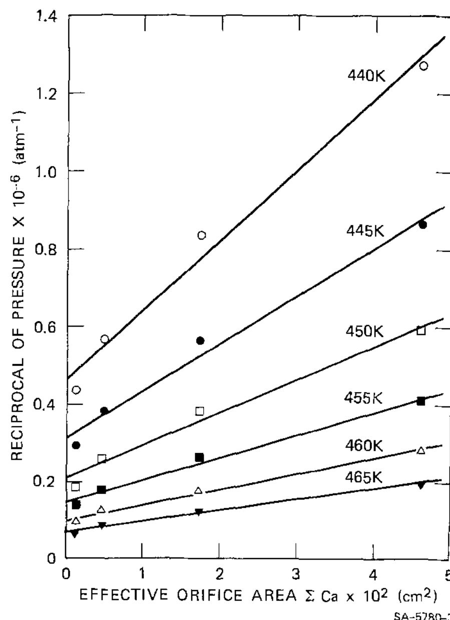

Fig. 3. Whitman-Motzfeldt extrapolation to zero orifice size

[12]). The x-ray diffraction pattern of the sample after the measurements was the same as the starting material.

Data Analysis

High temperature enthalpies.—The measured enthalpies were computer fitted with curves by polynomial functions as described by Justice (17). These functions were then used to calculate the smoothed values of enthalpies and derived thermodynamic properties at selected temperatures given in Table IV. Extrapolation of enthalpies from the last experimental measurement at 703.1°-772°K, the melting point adopted from Rahlfs and Fischer (7), was based on a reasonable projection of the smoothed values. The smoothed enthalpies are estimated to have an uncertainty of ±0.4%.

The smoothed enthalpies were fitted with an equation using the method described by Kelley (18). The derived equation is given below with the temperature range of validity. The average deviation of the equation from the smoothed data is <0.01%, and from the experimental values <0.1%.

$$H^\circ_T - H^\circ_{298}\ \text{(kcal/mole)} = 29.498 \times 10^{-3}T + 1.906 \times 10^{-6}T^2 + 62.3T^{-1} - 9.173;\ (298^\circ\text{-}772^\circ\text{K}) \quad [5]$$

Vapor pressures.—The equilibrium vapor pressures were analyzed by a modified Sigma-treatment (19) to derive the entropy and enthalpy changes associated with the sublimation reaction. In this treatment one calculates from each equilibrium pressure measurement a value for Sigma defined as

$$\Sigma = -R \ln P_{eq} - (\Delta fef\ \text{incr})$$

$$\Delta fef\ \text{incr} = \frac{1}{T}[(H^\circ_T - H^\circ_{298}) - T(S^\circ_T - S^\circ_{298})]_{gas} - \frac{1}{T}[(H^\circ_T - H^\circ_{298}) - T(S^\circ_T - S^\circ_{298})]_{solid}$$

The function (Δfef incr) depends only on the heat capacities of the gas and the solid. The heat capacity of the solid was obtained from Eq. [5]. The molecular constants of the gas have been established by measurements, and the heat capacity and absolute entropy are given in the JANAF Tables (5). An equation derived to represent the (Δfef incr) function in the Sigma treatment was

$$(\Delta fef\ \text{incr}) = -2.800 + 6.68 \times 10^{-3}T - 1.136 \times 10^{-6}T^2 + 8.06 \times 10^4/T^2\ (298^\circ \text{ to } 772^\circ\text{K}) \quad [6]$$

For a sublimation reaction like the present one

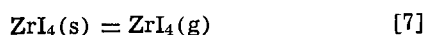

$$ZrI_4(s) = ZrI_4(g) \quad [7]$$

it can be shown (19) that the values of Sigma are related to the room temperature entropy and enthalpy of sublimation by the equation

$$\Sigma = \frac{\Delta H^\circ_{298}}{T} - \Delta S^\circ_{298} \quad [8]$$

Table IV. Smoothed high temperature thermodynamic properties of ZrI_4 (c)

T (°K)	C_p° (Cal/deg-mole)	$S^\circ_T - S^\circ_{298}$ (Cal/deg-mole)	$H^\circ_T - H^\circ_{298}$ (kcal/mole)
298	29.90	0	0
300	29.92	0.19	0.055
350	30.32	4.83	1.563
400	30.63	8.90	3.087
450	30.91	12.53	4.625
500	31.16	15.79	6.177
550	31.39	18.78	7.740
600	31.61	21.52	9.316
650	31.83	24.05	10.902
700	32.04	26.42	12.498
750	(32.25)*	(28.64)	(14.105)
772	(32.34)	(29.57)	(14.816)

* Values in parentheses are extrapolations.

The molecular weights were determined with cells A, B, and C and were equal to the molecular weight of ZrI_4 within about 5%, which is a reasonable experimental error for these measurements. This result, which is in agreement with the vapor density measurements of Rahlfs and Fischer (7), led to two conclusions. First, the vaporization was congruent, which means that from phase rule considerations the system acted as a one-component system, and the vapor pressure depended only on temperature and not on the amount of material removed during the vaporization study. Second, the gas was monomeric ZrI_4 with no measurable amounts of gaseous polymers. Therefore, the thermodynamic functions for the gas could be calculated from the molecular constant data available for ZrI_4.

Sale and Shelton (6) have made effusion-mass loss measurements on ZrI_4 using cells with three orifice sizes. A plot of reciprocal pressure against orifice size for their data was not linear, and they treated their data in a different way and derived the following equation for the equilibrium pressures

$$\log P_{eq}(\text{atm}) = 9.15 - 6342/T;\quad (\text{from } 425^\circ \text{ to } 500^\circ\text{K}) \quad [9]$$

Rahlfs and Fischer (7) measured the vapor pressure of ZrI_4 in a higher range of temperatures using a liquid tin manometer. They also measured the gas molecular weight by a vapor density method and found values in the range of 563-606, which are within experimental error of that of ZrI_4. Their vapor pressure measurements could be represented by the equation

$$\log p(\text{atm}) = 9.17 - 6455/T;\quad (\text{from } 558^\circ \text{ to } 671^\circ\text{K}) \quad [10]$$

Gerlach *et al.* (8) used an oscillating quartz fiber method to measure the vapor pressure, and gave the following equation for their data

$$\log p(\text{atm}) = 7.71 - 5730/T;\quad (\text{from } 393^\circ \text{ to } 453^\circ\text{K}) \quad [11]$$

The vapor pressure curves from these sources are shown in Fig. 4. In the lower pressure range the three sets of data are not in good agreement. The data of Ref. (6) and (8) are about a factor of two higher than the present data. We believe that the accuracy of the present data is significantly greater than that of the effusion study performed by Sale and Shelton (6), for the following reasons. The calibrations of the present cells, obtained from geometrical measurements, were checked by measuring the vapor pressure of KCl. The molecular weights of the effusing gas were determined and only when low molecular weight gases (presumably HI) had stopped effusing were measurements recorded. The orifice dependence of pressures followed the expected Whitman-Motzfeldt behavior. The results of Gerlach *et al.* were obtained by an unproven method of unknown reliability.

The present results are in excellent accord with the data of Rahlfs and Fischer as seen from Fig. 4. A Sigma treatment of these two sets of data yielded the following values for the sublimation reaction (Eq. [7])

$$\Delta H^\circ_{298} = 31.88 \pm 0.08\ \text{kcal/mole, and}$$

$$\Delta S^\circ_{298} = 46.9 \pm 0.16\ \text{cal/mole-degree}$$

The agreement between the two sets of data, as indicated by the relatively small standard deviations over the large pressure range (10^{-7}-1 atm), is very good. The vapor pressure equation derived from that treatment for ZrI_4 is

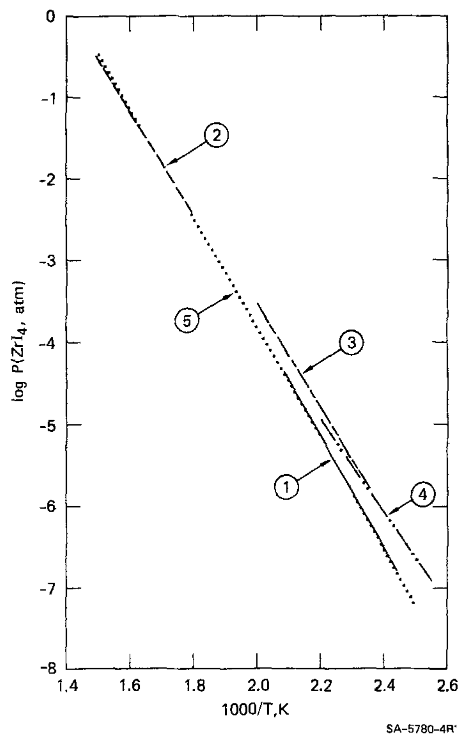

Fig. 4. Comparison of vapor pressure equations. 1, —, Present measurements, Eq. [4]. 2, - - -, data of Rahlfs and Fischer, Eq. [10]; 3, — - —, data of Sale and Shelton, Eq. [9]; 4, — · · —, data of Gerlach *et al.*, Eq. [11]; 5, ..., Sigma treatment, Eq. [12].

$$\log P(\text{atm}) = -\frac{1}{4.575}\left[\frac{31,880}{T} - 49.7 + 6.68 \times 10^{-3}T - 1.131 \times 10^{-6}T^2 + 8.06 \times 10^4/T^2\right]$$

(from 450° to 670°K) [12]

This equation is represented as a dotted line in Fig. 4.

Discussion

The measured enthalpies and derived quantities for ZrI_4 are about 2% lower than the estimates made in the JANAF Tables, and this reasonable agreement shows a good degree of acceptability for the estimation techniques.

The enthalpy measurements showed no indication for any thermal effects associated with phase transitions. That result was important in the interpretation of the vapor pressure data as follows. Stevenson and Wicks (20) found that the vapor pressure of solid hafnium tetraiodide decreased after the sample had been heated at 300°-310°C for some time. They attributed that behavior to the conversion of the solid from a metastable form to more stable forms. Because of the great similarity of the chemistry of zirconium and hafnium, we investigated the possibility of such a transformation in ZrI_4. We heated a sample of ZrI_4 in a sealed, evacuated Pyrex bulb for one week at 300°C. The x-ray pattern of the sample after heating was the same as that before heating and the same as that of the material used for the vapor pressure measurements. A series of torsion effusion vapor pressure measurements was made with the heat-treated sample in cell A. The results were about 5% below the values given in Table I. We consider that to be within the experimental error of the measurements. Therefore, we conclude that our measurements give the vapor pressure of the stable form of ZrI_4. (An alternative explanation for the low values obtained by Stevenson and Wicks in their run 2 is that they resulted from a reaction of the sample with the metallic container. The enthalpy of sublimation for their "metastable" HfI_4 is almost the same as that of ZrI_4. The very large change, namely 20 kcal/mole, to the "stable" form is more typical of a chemical reaction than a structural transformation.)

As indicated earlier, the thermodynamic quantities associated with vaporization can be used to derive related values for the solid or gas. The authors of the JANAF Tables have analyzed the data of Ref. (6) and (7) by a third law treatment; however, they used an estimated value for the absolute entropy of the solid. The sublimation thermodynamic data they obtained were $\Delta H°_{298} = 30.2$ kcal/mole, and $\Delta S°_{298} = 44.5$ cal/mole-degree. Those values differ somewhat from the present ones based on our second law treatment of the vapor pressures. We feel that the present values derived from experimental information are preferable to the JANAF values, which are based on the estimated entropy. Alcock *et al.* (21) have also analyzed the results of Ref. (6) and (7) and have derived an equation to fit them; however, for the reasons stated above we consider the present analysis to be more accurate.

The enthalpy of formation of solid ZrI_4 has been measured by Turnbull (22), and from his data the JANAF group has calculated an enthalpy of formation of -116.8 ± 1.5 kcal/mole for the solid. Therefore, the standard enthalpy of formation of the gas at 298°K is -84.9 ± 1.6 kcal/mole. This value differs from the JANAF Tables (-86.6 ± 2 kcal/mole) because of the new data and modified treatment.

The absolute standard entropy of the gas calculated from structure and molecular constant data was given in the JANAF Tables as 106.7 ± 0.03 cal/mole-degree; thus, the absolute entropy of the solid at 298°K becomes 59.8 ± 0.2 cal/mole-degree from our results. Our value is somewhat smaller than the JANAF value (62.2 ± 1 cal/mole-degree) that was estimated from data for other zirconium tetrahalides. We believe the present value is more accurate because it is based on measured quantities.

Acknowledgments

The authors are grateful to Dr. Donald L. Hildenbrand (SRI International) for the use of the torsion effusion-gravimetric apparatus and for extensive technical discussions.

Financial support for the vaporization research was provided by the U.S. Department of Energy, Division of Basic Energy Sciences under Contract No. E(04-3)-1339 to SRI International. Calorimetric measurements were performed at the Albany Metallurgical Research Center, Bureau of Mines, U.S. Department of the Interior, where chemical analyses were made by Robert R. Brown and x-ray diffraction analyses by Robert A. McCune.

Manuscript submitted Sept. 2, 1977; revised manuscript received Nov. 2, 1977.

Any discussion of this paper will appear in a Discussion Section to be published in the December 1978 JOURNAL. All discussions for the December 1978 Discussion Section should be submitted by Aug. 1, 1978.

Publication costs of this article were assisted by SRI International.

REFERENCES

1. B. Cox and J. C. Wood, in "Corrosion Problems in Energy Conversion and Generation," C. S. Tedmon, Jr., Editor, p. 275, The Electrochemical Society Softbond Symposium Series, Princeton, N. J. (1974).
2. F. R. Sale and R. A. J. Shelton, *J. Less Common Met.*, 9, 60 (1965).
3. R. Daake, Ph.D. Dissertation, Iowa State University, 1976.
4. E. M. Laren, *Adv. Inorg. Chem. Radiochem.*, **13**, 1 (1970).
5. JANAF Thermochemical Tables, The Dow Chemical Co., Midland, Michigan (December 31, 1976).

6. R. F. Sale and R. A. J. Shelton, *J. Less Common Met.*, **9**, 54 (1965).
7. O. Rahlfs and W. Fischer, *Z. Anorg. Allgem. Chem.*, **211**, 349 (1933).
8. J. Gerlach *et al.*, *Z. Phys. Chem. (Frankfurt)*, **53**, 135 (1967).
9. A. C. P. Pugh and R. F. Barrow, *Trans. Faraday Soc.*, **54**, 671 (1958).
10. D. L. Hildenbrand and W. F. Hall, *J. Phys. Chem.*, **67**, 888 (1963).
11. D. L. Hildenbrand, W. F. Hall, F. Ju, and N. D. Potter, *J. Chem., Phys.*, **40**, 2882 (1964).
12. D. L. Hildenbrand and D. T. Knight, *ibid.*, **51**, 1260 (1969).
13. K. H. Lau, D. Cubicciotti, and D. L. Hildenbrand, *ibid.*, **66**, 4532 (1977).
14. T. B. Douglas and E. G. King, in "High-Temperature Drop Calorimetry," Vol. 1, J. P. McCullough and D. W. Scott, Editors, Chap. 8, Butterworths, London (1968).
15. A. C. Victor and T. B. Douglas, *J. Res. NBS*, **67A**, 325 (1963).
16. Comite International des Poids et Mesures (The International Committee on Weights and Measures). The International Practical Temperature Scale of 1968. *Metrologia*, **5**, 35 (1969).
17. B. H. Justice, "Thermal Data Fitting with Orthogonal Functions and Combined Table Generation. The FITAB Program," pp. 49, Univ. Michigan, Ann Arbor, Mich., COO-1149-143 (1969).
18. K. K. Kelley, Bureau of Mines Bulletin 584, pp. 232, (1960).
19. D. Cubicciotti, *J. Phys. Chem.*, **70**, 2410 (1966).
20. F. D. Stevenson and C. E. Wicks, *J. Chem. Eng. Data*, **10**, 33 (1965).
21. C. B. Alcock *et al.*, in "Zirconium: Physico-Chemical Properties of Its Compounds and Alloys," Atomic Energy Review, Special Issue No. 6, IAEA, Vienna (1976).
22. A. G. Turnbull, *J. Phys. Chem.*, **65**, 1652 (1961).

Properties of Polycrystalline AlAs/GaAs on Graphite Heterojunctions for Solar Cell Applications

W. D. Johnston, Jr.* and W. M. Callahan

Bell Laboratories, Holmdel, New Jersey 07733

ABSTRACT

Polycrystalline heterojunction material of N-AlAs/p-GaAs and P-AlAs/n-GaAs was grown in a chloride arsine vapor-phase reactor on graphite substrates. P^+AlAs/p-n GaAs structures were produced as well by postgrowth Zn diffusion. Control of nucleation and ohmic contact of the GaAs layer to the graphite was achieved with Zn doping during growth, or Ge or Sn coating of the substrate prior to growth, for p- or n-type GaAs, respectively. The N-AlAs/p-GaAs material appears promising for possible solar cell applications, but we have not succeeded in overcoming the high spreading resistance due to grain boundary scattering in the AlAs layer.

An area of primary current interest in compound semiconductor materials research is the growth and characterization of thin polycrystalline films for devices potentially suitable for large-scale photovoltaic solar energy conversion.

Over a decade ago Vohl and co-workers (1) reported fabrication of Schottky barrier solar cells of polycrystalline GaAs with solar conversion efficiencies up to 5%. No significant improvement in the efficiency of thin-film polycrystalline cells of III-V semiconductor materials has been reported since. Little is known about the effect of grain boundaries on the minority or majority carrier properties of such films, nor is there any real understanding as yet of the range of control of film characteristics or grain boundary effects possible through variation of growth conditions, doping techniques, or substrate treatment.

The AlAs/GaAs heterojunction pair would appear to provide numerous potential advantages over other material combinations for polycrystalline thin-film solar cells. The device-related properties of single-crystal GaAs are well understood. $Al_xGa_{1-x}As$/GaAs single crystal solar cells grown by liquid phase epitaxy (LPE) claim the highest solar conversion efficiency yet demonstrated (2) for any solar cell. LPE is not well suited to large area growth of thin films on cheap foreign substrates, however, but single crystal cells with similar characteristics have also been prepared recently by halide transport vapor phase epitaxy (3). Preliminary work on an N-AlAs/p-GaAs/graphite thin film cell showed promise of high intrinsic efficiency and good minority carrier and junction properties (4). That work also disclosed an unanticipated difficulty with poor majority carrier transport, giving rise to unacceptably high spreading resistance in the N-AlAs upper layer. In this paper we present further results of our investigation of these N-AlAs/p-GaAs grown heterojunction cells. We have now also prepared grown-junction and diffused-junction P-AlAs/n-GaAs/graphite material for comparison; this material in present form has inferior characteristics to the N-on-p material, however.

We have attempted various doping schemes in an effort to ameliorate the top layer spreading resistance, which we have concluded arises from scattering of majority carriers in (or from) the depletion regions associated with grain boundary states. This resistance is thus thought to be similar to the blocking resistance at a metal-semiconductor contact. We have found that indeed appropriate doping by Zn diffusion does eliminate the grain boundary scattering in P-AlAs, but the conditions are such that the minority carrier properties (lifetime and p-n junction characteristics) are drastically compromised. We have not been able to obtain similar results in N-AlAs. The grain boundary scattering appears to be a fundamental problem which will be independent of growth process. It is certainly possible, however, that other growth techniques, operative at lower temperatures than the ~ 1000°C used in this work for the growth of the AlAs layer, may permit introduction of donor elements with better control, or eliminate the need for postgrowth diffusion with Zn.

Growth Technique

The growth apparatus was essentially unchanged from that described previously (4), and is comprised of Al_2O_3 ceramic components in a four-zone furnace.

* Electrochemical Society Active Member.
Key words: films, growth, photovoltaic, solar.

Substrates cut from Type 5890 PT graphite obtained from the Carbone Corporation, Boonton, New Jersey, were used exclusively, as our past experience had shown that polycrystal GaAs films on this material were tightly adherent in contrast to films on graphite from other suppliers which flaked off during or after growth. The typical structure for test cells is shown in Fig. 1. The critical features are the GaAs-graphite interface, No. 1, the junction, either at the heterointerface, No. 2, or somewhat within the GaAs, and the AlAs-top contact interface, No. 3. Control of the initial stage of GaAs growth ideally should result in low resistance ohmic conductivity across the GaAs-graphite interface and ensure uniform, pinhole-free coverage by the time the desired thickness, of the order of 5μm, is reached. The AlAs layer grows epitaxially (and preferentially) on the polycrystalline GaAs, reflecting and extending the morphology of the first layer. It is similar in all respects to growth on single crystal substrates as described in Ref. (2) and identical AlAs growth conditions were found to be optimum in this work. Heavy doping of the top surface at the last stage of (or after) growth is required to achieve an ohmic, low resistance contact to a transparent conducting oxide layer as shown in Fig. 1. This layer is not necessary if the AlAs can be made to have low lateral resistivity (~ 100 Ω/□) which permits a metallic grid contact to be used directly as for single crystal cells. This may be achieved by Zn diffusion following growth for P-AlAs, but we were unable to obtain sufficiently heavy donor concentration with Sn, Se, or S during or after growth to achieve ohmic contact of N-AlAs to transparent, conductive films of indium-doped tin oxide (ITO) (5) or Cd_2SnO_4 (6) films.

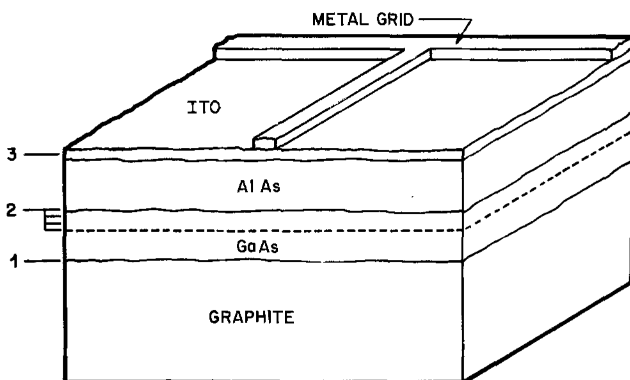

Fig. 1. Polycrystal cell structure. The p-n junction is located at interface No. 2 for N-AlAs/p-GaAs cells or just within the GaAs layer for diffused P^+AlAs/p-nGaAs structures. The AlAs layer is typically 10-20 μm thick, the GaAs layer 5-10 μm thick, the graphite substrate 350 μm thick.

Our initial observations confirmed that growth of undoped GaAs on the clean graphite substrate was nonpreferential relative to the Al_2O_3 ceramic walls of the growth reactor. We also observed that the density of nucleation and indeed whether any growth at all was obtained was relatively insensitive to substrate temperature, temperature gradient at the substrate, or gas flow parameters but was affected by geometrical relationships and the immediate past history of the reactor components. Reproducibility was obtained when the polycrystalline GaAs deposit over the reactor tube walls had reached a steady condition. Only periodic cleaning of a purely mechanical nature (scraping and vacuuming) was employed. These conditions leave much to be desired for carrying out precise doping studies or obtaining high purity material, but they are adequate for the qualitative investigations of the fairly heavily doped material reported here.

An early finding was that Zn doping drastically affected the nucleation of the GaAs layer to produce a continuous film rather than a panoply of nuggets. This difference is readily apparent in Fig. 2 which shows scanning-electron micrographs of undoped and Zn-doped polycrystalline GaAs grown under identical conditions (except for the temperature of the Zn metal source). Slight modification of the substrate position resulted in pinhole-free films over all of the 1 × 3 cm substrate except immediately contiguous to the Al_2O_3 substrate holder arms. Continuous films of this sort were only achieved at much greater total thickness for undoped GaAs growth on bare graphite. The level of

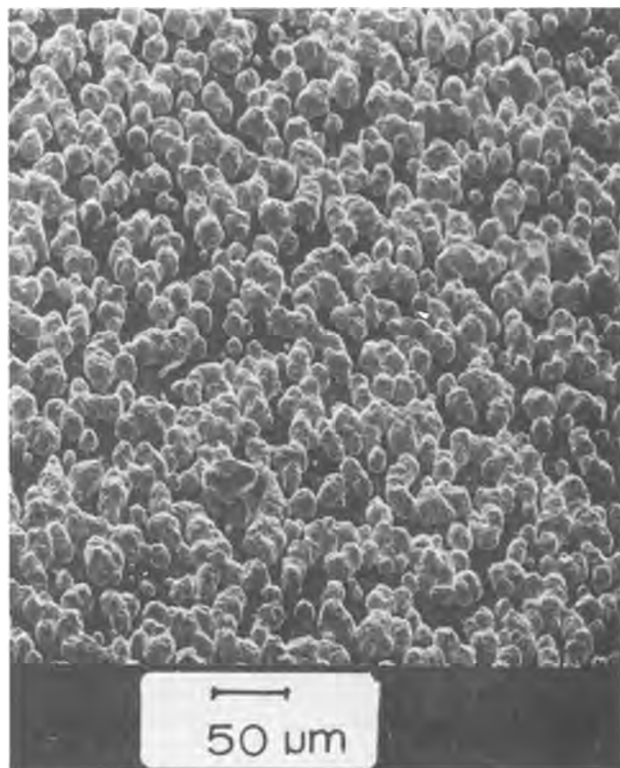

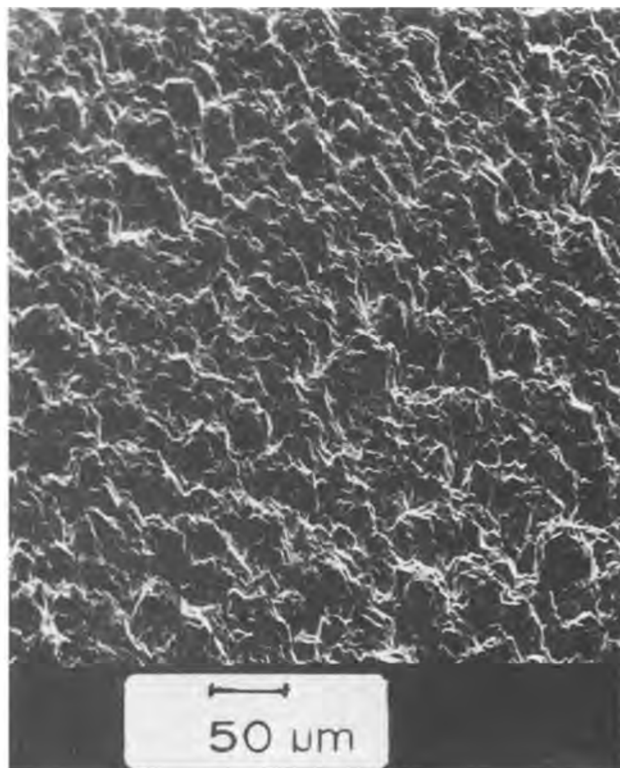

Fig. 2. SEM views of undoped (left) and Zn-doped (p ~ 10^{18} cm^3) GaAs grown on graphite under otherwise identical growth conditions

Zn doping necessary for this improved nucleation is consistent with that needed for good heterojunction performance ($p \sim 10^{18}cm^3$). An additional important, albeit fortuitous, result is that the p-GaAs layer so formed makes low resistance ohmic contact to the graphite.

Characterization of these polycrystalline semiconductor layers on conducting substrates is difficult. Photoluminescence spectra suggest a net ionized acceptor density in the $1 \sim 5 \times 10^{18}$ range, while capacitance voltage plots and reverse breakdown characteristics of heterodiodes formed with undoped AlAs favor the lower end of this range. Higher Zn concentration can be readily obtained, up to $2 \times 10^{19}cm^{-3}$ or greater, with increased Zn source temperature.

For an N-AlAs/p-GaAs heterodiode, the AlAs layer is grown without intentional dopant addition. Metallic contact to this layer is readily made with spark-welded Au-Sn(2%) alloy or sintered layers of Sn, Ni, and Au which may be evaporated or electrodeposited. Anodization (7) of the polycrystalline layer is not satisfactory for passivation and antireflective purposes. The high spreading resistance and rough surface also make it more difficult to obtain uniform electroplated contacts than on single crystal AlAs, and in contrast to results on that material (8), evaporated contacts are to be preferred for thin polycrystal layers.

We tried doping the AlAs layer with Se (introduced as H_2Se) and/or Sn (introduced as the metal and transported with HCl). Hall measurements on single crystal AlAs samples showed no increase in ionized donor concentration. We verified transport of Sn by weight loss measurements, but it was evidently not incorporated at the 1030°C growth temperature even at Sn/Al ratios of unity where the AlAs growth began to deteriorate. There was no observable effect for Se up to gas-phase Se/As ratios of 0.1. Postgrowth diffusion with As_2S_3 and elemental sulfur sources and from thin (≤ 50Å) layers of Sn, Sn-Ni, Sn-Au, and Sn-Ni-Au were evaluated in an effort to increase the surface doping to allow ohmic contact of the N-AlAs to ITO or Cd_2SnO_4 films. The latter were deposited in an rf plasma apparatus with various argon/oxygen ratios and sample temperatures. Of the various combinations, only evaporation of Sn, Ni, and Au in successive layers exceeding 50, 50, and 200Å, respectively, sintered at 450°C, produced the desired result. This contact is relatively opaque owing to the substantial amount of Au. Because of surface roughness, not all grains are effectively contacted with these small quantities of the metals. Whether ITO or Cd_2SnO_4 was used made no difference, although Cd_2SnO_4 could be deposited to form an ohmic contact on n-GaAs (Si-doped, $n \sim 2 \times 10^{18}cm^3$) to which ITO was always blocking.

In view of these difficulties with the N-AlAs top layer we attempted to prepare P-AlAs/n-GaAs structures since a shallow Zn diffusion (20 min at 550°C with a Zn_3As_2 or $ZnAs_2$ source) produces a high surface concentration of ionized acceptors and ohmic contact between P-AlAs and metallic conductors. Single crystal AlAs can be grown p-type, albeit heavy Zn concentration in the growth atmosphere must be used and growth conditions favoring minimum native donor concentration must be chosen (9). This material is heavily compensated ($n_a - n_d \sim 1 \times 10^{17}$, $n_a \sim n_d \sim 10^{18}$) but resistivity ($\sim 10$ Ω-cm) is not excessive for current flow transverse to the thin layer. Accordingly, work to control the nucleation and growth of n-type GaAs films on graphite was begun. Undoped "films" as in Fig. 2a become continuous when grown sufficiently thick (~ 100-200 μm) but they make blocking contact to the graphite and are, of course, far thicker than desired for inexpensive solar cells. Doping with H_2Se added to the gas stream or HCl-transported Sn, in contrast to the results with Zn, had no effect in improving the nucleation of film growth. Coating the substrates with electroplated Au and Sn-Ni alloy gave rise to dramatic VLS (vapor-liquid-solid) growth of Au-capped needles.

We also tried a series of substrates onto which 500Å layers of Si, Sn, or Ge had been evaporated. (This thickness is nominal and corresponds to thickness on monitor microscope slides—the actual surface area of the graphite greatly exceeds the projected area.) Electron micrographs of these samples are shown in Fig. 3 and 4. Since the evaporated films were thought to be amorphous and the Sn film is "liquid" at the 640°C GaAs growth temperature, it was not anticipated which films if any would favorably affect nucleation, and the initial intent was to ensure ohmic contact. All show improvement relative to nucleation on untreated graphite; Ge is the best, possibly reflecting the fact that the lattice constant of crystalline Ge is an excellent match for GaAs. The Sn-coated substrate shows nearly equivalent results, however, under conditions which certainly do not permit definition of a lattice constant whether the Sn film is truly liquid or not. Use of either Sn or Ge resulted in ohmic contact to the GaAs layers. No additional dopants were added to these layers; they are estimated to have background carrier concentrations $n \sim 5 \times 10^{17}cm^3$ from photoluminescence spectra.

Two techniques were employed to form heterodiodes to these n-GaAs films. AlAs was grown with up to 1% Zn vapor added to the gas phase, or undoped for subsequent deep Zn diffusion. Neither of these approaches was found satisfactory in regard to reproducibility, but the best diodes obtained, although inferior to the N-AlAs/p-GaAs devices, were in each case good enough to permit limited electrical characterization as described in the next section.

The growth conditions for the various combinations of AlAs and GaAs polycrystal layers we found to be optimum, in the sense primarily of best providing reproducible, pinhole-free layers, are summarized in Table I.

Electrical Characteristics

Rigorous characterization of this polycrystalline material is not possible by traditional methods, such as measurement of Hall conductivity, because of the highly conducting substrate and high spreading resistance of the layers. The heterojunction material may be represented conceptually as in Fig. 5, where diodes with characteristics similar to single crystal cells are connected in parallel between a conducting plane and the nodes of a resistance grid. The diode characteristics can be obtained with a broad area metallic top contact which shunts the spreading-resistance grid, and the spreading resistance in the top layer can be obtained between two stripe contacts provided the diode characteristics give adequate isolation from the conductive substrate. Physically this model corresponds to considering each grain as a heterojunction cell. Scanning electron micrographs of broken cross sections of this material suggest that this

Table I

Growth of	p-GaAs*	N-AlAs	n-GaAs**	P-AlAs
Substrate temperature (°C)	640	1030	640	1005
Subs. temp. gradient (°C/cm)	20	2	20	2
Source temperatures (°C)				
Ga	800	800	800	800
Al	1150	1150	1150	1150
Zn	325	<325	27	650
Flow rates (cm^3/min)				
A_sH_3	4	5	4	5
HCl over Ga	4	—	4	—
H_2 over Ga	200	10	200	10
HCl over Al	—	4	—	4
H_2 over Al	10	550	10	550
H_2 over Zn	50	5	10	220
H_2 carrier	200	720	200	720
Growth time (min)	60	30	60	~30
Film thickness (μm)	~10	~15	~10	~15

* On uncoated graphite substrate.
** On graphite coated with evaporated Sn or Ge film, $\sim 10^{-5}$ g cm^{-2} of nominal substrate area.

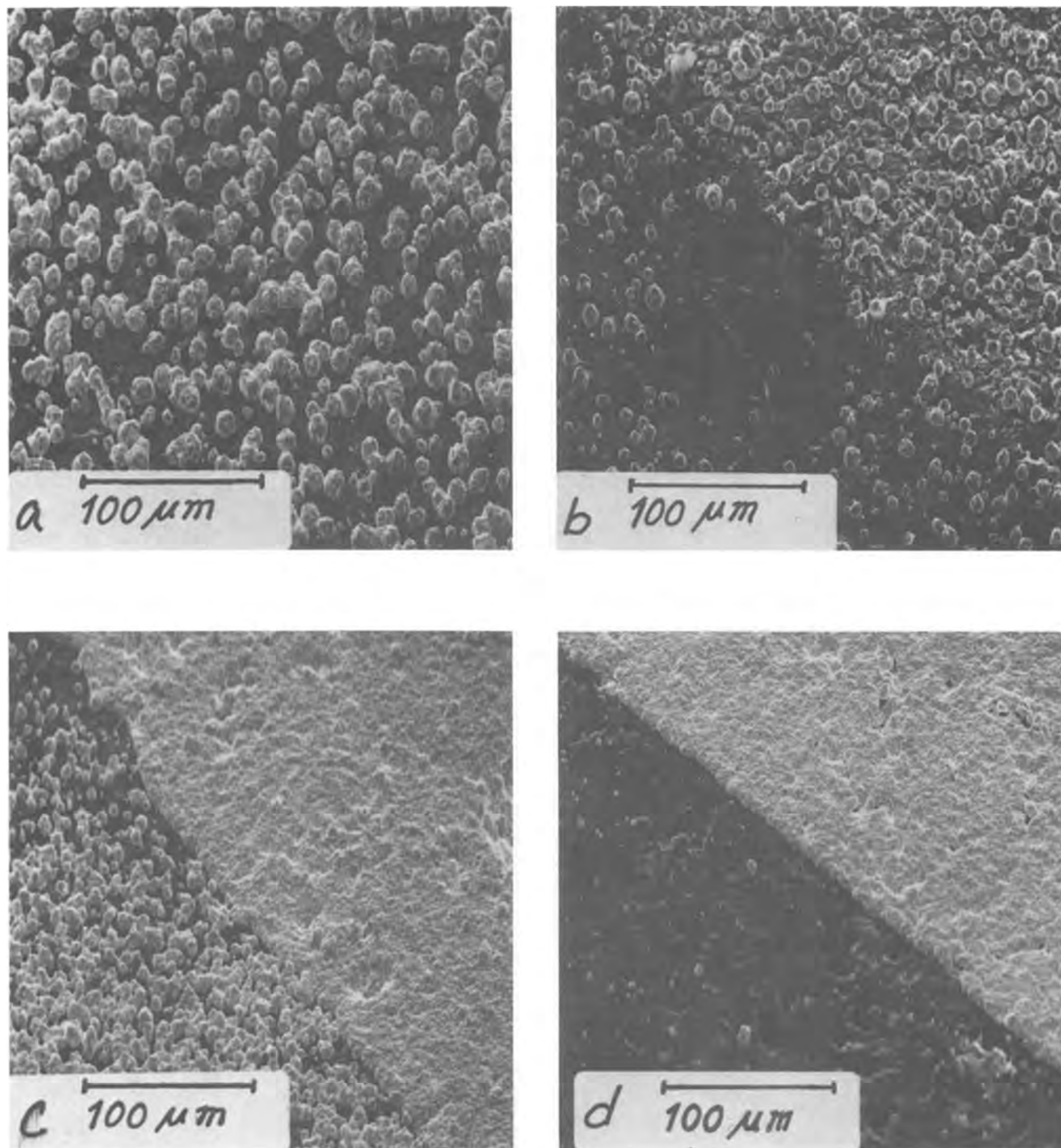

Fig. 3. SEM views of undoped GaAs grown on substrates partially coated (upper right portion of each view) with: a, nothing; b, 500Å Si; c, 500Å Ge; d, 500Å Sn. Growth conditions and times nominally identical.

is indeed a good picture—most grains appear to be columnar and continuous across the AlAs-GaAs interface.

In Fig. 6 typical log current-voltage data are presented for N-AlAs/p-GaAs and Zn-diffused P-AlAs/p-n GaAs samples. Electron beam-induced current (EBIC) examination in the scanning electron microscope indicated that for the N/p material the electrical junction coincided with the heterointerface, at least to within the estimated ±400Å resolution accuracy. For the P/n sample in Fig. 5, the junction appeared in EBIC traces to lie within 1000Å inside the GaAs. The diffusion coefficient for Zn in single crystal AlAs was determined to be 80 times larger than in single crystal GaAs under the conditions used here, so that there is a tendency for the AlAs layer to be completely diffused in spite of the irregularity of its surface and thickness, while the junction remains fairly close to the AlAs interface throughout the GaAs.

From the model of Fig. 5, we expect the dark current density-voltage relation for these diodes to be of the form

$$J = J_o\,[\exp\{e(V - JR_s)/nkT\}\ 1] + (V - JR_s)/R_p \qquad [1]$$

Here J_o is the reverse saturation current and n the "diode factor," R_s and R_p are the effective series and diode shunt specific resistances. Provided R_p exceeds a few hundred Ω-cm^2 and R_s is less than about 10 Ω-cm^2, the intermediate region of the plot of log J *vs.* V is linear. The slope in this region determines

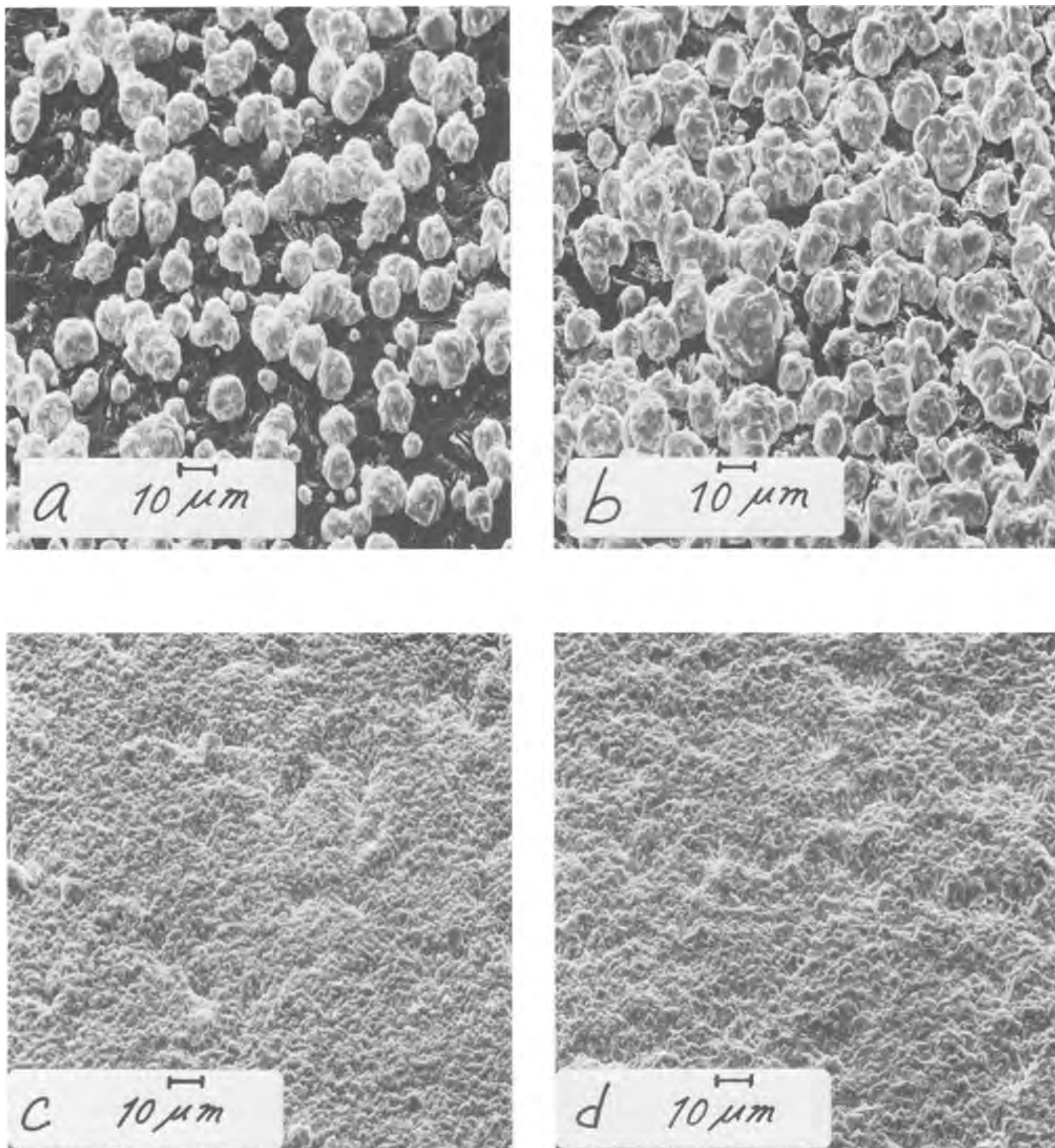

Fig. 4. SEM views at higher magnification of undoped GaAs grown on: a, uncoated graphite; b, Si (500Å); c, Ge (500Å); and d, Sn (500Å).

the diode factor n, which was generally between 1.9 and 2.0. R_s and R_p may be determined from the voltage and current offsets of the actual plot from the extrapolated linear portion, respectively. When the log J-V plot does not show a substantial linear region, as for the P/p-n diffused junction diode in Fig. 6, Eq. [1] may still be used by curve fitting, although as a practical matter such material is of little interest for solar cell application.

We attempted to produce P-AlAs/n-GaAs polycrystalline grown junctions using the conditions in Table I, with only a shallow Zn surface diffusion used for contacting. EBIC examination showed that the electrical junction was variably located within the AlAs layer; apparently some grains were grown p-type and others were not. This material showed good current-voltage characteristics with values of $R_p > 10^5$ Ω-cm^2 and $R_s < 5$ Ω-cm^2, but very low photocurrent response. Apparently either the native background donor concentration or the Zn incorporation varies from grain to grain. The larger (and presumably faster growing) grains remain n-type. There were no indications from EBIC scans of Zn incorporation preferentially along grain boundaries during growth. The relatively good diode characteristics permitted a lower-limit measurement of the spreading resistance which for this material exceeded 10^5 Ω/□.

The linear current-voltage characteristics of diffused P-AlAs/p-n GaAs and grown N-AlAs/p-GaAs polycrystal material are presented in Fig. 7. The detrimental effect on the potential fill factor arising from the shunt resistance in the diffused material is ap-

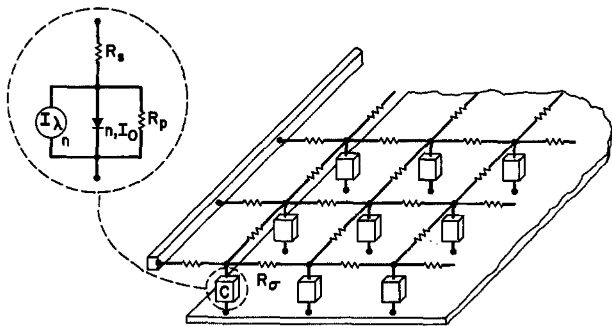

Fig. 5. Electrical equivalent circuit model of polycrystal heterojunction solar cell consisting of subunits (C) joined in parallel by a spreading resistance grid R_σ. The units (C) consist of the parallel combination of a current generator of quantum efficiency η, an idealized diode characterized by diode factor n and reverse dark current I_0, and shunt resistance R_p all in series with resistance R_s.

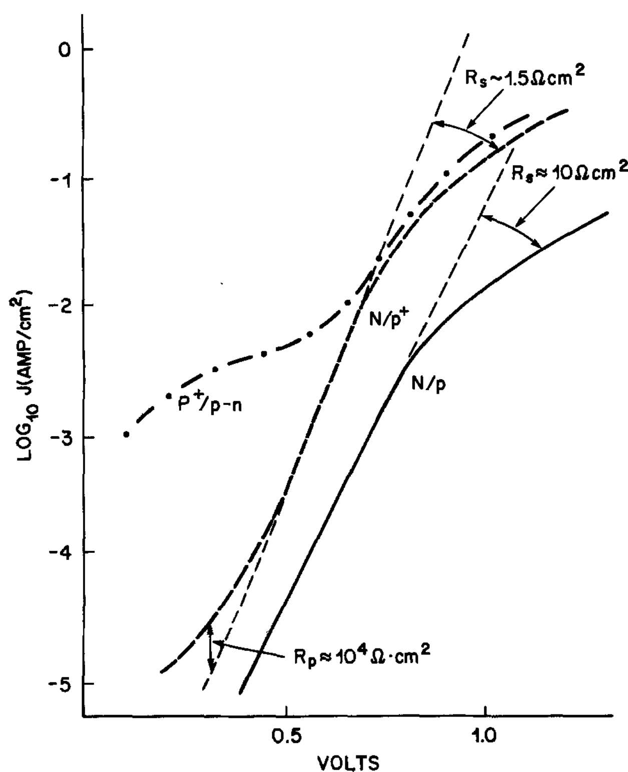

Fig. 6. Logarithmic current density-voltage characteristics for diffused P^+AlAs/p-nGaAs (dash-dot), and two grown N-AlAs/p-GaAs cells (dashed, $p^+ \sim 5 \times 10^{18}$; solid, $p \sim 10^{18}$). The two cells with lower R_s had evaporated top contacts, the other an electroplated metallization.

parent. This shunt resistance also makes analysis of the junction by capacitance-voltage measurement difficult and prevents determination of the top layer spreading resistance. The semiconductor layers can be removed as flakes of ~ 1mm² by arcing the substrate (which, in 300 μm thickness, is fairly flexible) and scribing along the GaAs-graphite interface with a scalpel tip. The resistance of these flakes (contacted on the AlAs layer) was typically 3000 Ω/□, at least three orders of magnitude lower than undiffused polycrystalline material. We were unable to separate the AlAs from the GaAs on these thin flakes, but it is reasonable to assume this reduction in resistance occurred in the diffused AlAs layer.

The diffused P-AlAs/p-n GaAs material shows poor photocurrent efficiency. The photocurrent spectrum shows a weak long wavelength response tail, and the response is low throughout the visible range. Power conversion efficiencies for natural sunlight were less

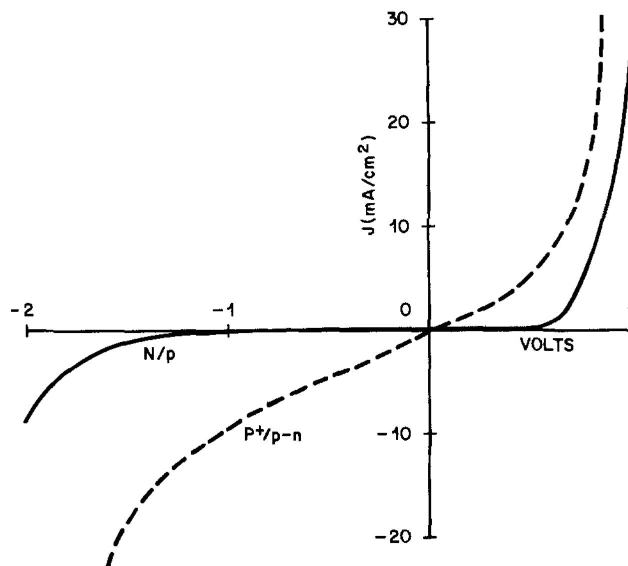

Fig. 7. Linear current density-voltage characteristics for N-AlAs/p-GaAs (solid) and P^+AlAs/p-n GaAs-diffused junction (dashed) cells.

than 1%. The photoluminescent spectra before and after diffusion showed the peak shift to longer wavelengths and broadening typical of Zn-diffused GaAs (10) with a weak tail extending below 1 μm. The precise reason for the very poor photoefficiency is not known at this time; perhaps the Zn diffuses preferentially along the grain boundaries and/or decorates them to form recombination centers. This would account qualitatively for the appearance of lower shunt resistance following diffusion as well. It is also true that the grain size is smaller in the n-GaAs films grown on Sn- or Ge-coated substrate (2-3 μm as compared to 3-5 μm for the Zn-doped p-GaAs). This should not, however, restrict the minority carrier diffusion length to excessively small values.

Discussion and Conclusions

The primary motivation for this work was to assess the possibility of fabricating thin-film, potentially cheap analogs of the high performance single crystal AlAs-GaAs heterojunction solar cells. In this context the best candidate still appears to be the combination of undoped AlAs on Zn-doped GaAs, resulting in a grown-junction, N on p structure. The Zn doping and nucleation of the GaAs layer can be reasonably well controlled, and good diode characteristics and high internal quantum efficiency result (4). Elimination of the high lateral resistance in the AlAs top layer requires that the doping level be raised at the top surface to provide an N^+ layer with a mobile carrier concentration in the high 10^{19} cm³ range, either to provide ohmic contact to a transparent conductive top window or to provide low resistance contact between AlAs grains. Our attempts to achieve this with Se or Sn during growth or with S diffusion after growth have not met with success.

The alternative p on n structure appears relatively unpromising in comparison. Zn doping during growth does not produce uniform P-type doping of the polycrystalline AlAs; some grains remain N-type. Postgrowth Zn diffusion does result in a sufficiently high surface doping that ohmic contact to pressed metals, silver paint, or transparent conductive oxides may be readily accomplished, and the contact between grains seems also to be rendered satisfactory. However, the diode characteristics are deteriorated by an increase in reverse saturation current and the appearance of significant, indeed dominant, ohmic shunt conductance. Changes in the photoluminescent spectra lead us to suspect that postgrowth Zn diffusion results in Zn aggregation along grain boundaries and that this is

the cause of the poor electrical behavior. The photocurrent response of these structures is also poor. This is not due to opacity of the Zn-diffused AlAs layer since the integrated photoluminescent efficiency of the GaAs layer does not change appreciably following diffusion. Evidently, recombination centers result from the Zn diffusion, either in the bulk of the grains or, more probably in our view, at the grain boundaries.

Several other findings are of interest. The observation that Zn-doped polycrystalline GaAs makes low resistance ohmic contact to graphite and that nucleation of a continuous film is facilitated by Zn doping, both at reasonable levels resulting in $p \sim 10^{18}cm^3$, was not anticipated. Advantage of this has been taken to obtain ohmic contact between graphite and thin films of other p-type semiconductors, notably InP, which form ohmic contact to p-GaAs but which cannot be made ohmic to graphite directly. Similarly the use of thin layers of Ge or Sn to obtain simultaneous ohmic contact and nucleation improvement may be of utility for Schottky barrier cell fabrication. It is not clear whether the nucleation improvement with Ge is due to the close lattice match to GaAs, but Sn at least should be useful for growth of other n-type III-V compounds or graphite.

Finally, we feel that there are limitations to the chloride transport growth system used in this work from the point of view of practicality for cheap, large-area fabrication, which are much more significant than for the earlier single crystal cell work. The growth of the GaAs film is slow, and relatively inefficient use of the reactants is made. The high temperature of the AlAs growth certainly contributes to the difficulty of obtaining high surface doping during growth and necessitates postgrowth diffusion. Lower temperatures can be used for growth of the AlAs layer by metal-organic pyrolysis, for instance (11), and for that reason such other growth techniques would appear more interesting for future work.

The stability of the semiconductor material is also a matter of concern if large-area terrestrial application is considered. The only cells which we have observed to undergo apparent deterioration over 6-12 months in a low humidity environment are those that were overcoated with ITO. Several of these showed separation of the ITO-semiconductor layer from the graphite, suggesting the graphite/GaAs interface is the weak point under strain. It does not seem that AlAs would require more stringent measures for encapsulation than other thin film semiconductor materials. The erosion products will be toxic, but that is true as well for all other materials being considered in the role of terrestrial photovoltaics save Si.

In conclusion, it appears that formidable difficulties, albeit not those initially anticipated, lie in the way of demonstration of a cheap thin film analog of the high performance AlAs/GaAs heterojunction cell, at least insofar as chloride transport growth is concerned.

Acknowledgment

It is a pleasure to thank Dr. L. A. Coldren for the deposition of high quality films of ITO and Cd_2SnO_4 on a number of polycrystalline and single crystal samples.

Manuscript submitted Oct. 28, 1977; revised manuscript received Dec. 28, 1977. This was Paper 247 presented at the Atlanta, Georgia, Meeting of the Society, Oct. 10-14, 1977.

Any discussion of this paper will appear in a Discussion Section to be published in the December 1978 JOURNAL. All discussions for the December 1978 Discussion Section should be submitted by Aug. 1, 1978.

Publication costs of this article were assisted by Bell Laboratories.

REFERENCES

1. P. Vohl, D. M. Perkins, S. G. Ellis, R. R. Addis, W. Hui, and G. Noel, *IEEE Trans.*, **ed-14**, 26 (1967).
2. L. W. James and R. L. Moon, in "Proceedings of the 11th IEEE Photovoltaic Specialist Conference," pp. 402-408, IEEE, New York (1975); J. M. Woodall and H. J. Hovel, *Appl. Phys. Lett.*, **30**, 492 (1977).
3. W. D. Johnston, Jr. and W. M. Callahan, *This Journal*, **123**, 1524 (1976).
4. W. D. Johnston, Jr. and W. M. Callahan, in "Proceedings of the 12th IEEE Photovoltaic Specialists Conference," pp. 934-938, IEEE, New York (1977).
5. D. B. Fraser, *Proc. IEEE*, **61**, 1013 (1973).
6. G. Haacke, *Appl. Phys. Lett.*, **28**, 622 (1976).
7. W. D. Johnston, Jr., *This Journal*, **123**, 442 (1976).
8. W. D. Johnston, Jr., *IEEE Trans.*, **ed-24**, 135 (1977).
9. W. D. Johnston, Jr., *J. Cryst. Growth*, **39**, 117 (1977).
10. H. C. Casey, Jr. and Frank Stern, *J. Appl. Phys.*, **47**, 631 (1976).
11. H. M. Manasevit, *This Journal*, **118**, 647 (1971). See also R. D. Dupuis, P. D. Dapkus, R. D. Yingling, and L. A. Moudy, *Appl. Phys. Lett.*, **31**, 201 (1977).

Technical Notes

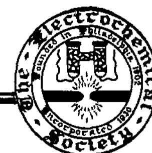

TiO_2 Antireflection Coatings by a Low Temperature Spray Process

H. J. Hovel

IBM Thomas J. Watson Research Center, Yorktown Heights, New York 10598

Antireflection coatings are an important aspect of solar cells and other optical devices. High efficiency Si and GaAs solar cells require coatings with absorption edges well below 4000Å and with refractive indexes of around 2. Films of TiO_2, Ta_2O_5, and Sb_2O_3 are among the best candidates to meet these requirements. TiO_2 is a particularly attractive material because it can be sprayed onto a sample in air (1-3), eliminating costly and time-consuming evaporation steps.

In the simplest spraying method, a nonoxidizing carrier gas such as N_2 or He is passed through a flask

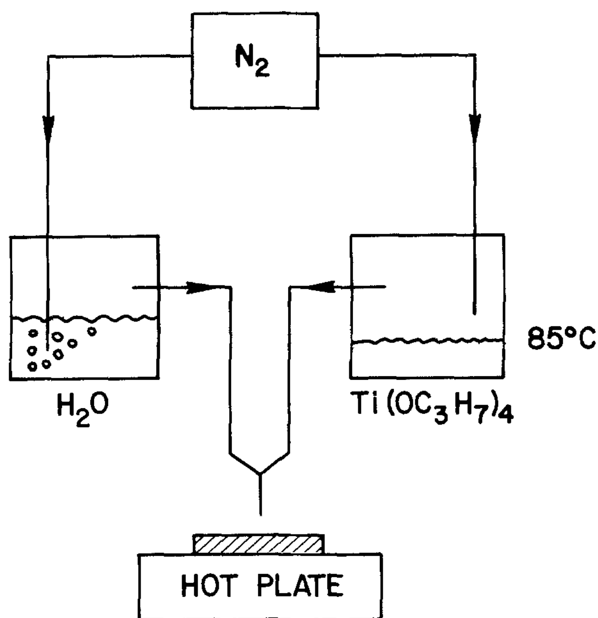

Fig. 1. TiO_2 film deposition system

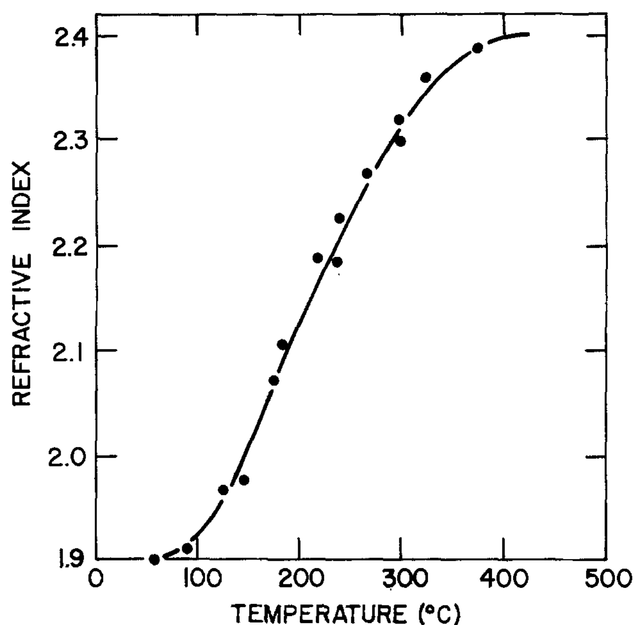

Fig. 2. Refractive index at 6328Å as a function of deposition temperature.

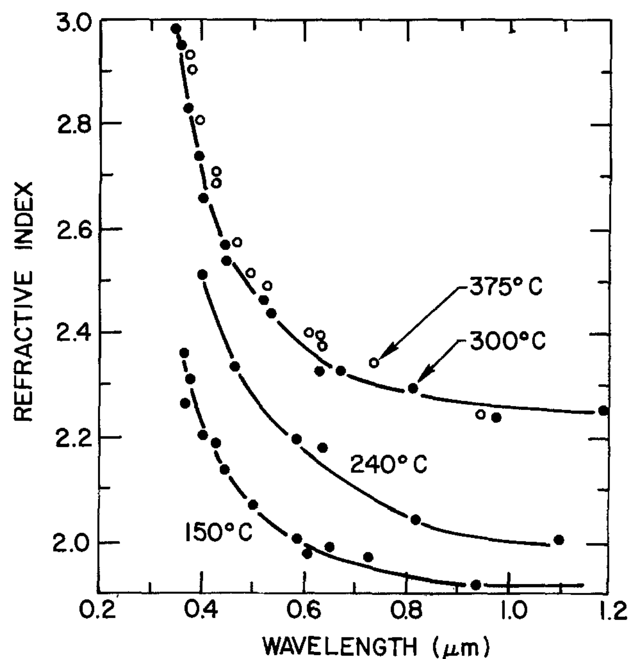

Fig. 3. Refractive index vs. wavelength for several deposition temperatures.

containing the liquid tetraisopropyl titanate (TPT) held at 80°-90°C (Fig. 1). A second stream of carrier gas is bubbled through a flask containing water at room temperature. The two gas streams are brought together at the output of a nozzle which is held from 1 to 2 cm away from the sample surface. The sample rests on a hot plate adjusted to the desired deposition temperature. Uniform coatings can be obtained by moving the nozzle (or sample) in a circular or figure-eight pattern. The deposition rate can be controlled within the range of 1-10Å/sec using different carrier gas flow rates. A certain amount of "trial-and-error" experimentation is required to find the optimum flow rates, TPT temperature, and nozzle-to-substrate distances which lead to TiO_2 coatings free from alcohols or solid TiO_2 particles (1). In the work reported here, flow rates of 500 cm^3/min (2-5Å/sec deposition), a TPT temperature of 85°C, and a distance of 1 cm were used.

The optical properties of the TiO_2 films depend very little on the deposition rate but depend strongly on the deposition temperature. In order to determine the temperature accurately, the 1 in. diam Si or Al_2O_3 substrates were backed with a liquid Ga/In/Sn mixture and placed upon a thick copper block sitting on the hot plate. A thermocouple was imbedded in the copper block, and the sample temperature was assumed to be the temperature indicated by the thermocouple.

The refractive index as a function of deposition temperature of TiO_2 films deposited on Si wafers is shown in Fig. 2. These measurements were made by ellipsometry using a He-Ne laser (6328Å). The index is around 1.9 for temperatures below 100°C, increases linearly between 120° and 340°C, and saturates at about 2.4 for temperatures above 400°C. The dispersion in the refractive index with wavelength is shown in Fig. 3 for films deposited at several different temperatures. (These data points were obtained from the reflectivity maxima and minima positions as a function of wavelength.) For any deposition temperature, the refractive index increases strongly at short wavelengths. Similar results have been reported by Hass (4) for oxidized evaporated titanium films and by Krylova *et al.* (5) for films deposited from $Ti(OC_2H_5)_4$ solution.

The optical absorption as a function of wavelength was obtained from the transmittance of TiO_2 films on Al_2O_3 substrates using a Beckman DK2 spectrometer. The absorption was least for films deposited at the lowest temperatures, as shown in Fig. 4. The absorption edge shifts to longer wavelengths with increasing deposition temperatures up to 200°C, reverts to a shorter wavelength between 200° and 240°C, and then continues its shift to longer wavelengths once more. Transmission electron micrographs of TiO_2 films deposited at various temperatures on GaAs indicate that there is a transformation in the films from an amorphous phase to a polycrystalline phase at a temperature between 200° and 300°C. This agrees well with published reports of a transition from the amorphous phase to the anastase form when films deposited below 200°C are annealed at 300°C or above (1, 4).

The effect of annealing on the refractive index of the TiO_2 films was also studied. Films deposited at 100°-150°C and then annealed at 300°-400°C for 1 hr experience an increase in refractive index of about 10% and a decrease in thickness by the same amount, leaving the optical thickness unchanged. Ad-

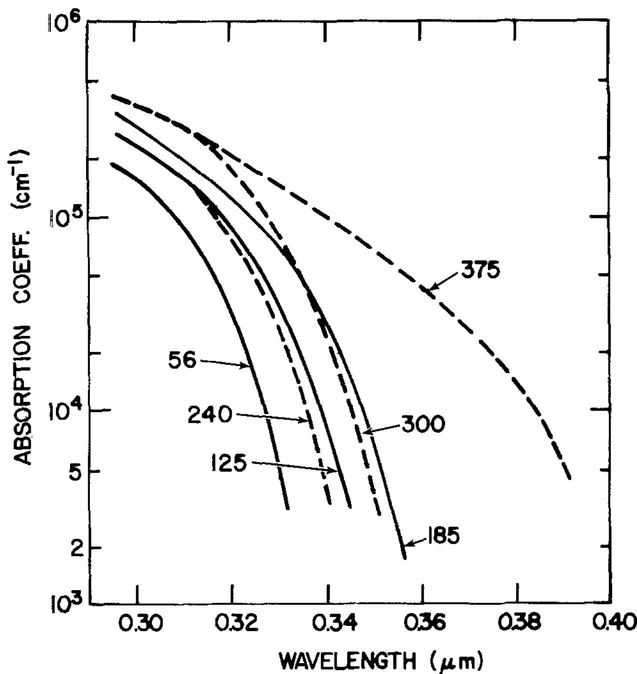

Fig. 4. Absorption coefficient vs. wavelength for several deposition temperatures.

ditional annealing for up to 6 hr brings no further changes.

The specular reflection as a function of wavelength of TiO_2 coated Si wafers is shown in Fig. 5. An index of 2 (150°C deposition) leads to a nearly ideal reflectance curve with less than 0.1% reflectance at the minimum. The results are identical for TiO_2-coated GaAs wafers.

Acknowledgments

I am indebted to G. Woolhouse, R. McGibbon, and R. Rutz for the transmission electron micrograph information.

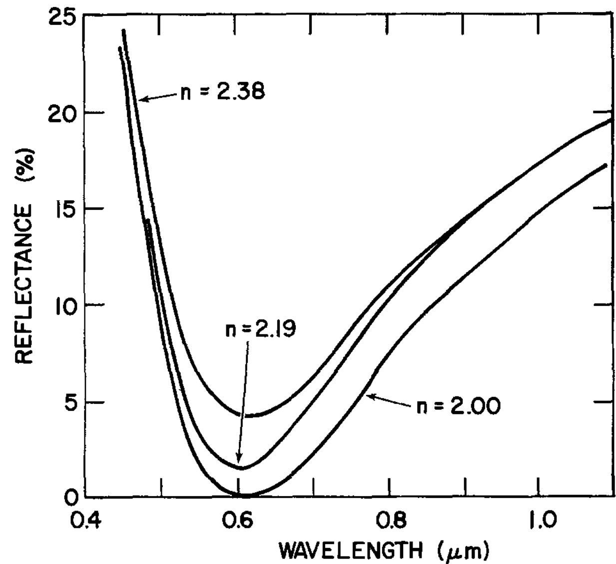

Fig. 5. Specular reflectance of TiO_2-coated silicon wafers

Manuscript submitted Dec. 8, 1978; revised manuscript received Feb. 8, 1978.

Any discussion of this paper will appear in a Discussion Section to be published in the December 1978 JOURNAL. All discussions for the December 1978 Discussion Section should be submitted by Aug. 1, 1978.

Publication costs of this article were assisted by IBM Corporation.

REFERENCES

1. E. T. Fitzgibbons, K. J. Sladek, and W. H. Hartwig, *This Journal*, **119**, 735 (1972).
2. K. L. Hardee and A. J. Bard, *ibid.*, **122**, 739 (1975).
3. M. Yokozawa, H. Iwasa, and I. Teramoto, *Jpn. J. Appl. Phys.*, **7**, 96 (1968).
4. G. Hass, *Vacuum*, **11**, 331 (1952).
5. T. N. Krylova and G. O. Bagdyk'yants, *Opt. Spectry* (USSR) (Eng. Transl.), **9**, 339 (1960).

The Effects of HCl Residual Treatment on MNOS Memory Transistors

R. M. McLouski* and M. C. Peckerar*

Westinghouse Electric Corporation, Advanced Technology Laboratories, Baltimore, Maryland 21203

and J. J. Schreurs

Westinghouse Electric Corporation, Research and Development Center, Pittsburgh, Pennsylvania 15235

HCl residual treatment improves the pulse and d-c responses of metal-nitride-oxide-semiconductor (MNOS) transistors prior to cycling (1). This treatment consists of exposing the native silicon surface to a gas mixture of HCl and N_2 at 750°C before subsequent processing of the MNOS structure. It has recently been shown that this treatment may not provide devices with long-term endurance and retention properties (2). However, studying the mechanism of time-zero improvement brought about by HCl treatment is valuable. Such study sheds light on the importance of prenitride surface treatment in MNOS performance. It also delineates the effects of processing on the thin-oxide tunnel layer of the transistor.

* Electrochemical Society Active Member.

Key words: HCl residual treatment, MNOS transistors, pulse, d-c responses.

In this paper the methods of preparation for the parts used in this study are described. The effects of different processing steps on the pulse clear, d-c write, and d-c clear levels are shown. Auger, sputtering, and ellipsometric analyses of the tunnel oxide layer are presented.

It is shown that HCl treatment makes the native silicon surface more resistant to nitrogen attack during the nitride deposition process. The nitrogen-incorporated layer does not provide as good a memory response as a layer which is more like silicon dioxide. A mechanism which explains this passivation with respect to nitrogen is proposed.

Fabrication of Samples

Two types of samples were employed for this study. There were MNOS test capacitors and monitor wafers

run along with the MNOS capacitors and withdrawn at various stages in processing for analysis. Fabrication of the structure proceeded as follows. Starting material was (100)-silicon (n-type), 4-8Ω-cm. Wafers were immersed in 48% HF solution (to remove any oxides present) for 2 min. Wafers were rinsed and sent through a series of sulfuric and nitric acid baths (to simulate the acid bath exposure of an MNOS-memory transistor during processing) followed by a 100:1 HF solution dip and rinse. Some surfaces received HCl residual treatment, others were set aside as controls. HCl residual treatment was accomplished by placing the wafers vertically on a quartz boat which was inserted into an open-tube furnace set at 750°C. Wafer surfaces were then exposed to a mixture of nitrogen and HCl gas in the furnace. HCl comprised 2, 5, and 10% of the total flow. Total gas flow was 2 liters/min. The time of HCl exposure was 10 min.

Immediately after HCl treatment wafers and controls were placed in a vertical nitride CVD reactor. A silicon nitride film of 495 ± 25Å was deposited on the wafer by the reaction of ammonia and silane gases on the hot wafer surfaces. Heating was accomplished by means of an rf-heated, silicon carbide-coated graphite susceptor. After nitride deposition, the wafers received an aluminum gate metallization. Aluminum was deposited by an electron-beam source through a shadow mask.

The completed structure can be shown to exhibit flatband voltage shifts after positive or negative biases. The shifts come about as a result of charges stored in the nitride-oxide interface region. For structures of equal nitride thickness, the shift after bias is roughly proportional to the change in charge stored in this region. The operation of these devices has recently been reviewed by Chang (3). *C-V* curves generated for these structures allow us to estimate flatband and threshold voltage shifts.

Electrical Measurements

Electrical measurements were performed on the *C-V* dots in the following fashion. A voltage of −20V was applied to the metal dot with respect to substrate ground for 60 sec, then the bias was removed. 15 sec later a high frequency *C-V* curve (referred to as the d-c write curve) was developed in a bias range from 0 to −20V. Next, the dot was biased at +6.0V. Bias was shifted rapidly negative to a value of −20V. The d-c clear curve was obtained by biasing the dot to +20V for 60 sec and then returning the dot to +6V. 15 sec later the device bias was swept from +6 to −20V and the *C-V* curve was developed over this bias range. Threshold voltages in the d-c written pulse cleared and d-c cleared state were estimated from these curves. [See Ref. (1) for further explanation of this technique.]

In Table I, the pulse and d-c thresholds obtained for the various processes are tabulated. Ten capacitors from each type of process studied were sampled. The mean threshold for the ten thresholds is recorded. As can be seen, HCl residual processing tends to make for more positive d-c clear thresholds. The pulse clear levels are also considerably more positive than those for non-HCl processing. D-c write levels are only slightly more positive. These represent significant improvements in device performance brought about by HCl. D-c hysteresis windows are larger. Pulse characteristics are closer to d-c characteristics.

Table I. Electrical performance of MNOS memory test capacitors processed with and without HCl treatment

Process	D-c write threshold (volts)	D-c clear threshold (volts)	Pulse clear threshold (volts)
Non-HCl treated	−12.5	+1.9	−3.2
2% HCl	−12.0	+3.7	+0.8
5% HCl	−11.0	+5.3	+1.0
10% HCl	−9.5	+4.6	+1.9

There is some improvement (*i.e.*, a more positive threshold shift) in pulse response on going from 2% to 5% HCl treatments. Going from 5% to 10% HCl there is further improvement in pulse response. However, d-c write is affected poorly (it has shifted positively also) with no attendant positive shift in d-c clear. Some pitting of the silicon surface is observed at the 10% level. Thus, the 10% HCl exposure is considered deleterious.

J-V measurements were also made on these capacitors (see Fig. 1). At the 5% HCl level there was no difference in *J-V* characteristics when compared with the non-HCl treated samples. This once again illustrates the often noted fact that conductivity in thin oxide MNOS devices is a nitride bulk limited phenomenon. (4).

An electrical parameter of prime importance in MNOS memory transistor fabrication is retention slope. As stated above, the effect of process in retention slope and endurance was previously reported (2). HCl treatment does not degrade the retention slope prior to

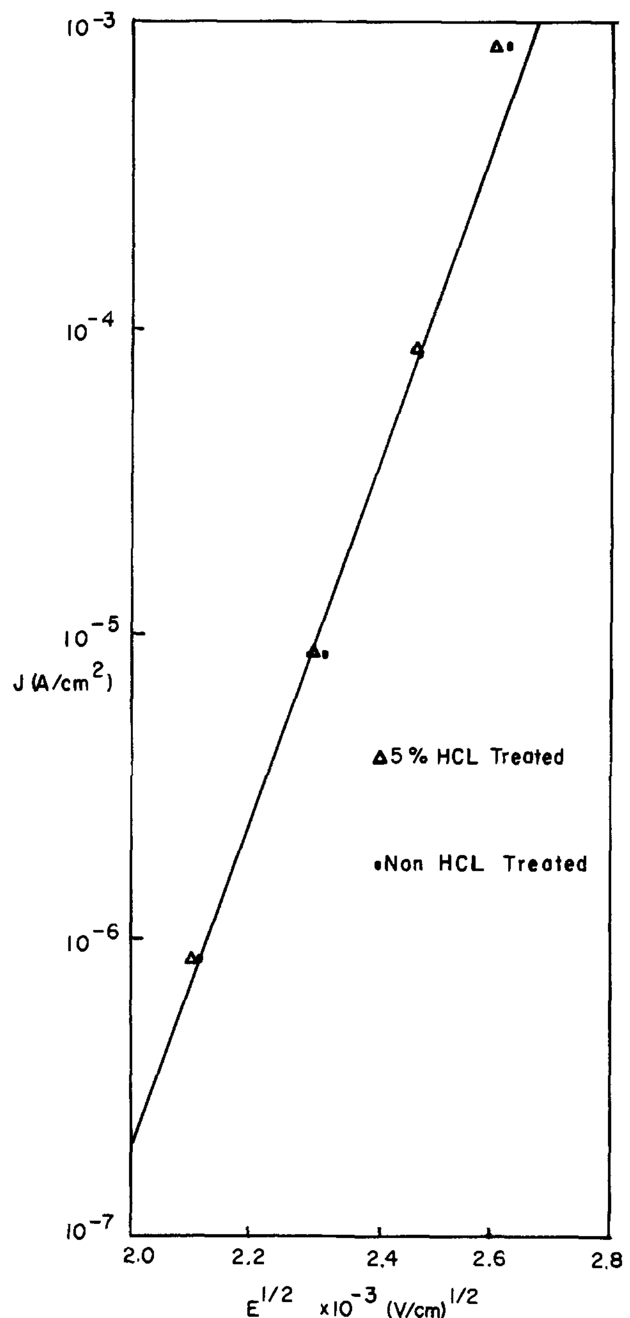

Fig. 1. *J-V* analysis of HCl and non-HCl-treated films. Four data points are included for comparison.

cycling. More recent comparisons of HCl- and non-HCl-treated transistor retention slopes prior to cycling support this claim. Two groups of fifteen transistors each were measured for retention slope prior to cycle stress. The mean retention slope of the write decay of the HCl-treated sample was 0.20 V/decade with a 0.06 V/decade standard deviation. That of the non-HCl treated film was 0.30 V/decade with a 0.16 V/decade standard deviation. Thus there is no statistically valid difference in retention slope between the two groups.

Auger, Sputtering, and Ellipsometric Analyses

Detailed Auger analyses of MNOS structures are reported elsewhere (5, 6). The aim of this research was to delineate changes in the oxide tunneling layer during processing. Wafers were drawn for analysis at the following points in processing (5 groups in all): (*i*) After 100:1 HF dip; (*ii*) after HF dip and sulfuric/nitric acid bath (prenitride clean); (*iii*) after HCl residual treatment at 5% HCl (to simulate actual memory transistor fabrication); (*iv*) after the prenitride depositor (PD) warm-up cycle in the vertical reactor (2 groups, one which had 5% HCl and one which received no HCl).

The PD warm-up cycle is the period the wafers spend in the nitride reactor while the susceptor is stabilized to temperature. This takes 15 min for the case at hand. During the first 14 min, the wafer is exposed to pure N_2 gas at atmospheric pressure. For the last 1 min of the cycle, NH_3 is introduced into the reactor. After the 15 min warm up, SiH_4 would normally be bled in and deposition would commence. For this study, wafers were withdrawn before this would occur.

Table II summarizes the results of Auger analyses performed on the surfaces of the 5 groups. A defocused beam is used to minimize damage produced by the incident electrons. The values of the peak-to-peak heights in the conventional derivative spectrum are given in arbitrary units. No attempt was made to normalize the signal strengths. The mixing of oxidized silicon and silicon-silicon spectra (between 1500 and 1619 eV) can be grouped into three categories according to the relative strengths of the observed peaks (Fig. 2): (a) the pattern characteristic of the HCl-treated samples. All high energy spectra revert to the (a) form after 2 min sputtering (Ar^+, 10 $\mu A/cm^2$; 10 Å/min removal rate). Patterns of the type (c) pass through a (b) stage before revealing the pure (a) silicon spectrum.

Those wafers which did not receive HCl treatment incorporated significantly more nitrogen during the PD warm-up cycle than those that did receive the treatment. The ratios of the nitrogen/oxygen signals for the HCl-treated specimens (column 5, Table II) are 7-50 times lower than those of the untreated samples (column 6, Table II). Column 2 represents clean silicon with some hydrocarbons, CO, and other contaminants absorbed to the surface. The high energy spectrum, which samples more of the deeper lying material, is virtually pure silicon-silicon.

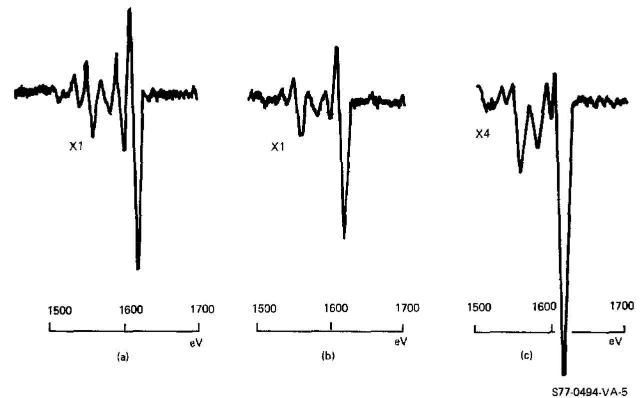

Fig. 2. Three types of $Si\text{-}SiO_2$ spectra between 1500 and 1700 eV. Primary electrons 5 keV modulation voltage, 3V peak-to-peak for curves (a) and (b), 6V peak-to-peak for curve (c). See text for discussion.

The prenitride cleaning cycle (PNC) yields spectra (column 3) which are indistinguishable from the HF-only spectra. Thus the acid baths following HF dip could not be responsible for nitrogen uptake. Nitric acid did not cause nitrogen uptake initially. In columns 4 and 5, the effect of the HCl treatment is seen to be the production of silicon-oxygen bonds, without significant nitrogen pickup. Enough of an oxide overlayer is produced to affect the high energy silicon spectrum. The thickness of the oxide layer is estimated to vary between 10 and 20Å. The sputtering times necessary to reduce the oxygen signals to reabsorption levels support this estimate. Also, during the predeposition warm-up cycle (PD), more free silicon is being oxidized as evidenced by the decrease of the 92 eV line with respect to the 75-85 eV oxide line.

Column 6 gives results obtained from wafers which were not treated with HCl residual. In one case, no 92 eV line was observed, but the nitrogen signal was as strong as the oxygen signal, indicating the formation of an oxynitride. The layer is thick enough to affect the high energy Si spectrum, but does not generate the characteristic (c) spectrum. In two other cases, incomplete or flawed oxide layers are produced (only one included in Table II), with a strong line at 92 eV and a high energy spectrum typical of pure (100) Si.

Ellipsometry of the thin native silicon oxide reveals an extremely thin, silicon-rich film. Using the McCrackin program (7), it is found that this film is approximately 13Å thick with an exceptionally high refractive index (averaging 1.97). Following the PD cycle, the untreated films thickened to about 17Å and the refractive index becomes an averaged value 1.89. Elipsometry of the HCl-treated films becomes impossible as a result of roughing of the surface. Attempts at ellipsometry of these films before the PD cycle would indicate that they are exceptionally thick (20-50Å). The refractive index was also high for these films

Table II. Summary of auger results

The numbers refer to peak-to-peak heights in the conventional dN(E)/dE-spectra obtained with a cylindrical mirror analyzer (arbitrary units.) Primary electrons 5 keV, modulation 3V peak-to-peak.

1 Element	2 HF only 1	2	3 HF + PNC 1	2	4 HF + PNC + HCl 1	5 HF + PNC + HCl + PD 1	2	6 HF + PNC + PD 1	2
Si (92 eV)	100	142	120	130	63	29	20	—	80
Si bonded with O (85 eV)	2	5	3	8	87	100	68	75*	58
Cl (183 eV)	<1	<1	<1	<1	<1	<1	<1	<1	<1
C (272 eV)	8	11	11	12	18	25	40	18	40
N (380 eV)	<1	<1	<1	<1	<1	5	5	100	20
O (505 eV)	100	93	97	107	183	250	185	104	140
F (650 eV)	<1	<1	<1	<1	<1	<1	<1	<1	<1
Si (1500-1619 eV) See text	A	A	A	**	C	C	C	B	A

* Not typical of oxide, more probably oxynitride.
** Not measured.

(averaging 1.7). The PD-cycled HCl-treated films are, according to the McCrackin program, thicker (ranging from 40-80Å) but of lower refractive index (1.22). This is in conflict with the sputtering results. The roughing and pitting of the surface, so evident at the 10% HCl level, probably explains these strange ellipsometric results. No ellipsometric estimate of film thickness can therefore be given for HCl-treated films.

None of the analytic techniques employed in this study were sufficient to determine the presence of hydrogen in the thin oxide films or at the oxide semiconductor interface. However, this was not judged to be a serious drawback. As Kooi has shown (8) heat-treatment of uncoverd oxides above 600°C for a few minutes is sufficient to drive off hydrogen from the oxide-semiconductor interface. After HCl treatment, the nitride reactor predeposition cycle keeps the uncovered tunnel oxides at temperatures in excess of 700°C in dry nitrogen for times longer than 10 min. Furthermore, annealing in hydrogen gas in place of HCl in the HCl-treatment cycle has no beneficial effect on d-c or pulse memory performance.

A Model for the Effect of HCl on the Tunnel Layer

The model for the effect of the HCl residual treatment on the thin oxide tunneling layer is shown in Fig. 3. Initially, the native oxide surface is far from homogeneous. There are regions in which silicon-oxygen bonding is not complete and impurities (probably carbon based, as that was the only atom other then silicon or oxygen which was detected) dot the surface. These departures from homogeneity are viewed as weak spots with respect to nitrogen attack during the PD warm-up cycle. HCl tends to etch out large agglomerates of impurities and regions of incomplete silicon-oxygen bonding without affecting a fully bonded silicon dioxide. This etching which is visibly evident at the 10% HCl level roughens the surface. When the HCl heat-treated surfaces are reexposed to air, a more perfect oxide film forms. This film is less susceptible to nitrogen inclusion.

Discussion

The improvement in device response comes about for three possible reasons. Even though the surfaces become rougher, the oxide films on HCl treated surfaces may remain thin through PD (as sputtering indicates). Untreated surfaces thicken nitrogen during PD. Thin tunnel layers allow for easier communication between nitride traps and the silicon, improving device pulse response (9). Also, the inclusion of nitrogen may adversely affect tunnel layer conductivity, degrading performance. A final possibility is that the rough surface contains many high field points, supplying more impetus for charge transfer, improving the device response.

This last possibility is viewed as least likely, due to the electrical performance data. The HCl at the 5% level is not so severe as to effect J-V characteristics. In addition, the retention slope is not at all degraded by HCl treatment. If this initial charge transfer into the insulator is mediated by high fields due to surface roughening only, this should show up as an increase in retention slope which is not observed.

There is some possibility of tunnel layer thickening during HCl treatment due to oxygen or water vapor present in the HCl treatment. This cannot be the cause of improved performance, though. As Wallmark and Scott (10) clearly show, such thickening leads to device hysteresis window degradation.

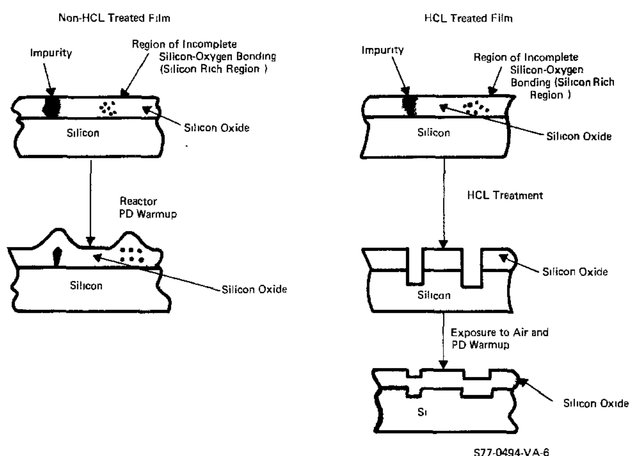

Fig. 3. Illustration of processing effects of MNOS tunnel layers

Summary and Conclusions

It has been shown that prenitride HCl surface treatment significantly affects the initial performance of MNOS devices. Untreated surfaces incorporate nitrogen during the predeposition warm-up cycle of a vertical reactor. Evidence points to nitrogen incorporation as being deleterious to device performance, degrading pulse response, and making d-c clears less positive. (However, the role of surface roughing from HCl gas has not been fully delineated, making this conclusion tentative at present.) HCl treatment makes the surface more resistant to nitrogen attack. This probably occurs because HCl etches away impurities and regions of incomplete silicon-oxygen bonding, (*i.e.*, silicon-rich regions). Silicon-oxygen bonding is promoted without any significant increase in oxide thickness. It is these impurities and/or silicon-enriched areas that are most susceptible to nitrogen attack during the prenitride reactor warm-up cycle.

Acknowledgments

The authors thank Dr. Herman Stein, of Sandia Laboratories, for many interesting and informative discussions concerning this work.

Manuscript submitted July 7, 1977; revised manuscript received Jan. 3, 1978.

Any discussion of this paper will appear in a Discussion Section to be published in the December 1978 JOURNAL. All discussions for the December 1978 Discussion Section should be submitted by Aug. 1, 1978.

Publication costs of this article were assisted by Westinghouse Electric Corporation.

REFERENCES

1. R. M. McLouski, Abstract 313, p. 805. The Electrochemical Society Extended Abstracts, Fall Meeting, Las Vegas, Nevada, Oct. 17-22, 1976.
2. M. H. White, J. W. Dzimianski, and M. C. Peckerar, *IEEE Trans. Electron Devices*, **ed.-24**, 577 (1977).
3. J. J. Chang, *ibid.*, **ed.-24**, 511 (1977).
4. C. M. Svensson, *J. Appl. Phys.*, **48**, 329 (1977).
5. J. S. Johannessen, C. R. Helms, W. E. Spicer, and Y. E. Strausser, *Thin Solid Films*, **32**, 311 (1976).
6. J. S. Johannessen, C. R. Helms, W. E. Spicer, and Y. E. Strausser, *IEEE Trans. Electron Devices*, **ed.-24**, 547 (1977).
7. F. L. McCrackin, NBS Tech. Note 497, April, 1969.
8. E. Kooi, "The Surface Properties of Oxidized Silicon," Springer-Verlag, New York (1967).
9. M. H. White and J. R. Cricchi, *IEEE Trans. Electron Devices*, **ed.-19**, 1280 (1972).
10. J. T. Wallmark, and J. A. Scott, *RCA Rev.*, **30**, 335 (1969).

MOS Characterization of Low Leakage Native Oxides on AlGaAs

E. H. Nicollian,* B. Schwartz,* L. A. Koszi, and N. E. Schumaker*

Bell Laboratories, Murray Hill, New Jersey 07974

It is reported here that a highly insulating native oxide on (36%) AlGaAs has been prepared that is comparable in dielectric strength to thermally grown SiO_2. This high dielectric breakdown strength and low electrical conductivity prior to breakdown are in contrast to those observed for anodically grown oxide films on GaAs with similarly evaporated gold electrodes which were conducting appreciable current even at an oxide thickness of 0.2 μm. The presence of the aluminum therefore makes the electrical conductivity of the anodic film on AlGaAs much less than that on an anodic film on GaAs below breakdown. However, the native oxides we grew on AlGaAs still had sufficiently large interface trap densities to make them unsuitable for most device applications at the present time. The reduction of these trap densities is the subject of continued development.

Experimental Procedures and Results

Sample preparation.—Two samples of nominally undoped 36% Al ternary material were grown by LPE on n^+ GaAs substrates doped with silicon to 1×10^{18} cm^{-3}. One of the epitaxial layers about 1.5 μm thick was found to be p-type from *C-V* curves, and the doping density was found to be 3×10^{16} cm^{-3} from the slope of a $(C_{ox}/C)^2$ *vs.* *V* curve (C_{ox} is the oxide layer capacitance, see Fig. 1). The second epitaxial layer, also about 1.5 μm thick, had an apparent n-type doping level of about 2×10^{15} cm^{-3} at 23°C (see Fig. 2). The substrate side of both samples was ohmically contacted by a Sn-Pd-Au metallization.

Because we had observed that GaAs and (36%) AlGaAs had different anodization characteristics, it was necessary to determine the thickness-voltage curve for the latter. Figure 3 shows the results of anodizing p-type Ge-doped to 3.5×10^{17} cm^{-3} (36%) AlGaAs in on aqueous solution of H_3PO_4 at a $pH = 2.5$. In the generation of the thickness data shown in Fig. 3, it was assumed that the refractive index for the native oxides on GaAs (1.80) (1) and AlGaAs are the same, and a calibrated GaAs color chart could therefore be used. Whereas 20 Å/V was the previously reported oxide growth parameter for GaAs (1), we note here that for AlGaAs, this parameter is only about 15 Å/V.

Both test samples were then anodized[1] to grow an oxide layer about 1200Å thick and then baked in a nitrogen purged oven at 250°C for 2 hr. Gold dots (either 127, 254, or 380 μm in diameter) were then evaporated, through a metal mask, directly onto the surface of the oxide.

Minority carrier response time.—Minority carrier response time (t_R) was measured because it is an important parameter in applications such as CCD's where long minority carrier response time means long retention time and low dark current. The minority carrier response time of an MOS capacitor is the time it takes for the system to reach thermal equilibrium after the applied field has been abruptly changed. The mechanism by which the system reaches thermal equilibrium is thermal generation of carriers in the space charge region of the semiconductor (2). The t_R was obtained in the AlGaAs samples by applying a step

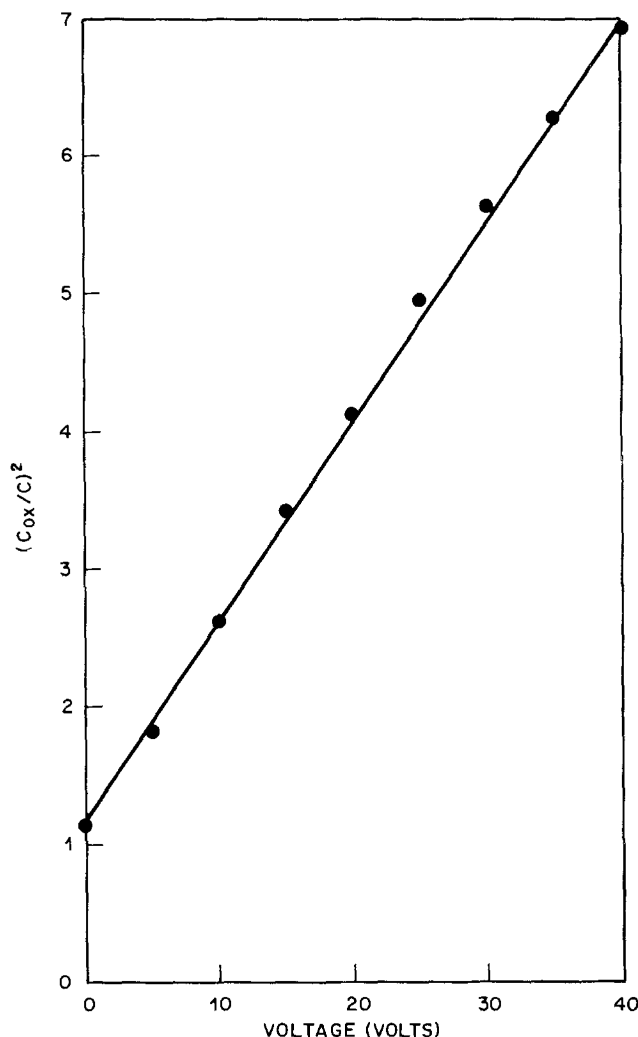

Fig. 1. $(C_{ox}/C)^2$ *vs.* *V* measured at 1 MHz with a voltage ramp of 0.1 V/sec on a p-type AlGaAs MOS capacitor with gold dots. $T = 23°C$.

voltage of 15V, which drove the semiconductor into deep depletion, and then measuring the time required to reach thermal equilibrium again; equilibrium was reached when the capacitance stopped increasing. Response times of 150, 250, and 300 sec were found on three different AlGaAs samples (3). These are relatively long response times and can be explained on the basis of the large bandgap of the AlGaAs (~1.53V) (4); because of the bandgap, the intrinsic carrier concentration, n_i, will be quite small. Thus, even though minority carrier lifetime may be short, the small value of n_i will determine the generation rate and the generation current will be relatively small, making t_R rather long (2). Such long values of t_R make this material attractive for such devices as CCD's.

Current vs. voltage characterization technique.—To measure the *I-V* characteristics and determine the breakdown voltage of the oxide layer, the samples were placed in a dry-nitrogen-purged light-tight box used to minimize spurious currents due to moisture

* Electrochemical Society Active Member.
Key words: compound semiconductor, oxides, metal oxide semiconductor.
[1] The back side was protected from the solution by being waxed down to a cover glass slide.

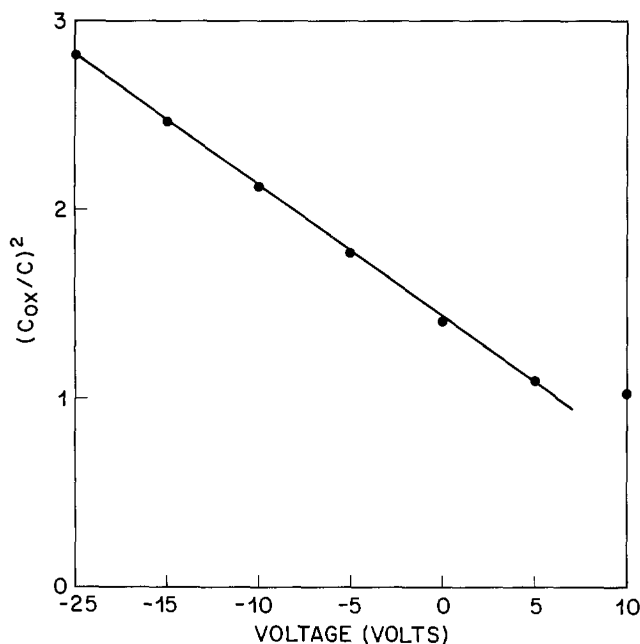

Fig. 2. $(C_{ox}/C)^2$ vs. V measured at 1 MHz with a voltage ramp of 0.1 V/sec on an n-type AlGaAs MOS capacitor with gold dots. $T = 23°C$.

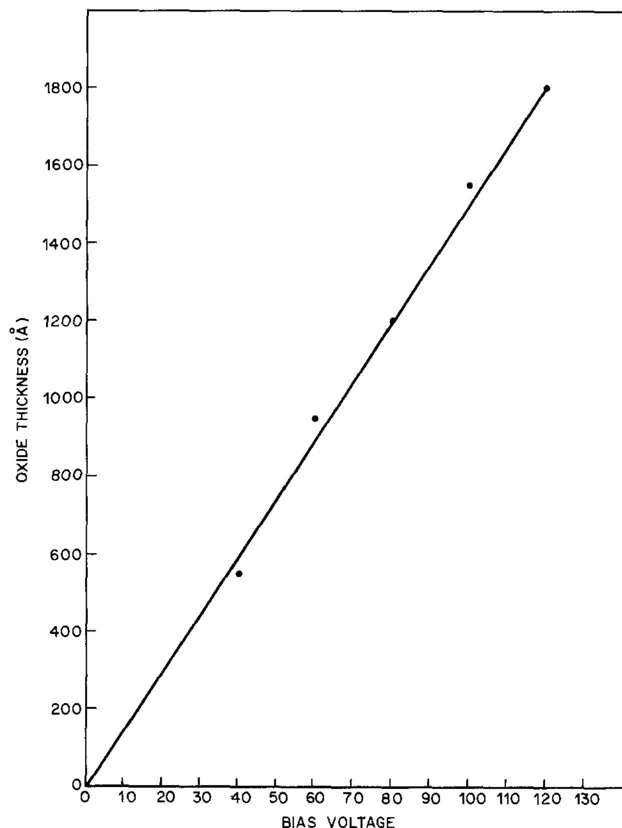

Fig. 3. Oxide thickness vs. applied bias for aqueous (pH = 2.5) anodization of (36%) AlGaAs.

leakage and photovoltaic effects. A voltage ramp of 0.2 V/sec was applied between a gold dot and the back contact of the wafer using a point probe to contact the gold dot. The resulting current was measured with a logarithmic picoammeter whose output was fed to the y-axis of an X-Y recorder. Feeding the output of the ramp generator to the x-axis of the X-Y recorder permitted the plotting of an I-V curve. To minimize spurious currents due to cable vibration, a rigid General Radio coaxial transmission line was used between

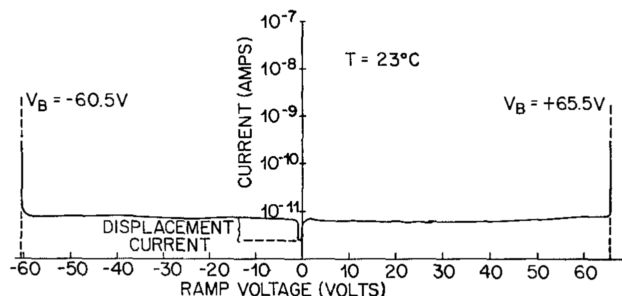

Fig. 4. Logarithm of current vs. voltage measured at 23°C for both positive and negative polarity. V_B is breakdown voltage. The sample was the same as in Fig. 1.

the point probe and the input of the picoammeter. The polarity of the ramp voltage is the polarity of the dot with respect to the back contact.

Results with gold gate electrode.—Figure 4 shows the resulting I-V characteristics of two representative MOS capacitors measured on the p-type AlGaAs epilayer, with Au-dots, for both positive and negative polarity. The only current measured prior to catastrophic breakdown was displacement current shown in Fig. 4 to be in the 10^{-12}A range. Breakdown voltage is defined as the voltage at which the current suddenly increases and is shown labeled as V_B in Fig. 4. Melting at various spots on the metal gate electrode is usually observed after breakdown and the MOS capacitor is invariably a short circuit. Thus, the measurement of breakdown voltage is destructive and each measurement must be made on a different dot. It is seen from Fig. 4 that breakdown with positive polarity occurred at +65.5V while with negative polarity, breakdown voltage was −60.5V. There were a minority of dots which broke down around 10V. On another p-type sample, breakdown voltages were +65 and −20V with a few dots which broke down at voltages as low as +38 and −20V.

The important thing to note is that for p-type material, the breakdown voltages were always higher for positive than for negative polarity. This effect follows from the fact that the voltage across the oxide near breakdown must be lower for positive than for negative polarity. At large positive values of gate voltage, the p-type semiconductor is in deep depletion because t_R is so long that minority carriers cannot follow the sweep rate. Therefore, the space charge region is much wider than it is at negative gate voltages where the semiconductor surface is in strong inversion. The semiconductor surface is in inversion at all negative gate voltages up to breakdown because of a large positive oxide charge density characteristic of these oxides (5). A smaller fraction of the applied voltage must appear across the oxide at positive polarity than at negative polarity because of the large difference in space charge widths. Similar reasoning applies for the n-type samples where the semiconductor surface is in deep depletion at high negative voltages and in inversion at large positive voltages because there is a large negative oxide charge density (5). For example, it was observed on an n-type sample that the breakdown voltages were +59 and −64V.

The breakdown field, which is the field across the oxide at breakdown, should be polarity independent. At large negative voltages, the p-type semiconductor is in inversion. Subtracting the voltage drop across the semiconductor space charge region, which cannot exceed 1.5V in inversion (band bending equal to the bandgap), from the breakdown voltage given in Fig. 4 as −60.5V gives 59V and a breakdown field of 4.9×10^6 V/cm where the oxide thickness was estimated to be 1200Å. This value of breakdown field and the observation that no leakage current (<0.01 pA) is measured prior to catastrophic breakdown makes this ox-

ide comparable to thermally grown SiO_2 with respect to room temperature dielectric breakdown strength. The resistivity of this film is estimated to be greater than 2×10^{17} Ω-cm.

There are two more observations, however, which indicate that the native oxide of AlGaAs is different from thermally grown SiO_2. The first is that the dielectric breakdown voltage decreases with storage time at room temperature. For example, the n-type sample exhibited a breakdown voltage of 180-200V immediately after it was prepared. After a few months, the breakdown voltages decreased into the 60V range. The second is that the breakdown voltages are temperature dependent decreasing with increasing temperature. Figure 5, which shows breakdown voltages on the same p-type sample as Fig. 4, but measured at 100°C, illustrates this observation. In Fig. 5, the breakdown voltages were +35.5 and −47V. Another pair of dots on the same sample yielded breakdown voltages of +33 and −41V. Notice that the breakdown voltage for positive polarity is less than for negative polarity, the reverse of what was measured at room temperature. Furthermore, the reduction in breakdown voltage for both polarities is rather large for a relatively small increase in temperature (100°C). The decrease in breakdown voltage with increasing temperature can be explained as follows. At high positive voltages, the semiconductor surface goes from deep depletion to inversion as temperature increases because minority carrier response time gets shorter with increasing temperature. Thus, the semiconductor surface space charge region decreases in width and the fraction of the applied voltage across the oxide increases with increasing temperature. The breakdown voltage for positive polarity decreases with increasing temperature as observed. For high negative voltages, the semiconductor surface goes from inversion to depletion as temperature increases. As temperature increases, the Fermi level moves toward midgap reducing net positive interface trap charge density sufficiently to allow gate bias to make the surface go from inversion to depletion. Thus, the space charge width again decreases with temperature and the fraction of the applied voltage across the oxide increases with increasing temperature. The breakdown voltage for negative polarity also decreases with increasing temperature as observed. Based on this reasoning, the breakdown voltage should decrease more for negative polarity than for positive polarity; but just the opposite occurs. The reason for this is not understood. As this reasoning does not explain all the observations, it is obviously an oversimplification of the true situation.

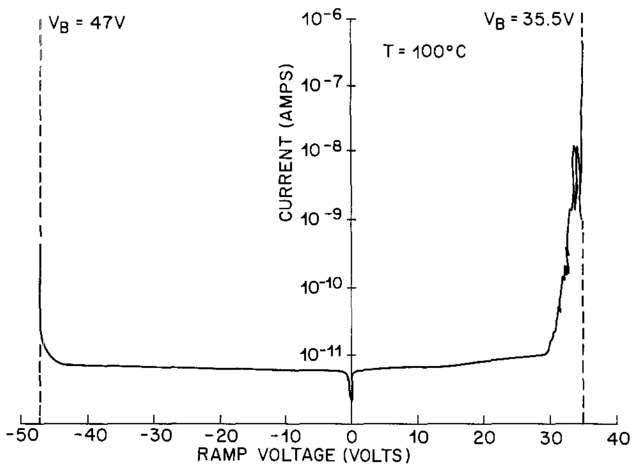

Fig. 5. Logarithm of current vs. voltage measured at 100°C for both positive and negative polarity. Sample is the same as in Fig. 1.

Conclusions

The long minority carrier response time and the high dielectric breakdown strengths observed make it appealing to pursue the development of native oxides on AlGaAs. The major problem in their use will be to reduce the large interface trap density sufficiently so that they no longer play such a dominant role in the MOS characteristics. The solution of this problem will result in an oxide which is quite suitable for numerous device applications.

Acknowledgments

The authors would like to thank A. Timko for measuring minority carrier response times of the AlGaAs samples, and G. E. Smith and J. R. Brews for a critical reading of the manuscript.

Manuscript submitted June 21, 1977; revised manuscript received Dec. 19, 1978. This was Paper 450 RNP presented at the Philadelphia, Pennsylvania, Meeting of the Society, May 8-13, 1977.

Any discussion of this paper will appear in a Discussion Section to be published in the December 1978 JOURNAL. All discussions for the December 1978 Discussion Section should be submitted by Aug. 1, 1978.

Publication costs of this article were assisted by Bell Laboratories.

REFERENCES

1. B. Schwartz, F. Ermanis, and M. Brastad, *This Journal*, **123**, 1089 (1976).
2. A. S. Grove, "Physics and Technology of Semiconductor Devices," John Wiley & Sons, Inc., New York (1967).
3. M. Zerbst, *Z. Agnew. Phys.*, **22**, 30 (1966).
4. S. M. Sze, "Physics of Semiconductor Devices," John Wiley & Sons, Inc., New York (1969).
5. E. H. Nicollian, B. Schwartz, D. J. Coleman, Jr., R. M. Ryder, and J. R. Brews, *J. Vac. Sci. Technol.*, **13**, 1047 (1976).

The "D.L.P." Model in $Ga_xIn_{1-x}P$:N Alloys Correlation with Electronic Properties

A. Marbeuf and J. C. Gillaume

CNRS, Laboratoire de Physique des Solides, Briand, 92190 Meudon/Bellevue, France

Several studies on $Ga_xIn_{1-x}P$ alloys have shown the interest of these materials for electroluminescent devices (1-4). If nitrogen is used as a dopant, the recombination of excitons bound to this isoelectronic impurity gives a luminescence in the green and yellow portion of the visible spectrum (5-8).

Mariette and Chevallier (8) have recently shown that enhancement of the external luminescence efficiency in nitrogen-doped alloys, when x decreases, is partly due to the band-structure effect on the radiative lifetime of the excitons bound to nitrogen atoms. On the other hand, the alloys have a different luminescence behavior when x is varied: for $x > 0.98$, the line due to nitrogen is similar to the so-called A-line which is usually observed in GaP:N, whereas for $x < 0.98$ nitrogen gives rise to a broader luminescent A_0-line at lower energy than that of the A-line (6, 8).

An explanation of this behavior can be obtained by using the thermodynamic model developed by Stringfellow (the Delta lattice parameter or "D.L.P." model) (9). Based on the Philips and Van Vechten dielectric theory (10, 11), this model uses the concept that the bonding energy of a semiconductor is proportional to the bandgap. Neglecting dehybridization and, for heteropolar alloys, bond ionicity effects, the bonding energy or atomization enthalpy ΔH^{at} may be written

$$\Delta H^{at} = Ka_o^{-2.5} \quad [1]$$

where K is a positive constant which can be evaluated from pseudobinary III V-III'V or III V-III V' systems (9).

In consequence, the activity coefficients in the solid will reflect the nature of the constituent atoms and the electronic properties of the material. From the "D.L.P." model, the free energy G^s of a crystal $A_{x1}{}^s B_{x2}{}^s C_{x3}{}^s D_{x4}{}^s$ depends on its lattice parameter a_o and its composition in the following manner

$$G^s = Ka_o^{-2.5} + RT\left[\sum_{i=1}^{2} x_i{}^s \log x_i{}^s + \sum_{j=3}^{4} x_j{}^s \log x_j{}^s\right] \quad [2]$$

In this note all the relations will be expressed in $1/K$ units.

Assuming Vegard's law, the chemical potentials $\mu_{ij}{}^s$ of the four binary III_iV_j systems can be expressed in the following manner

$$\mu_{ij}{}^s = 2.5\,Ka_o^{-3.5}[x_k{}^s x_j{}^s(a_{ij} - a_{kj}) + x_i{}^s x_{k'}{}^s(a_{ij} - a_{ik'}) + x_k{}^s x_{k'}{}^s(a_{ik'} + a_{kj} - 2a_{kk'})] + RT\log x_i{}^s x_j{}^s - Ka_o^{-2.5} \quad [3]$$

where a_{ij}, a_{kj}, etc . . ., represent the lattice parameters of the defined binary compounds AC, AD, BC, and BD which are given in the Table I, and where k and k' are indexes defined by

$$k = 1, 2 \quad k = i \quad \text{and} \quad k' = 3, 4 \quad k' = j$$

Because $-Ka_{ij}^{-2.5}$ is the standard chemical potential $\mu_{ij}{}^{os}$ of the III_iV_j compound, we can define the activity coefficient $\gamma_{ij}{}^s$

$$RT\log\gamma_{ij}{}^s = 2.5Ka_o^{-3.5}[x_k{}^s x_j{}^s(a_{ij} - a_{kj}) + x_i{}^s x_{k'}{}^s(a_{ij} - a_{ik'}) + x_k{}^s x_{k'}{}^s(a_{ik'} + a_{kj} - 2a_{kk'})] + K(a_{ij}^{-2.5} - a_o^{-2.5}) \quad [4]$$

assuming regular behavior of the solid solution between the four binary III_iV_j systems.

Table I. Lattice parameters used in the calculation of $\gamma_{ij}{}^s$

	GaP	GaN	InP	InN
a (Å)	5.4512 (9)	4.4894* (13)	5.8688 (9)	4.9919* (14)

* Parameters calculated from volume of the wurtzite-hexagonal cell.

A series of $Ga_xIn_{1-x}P$:N alloys were prepared by liquid phase epitaxy (LPE). The method described by Mariette *et al.* (12) was used. An In-rich melt was cooled down slowly from 830° to 800°C, and the four $\gamma_{ij}{}^s$ coefficients were calculated for the 830°C isotherm using relation [4] and the lattice parameters listed in Table I. The calculated dependence of $\log\gamma_{ij}{}^s$ (in $1/K$ units) *vs.* x, is shown in Fig. 1.

The $\log\gamma_{InN}{}^s$ curve clearly demonstrates that the interaction energy between InN and the $Ga_xIn_{1-x}P$ matrix is positive only for $x \lesssim 0.97$. This value does not depend on the doping concentration, since [N]

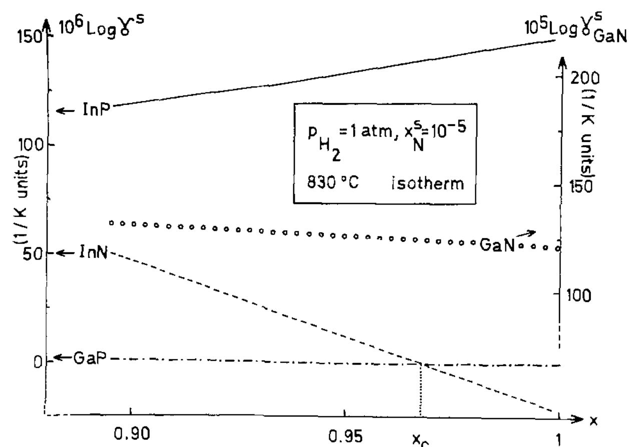

Fig. 1. Variation of the logarithm of the activity coefficients in the solid with alloy composition at 830°C.

Key words: D.L.P. model, $Ga_xIn_{1-x}P$:N alloys, electronic properties.

was varied between 10^{15} and 10^{19} atoms per cm^3. On the other hand, log $\gamma_{GaN}{}^s$ is always positive and becomes progressively greater as x decreases. Noting that the free energy of formation of InN is negative (−2.9 kcal·mole^{-1}) under the growing conditions at 830°C (15), whereas that of GaN is positive [1 kcal·mole^{-1}, Ref. (16)], then during the growth of alloys with $x < 0.97$ the more energetically favored NIn_4 tetrahedrons will be formed preferentially to NGa_nIn_{3-n} (n = 1, 2, 3) and even NGa_4 tetrahedrons. The ionic character f_i is more pronounced for In-N bonds than for Ga-N bonds [f_i In-N = 0.578, f_i Ga-N = 0.500 on the scale established by Philips, Ref. (10)]. Consequently, one can predict a different electronic behavior of nitrogen in $Ga_xIn_{1-x}P$:N alloys for $0.97 < x < 1$ and for $x \lesssim 0.97$, and so different luminescence spectra.

Experimentally, the critical value $x_c = 0.97$ corresponds to the appearance of the A_o-line, as previously described by Garbuzov and co-workers (6), and Mariette and Chevallier (8). These authors have noted that the short-range potential V created by nitrogen, more electronegative than phosphorus, should be different for the A-line and the A_o-line, which appears for $x < x_c$.

Indium is more electropositive than gallium, so that, for the NIn_4 tetrahedrons, the potential well created by nitrogen is surrounded by a curb which gives a greater effective potential. The A-line probably still exists for $x < x_c$ but becomes immersed into the A_o line.

Such effects cannot exist in GaP_yAs_{1-y}:N. Its lattice only contains NGa_4 tetrahedrons and P and As atoms, second neighbors of N-atoms, have a relatively small influence on the nature of Ga-N bonds. The electronic nitrogen behavior in GaP:N, GaP_yAs_{1-y}:N and $Ga_xIn_{1-x}P$:N is summarized in Fig. 2.

In recent work, Brühl and co-workers have shown the strong tendency of gallium and indium in $Ga_xIn_{1-x}P$ bulk-crystals toward segregation and have predicted that the effect of clustering should be more pronounced in as-grown epitaxial alloys (17). They also expect a strong effect of this nonrandom distribution on electronic properties created by doping.

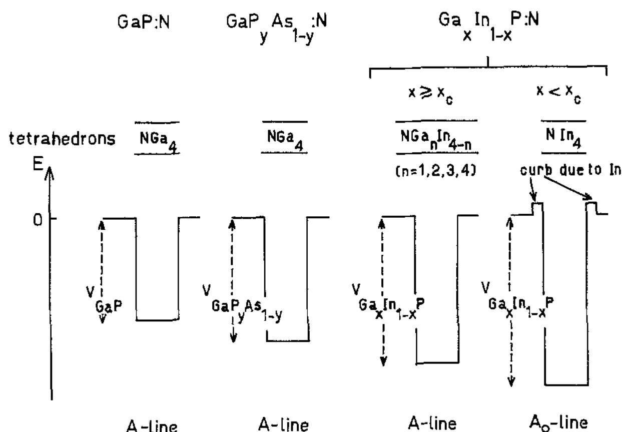

Fig. 2. Comparison of the potential well created by nitrogen in GaP, GaP_yAs_{1-y} and $Ga_xIn_{1-x}P$.

Hence, the "D.L.P." model connects the thermodynamic macroscopic properties to the electronic ones. A complete calculation of the quaternary phase diagram Ga-In-P-N can be considered. In relation with nitrogen-profile measurements, it should provide a precise knowledge of nitrogen-doping conditions in L.P.E. $Ga_xIn_{1-x}P$ alloys.

Acknowledgments

We thank D. Bourneix for his contribution to the LPE experiments and Doctors Chevallier, Ghazali, and Mariette for useful discussions and their interest for this work.

Manuscript submitted July 15, 1977; revised manuscript received March 2, 1978.

Any discussion of this paper will appear in a Discussion Section to be published in the December 1978 JOURNAL. All discussions for the December 1978 Discussion Section should be submitted by Aug. 1, 1978.

Publication costs of this article were assisted by the Laboratorie de Physique des Solides, CNRS.

REFERENCES

1. A. Onton and M. R. Lorenz, in "Proceedings of the 1970 Symposium on GaAs and Related Compounds," p. 222, Aachen, Germany (1970).
2. C. Alibert, G. Bordure, A. Laugier, and J. Chevallier, *Phys. Rev.*, **B6**, 1301 (1972).
3. G. B. Stringfellow, P. F. Linquist, and R. A. Burmeister, *J. Electron. Mater.*, **1**, 437 (1972).
4. M. H. Lee, N. Holonyak, Jr., W. R. Hitchens, J. C. Campbell, and M. Altarelli, *Solid State Commun.*, **15**, 981 (1974).
5. R. A. Logan, P. J. Dean, H. G. White, and W. Wiegmann, *J. Appl. Phys.*, **42**, 2328 (1971).
6. D. G. Garbuzov, S. G. Konnikov, P. S. Kop'ev, and V. A. Mishurnyi, *Sov. Phys. Semicond.*, **8**, 998 (1975).
7. J. C. Campbell, N. Holonyak, Jr., M. G. Craford, and D. L. Keune, *J. Appl. Phys.*, **45**, 4543 (1974).
8. H. Mariette and J. Chevallier, *ibid.*, **48**, 1200 (1977).
9. G. B. Stringfellow, *J. Cryst. Growth*, **27**, 21 (1974).
10. J. C. Philips, *Rev. Mod. Phys.*, **42**, 317 (1970).
11. J. C. Philips and J. A. Van Vechten, *Phys. Rev.*, **B2**, 2147 (1970).
12. H. Mariette, J. Bourneix, and A. Marbeuf, *Rev. Phys. Appl.*, **11**, 475 (1976).
13. M. Rodot, in "Les Matériaux Semi-Conducteurs," Vol. II, Dunod, Editor, Paris (1965).
14. K. Osamura, S. Naka, and Y. Murakami, *J. Appl. Phys.*, **46**, 3432 (1975).
15. Banque de données "Thermodata," Grenoble, France (1976).
16. C. D. Thurmond and R. A. Logan, *This Journal*, **119**, 622 (1972).
17. H. B. Brühl, L. Hildisch, H. Morwinski, W. Schmidt, and E. Schubert, *Phys. Status. Sol.*, **A39**, 133 (1977).

Phase-Memory Effect in a p-Type Photoconductor

Osamu Yoshie and Mitsuo Kamihara

Department of Electronics, Kogakuin University, Nishishinjuku, Shinjuku-ku, Tokyo, Japan

The phase-memory effect was previously found by one of the present authors in evaporated thin films of CdS and (Cd, Zn)S at low temperatures (1, 2). It was reported (2-5) that the memory effect in these films was due to trap-controlled high field domains caused by the field-quenching effect (6-8). The phase-memory

Key words: phase-memory effect, p-type photoconductor, Se film, domain velocity, maximum memory time.

effect was also found in bulk CdS single crystal (9) and Cr-doped GaAs single crystal (10). The mechanism of the memory effect in CdS was explained to be at least associated with both the deep hole traps and the deep electron traps (9). Thus, the phase-memory effect was investigated in detail in n-type semiconductors, while no reports have been made on it in p-type semiconductors. We have found and investigated the phase-memory effect in p-type thin films of Se.

Experimental

The thin films of Se (about 1 μm thick) were prepared by vacuum evaporation at $1 \sim 5 \times 10^{-5}$ Torr. A cleaved mica plate kept at room temperature was used as a substrate. After evaporation, the Se film was annealed at 100°C for 5 min in vacuum. The sample had a planar-type (gap-type) structure with silver paste electrodes (width: 1 ~ 2 mm, interelectrode spacing: 1 ~ 3 mm). The sample was illuminated with monochromatic light of wavelength approximately corresponding to the absorption edge of Se. The measurements were made at 40°K, and the probe potential of the sample was measured by a high impedance electrometer.

Results and Discussion

Figure 1 shows the very low frequency photocurrent oscillation in the Se film and the phase-memory effect for light interruption at 40°K. When the light illumination is turned off at a phase "P" during the periodic photocurrent oscillation, the oscillation stops and the current decays; by turning on the light again an arbitrary time later, the oscillation begins at the phase "P," which it had at the moment of turning off. This fact indicates that the phase of the oscillation can be memorized by turning off the light (light-controlled phase-memory effect). The above memory effect is also observed with regard to the probe potential of the sample. The traveling of the trap-controlled high field domain could not be confirmed since the crystallization of the Se film on the mica plate was very inhomogeneous. From the similarity to the phase-memory effect in CdS (2, 5, 6), however, we can deduce that the phase-memory effect in the Se film is also due to a trap-controlled high field domain. That is, the traveling high field domain stops and remains unchanged when the light is turned off during the domain traveling, and it begins to travel by turning on the light again. The observed maximum memory time has been confirmed to be longer than 12 hr at 40°K.

Figure 2(a) shows that the light-controlled phase-memory effect can also be observed even if the applied bias voltage is interrupted for an arbitrary time during the phase-memory state (nonvolatile phase-memory effect). This fact suggests that, if the bias voltage is interrupted during the phase-memory state, the dipole space-charge layer (*i.e.*, high field domain) disappears, but the layer-like spatial inhomogeneity of conductivity in the sample remains unchanged. Therefore, when the voltage is switched on again, the dipole space charge layer is reformed at the same position where the voltage was interrupted. The maximum memory time in this case has also been confirmed to be longer than 12 hr at 40°K.

Figure 2(b) shows that the phase-memory effect can also be observed when the bias voltage is interrupted

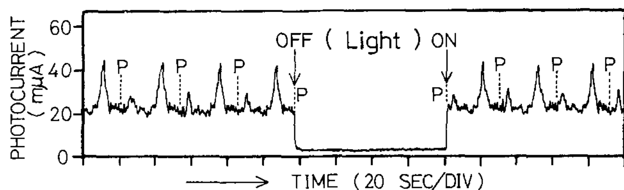

Fig. 1. Light-controlled phase-memory effect in a Se film at 40°K. Interelectrode spacing, 1.7 mm; bias voltage, 900V; illumination, 6700Å.

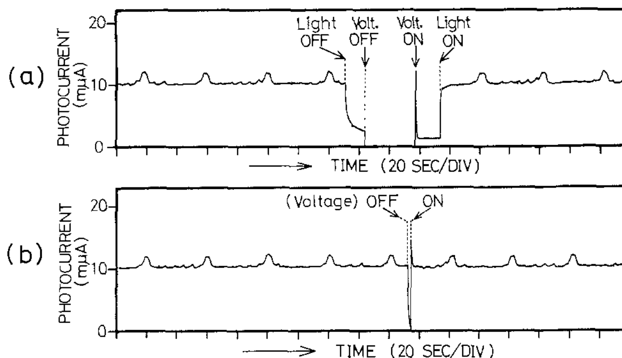

Fig. 2. (a) Nonvolatile phase-memory effect; and (b) voltage-controlled phase-memory effect at 40°K. Spacing, 1.7 mm; voltage, 200V; illumination, 6350Å.

for a very short time under light illumination (voltage-controlled phase-memory effect). In this case, if the voltage is interrupted for a time longer than 1 ~ 2 sec, the above memory effect can not be observed. This fact suggests that the layer-like spatial inhomogeneity of conductivity disappears in a certain time by light illumination under the condition of removed bias voltage.

It has been found that the dependence of the domain velocity v_d upon the light intensity B in the Se film is represented by $v_d = kB^x$ ($x = 0.7 \sim 1.0$), where k and x are constants and x is independent of the bias voltage. From this equation, it can be expected that if the light intensity decreases to zero during the domain traveling, the domain velocity also decreases to zero, *i.e.*, the domain stops and can remain unchanged; accordingly the light-controlled phase-memory effect can be expected.

We believe that the negative differential conductivity responsible for the domain formation is caused by the field-quenching effect which is defined for p-type photoconductors as a redistribution of trapped electrons from slow to fast recombination centers caused by an electric field, resulting in a shorter lifetime of the photoexcited free holes. Thus, the layer-like spatial inhomogeneity of conductivity in the sample is formed by the redistribution of the trapped charges. Therefore, if the trapping levels are deep enough or the temperature of the sample is sufficiently low, the thermal excitation of the trapped charges to the valence or to the conduction band is scarcely possible. Consequently, once a layer-like spatial inhomogeneity of conductivity is formed by the field quenching, it remains unchanged even if the light is turned off (light-controlled phase memory effect) or even if both the light and the bias voltage are turned off (nonvolatile phase-memory effect).

Acknowledgment

This work was supported in part by the Grant-in-Aid for Scientific Research from the Ministry of Education in Japan.

Manuscript submitted Nov. 14, 1977; revised manuscript received Jan. 10, 1978.

Any discussion of this paper will appear in a Discussion Section to be published in the December 1978 JOURNAL. All discussions for the December 1978 Discussion Section should be submitted by Aug. 1, 1978.

Publication costs of this article were assisted by Kogakuin University.

REFERENCES

1. O. Yoshie, Paper No. SSD73-37 presented at the Meeting of the Technical Group on Semiconductor and Semiconductor Devices, Institute of Elec-

tronics and Communication of Japan, September 1973.
2. O. Yoshie, *Jpn. J. Appl. Phys.*, **13**, 1177 (1974).
3. O. Yoshie, *ibid.*, **13**, 1303 (1974).
4. O. Yoshie, *ibid.*, **13**, 1671 (1974).
5. O. Yoshie, *ibid.*, **15**, 87 (1976).
6. K. W. Böer, *Z. Phys.*, **155**, 184 (1959).
7. K. W. Böer and W. E. Wilhelm, *Phys. Status Solidi*, **4**, 237 (1964).
8. G. A. Dussel and K. W. Böer, *ibid.*, **39**, 391 (1970).
9. O. Yoshie, *Jpn. J. Appl. Phys.*, **16**, 795 (1977).
10. O. Yoshie and M. Kamihara, Submitted to *This Journal*.

DISCUSSION SECTION

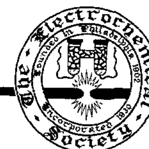

This Discussion Section includes discussion of papers appearing in the *Journal of The Electrochemical Society*, Vol. 124, No. 7, and 9, July and September 1977.

A Quantitative Model for the Diffusion of Phosphorus in Silicon and the Emitter Dip Effect

R. B. Fair and J. C. C. Tsai
pp. 1107-1118, Vol. 124, No. 7

F. A. Kroger:[1] The authors make an impressive effort to solve the problem of diffusion of P in Si. Although the proposed model appears to give a satisfactory representation of $D(x)$ (Fig. 15 in the paper being discussed), it does not give the proper dependence of n on C_T close to the surface. Also there are a few incorrect statements and inconsistencies that need correction. A new simple model is proposed in which only PV^- accounts for all the variations observed. In the following, numbers of references and equations are those of the paper under discussion.

1. The derivation of Eq. [6], intended to be the justification of Eq. [1], contains an inconsistency. Equation [5] (on which Eq. [6] is based) was derived from Eq. [4] with the unstated assumption $C_{P+} = n$. Experimentally, at high P concentrations, $C_T \approx 2n$ and thus $C_T = 2C_{P+}$. But $C_T = C_{P+} + C_{PV}$. Hence $C_{P+} = C_{PV-}$. But then $C_{P+} \neq n$, contrary to what was assumed! Evidently the more complete neutrality condition $C_{P+} = n + C_{PV-}$ has to be used. This leads to

$$C_{PV-} = \frac{Kn^3}{1 - Kn^2} \qquad \text{instead of Eq. [5]}$$

and

$$C_T = n + \frac{2Kn^3}{1 - Kn^2} \qquad \text{instead of Eq. [6]}$$

Here $K = K_V K_v K_P$ with

$K_v = C_V{}^\times, K_v = C_V{}^=/C_V{}^\times n^2,$

and $K_P = C_{PV}{}^-/C_P{}^+C_V{}^=$

2. For $n \approx C_{PV-} = ½\, C_{P+}$, $C_T = C_P + C_{PV-} = 3n$; for $n = 2C_{PV-} = 2/3\, C_{P+}$, $C_T = 2n$. Thus $C_{PV-} \leqq n$, and not $> n$ as assumed in Fig. 13.

3. Formulae [1] and [6] suggest that since $C_T = C_{P+} + C_{PV-}$, the first term represents C_{P+}, with $C_{P+} = n$, and the second C_{PV-}. This is not the case. At large C_T, $C_{P+} > n$ with $n \approx C_{PV-}$. Only at small C_T is $C_{P+} \simeq n$.

4. Equation [15] and the accompanying text suggest that the pair PV^- loses an electron to the conduction band when $E_F = E_c - 0.11$ eV. However, the energy indicated corresponds to the energy level of free $V^=$ and not of $V^=$ as present in the pair: the latter will have a level close to that of free V^-, at $E_c - 0.39$ eV. Therefore PV^- itself does not give up an electron. However, PV^- is in equilibrium with P^+ and $V^=$ through Eq. [12]. Therefore when $V^=$ loses an electron, $C_{V=}$ decreases and thus C_{PV-} decreases, reaction [12] proceeding to the left. On the other hand, the neutral associate, PV, remains at a low concentration because of its smaller binding energy. Equation [15] is correct as far as its left and right parts are concerned; the central part is in error. Equation [16] remains correct if $n = C_{P+}$ (which is correct when C_T has decreased sufficiently, *i.e.*, at 1000°C, $C_T \approx 10^{20}$ cm^{-3}). However, when $n = n_e$, C_{PV-} has no longer the value it has at the surface but must have decreased. Therefore one should not use [13], and [17] must be incorrect.

5. Expressions [2] and [7] for $D(n)$ are not as generally valid as the authors (and Shaw) believe. If X is the defect transporting the chemical element Y, with a total concentration C_T, the flux of X or Y is equal to

$$J_Y = J_X = -D_X \frac{\partial C_X}{\partial x} = -D_X \frac{\partial C_X}{\partial C_T} \frac{\partial C_T}{\partial x}$$

with $(D_Y)_{\text{effective}} = D_X \dfrac{\partial C_X}{\partial C_T}$

This effective diffusion coefficient is a function of concentration or, if X is charged, of the electron concentration or the Fermi level, if $\partial C_X/\partial C_T = f(C_T,n)$. This is the case, if X is a minority species. However, $\partial C_X/\partial C_T$ is constant if X is a majority species. Then $\partial C_X/\partial C_T = f =$ constant with $f = 1$ or a simple fraction. A situation in which $\partial C_X/\partial C_T$ is dependent on C_T but independent of n occurs when $C_T \approx C_{PVP}{}^\times$ with $C_{PV-} \approx C_{P+}$, PV^- being the P-carrying species. Owing to the triplet formation reaction $PV^- + P^+ \rightleftarrows PVP^\times$

$$\frac{C_{PVP}}{C_{PV-}C_{P+}} = K_T,\ C_{PV-} = f(C_T)$$

However, because of $P^+ + V^= \rightleftarrows PV^-$

$$\frac{C_{PV-}}{C_{P+}C_{V=}} = K_P \text{ or } C_{V=} = K_P{}^{-1}\frac{C_{PV-}}{C_{P+}} = K_P{}^{-1}$$

and, since $n \propto C_V{}^{1/2}$, n is also constant. One of these situations may apply to Si:As at high arsenic concentrations (see Fig. 11), arsenic being transported by AsV^- and not by $AsV^\times$ as assumed by the authors (see Fig. 6).

6. The conclusion that electric field effects play a role independent of the charge of a migrating species cannot be correct: the charge is the very reason for this effect. Reference (22) does not contain information proving that As migrates as As^+V^-. An argument that could possibly be based on Figure 11 was refuted above (see 5).

7. Reference (53) does not mention ΔH_V. The value $\Delta H_{V^\times} = 2.66$ eV is not mentioned in Ref. (22), but in ftn.[2] However, no values for ΔH_{V-} and $\Delta H_{V=}$ are given. It is unlikely that the latter should be larger than $\Delta H_{V^\times}$ if the Fermi level is at E_c (as stated); in that

[1] Department of Materials Science and Electrical Engineering and Chemistry, University of Southern California, University Park, Los Angeles, California 90007.

[2] *Phys. Rev. B*, **14**, 3551 (1976).

case energy is gained by the attachment of electrons to $V^\times$ and therefore ΔH_{V^-} and $\Delta H_{V^=} < \Delta H_{V^\times}$.

8. Figure 13 shows assumed profiles for PV^- and e^-, showing no gradient in the concentrations of these species at low x. This, of course, cannot be correct; if there is no gradient, there can be no diffusion. What must happen is that D is large and therefore the gradient required to maintain a flow of P is small. The actual penetration profiles (Fig. 4 and 15) indeed show a concentration gradient at the surface.

9. For the surface concentrations at 1000°C as given in Fig. 4, $C_T \approx 2.52n$. With $C_T = C_{PV^-} + C_{P^+}$ and $C_{P^+} = C_{PV^-} + n$, simple algebra shows that $n = 0.58\ C_{P^+} = 1.38\ C_{PV^-}$. Therefore $C_T = 8.3 \times 10^{20}$, $C_{P^+} = 5.8 \times 10^{20}$, $n = 3.29 \times 10^{20}$ and $C_{PV^-} = 2.5 \times 10^{20}$, all cm^{-3}. The pairing constant of Eq. [12], $K_{P^1} = C_{PV^-}/C_{P^+}C_{V^=} = 4 \exp E_b{}^=/kT$. For $E_b{}^= = 0.81$ eV and $T = 1000$°C, $K_{P^1} = 5.9 \times 10^3$ or 1.14×10^{-19} cm^{-3}. With this value of the constant and C_{PV^-} and C_{P^+} as given above, one finds $C_{V^=} = 3.8 \times 10^{18}$ cm^{-3}, much larger than the value 1.2×10^{15} cm^{-3} expected at $n = 2 \times 10^{20}$ cm^{-3}. The reason probably lies in the low value assumed for $E_b{}^=$. If $E_b{}^- = 0.55$ eV (which seems reasonable), $E_b{}^=$ should be ≈ 1.1 eV, giving $(K_{P^1})_{1000°C} = 3.5 \times 10^5 = 6.8 \times 10^{18}$ cm^3 and $C_{V^=} = 6.34 \times 10^{16}$ cm^{-3}, a more acceptable value. Concentrations of other defects at the surface are found using the equations and mass action constants

$$V^- + e^- \rightleftarrows V^=; \quad K_2 = \frac{C_{V^=}}{C_{V^-}n} = \left(\frac{h^2}{2\pi m_e{}^*kT}\right)^{3/2} \exp 0.11\ \text{eV}/kT$$

$$V^\times + e^- \rightleftarrows V^-; \quad K_1 = \frac{C_{V^-}}{C_{V^\times}n} = \left(\frac{h^2}{2\pi m_e{}^*/kT}\right)^{3/2} \exp 0.5\ \text{eV}\ kT$$

$$P^+ + V^- \rightleftarrows PV^\times; \quad K_P = \frac{C_{PV^\times}}{C_PC_{V^-}} = 4 \exp 0.55\ \text{eV}/kT$$

$$P^+ + V^\times \rightleftarrows PV^+; \quad K_{P^+} = \frac{C_{PV^+}}{C_{P^+}C_{V^\times}} = 4 \exp 0.25\ \text{eV}/kT$$

with $m_e{}^* = 1.25$, $(K_2)_{1000°C} = 8.6 \times 10^{-21}$ cm^3, $(K_1)_{1000°C} = 3 \times 10^{-19}$ cm^3, $(K_P)_{1000°C} = 1.2 \times 10^{-21}$ cm^3 and $(K_{P^+})_{1000°C} = 7.6 \times 10^{-22}$ cm^3. The result is: $C_{V^-} = 2.2 \times 10^{16}$, $C_{V^\times} = 2.2 \times 10^{14}$, $C_{PV^\times} - 1.53 \times 10^{17}$ and $C_{PV^+} = 9.7 \times 10^{13}$, all cm^{-3}.

10. Starting from the concentrations established by complete equilibrium at the surface (see above), one can calculate defect concentrations as $f(C_T)$ inside the crystal, making one of various possible assumptions: (*i*) assume that all processes except vacancy formation reach equilibrium, but that the vacancy concentration remains fixed at the value established at the surface, *i.e.*,

$$(C_V)_T = C_{PV^-} + C_{PV^\times} + C_{PV^+} + C_{V^=} + C_{V^-} + C_{V^\times} = 2.5 \times 10^{20}\ \text{cm}^{-3}$$

(*ii*) assume that all processes, including vacancy formation reach equilibrium (calculate n from

$$C_T = n + 2\,C_{PV^-} = n + \frac{7.72 \times 10^{-47}n^3}{1 - 3.86 \times 10^{-42}n^2}$$

(*iii*) assume (*ii*) up to a certain depth below the surface, and change to (*i*) at greater depths. Results of calculations according to (*i*) and (*ii*) using values of the constants as mentioned under 9 are given in Tables I and II. Although (*i*) seems to be best in line with the assumption of excess vacancy generation by splitting of PV pairs, Table I shows this model gives a decrease of n faster than proportional to C_T, contrary to what is observed (see Fig. 4). Case (*ii*) (Table II), on the other hand, shows the proper variation of n with C_T, but does not show the increase of C_{PV^+}/C_T or $C_{PV^\times}/C_T$ with decreasing C_T required to explain the increase of $D \propto n^{-2}$. Case (*iii*) may give the best over-all description.

Table III shows the result for the case that vacancy equilibration is frozen in ≈ 0.8 μm from the surface, where $C_T \approx 2 \times 10^{20}$ cm^{-3}. Table III shows that C_{PV} and C_{PV^+} are always << C_{PV^-} and therefore will not play an important role in P diffusion. On the other hand the ratio $r = C_{PV^-}/C_T$ shows the variation needed to explain the observed variation of D_P with concentration: r decreases with decreasing C_T from 8.3 to 2.1×10^{20}, accounting for the decrease of D_P; r increases from $C_T = 2 \times 10^{20}$ to $C_T = 7 \times 10^{19}$, accounting for the increase in D_P, r then becomes approximately constant at a value close to ½ (giving D_P= constant); r finally decreases (which should give a decreasing D_P) but by now we are well below the concentration (Fig. 6, $n = 10^{19}$) down to which D_P was measured. The agreement can probably be im-

Table I. Surface and bulk concentrations of various defects at 1000°C for fixed-vacancy concentration of 2.5 × 10²⁰ cm⁻³

	Surface concentrations	Bulk concentrations				
C_T	8.3×10^{20}	6×10^{20}	5.5×10^{20}	5.2×10^{20}	5.1×10^{20}	5.1×10^{20}
P^+	5.8×10^{20}	3.5×10^{20}	3.0×10^{20}	2.7×10^{20}	2.6×10^{20}	2.6×10^{20}
e^-	3.3×10^{20}	10^{20}	5.0×10^{19}	2.0×10^{19}	1.5×10^{19}	1.1×10^{19}
PV^-	2.5×10^{20}	2.5×10^{20}	2.5×10^{20}	2.5×10^{20}	2.5×10^{20}	2.5×10^{20}
$PV^\times$	1.5×10^{17}	5.1×10^{17}	1.0×10^{18}	2.6×10^{18}	3.3×10^{18}	4.7×10^{18}
$V^=$	6.3×10^{16}	1.1×10^{17}	1.2×10^{17}	1.4×10^{17}	1.4×10^{17}	1.4×10^{17}
V^-	2.2×10^{16}	1.2×10^{17}	2.8×10^{17}	7.9×10^{17}	1.1×10^{18}	1.5×10^{18}
$V^\times$	2.2×10^{14}	4.1×10^{15}	1.9×10^{16}	1.3×10^{17}	7.3×10^{17}	1.4×10^{18}
PV^+	9.7×10^{13}	1.1×10^{15}	4.3×10^{15}	2.7×10^{16}	1.5×10^{17}	2.8×10^{17}

Table II. Surface and bulk concentrations of various species at 1000°C, assuming equilibrium throughout

C_T	8.3×10^{20}	3.2×10^{20}	1.1×10^{20}	5.1×10^{19}	2.6×10^{19}	10^{19}	10^{18}
P^+	5.8×10^{20}	2.7×10^{20}	1.0×10^{20}	5.1×10^{19}	2.5×10^{19}	10^{19}	10^{18}
e^-	3.3×10^{20}	2.2×10^{20}	1.0×10^{20}	5.0×10^{19}	2.5×10^{19}	10^{19}	10^{18}
PV^-	2.5×10^{20}	5.1×10^{19}	4.0×10^{18}	4.9×10^{17}	6.0×10^{16}	3.9×10^{15}	3.9×10^{12}
$PV^\times$	1.5×10^{17}	4.7×10^{16}	8.2×10^{15}	2.0×10^{15}	5.0×10^{14}	7.9×10^{13}	7.9×10^{11}
$V^=$	6.3×10^{16}	2.7×10^{16}	5.7×10^{15}	1.4×10^{15}	3.6×10^{14}	5.7×10^{13}	5.7×10^{11}
V^-	2.2×10^{16}	1.5×10^{16}	6.6×10^{15}	3.3×10^{15}	1.7×10^{15}	6.6×10^{14}	6.6×10^{13}
$V^\times$	2.2×10^{14}	2.2×10^{14}	2.2×10^{14}	2.2×10^{14}	2.2×10^{14}	2.2×10^{14}	2.2×10^{14}
PV^+	9.7×10^{13}	4.5×10^{13}	1.7×10^{13}	8.4×10^{12}	4.2×10^{12}	1.7×10^{12}	1.7×10^{11}
C_{PV^-}/C_T	3.1×10^{-1}	1.6×10^{-1}	3.7×10^{-2}	9.6×10^{-3}	2.4×10^{-3}	3.9×10^{-4}	3.9×10^{-6}
$C_{PV^\times}/C_T$	1.85×10^{-4}	1.5×10^{-4}	7.6×10^{-5}	3.9×10^{-5}	2.0×10^{-5}	7.9×10^{-6}	7.9×10^{-7}
C_{PV^+}/C_T	1.2×10^{-7}	1.4×10^{-7}	1.6×10^{-7}	1.7×10^{-7}	1.7×10^{-7}	1.7×10^{-7}	1.7×10^{-7}

Table III. Surface and bulk-defect concentrations at 1000°C assuming constant total vacancy concentration at $C_T \leqq 2 \times 10^{20}$ cm^{-3}

	Complete equilibrium			ΣV = constant			
C_T	8.3×10^{20}	2.1×10^{20}	1.7×10^{20}	1.2×10^{20}	7.2×10^{19}	4.3×10^{19}	9.2×10^{18}
P^+	5.8×10^{20}	1.9×10^{20}	1.5×10^{20}	10^{20}	5.0×10^{19}	2.5×10^{19}	7.0×10^{18}
e^-	3.3×10^{20}	1.7×10^{20}	1.3×10^{20}	7.9×10^{19}	2.9×10^{19}	5.0×10^{18}	10^{18}
$V^=$	6.3×10^{16}	1.6×10^{16}	2.1×10^{16}	3.1×10^{18}	6.3×10^{16}	10^{17}	3.7×10^{16}
V^-	2.2×10^{16}	1.1×10^{16}	1.9×10^{16}	4.6×10^{18}	2.5×10^{17}	2.3×10^{18}	4.3×10^{18}
$V^\times$	2.2×10^{14}	2.2×10^{14}	5.0×10^{14}	2.0×10^{15}	3.0×10^{18}	1.6×10^{18}	1.43×10^{19}
PV^-	2.5×10^{20}	2.1×10^{19}	2.1×10^{19}	2.1×10^{19}	2.1×10^{19}	1.7×10^{19}	1.75×10^{18}
$PV^\times$	1.5×10^{17}	2.6×10^{16}	3.4×10^{16}	5.6×10^{16}	1.5×10^{17}	7.0×10^{17}	3.2×10^{17}
PV^+	9.7×10^{13}	3.2×10^{13}	5.6×10^{13}	1.5×10^{14}	1.1×10^{15}	2.9×10^{16}	7.6×10^{16}
C_{PV^-}/C_T	1.6×10^{-1}	10^{-1}	1.2×10^{-1}	1.8×10^{-1}	3.0×10^{-1}	4.0×10^{-1}	1.9×10^{-1}

proved by a slight modification of the various constants. Even the result as presented, however, seems sufficiently satisfactory to allow us to conclude that the entire diffusion behavior of P can be explained on the basis of PV^- as the only P-transporting species.

R. B. Fair and J. C. C. Tsai:[3] The first point raised by Professor Kroger concerns the relationships between ionized phosphorus concentration, C_{P^+}, the phosphorus-double ionized vacancy concentration, C_{PV^-}, and electron concentration, n, in P-doped Si. We have assumed $C_{P^+} = n$ to derive the equilibrium relation between total P concentration, C_T, and n. Therefore, C_{P^+} only refers to the unpaired P^+ atoms in the Si. Dr. Kroger's argument that this leads to an inconsistency is not valid. The claim that $C_T \simeq 2n$ is only true near $n = 2 \times 10^{20}$ cm^{-3} (see Fig. 5). Thus, $C_{P^+} = C_{PV^-}$ only at this concentration indicating that 50% of the P atoms are paired with $V^=$ vacancies. The total P concentration is

$$C_T = C_{P^+} + C_{PV^-} \qquad [1A]$$

At higher electron concentrations, $C_{PV^-} > C_{P^+}$ and the relation $C_{P^+} = n$ cannot be proven wrong by saying Eq. [1A] above is invalidated as Kroger argues.

If one prefers to account for the ionized P through the relation

$$C_{P^+} = n + C_{PV^-} \qquad [2A]$$

as Kroger proposes, the relationship between C_T and n still turns out approximately the same. On this basis

$$C_T = n + \frac{2Kn^3}{1 - Kn^2} \qquad [3A]$$

plots very nicely on our Fig. 5 with $K = 8.3 \times 10^{-42}$ cm^6. However if one uses Kroger's relation for C_{PV^-}, then

$$C_{PV^-} = \frac{Kn^3}{1 - Kn^2}$$

$$\propto n^5 (n \lesssim 1.5 \times 10^{20}) \qquad [4A]$$

Our Eq. [13] predicts $C_{PV^-} \propto n^3$ which is supported by the $n_s{}^3$ dependence of the tail region diffusion coefficient shown in our Fig. 9. Therefore, the data would suggest that using $C_{P^+} = n$ is still reasonable.

In order to make easier reference. the remaining comments will be numbered to coincide with the items in Kroger's discussion.

2. By using Eq. [4A] above it can be shown that for $C_T > 7.5 \times 10^{20}$ cm^{-3}, $C_{PV^-} > n$. Thus, at high concentrations, Fig. 13 is correct.

3. Again, it all depends upon how you wish to do your accounting. However, this argument Kroger presents is not valid since $n = C_{PV^-}$ is not generally true.

4. The tightly bound PV^- pair has a level at $E_C - 0.39$ eV. However at diffusion temperatures the vacancy can move to second and third neighbor sites without completely dissociating from the P^+ atom. This is a result of the distributed nature of the charge associated with a vacancy and the long-range Coulomb binding of the pair. During these excursions the effect of pair association on shifting the ionization energy of the vacancy's second acceptor level would be reduced. If the vacancy gives up an electron from this level while at a third neighbor site, the pair binding enthalpy would be reduced by ~0.3 eV and pair dissociation would be assured.

Equation [17] in our paper is not rigorously derived because of the simplifying assumption that the concentration of PV^- pairs at $n = n_e$ is proportional to the surface electron concentration ($\propto n_s{}^3$). The argument is that the PV^- concentration is relatively constant out to a distance that is within "jumping distance" of $n = n_e$. Thus, we assume only a "quasi-equilibrium" of PV^- pairs at $n = n_e$ which reflects the equilibrium conditions near the surface.

5. For the case of P in Si the flux equation for PV^- pairs must include an electric field term since the PV^- pairs are in equilibrium with C_{P^+} (and thus, n). One cannot dispute the fact that a built-in electric field exists in the diffused layer, since n decreases with increasing depth into the Si. Kroger's flux equation should be written as

$$J_Y = J_X = -D_x \frac{\partial C_x}{\partial C_T} \frac{\partial C_T}{\partial x} - D_x C_x \frac{1}{n} \frac{\partial n}{\partial x} \qquad [5A]$$

The total flux consists of PV^- (or $P^+V^=$) pairs, PV (or P^+V^-) pairs and PV^+ (or $P^+V^\times$) pairs. Thus

$$J_T = J_{PV^-} + J_{PV} + J_{PV^+} \qquad [6A]$$

At very high P concentrations, the dominant diffusing species is the PV^- pair. Thus

$$J_{PV^-} = -D^= \left[\frac{\partial C_{PV^-}}{\partial C_T} \frac{\partial C_T}{\partial x} + \frac{C_{PV^-}}{n} \frac{\partial n}{\partial x} \right]$$

$$= -D^= \left[1 + \frac{\partial n}{\partial C_T} \left(\frac{C_{PV^-}}{n} - 1 \right) \right] \frac{\partial C_T}{\partial x} \qquad [7A]$$

At values of $C_T \lesssim 7 \times 10^{19}$ cm^{-3}, $\partial n/\partial C_T \simeq 1$ and $C_{PV^-} << n$. Thus, $J_{PV^-} \simeq 0$. At $C_T \gtrsim 3 \times 10^{20}$ cm^{-3}, $\partial n/\partial C_T \simeq 1/3$ (from Fig. 5 in our paper). For the case of no electric field

$$J_{PV^-} = -D^= \left[1 - \frac{\partial n}{\partial C_T} \right] \frac{\partial C_T}{\partial x} \qquad [8A]$$

The ratio of J_{PV^-} (with E field)/J_{PV^-} (no field) varies from ~1.3 at $C_T = 3 \times 10^{20}$ cm^{-3} to 2.7 at $C_T = 1 \times 10^{21}$ cm^{-3}. Therefore, the effect of the built-in field on on the diffusion of PV^- pairs is important and is approximated by the field factor, $h \simeq 2$, in Eq. [2] and [7] from our paper.

For the case of As in Si, if AsV^- were the dominant species transporting As, an n^2 dependence would be observed for As diffusivity at high concentrations. However, As diffusivity increases linearly with n, supporting the $AsV^\times$ (or As^+V^-) pair model.

6. As we have just shown, the equilibrium distribution of electrons created by the unpaired P^+ atoms creates the built-in field which, in fact, influences P diffusion regardless of the charge state of the domi-

[3] Bell Laboratories, Reading, Pennsylvania 19604.

nant vacancy responsible for diffusion. Thus, for each kind of P-vacancy pair, an equation similar to Eq. [7A] above can be written.

7. We disagree that the formation enthalpy of V^- and $V^=$ should be less than for $V^\times$. True, energy is gained when an electron attaches to $V^\times$. However, because a vacancy has no central ion core, another carrier of opposite charge must be created (in the valence band). Thus, energy must be added to take an electron from the valence band to the conduction band, and ΔH_{V^-} and $\Delta H_{V^=} > \Delta H_{V^\times}$ by the ionization entropies ΔH_I^- and $\Delta H_I^=$, respectively. Van Vechten and Thurmond have discussed this in recent papers.[4,5]

8. Figure 13 is only claimed as a simplified, ideal profile.

9. We agree that the binding energy for the PV^- pair may be too low ($E_b^= = 0.81$ eV). Since we arrived at $E_b^=$ from the expression

$$E_b^= = \Delta H_{V^=} + Q_E^= - Q_I^=$$

where $\Delta H_{V^=} = 3.93$ eV is the formation enthalpy of $V^=$ vacancies, $Q_E^= = 1.25$ eV is the pair migration energy, and $Q_I^= = 4.37$ eV is the phosphorus diffusion energy, we are subtracting relatively large numbers from each other. With the uncertainty associated with these numbers, it is not unreasonable to be off by 0.3 eV in the calculation of $E_b^=$.

10. It is clear to us that none of the examples presented in Kroger's Tables I, II, or III are correct. As Kroger points out, the model presented in Table I yields a decrease in n faster than proportional to C_T, and the results in Table II cannot account for $D \propto n^{-2}$, both contrary to what is observed. However, the same can be said for the results in Table III where a large difference is calculated between C_T and n. Experimentally, $C_T = n$ for all concentrations below $\sim 5 \times 10^{19}$ cm^{-3} (see Fig. 5). The Table III model also predicts that P is only transported by PV^- pairs. This is unreasonable. The data in Fig. 7 of our paper show that for high concentration diffusions below 1000°C, the tail region diffuses faster than the surface region. For example, at 900°C the tail diffusivity is $\sim 10^{-13}$ cm^2/sec for a P profile with $C_S \simeq 5 \times 10^{20}$ cm^{-3}. The peak P diffusivity in the surface is 3×10^{-14} cm^2/sec. This result suggests that a different species is transporting P in the tail which we contend is the P^+V^- (or PV^x) pair and which has approximately a four times larger intrinsic diffusivity than the PV^- pair at 900°C. Also, the data in our Fig. 7 show that below $n \simeq 7 \times 10^{19}$ cm^{-3}, the diffusion coefficient of P no longer shows an n^2 dependence. When the surface concentration is also below $\sim 7 \times 10^{19}$ cm^{-3} (or $n_s/n_i \lesssim 7$), Fig. 11 shows that P diffusivity is constant (except for the electric field contribution). These two observations support our model that the PV^- pair only exists at high P concentrations ($n > n_e$). When $n_s/n_i \lesssim 7$, the dominant diffusing pair is the P-neutral vacancy ($P^+V^\times$) specie.

In conclusion, we feel that our model is valid to the extent that we have assumed quasi-equilibrium conditions at $n = n_e$ which reflects surface equilibrium. It is clear to us that this is the most consistent model to emerge among the dozen or so P diffusion models proposed over the past 20 years. However, our model does not predict the "anomalous" reduction in junction depth with increasing surface concentration as observed by Duffy *et al.*[6] Recent work by one of us (RBF) has shown that the misfit strain introduced by high concentrations of P causes the Si bandgap to be narrowed by as much as -0.13 eV at the P solubility limit. This bandgap shrinkage results in a reduction of PV^- pairs through mass action effects which can reduce P diffusivity by as much as 70%. These results are explained with our present model as a basis, and will be published in the near future.

[4] J. A. Van Vechten and C. D. Thurmond, *Phys. Rev. B*, 14, 3551 (1976).
[5] J. A. Van Vechten and C. D. Thurmond, *ibid.*, 14, 3539 (1976).
[6] M. C. Duffy, F. Barson, J. M. Fairfield, and G. H. Schwuttke, *This Journal*, 115, 84 (1968).

Auger Analysis of Thermally Oxidized GaAs Surfaces

I. Shiota, N. Miyamoto, and J. Nishizawa
(pp. 1405-1409, Vol. 124, No. 9)

R. W. Kee:[7] In the paper under discussion, there are several important errors made by the authors in analyzing the Auger depth profiles of thermally oxidized GaAs. The initial statement was made that the higher energy states, $L_3M_{4,5}M_{4,5}$, for Ga and As were used for in-depth profiling in order to avoid peak overlapping as observed in the lower energy range (<100 eV) and to obtain precise peak-to-peak values of their Auger signals. However, their Auger equipment parameters, specifically the modulation amplitude, time constant, and sweep rate which were 5 eV, 1 sec, and 6 eV/sec, respectively are such as to prevent accurate peak measurement. As shown in Fig. 1,

[7] Department of Electrical Engineering, Colorado State University, Fort Collins, Colorado 80523.

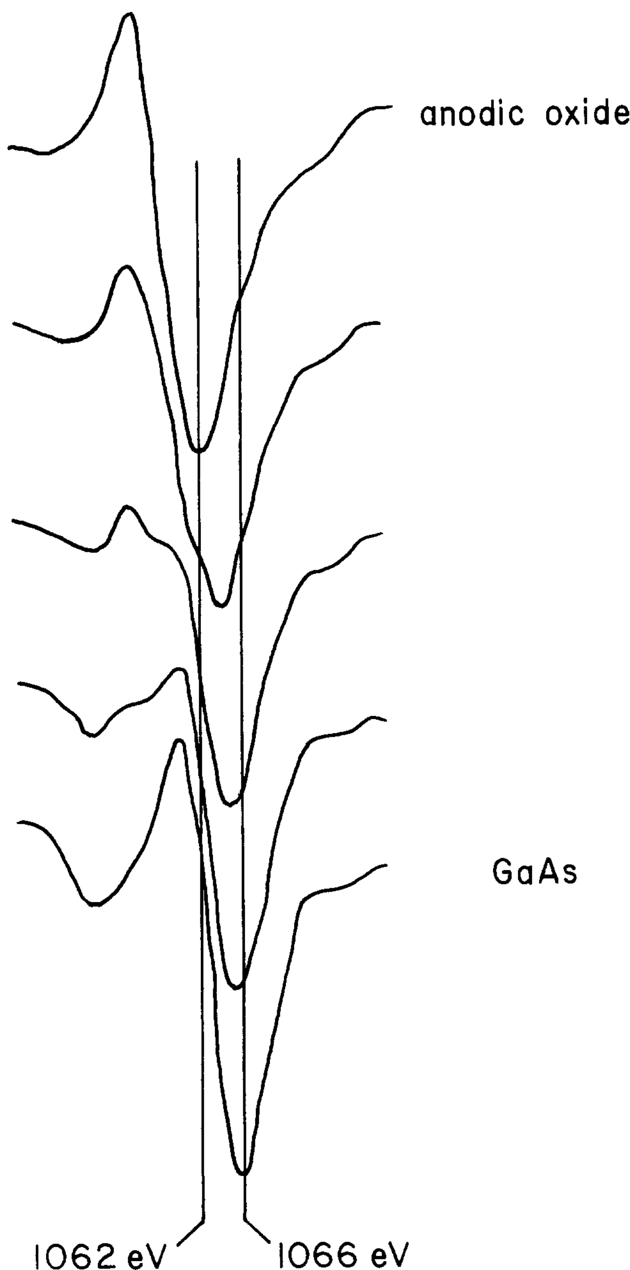

Fig. 1. Ga LMM Auger line progression from the outer anodically grown oxide, through the interfacial region, and into the GaAs substrate.

which was taken from work in our own laboratory on anodic oxide/GaAs structures, peak overlap occurs because the Ga LMM line for Ga_2O_3 is some 4 eV lower than that for GaAs, and since both chemical states are distinct.[8] The Ga LMM line progression of Fig. 1 was obtained by using a low modulation voltage of 2 eV, a reduced sweep rate of 1 eV/sec, and recording the individual Auger peaks for Ga while sputtering through the oxide and into the GaAs substrate.

Several researchers have found that the "valley" which occurs at the interface of a grown oxide/semiconductor[9,10] or metal[11] structure is merely an artifact due to the simultaneous addition of the Auger lines for a given element in two distinct chemical states, and does not necessarily indicate a depletion of that given element in or near the interface. The depletion or even accumulation of an element can only correctly be deduced when a concentration *vs.* depth profile has been constructed by taking into account the relative Auger sensitivities[12] for the elements involved and the effects of overlap of the two distinct states. It is important to note that the Auger sensitivity for an element can change with chemical state.[8,13] From Fig. 4 and 6 of the authors' paper, one observes that from simply considering the chemical configuration, *e.g.*, Ga_2O_3 (thermal oxide) and GaAs, Ga should occur in concentrations of 40% and 50%, respectively, however, the Auger peak-to-peak height for Ga in Ga_2O_3 is roughly 40% greater than that of GaAs, which is not consistent with their statements.

Upon construction of a concentration *vs.* depth profile by the authors, they will probably find that the occurrence of a Ga depletion at the oxide-GaAs interface is a phenomenon only observed in the Auger peak-to-peak profile, and is not found in the concentration *vs.* depth profile.

The authors' technique of defining the oxide thickness based upon whether the Auger peak ratio, 0/Ga, starts to decrease from the value of 1.75 for the bulk oxide, is rather unique since most researchers define the oxide thickness by drawing tangent lines to the 0 KLL peak-to-peak amplitudes and labeling the oxide thickness by either, where the 0 KLL peak height reaches 10% of its original value,[14] or where the tangent line in the interfacial region intersects the tangent line from the zero level of 0 KLL in the substrate.[9] If either of these conventions were employed in the present article, the constructed data values for the activation energy, E_a, would change due to the contribution of the increased interfacial width with increased oxide thickness. An additional complication would come from the Auger peak-to-peak height profile which was given in Fig. 5 for the 700°C thermal oxide on GaAs (111)B. If the depth profile results of Fig. 5 were reproducible, then the situation is indeed interesting, however, a misalignment of the ion and electron beams can also give a similar broadening of the interfacial region.[9]

I. Shiota, N. Miyamoto, and J. Nishizawa:[15] First of all, we must make a simple and important correction about a measuring parameter of AES; the time constant of the lock-in amplifier was not 1 sec, which was stated erroneously in the original paper, but 0.1 sec in all our AES measurements.

Now, the main point of the rebuttal made by R. W. Kee is that the Ga depletion observed

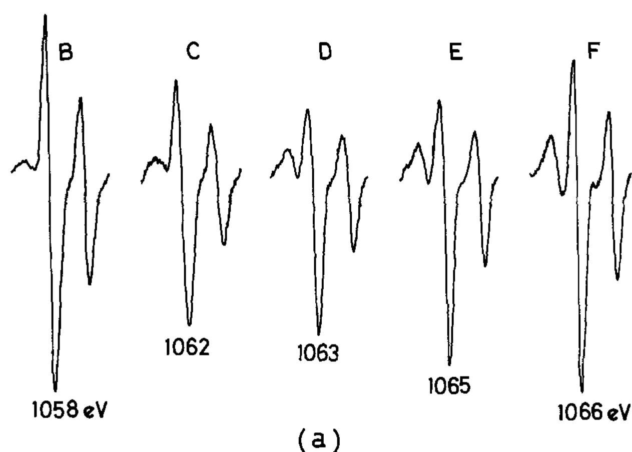

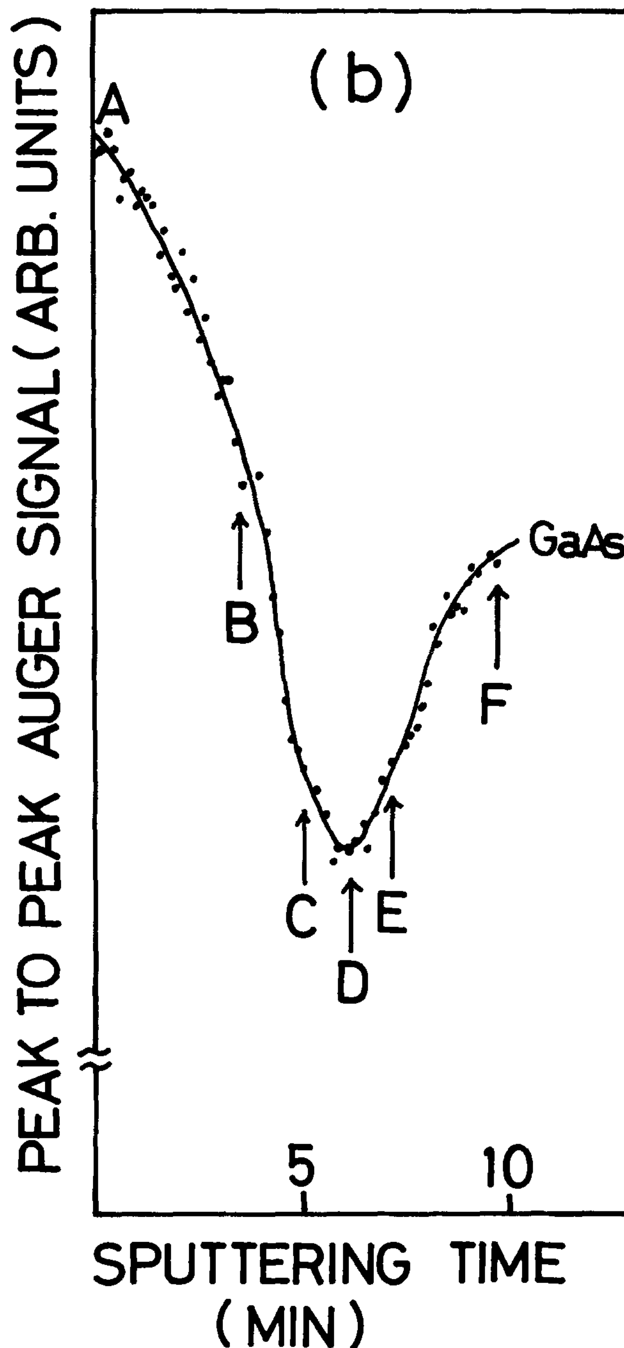

Fig. 2. The Ga $L_{2,3}M_{4,5}M_{4,5}$ Auger spectra. Each spectrum in (a) was resulted correspondingly from each point on depth-profile as shown in (b). Argon sputtering voltage is 2 kV and a Ga $L_3M_{4,5}M_{4,5}$ peak was monitored.

[8] R. W. Kee, Masters Thesis, Colorado State University, Ft. Collins, Colorado (1977).
[9] J. S. Johannessen, W. E. Spicer, and Y. E. Strausser, *J. Appl. Phys.*, 47, 3028 (1976).
[10] C. W. Wilmsen and R. W. Kee, *J. Vac. Sci. Technol.*, 14, 953 (1977).
[11] J. S. Solomon and V. Meyers, *Am. Lab.*, 8, 31 (1976).
[12] L. E. Davis, *et al.*, "Handbook of Auger Electron Spectroscopy," 2nd ed., Physical Electronics Ind., Inc., (1976).
[13] C. C. Chang, B. Schwartz, and S. P. Murarka, *This Journal*, 124, 922 (1977).
[14] W. E. Spicer, I. Lindau, and C. R. Helms, *Research/Development*, 28, 20 (1977).
[15] Research Institute of Electrical Communication, Tohoku University, Sendai, Japan 980.

near a thermal oxide-GaAs interface is merely an artifact characteristic of in-depth profiling by using peak-to-peak Auger height. It is of course most suitable to discuss the matter quantitatively from a concentration *vs.* depth profile as indicated, but it is even possible to deduce some conclusions based on a qualitative and a careful observation of the AES spectra and on the assistance from concrete phenomena concerned. In the case of SiO_2-Si interfaces, Si Auger peaks such as KLL one show a clear splitting into 1618 and 1606 eV in our spectrometer[16] leading to the apparent decrease in concentration of Si if only the over-all peak-to-peak height is monitored. At the thermal oxide-GaAs interface we could not observe any splitting of the $GaL_3M_{4,5}M_{4,5}$ peak as shown in Fig. 2. (Measuring parameters are the same as those of original depth profiling data and as follows; modulation amplitude 5 eV, scanning rate 6 eV/sec, and time constant 0.1 sec. No peak splitting was observed in the $GaL_3M_{4,5}M_{4,5}$ peak even under the more precise condition of MA 2 eV, SR 1 eV/sec, and $\tau = 0.1$ sec, while the lower part $GaM_{2,3}M_4M_4$ peaks showed a clear splitting as seen from a spectrum 3 of the original Fig. 3.) Auger peak shape varies in a rather simple manner, as going from oxide to GaAs and the positive peak suppression seen at the anodic oxide-GaAs interface is not so serious in our case.

Peak-to-peak width ΔE takes a maximum value around a point C located just outside the bottom of the valley and ΔE is equal at a point E and a point F. Therefore, the region from the point C to D seems to be the one with a largest chemical effect to the GaLMM Auger peak. Since the region E and F almost consist of Ga and As, there seems to be little difference in Auger sensitivity, especially in escape depth, comparing with that of GaAs bulk. This is supported from the fact that the appearance energy, ΔE, and the shape in Ga LMM peak are almost the same in E and F point.

From above qualitative discussions the decreasing trend from F to E seems to be fundamental, while around the bottom of the valley the tendency may be enhanced by the chemical effect. The same conclusion is conducted from the behavior of $GaM_{2,3}M_4M_4$ peak seen from spectra 4 and 5 in the original Fig. 3.

Further supports are obtained from such actual phenomena that there is observed a large orientation dependence in the shape of the valley and that the Ga valley is closely related to the As accumulation near the interface. We explained the reason of appearance of the Ga valley in the original paper as follows; it was responsible for a selective oxidation of GaAs with a resulting product of Ga_2O_3 and another constituent of As necessarily accumulated around the interface, in other words, the depletion of Ga was accompanied. Therefore, the Ga depletion at the interface is more easily generated by thermal oxidation than by anodic one because of a larger amount of As incorporation in the oxide state in the latter.

Finally, although our method to determine the oxide thickness is not always popular, we could not determine the thickness definitely by the conventional method because of a large dependence of the width of the interface region on oxidation conditions.

Analyzing point is a center of sputtered crater and so the edge effect can be safely ignored in our system.

[16] J. Ruzyllo, I. Shiota, N. Miyamoto, and J. Nishizawa, *This Journal*, 123, 26 (1976).

Electrolytic Etching of Aluminum from an Al-Al_3Ni Two-Phase Matrix in Aluminum Chloride Containing Molten Salts

C. L. Hussey, J. C. Nardi, L. A. King, and J. K. Erbacher
(pp. 1451-1454, Vol. 124, No. 9)

K. P. Quinlan and J. J. Hutta:[17] The paper by Hussey *et al.* describes an electrolytic procedure where aluminum is etched away from Al_3Ni fibers. These fibers are formed in an aluminum matrix utilizing a unidirectional solidification technique.[18] These fibers, when isolated, may possibly have wide applications extending from the area of catalysis[19] to microelectronic devices. In their electrolytic etching procedure, Hussey *et al.* used two molten salts containing aluminum chloride which requires inert atmospheres and high temperatures. We have developed a procedure where high quality Al_3Ni fibers can be obtained using 1*M* potassium hydroxide as the electrolyte. The method is carried out within a time period where the Al_3Ni fibers are not attacked by the 1*M* KOH. The advantages of a 1*M* KOH electrolyte over molten salts containing aluminum chloride are obvious.

Control potential electrolyses were accomplished with a potentiostat/galvanostat (Princeton Applied Research Corporation, Model 173) equipped with a current to voltage converter (PAR, Model 176). A universal programmer (PAR, Model 175) controlled the voltage output of the potentiostat. The cell consisted of a reference saturated calomel electrode, a platinum counterelectrode, and the aluminum-Al_3Ni ingot as the working electrode. The electrolyte was the 1*M* KOH solution. An agar-saturated KCl salt bridge was used with the calomel electrode. Contact to the Al-Al_3Ni ingot was made by wrapping platinum wire around the ingot. Electrolyses were carried out for 1 1/2 hr at a potential of -0.2V in unstirred solutions. Maximum anodic current was observed at -0.2V in the anodic polarization curve of the Al-Al_3Ni electrode. The current density decreased from an initial value of 0.02 to 0.01 A/cm^2 during the electrolyses. The ingot turned black and was composed of a matted mass of Al_3Ni fibers. Scanning electron micrographs of the product illustrated the preferential etching of aluminum leaving well-defined fibers. Energy-dispersive x-ray analysis verified their composition of aluminum and nickel.

The present method has the additional advantage of being applicable to a continuous process where the fibers can be removed and the KOH replenished.

[17] Department of the Air Force, Rome Air Development Center, Deputy for Electronic Technology, Hanscom AFB, Massachusetts 01731.

[18] R. W. Hertzberg, F. D. Lemkey, and J. A. Ford, *Trans. Met. Soc. AIME*, 233, 342 (1965).

[19] F. D. Lemkey, G. Golden, and C. S. Brooks, Annual Meeting Abstracts of the Materials Research Society, Cambridge, Massachusetts November 15-17, 1976.

JOURNAL OF THE ELECTROCHEMICAL SOCIETY

ACCELERATED

BRIEF COMMUNICATIONS

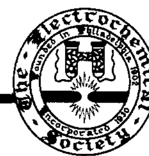

June 1978

Stress Corrosion Crack Initiation Sites in Zirconium Alloys Exposed to Iodine Vapor

D. D. Cubicciotti* and R. L. Jones

SRI International, Menlo Park, California 94025

Stress corrosion cracking (SCC), induced by fission products, is believed to be responsible for occasional service failures of the cladding of light water reactor fuel rods (1). It has been known for some time that iodine, an abundant fission product, is capable of promoting slow crack growth at cladding service temperatures in zirconium alloys (2). Both experimental results (2, 3) and theoretical considerations (4) indicate that the formation of a sharp crack in the metal surface is the key event in the overall iodine SCC failure process but it has proved difficult to elucidate the crack initiation mechanism (2).

We have recently completed an investigation of iodine-induced crack initiation and have found that the crack nuclei responsible for iodine-induced SCC failure invariably form at sites in the metal surface that contain unusually large local concentrations of alloying elements or impurities (3). In our study, samples of nuclear grade zirconium alloy sheet or thin walled tubing were deformed at about 600 K by pressing a 1.6 mm steel ball against them. As a result, a small region of the surface opposite the indenter was deformed to a strain of a few percent in biaxial tension while being exposed to a gas containing a small pressure of iodine vapor. After the test, the deformed region was cut out, cleaned by argon-ion milling, and examined for cracks in an SEM equipped with an energy dispersive X-ray analyzer.

In the absence of iodine, cracks in the metal were observed only under very severe mechanical conditions and were probably due to creep-rupture failure. When iodine was present cracks occurred under much milder mechanical conditions but not in the complete absence of strain. Therefore, we attributed the cracks formed in the presence of iodine to SCC. Two distinctly different types of iodine-induced cracks were observed in all materials tested (stress relieved Zircaloy-4, stress relieved Zircaloy-2, and annealed Zircaloy-2). Small cracks were observed in all samples strained in iodine, and in occasional samples relatively large cracks were also observed.

The small cracks, which were rarely larger than one or two grain diameters, generally formed at microstructural inhomogeneities (such as certain grain boundaries in recrystallized material) that would be expected to be associated with large local stress concentrations in an anisotropic material undergoing plastic flow. These crack initiation sites were not associated with any detectable chemical inhomogeneities. Some typical small cracks are shown in Figure 1. The larger cracks, which ranged in size up to ten or more grain diameters, were observed in about 30% of the samples and differed from the small cracks in that they were consistently associated with local concentrations of impurities (Al, Si, or Ti) or alloying elements, i.e., Fe, Cr, Sn.

To investigate the relation of these two types of cracks to iodine-induced SCC failure, two lengths of annealed Zircaloy-2 tube were pressurized for 30 minutes at 595 K with helium and iodine mixtures. The pressures were such that the nominal hoop stresses were 210 MPa and 310 MPa which are respectively below and above the threshold stress for iodine induced failure of the tubing, (~ 280 MPa, see Reference 3). Sections of the inner surfaces were ion cleaned and examined in the SEM. Small intergranular cracks similar to those in Figure 1 were observed in both samples. Larger cracks associated with chemical inhomogeneities occurred at many sites in the sample stressed at 310 MPa

*Electrochemical Society Active Member.

Key words: Cracking; Metals; Nucleation; Fission

but were not observed in the sample stressed at 210 MPa. An example of a larger crack is shown in Figure 2. The crack is associated with a local impurity concentration and follows the boundary of the impurity-rich region. The crack in Figure 2 is of exactly the same type as the larger cracks observed in the indenter tests.

We interpret these results to indicate that initiation of the cracks that result in iodine-induced SCC failure occurs most readily at sites in the metal surface that contain higher-than-average local concentrations of alloying additives or impurities. It is possible that microsegregation of alloying elements and impurities also plays an important role in crack initiation in other cases of SCC. If so, improved resistance to SCC failure may be achievable by devising treatments that eliminate microsegregation in component surfaces because the conditions required for crack initiation frequently define the SCC failure threshold for as-fabricated components.

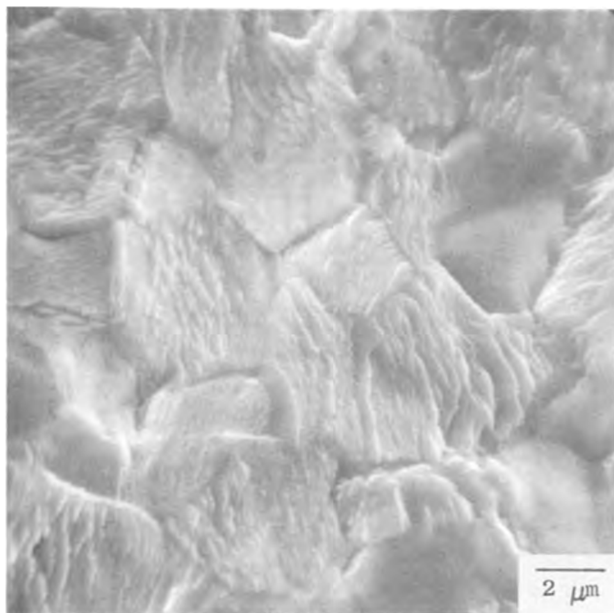

Figure 1: Annealed Zircaloy-2 Tubing Exposed to 40 Pa of Iodine at 590 K and Deformed ~ 5% in an Indenter Test. SEM Photograph of the Argon-Ion Cleaned Center of the Deformed Region Showing Typical Small Cracks.

ACKNOWLEDGMENTS

The authors are indebted to Drs. J.T.A. Roberts and H. Ocken of EPRI for many stimulating technical discussions. Thanks are due to Professor Stanley M. Howard, and Mr. Jan Terry for their help with the experiments. The research was funded by EPRI under Project Number RP 455-1.

REFERENCES

1. J.T.A. Roberts, et al., Nuclear Technology 35, 131 (1977).
2. B. Cox and J. C. Wood, Corrosion Problems in Energy Conversion and Generation, p. 275, C. S. Tedman, Jr., ed. (Electrochem. Soc., N.Y., 1974).
3. D. Cubicciotti and R. L. Jones, "EPRI-NASA Cooperative Project on Stress Corrosion Cracking of Zircaloys," EPRI NP 717, March 1978.
4. E. Smith and G. V. Ranjan, Proceedings: ANS Topical Meeting on Water Reactor Fuel Performance, p. 337, (St. Charles, Illinois, May 1977).

Manuscript submitted March 8, 1978; revised manuscript recieved March 21, 1978.

Publication costs of this article were assisted by SRI International.

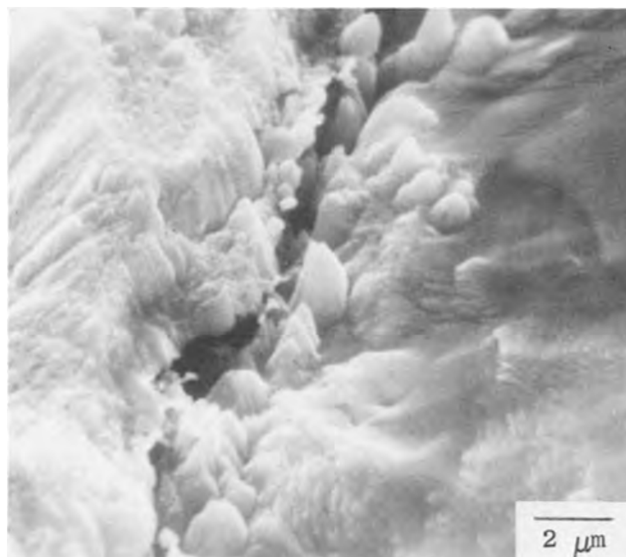

Figure 2: A Large Crack Observed in an Annealed Zircaloy-2 Pressure Test Specimen Stressed to 310 MPa at 595 K with Iodine Present. The Ridge of Light Material Contains Abnormal Concentrations of Sn, Ti, and Fe.

Reduction of Oxygen on Teflon-Bonded $NiCo_2O_4$/Graphite Electrodes

A. C. C. Tseung* and K. L. K. Yeung**

Department of Chemistry, The City University, St. John Street, London EC1, England

1. INTRODUCTION

King and Tseung (1)(2)(3) studied the reduction of O_2 on freeze-dried $NiCo_2O_4$ and found that it possessed high activity for the reduction of oxygen (∿ 250 mA/cm^2 at 0.65V, 5N KOH, iR corrected, 100% O_2 room temperature). However, the performance decreased to less than 2 mA/cm^2 within 2-3 hrs. X-ray and thermogravimetric measurements and solid state chemistry considerations suggest that the spinel $NiCo_2O_4$ phase, prepared by freeze-drying of the mixed nitrates, followed by thermal treatment at 400°C for 10 hrs, has the following electronic structure:

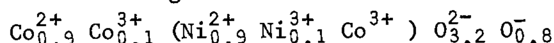

$$Co^{2+}_{0.9}\ Co^{3+}_{0.1}\ (Ni^{2+}_{0.9}\ Ni^{3+}_{0.1}\ Co^{3+})\ O^{2-}_{3.2}\ O^{-}_{0.8}$$

where cations outside the brackets are in tetrahedral sites and those inside the brackets are in octahedral sites. The existence of loosely bound O^- on the surface is most probably responsible for the high activity of $NiCo_2O_4$ at room temperature. It was thought that the decay in performance was associated with the substitution of OH^- into the lattice (2) and more probably the partial reduction of $NiCo_2O_4$ (4).

Some further investigation on the mechanism of decay is presented in this paper.

2. EXPERIMENTAL

Freeze-dried $NiCo_2O_4$ (1) was used as the catalyst in Teflon-bonded electrodes. The BET surface area was 40 m^2/g and the specific resistivity of the powder $NiCo_2O_4$ was less than 10 ohm-cm. A small number of $NiCo_2O_4$ electrodes were prepared by immersing 100 mesh nickel screens into 2M $Co(NO_3)_2.6H_2O$/1M Ni $(NO_3)_2.6H_2O$ solution, followed by thermal decomposition at 400°C in air. The process was repeated until the $NiCo_2O_4$ leading reached 35 to 40 mg/cm^2. These electrodes were examined by X-ray powder diffraction techniques before and after electrochemical testing.

Electrochemical testing was done on a 'floating' half cell. The potential of the working electrode was monitored with a Dynamic Hydrogen Electrode (DHE). A piece of Pt foil was used as the counter electrode. The potential of the working electrode was controlled by a Chemical Electronics Potentiostat.

3. RESULTS AND DISCUSSION

3.1. Cyclic Voltammetric Studies.--Figure 1 shows the cyclic voltammogram of a Teflon-bonded $NiCo_2O_4$ electrode operated in the floating mode in air, 5N KOH, room temperature. The electrode was continuously scanned from the open circuit voltage (Ca. 1.10 V) to 500 mV vs DHE.

There was a rapid decay over 1 hr. when the current density at 500 mV vs DHE decreased from 120 mA/cm^2 to 50 mA/cm^2. On the other hand, there is practically no change in the performance when the voltage is scanned continuously from open circuit to 750 mV. (Figure 2).

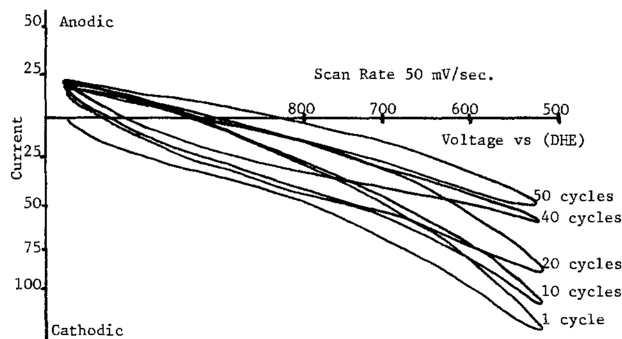

Fig.1. Cyclic Voltammogram of Teflon-bonded $NiCo_2O_4$ electrode from O.C.V. to 500 mV vs DHE, Air, room temperature, 5N KOH

As it is difficult to get clear X-ray powder diffraction patterns of the catalyst in a Teflon-bonded $NiCo_2O_4$ electrode, the electrodes prepared by direct decomposition of the mixed nitrates on nickel screens were used in the X-ray studies.

Table I. X-ray powder diffraction analysis of the $NiCo_2O_4$ electrode in 5N KOH at room temperature

Electrode	Potential (mV) (vs DHE)	Atmosphere	Time	Phases Present
1	500	Air	1 week	Co_2O_3, NiO, CoO, NiOOH, $CoO.H_2O$
2	750	Air	1 week	$NiCo_2O_4$ spinel
3	open circuit	Air	1 week	$NiCo_2O_4$ spinel
4	500	N_2	3 days	Co_2O_3, NiO, CoO, NiOOH, $CoO.H_2O$
5	750	N_2	3 days	$NiCo_2O_4$ spinel

The results clearly show that the $NiCo_2O_4$ spinel is stable at potentials above 750 mV vs DHE. At 500 mV vs DHE, the $NiCo_2O_4$ spinel structure is destroyed completely and the resultant product is a mixture of Co_2O_3, NiO, CoO, $CoO.H_2O$, NiOOH, none of which are active for O_2 reduction. Therefore, it is reasonable to assume that if a Teflon-bonded electrode is operated at or above 750 mV vs DHE, the performance should be stable. This is indeed the case — the performance of a Teflon-bonded $NiCo_2O_4$ electrode remained unchanged at 25 mA/cm^2, 750 mV, 5N KOH, Air over a test period of 130 hrs.

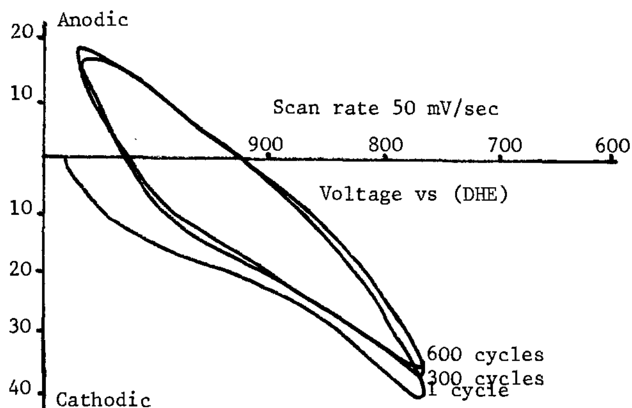

Fig. 2. Cyclic Voltammogram of Teflon-bonded $NiCo_2O_4$ electrode from O.C.V. to 700 mV vs DHE, Air, room temperature, 5N KOH.

Controlled-potential coulometric studies at 500 mV in a stream of N_2 showed that the reduction current is over 4 times greater than the amount required to reduce the loosely bound oxygen, thus giving additional evidence that the bulk of $NiCo_2O_4$ is reduced.

3.2. Performance of Teflon-bonded $NiCo_2O_4$/Graphite electrodes.—Since the current density of $NiCo_2O_4$ electrodes at or above 750 mV vs DHE is only of the order of 30 mA/cm^2 at room temperature, it is necessary to improve the performance by mixing $NiCo_2O_4$ with high surface area graphite (500 m^2/g). Previous work by Goldstein and Tseung (5) on the cobalt-iron oxide/graphite system showed that the reduction of oxygen can be treated as a two step process:

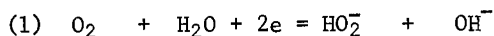

$$(1) \quad O_2 + H_2O + 2e = HO_2^- + OH^-$$

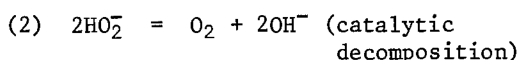

$$(2) \quad 2HO_2^- = O_2 + 2OH^- \text{ (catalytic decomposition)}$$

The evolved O_2 is then recycled for further reduction in (1). The maximum possible enhancement for a cobalt-iron oxide/graphite electrode is a doubling of a graphite electrode's i_o. Cobalt-iron oxide is a non-conductor which has good H_2O_2 decomposition activity but it cannot reduce oxygen. On the other hand, since $NiCo_2O_4$ is a good peroxide decomposition catalyst, as well as a relatively active oxygen reduction catalyst, we expect such combinations to be more active. The performance of Teflon-bonded $NiCo_2O_4$/graphite, and graphite electrodes at 20 and 70°C shows (Figure 3) that 10 wt% $NiCo_2O_4$/graphite electrodes give 200 mA/cm^2 at 750 mV, significantly better than graphite electrodes. Further optimization should lead to more significant improvements.

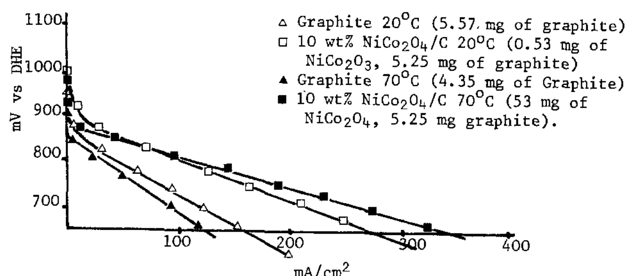

Fig. 3. V-i curves for Teflon-bonded 10 wt% $NiCo_2O_4$/C, and graphite electrodes supported on 100 mesh nickel screen 5N KOH, Air, iR corrected.

4. ACKNOWLEDGEMENT

This study was supported by the Science Research Council.

5. REFERENCES

1. W.J. King, A.C.C. Tseung, Electrochimica Acta, Vol. 19, 485 (1974).
2. W.J. King, A.C.C. Tseung, Electrochimica Acta, Vol. 19, 493 (1974).
3. W.J. King, A.C.C. Tseung, Brit. Pat. 1461764, 19 Jan. 1977.
4. G. Singh, M.H. Miles, S. Srinivasan, Paper presented at the NBS Meeting on Electrocatalysis, Washington, Dec.(1975).
5. J.R. Goldstein, A.C.C. Tseung, J. of Physical Chemistry, 76, 3646, (1972).

Manuscript Feb. 8, 1978; revised manuscript received Feb. 24, 1978.

*Active Member.
*Student Member.

Key words: oxygen reduction, nickel cobalt oxide, graphite, spinel.

JOURNAL OF THE ELECTROCHEMICAL SOCIETY

ELECTROCHEMICAL SCIENCE
—AND TECHNOLOGY

JULY
1978

Effects of Calcium, Potassium, and Iron Ions on Degradation of β″-Alumina

Itaru Yasui[1] and R. H. Doremus*

Department of Materials Engineering, Rensselaer Polytechnic Institute, Troy, New York 12181

ABSTRACT

The influence of calcium, potassium, and iron impurities in sodium-sulfur cells on β″-alumina electrolytes were studied. Sections of the ceramic were analyzed with the electron microprobe after cyclic electrolysis of the cells. No degradation by iron was detected. The distribution of potassium in the β″-alumina became more uniform as electrolysis proceeded, and the cell impedance increased by factors of two or three. Calcium was the most damaging impurity; even in small concentrations it caused large increases in cell impedance and calcium concentrated in the grain boundaries of the β″-alumina.

Impurities can degrade the performance and life of the β″-alumina electrolyte in a sodium-sulfur cell (1-6). In the absence of an electric field potassium exchanges with sodium in large grains in β-alumina in contact with a sodium source, and cracks result (6). In this work the influence of potassium, calcium, and iron impurities on degradation of β-alumina after cyclic electrolysis was studied with the electron microprobe and the scanning electron microscope. Calcium was found to be the most damaging impurity; even in small concentrations it causes large increases in the resistance of β″-alumina, and can also cause it to crack.

Experimental

Two different cells were used, as shown in Fig. 1. In one there was sodium inside the β″-alumina tube and sulfur-polysulfide outside; in the other there was Na_2S_4 in both chambers. Impurities were added to the outer chamber as sulfides.

Two different β″-aluminas were used, one with 9.0% Na_2O and 0.8% Li_2O (9.0-0.8) and the other with 8.85% Na_2O and 0.75% Li_2O (8.85-0.75).

The cells were baked at 350°C for 12 hr at 0.02 mm Hg before filling. Sulfur (sublimed) was dried under a reduced pressure at about 70°-80°C and sodium was filtered through a glass frit at about 150°C. Commercial Na_2S_4 (Alfa) was washed with toluene and then dried in vacuum at 130°C for 48 hr. All reactants were placed into the cell under a dry atmosphere and then melted into the cell. The cell was sealed with dry argon at a third of atmospheric pressure. For the Na/S cells 15g of Na and 30g of S were used.

The Na/S cells were first discharged until the composition of the outer chamber reached about Na_2S_4, and then charged and discharged in a 4 hr cycle. The current density was 25-30 mA/cm² for both charging and discharging, and this value was low enough to exclude the possibility of degradation due to the high current density mechanism. The composition of the outer chamber was near Na_2S_4, owing to the short cycle time and the low current density. Simulation cells were also operated in 4 hr cycles with a current density of 25-30 mA/cm².

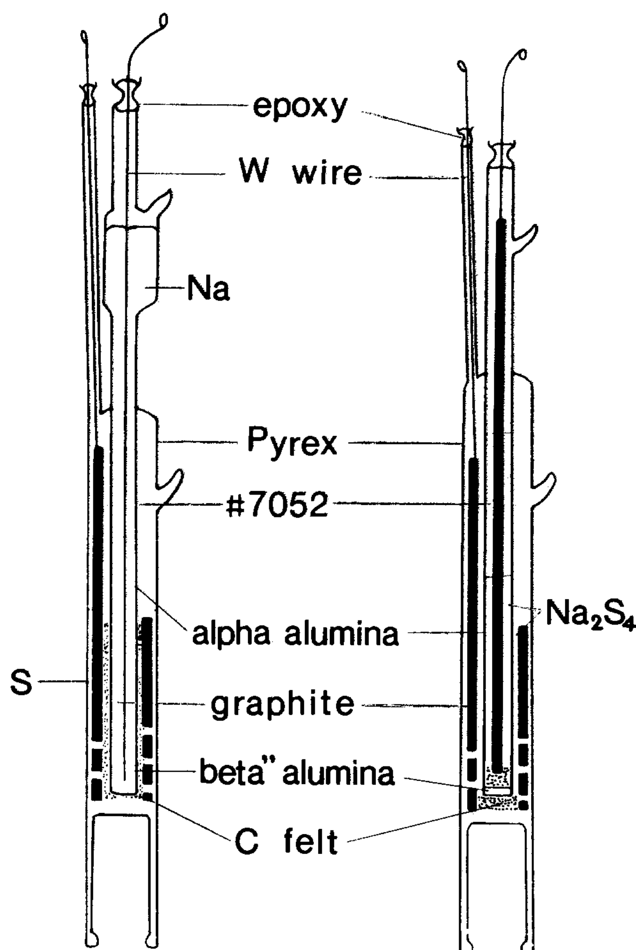

Fig. 1. Structures of Na-S cells and simulation cells

* Electrochemical Society Active Member.
[1] Present address: Institute of Industrial Science, University of Tokyo, Tokyo, Japan.
Key words: ceramics, cell, cracking, energy storage.

The temperature of the cells was 350°C. A conductivity bridge (Leeds & Northrup) was used to measure the impedance of the cell at 1000 Hz. After the cell was cooled down and disassembled, the β''-alumina electrolyte was cut into pieces (or rings) and some samples were analyzed with the electron microprobe or SEM equipped with EDA.

For microprobe (MAC-400) analysis a piece of the β''-alumina was mounted in epoxy resin and polished through 1μ diamond; water was used only for rough sanding and then any contact with water was avoided. The specimen was coated with carbon, distributions of impurities were photographed directly, and several spots were analyzed for the impurities. A back-scattered electron (BSE) image of the analyzed area was taken for identification in the optical microscope.

Standard β''-alumina samples containing known amounts of each of the impurities were prepared. Mixtures of Na_2CO_3, Li_2CO_3, $CaCO_3$, and Al_2O_3 (Linde B) were calcined at about 1000°C and then pressed into pellets, 1 cm diam and about 2 mm thick. These pellets were sintered at 1550°-1580°C for 10-20 min and then annealed at 1400°C for 2-3 hr, all in powder of the same composition.

Sample surfaces were observed in the SEM equipped with EDA (AMR-1000); they were coated with gold for observation or carbon for EDA. Optical micrographs of the analyzed area were taken after etching in HF-HNO_3.

An ion-exchange experiment was performed to clarify the difference between the results with and without electric current. A piece of β''-alumina (9.0-0.8) was immersed in a melt of either $NaNO_3$ or Na_2S_4 with impurity and analyzed with the microprobe and optical microscope.

Experimental Results

The results of cell operation are presented in Table I. The β''-alumina from cell Fe-1 had fine crystals on its surface, as shown in Fig. 2. EDA showed much sulfur and some sodium and calcium in these crystals and no iron in them. Microprobe analysis of a cross section of the ceramic showed less than 0.05 weight percent (w/o) iron; thus iron does not penetrate into the β''-alumina.

In cell K-1 cracks were found on the surface of the β''-alumina that contacted Na_2S_4 containing K^+; the cracks ran almost perpendicular to the surface. A nonuniform distribution of K^+ was observed in the microprobe in sections of β''-alumina from cells K-1 and K-2. The correspondence of the K^+-rich area to particular grains was not clear; large grains did not contain more K^+ than the surroundings. The K^+-rich region contained about 0.6-1.0 w/o of K_2O, showing that up to one tenth of the Na^+ ions in β''-alumina conduction paths were replaced with K^+ ions. The concentration of potassium in larger grains barely exceeded the detection limit, and it was estimated to be no more than 0.05 w/o. There were no appreciable differences in potassium concentrations along cracks.

In cells K-3 and K-4 the distribution of potassium was more uniform than in cells K-1 and K-2, suggesting that the potassium becomes uniformly distributed throughout the ceramic after long operation and that any stress resulting from the initial nonuniform distribution of potassium disappears gradually.

The Na_2S_4 from cell Ca-1 was washed out with methanol, and some white-gray powder was found on the graphite electrode and felt. Analysis of the powder by EDA showed Na, Ca, and S. X-ray diffraction of this powder showed complicated patterns and some peaks were identified as CaS, but most of them were not from CaS. This powder, therefore, was probably a mixture of CaS and some other compounds of Na, Ca, and S.

A section of the β''-alumina from cell Ca-1 was analyzed by means of the electron microprobe. Figure 3 shows the distribution of Ca and an optical micrograph of the same region and shows that Ca tends to take positions in grain boundaries or in smaller grains and that the larger grains contain less Ca than the surrounding regions. The Ca counts obtained for the large grains barely exceeded the background, indicat-

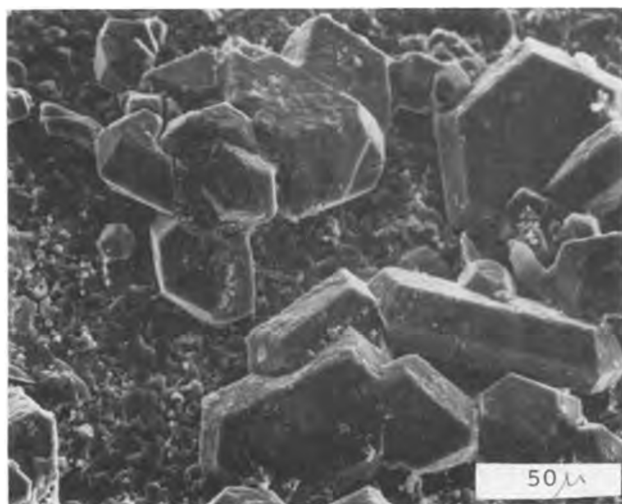

Fig. 2. A scanning electron micrograph of crystals found on the electrolyte of the cell Fe-1.

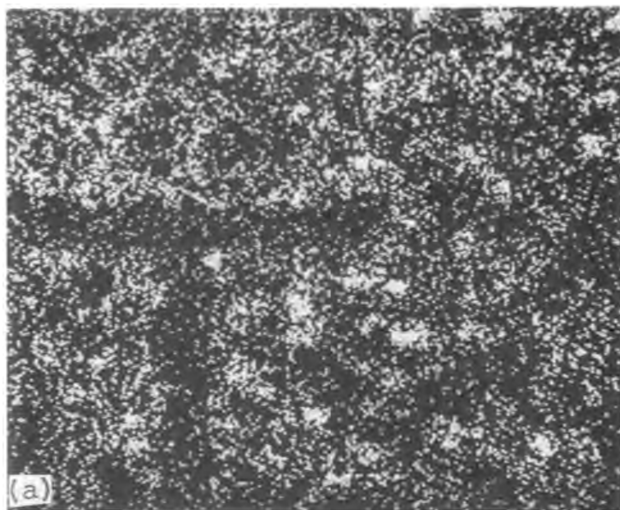

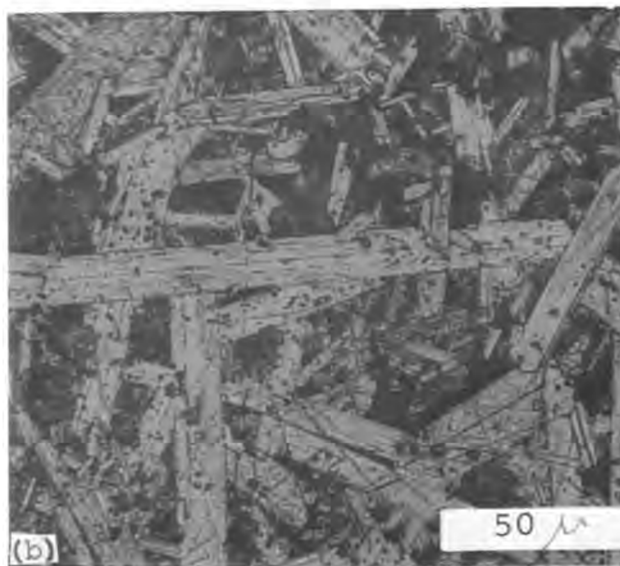

Fig. 3. Distribution of Ca in the electrolyte taken out of the cell Ca-1 and an optical micrograph of the same region.

Table I. Summary of cell designs

Name	Impurity (w/o)	Electrolyte	Cell	Duration days	Impedance	Cracks
Fe-1	FeS 1	9.0-0.8 disk	Na_2S_4	28	Constant	No
K-1	$K_2S_{3.5}$ 1	9.0-0.8 disk	Na_2S_4	9	Constant for 100 hr, then sharp increase and unstable	Yes
K-2	$K_2S_{3.5}$ 0.2	9.0-0.8 disk	Na_2S_4	6	Nearly constant	
K-3	$K_2S_{3.5}$ 0.2	8.85-0.75 tube	Na_2S_4	28	Slow increase to 3 times initial	No
K-4	$K_2S_{3.5}$ 0.2	8.85-0.75 tube	Na/S	33	Slow increase to 2 times initial	No
Ca-1	CaS 1	8.85-0.75 tube	Na/S	6	Rapid increase to 20 times initial in 50 hr, then unstable	No
Ca-2	CaS 0.2	8.85-0.75 tube	Na/S	16	Rapid increase to 20 times initial in 130 hr, then unstable	Yes
Ca-3	CaS 0.05	8.85-0.75 tube	Na/S	28	Slow increase to 8 times initial at 300 hr, then constant	No

ing that the concentration of CaO in large grains was less than 0.05 w/o. For the Ca-rich region the CaO concentration was estimated to be about 3-4 w/o. If each Ca^{2+} ion replaces two Na^+ ions, the formula of the ion exchanged β''-alumina can be written as

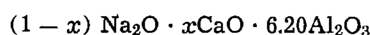

$$(1 - x)\ Na_2O \cdot xCaO \cdot 6.20Al_2O_3$$

with an x for the Ca-rich region of about 0.4-0.5.

Cracks were found on the electrolyte from cell Ca-2 that were different from cracks in the cells K-1 and K-2, and a small piece of the electrolyte came off from a part of surface. The cracks ran diagonally with respect to the surface, unlike cracks from K^+ impurity. Microprobe analysis showed that Ca^{2+} was not distributed evenly along the cracks (Fig. 4); the concentration of Ca was about the same as for cell Ca-1.

Pieces of β''-alumina (9.0-0.8) were kept in the outer chambers of the cells Ca-1 and Ca-2. Microprobe analyses of sections of these pieces are in Fig. 5 and 6, and show a high concentration of Ca in smaller grains or grain boundaries. The concentration of CaO in Ca-rich region was close to that of $CaO \cdot 6Al_2O_3$.

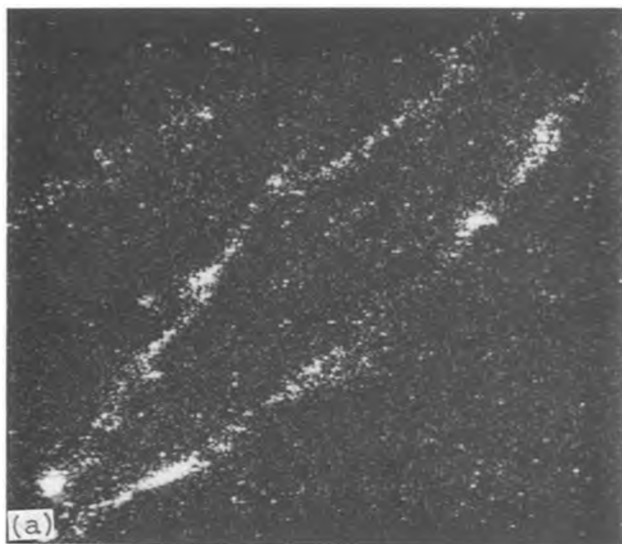

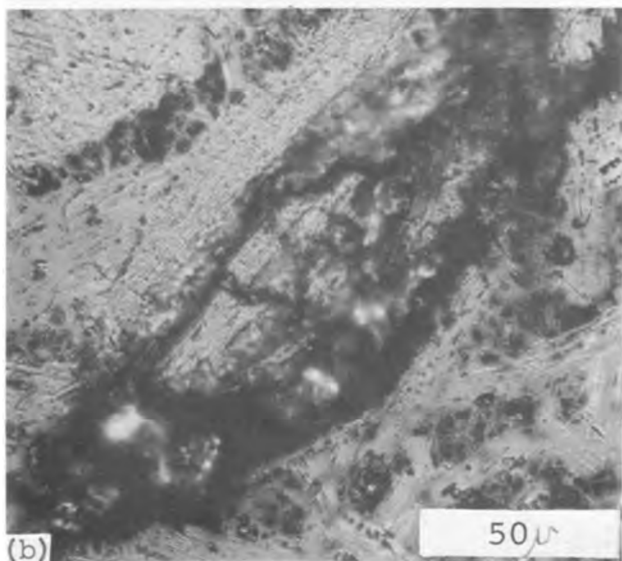

Fig. 4. Distribution of Ca along the cracks found in the electrolyte of the cell Ca-2.

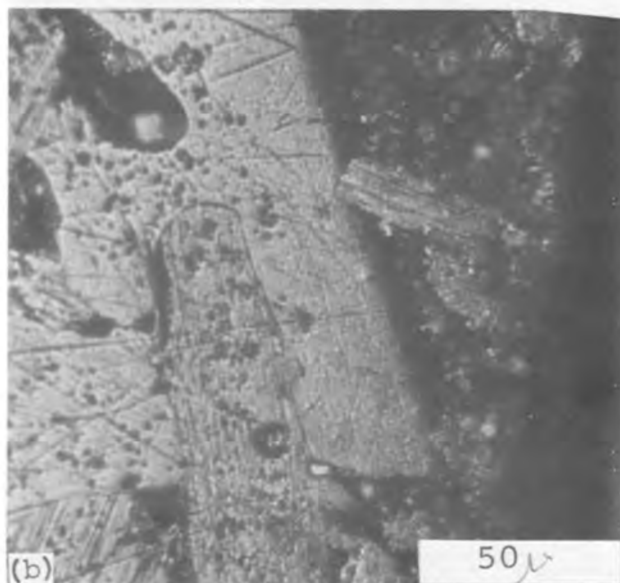

Fig. 5. Distribution of Ca in a piece of β''-alumina (9.0-0.8) which was kept in the sulfur chamber of the cell Ca-2.

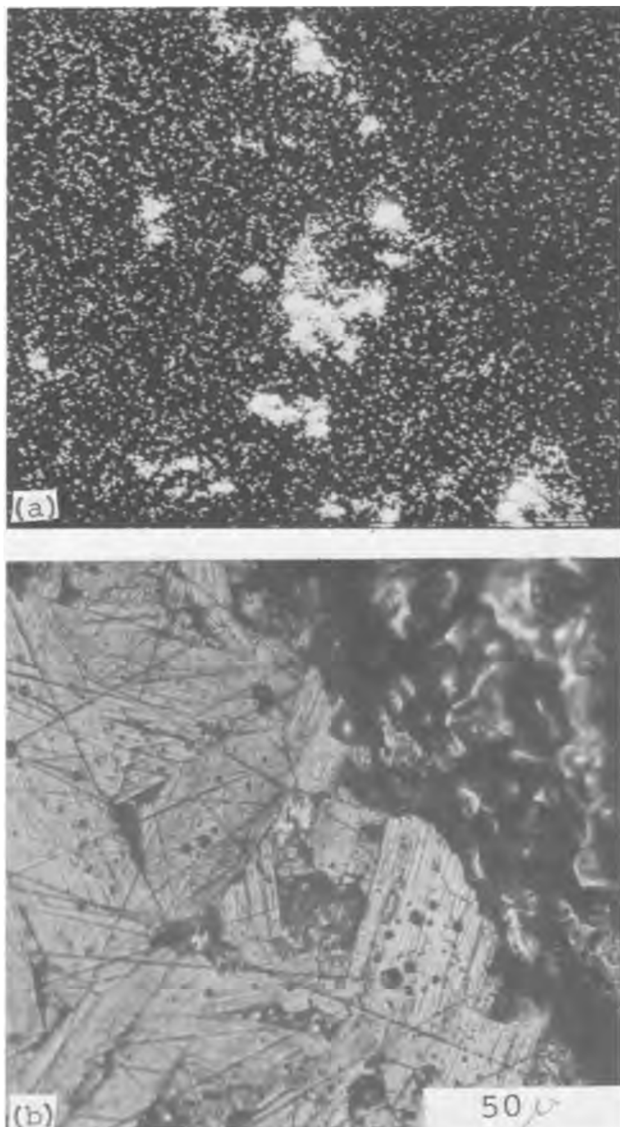

Fig. 6. Distribution of Ca in a piece of β″-alumina (9.0-0.8) which was immersed in the melt of Na_2S_4 containing 1.0 w/o of CaS. The surface of the ceramic cut with a slow speed diamond saw is shown here.

Discussion

Iron has been suggested as a degrading impurity for β″-alumina, because sodium-sulfur cells with stainless steel cases often fail at shorter lifetimes than expected. The present results indicate that iron does not deposit directly on the surface of β″-alumina or penetrate into it. Large amounts of iron compounds are found in the sulfide compartments of failed cells with stainless steel cases, and it is probable that these compounds interfere with cell operation and lead to failure.

In the absence of an electric field potassium penetrates into β″-alumina only in large grains in contact with the melt containing potassium; grain boundaries appear to act as barriers for potassium penetration (6). In contrast the present results show that with a cycling electric field the potassium slowly penetrates into the ceramic, becoming more uniformly distributed at longer cycle times. This result suggests that damage (cracking) from potassium impurity is more likely early in cell life, when the distribution of potassium in the β″-alumina is nonuniform. Once this critical period is past, damage from potassium probably becomes less likely. Small amounts (0.2% in the melt) of potassium can lead to increases by factors of two to three in the cell impedance.

Calcium was found in β″-alumina from failed sodium-sulfur cells in our laboratory (7), but has usually been ignored as a source of degradation of β″-alumina. The present results suggest that it can cause degradation in both conductivity and strength of β″-alumina. Figures 3 and 5 show that calcium concentrates in grain boundaries in β″-alumina either with or without an electric field. Quite small amounts of calcium (0.05% in the melt) can lead to large increases in impedance of the ceramic. This concentration of calcium in the grain boundaries can apparently also lead to cracking of the ceramic, as shown in Fig. 4. Thus calcium can seriously degrade the performance of β″-alumina in a sodium sulfur cell.

Manuscript submitted Sept. 6, 1977; revised manuscript received March 1, 1978.

Any discussion of this paper will appear in a Discussion Section to be published in the June 1979 JOURNAL. All discussions for the June 1979 Discussion Section should be submitted by Feb. 1, 1979.

Publication costs of this article were assisted by Rensselaer Polytechnic Institute.

REFERENCES

1. National Science Foundation Ann. Rep., Contract No. NSF-C805 (1975).
2. J. Fally, C. Lasne, Y. Lazennec, and P. Margotin, *This Journal*, **120**, 1292 (1973).
3. Y. Lazennec, C. Lasne, P. Morgan, and J. Fally, *ibid.*, **122**, 734 (1975).
4. M. D. Hames and J. H. Duncan, *SAE Trans.*, **84**, 988 (1975).
5. S. A. Weiner, *ibid.*, **84**, 662 (1975).
6. I. Yasui and R. H. Doremus, *J. Am. Ceram. Soc.*, **60**, 296 (1977).
7. National Science Foundation Ann. Rep., Contract No. NSF-C805 (1974).

Thermal Analysis of Lead-Acid Cells for Load-Leveling Applications

K. W. Choi* and N. P. Yao*

Argonne National Laboratory, Chemical Engineering Division, Argonne, Illinois 60439

ABSTRACT

Modeling studies have been conducted to determine the temperature field in a lead-acid cell contemplated for load-leveling applications, with daily duty cycles and a weakly equalization charge. The results show that under the proposed daily cycling and without a forced cooling, a maximum temperature rise of 16°C can be expected at the center of a proposed 9.76 kW-hr cell (48.26 cm length × 45.72 cm width × 127 cm height). For such tall lead-acid cells, reduction of cell length by about one-half would reduce the temperature rise by 7°-8°C without employing forced cooling. Conventional water cooling at the cell terminals has little effect in lowering the cell maximum temperature. Moreover, cooling may induce a large temperature gradient in the vertical direction of the cell, which may cause a nonuniform current distribution over the electrode leading to a gradual loss of cell capacity and cycle life. Practical cells in use often incorporate "air lift pump" that facilitates electrolyte stirring or an electrolyte circulation design to minimize the extreme temperature gradients. Gassing during the weekly equalization charge of loading-leveling cells may also enhance internal heat transfer, causing a more uniform temperature distribution. After the weekly equalization charge, the cell temperatures resume their initial values at the end of the rest period.

Thermal behavior in lead-acid batteries during cycling is an important factor affecting battery performance and cycle life. Temperature effects become even more critical for the advanced batteries employed in electrical vehicle propulsion and utility load-leveling applications. Poor battery design can result in significant temperature rise and temperature gradient in the battery during charge and discharge cycles. This temperature rise may cause enough variation in the physical and chemical properties of the battery components to lead to a gradual loss of cell capacity and cycle life. Baker, Gidaspow, and Wasan (1) have given a review for the thermal phenomena in fuel cells and batteries as well as the mathematical treatment to obtain the analytical solution for the temperature fields in fuel cells and batteries. They derived general solutions for maximum cell temperatures at steady state with a boundary condition of constant cell wall temperature. A similar approach has also been applied for the calculation of the maximum temperature in silver-zinc batteries at steady state and at isothermal wall conditions by Meredith and Uchiyama (2). The present work employs finite difference method to study transient thermal phenomena in load-leveling lead-acid cells under conditions of variable cell wall temperature. The same method was applied by us recently to a study of a transient thermal phenomena in lead-acid cells which were designed for electric vehicle propulsion (3). That study (3) addressed heat transfer behavior across the electrode, the electrolyte and their interface for a PbO_2 electrode; the temperature field in a composite lead-acid battery; and the proposed battery cooling methods. However, due to the difference in the battery specifications, construction, and use cycles for the batteries in electric vehicle propulsion and in load-leveling uses, it is expected that the thermal behavior of the batteries for the two applications will not be the same.

In the following, the temperature field and its variation in the cell designed for load-leveling use during daily duty cycles and weekly equalization charge are examined. This study also examines how the cell geometry and the cell designs (with and without water cooling at the electrode terminal) affect the temperature distribution. The proposed utility cycles for these calculations include five daily duty cycles and one weekly equalization charge per week. Three proposed cell designs, designated by Designs A, B, and C (with and without water cooling at the cell terminals) were analyzed. The design characteristics of the cells are summarized in Table I which compares the rated cell capacity and the dimensions of the respective cell designs (4, 5). The terminal water cooling was provided by running the coolant through cooling tubes next to the top of electrodes as shown in Fig. 1. The basic mathematical treatment is quite similar to that of the previous study (3); some modifications, however, have been added and will be discussed in the next section.

Mathematical Treatment

The elements within a single cell container consist of positive electrodes, negatives electrodes, separators and electrolyte. There are electrolyte reservoirs around the compact electrode element. As shown in Fig. 2 for a two-dimension cross section, region I represents the electrode element which is composed of the positive electrodes, negative electrodes, separators and electrolyte; and region II represents the electrolyte reservoir at the surrounding. Previous work (3) has shown that the compact electrode element may be regarded as a unit, and the averaged temperature may be assumed to represent the local temperature at any location within the electrode element, approximately. Following this approximation, Region I will be treated as a homogeneous medium with the averaged physical parameters (density, specific heat, thermal conductivity, and electrical conductivity) and the heat generated within the electrode element may be averaged over the whole region I.

Table I. Design characteristics of proposed lead-acid cells for utility load-leveling

Cell design designation	Type proposed by	Rated cell capacity (A-hr)[a]	Cell dimensions (L × W × H cm)
A	ESB (4) Type VLL 45	9760	48.26 × 45.72 × 127
B	Present study[b]	4500	22.12 × 45.72 × 121.92
C	Westinghouse (5)	2810	22.12 × 45.72 × 76.2

[a] At a 5 hr discharge rate.
[b] Basically a modified ESB design with a reduced cell length.

* Electrochemical Society Active Member.

Key words: lead-acid cells, utility load-leveling, temperature distribution, terminal water cooling.

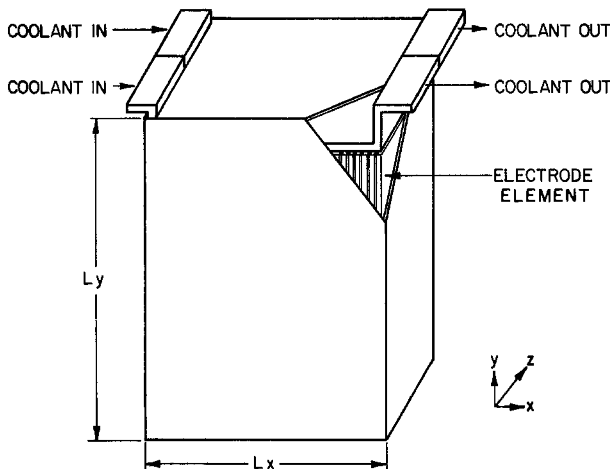

Fig. 1. Lead-acid cell for load-leveling application with a terminal water cooling design.

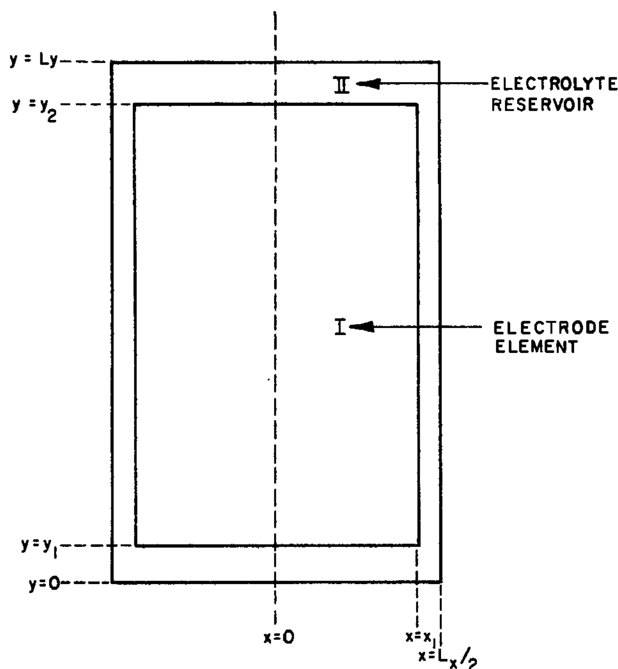

Fig. 2. Cell cross section in two-dimensions

In the previous study of the lead-acid cells for electric vehicle (EV) propulsion use (3), the temperature of the electrolyte in the top reservoir was assumed uniform because of limited amount of electrolyte in the reservoir. The numerical calculation was thus simplified. For the lead-acid cell in load-leveling use, the cell dimensions are much larger than that of the EV cells, and the energy density is not so critical as the EV cells. Generally there is large electrolyte reservoir around the compact electrode element so that the assumption of uniform temperature for the electrolyte reservoir is no longer applicable. Therefore in the following treatment, the numerical solutions for temperature field were obtained by matching region I (the electrode element) and region II (the electrolyte reservoir in the surrounding) with suitable boundary conditions. The calculation method is as follows.

For region I, the governing energy equation is written as

$$\rho\hat{C}\frac{\partial T}{\partial t} = k\frac{\partial^2 T}{\partial x^2} + k\frac{\partial^2 T}{\partial y^2} - \rho\hat{C}\,U\frac{\partial T}{\partial y} + \dot{q} \qquad [1]$$

where ρ, $\hat{C}$, k are the average density, specific heat, and thermal conductivity for the electrode element in region I, respectively. If gassing occurred in the cell during charge cycle, the thermal conductivity k is correlated similarly to the treatment in Ref. [3] as

$$k = k_o\,[1 + a(1 - \xi)i] \qquad [2]$$

where k_o is the thermal conductivity when there is no gassing, a is the gassing correlation constant. ξ is the current efficiency. i is the superficial current density on the electrode. U is the superficial velocity of the electrolyte in y-direction, which relates the electrolyte movement due to the change of electrode porosity in region I. $\dot{q}$ is the rate of internal heat production per unit volume. The velocity gradient may be expressed as

$$\frac{\partial U}{\partial y} = -\frac{\partial \epsilon}{\partial t} \qquad [3]$$

where ϵ is the porosity of the electrode element in region I. The derivative of ϵ with respect to time is written as

$$\frac{\partial \epsilon}{\partial t} = i\left\{\sum_{\substack{\text{solid phase}\\\text{product}}} s_i\overline{V}_i - \sum_{\substack{\text{solid phase}\\\text{reactant}}} s_i\overline{V}_i\right\} / n\mathbf{F}\,W_t \qquad [4]$$

based on the general expression for cell reaction as

$$\sum_{\text{reactant}} s_iM_iz_i = \sum_{\text{product}} s_iM_iz_i \qquad [5]$$

s_i is the stoichiometer coefficient of species i; z_i is the charge carried by species i; $\overline{V}_i$ is the partial molar volume of species i; n is the number of electron transfer for the cell reaction; and W_t is the total thickness of the positive electrode, the negative electrode and the separator. The rate of heat production per unit volume $\dot{q}$, is dependent on the cell reaction, temperature, cycling condition, current efficiency, and cell geometry. Following the derivation as in the previous study (3), $\dot{q}$ may be expressed as a combination of functions $f\left(i, \xi, W_t, V, \sum_j \Delta H_j^\circ\right)$ and $G\left(i, \xi, W_t, \sum_j \Delta C_{p,j}\right)$ as follows

$$\dot{q} = f\left(i, \xi, W_t, V, \sum_j \Delta H_j^\circ\right) + G\left(i, \xi, W_t, \sum_j \Delta C_{p,j}\right)\cdot(T - T_o) \qquad [6]$$

Function f represents the heat production due to the ohmic drop and the heats of cell reactions at the reference temperature (T_o). Function G represents the heat production due to temperature variation for the cell reactions. They may be expressed as

$$f\left(i, \xi, W_t, V, \sum_j \Delta H_j^\circ\right) = \frac{i}{W_t}\left[V - \xi\frac{\Delta H_r^\circ}{n_1\mathbf{F}} - (1 - \xi)\frac{\Delta H_g^\circ}{n_2\mathbf{F}}\right] \qquad [7]$$

and

$$G\left(i, \xi, W_t, \sum_j \Delta C_{p,j}\right) = -\frac{i}{W_t}\left[\xi\frac{\Delta C_{p,r}}{n_1\mathbf{F}} + (1 - \xi)\frac{\Delta C_{p,g}}{n_2\mathbf{F}}\right] \qquad [8]$$

where ΔH_r° and ΔH_g° are the heats of reaction for the faradaic cell reaction and the gas evolution reaction, respectively; n_1 and n_2 are the number of electron transfer for the cell reaction and the gassing reaction, respectively; $C_{p,r}$ and $C_{p,g}$ are the algebraic sums of species partial molar heat capacities for the cell reaction and the gassing reaction, respectively. V is the cell voltage. Other symbols have their initial meanings. For the electrolyte in the reservoir (region II), the energy equation is expressed as

$$\rho_l \hat{C}_l \frac{\partial T}{\partial t} = k_l \left(\frac{\partial^2 T}{\partial t^2} + \frac{\partial^2 T}{\partial y^2} \right) \quad [9]$$

where ρ_l, $\hat{C}_l$, and k_l are the density, specific heat, and thermal conductivity of the electrolyte, respectively. Similar correlation for the thermal conductivity due to gassing (Eq. [2]) will also be applied to the electrolyte in region II.

The initial and boundary conditions may be written as

$$\text{At } t = 0, \text{ any } x, \text{ and any } y, T = T_o \quad [10]$$

where

T_o is the initial cell (outer atmospheric) temperature.

$$\text{At } x = 0, \text{ any } y \frac{\partial T}{\partial x} = 0 \quad [11]$$

At $x = L_x/2$, any y

$$-k\left(\frac{\partial T}{\partial x}\right)_{x-\delta,y} + k\left(\frac{\partial T}{\partial y}\right)_{x,y+\delta} - k\left(\frac{\partial T}{\partial y}\right)_{x,y-\delta} = h(T - T_o) \quad [12]$$

where h, the heat transfer coefficient from the cell wall to the outer atmosphere,[1] is an infinitely small value.

At $y = 0$, any x

$$k\left(\frac{\partial T}{\partial y}\right)_{x,\delta} - k\left(\frac{\partial T}{\partial x}\right)_{x+\delta,y} + k\left(\frac{\partial T}{\partial x}\right)_{x-\delta,y} = h(T - T_o) \quad [13]$$

At $y = L_y$, any x

$$-k\left(\frac{\partial T}{\partial y}\right)_{x,y-\delta} - k\left(\frac{\partial T}{\partial x}\right)_{x+\delta,y} + k\left(\frac{\partial T}{\partial x}\right)_{x-\delta,y} = h(T - T_o) \quad [14]$$

At the interface between the electrode element of region I and the electrolyte of region II, the heat transfer across the two medium should be conserved. The boundary conditions at the interface may be written as

At $x = x_1$, $y_1 < y < y_2$

$$k\left(\frac{\partial T}{\partial x}\right)^{\mathrm{I}} = k_l\left(\frac{\partial T}{\partial x}\right)^{\mathrm{II}} \quad [15]$$

At $y = y_1$, any x

$$k\left(\frac{\partial T}{\partial y}\right)^{\mathrm{I}} = k_l\left(\frac{\partial T}{\partial y}\right)^{\mathrm{II}} \quad [16]$$

At $y = y_2$, any x

$$k\left(\frac{\partial T}{\partial y}\right)^{\mathrm{I}} = k_l\left(\frac{\partial T}{\partial y}\right)^{\mathrm{II}} \quad [17]$$

$(\partial T/\partial y)^{\mathrm{I}}$ and $(\partial T/\partial y)^{\mathrm{II}}$ represent the temperature gradients at region I and region II, respectively.

For the design with cooling at the top of the electrode (at $y = y_2$) the boundary condition may be rewritten as

At $y = y_2$, any x

$$-k\left(\frac{\partial T}{\partial y}\right)^{\mathrm{I}} + k_l\left(\frac{\partial T}{\partial y}\right)^{\mathrm{II}} = \Lambda(T - T_c) \quad [18]$$

where Λ is the averaged heat transfer coefficient across the cooling tube which relates to the material properties and geometries of the cooling tube.

[1] In the present calculation, constant values of h and T_o for a single cell were assumed. In a practical load-leveling battery plant which consists of hundreds of series-parallel connected single cells, the values of h and T_o will generally be affected by the heat transfer between the neighboring cells. However, the assumption of constant h and T_o will still be valid if proper air ventilation for cooling is provided for the space between the cells.

Numerical Calculation

Numerical solutions for Eq. [1]-[4] and [9] were obtained, subjected to the initial and boundary conditions (Eq. [10]-[18]) by finite difference method. Implicit alternating-direction (6, 7) techniques followed by an elimination algorithm were employed. The convergence criterion was set so that the difference between two successive solutions at all mesh points is less than 0.001%.

Description of daily duty cycles and weekly equalization charge.—The calculation was made for five daily duty cycles and one weekly equalization charge. For each daily duty cycle, the cell was discharged at constant current for 5 hr to 100% of the rated capacity, followed by 7 hr constant current charge and 2 hr taper charge. The cell potential was assumed to reach 2.35V at the end of the 7 hr constant current charge and was maintained at 2.35V for the 2 hr taper charge. About 84% of daily discharge capacity was delivered back to the cell at the end of the 7 hr constant current charge. At the end of the 2 hr taper charge, 100% of the daily discharge capacity was returned to the cell. Because the cell voltage was not allowed to exceed 2.35V during the daily charge, the current efficiency was assumed 100%. The weekly equalization charge was operated right after the end of the fifth daily charge cycle, which was a 5 hr constant voltage charge at 2.65V. About 20% excess of the rated capacity was charged to the cell during the 5 hr weekly equalization charge. As most of coulombs during this equalization charge would result in gassing, the current efficiency was assumed to be 5%. The variations of cell potential and cell current during the daily discharge and charge were represented in Fig. 3.

Physical parameters used in the calculation.—The heat of reaction (ΔH_r) for the cell faradaic reaction

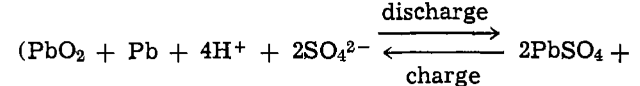

$$(PbO_2 + Pb + 4H^+ + 2SO_4^{2-} \underset{\text{charge}}{\overset{\text{discharge}}{\rightleftarrows}} 2PbSO_4 + 2H_2O)$$

varies with the electrolyte concentration and the electrolyte concentration changes during cell cycling. An empirical correlation for the dependence between ΔH_r and state of discharge (or charge) was made by assuming that the specific gravity of the electrolyte was equal to 1.12 at fully discharged state of the rated capacity, and equal to 1.28 at the fully charged state. Based on the reported values by Vinal (8), this correlation may be expressed as

$$\Delta H_r(298\text{K}) = 367{,}422 + 20{,}900\, Q + 11{,}520\, Q^2 \text{ J/mol} \quad [19]$$

where Q represent the state of charge. When the cell is fully discharged (the specific gravity of the electro-

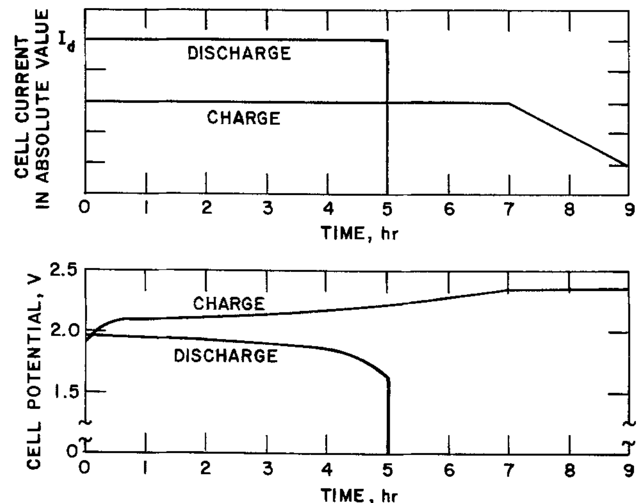

Fig. 3. Variations of cell potential and cell current with time during the daily discharge and charge cycles.

lyte is about 1.12), Q is equal to zero. Q is equal to 0.5 when the cell is charged to one-half of its rated capacity, and equal to 1.0 when the cell is fully charged (the specific gravity of the electrolyte is about 1.28).

The gas evolution reaction during charge may be generally expressed as

$$H_2O \rightarrow H_2 + \tfrac{1}{2} O_2 \quad [20]$$

since the dependence of the heat of the gas reaction to the acid concentration is quite small, the heat of gas reaction (ΔH_g) was assumed to be constant and is equal to 285,786.6 J/mol (9). The heat generation due to the changes of the species partial molar heat capacities with concentration and temperatures are also small. Therefore, the algebraic sums of the species partial molar heat capacities for the faradaic cell reaction ($\Delta C_{p,r}$) and for the gas reaction ($\Delta C_{p,g}$) were assumed constants, equal to -47.53 J/mol-K(8) and -32.89 J/mol-K(10), respectively.

The values of other parameters and data for calculations are listed below.

$a = 2500$ cm^2/A
$\rho\hat{C} = 2.85$ J/cm^3-K
$\rho_1\hat{C}_1 = 3.8087$ J/cm^3-K
$k_o = 0.04433$ W/cm-K
$k_1 = 0.00521$ W/cm-K
$V_{Pb} = 18.25$ cm^3/mole
$V_{PbO_2} = 25.54$ cm^3/mole
$V_{PbO_4} = 48.9$ cm^3/mole
$W_t = 0.9779$ cm
$h = 3.76 \times 10^{-4}$ J/cm^2-sec-K
$\Lambda = 0.2$ J/cm^2-sec-K

For Design A
$L_x = 48.26$ cm, $x_1 = 21.72$ cm
$L_y = 127.0$ cm, $y_1 = 10.16$ cm
$y_2 = 111.76$ cm

For Design B
$L_x = 22.12$ cm, $x_1 = 10.06$ cm
$L_y = 121.92$ cm, $y_1 = 8.13$ cm
$y_2 = 109.71$ cm

For Design C
$L_x = 22.12$ cm, $x_1 = 10.06$ cm
$L_y = 76.2$ cm, $y_1 = 5.08$ cm
$y_2 = 68.58$ cm

Results

The calculated temperature profiles for Cell Design A under the utility cycles (five daily duty cycles and one weekly equalization charge) are shown in Fig. 4 for the case without water cooling. In Fig. 4, curve 1 represents the profile for the maximum cell temperature near the cell center; curve 2 represents the temperature variation at the top of the electrode element (at $x = 0$, $y = y_2$); curve 3 is the temperature variation of the reservoir electrolyte 5.1 cm above the top of the electrode element (the height of the electrolyte above the top of the electrode element is 12.7 cm). These curves in Fig. 4 show that the temperatures profiles are similar throughout the daily duty cycles. A maximum temperature near the cell center (curve 1) may reach as high as 16°C above the ambient temperature. The temperature distribution in the vertical direction of the cell is not uniform, as shown by curves 1, 2, and 3. During the 5 hr weekly equalization charge at 2.65V, the temperature difference in the vertical direction is reduced somewhat due to vigorous gassing. After the weekly equalization charge, the cell temperatures return to nearly their initial temperature at the end of the 2 day rest period during the weekend. Figure 5 compares the profiles of maximum cell temperature for Cell Designs A, B, and C. Curve A is for the Cell Design A without cooling; curve A′ is for the Cell Design A with water cooling at the terminals. The water is circulated in such a rate that the coolant temperature may be assumed to be constant. For curve A′, the coolant temperature is set equal to 298°K; curve A″ is for the same design with a coolant temperature of 283°K. When water cooling is used, the location of maximum cell temperature is no longer near the cell center, but shifts downward from the terminal. Also shown in Fig. 5 are the maximum cell temperatures for Cell Design B (curve B) and for Cell Design C (curve C) without water cooling. Cell dimensions for the three cell designs were listed in Table I. The results with the Cell Design A showed that the water cooling has little effect in reducing the maximum cell temperatures (comparing curves A, A′, and A″ in Fig. 5). The water cooling essentially reduces the temperature at the region near the electrode terminals, as illustrated in Tables II and III. Tables II and III are the maps to show a complete temperature distribution over the one-half of the cell for Cell Design A under the conditions with and without water cooling. However, when the cell length of Design A is reduced from 48.26 to 22.12 cm (that of Design B), the maximum cell temperature in the absence of forced cooling is correspondingly reduced by nearly one-half, or 5°-6°C, as shown in Fig. 5. When the cell height is reduced from 122 cm (for Design B) to 76 cm (for Design C), the maximum cell temperature is reduced by only about 1°C. Figures 6, 7, and 8 compare the temperature profiles in the vertical direction for Cell Designs A, B, and C with and without water cooling. The results clearly show that a large temperature difference in the vertical direction is induced by the water cooling at the cell terminals.

Discussion

Cell Design A without forced water cooling.—Under the proposed utility cycles for load-leveling applications, the numerical results show that a maximum cell temperature (near the cell center) may rise by 16°C above the ambient temperature during daily charge cycles as shown by curve 1 in Fig. 4. The maximum temperature near the cell center is however not readily measurable experimentally. In practice, the electrolyte temperature in the top reservoir is usually measured. In this calculation, the electrolyte temperature 5.1 cm above the top of the electrode element (curve 3 in Fig.

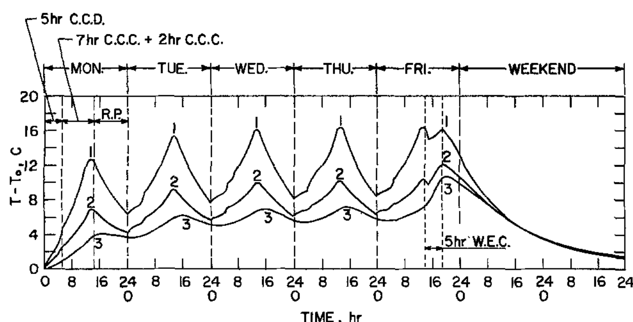

Fig. 4. Temperature variation during utility cycles for the Cell Design A. 1, Cell center; 2, top of electrode element; 3, electrolyte 5.1 cm above the top of electrode element.

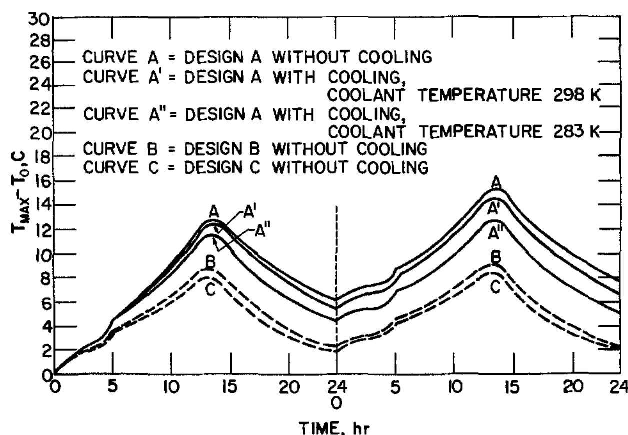

Fig. 5. A comparison of the maximum cell temperature for Cell Designs A, B, and C during the first and second daily cycles.

Table II. Temperature distribution of Cell Design A (ESB cell) at the end of the second daily charge cycle, with no water cooling

	Center axis $x = 0$			→| 2.19 cm |←							Side electrolyte reservoir
$y = L_y$ / Top electrolyte reservoir	2.78	2.76	2.73	2.68	2.61	2.52	2.41	2.31	2.21	2.13	2.12
Top electrolyte reservoir	4.04	4.02	3.98	3.89	3.78	3.64	3.47	3.28	3.07	2.86	2.65
Top electrolyte reservoir	6.12	6.10	6.02	5.90	5.73	5.50	5.22	4.89	4.50	4.07	3.64
$y = y_2$	9.18	9.16	9.04	8.85	8.62	8.30	7.89	7.37	6.73	5.79	5.01
Electrode element	10.44	10.40	10.29	10.10	9.84	9.51	9.10	8.62	8.09	7.53	6.31
Electrode element	11.56	11.52	11.41	11.22	10.95	10.61	10.20	9.71	9.20	8.64	7.32
Electrode element	12.52	12.48	12.37	12.17	11.89	11.54	11.12	10.64	10.09	9.50	8.08
Electrode element	13.32	13.28	13.16	12.95	12.67	12.30	11.87	11.36	10.79	10.16	8.66
Electrode element	13.96	13.92	13.79	13.58	13.28	12.90	12.45	11.92	11.33	10.67	9.11
Electrode element	14.45	14.41	14.28	14.06	13.75	13.37	12.90	12.35	11.74	11.06	9.44
Electrode element	14.82	14.78	14.04	14.42	14.10	13.71	13.23	12.67	12.04	11.34	9.69
Electrode element	15.08	15.03	14.90	14.67	14.35	13.95	13.46	12.89	12.25	11.54	9.86
Electrode element	15.24	15.19	15.06	14.83	14 51	14.10	13.60	13.03	12.38	11.67	9.96
Electrode element	15.31	15.27	15.13	14.90	14 57	14.16	13.67	13.09	12.44	11.72	10.01
Electrode element	15.30	15.25	15.11	14.88	14.56	14.15	13.65	13.08	12.43	11.71	10.00
Electrode element	15.19	15.15	15.00	14.78	14.46	14.05	13.56	12.99	12.34	11.63	9.93
Electrode element	15.00	14.95	14.81	14.58	14.27	13.87	13.38	12.81	12.17	11.47	9.79
Electrode element	14.68	14.64	14.50	14.28	13.97	13.58	13.10	12.54	11.91	11.23	9.58
Electrode element	14.24	14.20	14.07	13.85	13.55	13.16	12.70	12.16	11.55	10.88	9.28
Electrode element	13.66	13.62	13.49	13.28	12.98	12.61	12.16	11.64	11.05	10.41	8.87
Electrode element	12.90	12.86	12.74	12.53	12.25	11.88	11.45	10.95	10.38	9.77	8.31
Electrode element	11.96	11.92	11.80	11.60	11.32	10.97	10.55	10.06	9.52	8.94	7.56
$y = y_1$	10.83	10.78	10.67	10.48	10.21	9.87	9.45	8.95	8.40	7.83	6.57
Bottom electrolyte reservoir	9.54	9.51	9.40	9.22	8.97	8.63	8.21	7.68	7.02	5.90	5.26
Bottom electrolyte reservoir	6.37	6.35	6.27	6.15	5.98	5.75	5.47	5.13	4.76	4.35	3.95
Bottom electrolyte reservoir / $y = 0$	4.33	4.32	4.27	4.18	4.07	3.92	3.75	3.56	3.37	3.23	3.19

↓ 4.88 cm ↑

Electrode element ←→ ← Side electrolyte reservoir →

Center axis $x = 0$ $T - T_o$, C $x = x_1$ $x = L_x/2$

Table III. Temperature distribution of Cell Design A (ESB cell) at the end of the second daily charge cycle, with water cooling at terminals (coolant temperature 298°K)

	Center axis $x = 0$			→| 2.19 cm |←							Side electrolyte reservoir
$y = L_y$ / Top electrolyte reservoir	0.08	0.09	0.09	0.09	0.09	0.10	0.10	0.11	0.12	0.14	0.15
Top electrolyte reservoir	0.12	0.12	0.12	0.12	0.13	0.13	0.14	0.16	0.18	0.20	0.22
Top electrolyte reservoir	0.17	0.17	0.17	0.17	0.17	0.18	0.19	0.21	0.25	0.32	0.40
$y = y_2$	0.21	0.21	0.21	0.21	0.21	0.20	0.20	0.19	0.20	0.39	0.83
Electrode element	3.07	3.06	3.03	2.98	2.95	2.88	2.78	2.69	2.60	2.51	2.23
Electrode element	5.55	5.54	5.49	5.42	5.31	5.18	5.01	4.82	4.60	4.36	3.72
Electrode element	7.65	7.62	7.56	7.45	7.30	7.10	6.87	6.59	6.27	5.92	5.04
Electrode element	9.36	9.34	9.25	9.12	8.93	8.68	8.39	8.04	7.65	7.21	6.14
Electrode element	10.75	10.72	10.62	10.46	10.24	9.95	9.61	9.21	8.76	8.25	7.03
Electrode element	11.85	11.81	11.70	11.53	11.28	10.96	10.58	10.13	9.64	9.08	7.74
Electrode element	12.70	12.66	12.55	12.36	12.09	11.75	11.34	10.87	10.32	9.73	8.29
Electrode element	13.36	13.32	13.20	12.99	12.71	12.37	11.92	11.42	10.85	10.22	8.72
Electrode element	13.84	13.80	13.67	13.46	13.17	12.80	12.35	11.83	11.24	10.59	9.03
Electrode element	14.17	14.13	14.00	13.79	13.49	13.11	12.65	12.11	11.51	10.84	9.25
Electrode element	14.37	14.33	14.20	13.98	13.68	13.29	12.82	12.28	11.67	10.99	9.38
Electrode element	14.44	14.40	14.26	14.05	13.74	13.35	12.89	12.34	11.72	11.04	9.42
Electrode element	14.38	14.34	14.21	13.99	13.68	13.30	12.83	12.29	11.67	11.00	9.38
Electrode element	14.19	14.14	14.01	13.80	13.50	13.11	12.65	12.12	11.51	10.84	9.25
Electrode element	13.84	13.80	13.67	13.46	13.17	12.79	12.34	11.81	11.22	10.57	9.01
Electrode element	13.33	13.29	13.17	12.96	12.67	12.30	11.86	11.35	10.78	10.15	8.65
Electrode element	12.64	12.59	12.47	12.27	11.99	11.64	11.21	10.72	10.17	9.57	8.13
Electrode element	11.74	11.70	11.58	11.39	11.11	10.77	10.36	9.88	9.34	8.77	7.42
$y = y_1$	10.65	10.61	10.50	10.31	10.05	9.71	9.29	8.81	8.27	7.69	6.45
Bottom electrolyte reservoir	9.39	9.36	9.25	9.08	8.83	8.50	8.08	7.56	6.91	5.97	5.18
Bottom electrolyte reservoir	6.28	6.25	6.18	6.06	5.87	5.66	5.38	5.06	4.68	4.28	3.89
Bottom electrolyte reservoir / $y = 0$	4.27	4.25	4.20	4.12	4.01	3.86	3.69	3.50	3.32	3.18	3.14

↓ 4.88 cm ↑

Electrode element ←→ ← Side electrolyte reservoir →

Center axis $x = 0$ $T - T_o$, C $x = x_1$ $x = L_x/2$

4) was shown to rise by about 7°C relative to the ambient temperature during the daily charge cycles. During the weekly equalization charge, the rigorous gassing enhances the internal heat transfer and gives the rise of the electrolyte temperature in the top reservoir by as much as 10°C. The cell temperatures also become somewhat more uniform during the equalization charge due to the gassing (comparing curves 1, 2, and 3 in Fig. 4). The temperature variation throughout the daily duty cycles is almost identical. This suggests that for the similar system, computation of the temperature variation for one or two daily cycles will be adequate to estimate that for the remaining days of the week. After the weekly equalization charge, the cell temperatures return to their initial values at the end of 2 day rest period due to the natural air cooling.

Cell Design A with forced water cooling.—The numerical results, which are plotted in Fig. 5, indicate that the forced water cooling is not effective to reduce the cell temperature at the region away from the terminals. The location of maximum cell temperature shifts from the cell center to the region near the cell bottom as the water cooling is applied at the top terminals (see Fig. 6). The results further show that the maximum cell temperature is reduced by only about 0.8°C for a coolant temperature of 298°K, and by about 2.6°C for a coolant temperature of 283°K (Fig. 5 and 6). This ineffective terminal cooling is related to the limitation of internal heat conduction within the cell. The uneven cooling was shown to yield large temperature difference over the electrode in the vertical direction (Fig. 6). The temperature difference across the electrode in vertical direction is about 12°C for a coolant temperature of 298°K, and 27°C for a coolant temperature of 283°K. This temperature difference over the electrode may induce a nonuniform current distribution because of the change of electrolyte properties such as conductivity, viscosity, and species diffusivities. The nonuniform current distribution may further cause a nonuniform gassing over the electrode during the charge cycles. Therefore the region of the electrode with heavier gassing, may have a serious shedding and softening effects on the active materials. Also the utilization of active material may be very nonuniform due to the nonuniform current distribu-

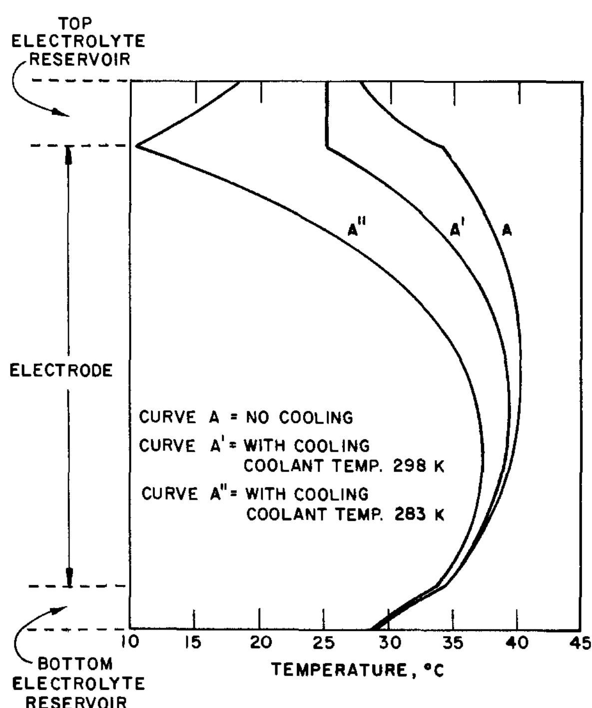

Fig. 6. Temperature distribution across the cell in the y-direction at the end of the second daily cycle for Cell Design A, $x = 0$. Cell dimensions: 48.26 cm L × 45.72 cm W × 127 cm H. Initial cell temperature: 25°C.

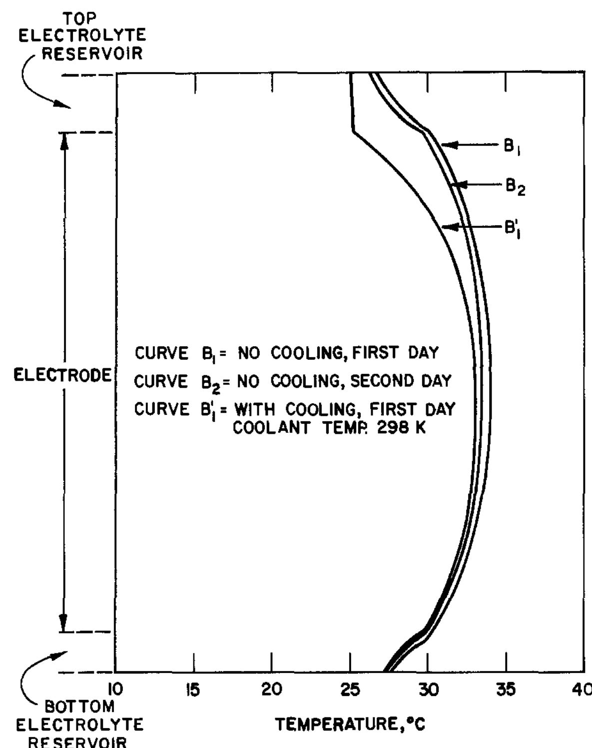

Fig. 7. Temperature distribution across the cell in the y-direction at the ends of daily charge cycles for Cell Design B, $x = 0$. Cell dimensions: 22.1 cm L × 45.72 cm W × 121.92 cm H. Initial cell temperature: 25°C.

tion. The part of the electrode which has poor utilization of active material may gradually become inactive. These effects as caused by the nonuniform temperature distribution, are interrelated and contribute to the deterioration of the cell capacity and cycle life as cycling continues without a proper thermal management.

Cell Designs B and C with and without forced water cooling.—When the cell length is slimmed from 48.26 cm for Cell Design A to 22.1 cm for Cell Design B, the maximum rise of cell temperature is accordingly reduced from 16° to 9°C (curvesA and B in Fig. 5) under the same proposed cycling conditions without forced cooling. When the cell height is reduced from 121.92 cm for Cell Design B to 76.2 cm for Cell Design C, the maximum cell temperature is reduced only by 1°C (curves B and C in Fig. 5). The results indicate that the heat transfer is preferred in the horizontal direction (x-direction) than the vertical direction (y-direction) because of the longer conduction path in the vertical direction of the tall cells. For Cell Design B and Cell Design C, the maximum temperature difference over the electrode may be about 3°-4°C under the proposed duty cycles without forced cooling (curves B_1 and B_2 in Fig. 7; curves C_1 and C_2 in Fig. 8). This temperature difference is tolerable for practical cell operation. The results suggest that without the forced cooling, the cell geometry plays an important role for effective heat transfer and for control of the temperature field provided that the ambient temperature could be properly controlled by air ventilation. When the forced water cooling is applied to the terminals, significant temperature gradients are induced for all three cell designs, and yet without the benefit of reducing significantly the maximum cell temperatures. The large temperature gradients may significantly be reduced by electrolyte circulation (3) or by the electrolyte stirring effected by an air lift pump (4).

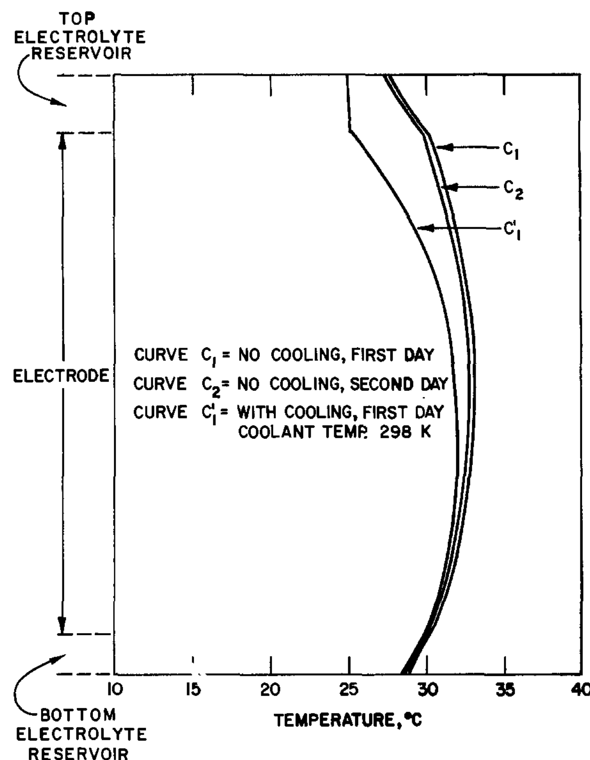

Fig. 8. Temperature distribution across the cell in the y-direction at the ends of daily charge cycles for Cell Design C, $x = 0$. Cell dimensions: 22.1 cm L × 45.72 cm W × 76.2 cm H. Initial cell temperature: 25°C.

The model.—In this study, the model treats the composite of grid, active materials of negative and positive plates, separator, and the electrolyte in the electrodes as a homogeneous medium. The composite is called the electrode element in the text. Since the grid has a much higher thermal conductivity relative to that of its surrounding (the grid surrounding consists of active materials of positive and negative plates, separator, and electrolyte), this often leads to a speculation that the heat generated in the cell may be effectively transferred through the grid and is released from the grid terminal to the outer atmosphere. One may therefore question the validity of the prediction

based on the present model which did not treat the heat transfer in the grid separately. What follows describes the basis for assuming homogeneity of the composite as treated in the present model.

In a lead-acid cell, most of the heat generated during cycling is contributed by the ohmic loss across the positive plate to the negative plate plus the activation. The contribution of heat due to the ohmic loss in the grid is relatively small, which is about 10% of the total heat generated. Therefore the heat released through the grid terminal to the outer atmosphere will be governed by the rates of heat transfer from the grid surrounding to the grid, from the grid interior to the grid terminal, and from the grid terminal to the outer atmosphere. A parallel but supportive model to describe the heat transfer processes in the grid and in its surrounding has been developed, and discussed in the Appendix.

The results from the supportive model in Appendix indicate that the temperatures of the grid and the grid surrounding are almost identical for Cell Design A during a daily cycle. The results furthermore show that the heat released from the grid terminal to the outer atmosphere is primarily limited by conduction in the grid. The amount of heat released from the grid terminal during the 14 hr daily operation (5 hr discharge plus 9 hr charge) is only about 15% of the total heat generated in the cell. The heat remaining in the cell contributes to the rise of cell temperature (see Fig. A-2). Furthermore a large temperature difference in the vertical direction of the cell is induced by the cooling of the grid terminal (see Fig. A-3). The results from the supportive model imply that (*i*) the heat released from the grid terminals in a tall cell design is not as effective as what has been commonly perceived, and (*ii*) temperatures of the grid and the grid surrounding are nearly identical so that they may be treated as a homogeneous medium in the heat transfer analysis of a whole cell. This assumption of a homogeneous medium was therefore adapted in the present model treatment.

Conclusion

Under the proposed utility cycles for lead-acid cells in load-leveling application, the daily cell temperature profiles are almost identical throughout the daily duty cycles. For a tall cell design (122-127 cm height), without forced water cooling, the maximum rise of cell temperature near the cell center may be reduced by about one-half, from 16° to 9°C, if the cell length is reduced, *e.g.*, from 48.26 cm for Cell Design A to 22.1 cm for Cell Design B. Reduction of the cell height, *e.g.*, from 121.92 cm for Cell Design B to 76.2 for Cell Design C, has little effect in reducing the maximum cell temperature. This preferential heat transfer in the horizontal direction, *i.e.*, through the cell case, than in the vertical direction, *i.e.*, through the terminals, is simply reflecting the longer conduction path in the vertical direction and that heat transfer within the cell is indeed limited by conduction. The above predicted results are based on the assumption of constant heat transfer coefficient from the cell wall to the ambient atmosphere of constant temperature. This assumption will be valid provided that adequate air ventilation exists for cooling the space between the cells in the load-leveling battery plant. The forced water cooling at electrode terminal has no significant effect in reducing the cell temperature at the region away from the terminal, but instead inducing a large temperature difference across the electrode. The large temperature gradients may cause a nonuniform current distribution over the electrodes leading to a gradual loss of cell capacity and cycle life. In practice, however, large battery cells, *e.g.*, lead-acid submarine cells, often incorporate "air lift pump" or electrolyte circulation design to minimize the temperature gradients within the cells. The gassing during equalization charge of load-leveling cells further enhances the internal heat transfer leading to a more uniform cell temperature distribution. After the weekly equalization charge, the 2 day rest period is enough to permit the cell temperature to return to its initial ambient temperature.

Acknowledgment

The authors acknowledge the support of this work by the Department of Energy, the Division of Energy Storage Systems.

Manuscript submitted Nov. 2, 1977; revised manuscript received March 9, 1978. This was Paper 91 presented at the Atlanta, Georgia, Meeting of the Society, Oct. 9-14, 1977.

Any discussion of this paper will appear in a Discussion Section to be published in the June 1979 JOURNAL. All discussions for the June 1979 Discussion Section should be submitted by Feb. 1, 1979.

Publication costs of this article were assisted by Argonne National Laboratory.

APPENDIX

Heat Transfer in the Electrode Grids and Their Surrounding in a Lead-Acid Cell

For a composite lead-acid cell, the arrangement of the electrode grids and their surrounding may be represented by Fig. A-1. Medium I in Fig. A-1 repre-

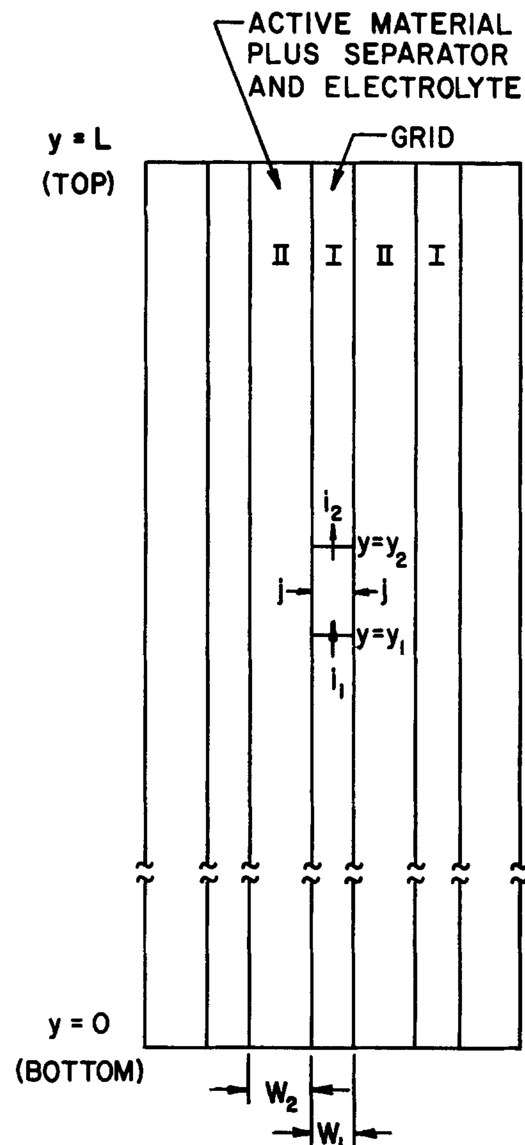

Fig. A-1. A cross section for the arrangement of the electrode grids and their surrounding in a composite cell.

sents the electrode grid; medium II represents the grid surrounding consisting of the active materials of positive and negative plates, separator, and electrolyte. For a tall cell design, the plate thickness is much smaller compared to the plate height. It is assumed that the temperature of the grid and its surrounding is uniform in the direction of the plate thickness. Only the temperature variations in the vertical direction are considered. In order to investigate the effectiveness of the heat being released through the grid terminal located at the top of the cell, the heat transfer through the side walls of the cell is not considered here. The mathematics are therefore simplified to a one-dimension model.

During cell cycling, the governing energy equations for the grid (medium I) and for the grid surrounding (medium II) may be expressed as

$$\rho_1 \hat{C}_1 \frac{\partial T_1}{\partial t} = k_1 \frac{\partial^2 T_1}{\partial y^2} + \dot{q}_1 \quad [A-1]$$

and

$$\rho_2 \hat{C}_2 \frac{\partial T_2}{\partial t} = k_2 \frac{\partial^2 T_2}{\partial y^2} + \dot{q}_2 \quad [A-2]$$

respectively. ρ_1 and ρ_2, $\hat{C}_1$ and $\hat{C}_2$, k_1 and k_2 represent the densities, specific heats, and thermal conductivities of the grid and the grid surrounding, respectively. $\dot{q}_1$ represents the rate of heat production in the grid, which is contributed by the ohmic loss and the heat transferred from the grid surrounding, and is expressed as follows

$$\dot{q}_1 = \left(\frac{2jy}{W_1}\right)^2 / K_1 + 2h(T_2 - T_1)/W_1 \quad [A-3]$$

where j represents the apparent current density over the plate. W_1 is the thickness and K_1 is the electrical conductivity of the grid. T_2 is the temperature of the grid surrounding. h is the heat transfer coefficient across the grid and the grid surrounding. $\dot{q}_2$ represents the rate of heat production in the grid surrounding, which is the major heat source in the cell, $\dot{q}_2$ is contributed by the electrochemical and chemical reactions plus the heat transferred from the grid. $\dot{q}_2$ may be expressed as

$$\dot{q}_2 = \left(jV - \sum_i j_i \Delta H_i / n_i \mathbf{F}\right) / W_2 - 2h(T_2 - T_1)/W_2 \quad [A-4]$$

where V is the potential difference between the positive and the negative grid, which may be approximately represented by the cell potential. W_2 is the thickness of the grid surrounding. Other parameters have already been described.

At the bottom of the cell, there is an electrolyte reservoir. By assuming that the heat transferred from the grid and from the grid surrounding to the bottom electrolyte reservoir is instantaneous, the boundary conditions at the bottom may be expressed as

$$y = 0, \quad \rho_l \hat{C}_l V_b \frac{\partial T_1}{\partial t} = k_1 \frac{\partial T_1}{\partial y} - h^*(T_1 - T_0) \quad [A-5]$$

$$\rho_l \hat{C}_l V_b \frac{\partial T_2}{\partial t} = k_2 \frac{\partial T_2}{\partial y} - h^*(T_2 - T_0) \quad [A-6]$$

where ρ_l and $\hat{C}_l$ are respectively the density and the specific heat of the electrolyte. T_0 is the outer atmospheric temperature. h^* is the heat transfer coefficient across the bottom cell wall to the outer atmosphere. V_b is the reservoir volume at the bottom.

At the top of the cell, the grid terminal is subjected to water cooling. The temperature of the grid terminal may be assumed equal to the coolant temperature (T_c). The boundary condition is then

$$y = L, \quad T_1 = T_c \quad [A-7]$$

For the top of the grid surrounding, following the same treatment as that for the bottom, the boundary condition is

$$y = L, \quad \rho_l \hat{C}_l V_t \frac{\partial T_2}{\partial t} = -k_2 \frac{\partial T_2}{\partial y} - h^*(T_2 - T_0) \quad [A-8]$$

where V_t is the reservoir volume at the top.

Equations [A-1] and [A-2] were solved subjected to the boundary conditions (Eq. [A-5]-[A-8]) by finite difference method. The Crank-Nicolson implicit techniques (11) followed by elimination algorithm was used. The calculation was carried out for a daily charge (5 hr discharge + 9 hr charge + 10 hr rest period) with the Cell Design A. The values of physical parameters for the calculation are

$\rho_1 = 11.34$ g/cm^3
$\rho_2 = 2.884$ g/cm^3
$\hat{C}_1 = 0.2196$ J/g-K
$\hat{C}_l = 1.054$ J/g-K
$W_1 = 0.128$ cm
$W_2 = 0.85$ cm
$T_0 = 298$°K
$k_1 = 0.353$ W/cm-K
$k_2 = 0.004725$ W/cm-K
$L = 101.6$ cm
$T_c = 298$°K

The numerical results show that the temperatures of the grid and the grid surrounding are nearly identical at any position in the vertical direction. Figure A-2 shows the temperature variation of the grid with time during the first daily cycle. In the figure, Q_t represents the total heat generated in the cell during the 14 hr cell operation; Q_{g1} represents the heat released from the grid terminal to the outer atmosphere during the same period; Q_{g2} represents the total heat released from the grid terminal to the outer atmosphere during the entire day (24 hr); r_1 is the percentage of the heat released from the grid terminal to the outer atmosphere relative to the total heat generated in the cell during the 14 hr cell operation; r_2 is the percentage of the total heat released from the grid terminal to the outer atmosphere relative to the total heat generated in the cell during the entire day. It is shown that the heat released from the grid terminal is limited by the heat conduction in the grid. Much of the heat generated remains in the cell and contributes to the rise of the cell temperature as shown in Fig. A-2. Figure A-3 shows that a large temperature difference over the grid will exist as result of the water cooling at the top grid terminal. The temperature distribution profiles over the grid during the daily cycle are also illustrated in Fig. A-3.

LIST OF SYMBOLS

a gassing correlation constant for the thermal conductivity
$\hat{C}$ average specific heat for the electrode element (J/g-K)
$\hat{C}_l$ specific heat of electrolyte (J/g-K)
$\Delta C_{p,j}$ algebraic sum of species partial molar heat capacities for reaction j (J/mol-K)
$\mathbf{F}$ Faraday's constant (96479 C/equiv.)
f internal heat production as a function of cell potential, heats of reaction, current density, current efficiency (J/cm^3-sec)
G internal heat production per degree Kelvin due to the contribution of current density, current efficiency and specific heats (J/cm^3-sec-K)
h convective heat-transfer coefficient on the cell container surface (J/cm^2-sec-K)
ΔH_j heat of reaction for reaction j (J/mol)
i apparent current density on the electrode surface (A/cm^2)
k average thermal conductivity of the electrode element (W/cm-K)
k_l thermal conductivity of electrolyte (W/cm-K)

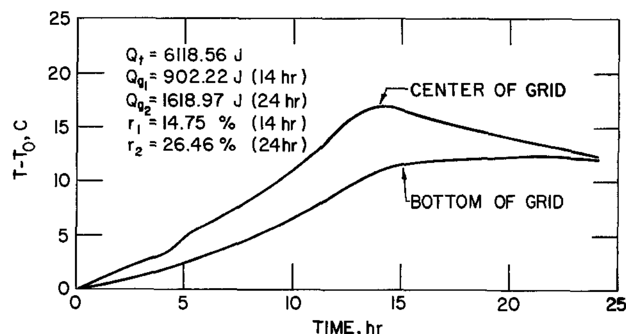

Fig. A-2. Temperature variation of the grid with time at the cell center and the cell bottom during first daily duty cycle.

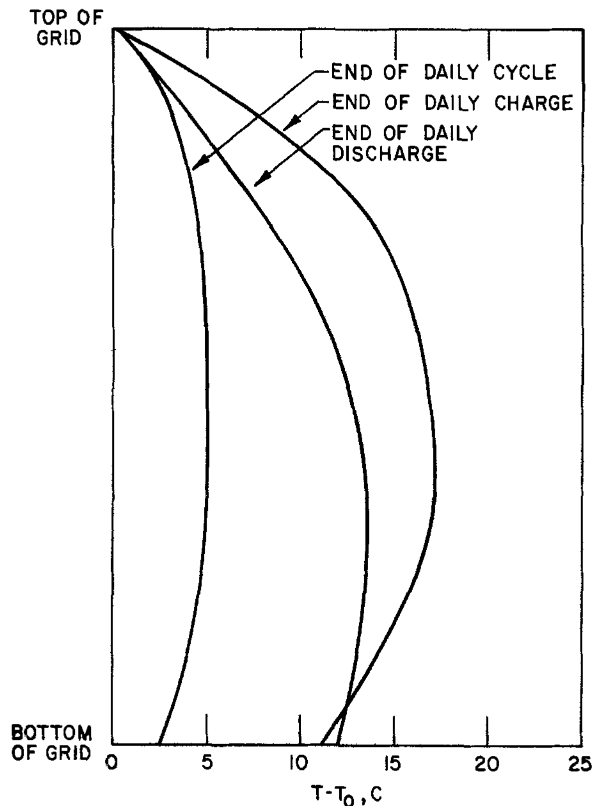

Fig. A-3. Temperature distribution over the grid during the first daily duty cycle.

k_o thermal conductivity of the electrode element for the case without gassing (W/cm-K)
L_x length of the cell (cm)
L_y height of the cell (cm)
M_i molecular weight of species i (g/mol)
n number of electron transfer for the electrode reaction
n_1 number of electron transfer for the cell reaction
n_2 number of electron transfer for the gassing reaction
Q state of charge
q rate of heat generated per unit volume (J/cm^3-sec)
s_i stoichiometric coefficient of species i in electrode reaction
t time (sec)
T temperature (K)
T_c coolant temperature (K)
T_o ambient temperature (K)
U velocity of electrolyte in y-direction (cm/sec)
V cell potential (volt)
$\overline{V}_i$ partial molar volume of species i (cm^3/mol)
W_t the combined thickness of positive electrode, separator, and negative electrode (cm)
x distance in x-direction (cm)
x_1 the distance from the central axis of the electrode element to the boundary of the electrode element in x-direction (cm)
y distance in y-direction (cm)
y_1 the distance from the cell bottom to the bottom of the electrode element in y-direction (cm)
y_2 the distance from the cell bottom to the top of the electrode element in y-direction (cm)
Λ the average heat transfer coefficient across the cooling tube (J/cm^2-sec-K)
ϵ electrode porosity
ξ current efficiency
ρ density of the electrode element (g/cm^3)
ρ_l density of the electrolyte (g/cm^3)

subscript

i species i
l electrolyte
x x-direction
y y-direction

REFERENCES

1. B. S. Baker, D. Gidaspow, and D. Wasan, "Advanced Electrochemistry and Electrochemical Engineering," P. Delahay and C. W. Tobias, Editors, Vol. 8, John Wiley and Sons, Inc. (1971).
2. R. E. Meredith, and A. A. Uchiyama, Proc. Intersociety Energy Conversion Engineering Conference, 32 (1968).
3. K. W. Choi and N. P. Yao, Argonne National Laboratory Report ANL-77-24, prepared for ERDA under contract W-31-109-Eng-38 (1977).
4. D. T. Ferrell, Jr. *et al.*, Prepared by ESB Inc. for Electric Power Research Institute under contract EPRI EM-375, project 419-1, Final Report, February (1977).
5. Westinghouse Electric Corp., ERDA contract E(49-18)-2114, Final Report Volume 1, 2, 3, December (1976).
6. J. Douglas, Jr., *J. Soc. Ind. Appl. Math.*, **3**, 42 (1955).
7. J. Douglas, Jr. and H. H. Rockford, Jr., *Trans. Am. Math. Soc.*, **82**, 421 (1956).
8. D. N. Craig, and G. W. Vinal, *J. Res. Nat. Bur. Stand.*, **24**, 475 (1940).
9. Handbook of Chemistry and Physics, 56th Edition (1975).
10. Selected Values of Chemical Thermodynamic Properties, Circular of the Nat. Bur. Stand. 500, U.S. Dept. of Commerce, Nat. Bur. Stand., February (1952).
11. J. Crank and P. Nicolson, *Cambridge Philos. Soc. Proc.*, **43**, 50 (1947).

Further Experimental Tests of the Convective Flow Theory of Zn Secondary Electrode Shape Change I

Drannan Hamby* and Jeffrey Wirkkala[1]

Linfield Research Institute, Linfield College, McMinnville, Oregon 97128

ABSTRACT

Additional experiments have been carried out to test the convective flow theory of zinc electrode shape change. The assumptions implied by the theory that overpotential and current distribution should be uniform over a flat rectangular porous zinc electrode operated with severely limited convective flow are not supported by these measurements. Several possible explanations of the observed behavior are suggested. Evidence of deterioration of anodic performance of the limited flow porous zinc electrode on cycling is presented. A flooded, non-vented Hg-HgO reference electrode without head space is described.

Choi, Bennion, and Newman have described a one dimensional mathematical model of the porous zinc secondary electrode with "normal" convection.[1,2] The model is based on the hypothesis that lateral movement of active material over the surface of the electrode, commonly called shape change, is determined primarily by convective flow driven by membrane pumping effects. In experiments designed to test the theory, material redistributions and volume average fluid flow rates in a zinc-silver oxide cell with "normal" convection were found to be in agreement with predictions based on the model (2). Zinc electrodes cycled in a cell designed to operate with severely limited convective flow in the zinc compartment showed insignificant material redistribution (2). During this latter series of experiments, several questions arose concerning the behavior of the zinc electrode when operated under limited flow conditions. It was observed that flooded, nonvented, limited flow cells constructed from porous zinc and silver electrodes having 12 and 6 A-hr theoretical capacities, respectively, would accept less than 1 A-hr of charge at charging rates from 15 to 30 mA/cm^2 before the onset of severe polarization. Qualitative, visual observation of used zinc electrodes from cells with limited convection in the zinc compartment indicated, through nonuniform zinc metal distribution, that current and potential distributions over the surface of the electrode were not uniform as implied by the convective flow theory.

It was found that the initial charge accepting capacity of the flooded, nonvented cells could be more than doubled by venting and enlarging the silver electrode compartment; however, capacity deteriorated with cycling. These and other observations indicated that the silver electrode was responsible for certain of the poor performance characteristics of these cells. However, since the cells were constructed without reference electrodes it was impossible to measure overpotentials at each working electrode, and, thereby, relate measured cell terminal potential differences to individual electrode behavior. Since one objective of our present investigations is to obtain information which will be useful in determining how the convective flow theory might be useful in the design of long-lived porous zinc secondary batteries, it was decided to design and operate a modified limited convection cell, incorporating several reference electrodes, which would provide information on the values of zinc electrode overpotential at various points over the zinc test electrode surface both on charge and discharge. In order to avoid confusion with phenomena associated with the silver electrode, it was decided to use a precharged zinc counterelectrode in the new cell.

* Electrochemical Society Active Member.
[1] Present address: a-dek Corporation, Newberg, Oregon.
Key words: battery, silver-silver oxide, mercury-mercuric oxide.
[2] Convection similar to that found in commercial cells.

Equipment and Procedures

Electrodes.—All electrodes used in this work to date have been furnished by AFAPL (Air Force Aero Propulsion Laboratory, Wright-Patterson Air Force Base, Ohio). The zinc electrodes come in the discharged state wrapped in Viskon (cellulose rayon) paper and consist of pressed, blended ZnO, HgO, and Teflon binder on expanded silver screen (3.23×10^{-2}g of Ag/cm^2). These electrodes are prepared according to the procedure described by Keralla (3). They are approximately 10.2 cm long, 6.4 cm wide, and 0.2 cm thick. Different batches of electrodes are found to vary slightly in composition, and different electrodes within the same batch differ in initial weight by as much as 8%. Previous analysis of both used and unused electrodes indicated a layered structure in the active material (2). By color, it appears that the layer near the collector screen is rich in HgO. This layer also appears finer grained, more coherent, and more firmly bound together than the material which covers it. The quantity of ZnO present on each electrode is adequate to yield a theoretical capacity, at 100% utilization, of approximately 12 A-hr. Initial HgO content in the electrodes is 33 mg HgO/g ZnO as determined in earlier work using an atomic absorption spectrophotometer (2). The silver electrodes also come in the discharged state. They have approximately the same apparent surface area, 66 cm^2, are 0.4 mm thick, and consist of porous sintered silver (1% palladium) on expanded silver screen. They were prepared according to the procedure of Falk and Fleischer (4). Estimated theoretical capacity of these electrodes at 100% utilization is 6.5 A-hr.

Acrylic electrode holders.—In Cell I the zinc test electrode faces a precharged zinc counterelectrode across two layers of 0.001 in. thick RAI P 2291 (40/20) separator.[3] Figure 1 illustrates the 1 in. thick acrylic holder for the porous zinc test electrode. The rectangular chamber milled into the center of the holder is just large enough to contain the dry electrode. The Hg, HgO reference electrodes designated, a through i, described more fully below, are located behind the test electrode. Sealed electrical contact is made to the test electrode through the cell wall, j, Fig. 1, and a, Fig. 2. Ports m and k are used for vacuum evacuation and filling of the cell with electrolytic solution. In the experiments to be described, the ports m and k are sealed after the filling operation is completed and the test electrode is normally operated flooded and not vented. Details of filling ports and port plugs are shown in Fig.

[3] RAI Corporation, 225 Marcus Boulevard, Hauppauge, New York 11787.

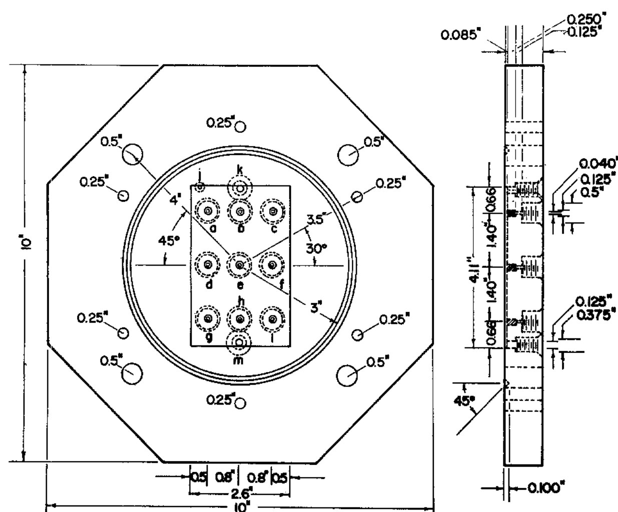

Fig. 1. Acrylic electrode holder for the zinc test electrode. Hg-HgO reference electrodes are designated a-i; k and m are filling ports; j is the electrode lead exit port.

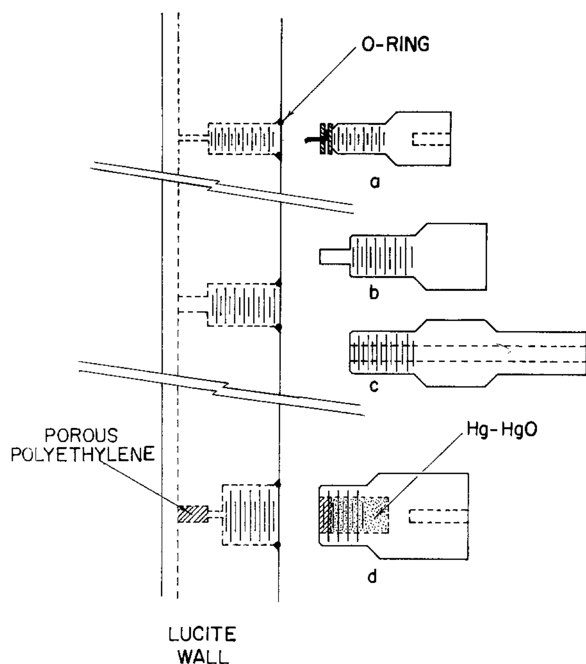

Fig. 2. (a) Schematic illustration of the arrangement for making sealed electrical contact to the electrode through the acrylic wall. (b) Filling port plug. (c) Attachment for vacuum filling through filling port. (d) The Hg-HgO electrode. Items labeled a, b, and c are silver plated brass. Item d, the container of the Hg-HgO paste is #304 stainless steel.

2. A large O ring, laid into the V groove surrounding the Zn electrode, seals the cell when the test electrode holder is bolted to the counterelectrode holder with six 0.25 in. bolts. The larger 0.5 in. holes are used to support the cell when in operation. During cell operation, convective flow rates in the zinc test electrode compartment are low, limited by pressure distortion of chamber dimensions and changes in partial molar volumes of materials participating in the cell reaction.

The acrylic holder for the zinc counterelectrode is similar to that for the test electrode. It also provides a milled rectangular chamber just large enough for its electrode. However, a 0.125 in. deep reservoir space is provided behind the counterelectrode and the compartment is normally vented through pipes attached to the filling ports. The counterelectrode and its reservoir are separated by a 0.125 in. thick sheet of porous polyethylene sheet.[4] To avoid distortion of the counterelectrode and its polyethylene backing plate due to pressure buildup in the test electrode chamber it was necessary to provide additional backing support for the polyethylene sheet. This was accomplished with additional sections of porous polyethylene sheet placed in the reservoir. Evacuation and filling ports and sealed electrical contact are as on the test electrode side. After all preparative procedures are complete, the cell is operated with the zinc electrodes positioned horizontally, the test electrode below the counter, with the counterelectrode filling ports used to connect the counterelectrode compartment to solution-filled reservoir tubes, gas collection tubes and external Hg-HgO in glass reference electrodes above the cell. During cell operation, the counterelectrode is always flooded but vented. Cell I in its normal, horizontal operating position is shown in Fig. 3.

Reference electrodes.—It was desired that convective flow be minimized in the test electrode chamber; therefore, a completely filled, nonvented reference electrode without head space was required. Use of a reference electrode of ordinary design, *i.e.*, an open electrode or an electrode which was vented or had head space would, because of pressure variations in the cell, result in periodic flow of fluid between the reference and test electrode chambers.

In preliminary experiments small electrodes fabricated from Cd, amalgamated Cd, commercial Cd negatives, and commercial nickel positives were all tested in the cell as reference electrodes; none of these performed satisfactorily. In all cases large differences (10-125 mV) in potential between apparently similarly prepared electrodes were observed and the potentials drifted erratically with time. The Hg-HgO system was then adapted to fit the needs of these experiments. The Hg and HgO used to prepare the electrodes were "Baker Analyzed" reagent-grade chemicals without further purification. Preparation of the Hg-HgO paste was done according to the procedure described by Falk and Salkind (5). The #304 stainless steel electrode holders shown in Fig. 2d were washed and then rinsed in distilled water and dried before the Hg-HgO paste was packed into the holders. In a preliminary experiment six of the Hg-HgO in steel references were prepared and placed in the cell wall. The cell container without zinc electrodes was then assembled and vacuum filled with the ZnO-saturated KOH solution. Two additional Hg-HgO electrodes in glass H cells (5) were prepared similarly and connected to the cell container with latex tubing filled with the same electrolytic solution. Initial potential differences between the eight electrodes, using one particular electrode as a

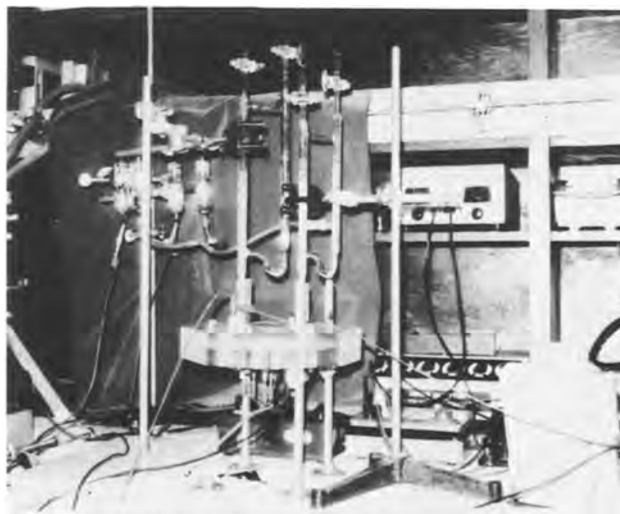

Fig. 3. Cell I in its normal, horizontal operating position. Gas collection burets are above the cell and above and to the left two external Hg-HgO in glass reference electrodes are visible.

[4] Obtained from ERB and Gray Scientific, Culver City, California, described as having an average pore size of 70 μm, designated F-13639.

reference, decreased with time to less than ± 0.2 mV after 28 hr. Daily observations of the electrodes over a seven-day period indicated that this level of agreement was being maintained over that period of time. Intentional polarization of one of the references by 0.25 mA indicated that the electrode had a fairly high resistance, 150Ω; however, after polarization for 10 sec at 0.25 mA the electrode returned to within less than 1 mV of its initial potential within about 1 sec.

Electrical equipment.—All cell-cycling experiments were carried out at constant current. Power sources were commercially available galvanostats. Potential differences across the cell terminals, *i.e.*, between the zinc test and zinc counterelectrode, were recorded continuously using one channel of a Hewlett-Packard 7100B two-channel recording voltmeter. A second, less sensitive, recording voltmeter was used in conjunction with a power resistor in series with the cell to monitor cell current to ± 25 mA. A Flexopulse Hg 108A6, repeat-cycle timer, was used as a reversing switch which allowed continuous variation in cell charge and discharge times. The switch also allowed for brief intervals of a few minutes duration with no cell current between half-cycles. Potential differences between the various Hg-HgO in steel reference electrodes and test, counter, or external, Hg-HgO in glass reference electrodes were monitored periodically using the other channel of the Hewlett-Packard recorder connected sequentially to different pairs of electrodes by an Eagle Signal Model MT-19 Step Switch controlled by another repeat-cycle timer.

Chemical analysis of used electrodes.—The distributions of metallic zinc and zinc compounds over electrode surfaces after cycling were of interest. The unused electrodes consist of mixtures of ZnO, HgO, and inert binder on expanded silver screen. Used electrodes contain, in addition to the substances listed above, metallic zinc and mercury, possibly various amalgams of zinc and silver, potassium hydroxide, and probably several hydroxides and hydroxy complexes of zinc (6). Selective dissolution methods for analysis were tested but found unsatisfactory because of air oxidation of electrolytic zinc. The following method was subsequently used to determine the distribution of zinc compounds over the electrodes. After removal from the cell each electrode was sectioned into fifteen samples and each section was labeled. Care was taken to record the position which the sample occupied on the electrode with respect to the electrode lead and the reference electrodes. Each section was treated with excess 6*N* HCl, the resulting solution filtered, buffered, and then titrated with standard EDTA and the result calculated and reported in terms of ZnO. It was subsequently learned that freezing the samples to prevent air oxidation of zinc and collection of the evolved H_2 upon treatment of the sample with acid would have permitted determination of both zinc metal and zinc compounds; however, at the time these electrodes were analyzed the rapidity of air oxidation of the electrolytic zinc was not realized, they were not frozen before storage, and the zinc metal information which was obtained from gas evolution data was not representative of the electrodes at the end of cycling.

Electrolytic solution.—The solution used for filling the cells was prepared from singly deionized distilled water and reagent-grade chemicals. KOH was first dissolved in water to prepare a concentrated solution. This solution was diluted to a specific gravity of 1.40 at 20°C. Fine grained reagent grade ZnO was then added in excess of the amount required to saturate the solution, and magnetic stirring continued for several days. The solution with excess crystalline ZnO was stored in tightly capped polyethylene bottles.

Cell filling.—Filling of the cell was carried out with the electrodes positioned vertically with respect to the earth's surface. The filling procedure in all cases involved evacuation of the cell and rubber filling lines by mechanical pumping followed by slow, simultaneous vacuum filling of the compartments with solution from a common reservoir. Following return of pressure in the filled cell to atmospheric, the cell was left to soak for at least 24 hr before the appropriate ports were plugged and cycling was begun.

Treatment of data.—The distribution of total zinc as ZnO over used and unused electrodes was determined. Because it is difficult to measure accurately the dimensions of the samples and because of total weight differences between different electrodes, the collector screen material is used to normalize the data. The normalization ratio used for each sample is

$$\frac{Q_{ZnO}}{Q_{ZnO^*}} = [W_{ZnO}{}^i/(W_{cs}{}^i\, 66.0\ \text{cm}^2/\sum_i W_{cs}{}^i)]/[\sum W_{ZnO}{}^i/66.0\ \text{cm}^2]$$

where $W_{ZnO}{}^i$ = weight of total zinc expressed as zinc oxide, sample i, and $W_{cs}{}^i$ = weight of collector screen, sample i. Assuming that the weight per unit area of the collector was uniform, the numerator of the normalization ratio Q_{ZnO}, is the weight of ZnO per unit area of sample. Similarly, the denominator, Q_{ZnO^*}, is the average weight of ZnO per unit area for the whole electrode. The ratio, Q_{ZnO}/Q_{ZnO^*}, compares the ZnO per unit area at a particular position on the electrode with the average value for the electrode as a whole and serves as a measure of electrode uniformity.

Comparisons of samples from used electrodes with samples from unused electrodes on the basis of the normalized data involves the assumption of uniformity of weight/area for the used collector screens.

Counterelectrode charging.—The zinc counterelectrodes were charged by assembling the cell with the counterelectrode in its normal position but with two porous silver electrodes in the test electrode compartment rather than the test electrode. Charging of the counter was normally carried out at 0.150A to a charge of 4.0-4.5 A-hr. The cell was then drained, opened, the silver electrodes replaced with the test zinc electrode, new membrane separator placed in the cell followed by cell closure and refilling. These operations were carried out as quickly as possible to avoid air oxidation of the charged counterelectrode.

Specific precycling treatment, Cell I.—Prior to counterelectrode charging the cell was vacuum filled with electrolyte and allowed to soak for 24 hr. Charging was carried out with the cell attached to the filling pipes. The counterelectrode was charged 29.5 hr at 0.150A and then 16.5 hr at 0.015A for a total of 4.67 A-hr. After placing the test electrode in the cell, the nine Hg-HgO reference electrodes in steel containers were prepared as described above and placed in the cell wall and the cell was again vacuum filled. The various reference electrodes were observed to be in agreement with one another to within ± 4 mV when cycling began approximately 48 hr after the final filling.

While the cell was still in the vertical position and attached to the filling tubes, it was taken through two complete cycles at 0.15A such that when the first-charge half-cycle started at the 1.0A rate there was nominally 0.63 A-hr charge on the test electrode and 4.04 A-hr charge on the counterelectrode.

Subsequent to the initial low current density cycles, the cell was vacuum-treated to remove gas and then carried through one complete cycle at 1.00A total cell current while still mounted in the upright position and attached to the filling pipes. This cycle was intended to provide data for comparison with cell data taken after the cell was placed in the horizontal position and the test electrode closed (no noticeable difference was observed in the two cases).

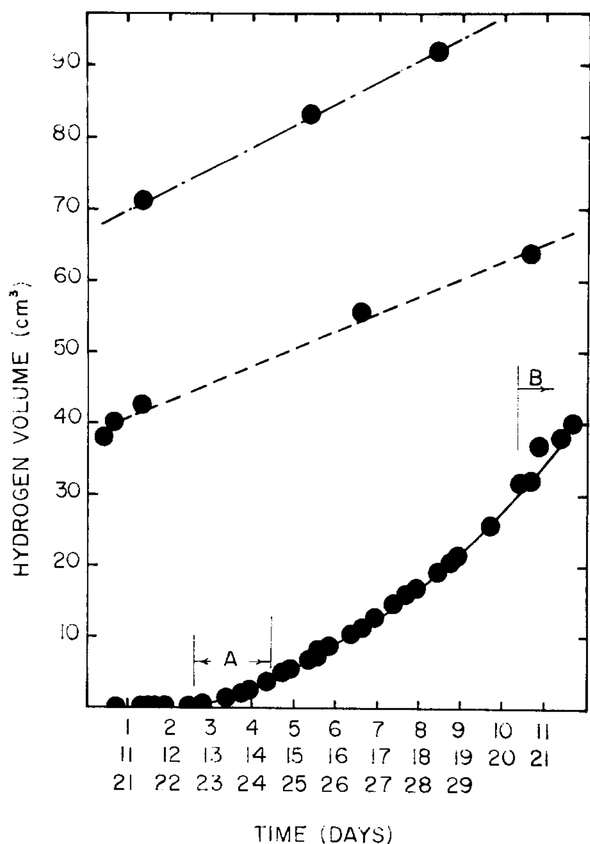

Fig. 4. Cumulative volume of gas at 25°C and 1 atm pressure evolved from the vented counterelectrode as a function of time.

The cell was then positioned horizontally, the test electrode closed, and the cell was cycled at 1.00A constant current; initial duration of each half-cycle was 2.0 hr but half-cycle lengths were decreased as cycling continued. Gas evolved from the counterelectrode chamber of the cell was trapped above the cell and the volume of evolved gas was measured as a function of time.

Results

The average cumulative amount of gas evolution from the vented counterelectrode was observed after the lower electrode was closed. The data are plotted in Fig. 4. The rate was observed to be very low during the initial 48 hr after closure but then to increase. After twelve complete cycles of operation at 1.00A the cell was subjected to several low current cycles at 0.150A (labeled period A, Fig. 4), to see if this might decrease the rate of gas evolution. It did not. The average rate of gas evolution decreased only after cycling of the cell was stopped (B, Fig. 4). The rate of gas production during cycling reached approximately 6.6×10^{-6} moles/hr corresponding to a loss of 4.3×10^{-4}g of zinc per hour.

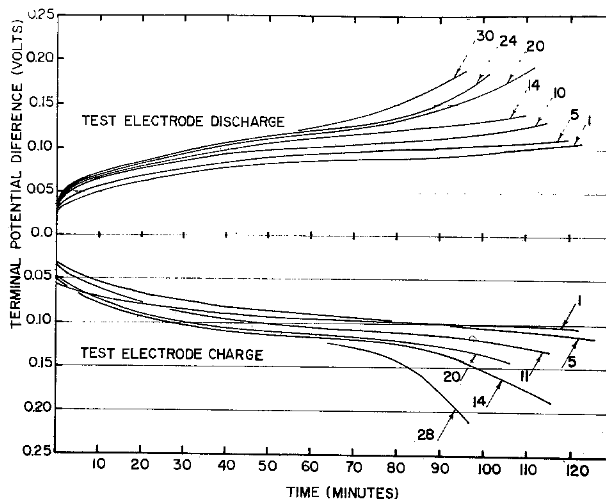

Fig. 5. Summary of behavior of Cell I during the first thirty cycles. Cycles are numbered. Potential differences between the zinc test electrode and zinc counterelectrode are plotted as functions of time.

A summary of Cell I behavior during the first thirty 1.00A, constant current cycles is shown in Fig. 5. As cycling continued, total cell polarization increased for both half-cycles. By adjusting half-cycle lengths total polarization was kept below 200 mV and symmetry of polarization of the cell during the half-cycles was approximately maintained; however, as cycling continued at constant current, both half-cycle lengths had to be shortened to avoid large values of cell polarization.

The presence of the Hg, HgO reference electrodes allowed periodic measurement of reference to test electrode potential differences at different areas over the test electrode surface. Some selected values of overpotential of the test electrode at different sites during charge and discharge are shown in Tables I and II. The data in Table I are from near the middle of the half-cycle and near the end. The trend which is illustrated is that the overpotential behavior of the test electrode on charge remains essentially the same as cycle number increases. This was found to be so even though there were sharp increases in some cases in the total cell polarization. On test electrode discharge, *i.e.*, when the test electrode was behaving as an anode, there were large increases in overpotential near the end of the half-cycle as cycle number increased, and, large differences in overpotential between different sites on the electrode began to appear. Although a well-defined pattern in the magnitudes of the overpotentials was not clearly developed in the early cycles, 2-20, a pattern did develop between cycles 20-23 (see Table II) which carried through for much of the remaining operation of the cell (with the obvious exception of electrode h). In Fig. 6-9 potential differences between the various Hg-HgO reference electrodes and the test electrode have been plotted to

Table I. Test electrode overpotential (mV), Cell I

	Cycle 2 Charge		Cycle 2 Discharge		Cycle 7 Charge		Cycle 7 Discharge		Cycle 12 Charge		Cycle 12 Discharge		Cycle 17 Charge		Cycle 17 Discharge		Cycle 23 Charge		Cycle 23 Discharge	
	Mid*	End	Mid	End	Mid	End	Mid	End	Mid*	End	Mid	End	Mid	End	Mid	End	Mid	End	Mid	End
a	−18	−23	+19	+24	−10	−18	+20	+28	−10	−17	+19	+35	−11	−20	+20	+35	−10	−18	+24	+ 93
b	−17	−23	+19	+23	−10	−17	+22	+27	−9	−22	+20	+29	−10	−21	+21	+28	−8	−17	+24	+41
c	−19	−24	+19	+25	−11	−21	+20	+30	−13	−21	+19	+48	−13	−19	+21	+42	−12	−19	+23	+103
d	−21	−26	+22	+32	−16	−24	+23	+40	−17	−24	+22	+49	−17	−25	+24	+41	−14	−23	+29	+92
e	−20	−25	+20	+25	−12	−20	+21	+28	−12	−22	+21	+35	−14	−24	+22	+29	−12	−20	+24	+35
f	−22	−26	+20	+26	−14	−22	+21	+31	−14	−21	+20	+38	−14	−20	+22	+33	−13	−20	+24	+78
g	−27	−30	+20	+25	−20	−27	+24	+39	−23	−25	+22	+54	−17	−24	+20	+35	−15	−22	+22	+52
h	−27	−30	+19	+25	−21	−26	+22	+34	−22	−26	+21	+49	−18	−25	+22	+34	−19	−25	+26	+116
i	−26	−29	+20	+26	−20	−25	+22	+35	−20	−24	+22	+46	−17	−23	+21	+31	−17	−23	+24	+76

* The values in this table are differences between reference to test electrode voltages with and without cell current.

Table II. Test electrode overpotential (mV) near end of discharge

	Cycle 20	Cycle 21	Cycle 22	Cycle 23
a	70	75	85	93
b	37	38	40	41
c	90	89	99	103
d	76	76	84	92
e	37	37	15	35
f	58	59	66	78
g	42	45	47	52
h	75	86	105	116
i	60	61	68	76

emphasize the development of differences in anodic overpotential between sites on discharge and the fact that certain sites near electrodes a, c, and d, and to a lesser extent f and i developed higher anodic overpotentials than others as the experiment progressed.[5]

The same pattern of test electrode behavior illustrated above was observed throughout all stages of cell cycling; *i.e.*, relatively low overpotential at all times and sites when the test electrode was acting as a cathode, even when total cell polarization was high, and large overpotential with large differences in between sites developing when the electrode was acting as an anode and total cell polarization was high. This phenomenon has now been observed in the operation of several similarly prepared cells and is believed to be typical of the electrode-cell design. Furthermore, additional measurements on the counterelectrodes in

[5] See Fig. 1 and 10 to relate reference electrode number to placement on the test electrode.

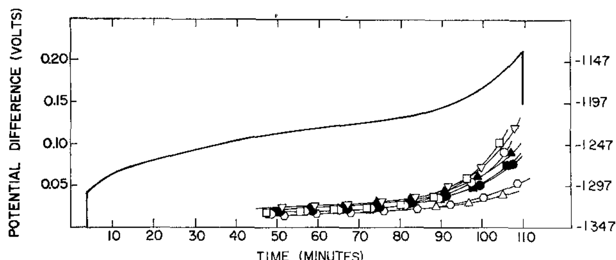

Fig. 6. Discharge half-cycle 23. Solid line—potential difference (left vertical axis) between test and counter zinc electrodes during discharge of the test electrode. Symbols for reference electrode to test electrode potentials are: a, ○; b, △; c, □; d, ▲; e, ⬢; f, ■; g, ⬡; h, ▽; i, ●. Reference to test electrode potential differences should be read from the right axis.

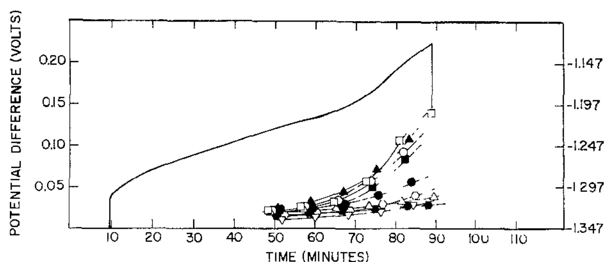

Fig. 7. Discharge half-cycle 41. See Fig. 6 for explanation of symbols.

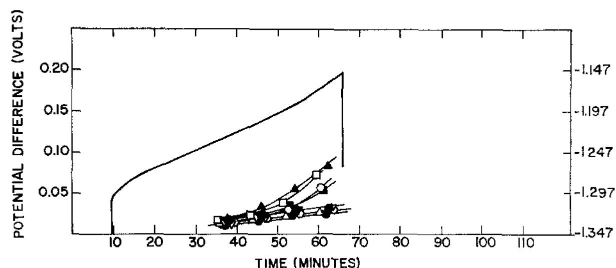

Fig. 8. Discharge half-cycle 54. See Fig. 6 for explanation of symbols.

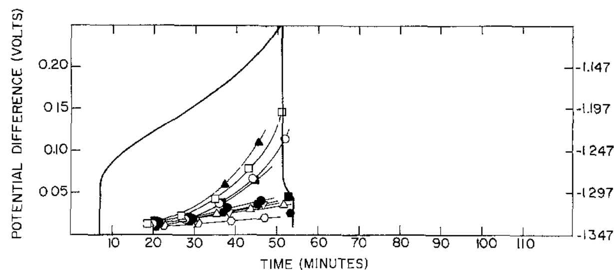

Fig. 9. Discharge half-cycle 78. See Fig. 6 for explanation of symbols.

similarly prepared cells indicate that they behave in a similar manner, *i.e.*, consistently low cathodic overpotential on charge, consistently higher overpotential on discharge, increasing in magnitude as cycling continues.

Additional features of the data taken during operation of Cell I, which deserve mention are (*i*) slow (hours) relaxation of the anodic overpotential at the test electrode, at the end of discharge and (*ii*) the observation of an irregular periodic fluctuation in test electrode overpotential after termination of cell current.

Cell I was operated through a total of 83 cycles at 1.00A constant-cell current. Near the end of testing the cycle lengths were greatly reduced, *e.g.*, discharge half-cycle 78 shown in Fig. 9 was 44 min in length. The test electrode was removed from the cell in the partially discharged condition after 83 cycles, sectioned, and analyzed by the gas evolution and EDTA titration technique described above. The results are summarized in Fig. 10. It was found that the reaction rate with HCl for the used electrode samples was much slower than that observed with pure granular zinc samples used in standardizing the method. Figure 11 illustrates volume of hydrogen gas evolved as a function of time for sample 2, test electrode, Cell I. These data are typical of the observed behavior.

The reference electrodes were checked against one another, and against the Hg-HgO in glass electrodes after cell relaxation several times during the experiment and at the end of the experiment. Agreement between members of the set was observed to improve as cycling continued, *e.g.*, after relaxation of the cell for 12 hr after 83 cycles eight of the electrodes were in agreement to ± 1 mV.

Visual observations indicated a significant resistive effect in the current collector on the distribution of metallic zinc over the electrodes on charge. This effect was most obvious when, after charging the counter-

Used electrode (left):

0.70 a +	0.93 b +	0.84 c +
0.96	0.80	1.24
0.83 + d	1.05 + e	1.21 + f
0.88	1.10	1.29
+ g 1.06	+ h 1.12	+ i 1.21

Unused electrode (right):

0.97	1.07	0.97
0.95	1.03	0.96
1.02	1.05	0.93
1.06	1.06	1.00
0.96	1.02	0.97

Fig. 10. Distribution of ZnO over the surface of a used (left) and an unused (right) electrode. Numbers given are ratios of Q_{ZnO}/Q_{ZnO}^* as defined in the text. Positions of the reference electrodes are indicated by crosses Current lead is in the upper left corner, side shown for the used electrode is the side toward the counterelectrode.

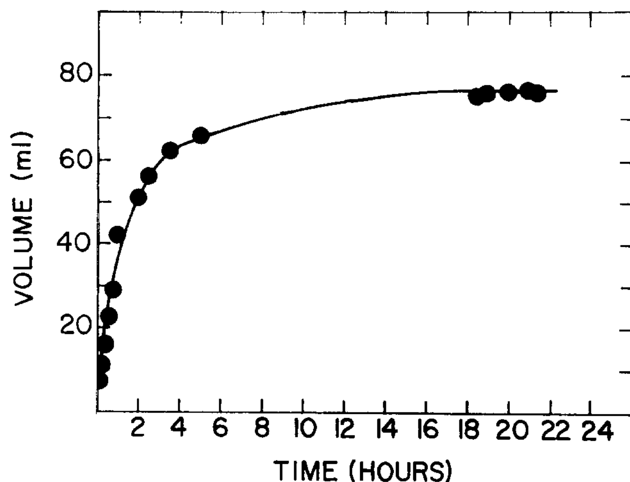

Fig. 11. Cumulative volume of hydrogen gas evolved (298°K and 1.0 atm) as a function of time for sample 2, test electrode.

electrode, the cell was opened and the counter could be observed in the charged condition. Zinc was most heavily plated near the lead with the amount per square centimeter apparently diminishing with distance from the tab.

Discussion and Conclusions

According to the initially published one dimensional convective flow theory (1), material redistributions as well as differences in potential and current distribution which develop longitudinally along porous zinc electrodes in cells with normal convection are caused by the membrane pumped flows. The theory implies that these effects would not develop if the convective flows were stopped. These implications are only partially supported by the measurements reported here. The development of nonuniformity of overpotential has been directly demonstrated and nonuniformity of current has been indicated by qualitative observations of zinc metal distribution after charge.

Data concerning active material distribution reported as ZnO over the test electrode surface, Fig. 10, are similar to those reported previously for an electrode operated under limited flow conditions (2) which reinforces our conclusions from the previous results that the rate of lateral shape change is significantly reduced by limiting convective flow parallel to the apparent electrode surface. The standard upon which this conclusion is based is the data reported by Choi for the longitudinal redistributions of zinc over the surface of zinc electrodes operated in cells with normal convection for periods of time and at operating currents similar to those reported here (2, 11). The redistributions in those cases were drastic and involved the depletion in zinc compounds to approximately 20% of their initial values over the end of the electrode nearest the cell reservoir. Thus, although the data in Fig. 10 do indicate some redistribution of material, the observed redistribution is much less than that reported by Choi for the same kind of electrode, operated under similar conditions of current density and number of cycles in a cell with normal convection.

These experiments indicate that some of the difficulties previously reported with respect to cycling cells with flooded, nonvented porous zinc electrodes with limited convection were the result of problems with the performance of the zinc electrode as an anode. Cycling of the flooded nonvented AFAPL zinc electrodes at constant cell current to approximately 15% of theoretical capacity in an environment in which convective flow is severely limited commonly results in the development of an average anodic overpotential which increases with number of cycles. No corresponding change in average cathodic overpotential has been observed. This observation is quite different from that reported by McBreen for a cell with normal convection (10). His observations indicated increasing cathodic overpotential on charge as cycling proceeded with large anodic overpotentials developing only after over 100 cycles.

In order to keep the anodic overpotential of the zinc electrode below a preset value it was found necessary to shorten the half-cycle duration as cycling continued, *i.e.*, the electrode capacity decreased, or the available zinc decreased. Vacuum refilling of the cell has some beneficial effect on capacity but does not restore the electrode to its initial state (2). The data indicate that the anodic effect is not limited to occurrence at the limited convection test electrode but occurs with equal severity at the vented counterelectrode. The rate of H_2 evolution from the cell is not great enough to explain the loss in available zinc.

Certain areas of the test electrode of Cell I exhibited consistently higher overpotentials than other areas over much of the lifetime of cell operation, *e.g.*, inspection of Fig. 6-9 indicates that areas near electrodes a, c, and d suffered, on the average, between cycles 23 and 78, the highest overpotentials; next, in order, were areas near electrodes f and i. On the average, during this same period, electrodes b, e, and h, those along the middle of the electrode, exhibited the smaller anodic overpotentials. Thus, a tendency toward greater overpotential at the top and outer edges on the electrode is discernible. Those areas a, c, and d which consistently exhibited the highest overpotentials suffered the greatest material loss; however, areas near f and i which exhibited, on the average, the next highest overpotentials, actually appear to have gained material. It is, therefore, difficult to conclude, on the basis of the data, that a correlation exists between observed overpotential and extent of material redistribution. The cause or causes of the observed increases in anodic overpotential on discharge remain a subject for further investigation. Passivation of porous zinc electrodes by thin film formation (called blockage of the second kind by some authors) has been suggested (7, 8) as has the development of anodic overpotential through plugging of the porous electrode through deposition of reaction products in the electrode pores (called blockage of the first kind by some authors) (12). Redistribution of zinc and zinc oxide parallel to the electric current flow, termed x-direction shape change as opposed to lateral shape change, has been suggested as an important limiting factor in the performance of certain porous zinc electrodes (12, 9). The separation of metallic zinc from the current collector has also been reported (2, 13) and serious concentration overpotential at the zinc electrode has been predicted (1). Data currently available on the cells of interest are not adequate to allow identification of which or to what extent each of these various possible mechanisms is contributing to the limitation of anodic performance of these particular electrodes.

Physical nonuniformities of real electrodes and membranes may contribute to the deviation of cell performance from theoretical predictions. In addition, the real electrodes differ from the original model in the resistive effect of the current collector; *i.e.*, the initial nonuniform zinc metal distributions observed on the charged counterelectrodes indicate a significant resistive effect in the current collector of the electrode which was not taken into consideration in modeling the electrode.

Acknowledgments

Financial support for this work has been provided by the United States Energy Research and Development Administration. We also wish to thank Prof. Douglas N. Bennion, UCLA, for his valuable discussions and constructive suggestions and Ms. Debbie Zahnle for her assistance in carrying out the chemical analyses.

Manuscript submitted Oct. 10, 1977; revised manuscript received March 9, 1978.

Any discussion of this paper will appear in a Discussion Section to be published in the June 1979 JOURNAL. All discussions for the June 1979 Discussion Section should be submitted by Feb. 1, 1979.

Publication costs of this article were assisted by Linfield College.

REFERENCES

1. K. W. Choi, D. N. Bennion, and J. Newman, *This Journal*, 123, 1616 (1976).
2. K. W. Choi, D. Hamby, D. N. Bennion, and J. Newman, *ibid.*, 123, 1628 (1976).
3. J. A. Keralla in "Zinc-Silver Oxide Batteries," A Fleisher and J. J. Lander, Editors, pp. 183-198, John Wiley and Sons, Inc., New York (1971).
4. S. U. Falk and A. Fleisher, *ibid.*, pp. 199-208.
5. S. U. Falk and A. Salkind, "Alkaline Storage Batteries," John Wiley and Sons, Inc., New York (1969).
6. R. Giovanoli, H. R. Oswald, and W. Feitknect, *Helv. Chim. Acta*, **49**, 1971 (1966).
7. Z. Nagy and J. O'M. Bockris, *This Journal*, **119**, 1129 (1972).
8. R. W. Powers, *ibid.*, **118**, 685 (1971).
9. D. N. Bennion, Quarterly Reports 1-4, Contract No. F44620-76-C-0098, AFOSR (1977).
10. James McBreen, *This Journal*, **119**, 1620 (1972).
11. K. W. Choi, Ph.D. Dissertation, School of Engineering, University of California, Los Angeles (1975).
12. W. G. Sunu, B. M. Eliash, and D. N. Bennion, Paper 45 presented at The Electrochemical Society Meeting, Atlanta, Georgia, Oct. 9-14, 1977.
13. T. Katan, J. R. Savory, and J. Perkins, Paper 44 presented at The Electrochemical Society Meeting, Atlanta, Georgia, Oct. 9-14, 1977.

Microelectrode Studies of Electrochemically Coprecipitated Cobalt Hydroxide in Nickel Hydroxide Electrodes

David F. Pickett*

U.S.A.F. Aero-Propulsion Laboratory, Aerospace Power Division, Wright-Patterson AFB, Ohio 45433

and J. T. Maloy*

Department of Chemistry, West Virginia University, Morgantown, West Virginia 26506

ABSTRACT

The role of electrochemically coprecipitated cobalt hydroxide and nickel hydroxide has been investigated at a nickel microelectrode for purposes of elucidating the effect of cobalt hydroxide on the electrode reactions of battery active nickel hydroxide. Hydroxide films were deposited onto the electrode surface from boiling ethanol solutions of $Ni(NO_3)_2$ in the presence and absence of $Co(NO_3)_2$; their behavior in 30% KOH solution was studied by cyclic voltammetry, chronoamperometry, and chronocoulometry. In general, the presence of coprecipitated cobalt hydroxide appears to render the charge-discharge reaction more reversible thereby allowing charging to occur at less positive potentials, this apparently increases the charging efficiency by minimizing concurrent oxygen evolution. The microelectrode was also used to characterize the cathodic deposition process for the nickel hydroxide.

The effect of cobalt hydroxide as a performance enhancing additive on the nickel hydroxide electrode has been known for some time (1). It has been reported that Edison was aware of the effect of cobalt hydroxide addition as early as 1908 (2). In 1925 it was confirmed that an addition of cobalt increased the capacity and life of the positive active material in nickel-iron and nickel-cadmium batteries (1). Cobalt is now used by most manufacturers, but barium, bismuth, cadmium, and lithium have been used as additives with similar effects. In general, it has been thought that these additives optimize the lattice imperfections in the electrode active material so that conductivity is increased and charging efficiency is improved.

Recently there have been quantitative empirical studies on the effect of cobalt addition to sintered plate electrodes. Ritterman, Lerner, and Seiger found that about 20 atom percent (a/o) of the active material as cobalt was optimum for electrodes manufactured using the chemical vacuum impregnation procedure (3), while Kroger found that about 10% was optimum for electrochemically impregnated electrodes (4). Workers at Bell Laboratories have also shown that additions of about 5% cobalt will extend the cycle life of electrochemically impregnated electrodes significantly (5).

* Electrochemical Society Active Member.
Key words: nickel hydroxide electrodes, alkaline cells, cobalt hydroxide additive, cyclic voltammetry, chronocoulometry.

The Air Force process for electrochemical impregnation (6) routinely uses 7-15% cobalt nitrate in the ethanolic nickel nitrate solution used in the preparation of positive plates to improve high temperature charge acceptance, extend the cycle life, and increase charge capacity.

This study was undertaken to gain a better understanding of why positive plate improvement should occur when cobalt hydroxide is coprecipitated with nickel hydroxide in the deposition process. Because the previous studies, which were conducted with large electrodes in actual working cells, had yielded little voltammetric data about the effect of cobalt hydroxide coprecipitation, it was decided that a microelectrode would be employed in this study to gain accurate potential information. Since nickel hydroxide microelectrodes were fabricated by cathodic deposition (6), some preliminary voltammetric studies were conducted to better understand this process. Most of the studies reported herein, however, were conducted with cathodically deposited nickel hydroxide electrodes immersed in 30% KOH. Charge-discharge characteristics were studied by slow scan cyclic voltammetry in a manner similar to that of MacArthur (7) and by double potential step chronoamperometry and chronocoulometry. Both types of experiments were conducted in the presence and absence of coprecipitated cobalt hydroxide.

Experimental

All experiments were conducted at a nickel working electrode with a Princeton Applied Research Model 170 electrochemical system (PAR). The working microelectrode was constructed by forcing a 0.05 in. nickel wire through a Teflon sleeve and grinding the end flat. The resulting disk electrode was then etched with 6M HCl and subjected to the cathodic deposition process to cover it with a uniform nickel hydroxide film. All experiments were conducted in a polyethylene cell fitted with a nickel auxiliary electrode. All potentials were measured against an aqueous KCl saturated calomel electrode (SCE) fitted with a 20 cm sidearm salt bridge with a pin-hole junction at its end. After every few hours of experimentation, the solution in the sidearm was withdrawn and replaced with fresh saturated KCl solution; in this manner it was possible to use the SCE reference even in 30% KOH solution.

Cathodic deposition of nickel hydroxide was carried out in an almost boiling ethanol-water [50 volume percent (v/o)] solution containing 1.8*M* $Ni(NO_3)_2$ alone and in the presence of 0.18*M* $Co(NO_3)_2$; typically, the potential of deposition was maintained at −1.5V *vs.* SCE. After charge-discharge studies in 30% KOH, the electrode surface was ground down and etched again with 6M HCl before being subjected to additional deposition. In order to characterize the voltammetry of the deposition process, some cyclic voltammetry experiments were conducted on $Ni(NO_3)_2$ solutions in ethanol-water mixtures containing KNO_3 as a supporting electrolyte. These experiments were conducted at an etched nickel electrode in quiescent solution at ambient temperature.

Charge-discharge studies were conducted in 30% KOH solution using the cell described above. It was soon discovered that charge or mass transport through the nickel hydroxide film was the current limiting step in the charge-discharge process; thereafter, and for most of this work reported herein, cyclic voltammetry and double potential step chronoamperometry and chronocoulometry experiments were conducted in stirred solutions. This technique has been used successfully in previous studies of membrane covered electrodes (8, 9). Cyclic voltammetry sweep rates employed were very slow. Double potential step experiments were initiated at the rest potential of a fully discharged electrode and after stepping to the desired charging potential for the desired time period of charge, the potential was returned to the initial rest potential for discharge measurements.

Cathodic Deposition Studies

In the Air Force process (6) for cathodic deposition of nickel hydroxide, sintered nickel plates are immersed in an ethanol-water solution of nickel nitrate at temperatures near the boiling point of the solution and cathodized at a constant current density (*ca.* 0.35 A/in.²) for a predetermined time (*ca.* 100 min). The current density that is selected is sufficient to cause the solvent supporting electrolyte system to decompose to liberate hydroxide ions. This may occur by the direct liberation of hydrogen gas at the electrode

$$H_2O + 2e \rightarrow H_2 + OH^- \quad [1]$$

or by reduction of the nitrate ion

$$\begin{array}{l} H_2O + NO_3^- + 2e \rightarrow NO_2^- + 2OH^- \\ \vdots \\ 6H_2O + NO_3^- + 8e \rightarrow NH_3 + 9OH^- \end{array} \quad [2]$$

where a variety of reduction products may form in addition to OH^-. This hydroxide ion then diffuses away from the electrode and reacts with a nickel ion present in the bulk of the solution to precipitate battery active nickel hydroxide within the pores of the nickel plaque

$$Ni^{+2} + 2OH^- \rightarrow Ni(OH)_2 \quad [3]$$

Of some concern in this process is the possible deposition of metallic nickel within the pores of the plaque material

$$Ni^{+2} + 2e \rightarrow Ni \quad [4]$$

because its presence would presumably exclude active material from the electrode. Initial experiments were directed towards the characterization of the deposition process to compare the relative likelihood of reactions [1] and [2] and reactions [3] and [4].

This was achieved by carrying out the voltammetry of a saturated KNO_3 solution at a nickel electrode. The results of multiple scans into anodic and cathodic background are shown in Fig. 1a and 2a, respectively. Figure 1a suggests that nickel ion reduction occurs at less negative potentials than hydroxide ion generation through solvent-supporting electrolyte decomposition. Note that the sweep into anodic background generates nickel ion which is electrodeposited in the vicinity of −1.0V *vs.* SCE (10) during sweep 2 of curve 1a. (This is also illustrated in sweeps 2 and 3 of curve 1b which were obtained from solutions containing a small amount of Ni^{+2}. The absence of a reduction wave during the first sweep indicates that the nickel electrode must first be activated to electrodeposit metallic nickel from nickel ions in solution.) Extrapolation of this result into the higher temperatures of the deposition process indicates that some care must be exercised during deposition to adjust the electrode potential sufficiently negative (at moderate current density in a galvanostatic deposition) to generate enough hydroxide ion to shield the electrode (by reaction [3]) from nickel deposition. Battery plates fabricated at low current densities by the Air Force process in preliminary experiments appeared gray in color and exhibited poor charging characteristics (11). These voltammetric results suggest that this was probably due to nickel deposition at potentials too positive for hydroxide generation.

Current
a
b
2
1
3
2
1
200 μA
1.0 0.0 −1.0
Potential (Volts vs SCE)

Fig. 1. Multiple scan voltammetry into the anodic background process for ethanol-water mixtures saturated with KNO_3. A bare nickel electrode was employed and the scan rate was 1 V/sec. Curve a: saturated KNO_3; curve b: saturated KNO_3 containing 2 g/liter $Ni(NO_3)_2$.

Figure 1b illustrates the effect of adding a small amount of Ni^{+2} to the saturated KNO_3. The large oxidation wave in the vicinity of 0.4V *vs.* SCE on the reversal of sweep 2 is probably due to the charging of $Ni(OH)_2$ formed during hydroxide ion generation at the activated electrode. The absence of a similar peak in curve 2b suggests that anodic activation of the nickel surface (prior to cathodic deposition) may also be beneficial to the formation of active material.

Figure 2 shows the effect of scanning into cathodic background without anodically activating the nickel electrode. Note that even in the presence of small concentrations of Ni^{+2} (Fig. 2b), the reduction wave at −1.0V *vs.* SCE is absent, just as it was in the first scans of 1a and 1b. This indicates that if this wave has been correctly assigned to the direct reduction of Ni^{+2}, this reduction readily takes place only at an anodically activated nickel electrode. In either the presence or absence of the nickel ion, however, the reduction of the NO_3^--solvent system generates a product that oxidizes in the vicinity of 0.6V *vs.* SCE. The only effect of nickel ion addition is the disappearance of the reversal of this oxidation wave upon scan reversal; compare the second scan of 2b with that of 2a. This indicates that the oxidation product of the cathodically generated species reacts with nickel ion. Since the same species forms in the presence and absence of nickel ion, the species that oxidizes at 0.6V *vs.* SCE is probably one of the products of nitrate reduction; see Eq. [2].

It has been proposed that nitrite ion formed during nitrate reduction causes the oxidation peak at 0.6V *vs.* SCE (12). This hypothesis was investigated by obtaining the voltammograms shown in Fig. 3. Note that while the product of nitrate reduction oxidizes at 0.55V *vs.* SCE, nitrite ion oxidizes at 0.85V *vs.* SCE under identical conditions. Thus, while it appears that nitrate ion reduction produces the hydroxide ion used in the deposition process, it also seems unlikely that the nitrate ion is reduced to nitrite. No further experiments were conducted to identify the product of nitrate ion reduction.

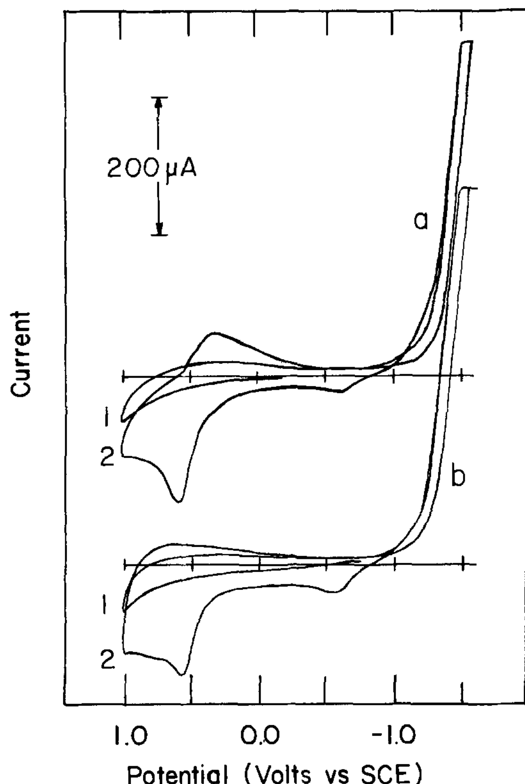

Fig. 2. Multiple scan voltammetry into the cathodic background process for ethanol-water mixtures saturated with KNO_3. See Fig. 1 for experimental details.

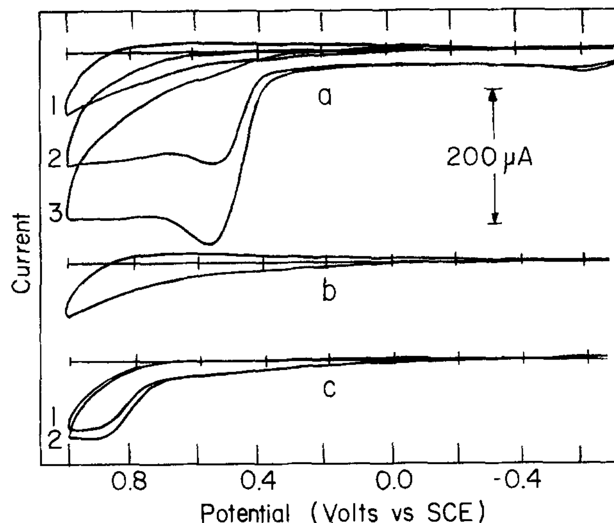

Fig. 3. An investigation of the products of nitrate reduction. Curve a, sweep 1, and Curve b: sweeps in saturated KNO_3 without reaching cathodic limit. Curve a, sweeps 2 and 3: the oxidation of the product of nitrate reduction formed during the cathodic background limiting process (not shown). Curve c: scans over the same range as curve b with 0.010M $NaNO_2$ added. The scan rate was 0.5 V/sec throughout, and the solution contained 2 g/liter $Ni(NO_3)_2$.

These studies also revealed deleterious effects if the cathodic deposition potential was too negative (at high galvanostatic current densities). When very negative potentials were employed (in the vicinity of −2.0V *vs* SCE), the green, hydrated nickel hydroxide formed on the surface of the electrode. This green hydroxide usually dislodged from the electrode surface during charge-discharge studies and was, therefore, unsatisfactory as an active material. Apparently, the generation of too much hydroxide ion causes the precipitation to occur at greater distances from the electrode. Thus, deposition occurs in a water-rich environment and the hydrated form of $Ni(OH)_2$ is loosely deposited on the electrode surface.

The above experiments suggest that potentiostatic control of the deposition process may result in superior loading of $Ni(OH)_2$ in positive plates. If this is prohibited due to cost or other considerations, great care must be exercised in the selection of an optimum current density for galvanostatic deposition.

Charge-Discharge Studies

Electrodes prepared by the cathodic deposition process were placed in 30% KOH solution for charge discharge studies. The charging process for electrodes of this type may be viewed as the conversion of $Ni(OH)_2$ (which exists in α and β forms) to NiOOH

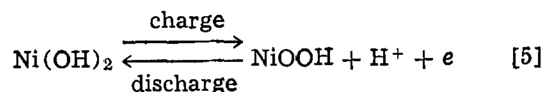

$$Ni(OH)_2 \underset{\text{discharge}}{\overset{\text{charge}}{\rightleftarrows}} NiOOH + H^+ + e \quad [5]$$

which remains in the charged state on the electrode surface (1). Alternately, one could write the charge-discharge reaction to emphasize the roles of OH^- and H_2O mass transport in rate-limiting either process

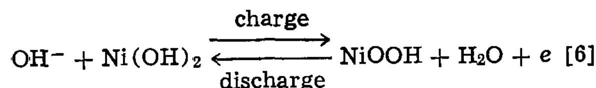

$$OH^- + Ni(OH)_2 \underset{\text{discharge}}{\overset{\text{charge}}{\rightleftarrows}} NiOOH + H_2O + e \quad [6]$$

Alternate reactions have been proposed (7, 13, 14) and proton diffusion has been proposed as the rate-limiting process (15). For simplicity, and because it provides solution species to control charge and discharge rates through diffusion and migration, Eq. [6] has been adopted as the model for this work.

In preliminary experiments, the electrodes prepared by the deposition process were subjected to slow scan cyclic voltammetry in 30% KOH; the results are shown in Fig. 4. In this figure, the behavior in the absence of coprecipitated cobalt hydroxide (curve a) is contrasted with the behavior in its presence (curves b, c, and d). Extremely slow scan rates (0.5 mV/sec) were employed in these studies; if rates much higher than 2 mV/sec were employed, the current maxima shown in Fig. 4 were not observed. (It is anticipated that a detailed discussion of the scan rate dependence at higher scan rates will be the subject of a future communication.) The appearance of current maxima even though the solution was being stirred during the experiment suggests that the rate of charge transfer is mass transport controlled (*i.e.*, by diffusion or migration) within the thin layer hydroxide film on the surface of the electrode. More importantly, Fig. 4 illustrates that the coprecipitation of cobalt hydroxide from a solution containing *ca.* 10% Co^{+2} allows the electrode to charge at a significantly less positive potential (0.13V instead of 0.23V *vs.* SCE). In addition, the charging process appears to occur more reversibly in the presence of coprecipitated cobalt hydroxide than in its absence (ΔEp is 75 mV instead of 150 mV). Thus, the cobalt additive apparently allows the charging process to occur more easily and more reversibly.

Regardless of the presence or absence of cobalt hydroxide, the voltammograms of Fig. 4 all exhibit a considerable increase in recorder noise when the charging process takes place. This 60 Hz noise persists so long as the active material remains in the charged state, but decreases upon discharge. This suggests that the impedance of the nickel hydroxide film increases appreciably in the charged state thereby increasing the probability of noise pickup. This hypothesis was verified by measuring a sixfold increase in cell resistance when the microelectrode was in the charged state instead of the discharged state. Thus, charge transfer appears to be controlled primarily by mass transport through a solid in which the conductivity depends upon the state of charge.

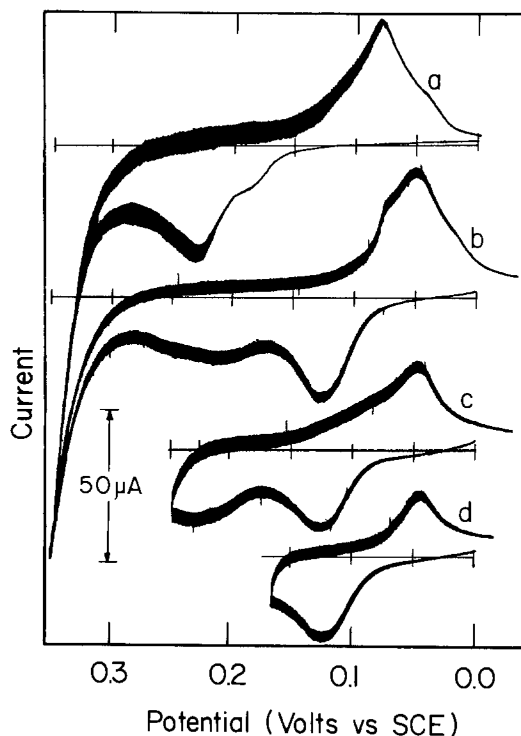

Fig. 4. Slow scan cyclic voltammetry of 30% KOH solutions at the nickel hydroxide electrode. Curve a: containing no coprecipitated cobalt hydroxide. Curves b c, and d: containing cobalt hydroxide coprecipitated from 1.8M $Ni(NO_3)_2$ containing 0.18M $Co(NO_3)_2$. The scan rate employed was 0.5 mV/sec. The solutions were stirred during the recording of these scans.

Typical quiescent solution cyclic voltammograms for nickel hydroxide electrodes containing coprecipitated cobalt are shown in Fig. 5. Although there is a variation in peak height with scan rate, there is not significant difference between voltammograms obtained using stirred or unstirred solutions (see Fig. 4). This indicates that convection is not an important mode of mass transport and that the mass transport that governs the voltammetry shown in Fig. 4 and 5 occurs primarily in the active layer of nickel hydroxide film and not in the solution in the vicinity of the electrode.

Characteristic cyclic voltammetry parameters obtained from Fig. 5 are shown in Fig. 6 as a function of sweep rate. In diffusion controlled cyclic voltammetry in liquid electrolytes, $i_{pa}/v^{1/2}$ is constant regardless of sweep rate for a kinetically uncomplicated redox reaction; for an adsorption process, i_{pa}/v is expected to be constant at different scan rates. In this system, neither condition is obtained, however, and

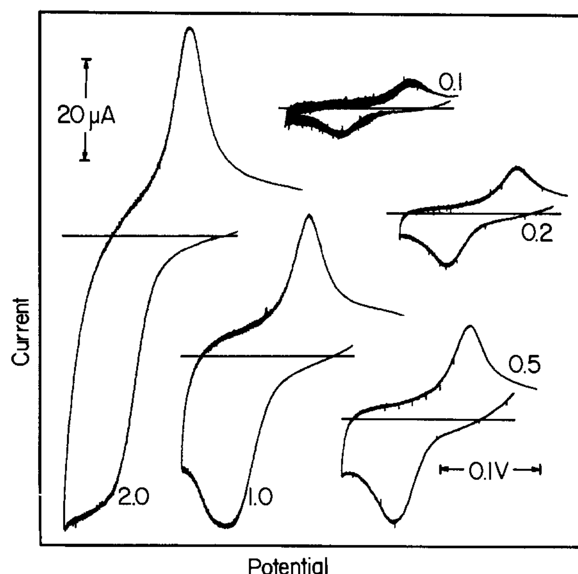

Fig. 5. Slow scan cyclic voltammetry of 30% KOH solution at a $Ni(OH)_2$ electrode containing some coprecipitated $Co(OH)_2$. Scan rates in mV/sec are shown associated with each figure. The solution was quiescent during the recording of these scans.

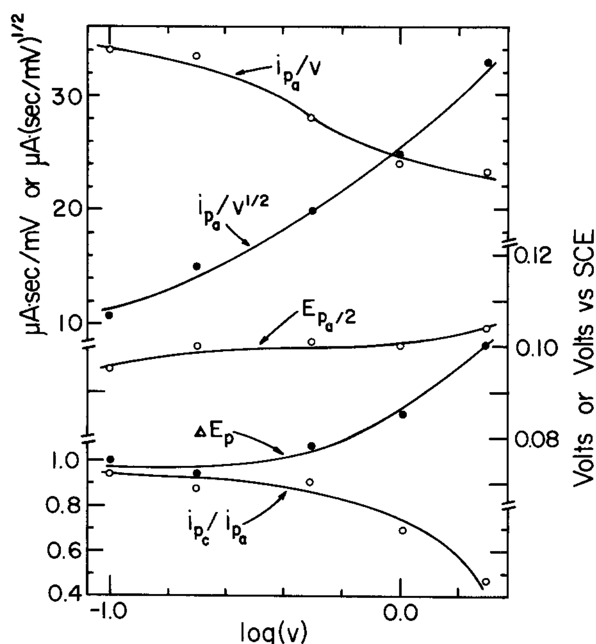

Fig. 6. The variation of cyclic voltammetry parameters with scan rate for a nickel hydroxide electrode (with cobalt hydroxide) in 30% KOH. The scan rate (in mV/sec) is shown logarithmically; other quantities have their usual electrochemical significance.

behavior somewhere between these two extremes might be proposed to explain the first two curves shown in Fig. 6. This behavior seems reasonable for a diffusion-controlled adsorption mechanism which takes place within the hydroxide film containing a limited number of chargeable sites. That the half-peak potential ($E_{pa/2}$) is fairly constant indicates that the same process is taking place at all scan rates. The peak to peak separation ($\Delta E_p = E_{pa} - E_{pc}$) generally increases at high scan rates from a minimum of 75 mV. Thus, on the basis of liquid electrolyte reversibility criteria, the reaction approaches reversibility only at low sweep rates. Since no attempt was made at iR compensation, increases in ΔE_p observed at higher sweep rates may be due to greater uncorrected potential differences at higher currents. Finally, it may be observed that the discharging to charging peak current ratio (i_{pc}/i_{pa}) generally decreases at higher scan rates from a near ideal value of 0.95. This may indicate that at the higher currents associated with faster sweep rates, the charging of the electrode is essentially complete, thereby allowing the generation of oxygen; this current would not be recovered upon discharge.

Chronoamperometric studies generally support the observations made on the basis of cyclic voltammetry. In addition, chronoamperometry reveals that the presence of coprecipitated cobalt hydroxide may cause charging to occur at a faster rate. Current-time curves in the absence of coprecipitated cobalt are shown at various charging potentials in Fig. 7; Fig. 8 shows this behavior in its presence. While curve 7a shows little more than double layer charging, curves 7b and 7c show both double layer charging currents and faradaic currents. At the potentials of curves 7e and 7f, the double layer charging current can no longer be distinguished from the faradaic current because the latter current is much higher at these potentials. At the intermediate charging potentials of curves 7b, 7c, and 7d, however, one may note that a delay time is necessary to achieve a maximum rate of charge. This may be contrasted with the behavior exhibited by all curves in Fig. 8 where no such delay time is observed in the presence of coprecipitated cobalt. Thus, at intermediate potentials, it appears that the presence of coprecipitated cobalt permits the charging to occur at a faster rate. Moreover, it also permits charging to occur at less positive potentials. (Compare the charging potentials of Fig. 7 with those in Fig. 8) This supports the observation made previously on the basis of cyclic voltammetry.

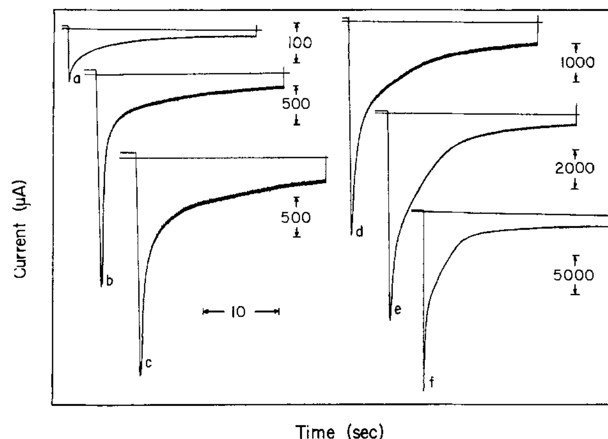

Fig. 8. Single step chronoamperometry of KOH solution at a nickel hydroxide electrode containing *ca.* 10% cobalt hydroxide. Potential steps to 0.10, 0.15, 0.20, 0.24, 0.28, and 0.32V *vs.* SCE were used in curves a through f, respectively.

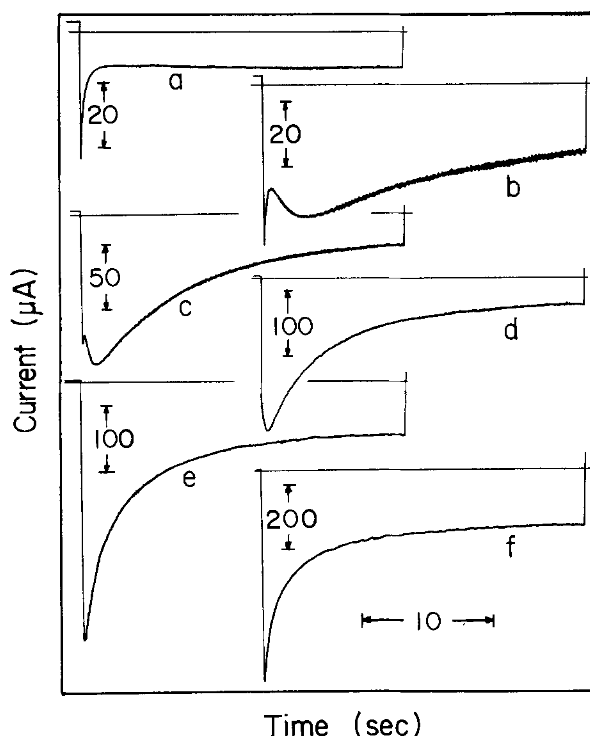

Fig. 7. Single potential step chronoamperometry of 30% KOH at a cobalt-free nickel hydroxide electrode. Curves a through f were obtained by stepping to 0.24, 0.26, 0.28, 0.30, 0.32, and 0.34V *vs.* SCE, respectively, to bring about the charging process.

Behavior like that shown in Fig. 7 has been reported by MacArthur (15) for similar electrodes; however, the mathematical model developed therein failed to explain the unexpected delay times observed in 7b, 7c, and 7d. No satisfactory model for this chronoamperometric behavior has yet been proposed. This thin layer cell problem is not unlike one considered recently in a study of immobilized enzyme electrodes (8, 9) in that mass transport and chemical reaction apparently take place in a film deposited on an electrode. Digital simulation techniques employed in the development of a mathematical model for the enzyme system appear to be applicable to this problem, and work is currently underway to model this chronoamperometric behavior using this technique.

Double potential step chronocoulometry was ultimately used to characterize the potential dependence of the rate of charge and the charging efficiency. A typical charge-time curve is shown Fig. 9. Here it is important to note that the initial potential and the potential of discharge were always maintained at the rest potential of a fully discharged electrode. With the electrode in a fully discharged state, then, the potential was stepped to some predetermined value

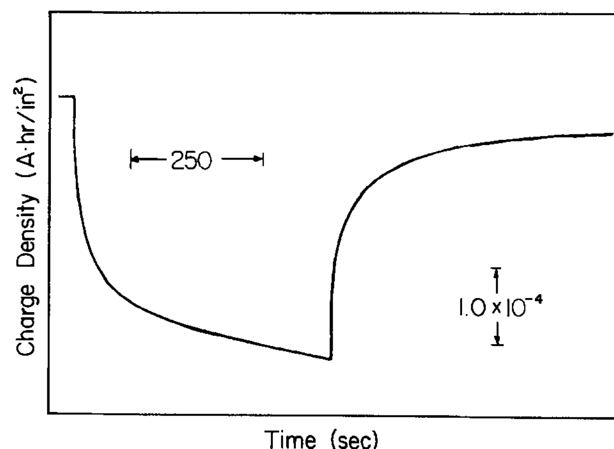

Fig. 9. Double potential step chronocoulometry using a nickel hydroxide electrode containing cobalt hydroxide. The potential was stepped from the rest potential (zero current) of a discharged electrode to +0.175V *vs.* SCE and then back to the rest potential after a 500 sec charge.

and the delivered charge was recorded as a function of time for a specified time interval. The potential was then returned to the initial value and the recovered charge was measured as a function of time until sufficient time had passed to restore the zero current condition. In this manner, the charge delivered and the charge recovered could be measured as a function of charging potential and time of charge.

Elimination of the latter quantity as a variable of interest was accomplished through the results illustrated in Fig. 10. In this experiment, the charging potential was always maintained at 0.175V *vs.* SCE, but the time of charge was varied. The time of discharge was also varied, but the zero current condition was always obtained. Thus, the charge that was recovered was always the maximum that it possibly could be. From the data in Fig. 10 and similar experiments, it soon became clear that complete charging of the microelectrode took place in less than 500 sec. Even though longer charging times were employed, these resulted in no additional recoverable charge when the microelectrode was discharged. Thus, for the electrode employed in these studies, 500 sec was found to be the maximum time necessary to achieve full charge. This time of charge was employed in all subsequent experiments.

The results of several 500 sec charges at various potentials are shown in Fig. 11. Panel I shows charge delivered as a function of charging potential in the

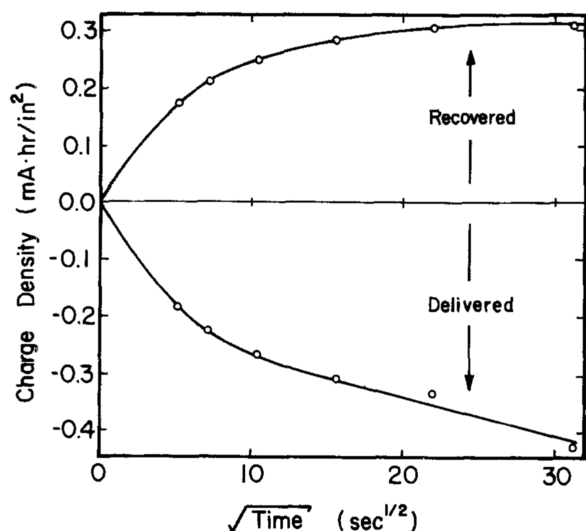

Fig. 10. A comparison of charge recovered to that delivered under potentiostatic conditions at various charging times. Experimental conditions are given in Fig. 9.

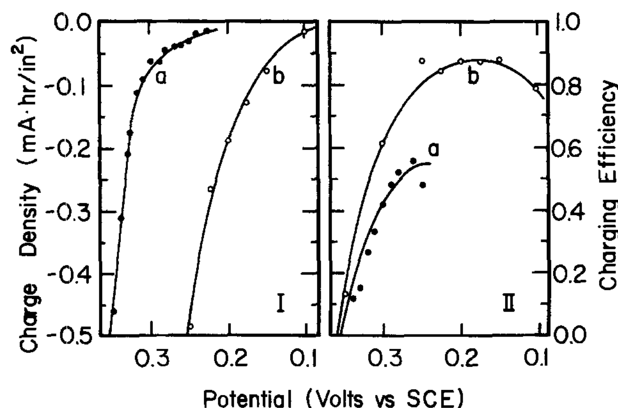

Fig. 11. Panel I: A comparison of charge delivered as a function of electrode charging potential in the presence and absence of coprecipitated cobalt hydroxide. Panel II: A comparison of charging efficiency under the same conditions. In either panel, curve a is for cobalt hydroxide absent; curve b, present. A 500 sec charge was employed throughout.

absence (curve a) and presence (curve b) of coprecipitated cobalt. From this panel, it is clear that the presence of coprecipitated cobalt allows charging to take place at less positive electrode potentials. Panel II shows the charging efficiency (charge recovered charge delivered) as a function of charging potential. In either curve, the charging efficiency falls off at more positive charging potentials because of concomitant oxygen evolution. Since coprecipitated cobalt (curve b) allows charging to occur at less positive potentials, however, less oxygen is evolved and much higher charging efficiencies are observed in its presence. Thus, the presence of cobalt hydroxide allows the electrode to be charged at less positive potentials (as indicated also by the voltammetry) and with greater efficiency because concomitant oxygen evolution is minimized. (This evidence that potentiostatic charging is less than 100% efficient even in the absence of any observable oxygen evolution is most intriguing. This aspect of this problem is being investigated in more detail because the potentiostatic charging efficiency should represent the maximum efficiency that can be obtained from an individual electrode within a cell.)

Data of the form of that given in Fig. 10 permit one to estimate the thickness of the $Ni(OH)_2$ film using Faraday's law and the known density of $Ni(OH)_2$ (2.5 g/cm^3). In this case, the film thickness is calculated to be 2.5 μm thick.

Conclusions

The microelectrode techniques used in this work have been shown to be useful in the study of solid film electrodes of this type. Mass transport (other than convection) occurring within the nickel hydroxide film has been found to determine the rate of the charge-discharge process. This observation suggests that the techniques developed above may be superior to conventional (Tafel plot) methods for studying electrode kinetics in this kind of electrode.

Some insight to the improvement of nickel hydroxide electrodes through cobalt hydroxide coprecipitation has been provided by this work. In general, coprecipitation increases potential range over which charging may occur and also makes the electron transfer process more reversible. Thus, coprecipitated cobalt hydroxide may be viewed as an electrocatalytic agent, but the mechanism of this catalysis is not known. Careful scrutiny of the voltammetry in Fig. 4 might lead one to propose that the presence of the cobalt causes the principal charge acceptor to be α-$Ni(OH)_2$ instead of β-$Ni(OH)_2$ as in the absence of cobalt, but no hard evidence exists to prove this conclusively. If this is the case, however, it appears that the improvement in reversibility could be due to the increased reversibility seen in charge-discharge studies of the α-$Ni(OH)_2$ form (7).

Acknowledgments

This work was supported by the Air Force Office of Scientific Research through contract grant F44620-75-C-0031 and grant AFOSR-76-2987. We acknowledge the administrative assistance of J. Fred O'Brien, Jr., Program Director of the 1975 USAF/ASEE Summer Faculty Research Program that made this collaboration possible.

Manuscript submitted Oct. 3, 1977; revised manuscript received March 24, 1978. This was Paper 49 presented at the Las Vegas, Nevada, Meeting of the Society, Oct. 17-22, 1976.

Any discussion of this paper will appear in a Discussion Section to be published in the June 1979 JOURNAL. All discussions for the June 1979 Discussion Section should be submitted by Feb. 1, 1979.

Publication costs of this article were assisted by the Air Force Office of Scientific Research.

REFERENCES

1. S. U. Falk and A. J. Salkind, "Alkaline Storage Batteries," John Wiley and Sons, New York (1969).

2. A. J. Salkind, Abstract 1, p. 9, The Electrochemical Society Extended Abstracts, Spring Meeting, Toronto, Canada, May 11-16, 1975.
3. P. R. Herman, S. Lerner, and H. N. Seiger, NASA Technical Report CR-72128, 1966.
4. H. H. Kroger, Air Force Technical Report AFAPL-TR-71-21, 1971.
5. D. W. Mauer and R. L. Beauchamp, Abstract 7, p. 23, The Electrochemical Society Extended Abstracts, Fall Meeting, Cleveland, Ohio, Oct. 3-7, 1971.
6. D. F. Pickett, U.S. Pat. 3,827,911 (1974).
7. D. M. MacArthur, *This Journal*, **117**, 422 (1970).
8. L. D. Mell and J. T. Maloy, *Anal. Chem.*, **47**, 299 (1975).
9. L. D. Mell and J. T. Maloy, *ibid.*, **48**, 1597 (1976).
10. See A. J. Arvia and D. Pasadas, "Nickel," in Encyclopedia of Electrochemistry of the Elements, 3, A. J. Bard, Editor, Marcel Dekker, Inc., New York (1975) and references contained therein.
11. J. W. Logsdon, Personal communication.
12. D. M. MacArthur, "Electrochemical Properties of Nickel Hydroxide Electrodes," in "Power Sources," 3, D. H. Collins, Editor, Oriel Press, Newcastle on Tyne, England (1971).
13. D. Tuomi, *This Journal*, **112**, 1 (1965).
14. P. C. Milner and U. B. Thomas in "Advances in Electrochemistry and Electrochemical Engineering," Vol. 5, P. Delahay and Tobias, Editors, Interscience, New York.
15. D. M. MacArthur, *This Journal*, **117**, 729 (1970).

Breakdown and Efficiency of Anodic Oxide Growth on Titanium

C. K. Dyer[1] and J. S. L. Leach

Department of Metallurgy and Materials Science, University of Nottingham, Nottingham NG7 2RD, England

ABSTRACT

The breakdown voltage, as defined by low coulombic efficiency of film formation, increases as the rate of anodic oxide growth on Ti increases. Ellipsometric determination of film thickness shows that the field across the oxide is not constant despite constant ionic flux. Changes in the ionic conductivity of the oxide are proposed to explain the nonlinear voltage/time behavior, and a range of high ionic conductivity is found at high growth rates preceding breakdown and crystallization.

The breakdown of anodic films on valve metals is usually accompanied by a significant decrease in the voltage gradient during growth at constant current density and there is gas evolution, sparking (1), crystallization (2), or a combination of these depending on the metal. The breakdown voltage of most valve metals depends on the metal and the electrolyte used in anodizing. Also, in the cases of Al and Ta, which may be considered typical valve metals, the breakdown voltage is independent of current density, and breakdown usually occurs after the passage of a fixed amount of charge or when a given thickness is reached (3, 4).

Titanium, which is also a valve metal, is reported to show indistinct breakdown at voltages as low as ~5V (2) but film growth continues to higher voltages with the formation of crystalline oxide (2) and oxygen evolution (1). Crystallization is also associated with breakdown of amorphous anodic oxide films on Al and Ta but generally at higher voltages than on Ti. In considering the breakdown behavior of these three valve metals, Yahalom and Zahavi (2) considered that while the link between crystallization and breakdown was established, cause and effect could not be distinguished; the authors assumed that prior to the low voltage breakdown on Ti, the anodic films were amorphous. The poorly defined breakdown behavior of Ti and the uncertainties as to the cause of breakdown and the prebreakdown condition of the anodic film prompted the present work. There is work which indicates that the cause of breakdown of some anodic films is a change in the oxide film such as generation of compressive stresses (3), while other reports show that there is a strong dependence on the anodizing electrolyte (5). In order to determine whether there are any changes within the oxide films on Ti during anodic growth, which might lead to breakdown, ellipsometric and weight gain measurements were made in the prebreakdown growth region to establish the film thickness and, therefore, the field strength and the film density. The coulombic efficiency of anodic film growth could then be determined.

As a result of the findings presented in this paper, we have considered it necessary to redefine the breakdown voltage (V_B) in terms of a change in efficiency of film growth since conventional ways to define it, such as by the change in slope of the voltage/time relation at constant current density, are deceptive in the case of Ti in that such changes are not always accompanied by a change in coulombic efficiency.

Experimental

Galvanostatic anodic film growth on Ti electrodes was measured by the change in cell voltage using a Cambridge potentiometric recorder in conjunction with a Tektronix 532 oscilloscope for the initial response to current. Application of constant current to polished Ti electrodes gives an initial voltage step followed by a voltage transient with slope (dV/dt) decreasing with time to a steady value (after ~2V). Extrapolation to $t = 0$ from this part of the voltage/time oscilloscope trace (of constant slope) was used as the origin for determination of the anodic film voltage. The intercept was subtracted from measured cell voltages to give a "film voltage" which excludes series contributions from sources such as electrolyte resistance and preexisting surface films. Ellipsometrically determined film thicknesses and the weight gains were plotted as a function of this film voltage in the present work.

Ellipsometry.—A manually operated ellipsometer was constructed using modified Glan-Thompson polarizing prisms mounted in divided circles which could be read to 2 min of arc. An additional divided circle carried a quarter-wave plate mounted between the polarizer and spectrometer stage. The light source was a 100W high-pressure Hg lamp. A narrow band mer-

[1] Present address: United Chemicon, Incorporated, Research and Development Laboratory, West Springfield, Massachusetts 01089.

Key words: amorphous, current density, ellipsometry, film.

cury green filter was incorporated in the telescope arm of the spectrometer and a photomultiplier tube was used to detect the intensity minima. The arrangement was aligned and calibrated as described by Archer (6).

An experimental cell machined from a solid "Perspex" cylinder had an open top. Light incident normally on an annealed glass window mounted in one side of the cell could also be incident normally on another similar window after 70° reflection at a flat electrode surface. Soft PTFE washers provided seals between the Perspex and the glass windows, which were found to be strain-free within the experimental accuracy of the system (intensity minima detectable to better than ~0.1°). The electrode surface could be centered in the cell (on the ellipsometer axis) and corrected for tilt by a finely adjustable clamp and stand.

Spectroscopically pure Ti rod (Table I) was cut, milled and abraded to expose a 0.33 cm² flat surface parallel to the rod axis at maximum rod width. The end of a Ti contact wire was inserted into a tapered hole in the curved surface of the specimen which provided good electrical contact. After degreasing in acetone the specimen and wire were anodized in 3 weight percent (w/o) ammonium hydrogen tetraborate at a high current density (50 mA/cm²) in order to grow an anodic film to a high voltage ~200V.

The specimen and contact wire were dried, coated with Araldite epoxy resin, and hot cured, which gave a leak-proof seal. Several coatings were applied and cured. Seals tested by anodizing to high voltage showed no color changes and, therefore, no further film growth below the hard transparent resin-covered surface. To reduce the risk of surface beveling during subsequent polishing, the specimen was mounted in thermosetting plastic in a standard metallurgical mounting press. The mounted specimen was abraded until the metal surface emerged, which was finally polished using alumina powder (5-30 nm particle diameter). Surfaces obtained in this way were satisfactorily flat. Surface treatments involving HF were avoided since this influences the film growth (7).

The cell was filled with electrolyte and eight readings of the azimuths of the polarizer (P) and analyzer (A) were taken, *i.e.* four pairs of values for minimum light intensity after reflection from the test surface. The ratio of the resultant reflected amplitudes in the plane of incidence and normal to this plane ($\tan \psi$) and the change in phase (Δ) were calculated from the mean P and A values (6) for the polished surface and after each increment in anodic film formation voltage under galvanostatic conditions. In Fig. 1, polar plots (8) of the vector, $\overline{Z} = (\tan \psi) e^{i\Delta}$, are compared with those derived from the Drude equations for theoretical values of the film thickness, d, the complex refractive indexes of the metal substrate and film [$\overline{n}_s = n_s (i - ik_s)$ and $\overline{n}_f = n_f (1 - ik_f)$, respectively] and the refractive index of the electrolyte, n_m (determined to four significant figures by Abbé refractometer). The rapid reaction of Ti with trace amounts of oxygen or water to form an oxide layer precluded attempts to measure the "bare" surface optical properties. Published data (9) for "atomically clean" Ti surfaces (after physical cleaning in UHV or chemical polishing) were unrelated to the present experimental results, giving data points unrealistically remote from extrapolations of the initial segments of the experimental polar plots in the direction of decreasing film thickness. Substrate constants n_s and k_s were determined by comparison with theoretical polar plots on the assumption of a

Table I. Ti rod composition (ppm) (Johnson Matthey Chemicals Limited)

Cu	40	Ni	8
Fe	20	Si	5
Sn	20	Mn	4
Al	10	Mg	<1

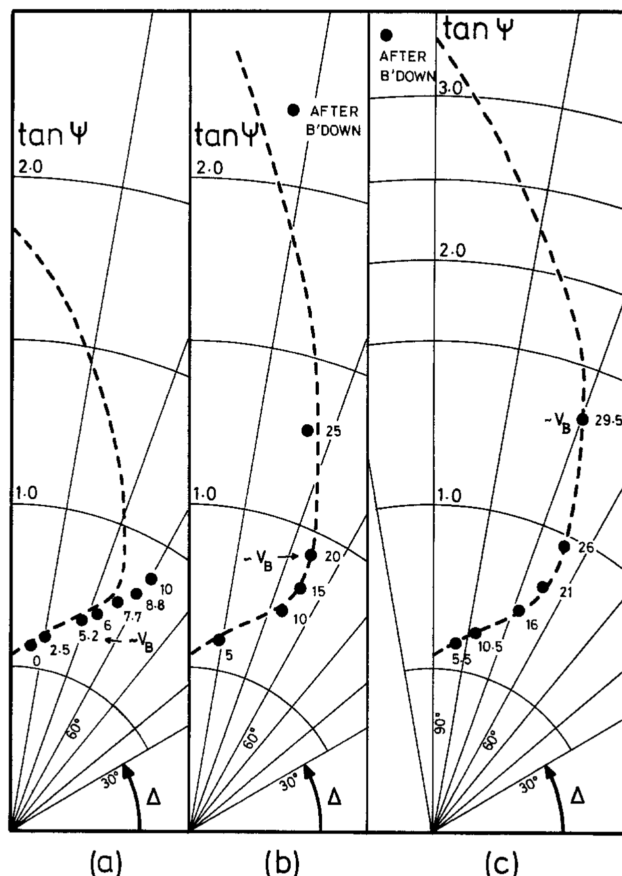

Fig. 1. Theoretical polar plots (– – –) of $\overline{Z} = (\tan \psi)e^{i\Delta}$ for substrate with $n_s = 2.0$, $k_s = 2.7$, and films with (a) $n_f = 2.008$, $k_f = 0$; (b) $n_f = 2.10$, $k_f = 0$; (c) $n_f = 2.14$, $k_f = 0$. Experimental data (●) at each film formation voltage (indicated) for (a) 1 mA/cm², (b) 10 mA/cm², (c) 50 mA/cm² anodic growth on Ti in carbonate buffer. $\lambda = 546.1$ nm, angle of incidence = 70°, $n_m = 1.335$.

constant film refractive index (to 1-3%) for different thicknesses. This gave a good fit to the data (to V_B) with $n_s = 2.0$ and $k_s = 2.7$ at wavelength $\lambda = 546.1$ nm (Fig. 1). The alternative, using as-polished P and A values to calculate n_s and k_s, led to a large increase then decrease in refractive index with increasing film thickness, which seems unlikely under conditions of galvanostatic anodic growth. With these substrate values, McCrackin's computer program (10) was used to check for constant film refractive index and to determine film thickness from the experimental data.

Interruption of film growth was necessary to allow time for measurement of P and A values with the manual ellipsometer. Some experiments were performed using an automatic ellipsometer, but its following-speed only allowed P and A values to be recorded during continuous anodic growth at ≤ 1 mA/cm². This equipment, which used a photoelectric detection system with Faraday effect modulation and with a Moiré fringe counting system, was sensitive to 0.002° changes and is described elsewhere (11).

Weight gain.—Specimens were weighed during film growth in order to determine the film density using the ellipsometric thickness data. 99.9% Ti foils (area ~70 cm²) were mechanically polished with alumina powder (particle diameter < 0.1 μm) then anodized in 3 w/o ammonium hydrogen tetraborate or a carbonate buffer solution at 1-50 mA/cm². Foil specimens were removed after increments in film formation voltage, washed, dried in air at ~150°C, and weighed on a microbalance to ± 10 μg.

Optical microscopy.—Anodic growth on the spectroscopically pure Ti specimen was observed *in situ* using a standard metallurgical microscope with water im-

mersion objectives. Crossed nicols were used in this microscope to detect the formation of crystalline TiO_2 during growth since the three crystalline forms of TiO_2 are noncubic and, therefore, birefringent. Cubic crystals or isotropic noncrystalline oxide would appear dark under crossed nicols.

Electrolytes.—All solutions were made from "analytically pure" reagents and doubly distilled water. Most work was done using a 3 w/o ammonium hydrogen tetraborate solution or a carbonate buffer solution (0.1M Na_2CO_3 + 0.1M $NaHCO_3$). At the highest current densities used (100 mA/cm²) the initial voltage step is ~20V in an ammonium hydrogen tetraborate solution, which means determination of film voltage is less accurate owing to the lower oscilloscope amplification which must be used. The carbonate buffer solution has an order of magnitude higher conductivity so that determination of the film voltage is inherently more accurate. A constant surface pH was also thought to be desirable in a study of film breakdown over the wide range of current densities used and anodic films of TiO_2 are known to be stable at the buffered pH of ~9.7 (12). The film voltage/time characteristics obtained for filmed Ti in this buffer solution were similar to those found in the borate solution. All experiments were carried out at room temperature.

Results

The film voltage/time characteristics of the mechanically polished Ti electrodes (Table I) were highly reproducible in either of the two electrolytes used (Fig. 2 and 3). In Tables II and III the details of these curves are shown in the form of the charge per volt. These details varied slightly on repolishing the specimen surface or between specimens, *i.e.*, charges per volt could differ by ± 12% and the extent of the voltage ranges of approximately constant slope could also vary by the same percentage, but the general characteristics remained the same.

The total charge passed, up to a particular voltage, can be determined from Fig. 2 and 3 where the abscissae show a rate of 0.5 C/cm²/division and 0.1 C/cm²/division, respectively, for all current densities. It is then clear from these figures that, for a given charge, the film voltage reached is higher at higher current densities but it is not obvious where breakdown occurs. The typical anodic film growth characteristic of nearly constant slope (dV/dt) after initial transients

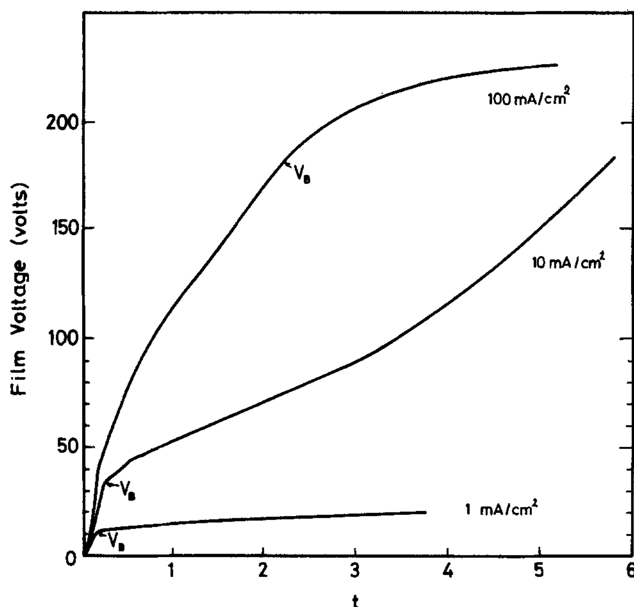

Fig. 2. Galvanostatic anodic film growth on a Ti electrode in 3 w/o ammonium borate solution at: 1 mA/cm² (t = 500 sec/div), 10 mA/cm² (t = 50 sec/div), 100 mA/cm² (t = 5 sec/div).

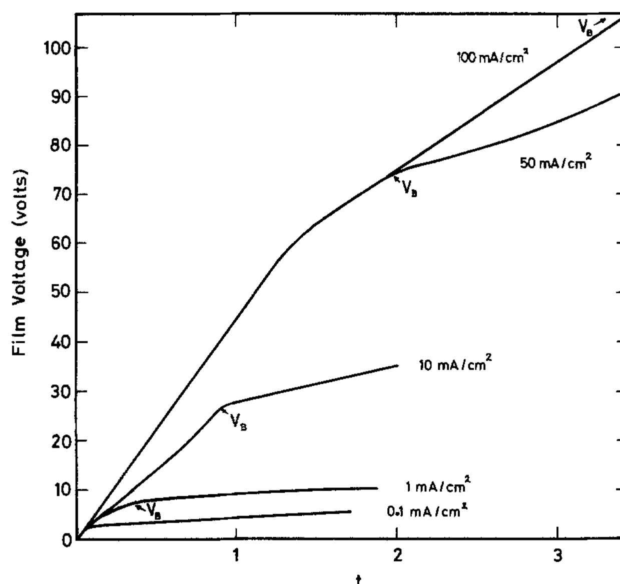

Fig. 3. Galvanostatic anodic film growth on a Ti electrode in 0.1M Na_2CO_3 + 0.1M $NaHCO_3$ solution at: 0.1 mA/cm² (t = 1000 sec/div), 1 mA/cm² (t = 100 sec/div), 10 mA/cm² (t = 10 sec/div), 50 mA/cm² (t = 2 sec/div), 100 mA/cm² t = 1 sec/div).

at constant current, only extends over a narrow initial voltage range which increases with current density in both electrolytes. There are significant changes of slope before the voltage/time curves develop a nearly constant gradient. We were concerned with these changes in slope at constant current density since a decrease would normally indicate breakdown.

Anodization at 1, 10, and 50 mA/cm² was followed by ellipsometry to establish the film thickness at different voltages on the same surface. At 1 mA/cm², film growth was followed continuously by the automatic ellipsometer but at 10 and 50 mA/cm² changes were too fast for automatic balancing and the growth was interrupted at 5V intervals while readings were taken with the manual ellipsometer.

Figures 4-6 show the derived thicknesses, from ellipsometric measurements, of films grown on a freshly polished surface anodized to the voltage shown, either continuously (Fig. 4) or with interruptions (Fig. 5 and 6). Changes in gradient (nanometers per volt) occurred at each current density. Repeated experiments on the same Ti specimen after repolishing the surface showed the same general behavior of variable slope

Table II. Coulombic charge per volt (per cm²) and derived film thickness from Eq. [1] (using optically derived densities from Table IV) during constant current anodization of Ti in 3 w/o ammonium borate)

		Film voltage range (V)	mC/V	nm/V	
(a)	100 mA/cm²	0-35	2.05	1.27	(ρ = 3.35)
		35-100	4.16	2.57	
		~100-180*	9.1	5.62	
		200 +	133 +		
(b)	10 mA/cm²	0-2	2.0	1.26	(ρ = 3.28)
		2-18	3.57	2.26	
		18-35	2.78	1.76	
		35*-40	45		
		40-49	22.5		
		49-90	27		
		90-200	12.5		
(c)	1 mA/cm²	0-2	2.0	1.34	(ρ = 3.09)
		2-9	5.5	3.68	
		11 + *	50 +		
(d)	0.1 mA/cm²	0-2	2.2		
		2-3	11		
		3 + *	20 +		

* Approximately the beginning of inefficient film growth (V_B).

Table III. Coulombic charge per cm^2 (during continuous constant current anodization of Ti in 0.1M Na_2CO_3 + 0.1M $NaHCO_3$) and derived film thickness per volt from Eq. [1] with optically derived values of ρ

		Film voltage range (V)	mC/V	nm/V	
(a)	100 mA/cm^2	0-56	2.38		
		56-120	4.46		
		~130*-150	22.76		
		~150-250	~100		
(b)	50 mA/cm^2	0-55	2.28	1.41	(ρ = 3.35)
		55-70	4.2	2.60	
		73*-78	12.5		
		78-88	7.3		
(c)	10 mA/cm^2	0-2	2.0	1.26	(ρ = 3.28)
		2-18	4.54	2.87	
		18-26	2.85	1.80	
		28*-36	12.5		
(d)	1 mA/cm^2	0-2.5	1.82	1.22	(ρ = 3.09)
		2.5-5.0	4.0	2.68	
		5-7.5	6.0	4.02	
		7.5*-9.5	11	7.37	
(e)	0.1 mA/cm^2	0-1	2.3		
		1-2	2.6		
		2*-3	28		
(f)	1.0 mA/cm^2	0-2	2.1		
		2-3	5.0		
		3.5-11.5	4.5	(10 mA/cm^2)†	
		11.5+ *	50+	(10 mA/cm^2)†	

* Approximately the beginning of inefficient film growth (V_B).
† Change to higher current density did not raise V_B to the values shown in (c).

(nm/V) differing only in the absolute values of the gradients by up to ± 12%. The data at $V = 0$ in Fig. 4-6 are for an as-polished surface before voltage is applied while all other data are corrected to exclude all but the voltage due to anodically grown film. The measurements on as-polished surfaces with no applied voltage gave an initial film thickness of 4.3 nm using $n_f = 2.008$ (Fig. 4) which was used to derive thicknesses of films grown at 1 mA/cm^2. There were no solutions for this initial film using the higher anodic

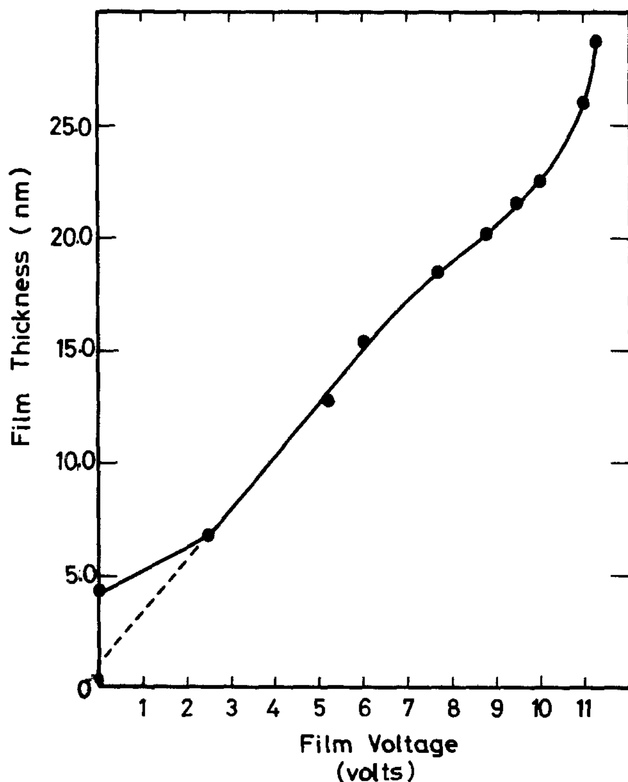

Fig. 4. Ellipsometric film thickness during interrupted anodization at 1 mA/cm^2 in 0.1M Na_2CO_3 + 0.1M $NaHCO_3$. λ = 546.1 nm, $n_f = 2.008 \pm 1\%$, $k_f = 0$. V_B ~5.2V.

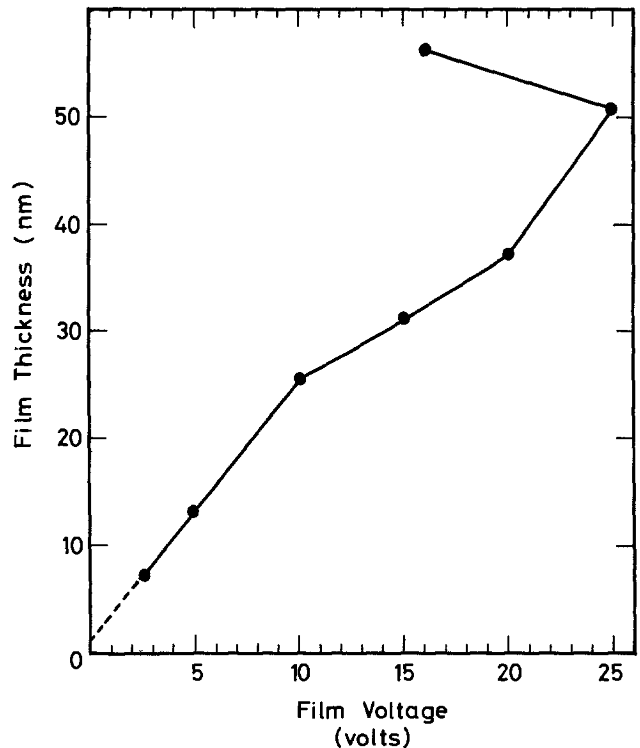

Fig. 5. Ellipsometric film thickness during interrupted anodization at 10 mA/cm^2 in 0.1M Na_2CO_3 + 0.1M $NaHCO_3$. λ = 546.1 nm, $n_f = 2.10 \pm 3\%$, $k_f = 0$. V_B ~20V.

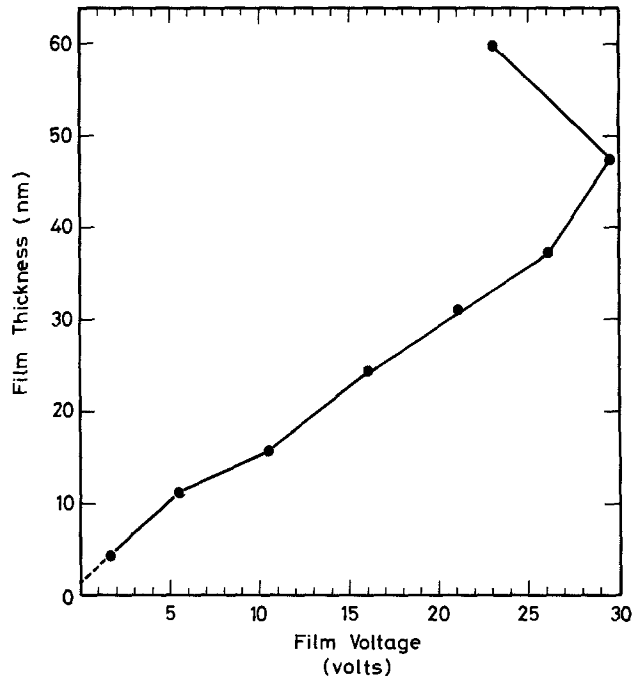

Fig. 6. Ellipsometric film thickness during interrupted anodization at 50 mA/cm^2 in 0.1M Na_2CO_3 + 0.1M $NaHCO_3$. λ = 546.1 nm, $n_f = 2.14 \pm 3\%$, $k_f = 0$. V_B ~29V.

film refractive indexes required in calculations for film growth at 10 or 50 mA/cm^2. The refractive index of this initial surface film is more than 3% below that of these anodic films and so is outside the limits set for the calculation where n_f is constant to 1-3%. Extrapolations from the first data points in Fig. 5 and 6 to $V = 0$ (and the 1 mA/cm^2 data excluding the data point at $V = 0$) do not pass through the origin as would be expected. This is probably due to overcorrection of the measured cell voltage because of extrapolation from the linear portion of the voltage/time oscilloscope trace.

Table IV. Coulometric and ellipsometrically determined film thickness/volt during 10 and 50 mA/cm² (interrupted) growth and 1 mA/cm² continuous growth in 0.1M Na_2CO_3 + 0.1M $NaHCO_3$ (from Fig. 4-6)

	Film voltage range (V)	(a) mC/V (±5%)	(b) nm/V (coulometric)†	(c) nm/V (ellipsometric)	% Coulombic efficiency (c)/(b) × 100
(a) 50 mA/cm²	1.8-26	2.2	(ρ = 3.35) 1.36	1.4	103
	26-29.5*	5.2	3.22	3.1	96
(b) 10 mA/cm²	2.5-10	3.8	(ρ = 3.28) 2.40	2.5	104
	10-20	2.0	1.26	1.2	95
	20*-25	8.53	5.39	2.6	48
(c) 1.0 mA/cm²	2.5-5.2	4.0	(ρ = 3.09) 2.68	2.3	86
	5.2*-7.5	6.0	4.02	2.3	57
	7.5-9.5	11.0	7.37	1.6	22

* V_B.
† Assuming optically derived densities.

Table IV shows the charge per volt passed during each stage of film growth followed ellipsometrically. The film density was estimated from the refractive index and weight gain (see Discussion section) so that the film thickness per volt could also be calculated from the charge passed. Comparison of this with the ellipsometrically determined thickness per volt shows the efficiency of film growth in Table IV. V_B is the voltage above which film growth proceeds at low coulombic efficiency. Ellipsometric experiments in ammonium borate solution also gave changes in gradient of film thickness/voltage relationships.

The effect of a change in current density on V_B, during continuous growth, is shown in Table III. After anodizing to only 3V at 1 mA/cm², an increase to 10 mA/cm² resulted in inefficient film growth above 11.5V which is considerably lower than if anodization had been at 10 mA/cm² throughout ($V_B \sim$ 28V). Anodizing history is therefore another factor in determining V_B.

The weight gain accompanying film growth is shown in Fig. 7 and was subject to an error of ± 0.3 μg/cm² in weighing.

At $\sim V_B$, optical microscopy showed local variations in color (indicative of different optical properties and/or thickness) and the presence of birefringent (noncubic crystalline) growths on which oxygen evolution was centered became apparent as the voltage increased above V_B. Below V_B the color was more uniform and no birefringence was observed.

Discussion

Film thicknesses derived from the ellipsometric measurements were not a linear function of film voltage (Fig. 4-6). There were changes in gradient (nm/V) during growth at 1 and 10 mA/cm² while at 50 mA/cm² there was film growth over a wide voltage range at small thickness per volt [column (c), Table IV]. These results suggest a variable oxide field strength during growth at constant current density. In the 10 and 50 mA/cm² experiments there were voltage ranges where the field strength was different by a factor of ~2× at the same current density. This behavior for an anodic film on a valve metal is usually associated with a change in the coulombic efficiency of oxide film growth. We will now try to determine this efficiency and its constancy during anodic growth, where a decrease in efficiency is linked with breakdown.

The ratio of the ellipsometrically determined film thickness with that expected from coulometry is a measure of coulombic efficiency of film growth. The calculation of coulometric thickness requires a knowledge of the film density and this we can derive in two ways: directly, from the refractive index of the film and, indirectly, from the weight gain data of the Ti foil assuming in the latter case the same thickness/voltage relationships as in the ellipsometric experiments. We will also consider the evidence in the present results for an amorphous film prior to breakdown.

Firstly, the assumption in this work of a constant film refractive index should be justified. We have already mentioned the experimental difficulty in obtaining a bare metal surface on Ti owing to its high reactivity with oxygen or water so that substrate optical constants cannot be determined directly. Immersion techniques cannot be used because suitable liquids for immersion have refractive indexes only up to ~1.7 and the lowest reported refractive index of TiO_2 is greater than 2.0 (13). Using n_s and k_s values calculated from ellipsometric readings of the as-polished specimen surface, we obtained an increase then decrease in refractive index from 2.27 to 2.29 to 2.07 for film growth at the 10 mA/cm² rate but the shape of the thickness/voltage relationship was similar to that shown in Fig 5, *i.e.*, the gradients were: 2.5 nm/V (2.5-10V), 1.2 nm/V (10-20V), and 2.8 nm/V (20-25V). At 50 mA/cm² there was also only a small difference in gradient (1.35 nm/V for the 0-26V range compared with 1.4 nm/V in Fig. 6) when using the apparent substrate constants derived from measurement of the polished specimen surface. The refractive index in this case

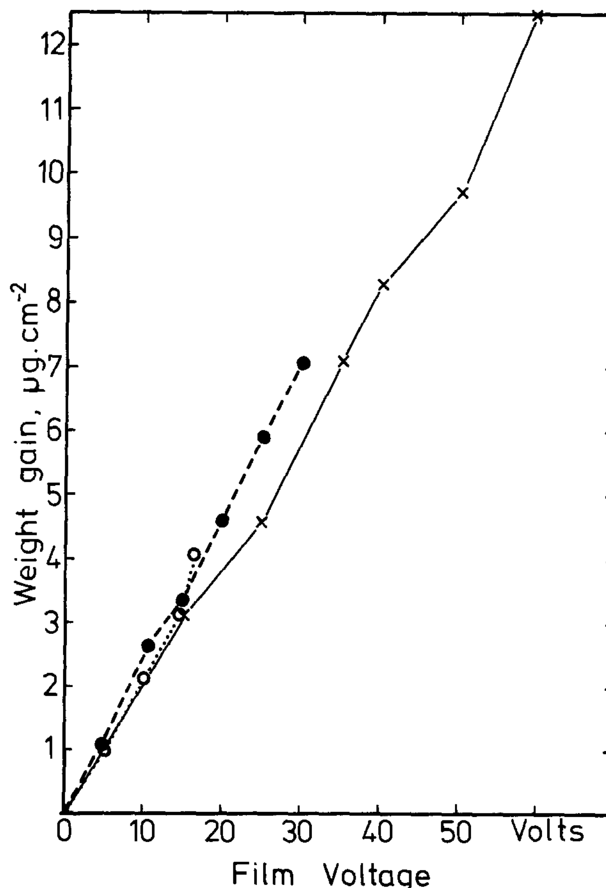

Fig. 7. Film voltage vs. weight gain of mechanically polished Ti sheet (annealed) during growth at 1 mA/cm² (○), 10 mA/cm² (●), 50 mA/cm² (×) in 0.1M $NaHCO_3$ + 0.1M Na_2CO_3.

varied from 2.26 to 2.16. The shape of the thickness/voltage curve at 1 mA/cm^2 was also only slightly altered by the use of as-polished substrate data. Data points were moved in the direction of greater film thickness by 2-3 nm for the three different film growth rates when as-polished substrate data were used.

Because we are cognizant of the inappropriate values for substrate constants obtained from as-polished surface measurements on Ti, we prefer to adopt the more reasonable assumption of a constant refractive index during anodic film growth, although it makes little difference to the results.

The relative insensitivity of n_f to variations in the thickness/voltage gradient in Fig. 4-6 is an interesting and important finding and is supported by observations from entirely different anodic oxides on Al (14). Here it was found that a change from amorphous to crystalline Al_2O_3 resulted in a 100% increase in growth field (at constant current), while the refractive index, as measured by an immersion technique, had only changed from 1.65 (15) to ~1.70. Structural changes in the anodic oxide films on Ti during growth might also be responsible for the changes in field strength.

Direct structural information on the anodic film on Ti is not easily acquired in the early stages of film growth. Other authors (2) have assumed that at least during the first 5V the film is amorphous, above this voltage they find crystalline TiO_2 (anatase) by electron diffraction of stripped 85V anodic oxide films, they report that the crystallinity in the films is apparent in polarized light. However, the problems of stripping very thin films (<10V) and the chance of crystallization in the electron microscope make convincing evidence for amorphous oxide prior to breakdown on Ti difficult to obtain.

In the present work, an *in situ* technique was used to test for amorphous oxide in the early stages of anodic growth. Optical microscopy of the specimen surface during film growth showed no birefringence under crossed nicols until gas evolution occurred. This must indicate the growth of an optically isotropic film such as an amorphous oxide, since the reported crystalline forms of TiO_2 are all noncubic. Better evidence that the growing film is initially amorphous is the low refractive index and density (Table V) of films compared with crystalline forms of TiO_2 which have refractive indexes in the range 2.49-2.90 (16) and densities in the range 3.90-5.5 g/cm^3 (16).

In discussing the breakdown of these anodic films during growth, we must consider whether the changes in gradient, dV/dt, are accompanied by a change in efficiency of formation of the barrier oxide film. Figures 2 and 3 show V/t curves where there are decreases in gradient. However, these would indicate breakdown only if accompanied by a decrease in coulombic efficiency for barrier film growth. Figures 4-6 only indicate the effect of oxide field strength during growth and provide no information about coulombic efficiency. However, in Table IV, the charge passed in each voltage range of anodic growth is tabulated (as mC/V) for the three growth rates and is seen to vary in the same direction as the thickness per volt, *e.g.*, at 10 mA/cm^2 both the charge and thickness per volt are decreased by ~50% in the 10-20V range compared with the 2.5-10V range. The actual film thickness, d, at a given voltage is given by the following equation

$$d = \frac{qM}{4F\rho} \cdot \eta \quad [1]$$

and

$$\eta = \frac{4dF\rho}{qM} \quad [2]$$

where M is the molecular weight of the oxide, ρ its density, and q is the charge passed. η is the fractional coulombic efficiency of oxide growth. To calculate η, a knowledge of the film density is required. Assuming the oxide has the same density as anatase [$\rho = 3.9$ g/cm^3 (16)] which has been reported in anodic films on Ti (2) (though at higher film voltages than used here) the maximum film thickness expected in the 2.5-5V range at 1 mA/cm^2 (*i.e.*, assuming 100% efficiency) is 2.1 nm/V. This is significantly below the ellipsometric value of 2.3 nm/V (Table IV) and is contradictory since 100% efficiency was assumed. The film density must be less than that of anatase. Similar calculations for the 10 and 50 mA/cm^2 rates lead to the same conclusion.

The optical polarizability of a crystalline oxide can be estimated (17) from the refractive index and density using the Lorentz-Lorenz relationship

$$\alpha_m = \frac{3M}{4\pi N\rho} \frac{(n_f^2 - 1)}{(n_f^2 + 2)} \quad [3]$$

where α_m is the molecular electronic polarizability and N is the Avogadro number. There are three crystalline forms of TiO_2: anatase, brookite, and rutile which are tetragonal, orthorhombic, and tetragonal, respectively. For comparison with the anodic TiO_2 which is optically isotropic, we will consider hypothetical crystalline oxides made of randomly oriented microcrystals of single crystal density so that average refractive indexes for the three crystal forms of TiO_2 are 2.5246, 2.6226, and 2.7545 (16) and densities are 3.9, 4.13, and 4.23 g/cm^3 (16) for anatase, brookite, and rutile, respectively. The respective values for α_{TiO_2} from Eq. [3] are 0.522, 0.508, and 0.515 $\times 10^{-23}$ cm^3 which, despite the different crystal systems and densities are remarkably similar. It is reasonable, then, to suppose that α_{TiO_2} for the anodic oxide is similar to an averaged value of 0.515 $\times 10^{-23}$ cm^3 between the crystal forms. This value would be for wavelength, $\lambda = 588.9$ nm but the correction for $\lambda = 546.1$ nm is only ~0.001 $\times 10^{-23}$ cm^3 and will be ignored.

Using an average value of α_{TiO_2} of 0.515 $\times 10^{-23}$ cm^3 and values of n_f as calculated in this work of 2.008, 2.10, and 2.14, Eq. [3] gives the following estimates of ρ: 3.09, 3.28, and 3.35 g/cm^3 for growth at 1, 10, and 50 mA/cm^2, respectively. The value of n_f for 1 mA/cm^2 growth is more accurate since it is derived from measurements with the automatic ellipsometer. Calculations of film thickness/volt using these film density values in Eq. [1] lead to the coulombic efficiencies shown in Table IV. In all the early stages of film growth, efficiency is nearly 100% and this is supported by the absence of gas evolution over these voltage ranges.

The film density can be independently calculated from the weight gains during anodization (Fig. 7) using the thicknesses per volt determined from ellipsometry shown in Table IV. Values derived in this way are shown in Table V and are within 10% of the average density calculated from the refractive indexes. Film growth, therefore, is highly efficient in the early stages of growth. It is important to note also that efficiency is ~100% over voltage ranges where the measured field strength is different by a factor of ~2× at the same current density. These changes in the field are not due to changes in ionic flux as might be anticipated from the well-known field-assisted ionic transport equation for anodic film growth which to a first approximation, can be written

$$i = i_0 \exp - (U/kT) \exp (qaE/kT) \quad [4]$$

Table V. Film densities derived from weight gain data (Fig. 7) and ellipsometric film thickness (Fig. 4-6)

Current density (mA/cm^2)	Film voltage range (V)	d (nm)	Weight gain ($\mu g/cm^2$)	TiO_2 ($\mu g/cm^2$)	ρ (g/cm^3)
1	0-7.5	14	1.6	4.0	2.86 ± 9%
10	2.5-25	44	5.35	13.37	3.04 ± 3%
50	2-29.5	43	5.20	13.00	3.02 ± 2%

where E is the field, U is the activation energy, q is the ionic charge, and a is the jump distance.

Coulombic data for continuous growth (in Tables II and III) have been used in Eq. [1] to calculate thicknesses per volt from the same densities used in Table IV. The derived values show apparent changes in field strength in similar sequences to those shown in Table IV. A more rapidly balancing ellipsometer would be required to determine film thicknesses and field strengths during continuous film growth at high rates. However, in common with interrupted growth data, Tables II and III also show a decrease in mC/V at 10 mA/cm^2, which implies an increase in field strength (assuming $\eta = 1$) at constant current density. The alternative explanation in the case of continuous growth is that there is an increase in efficiency at higher voltages which is contrary to experience of the breakdown phenomenon. In Tables II and III, high values of mC/V indicate that $V > V_B$.

We shall define breakdown for Ti as the beginning of the voltage range in which the efficiency is significantly below 100%. Such changes can be seen in Table IV and the voltage at the beginning of each range is denoted by V_B. At higher current densities (10 and 50 mA/cm^2), V_B appears at higher voltages than at 1 mA/cm^2. At 50 mA/cm^2 there is a decrease in field strength before breakdown (at 26-29.5V) and at 10 mA/cm^2, a decrease in efficiency to 48% cannot explain, in terms of Eq. [4], a decrease in field strength to less than half. The decrease in field strength at these current densities may not be attributed to joule heating (18) since these were interrupted growth experiments so that heat generated in the film was rapidly dissipated before the measurements were made. So, just before breakdown at 50 mA/cm^2, and associated with breakdown at 10 mA/cm^2, there may be an increase in ionic mobility such that a constant ionic flux is maintained at a lower field. This change in the intrinsic oxide field strength is delayed to higher voltages at faster growth rates as is breakdown and it may be that the increased ionic mobility is a precursor of breakdown.

The reasons for changes in intrinsic oxide field strength at constant ionic flux may be structural differences in the films which could significantly influence field-assisted ionic transport by, for instance, changing the activation energy (see Eq. [4]). Such changes could occur without affecting bulk properties such as density or refractive index by more than a few percent as has already been observed for anodic Al_2O_3 (14). However, unlike Al_2O_3, the structure during efficient oxide growth at high rates is not envisaged to be crystalline at any stage, since the film refractive index is approximately 15% below that of the least dense crystalline phase, anatase, and a crystalline oxide on Ti is associated with breakdown.

Evidence that breakdown is accompanied by crystallization was provided by optical microscopy which showed the presence of noncubic crystalline oxide at voltages $> V_B$. Oxygen evolution was sited on such crystalline regions leading to the low efficiency by which breakdown was defined. This is not unexpected as it is generally recognized that impurities have a greater influence on semiconduction in crystals than in noncrystalline materials (19) and anodic films are known to contain impurities such as electrolyte anions incorporated during anodic growth. So crystallization could result in high electronic conductivity which would enable the observed gas evolution to occur.

If the structural reorganization involved in formation of the crystalline oxide requires ease of ionic movement, then the increased ionic mobility found at high growth rates just before V_B could be the cause of breakdown on Ti.

Summary

The anodic film breakdown behavior of Ti is characterized by a change in film growth such that efficient growth of amorphous oxide gives way to a new anodic behavior: low efficiency oxide growth and gas evolution associated with crystalline oxide in the film. Changes in the slopes of the voltage/time relations at constant current density can occur at ~100% efficiency for growth indicating that there is a variable oxide field strength.

Breakdown occurs at higher voltages at higher rates of film growth. Just prior to breakdown at the highest growth rates there is a decrease in field strength in the oxide.

Acknowledgments

The authors wish to thank the Science Research Council for financial support, the Department of Mathematics and Physics, University of East Anglia, for the use of their automatic ellipsometer, and Dr. J. G. Wright, P.C.S. Hayfield, and M. A. Barrett for valuable discussions on ellipsometry.

Manuscript submitted May 11, 1977; revised manuscript received March 3, 1978.

Any discussion of this paper will appear in a Discussion Section to be published in the June 1979 JOURNAL. All discussions for the June 1979 Discussion Section should be submitted by Feb. 1, 1979.

REFERENCES

1. G. C. Wood and C. Pearson, *Corros. Sci.*, **7**, 119 (1967).
2. J. Yahalom and J. Zahavi, *Electrochim. Acta*, **15**, 1429 (1970).
3. J. Yahalom and T. P. Hoar, *ibid.*, **15**, 877 (1970).
4. J. Zahavi and J. Yahalom, *ibid.*, **16**, 89 (1971).
5. A. Aladjem, *J. Mater. Sci.*, **8**, 688 (1973).
6. R. J. Archer, "Manual on Ellipsometry," Gaertner Scientific Corporation, Chicago.
7. C. K. Dyer and J. S. L. Leach, To be published.
8. P. Hayfield, in "Advances in Corrosion Science and Technology," Vol. 2, M. G. Fontana and R. W. Staehle, Editors, p. 43 Plenum Press, New York (1972).
9. T. Smith and F. Mansfeld, *This Journal*, **119**, 663 (1972).
10. F. L. McCrackin, "A Fortran Program for Analysis of Ellipsometer Measurements," Nat. Bur. Stand. Tech. Note 479, U.S. Gov't Printing Office, Washington (1969).
11. C. C. Matheson, J. G. Wright, R. Gundermann, and H. Norris, *Surf. Sci.*, **56**, 196 (1976).
12. C. K. Dyer and J. S. L. Leach, *This Journal*, **125**, 23 (1978).
13. D. L. Johnson and L. C. Tao, *Surf. Sci.*, **16**, 390 (1969).
14. C. K. Dyer and R. S. Alwitt, *Electrochim. Acta*, **23**, 347 (1978).
15. M. A. Barrett and A. B. Winterbottom, 1st International Congress on Metallic Corrosion, p. 657, Butterworths, London (1961).
16. Handbook of Chemistry and Physics, 52nd ed., The Chemical Rubber Co., Cleveland (1971).
17. J. R. Tessman, A. H. Kahn, and W. Shockley, *Phys. Rev.*, **92**, 890 (1953).
18. D. A. Vermilyea, *Acta Met.*, **1**, 282 (1953); L. Young, *Trans. Faraday Soc.*, **50**, 153 (1954); *ibid.*, **52**, 502 (1956); *ibid.*, **53**, 229 (1957).
19. N. F. Mott and E. A. Davis, "Electronic Processes in Non-Crystalline Materials," Oxford University Press (1971).

Electropolishing of Titanium in Perchloric Acid-Acetic Acid Solution

I. Auger Electron Spectroscopy Study of Anodic Films

J. B. Mathieu,* H. J. Mathieu,** and D. Landolt**

Materials Department, Swiss Federal Institute of Technology, Lausanne, Switzerland

ABSTRACT

Anodic films on titanium formed in a perchloric acid-acetic acid electropolishing electrolyte were investigated by Auger electron spectroscopy (AES) depth profile analysis. Films formed in 1*N* H_2SO_4 at different potentials were used as standards for determining sputter rate and stoichiometry. Obtained results show linear film growth to occur up to the onset of electropolishing when film thickness abruptly decreases and becomes independent of potential. The electropolishing film observed by AES contains chloride ions, the concentration of which exhibits a maximum at the metal-film interface.

Perchloric acid-acetic acid electrolytes are commonly used in metallurgical laboratories for electropolishing of titanium (1). Anode potentials as high as 25-40V are necessary to achieve good polishing indicating that anodic films play an important role. Recently Auger electron spectroscopy (AES) has become available as a powerful technique for surface analysis which allows one to study chemical composition of outermost surface layers with high resolution (2). By combining AES analysis with atom layer removal by argon ion sputtering concentration depth profiles can be determined. The applicability of this technique to the investigation of thickness and stoichiometry of titanium oxide films has recently been investigated (3) and it was concluded that useful information can be obtained provided complicating effects resulting from beam-surface interactions and from impurity adsorption are taken into account properly.

The purpose of the present study is to investigate the thickness and chemical nature of anodic films formed on titanium at different stages of the polishing process by using AES. In a subsequent paper polarization behavior and dissolution stoichiometry of titanium in perchloric acid-acetic acid electropolishing solution will be discussed (4).

Experimental

A preliminary series of experiments were performed with films produced by anodizing in 1*N* sulfuric acid (5). For this purpose 7 mm diam titanium disks were electrochemically polished in a solution of 30 ml $NaClO_4$, 270 ml methanol, and 175 ml butyl cellosolve at a potential of 25V and a temperature of $-10°C$. After this the samples were rinsed and then anodized for 5 min at constant voltage ranging from 5 to 35V at a temperature of 25°C. This procedure leads to the formation of TiO_2 films, the thickness of which increases linearly with potential at a rate of approximately 25 Å/V (5, 6).

Rotating disk electrodes as well as stationary electrodes were employed for anodization in perchloric acid-acetic acid solution. The rotating disk electrode was fabricated from a 7 mm diam titanium rod (99.97%, Materials Research) embedded in a 15 mm diam Teflon cylinder. Rotation rate was 1200 rpm in all experiments. A cylindrical platinum counterelectrode of 45 mm diam and a saturated mercury sulfate reference electrode with a Luggin capillary perpendicular to the disk surface were employed. The electrolyte solution was prepared by mixing 1000 ml glacial acetic acid ($\rho = 1.05$) with 100 ml 70% perchloric acid ($\rho = 1.67$). Electrolyte composition corresponded to 1.1 mole/liter $HClO_4$ and 15.9 mole/liter CH_3COOH. The temperature during experiments was 25°C. Before each run the titanium anode was mechanically polished on 6 μm diamond paste, then washed and rinsed with double distilled water. Starting from open circuit a voltage ramp of 20 mV/sec was applied until a preset potential was reached at which the anodization was stopped. The titanium rotating disk electrode was then removed from the cell and was cut carefully parallel to its surface such that an approximately 2 mm thick disk was obtained. Stationary electrodes consisted of a thin titanium disk insulated on three sides and therefore no cutting operation was needed. The thin metal disks were washed with soap solution, rinsed with distilled water, and dried with acetone before being inserted into the vacuum system for AES analysis.

A potentiostat (Amel Type 552) with function generator (Amel Type 564) was used as power supply. To allow potentiostatic operation at anode potentials of up to 50V an operational amplifier with voltage divider was employed in the reference electrode circuit. Potentials were measured with an electrometer and recorded as function of current using an X-Y recorder.

AES analysis was performed using a commercial apparatus (Physical Electronics Model 545 A) including UHV system and cylindrical mirror analyzer. After insertion of the samples to be analyzed, the apparatus was evacuated to a base pressure of approximately 10^{-9} Torr. High purity argon was then leaked in and the pressure was allowed to increase to 5.0×10^{-5} Torr for *in situ* argon ion sputtering. Ion beam energy was 2 kV in all experiments. AES analysis was performed at a primary electron beam energy of 5 keV and a current of 3-20 μA.

Most concentration depth profiles were derived from complete Auger spectra recorded at different sputter times, but in some cases peak amplitudes were plotted directly as a function of time using a multiplexer unit. The amplitudes of the following peaks were monitored: 381 eV titanium, 416 eV titanium, 508 eV oxygen, 181 eV chlorine, 270 eV carbon, and 145 eV sulfur. For a more detailed discussion of the Auger spectra of different titanium oxides the reader is referred to Ref. (3).

Results

Films formed in H_2SO_4.—Figure 1 shows AES concentration depth profiles for oxygen, titanium (Ti_1 = 381 eV peak, Ti_2 = 416 eV peak), sulfur, and carbon for a film produced at 7.5V. The oxygen peak-to-peak

* Electrochemical Society Student Member.
** Electrochemical Society Active Member.

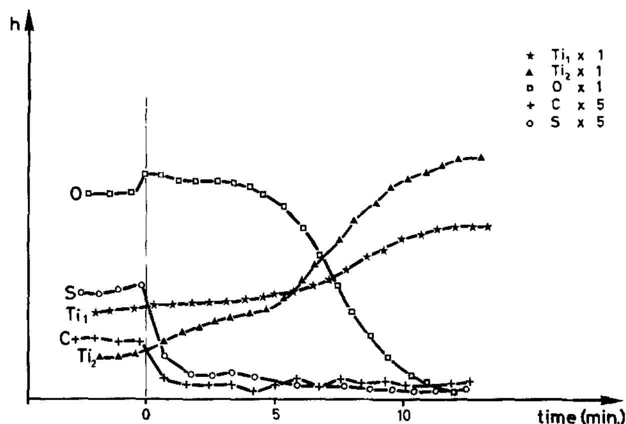

Fig. 1. AES concentration depth profile of titanium oxide film produced by anodizing in H_2SO_4 at 7.5V. h = peak amplitude in arbitrary units.

amplitude exhibits a plateau within the bulk oxide, then decreases at the oxide-metal interface to become zero in the metal. The amplitudes of the two titanium peaks [Ti_1] and [Ti_2] increase at the oxide-metal interface. In the oxide the [Ti_1] amplitude is higher than the [Ti_2] amplitude but in the metal the inverse is true. This change in relative peak height is due to differences in the shape of the titanium peaks between oxide and metal (3). For the purposes of the present study the behavior is of no further consequence. Sulfur and carbon are present at the outer oxide surface in noticeable amounts because of adsorption of sulfate from the electrolyte and of carbon compounds from the air or the UHV system. In the interior of the oxide the magnitude of the Auger signals for these elements is of the order of the background noise only and therefore essentially zero.

Film thickness can be deduced from concentration depth profiles using the relation $l = v_o t_l$, where l is the film thickness, v_o is the sputter rate, and t_l is the time needed for sputtering through the film. For oxide films one usually defines t_l as the time at which the oxygen peak amplitude at the metal-oxide interface has decreased to 50% of its steady-state value in the oxide (3).

In Fig. 2 measured t_l values for titanium oxide films formed in 1N H_2SO_4 are given as a function of anodizing potential. A linear increase in t_l with potential is observed. Since film thickness is also a linear function of anodizing voltage it follows that the sputter rate v_o is constant, *i.e.*, independent of film thickness. Assuming a film formation constant of 25 Å/V the sputter rate v_o was evaluated from the slope of the straight line and used for estimating film thickness from depth profile data. For the oxide film formed under open-circuit conditions (−0.3V *vs.* SCE) a value of 70Å was thus obtained in satisfactory agreement with values published in the literature (6).

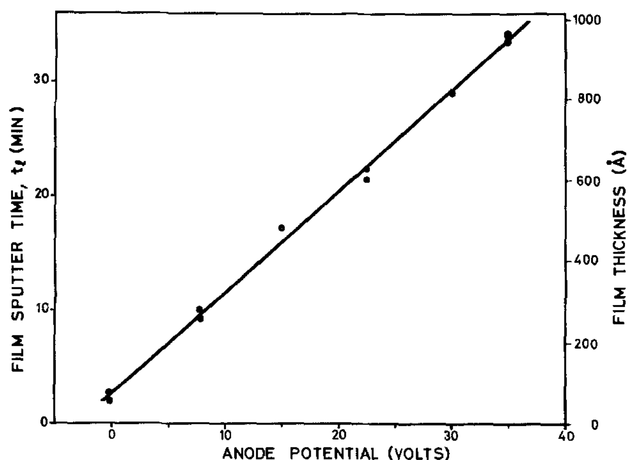

Fig. 2. Film sputter time, t_l, and estimated thickness of titanium oxide films produced by anodizing in H_2SO_4 as a function of potential.

For studying the stoichiometry of titanium oxide films by AES depth profile analysis it is usually preferable to use relative rather than absolute peak amplitudes (3). In Fig. 3 the amplitude ratio Q defined by Eq. [1] is plotted as a function of sputter time for different H_2SO_4 formed films

$$Q = \frac{h_o}{h_l} \quad [1]$$

In Eq. [1] h_o is the amplitude of the 508 eV oxygen peak and h_l the amplitude of the 381 eV titanium peak. The data of Fig. 3 show that the steady-state plateau value, Q_p, is reproducible. For the given Auger analysis conditions its value depends on oxide stoichiometry which for sulfuric acid formed films corresponds to TiO_2 (3). Film thickness may be deduced from Q *vs.* time profiles by determining the film sputter time t_l which now corresponds to the time necessary for Q to reach the value Q_l given by Eq. [2]

$$Q_l = \frac{h_{op}}{(h_{lp} + h_{lm})} \quad [2]$$

Here h_{op} and h_{lp} are the amplitudes of the oxygen peak and the 381 eV titanium peak in the steady-state plateau region in the oxide and h_{lm} is the steady-state 381 eV titanium peak amplitude in the metal. In Fig. 3, Q_p and Q are given by the broken lines. It may be noted that t_l defined by Eq. [2] does not exactly correspond to the t_l defined above in terms of oxygen amplitude only. The reason is that the increase in [Ti_1] peak amplitude at the oxide-metal interface is not symmetrical to the decrease in oxygen peak amplitude (see Fig. 1). In the present study differences in film thickness estimated by the two methods were within experimental error, however. A considerable advantage of the use of Q *vs.* time profiles is the possibility of using thick films exhibiting well-defined amplitude plateaus for evaluating Q_l which subsequently may serve for determining the thickness of thin films which do not exhibit a well-defined plateau (Fig. 3).

Films formed in perchloric acid-acetic acid solution.—The anodic polarization behavior of titanium rotating disk electrodes in perchloric acid-acetic acid solution is illustrated by Fig. 4. Each point shown corresponds to a different experiment performed by scanning from open circuit up to the potential indicated. Because each such experiment corresponded to a newly prepared anode surface, the points of Fig. 4 show considerable scattering. Anodic films formed during the different potential scan experiments were subjected to AES depth profile analysis and the amplitude ratio Q

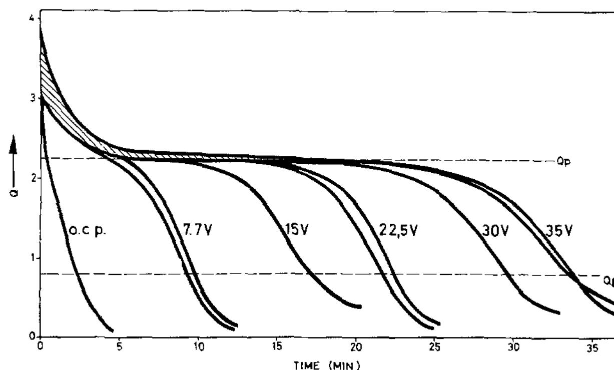

Fig. 3. Relative oxygen amplitude Q as a function of sputter time for titanium oxide films produced by anodizing in H_2SO_4 at different potentials or by immersion at open circuit (ocp).

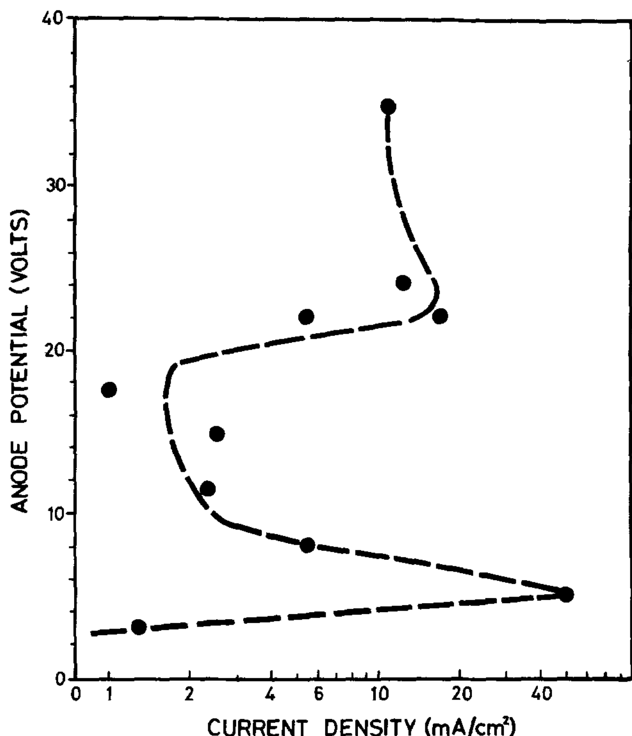

Fig. 4. Potentiodynamic polarization curve (schematic) for titanium rotating disk anode in perchloric acid-acetic acid solution. The experimental points given correspond to the depth profile experiments of Fig. 5 and 6.

was determined as a function of sputter time. Obtained results corresponding to the experimental points of Fig. 4 are shown in Fig. 5. Also indicated in the figure is the steady-state value Q_p for H_2SO_4 formed films. This value corresponds quite well to the steady-state value of Q measured for perchloric acid-acetic acid formed films indicating that film stoichiometry is the same in both cases, namely TiO_2. The plateaus for perchloric acid formed films are less well defined, however, and transition zones at the oxide metal interface are broader than in case of H_2SO_4 formed films. This is in part due to the different polishing procedure employed in the two sets of experiments: electrode surfaces anodized in H_2SO_4 were prepared by electropolishing, while those anodized in perchloric acid-acetic acid solution were prepared by mechanical polishing.

The film sputter time t_l was determined from Q *vs.* t graphs as described above and film thickness was estimated by assuming that the sputter rate for $HClO_4$ formed films is equal to that of H_2SO_4 formed films. This assumption appears justified in view of the similar composition of the films. Measured film sputter times as a function of anode potential are given in Fig. 6. The data indicate that above an anodizing potential of 2-3V film thickness increases with potential in a linear fashion up to a potential of *ca.* 22V. At this potential observation of the sample surface shows coexistence of thick colored films and bright pits (4). At higher potentials measured sputter times decrease drastically and become independent of potential. The abrupt change in measured sputter time coincides with the onset of electropolishing. The measurements shown in Fig. 6 were performed without the simultaneous use of oxide standards for calibrating sputter rates and therefore no film thickness values are given. However, an identical series of measurements was carried out with a stationary electrode. Before each depth profile the sputter rate was newly calibrated using H_2SO_4 formed titanium oxide film. Results are given in Fig. 7 in which film thickness is plotted as a function of potential. It follows that film thickness increases up to *ca.* 400Å before breakdown occurs at a voltage of *ca.* 20V. For samples polarized under elec-

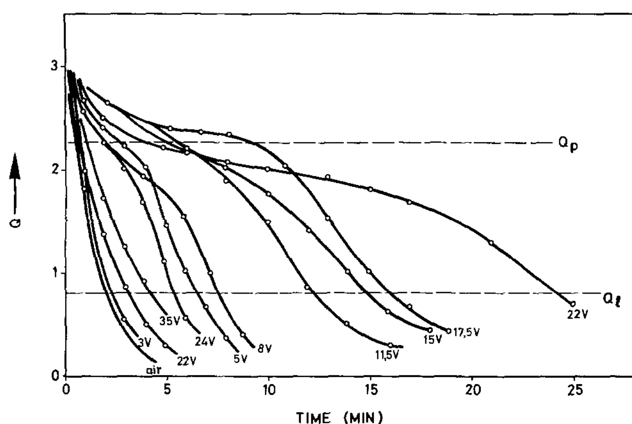

Fig. 5. Relative oxygen amplitude Q as a function of sputter time for titanium oxide films formed in perchloric acid-acetic acid solution at different potentials or formed in air.

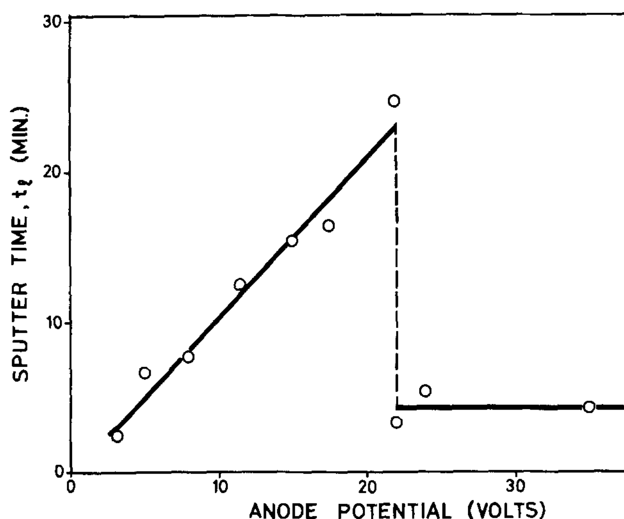

Fig. 6. Film sputter time as a function of anode potential for anodic films formed on rotating disk electrode in perchloric acid-acetic acid solution.

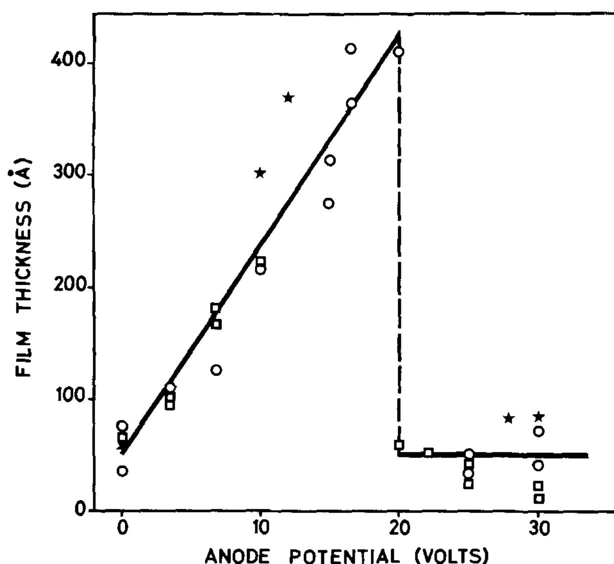

Fig. 7. Estimated film thickness as a function of anode potential for anodic films formed in perchloric acid-acetic acid solution. □ ○, Stationary electrode, two independent sets of experiments; *, rotating disk electrode, 1200 rpm.

tropolishing conditions measured film thicknesses scatter considerably but they are always smaller than 100Å, *i.e.*, of the same order as that of natural oxide films formed in air.

To characterize the chemical composition of the films, concentration depth profiles for Ti, O, C, and Cl were determined using the multiplexing unit. Typical results are given in Fig. 8-10. The titanium amplitudes shown correspond to the larger of the two titanium peaks, *i.e.*, to the 381 eV peak in the oxide and to the 416 eV peak in the metal (cf. Fig. 1). Figure 8 shows a film formed by scanning up to 12V. The data are typical for concentration depth profiles obtained with films in the prepolishing region where film thickness increases linearly with potential. The strong carbon signal at the outer oxide surface is due to adsorption

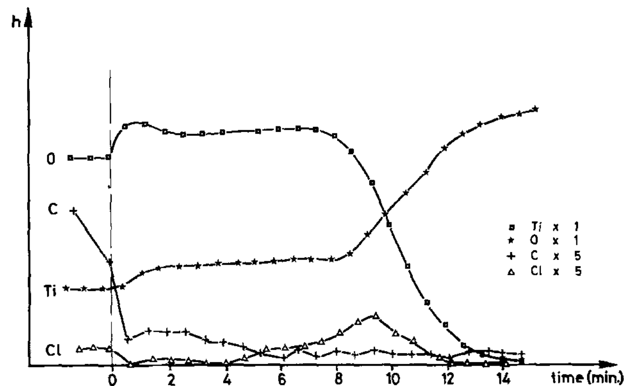

Fig. 8. Concentration depth profile of anodic film typical for the prepolishing region obtained by scanning to a potential of 12V.

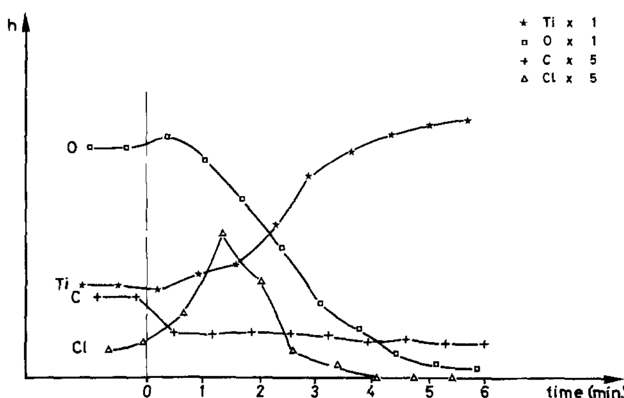

Fig. 9. Concentration depth profile of anodic film formed for the electropolishing region obtained by scanning to a potential of 28V.

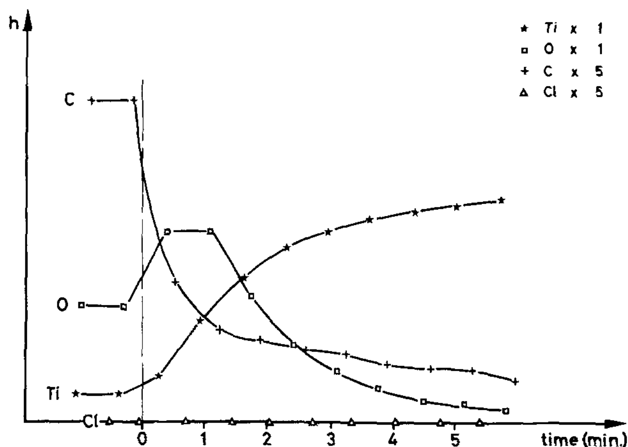

Fig. 10. Concentration depth profile of natural oxide film on mechanically polished titanium.

of carbon compounds taking place during or after the polarization experiments. Only a weak carbon signal is observed in the interior of the oxide. This signal could well be an experimental artifact (3) and will therefore not be considered for further interpretation. The same holds true for the carbon signals of Fig. 9 and 10. Of particular interest is the behavior of the chlorine peak amplitude. At the outer oxide surface it exhibits a definite value indicating the presence of adsorbed species. After removing the outermost surface layers by sputtering the chlorine amplitude decreases to a very small value which is of the same order of magnitude as the background noise. However, on approaching the oxide-metal interface the chlorine amplitude increases again and a clearly defined maximum is reached before the amplitude decreases to zero in the interior of the metal. It is concluded that chlorine species such as perchlorate or chloride ions may accumulate at the metal oxide interface. Figure 9 shows concentration depth profile data for the electropolishing region. Compared to the data of Fig. 8 the chlorine amplitude is larger and chlorine species are present throughout the film. A pronounced maximum is again observed near the oxide-metal interface. For comparison, Fig. 10 shows concentration depth profiles of a thin oxide film formed by exposure of a mechanically polished sample to air. No chlorine signal is observed in this case which proves that the chlorine observed in Fig. 8 and 9 is indeed due to anodization in perchloric acid.

Discussion

The data of the present study show that when titanium is anodically polarized in a perchloric acid-acetic acid electropolishing electrolyte anodic films grow in a similar way as in H_2SO_4 anodizing solution. From the data of Fig. 7 one deduces a growth constant of 20 Å/V which is somewhat lower than the growth constant of 25 Å/V typical for H_2SO_4 formed films. However, the accuracy of the growth constant derived for perchloric acid-acetic acid formed films is limited because of the ill-defined transition zones in the Q *vs.* t profiles and, furthermore, growth conditions for perchloric acid-acetic acid and H_2SO_4 formed films were not identical. Therefore no further interpretation of observed growth constants is warranted.

According to the data of Fig. 3 and 5 the oxide formed in perchloric acid-acetic acid solution is TiO_2 because observed Q_p values correspond to those of H_2SO_4 formed films measured under identical analyzing conditions. This conclusion is strictly valid for films anodized in the prepolishing region because they exhibit well-defined steady-state Q_p values. However, comparing the Q *vs.* t plots (Fig. 5) for 24 and 22V films corresponding to electropolishing conditions with those for 5 and 3V films corresponding to the prepolishing region one observes a close similarity. This suggests that the oxygen-titanium ratio for electropolishing films corresponds also approximately to TiO_2. However, the electropolishing films contain much more chlorine than the films formed in the preelectropolishing region. This is illustrated by the data of Fig. 8 and 9. A quantitative interpretation of these data taking into account matrix effects and possible preferential sputtering effects is not possible, but, following Ref. (7) a semiquantitative estimation of the chlorine concentration can be made using Eq. [3]

$$C_i = \frac{h_i/s_i}{\Sigma\, h_j/s_j} \quad [3]$$

Here C_i is the concentration of element i (chlorine) in atomic percent, h_i is the amplitude of the chlorine Auger signal, and s_i is the so-called "sensitivity factor," an empirically determined parameter characteristic for each element (7). According to this the chlorine concentration at the interface is estimated to be

approximately 1% for the 12V film of Fig. 8 and approximately 4% for the 28V film of Fig. 9.

To learn more about the chemical nature of the chlorine species detected by AES analysis samples polarized in the prepolishing and in the polishing region were subjected to ESCA analysis. The analysis was carried out using the equipment and procedures described by Augustinsky *et al.* (8, 9).

In the pitting region chlorine was found to be present in form of Cl^- (binding energy of Cl 3/2 p at 205-207 eV with respect to Cl 1s at 290 eV) and ClO_4^- (binding energy of Cl 3/2 p at 213-215 eV). In the polishing region, on the other hand, only Cl^- but no ClO_4^- could be detected in the film. From the ESCA data the total chlorine concentration was estimated at 1-2 atomic percent (a/o) for both films in reasonable agreement with the AES results.

Based on the different data available the AES concentration depth profiles for chlorine in the prepolishing region can be explained by postulating that the prepolishing film contains flaws which allow the perchlorate ion to penetrate up to the metal surface where it is reduced to chloride. Only strongly adsorbed species are detected in the AES analysis of anodized samples because other species will have been removed by washing the anode after polarization experiments. For this reason perchlorate or chloride ion dissolved in the electrolyte, which during anodization fills the microscopic flaws, do not appear in the AES spectra and the observed chlorine concentration within the film is therefore negligibly small. On the other hand, at the metal-oxide interface chloride ion adsorbed at the metal give rise to a well-defined AES signal. The measured signal intensity corresponds to the average chloride concentration on the analyzed surface area but according to the proposed flaw model the chloride concentration should be highly localized. It is therefore concluded that at the bottom of flaws the chloride concentration is much higher than the measured average value of 1%.

AES analysis of surfaces polarized under electropolishing conditions reveals the presence of a thin layer contaminated by chlorine species, the concentration of which is maximum at the metal-film interface. Only Cl^- but no ClO_4^- was detected by ESCA and therefore it is concluded that the latter ion upon entering into contact with the metal surface is reduced. This conclusion is supported by stoichiometric measurements (4) and it is in agreement with observations made during aluminum corrosion in presence of oxidizing anions (9). Several authors have postulated that electropolishing requires the presence of a thin porous film which is permeable to cations (10-12) while others (13, 14) proposed that electropolishing proceeds in presence of an anhydrous layer of adsorbed anions. The AES data presented here show that electrolyte anions may indeed enter into contact with the metal surface since the chlorine signal amplitude there goes through a maximum. AES depth profile analysis also reveals the presence of an oxide film, the thickness of which corresponds roughly to the thickness of the natural oxide film formed in air. Since AES is not a method permitting *in situ* measurements under anodic polarization conditions it is very possible that part of the observed AES signals are the result of oxidation reactions which took place after the polarization experiments, *i.e.*, in the electrolyte solution after current cutoff or during the transfer of the anode from the electrochemical cell to the Auger apparatus. The present AES data can therefore be interpreted in terms of the thin porous oxide film concept of electropolishing as well as in terms of the adsorbed anhydrous anion layer concept.

Conclusions

1. The present study illustrates that AES depth profile analysis is a useful method for the investigation of the thickness and chemical composition of electropolishing films as a function of formation conditions.

2. Anodic polarization of titanium in perchloric acid-acetic acid electropolishing solution leads to formation of an anodic film of TiO_2 which grows linearly with potential up to 20-22V when electropolishing sets in coinciding with removal of the prepolishing film.

3. AES concentration depth profile analysis in the prepolishing region indicates that prepolishing film removal is initiated by penetration of ClO_4^- ions through flaws and reaction to Cl^- under simultaneous metal dissolution thus leading to film removal by under-cutting.

4. After electropolishing the anode is covered by a thin Cl^- contaminated oxide layer, the thickness and nature of which is comparable to the natural oxide film. Present AES and ESCA experiments do not indicate whether this film is present under electropolishing conditions or is formed only after completion of anodic polarization experiments.

Acknowledgment

The authors thank Mr. D. E. McClure for his experimental assistance and Dr. Augustinsky and Dr. Sanchez, of the University of Geneva, for carrying out the ESCA analysis. This work was supported by the "Fondation pour l'encouragement de la recherche scientifique" (FERS), Bern, Switzerland.

Manuscript submitted Dec. 20, 1977; revised manuscript received Feb. 6, 1978.

Any discussion of this paper will appear in a Discussion Section to be published in the June 1979 JOURNAL. All discussions for the June 1979 Discussion Section should be submitted by Feb. 1, 1979.

Publication costs of this article were assisted by the Swiss Federal Institute of Technology.

REFERENCES

1. W. J. Mc G Tegart, "Polissage electrolytique et chimique des métaux," p. 85, Dunod, Paris (1960).
2. P. W. Palmberg, *Anal. Chem.*, **45**, 549 A (1973).
3. H. J. Mathieu, J. B. Mathieu, D. E. McClure, and D. Landolt *J. Vac. Sci. Technol.*, **14**, 1023 (1977).
4. J. B. Mathieu and D. Landolt, *This Journal*, **125**, 1044 (1978).
5. L. Arsov, M. Froelicher, M. Froment, and A. Hugot-Le-Goff, *J. Chim. Phys.*, **72**, 3 (1975).
6. F. Dalard, G. Montelly, and J. C. Sohm, *Surf. Technol.*, **4**, 367 (1976).
7. "Handbook of Auger Electron Spectroscopy," 2nd ed., L. E. Davis, N.C. Mac C Donald, P. W. Palmberg, G. E. Riach, and R. E. Weber, Editors, Physical Electronics Ind., Eden Prairie, Minnesota (1976).
8. J. Augustinsky, H. Berthou, and J. Painot, *Chem. Phys. Lett.*, **44**, 221 (1976).
9. J. Augustinsky and J. Painot, *This Journal*, **123**, 841 (1976).
10. T. P. Hoar and J. A. S. Mowat, *Nature (London)*, **165**, 64 (1950).
11. M. Turner and P. A. Brook, *Electrodeposition Surf. Treat.*, **2**, 245 (1973-1974).
12. K. Kojima and C. W. Tobias, *This Journal*, **120**, 1202 (1973).
13. M. Froment, *Corros. Anticorros.*, **6**, 142 (1958).
14. I. Epelboin, *Z. Elektrochem.*, **62**, 813 (1958).

Electropolishing of Titanium in Perchloric Acid-Acetic Acid Solution

II. Polarization Behavior and Stoichiometry

J. B. Mathieu* and D. Landolt**

Materials Department, Swiss Federal Institute of Technology, Lausanne, Switzerland

ABSTRACT

Anodic polarization behavior and reaction stoichiometry during electropolishing of titanium in perchloric acid-acetic acid solution has been investigated using a rotating cylinder electrode. Formation and breakdown of anodic films result in strongly time-dependent polarization behavior. The onset of electropolishing coincides with a current plateau in the potentiostatic polarization curve but solution side mass transfer effects are masked by the presence of a layer of reaction products. The apparent valence of dissolution in perchlorate-containing solution is unusually low because perchlorate ion is reduced at the anode.

Electropolishing includes smoothing and brightening of a metal surface by anodic dissolution (1). Smoothing is usually associated with a diffusion-controlled dissolution process but no agreement exists in the literature as to the nature of the diffusion-limiting species. According to some authors diffusion of acceptor ions or water molecules from the bulk toward the anode is rate limiting (2-4) while others consider diffusion of anodic dissolution products from the anode toward the bulk solution to be the rate-controlling process (5-7). According to both views smoothing occurs because the diffusion path from protruding parts of a rough surface is smaller than from receding parts and hence dissolution of protruding parts is favored. A diffusion-controlled mechanism of smoothing is consistent with the observation that electropolishing occurs usually in the presence of a highly viscous layer at the anode (Jacquet layer) (8). The latter has the effect of slowing down diffusion processes, thus favoring the establishment of diffusion-controlled dissolution conditions. According to Hoar (9, 10) brightening requires the presence at the anode of a thin solid film which is permeable to metal cations. The film which covers the surface uniformly suppresses the influence of crystallographic orientation on dissolution and thus prevents crystallographic etching of the anode. A similar concept has been advanced by Epelboin and coworkers (4, 11, 12) who postulate the presence of an anhydrous layer as a condition for brightening. The existence of thin surface layers responsible for brightening has been deduced from mercury drop wetting experiments (9), polarization curves (1), and impedance measurements (4).

The majority of studies on the mechanism of electropolishing have been performed with copper in phosphoric acid solution (1, 2, 5, 7, 13-19) but relatively little is known about the phenomena leading to electropolishing of valve metals which are capable of forming thick oxide films. Garreau and Epelboin (20) studying electropolishing of aluminum in perchlorate-ethanol solution concluded that electropolishing occurred under diffusion control but limiting current plateaus were masked by heating effects. On the other hand, Ippolitova and Korovin (21) found no evidence for diffusion-limited conditions during electropolishing of tantalum in a solution of HF, H_2SO_4, and ethylene glycol.

The most common electropolishing electrolytes for titanium are mixtures of perchloric acid and acetic-acid (8). Good electropolishing is obtained at anode potentials of 20-30V but little is known about the mechanisms involved. Froment (22) studying the stoichiometry of dissolution of various metals including titanium in perchloric acid-acetic acid electrolytes found that the perchlorate ion is being reduced during the dissolution process. He postulated that Ti^{+} and Ti^{2+} ions are formed by anodic dissolution and subsequently react with the perchlorate ion. On the other hand, it is well known that usually in aqueous solution titanium dissolves to Ti^{3+} or Ti^{4+} (23). Johnson and Shreir (24) measured anodic polarization curves for titanium in 3M $AlCl_3$-diethyl ether solutions at a stationary electrode. They found a current plateau in the potential region where electropolishing occurred but the nature of this plateau was not further investigated. Beck (25, 26) studying pitting of titanium in different chloride and bromide electrolytes found brightening to occur at the bottom of pits and he attributed this behavior to the presence of a salt film. Powers and Wilfore (27) studying ECM behavior of titanium also found evidence for pitting and brightening. According to these authors brightening of the entire surface occurs at high current densities when individual pits merge together.

In a previous paper (28) Auger electron spectroscopy was employed to study chemical composition and thickness of the solid films formed anodically on the titanium in perchloric acid-acetic acid electropolishing solution. It was found that a thick TiO_2 film grows linearly with applied potential up to the potential where electropolishing sets in which leads to an abrupt decrease in film thickness. The anodic layer observed after completion of experiments is of the same nature and thickness as the natural oxide film and it contains substantial amounts of chloride. The aim of the present paper is to investigate the electrochemical behavior of titanium in perchloric acid-acetic acid electropolishing electrolytes in order to elucidate the processes leading to removal of the protecting titanium oxide film at high potential and to study the role of mass transfer in the polishing process. For this purpose potentiostatic and galvanostatic polarization measurements were performed under controlled hydrodynamic conditions, and anodic reaction stoichiometry as well as surface texture resulting from dissolution were investigated.

Experimental

Polarization measurements were performed on a rotating cylinder electrode of 1 cm diam and 0.7 cm height. Rotation rates ranged up to 6000 rpm. A cylindrical platinum wire mesh electrode of approximately 3 cm diam served as counterelectrode. Anode poten-

* Electrochemical Society Student Member.
** Electrochemical Society Active Member.

tials were measured against a mercury sulfate reference electrode.

A potentiostat (Tacussel PRT 100-2) was used as current source. To allow potentiostatic operation at anode potentials of up to 50V an operational amplifier with a voltage divider at its output was inserted between reference electrode and reference signal input of the potentiostat. Potentiostatic polarization curves were measured using a slow sweep generator Amel Type 564 to drive the potentiostat. In addition, potentiostatic and galvanostatic experiments were performed by applying a potential or current step while following the resulting current or potential response of the anode as a function of time.

Weight loss measurements at different applied potentials and/or currents were performed in a separate cell in which a stationary cylindrical titanium rod inserted from the bottom served as anode. The charge passed during an experiment was measured using a current integrator (Amel Type 558). The apparent valence of dissolution was calculated using Eq. [1]

$$n = \frac{MQ}{\Delta m \mathbf{F}} \quad [1]$$

Here n = apparent valence of dissolution, M = molecular weight of titanium, Q = electric charge passed, Δm = measured weight loss of the anode, $\mathbf{F}$ = Faraday constant.

In a few experiments, the amount of Cl^- ion produced was determined by potentiometric titration. All experiments were performed with 99.5% pure titanium (Kobe). The composition given by the supplier is: H, $\leq$0.01%; O, $\leq$0.2%; N, $\leq$0.05%; Fe, $\leq$0.25%; and Ti, remainder. Perchloric acid-acetic acid electrolytes were prepared by mixing 70% $HClO_4$ with 100% acetic acid (Merck). Unless otherwise noted, experiments were performed in a solution containing 10 cm^3 conc $HClO_4$ per 100 cm^3 glacial acetic acid which corresponds to a $HClO_4$ concentration of 1.1 mole/liter. Preliminary experiments had shown that good electropolishing can be achieved in this solution. The temperature was maintained at 25°C. Before experiments, the samples were mechanically polished with 600 emery paper, washed and rinsed with double-distilled water.

Results

Figure 1 shows potentiodynamic polarization curves obtained at a scan rate of 100 mV/sec using a rotating cylinder anode at various rotation rates. The curves exhibit a passive zone ranging up to approximately 15V. The current then increases steeply until a maximum is reached at approximately 22V which corresponds to the beginning of electropolishing. The value of the current at or below the maximum was independent of rotation rate. The electrode appearance in the passive region was yellowish due to the presence of an anodic film. With increasing potential, the color turned to dark blue and local film attack and gas evolution were observed. In the electropolishing region white solid reaction products spalled off the anode. No well-defined diffusion-limited currents were observed under polishing conditions but the shape of the current voltage curves above the current maximum at *ca.* 22V depended on rotation rate (Fig. 1). In a second series of experiments, a constant potential was applied to the anode and the current was followed as a function of time. Typical data obtained at a rotation rate of 3000 rpm are given in Fig. 2. At relatively low potentials, the current decreases with time due to growth of an anodic film. At higher potentials, the current decreases first and then increases while exhibiting irregular fluctuations. The behavior indicates that film breakdown takes place. To gain more insight into the time-dependent polarization behavior galvanostatic measurements were performed. Typical data are given in Fig. 3. At low currents (1.7 mA/cm^2), the potential increases linearly with time up to a limiting value close to 20V. At currents > 10 mA/cm^2, the initial potential rise is followed by a characteristic overshoot and at still higher current densities, correspond-

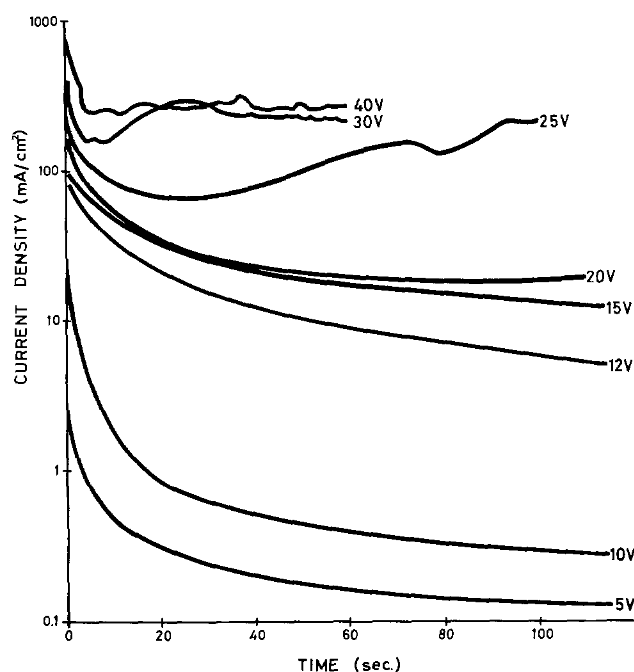

Fig. 2. Variation of current with time measured with rotating cylinder electrode at 3000 rpm at different constant potentials.

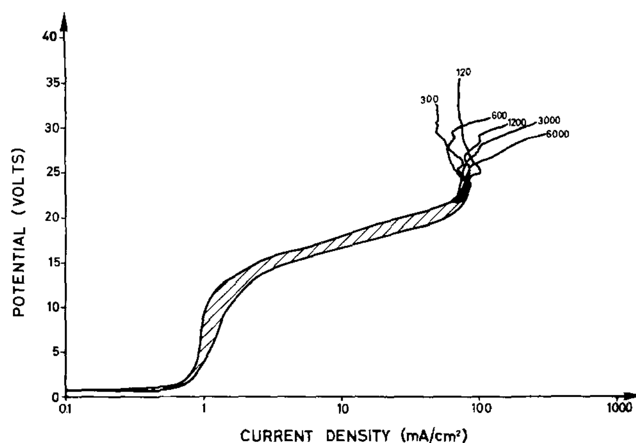

Fig. 1. Potentiodynamic polarization curves measured with rotating cylinder electrode at different rpm. Scan rate 100 mV/sec.

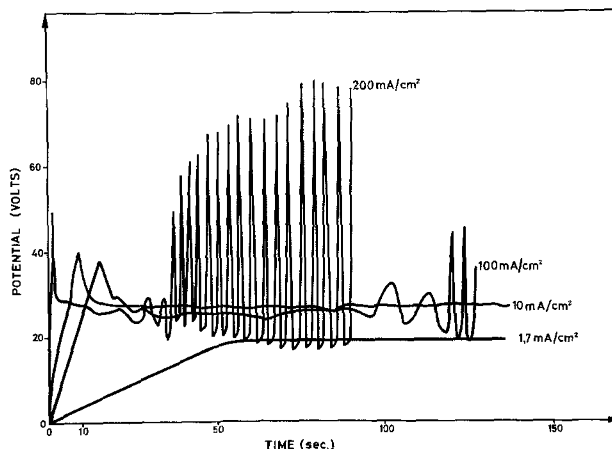

Fig. 3. Variation of anode potential with time measured with rotating cylinder electrode at 3000 rpm at different constant current densities.

ing to electropolishing, periodic oscillations occur. The oscillation amplitude is of many volts and it depends on current density. This is illustrated by Fig. 4 which gives average steady-state potential values measured at constant current for two different rotation rates. Three zones corresponding to no visible attack of the anode surface, to pitting, and to polishing are schematically indicated in the figure. Measured steady-state potential values in the first zone are 20V, independent of current density. Rotation rate did not affect obtained results in a systematic way.

The appearance of the anode surface corresponding to prepolishing and to polishing conditions is illustrated by the scanning electron microscope pictures of Fig. 5-7. Figures 5 and 6 show a sample surface after polarization for 100 sec at a current density of 45 mA/cm^2 and a rotation rate of 3000 rpm. Three types of surface textures are visible; passive, nonattacked areas where mechanical polishing marks are still present; areas showing noncrystallographic, more or less hemispherical pits; and areas covered by loosely adherent dissolution products. The dissolution products could be removed easily by scraping, revealing underneath a bright pitted surface (Fig. 6). The products were of white color, distinctly different from the adjacent passive film. X-ray analysis showed no diffraction pattern, indicating that the dissolution products were amorphous. Figure 7 illustrates an electropolished surface obtained by polarizing anodically for 100 sec at 200 mA/cm^2 and 3000 rpm. The surface exhibits irregular

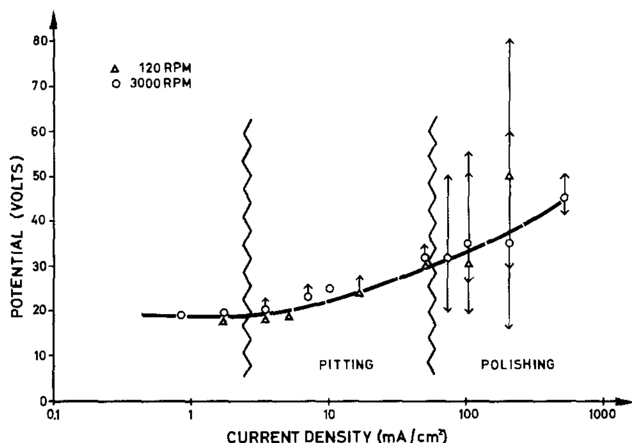

Fig. 4. Approximate steady-state values for current-voltage curve measured by galvanostatic polarization at rotating cylinder electrode at 120 and 3000 rpm.

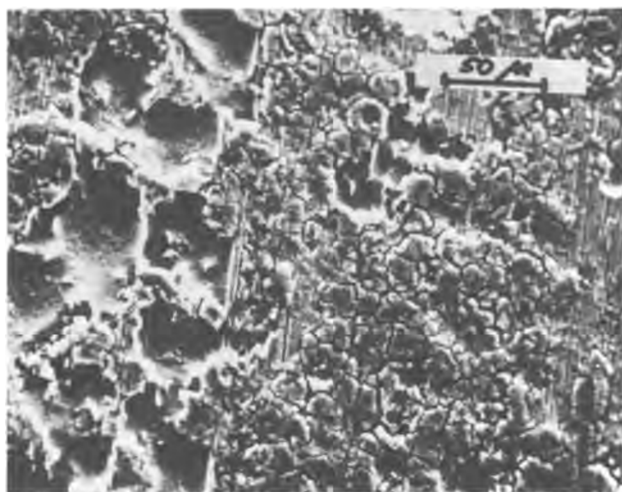

Fig. 5. SEM micrograph of anode surface polarized at 45 mA/cm^2 for 100 sec. Rotating cylinder electrode 3000 rpm; magnification 300×.

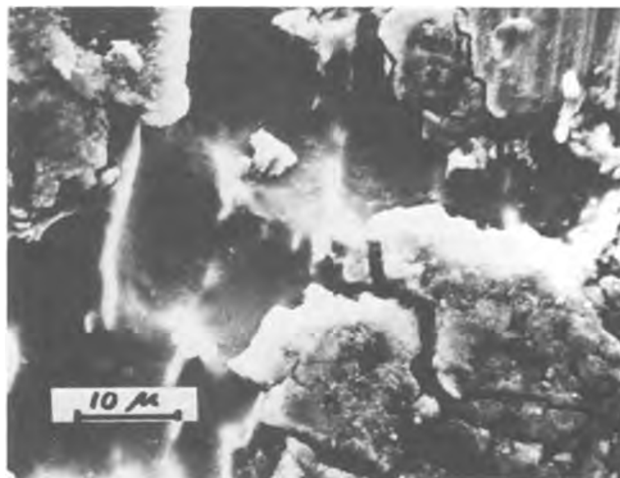

Fig. 6. Same surface as Fig. 5 showing bright areas underneath film of loose reaction products; magnification 1500×.

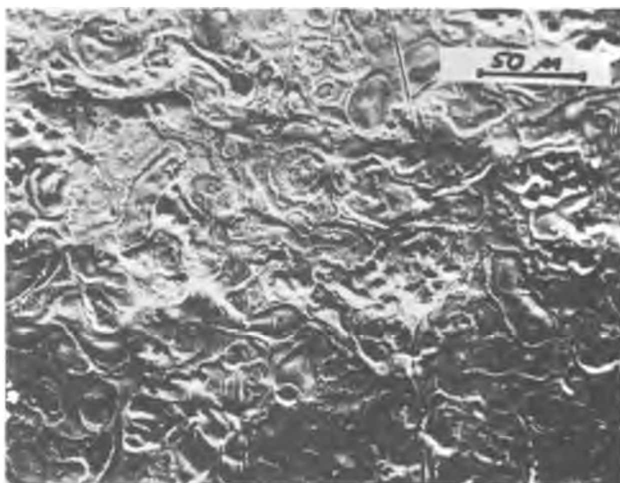

Fig. 7. SEM micrograph of electropolished anode surface polarized at 200 mA/cm^2 for 100 sec. Rotating cylinder electrode, 3000 rpm; magnification 300×.

waviness reminiscent of the pitting-type attack of Fig. 5 and 6.

The apparent valence for dissolution was determined from weight-loss measurements performed on a stationary electrode at constant applied potential. Results are given in Fig. 8. In perchloric acid containing so-

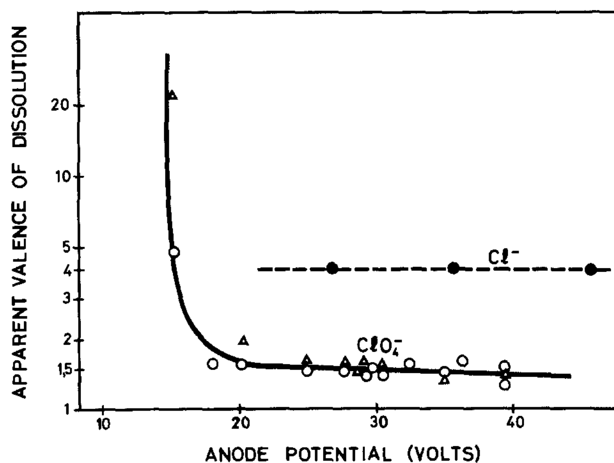

Fig. 8. Apparent valence of dissolution measured with rotating cylinder electrode in $HClO_4$ and HCl containing acetic acid electrolyte at different applied potentials. Electrodes were pretreated by mechanical (○, ●) and by electrochemical (△) polishing.

Table I. Stoichiometry

	Q, charge passed (coulomb)	Δm, weight loss (mg)	n, apparent valence	m_{Cl}, mass of Cl^- in electrolyte (mg)	Q_{Cl}, charge corresponding to Cl^- (coulomb)	n_{corr}, corrected valence
1	300	101.8	1.46	18.7	410	3.46
2	300	107.8	1.39	22.2	480	3.61
3	300	98	1.52	22.16	480	3.95
4	300	102.1	1.46	21.17	460	3.69

lution at potentials below 20V the apparent valence is very high indicating that little dissolution takes place. At higher potentials, on the other hand, the apparent valence is 1.3-1.6 independent of potential. Table I shows that the perchlorate ion is reduced during the anodic dissolution process in agreement with previous findings by Froment (22). The data were obtained by carrying out electropolishing experiments in a small electrolyte volume and measuring the amount of chloride formed by potentiometric titration. A corrected value for the apparent valence of dissolution n_{corr} was calculated using Eq. [2]

$$n_{corr} = \frac{M(Q + Q_{Cl})}{\Delta m F} \quad [2]$$

Here Q_{Cl} is the equivalent charge corresponding to reduction of perchlorate to chloride according to Eq. [3]. It was calculated from the amount of chloride ion found by chemical analysis

$$ClO_4^- + 8H^+ + 8e = Cl^- + 4H_2O \quad [3]$$

Numerical values for n_{corr} are given in the last column of Table I. For all experiments n_{corr} is between 3.5 and 4. A few experiments were performed in acetic acid electropolishing solutions in which part or all of the $HClO_4$ was replaced by HCl. The apparent valence in an acetic acid solution containing 0.55M $HClO_4$ and 0.55M HCl was equal to that found for 1.1M $HClO_4$ acetic acid electrolytes and the electropolishing behavior was generally the same. In an acetic acid solution containing 1.1M HCl and no $HClO_4$, on the other hand, the apparent valence for dissolution was $n = 4$. Obtained data points are indicated in Fig. 8.

Discussion

It was not possible to measure steady-state polarization curves in the present study because the polarization behavior was found to be a function of time. Obtained results depended on the experimental technique employed as well as to a lesser extent on surface treatment and electrode geometry. The reason for this behavior lies in the previously observed formation and removal of anodic films (28). Indeed, if titanium in perchloric acid-acetic acid solution is anodically polarized to potentials below a critical breakdown potential a thick passivating film of TiO_2 is formed. Under potentiostatic conditions this leads to a steady decrease of observed current with time (Fig. 2), under galvanostatic conditions to a slow rise in potential (Fig. 3). If the anode is polarized above the critical breakdown potential pitting occurs. This is evidenced by the SEM micrographs of Fig. 5 and 6 as well as by the polarization data of Fig. 1-3 which exhibit a current or potential *vs.* time behavior typical for metals undergoing pitting (29); under potentiostatic conditions the current increases autocatalytically with time while under galvanostatic conditions typical potential overshoots are observed. Following the criteria defined by Smialovska and Czachor (29) the critical potential for pit nucleation in the galvanostatic and potentiostatic step experiments is $20V < E_{np} < 25V$ while a somewhat lower value is deduced from the potentiodynamic data of Fig. 1.

Dissolution from pits proceeds at a high rate leading to formation of solid reaction products and to local surface brightening (Fig. 7). The loose solid products which apparently consist of amorphous TiO_2 accumulate near the anode surface where they form a gelatinous layer reminiscent of the viscous layer originally described by Jacquet (8). The existence of a current plateau (Fig. 1) at high potentials suggests a diffusion-controlled process, but the presence of the viscous product layer, as well as the heterogeneous nature of the anodic attack tend to mask the influence of solution side mass transfer processes on limiting current. As a consequence the anodic polarization behavior depended only little on rotation rate of the titanium cylinder electrode except for the fact that at sufficiently high rotation rates the highly viscous layer could be mechanically removed by shear forces thus leading to an increase in observed currents (Fig. 1).

The data of Fig. 8 show an apparent valence of dissolution for titanium which is unusually low. Different explanations have been advanced in the literature to explain such low value. According to Straumanis and co-workers (30, 31) abnormally low valences in metal dissolution are usually due to anodic disintegration, *i.e.*, selective attack of grain boundaries leading to removal of metallic particles from the anode. However, such a mechanism can be excluded in the present case for different reasons. First of all, no selective grain boundary attack is apparent in the micrographs in Fig. 5-7 and no evidence of metallic titanium could be found in the dissolution products by x-ray analysis. Titanium metal does not corrode rapidly in the solutions employed here and therefore it is not likely that metallic particles after breaking away from the anode could have completely corroded before analysis was carried out. Another explanation for unusually low valence of dissolution has been given by Epelboin and co-workers (11, 32). According to these authors anodic dissolution of aluminum and beryllium in anhydrous perchlorate media leads to formation of monovalent species which in turn may react chemically with perchlorate ion in a homogeneous reaction following dissolution. Such a mechanism has been postulated for titanium dissolution in perchlorate electrolytes by Froment (22). No direct observation of the subvalent species has been possible up to now, however, and it must be assumed that if they exist they are extremely short lived (33).

Recently Neumann and Klimmek (34) studied the stoichiometry of anodic dissolution of molybdenum in mixed organic solvent-water electrolytes. They found an apparent valence of 3 in the presence of perchlorate but an apparent valence of 6 in the presence of chloride. The present data for titanium show a similar behavior. Under otherwise identical conditions, an apparent valence of 1.3-1.6 is observed in acetic acid containing 1.1M $HClO_4$ or 0.55M $HClO_4$ + 0.55M HCl, but an apparent valence of 4 in acetic acid containing 1.1M HCl. If dissolution would involve formation of a dissolved subvalent species which subsequently could react chemically in the electrolyte the apparent valence for dissolution should be the same for $HClO_4$ and HCl containing acetic acid solution since homogeneous chemical reactions following the charge transfer step do not affect weight loss. In view of the observed differences in apparent valence between $HClO_4$ and HCl containing solutions it is therefore concluded that the perchlorate ion intervenes directly at the metal sur-

face where it apparently reacts with adsorbed reaction intermediates of the dissolution process such as monovalent adsorbed ions or metallic adatoms. Stoichiometric measurements do not allow us to identify the reacting titanium species. The term "anodically activated titanium surface" will therefore be used independent of the exact nature of the reacting species.

It is interesting to note that the observed low values for the apparent valence are apparently not due to the anhydrous nature of the solution employed but to the presence of perchlorate ion. Indeed, recent experiments on high rate dissolution of titanium performed in our laboratory showed that similarly low values for the apparent valence of dissolution as in the present study are obtained in aqueous 5M $NaClO_4$ solution provided the critical potential for film breakdown is exceeded.

The proposed reaction of perchlorate ion with an anodically activated titanium surface poses an apparent paradox since for such a reaction to be thermodynamically possible the anode potential at the metal surface must be more cathodic than the reversible potential for reaction [3], the standard potential of which is 1.386V (35). On the other hand, the data of Fig. 1-4 show that measured anode potentials under polishing conditions are $>$ 20V. To explain the discrepancy one has to postulate that the actual potential at the reaction sites is different from that measured experimentally. It is well established that local potentials in corrosion pits can be much more negative than the apparent over-all anode potential (36, 25). Beck studying pitting of titanium in HBr observed hydrogen evolution at over-all anode potentials of several volts (25). He proposed that the principal factor causing the local potential differences was the ohmic resistance of a thin salt film. Since under present experimental conditions similar films of solid reaction products were present, it is very possible that local anode potentials at the metal surface were indeed much lower than those imposed externally. A separate experiment in a nonstirred electrolyte was performed in which anodically produced gas was collected and subjected to gas chromatographic analysis. Hydrogen as well as oxygen were found. The total amount of gas evolved was small, however, and therefore did not affect the over-all charge balance of Table I.

The proposed hypothesis involving reduction of perchlorate ion by reaction with an anodically activated titanium surface is consistent with the AES and ESCA data described in a previous study (28) which showed a chloride ion to exist at the film-metal interface in the breakdown and polishing region. According to present results passive film breakdown is initiated at discrete sites leading to dissolution by pitting. It is likely that these sites correspond to preexisting flaws in the anodic film which allow the perchlorate ions to penetrate into the film under the influence of the electric field and to react at the metal interface. With increasing potential the fraction of the surface accessible to anions increases and eventually the protecting TiO_2 film is completely removed by way of undercutting due to lateral growth of pits.

Conclusions

1. To achieve electropolishing of titanium in perchloric acid-acetic acid solutions anode potentials in excess of 20V are required to cause breakdown of the anodic film of TiO_2 which protects the metal from dissolution at lower potentials. Electropolishing is the result of merging together of bright pits.

2. Electropolishing coincides with the appearance in the current voltage curve of a current maximum or plateau. Its value depends little on hydrodynamic conditions because a gelatinous matrix consisting of solid reaction products covers the anode and masks the influence of convection on anodic mass transport processes.

3. During anodic dissolution under electropolishing conditions perchlorate ion is reduced to chloride which leads to an apparent valence of dissolution of 1.3-1.6 independent of applied current or potential.

4. Dissolution experiments performed in chloride and chloride containing perchlorate electrolytes and previous ESCA and AES analysis of electropolishing films provide strong evidence that perchlorate reduction proceeds by a heterogeneous reaction on an anodically activated titanium surface. This suggests that the effective anode potential at the metal surface is much lower than that measured externally.

Manuscript submitted Dec. 20, 1977; revised manuscript received Feb. 6, 1978.

Any discussion of this paper will appear in a Discussion Section to be published in the June 1979 JOURNAL. All discussions for the June 1979 Discussion Section should be submitted by Feb. 1, 1979.

Publication costs of this article were assisted by the Swiss Federal Institute of Technology.

REFERENCES

1. T. P. Hoar and G. P. Rothwell, *Electrochim. Acta*, **9**, 135 (1964).
2. C. Wagner, *This Journal*, **101**, 225 (1954).
3. I. Edwards, *ibid.*, **100**, 223C (1953).
4. I. Epelboin, "Proceedings of Surface 66," p. 161, Forster Verlag, Zurich (1967).
5. W. C. Elmore, *J. Appl. Phys.*, **11**, 797 (1940).
6. J. K. Higgins, *This Journal*, **106**, 999 (1959).
7. K. Kojima and C. W. Tobias, *ibid.*, **120**, 1029 (1973).
8. W. J. McTegart, "Polissage électrolytique et chimique des métaux," Dunod, Paris (1960).
9. T. P. Hoar and J. A. S. Mowat, *Nature (London)*, **165**, 64 (1950).
10. T. P. Hoar, D. C. Mears, and G. P. Rothwell, *Corros. Sci.*, **5**, 279 (1965).
11. I. Epelboin, *Z. Elektrochem.*, **62**, 813 (1958).
12. M. Daguenet and M. Froment, *C. R. Acad. Sci. Paris*, **260**, (21) 5534 (1965).
13. P. A. Jacquet, *Trans. Electrochem. Soc.*, **69**, 629 (1936).
14. M. C. Petit, *Electrochim. Acta*, **8**, 217 (1963).
15. Z. Zembura, *Bull. Acad. Pol. Sci*, **XI**, No. 5, 271 (1963).
16. M. Turner and P. A. Brook, *Electrodeposition Surf. Treat.*, **2**, 245 (1973-1974).
17. S. I. Krichmar and A. Ya Pronskaya, *Russ. J. Phys. Chem.*, **39**, 730 (1965).
18. T. P. Hoar and G. P. Rothwell, *Electrochim. Acta*, **9**, 135 (1964).
19. S. I. Krichmar, A. Ya Pronskaya, and K. F. Afendik, *Elektrokhimiya*, **2**, 967 (1966).
20. M. Garreau and I. Epelboin, *J. Chim. Phys.*, **11/12**, 1515 (1966).
21. L. A. Ippolitova and N. V. Korovin, *Elektrokhimiya*, **10**, 517 (1974).
22. M. Froment, *Corros. Anticorros.*, **7**, 98 (1959).
23. M. J. Blackburn, J. A. Feeney, and T. R. Beck, in "Advances in Corrosion Science and Technology," Vol. 3, M. Fontana and R. Staehle, Editors, pp. 113ff, Plenum Press, New York (1973).
24. A. J. Johnson and L. L. Shreir, *Corros. Sci.*, **5**, 269 (1965).
25. T. R. Beck, *This Journal*, **120**, 1311, 1318 (1973).
26. T. R. Beck, *Corrosion (Houston)*, **33**, 9 (1977).
27. R. W. Powers and J. F. Wilfore, in "Fundamentals of Electrochemical Machining," Ch. L. Faust, Editor, p. 135, The Electrochemical Society Softbound Symposium Series, Princeton, N.J. (1971)
28. J. B. Mathieu, H. J. Mathieu, and D. Landolt, *This Journal*, **125**, 1039 (1978).
29. S. Smialovska and M. Czachor, in "Localized Corrosion," R. W. Staehle *et al.*, Editors, p. 353, NACE-3 (1974).
30. M. E. Straumanis, *This Journal*, **108**, 1087 (1961).
31. W. J. James and M. E. Straumanis, *ibid.*, **118**, 1960 (1961).
32. H. Aida, I. Epelboin, and M. Garreau, *ibid.*, **118**, 243 (1971).
33. W. J. James, in "Advances in Corrosion Science and

Engineering," Vol. 4, M. Fontana and R. Staehle, Editors, p. 85, Plenum Press, New York (1974).
34. Th. Neumann and M. Klimmek, *Werkst. Korros.*, 25, 906 (1974).
35. M. Pourbaix, "Atlas of Electrochemical Equilibria," Pergamon Press, p. 196.
36. R. P. Frankenthal and H. Pickering, *This Journal*, **119**, 1297, 1304 (1972).

Linear Defects Observed in Nickel Electrodeposits

S. Nakahara*

Bell Laboratories, Murray Hill, New Jersey 07974

ABSTRACT

During the course of a transmission-electron microscope characterization of nickel electrodeposits, it was found that deposits contain a high density ($\sim 1 \times 10^{15}/cm^3$) of linear defects whose image contrast is not the same as is expected from dislocation lines. A detailed analysis of these defects using electron diffraction techniques showed that these images are similar to a line of dilatation. It has been suggested that these linear defects probably are generated at growth steps as a result of the incorporation of hydrogen during electrocrystallization.

Recently, the inclusion of hydrogen in the form of gas bubbles was found to cause a loss in the ductility of electroless copper films (1). This loss was attributed to high pressure ($\sim 10^4$ atm) hydrogen gas bubbles, resulting in the so-called hydrogen embrittlement. In most electroplating systems in which the cathodic reactions involve both metal deposition and hydrogen evolution, the incorporation of hydrogen into deposits is inevitable as indicated by the high hydrogen content detected in electrodeposited metals (2). Consequently, hydrogen in electrodeposited films is known to greatly influence their mechanical properties such as ductility (3) and internal stress (4). A study of electrodeposited films, therefore, is of practical importance in understanding the relationship between incorporated hydrogen and mechanical properties.

A transmission-electron microscope (TEM) study was made on the structure of nickel electrodeposits to determine if hydrogen was incorporated as inclusions. During the course of this investigation, we discovered a high density of linear defects whose image contrast was different from that of dislocation lines. In order to understand the nature of these defects, a detailed analysis of their image contrast was carried out using TEM. This paper reports a preliminary account of this study and attempts to discuss the role of hydrogen in the formation of these linear defects.

Experimental

Nickel films were electrodeposited on a (001) copper film, as well as on a sheet of annealed OFHC polycrystalline copper. The composition of the electrolyte was 0.43M $NiSO_4 \cdot 6H_2O$ and 0.5M H_3BO_3. The pH of the bath was adjusted to 1.5. Plating was carried out at room temperature and at current densities of 5 and 15 mA/cm^2. Nickel films were stripped off the substrate in a copper-stripping solution (500 g/liter CrO_3 and 50 g/liter H_2SO_4). Specimens for TEM observation were jet polished in an electrolyte known as Borrmann solution (5). All TEM micrographs were taken using a JEM 200 microscope operated at an accelerating voltage of 200 kV.

Results

The structure of a (001) nickel film which was plated epitaxially on (001) copper film at a current density of 5 mA/cm^2 was carefully examined using several reflections under the so-called two-beam conditions (6) in TEM. Figure 1(a), 1(b), and 1(c) show micrographs of the film taken with reflecting vectors $\bar{g}$ = 200, $2\bar{2}0$, and $\bar{1}3\bar{1}$, respectively. Dislocations and growth twins are seen to exhibit various contrast features for these three reflections. Symbols x, y, and z indicate images of dislocations. In addition to the usual images of dislocations and growth twins, a high density of defects that exhibits a faint strain contrast as indicated by four fine arrows is also seen in Fig. 1(c). The existence of black-white oscillatory features suggests that the defects are linear along the direction of the oscillation. These linear defects (LD's) were not readily discernible with low-order $\bar{g}$'s such as 111, 200, and 220. Imaging with 311 type reflections was found to be most useful in obtaining detectable images of these defects. A subsequent characterization of these defects, therefore, was made using 311 type reflections. Typical results are shown in detail in Fig. 2 where $\bar{g}$ = 311. Examples of the LD's are indicated by symbol C, while that of dislocation is shown by symbol D. It can be seen clearly that the strain contrast associated with these LD's is much weaker than that associated with dislocation (compare C with D). It also appears that the image topography of the defects is different from that of dislocations. The density of these LD's was found to be $\sim 1 \times 10^{15}/cm^3$, which is much higher than that of grown-in dislocations ($\sim 6 \times 10^{13}/cm^3$) in these films.

In Fig. 2, a careful examination of the LD's in comparison with the images of dislocations indicates that the LD images possess a black-white oscillatory feature which has a periodicity of the order of the extinction distance for the operating reflecting vector $\bar{g}$. These oscillations, therefore, indicate that the LD's must be inclined in the foil. Stereoscopic analysis showed that the defects were indeed inclined in a form of linear segments which appear to be spacially distributed as a network. Furthermore, it was found that most of the LD's terminate inside the foil, as opposed to dislocations which except for small dislocation loops, terminate at the top or bottom surface of the film. This evidence, therefore, supports the hypothesis that the LD's are not dislocations.

In order to analyze further the nature of these LD's, in particular, relative to dislocations, the images were taken using $\pm\bar{g}$ reflections. Figures 3(a) and 3(b) show micrographs taken with $\bar{g}$ = $\bar{3}11$ and $3\bar{1}\bar{1}$, respectively. The images of dislocations are indicated by symbols x and y. Changing the reflecting vector, $\bar{g}$, from $+\bar{g}$ to $-\bar{g}$ results in the inversion of the image

* Electrochemical Society Active Member.

Key words: transmission electron microscopy, line of dilatation, thin films, hydrogen inclusion.

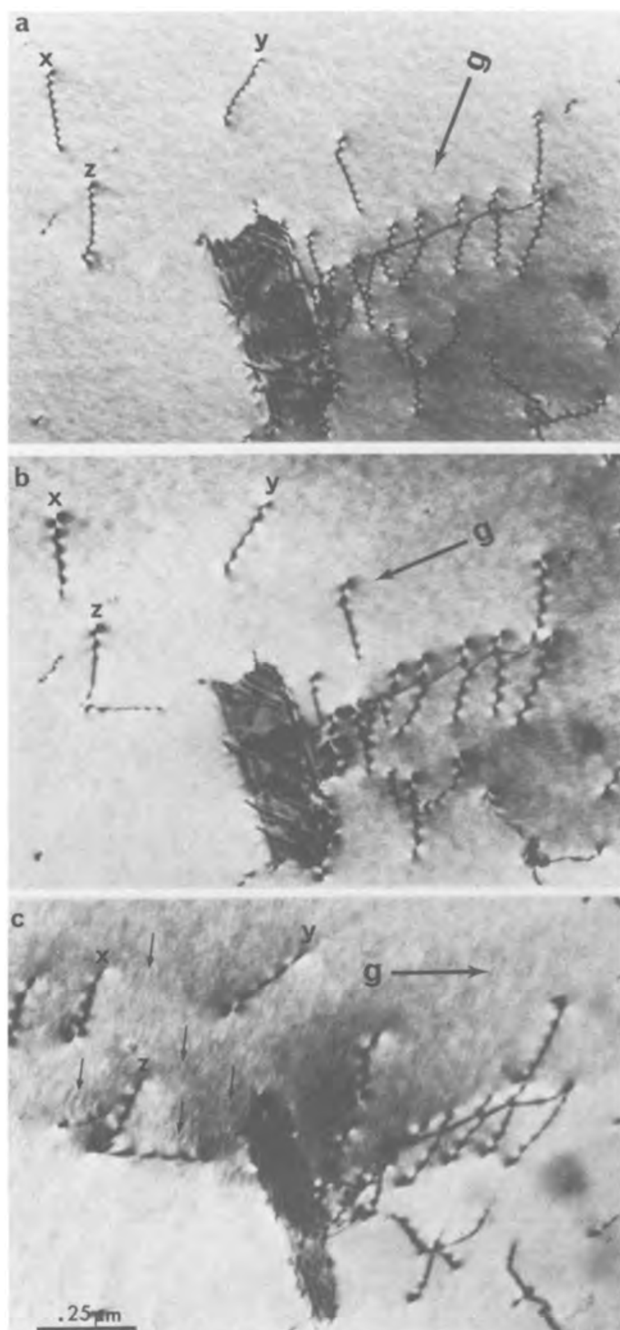

Fig. 1. TEM micrographs of a (001) nickel film imaged with (a) $\bar{g} = 200$; (b) $2\bar{2}0$; and (c) $\bar{1}3\bar{1}$. Symbols x, y, and z indicate dislocations. Four fine arrows in (c) mark the images of linear defects.

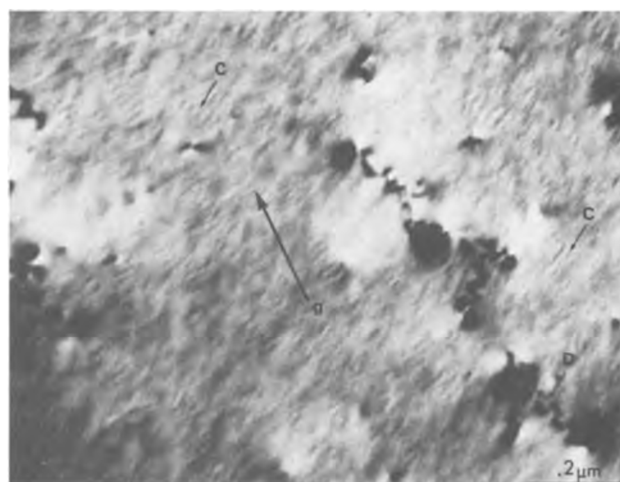

Fig. 2. TEM micrograph of a (001) nickel film imaged with $g = \bar{3}11$. Symbols C and D indicate the images of linear defects and dislocation, respectively.

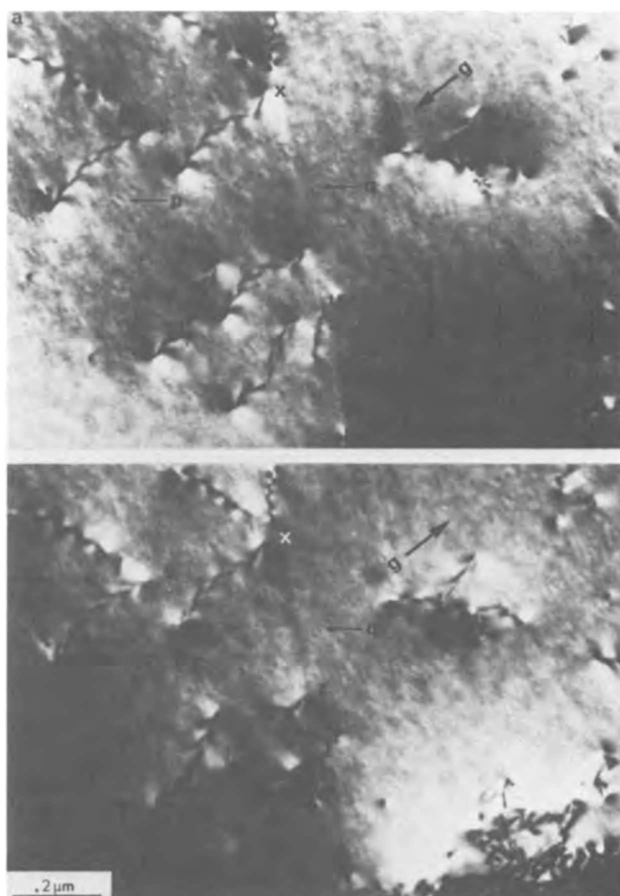

Fig. 3. Structure of a (001) nickel foil imaged with (a) $\bar{g} = \bar{3}11$; and (b) $3\bar{1}\bar{1}$. The micrograph was taken along a zone axis near 103. The images of dislocations are indicated by symbols x and y; those of LD's are shown by symbols p and q.

of a threading dislocation about the center of the image, i.e, the image is reversed with respect to the top and bottom surfaces of the foil and side for side with respect to the dislocation line. On the other hand, no such inversion occurs in the images of LD's as indicated by symbols p and q. Furthermore, it is seen that the LD images taken with the reflecting vector $+\bar{g}$ bear no relationship to those obtained with the reflecting vector $-\bar{g}$. In addition to the $\pm\bar{g}$ behavior of the image contrast, the images of the LD's contain a center of inversion (see Fig. 3). This symmetry property, however, does not exist for images of a dislocation. Based upon the symmetry properties of defect images obtained from theoretical micrographs (7), it can be concluded that the observed LD is not a dislocation, but a line of dilatation. The condition for invisibility of a line of dilatation is that the reflecting vector lies exactly along the dilatational line (7). In order to achieve such invisibility condition it was necessary to determine the direction of the line of dilatation.

The determination of the direction of the line of dilatation was made using the standard stereographic trace analysis. Figure 4 shows a micrograph of the (001) nickel foil imaged with $\bar{g} = \bar{3}11$ along its projected direction $\bar{z} \sim [1\bar{1}4]$. Most of the observed LD's were found to project along three major directions. In

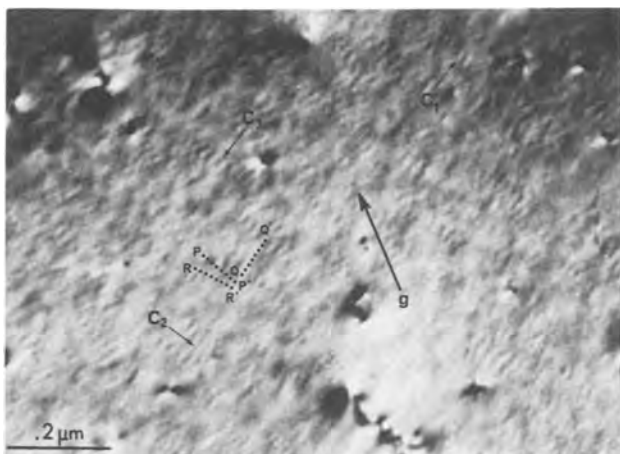

Fig. 4. TEM micrograph of a (001) nickel film imaged with $g = \bar{3}11$. Three dotted lines indicated by symbols PP', QQ', and RR' correspond to the line direction of LD's denoted by C_1, C_2, and C_3, respectively. $\bar{z} = \bar{1}\bar{1}4$.

Fig. 4, these three projected directions onto the ($\bar{1}\bar{1}4$) plane are indicated by symbols PP', QQ', and RR' which correspond to those of the LD's denoted by C_1, C_2, and C_3, respectively. The (001) stereogram in Fig. 5 shows the result of plotting great circles which correspond to the traces of the LD, C_1, obtained from the projections along [001], [103], and [125] directions. As seen in Fig. 5, within the experimental accuracy, the LD, C_1, lies approximately along the [001] direction, which is coincident with the foil normal. Similarly, the defects C_2 and C_3 were found to lie along the [100] and [010] directions, respectively. All the observed LD's in the (001) nickel foil are, therefore, found to lie primarily along <001> type directions.

The condition for invisibility of a line of dilatation can be achieved if the reflecting vector is chosen to lie exactly along the line of dilatation. It was possible to obtain such reflecting vectors for LD's labeled C_2 and C_3. For testing the invisibility condition h00 and 0h'0 type reflecting vectors were chosen for LD's, C_2, and C_3, respectively. The choice of 200 or 020 reflection, however, failed to give an unambiguous condition for invisibility, as the reflection itself does not produce detectable images of LD's. The use of 400 or 040 reflection nearly satisfied the invisibility condition for defects C_2 or C_3, although such detectability was also found to be rather difficult due to the relatively high order reflection. The difficulties encountered for achieving an invisibility condition are discussed further in the following section.

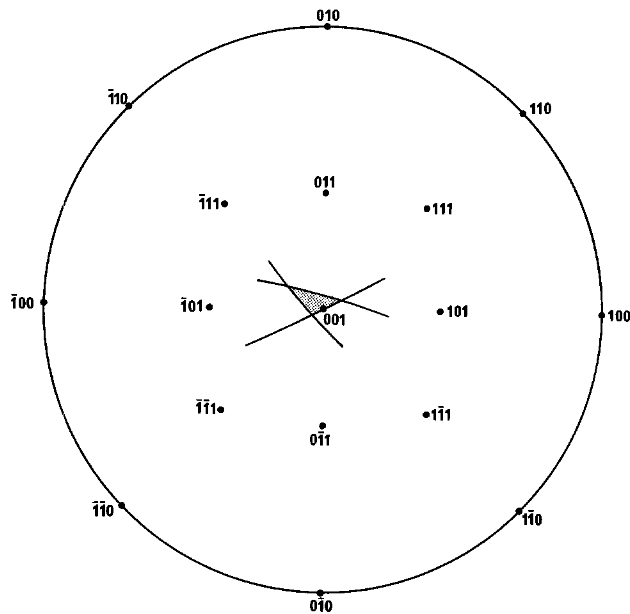

Fig. 5. A (001) stereogram showing the result of plotting great circles which correspond to the traces of the LD marked in Fig. 4, obtained from the projections along 001, 103, and $\bar{1}25$.

Discussion

It is, to the best of author's knowledge, the first time that lines of dilatation have been observed in electrodeposited nickel films. The fact that low order reflections such as $\bar{g} = 111$, 200, and 220, do not provide appreciable strain contrast from these defects undoubtedly accounts for the fact that they have not been observed. It is, however, rather surprising to find that LD's exist in such a high density ($\sim 1 \times 10^{15}/\text{cm}^3$), which is about more than one order of magnitude higher than the density of grown-in dislocations ($6 \times 10^{13}/\text{cm}^3$).

The crystallographic alignment of the observed LD's along <001> in (001) nickel foils resembles that of organic molecules incorporated in copper electrodeposits. It was recently found (8) that a chain of O-phenanthroline molecules, which are deliberately added to an electrolyte as an addition agent, are incorporated into (001), (011), and (103) copper foils along <001>. From morphological studies, it was concluded that the molecules are adsorbed at growth steps (multi-atomic steps) during growth processes and are subsequently incorporated into the deposit at the steps. This result clearly suggests that the observed lines of dilatation must have been generated at the growth steps of (001) planes by the incorporation of impurities during the crystallization process. In fact, morphological studies using a scanning electron microscope have shown that (001) nickel foils contained primarily three growth facets which are bounded by (001), (010), and (100) planes. On these growth facets, therefore, there are three stair steps along [100], [010], and [001], respectively. It can be easily seen that these stair steps can serve as the most probable sites for trapping gaseous and/or organic impurities. In the present experiment, the former impurity is likely to be hydrogen; the latter could be a trace of organic contaminant which is left in the electrolyte. As the electrolyte has been highly purified, it is not likely that a high density of organic impurities is incorporated in the form of lines of dilatation. Hence, impurities forming the observed LD's are most likely to be hydrogen. It should also be pointed out that the deliberate use of low pH($\sim$1.5) in the bath further increases the probability of incorporating hydrogen into the deposit. Figure 6 shows a proposed model

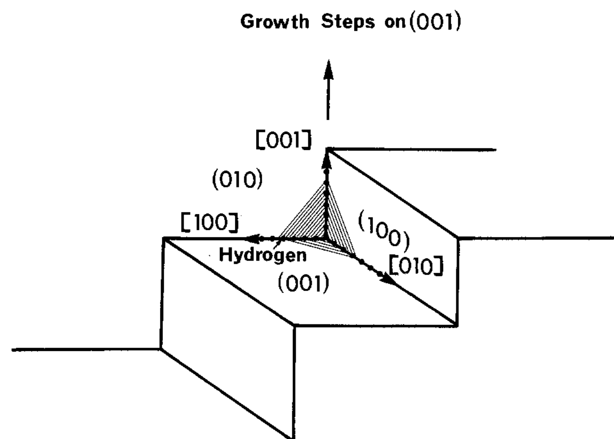

Fig. 6. Schematic illustration showing how a line of hydrogen molecules can be trapped along [100], [010], and [001] and subsequently incorporated into (001) deposit.

which illustrates how lines of hydrogen molecules can be trapped and then incorporated at growth steps along <001>. If this proposed model is correct, it is expected that the geometry and distribution of lines of dilatation should closely follow the pattern of growth facets on the (001) nickel foil. Furthermore, from this model it is easy to understand why such a high density ($\sim 1 \times 10^{15}/cm^3$) of LD's can be incorporated during the film growth.

Since this model predicts that LD's are generated at growth steps, it might be possible to change the LD structure by changing the structure of growth steps. In order to test this hypothesis, the deposition rate was varied by raising the current density from 5 to 15 mA/cm^2. Figure 7 shows the structure of a nickel film plated at a current density of 15 mA/cm^2 on a textured copper foil. The image was taken with $\bar{g} = 311$. Figure 7 shows that under this condition there are many features similar to the images of spherical inclusions whose strain field is indicated by three arrows. Although the images of these randomly distributed inclusions are visible in high density, inclusions of the type found in the (001) nickel films plated at 5 mA/cm^2 are not observed. These spherical-like inclusions were studied under so-called kinematical imaging conditions (6) using the defocus contrast technique (9). The defocus contrast revealed that the images of inclusions behave effectively like spherical voids. In other words, the inclusions are seen as white dots surrounded by black rings in the underfocused condition, and as black dots surrounded by white rings in the overfocused condition. This observation led us to conclude that the observed inclusions are pressurized spherical voids, probably containing hydrogen. The question then arises as to whether or not these inclusions bear any relation to the LD's.

A further close examination of the image features in Fig. 7 revealed that the images of closely spaced spherical inclusions somewhat resemble those of LD's. This observation motivated us to consider the possibility that LD's are, in fact, composed of strings of closely spaced spherical voids. Based upon this assumption, a (001) nickel film was reexamined to see if the LD's are associated with voids. Although high resolution defocus contrast technique was used, the presence of voids could not be assessed due to the resolution limit of the microscope (~5A). Therefore, it was concluded that if voids are present, they must be less than 5A in size. If the observed LD's are strings of spherical voids rather than lines of dilatation, they would not be invisible for a reflection which is parallel to them but show strong contrast, as pointed out by Borggreen and Thölén in their computer-simulation work (10). As described in the previous section, some difficulties were encountered in obtaining an unambiguous invisibility condition and this might be related partly to the fact that the LD's are not exactly pure lines of dilatation but are strings of spherical voids in a microscopic sense. Another possible explanation for this difficulty is, of course, that the LD's do not lie exactly along <001> directions. Nevertheless an increase in current density appears to modify the structure of growth steps, and consequently to change LD's into randomly distributed spherical voids. These results strongly suggest that this type of linear defects might be found in other thin films if the process of film formation involves the incorporation of gaseous and/or organic impurities. It should be pointed out, however, that strain fields associated with these defects might be extremely small and the use of high order reflections will be essential for their detection.

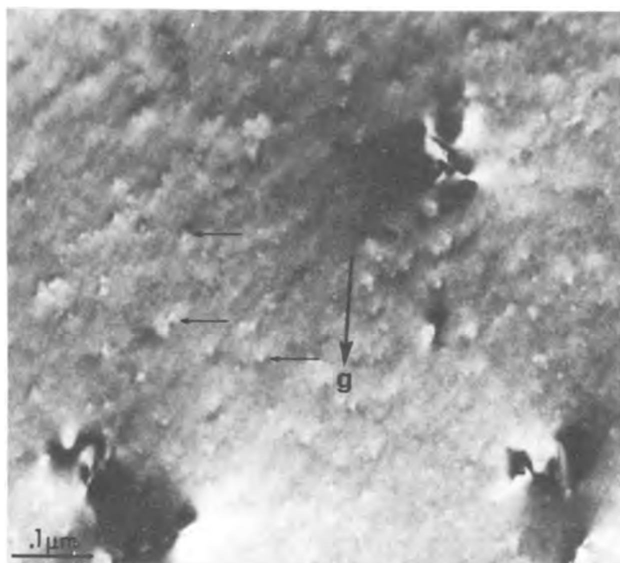

Fig. 7. TEM micrograph of a nickel film plated at a current density of 15 mA/cm^2 on a textured OFHC copper foil. The image was taken with $\bar{g} = 311$. Arrows indicate images of spherical inclusions.

The presence of such a high density of LD's in electrodeposited films is certainly expected to influence the level of internal stresses and, therefore, their contribution to the internal stress in electrodeposited films must be considered. Although most of the internal stress analyses in thin films has been based primarily upon stress gradient that is caused by variations in the density of grown-in dislocations along the direction of growth (11), the fact that the LD's are distributed along specific crystallographic directions <100> suggests that the LD's might contribute even more significantly to an anisotropy of internal stress in electrodeposited nickel films than do randomly distributed grown-in dislocations.

Further work will be required to determine whether the LD's are lines of expansion or lines of compression. The fact that the LD's were not found in very thin (<300A) foils indicates that mobile impurities incorporated along lines of dilatation might have escaped as the line segments intersect the film surfaces. This evidence appears to imply that gaseous impurities, such as hydrogen, are trapped along LD's but may be released at surfaces in thin areas of the film. Although the presence of hydrogen along the dilatational line still must be proven it is interesting to mention that LD's still were found in (001) foils after storage for as long as four years. Thermal stability of the LD's at various temperatures will be the subject of a future publication. Presently, a theoretical analysis based on computer-simulated electron micrographs is being carried out in order to determine the compressive or tensile nature of these LD's.

Acknowledgments

The author wishes to thank Dr. D. M. Maher for his experimental and technical guidance in obtaining our initial results without which the present work could not have been obtained. Thanks are also due to Drs. G. Y. Chin, S. Mahajan, and D. M. Maher for their constructive comments on this manuscript.

Manuscript submitted Feb. 6, 1978; revised manuscript received March 14, 1978.

Any discussion of this paper will appear in a Discussion Section to be published in the June 1979 JOURNAL. All discussions for the June 1979 Discussion Section should be submitted by Feb. 1, 1979.

Publication costs of this article were assisted by Bell Laboratories.

REFERENCES

1. Y. Okinaka and S. Nakahara, *This Journal*, **123**, 475 (1976).

2. D. P. Smith, "Hydrogen in Metals," p. 38, The University of Chicago Press, Chicago, Illinois (1948).
3. A. K. Graham, in "Electroplating Engineering Handbook," 3rd ed. p. 231, A. K. Graham, Editor, Van Nostrand Co., New York (1972).
4. W. H. Cleghorn and J. M. West, *Trans. Inst. Met. Finish.*, **45**, 43 (1967).
5. G. Thomas, "Transmission Electron Microscopy of Metals," p. 150, John Wiley & Sons, Inc., New York (1967).
6. P. B. Hirsch, A. Howie, R. B. Nicholson, D. W. Pashley, and M. J. Whelan, "Electron Microscopy of Thin Crystals," Butterworths, London (1965).
7. P. Humble, *Aust. J. Phys.*, **22**, 51 (1969).
8. S. Nakahara and A. Staudinger, Paper 262 presented at The Electrochemical Society Meeting, Las Vegas, Nevada, Oct. 17-22, 1976.
9. S. Nakahara and Y. Okinaka, in "Properties of Electrodeposits—Their Measurements and Significance," R. Sard, H. Leidheiser Jr., and F. Ogburn, Editors, Chap. 3, The Electrochemical Society Softbound Symposium Series, Princeton, N.J. (1974).
10. K. Borggreen and A. R. Thölén, *Phys. Status Solidi. A*, **39**, 223 (1977).
11. L. Souzis and R. Weil, *Surf. Technol.*, **4**, 41 (1976).

The Liquid Phase Epitaxy of $Al_yGa_{1-y}As_{1-x}Sb_x$ and the Importance of Strain Effects near the Miscibility Gap

R. E. Nahory, M. A. Pollack, E. D. Beebe, and J. C. DeWinter

Bell Laboratories, Holmdel, New Jersey 07733

and M. Ilegems*

Bell Laboratories, Murray Hill, New Jersey 07974

ABSTRACT

A study is presented of the liquid phase epitaxial growth of the quaternary mixed crystal $Al_yGa_{1-y}As_{1-x}Sb_x$. Samples were grown over the composition range $0 < x < 0.2$, $0 < y < 0.6$, at temperatures from 785° down to 715°C, below which a miscibility gap in solid composition was observed. With the inclusion of strain energy terms, a phase diagram calculation was found to describe all of the experimental results. Although strain effects on composition are small, in general, using this model, they are significant in the region of the miscibility gap.

The quaternary mixed crystal $Al_yGa_{1-y}As_{1-x}Sb_x$ has found application in such optoelectronic devices as lasers (1, 2), LED's (3), and photocathodes (4, 5). Its preparation was first reported by Sugiyama and Saito, who briefly described its use in a double heterostructure (DH) laser (1). Advances in the preparation of this material have since permitted such DH lasers to operate continuously at room temperature at wavelengths near 1 μm (2).

Very little data have so far been available on the growth and characterization of $Al_yGa_{1-y}As_{1-x}Sb_x$ (4, 5). In one study, limited to low Sb concentrations, $x \leq 0.065$, it was shown that the addition of Al to the ternary $GaAs_{1-x}Sb_x$ system had only a small effect on the Sb to As ratio in the solid (4). At higher Sb concentrations, our study of the Al-Ga-As-Sb phase diagram demonstrates that the addition of Al does significantly reduce the incorporation of Sb into the solid. In this study, layers were grown by liquid phase epitaxy with compositions over the range $0 < x < 0.2$, $0 < y < 0.6$, at temperatures between 715° and 785°C. Below 715°C, a miscibility gap was observed in the solid compositions of the grown layers. A phase diagram calculation has been carried out which provides good quantitative agreement with all of the experimental liquidus and solidus data. Lattice strain energy was found to significantly affect the results in the vicinity of the miscibility gap under the present conditions of epitaxial growth. The bandgaps of all the grown layers, along with the compositions, have permitted a mapping of the bandgap-lattice constant space of the $Al_yGa_{1-y}As_{1-x}Sb_x$ mixed crystal system.

* Electrochemical Society Active Member.

Experimental Methods

Liquid phase epitaxial growth was carried out in a horizontal, multiwell graphite boat and slider assembly in a flowing H_2 ambient. Solutions were prepared from elemental Ga (99.9999% pure), Sb (99.9999% pure), and Al (99.999% pure), with undoped polycrystalline GaAs as a source of As. The atomic fraction of Al in the liquid, X_{Al}^l, was varied over the range 0-0.007, while X_{As}^l was in the range $\approx$0.004-0.007. The As solubility could only be estimated in these experiments, because an amount of GaAs in excess of that required for saturation was always used. All solutions were prepared with a fixed Sb to Ga weight ratio of 1.074, resulting in $X_{Ga}^l \simeq 0.62$ and $X_{Sb}^l \simeq 0.37$.

The epitaxial quaternary solid solutions were grown at a cooling rate of 0.6°C/min on substrates consisting of three compositionally step-graded $GaAs_{1-x'}Sb_{x'}$ layers which served to accommodate the lattice-mismatch with the GaAs (100) seed. The double seed technique used for successful preparation of DH lasers (2) was used to equilibrate the growth solutions. In each case, the first two step-graded $GaAs_{1-x'}Sb_{x'}$ layers were grown with $x' = 0.03$ ($X_{Sb}^l = 0.09$, 792°-790°C) and $x' = 0.06$ ($X_{Sb}^l = 0.18$, 790°-788°C). The third "matching" layer was then grown with $X_{Sb}^l = 0.27$ from 788°C down to the starting temperature for the quaternary layer. This layer continuously graded in composition and lattice constant during growth and provided a reasonable lattice match for the quaternary. During the growth of the third layer, the quaternary solution was in contact with the equilibrating seed and, therefore, became partially depleted of Al. As a result, although the initial value of X_{Al}^l was known

accurately, the exact value at the time of growth was not well known. Finally, each quaternary layer was grown on such a graded substrate by cooling over 15° to a final temperature T between 715° and 770°C.

The solid composition at the surface of each $Al_yGa_{1-y}As_{1-x}Sb_x$ sample was measured with an x-ray microprobe analyzer. The compositions were determined using Colby's "MAGIC" computer program (6) by comparing the x-ray intensities of the quaternary unknowns to those of the same elements measured on GaAs, Sb, and Al standards. Room temperature bandgaps for most of the samples were determined from photoluminescence spectra, which were excited by a pulsed u.v. N_2 laser (3371Å) and analyzed with a ¾ meter spectrometer and S-1 photomultiplier. The bandgap E_g was taken as the peak of the photoluminescence curve in each case.

Experimental Results

Liquid and solid compositions.—Table I summarizes the experimental results for 14 different samples. The measured compositions x and y are given, along with the room temperature bandgaps E_g, for different initial X_{Al}^l and final growth temperatures T. Using Vegard's law (Eq. [B-2], Appendix B), the lattice constants a of the quaternaries have been calculated and are included in the table. The values of X_{Al}^l are those of the initial solutions, which were then partially depleted by the equilibrating seed as discussed above. In one case, for the initial growth (near the interface with the substrate) of sample B at 785°, this depletion amounted to only 3° growth on the equilibrating seed and could be neglected. By microprobe analysis of an angle-lapped section of B, the initial growth composition corresponding to $X_{Al}^l = 3.87 \times 10^{-3}$ and 785°C was determined, and is given as A in Table I. This particular data point was used to fit the phase diagram calculation described below.

Several conclusions can be drawn immediately from the data of Table I. It is clear that the addition of Al decreases the incorporation of Sb into the quaternary. By comparing the 760°C data of samples C, D, and E or the 730°C data of samples H, I, and J, a significant decrease of x with increasing y is evident. Such a strong dependence of x on y was not established in the earlier report of epitaxial growth in this system (4). On the other hand, when y was held approximately constant and the growth temperature reduced (for example in the series D, F, G, I, and L) x increased as it does in the limiting case of $GaAs_{1-x}Sb_x$ (7). Note that the apparent decrease of y with decreasing growth temperature for a constant starting value of X_{Al}^l (in samples A, B, D, F, G, H, and K) is due to Al depletion by the equilibrating seed and is therefore only an artifact of the growth procedure.

Table I. Al-Ga-As-Sb liquidus and solidus data*

Sample	T (°C)	$X_{Al}^l(10^{-3})$ (initial)	x	y	a (calc) (A)	E_g (eV)
A	785	3.87	0.085	0.397	5.6954	—
B	770	3.87	0.090	0.350	5.6972	1.6926
C	760	1.55	0.130	0.108	5.7122	1.3403
D	760	3.87	0.107	0.313	5.7044	1.6260
E	760	5.41	0.099	0.422	5.7021	1.8126
F	750	3.87	0.114	0.316	5.7076	1.6207
G	740	3.87	0.137	0.275	5.7175	1.5536
H	730	3.87	0.183	0.206	5.7372	1.3462
I	730	4.79	0.162	0.317	5.7294	1.5834
J	730	7.73	0.138	0.575	5.7219	—
K	725	3.87	0.182	0.208	5.7368	1.3946
L	720	4.64	0.195	0.274	5.7436	1.5074
M	715	5.41	0.190	0.353	5.7426	1.6926
N	~715	5.41	0.189	0.311	5.7415	—

* All solutions had liquidus compositions $X_{Ga}^l \simeq 0.62$, $X_{Sb}^l \simeq 0.37$, and were saturated with As using excess GaAs. Except for sample A, the X_{Al}^l's were not equilibrium compositions, but were chosen initial values, as described in the text. All samples were grown through 15° to a final temperature T. The solid compositions x,y at the sample surfaces were measured with an electron microprobe and the lattice parameter a was calculated with Vegard's law. The bandgaps E_g were determined from photoluminescence spectra at room temperature. For sample N, the composition was measured just before the abrupt change corresponding to the miscibility gap at ~715°.

A striking change in the morphology of the samples occurred when growth was continued below 715°C. Above this temperature, the surfaces of the layers were shiny but had a crosshatched appearance. This structure, observed as well in graded $GaAs_{1-x'}Sb_{x'}$ layers (7), consists of microscopic ridges and valleys aligned along the [110] directions and is believed to arise from spatial deposition rate variations originating in misfit dislocation networks. Below 715°C, the surface became very rough, and a microprobe analysis in the appropriately angle-lapped layer revealed that the composition had changed abruptly during growth. Figure 1 shows the measured composition of this layer as a function of distance from the $GaAs_{1-x'}Sb_{x'}$ "matching layer" substrate. At 725°, growth of the quaternary first began with $x = 0.189$, $y = 0.311$. The composition remained nearly constant for about 3 μm until a temperature estimated to be about 715°C (given as sample N in Table I). Slightly below this point, the composition jumped to $x \approx 0.8$, $y \approx 0.04$, indicating the existence of a miscibility gap at this temperature under these conditions of growth. The significance of this miscibility gap region is discussed later.

Compositional dependence of the bandgap.—Figure 2 shows the compositional dependence of the bandgap for the data of Table I, in the form of E_g *vs.* lattice constant a. The points are the measured values for the different samples, and the curves are calculated bandgap-lattice constant isoconcentration lines. They are shown solid in the region where the direct bandgap is lowest and dashed in the region where an indirect bandgap has the lowest energy. The dotted curve is the boundary between these two regions. The direct bandgap of the quaternary has been approximated by

$$E_g(x, y) = E_g(0, 0) + Ax + Bx^2 + Cy + Dy^2 + Exy + Fxy^2 + Gyx^2 \quad [1]$$

The direct bandgap variations for three of the limiting ternaries give $E_g(0, 0) = 1.43$, $A = -1.9$, $B = 1.2$ eV for $GaAs_{1-x}Sb_x$ (7), $C = 1.042$, $D = 0.468$ eV for $Al_yGa_{1-y}As$ (8), and $C + E + G = 1.129$, $D + F = 0.368$ eV for $Al_yGa_{1-y}Sb$ (9). The bandgap variation

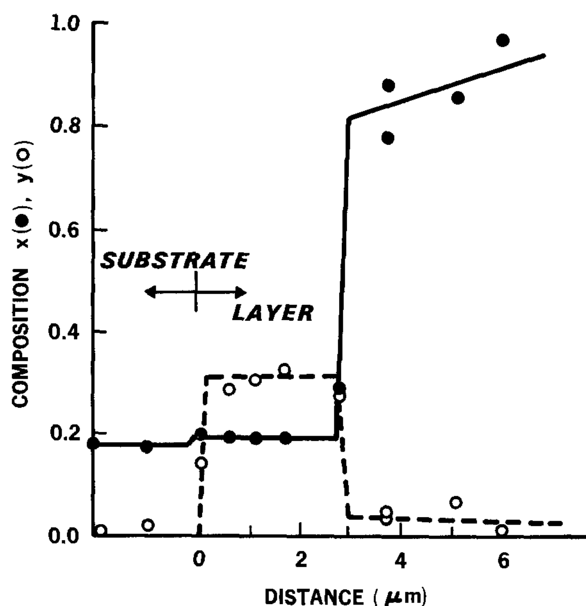

Fig. 1. Composition x, y *vs.* distance for sample N (grown from 725° to 710°C), obtained by electron microprobe measurements on an angle-lapped section. At a distance of 3 μm into the layer, the composition jumps abruptly, corresponding to the miscibility gap at ~715°C.

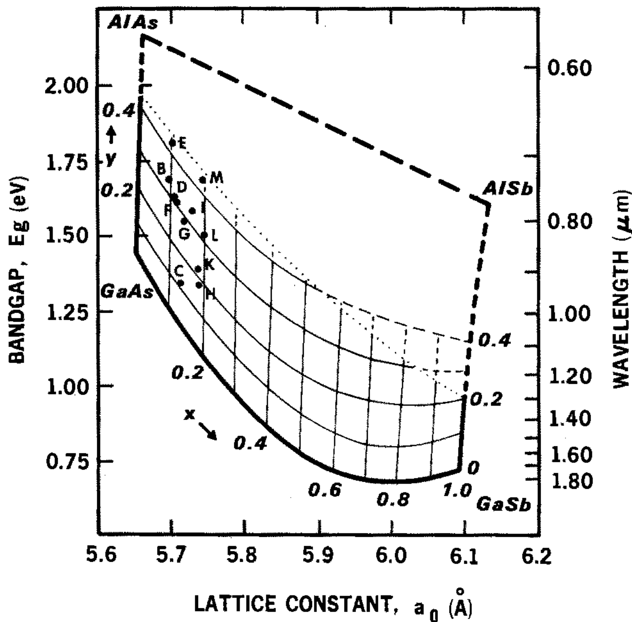

Fig. 2. Bandgap vs. lattice constant of $Al_yGa_{1-y}As_{1-x}Sb_x$. The points are measured values (Table I) and the curves are calculated isoconcentration lines. The dotted line separates the direct bandgap region (solid curves) and the indirect bandgap region (dashed curves).

for $AlAs_{1-x}Sb_x$ being unknown, a least squares fit of the data was used to determine E and G separately. It is clear from Eq. [1] that this determination cannot be very precise for a limited range of x, but the values obtained from the fit give the result $E \approx 1.0$ and $G \approx -0.9$ eV so that in eV

$$E_g(x, y) = 1.43 - 1.9x + 1.2x^2 + 1.042y + 0.468y^2 + 1.0xy - 0.1xy^2 - 0.9x^2y \quad [2]$$

The dashed curves for the indirect bandgap near the $Al_yGa_{1-y}Sb$ limit have been estimated from Ref. (9).

Quaternary Phase Diagram

The Al-Ga-As-Sb quaternary phase diagram can be calculated using the model and computational procedure outlined in Appendix A, as taken from the work of Ilegems and Panish (10) and Jordan and Ilegems (11). Table II lists the parameters used in the calculation, including the temperatures of fusion T^F, entropies of fusion ΔS^F, and interaction parameters α for the binary pairs in the liquid and β for the ternaries in the solid. The interaction parameters $\alpha_{As\text{-}Sb}$ and $\beta_{GaAs\text{-}GaSb}$ were taken from previous work on the Ga-As-Sb system over the same temperature range studied here (7). The parameter $\beta_{AlAs\text{-}AlSb}$ was obtained from $\beta_{GaAs\text{-}GaSb}$ by applying the δ-lattice-parameter model (12) and scaling according to $(\Delta a)^{2.5}$. The other parameters have been taken from Panish and Ilegems (13).

Table II. Parameters used in the phase diagram calculation*

	T^F (°K)	ΔS^F (eu/mole)	α,β (cal/mole)	a (Å)
Al-As	2043	15.60	$-12.0T + 600$	5.6622
Ga-As	1511	16.64	$-9.16T + 5160$	5.65321
Al-Sb	1338	14.74	-6000†	6.1355
Ga-Sb	983	15.80	$-6.0T + 4700$	6.09593
Al-Ga			104	
As-Sb			-600‡	
AlAs-GaAs			0	
AlSb-GaSb			0	
AlAs-AlSb			4700†	
GaAs-GaSb			4000‡	

* Parameters include the temperatures of fusion T^F, entropies of fusion ΔS^F, binary lattice parameters a, and the interaction parameters α for the liquid and β for the solid.** Except as noted, all parameters are from Ref. (13).

** The interaction parameters β are related to α_{12}^s and α_{34}^s of Appendix A by

$$\alpha_{12} = x\beta_{AlSb\text{-}GaSb} + (1 - x)\beta_{AlAs\text{-}GaAs}$$

$$\alpha_{34} = y\beta_{AlAs\text{-}AlSb} + (1 - y)\beta_{GaAs\text{-}GaSb}$$

† Present work.

‡ Ref. (7).

The only parameter not known sufficiently well in this temperature range from other sources is $\alpha_{Al\text{-}Sb}$. It was therefore evaluated by fitting the experimental liquidus and solidus data of sample A (Table I) at 785°C, as shown in Fig. 3. A value of $\alpha_{Al\text{-}Sb} = -6000$ cal/mole gives good agreement between calculated and measured (sample A) compositions $y = 0.397$ and $X_{Al}^l = 3.87 \times 10^{-3}$. Note from Fig. 3 that y is only weakly dependent on temperature between 785° and 745°C. This feature could not be verified experimentally because of the Al depletion already discussed.

A comparison of the results of the phase diagram calculation with the experimental solidus data of Table I is made in Fig. 4. The solid lines are the com-

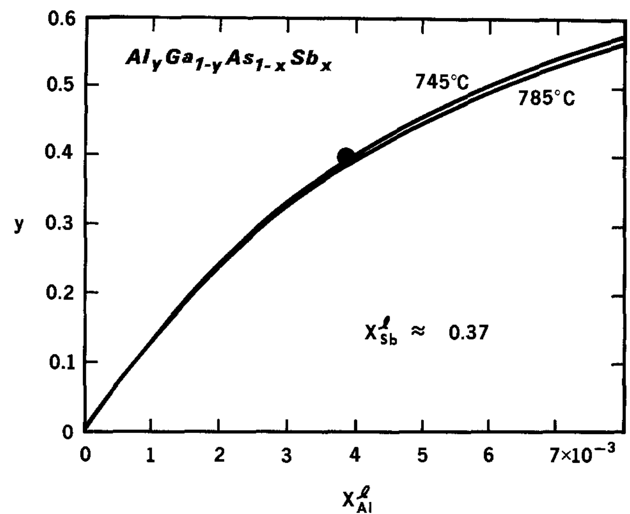

Fig. 3. Compositions y in the solid vs. X_{Al}^l in the liquid. The point corresponds to the measurements on sample A, and the curves are calculated at two different temperatures.

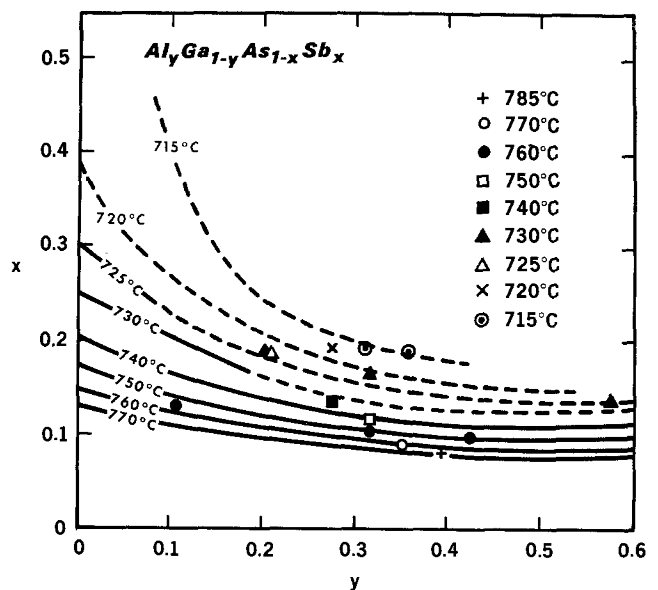

Fig. 4. Section of the Al-Ga-As-Sb phase diagram showing the solidus compositions x vs. y. The points correspond to the data of Table I. The dashed curves are obtained with the inclusion of strain energy effects. The solid curves are isotherms calculated in the strain-free case and are essentially unchanged by the inclusion of strain effects during continuous growth, as discussed in the text.

puted isotherms of x vs. y at temperatures between 725° and 770°C. The calculation follows the trends of the experimental results: x increases with decreasing temperature for a fixed value of y, and at a given temperature x decreases as y increases. Detailed comparison of the data with the calculated curves shows good agreement over the range 770°-740°. The epilayer compositions fall on calculated isotherms about 10°C lower than the final growth temperatures, but this deviation is quite small considering that no parameters were adjusted to specifically fit the experimental solidus points. This 10° difference may in fact be significant and due to a phenomenon previously observed in the Ga-As-Sb system (7). There, 10° of constitutional supercooling, arising from As-diffusion-limited growth, was observed for the same cooling rate of 0.6°C/min.

A striking discrepancy between the calculated phase diagram and the data occurs at temperatures below 740°C. Sections of the solid curves do not exist in this region of Fig. 4 since the calculation predicts a miscibility gap, with an abrupt jump in composition toward the GaSb limit, as the temperature is lowered. The compositional width of the predicted gap is a function of temperature: For example at 730°C it exists for $y > 0.2$, while at 725°C it should occur for $y > 0.1$. Experimentally, however, seven epilayers (samples H-N) have been grown below 740° in this region where the phase diagram calculation shows no solid solution miscibility. For instance, for a constant $y \approx 0.3$, the miscibility gap has not been observed until a temperature slightly below 715°C (Fig. 1). No changes in either the value of $\beta_{AlAs\text{-}AlSb}$ or the adjustable parameter $\alpha_{Al\text{-}Sb}$ could be made which would shift the calculated gap region from 740° to the observed 715°C at $y = 0.3$ without causing drastic disagreement with the known $y = 0$ ternary boundary (7) or with the data measured above 740°C.

Strain Energy Effects

We propose that this discrepancy can be resolved by the inclusion of lattice mismatch strain energy effects in the phase diagram calculation (14, 15). The details of the calculation are described in Appendix B. The mismatch strain energy is proportional to $(a - a_o)^2$, where a is the lattice parameter of the growing layer and a_o is that of the underlying layer. The contribution of this term to the free energy should be especially important in situations where solid compositions (and lattice parameters) can vary rapidly during growth, as in the region near a miscibility gap. In the neighborhood of such a gap there are two widely different compositional ranges of the solid in near-equilibrium with the liquid phase at a given temperature. With lowering temperature, the crystal tends to grow near the composition which minimizes the strain energy and thus continues to change composition slowly, rather than abruptly jump across the miscibility gap. At a sufficiently low temperature the strain energy term no longer dominates the free energy and a rapid change in composition finally occurs. This phenomenon would be observable as an effective reduction in the miscibility gap temperature, in agreement with the experimental results.

To quantitatively include this effect in the calculation, we note that the strain energy term can be written in the form

$$G^{st} = \sigma \left(\frac{a - a_o}{a_o} \right)^2 \text{ cal mole}^{-1} \qquad [3]$$

where σ is an elastic coefficient dependent on the material. This term has been included in the phase diagram calculation as described in Appendix B. The calculation was carried out successively at small temperature intervals, $\Delta T = 1°$, beginning at a temperature corresponding to the start of experimental growth. At each step, a_o was taken as the lattice constant of the composition calculated at the previous step. In this way the composition was calculated step-by-step for each temperature as the crystal grew, accounting for the changing lattice parameter of the underlying material. The temperature intervals of 1° used in the calculation were found to be adequately small to describe the continuous crystal growth. The calculation was continued to lower and lower temperatures, until an abrupt change of composition occurred. For any nonzero value of σ, the temperature at which this change occurs is lower than the miscibility gap temperature in the absence of the strain energy term.

The value of the elastic coefficient which lowers the calculated miscibility gap temperature to the observed range near 715°C was found to be $\sigma \approx 1 \times 10^5$ cal mole^{-1}. The computed results for this value are shown by the dashed isotherms in Fig. 4. For the region below 740° down to 715°C the dashed isotherms are now in good agreement with the experimental data points. In the region of the original solid isotherms, away from a miscibility gap, the inclusion of the strain energy has a negligible effect. This is because, as shown in Appendix B, the magnitude of the strain energy contribution to the total free energy of mixing is, in general, quite small. The inclusion of the strain energy term, therefore, has only a small effect on the solid composition, except near the miscibility gap, where a small change in the free energy of mixing is sufficient to cause a large shift in the solid composition. The magnitude of the elastic coefficient obtained by the above curve-fitting procedure, $\sigma \sim 1 \times 10^5$ cal mole^{-1}, is close to, but somewhat smaller than, the value 6×10^5 cal mole^{-1} estimated (Appendix B) from the elastic properties of the material (16). This difference, however, is reasonable in view of the fact that the theoretical prediction should give only an upper limit to the strain effects, since it ignores strain-relieving mechanisms such as interfacial misfit dislocations.

Conclusions

We have discussed the liquid phase epitaxial growth of the quaternary mixed crystal $Al_yGa_{1-y}As_{1-x}Sb_x$ over a wide range of compositions, $0 < x < 0.2$, $0 < y < 0.6$, at temperatures between 715° and 785°C. An abrupt change in composition has been observed in samples grown through ~715°, corresponding to a miscibility gap in the solid solution. The entire growth region investigated, including the miscibility gap, is successfully described by a phase diagram calculation. It was found that strain energy contributions to the free energy of mixing are required to bring the calculated results into agreement with the experimental data for temperatures in the region of the miscibility gap. Except for the miscibility gap region, the strain energy is shown to have a negligible effect on the phase diagram of the Al-Ga-As-Sb system. This strain energy model should be generally valid for all III-V solid solutions, but it alone cannot explain the strong lattice-pulling effects reported in some of these systems (14, 17, 18).

Manuscript submitted Sept. 14, 1977; revised manuscript received Jan. 27, 1978.

Any discussion of this paper will appear in a Discussion Section to be published in the June 1979 JOURNAL. All discussions for the June 1979 Discussion Section should be submitted by Feb. 1, 1979.

Publication costs of this article were assisted by Bell Laboratories.

APPENDIX A

Quaternary Phase Diagram Calculations in the Equilibrium (No Strain) Case

A general technique for solving the solid-liquid equilibrium in quaternary systems involving compound semiconductors forming continuous series of solid solutions of the type $A_u\, B_{1-u}\, C_v\, D_{1-v}$ was pre-

sented in Ref. (10-11). (We retain the u, v notation here to be consistent with Ref. (11), and note that $u = y$ and $v = 1 - x$.) Explicit equilibrium equations were obtained for the case where the quaternary solid solution may be approximated by a regular mixture of the atoms A, B, C, and D subject to the site restrictions of the zinc blende lattice, and where the thermodynamic properties of the quaternary liquid may be approximated through the use of the simple-solution model.

The equilibrium equations between liquid and solid phases are written, in general form, in terms of the chemical potentials

$$\mu_{ij}^s = \mu_i^l + \mu_j^l \qquad \text{[A-1]}$$

where

$$ij = AC, AD, BC, BD$$

or, equivalently,

$$ij = 13, 14, 23, 24$$

for the four binary components of the quaternary solid. Of the four equations [A-1] only three are independent because of the relation

$$\mu_{13}^s + \mu_{24}^s = \mu_{14}^s + \mu_{23}^s \qquad \text{[A-2]}$$

The chemical potentials of the binary components, μ_{ij}^s, can be expressed in terms of the chemical potentials of the pure binary compounds (superscript o) according to

$$\mu_{ij}^s(T) = \mu_{ij}^{os}(T) + RT \ln x_i^s x_j^s + RT \ln \gamma_{ij}^s \qquad \text{[A-3]}$$

where $x_i^s x_j^s$ is the mole fraction of the binary component ij in the quaternary solid (random mixing on each sublattice) and γ_{ij}^s is the corresponding activity coefficient. The activity coefficients are obtained by partial differentiation of the excess free energy of mixing, G_M^e

$$RT \ln \gamma_{ij}^s = \frac{\partial G_M^e}{\partial n_{ij}} \qquad \text{[A-4]}$$

where n_{ij} represents the number of moles of component ij in n moles of the quaternary solid ($n = n_{13} + n_{23} + n_{14} + n_{24}$).

It has been shown that (11)

$$G_M^e = \frac{1}{n} [\alpha_{12}^s n_1 n_2 + \alpha_{34}^s n_3 n_4 + \alpha_c^s (n_{14} n_{23} - n_{13} n_{24})] \qquad \text{[A-5]}$$

where n_i represents the number of moles of component i. The quantities α_{12}^s and α_{34}^s are the interaction parameters for mixing on the Group III and Group V sublattices, respectively, while α_c^s is a combination of the interaction energies between elements residing on different sublattices. It can be verified that the γ_{ij}^s's obey the condition

$$RT \ln [\gamma_{14}^s \gamma_{23}^s / \gamma_{13}^s \gamma_{24}^s] = \alpha_c^s \qquad \text{[A-6]}$$

After making the appropriate substitutions for the chemical potentials in the four equilibrium equations [A-1], and after combining (10) all terms which depend on the composition X^l and parameters of the liquid phase together in the quantity Q_{ij}, the equilibrium equations are obtained in the simple form

$$\ln \gamma_{ij}^s x_i^s x_j^s = Q_{ij}; \quad ij = 13, 14, 23, 24 \qquad \text{[A-7]}$$

Again, only three out of the four equations [A-7] are linearly independent in accordance with the condition [A-2]. For the computer solution of the phase equilibrium, these three independent equations, rearranged in an equivalent symmetrical form as given in Ref. (10), are solved for u, v, X_4^l for a given set of input values X_2^l, X_3^l, and T using the numerical constants listed in Table II.

APPENDIX B

Quaternary Phase Diagram Calculation in the Elastic Strain Case

When the epitaxial layer is elastically strained such that its lattice constant a is made to conform to the lattice constant a_o of the underlying layer, there is an additional strain contribution to the total excess free energy of mixing

$$G_M^{e,\text{total}} = G_M^e + G_M^{st} \qquad \text{[B-1]}$$

The lattice constant of the quaternary solid is given by Vegard's law

$$a = uv\, a_{13} + u(1 - v) a_{14} + (1 - u) v a_{23} + (1 - u)(1 - v) a_{24} \qquad \text{[B-2]}$$

where the a_{ij} are the lattice constants of the binary compounds ij, given in Table II, and $u = y$ and $v = 1 - x$.

The strain energy contribution, evaluated per mole of epitaxial layer growth, can be estimated from the expressions given by Jesser and Kuhlmann-Wilsdorf (15)

$$G_M^{st} = \sigma \left(\frac{a - a_o}{a_o} \right)^2 \qquad \text{[B-3]}$$

with

$$\sigma = 2C \frac{1 + \nu}{1 - \nu} V_m \qquad \text{[B-4]}$$

where C is the interfacial shear modulus of the layer [$C = \frac{1}{2} c_{44}$ for growth on the (100) plane], ν the Poisson ratio, and V_m its molar volume. In these equations it is assumed that the thickness of the epitaxial layer is much smaller than that of the underlying layer so that the strain energy contribution from this underlying layer can be neglected.

To quantitatively include the effects of strain in the phase diagram calculation we evaluate the activity coefficients γ_{ij}^s in the solid solution, as in [A-4]

$$RT \ln \gamma_{ij}^s = \frac{\partial}{\partial n_{ij}} (G_M^e + G_M^{st}) \qquad \text{[B-5]}$$

For the strain contribution (superscript st), one obtains

$$RT \ln \gamma_{ij}^{s,st} = \frac{\partial}{\partial n_{ij}} \left[\sigma \left(\frac{a - a_o}{a_o} \right)^2 n \right] \qquad \text{[B-6]}$$

Finally, after differentiation

$$RT \ln \gamma_{ij}^{s,st} = \frac{\sigma}{a_o^2} (a - a_o)(2a_{ij} - a - a_o) \qquad \text{[B-7]}$$

In order for the $\gamma_{ij}^{s,st}$'s to satisfy condition [A-6], it is required that

$$\gamma_{13}^{s,st} \gamma_{24}^{s,st} / (\gamma_{14}^{s,st} \gamma_{23}^{s,st}) = 1 \qquad \text{[B-8]}$$

or after substitution that

$$a_{13} + a_{24} = a_{14} + a_{23} \qquad \text{[B-9]}$$

In general, an exact equality is not expected in [B-9], in view of the approximate formalism used to express G_M^{st}. In the AlGaAsSb system, however, $a_{13} \approx a_{23}$, and $a_{14} \approx a_{24}$, so that the relation [B-9] is closely satisfied. Therefore, in the computer calculation, which requires [B-9] to be an exact equality, the lattice constant values used in the evaluation of γ_{ij}^{st} [B-7] were replaced by average values: a_{13} and a_{23} by $(a_{13} + a_{23})/2$, a_{14} and a_{24} by $(a_{14} + a_{24})/2$.

An order of magnitude estimate of the strain contribution can be made taking the following values (16) to be representative of the $Al_uGa_{1-u}As_vSb_{1-v}$ quaternary with $u \sim 0.3$, $v \sim 0.8$, and $T \sim 1000°K$

$$\nu = 0.3$$
$$c_{44} = 5.1 \times 10^{11} \text{ dynes cm}^{-2} = 1.22 \times 10^4 \text{ cal cm}^{-3}$$
$$V_m = 28.6 \text{ cm}^3 \text{ mole}^{-1}$$

which yields

$$\sigma \sim 6 \times 10^5 \text{ cal mole}^{-1}$$

Since the maximum lattice mismatch which can be elastically accommodated without the generation of mismatch dislocations is expected to be well below 1%, the maximum strain energy contribution to the free energy of mixing is, from [B-3]

$$G_M^{st} << 60 \text{ cal mole}^{-1}$$

This value should be compared with the excess free energy of mixing in the absence of strain, evaluated using [A-5] and the parameters of Table II

$$G_M^e \sim 660 \text{ cal/mole}$$

Therefore, $G_M^{st} << G_M^e$, so that this strain energy contribution generally will have only a minor effect on the equilibrium solid composition. In cases near a miscibility gap, however, such a small change in $G_M^{e,total}$ may lead to large shifts in solid composition. These conclusions are verified by the detailed calculations carried out for the $Al_uGa_{1-u}As_vSb_{1-v}$ system as discussed in the text.

REFERENCES

1. K. Sugiyama and H. Saito, *Jpn. J. Appl. Phys.*, **11**, 1057 (1972).
2. R. E. Nahory, M. A. Pollack, E. D. Beebe, J. C. DeWinter, and R. W. Dixon, *Appl. Phys. Lett.*, **28**, 19 (1976).
3. R. E. Nahory, M. A. Pollack, E. D. Beebe, and J. C. DeWinter, *ibid.*, **27** 356 (1975).
4. G. A. Antypas and R. L. Moon, *This Journal*, **121**, 416 (1974).
5. J. S. Harris, Jr., and R. Sahai, Technical Report AFAL-TR-74-68, April 1974, Science Center, Rockwell International (unpublished).
6. J. W. Colby, in "Advances in X-Ray Analysis," Vol. II, p. 287, Plenum Press, New York (1968); J. W. Colby, Proceedings of Sixth National Conference on Electron Probe Analysis, p. 17 (1971).
7. R. E. Nahory, M. A. Pollack, J. C. DeWinter, and K. M. Williams, *J. Appl. Phys.*, **47**, 1607 (1977).
8. A. Onton, M. R. Lorenz, and J. M. Woodall, *Bull. Am. Phys. Soc.*, **16**, 371 (1971).
9. Keh-Yung Cheng, Technical Report 5111-5 (1975) Stanford Electronics Laboratory, Stanford University (unpublished).
10. M. Ilegems and M. B. Panish, *J. Phys. Chem. Solids*, **35**, 409 (1974).
11. A. S. Jordan and M. Ilegems, *ibid.*, **36**, 329 (1975).
12. G. B. Stringfellow, *J. Cryst. Growth*, **27**, 21 (1974).
13. M. B. Panish and M. Ilegems, in "Progress in Solid State Chemistry," Vol. 7, H. Reiss and J. O. McCaldin, Editors, p. 39, Pergamon, New York (1972).
14. G. B. Stringfellow, *J. Appl. Phys.*, **43**, 3455 (1972).
15. W. A. Jesser and D. Kuhlmann-Wilsdorf, *Phys. Status Solidi*, **19**, 95 (1967).
16. M. Neuberger, "Handbook of Electronic Materials," Vol 2, "III-V Semiconducting Compounds," IFI/Plenum, New York (1971).
17. G. A. Antypas and L. W. James, *J. Appl. Phys.*, **41**, 2165 (1970).
18. J. P. Hirth and G. B. Stringfellow, *ibid.*, **48**, 1813 (1977).

The Anodic Decomposition Pathways of *Ortho*- and *Meta*-substituted Anilines

Rodney L. Hand[1]

Department of Chemistry, University of Idaho, Moscow, Idaho 83843

and Robert F. Nelson*

Department of Chemistry, University of Georgia, Athens, Georgia 30602

ABSTRACT

A survey of the anodic electrochemistry of a number of *ortho*- and *meta*-substituted anilines in 6*N* H_2SO_4 at carbon paste and graphite cloth electrodes has been carried out. It was found that the electrogenerated cation radicals decompose to form the correspondingly substituted benzidines and 4-aminodiphenylamines by tail-to-tail and head-to-tail coupling routes, respectively, in agreement with previous studies. Steric restraints hinder or exclude benzidine formation in some systems. The 4-aminodiphenylamines undergo hydrolytic degradation by different routes for the *ortho*- and *meta*-substituted derivatives, but in both cases 2-substituted *p*-benzoquinones are the end product. The quinones with electron-withdrawing substituents undergo a 1,4-addition of water to form substituted trihydroxybenzene derivatives which are also electroactive. Products and intermediates formed were verified, where possible, by comparison with authentic samples. Preparative-scale electrolyses resulted in substantial yields of some of the substituted *p*-benzoquinones of a magnitude comparable with chemical oxidations. A reaction mechanism is proposed which is consistent with the electroanalytical data and products formed for the series of compounds.

Recent articles have contributed significantly to our understanding of the decomposition pathways of ring-substituted anilines. Bacon and Adams have found that *para*-substituted anilines couple head-to-tail to form the corresponding diphenylamines and that aniline and o-toluidine couple head-to-tail and tail-to-tail to form the corresponding diphenylamines and benzidines in a *p*H-dependent process (1). Wawzonek and McIntyre have shown that aniline and a number of ring-substituted anilines couple head-to-head to form hydrazo compounds in acetonitrile with pyridine (2) and in aqueous alkaline solutions (3). These various coupling reactions are summarized below

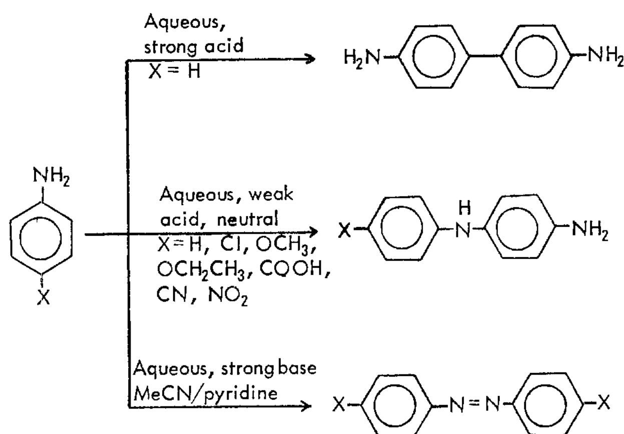

The reaction mechanism proposed by Bacon and Adams involved cation radical coupling reactions (or, alternatively, in view of considerable circumstantial but no conclusive evidence as to the existence of these cation radicals, a dication-parent aniline coupling reaction) to form the benzidines and diphenylamines. The reaction mechanism did not appear to account for the observed *p*H dependence of the benzidine-to-diphenylamine ratio in the aniline and o-toluidine systems.

Wawzonek and McIntyre proposed initial generation of the cation radical via a one-electron oxidation. The cation radical was subsequently deprotonated (pyridine as the base in MeCN/pyridine and the parent aniline as the base in MeCN) to give the neutral free radical. The neutral free radicals then coupled to form diphenylamines and hydrazo compounds which were further oxidized. The diphenylamine-to-hydrazobenzene ratio was reportedly controlled by the ring substituent present though no general conclusions as to substituent effects were presented or evident.

A later study of N-alkylanilines in MeCN and aqueous solutions again demonstrated the formation of diphenylamines and benzidines (4). The diphenylamine-to-benzidine ratio was observed to increase with decreasing bulk of the alkyl substituent, increasing *p*H, increasing parent concentration, and decreasing current density. To explain these observations, two discrete decomposition pathways were proposed for the electrogenerated aniline cation radicals. N-ring coupling of a neutral free radical and parent amine to give diphenylamines was proposed when the cation radical-to-parent ratio was low (low curent density, high parent concentration) and deprotonation of the cation radical was facilitated (increasing *p*H). Direct coupling of cation radicals was proposed when the cation radical-to-parent ratio was high (high current density, low parent concentration) and solution conditions were not conducive to deprotonation (low *p*H). The reaction mechanism is somewhat speculative but did account for the observed product distributions as a function of solution conditions.

In an effort to relate these studies more clearly and to provide additional insight into the reaction mechanism through observations of steric and electronic ring substituent effects, we have investigated the electrochemistry of a series of *ortho*- and *meta*-substituted anilines in strong acid solution. The results of this study are reported herein.

Experimental

Solvents, supporting electrolytes, and reagents.—All aqueous solutions were prepared from doubly distilled water and reagent grade H_2SO_4 or standard buffer re-

* Electrochemical Society Active Member.

[1] Present address: Allied Chemical Corporation, Idaho Falls, Idaho 83401.

Key words: organic, electrode, EPR, voltammetry.

agents. o-N,N-dimethylaminoaniline hydrochloride (Eastman), o-phenylenediamine dihydrochloride (Eastman), o-methoxyaniline (Eastman), o-methylaniline (Eastman), o-fluoroaniline (Aldrich), o-chloroaniline (Aldrich), o-bromoaniline (Columbia Organic Chemicals), o-iodoaniline (Aldrich), o-acetylaniline (Aldrich), ethyl anthranilate (Eastman), o-trifluoromethylaniline (Maumee Chemical Corporation), and o-cyanoaniline (Aldrich) were obtained commercially and used without further purification. o-Nitroaniline (Eastman) was obtained commercially and purified by column chromatography. 2-Aminobiphenyl was obtained from Aldrich and purified by benzene/alumina (Woelm) chromatography and recrystallization from benzene/ethanol. *m*-N,N-dimethylaminoaniline hydrochloride (Eastman), *m*-methoxyaniline (Aldrich), *m*-chloroaniline (Aldrich), *m*-bromoaniline (Matheson, Coleman and Bell), *m*-iodoaniline (Aldrich), *m*-trifluoromethylaniline (Maumee Chemical Corporation), *m*-cyanoaniline (Aldrich), and *m*-nitroaniline (Eastman) were obtained commercially and used as received. 3,3'-Dimethoxybenzidine (Aldrich), 3,3'-dimethylbenzidine (Eastman), and 3,3'-dichlorobenzidine (K and K) were obtained commercially and purified by recrystallization. 3,3'-Dinitrobenzidine was prepared by a standard method (5), as were 2,2'-dichloroazobenzene and 3,3'-dichloroazobenzene (6). 2,2'-Dicyanoazobenzene and 2,2'-dinitroazobenzene were prepared by a hypochlorite oxidation of the corresponding anilines in neutral aqueous media (7). Hydroquinone (Aldrich), 2-methylhydroquinone (Aldrich), 2-chlorohydroquinone (Pfaltz and Bauer), 2-bromohydroquinone (Pfaltz and Bauer), and catechol (Aldrich) were obtained commercially and used without further purification. 2-Nitrohydroquinone was prepared by a standard literature method (8), as was the 2-methoxyhydroquinone (9). Ethyl-2,5-dihydroxyanthranilate was prepared by esterification of 2,5-dihydroxybenzoic acid (Pfaltz and Bauer). 4-Amino-3-methylphenol and 4-amino-2-methylphenol were obtained commercially (Eastman) and used without further purification. All other materials were reagent grade and used without further purification.

Instruments, cells, and electrodes.—The instrument used for the electroanalytical studies was a standard operational amplifier-based potentiostat-amperostat employing a three-electrode configuration. Current-voltage and current-time curves were monitored with a Hewlett-Packard 7030 X-Y recorder. Coulometric *n*-values were obtained with a Wenking 68FR 0.5 fast-rise potentiostat equipped with a digital integration system. Preparative electrolyses were effected with a "home-built" ±65V ±2.5A potentiostat (10).

Electroanalytical studies.—The electroanalytical experiments were conducted in a one-compartment cell containing a carbon paste working electrode, platinum wire auxiliary electrode, and aqueous SCE reference electrode. The carbon paste was prepared by mixing 4g of powdered graphite (Ultra Carbon Corporation, WCP-1-M, Lot 989-2) and 6 ml of Nujol mineral oil. A new carbon paste surface was prepared for each individual aqueous electroanalytical experiment.

In the chronoamperometry experiments, the initial potentials were always at least 200 mV cathodic of the peak potentials of the substituted anilines and the final potentials were at least 100 mV anodic of the peak potentials unless otherwise stated.

Coulometric *n*-values were obtained in a two-compartment cell using a carbon rod auxiliary electrode, a carbon cloth working electrode, and a SCE reference electrode. The working and auxiliary compartments were separated by a porous sintered glass frit. The coulometry experiments were terminated when the electrolysis current was 1% of the initial current or when a steady-state current was reached (typically 1-5% of the initial current). Background corrections were obtained by electrolyzing the appropriate solvent and supporting electrolyte for various times at the appropriate potential. In all cases oxidation potentials were at least 100 mV anodic of the parent peak potential. A typical coulometry experiment involved the oxidation of approximately 60 mg of substituted aniline in 50 ml of 6*N* H_2SO_4. Typical initial currents were 250 mA and typical final currents were 2.5 mA.

Preparative electrolyses.—Preparative electrolyses were conducted in a two-compartment cell using a carbon rod auxiliary electrode, a carbon cloth working electrode backed by a platinum foil (10 × 20 cm), and a SCE reference electrode. The cells were 400 and 600 ml beakers and the auxiliary and working compartments were separated by a porous ceramic cup (25 mm diam, 76 mm height), Coors Model No. 70001. Electrical contact to the working electrode was made at several points to avoid local potential gradients. Oxidation potentials were at least 100 mV anodic of parent peak potentials, and electrolyses were terminated when a low steady-state current was reached. A typical preparative electrolysis involved the oxidation of 1g of substituted aniline in 300 ml of 6*N* H_2SO_4. Typical initial currents were 2.5A and typical final currents were from 25-100 mA. Electrolysis times were usually on the order of 1 hr.

Preparative chemical oxidations.—Chemical oxidations were performed under the same solution conditions as the electrochemical oxidations, *i.e.*, 1g of substituted aniline in 300 ml 6*N* H_2SO_4. $(NH_4)_2Ce(NO_3)_6$ and $Ce(SO_4)_2$ were used as chemical oxidants. The chemical oxidant was added in excess or until the disappearance of the parent aniline peak in cyclic voltammograms of the solution was observed.

Product isolation.—Following electrochemical reduction at 0.2V the 6*N* H_2SO_4 electrolysis solutions were extracted several times with benzene. The solution pH was then raised to pH 2-3 with Na_2SO_3 and the benzene extractions were repeated. Extractions were again repeated at *p*H 4-5, *p*H 7-8, and *p*H 10-11. Relatively small amounts of reasonably pure substituted hydroquinones were isolated from the 6*N* H_2SO_4 extracts. From *p*H 2-3 to *p*H 7-8 substituted hydroquinones, increasing quantities of substituted benzidines, increasing quantities of aniline "polymers," and any remaining unoxidized parent aniline were isolated. At *p*H 10-11, only unidentified intractable, highly colored "tars" or "polymers" and small amounts of substituted benzidines were isolated. The benzene extracts were concentrated and chromatographed on neutral alumina. Unoxidized anilines were eluted with benzene, benzidines, and then hydroquinones with $CHCl_3$ and hydroquinones and polymers with acetone.

Results

The electrochemistry of these compounds in 6*N* H_2SO_4 can be broadly characterized as involving coupling reactions followed by a series of hydrolysis and substitution steps; the initially formed cation radicals couple tail-to-tail and/or head-to-tail to form substituted benzidines and/or diphenylamines. The benzidines are oxidized onto chemically inert dications for an over-all two-electron process. The diphenylamines are also oxidized to the dication state, but these dications undergo two succesive hydrolysis steps to generate a molecule of the parent aniline and one of the correspondingly substituted *p*-benzoquinone, an over-all process involving four electrons per parent aniline molecule. In some cases, the 2-substituted benzoquinones undergo a 1,4-addition reaction to generate a substituted trihydroxybenzene, which can then undergo an additional two-electron step, leading to a maximum *n*-value of 6. The results and discussion given below illustrate how and why these processes can be correlated with the various substituents in the *ortho*- and *meta*-substituted anilines studied.

Table I. Electroanalytical data for *ortho*- and *meta*-substituted anilines in 6*N* H_2SO_4

Compound	$Ep/2$[a]	$ip/V^{1/2}C$[b]	n	$it^{1/2}/C$[c]	n	Coul-n[d]
o-NH_3	[i]	41.3-40.5	1.92-1.88[R]	65.3-49.1	2.18-1.64	2.32
o-NMe_2	0.79	32.9-31.5	1.53-1.47[D]	66.7-61.2	2 23-2.04	2.25
o-OMe	0.79	39.9-38.1	1.86-1.77[R]	59.6-55.0	1.99-1.83	2.48
o-Phenyl	0.92	43.7-42.8	2.03-1.99[R]	91.3-74.9	3.04-2.50	2.83
o-Me	0.90	51.2-2.49	2.3[illegible]-2.29[R]	78.4-66.7	2.61-2.22	3.20
o-*i*-Propyl	0.89	43.1-41.4	2.01-1.93[R]	69.5-60.2	2.32-2.01	3.04
o-F	0.97	50.7-47.9	2.36-2.23[R]	75.7-62 5	2.52-2.08	3.02
o-Cl	0.96	43.8-42.7	2.04-1.99[R]	82.6-75.2	2.75-2.51	2.82
o-Br	0.97	44.6-43.2	2.07-2.01[R]	102-77.6	3.40-2 59	2.90
o-I	0.95	39.7-38.6	1.85-1.80[R]	99.4-78.1	3.31-2.60	3.05
o-COMe	1.01	52.5-47.7	2.44-2.22[D]	151-111	5.02-3.71	3.65
o-COOEt	1.00	54.6-48.7	2.54-2.26[D]	150-107	5.01-3.58	3.94
o-CF_3	1.06	58.8-52.1	2.74-4.42[I]	126-84.0	4.19-3.02	3.67
o-CN[e]	1.02	63.4	2.95	138-107	4.58-3.55	4.08
o-NO_3	1.07	90.5-83.4	4.21-3.88[D]	133-128	4.42-4.26	4.19
m-NMe_2	0.90	26.4-20.6	1.24-0.97[D]	76.5-58.1	2.55-1.94	4.54
m-OMe	0.90	44.9-40.9	2.09-1.86[D]	86.4-81.1	2 88-2.70	3.53
m-Me	0.92	51.2-47.6	2.38-2.21[D]	99.0-76.5	3.30-2.55	3.80
m-F	1.01	53.6-50.8	2.49-2.36[R]	158-115	5.25-3.82	4.58
m-Cl	1.01	52.8-51.2	2.46-2.38[R]	134-114	4.48-3.79	4.08[f]
m-Br	1.00	56.6-50.2	2.63-2.33[I]	122-113	4.06-3.78	2.98[f]
m-I	0.97	52.5-47.6	2.44-2.21[I]	96.3-85.3	3.21-2.84	2.99[f]
m-CF_3	1.08	55.9-50.7	2.60-2.36[I]	116-84.5	3.86-2.82	2.21[f]
m-CN	1.12	56.1-54.4	2.61-2.54[R]	102-85.4	3.40-2.84	2.20[f,g]
m-NO_2	1.12	54.4-43.3	2.53-2.48[R]	92.1-85.8	3.07-2.86	2.48[f,g]
Model		43.0[h]	2.00[h]	60.0[h]	2.00[h]	

[R] Random variation of data.
[D] Peak current quotient decreases as scan rate increases.
[I] Peak current quotient increases as scan rate increases.
[a] In volts *vs.* SCE.
[b] Data taken from linear-scan chronoamperometry curves. Scan rates were varied from 2 to 25 V/min.
[c] Data taken from chronoamperometric current-time curves. In all cases values increased with increasing time.
[d] Data taken from controlled-potential exhaustive electrolyses.
[e] Severe filming, data from single scan rate of 2 V/min.
[f] Electrode filming was observed in these systems.
[g] Background limit of 1.2V prevents exhaustive electrolysis.
[h] Averaged data taken from hydroquinone and 2-methylhydroquinone and used for comparison as a model two-electron system.
[i] Two poorly defined anodic waves, $Ep/2$ approximately 0.66 and 0.82.

The electroanalytical data for the *ortho*- and *meta*-anilines in 6*N* H_2SO_4 are shown in Table I. The electroanalytical data for two model two-electron compounds, hydroquinone and 2-methylhydroquinone, were averaged and used as a basis for comparison. Electrode filming was encountered in long-term experiments for all but the electron-donating substituents and signs of filming are evident in voltammograms of many of the substituted anilines. The extent to which filming affected the electroanalytical data is unknown, although the data presented in Table I are easily reproducible within the ±5% normally attributed to the reproducibility of the carbon paste electrode surface. The onset of large background currents begins at 1.2V (*vs.* SCE) and therefore the maximum potential used for chronoamperometry and coulometry experiments was 1.2V. This limit resulted in chronoamperometry and coulometry experiments being performed 80 mV anodic of the peak potential in the *meta*-trifluoromethylaniline and *ortho*-nitroaniline systems and 20 mV anodic of the peak potentials in the *meta*-cyanoaniline and *meta*-nitroaniline systems.

The peak current data for the anilines generally indicate an n-value of near two at short times with a gradual increase as the ring substituent becomes more electron withdrawing. The n-value of two is consistent with the initial formation of benzidines and diphenylamines via a fast ECE process (4).

The chronoamperometric data are more sensitive to changes in n-values caused by the hydrolysis reactions in these systems due to the 1-10 sec time gate available. The chronoamperometric data in Table I reflect the relative amounts of benzidine and diphenylamine formed from the parent aniline. The n-values increase from near two for the electron-donating groups to over five for the electron-withdrawing groups. This trend reflects the increase in dephenylamine formation as the *ortho* substituent becomes more electron withdrawing, the decomposition of the diphenylamines, and the decomposition reaction of the quinones. The higher n-values for the corresponding *meta*-anilines reflect the increased diphenylamine formation in the *meta* systems. The low n-values for *meta*-trifluoromethyl-, *meta*-cyano- and *meta*-nitroaniline reflect incomplete oxidation due to the +1.2V background limit and filming. Filming could also be a factor for *ortho*-chloro- through *ortho*-nitroaniline and *meta*-chloro through *meta*-iodoaniline, as filming was observed in the longer term experiments in these systems.

The coulometric data indicate the long-term behavior of these systems. Again, the n-values increase as the ring substituent becomes more electron withdrawing, reflecting the increased diphenylamine formation and ensuing follow-up reactions. The higher n-values for the corresponding *meta*-anilines again reflect the increased diphenylamine formation in the *meta* systems. Incomplete electrolysis due to filming and/or background limitations were observed for *meta*-chloro through *meta*-nitroaniline. Filming could also be a factor in the *ortho*-chloro- through *ortho*-nitroaniline systems.

Following is a brief treatment of the various groups of compounds studied that could be lumped together as a result of similar electrochemical behavior. These data are critical to understanding the rationalizations forwarded in the Discussion section.

o-Phenylenediamine, o-N,N-dimethylaminoaniline, m-N,N-dimethylaminoaniline.—The cyclic voltammograms and electroanalytical data for the phenylenediamines indicate behavior markedly different from the remainder of the *ortho*- and *meta*-substituted anilines. The decomposition pathways for the phenylenediamines were not pursued.

o-Methoxyaniline, m-methoxyaniline, o-methylaniline, m-methylaniline, o-isopropylaniline, and o-phenylaniline.—The *ortho* compounds in this group exhibited nearly identical behavior on cyclic voltammograms, an example of which is shown in Fig. 1 for the methoxy derivative. The couple labeled "1" is assigned to the 2-substituted quinone/hydroquinone couple which can be generated by successive hydrolyses of the 2′,3-disubstituted-4-aminodiphenylamines and the 2,3′-disubstituted-4-aminodiphenylamines resulting from head-to-tail coupling in the *ortho*- and *meta*-aniline systems, respectively

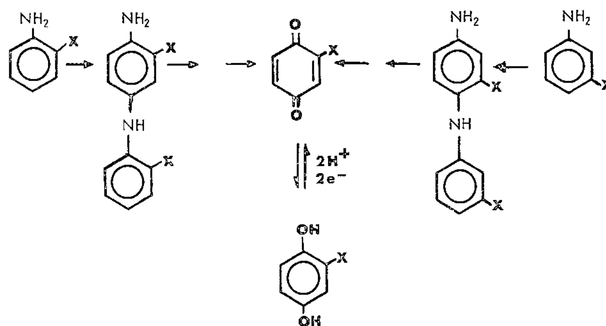

These quinone/hydroquinone couples were identified by matching of cyclic voltammograms (Fig. 1) and ESR spectra, in the case of the methyl derivative, with authentic samples.

The couples labeled "2" are assigned to the substituted 4-aminodiphenylamines generated by head-to-tail coupling or an intermediate in the two-step hydrolysis reaction which generates the 2-substituted quinone (see the Discussion section). Some uncertainty exists as to the identity of this couple as it was not possible to isolate the compounds responsible for it; comparisons with authentic samples were not possible as the compounds which could be responsible for this couple are not commercially available and their preparations would be difficult and time-consuming, since the aminodiphenylamines are easily air oxidized.

The couple labeled "3" in Fig. 1 was assigned to the 3,3′-disubstituted benzidines generated by tail-to-

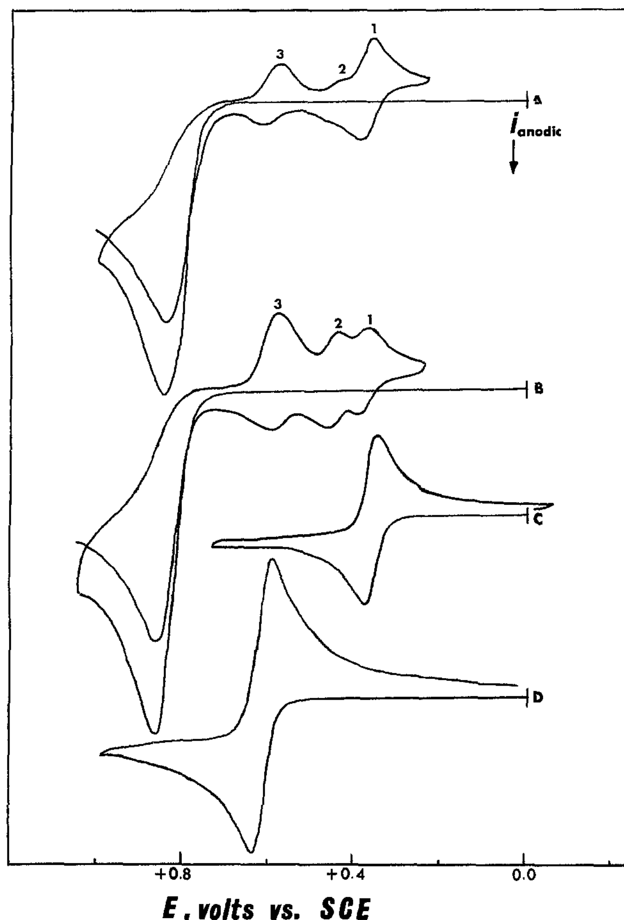

Fig. 1. Cyclic voltammograms in 6N H_2SO_4 at carbon paste. Curve A, 1.1 × 10^{-3}M o-methoxyaniline, sweep rate = 50 mV/sec; curve B, same, sweep rate = 450 mV/sec; curve C, o-methoxyhydroquinone; curve D, 3,3′-dimethoxybenzidine.

tail coupling; this assignment was confirmed by matching of cyclic voltammograms (Fig. 1) and optical spectra of products isolated from mass electrolyses with authentic samples. The 3,3′-disubstituted benzidines, the substituted 4-aminodiphenylamines (or intermediates) and the 2-substituted hydroquinones are clearly visible on cyclic voltammograms and the quinone-to-diphenylamine ratio clearly increases as the scan rate is decreased. The short time gate (peak current) n-value of approximately two is consistent with the formation of benzidines and diphenylamines via a fast ECE process and hydrolysis of the diphenylamines (or intermediates). The benzidine/diphenylamine ratio is also affected by steric considerations; in going from methyl to isopropyl to phenyl as the *ortho* substituent the relative amount of benzidine increases due to the steric crowding involved in diphenylamine formation with a bulky *ortho* substituent. In addition, the diphenylamine in the phenyl system appears to be more stable than that in the methyl analog, due, presumably, to the steric effect on the hydrolysis rate of the central nitrogen.

Numerous preparative-scale mass electrolyses were performed on *ortho*-methoxy- and *ortho*-methylaniline. The n-values resulting from these electrolyses were slightly higher (2.9 *vs.* 2.48 and 3.4 *vs.* 3.20) than those obtained in the coulometry experiments. The n-values resulting from the reduction of the oxidized preparative-scale electrolysis solutions were 0.6 for *ortho*-methoxyaniline and 1.2 for *ortho*-methylaniline. Both reduction n-values are lower than would be expected, indicating formation of electroinactive species, *i.e.*, tars and polymers. Large amounts of an insoluble precipitate, reminiscent of those obtained in aniline electrolyses, were obtained in the *ortho*-methoxyaniline oxidations. Crude yields of isolable product averaging 25% for *ortho*-methoxyaniline and 40% for *ortho*-methylaniline were obtained from the electrolysis solutions according to the work-up procedure described in the Experimental section; no attempts were made to maximize the product yields. The crude products were purified according to the procedure in the Experimental section. Interestingly, chemical oxidation of o-methylaniline produced only 2-methylhydroquinone in an approximately 40% yield.

The cyclic voltammograms of *meta*-methoxyaniline indicate that the major product is the diphenylamine or intermediate, as shown in Fig. 2. In addition, two small couples are visible anodic of the diphenylamine couple; the less anodic corresponds in potential to the *p*-*p*-benzidine for this system and the minor redox pair (arrows) could be due to the o-*p*-benzidine, although the latter assignment is purely speculative. The cyclic voltammograms of *meta*-methylaniline (Fig. 2) show only the single product identified as the diphenylamine or intermediate. The higher n-values obtained in the electroanalytical experiments for *meta*-methyl- and *meta*-methoxyaniline reflect the increased diphenylamine formation (and subsequent hydrolysis reactions) over their *ortho* analogs. Preparative-scale mass electrolyses for these two compounds were similar to those for *ortho*-methyl- and *ortho*-methoxyaniline. Forward n-values were slightly above those obtained from coulometric determinations and reverse n-values were 0.8 for *meta*-methylaniline and 0.4 for *meta*-methoxyaniline, again indicating formation of electroinactive species. Cyclic voltammograms following mass electrolysis indicated that the major product for *meta*-methoxyaniline was the same product obtained in the coulometry experiments. The product has not been

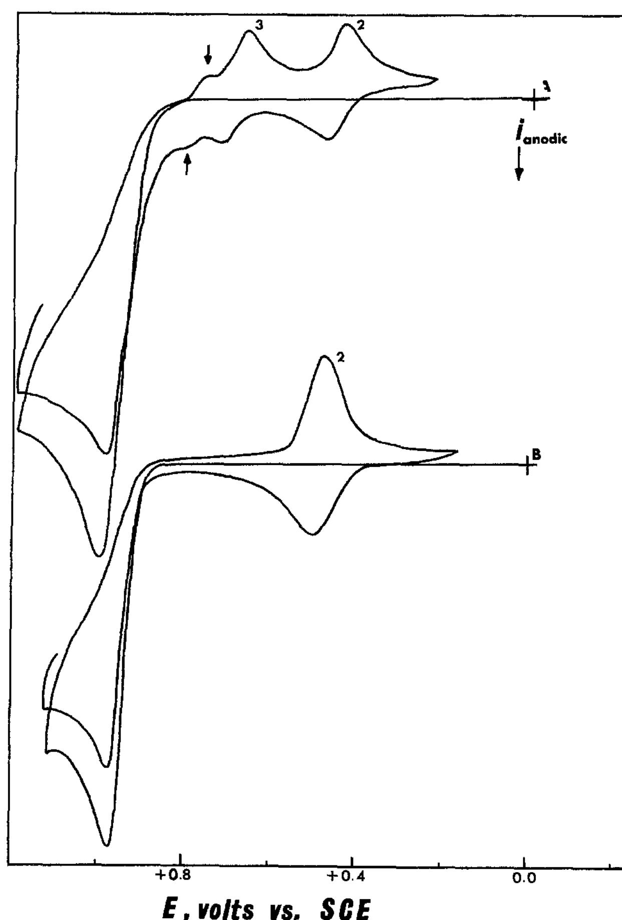

Fig. 2. Cyclic voltammograms in 6N H_2SO_4 at carbon paste. Curve A, 2.12 × 10^{-3}M m-methoxyaniline, sweep rate = 100 mV/sec; curve B, 1.18 × 10^{-3}M m-methyaniline, sweep rate = 150 mV/sec.

positively identified but is presumed to be 2-methoxy-*para*-aminophenol. Cyclic voltammograms of *meta*-methylaniline following mass electrolyses indicate the final product in this system is 2-methylhydroquinone, whereas 2-methyl-*para*-aminophenol was found to be produced in the short coulometry experiments. This result is consistent with the known slow hydrolysis of 2-methyl-*para*-aminophenol to 2-methylhydroquinone (11).

In addition to the products identified and identification methods described in the above discussions, cyclic voltammograms of authentic samples of 2-methylhydroquinone, 2-phenylhydroquinone, and 3,3'-dimethylbenzidine matched product couples in voltammograms of their respective amines.

o-Fluoroaniline, o-chloroaniline, o-bromoaniline, o-iodoaniline, m-fluoroaniline, m-chloroaniline, m-bromoaniline, and m-iodoaniline.—The *ortho*-substituted compounds in this group exhibited nearly identical behavior on cyclic voltammograms. The 3,3'-disubstituted benzidines, substituted 4-aminodiphenylamines (or intermediates), and 2-substituted hydroquinones are clearly visible in the voltammograms and the quinone-to-diphenylamine ratio increases as the scan rate decreases as shown in Fig. 3. The cyclic voltammograms of the *meta*-substituted compounds show little variation with scan rate and, with the exception of *m*-fluoroaniline, show only the single product couple identified as the diphenylamine or intermediate. The second product couple in the *meta*-fluoroaniline voltammogram corresponds in potential to that which would be expected for the 2,2'-disubstituted benzidine. The similar behavior of the *ortho* compounds, and the similar behavior of the *meta* compounds lead to the conclusion that there is little difference between the electronic effects of the various halogens, and the absence of the 2,2'-disubstituted benzidines in the *meta*-chloro-, *meta*-bromo-, and *meta*-iodoaniline systems is, therefore, attributed to steric effects.

The higher short time-gate *n*-values reflect the increased diphenylamine formation for the *meta* compounds and the increased hydrolysis rates of the diphenylamines in both the *ortho* and *meta* systems due to the electronegative halogen substituents. The higher long time-gate *n*-values for the *meta*-substituted anilines (*meta*-bromo- and *meta*-iodoaniline film the electrode) again reflect the increased diphenylamine formation and, in addition, some decomposition of the hydroquinone to the substituted trihydroxy compound.

Cyclic voltammograms following coulometry experiments for the *ortho*-halogens indicate only benzidine and hydroquinone as products (Fig. 4). Similar voltammograms for the *meta*-substituted anilines indicate the presence of large quantities of hydroquinone, small amounts of the trihydroxy compound, and small amounts of the substituted *para*-aminophenol. The fact that the hydroquinone was the almost exclusive product indicates that the halogen-substituted *para*-aminophenols hydrolyze faster than the methoxy- and methyl-aminophenols, which were the major products following coulometric determinations for the *meta*-methyl- and *meta*-methoxyanilines. The increased hydrolysis rate for the halogen-substituted *para*-aminophenols is consistent with the expected substituent effect.

Numerous preparative-scale mass electrolyses were performed on *ortho*- and *meta*-chloroaniline. Filming was severe for both of these compounds and meaningful *n*-values could not be obtained. Several electrode changes were required to effect even partial electrolyses (50-75%) of these anilines. Crude yields of isolable products averaging 35% were obtained by the work-up procedure described in the Experimental section; the crude products were purified according to the procedure in the Experimental section. 2-Chlorohydroquinone was identified as the product from both *ortho*- and *meta*-chloroaniline electrolyses by matching ESR spectra of the corresponding semiquinone radical, generated by chemical oxidation in an O_2-saturated aqueous $NaHCO_3$ solution, with an authentic sample, and 3,3'-dichlorobenzidine was identified as a product from *ortho*-chloroaniline electrolyses by the same procedures described for the 3,3'-dimethoxybenzidine.

Chemical oxidations of *ortho*- and *meta*-chloroaniline produced approximately 40% yields of the 2-chlorohydroquinone.

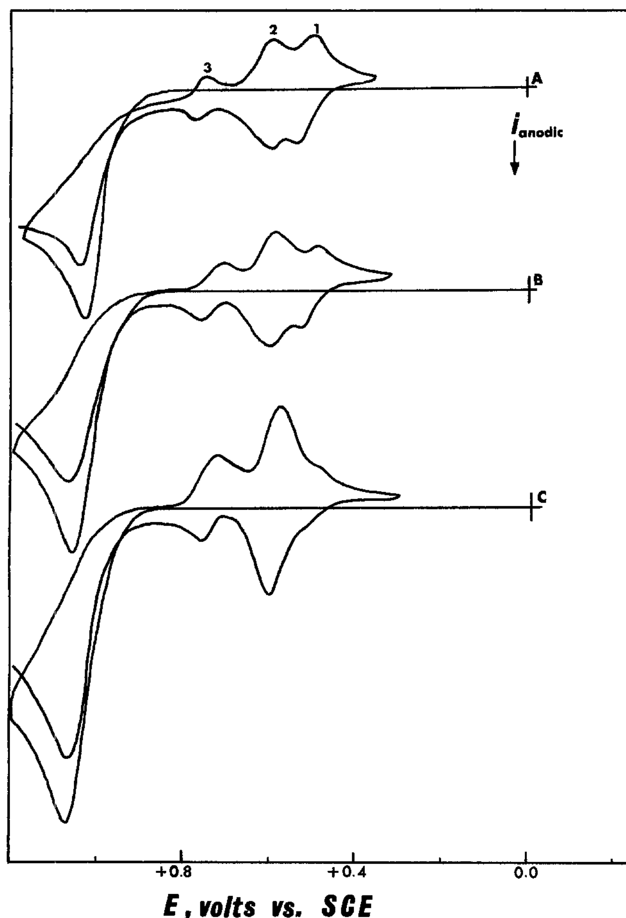

Fig. 3. Cyclic voltammograms in 6N H_2SO_4 at carbon paste, $2.86 \times 10^{-3}M$ o-chloroaniline. Curve A, sweep rate = 17 mV/sec; curve B, sweep rate = 100 mV/sec; curve C: sweep rate = 583 mV/sec.

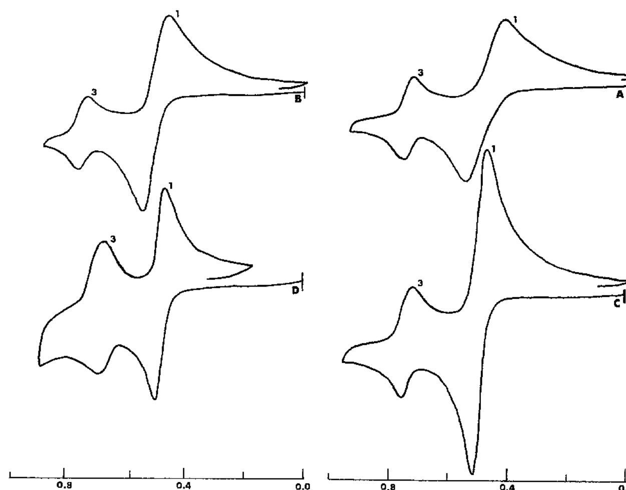

Fig. 4. Cyclic voltammograms in 6N H_2SO_4 following exhaustive electrolysis. Curve A, $10^{-3}M$ o-fluoroaniline; curve B, $10^{-3}M$ o-chloroaniline; curve C, $10^{-3}M$ o-bromoaniline; curve D, $10^{-4}M$ o-iodoaniline.

o-Aminoacetophenone, ethyl anthranilate, o-trifluoromethylaniline, o-cyanoaniline, o-nitroaniline, m-trifluoromethylaniline, m-cyanoaniline, and m-nitroaniline.—The compounds in this group exhibited similar, though far from the nearly identical, behavior to the compounds in the previous groups.

o-Aminoacetophenone and ethyl anthranilate are similar in the complexity of their cyclic voltammograms. This complexity makes interpretations difficult, but an inspection of these curves indicates that the amounts of couple "4" identified as the substituted trihydroxy compound, and couple "2," the diphenylamine or intermediate, vary with scan rate in a manner that suggests couple "2" decomposes to generate the trihydroxy compound, presumably through the quinone. The higher n-values for the peak-current data reflect the increased diphenylamine formation and the increased rate of the follow-up hydrolysis reactions. The chronoamperometric n-values of about 5 are consistent with partial formation of the trihydroxy compound via the 1,4-addition reaction mentioned previously. The cyclic voltammograms of ethyl anthranilate following electrolysis for coulometric determinations indicate the major long-term product is the trihydroxy compound, as shown by comparison with an authentic sample of ethyl-2,5-dihydroxybenzoate in Fig. 5; the small couple "4" is the trihydroxy compound, formed by hydrolysis of the quinone.

Benzidine formation could not be verified for these compounds due to the complexity of the cyclic voltammograms and the absence of authentic samples, but redox couples are present whose potentials, based on comparisons with systems known to generate benzidines, would indicate benzidine formation.

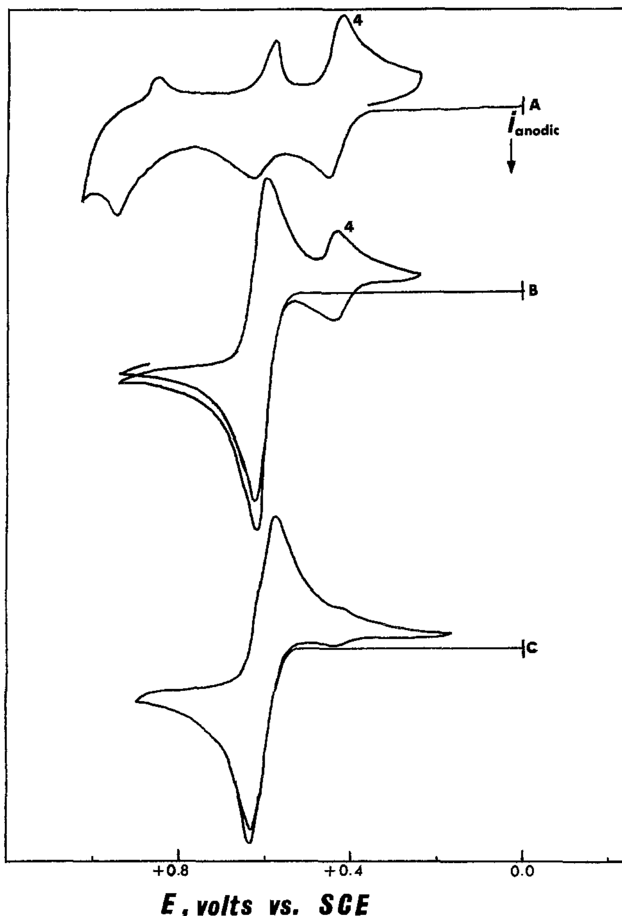

Fig. 5. Cyclic voltammograms in 6N H_2SO_4 at carbon paste. Curve A, $10^{-4}M$ ethylanthranilate following exhaustive electrolysis, sweep rate = 100 mV/sec; curve B, $1.76 \times 10^{-3}M$ ethyl-2,5-dihydroxybenzoate, sweep rate = 33 mV/sec; curve C, same as B, sweep rate = 350 mV/sec.

o-Trifluoromethylaniline and *m*-trifluoromethylaniline exhibit the common product couple which has been characteristic of all of the *ortho-meta* pairs. The diphenylamine or intermediate is the only product couple visible in the *meta* system, while the substituted benzidine and a small amount of the trihydroxy compound are also visible in the *ortho* system. Cyclic voltammograms of *ortho*-trifluoromethylaniline following electrolysis for coulometric determinations indicate the presence of the 2,2′-disubstituted benzidine, the diphenylamine (or intermediate), or hydroquinone (the voltammogram is not well defined), and the trihydroxy compound. Similar voltammograms for *meta*-trifluoromethylaniline indicate the major product is the substituted *para*-aminophenol with small amounts of the substituted trihydroxy compound.

o-Cyanoaniline and *m*-cyanoaniline reinforce trends that were only vaguely apparent in the *ortho*- and *meta*-trifluoromethylaniline systems. Cyclic voltammograms of *ortho*-cyanoaniline show only the trihydroxy couple at low scan rates, and small amounts of the diphenylamine or intermediate plus the trihydroxy couple at high scan rates. Cyclic voltammograms following coulometric determinations indicate that the trihydroxy compound is the major product. Cyclic voltammograms of *meta*-cyanoaniline show large amounts of the diphenylamine or intermediate, small amounts of the trihydroxy compound, and small amounts of an unidentified low-potential product. Cyclic voltammograms folowing coulometry indicate two major products, 2-cyano-*para*-aminophenol and the trihydroxy compound.

The identification of couple "2" as the diphenylamine or intermediate in both the trifluoromethyl- and cyano-systems was made on the basis of the difference in behavior of couple "2" between the *ortho*- and *meta*-systems. In both the *m*-trifluoromethyl- and *m*-cyanoaniline systems, couple "2" appeared to be considerably more stable than the corresponding couple in the *ortho* systems. The difference in stability could not be explained if couple "2" were hydroquinone, as the same 2-substituted hydroquinone would result in both the *ortho*- and *meta*-systems. The identification of couple "2" as the diphenylamine or intermediate forces the conclusion that the substituted quinone, once generated, rapidly undergoes 1,4-addition to the trihydroxy compound, as a couple for this quinone is not visible in the cyclic voltammograms. This is consistent with the electrochemistry of the hydroquinones containing electron-withdrawing substituents (Fig. 5 and 6), as well as their published rate-constant data (11, 12).

m-Nitroaniline exhibits behavior similar to the preceding compounds while o-nitroaniline appears to decompose by a different, as yet unidentified, pathway. Voltammograms of *m*-nitroaniline indicate the formation of the diphenylamine or intermediate, small amounts of the quinone, the substituted trihydroxy compound, and an unidentified low-potential product. Cyclic voltammograms following coulometry show the substituted trihydroxy compound as the major product, as shown in Fig. 6. Cyclic voltammograms of *ortho*-nitroaniline indicate the major product is not the substituted trihydroxy compound. The product couple is cathodic of the trihydroxy couple in the *m*-nitroaniline system and the 2-nitrohydroquinone system. Voltammograms of various possible products, 2,2′-dinitroazobenzene, 3,3′-dinitrobenzidine, 2-nitrohydroquinone, o-benzoquinonedioxime peroxide, o-benzoquinonedioxime, and 2-nitrophenol failed to account for the product couple. Further investigation of the various possible products, synthesis and investigation of the diphenylamine, and investigation of other possible decomposition pathways will be required to establish the identity of the product couple in the *ortho*-nitroaniline system.

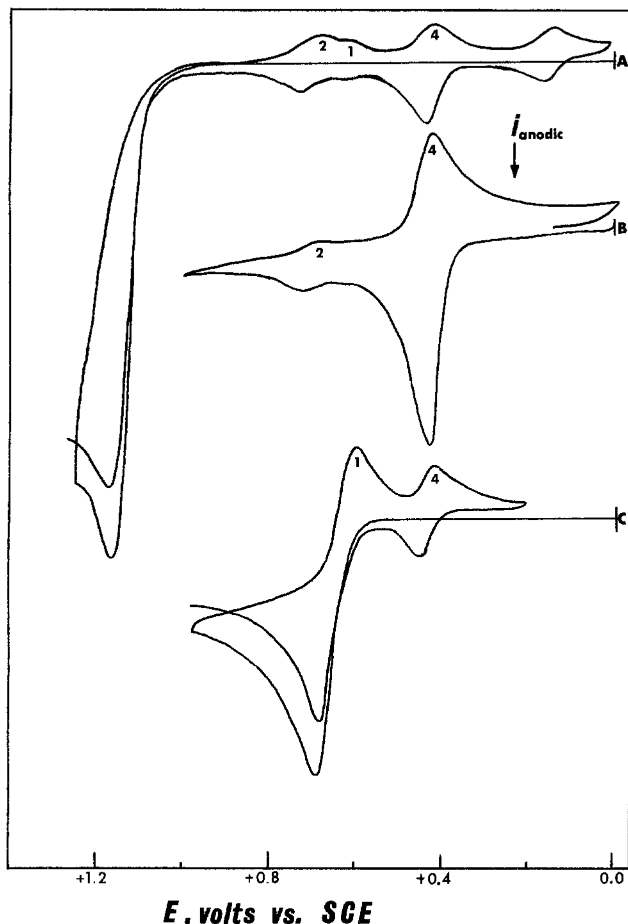

Fig. 6. Cyclic voltammograms in 6N H_2SO_4 at carbon paste. Curve A, 1.2 × 10^{-3}M *m*-nitroaniline, sweep rate = 50 mV/sec; curve B, same solution as A following exhaustive electrolysis at +1.2V, sweep rate = 100 mV/sec; curve C, 8.5 × 10^{-4}M 2-nitrohydroquinone, sweep rate = 250 mV/sec.

The electroanalytical data for all of the *ortho*- and *meta*-electron-withdrawing substituents are a bit suspect because of filming and background problems. The peak current data for all but *ortho*-nitroaniline indicate processes consistent with those of the preceding compounds. The higher n-values simply reflect the increased diphenylamine formation and the increased rates of the follow-up reactions. The short time-gate n-value for *ortho*-nitroaniline indicates a rapid four-electron process. The chronoamperometric data reflect the same trends as the peak current data but are complicated by filming and background limits.

Preparative-scale electrolyses and chemical oxidations of several members of this group were quite unsuccessful. The only electroactive species present in solution following oxidation were unoxidized parent aniline and a small amount of 3,3′-disubstituted benzidine in the *ortho*-trifluoromethylaniline system. Filming was severe in all cases, and numerous electrode changes were required to effect even partial oxidations. Large quantities of precipitates formed in these systems and, in all cases, voltammograms of the precipitates indicated they were electroinactive. Attempts to purify and identify the precipitates or constituents of the precipitates were unsuccessful. The behavior of these compounds indicates that the decomposition products are not stable to prolonged electrolysis and are presumably involved in multiple coupling reactions to generate products of an unknown composition.

The failure to isolate products from electrolysis solutions and the lack of authentic samples, except for several of the 2-substituted hydroquinones, necessitated considerable speculation for identification of the product couples in this group of compounds. The speculation was, however, based on the established reaction pathways of the previous groups of compounds and the established 1,4-addition reaction of quinones with electron-withdrawing substituents (11-13). Additional studies involving synthesis of the substituted diphenylamines and substituted quinones will be necessary to firmly establish the identification of the various product couples in this group of compounds. For the survey purposes of the present study, however, their behavior, as well as it could be elucidated, is consistent with trends noted for the more electron-donating substituents.

Discussion

The chemistry involved in these systems is complex but orderly. Summarizing, the couples labeled "3" in the cyclic voltammograms can be assigned to the substituted benzidines generated by tail-to-tail coupling of the anilines. Cyclic voltammograms indicate that the amount of benzidines formed decreases as the ring substituent in the *ortho* series becomes more electron withdrawing, in agreement with the previously proposed mechanism (4) whereby as the amine nitrogen becomes more acidic deprotonation of the electrogenerated cation radical is facilitated, leading to diphenylamine formation. Couples corresponding to the 2,2′-disubstituted benzidines are visible only in the methoxy, methyl, and fluoro derivatives in the *meta*-substituted anilines, and the relative amounts are consistent with the trend seen in the *ortho* systems, but here the overriding consideration for *para-para* coupling appears to be steric in nature.

The couples labeled "4" in the cyclic voltammograms are decomposition products of the 2-substituted *para*-benzoquinones (the "1" couples). Investigations of the 2-substituted hydroquinones have demonstrated that *mono*-substituted hydroquinones with electron-withdrawing substituents (—NO_2, —CHO, —$COCH_3$, COOH) undergo a nucleophilic 1,4-addition of water to form the substituted trihydroxy compounds (14-16). The reaction mechanism is shown below

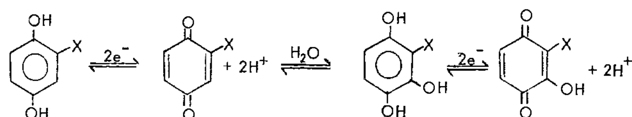

Of particular interest is the fact that the product of the 1,4-addition is a substituted hydroquinone which is susceptible to further oxidation giving an over-all four-electron process. The end products of the hydrolysis reactions in the *ortho*- and *meta*-substituted aniline systems are substituted *para*-benzoquinones which, according to the reaction mechanism present above, could undergo a 1,4-addition and a subsequent two-electron oxidation. The addition of this decomposition pathway to the previously established mechanism indicates that a maximum n-value of 6 electrons could be obtained for anilines with an electron-withdrawing substituent. The rate of the 1,4-addition reaction was found to increase as the 2-substituent becomes more electron withdrawing (11, 12), and in all cases the rate is fast enough to be evidenced in coulometric n-value determinations, as can be seen in Fig. 5 and 6.

The couples denoted as "2" in the cyclic voltammograms have been referred to as "diphenylamines or intermediates," that is as the appropriately substituted 4-aminodiphenylamine formed by head-to-tail coupling or a derivative generated by hydrolysis of the diphenylamine; a discussion of the hydrolysis chemistry of these systems follows.

Studies of the hydrolysis mechanism and reaction rates of a family of related compounds, various substituted *para*-aminophenols, have produced the following reaction pathway (14, 15, 17-19).

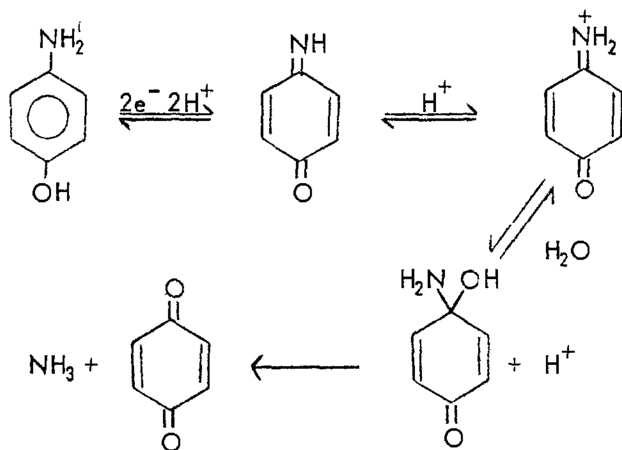

Correlations between hydrolysis rates and substituent effects for this general reaction have been successfully demonstrated only for N-(*para*-phenyl) substituted *para*-aminophenols (16, 20). For this class of aminophenols, the hydrolysis rate was found to increase as the N-*para*-phenyl substituent became more electron withdrawing (see Table II) Correlations for the ring-substituted *para*-aminophenols were largely unsuccessful (15, 21). One difficulty that possibly precluded establishing general substituent effects was that there were only a few substituted *para*-aminophenols involved in the correlation study. Inspection of the limited available hydrolysis rate data for *para*-aminophenols collected in Table II permits the following tentative conclusion: Substituents *ortho* to the N-C bond increase the hydrolysis rate, probably due to facilitating the formation of the tetrahedral carbinolamine intermediate, and substituents *meta* to the N-C bond decrease the hydrolysis rate. In addition, from Leedy's work we would expect the hydrolysis rate to increase as the substituent becomes more electron withdrawing, as seen in Table II.

In addition to the *para*-aminophenols, 4-aminodiphenylamine (4-ADPA) and the various substituted derivatives resulting from head-to-tail coupling in the N-alkylanilines system have been shown to undergo hydrolyses to *para*-benzoquinone and aniline or an N-alkylaniline (4, 16). Leedy proposed that the hydrolysis of 4-ADPA proceeds in a two-step mechanism as shown below

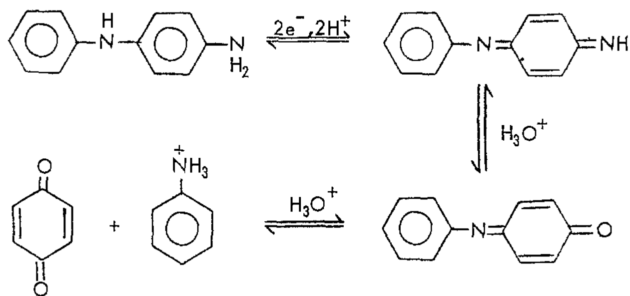

This proposal was based on HMO calculations of the fully protonated diimine and not on experimental observations (16). Cyclic voltammograms of 4-ADPA and mass electrolysis of 4-ADPA show only aniline, *para*-benzoquinone, and 4-ADPA. The intermediate in this mechanism, N-phenyl-*para*-benzoquinoneimine, was not detected in solution. The only plausible alternative mechanism is shown below

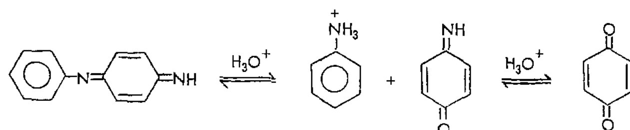

Again, the intermediate in this mechanism, *para*-benzoquinoneimine, was not detected in solution (16). In view of the experimental evidence, or the lack

Table II. Hydrolysis rates of substituted *p*-benzoquinoneimines

Parent compound	Medium	K (sec⁻¹)
NH_2, OH [1]	$0.51M$ H_2SO_4 $0.051M$ H_2SO_4	0.0194 0.102
NH_2, CH_3, OH [1]	$0.51M$ H_2SO_4 $0.051M$ H_2SO_4	0.09 0.30
NH_2, CH_3, OH [1]	$0.05M$ H_2SO_4	0.003
R, NH, OMe [2]	50% acetone/ 50% $1M$ $HClO_4$	
R = OMe		0.010
R = H		0.040
R = NO_2		0.063

[1] Data taken from Ref. (19).
[2] Data taken from Ref. (20).

thereof (especially the absence of either intermediate), it was not possible to determine which mechanism was operative though the former was favored on the basis of HMO calculations. If the two decomposition pathways are drawn for the diphenylamines in the *ortho*- and *meta*-substituted aniline systems, the intermediates shown below would result

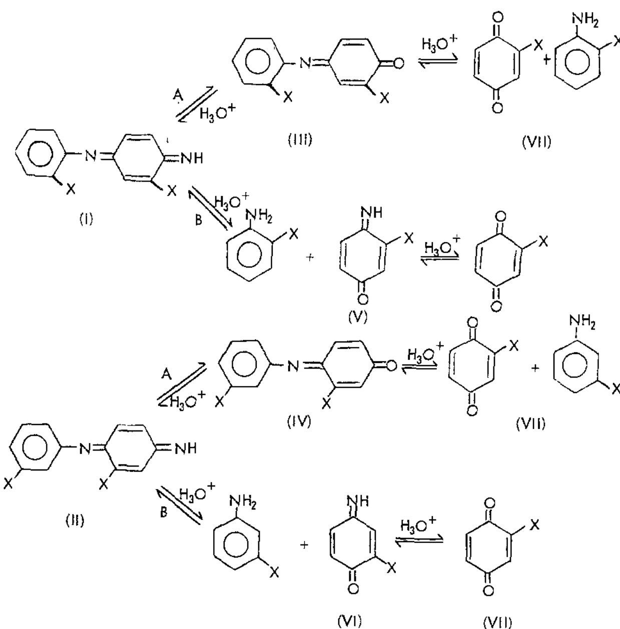

If the decomposition pathways for diimines (I) and (II) are evaluated in terms of the somewhat speculative conclusions reached from the data in Table II, then path A would be favored for diimine (I) and path B for diimine (II). Path A would be favored for diimine (I) because of the substituent *ortho* to the N-C double bond and path B would be favored for diimine (II) for the same reason. Continuing along the same lines, the N-phenyl-*para*-benzoquinoneimine (III) would be expected to decompose faster than the *para*-benzoquinoneimine (VI) because of the influence of the *ortho* substituent.

The cyclic voltammetric data presented indicate that the *ortho*- and *meta*-substituted anilines appear to have a common product in couple "2." However, couple "2" in the *meta* systems appears to be considerably more stable than couple "2" in the *ortho* systems. Figure 7 shows the cyclic voltammograms of several of the *ortho*- and *meta*-substituted anilines following exhaustive electrolysis for coulometric determinations. These voltammograms indicate the long-term behavior of the compounds and verify trends seen in Fig. 1-3 for couple "2." The compounds responsible for couple "2" in the *ortho* systems appear to have completely hydrolyzed to to the quinones, while the hydrolysis of couples "2" in the *meta* systems varies from nearly none for the *meta*-methoxy and *meta*-methylanilines to nearly complete hydrolysis for the more electronegative substituents. The stability of couple "2" in the *meta*-methoxy and *meta*-methyl systems provides additional mechanistic information when the coulometric n-values in Table I are considered. The n-values for both of these compounds approach four, indicating that the formation of the substituted *para*-benzoquinones in these two systems are not necessary to reach this n-value. The n-value of near four eliminates the substituted 4-aminodiphenylamine as couple "2" (unless, of course, the DPA has the same peak potential as the *para*-benzoquinoneimine and is responsible for couple "2" prior to exhaustive electrolysis) and, if pathway A for the diimine (II) were followed, formation of the *para*-benzoquinone would be necessary to attain an n-value of four. The above considerations reasonably establish path B as the decomposition pathway of the diimine (II) generated in the *meta*-anilines systems. Additional verification is possible for the *meta*-methylaniline system, as a cyclic voltammogram of 2-methyl-*para*-aminophenol (Fig. 8) matches the voltammogram of *meta*-methylaniline following electrolysis, both in peak potential and wave shape.

The hydrolysis pathway for the *ortho*-anilines remains to be resolved. A cyclic voltammogram of 3-methyl-*para*-aminophenol does not match with any couples seen in the voltammograms of *ortho*-methylaniline either before or after electrolysis, further suggesting that pathway A is being followed for the *ortho*-aniline systems. As couple "2" is not visible for *ortho*-anilines in the cyclic voltammograms following electrolysis, and as there is no difference in n-values between the diimine (I) and the N-phenyl-*para*-benzoquinoneimine (III), there is little to choose from to identify one or the other as couple "2" in the *ortho*-aniline cyclic voltammograms. Based on the behavior of the *meta*-aniline systems, however, the *para*-benzoquinoneimine (III) would be expected to be responsible for couple "2" in the *ortho*-aniline systems [again, unless the diphenylamine has the same peak potential as (III)].

Therefore it appears that the diimine (I), generated in the *ortho*-aniline systems, undergoes a rapid hydrolysis to the N-phenyl-*para*-benzoquinoneimine (III) which slowly hydrolyzes to the substituted *para*-benzoquinone (VII), and the diimine (II), generated

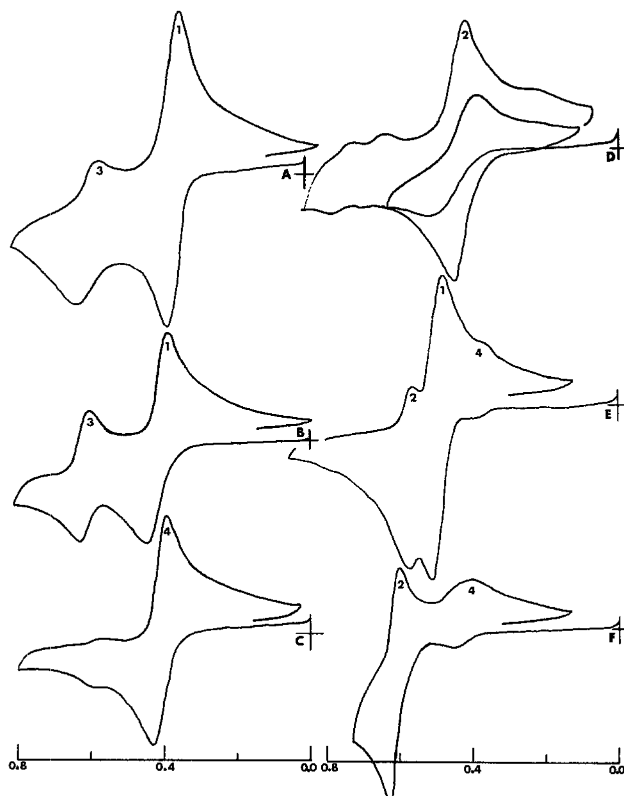

Fig. 7. Cyclic voltammograms in 6N H_2SO_4 at carbon paste following exhaustive electrolysis of 1.0 × $10^{-3}M$ solutions. Curve A, o-methoxyaniline; curve B, o-methylaniline; curve C, o-cyanoaniline; curve D, m-methoxyaniline; curve E, m-bromoaniline; curve F, m-trifluoromethylaniline.

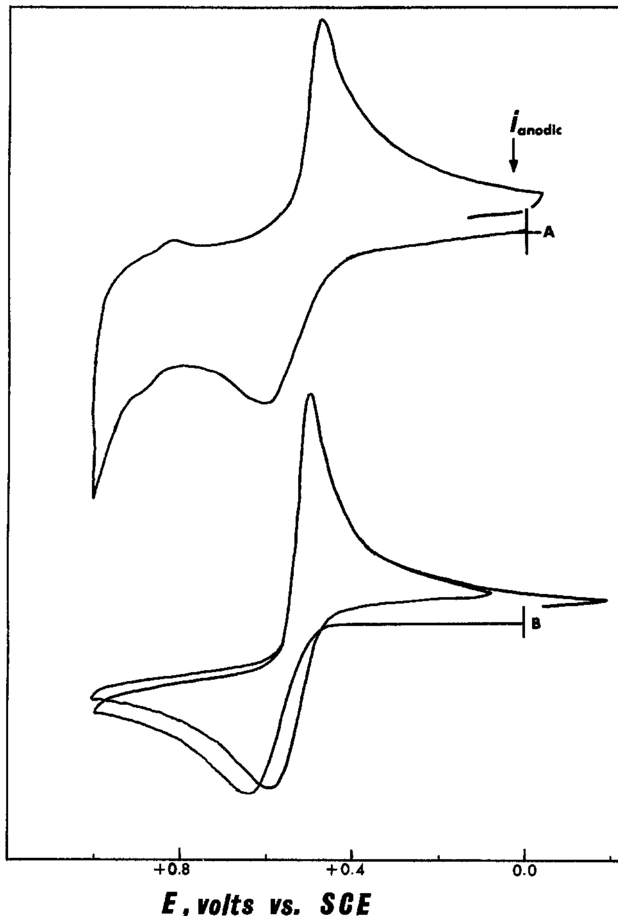

Fig. 8. Cyclic voltammograms in 6N H_2SO_4 at carbon paste. Curve A, 1 × $10^{-4}M$ solution of m-methylaniline following exhaustive electrolysis, sweep rate = 100 mV/sec; curve B, 6.8 × $10^{-4}M$ 2-methyl-p-aminophenol, sweep rate = 100 mV/sec.

in the *meta*-aniline systems, undergoes a rapid hydrolysis to the *para*-benzoquinoneimine (VI) which slowly hydrolyzes to the *para*-benzoquinone (VII).

The alternative to that proposed above would involve identifying the substituted diphenylamines as couple "2" in the cyclic voltammograms presented. The decomposition pathway of diimine (I) would then involve a slow hydrolysis of the 4-amino group followed by rapid completion of the hydrolysis sequence to give the substituted *para*-benzoquinone, and the decomposition of diimine (II) would involve a slow hydrolysis of the center amine.

The only difference in the two proposals is the reaction rate of the first hydrolysis step. If couple "2" in the voltammograms is the diphenylamine, then the first hydrolysis is slow (more rapid for the *ortho*'s than the *meta*'s), while if couple "2" is the N-phenyl-*para*-benzoquinoneimine (*ortho's*) or the *para*-benzoquinoneimine (*meta*'s), then the first hydrolysis is rapid. In addition, if the substituted diphenylamine is couple "2" this necessitates that the diphenylamine and the substituted *para*-benzoquinoneimine in the *meta* system have the same peak potential.

Resolution of this "fine" point must await synthesis of the diphenylamines and the intermediates or generation of more data on substituent effects on hydrolysis rates.

With the exception of the low potential couple in the *ortho*-cyano- and *ortho*-nitroaniline systems, the couples labeled "1" through "4" appear to adequately describe the decomposition pathways of the *ortho*- and *meta*-substituted anilines. For the *ortho*-anilines, benzidine formation decreases and diphenylamine formation increases as the *ortho*-substituent becomes more electron withdrawing. In addition, as the *ortho*-substituent becomes more electron withdrawing, the diphenylamines decompose more rapidly to the quinones and the quinones begin decomposing to the trihydroxy compounds. The same trends are reflected in the *meta* systems, except that there is much less benzidine formation and the diphenylamine or intermediate (substituted *p*-aminophenol) appears to be more stable.

The general reaction mechanism for the *ortho*- and *meta*-substituted anilines is shown in Fig. 9. This reaction mechanism is similar to that proposed for the N-alkylanilines except that the hydrolysis reactions of the diphenylamines are shown to occur by two discrete pathways and the 1,4-addition reaction of the quinones with electron-withdrawing substituents has been added. In addition, the diphenylamines derived from *meta*-substituted anilines are shown hydrolyzing to the corresponding substituted *p*-quinoneimines and thence to the analogous *p*-benzoquinones. The reaction mechanism depicts diphenylamine formation occurring by deprotonation of the cation radical and reaction with a parent aniline molecule in accordance with our previous observations for the N-alkylanilines. The observed effects of substituents on the diphenylamine-to-benzidine ratio in this present study are consistent with this pathway. The diphenylamine-to-benzidine ratio increases as the substituent becomes more electron withdrawing, presumably by more facile deprotonation of the primary cation radical.

Substituted azobenzenes and/or substituted hydrazobenzenes were not detected during the course of this work and initial formation of the hydrazobenzenes, followed by a benzidine rearrangement, is not proposed as an over-all mechanism, since product distributions were not consistent with those obtained from benzidine rearrangements. A particularly striking example involves the oxidation of *meta*-methylaniline in which no 3,3'-dimethylbenzidine was detected, whereas acid-catalyzed rearrangemnts of 3,3'-dimethylhydrazobenzene result in quantitative yields of 3,3'-dimethylbenzidine (22). Therefore, rather than proposing initial formation of the hydrazobenzene in all solutions, and

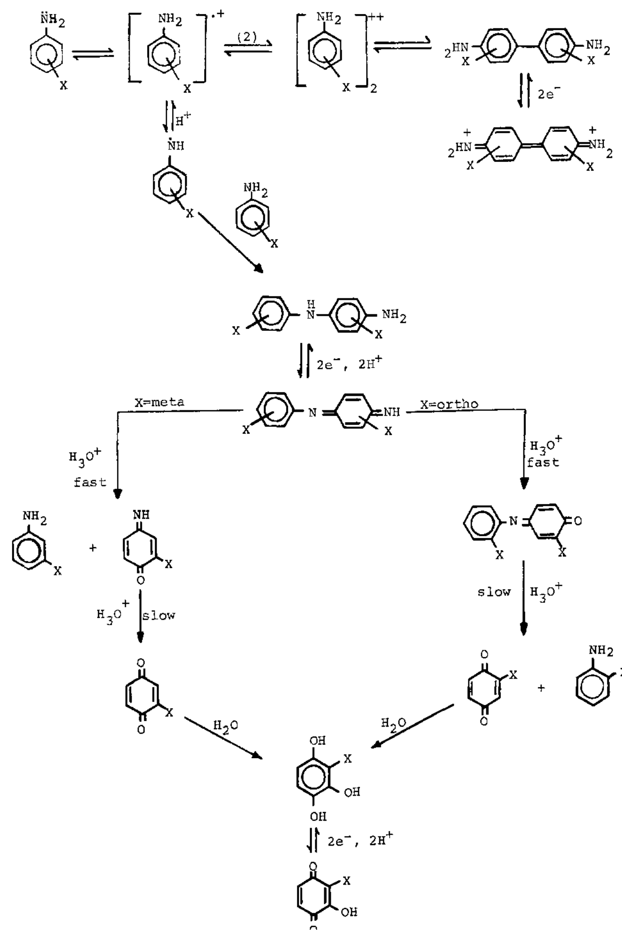

Fig. 9. Proposed reaction pathways for the *ortho*- and *meta*-substituted anilines in 6*N* H_2SO_4.

subsequently proposing that the stability of the hydrazobenzene is the factor which affects product distributions as a function of pH, we would propose that as the solutions become more basic, deprotonation is facilitated and the resulting free radicals couple in basic solutions to form the hydrazo compounds, as in the work of Wawzonek (2, 3).

It is anticipated that studies now under way will show that with increasing pH (compared to 6*N* H_2SO_4) the *ortho*- and *meta*-anilines will, upon electro-oxidation, form less benzidines, more diphenylamines (and attendant hydrolysis products), and, eventually, azo- and hydrazobenzenes.

Acknowledgments

Thanks are due to Dr. R. N. Adams and Dr. D. E. Smith for their support and encouragement.

Manuscript submitted Feb. 28, 1978; revised manuscript received March 1, 1978.

Any discussion of this paper will appear in a Discussion Section to be published in the June 1979 JOURNAL. All discussions for the June 1979 Discussion Section should be submitted by Feb. 1, 1979.

REFERENCES

1. J. Bacon and R. N. Adams, *J. Am. Chem. Soc.*, **90**, 6596 (1968).
2. S. Wawzonek and T. W. McIntyre, *This Journal*, **114**, 1025 (1967).
3. S. Wawzonek and T. W. McIntyre, *ibid.*, **119**, 1270 (1972).
4. R. L. Hand and R. F. Nelson, *J. Am. Chem. Soc.*, **96**, 850 (1974).
5. E. D. Bergmann and M. Benton, *J. Org. Chem.*, **19**, 1594 (1954).
6. R. B. Carlin and W. O. Forshey, Jr., *J. Am. Chem. Soc.*, **72**, 793 (1950).

7. A. G. Green and F. M. Rowe, *J. Chem. Soc.*, **101**, 2443 (1913).
8. M. J. Astle and S. P. Stephenson, *J. Am. Chem. Soc.*, **65**, 2399 (1943).
9. H. G. H. Erdtman, *Proc. R. Soc. London, Ser. A*, **143**, 177 (1934).
10. R. L. Hand and R. F. Nelson, *Anal. Chem.*, **48**, 1263 (1976).
11. L. Papouchado, G. Petrie, and R. N. Adams, *J. Electroanal. Chem.*, **38**, 389 (1972).
12. L. Papouchado, Ph.D. Thesis, University of Kansas (1970).
13. L. Papouchado, G. Petrie, G. H. Sharp, and R. N. Adams, *J. Am. Chem. Soc.*, **90**, 5620 (1968).
14. M. D. Hawley, Ph.D. Thesis, University of Kansas (1966).
15. P. A. Malachesky, G. Petrie, D. W. Leedy, and R. N. Adams, Abstracts of Army Research Office Symposium on Synthetic and Mechanistic Aspects of Electroorganic Chemistry, Durham, N.C., 1968, p. 235.
16. D. W. Leedy, Ph.D. Thesis, Kansas University (1968).
17. W. K. Snead and A. E. Remick, *J. Am. Chem. Soc.*, **79**, 6121 (1957).
18. P. A. Malachesky, K. B. Prater, G. Petrie, and R. N. Adams, *J. Electroanal. Chem.*, **16**, 41 (1968).
19. D. Hawley and R. N. Adams, *ibid.*, **10**, 376 (1965).
20. D. W. Leedy and R. N. Adams, *J. Am. Chem. Soc.*, **92**, 1646 (1970).
21. G. Petrie, Ph.D. Thesis, Kansas University (1970).
22. R. B. Carlin and R. C. Odioso, *J. Am. Chem. Soc.*, **76**, 2345 (1954).

Studies of Ruthenium-Oxy Species in Basic Solutions by Cyclic Voltammetry

Kim W. Lam, Keith E. Johnson,* and Donald G. Lee

Department of Chemistry, University of Regina, Regina, Saskatchewan, Canada S4S 0A2

ABSTRACT

Ruthenium(VI) solutions in alkaline media have been investigated by cyclic voltammetry using platinum and ruthenium dioxide electrodes. Four pairs of peaks were observed. The oxidation states of the electrolysis products were evaluated by coulometry and absorption spectra. The first and second pairs of peaks correspond, respectively, to the oxidation reduction of Ru(VIII)/Ru(VII) and Ru(VII)/Ru(VI) with a catalytic reaction. The third pair shows reduction of Ru(VI) to Ru(IV) with a following reaction giving ruthenium dioxide. The electron transfer product is postulated as $Ru(OH)_6^{-2}$. The last or most cathodic pair revealed a reduction peak composed of two waves. The first is from the reduction of the electrode surface oxide layer or adsorbed oxygen and the second, the reduction of Ru(IV) to Ru(III). The corresponding pairs of peaks are also observed from ruthenium dioxide electrodes in sodium hydroxide solutions.

During the last few years the ruthenium dioxide electrode has attracted considerable interest due to its corrosion-resistant properties and low overpotential for chlorine and oxygen evolution. However, little is known about its electrochemical reactions and for those (1-3) reported, the electrode was used in acidic media where it exhibits more corrosion-resistant characteristics. Difficulties in examining its electrochemical surface properties, besides those encountered in identifying its oxidation or reduction products, arise from its ill-resolved current-potential curve and potential-time charging curve. Here we have indirectly characterized its surface reactions through the investigation of ruthenium-oxy species in alkaline solutions.

The higher oxidation states of ruthenium exist only as oxy-species in basic media with ruthenate being most stable. However, a survey of the literature revealed that few have reported on the voltammetric behavior of ruthenate. The earlier studies (4, 5) determined the standard potentials of Ru(VIII)/Ru(VII) and Ru(VII)/Ru(VI) couples and touched on the disproportionation reaction of ruthenate (5) and perruthenate (6), but attempts to follow ruthenate reduction reactions failed. Though two other reports (7, 8) have appeared recently, the results and conclusions drawn were contradictory because of uncertainties in coulometric results and current-potential profiles. In one (7) it was postulated that ruthenate reduces first to ruthenium dioxide, then to Ru(III), and finally to the metal itself; the other (8) proposed that ruthenium dioxide, the final electrolysis product, was formed via Ru(V). We have obtained experimental results from cyclic voltammetry which offer a different point of view and which resolve the earlier uncertainties. The present paper reports on the electroreactions of the various ruthenium-oxy species, while the kinetics of the proposed mechanisms are reported in a later paper.

Experimental

Stock ruthenate solutions were prepared by oxidizing ruthenium dioxide (Ventron, Alfa Products) with commercial bleach (9). The product was extracted into carbon tetrachloride and washed several times with distilled water to remove traces of bleach and any water-soluble inorganic materials (10). The ruthenium tetroxide was then extracted into portions of from 0.1 to 0.5M sodium hydroxide solutions in which it reacted to give perruthenate (11). If perruthenate was desired, the solution was immediately stored in a freezer where crystals were observed to form. To obtain ruthenate the solution was allowed to stand at room temperature for several days or heated gently overnight (12). Spectroscopically pure ruthenate or perruthenate solutions of about 0.03M were obtained by this method. The concentrations of solutions prepared by diluting the stock with sodium hydroxide solutions were calculated from the molar absorptivities of 2150 at 385 nm for perruthenate and 1730 at 465 nm for ruthenate (13). The absorbance values were measured using a Unicam SP500 spectrophotometer while spectra were taken on a Beckman DK-2A spectrophotometer. The basicities of any one series of solutions were either measured

* Electrochemical Society Active Member.

Key words: cyclic voltammetry, catalytic waves, ruthenium oxides, ruthenium dioxide electrode.

by a pH meter (Radiometer PHM-4d) with a high pH glass electrode (Beckman) or by titration with potassium hydrogen phthalate after reduction of the oxidant to eliminate any obscuring color.

All electrochemical techniques were performed on a Princeton Applied Research Model 170 electrochemistry system. The instrument is equipped with an X-Y recorder having a rise time of approximately 0.3 sec such that rather accurate voltammograms with sweep rates as fast as 200-500 mV sec^{-1} can be obtained without using an oscilloscope.

The cell used was of conventional three-electrode design. The stability of the silver-silver chloride reference electrode was checked from time to time by comparing its potential with other silver-silver chloride electrodes or calomel electrodes. A double salt bridge was used in conjunction with the reference electrode. It consisted of 1M potassium chloride in contact with the electrode and whatever electrolyte (whose ionic strength was also adjusted to 1M by addition of sodium perchlorate) was being used in contact with the test solution. The tip of the second bridge was brought as close to the working electrode as possible but not close enough to interfere with diffusion. The use of a double salt bridge is a necessity since chloride ion can cause the decomposition of the ruthenate solution (4). The counterelectrode was a coiled platinum wire. In performing coulometric experiments it was isolated in a separate compartment, one end of which was in contact with the test solution through a fine fritted disk. The working electrode was a platinum electrode or a ruthenium dioxide electrode. Though a gold electrode was tried, it did not seem to offer any advantage over platinum.

Ruthenium dioxide electrodes were prepared following the procedure given in the literature (2) by thermal decomposition of ruthenium trichloride in air at 350°-400°C on a metal support of either platinum, tantalum, or titanium. Electrodes generated electrochemically were also prepared. It was found that films deposited by controlled potential in a quiescent solution gave better adhesion than with a small controlled current. Better surface uniformity, as evident from observations with a microscope, was also obtained by cycling the electrode several times between its oxidation and reduction potentials with a fast sweep. However, care was taken such that the electrode was not allowed to be swept past its cathodic limit or the film could collapse rather easily (2).

All other working electrodes were made of platinum wire (0.02 in. diam) with exposed lengths of approximately 4 and 7 mm. The electrodes were soaked in dilute nitric acid between use and cycled over the potential range employed before running the experiment. Any ruthenium dioxide deposited on the electrode could be removed either by electrochemical or chemical oxidation with permanganate (14). In coulometric experiments, the electrode used was a platinum wire gauze. Its apparent area was 43.2 cm^2. The solution volume was 50 ml. Stirring was achieved with a magnetic stirring bar and by bubbling nitrogen. Before running the experiment, the wire gauze electrode was subjected to oxidation or reduction in a blank solution depending on the potential chosen for the experiment. Coulometric data were recorded as charge-time curves through an electronic current integrator. Whenever the charge-time curve exhibited a sloping plateau, a line drawn through the origin and parallel to the slope was used as the base line to measure the charge instead of using the blank recorded immediately before the experiment.

Results and Discussion

A composite current-potential curve of ruthenate derived from several voltammograms with potential ranges of 1.0-0.1, 0.7- −0.25, 0.3- −0.8, and 0.1- −1.1V is shown in Fig. 1. Four pairs of peaks are observed. The cathodic and anodic peaks are labeled correspondingly in Roman numerals. The cyclic voltammogram of

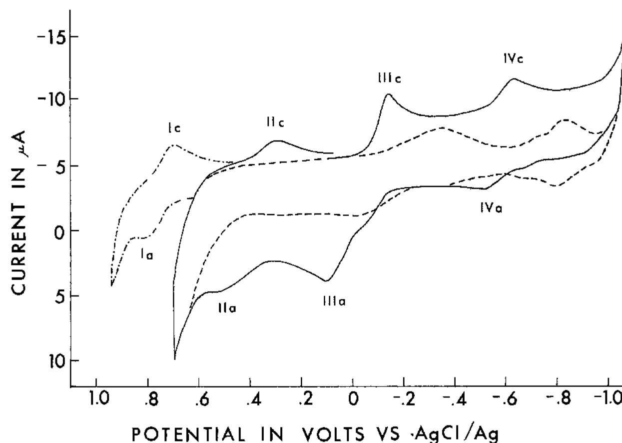

Fig. 1. Composite diagram drawn from cyclic voltammograms of ruthenate. Scan rate was 50 mV/sec; ——— ruthenate concentration was 2.56 × 10^{-4}M in 2M NaOH; – – – – blank, 2M NaOH; –·–·–· ruthenate concentration was 2.56 × 10^{-4}M in 8.5 × 10^{-3}M NaOH.

the platinum electrode in a blank solution is also reproduced for reference. However, it does not represent the true blank when ruthenate is added due to changes in surface conditions which are discussed later. Thus, the magnitudes of the well-known platinum oxide peaks should not be taken seriously. To avoid a prominent platinum oxide peak overshadowing the ruthenate reduction peaks in scanning toward the cathodic limit, the starting or initial potential was set at about +0.1V where oxidation of the electrode does not occur to an appreciable extent.

Peak I.—The pair of peaks labeled I is observed only with less basic solutions (below approximately pH =12) where the anodic limit of the platinum electrode is pushed to more positive potentials. Attempts to determine the number of electrons transferred by coulometric oxidation of ruthenate or perruthenate solutions were unsuccessful. The charge-time curve, except for an initial exponential rise, was continuously rising, making measurements impossible. The same trend was also observed when the electrolysis potential was set on the rising portion of the oxidation peak which was more than 150 mV negative of the anodic limit. Thus, the continuing supply of charge was not due to the electrolysis of the supporting electrolyte. The u.v.-visible absorption spectrum of the electrolysis product is similar to that of perruthenate. Coulometric reductions of the electrolysis product to perruthenate required between 0.5 and 1e.

Cyclic voltammetry of perruthenate solutions gives well-defined anodic and cathodic peaks for scan rates of 10 mV sec^{-1} or greater. However, the appearance of peaks is more likely to be observed at lower hydroxide concentrations. For scan rates below 5 mV sec^{-1} peaks are not observed. Instead, the anodic wave rises to a sloping plateau which blends into the anodic limit, while on reversing the scan, the cathodic wave simply returns to the foot of the anodic wave. The voltammograms are shown in Fig. 2 where the initial scan is toward the anodic direction. The voltammograms have been corrected for the blank. Two interesting points can be observed from this figure: (*i*) the current around the switching potential in the voltammogram for 1 mV sec^{-1} curves back toward the zero current line after reaching a maximum current; and (*ii*) the anodic current, $i/\sqrt{v}$ (v stands for scan rate), is higher for slower scan rates. The first effect is due to the subtraction of the blank. Before the subtraction, the wave rises to a sloping plateau.

The effect of scan rate on the anodic peak current is shown in Fig. 3. The shape of the voltammograms and the effect of the scan rate (15) strongly suggests that perruthenate is catalytically regenerated after being

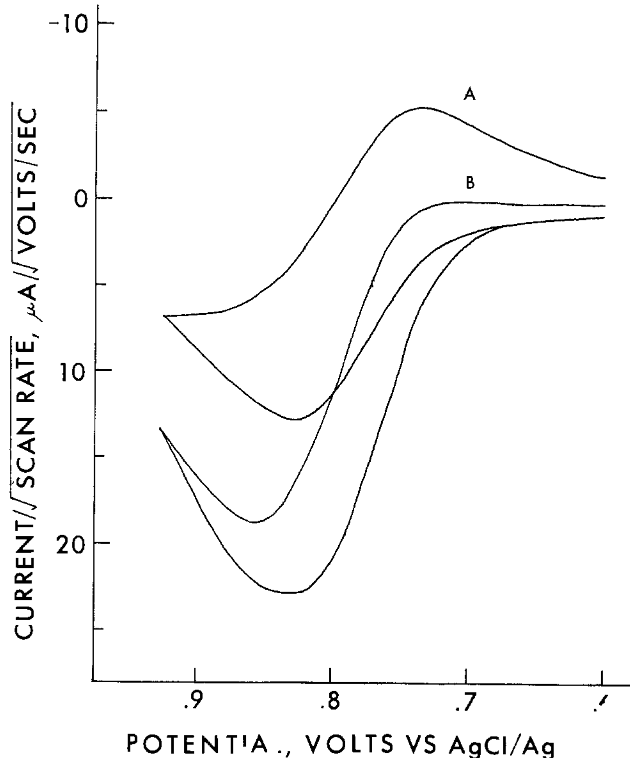

Fig. 2. Cyclic voltammograms of perruthenate oxidation. Initial sweep was in the anodic direction. Perruthenate concentration was ~ 2×10^{-4}M in 5×10^{-3}M NaOH and 1M $NaClO_4$. Scan rate was A, 100 mV/sec; B, 1 mV/sec.

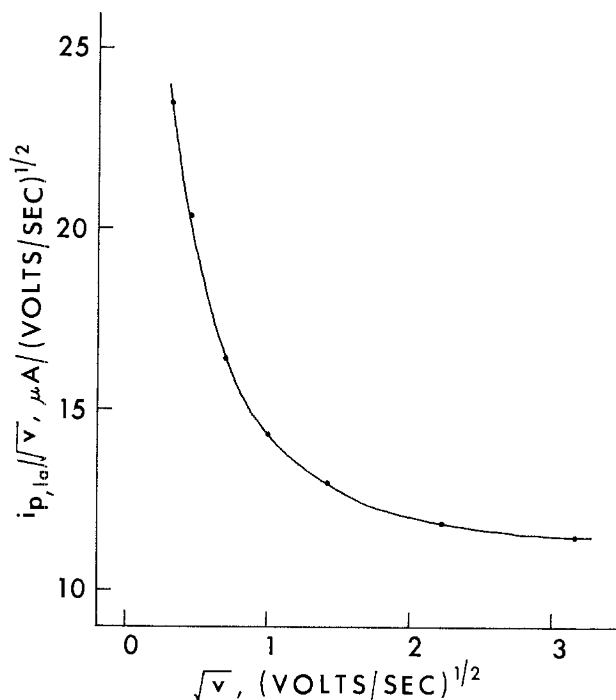

Fig. 3. Effect of scan rate on anodic peak current of perruthenate oxidation. Perruthenate concentration was ~ 2×10^{-4}M in 5×10^{-3}M NaOH and 1M $NaClO_4$.

oxidized. This in turn fits the coulometric observations. For the catalytic case the kinetics affect the voltammogram less at higher scan rates. It is found that for a hydroxide concentration of 1×10^{-3}-1×10^{-2}M, the voltammograms for a scan rate of approximately 20 mV sec^{-1} fit those of a simple reversible case with one electron being transferred. However, separation between the anodic and cathodic peaks is about 80 mV, which is greater than that predicted for the simple reversible system. As the scan rate increases or decreases from approximately 10 or 20 mV sec^{-1}, anodic and cathodic peak separation becomes larger. The ratio of the cathodic to anodic peak currents, though difficult to estimate because of uncertainties in the cathodic baseline, is seen to be approximately one (using scan rates of from 0.5 to 200 mV sec^{-1}). The above then suggests the following reaction scheme

$$RuO_4^- \leftrightarrow RuO_4 + e^- \quad [1a]$$

$$4RuO_4 + 4(OH^-) \rightarrow 4RuO_4^- + 2H_2O + O_2 \quad [1b]$$

which is consistent with the fact that ruthenium tetroxide is known to react with hydroxide to give perruthenate (11). The electron transfer, though reversible, may not be as fast, since, as observed by increasing the scan rate, anodic and cathodic peak separation becomes larger. The separation increases from about 80 mV at 20 or 10 mV sec^{-1} to 100 mV at 100 mV sec^{-1}. Likewise, the peak width $(Ep - Ep/2)$ increases from 57 to 63 mV.

From the reaction scheme, the curving near the anodic limit for slow scan rates can be explained as follows. At slower scan rate or higher hydroxide concentrations the catalytic reaction exerts more effect. One of the products of the catalytic reaction is oxygen which is also a product of the anodic limit reaction. Thus, the liberation of oxygen from the catalytic reaction pushes the anodic limit to a slightly more positive potential which in effect means the magnitude of the blank voltammogram in this region decreases. The voltammograms drawn in Fig. 2 had only their respective apparent blank voltammograms subtracted from them and thus are overly corrected giving the curving shape.

The formal potential for the redox couple can be determined from the potential midway between the cathodic and anodic peak potentials or where no peaks are observed from the average of the anodic and cathodic half-wave potentials. The average results of five sets of experiments are given in Table I. Within each set of experiments, one to three solutions were used. The solutions had the same initial hydroxide but different ruthenium concentrations. A number of scan rates were used and each was repeated several times. For each scan rate the results were averaged. The averaged results for all scan rates were again averaged and these averaged values are given in Table I. The reproducibility of the results within each set of experiments was generally good (within ±3 mV). However, the reproducibility of the anodic or cathodic peak potentials was ±6 mV. The potential thus determined at an ionic strength of 1M is 1.00V *vs.* the standard hydrogen electrode. This value agrees exactly with that of Silverman and Levy (4) whose value was, however, approximately corrected for activity coefficients.

Peak II.—The properties of peak II are similar to peak I. Coulometric oxidation of the ruthenate solution after the peak potential also gave a continuously rising charge-time curve preceded by an initial exponential rise. However, the rise, which is dependent on

Table I. Determination of formal potential for RuO_4/RuO_4^-

Number of solutions	3	2	1	2	1
NaOH, (M)	1×10^{-3}	1×10^{-3}	5×10^{-3}	8.5×10^{-3}	1×10^{-2}
Ruthenium species	RuO_4^-	RuO_4^-	RuO_4^-, RuO_4^{-2}	RuO_4^{-2}	RuO_4, RuO_4^-
Number of scan rates used	5	5	6	6	5
Average potential (V)	0.997	1.002	1.004	0.983	0.999
Reproducibility (mV)	±3	±1	±2	±6	0

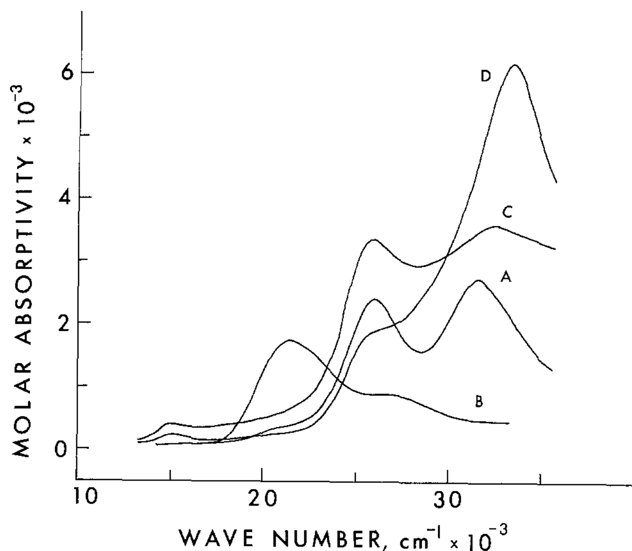

Fig. 4. Spectra of ruthenate electrolysis products. A, Ru(VII) in 8.5×10^{-2}M NaOH; B, Ru(VI) in 4M NaOH; C, Ru(IV) in 4M NaOH; D, Ru(III) and Ru(IV) in 4M NaOH.

the amounts of both hydroxide and ruthenate, is so much slower than in the previous case that the charge can be determined after drawing a baseline parallel to the sloping plateau. The number of electrons required was found to be 1.1 ±0.1. Figure 4, curve A shows the spectrum of the electrolysis product. It is identical to that of perruthenate (13). The spectrum is shown here for comparison with other spectra to be discussed later. The spectra reproduced have not been corrected for instrumental baseline and the molar absorptivities are thus higher than the literature values.

The cyclic voltammograms have properties similar to those of perruthenate oxidation, except in this case the baseline (or the anodic limited reaction) has a lesser influence and depending on the hydroxide or ruthenate concentration a plateau instead of a peak may be seen on the oxidation wave. The shape of the voltammogram and the effect of scan rate on the anodic peak current again indicate that a catalytic reaction is involved. Thus, the reaction for peak II may be written as

$$RuO_4^{-2} \rightleftharpoons RuO_4^- + e \quad [2a]$$

$$4RuO_4^- + 4(OH^-) \rightarrow 4RuO_4^{-2} + 2H_2O + O_2 \quad [2b]$$

Besides the catalytic reaction, no other side reactions can be detected (except at low pH where the decomposition of ruthenate to ruthenium dioxide exerts an influence on the voltammogram). This is supported by the observation that the ratio of the cathodic to anodic peak currents has a value of unity. (Baselines for measuring cathodic peak currents were established by holding the electrode potential at about +0.6V before sweeping cathodically). Thus, the only difference between reaction schemes [1] and [2] is that in the present system, the electron transfer kinetics plays a more important role and the catalytic reaction rate is much slower. The slower electron transfer rate can be observed from the wider peak separation. For the same scan rate the separation is about twice as wide. The current, which is controlled by both electron transfer and chemical kinetics, is smaller than that of Ru(VII)/Ru(VIII). For example, in 8.5×10^{-3}M sodium hydroxide with 2.4×10^{-4}M perruthenate or ruthenate, the peak current for Ru(VII)/Ru(VIII) at a scan rate of 5 mV sec^{-1} is 3.2 times as large. Although electron transfer kinetics may have caused the peak current for Ru(VI)/Ru(VII) to be smaller, the difference is so large that it cannot be attributed to the slower electron transfer rate alone. Comparing the case where the electron transfer is completely reversible without chemical complications with the irreversible system and assuming the transfer coefficient is 0.5, the peak current for the reversible system is theoretically only 1.27 times larger than for the irreversible case. Thus, the homogeneous reduction of perruthenate by hydroxide occurs at a slower rate than that of the tetroxide.

The average of the cathodic and anodic peak potentials of half-peak potentials should correlate to the standard potential of the redox couple. However, unlike Ru(VIII)/Ru(VII), the average potential for Ru(VII)/Ru(VI) is highly dependent on the ionic strength of the solution. Furthermore, it is affected by both the hydroxide and ruthenate concentrations. The effects do not affect the over-all reaction scheme proposed above, but do indicate a more complicated mechanism for the catalytic reaction involving a rate-determining step in which the stoichiometric ratio of perruthenate to hydroxide is not equal to one. (These results together with the detailed mechanism are reported in an upcoming paper.) It suffices to say here that the average potential does fall in the same potential region as reported in the literature (4, 5) for Ru(VII)/Ru(VI).

Peak III.—The reduction of ruthenate has raised a few questions in the past; even the nature of the reduction product has been uncertain (4, 7, 8). It seems appropriate at this time, with the recent surge of interest in the ruthenium dioxide electrode, to reexamine the reduction of ruthenate.

Coulometric reduction of ruthenate solution, after first reducing the platinum electrode used, gave very well-defined charge-time curves with an initial rise to a horizontal plateau. The number of electrons obtained for ten determinations with the electrode potential set on the rising or decaying portions of the wave was 2.00 ±0.06. The electrolysis product was obtained simultaneously in three forms, as a film deposited on the electrode (the color can be an orange-brown, purplish-blue, or black depending on the potential chosen and the amount of ruthenate used), as a black precipitate, and as a pale yellowish-green solution. Prolonged electrolysis for 12 hr or more did not change the yellowish-green solution or the number of electrons obtained. The solution upon standing for a period of time gave a clear solution with a black precipitate. Coulometric oxidation of either the film or the yellowish-green solution gave the characteristic orange color of ruthenate. (The yellowish-green solution was subjected to either centrifugation or filtration through a sintered glass crucible before oxidation.) The absorbances of the resulting ruthenate solutions were measured and the number of electrons obtained for both the film and the solution was between 1.70 and 1.85. The result was expected to be low since the ruthenate solution obtained was rather dilute and error was introduced in taking its absorbance value. Thus, the over-all reaction for the reduction of ruthenate involves two electrons and since no other complexing agent except hydroxide was in the solution, the ruthenium in the final electrolysis product had an oxidation state of (IV). [The uncertainty associated with the coulometric oxidation of the products may not account for the low electron value. The products, then, may have an oxidation state of slightly higher than (IV).]

The black precipitate, which also includes drop-offs from the film, showed no x-ray diffraction pattern. X-ray diffraction was also taken of commercial hydrated ruthenium dioxide and as reported in the literature (16), no pattern was observed. A diffraction pattern was not taken from the film since the authors have not developed a method to remove sufficient quantities from the electrode.

Figure 4, curve C, shows the u.v.-*vis*. spectrum of Ru(IV) in 4M NaOH. The molar absorptivity values should be within ±10%. The spectrum, though it resembles that of perruthenate, is quite distinctive. Besides differences in molar absorptivity and major band maximum positions, a small band maximum at 670 ± 10 nm is observed. The spectrum is that expected for an octahedrally coordinated $4d^4$ system (17). Thus,

disproportionation of ruthenate to perruthenate and ruthenium dioxide is not involved in the reaction. Interpretation of the spectrum extending into the infrared region will be reported in another paper.

In cyclic voltammetry, the effects of scan rate on the voltammogram are shown in Fig. 5. On the cathodic sweep, where ruthenate is reduced, the peak current, $i_p/\sqrt{v}$, either increases or decreases as the scan rate increases, depending on the concentration of ruthenate. The effect of scan rate on the cathodic peak current is shown in Fig. 6. It can be observed that for low ruthenate concentrations, the peak current, $i_p/\sqrt{v}$, decreases as the scan rate increases, while at higher concentrations the reverse trend is observed. The pattern shown indicates a chemical reaction is involved following the electron transfer (15). The chemical reaction is irreversible but shows some limited reversible characteristics for ruthenate concentrations of greater than 4×10^{-4}M. It was also noticed that aged solutions showed increasing irreversibility for the reaction. A gradual shift of the curves in Fig. 6 into the shape of curve A was observed. The negative slope of the curves became steeper and started at a slower scan rate. At the same time, solutions of low ruthenate concentration showed increasing visible signs of decomposition. (Stock solutions can be stored for months without deterioration.)

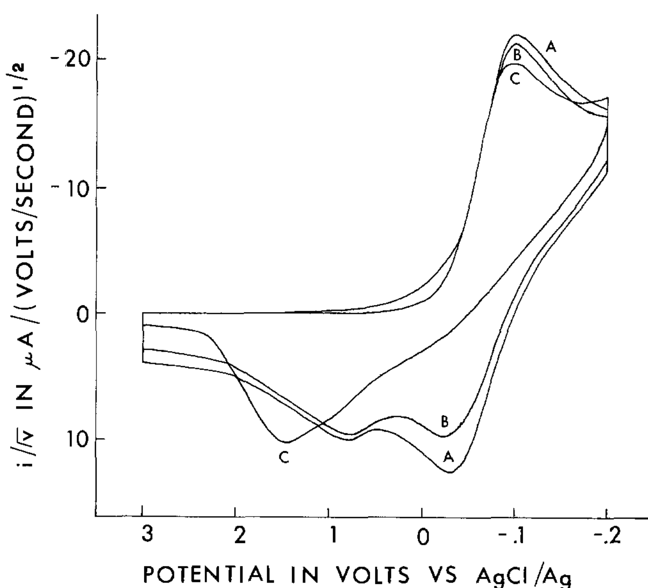

Fig. 5. Cyclic voltammograms of ruthenate reduction showing the effect of scan rate. Ruthenate concentration was 2.0×10^{-4}M in 1M NaOH. Scan rate was: A, 100 mV/sec; B, 50 mV/sec; C, 5 mV/sec.

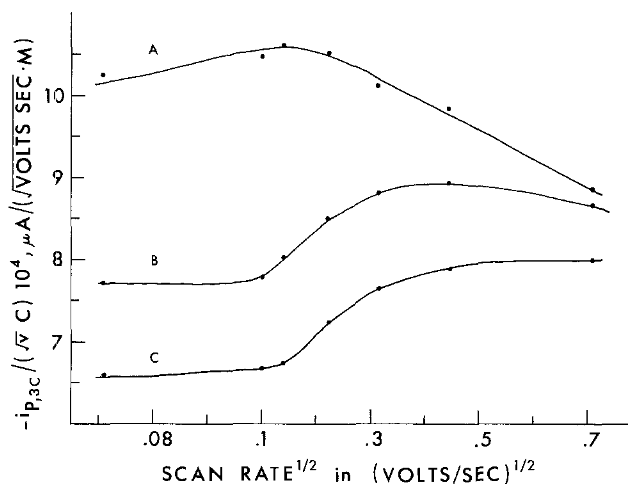

Fig. 6. Effect of scan rate on the cathodic peak current of ruthenate reduction. Ruthenate concentration was: A, 1.0×10^{-4}M in 1M NaOH; B, 4.0×10^{-4}M; C, 6.0×10^{-4}M.

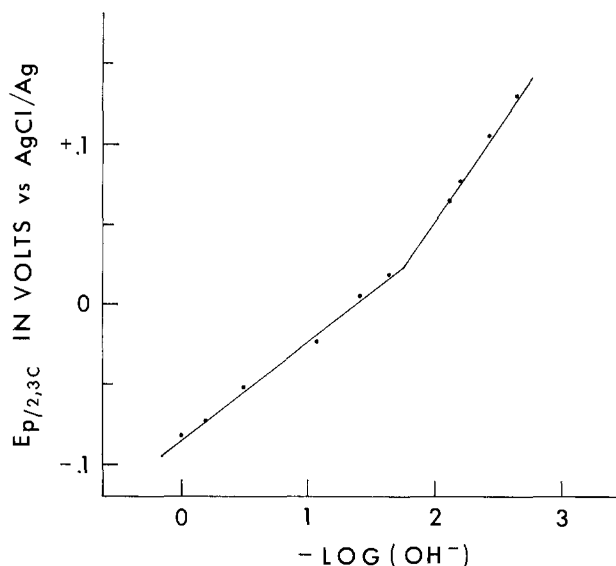

Fig. 7. Effect of hydroxide concentration on the cathodic half-peak potential of ruthenate reduction. Ruthenate concentration was 1.7×10^{-4}M. Scan rate was 50 mV/sec.

The effect of the hydroxide concentration on the voltammogram is shown in Fig. 8. The reduction wave shifts cathodically on increasing the hydroxide concentration, and a corresponding slight increase in peak current is observed. (For low hydroxide concentrations, the peak current also increases very slightly.) The shift of the cathodic peak or half-peak potentials as a function of hydroxide concentration is shown in Fig. 7. Two slopes are observed. For low hydroxide concentrations (below $\sim 1 \times 10^{-2}$M), the shift is approximately -120 mV per decade increase in hydroxide concentration, while at higher concentrations, the average of the least squares slopes of four sets of experiments is -60 ± 1.5 mV/decade. Though the reproducibility of the least-square slope is good, the reproducibility of the peak or half-peak potentials for the same hydroxide concentration from one set of experiments to another is rather poor. A 10 mV shift of the plot along the potential axis is not uncommon. This poor reproducibility was probably due to changes in the electrode surface conditions and, more importantly, the different degree of deteriorations of the ruthenate solutions. Nevertheless, the plot indicates that at high hydroxide concentrations the ratio of $(OH^-)/(e^-)$ is unity, while at low concentrations the ratio is two.

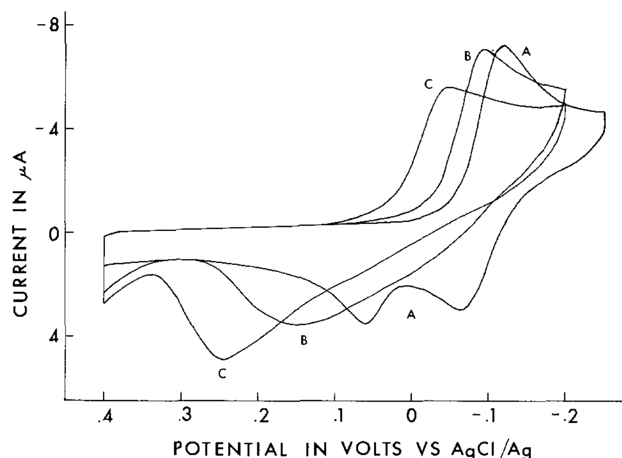

Fig. 8. Cyclic voltammograms of ruthenate reduction showing the effect of hydroxide concentration. Ruthenate concentration was 2.3×10^{-4}M. Scan rate was 50 mV/sec. Hydroxide concentration was: A, 4.0M; B, 0.6M; C, 0.1M.

From the above coulometric and cathodic sweep results, the reaction scheme for ruthenate reduction may be written as

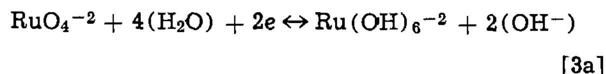

$$RuO_4^{-2} + 4(H_2O) + 2e \leftrightarrow Ru(OH)_6^{-2} + 2(OH^-) \quad [3a]$$

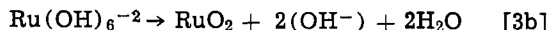

$$Ru(OH)_6^{-2} \rightarrow RuO_2 + 2(OH^-) + 2H_2O \quad [3b]$$

The proposed reaction scheme is further supported by the anodic waves of the cyclic voltammograms. Two peaks, instead of one, are observed. This confirms that two electroactive products are produced as the result of the reduction. The more cathodic (negative) peak appears only at higher scan rates as shown in Fig. 5. (This anodic peak together with the cathodic composes the normal cyclic voltammogram for a chemical reaction following the electron transfer when the chemical reaction does not further produce an electroactive product.) The appearance of the peak also depends on the concentration of hydroxide and ruthenate. These effects are shown in Fig. 8 and 9 and are in accord with the proposed reaction. The more positive peak, however, appears under any conditions but is comparatively very small when the ruthenate concentration is small and the scan rate is fast. The shift of the peak potential as a function of hydroxide concentration is -125 ± 3 mV/log(OH) for four sets of determinations. The peak shows all signs such as the sharpness of the peak and the noisy characteristics of the current of a deposit on a solid electrode being reoxidized. The reaction for this peak is thus

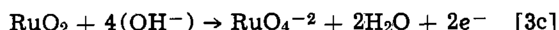

$$RuO_2 + 4(OH^-) \rightarrow RuO_4^{-2} + 2H_2O + 2e^- \quad [3c]$$

Only the above two-electron transfer (no one-electron reaction) was detected. Though it has been claimed (17) that a ruthenium (V) species, Na_3RuO_4, can be produced chemically, attempts to reproduce the experiment thus far in this laboratory have failed and no Na_3RuO_4 has ever been found.

Peak IV.—The last pair of peaks was usually obscured by a huge platinum oxide peak occurring immediately before it. To observe the cathodic peak, a reduced platinum electrode must be used.

Coulometric reduction of ruthenate solutions gave charge-time curves with a sloping plateau after an initial rise. Baselines drawn parallel to the plateaus gave the number of electrons as 2.8 ± 0.15 for four determinations. The forms of the electrolysis products are similar to the previous case (reduction to ruthenium dioxide). The film deposited on the electrode can be dissolved in hydrochloric or nitric acid solutions but not in sulfuric acid. Coulometric oxidation of the film or the light green solution back to ruthenate gave the number of electrons between 3.2 and 3.4. The results were high due to the oxidation of the platinum electrode itself, uncertainty in measuring the small absorbance values of the resulting ruthenate solutions, and the relatively large initial charging current. Thus, the number of electrons involved in the over-all reaction is three and the oxidation state of ruthenium in the electrolysis product is III or slightly higher.[1] The u.v.-visible spectrum of the light green solution is shown in Fig. 4, curve D. The spectrum shows that the solution contains a new species besides Ru(IV). The products are susceptible to air oxidation since the solution, upon standing for a couple of days, gave a spectrum similar to curve C.

In cyclic voltammetric experiments, the peak is rather broad and usually seems to have a shoulder on the rising portion of the wave even though the platinum electrode had already been reduced and no platinum oxide peaks should occur. This shoulder can be diminished to an undetectable level if a fast scan rate is used and the voltammogram recorded immediately after a previous sweep. To examine whether this is a composite peak of two or more waves, a slower scan rate was used and the solutions were stirred to enhance the shoulder even more. [These were the conditions used by a previous investigator (7) who first observed the shoulder wave.] The cyclic voltammograms for a stirred and a quiescent solution are shown in Fig. 10. The reproducibility of this shoulder wave is extremely poor and no correlation with the other peaks or any trend in experimental parameters could be detected. However the magnitude of the wave does increase with increasing stirring rate or ruthenate concentration. The same enhancement effect can also be observed if the initial potential is slightly more positive or in other words when the electrode is partially oxidized. The voltammogram recorded with a partially oxidized electrode is shown in Fig. 11 where the shoulder wave is seen to merge with peak IV. This merging of the shoulder wave with peak IV is gradual with a positive increment of the initial electrode potential from +0.1V. This huge composite peak IV was the one observed by another investigator (8) who used a rotating electrode. The same huge wave can also be observed if a high ruthenate concentration (1×10^{-3}M) is used even though the initial potential starts at a more negative value than +0.1V. Thus, all indi-

[1] In a paper by Trojanek (18), which appeared during the preparation of this manuscript, the author compared the areas of peaks IIIa and IVa and found that they were in the ratio of 2:1. Hence, the author concluded that the final product of ruthenate reduction probably has a +III oxidation state.

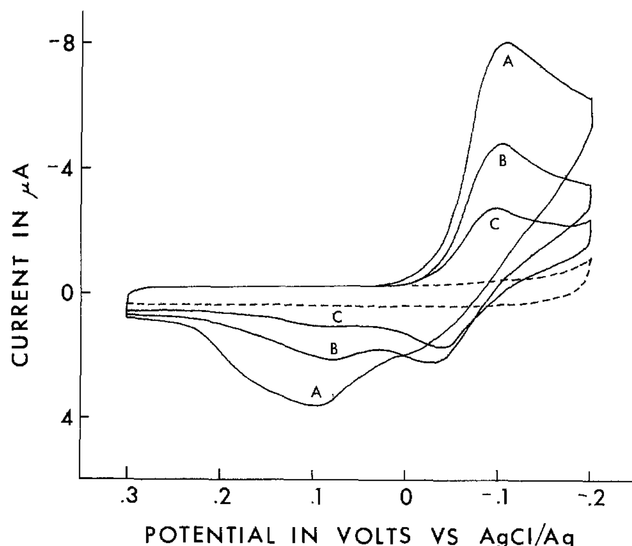

Fig. 9. Cyclic voltammograms of ruthenate reduction showing the effect of ruthenate concentration. Scan rate was 50 mV/sec. Ruthenate concentration was: A, 4.0 × 10^{-4}M in 1M NaOH; B, 2.0 × 10^{-4}M; C, 1.0 × 10^{-4}M. --- blank, 1M NaOH.

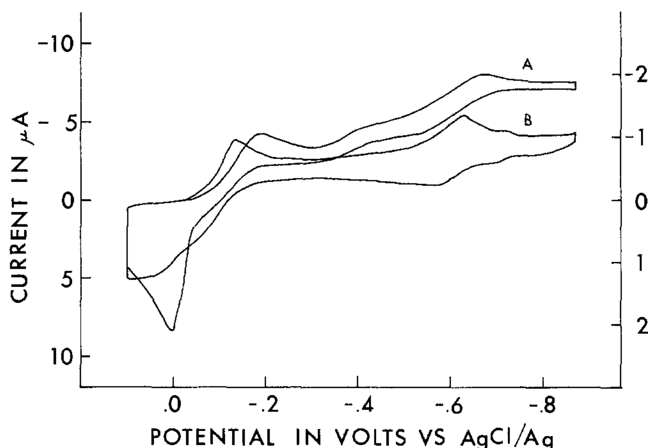

Fig. 10. Cyclic voltammograms of ruthenate reduction showing the ruthenium dioxide reduction peaks. Sweep began at + 0.1V. Ruthenate concentration was 2.0 × 10^{-4}M in 1M NaOH. Scan rate was 2 mV/sec. A, solution was stirred; current scale is on the left. B, solution was quiet; current scale is on the right.

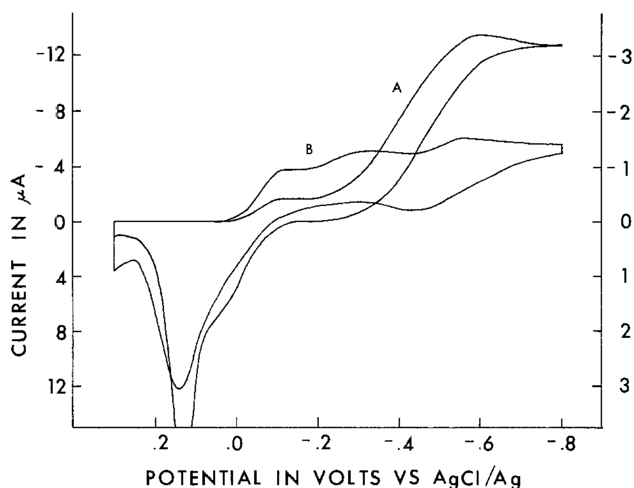

Fig. 11. Cyclic voltammograms of ruthenate reduction showing the ruthenium dioxide reduction peaks. Sweep began at + 0.3V. Other parameters were the same as in Fig. 12.

cations point to the possibility that ruthenate in the solution oxidizes the platinum electrode which in turn produces the platinum oxide peak. Oxidation of the platinum electrode by electroactive species is not uncommon. In the present case, the reduction of ruthenate to ruthenium dioxide occurs at a potential slightly more positive than the oxidation wave of the platinum electrode and thus the possibility of the oxidation of the electrode by ruthenate cannot be discarded.

Figure 12 shows that the platinum electrode is indeed oxidized by ruthenate. Curves A and B in Fig. 12 are, respectively, cyclic voltammograms for an oxidized and a reduced platinum electrode. It can be seen that for the reduced electrode, no sign of the platinum oxide peak is observed. Curve C is also a voltammogram of a reduced electrode, but immediately after reducing the electrode was soaked in a quiet 1×10^{-3}M ruthenate solution for about 2 min and then the electrode was washed with distilled water before recording the voltammogram. In this voltammogram the platinum oxide peak reappears. Thus, the experimental results strongly suggest that the shoulder on peak IV is due to the reduction of platinum oxide. To further confirm this, voltammograms were recorded from an electrolytically plated ruthenium dioxide electrode in sodium hydroxide solutions. The solutions were thoroughly deaerated with nitrogen to avoid further adsorption of oxygen on the electrode [a process favored by ruthenium dioxide (16)]. The resulting voltammograms showed no sign of the shoulder wave.

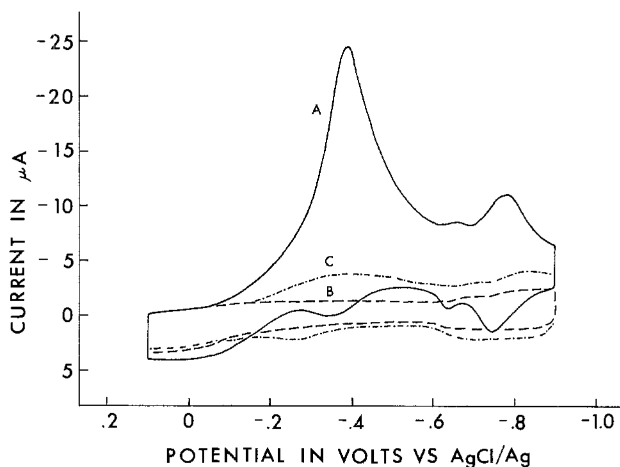

Fig. 12. Cyclic voltammograms of platinum electrode in 1M NaOH. Scan rate was 50 mV/sec. A, electrode was oxidized at + 0.8V before sweep; B, electrode was reduced at —0.9V before sweep; C, same as B but the reduced electrode was soaked in 1×10^{-3}M ruthenate for ~ 2 min and then washed in distilled water before sweep.

The various experimental parameters which affect the peak current are not discussed here since the theory for consecutive reactions starting from solution to solid, then from solid to solid (or a theory simply from solid to solid) has not been developed. However, the effect of hydroxide concentration on the peak potential can be observed easily. The average least-squares slope for plots of both the cathodic and anodic peak potential *vs.* log(OH) is 59 ± 2 mV for three sets of experiments using a platinum electrode, a chemically prepared ruthenium dioxide electrode in hydroxide solution and in ruthenate solution. The measurement of the peak potentials was in fact not very accurate due to the somewhat rounded nature of the peak especially when the ruthenium dioxide electrode was used. The plots, similar to the previous system for peak III, shift 10-15 mV along the potential axis from one to another. The reproducibility of the slope was surprisingly good and the result indicates that the ratio of OH^-/e^- is one. From the above coulometric and voltammetric observations, the over-all reaction responsible for peak IV is postulated as

$$2RuO_2 + H_2O + 2e \leftrightarrow Ru_2O_3 + 2(OH^-) \quad [4]$$

Ruthenium dioxide electrode.—Ruthenium dioxide electrodes freshly prepared by chemical methods give very ill-defined voltammograms (Fig. 13, curve B) except for a pair of prominent peaks immediately following the anodic limit. Slightly deteriorated electrodes, however, provide more defined voltammograms. This was also noticed by previous investigators (1, 2) who ran the electrode in acidic media. The slightly deteriorated condition can be achieved by sweeping or holding the electrode potential past the cathodic limit where the electrode on prolonged standing can collapse very easily. However, the best voltammograms obtained were not very well defined. On the other hand, running the electrode in a ruthenate solution enhances all the ill-defined waves so that they can be observed with ease (Fig. 13, curve A). These waves or peaks coincide exactly with those discussed above for the oxidation and reduction of ruthenate. The first pair of peaks following the anodic limit corresponds to the redox reaction of the $RuO_4^-/RuO_4^=$ couple. The second pair corresponds to that of RuO_4^{-2}/RuO_2 and the third or the most cathodic pair corresponds to RuO_2/Ru_2O_3.

Once these waves have been identified, their behavior can be followed as was shown in the discussion of the RuO_2/Ru_2O_3 reaction above. The behavior of the most positive pair is almost exactly the same as the RuO_4^-/RuO_4^{-2} couple even though it can only be observed qualitatively due to its close proximity to the

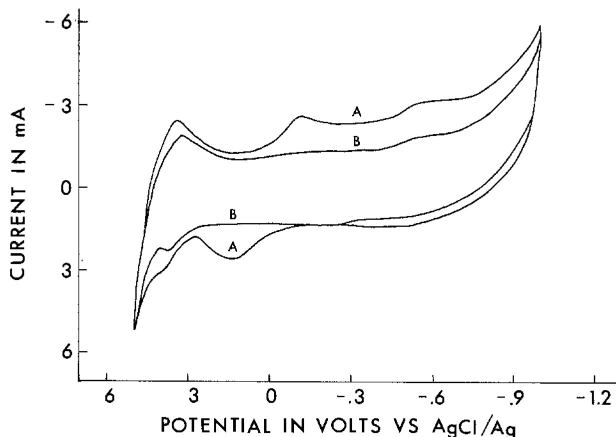

Fig. 13. Cyclic voltammogram of ruthenium dioxide electrode. The scan rate was 50 mV/sec. The solution was: A, 5.4×10^{-4}M ruthenate in 1M NaOH; B, 1M NaOH.

oxygen evolution limit. The only difference between this pair and that of the ruthenate oxidation reaction is in the shift of the average of the cathodic and anodic peak potentials with the hydroxide concentration. For the ruthenium dioxide electrode, the shift is in the cathodic direction with increasing hydroxide concentrations, while in the ruthenate solutions, the shift is in the opposite direction (these effects will be discussed in another paper on the detailed mechanism of ruthenate oxidation). The difference in this behavior is probably due to the nature of the surface as opposed to solution phenomena, since adsorbed oxygen may have been involved in the oxidation of ruthenium dioxide. Nevertheless, the rate of shifts for both, but not their sign, are approximately the same (they differ by ~3 mV). At low hydroxide concentration, however, the anodic peak may possibly be the composite of the oxidation of ruthenium dioxide to ruthenate and then to perruthenate since in voltammograms obtained with a platinum electrode in ruthenate solutions having low hydroxide concentrations, the ruthenium dioxide oxidation peak actually overshadows the ruthenate oxidation wave (Fig. 14). The wave for the RuO_4^{-2}/RuO_2 couple is rather flat and broad, and when freshly prepared electrodes are used it often blends with that of the RuO_2/Ru_2O_3 couple such that one continuous wave is observed. A few sweeps passing the anodic or cathodic limit distinguishes the two waves in that the magnitude for the RuO_2/Ru_2O_3 wave increases while the RuO_4^{-2}/RuO_2 wave remains the same. This, together with the observation that the electrode can withstand several sweeps past the anodic limit, indicates that it can resist oxidation or dissolution much

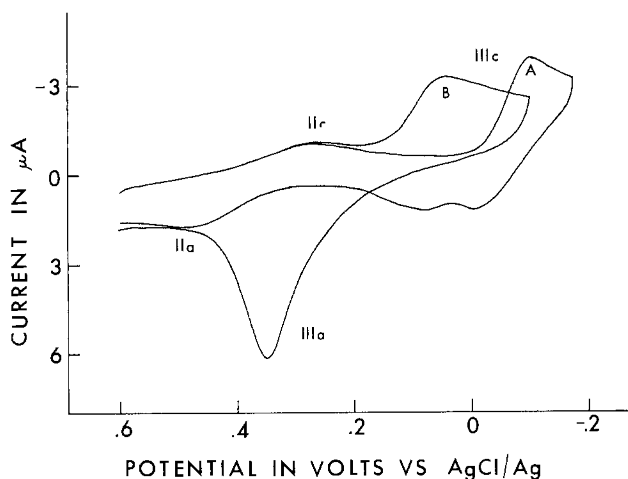

Fig. 14. Cyclic voltammograms showing the overlap of the ruthenium dioxide and ruthenate oxidation peaks. The scan rate was 50 mV/sec. The solution was 1.7×10^{-4}M ruthenate in A, 0.32M NaOH; B, 3.8×10^{-3}M NaOH. The ion strength of the solution was 1M by adding sodium perchlorate.

better than reduction or rearrangement of the crystal lattice, providing the electrode with corrosion resistant characteristics.

During the course of the investigation it was observed that hydrated ruthenium dioxide can undergo partial air oxidation to ruthenate in high hydroxide concentration solutions (> 1M). It is also known that in low hydroxide concentrations, ruthenate decomposes to ruthenium dioxide. Thus, without complexation reactions, the electrode should perform longer in lower pH media.

Acknowledgment

This work was supported in part by the National Research Council of Canada through operating grants to K.E.J. and D.G.L.

Manuscript submitted Oct. 10, 1977; revised manuscript received March 16, 1978.

Any discussion of this paper will appear in a Discussion Section to be published in the June 1979 JOURNAL. All discussions for the June 1979 Discussion Section should be submitted by Feb. 1, 1979.

Publication costs of this article were assisted by the University of Regina.

REFERENCES

1. S. Hadzi-Jordanov, H. Angerstein-Kozlowska, and B. E. Conway, *J. Electroanal. Chem.*, **60**, 359 (1975).
2. D. Galizzioli, F. Tantardini, and S. Trasatti, *J. Appl. Electrochem.*, **4**, 57 (1974).
3. J. Llopis and M. Vazquez, *Electrochim. Acta*, **11**, 633 (1966).
4. M. D. Silverman and H. A. Levy, *J. Am. Chem. Soc.*, **76**, 3319 (1954).
5. R. E. Connick and C. R. Hurley, *ibid.*, **74**, 5012 (1952).
6. R. E. Connick and C. R. Hurley, *J. Phys. Chem.*, **61**, 1018 (1957).
7. P. Eichner, *Bull. Soc. Chim. Fr.*, **6**, 2015 (1967).
8. M. B. Bardin and N. F. Tkhan, *Zh. Anal. Khim.*, **30**, 549 (1975).
9. S. Wolfe, S. K. Hasan, and J. R. Campbell, *J. Chem. Soc. D.*, 1420 (1970).
10. D. G. Lee and M. Van den Engh, in "Oxidation in Organic Chemistry, Part B," W. S. Trahanovsky, Editor, p. 177, Academic Press, New York (1973).
11. G. Nowogrocki and G. Tridot, *Bull. Soc. Chim. Fr.*, **4**, 684 (1965).
12. D. G. Lee, D. T. Hall and J. H. Cleland, *Can. J. Chem.*, **50**, 3741 (1972).
13. R. P. Larsen and L. E. Ross, *Anal. Chem.*, **31**, 176 (1959).
14. T. Hara and E. B. Sandell, *Anal. Chim. Acta*, **23**, 65 (1960).
15. R. S. Nicholson and I. Shain, *Anal. Chem.*, **36**, 706 (1964).
16. J. M. Fletcher, W. E. Gardner, B. F. Greenfield, M. J. Holdoway, and M. H. Rand, *J. Chem. Soc. A*, 653 (1968).
17. J. R. Dickinson and K. E. Johnson, *Mol. Phys.*, **19**, 19 (1970).
18. A. Trojanek, *J. Electroanal. Chem.*, **81**, 189 (1977).

Some Electrocapillary-Type Behaviors of Gold Electrode

Kaung-Far Lin

Department of Industrial Chemistry and Chemical Engineering, National Tsing Hua University, Taiwan, China

ABSTRACT

The effect of activity on potential of interfacial tension maximum in aqueous solutions of I^-, Br^-, and Cl^- is investigated for gold electrodes. It is seen that the potential decreases with ion concentration at a rate of $-0.1V$/decade in activity for I^- and Br^-. Electrocapillary-type curves for $0.1N$ $N(CH_3)_4OH$ is found to almost coincide with that for $0.1N$ KOH. Change in interfacial tension for I^- and Br^- is of the same magnitude in methanol solution as in aqueous solution.

The electrocapillary behavior of mercury is very well known in the literature. However, much less data is available for solid metals. Electrocapillary-type curves (interfacial tension *vs.* potential) for solid metals have been recently reported by Bockris *et al.* (1, 2) and Beck *et al.* (3, 4). A rather thorough study of the electrocapillary-type phenomena on gold electrode has been made by Lin *et al.* (5). Information about gold electrode is complemented in this study by showing the effect of activity (or concentration) on the observed potential of electrocapillary maximum and comparing interfacial tension curves in organic solution and aqueous solution.

Experimental

Gold ribbon ($0.000127 \times 0.318 \times 50$ cm) with purity 99.99% is used. The interfacial tension is measured by an extensometer. The design and characteristics of the extensometer have been presented previously (3-5). The experimental procedure is the same as those in the previous reports. The potential is relative to standard hydrogen electrode (V_{she}). The potential span is limited in the range that there is no appreciable faradaic current and Joule heating. For small value of linear strain ($\Delta L/L < 10^{-7}$), bulk and surface elastic moduli can be regarded as a constant. Thus a linear relationship between interfacial tension and length of gold ribbon is valid.

Results and Discussion

Activity effect of anions.—It was observed that the surface active anions I^-, Br^-, and Cl^- shift the potential of interfacial tension maximum in a negative direction for gold (5). A series of electrocapillary-type curves are measured for these ions in various concentrations in a small potential span around the interfacial tension maximum and the potential of interfacial tension maximum is thus determined. Figures 1, 2, and 3 show the original electrocapillary-type curves for 4, 1, 0.1, 0.01, and 0.001M aqueous solutions of KI, KBr, and KCl.[1] The activity coefficients of potassium salts in aqueous solution are available in the literature (6). The effect of activity of anions on the potential of interfacial tension maximum is shown in Fig. 4. It can be seen that the potential of interfacial tension maximum changes with activity at a rate of -0.1 V/decade for strongly adsorbed I^- and Br^-, like that observed on mercury (7). However, the potential of interfacial tension maximum for Cl^- decreases with activity nonlinearly on a semilog scale.

Bode *et al.* obtained slopes of lines of -0.050, -0.045, -0.040 V/decade in activity for I^-, Br^-, and Cl^- by open-circuit scrape method for gold electrode (8). The potentials of interfacial tension maximum in Fig. 1 are generally more negative than other reported values (8-10). This trend is also observed for $SO_4^{=}$, ClO_4^-, and NO_3^- though measured change in interfacial tension and charge density is in agreement with the Lippmann equation in electric double layer region (5). The reason for this discrepancy is not exactly known.

Cation adsorption.—It was known that tetra-alkylammonium cations are specifically adsorbed on mercury (11). A tetra-alkylammonium ion would be ex-

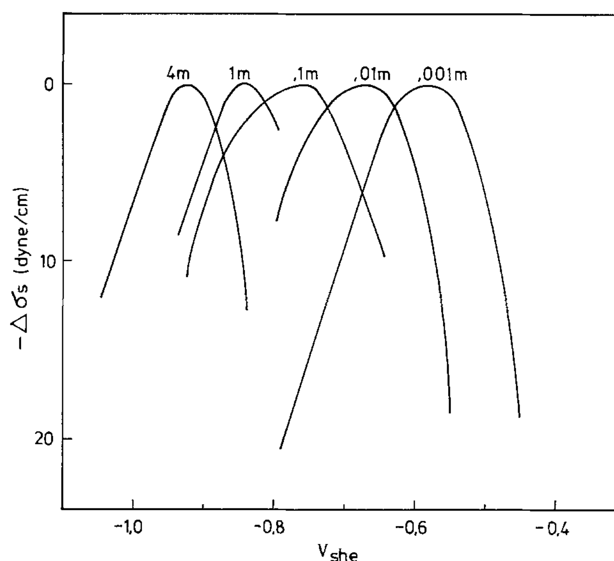

Fig. 1. Electrocapillary-type curves for 4, 1, 0.1, 0.01, and 0.001M aqueous solutions of KI.

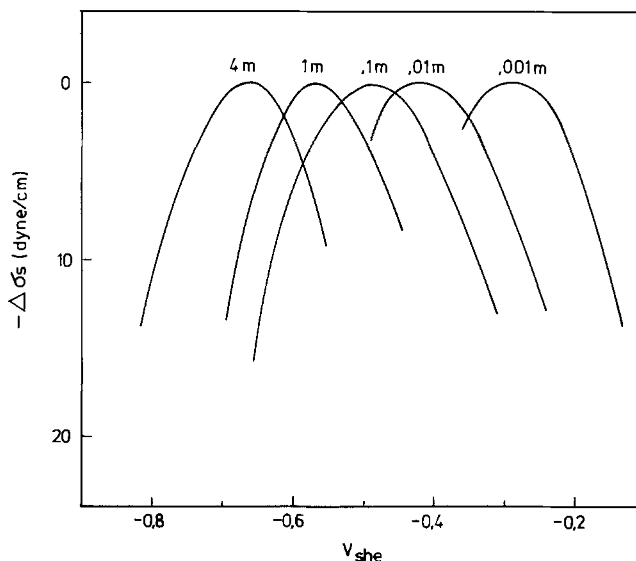

Fig. 2. Electrocapillary-type curves for 4, 1, 0.1, 0.01, and 0.001M aqueous solutions of KBr.

Key words: electrode, capacitance, stress-strain.

[1] The extensometer can measure the change in interfacial tension, not the absolute value. In Fig. 1, 2, and 3, interfacial tension values are arbitrarily set at zero for interfacial tension maximum in various solutions.

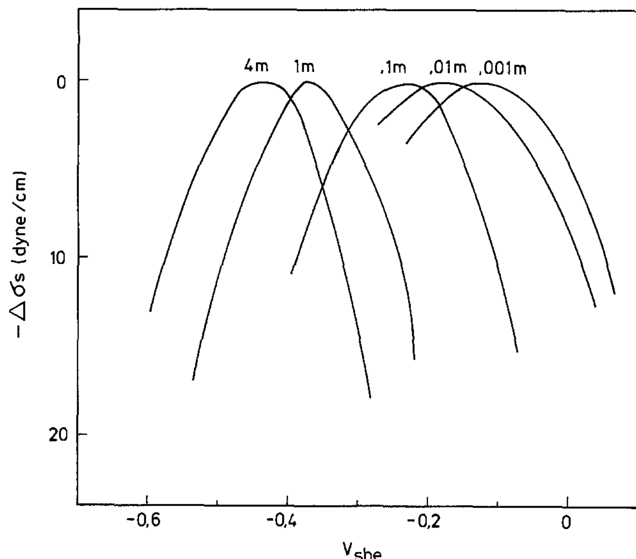

Fig. 3. Electrocapillary-type curves for 4, 1, 0.1, 0.01, and 0.001M aqueous solutions for KCl.

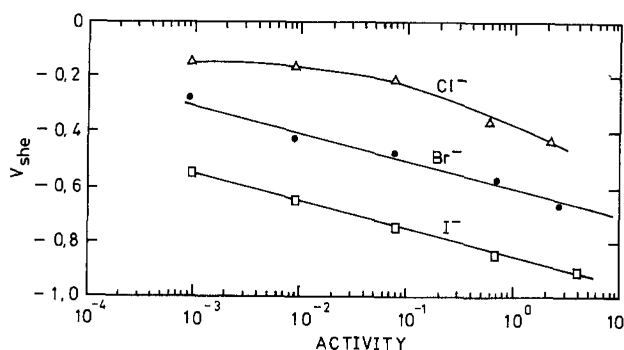

Fig. 4. Effect of activity on potential of interfacial tension maximum in potassium salt.

pected to shift the potential of interfacial tension maximum anodically if it is specifically adsorbed on gold electrode. However, experimental interfacial tension curves for 0.1*N* KOH and 0.1*N* $N(CH_3)_4OH$ almost coincide in Fig. 5. This anomaly can be explained by the fact that, for gold electrodes, adsorption of an anion is enhanced by the large tetramethyl ammonium cation and the metal-anion interaction is stronger than the metal-cation interaction. Thus the anion is nearer to the metal than the cation and a metal-anion-cation bridge is formed. The over-all effect is that there is not much difference in interfacial tension curve for 0.1*N*

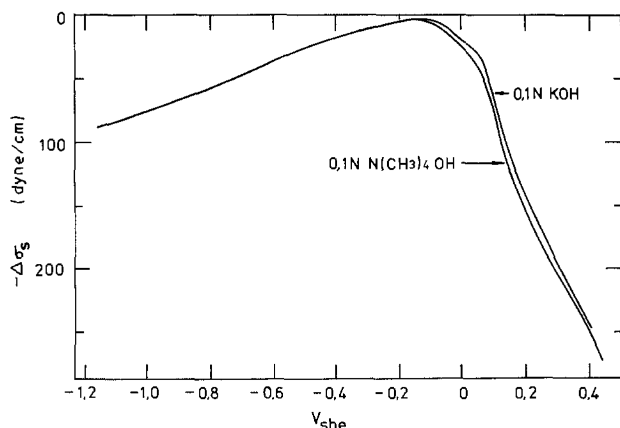

Fig. 5. Interfacial tension curve for aqueous 0.1*N* KOH and 0.1*N* $N(CH_3)_4OH$.

KOH and 0.1*N* $N(CH_3)_4OH$, just like there is not much difference in potentials of zero charge for NaOH and $N(CH_3)_4OH$ in different concentrations (12). The enhancement of anion adsorption by tetra-alkylammonium ion and the formation of metal-anion-cation bridges have been invoked in explaining observed peak potential for gold and silver electrodes (12) and some kinetic processes (13).

Organic solvent.—Interfacial tension curves for 0.1*N* NaI and 0.1*N* NaBr in methanol (ACS reagent grade) are shown in Fig. 6. (The two curves are matched at the negative potential side). It is seen that I^- is more strongly adsorbed on gold than Br^-, with potential of interfacial tension maximum at -0.96 V_{she} and -0.31 V_{she}, respectively. The shift in potential of interfacial tension maximum is thus 0.65V, as compared to 0.2V for 1*N* I^- and Br^- in methanol on mercury (14). For a gold electrode, change in interfacial tension with potential in methanol is of the same magnitude as that in aqueous solution, but shift in potential of interfacial tension maximum for I^- and Br^- is 0.28V in an aqueous solution (5).

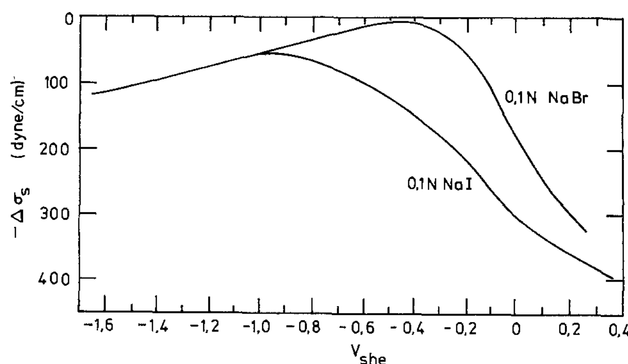

Fig. 6. Interfacial tension curve for 0.1*N* NaI and 0.1*N* NaBr in methanol.

Acknowledgment

The guidance of Dr. T. R. Beck in the course of this work is appreciated.

Manuscript submitted Sept. 13, 1977; revised manuscript received March 1, 1978.

Any discussion of this paper will appear in a Discussion Section to be published in the June 1979 JOURNAL. All discussions for the June 1979 Discussion Section should be submitted by Feb. 1, 1979.

REFERENCES

1. R. A. Fredlein, A. Damjanovic, and J. O'M Bockris, *Surf. Sci.*, **25**, 261 (1971).
2. R. A. Fredlein and J. O'M Bockris, *ibid.*, **46**, 441 (1974).
3. T. R. Beck, *J. Phys. Chem.*, **73**, 466 (1968).
4. T. R. Beck and K. W. Beach, in "Electrocatalysis," M. W. Breiter, Editor, pp. 357-364, The Electrochemical Society Softbound Symposium Series, Princeton, N.J. (1974).
5. K. F. Lin and T. R. Beck, *This Journal*, **123**, 1146 (1976).
6. W. M. Latimer, "The Oxidation States of the Elements and Their Potentials in Aqueous Solutions," Prentice-Hall Inc., New York (1952).
7. D. C. Grahame, *J. Am. Chem. Soc.*, **80**, 4201 (1958).
8. D. D. Bodé, Jr., T. N. Andersen, and H. Eyring, *J. Phys. Chem.*, **71**, 792 (1967).
9. R. S. Perkins, R. C. Livingston, T. N. Andersen, and H. Eyring, *This Journal*, **69**, 3329 (1965).
10. J. Clavilier and N. Van Huong, *J. Electroanal. Chem.*, **41**, 193 (1973).
11. M. V. A. Devanathan and M. J. Fernade, *Trans. Faraday Soc.*, **58**, 368 (1962).
12. D. D. Bodé, Jr., T. N. Andersen, and H. Eyring, *This Journal*, **114**, 72 (1967).
13. A. N. Frumkin, *Trans. Faraday Soc.*, **55**, 156 (1959).
14. W. K. Paik, M. A. Genshaw, and J. O'M. Bockris, *J. Phys. Chem.*, **74**, 4266 (1970).

A Detailed Treatment of the Reaction Zone for Electron-Transfer Chemiluminescence

J. Lee Morris, Jr., and Larry R. Faulkner*

Department of Chemistry, University of Illinois, Urbana, Illinois 61801

ABSTRACT

Techniques of digital simulation have been used to model the reaction zone yielding chemiluminescence in conventional double or triple potential step experiments. Each simulation describes the steady state achieved within a fixed volume into which the reactant radical ions are injected at a constant rate. Thus each simulation depicts a single point along the luminescence decay curve. Other points are examined via simulations involving different rates of reactant injection. Radical ion annihilation, triplet-triplet annihilation, first-order triplet decay, and triplet quenching by the radical ions are all modeled directly. Problems associated with the simulation of a steady state are discussed in detail. The results of simulations for various sets of realistic rate parameters are compared with the predictions of a simplified treatment of the reaction zone as a homogeneous region of constant width. The impact of quenching by radical ions is evaluated quantitatively for the first time. The results show that one can usually expect triplet lifetimes to be controlled by these species at times early in the light pulse. The importance of this conclusion to the usual interpretation of magnetic effects is discussed.

Light transients produced in electrochemical step experiments have been carefully studied since Feldberg first recognized the value of their shapes for mechanistic diagnosis (1, 2). In these experiments (3, 4), two high energy reactants (*e.g.*, the anion and cation radicals of an aromatic precursor) are generated sequentially at a planar microelectrode in a quiescent solution at diffusion-controlled rates. The first reactant is deposited in the diffusion layer during the forward step, which lasts for a period t_f. Light arises during the reversal step, when the second reactant is produced at the electrode, diffuses outward, and meets the first reactant in a reaction zone located within the diffusion layer. If energy permits, the emitting state can be produced directly by the reactant annihilation (S route). Alternatively, the chemistry may yield triplet intermediates, which can themselves annihilate to produce emitting singlets (T route).

Feldberg noted that these two mechanisms could be distinguished from the form of the light decay, as reflected in the slope of a linear plot of log I *vs.* $(t_r/t_f)^{1/2}$, where I is light intensity and t_r is time measured into the second step from its start (2). The predicted slope for an S-route system requires no model of the reaction zone and is well defined by diffusion. The T mechanism is much more complex, and predictions of the corresponding decay function require a model of the reaction zone. Feldberg took this zone as a small region of fixed thickness into which the reactants are injected at a rate controlled by diffusion (2). Triplets were regarded as being uniformly distributed over the zone, and their concentration was assumed to be at a virtual steady state. This basis simplifies the problem greatly, and the intensity decay is readily defined within its framework. The slope magnitude of a Feldberg plot was expected to exceed that for an S-route case, but it should never be larger than twice that lower limit. Later work by others sought to develop quantitative techniques for extracting mechanistic information from the light transients (3-7).

Finding experimental systems that are explicable in terms of the theory has proved very difficult, despite the fact that the electrochemical features are often quite well behaved (8, 9). Feldberg slopes are frequently 4-6 times larger than the S-route value, and only rarely are T-route shape functions followed over a wide time range, even when reaction energy dictates a T mechanism (10-12). Part of the problem is that Feldberg plots are linear only for $t_r/t_f \geqq 0.2$, when most of the light pulse has passed, and the reactant levels are easily perturbed by side reactions (13). Another aspect is that the simplifications introduced in the Feldberg model may be too restrictive to allow an accurate prediction of decay functions, except in special cases.

In this paper, we present a technique for obtaining detailed models of the reaction zone. Calculations for realistic experimental situations allow an evaluation of the assumptions underlying the simplified model. In addition, they provide rationale for a number of anomalous observations, and they yield insight into the fundamentals of important experimental methods.

The Simplified Model

We consider only the case in which the two reactant ions are produced from the same precursor, P. The reaction scheme is given by [1]-[8]

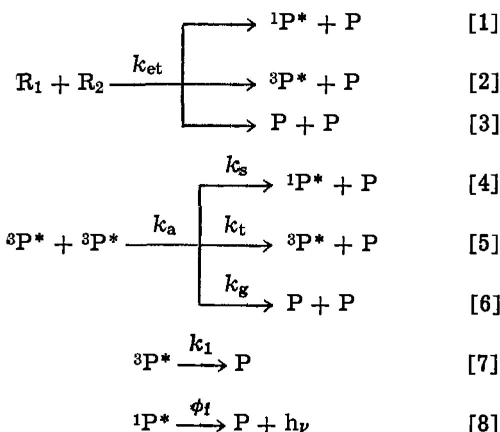

where R_1 and R_2 are the reactants and $^1P^*$ and $^3P^*$ are excited singlet and triplet precursors. The parameter k_1 is the first-order rate constant for triplet decay, and ϕ_f is the fluorescence efficiency of $^1P^*$.

Reactions [1]-[3] take place at a rate controlled by diffusion of R_1 and R_2 into the reaction zone (2, 5). That rate is N (moles per second), and the reaction zone volume is V_r. The kinetics of triplet formation by [2] and decay by [4]-[7] leads to an analytical expression for the triplet concentration, *viz.*

* Electrochemical Society Active Member.

Key words: chemiluminescence, diffusion, kinetics, simulation.

$$[^3P^*] = \frac{-1 + [1 + 8\,k_a(1-g)\tau^2 L/V_r]^{1/2}}{4\,k_a(1-g)\tau} \quad [9]$$

The steady-state approximation for $^3P^*$ has been invoked, and the reaction zone has been taken as homogeneous. The various symbols in [9] are defined as follows: $k_a = k_s + k_t + k_g$, $\tau = 1/k_1$, $g = k_t/2k_a$, $L = \phi_t N$. The parameter ϕ_t is the triplet yield of radical ion annihilation. Using the additional relationships [10] and [11]

$$I = \phi_f \phi_{tt} k_a [^3P^*]^2 V_r \quad [10]$$

$$V_r = fA(Dt_f)^{1/2} \quad [11]$$

one can develop a relationship for the T-route intensity in dimensionless terms

$$\omega_i = \beta[1 - (1 + \alpha\omega_n/\beta)^{1/2}] + 0.5\,\alpha\omega_n \quad [12]$$

Here ϕ_{tt} is the singlet production efficiency of triplet-triplet annihilation k_s/k_a, D is the diffusion coefficient, and A is the electrode area. Equation [11] essentially defines f as a dimensionless reaction zone thickness, which is taken as a constant throughout the experiment. In [12], $\omega_i = It_f^{1/2}/AD^{1/2}C_P^*$ and is the dimensionless intensity; $\omega_n = Nt_f^{1/2}/AD^{1/2}C_P^*$ and is the dimensionless ion annihilation rate; $\alpha = \phi_t\phi_{tt}\phi_f/(1 - g)$; $\beta = ft_f\phi_f\phi_{tt}/8k_a\tau^2C_P^*(1 - g)^2$; and C_P^* is the bulk precursor concentration. Since ω_i can be determined experimentally and ω_n can be readily calculated theoretically, the simplified treatment allows the evaluation of α and β from real data, in principle. Estimates of the triplet yield ϕ_t could be obtained from reliable α's.

There are at least three important deficiencies in the treatment: (*i*) Time-dependent triplet quenching by radical ions is not considered. (*ii*) The reaction zone thickness is assumed to remain constant throughout the experiment. (*iii*) The reaction zone is taken as a homogeneous region.

The presence of radical ions in and around the reaction zone bears importantly on all three of these issues. These species have been shown to deactivate triplets readily (14, 15), and a detailed treatment must implicate kinetics reflecting this activity. If radical ion quenching has a large influence on the triplet lifetime, then that lifetime will show a time dependence as the radical ion concentrations decrease during the course of the experiment. Since the triplet lifetime partially determines the size of the reaction zone, it is evident that the radical ion concentrations will also play a role in controlling the thickness of the zone, f, along the dimensionless diffusion axis. A time-dependent lifetime would imply a time-dependent f. Finally, we note that the relative competitiveness of quenching by radical ions and triplet-triplet annihilation changes across the reaction zone, because both triplets and radical ions are inhomogeneously distributed. One of our goals here is to use a detailed model to evaluate the practical impact of these factors on the light decay.

Formulation of the Problem

Most aspects of the computer program developed to model the reaction zone involve well-known digital simulation techniques (16, 17) and need not be discussed. Most of the notation used here corresponds to common practice in dealing with electrochemiluminescence (ECL). There are, however, several features of this particular simulation that are unique and require amplification. These include: (*i*) the basic spatial features of the reaction zone, (*ii*) the means of ascertaining the stopping point for the simulation, and (*iii*) the methods for evaluating the rates of ion and triplet annihilation.

Any consideration of the reaction zone begins with the concentration profiles of the radical ions during the second step of the experiment. Figure 1 shows a typical case. The reaction zone is the region where

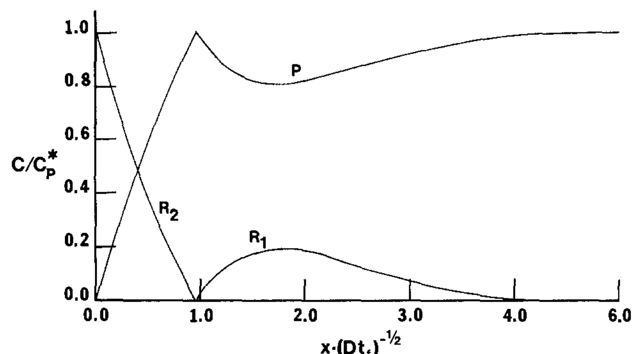

Fig. 1. Concentration profiles in the diffusion layer at $t_r/t_f = 0.4$

the profiles for R_1 and R_2 meet. This region is very thin compared to the thickness of the whole diffusion layer, hence the rate of ion injection into the reaction zone is dictated by the slopes of the essentially linear profiles on either side (13). The time scale over which the profiles evolve is much longer than those of the steps in reaction scheme [1]-[8], hence a steady-state condition essentially prevails within the zone (7). The rate of ion injection, therefore, equals the rate of ion annihilation N (or ω_n, in dimensionless format). This parameter is determined only by basic considerations of diffusion and is readily calculated (13). For any time t_r/t_f, there is a corresponding ω_n value.

Thus, the problem is to model the steady-state condition for a reaction zone into which reactants are injected from opposite sides at a fixed rate. The digital arrays representing various species are initialized arbitrarily, then they are manipulated according to the dynamic laws until a steady condition is reached.

Initialization.—The starting concentration profiles of the reactants R_1 and R_2 are chosen to be linear functions. Their concentrations are largest at opposite sides of the zone and decrease to zero at the center The concentration of the precursor P is chosen such that the sum of all fractional concentrations ($f_i \equiv C_i/C_P^*$, where i is any species) in any box is unity. This relationship always holds for the present case, in which all species have the same diffusion coefficient (13).

Since the radical ion annihilation rate changes over a long time scale, a simulation at steady state yields a picture of the system for essentially a single experimental time. A series of simulations for discrete values of ω_n must be carried out to cover a wide time range. Once one sets ω_n for a given simulation, one has fixed the injection rates of R_1 and R_2 and, thus, the gradient in their concentrations at the two boundaries. This gradient is the slope used for the initial linear profiles. It allows one to fix the initial difference in fractional concentration between adjacent boxes in the simulation, if one first determines the size of the zone to be considered and the number of boxes in that zone.

We have chosen to define the reaction zone size in terms of the rates of diffusion and electron transfer. Thus the actual zone width, d, along the diffusion axis is given by

$$d \equiv v\left(\frac{D}{k_{et}C_P^*}\right)^{1/2} \quad [13]$$

where D is the diffusion coefficient, k_{et} is the over-all rate constant for electron transfer, and v is a scale factor to be optimized. It is easy to see that $(k_{et}C_P^*)^{-1}$ has the units of time and defines a time scale for the electron transfer reaction. Therefore, the value of v is the size of the reaction zone in terms of diffusion lengths on this time scale. This parameter is a simulation variable and can be selected at will, but it must be large enough to accommodate all of the reaction events of interest. Ideally, it is no larger. Using this definition, that of the model diffusion co-

efficient, D_M

$$D_M \equiv \frac{D\Delta t}{\Delta x^2} \quad [14]$$

and the dimensionless redox rate constant κ

$$\kappa = k_{et} t_f C_P{}^* \quad [15]$$

we arrive at useful expressions for the space and time increments, Δx and Δt, that characterize the simulation

$$\Delta x = \frac{v}{(j_{max} - 1)} \left(\frac{Dt_f}{\kappa} \right)^{1/2} \quad [16]$$

$$\Delta t = \frac{v^2 D_M t_f}{\kappa (j_{max} - 1)^2} \quad [17]$$

Here, it is understood that the distance d is represented by boxes numbered from 1 to j_{max}, so that $d = (j_{max} - 1)\Delta x$.

The value of J, the difference in fractional concentrations between adjacent boxes in the initial linear concentration profiles of R_1 and R_2, can now be determined to be

$$J = \frac{\omega_n v}{\kappa^{1/2}(j_{max} - 1)} \quad [18]$$

See the Appendix for details. This relation provides the means for initializing the simulation.

Let us note a few differences between the simulation technique presented here and that which is utilized in the more familiar case of semi-infinite linear diffusion. In the latter case, the time resolution is specified by the number of iterations corresponding to some experimental period (16, 17), whereas the number of boxes required for spatial representation is not directly controlled. Therefore, the over-all size of the region to be described is initially unknown. In the steady-state case presented here, the over-all size of the reaction region and the number of boxes representing it are specified at the start, thus the spatial resolution is initially defined in direct terms. Time resolution is defined indirectly through D_M, and the number of iterations required to achieve steady state is completely unknown. Whereas the number of iterations is the chief simulation variable in the semi-infinite case, the reaction zone scaler is the chief variable for the present model. Since the number of iterations cannot be preset in this case, some other indicator must be devised for stopping the simulation when steady state is reached.

Boundary conditions.—The key constraint on the model is that the two radicals are injected from opposite sides at steady rates corresponding to the value of ω_n chosen for the simulation. This condition is enforced for R_2 by maintaining its fractional concentrations in boxes 1 and 2 at the constant difference J. After each iteration, the fractional concentration in box 1 is adjusted appropriately. For species R_1, the boundary condition is enforced in boxes $j_{max} - 1$ and j_{max} in exactly the same way. The zone width parameter v is always sufficiently large that radical ions do not diffuse through the zone and triplets do not diffuse out of it.

Dynamics.—The chemical reactions that must be considered in the reaction zone are (*i*) electron transfer, (*ii*) triplet-triplet annihilation, (*iii*) first-order triplet decay, and (*iv*) quenching of triplets by radical ions. The expressions used to determine the changes in the various fractional concentrations in each box during each iteration are listed below. They are derived by conventional techniques for treating homogeneous processes (16, 17)

$$-\Delta f_{R_1} = -\Delta f_{R_2} = \Delta f_T/\phi_t = \Delta f_P/(2 - \phi_t) = \frac{v^2 D_M f_{R_1} f_{R_2}}{(j_{max} - 1)^2} \quad \text{electron transfer} \quad [19]$$

$$-\Delta f_T = \Delta f_P = \frac{2v^2 D_M}{(j_{max} - 1)^2}(1 - g)\left(\frac{k_a}{k_{et}}\right) f_T{}^2 \quad \text{triplet-triplet annihilation} \quad [20]$$

$$-\Delta f_T = \Delta f_P = \frac{v^2 D_M}{(j_{max} - 1)^2}\left(\frac{k_1}{k_{et} C_P{}^*}\right) f_T \quad \text{first-order triplet decay} \quad [21]$$

$$-\Delta f_T = \Delta f_P = \frac{v^2 D_M}{(j_{max} - 1)^2}\left(\frac{k_q}{k_{et}}\right) f_T f_Q \quad \text{radical-ion quenching} \quad [22]$$

Here, the f_i's are fractional concentrations of species denoted by the subscripts, where T signifies the triplet $^3P^*$, and Q stands for both radical quenchers R_1 and R_2, which are assumed to destroy triplets equally effectively by rate constant k_q, *i.e.*

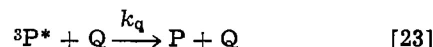

$$^3P^* + Q \xrightarrow{k_q} P + Q \quad [23]$$

Thus, $f_Q = f_{R_1} + f_{R_2}$. The singlet $^1P^*$ is not specifically modeled because its lifetime is too short to permit significant concentrations at steady state. These reactions are allowed to occur sequentially in the simulation at the end of each iteration, just after diffusion of all species.

Steady-state criterion.—The simulation is stopped at the earliest point where the values of the total radical ion reaction rate and the total triplet-triplet annihilation rate cease to change significantly in successive iterations. The total electron transfer rate is given by ω_n, and the total triplet-triplet annihilation rate is given in dimensionless terms by an analogous parameter ω_t, which for a T-route system is directly proportional to ω_i

$$\omega_t = \omega_i/\phi_f \phi_{tt} \quad [24]$$

Both ω_i and ω_t can be determined from the input parameters for the simulation and the concentration profiles at the end of each iteration. It was necessary to monitor both functions, because they approached steady state at different rates. Their values can be calculated at any time from the following expressions, which are derived in the Appendix

$$\omega_n = \frac{v\kappa^{1/2}}{(j_{max} - 1)}\left[\sum_j f_{R_1}(j) f_{R_2}(j) + \frac{(j_{max} - 1)^2}{v^2 D_M} \sum_k f_l(k)\right] \quad [25]$$

$$\omega_t = \left(\frac{k_a}{k_{et}}\right)\left[\frac{v\kappa^{1/2}}{(j_{max} - 1)}\right] \sum_j f_T{}^2(j) \quad [26]$$

The second term in [25] is introduced to account for those boxes in which the extent of the redox reaction is limited by the concentration of R_1 or R_2. The fractional concentration f_l refers to the limiting value f_{R_1} or f_{R_2}. The summation in the first term runs over all boxes j where a limiting reagent is not found. The summation in [26] runs over all boxes in the zone.

The validity of using ω_t and ω_n to determine the steady state was tested by monitoring the ratio of ω_t to ω_n for a special case. In the absence of triplet decay and radical ion quenching, all triplets must undergo triplet-triplet annihilation, and one obtains simply from stoichiometric factors

$$\frac{\omega_t}{\omega_n} = \frac{0.5\alpha}{\phi_f \phi_{tt}} = \frac{0.5\,\phi_t}{(1 - g)} \quad [27]$$

For the simulations considered here, where $\phi_t = 1$ and $g = 0.37$, Eq. [27] produces the numeric ratio $\omega_t/\omega_n = 0.794$. A valid simulation must predict this result. In addition, the value of ω_n calculated from

[25] ought to agree with the assigned value used to fix the injection rates of R_1 and R_2.

In general, we found that the ratio ω_t/ω_n was quite independent of model variables and was very close to 0.794. However, the individual values of ω_t and ω_n were significantly sensitive to the spatial resolution of the simulation. This effect is illustrated by the results in Table I. The reasons behind it are not fully understood. In part, it seems to stem from the ordered manner in which diffusion and the chemical processes are effected in the model. The sequential handling of processes that are actually concurrent may lead to a slightly erroneous steady state. Still, the important ratio ω_t/ω_n is reliably predicted, and the zone width parameter can be optimized so that the assigned and calculated values of ω_n agree very closely. The zone width scaler values listed in Table II for various values of ω_n yield agreement within 1% for a 51 box simulation. These values of v were used to obtain results reported below. They increase as ω_n falls, because the reaction zone expands as the concentrations and the gradients of the radicals decline.

Results and Discussion

The simplified view of the ECL reaction zone as a homogeneous region of light emission is a good first approximation for the case of (*i*) an infinitely fast ion annihilation rate, (*ii*) a very short triplet lifetime, and (*iii*) no triplet quenching by radical ions. However, the results of the simulations reported below indicate that this treatment cannot be extended to cases with realistic reaction parameters. In our work, we have assumed that the electron transfer rate constant is on the order of 10^{10} M^{-1} sec^{-1}. This figure accords with the few available experimental measurements (6, 18). For $t_f = 1$ sec, and $C_P^* = 10^{-3}M$, we arrive at $\kappa = 10^7$, which is a constant for all simulations. The rate constants k_a and k_q are probably significantly smaller than k_{et} (14, 19-25), hence we have used ratios (k_a/k_{et}) and (k_q/k_{et}) equal to 0.1 in our simulations. It is important to recognize that the values of κ, (k_a/k_{et}), and (k_q/k_{et}) must lie fairly near our choices, because the rate constants determining them are diffusion controlled (or nearly so) and should not vary much from system to system. In contrast, the rate constant for first-order triplet decay, k_1, has wide latitude. In carefully deaerated solutions, it probably corresponds to a lifetime $\tau_{max} = 1/k_1$ of perhaps 100 μsec. Under more favorable conditions, τ_{max} could approach or exceed 1 msec. Poor purity could produce a value as short as 1 μsec.

Table I. Dependence of simulation performance on zone width*

v	ω_n	ω_t	ω_t/ω_n
50	29.08	23.23	0.799
60	34.74	27.75	0.799
70	40.37	32.24	0.799
76†	30.15	24.11	0.799
80	31.67	25.33	0.800
90	28.23	22.65	0.802
100	26.34	21.21	0.805

* $\omega_n = 30$ (assigned), $j_{max} = 51$, $\kappa = 10^7$, $(k_1/k_{et}C_P^*) = 0$, $(k_a/k_{et}) = 10$, $(k_qk_{et}) = 0$, $\phi_t = 1$, $g = 0.37$, $D_M = 0.45$.
† Optimal v.

Table II. Optimal values of the zone width scaler*

Assigned ω_n	Optimized v
30	76
15	92
10	107
5	129
1	179
0.1	291

* $j_{max} = 51$, $\kappa = 10^7$, $(k_1/k_{et}C_P^*) = 0$, $(k_a/k_{et}) = 10$, $(k_q/k_{et}) = 0$, $\phi_t = 1$, $g = 0.37$, $D_M = 0.45$.

Shorter values would probably lead to complete loss of T-route emission and are not of interest. In all of our simulations, we assume that the electron transfer reaction produces triplets with efficiency $\phi_t = 1$.

Structure of the reaction zone.—Figures 2a and 2b illustrate the inhomogeneity of the reaction zone under realistic conditions. The radical ion profiles overlap considerably in the light emitting region, and the total radical ion concentration at the center is sizable. The illustrated case is for $\omega_n = 30$ and would apply at a point just earlier than $t_r/t_f = 0.001$. These results indicate that for a typical ECL experiment, where the bulk precursor is present at a 1 mmole level, the radical ion concentration is near $5 \times 10^{-5}M$ in the very early part of the light transient. Such a concentration is large enough to completely overshadow first-order decay, unless k_1 provides for triplet lifetimes less than 10 μsec.

This conclusion is very important for its bearing on the interpretation of magnetic effects. The rationale now offered for the magnetic enhancements that are universally seen for energy deficient systems rests on the assumption that triplet disappearance (aside from annihilation) is almost totally controlled by the radical ions (3, 4, 14, 15, 26, 27). Our present results strongly support the validity of that assumption, at least for the earliest experimental times, where magnetic measurements have usually been made.

At later times, when ω_n falls, the mean radical concentration across the light emitting region also declines, and first-order processes may regain control of triplet decay. For example, $\omega_n = 1$ yields a mean concentration near $5 \times 10^{-6}M$. This level would dominate triplet deactivation only in systems with τ_{max}

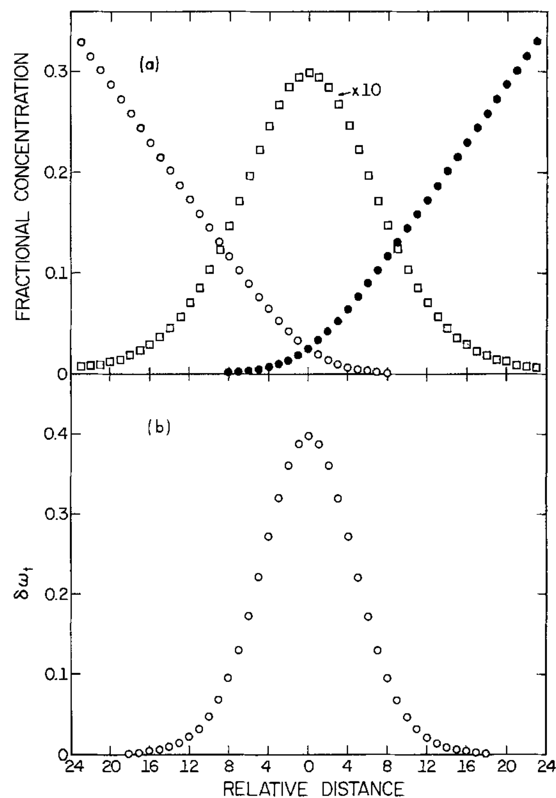

Fig. 2. Distributions across the reaction zone. (a) Concentration profiles: filled circles, R_1; open circles, R_2; squares, triplets. (b) Triplet-triplet annihilation rate; each point represents the contribution to ω_t made in a single box. Parameters: $\phi_t = 1$, $\kappa = 10^7$, $(k_a/k_{et}) = 0.1$, $(k_q/k_{et}) = 0.1$, $(k_1/k_{et}C_P^*) = 10^{-3}$, $j_{max} = 51$, $D_M = 0.45$, $g = 0.37$, $\omega_n = 30$. Distance axis is relative to the center of the reaction zone and is in units of Δx. For $t_f = 1$ sec, $C_P^* = 10^{-3}M$, and $k_{et} = 10^{10}$ M^{-1} sec^{-1}, this simulation corresponds to $t_r \sim 1$ msec and a first-order triplet lifetime of 100 μsec.

$= 1/k_1 \lesssim 100$ μsec. The corresponding experimental time is $t_r/t_f = 0.236$.

Also of interest is the distribution of light emission, which for a T-route system is directly proportional to the rate of triplet-triplet annihilation. The distribution for that process is shown in Fig. 2b. It is significantly narrower than the over-all reaction zone, because there is a square dependence on $[^3P^*]$, and because triplet-triplet annihilation becomes uncompetitive in the wings of the triplet distribution. For the conditions applicable to Fig. 2b, the width of the distribution at half-height is on the order of $10(D/k_{et}C_P^*)^{1/2}$, which amounts to about 10^{-5} cm for typical values of D, k_{et}, and C_P^*. At later times, the zone widens considerably, as one sees in Fig. 3, which gives the distribution of intensity with distance from the center. To facilitate comparisons of breadth, the curves in the figure have been normalized to unit height. Of course, the absolute intensity decreases with time, due to the steadily decreasing availability of R_1.

In general, the broadening of the emitting region results from three effects. The first of these is the increased overlap in the profiles of R_1 and R_2 as time proceeds. With decreasing ω_n, the concentrations of the radicals in the reaction region fall, hence the two reactants can penetrate their opposing profiles to greater distances before annihilation is assured.

A second factor reflects an interplay between the first-order lifetime τ_{max} and the rate of triplet-triplet annihilation. Since the latter factor depends on the square of the triplet concentration, its effect decreases with time as ω_n and the triplet concentration fall off. Triplet-triplet annihilation in these systems is often competitive with first-order decay; thus, the triplets live longer as the experiment proceeds and are able to diffuse further before deactivation.

The third effect leading to a broadening of the intensity distribution is the time dependence of triplet quenching by radical ions. This process also controls the actual triplet lifetime to a significant degree. Since the ion concentrations decrease steadily during the experiment, the triplet lifetime again increases monotonically, and the emission zone widens.

The triplet concentrations shown in Fig. 2a approach the highest that can be achieved, because ω_n is very large, and ϕ_t has been set to unity. The calculated level is on the same order as that of the radical ions and shows that triplet-triplet annihilation can indeed be competitive with other processes for deactivating triplets, particularly at early times. Annihilation efficiencies near 50% seem possible. At later times, the competitiveness of annihilation always declines, hence light from the T route must decay faster than ω_n does.

Effective width of the reaction zone.—The curves depicted in Fig. 4-6 illustrate the effect of triplet lifetime on the effective size of the emitting region. The circles in each figure represent simulations in which triplet quenching by radical ions is deleted; *i.e.*, $(k_q/k_{et}) = 0$. In those cases, the triplet lifetimes are constant with time, aside from the effect of annihilation, and the simplified treatment can be tested by direct comparison with the simulations.

Our test of the adequacy of that treatment is to examine the time dependence of the effective zone width parameter f, which is defined in [11]. It is

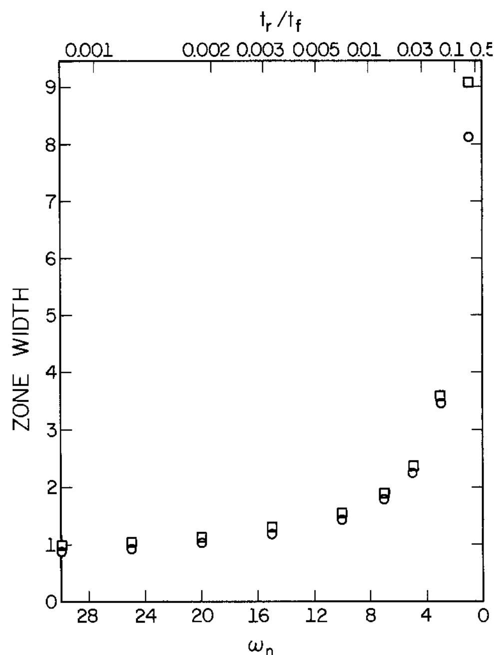

Fig. 4. Variation of effective zone width with ω_n. Circles show f vs. ω_n for $(k_q/k_{et}) = 0$. Squares show $f(\tau_{max}/\tau)^2$ vs. ω_n for $(k_q/k_{et}) = 0.1$. Both curves have ordinates multiplied by 100. All unspecified parameters are the same as for Fig. 2, except $(k_1/k_{et}C_P^*) = 0.1$. For $t_f = 1$ sec, $C_P^* = 10^{-3}$M, and $k_{et} = 10^{10}$ M^{-1} sec^{-1}, these curves correspond to $\tau_{max} = 1$ μsec.

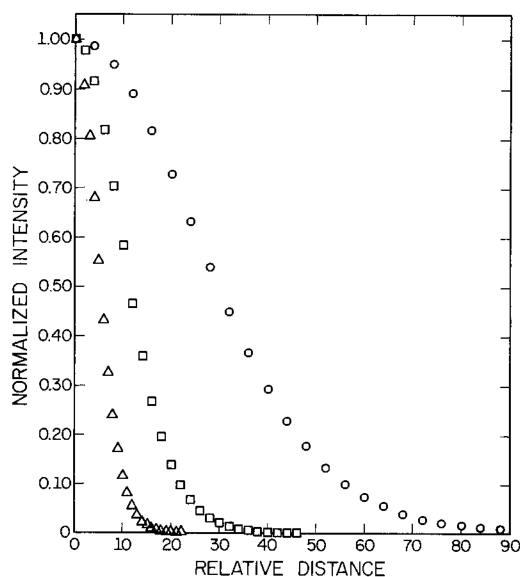

Fig. 3. Normalized intensity distributions as a function of ω_n. Same conditions as for Fig. 2. Circles, $\omega_n = 0.1$; squares, $\omega_n = 3$; triangles, $\omega_n = 30$.

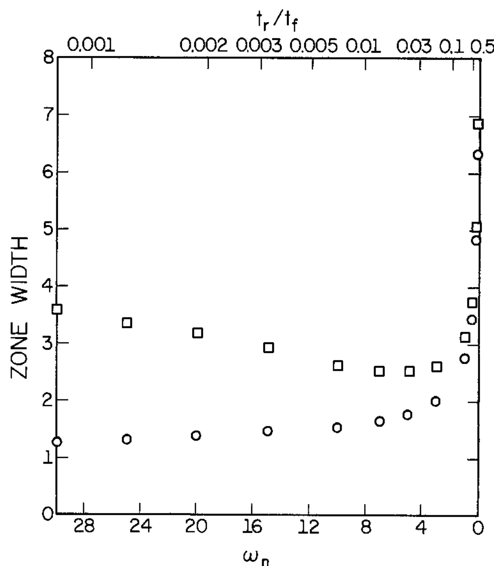

Fig. 5. Variation of effective zone width vs. ω_n. All details are the same as for Fig. 4, except $(k_1/k_{et}C_P^*) = 10^{-2}$. For $t_f = 1$ sec, $C_P^* = 10^{-3}$M, and $k_{et} = 10^{10}$ M^{-1} sec^{-1}, these curves correspond to $\tau_{max} = 10$ μsec.

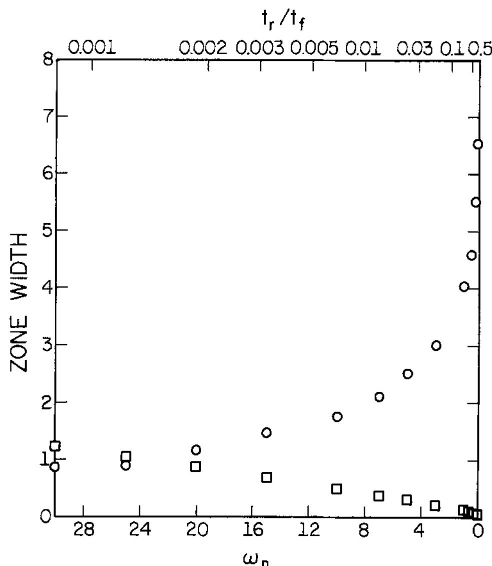

Fig. 6. Variation of effective zone width vs. ω_n. All details are the same as for Fig. 4, except $(k_1/k_{et}C_P^*) = 10^{-3}$. For $t_f = 1$ sec, $C_P^* = 10^{-3}$M, and $k_{et} = 10^{10}$ M^{-1} sec^{-1}, these curves correspond to $\tau_{max} = 100$ μsec. The squares have not been scaled upward, hence their true ordinates are ~100 times larger than those of the circles.

easy to obtain the value of f for any given reaction situation. The simulation yields ω_t for a particular set of dynamic parameters and a single defined value of ω_n. Equations [12] and [14] link ω_t and ω_n in an explicit manner for any set of dynamic conditions. Only f is freely adjustable. One can, therefore, calculate it from the simulated ω_t corresponding to any ω_n. This job is readily accomplished by the Newton-Raphson technique. The time dependence of f is important, because an assumption that it is constant underlies every proposed scheme for evaluating dynamic parameters from T-route decay curves.

The figures indicate that, in the absence of triplet quenching by radical ions, the effective size of the zone is strongly time dependent. It remains constant within a factor of two until ω_n reaches a value near 5 ($t_r/t_f \cong 0.02$). Smaller values of ω_n, applicable at later times, lead to drastic increases in effective zone size. This result in itself precludes the use of Feldberg plots for extracting dynamic parameters, because the plots utilize data only for values in the range $0.2 \leq t_r/t_f \leq 1.0$, where f changes most rapidly. The frequent experimental observation of Feldberg slopes steeper than -2.90 may manifest the expanding f. We shall address that aspect in more detail below.

It is interesting that changing the triplet lifetime τ_{max} from 1 to 100 μsec has little effect on the f function. This result suggests that the main determinant of effective zone thickness is not triplet diffusion, but overlap of the reactant profiles, unless τ_{max} is very long. The details of the f curve change from case to case, because the competitiveness of triplet-triplet annihilation varies in a complex way across the zone, and f must accommodate these spatial aspects.

The squares in Fig. 4-6 correspond to simulations in which the triplets are quenched by the radicals with $(k_q/k_{et}) = 0.1$. Simulated ω_t values were obtained for various sets of conditions in a straightforward manner, but comparisons with [12] and [24] were complicated by the fact that the triplet lifetime τ (which appears in β) varies across the reaction zone in a complex fashion. Our approach was to treat the aggregate $f(\tau_{max}/\tau)^2$ as an adjustable parameter that can be used to bring the simulated results and the simplified treatment into agreement. Applications of the simplified approach demand only that this aggregate be reasonably constant, and that is our concern here. The value of $f(\tau_{max}/\tau)^2$ is readily calculated for any set of conditions by the Newton-Raphson method.

The behavior of this function depends markedly on the value of the first-order lifetime τ_{max}. For very short τ_{max} (Fig. 4), radical ions are not competitive quenchers, hence $(\tau_{max}/\tau) \to 1$, and one obtains the f function defined earlier without quenching by radical ions.

For intermediate τ_{max} (Fig. 5), the radical ions are effective quenchers at early times. Thus $(\tau_{max}/\tau) > 1$, and $f(\tau_{max}/\tau)^2$ lies well above the f curve obtained without quenching by radicals. At later times, the concentrations of R_1 and R_2 decline, and they become less effective quenchers. The value of (τ_{max}/τ) then approaches unity, and the plot of $f(\tau_{max}/\tau)^2$ converges on that of f. Figure 5 is especially clear in showing that the effect of triplet quenching by the ions is greatest in the early part of the experiment. This point bears significantly on the interpretation of magnetic effects, as we have noted above. Since the intensity enhancement, according to current interpretation, is dependent on the degree of triplet quenching by the reactant ions, the largest positive field effect ought to occur on the height of the light pulse.

Figure 6 shows that triplets with long τ_{max} will be dominated in an ECL experiment by the radical ions. Since $(\tau_{max}/\tau) >> 1$, $f(\tau_{max}/\tau)^2$ lies far above the f curve obtained without quenching by radicals. (Note that the squares have been scaled down, relative to the circles, by a factor of 100.) As time proceeds, (τ_{max}/τ) becomes smaller, because the radical concentrations fall, and the curve of $f(\tau_{max}/\tau)^2$ approaches that of f. Even so, the rightmost square lies slightly above the corresponding circle.

Treatment of experimental data.—The results of the previous section show clearly that one cannot expect $f(\tau_{max}/\tau)^2$ to remain constant with time in any experiment. Thus, Eq. [12] does not straightforwardly describe the decay of emission from the T route, and treatments based on it can generally be expected to give only roughly approximate quantitative results. This statement is especially valid when a wide range of t_r/t_f is to be considered. Figures 4-6 suggest that reasonably good behavior might be encountered for times earlier than perhaps $(t_r/t_f) = 0.1$.

In the region used for Feldberg plots ($0.2 \leq t_r/t_f \leq 1.0$), $f(\tau_{max}/\tau)^2$ generally changes rather rapidly, and β changes in the same manner. One can expect to see nonlinear plots or plots with slopes steeper than the predicted upper limit of -2.90. Complications from side reactions may exacerbate these effects (13).

We propose to replace the Feldberg slope, as a diagnostic criterion, with a plot of ω_i/ω_n *vs.* t_r/t_f. Since ω_i/ω_n is the instantaneous chemiluminescence efficiency, it should start at some finite value and decay to zero at long times, if light arises via the T route. For an S-route process, however, ω_i/ω_n should be constant throughout the experiment. If a mixed ST process is encountered, ω_i/ω_n ought to decay to a constant, nonzero value that represents the S-route component.

In general, reliable quantitative efficiencies for the S route should be readily accessible from these plots. Useful estimates of T-route parameters might be obtained from the extrapolated intercepts at $t_r = 0$, but a theoretical basis for that operation would have to be established beforehand.

Acknowledgment

We are grateful to the National Science Foundation for supporting this work under Grant MPS-75-05361.

Manuscript submitted Oct. 14, 1977; revised manuscript received Feb. 27, 1978.

Any discussion of this paper will appear in a Discussion Section to be published in the June 1979 JOURNAL. All discussions for the June 1979 Discussion Section should be submitted by Feb. 1, 1979.

Publication costs of this article were assisted by the University of Illinois.

APPENDIX

Derivation of Eq. [18].—The radical ion reaction rate N can be expressed as the product of the area of the diffusion field A and the flux of R_1 at the outer edge of the reaction zone

$$N = \frac{AD}{\Delta x}[C_{R_1}(j_{max}) - C_{R_1}(j_{max} - 1)]$$

$$= \frac{ADC_P^*}{\Delta x}[f_{R_1}(j_{max}) - f_{R_1}(j_{max} - 1)] \quad \text{[A-1]}$$

Substituting for Δx and defining $J = f_{R_1}(j_{max}) - f_{R_1}(j_{max} - 1)$ one has

$$N = \frac{AD^{1/2}C_P^*\kappa^{1/2}J(j_{max} - 1)}{vt_f^{1/2}} \quad \text{[A-2]}$$

Rearrangement of [A-2] and substitution according to the definition of ω_n yields [18].

Derivation of Eq. [25].—The total reaction rate N is given by the sum of the reaction rates in the boxes of the zone. The reaction rate in a given box is given by the product of the volume of the box and the conventional reaction rate (moles per second) within the box. This relationship is expressed

$$N = \Delta x A\left[\sum_j k_{et}C_{R_1}(j)C_{R_2}(j) + \sum_k C_l(k)/\Delta t\right] \quad \text{[A-3]}$$

The first summation in [A-3] accounts for all boxes within the zone in which the extent of reaction is rate limited. In some boxes, however, the extent of reaction is limited by one of the radicals whose concentration is less than the product $k_{et}C_{R_1}(k)C_{R_2}(k)\Delta t$. For these cases, the second summation is required, where C_l is the concentration of the limiting radical and the index k runs only over pertinent boxes. Equation [A-3] can be rearranged, with appropriate substitutions, to

$$N = \frac{vt_f^{1/2}AD^{1/2}C_P^*}{(j_{max} - 1)\kappa^{1/2}}\left[\sum_j k_{et}C_P^*f_{R_1}(j)f_{R_2}(j) + \sum_k \frac{f_l(k)\kappa(j_{max} - 1)^2}{v^2D_Mt_f}\right] \quad \text{[A-4]}$$

Rearrangement to give ω_n yields [25].

Derivation of Eq. [26].—Since only the T route to emission is considered here, the intensity of emitted light is given by

$$I = \Delta x A\phi_{tt}\phi_f \sum_j k_aC_T^2(j) \quad \text{[A-5]}$$

which can be expanded to

$$I = \frac{vt_f^{1/2}AD^{1/2}C_P^{*2}\phi_{tt}\phi_f k_a}{(j_{max} - 1)\kappa^{1/2}} \sum_j f_T^2(j) \quad \text{[A-6]}$$

Following the same procedure as above for simplification and rearrangement, we arrive at [26], which is written in terms of $\omega_t \equiv It_f^{1/2}/(AD^{1/2}C_P^*\phi_{tt}\phi_f)$.

REFERENCES

1. S. W. Feldberg, *J. Am. Chem. Soc.*, **88**, 390 (1966).
2. S. W. Feldberg, *J. Phys. Chem.*, **70**, 3928 (1966).
3. L. R. Faulkner, *MTP Int. Rev. Sci.: Phys. Chem., Ser. Two*, **9**, 213 (1976), and references cited therein.
4. L. R. Faulkner and A. J. Bard, *Electroanal. Chem.*, **10**, 1 (1977), and references cited therein.
5. R. Bezman and L. R. Faulkner, *J. Am. Chem. Soc.*, **94**, 3699 (1972).
6. R. P. Van Duyne and S. F. Fischer, *Chem. Phys.*, **5**, 183 (1974).
7. L. R. Faulkner, *This Journal*, **122**, 1190 (1975).
8. P. R. Michael, Ph.D. Thesis, University of Illinois at Urbana-Champaign (1976).
9. P. R. Michael and L. R. Faulkner, *J. Am. Chem. Soc.*, **99**, 7754 (1977).
10. J. Chang, D. M. Hercules, and D. K. Roe, *Electrochim. Acta*, **13**, 1197 (1968).
11. E. W. Grabner and E. Brauer, *Ber. Bunsenges. Phys. Chem.*, **76**, 106 (1972).
12. R. Bezman, P. R. Michael, J. L. Morris, Jr., and L. R. Faulkner, Unpublished results (1970-1977).
13. L. R. Faulkner, *This Journal*, **124**, 1724 (1977).
14. L. R. Faulkner and A. J. Bard, *J. Am. Chem. Soc.*, **91**, 6497 (1969).
15. H. Tachikawa and A. J. Bard, *Chem. Phys. Lett.*, **26**, 10 (1974).
16. S. W. Feldberg, *Electroanal. Chem.*, **3**, 199 (1969).
17. J. T. Maloy, in "Laboratory Techniques in Electroanalytical Chemistry," P. T. Kissinger, Editor, Marcel Dekker, New York, In press.
18. S. Arai, A. Kira, and M. Imamura, *J. Chem. Phys.*, **54**, 5073 (1971).
19. G. Porter and M. R. Wright, *Discuss. Faraday Soc.*, **27**, 18 (1959).
20. C. A. Parker, "Photoluminescence of Solutions," Elsevier, Amsterdam (1968).
21. K. Kikuchi, H. Kokubun, and M. Koizumi, *Bull. Chem. Soc. Jpn.*, **41**, 1545 (1968).
22. F. Tfibel and L. Lindqvist, *Chem. Phys.*, **10**, 471 (1975).
23. D. K. K. Liu and L. R. Faulkner, *J. Am. Chem. Soc.*, **100**, 2635 (1978).
24. R. E. Schwerzel and R. A. Caldwell, *ibid.*, **95**, 1382 (1973).
25. J. A. Green and L. A. Singer, *ibid.*, **96**, 2730 (1974).
26. L. R. Faulkner, H. Tachikawa, and A. J. Bard, *ibid.*, **94**, 691 (1972).
27. P. W. Atkins and G. T. Evans, *Mol. Phys.*, **29**, 921 (1975).

Hole Reactions from d-Energy Bands of Layer Type Group VI Transition Metal Dichalcogenides: New Perspectives for Electrochemical Solar Energy Conversion

Helmut Tributsch

Fritz-Haber-Institut der Max-Planck-Gesellschaft, Berlin, Germany

ABSTRACT

Holes, photogenerated in d-energy bands of covalent semiconducting layer-type group VI-transition metal dichalcogenides react electrochemically differently from holes generated in semiconductors with valence bands based on p-orbitals (*e.g.*, CdS, ZnO, CdSe, GaAs). They do not constitute broken crystal bonds and do therefore not lead directly to an anodic photodecomposition of the electrode. The chemical character of these holes as missing d-electrons, on the other hand, gives rise to very specific electrochemical surface reactions with electron donors such as I^-, Br^-, and even OH^-, for example. The specific nature of the interfacial charge transfer complexes formed, their advantageous effect on the potential distribution in the electrode surface, and their favorable oxidation potential (in the case of the photoreaction with OH^- ions), respectively, may be the clue to a promising new approach to several unaccomplished goals of photoelectrochemical research, among them the construction of stable regenerative electrochemical solar cells and the oxidation of water with visible light. Photoelectrochemical measurements performed with $MoSe_2$ single crystals as well as experiments on solar energy conversion and photoelectrochemical reactions with water induced by visible and near infrared light are described as experimental evidence in support of this finding.

Recently, there have been considerable efforts to improve chemical stability of compound semiconductor electrodes (CdS, CdSe, CdTe, GaAs, GaP) for solar energy conversion in semiconductor liquid junction cells (1-9). Sulfide-polysulfides, telluride-polytellurides, or selenide-polyselenides (7,8) in the electrolyte or ultrathin noble-metal layers deposited onto the semiconductor electrode (6) have, with some success (7), been applied to reduce photocorrosion of the electrode surface.

The author's approach to the problem of light-induced photodecomposition was based on an entirely different idea; instead of trying to reestablish bonds broken by electron excitation in metal chalcogenides of considerable polar character or to prevent transport of reaction products, a search was initiated for new substrates which should provide favorable optical transitions between nonbonding orbitals which would therefore not affect the original bonding situation in the semiconductor surface. Such a property of a photoelectrode would not only appear to be interesting for continuously operating redox-photoelements but also for solar cells aimed at a photoelectrochemical dissociation of water for the purpose of generation of fuel.

A detailed theoretical analysis, mostly based on energetic and kinetic considerations, focused attention to $d \rightarrow d$ electron excitation in transition metal compounds and an approximation procedure to identify compounds with suitable energetically low-lying d-bands led to a simple criterion: to screen transition metal dichalcogenides for those with the smallest metal-metal distances (10). The analysis of 70 compounds showed that suitable target substrates had to be searched for among largely covalent layer-type compounds and not among more polar compounds of pyrite structure. As theoretically most promising layer compounds, WS_2 and MoS_2, and second in the line, $MoSe_2$ and WSe_2 were identified.

The experimental investigation of MoS_2 confirmed good photoelectrochemical activity. As expected, electrochemical hole reactions from d-bands of layer-dichalcogenides belonging to nonbonding orbitals of the transition metal were different as compared to hole reactions from anion p-bands in semiconductors of more polar bonding character (CdS, CdSe, PbS, GaAs). Instead of an anodic photodecomposition into metal ions and the chalcogenide in molecular form, upon illumination with visible light between 400 and 715 nm, MoS_2 reacts with water. The main reaction product is sulfate (11), however, at low anodic potentials the liberation of small quantities of oxygen could be traced by polarographic techniques (10). Evidence was given, that the mechanism leading to the photoelectrochemical oxidation of water is initiated by a hole-mediated transition of molybdenum from the four-valent to the five-valent state. An additional bonding possibility for OH^- ions is thus created from which electrons can subsequently be transferred to recombine with holes in the low lying d_z2-band of MoS_2 (10). Since the flatband potential of MoS_2 is found remarkably far in the anodic range, it became possible to construct a regenerative solar cell, in which p-MoS_2 is operating as a photocathode at which a suitable oxidizing agent of a redox couple is reduced (12).

The present paper extends investigations to $MoSe_2$. The basic scientific objective is an attempt to generalize and test the derived theoretical considerations on photoelectrochemical hole reactions from low-lying d-bands of transition metal compounds (10), the attempt to construct a regenerative solar cell with n-type MoSe as well as an investigation of whether light quanta of only 1.4 eV corresponding to infrared light of up to approximately 900 nm would be sufficient to initiate an oxidative reaction with water.

Experimental Methods and Materials

$MoSe_2$ crystals, grown by iodine-transport from the gas phase were obtained from the Kristallographisches Institut of the University of Freiburg (Prof. R. Nitsche). The surface dimensions of the thin layer crystals $d \lesssim 2 \times 10^{-1}$ mm were between 5 and 50

mm^2. Their appearance was similar to that of MoS_2, gray and metallic bright. They were contacted and embedded into a Teflon mounting according to a procedure described in Ref. (11). The surface preparation occurred through mechanical cleavage of the crystals by means of an affixed and subsequently pulled off adhesive tape or through a method especially elaborated for layer crystals, which is based on the abrasive action of a controlled water jet (11). The experiments were performed in a standard three electrode electrochemical glass cell with a saturated calomel reference electrode in water (0.1M KCl) as an electrolyte and an Ag/0.01M $AgClO_4$ reference electrode in acetonitrile (0.1M $LiClO_4$). Electrochemical measurements were made with a potentiostat and current-voltage curves plotted dynamically with a scanning speed of 4 mV/sec. Capacitive phase shift measurements were made with the lock-in technique. The light source was a xenon XBO-150W lamp. For the infrared portion of the photocurrent spectrum a 100W tungsten halogen lamp was used. The monochromator was a Bausch and Lomb high intensity model with interchangeable blazes for the visible and the infrared region.

Solid-State Properties of $MoSe_2$

Transition metal dichalcogenides with two-dimensional layer structures have received much attention from solid-state physicists (13-20). However, only partial experimental information is available for $MoSe_2$ (20-23). The basic structural unit of this compound is a sandwich of three planes: selenium-molybdenum-selenium. Within the planes the atomic alignment is in hexagonal packing. The Se-Mo-Se sandwiches are only loosely bound together through van der Waals forces. The most abundant hexagonal 2 H-polytype has two sandwiches per unit cell along the c-axis. The bonding character of $MoSe_2$ is mainly covalent and indicated by short Mo-Se and Se-Se distances. Hall measurements yielded electron mobilities of the order of 100 $cm^2\ V^{-1}\ sec^{-1}$ (16). Electrical measurements have been reported by several authors. P-type conduction (doping with Nb) as well as n-type conduction (doping with Re) have been shown to exist (13, 21). As in other layered transition metal dichalcogenides there is a pronounced anisotropy of electrical conduction. It is considerably (two to three orders of magnitude) larger parallel to the planes. Perpendicular to the planes, conduction occurs by a hopping mechanism (13).

Detailed band calculations apparently do not yet exist for $MoSe_2$. Sufficiently reliable information can, however, be deduced from theoretical work on MoS_2 (20, 24, 25) and from spectroscopic data on $MoSe_2$ (13). In MoS_2 the conduction band is approximately 3 eV wide and based on four of the six Mo 4d orbitals ($4d_{xy}$, $4d_{x2-y2}$), with antibonding admixtures of S 3p orbitals (Fig. 1). Separated by a hybridization gap (20) and approximately 1.75 eV below (as determined from the anodic photocurrent spectrum measured in the electrochemical cell arrangement) there is the energy band derived from the nonbonding Mo $4d_{z2}$ orbital holding two electrons per MoS_2. It is approximately 1 eV wide (electrons in this energy band do not contribute to the transition metal-dichalcogene bonding; however, the width of the band indicates that there is some bonding interaction among transition metal atoms). Below and slightly overlapping (0.1 eV) with the Mo d_2-band is the principal 3p valence band. Optical excitation in the visible spectral range consequently involves d → d transitions, a fact which has also been confirmed experimentally by parametric resonance measurements of holes (26). Transitions from the sulfur 3p to the unoccupied molybdenum 4d bands are only expected to occur in the near ultraviolet region (20). A series of details on excitons and electron-transitions are known for MoS_2 (13) which are not considered here for reasons of simplicity.

The main difference between the energy scheme of MoS_2 and $MoSe_2$ is that the d-hydbridization gap in $MoSe_2$ will be decreased to approximately 1.4 eV [a value determined from the electrochemical photocurrent spectrum and somewhat larger than a value of 1.1 eV deduced from solid-state measurements (23)] and the Mo d_{z2} band is more narrow due to weaker atomic interactions. This is shown in Fig. 1 together with the energetic position of redox couples in an aqueous electrolyte which is in contact with these molybdenum compounds as determined electrochemically by electron transfer studies in the dark and during illumination (investigated redox couples were H^+/H_2, I^-/I_2, $Fe(CN)_6{}^{-3/-4}$, Quinhydrone, $Fe^{2+/3+}$, Br^-/Br^2, $Ce^{3+/4+}$). Photoreactions in the near infrared and in the red region of the $MoSe_2$ spectrum have therefore to be expected to arise essentially from molybdenum d → d transitions. Light of shorter wavelength will in addition involve electron excitation from Se 4p orbitals. Holes generated in $MoSe_2$ electrodes will be available for surface reactions near the upper edge of the Mo 4 $d_z{}^2$ band and consequently do not represent missing chemical bonds such as, for example, holes in CdSe.

Experimental Results

The current voltage dependence of covalent $MoSe_2$ crystals is characterized by a behavior which is qualitatively different from that obtained for well-investigated semiconductor electrodes with valence bands derived from p-orbitals of the electronegative component such as ZnO, CdS, or GaAs (Fig. 2). The observed pronounced anodic photoeffect would appear to be typical for n-type semiconductors. However, when compared with the cathodic electrode behavior, there is no characteristic limiting behavior in the anodic region. In addition there is a slow and small photoeffect in the cathodic region. Capacitive phase-shift measurements (because of the difficulty of determining a reliable representative electrical circuit, no attempt has been made to specify the absolute capacitance) also lead to results which are not consistent with the experience from well-investigated semiconductors of similar bandgap since $MoSe_2$ electrodes like MoS_2 electrodes produce a pronounced capacitive minimum (Fig. 2). It is difficult to imagine an inversion of the space-charge layer within a narrow potential range in a semiconductor with a 1.4 eV bandgap. It is therefore suggested that kinetic phenomena and space-charge effects are jointly responsible for these capacitive properties. The clue to this peculiar electrochemical behavior of $MoSe_2$ are hole reactions from Mo-4 $d_z{}^2$ bands with water. They are clearly manifested by the

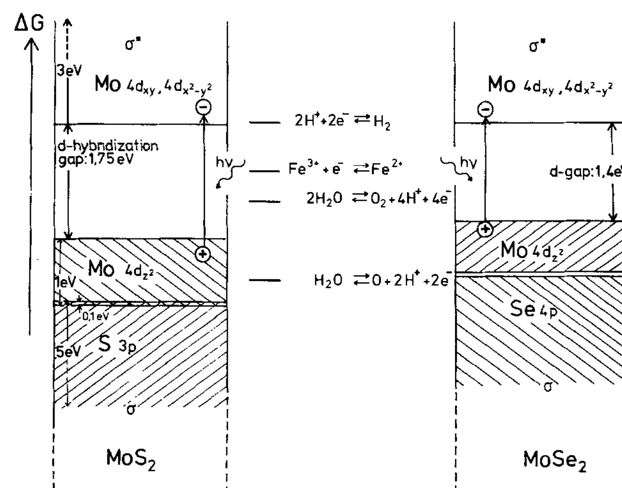

Fig. 1. Simplified energy schemes of MoS_2 and $MoSe_2$ as compared with the energetic position of redox couples in an aqueous electrolyte (acid solution, pH 1).

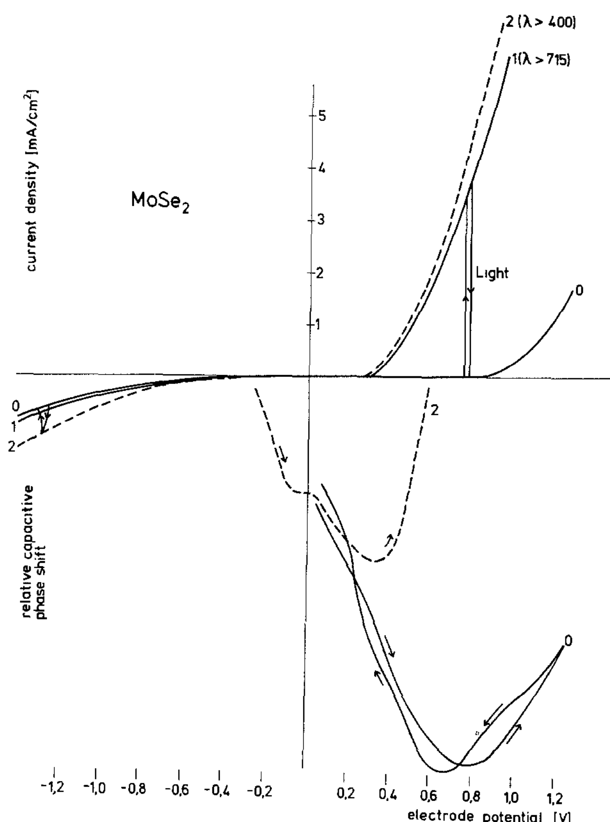

Fig. 2. Dynamic current voltage curves and relative capacitive phase shift (500 Hz) of $MoSe_2$-electrodes 0, dark effect; 1, illumination with $\lambda > 715$ nm (150W xenon lamp); 2, illumination with $\lambda > 400$ nm. Electrolyte, citrate buffer, pH 2/0.1M KCl. Potential sweep: 4 mV/sec.

kind of electrochemical reaction products which are obtained from the anodic reaction as well as evident from the current voltage behavior of $MoSe_2$. When a $MoSe_2$ electrode was illuminated with visible and near infrared light (xenon lamp, $\lambda > 400$ nm) and a photocurrent drawn at a potential of 0.6V (Fig. 2) for a prolonged time to yield a turnover of 26C of electric charge, only traces of elemental selenium were found on the electrode surface. However, there was an accumulation of soluble selenium in the electrolyte (citrate/HCl-buffer, pH 2; 0.1M KCl) in the form of selenic acid and a red deposit of elemental selenium formed on the Pt counterelectrode. The latter was found to be the result of an electrochemical reduction of selenic acid from the electrolyte to elemental selenium. A quantitative analysis confirmed the following anodic photoelectrochemical reaction as predominant reaction path (h^+ = holes)

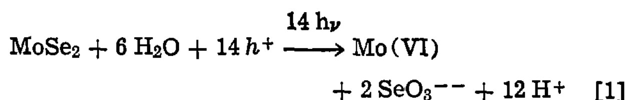

$$MoSe_2 + 6\,H_2O + 14\,h^+ \xrightarrow{14\,h\nu} Mo(VI) + 2\,SeO_3^{--} + 12\,H^+ \quad [1]$$

Of 3.13 mg originally crystal bound selenium, 1.83 mg were subsequently found in soluble form in the electrolyte and slightly more than 1 mg as elemental selenium on the counterelectrode. (Mo and soluble Se were measured photometrically with thiocyanate complex and diaminobenzidine, respectively.) The involvement of water in the anodic hole reaction was thus confirmed for $MoSe_2$. In addition, the anodic liberation of soluble SeO_3^{--} and its subsequent cathodic reduction to elemental selenium was recognized as the mechanism essentially responsible for the small and relatively slow cathodic photoeffect, observed during the cyclic plot of current-voltage characteristics (Fig. 2); it results from a thin p-conducting deposit of selenium with an approximate absorption edge of 1.9 eV. It could be confirmed, that, with respect to the photoeffect of $MoSe_2$ (bandgap = 1.4 eV), its spectral response was shifted toward shorter wavelengths and the cathodic photocurrent could be clearly increased by adding SeO_3^{--} to the electrolyte. The mechanism of the anodic photoreaction of $MoSe_2$ with water is especially interesting, since it can proceed even with near infrared light up to 900 nm.

Figure 3 shows the spectral dependence of the anodic photocurrents of $MoSe_2$ on the wavelength of the incident light and compares it with the corresponding photocurrent spectrum of MoS_2. With both systems the photocurrent output gradually drops toward the u.v. region although the light absorption in the bulk continues to increase (13). It is suggested that the photocurrents of these layer crystals essentially arise from d → d phototransitions (compare Fig. 1 and 3) and are for some unknown reasons suppressed if sulfur p-orbitals are involved. In order to get some insight into the mechanism which enables holes from a d-band to react with OH^- ions at energy levels close to the thermodynamic 2-electron transfer oxidation potential of water (1.23V) and considerably more negative than the 1-electron transfer potential ($\sim$ 2V) (Fig. 1), some experiments have been performed with organic electrolytes. If $MoSe_2$ is in contact with acetonitrile (0.1M $LiClO_4$) the anodic photocurrents are very small and can be attributed to traces of water in the organic solvent. They systematically decrease with increasing purification from water (molecular sieve).

The photocurrents can be made to increase if a suitable reducing agent such as hydroquinone is added to the acetonitrile (Fig. 4b). Photocurrents consequently only pass the interface if electrons are transferred into the electrode to recombine with holes which cannot leave the electrode surface by means of liberating ions from the solid. If instead of a typical reducing agent water is added to the organic electrolyte, photocurrents are produced in the same way (Fig. 4a). With photogenerated d-holes it apparently reacts efficiently as an electron donor. This behavior has not been observed with nonlayered semiconductor electrodes until now. CdS, for example, the valence bandedge of which is situated at much more positive redox potentials than that of $MoSe_2$ [its energy band scheme approximately corresponds to that of $MoSe_2$ (Fig. 1) without the low-lying 4 d_{z^2} band] does not react photoelectrochemically with water. Anodic photocurrents which result from a photodecomposition of CdS continue to flow in presence of oxidation resistant organic electrolytes in contrast to the situation with d-band conductors such as MoS_2 or $MoSe_2$. Here it is necessary that a hole oxidizes an OH^- ion or water (or another oxidizable

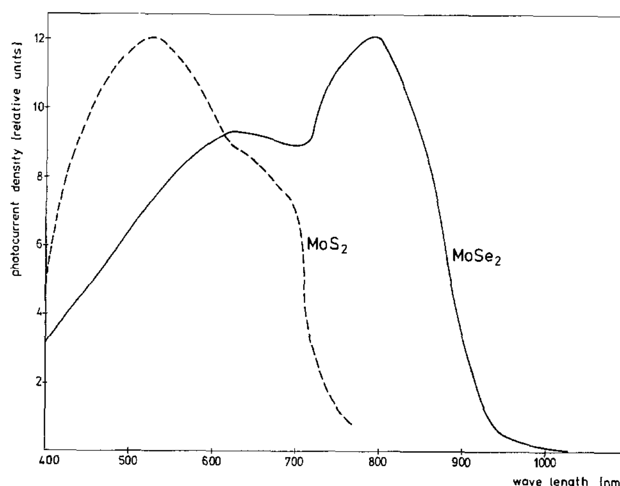

Fig. 3. Spectral dependences of anodical photocurrents of $MoSe_2$ normalized to constant quantum density (citrate/HCl-buffer, pH 2, and MoS_2 (0.1M KCl)).

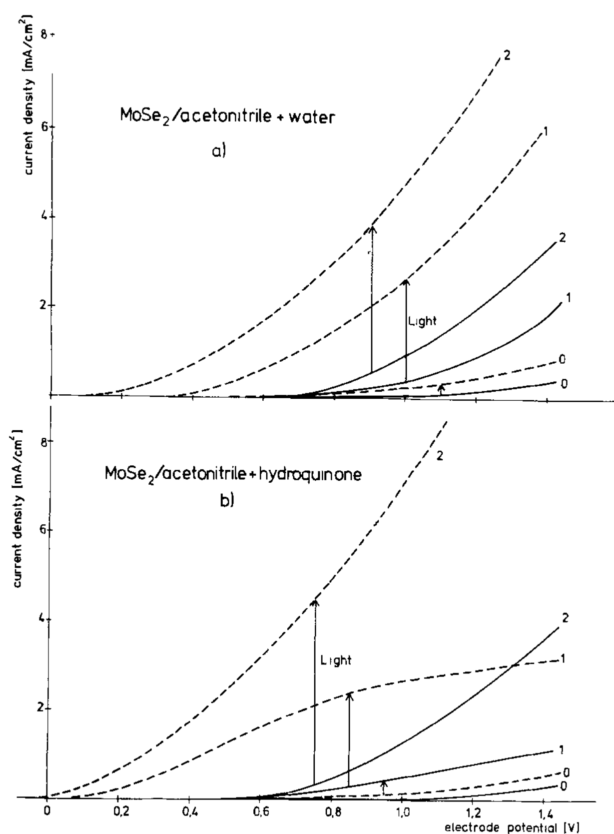

Fig. 4. Anodic photocurrents of $MoSe_2$ in acetonitrile (0.1M $LiClO_4$, 0.03% H_2O), reference electrode, Ag/0.01M $AgClO_4$. (a) Effect of water-additions. 0, 0.03 v/o H_2O; 1, 1.55 v/o H_2O; 2, 5.2 v/o H_2O. (b) Effect of hydroquinone-addition (photocurrent, dotted curves). 0, no HQ; 1, 4.25 $\times$ 10^{-3} HQ; 2, 1/10 saturated solution of HQ.

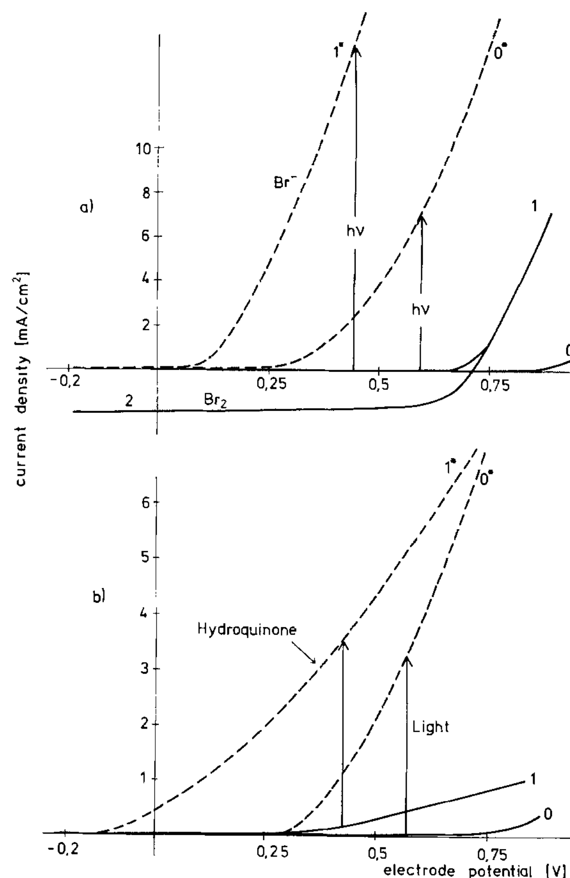

Fig. 5. Negative shift of anodic onset of photocurrents (*) and dark currents upon addition of Br^- (a) and hydroquinone (b) to an aqueous electrolyte (0.1M KCl); 0,0: aqueous electrolyte; 1,1: after addition of reducing agent. 2 in (a): cathodic reduction of Br_2.

agent) in the electrolyte to produce charge transfer across the layer crystal-electrolyte interface. The oxidation of OH^- ions or water molecules has therefore to be considered the primary step of the mechanism leading to the generation of anodic photocurrents, although the principal oxidation product is not oxygen, but selenic acid (compare reaction [1]). It is therefore justified to conclude that holes in energy bands derived from d-orbitals are reacting electrochemically differently from holes in energy bands derived from p-orbitals. Support for this conclusion may also be found in the observation that $ZrSe_2$ and $HfSe_2$, which have the same layer structure as $MoSe_2$ but an empty d_{z^2}-band (compare Fig. 1) and consequently hole reactions from Se p-bands, do anodically produce elemental selenium and not selenic acid. The peculiarity of hole reactions from d-bands is also evident from the interaction of redox couples of less positive redox potential with the $MoSe_2$-electrode. If an anodic potential is applied to an illuminated n-type semiconductor and if suitable electron donors are available in the electrolyte, the migration of holes, generated in the space charge layer, to the electrode surface should be the rate-limiting process controlling the onset of anodic photocurrents. With $MoSe_2$ the onset of anodic photocurrents is, however, strongly dependent on the type of redox couple added to the electrolyte. Redox couples, the oxidation potential of which is more positive than that of water, generally shift the onset of photocurrents and dark currents toward more negative electrode potentials. Figures 5 and 6 demonstrate the effect of hydroquinone, Br^- and I^-. They shift the photocurrent onset up to approximately 0.4, 0.25, and 0.6V, respectively. Figure 6 shows how additions of I^- ions gradually suppress the photocurrent resulting from the oxidation of water and build up new photo and dark currents arising from the oxidation

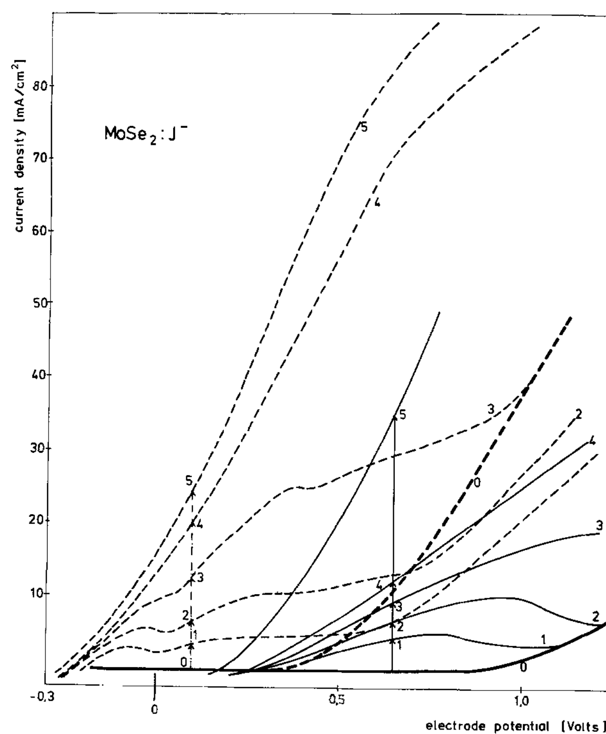

Fig. 6. Influence of I^- on the anodic dark currents and photocurrents (broken lines) of $MoSe_2$ (in order to keep the redox potential constant, I_2 was also added at a concentration ten times smaller than that of I^-). 0, 0.5M Na_2SO_4, no KI; 1, 10^{-1}M KI; 2, 2 $\times$ 10^{-1}M KI; 3, 5 $\times$ 10^{-1}M KI; 4, 1M KI; 5, sat. solution of KI. Illumination, 150W xenon, $\lambda > 615$ nm. Scanning (4 mV/sec) in direction of increasing positive electrode potential.

of iodide. Most remarkably the onset of the new dark current which leads to the formation of iodine is finally more negative than the original photocurrent arising from the oxidative reaction with water.

The fact that certain redox couples produce large photocurrents through $MoSe_2$ electrodes at potentials which they also would produce at a metal electrode, the standard redox potential of I^-/I_2 in aqueous solution which adjusts itself at the metal counterelectrode is, for example, + 0.293V against a SCE (compare Fig. 6), indicates that this effect could be used to drive regenerative electrochemical solar cells. Since the photoreaction with water only starts at more positive electrode potentials and since it is, in addition, suppressed in the presence of a suitable redox couple (*e.g.*, I^-/I_2) there is also a good chance that $MoSe_2$ photoelectrodes would be corrosion resistant. Solar cells, based on d → d electron transitions in combination with anodic electron transfer from Fe^{2+} and I^- respectively have actually been put into operation and are described elsewhere in more detail (27). With the $MoSe_2$:I^-/I_2 solar cell (current-voltage behavior in Fig. 6) photocurrent densities of 23 mA/cm^2 and photopotentials of 0.55V were produced. At moderate light intensities (21 mW/cm^2) energy conversion efficiencies between 4-5% were found for illumination with red and near infrared light. Longtime experiments actually suggest an apparently corrosion-free operation of the cell: Photocurrent densities between 10 and 12 mA/cm^2 were drawn over a load resistance of 100Ω over a period of more than 120 days without any visible deterioration of the performance of the approximately 1/10 of a mm thick $MoSe_2$ electrode (Fig. 7). It seems that only electrons and no ions are passing the $MoSe_2$/electrolyte + I^-/I_2 interface.

An important problem (it is the clue to the anodic stability of the $MoSe_2$ electrochemical solar cell) is the question, why reducing agents such as I^- or Fe^{2+} are photo-oxidized at more negative potentials than OH^- ions although all three systems should energetically be placed above the Mo 4 d_{z^2} "valence"-band and the oxidation controlled by the availability of holes which reach the electrode surface. An investigation of capacitive phase shifts at $MoSe_2$ electrodes [measurement of $U = (2U_m/\pi) \cos\phi \approx (2U_m/\pi)\phi$ with lock in technique] has provided some interesting insight into this phenomenon (Fig. 8). When they are in contact with neutral 0.5M KCl or Na_2SO_4 solution a pronounced minimum is found between +0.5 and +0.6V. When I^-/I_2 is added, this minimum is gradually, with increasing concentration of the redox couple, shifted toward more negative potentials. At a concentration of

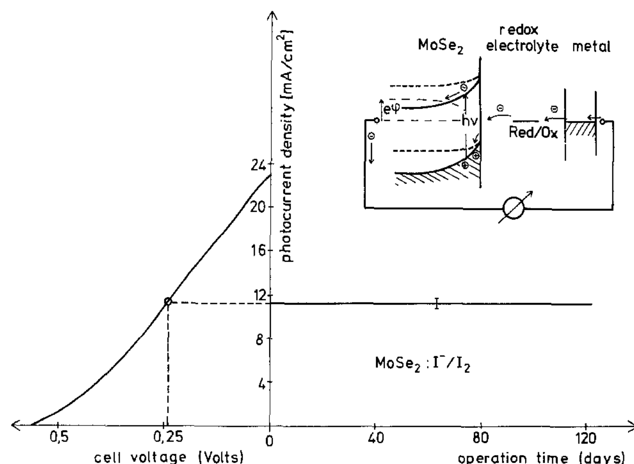

Fig. 7. Operation mode, power characteristic, and stability of $MoSe_2$: I^-/I_2 solar cell. Electrolyte, 1M I^-, 10^{-1}M I_2 (water); work resistance, 100Ω; access of air, no stirring; 150W xenon lamp, λ > 615 nm.

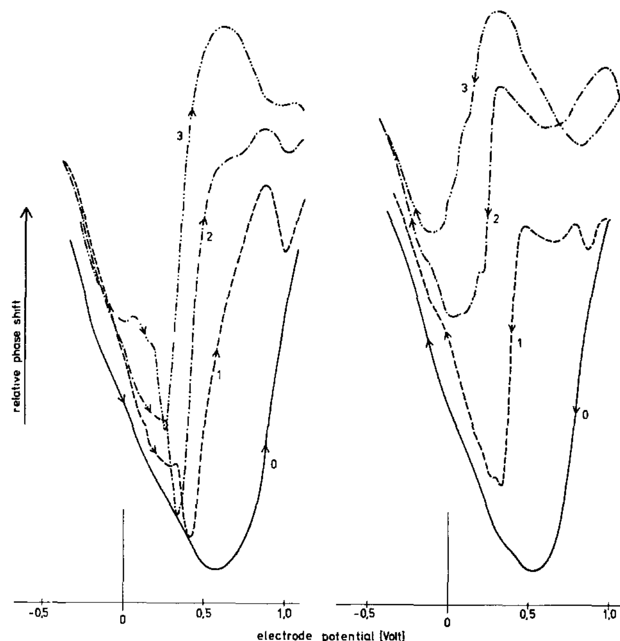

Fig. 8. Dependence of the capacitive phase-shift minimum of $MoSe_2$ on additions of the I^-/I_2 redox system for scanning in opposite potential directions. Potential sweep: 15 mV/sec. Frequency 500 Hz, N_2-bubbling. 0, 0.5M Na_2SO_4; 1, 1.3 × 10^{-3}M KI, 1.3 × 10^{-4}M I_2; 2, 8 × 10^{-3}M KI, 8 × 10^{-4}M I_2; 3, 10^{-1}M KI, 10^{-2}M I_2.

10^{-1}M KI and 10^{-2}M I_2 it is found at +0.25 (for the curve plotted in anodic direction) and at −0.1V (for the curve plotted in cathodic direction). Concurrently same major changes of the shape of the curve occur and finally an additional, smaller minimum appears on the positive potential side (Fig. 8). It was originally not entirely evident why an n-type semiconductor with a forbidden bandgap as large as 1.4 eV can have such a pronounced capacitive phase shift minimum. This would presuppose that the charge in the space-charge layer can be inverted within a surprisingly narrow potential range. Since this is not easily possible through thermal activation across a 1.4 eV gap from the Mo 4 d_{z^2} to the Mo 4 d_{xy,x^2-y^2} conducting band, it has to be examined whether the minimum is obtained by the combination of a space charge effect and a kinetic phenomenon on the electrode surface. Such a situation is actually confirmed experimentally. The capacitive phase shift-branch at more negative potentials may be considered relatively stable, while the position of the positive branch is strongly dependent on the presence of the reducing agent (iodide) in the electrolyte so that the minimum is not only shifted but also becoming more narrow with increasing concentration of I^- (compare Fig. 8). The positive branch of the capacitive phase shift may therefore be regarded a consequence of the reaction of an oxidizable agent (*e.g.*, OH^-, I^-) with the electrode surface. A support for this conclusion is also the fact that the capacitive phase shift minimum is to be found near the onset of anodic oxidation currents and correspondingly shifted with increasing concentration of the electron donor (compare Fig. 6 and 8). Additional evidence may also be deduced from the observation that illumination, in absence of I^-/I_2, shifts the capacitive minimum to negative potentials (Fig. 2) and that anodic polarization of the electrode in presence of I^-/I_2 is followed by a similar negative shift of the capacitive minimum (compare scanning of capacitive curves into positive and negative potential directions in Fig. 8). The information content of the phase-shift measurements is, as presented, somewhat ambiguous. At the moment, it is not possible to deduce the real interface capacitance due to the lack of information needed to design a representative electrical

circuit for layer crystal interfaces. Necessary measurements of frequency behavior and the influence of redox agents are presently being performed.

Several additional experimental observations seem worth mentioning. The reducible components of the redox couples investigated (I_2, Br_2, quinone, Fe^{3+}) always produce cathodic dark currents at the $MoSe_2$ electrode. They are generally overlapping the potential range in which photocurrents are produced and, especially with I^-/I_2 and Br^-/Br_2 they directly pass over into the anodic dark current which arises from the oxidation of I^- and Br^-, respectively (*e.g.*, Fig. 5a, curve 2). Cathodic dark currents and anodic photocurrents are therefore superposed on each other. If I_2 or Br_2 is absent from the electrolyte and the electrode illumination switched off, a cathodic dark current, arising from the reduction of anodically formed I_2 or Br_2 will flow for a short time. There is also some photoenhancement of the cathodic reduction current in form of a very slow photo or temperature effect (observed with Br^-/Br_2). The superposition of anodic and cathodic reactions occurring in the same potential region makes the systems kinetically relatively complicated. An indication for intricate reactions is also the occurrence of electrochemical current oscillations which have frequently been observed with the $MoSe_2$: I^-/I_2 system in the potential range between + 0.5 and + 1.0V. They are a definite sign of proceeding autocatalytic surface reactions.

Discussion

The experimental observation that near infrared light leads to an anodic photoreaction of $MoSe_2$ in presence of water but not in presence of acetonitrile, and the fact that selenic acid is found to be the main reaction product leaves practically no doubt that the formation of a chemical bond between the illuminated semiconductor and water (OH^-) is involved in this reaction. Additional arguments against a following reaction of water with a hypothetical photodissolution product of $MoSe_2$ are that (*i*) photocorrosion does not occur if the oxidation reaction involves a reducing agent (*e.g.*, I^-) which does not form a soluble compound with selenium (compare long time experiment of Fig. 7), (*ii*) the oxidation product (H_2SeO_3) does not form with CdSe although this compound photocorrodes, and (*iii*) that elemental selenium, not selenic acid is found anodically at $HfSe_2$ and $ZrSe_2$ electrodes which have the same structure as $MoSe_2$ but in which hole reactions occur from p-bands below the empty d_{z^2} band (compare Fig. 1). A bond formation between illuminated $MoSe_2$ and OH^- ions is the only mechanism explaining the energetic feasibility of a reaction with water without having to postulate a theoretically ideal one-step 2-electron transfer reaction near its thermodynamic standard redox potential (+ 1.23V). A chemical bonding as an intermediate step also explains why a transition from MoS_2 to $MoSe_2$, corresponding to a shift of the Mo 4 d_{z^2} bandedge toward negative redox potentials by approximately 0.35 eV (compare also Fig. 3) is not reflected in a significant change of the semiconductors photooxidative reactivity with water. In both cases, with MoS_2 as well as with $MoSe_2$, there is apparently sufficient interaction energy to discharge OH^- ions: The chemical interaction of an OH^- ion with a surface hole in the d-band will result in the formation of a complex which is apparently characterized by an occupied electronic state situated above the edge of the 4 d_{z^2} energy band. It can be further oxidized by an additional hole in the d-band. Why is there a formation of a chemical bond when a d-hole reaches the semiconductor surface? Is it possible that missing d-electrons convert a layer crystal surface which only exhibits van der Waals interactions into a surface forming chemical bonds with molecules capable of donating electrons? Previous studies performed to analyze the photoelectrochemical reaction of water with MoS_2 electrodes (10) have yielded a reasonable qualitative explanation. In contrast to holes in energy bands derived from p-orbitals (*e.g.*, CdS, ZnO), which represent broken polar bonds, holes in d-bands of molybdenum dichalcogenides mean an increase of the valence state of molybdenum. A transition from Mo(IV) to $Mo(V)^+$ in the electrode surface, however, would be paralleled by a reorganization of electron densities leading to changes in the crystal geometry and to the liberation of an additional bond. OH^- ions would interact with it to produce a Mo(V)-(OH) complex. The corresponding electronic level rises above the edge of the Mo 4 d_{z^2} band and will serve as trap for holes which further oxidize the complex (Fig. 9). The finding of this investigation that reducing agents such as I^-, Br^-, hydroquinone, $Fe(CN)_6^{4-}$, or Fe^{2+} shift the anodic onset of $MoSe_2$ photocurrents (in the presence of water) and induce dramatic changes in the potential structure of the double layer (as measured with the I^-/I_2 redox couple) provides convincing additional support for the formation of complexes between electron donors and surface states produced by d-holes. OH^- ions are included in the list of complexing electron donors. Experimental consequences are a *p*H dependent onset of anodic photocurrents and a *p*H and water-dependent capacitive behavior. The peculiarity of individual complexes explains the observations that potential shifts in the current voltage behavior do not reflect a simple relation with redox potentials and their specific importance as transition states for photoactivated electron transfer makes it understandable why high photocurrents can pass the electrode surface for a long time without leading to inhibition phenomena, typical for many electrochemical processes: If the Mo(V)-Red (Red = reducing agent) surface complex is oxidized by holes from the lower Mo 4 d_{z^2} energy band (Fig. 9), the bond of the original electron donor is simply broken and the oxidized reactant desorbed. (It is presently not yet known to what extent half crystalline sites are favored in this complex formation). It is also relatively easy to understand why the presence of a reducing agent such as I^- suppresses the photoreaction of $MoSe_2$ with OH^- ions. The potential drop, which the complex-formation of I^- with the surface produces, generates a relative shift between energy levels in the electrode surface and in the electrolyte (Fig. 9c). Electron transfer from OH^- is thus suppressed while transfer from I^- is still possible and the generation of photocurrent is considerably facili-

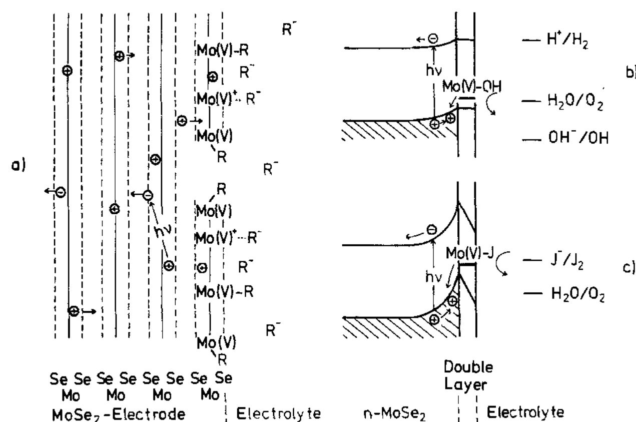

Fig. 9. Complex formation between d-hole and electron donor (R^-) on the surface of a layer crystal ($MoSe_2$). (a) Structural scheme of $MoSe_2$-electrode surface, (the surface Se-Mo-Se sandwich is interrupted to show possible electrochemical attack parallel to layers). (b) and (c), respectively, energy scheme visualizing its function during the photoelectrochemical oxidation of water (OH^-) and its role in the generation of a double layer and space charge layer favorable for electron transfer during regenerative solar energy conversion.

tated through the induced positive charge in the space-charge layer.

These arguments provided for a complex formation between reducing agents and vacant d-states in transition metal-dichalcogenide layer crystals receive substantial support from the remarkable crystal-chemical property of these compounds. They belong to a class of lamellar hosts capable of intercalating organic compounds between the composite sheets of their chalcogenide-transition metal-chalcogenide sandwiches (15, 28-34). A most interesting detail is that the guest molecules have to be Lewis bases (*e.g.*, ammonia, pyridine) or electron donating species (such as alkali metals) and another one that the intercalate formation with organic molecules works well with layer crystals belonging to Group V transition metals (TaS_2, NbS_2), in which the low energy d-bands are only half filled, giving them metallic character, but not with those belonging to Group VI transition metals (MoS_2, WS_2) which are semiconductors with full d-bands (29). The experimental observation that the ability to form organic intercalation complexes disappears with the filling of the low energy d-band (29) and the finding that the interaction responsible for intercalation involves a donation of electron charge from the nitrogen of the organic or from the inorganic electron donor to the layer crystal (29, 33) leaves no doubt that vacant low lying d-orbitals play a crucial role as electron acceptors during complex formation. Since holes photogenerated or anodically formed in molybdenum dichalcogenide electrodes would create the necessary preconditions for this complex formation with electron donating compounds it may be concluded that the complex-formation described in our photoelectrochemical study is deducible to the same kind of electronic interaction which is responsible for intercalate formation. A detailed molecular understanding of the electronic structure of these transition complexes will therefore go parallel with a better understanding of intercalate formation which is still very fragmentary. An obvious conclusion, which has already been successfully tested experimentally, is that electrochemical studies of the reaction of transition metal dichalcogenide layer crystal electrodes with intercalating compounds will be most instructive for a better comprehension of the mechanism of intercalation.

The finding that photogenerated holes from d-bands of Group VI transition metal layer-semiconductors react with oxidizable agents by way of formation of charge transfer-transition complexes could have major consequences for future developments in photoelectrochemistry and photoelectrochemical energy conversion. One important conclusion is that photoassisted or photopowered oxidation of water with visible light or even near infrared light may be an achievable goal with suitable hole reactions from d-bands. Experimental studies performed with MoS_2 have demonstrated photoelectrochemical oxygen evolution from water, although it is only a subordinate process and in the long run most of the light energy is channeled into sulfate formation because of the reactive intermediate's attack on crystal bound sulfur (10). Once the energetically efficient d-band mechanism of photoelectrochemical oxidation of water is thoroughly understood, it may be tried to produce favorable d-bands for hole reactions in more oxidation resistant electrodes or it may be tried to improve oxygen evolution catalytically. Attempts in this direction have already been started with MoS_2 (10). It is interesting to note that a d-hole mediated valence increase of a transition metal compound to yield a transition metal hydroxide which can further be oxidized to liberate molecular oxygen might not be a newly discovered mechanism but applied in one of the most basic processes of life. Why exactly are holes from reaction centers in photosynthetic systems channeled into an oxidation complex for water which is based on a transition metal (manganese) which is apparently being oxidized (35) (necessarily by an extraction of d-electrons) as intermediate step toward oxygen evolution?

Experiments with the photooxidation of water at MoS_2 and $MoSe_2$ electrodes suggest that such a mechanism is kinetically or energetically reproducible with hole reactions from d-bands of a semiconductor provided a secondary destructive oxidation by reactive intermediate compounds is avoided by appropriate chemical bonding in the neighborhood of the transition metal reaction center.

The inability of holes in an energy band derived from nonbonding d-orbitals to initiate anodic photocorrosion, in combination with their specific charge transfer interaction with reducing agents have finally provided a basis for regenerative electrochemical solar cells which seem to be sufficiently stable to be developed for practical use (27). The experimental evidence suggests that it is much more reasonable not to break chemical bonds in a photoelectrode surface at all than to try to repair them by complicated successive chemical reactions from the electrolyte.

From theoretical points of view tungsten dichalcogenides will photoelectrochemically behave very similarly to molybdenum dichalcogenides and interesting additional experience on d-band electrochemistry will be obtained from Group IV and V transition metal layer crystals. Preliminary studies of several among the latter compounds have confirmed unusual electrochemical mechanism also there. For example, anodic photocurrents in the mA/cm^2 range have been observed with $2H\text{-}TaS_2$ (and NbS_2) although its solid-state behavior is typically metallic with hole concentrations exceeding 10^{22} cm^{-3}. Mixed layer compounds which would permit a gradual filling of d-bands should be promising substrates for research into d-hole reactions as well.

There is one important circumstance to be considered, when dealing with d-hole reactions in which the formation of specific surface complexes is involved. It will not be admissible to apply the simplified theoretical concepts developed for electron transfer between semiconductor electrodes and redox couples in the electrolyte which neglect chemisorption of the reactants. The closest approach to the problem of d-hole reactions may be a theoretical model which has been discussed as a special reaction type of electrocatalysis (36). It is the case of surface states on an electrode which strongly interact with both the electronic bulk of the electrode and the redox couple in the electrolyte.

Acknowledgment

This work became possible through a grant on applied sulfide electrochemistry from the Deutsche Forschungsgemeinschaft. The author thanks Prof. Gerischer for supporting the project and for interesting discussions. The technical help received from Mrs. C. Lober is gratefully appreciated.

Manuscript submitted Oct. 26, 1977; revised manuscript received March 9, 1978.

Any discussion of this paper will appear in a Discussion Section to be published in the June 1979 JOURNAL. All discussions for the June 1979 Discussion Section should be submitted by Feb. 1, 1979.

REFERENCES

1. H. Gerischer, *J. Electroanal. Chem.*, **58**, 236 (1975).
2. H. Gerischer and J. Gobrecht, *Ber. Bunsenges. Phys. Chem.*, **80**, 327 (1976).
3. B. Miller and A. Heller, *Nature (London)*, **262**, 680 (1976).
4. G. Hodes, J. Manassen, and D. Cahen, *ibid.*, **261**, 403 (1976).
5. A. Heller, K. C. Chang, and B. Miller, *This Journal*, **124**, 697 (1977).
6. Y. Nakato, K. Abe, and H. Tsubomura, *Ber. Bunsenges. Phys. Chem.*, **80**, 1002 (1976).

7. K. C. Chang, A. Heller, B. Schwartz, S. Menezes, and B. Miller, *Science*, **196**, 1097 (1977).
8. (a) A. B. Ellis, S. W. Kaiser, and M. S. Wrighton, *J. Am. Chem. Soc.*, **98**, 6418 (1976); (b) A. B. Ellis, S. W. Kaiser, and M. S. Wrighton, *ibid.*, **98**, 6418 (1976); (c) A. B. Ellis, S. W. Kaiser, and M. S. Wrighton, *ibid.*, **98**, 6855 (1976).
9. H. Gerischer, lecture given at International Conference on the Photochemical Conversion and Storage of Solar Energy, London, Ontario, Aug. 1976.
10. H. Tributsch, *Z. Naturforsch.*, **32a**, 972 (1977).
11. H. Tributsch and J. C. Bennett, *J. Electroanal. Chem.*, **81**, 97 (1977).
12. H. Tributsch, *Ber. Bunsenges Phys. Chem.*, **81**, 361 (1977).
13. J. A. Wilson and D. A. Yoffe, *Adv. Phys.*, **18**, 193 (1969).
14. B. L. Evans and P. A. Young, *Proc. R. Soc. London, Ser. A*, **284**, 402 (1965).
15. A. D. Yoffe, in Annual Review of Material Science, Vol. 3, R. A. Huggins, Editor, p. 147, Annual Review, Palo Alto (1973).
16. R. Fivaz and E. Mooser, *Phys. Rev.* **163**, 743 (1967).
17. A. D. Sounder and D. E. Brodie, *Can. J. Phys.*, **49**, 2565 (1971).
18. A. R. Beal, J. C. Knights, and W. Y. Liang, *J. Phys.*, **C5**, 3531 (1972).
19. R. F. Frindt and A. D. Yoffe, *Proc. R. Soc. London, Ser. A*, **273**, 69 (1963).
20. L. F. Mattheiss, *Phys. Rev.*, **8D**, 3719 (1973).
21. F. Levy, Ph. Schmid, and H. Berger, *Phil. Mag.*, **34**, 1129 (1976).
22. V. L. Kalikhman and L. L. Pravoverova, *Inorg. Mater.*, **10**, 1021 (1974).
23. A. M. Goldberg, A. R. Beal, F. A. Levy, and E. A. Davis, *Phil. Mag.*, **32**, 367 (1975).
24. R. V. Kasowski, *Phys. Rev. Letts.*, **30**, 1175 (1973).
25. K. Wood and J. B. Pendry, *ibid.*, **31**, 1400 (1973).
26. R. S. Title and M. W. Schafer, *ibid.*, **28**, 808 (1972).
27. H. Tributsch, *Ber. Bunsenges. Phys. Chem.*, In press.
28. F. R. Gamble, F. J. Di Sao, R. A. Klemm, and T. H. Geballe, *Science*, **168**, 568 (1970).
29. F. R. Gamble and J. H. Osiecki, *J. Phys. Chem.*, **55**, 3525 (1971).
30. B. G. Silbernagel and F. R. Gamble, *Phys. Rev. Lett.*, **32**, 1436 (1974).
31. W. Rüdorff and H. H. Sick, *Angew. Chem.*, **71**, 127 (1959).
32. A. Weiss and R. Ruthardt, *Z. Naturforsch.*, **24b**, 355 (1969).
33. R. Schöllhorn and H.-D. Zagefa, *Angew. Chem.*, **89**, 193 (1977).
34. M. Dines and Ricardo Levy, *J. Phys. Chem.*, **79**, 1979 (1975).
35. M. Calvin, *Science*, **184**, 375 (1974).
36. H. Gerischer, in "Electrocatalysis on Nonmetallic Surfaces," A. D. Franklin Editor, National Bureau of Standards, Gaithersburg, Maryland (1975).

X-Ray Photoelectron Spectroscopic Studies of RuO_2-Based Film Electrodes

Jan Augustynski, Lucette Balsenc, and Jean Hinden

Département de Chimie Minérale, Analytique et Appliquée, Université de Genève, Geneva, Switzerland

ABSTRACT

The nature and relative amounts of the different species present in the surface region of RuO_2 and RuO_2-TiO_2 film electrodes, before and after an anodic polarization in 4M aq NaCl solution, have been determined by means of x-ray photoelectron spectroscopy. The existence of a surface defect structure of RuO_3, analogous to that found on RuO_2 powder, has been confirmed for both the RuO_2 and RuO_2-TiO_2 electrodes. Two different chlorine species, identified as chloride ions and adsorbed atomic chlorine, have been shown to be present on the surface of the electrodes used as anodes for the chlorine evolution.

Successful industrial application of the dimensionally stable anodes (DSA) in chlor-alkali cells during recent years (1-3) has attracted considerable interest to the electrocatalytic properties of transition metal oxides, especially those exhibiting metallic conductivity as RuO_2 or IrO_2. A number of authors have studied the kinetics of chlorine evolution on RuO_2-based electrodes (4-10). The low-slope linear Tafel behavior up to very high anodic current densities has been generally reported for the latter reaction on pure RuO_2 film electrodes as well as on mixed RuO_2-TiO_2 electrodes containing at least 20 mole percent (m/o) of RuO_2 (7). However, apparently, some disagreement exists about the mechanism of this reaction and the nature of the rate-determining step (8, 10).

In the present paper, recent results obtained by x-ray photoelectron spectroscopy (XPS) concerning the chemical constitution of the surface region of RuO_2 film electrodes are discussed. Data are given for both pure RuO_2 and mixed oxide RuO_2-TiO_2 films prepared by thermal decomposition in air of $RuCl_3$ and $TiCl_3$ on metallic titanium supports. Spectra have been obtained for freshly prepared RuO_2 and RuO_2-TiO_2 electrodes and for electrodes being employed as anodes in the electrolysis of 4M aq NaCl solution. Distinct changes in the composition of the 20-30Å outermost layer of the electrodes, subsequent to the polarization at anodic potentials and chlorine evolution, are to be expected. These changes could affect the oxidation state of ruthenium atoms, the degree of hydration, and the adsorption of chloride-chlorine species.

Key words: anodes, chlorine evolution, surface analysis.

The results of this study are, thus, likely to permit a better understanding of the peculiar features of RuO_2-based electrode materials, *i.e.*, of their low overpotential for chlorine evolution and excellent corrosion resistance to anodic potentials. The latter have been tentatively assigned (4) to the nonstoichiometric character of the thermally deposited oxide films and also to chloride ion adsorption which is supposed to prevent the surface oxidation of the electrode.

Experimental

The photoelectron spectra were obtained with a Varian IEE spectrometer using $MgK\alpha_{1,2}$ x-rays at 1253.6 eV. Basic pressure in the sample chamber was 10^{-6}-10^{-7} Torr. Binding energies were referred to the carbon ls electron peak due to residual pump oil on the sample surface and are given relative to the zero kinetic energy level, taking 290.0 eV as the C ls binding

energy in vacuo (11). The deconvolutions of the multiple signals were performed graphically with gaussian peak shapes (12). The relative concentrations of the various species were calculated from the corresponding XPS peak intensities. The relative photoelectron line sensitivities referred to the fluorine 1s signal (13, 14) were used for this purpose. Measured concentrations were reproducible within 15%.

The electrodes were prepared by depositing a thin film of RuO_2 or RuO_2-TiO_2 on cylindrical titanium samples of about 6.5 cm^2 area. Commercial 99.5% Ti rods were used. All electrodes were first etched in 20% hydrochloric acid at 100°C for 60 min, then washed with distilled water, and dried. Coatings were applied using a brush, layer by layer, from solutions of the corresponding chlorides. The solution of $RuCl_3$ was prepared by dissolving first $RuCl_3$ aq (Fluka) in 20% HCl aq and evaporating to dryness by gentle heating. The residue was then dissolved in isopropanol. The solution containing both ruthenium and titanium chlorides was obtained by adding to the $RuCl_3$ solution a solution of 15% $TiCl_3$ in HCl (Analar grade, Merck) and a few drops of H_2O_2. The individual layers were first dried at 60°C and then fired at 450°C for 10 min in an oven with forced air circulation. The whole electrode, coated with 6 layers and having a thickness of about 5 μm, was finally annealed at the same temperature for 60 min.

The electrolyses were carried out in a two-compartment cell containing an acidified (pH 2) 4M NaCl solution. Analar grade NaCl and triply distilled water were used. The electrodes were polarized anodically at 200 mA ($\sim$30 mA cm^{-2}) for 4 hr at 20°C. After being removed from the cell, the electrodes were carefully washed with distilled water and dried in a desiccator for at least 24 hr.

Barium ruthenate $BaRuO_4 \cdot H_2O$ was synthesized as described in (15). All ruthenium compounds submitted to XPS analysis were first characterized using x-ray diffraction.

Results

In their XPS study of the surface chemistry of a series of ruthenium-oxygen compounds Kim and Winograd (16) have reported the existence on the surface of RuO_2 (both powder and single crystal) of an additional, higher valency ruthenium compound identified as RuO_3. Their observation has been confirmed by the present authors (17) in the case of RuO_2 and RuO_2-TiO_2 coatings on titanium metal. Figure 1 shows the photoelectron spectra of Ru 3p region for RuO_2 powder (Koch-Light) and RuO_2 coating on titanium obtained by thermal decomposition of $RuCl_3$ in air. Both spectra (a and b) are quite similar, each of them being apparently composed of double signals. The corresponding O 1s electron spectra are even more complex (Fig. 2) showing, besides two larger peaks associated with two Ru compounds, two smaller signals due to water and adsorbed gases as are discussed later. By comparing the relative concentrations of the Ru and O species (Table I) a Ru/O atomic ratio of about 1:2 (corresponding to RuO_2) is obtained for the largest signals, while the Ru/O ratio for Ru and O signals shifted to higher binding energies agrees reasonably well with the formula of RuO_3.

To ascertain further the nature of multiple Ru signals in the RuO_2 spectra we have examined by means of XPS a well-defined compound of Ru(VI)-$BaRuO_4$. As shown in Table II, the position of the smaller Ru peak in the RuO_2 spectra corresponds indeed quite well, for various electron levels, to the binding energy of Ru(VI) in $BaRuO_4$.

Thus, the analysis of XPS spectra strongly suggests that the surface region of freshly prepared RuO_2 film electrode contains, in an analogous manner to RuO_2 powder, an appreciable amount of RuO_3. Assuming the XPS effective depth in the range of 20-30Å, the Ru(VI)/Ru(IV) atomic ratio of about 1:2 could be tentatively interpreted[1] in terms of a 7-10Å outermost surface layer of RuO_3. This situation, therefore, would be similar to that of some noble metals covered with thin oxide films, with the difference that, in the present case (of RuO_2), the metal is substituted by the electronically conducting oxide.

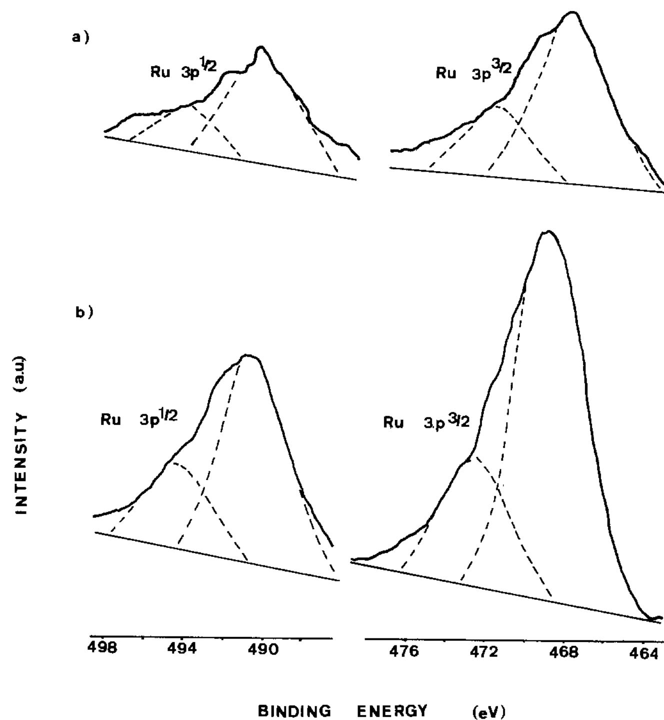

Fig. 1. X-ray photoelectron spectra of Ru 3p region of (a) RuO_2 powder, and (b) RuO_2 deposit on titanium.

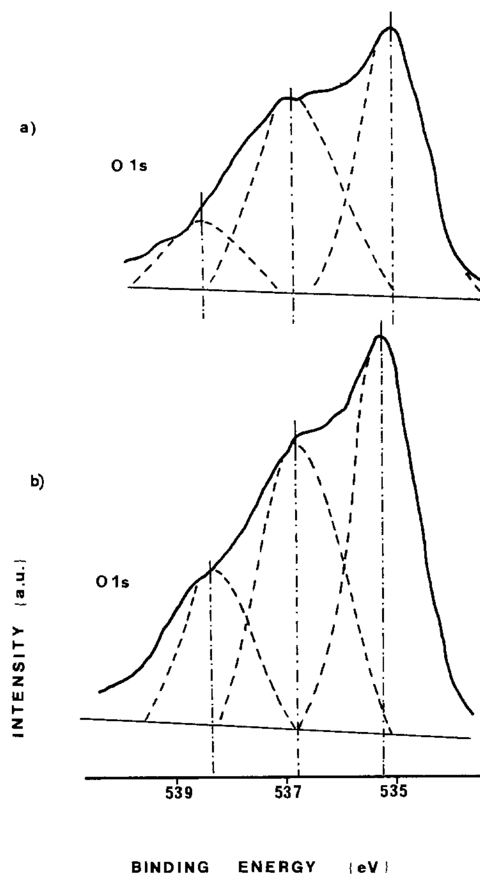

Fig. 2. Oxygen 1s photoelectron signals for (a) RuO_2 powder, and (b) RuO_2 deposit on titanium.

[1] Another possibility is that RuO_3 exists on the surface in a mixture with RuO_2.

Table I. Relative amounts of different Ru and O species identified on the surface of RuO_2 powder and RuO_2 deposit on titanium

	Ru(VI)/Ru(IV)	O/Ru
RuO_2 powder	0.47	2 (largest signals) 3.13 (smaller signals)
RuO_2 deposit on Ti	0.49	2 (largest signals) 3.06 (smaller signals)

Since in industrial applications the so-called RuO_2 electrode consists most frequently of a mixed oxide RuO_2-TiO_2 film on Ti, it was also interesting to characterize Ru species in TiO_2 environment. The mixed RuO_2-TiO_2 deposit, containing about 22 atomic percent (a/o) of Ru as a metal and prepared in the same manner as RuO_2 films, was first examined by x-ray diffraction. As shown in Table III, the principal diffraction lines for the RuO_2-TiO_2 sample are placed between the values relative to RuO_2 and those of rutile form of TiO_2 indicating that the deposit is constituted[2] by the solid solution of both oxides. As in the case of pure RuO_2, various Ru levels in the XPS spectra of mixed RuO_2-TiO_2 deposit are composed of double signals assigned above to RuO_2 and RuO_3. In comparison with the spectra of pure RuO_2 film we observed neither detectable shift in the positions of Ru peaks (Table II) nor a significant change in the Ru(VI)/Ru(IV) ratio.[3] It must be noted that the Ru(total)/Ti atomic ratio obtained from the photoelectron peak intensities (about 0.15) is appreciably lower than the corresponding mean film composition (0.28). This result implies that some preferential diffusion processes have probably taken place during final heat-treatment of the electrodes.

The oxygen 1s electron signal for mixed RuO_2-TiO_2 film (Fig. 3a), appears to be less complex than that of pure RuO_2 and can be resolved into two peaks. From comparison with the spectra of pure TiO_2 and RuO_2 the larger O 1s peak is assigned to oxygen species associated with Ti(IV) and Ru(IV), the corresponding binding energies being practically the same. The smaller O 1s signal,[4] the position of which agrees well with that of the hydration water peak in the TiO_2 spectrum, is shifted about 2 eV to lower binding energies with respect to the O 1s peak attributed to water in the RuO_2 spectrum (Table II).

The photoelectron spectra obtained with RuO_2 and RuO_2-TiO_2 deposits on Ti used as electrodes for anodic chlorine evolution show some significant differences with respect to those of freshly prepared samples.

[2] In addition to the rutile-type RuO_2-TiO_2 solid solution we have also found some nontransformed TiO_2-anatase.
[3] Also the Ti 2p electron spectra from pure TiO_2 (rutile) and from Ti species in the RuO_2-TiO_2 electrode were fairly identical.
[4] Due to the small relative concentration of Ru(VI), the oxygen associated with these species cannot be distinguished from the oxygen of water.

Table III. Principal x-ray diffraction lines for RuO_2, TiO_2-rutile, TiO_2-anatase, and RuO_2-TiO_2 mixed oxide

RuO_2	RuO_2/TiO_2 mixed deposit	TiO_2 rutile	TiO_2 anatase
3.17	3.23	3.25	3.52
2.55	2.50	2.487	2.378
2.243	2.28	2.297	2.332
1.685	1.687	1.6874	1.892
1.586	1.615	1.6237	1.666
1.349	1.355	1.360	1.481

These differences essentially concern the spectra of oxygen and chlorine levels, the Ru binding energies and the Ru(VI)/Ru(IV) and Ru/Ti ratios remaining practically unchanged. As could be expected, the O 1s signals assigned to water and adsorbed oxygen are clearly enhanced for both RuO_2 and RuO_2-TiO_2 electrodes (Fig. 3b).

On account of exceptional characteristics of RuO_2 electrode with regard to the anodic chlorine evolution, it was, of course, important to obtain some more detailed information about the nature and the relative concentrations of chlorine species present on the film surface. In this connection it must be mentioned that the freshly prepared RuO_2 deposit already contains a certain quantity of chlorine (18, 19) resulting from incomplete decomposition of $RuCl_3$ during the heating at 450°C. As a matter of fact, the photoelectron spectrum of Cl 2p level for freshly prepared RuO_2 film (Fig. 4a) clearly shows the presence of two different chlorine species. Since the chlorine 2p electron spectrum consists normally of two signals, due to spin-orbit splitting, the larger $2p^{3/2}$ and the smaller $2p^{1/2}$ placed at higher binding energies, the middle (largest) peak at Fig. 4a must result from the superposition of the $2p^{1/2}$ signal arising from first Cl species and the $2p^{3/2}$ signal characteristic of second Cl species. According to the generally observed tendencies, the binding energy for a given electron level increases together with the oxidation state of the element. Consequently, the lower binding energy Cl $2p^{3/2}$ peak originates, in our opinion, from the chloride ions[5] in RuO_2 crystal lattice, whereas the second Cl $2p^{3/2}$ peak is assigned to adsorbed (atomic) chlorine.[6] This is supported by the fact that the higher binding energy Cl $2p^{3/2}$ peak strongly increases after the RuO_2 electrode has been polarized in the region of the chlorine evolution potential (Fig. 4b). While the amount of adsorbed atomic chlorine rises from about 3 a/o[7] before electrolysis to near 15 a/o[7] after electrolysis, the chloride content changes only from 4 to 6 a/o[7] (Table IV) under the same conditions.

[5] The assignment of this peak is based on the comparison with the binding energies obtained for Cl^- species incorporated into the oxide films on titanium or aluminum.
[6] In the Discussion section we propose an alternative assignment of this peak.
[7] Values reported to Ru(IV).

Table II. Ru and O binding energies of various ruthenium-oxygen compounds

Compound	Binding energy (eV) ±0.2 eV			
	Ru $3d^{5/2}$	Ru $3p^{3/2}$	Ru $3p^{1/2}$	O 1s
RuO_2 powder	286.3 and 287.9	468.1 and 471.5	490.1 and 493.4	535.0, 536.8, and 538.4
RuO_2 deposit on Ti	286.5 and 288.1	468.4 and 471.9	490.5 and 493.9	535.25, 536.8, and 538.35
RuO_2-TiO_2 deposit on Ti	286.3 and 287.7		490.3 and (494.3)	534.5 and 536.3
$BaRuO_4 \cdot H_2O$	288.5	470.8	493.4	535.6

Table IV. Binding energies and relative concentrations of Cl species detected in RuO_2 and RuO_2-TiO_2 film electrodes

	RuO_2 film as prepared	RuO_2-TiO_2 film as prepared	RuO_2 electrode after electrolysis	RuO_2-TiO_2 electrode after electrolysis
Binding energy of Cl $2p^{3/2}$ electron (eV) ±0.2 eV	203.0 and 204.5	202.7	203.0 and 205.2	203.6 and 205.6
Relative concentrations (a/o)	4* and 3*	4**	6* and 15	4** and 32**

* Values reported to Ru(IV).
** Values reported to the sum of Ti(IV) and Ru(IV).

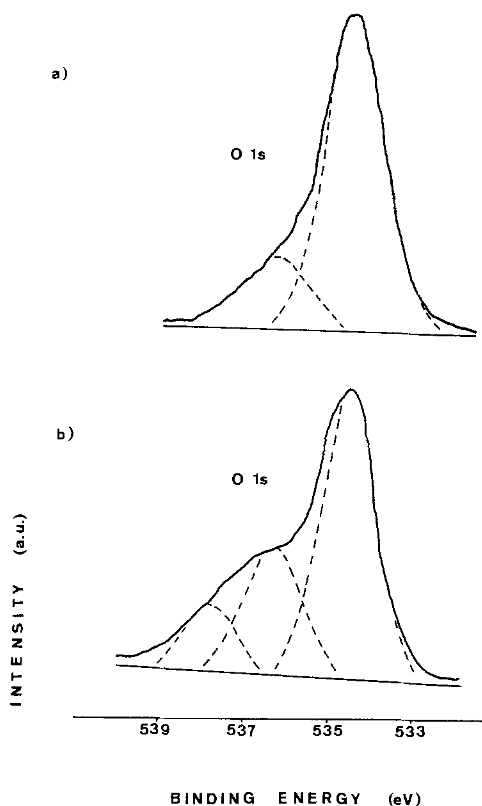

Fig. 3. Oxygen 1s photoelectron signals for RuO_2-TiO_2 deposit on titanium: (a) as prepared, (b) after electrolysis in 4M NaCl solution.

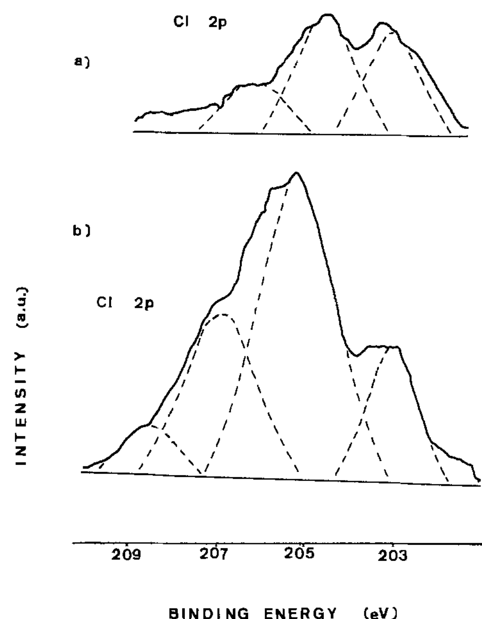

Fig. 4. X-ray photoelectron spectra of Cl 2p region for RuO_2 deposit on titanium: (a) as prepared, (b) used as an anode for chlorine evolution.

The Cl 2p electron spectrum of a freshly prepared RuO_2-TiO_2 deposit shows the presence of a single chlorine species (Fig. 5a), which is characterized by the same binding energy as the one assigned to chlorides in RuO_2 (Table IV). It is interesting to note that the relative concentration of the residual chlorides in RuO_2-TiO_2 coating, calculated with respect to the sum of Ti(IV) and Ru(IV) concentrations, is equal to that found for pure RuO_2 films (4 a/o). This result suggests that the degree of chloride doping in the RuO_2-TiO_2 coatings obtained by thermal decomposition of $RuCl_3$ and $TiCl_3$ rather depends on the annealing temperature than on the ruthenium content.

After using the RuO_2-TiO_2-coated electrode as an anode for the chlorine evolution from 4M NaCl solu-

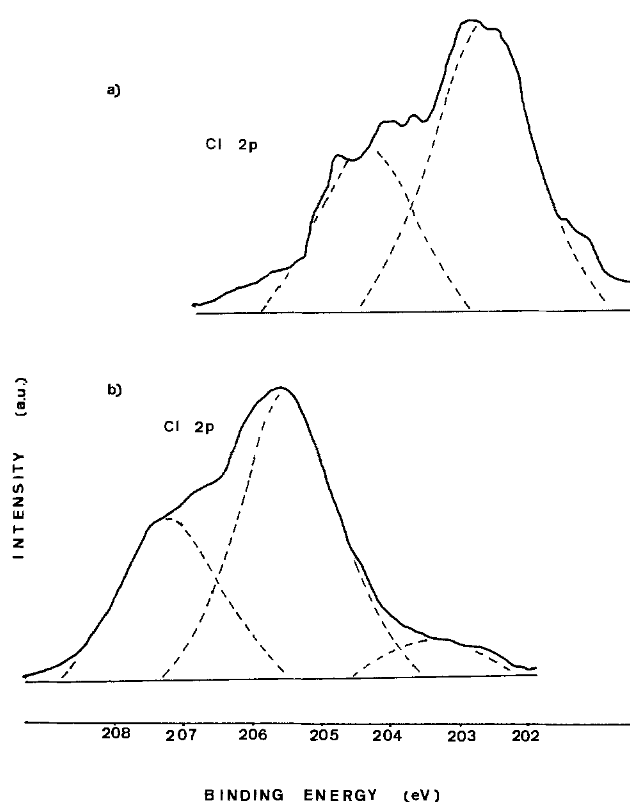

Fig. 5, X-ray photoelectron spectra of Cl 2p region for RuO_2-TiO_2 deposit on titanium: (a) as prepared, (b) used as an anode for chlorine evolution.

tion, a strong additional signal appears in the photoelectron spectrum; this is due to adsorbed atomic chlorine[8] (Fig. 5b). Rather surprisingly, the extent of Cl adsorption found on the RuO_2-TiO_2 electrode is higher than that on the RuO_2 electrode: 32 a/o compared with 15 a/o.

Discussion

Notwithstanding the fact that the XPS analysis is performed outside an electrochemical cell, under high vacuum conditions, the existence of a RuO_3 defect structure on the surface of RuO_2-based film electrodes seems to be definitely established. As a matter of fact, the Ru(VI) species have been detected on the surface of all the kinds of RuO_2 examined by photoelectron spectroscopy; *i.e.*, single crystal of RuO_2 (16), commercially obtained or freshly prepared RuO_2 powder (16, 17), and RuO_2 film electrode. The Ru(VI) species have been equally identified on the surface of the mixed oxide RuO_2-TiO_2 film electrode, wherein RuO_2 forms a solid solution with TiO_2. Moreover, the relative amounts of RuO_3 to RuO_2 do not appear to be significantly influenced by such experimental conditions as the pressure in the sample chamber of the spectrometer (16, 20) and the duration of x-ray irradiation. Finally, the same Ru(VI) species are still present on the surface of RuO_2 and RuO_2-TiO_2 film electrodes which have been used as anodes for the chlorine evolution.

All these results suggest that RuO_3 may be the species responsible for the good stability of RuO_2 electrodes at anodic potentials where, according to the thermodynamic data (21),[9] formation of RuO_4 should take place.

Another significant point in relation to the specific properties of thermally deposited RuO_2 electrodes is the substantial chemical shift of the O 1s signal assigned to water in RuO_2 with respect to the corresponding signals for TiO_2 and for other hydrated ox-

[8] As shown in Table IV, this signal is placed at the same binding energy as in the case of RuO_2 electrode.

[9] It must be noted, however, that the known thermodynamic data concern actually a hydrated ruthenium dioxide $RuO_2 \cdot 2H_2O$.

ides such as $Al_2O_3 \cdot xH_2O$.[10] This shift may be interpreted in terms of a particularly weak bonding (*i.e.*, of a nondissociative adsorption) of water by the oxide.

The photoelectron spectra of Cl 2p level for the RuO_2 and RuO_2-TiO_2 electrodes polarized anodically in 4M NaCl show the presence of a large amount of Cl species which have been assigned to adsorbed atomic chlorine. As a matter of fact, the relative concentrations of these species given in Table IV seem to indicate that the degree of surface coverage by Cl_{ads} must be roughly equal to unity ($\theta \approx 1$), assuming one Cl atom per Ru or (and) Ti atom. It is interesting to consider this result in connection with the postulated mechanisms of the $Cl^- - e = \frac{1}{2} Cl_2$ reaction at RuO_2 and RuO_2-TiO_2. According to Ref. (4) and (10), the observed low Tafel slopes ($b = dV/d \ln i = RT/2F$ to $2\,RT/3F$) are consistent with the

$$Cl^- \leftrightarrows Cl_{ads} + e \quad [1]$$

$$2Cl_{ads} \rightarrow Cl_2(\text{rds}) \quad [2]$$

reaction pathway, the second step being the rate-determining step (rds). In the case of radical recombination controlled kinetics (Eq. [2]), $dV/d \ln i = RT/2F$ corresponds to moderate surface coverage conditions, while for $\theta \rightarrow 1$ a transition of Tafel slope to ∞ (the limiting anodic current) is expected. The above mechanism (4) has been refuted by Erenburg *et al.* (8) on the basis of the observed dependence of the overpotential on the chloride concentration and of the anodic reaction order with respect to Cl^- ions equal to +1. After detailed analysis of various possible reaction schemes these authors have proposed an alternative three-step mechanism

$$Cl^- \rightleftarrows Cl_{ads} + e \quad [3]$$

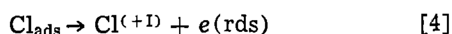

$$Cl_{ads} \rightarrow Cl^{(+I)} + e(\text{rds}) \quad [4]$$

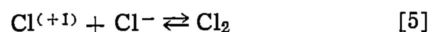

$$Cl^{(+I)} + Cl^- \rightleftarrows Cl_2 \quad [5]$$

with the second charge-transfer step (Eq. [4]) as rate controlling. The rds is assumed barrierless at low overvoltages, corresponding to $\alpha = 1$ with $b = dV/d \ln i = RT/(\alpha + 1)F$, where α is the true transfer coefficient. At higher overvoltages, where a transition to normal process is expected, a Tafel slope of about $2RT/3F$ was obtained (9) in agreement with $b = RT/(\alpha + 1)F$ for $\alpha = 0.5$. However, the reaction mechanism suggested by Erenburg *et al.* clearly implies $\theta << 1$, *i.e.*, very low coverage by atomic chlorine on the electrode, which is in disagreement with our results. In this connection it must be pointed out that certain points of measurements carried out by the latter authors are subject to criticism. In particular, sulfuric acid added in excess to chloride solutions, in order to suppress secondary double layer ionic distribution effects in the determination of the reaction order, can hardly be considered in this case as a nonspecifically adsorbing supporting electrolyte. Indeed, as shown by preliminary XPS analyses, SO_4^{2-} ions strongly interact with both RuO_2 and TiO_2.

In any case, further experimental information is needed before definite mechanistic conclusions can be made. These must involve the examination of a possible role which Ru(VI) species could play in the chlorine evolution process, *e.g.*, through the following reaction sequence

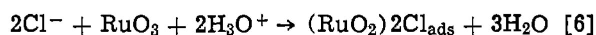

$$2Cl^- + RuO_3 + 2H_3O^+ \rightarrow (RuO_2)2Cl_{ads} + 3H_2O \quad [6]$$

and

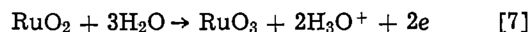

$$RuO_2 + 3H_2O \rightarrow RuO_3 + 2H_3O^+ + 2e \quad [7]$$

Finally, the possibility that the chlorine species detected by our XPS measurements are not Cl_{ads} atoms but adsorbed ClO^- ions cannot be completely excluded. These species could be produced in a secondary chemical reaction or originate (as intermediates) from a reaction pathway of the kind

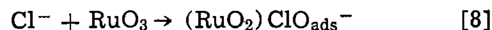

$$Cl^- + RuO_3 \rightarrow (RuO_2)ClO_{ads}^- \quad [8]$$

Eq. [7] and

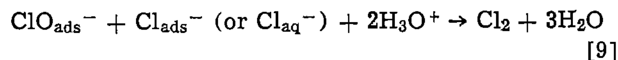

$$ClO_{ads}^- + Cl_{ads}^- \text{ (or } Cl_{aq}^-) + 2H_3O^+ \rightarrow Cl_2 + 3H_2O \quad [9]$$

Reaction [9] presents an analogy with the third step (Eq. [5]) in the mechanism postulated by Erenburg *et al.*

Acknowledgments

The authors are very much indebted to Dr. H. Berthou for the assistance with XPS measurements. The research has been partially supported by the Swiss National Science Foundation.

Manuscript submitted June 14, 1977; revised manuscript received Feb. 14, 1978.

Any discussion of this paper will appear in a Discussion Section to be published in the June 1979 JOURNAL. All discussions for the June 1979 Discussion Section should be submitted by Feb. 1, 1979.

Publication costs of this article were assisted by the Université de Genève.

REFERENCES

1. O. De Nora, *Chem. Ing. Tech.*, **42**, 222 (1970).
2. O. De Nora, *ibid.*, **43**, 182 (1971).
3. S. D. Argade and F. B. Leitz, *This Journal*, **124**, 12C (1977).
4. G. Faita and G. Fiori, *J. Appl. Electrochem.*, **2**, 31 (1972).
5. A. T. Kuhn and C. J. Mortimer, *This Journal*, **120**, 231 (1973).
6. R. G. Erenburg, L. I. Krishtalik, and V. I. Bystrov, *Elektrokhimiya*, **8**, 1740 (1972).
7. I. E. Veselovskaya, E. K. Spasskaya, V. A. Sokolov, V. I. Tkachenko, and L. M. Yakimenko, *ibid.*, **10**, 70 (1974).
8. R. G. Erenburg, L. I. Krishtalik, and I. P. Yaroshevskaya, *ibid.*, **11**, 1068 and 1072 (1975).
9. R. G. Erenburg, L. I. Krishtalik, and I. P. Yaroshevskaya, *ibid.*, **11**, 1236 (1975).
10. I. R. Burrows, J. H. Entwisle, and J. A. Harrison, *J. Electroanal. Chem.*, **77**, 21 (1977).
11. C. K. Jørgensen and H. Berthou, *Chem. Phys. Lett.*, **31**, 416 (1975).
12. C. K. Jørgensen and H. Berthou, *K. Dan. Vidensk. Selsk. Mat. Fys. Medd.*, **38**, No. 15 (1972).
13. C. D. Wagner, *Anal. Chem.*, **44**, 1050 (1972).
14. H. Berthou and C. K. Jørgensen, *ibid.*, **47**, 487 (1975).
15. E. E. Mercer and D. T. Farrar, *Can. J. Chem.*, **47**, 581 (1969).
16. K. S. Kim and N. Winograd, *J. Catalysis*, **35**, 66 (1974).
17. J. Augustynski, L. Balsenc, and J. Hinden, Presented at the Symposium on Novel Electrode Materials (Chemical Society), Brighton, September 25-26, 1975.
18. S. Pizzini, G. Buzzanca, C. Mari, L. Rossi, and S. Torchio, *Mater. Res. Bull.*, **7**, 449 (1972).
19. C. Iwakura, H. Tada, and H. Tamura, *Electrochim. Acta*, **22**, 217 (1977).
20. J. Augustynski, L. Balsenc, J. Hinden, and J. P. Coad, To be published.
21. M. Pourbaix, "Atlas d'Equilibres Electrochimiques á 25°C," p. **343**, Gauthier-Villars, Paris (1963).

[10] In the case of other oxide films analyzed in our laboratory (TiO_2, Al_2O_3, Cr_2O_3, and MoO_{2+x}) the binding energies (BE) attributed to adsorbed H_2O species were comprised between 536 and 537 eV; consequently the value of O 1s BE for H_2O_{ads} on the RuO_2 electrode (538.4 eV) may be considered as anomalously high.

A Rotating Ring-Disk Electrode Study of the Underpotential Deposition of Mercury on Gold

W. G. Sherwood*,[1] and Stanley Bruckenstein*

Department of Chemistry, State University of New York at Buffalo, Buffalo, New York 14214

ABSTRACT

The isotherm for the underpotential deposition (UPD) of mercury from $0.2M$ H_2SO_4 solutions of mercurous or mercuric ions is the same. At the equilibrium potential of a liquid mercury electrode in either of the solutions, the surface coverage of mercury species is 1.9×10^{-9} g·atom/cm^2. However, only faradaic charge sufficient to deposit 1.7×10^{-9} g·atm/cm^2 of Hg(O) is consumed and $\sim 2 \times 10^{10}$ g·atm/cm^2 of $(Hg(I))_2$ appear to be adsorbed along with the UPD Hg(O).

Underpotential deposition (UPD) involves the deposition of a metal ion on a foreign metal substrate at potentials anodic to the equilibrium potential of the metal/metal ion couple. UPD is usually observed for the first few atom-layers of the metal (adatom) deposited on the electrode (1-28), and the process is sometimes accompanied by the adsorption of submonolayer quantities of the metal ion (adion) (9, 10, 18, 26-28). Some authors prefer to consider the deposition process to produce a single species carrying a partial charge rather than a mixture of adatoms and adions. Neither view can be distinguished from the other by electrochemical methods.

We report here the results of a study of the UPD of Hg on Au from dilute $(Hg(I))_2$ or Hg(II) in $0.2M$ H_2SO_4 solutions. The issues to which our study were directed were the determination of (*i*) the mercury coverage at the Nernst potential for the $(Hg(I))_2$/Hg couple, (*ii*) the UPD isotherm in $(Hg(I))_2$ and Hg(II) solutions, and (*iii*) the net charge of the adsorbed species as a function of deposition potential.

Experimental

Circuitry and electrodes.—The electrochemical equipment and supporting circuitry used have been described elsewhere (29). Additional circuitry was added to the standard four-electrode potentiostat in order to perform deposition experiments at 0.1 mV anodic to the Nernst potential (Fig. 1). Using a saturated calomel reference electrode, ten monolayers of Hg were deposited on a gold electrode, and then the current was set equal to zero by disconnecting the auxiliary electrode. After the Hg-coated electrode reached equilibrium, potentiometer P was adjusted until the output of inverter I was -10.0 mV. The output of follower F_2 was then injected through a 10^4 Ω resistor into the input of amplifier CA by closing switch S. The auxiliary electrode was connected in order to deposit Hg on a rotating disk electrode at 0.1 mV anodic of the Nernst potential.

The data reported here were obtained using a rotating gold disk-gold ring electrode RRDE. Its dimensions were $r_1 = 0.379$ cm, $r_2 = 0.402$ cm, and $r_3 = 0.484$ cm, $N = 0.34$ and $S = 0.63$. All potentials are reported with respect to the saturated calomel electrode (SCE).

The surface roughness of the gold disk was calculated by the method of Brummer and Makrides (30), which gives the charge required to oxidize a 1.00 cm^2 gold surface at 1.2V.

Mercury surface coverage was calculated by assuming that one monolayer of mercury on gold requires 336 μC/cm^2 to be oxidized to soluble Hg(II). This assumption is justified in the Results and Discussion section.

* Electrochemical Society Active Member.
[1] Present address: AMAX, Incorporated, Extractive Metallurgy Laboratory, Golden, Colorado 80401

Experimental procedure.—The potential sequence used to obtain the data reported is given in Table I. Digital data acquisition and control techniques are given elsewhere (29). Data acquisition was initiated at step 6 and the rotation speed, ω, set to zero at step 5 if stationary anodic stripping data were desired. The disk potential scan was performed at $\omega = 0$ if only disk electrode data were desired. The stationary disk electrode potential scans were performed to minimize the steady-state background current associated with the oxidation of $(Hg(I))_2$ during the anodic potential scan. Step 8 resets the digital sequencer to step 1, allowing signal averaged data acquisition, when this is required. Data for the potential-charge curves were obtained at 0.1V intervals near the anodic limit of the underpotential region, and at smaller potential intervals near the cathodic limit of the underpotential region. The 5 min time interval allowed for underpotential deposition was sufficient to achieve equilibrium coverage of Hg on Au at the deposition potential of interest.

Results and Discussion

Determination of the Nernst potential.—The Nernst potential for the Hg(I)/Hg couple in $2 \times 10^{-5}M$ $(Hg(I))_2$ $-0.2M$ H_2SO_4 solution was determined using the gold disk of the RRDE. First, the Au disk was potentiostated at 0.0V and $\omega = 2500$ rpm, where the reduction of $(Hg(I))_2$ to Hg(O) occurs under convective diffusion control. After deposition of more than 10 layers of Hg(O), the disk current, i_D, was set equal to zero and the disk potential was monitored. The rest potential attained by the gold disk is the equilibrium potential for the Hg(I)/Hg couple, *i.e.*, 0.398V in $2.0 \times 10^{-5}M$ $(Hg(I))_2$ $-$ $0.2M$ H_2SO_4 for our particular SCE.

In order to verify that on the gold disk mercury coverages greater than 10 layers behave as metallic mercury for the time of each experiment, a mercury

Fig. 1. Circuit for UPD at 0.1 mV anodic to Nernst potential

Table I. Sequence for underpotential deposition and stripping of Hg

Step No.	Disk potential (V)	Purpose of step	Ring potential (V)	Purpose of step	Time
1	1.20	Pretreat $\omega = 0$ rpm	1.20	Pretreat	1 min
2	0.00	Reduce Au $\omega = 0$ rpm	1.20	Pretreat	3 sec
3	E_{DEP}	Deposit Hg $\omega = 2500$ rpm	1.20	Pretreat	4 min
4	E_{DEP}	Deposit Hg $\omega = 2500$ rpm	0.0 or 1.0	Stabilize for coll.	1 min
5	E_{DEP}	Deposit Hg $\omega = 2500$ rpm	0.0 or 1.0	Set rotation	5 sec
6	Scan anodic	Data acq. $\omega = 0$ or 2500 rpm	0.0 or 1.0	Collect products	As required
7	1.60	Clean $\omega = 2500$ rpm	1.60	Clean	2 min
8	Reset	Sig. avg.	Reset	Sig. avg.	1 msec

pool was substituted for the SCE reference electrode, and the potential of the mercury coated gold electrode was measured *vs.* the mercury pool. The potential measured in this experiment was 0.0 mV.

Hg(O) layer thickness at the Nernst potential.—Anodic stripping method.—The gold disk of the RRDE was potentiostated 0.1 mV anodic to the Nernst potential for 5, 10, and 120 min. Then the amount of mercury deposited for each time was determined by anodic stripping. No time dependent increase in stripping charge was noted, and all data agreed within 2% of the value obtained after 5 min, 340 $\mu C/cm^2$ (1.76×10^{-9} g·atom/cm^2 of mercury).

The only time effect found at the above potential was that the stripping potential shifted 30 mV more anodic after a 120 min wait. The time stability of mercury in the gold surface demonstrates the large interaction energy of the UPD process, an energy which exceeds that for bulk amalgam formation.

Deposition at potentials 1.0 mV cathodic of the Nernst potential produced time dependent anodic charges under the stripping peaks, as would be expected for ordinary metal deposition.

The charge corresponding to electrooxidizing one atom layer of mercury on gold as Hg(II) was calculated by assuming that the zero-valent mercury atoms form a close-packed array on the gold surface. Thus the maximum coverage for one layer of Hg atoms is proportional to the ratio of the square of the radii of Hg and Au. The atomic radius of Au is 1.44Å. However, the reported radii for Hg vary somewhat between 1.50 and 1.73Å (23), and the best value of r_{Hg} cannot be selected on the basis of these data.

Bowles (25) presented evidence that mercury deposits on Pt in a square lattice. Using this assumption, Hassan, Untereker, and Bruckenstein (19) showed that if the $r_{Hg} = 1.57$Å, the charge calculated for stripping one geometric monolayer of mercury from a platinum electrode coincides with the amount of mercury required to inhibit all hydrogen adsorption on the same platinum electrode. Therefore, it is assumed here that 1.57Å is also the correct value for the radius of UPD Hg on Au and that a monolayer is 1.74×10^{-9} g·atom/cm^2. We calculate, then, that the charge required to strip one monolayer of mercury on gold as Hg(II) is 336 $\mu C/cm^2$. This value coincides, within experimental error, with the amount found above for the quantity of Hg(II) stripped after UPD 0.1 mV anodic of the Nernst potential. This remarkable result indicates that one atom layer of mercury on a gold substrate behaves as if it were bulk mercury in a potentiometric experiment.

$(Hg(I))_2$ direct reduction method.—When an oxidized gold disk electrode is reduced at 0.0V and $\omega = 0$ rpm and the potential subsequently stepped to 0.40V at $\omega = 2500$ rpm in solution of $2.0 \times 10^{-5}M$ $(Hg(I))_2$ and 0.2*M* H_2SO_4, the disk current, i_D, *vs.* time, *t*, curve of

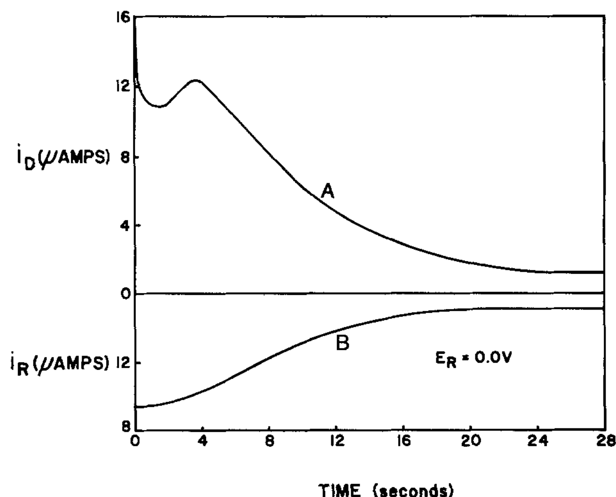

Fig. 2. RRDE-current-time responses during UPD of Hg. Curve A, disk; curve B, ring. Disk potential = 0.40V; ring potential = 0.0V; ω = 2500 rpm; $C_{H_2SO_4}$ = 0.2*M*; and $C_{Hg(I)}$ = $2.0 \times 10^{-5}M$.

Fig. 2, Curve A, results. The time required to obtain 99% of the equilibrium coverage of Hg is approximately 30 sec. After 300 sec, i_D had diminished to 7 nA. Integration of the area under the i_D *vs.* *t* curve, yields an apparent charge density of 164 $\mu C/cm^2$ for reaction [1], *i.e.*, 1.70×10^{-9} g·atom/cm^2 of Hg were deposited.

$$(Hg(I))_2 + 2e \rightleftarrows 2Hg(O)_{UPD} \qquad [1]$$

However, during the initial 3 sec waiting period at the start of the experiment when $\omega = 0$ (step 2 in Table I), we calculate that 0.12×10^{-9} g·atom/cm^2 of $Hg(O)_{UPD}$ forms as a result of semi-infinite linear diffusion to the stationary disk electrode. Thus the total $Hg(O)_{UPD}$ formed is 1.82×10^{-9} g·atm/cm^2. This coverage agrees well with that calculated using Eq. [2] to interpret the anodic stripping of the underpotential deposit produced potentiostatically at 0.399V. Equation [2] is shown below to describe the anodic stripping process.

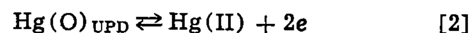

$$Hg(O)_{UPD} \rightleftarrows Hg(II) + 2e \qquad [2]$$

Ring shielding method.—The ring current, i_R, *vs.* *t* response of a rotating ring disk electrode corresponding to the i_D *vs.* *t* experiment described above is shown in Fig. 2, Curve B. The ring electrode was potentiostated at 0.0V during this experiment, and the consumption of $(Hg(I))_2$ via reaction [1] was monitored. The ring electrode remains partially shielded for the first 15 sec, after which the ring electrode current approaches the limiting value for the reduction of $(Hg(I))_2$. The integral of the i_R *vs.* *t* curve, when divided by *N*, yields a value of 184 $\mu C/cm^2$ for the amount of $(Hg(I))_2$ consumed on the gold disk of the RRDE, only in fair agreement with the anodic stripping and the direct reduction experiments. This experiment indicates 1.91×10^{-9} g·atom/cm^2 of mercury species has been consumed at the gold disk.

Figure 3 shows both i_D *vs.* *t* and $-i_R/N$ *vs.* *t* curves for the experiment described above. In the absence of adsorption or other phenomena that consume $(Hg(I))_2$ at the disk electrode via a nonfaradaic mechanism, the two curves of Fig. 3 should superimpose. However, the ring electrode shielding observed during the first 16 sec indicates that a nonfaradaic process is consuming $(Hg(I))_2$ at the disk electrode. The charge density under the shaded region of Fig. 3, Q_{ads}, equals (368 − 328) or 40 $\mu C/cm^2$. Evidence is given below that this difference can be represented as the adsorption of 2.1×10^{-10} g·atom/cm^2 $(Hg(I))_2$ that occurs on a reduced Au electrode simultaneously with the underpotential deposition of Hg.

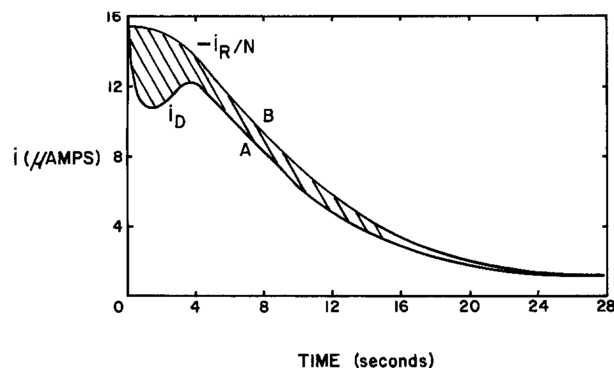

Fig. 3. Comparison of time dependence of the disk current and flux of $(Hg(I))_2$ removed at the disk. Data of Fig. 2. Curve A, disk current; Curve B, current equivalent to flux removed at disk electrode calculated from $-i_R/N$.

UPD in $(Hg(I))_2$ solutions.—Anodic stripping charge. —To obtain the relationship between charge and potential in the underpotential region, mercury was deposited on various potentials, E_{DEP}, ($1.00V \geqq E_{DEP} \geqq 0.398V$), and subsequently oxidized from the electrode via a linear anodic potential sweep. In these experiments, the rotator was turned off prior to stripping the UPD deposit to avoid interference due to the steady-state oxidation of $(Hg(I))_2$, since the latter process occurs simultaneously with the oxidation of Hg(O) from the Au electrode. Figure 4 shows a typical *i-E* curve obtained following deposition at 0.42V. The anodic stripping charges obtained following deposition at various potentials in the underpotential region are summarized in column 2 of Table II and are plotted in curve A of Fig. 5. Values obtained in this manner are termed "$Q_{D,\omega=0}$."

If, following deposition, the initial potential scan was made in the cathodic direction, a peak (Fig. 4, peak "P") was observed at 0.2V. The charge under this peak (Q_{ads}^P) increased with increasingly cathodic deposition potentials (column 6, Table II). RRDE experiments showed that the disk reduction process associated with the cathodic peak does not consume or produce any oxidizable or reducible species. This result again suggested the presence of an adsorbed species on the electrode surface, such as $(Hg(I))_2$ (or Hg(II)), and further RRDE anodic stripping experiments were conducted.

Ring collection. The anodic stripping experiments described in the preceding section were repeated at ω = 2500 rpm, and both the i_D-E_D and i_R-E_D responses were recorded first at E_R = 0.0V and then at 0.80V. These data are shown in Fig. 6 and 7. The disk electrode stripping curves for deposition potentials of 0.60 and 0.45V, and the corresponding ring electrode responses at 0.0 and 1.0V demonstrated that Hg(II) was the sole product of the electrooxidation of underpotential mercury.

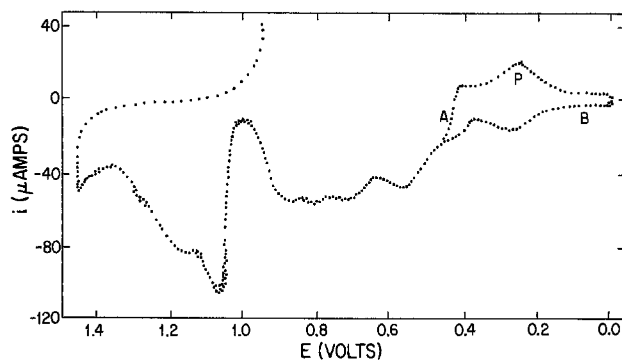

Fig. 4. Current-potential curves at a stationary gold disk electrode following UPD of Hg at 0.42V. dE/dt = 50 mV/sec. $C_{H_2SO_4}$ = 0.2*M* and $C_{Hg(I)} = 2.0 \times 10^{-5}M$.

Table II. Charge data for underpotential deposition and adsorption from Hg(I) solutions

Charge density, μC/cm²

E_{DEP} (V)	$Q_{D,\omega=0}$[a]	$Q_{D,\omega=2500}$[b]	Q_R^*[c]	$Q_R^* - Q_{D,\omega=2500}$[d]	Q_{ads}^P[e]
0.90	18	16	23	7	8
0.80	74	73	93	20	23
0.70	138	134	173	39	42
0.60	179	181	227	46	49
0.50	255	250	301	51	54
0.45	294	286	337	51	54
0.44	300	297	349	52	53
0.43	312	314	365	51	54
0.42	326	322	374	52	55
0.41	335	333	385	52	54
0.40	339	340	392	52	54

[a] $Q_{D,\omega=0}$: Disk electrode anodic stripping charge obtained at ω = 0 rpm.
[b] $Q_{D,\omega=2500}$: Disk electrode anodic stripping charge obtained at ω = 2500 rpm.
[c] Q_R^*: Ring electrode collection data (divided by the RRDE collection efficiency, *N*) obtained for disk electrode anodic stripping experiments at ω = 2500 rpm.
[d] $Q_R^* - Q_{D,\omega=2500}$: The difference between the ring electrode and disk electrode charge density values for a given E_{DEP} corresponds to the charge equivalent to adsorbed $(Hg(I))_2$ or Hg(II).
[e] Q_{ads}^P: The charge corresponding to peak "P" in Fig. 4; agreement with column 5 data indicates the peak results from reduction of adsorbed Hg(I) or Hg(II).

The disk and ring electrode charges for similar experiments at various deposition potentials are summarized, respectively, in columns 3 and 4 of Table II. $Q_{D,\omega=2500}$ is used to designate disk electrode data obtained in the above experiments, and Q_R^* designates the corresponding ring electrode data, divided by the RRDE collection efficiency (Q_R/N). The ring electrode data are plotted in curve B of Fig. 5.

Values of Q_R^* are all larger than $Q_{D,\omega=2500}$. This difference indicates the collection at the ring electrode of a reducible species that has been desorbed from the disk electrode via a nonfaradaic mechanism. This inference is consistent with the conclusion drawn earlier that either $(Hg(I))_2$ or Hg(II) is adsorbed on the reduced gold electrode during the UPD process. Two possible adsorption reactions are given by Eq. [3] and [4].

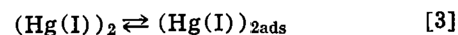

$$(Hg(I))_2 \rightleftarrows (Hg(I))_{2ads} \quad [3]$$

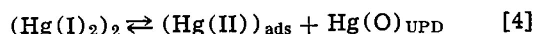

$$(Hg(I)_2)_2 \rightleftarrows (Hg(II))_{ads} + Hg(O)_{UPD} \quad [4]$$

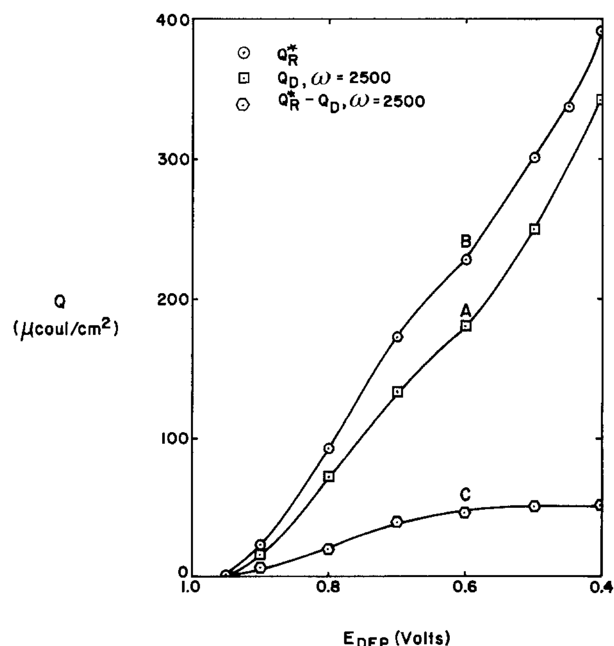

Fig. 5. Potential dependence of charge density at gold disk of RRDE. Curve A, ring collection data divided by *N*, Q_R^*; curve B, disk stripping data, $Q_{D,\omega=2500}$; curve C, charge equivalent to adsorbed mercury species, $Q_R^* - Q_{D,\omega=2500}$.

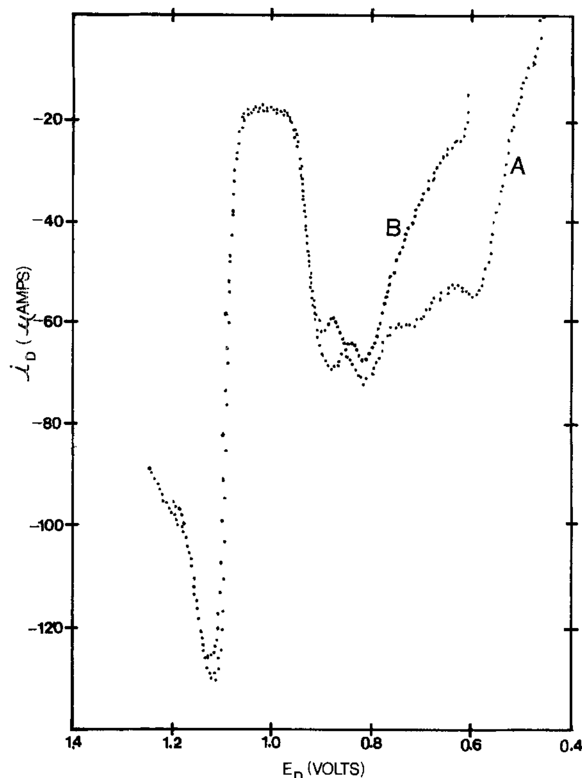

Fig. 6. Rotating disk electrode anodic stripping curves. Curve A, $E_{DEP} = 0.45V$; Curve B, $E_{DEP} = 0.60V$. $\omega = 2500$ rpm, $dE/dt = 50$ mV/sec, $C_{H_2SO_4} = 0.2M$ and $C_{Hg(I)} = 2.0 \times 10^{-5}M$.

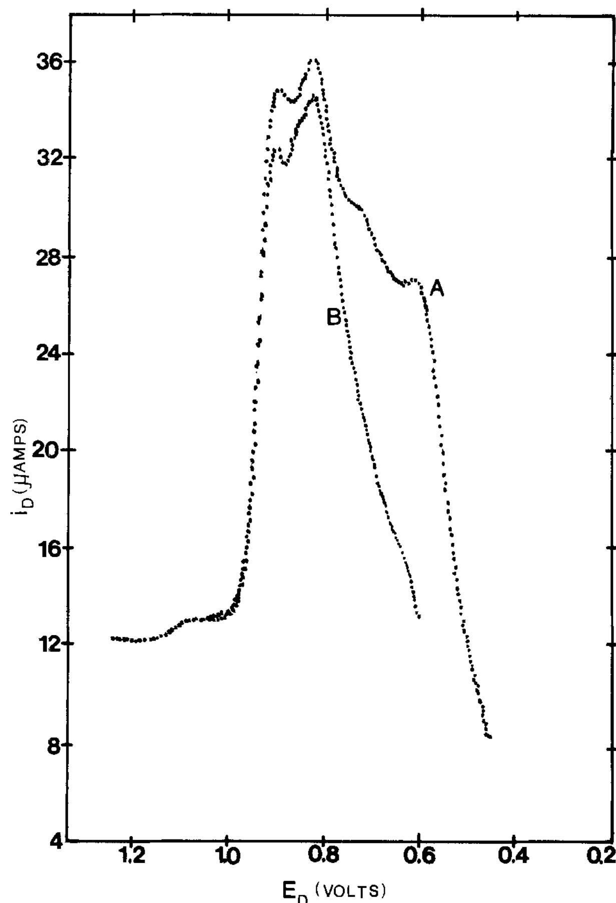

Fig. 7. Ring electrode collection curves of disk of RRDE used in Fig. 6. Curves A and B as in Fig. 6. $E_R = 0.0V$.

These are indistinguishable on the basis of the existing data, as is the possible existence of a partially discharged Hg species produced during the UPD process

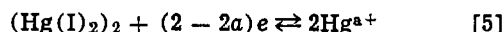

$$(Hg(I)_2)_2 + (2 - 2a)e \rightleftarrows 2Hg^{a+} \quad [5]$$

The desorption path is the reverse of the adsorption path. If the charge associated with peak "P" ($Q_{ads}{}^P$) of Fig. 4 is that required to reduce the adsorbed mercury species, and the difference between the ring and disk electrode charges measured in the above experiments ($Q_R{}^* - Q_{D,\omega=2500}$) is attributed to the desorption of the same mercury species, then the relationship

$$Q_R{}^* - Q_{D,\omega=2500} = Q_{ads}{}^P \quad [6]$$

should hold at each deposition potential. Comparison of the above difference (column 5, Table II and curve C, Fig. 5) with the $Q_{ads}{}^P$ (column 6, Table II), indicates that Eq. [6] is obeyed over the entire underpotential deposition range. Again, the results do not permit distinguishing between the various mechanisms, although the existence of peak "P" is suggestive of a surface species undergoing charge transfer, rather than some double layer process.

An excellent method for visualizing the potential region over which the adsorbed mercury species desorbs is to compare I_D-E_D curves with i_R/N-E_D curves obtained simultaneously during the anodic stripping of the underpotentially deposited Hg. Typical curves for deposition at 0.45V are shown in Fig. 8. The shaded area between the curves represents the charge associated with the adsorbed mercury species present on the reduced gold electrode.

UPD Hg(II) solutions.—Experiments identical to those described in the previous sections for $(Hg(I))_2$ were also performed using $2.0 \times 10^{-5}M$ Hg(II). The zero-current rest potential was determined to be 0.399V using the methods described in the section dealing with the establishment of the Nernst potential in $(Hg(I))_2$ solution. Here, as in the $(Hg(I))_2$ case the rest potential was independent of the electrode rotation rate over the range 400-4900 rpm. Since the potential in $(Hg(I))_2$ and Hg(II) solutions are identical for practical purposes in our experiments, the reaction

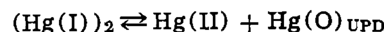

$$(Hg(I))_2 \rightleftarrows Hg(II) + Hg(O)_{UPD}$$

must be very fast at the electrode surface, and lie far to the right. This conclusion has been confirmed by coulostatic experiments reported elsewhere (31).

Anodic stripping and ring collection curves obtained after potentiostating the disk electrode in the UPD region are essentially indistinguishable from those obtained in $(Hg(I))_2$ solutions. Note that the stripping data obtained at $\omega = 2500$ rpm are not complicated by the background oxidation of $(Hg(I))_2$ that was present in the previous experiments. Peak "P" (Fig. 4) is also

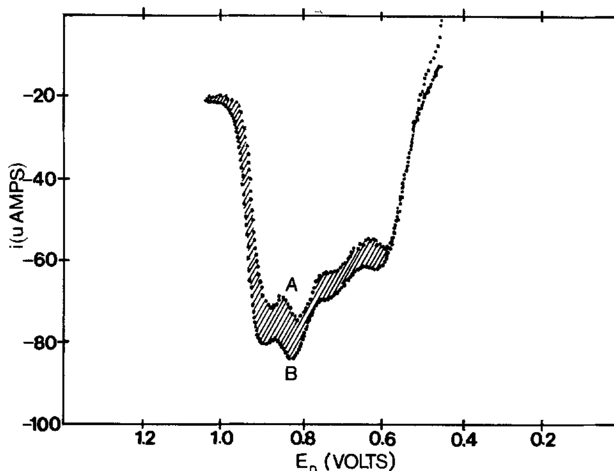

Fig. 8. Comparison of potential dependence of disk current and flux of $(Hg(I))_2$ removed at the disk. Data of Fig. 6 and 7. Curve A, disk current; curve B, current equivalent to flux removed at disk electrode calculated from i_R/N.

Table III. Charge data for underpotential deposition and adsorption from Hg(II) solutions

E_{DEP} (V)	Charge density, $\mu C/cm^2$ Q_D[a]	Q_R^*	$Q_R^* - Q_{D,\omega=2500}$	Q_{ads}^P
0.90	16	24	8	6
0.80	73	97	24	27
0.70	139	175	36	39
0.60	178	229	51	48
0.50	249	299	50	53
0.45	283	334	51	52
0.40	341	392	51	53

[a] Q_D is disk electrode anodic stripping data obtained at ω = 2500 rpm; all other charge values are as defined in Table II.

observed during stationary cathodic scans following the deposition of Hg(O) at underpotential from Hg(II) solutions.

The potential-charge data for the Hg(II) experiments are tabulated in Table III. The similarity between these data and corresponding $(Hg(I))_2$ data again suggest that deposition and adsorption from Hg(II) solutions proceed through a common intermediate.

Conclusions

Just anodic of the Nernst potential, one monolayer of Hg deposits on gold at underpotential from mercurous or mercuric solutions. UPD mercury does not diffuse into the bulk of the gold electrode because of the strong interactions between mercury and surface gold atoms. $(Hg(I))_2$ (or Hg(II)) coadsorb with $Hg(O)_{UPD}$ on a reduced gold electrode in 0.2*M* H_2SO_4 over a wide potential range, $1.0V \geqq E_{DEP} \geqq 0.40V$. This adsorption increases at more cathodic deposition potentials, and it reaches a maximum of 54 $\mu C/cm^2$ at the Nernst potential.

Electrooxidation of Hg(O) in the underpotential region produces Hg(II) in four overlapping stripping peaks. Deposition of bulk Hg does not occur until potentials cathodic of the Nernst potential, and then only after one monolayer of $Hg(O)_{UPD}$ has been deposited.

Acknowledgment

This work was supported by the Air Force Office of Scientific Research under Grant No. 74-2572.

Manuscript submitted Jan. 9, 1978; revised manuscript received March 6, 1978.

Any discussion of this paper will appear in a Discussion Section to be published in the June 1979 JOURNAL. All discussions for the June 1979 Discussion Section should be submitted by Feb. 1, 1979.

REFERENCES

1. B. J. Bowles, *Electrochim. Acta*, **10**, 731 (1965).
2. B. J. Bowles *Nature (London)*, **212**, 1456 (1966).
3. B. J. Bowles, *Electrochim. Acta*, **15**, 589 (1970).
4. B. J. Bowles, *ibid.*, **15**, 737 (1970).
5. M. W. Breiter, *Trans. Faraday Soc.*, **65**, 2197 (1969).
6. J. W. Schultz, *Ber. Bunsenges Phys. Chem.*, **74**, 7 (1970).
7. G. W. Tindall and S. Bruckenstein, *Anal. Chem.*, **40**, 1051 (1968).
8. G. W. Tindall and S. Bruckenstein, *Electrochim. Acta*, **16**, 235 (1971).
9. T. M. Riedhammer, Ph.D. Thesis, State University of New York at Buffalo, Buffalo, New York (1977).
10. D. F. Untereker, Ph.D. Thesis, State University of New York at Buffalo, Buffalo, New York (1973).
11. J. D. E. McIntyre and D. M. Kolb, Symp. Faraday Soc., No. 4, 99-113 (1970).
12. G. D. Zakumbaeva, F. M. Toktabaeva, and D. V. Sokol'skii, *Electrokhimiya*, **6**, 777 (1970).
13. S. Gilman, *This Journal*, **118**, 1953 (1971).
14. E. Schmidt and H. R. Gygax, *J. Electroanal. Chem.*, **12**, 300 (1966).
15. E. Schmidt and H. R. Gygax, *ibid.*, **13**, 378 (1967).
16. E. Schmidt and H. R. Gygax, *ibid.*, **14**, 126 (1967).
17. D. J. Astely, J. A. Harrison, and H. R. Thirsk, *ibid.*, **19**, 325 (1968).
18. S. H. Cadle and S. Bruckenstein, *Anal. Chem.*, **44**, 1993 (1972).
19. G. D. Robbins and C. G. Enke, *J. Electroanal. Chem.*, **23**, 343 (1969).
20. M. Z. Hassan, D. F. Untereker, and S. Bruckenstein, *ibid.*, **42**, 161 (1973).
21. W. J. Lorentz, I. Moumtzes, and E. Schmidt, *ibid.*, **33**, 121 (1971).
22. E. Schmidt and W. J. Lorentz, *Ber. Bunsenges. Phys. Chem.*, **75**, 71 (1971).
23. D. P. Sandoz, R. M. Peekma, H. Freund, and C. F. Morrison, Jr., *J. Electroanal. Chem.*, **24**, 165 (1970).
24. D. Grdenic', *Quarterly Reviews*, **19**, 303 (1965).
25. B. J. Bowles, *Nature (London)*, **212**, 1456 (1966).
26. V. A. Vicente, Ph.D. Thesis, State University of New York at Buffalo, Buffalo, New York (1973).
27. V. A. Vicente and S. Bruckenstein, *Anal. Chem.*, **45**, 2036 (1973).
28. V. A. Vicente and S. Bruckenstein, *ibid.*, **44**, 297 (1972).
29. W. G. Sherwood, Ph.D. Thesis, State University of New York at Buffalo, Buffalo, New York, September 1977, Chapter II.
30. S. B. Brummer and A. C. Makrides, *This Journal*, **111**, 1122 (1964).
31. W. G. Sherwood, D. F. Untereker, and S. Bruckenstein, *ibid.*, In press.

The Kinetics of the Oxygen Reduction Reaction on Gold in Alkaline Solution

R. W. Zurilla,*,[1] R. K. Sen,* and E. Yeager**

Case Laboratories for Electrochemical Studies and the Chemistry Department, Case Western Reserve University, Cleveland, Ohio 44106

ABSTRACT

The kinetics of the O_2 cathode have been examined on Au in alkaline electrolytes using the rotating ring-disk method. Only the series mechanism is operative. The cathodic and anodic kinetic data for the O_2/HO_2^- couple support the mechanism

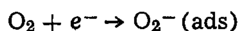

$$O_2 + e^- \rightarrow O_2^-(\text{ads})$$

$$2\,O_2^-(\text{ads}) + H_2O \rightarrow HO_2^- + O_2 + OH^-$$

The further reduction of HO_2^- to OH^- is first order in HO_2^- and involves a rate-controlling step with very little potential dependence.

Several studies (1-4) indicate that O_2 reduction on Au in alkaline solutions proceeds only by the series mechanism with HO_2^- (ads) as an intermediate in the reduction process. Some questions persist, however, regarding the mechanism involved in the reduction process to peroxide (1-4) as well as the peroxide elimination step. To resolve some of these questions the present study has involved kinetic measurements of O_2 reduction on Au in alkaline solution of high purity.

Experimental

The experiments were carried out in an all-Teflon cell, using a Au rotating ring-disk electrode, the details of which are available elsewhere (5). The gold was obtained from Alfa Products Division of the Ventron Corporation and had a purity of 99.999% according to the supplier. The Au disk (0.5 cm diam, 0.196 cm^2 area) and ring (0.89 cm OD, 0.62 cm ID, 0.32 cm^2 area) electrodes were mechanically polished in successive stages with the following materials: (*i*) silicon carbide paper, 600 grit (3M Company); (*ii*) crocus cloth (Behr-Manning Company); (*iii*) AB alumina, 600 grit (Buehler Limited); (*iv*) AB alpha alumina, 0.3μ (Buehler Limited); and (*v*) AB gamma alumina, 0.05μ (Buehler Limited). When the electrodes attained a mirror finish, they were soaked in 6*M* NaOH (16 hr), 1:1 H_2SO_4-HNO_3 (16 hr), 1:1 HNO_3-H_2O (12 hr), and then washed and stored in triply distilled water. The electrodes thus prepared are probably in a slightly oxidized state. Therefore, prior to the electrochemical measurements the Au disk electrode was cycled several times between +0.9 and +0.25V *vs.* RHE at a sweep rate of 1 V/min. Such treatment yields an electrode surface which is in the reduced state. Linear sweep voltammetry for Au over a sufficiently wide potential range in alkaline solutions indicates that the anodic film is reduced at ~0.85V *vs.* RHE. Diaphragm-type β Pd-H electrodes, fed from the rear with H_2, were used as the reference and counterelectrodes. Unless otherwise indicated all potentials are expressed relative to the β Pd-H electrode, which exhibits the reversible hydrogen electrode (RHE) potential.

A 50% stock solution of NaOH was prepared from special low carbonate NaOH pellets (J. T. Baker). The solubility and hence maximum concentration of Na_2CO_3 in this solution is very low ($10^{-4}M$). Over a period of several months the 50% solution was decanted several times to remove the precipitated Na_2CO_3. The 0.1*M* NaOH solution used in the present study was prepared from this stock solution with care to avoid recontamination with CO_2.

Preelectrolysis of the 0.1*M* NaOH solution was carried out with two interconnected Au foil cathodes (total area ~45 cm^2) in the main compartment of the cell. The maximum current density during preelectrolysis was 10 μA/cm^2. In prior studies many workers have used Pt for the preelectrolysis electrodes. Under anodic conditions, however, even in alkaline solutions Pt may be introduced in the solution and subsequently redeposited on the working electrode during electrochemical measurements. To check on this, various metals were used as preelectrolysis anodes, namely Pt, Au, Ni, and β Pd-H (H_2 fed from the rear). In all instances preelectrolysis was carried out for a minimum of 40 hr with purified He bubbling through the solution. The two preelectrolysis cathodes were usually maintained at −0.40V, whereas the corresponding anode potentials were for Pt ~1.5V *vs.* the β Pd-H reference, Au ~1.7V, Ni ~1.8V, and β Pd-H ~0.0V. In addition two unbiased Au foil electrodes (~22 cm^2 each) were introduced in the main compartment of the cell at a rest potential of +0.9V during preelectrolysis to adsorb impurities.

O_2 reduction was then studied with the solutions preelectrolyzed in the presence of the various anodes. The Tafel plots diffusion corrected are as shown[2] in Fig. 1. The current i_1 indicated in Fig. 1 is that portion of the disk current that results in the formation of adsorbed HO_2^- and i_D is the diffusion-limited current for this process. The method of calculation and significance of i_1 are discussed later. The use of Pt as the preelectrolysis anode yields different results. This is attributed to Pt contamination of the solution. For all further results presented in this article, only β Pd-H anodes were used during preelectrolysis.

Results

O_2 reduction.—The disk and ring currents as a function of the disk potential for O_2 reduction on Au in 0.1*M* NaOH at 2500 rpm are shown in Fig. 2. The ring was held at +1.05V where prior measurements indicate that H_2O_2 oxidation is diffusion controlled. A small residual ring current (<5 μA) was observed with the disk in the potential range 0.93-0.89V, even though the disk current was essentially zero. This residual ring current was rotation dependent and amounted only to a few percent of the ring current in the current-potential plateau region for the disk. This background ring current is probably due to traces of HO_2^- in solution and was subtracted from the observed ring currents in the data shown in Fig. 2.

* Electrochemical Society Active Member.
** Electrochemical Society Honorary Member.
[1] Present address: Ford Motor Company, Research and Engineering Center, Dearborn, Michigan 48100.

Key words: metals, electrode, adsorption, catalysis.

[2] Cathodic currents are taken as positive.

Fig. 1. Tafel plots for O_2 reduction on Au measured at 2500 rpm and 2 V/min in O_2-saturated 0.1*M* NaOH preelectrolyzed with β Pd-H (○), Au (●), Ni (△), and Pt (□) anodes with Au cathodes. Disk area, 0.196 cm^2; temperature, 26°C; i_D = 0.66 mA.

Fig. 2. Comparison of disk and ring currents with calculated current (i_1) for O_2 reduction to HO_2^- for Au disk electrode at various potentials in O_2-saturated 0.1*M* NaOH at 26°C. Rotation rate, 2500 rpm; sweep rate, 1 V/min; *N*, 0.43; disk electrode area, 0.196 cm^2.

The hysteresis in the disk polarization curves was negligible between the cathodic and anodic voltage sweeps. The collection efficiency *N* for the disk-ring electrode system was calculated to be $N = 0.43$ from the geometry of the disk and ring electrodes, using the treatment of Albery and Bruckenstein (6).

If the series mechanism is assumed to be operative for O_2 reduction on Au in alkaline media, the reaction sequence can be represented as

$$\begin{array}{lccccc} \text{electrode surface} & O_2 & \xrightarrow{i_1} & HO_2^-\ (\text{ads}) & \xrightarrow{i_2} & \text{products} \\ & \uparrow & & i_4 \downarrow \uparrow i_5 & & \\ & & & (HO_2^-)_e & & \\ & & & \downarrow i_R/N & & \\ \text{bulk solution} & O_2 & & HO_2^- & & \end{array}$$

where i_2 is the current associated with the electrochemical reduction of HO_2^-, i_R is the ring current, i_4 and i_5 are the rates of desorption and adsorption of HO_2^- expressed as currents, and HO_2^- and $(HO_2^-)_e$ correspond to solution phase peroxide in the bulk and at the electrode surface, respectively. This reaction scheme predicts the relationship (5)

$$\frac{i}{i_R} = \frac{(2k_2/k_4) + 1}{N} + \frac{2k_2k_5(1.61\nu^{1/6})}{k_4ND_p^{2/3}\omega^{1/2}} \quad [1]$$

where i is the experimentally measured disk current, D_p is the diffusion coefficient of HO_2^-, ν is the kinematic viscosity of the electrolyte, ω is the electrode rotation rate, *N* is the collection efficiency, and the *k*'s are the rate constants of the steps indicated by the subscripts.

Equation [1] predicts a linear relationship between i/i_R and $\omega^{-1/2}$ for a given potential and the intercept can be greater than $1/N$ depending on the rate constants for steps 2 and 4. Damjanovic *et al.* (4) have stated that i/i_R *vs.* $\omega^{-1/2}$ plots having intercepts greater than $1/N$ are proof that the parallel mechanism is operative. This analysis shows that such is not a proof. Recently Tarasevich *et al.* (2) and Wroblowa *et al.* (3) have also arrived at the same conclusion regarding the analysis of Damjanovic *et al.* (4).

If $2k_2/k_4 << 1$, then Eq. [1] rearranges to

$$\frac{i}{i_R} = \frac{1}{N} + \frac{2\overline{k_2}(1.61\nu^{1/6})}{ND_p^{2/3}\omega^{1/2}} \quad [2]$$

where $\overline{k_2} = k_2k_5/k_4$.

A plot of i/i_R *vs.* $\omega^{-1/2}$ obtained from the experimental data of the present study is shown in Fig. 3. The extrapolations of the linear plots in Fig. 3 to $\omega^{-1/2} = 0$ yields an intercept which is independent of the disk potential and its magnitude (2.2) approximately equals $1/N$. Since this behavior fits Eq. [2], the O_2 reduction on Au in 0.1*M* NaOH appears to proceed via the series mechanism. Furthermore it confirms that $k_4 >> k_2$.

Fig. 3. Ratio of the disk to ring currents obtained for O_2 reduction for Au electrodes at various disk potentials in O_2-saturated 0.1*M* NaOH plotted against $\omega^{-1/2}$. Disk area, 0.196 cm^2; sweep rate, 1 V/min; temperature, 26°C; ring potential, 1.05V.

The expressions for i_1 and i_2 obtained from the reaction scheme presented above are

$$i_1 = \frac{i + (i_R/N)}{2} \quad [3a]$$

and

$$i_2 = i - i_1 \quad [3b]$$

With the disk-ring data obtained in the present study, i_1 can be calculated at various potentials for a particular rotation rate. The results of such calculations at 2500 rpm are shown in Fig. 2 and indicate that at all cathodic potentials the experimental disk currents are larger than the calculated i_1 values. The difference is due to the further reduction of HO_2^- (i_2).

If the kinetics are first order with respect to dissolved O_2, the corrected disk current i_1 is related (7) to rotation rate ω by the equation

$$\frac{1}{i_1} = \frac{1}{(i_1)_k} + \frac{1}{B\sqrt{\omega}} \quad [4]$$

where $(i_1)_k$ is the kinetic limiting current for O_2 reduction to HO_2^- and $i_D = B\sqrt{\omega}$ is the corresponding diffusion limiting current. Figure 4 shows a plot of $1/i_1$ *vs.* $\omega^{-1/2}$ obtained from the present experimental data. The linearity of the plot indicates that O_2 reduction is first order with respect to dissolved O_2. The experimental value of B obtained from Fig. 4 is 0.013 mA $(rpm)^{-1/2}$ which compares favorably with the calculated value of 0.014 mA $(rpm)^{-1/2}$ using Newman's (8) expression for B and the data of Gubbins and Walker (9) for the solubility and diffusion coefficient of O_2 in 0.1*M* NaOH.

If the experimentally measured disk currents are used directly to construct Tafel plots, the slope turns out to be a function of the rotation rate. This apparent change of Tafel slope with rotation rate is caused by a failure to consider the contribution made to the disk current by HO_2^- reduction. When the corrected disk current (i_1) is used, the Tafel slope is independent of rotation rate and has a value of −120 mV/decade as shown in Fig. 5. The values of i_D for these plots were calculated from the B value obtained from Fig. 4 and

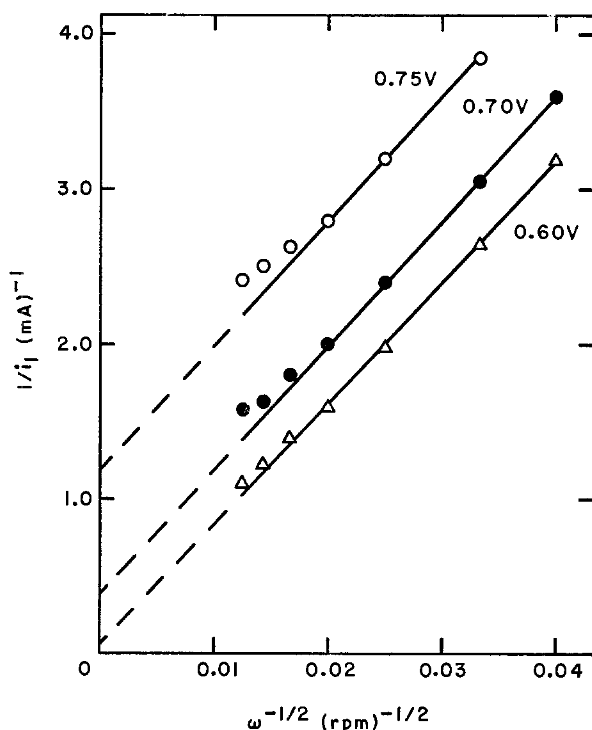

Fig. 4. Plot of $1/i_1$ vs. $\omega^{-1/2}$ for the reduction of O_2 on Au at various disk potentials in O_2-saturated 0.1*M* NaOH. Electrode area, 0.196 cm^2; sweep rate, 1 V/min; temperature, 26°C.

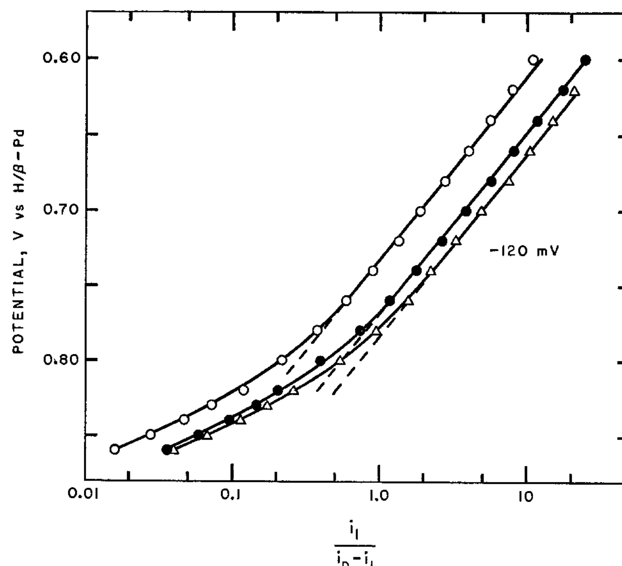

Fig. 5. Tafel plots constructed from corrected disk currents (i_1) for O_2 reduction on Au in O_2-saturated 0.1*M* NaOH at 26°C. Disk area, 0.196 cm^2; sweep rate, 1 V/min, ○, 6400 rpm; i_D = 1.04 mA. ●, 1600 rpm; i_D = 0.52 mA. △, 900 rpm; i_D = 0.39 mA.

the rotation rate. Deviations from Tafel linearity begin at a potential of +0.77V. These deviations are caused most likely by a contribution to the disk current by the back-reaction of HO_2^- to O_2, which decreases the net observed cathodic current. The observed −120 mV/decade Tafel slope implies rate control by an initial one-electron transfer step.

Investigations of 0.1*M* NaOH solutions containing O_2 and $8.8 \times 10^{-4}M$ HO_2^- were carried out to detect possible coupling of the O_2 and HO_2^- reduction processes and any inhibition effects of the O_2 reduction reaction caused by the presence of HO_2^- in the bulk solution. The Tafel plots for O_2 reduction obtained in this case superimpose with the ones obtained in the absence of any HO_2^- in the Tafel linear range. Therefore, the rotating disk-ring data do not indicate any kinetic coupling.

The experiments with peroxide added to the solution were also used to evaluate the stoichiometric number ν with the help of the equation

$$\left(\frac{\partial \eta_a}{\partial i_1}\right)_o = \frac{-RT}{n\mathbf{F}} \cdot \frac{\nu}{(i_o)_a} \quad [5]$$

where $(\partial\eta_a/\partial i_1)_o$ is the activation polarization resistance evaluated at $\eta = 0$ for O_2/HO_2^- couple, $(i_o)_a$ is the apparent exchange current for this couple evaluated from the Tafel slope, and n is the over-all number of electrons transferred per mole of O_2 ($n = 2$). The activation polarization resistance was determined by correcting the experimentally determined over-all polarization resistance $(\partial\eta/\partial i_1)_o$ for mass transport by the equation

$$\left(\frac{\partial \eta_a}{\partial i_1}\right)_o = \left(\frac{\partial \eta}{\partial i_1}\right)_o - \left(\frac{\partial \eta_d}{\partial i_1}\right)_o \quad [6]$$

The mass transport resistance $(\partial\eta_d/\partial i_1)_o$ is defined by

$$\left(\frac{\partial \eta_d}{\partial i_1}\right)_o = \frac{RT}{n\mathbf{F}}\left[\frac{1}{i_D} + \frac{1}{i_d}\right] \quad [7]$$

where i_D and i_d are the diffusion-limiting currents for O_2 reduction and HO_2^- oxidation. The over-all polarization resistance $(\partial\eta/\partial i_1)_o$ was determined from a plot of η *vs.* i_1 at small η with i_1 calculated from the disk-ring data. This procedure for the evaluation of $(\partial\eta/\partial i_1)_o$ was used to eliminate contributions to the disk current from HO_2^- reduction.

Table I. Parameters for the evaluation of the apparent stoichiometric number (ν) for the reduction of O_2 on Au in O_2-saturated 0.1*M* NaOH containing $8.8 \times 10^{-4}M$ HO_2^- at 26°C. Electrode area, 0.196 cm².

rpm	900	2500	4900
i_D (mA)	0.40	0.66	0.93
i_d (mA)	0.20	0.33	0.47
$(i_o)_a$ (mA)	0.18	0.17	0.18
$\left(\frac{\partial\eta}{\partial i_1}\right)_o \left(\frac{V}{mA}\right)$	−0.24	−0.21	−0.17
$\left(\frac{\partial\eta_d}{\partial i_1}\right)_o \left(\frac{V}{mA}\right)$	−0.10	−0.06	−0.04
$\left(\frac{\partial\eta_a}{\partial i_1}\right)_o \left(\frac{V}{mA}\right)$	−0.14	−0.15	−0.13
Apparent ν	2.0	2.0	1.8

Values of the stoichiometric number calculated by use of the above equations are listed in Table I together with values for the various parameters involved in the computations. These results indicate an apparent stoichiometric number of 2 for the O_2/HO_2^- couple.

The *p*H dependence of the O_2 reduction was examined in the range 11.5-12.7 by adding $HClO_4$ to the 0.1*M* NaOH. At constant electrode potential, the disk current was essentially independent of *p*H in this range and hence the O_2 reduction to peroxide is considered to be zero order with respect to OH^-.

HO_2^- oxidation.—The oxidation of HO_2^- on Au in He-saturated 0.1*M* NaOH containing $1.34 \times 10^{-2}M$ HO_2^- exhibits a well-defined limiting current. Figure 6 shows experimental current-potential curves for HO_2^- oxidation at various rotation rates. Hysteresis was negligible between the curves measured with increasing and decreasing anodic potentials, provided the maximum potential did not exceed 1.1V. The rotation dependence of the potential corresponding to $i = 0$ is attributed to the heterogeneous decomposition of HO_2^- according to the reactions

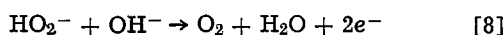

$$HO_2^- + OH^- \rightarrow O_2 + H_2O + 2e^- \quad [8]$$

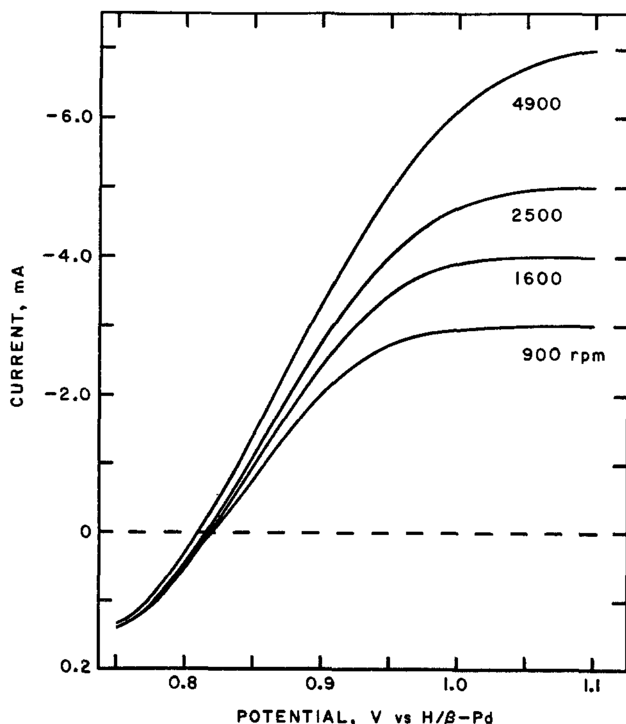

Fig. 6. Oxidation of HO_2 at various rotation rates (rpm) on Au in He-saturated 0.1*M* NaOH containing $1.34 \times 10^{-2}M$ HO_2^- at 26°C. Electrode area, 0.196 cm²; sweep rate, 1 V/min².

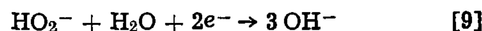

$$HO_2^- + H_2O + 2e^- \rightarrow 3\,OH^- \quad [9]$$

or the total reaction

$$2HO_2^- \rightarrow O_2 + 2\,OH^- \quad [10]$$

When the back-reaction for HO_2^- oxidation is negligible, the kinetics at constant *p*H and potential follow the relationship

$$i = -k[HO_2^-]_e^m \quad [11]$$

where *k* is the rate constant and *i* the current for HO_2^- oxidation, *m* is the reaction order, $[HO_2^-]_e$ is the concentration of HO_2^- at the electrode surface. With the use of the relation

$$\frac{[HO_2^-]_e}{[HO_2^-]} = \frac{i_d - i}{i_d} \quad [12]$$

where $[HO_2^-]$ is the bulk concentration of HO_2^-, Eq. [11] becomes

$$i = k[HO_2^-]^m \left[\frac{i_d - i}{i_d}\right]^m \quad [13]$$

By plotting log (*i*) *vs.* log $[(i_d - i)/i_d]$ at different rotation rates and constant potential, the slope *m* can be determined. Such plots are shown in Fig. 7 for the oxidation of HO_2^- on Au in He-saturated $1.34 \times 10^{-2}M$ HO_2^- + 0.1*M* NaOH. The plots for 0.95 and 1.00V indicate a reaction order of ~½ while that at 0.90V indicates ~1. The most likely explanation for this apparent discrepancy is that at 0.90V the HO_2^- is undergoing reduction to OH^- according to Eq. [9], and O_2 formed at the electrode by the oxidation of HO_2^- is contributing a cathodic current.

If the oxidation of HO_2^- is one-half order with respect to HO_2^-, the disk current at a given potential is related to the rotation rate (7) by

$$\frac{1}{i^2} = \frac{1}{(i_k)^2} + \frac{1}{B\,i\sqrt{\omega}} \quad [14]$$

where i_k is the kinetic limiting current for HO_2^- oxidation and $B = \overline{B}/[HO_2^-]$. Plots of $1/i^2$ *vs.* $1/i\sqrt{\omega}$ for various potentials are given in Fig. 8 for the same set of experimental data. The linearity and parallel slopes at 0.95 and 1.00V provide further evidence of $m = ½$ at these potentials. While the plot is linear also at 0.90V, the slope deviates from that at more anodic potentials. This deviation in slope at 0.90V is not surprising in view of the difference found also in Fig. 7 at this potential. The values of $\overline{B}$ calculated from the plots in Fig. 8 are 7.7 and 7.8 in mA^{-1} $(rpm)^{-1/2}$ for 0.95 and 1.00V as compared with a value of 7.6 determined under conditions of pure diffusion HO_2^- control from a plot of $1/i$ *vs.* $1/\sqrt{\omega}$ for a $2.5 \times 10^{-3}M$ HO_2^- + 0.1*M* NaOH at 1.05V. The value of $\overline{B}$ calculated from Fig. 8 for 0.90V, however, is 6.1 which deviates substantially from the expected value.

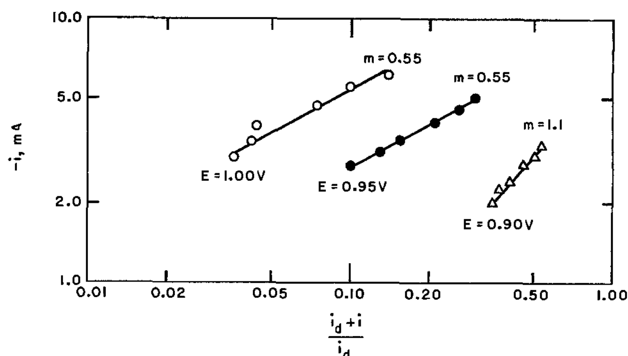

Fig. 7. Reaction order (*m*) for oxidation of HO_2^- on Au in He-saturated 0.1*M* NaOH containing $1.34 \times 10^{-2}M$ HO_2^-. Electrode area, 0.196 cm²; temperature, 26°C; sweep rate, 1 V/min.

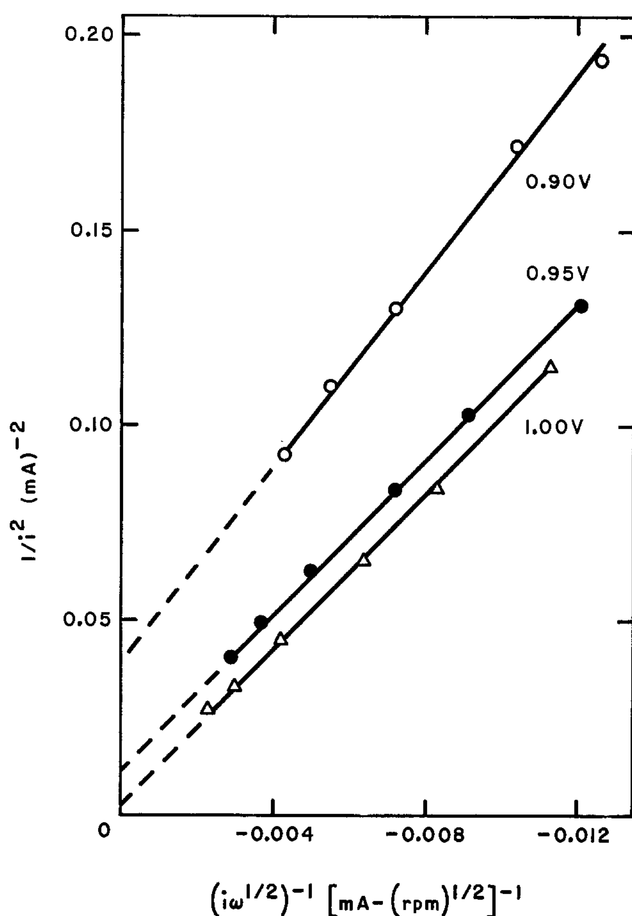

Fig. 8. Plot of $1/i^2$ vs. $(i\omega^{1/2})^{-1}$ for the oxidation of HO_2^- on Au at various potentials in He-saturated 0.1*M* NaOH containing 1.34 × 10^{-2}*M* HO_2^- at 26°C. Electrode area, 0.196 cm^2; sweep rate, 1 V/min.

It is unfortunate that the reaction orders can be examined for the HO_2^- oxidation step only relatively close to the HO_2^- diffusion-limiting current using the rotating disk data. This makes it difficult to obtain accurate values for m by this approach. Even so, the reaction order data in Fig. 7 and 8 support a value of $m = ½$ with respect to HO_2^-. In the later discussion of mechanism it is shown that a HO_2^- reaction order of one-half is compatible with the stoichiometric number of 2 evaluated from the combined rotating disk-ring data whereas a HO_2^- reaction order of 1 is not.

The pH dependence of the HO_2^- oxidation was also examined over the range 11-12.7 at 0.95 and 1.00V by adding varying amounts of concentrated $HClO_4$ to an O_2 saturated 0.1*M* NaOH + 7.8 × 10^{-4}*M* HO_2^-. The results are shown in Fig. 9 in terms of a function of the current density i and the limiting current densities i_D and i_d corresponding to the values for O_2 and HO_2^- transport, respectively. The use of this function is prompted by mechanistic considerations discussed later. The OH^- reaction order corresponds to the slope in the log-log plot and is ~½. Measurements at lower pH's than 11 gave erratic results probably because of OH^- transport problems. The pK of H_2O_2 is ~12, which also can lead to complications at pH less than this value.

HO_2^- reduction.—Investigations of the reduction of HO_2^- on Au were conducted in He-saturated 0.1*M* NaOH. Reproducible results were difficult to obtain due to the decomposition of HO_2^- which introduced O_2 into the solution. Nonetheless, reliable results for HO_2^- reduction on Au were obtained by performing the experiments in reasonably short time. The results obtained in 0.1*M* NaOH solutions plus 2.5 × 10^{-3}*M* HO_2^- are shown in Fig. 10 and 11.

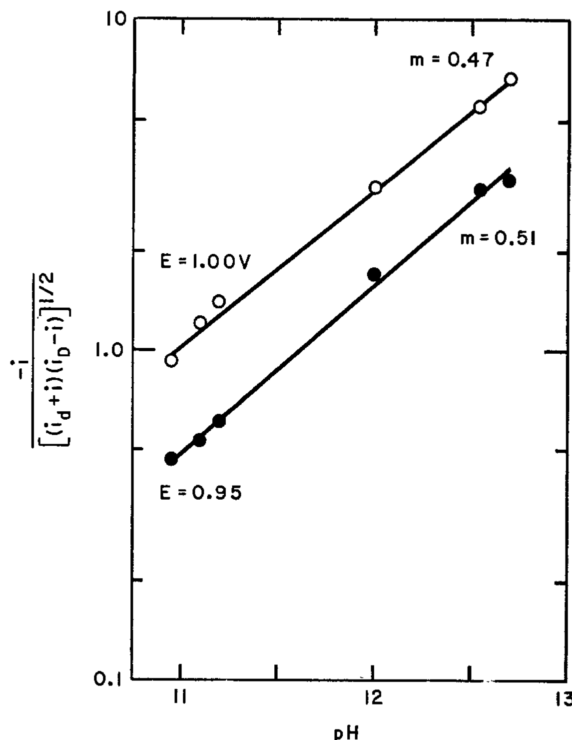

Fig. 9. Dependence of oxidation of HO_2^- on pH for Au electrode in O_2-saturated 0.1*M* NaOH and small amounts of 70% $HClO_4$ + 7.8 × 10^{-4} HO_2^-. Electrode area, 0.196 cm^2; rotation rate, 2500 rpm; temperature, 26°C.

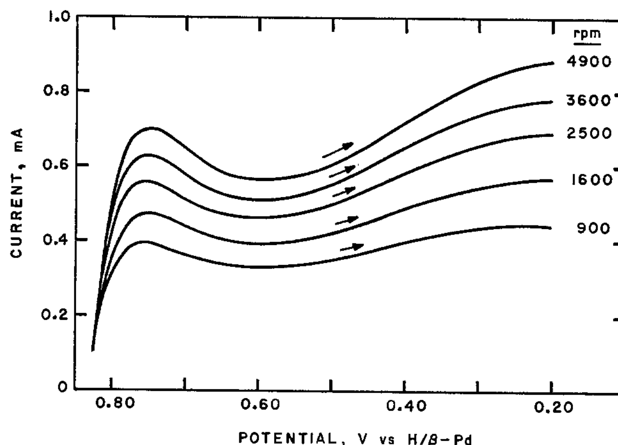

Fig. 10. Reduction of HO_2^- in He-saturated 0.1*M* NaOH containing 2.5 × 10^{-3}*M* HO_2^- at 26°C. Electrode area, 0.196 cm^2; sweep rate, 4 V/min.

The i vs. E plots in Fig. 10 have a rather strange shape. The $1/i$ vs. $1/\sqrt{\omega}$ plot in Fig. 11 indicates that the current even at the most cathodic potentials examined is still under combined kinetic and diffusion control. The kinetic currents $(i_2)_K$ obtained from the intercepts in Fig. 11 have very little potential dependence over a wide range of potentials (0.2-0.75V) and correspond to a value of $k_2 \cong 0.01$ cm/sec. The lack of potential dependence of k_2 suggests that the rate-controlling step and any step preceding it do not involve electron transfer.

Mechanistic Considerations

The kinetic data for O_2 reduction and HO_2^- oxidation on Au in alkaline solution are compatible with the following mechanism

Step I

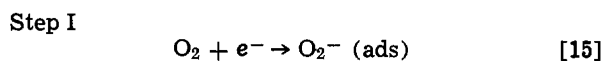

$$O_2 + e^- \rightarrow O_2^- \text{ (ads)} \quad [15]$$

Step II

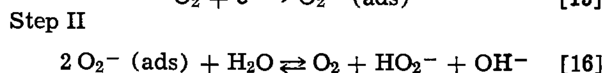

$$2\,O_2^- \text{ (ads)} + H_2O \rightleftarrows O_2 + HO_2^- + OH^- \quad [16]$$

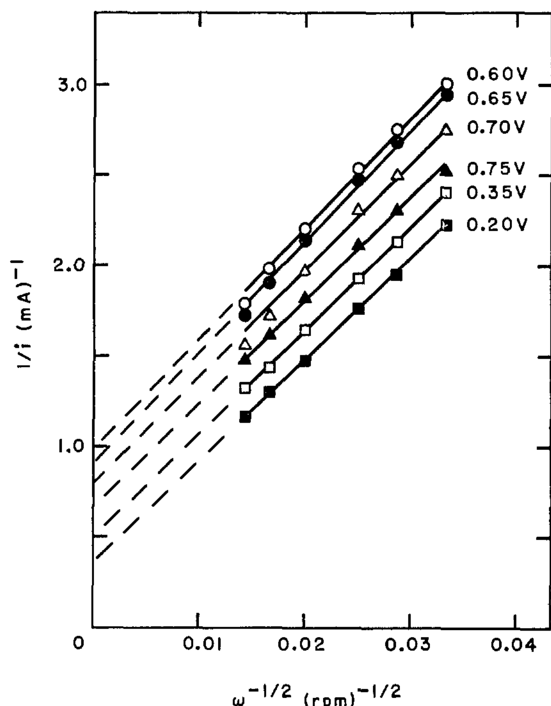

Fig. 11. $1/i$ vs. $\omega^{-1/2}$ plots for the reduction of HO_2^- on Au at various potentials in He-saturated 0.1M NaOH containing $2.5 \times 10^{-3}M$ HO_2^- at 26°C. Electrode area, 0.196 cm²; sweep rate, 4 V/min.

This mechanism satisfies the requirement of a Tafel slope of −120 mV/decade, a stoichiometric number of 2, and the observed reaction orders with respect to O_2 ($m = 1$), OH^- ($m = 0$) for the reduction, and HO_2^- ($m = 1/2$) and OH^- ($m = 1/2$) for the peroxide oxidation. Further it does not involve the cleavage of the O-O bond prior to the formation of HO_2^-. Isotopic experiments on various surfaces (10, 2) provide strong evidence that all of the peroxide oxygen originates from the O_2 and not H_2O or OH^- and that the O-O bond is not ruptured.

The dismutation step II is rather surprising. Since the rate of the reverse of step I is negligible, step II is not just the simple electrochemical oxidation of the superoxide $O_2^{\overline{\cdot}}$ coupled with its further reductions. Further, it is unlikely that step II proceeds by the desorption of $O_2^{\overline{\cdot}}$, followed by the second-order homogeneous reaction

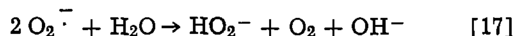

$$2\,O_2^{\overline{\cdot}} + H_2O \rightarrow HO_2^- + O_2 + OH^- \quad [17]$$

The slopes of the $1/i_l$ vs. $1/\sqrt{\omega}$ plots in Fig. 4 correspond to those of $2e^-$ per O_2 transported through the Nernst layer. Consequently if Eq. [17] contributes significantly to the HO_2^- formation this reaction must proceed sufficiently fast to be essentially complete within a distance small compared to the Nernst diffusion layer thickness. Thermodynamics imposes an upper limit on the $O_2^{\overline{\cdot}}$ concentration adjacent to the electrode. Recent estimates (11, 12) of the standard reduction potential for the reaction

$$O_2 + e^- \rightarrow O_2^{\overline{\cdot}} \quad [18]$$

indicate $E° = -0.28V$ vs. SHE or $+0.55V$ vs. β Pd-H. At a potential of, for example, 0.75V vs. β Pd-H (see Fig. 4), the upper limit for the $O_2^{\overline{\cdot}}$ concentration (calculated from the Nernst equation) is $\sim 10^{-3}M$. The upper limit for the second-order rate constant for Eq. [17], however, has been shown (13) to be 100 M^{-1} sec^{-1}. Assuming that the reaction must occur in an electrolyte layer of $X = 10^{-3}$ cm thickness, the upper limit on the rate of Eq. [17] expressed in units of current density is

$$i = 2\mathbf{F}k(C_{O_2^{\overline{\cdot}}})^2 V = 2 \times 10^{-5}\ \text{A/cm}^2 \quad [19]$$

where $\mathbf{F}$ is the Faraday, $k = 10^2$ M^{-1} sec^{-1}, $C_{O_2^{\overline{\cdot}}} = 10^{-3}M$, and $V = (10^{-3}$ cm$)(1$ cm$^2) = 10^{-6}$ liters. The observed current density i_l at this potential and a rotation rate of 2500 rpm is 1.8×10^{-3} A/cm² or two orders of magnitude greater. Thus it appears that step II is definitely a surface process involving the direct interaction of two $O_2^{\overline{\cdot}}$ adsorbed radicals.

With step I slow and step II fast, the current for O_2 reduction is

$$i = (i_o)_I \left[\frac{i_D - i}{i_D} \exp \frac{-\alpha_I \mathbf{F} \eta}{RT} - \left(\frac{i_d + i}{i_d} \cdot \frac{i_D - i}{i_D} \right)^{1/2} \exp \frac{(1-\alpha_I)\mathbf{F}\eta}{RT} \right] \quad [20]$$

where $(i_o)_I$ and α_I are the apparent exchange current density and transfer coefficient for step I, i_D and i_d are the diffusion limiting current densities for O_2 reduction and HO_2^- oxidation involving the over-all transfer of two electrons, and $\eta = E - E_r$, with E_r the reversible potential of the O_2/HO_2^- couple. For Eq. [20] the current density i is negative for net oxidation currents and positive for the reduction currents. Equation [20] also assumes that the surface coverage of O_2^-(ads) is small.

For ease in testing the proposed reaction scheme Eq. [20] is rearranged to the following form

$$\eta = \frac{2.3RT}{\alpha_I \mathbf{F}} \log \frac{(i_o)_I}{i_D} - \frac{2.3RT}{\alpha_I \mathbf{F}} \log X \quad [21]$$

where

$$X = \frac{i/(i_D - i)}{1 - \left[\frac{i_D(i_d + i)}{i_d(i_D - i)} \right]^{1/2} \cdot \exp \frac{\mathbf{F}\eta}{RT}} \quad [21a]$$

Thus a plot of η vs. log X should be linear over the whole potential range in which anodic and cathodic currents are observed and the linear plot should have a slope of $-(2.3\,RT/\alpha_I\mathbf{F}) = -120$ mV when $\alpha_I = 0.5$.

Plots of η vs. log X are given in Fig. 12 for the polarization curves measured at 900, 2500, and 4900 rpm for the oxidation of HO_2^- and reduction of O_2 on Au in O_2-saturated 0.1M NaOH containing $8.8 \times 10^{-4}M$ HO_2^-. The cathodic disk currents were corrected for HO_2^- reduction using the ring current data and the appropriate equation. The linear plots in Fig. 12 show the expected translation with rotation rate in the ratio of the diffusion currents i_D and have a slope of ~ -120 mV/decade which corresponds to $\alpha_I = 0.5$. The plots in Fig. 12, therefore, are a good verification of the reaction mechanism represented by Eq. [15] and [16]. The exchange current density $(i_o)_I$ calculated from Fig. 12 is ~ 0.9 mA/cm² for the O_2-saturated $8.8 \times 10^{-4}M$ HO_2^- + 0.1M NaOH solution at 26°C.

The observed pH dependence of the anodic oxidation of HO_2^- to O_2 (Fig. 9) can also be explained on the basis of steps I and II. The oxidation current is related to the molar concentrations of O_2, HO_2^-, and OH^- at the electrode surface by the equation

$$i = -2\mathbf{F}\overleftarrow{k}_I K_{II}^{-1/2}[O_2]_e^{1/2}[HO_2^-]_e^{1/2}[OH^-]_e^{1/2} \quad [22]$$

where $\overleftarrow{k}_I$ is the reverse rate constant for step I and K_{II} the equilibrium constant for step II. Correcting for diffusion of HO_2^- and O_2, Eq. [22] becomes

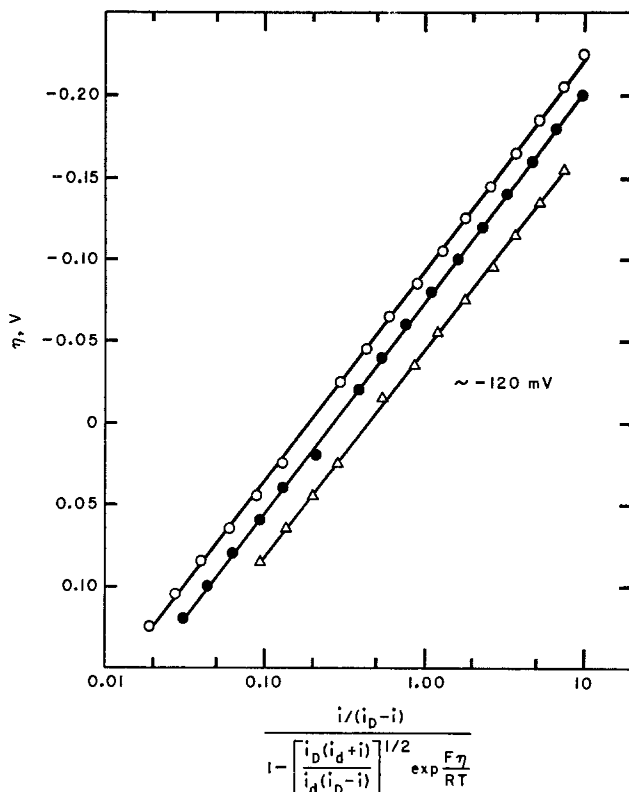

Fig. 12. Oxidation of HO_2^- and reduction of O_2 on Au in O_2-saturated 0.1M NaOH containing $8.8 \times 10^{-4}M$ HO_2^- at 26°C. Electrode area, 0.196 cm^2; sweep rate, 2 V/min; $E_r = 0.83V$. ○, 4900 rpm; $i_D = 0.93$; $i_d = 0.47$. ●, 2500 rpm; $i_D = 0.66$; $i_d = 0.34$. △, 900 rpm; $i_D = 0.40$; $i_d = 0.20$ mA.

$$\frac{i}{[(i_d + i)(i_D - i)]^{1/2}} = \overleftarrow{k}_I K_{II}^{-1/2}(i_d \cdot i_D)^{1/2}[O_2]^{1/2}[HO_2^-]^{1/2}[OH]^{1/2} \quad [23]$$

where $[O_2]$, $[HO_2^-]$, and $[OH^-]$ are the bulk concentrations. The plot in Fig. 9 verifies the one-half order dependence on $[OH^-]$. Equation [20] also predicts a one-half order dependence on O_2 for the oxidation of HO_2^-. This reaction order was not checked in the present work.

Only the reduction process could be studied for the HO_2^-/OH^- couple. The process is first order with respect to HO_2^-. A surprising result is that even at very cathodic potentials (0.2V) the process is still under partial kinetic control. The rate constant for the process has a very small potential dependence. This suggests that a chemical step proceeding the electron transfer is rate controlling. Such a step might be

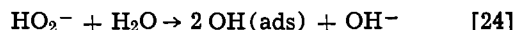

$$HO_2^- + H_2O \rightarrow 2\,OH(ads) + OH^- \quad [24]$$

The small variation of the rate constant with potential may be just secondary changes due to the potential dependence of the state of adsorption of anions and other features of the surface.

Acknowledgments

The authors are pleased to acknowledge the support of this research by the U.S. Office of Naval Research. One of the authors (RWZ) wishes to express appreciation to the National Aeronautics and Space Administration for a fellowship.

Manuscript submitted April 11, 1977; revised manuscript received Feb. 23, 1978.

Any discussion of this paper will appear in a Discussion Section to be published in the June 1979 JOURNAL. All discussions for the June 1979 Discussion Section should be submitted by Feb. 1, 1979.

Publication costs of this article were assisted by Case Western Reserve University.

REFERENCES

1. B. A. Podlibner and L. N. Nekrasov, *Electrokhimiya*, **5**, 340 (1960).
2. M. R. Tarasevich, K. A. Radyushkina, V. Yu. Filinovskii, and R. Kh. Burstein, *ibid.*, **6**, 1522 (1970).
3. H. S. Wroblowa, Y. D. Pan, and G. Razumney, *J. Electroanal. Chem.*, **60**, 195 (1976).
4. A. Damjanovic, M. A. Genshaw, and J. O'M. Bockris, *ibid.*, **15**, 173 (1967).
5. R. W. Zurilla and E. Yeager, Technical Report No. 23, Office of Naval Research Contract No. N00014-67-C-0389, Case Western Reserve University (1969).
6. W. J. Albery and S. Bruckenstein, *Trans. Faraday Soc.*, **62**, 1920 (1966).
7. V. G. Levich, "Physicochemical Hydrodynamics," Prentice Hall International, Inc., Englewood Cliffs, N.J. (1962).
8. J. Newman, *J. Phys. Chem.*, **70**, 1327 (1966).
9. K. E. Gubbins and R. D. Walker, *This Journal*, **112**, 469 (1965).
10. M. Davies, M. Clarke, E. Yeager, and F. Hovorka, *ibid.*, **106**, 56 (1959).
11. J. Divisek and B. Kastening, *J. Electroanal. Chem.*, **65**, 603 (1975).
12. E. Yeager, in "Proceedings of the Workshop on Electrocatalysis on NonMetallic Surface," National Bureau of Standards, Dec. 9-12, 1975.
13. D. Behar, G. Czapski, J. Rabani, L. M. Dorfman, and H. A. Schwarz, *J. Phys. Chem.*, **74**, 3209 (1970).

Technical Note

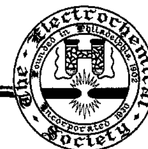

A Practical Electrochemical Transport Equation for Concentrated Solutions

Aharon S. Roy*,[1]

Energy and Metals and Ceramics Divisions, Oak Ridge National Laboratory, Oak Ridge, Tennessee 37830

Most electrochemical energy-related processes employ concentrated electrolytic solutions or fused salts. Notable are storage batteries and fuel cells. Analysis of the transport behavior of the various species of the liquids involved is useful for optimizing the system. However, the conventional transport equations in the literature for nondilute solutions, either of the linear phenomenological or the friction-coefficients form, require thermodynamic data which is often difficult to obtain. When the conventional Stefan-Maxwell form is used, an additional difficulty is involved when transport with respect to stationary axes is needed as the mathematical inversion required is quite complicated with multicomponent liquids (1-4). It would be very helpful if a practical, simplified transport model could be devised which would relate to gradients of concentrations and to the gradient of the electrical potential as the driving forces and which would give directly a flux expression with respect to stationary axes. This is the purpose of the present work. This approach (5, 6) constitutes a marked deviation from the conventional ones in the field.

Diffusional Fluxes, Velocities, and Transport Coefficients

For simplicity, the molar system (5, 6) is depicted for the present work. For isothermal and isobaric conditions, the total electrochemical transport $\mathbf{N}_i$ (mole/cm^2-sec) of component i will be the sum of three fluxes of i. One is by virtue of the bulk (molar-average) velocity $\mathbf{v}^*$ (cm/sec) and the other two are diffusion fluxes (relative to $\mathbf{v}^*$): migration, $\mathbf{J}_i^{*(E)}$ and ordinary, $\mathbf{J}_i^{*(x)}$, diffusion fluxes

$$\mathbf{N}_i = c_i\mathbf{v}^* + \mathbf{J}_i^{*(E)} + \mathbf{J}_i^{*(x)} \quad [1]$$

where c_i is the concentration of component i (mole/cm^3). The following relations hold (1-8)

$$\mathbf{v}^* = \Sigma_k x_k \mathbf{v}_k \quad [2]$$

$$\mathbf{J}_i^{*(E)} = c_i\mathbf{w}_i^{*(E)} = -cx_i u_i^* \nabla\phi \quad [3]$$

$$\mathbf{J}_i^{*(x)} = c_i\mathbf{w}_i^{*(x)} = c\Sigma D_i{}^*{}_k{}' \nabla x_k \quad k = 3, 4, \ldots, n) \quad [4]$$

where x_k is the molar fraction, $\mathbf{v}_k$ the velocity of component k, $c = \Sigma_k c_k$, and Σ_k stands for summation for all components (k = 1, 2, . . ., n). $\mathbf{N}_i$, $\mathbf{v}^*$, and $\mathbf{v}_k$ are measurable with respect to a fixed frame of reference (*e.g.*, the porous disk of Fig. 1). $\mathbf{w}_i^{*(E)}$ is the migration diffusion velocity of i, measurable, in absence of concentration gradients, by

$$\mathbf{w}_i^{*(E)} = \mathbf{v}_i - \mathbf{v}^* \quad [5]$$

which, with the electrostatic potential gradient [or (−) field], $\nabla\phi$, as driving force, defines the mobility of i, u_i^*. $\mathbf{w}_i^{*(x)}$ is the ordinary-diffusion velocity of i, measurable in the absence of electric field by

$$\mathbf{w}_i^{*(x)} = \mathbf{v}_i - \mathbf{v}^* \quad [6]$$

which, with the concentration gradient, ∇x_k, as driving force, defines the ordinary diffusivities $D_i{}^*{}_k{}'$.

Including the practical transport coefficients u_i^* and $D_i{}^*{}_k{}'$, Eq. [1] takes the form of a practical electrochemical transport equation

$$\mathbf{N}_i = c_i\mathbf{v}^* + c\Sigma D_i{}^*{}_k{}' \nabla x_k - c_i u_i^* \nabla\Phi, \quad (k = 3, 4, \ldots, n) \quad [7]$$

Note that only one driving force is used for defining mobilities for all components, whereas many driving forces exist for the ordinary diffusion of each component. For migration, an n-component liquid (6) gives rise to n mobilities u_i, of which $n - 1$ are independent. This is because of the constraint resulting from the definition of diffusion by which the summation of the diffusional fluxes for all components is zero. For instance, for a 4-component liquid, the constraint is (by Eq. [3], [5], and [2])

$$\Sigma_k x_k u_k^* = x_1u_1^* + x_2u_2^* + x_3u_3^* + x_4u_4^* = 0 \quad [8]$$

For ordinary diffusion the concentration gradient of any component is a driving force for all components. This leads to multicomponent or cross-term diffusivities, $D_i{}^*{}_k{}'$, of which a certain number are necessary in order to define the transport system (8-10). n^2 diffusivities may be written of which $(n-2)^2$ are independent [$(n-1)^2$ for nonelectrolytes (10)]. For instance, consider a four-component fused-salt solution composed of the components M, X, N, and Y, where M and N are, say, monovalent metals and X and Y are halogens. Indexing these components consecutively by 1, 2, 3, and 4, one may write an ordinary diffusion flux equation including four multicomponent ordinary diffusivities for the total ordinary diffusion flux of component 1

$$\mathbf{J}_1^{*(x)} = c(D_1{}^*{}_1{}')\nabla x_1 + c(D_1{}^*{}_2{}')\nabla x_2 + c(D_1{}^*{}_3{}')\nabla x_3 + c(D_1{}^*{}_4{}')\nabla x_4 \quad [9]$$

With similar equations also for fluxes of components 2, 3, and 4, sixteen diffusivities are thus written. However, two restricting relationships reduce the number of the independent gradients by two, so that the number of diffusivities decrease to eight [$n(n-2)$]. One relationship is by definition of concentration and their gradients: with n components there are only $n-1$ independent concentration gradients (summation of mole-fractions is unity, the gradient of which is zero)

$$\Sigma_k \nabla x_k = \nabla x_1 + \nabla x_2 + \nabla x_3 + \nabla x_4 = 0 \quad [10]$$

The other is the condition of electroneutrality which leads to ($z_1 = z_3 = 1$; $z_2 = z_4 = -1$)

$$\Sigma_k z_k \nabla x_k = \nabla x_1 - \nabla x_2 + \nabla x_3 - \nabla x_4 = 0 \quad [11]$$

* Electrochemical Society Active Member.
[1] On leave from Department of Chemical Engineering, Ben Gurion University of the Negev, Beer-Sheva, Israel.

Key words: electrolyte, cell, diffusion.

Altogether, only $(n - 2)$ gradients are independent. For our example, Eq. [10] and [11] yield

$$\nabla x_3 = -\nabla x_1 \quad \text{and} \quad \nabla x_4 = -\nabla x_2 \qquad [12]$$

Consequently, the total ordinary diffusion flux of component 1 is now represented by only two diffusivities (which bear explicit relationships to those of Eq. [9])

$$J_1^{*(x)} = cD_1{}^*{}_1{}'\nabla x_1 + cD_1{}^*{}_2{}'\nabla x_2 \qquad [13]$$

Similar equations hold also for the fluxes of components 2, 3, and 4. Of the resulting eight diffusivities only four $[(n - 2)^2$ in general] are independent due to two additional restrictions (Eq. [19], [22]). The cross-term diffusivities are not equal in general to the binary-solution diffusivities of the respective components.

The transport coefficients u_i^* and $D_i{}^*{}_k{}'$ are a function of state (composition and temperature) (8-11), *i.e.*, they are not a function of the magnitude of the gradients for most practical purposes (for fields up to about 10,000 V/cm and concentration gradients of virtually no limitation). The property of being a function of state holds equally well independently of how the gradients are defined (11), whether in terms of thermodynamic activities, molar or mass concentrations, or fractions of them, etc. It is this very property of being a function of state which is responsible for the additivity of the diffusion fluxes and their measurability independently of each other, a property that can be utilized for devising methods for measuring the transport coefficients.

A Method for Measuring Mobilities

An experimental measurement may follow one of the conventional methods for measuring migration transport of which the Hittorf method is typical. However, a special treatment of the experimental results is necessary (Eq. [16]) in order to adapt them for use with the practical transport equation. Figure 1 illustrates the principle of the Hittorf method. With uniform liquid composition (all $\nabla c_i = 0$) at the measuring zone (the porous disk) to enable compliance with Eq. [5], the transport of all components i under an electrical field (imposed by the two electrolysis electrodes shown) gives expression to measurable migration fluxes. The electrical field is defined by the potential difference across the disk as is measurable by two equal reference electrodes (12).

However, due to volume changes occurring in the two compartments across the disk during the transport experiment, the measured velocity of any component i across the disk will include also a hydrodynamic part (which depends on experimental conditions). Because this part is equally imposed on all components, it is possible to get rid of it (and thus obtain a transport coefficient which is a function of state) by resorting to relative migration-velocities (and mobilities) with respect to an arbitrarily chosen reference component s of the liquid

$$\mathbf{w}_{k/s}{}^{*(E)} = \mathbf{w}_k{}^{*(E)} - \mathbf{w}_s{}^{*(E)} \qquad [14]$$

Only $\mathbf{w}_{k/s}{}^{*(E)}$ is known from experiment. $\mathbf{w}_k{}^{*(E)}$ is still unknown. The latter can be derived by use of the relation

$$\Sigma_k x_k \mathbf{w}_k{}^{*(E)} = 0 \qquad [15]$$

(by definition of diffusion, Eq. [2] and [5]) with the function

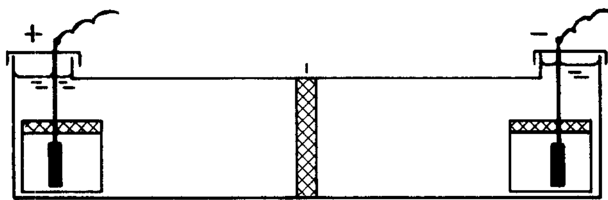

Fig. 1. A schematic representation of a migration cell

$$\mathbf{w}_i{}^{*(E)} = \Sigma x_k(\mathbf{w}_i{}^{*(E)} - \mathbf{w}_k{}^{*(E)})$$
$$= \Sigma x_k(\mathbf{w}_{i/s}{}^{*(E)} - \mathbf{w}_{k/s}{}^{*(E)} \qquad [16]$$

From Eq. [16] $u_i{}^{*(E)}$ is directly obtained by use of Eq. [3] ($\nabla\Phi$ across the disk and c_i are known).

One transport experiment yields n migration fluxes, (velocities and mobilities), of which $n - 1$ are independent, due to Eq. [15]. Being a function of state the mobilities found in an experiment with a uniform composition and in a particular electrical field will be applicable for a wide range of electrical fields and also usable within a very wide range of concentration gradients for a defined state. Similar considerations hold also for diffusivities.

A Method for Measuring Diffusivities

A possible method follows a typical conventional technique, *e.g.*, the diffusion cell with a porous disk. Here, too a special new treatment of the experimental results will render them applicable for use with the practical transport equation. Figure 2 represents a schematic of the diffusion cell. The two compartments on the two sides of the disk contain liquids with a defined difference in their composition and maintain a controlled concentration gradient across the disk. Each compartment is kept mixed at a nearly uniform composition and the fluxes across the disk during a certain period are measured by a material balance and chemical analysis. The concentration gradients for our example system are illustrated in Fig. 3. For the purpose of defining the state to which the diffusivity is assigned, the choice of the average composition of the gradient is fair enough, as is illustrated by point 0. The plane shown in the middle of the gradient lines thus specifies the state.

Each experiment is performed with only one independent concentration gradient existing. For our example, ∇x_1 $(= -\nabla x_3)$ is the only nonzero gradient $(\nabla x_2 = \nabla x_4 = 0)$. There are no electrolysis electrodes in the two compartments and there is no net electric current crossing the disk (electroneutrality forbids continuous accumulation of substantial electric charge in any macroscopic liquid volume), namely an over-all electrical field $-\nabla\Phi$ of zero value.

The electrical field $(-\nabla\Phi)$ of our consideration (for use in Eq. [7]) is defined by the addition of electric potential difference over the cell emf (13, 14)

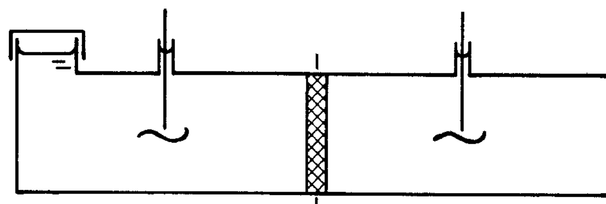
Fig. 2. A schematic representation of an ordinary diffusion cell

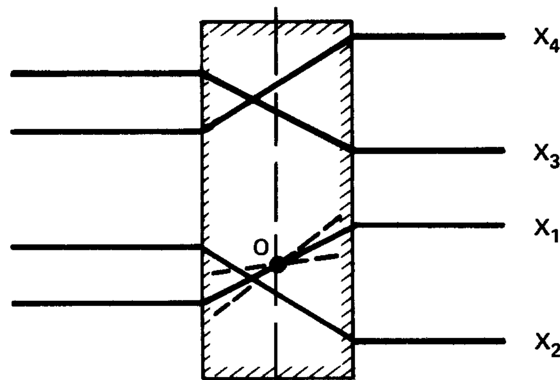

Fig. 3. A schematic representation of molar fraction gradients inside the porous disk (expanded) of the diffusion cell.

[measured by reference electrodes (12)] due to the passage of net electric current density **i** via two electrolysis electrodes. Both electric current and potential difference are externally measured.

As with the case of mobility measurement, here too the observed velocity of component i across the disk includes an undesirable hydrodynamic part due to volume changes which usually accompany any transport process. Again, this part is eliminated by recording only relative velocities with respect to a reference component s

$$\mathbf{w}_{k/s}^{*(x)} = \mathbf{w}_k^{*(x)} - \mathbf{w}_s^{*(x)} \quad [17]$$

Similarly to Eq. [14]-[16], the ordinary diffusion velocity is derived by the appropriate summation function based on the relative transport data

$$\mathbf{w}_i^{*(x)} = \Sigma x_k (\mathbf{w}_{i/s}^{*(x)} - \mathbf{w}_{k/s}^{*(x)}) \quad [18]$$

Each experiment for $\nabla x_k \neq 0$ yields n (i = 1, 2, ..., n) $D_i{}^*{}_k{}'$ diffusivities of which $n - 2$ are independent, due to two restrictive relationships. In our first experiment for example, with ∇x_1 as the only nonzero gradient, only the first term on the right of Eq. [13] is nonzero and thus the measured flux $\mathbf{J}_1^{*(x)}$ yields $D_1{}^*{}_1{}'$. Similarly, a measured $\mathbf{J}_2^{*(x)}$ will yield $D_2{}^*{}_1{}'$, etc. As the summation of all these diffusion fluxes is zero, the resulting restrictive relationship between the derived diffusivities is

$$D_1{}^*{}_1{}' + D_2{}^*{}_1{}' + D_3{}^*{}_1{}' + D_4{}^*{}_1{}' = 0 \quad [19]$$

Another restrictive relationship is obtained from the constraint that no net electric current occurs

$$\Sigma z_i \mathbf{J}_i^{*(x)} = 0 \quad [20]$$

$$z_1 D_1{}^*{}_1{}' + z_2 D_2{}^*{}_1{}' + z_3 D_3{}^*{}_1{}' + z_4 D_4{}^*{}_1{}' = 0 \quad [21]$$

which, for the numerical values of z from our example, gives

$$D_1{}^*{}_1{}' - D_2{}^*{}_1{}' + D_3{}^*{}_1{}' - D_4{}^*{}_1{}' = 0 \quad [22]$$

From Eq. [19] and [22] it follows (compare Eq. [12]) that

$$\text{(a) } D_3{}^*{}_1{}' = -D_1{}^*{}_1{}' \quad \text{(b) } D_4{}^*{}_1{}' = -D_2{}^*{}_1{}' \quad [23]$$

This reduces the array of independent diffusivities from eight to four (now only two equations of the type of Eq. [13] are independent) requiring only two ordinary diffusion experiments in our example. In general this means $(n - 2)^2$ independent diffusivities and $n - 2$ experiments. Altogether, the number of experiments required for obtaining both the mobilities and the diffusivities for each state point is $1 + n - 2 = n - 1$. As functions of state the diffusivities are not function of the magnitude of the gradients under which they were measured and therefore they are applicable for any mixed gradients condition.

Conclusion

Experience shows that transport coefficients are generally not supposed to depend on the magnitude of the fluxes and of the forces within very wide ranges. Irreversible thermodynamics, which heavily depends on this concept, do not necessarily require the use of chemical or electrochemical potentials or friction coefficients for all purposes. Separate transport coefficients for different driving forces, such as concentration and electrostatic potential gradients, can be arbitrary functions of state variables (9, 11). This enables both definition and planning of measurement of coefficients, one type at a time, as demonstrated above.

When we have all the independently measured data concerning $u_i{}^*$, which are $n - 1$ in number, and on $D_i{}^*{}_k{}'$, which are $(n - 2)^2$ in number, the general transport equation (Eq. [7]) becomes usable with all its necessary transport coefficients known. Other systems may be analyzed easily by following the pattern used in our example of the M, X, N, Y system. The number of experiments required and the number of independently measurable transport coefficients for several systems are demonstrated in Table I.

Table I. The number of independently measurable transport coefficients for several systems

System	Global number of components n	Number of independent mobilities* $n - 1$	Number of independent diffusivities $(n - 2)^2$	Thermodynamic min. (Onsager) number of independent diffusivities $(n - 1)(n - 2)/2$
M,X	2	1	0	0
M,N,X	3	2	1	1
M,N,X,Y	4	3	4	3
M,N,P,X,Y	5	4	9	6
M,N,P,X,Y,Z	6	5	16	10

* This column also indicates the total number of transport experiments necessary for each state point.

The last column on the right of Table I gives the minimum number of independent diffusivities which can be arrived at by the use of Onsager's symmetrical reciprocal law, applicable when appropriate thermodynamic driving forces are used. Though a smaller number of coefficients is obtained by this method, the effort required in attempting to obtain thermodynamic data far exceeds that involved in obtaining a few more simple experimental data, as shown above for the practical model. The inapplicability of Onsager's symmetrical reciprocal law to the practical transport coefficients is not a real disadvantage when it is realized how difficult it is, if at all possible, to measure chemical or electrochemical potentials for most nondilute systems. This may explain the limited application of the symmetrical-coefficients approach for solving practical problems in concentrated solutions for many years (15). It seems that both conceptual and experimental difficulties prevent their wide use (15).

The practical electrochemical transport equation has potential advantages at least for some particular systems. It is considerably simplified as compared to some other formalisms. It is related to single component concentrations, it is relatively less dependent on the complications involving both the definition and the elaborate measurements of many ionic activities, its coefficients are relatively readily measurable, it is directly expressed with respect to stationary axes, and it clearly reflects the different contributions of the different driving forces to the transport phenomena.

Acknowledgment

It is a pleasure to thank J. Braunstein for helpful discussions.

This research was sponsored by the Division of Physical Research, U.S. Department of Energy under contract W-7405-eng-26 with the Union Carbide Corporation.

Manuscript submitted April 11, 1977; revised manuscript received March 15, 1978. This was Paper 402 presented at the Philadelphia, Pennsylvania, Meeting of the Society, May 8-13, 1977.

Any discussion of this paper will appear in a Discussion Section to be published in the June 1979 JOURNAL. All discussions for the June 1979 Discussion Section should be submitted by Feb. 1, 1979.

Publication costs of this article were assisted by Oak Ridge National Laboratory.

REFERENCES

1. E. N. Lightfoot, E. L. Cussler, and R. B. Rettig, *Am. Inst. Chem. Eng. J.*, **8**, 708 (1962).
2. J. S. Newman, D. Bennion, and J. W. Tobias, *Ber. Bunsenges. Phys. Chem.*, **69**, 608 (1965).
3. J. S. Newman, *Adv. Electrochem. Electrochem. Eng.*, **5**, 87 (1967).
4. J. S. Newman, "Electrochemical Systems," Prentice Hall, Englewood Cliffs, N.J. (1973).

5. A. S. Roy, in "Proceedings of the Symposium on Electrode Materials and Processes for Energy Conversion and Storage," J. D. E. McIntyre, S. Srinivasan, and F. G. Will, Editors, pp. 1009-1022, Proc. Vol. 77-6, The Electrochemical Society, Inc., Princeton, N.J. (1977).
6. A. S. Roy, in "Advances in Heat Transfer," T. F. Irvine and J. P. Harnett, Editors, pp. 195-282, Academic Press, New York (1976).
7. R. B. Bird, W. E. Stewart, and E. N. Lightfoot, "Transport Phenomena," Chap. 3, 16, and 18, John Wiley & Sons, Inc., New York (1960).
8. R. B. Baldwin, P. J. Dunlop, and L. J. Gosting, *J. Am. Chem. Soc.*, **77**, 5235 (1955).
9. S. R. Degroot and P. Mazur, "Non-Equilibrium Thermodynamics," North Holland Publishing Co., Amsterdam, (1962) (particularly Chapter XI).
10. L. Onsager, *Ann. N.Y. Acad. Sci.*, **46**, 241 (1945).
11. R. Haase, "Thermodynamics of Irreversible Processes," Addison-Wesley, Reading, Mass. (1969) (particularly pp. 98 and 272).
12. D. J. G. Ives and G. J. Janz, Editors, "Reference Electrodes Theory and Practice," Academic Press, New York (1961).
13. E. A. Guggenheim, Thermodynamics," Chap. 8, North Holland Publishing Co., Amsterdam (1967).
14. J. Braunstein and H. Braunstein, Chap. 18 in "Pure and Applied Chemistry, Experimental Thermodynamics," Vol. II, "Experimental Thermodynamics of Non Reacting Fluids," B. Le Neidre and B. Vodar, Editors, Butterworth and Co., Ltd., London (1975).
15. A. Sanfeld, Free University of Brussels, Brussels, Belgium, Private communications in 1974 and 1975.

Erratum

In reference to the paper "Preparative Electrolyses at Graphite Paste Electrodes," by K. D. Wolter and J. T. Stock, which appeared on pp. 531-533 in the April 1978 JOURNAL, Vol. 125, No. 4, several things should be noted.

First, the authors overlooked the fact that a paper based on Colaruotolo's Ph.D. dissertation (Ref. 2) had actually appeared in *This Journal*, **120**, 773 (1973).

Second, it should have been stressed that Colaruotolo and co-workers were the first to show the feasibility of graphite paste as a material for preparative-scale electrolytes.

Finally, a paper by Bobbitt, Colaruotolo, and Huang [*This Journal*, **120**, 773 (1973)] should be added as Ref. (2a). This 1973 paper clearly shows for the first time that graphite paste can be used as electrode material for preparative-scale electrolyses and gives examples of actual products that were obtained at such electrodes.

JOURNAL OF THE ELECTROCHEMICAL SOCIETY

SOLID-STATE SCIENCE
AND TECHNOLOGY

JULY
1978

Interaction of NO_x and Cu at Various Relative Humidities

Rudolf Schubert

Bell Laboratories, Columbus, Ohio 43213

ABSTRACT

It has been shown that NO_2 (2 ppm) in air at room temperature does not react (<1%) with Cu at relative humidities $\lesssim$ 65%. At RH $\gtrsim$ 65% the Cu appears to act as a catalyst to reduce NO_2 to NO. The maximum activity occurs at 100% RH with ~70% of the NO_2 being reduced. It is further shown that at 65% $\lesssim$ RH $\lesssim$ 100%, NO (0-1.3 ppm) and Cu do not interact in air. At the RH generally found in air-conditioned electronic equipment areas, NO_2 and NO should not cause any significant deterioration of exposed Cu.

If one reduces the thickness of the electroplated gold over copper on electrical connector contacts, more Cu is exposed to the atmosphere through pores in the Au electroplate and by diffusion through the Au (1). The exposed Cu may interact with oxides of nitrogen and water vapor from the atmosphere. The combination of these compounds might be expected to form nitric acid and hence insulating corrosion deposits on connector contacts over a multiyear life span. The reaction of exposed Cu through porous Au to concentrated HNO_3 vapor is well known from the nitric acid porosity test (2). In this test the Cu reacts through the Au pores and leaves a visible insulating product, providing a measure of Au porosity. This test is a highly accelerated condition as compared to the field situation, and the test in all likelihood does not reflect field performance.

This paper reports the investigation of the interaction of NO_2, H_2O vapor, and Cu filings in air. Oxides of nitrogen at the ppm level were continuously monitored after passing over Cu particles at various relative humidity (RH) levels. The reduction of NO_2 to NO as a function of RH with no copper nitrate formation is reported. These data, known RH data in air-conditioned electronic equipment locations, and estimated vapor pressure of HNO_3 over copper nitrates are taken to indicate a negligible rate of formation of copper nitrates in air-conditioned electronic equipment areas.

Experimental

The apparatus consisted of a Bendix oxides of nitrogen analyzer, Model No. 8101-B, and a gas flow system. The detector measures the chemiluminescence occurring during the reaction of NO and instrument-generated ozone. Different oxides of nitrogen are measured by alternately analyzing the gas stream for NO and then a sample in which all the NO_2 has been reduced; a difference measurement then determines the amount of NO_2 in the sample. Figure 1 is a schematic of the system.

To minimize gas-system interactions, glass and Teflon tubing were the primary components in the flow system. However, there were stainless steel fittings on the flowmeters and detector. Connections between the glass and Teflon were made by using Tygon tubing clamped over a glass-Teflon butt joint such that a minimum of Tygon tubing was exposed to the gas.

Key words: environment, metals, connectors, catalysis, corrosion.

Oxygen used in the ozone generator of the photometric detector was 99.95% pure. Laboratory room air was used to calibrate the zero point of the detector. Linde zero-grade air ($\leq$ 1 ppm total hydrocarbons, $\leq$ 3 ppm H_2O) doped with ~ 1.8 ppm NO_2 was used to investigate the interaction between NO_2 and Cu. This concentration was determined by maximizing the detector reading on the 5 ppm full scale mode with the tank gas flowing directly into the detector. Although the absolute value is somewhat arbitrary since no full-scale calibration standard was available, it is believed to be accurate to within a factor of 2 with the relative values being accurate to within ± 5% of the full-scale reading. Relative humidity in the NO_2/air mixture was varied by adjusting the percentage of the mixture passing through a fritted glass water bubbler. Direct RH measurements were deemed unnecessary and the percentages of RH listed below should be approximately correct. With 100% of the test atmosphere passing through the H_2O bubbler a slight fogging of the tubing occurred, indicating saturated water vapor. Other RH percentages were calculated as a proportion

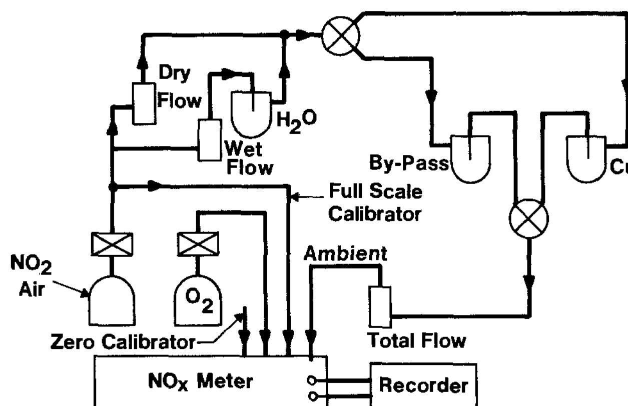

Fig. 1. Schematic of flow system. Dry flow and wet flow are gas flow meters. The by-pass section of the apparatus is to insure that the apparatus is not altering the doped gas before the exposure to the Cu filings.

of the dry-to-saturated air. As expected, no loss of NO_2 was detected when bubbling the doped air through the water.

Interaction of the test atmosphere and Cu was achieved by placing 2.6g of fresh Cu filings in the base of a fritted glass bubbler tube (~ 5 mm diam) and passing the gas up through the Cu at a flow rate of 250 ml/min. No attempt was made to prevent the Cu from oxidizing before the experiment began since the experiment was being carried out in air. The total Cu surface area is calculated to be well in excess of 2×10^3 cm^2 from particle size determination by microscope photographs of samples of the powder.

Data were taken in the following order: 0, 50, 100, 75, 84, and 100% RH on the same Cu sample. At each of these RH's several cycles were carried out; all cycles were at 1.8 ppm NO_2. A cycle consisted of setting the meter zero with room air; setting the full scale span adjustment with dry NO_2/air; measuring the NO and NO_2 values passing through the system at a given RH; and finally measuring the NO and NO_2 values passing through the equivalent system with Cu particles. Typically 2-3 days were used for one complete cycle. All data were recorded dynamically on a strip chart recorder. Measurements reported herein are after steady state was established, approximately 2 hr after any change in the cycle.

Results and Discussion

NO_2 levels measured in doped air were 1.8 ppm when fed directly from the cylinder to the detector. The same level of NO_2 was found after the gas stream had been bubbled through the water and through the bypass system without Cu. No NO was detected ([NO] < 0.02 ppm) in the NO_2-doped air at all RH's used.

NO_2-doped air was found to react with OFHC Cu particles at a rate which is very humidity dependent. NO_2 did not react at 0 and 50% RH as indicated by a constant [NO_2] of 1.8 ppm. Nor was NO (< 0.02 ppm) detected at these RH's. At 100% RH more than 70% of the NO_2 has interacted with the Cu to form NO. Both the increase in [NO] and the decrease in [NO_2] as a function of RH are plotted in Fig. 2. Before interacting with the Cu, 1.8 ppm NO_2 was present, and after the interaction 0.53 ppm NO_2 and 1.3 ppm NO were present at 100% RH. Thus the sum of NO_x molecules appears to have been conserved in the gas phase within the limits of our instrumentation.

Upon inspection, the Cu particles appeared to have oxidized, as would be expected from exposure to moist air. They were slightly brown in color but no trace of blue could be seen, which is the color of $Cu(NO_3)_2 \cdot n\,H_2O$. Tests with 1, 2, 4 phenol bisulfonic acid, which is a specific nitrate test, indicated no nitrate.[1] The vapor pressure of HNO_3 over $Cu(NO_3)_2 \cdot 3H_2O$ is estimated from vapor pressures of other organic and inorganic compounds with similar mass and boiling point to be of the order of 500 ppm at room temperature.[2] Thus, at the low partial pressures of our experiment it is expected that if a copper nitrate is formed it would also rapidly dissociate. Therefore, it appears that in this case virtually no copper nitrate is formed.

The interaction of NO_2 and H_2O is described by

$$3NO_2 + H_2O \rightarrow 2HNO_3 + NO \quad [1]$$

This reaction is very slow, if one assumes an ideal gas, since its rate is proportional to the cube of the [NO_2]. It could have been observed in this experiment at 5% of the [NO_2] by looking for an increase in the NO

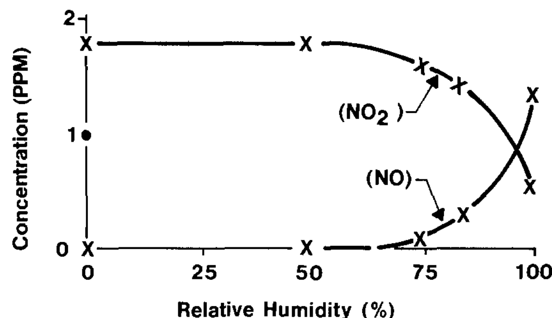

Fig. 2. Plot of concentration of NO and NO_2 (ppm) in zero-grade air vs. relative humidity when it is passed over OFHC Cu particles.

concentration. An increase in [NO] was not seen before exposure to Cu and is in agreement with the other results of trying to remove NO_2 from stack gases by scrubbing (5).

The reaction between Cu and nitric acid fumes in the solid-gas case is

$$3Cu + 8HNO_3 \leftrightarrow 2NO\uparrow 3Cu\,(NO_3)_2 + 4H_2O\uparrow \quad [2]$$

In solution at low concentration, the reaction proceeds slowly but as (3)

$$8H^+ + 2NO_3^- + 3Cu = 3Cu^{++} + 2NO\uparrow + 4H_2O \quad [3]$$

At the low partial pressures of our experiments it is not known whether the Cu is simply acting as a catalyst in the NO_2 reduction or if the Cu is being oxidized by reaction [3].

It is difficult to distinguish between reactions [2] and [3]. In both cases NO is liberated. The fact that no copper nitrate was seen does not rule out reaction [2] since the concentration of NO_2 and HNO_3 is much less than the dissociation vapor pressure of HNO_3 from copper nitrate (~ 500 ppm). Thus, it is concluded that either the solid-gas reaction or the quasisurface solution-solid reaction can explain our results.

A small fraction of the evolved NO may be lost in the air before the detector by

$$2NO + O_2 \leftrightarrow 2NO_2 \quad [4]$$

This is believed to be negligible due to the short time path between evolution and detection, as well as a rate dependence on the square of the [NO], assuming ideal gases.

The interaction of $NO_2/Cu/H_2O$ is amply demonstrated in Fig. 2. The importance of RH affecting corrosion rates has been known to some extent for a long period of time (6), however, the published literature for low concentrations is scarce and generally on slightly different systems. Aziz and Godard (7) find that SO_2 interacts with Cu to cause corrosion at RH $>$ 63%. Vernon (8) indicates that even with the inclusion of particles minimal corrosions occurred at RH $<$ 60%. Abbott *et al.* (9) also find RH an important component of corrosion tests. Thus RH is an important consideration for control of sensitive electronic equipment corrosion.

Recent studies of RH in eight locations which were air conditioned to handle large amounts of electronic equipment show that the RH was $<$60% RH for $>$90% of the time over a one year cycle (10). This RH data coupled with Fig. 2 would seem to indicate that NO_2 would not be a problem as far as Cu surfaces are concerned. This is reinforced by noting from Fig. 2 that, rather than copper nitrate forming, the Cu acts as a catalyst in reducing NO_2 to NO.

Conclusions

It is shown that NO_2 (1.8 ppm) does not interact with Cu surfaces at RH $\lesssim$ 65%. Furthermore, even at higher RH the NO_2 is reduced to NO without appreciable formation of $Cu(NO_3)_2 \cdot n\,H_2O$. At the RH gen-

[1] The 1, 2, 4 phenol bisulfonic test is capable of detection ~2 μg of $Cu(NO_3)_2 \cdot n\,H_2O$. Thus for our flow conditions we would have been able to see a test reaction if only 0.1% of the gas had reacted when using a test sample of Cu of 40 mg.

[2] If one plots the vapor pressure *vs.* temperature for N_2O_4, N_2O_5, NH_2OH, C_2H_5NO, and H_2SO_4 the slopes are between 2 and 4. At 170°C the vapor pressure of HNO_3 over $Cu(NO_3)_2 \cdot 3H_2O$ is one atmosphere. Using the above slopes and extrapolating to room temperature, the vapor pressure of interest is between 100 and 1000 ppm. In all cases the vapor pressure of HNO_3 over $Cu(NO_3)_2 \cdot 3H_20$ is much greater than the 1.8 ppm [NO_2] (4).

erally found in air-conditioned electronic equipment locations NO_2, up to several ppm, should not cause any significant deterioration of exposed Cu surfaces over what is normally found in pure air. It is also shown at RH > 65% that NO does not interact with Cu in any readily detectable amounts.

Acknowledgments

The author thanks E. T. Eisenmann for helpful discussions.

Manuscript submitted Nov. 1, 1977; revised manuscript received March 9, 1978.

Any discussion of this paper will appear in a Discussion Section to be published in the June 1979 JOURNAL. All discussions for the June 1979 Discussion Section should be submitted by Feb. 1, 1979.

Publication costs of this article were assisted by Bell Laboratories.

REFERENCES

1. H. G. Tompkins and M. R. Pinnel, To be published in *J. Appl. Phys.*
2. "1977 Annual Book of ASTM Standards," Part 44, Stand. B583-73, ASTM, Philadelphia (1977).
3. B. H. Mahan, "University Chemistry," 3rd ed., p. 644, Addison-Wesley, Reading, Mass (1975).
4. "The Handbook of Chemistry and Physics," 50th ed, R. C. Weast, Editor, Sect. B and D, The Chemical Rubber Co., Cleveland (1969).
5. A. P. Altschuller, "Air Pollution," Vol. III, 2nd ed., A. C. Stern, Editor, p. 206, Academic Press, New York (1968).
6. W. H. J. Vernon, *J. Chem. Soc.*, 2273 (1926).
7. P. M. Aziz and H. P. Godard, *Corrosion (Houston)*, **15**, 39 (1959).
8. W. H. J. Vernon, *Trans. Faraday Soc.*, **31**, 1668 (1935).
9. W. H. Abbott, D. N. Williams, J. F. Dettorre, E. S. Bartlett, and H. R. Ogden, "Third Annual Summary Rep.," Battelle Memorial Institute, Columbus, Ohio (1968).
10. P. A. Baker and K. F. Bradford, Unpublished data.

The Criterion for the Onset of Internal Oxidation Beneath the External Scales on Binary Alloys

W. W. Smeltzer*[,1] and D. P. Whittle

Department of Metallurgy and Materials Science, University of Liverpool, Liverpool L69 3BX, England

ABSTRACT

Ternary diffusion theory is used to establish a criterion for the onset of an internal oxidation zone beneath the external scale when oxidizing conditions favor formation of the oxide of the less noble metal in a binary alloy. The problem is posed in terms of ternary solution thermodynamics and diffusion and is correlated to the locus of the virtual diffusion path on the ternary alloy-oxygen isotherm. External scale formation alone occurs when the virtual diffusion path in the alloy phase contacts the oxygen solubility curve for the alloy. External scale formation accompanied by internal oxidation occurs when the virtual diffusion path for the alloy leads to oxygen supersaturation and oxide precipitation by cutting into and across the two-phase alloy/oxide field. These assertions can be used to define a limiting bulk atom fraction of the selectively oxidized solute, $N_A{}^{O*}$, in the alloy above which internal oxidation does not occur: $N_A{}^{O*}$ satisfies

$$\epsilon_O{}^A(N_A{}^{O*})^2 + \left\{ \frac{1-F(u)}{F(u)}\left[1+\left(\frac{D_{OO}}{D_{AA}}\right)^{1/2}\frac{u}{\nu}\pi^{1/2}\right] - \epsilon_O{}^A[1+F(u)] \right\}$$

$$(N_A{}^{O*}) + \left\{ \epsilon_O{}^A F(u) - (1-F(u)) - \left(\frac{D_{OO}}{D_{AA}}\right)^{1/2}\frac{1-F(u)}{F(u)}\frac{u}{\nu}\pi^{1/2} \right\} = 0$$

where $\epsilon_O{}^A$ is the Wagner interaction coefficient between oxygen and A in the alloy, D_{AA} and D_{OO} are the direct diffusion coefficients of A and oxygen in the alloy, ν is the atomic ratio of oxygen to A in the oxide AO_ν, $F(u)$ is an auxiliary function

$$F(u) = \pi^{1/2}u \exp(u^2) \operatorname{erfc}(u)$$

and u replaces $(k/2D_{AA})^{1/2}$ with k as the corrosion constant for the parabolic rate of recession of the alloy/surface scale interface. Typical ranges of parameters applicable to a variety of alloy systems are used to show the effects of the diffusion coefficients, scaling constants, and interaction parameters on the limiting value $N_A{}^{O*}$.

A limiting condition has been determined by Wagner (1) from an analysis of the diffusion processes for the onset of an internal oxidation zone beneath the external scale when oxidizing conditions favor the formation of the oxide of the less noble metal in a binary alloy. In this treatment, he assumed that metal and oxygen diffuse down their own individual gradients established by the formation of the pure binary oxide and that both metal and oxygen exhibit ideal solution behavior in the alloy. The criterion for defining the onset of internal oxidation is when conditions exist at the alloy side of the scale/alloy interface for the product of the metal and oxygen concentrations to exceed the solubility product of the binary oxide. By this means a minimum composition of the less noble metal in the binary alloy, above which internal oxidation will not occur, can be ascertained in terms of the

* Electrochemical Society Active Member.
[1] Department of Metallurgy and Materials Science, McMaster University, Hamilton, Ontario, L8S 4M1 Canada.
Key words: oxidation, alloys.

metal and oxygen diffusivities in the alloy and the parabolic rate constant for external scale growth.

The purpose of this paper is to expand this analysis by treating the binary alloy plus oxygen as a true ternary system, since Whittle *et al.* (2) have shown recently that the oxygen flux into the alloy under these circumstances can readily arise from either or both the oxygen and metal gradients in the alloy, and depending on the thermodynamic properties of the alloy solid solution, the latter can be the more significant. Thus the problem is posed in terms of the underlying ternary solution thermodynamics and diffusion, and using appropriate approximations, equations are then derived for the onset of internal oxidation based on the following two assertions relating the locus of the virtual diffusion path on the ternary alloy-oxygen isotherm: (*i*) External scale formation alone occurs when the virtual diffusion path in the alloy phase contacts the oxygen solubility curve for the alloy. In this case, the virtual path corresponds to the actual diffusion path during the oxidation reaction. (*ii*) External scale formation accompanied by internal oxidation occurs when the virtual diffusion path for the alloy cuts into and across the two-phase alloy-oxide field. This path leads to oxygen supersaturation and oxide precipitation, and, as a consequence, the virtual diffusion path does not correspond to the actual path followed during the oxidation reaction.

The Wagner Criterion for Internal Oxidation

The parabolic growth by metal transport of a scale AO_ν on an alloy A-B with concurrent diffusion of oxygen into the alloy is shown schematically in Fig. 1a. The concentration profiles in the alloy phase are described by the appropriate solutions of Fick's second law, under the assumption of concentration-independent diffusivities

$$N_A = N_A^\circ - (N_A^\circ - N_A')\frac{\operatorname{erfc} x/2\sqrt{D_{AB}t}}{\operatorname{erfc}\sqrt{k/2D_{AB}}}; \quad x \geq X \quad [1]$$

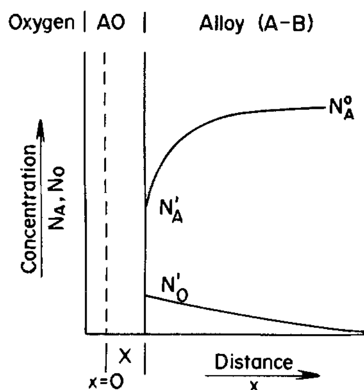

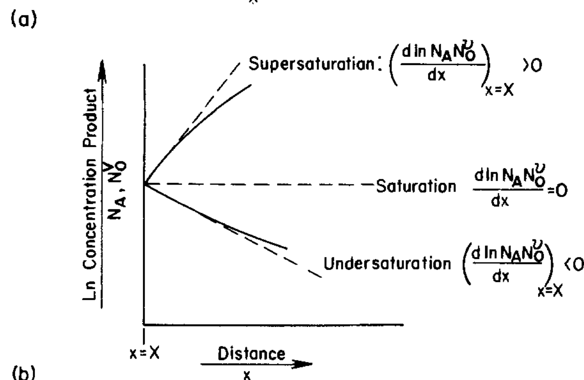

Fig. 1. The oxide scale/alloy model with symbols corresponding to those in the text. (a) Cross-section showing concentrations of solute A and oxygen in the underlying alloy. (b) The product $N_A N_O^\nu$ as a function of distance in the underlying alloy demonstrating the three possibilities.

$$N_O = N_O'\frac{\operatorname{erfc} x/2\sqrt{D_O t}}{\operatorname{erfc}\sqrt{k/2D_O}}; \quad x \geq X \quad [2]$$

where N_A°, N_A', and N_A are the atom fractions of A in the bulk alloy, at the alloy/scale interface, and locally at distance x and time t, respectively, where position x is measured from the original alloy surface. N_O' and N_O are the corresponding atom fractions of oxygen. D_{AB} and D_O are the interdiffusion coefficient and the oxygen diffusion coefficient in the alloy, respectively. The position of the actual alloy surface X at any time is related to the corrosion constant, k, by

$$X = \sqrt{2kt} \quad [3]$$

Since pure oxide, AO_ν, is assumed to form, a mass balance at the alloy/scale interface leads to

$$\frac{1}{V_M}\frac{dX}{dt} = \frac{N_A'}{V_M} - \frac{D_{AB}}{V_M}\frac{\partial N_A}{\partial x}\Bigg|_{x=X} \quad [4]$$

where V_M is the molar volume of the alloy. Substitution of [1] and [3] into [4] gives

$$N_A' = \frac{N_A^\circ - F(u)}{1 - F(u)} \quad [5]$$

where u replaces $\sqrt{k/2D_{AB}}$ and the auxiliary function $F(u)$ is given by

$$F(u) = \sqrt{\pi}\, u \exp u^2 \operatorname{erfc} u \quad [6]$$

The following equilibrium defines the relationship between the oxide and alloy components at the alloy/oxide interface

$$AO_\nu = A\,(\text{alloy}) + \nu O\,(\text{alloy}) \quad [7]$$

enabling a solubility constant K to be defined such that

$$K = N_A' \cdot N_O'^\nu \text{ at } x = X \quad [8]$$

Accordingly, the criterion for internal oxidation then becomes whether the product $N_A \cdot N_O^\nu$ exceeds the solubility constant at positions within the alloy, away from the interface. Thus, the value of $\frac{\partial}{\partial x}(N_A \cdot N_O^\nu)$ at $x = X$ is examined. Using [1], [2], [3], [6], and [8]

$$\left[\frac{\partial}{\partial x}(N_A \cdot N_O^\nu)\right]_{x=X} = \frac{2}{\sqrt{\pi}}\frac{1}{2\sqrt{D_{AB}t}}K\left[\frac{N_A^\circ - N_A'}{N_A'}\frac{\exp(-k/2D_{AB})}{\operatorname{erfc}\sqrt{k/2D_{AB}}} - \nu\left(\frac{D_{AB}}{D_O}\right)^{1/2}\frac{\exp(-k/2D_O)}{\operatorname{erfc}\sqrt{k/2D_O}}\right] \quad [9]$$

If $[\partial/\partial x(N_A \cdot N_O^\nu)]_{x=X} < 0$: the alloy is unsaturated and there is no internal oxidation.

If $[\partial/\partial x(N_A \cdot N_O^\nu)]_{x=X} = 0$: the alloy is saturated and at the limit for internal oxidation.

If $[\partial/\partial x(N_A \cdot N_O^\nu)]_{x=X} > 0$: the alloy is supersaturated directly behind the scale/alloy interface and internal oxidation is possible.

These three possibilities are shown schematically in Fig. 1b.

Equation [9] may be simplified further since in most systems

$$D_O >> k \text{ and } D_{AB} \quad [10]$$

and thus

$$\operatorname{erfc}(\sqrt{k/2D_O}) \cdot \exp\left(\frac{k}{2D_O}\right) \simeq 1 \quad [11]$$

The criterion for internal oxidation therefore becomes

$$\frac{N_A^\circ - N_A'}{\nu N_A'}\left(\frac{D_O}{D_{AB}}\right)^{1/2}\frac{\exp(-k/2D_{AB})}{\operatorname{erfc}\sqrt{k/2D_{AB}}} > 1 \quad \text{(internal oxidation)} \quad [12]$$

Equation [12] may be utilized to define the limiting atom for mole fraction of solute A above which internal oxidation would not occur. Upon the use of [5] and [6] to define N_A' and the auxiliary function $F(u)$ with u replacing $\sqrt{k/2D_{AB}}$, Eq. [12] becomes

$$N_A^{\circ} \geq \frac{F(u) + \frac{1}{\nu}\left(\frac{D_O}{D_{AB}}\right)^{1/2} u\pi^{1/2}}{1 + \frac{1}{\nu}\left(\frac{D_O}{D_{AB}}\right)^{1/2} u\pi^{1/2}} \quad \text{(no internal oxidation)} \quad [13]$$

The Ternary Representation of the Wagner Criterion for Internal Oxidation

The oxidation model considered by Wagner can be placed into a ternary thermodynamic and diffusion formalism using the A-B-O ternary isotherm and the placement of the representative diffusion paths on this isotherm. The previously discussed oxidation model corresponds to the phase diagram shown in Fig. 2. Diffusion path (Fig. 2, 1) corresponds to the formation of an external AO_ν scale only. In this case, the virtual diffusion path is constructed as tangenting the oxygen solubility curve in the alloy which is assumed to increase in slope with increasing B content of the alloy in accord with Eq. [8]. Here the virtual diffusion path corresponds to the actual diffusion profile in an alloy sample oxidizing by parabolic kinetics. Path (2, Fig. 2) corresponds to the case for external scale formation accompanied by internal oxidation. Here, the virtual diffusion path cuts into the two-phase AO_ν + alloy field leading to oxygen supersaturation. The relief of this supersaturation causes formation of internal oxide precipitates in the alloy beneath the external scale. Consequently, the criterion of Wagner for the presence or absence of internal oxidation based on the concentration gradients of metal and oxygen and their relationships to oxygen supersaturation now becomes a relationship between the diffusional composition path and the oxygen solubility curve in the ternary A-B-O isotherm.

The equivalence of the Wagner approach to that described by a limiting application of ternary diffusion theory is now demonstrated. The slope of the solubility curve at the composition corresponding to the alloy/surface scale interface (N_A', N_O') is obtained from Eq. [8]

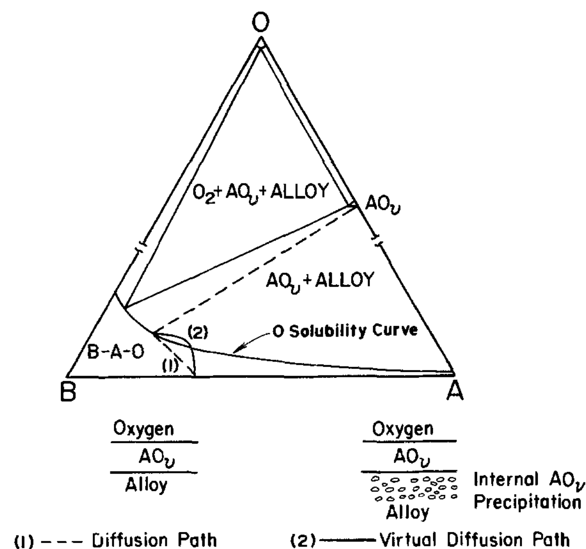

Fig. 2. The diffusion path for metal and oxygen superimposed on the A-B-O ternary isotherm. Diffusion path labeled (1) corresponds to the formation of an external AO_ν scale only. Path labeled (2) corresponds to the case of external scale formation accompanied by internal oxidation.

$$\left(\frac{dN_O}{dN_A}\right)^{\text{Sol.}}_{x=X} = -\frac{N_O'}{\nu N_A'} \quad [14]$$

In addition, the gradient of the virtual diffusion path (DP) at the alloy/scale interface

$$\left(\frac{dN_O}{dN_A}\right)^{\text{DP}}_{x=X} \quad [15]$$

can also be calculated to determine the manner in which DP contacts the solubility curve at the interfacial composition

$$\left(\frac{dN_O}{dN_A}\right)^{\text{DP}}_{x=X} = \left(\frac{\partial N_O}{\partial x} \bigg/ \frac{\partial N_A}{\partial x}\right)_{x=X} \quad [16]$$

and using Eq. [1]-[3] along with the approximation introduced as Eq. [11]

$$\left(\frac{dN_O}{dN_A}\right)^{\text{DP}}_{x=X} = -\frac{N_O'}{N_A^{\circ} - N_A'}\left(\frac{D_{AB}}{D_O}\right)^{1/2} \frac{\text{erfc}\,(k/2D_{AB})^{1/2}}{\exp -k/2D_{AB}} \quad [17]$$

These two gradients, Eq. [14] and [17] can now be compared to define the conditions of oxidation. Thus, for internal oxidation to occur

$$\left(\frac{dN_O}{dN_A}\right)^{\text{DP}}_{x=X} \geq \left(\frac{dN_O}{dN_A}\right)^{\text{Sol.}}_{x=X} \quad [18]$$

or substituting Eq. [15] and [17]

$$\frac{N_O'}{\nu N_A'} \geq \frac{N_O'}{N_A^{\circ} - N_A'}\left(\frac{D_{AB}}{D_O}\right)^{1/2} \frac{\text{erfc}\,(k/2D_{AB})^{1/2}}{\exp -k/2D_{AB}} \quad [19]$$

Rearrangement of [19] shows it is identical to the Wagner criterion as given in [13].

Although both approaches arrive at the same result, it will now be shown that the ternary analysis is more appropriate for interpreting less restrictive models.

Ternary Diffusional Analysis of the Transition from Internal Oxidation to External Scale Formation

As has been emphasized, external scale formation accompanied by a zone of internal oxidation will occur when the calculated virtual diffusion paths cuts into and across the two-phase alloy-oxide field. On the other hand, external scale growth only occurs when the virtual diffusion path for the alloy phase contacts the oxygen solubility curve and in the limit becomes a tangent to it. Accordingly, in formulating more general expressions for this criterion, particularly where nonideal thermodynamic behavior prevails, two aspects are involved: firstly, the thermodynamics of oxygen solubility in the alloy, and especially the magnitude of the solubility and its variation with composition, and secondly, the effects of thermodynamic interaction on the diffusion profiles in the alloy, and hence on the shape of the diffusion path. These two calculations on oxygen solubility and ternary diffusion are then coupled to describe internal oxidation and scale growth.

Oxygen solubility in a binary alloy involving ternary interaction.—Liquid binary alloys, in which one element is selectively oxidized from the solvent metal often exhibit a minimum in the oxygen solubility curve. Using the Wagner formalism for solution thermodynamics involving ternary interaction, St. Pierre and Blackburn (3) and Feldman and Kirkaldy (4) have derived solubility relations to interpret the experimental oxygen solubility curves in iron melts. A similar formalism is used here to interpret the oxygen solubility curves in solid binary alloys.

Expressions derived from the Gibbs-Duhem relationship, or from the equilibrium constant of the oxide with oxygen dissolved in the alloy describe the variation of the oxygen solubility curve with alloy compo-

sition. The latter method is used here as interest focuses on formation of an oxide containing negligible concentration of the solvent metal. The oxide-alloy equilibrium may therefore be written as

$$A_{1-\delta}B_\delta O_\nu = (1 - \delta)\,A + \delta B + \nu O \qquad [20]$$

where A, B, and O refer to alloy compositions and B is the solvent metal such that its concentration in the oxide is small ($\delta << 1$). Accordingly for a constant activity of the oxide $A_{1-\delta}B_\delta O_\gamma$

$$\ln K = \ln a_A^{1-\delta} a_B^{\delta} a_O^{\nu} = \ln N_A^{1-\delta} N_B^{\delta} N_O^{\nu} + \ln \gamma_A^{1-\delta}\gamma_B^{\delta}\gamma_O^{\nu} \qquad [21]$$

where K is the equilibrium constant. The oxygen solubility curve for the alloy is then defined by

$$\frac{d \ln K}{dN_A} = 0 \qquad [22]$$

If the dissolved oxygen concentration in the solvent metal B is very small, the activity coefficients in [21] can be expressed according to the Wagner formalism

$$\ln \gamma_A = \ln \gamma_A^\circ + \epsilon_A^O N_O + \epsilon_A^A N_A \qquad [23]$$

$$\ln \gamma_O = \ln \gamma_O^\circ + \epsilon_O^O N_O + \epsilon_O^A N_A \qquad [24]$$

$$\ln \gamma_B = 0; \quad N_B \simeq 1 - N_A \qquad [25]$$

Substituting [23]-[25] in [22] using [21] and remembering that $\epsilon_O^A = \epsilon_A^O$, gives

$$\left\{ \frac{1-\delta}{N_A} - \frac{\delta}{1-N_A} + (1-\delta)\epsilon_A^A + \nu\epsilon_O^A \right\} + \left\{ \frac{\nu}{N_O} + (1-\delta)\epsilon_O^A + \nu\epsilon_O^O \right\} \frac{dN_O}{dN_A} = 0 \qquad [26]$$

It follows then, that the gradient of this solubility curve can be calculated at $x = X$, the interface between alloy and growing surface scale. Under the restrictions that $\delta << 1$ and $N_A' << 1$, Eq. [26] becomes

$$\left(\frac{dN_O}{dN_A} \right)^{\text{Sol.}}_{x=X} - \frac{N_O'}{N_A'} \left(\frac{1 + N_A'\epsilon_A^A + \nu N_A'\epsilon_O^A}{\nu + N_O'\epsilon_O^A + \nu N_O'\epsilon_O^O} \right) \qquad [26a]$$

[26a] reduces to [14] earlier if ϵ_A^A, ϵ_O^O, and ϵ_O^A are zero.

Equation [26] can be utilized to define the minimum in the oxygen solubility curve since at this point dN_O/dN_A will be zero. Thus, again with $\delta << 1$

$$N_A^* = -\frac{1}{\nu\epsilon_O^A + \epsilon_A^A} \qquad [27]$$

where N_A^* is the atom fraction of A at the minimum in the solubility curve (3, 4). When A and B are neighboring transition metals in the periodic table they often exhibit Henrian solution behavior, and $\epsilon_A^A = 0$, thereby simplifying [27] to

$$N_A^* \simeq \frac{1}{\nu\epsilon_O^A} \qquad [28]$$

Oxygen solubility in a binary alloy involving Henrian and non-Henrian solution behavior.—A distinction between Henrian and non-Henrian solution behavior is essential when coupling thermodynamic and diffusional parameters to interpret reaction kinetics. It is only for the latter case of non-Henrian behavior that the slope of the oxygen solubility curve and the coupling of diffusion fluxes on the two independent compositional profiles become significant. Equation [28] has demonstrated the role of a non-Henrian interaction parameter ϵ_O^A in determining the existence of a minimum in the oxygen solubility curve, and it is appropriate here to compare Henrian and non-Henrian oxygen solubility.

Equation [21] for the oxide equilibrium reaction assuming the oxide to be essentially pure AO_ν becomes for Henrian (H) and non-Henrian (NH) behavior

$$\ln K = \ln(\gamma_A^\circ N_A)_H (\gamma_O^\circ N_O)^{\nu}{}_H \qquad [29]$$

$$\ln K = \ln(\gamma_A^\circ N_A)_{NH} (\gamma_O^\circ N_O)^{\nu}{}_{NH} + (\epsilon_A^A + \nu\epsilon_O^A) N_A + (\epsilon_O^A + \nu\epsilon_O^O) N_O \qquad [29a]$$

where the activity coefficients were defined in [23]-[25]. Because the oxygen solubility is very small ($\sim$ 10-1000 ppm), $N_O << 1$ and also the solute element (A) in the binary alloy has been regarded as exhibiting Henrian behavior ($\epsilon_A^A = 0$), [29] and [29a] yield

$$\frac{(N_O)_{NH}}{(N_O)_H} = \exp(-\epsilon_O^A N_A) \qquad [30]$$

If the Henrian activity coefficients were known, an equilibrium constant could be defined

$$K_H = \frac{K}{\gamma_A^\circ (\gamma_O^\circ)^\nu} \qquad [31]$$

such that

$$(N_O)_{NH} = \left(\frac{K_H}{N_A} \right)^{1/\nu} \exp(-\epsilon_O^A N_A) \qquad [32]$$

Expressions [31] and [32] allow, in principle, the oxygen solubilities for Henrian and non-Henrian solution behavior of oxygen in a binary alloy to be compared.

A similar shape of oxygen solubility curve is obtained for Henrian solution behavior since values of the activity coefficients remain constant irrespective of the composition of the alloy solid solution. Figure 3a presents the ratio of the non-Henrian oxygen solubility to that of Henrian oxygen solubility as given by Eq. 30. In this case component A is the less-noble alloying element in the solid solvent B. As can be seen, positive values of the interaction coefficient ϵ_O^A decrease the solubility, the decrease being more pronounced, the larger the interaction coefficient. The

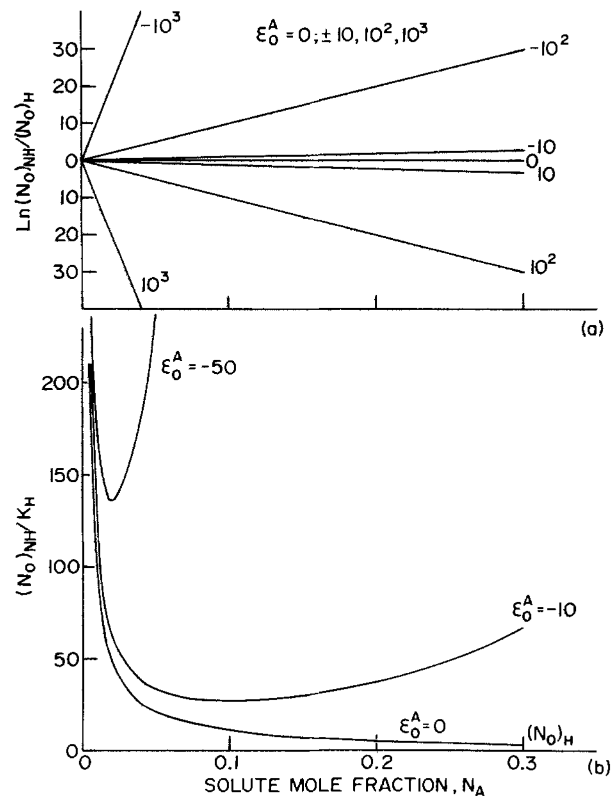

Fig. 3(a) The ratio of non-Henrian oxygen solubility to that of Henrian oxygen solubility as a function of alloy composition for different Wagner interaction parameters according to Eq. [30]. (b) The shape of the oxygen solubility curve for nonideal behavior as a function of the Wagner interaction parameter according to Eq. [32] and $\nu = 1$.

converse is found when $\epsilon_O^A < 0$, oxygen solubility increasing with larger negative values of the interaction coefficient. Figure 3b illustrates the variation and shape of the oxygen solubility curves for different negative values of ϵ_O^A. These solubility curves exhibit minima of larger oxygen concentrations which occur at smaller values of N_A with larger negative values of ϵ_O^A. The absolute slopes of the curves on either side of the minima also markedly increase as ϵ_O^A increases in negative value.

The Ternary Oxidation Model

The relatively simple diffusion model, similar to that considered by Wagner (1) is shown schematically in Fig. 4: The ternary oxide $A_{1-\delta}B_\delta O_\nu$ is assumed to correspond closely with the composition of the binary oxide ($\delta << 1$) and the oxygen solubility curve may exhibit a minimum.

Oxygen is the only component which is regarded as diffusing on both its own and the metal gradient. This assumption is realistic in that its concentration is small, and it diffuses interstitially at a rate much more rapid than the metallic species by substitutional vacancy mechanisms. Accordingly

$$D_{OO} >> D_{AA} \text{ and } |\partial N_O/\partial x| << |\partial N_A/\partial x| \quad [33]$$

and the flux equations describing diffusion in the alloy may be written as

$$j_A = -D_{AA}\frac{\partial N_A}{\partial x} \quad [34]$$

$$j_O = -D_{OO}\frac{\partial N_O}{\partial x} - D_{OA}\frac{\partial N_A}{\partial x} = -D_{OO}\left(\frac{\partial N_O}{\partial x} + \epsilon_O^A N_O \frac{\partial N_A}{\partial x}\right) \quad [35]$$

where the dilute solution approximation has been substituted for the off-diagonal diffusion coefficient D_{OA} (5)

$$D_{OA} = D_{OO}\epsilon_O^A N_O \quad [36]$$

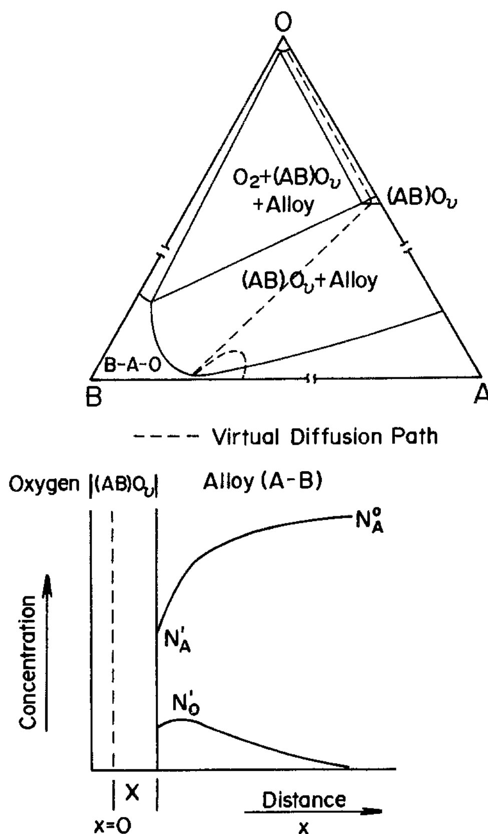

Fig. 4. The ternary oxidation model

The divergence of the fluxes may be written

$$\frac{\partial N_A}{\partial t} = \frac{\partial}{\partial x}\left(D_{AA}\frac{\partial N_A}{\partial x}\right) = D_{AA}\frac{\partial^2 N_A}{\partial x^2} \quad [37]$$

$$\frac{\partial N_O}{\partial t} = \frac{\partial}{\partial x}\left| D_{OO}\left(\frac{\partial N_O}{\partial x} + \epsilon_O^A N_O\frac{\partial N_A}{\partial x}\right)\right| = D_{OO}\frac{\partial^2 N_O}{\partial x^2} + D_{OO}\epsilon_O^A\frac{\partial}{\partial x}\left(N_O\frac{\partial N_A}{\partial x}\right) \quad [38]$$

where it has been assumed that D_{AA} and D_{OO} are independent of composition.

Since ternary interactions have been assumed not to influence the diffusion of A, the solution of [37] is that due to Wagner (1) given earlier in Eq. [1], with Eq. [5] giving N_A', the mole fraction of A at the alloy/scale interface, $x = X = (2kt)^{1/2}$. The solution of [38] gives the oxygen profile in the alloy. A modification of a solution presented by Bolze *et al.* (6), which assumes that the off-diagonal coefficient, D_{OA}, and the direct coefficient, D_{OO}, are constant, gives

$$N_O = \frac{D_{OA}}{D_{OO}}(N_A^o - N_A')\frac{\text{erfc}(x/2\sqrt{D_{AA}t})}{\text{erfc}(k/2D_{AA})^{1/2}} + N_O'\frac{\text{erfc}(x/2\sqrt{D_{OO}t})}{\text{erfc}(k/2D_{OO})^{1/2}} - \frac{D_{OA}}{D_{OO}}(N_A^o - N_A')\frac{\text{erfc}(x/2\sqrt{D_{OO}t})}{\text{erfc}(k/2D_{OO})^{1/2}} \quad [39]$$

N_O' is the mole fraction of oxygen at the alloy/scale interface, which is also the oxygen solubility limit for an alloy of composition N_A'. Equation [39] can be used to give the gradient of the oxygen profile at this interface, $x = X$

$$\left(\frac{\partial N_O}{\partial x}\right)_{x=X} = \frac{N_A^o - N_A'}{(\pi D_{OO}t)^{1/2}}\left\{\frac{D_{OA}}{D_{OO}} - \frac{D_{OA}}{(D_{OO}D_{AA})^{1/2}}\frac{\exp(-k/2D_{AA})}{\text{erfc}(k/2D_{AA})^{1/2}} - \frac{N_O'}{N_A^o - N_A'}\right\} \quad [40]$$

where the approximation given in [11] has been used. The gradient of the metal profile at $x = X$ is obtained from [1], and combining this with [40] provides an expression for the slope of the virtual diffusion path in the alloy at the point where it contacts the surface scale

$$\left(\frac{dN_O}{dN_A}\right)^{DP}_{x=X} = \left(\frac{D_{AA}}{D_{OO}}\right)^{1/2}\frac{\text{erfc}(k/2D_{AA})^{1/2}}{\exp(-k/2D_{AA})}\left\{-\frac{D_{OA}}{D_{OO}} - \frac{D_{OA}}{(D_{OO}D_{AA})^{1/2}}\frac{\exp(-k/2D_{AA})}{\text{erfc}(k/2D_{AA})^{1/2}} - \frac{N_O'}{N_A^o - N_A'}\right\} \quad [41]$$

If ternary interaction were negligible, and $D_{OA} = 0$, [41] reduces to [15] given earlier, with D_{AA} equivalent to D_{AB}, the interdiffusion coefficient in the binary alloy.

Upon substitution of [36] for the constant off-diagonal coefficient, at the specific value corresponding to N_O', the atom fraction of oxygen at the alloy/scale interface, [41] becomes

$$\left(\frac{dN_O}{dN_A}\right)^{DP}_{x=X} = -N_O'\left(\frac{D_{AA}}{D_{OO}}\right)^{1/2}\frac{\text{erfc}(k/2D_{AA})^{1/2}}{\exp(-k/2D_{AA}}\left\{\frac{1}{N_A^o - N_A'} + \epsilon_O^A\left(\frac{D_{OO}}{D_{AA}}\right)^{1/2}\frac{\exp(-k/2D_{AA})}{\text{erfc}(k/2D_{AA})^{1/2}} - \epsilon_O^A\right\} \quad [42]$$

This tangent to the compositional profile of the virtual diffusion path has to be compared to the tangent to the solubility curve at the composition of the alloy/scale interface (N_A', N_O') as given by [26a]. Equation [42] then provides the limiting criterion for transition from external scale formation accompanied with internal oxidation, to external scale formation only. Thus, for internal oxidation to occur, condition [18] must be satisfied, irrespective of the composition N_A' on the solubility curve: N_A' can be ahead of the oxygen minimum solubility, at this minimum, or on the ascending curve. Substitution of [42] and [26a] into [18] gives

$$\frac{N_A^o - N_A'}{N_A'}\left(\frac{1 + N_A'\epsilon_A^A + \nu N_A'\epsilon_O^A}{\nu + N_O'\epsilon_O^A + \nu N_O'\epsilon_O^O}\right)\left(\frac{D_{OO}}{D_{AA}}\right)^{1/2}\frac{\exp(-k/2D_{AA})}{\operatorname{erfc}(k/2D_{AA})^{1/2}} \left\{\frac{1}{1 + (N_A^o - N_A')\,\epsilon_O^A\left[\left(\frac{D_{OO}}{D_{AA}}\right)^{1/2}\frac{\exp(-k/2D_{AA})}{\operatorname{erfc}(k/2D_{AA})^{1/2}} - 1\right]}\right\} > 1 \quad [43]$$

Equation [43] may be utilized to define the limiting atom fraction of solute A above which internal oxidation of the alloy would not occur, using [5] and [32], respectively, to define N_A' and N_O'. However, first it is appropriate to introduce the following simplification, since ϵ_A^A and ϵ_O^O are generally much less than ϵ_O^A, $N_O' << N_A'$

$$\frac{1 + \epsilon_A^A N_A' + \nu\epsilon_O^A N_A'}{\nu + \epsilon_O^A N_O' + \nu\epsilon_O^O N_O'} \simeq \frac{1 + \nu\epsilon_O^A N_A'}{\nu} \quad [44]$$

Thus rearrangement of Eq. [43] gives

$$\frac{N_A^o - F(u)}{1 - N_A^o} \geq \frac{\sqrt{\pi}}{\nu}u\sqrt{\frac{D_{OO}}{D_{AA}}}\left\{\frac{1 + \nu\epsilon_O^A N_A^o - F(u)[1 + \nu\epsilon_O^A]}{1 + \sqrt{\pi}u\epsilon_O^A\sqrt{\frac{D_{OO}}{D_{AA}}}(1 - N_A^o) - F(u)[\epsilon_O^A(1 - N_A^o) + 1]}\right\} \quad [45]$$

where the auxiliary function $F(u)$ is defined by [6] and as earlier, u replaces $\sqrt{k/2D_{AA}}$. In the case of ideal behavior, when $\epsilon_O^A = 0$, [45] reduces to [13] earlier; that given by Wagner (1).

Oxygen flux into the alloy.—It is appropriate here to compare the fluxes of oxygen into the alloy in the two limiting cases in which oxygen is free from, or includes ternary interaction. The metal concentration gradient has been assumed to be identical in each case. The oxygen fluxes are as follows:

No interaction

$$j_O = D_{OO}(\partial N_O/\partial x)_{x=X} \quad [46]$$

Including ternary interaction

$$j_O = -D_{OO}\left(\frac{\partial N_O}{\partial x} + \epsilon_O^A N_O'\frac{\partial N_A}{\partial x}\right)_{x=X} \quad [47]$$

Using the approximation in Eq. [11], together with Eq. [2], [40,] and [1]

$$\left(\frac{\partial N_O}{\partial x}\right)_{x=X}[\text{no interaction}] = -(N_O')_H/(\pi D_O t)^{1/2} \quad [48]$$

$$\left(\frac{\partial N_O}{\partial x}\right)_{x=X}[\text{interaction}] = -\frac{(N_O')_{NH}}{(\pi D_{OO}t)^{1/2}}\left\{1 + \epsilon_O^A(N_A^o - N_A')\left[\left(\frac{D_{OO}}{D_{AA}}\right)^{1/2}\frac{\exp - k/2D_{AA}}{\operatorname{erfc}(k/2D_{AA})^{1/2}} - 1\right]\right\} \quad [49]$$

$$\left(\frac{\partial N_A}{\partial x}\right)_{x=X} = \frac{N_A^o - N_A'}{(\pi D_{AA}t)^{1/2}}\frac{\exp - k/2D_{AA}}{\operatorname{erfc}(k/2D_{AA})^{1/2}} \quad [50]$$

where $(N_O')_H$ and $(N_O')_{NH}$ are the oxygen solubilities at the particular metal concentration existing at the alloy/scale interface corresponding to Henrian and non-Henrian thermodynamic behavior, respectively. Thus

$$\frac{j_O(\text{no interaction})}{j_O(\text{interaction})} = \frac{(N_O')_H}{(N_O')_{NH}}\frac{1}{[1 - \epsilon_O^A(N_A^o - N_A')]} \quad [51]$$

When ternary interactions are considered, the total oxygen flux, as given by Eq. [47], consists of two parts: that along the oxygen gradient itself, j_O^O, and that along the metal gradient, j_O^M

$$j_O(\text{interaction}) = j_O^O + j_O^M \quad [52]$$

$$j_O^O = -D_{OO}(\partial N_O/\partial x)_{x=X} \quad [53]$$

$$j_O^M = -D_{OO}\epsilon_O^A(N_O')_{NH}(\partial N_A/\partial x)_{x=X} \quad [54]$$

The latter contribution to the flux, of course, does not exist in the case of Henrian or noninteractive behavior. However, in the former, the flux of oxygen along its own gradient has also been modified from that of Henrian behavior due to the ternary interaction since the oxygen concentration gradients are different in the two cases. Equations [48] and [49] give these gradients for Henrian and non-Henrian behavior, respectively; an increasingly negative interaction parameter ϵ_O^A causes the oxygen gradient to become more positive and thus retards the inward diffusion of oxygen. The contributions to the total oxygen flux by the oxygen and metal gradients can be compared for the ternary oxidation model

$$\frac{j_O^O}{j_O^M} = -\left\{1 + \left(\frac{D_{AA}}{D_{OO}}\right)^{1/2}\frac{\operatorname{erfc}(k/2D_{AA})^{1/2}}{\exp - k/2D_{AA}}\left[\frac{1}{\epsilon_O^A(N_A^o - N_A')} - 1\right]\right\} \quad [55]$$

A comparison of Eq. [53] to [54] demonstrates that the above flux ratio is negative when the influence of the interaction causes the oxygen gradient at the alloy/scale interface to become positive. Moreover, the oxygen flux along the metal gradient is always greater in magnitude than that along the oxygen gradient (the absolute value of the ratio in Eq. [55] is always less than 1), and so the net oxygen flux is always into the alloy.

In our earlier paper (2) oxygen diffusion under the influence of its own gradient was neglected, and the oxygen flux into the alloy under Henrian behavior, Eq. [46], was compared with that under interactive conditions along the metal gradient only, j_O^M in Eq. [54]. This comparison upon using Eq. [48] and [50] becomes

$$\frac{j_O(\text{no interaction})}{j_O^M(\text{interaction})} = -\frac{(N_O')_H}{(N_O')_{NH}}\left(\frac{D_{AA}}{D_{OO}}\right)^{1/2}\frac{1}{\epsilon_O^A(N_A^o - N_A')}\frac{\operatorname{erfc}(k/2D_{AA})^{1/2}}{\exp - k/2D_{AA}} \quad [56]$$

This is identical to the expression in our earlier paper (2) for the special case when $(N_O')_H \simeq (N_O')_{NH}$ and $k/2D_{AA}$ is relatively small

$$\text{erfc}(k/2D_{AA})^{1/2} \exp(k/2D_{AA}) \simeq 1$$

Discussion

An extreme limitation in attempts to apply conclusions from the preceding analysis to practical systems is the lack of data on oxygen solubilities in solid binary alloys and of ternary interaction parameters. Limited data are available for liquid iron alloys and Table I summarizes these from Ref. (4): Ranges of values are given in some instances, and these represent either experimental values [refer to Ref. (4) for the original reference] or values calculated theoretically from oxygen solubility curves.

Table I and the value $\epsilon_O{}^O = -13.9$ indicate that the neglect of $\epsilon_A{}^A N_O'$, $\epsilon_O{}^A N_O'$ and $\nu\epsilon_O{}^O N_O'$ in arriving at Eq. [45]-[44] is justified, particularly in view of the very low value of N_O', the atom fraction of oxygen at the alloy/scale interface. $\epsilon_O{}^A$, the interaction coefficient for oxygen with the alloying additions which would be selectively oxidized from transition metal alloys can have high negative values, even at 1600°C; extrapolation of known values demonstrates that these become even more negative with decreasing temperature.

The criterion then which determines whether the virtual diffusion path contacts the oxygen solubility curve for the alloy at a tangent or cuts into and across the two-phase alloy-oxide field is given in Eq. [45]. This condition can be used to define a limiting bulk atom fraction of the selectively oxidized solute, A, in the alloy above which internal oxidation would not occur. Equation [45] can be rearranged as a quadratic in $N_A{}^{o*}$, the critical atom fraction

$$\epsilon_O{}^A (N_A{}^{o*})^2 + \left\{ \frac{1-F(u)}{F(u)} \left[1 + \frac{u}{\nu}\left(\frac{\pi D_{OO}}{D_{AA}}\right)^{1/2} \right] - \epsilon_O{}^A[1+F(u)] \right\} (N_A{}^{o*}) + \left\{ \epsilon_A{}^O F(u) - [1-F(u)] - \frac{u}{\nu}\left(\frac{\pi D_{OO}}{D_{AA}}\right)^{1/2} \frac{1-F(u)}{F(u)} \right\} = 0 \quad [57]$$

where as before u replaces $(k/2D_{AA})^{1/2}$ and $F(u)$ represents the auxiliary function defined in Eq. [6]. Although exact calculation of Eq. [57] is not possible at this stage, it is nevertheless appropriate to carry out order of magnitude calculations to examine the influence of the various parameters involved. Clearly $N_A{}^{o*}$ depends on the interaction parameter $\epsilon_O{}^A$, the two diffusion coefficients D_{AA} and D_{OO}, and alloy/oxide interface recession rate constant k, which in turn is directly related to the diffusion coefficient of the ionic species responsible for scale growth.

It is appropriate then to consider the ranges of values which these parameters can take. Primarily, concern is with binary alloys composed of metals which have widely different affinities for oxygen: Fe, Ni, and Co-base alloys with solute additions of Cr or Al which tend to form Cr_2O_3 or Al_2O_3 protective scales. The growth rates of these latter two oxides depend marginally on the particular alloy involved: However, typical parabolic rate constants at 1000°C may be taken as 1×10^{-10} and 8×10^{-14} g^2 cm^{-4} sec^{-1}, respectively (7). These parabolic rate constants in terms of weight increase per unit surface area, the conventional k_p, are related to the alloy recession rate constant through

$$k = (2V_A/\nu M_O)^2 k_p \quad [58]$$

where V_A is the molar volume of the alloy, M_O the gram molecular weight of oxygen, and ν the ratio of oxygen ions to metal cations in the oxide AO_ν. Thus, the rate constant k has values of approximately 8.0×10^{-12} and 6.4×10^{-15} cm^2 sec^{-1} for Cr_2O_3 and Al_2O_3 growth at 1000°C, respectively.

Alloy interdiffusion coefficients, which are essentially equivalent to D_{AA}, are summarized in Table II along with the appropriate oxygen diffusivities: Again the data are at 1000°C and are only intended to represent order of magnitude values.

Thus, approximate values of the ratios k/D_{AA} and D_{OO}/D_{AA} pertinent to the Cr_2O_3 and Al_2O_3-forming systems are given in Table III.

As was seen in Table I, the interaction parameter $\epsilon_O{}^A$ is likely to lie in the range -10 to -500. Positive values need not be considered since these would correspond to noble metals, with low oxygen affinities, and thus unlikely to be selectively oxidized.

Wagner (15) and Whittle (16) have derived the following relationship to define the limiting bulk mole fraction of A required to form the surface scale AO_ν

$$N_A{}^{o*} = F[(\tfrac{1}{2}k/D_{AA})^{1/2}] \quad [59]$$

upon assuming that oxygen diffusion in the alloy can be ignored. Equation [57] also leads to Eq. [59] when $\epsilon_O{}^A = 0$ and D_{OO}/D_{AA} is ignored. Only the diffusion of the selectively oxidized solute is involved, and the condition represents the criterion that the concentration of the solute at the alloy/scale interface must not fall below the value at which the oxide AO_ν becomes thermodynamically unstable. In practice, where there is a wide difference in stability between the oxides of the various components, this concentration at the alloy/scale interface is virtually zero. The limiting condition defined by Eq. [59] is shown as one of the curves in Fig. 5 where $N_A{}^{o*}$ is plotted as a function of k/D_{AA} for different ratios of D_{OO}/D_{AA}. For this limiting case, $D_{OO}/D_{AA} = 0$, and with increasing values of k/D_{AA}, that is, either the scaling rate increases or the diffusion rate in the alloy decreases, the limiting bulk concentration increases.

One may develop a more realistic model by considering finite oxygen diffusivities in the alloy but with no interaction. Equation [57] then reduces to Eq. [13] earlier: This is Wagner's pseudobinary model. $N_A{}^{o*}$ is shown as a function of k/D_{AA} and D_{OO}/D_{AA} for this condition in Fig. 5. As would be expected, increase in the relative rate of oxygen diffusion in the alloy to that of the alloying element increases the critical bulk atom fraction of A required for exclusive external oxidation.

Table I. Oxygen solubility data in liquid iron alloys at 1600°C (4)

System	$N_O{}^{Sol.}$ (min)	N_A (min)	$\epsilon_A{}^A$	$\epsilon_O{}^A$
V_2O_5/Fe-V-O	0.00055/0.00061	0.0273/0.0350	3.2	−22.0/−38 6
Ti_2O_3/Fe-Ti-O	0.00011/0.0019	0.0093/0.0122	9.0	−73.0/−222.0
Al_2O_3/Fe-Al-O	0.00024	0.0018	5.3	−360.0/−433.0
Cr_2O_3/Fe-Cr-O	0.00028/0.0010	0.0747/0.0906	0.0	−7.0/−12.7
NbO_2/Fe-Nb-O	0.00060/0.00073	0.0097/0.0115	3.2	−45.0/−54.0

Table II. Alloy and oxygen interdiffusion coefficients at 1000°C

System	D_{AA} (cm^2/sec)	D_{OO} (cm^2/sec)
Fe-Cr	6×10^{-10} (8)	7×10^{-8} (in Fe) (9)
Ni-Cr	2×10^{-11} (10)	4×10^{-9} (in Ni) (11)
Co-Cr	4×10^{-12} (12)	
Fe-Al	5×10^{-9} (13)	
Ni-Al	2×10^{-10} (14)	

Table III. Values of the ratios k/D_{AA} and D_{OO}/D_{AA} for (Fe, Ni, Co)-(Cr, Al) systems

System	k/D_{AA}	D_{OO}/D_{AA}
Fe-Cr	0.013	117
Ni-Cr	0.4	200
Co-Cr	2	—
Fe-Al	1.2×10^{-6}	14
Ni-Al	3.2×10^{-5}	20

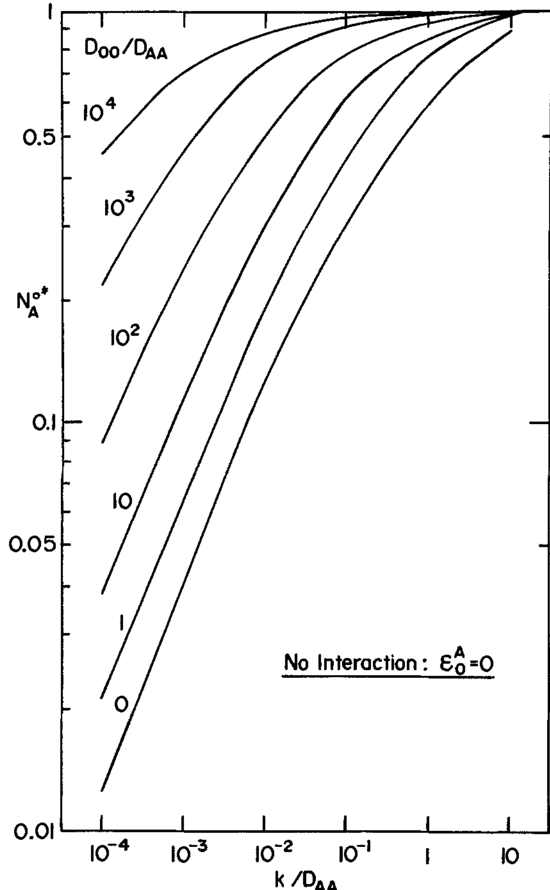

Fig. 5. The critical atom fraction of A in the alloy, N_A^{o*}, for exclusive external oxidation as a function of k/D_{AA} and D_{OO}/D_{AA}: no interaction.

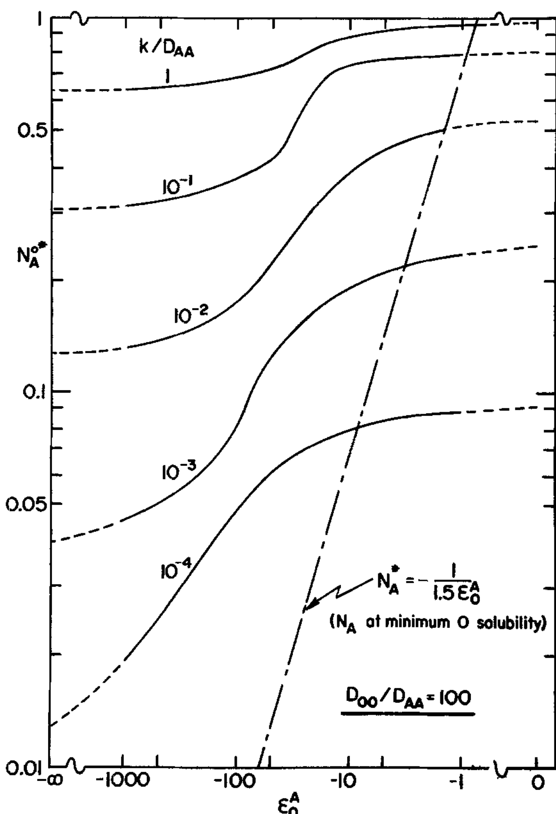

Fig. 6. The critical atom fraction of A in the alloy, N_A^{o*}, for exclusive external oxidation as a function of k/D_{AA} and the interaction parameter ϵ_O^A. $D_{OO}/D_{AA} = 100$.

Finally the ternary model involving non-Henrian interaction: Fig. 6 shows N_A^{o*} as a function of ϵ_O^A and k/D_{AA} at a value of $D_{OO}/D_{AA} = 100$. The critical atom fraction N_A^{o*} lies on each calculated curve between two limiting values depending on ϵ_O^A: The upper value at $\epsilon_O^A = 0$ corresponds to Henrian thermodynamic behavior, the lower limiting value at $\epsilon_O^A = -\infty$ is identical to Eq. [59] above. However, this is not because oxygen diffusion in the alloy becomes insignificant but with large negative values of ϵ_O^A the minimum in the oxygen solubility curve decreases to lower alloy solute concentrations as shown in Fig. 6, and the solubility rises more sharply after this minimum (Fig. 3b). Thus, although the diffusional flux of oxygen into the alloy may be substantial, the oxygen solubility curve is very steep and the alloy does not become saturated with respect to AO_ν because the diffusion path does not cut into the two-phase alloy and oxide field.

Within the reasonable range of interaction coefficients, ϵ_O^A, referred to earlier, -500 to -10, the critical mole fraction of solute for exclusive external scale formation, N_A^{o*}, is most affected by non-Henrian behavior. Furthermore, as soon as oxygen diffusion in the alloy becomes significant, particularly when the alloy diffusion coefficient is small and relatively large depletions exist, the interaction between dissolved oxygen and the solute must be significant, otherwise only alloys rich in the solute A would be able to form exclusively an external scale. The two upper curves in Fig. 6 may not be particularly significant because the simple model of thermodynamic behavior based on Wagner interaction coefficients is not expected to remain valid at solute concentrations exceeding about 30 atomic percent. However, the alloy composition near the alloy/scale interface is more important in determining whether a dilute solution approximation can be used. This is shown in Fig. 7 for the cases where the bulk atom fraction is the critical value to prevent internal oxidation, N_A^{o*} as shown in Fig. 6. The critical concentrations at the alloy/scale interface, N_A', are calculated as a function of the ratio k/D_{AA} and ϵ_O^A with $D_{OO}/D_{AA} = 100$, using Eq. [5]. Thus, the simple interactive solution model is probably valid for

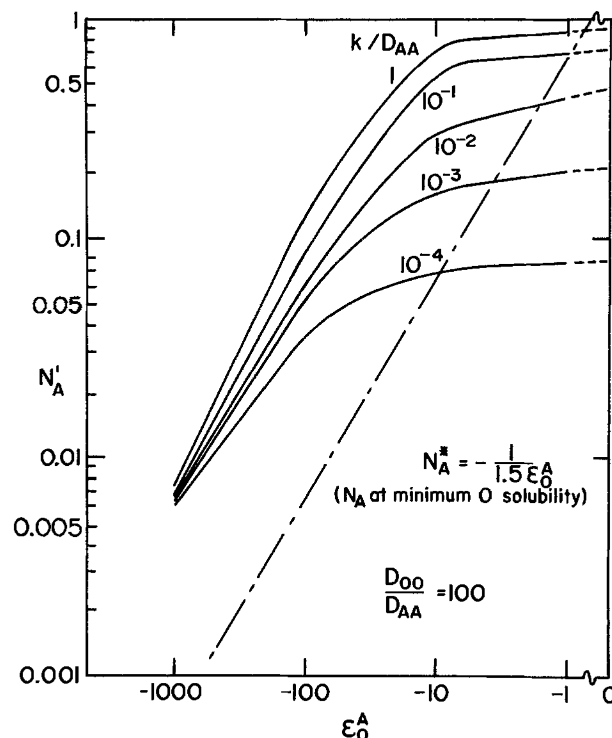

Fig. 7. The atom fraction of A at the alloy/scale interface, N_A', corresponding to the transition from internal to external scale formation as a function of $k/2D_{AA}$ and the interaction parameter ϵ_O^A. $D_{OO}/D_{AA} = 100$.

all the situations other than where k/D_{AA} is relatively large, and the interaction is weak corresponding to small negative values of ϵ_O^A. Figrue 7 also indicates that in most instances the critical concentration corresponds to a point on the solubility curve to the right of the oxygen solubility minimum, that is, on the ascending part of the solubility curve.

The distinction between Henrian and non-Henrian thermodynamic behavior of oxygen in the alloy on both the oxygen solubility curve and the diffusion path is demonstrated in Fig. 8. The oxygen solubility curves have been calculated according to Eq. [32] for different values of the interaction parameter, ϵ_O^A, using a value for the Henrian solubility product, K_H, (defined in Eq. [31]) of 10^{-12}. As was pointed out earlier, the solubility curves exhibit minima of larger oxygen concentrations and at smaller base metal concentrations as ϵ_O^A becomes more negative. The absolute slopes of the curves behind the minima also markedly increase as ϵ_O^A increases in negative value. The curve for Henrian behavior, $\epsilon_O^A = 0$, shows no minimum. Diffusion paths are also included in Fig. 8. These have been calculated using Eq. [39] and [1] to give the oxygen and metal concentration profiles, respectively, and then eliminating the variable $x/\sqrt{t}$ from the two expressions; the following values of the diffusion parameters were used: $k = 10^{-12}$, $D_{AA} = 10^{-10}$, $D_{OO} = 10^{-8}$, and $\nu = 1.5$. The diffusion cofficients and the alloy recession rate constant all have the same units. The diffusion paths correspond to a bulk alloy compostion, $N_A°$, of 0.178 which is the critical value necessary to prevent internal oxidation under these conditions when ϵ_O^A has a value of -100: This is shown in Fig. 6. At small negative values of the interaction coefficient, this particular alloy composition is not sufficient to prevent internal oxidation and the slope of the diffusion path is greater than that of the solubility curve at the point corresponding to the alloy/scale interface. Thus, the diffusion path cuts into the two-phase alloy and oxide phase field as shown in Fig. 8. Increase in the negative value of the interaction parameter increases the slopes of both the diffusion path and the oxygen solubility curve and it is the interplay between these two factors which governs the critical atom fraction of solute in the alloy necessary to prevent internal oxidation.

Of course, it must be remembered that internal oxide and a surface scale are formed when the virtual diffusion path cuts into the alloy and oxide phase field. This internal oxide precipitation confines the actual diffusion path along the solubility curve in the alloy. The effective removal of a fraction of the solute A diffusing to the alloy/scale interface to form the surface scale must then be taken into account. Certainly, this modified diffusion path leads to a reduced concentration of A at the alloy/scale interface. However, it may not necessarily be reduced such that other less stable oxides of the solvent metal are formed. It is not possible to proceed further and calculate actual diffusion paths for these limiting cases without detailed knowledge of the alloy-oxygen solubility curves.

Equation [51] compares the flux of oxygen into the alloy from the alloy/scale interface under the assumption of Henrian and non-Henrian thermodynamic behavior. Figure 9 shows this ratio, j_O^H/j_O^{NH}, as a function of the interaction parameter, ϵ_O^A, with various values of k/D_{AA}. The value of k/D_{AA} determines the metal concentration profile in the alloy and, in particular, the concentration of A at the alloy/scale interface for a given bulk alloy content of A, $N_A°$. The curves in Fig. 9 have been calculated for $N_A° = 0.2$: this alloy content is sufficient to prevent internal oxidation under these conditions ($k/D_{AA} = 10^{-2}$, $D_{OO}/D_{AA} = 10^2$) only when ϵ_O^A is less than a certain value, as indicated by the arrows in Fig. 9 for the various ratios of k/D_{AA}.

The concentration of A at the alloy/scale interface, N_A', is independent of ϵ_O^A; N_O', however, the concentration of oxygen, is strongly dependent on ϵ_O^A increasing markedly with increasing negative values of ϵ_O^A as shown in Fig. 8. Thus, there are two factors contributing to the decreased flux of oxygen into the

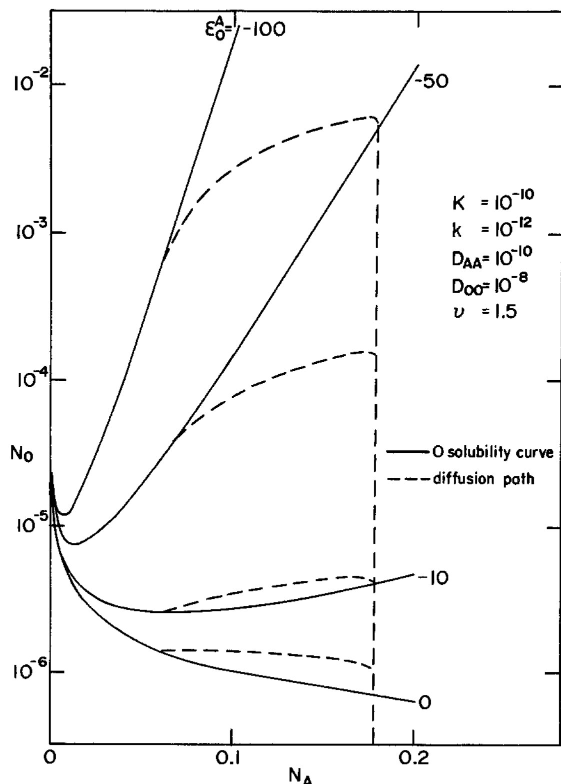

Fig. 8. The oxygen solubility curve according to Eq. [32] with $k = 10^{-10}$ and $\nu = 1.5$ with diffusion paths superimposed for an alloy of $N_A° = 0.178$: $k = 10^{-12}$, $D_{AA} = 10^{-10}$, $D_{OO} = 10^{-8}$.

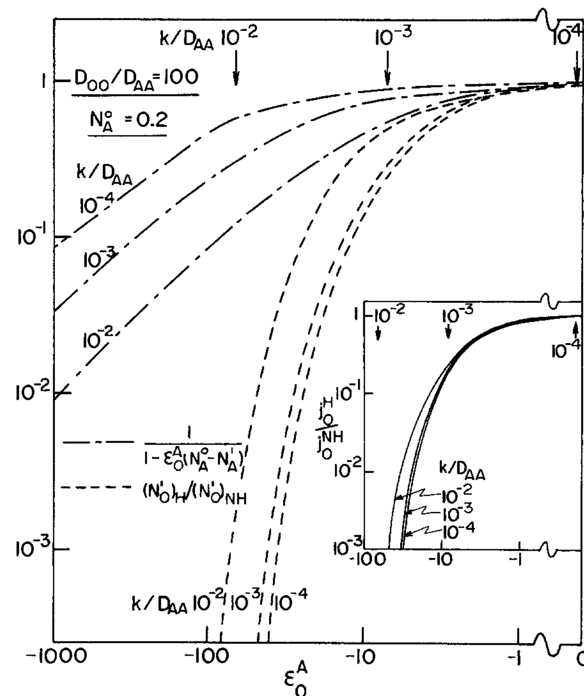

Fig. 9. The ratio of oxygen flux at the alloy/scale interface with Henrian thermodynamic behavior to that with non-Henrian behavior for an alloy of $N_A° = 0.2$. The ratio of solubilities and the effective diffusion coefficient are also shown. Conditions to the left of the vertical arrows correspond to exclusive surface scale formation, and to the right, combined internal and external oxidation for the indicated ratio of k/D_{AA}. $D_{OO}/D_{AA} = 100$.

alloy under Henrian behavior $(j_O^H/j_O^{NH}) < 1$: the decreased oxygen solubility in the alloy as represnted by the term, $(N_O')_H/(N_O')_{NH}$, and a decreased effective diffusion coefficient because under Henrian behavior the only driving force for oxygen diffusion inward is its own concentration. These two factors are shown separately in Fig. 9. The former, relating to the change in oxygen solubility, is the more important term: It decreases as k/D_{AA} decreases since as the metal gradient decreases the diffusion path contacts the oxygen solubility curve at higher oxygen concentrations. In contrast, the effective diffusion parameter, $1/1 - \epsilon_A{}^o(N_A{}^o - N_A')$, increases as k/D_{AA} decreases since the reduced metal gradients correspond to a reduced driving force for oxygen inward. For $\epsilon_O{}^A$ values in the range of interest, -10 to -100, the oxygen flux under interactive conditions is always very much larger than when Henrian solution of oxygen in the alloy prevails.

An extreme limitation in trying to apply the conclusion of the preceding analysis is the lack of oxygen solubility data in binary alloys and of ternary interaction parameters: Suitable thermodynamic models of solution behavior have also not been developed to permit order of magnitude calculations. The measured oxygen solubilities in pure metals whose oxides grow by cation transport are exceedingly small, of the order of parts per million, and consequently experimental determination is extremely difficult, particularly since the variation of this solubility as a function of the solute alloying element content is required. However, measurement of oxygen activities in saturated binary alloys may be sufficient. Ternary A-B-O phase diagrams can be readily related to oxygen activity/alloy diagrams in which log a_o is shown as a function of the atom fractions of metal in all the possible phases. Moreover, diffusion paths can readily be superimposed on these diagrams, in the same way as on phase diagrams referred to earlier. Several of these diagrams for transition metal alloys-oxygen are already available (17), for example: Fe-Ni-O, Fe-Cr-O, and Ni-Cr-O, having been determined by electrochemical and gas equilibration methods.

Defining the oxygen activity, $a_O{}^S$, on the oxygen solubility curve, accordng to the Wagner formalism

$$\ln a_O{}^S = \ln N_O{}^S + \ln \gamma_O{}^S$$

$$= \ln N_O{}^S + \ln \gamma_O{}^o + \epsilon_O{}^O N_O{}^S + \epsilon_O{}^A N_A{}^S \quad [60]$$

the slope of the solubility curve is given by

$$\left(\frac{dN_O}{dN_A}\right)^{\text{Sol.}} = \left[\frac{1}{a_O{}^S}\left(\frac{da_O{}^S}{dN_A}\right) - \epsilon_O{}^A\right]\frac{N_O{}^S}{1 + \epsilon_O{}^O N_O{}^S}$$

$$\simeq \left[\frac{1}{a_O{}^S}\left(\frac{da_O{}^S}{dN_A}\right) - \epsilon_O{}^A\right] N_O{}^S \text{ for } \epsilon_O{}^O N_O{}^S << 1 \quad [61]$$

Thus, the limiting criterion separating the transition from exclusive external oxidation to combined internal and external oxidation as given in Eq. [18] using Eq. [42] for the gradient of the diffusion path, and Eq. [61] in place of [26a] for the gradient of the solubility curve, may be written as

$$-\left(\frac{D_{AA}}{D_{OO}}\right)^{1/2} \frac{\operatorname{erfc} u}{\exp - u^2} \left\{ \frac{1}{N_A{}^o - N_A'} + \epsilon_O{}^A \left(\frac{D_{OO}}{D_{AA}}\right)^{1/2} \frac{\exp - u^2}{\operatorname{erfc} u} - \epsilon_A{}^O \right\}$$

$$\geqq \left[\frac{1}{a_O{}^S}\left(\frac{da_O{}^S}{dN_A}\right) - \epsilon_O{}^A\right] \quad [62]$$

u represents the ratio $(k/2D_{AA})^{1/2}$ as earlier. The differential term, $1/a_O{}^S\ (da_O{}^S/dN_A)$ can be determined from the ln a_O as a functiion of N_A data referred to earlier. The interaction parameter, $\epsilon_O{}^A$, can be obtained if the alloy composition at the minimum oxygen solubility is known. At the minimum, $(dN_O/dN_A) = 0$ and thus Eq. [61] gives

$$\epsilon_O{}^A = 1/a_O{}^S \left(\frac{da_O{}^S}{dN_A}\right)_{(N_O)\min.} \quad [63]$$

Accordingly, it is not necessary to know the absolute value of the minimum oxygen solubility, but only the atom fraction, N_A, at which this minimum occurs. Possibly, electrochemical thermodynamic and coulometric techniques using solid electrolytes could be used to determine these parameters.

The concepts outlined in this paper may be extended to the oxidation of ternary alloys. For example, it has been known for several decades that the addition of an alloying element which forms an oxide preferentially to the solvent metal often prevents the internal oxidation of the alloying element in a binary alloy which forms the most stable oxide .The addition of Cr to Fe-, Ni-, or Co-Al alloys leads to the formation of Al_2O_3 solely as an external scale at Al concentrations much less than required in the binary alloys. Following a suggestion by Wagner (18) this phenomenon has usually been described as due to a gettering action by the element whose oxide is of intermediate stability, even though only Al_2O_3 is formed during steady-state oxidation. The function of the additional element according to our diffusional analysis is to ensure that the diffusion path only contacts or in the limit tangents the oxygen solubility surface at an area where Al_2O_3 exists in equilibrium with the alloy.

Summary

The pseudobinary model considered by Wagner for the onset of internal oxidation beneath the external scale based on the criterion that conditions must exist at the alloy side of the scale/alloy for the product of the selectively oxidized metal and oxygen concentrations to exceed the solubility of the binary oxide has been expanded into a ternary thermodynamic and diffusional formalism using the A-B-O isotherm and the placement of the representative diffusion paths on this isotherm. The Wagner formalism for interaction coefficients was utilized to interpret the ternary solution thermodynamics and the Fickian type diffusion. It was possible to demonstrate, firstly, that external scale formation accompanied by internal oxidation occurs when the virtual diffusion path for the alloy cuts into and across the two phase alloy-oxide field and, secondly, that a limiting atom fraction of the selectively oxidized solute alloying element for external scale formation alone can be defined by the diffusion path in the alloy which tangents the oxygen solubility curve for the alloy. Typical ranges of interaction parameters applicable to cobalt, iron, and nickel-base alloys were used to show the effects of the diffusion coefficients, scaling constants, and interaction parameters on this limiting solute alloying element concentration. In the case of non-Henrian solution behavior of oxygen, this critical alloy composition corresponds generally to a point on the solubility curve to the right of the oxygen solubility minimum, that is, on the ascending part of the solubility curve.

Acknowledgments

The authors gratefully acknowledge helpful discussions with J. S. Kirkaldy and the financial support of the Science Research Council in the form of a Senior Visiting Fellowship (WWS).

Manuscript submitted Aug. 2, 1977; revised manuscript received Feb. 6, 1978.

Any discussion of this paper will appear in a Discussion Section to be published in the June 1979 JOURNAL. All discussions for the June 1979 Discussion Section should be submitted by Feb. 1, 1979.

Publication costs of this article were assisted by McMaster University.

REFERENCES

1. C. Wagner, *Corros. Sci.*, **8**, 889 (1968).
2. D. J. Whittle, D. J. Young, and W. W. Smeltzer, *This Journal*, **133**, 1073 (1976).
3. G. R. St. Pierre and R. D. Blackburn, *Trans. Metall. Soc. AIME*, **242**, 24 (1968).
4. S. E. Feldman and J. S. Kirkaldy, *Can. Met. Quart.*, **13**, 625 (1974).
5. J. S. Kirkaldy and G. R. Purdy, *Can. J. Phys.*, **40**, 208 (1962).
6. G. Bolze, D. E. Coates, and J. S Kirkaldy, *Trans. ASM*, **62**, 794 (1969).
7. G. C. Wood, I. G. Wright, T. Hodgkiess, and D. P. Whittle, *Werkst. Korros.*, **21**, 900 (1970).
8. F. N. Tavadze, M. L. Bernshtein, K. I. Dzhngeli, and M. N. Surmava, *Akad. Nauk Gruz. SSR*, **69**, 389 (1973).
9. R. J. Borg, D. Y. F. Lai, and O. H. Krikorian, University of California, Dept. Rept. No. UCRL 7124 (1962).
10. A. Davin, V. Leroy, D. Coutsouradis, and L. Habraken, *Cobalt*, **19**, 51 (1963).
11. C. B. Alcock and P. B. Brown, *Met. Sci. J.*, **3**, 116 (1969).
12. A. Green, D. P. Whittle, J. Stringer, and N. Swindells, *Scripta Met.*, **7**, 1079 (1973).
13. K. Hirano and A. Hishinuma, *Nippon Kinzoku Gakkaishi*, **32**, 516 (1968).
14. R. Sivakumar, N. B. Menon, and L. L. Siegle, *Metall. Trans.*, **4**, 396 (1973).
15. C. Wagner, *This Journal*, **99**, 369 (1952).
16. D. P. Whittle, *Oxid. Met.*, **4**, 171 (1972).
17. A. D. Pelton and W. T. Thompson, *Prog. Solid State Chem.*, **10**, 119 (1976).
18. C. Wagner, *Corros. Sci.*, **5**, 751 (1965).

Chemical Mechanisms in Photoresist Systems

Part II. Thermal Reactions of a Bisazide Resist

Shigeki Shimizu[1]

School of Chemistry, Rutgers, The State University of New Jersey, New Brunswick, New Jersey 08903

ABSTRACT

We have investigated the thermal reaction of a negative photoresist (cyclized polyisoprene + bis(4-azidobenzal)cyclohexanone) by infrared spectroscopy. Two major thermal crosslinking reactions were observed, one is the oxidative polymerization of cyclized polyisoprene and the other is the decomposition of bisazide. At 100°C, the oxidative crosslinking in air proceeds about three times faster than the bisazide crosslinking. The activation energies of these reactions were determined as 32 and 23 kcal/mole, respectively. Extensive crosslinking of cyclized polyisoprene tends to retard the bisazide decomposition reaction. This retardation is attributed to a cage effect of the increasing rigid matrix.

Thermal fog stands in the way of any organic imaging systems (1). In photoresists thermal fog may become a problem, especially in the process of prebaking. Prebaking is generally thought necessary to get hard films and good adhesion of polymer to the Si wafer, but it can also cause thermal fog at higher temperature or longer prebaking times. DeForest (2) shows allowable prebaking times for several types of commercial photoresists at different prebaking conditions. Nakane (3) did a more quantitative study on a positive-type resist, observing u.v. absorption and thermal decomposition of quinone diazide. Working with a negative photoresist, Moreau *et al.* (4) studied photo crosslinking of bisazide-cyclized polyisoprene and reported enhanced sensitivity at higher temperatures.

We have conducted a mechanistic study on thermal reactions of a related negative resist (bis(4-azidobenzal)-cyclohexanone + cyclized polyisoprene) by infrared spectroscopy, thus gaining some information on the rate of removal of bisazide and the rate of polymer immobilization by the thermal reactions. The decreased importance of direct bisazide crosslinking in the over-all thermal reactions in air is explored in detail.

Results and Discussion

Comparison of crosslinking efficiency between the thermal reactions and the photoreactions of bisazide resist.—When equal amounts of bisazide are decomposed thermally and photochemically, we might at first assume that they form equal amounts of bisamine-crosslink in a negative photoresist. We can obtain the information on the extent of the crosslinking reaction by comparing the film thickness of photoresist before and after development (dissolve in benzene for 3 min).

Figure 1 shows the percentage of polymer retention after development) *vs.* the percentage of decomposed bisazide. There is a great difference between thermal

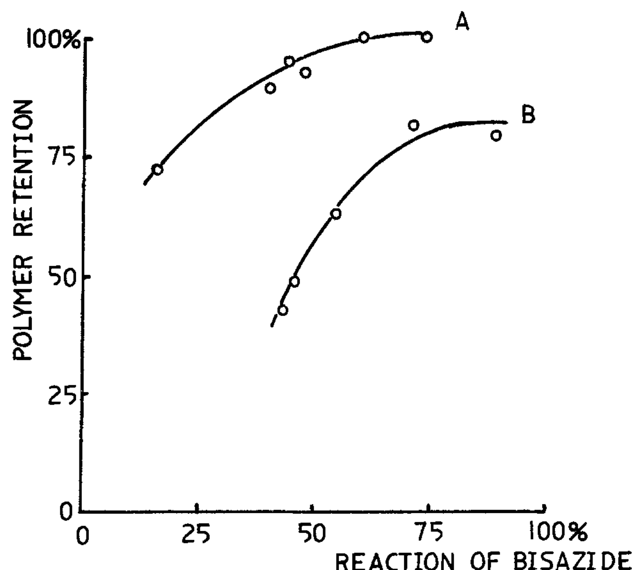

Fig. 1. Crosslinking *vs.* reacted bisazide in photo and thermal reactions of photoresist. Photoresist: 3% bisazide, 1.2 μm coating on Si. A:thermal reaction at 100°C in air; B:photoreaction by 365 nm dosing at 25°C at 3.6 mJ/cm^2 min under N_2.

[1] Present address: Mitsubishi Chemical Industries, Research Laboratory, 1000 Kamoshida, Midori-ku, Yokohama, Japan.

Key words: film, infrared, oxidation, polymerization.

and photoreaction. At 100°C in air and with no exposure, about 70% of the cyclized polyisoprene is retained after only 15% decomposition of bisazide. The retention of 70% of polymer, after thermal reactions have decomposed only 15% of the bisazide, clearly indicates that at least one additional thermal crosslinking reaction is operating independent of the bisazide. To retain this fraction of the polymer by room temperature photocrosslinking under N_2 requires 55% reaction of bisazide (at 3%/wt. loading).

Thermal crosslinking of cyclized polyisoprene.—We made several coatings of cyclized polyisoprene (no bisazide added) on Si wafers and observed their crosslinking by comparing film thickness before and after development. Figure 2 shows the percentage of polymer retention (after development) at different temperatures and heating times. It shows that cyclized polyisoprene crosslinks thermally without the aid of bisazide. This is the main reason why the thermal crosslinking in Fig. 1 proceeds further than the photo crosslinking when identical amounts of bisazide are decomposed. The small difference between 80% polymer retention in film 2C (no bisazide) *vs.* 97% retention in film 2D (3% bisazide) on the time-independent retention plateau at 5 hr (100°C) is assigned to the effect of bisazide crosslinking.

We observed *IR* spectra of cyclized polyisoprene upon heating. When a film is heated at 100°C in air for 24 hr, the *IR* spectrum shows a tremendous change, indicating the formation of OH groups (3500 cm^{-1}), isolated C=O groups (1720 cm^{-1}) and conjugated C=O groups (1670 cm^{-1}), as in Fig. 3. The formation of these groups can be explained as the termination products of oxidative radical reactions that are initiated by the thermal decomposition of peroxide. The peroxides are unstable and their *IR* absorption cannot be identified in Fig. 3. It is well known that oxygen reacts with polyolefins to form peroxide, which initiates radical crosslinking upon heating (5).

Both crosslinking and chain scission reactions are reported to occur in the oxidative heating of unsaturated polyolefins, the former leading to gels and the latter decreasing the viscosity (5). In the case of cyclized polyisoprene, oxidative crosslinking apparently predominates over oxidative chain scission since heating in air does immobilize the polymer instead of increasing its solubility.

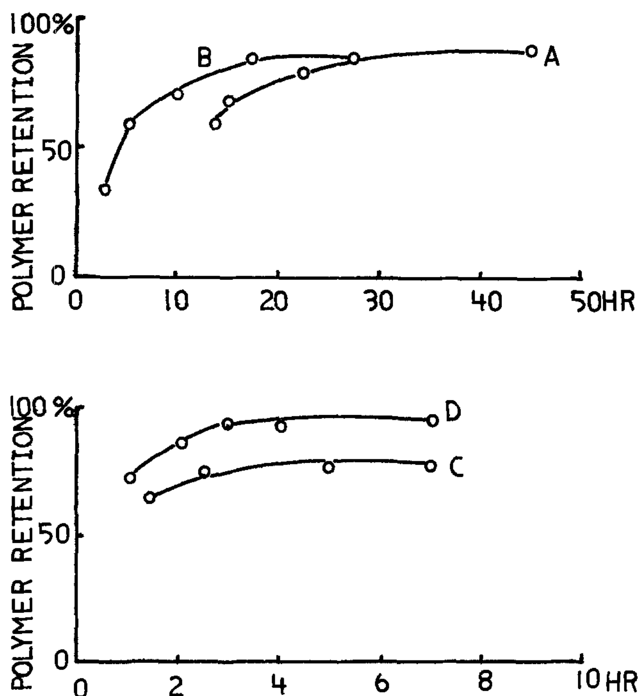

Fig. 2. Thermal crosslinking of cyclized polyisoprene in air as observed in terms of percent polymer retention on development with benzene for 3 min. A = 82°C, 0% bisazide, 1.0 μm coating on Si; B = 90°C, 0% bisazide, 1.0 μm coating on Si; C = 100°C, 0% bisazide, 1.0 μm coating on Si; D = 100°C, 3% bisazide, 1.2 μm coating on Si.

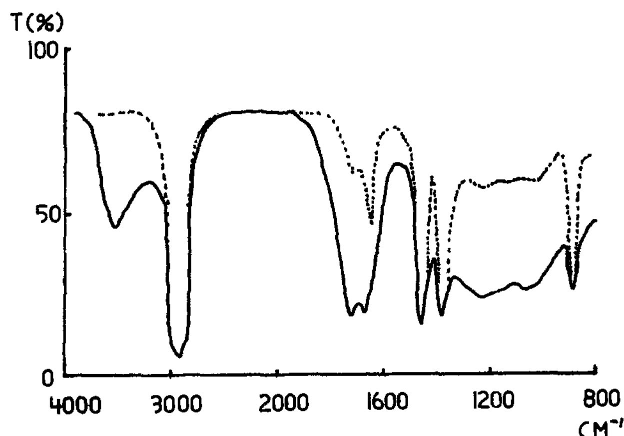

Fig. 3. *IR* spectra of cyclized polyisoprene film on NaCl. ——— 100°C, in air, 24 hr; - - - - - control, no thermal treatment.

The crosslinking of cyclized polyisoprene also proceeds in vacuum, though at a slower rate than in air.[2] This crosslinking can be attributed to the small amount of residual catalyst for the cyclization (p-toluene sulfonic acid), which might initiate the intermolecular reaction analogous to the intramolecular cyclization (10). The crosslinking in vacuum can be reduced to one-fourth by washing the polymer solution (15% in xylene) in 0.1*N* NaOH aqueous solution for 3 hr.

There is also a report that polycyclized polyisoprene is formed when polyisoprene is heated in vacuum between 200° and 300°C (6). This polycyclized polyisoprene shows no vinylidene absorption like that which is observed in partially cyclized polyisoprene (7). The *IR* spectra of our films of cyclized polyisoprene show no decrease of the vinylidene absorption (875 cm^{-1}) after heating in vacuum at 110°C for 72 hr, indicating no further intramolecular cyclization around this temperature.

Thermal decomposition of bisazide in photoresists.—Figure 4 shows the plot of the logarithm of *IR* azido absorbance *vs.* time of heating in air. The decrease of azido absorbance shows a retardation as the thermal reaction proceeds somewhat similar to that observed in the photoreaction (8).

Making several coatings with different azide concentrations, we compared azide decomposition characteristics between thermal and photoreaction. In Fig. 5A, two coatings (I *vs.* II) with different azide concentration show different retardation characteristics upon exposure. Films coated with higher azide concentration show more retardation because of greater generation of bis-amine (reacted bisazide) which works as an energy acceptor for photoexcited bisazide and lowers the quantum yield of bisazide photodecomposition. In thermal reaction (Fig. 5B), two coatings at different azide concentrations showed the same characteristic retardation curve (I *vs.* II), in great contrast with the photoreaction. It can be concluded immediately that the energy transfer, characteristic of the photoreaction, is not operating in the thermal decomposition retardation.

We made extended observations on the retardation of bisazide decomposition at 90° and 100°C in air and compared these with the data on oxidative polymerization of cyclized polyisoprene. At 90°C, the retardation of azide decomposition becomes constant on the log (absorbance) *vs.* time plot after 17 hr (Fig. 6A), a

[2] We estimate that the reaction rate of normal, unwashed polymer for crosslinking in vacuum is about one-fifth the rate for oxidative crosslinking in air. The measurement was difficult to perform in vacuum since the oven developed thermal gradients in the absence of a circulating atmosphere, and film temperature was poorly controlled.

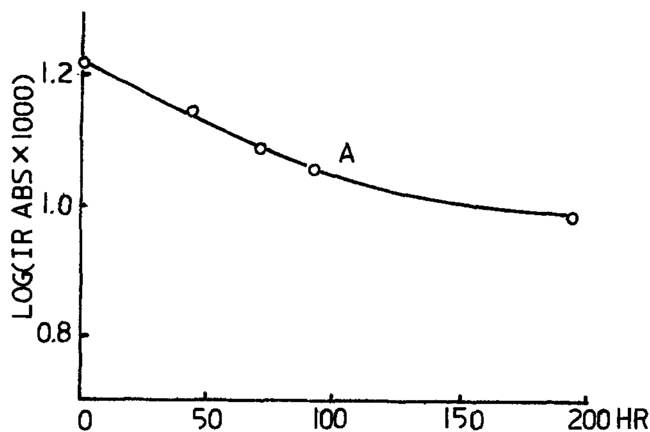

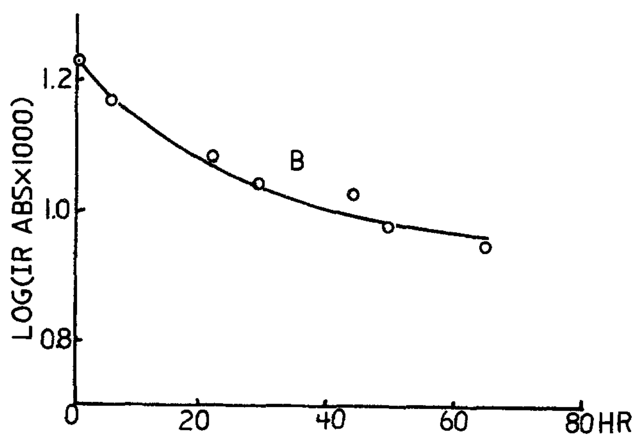

Fig. 4. Thermal decomposition characteristics of bisazide in photoresists. Photoresist = 3% bisazide, 1.2 μm coating on Si. A = 60°C in air; B = 80°C in air. The infrared absorbance is observed at 2110 cm^{-1}, the well-isolated and sharp band of the bisazide.

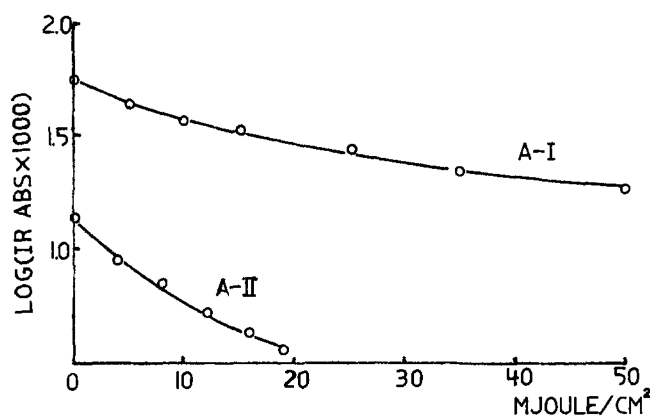

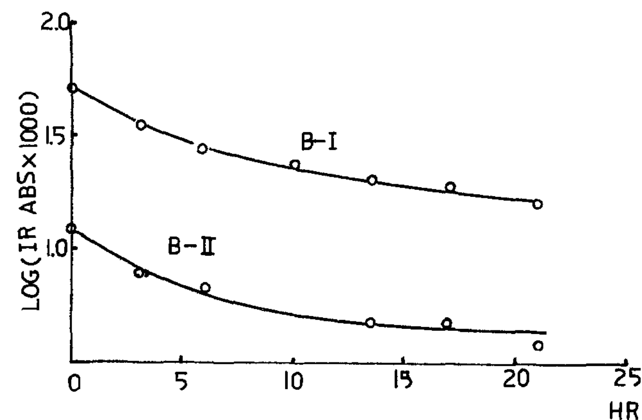

Fig. 5. Comparison of the concentration dependence of photo and thermal decomposition of bisazide in photoresists. A:photoreaction at 365 nm at 25°C, 5.0 mJ/cm^2 min; B:thermal reaction at 100°C in air; I:4.6% bisazide, 2.7 μm coating on Si; II:0.9% bisazide, 2.7 μm coating on Si.

time corresponding to the time when the percentage of polymer retention after development reaches its saturation value (Fig. 2B). This same correlation can also be observed at 100°C after 3 hr by comparing the retardation of azide decomposition in Fig. 6B with the oxidative crosslinking in Fig. 2C.

Thus this retardation can well be explained by the cage effect of crosslinked polyisoprene. The cage effect is an inhibition of a dissociation reaction by a relatively rigid solvent or polymer medium which prevents that degree of nuclear motion necessary to accomplish bondbreaking. It is a familiar effect in studies of photodissociation in glassy matrixes. Crosslinking makes the polymer matrix more rigid and does seem to make the thermal decomposition of bisazide increasingly difficult.

Activation energy of thermal reactions.—By assuming that the same amount of thermal and photodecomposition of bisazide produce the same amount of bisamine crosslinks we can compare the crosslinking reaction rates by bisazide decomposition and oxidative polymerization.

Figure 1-B shows that 48% bisazide photodecomposition causes 60% (after development) polymer retention when the azide concentration is 3% based on polymer. Oxidative thermal polymerization of cyclized polyisoprene can be neglected at room temperature over the elapsed time of the experiment. From the initial slope of thermal decomposition of bisazide in Fig. 4 and 6 we can obtain the reaction times that are required for 48% decomposition of bisazide.

The corresponding time for 60% polymer retention (after development) by oxidative polymerization of azide-free polyisoprene can also be obtained from Fig. 2.

The reciprocals of these times for 60% retention of polymer can be interpreted as solid-state reaction rate constants, and by plotting the logarithm of rate constants *vs.* (1) temperature we obtain the activation energies of bisazide decomposition and oxidative self-polymerization of cyclized polyisoprene. In Fig. 7 the two reaction rate constants cross around 65°C, indicating that oxidative crosslinking causes more "thermal fog" than bisazide decomposition at the normal prebaking temperature (80°C) and at the normal azide concentration (3%).

The activation energy of bisazide decomposition is 23 kcal/mole, whereas that of oxidative self-polymerization is 32 kcal/mole.[3] The activation energy of bisazide looks very low, but it is in accord with the previous work (9) on substituted 2-azidobiphenyls whose activation energies can be as low as 25.5 kcal/mole when the azido group is conjugated with various electron donating groups in para-position. This low activation energy is presumed to be the energy for rupture of a single azide bond. (If two groups could be broken directly with 23 kcal of energy, a gross instability of the bisazide molecule would be implied.) This low value can also be used indirectly to support the observed single photon simultaneous cleavage of bisazide molecules (8). The input of 80 kcal of optical energy plus the actual exothermal bond-breaking of the first azido group can be considered as producing an energy-rich azidonitrene whose azide group is cleaved before vibrational deactivation can occur. Our photochemi-

[3] This oxidation crosslinking also includes the slower nonoxidative acid crosslinking mentioned above. Measured activation energies for the nonoxidative crosslinking fluctuated between 27 and 35 kcal/mole because of the difficulty of maintaining precise temperature control in vacuum. Since this is a minority reaction with an activation energy comparable to the oxidative crosslinking reaction, no correction was introduced in determining the energy of 32 kcal. Any such correction should have a trivial effect.

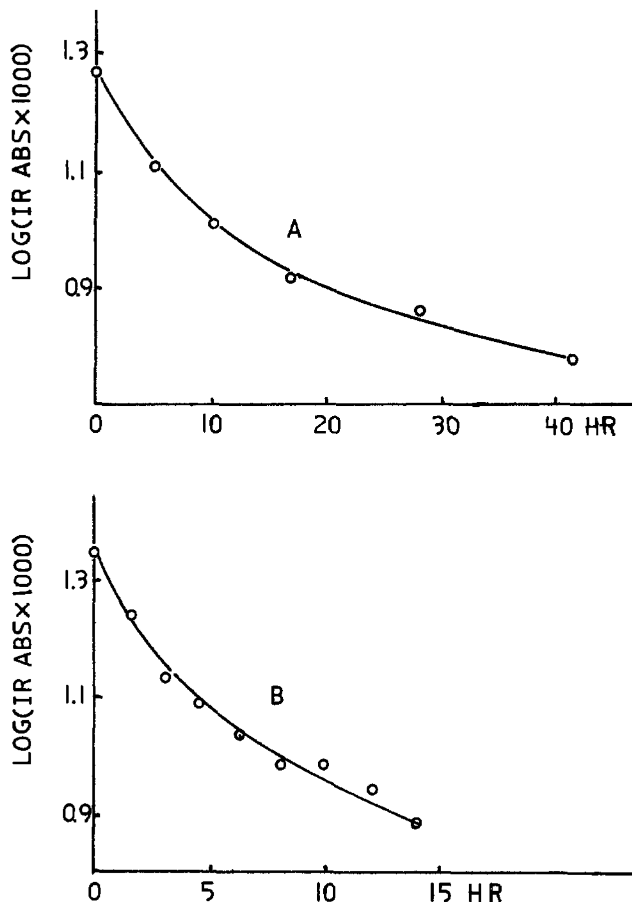

Fig. 6. Thermal decomposition characteristics of bisazide in photoresist showing retardation of the reaction as crosslinking becomes extensive:compare with Fig. 2. Photoresist:3% bisazide, 1.2 μm coating on Si. A:90°C in air; B:100°C in air.

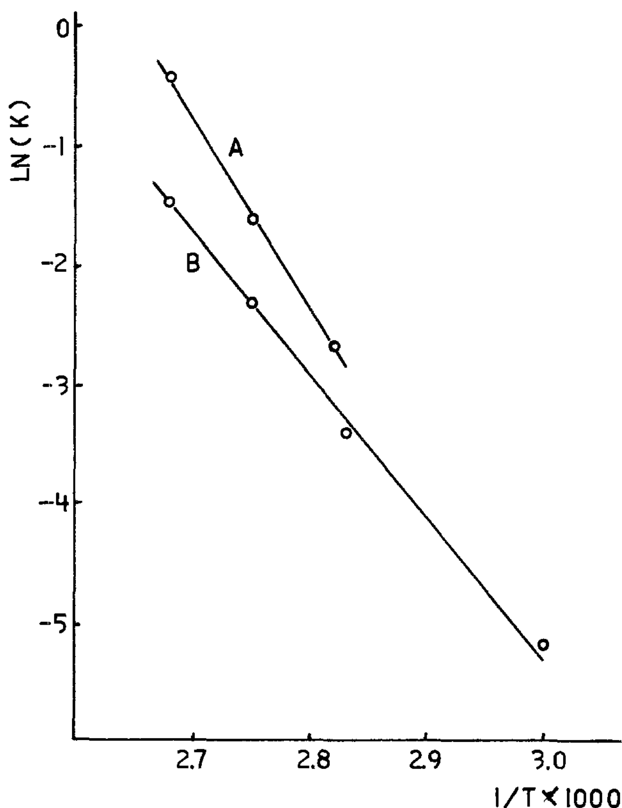

Fig. 7. Thermal reaction rate constants as calculated from reciprocal times for retention of 60% of polymer film on development. A:oxidative polymerization of cyclized polyisoprene; B:bisazide decomposition.

cally inclined friends all seem to be uneasy with the concept of a truly simultaneous cleavage, but are quite at home with a triggered second cleavage which is experimentally indistinguishable from a simultaneous bisazide photochemical cleavage (8).

We conducted further studies of the thermal decomposition mechanism of bisazide to confirm whether both azido groups decompose in concert or stepwisely. However, the self-crosslinking of cyclized polyisoprene made the extraction of low molecular weight azido compound much more difficult (8) and we could not obtain a clear answer. *IR* azido absorption (2110 cm^{-1}) showed no shift in the course of thermal decomposition of bisazide and we find no information supporting the stepwise mechanism.

Experimental

The same materials and chemicals (photoresist, Si wafer), the same analytical methods (*IR* expansion, u.v. specular reflectance) and the same exposing apparatus (Hg lamp, filter, photomultiplier) were used as the previous work (8). Thermal reaction was conducted in a steel box (11 × 14.5 × 20 cm) with heater (300W), fan, wafer holder, quartz window, and thermistor (Yellow Spring Company, Model-621). By combining thermistor controller (Yellow Spring Company, Model-63RC) and variac, precise temperature control (± 0.1°C) was obtained.

Two methods of optical thickness gauging were used. The first was measurement of the interference fringes of the cast film on the Si wafer, as measured in a Cary Model 14 spectrophotometer with integrating sphere attachment operating in the total reflectance mode. With the peak reflection wavelengths converted to reciprocal wavelengths (cm^{-1}), successive interference maxima are separated by $\Delta\tilde{\nu} = (2nt)^{-1}$ where n is the refractive index of the film and t is the thickness in centimeters. The refractive index of partially cyclized polyisoprene was taken to be 1.541 for this measurement. Reflectance maxima should be measured at the longest convenient wavelengths to minimize errors from optical phase shifts at the silicon surface. These same interference maxima can be observed from films coated on NaCl, though with much reduced amplitude.

The reflectance method was used to calibrate the intensity of the CH absorption as measured by the Perkin-Elmer Model 521 spectrometer at a frequency of 2929 cm^{-1}. The attenuation constant obtained was $k = 1.18 \cdot 10^3$ cm^{-1} from the equation $\log_{10}(I_o/I) = kt$. Note that this value is subject to change as polyisoprenes of different cyclicity are examined. When the polymer film has been coated on a silicon wafer, a zero-absorption baseline must be constructed between 3300 and 2500 cm^{-1} to compensate for the low transmission of silicon in the near infrared. Routine thickness measurements were made by the infrared method, and are considered accurate to ±3% relative, to ±5% absolute.

Conclusion

From the *IR* study on the thermal reaction of bisazide-cyclized polyisoprene photoresist, we obtained the following conclusions.

1. Two major kinds of thermal reaction are observed in this photoresist, one is oxidative self-polymerization of cyclized polyisoprene and the other is the expected bisazide reaction.

2. The activation energies of these two reactions are 32 and 23 kcal/mole, respectively, and at the prebaking conditions of photoresist preparation, oxidative crosslinking predominates over bisazide crosslinking.

3. The thermal decomposition reaction of bisazide is retarded in the later stage of reaction, and this can be explained as a cage effect of crosslinked polyisoprene.

Acknowledgment

The author would like to thank Dr. George R. Bird for many helpful suggestions and discussions.

Manuscript submitted May 23, 1977; revised manuscript received March 10, 1978.

Any discussion of this paper will appear in a Discussion Section to be published in the June 1979 JOURNAL. All discussions for the June 1979 Discussion Section should be submitted by Feb. 1, 1979.

REFERENCES

1. W. D. Pandolfe and G. R. Bird, "Unconventional Photographic Systems Symposium," p. 19 SPSE, Washington, D.C. (1975).
2. W. DeForest, "Photoresist," p. 102, McGraw Hill, New York (1976).
3. H. Nakane, "4th Symposium on Semiconductor and IC Processing," p. 50, April 19-20, Tokyo (1973).
4. N. J. Clecak, R. J. Cox, and W. M. Moreau, *Polym. Sci. Eng.*, **14**, 491 (1974).
5. H. F. Mark, N. G. Gaylord, and N. M. Bikales, "Encyclopedia of Polymer Science and Technology," Vol. 7, p. 838 Wiley-Interscience, New York (1964).
6. H. Staudinger and E. Geiger, *Helv. Chem. Acta.*, **9**, 549 (1926).
7. R. K. Agnihotri, D. Falcon, and E. C. Fredericks, *J. Polym. Sci., Part A-1*, **10**, 183 (1972).
8. S. Shimizu and G. R. Bird, *This Journal*, **124**, 1394 (1977).
9. P. A. Smith and J. H. Hall, *J. Am. Chem. Soc.*, **84**, 480 (1962).
10. R. K. Agnihotri, D. L. Falcon, F. P. Hood, L. G. Lesoine, C. D. Needham, and J. A. Offenbach, *Photo. Sci. Eng.*, **16**, 443 (1972).

Luminescence of Rare Earth-Activated Tellurate Perovskites

R. R. Neurgaonkar,* L. E. Cross, and William B. White*

Materials Research Laboratory, The Pennsylvania State University, University Park, Pennsylvania 16802

ABSTRACT

$M_2^{2+}R^{2+}TeO_6$, where M^{2+} = Ba, Sr, Ca, or Cd and R^{2+} = Ba, Sr, Ca, Cd, Mg, or Zn, crystallize with ordered (Fm3m) or ordered-distorted ($P2_1$) perovskite structures, and can be used as hosts for rare earth activated luminescence. Rare earths (Ln^{3+}) were introduced according to the substitution $2R^{2+} \rightarrow Ln^{3+} + Na^+$, $Ln^{3+} = Eu^{3+}, Tb^{3+}, Dy^{3+}$, or Er^{3+}. The Eu^{3+} emission depends strongly on the ordering of the perovskite structure. The $^5D_0 \rightarrow {}^7F_1$ transition is dominant when Eu^{3+} occupies a site with symmetry O_h in the Fm3m ordered perovskite, whereas the Eu^{3+} emission is the $^5D_0 \rightarrow {}^7F_2$ transition in the ordered-distorted perovskite structure. Only Ca_2MgTeO_6 is an effective host for Tb^{3+}-, Dy^{3+}-, and Er^{3+}-activated luminescence.

The first report of the substitution of Te^{6+} in perovskite was by Merz (1) in 1956. He synthesized Ba_3TeO_6 and Sr_3TeO_6 and reported that they are isotypic with Ba_3UO_6. Subsequently, Bayer (2-5) prepared the Te^{6+}-containing $M_2^{2+}R^{2+}TeO_6$ compounds where M = Ba, Pb, or Sr and R = Mg, Cd, Ca, etc., and it was he who put forward the idea that some of these compounds are ferroelectrics. Sleight and Ward (6) also reported the synthesis of Ba_2CaTeO_6 and Ba_2MgTeO_6 types of perovskites. More recently, Politova and Venevstev (7) reinvestigated the crystal structure and dielectric properties of the Te^{6+}-containing perovskite compounds with compositions $M_2^{2+}R^{2+}TeO_6$, $(M^{3+}M^{2+})R^+TeO_6$, and $(M^{1+}M^{3+})R^{2+}TeO_6$, where M^{2+} = Ba, Pb, Sr, Ca, or Cd, M^{3+} = Bi or La, M^{1+} = Na, R^+ = Na or Li, R^{2+} = Mn, Mg, Co, Zn, Cd, or Ca. Their investigations show that all of these compounds belong either to ordered (Fm3m) or ordered-distorted ($P2_1$) perovskite structures. Further, they confirmed that most of these compounds exhibit phase transitions at high temperatures, some of which have large dielectric anomalies.

Blasse and Bril (8) reported the luminescence of tungsten-activated tellurates. Corsmit *et al.* (9) also used the vibrational spectra to characterize the ordering schemes in these compounds.

This paper reports on the fluorescence of Eu^{3+}-, Tb^{3+}-, Dy^{3+}-, and Er^{3+}-activated $M_2^{2+}R^{2+}TeO_6$, where M = Ba, Sr, Ca, or Cd and R = Ba, Sr, Ca, Cd, Zn, or Mg. The objective is to examine the effects of the two ordering schemes on the luminescent emission of rare earth ions, especially Eu^{3+}.

Experimental

The rare earth activated $M_2^{2+}R^{2+}TeO_6$ compounds were prepared by solid-state reactions as described by Bayer (2). Compositions were first fired in air at 800°C to oxidize the tellurium to Te^{6+}. To avoid tellurium loss, the final firings were made in sealed silica tubes at 1000°-1150°C. Each preparation was checked for phase identification and phase purity by x-ray powder diffraction methods. In all cases the powder patterns were in good agreement with the literature (1-7).

The luminescent emission spectra were measured using powder plaques excited by the 253.7 nm line of a 150W mercury lamp. The emission spectrometer was a 1m Jarrell-Ash scanning monochromator with an RCA 31034 photomultiplier cooled to −40°C. The photomultiplier has a fairly flat response over the spectral range examined and no corrections for photomultiplier response were made. The spectra that appear in the figures are direct tracings from strip-chart records of the photomultiplier current. Spectrometer slit widths were in the range of 30-60 μm.

Several exceptions to the findings reported in the literature were uncovered in the course of synthesis of the phosphors. Sr_2MgTeO_6 has been reported to crystallize in space group Fm3m. The results of the present work showed that the attempted synthesis of this compound with or without Eu^{3+} and Na^+ resulted in a mixture of two phases. There is some disagreement over the structure of Sr_3TeO_6 with earlier literature (1, 10, 11) assigning it to space group $P2_1$, whereas a recent paper by Politova and Venevtsev (7) claims it belongs to Fm3m. The results of the present x-ray analysis indicate that Sr_3TeO_6 with or without Eu^{3+} + Na^+ prepared at 1100°C could only be indexed on space group $P2_1$.

Complete replacement of the octahedral cation by a combination of Eu^{3+} + Na^+ was successful in $M_2^{2+}R^{2+}TeO_6$, M = Ba or Sr. Both the $Ba_2[Eu_{.50}Na_{.60}]TeO_6$ and $Sr_2[Eu_{.50}Na_{.50}]TeO_6$ phases crystallized in the space group Fm3m.

* Electrochemical Society Active Member.

Key words: luminescence, rare earths, europium, perovskite structure, tellurates, ordered structures.

Table I. Luminescence of Eu^{3+} in $M_2^{2+}R^{2+}TeO_6$

Composition	Space group	Luminescence	Relative intensity $^5D_0 \rightarrow {}^7F_2$	Relative intensity $^5D_0 \rightarrow {}^7F_1$
$Ba_2Mg_{1-2x}Eu_xNa_xTeO_6$	Fm3m	Orange (M)	1.5	10
$Ba_2Ca_{1-2x}Eu_xNa_xTeO_6$	Fm3m	Orange (M)	1.5	10
$Ba_2Eu_{.50}Na_{.50}TeO_6$	Fm3m	Orange (MS)	3	10
$Sr_2Ca_{1-2x}Eu_xNa_xTeO_6$	Fm3m	Orange (S)	2	10
$Sr_2Eu_{.50}Na_{.50}TeO_6$	Fm3m	Orange (S)	3.5	10
$Ba_2Ba_{1-2x}Eu_xNa_xTeO_6$	$P2_1$	Red (M)	10	6
$Sr_2Sr_{1-2x}Eu_xNa_xTeO_6$	$P2_1$	Red (M)	10	2.5
$Ca_2Ca_{1-2x}Eu_xNa_xTeO_6$	$P2_1$	Red (S)	10	2
$Cd_2Cd_{1-2x}Eu_xNa_xTeO_6$	$P2_1$	Red (S)	10	2
$Sr_2Zn_{1-2x}Eu_xNa_xTeO_6$	$P2_1$	Red (M)	10	4
$Ca_2Mg_{1-2x}Eu_xNa_xTeO_6$	$P2_1$	Red (VS)	10	1.5
$Cd_2Mg_{1-2x}Eu_xNa_xTeO_6$	$P2_1$	Red (S)	10	1.5

$x \rightarrow$ 1-10 m/o, M = medium, MS = medium strong, S = strong, VS = very strong.

Luminescence of Eu^{3+}-Activated Phosphors

The $M_2^{2+}R^{2+}TeO_6:Eu^{3+}$ compounds are luminescent under 253.7 nm excitation. Both Fm3m and $P2_1$ forms are luminescent, but with considerable differences in luminescence behavior. The results for the compounds investigated are summarized in Table I.

Figure 1 shows spectral energy distribution of the emission of Eu^{3+}-activated $Ba_2R^{2+}TeO_6$ (R = Ca or Mg) and Sr_2CaTeO_6. The spectra of Eu^{3+} contain lines which can be attributed to the transitions $^5D_0 \rightarrow {}^7F_J$, where J = 0, 1, 2, 3, and 4. The $^5D_0 \rightarrow {}^7F_1$ magnetic dipole transition is unsplit and very intense. The transitions corresponding to $^5D_0 \rightarrow {}^7F_4$, $^5D_0 \rightarrow {}^7F_3$, $^5D_0 \rightarrow {}^7F_2$, and $^5D_0 \rightarrow {}^7F_0$ are all weak and broad.

The spectral energy distributions of Eu^{3+} in $Sr_2[Eu_{0.5}Na_{0.5}]TeO_6$ and $Ba_2[Eu_{0.5}Na_{0.5}]TeO_6$ are given in Fig. 2. It can be seen that the magnetic dipole transition is dominant for both the phases.

The spectra of the ordered-distorted perovskite structures are entirely different from the spectra of the ordered compounds. The spectral energy distribution of the emission of $M_3^{2+}TeO_6:Eu^{3+}$ (M = Ba, Sr or Ca), $M_2^{2+}MgTeO_6:Eu^{3+}$ (M = Ca or Cd) and

Fig. 1. Emission spectra of Eu^{3+} in $Ba_2R^{2+}TeO_6$ (R = Ca or Mg) and Sr_2CaTeO_6.

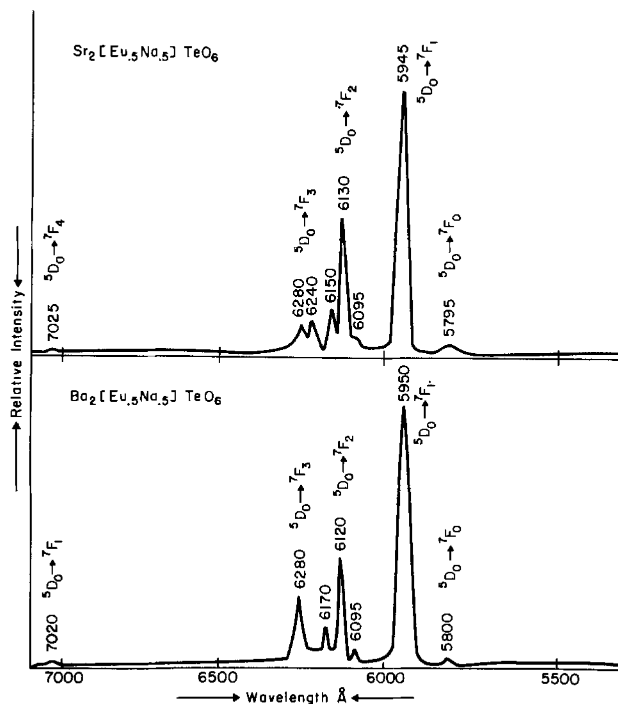

Fig. 2. Emission spectra of Eu^{3+} in $M_2^{2+}[Eu_{0.5}Na_{0.5}]TeO_6$. M = Ba or Sr.

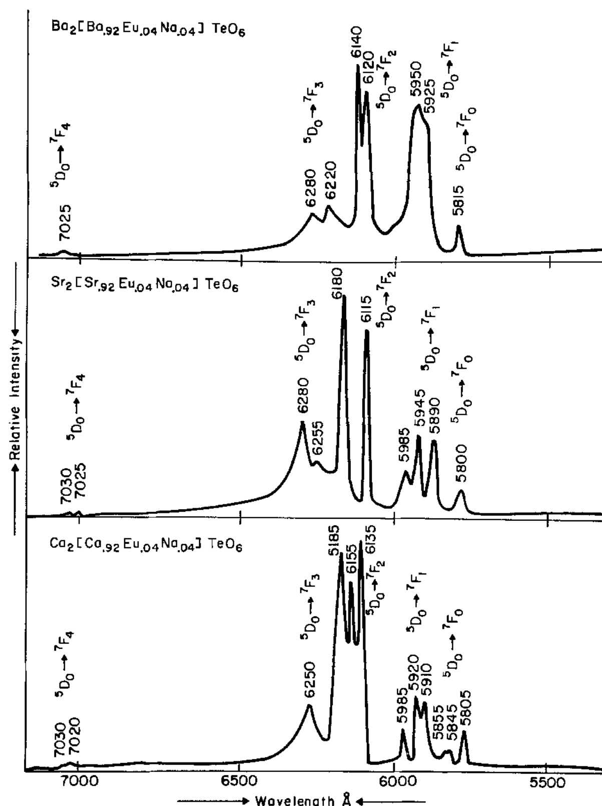

Fig. 3. Emission spectra of Eu^{3+} in $M_3^{2+}TeO_6$. M = Ba, Sr, or Ca.

$Sr_2ZnTeO_6:Eu^{3+}$ are given in Fig. 3 and 4. Since emission spectra of $Ca_3TeO_6:Eu^{3+}$ and $Cd_3TeO_6:Eu^{3+}$ are similar, no separate figure is given for the latter compound. The strong Eu^{3+} emission that appears from all compounds is the forced electric dipole transition $^5D_0 \rightarrow {}^7F_2$ as expected from the distorted structure. The transitions $^5D_0 \rightarrow {}^7F_4$, $^5D_0 \rightarrow {}^7F_3$, and $^5D_0 \rightarrow {}^7F_0$ are weak in both the systems and are not affected by the changes in crystal symmetry.

The spectroscopic results confirm the x-ray findings concerning the structure of Sr_3TeO_6. The similarity of the Eu^{3+} emission in this host to that of the other

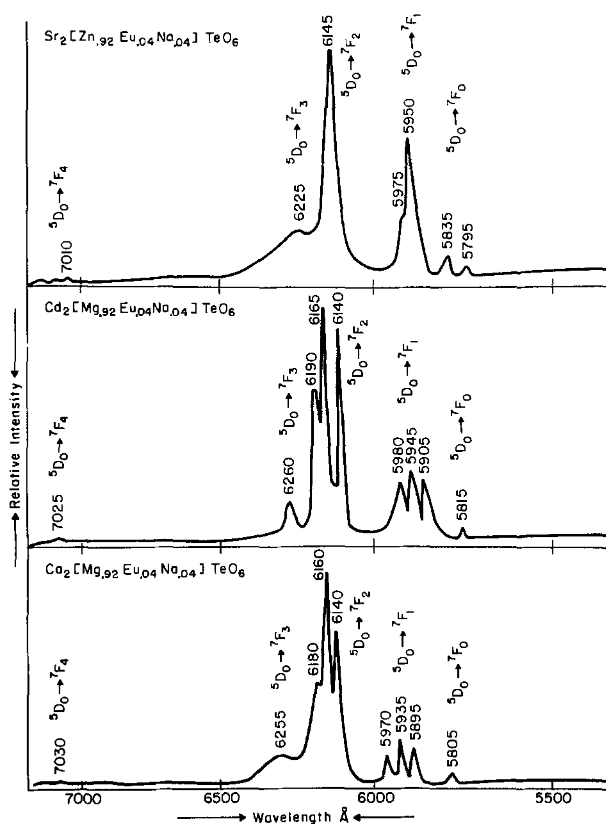

Fig. 4. Emission spectra of Eu^{3+} in $M_2^{2+}MgTeO_6$ and Sr_2ZnTeO_6. M = Ca or Cd.

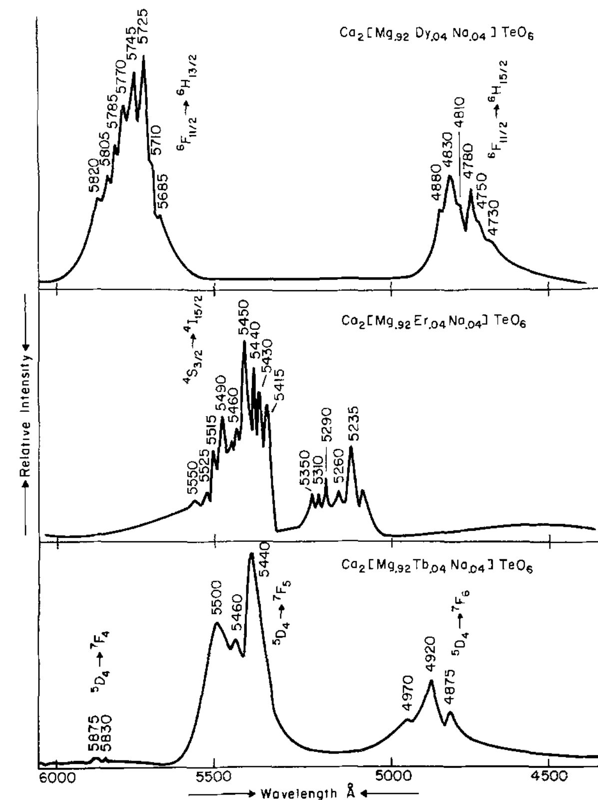

Fig. 5. Emission spectra of Tb^{3+}, Dy^{3+}, and Er^{3+} in Ca_2MgTeO_6.

ordered-distorted perovskites leaves little doubt that the space group is $P2_1$ rather than Fm3m.

Luminescence from Other Rare Earth Activators

Table II summarizes compositions and luminescence color for Tb^{3+}-, Dy^{3+}-, and Er^{3+}-activated $M_2^{2+}R^{2+}TeO_6$ (M^{2+} = Ba^{2+}, Sr^{2+}, Cd^{2+} or Ca; R^{2+} = Mg^{2+} or Ca^{2+}). The Dy^{3+}- and Er^{3+}-activated phases showed luminescence under 365 nm excitation.

Ca_2MgTeO_6 was found to be the only effective host for Tb^{3+}-, Dy^{3+}-, and Er^{3+}-activated luminescence. Dy^{3+}-activated Cd_2MgTeO_6 showed typical yellow luminescence. Although a very feeble green luminescence was noted for Tb^{3+}- or Er^{3+}-activated Sr_2CaTeO_6, the compounds belonging to the space group Fm3m do not exhibit intense luminescence when activated with Tb^{3+}, Dy^{3+}, or Er^{3+}.

Figure 5 shows the spectral energy distribution of Tb^{3+}-, Er^{3+}-, and Dy^{3+}-activated Ca_2MgTeO_6. The Tb^{3+} spectra consist of the transitions $^5D_4 \rightarrow {}^7F_J$, J = 6, 5, 4, and 3. The transition $^5D_4 \rightarrow {}^7F_5$ is stronger, while $^5D_4 \rightarrow {}^7F_6$, $^5D_4 \rightarrow {}^7F_4$, and $^5D_4 \rightarrow {}^7F_3$ transitions are weak. The transition $^5D_4 \rightarrow {}^7F_3$ is not shown in Fig. 5 since it is very weak and can be seen only at much higher sensitivity settings of the spectrometer. The Dy^{3+} spectra arise from the two transitions corresponding to $^6F_{11/2} \rightarrow {}^6H_{13/2}$ and $^6F_{11/2} \rightarrow {}^6H_{15/2}$. The Er^{3+} luminescence spectra appear in the green region. All lines indicated in the region 5400-5550Å were identified as the transition from $^4S_{3/2} \rightarrow {}^4I_{15/2}$. Ozawa (12) also noted similar spectra for Er^{3+}-activated $BaYb_2F_8$ under infrared excitation.

Table II. Luminescence of Tb^{3+}, Dy^{3+}, and Er^{3+} in $M_2^{2+}R^{2+}TeO_6$

Composition	Space group	Luminescence	Main emission peak
$Ba_2Ca_{1-2x}Tb_xNa_xTeO_6$	Fm3m	No luminescence	—
$Ba_2Ca_{1-2x}Dy_xNa_xTeO_6$	Fm3m	No luminescence	—
$Ba_2Ca_{1-2x}Er_xNa_xTeO_6$	Fm3m	No luminescence	—
$Sr_2Ca_{1-2x}Tb_xNa_xTeO_6$	Fm3m	Green (VW)	—
$Sr_2Ca_{1-2x}Dy_xNa_xTeO_6$	Fm3m	No luminescence	—
$Sr_2Ca_{1-2x}Er_xNa_xTeO_6$	Fm3m	Green (VW)	—
$Ca_2Mg_{1-2x}Tb_xNa_xTeO_6$	$P2_1$	Green (M)	$^5D_4 \rightarrow {}^7F_5$
$Ca_2Mg_{1-2x}Dy_xNa_xTeO_6$	$P2_1$	Yellow (S)	$^6F_{11/2} \rightarrow {}^6H_{13/2}$
$Ca_2Mg_{1-2x}Er_xNa_xTeO_6$	$P2_1$	Green (M)	$^4S_{3/2} \rightarrow {}^4I_{15/2}$
$Cd_2Mg_{1-2x}Tb_xNa_xTeO_6$	$P2_1$	No luminescence	—
$Cd_2Mg_{1-2x}Dy_xNa_xTeO_6$	$P2_1$	Yellow (M)	$^6H_{11/2} \rightarrow {}^6H_{15/2}$
$Cd_2Mg_{1-2x}Er_xNa_xTeO_6$	$P2_1$	No luminescence	—

x = 1-10 m/o, VW = very weak, M = medium, S = strong.

Discussion and Conclusions

The discussion that follows deals with the Eu^{3+}-activated compounds, since only for these phosphors are systematic data available.

The cubic compounds are a superstructure built on the perovskite structure by the ordering of the octahedral cations. As a result of the ordering, the point symmetry of the 12-fold coordinated cations becomes $\bar{4}3m$. Although the 12 nearest-neighbor anions still form a symmetric array, the next-nearest neighbor cations are alternately Te^{6+} and the R^{2+} cation. The resulting configuration is that of two interpenetrating cation tetrahedra, and the center of symmetry is lost on the 12-fold site. The octahedral site retains symmetry m3m and thus is strictly centrosymmetric both with respect to the anion octahedron and with respect to the array of M^{2+} next-nearest-neighbor cations. The spectra of Eu^{3+} in these structures is dominated by the magnetic dipole line which usually appears only when Eu^{3+} occupies a centrosymmetric site. It can be concluded, therefore, that the Eu^{3+} activator enters these structures preferentially on the octahedral site. The relative intensities of the $^7F_1$ and $^7F_2$ transitions are known to be hypersensitive to the environment of the Eu^{3+} ion (13). The possibility that Eu^{3+} might be on the 12-fold site and exhibit only the $^7F_1$ magnetic dipole line because of the regular oxygen array can be excluded by the observations of Blasse (14) who showed that the next-nearest-neighbor cation symmetry also profoundly affects the relative intensities when the cations have large differences in charge.

Substitution of the rare earths in the six fold coordinated site of $Ba_2R^{3+}M^{5+}O_6$, R = rare-earths, M = Nb, Ta, Re, etc., ordered perovskite structure is known

and reported by several workers (15-18). Blasse *et al.* (19) also reported the magnetic dipole transition for Eu^{3+}-activated Ba_2GdNbO_6 ordered perovskite phase, indicating that Eu^{3+} replaces the octahedrally coordinated Gd^{3+} ion. The line corresponding to the transition $^5D_0 \rightarrow {}^7F_1$ does not split in Oh symmetry. The results of the present investigation are in excellent agreement with earlier findings.

The spectra of the monoclinic structures are more diverse than the cubic structures. In all compounds the forced electric dipole transition is dominant. In four of the compounds, Sr_3TeO_6, Ca_3TeO_6, Ca_2MgTeO_6, and Cd_2MgTeO_6, the $^7F_2$ level appears as a cluster of sharp crystal field lines. The $^7F_1$ level is separated into three components, the maximum that may appear. Detailed structure determinations are not available for the tellurate compounds, but the octahedral site in the isostructural alkaline earth uranates (10) is known to be quite distorted. In Ba_3TeO_6 the magnetic dipole line is much stronger in proportion to the other compounds and appears as a broad band. The monoclinic structures were originally described as pseudocubic and the barium compound is perhaps more nearly isometric than the others. In two of the compounds, Ca_3TeO_6 and Sr_2ZnTeO_6, the nondegenerate $^7F_0$ line appears in at least two components. This can only be accounted for if Eu^{3+} appears on more than one site in these structures. Finally, the emission spectrum of Sr_2ZnTeO_6 is distinctly different from the other compounds. The separation of the crystal field levels is much smaller, and the individual J-multiplets appear as roughly single rather broad lines. It is tempting to argue that Eu^{3+} is partitioned onto the 12-fold site in this structure with the intensity of the forced electric dipole line derived from distortion of the site.

These phosphors provide a useful demonstration of the importance of next-nearest-neighbor effects and the effects of structural order on luminescence behavior. They also show that the Eu^{3+} ion shows a pronounced site preference for 6 coordinated sites in these structures.

Acknowledgments

This research was supported by the National Science Foundation under Grant No. DMR74-00340.

Manuscript submitted Feb. 22, 1977; revised manuscript received Feb. 22, 1978.

Any discussion of this paper will appear in a Discussion Section to be published in the June 1979 JOURNAL. All discussions for the June 1979 Discussion Section should be submitted by Feb. 1, 1979.

Publication costs of this article were assisted by The Pennsylvania State University.

REFERENCES

1. G. Merz, Dissertation, Technische Hochschule Karlsruhe, Germany (1956).
2. G. Bayer, *J. Am. Ceram. Soc.*, **46**, 604 (1963).
3. G. Bayer, U.S. Pat. 3,309,168 (1967).
4. G. Bayer, U.S. Pat. 3,309,169 (1967).
5. G. Bayer, *Fortschr. Miner.*, **46**, 41 (1969).
6. A. W. Sleight and R. Ward, *Inorg. Chem.*, **3**, 292 (1964).
7. E. D. Politova and Y.u. N. Venevtsev, *Mater. Res. Bull.*, **10**, 319 (1975).
8. G. Blasse and A. Bril, *J. Solid State Chem.*, **2**, 291 (1970).
9. A. F. Corsmit, H. E. Hoefdraad, and G. Blasse, *J. Inorg. Nucl. Chem.*, **34**, 3401 (1972).
10. H. M. Rietveld, *Acta Cryst.*, **20**, 508 (1966).
11. J. A. Balio and S. Natansonhn, *J. Appl. Crystallogr.*, **2**, 252 (1969).
12. L. Ozawa, *This Journal*, **119**, 1783 (1973).
13. G. Blasse, *Chem. Phys. Lett.*, **20**, 573 (1973).
14. G. Blasse, A. Bril, and W. C. Nieuwpoort, *J. Phys. Chem. Solids*, **27**, 1587 (1966).
15. C. Keller, *J. Inorg. Nucl. Chem.*, **27**, 321 (1965).
16. F. Galasso and W. Darby, *J. Phys. Chem.*, **66**, 131 (1962).
17. L. Brixner, *J. Inorg. Nucl. Chem.*, **15**, 352 (1966).
18. F. Galasso, G. Layden, and D. Flinchbaugh, *J. Chem. Phys.*, **44**, 2703 (1966).
19. G. Blasse, "Proceedings of the International Conference on Luminescence," Akadamiai Kiado, Budapest (1968); 1647-1650 (1966).

Investigation of Luminescence in Ge-Doped Sodalite Powders

Lee T. Todd, Jr.

Department of Electrical Engineering, University of Kentucky, Lexington, Kentucky 40506

ABSTRACT

A new class of cathodochromic materials, germanium-doped sodalite: Br, are described. They exhibit both a bright luminescence at room temperature and a long lifetime, high contrast coloration mode. The effect of hydrogen annealing on the initial reflectance, luminescent intensity, and FB location are studied. The FB energy is shown to initially increase with increasing germanium concentration up to 9% and then to decrease with higher germanium concentration. A technique is outlined for determining the luminescence generated within a powdered sample that possesses an absorption band. This technique is used to determine the effect of electron beam coloration on the luminescent centers. It is shown that the formation of thermally erasable F centers quenches luminescent centers while the formation of optically erasable F centers does not.

The coloration properties of sodalite and the luminescent properties of doped synthetic sodalites have been extensively studied (1-11). Sulfur (3-9), oxygen (7, 8, 10), manganese (7, 10), and iron (7, 10, 11) are the most common dopants investigated. This paper discusses germanium-doped sodalite powders (12, 13) which emit a bright green luminescence under ultraviolet radiation and exhibit a long lifetime, high contrast, and thermally erasable coloration. Figure 1 shows excitation and emission spectra of the luminescence. The effect of material preparation on the initial reflectance, luminescence intensity, and position of the FB peak absorption is presented. A method of obtaining the luminescence intensity generated within colored powders using observed luminescence intensity measurements is outlined and employed to determine the effect of FB coloration on generated luminescence.

Key words: cathodochromism, emission spectra, reflectance spectra, F centers.

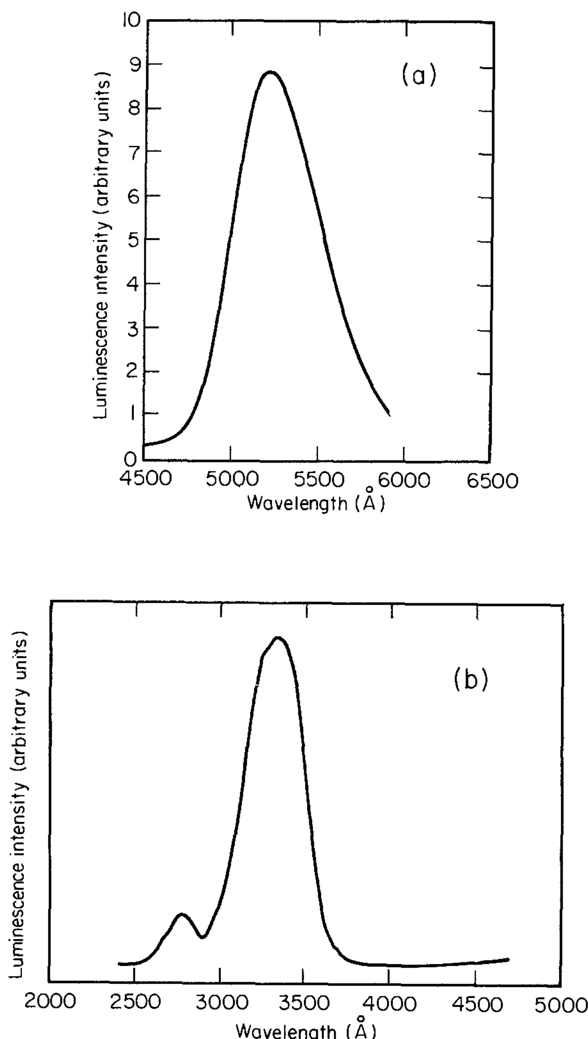

Fig. 1. Luminescence (a) and excitation (b) spectra of Ge-doped sodalite:Br.

Experimental

Material preparation and measurement techniques.—Using a hydrothermal method (14, 15), sodalite materials were grown by combining chemicals according to the equation

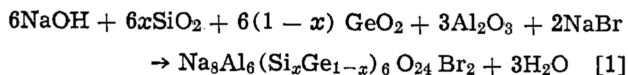

$$6NaOH + 6xSiO_2 + 6(1-x)\ GeO_2 + 3Al_2O_3 + 2NaBr \rightarrow Na_8Al_6(Si_xGe_{1-x})_6\,O_{24}\,Br_2 + 3H_2O \quad [1]$$

where x is the atomic percent (a/o) silicon. The sodium bromide and sodium hydroxide were reagent grade, while the SiO_2, GeO_2, and Al_2O_3 were three nines pure. The powders were identified as sodalite by x-ray powder diffraction; the amount of germanium in each sample was determined with an electron microprobe (15). Materials were grown containing 0, 1, 2, 3, 9, 28, and 64 a/o germanium substituted for silicon. Annealing in a hydrogen atmosphere sensitized the powders to permit both coloration and luminescence.

Samples made by depositing the sodalite powders onto aluminum slides [using conventional powder settling techniques (16)], were colored by electron beam exposure in a demountable CRT system and u.v. light. Diffuse reflectance spectra were measured with a Cary-14 spectrophotometer equipped with a diffuse reflectance integrating sphere: Typical luminescent and excitation spectra, measured with equipment described by Jenssen (17), are shown in Fig. 1. The excitation source was a 1000W Xenon lamp and a Bausch and Lomb high intensity monochromator. The detection system included a 400 Hz chopper, a McPherson 0.3 meter Model 218 Grating Monochromator, and an RCA C7164R photomultiplier.

Determination of generated luminescence.—The F-center absorption band for the materials studied was about 1000Å wide and was centered at approximately 5550Å. Therefore, the absorption band overlapped the luminescent emission band and caused the observed, or measured, emission to be less than the emission generated by the luminescent centers. Melamed's (18) theory of luminescent powders was used to determine the generated luminescence from experimental measurements of diffuse reflectance and luminescent spectra.

If the exciting radiation is very strongly absorbed, one may assume that the excitation is consumed in a single layer. For this case, Melamed shows that the observed luminescent intensity $J(E)$, can be corrected to give the intensity of the generated luminescence, $J'(E)$, by applying the formula

$$J'(E) = J(E)\,\frac{(1-2xm_e)_E}{(R_1-2xm_e)_E} \quad [2]$$

where R_1 is the diffuse reflectance from the first layer of particles and the subscript E denotes that the quantity in parenthesis is measured at the energy of the emission. The value of m_e depends on the index of refraction and is 0.10 for sodalite:Br, $n = 1.485$. The parameter x is given by

$$x = \frac{x_u}{1-(1-2x_u)T} \quad [3]$$

where T is the percent transmission through a particle and x_u is a geometrical factor that depends on the characteristics of the powder particles. Faughnan *et al.* (19) have determined a value of $x_u = 0.143$ for settled screens of sodalite: Br. The general formula for R_1 calculated by Melamed is

$$R_1 = 2xm_e + \frac{x(1-2xm_e)T(1-m_eR)}{(1-m_eR)-(1-x)(1-m_e)TR} \quad [4]$$

where R is the diffuse reflectance for all layers beneath the first. Because the maximum value of x is one-half and because m_e is small, Eq. [4] can be reduced, with only a small error, to

$$R_1 = \frac{xT}{1-(1-x)TR} \quad [5]$$

For an uncolored sample, $R_1 = R$ but $R_1 < R$ when the sample is colored. From Eq. [3] and [5] and the value $x_u = 0.143$, an equation for T in terms R_1 and R can be obtained

$$T = \frac{1+6RR_1+5R_1}{10RR_1} - \sqrt{\left[\frac{1+6RR_1+5R_1}{10RR_1}\right]^2 - \frac{7}{5R}} \quad [6]$$

Using the measured values of R, R_1, and $J(E)$ in Eq. [2], [3], and [4], the value of generated luminescence intensity, even in the presence of an absorption band, can be obtained. Considering the accuracy with which the luminescence intensity and the diffuse reflectance can be measured, the generated luminescence is determined within ±1%.

Results

Effect of hydrogen annealing on initial reflectance.—Although undoped sodalite powders remain highly reflective if annealed at 200°C above an optimum value for maximum coloration efficiency of about 700°C, germanium-doped powders turn dark at relatively low annealing temperatures. The degree of discoloration depends on the annealing temperature and the amount of germanium in the sample. Figure 2a shows the diffuse reflectance at 5000Å for five sodalite: Br samples, containing different percents of germanium annealed in hydrogen at various temperatures for 15 min. De-

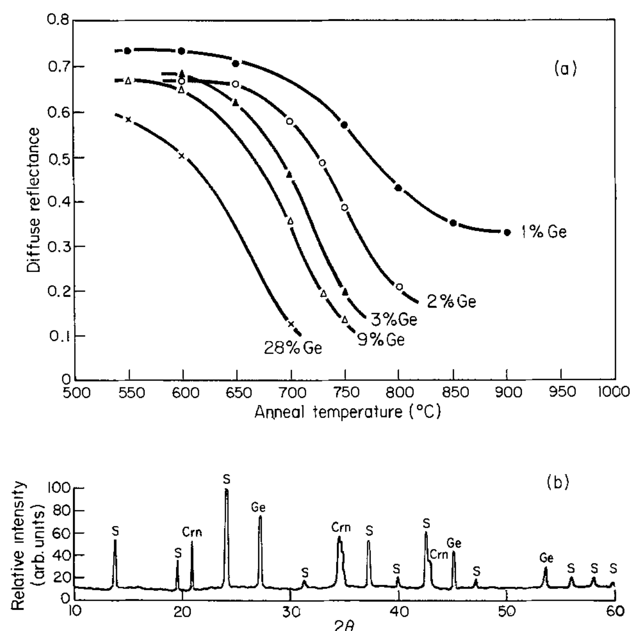

Fig. 2. Initial reflectance of Ge-doped sodalite:Br as a function of Ge concentration and anneal temperature for an annealing time of 15 min (a), and x-ray powder pattern of sample annealed at 800°C for 15 min (b).

creased reflectance is caused by the powder darkening as the annealing temperature increases. That is, the higher the germanium content, the lower the reflectance at a given annealing temperature. This reduction is also influenced by the lattice parameter increasing with germanium concentration (15) which affects diffusion rates and, therefore, the sensitizing properties of the material. Improved sensitization can be achieved by annealing for a longer time at a temperature below the break in the reflectance curves of Fig. 2a. This improvement is limited, however, because the initial reflectance also decreases with increasing anneal time at a fixed temperature.

Black coloration of over-annealed powders is due to the precipitation of germanium metal. Figure 2b is an x-ray powder pattern of $Na_6Al_6(Si_{0.91}Ge_{0.09})_6O_{24} \cdot 2NaBr$ annealed in hydrogen at 800°C for 15 min. In addition to the strong sodalite peaks, denoted by S, there are six other lines. The three lines, Ge, at 27.3° ($d = 3.280Å$), 45.2° (2.006Å), and 53.7 (1.708Å) are due to germanium metal as indicated by the excellent agreement between the observed lines and the standard lines for germanium. Another strong line, Crn, is shown in Fig. 2b at 20.9° ($d = 4.230Å$). This coincides very closely with the location of the strongest peak of high carnegieite (17, 18). It is believed that this phase occurs because of excessive loss of NaBr at high annealing temperatures.

Effects of hydrogen annealing on luminescence intensity.—The hydrogen annealing process also strongly affects the intensity of the luminescence emission. Figure 3 summarizes the results of an experiment in which materials with the composition $Na_6Al_6(Si_{0.97}Ge_{0.03})_6O_{24} \cdot 2NaBr$ were annealed at various temperatures for 15 min. The luminescence intensity is negligible for anneal temperatures less than 600°C, but increases rapidly with increasing anneal temperature. The observed emission must be corrected for reabsorption since Ge precipitation occurs upon annealing, causing the material to darken. Once corrected, the peak emission occurs at 750°C, 20° above the peak of the observed intensity. This correction explains the spectrum shift in Fig. 3. The observed intensity begins to decrease at 730°C even though new luminescent centers are being created due to reabsorption caused by germanium precipitation, while the corrected luminescence curve increases between these temperatures because the ef-

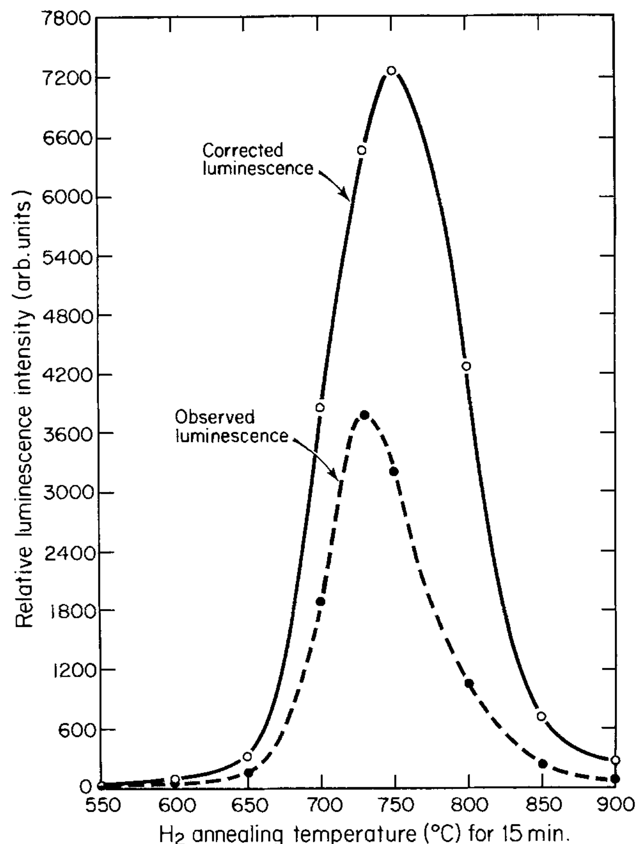

Fig. 3. Luminescence intensity of $Na_6Al_6(Si_{0.97}Ge_{0.03})_6O_{24} \cdot 2NaBr$ as a function of H_2 anneal temperature for an annealing time of 15 min.

fect of reabsorption has been removed. Above 750°C, the corrected luminescence also begins to decrease. It is believed that this is caused by the conversion of the sodalite structure into either nepheline or high carnegieite (14, 21). High carnegieite, $Na_4Al_4Si_4O_{16}$, has the same chemical formula as nepheline but is cubic while nepheline is hexagonal.

Luminescence intensity is also affected by hydrogen annealing time at a given temperature. Figure 4 shows the luminescence intensity of the powder discussed above at various annealing times at 700°C. The emission increases almost linearly between 0 and 25 min and then saturates. It appears that annealing times above 45 min causes a decrease in the emission. Figures 3 and 4 show that the annealing temperature, not the annealing time, determines the maximum luminescence intensity because annealing at 730°C for only 15 min results in a higher emission than obtained when annealing at 700°C for times much longer than 15 min.

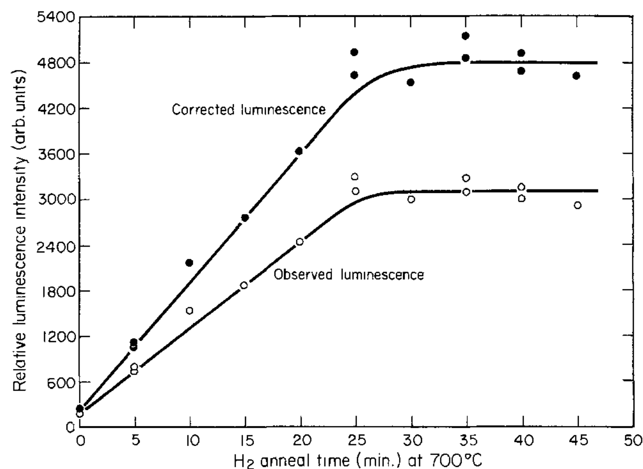

Fig. 4. Luminescence intensity of $Na_6Al_6(Si_{0.97}Ge_{0.03})_6O_{24}$ $2NaBr$ as a function of H_2 anneal time at 700°C.

The best luminescent materials contained less than 9% germanium substituted for silicon. The strongest emission was observed using a material containing 3% germanium which was annealed in hydrogen at 730°C for 30 min. When excited by a 20W ultraviolet lamp, this material exhibits a 14 f-L emission. Samples containing 28 and 54% germanium are difficult to sensitize because the material darkens at very low annealing temperatures and the luminescence intensity observed with these samples was almost negligible.

Effect of Ge concentration on F band absorption peak.—Though the positions of the excitation and emission bands are unaffected by germanium concentration, the location of the F band is strongly affected by the germanium concentration. A study of the effect of germanium substitution in bromine sodalite on the location of the F band peak is complicated by the fact that the F band position is also a function of the hydrogen annealing temperature and time. Figure 5 shows that the wavelength of the peak absorption for a bromine sodalite sample containing no germanium varies from 5400 to 6300Å when the annealing temperature is varied from 600° to 800°C. Therefore, there is not a unique F band peak wavelength for each germanium composition, but a range of values. To avoid this problem and obtain an F band peak wavelength characteristic of the germanium content, the samples used in this part of the investigation were annealed for 15 min at 600°C to minimize the shift of the peak due to annealing. The F band locations were determined from diffuse reflectance spectra of settled screen samples. The results are presented in Table I. These data indicate that the incorporation of Ge causes the lattice parameter to increase almost linearly starting from zero Ge concentration (15). One would expect that this lattice expansion would cause the F center potential well to expand and hence E_F to decrease. However, the data in Table I show that E_F first increases and then decreases as germanium is added. Rizzo (22) observed this same behavior when using ESR to measure the effect of germanium substitution on the hyperfine constant of the trapped electron. He found that the interaction of the trapped electron with its surrounding sodium nuclei increased and then decreased as germanium was added. Therefore, at low

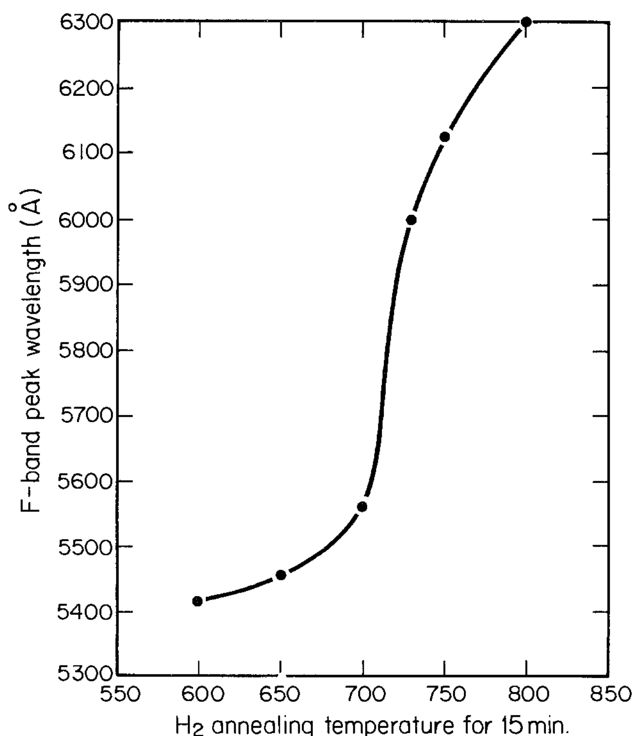

Fig. 5. Sodalite:Br F band peak wavelength as a function of H_2 annealing temperature.

Table I. F band peak location as a function of Ge concentration

A/o Ge	a_0 (Å)[12]	λ_{peak} (Å)	E_F (eV) $= \frac{hc}{\lambda_{peak}}$
0	8.914	5420	2.294
1	8.919	5400	2.302
3	8.921	5375	2.313
9	8.932	5365	2.317
28	8.973	5515	2.253
54	9.042	5800	2.143

Ge concentrations another effect must be occurring to produce the energy shift in the opposite direction from the lattice expansion shift. This effect could, for example, be a perturbation of the F center wavefunctions which could cause a shift in the absorption band. The perturbation may be less significant at higher Ge concentrations where E_F decreases with lattice expansion. The data in Table I show that E_F begins decreasing at a germanium concentration of nine atomic percent. The logarithm of the energy of the trapped electron, $E_F = hc/\lambda_{peak}$, is plotted in Fig. 6 *vs.* the lattice parameter to show the exponential dependence of E_F on a_0. Above 9% Ge, E_F can be represented by

$$E_F = (2.37 \times 10^6)\, a_0^{-6.32} \quad [7]$$

The exponential dependence in Eq. [7] is much stronger than that observed in the alkali halides which is represented by the Mollwo-Ivey relation

$$E_F = 17.7\, a_0^{-1.84} \quad [8]$$

However, the exponential dependence in Eq. [7] is less than that observed for sodalite when substitutions are made into the halogen site. From the data of Taylor *et al.* (6), one can calculate for this case

$$E_F = (7.15 \times 10^9)\, a_0^{-10} \quad [9]$$

Therefore, substituting into the cage framework rather than into the center of the cage produces a more subtle effect on the position of the F band peak.

Effect of F band coloration on luminescent intensity.—Coloration of these materials greatly quenches the observed luminescence. Some quenching was expected because the F band and emission band overlap, but the reduction in intensity was larger than that due merely to reabsorption. To determine the cause of this reduction, luminescence intensity as a function of F band absorption was measured. First, initial reflectance and luminescence spectra of the uncolored slide were measured. The slide was then lightly colored with ultraviolet light and the resulting reflectance and lumin-

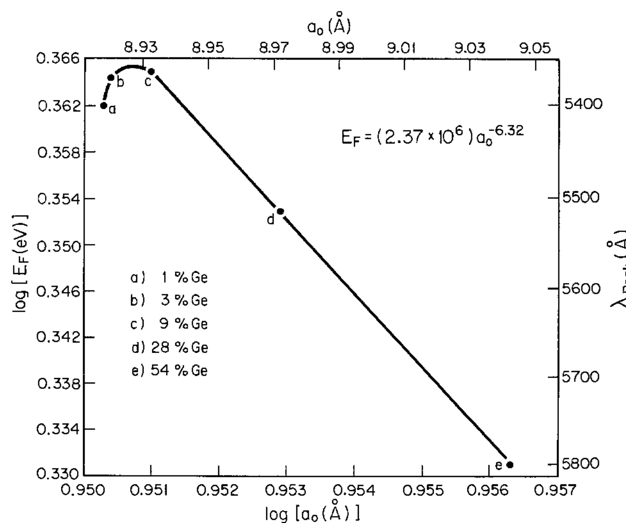

Fig. 6. The dependence of the F band peak wavelength on the lattice parameter of Ge-doped sodalite:Br.

Table II. The dependence of the generated luminescence intensity on the degree of F band coloration

Number of exposures	Measured lum. intensity $J(E)$ at 5250Å (arb. units)	Diffuse reflectance R_1 at 5450Å ±0.002	Absorption $1 - R_1$ at 5450Å ± 0.002	F band peak absorption at 5450Å ± 0.002	Diffuse reflectance R_1 at 5250Å ± 0.002	Generated lum. intensity $J(E)$ at 5250Å (arb. units) ± 1%
0	3050 ± 20	0.656	0.344	0	0.645*	5000
2	2610 ± 20	0.584	0.416	0.072	0.575	4860
5	2250 ± 20	0.504	0.496	0.152	0.495	4950
12	1255 ± 10	0.396	0.604	0.260	0.385	3670
20	300 ± 2	0.218	0.782	0.438	0.203	1860

* The value of R used in Eq. [6].

escence spectra determined. This procedure was continued by increasing the sample coloration and measuring the spectra after each exposure until the contrast saturated. Darker coloration was obtained by electron beam exposure. Table II lists the parameters used to calculate the corrected luminescence and the F band absorption along with a few sample calculations. The luminescence peak occurred at 5250Å while the F band peak was at 5450Å. Figure 7 shows both the observed and corrected luminescence intensities as a function of F band absorption. The observed luminescence decreases almost linearly with increased coloration. The corrected intensity is essentially constant for low F band absorption, however, and then decreases almost linearly with increasing absorption. The region in which the corrected luminescence intensity remains constant coincides with the region of photoerasable coloration, *i.e.*, that portion of the coloration that can be erased by light, while the decrease in corrected intensity coincides with the region of thermally erasable coloration. This correlation was confirmed by repeating the above experiment but, in addition, thoroughly optically bleaching the sample after each exposure and before measuring the luminescence and diffuse reflectance spectra. The results of this experiment are shown in Fig. 8. In this case, the corrected luminescence decreases over the entire range of coloration. These two experiments indicate that the reduction in observed luminescence due to photoerasable coloration results entirely from partial reabsorption of the generated emission by the F centers. Thermally erasable coloration causes the observed luminescence to decrease not only due to reabsorption, but also as a result of an additional quenching mechanism. For example, in zero ambient light and under ultraviolet excitation, a sample with an emission of 14 f-L from an uncolored area emitted only about 0.1 f-L in a colored area giving a contrast ratio of approximately 140:1. This sample exhibits a reflective contrast ratio of 15:1 in high ambient light.

Summary

Germanium-doped, sodalite:Br powders were prepared and shown to exhibit luminescence at 5250Å with an excitation band at 3465Å. The materials also possess a long lifetime, high contrast, cathodochromic coloration mode. The luminescent intensity depends strongly on both the hydrogen-annealing temperature and duration. The luminescence initially increases with increasing annealing temperature and then decreases at higher temperatures due to structural collapse. The sample with the highest luminescent intensity, *i.e.*, 14

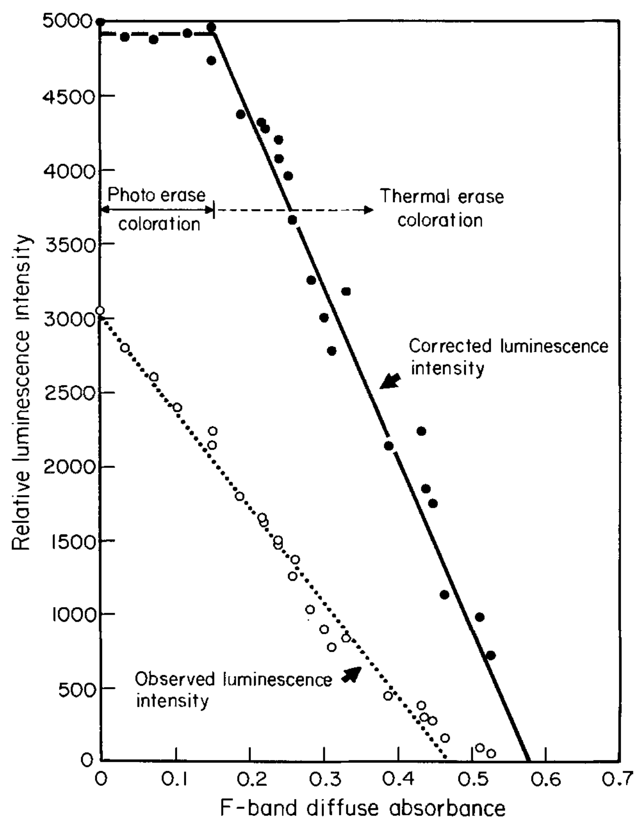

Fig. 7. Luminescence intensity as a function of F band absorption for $Na_6Al_6(Si_{0.99}Ge_{0.01})_6O_{24} \cdot 2NaBr$ annealed at 700°C for 30 min.

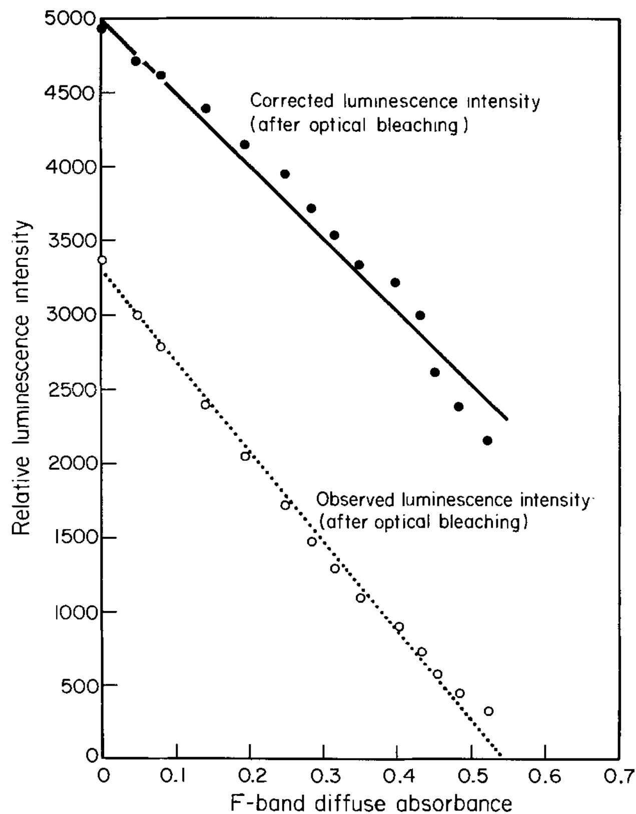

Fig. 8. Luminescence intensity as a function of F band absorption (after optical bleaching) for $Na_6Al_6(Si_{0.99}Ge_{0.01})_6O_{24} \cdot 2NaBr$ annealed at 700°C for 30 min.

f-L, contained 3% germanium and was annealed at 730°C for 30 min.

The sensitizing of germanium-doped powders is complicated by the precipitation of germanium at relatively low anneal temperatures. This causes the powder to appear black and reduces the initial reflectance. This effect becomes more pronounced with higher germanium concentrations. Samples containing less than 9% Ge have very good luminescent and cathodochromic properties while those above 9% are very difficult to sensitize.

The F band energy was shown to increase with increasing germanium concentration up to 9% and then to decrease with higher concentrations. Above 9% germanium, the F band energy was shown to obey the relationship

$$E_F = (2.37 \times 10^6)\, a_0^{-6.32} \qquad [10]$$

Electron beam coloration of these materials greatly reduces the observed luminescence. While some of this reduction results from absorption of the generated luminescence by F centers, a further reduction results from the quenching of luminescent centers. It was shown that the formation of thermally erasable F centers results in the quenching of luminescent centers while the formation of optically erasable F centers does not.

Experiments are being conducted to measure the effect of electron beam coloration on the intensity of an absorption band that is attributed to the luminescent center. Other experiments are being considered to determine a model for the luminescent mechanism.

Acknowledgments

The author gratefully acknowledges the assistance of E. F. Farrell in the growth of the materials and the x-ray diffraction measurements, Dr. H. P. Jenssen for his assistance and the use of his M.I.T. laboratory facilities for luminescence measurements, Dr. A. Linz and Professor D. J. Epstein for many helpful discussions, and Gail McAlister and Dr. Margaret Somers for their assistance in the preparation of the manuscript.

This work was supported by the Advanced Research Projects Agency under Contract No. SD-90 and DAHC-15-67-C-0222, and by the National Science Foundation under Grant No. H33635 and DMR75-10620. Personal financial support for the author was provided by the John and Fannie Hertz Foundation. The experimental work was conducted at the Crystal Physics Laboratory at M.I.T., Cambridge, Massachusetts.

Manuscript submitted Aug. 22, 1977; revised manuscript received Feb. 22, 1977.

Any discussion of this paper will appear in a Discussion Section to be published in the June 1979 JOURNAL. All discussions for the June 1979 Discussion Section should be submitted by Feb. 1, 1979.

REFERENCES

1. P. M. Heyman, I. Gorog, and B. W. Faughnan, *IEEE Trans. Electron Devices*, **ed-18**, 685 (1971).
2. I. F. Chang, *This Journal*, **121**, 815 (1974).
3. I. F. Chang and A. Onton, *J. Electron. Mater.*, **2**, 17 (1973).
4. R. D. Kirk, *This Journal*, **101**, 461 (1954); *Am. Mineral.*, **40**, 22 (1955).
5. W. G. Hodgson, J. S. Brinen, and E. F. Williams, *J. Chem. Phys.*, **47**, 3719 (1967).
6. M. J. Taylor, D. J. Marshall, P. A. Forrester, and S. D. McLaughlan, *Radio Electron Eng.*, **40**, 17 (1970).
7. C. Z. Van Doorn, D. J. Schipper, and P. T. Bolwijn, *This Journal*, **119**, 85 (1972).
8. S. K. Deb and S. B. Gallivan, *J. Lumin.*, **5**, 348 (1972).
9. T. Takeda and A. Watanabe, *This Journal*, **120**, 1414 (1973).
10. C. Z. Van Doorn and D. J. Schipper, *Phys. Lett*, **34A**, 139 (1971).
11. W. Phillips, *This Journal*, **117**, 1557 (1970).
12. L. T. Todd, Jr., E. F. Farrell, and A. Linz, *IEEE Trans. Electron Devices*, **ed-23**, 1183 (1976).
13. L. T. Todd, Jr.. E. F. Farrell, and A. Linz, U.S. Pat. 3,911,315 (1975).
14. L. T. Todd, Jr., Ph.D. Thesis, M.I.T., Cambridge, Mass. (1973).
15. M. S. Perlmutter, L. T. Todd, Jr., and E. F. Farrell, *Mater. Res. Bull.*, **9**, 65 (1974).
16. W. Espe, "Materials of High Vacuum Technology," Vol. 3, p. 122, Pergamon Press, Inc., Elmsford, N.Y. (1968).
17. H. P. Jenssen, Ph.D. Thesis, M.I.T., Cambridge, Mass. (1971).
18. N. T. Melamed, *J. Appl. Phys.*, **34**, 560 (1963).
19. B. W. Faughnan, I. Gorog, P. M. Heyman, and I. Shidlovsky *Proc. IEEE*, **61**, 291 (1973).
20. D. Taylor, *Min. Mag.*, **36**, 761 (1968).
21. D. J. Schipper, T. W. Lathouwers, and C. Z. Van Doorn, *J. Am. Ceram. Soc.*, **56**, 523 (1973).
22. J. F. Rizzo, S. M. Thesis, M.I.T., Cambridge, Mass. (1973).

Passivating CVD Molybdenum Films Against Infrared Reflection Losses Caused by Oxidation

G. E. Carver, H. S. Gurev,* and B. O. Seraphin

Optical Sciences Center, University of Arizona, Tucson, Arizona 85721

ABSTRACT

Thin film reflectors of molybdenum deposited by CVD can be passivated against oxidation by overcoating them with either a thin film of aluminum oxide (500Å) or silicon nitride (300Å). A set of such molybdenum films were exposed to open air at 500°C for 160 min without measurable deterioration of their infrared reflectance. This demonstrates the feasibility of using refractory metal reflectors in high temperature photothermal converters without risking reflectance losses caused by oxidation. It also established the possibility of integrating the refractory metal reflector into the deposition sequence of converter fabrication by CVD.

The spectral selectivity required for photothermal solar energy converters can be provided by a sequence of thin films. Antireflection coating and thin film absorbers operating in the visible range, covering a thin film reflector operating in the infrared are the major components of a converter. Previous work has demonstrated the feasibility of fabricating these thin

* Electrochemical Society Active Member.

Key words: refractory metal reflector, photothermal conversion, high temperature anneals.

film stacks by CVD (1). The method is economically particularly attractive for solar technology since it proceeds at atmospheric pressure, thereby facilitating large scale flow-through operation without the restrictions and costs of vacuum-based techniques. In addition, fabrication by CVD requires exposure of the growing stack to temperatures in excess of 700°C. As a consequence, the final system is well suited for long-term operation at temperatures of 500°C. However, the high temperatures of fabrication and operation present difficulties. If highly reflective noble metals such as silver are used, the reflective film tends to agglomerate during fabrication, resulting in reduced infrared reflectance. As an alternative, refractory metals of superior thermal stability can serve as reflectors. In contrast to films prepared by physical vapor deposition, thin films of molybdenum deposited by CVD compete in their infrared reflectance with the high reflectance of the bulk material (2). Having profited from the thermal and optical properties of molybdenum, problems still arose concerning the strong oxidation tendency of this refractory metal, especially at the temperatures of converter operation. We consequently studied methods of passivating CVD molybdenum thin films with respect to preserving their infrared reflectance. The results of tests in which a set of passivated molybdenum films was exposed to open air at 500°C for 160 min is reported. Within reflectometer accuracy, the infrared reflectance of the passivated films remained unchanged throughout this period of time. Two typical samples were further heated and failed to determine a lifetime limit.

Sample Set

Twenty-one samples were deposited by thermal decomposition of molybdenum carbonyl [$Mo(CO)_6$]. An important aspect of this process is the possibility of incorporating traces of oxide and carbide phases within the molybdenum matrix. Anticipating that these oxides and carbides could alter metallurgical interactions between the metallic film, passivator, and atmosphere, we included deposits of differing impurity content within our sample set. This was done by varying the deposition temperature of the metallic films, as it is known that the end products of the thermal decomposition of $Mo(CO)_6$ are a function of temperature (3). Films were deposited at temperatures ranging from 200° to 350°C. All samples were deposited on fused silica and range in thickness from 600-1800Å. As explained below, four different methods of passivation were tested. Sample subsets were assembled for use with each passivator, along with an additional subset which was not passivated for reasons of comparison. Each subset includes samples of different deposition temperature. The top two rows of the figure summarizes this information. In addition to variations of the purity amongst the sample set, the large surface-

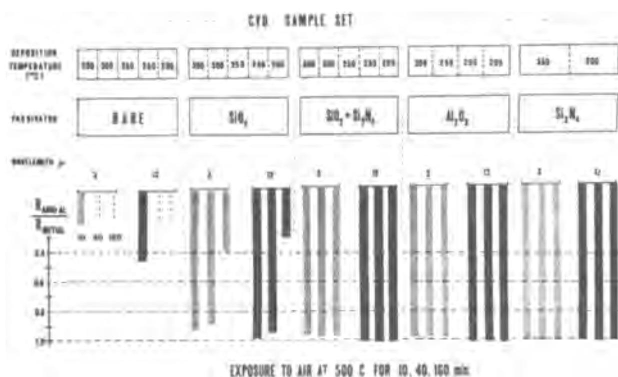

Fig. 1. Ratios of the reflectance of passivated, annealed CVD molybdenum films to as-deposited reflectance values at 3 and 12 μm for samples which have been annealed in air at 500°C for 10, 40, and 160 min using different passivators.

to-thickness ratio of a thin film can force structural differences from the bulk. In order to study the influence of these parameters on the passivation, we included in our test samples of bulk molybdenum which were polished to a specular finish.

Choice of Passivators

For purposes other than the stabilization of the optical properties, passivation of molybdenum is routinely accomplished with a few thousandths of an inch of molybdenum silicides when structural strength, impact resistance, and/or thermal shock resistance of the object to be passivated is of interest (4). The fact that our application requires preservation of the high infrared reflectance of the passivated films places more stringent requirements on the passivators. The high infrared emittance, ranging from 0.4-0.8 (5), of these silicide layers precludes their use as passivators in solar applications. However, the mechanism by which the silicides operate suggests a passivator for our application. During heating, the silicide reacts with oxygen to form a thin layer of SiO_2 on the outer surface which acts as the protective layer (6). Thus we coated one subset of our molybdenum films with 500Å of SiO_2 by evaporation. These layers are thin enough to render the infrared reflectance of the metal unaltered by the passivator. Other subsets were passivated with 500Å of Al_2O_3 which was also deposited by evaporation. In addition, a passivating layer of 300Å thickness of Si_3N_4 was applied to a sample subset by chemical vapor deposition from a $SiH_4/NH_3/He$ gas mixture at a temperature of 750°C. It is remarkable that the reflectance of the Mo films thus coated did not change in the CVD process, indicating that the absence of oxygen in the reaction chamber permitted heating of the Mo films up to temperatures above 700°C without adverse effects. In order to guarantee the survival of the Mo films during Si_3N_4 deposition, we applied 500Å of SiO_2 to a subset of metal films before the CVD step. As mentioned above, bulk molybdenum samples were also passivated. Similar Al_2O_3 and SiO_2 layers were used on the bulk samples.

Testing Procedures

Using a PE 137 spectrophotometer, we measured the near-normal incidence specular reflectance of all samples, (*i*) after deposition of the metal; (*ii*) after passivation; and (*iii*) after each step of the lifetime test. Concerning the vertical scale of the figure, $R_{initial}$ refers to the reflectance before application of the passivating layer, and R_{anneal} to the reflectance after annealing the sample for the times given. The quotient is therefore indicative of conservation or deterioration of the infrared reflectance. All samples were heated in air in a furnace of near-constant temperature profile varying only from 502° to 504°C over the area utilized. Reflectances were measured after exposure to this condition for 10, 40, and 160 min, respectively.

Results

All results for the metallic films are summarized in the figure where light and dark bars indicate values of R_{anneal} over $R_{initial}$ at 3 and 12 μm, respectively, for each sample subset after each of the three anneal periods. Each bar represents an average calculated over all samples in each subset, each sample being characterized by deposition temperature, and consequently by impurity content. Changes in reflectance varied only slightly among samples within each subset. Therefore, variations of impurity content within the metallic films due to different deposition temperatures are seen to be of little consequence concerning passivation.

One sample subset and the bulk molybdenum sample were passivated by 500Å of SiO_2. They deteriorated in their reflectance after 40 min of anneal in open air at 500°C. In addition, measurements of reflectance of these samples in the visible and near infrared indicate

a shift of the first interference fringe to longer wavelengths during exposure. This indicates an increase in the optical thickness of the dielectric layer above the metallic surface. It can be assumed that the fringe shift is caused by a growth of molybdenum oxide at the metal-dielectric interface which in turn eventually consumes the metal and destroys the reflectance. Incomplete densification (7) of the silicon dioxide layers may explain the partial failure of these samples.

Similar fringe shifts are seen after 40 min of exposure in the reflectance measurements on unpassivated bulk molybdenum. In this case, the shifts result from an oxide growth on the outer metallic surface. As the dielectric thickness increases, fringe minima shift towards the infrared and reduce reflectance values. Oxide absorption bands also contribute to infrared reflectance losses for these unprotected bulk molybdenum surfaces. It can be assumed that the unpassivated subset of molybdenum films was consumed by oxide growth resulting in complete reflectance loss within 10 min of exposure.

The Al_2O_3 and Si_3N_4 passivators protected their respective subsets through at least 160 min in air at 500°C without loss of infrared reflectance. Aluminum oxide preserves the reflectance of bulk molybdenum under the same conditions. No lifetime limit was found as two typical samples were tested for an additional 6 hr without reflectance degradation. Reflectance measurements in the visible range indicated that the dielectric layer overcoating these samples did not change in thickness as the first order fringe minima remained at the same wavelength throughout all tests. In some cases reflectance values increased slightly after the first anneal, indicating a possible outgassing and/or structural improvement of the film caused by heating.

Conclusions

Both thin layers of Al_2O_3 and Si_3N_4 can passivate thin molybdenum films deposited from the vapor phase without degrading their infrared reflectance against exposure to air at 500°C for 160 min. Thin layers of SiO_2 preserved the reflectance for nearly 40 min at 500°C. These results establish the possibility of integrating refractory metal reflectors into the deposition sequence of photothermal converter fabrication by CVD. In addition, in the event of accidental exposure of a photothermal converter to air during operation, the metallic reflectors would easily survive the ensuing cooldown period prior to enclosure repair without suffering oxidation induced reflectance losses.

Acknowledgments

This report is based on efforts supported by ERDA Grant No. E(29-2) 3673 and NSF Grant DMR 75-01267. Supplementary information can be found in the progress reports of this grant. The authors wish to thank D. C. Booth and K. D. Masterson for assisting in film deposition and optical measurements.

Manuscript submitted Nov. 2, 1977; revised manuscript received March 7, 1978.

Any discussion of this paper will appear in a Discussion Section to be published in the June 1979 JOURNAL. All discussions for the June 1979 Discussion Section should be submitted by Feb. 1, 1979.

Publication costs of this article were assisted by the University of Arizona.

REFERENCES

1. B. O. Seraphin, Annual Progress Report, NSF-RANN Grant No. SE-GI-36731X, (1973-1975); R. E. Hahn and B. O. Seraphin, *J. Vac. Sci. Technol.*, 12, 905 (1975).
2. H. S. Gurev, G. E. Carver, and B. O. Seraphin, International Symposium on Solar Energy, J. B. Berkowitz and I. A. Osh, Editors, The Electrochemical Society Softbound Symposium Series, Princeton, N.J. (1976).
3. J. J. Lander and L. H. Germer, Technical Pub. 2259, AIME (1947).
4. A. G. Quarrell, "Niobium, Tantalum, Molybdenum and Tungsten," Session III, pp. 181-273, Elsevier Publishing Company, New York (1961).
5. Y. S. Touloukian, "Thermophysical Properties of High Temperature Solid Materials," Vol. 6, Part II, pp. 1469-1471, Macmillan Company, New York (1967).
6. A. G. Quarrell, "Niobium, Tantalum, Molybdenum and Tungsten," Session III, p. 272, Elsevier Publishing Company, New York (1961).
7. L. I. Maissel and R. Glang, "Handbook of Thin Film Technology," pp. 11-48, McGraw-Hill Book Company, New York (1970).

Thickness Uniformity of GaAs Layers Grown by Electroepitaxy

L. Jastrzebski, Y. Imamura,[1] and H. C. Gatos*

Department of Materials Science and Engineering,

Massachusetts Institute of Technology, Cambridge, Massachusetts 02139

ABSTRACT

The thickness profiles of GaAs layers grown by electroepitaxy (current-controlled liquid phase epitaxy) were investigated in conjunction with experimental growth parameters. It was found that defective electrical contacts to the substrate and variations in the dissolution depth of the substrate by the gallium contact layer lead to random fluctuations in the epitaxial layers. Convective flow in the solution due to horizontal gradients in the solution caused by joule heating leads to systematic variations in the thickness of the epilayers. Experimental procedures are presented for minimizing or essentially eliminating both types of thickness variations.

Current-controlled liquid phase epitaxy, referred to from here on as electroepitaxy, of semiconductors and other compounds utilizes current flow through the growth interface while the temperature of the system is maintained constant (1). Growth of semiconductors such as InSb (1), GaAs (2-6), InP (7), and GaAlAs (8-10) as well as garnet layers (11) has been successfully achieved by electroepitaxy. Furthermore, electro-

* Electrochemical Society Active Member.
[1] Permanent address: ECL, Nippon Telegraph and Telephone Public Corporation, Tokyo, Japan.
Key words: GaAs, LPE, electroepitaxy, layer thickness, uniformity.

epitaxy has been employed for the study of growth kinetics of GaAs layers and Si segregation from Si-doped solutions; in these studies the amphoteric doping behavior of Si has been elucidated and attributed to the formation of As-Si-Ga complexes in solution from which Si can be incorporated into Ga or As sites during growth depending on temperature (6). The electrical properties of GaAs layers and p-n junctions grown by electroepitaxy (*i.e.*, mobility, minority carrier diffusion length, and *I-V* characteristics) were found to be as good as in layers (or p-n junctions) grown under the same conditions by thermal cooling (5); similarly, parameters of DH GaAlAs layers were found to be comparable to those prepared by classical methods (10).

During electroepitaxy it has been found that joule heating can play a significant role and that a.c. must be applied prior to the direct current for successful growth (8). Other investigators, on the other hand, have not encountered any interference from joule heating (2). Furthermore, convection in the solution was found to be very significant in some experiments (12); however, its origin has not been clarified.

It was the purpose of the present work to study in detail the extent of joule heating and its effects on the thermal gradients in the growth cell and on convection in the solution; it was also the purpose of this work to study the thickness uniformity of the epitaxial layers as affected by joule heating and other experimental parameters.

Apparatus and Procedure

The apparatus employed in the present study is shown schematically in Fig. 1. The growth cell, operated in a furnace with a cylindrical gold reflector, is a modified version of that commonly employed in LPE to permit a controlled flow of electric current through the growth interface. Thus, two stainless steel electrodes are threaded, one each into the top and bottom graphite segments; the two segments are electrically isolated with boron nitride and current can flow only when the seed is brought into contact with the solution by means of a boron nitride slide. Monitoring thermocouples are positioned 1 mm from the seed and the solution. During growth the controlled thermocouple can be either in position C near the seed or in position B near the heating element for reasons to be discussed below.

GaAs substrates (1.2×1.2 cm) with the (100) orientation were employed; their thickness varied from 200 to 300 μm; they were Cr doped (semi-insulating at room temperature). A uniform electrical contact on one side of the substrate was established with a 150 μm thick gallium layer[2] (details on this contact are discussed later). Depending on the dimensions of the solution well, the growth area was 1.4, 1.0, 0.5, and 0.2 cm^2. The layers were Ge doped (p-type) to a level of about 1.0×10^{18}; other dopants such as Te, Sn, and Si led to similar results. The height of the solution was varied from 0.2 to 2 cm.

In a typical growth experiment the cell was brought to the desired temperature (from 800° to 1000°C) and the solution was equilibrated over a dummy substrate for a period ranging from 2 to 5 hr depending on the height of the melt. The substrate was then brought into contact with the melt and electric current was passed through the growth interface at a density of 0.3-60 A/cm^2; the substrate had a positive polarity with respect to the solution.

Interface demarcation (13) (for the determination of the microscopic growth rate) was introduced by passing through the growth interface 40A current pulses of 0.5 sec duration; depending on the growth rate, the pulse frequency was varied for optimum resolution. Growth was terminated by switching the current off and the substrate was isolated from the solution by moving the slide. The epitaxial layer ranged in thickness from 1 to 150 μm and the growth time from a few minutes to a few hours.

After growth the layers were cleaved along the diameter parallel to the horizontal direction of the cell, etched in AB etchant, and studied by interference contrast microscopy.

The total electrical resistance of the system at 900°C (including stainless steel electrodes, graphite segments, solution, and substrate) for a number of runs was found to range from 0.19 to 0.25Ω. Upon removing the substrate and allowing the solution to make electrical contact between the two graphite segments, no change in resistance was observed; the resistivity of the

[2] Electrical contacts made by evaporating metals such as Pt, Au, Ag, and Pb or by soldering In and Sn did not give satisfactory results.

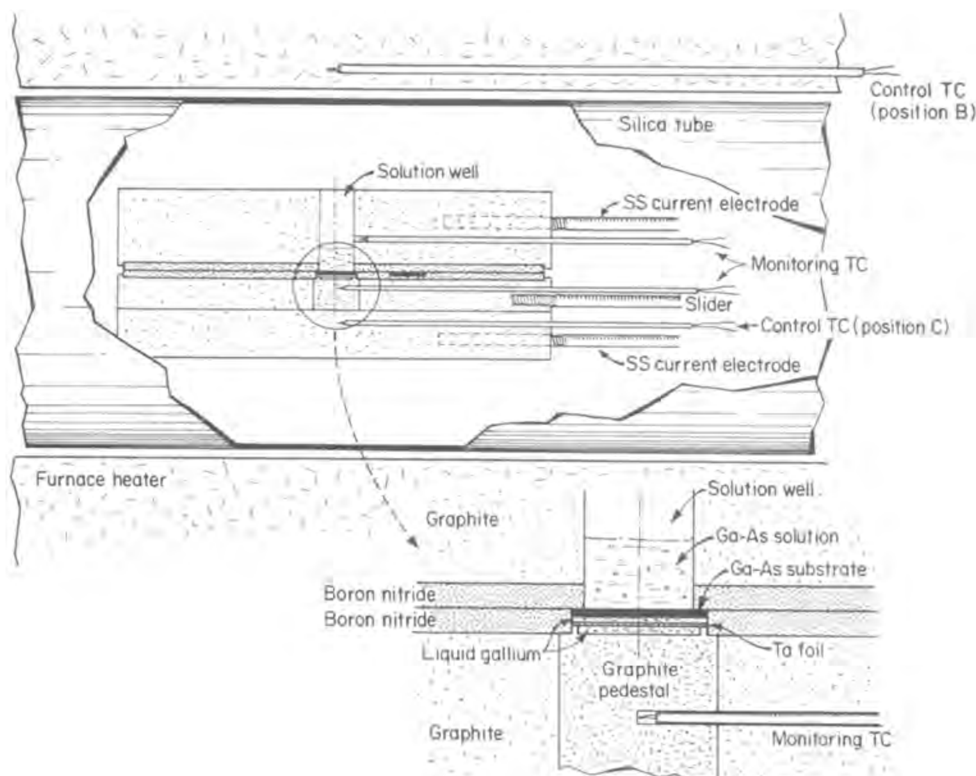

Fig. 1. Schematic diagram of the electroepitaxy apparatus.

graphite segments was estimated to be a few milliohms, taking the resistivity of the graphite to be 10^{-3} Ω-cm; the resistance of stainless steel electrodes was found to be 0.07-0.09Ω. Thus, there is resistance of about 0.1-0.16Ω unaccounted for which must be attributed to the stainless steel-graphite contacts. As is discussed below, this resistance leads to localized joule heating on the right-hand side of the growth cell.

Experimental Results and Discussion

Thermal effects associated with electroepitaxy.—Effect of joule heating on the temperature profile.—Temperature measurements, after thermal equilibration of the growth apparatus, were carried out along a horizontal line 2 mm below the substrate employing a thermocouple as indicated in Fig. 1. The results in the absence and presence of current flow (20A) are plotted in Fig. 2. It is seen that the temperature profile (curve A) is significantly changed in the presence of current flow (curves B and C).

In the absence of current flow the location of the control thermocouple (position B or C indicated in Fig. 1) does not affect the equilibrium temperature profile. However, in the presence of current flow the location of the control thermocouple plays an important role. In the presence of current flow (20A) and with the control thermocouple in position B, near the heating element, (curve B in Fig. 2) the substrate temperature increases by about 8°C and the thermal gradients on either side of the temperature maximum become steeper; furthermore, the temperature maximum is shifted to the right. This shift and the fact that the gradient to the left-hand side of the temperature maximum is greater than that to the right-hand side of the maximum indicate that joule heating is concentrated in the graphite segments of the growth cell on the right-hand side of the substrate. Thus, the joule heating appears to be associated with the stainless steel electrode-graphite contacts which represent half of the electrical resistance of the entire growth system, as pointed out above.

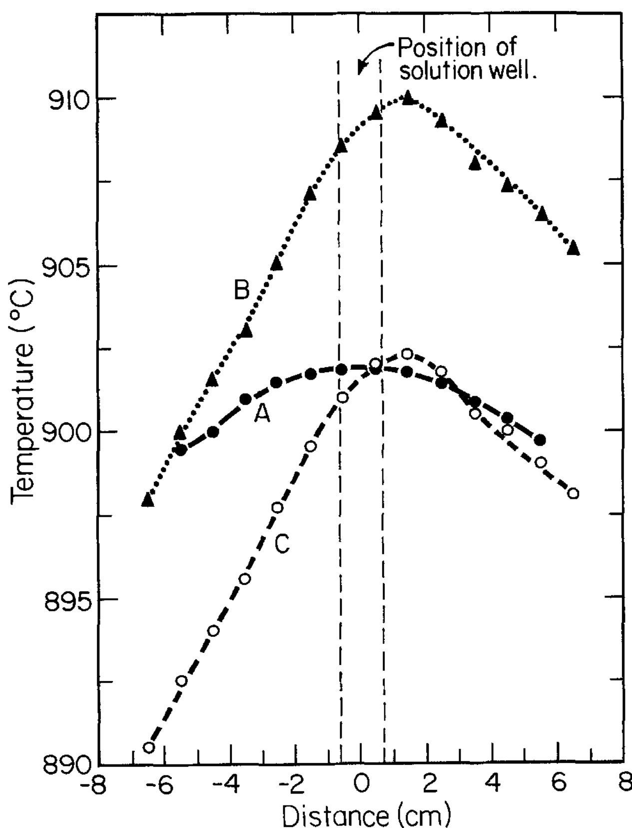

Fig. 2. Horizontal temperature profile in growth cell. Curve A temperature profile in the absence of current; curve B and C temperature profiles during current flow (20A) with the controlled thermocouple in positions B and C, respectively from Fig. 1.

With the control thermocouple in position C near the substrate (Fig. 1), the thermal profile after equilibration in the presence of current flow (curve C, Fig. 2) indicates also significant joule heating at the stainless steel electrode-graphite contacts (different thermal gradients about the maximum). However, the substrate and solution temperature is changed to a relatively small extent. The same curves as in Fig. 2 were obtained 4 mm above the solution (having a height of 0.5 cm) by traversing a monitoring thermocouple through a graphite plug resting on the solution.

It is, thus, shown that joule heating in electroepitaxy establishes a new thermal equilibrium characterized by steeper thermal gradients than the thermal equilibrium prior to the flow of electric current. The new thermal equilibrium is established in about 5 min after the current flow is initiated, as shown in Fig. 3 for an initial temperature of 902°C and a current of 20A.

In the present growth system the thermal gradients, after thermal equilibration, were found to be a function of the electric power. The measured thermal gradient across the solution as a function of electric power (resistance of the system 0.25Ω) is shown in Fig. 4. This horizontal thermal gradient is a potential cause of thermal instability in the solution and could lead to convective flow. The effects of such flow on the uniformity of the epitaxial layers are discussed below.

Effect of the joule heating on the growth process.—As was shown in Fig. 2, with the controlled thermocouple near the heating element (position B in Fig. 1) the temperature of the substrate and the solution increases by about 8°C during flow of 20A. Accordingly, in this case, it was possible to carry out electroepitaxy only after alternating current (a.c.) was passed through the system prior to direct current (d.c.) consistent with results reported previously (8). During a-c flow substrate dissolution took place and the As concentration in the solution reached a new equilibrium value, corresponding to the increased temperature brought about by joule heating (910°C for a current of 20A). Thus, after substituting d.c. for a.c., electroepitaxy was carried out at 910°C, *i.e.*, 8°C higher than set by the temperature controller. When the control thermocouple was near the substrate (position C in Fig. 1) the temperature of the solution and the substrate did not change during current flow as the control thermocouple sensed the joule heating and thus reduced the power to the heating element. Thus, in this

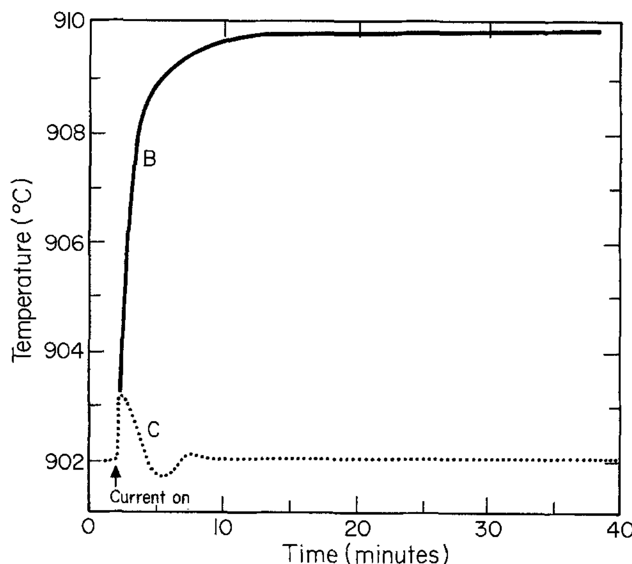

Fig. 3. Thermal equilibration after applying current. Curves B and C were obtained with the controlled thermocouple in positions B and C, respectively from Fig. 1.

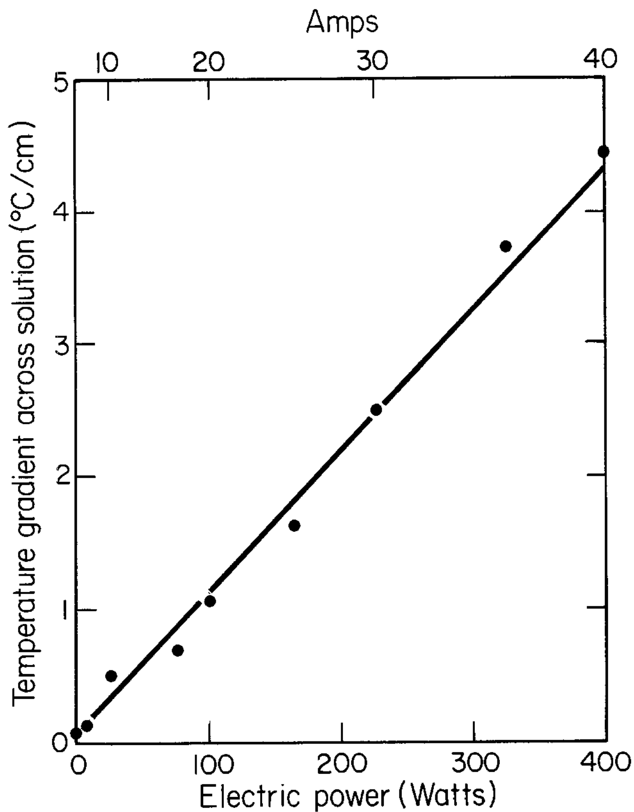

Fig. 4. Temperature gradient across the solution vs. electric power at 902°C.

case no substrate dissolution took place and electroepitaxy was carried out without applying a.c. prior to d.c.

The above results can account for the discrepancy in electroepitaxy findings reported in the literature: one group (8) found extensive backmelting of the substrate upon passage of current and could obtain growth only when a.c. was applied prior to d.c.; a second group (2) experienced no difficulties in carrying out electroepitaxy and found it unnecessary to introduce a.c. In the light of the present results, differences in the effect of joule heating on the thermal configuration of the growth cell resulting from differences in experimental arrangement are the apparent cause of this discrepancy.

Minimization of temperature gradients due to joule heating.—In order to decrease joule heating the cross section of the stainless steel rods was increased by a factor of ten (from 0.1 to 1 cm^2). In addition, the contact area between the rods and the graphite was increased by welding a 2 cm^2 stainless plate at the end of the rods. These modifications decreased the resistance of the system from 0.19-0.25Ω down to 0.05-0.08Ω. In turn, the horizontal temperature gradient across the solution was reduced from 1.4° to 0.4°C/cm for a current flow of 20A at 902°C.

In order to decrease further the horizontal temperature gradient across the solution, the following procedure was employed. Prior to growth the graphite segments were positioned in the furnace so that the horizontal temperature gradient in the solution was of the same magnitude but of opposite sign to the horizontal temperature gradient change caused by the joule heating. Thus, during current flow, the resulting horizontal gradient in the solution was minimized. The smallest gradient achieved across the solution was 0.05°C/cm for a solution temperature of about 900°C, a current flow of 25A, and a total system resistance of 0.05Ω. In most experiments at this temperature and for the same current flow the horizontal gradient ranged from 0.1 to 0.15°C/cm (resistance range 0.05-0.08Ω) as shown in Fig. 5.

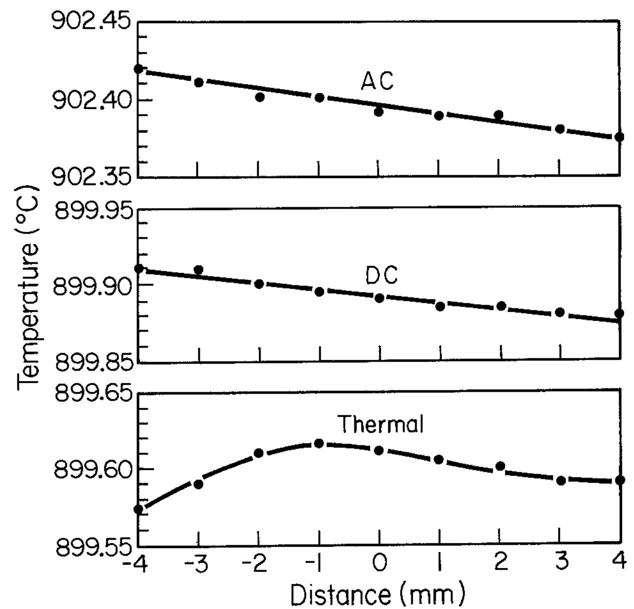

Fig. 5. Horizontal temperature gradient in the solution while passing 25A a.c. (upper curve), 25A d.c. (middle curve), and no current (lower curve). Data obtained with Cr-doped 1 mm thick substrate.

It has been reported (12) that Peltier cooling can lead to horizontal temperature gradient changes (over and above those introduced by joule heating). No such effects were found in the present study. Thus, it is seen in Fig. 5 that passing 25A a.c. (no Peltier cooling) instead of d.c. under identical experimental conditions the horizontal temperature gradient in the solution remains the same, although with d.c., the average temperature decreased about 2.5°C due to Peltier cooling.

Layer thickness uniformity.—The uniformity of the layer thickness was studied in conjunction with various growth conditions such as current density, extent of joule heating, solution height, and the nature of the electric contact to the substrate. Two types of thickness fluctuations were observed: random fluctuations associated with nonuniform current flow through the substrate and systematic fluctuations associated with temperature gradients or convective flow in the solution.

Random thickness fluctuations.—Random fluctuations of the layer thickness associated with nonuniform current density were found to originate in nonuniform electric contacts to the substrate and in variations of the substrate thickness.

Thus, Fig. 6a depicts an epilayer grown in 1 hr under a current density of 5 A/cm^2 at 850°C (substrate thickness 400 μm, n-type 10^{18} $carriers/cm^3$). On some areas of the substrate (identified by numbers) essentially no growth took place. These areas correspond to areas of poor electric contact to the substrate, where gallium did not wet the substrate. They are identified by numbers in Fig. 6b, corresponding to the numbers on the epilayer of Fig. 6a.

Fluctuations in substrate thickness were also found to originate in nonuniform dissolution depth of the substrate by the gallium layer used for electric contact. These variations in the substrate thickness led to variations in the resistance across the substrate and thus in fluctuations in layer thickness. They were particularly pronounced in thin substrates (of the order of 300 μm) where dissolution by gallium represented a significant part of their thickness, since a minimum thickness of about 150 μm of a gallium layer was found to be necessary for a satisfactory spread of gallium over the substrate surface.

Nonuniformities in the ohmic contacts were eliminated by placing the layer of Ga on the substrate (~150 μm), then a Ta foil (~50 μm thick), and then a second thin layer of Ga which served as the contact

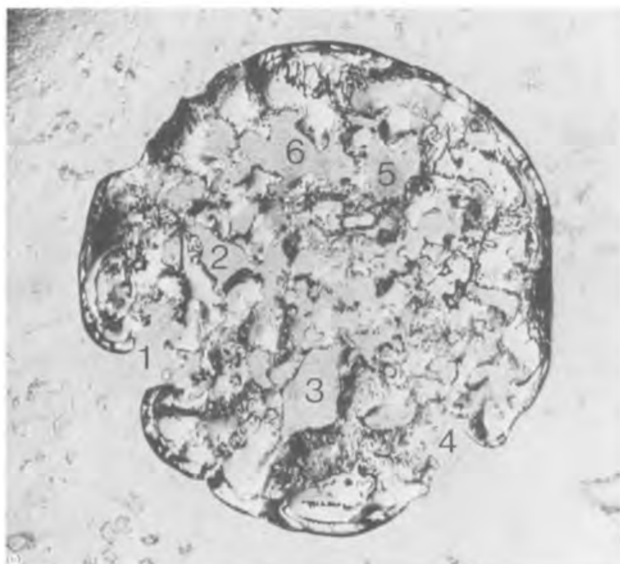

Fig. 6. Defects in the epilayer caused by a defective electric contact. The numbers indicate the defects (a) in the epilayers; and (b) in the corresponding defects in the electric contact.

between the Ga foil and the graphite pedestal (Fig. 1) (2). This assembly was heated at 940°C for 1½ hr prior to the growth experiment. At this temperature Ga is quite soluble in Ta so that the extent of the dissolution of the substrate by the Ga layer is significantly decreased and the electric contacts become very uniform as indicated by the elimination of the random fluctuations of the epilayer thickness. Thus, the role of the Ta foil is to decrease the effective thickness of the gallium layer involved in establishing the electric contact with the substrate.

Systematic thickness variations. Large horizontal temperature gradients in solution.—Epitaxial layers were grown from solutions with a horizontal thermal gradient of 2.5°C/cm at 900°C and a current flow of 30A (resistance of the system 0.25Ω). The substrate was n-type (2×10^{17} carriers/cm^3), its thickness was 450 μm, and its area 1.2 cm^2. Three solution heights were used—0.3, 0.6, and 1.2 cm. The results are shown in Fig. 7.

It should be first pointed out that the increased thickness near the edge of the epilayers is due to the fact that the diameter of the pedestal is larger than the diameter of the solution well, which leads to an increased current density near the wall of the well. When the diameter of the pedestal is smaller than the diameter of the solution well, the thickness of the layers near their periphery is decreased (see below) due to decreased current density. In the subsequent discussion of thickness variations, the thickness near the edges will not be taken into consideration.

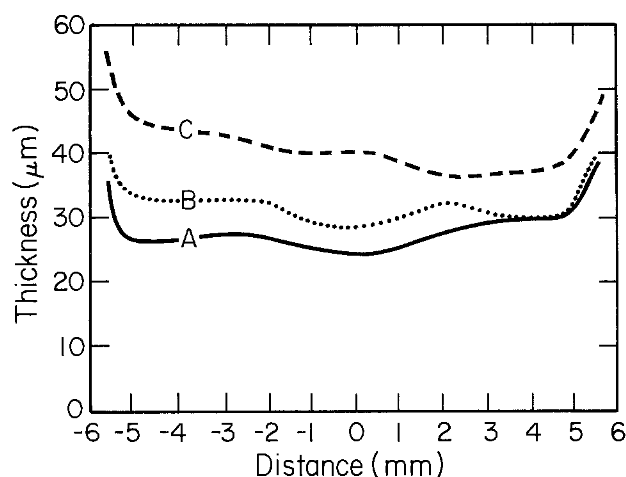

Fig. 7. Thickness profiles after 10 min of growth in the presence of a large horizontal temperature gradient (2.5°C/cm) at 900°C with a current of 30A; solution height: curve A, 0.3 cm; B, 0.6 cm; C, 1.2 cm.

A comparison of the layer thickness after 10 min of growth shows that when the solution height increases from 0.3 to 0.6 cm, the growth rate increases by 15%; when the height increases from 0.6 to 1.2 cm the growth rate increases by 35%. This increase in growth rate with increasing solution height indicates increased transport of As to the growth interface which is attributed to increased convective flow (12).

If the As transport to the interface is controlled by convective flow, the thickness profiles B and C in Fig. 7 must reflect the pattern of the convective flow (14). The thickness variations in case A of Fig. 7 are not controlled by convective flow, as is discussed below.

It is of interest to consider the magnitude of the Grashof number, Gr, (a criterion of convective flow) for the above solution

$$\mathrm{Gr} = \frac{\alpha g}{\nu^2} \Delta T h^4 / w \qquad [1]$$

where α is the coefficient of thermal expansion (10^{-4}) (15); ν is the kinematic viscosity (10^{-3} cm^2/sec) (15); g is the gravitational constant (10^3 cm/sec^2); ΔT is the horizontal temperature difference across the solution (~2.5°C), h is the solution height, and w is the width of the cell (1.2 cm). Thus, for h = 1.2, 0.6, and 0.3, Gr is approximately 2×10^5, 5×10^4, and 2×10^3, respectively. In solutions with a Grashof number of this magnitude and a Prandtl number ($\mu c_p/\kappa$, where κ is the thermal conductivity, μ is the absolute viscosity, and c_p is the specific heat) of about 10^{-2}, which is typical for metallic solutions (16), significant convective flow should be present. Thus, for Gr of the order of 10^4 the flow velocity should be about 10^{-2} cm/sec (16).

It is of interest to point out that the growth rate and the thickness profile of the layers grown from solutions with a height of 0.3 cm (Gr $\simeq 2 \times 10^3$) is the same as that of layers grown from solutions with the same height under the same current density but with a ΔT across the solution an order of magnitude less (Gr $\approx 10^2$) than that in the above experiment. As is seen below, the layers grown under very small horizontal thermal gradients exhibit no thickness variations attributable to convective flow. Thus, in the case A of Fig. 7 (Gr $\approx 2 \times 10^3$) convective flow (expected to be about 10^{-3} cm/sec) (16) does not seem to cause variations in the layer thickness.

On the basis of the experimental values and the above approximate calculations it appears that the growth process in the present case is not affected by convective flow until Gr exceeds a value of the order of 10^4. It is not understood at this time why such a

relatively high value of Gr is necessary before significantly convective flow is present in the solution to affect the growth process. It is possible that a stabilizing solute (As) boundary layer is present. However, no quantitative data are available at this time to determine the thickness of such a stabilizing solute layer.

Systematic thickness variations. Very small horizontal temperature gradients in solution.—Very small horizontal thermal gradients in the solution were obtained by the procedure described above whereby the position of the growth cell in the furnace was so chosen as to compensate the gradients that joule heating would introduce. Employing this procedure, layers 0.5 cm^2 were grown at 900°C on semi-isolating Cr-doped substrates 350-450 μm thick from solutions varying in height from 0.5 to 1.2 cm under current densities of 5, 25, 50, and 60 A/cm^2. The horizontal gradients ranged from 0.05°C/cm for a current density of 5 A/cm^2 to 0.15°C/cm for current density of 60 A/cm^2 (the temperature was higher at the side of the current carrying rods).

The results are shown in Fig. 8 and 9 for a solution height of 0.7 cm. Excluding the thickness near the edges, for reasons pointed out above, it is seen (Fig. 8) that for a current density of 5 A/cm^2 there is a decrease in thickness from right to left. As the current density increases (Fig. 8) the thickness becomes fairly uniform. This fact and the fact that the growth rates were found to be independent of the solution height indicate that no convective flow was present affecting the growth process.

The decrease in thickness from right to left in Fig. 8 is believed to be associated with the systematic small

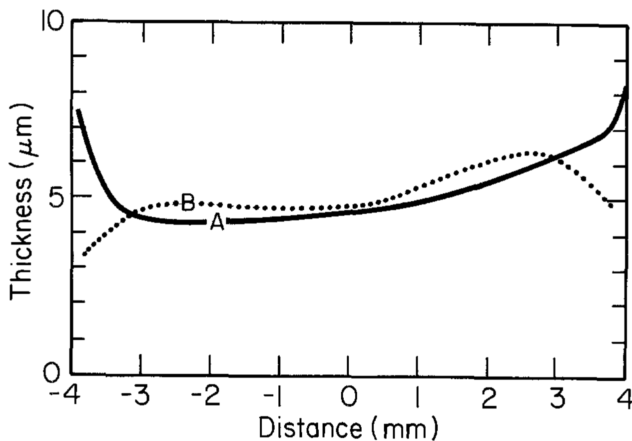

Fig. 8. Thickness profiles after 10 min of growth at 900°C with a current density of 5 A/cm^2 in the presence of a very small temperature gradient. Curves A and B were obtained with graphite pedestals of different diameters (see text).

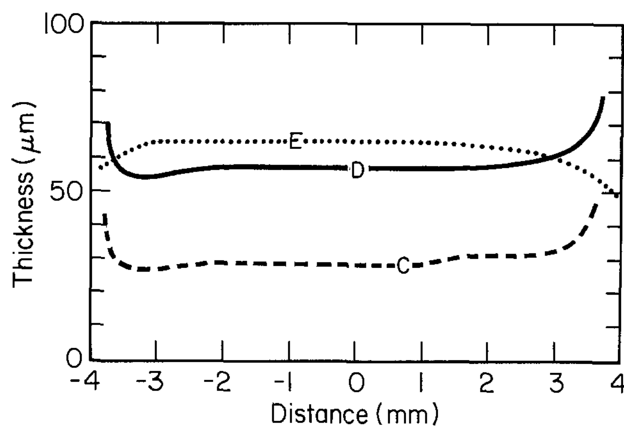

Fig. 9. Thickness profiles after 10 min of growth at 900°C in the presence of a very small temperature gradient: current density; curve C, 25 A/cm^2; D, 50 A/cm^2; E, 60 A/cm^2.

variation of the current density across the growth interface due to the geometry of the system. Since both current-carrying rods are located on one side of the growth cell, it is expected that the resistance to current flow will be smallest, the current density will be largest, and thus the thickness of the layer will be largest on that side of the cell.

At increased current densities (Fig. 9) apparently the effect of the current density gradient (an increase in growth rate from right to left) is essentially compensated by the effect of the 0.15°C/cm horizontal thermal gradient (an increase of the growth rate from left to right); another compensating factor is perhaps diffusion of As from areas of higher current density [higher As concentration due to electromigration (4)] to areas of lower current density (lower As concentration).

Summary

Although electroepitaxy has been used for several years for the successful growth of III-V compound layers and devices, the role of various experimental parameters on the characteristics of the layers has not as yet been extensively studied. The present work is concerned with parameters affecting the thickness uniformity of the layers.

Two types of epilayer thickness variations were observed: random fluctuations and systematic variations. The random fluctuations were found to be associated with nonuniform current density at the growth interface, resulting from random defects in the electric contact to the substrate. Random fluctuations were also found to result from fluctuations in the resistance across the substrate, which in turn were caused by fluctuations in the depth of substrate dissolution by the Ga contact layer. For relatively thin substrates the dissolution depth represented a significant fraction of their thickness since a relatively thick layer of Ga (~150 μm) is necessary for a satisfactory spread. These fluctuations were eliminated by placing a tantalum foil in contact with the gallium layer. This foil dissolves part of the gallium when the assembly is heated to establish electric contact. Thus, the Ta foil essentially decreases the effective thickness of the gallium layer and thus the extent of dissolution of the substrate by the gallium.

In the presence of convection in the solution the thickness profile of the layers was found to reflect the convective flow pattern in the solution. The primary cause of convection was identified with the horizontal temperature gradients resulting from joule heating which was found to be more pronounced at the contacts of the current carrying rods and the graphite segments. Convective flow affecting the growth was observed for Grashof numbers greater than about 10^4. Convective interference was eliminated by minimizing the temperature gradient across the solution through reduction of the system's resistance and by positioning the solution well in the furnace so that the horizontal gradient in the solution prior to current flow was of the same magnitude but opposite sign to that induced by joule heating. The thickness profiles of the layers grown without convective interference were found to reflect the gradient of the current density across the growth interface associated with the geometry of the growth system and a very small horizontal temperature gradient due to joule heating. These two effects compensated each other at high current densities, and thus epilayers with the most uniform thickness were obtained at current densities of 50-60 A/cm^2.

Although random thickness fluctuations and convective interference were minimized or essentially eliminated, work for achieving epilayers with perfectly uniform thickness continues.

Acknowledgment

The authors acknowledge with gratitude the financial support of the National Science Foundation. They are grateful to Drs. J. Lagowski, E. P. Martin, Jr., and

Professor A. F. Witt for stimulating discussions. In addition, they are grateful to Dr. Lagowski for his suggestion that current-controlled liquid phase epitaxy be called electroepitaxy.

Manuscript submitted Nov. 21, 1977; revised manuscript received March 15, 1978.

Any discussion of this paper will appear in a Discussion Section to be published in the June 1979 JOURNAL. All discussions for the June 1979 Discussion Section should be submitted by Feb. 1, 1979.

Publication costs of this article were assisted by the Massachusetts Institute of Technology.

REFERENCES

1. M. Kumagawa, A. F. Witt, M. Lichtensteiger, and H. C. Gatos, *This Journal*, **120**, 583 (1973).
2. D. J. Lawrence and L. F. Eastman, *J. Cryst. Growth*, **30**, 267 (1975).
3. D. J. Lawrence and L. F. Eastman, *J. Electron. Mater.*, **6**, 1 (1976).
4. L. Jastrzebski, H. C. Gatos, and A. F. Witt, *This Journal*, **123**, 1121 (1976).
5. L. Jastrzebski and H. C. Gatos, in "Proceedings of the 6th International Symposium on GaAs and Related Compounds," St. Louis, Institute of Physics Conf. Ser. 33b, p. 88, Bristol and London (1976).
6. L. Jastrzebski and H. C. Gatos, Paper submitted to *J. Cryst. Growth*, **42**, 309 (1977).
7. A. Abdul-Fadl and E. K. Stefanakos, *ibid.*, **39**, 341 (1977).
8. J. J. Daniele and C. Michel, in "Proceedings of the Symposium on GaAs and Related Compounds," Deauville, France, Institute of Physics and Phys. Soc. London, p. 155 (1975).
9. J. J. Daniele, *Appl. Phys. Lett.*, **27**, 373 (1975).
10. J. J. Daniele, D. A. Cammack, and P. M. Asbeck, *J. Appl. Phys.*, **48**, 914 (1977).
11. L. Jastrzebski, H. C. Gatos, and A. F. Witt, *This Journal*, **124**, 633 (1977).
12. J. J. Daniele, Results presented at ICCG-5, Boston, July 1977.
13. M. Lichtensteiger, A. F. Witt, and H. C. Gatos, *This Journal*, **118**, 1013 (1971).
14. K. M. Kim, A. F. Witt, and H. C. Gatos, *ibid.*, **119**, 1218 (1972); K. M. Kim, A. F. Witt, and H. C. Gatos, *ibid.*, In press.
15. S. I. Long, J. M. Ballantyne, and L. F. Eastman, *J. Cryst. Growth*, **26**, 13 (1974).
16. M. J. Steward and F. Weinberg, *ibid.*, **12**, 217 (1972).

Silicon Oxidation Studies: The Oxidation of Heavily B- and P-Doped Single Crystal Silicon

E. A. Irene* and D. W. Dong*

IBM Thomas J. Watson Research Center, Yorktown Heights, New York 10598

ABSTRACT

The present oxidation study covers the 780°-1150°C temperature range using 0.001 Ω-cm Si which is heavily B- and P-doped Si ($6\text{-}8 \times 10^{19}$ cm^{-3}) in dry O_2 (<1 ppm H_2O). Emphasis is on the lower temperatures thereby extending the scope of already published studies. For 0.001 Ω-cm Si at temperatures greater than 1000°C, the over-all oxidation rates were found to conform to the order

B doped > P doped > STD

(where STD is 2 Ω-cm B-doped Si), which is in agreement with published results for the higher temperatures. However, for the lower oxidation temperatures of the present study (≤1000°C), the order for the over-all oxidation rates was found to be

P doped > B doped ≥ STD

The oxidation data was taken using an automated ellipsometer *in situ* and was analyzed using a linear-parabolic oxidation model. The resulting linear rate constants could be correlated with well-known B depletion and P accumulation effects near the Si-SiO_2 interface while a consideration of the structural roles of B and P in the SiO_2 network was necessary to explain the parabolic rate constants. Phase separation of B_2O_3 occurred in the SiO_2 grown on B-doped Si and Si precipitation was observed in all the oxides grown at 1150°C but neither of these phenomena are believed to affect the oxidation kinetics. The extended temperature range showed non-Arrhenius behavior which could explain the divergent activation energies reported from published studies.

An understanding of the oxidation kinetics for single crystal silicon which has been heavily doped (~10^{20} cm^{-3}) with donor or acceptor impurities is important in the practice of planar technology. Previous studies on this topic (1-5) have shown that a redistribution of the electrically active impurities (As, B, P, etc.) occurs during the thermal oxidation of Si. Specifically, it was discovered (3, 4) that during oxidation the acceptor impurities studied (Al, B, Ga, and In) depleted near the Si surface while the donor impurities studied (As, P, Sb) piled up at the Si surface. The extent to which the redistribution occurs depends on the oxidation temperature and ambient 3-5). At lower temperatures and in an H_2O-containing oxidation ambient, B depletes more and P accumulates more. In order to understand these observations several factors are important. First, the relative solubilities of the impurity in Si and SiO_2 are important with donor impurities usually being relatively more soluble in Si (3). Second, the diffusivity of the impurity in SiO_2 is important with B having a slightly larger value than P at lower temperatures (6) but in an H_2O-containing ambient the diffusivity of B in SiO_2 increases several orders of magnitude.

By utilizing the linear-parabolic model for Si oxidation (7) in conjunction with the published redistribution effects and the fact that the Si dopants increase the oxidation rate when they affect it at all (5), the kinetics of the oxidation of heavily B- and P-doped Si can be qualitatively predicted. In the

* Electrochemical Society Active Member.
Key words: oxidation kinetics, impurities, thermal oxidation.

linear-parabolic model, the linear rate constant, k_L, is correlated with the reaction between the Si surface and oxidant, while the parabolic rate constant, k_P, is related to the diffusion of oxidant through the SiO_2 film. Then, it is predicted that at lower oxidation temperatures (<1000°C) where P accumulates and B depletes maximally, an accumulation of P at the Si surface will increase k_L maximally and the depletion of B from the surface should yield a minimal effect on k_L. At higher temperatures, where the B depletion is less, the effect on oxidation of a heavily B-doped Si surface on k_L should be observed. In order to predict changes in k_P values, the structural implications of B and P on the SiO_2 network must be assessed (8, 9). The role of P in SiO_2 is to substitute for Si in the network. The P in SiO_2 is tetrahedrally surrounded by O atoms similarly to Si in Si-O_4 tetrahedra, except that in the P-O_4 tetrahedra one of the O atoms is doubly bonded to P which precludes that O atom from bridging to an adjacent tetrahedron. A loosening of the SiO_2 network results. The net effect of this loosening on oxidation kinetics would be to increase k_P and it would be more pronounced at lower experimental temperatures where other network loosening mechanisms are minimized (such as thermal expansion and thermal vibration). The substitution of B in the SiO_2 network is difficult in low alkali SiO_2. This is due to the fact that B preferentially forms a three coordinate planar trigonal arrangement of O atoms which is structurally incompatible with the Si-O_4 tetrahedra. Consequently, a study aimed at defining the subliquidus miscibility gap in the SiO_2-B_2O_3 system (10) has shown that phase separation extends to the Si phase boundary with an upper consolute temperature of ~520°C. However, the effect of phase separation on the oxidation kinetics would be minimal because the amount of B_2O_3 phase is less than 1 mole percent (m/o) and the separation would not occur above 600°C, *i.e.*, during oxidation. An alternate mechanism has been proposed (11) in which a large number of oxygen vacancies are created when B cations enter the SiO_2 network. These defects occur as BO_3 is oxidized to BO_4 and are most likely to occur at higher temperatures where thermal vibrations create the greatest number of broken bonds. Therefore, the effect of B should be to increase k_P predominantly at high temperatures.

In order to test these predictions of the effect of B and P on k_L and k_P values, the oxidation data already published (5) needs to be extended to cover a broader temperature range, in particular lower temperatures. Also, the data need to be generated in a well-defined ambient and analyzed according to the linear-parabolic model. For these purposes an automated ellipsometer which can observe oxidation *in situ* (12, 13) was used to obtain oxidation data in pure dry O_2 (<1 ppm H_2O) (13, 14) over the temperature range 780°-1040°C and with point by point measurements up to 1150°C. The resulting data were analyzed for k_L and k_P values using a previously developed iterative least squares technique (13). Transmission electron microscopy (TEM) was used to survey whether any obvious morphological changes could explain the kinetic results.

Experimental Procedures

Wafer preparation.—The B-, P-, and As-doped Si slices were commercially acquired 3.2 cm diam, 0.025 cm thick, <100> oriented chem-mechanically polished Si slices. They were purchased as having a nominal bulk resistivity of 0.0008-0.0012 Ω-cm. Measurements at our laboratory yielded average values of 0.0016 Ω-cm for B-doped, 0.0009 for P-doped, and 0.0022 for As-doped material, all values within ±5% across the wafers. These resistivity values correspond to concentrations of about 6×10^{19} cm^{-3} for B-doped and 8×10^{19} cm^{-3} for P-doped material.

Prior to oxidation the wafers were thoroughly cleaned by a previously detailed procedure (14). For transmission electron microscopy observations, 3 × 3 mm chips of Si with the SiO_2 film on one side were prepared by a previously outlined procedure (15).

Gas purity.—The moisture content of O_2 and its effect on Si oxidation kinetics has been the subject of several previous studies at our laboratory (13, 14, 16). The gaseous O_2 used for the present study is from boil-off of liquid oxygen and has been purified by a previously published procedure (14) which removes hydrocarbons and thereby reduces the H_2O content to less than 1 ppm as measured at the oxidation tube exit under oxidation conditions.

Ellipsometry.—The automated ellipsometer which can measure oxide thickness while oxidation is occurring, *in situ*, has been described previously (12). The procedures for the use of the automated ellipsometer, temperature calibration, and optical constants used for ellipsometry calculations have also been previously published (12, 13). The analyses of thickness (d) and time (t) data have been done by a linear least squares technique (13). Preliminary ellipsometry measurements made on oxide grown on heavily B- and P-doped Si have shown that the doping does not alter the optical constants or procedures used for the ellipsometry performed on undoped silicon.

Results and Discussion

Over-all oxidation rates.—From the thickness-time oxidation data presented in Fig. 1a-f, several observations can be made. First, when B and P affect the oxidation rate, both dopants enhance the rate as previously reported [see for example Ref. (5)]. At the higher experimental temperatures (1040° and 1150°C) and for thicker films the heavily B-doped Si exhibits a higher over-all rate than P-doped and lightly doped Si, again in nominal agreement with a previous study (5). However, at lower oxidation temperatures, the heavily P-doped Si exhibits the highest over-all rate and the heavily B-doped Si has about the same rate as lightly doped material. Although, this is not in agreement with published results (5), our results are more extensive at the lower temperatures and the trends in our data are predictable based on published depletion and accumulation effects (3-5) as presented below. The crossover in the oxidation rates between the heavily P- and B-doped Si occurs for the 1040°C oxidation at about 2000Å. Finally, one experiment using heavily As-doped Si displayed the same oxidation behavior as for heavily P-doped Si but with a slightly lower over-all oxidation rate. In order to gain further insight into the "crossover" behavior between P and B as a function of temperature the linear, k_L and parabolic, k_P rate constants need to be considered.

Rate constants.—The k_L and k_P values are shown in Table I. The errors associated with the 780°-1040°C data are less than 10% and are primarily due to the approximate nature of the linear-parabolic model (13). For the 1150°C data the errors are estimated to be larger but less than 20%, and the increase is due to larger curve fitting errors with the fewer available data points. In accordance with the predictions made earlier which are directly deduced from previous impurity redistribution studies (3-5), the k_L values for B at the lower oxidation temperatures do not show any enhancement effect due to B, since B is expected to deplete maximally at these temperatures; P shows an enhancement effect on k_L at all temperatures due to the accumulation effect. Also as predicted, at the highest temperatures of the present study (1150°) where the B-depletion effect is minimum, the k_L is considerably higher than for P. The fact that the over-all rate for heavily P-doped Si is greater than B for the thinner films even at 1040°C is clearly seen as a k_L effect. For thinner films k_L is dominant and k_L for heavily P-doped Si is greater than k_L for heavily B-doped Si up to 1040°C.

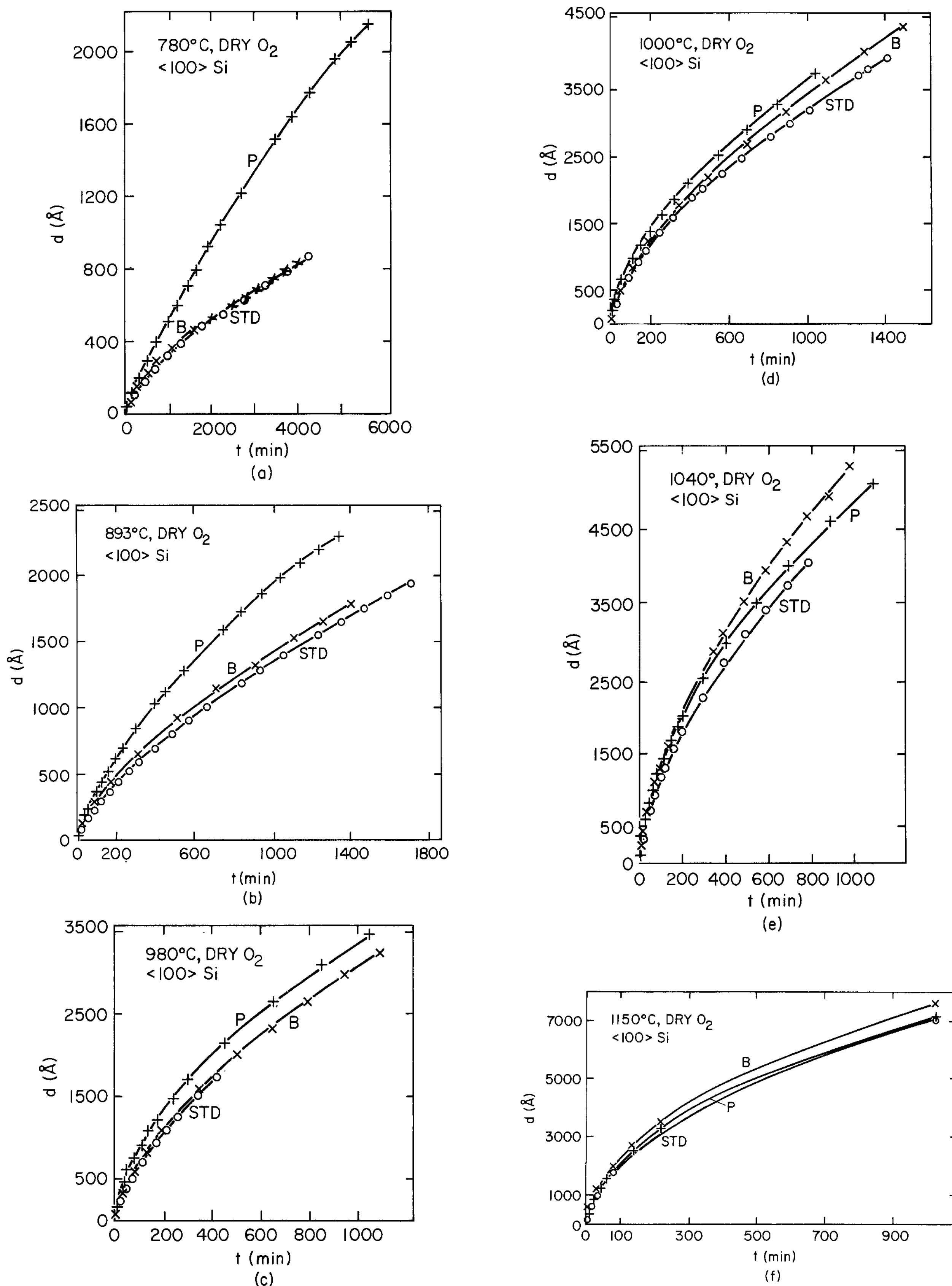

Fig. 1. Plots of SiO_2 film thickness, *d* (Å), *vs.* oxidation time, *t* (min), for heavily B (X), and P (+) doped Si against lightly doped Si (O) showing every fifth data point at (a) 780°C, (b) 893°C; (c) 980°C; (d) 1000°C; (e) 1040°C; and (f) 1150°C, all the data are shown.

Therefore, the crossover which occurs for larger thicknesses at 1040°C must be a k_P effect. The observation that both heavy B and P doping of Si causes an increase in k_L may be related to the fact that these impurities cause a substantial increase in the total (neutral plus ionized) vacancy concentration in Si (17). An enhanced vacancy concentration at the Si surface increases the number of Si atoms exposed to oxidant (by forming ledges, steps, etc.) thereby enhancing the amount of reaction at the surface.

The k_P for heavily P-doped Si is clearly greater than the standard at the lower temperatures as predicted. The network loosening attributable to P is lost at high temperatures where thermal vibrations

Table I. Rate constants obtained from linear least squares analysis of the oxidation data

Oxidation temp (°C)	k_L (A/min)*			k_P (A^2/min)*			d_o (A)**		
	STD	B	P	STD	B	P	STD	B	P
780	0.56	0.58	0.52	265	244	2,880	50	30	150
893	2.2	2.4	3.9	4,350	4,000	6,900	340	210	190
980	7.7	8.5	17	14,000	14,100	14,000	380	200	300
1000	12	13	21	14,300	16,000	16,000	350	350	370
1040	26	25	40	24,000	35,700	26,300	200†	200†	200†
1150	90	170	140	53,000	60,000	52,000	200†	200†	200†

* The maximum spread in k_L and k_P values is less than ± 10%.
** The errors in d_o values are estimated to be ± 50A for STD values and ± 100A for B and P data. The 1150°C data has a larger error of about ± 150A due to having only 10 data points per curve.
† 200A represents the maximum value considering a large scatter.

and expansion dominate. However, even larger amounts of P in SiO_2 than in the present study should extend the enhanced k_P to higher temperatures.

In addition to the enhanced k_L for heavily B-doped Si at high temperatures due to less B depletion, the k_P for B is also enhanced. This latter effect is consistent with Kang's arguments (11) which are predicated on defect equilibria being shifted toward larger defect concentrations at higher temperatures. The B effect on k_P requires many network bonds to be broken as $B\text{-}O_3$ changes coordination to become $B\text{-}O_4$. This can most easily occur at higher temperatures where the network vibrations are largest and simultaneously during interstitial diffusion of oxidant where there exist large forces exerted on the network. The net effect of B on k_P is a large enhancement at temperatures above 1000°C and hence gives rise to the crossover between P and B.

It is also interesting to note the variation of d_o values with temperature. As defined in the present study, d_o represents the upper thickness limit of the initial oxidation regime which does not conform to linear parabolic kinetics (7, 13, 14). The values of d_o are found using the iterative linear least squares analysis previously described (13). From Table I it is seen that d_o values for all the samples increase with temperature in the low temperature regime as previously reported for lightly doped material (13) but at higher temperatures the d_o values decrease. The smaller values of d_o mean that the oxidation data conform to linear-parabolic kinetics earlier during oxidation. The observation that d_o values go through a maximum near 1000°C suggests a change in oxidation mechanism near this temperature. The values of d_o near 200Å for higher temperature oxidation data agrees with a previous study (7).

Activation energies.—With k_L and k_P values over an extended temperature range, further insight into the oxidation mechanism may be obtained by interpreting the activation energies calculated according to an Arrhenius equation of the form

$$k = k_o e^{-Ea/RT}$$

Figure 2 shows that neither the linear nor parabolic rate constants obey the above Arrhenius equation. This probably means that both k_L and k_P represent a composite rate constant rather than a kinetically simple step. Therefore, a straightforward interpretation of the E_a values is not possible.

The curvature of the Arrhenius plots suggests that the discrepancies which exist between previous studies (7, 13) may be due to the different temperature ranges used. To clarify this situation, E_a values were calculated by least squares analysis of four k_L and k_P values at the lower temperatures (780°, 893°, 980°, and 1000°C) and separately using four k_L and k_P values at the highest four temperatures (980°, 1000°, 1040°, and 1150°C). These E_a values as well as the literature values are compared in Table II. Since one study considered mainly higher temperature data (7) and the other lower temperature data (13), the discrepancy

Table II. Arrhenius activation energies comparison for the high and low temperature regimes

Temp range	$E_{a,L}$ (eV)			$E_{a,P}$ (eV)		
	STD	B	P	STD	B	P
980°-1150°C (4 points)	2.2	2.7	2.0	1.3	1.3	1.2
780°-1000°C (4 points)	1.6	1.6	1.9	2.1	2.2	2.1
780°-1150°C (6 points)	1.8	1.9	2.0	1.9	2.0	1.8
Deal and Grove (7) 900°-1200°C	2.0	—	—	1.2	—	—
Irene and van der Meulen (13) 780°-980°C	1.5	—	—	2.3	—	—

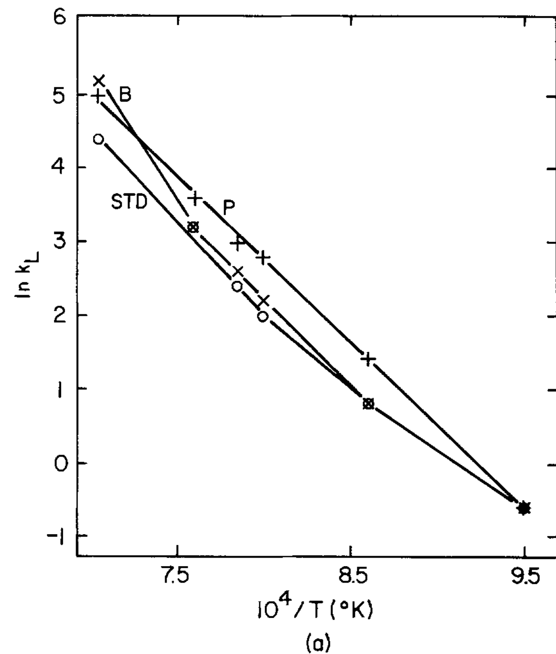

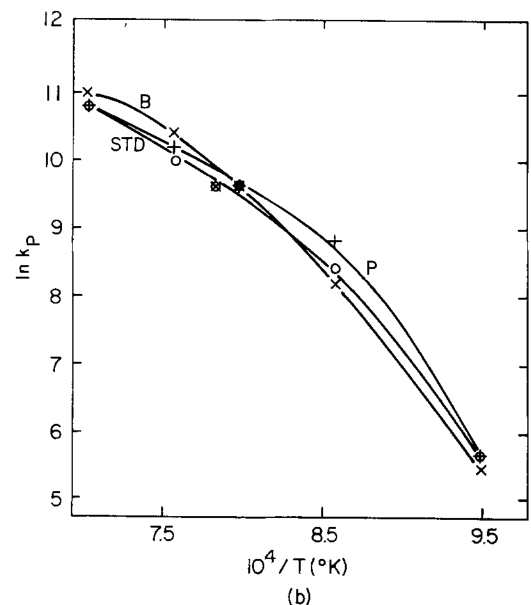

Fig. 2. Arrhenius plots of (a) ln k_L vs $1/T$ and (b) ln k_P vs. $1/T$ for the data from Table I.

is clearly due to the non-Arrhenius behavior. Even though one study (7) used <111> Si while the other used <100> Si, it was previously shown (14) that there is less than ±0.2 eV difference between E_a values for <111> and <100> Si orientations in the same temperature interval.

Transmission electron microscopy (TEM).—Samples of SiO_2 grown on heavily P- and B- doped Si as well as lightly doped Si at 780° and 1150°C were compared by TEM. The TEM investigation was directed at finding microstructure (such as voids or channels) which could account for the differences in diffusion behavior. However, except for two observations relating to the appearances of microphases and described below, there were no differences in the different films resolvable in the present TEM study. As to be discussed, the microphase phenomena cannot explain the kinetic results. Therefore, based on this negative TEM result, it is concluded that the diffusion enhancement caused by P in SiO_2 at lower temperatures and B in SiO_2 at higher temperatures is due to the creation of smaller defects (<20Å) than resolvable in the present study by TEM and probably involves network defects as hypothesized by Kang (11).

As shown in Fig. 3, certain areas of the SiO_2 films grown on heavily B-doped Si at 1150°C and to a lesser extent on 780°C grown SiO_2 displayed an amorphous microphase. Since B_2O_3 is expected to phase separate due to structural incompatibilities (8-10), we believe that the microphase is amorphous B_2O_3. As estimated from the micrographs the B_2O_3 phase comprises about 0.5% by volume of the film. However, since the regions of SiO_2 film which displayed phase separation were widely separated, a more realistic estimate would be about 0.05%. If all the B were incorporated in the SiO_2, about 0.3% B_2O_3 would be expected. Considering the large errors in estimating the volumes from micrographs and the possibility of loss of B during oxidation, the agreement is reasonable. Because phase separation in the amorphous B_2O_3-SiO_2 system occurs on cooling from the oxidation temperature to about 520°C (the upper consolute temperature), there should be no effect on the oxidation kinetics.

In addition to the B_2O_3 microphase in B-containing SiO_2 samples, Si islands were observed in all the SiO_2 films grown at 1150°C, and an example is shown in Fig. 4. The distribution is sparse as most areas observed has no Si islands. Selected area diffraction and dark field techniques positively identified the islands as crystalline Si (Fig. 4). Only rarely was the same structure seen for films grown at lower temperatures. The fact that this microstructure occurs predominantly at the high temperatures suggests that a disproportionation reaction with chemical transport is taking place. A reaction such as

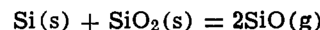

$$Si(s) + SiO_2(s) = 2SiO(g)$$

goes further to the right at higher temperatures near the Si-SiO_2 interface The gaseous SiO produced diffuses away from the interface into the SiO_2 film and equilibrates producing Si(s) and SiO_2(s). At the high temperatures a larger amount of SiO(g) is produced, and the Si which comes from SiO has enough mobility to form islands. Thermochemical calculations have shown that at 1150°C the partial pressure of SiO(g) is about 10^{-3} atm. That pressure of SiO(g) would provide a pressure of Si(g) of more than 10^{-6} atm at 1150°C. At 1150°C the saturation pressure for Si is about 2×10^{-5} atm. Therefore considering a nonideal system the conditions for the production of free Si in SiO_2 can occur. However, since this effect was seen for the standard, as well as for B- and P-doped SiO_2 films

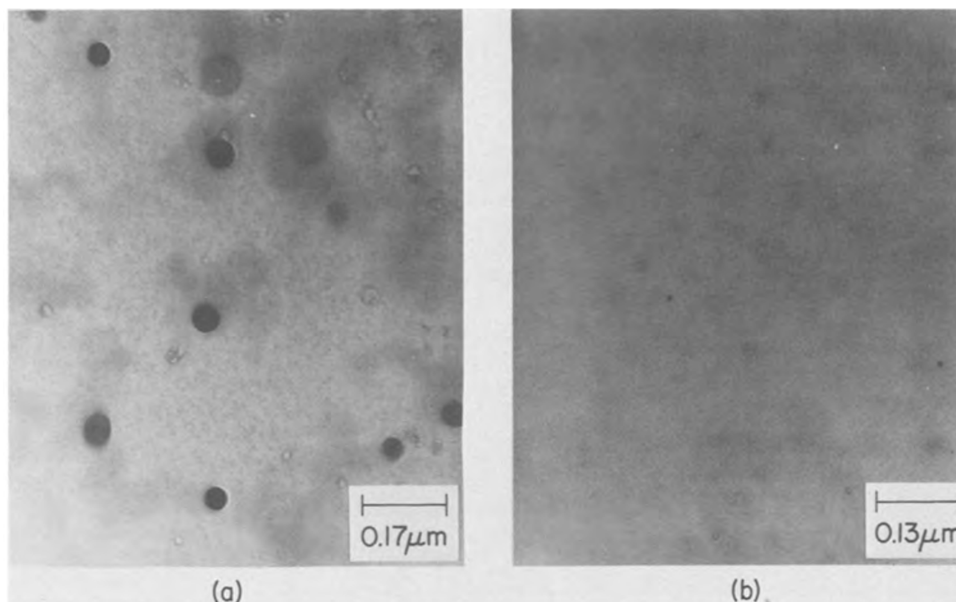

Fig. 3. TEM micrographs showing B_2O_3 phase separation at (a) 1150°C and (b) 780°C in SiO_2 films grown on heavily B-doped Si.

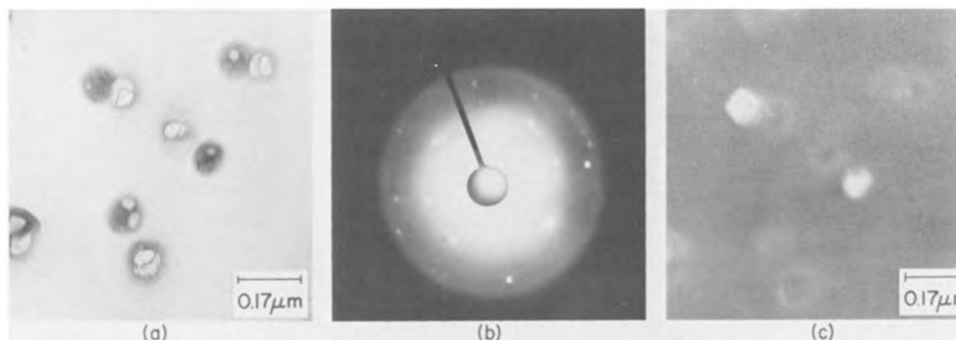

Fig. 4. TEM micrographs showing typical Si island formation in SiO_2 films grown at 1150°C on lightly doped Si (a) bright field, (b) selected area diffraction, (c) dark field.

at 1150°C, no impurity driven effect on oxidation is attributed to the Si precipitation.

Since this study deals with the oxidation of heavily B- and P-doped Si, the B_2O_3 phase separation effect and the Si precipitation effect will be discussed at greater depth in a future publication.

Conclusions

From an extension of the oxidation data for heavily B- and P-doped Si to lower temperatures and an analysis of the data in terms of the linear-parabolic model several conclusions are made:

1. P primarily increases the over-all oxidation rate at lower temperatures while B is more effective at the higher oxidation temperatures.
2. The accumulation of P and depletion of B at the Si surface explain the variation of k_L values with temperature.
3. The enhancement effect of P on k_P is due to a loosening of the SiO_2 network. When P substitutes for Si in Si-O_4 tetrahedra, fewer bridging oxygens are provided. The net loosening effect is most pronounced at lower temperatures where other network loosening factors are smaller.
4. The enhancement of k_P due to B is due to the creation of defects when B-O_3 is oxidized to B-O_4. This mechanism is favored at higher temperatures where bonds are more likely to be broken.
5. TEM supports the atomistic arguments to explain the k_P results, since no morphological differences were found in the various oxides which could be correlated with an enhanced diffusion of oxidant.
6. Over the extended temperature range of the present study, the Arrhenius relationship is not obeyed. Hence there is no straightforward interpretation of E_a values. However, divergent results from two previous studies (7, 13) are explained based on the Arrhenius plots.

Acknowledgments

The authors gratefully acknowledge helpful discussions with Drs. T. Takamori and J. A. Van Vechten and the help of Drs. A. B. Fowler, R. Ghez and D. R. Young in reviewing this manuscript and of Dr. J. Blum for the silicon substrate resistivity measurements. This research was partially supported by the Defense Advanced Research Projects Agency and monitored by the Deputy for Electronic Technology, RADC, under Contract F19628-76-C-0249.

Manuscript submitted Dec. 12, 1977; revised manuscript received Feb. 15, 1978.

Any discussion of this paper will appear in a Discussion Section to be published in the June 1979 JOURNAL. All discussions for the June 1979 Discussion Section should be submitted by Feb. 1, 1979.

Publication costs of this article were assisted by the IBM Corporation.

REFERENCES

1. M. M. Atalla and E. Tannebaum, *Bell Syst. Tech. J*, **39**, 933 (1960).
2. F. Leuenberger, *J. App. Phys.*, **33**, 2911 (1962).
3. A. K. Grove, O. Leistiko, and C. T. Sah, *ibid.*, **35**, 2695 (1964).
4. B. E. Deal, A. S. Grove, E. H. Snow, and C. T. Sah, *This Journal*, **112**, 308 (1965).
5. B. E. Deal and M. Sklar, *ibid.*, **112**, 430 (1965).
6. M. Ghezzo and D. M. Brown, *ibid.*, **120**, 146 (1973).
7. B. E. Deal and A. S. Grove, *J. Appl. Phys.*, **36**, 3770 (1965).
8. A. E. R. Westman, in "Modern Aspects of the Vitreous State," J. D. Mackenzie, Editor, chap. 4, Butterworths and Co. Ltd., Washington (1960); P. J. Bray and A. H. Silver, *ibid.*, chap. 5.
9. R. Doremus, "Glass Science," chap. 3, John Wiley & Sons Inc. New York (1973).
10. R. J. Charles and F. E. Wagstaff, *J. Am. Ceram. Soc.*, **51**, 16 (1968).
11. K. D. Kang, PhD. Thesis, Ohio State University (1962).
12. Y. J. van der Meulen and N. C. Hien, *J. Opt. Soc. Am.*, **64**, 804 (1974).
13. E. A. Irene and Y. J. van der Meulen, *This Journal*, **123**, 1380 (1976).
14. E. A. Irene, *ibid.*, **121**, 1613 (1974).
15. E. A. Irene, V. J. Silvestri, and G. R. Woolhouse, *J. Electron. Mater.*, **4**, 409 (1975).
16. E. A. Irene and R. Ghez, *This Journal*, **124**, 1757 (1977).
17. J. A. Van Vechten and C. D. Thurmond, *Phys. Rev. B*, **14**, 3539 (1976).

High Oxygen Czochralski Silicon Crystal Growth Relationship to Epitaxial Stacking Faults

L. E. Katz* and D. W. Hill

Bell Laboratories, Allentown, Pennsylvania 18103

ABSTRACT

With larger diameter Czochralski-grown silicon crystals an increase in the oxygen content is observed. Oxygen in excess of the solubility limit will precipitate resulting in bulk crystal defects which can modify gettering of impurities known to degrade electrical characteristics. In this study we have investigated crystal growth parameters and related them to the properties of the crystal. Wafers were processed from crystals grown under various conditions. Defect formation was evaluated as a function of processing and related to the crystal properties. By growing 2 in. diam crystals at high seed rotation rates so as to maximize the oxygen content, we were able to suppress saucer etch pit formation and epitaxial stacking fault formation. The high oxygen content crystals behaved in the same manner as 3 in. diam crystals with respect to defect formation.

With the general introduction of larger diameter (3 in. or greater) Czochralski grown silicon crystals the oxygen content becomes of increasing concern due to the greater incorporation into the crystal during crystal growth and subsequent modification of defect formation during processing. Recently, correlations between process-induced defects and the interstitial oxygen content of the wafers being processed have been made (1-3). Defects studied have typically been saucer or shallow etch pits, oxidation-induced stacking faults, bulk stacking faults, epitaxial stacking faults, and precipitates.

* Electrochemical Society Active Member.

Key words: crystal growth, epitaxial stacking faults, oxygen in silicon, silicon defects.

The interstitial oxygen content can be controlled simply by selecting those crystals or wafers with the lowest oxygen content, by heat-treatment of the wafers to lower the interstitial oxygen content near the wafer surface (4), or by crystal growth modification.

Conceptually, oxygen in silicon can be both beneficial and harmful. Oxygen in excess of the solubility limit can precipitate with the subsequent formation of bulk stacking faults bounded by partial dislocations. Such defects, if penetrating the active device area, may prove harmful to junction characteristics. On the other hand, proper control over the positioning of the oxygen-induced defects can be potentially beneficial since they can act as gettering sites. Ideally, one might prefer to have the surface and perhaps the first 20-30 μm in depth void of bulk oxygen defects, while confining the bulk oxygen defects to the central portion (in depth) of the wafer. This can be controlled by proper processing (4).

It has been found that epitaxial stacking faults sometimes formed during standard buried collector integrated circuit fabrication (3). The nucleation sites for the stacking fault formation were suppressed in the regions which received an Sb buried collector diffusion. If the diffusion was carried out from an ion implanted source, subsequent formation of the epitaxial stacking faults was also suppressed in the non-Sb diffused regions. This was attributed to implant damage lateral gettering (3). A study of the epi stacking fault nucleation and growth mechanism (5) for similar standard buried collector transistor processing as discussed above indicates the nucleation process to be complicated and involving precipitates, dislocation, and voids as well as Ni and/or Cu contamination. The purpose of the work described in this paper was to: (*i*) investigate crystal growth parameters and relate these to the various characteristics of the crystal (interface shape, radial resistivity variation, and carbon and oxygen content using ASTM procedure F-121); (*ii*) process wafers from the various crystals through buried collector and epitaxial deposition and evaluate defect formation following each high temperature operation; and (*iii*) correlate the defect formation with the crystal properties.

Experimental

Dislocation-free silicon single crystals doped to $10^{15}/cm^3$ range and of (111) orientation were grown from 5.5 kg melts. Typically, the seed and the crucible containing the molten silicon are counter rotated. The crystal growth variables studied here were seed and crucible rotation rates which were varied from 5 to 40 rpm (seed) and 2 to 20 rpm (crucible). Following crystal growth, a section ~25 cm long from the seed end of each crystal was heat-treated to annihilate the donors formed during crystal growth. The remainder of each crystal was intentionally not heat-treated for comparative purposes. Following centerless grinding, slicing, and polishing, wafers were processed through epitaxial deposition. An outline of the processing sequence is presented in Table I. Two lots of 100 wafers each were processed. Each lot contained random wafers from the first section (seed end) of each crystal. The first section consisted of two parts, A and B, where A was subjected to the oxygen stabilization heat-treatment and B was not. Wafers from each of the sections were removed for analysis following each high temperature operation.

Table I. Processing sequence

1. Clean
2. Initial oxidation
3. Photoresist
4. Open windows
5. Clean
6. Sb predeposition from Sb_2O_5
7. Glass removal
8. Sb drive-in
9. Clean
10. Epi (~$1 \times 10^{16}/cm^3$ n-type, 6-8 μm)

Table II. Rotation rates and carbon and oxygen content of seed and rear end of crystal

RPM		Oxygen (PPMA)		Carbon (PPMA)	
Seed	Cruc	Seed	Rear	Seed	Rear
40	20	58	37	0.37	1.35
40	10	45	28	0.37	1.10
40	2	52	33	N.D.	1.03
20	20	51	33	0.36	2.00
20	10	33	28	1.11	2.95
20	2	41	26	0.57	2.42
10	5	35	26	1.11	3.21
5	2	34	27	0.57	2.02

The crystals were evaluated with respect to (*i*) carbon and oxygen content using infrared techniques (6),[2] (*ii*) solid-liquid interface shape using chemical etching (8), (*iii*) radial and longitudinal resistivity uniformity using the spreading resistance technique, and (*iv*) defect formation and distribution using the Secco etch (9) for wafers processed up to epi and interference contrast microscopy for the epi wafers.

Experimental Results and Discussion

Crystal properties.—Carbon and oxygen content.— Table II shows the seed and crucible rotation rates as well as carbon and oxygen content at the seed and rear end of the heat-treated section of the crystal. The rear in this case represents a distance approximately 25 cm from the seed end representing ~1/3 of the solidified portion of the crystal. An oxygen stabilization heat-treatment was carried out prior to infrared analysis. This treatment did not appreciably change the measured oxygen content. Carbon detection limits are ~0.35 ppm with the technique used, whereas all oxygen levels reported are well above detection limits. It is apparent that the oxygen concentrations are highest at the seed end of each section. The high seed rotation rate increases the oxygen content and the carbon behaves in an inverse manner to oxygen. Oxygen profiles were also taken across wafers from the various crystals. Results are similar to those presented by Rozgonyi *et al.* (3) and show that the peripheral regions of a wafer have lower oxygen content than the center.

The equilibrium segregation coefficient of oxygen in silicon is ~1 (10, 11) while that of carbon in silicon is ~0.07 (12). It is expected that vigorous crystal rotation may result in a departure from equilibrium. Kaiser and Breslin (11) have determined that the oxygen content of liquid silicon at its melting point is proportional to the bare silicon surface. Carruthers *et al.* (4) have shown that macro and microsegregation are dominated by thermal convection flows in the melt. In Czochralski growth, forced convection as accomplished by crystal rotation is used to modify the effects of thermal convection. Those authors (13) have discussed theoretically the effect of the thermal convection flows on segregation behavior. Hrostowski and Kaiser (14) have shown that crystals produced without rotation contain less oxygen than those which are rotated. This is presumably due to the stirring action of the rotating crystal supplying melt with high oxygen concentration to the growing interface (10). Their (14) observations are in line with the experimental observations presented here.

Interface shape.—Etching (8) of longitudinal sections taken from the seed end of the crystal after heat-treatment revealed there was little effect of seed or crucible rotation rate (over the range investigated) on the solid-liquid interface shape which was concave toward the melt. No faceting was observed. Interface shape is important since it is one factor related to the radial solute distribution, *i.e.*, radial resistivity uniformity. The lack of an interface facet is generally necessary in achieving good radial resistivity uniformity.

[2] For a more complete discussion see, Ref. (7).

Resistivity uniformity.—Radial resistivity traces using the spreading resistance technique were taken across the entire 2 in. diam. of heat-treated (oxygen stabilized) sections from each crystal. Readings were taken every 250 μm across the wafer. Results showed no clear cut trend. Flatter resistivity traces seemed to be associated with the 20 and 40 seed rpm. Absolute values in terms of concentration correlated with the bulk doping level.

In addition, longitudinal spreading resistance traces were taken at 5 μm intervals on sections cut parallel to the growth axis. Typically, a distance ~0.7 mm was scanned. Generally, the resistance profiles were flat to within a few percent.

Processing results.—Wafers from each crystal were processed through buried collector and epi. Figure 1 after initial oxidation and Secco etching (3) shows the various macroscopic etching patterns observed on wafers from three crystals. These are typical of the etching patterns observed for all oxidized wafers examined. The photographs were taken in dark field, hence regions which show up as light on the photograph appear as cloudy to the naked eye. These regions will be referred to as cloudy etched regions. Regions which are dark in the photograph are clear to the naked eye and will be referred to as clear etched regions. We define three types of etching patterns shown in Fig. 1 as: Type 1, uniform etch pattern, cloudy to the naked eye across the entire wafer; type 2, radial etch pattern, clear and cloudy etch regions; type 3, edge etch pattern, clear over most of the wafer and cloudy at the edge. The vast majority of wafers grown at 40 seed rpm exhibited type 3 behavior shown in Fig. 3. In most cases such wafers were clear across the entire wafer. Pattern type 1 and 2 were observed on wafers taken from crystals grown with a seed rotation rate of 20 rpm and below with type 1 being more prevalent at the lower seed rotation rate. There was no correlation with crucible rotation rate. It will later be shown that the clear etched regions do not result in epitaxial stacking faults whereas the cloudy regions do. In addition, wafers which were not subjected to the buried collector processing did not result in epitaxial stacking fault formation.

Figure 2 shows higher magnification photographs of the clear and cloudy Secco etch regions for type 2 wafer from Fig. 1. The cloudy region, Fig. 2a, shows a high density of "saucer pits" (~10^7/cm^2) along with

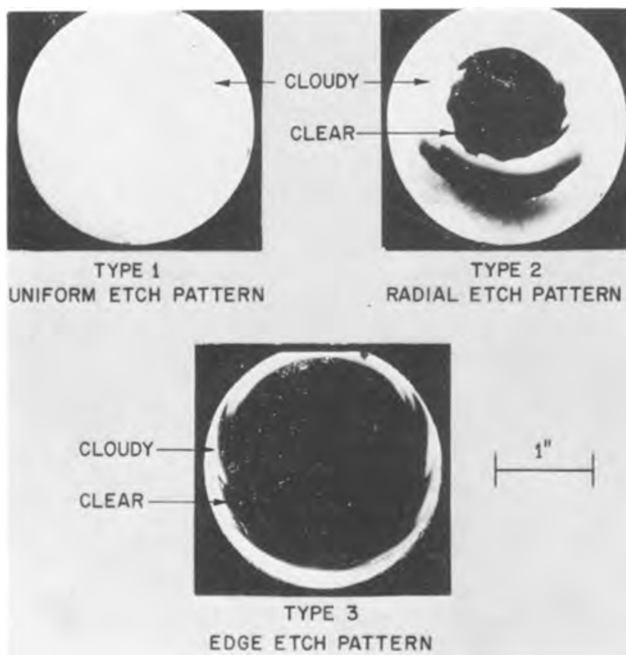

Fig. 1. Secco etched wafers after initial oxidation

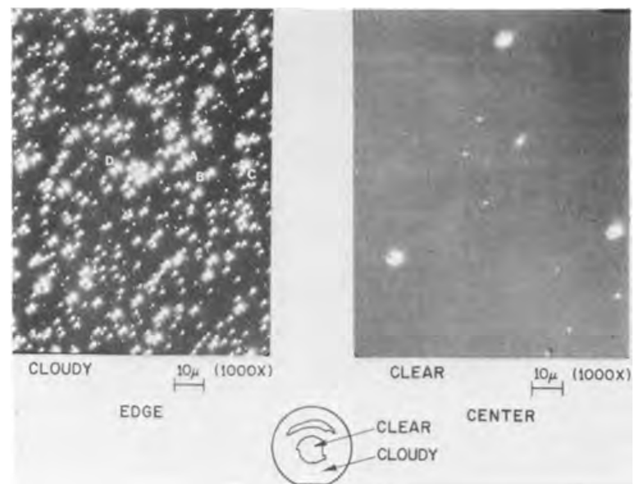

Fig. 2. Secco etched wafer after initial oxidation, clear and cloudy regions (a, left; b, right).

a lower density of oxidation-induced stacking faults (labeled A, B, C, and D). The saucer pits are generally not observed in the clear etch regions, but stacking faults at a nonuniform density ~10^2-10^3/cm^2 are often seen (Fig. 2b). The defects which we labeled A, B, C, and D in Fig. 2a have been identified by transmission electron microscopy as stacking faults (15). Type 1 and 3 wafers also showed similar etching and defect behavior as shown in Fig. 2a for cloudy regions and Fig. 2b for clear regions.

In order to determine whether the stacking faults were present in depth, 0.002 in. of material was removed by Syton polishing from a type 3 wafer. Results after etching, showed that stacking faults were still present in the clear etch regions. This demonstrates that bulk stacking faults were present in these wafers. Regions which etched cloudy still showed a high density of small saucer pits along with an occasional bulk stacking fault. Examination in cross section of cleaved wafers confirmed these observations.

The same gross etch pattern observed after initial oxidation (Fig. 1) followed through the buried layer processing with each high temperature operation. Thus wafers showing type 3 behavior after initial oxidation showed type 3 behavior after predeposition and drive-in. Similar wafers showing type 1 and 2 characteristics followed through the processing sequence showing the same behavior. As we show later, those areas etching "cloudy" on any type wafer resulted in epi stacking faults in the nondiffused regions. Those areas etching "clear" showed no epi stacking faults.

Secco etch results after predeposition are shown in cloudy and clear area, both diffused and nondiffused in Fig. 3 for type 2 and type 3 wafers. A similar study following drive-in is shown in Fig. 4. As is evident a high density of saucer pits is observed in cloudy etch regions, but a much lower density or complete absence is observed in clear etch regions.

Figure 5 shows the appearance of diffused and nondiffused regions, in unetched samples, following epitaxial deposition. Those defects in the photos which are V-shaped or triangular in appearance are epitaxial stacking faults. The photograph on the left was obtained from a type 1 sample whereas the one on the right was obtained from a clear region in a type 3 sample. Examination of over 100 wafers led to the firm conclusion that regions which exhibit cloudy etch behavior, as evidenced by a high density of saucer pits, will result in the formation of stacking faults in nondiffused regions during epitaxial deposition. In addition, regions which exhibit clear etch behavior do not reveal epitaxial stacking faults. In this particular study no deleterious effects were observed as a result of the high oxygen content.

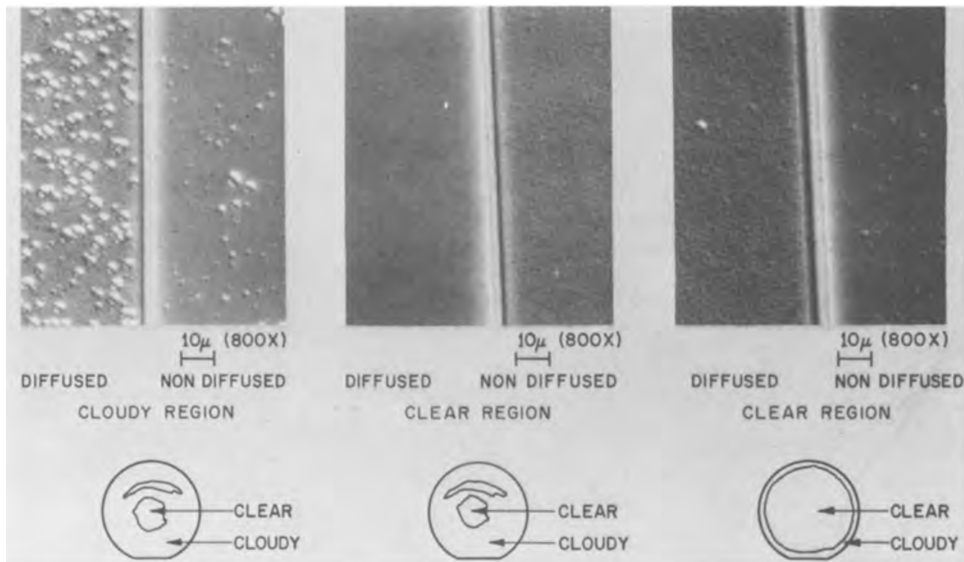

Fig. 3. Secco etched wafer after Sb predeposition.

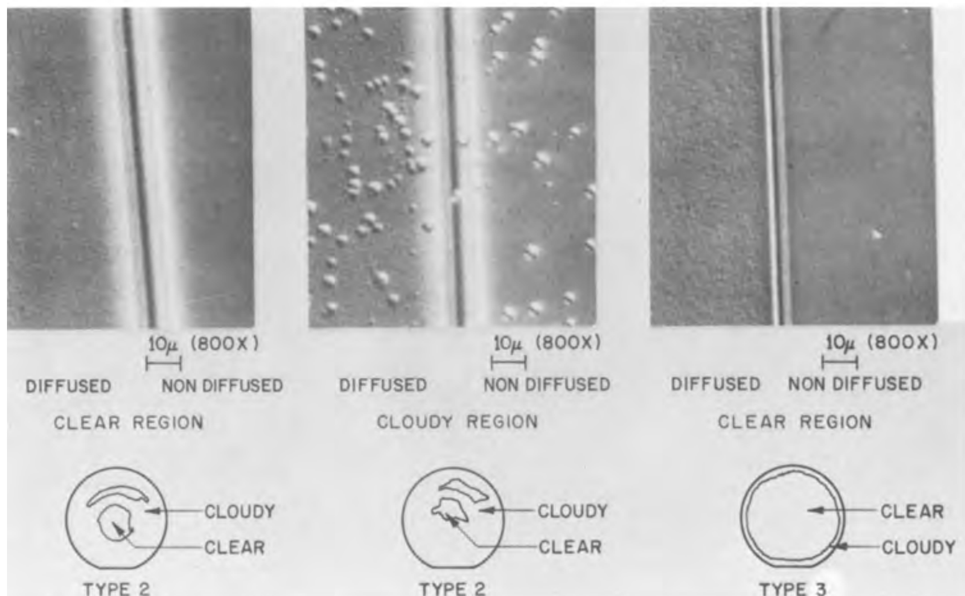

Fig. 4. Secco etched wafer after Sb drive-in.

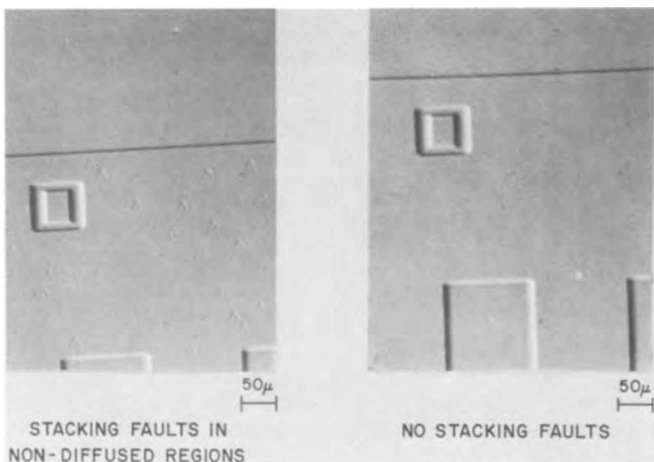

Fig. 5. Post epitaxial surfaces, (a, left) shows stacking faults in the nondiffused regions and (b, right) shows no stacking faults.

Correlation of defect formation with crystal characteristics.—Upon examination of wafers following epitaxial deposition, five categories of epitaxial stacking fault severity were chosen; they are (*i*) none, (*ii*) stacking faults at edge, (*iii*) radial distribution (from

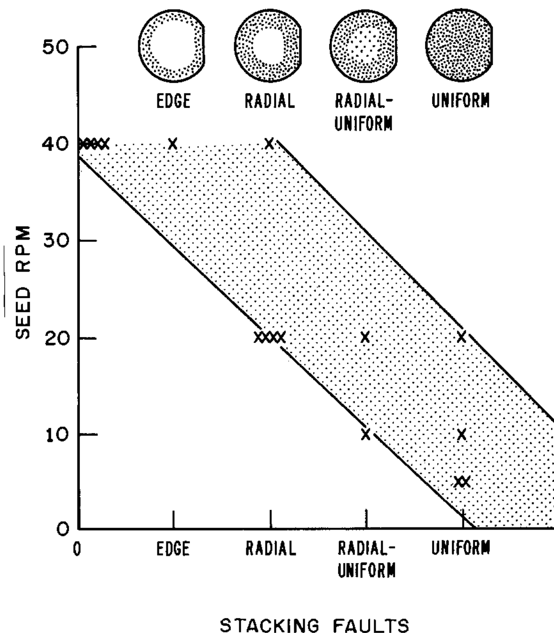

Fig. 6. Degrees of stacking fault formation as related to seed rotation rate.

edge part way toward center), (*iv*) radial to uniform distribution, and (*v*) uniform distribution. After all wafers were examined, the effect of crucible rpm on stacking fault formation was studied and no correlation was obtained. However, a similar study of seed rpm *vs.* stacking faults, Fig. 6, showed that high seed rpm, *i.e.*, 40 rpm, practically eliminated the epitaxial stacking fault problem; thirty-one out of thirty-six wafers from six different ingots showed no epi stacking faults at all. All wafers obtained from crystals grown at 20, 10, and 5 rpm showed stacking faults; sixty-four out of sixty-four wafers examined showed epi stacking faults. No difference was observed between heat-treated and nonheat-treated ingots for both high rpm and low rpm with respect to epi stacking fault formation. Presumably the initial oxidation equalizes the "heat-treated" and "nonheat-treated" wafers with respect to oxygen precipitation.

The radial oxygen profiles from our wafers and also those of others (3, 4) show that a correlation exists between radial stacking fault density and radial oxygen profile; namely, that the edge regions have lower oxygen levels than the central regions. In crystals grown at low turn rates, 20 rpm and lower, the epi stacking faults are observed most predominantly at the edge where the oxygen is lowest. Once the oxygen level becomes higher, even at the edge such as in the 40 rpm crystals, a drastic reduction in stacking fault level is observed. It thus appears that a strong correlation exists between (low) oxygen and stacking fault formation. This does not preclude a similar correlation with (high) carbon.

Since the epi stacking faults generally were not present in the 3 in. diam crystals where the oxygen content is typically near 40 ppm, it appears this value of the oxygen content is approximately the threshold above which the saucer pit formation is suppressed, presumably due to a gettering action by oxygen-induced defects. Thus by changing the crystal growth parameters we were capable of growing 2 in. diam crystals which exhibited properties of normal 3 in. diam crystals.

In analyzing the defect mechanisms involved, we must first consider those defects appearing at the initial oxidation. In lower oxygen content regions a high density of saucer pits was observed ($\sim 10^7/cm^2$) along with a much lower density of stacking faults. In high oxygen regions the predominant defect was the stacking fault which appeared in low density. Based on evidence obtained when 0.002 in. of silicon was removed after oxidation (which indicated the primary defect as stacking faults in high oxygen regions and saucer pits in low oxygen regions), it must be concluded that at least some of the stacking faults observed prior to the 0.002 in. removal are bulk stacking faults. These bulk stackings are presumably nucleated by the bulk oxygen precipitation in high oxygen regions. In addition, the high oxygen concentration presumably acts to suppress the saucer pit formation to a large enough degree that on further processing they do not form. The high oxygen content is just as effective in preventing subsequent epi stacking faults as implant buried layer gettering; however, the mechanisms are different. With implanted buried layers the gettering of the nondiffused regions takes place laterally whereas the oxygen gettering takes place immediately on the initial oxidation and appears to be a bulk effect.

A calculation of approximate defect densities of some of the defects observed shows:

surface stacking faults—low O_2 area $\sim 10^5$-$10^6/cm^2$
surface stacking faults—high O_2 area $\sim 10^2$-$10^3/cm^2$
saucer pits—low O_2 area $\sim 10^7/cm^2$
epitaxial stacking faults—low O_2 area $\sim 10^4/cm^2$.

A separate transmission electron microscope study has been carried out to determine the nucleating defects for the epitaxial stacking fault (5). This study showed that the stacking fault nucleation correlated well with the presence of defect centers resulting from metallic contamination of the epi-substrate interface.

Conclusions

We have shown here that altering crystal growth parameters can produce crystals which have significantly different defect properties. Increasing the oxygen content of 2 in. diam wafers suppresses epitaxial stacking fault formation in nonburied layer regions, thus making the 2 in. crystals behave similarly to 3 in. crystals. The high oxygen concentration prevents the formation of epi stacking fault nuclei.

As we emphasized earlier, high oxygen content wafers can result in the formation of process-induced defects. Bulk oxygen defects, properly positioned, can provide a beneficial gettering effect. Hence when using high oxygen content silicon an understanding and control over the distribution of oxygen in depth is important. Additionally, control must be exercised as to whether the oxygen is present in interstitial form or in a precipitated form.

Acknowledgments

The authors wish to thank C. W. Pearce, of the Western Electric Company, and P. H. Langer and G. A. Rozgonyi, of Bell Laboratories, for the input with respect to analytical data and useful discussions.

Manuscript submitted Nov. 21, 1977; revised manuscript received Feb. 16, 1978.

Any discussion of this paper will appear in a Discussion Section to be published in the June 1979 JOURNAL. All discussions for the June 1979 Discussion Section should be submitted by Feb. 1, 1979.

Publication costs of this article were assisted by Bell Laboratories.

REFERENCES

1. C. W. Pearce and G. A. Rozgonyi, in "Semiconductor Silicon 1977," H. R. Huff and E. Sirtl, Editors, p. 606, The Electrochemical Society Softbound Symposium Series, Princeton, N.J. (1977).
2. T. Y. Tan, E. E. Gardner, and W. K. Tice, Paper 70 presented at the Electrochemical Society Meeting, Philadelphia, Pa., May 8-13 1977.
3. G. A. Rozgonyi, R. P. Deysher, and C. W. Pearce, *This Journal*, **123**, 1910 (1976).
4. G. A. Rozgonyi and G. W. Pearce, *Appl. Phys. Lett.*, To be published.
5. P. M. Petroff, L. E. Katz, and A. Savage, in "Semiconductor Silicon 1977," H. R. Huff and E. Sirtl, Editors, p. 761, The Electrochemical Society Softbound Symposium Series, Princeton, N.J. (1977).
6. Annual Book of ASTM Standards, F121 and F123, American Society for Testing and Materials, Philadelphia, Pa. (1970).
7. J. R. Patel, in "Semiconductor Silicon, 1977," H. R. Huff and E. Sirtl, Editors, p. 521, The Electrochemical Society Softbound Symposium Series, Princeton, N.J. (1977).
8. M. Kamper, *This Journal*, **117**, 261 (1970).
9. F. Secco d'Aragona, *ibid.*, **119**, 948 (1972).
10. W. Kaiser and P. H. Keck, *J. Appl. Phys.*, **28**, 882 (1957).
11. W. Kaiser and J. Breslin, *ibid.*, **29**, 1292 (1958).
12. T. Nozaki, Y. Yatsurugi, and N. Akujama, *This Journal*, **117**, 1566 (1970).
13. J. R. Carruthers, A. F. Witt, and R. E. Reusser, in "Semiconductor Silicon 1977," H. R. Huff and E. Sirtl, Editors, p. 61, The Electrochemical Society Softbound Symposium Series, Princeton, N.J. (1977).
14. H. J. Hrostowski and R. H. Kaiser, *Bull. Am. Phys. Soc. Ser. II*, *k*, 294 (1956).
15. P. M. Petroff and G. A. Rozgonyi, Private communication.

Output Stability of n-CdSe/Na_2S-S-NaOH/C Solar Cells

A. Heller,* G. P. Schwartz, R. G. Vadimsky, S. Menezes, and B. Miller*

Bell Laboratories, Murray Hill, New Jersey 07974

ABSTRACT

When operated at the current densities in excess of 10 mA/cm^2 that are typical of efficient solar-irradiated photovoltaic cells, n-CdSe/1M Na_2S-1M S-1M NaOH/C semiconductor-liquid junction cells deteriorate with time. In CdSe electrodes that have lost activity, formation of a CdS-enriched film has been detected by means of Auger spectroscopy and electron beam-induced luminescence. Such a layer is a barrier to the flow of holes to the surface. The rate of deterioration increases with light flux, usually decreases with stirring, and depends on the crystal face exposed to the solution. Addition of small amounts of elemental selenium to the solution substantially improves the stability by preventing excessive sulfide enrichment of the surface. For example, with 0.5M Se added, the output of $\langle 11\bar{2}0 \rangle$ face electrodes run at 35 mA/cm^2 is essentially unchanged beyond 2×10^4 C/cm^2 charge passage.

Although numerous photoelectrochemical (1) and photochemical (2) systems have been cited as potentially useful solar to electrical power converters, none, to the authors' knowledge, has as yet simultaneously achieved high efficiency, low cost, and long-term output stability. Recently we have addressed some of these issues (3-10) and have shown that 7-9% solar to electrical conversion efficiency can be achieved with single crystal-based cells (3-6), that semiconducting photoelectrodes can be formed by the relatively economic means of metal anodization (7) or of hot pressing and annealing a powdered semiconductor (8), that cells with polycrystalline photoelectrodes reach 70% of the efficiency of cells with single crystals (8), and that a stable power output can be maintained in a semiconductor liquid junction solar cell by controlled, very slow etching of the surface of a photoelectrode (5). We noted, however, that in some of the more interesting cells, including the n-CdSe/Na_2S-S-NaOH/C cell for which we have examined single crystal, pressure-sintered polycrystalline, and anodically formed CdSe films, the power output deteriorates during operation (5). While confirming practically no weight change (9-11) in the photoelectrode upon prolonged use, we noted very substantial, and occasionally very rapid, drop in the power output of the cell at solar irradiance levels.[1] The constancy of weight is only poorly predictive of the stability of an electrode. While the photoelectrode may not dissolve, a film which blocks the flow of holes to the liquid junction may form, causing both current and voltage losses.

In this paper we examine how the output current of the n-CdSe/Na_2S-S-NaOH/C cell is affected by the interposition of a blocking film and the conditions under which this results. We find that a slight modification in the composition of the aqueous solution diminishes the tendency to form an inhibiting film and stabilizes the power output of the cells.

Experimental

The materials, solutions, light sources, electrochemical cells, and instrumentation were similar to those described earlier (4-8). Both single crystal (4) and polycrystalline, hot-pressed (8) CdSe electrodes were used. Their surface treatment was carried out in four steps prior to each run. First, the electrodes were etched for 30 sec in 4:1 HCl:HNO_3 (stored in a glass-stoppered bottle to reduce escape of vapors), then rinsed in distilled water. Next they were immersed 30 sec in a 10% aqueous KCN solution to dissolve any selenium that may be present following oxidation by the aqua regia. The electrode is then rinsed again in distilled water and used. This sequence of treatments to which we now add the KCN step provides a more reproducible electrode with a more consistent open-circuit voltage and better short-circuit current than those we previously observed.

We find that impurities introduced by storage of "analytical grade" $Na_2S \cdot 9H_2O$ crystals in dark glass bottles accelerate the deterioration of the CdSe photoanodes. Therefore, the crystals were purified until the results obtained were identical to those with Na_2S solutions prepared by bubbling H_2S into an aqueous NaOH solution. Also, the solutions were best formulated from the components directly in the electrochemical cells under a positive nitrogen pressure. Prolonged exposure to air induces earlier deterioration and stability runs were maintained under nitrogen.

Runs to measure the effect of stirring were accomplished with magnetic bars; in these cases the electrodes were stationary. The trends in such data were verified by separate experiments with CdSe rotating-disk electrodes (8), although only curves with magnetically stirred or quiet solutions are cited here.

In extended runs the cells were operated with 1Ω precision resistor loads between photoanode and carbon cathode to approximate short circuit, and the voltage (0-10 mV) across the resistor was monitored.

The CdSe surfaces were prepared for the Auger/e-beam luminescence experiments as follows: the photoanode control specimens were etched as earlier described, then immersed in a 0.5M Na_2S solution and rinsed with deionized water. The photoanodes which saw Na_2S-S-NaOH solutions were rinsed with 0.5M Na_2S and deionized water. The equipment used for the Auger spectroscopy and for the luminescence experiments consisted of a PHI ESCA/Auger spectrometer (Model 548). The 376 eV Cd, 153 eV S, and 1315 eV Se Auger peaks were monitored.

Results

Figure 1 shows the dependence of the short-circuit current density on the charge per unit area passed through two stationary photoelectrodes of different crystal faces when individually operated in unstirred 1M Na_2S-1M S-1M NaOH solution with a one ohm load to a carbon cathode. That the drop in current density is due entirely to the photoelectrode, and not to the solution or to the counterelectrode, was shown by the fact that mild etching of the semiconductor at any time restores the cell output to its initial value. As seen in Fig. 1, the relative rate of loss in current density for either crystal face depends on the initial current density and thus the light flux. The stability is expressed in coulombs/cm^2 rather than time. This

* Electrochemical Society Active Member.

Key words: semiconductors, photoelectrochemistry, photoanodes, liquid junctions.

[1] G. Hodes, J. Manassen, and D. Cahen have indicated that electrode to be long lived at lower output levels (efficiencies). We are concerned with maintaining the initial higher values of which we have determined this system to be capable.

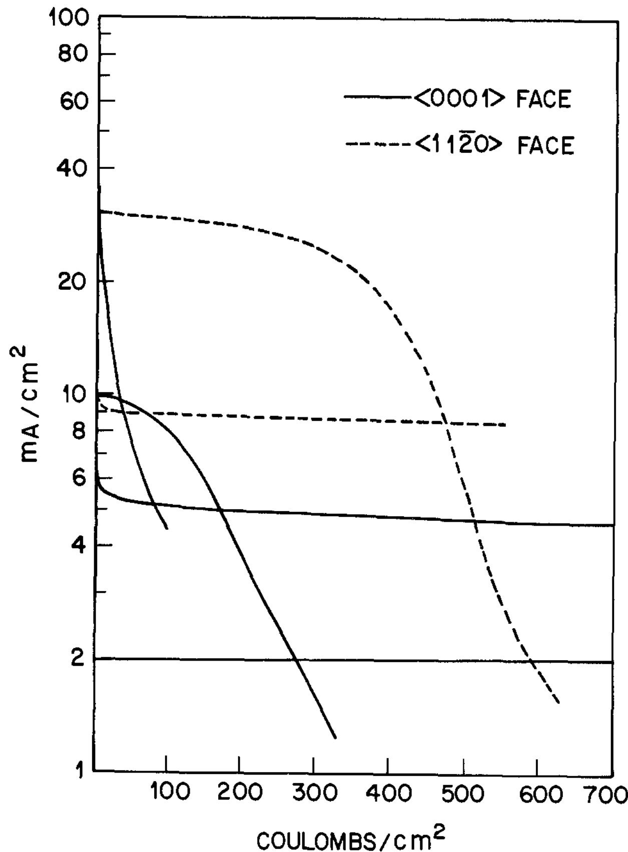

Fig. 1. Dependence of the short-circuit current stability of two n-CdSe photoanodes in a 1M Na_2S-1M S-1M NaOH solution on the initial current density (light flux). Solid lines are for <0001> face electrodes; dashed for <11$\bar{2}$0>. The solutions are not stirred.

allows us to compare electrode stability for different light fluxes along an axis expressing charge capacity, which is the significant factor for an energy source. For the <0001> face electrodes, light fluxes producing >10 mA/cm^2 evince nearly total deterioration in less than 400 C/cm^2. At lower fluxes stability is better maintained, and at 2 mA/cm^2 no deterioration is observed up to 700 C/cm^2. The behavior of the <11$\bar{2}$0> face is similar except that higher currents are tolerated. The curves for either face cross over, showing that initial operation at higher current densities results in lower activity after the passage of a sufficient charge in spite of the higher light flux. The <0001> and <000$\bar{1}$> planes consist of either Cd or Se atoms, the ions of opposite charge lying slightly below the plane. The <11$\bar{2}$0> plane contains an equal number of Cd and Se atoms.

Figure 2 shows the effect of stirring on the stability of the short-circuit current density of a freshly etched photoanode. The results shown are for the <0001> face, which deteriorates more rapidly (see above). Improved stability upon stirring is observed throughout the range of current densities studied (to 45 mA/cm^2) and is most pronounced for rapidly deteriorating electrodes. The long-term drop of the output cannot be simply ascribed to depletion at the electrode surface of electroactive species (which may be in sluggish equilibrium) since recovery of a previously unstirred cell with a deteriorated electrode cannot be achieved by stirring.

Figure 3 shows the effect on stability of the addition of elemental selenium to the 1M Na_2S-1M S-1M NaOH solution. Small concentrations of selenium dramatically improve the constancy of the short-circuit current density, even at a light flux sufficient to generate over 40 mA/cm^2. At 0.05M Se concentrations (not shown) there is virtually no change from the initial 35 mA/cm^2 short-circuit current density of a

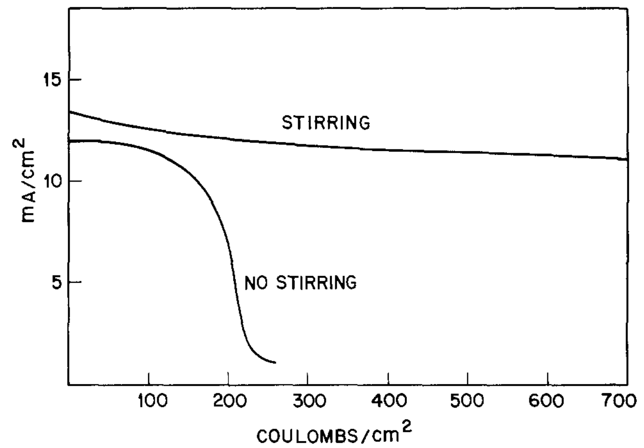

Fig. 2. Dependence of the short-circuit current stability on an n-CdSe <0001> face photoanode in a 1M Na_2S-1M S-1M NaOH solution on stirring.

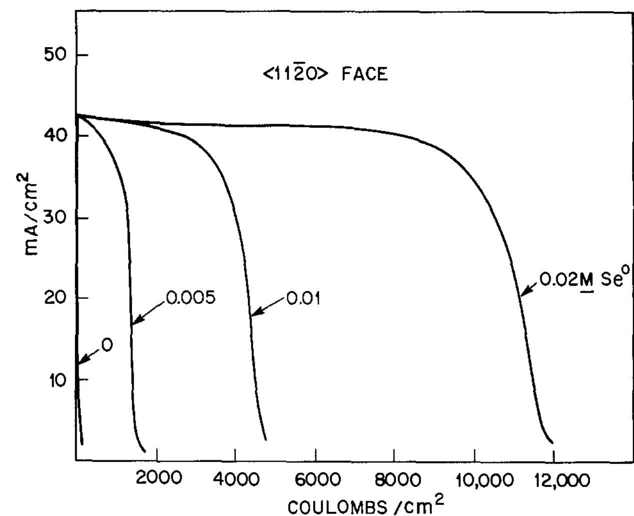

Fig. 3. Effect of Se addition on the short-circuit current output stability of an n-CdSe <11$\bar{2}$0> face photoanode in a 1M Na_2S-1M S-1M NaOH solution.

stationary, unstirred <11$\bar{2}$0> photoanode run to 20,000 C/cm^2.

Auger analysis of the near surface region was performed on freshly etched and deteriorated photoanodes. The near surface depth from which 95% of the Auger intensity emanates is given by 3λ cos 42.3°, where λ is the mean free path for an electron and the cosine term accounts for the collection geometry of our cylindrical mirror analyzer. Published values (12) for the dependence of λ on the electron's kinetic energy allow us to estimate detection depths ranging from roughly 11Å for sulfur LVV (153 eV) to 40Å for selenium LMM (1315 eV) transitions.

Deteriorated photoanodes evidenced an appreciable sulfur intensity (typically S(153 eV)/Cd(376 eV) ≈ 1.5) even after repeated rinsing to remove the physically adsorbed electrolyte. None of the surfaces was ion sputtered prior to measurement, and total contaminant levels due to carbon, oxygen, and Na_2S (detected by Na) varied from practically zero to an estimated 40% of the surface composition on various electrodes. The conversion of contaminant intensities into an atomic percentage of the detected volume is quite approximate because of errors in sensitivity factors and the assumption of a homogeneous distribution of elements in the surface.

However, the measurements systematically revealed a reduction in the Se/Cd intensity ratio on deteriorated electrode surfaces. The starting etched surface (Se × 10)/Cd ratio was 0.85, which is close to that of

samples of pure CdSe powder (0.83 ± 0.06). The corresponding ratios for samples run at light intensities which produced current densities of 2.5 and 20 mA/cm² were 0.61 and 0.34, respectively. This reduction in the observed Se/Cd ratio cannot be explained by a deposited sulfur or contaminant overlayer because the energy dependence of the inelastic mean-free path for electrons scales roughly as $\sqrt{E}$ (for $E \gtrsim 50$ eV) (12). Any such blocking layer would thus attenuate the low kinetic energy Cd intensity (376 eV) relatively more than the Se signal (1315 eV), thus increasing the Se/Cd ratio in contrast to what was observed.

During the Auger measurements, electron beam-stimulated luminescence in the red was observed. Of the many products whose existence was probable on the surface (CdSe, $CdS_{1-x}Se_x$, CdS, CdO, $Cd(OH)_2$, Na_2S, free S), CdS and $CdS_{1-x}Se_x$ (with $x << 1$) are unique in luminescing in the red. This luminescence was observed on samples simply immersed in the 1M Na_2S-1M S-1M NaOH solution, indicative of a CdSe → CdS replacement reaction even without passage of current. Qualitative visual observation of the luminescence intensity indicated a distinct increase in brightness on deteriorated electrode surfaces. Thus, both electron beam-stimulated luminescence and Auger studies are consistent with extensive surface substitution of CdS for CdSe in deteriorated electrodes.

The observation of luminescence on freshly etched, working electrodes which were immersed in sulfide-polysulfide solutions indicates that some replacement of the CdSe by CdS can be tolerated. Following passage of 1000 C/cm², the thickness of the zone in which CdS is detected is about 50-80Å, as estimated from the signal attenuation of the Se intensity and an electron inelastic mean free path of 15-25Å at 1315 eV.

Surfaces of electrodes run in 1M Na_2S-1M S-1M NaOH solutions containing 0.075M Se (in which they are stable) maintain their selenium surface content. Thus, while passage of 1000 C/cm² at a light flux producing an initial current density of 20 mA/cm² reduces the Auger Se/Cd peak intensity ratio by a factor of 2 on a <11$\bar{2}$0> face, there is no change in the same ratio when the solution contains 0.075M Se. Furthermore, the (Se × 10)/Cd peak intensity ratio drops from 0.83 to ~0.34 when 150 C/cm² are passed in the 1M Na_2S-1M S-1M NaOH at 20 mA/cm² through a polycrystalline photoanode, which deteriorates in that period. At low current densities (2.5 mA/cm²) at which the polycrystalline electrode remains active, the (Se × 10)/Cd ratio is 0.61 following the passage of the same charge.

Figure 4 compares the transmittance of the 1M-Na_2S-1M S-1M NaOH and the 1M Na_2S-1M S-1M-NaOH-0.075 Se solutions. Figure 5 compares the efficiencies (current-voltage curves) of two cells, one with a 1M-Na_2S-1M S-1M NaOH solution, and another with the same solution to which 0.075M Se has been added. As expected from Fig. 4, addition of Se decreases the short-circuit current. This >12% loss is, however, partly compensated for by an increase in the fill factor (from 0.50 to 0.55) and in the open-circuit voltage (from 0.755 to 0.765V). The net result is that 97% of the original solar to electrical conversion efficiency of 7.1% for the crystal used is retained in the solution of sharply improved output stability.

Exposure of the sulfur-sulfide solution to air during (or before) CdSe cell operation causes premature failure of the semiconductor electrode. Etching of the surface restores activity for only a very brief time (a few coulombs/cm²) in such an air exposed solution after initial failure. Although quantitative measurements of oxidative conversion of the solutions were not made, little or no visible bleaching of color could be detected after air exposures sufficient to make the cells deteriorate rapidly; these effects cannot be repressed by selenium additions and air access must be rigorously excluded.

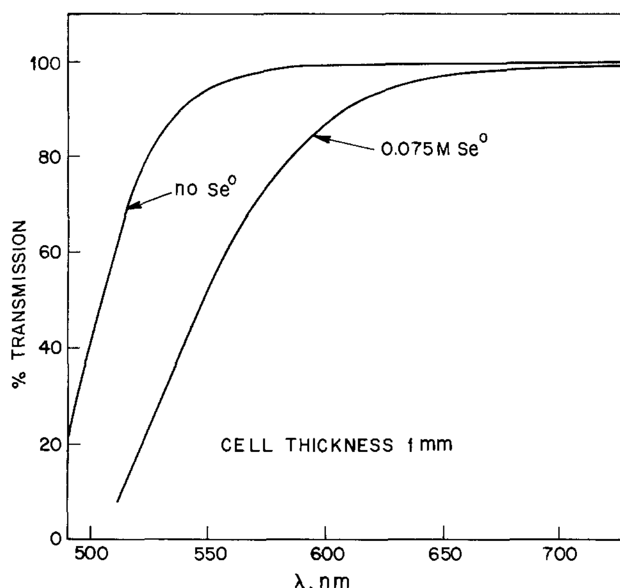

Fig. 4. Comparison of the transmittances of 1M Na_2S-1M S-1M NaOH and 1M Na_2S-1M S-1M NaOH-0.075M Se° solutions. The sample thickness is 1 mm.

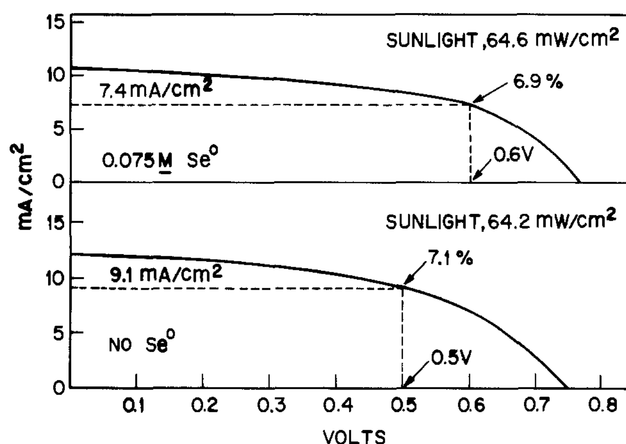

Fig. 5. Current-voltage curves under nearly identical solar irradiance for the same n-CdSe crystal run in 1M Na_2S-1M S°-1M NaOH with and without 0.075M Se present. Without Se(bottom): insolation 64.2 mM/cm²; open-circuit voltage 0.755; short-circuit current 12.1 mA/cm². With 0.075M Se (top): insolation 64.6 mW/cm²; open-circuit voltage 0.765; short-circuit current 10.6 mA/cm. Maximum efficiency parameters are indicated.

Polycrystalline hot-pressed CdSe photoanodes (8) deteriorate less rapidly than electrodes made with single crystal electrodes with <0001> faces exposed to the solution, but more rapidly than electrodes with exposed <11$\bar{2}$0> faces. Improvements upon addition of Se to the solutions parallel those described for <11$\bar{2}$0> electrodes, both for polycrystalline and <0001> photoanodes.

Discussion

Surface processes at CdSe in sulfide-polysulfide solution depend on the equilibria and kinetics of exchange processes typified by

$$CdSe(s) + S^{=} \rightarrow CdS(s) + Se^{=} \quad [1]$$

These will be modified by reactions

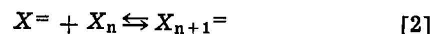

$$X^{=} + X_n \leftrightarrows X_{n+1}^{=} \quad [2]$$

for both sulfur and selenium and the existence of mixed complexes such as $S_pSe_q^{=}$, as well as incorporation of OH^-. Literature tabulations of the free energy of formation for CdS (13-15) and CdSe (16-19) show variations in excess of 5 kcal/mole. If we adopt the

NBS thermochemical compilation value of ΔG°_{298}(CdS) (15) = −37.4 kcal/mole and use the average of Ref. (16-19) for ΔG°_{298}(CdSe) = −24 kcal/mole, then the reaction

$$CdSe(s) + S(s) \rightarrow CdS(s) + Se(s) \quad [3]$$

is favored by ~13 kcal/mole. However, from standard electrode potentials of chalcogen/chalcogenide couples (−0.92V, Se and −0.50V, S) (20), the reaction

$$Se + S^{=} = Se^{=} + S \quad [4]$$

is thermodynamically unfavorable by 19 kcal/mole. Addition of Eq. [3] and [4] would imply that Eq. [1] is unfavorable by roughly 6 kcal/mole. Other sources however quote −0.78V for the Se/$Se^{=}$ couple (21), which reduces the instability of Eq. [4] by 6.5 kcal/mole. Our own potential measurements in fact are close to this more positive value. In view of the uncertainties in the tabulated free energies for reactions [3] and [4] and our omission of equilibria implied by Eq. [2], one cannot make a compelling argument concerning the relative thermodynamic stability of either bulk CdS or CdSe under the conditions of these experiments.

However, our Auger/luminescence observations indicate that exposure of an area of CdSe crystals to a volume of pure (*i.e.*, selenium-free) polysulfide will cause some exchange at the surface (with $Se^{=}$ either transported to the bulk or oxidized to the elemental state) until an over-all equilibrium is reached. A molecular layer contributes approximately 10^{-9} moles/cm^2 and therefore to a 10 cm^3 volume 10^{-7} molar concentration of the dissolved species. From the standard potential difference driving reaction (4) the concentration of $Se^{=}$ in the presence of excess polysulfide must be small if the total selenium content results from the CdSe crystal and any impurity content of the polysulfide solution. Auger spectroscopy data here and electron microprobe and x-ray diffraction results by Manassen *et al.* (11) point to sulfur and CdS on the surface when CdSe is removed from sulfide solutions. That the sulfur represents more than absorbed or occluded material and is actually bound as CdS is substantiated here by the red luminescence seen when the previously immersed n-CdSe specimen is stimulated by electron bombardment. The luminescence of freshly etched n-CdSe is practically undetected by the human eye which is insensitive at the 1.7 eV bandgap energy corresponding to 720 nm. The presence of 2.4 eV bandgap CdS shifts the emission into the visible.

The sulfur-containing layer resulting solely from immersion of n-CdSe in sulfide-polysulfide solution is very thin. In these thin films, electrons may tunnel from the solution to the semiconductor to enable photoanodic oxidation of electrolyte ions. However, development of thick layers of $CdSe_{1-x}S_x$, as measured by Auger spectroscopy, is associated with a blockage of current flow through the photoanode of the cell.

Two possible reasons for this blocking action are the following. First, and most important, a heavily doped large bandgap n-type semiconductor on a similar semiconductor of smaller bandgap blocks the passage of holes to the surface. From the electron affinities of CdS and CdSe, it is known (22) that the conduction band of CdS is closer to the vacuum level by about 0.2 eV. Under short-circuit conditions, the Fermi levels of the four phases are equal relative to vacuum, as shown in Fig. 6. At the interface of CdS and CdSe band bending of about 0.2 eV may exist, depending on the relative doping level. (We ignore the band bending due to the solution interface since the depletion layer is much thicker than the scale of this figure.) The major consequence of the presence of a CdS layer will, however, be the barrier-to-hole transfer between the valence bands (and ultimately to the solution interface) which amounts to

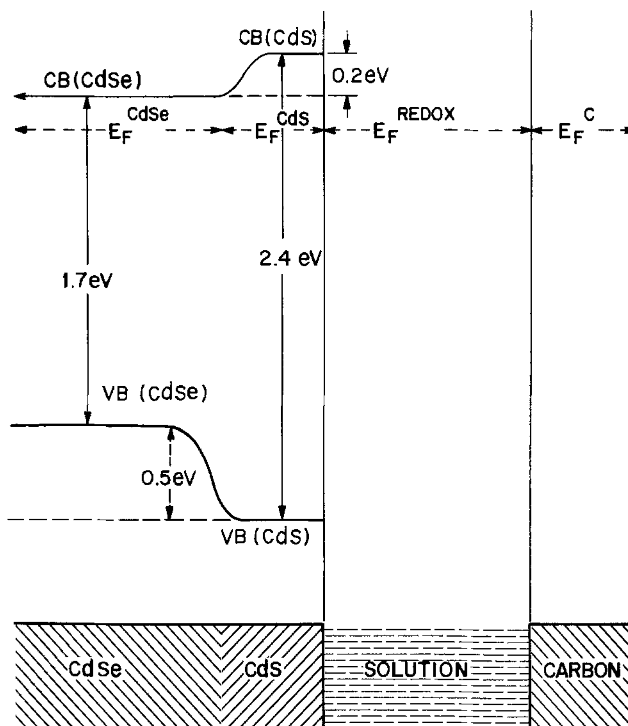

Fig. 6. Schematic diagram showing a barrier for hole transport from an n-CdSe photoanode to a redox couple solution by an n-CdS surface layer under short-circuit conditions. To keep the diagram simple, the band bending in the depletion region is not shown.

0.7-0.2 eV. This barrier is progressively lowered as x decreases in the series of compounds $CdSe_{1-x}S_x$, accounting for our observation that the current is not blocked unless x is high. Liquid junction cells with $CdSe_{1-x}S_x$ photoanodes were recently studied by Noufi, Kohl, and Bard (23).

A second reason for current blockage is lattice mismatch. If a layer of CdS is deposited on CdSe there is an abrupt shrinkage in the interatomic distance. The resulting stresses are known to be relieved by the formation of nonstoichiometric compounds in which the element forming stronger bonds with itself (*i.e.*, is more metallic) dominates. In the case of cadmium sulfide, the interface is likely to be Cd rich. Such a layer would introduce a discontinuity and block the flow of holes to the liquid interface even if the bandgaps of CdS and CdSe were equal. Furthermore, even in the absence of this interface the defects at the interface may be traps and thus sites for carrier recombination.

Passage of current appears to promote the exchange of ions that results in a current reducing film (Fig. 1). At low levels of illumination (cell current density ≤ 2 mA/cm^2) no decline in current is observed, but at levels normal to solar illumination (≥10 mA/cm^2 cell output) blocking layers are eventually formed. An explanation may lie in the possibility that at sufficiently high light intensities the concentration of the kinetically most active electron donor-hole acceptor species at the electrode surface may become depleted due to slow equilibria in spite of a relatively small reduction of the total $S^{=}$ containing species concentration in these molar solutions. The rates of reactions like Eq. [2] may become limiting. Photocorrosion may then become competitive and be followed by reprecipitation of the more prevalent chalcogenide

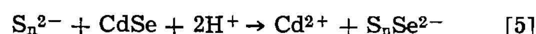

$$S_n^{2-} + CdSe + 2H^+ \rightarrow Cd^{2+} + S_nSe^{2-} \quad [5]$$

$$Cd^{2+} + 2S_n^{2-} \rightarrow CdS + S_{2n-1}^{2-} \quad [6]$$

Such depletion at high current density may also account for the fact that stirring or rotation of elec-

trodes decelerates the degradation process (Fig. 2 and 3). Finally, however, this sort of inhibition produces a less active surface for which stirring no longer improves the current.

Our model for current blockage predicts that maintenance of an adequate amount of selenium in the surface film should reduce or eliminate the photoanode deterioration problem; it is also obvious from thermodynamic arguments that the film will become richer in Se as the concentration of the element in the solution increases. These conclusions are supported by the plots in Fig. 3 in which the deterioration at 0-0.02M Se° concentrations in a 1M Na_2S-1M NaOH solution is shown. Cell life increases dramatically with the Se concentration. Our data indicates that with 0.05-0.075M Se added, runs at solar irradiance levels ought to have a stable output well beyond our 2×10^4 C/cm^2 cutoff.

As seen in transmittance data of Fig. 4 and in the 12% drop of short-circuit current in Fig. 5, some quantum efficiency loss results upon addition of 0.075M Se. However, this is practically compensated by a slightly higher open-circuit voltage and a significantly better fill factor in the presence of selenium. Possible sources of these positive features of the Se stabilized solution are a higher open-circuit voltage caused by a negative shift of the flatband potential, faster rates for the electrochemical oxidation, and reduction of losses due to hole transfer across the sulfide containing barrier, the latter two leading to fill-factor improvement.

In summary, we show in this paper that (*i*) absence of weight loss is not adequately predictive of stability of photoelectrodes; (*ii*) the deterioration of n-CdSe in sulfide-polysulfide solutions derives from a CdS-rich film which blocks the flow of current; (*iii*) if the CdS film contains an adequate amount of CdSe the flow of current is not blocked; and (*iv*) an adequate amount of CdSe in the film that is formed can be assured by adding a small amount of elemental selenium to the sulfide-polysulfide solution.

Acknowledgments

The authors wish to thank K. C. Chang for his participation in early phases of the stability studies, M. Robbins for his cooperation in supplying CdSe specimens, and J. L. Bernstein for structural interpretation.

Manuscript submitted Dec. 19, 1977; revised manuscript received March 14, 1978. This was Paper 416 presented at the Seattle, Washington, Meeting of the Society, May 21-26, 1978.

Any discussion of this paper will appear in a Discussion Section to be published in the June 1979 JOURNAL. All discussions for the June 1979 Discussion Section should be submitted by Feb. 1, 1979.

Publication costs of this article were assisted by Bell Laboratories.

REFERENCES

1. "Semiconductor Liquid Junction Solar Cells," A. Heller, Editor, The Electrochemical Society, Softbound Symposium Series, Princeton, N.J. (1977).
2. "Photochemical Conversion and Storage of Solar Energy," Proceedings of an International Conference at London, Ont., J. R. Bolton, Editor, Academic Press, New York (1976).
3. A. Heller, K. C. Chang, and B. Miller, in "Semiconductor Liquid Junction Solar Cells," A. Heller, Editor, p. 186, The Electrochemical Society Softbound Symposium Series, Princeton, N.J. (1977); *J. Am. Chem. Soc.*, **100**, 684 (1978).
4. A. Heller, K. C. Chang, and B. Miller, *This Journal*, **124**, 697 (1977).
5. K. C. Chang, A. Heller, B. Schwartz, S. Menezes, and B. Miller, *Science*, **196**, 1097 (1977).
6. B. Miller and A. Heller, in "Proceedings of the Symposium on Materials and Processes for Photovoltaic Energy Conversion," The Electrochemical Society, Princeton, N.J. May (1977).
7. B. Miller and A. Heller, *Nature (London)*, **262**, 680 (1976).
8. B. Miller, A. Heller, M. Robbins, S. Menezes, K. C. Chang, and J. Thomson, Jr., *This Journal*, **124**, 1019 (1977).
9. A. B. Ellis, S. W. Kaiser, and M. S. Wrighton, *J. Am. Chem. Soc.*, **98**, 1645 (1976).
10. A. B. Ellis, S. W. Kaiser, and M. S. Wrighton, *ibid.*, **98**, 1635 (1976); *ibid.*, **98**, 6855 (1976).
11. G. Hodes, J. Manassen, and D. Cahen, *Nature (London)*, **261**, 403 (1976).
12. C. J. Powell, *Surf. Sci.*, **44**, 29 (1974).
13. Gmelin, "Handbuch der Anorganischen Chemie," Cadmium System No. 33, p. 594, and references therein, Verlag Chemie, Weinheim/Bergstrasse, Germany (1959).
14. J. G. Gibson and J. L. Sudworth, "Specific Energies of Galvanic Reactions and Related Thermodynamic Data," pp. 159-163, Chapman and Hall, Ltd., London (1973).
15. D. D. Wagman, W. H. Evans, V. B. Parker, I. Halow, S. M. Bailey, and R. H. Schumm, NBS Tech. Note 270-3 (1968).
16. V. A. Kireev, *J. Gen. Chem. (USSR)*, **16**, 1569 (1946).
17. Gmelin, "Handbuch der Anorganischen Chemie," Cadmium System No. 33, p. 133 and references therein, Verlag Chemie, Leipzig-Berlin (1925).
18. J. Drowarf and P. Goldfinger, *J. Chim. Phys.*, **55**, 721 (1958).
19. P. Goldfinger and M. Jeunehomme, *Trans. Faraday Soc.*, **59**, 2851 (1963).
20. L. G. Sillén, "Stability Constants of Metal-Ion Complexes," The Chemical Society, London (1964).
21. "Lange's Handbook of Chemistry," 10th ed., p. 1225, McGraw-Hill, New York (1969).
22. A. H. Nethercot, *Phys. Rev. Lett.*, **33**, 1088 (1974).
23. R. N. Noufi, P. A. Kohl, and A. J. Bard, *This Journal*, **125**, 375 (1978).

Growth Kinetics and Catalytic Effects in the Vapor Phase Epitaxy of Gallium Nitride

S. S. Liu*,[1] and D. A. Stevenson**

Department of Materials Science and Engineering, Stanford University, Stanford, California 94305

ABSTRACT

The kinetics of the heteroepitaxial film growth of GaN on sapphire by chemical vapor deposition was investigated under a variety of experimental conditions. The growth rate was observed to be linear with time for all conditions studied and was found to be significantly influenced by the following factors: composition of the reactants in the vapor, temperature in the reaction zone, substrate orientation, and dopant concentration. The Gibbs free energy change for the main deposition reaction was evaluated as a function of temperature and reactant composition using available thermochemical data and compared with the observed deposition rate. An apparent discrepancy between predicted and observed deposition rate was attributed to local differences in NH_3 composition due to decomposition and/or to the uncertainty in available thermochemical data. Significant observations are reported concerning the decomposition kinetics of NH_3 in different growth ambients.

Gallium nitride (GaN), a III-V compound semiconductor, has a direct bandgap of 3.4 eV at room temperature (1, 2) and crystallizes in the wurtzite structure. Nominally pure GaN is invariably an n-type conductor with the carrier concentration in the 10^{18}-10^{19} cm^{-3} range and resistivity in the 10^{-2}-10^{-3} Ω-cm range (3-7), the donors presumably being native defects such as nitrogen vacancies (3, 5, 8, 9) or gallium interstitials. Attempts to change the carrier type by p-type doping have been unsuccessful, presumably due to self-compensation; however, addition of group II elements such as Mg (3) and Zn produce insulating material (10-12). The large direct bandgap has prompted interest in this material for optoelectronic devices and recently GaN metal-insulator-semiconductor (MIS) light emitting diodes have been reported that emit violet (13), blue (10), green (11), and yellow (12) light. In addition, the piezoelectric properties and high acoustic velocities in this material make it attractive for acoustic devices (14). A major problem encountered in these device applications has been the quality of the material, particularly the reproducibility in the synthesis of material suitable for devices. The preparation of this material is an intriguing and challenging problem.

Gallium nitride is chemically inert but thermally unstable; GaN decomposes into the component elements prior to melting (15-18) (the normal decomposition temperature is ~800°C) and the high temperature and pressure for the coexistence of solid and liquid [estimated to be 2000°C and 10^5 atm (19)] make melt growth unfeasible. All practical methods for the synthesis of GaN utilize an active source of nitrogen, such as ammonia, NH_3. The most promising growth technique for device material has been the heteroepitaxial chemical vapor deposition utilizing NH_3, a vapor source of Ga (usually GaCl), and a sapphire substrate. A significant feature of this process is the use of NH_3 as an active nitrogen source under conditions where NH_3 is thermodynamically unstable. Thus, factors influencing the kinetics of NH_3 decomposition are highly relevant to this deposition process.

The present work was undertaken to interrelate the growth conditions, the growth kinetics, and the film characteristics for the heteroepitaxial deposition of GaN films. We present the following relevant observations and analyses: a development of the thermodynamics for the deposition reaction, measurements of the catalytic decomposition of NH_3 in typical growth environments, and measurements of growth kinetics under a variety of experimental conditions. These experimental observations are discussed in terms of the optimum conditions for GaN film growth for device applications.

Gallium nitride growth apparatus.—A previous study (20) has established the main GaN deposition reaction to be

$$GaCl_{(g)} + NH_{3(g)} = GaN_{(s)} + H_{2(g)} + HCl_{(g)} \quad [1]$$

for the conditions used in the present investigation. The growth apparatus is a conventional hot wall open flow reactor and is diagrammed schematically in Fig. 1. The essential zones of the reactor are a source zone where $GaCl_{(g)}$ is generated by passing HCl over Ga, a mixing zone where $GaCl_{(g)}$ is mixed with $NH_{3(g)}$, and the deposition zone where the reaction mixture produces a deposit of GaN on the substrate as well as on the reactor walls. A sidearm, containing a crucible filled with Mg, is used to introduce Mg vapor into the mixing zone for the purpose of Mg doping. The temperature of the Mg source and the carrier gas flow rate determine the relative amount of Mg introduced. A stopcock and forechamber accommodate the introduction and withdrawal of the substrate without cooling the system to room temperature, thus facilitating several successive runs with a minimum of interruption. Palladium-diffused hydrogen was the carrier gas for all components. Thermocouples were used to monitor the temperature of the Mg source crucible and the substrate. Sapphire substrates of either basal plane orientation (0001) or R-plane orientation $(1\bar{1}02)$ were used. Further details of the process, such as specific temperatures and flow rates, are given in the discussion below and in a previous publication (13).

Basic reaction.—There are four reactions of central interest for the GaN deposition, two concerning the supply of reactants to the reaction chamber and two concerned, respectively, with the formation and depletion of GaN. The Ga source reaction is its conversion to GaCl by the reaction

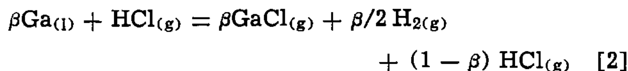

$$\beta Ga_{(l)} + HCl_{(g)} = \beta GaCl_{(g)} + \beta/2\, H_{2(g)} + (1-\beta)\, HCl_{(g)} \quad [2]$$

where β is the conversion efficiency. At the temperature in question, the equilibrium conversion efficiency is essentially unity; however, the extent of attainment of equilibrium depends on several factors, principally the residence time of the $HCl_{(g)}$ over the liquid Ga source, the Ga surface area, and the nature of the stir-

* Electrochemical Society Student Member.
** Electrochemical Society Active Member.
[1] Present address: Intel Corporation, Santa Clara, California 95051.

Fig. 1. Schematic diagram of the open-flow vapor growth system for preparing GaN

ring of the gaseous environment in the source zone. The other reaction that concerns the source of reactants is the decomposition of $NH_{3(g)}$

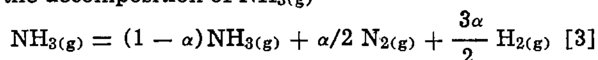

$$NH_{3(g)} = (1-\alpha)NH_{3(g)} + \alpha/2\ N_{2(g)} + \frac{3\alpha}{2} H_{2(g)} \quad [3]$$

where α is the degree of dissociation and is influenced principally by the temperature, partial pressure of $NH_{3(g)}$, the residence time of NH_3 in the reaction zone, and the catalytic nature of the environment in the reaction zone. The main formation reaction of GaN was given in Eq. [1]. As was already mentioned, GaN is unstable at elevated temperatures and tends to decompose into the elements

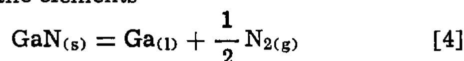

$$GaN_{(s)} = Ga_{(l)} + \frac{1}{2} N_{2(g)} \quad [4]$$

It is informative to compare the standard Gibbs free energy changes for the last three reactions, as given in Fig. 2. It is obvious from this figure that the decomposition of NH_3 and GaN is overwhelmingly favored in the temperature regime of interest (growth temperatures *ca.* 1200°-1400°K). The fact that epitaxial growth actually occurs at these temperatures is a consequence of the sluggishness of the NH_3 decomposition. It is appropriate to consider the influence of the extent of ammonia decomposition, α, and the conversion efficiency to GaCl, β, on the driving force for the deposition reaction by applying the reaction isotherm to Eq. [1]

$$\Delta G = \Delta G^\circ + RT \ln(a_{GaN}a_{HCl}a_{H_2})/(a_{GaCl}a_{NH_3}) \quad [5]$$

where a's are the activities of the different species denoted by the subscripts and ΔG and ΔG° are the change in Gibbs free energy and the standard Gibbs free energy, respectively.

Assuming that the gaseous species are ideal and GaN is a pure phase, then

$$a_{GaN} = 1,\quad a_{HCl} = (1-\beta)p_{HCl},\quad a_{GaCl} = \beta p_{HCl},$$
$$a_{H_2} = p_{H_2} + \beta/2\ p_{HCl} + 3\alpha/2\ p_{NH_3},\quad a_{NH_3} = (1-\alpha)p_{NH_3}$$

The flow rate of HCl is much smaller than that of NH_3 or H_2, or

$$p_{HCl} << p_{NH_3}\ p_{H_2}$$

and the total pressure is 1 atm, thus

$$p_{H_2} = 1 - p_{NH_3}$$

and we may write

$$\Delta G = \Delta G^\circ + RT\{\ln(1-\beta/\beta) + \ln[1 + (3\alpha/2 - 1)p_{NH_3}]/(1-\alpha)p_{NH_3}\} \quad [6]$$

Here

$$\Delta G^\circ = (\Delta G^\circ_{GaN} + \Delta G^\circ_{HCl} + \Delta G^\circ_{H_2}) - (\Delta G^\circ_{GaCl} + \Delta G^\circ_{NH_3})$$

and ΔG°'s are the standard Gibbs free energy of formation for each species in question. Literature values for ΔG° as a function of T (in °K) are

$$\Delta G^\circ_{GaN} = 1.34 \times 10^{-2} T^2 - 15.27T + 1.48 \ (15)$$
$$\Delta G^\circ_{GaCl} = 2.14 \times T \ln T - 29.42T - 1.68 \times 10^4 \ (21)$$
$$\Delta G^\circ_{HCl} = 1.41 \times T \ln T - 12.71T - 2.08 \times 10^4 \ (21)$$

with $\Delta G^\circ_{H_2} = 0$ and $\Delta G^\circ_{NH_3}$ taulated in the JANAF table (22).

ΔG° and ΔG can therefore be plotted as a function of T with different values of α and β, as shown in Fig. 3 and 4. As can be seen in these figures, ΔG° and all ΔG's go through a maximum as temperature changes. The peak shifts toward the lower temperature side with decreased value as either α increases or β decreases. This indicates the existence of an optimum temperature as far as the local thermodynamic affinity is concerned. The broken lines in the figures indicate the temperature regime commonly used for growth.

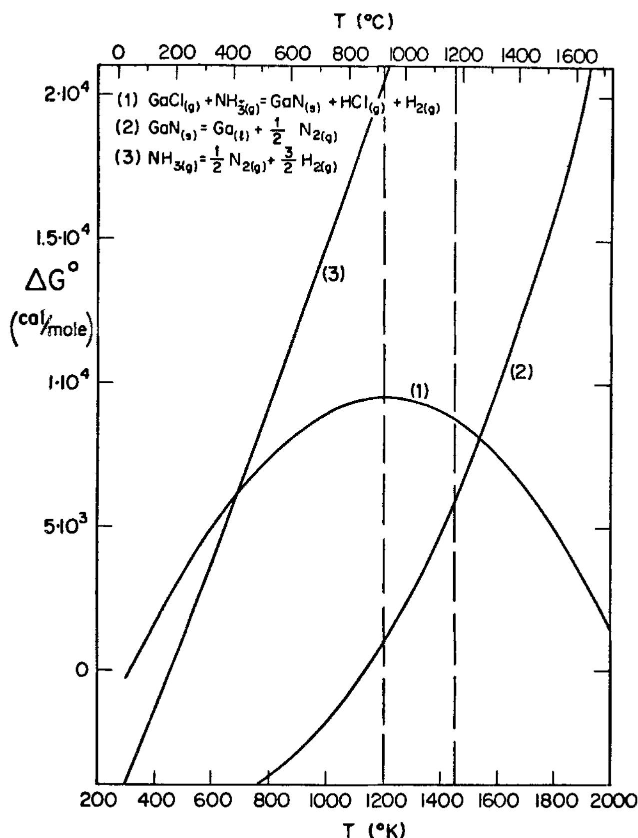

Fig. 2. Plot of ΔG° *vs.* *t* for three possible reactions in the deposition zone.

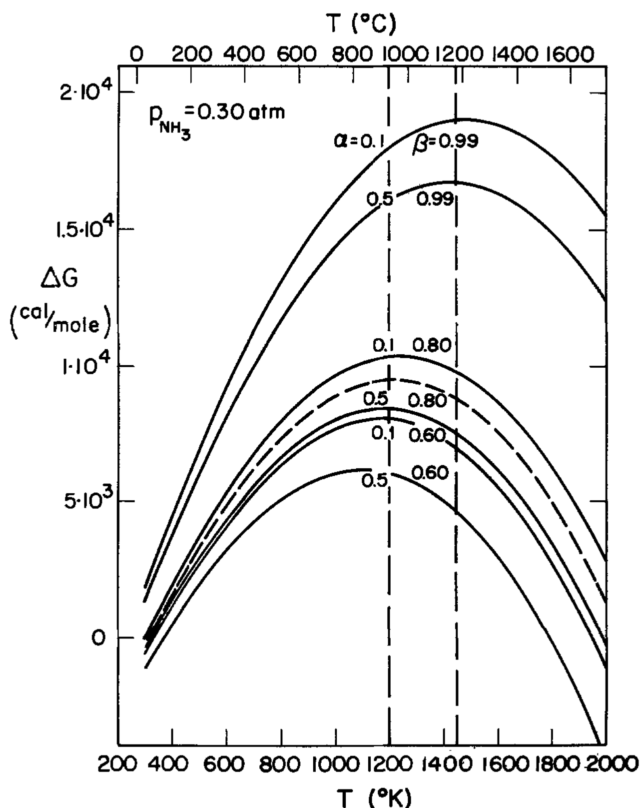

Fig. 3. Plot of ΔG *vs.* *T* for $p_{NH_3} = 0.30$ atm

It should be noted that the affinity in question is the initial affinity and as the reaction proceeds the concentration of HCl increases and causes the affinity to decrease in accord with Eq. [5].

Experimental

It is obvious from the foregoing discussion that the concentrations of $GaCl_{(g)}$ and $NH_{3(g)}$ are key factors

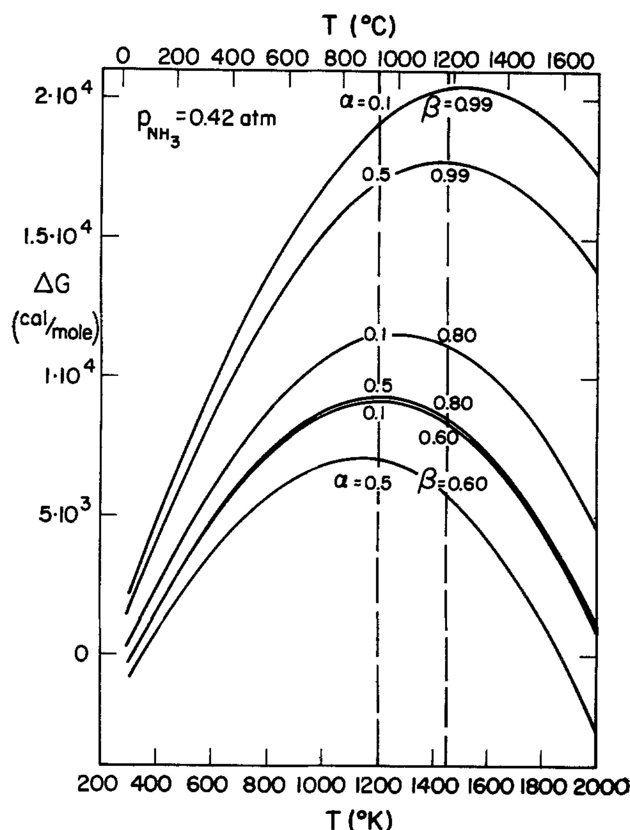

Fig. 4. Plot of ΔG *vs.* *T* for $p_{NH_3} = 0.42$ atm

in determining the basic thermodynamic driving force for the deposition reaction. Hence, factors affecting their concentration will certainly influence the nature of the GaN deposit. In this section we describe the techniques that were employed to study the conversion efficiency of $Ga_{(l)}$ to $GaCl_{(g)}$ and the parameters involved in the decomposition of NH_3. In addition, we describe techniques that were used to measure the growth rate of the deposits under a variety of experimental conditions.

Determination of the Ga-GaCl conversion and the extent of NH_3 *decomposition.*—Both the Ga-GaCl conversion and the extent of NH_3 decomposition were accomplished by a straightforward acid-base titration technique. For all determinations, the actual growth system was used (Fig. 1) with the addition of a manometer connected to the sidearm to monitor the pressure of the system and the addition of a series of three traps at the outlet to trap the effluent gases for analysis. The three traps were used to ensure that there was complete trapping of the gas in question. The conditions of temperature, gas composition, and gas flow rates spanned the range of interest for the actual epitaxial growth procedure. In the case of the Ga-GaCl conversion, a mixture of HCl and H_2 gases was flowed over the Ga boat in the source zone and the unreacted HCl collected in a series of three aqueous traps. The total HCl collected was determined by titration with a standard 0.1*N* NaOH solution. The actual HCl flow rates were checked by running the experiment without the presence of Ga, thus, no conversion of the HCl. A cross check on the Ga-GaCl conversion was obtained by measurement of the weight loss of the Ga boat in the source zone. In the case of the NH_3 decomposition study, the approach was similar except that in this case a NH_3-H_2 gas mixture, after passing through the furnace, was passed through a series of traps containing HCl; the first trap contained a standardized 5*N* HCl and the second and third 1*N* HCl. The respective flow rates of NH_3 and H_2 were 1060 and 1440 ml/min and the back pressure caused by the traps was approximately 0.8 psi, a pressure well below the level corre-

sponding to any significant leak rate. The amount of NH_3 trapped was determined by titration of the remaining HCl in all three traps using a standard 1*N* NaOH solution. In these experiments, an appreciable amount of time was allowed for the system to reach a steady state before sampling of the effluent was begun. The NaOH and the HCl solutions were standardized using potassium biphthalate weighed on a Mettler microbalance. The indicators used in the standardization and the HCl titration were o-cresolphthalein and methyl red, respectively. Similar to the HCl case, the actual flow of NH_3 was checked by flowing the gases through a cold furnace under conditions such that no decomposition would occur.

Growth rate determination.—The growth of GaN was determined by weighing the sapphire substrate on a Mettler microbalance prior to and subsequent to the GaN deposition for a given time of deposition with specified deposition conditions. The growth rate, expressed in terms of micrometers per minute was obtained by converting the weight gain to thickness. The latter assumption was justified as reasonable by observations of the deposit using both optical and scanning electron microscopy. The growth rate was also determined by direct thickness measurements by fracturing the sample and viewing the layer in cross section with a vernier lens, using optical microscopy.

Experimental Results

Conversion efficiency of HCl to GaCl (β) and the extent of decomposition of NH_3 (α).—The quantities β and α are essential for the prediction of the affinity of the main deposition reaction and were determined for a variety of experimental conditions in the range of interest for actual deposition systems. Figure 5 shows the results of the determination of the HCl conversion efficiency as a function of the HCl flow rate at a temperature of 950°C. As expected, the conversion efficiency decreases as the flow rate increases, presumably due to a decreased residence time. For the highest flow rate studied, the conversion efficiency was ~97% as compared with ~99% for the slowest flow rate (which was ~1/10 of the maximum). Thus, for all the conditions used in the present study, the conversion may be regarded as complete.

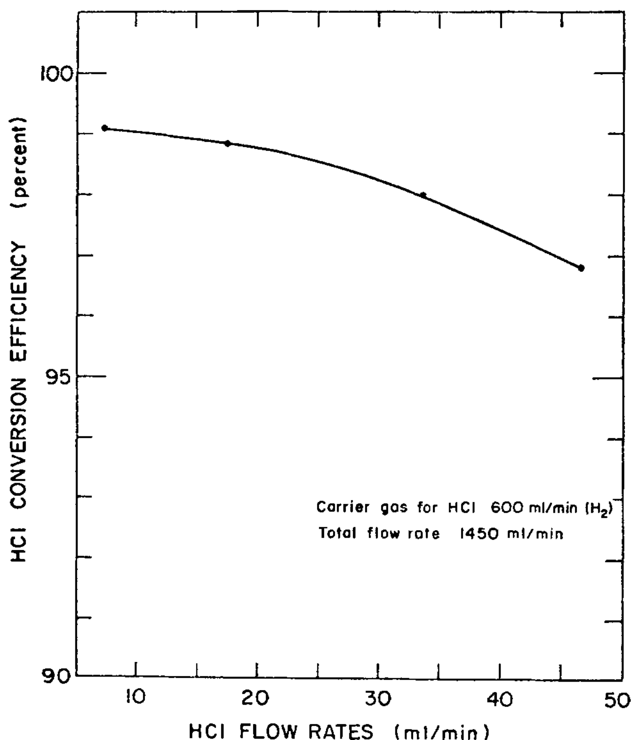

Fig. 5. Plot of the HCl conversion efficiency vs. HCl flow rates for a temperature of 950°C.

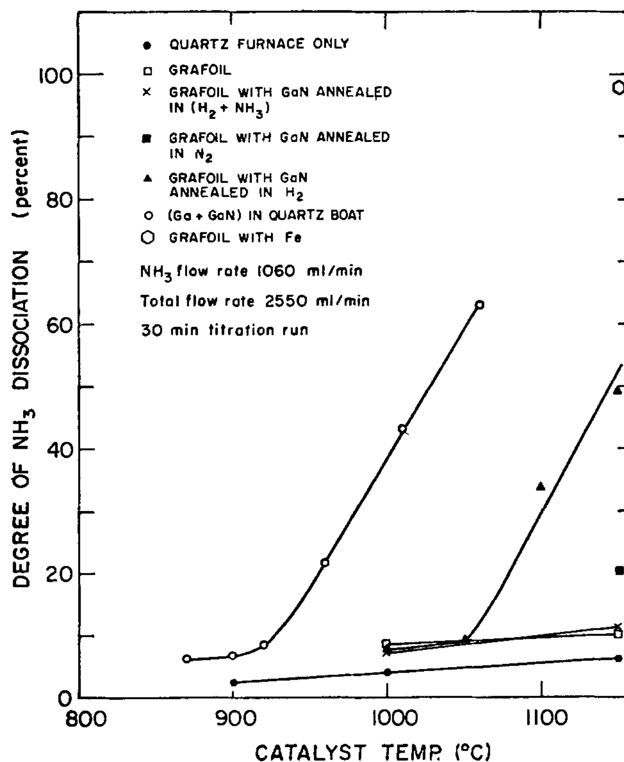

Fig. 6. Plot of the degree of NH_3 decomposition vs. the temperature of different catalytic environments prepared in the growth furnace.

The degree of NH_3 dissociation was determined as a function of temperature for several different environments and the results are summarized in Fig. 6. As shown by this figure, if the NH_3 contacts only pure quartz tubes (vitrified or devitrified) or a new graphite liner (Grafoil) the degree of dissociation is linear with temperature and ranges between 2 and 5 and 10%, respectively, for the temperature interval of 900°-1150°C. If, however, GaN is predeposited on the Grafoil liner, the thermal history of the liner becomes important. When the predeposited GaN was annealed in an ambient of NH_3 sufficient to prevent decomposition of GaN, the extent of decomposition was the same as for the pure graphite environment. When GaN is annealed in pure N_2 or pure H_2 prior to exposure to NH_3, a significant enhancement in α occurs at elevated temperatures, with an apparent threshold temperature of ~1050°C for the H_2 annealing case. To ascertain the reason for the enhanced catalytic effect and the significance of an apparent threshold temperature, the surfaces of GaN were examined by scanning electron microscopy (SEM) after appropriate anneals and the results are shown in Fig. 7. After annealing in a pure H_2 ambient at 1000°C for 1 hr, the appearance of Ga droplets due to the decomposition is easily detected. Subsequent annealing in a NH_3-containing ambient results in a uniform texture if annealing is carried out at a temperature below the threshold temperature, presumably due to the reformation of GaN from the Ga droplets. By contrast the droplets will persist if the annealing with NH_3 is performed above the threshold temperature. The supposition of the presence of Ga in the SEM micrographs was confirmed using x-ray diffraction. Since GaN itself was shown to have little influence on the decomposition of NH_3, there are two possible reasons for the anomalous enhancement in the catalytic decomposition of NH_3 caused by the partial decomposition of GaN: the presence of pure liquid Ga, or the coexistence of Ga-GaN.

To determine the role of liquid Ga, a sample of pure Ga was placed in a boat located at the NH_3 inlet. There was no significant influence on the NH_3 decomposition for temperatures below 1000°C and a thin coat

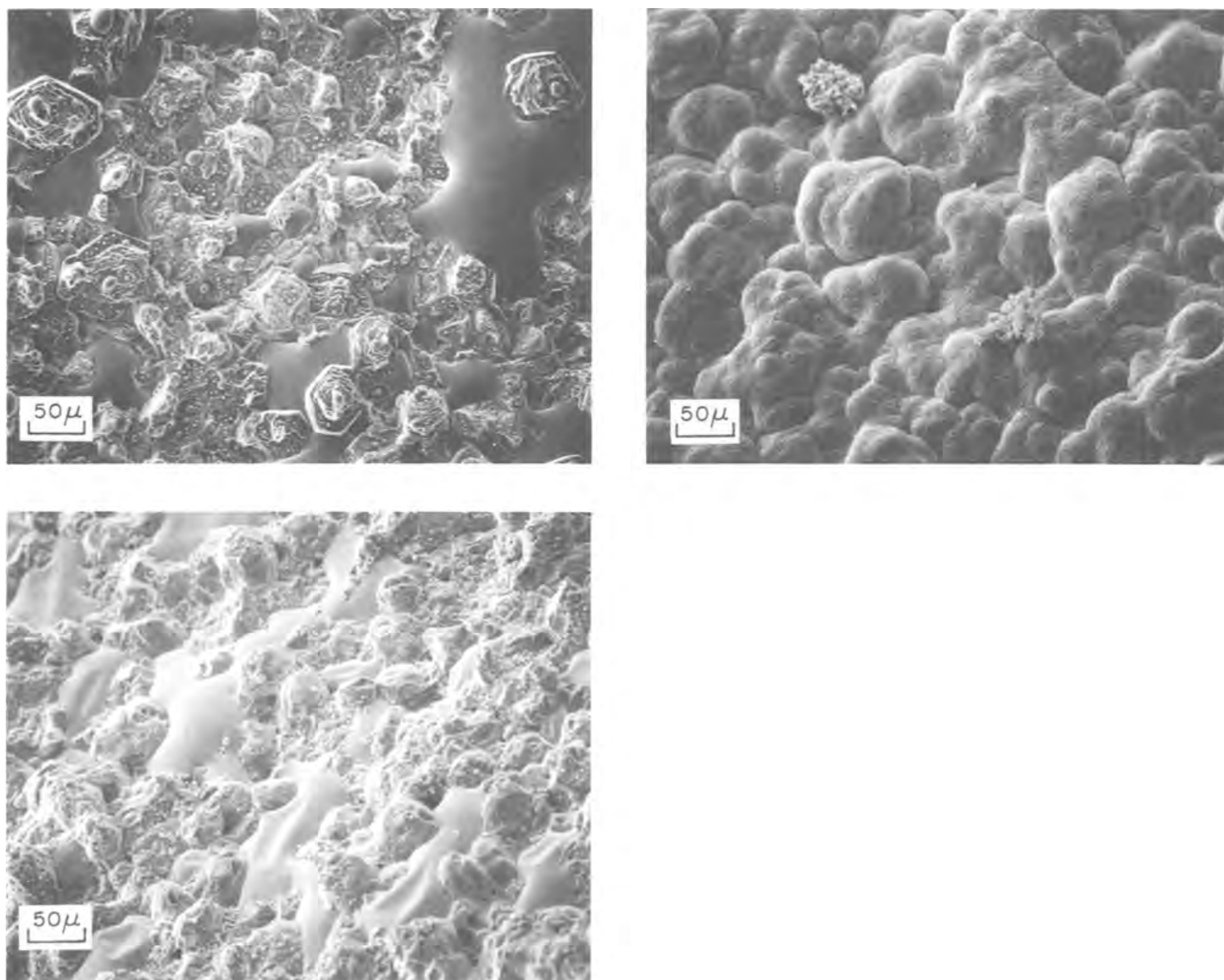

Fig. 7. Secondary emission micrographs of GaN-predeposited Grafoil liner: (a, left) after annealing in H_2-only ambient for 1 hr at about 1000°C after passing NH_3 through the liner shown in (a) for 30 min; (b, right) at temperatures below the "threshold" point; and (c, bottom) at temperatures above the "threshold" point.

of GaN formed on the Ga. Above 1025°C, however, a dramatic change occurred; significantly more NH_3 was decomposed and the Ga reacted to form a large amount of dark gray spongy material which filled the tube but did not block the gas flow. Between 1000° and 1025°C, a golden spongy material was generally formed with no enhancement in the extent of NH_3 decomposition. The fact that pure Ga reacts with NH_3 at all temperatures investigated implies that it does not decompose NH_3 rapidly, otherwise NH_3 would not be available for the formation of GaN.

The material obtained above 1025°C was analyzed by x-ray diffraction and by chemical analysis. It was found to be a conglomerate containing about 60% Ga and 40% GaN in polycrystalline form. The SEM micrographs of this material, Fig. 8, demonstrated the general porosity of the materials (Fig. 8a) which was the result of the formation of numerous fine dendritic crystallites (Fig. 8b). The Ga in the conglomerate was removed with aqua regia exposing micrometer-sized GaN dendrites (Fig. 8c). The catalytic nature of this conglomerate material was investigated by placing a sample near the NH_3 inlet and performing the titration analysis as previously described. The results, shown in Fig. 6, show a similar behavior to the hydrogen-annealed GaN material except that the "threshold" temperature is lower. This confirms that the coexistence of Ga and GaN has a significant catalytic effect for the decomposition of NH_3. The lower threshold temperature for the conglomerate material is presumably the result of more total surface area.

For comparison purposes, the catalytic activity of a well-known catalyst for NH_3 decomposition was evaluated in our system. The catalyst was fine Fe particles obtained by decomposition of $FeCl_3$ on Grafoil in a hydrogen ambient and caused virtually complete decomposition of the NH_3 at 1150°C, as seen from Fig. 6, and it is known that this catalyst is of comparable effectiveness at lower temperatures as well. It must be emphasized that the GaN-Ga conglomerate would not be an effective commercial catalyst for ammonia synthesis; however, its catalytic effect would certainly influence the chemical vapor deposition of GaN.

Growth rate studies.—The growth rate of heteroepitaxial GaN depends on the following parameters: the growth temperature, the flow rate of reactants, substrate orientation, growth environment, and Mg-doping.

To study the influence of these growth variables, different temperature profiles, providing growth temperatures within the range of interest as indicated in Fig. 2-4, were investigated and two representative profiles selected for more extensive examination. The results are summarized in Fig. 9 and 10 for average temperatures of 1050° and 950°C, respectively. The modest increase in the furnace temperature during actual growth (the dashed curve) as compared to the profile when only H_2 carrier gas is passed through the furnace (the solid curve) is attributed to the exothermic nature of the reaction. Since it was established that the growth rate is linear, for given growth conditions (Fig. 11), the growth rate for each individual condition may

Fig. 8. Secondary emission micrographs of Ga-GaN mixture: (a, left) at 50×; (b, right) at 2500×; and (c, bottom) at 2500×, after removing Ga.

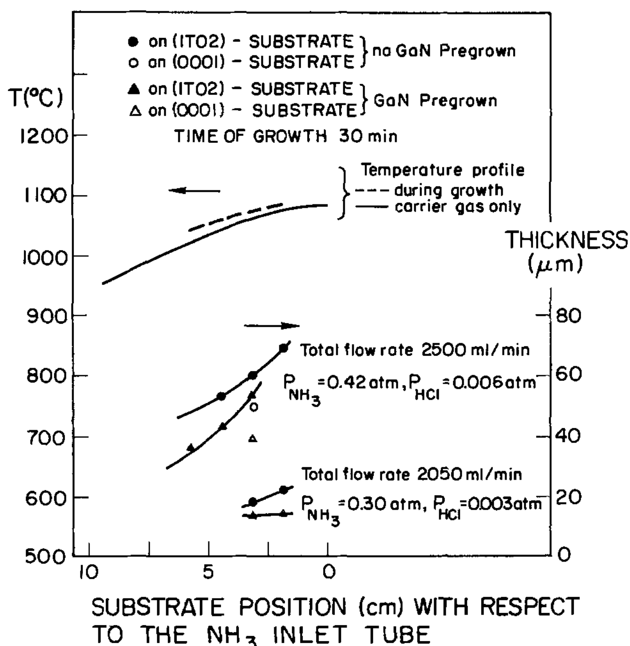

Fig. 9. Plot of growth temperature (>1000°C) and undoped GaN layer thickness *vs.* substrate position.

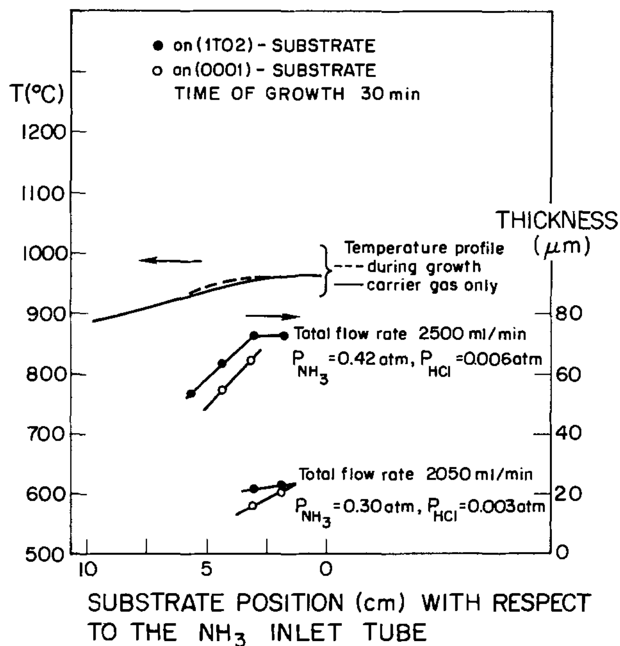

Fig. 10. Plot of growth temperature (<1000°C) and undoped GaN layer thickness *vs.* substrate position.

be obtained from the layer thickness after 30 min of growth. Several important trends that are apparent from these graphs may be summarized as follows:

(*i*) *Growth temperature.*—Comparison of identical substrate positions for the high and low temperature cases established that the growth rate decreases with

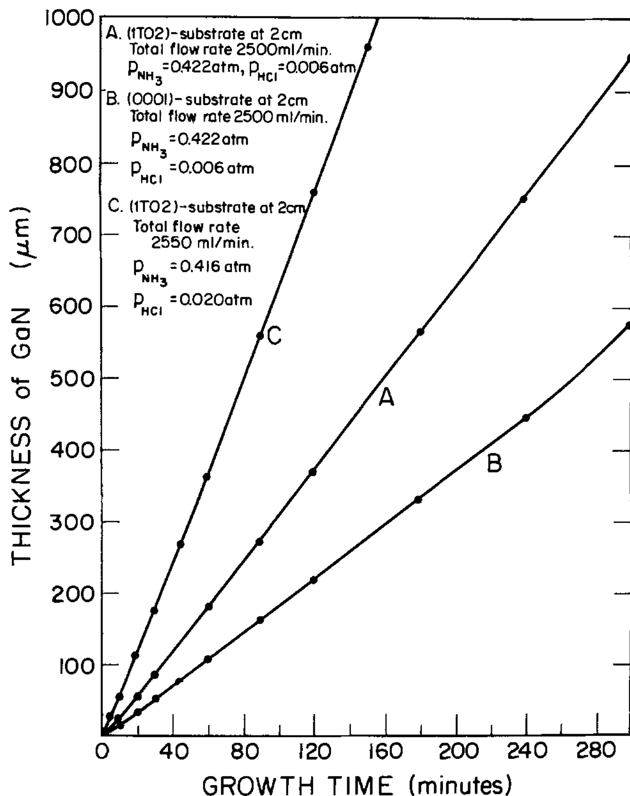

Fig. 11. Plot of undoped GaN layer thickness vs. growth time

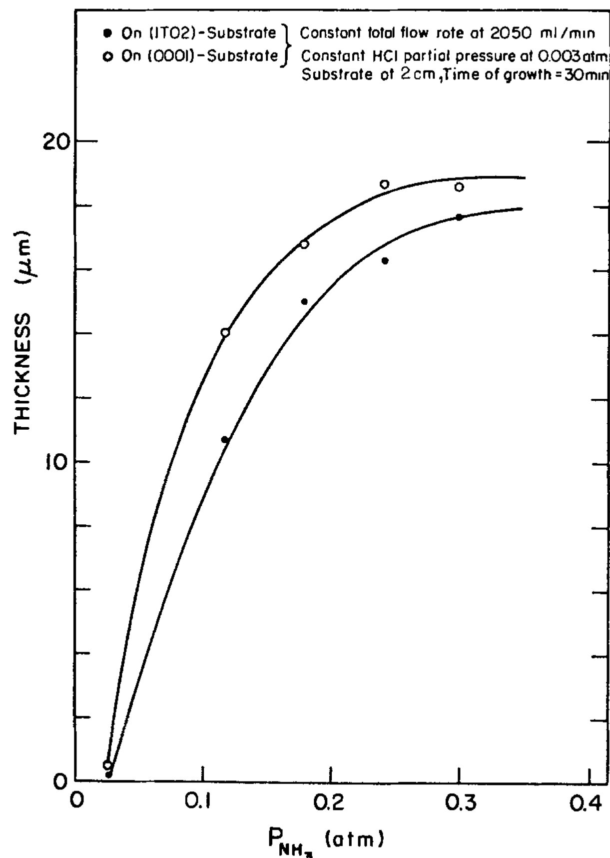

Fig. 12. Plot of undoped GaN layer thickness vs. p_{NH_3} for constant p_{GaCl}.

increasing temperature within the temperature regime of interest for both R-plane and basal-plane substrates. The temperature gradient at a specific growth site is generally not a major factor unless it is extremely shallow or steep. For shallow gradients, the heat of reaction is not conducted away as rapidly and the temperature increases as growth proceeds with a consequent influence on the growth rate and the surface morphology. For steep gradients, there is evidence of a homogeneous reaction in the gas stream prior to the heterogeneous reaction at the substrate.

(*ii*) *Flow rate*.—The influence of gas flow rate concerns the total flow rate, the carrier gas flow rate, and the flow rates of the reactant gases (HCl and NH_3). The influence of changing the individual reactant gas flow rates was most extensively studied. The results for two sets of NH_3 and HCl flow rates, with the hydrogen carrier gas flow rate kept constant, are shown in Fig. 9 and 10, and the influence of varying individual reactant gas flow rate is described in Fig. 11 and 12. It is evident that the growth rate increases with increasing flow rates of the reactant gases if either one or both rates are increased.

(*iii*) *Substrate position*.—As shown in Fig. 9 and 10, the growth rate decreases as the substrate position is moved downstream from the NH_3 inlet, presumably due to the depletion of the reactant species caused by deposition on the Grafoil liner prior to encountering the substrate.

(*iv*) *Substrate orientation*.—The growth rate on the (1$\bar{1}$02) or R-plane orientation was observed to be greater than that on the (0001) or basal-plane orientation for all the conditions investigated in this study, as shown in Fig. 9-12.

(*v*) *Growth environment*.—The enhanced NH_3 decomposition caused by the coexistence of Ga-GaN, as described in the previous section, has a direct influence on the growth rate at temperatures where part of the system is above the threshold temperature of ~1000°C for enhanced ammonia decomposition (cf. Fig. 6). Thus, for the higher temperature series, described in Fig. 9, there is a significant decrease in the growth rate if the growth environment includes Ga-GaN coexistence, as the result of the annealing of pregrown GaN in a H_2 ambient. For the low temperature series, however, where there is no part of the system above the threshold temperature (Fig. 10), there is no difference observed for two different growth environments.

(*vi*) *Mg-doping*.—A previous study (1) had shown that the rate of GaN deposition was lower during Mg doping than during growth prior to the doping. This implied that either Mg doping retarded the growth rate or the growth rate was not linear with time (*i.e.*, the growth rate was smaller at later times when Mg doping was occurring). The present study has established that the growth rate of the undoped layer is linear with time, thus Mg doping must decrease the growth rate. This decrease was established experimentally, with the results shown in Fig. 13. As can be seen from this graph, there is a substantial decrease in growth rate for either substrate orientation as the partial pressure of the Mg (as controlled by the temperature of the Mg reservoir) is increased in the growth system.

Discussion

Catalytic effect.—It has been established in this study that the growth environment can significantly influence the extent of NH_3 decomposition; limited decomposition occurs in quartz and graphite environments (up to ~10%) whereas more extensive decomposition occurs (up to ~60%) above a threshold temperature of 950°-1050°C if Ga and GaN coexist. It is appropriate to compare these results with previous investigations and to speculate on the causes and implications of this behavior. Other workers (20, 23) have reported that graphite and devitrified quartz exhibit catalytic effects for NH_3 decomposition in various vapor growth systems. As established in the present study, however, their influence is relatively modest compared to the Ga-GaN mixture. Recently, Raman spectroscopy has been applied to profile the NH_3 composition in the vicinity of a graphite susceptor in a CVD system and

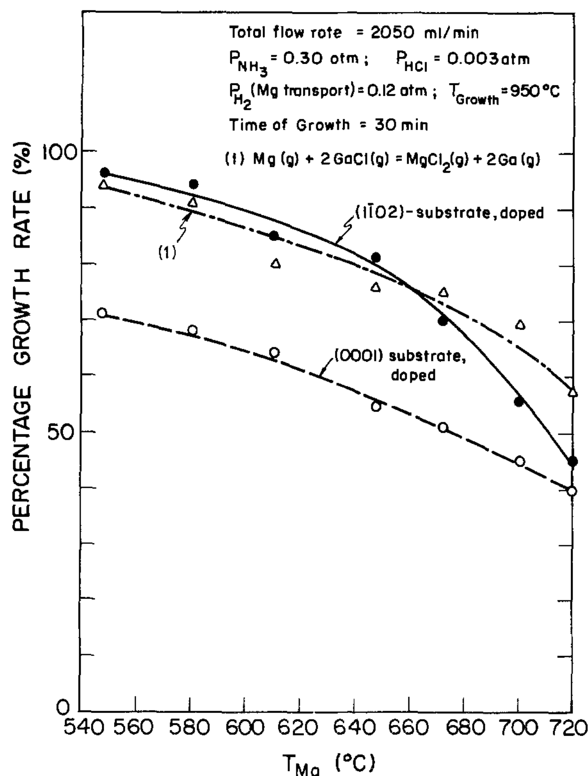

Fig. 13. Plot of percentage growth rate (with respect to the undoped) for doped GaN layer vs. Mg source temperature.

the catalytic effect of graphite confirmed (24). (This latter work, which measures the NH_3 concentrations at individual points, should be contrasted to the integral effects obtained in the previous studies and in the present work.) Our results of the modest catalytic effect of quartz and graphite for the decomposition of NH_3 are thus in agreement with the present literature.

Our significant finding, however, concerns the more pronounced enhancement of NH_3 decomposition with the coexistence of Ga-GaN above a threshold temperature. The need for the coexistence of both Ga and GaN clearly implies a critical interaction between the two components. This is analogous to the interaction between metal and support in the case of supported-metal catalysts (25, 26) except that there is no clear definition of which component plays the role of support in the present case. Two types of interaction might be possible: either a "bifunctional" catalyst (27) in which one reaction occurs on one component to yield an intermediate product which further reacts on the other component, with neither one capable of producing the enhanced effect alone, or a modification of the chemical properties of one of the components at the interface (28). For the latter case, the enhancement might be caused by a modification of one or more of the following at the interface: the electronegativity of the metal, the surface composition, and the surface structure. There is no clear evidence to allow an evaluation of the relative merits of possible mechanisms and detailed account of catalytic mechanisms is beyond the scope of this study.

The implications of these results are obvious. Since several runs are made in succession in the same reaction zone in a typical growth system, the treatment of this zone between runs will clearly influence the basic driving force for the deposition reaction, particularly in the early stages of the deposition. Furthermore, the early stage of the deposition is critical since the initial nucleation will have a pronounced influence on the deposition in general. It was found that the morphology of the GaN is changed if GaN is grown in the presence of coexisting Ga-GaN as would be expected from the decrease in the affinity for the reaction that results from the NH_3 decomposition. Another example is the procedure established to improve the microstructure for GaN light emitting diodes by use of higher affinities at the early stage of growth. This was achieved by the use of Ar gas instead of H_2 gas as a carrier gas (29). Furthermore, if nitrogen vacancies are the dominant donors in GaN that are responsible for the large intrinsic electron concentration, their concentration would be expected to vary with a change in the chemical potential of nitrogen which is clearly a function of the NH_3/H_2 ratio. Obviously, in cases where one wishes to maximize the affinity of a reaction involving nitrogen as a reactant, one should avoid conditions conducive to the decomposition of NH_3. The general concept of catalytic potency of the reactor environment will certainly be important for other CVD processes, such as the synthesis of GaAs and GaP, especially when NH_3 is used as a dopant.

Growth kinetics.—The experimental observations concerning the growth rate of GaN heteroepitaxial layers can be summarized as follows: (*i*) the growth rate is constant with respect to time; (*ii*) the growth rate decreases with increasing temperature within the temperature range of 850°-1150°C; (*iii*) the growth rate increases with increased flow rate of NH_3 and/or HCl, and generally saturates; (*iv*) the growth rate is a function of the substrate position in the gas stream, it decreases as the substrate position is moved further downstream; (*v*) the growth rate depends on the catalytic nature of the growth environment and decreases under conditions of greater NH_3 decomposition; (*vi*) the growth rate is significantly more rapid on R-plane substrates as compared to basal-plane substrates; (*vii*) the concurrent incorporation of Mg in the deposit, produced by the presence of Mg vapor in the growth zone, decreases the growth rate substantially.

The temperature dependence of the growth rate is an apparent contradiction to predictions based on thermodynamics, as illustrated in Fig. 3 and 4. Since, in the majority of the growth runs studied, the extent of NH_3 decomposition in the bulk stream was less than 10%, one would predict an increase in the equilibrium extent of reaction with increasing temperature in the temperature range studied. One would also expect the relative attainment of equilibrium to increase with increasing temperature since the detailed kinetic processes involved should be enhanced with increasing temperature. This apparent contradiction may be the result of a combination of two or more factors: inaccurate literature values for the thermodynamic data and the discrepancy between the bulk extent of decomposition of NH_3 and the local extent of decomposition in the vicinity of the reaction interface. The weakest factor in the development of the thermodynamics of the deposition reaction is the standard Gibbs free energy of formation for GaN (15). These values were estimated since direct measurements of the standard enthalpy of formation, entropies, and heat capacities are not available at present. Thus, a discrepancy in the values that would displace the maximum in the curves in Fig. 3 and 4 downward by ~250°K is not an unreasonable expectation. Furthermore, it must be noted that the extent of decomposition of NH_3 that was experimentally determined in the present study was an integrated effect. It is possible and indeed probable, based on the recent work of Sedgwick (24), that the local extent of decomposition would shift the maxima in these curves to lower temperatures. It is obvious that in nonuniform reacting systems, such as CVD reactors, an *in situ* analysis technique for composition and temperature, with fine space resolution, is necessary to rigorously establish the thermodynamics near an interface.

The relative importance of two rate-limiting mechanisms in the epitaxial growth, mass transfer and surface reaction, cannot be clearly established for the present CVD system, but there is some evidence that it is a mixed controlled case. While there is a definite dependence of growth rate on the substrate and crys-

tal orientation (item *vi*), an observation commonly used to imply the existence of a surface reaction-controlled process, there is a dependence on the rate of supply of the reactants (items *iii* through *v*), commonly associated with mass transfer control mechanism. It is certainly clear that the reaction is not surface catalyzed since the deposition is not restricted to a definite surface and nucleation is easily accomplished. (These two conclusions are based on the fact that the deposition of GaN is not surface sensitive; for conditions used in typical growths, polycrystalline GaN can be deposited on practically any surface in the growth chamber, such as the fine textured Grafoil liner and fused quartz substrate holder.) It appears that there may be a homogeneous reaction producing a precursor for the GaN deposit. Indeed, in the presence of steep temperature gradients, noncoalescent randomly oriented GaN clusters appear on single crystal sapphire substrates and, for extreme conditions, ultrafine powders (~100Å) of GaN are formed (30).

The pronounced decrease in the growth rate caused by Mg doping, as illustrated in Fig. 13, might arise for two reasons: the displacement reaction between Mg and GaCl to produce a less reactive source of Ga, and the poisoning of the growth surface by the adsorption of Mg or MgCl. The Gibbs free energy of formation of GaCl is about −35 kcal/mole at the growth temperature (21), whereas it is −110 kcal/mole for $MgCl_2$ (22). Thus the displacement reaction

$$Mg(G) + 2GaCl(G) = MgCl_2(G) + 2Ga(G)$$

should be complete in the vapor, if kinetic factors are favorable. From the geometrical configuration of the growth reactor (Fig. 1) the reaction will take place between the sidearm entrance and the NH_3 inlet tube; thus, GaCl will be depleted before mixing with NH_3. Since in the growth of insulating layers, it is necessary to have a partial pressure of Mg that is 10-20% of the value for the partial pressure of GaCl in order to fully compensate the native donors in GaN, the depletion of the GaCl concentration due to this reaction can be significant.

One may calculate the decrease in the growth rate due to the addition of Mg, making the assumption that the above reaction goes to completion and that the reduced Ga does not react to form GaN. Comparison of such calculations with observations for the R-plane substrates (Fig. 13) shows good agreement at lower Mg concentrations, whereas the actual growth rate is depressed even further at Mg concentrations corresponding to full electrical compensation. This implies a surface poisoning effect at these higher concentrations, in addition to the depletion effect. It is also noticed in this regime of Mg concentration that there is a change in the surface morphology (31), as might be expected for a surface poisoning effect. The proposed surface poisoning effect correlates to a detrimental change in the substrate surface. This change may be caused either by a high Mg concentration in the lattice inducing a change in the GaN layer surface morphology or the presence of adsorbed Mg species on the growth surface. For growth on the basal plane, a pronounced effect was observed even at low Mg source temperatures, which is consistent with our observation that surface morphologies are altered with low Mg concentration for the basal-plane substrate (31).

Summary

The nature of the growth ambient in the chemical vapor deposition of GaN was found to influence the extent of NH_3 decomposition. Pure quartz, graphite, and GaN surfaces had a minor influence on the decomposition (up to a maximum of ~10%) whereas the coexistence of Ga and GaN caused extensive decomposition (up to ~60%) for the temperature range of 950°-1050°C. The catalytic effect of the growth environment is thus a significant variable when NH_3 is used as a reactant or dopant in chemical vapor deposition processes.

Several significant trends in the growth rate of GaN are reported for typical growth conditions: (*i*) The growth rate is linear with time. (*ii*) The growth rate decreases with increasing temperature, in the range 850°-1150°C. (*iii*) The growth rate increases with increasing reactant composition. (*iv*) The growth rate decreases as the substrate is located further downstream. (*v*) The growth rate decreases when the growth environment favors the catalytic decomposition of NH_3. (*vi*) The growth rate is more rapid on R-plane sapphire substrates than on basal plane sapphire substrates. (*vii*) The growth rate decreases substantially when Mg is concurrently incorporated in the deposit.

An apparent discrepancy between the temperature dependence of the growth rate and the Gibbs free energy is noted and it is postulated that the discrepancy arises from local variations in NH_3 concentration caused by decomposition and/or by incorrect thermodynamic data for the reactant species.

Manuscript submitted Nov. 30, 1977; revised manuscript received March 1, 1978.

Any discussion of this paper will appear in a Discussion Section to be published in the June 1979 JOURNAL. All discussions for the June 1979 Discussion Section should be submitted by Feb. 1, 1979.

Publication costs of this article were assisted by Intel Corporation.

REFERENCES

1. H. P. Maruska, Ph.D. Thesis, Stanford University (1973).
2. T. L. Chu, *This Journal*, **118**, 1200 (1971).
3. H. P. Maruska and J. J. Tietjen, *Appl. Phys. Lett.*, **15**, 327 (1969).
4. H. M. Manasevit, F. M. Erdmann, and W. I. Simpson, *This Journal*, **118**, 1864 (1971).
5. J. J. Hsieh, Ph.D. Thesis, University of Southern California (1971).
6. R. Dingle, D. D. Sell, S. E. Stokowski, P. J. Dean, and R. B. Zetterstrom, *Phys. Rev. B*, **3**, 497 (1971).
7. R. Dingle and M. Ilegems, *Solid State Commun.*, **9**, 175 (1971).
8. A. Rabenau, "Compound Semiconductors," Vol. 1, chap. 19, Reinhold, New York (1962).
9. M. Ilegems and H. C. Montgomery, *J. Phys. Chem. Solids*, **34**, 885 (1973).
10. J. I. Pankove, E. A. Miller, and J. E. Berkeyheiser, *J. Lumin.*, **5**, 84 (1972).
11. J. I. Pankove, E. A. Miller, and J. E. Berkeyheiser, *RCA Rev.*, **32**, 383 (1971).
12. J. I. Pankove, E. A. Miller, and J. E. Berkeyheiser, *J. Lumin.*, **6**, 54 (1973).
13. H. P. Maruska, W. C. Rhines, and D. A. Stevenson, *Mater. Res. Bull.*, **7**, 777 (1972).
14. M. T. Duffy, C. C. Wang, G. D. O'Clock, Jr., S. H. McFarlane III, and D. J. Zanzucchi, *J. Electron. Mater.*, **2**, 359 (1973).
15. C. D. Thurmond and R. A. Logan, *This Journal*, **119**, 622 (1972).
16. J. B. MacChesney, P. M. Bridenbaugh, and P. B. O'Conner, *Mater. Res. Bull.*, **5**, 783 (1970).
17. R. Groh, G. Gerey, L. Bartha, and J. I. Pankove, *Phys. Status Solidi A*, **26**, 353 (1974).
18. Y. Morimoto, *This Journal*, **121**, 1383 (1974).
19. A. G. Fischer, *Solid State Electron.*, **2**, 232 (1961).
20. V. S. Ban, *This Journal*, **119**, 761 (1972).
21. D. J. Kirwan, *ibid.*, **117**, 1572 (1970).
22. D. R. Stull, "JANAF Thermochemical Tables," (1967).
23. D. D. Roccasecca, R. H. Saul, and O. G. Lorimor, *This Journal*, **121**, 962 (1974).
24. T. O. Sedgwick and J. E. Smith, Jr., *ibid.*, **123**, 254 (1976).
25. M. Boudart, *Adv. Catalysis*, **20**, 153 (1969).
26. A. D. O. Cinneide and J. K. A. Clarke, *Catalysis Rev.*, **7**, (2), 213 (1972).
27. J. H. Sinfelt, *Adv. Chem. Eng.*, **5**, 37 (1964).
28. G. M. Schwab, *Discuss. Faraday Soc.*, **41**, 252 (1966).
29. G. Jacob, R. Madar, and J. Hallais, *Mater. Res. Bull.*, **11**, 445 (1976).
30. F. Q. Johnson and D. A. Stevenson, To be published.
31. S. S. Liu, T. L. Cass, and D. A. Stevenson, To be published.

High Speed Implementation and Experimental Evaluation of Multilayer Spreading Resistance Analysis

Donald C. D'Avanzo,* Robert D. Rung,,[1] Arnon Gat, and Robert W. Dutton**

Department of Electrical Engineering, Stanford University, Stanford, California 94305

ABSTRACT

An efficient implementation of multilayer potential analysis for spreading resistance measurements is described. A precalculated partial integral technique reduces computation time by a factor of 20 with no significant loss of accuracy. Spreading resistance measurements on beveled samples are compared to spreading resistance and four-point probe measurements on anodically sectioned samples and to Schottky C-V measurements. The results demonstrate the accuracy, versatility, and limitations of the technique.

Spreading resistance measurements on beveled samples allow convenient, high resolution determination of arbitrary impurity profiles in semiconductor devices (1, 2). Mechanical manipulation of the probes, probe tip design, bias conditions, and sample preparation have been optimized so that repeatable contacts can be achieved over a wide range of resistivities (1). Calibration curves can be generated from measurements on homogeneous samples to account for nonideal contact phenomena such as piezoresistive effects, contact potentials, and noncircular contact area, so that the resistivity of a homogeneous sample can be inferred directly from the spreading resistance measurement. However, for nonuniformly doped semiconductors the resistivity profile distorts the potential distribution beneath the probes resulting in a spreading resistance measurement which depends on the resistivities throughout the structure. A relationship between surface resistivity and measured spreading resistance which incorporates the effect of the nonuniform profile must be utilized to derive an impurity profile from the measured data.

Several methods have been developed for calculating spreading resistance "correction factors" on nonuniform samples. The simplest approach utilizes a two-layer model in which a single homogeneous layer of finite thickness is separated from a semi-infinite substrate by a perfectly insulating or perfectly conducting boundary. Analytical expressions for the correction factor can be derived for this idealized geometry by solving for the potential distribution with the method of images (3, 4). This approach is attractive for concentration profiles which change a negligible amount in a distance comparable to the contact radius, approximately 3 μm. However, a more sophisticated model is essential for the accurate analysis of measurements on the shallow diffusions, implantations, and epitaxial layers characteristic of modern integrated circuit technology.

Recent correction factor schemes have utilized a multilayer model in which the continuous concentration profile is approximated by a staircase function, Fig. 1. Each layer is assumed to have uniform concentration and finite thickness, equal to the distance between measurement points. If a p-n junction exists within one probe radius of the surface then a differential spreading resistance technique, analgous to four-point probe incremental sheet resistance, can be applied (5, 6). The resulting correction factors are explicit functions of the profile slope and are fairly accurate for shallow structures. A second approach solves for the potential distribution in the multilayer structure by the image method (7). Calculation of the correction factors requires a summation over the infinite series of image charges generated by each probe. The accuracy and range of applicability of this technique have yet to be established.

Of all the correction factor algorithms multilayer analysis (8-11) most nearly reflects the true physical nature of spreading resistance measurements on nonuniformly doped samples. It is basically a technique for solving Laplace's equation for the idealized multilayer geometry of Fig. 2. The semiconductor is assumed to be planar and of infinite extent in the Z and r directions. The sample is divided into layers of homogeneous resistivity and finite thickness Δh where Δh usually corresponds to the distance between measurement points. The probes are separated by a distance D and are assumed to make ideal contacts with the semiconductor surface, *i.e.*, the contact area is flat and circular of radius a, and all barrier potential and piezoresistive effects are neglected. These effects are often incorporated into the correction factor calculation empirically through a calibration curve (1, 2). With these assumptions Laplace's equation can be solved for the potential distribution in each of the layers. The expression for the correction factor, CF is derived directly from the surface potential V_1

$$CF = \frac{4}{\pi} \int_0^\infty \{1 + 2\theta\} \left\{ \frac{J_1(\lambda a)}{\lambda a} - \frac{J_0(\lambda D)}{2} \right\} \frac{\sin \lambda a}{\lambda} d\lambda$$

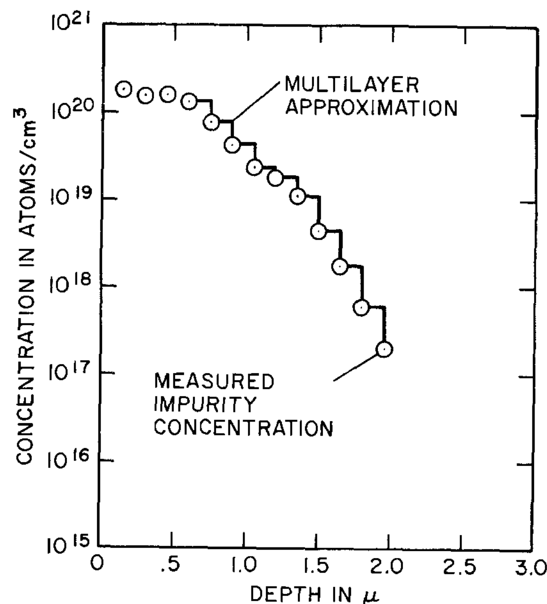

Fig. 1. Multilayer approximation to an impurity concentration profile.

* Electrochemical Society Active Member.
** Electrochemical Society Student Member.
[1] Present address: Hewlett Packard Laboratories, Palo Alto, California 94305.

Key words: spreading resistance, impurity profile, sheet resistance, emitter dip effect, p-n junction.

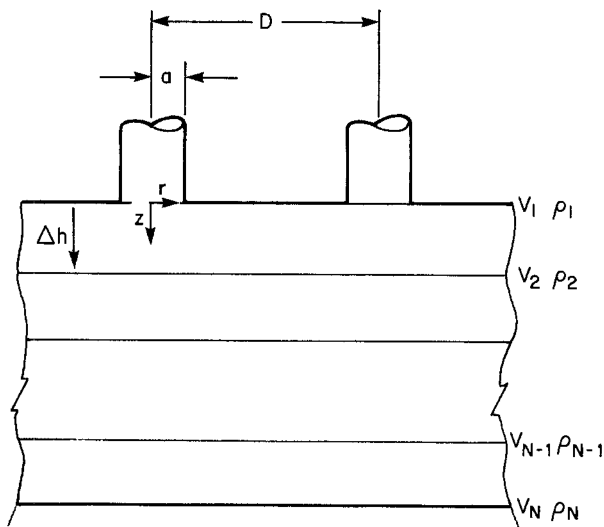

Fig. 2. Idealized multilayer geometry. *D* is the distance between the probes, *a* is the contact radius, Δh is the layer thickness, V_i are the potentials at each interface, and ρ_i are the resistivities of each layer.

The zero and first-order Bessel functions, J_0 and J_1, are characteristic of solutions to Laplace's equation for problems with cylindrical symmetry. The integration factor, θ, is derived from the boundary conditions of current and voltage continuity at each interface and is therefore dependent on all the resistivities ρ_1 through ρ_N as well as the layer thickness and the integration variable, λ. The infinite integral is required to satisfy the boundary conditions at each interface and the surface.

Multilayer potential analysis is generally applicable to any type of resistivity profile and its accuracy for measurement in beveled samples is limited mainly by the assumptions of planar geometry and charge neutrality. General application of this method has been inhibited by the complexity of the calculations. Originally, over 10,000 integrand evaluations were required to insure convergence of the integral resulting in excessive computation time and limiting the usefulness of this approach. Several authors simplified the computations by limiting or partitioning the number of layers (11-14). Others simplified the calculation of θ (which originally required the solution of a $2N$ by $2N$ matrix) first by power law interpolation (11, 14) and later by the derivation of exact recurrence formulas (15, 16). Recently an integration scheme has been devised which significantly reduces the number of integrand evaluations (17). The foregoing methods increase the efficiency of multilayer analysis but still include the time-consuming evaluation of the infinite integral. The following section describes an approach which removes the resistivity dependence from the integrand so that the integrals can be precalculated and stored. This particular implementation, called precalculated partial integrals, reduces the computation time by a factor of 20 as compared to an implementation including the recurrence formula calculation of θ.

Spreading resistance measurements on beveled samples are compared to spreading resistance and four-point probe measurements on anodically sectioned samples and Schottky *C-V* measurements. The results indicate several limitations inherent in the application of multilayer potential analysis to spreading resistance measurements on beveled samples.

Precalculated partial integrals.—The integration factor, θ, is a well-behaved function of λ and can be readily approximated by interpolation. θ is evaluated exactly at several judiciously chosen values of λ (the λ_i's in the following discussion) while in the intervals between λ_i's θ is approximated by the interpolation function. Figure 3 shows the exact evaluations of $1 + 2\theta$ (open circles) and a cubic natural spline interpolation (solid line) for 2 and 33 layers. For these examples, the interpolation error does not exceed 1% and is less than the error resulting from power law interpolation. For the cubic spline approximation, a distinct cubic polynomial is determined in each interval with the first and second derivatives constrained to be continuous at the boundaries. The expression for the integration factor becomes

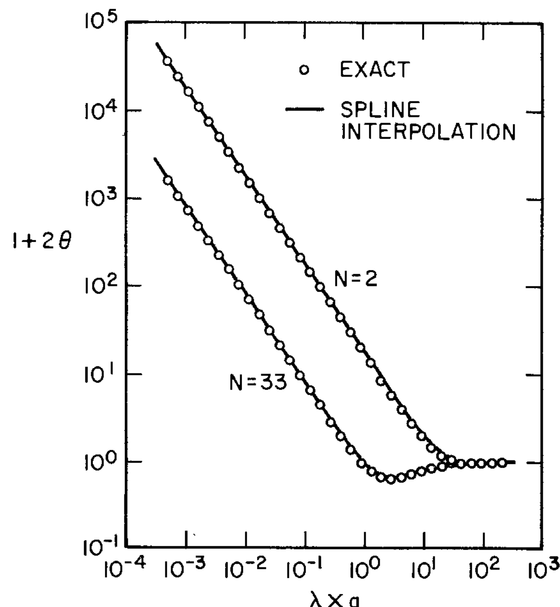

Fig. 3. Spline interpolation of the integration factor, $1 + 2\theta$, for 2 and 33 layers. λ is the integration variable and *a* is the contact radius.

$$1 + 2\theta(\lambda) = A_i\lambda^3 + B_i\lambda^2 + C_i\lambda + [1 + 2\theta(\lambda_i)]$$

for $\lambda_i \leq \lambda < \lambda_{i+1}$. A_i, B_i, and C_i are the cubic polynomial coefficients and are constant over the intervals between λ_i and λ_{i+1}.

The spline approximation for $(1 + 2\theta)$ can be substituted into the expression for the correction factor and the integral can be divided into partial integrals with limits of integration corresponding to the interpolation interval boundaries. The resulting expression is

$$CF = \frac{4}{\pi}\sum_{i=1}^{m-1}\left\{ A_i\int_{\lambda_i}^{\lambda_{i+1}} \lambda^3 f(\lambda)d\lambda + B_i\int_{\lambda_i}^{\lambda_{i+1}} \lambda^2 f(\lambda)d\lambda + C_i\int_{\lambda_i}^{\lambda_{i+1}} \lambda f(\lambda)d\lambda + D_i\int_{\lambda_i}^{\lambda_{i+1}} f(\lambda)d\lambda \right\}$$

where

$$f(\lambda) = \left\{ \frac{J_1(\lambda a)}{\lambda a} - \frac{J_0(\lambda D)}{2} \right\} \frac{\sin(\lambda a)}{\lambda}$$

$$\lambda_1 = 0$$

and λ_m, the upper integration limit, is chosen to insure convergence of the integrals. The spline coefficients are constant over the interpolation intervals and can be removed from the integration. The resulting integrands are independent of resistivity and layer thickness and can therefore be precalculated and stored for any given contact radius and probe separation.

The method of precalculated partial integrals significantly reduces computation time without compromising the inherent accuracy of multilayer potential analysis. Figure 4 shows the uncorrected and corrected profiles for an epi-buried layer structure. A full multilayer implementation including the recurrence formula

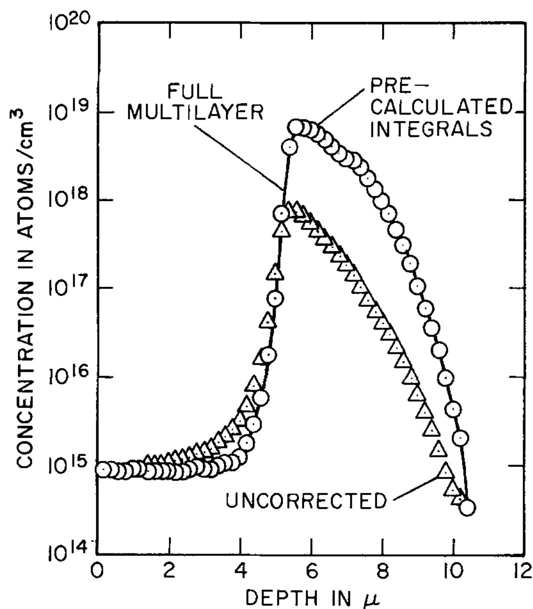

Fig. 4. Comparison of full multilayer and precalculated partial integral analysis of an epi-buried layer structure, including the corrected and uncorrected impurity profiles (a), and tabulated execution times and maximum percent deviation, (b).

	Execution time (min	Max. deviation of impurity concentration (%)	Limiting computation step per iteration
Full multilayer	50	0.1	10,000 integrand evaluations
Precalculated partial integrals	2.5	0.1	Calculation of 280 spline coefficients

calculation of θ required over 50 min on an HP 2100 minicomputer with a memory cycle time of 1 μsec. In comparison, use of precalculated partial integrals reduced the execution time by a factor of 20 to less than 2.5 min while introducing a maximum deviation in concentration of only 0.1%.

The error introduced by spline interpolation of $1 + 2\theta$ is apparently negligible. However, the approximations inherent in multilayer potential analysis can be a source of inaccuracy in isolated portions of certain types of impurity profiles. The comparative results of the next section demonstrate some of these limitations as well as the general utility of the multilayer method.

Comparative Results

To verify the accuracy of multilayer potential analysis on beveled samples, several impurity profiles have been measured by alternative methods including four-point probe incremental sheet resistance, two-point probe incremental spreading resistance, and Schottky C-V.

For the incremental sheet resistance method material is removed in 500Å layers by anodic sectioning. Successive sheet resistance measurements are made with a four-point probe and the resistivity is calculated from the standard incremental conductance model (18).

Incremental spreading resistance also utilizes anodic sectioning to remove material. However, in this case, measurements are made with a two-point spreading resistance probe and the data are analyzed with multilayer potential theory. The incremental spreading resistance technique offers an excellent test of multilayer theory, since the planar geometry and absence of junction space charge regions in the anodically sectioned samples are consistent with the assumptions of the multilayer model

The alternative measurement techniques are compared to the standard two-point probe spreading resistance on beveled surfaces, corrected by multilayer analysis. The beveled samples were polished with water soluble abrasives (Metadi, Quso, or Syton) on Plexiglas in an SSM LP Machine.[2] Angles on the order of 16′ to 1° were measured with the small angle measurement technique (SAM) (19) or multibeam interferometry. The spreading resistance measurements were made with a commercially available automatic probe, the ASR 100.[2]

The first example is a fairly deep phosphorus emitter diffusion into a 4 Ω-cm p-type substrate. Figure 5 compares the concentration profiles measured by incremental spreading resistance and incremental sheet resistance. Agreement in profile shape and absolute concentration values is excellent. Figure 6 compares incremental spreading resistance on an anodically sectioned surface to spreading resistance on a beveled surface. Agreement is good throughout most of the diffusion, including junction depths and peak concentrations as well as in the familiar dip due to concentration-dependent diffusivity. However, significant

[2] Available from Solid Measurements, Monroeville, Pennsylvania.

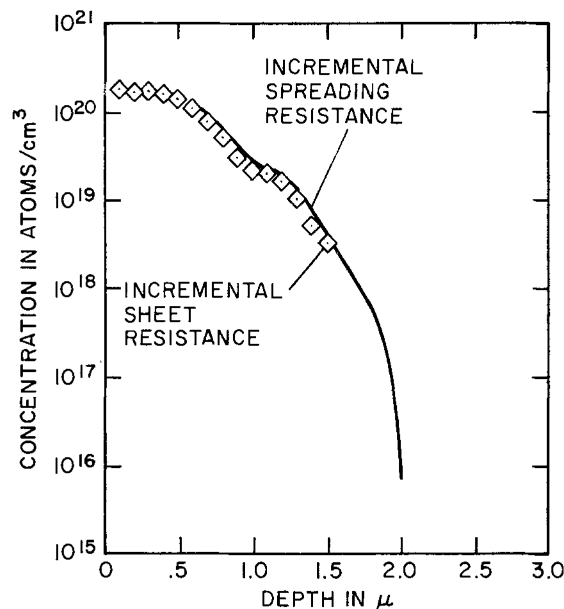

Fig. 5. Incremental spreading resistance (—), and incremental sheet resistance (◇) for a phosphorus diffusions.

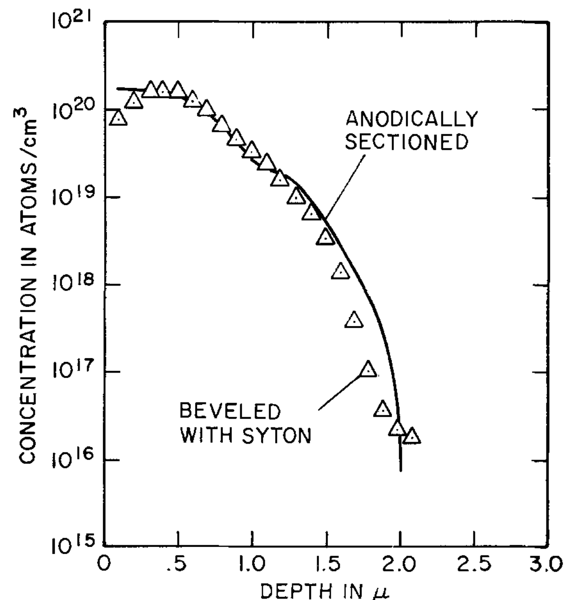

Fig. 6. Incremental spreading resistance (—), and beveled spreading resistance (△) for the phosphorus diffusion.

Table I. Calculated and measured sheet resistance for 2 μm phosphorus diffusion

Calculated from	Sheet resistance (Ω/□)
Beveled spreading resistance	7.5
Incremental spreading resistance	6.3
Incremental sheet resistance	6.5
Measured by four-point probe	6.3 ± 5%

discrepancy exists at the surface where the concentration on the beveled sample falls below the concentration on the anodically sectioned sample. This effect, which has been observed by others (11), is in some way caused by the bevel geometry and is consistently present as is shown in the following examples. Probable causes of the surface anomaly are discussed in a later section.

As an additional verification of the measurement accuracy sheet resistance values were calculated by integrating the corrected conductivity profiles and compared to the sheet resistance measured by a four-point probe, Table I. The calculated values for both the incremental spreading resistance and incremental sheet resistance profiles are in excellent agreement with the measurement The slightly higher value for beveled spreading resistance is a result of the decreased surface concentrations.

The second sample is a three layered structure which forms the source, channel, and drift regions in VMOS and DMOS transistors (20). The channel region is formed by boron implantation into an n^- substrate while the source region is diffused from an arsenic-doped oxide. Incremental spreading resistance is compared to incremental sheet resistance in Fig. 7 and beveled spreading resistance in Fig. 8. Agreement between the two incremental profiles is excellent throughout the n^+ source, but both demonstrate a considerably higher surface concentration than the beveled spreading resistance. In the channel region beveled spreading resistance falls below incremental spreading resistance near the source junction but follows it closely throughout the rest of the p diffusion. The discrepancy near the junction may be caused by the presence of the space charge region in the beveled sample. Since all the n-type material has been removed by anodic sectioning there is no space charge region extending into the channel for the incremental case.

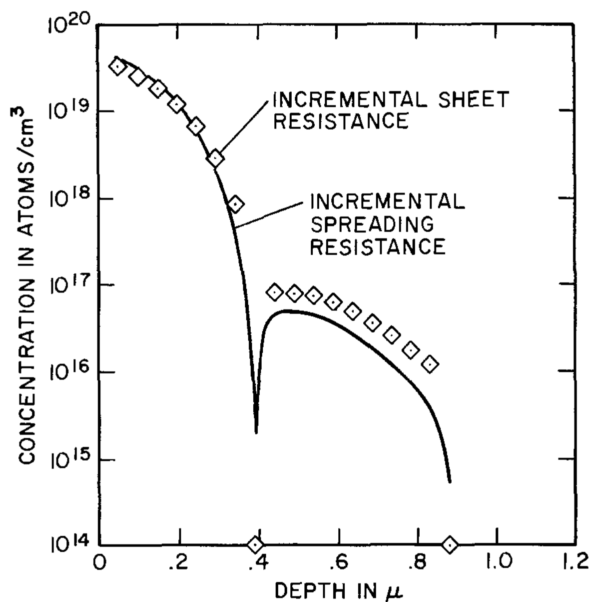

Fig. 7. Incremental spreading resistance (—), and incremental sheet resistance (◇) for the source-channel region of a DMOS/VMOS transistor.

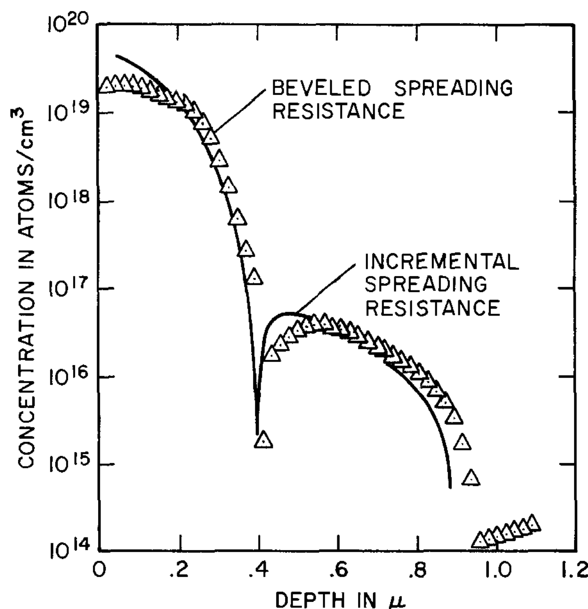

Fig. 8. Incremental spreading resistance (—), and beveled spreading resistance (△) for the DMOS/VMOS process.

The channel concentrations from incremental sheet resistance are approximately 30% higher than the values derived from the two spreading resistance methods. To further evaluate these results calculated sheet resistance is compared to measured values in Table II, where channel resistance is measured on a pinched base resistor. Incremental spreading resistance agrees best with the measured values, both in the source and channel regions, while beveled spreading resistance is high in both regions due to the low concentration at the surface and at the source junction. The high concentrations of the incremental sheet resistance profile result in a calculated channel sheet resistance which is about 30% lower than the measured. The discrepancy may be attributed to the inaccuracy of the four-point probe measurement for narrow, lightly doped layers with sheet resistance on the order of 10 kΩ/□. Table III compares the calculated (from beveled spreading resistance) and measured sheet resistance values for several channel implants and drive-in schedules. The difference never exceeds 15% for channel lengths between 0.5 and 2.0 μm.

The third example is a high frequency bipolar transistor with a diffused phosphorus emitter and a boron base resulting in an emitter junction depth and base

Table II. Calculated and measured sheet resistances for VMOS/DMOS profile

Calculated from	Sheet resistance (Ω/□) Source	channel
Beveled sheet resistance	139	15.6×10^3
Incremental spreading resistance	98	14.7×10^3
Incremental sheet resistance	117	9.4×10^3
Measured	99 ± 5%	$14.0 \times 10^3 \pm 15\%$

Table III. Channel sheet resistance

		Channel sheet resistance		
Wafer	Channel length (μm)	Integrated spreading resistance profile (kΩ/□)	Pinched base resistor (kΩ/□)	% Difference
1	0.48	15.8	13.90	12
2	0.82	—	6.86	—
3	1.05	36.7	31.30	15
4	1.98	10.0	9.50	5
5	2.20	6.9	9.50	13
6	1.90	7.6	7.10	7

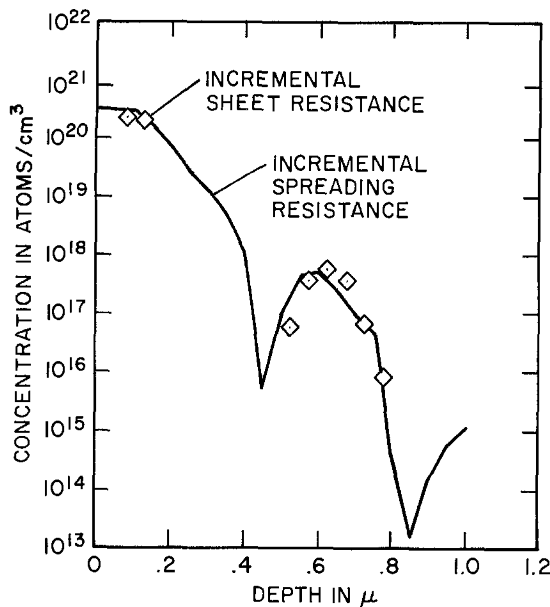

Fig. 9. Incremental spreading resistance (—), and incremental sheet resistance (◇) for the emitter and base of a bipolar transistor.

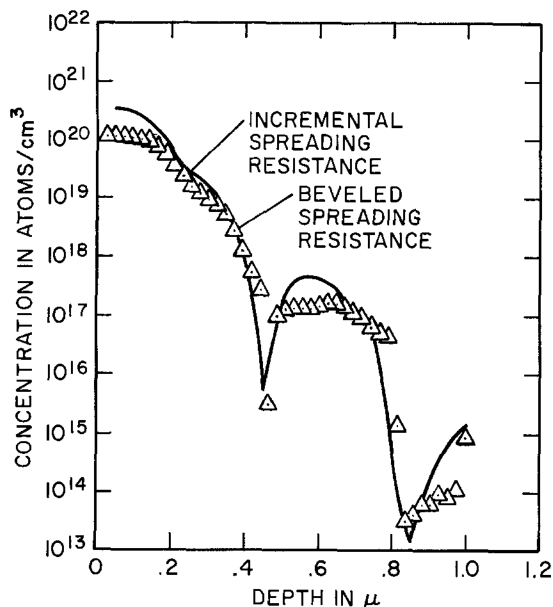

Fig. 10. Incremental spreading resistance (—), and beveled spreading resistance (△) for the bipolar transistor.

width of approximately 0.4 μm. The comparisons in Fig. 9 and 10 demonstrate the same regions of discrepancy and correspondence observed in the previous example. Comparisons of the calculated and measured sheet resistance values, Table IV, again verify the excellent accuracy of multilayer potential theory applied to anodically sectioned structures and demonstrate the limitations of the measurement on beveled samples

The over-all repeatability of the spreading resistance method on beveled samples is demonstrated in

Table IV. Measured and calculated sheet resistance for the bipolar transistor

Calculated from	Sheet resistance (Ω/□) Emitter	Base
Beveled spreading resistance	38.3	6.9×10^3
Incremental spreading resistance	17.2	4.5×10^3
Incremental sheet resistance	—	4.7×10^3
Measured	16.1 ± 5%	

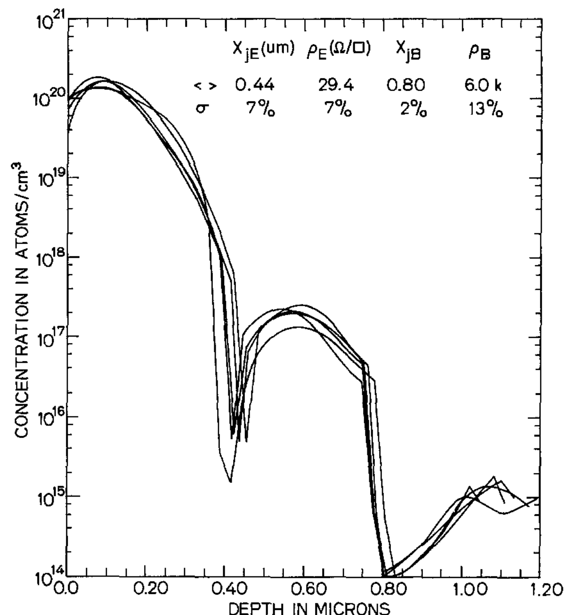

Fig. 11. Comparison of beveled spreading resistance measurements on samples taken from the same bipolar wafer. The tabulated results are the average (< >), and standard deviation in percent of the average (σ), for the emitter (X_{jE}) and base (X_{jB}) junction depths and the calculated sheet resistances in the emitter (ρ_E), and in the base (ρ_B).

Fig. 11. For this experiment a single high frequency bipolar wafer was chosen, from which one sample per week was scribed, beveled, measured, and analyzed. As can be seen from the tabulated statistics repeatability in junction depths and calculated sheet resistances is very good. As can be expected the regions demonstrating the least repeatability are at the surface and in the base near the emitter junction.

The final example, Fig. 12, compares Schottky C-V and beveled spreading resistance measurements for a shallow n^- epitaxial layer on an n^+ buried layer. The two step epitaxial layer process was designed to minimize autodoping. The resulting dip in concentration at the epi-buried layer interface is detected by both profiling techniques. This structure demonstrates the over-all range and versatility of the spreading resistance method which is capable of measuring the epitaxial layer, and the buried layer while the C-V technique is limited by breakdown to the lightly doped epitaxial layer.

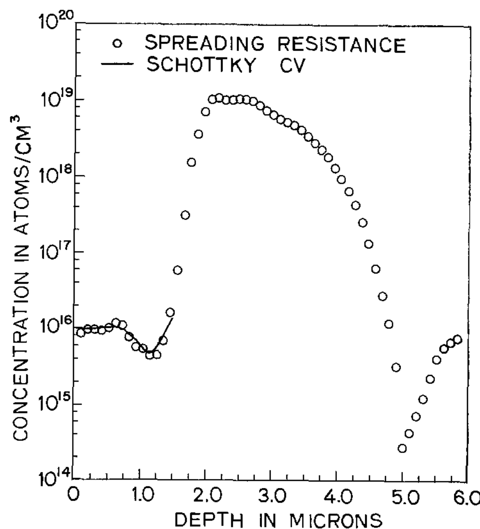

Fig. 12. Beveled spreading resistance (○), and Schottky C-V (—) for an epi-buried layer profile.

Discussion

The preceding comparative measurements demonstrate the utility and accuracy of the spreading resistance technique in combination with multilayer potential analysis. The comparisons of incremental spreading resistance with incremental and total sheet resistance measurements suggest that the multilayer model accurately (to within 10%) describes spreading resistance measurements on idealized planar structures with junction depths on the order of 0.5 μm and larger. However, measurements on beveled samples indicate that the bevel geometry introduces second-order effects which result in significant underestimation of diffused profiles near the Si-SiO_2 interface and in the vicinity of junctions. Several probable causes for these discrepancies are discussed.

The multilayer model assumes a semi-infinite planar geometry so that cylindrical symmetry can be invoked in the solution to Laplace's equation. The bevel geometry only approximates this situation in the limit of small bevel angles. The two dimensional asymmetry in a beveled structure will distort field and potential distributions as insulating interfaces are approached. This phenomenon can be expected to effect the results similarly at material interfaces such as Si-SiO_2 and Si-air and metallugical junctions. In both cases the sampling volume of the measurement is diminished due to the presence of an insulating boundary resulting in higher values of measured resistance and lower corrected concentrations. While exact analysis of the edge effect would require three-dimensional solutions, two-dimensional analysis of limiting cases in conjunction with empirical corrections may prove useful.

In practice the bevel geometry is never ideal in the sense that two flat planes intersect at an obtuse angle. Instead the beveled surface tends to curve or round, especially at the Si-SiO_2 interface. Figure 13 shows surface profiilometer plots for two beveled samples, one prepared with mechanical diamond polish, Metadi, in an aqueous medium and the other with the chem-mechanical, silica polish, Syton. Rounding extends several micrometers into the beveled surface for both samples and is more pronounced in the case of the chem-mechanical polish. The relatively high viscosity of the Syton mixture may be responsible for the excessive rounding. The analysis procedure assumes a fixed vertical distance between each measurement point, which is derived from a bevel angle measurement and the horizontal stepping distance. For the curved bevel surface actual vertical spacing will increase with increasing depth. In general, the bevel angle measurement will be an average over the surface so that the distance between points will tend to be overestimated near the bevel edge and corrected concentrations will be diminished. Possible solutions to this particular problem include optimization of the beveling process to minimize rounding and quantitative measurement of the bevel contour.

As previously mentioned, the presence of space charge in beveled samples may be responsible for the discrepancy on the lightly doped side of p-n junctions. Multilayer potential analysis, which is a solution to Laplace's equation, inherently neglects the effects of space charge. Since spreading resistance is an electrical measurement, only mobile carriers can be detected resulting in an underestimation of impurity concentrations in space charge regions.

An additional source of inaccuracy arises for measurements of p-type profiles due to the nonideal nature of the calibration. Figure 14 is a typical p-type calibration for samples polished in Metadi. The curve is generated by measuring spreading resistance on a number of uniformly doped samples of varying resistivities. The effective contact radius is derived from a power law fit to the measured data so that $Rm = C\rho^m$ and $a = 1/(2C)$. An exponent of 1.0 would imply a constant contact radius as is assumed in the multilayer model. For n-type calibrations m is consistently on the order of 0.95 while for p-type it decreases to 0.85. The deviation from unity results in underestimation of p-type concentrations greater than 10^{18} cm^{-3}. The degree of nonlinearity in the calibration curve is highly dependent on sample preparation and is consistently higher for mechanical polishes such as Metadi in comparison to chem-mechanical abrasives, including Syton and Quso (2). The trends indicate that the effects of nonideal contact phenomena, such as barrier potentials, and piezoresistance, increase with increasing surface damage. The nonlinearity in the calibration curve can be compensated by including an empirical barrier resistance into the correction algorithm (2, 6).

Finally, finite probe penetration and surface extent will ultimately limit the achievable vertical resolution. For this work probe loading was a nominal 20g resulting in a contact radius of about 3.0 μm. Considerable error can be expected from profile smearing at this load for junction depths less than 0.2-0.3 μm. Lighter loads on the order of 6g reduce the contact radius to less than a micrometer significantly increasing potential resolution.

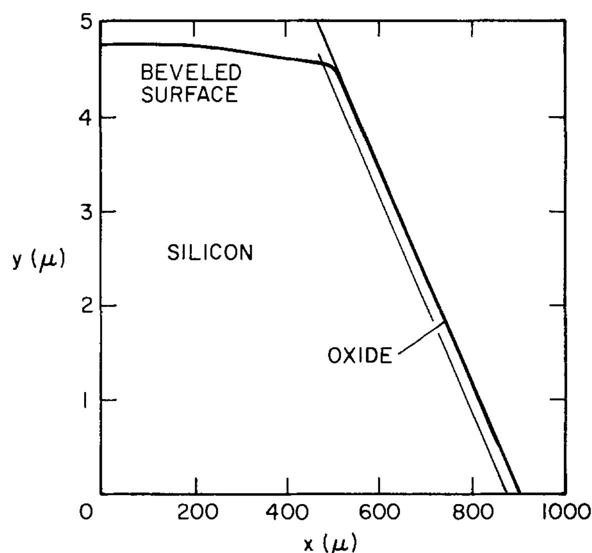

(a) METADI, BEVEL ANGLE = 34′, $T_{ox} \approx 2000$ Å

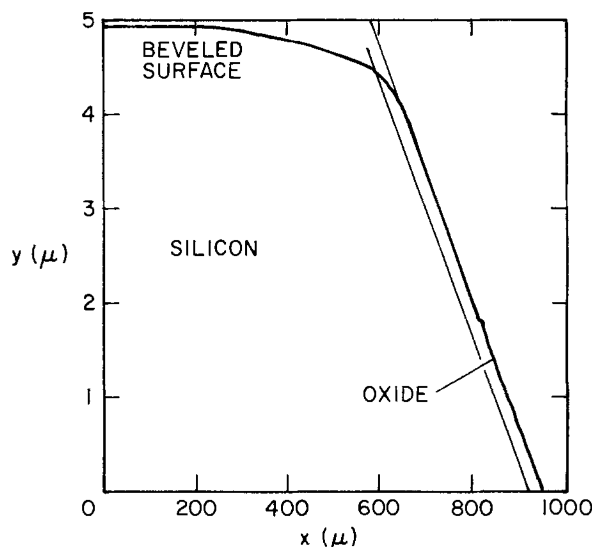

(b) SYTON, BEVEL ANGLE = 34′, $T_{ox} \approx 2000$ Å

Fig. 13. Surface profilometer plots for samples with 34′ angles beveled in Metadi (a), and Syton (b).

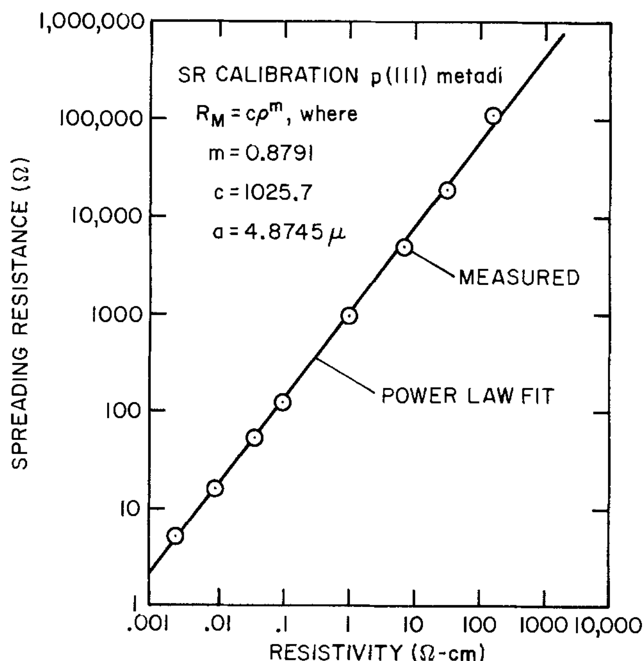

Fig. 14. Spreading resistance calibration for p-type, (111) orientation samples beveled in Metadi. The measured values (⊙), are approximated by a power law fit (—).

Conclusion

The spreading resistance technique is a potentially powerful tool for measuring arbitrary impurity profiles in semiconductors. An accurate data analysis scheme is essential for the determination of shallow profiles. Of the methods currently available, multilayer potential analysis is most consistent with the physical nature of the measurements An implementation of multilayer analysis has been presented which reduces computation time by a factor of 20 with no significant loss of accuracy. Comparative results demonstrated the excellent accuracy of the model for junction depths of 0.5 μm and larger as well as limitations for the application of the method to beveled structures. Proposals for future development include theoretical investigation of three dimensional bevel edge effects, quantitative measurement of the bevel contour, analysis of space charge effects, and physical investigation of the metal probe-semiconductor contact and its effect on calibration measurements.

Acknowledgment

The authors gratefully acknowledge the contributions of Bob Kopp, Conrad Dell'Oca, and the HP ICL staff for multibeam interferometer measurements, surface profilometer measurements, several sample wafers, and the Schottky *C-V* measurements. Research support is gratefully acknowledged from Hewlett-Packard Company through an Industrial Grant from Corporate Engineering, also from National Science Foundation under Grant No. Eng. 74-12151.

Manuscript submitted Nov. 20, 1977; revised manuscript received Feb. 22, 1978. This was Paper 300 presented at the Las Vegas, Nevada, Meeting of the Society, Oct. 17-22, 1976.

Any discussion of this paper will appear in a Discussion Section to be published in the June 1979 JOURNAL. All discussions for the June 1979 Discussion Section should be submitted by Feb. 1, 1979.

Publication costs of this article were assisted by Stanford University.

REFERENCES

1. R. G. Mazur and D. H. Dickey, *This Journal,* **113,** 3 (1966).
2. D. C. D'Avanzo, R. D. Rung, and R. W. Dutton, Stanford Electronics Laboratories, Technical Report No. 5013-2 (February 1977).
3. D. H. Dickey, Abstract 57, p. 151, The Electrochemical Society Extended Abstracts, Spring Meeting, Pittsburgh, Pennsylvania, April 15-18, 1963.
4. D. H. Dickey, in NBS Spec. Pub. 400-10, J. R. Ehrstein, Editor (June 1974).
5. D. H. Dickey, 250 RNP presented at The Electrochemical Society Meeting, Dallas, Texas, October 5-9, 1975.
6. O. Kudoh, K. Uda, Y. Ikushima, and M. Kamoshida, *This Journal,* **123,** 11 (1976).
7. E. Nagusawa and M. Matsumura, *Solid-State Electron,* **20,** 507 (1977).
8. P. A. Schumann and E. E. Gardner, *This Journal,* **116,** 87 (1969).
9. P. A. Schumann and E. E. Gardner, *Solid State Electron.,* **12,** 371 (1969).
10. T. H. Yeh and K. H. Khokani, *This Journal,* **116,** 10 (1969).
11. G. A. Lee, in NBS Special Publication 400-10, J. R. Ehrstein, Editor (June 1974).
12. B. L. Morris, P. H. Langer and J. C. White, in *ibid.*
13. T. E. Hendrickson, *This Journal,* **122,** 11 (1975).
14. S. M. Hu, *Solid-State Electron.,* **15,** 7 (1972).
15. S. C. Choo, M. S. Leong, and K. L. Kuan, *ibid.,* **19,** 7 (1976).
16. Y. Lida H. Abe, and M. Kondo, *This Journal,* **124,** 7 (1977).
17. S. C. Choo, M. S. Leong, H. L. Hung, Ling Pi, and L. S. Tan, *Solid State Electron.,* **20,** 10 (1977).
18. J. C. C. Tsai, *Proc. IEEE,* **5,** 9 (1969).
19. A. H. Tong, E. F. Gorey, and C. P. Schneider, *Rev. Sci. Instrum.,* (February 1972).
20. D. C. D'Avanzo, S. R. Combs, and R. W. Dutton, *J. IEEE Solid-State Circuits,* **sc-12,** 4 (1977).

Abnormal Undercutting in Etched Cr/Au Films

Y. Nemirovsky

Department of Electrical Engineering, Technion-Israel Institute of Technology, Haifa, Israel

and I. A. Blech and J. Yahalom

Department of Materials Engineering, Technion-Israel Institute of Technology, Haifa, Israel

ABSTRACT

The etching of gold films deposited on chromium adhesion layers in iodine solution creates cavities at the base of the films. These cavities or abnormal undercutting are revealed and studied by means of the scanning electron microscope. The abnormal undercutting causes the lifting of gold in the etching of high resolution patterns. The alkali cyanide etching solution creates normal undercutting and its use is recommended. It is suggested that the abnormal undercutting results from the formation of an electrochemical cell in the final stage of the etching process when the chromium layer and the gold layer are simultaneously exposed to the electrolyte. The partial oxidation reaction of gold dissolution at the gold surface is balanced by triiodide reduction at the chromium surface as well as at the gold surface. The electrochemical cell formation accelerates the etching of gold near the chromium-gold boundary and causes the formation of cavities. The mechanisms for the normal and abnormal undercutting processes are discussed.

One of the most commonly used metal systems in solid-state technology is Cr-Au layers. This combination is often used for microstrip MIC's for multilayer thin film MIC's as well as for hybrid circuitry in general (1). Cr-Au is also often used as metallization for interconnections and bonding pads in semiconductors other than Si (2).

Because of its great technological importance and the common trouble of gold lifting in the etching of high resolution patterns, the study of the undercutting of etched gold lines was undertaken. The etchants which were employed are the commonly recommended, commercially available etchants, *i.e.*, the iodine etch and the alkali cyanide solutions.[1]

It was found that while the alkali cyanide solution created normal undercutting, the iodine etch caused an abnormal undercut. At high magnification the optical microscope revealed what appeared to be a small degree of undercut—seemingly very favorable for fine lines. However, the scanning electron microscope (SEM) showed that narrow but deep penetrating cavities were formed at the base of the etched lines.

The damaging nature of the phenomenon manifests itself in the lifting of the gold where fine lines in patterns of high resolution are etched. The gold is lifted mainly during the second stage of the etching process. The chromium etching solution penetrates through the cavities and etches away the entire chromium adhesion layer from underneath the gold.

In this paper the undesired phenomena of cavities under etched gold are studied by means of the SEM. A mechanism for the abnormal undercut of gold films on chromium with the iodine etch is proposed. In the discussion the various etching processes of gold are theoretically evaluated.

Experimental

Pattern etching.—Gold was etched with the iodine etch in the presence of conventional positive photoresists and with alkali cyanide solutions containing peroxide in the presence of conventional negative photoresists. Negative photoresists were employed because of the high *p*H of the solution. Iodine etch is made from 400g KI, 100g I_2, and 400 ml of water. Alkali cyanide powder with the proper amount of peroxide is available commercially. Chromium was etched with either concentrated HCl and hydrazine or with an alkaline ferricyanide etch (3). For both layers the etching is selective.

Substrates.—The layers used for the etching experiments were from varied origin: Sputtered or evaporated Cr/Au films with a chromium layer of 500-1000Å and a gold layer about 0.5 μm thick and commercially Cr-Au-coated substrates with an additional electroplated gold layer of several microns. The layers were deposited on glass, sapphire, and alumina. While the texture of the films was dependent on the nature of the substrate, the observed phenomena were general and independent of the substrate or the photoresist. Normal or abnormal undercut developed only as a direct result of the specific etching solution which was used.

Results and Discussion

Figure 1 shows the profile and surface of 6 μm thick gold film etched at room temperature with iodine solution. The cavity which is formed at the base of the gold line is clearly seen. Figure 2 shows a schematic diagram of the film cross section showing the deep cavities which are referred to as abnormal undercutting.

In order to measure quantitatively the depth of the cavity in relation to the film thickness and time of exposure to the etching solution, the etched films were overexposed to the chromium etching solution. The lines lifted, were turned over, and photographed again.

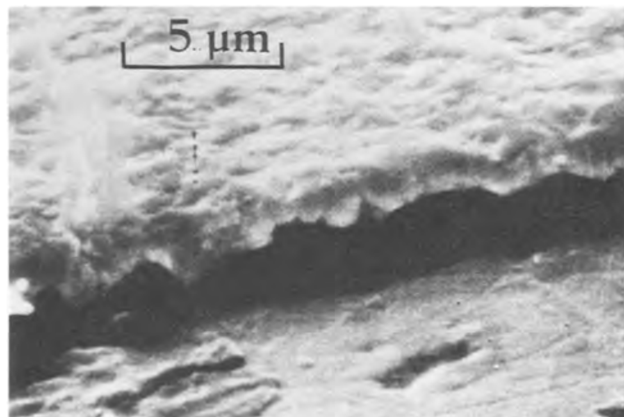

Fig. 1. SEM micrograph of a gold line edge etched with iodine solution. A deep cavity is seen underneath.

Key words: films, circuits, corrosion, etching.

[1] Source of sodium cyanide mixture; MacDermit, Waterbury, Connecticut.

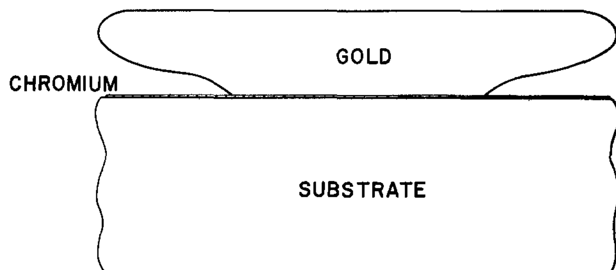

Fig. 2. A schematic cross section showing the abnormal undercutting of a Cr/Au line etched with iodine solution.

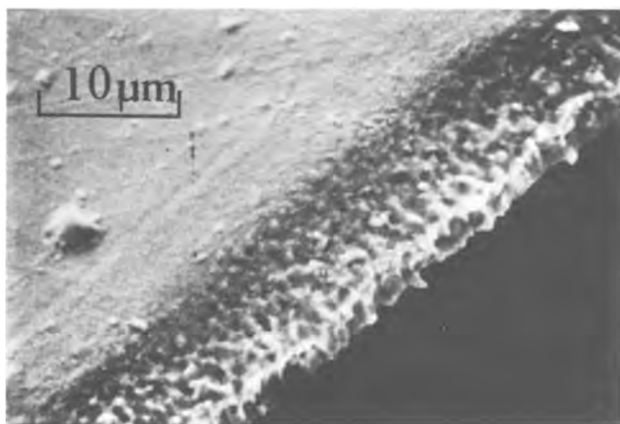

Fig. 3. SEM micrograph of the base of the gold line etched with iodine solution.

Figure 3 is a top view of the base of the etched line. Another technique which was employed was to evaporate Cr/Au films on glass substrate and then measure the degree of abnormal undercut through the backside of the transparent substrate using an optical microscope. The cavities extended quite often 10 μm underneath the gold film.

Finally, Fig. 4 shows the successive stages of the etching process of a 6 μm thick gold film. Figure 4 was obtained by interruption of the etching at different stages of the process, removal of the photoresist, and recording the result by the SEM. Figure 4a shows the morphology of the gold edge when the etchant has not yet reached the chromium. No cavities are observed at this stage. Figure 4b shows the edge shortly after the etchant reached the chromium interface. The chromium is first seen at the gold edge but some holes can be seen elsewhere in the film. Subsequently more holes appear in the field and a cavity develops around each hole and the film edge. When the entire gold is finally etched away, a deep cavity remains under the gold edge (Fig. 4c).

Figure 5 shows the profile and surface of gold film etched with the alkali cyanide solution. It clearly indicates the proper way of etching fine-lines of gold. The etching process is referred to as normal undercutting because of the uniform slope at the film edge devoid of any reentrant slopes or cavities.

The rate of the etching process in the iodine solution was then compared with that of a pure gold surface and a couple of gold with chromium. The exposed area of the latter was about ten times larger than that of gold. The etching rate increased from 30 to 200 nm/sec by the couple, the gold being the anode. In the actual etching process (see Fig. 4) the etch rate of gold at the final stage is increased significantly since the area of the chromium surface which is exposed to the etching solution rapidly increases (8).

The actual behavior of the couple Cr/Au during etching in the iodine solution indicates that the gold acts as the anode in respect to the exposed chromium. The potential of the chromium surface which was measured against the gold surface at open circuit was found to be approximately 3 mV. The relatively active potential of the gold could possibly be the result of formation of a complex, iodoaurate (AuI_2^-) as the anodic product. The chromium is expected to be passivated at the prevailing mixed potential when both are in contact and exposed simultaneously to the solution. The galvanic cell created between the gold and the exposed chromium thus enhances gold etching near the junction and causes the observed undercut if free gold dissolution is assumed in the electrolyte.

The open-circuit conditions leading to the observed polarity between chromium and gold is schematically illustrated in Fig. 6.

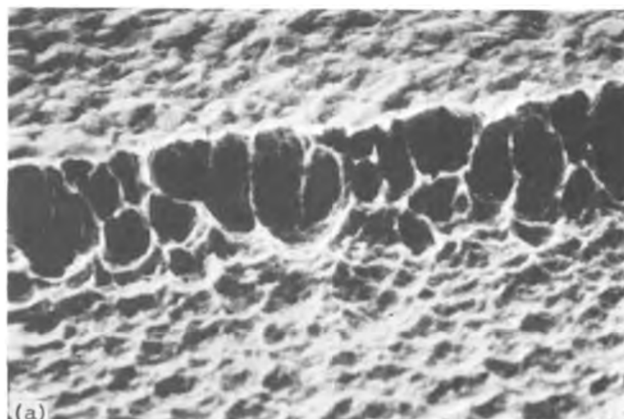

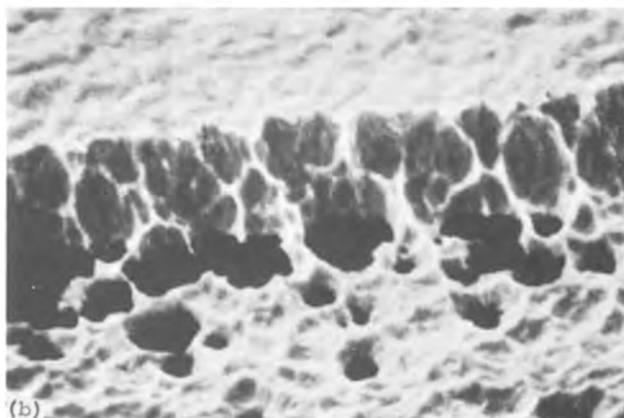

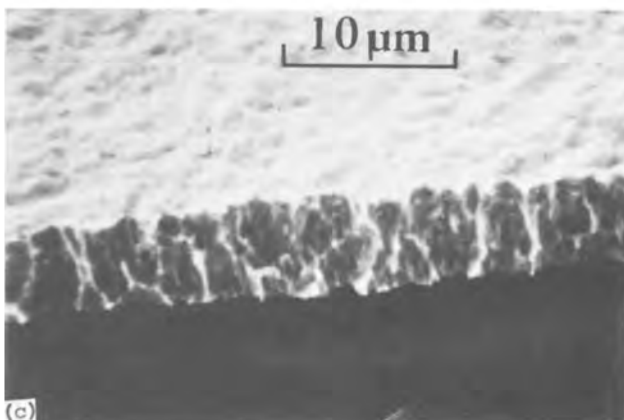

Fig. 4. The development of holes and cavities during successive stages of the etching process with iodine solution: (a) Film edge just before reaching the Cr interface; (b) holes form at the film edge and in the field; (c) after completion a deep cavity formed under the gold edge.

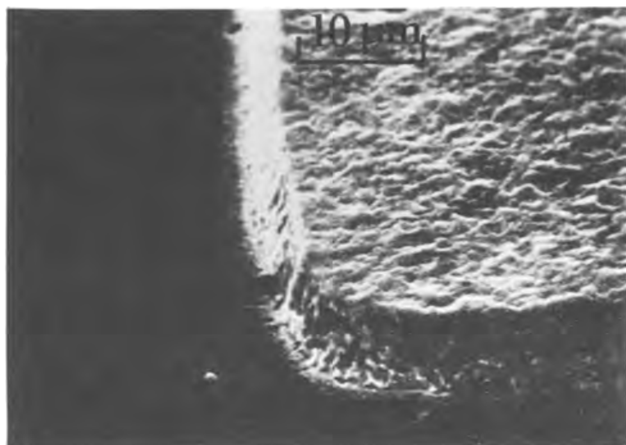

Fig. 5. SEM micrograph of gold film etched with alkali cyanide solution showing normal undercutting.

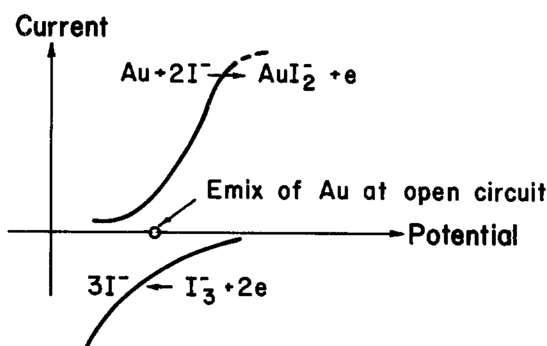

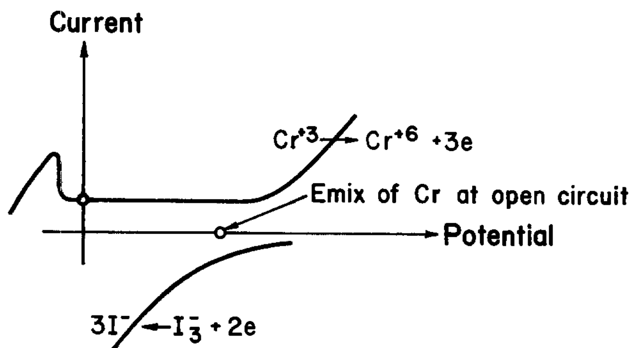

Fig. 6. Schematic diagram of the current-voltage curves for etching of gold and the passivation of chromium in iodine solution.

In the cyanide solution, where no undercutting took place, the gold was nevertheless still found to be at a more negative potential than the chromium. The potential of a chromium surface against a gold surface at open circuit in the alkali cyanide solution was found to be +250 mV. The active potential of gold is due to the formation of stable complexes. The cathodic depolarizer is hydrogen peroxide. Under such conditions the exposed chromium is again expected to be passivated (7). The complete selectivity in the etching of gold which was observed would indicate passivity for the chromium layer. The fact that no enhancement of dissolution occurred in this case at the gold adjacent to the chromium layer in spite of the galvanic cell created between them should indicate limiting-current conditions at the gold surface. The current in this case is con-

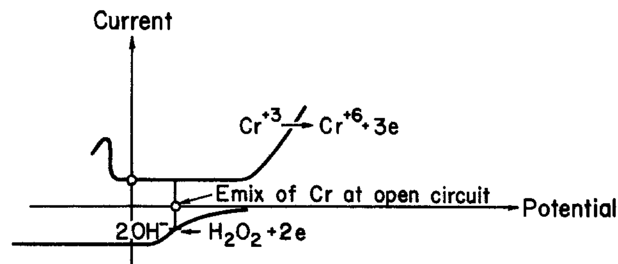

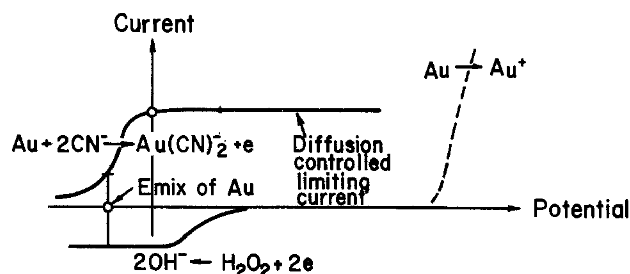

Fig. 7. Schematic diagram of the current-voltage curves for the etching of gold in the alkali cyanide solution.

trolled by the diffusion of the cyanide ions. The open-circuit situation is schematically illustrated in Fig. 7.

Summary

It has been shown that the iodine etchant for gold films which are deposited on chromium adhesion layers forms cavities at the base of the films. This abnormal undercutting causes the lifting of gold in the etching of high resolution patterns.

It is believed that the cavities are created at the final stage of the etching process when the chromium and gold layers are simultaneously exposed to the electrolyte. The gold acts as the anode and the chromium becomes the cathode. The electrochemical cell formation accelerates the etching of gold near the chromium-gold boundary and causes the formation of cavities.

In the alkali cyanide etchant abnormal undercutting is avoided due to the limiting diffusion of the cyanide ions. The use of alkali cyanide solution is therefore recommended for the etching of fine lines.

Manuscript submitted Sept. 23, 1977; revised manuscript received Feb. 15, 1978.

Any discussion of this paper will appear in a Discussion Section to be published in the June 1979 JOURNAL. All discussions for the June 1979 Discussion Section should be submitted by Feb. 1, 1979.

REFERENCES

1. D. M. Mattox, *Thin Solid Films*, **18**, 173 (1973).
2. J. Shappir, S. Margalit, and I. Kidron, *IEEE Trans. Electron Devices*, **ed 22** (1975).
3. L. I. Maissel and R. Glang, "Handbook of Thin Film Technology," McGraw-Hill, Inc., New York (1970).
4. K. J. Vetter, "Electrochemical Kinetics," Academic Press, New York (1967).
5. W. M. Latimer, "Oxidation Potentials," Prentice-Hall, Inc., Englewood Cliffs, New Jersey (1952).
6. K. J. Vetter and D. Berndt, *Z. Elektrochem*, **62**, 378 (1958).
7. M. Pourbaix, "Atlas D'equilibres Electrochimiques," Gauthier-Villars, Paris (1963).
8. J. J. Kelly and C. H. de Minjer, *This Journal*, **122**, 931 (1975).

Perturbation of Parabolic Kinetics Resulting from the Accumulation of Stress in Protective Oxide Layers

H. E. Evans, D. J. Norfolk, and T. Swan

Berkeley Nuclear Laboratories, Central Electricity Generating Board, Berkeley, Gloucestershire, England

ABSTRACT

A frequent observation in metal oxidation is the development of subparabolic kinetics, variously described as cubic or quartic. Although a number of detailed mechanisms have been proposed to account for this effect, none seem generally applicable. This paper presents a model of the oxidation process which is divorced from such restrictions. It is argued that deviations from parabolic behavior occur as a result of the concurrent development of stresses within the oxide. It is shown that the presence of stress fields can influence significantly the rate of transport of vacancy defects within the oxide such that tensile stresses produce positive deviations and compressive stresses, negative deviations from parabolic behavior. The model is applied in detail to Zircaloy-2 oxidation at 773°K. It is predicted that the kinetics should be insensitve to the oxygen potential of the environment and this has been confirmed by previous experimental work. In addition, the absolute value of the oxidation rate is closely predicted using measured values of diffusion coefficients and the observed gradual departure from parabolic kinetics with increasing oxide thickness is accounted for.

Simple models for the protective oxidation of metals based on reaction control by the diffusion of species across the oxide layer predict parabolic kinetics, *viz*

$$\xi = k_p t^{1/2} \quad [1]$$

where ξ is the oxide thickness, t is elapsed time, and k_p is the parabolic rate constant. However, there are many instances where reaction rates decline more rapidly than parabolic kinetics predict, *e.g.*, on zirconium (1), Zircaloy-2 (1), nickel (2-4), titanium (5), tantalum (5), and copper (5). No entirely satisfactory explanation has been given of this behavior. Thus, both Mott (6) and Anderson (7) have argued that the existence of space-charge effects within the oxide could produce such a departure from parabolic kinetics but this is likely to be important only for thin films. Irving (8) using Whipple's analysis (9) for diffusion in a polycrystalline aggregate attempted to demonstrate that cubic-type kinetics could occur if the dominant diffusion paths were grain boundaries, but Gibbs (10) has emphasized the shortcomings of this approach. There is good evidence, however, that mass transport in growing oxides can occur predominantly along short-circuit paths [*e.g.*, (11, 12)] and any variation with time in the density of such paths will lead to departures from parabolic kinetics.

On this basis a number of authors (13-16, 18) have developed a "decay" hypothesis which accounts for subparabolic kinetics by a decrease in the density of paths. More explicitly, observations of a tendency for increased oxide grain size with increasing oxide thickness (15-17) combined with the assumption that grain boundaries are the only important short-circuit routes can account for cubic (18) or even quartic (19) oxidation kinetics. This view gives rise to two reservations. The first is the assumption that grain boundaries are the only significant short-circuit paths, whereas calculation (14) and observation (15, 16) show that both dislocations and subboundaries are also important. The second reservation is that the evidence for an increasing oxide grain size is based on comparatively few observations for Zircaloy (17, 18), where data for only one pretransition film were presented. An additional difficulty with these measurements is that the scatter in grain size in any one transverse section was very large and resulted in considerable overlap of size ranges from one part of the film to another. Bearing in mind that observations of subparabolic kinetics are a frequent occurrence [for a summary of data on Zircaloy see Ref. (19)] the purpose of this paper is to present an alternative theory which does not require a systematic variation of structure with extent of oxidation. It is still recognized that short-circuit diffusion can occur, but the over-all density of such paths (*e.g.*, dislocations, subboundaries, and grain boundaries) is taken as constant.

An additional factor in the reported examples of nonparabolic behavior seems to be the development of compressive stress within the oxide. Thus, Pawel and Campbell (20) attribute at least part of their observed curvatures in specimens of tantalum and niobium to stresses within the oxide film; Tylecote and Appleby (21) consider that low temperature oxides grown on copper contain stresses which Borie *et al.* (22) attribute to epitaxy; Engell and Wever (23) have suggested the presence of strong compressive stresses in films of NiO and FeO; Roy and Burgess (24) have measured average stress levels of 1.7×10^9 nm^{-2} in films grown on Zircaloy-2 in oxygen and 1.1×10^9 nm^{-2} in films grown on zirconium. Accepting that the defects which control oxidation are in equilibrium at the oxide/metal and oxide/environment interfaces, the presence of stress may influence defect migration in two ways. The first arises because oxidation generally causes changes in solid volume at one or both of the interfaces. In the presence of stress such volume changes involve mechanical work and so displace the equilibrium positions of the interfacial reactions. Defect concentrations at either interface consequently vary with stress. This aspect is considered in this paper for the example of vacancy defects. The second arises because the volume occupied by a defect is different from that of a normal lattice site. The presence of a stress gradient within the oxide therefore imposes a bias on the random migration of defects. This is considered in the present work when the general transport equation is solved for particular distributions of stress. A comparison of the theory is then made with experimental data on Zircaloy-2 since reasonable measurements of stress exist for this material.

Because of this, the theory is developed for a metal M forming a stable dioxide MO_2 which grows by the formation of oxide at the oxide/metal interface. The volume increase so produced results in the accumulation of compressive stresses within the oxide. The

Key words: metal, oxidation, oxide layer stress.

oxide ions are transported to this interface by a vacancy-exchange mechanism. It is assumed that departures from stoichiometry are accommodated by single vacancies and that space-charge effects are negligible. It should be pointed out that the choice of this specific example does not detract from the generality of the concepts used. A further purpose of this paper is to make a numerical evaluation of the effect for this particular case.

Influence of Stress on Vacancy Equilibria

At the oxide/metal interface diffusing oxide ions are incorporated into the metal lattice to form a substoichiometric oxide, MO_{2-y}, and an anion vacancy within the original oxide layer. This is illustrated in Fig. 1. The over-all reaction may be written

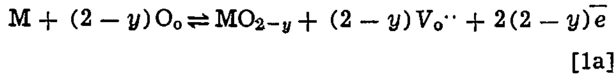

$$M + (2-y)O_o \rightleftharpoons MO_{2-y} + (2-y)V_o^{\cdot\cdot} + 2(2-y)\bar{e} \quad [1a]$$

For convenience, this reaction can be split into two parts, the first describing the formation of gaseous oxygen by dissociation of the oxide, *i.e.*

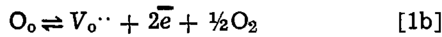

$$O_o \rightleftharpoons V_o^{\cdot\cdot} + 2\bar{e} + \tfrac{1}{2}O_2 \quad [1b]$$

and the second, describing the oxidation of the metal by oxygen

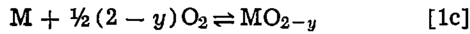

$$M + \tfrac{1}{2}(2-y)O_2 \rightleftharpoons MO_{2-y} \quad [1c]$$

Here O_o is a lattice oxygen ion, $V_o^{\cdot\cdot}$ is a doubly charged anion vacancy, $\bar{e}$ is an electron, and O_2 is a molecule of oxygen in the gaseous phase.

At the oxide/atmosphere interface, vacancies react with oxygen and are replaced by oxide ions; this is the reverse of reaction [1b]. This model assumes that the vacancy concentration at oxide interfaces is dictated by the local oxidation potential and that the concentration arising from extrinsic factors (*e.g.*, impurities) is negligible.

Since the rate of oxidation is limited by vacancy diffusion through the oxide, the chemical reactions in which vacancies are formed are in equilibrium at both the inner and outer interfaces. The respective volume changes for the reactions [1b] and [1c] are

$$\Delta\Omega_B = (\Omega_{O_o} - \Omega_{V_o^{\cdot\cdot}}) \quad \text{and} \quad \Delta\Omega_A = (\Omega_{MO_{2-y}} - \Omega_M)$$

where Ω_M is the volume of a metal atom; $\Omega_{MO_{2-y}}$ the volume of the oxide per metal atom; Ω_{O_o} the volume of an anion in the oxide and $\Omega_{V_o^{\cdot\cdot}}$ the volume of a doubly charged anion vacancy. The over-all volume change $\Delta\Omega$ is then

$$\Delta\Omega = \Delta\Omega_A - (2-y)\Omega\Delta_B$$

When $\Delta\Omega$ is positive (volume increase) the oxide experiences a compressive stress of hydrostatic component $(-\sigma)$ and further oxide growth has to do work against this stress.

Under these conditions the chemical potentials of the various constituents are

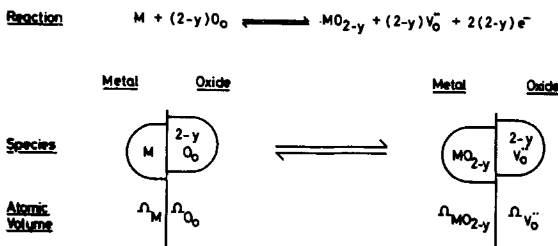

Fig. 1. Model of the oxidation process at the metal/oxide interface.

$$\mu_{O_o} = \mu^\circ_{O_o} + kT \ln \frac{[O_o]}{[O_o]^\circ} - \sigma\Omega_{O_o} \quad [2a]$$

$$\mu_{V_o^{\cdot\cdot}} = \mu^\circ_{V_o^{\cdot\cdot}} + kT \ln \frac{[V_o^{\cdot\cdot}]}{[V_o^{\cdot\cdot}]^\circ} - \sigma\Omega_{V_o^{\cdot\cdot}} \quad [2b]$$

$$\mu_e = \mu^\circ_e + kT \ln \frac{[m]}{[m]^\circ} \quad [2c]$$

$$\mu_{O_2} = \mu^\circ_{O_2} + kT \ln \frac{p}{p^\circ} \quad [2d]$$

where the subscripts are self-explanatory and the superscript "o" represents a standard state which is stress free and contains concentrations of oxide ions, vacancies, and electrons in equilibrium with an oxygen pressure p°. These concentrations are related by the equations

$$[O_o] + [V_o^{\cdot\cdot}] = N$$

where N is the number of lattice sites, and

$$[m] = 2[V_o^{\cdot\cdot}]$$

where $[m]$ is the concentration of electrons. It should be noted that σ in Eq. 2 is negative if compressive. Expression [2b] is obtained by envisaging the vacancy as being created by removal of an interior ion to a surface step, thereby increasing the total number of lattice sites by 1.

Applying the equilibrium condition that $\Sigma\, \mu_i dn_i = 0$ to Eq. [2] and noting that $[m]/[m]^\circ = [V_o^{\cdot\cdot}]/[V_o^{\cdot\cdot}]^\circ$ and that, for realistic stoichiometries, $[O_o]/[O_o]^\circ \approx 1$ it can be shown that the equilibrium vacancy concentration is given by

$$[V_o^{\cdot\cdot}] = K[V_o^{\cdot\cdot}]^\circ (p/p^\circ)^{-1/6} \exp \frac{-\sigma\Delta\Omega_B}{3kT} \quad [3]$$

where $K = \exp(-\, \Sigma\, \mu^\circ_i dn_i/3kT)$ and p is the local value of the oxygen pressure. Since the standard state is also at equilibrium, $K = 1$.

In particular, at the oxide/metal interface the oxygen partial pressure is set by the dissociation pressure of the oxide via the equilibrium of reaction [1c]. If σ_I is the value of σ at the interface, the chemical potentials of the constituents of reaction [1c] become

$$\mu_{MO_{2-y}} = \mu^\circ_{MO_{2-y}} - \sigma_I\Omega_{MO_{2-y}} \quad [4a]$$

$$\mu_M = \mu^\circ_M - \sigma_I\Omega_M \quad [4b]$$

$$\mu_{O_2} = \mu^\circ_{O_2} + kT \ln p/p^\circ \quad [4c]$$

Here again σ_I is negative if compressive and the μ°'s refer to stress-free, standard states. Applying the equilibrium condition $\Sigma\, \mu_i dn_i = 0$ to Eq. [4] it can be shown, after some algebra, that the oxygen partial pressure, p_σ, in the presence of a stress is related to the stress-free value, $p_{diss.}$, by

$$p_\sigma = p_{diss.} \exp\left[-\frac{\sigma_I\Delta\Omega_A}{kT}\left(\frac{2}{2-y}\right)\right] \quad [5]$$

At the oxide/environment interface, the stresses in the oxide will have a negligible effect on the oxygen partial pressure. The latter will be the equilibrium value set by the environment and is designated p_s.

The Transport Equation

General solution.—The driving force for anion vacancy diffusion is the negative gradient of the difference $(\mu_{V_o^{\cdot\cdot}} - \mu_{O_o})$. The flux of vacancies, j_v, is obtained from the Nernst-Einstein equation

$$j_v = -\frac{D_v[V_o^{\cdot\cdot}]}{kT} \frac{\partial}{\partial x} (\mu_{V_o^{\cdot\cdot}} - \mu_{O_o}) \quad [6]$$

where x is the distance coordinate originating at the oxide/environment interface. D_v is an effective vacancy-diffusion coefficient which allows for short-

circuiting paths, and the ensuing treatment assumes that lateral diffusion at the oxide/metal interface is so rapid that the oxide continues to grow uniformly. The preceding derivations of chemical potentials will still apply to diffusion along such paths provided that the process is one of vacancy/atom exchange. This is considered a reasonable assumption.

Substitution of the general Eq. [2a] and [2b] in Eq. [6] then gives

$$j_V = -\frac{D_V[V_o^{\cdot\cdot}]}{kT}\frac{\partial}{\partial x}\left\{\mu^{\circ\prime} + \sigma\Delta\Omega_B + kT\ln\frac{[V_o^{\cdot\cdot}]}{[V_o^{\cdot\cdot}]^\circ}\right\} \quad [7]$$

where $\mu^{\circ\prime} = \mu^\circ{}_{V_o^{\cdot\cdot}} - \mu^\circ{}_{O_o}$, $\Delta\Omega_B = \Omega_{O_o} - \Omega_{V_o^{\cdot\cdot}}$ and for realistic stoichiometries $[O_o]/[O_o]^\circ \approx 1$. In order to preserve the convention of expressing vacancy concentrations in terms of oxygen partial pressure, Eq. [3] can be substituted in the form

$$\frac{[V_o^{\cdot\cdot}]}{[V_o^{\cdot\cdot}]^\circ} = \left(\frac{p}{p^\circ}\right)^{-1/6}\exp\left(-\frac{\sigma\Delta\Omega_B}{3kT}\right) \quad [8]$$

Insertion of this into Eq. [7] and differentiating gives the transport equation

$$j_V = -D_V\frac{[V_o^{\cdot\cdot}]}{kT}\left(\frac{p}{p^\circ}\right)^{-1/6}\exp\left(\frac{-\sigma\Delta\Omega_B}{3kT}\right)\left(\frac{2}{3}\Delta\Omega_B\frac{\partial\sigma}{\partial x} - \frac{kT}{6}\frac{\partial\ln p}{\partial x}\right) \quad [9]$$

This equation describes the vacancy flux in terms of both a stress gradient and a concentration gradient, but these cannot be easily separated because the concentration gradient is also a function of stress. If we now define a new variable

$$P^* = [V_o^{\cdot\cdot}]^\circ\left(\frac{p}{p^\circ}\right)^{-1/6}\exp\left(\frac{2\sigma\Delta\Omega_B}{3kT}\right) \quad [10]$$

then

$$\frac{\partial P^*}{\partial x} = \exp\left(\frac{2\sigma\Delta\Omega_B}{3kT}\right)\left(\frac{p}{p^\circ}\right)^{-1/6}\frac{[V_o^{\cdot\cdot}]^\circ}{kT}\left(\frac{2\Delta\Omega_B}{3}\frac{\partial\sigma}{\partial x} - \frac{kT}{6}\frac{\partial\ln p}{\partial x}\right) \quad [11]$$

Substituting Eq. [9] in [11] gives

$$\frac{\partial P^*}{\partial x} = -\frac{j_V}{D_V}\exp\left(\frac{\sigma\Delta\Omega_B}{kT}\right) \quad [12]$$

This can be integrated noting that, as pseudosteady-state conditions are assumed, j_V is constant with x for any given oxide thickness ξ. Thus

$$j_V = \frac{-D_V(P^*_I - P^*_s)}{\int_0^\xi \exp\left(\frac{\sigma\Delta\Omega_B}{kT}\right)dx} \quad [13]$$

where P^*_I is the value of P^* at the inner oxide interface, $x = \xi$, and P^*_s is the corresponding value at the surface $x = 0$. To obtain explicit expressions for the oxidation rate, it is necessary to know the variation of σ with x and examples are considered below. In the limiting case of uniform or zero stress throughout the oxide Eq. [13] reverts to parabolic form.

Specific solutions.—Stress concentrated at the inner (oxide/metal) interface, (Case I).—Measurements of stress distribution through an oxide layer are particularly difficult to make. Roy and Burgess (24) have attempted to do so with both zirconium and Zircaloy-2 by determining the change in average stress on solution of part of the oxide during annealing. The technique is crude, but the results indicate that approximately 70% of the stress may be associated with the 10% of the oxide thickness adjacent to the metal. The data are not sufficiently extensive to allow the fitting of a meaningful distribution function, but do show that a model of the oxide in which the stress is considered zero everywhere except at the oxide/metal interface, may not be unreasonable. This is shown diagramatically in Fig. (2a). Under these circumstances, the denominator of Eq. [13] reduces to ξ and the equation becomes

$$j_V = -\frac{D_V}{\xi}(P^*_I - P^*_s) \quad [14]$$

where, from Eq. [5] and [10]

$$\left[\begin{aligned} P^*_I &= [V_o^{\cdot\cdot}]\frac{P_{diss}}{p^\circ}^{-1/6}\exp -\frac{\sigma_I\Delta\Omega_B}{3kT}\exp\frac{\sigma_I}{kT}\left\{\left(\frac{\Delta\Omega_A}{3(2-y)} + \Delta\Omega_B\right)\right\} \\ \text{and}\quad P^*_s &= [V_o^{\cdot\cdot}]^\circ\frac{p_s}{p^\circ}^{-1/6}\end{aligned}\right] \quad [15]$$

where p_s is the oxygen partial pressure at the surface of the oxide.

The flux of oxygen ions arriving per unit area of metal surface is then the negative of Eq. [14] so that, as the volume of oxide produced per ion is $\approx (\Omega_{MO_{2-y}}/2)$, the oxide growth rate is

$$(d\xi/dt) = \frac{D_V\Omega}{2\xi}(P^*_I - P^*_s) \quad [16]$$

where the symbol $\Omega_{MO_{2-y}}$ has been abbreviated to Ω.

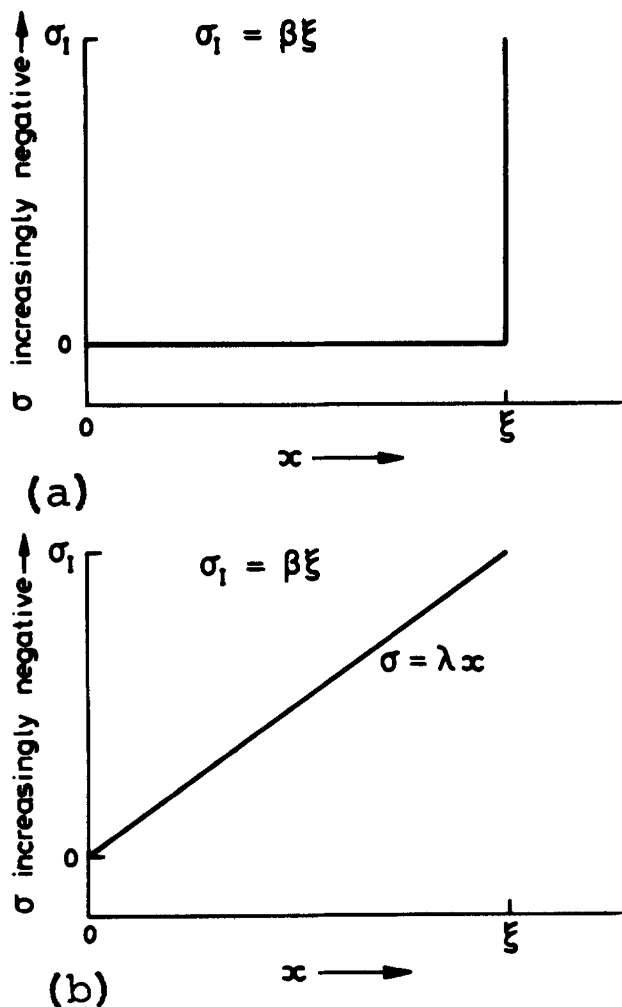

Fig. 2. Assumed stress distribution in oxide layers. (a) Stress concentrated at inner interface; (b) linear stress gradient with zero stress at oxide/environment interface.

Noting, in addition, that Roy and Burgess (24) find an approximately linear relationship between oxide thickness and stress, *i.e.*, in the context of this approximation

$$\sigma_I = \beta\xi \qquad [17]$$

where β is an empirical constant, the oxidation rate can be obtained finally as

$$\left(\frac{d\xi}{dt}\right) = \frac{D_V\Omega[V_o^{\cdot\cdot}]^o}{2\xi(p^o)^{-1/6}} \left\{ p_{\text{diss.}}^{-1/6} \exp\left(-\frac{\sigma_I \Delta\Omega_B}{3kT}\right) \exp\left\{\frac{\beta\xi}{kT}\left[\frac{\Delta\Omega_A}{3(2-y)} + \Delta\Omega_B\right]\right\} - p_s^{-1/6} \right\} \qquad [18]$$

It is clear that with compressive stresses at the oxide/metal interface, (*i.e.*, β is negative) the oxidation rate decreases below parabolic with time. Parabolic kinetics pertain in a stress-free oxide ($\beta = 0$) and with tensile stresses present the rate will be higher than parabolic.

A linear compressive stress gradient, (Case II).—Calculations [*e.g.*; (25)] of the stress distribution within anion deficient oxides inevitably predict a linear gradient. The compressive stress at the inner interface decreases in value through the oxide and acquires tensile values at the outer surface depending on the stress borne by the metal substrate. Simply for comparative purposes with the result of the preceding section, the outer surface stress is again taken as zero and the stress σ_I is assumed to obey Eq. [17] (with β negative). The stress distribution within the oxide is then

$$\sigma = \frac{\sigma_I x}{\xi} = \lambda x \qquad [19]$$

and this is shown diagramatically in Fig. (2b). The denominator of Eq. [13] is now

$$\int_0^\xi \exp\left(\frac{\lambda x \Delta\Omega_B}{kT}\right) dx = \frac{kT}{\lambda\Delta\Omega_B}\left\{\exp\left[\frac{\lambda\xi\Delta\Omega_B}{kT}\right] - 1\right\} \qquad [20]$$

Since the values of P^*_I and P^*_s are the same in both Case I and Case II, the ratio of the rates for the two cases is

$$R = \frac{\text{Case II}}{\text{Case I}} = \frac{\xi}{\dfrac{kT}{\lambda\Delta\Omega_B}\left\{\exp\left[\dfrac{\lambda\xi\Delta\Omega_B}{kT}\right] - 1\right\}} \qquad [21]$$

i.e.

$$R = \frac{A}{(\exp A) - 1}, \quad \text{where } A = \frac{\sigma_I \Delta\Omega_B}{kT} \qquad [22]$$

It follows from Eq. [18] and [22] that the oxidation rate for the linear-compressive-stress case is

$$\left(\frac{d\xi}{dt}\right) = \frac{\dfrac{D_V\Omega[V_o^{\cdot\cdot}]\lambda\Delta\Omega_B}{2kT(p^o)^{-1/6}}\left\{p_{\text{diss.}}^{-1/6}\exp\left(-\dfrac{\sigma_I\Delta\Omega_B}{3kT}\right)\exp\left\{\dfrac{\beta\xi}{kT}\left[\dfrac{\Delta\Omega_A}{3(2-y)} + \Delta\Omega_B\right]\right\} - p_s^{-1/6}\right\}}{\exp\left[\dfrac{\lambda\xi\Delta\,\Omega_B}{k\,T}\right] - 1} \qquad [23]$$

The ratio, R, of rates (expression [22]) is plotted as a function of A in Fig. 3 for σ_I compressive. Clearly, the two solutions predict rates which are negligibly different, say $\leq 20\%$ in ratio, for $-A \leq 0.38$, the rate in Case II being the larger. The error, however, becomes increasingly large with higher values of σ_I and the ratio is ~ 2 at $-A = 1.6$.

An interesting feature in both cases (Eq. [18] and [23] is that the predicted oxidation rate will become zero when the (compressive) interfacial stress, $(-\sigma_I)$ is

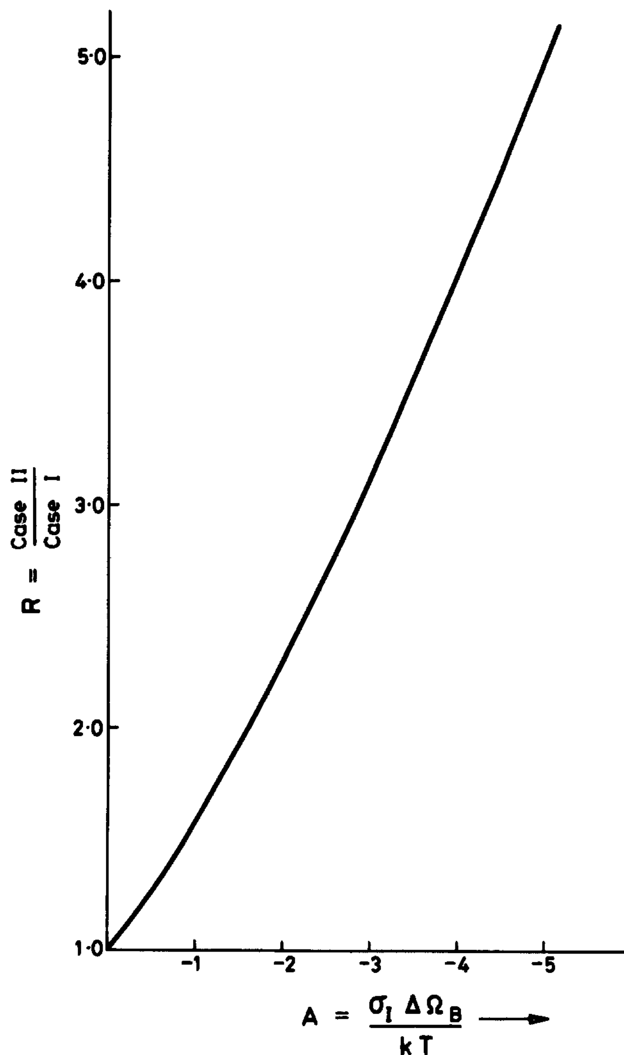

Fig. 3. Ratio of rates for Case II and Case I, vs. A

$$(-\sigma_I) = -\frac{kT\ln\left(\dfrac{p_s}{p_{\text{diss.}}}\right)^{-1/6}}{\left[\dfrac{\Delta\Omega_A}{3(2-y)} + \dfrac{2\Delta\Omega_B}{3}\right]} \qquad [24]$$

Application to Zircaloy-2

There must be some uncertainty over the correct value of $\Delta\Omega_B = (\Omega_{O_o} - \Omega_{V_o^{\cdot\cdot}})$, but if the vacancy volume is taken, reasonably, as 0.7 of that of the ion, $\Delta\Omega_B$ becomes 0.3×10^{-29} m^3. Using Roy and Burgess' (24) measurements, the maximum value of $(-\sigma_I)$ obtainable at 773°K (at least) is $\simeq 1.7 \times 10^9$ nm^{-2}, so that the maximum value of A at this temperature is ~ 0.45. Reference to Fig. 3 shows that the ratio of oxidation rates for the two stress distributions previously discussed is ~ 1.25 for this particular value. Since this error exists only during the late stages of protective oxidation, it seems adequate to use the simplified stress distribution of Case I.

Taking a typical value of $\Delta G°$ for the oxidation reaction of 950 kJ mole O_2^{-1} (26) gives $p_{\text{diss.}}^{-1/6} = 2 \times 10^{10}b^{-1/6}$. It is clear that the first pressure term in the main bracket of Eq. [18] is dominant and the

second may therefore be neglected for all likely values of p_s. It follows that the inhibition condition of Eq. [24] is unlikely to apply to Zircaloy oxidation and the oxidation rate will be essentially independent of the oxidation potential of the environment. The latter is in fact found experimentally (cf. the data sources shown in Fig. 5). In addition, the large values of $p_{diss.}^{-1/6}$ will dominate any extrinsic effects due to trace impurities and permits application of the present analysis to Zircaloy oxidation.

The expression for the oxidation rate now becomes

$$\left(\frac{d\xi}{dt}\right) = \frac{D_v\Omega[V_o^{\cdot\cdot}]^\circ}{2\xi}\left(\frac{p_{diss.}}{p_o}\right)^{-1/6} \exp\left(-\frac{\sigma_I\Delta\Omega_B}{3kT}\right)\exp\left(\xi\Delta\Omega_\sigma\right) \quad [25]$$

where

$$\Delta\Omega_\sigma = \frac{\beta}{kT}\left(\frac{\Delta\Omega_A}{3(2-y)} + \Delta\Omega_B\right)$$

The term $(D_v\Omega/2)\ [V_o^{\cdot\cdot}]^\circ (p_{diss.}/p_o)^{-1/6} \exp(-\sigma_I\Delta\Omega_B/3kT)$ may be rewritten using Eq. [8] when it becomes $(D_v\Omega/2)\ [V_o^{\cdot\cdot}]^{diss.}$ where $[V_o^{\cdot\cdot}]^{diss.}$ is the vacancy concentration in equilibrium with the oxygen potential at the oxide metal interface. The quantity $(\Omega/2)\ [V_o^{\cdot\cdot}]^{diss.}$ is the fractional vacancy concentration N_v so that the product D_vN_v is equivalent to the diffusion coefficient for anions, $D_o^{diss.}$, at the inner interface. The rate expression thus becomes

$$\frac{d\xi}{dt} = \frac{D_o^{diss.}}{\xi}\exp\left(\xi\Delta\Omega_\sigma\right) \quad [26]$$

This can be integrated using the initial condition that $\xi = 0$ when $t = 0$ to give

$$(1 + \xi\Delta\Omega_\sigma)\exp(-\xi\Delta\Omega_\sigma) = 1 - D_o^{diss.}(\Delta\Omega_\sigma)^2 t \quad [27]$$

This relationship between oxide growth and time can be evaluated if $D_o^{diss.}$ is known. Because of the low values of $p_{diss.}$ there are no direct measurements on bulk specimens, but an adequate compromise would be to obtain values from oxide films. This has the advantage that since $D_o^{diss.}$ has a large contribution from short-circuit paths (11) the value obtained from films will reflect accurately the oxide structure existing during the oxidation process. Cox and Pemsler (11) present a number of measurements of D_o, but of these the one obtained by Cox and Roy (27) is deemed to be the most reliable since it was obtained by a method which measured the transport of oxygen directly. At 773°K the value is 1.0×10^{-16} m² sec⁻¹.

Comparison with experimental reaction rates.—A direct check of the present theory may be made only at 773°K since it is only for this temperature that β may be established from the data of Roy and Burgess. The dependence of oxide stress on thickness is very variable but three cases are presented in Fig. 4 for different values of β and compared with the simple parabolic case where $\beta = 0$. The β values of -6.5×10^{14} and -2.5×10^{14} nm^{-3} present the extremes of the data presented by Roy and Burgess (24). The intermediate value of -3.4×10^{14} nm^{-3} represents a subjective average value of β for specimens of a thickness similar to fuel tube material. As expected, the departure from parabolic kinetics increases with increasing compressive stress (*i.e.*, increasing $-\beta$). The value of β applicable to pretransition behavior may be derived if it is assumed that the oxide fractures at the kinetic transition at $\simeq$ 34 g·dm^{-2} (2.3 μm).[1] If Young's modulus (E) for ZrO_2 is taken as 2.1×10^{11} nm^{-2} (28) and the fracture ductility ϵ_f as ~0.01 (25) then the uniaxial rupture stress is $\sigma_F = E\epsilon_f = 2.1 \times 10^9$ nm^{-2}. For a 2.3 μm oxide thickness this gives $\beta_{max} = 6.1 \times 10^{14}$ nm^{-3} if a biaxial stress state is assumed. This value is in good agreement with the upper value deduced from the data of Roy and Burgess (24) for relatively thin oxides, and is used in the comparison below. Other numerical data used in these calculations are $\Delta\Omega_A = (\Omega_{ZrO_{2-y}} - \Omega_{Zr}) = 1.0 \times 10^{-29}$ m³ and $y = 0.04$ giving a stoichiometry of $ZrO_{1.96}$ at the inner interface.

[1] To convert $X\mu$m to W mg · dm^{-2} the formula 0.0675W = X has been used.

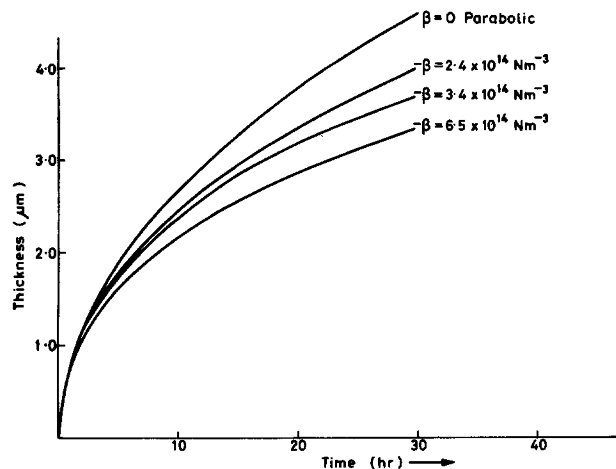

Fig. 4. Theoretical plots of thickness against time from Eq. [28]

Figure 5 shows 500°C (773°K) experimental data for oxide thickness plotted against time determined by a number of different authors for Zircaloy-2. The solid line on this graph is a plot of Eq. [27] with $\beta = -6.5 \times 10^{14}$ nm^{-3}. Clearly, the theory is capable of predicting not only the absolute rate, but also the gradual deviation from parabolic behavior with increasing oxide thickness up to the point of the kinetic transition at 34 mg·dm^{-2}.

Conclusions

A model has been developed which describes the effect of a stress field within the oxide film on the rate of vacancy transport.

The oxidation kinetics for oxides which accumulate compressive stress during growth are predicted to be slower than parabolic; those for oxides which accumulate tensile stress will be faster than parabolic.

When applied to Zircaloy-2 corrosion at 773°K, the model yields kinetics in good agreement with experimental data predicting both the absolute rate and the increasing deviation from parabolic kinetics with oxide thickness. Comparison of theory with experiment at other temperatures is not possible due to lack of data.

The model predicts that Zircaloy-2 corrosion rates should be independent of the oxidation potential of the environment while the rate-controlling step remains anion diffusion within the oxide. This is in agreement with experiment.

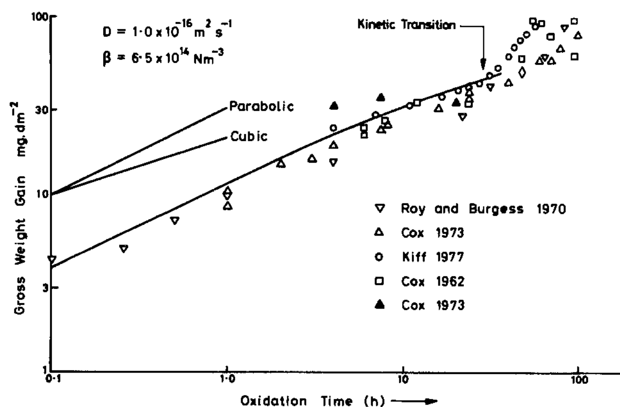

Fig. 5. Comparison of theoretical line from Eq. [28] with experimental Zircaloy corrosion data at 773°K.

Acknowledgments

We are grateful to Mr. R. Kiff for permission to use his oxidation data at 773°K prior to their publication. This paper is published by permission of the Central Electricity Generating Board.

Manuscript submitted Sept. 22, 1977; revised manuscript received March 8, 1978.

Any discussion of this paper will appear in a Discussion Section to be published in the June 1979 JOURNAL. All discussions for the June 1979 Discussion Section should be submitted by Feb. 1, 1979.

Publication costs of this article were assisted by Berkeley Nuclear Laboratories.

REFERENCES

1. B. Cox, NACE Conference Proceedings, "High Temperature High Pressure Electrochemistry in Aqueous Solutions" (1972).
2. H. J. Engell, K. Hauffe, and B. Ilschner, *Z. Elektrochem.*, **58**, 478 (1954).
3. G. A. Gulbransen and K. F. Andrew, *This Journal*, **101**, 128 (1954).
4. K. Hauffe, L. Pethe, R. Schmidt, and S. R. Morrison, *ibid.*, **115**, 456 (1968).
5. J. T. Waber, *J. Chem. Phys.*, **20**, 734 (1952).
6. N. F. Mott, *Trans. Faraday Soc.*, **36**, 472 (1940).
7. S. Anderson, *Phys. Rev.*, **69**, 52 (1946).
8. B. A. Irving, *Corros. Sci.*, **5**, 471 (1965).
9. R. T. P. Whipple, *Phil. Mag.*, **45**, 1225 (1954).
10. G. B. Gibbs, *Corros. Sci.*, **7**, 165 (1967).
11. B. Cox and J. P. Pemsler, *J. Nuc. Mat.*, **28**, 73 (1968).
12. J. Stringer, "Defects and Transport in Oxides," p. 495, Plenum Press, New York (1974).
13. E. A. Gulbransen and K. F. Andrew, *Trans. Am. Inst. Min. Metall. Eng.*, **185**, 515 (1949).
14. W. W. Smeltzer, R. R. Haering, and J. S. Kirkaldy, *Acta Metall.*, **9**, 880 (1961).
15. J. M. Perrow, W. W. Smelter, and R. K. Ham, *ibid.*, **15**, 577 (1967).
16. J. M. Perrow, W. W. Smeltzer, and J. D. Embury, *ibid.*, **16**, 1209 (1968).
17. G. P. Sabol, S. G. McDonald, and G. P. Airey, "Zirconium in Nuclear Applications," ASTM-STP, **551**, 435 (1974).
18. G. P. Sabol and S. B. Dalgaard, *This Journal*, **122**, 316 (1975).
19. B. Cox and R. A. Ploc, *ibid.*, **122**, 1744 (1975).
20. R. E. Pawel and J. J. Campbell, *Acta. Metall.*, **14**, 1827 (1966).
21. R. F. Tylecote and W. K. Appleby, *Werkst. Korros.*, **23**, 855 (1972).
22. B. Borie, C. J. Sparks, and J. V. Cathcart, *Acta. Metall.*, **10**, 691 (1962).
23. H. J. Engell and F. Wever, *ibid.*, **5**, 695 (1967).
24. C. Roy and B. Burgess, *Oxid. Met.*, **2**, 235 (1970).
25. J. C. Greenbank and S. Harper, *Electrochem. Technol.*, **4**, 88 (1966).
26. J. F. Elliott and M. Gleiser, "The Thermochemistry of Steelmaking," Pergamon Press, New York (1960).
27. B. Cox and C. Roy, *Electrochem. Technol.*, **4**, 121 (1966).
28. C. F. Smith and W. B. Crandall, *J. Am. Ceram. Soc.*, **47**, 624 (1964).
29. B. Cox, A.E.C.L. Rep. 4448 (1973).
30. B. Cox, Proc. USAEC Symposium on Zircaloy Fuel Development, Calif. Paper 16 (1962).
31. R. Kiff, Unpublished work (1977).

Technical Notes

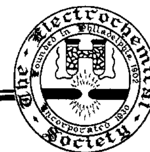

Localized Avalanche Breakdown on GaAs Electrodes in Aqueous Electrolytes

J. C. Tranchart, L. Hollan, and R. Memming[1]

Laboratoires d'Electronique et de Physique Appliquée, 94450 Limeil-Brévannes, France

GaAs electrodes have been the subject of various electrochemical studies (1-4). It has been shown that the basic anodic process in aqueous electrolytes is the anodic dissolution of the GaAs electrode (2) whereas the cathodic process is mainly due to hydrogen evolution (2, 4). The first process occurs via the valence band, *i.e.*, holes are consumed. Using n-type electrodes in the dark, the corresponding anodic current is limited to a very low value since only few holes are available. In the case of hydrogen evolution, a process involving electrons from the conduction band, a corresponding limiting cathodic current is expected for p-type electrodes.

These effects, typical for semiconductor electrodes, have been found with many other materials. It is interesting to note, however, that in all cases reported in the literature, the limiting currents at GaAs electrodes controlled by the diffusion of minority carriers toward the surface, remain at low levels only for small electrode potentials (< 1-2V). At higher potentials a steep current rise has always been observed. In the present paper the mechanism of this current rise is studied in more detail.

Experimental

The samples used in this study are grown in our laboratory by vapor phase epitaxy on (100) n^+ substrates (5). The layers are sulfur doped in the range of 10^{15}-10^{18} cm^{-3} and their thicknesses are chosen greater than 10 μm in order to avoid any substrate or interface effects. These layers show a much lower density of defects than the more often studied bulk material and, also, lower carrier concentration layers are available. Tin ohmic contacts are soldered by short annealing (< 1 min) in pure H_2 atmosphere at 400°C. The samples are etched in a H_2SO_4, H_2O_2, H_2O (5:1:1) solution just before mounting in a classical electrochemical cell where the sample area is limited and defined by an O-ring. The commonly used electrolyte is a 1*N* NaOH solution.

Results and Discussion

Typical current potential curves, as obtained with epitaxial layers of n-GaAs, are shown in Fig. 1. The

[1] Permanent address: Philips Forschungslaboratorium GmbH, 2000 Hamburg 54, Germany.

Key words: defects, doping, semiconductor.

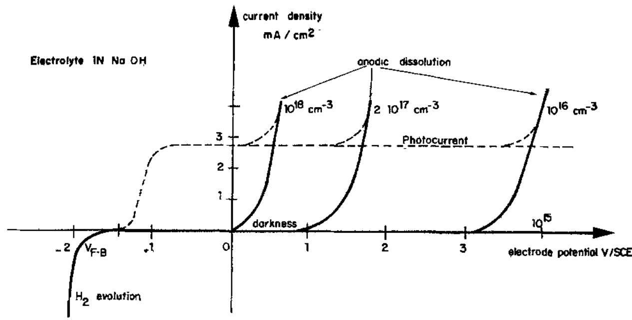

Fig. 1. Current-potential curves for n GaAs (epitaxial layers on GaAs substrates in 1N NaOH).

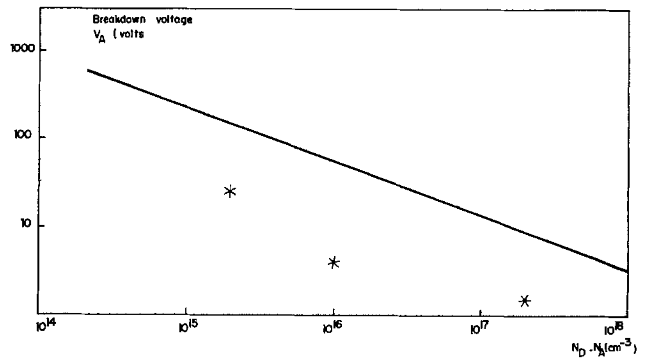

Fig. 2. Breakdown voltage vs. concentration of GaAs. Continuous line, calculated values; *, experimental values from anodic polarization.

limiting anodic current could be kept at a very low level for layers of a rather small carrier density. In the case of a doping level of 10^{15} cm^{-3}, an extremely low anodic current has been observed up to about 20-30V. The breakdown occurs at lower potentials for electrodes of higher carrier densities (Fig. 1).

The question arises whether the increase of the anodic current at n-type is due to a tunneling of electrons through the space-charge layer or to an ava-

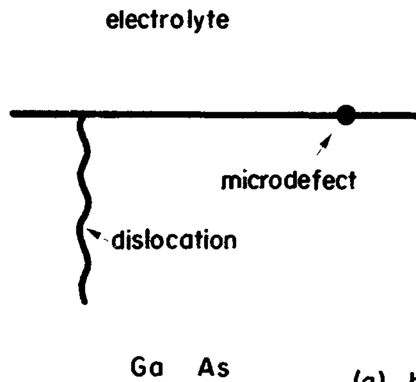

(a) before avalanche (x 90)

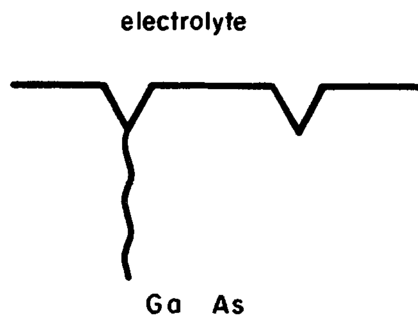

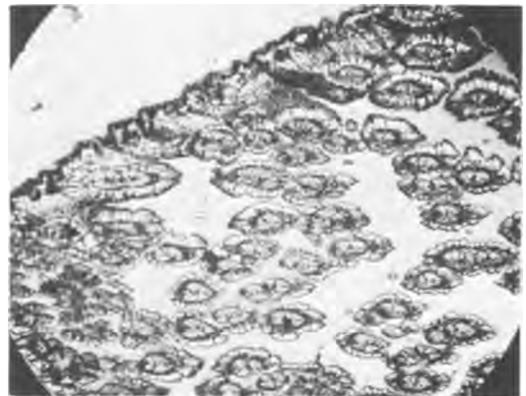

(b) after avalanche

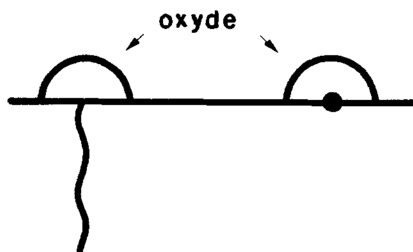

(c) anodic oxydation

Fig. 3. Schematic presentation of defects in n GaAs electrodes during anodic dissolution and anodic oxidation.

lanche breakdown. Both mechanisms can occur if the band bending is larger than the bandgap of 1.4 eV. This condition is fulfilled for $V > 0$ since the flatband potential occurs at -1.4 V/SCE, as determined from capacity measurements. The thickness of the space-charge layer, however, is of the order of several hundred angstroms for $N_D = 10^{18}$ cm^{-3} (6, 7) so that any tunneling process has to be ruled out at doping levels $N_D \leq 10^{18}$ cm^{-3}.

The avalanche process was investigated in more detail. In Fig. 2 the potentials at which breakdown occurs *vs.* the carrier density are represented. These values are lower than the calculated bulk avalanche values represented by the continuous line (8). These calculated values have been confirmed experimentally by several authors using solid-state diodes (9) and in our laboratory using Schottky diodes and epitaxial material (10) Furthermore, the values obtained by anodic oxidation are the same (11, 12). We assume, therefore, a localized avalanche mechanism starting at surface defects, dislocations, or dopant variation, as schematically shown in Fig. 3a and 3b. According to this model, a microbreakdown occurs which induces a short etching around the defect (Fig. 3b). The latter process is confirmed by the occurrence of etch pits after the avalanche breakdown as shown on the microscopic pictures in Fig. 3b and also observed by others (13). A further support for this mechanism is given by the current-potential curve itself. For example, an n-type GaAs electrode of $N_D = 10^{15}$ cm^{-3} can be initially polarized up to 25V before avalanche breakdown occurs (Fig. 4). As the potential is then decreased, the current remains at a higher level. A low current is only obtained again below about 2V. As the potential is increased again, the current rises at about 2V (see curve 3 in Fig. 4). Thus, as soon as some defects have been developed avalanche breakdown occurs at much lower potentials. Accordingly, the presence of defects determines the avalanche breakdown, their density, and the limiting anodic current at n-GaAs electrodes. Since the quality of the material plays such a dominant role, small currents up to very large potentials can only be observed by using epitaxial layers in which the density of defects could be kept at a sufficiently low level.

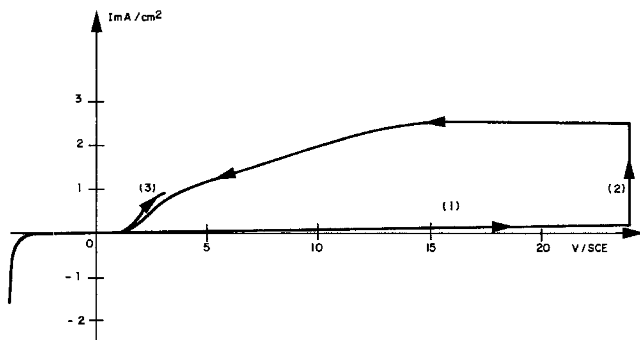

Fig. 4. Current potential curve for n GaAs ($N_D = 2 \cdot 10^{15}$ cm^{-3}) in 1*N* NaOH. (1) First anodic potential scan; (2) breakdown; (3) second scan.

It should be emphasized that the situation is quite different for electrolytes of neutral *p*H values. In this case, anodic oxidation occurs which is an autolimiting process: any initial avalanche, localized on a defect, leads immediately to an oxide formation, as shown schematically in Fig. 3c. The local resistance is strongly increased and etching at the defect is stopped. So, in this case the avalanche is not controlled any more by the defects but only by the bulk properties, as has been observed by Colquhoune and Hartnagel (11) and by ourselves (12). As mentioned above, in these conditions the experimental values fit well with the theoretical curve calculated for a bulk avalanche process (Fig. 2).

Acknowledgments

The authors wish to thank the Director of the Laboratoires d'Electronique et de Physique Appliquée for permission to publish this contribution. They are grateful to Mrs. E. Boucherez for technical assistance and to D. Bois and Professor A. Deschanvres for helpful discussion.

This work has been supported by the Délégation Generale a la Recherche Scientifique et Technique.

Manuscript submitted Dec. 20, 1977; revised manuscript received March 14, 1978.

Any discussion of this paper will appear in a Discussion Section to be published in the June 1979 JOURNAL. All discussions for the June 1979 Discussion Section should be submitted by Feb. 1, 1979.

Publication costs of this article were assisted by the Laboratoires d'Electronique et de Physique Applique.

REFERENCES

1. Y. V. Pleskov, *Doklady Akad., Nauk SSSR*, **143**, 1399 (1962).
2. H. Gerischer, *Ber. Bunsenges. Phys. Chem.*, **69**, 578 (1965).
3. W. W. Harvey, *This Journal*, **114**, 1275 (1967).
4. K. D. N. Brummer, *This Journal*, **114**, 1275 (1967).
5. L. Hollan, *Inst. Phys. Conf. Ser.*, **24**, 22 (1975).
6. R. Memming and F. Mollers, *Ber. Bunsenges. Phys. Chem.*, **76**, 475 (1972).
7. B. Pettinger, H. R. Schoppel, T. Yokoyama, and H. Gerischer, *Ber. Bunsenges. Phys. Chem.*, **78**, 1024 (1974).
8. G. E. Stillman, C. M. Wolfe, J. A. Rossi, and A. G. Foyt, *Appl. Phys. Lett.*, **24**, 471 (1974).
9. S. Z. E. Logan, *J. Phys. Soc., Jpn.*, **21**, 439 (1966).
10. A. Mircea, Private communication.
11. A. Colquhoune and H. Hartnagel, *Solid State Electron.*, **19**, 819 (1976).
12. J. C. Tranchart, A. Farrayre, and L. Hollan, "Coll. Mat. et Tech. Microélectr., Montpellier," Nov. 16-19, 1976, Suppl. au n° 183, *Le Vide*, **77** (1976).
13. T. Ambridge and M. M. Faktor, *Inst. Phys. Conf. Ser.*, **24**, 320 (1975).

Stabilized Fused-Quartz Tubes with Reduced Sodium Diffusion for Semiconductor Device Technology

K. M. Eisele

Institut für Angewandte Festkörperphysik der Fraunhofer Gesellschaft, Eckerstrasse 4, D-7800 Freiburg, Germany

and R. Ruthardt

Heraeus Quarzschmelze GmbH, Postfach 463, D-6450 Hanau, Germany

Fused quartz can be produced with a sodium content below 1 ppm. But for high temperature applications it is not only the amount of sodium in a material that matters but also the velocity with which it diffuses through the tube walls. The importance of the diffusion coefficient becomes evident when considering that the hot ceramics of a furnace present a nearly inexhaustible source of sodium. The diffusion coefficient of sodium in fused quartz depends very much on the type of fused quartz and can vary three orders of magnitude (1-3). In addition, due to its specific structure, fused quartz offers the advantage of permitting modification by replacing some of the four positively charged silicon atoms by atoms with lower positive charge which can equally well be incorporated into the spatial network of the silicon dioxide. These defect points with a deficit of positive charge then serve as a kind of trap for the diffusing sodium.

As the latest stage in fused-quartz diffusion tube development stabilized fused-quartz diffusion tubes (CFQ_{st}) obtain a high temperature stability from a layer of crystobalit on their outside. The patent literature (4, 5) points out that in these materials the diffusion of impurities is reduced. The results of investigations of this phenomenon are the subject of this paper. A more detailed report will be given elsewhere. Principally we have chosen a mass spectroscopic method to compare the sodium diffusion through stabilized fused-quartz CFQ_{st} with other vitreous silica materials for which the diffusion coefficients are already known.

Experimental

A test tube, 25 mm diam, was closed at one end and fused to a metal flange at the open end. It was connected to a vacuum chamber with a quadrupole mass spectrometer and an ionization pressure gauge (Fig. 1). The tube to be tested was surrounded by a larger tube made of regular CFQ-type fused quartz. Within it sodium vapor was guided along the surface of the test tube by a nitrogen gas stream. All parts could be degassed by heating to 120°C. In a well-degassed state the pressure in the system was $1 \cdot 10^{-8}$ Torr. The concentric glass tubes were positioned in a furnace whose temperature profile was determined for a nominal temperature of 1000°C. To immerse the test tube in sodium vapor during the diffusion experiment a molybdenum boat filled with metallic sodium was deposited at an exactly known temperature zone of the outer fused-quartz tube. By this means sodium will appear at the ionizer of the mass spectrometer if its vapor pressure at a given temperature is higher than the partial pressure of sodium in the vacuum system, provided it is not held by any mechanism to the surface at which it appears by the diffusion process or by condensation. To confirm that the prerequisites of the experiment are given, the following test was performed: A few pieces of a sodium containing silicate glass were placed in a fused quartz tube identical to the actual test tubes. Then the silicate glass was slowly heated and the sodium arriving at the mass spectrometer observed. When the temperature was raised, a spontaneous increase in the amount of sodium was observed which dropped again after passing through a maximum (Fig. 2). This drop can be explained by the process first being governed by a desorption process of the sodium at the surfaces of the soft glass and afterwards by the outdiffusion of sodium from the bulk. A better picture was obtained when the sample cooled off whereby the sodium level decreased corresponding to the lowering temperature (Fig. 3). This result proved that the sodium already leaves the surface at moderately high temperatures, a necessary condition for the feasibility of the actual experiment.

For a quantitative comparison of all contributions to the total pressure it is required that in the mass range of interest the sensitivity of the spectrometer remains the same. The mass spectrometer employed permitted adjustment of the sensitivity by applying a bias to opposite poles of the mass filter. Furthermore it is important for the comparison of the spectra that during the experiments all parameters that do not linearly affect the signal amplitude must be kept constant. This refers to resolution, pole bias, ΔM, SEM voltage, ionization- and extraction-voltages.

Key words: semiconductors, fused-quartz, sodium diffusion.

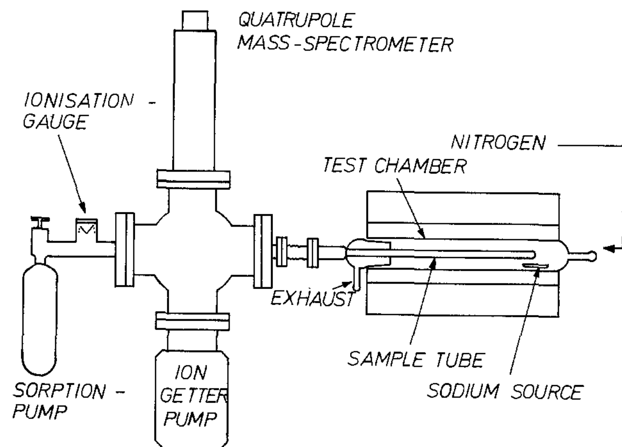

Fig. 1. Schematic of the apparatus used for the measurements

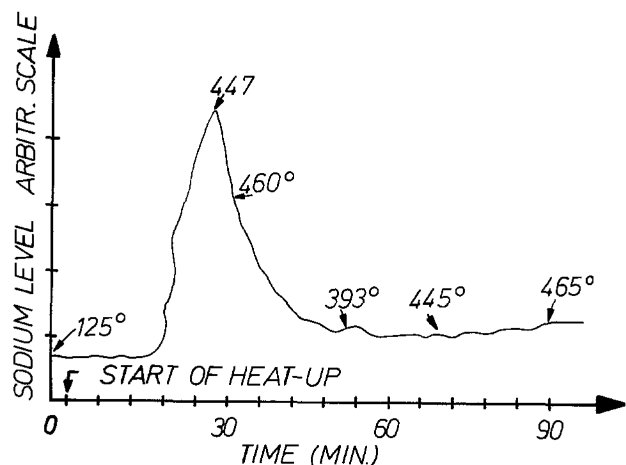

Fig. 2. Emanation of sodium from moderately heated soft glass

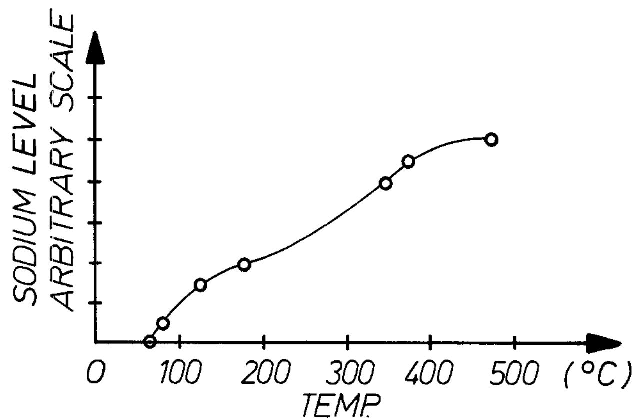

Fig. 3. Decrease of sodium level with decreasing temperature of the soft glass.

A mass spectrum was taken before exposing the test tube to sodium, and then the sodium level was monitored continuously during the exposure until a second total spectrum was recorded for the purpose of calibration. The amplitudes of all the lines in the spectra were measured in millimeters from the recorded graphs, divided by the ionization cross section to determine the partial pressure of sodium from the total pressure readings.

Kinetic gas theory yields the molecular velocity

$$V = \sqrt{\frac{3\,kT}{m}}$$

where k is Boltzmann's constant, T absolute temperature, m molecular mass of Na. The gas density of each component present is

$$\rho = \frac{3p}{V^2} = \frac{pm}{kT}$$

where p is its partial pressure. Then the number of particles causing this partial pressure is

$$n = \frac{\rho}{m} = \frac{p}{kT}$$

We can therefore plot the number of sodium atoms in the vacuum chamber during the time sodium vapor is surrounding the sample tube. It is necessary to point out that the temperature to be used in this equation is room temperature, and not the temperature of the fused-quartz tube, because only a relatively small surface of the total system is at a higher temperature than 30°C.

For a quantitative evaluation of the mass spectra not only equal sensitivity for all masses is required, but also the ionization probability of the various molecules or atoms has to be considered. For some atoms, especially the noble gases, ionization probabilities have been measured (6), but for our range of interest such measurements are not available. Therefore we used the calculated theoretical values for ionization cross sections of Mann (7) to correct the amplitudes of the measured spectral lines.

Results

The number of sodium atoms per cubic centimeter in the vacuum chamber is plotted in Fig. 4 against the time beginning with zero at the moment the molybdenum boat filled with sodium is moved into the zone where the furnace is between 500° and 600°C. The three types of fused quartz tubes tested were of the type CFQ, made of natural quartz crystal, of Suprasil, made from synthetic vitreous silica, and finally of CFQ_{st}, made from natural quartz and stabilized as mentioned before.

For the CFQ-tube the increase of the sodium partial pressure is most pronounced. It begins at 1208 cm^{-3}, reaches a maximum of 2243 cm^{-3}, and at the end

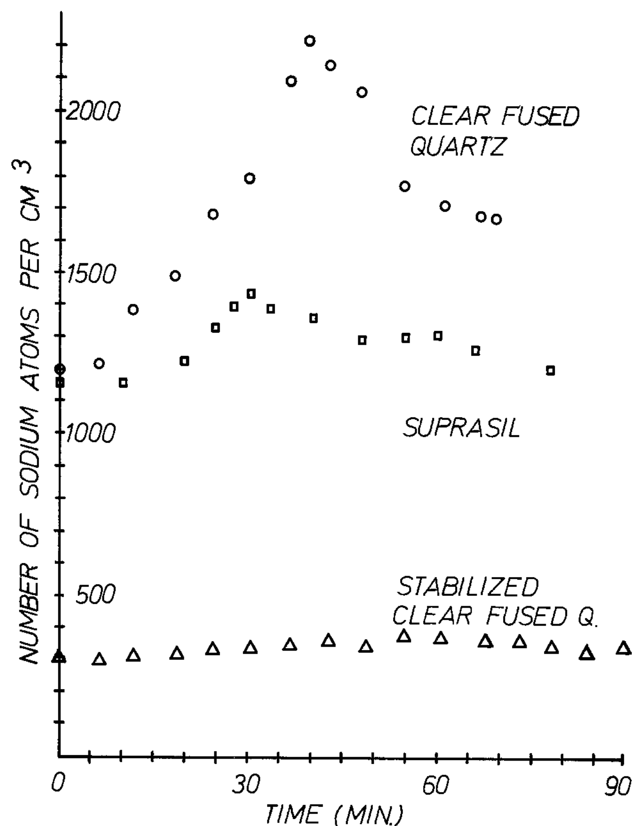

Fig. 4. Increase in time of the sodium level in the vacuum chamber after the sodium source has been placed at a predetermined temperature zone of the furnace.

stands at 1680 cm^{-3}. The Suprasil tube started with 1150 cm^{-3} sodium atoms. After exposure to the sodium vapor the level increased to 1442 cm^{-3} and dropped then to 1225 cm^{-3}. The material CFQ_{st} clearly withstood the sodium diffusion best. The sodium level only increased from 295 to 377 cm^{-3}.

The behavior with time was similar with all tubes. Generally 30-35 min after exposure to sodium the level reached a maximum. For demonstrative purposes we made the simplifying assumption that the level rises linearly and calculated the increase of sodium atoms per minute. This showed even more clearly the advantage of the CFQ_{st} tube. The rate of increase with Suprasil was less than half found with CFQ material, and CFQ_{st} was another factor 1/7 lower than Suprasil. Altogether stabilization brought a reduction by a factor of 1/15. After 30-35 min the sodium supply had evaporated and the sodium level decreased again to settle slightly higher than it was prior to the experiment.

Conclusion

The results obtained for CFQ and Suprasil are as expected from their different diffusion coefficients.

Stabilized clear fused-quartz CFQ_{st} exhibits even lower permeability for sodium than Suprasil. This is to be expected because the stabilization is achieved by infusing a metal oxide into the quartz which according to a hypothesis of Ligenza (8) forms a sodium-metal complex which diffuses as an entity. If, for example, a sodium-aluminum-oxide complex has the diffusion coefficient of aluminum, the diffusion coefficient of which has been measured by Frischat (9) to be $1.3 \cdot 10^{-13}$ cm^2/sec at 998°C, then a sodium atom attached to aluminum affords a time longer by a factor of 30,000 to diffuse through a given fused-quartz thickness than a sodium attached to silicon and oxygen only. This fact gives CFQ_{st}-type diffusion tubes especially favorable properties for application in semiconductor device manufacture. This becomes distinctly clear when comparing the diffusion coefficient of sodium at 1000°C

through CFQ $9 \cdot 10^{-6}$ cm²/sec (2), through silicon $4.45 \cdot 10^{-7}$ cm²/sec (10), and through Suprasil $9 \cdot 10^{-9}$ cm²/sec (3). Because the measurements presented in this paper show the superiority of CFQ_{st} over Suprasil one must conclude that as far as diffusion of sodium is concerned diffusion tubes made of fused-quartz type CFQ_{st} are presently singularly preferable for the manufacture of integrated circuits.

Acknowledgments

The authors wish to express their gratitude to Dr. K. H. Rau for his interest expressed in constructive remarks concerning this work.

Manuscript submitted Oct. 19, 1977; revised manuscript received Feb. 6, 1978.

Any discussion of this paper will appear in a Discussion Section to be published in the June 1979 JOURNAL. All discussions for the June 1979 Discussion Section should be submitted by Feb. 1, 1979.

Publication costs of this article were assisted by the Insitut für Angewandte Festkorperphysik der Fraunhofer Gesellschaft.

REFERENCES

1. G. H. Frischat, "Ionic Diffusion in Oxide Glasses," Trans. Tech. Publications, Diffusion Monograph Series No. 3/4, 128 (1975).
2. G. H. Frischat, *J. Am. Ceram. Soc.*, **51**, 528 (1968).
3. G. H. Frischat, *Z. Angew. Physik*, **25**, 163 (1968).
4. P. Baeumler *et al.* DT 1 696 061 (1968); K. H. Hoefer *et al.*, U.S. Pat. 3,776,809 (1971); P. Baeumler *et al.*, U.S. Pat. 3,927,697 (1973).
5. K. H. Rao, DT 2 038 564 (1970); U.S. Pat. 3,957,476 (1973).
6. Handbook of the American Institute of Physics, pp. 5-138, New York (1963).
7. J. B. Mann, "Recent Developments in Mass Spectroscopy," Proceedings of the International Conference in Mass Spectrometry, K. Ogata and T. Hayakawa, Editors, p. 814, University Park Press, Tokyo (1970).
8. J. R. Ligenza, Paper presented at the Workshop "Radiation Effects in MOS Technology," Washington, D.C. (1973).
9. G. H. Frischat, *J. Am. Ceram. Soc.*, **52**, 625 (1969).
10. B. L. Sharma, "Diffusion in Semiconductors," Trans. Tech. Publications, Clausthal-Zellerfeld (1970).

JOURNAL OF THE ELECTROCHEMICAL SOCIETY

ACCELERATED
BRIEF COMMUNICATIONS

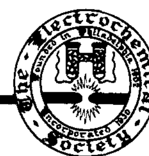

JULY
1978

A Device of Electrostatic Lens for Electron Microscopy

S. Yamaguchi*

National Institute for Researches in Inorganic Materials, Sakura-mura Niihari-gun Ibaraki-ken, 300-31, Japan

One can charge up a dielectric substance with electrons in vacuum. Strength of the electrostatic field produced at the surface of this dielectric is very high, to wit, about 10000 kV/cm in the case of dielectric ruby (1). It was attempted here to turn this field to account for microscopy.

Construction of an electrostatic lens for microscopy is illustrated in Fig.1. This lens is a small brass cylinder (outside and inside diameters: 3 and 2 mm, height: 2 mm) which is filled with dielectric substance. There are disposed here the two electrodes of aluminum sheets with mirror surfaces. There are pinholes along the central axis of the lens. The electrostatic field realized in this lens remained stationary, insofar as stationary monochromatic electron beam was running along the central axis of the lens. The focal length of the lens could be changed by controlling the current density and the accelerating voltage of the electron beam applied. Amorphous glass, paraffin or polyethylene served as the dielectric for the lens illustrated in Fig.1. A brass wire gauze with standard mesh size has been employed as an object for testing electron optical ability of the device concerned.

The electron micrograph observed from the object with a single lens

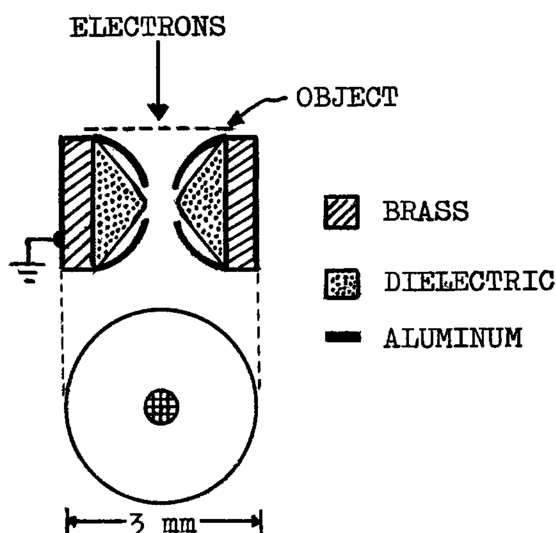

Fig. 1 Electrostatic lens which works only when an electron beam is running along its central axis.

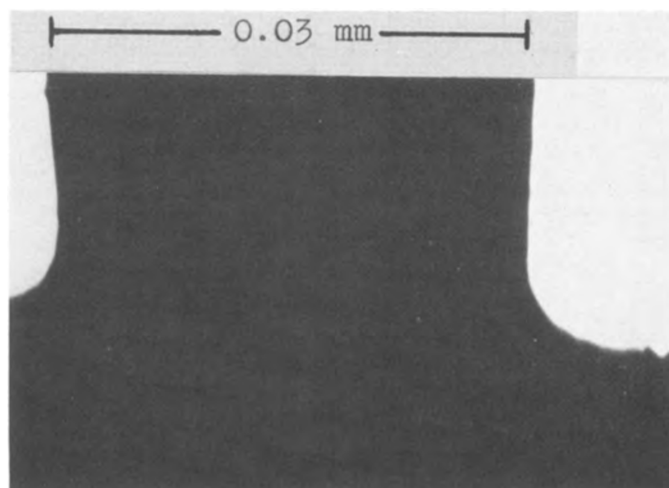

Fig. 2 Electron micrograph of a wire gauze.

*Electrochemical Society Active Member. Key words: electrostatic lens, dielectrics, electron diffraction.

is reproduced in Fig.2. This figure is referred to the photomicrograph of the same object that is seen in Fig.3. Fig.2 demonstrates that the electrostatic lens here devised performed well for microscopy. Here the beam current, the potential difference for accelerating the electrons and the diameter of the electron flux were 0.05 mA, 75 kV and 0.1 mm.

It was possible to observe diffraction pattern from an object placed on the gauze support. Only the lens was removed out of the electron path in the microscope by a mechanical means, and so the object alone remained in situ. This was easy to do, since the lens of interest was small and light enough to be moved. The diffraction pattern observed from a thin foil of gold that was placed on the support is shown in Fig.4. This figure was precisely analysed, because the distance between the object and the photographic emulsion was fixed to be 50 cm. It is impossible, on the other hand, for the conventional magnetic lens microscope to carry out this diffraction procedure.

In the present study, a simple way for observing electron microscopic and diffraction figures was devised, in which solid state properties of dielectrics were utilized in order to give rise to a strong electrostatic field for microscopy.

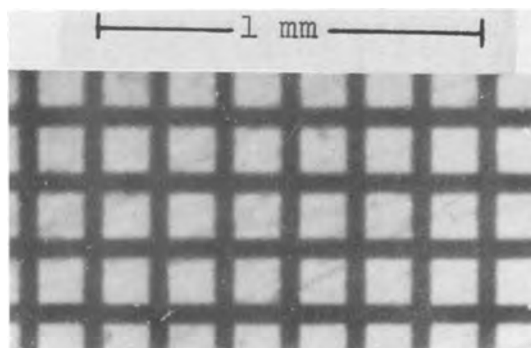

Fig. 3 Photomicrograph of the gauze.

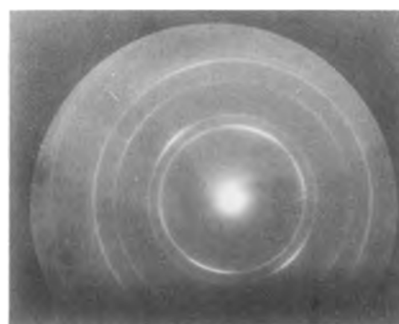

Fig. 4 Diffraction pattern from a gold foil placed on the object support in Fig.1.

REFERENCE

1. S. Yamaguchi, J. Appl. Phys., 46, 439 (1975).

Manuscript submitted Feb. 9, 1978, revised manuscript received March 27, 1978.

Publication costs of this article were assisted by the National Institute for Researches in Inorganic Materials.

JOURNAL OF THE ELECTROCHEMICAL SOCIETY

ELECTROCHEMICAL SCIENCE
AND TECHNOLOGY

AUGUST
1978

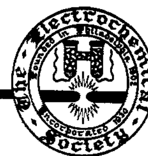

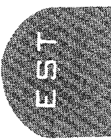

Steady-State Composition Profiles in Mixed Molten Salt Electrochemical Devices

I. Lithium/Sulfur Battery Analogs

C. E. Vallet and J. Braunstein*

Oak Ridge National Laboratory, Chemistry Division, Oak Ridge, Tennessee 37830

ABSTRACT

During charge or discharge of batteries with a binary molten salt mixture as the electrolyte, composition gradients are produced by the electrode reactions and the differences in mobilities of the electroactive and nonelectroactive ions. The effects of current density, electrode separation, and initial composition of the electrolyte are predicted by an analytical solution of the flux equations derived with transport properties similar to those of LiCl-KCl mixtures. Numerical solution of the flux equations predicts the composition profiles in lithium sulfur battery analogs with LiCl-KCl mixtures of differing compositions. Either complete depletion of the electroactive constituent at one electrode, or precipitation of a solid phase at the electrodes, could result from the predicted composition gradients. Changes in electrolyte composition at the electrodes may also affect J-phase formation at the sulfur electrode during discharge.

Electrochemical devices employing mixed electrolytes and operated at high current densities, such as molten salt batteries and fuel cells (1, 2), are subject to composition gradients resulting from the faradaic and migrational processes occurring at the electrodes, a phenomenon we have referred to as migrational polarization. Since such composition gradients can have significant effects on the performance of molten salt batteries and fuel cells, an understanding of the phenomenon and its characterization is important to design and modeling studies (3).

In a previous paper (2), the time evolution of composition at the electrodes and simulated composition profiles were computed by finite difference solution of the nonlinear partial differential equation of transport (3) for a molten salt battery analog and for a molten salt fuel cell analog. For both cases considered a limiting steady-state composition gradient was indicated. In this paper we present an analytical solution of the flux equations for the steady-state composition gradient in binary molten salt mixtures analogous to molten salt battery electrolytes (LiCl-KCl). Porosity of electrodes and of the electrolyte support must have important effects and will be treated in subsequent work, as will coupling of the mass flows to thermal energy flows. Here we concentrate on the effects of current density, initial electrolyte composition, electrode separation, and ion mobilities on steady-state migrational polarization and on possible phase separation in mixed electrolytes at high current density.

Flux Equations and Boundary Conditions

The electrochemical flux equations for a binary electrolyte designated LC-KC have been derived previously (2) for the cases where: (*i*) one of the two like-charged ions is produced at one electrode and consumed at the other [Ref. (2), Equation 3]; and (*ii*) the common ion is produced at one electrode and consumed at the other [Ref. (2), Equation 14]. The general one dimensional flux expressions may be written

$$-J_L^* = D\frac{\partial C_L}{\partial \xi} - M_L^*\, I/\mathbf{F} \qquad [1]$$

$$-J_K^* = D\frac{\partial C_K}{\partial \xi} - M_K^*\, I/\mathbf{F} \qquad [2]$$

where the J_i^*'s are the flows of ions i (in equivalents) relative to the reference frame*. D is interdiffusion coefficient of L and K, the C_i's are the equivalent concentrations, the M_i^*'s are migrational terms related to the transference numbers in the appropriate reference frame, and flows, concentrations, and migrational terms also satisfy the relations

$$I/\mathbf{F} = J_L^* + J_K^* - J_C^*; \quad C_L + C_K = C_C; \quad M_L^* + M_K^* = 1 + M_C^* \qquad [3]$$

where I is the current density. ξ is a distance variable, which in a pseudoconstant volume system is the distance from an electrode. For systems of variable volume, ξ can be defined such that equal distance increments contain equal numbers of the common ion, in order to compensate for the volume change of the electrolyte with composition change (3). In a system with fixed electrodes, this volume change may introduce an additional flow term or stress term which will be dealt with in subsequent work, although the general features of the shapes of the composition profiles will remain.

For the case where the electrode reactions consume and produce one of the two like-charged ions (rather than the common ion C), as for an Li electrode in an LiCl-KCl melt, the common ion C is conveniently

* Electrochemical Society Active Member.

Key words: LiCl, KCl, battery, diffusion, migration.

taken as the reference frame. The migrational terms in this case become simply the Hittorf transference numbers, *i.e.*, the transference numbers of ions L and K relative to the common ion C

$$M_L{}^C = t_L{}^C; \quad M_K{}^C = t_K{}^C; \quad M_C{}^C = 0 \qquad [4]$$

For the case where the common ion, C, of the mixture reacts at electrodes, as for a chlorine electrode in an LiCl-KCl melt or a CO_2-O_2 electrode in a carbonate melt, the fluxes are more conveniently taken relative to the electrode surface (2), which in a constant volume system is simply related to the common ion reference frame. In this case, $J_C{}^V = -I/\mathbf{F}$ and the migrational terms are

$$M_L{}^V = t_L{}^C - X_L; \quad M_K{}^V = t_K{}^C - X_K \quad \text{and} \quad M_C{}^V = -1 \qquad [5]$$

The boundary conditions at the two electrodes separated by a distance Ξ, are, when the cation L reacts at electrodes

$$J_L{}^C = I/\mathbf{F} \text{ at } \xi = 0 \text{ and } \xi = \Xi$$

$$J_K{}^C = 0 \text{ at } \xi = 0 \text{ and } \xi = \Xi \qquad [6]$$

When the common anion C reacts at electrodes the boundary conditions are

$$J_L{}^V = J_K{}^V = 0 \text{ at } \xi = 0 \text{ and } \xi = \Xi \qquad [7]$$

In a constant volume system, $X_L = VC_L$, where V is the equivalent volume. Here V will represent the mean partial equivalent volume of L and K. The use of equivalents rather than moles in Eq. [1] makes the equation general for charge symmetric or charge unsymmetric mixtures (4).

The Steady State

The concentration changes with time are given by

$$\frac{\partial C_K}{\partial t} = -\frac{\partial J_K{}^*}{\partial \xi} \qquad [8]$$

Equation [6], written with the fluxes from Eq. [1] and [4], is a nonlinear partial differential equation whose solutions we have computed by finite difference methods (3). Stationary composition profiles with respect to time were found (2) numerically in some cases, and an analytical solution for the steady state is possible. In the steady state the concentrations remain unchanged at all points between the electrodes, and Eq. [8] becomes

$$\frac{\partial C_K}{\partial t} = 0 = -\frac{\partial J_K{}^*}{\partial \xi} \qquad [9]$$

Since the flux of K vanishes (Eq. [6] and [7]) at the electrode surfaces for the cases where either L or C reacts at electrodes, Eq. [9] requires that it vanish at all points between the electrodes

$$J_K{}^* = 0; \quad 0 \leq \xi \leq \Xi \qquad [10]$$

The differential equation of the steady-state composition profile becomes, by Eq. [2]

$$\frac{\partial C_K}{\partial \xi} = \frac{M_K{}^* I}{\mathbf{F} D} \qquad [11]$$

Since $M_K{}^*$, D, and C_K are functions of composition only, Eq. [11] is an ordinary differential equation which can always be integrated if the functions $M_K{}^*$ and D are known. However, some simple but plausible forms of composition dependence of M_K and D lead to especially simple analytical solutions which provide insight into the effects of various parameters on the composition gradients between the electrodes.

Lithium/Sulfur Battery Analog

In a lithium/sulfur battery with an LiCl-KCl mixture as the electrolyte, lithium cations are produced at one electrode and are consumed at the other electrode. Consequently, the migrational term in Eq. [2] is the transference number of potassium relative to chloride ions. During charge the sulfur electrode is the positive anode, at which the lithium cations enter the electrolyte; lithium cations leave the electrolyte at the negative lithium alloy cathode. During discharge, the negative lithium alloy electrode becomes the anode at which lithium cations are produced in the electrolyte; lithium ions leave the electrolyte at the positive sulfur cathode. Thus, during either charge or discharge, the flows of ions are in the same direction relative to anode or cathode rather than relative to the positive or negative electrode. Calculated composition gradients from anode to cathode, therefore, refer to gradients from the negative (Li) electrode to the positive (S) electrode on discharge and in the reverse direction on charge.

Steady-state composition profiles.—Analytical solution.—A very simple case to treat, which is a not unreasonable approximation of the LiCl-KCl system, is that of a constant volume system with a constant interdiffusion coefficient and with a transference number of potassium equal to the mole fraction X_K. Equation [11] becomes

$$\frac{d \ln C_K}{d\xi} = \frac{d \ln X_K}{d\xi} = \frac{VI}{\mathbf{F}D} = q \qquad [12]$$

which is readily integrated to give

$$C_K = C_K' e^{q\xi} \qquad [13]$$

where C_K' is the concentration of K at the anode ($\xi = 0$). It is thus seen that the predicted composition gradient with this model is not linear but exponential (although not far from linear in appearance for small electrode separations).

The value of the steady-state concentration at the anode, C_K', can be obtained from the conservation condition, since the number of equivalents (N_K) of K between the electrodes remains constant

$$N_K = \int_0^{\Xi} C_K d\xi = \overline{C}\Xi \qquad [14]$$

where $\overline{C}$ is the initial uniform melt composition. The steady-state composition profile (Eq. [13]) may thus be written in terms of the initial ($\overline{X}$, $\overline{C}$) and steady-state ($X(\xi)$, $C(\xi)$) values of the equivalent fraction or volume concentration of K

$$\frac{C(\xi)}{\overline{C}} = \frac{X(\xi)}{\overline{X}} = \frac{q\Xi}{e^{q\Xi} - 1} e^{q\xi} \qquad [15a]$$

Numerical solution.—A more exact description of transport in LiCl-KCl can be provided by using the partial equivalent volumes $\overline{V}_L = 28.4$ cm³ and $\overline{V}_K = 49$ cm³ obtained from density measurements (5) and the Hittorf measurements (6) of the transference number of potassium relative to chloride, which can be represented over the entire composition range by

$$t_K{}^C = X_K + (X_K - 0.2)\, X_K - 0.8\, X_K{}^3 \quad 0 \leq X_K \leq 1 \qquad [16]$$

The transference number is equal, within 10%, to the mole fraction X_K. The interdiffusion coefficient of the melt probably varies little with composition, as in similar melts (7). We assumed in our calculations the value of 1×10^{-5} cm² sec⁻¹ for the interdiffusion coefficient of lithium and potassium. Although the steady-state differential equation (Eq. [11]) and the conservation condition (Eq. [14]) can also be readily integrated, they result in a pair of transcendental equations whose solution requires numerical methods. In such cases it is more reasonable to solve the partial differential equation (Eq. [8]) numerically since this solution can provide the composition profiles at any time rather than at steady state only.

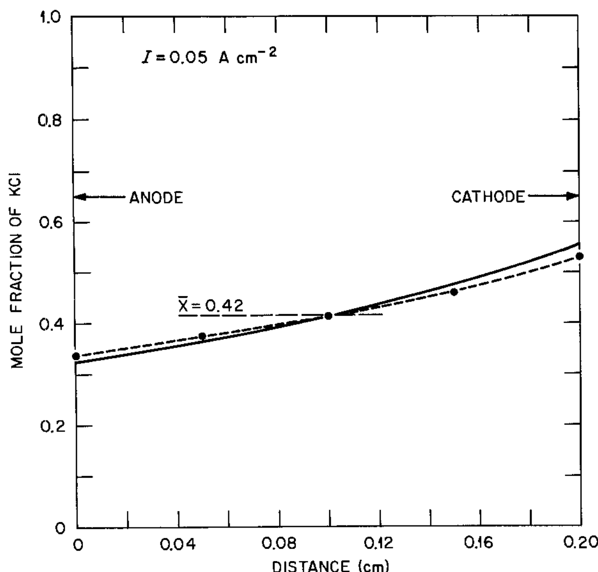

Fig. 1. Steady-state composition profile numerically calculated ——— with differing partial molar volumes and experimental (6) transference number of LiCl-KCl, - - - - with constant equivalent molar volume $V = 37$ cm³ equiv.⁻¹ and $t_K^C = X_K$, ● analytical solution with $V = 37$ cm³ equiv.⁻¹ and $t_K^C = X_K$.

Figure 1 shows steady-state composition profiles calculated for a 0.42 KCl-0.58 LiCl mixture with constant current density of 50 mA cm^{-2} and electrode separation of 0.2 cm. The profile calculated analytically by Eq. [15a] with a constant volume (37 cm^3 $equiv.^{-1}$) and transference number equal to the mole fraction coincides with the numerically calculated profile for the same volume and transference number. Even the profile calculated numerically with unequal equivalent volumes, and with the transference number given by Eq. [16], differs by less than 5% from the analytical solution for equal equivalent volumes. The simple analytical solution (Eq. [15a]) thus provides a very useful approximation to the steady-state composition profile for evaluation of the effects of current density, electrode separation, and initial composition on concentration gradients.

Effect of current density and electrode separation on concentration gradients.—Equation [15a] may be rewritten in terms of a dimensionless parameter, $Q = VI\Xi/\mathbf{F}D$, and a fractional distance between the electrodes $0 \leq \theta = \xi/\Xi \leq 1$

$$X(\theta) = X'e^{Q\theta} \quad [17a]$$

with the compositions at electrodes

$$\text{(anode)} \quad \xi = 0; \quad X' = \frac{\overline{X}Q}{e^Q - 1} \quad [17b]$$

$$\text{(cathode)} \quad \xi = \Xi; \quad X'' = \frac{\overline{X}Q}{e^Q - 1} e^Q \quad [17c]$$

The effects of current density and electrode separation thus appear through the value of their product in the parameter Q. For a fixed current density, the slope of the steady-state profile remains nearly unchanged as the distance between the electrodes is changed, but the difference of concentration between the two electrodes will decrease with decreasing electrode separation. This can be seen readily from a linear approximation of Eq. [15a]. For very low current densities and very small electrode separations, Eq. [15a] can be approximated by expansion of the exponential, as

$$X(\xi) \rightarrow X(0)\,[1 + q\xi]$$

or

$$X(\xi) \xrightarrow[(q \to 0)]{} \overline{X}\left[1 + q\left(\xi - \frac{\Xi}{2}\right)\right] \quad [15b]$$

Even for values of $q\Xi$, for which the truncated expansion is not strictly valid, the profiles in many cases do not, in fact, differ greatly from linearity, as seen in profiles A and B in Fig. 3, for which $q\Xi \simeq 1$. Increasing current at fixed electrode separation leads to increased slope and increased composition differences between the electrodes.

Effect of initial composition; chronopotentiometric transition.—An example of the magnitude of the composition gradient is given in the following calculation. Since in LiCl-KCl melts the diffusion coefficient is probably of the order of 10^{-5}, the quantity $\mathbf{F}D$ is approximately one, hence $Q \approx VI\Xi$. A mean value of the equivalent volume is about 35 cm^3 $equiv.^{-1}$, so that a plausible approximation to the steady-state concentration profile for the free electrolyte case, neglecting convection, would be

$$\frac{X(\theta)}{\overline{X}} = \frac{35I\Xi}{e^{35I\Xi} - 1} e^{35I\Xi\theta}$$

For Ξ of the order of 0.2 cm and for a current density of 200 mA cm^{-2}, the compositions along the steady-state profile fall within the range

$$0.46\overline{X} < X(\theta) < 1.86\overline{X} \quad [18]$$

In a real system X cannot exceed unity. Equation [18] indicates that before attainment of a steady state, the composition $X = 1$ would be attained at the cathode ($\theta = 1$) at this current density and electrode separation and for initial equivalent fractions $\overline{X}_K > 0.538$; *i.e.*, the vicinity of the cathode would be completely depleted of the electroactive constituent L, and maintenance of constant current would require the potential to be increased to where another electrode process would take place. This is the analog of a chronopotentiometric transition (4, 8). At low temperatures, however, precipitation of the constituent being enriched (K) might occur before the chronopotentiometric transition could be reached. The increase in X_K (and corresponding decrease in X_L) occurs always at the cathode, where Li^+ is being consumed from the electrolyte, *i.e.*, at the sulfur (positive) electrode in the Li/S battery on discharge and at the lithium (negative) electrode on charge.

Conditions for attainment of steady state.—Attainment of the steady state rather than a chronopotentiometric transition requires that X'', as calculated in Eq. [17c], be less than unity, which leads to

$$\overline{X} < \frac{e^Q - 1}{Qe^Q} \quad [19]$$

For a given value of the parameter Q (or of the product $I\Xi$), the calculation indicates a decreasing steady-state composition difference between the electrodes with decreasing initial concentration of the nonelectroactive component. Since the initial rate of change of composition is proportional to the current, while the steady-state composition is determined by the parameter Q (or product $I\Xi$), high current favors a rapid approach to the steady state (or transition). At a given initial composition, furthermore, low current densities and small electrode separations (*i.e.*, low values of Q) favor the steady state rather than transition. When inequality [19] is not satisfied (*i.e.*, for higher initial composition or for higher values of Q), the composition at the cathode ($\xi - \Xi$) becomes pure nonelectroactive constituent before the steady state can be reached, and this complete depletion of the electroactive constituent from the cathode region is the analog of a chronopotentiometric transition. Figure 2 is the plot of the right-hand side of inequality [19] *vs.* the values of the parameter Q calculated with a partial equivalent volume of 35 cm^3 $equiv.^{-1}$. The plot distinguishes the values of Q and of the initial composi-

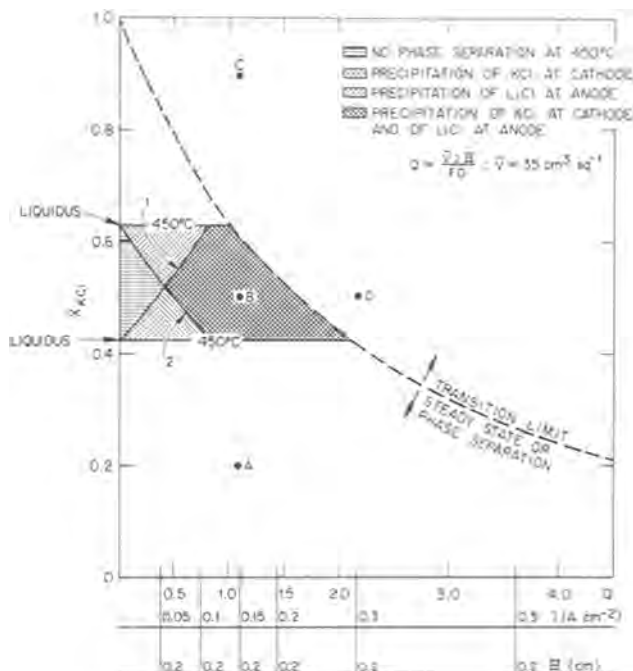

Fig. 2. Conditions for phase separation, transition, or steady state in analog of Li/LiCl-KCl/S battery. A, $X_{KCl} = 0.2$; $I = 0.15$ A cm^{-2}; $\Xi = 0.2$ cm. B, $X_{KCl} = 0.5$; $I = 0.15$ A cm^{-2}; $\Xi = 0.2$ cm. C, $X_{KCl} = 0.9$; $I = 0.15$ A cm^{-2}; $\Xi = 0.2$ cm. D, $X_{KCl} = 0.5$; $I = 0.3$ A cm^{-2}; $\Xi = 0.2$ cm. Curve 1, left-hand side of inequality [20]; curve 2, right-hand side of inequality [20].

tion leading to the establishment of a steady-state composition gradient from those leading to a chronopotentiometric transition by complete depletion of LiCl at the cathode. A and B represent conditions for which a steady state is predicted, while C and D are cases of transition. Composition profiles in these four cases are shown in Fig. 3. The two numerically obtained steady-state profiles A and B are identical to the corresponding analytical profiles. The profiles C and D show

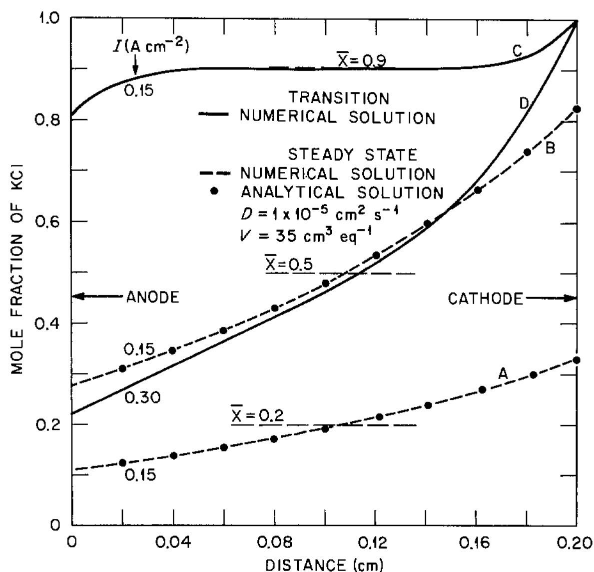

Fig. 3. Effect of initial composition and current density on composition profiles with $V = 37$ cm^3 equiv.$^{-1}$ and $t_K^C = X_K$. A, Steady state: numerical (– – – –); analytical (●); $\overline{X}_{KCl} = 0.2$, $I = 0.15$ A cm^{-2}. B, Steady state: numerical (– – – –); analytical (●); $\overline{X}_{KCl} = 0.5$, $I = 0.15$ A cm^{-2}. C, Transition numerically calculated for $\overline{X}_{KCl} = 0.9$, $I = 0.15$ A cm^{-2}. D, Transition numerically calculated for $\overline{X}_{KCl} = 0.5$, $I = 0.3$ A cm^{-2}.

the chronopotentiometric transitions predicted in Fig. 2.

Conditions for avoidance of phase separation.—In experimental devices, precipitation of a solid phase at one electrode could limit the current density and other performance characteristics. In molten salt batteries, the initial compositions are often eutectics [or other mixtures chosen to optimize melting temperatures, conductance, and other physical and chemical properties (9, 10)]. The composition gradient between the two electrodes must be kept in a range where the mixture is liquid in order to avoid the precipitation of a solid phase. Thus the compositions at the two electrodes, X' and X'' in Eq. [17b] and [17c], must fall within the range of the liquidus compositions, designated X_I and X_{II}, respectively, at the temperature in question. The initial composition must therefore satisfy the inequalities

$$X_I \frac{e^Q - 1}{Q} \leq \overline{X} \leq X_{II} \frac{e^Q - 1}{Qe^Q} \qquad [20]$$

Comparison of the third term in Eq. [20] with the right-hand side of Eq. [19] shows, since $X_{II} < 1$, that phase separation may prevent attainment of the steady state even though the conditions for avoidance of a transition are satisfied. Precipitation of the component being enriched at the anode is predicted if the left-hand side of the inequality Eq. [20], plotted in curve 1 in Fig. 2, is violated, *i.e.*, for points below curve 1; and precipitation of the other component is predicted at the cathode if the right-hand side, plotted in curve 2, is violated, *i.e.*, for points above curve 2. Only in the region between these two curves and the ordinate would the steady state be predicted rather than transition or phase separation. In the LiCl-KCl eutectic composition at 450°C, phase separation would occur (11) for $Q \geq 0.22$, *e.g.*, with electrode separation of 0.15 cm, phase separation is expected at current densities greater than 40 mA cm^{-2}. At temperatures above the melting point of KCl, with the same electrode separation, a steady state would be predicted at currents below 240 mA cm^{-2}, and a higher current would result in transition. Thus the blocking of the approach to the steady state might result at either electrode depending on the conditions of current density, electrode separation, initial composition, and operating temperature. At a temperature of 400°-430°C, with LiCl-KCl eutectic, Askew and Holland (12) reported that the lithium electrode was markedly polarized at current densities exceeding 500 mA cm^{-2}. They conjectured that this polarization was caused by precipitation of solid LiCl at the anode. Our calculations suggest that under the conditions of the experiment both LiCl precipitation at the anode and KCl precipitation at the cathode might be expected, but KCl precipitation at the cathode would probably occur first as the current density is increased.

Example of development of steady state, transition, or phase separation.—Figure 4 shows composition profiles numerically calculated for LiCl-KCl melts of the same compositions as in Fig. 3 but with the transference number given by Eq. [16] and the different equivalent volumes of LiCl and KCl. A′ and B′ are composition profiles for initial compositions of 0.2 and 0.5 mole fraction KCl, respectively, at a current density of 0.15 A cm^{-2}. For both cases, A′ and B′, the simple analytical expression (Fig. 2) is consistent with a steady state. The calculation with variable volume and mobilities shows the expected steady state for case A′ but a chronopotentiometric transition for B′ occurring after about 6 min in a situation where the values of Q and $\overline{X}$ are close to the condition for attainment of steady state. The numerically calculated profile B′ exhibits only upward curvature, similar to the shape of the numerical steady-state profile A′. E′ is a steady-state profile calculated for $\overline{X} = 0.5$ and a lower cur-

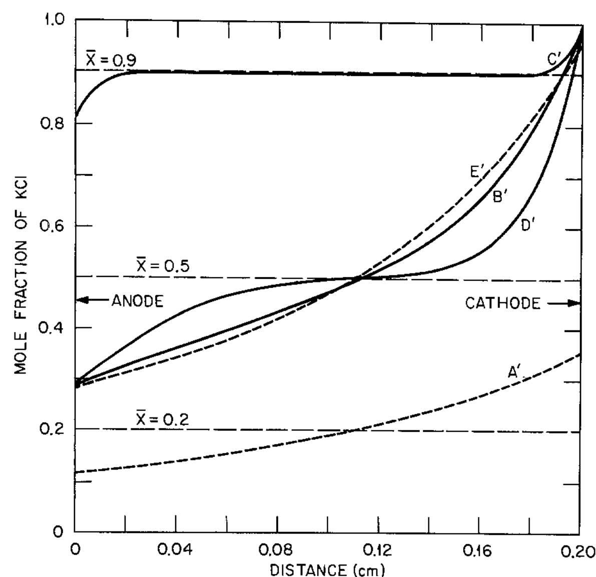

Fig. 4. Steady-state profiles (----) and profiles at transition (—+—) numerically calculated with differing partial equivalent volumes and transference number from Ref. (6). A′, $\overline{X}_{KCl}$ = 0.2; I = 0.15 A cm^{-2}. B′, $\overline{X}_{KCl}$ = 0.5; I = 0.15 A cm^{-2}. C′, $\overline{X}_{KCl}$ = 0.9; I = 0.15 A cm^{-2}. D′, $\overline{X}_{KCl}$ = 0.5; I = 0.3 A cm^{-2}. E′, $\overline{X}_{KCl}$ = 0.5; I = 0.1 A cm^{-2}.

rent density of 0.1 A cm^{-2}. As shown in curve B of Fig. 3, the calculation for the initial composition and current density of curve B′, but with the mean equivalent volume and transference number $t_K^c = X_K$, leads to prediction of a steady state, but one close to transition. Thus the effect of disparity of $\overline{V}$ values is small and appears only near the border between transition and steady-state.

The profile C′ in Fig. 4 corresponds to the composition 0.1LiCl-0.9KCl at a current density of 0.15 A cm^{-2}. It is calculated at the transition time, which is a little more than 4 sec. The simple analytical expression (Fig. 2) also predicts transition at this composition and current density. The transition shown in D′, corresponding to $\overline{X}$ = 0.5 and I = 0.3 A cm^{-2}, is attained after 85 sec, the profile showing downward curvature near the anode and upward curvature near the cathode. A transition also is predicted from the value of the parameter Q with the mean equivalent volume of 37 cm^3 $equiv.^{-1}$. The simple calculation in terms of the parameter Q, a mean equivalent volume and a transference number equal to the mole fraction is thus useful and reliable for predicting conditions for steady state or transition. Only small differences from the numerical solution appear, and these only near the border between transition and steady state.

Relaxation of composition gradients and chemical effects.—Composition gradients in operating cells have received little attention. Postoperative examinations, conducted after a slow cooling of the cell, may show little composition change. In Fig. 5, our calculation simulates the relaxation of compositions at anode and cathode after cessation of current flow following establishment of a steady-state composition profile. The initial composition is 0.5KCl-0.5LiCl, the current density for establishing the gradient is 100 mA cm^{-2}, and the electrode separation is 0.2 cm. The electrolyte composition between the electrodes extends from 0.28 to 0.96 mole fraction of KCl on cessation of current flow. The gradient relaxes after 2.5 min to a composition range 0.36-0.69; after 10 min the range is 0.45-0.56. Since cooling and disassembly of cells may take even longer, these gradients may be difficult to detect by chemical analysis. A relaxation in agreement with that predicted has been observed (13) by means of potential changes

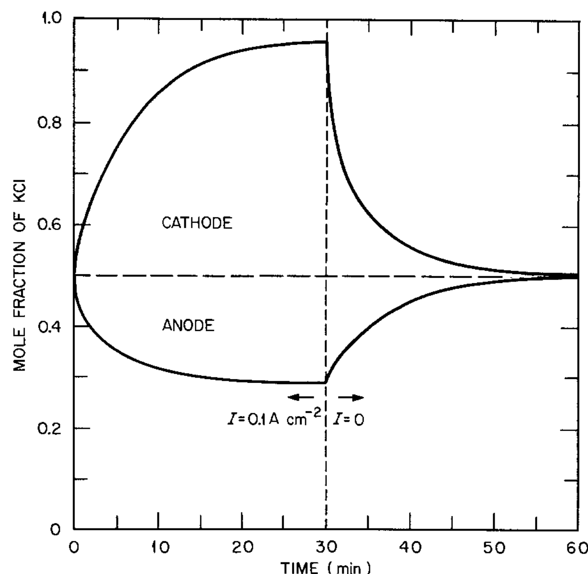

Fig. 5. Composition changes with time at the cathode and at the anode (during charge or discharge) followed by relaxation on open circuit.

of both electrodes in an analogous system, $Ag/AgNO_3$-KNO_3/Ag.

The composition profiles we predict by considering diffusion and migration in the electrolyte are consistent with observations made on the formation of J-phase (possibly $LiK_6Fe_{24}S_{26}Cl$) at the cathode of Li/S cells on discharge (10). A recent report (14) on the effects of electrolyte composition on the formation of J-phase during the discharge of FeS electrodes shows that increasing the LiCl concentration from 58 to 70 mole percent (m/o) eliminated the J-phase. Figure 6 shows predicted steady-state composition profiles in the mixtures 0.58LiCl-0.42KCl and 0.7LiCl-0.3KCl with electrode separation of 0.2 cm and current density of 0.05 and 0.1 A cm^{-2}. In the first mixture, where J-phase has been reported (14), the steady-state composition of the melt near the cathode is calculated to be about 0.5LiCl at 0.05 A cm^{-2}; in the other mixture, where no J-phase is reported, the calculated composition at the cathode is 0.64 mole fraction LiCl at the same current density. This is consistent with recent thermodynamic calculations (15) indicating that J-phase formation could be prevented by increasing the ratio of the activities of LiCl to KCl in the electrolyte. Choice of initial compo-

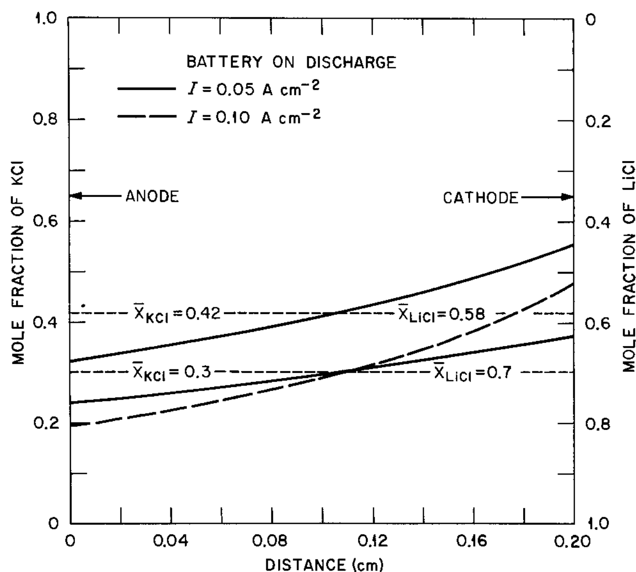

Fig. 6. Steady-state composition profiles: dependence on initial composition and on current density.

sition alone, however, independent of current density and electrode separation, may be insufficient to eliminate J-phase formation. An increase of the current density or of the electrode separation may lead to compositions at the cathode in the range favoring J-phase formations even for melts with the higher lithium chloride content. For example, in Fig. 6 the dashed curve is the steady-state composition profile calculated for the melt with the higher LiCl content but at 0.1 A cm^{-2}. The composition of about 58 m/o LiCl predicted at the cathode is close to the value predicted at the lower current in the melt of lower LiCl content. Doubling the electrode separation, instead of the current density, would lead to a similar composition at the cathode.

Conclusions

Composition gradients in analogs of Li/S batteries (with LiCl-KCl as the electrolyte) are predicted to result from the faradaic, migrational, and diffusive processes. A simple, useful analytical expression has been derived for steady-state composition profiles in terms of a single parameter, Q, incorporating the current density, the mean equivalent volume, the electrode separation, and the interdiffusion coefficient. A steady-state composition gradient, a chronopotentiometric transition, or phase separation are predictable from the value of Q, together with the initial composition and the phase diagram of the system. Numerical solution of the diffusion-migration equation has been used to calculate profiles at the transition time, at other times prior to reaching the steady state, or for unequal equivalent volumes of the mixture components and unequal mobilities of the two like-charged ions. However, comparison of computed steady-state profiles shows little difference between results from the simple analytical expression and from the numerical solution with equivalent volumes and mobilities corresponding to LiCl-KCl.

Composition gradients have been recognized in aqueous fuel cells (16, 17) and electrolyzers (18-20), but have received little prior attention in connection with molten salt batteries. Since they may result in the depletion of the electroactive constituent at one electrode, or in phase separation, they must be taken into account in the chemistry and phase equilibria of the electrolytes. Further refinements in the predictions will require attention to convection and to the porosity of the electrolyte matrix.

Acknowledgment

This research was sponsored by the Division of Materials Science, Office of Basic Energy Sciences, U.S. Department of Energy, under contract W-7405-eng-26 with the Union Carbide Corporation.

Manuscript received Jan. 3, 1978.

Any discussion of this paper will appear in a Discussion Section to be published in the June 1979 JOURNAL. All discussions for the June 1979 Discussion Section should be submitted by Feb. 1, 1979.

Publication costs of this article were assisted by the Oak Ridge National Laboratory.

LIST OF SYMBOLS

- C — common anion Cl^-
- $\overline{C}$ — initial concentration (equiv. cm^{-3})
- C_i — concentration of i (equiv. cm^{-3})
- C_i' — concentration of i at the anode (equiv. cm^{-3})
- D — interdiffusion coefficient
- $\mathbf{F}$ — Faraday (96,487C)
- I — current density (A cm^{-2})
- J_i^* — flow of i relative to the reference frame *
- K — potassium chloride, or potassium
- L — lithium chloride, or lithium
- M_i — migrational term relative to i
- M_i^j — migrational term relative to i in the reference frame j
- N_i — number of equivalents i
- Q — parameter $= VI\Xi/\mathbf{F}D$
- q — parameter $= VI/\mathbf{F}D$
- t — time
- t_i^j — Hittorf transference number of ion i relative to j
- V — mean value of the equivalent volume (cm^3 $equiv.^{-1}$)
- $\overline{V_i}$ — partial equivalent volume of i (cm^3 $equiv.^{-1}$)
- $\overline{X}$ — initial composition (mole fraction)
- X' — composition at anode (mole fraction)
- X'' — composition at cathode (mole fraction)
- X_i — mole fraction of component i
- X_I and X_{II} liquidus compositions
- θ — fractional distance $= \xi/\Xi$
- Ξ — electrode separation
- ξ — distance variable

REFERENCES

1. J. Braunstein, H. R. Bronstein, S. Cantor, D. Heatherly, and C. E. Vallet, Oak Ridge National Laboratory Report ORNL/TM-5886, May 1977.
2. J. Braunstein and C. E. Vallet, in Proceedings of the Symposium on Electrode Materials and Processes for Energy Conversion and Storage, p. 559, The Electrochemical Society Softbound Symposium Series Princeton, N. J. (1977).
3. C. E. Vallet and J. Braunstein, *J. Phys. Chem.*, **81**, 2438 (1977).
4. C. E. Vallet, H. R. Bronstein, and J. Braunstein, *This Journal*, **121**, 1429 (1974).
5. E. R. Van Artsdalen and I. S. Yaffe, *J. Phys. Chem.*, **59**, 118 (1955).
6. C. T. Moynihan and R. W. Laity, *ibid.*, **68**, 3312 (1964).
7. J. Richter, *J. Chem. Eng. Data*, **18**, 400 (1973).
8. P. Delahay, "New Instrumental Methods in Electrochemistry," p. 179, Interscience Publishers, Inc., New York (1954).
9. "High Performance Batteries for Off-Peak Energy Storage and Electric Vehicle Propulsion," Prog. Report ANL 76-98 (December 1976).
10. R. K. Steunenberg and M. F. Roche, in Proceedings of Symposium on Electrode Materials and Processes for Energy Conversion and Storage, p. 869 The Electrochemical Society Softbound Symposium Series, Princeton, N.J. (1977).
11. A. Grothe and C. A. Piel, *Z. Elektrochem.*, **54**, 215 (1950).
12. B. A. Askew and R. Holland, Abstract 56, p. 138, The Electrochemical Society Extended Abstracts, Fall Meeting, Boston, Mass., October 7-11, 1973.
13. D. E. Heatherly and C. E. Vallet, Paper presented at the Council Committee on Technician Activities, American Chemical Society, Chicago, Aug. 28-Sept. 2, 1977.
14. "Development of Lithium/Metal Sulfide Batteries at Argonne National Laboratory: Summary Report for 1976, ANL-77-18, March 1977, p. 21; C. A. Melendres, C. G. Sy, and B. Tani, *This Journal*, **124**, 1060 (1977).
15. M. L. Saboungi, J. J. Marr, and M. Blander, Abstract 37, p. 101, The Electrochemical Society Extended Abstracts, Fall Meeting, Atlanta, Ga., Oct. 9-14, 1977.
16. M. L. Miller and H. J. Fornasan, *This Journal*, **115**, 330 (1968).
17. J. T. Lundquist and W. M. Vogel, *ibid.*, **116**, 1066 (1969).
18. C. R. Wilke, M. Eisenberg, and C. W. Tobias, *ibid.*, **100**, 513 (1953).
19. L. Hsueh and J. Newman, *Ind. Eng. Chem. Fundam.*, **10**, No. 4, 615 (1971).
20. C. G. Smith and R. H. Muller, Lawrence Berkeley Laboratory Annual Report LBL-6016, p. 209 (1976).

Electrochemical Behavior of Titanium and Some Titanium Alloys under Tensile Stress in Boiling Sulfuric Acid and Acidic Chloride Solutions

D. Sinigaglia

Istituto di Chimica-Fisica, Elettrochimica e Metallurgia, Politecnico di Milano, Piazza Leonardo da Vinci, 32, 20122 Milano, Italy

and G. Taccani, B. Vicentini, and G. Dallaspezia

Laboratory of Technology for Non-traditional Metals (L.T.M.), C.N.R. Via Induno, 10, Cinisello Balsamo, Milano, Italy

ABSTRACT

The anodic and cathodic polarization behavior of titanium and four commercial alloys (Ti-5Al-2.5Sn; Ti-6Al-4V; Ti-8Al-1Mo-1V; Ti-13V-11Cr-3Al) has been investigated in boiling acidic chloride solutions (0.1M HCl; 0.1M HCl + 0.5M NaCl; 0.1M HCl + 5M NaCl) and in 0.1M H_2SO_4 solution as a function of tensile stress (equal to $0.9\sigma_y$). All materials exhibit an active to passive transition. Pitting corrosion was observed at very noble potentials for the Ti-5Al-2.5Sn; Ti-6Al-4V, and Ti-8Al-1Mo-1V alloys, and a transpassive behavior was observed for the Ti-13V-11Cr-3Al alloy. The kinetics of the hydrogen evolution reaction (HER) is substantially facilitated by increasing the chloride concentration and by going from the most dilute chloride solutions to dilute sulfuric acid solutions. The tensile stress does not modify in our experimental conditions (of aggressive medium, temperature, surface state, and stress type and level, etc.) the electrochemical behavior of all materials examined.

Titanium and its alloys have found, despite their high cost, fairly extensive application in the naval, aeronautic, and chemical industries thanks to their high strength/weight ratio and to their good resistance to general and localized corrosion in various environments. Titanium and its alloys are characterized by the tendency to be easily passivated, by stable passivity over a wide range of potential and temperature, and by insensitivity to the detrimental effect of aerated or other oxygen-containing chloride solutions.

However, it is well known that these materials are susceptible to pitting and crevice corrosion (1-5) in the hot concentrated solutions employed in desalination plants and to stress corrosion cracking (6-9). In particular, stress corrosion cracking is promoted by crevices, as Brown and collaborators have clearly demonstrated (9).

Many authors have studied the corrosion behavior of titanium and its alloys in sulfuric acid (11-17), in acidic sulfate solutions (18), in hydrochloric acid (10, 19), and in halide solutions of various pH (20-24), mostly at ambient temperature. Most studies concern the anodic dissolution mechanism in the active and passive range, the active-passive transition *vs.* temperature, acidity, and aggressive anions of the solution, and also the effect of alloy composition and microstructures. The corrosion and primary passivation potentials, the critical and passivation current density, and the critical pitting potential values have been reported in these papers.

Other studies (17, 23) have examined the cathodic hydrogen evolution process on these materials with the determination of the rate-controlling step and of parameters such as the exchange current density, the transfer coefficient, the reaction order, and the Tafel slope.

With reference to what has been reported above it appears that the tensile stress effect on the electrochemical behavior of titanium and its alloys in boiling acidic chloride solutions has not been systematically examined apart from some results of Wijman in 10% H_2SO_4 + 8% HCl at room temperature (25) and from the paper of Levy (5) which is, however, restricted to the 0.17M sodium chloride solution (approximate NaCl concentration in blood, plasma, and lymph) and to Hank's physiological solution (a fairly close imitation, from the chemical viewpoint, of the fluid in muscle and bone) at a temperature of 37°C.

The present investigation was undertaken to obtain a more complete understanding of the role of the tensile stress on the anodic dissolution process (in the active condition), on the formation and stability of the passivating films, hence on localized corrosion, *i.e.*, on pitting, crevice, and stress corrosion cracking, and on the cathodic hydrogen evolution process. For this reason, the electrochemical behavior of titanium and four commercial alloys (Ti-5Al-2.5Sn; Ti-6Al-4V; Ti-8Al-1Mo-1V; Ti-13V-11Cr-3Al) was investigated in boiling acidic chloride solutions with stressed specimens to 90% yield strength and unstressed tensile specimens as electrodes, and was extended to boiling 0.1M HCl and 0.1M H_2SO_4 solutions for comparison.

Experimental

Materials.—Chemical composition, factory heat-treatment, microstructures, and yield strength of the titanium Contimet 35 and of the alloys used in this work are given in Table I. The conventional test specimens were cut from 1.0 mm thick sheet, degreased for 15 min in 90% ethanol (reagent grade chemical), washed in boiling distilled water, and then dried with pure ethanol. The specimen surface area, equal to nearly 9 cm^2, was accurately outlined with two silicon rubber gaskets (see details in Fig. 1) and was measured after every experiment.

Solutions.—The following solutions were used at their boiling temperature (100°-105°C): 0.1M HCl (I); 0.1M HCl + 0.5M NaCl (II); 0.1M HCl + 5.0M NaCl (III); 0.1M H_2SO_4 (IV). Reagent grade chemicals and bidistilled water (3 μS specific conductivity) were

Key words: hydrogen evolution reaction, localized corrosion, passivity, tensile stress, titanium and titanium alloys, transpassivity.

Table I. Chemical composition, heat-treatment, and microstructure of titanium and the alloys used (1.0 mm sheet)

Material	Heat-treatment	Chemical composition (weight percent)											Y.S. (at 100°C) (mn/m²)
		Fe	C	N	O	H	Al	V	Mo	Sn	Cr	Ti	
Ti (α)	10 min, 700°C/a.c.	0.06	0.026	0.008	0.12	0.003	—	—	—	—	—	Bal.	170
Ti-5Al-2.5Sn (α)	15-20 min, 780°C/a.c.	0.25	0.022	0.018	0.18	0.006	5.27	—	—	2.54	—	Bal.	695
Ti-6Al-4V (α + β)	30 min, 750°C/a.c.	0.13	0.024	0.010	0.13	0.009	6.0	4.2	—	—	—	Bal.	850
Ti-8Al-1Mo-1V α(+ β)	1 hr, 790°C/a.c.	0.04	0.024	0.010	0.09	0.010	8.0	1.0	1.0	—	—	Bal.	850
Ti-13V-11Cr-3Al (β)	15-20 min, 790°C/a.c.	0.15	0.028	0.028	0.13	0.04	3.1	13.5	—	—	10.6	Bal.	790

employed. Molar concentrations are referred to 25°C without taking in to account variation in density with temperature. The solution volume, referred to 1 cm² of the electrode surface area, was equal to approximately 50 ml.

Cell and electrode arrangements.—The stressed specimen polarization cell is a Pyrex glass standard cell (26). It consists of two compartments joined by a bridge containing a fritted glass disk. The first compartment is a 0.5 liter spherical flask with five necks to introduce the working electrode, the gas inlet and outlet tubes, the thermometer, the condenser, and the Haber-Luggin probe; the second compartment is a cylindrical flask containing the platinum auxiliary electrode. It was necessary to design the special electrode arrangement shown in Fig. 1, which is able to apply an uniaxial tensile stress on the plate working electrode and to minimize or avoid the crevice effect.

Teflon, Vyton, and silicon rubber were the insulating materials selected because of their chemical inertness in hot acidic solutions. The cell and all the Teflon parts in contact with the solutions were washed in hot chromic solution, rinsed several times in distilled water, and dipped in the test solution with the Vyton and silicon rubber parts.

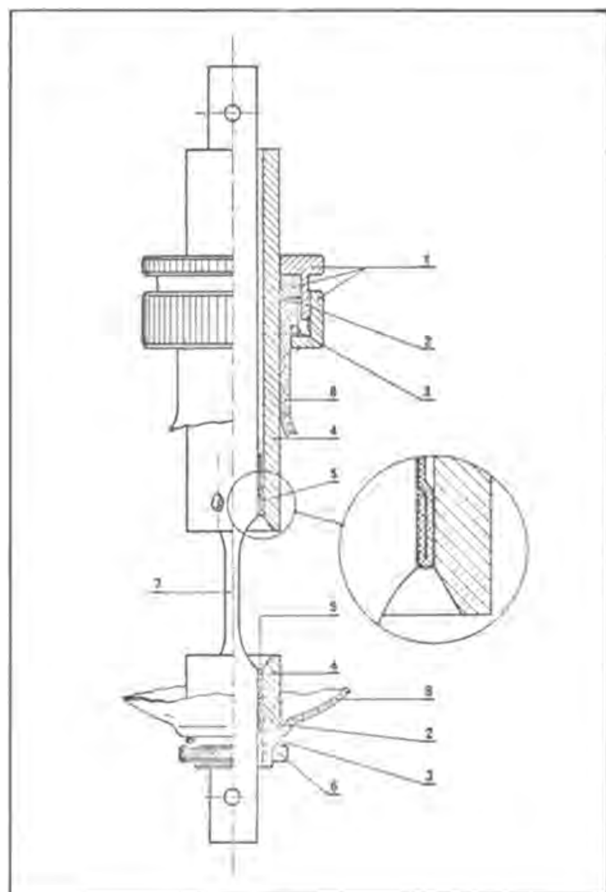

Fig. 1. Electrode assembly used for electrochemical measurements: 1, upper polypropylene seal; 2, Vyton O-ring; 3, neoprene O-ring; 4, Teflon seal; 5, silicon rubber gasket; 6, AISI 304 hold-down nut; 7, specimen; 8, Pyrex glass cell.

Electrochemical procedure.—The electrochemical cell and the electrode assembly were mounted in the tensile machine (Model Unisteel with arm 1:30 length ratio) keeping the specimen unstressed. The solution was poured into the cell at room temperature and then high purity nitrogen was bubbled through the solution at a rate of 10 liters/hr for 24 hr to ensure a very low oxygen concentration in the solution. During this time the specimen was in the passive state.

The solution cell was then heated with a glass wool mantel and the electrode potential recorded. The potential of the unstressed specimen at first decreases slowly and then falls quickly in the active direction. The specimen in the active state was then stressed at a tensile stress level equal to 90% of yield strength and after 5 min (carefully controlled) was polarized. The applied stress virtually does not change the specimen potential.

For anodic polarization, the potentiodynamic method was used at a sweep rate of 20 mV/min up to 2V *vs.* SCE; for cathodic polarization, the potentiostatic method was used (steps of 20 mV for 30 sec). At each step the polarization was interrupted for 5 sec. All polarizations were performed in triplicate. The electronic device (*i.e.*, potentiostat, electrometer, recorder, and so on), have previously been described (27). All potentials are referred to the saturated calomel electrode (SCE), which was kept at room temperature and joined with a potassium chloride agar-agar salt bridge to a Luggin probe positioned 1-2 mm from the specimen surface. The potential values were not corrected for the small ohmic drop and for Sorel thermal potential errors.

Results and Discussion

The anodic polarization curves of the unstressed and stressed titanium and Ti-8Al-1Mo-1V alloy are given in Fig. 2 and 3 as examples of the behavior of the

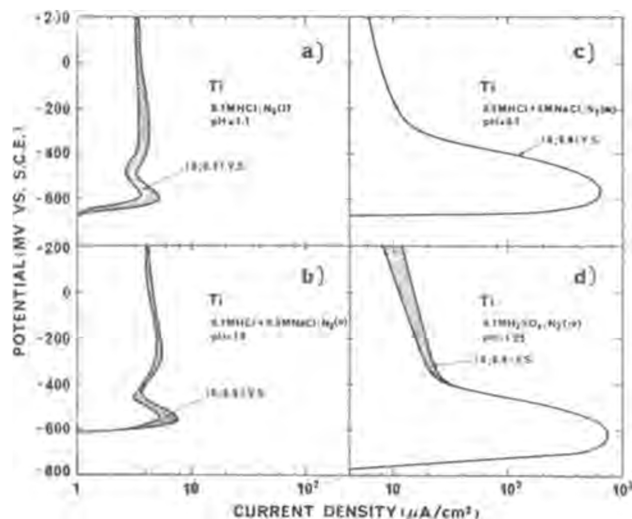

Fig. 2. Anodic polarization curves of unstressed and stressed titanium in various deaerated solutions at boiling point (Y.S. = yield strength).

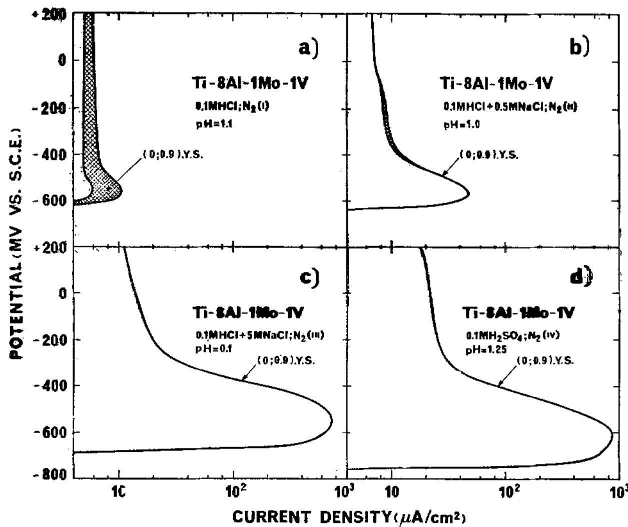

Fig. 3. Anodic polarization curves of unstressed and stressed Ti-8Al-1Mo-1V alloy in various deaerated solutions at boiling point (Y.S. = yield strength).

tested materials. The most important parameters for a quantitative classification of the corrosion behavior of active-passive metallic materials are summarized in Table II.

The anodic curves were plotted up to + 200 mV *vs.* SCE since the current density was practically constant and less than 10 $\mu A/cm^2$ at more noble potentials, *e.g.*, up to 2000 mV *vs.* SCE for titanium and up to the potential values, summarized in Table III, for the titanium alloys. The potential above which the titanium alloys' anodic current density markedly increased is reported in Table III; this potential indicates the breakdown of passivity, that is, the onset of pitting in the case of Ti-5Al-2.5Sn, Ti-6Al-4V, and Ti-8Al-1Mo-1V alloys, and for the onset of the transpassive corrosion in the case of the Ti-13V-11Cr-3Al alloy. The pitting occurs generally on the edges, *i.e.*, on the transversal cut surfaces and never beneath the silicon rubber gasket. The data are in good agreement with the values reported by Griess (1) and Levy and Sklover (10) for the same titanium alloys.

From the examination of all the anodic polarization data, we can formulate the following remarks.

Titanium.—In solutions I and II, titanium exhibits only a slight active-passive transition (Fig. 2a and b)

Table III. Breakdown potential (mV *vs.* SCE) of unstressed and stressed specimens

Solution		Alloy: Ti-5Al-2.5Sn (α)	Ti-6Al-4V ($\alpha + \beta$)	Ti-8Al-1Mo-1V ($\alpha + \beta$)	Ti-13V-11Cr-3Al* (β)
0.1M HCl	US**	1650	1625	1580	N.D.
	S	1800	1570	1430	N.D.
0.1M HCl + 0.5M NaCl	US	1540	1570	1360	725
	S	1500	1565	1290	725
0.1M HCl + 5.0M NaCl	US	1300	1485	1170	825
	S	1140	1470	1020	825

* For this alloy the values reported refer to the initiation of transpassive behavior.
** US = unstressed specimen; S = stressed specimen.

but a more pronounced one is observed in solutions III and IV (Fig. 2c and d). In solutions I and II, there was an initial transient drop in corrosion potential followed by an increase as the passive film was reformed (see Fig. 4). A similar activation and repassivation phenomenon was observed by the authors in 0.1M H_2SO_4 at 40°C (28).

From the Fig. 2 it is also noted that the active anodic loop spreads out when the chloride anion concentration increases. This effect is more evident when solution II is compared with solution III. In 0.1M H_2SO_4 (solution IV) the anodic loop is practically equal to that of the most concentrated chloride solution (III), but shifted in the less noble direction.

Therefore, it is important to point out that according to Griess (1) the chloride anion catalytic effect on the titanium active-passive transition is not only direct [*i.e.*, by increasing the water-complex reactivity through the substitution of coordination water with the anion or by means of anion preferential adsorption on the metallic surface, the anion functioning as a "bridge" between the metallic phase and the solution (29)], but above all indirect by increasing the activity or reactivity of the other ions in the solution which are operating in the heterogeneous charge transfer reaction, *i.e.*, in this particular case, H^+ ions. In fact comparing solution II with solution III, the chloride anion concentration is increased by nearly 10 times and the *p*H value is decreased from 1.0 to 0.1 [and so the H^+ activity is increased by nearly 8 times (1)]. On comparing Fig. 2a with d (the solutions have the same *p*H), it is evident that the SO_4^{2-} anion has a stronger acceleration action on the titanium active dissolution than the Cl^- anion.

Table II. Summary of corrosion potential E_{corr} (mV *vs.* SCE) of primary passivation potential E_{pp} (mV *vs.* SCE) and critical current density i_{cp} ($\mu A/cm^2$) for unstressed and stressed specimens*

Solution			Material: Ti Contimet 35	Ti-5Al-2.5Sn	Ti-6Al-4V	Ti-8Al-1Mo-1V	Ti-13V-11Cr-3Al
0.1M HCl (I)	US	$E_{corr.}$	−630	−635	−645	−620	—
		E_{pp}	−595	−575	−575	−560	—
		i_{cp}	5.3	13.5	26.4	11.0	—
	S	$E_{corr.}$	−660	−635	−620	−600	—
		E_{pp}	−585	−575	−575	−560	—
		i_{cp}	3.6	11.0	7.0	6.0	—
0.1M HCl + 0.5M NaCl	US	$E_{corr.}$	−605	−655	−675	−640	−655
		E_{pp}	−550	−585	−575	−565	−585
		i_{cp}	5.4	63	85	50	125
	S	$E_{corr.}$	−608	−660	−660	−640	−655
		E_{pp}	−550	−575	−590	−555	−595
		i_{cp}	7.6	90	70	45	145
0.1M HCl + 5.0M NaCl	US	$E_{corr.}$	−680	−685	−725	−680	−700
		E_{pp}	−550	−550	−575	−545	−580
		i_{cp}	650	1115	725	740	1345
	S	$E_{corr.}$	−675	−685	−735	−685	−700
		E_{pp}	−565	−565	−570	−550	−580
		i_{cp}	645	950	800	745	1440
0.1M H_2SO_4 (IV)	US	$E_{corr.}$	−775	−750	−840	−750	−800
		E_{pp}	−635	−600	−635	−620	−635
		i_{cp}	590	1220	1075	915	1240
		$E_{corr.}$	−765	−750	−835	−750	−775
	S	E_{pp}	−640	−620	−645	−620	−645
		i_{cp}	625	1135	1065	920	1330

* Passivity current density (at 0 mV *vs.* SCE) $\leqq$ 10 $\mu A/cm^2$. US = unstressed specimen; S = stressed specimen.

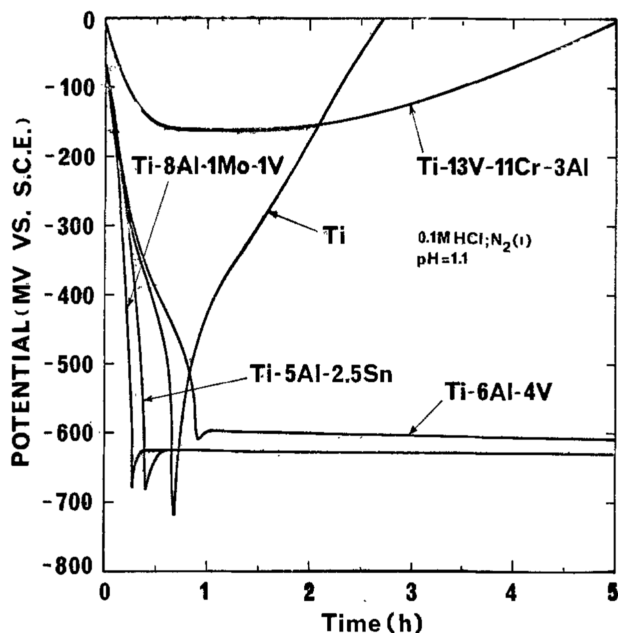

Fig. 4. Potential-time curves of unstressed titanium and unstressed Ti-5Al-2.5Sn, Ti-6Al-4V, Ti-8Al-1Mo-1V, and Ti-13V-11Cr-3Al alloys in deaerated 0.1M HCl at boiling point.

The effect of the applied tensile stress on the titanium anodic behavior is practically negligible, the difference observed being due to scatter in the experimental data. In any case, the titanium remains passive up to a potential of 2V *vs.* SCE in the acidic chloride solutions tested.

Ti-5Al-2.5Sn.—This alloy has an evident active-passive transition behavior in all solutions tested. The chloride and sulfate anions and the applied tensile stress effects are similar to those observed and discussed for titanium. Unlike titanium, the Ti-5Al-2.5Sn alloy is susceptible to pitting corrosion in all the acidic chloride solutions tested. An important point is the lack of tensile stress effect on the pitting resistance evaluated as breakdown potential (see Table III).

Ti-6Al-4V and Ti-8Al-1Mo-1V.—These alloys have, as shown in Fig. 3 for the Ti-8Al-1Mo-1V alloy, the same anodic behavior as the Ti-5Al-2.5Sn discussed above (see also Tables II and III).

Ti-13V-11Cr-3Al.—This alloy has the same anodic primary loop as the alloys discussed above. In particular this alloy is not susceptible to pitting corrosion in all the acidic chloride solutions tested, according to Levy and Sklover (10), but it is susceptible to transpassive dissolution, as shown in Fig. 5 and reported in Table III.[1] This alloy does not spontaneously shift to the active state in 0.1M HCl (Fig. 4).

Figures 6 and 7 show, for example, the cathodic polarization curves of the Ti-6Al-4V and Ti-5Al-2.5Sn alloys *vs.* the chloride or sulfate concentration and the applied tensile stress. A comparison of the curves allows the following remarks to be made concerning the cathodic hydrogen process.

(*i*) The titanium and Ti-6Al-4V alloy (Fig. 6) have substantially the same kinetics of the hydrogen evolution reaction (HER), *i.e.*, characterized for equal polarization by the same cathodic current density values and by the presence of a linear Tafel region with slope of 200 mV/decade in boiling chloride solutions (I, II, and III) and of 400 mV/decade in boiling 0.1M H_2SO_4 (IV). These high values of the Tafel slopes suggest the presence of a mixed oxide film of TiO_2 and Ti_2O_3, as shown by Tomashov *et al.* (30), on the titanium and on the Ti-6Al-4V alloy surface.

The cathodic polarization, measured as $\Delta E = E(i_{cat.}) - E_{corr.}$ at $i_{cat.} = 10^3$ $\mu A/cm^2$, decreases with increasing chloride concentration (I: $\Delta E = 250$ mV; II: $\Delta E = 180$ mV; III: $\Delta E = 75$ mV) and going from the most dilute solutions (I and II) to 0.1M H_2SO_4 solution (IV: $\Delta E = 50$ mV). It has been observed in the cathodic polarization of titanium in 0.1M HCl + 0.5M NaCl solution that, at approximately − 1.1V *vs.* SCE, deviations from linear Tafel behavior commenced with an anomalous increase in the cathodic current density. In agreement with the interpretation reported by Thomas and Nobe (17) a possible explanation of this phenomenon is the complete reduction of the oxide film or the possible hydride formation from the oxides at this potential and the subsequent hydrogen ion discharge on oxide-free titanium.

(*ii*) The Ti-5Al-2.5Sn (Fig. 7), Ti-8Al-1Mo-1V, and Ti-13V-11Cr-3Al have the same kinetics of hydrogen evolution reaction (HER), *i.e.*, characterized for equal polarization by the same cathodic current density values and by the absence of a linear Tafel region. The

[1] The complex formed by the hexavalent chromium ion and diphenylcarbazide was spectrophotometrically detected at the end of each anodic polarization. The presence of this complex was particularly evident in 0.1M H_2SO_4 solution.

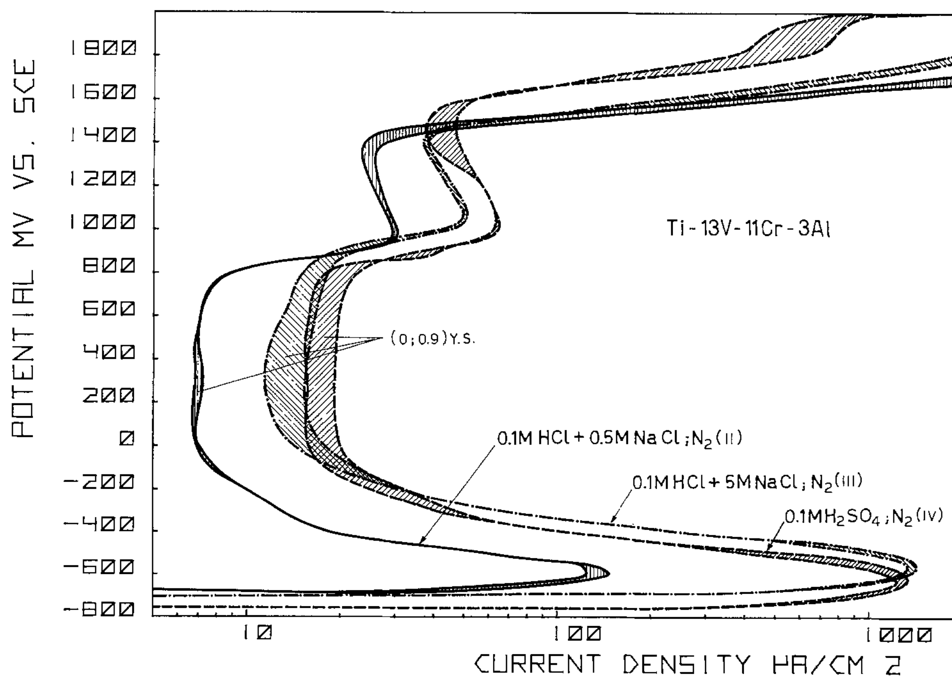

Fig. 5. Anodic polarization curves of unstressed and stressed Ti-13V-11Cr-3Al alloy in various deaerated solutions at boiling point. (Y.S. = yield strength).

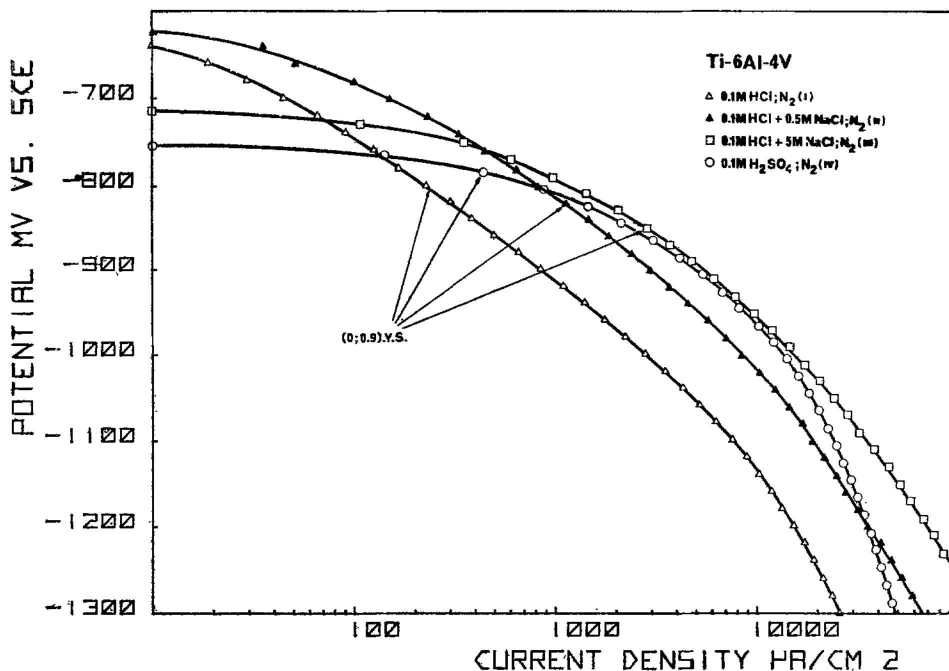

Fig. 6. Cathodic polarization curves of unstressed and stressed Ti-6Al-4V alloy in various deaerated solutions at boiling point (Y.S. = yield strength).

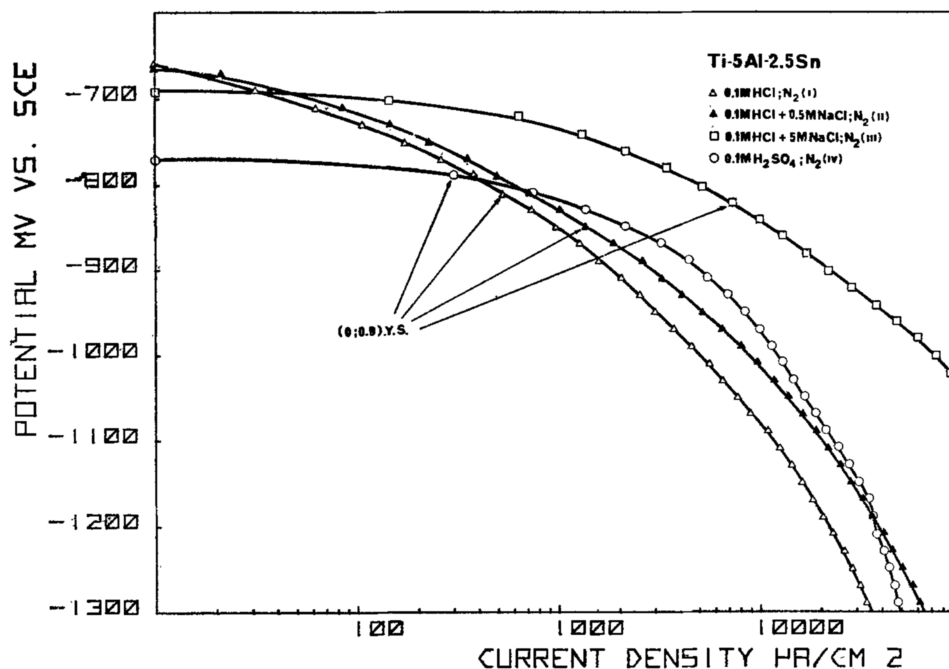

Fig. 7. Cathodic polarization curves of unstressed and stressed Ti-5Al-2.5Sn alloy in various deaerated solutions at boiling point (Y.S. = yield strength).

cathodic polarization, measured in (*i*), decreases with increasing chloride concentration and going from the most dilute chloride solutions (I and II) to 0.1M H_2SO_4 solution (IV). Moreover the HER of these alloys tends to take place more easily.

(*iii*) The cathodic behavior of titanium and the alloys studied is independent of the tensile stress applied in all the solutions.

Conclusions

The study of the electrochemical and corrosion behavior of titanium and the alloys (Ti-5Al-2.5Sn, Ti-6Al-4V, Ti-8Al-1Mo-1V, and Ti-13V-11Cr-3Al) under tensile stress in boiling sulfuric acid and acidic chloride solutions indicated that:

1. All the materials exhibit an active anodic loop (except the Ti-13V-11Cr-3Al in 0.1M HCl) with an active-passive transition characterized by the same primary passivation potential values. The critical current densities increase in the order: Ti <Ti-8Al-1Mo-1V <Ti-5Al-2.5Sn <Ti-6Al-4V <Ti-13V-11Cr-3Al. Passivity characterized by a low current density value ($\simeq$ 10 $\mu A/cm^2$) indicates the formation of a very protective film.

(*ii*) Unlike titanium, the alloys Ti-5Al-2.5Sn, Ti-6Al-4V, and Ti-8Al-1Mo-1V are susceptible to pitting corrosion (generally on the sample edges) and the alloy Ti-13V-11Cr-3Al to transpassive anodic dissolution. Since the pitting phenomena, in absence of crevices, appear at very high potentials ($\simeq$ 1000 mV *vs. SCE*), that is, an aggressive environment with a very high oxidizing power is required, the alloys have the same resistance to pitting corrosion as titanium but better mechanical properties.

(*iii*) The kinetics of cathodic hydrogen evolution is substantially facilitated by increasing chloride concentration. Therefore, it is possible to conclude that the active corrosion rate of titanium and the alloys examined increases with the chloride anion content in acidic solutions.

(*iv*) Tensile stress has no appreciable effect on anodic and cathodic behavior in the experimental conditions

tested (*i.e.*, of aggressive medium, temperature, surface state, and stress type and level).

Manuscript submitted Nov. 17, 1977; revised manuscript received March 27, 1978.

Any discussion of this paper will appear in a Discussion Section to be published in the June 1979 JOURNAL. All discussions for the June 1979 Discussion Section should be submitted by Feb. 1, 1979.

Publication costs of this article were assisted by L.T.M.-C.N.R. Laboratory Cinisello Balsamo.

REFERENCES

1. J. C. Griess, Jr. *Corrosion (Houston)*, **24**, 96 (1968).
2. F. Mazza, *ibid.*, **23**, 223 (1967).
3. A. Takamura, *ibid.*, **23**, 306 (1967).
4. E. G. Bohlmann and F. A. Posey, in Proceedings of 1st International Symposium on Water Desalination, Washington, D.C, Oct. 3-9, 1965.
5. T. Koizumi and S. Furuya, in "Titanium Science and Technology," Vol. 4, R. I. Jaffee and H. M. Burtes, Editors, pp. 2383-2393, Plenum Press, New York (1973); L. C. Covington, *ibid.*, pp. 2395-2403; M. Levy *et al.*, *ibid.*, pp. 2459-2474; A. C. Fraker *et al.*, *ibid.*, pp. 2447-2457.
6. C. M. Chen, F. H. Beck, and M. G. Fontana, *Corrosion (Houston)*, **4**, 135 (1970).
7. L. Fu-Shiong and R. F. Hochman, *ibid.*, **28**, 182 (1972).
8. M. H. Peterson *et al.*, *ibid.*, **23**, 142 (1967).
9. B. F. Brown, in "The Theory of Stress Corrosion Cracking in Alloys," J. C. Scully, Editor, NATO Science Committee Research Evaluation Conference, Ericeira, March 29-April 2, 1971.
10. M. Levy and G. N. Sklover, *This Journal*, **116**, 323 (1969).
11. J. M. Peters and J. R. Myers, *Corrosion (Houston)*, **23**, 326 (1967).
12. J. A. Petit and F. Dabosi, *C. R. Acad. Sci. Ser. C.*, **15**, 773 (1972).
13. M. Levy, *Corrosion (Houston)*, **23**, 236 (1967).
14. D. Sinigaglia, G. Taccani, and B. Vicentini, *Werkst. Korros.*, **24**, 1027 (1973).
15. M. J. Mandry and G. Rosenblatt, *This Journal*, **119**, 29 (1972).
16. R. D. Armstrong, J. A. Harrison, H. R. Thirsch, and R. Whitfield, *This Journal*, **117**, 1003 (1970).
17. N. T. Thomas and K. Nobe, *ibid.*, **117**, 622 (1970).
18. E. J. Kelly, in Proceedings of 5th International Congress on Metallic Corrosion, Tokyo, May 21-27, 1972.
19. N. T. Thomas and K. Nobe, *Corrosion (Houston)*, **29**, 118 (1973).
20. N. Hackerman and C. D. Hall, *This Journal*, **101**, 321 (1954).
21. I. Dugdale and J. B. Cotton, *Corros. Sci.*, **4**, 397 (1964).
22. J. A. S. Green and R. M. Latanision, *Corrosion (Houston)*, **29**, 386 (1973).
23. N. T. Thomas and K. Nobe, *This Journal*, **116**, 1748 (1969).
24. A. J. Sedriks *et al.*, in "Titanium Science and Technology," Vol. 4, R. I. Jaffee and H. A. Burte, Editors, pp. 2431-2445, Plenum Press, New York (1973).
25. H. Wijsman, Discussion to the paper of S. Henrikson, Lectures held at the IVth Scandinavian Corrosion Congress (NKM), November 24-27, 1964, Helsinki, Finlandia.
26. N. D. Greene, Experimental Electrode Kinetics, Rensselaer Polytechnic Institute, Troy, New York (1965); R. E. Geisent *et al.*, *Corrosion-Nace*, **32**, 407 (1976).
27. B. Mazza, P. Pedeferri, D. Sinigaglia, A. Cigada, L. Lazzari, G. Re, and D. Wenger, *This Journal*, **123**, 1157 (1976).
28. B. Vicentini, D. Sinigaglia, and G. Taccani in Proceedings of 6th International Congress on Metallic Corrosion, Sydney, December 3-9, 1975, In print.
29. R. Piontelli, *Electrochim. Met.*, **1**, 5 (1966).
30. N. D. Tomashov *et al.*, *Proc. Acad. Sci. USSR, Phy. Chem. Sec.*, **141**, 927 (1961).

Effect of Molybdenum on the Pitting Potential of High Purity 18% Cr Ferritic Stainless Steels

J. R. Galvele,*[1] J. B. Lumsden,[2] and R. W. Staehle*

The Ohio State University, Columbus, Ohio 43210

ABSTRACT

The anodic behavior of high purity 18% Cr ferritic stainless steels, with a content from 0 to 5% molybdenum, was studied in 1*N* NaCl and in 1*N* HCl solutions. The studies were complemented by Auger electron spectroscopy analysis of the films in HCl solutions. It was found that the effect of molybdenum on the pitting potential of these alloys in NaCl solutions could be rationalized assuming that pit initiation is related to localized acidification at the metal-solution interface. The Auger analysis showed a high concentration of chloride ions in the films formed in HCl solutions. No molybdenum enrichment was found in the films. The anodic behavior of these alloys in HCl solutions was related to the formation of a slowly dissolving salt layer of $CrCl_3$ on the alloy surface. The results suggest that molybdenum exerts its influence by reducing the dissolution rate of the salt layer.

It is well documented in the literature (1-4) that molybdenum has a beneficial effect on the resistance of stainless steels to pitting in NaCl solutions. It was first assumed (5, 6) that molybdenum was enriched in the surface film, increasing its chemical resistance. Nevertheless, recent Auger electron spectroscopy (AES) analysis (7, 8) has shown that no molybdenum was enriched in the oxide film of molybdenum containing stainless steels.

Recent work on the pitting of metals (9) has indicated that many of the variables that affect the pitting potential can be related to localized acidification. According to this mechanism the alloying elements exert their effects by changing the anodic behavior in the acid solutions which exist inside pits. Then, the effect of molybdenum should not be found in enrichment in the oxide film, but rather in changing the anodic kinetics of the alloys in the pit-like solutions.

* Electrochemical Society Active Member.
[1] Present address: Comision Nacional Energia Atomics, Buenos Aires, Argentina.
[2] Present address: North American Rockwell, Science Center, Thousand Oaks, California 91360.

In the work reported herein, it was attempted to verify such a mechanism. Pitting potential measurements obtained by techniques such as scratching the metal surface (10) give the potential at which pits start from very small dimensions and grow to visible sizes. In the initial steps of pit growth no substantial changes of the electrolyte concentration should be found (9, 11); it was concluded that the chloride concentration inside the pits at the initial stage, for surfaces exposed to a 1*N* NaCl solution, should also be 1*N*. The pH inside pits has been measured for large pits only (12, 13) and values between 0 and 1 have been reported. No measurements have been reported for the initial stages of pit growth. Thus a 1*N* HCl solution was chosen in the present work to represent the pit-like solution.

Very good correlation was found between the values of pitting potential predicted by the acidification mechanism and those reported by Lizlovs and Bond (3) for the same alloys in a 1*N* NaCl solution.

Materials

The materials employed were high purity ferritic stainless steels having 18% Cr and containing 0-4.75% Mo. All the steels were annealed at temperatures which avoid the formation of chi and sigma phases. The alloys containing 0, 1, and 2% Mo were heat-treated for 1 hr at 815°C and then water quenched. The alloy containing 4.75% Mo was heat-treated for 1 hr at 980°C, followed by water quenching. Metallographic examination did not show the presence of intermetallic phases in any of the materials. The chemical composition of the alloys is given in Table I.

Experimental

The samples for the electrochemical measurements were mounted in bakelite metallographic mounting and mechanically polished; the final polish was alumina No. 3. An epoxy was used to mask the borders of the samples leaving exposed an area of approximately 1 cm^2. Electrical contact was made by drilling a hole through the mounting. The solutions were prepared with analytical-grade reagents and double distilled water and were deaerated with high purity argon. All the measurements were made at room temperature (24°C). Potentials were measured with respect to the saturated calomel electrode.

The polarization curves were determined in steps of 50 mV with the potential held constant for 10 min before the current was recorded. General dissolution occurred at potentials below −0.200V SCE. Above this potential pits were found on the surface.

Pitting-potential values were measured by the scratch technique described by Pessal and Liu (10). While the samples were kept at constant potential, the surface of the metal was scratched with an SiC point mounted on the Luggin capillary. The change of current with time was recorded to determine the repassivation time. After repassivation the potential was charged 25 mV and the surface was again scratched. This procedure was repeated until a potential was reached at which repassivation no longer occurred, *i.e.*, the pitting potential.

Pits were allowed to grow at constant potential and the mean current density inside the pits was calculated. All the pits observed were hemispherical; most of them were covered by a thin oxide film. This film was removed by light mechanical polishing. Measurements of the diameter of the pits were made under a microscope at 100 times. Assuming that the pit grew at a constant rate, the current density inside the pits was calculated

$$\text{Current density (A/cm}^2) = \frac{rd\mathbf{F}}{tE} \quad [1]$$

where r is the pit radius (in cm), d is the alloy density (in g/cm^3), **F** is the Faraday constant, t is the exposure time (in seconds), and E is the equivalent weight of the alloy. Assuming that iron dissolves as Fe^{2+} and chromium as Cr^{3+}, the mean equivalent weight is $E = 25$ g-equiv.

Table I. Chemical composition of the ferritic stainless steels

Stainless steel type	Element, w/o			
	Cr	Mo	C	N
18Cr-0 Mo	17.35	<0.01	0.002	0.003
18Cr-1Mo	17.53	1.14	0.003	0.004
18Cr-2Mo	17.61	2.02	0.004	0.004
18Ca-4.75Mo	17.38	4.75	0.004	0.004

Results

The pitting potential of these alloys in 1*N* NaCl solution has been reported previously by Lizlovs and Bond (3, 4). However, some of the measurements were repeated in the present work. Figure 1 shows a typical example of the results. This figure gives the current-time response of the 18Cr-1Mo alloy. The alloy was exposed at constant potential to a 1*N* NaCl solution. Up to +0.175V SCE, a current transient was observed after scratching the surface which returned to the initial value after 10-15 sec. Although the potential was kept constant for another 5-10 min, no further changes in the current were observed. This behavior was independent of the number of times the surface was scratched. At +0.200V SCE and after scratching, the current density was followed by a current increase, which after 1 min was 6×10^{-5}A, after 5 min reached 1.5×10^{-4}A, and was still increasing after 30 min. Microscopic observation of the samples showed that pits were nucleated along the scratch line.

The pitting potential values found in these experiments were in accordance with those reported by Lizlovs and Bond. After the current started to increase, samples were kept at constant potential for approximately 20-30 min to allow the pits to grow. Then they were removed from the cell and the mean radius of the pits was measured under the microscope. The current density inside the pits was calculated with Eq. [1], and the values found are given in Table II. The value obtained at the pitting potential was approximately 5×10^{-1} A/cm² for all the alloys tested.

Another important observation from these experiments is that in the range of 25 mV a transition from

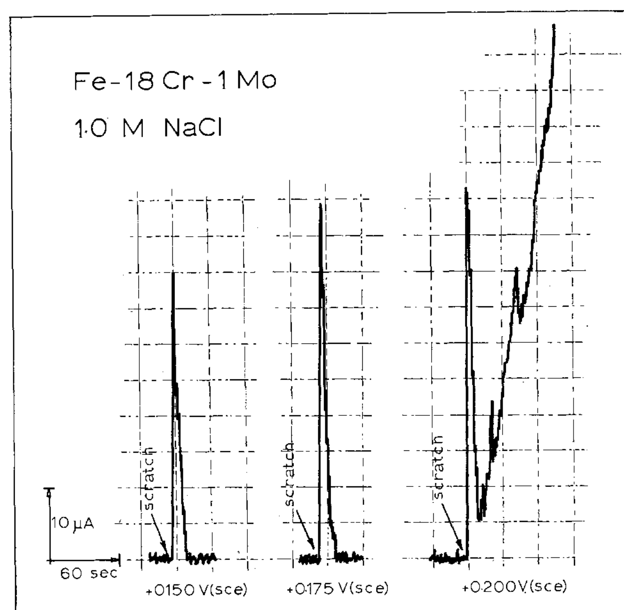

Fig. 1. Typical current-time curves recorded after scratching the metal surface with an SiC point, at constant potential. Type 18 Cr-1Mo ferritic stainless steel in deaerated 1*N* NaCl solution at 24°C.

Table II. Calculated current density inside the pits, at constant potential, deaerated 1*N* NaCl solution at 24°C

Stainless steel type	Potential V (SCE)	Current density (A/cm^2)
18Cr-0 Mo	+0.200	7.43×10^{-1}
18Cr-1Mo	+0.200	3.55×10^{-1}
18Cr-2Mo	+0.300	5.11×10^{-1}
18Cr-4.75Mo	+0.525	4.37×10^{-1}

repassivation after scratching to pitting after scratching takes place. It is concluded that no pits are nucleated, for example in Fig. 1, after scratching +0.175V SCE. Otherwise, even if the current density inside the pits was one order of magnitude lower than at +0.200V SCE, current changes should have been observed after a 5-10 min exposure at constant potential.

Anodic Behavior in 1*N* HCl Solution

Anodic polarization curves were measured for all the alloys in deaerated 1*N* HCl solution at 24°C (Fig. 2). The corrosion potential was found to increase with the molybdenum content, as shown in Fig. 3. The alloy with 4.75% Mo had a corrosion potential approximately 100 mV higher than that of the 18Cr-0 Mo alloy.

As the potential was increased above the corrosion potential, the current density also increased and the surface of the samples showed generalized etching. The current density continued to increase with potential up to approximately −0.300V, above which it began to decrease. At −0.200V the current density reached a minimum value, increasing again at higher potentials. Current densities which did not vary with time were found between the corrosion potential and −0.200V. For higher potentials the current density increased with time. All the samples exposed at potentials higher than −0.200V pitted.

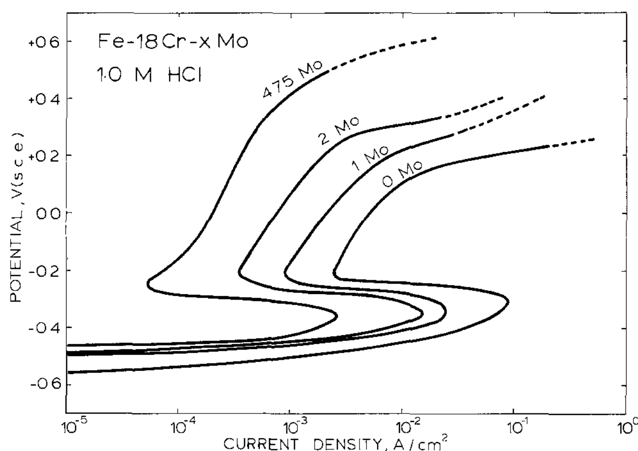

Fig. 2. Anodic polarization curves for Type 18Cr-X Mo ferritic stainless steels in deaerated 1*N* HCl solution at 24°C.

This time-dependent behavior at high potential was confirmed with the scratch technique. An 18Cr-1Mo alloy was exposed to the 1*N* HCl solution at constant potential. It was observed that at −0.400 and −0.300V the stationary current density was not affected by scratching the metal surface. The current density was also stable at −0.200V. After scratching the surface at this potential, the current increased but returned almost immediately to the initial value. At −0.100V, on the other hand, the current increased after scratching, and continued to increase with time. Pits were observed along the scratch.

These results show that curves like those in Fig. 2 are real polarization curves with true current densities only between the corrosion potential and −0.200V. For higher potentials the true polarization curve is not given by Fig. 2. To overcome this difficulty, constant potential experiments were performed with all the alloys at potentials higher than −0.200V. After exposure the pits were measured with a microscope, and the current density inside the pits was calculated using Eq. [1]. Figure 4 shows the composite polarization curves obtained by direct measurement below −0.200V, plus calculated current density values for higher potentials.

Figure 4 shows that the 18Cr-X Mo alloys underwent active dissolution between the corrosion potential and −0.200V. The current density in this zone, as reported by Lizlovs and Bond (3), was strongly affected by the molybdenum content of the alloy; the dissolution rate for the 18Cr-4.75Mo alloy was approximately two orders of magnitude lower than that for the 18Cr-0 Mo alloy. The active dissolution zone was followed by a reduction in the current density which could not be taken as a true passivation because of the high current densities involved. Above −0.200V (SCE) a process of localized corrosion entered into competition with the pseudopassivity. This transition took place at the same potential for all the alloys tested; thus it was not affected by the molybdenum content of the alloy. The current densities calculated, on the other hand, were strongly affected by the molybdenum content being almost two orders of magnitude lower for the 18Cr-4.75Mo alloy than for the 18 Cr-0 Mo alloy. The current density in this region followed a logarithmic law, with a slope ranging from 150 to 200 mV.

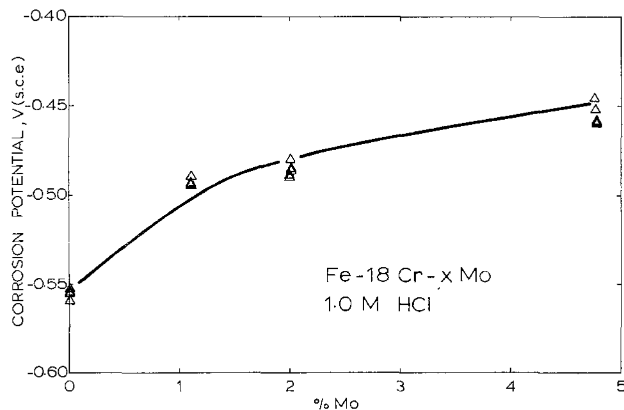

Fig. 3. Corrosion-potential values measured for Type 18Cr-X Mo ferritic stainless steels in deaerated 1*N* HCl solution at 24°C.

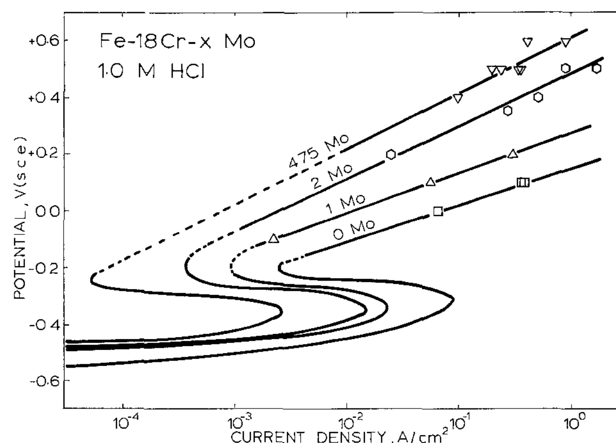

Fig. 4. Composite anodic polarization curves for Type 18Cr-X Mo ferritic stainless steels in deaerated 1*N* HCl solution at 24°C. Below −0.2V SCE direct current density measurements; above −0.2V SCE current density calculated with Eq. [1].

AES Analysis of Films Formed in HCl Solutions

AES analysis was used to identify the products responsible for the pseudo-passivity found in the anodic polarization curves. The samples were polarized in the active zone to dissolve any air-formed film, and then the potential was switched to −0.200V. Two different techniques were used to remove the samples from the cell. In one the potentiostat was switched off and the sample was removed, and washed with distilled water. It was then dried with hot air. In the second procedure, the technique used by Vetter and Strehblow (14) was applied. In this technique a layer of benzene is poured over the electrolyte in the cell. The sample is slowly removed from the electrolyte into the benzene layer without switching off the potentiostat. They were then washed with acetone and dried. The AES results were the same for both procedures.

Figures 5 and 6 show typical examples of the results found with AES analysis. The results are given as in previous publications (7, 15). It is assumed that the normalized peak heights are approximately proportional to the elemental concentration. Figure 5 gives the Auger analysis of the 18Cr-4.75Mo alloy which was polarized for 90 min at −0.400V. Figure 6 shows the Auger results for the same alloy which was polarized for 90 min at −0.400V, followed by 10 min at −0.200V.

The sputtering technique used removed about 3Å/min. No enrichment in molybdenum was found in the films on any of the alloys tested. There was a slight depletion of iron in the film plus a small enrichment in chromium. The oxygen content decreased uniformly from a high value in the near-surface layers until the metal-oxide interface was reached. One important feature found in this analysis was the high content in chloride in films formed at −0.200V and above. This is different from that which was reported for these alloys in NaCl solutions (8). The amount of chloride in the film increased with potential for potentials higher than −0.200V. There was also a tendency for alloys with higher Mo contents to have larger amounts of chloride in the film. However, the latter conclusion must still be taken as tentative. A few examples were found in which there was no change in the chloride content with Mo concentration in the alloy.

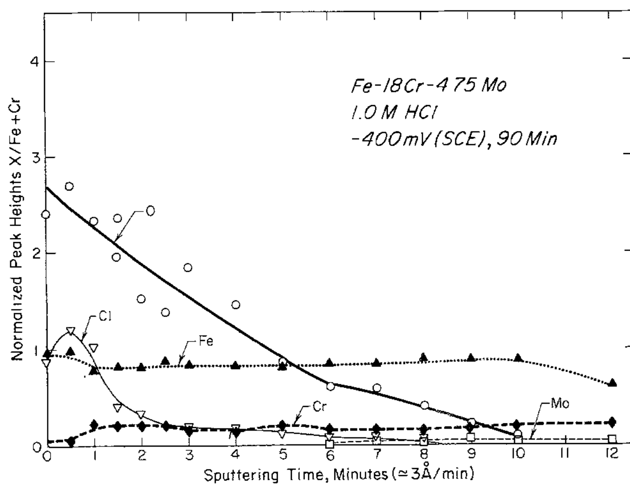

Fig. 5. Auger normalized peak heights vs. sputtering time for Type 18Cr-4.75Mo stainless steel polarized for 90 min at −0.400V SCE.

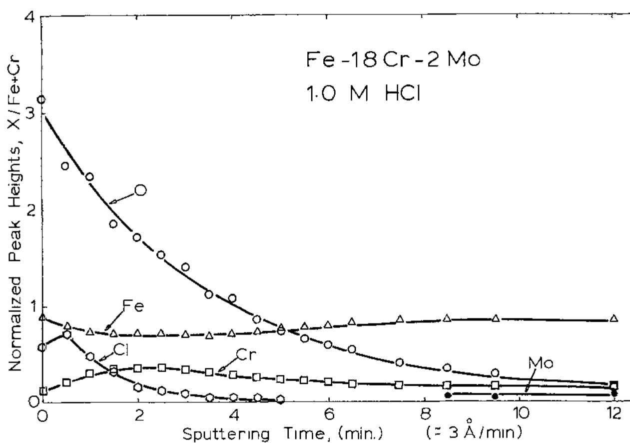

Fig. 6. Auger normalized peak heights vs. sputtering time for Type 18Cr-4.75Mo ferritic stainless steel polarized for 90 min at −0.400V SCE plus 10 min at −0.200V SCE in deaerated 1*N* HCl solution at 24°C.

Theoretical Pitting-Potential Calculation

According to the mechanism of localized acidification (9), the pitting potential of a metal or alloy in a neutral solution can be evaluated from the anodic behavior of the same metal or alloy in a low pH solution. The pitting potential in the neutral solution is given by

$$E_p = E_c{}^* + \eta + \phi + E_{inh} \qquad [2]$$

where E_p is the pitting potential, $E_c{}^*$ is the corrosion potential in the acidified solution, η is the polarization necessary to obtain a current density high enough to maintain acidity inside the pit, ϕ is the potential drop inside the pit, and E_{inh} is the contribution to the pitting potential due to inhibitors in the media.

$E_c{}^*$ was taken from Fig. 3, and η was taken from Fig. 4, assuming that the current density inside the pits at the pitting potential was 0.5 A/cm^2 (Table II). The values from Fig. 4 include the potential drop inside the pit; a high ϕ arises because of the technique used to evaluate the current density values. E_{inh} is ignored since no inhibitors were used in the measurement of the pitting potential in NaCl solutions.

Table III shows the calculated pitting potential values, as given by Eq. [2], compared with the experimental values reported by Lizlovs and Bond (3, 4). A very good correlation was found between the calculated pitting potential values and the experimental ones.

Discussion and Conclusions

Very good agreement was found between the pitting potential values predicted by Eq. [2] and those found experimentally. It is interesting to note that the pseudopassivity found in the polarization curves of the stainless steels in HCl solutions results in a high contribution of η to the pitting potential. In some systems, like high purity iron (16), high purity zinc (17), high purity cadmium (18), Al-Cu alloys (19), and Al-Zn alloys (11) in NaCl solutions, high current densities are obtained in acid solutions with small polarizations. In these cases the contribution of η to the pitting potential was small, and the pitting potential was found to be close to the corrosion potential inside the pit, $E_c{}^*$. In other systems, for example pure nickel (20), pure aluminum (19), Al-Mg (19), and 18 Cr-X Mo alloys in NaCl solutions, sizable polarizations had to be applied to obtain the necessary current density.

In the system studied in the present work, η is an important component of the pitting potential. The ex-

Table III. Pitting-potential values for 18Cr-X Mo alloys in 1*N* NaCl solution, calculated with Eq. [2], and compared with the experimental values reported by Lizlovs and Bond (4)

Stainless steel type	$E_c{}^*$	+	η	=	E_p	Experimental pitting potential V (SCE)
18Cr-0 Mo	−0.55	+	0.67	=	0.12	0.10-0.14
18Cr-1Mo	−0.49	+	0.74	=	0.25	0.16-0.22
18Cr-2Mo	−0.48	+	0.88	=	0.40	0.22-0.34
18Cr-4.75Mo	−0.45	+	1.00	=	0.55	0.52-0.56

perimental results described above could be used to attempt an explanation for this behavior. Lizlovs and Bond (3) reported that molybdenum had a big effect on the pitting potential of the ferritic stainless steels, and that the higher the chromium content of the alloys the more pronounced the effect of molybdenum. From the AES analysis it was found that there was a high chloride content in the film formed in the pseudopassive region in HCl solutions. The pseudopassivity could be due to the accumulation of a salt film of chromic chloride on the alloy surface. It is known that the dissolution rate of $CrCl_3$ is very slow (21, 22). The molybdenum could act by reducing this rate still further. The detailed mechanism by which this process occurs is not yet clear, but it is known that the presence of certain metal ions can change the dissolution rate of $CrCl_3$. For example, it was reported that in the presence of either Cr^{2+} or $SnCl_2$, the dissolution rate of $CrCl_3$ is significantly accelerated (21, 22). It is possible that molybdenum retards the dissolution rate of $CrCl_3$. According to Hedinfor *et al.* (21) the presence of oxidizing agents reduces the dissolution rate of $CrCl_3$. This agrees with recent publications (23) where it was reported that pitting corrosion of stainless steels was inhibited by the presence of MoO_4^{2-} ions in the solution.

From the above results it can be concluded that there are two ways by which the resistance of an alloy to pitting can be improved. One is by increasing E_c^*, *e.g.*, by accelerating the cathodic reaction inside the pit, and the other one is by increasing the value of η, *i.e.*, by reducing the dissolution rate of the metal in the acid solution.

Two processes of pitting were described in the present work. One was found in neutral NaCl solutions. There pitting started as the result of localized acidification, and Eq. [2] accounted for the effect of molybdenum on the pitting potential of the alloy. The other one was observed in HCl solutions. The pitting initiation potential was not affected here by the molybdenum content of the alloy. Molydenum changed the rate of pit propagation. The potential of pit initiation for 18Cr-X Mo alloys in HCl solutions could be related to either the potential of formation of $CrCl_3$ or to a potential-dependent dissolution rate of $CrCl_3$.

Acknowledgment

Support from the National Science Foundation, Contract No. DMR76-20807, is gratefully acknowledged.

Manuscript submitted June 3, 1977; revised manuscript received March 27, 1978.

Any discussion of this paper will appear in a Discussion Section to be published in the June 1979 JOURNAL. All discussions for the June 1979 Discussion Section should be submitted by Feb. 1, 1979.

Publication costs of this article were assisted by Ohio State University.

REFERENCES

1. S. Szklarska-Smialowska, in "Localized Corrosion," R. W. Staehle, B. F. Brown, J. Kruger, and A. Agrawal, Editors, p. 312, NACE, Houston (1974).
2. E. A. Lizlovs and A. P. Bond, *This Journal*, **116**, 547 (1969).
3. E. A. Lizlovs and A. P. Bond, *ibid.*, **122**, 719 (1975).
4. E. A. Lizlovs and A. I. Bond, *Corrosion (Houston)*, **31**, 219 (1975).
5. T. N. Rhodin, *ibid.*, **12**, 123t (1956).
6. T. N. Rhodin, *ibid.*, **12**, 465t (1956)
7. J. B. Lumsden and R. W. Staehle, *Scripta Met.*, **6**, 1205 (1972).
8. A. E. Yaniv, J. B. Lumsden, and R. W. Staehle, *This Journal*, **124**, 490 (1977).
9. J. R. Galvele, *ibid.*, **123**, 464 (1976).
10. N. Pessall and C. Liu, *Electrochim. Acta*, **16**, 1987 (1971).
11. K. J. Vetter and H. H. Strehblow, Ber. Bunsenges. *Phys. Chem.*, **74**, 1024 (1970).
12. B. E. Wilde and E. Williams, *Electrochim. Acta*, **16**, 1971 (1971).
13. T. Suzuki, M. Yamabe, and Y. Kitamura, *Corrosion (Houston)*, **29**, 18 (1973).
14. K. J. Vetter and H. H. Strehblow, in "Localized Corrosion," R. W. Staehle, B. F. Brown, J. Kruger, and A. Agrawal, Editors, p. 240, NACE, Houston (1974).
15. J. B. Lumsden and R. W. Staehle, in "Passivity and Its Breakdown on Iron and Iron Base Alloys," R. W. Staehle and H. Okada Editors, p. 75, NACE, Houston (1976).
16. C. J. Semino and J. R. Galvele, *Corros. Sci.*, **16**, 297 (1976).
17. M. G. Alvarez and J. R. Galvele, *Corrosion (Houston)*, **32**, 285 (1976)
18. M. G. Alvarez and J. R. Galvele, in "II Congreso Latinoamericano de Electroquimica," Rio de Janeiro, October 1974.
19. I. L. Muller and J. R. Galvele, *Corros. Sci.*, In press.
20. G. M. Alvarez and J. R. Galvele, To be published
21. A. Hendifar, W. F. Libbz, and G. L. Zimmerman, *J. Phys. Chem.*, **78**, 1923 (1974).
22. C. F. Baes and R. E. Mesmer, "The Hydrolysis of Cations," p. 211, John Wiley & Sons, New York (1976).
23. K. Sugimoto and Y. Sawada, *Corrosion (Houston)*, **32**, 347 (1976).

The Calcium Anode in Molten Nitrate Electrolytes

M. H. Miles,* D. A. Fine, and A. N. Fletcher*

Naval Weapons Center, Chemistry Division, Research Department, China Lake, California 93555

ABSTRACT

The electrochemical behavior of the calcium anode in molten nitrates was determined using constant current methods. Investigations were made in both $LiNO_3$ and KNO_3 at 350°C and in KNO_3-$LiNO_3$ (60-40 mole percent) over a temperature range of 250°-400°C. Differential scanning calorimetry studies were also made on calcium in many nitrate mixtures. No exothermic reactions were detected for calcium in any pure alkali metal nitrate melt; however, chemical reactions were apparent for many calcium-molten nitrate systems which contained added halide salts. The rate of the calcium electrode reaction is determined largely by the passivating oxide film formed on calcium in molten nitrates. The addition of halides that promote breaks in the film can greatly improve both the electrode kinetics and the open-circuit potential. With sufficient breakdown of the passivating layer, high current densities can be obtained for the calcium anode with very little polarization. The effectiveness of the added halides in reducing polarization generally decreased in the order $I^- > Br^- > Cl^- > F^-$. The experimental results can be explained by a passivating layer model involving specific adsorption of anions at the CaO/solution interface.

Molten nitrates are attractive for possible use in thermal batteries due to their favorable physical properties which include low melting points and high electrical conductivities. In addition, alkali metal nitrate melts are stable over a reasonable temperature range, have low volatility, and have a viscosity and surface tension similar to aqueous solutions (1, 2). Thermal batteries fulfill unique military applications which require rapid activation and high discharge rates for short time periods (3). Generally, thermal batteries operate at temperatures between 500° and 600°C using the LiCl-KCl [59-41 mole percent (m/o)] eutectic which melts at 352°C. Much lower melting points are possible with nitrate electrolytes; for example, KNO_3-$LiNO_3$ (57-43 m/o) melts at 132°C and KNO_3-$LiNO_3$-$NaNO_3$ (53-30-17 m/o) melts at 120°C (1, 2). Furthermore, problems associated with formation of a calcium-lithium alloy, $CaLi_2$, at the calcium anode in LiCl-KCl melts (3, 4) could be eliminated or perhaps controlled with the use of molten nitrates.

Since molten nitrates are strong oxidizing agents (5), a passivating film on the calcium surface is required to restrict the corrosive reaction of the molten nitrate with the calcium anode. This protective layer must also permit the passage of calcium ions into the solution during battery operation. Ideally, this film would act as a solid electrolyte interphase between the metal and solution and would be a good electronic insulator (6, 7). The formation of such passivating layers has been reported for the magnesium electrode in thionyl chloride solutions (6) as well as for the lithium anode in aqueous electrolyte (8, 9).

Alhough calcium anodes are often used in thermal batteries, there is very little literature data on the dissolution process for calcium in molten salts or in any other type of solution (10-14). The electrochemical behavior of calcium metal is reported in this paper, and experimental conditions are defined which yield promising results for the use of this anode in molten nitrates. The addition of certain salts is required to attack the passivating film sufficiently to permit high current densities with very little polarization.

Experimental

The electrochemical cell and electrodes are shown in Fig. 1. The calcium electrode was cut from sheet (ROC/RIC), 99%, 0.5 mm thick and generally had a geometrical area close to 1 cm². The major impurity in the metal is magnesium. The calcium sample was cleaned by treatment with dilute nitric acid in dimethyl formamide (DMF) until a bright, metallic surface was obtained and then rinsed in DMF. Connection to the working electrode was made by spot-welding the calcium metal to the aluminum lead wire. The back side and edges of the calcium electrode and the portion of the aluminum wire exposed to the solution were masked off by using a thin layer of Sauereisen cement (No. 1) which was quickly dried with use of a heat gun. The calcium surface was then recleaned with the nitric acid in DMF just prior to use. When the calcium electrode is placed in molten nitrates, a dark oxide forms on the electrode surface. By use of the external nickel lead wire, the calcium electrode was positioned within 1-2 mm of the tip of the Luggin capillary. A magnesium electrode cut from sheet (ROC/RIC), 99.8%, was prepared in a similar manner and used in several experiments.

All potentials were measured against a $Ag/AgNO_3$ (0.1m) reference electrode in KNO_3-$NaNO_3$ (50-50 m/o). A Tesla coil spark was used to form a minute hole through the glass tip of the reference electrode. This hole provided contact while allowing only minimal electrolyte leakage. The electrolytic resistance through this opening was generally greater than 10,000Ω. Small asbestos fibers sealed in glass were also used with good results when the fibers were kept small to minimize electrolyte leakage. The Ni/Ag junction of the reference electrode and the Ni/Al junction of the working electrode were positioned at about the same level in the cell to cancel thermocouple effects due to temperature gradients. A series of reference electrodes was kept for internal checks which generally gave potential readings within 10 mV. A platinum wire coil sealed to the cell wall served as the counterelectrode.

Temperature control was maintained by placing the electrochemical cell in a fluidized sand bath (Tecam) and measuring the temperature of the bath adjacent to the cell with both a digital thermocouple thermometer and a dial thermometer. The temperature readings generally agreed within 5°C. The electrochemical measurements were made using a Beckman Electroscan 30 instrument.

Molten salt solutions were prepared from reagent grade chemicals which were dried overnight in a vacuum oven at 150°C. Exactly 28g of nitrate salt were used in each experiment. When not in use, these salts

* Electrochemical Society Active Member.

Key words: calorimetry, current efficiencies, corrosion, halides, passivating layer.

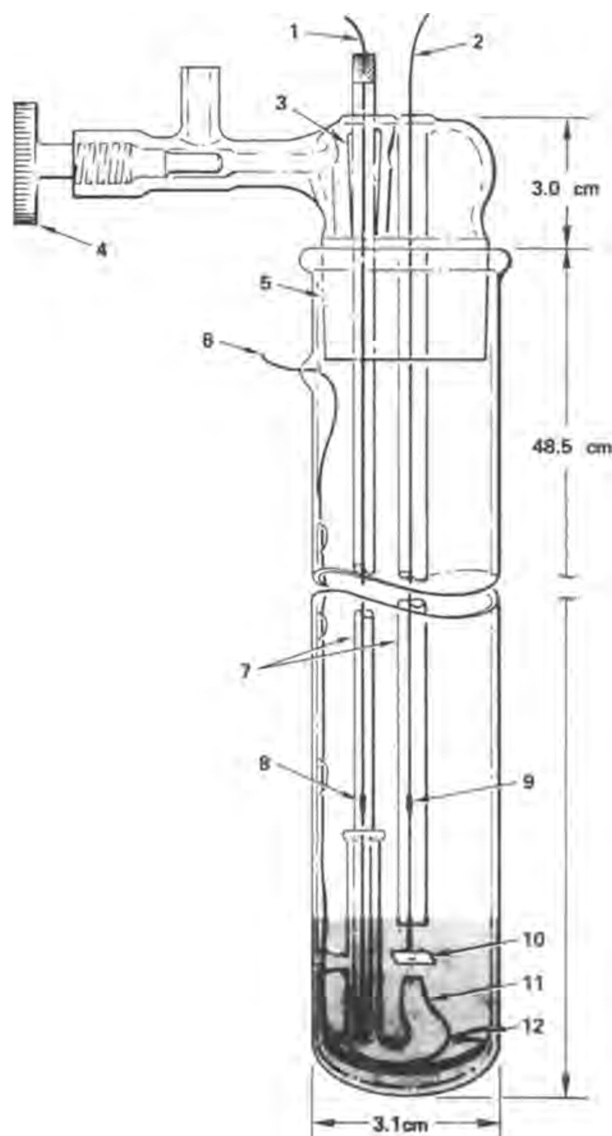

Fig. 1. Sketch of the electrochemical cell. 1, Reference electrode; 2, working electrode lead; 3, 7/25 standard tapered joint; 4, Teflon valve; 5, 29/26 standard tapered joint; 6, counterelectrode lead; 7, nickel lead wires; 8, Ni/Ag junction; 9, Ni/Al junction; 10, calcium electrode; 11, Luggin capillary; 12, platinum coil counterelectrode.

were stored in a desiccator containing anhydrous calcium sulfate (indicating Drierite).

The chemical reactivity of calcium with the various molten salt mixtures was determined using a differential scanning calorimeter (Perkin-Elmer DSC-1b). A temperature scan rate of 10°C/min was selected, and the resulting endotherms and exotherms were recorded using a strip chart recorder (Honeywell Electronik 194). For safety reasons, small samples were tested by this method before studies on larger samples in electrochemical cells were made. However, violent reactions of calcium with pure alkali metal nitrates were never observed, in contradiction to results reported by Brough and Kerridge (15).

Results

The electrochemical behavior of the calcium anode in molten nitrates was determined galvanostatically. Potential measurements were recorded at current settings of 100, 30, 10, 3, 1, and 0.3 mA/cm². Open-circuit potentials were also determined. The potential was generally recorded over a time period of 30-100 sec and was usually quite steady; however, the variation

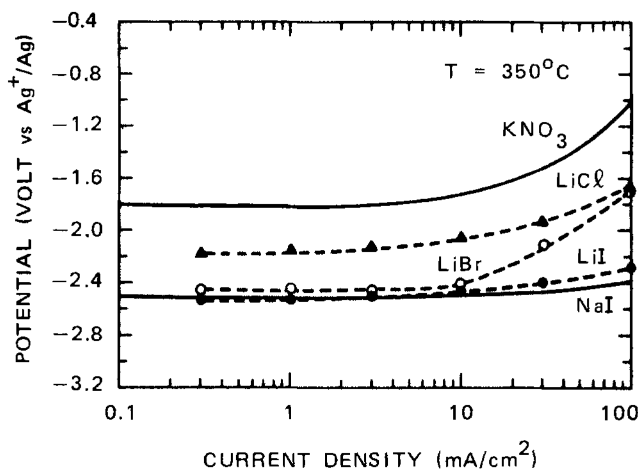

Fig. 2. Current density-potential measurements for the calcium anode in molten KNO_3 at 350°C. Effects of addition of 5 m/o LiCl, LiBr, LiI, or NaI to molten KNO_3.

was often greater at the higher current densities. Results for the calcium anode in molten KNO_3 at 350°C are shown in Fig. 2. The potential-current density line for calcium dissolution in pure KNO_3 represents the average results of nine different experiments. The standard deviation for the measured potentials ranged from ±0.14V at 100 mA/cm² to ±0.040V at 1 mA/cm². The other potential-current density lines in Fig. 2 show how additions of 5 m/o LiCl, LiBr, LiI, or NaI to the molten KNO_3 improve the performance of the calcium anode. For example, the addition of 5 m/o NaI changes the potential at 100 mA/cm² by more than 1.3V. The results shown for the addition of NaI represent the average of four different experiments. The good reproducibility of these experiments is reflected by the small standard deviations of ±0.022V at 100 mA/cm² and ±0.025V at 1 mA/cm². The results shown in Fig. 2 for solutions containing 5 m/o LiCl, LiBr, or LiI were obtained from single experiments which were repeated at least once to check for reproducibility. Table I summarizes the effect of other added salts on the calcium anode.

Constant current investigations of the calcium anode in molten $LiNO_3$ systems at 350°C are shown in Fig. 3. The addition of either LiCl or LiBr reduces the polarization. The amount of added salt also has a marked effect; *i.e.*, 10 m/o LiCl is much more effective in reducing polarization than the 5 m/o LiCl. In $LiNO_3$ containing 10 m/o LiCl, the open-circuit potential for the calcium anode was −2.83V at 350°C, and the polarization was small at the lower current densities. The current-potential line for calcium in pure $LiNO_3$ represents the average of four different experiments with standard deviations of ±0.056V at 100 mA/cm² and ±0.017V at 1 mA/cm², while the results for solutions containing 10 m/o LiCl represent the average of five experiments in which the standard deviation was ±0.155V at 100 mA/cm² and ±0.044V at 1 mA/cm².

Figure 4 shows the temperature effect on the potential-current density measurements for the calcium anode in KNO_3-$LiNO_3$ (60-40 m/o) containing 10 m/o LiCl. At the higher current densities, the polarization

Table I. Effect of potassium salts on the calcium anode in molten KNO_3 at 350°C

Electrolyte	Electrode potentials *vs.* Ag^+/Ag (V) 100 mA/cm²	10 mA/cm²	1 mA/cm²	Open circuit
KNO_3 + 5 m/o KF	−0.2	−1.2	−1.68	−2.7
KNO_3 + 5 m/o KCl	−1.6	−2.16	−2.22	−2.22
KNO_3 + 5 m/o KBr	−1.34	−1.81	−1.85	−1.85
KNO_3 + 5 m/o KI	−2.20	−2.32	−2.41	−2.41
Pure KNO_3	−1.02	−1.71	−1.81	−1.81

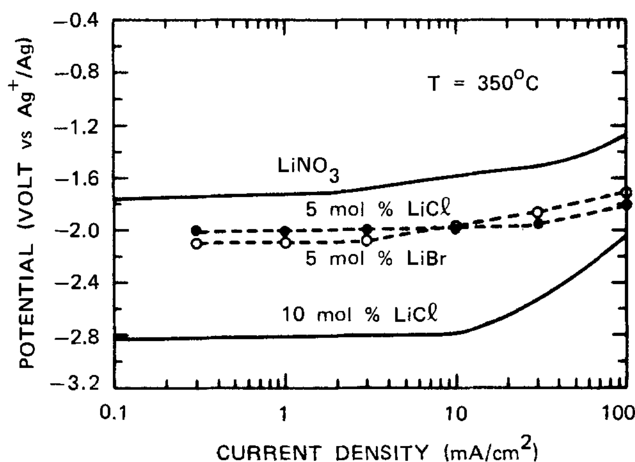

Fig. 3. Current density-potential measurements for the calcium anode in molten $LiNO_3$ at 350°C. Effects of addition of 5 m/o LiCl, 5 m/o LiBr, or 10 m/o LiCl to molten $LiNO_3$.

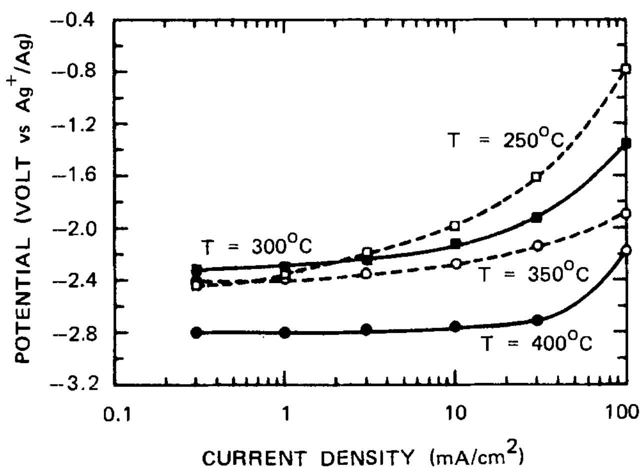

Fig. 4. Effect of the temperature on current density-potential measurements for the calcium anode in KNO_3-$LiNO_3$ (60-40 m/o) containing 10 m/o LiCl.

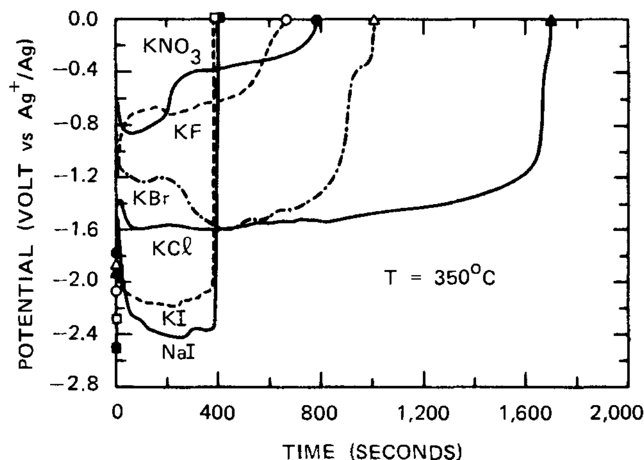

Fig. 5. Anodic dissolution of calcium at 100 mA/cm² in molten KNO_3 at 350°C. Effects of addition of 5 m/o halide salts: ■, NaI; □, KI; ▲, KCl; △, KBr; ○, KF; ●, pure KNO_3.

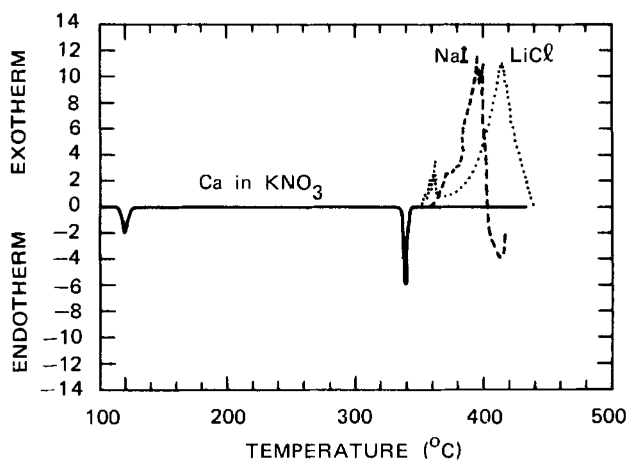

Fig. 6. Differential scanning calorimetry studies of calcium in KNO_3. Effects of addition of 5 m/o NaI or 5 m/o LiCl.

is greatly reduced as the temperature is increased from 250° to 400°C. The temperature effect is small at low current densities except for a notable improvement in the performance of the calcium electrode between 350° and 400°C.

Constant current experiments at 100 mA/cm² were used to determine the long-term behavior of the calcium anode as well as the current efficiency for the dissolution process. Potential *vs.* time plots are shown in Fig. 5 for the calcium anode in molten KNO_3 containing 5 m/o of various salts. Results in pure KNO_3 are also included for comparison. When dissolution of the calcium anode is complete, a sudden shift in the potential to large, positive values is observed. The most electronegative potentials are obtained when 5 m/o of NaI or KI is added; however, the short dissolution time periods indicate extensive reaction of calcium with the electrolyte when iodides are present. Since the calcium electrode weight was in the neighborhood of 70 mg/cm², the electrochemical dissolution of the electrode at 100 mA/cm² would require about 3400 sec if two electrons per calcium atom were obtained. The actual electron yields per calcium atom in various experiments are presented in Table II. Both the type of added salt and the experimental temperature affect the number of electrons obtainable per calcium atom. It is interesting to note that calcium in KNO_3 + 5 m/o KCl gave exactly one electron per calcium atom while smaller yields were obtained in all other experiments. In an experiment using a magnesium electrode in molten KNO_3 at 350°C, however, anodic dissolution at 100 mA/cm² gave a yield of 1.8 electrons per magnesium atom. The experimental potentials obtained using magnesium were generally about 0.8V less negative than those obtained with calcium.

Figure 6 shows differential scanning calorimetry (DSC) results for calcium in KNO_3 systems when a temperature scan rate of 10°/min is used. The actual baseline has been adjusted in this figure to make it horizontal. For calcium in pure KNO_3 (solid line), a lattice transition occurs at 120°C (129°C, lit.), and the KNO_3 melts at about 338°C (334°C, lit.). No exothermic reaction of calcium with molten KNO_3 is observed. In the presence of 5 m/o NaI (dashed line) or 5 m/o LiCl (dotted line), exothermic reactions are easily detected beginning at about 350°C.

Table III presents a partial summary of many other DSC studies of calcium in molten nitrate systems. No

Table II. Electron yield per calcium atom in molten nitrate systems

Electrolyte*	Temperature (°C)	e^-/Ca atom
$LiNO_3$ + 10 m/o LiCl	350	0.15
KNO_3 + 5 m/o NaI	350	0.22
KNO_3 + 5 m/o KI	350	0.22
KNO_3-$LiNO_3$ + 10 m/o LiCl	400	0.38
KNO_3-$LiNO_3$ + 10 m/o LiCl	350	0.50
KNO_3	350	0.52
KNO_3 + 5 m/o KF	350	0.52
KNO_3 + 5 m/o KBr	350	0.62
KNO_3-$LiNO_3$ + 10 m/o LiCl	300	0.75
$RbNO_3$-KNO_3 (70-30 m/o)	350	0.79
KNO_3-$LiNO_3$ + 5 m/o KCl	250	0.80
KNO_3-$LiNO_3$ + 10 m/o LiCl	250	0.88
KNO_3 + 5m/o KCl	350	1.0

* KNO_3-$LiNO_3$ mixture was 60-40 m/o.

Table III. DSC studies of calcium in nitrate/halide mixtures

Nitrate	Halide	Halide (m/o)	Endotherms (°C)*	Exotherms (°C)†
$LiNO_3$	KF	10.2	115, 125, 240	None
	LiCl	10.0	230	372, m
	KCl	10.2	164, 240	None
	KBr	10.2	220	365, s
	KI	10.3	240	340, s
$NaNO_3$	NaF	10.0	305	385, m
	KF	10.8	290	400, m
	CaF_2	9.9	310	414, w
	KCl	10.3	218, 282	415, m
	$CaCl_2$	10.3	280	350, s
	NaBr	10.2	300	395, m
	KBr	10.2	220, 285	405, s
	NaI	10.0	300	345, s
	KI	10.2	280	345, s
KNO_3	KF	10.9	118, 315	370, s
	KCl	10.5	120, 330	None
	KBr	10.3	116, 340	None
	KI	9.2	120, 345	386, s
$Na_{0.5}K_{0.5}NO_3$	KF	12.4	115, 220	390, m
	LiCl	10.5	114, 220	405, m
	KCl	12.7	118, 220	390, m
	NaBr	9.5	115, 214	398, s
	KBr	11.5	118, 215	410, s
	KI	10.1	120, 230	400, s
$RbNO_3$	NaF	11.1	160, 235, 317	388, m
	KF	11.0	150, 160, 260	357, s
	CaF_2	10.5	163, 235, 294, 320	None
	KCl	10.3	160, 325	None
	KBr	10.3	160, 290	435, w
	KI	10.2	165, 295	394, m

* Highest temperature is that of the melting endotherm; others are lattice transitions.

† The temperature given is that of the highest peak of the exotherm. Most exotherms were broad and many had several peaks. s = strong, m = moderate, and w = weak.

exothermic reactions were observed for calcium in any pure alkali metal nitrate melt. Exothermic reactions, however, were apparent for many calcium-nitrate systems which contained halide salts. Generally, with halide present but calcium absent, no exothermic reactions were detected in the molten nitrates; therefore the reactions involve the calcium metal. The magnitude of the exotherm usually increased with increasing concentration of the halide salt. In fact, at salt concentrations much above 10 m/o LiCl in $LiNO_3$, explosive reactions with calcium were observed near 400°C. Calcium with silver nitrate gave a violent reaction with a flash of light as soon as the silver nitrate melted. Evidence for metallic silver shows that this was simply the reaction of calcium metal with silver ions; $Ca + 2Ag^+ \rightarrow Ca^{++} + 2Ag$. This reaction becomes slower and controllable in KNO_3-$AgNO_3$ mixtures containing lower concentrations of silver ions.

Discussion

Examination of Fig. 2 and 3 and Table I suggests that both kinetic and thermodynamic properties are influenced by the passivating film on the calcium electrode. For example, Fig. 2 shows that the overvoltage at high current densities is greatly reduced when NaI or LiI is added to molten KNO_3 and a more negative open-circuit potential (OCP) is also established. In the absence of resistive films, most metal-metal ion electrode reactions in molten salts show high exchange current densities and very little true polarization (10).

The experiments show somewhat erratic trends on addition of halide salts to the molten nitrates. Judging from the potentials measured at 100 mA/cm² (Fig. 5 and Table I), the effectiveness of the added salt decreases in the order KI > KCl ~ KBr > KF while the current efficiencies (Table II) decrease in the order of KCl > KBr > KF > KI. The DSC studies (Table III) indicate that the ability of the halide salt to promote exothermic reactions with calcium decreases in the order KF ~ KI >> KBr ~ KCl in molten KNO_3 while the order is KI ~ KBr >> KCl ~ KF in molten $LiNO_3$. Figure 2 shows that the effectiveness of lithium salts added to molten KNO_3 decreases in the order LiI > LiBr > LiCl.

The experimental results for the calcium anode in molten nitrates can be interpreted in terms of the passivating layer model proposed in Fig. 7. A similar model has been used by Peled and Straze (6) to explain the behavior of the magnesium electrode in thionyl chloride solutions. Two interfaces are present in this model; the calcium/passivating layer interface involving the formation of calcium ions and the passivating layer/solution interface involving the passage of calcium ions into the solution. For calcium in molten nitrates, the passivating layer likely consists of CaO since electrodes which had become completely passivated in molten nitrates yielded the characteristic precipitate of $Ca(OH)_2$ when placed in water. Studies of the reaction of calcium in the $LiNO_3$-KNO_3 eutectic indicate that the net reaction is

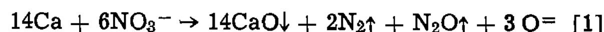

$$14Ca + 6NO_3^- \rightarrow 14CaO\downarrow + 2N_2\uparrow + N_2O\uparrow + 3\,O^= \quad [1]$$

according to analyses of the precipitate and gaseous products (15). In many experiments in this study, the slow evolution of colorless gas could be detected at the calcium electrode. This reaction also accounts for the relatively large exotherms shown in Fig. 6 since about 2900 cal are evolved per gram of calcium reacted compared with only 28 cal per gram for the heat of fusion of KNO_3.

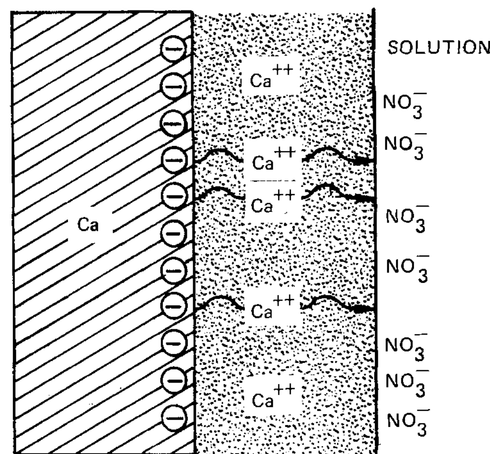

Fig. 7. Passivating layer model for the calcium anode in pure molten nitrates. The passivating layer is positively charged due to the excess concentration of calcium ions within the film. An excess of anions are electrostatically attracted to the passivating layer/electrolyte interface. Only anions at the interface are shown. A nonuniform distribution of anions is expected due to the preferential transfer of calcium ions through cracks or other imperfections in the passivating layer.

Corrosion of a metal requires both an anodic area where metal ions are transferred and a cathodic area where the surplus electrons can be transferred (16, 17). In battery systems, the corrosion rate of active metal anodes depends on the solubility of the protective film and on the transference number of the film for electrons (7). The slow corrosion rate for calcium in pure molten nitrates indicates a small transference number for electrons in the passivating layer as would be expected for an ionic compound such as calcium oxide. Assuming molten nitrates form ideal solutions (18), an unusually low solubility of 0.04 m/o is calculated for CaO at 350°C. The low solubility observed in molten nitrates for the CaO formed on the electrode surface indicates approximate agreement with this calculated value.

Oxidizing agents such as nitrates can act as anodic corrosion inhibitors by repairing faults in protective oxide films (16). As sketched in Fig. 7, the negative nitrate ions would normally be favorably positioned adjacent to the positively charged film. The adsorption of anions on electrodes, however, decreases in the order $I^- > Br^- > Cl^- \sim NO_3^- > F^-$ (19-21). The added I^- would displace NO_3^- from the electrode surface, thereby preventing the repairing of the film when

a break occurs. Pitting corrosion, which was usually observed with the effective salts, is believed to be caused by the inability of anodic inhibitors to rectify every fault in the protective oxide film (16). Other studies on active metals have also shown that halides have a tendency to promote pitting (22).

The effectiveness of iodide ions in reducing the polarization of the calcium anode may also be enhanced by their tendency to become oxidized in molten nitrates (1)

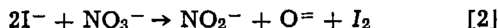

$$2I^- + NO_3^- \rightarrow NO_2^- + O^= + I_2 \qquad [2]$$

In fact, iodide salts could not be used in molten $LiNO_3$ at 350°C due to the rapid production of violet iodine fumes. In molten KNO_3, however, the reaction was much slower. Some yellow coloration developed at 350°C as the iodide salt dissolved to give regions of high local concentrations of iodide ions, but this gradually dissipated. Specific adsorption of iodide ions at the electrode surface giving high local concentrations could lead to reaction with nitrate ions to form I_2 or I_3^-. Faults developing in the passivating film enabling the iodine to react directly with calcium metal could account for the low current efficiencies (0.22 e^-/Ca atom) obtained in the presence of NaI and KI.

Since fluoride ions have a smaller tendency for anion adsorption than nitrate ions, their addition to the molten nitrate would have little effect on the passivating layer/solution interface. Breaks in the oxide film would be readily repaired by the chemical reaction of calcium with adsorbed nitrate ions leading to high overvoltages. In Fig. 5 the anodic dissolution of calcium in KNO_3 + 5 m/o KF is similar to that obtained in pure KNO_3. Both experiments gave large polarizations and low current efficiencies of 0.52 e^-/Ca atom (Table II). No pitting of the electrode surface took place in either experiment and a thick, brittle film gradually formed which had a final weight greater than the initial weight of the calcium. The increase in both the film thickness and the anodic polarization with the discharge time suggests that anions are injected into the passivating layer during discharge (7). In the presence of other salts such as KI or KCl, the calcium electrode was completely consumed so that only the Sauereisen backing remained. Experiments using KNO_3 + 5 m/o KF gave the electronegative open-circuit potentials expected for calcium, but these were unstable and unusually large polarizations occurred on drawing anodic currents. This may result from the penetration of the small fluoride ions into the film lattice and precipitation of CaF_2 clogging the pores of the film during anodic dissolution of the calcium.

The addition of chloride and bromide ions to molten nitrates generally gave results intermediate to those found for iodide and fluoride ions. Both apparently displace adsorbed nitrate ions sufficiently to permit breaks to exist in the passivating film. It is interesting to note that infrared studies in molten KNO_3-$Ca(NO_3)_2$ mixtures show that Cl^- ions can also displace NO_3^- ions from the $Ca^{2+}\cdot\cdot ONO_2^-$ complexes (23). The highest current efficiency observed (1.0 e^-/Ca atom) involved the use of 5 m/o KCl in KNO_3. A possible explanation is that chloride ions displace nitrate ions at the surface of the calcium oxide film which prevents the chemical reaction of calcium metal with nitrate ions when breaks in the film occur. Furthermore, the chloride ions are not oxidized by nitrate ions, hence, unlike iodide ions, they do not contribute to any other chemical reaction of calcium. In $LiNO_3$-KNO_3 melts, it is reported that iodide was oxidized by nitrate ions at 147°C, bromide ions reacted at 300°C, while chloride ions did not react until 470°C (1). The reactivity of the halides would be even less in pure KNO_3 since the lithium ion is a stronger Lux-Flood acid than the larger potassium ion (1, 24). The low current efficiency found for $LiNO_3$ + 10 m/o LiCl (0.15 e^-/Ca atom) may reflect the possible formation of the liquid $CaLi_2$ alloy (mp = 230°C) where breaks in the passivating film occur causing rapid corrosion.

The fact that exactly 1.0 e^-/Ca atom was obtained for the calcium anode in KNO_3 + 5 m/o KCl suggests that Ca^+ may be involved in the electrode reaction. Other experimenters have also proposed this possibility (12, 13, 25). The calcium electrode reaction in molten nitrates may then involve the steps

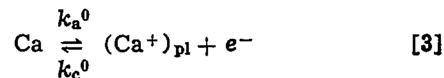

$$Ca \underset{k_c^0}{\overset{k_a^0}{\rightleftharpoons}} (Ca^+)_{pl} + e^- \qquad [3]$$

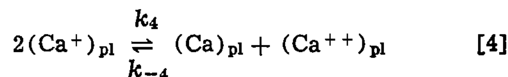

$$2(Ca^+)_{pl} \underset{k_{-4}}{\overset{k_4}{\rightleftharpoons}} (Ca)_{pl} + (Ca^{++})_{pl} \qquad [4]$$

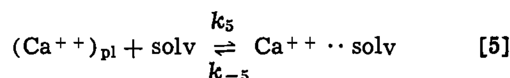

$$(Ca^{++})_{pl} + \text{solv} \underset{k_{-5}}{\overset{k_5}{\rightleftharpoons}} Ca^{++}\cdot\cdot\text{solv} \qquad [5]$$

where the parentheses denote a substance within the passivating layer. If the calcium atoms produced by the disproportionation reaction become isolated from the electrode and react with the solvent or solute, then the maximum current efficiency expected would be 1.0 e^-/Ca atom.

According to the above reaction mechanism, the current density would be given by

$$i = \mathbf{F}\cdot k_a^0 \cdot \exp\left(\frac{\alpha \mathbf{F} E}{RT}\right) - \mathbf{F}\cdot k_c^0 \cdot (a_{Ca^+})_{pl} \cdot \exp\left[\frac{-(1-\alpha)\mathbf{F}E}{RT}\right] \qquad [6]$$

where k_a^0 and k_c^0 are the formal anodic and cathodic rate constants at zero potential (26). The open-circuit potential (OCP) where $i = 0$ would then be

$$E_{OCP} = \frac{RT}{\mathbf{F}}\ln\frac{k_c^0}{k_a^0} + \frac{RT}{\mathbf{F}}\ln (a_{Ca^+})_{pl} \qquad [7]$$

When reaction [5] reaches equilibrium, then

$$(a_{Ca^+})_{pl} = \left(\frac{a_{Ca^{++}..solv}}{K_4K_5}\right)^{1/2} \qquad [8]$$

hence the equilibrium potential is

$$E_{eq} = \frac{RT}{\mathbf{F}}\ln\frac{k_c^0}{k_a^0} - \frac{RT}{2\mathbf{F}}\ln K_4K_5 + \frac{RT}{2\mathbf{F}}\ln a_{Ca^{++}..solv} \qquad [9]$$

where K_4 and K_5 are the equilibrium constants of the corresponding reactions. Equation [9] is simply the Nernst equation for the calcium electrode reaction with the first two terms representing the standard potential. The difference between the open-circuit potential and the true equilibrium potential is given by

$$\Delta E = E_{OCP} - E_{eq} = \frac{RT}{\mathbf{F}}\ln (a_{Ca^+})_{pl} + \frac{RT}{2\mathbf{F}}\ln K_4K_5 - \frac{RT}{2\mathbf{F}}\ln a_{Ca^{++}..solv} \qquad [10]$$

Although the passivating film does not affect the equilibrium potential, it can make the kinetics of reaction [5] so slow that true equilibrium cannot be readily attained during open-circuit potential measurements. The activities of Ca^+ and Ca^{++} in the passivating layer, therefore, build up to unusually high levels producing a positive shift in the open-circuit potential. Judging from the large shifts observed (Fig. 2 and 3), the activity of Ca^+ in the passivating layer may become 5-8 orders of magnitude larger than its equilibrium value. Addition of halides which produce breaks in the passivating film allows the excess calcium ions

to pass into the solution, thereby restoring the true equilibrium potential.

Chronopotentiometric studies of the lithium anode in aqueous electrolytes indicate that a concentration gradient of Li^+ ions exists across the oxide layer even at open circuit (9). Investigations of the calcium electrode in aqueous electrolytes show that the addition of chloride ions affects both the passivation and the observed open-circuit potential (14). The kinetic study of the magnesium electrode in thionyl chloride solutions shows that the migration of Mg^{++} through a passivating layer is the rate-determining step (6).

Conclusions

The protective oxide film formed by calcium in molten nitrates greatly influences the kinetics of the anodic reaction. The slow step appears to be the migration of calcium ions across the passivating film and into the solution. The addition of I^- and other halides capable of displacing NO_3^- ions from the passivating layer/solution interface promotes breaks in the film to give faster kinetics and more electronegative open-circuit potentials. High current densities can then be obtained with very little polarization. Therefore, the calcium anode in molten nitrates looks promising for applications in high discharge rate thermal batteries operating at temperatures between 300° and 400°C. A maximum current efficiency of 1.0 e^-/Ca atom observed experimentally suggests the involvement of monovalent Ca^+ in the electrode reaction. Results in molten $LiNO_3$ were often quite different from those in KNO_3 due to the stronger oxidizing power of the $LiNO_3$, and also, perhaps, to the formation of the liquid $CaLi_2$ alloy in molten $LiNO_3$.

Acknowledgments

The authors wish to thank Dr. S. Ruven Smith for bringing to their attention the Tesla coil technique of making pin holes in glass. A summer research position in 1977 for M. H. M. is gratefully acknowledged.

Manuscript submitted Dec. 13, 1977; revised manuscript received March 10, 1978. This was Paper 555 presented at the Seattle, Washington, Meeting of the Society, May 21-26, 1978.

Any discussion of this paper will appear in a Discussion Section to be published in the June 1979 JOURNAL. All discussions for the June 1979 Discussion Section should be submitted by Feb. 1, 1979.

Publication costs of this article were assisted by the Naval Weapons Center.

REFERENCES

1. D. H. Kerridge, in "Inorganic Chemistry: Main Group Elements, Groups V and VI," Series 1, Vol. 2, C. C. Addison and D. B. Sowerby, Editors, pp. 30-60, Butterworths, London (1972).
2. R. K. Jain and H. C. Gaur, *J. Electroanal. Chem. Interfacial Electrochem.*, **78**, 1 (1977).
3. C. W. Jennings, in "The Primary Battery," Vol. II, G. W. Heise and N. C. Cahoon, Editors, pp. 263-293, John Wiley & Sons, Inc., New York (1975).
4. R. P. Clark and K. R. Grothaus, *This Journal*, **118**, 1680 (1971).
5. J. Jordon, *J. Electroanal. Chem. Interfacial Electrochem.*, **29**, 127 (1971).
6. E. Peled and H. Straze, *This Journal*, **124**, 1030 (1977).
7. E. Peled, Paper 4 presented at The Electrochemical Society Meeting, Atlanta, Georgia, Oct. 9-14, 1977.
8. E. L. Littauer and K. C. Tsai, *This Journal*, **123**, 771 (1976).
9. E. L. Littauer and K. C. Tsai, *ibid.*, **123**, 964 (1976).
10. H. A. Laitinen and R. A. Osteryoung, in "Fused Salts," B. R. Sundheim, Editor, pp. 264-282, McGraw-Hill, New York (1964).
11. S. Toshima, in "Encyclopedia of Electrochemistry of the Elements," A. J. Bard, Editor, pp. 420-422, Marcel Dekker, Inc., New York (1973).
12. M. L. Rumpel, A. W. Davidson, and J. Kleinberg, *Inorg. Chem.*, **2**, 810 (1963).
13. A. L. Rotinyan, V. I. Zabolotskii, and K. I. Tikhonov, *Elektrokhimiya*, **9**, 225 (1973); *C. A.*, **78**, 118429k (1973).
14. J. F. Cooper and P. K. Hosmer, Paper 54 presented at The Electrochemical Society Meeting, Atlanta, Georgia, Oct. 9-14, 1977.
15. B. J. Brough and K. H. Kerridge, *Inorg. Chem.*, **4**, 1353 (1965).
16. E. C. Potter, "Electrochemistry: Principles and Applications," pp. 231-253, Cleaver-Hume Press, Ltd., London (1961).
17. J. O'M. Bockris and A. K. N. Reddy, "Modern Electrochemistry," Vol. 2, pp. 1267-1350, Plenum Press, New York (1970).
18. G. N. Lewis and M. Randall, "Thermodynamics," Revised by K. S. Pitzer and L. Brewer, 2nd. ed., chap. 18, McGraw-Hill Book Co., New York (1961).
19. P. Delahay, "Double Layer and Electrode Kinetics," pp. 53-65, John Wiley & Sons, Inc., New York (1965).
20. M. H. Miles and P. M. Kellett, *This Journal*, **117**, 60 (1970).
21. K. F. Lin and T. R. Beck, *ibid.*, **124**, 239C (1977).
22. J. Augustynski, *Corros. Sci.*, **13**, 955 (1973).
23. R. E. Hester and K. Krishnan, *J. Chem. Phys.*, **46**, 3405 (1967).
24. A. M. Shams El Din and A. A. El Hosary, *J. Electroanal. Chem. Interfacial Electrochem.*, **16**, 551 (1968).
25. R. D. Goodenough and V. A. Stenger, in "Comprehensive Inorganic Chemistry," Vol. 1, A. F. Trotman-Dickenson, Editor, pp. 624-625, Pergamon Press Ltd., Oxford (1973).
26. P. Delahay, "New Instrumental Methods in Electrochemistry," pp. 32-36, Interscience Publishers, Inc., New York (1954).

Analysis of SnNi Electroplate by Secondary Ion Mass Spectrometry, Ion Scattering Spectrometry, and Rutherford Backscattering

Rudolf Schubert

Bell Laboratories, Columbus, Ohio 43213

ABSTRACT

Two batches of SnNi electroplate, expected to be composed of equal atomic amounts of Sn and Ni, have been examined by secondary ion mass spectrometry, ion scattering spectrometry, and Rutherford backscattering. Tin oxides and hydroxides were found in the surface region, which is Sn-rich; no Ni oxides or hydroxides were seen. The Sn/Ni ratio for the two batches was 45/55 and 52/48 a/o. After Ar^+-sputter cleaning, films of the type which occur during and immediately after electroplating could not be reproduced in 10^{-6} Torr O_2. The regenerated films contained substantial amounts of nickel oxides and hydroxides.

Electroplated metastable SnNi is of technological interest for a broad range of metallic coating applications. It is suitable as a decorative coating and as a protective corrosion barrier (1). Usage as one of the electroplated components of electrical components has also been proposed (2). Its main attractive feature is that surface films on electroplated SnNi form rapidly in air or most aqueous solutions and exhibit a high degree of passivity to further corrosion (3-5). In order to understand the nature of these films, a detailed analysis is important.

With reasonable care during electroplating, the deposit is expected to have equiatomic composition (3), although a broad range of compositions can be plated (6). Current knowledge of the surface film composition has been obtained through Auger electron spectroscopy (AES), electron spectroscopy for chemical analysis (ESCA), and passivation potential curves. AES studies show the surface to be a tin-rich oxide (7) or a nickel polystannate (8). These two results are not in conflict since AES does not detect hydrogen nor chemical bonding in general. The ESCA study has reached a similar conclusion (9). Passivation-potential techniques indicate that the surface is nickel stannate (3, 4), however, with films that are only tens of angstroms thick (7, 9), electrochemical techniques are not sufficient to give an unambiguous analysis.

This paper describes the surface analysis of SnNi electroplate by three techniques; Rutherford backscattering (RBS), ion-scattering spectrometry (ISS), and secondary ion mass spectrometry (SIMS).

Experimental

The SIMS experiments were carried out in a stainless steel ion pumped UHV system. These included molecular composition depth profiles and film regeneration with O_2 exposure. A 2 keV focused Ar^+ ion source with variable current density has been described previously (10). Detection of secondary ions is made through an energy filter and quadrupole mass spectrometer equipped with an electron multiplier; this has also been previously described (11).

Ion-scattering spectroscopy experiments were done on a commercially available 3M ISS machine. 2 keV $^4He^+$ ions were used as the primary beam with the scattered ions being detected at 138° to the incident ions. Rutherford backscattering with 2 MeV $^4He^+$ ions was also carried out on the same samples used for the ISS measurements. Both of the techniques complement the SIMS measurements. RBS yields quantitative (12) elemental data (± 5% of component values) from a depth of approximately 1000Å, thus providing a quantitative bulk analysis to check the steady-state ISS values after sputtering through the surface film. One can now use these bulk values to find quantitative elemental data with depth profiling as the low energy ions sputter into the sample.

Electroplated SnNi samples were prepared at two separate times. Both sets of samples were plated in a conventional fluoride bath (13) with the current density (20 mA/cm^2), bath temperature (75°C), time and bath pH monitored and controlled. One set of samples was plated on stainless steel strips (SnNi/SS) which yielded chips (~15 mm^2) of SnNi when a bending (14) stress was applied to the plated stainless steel. All measurements were made on the surface opposite that in contact with the stainless steel. The second set of samples was barrel plated on Cu coupons (SnNi/Cu). Plating thickness was several microns. In addition, pure Ni and pure Sn samples were used to calibrate the spectrometers for relative sensitivity and oxidation studies.

Results

Typical relative intensities of the positive and negative Ni and positive Sn containing secondary ions from natural air-formed surface oxide films are listed in Table I for pure material. Also listed are the relative

Key words: corrosion, surface films, depth profies, oxidation.

Table I. Relative* intensities of Ni- and Sn-containing secondary ions from pure Ni and Sn

	$^{58}Ni^+$	$^{58}Ni_2^+$	$^{58}NiOH^+$	$^{58}NiO^-$	$^{58}NiO_2^-$	$^{120}Sn^+$	$^{120}SnH^+$	$^{120}SnO^+$	$^{120}SnOH^+$
Air-oxidized natural film pure metals	91	3.2	<0.65	17	23	1000	3.7	8	12
After sputter cleaning	82	ND	ND	ND	ND	64	ND	ND	ND
After O_2 exposure of 1100L	1500	7.8	10	NM	NM	128	ND	3.2	ND
After O_2 exposure of 3300L						256	ND	4	ND

ND—not detected.
NM—not measured.
* Relative to $^{120}Sn^+$-air oxidized natural film.

Table II. Relative* intensities of Ni- and Sn-containing secondary ions from SnNi/SS electroplate surface

	$^{58}Ni^+$	$^{58}NiO^+$	$^{58}NiOH^+$	$^{58}NiO^-$	$^{58}NiO_2^-$	$^{120}Sn^+$	$^{120}SnH^+$	$^{120}SnO^+$	$^{120}SnOH^+$
Natural film from plating bath and air	380	ND	ND	ND	ND	1000	10	11	24
After sputter cleaning	19	ND	ND	ND	ND	29	ND	ND	ND
After O_2 exposure of 6000L	680	15	18	NM	NM	140	T	9.6	37
After O_2 exposure of 19,000L	1040	34	25	NM	NM	150	T	9.6	59

ND—not detected.
NM—not measured.
T—trace.
* Relative to $^{120}Sn^+$—natural film from plating bath and air.

intensities of positive ions formed after the surfaces were sputtered clean. For sputter-cleaned data, the precision of the data is ± 50%. Exposure for up to 3.3 × 10^{-3} Torr sec of O_2 in the vacuum system was made. The SIMS ion beam was on during the O_2 exposure, however, its effect is negligible since the arrival rate of O_2 to Ar ions is ~10^3. During oxygen exposure, H_2O and H_2 were less than 1% of the total pressure of 2 × 10^{-6} Torr. Similar results are presented for SnNi/SS electroplate in Table II.

Depth profiles of both batches of SnNi electroplate were made with positive ion-detection SIMS. Six segments of the mass range from 1 to 140 were scanned repeatedly using a 6 amu width. These segments were at amu's 1-7, 12-18, 57-63, 73-79, 118-124, and 134-140. By scanning segments of the mass range one could check for the proper isotopic abundance and chemical combinations with hydrogen. Segment scanning also allows one to skip the mass ranges where there are no masses of interest. Depth profiles of H, CH, Ni, Sn, ^{120}SnH, $^{119}SnOH$ and ^{120}SnO, and $^{120}SnOH$ are shown for SnNi/SS and SnNi/Cu in Fig. 1 and 2, respectively. NiH^+, NiO^+, or $NiOH^+$ were not seen in positive SIMS in the samples with naturally formed films, nor was NiO^- or NiO_2^- seen by using negative SIMS. The above data are typical of three samples from each electroplating batch.

Impurity differences between the two electroplated sample batches exist. SnNi/Cu samples had approximately 10 times more Ca and CaOH present than the SnNi/SS. The total Ca impurity was still only a fraction of a percent. Higher Ca concentrations are attributed to a leak between the electrodeposition bath and the cooling system bath.

Two samples of each batch were also analyzed by RBS using 2 MeV $^4He^+$. Results showed different amounts of Sn and Ni in the two batches. The SnNi/Cu had a Sn/Ni = 45/55 atomic percent (a/o) and the SnNi/SS had a Sn/Ni = 52/48 a/o. This is a greater difference than the ±2% precision of the samples analyzed and the accepted component accuracy of ±5% for the RBS technique (12).

The same two samples were then sputter profiled by ISS with a sputtering rate of ~0.5 Å/min. As expected, only Sn and Ni peaks were distinctly seen. A typical profile (±2% precision) from each electroplate

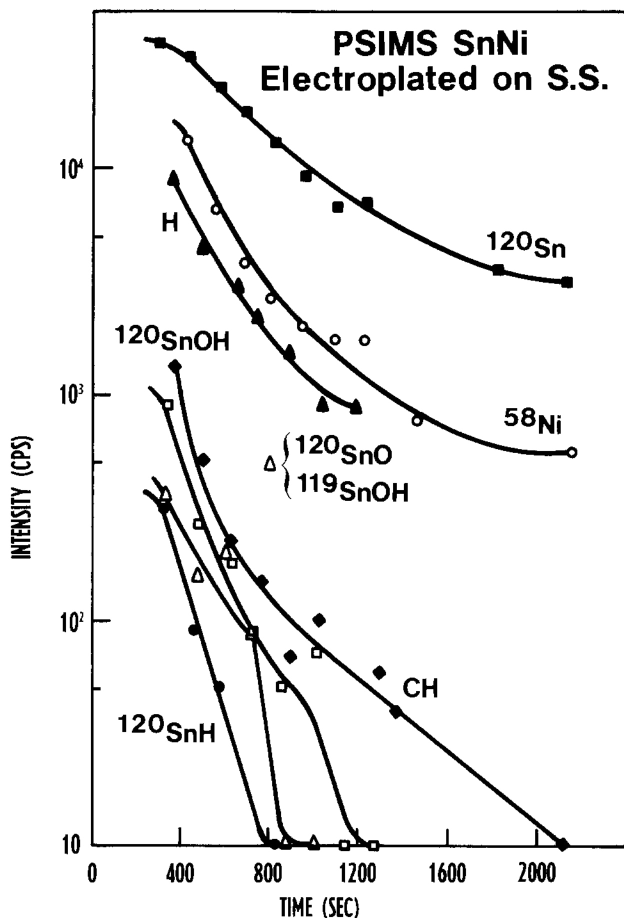

Fig. 1. Positive SIMS depth profile of electroplated SnNi on stainless steel. No NiH^+ or $NiOH^+$ were seen in the positive spectrum, nor were NiO^- or NiO_2^- seen in the negative spectrum. Primary 2 keV Ar^+ beam density was 0.065 μA/cm² which equals 4 × 10^{12} Ar^+/sec-cm². The surface monolayer of material was lost during sample alignment and beam stabilization. Data has been adjusted for isotopic abundances.

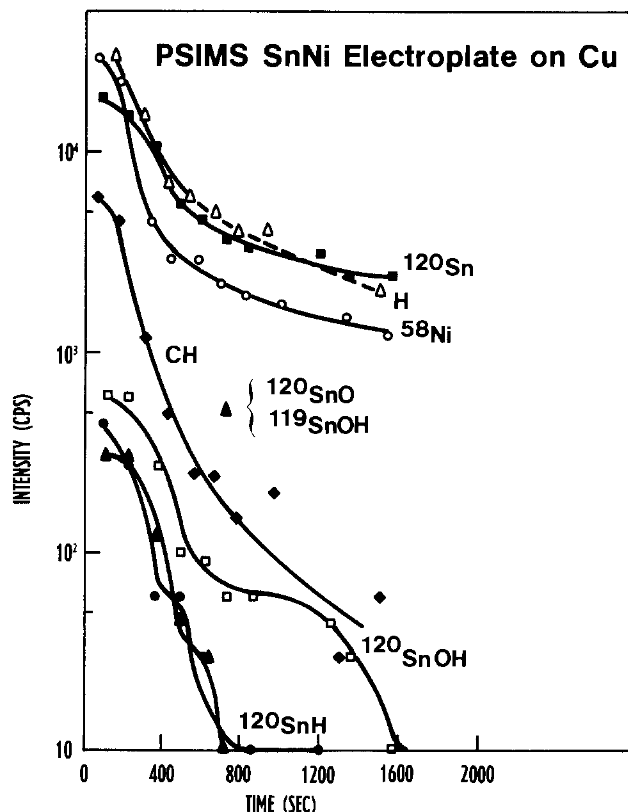

Fig. 2. Positive SIMS depth profile of electroplated SnNi on OFHC Cu coupons. Comments of Fig. 1 are applicable here also.

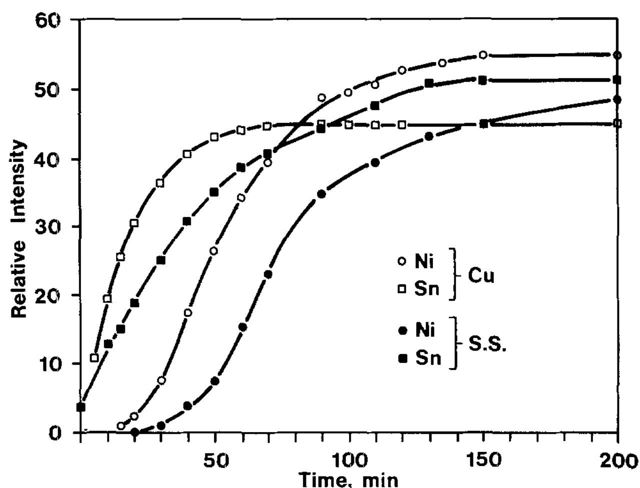

Fig. 3. Depth profiles determined by ISS on electroplated SnNi. Signals were normalized from RBS data on Cu-backed samples such that the total signal was 100%. Assuming a sputtering rate of unity, the sputtering rate is calculated as ~0.5 Å/min.

batch is shown in Fig. 3. The data were normalized such that the Sn/Ni ratio of the samples on Cu at steady state was the same as for RBS and the total was 100%. The same normalization factor was then applied to the SnNi/SS sample and the Sn/Ni ratio was found to be 52/48 after steady state was achieved, indicating consistency between ISS and RBS techniques.

The lack of ISS signal for the initial times in Fig. 3 is very normal for air-exposed samples which have not been cleaned in UHV. ISS ($^4He^+$) does not detect H at all. The sensitivity to C is also extremely poor. In general, hydrocarbons and other air contaminants neutralize the reflected beam and shadow the underlying metal atom (15).

Discussion

Pure Sn and Ni.—All the data in Tables I and II are normalized to a $^{120}Sn^+$ signal of 1000 for a natural air-formed film. The effects of oxygen on the ion yields of pure Ni samples are in agreement with other work (16), but no data could be found for Sn. It is important to note the different surface chemistry occurring in samples that have been sputter cleaned and then exposed to O_2 as compared to air-formed films. In Table I one sees that the $^{58}Ni^+$ signal from an air-formed film on Ni is approximately 16 times lower than the signal from an O_2 exposure after sputter cleaning. It is well known that oxygen strongly enhances the secondary ion yields of most elements (17). This is an electronic surface structure or chemical-bonding effect due to the interaction with the electronegative oxygen. Table I also shows that the $^{120}Sn^+$ signal behaves substantially different than the Ni. The Sn^+ yield is greatest after a natural air film has formed. Obviously the interaction of the other gases contained in air also plays a role in the film formation since the SIMS signals are so different between air and oxygen formed films. Although the exposure is much smaller in this experiment as compared to the air exposure of the native film, it is not probable that the oxides formed would decrease with longer exposures and reach the low Ni^+ yield of air-formed films. The data in no way suggest that there is more or less metal present at the surface, but rather that the surface matrix is a different chemical entity for the two formation conditions.

SnNi electroplate.—This matrix effect is also very evident in the SnNi electroplate. In the initial film the Ni SIMS signal was higher than the signal from the pure Ni, whereas by ISS, as discussed below, and Auger (7, 14) the Ni concentration was actually less than 50% in the near surface region. Conversely, substantially greater O_2 exposures are needed to enhance the Ni^+ signal from the electroplate as compared to the pure material when normalized to the 120 Sn signal. The Sn^+ is also less enhanced by O_2 exposure when it is in the SnNi matrix. However, the Ni and Sn hydroxide signals were much larger in the regenerated film than in the initial film, even though less than 1% of the gas was H_2O and H_2. As expected, Table I and II do not have a one-to-one correspondence, but the trends of both Sn and Ni are similar with regards to ion yields even though their matrixes are substantially different.

From the above discussion it is evident that caution must be used when interpreting results of cleaned surfaces as compared to electroplated and air-formed surfaces, as has been reported by others (18).

Sharma and Thomas (18) have reported that sputtering of the surface and later exposure to air and O_2 does not reproduce the native surface films. Recently, Antler (19) has reported that partial etching in a HCl bath *vs.* complete etching appears to have different regrowth kinetics of films as determined by contact-resistance measurements. This paper shows that Ni compounds form much more readily on the sputter-cleaned surface than on the native electroplate.

Typical SIMS depth profiles shown in Fig. 1 and 2 from the two batches of electroplated material indicate that the batches are not the same. Looking at the figures one sees that the bulk ratios of Sn to Ni are different. However, the ratio differences are much greater than the precision of ±2% per component from RBS, ISS, and AES measurements (7,8,14). (Sn/Ni)Cu is 2/1 and (Sn/Ni)SS is ~6/1. Since SIMS data derived from an Ar^+ beam are not quantitative with present theories (20-22), the SIMS depth profiles indicate only relative depth, chemical compounds, and approximate concentrations.

Figures 1 and 2 also show a hydrocarbon signal. Only mass 13 is plotted, although many others are present. They appear to be surface contaminants as is found on all samples which have been in room air. The H^+ signal is much higher at deeper levels from the surface in the Cu-backed film as is the $SnOH^+$ signal. It cannot be said what percentages of the H^+ signal were due to free hydrogen in the film, decomposition of hydrocarbons, or to decomposition of tin hydroxide. At no time could NiO^+ or $NiOH^+$ ions nor any negative Ni oxide ions be detected in the native film. It is calculated from Table I, Row I [also Ref. (15)] that the routine lower detection limit of nickel oxides with SIMS is of the order of 0.5% of the surface concentration of Ni. This work is in agreement with ESCA results (9) which required signal time averaging of $>6.5 \times 10^4$ sec to indicate nickel hydroxides.

The conclusion drawn from the above discussion is that the two batches of electroplate have different compositions and surface films after electroplating.

It is very questionable if the differences are attributable to the two different substrate materials (Cu and stainless steel), since in both batches the electroplate is several microns thick. Similarly, length of time in the laboratory environment should not be a factor since the SnNi/SS film has less oxide but is 12 months older. Atomic surface composition and possibly surface chemical structure (*i.e.*, the different Sn/Ni ratios reported above), appear to play a major role.

Conclusions

Two batches of electroplated SnNi were carefully plated under controlled conditions and expected to have equal atomic percentages of Sn and Ni. They have subsequently been examined by SIMS, RBS, and ISS. RBS has shown the Sn/Ni ratio to vary from 45/55 to 52/48 a/o. In both cases the surface regions were Sn rich as found by ISS. Natural surface films were shown to be primarily Sn oxides and hydroxides;

no Ni oxides or hydroxides were found. Surface films formed in 10^{-6} Torr of O_2 after removal of native films by Ar^+ sputter cleaning were not the same as the original films since they contain substantial amounts of nickel oxides and hydroxides.

Acknowledgments

The author thanks G. V. McIlhargie for supplying the samples. RBS and ISS measurements were made by J. C. Nelson of Sandia Laboratories.

Manuscript submitted Oct. 14, 1977; revised manuscript received March 20, 1978.

Any discussion of this paper will appear in a Discussion Section to be published in the June 1979 JOURNAL. All discussions for the June 1979 Discussion Section should be submitted by Feb. 1, 1979.

Publication costs of this article were assisted by Bell Laboratories.

REFERENCES

1. International Nickel Co., *Nickel Top.*, **27**, 11 (1974).
2. G. C. Wilson, *Trans. Inst. Metal Finish.*, **50**, 109 (1972).
3. M. Clarke and S. C. Britton, *Corros. Sci.*, **3**, 207 (1963).
4. M. Clarke and R. G. P. Elbourne, *ibid.*, **8**, 29 (1968).
5. M. Antler, M. Feder, C. F. Hornig, and J. Bohland, *Plate. Surf. Finish.*, **63**, 30 (1976).
6. P. K. Dutta and M. Clarke, *Trans. Inst. Met. Finish.*, **46**, 20 (1968).
7. H. G. Tompkins and J. E. Bennett, *This Journal*, **123**, 1003 (1976).
8. T. P. Hoar, M. Talerman, and E. Trad, *Nat. Phys Sci.*, **244**, 41 (1973).
9. J. H. Thomas III and S. P. Sharma, *J. Vac. Sci. Technol.*, **14**, 1168 (1977).
10. R. Schubert, *ibid.*, **11**, 903 (1974).
11. R. Schubert and J. C. Tracy, *Rev. Sci. Instrum.*, **44**, 487 (1973).
12. J. W. Mayer and A. Turos, *Thin Solid Films*, **19**, 1 (1973).
13. Technical Data Sheet 140, Metal and Thermit Corp., Rahway, N.J. (1955).
14. J. E. Bennett and H. G. Tompkins, *This Journal*, **123**, 999 (1976).
15. H. H. Brongersma and T. M. Buck, Paper submitted to *Nucl. Instrum. Meth.*
16. A. Benninghoven, *Surf. Sci.*, **53**, 596 (1975).
17. C. A. Anderson, *Int. J. Mass. Spectrom. Ion Phys.*, **2**, 61 (1969) and **3**, 412 (1970).
18. S. P. Sharma and J. H. Thomas III, *Anal. Chem.*, **49**, 7, 987 (1977).
19. M. Antler, *This Journal*, **125**, 420 (1978).
20. C. A. Anderson and J. R. Hinthorne, *Anal. Chem.*, **45**, 1421 (1973).
21. A. E. Morgan and H. W. Werner, *ibid.*, **48**, 699 (1976).
22. D. S. Simons, J. E. Baker, and C. A. Evans, Jr., *ibid.*, **48**, 1341 (1976).
23. L. DeGalan, R. Smith, and J. D. Winefordner, *Spectrochim. Acta.*, **23B**, 521 (1968).

On the Functioning and Malfunctioning of Dimercaptothiadiazoles as Leveling Agents in Circuit Board Plating from Copper Pyrophosphate Baths

Dennis Tench* and Cameron Ogden*

Rockwell International Science Center, Thousand Oaks, California 91360

ABSTRACT

Foldback of copper electrodeposits to form lines of demarcation and voids in circuit board through-holes plated from pyrophosphate baths containing dimercaptothiadiazole brightening additives has been studied on rotating planar electrodes prepared from cross sections of actual multilayer circuit boards. The macro surface roughness of deposits was used as a quantitative measure of foldback to show that this problem results from a deficiency of the brightener at the electrode surface. Cyclic voltammetric data for a rotating Pt-disk electrode are presented which show that higher concentrations of the brightener inhibit or decelerate the copper deposition rate, whereas lower concentrations exert an accelerating effect. A mechanism is proposed to explain how acceleration of deposition occurs and how the brightener functions to induce leveling or malfunctions to produce foldback. Scanning-electron micrographs revealing deposit morphology are presented in support of this mechanism.

A key process in the manufacture of multilayer circuit boards is the plating of through-hole interconnections, which involves both electroless and electrodeposition methods. When high reliability is required, as in military and space applications, through-holes are frequently electroplated from copper pyrophosphate baths (1). An organic leveling additive widely used is proprietary brightener PY61-H (2, 3), whose active ingredient is a dimercaptothiadiazole. To our knowledge, the mechanism by which this additive functions to produce leveling has not previously been reported.

An important problem in through-hole plating from pyrophosphate baths is foldback of copper electrodeposits to form lines of demarcation and voids, as illustrated by the cross section in Fig. 1. In addition to being cosmetically undesirable, folded-back deposits may fail on thermal cycling or be too thin to meet specifications. This problem occurs predominantly at the insulator-conductor boundaries, especially after positive etch-back. The latter procedure recesses the insulating layers relative to the conducting sheets, forming ring-shaped pockets where conventional solution agitation is expected to be less effective in maintaining adequate concentrations of solution species. This suggests that mass transport in the electrolyte is an important factor in the foldback problem. Irregular deposition of copper can result from Cu^{++} depletion within substrate recesses, and this effect has recently been treated

* Electrochemical Society Active Member.

Key words: electroplating, copper pyrophosphate, dimercaptothiadiazoles, leveling mechanism, foldback.

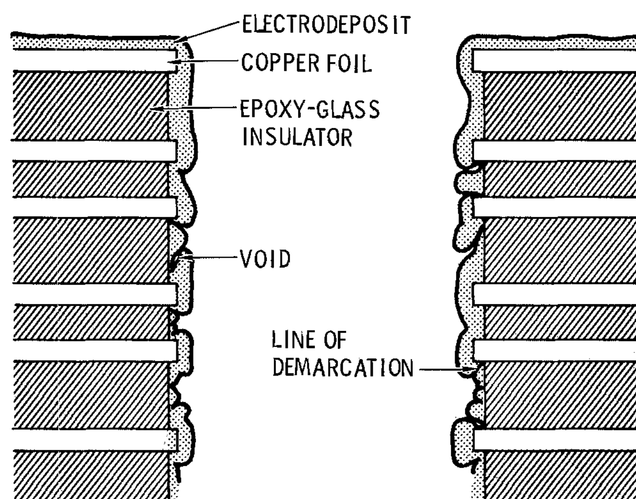

Fig. 1. Representation of foldback of the copper electrodeposit in a circuit board plated through-hole.

quantitatively for the acid copper sulfate system in the literature (4, 5). However, our results show that foldback is a special case involving brightener depletion, with Cu^{++} ion transport playing only a secondary role.

Experimental Details

Rotating circuit board electrodes.—Electrodes were prepared for foldback studies by mounting 3 mm^2 circuit board cross sections (having 12 copper layers) flush with the ends of 12 mm diam Teflon right cylinders which could be rotated for accurate mass transport control in the solution. This type of electrode is illustrated schematically in Fig. 2, where parallel lines on the circuit board material represent alternate copper layers of ~0.05 mm thickness separated by 0.1-0.3 mm of epoxy-fiberglass insulator. The mounting material (Hysol epoxy R9-2039/H9-3469) used to seal the circuit board cross sections in the 7 mm diam holes in the Teflon cylinders was chosen because of its similarity to the G-10 epoxy (Mica Corporation) used in circuit board construction. Electrical contact was made to a rotating shaft through the threaded brass connector, which was bonded to the circuit board electrode by low temperature soldering.

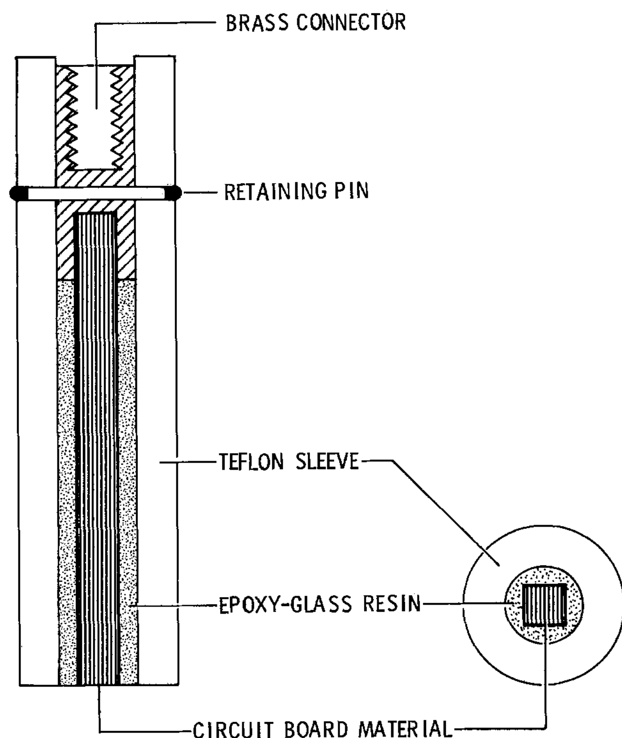

Fig. 2. Representation of a planar rotating circuit board electrode

Circuit board electrode pretreatment.—After fabrication, electrodes were polished on 600 grit SiC paper before undergoing etch-back, conditioning, and activation treatments identical to those generally used to process actual circuit boards. All baths used for these treatments were proprietary formulations of Enthone, Incorporated, except the deionized water rinses, copper pyrophosphate plating baths (M&T Chemicals, Incorporated), and H_2SO_4 and HF solutions. All baths operated at room temperature, except Enplate 453 and copper pyrophosphate, which were maintained at 55°C. During the pretreatment procedure, the electrode was always rotated at ~200 rpm. Details of this procedure follow.

The etch-back procedure removes epoxy-fiberglass insulator material smeared onto the copper layers by polishing (drilling in the case of through-holes), and recesses the insulating layers relative to the conducting sheets. The etch-back sequence is 60 sec in >94% H_2SO_4, rinse; 30 sec in >42% HF, rinse; and 5 sec in >94% H_2SO_4, which is followed by a rinse. Positive etch-back is accomplished by repeating the normal etch-back sequence. The former procedure further recesses the epoxy-fiberglass, resulting in an interlocking structure within the plated through-holes. Unless otherwise indicated, only the normal etch-back procedure was used in the studies described here. This leaves the surface reasonably flat, so that the electrode more closely approximates a rotating disk as described by Levich (6).

The conditioning procedure used after etchback is 150 sec in the Enplate 453, 60 sec rinse, and 60 sec in AD 481, which is followed by a 60 sec rinse. Enplate 453 is a strongly alkaline solution which conditions and cleans the through-holes and outsides of the circuit board. Enthone AD 481 is an ammonium persulfate solution that reduces and etches the copper layers, leaving clean active surfaces.

The insulating surfaces are prepared for electroplating by electroless copper deposition. This involves a cleaning and conditioning sequence of 180 sec in Enplate 453, rinse, 180 sec in Enplate 50104 (concentrated HCl solution), rinse, 60 sec in AD 481, rinse, 60 sec in Enplate 11105 (HCl-chloride solution) and 60 sec in another Enplate 11105, followed by activation. The latter involves adsorption of reduced Pd on the epoxy-fiberglass and copper surfaces from a mixed Pd-Sn chloride solution (180 sec in Activator 443), followed by a rinse, removal of excess metal chlorides in Accelerator 09043 (180 sec), and then another rinse. The adsorbed Pd catalyzes the electroless reduction of Cu^{+2} by formaldehyde in the electroless copper bath Cu 404 (360 sec), producing a thin layer of Cu over the surface (~1.5 μm thick). In the laboratory studies, any electroless Cu deposited on the Teflon mounting material was removed by scraping.

Circuit board plating conditions.—Copper electrodeposition on the rotating electrodes was performed from air-saturated copper pyrophosphate solutions prepared from plating bath concentrates C10XB, C11XB, and PY61-H obtained from M&T Chemicals, Incorporated. Baths typically had a pH of 8.3 and contained 22.5 g/liter Cu^{++}, 173 g/liter $(P_2O_7)^{-4}$, and 2.25 g/liter NH_3. Before use, baths were conditioned for 16 hr at 50°C and the temperature was maintained at 55° ± 1°C during electrodeposition by water circulated around the 150 ml jacketed glass cell from a Haake FT circulator-controller. The OFHC copper coil anode was dipped directly into the bath. Electrical contact to the cathode was made via silver-graphite brushes and the electrode rotation was controlled by a Motomatic E-550M controller and d.c. motor. Cell current was maintained at 38 mA/cm^2 (35 ASF) by a

Keithley Model 227 constant current source. Plating time was 60 min so that the average deposit thickness was 0.05 mm.

Cross section preparation.—After electroplating, a 1-2 mm slice was removed from the plated end of the cylindrical electrode using a low speed diamond saw. The disk obtained was mounted in Buehler Epoxide resin (20-8130) to protect the electroplate. A section of the disk was then cut perpendicular to both the plated surface and the parallel laminated copper sheets. This procedure exposed a cross section of the electroplate across alternating copper and epoxy-fiberglass circuit board layers. The surface of the cross section was then polished on successively finer aqueous alumina powder slurries to a 1 μm particle size to facilitate examination of the macro features of the deposit and substrate. For microstructure examination, samples were then etched for 2-3 sec in a mixture of concentrated acids (65% acetic, 34% nitric, and 1% hydrochloric).

Rotating Pt disk electrode studies.—The effect of brightener concentration on the rate of copper electrodeposition was investigated by voltammetrically cycling a rotating (2500 rpm) Pt disk electrode at 50 mV/sec from -0.700 to $+1.000$V *vs.* SCE (saturated calomel electrode) in air-saturated copper pyrophosphate baths at 55°C. Typical voltammetry curves are shown in Fig. 3 for baths containing 0.0 and 1.8 ml/liter PY61-H. Deposition of copper occurs between -0.3 and -0.7V for both sweep directions and the copper deposit is removed from the inert electrode by oxidation, *i.e.*, stripped, on the anodic sweep between -0.3 and -0.05V *vs.* SCE. The area under the stripping peak corresponds to the charge required to oxidize the copper deposit and is proportional to the average deposition rate for that cycle (7). At a concentration of 1.8 ml/liter, it is evident from Fig. 3 that the brightener decelerates Cu deposition.

The test electrode was a 99.95% Pt disk of 0.13 cm^2, which was mounted concentric and flush with the end of a 12 mm diam Kel-F cylinder by compression molding at elevated temperature. After mounting, the electrode was polished on successively finer aqueous alumina powder slurries to 1 μm particle size and then potential cycled to steady state in a bath containing no PY61-H. Both the Pt-40% Rh counterelectrode and commercial SCE were dipped directly in the cell. The indicator electrode potential was controlled relative to the SCE reference with a PAR Model 173 Potentiostat/Galvanostat in conjunction with a PAR Model 175 Universal Programmer. Steady-state voltammograms were generally obtained after 3-5 cycles. Anodic current peaks were integrated electronically to -0.05V *vs.* SCE using a PAR Model 179 Digital Coulometer.

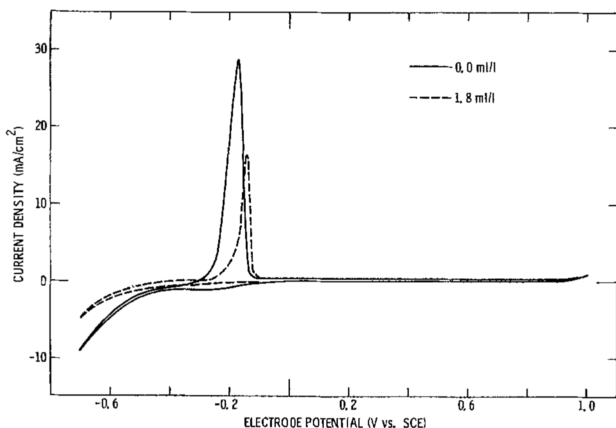

Fig. 3. Steady-state linear sweep cyclic voltammograms at 50 mV/sec for a Pt disk electrode rotating at 2500 rpm in copper pyrophosphate plating baths at 55°C containing 0.0 and 1.8 ml/liter of PY61-H.

Results and Discussion

The cause of foldback.—Cross sections of electrodeposits obtained on rotating circuit board electrodes at low (45 rpm) and moderate (95 rpm) rotation rates in baths containing 2.0 ml/liter of PY61-H are shown in Fig. 4 and 5, respectively. It is evident from these figures that foldback can be studied on rotating planar electrodes and that increased mass transport (faster electrode rotation) mitigates the problem. Similar experiments with positively etched-back electrodes show an increased incidence of foldback at the insulator-conductor boundaries, in agreement with studies of actual circuit board through-holes.

Since the activity of the brightener increases with bath heating time and varies by as much as 60% for different PY61-H batches (7), only the relative concentrations are really significant. To minimize errors caused by variations in brightener activity, baths were always prepared fresh using the same PY61-H batch and were heat-treated at 50°C for a specific amount of time (16 hr) before use. Time at operating temperature may be necessary to promote formation of a copper complex or polymerization of the brightener to an active form.

To facilitate data handling and display, a quantitative measure of foldback is desirable. To generate such numbers, advantage can be taken of the disrup-

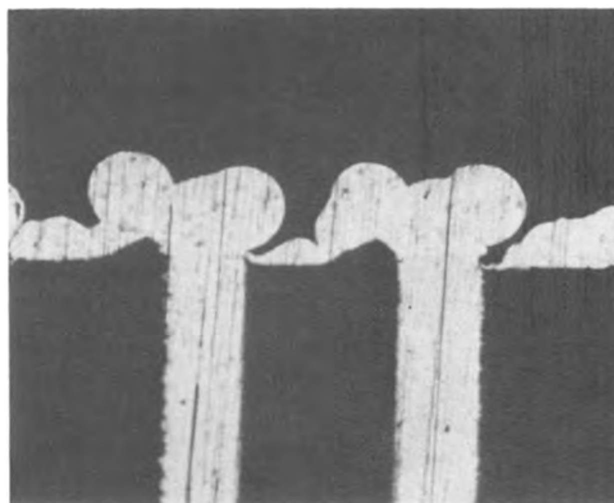

Fig. 4. Optical micrograph at 225 times of a planar circuit board electrode cross section after plating at 55°C from a copper pyrophosphate bath (2.0 ml/liter PY61-H) at 45 rpm (light areas are copper).

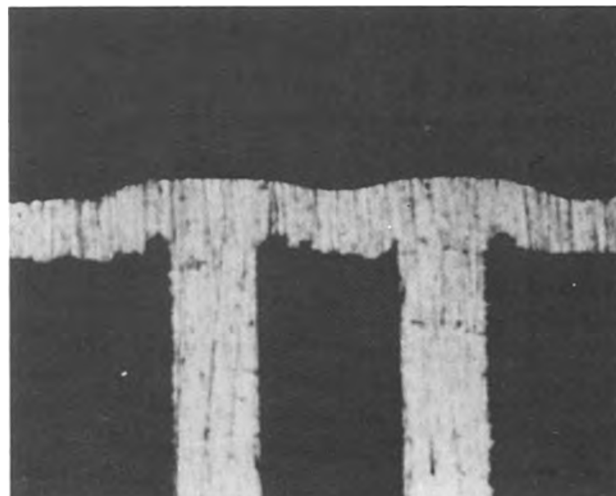

Fig. 5. Same as Fig. 4 except at 95 rpm

tions in the electrodeposit contour which result from foldback. Referring to Fig. 6, we define the foldback ratio (R_{FB}) as the length (L) along the contour of the electrodeposit surface divided by the corresponding distance (D) along the substrate. Thus, R_{FB} is larger as foldback becomes more severe and approaches unity as the problem disappears. Foldback ratios were measured from 330 times enlargements of electrodeposit cross sections.

Values of R_{FB} are plotted in Fig. 7 as a function of electrode rotation rate (ω) for various concentrations of PY61-H. It is evident from these curves that foldback is caused by insufficient brightener at the electrode surface. At the highest bulk brightener concentration (3.0 ml/liter), foldback is appreciable only at the lower rotation rates (<40 rpm) for which mass transport is slow, resulting in brightener depletion at the surface. For the lowest bulk brightener level (0.5 ml/liter), foldback is appreciable even at the highest rotation rate. This interpretation is based on the assumption that brightener is consumed at the electrode by inclusion in the deposit, which was shown to be the case by XPS analysis of deposits obtained on a Cu disk electrode rotating at 2500 rpm in baths at 55°C

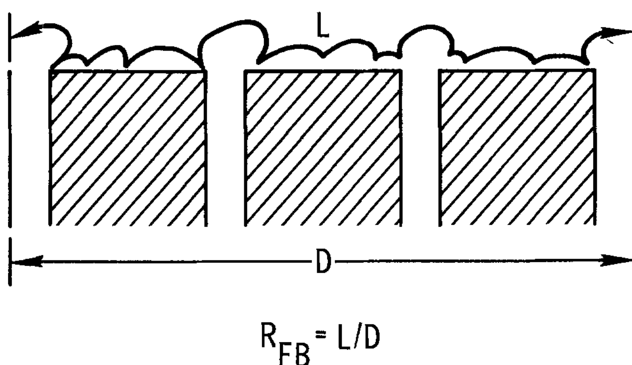

Fig. 6. Representation of a rotating circuit board electrode cross section illustrating the foldback ratio (R_{FB}).

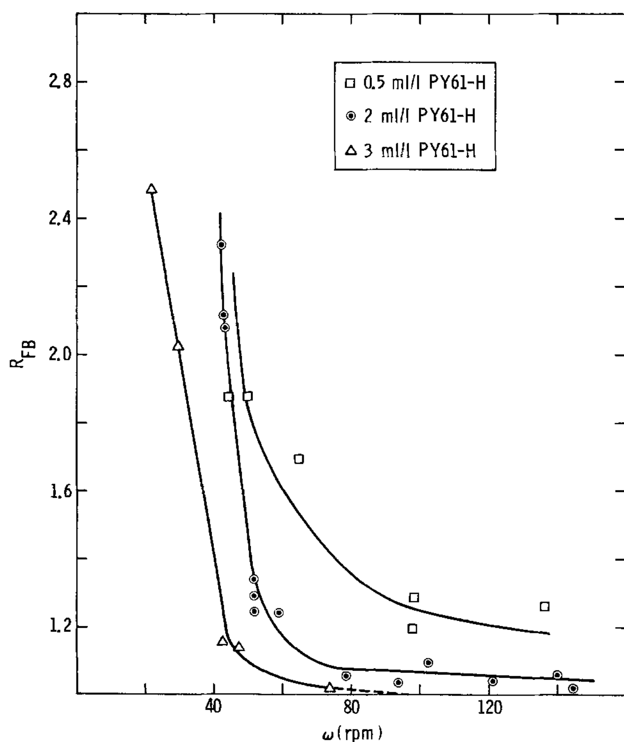

Fig. 7. Plots of foldback ratio (R_{FB}) vs. rotation rate (ω) of planar circuit board electrodes plated at 55°C from copper pyrophosphate baths containing various concentrations of PY61-H.

containing 2.0 ml/liter of PY61-H. An appreciable concentration of sulfur (0.3-0.6 atom percent) was detected.

The relationship between foldback and brightener concentration is more clearly illustrated by the topograph of foldback ratio *vs.* brightener level and current density shown in Fig. 8 for an electrode rotation of 100 rpm. This topograph is based on about 75 data points. Since brightener is consumed more rapidly at higher deposition rates, R_{FB} increases sharply with current density for the lower bulk brightener levels. Above 2 ml/liter, however, brightener depletion is less severe and foldback is suppressed even at the higher current densities. The increase in R_{FB} with increasing current density and decreasing PY61-H concentration is much more pronounced for similar plots at lower rotation rates. Dashed lines are used at the lower PY61-H concentrations since the data scatter is considerable in this region. Also, as the brightener concentration approaches zero, irregularities in the deposit contour result more from the absence of leveling than from the effects of insufficient brightener which are discussed below. This change of mechanism also accounts for the apparent decrease in R_{FB} at lower brightener concentrations.

Because of decreased mass transport of brightener to recessed areas of the electrode, foldback is generally more pronounced for positively etched-back surfaces and less evident for unetched samples, as shown in Fig. 9. Thus, at a given bulk brightener concentration, more vigorous agitation is required to prevent foldback when positive etch-back is used.

A mechanism proposed.—The mechanism by which the PY61-H brightener functions to induce uniform deposition of copper (leveling) and malfunctions to produce foldback can be understood from the voltammetric results for a rotating Pt disk electrode summarized in Fig. 10. As explained above, the copper stripping peak area (A_r) is a measure of the rate of copper electrodeposition. Since the absolute magnitude of A_r depends somewhat on the electrode pretreatment, only the relative values are significant. It is evident that the brightener accelerates the rate of electrodeposition at lower concentrations, but exerts a decelerating effect at higher levels. In actual circuit board plating, freshly prepared baths generally contain 2.0 ml/liter of PY61-H, so that the brightener presumably induces deceleration when functioning properly.

The results above are consistent with the view that the effectiveness of the brightener in producing leveling results from its ability to either decelerate or accelerate deposition of copper. Thus, as brightener is depleted at the electrode by inclusion in the deposit,

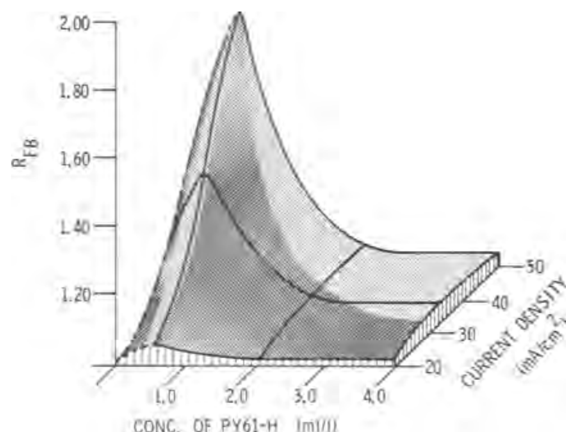

Fig. 8. Topographical plot of foldback ratio (R_{FB}) vs. current density and PY61-H concentration for planar circuit board electrodes rotated at 100 rpm during plating at 55°C from copper pyrophosphate baths.

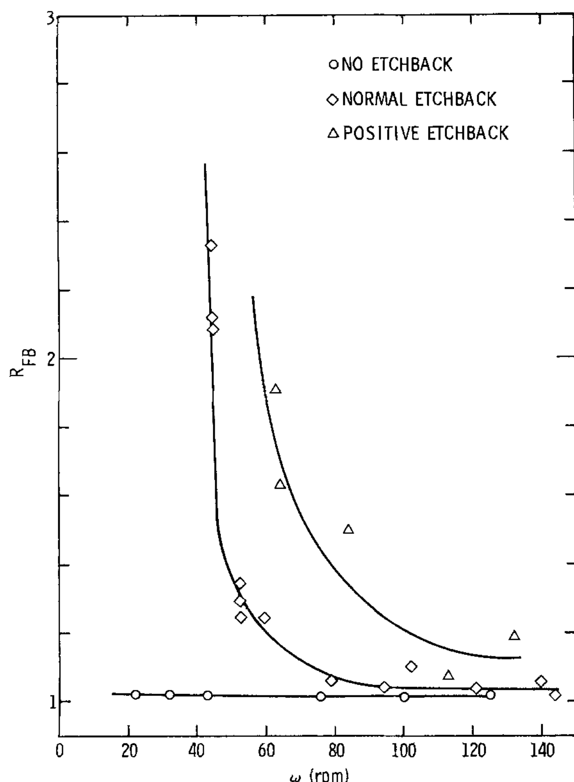

Fig. 9. Plots of foldback ratio (R_{FB}) vs. rotation rate (ω) of planar circuit board electrodes receiving various pretreatments before plating at 55°C from copper pyrophosphate baths containing 2.0 ml/liter of PY61-H.

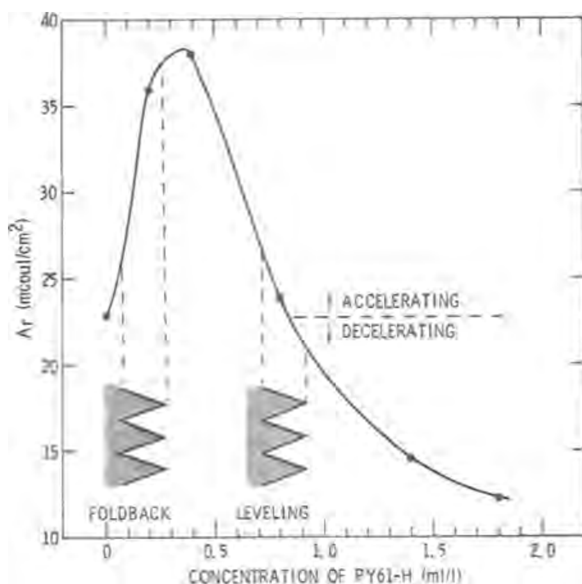

Fig. 10. Brightener concentration dependence of the steady-state Cu stripping peak area (A_r) for a rotating (2500 rpm) Pt disk electrode cycled at 50 mV/sec between −0.700 and 1.000V vs. SCE in copper pyrophosphate baths at 55°C. Inserts represent micro or macro surface roughness of substrates during plating.

its concentration at micro and macro peaks remains sufficient to inhibit deposition, as long as solution agitation and bulk brightener level are adequate. At the same time, because of reduced solution agitation in recesses, the brightener concentration becomes sufficiently depleted that acceleration of deposition occurs. Referring to Fig. 10, the brightener concentration at substrate peaks remains in the "decelerating" range, while that at recesses moves to the "accelerating" region. Hence, peaks are plated more slowly than without brightener and recesses are plated more rapidly, so that very efficient leveling results. Of course, either acceleration or deceleration alone would also level the deposit by the generally accepted mchanism (8), but the two operating together should be most effective.

Foldback, then, occurs when solution agitation or the PY61-H level becomes inadequate, resulting in sufficient depletion of brightener concentration at the electrode to produce acceleration of deposition at peaks in the substrate. At the same time, enhancement of deposition in recesses is reduced because of even more severe brightener depletion. In this case, the brightener concentration is always in the "accelerating" range, but at surface protrusions it is nearer to the maximum acceleration in Fig. 10. Thus, substrate peaks grow more rapidly than recesses, folding back over the latter. As foldback proceeds, the problem is compounded by increasingly restricted fluid flow to the recesses, perhaps resulting in severe depletion of copper pyrophosphate ions. Depletion of the latter species may also play some role in the early stages of foldback.

Additional insight is provided by comparison of electron micrographs taken along folded-back deposits with those obtained on flat copper disk electrodes rotating at 2500 rpm in baths containing known concentrations of brightener. Our data of the latter type show that deposits are: coarse-grained when the brightener concentration at the electrode surface is too small to appreciably affect the electrodeposition rate; composed of fine nodules less than 1 μm in diameter when the brightener exerts an accelerating effect; and extremely fine-grained when the effect is decelerating. In Fig. 11 and 12, typical electron micrographs are shown, respectively, for the bottom of a crevice and the top of a peak on the same folded-back deposit plated with electrode rotation of 45 rpm from a bath containing 2.0 ml/liter of PY61-H. Although the bulk additive concentration falls in the decelerating

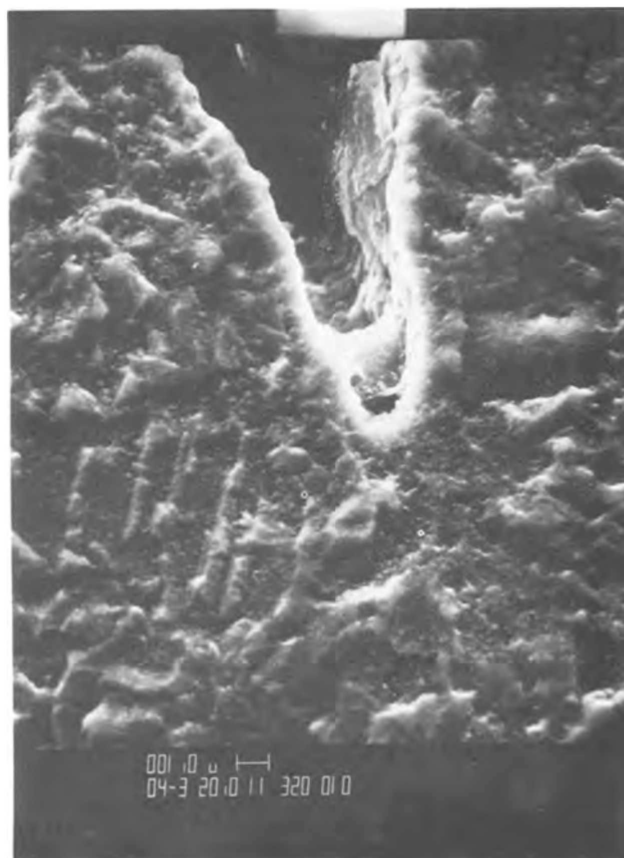

Fig. 11. Cross-sectional scanning electron micrograph at 4000 times of the bottom of a crevice on a folded-back deposit plated on a circuit board electrode rotating at 45 rpm in a copper pyrophosphate bath at 55°C containing 2.0 ml/liter of PY61-H.

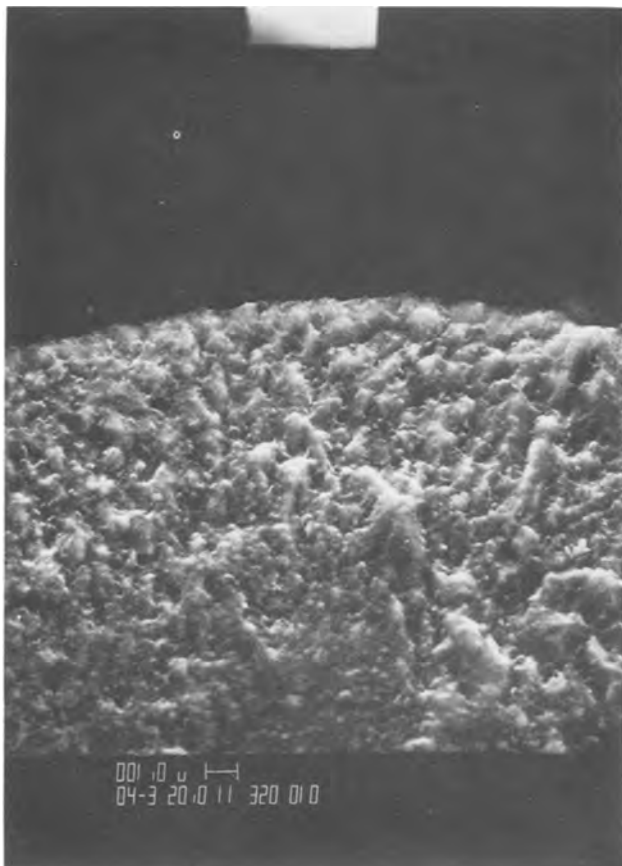

Fig. 12. Cross-sectional scanning electron micrograph at 4000 times of a peak on a folded-back deposit plated under the same conditions as for Fig. 11.

range, it is evident from the coarse-grained structure in Fig. 11 that the brightener is severely depleted within substrate recesses and has little effect on the electrodeposition rate. On the other hand, the fine nodular structure in Fig. 12 indicates that the folded-back peaks result from locally accelerated electrodeposition caused by less severe brightener depletion at the surface protrusions. This provides additional support for the mechanism proposed to explain foldback.

A possible mechanism by which the brightener can accelerate copper deposition at one concentration while inhibiting it at another can also be inferred from the deposit morphology observed under various plating conditions. In the absence of organic addition agents, which would interrupt grain growth, large-grained deposits (see Fig. 11) are typically obtained from copper pyrophosphate baths (9). Likewise, baths containing organic additives have generally been found to produce extremely fine-grained deposits (3), presumably because the organics adsorb at normal growth sites (kinks and steps) and force renucleation (10). It is proposed here that acceleration of electrodeposition occurs when the coverage of growth sites by brightener molecules is in the intermediate range, resulting in a large number of isolated growth centers. In this case, individual grains resemble dendrites or nodules growing out into the solution. The rate of electrodeposition is enhanced by the concomitant increase in the actual surface area of the electrode and because solution mass transport is increased by spherical diffusion to the tips of the protrusions (11). The resulting fine nodular deposit structure is evident in Fig. 12. At higher brightener concentrations, nodules do not form since most growth sites are blocked by adsorption of brightener molecules soon after nucleation. In this case, renucleation must occur much more often, so that fine-grained deposits are obtained and the deposition rate is decreased at a given electrode potential.

Nodules formed at high rotation rates (~2500 rpm) when the bulk brightener concentration is in the accelerating range are always an order of magnitude smaller than those obtained by lowering the electrode rotation rate at constant bulk brightener level to achieve the same concentration of brightener at the electrode surface. This result indicates that the depletion of Cu^{++} ions also contributes significantly to the growth of nodules when the solution mass transport rate is low.

It is interesting to note that, although leveling is induced only at brightener concentrations greater than that producing maximum acceleration of deposition, some brightening is produced over the entire concentration range. The latter occurs because specular reflection is increased by grain refinement, which is observed even for the lower brightener concentrations that produce fine nodular deposits. For leveling, however, the deposition rate within surface recesses must be faster than at surface protrusions where the brightener concentration is generally higher.

Although foldback has been shown to result from a deficiency of brightener at the electrode surface, other factors may also contribute indirectly to the problem. For example, the quality of the electroless deposit may be important since flaws in the conductive layer could act as centers for the initiation of foldback. The quality of the electroless deposit may in turn depend on the nature and pretreatment of the laminate used.

Conclusions

In through-hole plating from copper pyrophosphate baths, foldback of the electrodeposit to form lines of demarcation and voids has been shown to result from a deficiency of brightener at the electrode surface. Foldback can be understood from the voltammetric results which show that higher concentrations of brightener decelerate the deposition rate, whereas lower concentrations exert an accelerating effect. It is proposed that accelerated deposition results from nodular growth of centers isolated by partial coverage of growth sites by brightener molecules. When functioning properly, the brightener induces leveling by inhibiting deposition at peaks where its concentration remains high, and enhancing deposition in recesses where its concentration becomes depleted as it is included in the deposit. Foldback occurs when insufficient electrolyte agitation or additive level results in a low brightener concentration at the electrode surface, producing acceleration of deposition at the peaks. Thus, the problem can be controlled by maintaining an adequate brightener level and efficient solution agitation.

Acknowledgments

The authors are indebted to Dr. Alan Harker for performing the XPS analysis, Mr. John White for performing some of the experiments, and Mr. Joe Nagy of Enthone, Incorporated, for providing the plating bath concentrates.

Manuscript submitted Nov. 22, 1977; revised manuscript received Feb. 27, 1978.

Any discussion of this paper will appear in a Discussion Section to be published in the June 1979 JOURNAL. All discussions for the June 1979 Discussion Section should be submitted by Feb. 1, 1979.

Publication costs of this article were assisted by Rockwell International.

REFERENCES

1. J. W. Dini, in "Modern Electroplating," 3rd ed., F. A. Lowenheim, Editor, p. 205, Wiley-Interscience, New York (1974).
2. F. H. Wells and D. M. Lyde, Brit. Pat. 939,997 (1960).

3. P. Hinton, M.S. Thesis, University of Arizona, Tucson (1968).
4. T. Kessler and R. Alkire, *This Journal,* **123**, 990 (1976).
5. T. Kessler and R. Alkire, *Plating (East Orange, N.J.),* **63**, 22 (1976).
6. V. G. Levich, "Physicochemical Hydrodynamics," Prentice-Hall, Englewood Cliffs, N.J. (1962).
7. D. Tench and C. Ogden, *This Journal,* **125**, 194 (1978).
8. S. A. Watson and J. Edwards, *Trans. Inst. Met. Finish.,* **34**, 167 (1957).
9. V. A. Lamb, C. E. Johnson, and D. R. Valentine, *This Journal,* **117**, 281, 341, 381 (1970).
10. E. H. Lyons, Jr., in "Modern Electroplating," 3rd ed., F. A. Lowenheim, Editor, p. 26, Wiley-Interscience, New York (1974).
11. J. O'M. Bockris and A. K. Reddy, "Modern Electrochemistry," Vol. 2, p. 1219, Plenum Press, New York (1970).

Surface Properties of Nickel after Each Step of the Activation Process for Nickel Plating

Tennyson Smith and G. Lindberg

Rockwell International Science Center, Thousand Oaks, California 91360

ABSTRACT

The surface properties of nickel, after each step of the activation process for nickel plating, have been measured with ellipsometry, surface potential difference (SPD), photoelectron emission (PEE), water contact angle (ϕH_2O), and Auger electron spectroscopy (AES). The unique properties of properly activated nickel are compared with those for improperly prepared nickel and reveal the requirements for proper activation.

Properly activated nickel (anodic etch in H_3PO_4, rinse, cathodic activation in H_2SO_4, rinse) yields strong adhesion of the electrodeposited nickel to the substrate. A properly activated surface allows a uniform layer of nickel plate with a strong bond, whereas on an improperly activated surface, nickel is deposited in patches in the early stages of nucleation. The detailed description of the physical and chemical properties of the metal surface after each step of the activation process and the relationship of surface properties to successful plating has not been known.

Linford *et al.* (1) have prepared a literature review of the effects of contamination films (organic and inorganic, *e.g.*, oxides) in electroplating. They concluded that due to the active nature of metals that have been cleaned of all contamination, it is virtually impossible to place an absolute clean surface in the electroplating bath. There will always be a thin layer of oxide or oxide and other contaminants. Although the presence of oxide films is generally considered to be detrimental to plating, Linford *et al.* (1) indicate the presence of an oxide film may either prevent or promote adhesion depending on the circumstances. Almost all of the conclusions concerning the presence or absence of oxide between the substrate and the plate are based on indirect rather than direct observations.

Proposed mechanisms for plating at the interface include reduction of the oxide in the plating bath followed by plating on bare metal, plating on top of or in the pores of the oxide or lack of plating, depending on the conductivity of the oxide. Linford *et al.* state "there is no direct evidence to substantiate any of these mechanisms" (1). There is also little conclusive evidence as to whether very thin films are reduced by cathodic reduction in electrolysis or plating baths. They conclude that the structure of electrodeposits is controlled by the relative rates of crystal nucleation and growth and that the early stage of nucleation is dramatically affected by substrate topography and electric fields associated with sharp points, ledges, and ridges (*i.e.*, roughness on an atomic scale).

A more recent investigation (2) reveals that contamination from exposure to air causes isolated 3-D nuclei to form as well as larger blocklike growths, in contrast to smooth monolayer-type growths for uncontaminated surfaces. No effort was made to discover the nature of the contamination.

The lack of information available from the literature concerning detailed analysis of the state of metal surfaces prior to plating is due to the difficulty in the past of analyzing the region of interest, *i.e.*, the first few atom layers on the surface. Recent advances with respect to surface analysis make it possible to make such a study. The surface tools that have been used in this investigation are: light scattering, ellipsometry, surface potential difference (SPD), photoelectron emission (PEE), water contact angle (ϕH_2O), and Auger electron spectroscopy (AES). In addition, a technique has been developed for simultaneous ellipsometry and Auger spectroscopy during removal of films (EARF) by heating samples in ultra-high vacuum to evaporate the films, layer by layer, from the outer surface. The properties that are probed by these tools are listed in Table I. Interpretations of the experimental parameters revealed by these tools are given in Ref. (3).

The physical and chemical state of the nickel surface after each step of the proper activation process for plating nickel on nickel have been evaluated with these surface physics tools. Investigations were also made during and after steps that are not used in the proper treatment, but may be involved by inadvertent errors in the activation process.

Prior to the activation process, the electrodeposited nickel (EDNi) samples were wet-polished with silicon

Table I. Surface tools and the physical properties they probe

Tool	Properties
Profilometer	Roughness, topography
Light scattering	Roughness
Ellipsometry	Film thickness, film refractive index
(SPD) surface potential difference	Dielectric properties (outer dipole layer)
(ϕH_2O) water contact angle	Surface energy (outer atom layer)
(PEE) photoelectron emission	Film electron emission and attenuation properties
(AES) Auger electron spectroscopy	Elemental composition in outer 20A
(EARF) ellipsometry and Auger spectroscopy during removal of films	Depth profile of film thickness, optical properties and chemical composition

Key words: ellipsometry, Auger spectroscopy, surface potential difference, photoelectron emission.

carbide and cleaned in a mild alkaline cleaner (21g Vitro Klene[1] in 400 ml water, referred to as VK) at 80°C for 10 min. The first activation step is anodic etch (AE) in 81.5% by volume H_3PO_4, for 90 sec at 100 mA/cm^2 and room temperature, followed by a rinse in deionized water. The second activation step is cathodic activation (CA) in 25% by volume H_2SO_4, for 90 sec at 100 mA/cm^2 and room temperature, followed by a rinse in deionized water. VK alone or one of the activation steps by itself yield poor nickel adhesion (4).

Experimental Results

Film properties after each step.—Table II gives reproducible values (within ~ 10%) of equivalent film thickness (from ellipsometry), SPD, PEE, ϕH_2O, and Auger peak-to-peak heights (APPH) for carbon, phosphorus, sulfur, and silicon, relative to the APPH for the 850 eV peak of nickel. The term "equivalent film thickness" refers to an equivalent nickel oxide film of refractive index 2.6 and absorption index of zero. The nickel samples were rinsed and dried in flowing nitrogen after each step to prepare them for analysis with the surface tools.

No activation, VK only.—All samples were cleaned in Vitro Klene. "No activation" indicates the samples were polished but not activated. According to Table II the VK samples have an oxide film which is about 22Å thick. Removal of this oxide is indicated by the drift of the triangles in Fig. 1, up and to the left.[2]

The lowest value of Δ for the triangles corresponds to about 20Å of oxide. The highest value of Δ corresponds to a porous film of pure metal. For the porous film of pure metal, the ellipsometer cannot distinguish between a 20Å layer with about 50% porosity and a layer of about 300Å with about 5% porosity.

After VK, Table II reveals SPD to be approximately zero; this is because the reference electrode is also a nickel foil with natural oxide. That is, the work function of the sample and reference are about the same. The absolute value of SPD is difficult to interpret but the change from one treatment to another can be interpreted in terms of the changes in the outer dipole layer (3). The photoelectron emission has previously (3) been shown to come from the nickel oxide rather than the underlying metal. The attenuation index for nickel oxide (3) is ~ 71Å. The nickel oxide thickness calculated from the emission current proves to be approximately that from ellipsometry, 22Å. The low contact angle for water on VK nickel indicates that the surface is clean of low energy contamination.

One must not interpret the magnitude of the APPH ratio in Table II as relative surface concentration of one element with respect to another. The magnitude is strongly dependent on the position of the peak in the spectrogram. However, there is direct relative relation between the magnitude of the APPH ratio, for a given element, from one surface treatment to another, and the surface concentration of that particular element. For example, the fact that APPH(X)/APPH(Ni) is 15 for X = Si and 3.5 for X = C does not mean that

[1] TURCO Products, Wilmington, California.

[2] It should be noted in comparing Δ, ψ values in EARF with those not in EARF, that the angle of incidence is 79.2° in EARF as compared to 70° for other experiments. Δ is the phase shift and ψ is the arctan of the amplitude ratio, respectively, of the orthogonal components of reflected polarized light from ellipsometry.

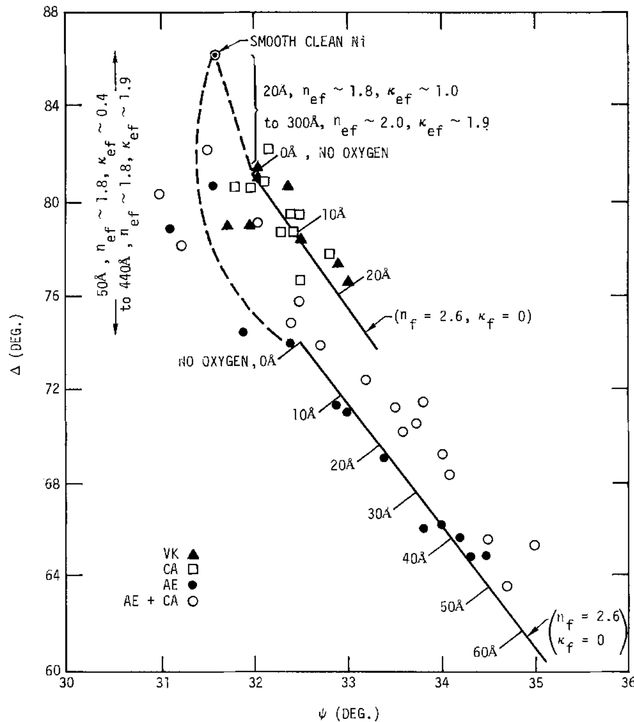

Fig. 1. Δ vs. ψ plots for the removal of films in EARF

there is about four times as much Si as C. However, the ratio of 15 for Si in the VK treatment and 4 in the CA treatment indicates that there is about four times as much Si on the surface after the VK treatment as after the CA treatment. The large silicon and carbon APPH ratios may be due to SiC particles from the mechanical polishing. As noted in Table II the AE treatment seems to remove these particles (APPH Si = 0).

The results for surface topography, from profilometry and light scattering measurements, are not reported in Table II, but indicate that compared to smooth polished nickel, the Vitro Klened samples which had been polished with 600 SiC paper are very rough (rms roughness ~ 0.25 μm for VK *vs.* 0.0005 μm for smooth nickel).

Cathodic activation only.—If a Vitro Klened sample is subjected to cathodic activation without prior anodic etch, the equivalent oxide film thickness and optical properties have not been changed (see Table II and open squares, Fig. 1) but the nature of the film has. The outer dipole layer has changed to increase SPD to 0.46V (due to a dipole layer with positive end pointing away from the surface), the emission yield has doubled, and the contact angle cannot be reduced below 20°. Most of the silicon (but not all) has been removed and sulfur has been increased. The ratios of the sulfur, carbon, and chlorine peaks in the CA film to that for a proper treatment (AE + CA) are plotted as a function of depth into the oxide film in Fig. 2. For CA only, oxygen and chlorine are in the outer atomic layer, whereas sulfur and carbon are found throughout the 20-30Å film. It is concluded that the sulfuric acid cathodic activation of a Vitro Klened sample has

Table II. Surface properties of films on nickel after each activation step

Surface treatment	Surface properties							
	Film thickness (Å)	SPD (V)	PEE (A × 10^{11})	ϕH_2O (deg)	APPH/APPH(Ni)			
					C	P	S	Si
No activation (VK)	22	−0.10	100	4	3.5	0.0	0.4	15.0
Cathodic activation (CA)	22	0.46	200	20	1.4	0.0	1.0	4.0
Anodic etch (AE)	65	0.20	400	3	1.2	1.2	0.0	0.0
AE + CA	65	0.46	400	7	0.7	0.0	0.1	0.0

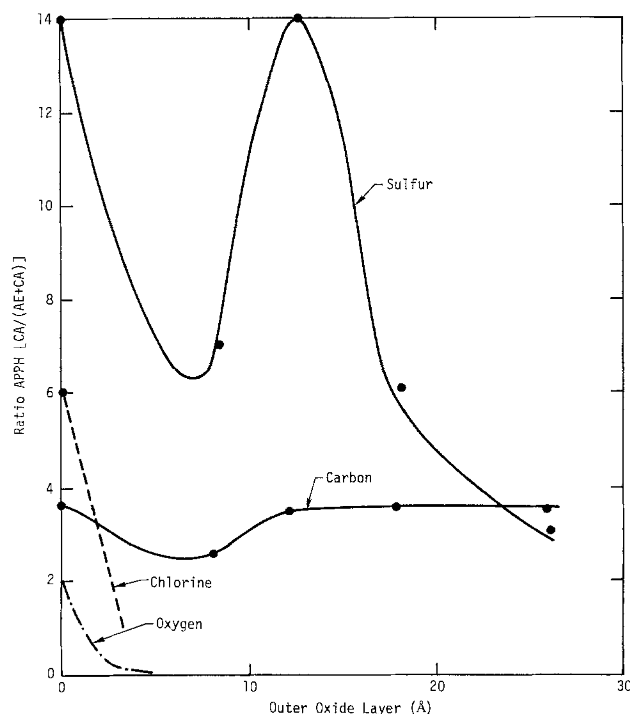

Fig. 2. Auger peak-to-peak height (APPH) profile for elements of the outer atomic layers of the film formed during cathodic activation of nickel to that formed in AE + CA.

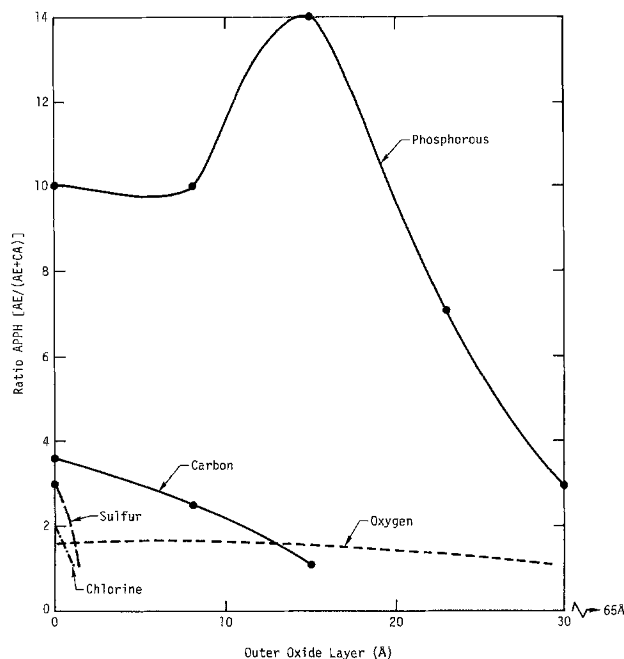

Fig. 3. APPH profile for elements in the outer atomic layers of the film formed during anodic etch of nickel.

changed the air-formed oxide film to a sulfide-carbide film, with resultant changes in SPD, PEE, and ϕH_2O, but essentially no change in thickness or optical properties.

The surface roughness, as measured by profilometry and light scattering, is essentially unchanged by CA, which has to be expected since no metal removal should occur during application of a cathodic current.

Anodic etch only.—If a Vitro Klened sample is subjected to anodic etch but not cathodically activated, a new equivalent film (~ 65Å) is observed after the AE step. Note that this 65Å film is measured *in situ* in the phosphoric acid but remains unchanged if the sample is removed, rinsed, and dried. It is only slightly changed (remove 3 or 4Å) by exposure to vacuum. Figure 1 (solid circles) shows the Δ *vs.* ψ results obtained by EARF for another AE sample. The lowest value of Δ and the largest value of ψ correspond to about 50Å of oxide on or within a porous layer of pure nickel. Heating to about 500°C in the UHV system drives off the oxide, following the theoretical curve for 50-0Å, at which point almost no oxygen is observed by AES. Further heating drives Δ and ψ toward the value for smooth clean nickel due to some sintering. The ellipsometer indicates that the porous nickel film remaining after heating has a thickness between 50Å with about 75% porosity and 440Å with just a few percent porosity. In contrast continued heating after removal of oxide from VK or VK + CA treated samples does not drive Δ, ψ toward the smooth-clean values, indicating that these surfaces are rough but not porous.

The SPD for the AE sample (see Table II) is only increased half as much as for CA, but the PEE is doubled due to the increased oxide thickness. Although the surface is very wettable (ϕH_2O ~ 3°), the carbon and phosphorus peaks are large. There is no sulfur or silicon at the outer surface of the oxide.

Figure 3 shows a profile after anodic etch alone, which is similar to Fig. 2. Relative to the proper treatment (AE + CA), sulfur and chlorine are only in the outer atomic layer, phosphorus and carbon are predominant in the outer 20-30Å whereas oxygen remains fairly uniform throughout the 60-80Å films. It is concluded that AE leaves an oxide that is primarily nickel phosphate in the outer part of the film.

The anodic etch has little effect on the rms surface roughness, but does increase the autocorrelation length (roughness wavelength) and thus smooths the surface with respect to VK only.

Proper treatment (AE + CA).—If a Vitro Klened sample is subjected to proper treatment, *i.e.*, anodic etch followed by cathodic activation, the anodic film is either changed in physical and electrical character but not removed or, if it is removed, another film of about the same average thickness but different properties replaces it. The film formed by AE + CA is observed *in situ* in the activation solutions and is only slightly changed upon rinsing and drying and under vacuum. The EARF results are seen in Fig. 1 (open circles).

The CA treatment following AE produces an outer dipole layer similar to that for CA after VK in the absence of AE. The change in dielectric properties is noted by the change of SPD from 0.2V (AE) to that of a CA-type outer surface (0.46V). The lack of change of PEE due to CA after AE is further confirmation of a film of thickness similar to that existing after AE. However, CA has reduced the carbon and phosphorus levels, and there is very little sulfur in the film after AE and AE + CA (see Table II). The low contact angle indicates a low level of nonpolar organic contamination. The most significant effect of the CA treatment after AE is to remove phosphorus which had been deposited in the AE step and to substantially decrease the carbon content in the outer layers.

Surface roughness, as measured by profilometry and light scattering, is unchanged by the CA treatment after AE. This is to be expected, since although the film chemistry was changed to CA, the film thickness was not, and even if it had been removed, 60-80Å removal would have little effect on topography.

Surface contamination from process solutions.—It had been noted that reproducible water contact angles were obtained on Vitro Klened samples (ϕH_2O ~ 3°, always wettable), whereas irreproducible contact angles were obtained for AE, CA, or AE + CA. Table III shows the effect of transfer of organic contamination from the surface of process solutions to the nickel sample upon removal of the sample. A series of experiments was performed in which the organic sur-

Table III. Surface properties of EDNi after each activation step. Effect of surface contamination from process solutions

Sample	Treatment	Surface properties					
		Δ (deg)	ψ (deg)	Film thickness (Å)	SPD (V)	PEE ($A \times 10^{11}$)	ϕH_2O (deg)
13 Samples	Polish and Vitro Klene	117.6	34.9	22	−0.12	112	4
	Anodic etch only						
1	Standard preparation						16
2	Clean solution surfaces	107.5	34.8	65	0.25	400	3
3	Clean solution surfaces + triple distilled H_2O	109.5	35.0	58	0.19	360	3
3	5 hr later						10
	Cathodic activation only						
4	Standard preparation						30
5	Clean solution surfaces						23
6	Clean solution surfaces						33
7	Clean solution surfaces						18
8	Clean solution surfaces						22
9	Clean solution surfaces	117.7	35.5	22	0.46	210	20
10	Clean solution surfaces	118.2	34.3	19	0.40	210	23
11	Clean solution surfaces + triple distilled H_2O						22
11	After 5 hr						39
	Anodic etch + cathodic activation						
12	Standard preparation						34
13	Clean solution surfaces	109.3	35.0	58	0.49	480	7
14	Clean solution surfaces + triple distilled H_2O						7
14	After 5 hr						16

face contamination from the surface of the activation solution was removed by suction prior to sample entrance and exit. It is seen in Table III that except for CA alone, a dramatic decrease in ϕH_2O resulted (samples 2, 3, 13, and 14). Exposure of the samples to laboratory air for 5 hr caused an increase of about 10° in ϕH_2O in each case, indicating slow contamination. The contact angle for CA only is invariably 20° regardless of cleaning procedures. Either the sulfide film has a lower surface energy or this film attracts contamination much faster and more strongly than the others.

Table IV gives results for a Ni sample that had been processed through AE + CA but was highly contaminated. The unusually high contamination resulted from the VK step, as evidenced by the large contact angle ($\phi H_2O = 26°$), and after the AE + CA step ($\phi H_2O = 46°$). The Auger carbon peak was so large that other elements could not be observed and therefore the actual peak-to-peak heights are reported rather than the ratio with respect to the Ni 850 eV peak. After 30 min of Ar^+ sputtering, the carbon peak was 60. The sample was moved during the next Auger sweep, which increased the carbon peak observed on the new area to 180. Exposure to the electron beam rapidly decreased the carbon peak. This indicates that the gross organic contamination is easily removed by the electron beam. A means for detecting the type of carbon on the surface has therefore been discovered because the rate of decrease of the carbon peak is directly related to the heat of adsorption of the contamination. Figure 4 is a plot of Δ *vs.* ψ for the contaminated sample. The data fall along the theoretical curve between zero and 60Å of nickel oxide on or within a nickel film, but then follow the theoretical curve for an organic film of about 50Å on top of the oxide.

For some samples, the regrowth of oxide after cleaning by EARF was monitored by ellipsometry during exposure of the clean metal to air. Figure 4 shows that just prior to AE + CA (after VK) the oxide film was about 14Å and after exposure to air about 10Å. All such measurements reveal that exposure of clean

Table IV. EARF surface properties of EDNi after activation (AE + CA) but contaminated in the process

Time (total min)	History	Ellipsometry			Auger spectroscopy APPH									
		Δ (deg)	ψ (deg)	Film thickness (Å)	Ni	O	C	S	P	N	Cl	Si	Ca	Other
	Vitro Klene	76.8	33.0,	$\phi H_2O = 26°$, SPD = 0.06, PEE = 100×10^{-11}A										
	AE + CA	63.7	35.2,	$\phi H_2O = 46°$, SPD = 0.46, PEE = 290×10^{-11}A										
	Evacuate UHV	64.5	35.0											
					0	0	Lge.	0	0	0	0	0	0	0
10	Ar^+ 3 μA	66.8	33.9											
					0	0	Lge.	0	0	0	0	0	0	0
30	Ar^+ 3.5 μA	67.7	33.5											
					5	25	60	0	0	0	0	0	0	0
	Move sample				0	7	180	5	0	3	10	0	0	0
30	Ar^+ 3.5 μA	68.0	33.4											
0	Heat													
26	355°C	69.8	33.5											
29	355°C	70.5	33.1											
34	420°C	72.3	32.8											
39	420°C	74.5	32.5											
					16	8	30	220	0	0	0	0	0	0
48	420°C	74.4	32.5											
52	420°C	75.4	32.3											
56	420°C	75.8	32.2											
61	420°C	76.8	32.1											
73	460°C	77.5	32.0											
76	460°C	77.8	31.8											
81	500°C	78.4	31.8											
					23	0	0	500	0	0	0	0	0	0
116	Ar^+ 3.5 μA	78.0	31.8											
16 hr	Ar^+ 3.5 μA	78.1	31.4											
					8	25	30	0	0	0	0	0	0	0
	Expose to air	77.4	32.5											
72 hr		75.7	32.7	$\phi H_2O = 43°$, SPD = 0.02, PEE = 130×10^{-11}										

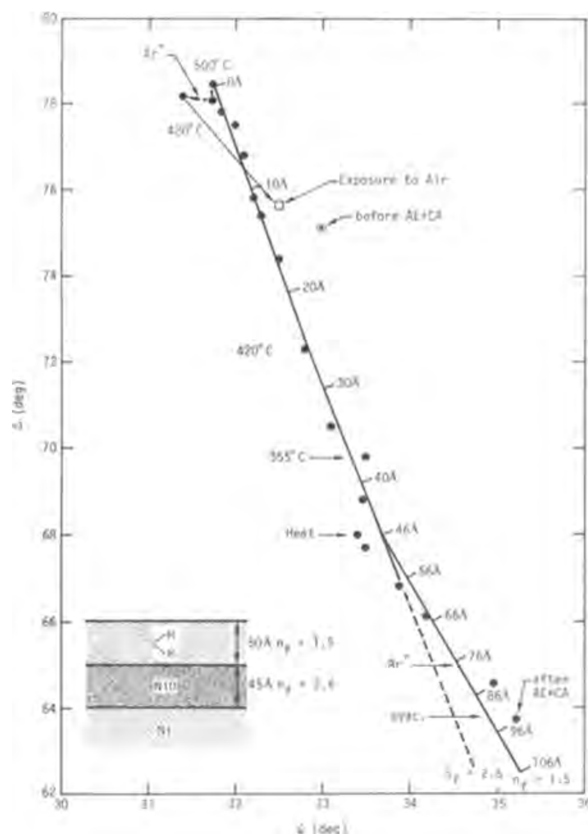

Fig. 4. A Δ vs. ψ plot for the removal of films formed before and after AE + CA on electrodeposited nickel.

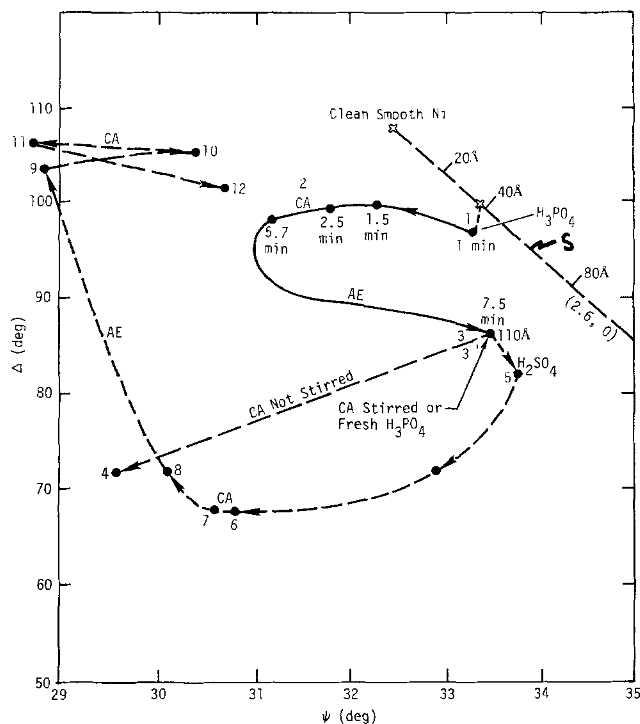

Fig. 5. A Δ vs. ψ plot, tracking the film formation and roughening of nickel during AE and CA in H_3PO_4, and H_2SO_4, respectively.

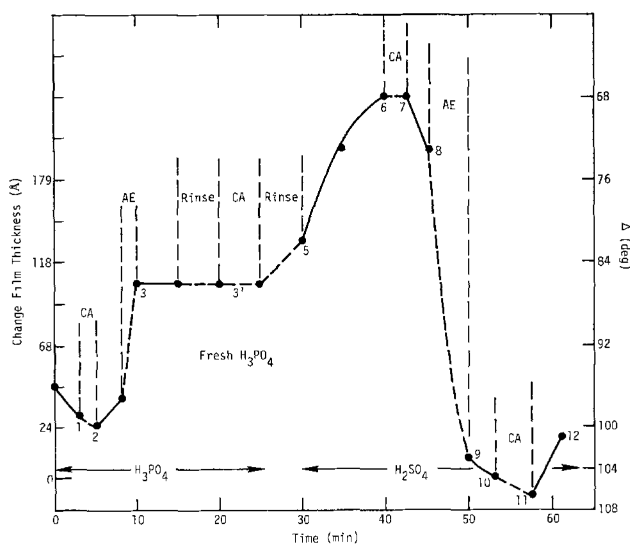

Fig. 6. Changes of Δ and corresponding film thickness during activation of Ni in H_3PO_4 and H_2SO_4.

nickel to air produces a film of oxide about 10Å thick within seconds, after which very little further film growth occurs in many hours. This result is consistent with reported (5) oxidation of clean nickel and confirms the interpretation of the ellipsometric results.

In situ ellipsometry during activation.—Ellipsometric measurements were performed *in situ* as the activation steps were made in the acid solutions. Figure 5 is a Δ-ψ plot tracking a nickel surface from VK into H_3PO_4 followed by CA, AE, and CA again (with and without stirring).[3] The drastic variations in ψ during these steps led us to make a careful study of the interpretation of ellipsometry during polarization. The results of this study are given in Ref. (6). The significant conclusion is that changes in Δ reflect changes in film thickness, whereas changes in ψ reflect changes in thickness and surface roughness, but predominantly in surface roughness. Values of ψ move to the left of the dashed curve for oxide on a smooth nickel surface (labeled S in Fig. 5) with increased roughness.

After VK, the sample had a film about 40Å thick. The coordinates of such a film in H_3PO_4 ambient are identified as the open crosses along curve S in Fig. 5. Figure 6 tracks the estimated film thickness that corresponds to Fig. 5. The first measurement in solution corresponds to point 1 at 1 min (Fig. 5). On the basis of the study in Ref. (6), exposure of the 40Å film to H_3PO_4 for 2.5 min (Fig. 5) has greatly roughened the surface, *i.e.*, the surface is dissolving. Cathodic treatment in H_3PO_4 between 2.5 and 5.7 min (point 2) produces no decrease in film thickness, only continued roughening. Anodic etch between 5.7 and 7.5 min moved the Δ-ψ coordinates to point 3. The shift of ψ to higher values indicates smoothing of the surface at the submicroscopic level and the decrease in Δ indicates formation of a film during or immediately following AE. It should be noted that measurement of Δ and ψ cannot be performed during AE or CA due to the copious gas bubble evolution. It is emphasized that after AE, the surface is still quite rough, otherwise point 3 would have moved to the dashed curve for film growth on a smooth substrate (curve S). These results are consistent with the analysis of Fig. 1 after AE. The formation of a rough surface (from recrystallization of dissolved nickel by cathodic reduction of dissolved nickel), as indicated by the large decrease in ψ to point 4 in Fig. 6, is evidence of a similar condition, but to a lesser extent, at point 3 after AE.

Removing the nickel from the H_3PO_4, rinsing, and placing in H_2SO_4 moves the Δ-ψ coordinates to point 5 (Fig. 5), which is only slightly changed from position 3 in the H_3PO_4. Exposure to H_2SO_4 moves Δ-ψ along the dashed line to position 6. This corresponds to the formation of a porous film somewhat similar to that observed after CA in unstirred H_3PO_4 (point 4),

[3] The experiments described in this section do not correspond to the correct activation procedure but were considered to evaluate the reaction occurring during the individual steps of the process.

i.e., H_2SO_4 is dissolving and reprecipitating a corrosion product film. The cathodic activation treatment between points 6 and 7 has little effect on the Δ-ψ coordinates, but has changed the film from a growth mode to a dissolution mode, as indicated by movement to position 8. Anodic etch moves Δ-ψ to 9, which corresponds to a thin but very rough film. Exposure to H_2SO_4 after AE drives Δ-ψ to a higher value (point 10, a smoother surface) but an additional CA step roughens it to point 11. Subsequent exposure to H_2SO_4 tends to smooth the surface again, moving Δ-ψ to position 12. At this point the experiment was terminated.

Effect of acid exposure.—Since exposure to acids in the absence of applied currents after the activation treatment may be detrimental to the plating process, nickel samples were Vitro Klened, treated with AE, CA, or AE + CA, and then exposed to H_2SO_4 or H_3PO_4 to establish the effect of exposure to acid on the surface activity. Figures 7, 8, 9 show Δ, ψ, and estimated film thickness changes as a function of time in these acids after each treatment. After VK the 30Å air-formed oxide layer dissolves in H_3PO_4 but a porous nickel film of corrosion products deposits in H_2SO_4 as noted by the decrease in Δ and ψ. The behavior in

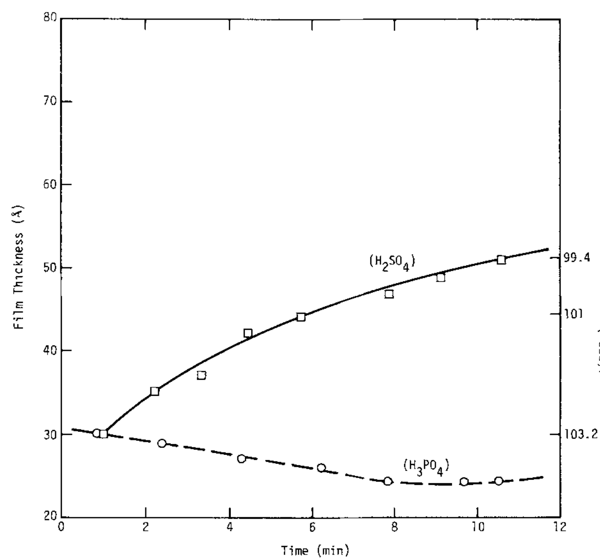

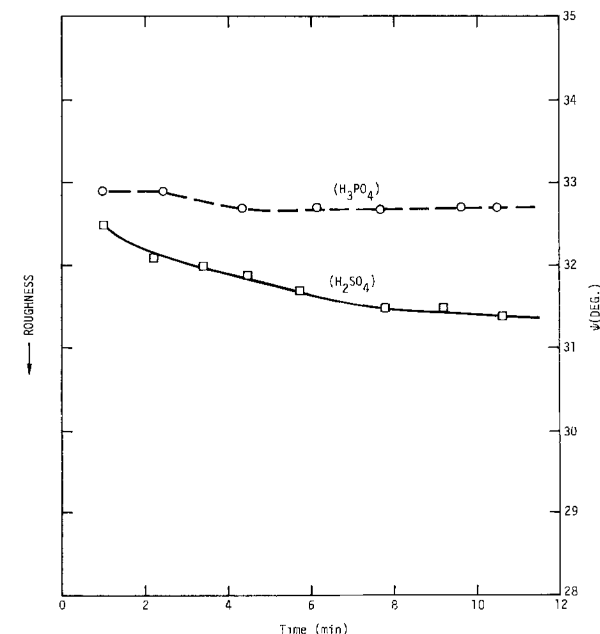

Fig. 7. Δ and ψ plot for EDNi in H_2SO_4 and H_3PO_4 after VK, showing estimated change in film thickness and roughness.

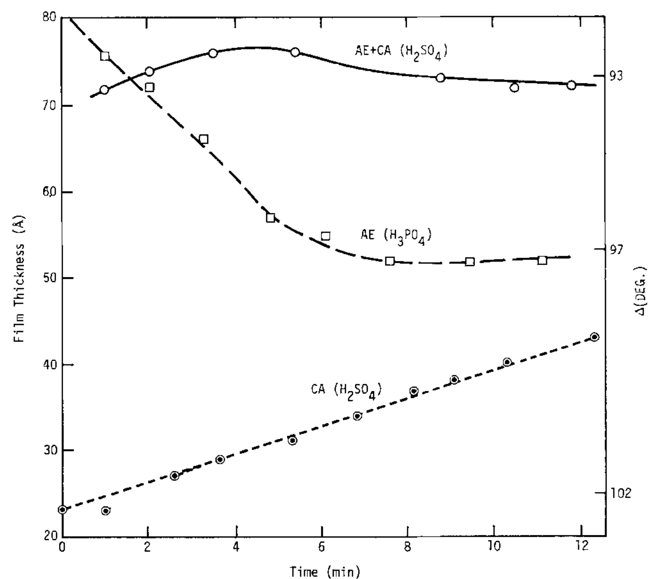

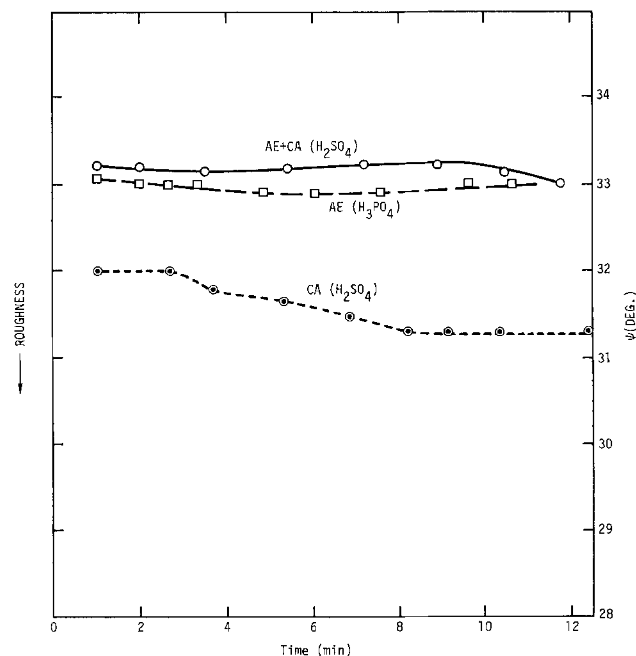

Fig. 8. Δ and ψ plot for nickel in H_2SO_4 and H_3PO_4 after AE, CA, and AE + CA, showing estimated changes in film thickness and roughness.

H_2SO_4 is about the same after CA (Fig. 8) as after VK only (Fig. 7). After AE, exposure to H_3PO_4 dissolves about 30Å of the 80Å film, *i.e.*, the outer layer of nickel phosphate may be removed. Figure 9 tracks Δ, ψ, film thickness, and corrosion potential (corrected) in H_2SO_4 after various treatments. About 30Å of the 80Å formed in AE dissolves in H_2SO_4 as it did in H_3PO_4, *i.e.*, the H_2SO_4 may also remove the phosphate layer and then allows the continued formation of oxide or corrosion product layers. If cathodic activation is performed after AE, the phosphate layer is replaced by an oxide which does not dissolve in H_2SO_4. This film continues to grow in H_2SO_4 as it did after AE (but after dissolution of the phosphate layer). This interpretation is in need of verification by surface analysis by EARF after exposure to these acids. If this interpretation is correct, the large decrease in corrosion potential in the first 2 min (after AE, Fig. 9), which from an electrochemical standpoint results from breakdown of a passive film, corresponds to dissolution of the outer phosphate layer. The trend of film growth in H_2SO_4 is the same as for the sample in Fig. 8, but somewhat

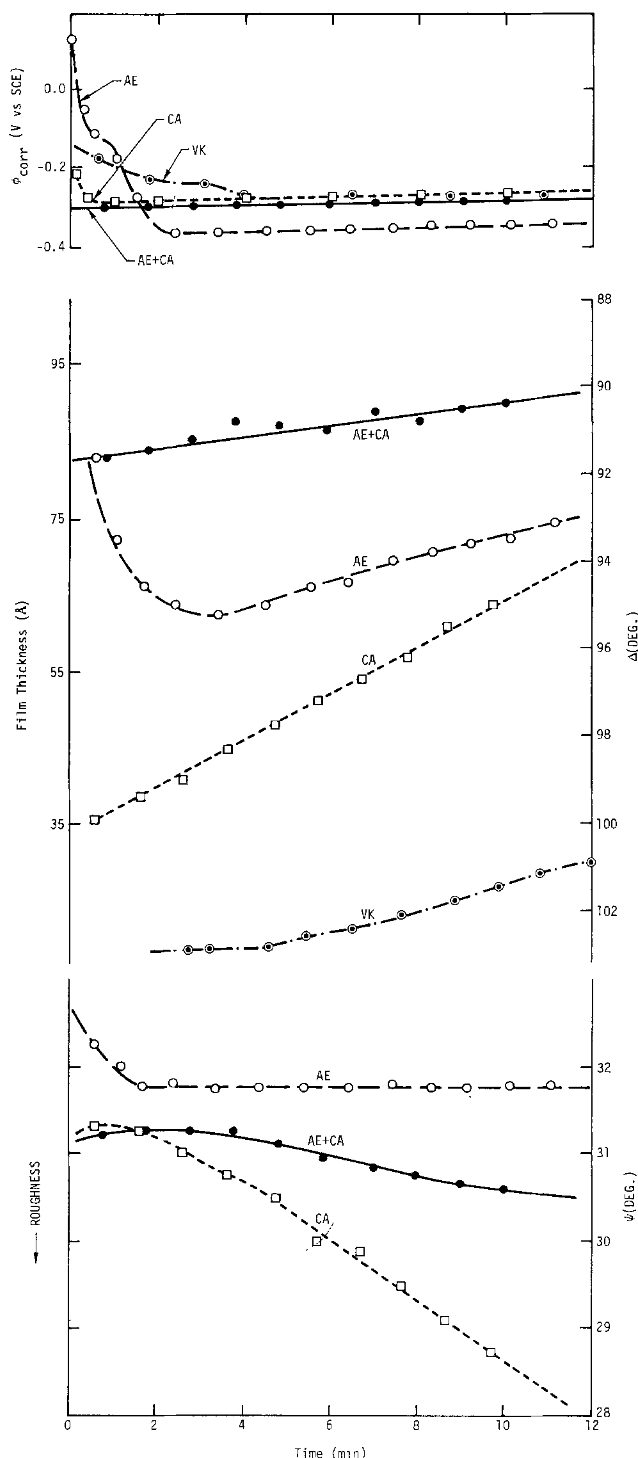

Fig. 9. EDNi in H_2SO_4 after AE, CA, and AE + CA

faster. The film on a VK sample is initially thinner than for the other treatments and slowly grows in H_2SO_4.

Exposure to acids always increases SPD and ϕH_2O. It may increase or decrease the film thickness and corresponding PEE's depending on the activation treatment, as seen above. Light scattering reveals little change in surface roughness due to acid exposure, whereas changes in ψ indicate roughening on a submicroscopic scale (porous film deposition) by exposure to H_2SO_4.

Solubility in nickel sulfamate.—It has been shown in the preceding that each step of the activation process produces a film with unique surface properties. It is supposed that the unique properties of the correct treatment (AE + CA) are responsible for its unique nickel plating success, but the reason is still obscure. One hypothesis, proposed in the literature (1), is that proper plating occurs only if the plating bath and plating current first remove any films so that nickel is plated on clean, bare nickel. Another hypothesis (1) is that nickel can plate on oxide films if they have certain properties. We have attempted to determine if the film formed on properly treated (AE + CA) nickel is removed in the plating bath, whereas the film formed on improperly prepared nickel (AE only) is not.

This is a very difficult problem to resolve with ellipsometry, because the nickel sulfamate bath is opaque to the red laser light, making *in situ* measurements impossible. To avoid these problems, nickel treated with AE only was placed in nickel sulfamate plating bath for various lengths of time without current flow, removed, rinsed, dried, and examined with ellipsometry to see if the film had dissolved. The same experiment was conducted with a properly treated (AE + CA) nickel sample. Figure 10 indicates that there is no dramatic difference between the change in film thickness for exposure to the Ni sulfamate bath after AE only and AE + CA. The slight tendency for the properly treated surface to exhibit slow dissolution of the film as compared to the tendency to increase the film thickness for the improperly treated surface may be greatly accentuated by applying the plating current. Unfortunately, ellipsometry cannot distinguish between reduction of oxide film on nickel and growth of a nickel deposit on the oxide. The resolution of this problem must await careful experiments to monitor the presence or absence of oxide between the plate and substrate by sputtering through the plate and monitoring with AES or ESCA.

Summary and Conclusions

Each step of the preparation of nickel for electroplating involves complex physical and chemical changes that we have attempted to elucidate with various sophisticated surface tools. Based on all results the schematic representation of the condition of the surface after each step of the activation process is given in Fig. 11.

Mechanical polish and VK of the samples leave them with about 20Å of oxide, some embedded silicon carbide polish particles, but little organic contamination. If the VK sample is treated with CA in H_2SO_4, the film is replaced by nickel sulfide of about the same thickness. However, if the sample is treated with AE after VK, the oxide is dissolved. Rapid dissolution of nickel (~5 μm/hr) (4) leaves particles of nickel and a saturated solution of nickel ions near the nickel surface. Turning off the anodic current, or removing

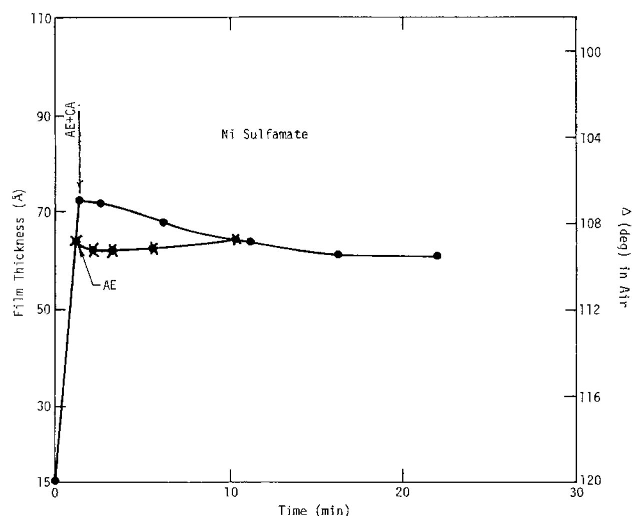

Fig. 10. Plot of Δ and corresponding film thickness on nickel after AE only and after AE + CA, as a function of exposure time.

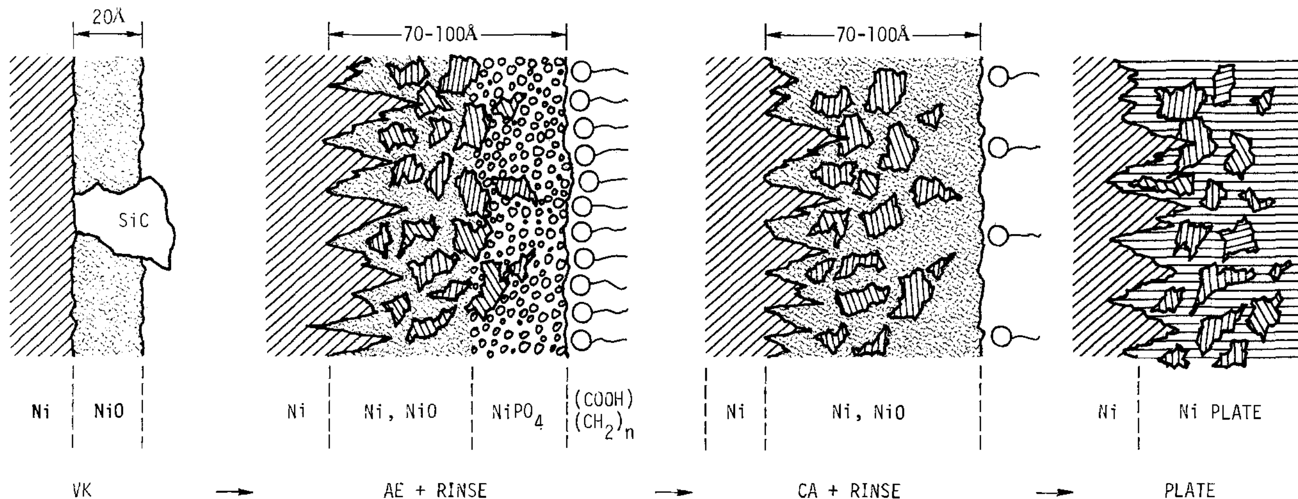

Fig. 11. Schematic representation of surface after each step

the sample from the solution, causes precipitation of small particles of nickel and precipitation of a porous layer of nickel phosphate, particularly at the outer surface. Rinsing removes phosphoric acid from the porous layer and oxidizes the porous nickel, particularly within the layer.

If the sample with AE treatment only is placed in the sulfamate plating bath, the phosphate layer cannot be reduced and plating occurs only at a few active points where reduction can occur. Nonuniform nucleation and growth of the deposit yield a weak interface and poor bonding. However, if the CA is carried out after AE, the phosphate film is reduced and perhaps the oxide film is also reduced, but upon stopping the current and rinsing of the sample, the porous nickel surface is reoxidized. The reoxidized nickel surface can, however, be reduced in the plating bath and plating occurs within and on the porous nickel. The result is a uniform plate with strong, tough bonding.

There appear to be three requirements for achieving a satisfactory deposit with a strong bond to the substrate: (*i*) a large concentration of nucleation sites, provided by the roughening and precipitation of nickel nuclei during and following AE (revealed by ellipsometry), (*ii*) reduction of the phosphate layer and reformation of an oxide that can be reduced in the plating bath (revealed by AES), and (*iii*) organic contamination must be reduced below some critical level.

If this mechanism is valid, other experiments could reveal possible alternative activation procedures that may be simpler and therefore less expensive and perhaps more reliable.

Acknowledgments

We are pleased to acknowledge the help and many suggestions of F. Mansfeld. This study was funded by the Rocketdyne Division of Rockwell International.

Manuscript submitted Jan. 30, 1978; revised manuscript received March 20, 1978.

Any discussion of this paper will appear in a Discussion Section to be published in the June 1979 JOURNAL. All discussions for the June 1979 Discussion Section should be submitted by Feb. 1, 1979.

Publication costs of this article were assisted by Rockwell International Science Center.

REFERENCES

1. H. B. Linford, D. O. Feder, and A. Venkateswarlu, American Electroplaters Society, Research Report No. 42 (1951).
2. H. L. Gaigher and G. N. van Wyke, *Electrochim. Acta*, **18**, 849 (1973).
3. T. Smith, *J. Appl. Phys.*, **46**, 1553 (1975).
4. F. Mansfeld, Technical Report SCTR-76-11, Science Center Rockwell International (1976).
5. O. Kubaschewski and B. E. Hopkins, "Oxidation of Metals and Alloys," Butterworths, London (1962).
6. T. Smith and F. B. Mansfeld, Paper submitted *This Journal.*

Catalysis of the Electroreduction of Allyl Chloride by Cobalt 2,2′-Bipyridine Complexes

Shlomo Margel and Fred C. Anson*

Arthur Amos Noyes Laboratory, California Institute of Technology, Pasadena, California 91125

ABSTRACT

The electrochemical reduction of allyl chloride is strongly catalyzed in the presence of cobalt complexes of 2,2′-bipyridine. A prominent reaction product of the catalyzed reduction is 1,5-hexadiene. Voltammetry, coulometry, and gas chromatographic data are presented and analyzed and a mechanistic scheme proposed to account for the catalytic action of the cobalt-2,2′-bipyridine complexes.

Recently we reported studies (1) which examined a previous claim (2) that the electroreduction of acrylonitrile in acetonitrile was catalyzed by a complex of cobalt with 2,2′-bipyridine. These studies demonstrated the absence of such catalysis for acrylonitrile and a number of other vinyl monomers but one substrate, allyl chloride, did exhibit a very large enhancement in its reduction rate in the presence of cobalt 2,2′-bipyridine complexes. This report summarizes our experimental observations with this system and presents a possible reaction scheme to account for the observed catalysis.

Experimental

Reagents.—The solvent was prepared from spectroscopic grade acetonitrile which was stirred over CaH_2 for 24 hr, distilled near room temperature under reduced pressure, and stored under argon. Polarographic grade tetraethylammonium perchlorate (TEAP) (Southwestern Analytical Company) was vacuum dried and used as the supporting electrolyte without additional purification.

$Co(bipy)_3(ClO_4)_3$, $Co(bipy)_3(ClO_4)_2$ (bipy ≡ 2,2′-bipyridine), and $Co(phen)_3(ClO_4)_2$ (phen ≡ 1,10-phenanthroline) were prepared as previously described (1). Solutions of $Co(bipy)_2(ClO_4)_2$ were prepared by mixing $Co(ClO_4)_2$ and 2,2′-bipyridine in a molar ratio of 1:2 in acetonitrile. Allyl chloride (Eastman) and allyl alcohol (Aldrich) were distilled just prior to their use.

Apparatus.—Cyclic voltammograms were obtained with a Princeton Applied Research (PAR) Model 173 potentiostat driven by a PAR Model 175 programmer. Current-voltage curves were recorded with a Tektronix Model 564 storage oscilloscope and photographed with a Tetronix Model C-12 camera. Controlled potential coulometry was conducted with the same potentiostat equipped with a Model 179 digital coulometer. A three-compartment electrochemical cell was employed with double isolation of the Ag/0.1M Ag^+ reference electrode against which all potentials are quoted. Solutions were deoxygenated with prepurified argon which was passed successively through aqueous chromous chloride solution, a calcium chloride drying tower, and purified acetonitrile before entering the test solution. Concentrations of allyl chloride and 1,5-hexadiene were monitored gas chromatographically with a Hewlett-Packard Model 5830 chromatograph using a 12 ft column packed with Carbowax 20M on Chromosorb W.

Results

Of the three characteristic voltammetric waves exhibited by $Co(bipy)_3^{3+}$ in acetonitrile (1, 2) the second is the first to be affected by the presence of allyl chloride. In addition, as was true for acrylonitrile (1), a new wave appears between the original second and third waves. These features are shown in Fig. 1. The peak current of the new wave with a peak potential near −1500 mV increases at the expense of the third wave ($E_p = -1950$ mV) as the concentration of added allyl chloride is increased (Fig. 1). At a fixed concentration of allyl chloride the ratio of peak current to square root of scan rate for the new wave at first increases as the scan rate decreases (Fig. 2) but eventually decreases again at very low scan rates. The magnitude of the wave is also suppressed by the presence of excess 2,2′-bipyridine (Fig. 2).

The behavior is rather similar to that obtained with acrylonitrile and is consistent with an analogous interpretation of the origin of the new wave (1): It corresponds to the reduction of a mixed allyl chloride, 2,2′-bipyridine complex of cobalt(I) that is the product of reaction [1]

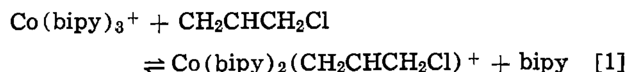

$$Co(bipy)_3^+ + CH_2CHCH_2Cl \rightleftharpoons Co(bipy)_2(CH_2CHCH_2Cl)^+ + bipy \quad [1]$$

However, in contrast with the cobalt(I) acrylonitrile system, the mixed complex with allyl chloride is unstable with respect to intramolecular reduction of the coordinated allyl chloride by the cobalt(I). This reaction, which results in the regeneration of cobalt(II) at the electrode surface, is the reason that the addition of allyl chloride causes the peak current of the wave corresponding to the reduction of cobalt(II) to cobalt(I) to exceed its value in the absence of allyl chloride (Fig. 2) except at scan rates high enough to prevent reaction [1] (and the subsequent intramolec-

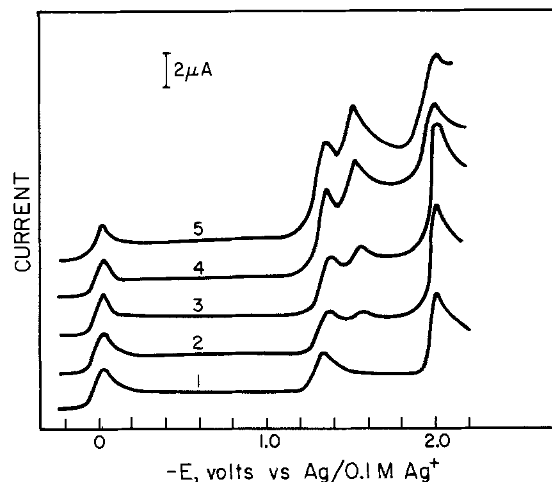

Fig. 1. Effect of allyl chloride on linear scan voltammograms for 1 mM $Co(bipy)_3^{3+}$ in acetonitrile. Allyl chloride concentrations: curve 1, 0; curve 2, 1 mM; curve 3, 5 mM; curve 4, 30 mM; curve 5, 0.1M. Supporting electrolyte: 0.1M TEAP. Scan rate: 0.5 V sec^{-1}. Platinum electrode area: 0.43 cm^2.

* Electrochemical Society Active Member.

Key words: catalysis, π-coordination, intramolecular.

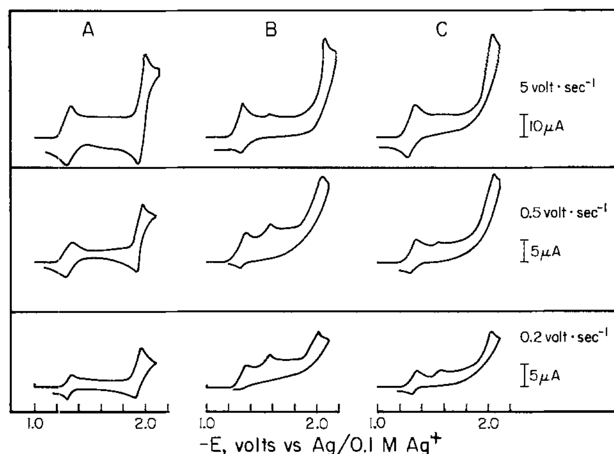

Fig. 2. Effect of allyl chloride on cyclic voltammograms for 0.5 mM $Co(bipy)_3^{2+}$ in acetonitrile. Allyl chloride concentrations: A, 0; B, 10 mM; C, 10 mM + 2 mM 2,2'-bipyridine. Supporting electrolyte: 0.1M TEAP. Platinum electrode area: 1.6 cm^2.

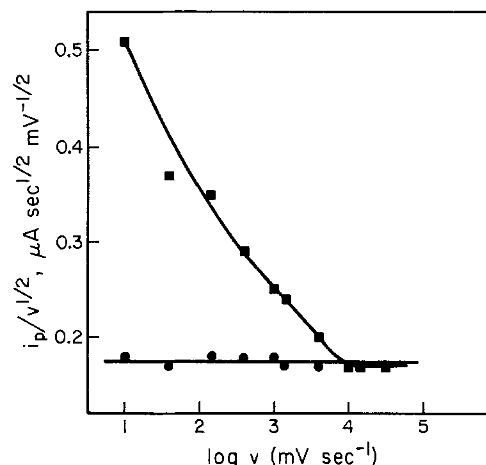

Fig. 4. Scan rate dependence of the ratio of voltammetric peak current, i_p, to square-root of scan rate for reduction of $Co(bipy)_3^{2+}$ to $Co(bipy)_3^{+}$. ●, 0.5 mM $Co(bipy)_3^{2+}$; ■, 0.5 mM $Co(bipy)_3^{2+}$ + 10 mM allyl chloride. Other conditions as in Fig. 2.

ular reduction reaction) from proceeding significantly from left to right.

The instability of the mixed cobalt(I)-allyl chloride complex made it impossible to evaluate the equilibrium constant for reaction [1] from cyclic voltammetric data as was done for the acrylonitrile complex. However, from the qualitative observation that larger concentrations of allyl chloride than of acrylonitrile are required to cause the formation of the new wave, it seems likely that the equilibrium constant is smaller for the allyl chloride complex.

The voltammograms in Fig. 3 show that substitution of $Co(bipy)_2^{+}$ for $Co(bipy)_3^{+}$ significantly increases the rate at which reaction [1] proceeds from left to right (the same is true for the analogous reaction involving acrylonitrile). In the case of $Co(bipy)_3^{+}$ the slow step is apparently the loss of one of the coordinated 2,2'-bipyridine ligands.

No evidence of the formation of a mixed complex was obtained when $Co(bipy)_3^{+}$ was exposed to allyl alcohol or when $Co(phen)_3^{+}$ was exposed to even large excesses of allyl chloride.

Note that the rate of the reduction of the coordinated allyl chloride is apparently slower than the rate at which it coordinates to $Co(bipy)_3^{+}$ or $Co(bipy)_2^{+}$. Otherwise, the new wave in Fig. 2 and 3 arising from the reduction of the mixed complex would not appear. Instead, the wave corresponding to the reduction of cobalt(II) to cobalt(I) would merely increase in magnitude as all of the allyl chloride was reduced.

The ratio of peak current to square root of scan rate for the reduction of $Co(bipy)_3^{2+}$ to $Co(bipy)_3^{+}$ becomes strongly dependent on scan rate in the presence of allyl chloride as shown in Fig. 4. Only at scan rates high enough to prevent reaction [1] from proceeding does the ratio of i_p to $v^{1/2}$ decrease to its value in the absence of allyl chloride.

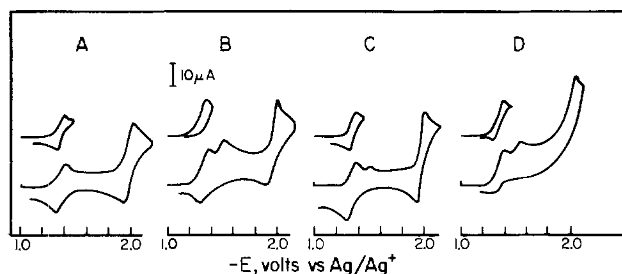

Fig. 3. Comparison of cyclic voltammograms for $Co(bipy)_3^{2+}$ and $Co(bipy)_2^{2+}$ in the presence of allyl chloride. Concentrations of cobalt complex: 1.0 mM; A, $Co(bipy)_2^{2+}$; B, $Co(bipy)_2^{2+}$ + 1 mM allyl chloride; C, $Co(bipy)_3^{2+}$ + 1 mM allyl chloride; D, $Co(bipy)_3^{2+}$ + 11 mM allyl chloride. The small upper voltammograms in each case show the response obtained if the potential scan is reversed just after the first (Co(II) → Co(I)) peak. Scan rate: 0.5 V sec^{-1}. Other conditions as in Fig. 2.

The behavior of the anodic half of the cyclic voltammograms in Fig. 2 and 3 is also understandable on this basis: Little or no wave is observed for the oxidation of $Co(bipy)_3^{+}$ and $Co(bipy)_2^{+}$ under conditions where the mixed complex is formed because the product of its further reduction is apparently not oxidizable. The anodic wave for Co(I) → Co(II) appears only under conditions where most of any allyl chloride present has been consumed so that $Co(bipy)_3^{+}$ or $Co(bipy)_2^{+}$ can persist at the electrode surface and be reoxidized.

By using a mercury electrode it proved possible to use the anodic depolarization of mercury at +400 mV to monitor the concentration of chloride ion released as the allyl chloride was reduced. There was a good correlation between the magnitude of the anodic wave due to chloride and the increase in the peak current of the wave for the reduction of cobalt(II) to cobalt(I).

Controlled Potential Coulometry

Electrolysis of solutions of $Co(bipy)_3^{2+}$ in acetonitrile at −1400 mV results in the quantitative formation of the intensely blue $Co(bipy)_3^{+}$ ion (1). If allyl chloride is present during such an electrolysis, the deep blue color does not develop during the initial stages of the electrolysis. Gas chromatographic analysis of the solution shows that the allyl chloride is consumed and 1,5-hexadiene is produced as the electrolysis proceeds (Fig. 5). The blue color of the $Co(bipy)_3^{+}$ ion persists in the solution only after all of the allyl chloride has been removed. The yield of 1,5-hexadiene and the quantity of charge required to reduce the allyl chloride are functions of the relative amounts of allyl chloride and cobalt complex present. Table I summarizes the coulometric data. When the ratio of allyl chloride to $Co(bipy)_3^{+}$ is small, *e.g.*, experiments 1 and 2 in Table I, the reduction consumes precisely one electron per molecule of allyl chloride and a prominent reaction product is 1,5-hexadiene (the other reaction products were not determined). As this ratio increases allyl chloride disappears from the solution before one electron per molecule is consumed (experiments 3 to 7, Table I), the more so the higher the concentration of allyl chloride. Gas chromatograms of the solutions resulting from such electrolyses (Fig. 6) contain a series of ill-defined peaks corresponding to components with high retention times as would be expected for oligomers of allyl chloride.

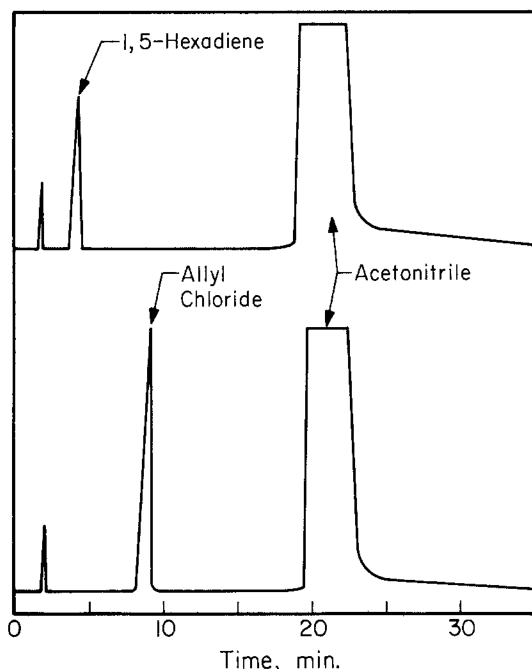

Fig. 5. Gas chromatograms of electrolysis solution before (lower chromatogram) and after (upper chromatogram) exhaustive electrolysis at −1.4V *vs.* Ag/0.1M Ag^+ at a platinum gauze electrode. Initial solution composition: 10 mM $Co(bipy)_3^{2+}$, 10 mM allyl chloride, 0.2M TEAP. The small peak with a retention time near 3 min was obtained in all chromatograms and may be an impurity in the solvent.

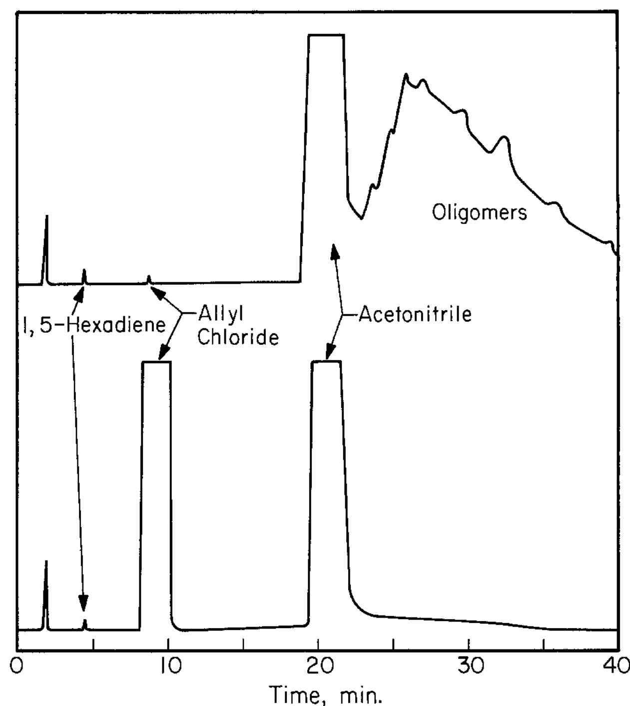

Fig. 6. Gas chromatograms of electrolysis solutions before (lower chromatogram) and after (upper chromatogram) exhaustive electrolysis at −1.4V *vs.* Ag/0.1M Ag^+. Initial solution composition: 4 mM $Co(bipy)_3^{2+}$, 5.7M allyl chloride, 0.2M TEAP. Other conditions as in Fig. 5.

During the electrolysis for experiment 7 in Table I a small amount of a white, pastelike solid precipitated from the solution. The solid was collected, washed with water, and vacuum dried at room temperature. Elemental analyses of the solid showed: (percentages) C, 47.5; H, 6.3; Cl, 44. Calculated for $(CH_2CHCH_2Cl)_n$: C, 47.1; H, 6.5; Cl, 46.4. Thus, at high ratios of allyl chloride to cobalt(I) polymerization of the allyl chloride ensues and is the major pathway by which it is removed from electrolysis solutions.

It is not necessary for the allyl chloride to be present during the electrolytic reduction of $Co(bipy)_3^{2+}$ to $Co(bipy)_3^+$ in order to achieve the reduction of allyl chloride. For example, the addition, under argon, of 0.1 mM of allyl chloride to 10 ml of a 10 mM solution of $Co(bipy)_3^+$ prepared by the electrolytic reduction of $Co(bipy)_3^{2+}$ resulted in the rapid fading of the intense blue color of the solution. Gas chromatographic analysis showed that all of the allyl chloride had been consumed and about 50% had been converted to a 1,5-hexadiene. Cyclic voltammograms of the resulting solution were indistinguishable from those obtained with a fresh solution of $Co(bipy)_3^{2+}$.

The cobalt catalyzed reduction of allyl chloride may also be carried out chemically using borohydride as the reductant since sodium borohydride rapidly reduces $Co(bipy)_{3\text{ or }2}^{2+}$ to $Co(bipy)_{3\text{ or }2}^{+}$.

Table I. Coulometric data for the catalyzed reduction of allyl chloride in the presence of $Co(bipy)_3^+$*

Expt. No.	$[Co(bipy)_3^{2+}]$ (mM)	$[CH_2CHCH_2Cl]$ (mM)	n_{app}**	Yield of 1,5 hexadiene (%)
1	10	5	1.0	53
2	10	10	1.0	50
3	2	10	0.89	41
4	2	30	0.63	26
5	2	100	0.32	4
6	2	500	0.11	~1
7	4	5700	0.01	~1
8	0	10‡	2.0	§

* Reduction at a platinum gauze electrode maintained at −1400 mV *vs.* Ag/0.1M Ag^+ in acetonitrile. Supporting electrolyte: 0.1M tetraethylammonium perchlorate; solution volume: 10 ml.
** n_{app} is the ratio of the charge consumed up to the point at which the blue color of $Co(bipy)_3^+$ first appeared to the calculated charge for the one-electron reduction of the allyl chloride present.
† The fate of the reduced allyl chloride which did not appear as 1,5-hexadiene was not determined.
‡ Electrode potential was −2600 mV.
§ Products were not monitored. Allyl chloride is reported to be reduced to a mixture of 1,5-hexadiene and 1-propene under these conditions (3, 4).

Discussion

The reduction of allyl chloride in the absence of cobalt complexes at mercury electrodes occurs near −2.6V (*vs.* Ag/0.1M Ag^+) in nonaqueous solvents and the polarographic limiting current corresponds to two electrons per molecule of allyl chloride (3). Nevertheless, the primary reduction product of nonexhaustive electrolysis in which the concentration of allyl chloride is maintained relatively high is 1,5-hexadiene (4) which requires only one electron per allyl chloride molecule (1-propene is also formed). These results have been rationalized (4) in terms of a chemical reaction between allyl chloride and allyl carbanion, the primary, two-electron reduction product.

In exhaustive, controlled potential electrolysis of 10 mM solutions of allyl chloride with platinum electrodes we obtained rapid, clean, two-electron reduction at −2.6V in acetonitrile which we presume leads to the quantitative formation of 1-propene (no 1,5-hexadiene was detected by gas chromatography). The essential difference produced by the addition of cobalt-2,2′-bipyridine complexes to the electrolysis solution is the conversion from the two-electron reduction which yields allyl carbanion to a one-electron reduction yielding the allyl radical. The Scheme summarizes the proposed course of the reduction of allyl chloride both in the presence and in the absence of cobalt-2,2′-bipyridine complexes.

Scheme

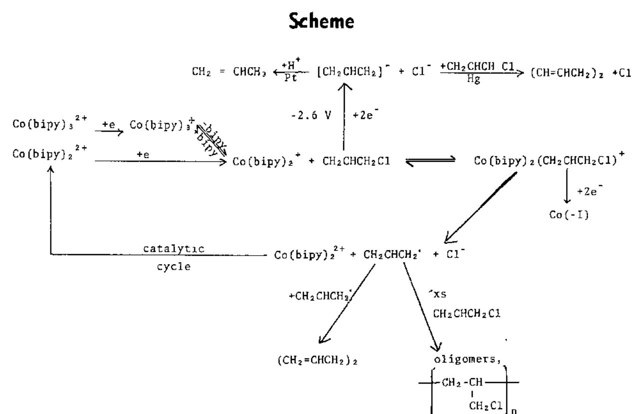

In the absence of cobalt a very negative electrode potential (−2.6V) is required for the reduction of allyl chloride but quantitative reduction can be achieved at −1.4V in the presence of $Co(bipy)_3^{2+}$ (or $Co(bipy)_2^{2+}$). In the catalytic cycle which leads to the reduction, $Co(bipy)_3^{2+}$ is regenerated and this accounts for the enhancement of the reduction wave for this complex in the presence of allyl chloride (Fig. 1-3).

The proposition that the catalytic reduction involves an intermediate in which the allyl chloride is bonded to a complex of cobalt(I) and 2,2′-bipyridine is supported by several pieces of evidence: (*i*) Addition of 2,2′-bipyridine inhibits and eventually eliminates the catalytic reduction of allyl chloride (Fig. 2) even though the production of $Co(bipy)_3^+$ is not impeded; (*ii*) the rate of the catalyzed reduction (as measured by the extent of the enhancement of the cobalt(II) reduction wave in cyclic voltammograms) is much higher when $Co(bipy)_2^+$ is used as catalyst (Fig. 3); (*iii*) the new voltammetric wave at −1500 mV produced by the addition of allyl chloride to solutions of $Co(bipy)_3^{2+}$ resembles in all regards the similar wave produced by acrylonitrile which is believed (1) to correspond to a stable, π-bonded, mixed complex in which the cobalt(I) is reduced to cobalt(−I). With acrylonitrile, the mixed complex is stable toward an intramolecular oxidation-reduction reaction, but with the more readily reducible allyl chloride the mixed complex decomposes as depicted in the Scheme.

The release of chloride anion in the decomposition of the mixed complex was confirmed by the appearance of an anodic wave at +400 mV when a mercury electrode was used to record cyclic voltammograms. That the other initial decomposition product is allyl radical is supported by the coulometric data (Table I). One electron per allyl chloride molecule is consumed in controlled potential electrolyses at ratios of allyl chloride to cobalt near unity. In addition, the appearance of oligomers of allyl chloride at higher ratios (Table I) is a strong indication that allyl radicals are present since the polymerization of allyl chloride requires radical (or cationic) initiation (5).

A rival mechanism for the decomposition of the mixed complex might involve the formation of a π-allyl anion complex of Co(III) similar to a species prepared by Bercaw *et al.* (6) from reaction of allyl alcohol with a mixed cyano and phosphine complex of cobalt(I). Such a reaction sequence seems less attractive for the cobalt 2,2′-bipyridine complexes because $Co(bipy)_2^{3+}$ is a rather strong oxidant ($E_f \sim -70$ mV *vs.* Ag/0.1M Ag^+) and allyl anion is so powerful a reductant ($E_{1/2} \sim -2.0$V *vs.* Ag/0.1M Ag^+) (3) that rapid decomposition of such a complex to $Co(bipy)_2^{2+}$ and allyl radical would be favored unless extraordinary stability were attributed to the bond between cobalt(III) and the π-allyl anion.

Conclusions

The primary purpose of this communication was to point out the remarkable effectiveness of cobalt-2,2′-bipyridine complexes as catalysts in the electroreduction of allyl chloride. The potential where the reduction commences becomes *ca.* 1.2V less negative in the presence of the catalyst. The mechanism proposed for the catalysis includes the initial formation of a π-complex between allyl chloride and $Co(bipy)_2^+$ which parallels the recently described coordination chemistry of $Co(bipy)_2^+$ and acrylonitrile (1). In the latter case, the lower reactivity of acrylonitrile terminates the reaction sequence with the coordination but with allyl chloride an intramolecular oxidation-reduction reaction ensues. Allyl bromide is itself reduced at potentials only slightly more negative than that at which $Co(bipy)_3^{2+}$ is reduced but addition of the latter does result in the catalyzed reduction of allyl bromide.

The ability of a number of activated olefins to form π-bonds with low valent cobalt-2,2′-bipyridine complexes (1) suggests that these complexes may serve a general role as catalytic agents for the reduction of sufficiently activated (*e.g.*, allyl chloride but not allyl alcohol or acrylonitrile) coordinated molecules.

Acknowledgments

This work was supported by the National Science Foundation. A Chaim Weizmann Fellowship supplied partial support for S.M.

Manuscript submitted Sept. 12, 1977; revised manuscript received *ca.* March 25, 1978.

Any discussion of this paper will appear in a Discussion Section to be published in the June 1979 JOURNAL. All discussions for the June 1979 Discussion Section should be submitted by Feb. 1, 1979.

REFERENCES

1. S. Margel, W. Smith, and F. C. Anson, *This Journal*, **125**, 241 (1978).
2. N. Tanaka and Y. Sato, *Bull. Chem. Soc. Jpn.*, **41**, 2059 (1968).
3. J. P. Petrovich and M. M. Baizer, *Electrochim. Acta*, **12**, 1249 (1967).
4. M. M. Baizer and J. L. Chruma, *J. Org. Chem.*, **37**, 1951 (1972).
5. E. Schildknecht, "High Polymers," Vol. XXVIII, p. 156, 707, Wiley Interscience, New York (1973).
6. J. E. Bercaw, L. Y. Goh, and J. Halpern, *J. Am. Chem. Soc.*, **94**, 6534 (1972).

Interfacial Behavior of *D*-Ribose, 2′-Deoxy-*D*-Ribose, and *D*-Ribose 5′-Phosphate

Viktor Brabec, Sherril D. Christian, and Glenn Dryhurst

Department of Chemistry, University of Oklahoma, Norman, Oklahoma 73019

ABSTRACT

The adsorption of *D*-ribose, 2′-deoxy-*D*-ribose, and *D*-ribose 5′-phosphate at the mercury electrode-electrolyte solution interface at *p*H 8.0 (0.5*M* NaF plus 0.01*M* Na_2HPO_4) has been studied by electrocapillary measurements. Each of these compounds is only weakly adsorbed with the free sugars being adsorbed at potentials close to the potential of zero charge (electrocapillary maximum potential). *D*-ribose 5′-phosphate, being extensively ionized at *p*H 8.0, is adsorbed mainly at a positively charged electrode. The areas occupied by these molecules at monolayer surface saturation suggest that they are all adsorbed with the average plane of atoms of the 5-membered sugar ring parallel to the electrode surface, *i.e.*, in a flat surface orientation. Information about the interfacial behavior of these sugars and sugar phosphate has been used to interpret in more detail the interfacial conformation of purine and pyrimidine nucleosides and nucleotides adsorbed at an electrode surface. It appears that pyrimidine nucleosides and nucleotides, such as uridine and uridine 5′-monophosphate, are adsorbed with the planar pyrimidine base adsorbed in a flat orientation on the electrode. The sugar residues must be adsorbed perpendicular to the electrode surface. Since pyrimidine nucleosides and nucleotides preferentially adopt an *anti* conformation, these molecules occupy significantly more surface area than the base. On the other hand, purine nucleosides and nucleotides, such as those of adenine, adopt a *syn* conformation in the adsorbed state at monolayer surface saturation. Again the purine base is adsorbed in a flat orientation on the electrode. This results in the sugar or sugar phosphate residues being largely rotated out of the plane of the electrode surface so that the adenine moieties can pack closely together. It is for this reason that the areas occupied by adenine, deoxyadenosine, and deoxyadenosine 5′-monophosphate are close to those observed for the free purine base.

Recent reports from this laboratory have described the interfacial behavior of adenine (1), thymine (2), and uracil (3) and their nucleosides and nucleotides at the mercury-aqueous solution interface at *p*H 8-9. These purines and pyrimidines are found naturally in all living organisms, particularly as components of nucleic acids. We are attempting to interpret the interfacial behavior of the purine and pyrimidine constituents of nucleic acids with a view to ultimately understanding the interfacial behavior of the complex nucleic acids themselves. There is considerable literature evidence that the nucleic acids are extensively associated with charged biological surfaces, such as the surfaces of mammalian cells and other biological membranes (4-7). There are indications that interactions of nucleic acids with biological interfaces (adsorption and subsequent conformational changes) are a prerequisite for the manifestation of the biological effects of these polynucleotides in mammalian systems *in vivo* and *in vitro* (8-10). It has also been known for some time that electric fields having magnitudes equivalent to those existing within the inner double layer at a charged cell surface-biological fluid interface affect the conformation of various polynucleotides in solution (11-13).

Recent work by Brabec and Palecek (14) strongly suggests that various double-stranded polynucleotides unfold at certain potentials at a mercury electrode.

We are employing a mercury electrode-electrolyte solution interface as a model of a biological surface-biological fluid interface to study the interfacial behavior of the constituents of nucleic acids and, ultimately, of natural and biosynthetic polynucleotides.

All of the compounds that we have studied exhibit an initial adsorption region where they are adsorbed with the virtually planar purine or pyrimidine residue in a flat orientation on the electrode surface. This region has been referred to as the dilute adsorption region (1-3, 15). In the case of thymine and uracil a surface reorientation process occurs at critical concentrations and potentials such that the molecules adopt a perpendicular stance on the electrode (3, 16). We suspect that a similar reorientation occurs with the adenine derivatives although this is currently being investigated.

In order to facilitate further discussion some results relevant to this paper for adenine and uracil and their nucleosides and nucleotides in the dilute adsorption region are presented in Table I. It will be noted that in the adenine series the areas occupied by adenine and its nucleosides and nucleotides are very similar. This has been interpreted (1) as indicating that primarily the adenine residue is adsorbed to the electrode

Table I. Adsorption parameters for adenine, uracil, and their nucleosides and nucleotides in the dilute adsorption region

Compound	Buffer system	ΔG°*/cal	Area/Å² per molecule	Reference
Adenine	Borate, *p*H 9.0**,†	−4428	55 ± 4	(1)
Deoxyadenosine	Borate, *p*H 9.0	−5695	55 ± 4	(1)
Deoxyadenosine 5′-monophosphate	Borate, *p*H 9.0	−4948	67 ± 8	(1)
Adenine	Fluoride, *p*H 8.0‡	−4413	53 ± 3	§
Adenosine	Fluoride, *p*H 8.0	−5832	55 ± 3	
Adenosine 5′-monophosphate	Fluoride, *p*H 8.0	−4887	63 ± 2	§
Uracil	Fluoride, *p*H 8.0†,‡	−2996	64 ± 3	(3)
Uridine	Fluoride, *p*H 8.0	−4177	104 ± 4	(3)
Uridine 5′-monophosphate	Fluoride, *p*H 8.0	−3863	120 ± 4	(3)

* Standard free energy of adsorption at the electrocapillary maximum potential for pure background electrolyte solution, based on infinite dilution standard states for the adsorbate, both in solution (at unit molarity) and on the surface (at unit value of $\theta/1 - \theta$). In fluoride buffer the ECM occurs at −0.433V; for the borate buffer the ECM potential is −0.500V.

** $Na_2B_4O_7$, KCl, HCl buffer *p*H 9, ionic strength 0.5.

† There is no significant difference between the adsorption results at *p*H 8.0 in fluoride solution and *p*H 9.0 borate buffer (15).

‡ 0.5*M* NaF with 0.01*M* Na_2HPO_4, *p*H 8.0.

§ From work in progress in this laboratory.

surface with substituent ribose, deoxyribose, ribosephosphate, or deoxyribosephosphate groups being largely tilted away from the electrode surface at surface saturation, *i.e.*, as $\theta \to 1$. However, in the case of the uracil series, the areas occupied by the nucleoside and nucleotide are significantly larger than for the free base. This has been interpreted (3, 16) as indicating that substituent sugar or sugar-phosphate groups remain in the vicinity of the electrode surface at surface saturation.

The standard free energy of adsorption of these various purine and pyrimidine derivatives reveal that the nucleosides and nucleotides have significantly larger negative ΔG° values than the free bases (Table I). The ΔG° values reported in Table I are those at the ECM potential for the supporting electrolyte. The same general trend is also noticed at the potentials of maximum adsorption of each species, which are normally within *ca.* 50 mV of the ECM potential for pure supporting electrolyte solution. These observations imply that the sugar and sugar phosphate residues enhance the adsorption of these compounds at potentials in the region of maximum adsorption.

This investigation was initiated, therefore, to elucidate the interfacial behavior of *D*-ribose, 2′-deoxy-*D*-ribose, and *D*-ribose 5′-phosphate at the mercury-solution interface. The very high cost of 2′-deoxy-*D*-ribose 5′-phosphate precluded an investigation of this material, although we expect it to parallel *D*-ribose 5′-phosphate.

Experimental

Chemicals.—*D*-Ribose, 2′-deoxy-*D*-ribose, and *D*-ribose 5′-phosphate were obtained from Calbiochem and were used without further purification. All measurements were performed in 0.5*M* sodium fluoride with 0.01*M* Na_2HPO_4, *p*H 8.0. Samples were weighed directly into this supporting electrolyte solution and, after dissolution, deaerated with water-saturated nitrogen before study.

Differential capacitance measurements.—Differential capacitance measurements were obtained by the phase-selective a-c polarographic method outlined in previous reports (1, 2). Differential capacitance *vs.* potential (*C vs. E*) curves for *D*-ribose, 2′-deoxy-*D*-ribose, and *D*-ribose 5′-phosphate were not coincident with the *C vs. E* curve of pure background electrolyte solution at very negative potentials. It was not possible, therefore, to use the double back-integration method of Grahame *et al.* (17) to calculate interfacial tension values.

Direct interfacial tension measurements.—An apparatus for interfacial tension measurements, similar to that used by Hansen *et al.* (18) and described in detail elsewhere (16), was utilized. A J-shaped Pyrex capillary was employed; this capillary was siliconized. With this capillary, the pressure at a particular applied potential necessary to cause mercury drops to form at the capillary tip was measured with a Mensor Corporation Quartz Manometer pressure gauge. This method is, of course, a maximum bubble pressure experiment. The internal radius, *r*, of the J-shaped capillary at its tip was 0.004105 cm; hence, the total measured pressure, Δp, is directly proportional to the interfacial tension, γ, by the relationship

$$\gamma = \frac{\Delta p}{2r} \quad [1]$$

The value of *r* was determined with 0.10*N* $HClO_4$ where the interfacial tension at −0.500V at 25°C is 425.56 dyne cm^{-1} (18). All potentials are referred to the saturated calomel electrode at 25°C.

Measurements of interfacial tension were normally taken at 50 mV intervals between −0.2 and −1.8V.

In order to obtain charge values from interfacial tension measurements, the electrocapillary data were first fitted to a sixth-order polynomial of the type $\gamma = A_1(E - E_{ECM})^2 + A_2(E - E_{ECM})^3 + \ldots A_5(E - E_{ECM})^6$, where E_{ECM} is the potential of the electrocapillary maximum. A nonlinear least squares procedure was employed to obtain optimum values of all parameters. The root mean square (rms) deviation observed over all concentrations for each adsorbate never exceeded 0.1 dyne cm^{-1}. The use of polynomials of higher degrees did not improve the γ *vs. E* fit. Charge, *q*, *vs.* potential, *E*, curves were then obtained by analytical differentiation of the fitted electrocapillary curves with respect to potential.

Results and Discussion

Because it was necessary to employ quite high concentrations of the sugars studied in order to obtain significant changes in interfacial tension, the activities of each compound were measured over the entire concentration range of interest in fluoride buffer *p*H 8.0. Solute activities were inferred from surface spreading pressure-surface charge data by methods which have been outlined elsewhere (19). In the case of *D*-ribose, 2′-deoxy-*D*-ribose, and *D*-ribose 5′-phosphate there was no evidence for activity being different from concentration even at the highest bulk-solution concentrations used (*vide infra*).

Typical electrocapillary curves (γ *vs. E*) for *D*-ribose, 2′-deoxy-*D*-ribose, and *D*-ribose 5′-phosphate are shown in Fig. 1. These curves indicate that all three compounds are adsorbed, *i.e.*, decrease interfacial tension compared to pure supporting electrolyte solution. *D*-ribose 5′-phosphate is adsorbed extensively only at potentials more positive than about −0.6V.

From γ *vs. E* data of the type presented in Fig. 1 the surface spreading pressure, π, as a function of electrode potential, *E*, and solute activity, *a*, was calculated from Eq. [2]

$$\pi = \gamma_w(E) - \gamma(E) \quad [2]$$

where γ_w is the value of the interfacial tension for the pure background electrolyte solution at $a = 0$.

For each compound studied, plots of π *vs.* the logarithm of the solute activity had the same geometrical shape at different potentials and, hence, were superimposable by abscissa translation (Fig. 2). The calculated curve in Fig. 2 represents the least squares fit of π, *a*, and *E* data to the empirical equation

$$\pi = A\{\ln[1 + Ba]\}\left[1 + \frac{\alpha a}{(1 + Ba)^2} + \frac{\beta_a{}^2}{(1 + Ba)^3} + \cdots\right] \quad [3]$$

In this equation *A* is equal to $\Gamma_m RT$, where Γ_m is the surface excess of the solute at $\theta = 1$. The detailed method of applying this equation has been outlined in previous reports (2, 3, 16).

Once a composite fit was obtained for data at several potentials, the same functional form was used to fit data at fixed potentials. In performing these fits it was assumed that the value of $\Gamma_m RT$ (or *A* in Eq. [3]) was constant, which is quite reasonable considering the excellent composite π *vs.* ln *a* fits. Analytical differentiation of the π *vs.* ln *a* fits obtained at fixed potentials gives, according to the Gibbs equation (Eq. [4])

$$\Gamma = \frac{1}{RT} \cdot \frac{d\pi}{d \ln a} \quad [4]$$

the value of ΓRT corresponding to each activity at each electrode potential.

The congruence of adsorption isotherms with respect to both potential and charge was tested for in the following fashion (2, 3, 16). In order to test for congruence with respect to potential plots of charge, *q vs.* ΓRT were prepared at fixed potentials. Throughout ranges of potential where *q vs.* ΓRT plots are linear the

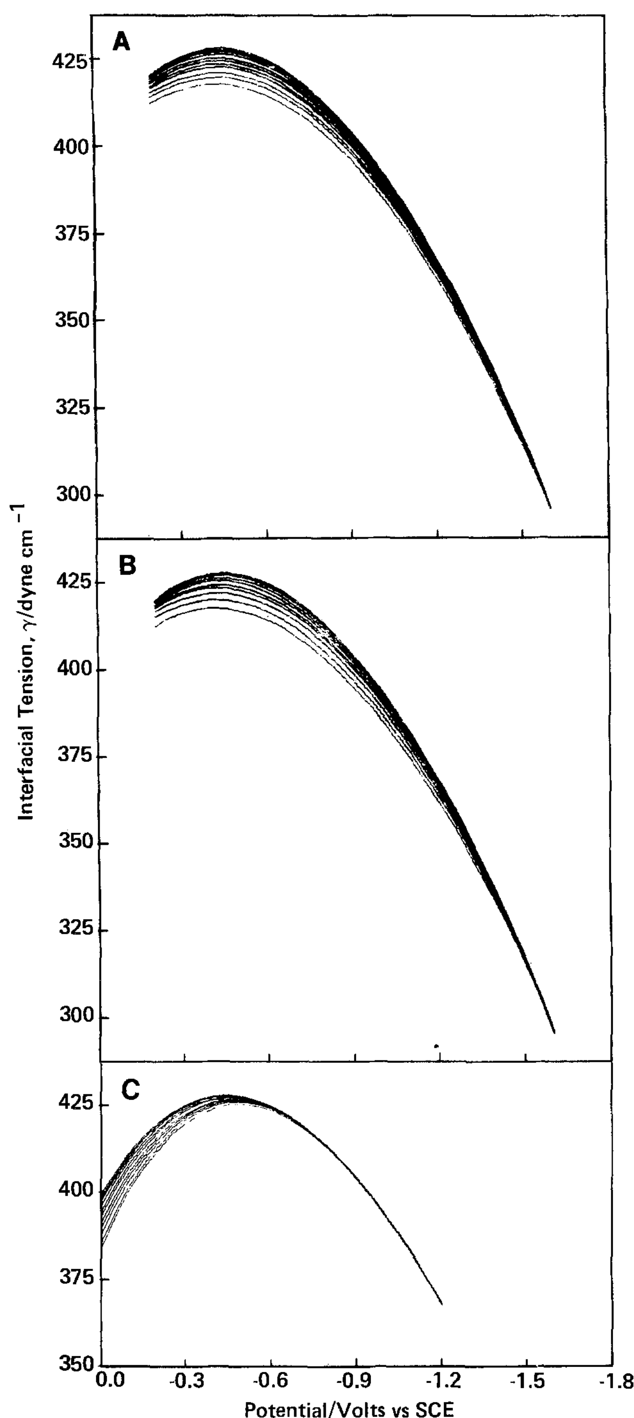

Fig. 1. Electrocapillary curves for (A) *D*-ribose (0-300 mM), (B) 2′-deoxy-*D*-ribose (0-100 mM), and (C) *D*-ribose 5′phosphate (0-200 mM) in 0.5*M* NaF with 0.01*M* Na_2HPO_4 buffer *p*H 8.0. Interfacial tension, γ, was measured by the maximum bubble pressure method.

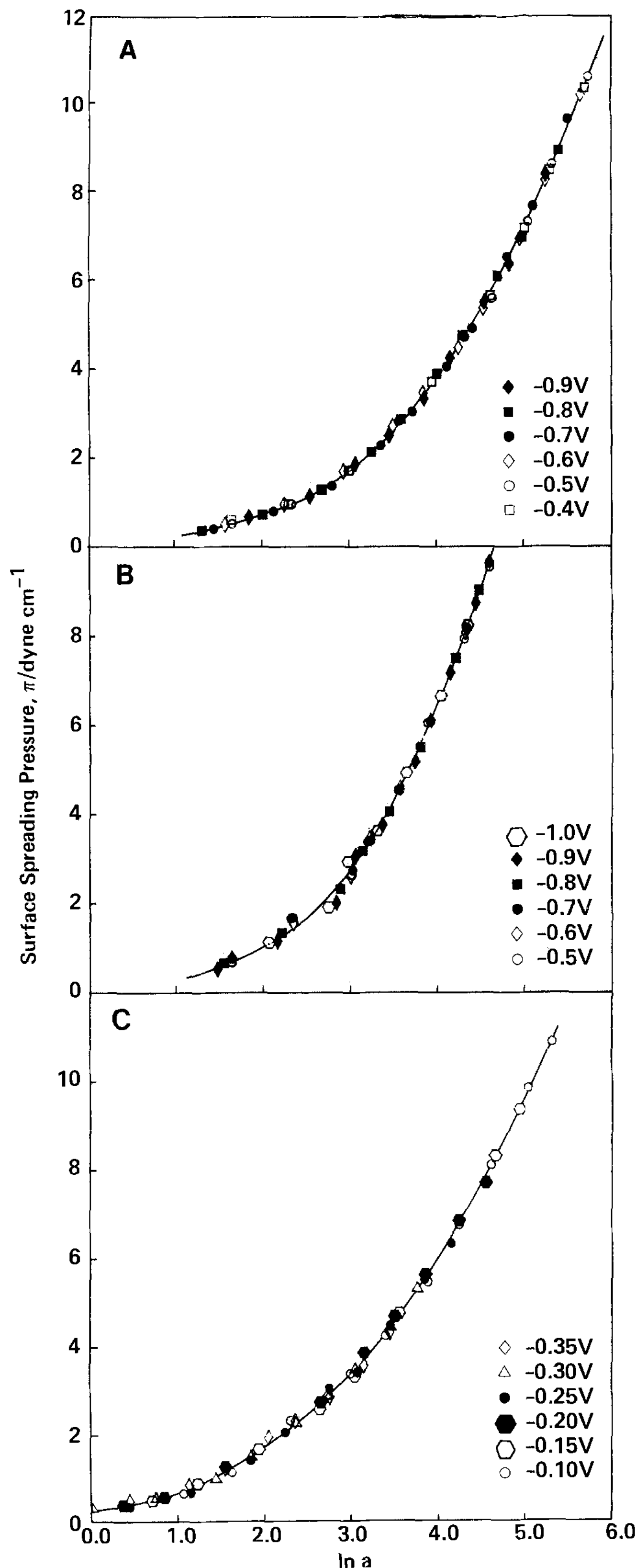

Fig. 2. Composite π *vs.* ln *a* plots for (A) *D*-ribose, (B) 2′deoxy-*D*-ribose, and (C) *D*-ribose-5′-phosphate in 0.5*M* NaF with 0.01*M* Na_2HPO_4 *p*H 8.0. Potentials for each point are indicated in the figure. Data were obtained from maximum bubble pressure experiments. The solid line is the best least squares fit of all π, *a*, *E* data. The rms deviation in π from the calculated curve for (A) is 0.094 dyne cm^{-1}, (B) 0.133 dyne cm^{-1}, and for (C) 0.096 dyne cm^{-1}.

isotherms must be congruent with respect to potential. Charge values at each potential and solute activity were obtained by analytical differentiation of electrocapillary curves (see Experimental). The values of ΓRT at the same potential and solute activity were obtained by analytical differentiation of individual π *vs.* ln *a* curves and hence are independent of any adsorption model. Typical *q* *vs.* ΓRT data for *D*-ribose, 2′-deoxy-*D*-ribose, and *D*-ribose 5′-phosphate are shown in Fig. 3. It is clear that for *D*-ribose and 2′-deoxy-*D*-ribose (Fig. 3A and B) the isotherms are congruent with respect to potential between at least -0.2 and -1.1V. In the case of *D*-ribose 5′-phosphate (Fig. 3C), however, the congruence conditions prevail between -0.1 and *ca.* -0.4V. At potentials more negative than -0.4V ΓRT values become extremely small. It is possible that the reason for the apparent noncongruence

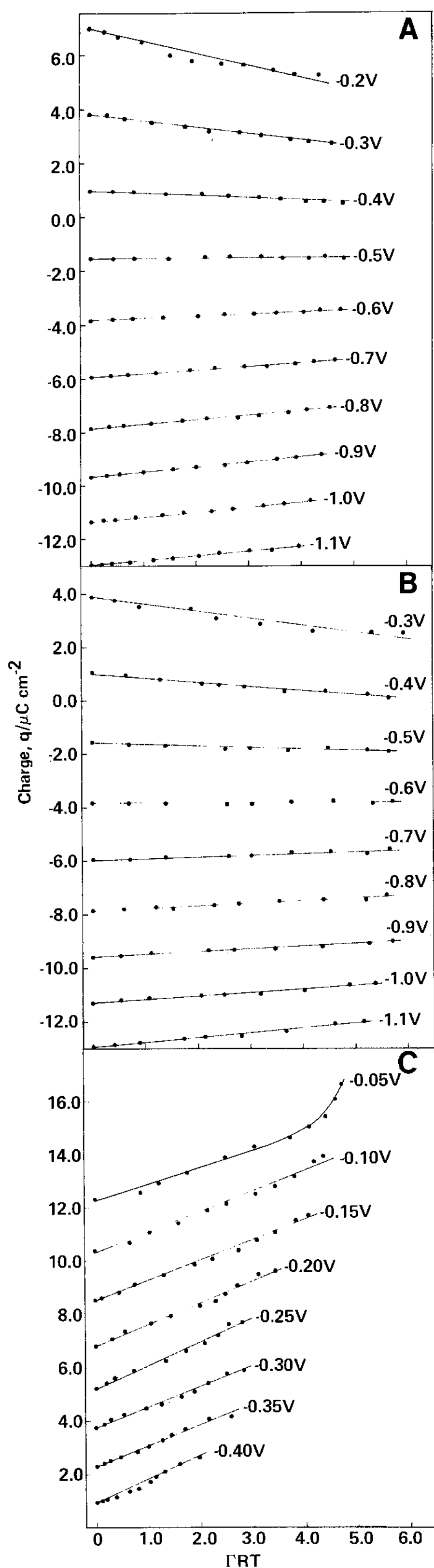

Fig. 3. Test of congruence of electrosorption isotherms with respect to potential in 0.5M NaF with 0.01M Na_2HPO_4 pH 8.0 for (A) D-ribose, (B) 2′-deoxy-D-ribose, and (C) D-ribose 5′-phosphate. Potential values are shown in the figure. Data obtained from maximum bubble pressure results.

of the isotherms of D-ribose 5′-phosphate at −0.05V (Fig. 3C) is that at this positive potential significant oxidation of the mercury electrode begins to take place.

Nevertheless, the plots shown in Fig. 3 indicate that, over the range of accessible potentials were the compounds adsorb to an appreciable extent, the adsorption isotherms are congruent with respect to potential.

Plots of potential, E *vs.* ΓRT at fixed charge values were prepared to decide whether the electrosorption isotherms were congruent with respect to charge (2, 3, 16). Excellent linear relationships between E and ΓRT were noted over a relatively large range of charge values (Fig. 4) which implies that the electrosorption

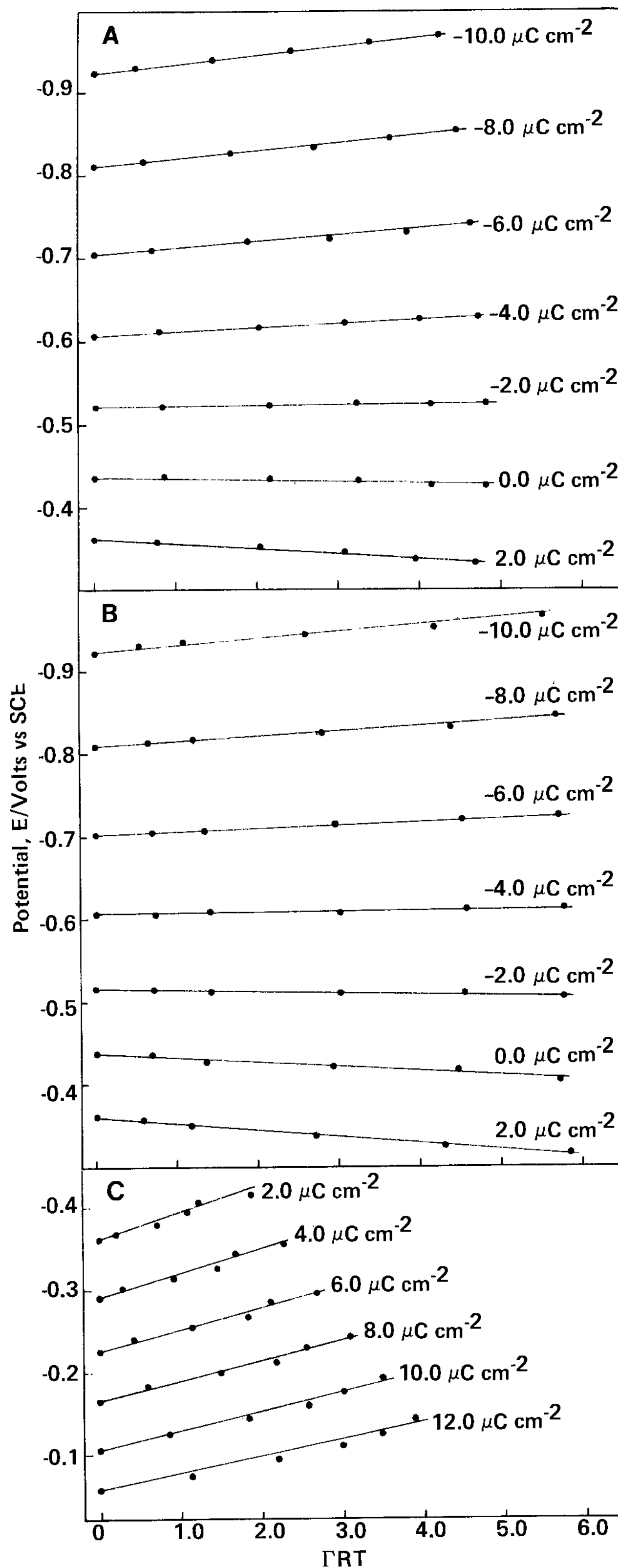

Fig. 4. Test of congruence of electrosorption isotherms with respect to charge in 0.5M NaF with 0.01M Na_2HPO_4 pH 8.0 for (A) D-ribose, (B) 2′-deoxy-D-ribose, and (C) D-ribose 5′-phosphate. Charge values are shown in the figure. Data obtained from maximum bubble pressure results.

of the sugars and sugar phosphate is apparently congruent with respect to charge.

The observation that the adsorption isotherms of these compounds are congruent with respect to both potential and charge has been noted for other compounds (16). Such behavior is expected for organic solutes having relatively large C' values [where C' is the capacitance at complete monolayer saturation and which is assumed to be constant and independent of potential (20)], at relatively low surface activity (21).

Since the electrosorption isotherms of *D*-ribose, 2′-deoxy-*D*-ribose, and *D*-ribose 5′-phosphate are all congruent with respect to potential, π, E, and a data were fitted to the Frumkin isotherm model. The fixed potential form of the Frumkin equation is shown below (Eq. [5])

$$\frac{\theta}{1-\theta} = Ba \exp 2\alpha\theta \qquad [5]$$

where θ is the fractional surface coverage, and B and α are constants depending on interactions between the adsorbed molecules and the electrode surface and on lateral intermolecular interactions between the adsorbed organic molecules, respectively. The constant B is dependent on potential according to Eq. [6] (22)

$$B = B_0 \exp -[\phi/\Gamma_m RT] \qquad [6]$$

where the function ϕ is defined in Eq. [7]

$$\phi = [\gamma_w(O) - \gamma_w(E)] + C'EE_N - \frac{C'E^2}{2} \qquad [7]$$

In this expression E is the potential relative to the ECM potential for the pure supporting electrolyte solution, E_N is the ECM potential for $\theta = 1$, and γ_w is the interfacial tension for the pure electrolyte solution. The term B_0 in Eq. [6] is the value of the constant B at the ECM potential for pure electrolyte solution. Combination of Eq. [5] and [6] gives the generalized form of the Frumkin equation (Eq. [8])

$$\frac{\theta}{1-\theta} = B_0 a \exp (2\alpha\theta) \cdot \exp -[\phi/\Gamma_m RT] \qquad [8]$$

The parameters C', E_N, α, B_0, and Γ_m are evaluated from Eq. [7] and [8] by a nonlinear least squares method described extensively elsewhere (1, 2, 16).

Some reduced isotherms for all three solutes studied are shown in Fig. 5. Experimental ΓRT values were obtained by differentiation of π *vs.* ln a plots at individual potentials. The solid curve is the best fit of all π, E, and a data to the Frumkin model. The individual experimental points, which were obtained without assuming an adsorption model, were in excellent agreement with the calculated Frumkin isotherm. The superimposability of the isotherms at various potentials shown in Fig. 5 may also be regarded as a test of congruence of the electrosorption isotherms as a function of potential (23).

Detailed results of analysis of π, E, and a data for *D*-ribose, 2′-deoxy-*D*-ribose, and *D*-ribose 5′-phosphate are presented in Table II. A number of conclusions may be drawn from these results and those presented elsewhere in this report. First, the free energy of adsorption, $\Delta G°$, at the ECM potential indicates that in the potential regions where adenine, uracil, and their derivatives are most strongly adsorbed (*ca.* −0.4 to −0.6V) the sugar and sugar phosphate groups are significantly less strongly adsorbed than the molecules which contain a purine or pyrimidine base residue. The sugar and sugar phosphate groups are not appreciably adsorbed at very negative potentials.

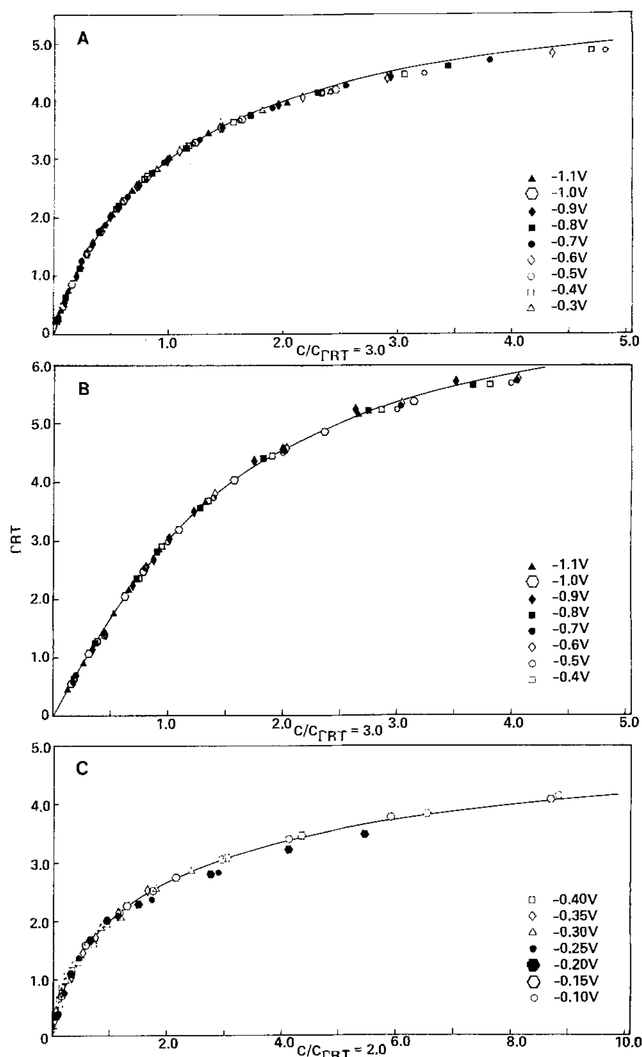

Fig. 5. Reduced adsorption isotherms in 0.5*M* NaF with 0.01*M* Na_2HPO_4 *pH* 8.0 for (A) *D*-ribose, (B) 2′-deoxy-*D*-ribose, and (C) *D*-ribose 5′-phosphate. The solid line is the best fit of all π, E, and a data to the generalized Frumkin equation with (A) $\alpha = 0.28$, $B_0 = 16.45 \times 10^3$, $\Gamma_m RT = 6.76$, $C' = 17.42$ μF cm^{-2}, $E_N = -0.414$V; (B) $\alpha = 0.41$, $B_0 = 20.83 \times 10^3$, $\Gamma_m RT = 7.47$, $C' = 17.86$ μF cm^{-2}, $E_N = -0.395$V; and (C) $\alpha = -0.91$, $B_0 = 3.83 \times 10^3$, $\Gamma_m RT = 5.86$, $C' = 33.68$ μF cm^{-2}, $E_N = -0.539$V. Potentials are shown in the figure.

Table II. Parameters of the generalized Frumkin equation for *D*-ribose, 2′-deoxy-*D*-ribose, and *D*-ribose 5′-phosphate determined from maximum bubble pressure measurements at *pH* 8.0*

Compound	α	C'** (μF cm^{-2} cal)	$\Delta G°$† (cal)	E_N‡ (volt *vs.* SCE)	Γ_m/mole (cm^{-2} × 10^{10})	Area per molecule
D-ribose	−0.28 ± 0.11	17.42	−1657	−0.414 ± 0.002	2.73	61 ± 4
2′-deoxy-*D*-ribose	0.41 ± 0.11	17.85	−1796	−0.395 ± 0.005	3.01	55 ± 6
D-ribose 5′-phosphate	−0.91 ± 0.35	33.68	−794	−0.539 ± 0.023	2.37	70 ± 11

* 0.5*M* NaF with 0.01*M* Na_2HPO_4, *p*H 8.0.
** Capacitance of monolayer covered electrode surface.
† Standard free energy of adsorption at the ECM potential for pure background electrolyte solution based on infinite dilution standard states for the adsorbate both in solution (at unit molarity) and on the surface (at unit value of $\theta/1-\theta$). $\Delta G° = -RT \ln B_0$.
‡ ECM potential when $\theta = 1$.

The area occupied by D-ribose is 61Å^2, by 2'-deoxy-D-ribose 55Å^2, while that occupied by D-ribose 5'-phosphate is 70Å^2 (Table II).

In order to decide from the latter values the probable surface orientation of each of the molecules, projected areas were calculated based on their crystal structures (24). These areas were calculated for each molecule in two orientations. The first was the area that the molecule would be expected to occupy when the approximately planar sugar ring system is in a flat orientation on the electrode surface [specifically, with the plane formed by the C'(1), O'(1), and C'(4) atoms parallel to the electrode surface]. The second was the area the molecule should occupy when the approximately planar sugar ring is perpendicular to the electrode surface [*i.e.*, the plane formed by C'(1), O'(1), and C'(4) atoms]. These areas were calculated using the ORTEP programs of Johnson (25). Some typical projected areas for D-ribose, 2'-deoxy-D-ribose, and D-ribose 5'-phosphate with the sugar ring in a flat surface orientation are shown in Fig. 6. Projected areas for the same molecules with the sugar ring in a perpendicular surface orientation are presented in Fig. 7. It should be noted that the areas shown in Fig. 6 and 7 are based on the C'(3)-*endo* conformation of D-ribose and the C'(2)-*endo* conformation of 2'-deoxy-D-ribose. These conformations were used because in RNA D-ribose is in the C'(3)-*endo* form while in the common form of DNA (B-DNA) the 2'-deoxy-D-ribose occurs in the C'(3)-*endo* conformation. An excellent review of the conformation of purine and pyrimidine bases, nucleosides, and nucleotides has been prepared by Ts'o (26).

The projected areas occupied by D-ribose, 2'-deoxy-D-ribose, and D-ribose 5'-phosphate in the flat surface orientation are 52, 39, and 59Å^2, respectively (Fig. 6). When in a perpendicular surface orientation the projected areas occupied by D-ribose and 2'-deoxy-D-ribose are 43 and 45Å^2, respectively, while for D-ribose 5'-phosphate the area with the perpendicular orientation of the sugar, 61Å^2, is essentially identical to that observed for the flat orientation of the sugar, 59Å^2 (Fig. 7).

Comparison of the projected areas shown in Fig. 6 and 7 with the measured areas at the electrode surface at surface saturation (Table II) clearly supports the view that in the case of D-ribose the molecule is probably adsorbed at the electrode surface in a flat orientation.

Since the projected area of 2'-deoxy-D-ribose in the flat and perpendicular orientations (39 and 45Å^2, respectively) are so similar it is difficult to be certain of the real surface orientation. However, by analogy with D-ribose it seems reasonable to assume that the flat orientation is more likely. The projected area of D-ribose 5'-phosphate is also virtually the same when the sugar residue is flat or perpendicular to the electrode and both areas are close to that observed from experimental measurements. However, in view of the flat surface orientation of the free sugars, it is probable that the sugar phosphate is also adsorbed with the sugar in a flat orientation.

Interfacial behavior of nucleosides and nucleotides.—The results presented in this report indicate that D-ribose, 2'-deoxy-D-ribose, and D-ribose 5'-phosphate are relatively weakly adsorbed (Table II) and only at potentials close to the ECM potential for pure supporting electrolyte solution. The electrode areas occupied by these molecules at surface saturation have been measured experimentally and indicate that they are probably adsorbed with the sugar ring in a flat surface orientation.

These results may be used to better understand the surface conformation of purine and pyrimidine nucleosides and nucleotides at the electrode/solution interface. Typical adsorption parameters for adenine and uracil and their nucleosides and nucleotides are presented in Table I.

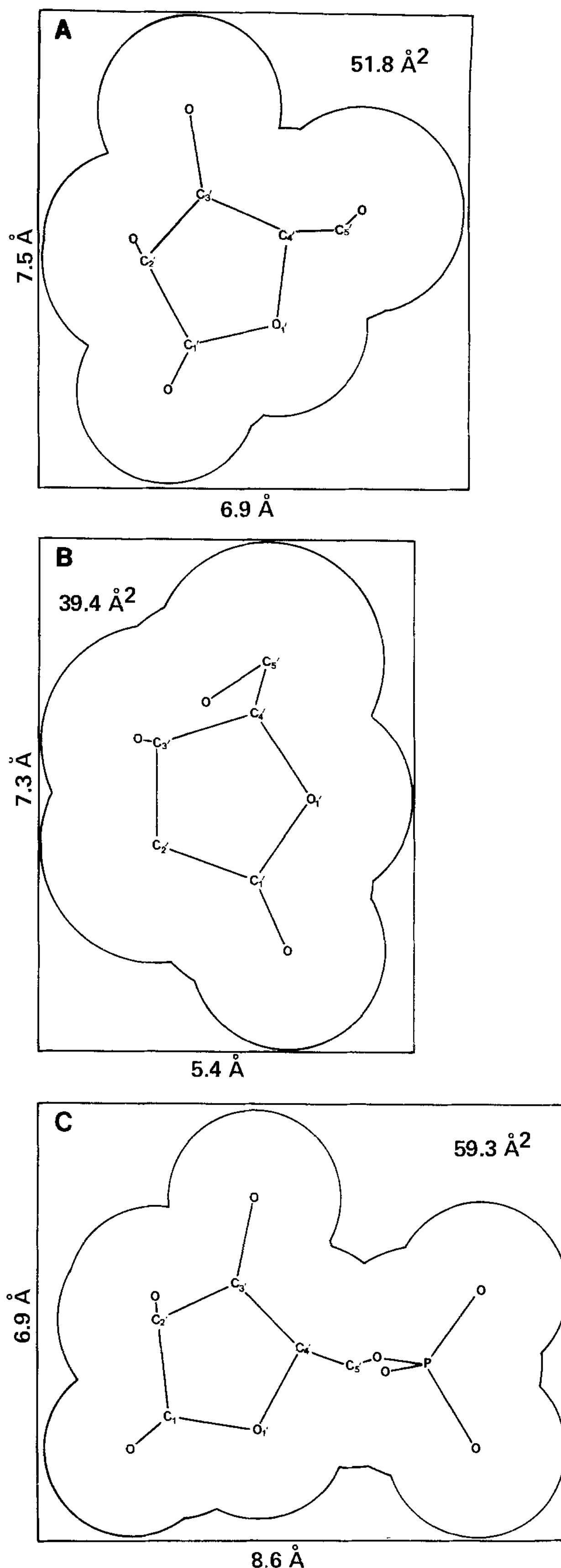

Fig. 6. Projected areas occupied by (A) D-ribose, (B) 2'-deoxy-D-ribose, and (C) D-ribose 5'-phosphate when the sugar ring is in a flat surface orientation. The projections refer to the C(3) *endo* conformation of the ribose residue and C'(2) *endo* conformation of deoxyribose.

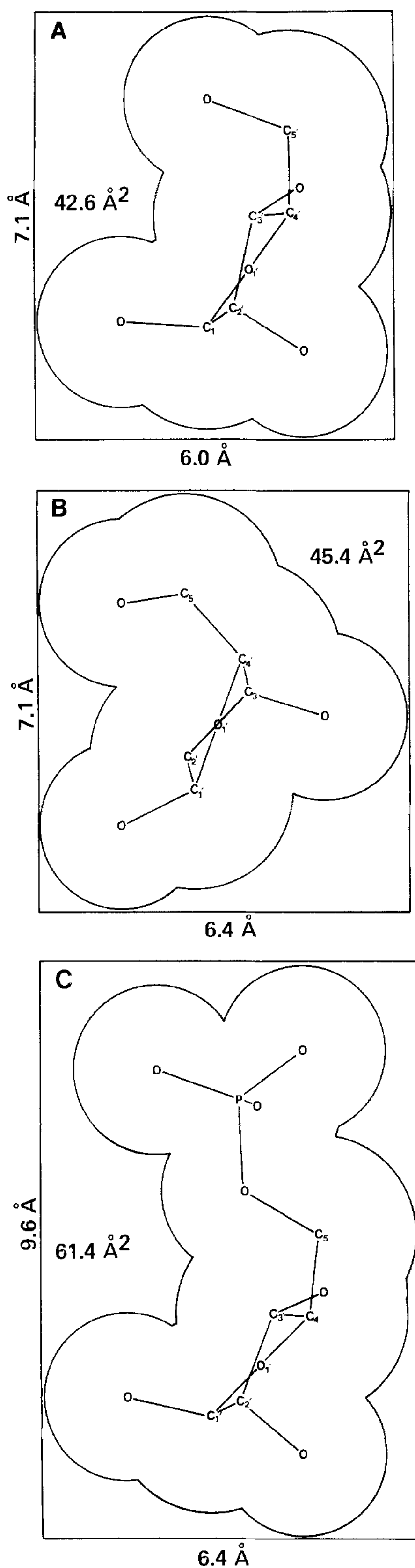

Fig. 7. Projected areas occupied by (A) *D*-ribose, (B) 2'-deoxy-*D*-ribose, and (C) *D*-ribose 5'-phosphate when the sugar ring is in a perpendicular surface orientation. The projections refer to the C'(3) *endo* conformation of the ribose residue and C'(2) *endo* conformation of the deoxyribose residue.

In considering the adsorption of such purine and pyrimidine nucleosides and nucleotides it seems reasonable to conclude that the base residue will preferentially adsorb with the planes of the rings parallel to the surface. This is so because the base is always more strongly adsorbed than the sugar or sugar phosphate residue (compare $\Delta G°$ values in Tables I and II). If the purine or pyrimidine base residue is adsorbed with plane of the ring parallel to the electrode surface, then it is clearly impossible for the sugar residue to adopt a similar surface orientation because the average plane of atoms in the sugar ring is approximately perpendicular to the base ring system (26).

The conformations of purine and pyrimidine nucleosides and nucleotides can be better understood by consideration of the sugar-base torsion angle, ϕ_{CN}, and the related *syn* and *anti* conformations which are defined in Fig. 8.

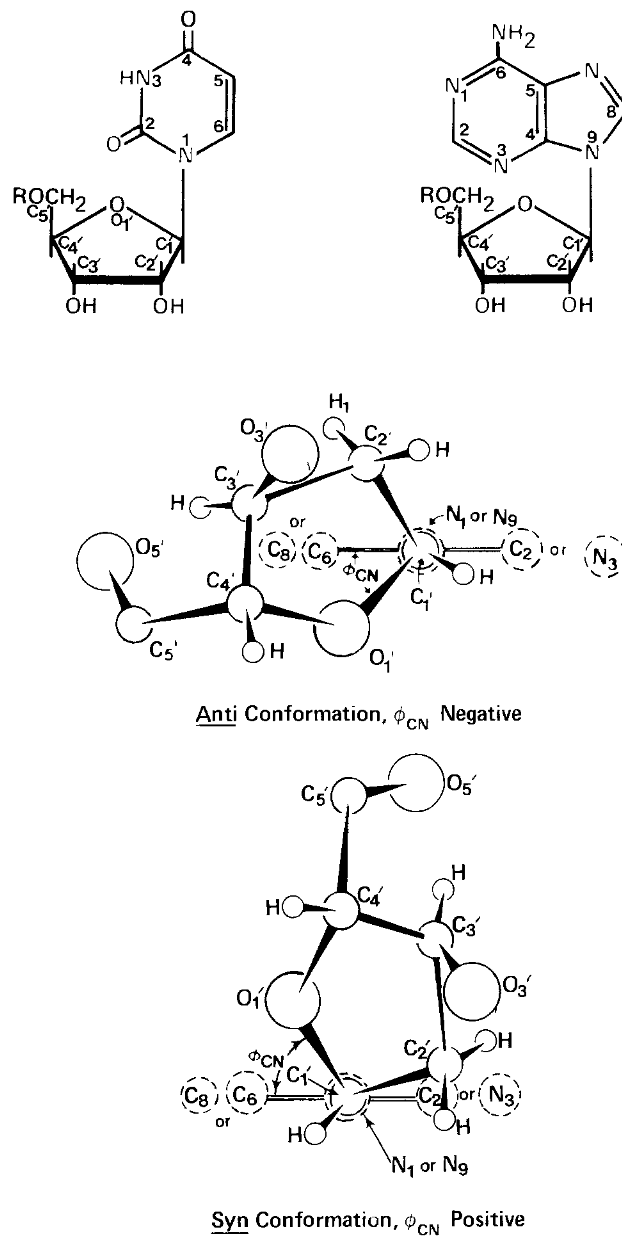

Fig. 8. Schematic illustration of the torsion angle in a pyrimidine or purine nucleoside [after Ts'o (26) and Hashemeyer and Rich (27)]. The plane of the base is viewed end-on with the glycosyl bond between C'(1) and *N*(1) (for a pyrimidine) or *N*(9) (for a purine) of the base perpendicular to the page. The torsion angle, ϕ_{CN}, is the dihedral angle between the plane of the base and the plane formed by the C'(1) to *N*(1) bond. The torsion angle is zero when *O*'(1) lies directly in front of C(6) [or C(8) for a purine] and positive angles are measured when C'(1) to *O*'(1) is rotated in a clockwise direction when viewing from C'(1) to *N*. When ϕ_{CN} is negative (*ca.* $-30°$) the system is in an *anti* conformation. When ϕ_{CN} is positive (*ca.* $+150°$) the system is in a *syn* conformation (28).

Extensive x-ray diffraction studies have revealed that pyrimidine nucleosides and nucleotides, including those of uracil, have negative values of ϕ_{CN} and exist in the *anti* conformation (26). In the case of thymidine ϕ_{CN} is $-39°$ (29) while for uridine the value is probably similar (26). In the case of deoxyadenosine [$\phi_{CN} = -3°$ (30)] the *anti* conformation is also adopted. However, the extensive studies of Haschemeyer and Rich (27) and others (31, 32) indicate that for the pyrimidine nucleosides and nucleotides the barriers between the *syn* and *anti* conformations are large. On the other hand, the steric barrier to the interconversion between *syn* and *anti* conformations in purine nucleosides and nucleotides is very low. The difference in energy between the *syn* and *anti* forms in the purine systems is probably quite small, although somewhat larger energy differences may exist for the pyrimidine systems.

In the *anti* conformation with a value of ϕ_{CN} of about $-30°$ and the base plane parallel to the electrode surface molecular models reveal that the surface area occupied by uridine should be equal to the projected area of the base [53Å^2 (3)] plus the projected area of the *D*-ribose moiety in a perpendicular orientation [43Å^2 (Fig. 7)] for a total area of 97Å^2. This is very close to the area occupied by uridine measured by capacitance and maximum bubble pressure techniques [104Å^2, Table I (2)]. Similarly, the area occupied by uridine 5′-monophosphate should, on the basis of the above conformation, be the area of base [53Å^2 (3)] plus that of the perpendicular sugar with attached phosphate [61Å^2, Fig. 7] or 114Å^2, which again compares very well with the experimentally determined surface occupied of 120Å^2 (Table I).

Thus, these results seem to support the general conclusion that the nucleosides and nucleotides of uracil adopt the expected *anti* conformation on the electrode surface. It should also be stressed that in the latter conformation the almost perpendicular sugar residue and the phosphate residue are in close vicinity to the electrode surface and occupy projected areas very similar to that shown in Fig. 7C. Although we have not presented the data in this report, the interfacial behavior of thymine, thymidine, and thymidine 5′-monophosphate may be rationalized by the same arguments presented for the uridine systems.

In the case of adenine and its nucleosides and nucleotides, experimental measurements (Table I) reveal that the nucleotide occupies only about 20% more surface than the nucleoside which in turn occupies an area very similar to the parent base. This behavior can be rationalized by the fact that little energy is required to cause rotation about the $N(9)$- $C'(1)$ glycosyl linkage; *i.e.*, adenosine or adenosine 5′-monophosphate can readily adopt either the *syn* or *anti* conformations. In the *syn* conformation (*i.e.*, positive values of ϕ_{CN}) molecular models reveal that the sugar ring oxygen (O′(1)) and the $C'(5)H_2OH$ or $C'(5)$-H_2OPO_3 groups can be moved completely out of the plane of the surface. The net result is that in the closely packed monolayer (at $\theta \rightarrow 1$), the adsorbed nucleoside or nucleotide molecules attach with $C'(1)$ and $C'(2)$ in close proximity to the plane of the surface and with $C'(3)$, $C'(4)$, and $C'(5)$ and the ring oxygen elevated above the plane of the electrode. This arrangement permits the adenine moiety to have maximum contact with the mercury and to adsorb in a two-dimensional array with relatively little increase in the area over that of the purine itself.

Some additional comments may be made relative to the values of $\Delta G°$ for the sugars, sugar phosphates, nucleosides, and nucleotides. As has been noted above, it seems unlikely on structural grounds that both the purine or pyrimidine ring and the average plane of the sugar ring will simultaenously lie in the plane of the surface. Therefore, it is somewhat surprising that the sum of $\Delta G°$ values for the sugar (or sugar phosphate) and the free bases nearly equals $\Delta G°$ for the nucleosides (or nucleotides). Thus, the increase in $-\Delta G°$ (from base to nucleoside) is on average about 1290 cal/mole for the three systems, compared to $-\Delta G° =$ 1700 cal/mole for *D*-ribose and 1800 cal/mole for 2′-deoxy-*D*-ribose, and the increase in $-\Delta G°$ from base to nucleotide averages 620 cal, compared to $-\Delta G° = 800$ cal for *D*-ribose 5′-phosphate. It may be that the free energy of adsorption for ribose and ribose phosphate is not very different if these molecules adsorb in the plane of the Hg or nearly perpendicular to it, with the ring oxygen and 5′ polar groups close to the surface.

The fact that the nucleosides and nucleotides of adenine have values of $\Delta G°$ significantly more negative than adenine, but nearly the same molecular areas as adenine, requires further explanation. Note that $\Delta G°$ refers to the standard free energy of adsorption at low degrees of coverage, in the region where the adenine moiety of the nucleoside or nucleotide will not be able to displace sugar and sugar-phosphate groups from the surface. We propose, therefore, that at small values of θ the nucleosides and nucleotides of adenine adsorb similarly to uridine and uridine 5′-monophosphate, with the sugar oxygen and the $C'(5)CH_2OH$ or phosphate ester groups near the surface. At large values of θ, rotation about the $N(9)$-$C'(1)$ bond occurs to permit as large a fraction of the surface as possible to be covered with the purine rings. Thus, values of Γ_{max} and area per molecule (which reflect the dependence of π on ln activity in the limit as $\theta \rightarrow 1$) do not vary greatly in the series base-nucleoside-nucleotide for adenine even though the sugar and sugar phosphate groups contribute to the adsorption free energy at low values of θ. The reorientation which supposedly occurs as θ increases does not lead to sizable deviations from the Frumkin equation; this relation applies wth a single set of B_o, α, and Γ_{max} values throughout a wide range of potentials and surface concentrations.

Acknowledgments

The authors would like to thank Dr. Eric Enwall for assistance in computing molecular areas. This work was supported by the National Institutes of Health through Grant No. GM-21034.

Manuscript submitted Sept. 6, 1977; revised manuscript received March 27, 1978.

Any discussion of this paper will appear in a Discussion Section to be published in the June 1979 JOURNAL. All discussions for the June 1979 Discussion Section should be submitted by Feb. 1, 1979.

REFERENCES

1. H. Kinoshita, S. D. Christian, and G. Dryhurst, *J. Electroanal. Chem.*, **83**, 151 (1977).
2. H. Kinoshita, S. D. Christian, and G. Dryhurst, *ibid.*, **85**, 377 (1977).
3. V. Brabec, S. D. Christian, and G. Dryhurst, *Biophys. Chem.*, **7**, 253 (1978).
4. A. T. Ganesan and L. Lederberg, *Biochim. Biophys. Res. Commun.*, **18**, 824 (1965).
5. A. Ryter, *Bact. Rev.*, **32**, 39 (1968).
6. D. E. Comings, *Ann. J. Human Genetics*, **20**, 440 (1968).
7. R. L. O'Brian, A. B. Sanyal, and R. H. Stanton, *Exp. Cell. Res.*, **76**, 106 (1972).
8. A. V. Field, A. A. Tytell, P. G. Lampson, and M. R. Hilleman, *Proc. Nat. Acad. Sci. U.S.A.*, **58**, 1004 (1967).
9. P. L. Schell, *Biochim. Biophys. Acta*, **240**, 472 (1971).
10. B. Janik and R. G. Sommer, *Biopolymers*, **12**, 2803 (1973).
11. T. L. Hill, *J. Am. Chem. Soc.*, **80**, 2142 (1958).
12. O. T. O'Konski and N. C. Stellwagen, *Biophys. J.*, **5**, 607 (1965).
13. E. Neumann and A. Katchalsky, *Proc. Nat. Acad. Sci., U.S.A.*, **69**, 993 (1972).
14. V. Brabec and E. Palecek, *Biophys. Chem.*, **4**, 79 (1976).

15. D. Krznarik, P. Valenta, and H. W. Nurnberg, *J. Electroanal. Chem.*, **65**, 863 (1975).
16. V. Brabec, S. D. Christian, and G. Dryhurst, *ibid.*, **85**, 389 (1977).
17. D. C. Grahame, E. M. Coffin, J. P. Cummings, and M. A. Poth, *J. Am. Chem. Soc.*, **74**, 1207 (1952).
18. D. E. Broadhead, R. S. Hansen, and G. W. Potter, *J. Colloid Interface Sci.*, **31**, 61 (1969).
19. S. D. Christian, G. Dryhurst, V. Brabec, and J. G. Baker, *ibid.*, **62**, 454 (1977).
20. B. B. Damaskin, O. A. Petrii, and V. Batrakov, "Adsorption of Organic Compounds on Electrodes," p. 112, Plenum Press, New York (1971).
21. B. B. Damaskin, *Elektrokhimiya*, **11**, 428 (1975).
22. B. B. Damaskin, O. A. Petrii, and V. Batrakov, "Adsorption of Organic Compounds on Electrodes," p. 113, Plenum Press, New York (1971).
23. H. Nakadomari, D. M. Mohilner, and P. R. Mohilner, *J. Phys. Chem.*, **80**, 1761 (1976).
24. S. Arnott, S. D. Doren, and A. J. Wonacott, *Acta Cryst.*, **258**, 2192 (1969).
25. C. K. Johnson, ORNC Publication No. 3794 (1966).
26. P. O. P. Ts'o, in "Basic Principles of Nucleic Acid Chemistry," Vol. I, P. O. P. Ts'o, Editor, p. 453, Academic Press, New York (1974).
27. A. E. V. Haschemeyer and A. Rich, *J. Mol. Biol.*, **27**, 369 (1967).
28. J. Donohue and K. N. Trueblood, *ibid.*, **2**, 363 (1960).
29. P. Tollin, H. R. Wilson, and D. W. Young, *Nature (London)*, **217**, 1148 (1968).
30. D. G. Watson, D. J. Sutor, and P. Tollin, *Acta Cryst.*, **19**, 111 (1965).
31. V. Sasisekharan, A. V. Lakshminarayanan, and G. N. Ramachandran. *Conform. Biopolym.*, Pap. Int. Symp., 1967, Vol. 2, p. 641 (1967).
32. A. V. Lakshminarayanan and V. Sasisekharan, *Biochim. Biophys. Acta*, **204**, 49 (1970).

Measurement of Electrochemical Reactions at the Anodized Tantalum Electrode

R. B. Diegle* and C. R. Hassler

Battelle, Columbus Laboratories, Columbus, Ohio 43201

ABSTRACT

Electrochemical activity occurring at anodized tantalum and platinum electrodes was evaluated *in vitro* during pulsed d-c stimulation. The pH of physiological saline was used as an indicator of electrochemical charge transfer at the electrodes, pH change being proportional to the amount of reaction products created by electrochemical processes. The pH changes produced by platinum were large and predictable by electrochemical theory, whereas no detectable changes occurred at either tantalum anode or cathode. It has thus been demonstrated that anodized tantalum can be used as a nearly ideal capacitor electrode, and therefore it is suitable for stimulating tissue *in vivo* in the absence of undesirable faradaic reactions.

Healing of bone in laboratory animals and in humans has been shown to be accelerated if the fracture site is subjected to electrical stimulation by means of implanted electrodes (1-6). Investigators have also demonstrated that rapid healing can occur if the fractured region is merely exposed to an electromagnetic field from a coil placed near the fracture but external to the body (7-9). Results from the former group of experiments suggest that the cause of accelerated healing may be related to either (*i*) the presence of an electric field within the tissue; or (*ii*) altered body fluid chemistry near the electrodes. Concerning item (*ii*), faradaic electrode reactions occur which may include oxygen reduction and hydrogen ion reduction leading to a pH increase at the cathode, and acidification at the anode due to oxidation of water. (The extent of such changes on local chemistry and the resultant effects on bone growth presently are not well characterized, but such changes conceivably could be important.) Because invasive electrodes are not used in the technique employing electromagnetic fields, results from this technique suggest that healing can be produced solely by the presence of an electromagnetic field, and in the absence of changes in body fluid chemistry produced by electrochemical charge transfer in the classical sense.

This present work complements earlier research which sought in part to determine whether accelerated healing results from an electric field or an altered body fluid chemistry (6). The earlier program used both platinum electrodes, which permitted faradaic reactions and hence changes in electrolyte chemistry, and also anodized tantalum. Anodized tantalum was used as a capacitor electrode to prevent electrochemical reactions by insuring charge transfer in a capacitive mode only. That is, a capacitor electrode causes ionic current flow in the body fluids due to the electric field present, but it prevents classical electrochemical reactions from occurring at the anode and cathode and attendant large changes in chemistry of the fluids.

Attempts have been made previously in recent years to pass current in a capacitive rather than faradaic mode. The underlying principle is that electrical charge transfer across the metal-electrolyte interface is suppressed because current is passed by transient charging and discharging of the double layer across a dielectric. The first reported example of an insulated, or capacitor-type, electrode was by Mauro in 1960 (10); his electrode consisted of Teflon[R]-coated wire coiled within a plastic chamber, which was filled with Ringer's solution and had a small opening at the stimulation site to concentrate the ionic current. An improved capacitor electrode was devised by Schaldach (11) for cardiac pacemakers. It consisted of an insulated metallic tip on the end of a transvenous catheter; the tip was covered with a thin layer of tantalum pentoxide, Ta_2O_5, which is a good dielectric material, possessing extremely high electrical resistance and a large dielectric constant. Guyton and Hambrecht (12) improved the charge-storage capacity of the tantalum electrode still further by using a porous sintered electrode, which increased the total surface area by a factor of nearly 90 over the projected area. These porous electrodes were used for surface stimulation of the human visual cortex. Other investigators

* Electrochemical Society Active Member.

Key words: healing, bone, electric field, dielectric.

have used capacitor electrodes to electrically augment the healing of bone (6, 13, 14). In two studies (6, 14), anodized tantalum electrodes were implanted within osteotomies to effect accelerated healing in the absence of detrimental faradaic reactions which can destroy bone, especially near the anode.

Relatively few investigators have undertaken to characterize *in vitro* the performance of the anodized tantalum electrode, specifically, its effectiveness in accomplishing the desired objectives of suppressing electrochemical reactions. Pilla (15) performed an *in vitro* comparative evaluation of tantalum, titanium, stainless steel, and platinum by using a potential sweep method to determine overvoltages for faradaic activity. He demonstrated that tantalum and titanium, unlike stainless steel and platinum, exhibit little faradaic current over a nearly 2V potential range in Ringer's and McCoy's tissue culture media. He concluded that these metals, therefore, would be better suited for pulsed current stimulation and minimization of tissue damage. Guyton and Hambrecht (12) used pH paper to show that the level of electrochemical activity at porous anodized tantalum anodes was significantly reduced relative to that occurring at platinum. Again, no quantitative comparison was made, and an indifferent metal electrode was used as cathode.

In the earlier study (6) it was demonstrated that healing of rabbit calvaria can be accelerated by using anodized tantalum as well as platinum for electrodes. It was therefore initially concluded that the electric field alone is responsible for healing. However, during these *in vivo* experiments, anodized tantalum had been used not only as the anode but also as the cathode. It has been demonstrated (16, 17) that tantalum pentoxide is an extremely leaky dielectric under forward (metal negative) bias, and the question arose as to whether the desired objective of preventing electrochemical reactions had been achieved. Therefore, the *in vitro* research reported herein was performed to determine the degree to which tantalum electrodes actually suppress electrochemical activity under experimental conditions simulating those used in the previous *in vivo* studies.

Experimental

Material and preparation.—Tantalum for the earlier *in vivo* research and for this study was obtained from Materials Research Corporation as 0.25 mm diam wire of 99.996+% purity. High purity material was used to minimize flaws in the Ta_2O_5 dielectric and therefore to maximize its electrical resistivity. Before anodization the wire was coiled in the form of a helix of 1 cm^2 surface area and etched for 10 sec in a chemical polishing solution consisting of a 5:2:2 (volume) mixture of commercial strength analytical reagent grade H_2SO_4, HNO_3, and HF (18). This etch was followed by a 10 sec immersion in 48% HF to remove the chemical polishing residue, a quick water rinse, and anodization in 0.2*N* H_2SO_4. Anodization was performed at a constant current density of 1 mA/cm^2 until a total cell voltage of 20V was reached, at which time the current was allowed to decay at constant applied voltage to $2 \cdot 10^{-5}$ A/cm^2. The electrode was removed without mechanical contact with the anodized region and inserted into a glass electrode holder for mounting in the cell.

Capacitance of the anodized electrodes was measured at a frequency of 60 Hz with a General Radio Model 1650-B impedance bridge and General Radio Model 1310-A external oscillator. Measurements were made in 0.9% NaCl solution (physiological saline) by using a platinum counterelectrode of many square centimeters area, to minimize its series capacitance contribution.

Electrolytes were prepared with analytical reagent-grade chemicals and distilled water. Ringer's solution was a commercial preparation.

Electrochemical cell.—Change of pH as function of charge passed was used to measure the degree to which tantalum prevented electrochemical charge transfer during current flow. For this purpose an electrochemical cell was constructed from Teflon[R] as shown in Fig. 1. The separate anode and cathode compartments, which were connected by a string bridge saturated with electrolyte, permitted measurement of pH of anolyte and catholyte in the absence of diffusional mixing. Figure 1(b) shows the placement of the helical wire and pH electrodes (Corning semi-micro combination electrode) within one of the chambers. In practice, the string bridge was thoroughly rinsed to remove electrolyte from the previous experiment, and the cell was filled with 0.75 ml electrolyte in the chamber in which pH was to be measured and 1 ml in the other chamber. If an anodized tantalum electrode was used, it had been reanodized after insertion into the cell to heal any damaged areas to the dielectric created during mounting in the glass capillary and positioning within the cell. The pH electrode was carefully inserted into one chamber and the pH reading was allowed to stabilize. Pulsating direct current was next applied and the pH was continuously recorded on a strip chart recorder connected to the proportional output of the meter.

Electrical circuitry.—The circuitry used to deliver the current consisted of a pulse generator/constant current generator combination adjusted to give square wave d-c pulses. When tantalum electrodes were used, a reed relay microswitch was placed in the circuit to short the electrodes between pulses and thereby discharge them from the previous pulse. The waveform used throughout most of this work consisted of a square wave with an amplitude of 1 mA, duration of 5 msec, and repetition rate of 60 Hz. The waveform was adjusted and monitored by means of an oscilloscope connected to the electrochemical cell prior to and during each experiment. This waveform, therefore, provided a current density of 1.0 mA/cm^2 with a duty cycle of 30%; *i.e.*, the current was applied for 30% of the duration of each experiment.

Dielectric resistance.—Electrical resistance of the Ta_2O_5 dielectric layer was measured under forward

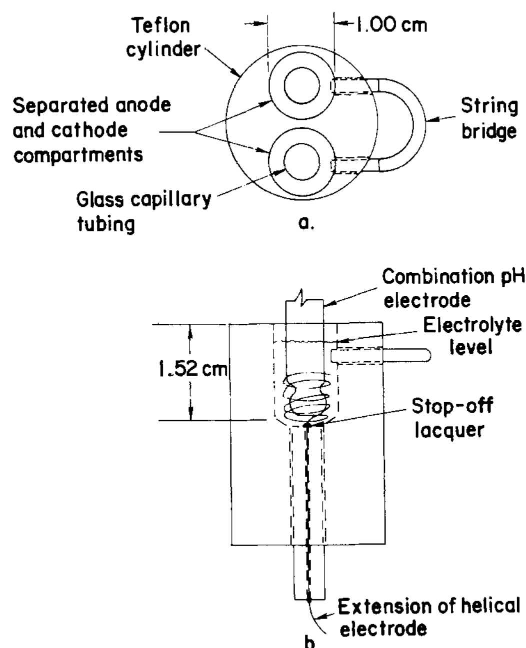

Fig. 1. Schematic diagram of the electrochemical cell used for electrode evaluation. (a) Top view, illustrating separated anode and cathode compartments and string bridge; (b) side view illustrating placement of spiral electrode and combination *pH* electrode.

bias by potentiostatically polarizing an anodized tantalum electrode in a stepwise manner to ever-increasing cathodic potentials and recording the steady-state or near-steady-state current flow through a microammeter. Potentials were measured relative to a saturated calomel electrode (SCE) with a high impedance Keithley electrometer.

Miscellaneous measurements.—Additional experiments included measuring the impedance of the string bridge, developing an equivalent circuit model of the electrochemical cell, and measuring *in situ* electrode potentials during direct current pulsing. Electrode potentials were measured between the anode or cathode and an SCE immersed directly in the anolyte or catholyte. The leads were connected directly to an oscilloscope differential amplifier to prevent distortion by interface circuitry, such as an electrometer.

Results

pH measurements.—Results of pH measurements made on platinum and anodized tantalum in physiological saline are shown in Fig. 2.

The curves designated "theoretical" were calculated on the basis that all charge produces electrochemical reactions at the anode and cathode. It was assumed that the only possible reactions in catholyte and anolyte were

$$H_2O + e = \tfrac{1}{2} H_2 + OH^-, \text{ cathode} \quad [1]$$

$$\tfrac{1}{4} O_2 + \tfrac{1}{2} H_2O + e = OH^-, \text{ cathode} \quad [2]$$

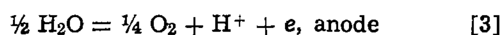

$$\tfrac{1}{2} H_2O = \tfrac{1}{4} O_2 + H^+ + e, \text{ anode} \quad [3]$$

The possibility of another anodic reaction

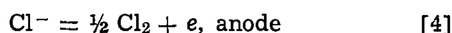

$$Cl^- = \tfrac{1}{2} Cl_2 + e, \text{ anode} \quad [4]$$

was considered, but experimental results indicated that it did not participate to a detectable degree in the reaction scheme, presumably because it occurs at a potential well anodic to that required for reaction [3]. Inspection of Eq. [1]-[3] shows that the passage of current produces, in physiological saline, only reactions which directly change the pH (see "Discussion" for further treatment). In addition, an equivalent pH change is produced in the catholyte regardless of how the charge is apportioned between reactions [1] and [2]. Therefore, electrochemical charge transfer in physiological saline produces changes in an easily monitored and well-understood quantity, namely, pH.

To calculate the expected pH change if all of the charge enters into the electrochemical reactions shown above, we proceed as follows. The charge Q passed in any time interval is

$$Q = It\alpha \quad [5]$$

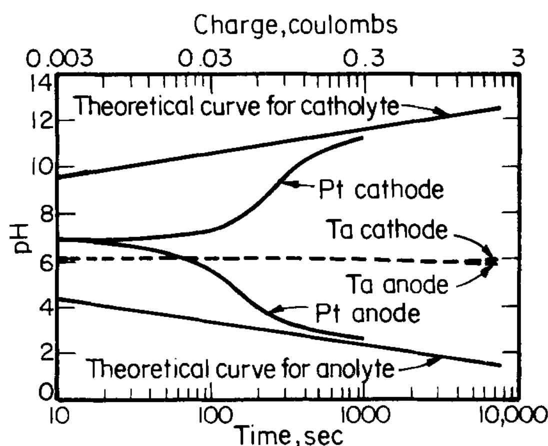

Fig. 2. pH vs. time (or charge) for platinum and anodized tantalum electrodes in physiological saline. Waveform: square d.c.; amplitude 1 mA; duration 5 msec; repetition rate 60 Hz. Theoretical curves were calculated for reactions [1]-[3], see text.

in which I is the current and α is the duty cycle of the wave form, *i.e.*, the fraction of time during which the pulse is applied. The moles reacted, M, is

$$M = \frac{Q}{n\mathbf{F}} = \frac{It\alpha}{n\mathbf{F}} \quad [6]$$

in which n is the number of equivalents per mole and $\mathbf{F}$ is the Faraday, 96,500C per equivalent. The resulting concentration, m, of reaction product is

$$m = \frac{M^o + M}{V} = \sim \frac{M}{V} \quad [7]$$

in which M^o is the initial amount of product at time $t = 0$, M is the amount produced by current flow, Eq. [6], and V is the electrolyte volume. For the conditions used in this study, M (the amount of H^+ or OH^-) greatly exceeded M^o within a few seconds after application of current, so that the approximation in Eq. [7] is justified.

For the anolyte m gives the concentration of H^+, such that

$$pH = -\log a_{H^+} \cong -\log m \cong -\log \frac{It\alpha}{Vn\mathbf{F}} \quad [8]$$

(It was found that for the concentration of electrolyte used, a good approximation of pH was obtained by substituting the molar concentrations of H^+ and OH^- for the activities, a_{H^+} and a_{OH^-}). For the catholyte the expression for pH is

$$pH = -\log \frac{K_w}{(OH^-)} \cong 14 - \log \frac{Vn\mathbf{F}}{It\alpha} \quad [9]$$

K_w is the ionization constant of water, which at 22°C is $1.0 \cdot 10^{-14}$.

As evident in Fig. 2, agreement between the theoretical, or calculated, pH curves and those produced with platinum electrodes is very good for times exceeding about 1000 sec. Poor agreement at shorter times is due simply to the delay in diffusive mixing of reaction products formed at the platinum-electrolyte interface with the bulk of the electrolyte. This delay in mixing was demonstrated by shutting the current off at shorter time intervals and monitoring pH: it continued to drift until it approached the theoretical value. Likewise, reapplication of the current was followed by a slight delay in pH change while the reaction products were migrating toward the pH electrode.

The curves obtained with anodized tantalum indicate that no pH change, outside of experimental drift, occurred at times exceeding 7000 sec.

Results of similar experiments conducted in lactated Ringer's and Dulbecco's tissue culture media are shown in Fig. 3. The change in pH produced by platinum in these culture media at a particular time was less than that in physiological saline because not only were the former electrolytes strongly buffered, but electrochemical reactions were possible other than those which directly affect pH. Examples include oxidation and reduction of carbonate, bicarbonate, phosphate, and sulfate ions, and in addition, organic species in Dulbecco's. There was again no evidence of pH change produced by anodized tantalum.

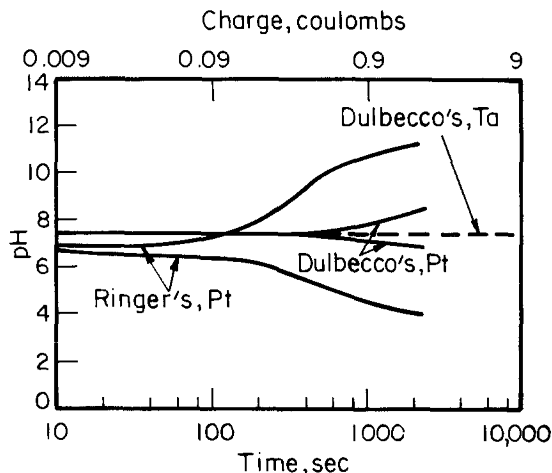

Fig. 3. pH *vs.* time (or charge) for platinum and anodized tantalum electrodes in lactated Ringer's and Dulbecco's tissue culture media. Waveform: square d.c.; amplitude 1 mA; durotion 5 msec; repetition rate 60 Hz.

The effect with tantalum electrodes of increasing the duration of the current pulse from 5 to 15 msec is shown in Fig. 4. It is evident that some pH change occurred at times exceeding 400 sec, although the rate of change is still considerably less than that for platinum, Fig. 2.

Electrode potential measurements.—Electrode potential-time traces of tantalum anode and cathode are shown in Fig. 5 together with the square-wave current pulse used to produce them. The anode reached a potential of 7V (SCE) by the end of the pulse, and it was not completely discharged between pulses. [The potential of discharged tantalum in physiological saline was about 0 ± 0.2V (SCE)]. The cathode reached −2.6V (SCE) during pulse application and was completely discharged between pulses.

Dielectric resistance.—Anodic potentiostatic polarization of anodized tantalum in physiological saline to potentials exceeding 10V (SCE) did not produce detectable current flow (>10^{-7} A/cm^2). Therefore the direct current leakage resistance of the Ta_2O_5 under reverse bias exceeded $10^8\Omega$, which is in agreement with previously published values (17).

Results of cathodic polarization are illustrated in Fig. 6 for two electrolytes. Physiological saline was used because it was the working electrolyte throughout most of this study. In addition, a 0.1M $Ce(SO_4)_2$/1M H_2SO_4 solution was used to eliminate polarization

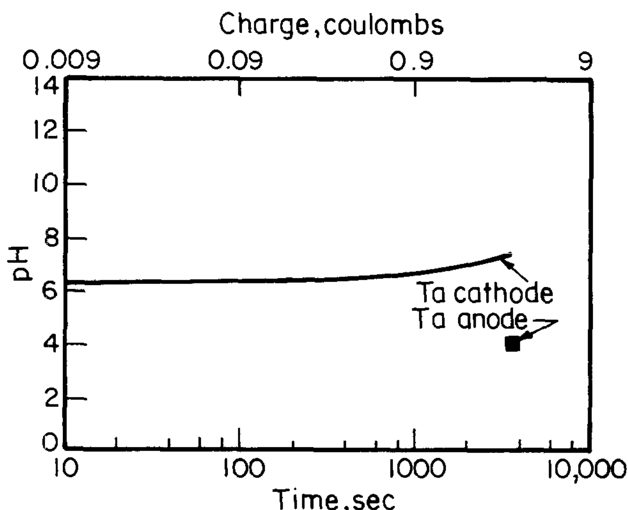

Fig. 4. pH *vs.* time (or charge) for anodized tantalum cathode in physiological saline. Waveform: square d.c.; amplitude 1 mA; duration 15 msec; repetition rate 60 Hz.

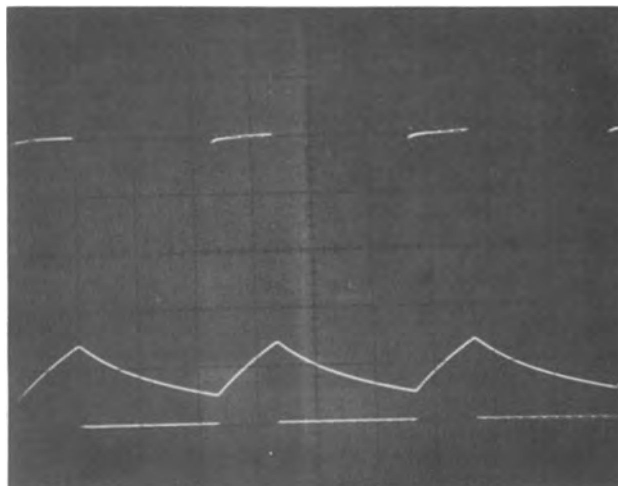

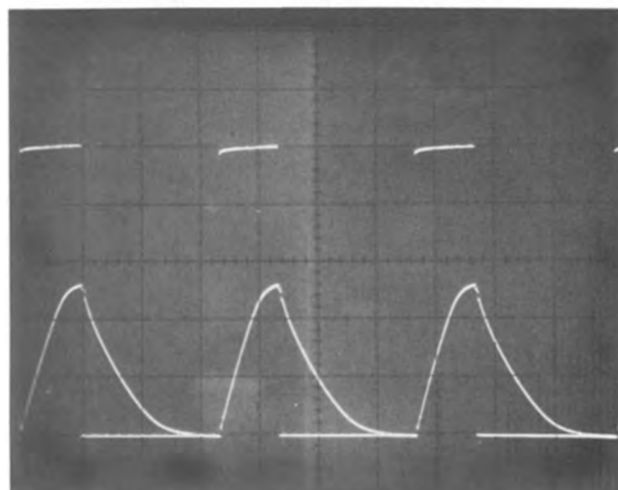

Fig. 5. Current-time and potential-time behavior of anodized tantalum electrodes in physiological saline. Potentials measured relative to the saturated calomel electrode. (a) Tantalum anode: Current, 200 μA/vertical division; potential, 5V (SCE)/vertical division; time, 5 msec/horizontal division; (b) tantalum cathode: As in (a), except 1V (SCE)/vertical division.

due to charge transfer involved in reactions 1-3 (17); such polarization is minimal for reactions involving the change of valence of a metallic ion, *e.g.*, ceric to cerous ion. The 0.6V cathodic shift of the curve for physiological saline was presumably caused by the overvoltage required to drive reactions [1] and [2].

Discussion

It should be emphasized at this point that physiological saline was chosen as the working electrolyte, rather than a more complex tissue culture medium, because it permitted quantification of leakage current through the Ta_2O_5 dielectric film. That is, any current which passed through the dielectric produced electrochemical changes which of necessity changed the pH. Therefore, simply monitoring pH enabled quantification of this leakage current. It is not implied that pH is all-important in producing accelerated bone growth, nor that electrochemical reactions occurring *in vivo* would not include oxidation and reduction of species other than those shown in reactions [1]-[4]. Physiological saline was used merely to enable convenient detection of electronic charge transfer *in vitro*; because such charge transfer does not occur *in vitro* for anodized tantalum, it can be stated with considerable confidence that it also does not occur *in vivo*, and thus neither do the many electrochemical reactions which otherwise would be possible.

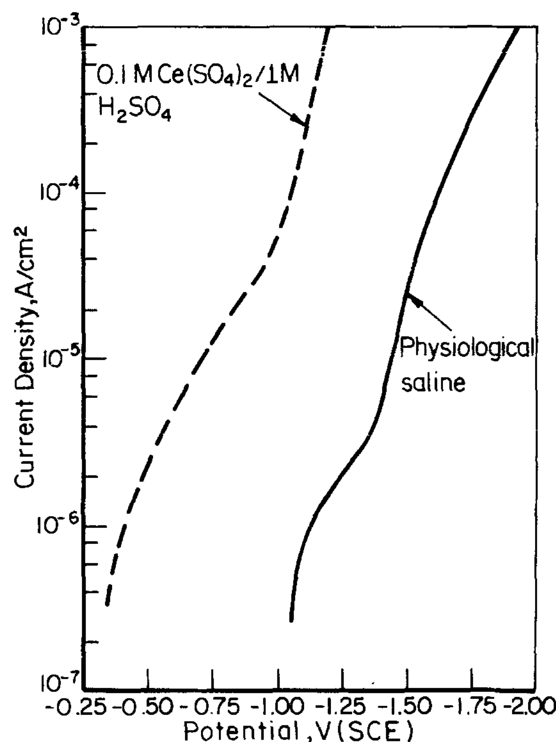

Fig. 6. Pseudosteady state current density vs. electrode potential of tantalum anodized to 20V, then polarized in ceric sulfate solution and physiological saline.

The major observation from this research is that anodized tantalum, used both as anode and cathode in pulsed d-c circuitry, functions as a nearly perfect capacitor electrode. This fact is evident from the lack of significant pH change created by tantalum electrodes, Fig. 2. Leakage through the dielectric of even 1% of the total charge passed in 7000 sec would have produced a pH change of over 3 units. The excellent capacitor behavior of anodized tantalum is reinforced by the results obtained in Ringer's and Dulbecco's tissue culture media, Fig. 3.

The absence of electrochemical activity at the tantalum anode was expected, in light of the excellent dielectric properties of Ta_2O_5 under reverse bias and the results of previous research. Indeed, Guyton and Hambrecht (12) demonstrated semiquantitatively that anodized tantalum behaves well as a capacitor anode; but they used an indifferent platinum electrode as cathode in their work on the presumption that anodized tantalum does not function well as a cathode. However, this present research has demonstrated that anodized tantalum can also function effectively as a capacitor when used as a cathode.

It is not clear why there was no net charge transfer through the cathode dielectric. Figure 5 indicates that the electrode attained a potential of -2.6V (SCE) at the completion of the 5 msec current pulse. Reference to Fig. 6 shows that, at near-steady state, a current density in physiological saline of 1 mA/cm^2 was attained at -1.93V (SCE). It is apparent that current-potential dependence between the transient (pulse) and steady-state measurements do not agree. This differing behavior was presumably not due to unusual properties of the particular Ta_2O_5 films grown in this study, because the film conductivity as measured in ceric sulfate electrolyte was quite similar to that determined in previous work (19). It is concluded that the conductivity of the Ta_2O_5 may be time dependent under forward bias such that insignificant current passed within 5 msec, or perhaps a symmetric oxidation-reduction reaction occurred at the cathodic electrode-electrolyte interface. Such a reaction would involve oxidation, during electrode shorting, of chemical species produced by reduction reactions occurring during application of the current pulse, such that no net change occurred in catholyte chemistry.

The reason for the slight pH shift illustrated in Fig. 4 is that the charge-storage capacity of the electrodes was exceeded by the 5 msec pulse. That is, the maximum amount of charge, Q_m, which can be stored in an anodized metal electrode is

$$Q_m = V_a \cdot C \qquad [10]$$

in which V_a is the voltage to which the film was grown (the anodization voltage) and C is the capacitance. Anodization of the tanatalum wire to 20V produced a total capacitance for 1 cm^2 electrode area of 0.6-0.8 μF, in good agreement with published values (20). Therefore, taking C as 0.7 μF

$$Q_m = 20\text{V} \cdot 7 \cdot 10^{-7}\text{F}$$
$$= 14 \cdot 10^{-6}\text{C}$$
$$= 14\,\mu\text{C}$$

In practice, an anodized electrode is usually operated at no more than about 80% of V_a to prevent additional film growth and to minimize electronic leakage current. Thus, a more conservative value for Q_m is about 11 μF. The charge contained in each 15 msec pulse was 15 μC, which exceeded Q_m by 34%. The pH shift in Fig. 4 was therefore caused by electrochemical reaction produced by a small rate of anodization in the anolyte and electronic leakage in the catholyte. The preceding analysis indicates one of the basic limitations of the capacitor electrode, namely, that the quantity of charge which can be passed per pulse is limited by the electrode capacitance. The total capacitance of an electrode of given outside dimensions can be greatly increased by using a porous structure (12).

The equivalent model circuit of the electrochemical cell is shown in Fig. 7. The anode capacitance, C_a, is 0.7 μF, and the string bridge resistance, R_b, is 20,000Ω. The diode in parallel with C_c simulates the low electronic resistance of Ta_2O_5 under forward bias. No resistance was required in parallel with C_a due to the extremely low leakage under reverse bias. Use of the preceding values, which were determined from measurements of the individual components of the actual electrochemical cell, resulted in excellent simulation of the waveforms shown in Fig. 5 and of the waveform across the entire cell (not shown).

The behavior of anodized tantalum was measured at only one frequency, namely, 60 Hz. This is because the primary objective of this research was to simulate *in vitro* the behavior of tantalum in the previous *in vivo* study, for which the frequency of stimulation was predominantly 60 Hz. A more complete indication of the behavior of anodized tantalum as a capacitor electrode can be acquired by using a range of frequencies, and this is recommended for future research involving tantalum.

Conclusions

It has been quantitatively demonstrated that anodized tantalum behaves as a nearly ideal capacitor when used within its charge storage capability in a pulsed-current circuit. This supports the premise of earlier *in vivo* research (6) and suggests that healing is the result of an applied electric field, not of changes in local electrolyte chemistry. Significantly, anodized tantalum can be used as a cathode as well as an anode, thereby eliminating the need for an indifferent metal electrode or the use of a continuous positive bias voltage on the cathode. (It is emphasized that this latter conclusion has been demonstrated only for the specific circuit and frequency used in this research.) Absence of pH change at the cathode may be due either to significant capacitive behavior of the tantalum cathode for short times upon cathodic polarization, or to symmetric

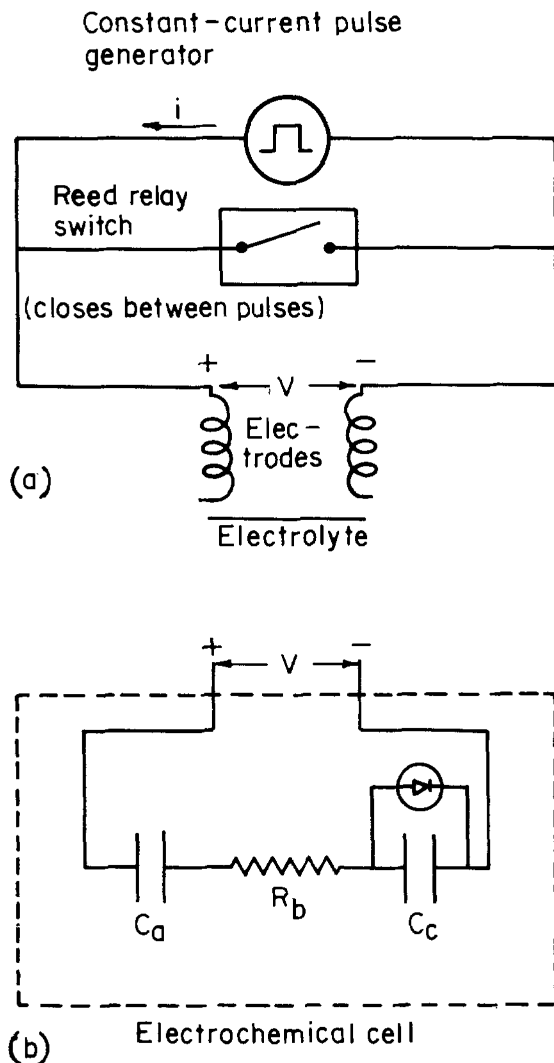

Fig. 7. (a) Stimulating circuit used in this research; (b) equivalent model of electrochemical cell, including tantalum anode (C_a), tantalum cathode (C_c), and string bridge (R_b).

oxidation-reduction reactions resulting in no net change in catholyte chemistry.

Acknowledgments

The authors gratefully acknowledge discussions with E. G. Rybicki and K. D. Cummings, technical assistance rendered by K. D. Cummings, and the loan of pH measuring equipment by R. L. Foltz, all of Battelle. Critical review of the manuscript by D. A. Vermilyea of the General Electric Company is also appreciated. This program was sponsored by the Battelle Institute.

Manuscript submitted Jan. 25, 1977; revised manuscript received *ca.* Dec. 1, 1977.

Any discussion of this paper will appear in a Discussion Section to be published in the June 1979 JOURNAL. All discussions for the June 1979 Discussion Section should be submitted by Feb. 1, 1979.

Publication costs of this article were assisted by Battelle Institute.

REFERENCES

1. C. A. L. Bassett, R. J. Pawluk, and R. O. Becker, *Nature (London)*, **204**, 652 (1964).
2. Z. B. Friedenberg, E. T. Andrews, B. I. Smolenski, B. W. Pearl, and C. T. Brighton, *Surg. Gynecol. Obstet.*, **131**, 894 (1970).
3. Z. B. Friedenberg, P. G. Roberts, Jr., N. H. Didizian, and C. T. Brighton, *J. Bone Joint Surg.*, **53-A**, 1400 (1971).
4. Z. B. Friedenberg, L. M. Zemsky, R. P. Pollis, and C. T. Brighton, *J. Bone Joint Surg.*, **56-A**, 1023 (1974).
5. L. S. Lavine, I. Lustrin, R. A. Rinaldi, and A. R. Liboff, *Science*, **175**, 1118 (1972).
6. C. R. Hassler, E. F. Rybicki, R. B. Diegle, and L. C. Clark, *Clin. Orthop. Relat. Res.*, **124**, 9 (1977).
7. C. A. L. Bassett, R. J. Pawluk, and A. A. Pilla, *Ann. N.Y. Acad. Sci.*, **238**, 242 (1974).
8. C. A. L. Bassett, R. J. Pawluk, and A. A. Pilla, *Science*, **184**, 575 (1974).
9. C. A. L. Bassett, A. A. Pilla, and R. J. Pawluk, *Clin. Orthop. Relat. Res.*, **124**, 128 (1977).
10. A. Mauro, *Science*, **132**, 356 (1960).
11. M. Schaldach, *Trans. Am. Soc. Artif. Intern. Organs*, **17**, 29 (1971).
12. D. L. Guyton and F. T. Hambrecht, *Med. Biol. Eng.*, **12**, 613 (1974).
13. L. Klapper and R. E. Stallard, *J. Dent. Res.*, **54-A**, 130 (1975).
14. L. Klapper and R. E. Stallard, Paper presented at the American Association for Dental Research, New York, April, 1975.
15. A A. Pilla, *Ann. N.Y. Acad. Sci.*, **238**, 149 (1974).
16. L. Young, "Anodic Oxide Films," Chap. 1, Academic Press, New York (1961).
17. D. A. Vermilyea, *This Journal*, **112**, 1232 (1965).
18. W. J. McG. Tegart, "The Electrolytic and Chemical Polishing of Metals," Pergamon Press, London (1956).
19. D. A. Vermilyea, *J. Appl. Phys.*, **36**, 3663 (1965).
20. L. Young, "Anodic Oxide Films," Chap. 6, Academic Press, New York (1961).

Electrode Kinetics of Heme and Electron-Transfer Mechanisms of Heme and Hemoproteins

Karl M. Kadish*,[1] and Joseph Jordan

Department of Chemistry, Pennsylvania State University, University Park, Pennsylvania 16802

ABSTRACT

The electroreduction of ferriheme was investigated by controlled potential coulometry, polarography, and cyclic voltammetry in solvent systems ranging from pure water to ethanol water mixtures containing as much as 75% ethanol. In pure water, ferriheme was dimerized and was reduced by a one electron transfer to a mixed ferric-ferrous intermediate whose disproportionation yielded a dimeric ferroheme product. Redox reactivities of hemoproteins and relevant electrochemical kinetics are intercompared critically with the aid of R. A. Marcus' unified theory of electron transfer.

Electron-transfer reactivities of hemoglobin, myoglobin, and cytochrome c are of evident interest in the context of their biological relevance. The first two function *in vivo* as oxygen transport (or storage) moieties, while cytochrome c is outstandingly efficient as an "electron transferor" (1,2). The very fact that oxymyoglobin and oxyhemoglobin are capable of existence for appreciable time periods is due to sluggish redox kinetics; the heme iron in oxyhemoglobin remains divalent even though thermodynamics (*i.e.*, differences in the standard potentials of the redox couples hemoglobin/methemoglobin and myoglobin/methmyoglobin on the one hand and water/oxygen on the other hand) require virtually complete conversion to the ferric state (3).

The electroreduction of ferriheme has been studied extensively in aqueous and nonaqueous media (4-9). Tailor-made synthetic "model oligohemochromes" (2-3 heme units linked by poly-4 vinylimidazole or poly-L-histidine chains) exhibit ferrous-ferric electron transfer reactivities decreased (9) by a factor of 10^{18}-10^{28}. On the other hand, electroreduction of ferriheme itself is diffusion controlled at the dropping mercury electrode in aqueous solution and involves dimeric or monomeric species depending on pH (8).

In a preliminary communcation (10) we have reported the formation of the transient ferrous-ferric hybrid II, *viz.*

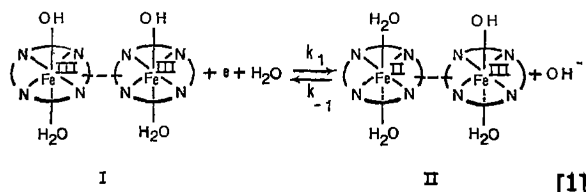

where the tetrapyrrole ring denotes protoporphyrin IX with its normal side chains.

Results are presented and discussed in this paper substantiating that the disproportionation reaction

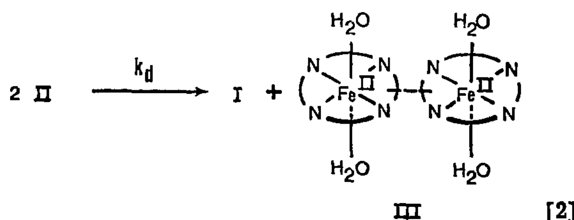

was the rate-determining step in the over-all process

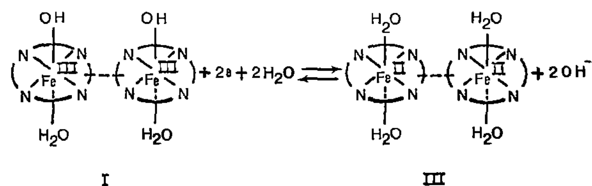

occurring in aqueous solutions of pH 9.5-12.5.

The formulation of the several species in pure water solvent in Eq. [1]-[3] was predicated by assignments of the two axial ligands which have been substantiated conclusively in previous relevant work (8), *viz.*, in the case of Fe(III), OH^- coordinated at one Z position and H_2O at the other; in the case of Fe(II), water coordinated at both Z positions. The nature of the dimer bond in the compounds I, II, and III is not known in aqueous solution. Oxo-bridging (4a) is inconsistent with the established axial ligand assignments. Apparently, two discrete types of dimers may prevail, depending on *pH* (8). However, the question of the dimerization bond is only of periferal interest in the context of the present paper.

In this work we report an estimate of the electrochemical standard (formal) rate constant of reaction [1] which prevailed at the appropriate standard (formal) potential $E°$ where $k_{+1} = k_{-1} = k_1°$. Likewise, we have measured the rate of the reaction

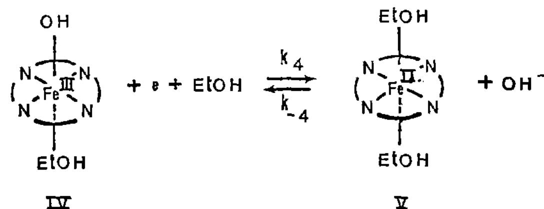

and found that the specific rate constants $k_1°$ and $k_4°$ were of the same order of magnitude as the specific rate constant $k_5°$ of the dicyanohemochrome couple

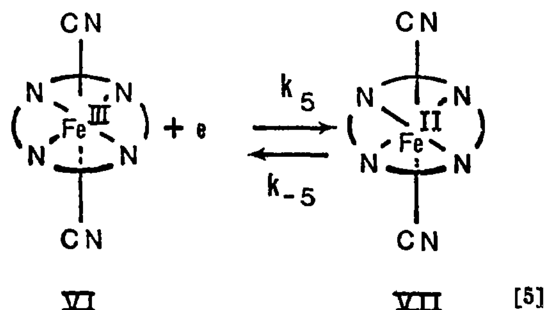

* Electrochemical Society Active Member.
[1] Present address: Department of Chemistry, University of Houston, Houston, Texas 77004.

Key words: ferriheme, disproportionation, cyclic voltammetry, Marcus theory.

which has been previously determined in another laboratory (7).

We have calculated rationally comparable hypothetical rate assignments (*vide infra*) for hemoglobin, myoglobin, and cytochrome c based on the unified electron transfer theory, developed by Marcus (11). A critical assessment of these data (presented later on in this writeup) revealed remarkable features of internal consistency. This led us to postulate that in compounds I-VII, as well as in myoglobin and hemoglobin, electron transfer occurred through similar "hindered paths" via the porphyrin plane.

Experimental Methodology

Apparatus and procedure.—All measurements were made with a three-electrode system using a controlled potential polarograph, assembled from operational amplifiers (Heath Company, Benton Harbor, Michigan). A hanging mercury drop electrode, HMDE, of Kemula's design (Model E-410, Metrohm Limited, Herisau, Switzerland) served as the indicator electrode. The capillary was Kemula's Model EA-842, having a 12 cm length and drop diameter to 0.83 mm. The reference electrode was a commercial saturated calomel half-cell, and platinum served as counterelectrode. The voltage waveform was generated with the aid of a variable frequency function generator (Wavetek, San Diego, California), which could be dialed directly and measured to an accuracy of 0.5%. The waveform from the signal generator consisted of the first arm of a triangular wave for linear sweep and both arms for cyclic sweep; linearity of the potential scan was verified by substitution of a standard resistor for the cell.

One of two detectors was used as a readout device depending on the sweep rate employed. For voltage scans less than 150 mV/sec, voltammograms were recorded with a Model 7000A X-Y recorder (Hewlett Packard, Pasadena, California), while for sweeps greater than 120 mV/sec, the detector was a Model 503 oscilloscope (Tektronix, Beverton, Oregon), which was equipped with a camera for recording the trace.

For peak polarography (linear sweep and cyclic voltammetry) a 100 ml jacketed reaction flask served as the electrolysis cell into which the three electrodes were placed. A tube was inserted into the cell for bubbling nitrogen through the solution, thus facilitating the removal of dissolved oxygen. After deaeration, the bubbler was raised above the solution and a nitrogen atmosphere maintained in the supernate during electrochemical experiments. Nitrogen was prepurified by passing it through two vanadous scrub solutions, a basic wash solution, and finally through a portion of the test solution before entering the cell. The last bubbling step prevented the cell from losing or gaining volatile components during deaeration. The lid of the cell was made of Teflon and machined to fit the cell. Holes were drilled in the lid to allow insertion of the three electrodes along with the nitrogen inlet tube. The lid was further equipped with an orifice for the insertion of a dropping mercury electrode so that conventional steady-state d-c polarograms could be run on the same test solution. The electrolysis cell was maintained at 25.00° $\pm$ 0.05°C by circulation of water through the cell jacket from a constant temperature bath controlled by a thermistor thermoregulator. In order to eliminate uncompensated IR losses resulting from the resistance of the HMDE capillary, a "positive feedback" circuit was used in which part of the current output was returned to the potential input (12). If IR drop was not compensated for, a distortion or shift in the position and height of the peak would occur at high scan rates (13). Since mechanistic sequences of electrode reactions were diagnosed in this study with the aid of the shifts of peak potential with scan, it was essential that no IR drop remain uncorrected.

The over-all number of electrons (faradays per mole of electroreduced ferriheme) transferred in reactions [3] and [4] was determined by controlled potential coulometry. A modified Wenking Model 61-TR potentiostat (supplied by Brinkmann, Westbury, New York) was used to control the potential at which experiments were run. Electronic integration of the current-time curve was achieved by means of an operational amplifier difference integrator (14) yielding a voltage output that was recorded on a strip chart recorder (supplied by Varian Associates, Palo Alto, California). The coulometric cell was similar to that used for peak polarography and described in the preceding paragraph. A large coiled platinum wire served as the anode and was separated from the catholyte compartment by means of a fritted disk which fitted into the center of the cell. A stirred mercury pool, area 7 cm^2, served at the cathode and a saturated calomel electrode was the reference electrode. Stirring of the solution was achieved by means of a magnetic stirring bar positioned atop the mercury pool and actuated by a motor beneath the cell. Deaeration of both the anodic and cathodic chambers was rigorously controlled before beginning the experiment, and nitrogen was passed over the solution in both compartments during the experiment with the aid of a Y tube connector.

Chemicals.—Several buffer solutions (15) were employed in the pH range 9.5-12.5, *viz.*, in the systems potassium bicarbonate-carbonate, potassium biphosphate-phosphate, and potassium hydroxide, the pH ranges were 9.5-11, 10.9-12, and 12-12.5, respectively. pH was monitored with the aid of a Model 801 digital pH meter (supplied by Orion Research, Cambridge, Massachusetts) using a Beckman glass electrode and a fiber-type saturated calomel reference half-cell. Reagent grade chemicals and triply distilled water were used throughout this investigation. Hemin chloride (FW 651.59, Nutritional Biochemical Corporation, Cleveland, Ohio) served as the source material for preparing ferriheme solutions in the range of concentrations between 5×10^{-4} and 10^{-3}F. Experiments were advisedly restricted to this narrow concentration range in order to minimize interfering complications due to adsorption at the electrode interface (8). The ionic strength was maintained in a range between 0.1-0.2 by adding potassium chloride when necessary.

Units, sign conventions, etc.—Potentials reported in this paper are referred to the normal hydrogen electrode (NHE) in accordance with the 1972 Manual of Physico Chemical Nomenclature of the International Union of Pure and Applied Chemistry (IUPAC) (16). The relevant sign convention is the reverse of the one used in Latimer (17), *i.e.*, a more positive potential is more anodic (oxidizing) and a more negative potential more cathodic (reducing).

Electric double layer and specific adsorption effects.—Specific adsorption effects were negligible under the experimental conditions due to the prevailing high ionic strength. Results reported in this paper have been advisedly restricted to those ranges where specific adsorption could be ascertained to cause no appreciable distortions of the current-voltage curves. At high scan rates ($v > 1$ V/sec in ethanol-water mixtures and, $v > 12$ V/sec in pure water) adsorption effects were evident and could be identified by the variation of peak currents as a function of scan rate (linear dependence on sweep rate, etc.). Since it is known that adsorption distorts current voltage curves, these high scans were not employed in the measurement of electrochemical rate constants (and were indeed not needed in the determination of the mechanism described in this paper). Thus, higher values of Nicholson's (18) dimensionless parameter ψ (Eq. [7] below) were not used where interpretations would be open to question due to the presence of adsorption.

Table I. Controlled potential coulometry of $6.00 \times 10^{-4}M$ ferriheme[a] in various ethanol-water mixtures containing 0.1M KOH

Ethanol present (percent by volume)	Faradays found ($\times 10^{6}$)	Faradays per mole of Fe(III) converted to Fe(II)[b]
0.0	5.9 ± 0.2	0.98 ± 0.03
25.0	5.9 ± 0.1	0.98 ± 0.02
75.0	5.8 ± 0.2	0.97 ± 0.03

[a] 100 ml samples of $6.0 \times 10^{-4}F$ ferriheme were electrolyzed at potentials corresponding to 99.9% conversion of Fe(III) to Fe(II).
[b] Corrected for background (residual current) effects; precision expressed as standard deviation of the mean of three replicates.

Results

Coulometric verification of "over-all" electrode process.—It has previously been substantiated (6, 8) that ferriheme yielded diffusion-controlled steady-state polarograms at the DME, both in pure water and in ethanol-water mixtures containing 25-30% EtOH. The relevant current-voltage curves had the sigmoid shape of classical polarographic waves whose mathematical analysis invariably suggested the transfer of 1 faraday per gram atom of iron. This correspondence has previously been verified in our laboratories by controlled potential coulometry in aqueous solutions over a range of pH 8-13. In the present investigation this relationship was reinvestigated and again verified over the broader domain of solvent compositions ranging from pure water to 25% water-75% ethanol. The relevant current time integrals are listed in Table I.

Cyclic voltammetry in ethanol-water mixtures.—Cyclic voltammograms of ferriheme were obtained at Kemula's HMDE in the presence of 25-75% ethanol, at potential sweep rates in the range between 0.01-1.0V/sec. A typical cyclic voltammogram of ferriheme is illustrated in Fig. 1. The analytic geometry of the relevant curves was invariant up to scan rates of $v = 0.1$V/sec. The corresponding peak currents were a linear function of $v^{1/2}$ and the anodic and cathodic peaks were separated by 0.057V (2.2 RT/nF, where $n = 1$). However, at higher scan rates the separation between the anodic and cathodic peak potentials ($E_{p,a}$; $E_{p,c}$) appeared to increase slightly, *viz.*, to the 0.061-0.062V range. At any given scan rate peak potentials varied as a function of pH in accordance with Eq. [6]

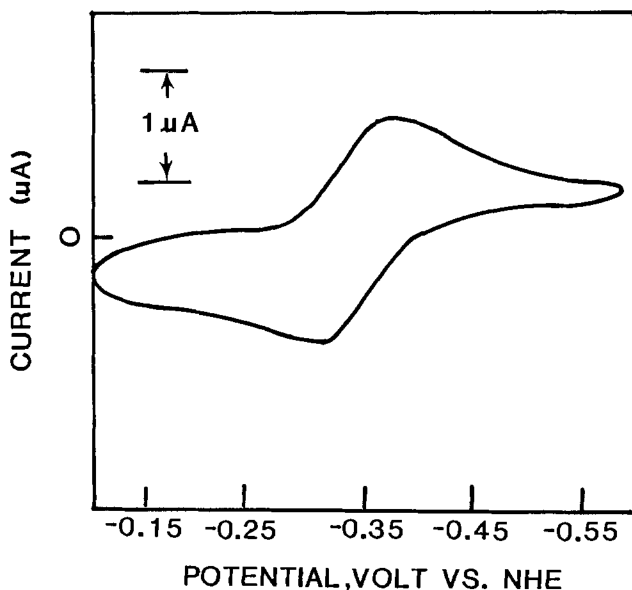

Fig. 1. Cyclic voltammogram of $5 \times 10^{-4}F$ ferriheme in 50% ethanol-water mixture: $pH = 9.96$ (carbonate-bicarbonate buffer); ionic strength = 0.14; scan rate = 0.21 V/sec.

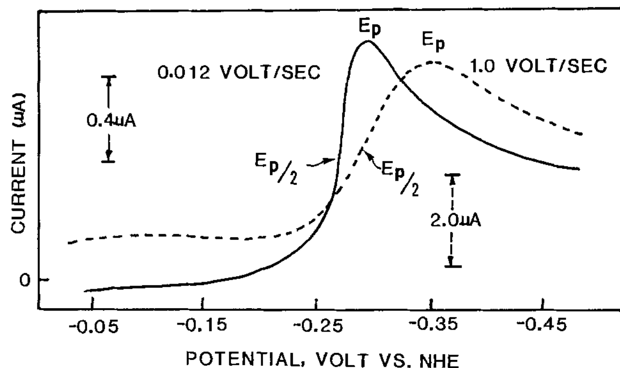

Fig. 2. Cathodic peak voltammogram of $9.1 \times 10^{-4}F$ ferriheme in aqueous carbonate-bicarbonate buffer of pH 9.96, ionic strength = 0.14.

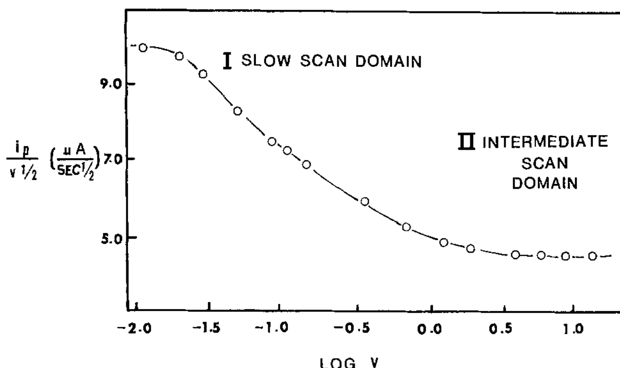

Fig. 3. "Diagnostic plots" of $i_p/v^{1/2}$ vs. scan rate. The value of $i_p/v^{1/2}$ is proportional to the current function maximum χ_P.

$$\frac{\Delta E_{p,c}}{\Delta pH} = \frac{\Delta E_{p,a}}{\Delta pH} = \frac{-2.3RT}{F} = -0.059\text{V at } 25°\text{C} \quad [6]$$

Peak polarography in aqueous solutions at pH 9.5-12.5.—Cathodic linear sweep voltammograms of ferriheme varied between two extreme analytic geometries depending on potential scan rates. Representative current voltage curves are shown in Fig. 2 [similar results obtained under somewhat different experimental conditions have been reported in Ref. (12)]. Plots of variation of the quantity, $i_p/v^{1/2}$, as a function of v (in a given solution of ferriheme) yielded interesting sigmoid curves are illustrated in Fig. 3. The quantity $i_p/v^{1/2}$ is an experimentally accessible proportional measure of the well-known "peak current function" which was used in this investigation as an important diagnostic criterion for identifying reaction mechanisms (see Discussion Section).

The difference between the peak potential (E_p) and the half-peak potential ($E_{p/2}$) is a convenient parameter for characterizing relevant analytic geometries. Observed $E_{p/2}$-E_p assignments are listed as a function of scan in Table II. Peak potentials were essentially invariant at potential scan rates in a range between 3

Table II. Variation of $E_p - E_{p/2}$ with potential scan rate[a,b]

Potential scan rate (V/sec)	$E_p - E_{p/2}$ (V)	$\frac{2.2\,RT}{F(E_p - E_{p/2})} = n$
0.02	0.028	2.00
0.09	0.034	1.65
0.15	0.040	1.40
0.50	0.047	1.19
6.00	0.058	0.97

[a] From cathodic peak polarograms exemplified in Fig. 2.
[b] The dimensionless quantity listed in the last column is equal to the "average number of electrons" transferred per molecule of the electroreducible species (see Discussion).

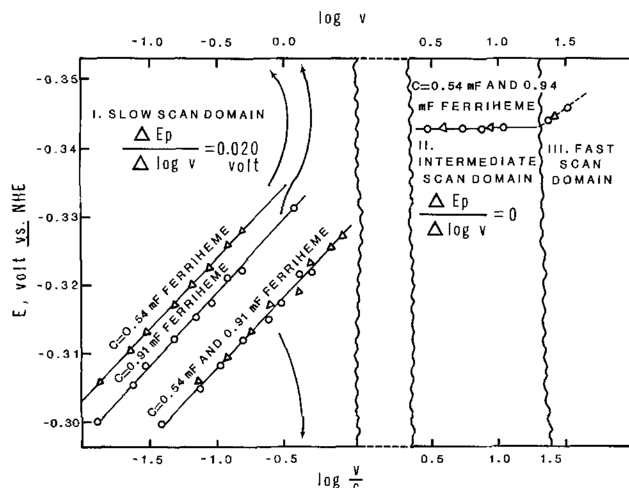

Fig. 4. Experimental cathodic peak potentials for the reduction of ferriheme plotted vs. log v and log v/C. Different curves are obtained for each concentration in domain I while in domain II and III all concentrations yield the same curve.

and 12 V/sec (Fig. 4). However, E_p became gradually more positive as scan rates decreased in the range between 1.0 and 0.01 V/sec and shifted to progressively more negative values when scan rates were increased beyond 12 V/sec. Thus a plot of E_p *vs.* log v had three discrete domains, as is apparent in Fig. 4 and outlined below.

In the "slow scan domain" reported qualitatively in Ref. (12) the plot of E_p *vs.* log v (see upper abscissa scale) yielded a family of parallel lines of slope 0.020V ($2.3\ RT/3\mathbf{F}$), each corresponding to a specified concentration of ferriheme. Two of these ($C = 0.54$ m**F** and 0.91 m**F** ferriheme) are shown in the figure. Using as abscissa log v/c (lower scale) in lieu of log v, caused these discrete lines to coalesce into a single line of the same slope.

In the "intermediate scan domain" the peak potential was independent of the concentration of ferriheme, as well as of scan rate. Cyclic voltammograms recorded in the "intermediate scan domain" yielded normal diffusion-controlled anodic and cathodic peaks separated by 0.057V. In this range the pH dependence of the current voltage curve was the same as described by Eq. [6].

In the "fast scan domain," peak potentials were independent of ferriheme concentration (but varied slightly with scan rate).

Discussion

Kinetics and mechanisms of electroreduction of ferriheme to ferroheme.—Our experimental findings are accounted for by the following interpretation. Considering solely initial (stable) reactants and ultimate products (*i.e.*, disregarding transient intermediates), one faraday of electricity was transferred per mole of iron under all experimental conditions prevailing in this investigation.

The main contribution of the experiments described in this paper was to unravel mechanisms and estimate rate constants of electron-transfer and coupled chemical reactions. Our interpretive rationale relied on the fact that an electrode reaction involved invariably at least two types of competing rate processes, *viz.*, diffusion to and from the electrode surface on the one hand and electron transfer on the other hand. Under the experimental conditions, diffusion rates were inversely proportional to the thickness of the concentration polarization layer $\delta = (\pi Dt)^{1/2}$. In classical polarography at the dropping mercury electrode ($3 < t < 6$ sec) diffusion was the rate-controlling "slow step" yielding "Nernst reversible" current-voltage curves whose shapes were determined solely by the initial reactants and final products. Consequently, our previously reported steady-state polarograms of hemin (8) were not illuminating with respect to electrooxidation-reduction kinetics and mechanisms. In the present investigation we made judicious use of rapid potential scan rates at a HMDE to minimize t, thus providing "time windows" sufficiently small to permit measurements prior to increase of δ to levels where diffusion takes over as the slow rate-determining step.

Rate constants of electron transfer effective at the formal potential were evaluated from the expression (18)

$$\psi = \left(\frac{D_{III}{}^{\alpha}}{D_{II}}\right)\frac{k^o}{\left(\pi D_{III}\frac{n\mathbf{F}v}{RT}\right)^{1/2}} \approx \frac{k^o}{\left(\pi D\frac{n\mathbf{F}v}{RT}\right)^{1/2}} \quad [7]$$

In Eq. [7], k^o is the standard (formal) rate constant expressed in centimeters per second and is correlated as follows with the actual electrooxidation and electroreduction rate constants effective at any potential E

$$k_{red} = k^o \exp\left(\frac{-\alpha n\mathbf{F}}{RT}[E - E^o]\right) \quad [8]$$

$$k_{ox} = k^o \exp\left([1-\alpha]\frac{n\mathbf{F}}{RT}[E - E^o]\right) \quad [9]$$

where $0 < \alpha < 1$ is the transfer coefficient and E^o denotes the formal potential (18). In accordance with the concepts of the Marcus theory (11) we have elected to use k^o for intercomparing rates of different electrode reactions. The other symbols in Eq. [7] have the following connotation: D, diffusion coefficient (cm^2/sec) of the relevant ferri- and ferroheme species (identified by the subscripts III and II, respectively); v, the potential scan rate expressed in V/sec; ψ, Nicholson's dimensionless parameter (*vide infra*), which was accessible from anodic and cathodic peak-potential separations and recorded as a function of the scan rate, v. The latter was manipulated as an experimental variable.

The approximation $D_{III} = D_{II} = D$, incorporated in Eq. [7] was warranted by the similarity in molecular size between ferroheme and ferriheme. The rate-determining step of the electroreduction of ferriheme in the presence of ethanol was found to be indistinguishable from the over-all reaction [4]. The latter has been unambiguously substantiated in previously published work (7, 9) and was verified in this paper.

Application of Eq. [7] yielded the estimate $k_4{}^o \geqq 0.2$ cm/sec. This assignment holds for the entire range of solvent composition investigated, *i.e.*, between 25% ethanol-75% water to 75% ethanol-25% water. From Eq. [6] it appears that hydroxyl-ethanol ligand exchange occurred concomitantly with the electron transfer and was kinetically inseparable (*i.e.*, the ligand exchange per se was fast, compared to electron transfer).

It was previously shown (8) that both ferriheme and ferroheme were dimerized in the aqueous solutions used in the present investigation and that the over-all reaction 3 was diffusion controlled at the DME. This was confirmed in the "limiting case" when slow scan rates (0.01 V/sec) at the HMDE were used (Fig. 2, solid curve), yielding a separation between half-peak ($E_{p/2}$) and peak potential (E_p) which corresponded indeed to a Nernst-reversible two-electron transfer: the quantity

$$n = \frac{2.2RT}{\mathbf{F}(E_{p/2} - E_p)} \quad [10]$$

listed in the last column of Table II represents a measure of the number of faradays per mole involved in a diffusion-controlled reaction of the type: Ox + $ne \rightleftharpoons$ Red.

As can be seen in Table II the apparent value of n decreased gradually with increased potential scan rates. At a scan rate of 0.02 V/sec, Eq. [10] yielded $n = 2.00$ while at scan rate of 6 V/sec, Eq. [10] yielded $n = 0.97$, corresponding to a diffusion-controlled one-electron transfer. This is remarkable behavior, accounted for as follows: Within the 'time window" of slow potential scans, reaction [3] was completed *in toto*, the rate-determining step being the diffusion of the ferriheme dimer I from the bulk of the solution to the HMDE surface. Diffusion of that species remained the rate-determining process at fast scan rates as well. However, when $v = 6$ V/sec the small "time window" effectively isolated reaction [1] and excluded from "peak polarographic visibility" a slower follow-up process necessary to complete the two-electron reduction. Evidence for the follow-up reaction and a conclusive clue as to its nature transpires from Fig. 3 and 4. Peak potentials plotted in Fig. 4 were invariant in domain II where $n = 1$. In contradistinction, E_p shifted anodically with decreasing scan rates in domain I. Such behavior is known to be a diagnostic criterion for the occurrence of a chemical reaction following charge transfer (19). Such sequences include an electrochemical reaction followed by a rate-determining chemical reaction (EC); and an ECE (electrochemical-chemical-electrochemical reaction sequence) or ED (electrochemical reaction followed by a rate-determining disproportionation step). Figure 3 is based on a special analog of the Randles-Sevcik Eq. (20), *viz.*

$$i_p = (n_i\mathbf{F}A)(\pi D n_i \mathbf{F}/RT)^{1/2} v^{1/2} C \chi_P \qquad [11]$$

where n_i denotes the number of electrons involved in the initial electrochemical reaction; A and C denote the area of the electrode and the bulk concentration of the electroactive species, respectively. χ_P is a dimensionless "current function maximum" which is accessible on the basis of theoretical calculations. In a given solution at a given electrode area, A and C are constant and therefore

$$i_p/v^{1/2} \text{ is proportional to } \chi_P \qquad [12]$$

Equation [12] is the rationale for the choice of ordinates in Fig. 3. In the intermediate scan domain, substitution of $n_i = 1$ (based on the experimental n, Table II, Column 3) into Eq. [11] yielded $\chi_P = 0.45$ which is in excellent agreement for a diffusion-controlled process (20-21) and thus eminently compatible with Eq. [1]. A drastic increase in $i_p/v^{1/2}$ with the decreasing scan rates is strikingly apparent in Fig. 3. At slow scans a limit corresponding to $\chi_P \approx 1.0$ was attained. This assignment of χ_P is compatible only with the sequences ECE and ED (22, 23), eliminating all other alternatives (19, 24-28). Of these, ECE can be counted out on the basis of the experimental finding that in scan domain I of Fig. 4

$$\frac{\Delta E_p}{\Delta \log v} = -\frac{2.3RT}{3\mathbf{F}} = -0.020\text{V at } 25°\text{C} \qquad [13]$$

This finding is compatible with the following theoretical relationships appropriate for an ED sequence (22, 23) *viz.*

$$n_i(E_p - E°) = \frac{RT}{3\mathbf{F}}(\ln \rho_2 - \text{const.}) \qquad [14]$$

$$\rho_2 = \frac{RT}{n\mathbf{F}}\frac{k_2 C}{v} \qquad [15]$$

where k_2 is the appropriate second-order disproportionation rate constant and n_i denotes the number of electrons involved in the electrochemical step which precedes the disproportionation. In contradistinction, for an ECE mechanism where the "interposed chemical reaction" has first-order kinetics, theory predicts (22)

$$\frac{\Delta E_p}{\Delta \log v} = -\frac{2.3RT}{2\mathbf{F}} = -0.030\text{V at } 25°\text{C} \qquad [16]$$

because

$$n_i(E_p - E°) = \frac{RT}{2\mathbf{F}}(\ln \rho_1 - \text{const.}) \qquad [17]$$

$$\rho_1 = \frac{RT}{n\mathbf{F}}\frac{k_1}{v} \qquad [18]$$

where k_1 is the first-order rate constant of the interposed chemical reaction. The ρ's in Eq. [15] and [18] are dimensionless parameters which differ by the factor C (concentration, which appears in Eq. [15], but is conspicuous by its absence in Eq. [18]). The reason for the difference between ρ_1 and ρ_2 is inherent in the second-order kinetics of the disproportionation process. A consequence of Eq. [15] and [18] was that plots of E_p *vs.* log v for two different ferriheme concentrations were parallel and separated by an intercept of 2.3 $RT/3\mathbf{F}$ log C. The two lines merged when E_p was plotted *vs.* log v/C in lieu of log v (Fig. 4, lower curve). The internal consistency of these findings established unambiguously the sequence of reactions [1] and [2] as the mechanism of the over-all reaction [3]. It should be noted that the rate-determining step was the disproportionation process 2 ($k_2 = 6 \times 10^5$ M^{-1} sec^{-1}).[2] Nevertheless, we succeeded in estimating the standard rate constant for the faster reaction [1]. This was accomplished with the aid of Eq. [7] yielding a $k_1° \geqq 0.8$ cm/sec.

Comparison of electron transfer reactivities of simple heme moieties and of hemoproteins.—Data presented in this paper have enriched somewhat the information available on the electrode kinetics in aqueous media (including ethanol-water mixtures up to 75% ethanol) of the process Fe(III) + $e \rightleftarrows$ Fe(II) occurring in low molecular weight (MW < 1500) heme entities. Combined with earlier experimental findings reported in the literature, we now have estimates of relevant electrochemical rate constants for systems ranging in complexity from the simplest monomers with symmetrically coordinated axial (Z) ligands (*e.g.*, the dicyanohemi(o)chromes, VI and VII, through monomeric hemes with asymmetric Z ligands (*e.g.*, the hydroxy ethanolato ferriheme, IV) to the dimeric ferri- and ferroheme moieties I, II, and III.

It is of evident interest to correlate these electrochemical rates with the kinetics of the ferrous-ferric redox processes as it occurs in macromolecular hemoproteins (10^4 < MW < 10^5). However, no direct comparison of electrode kinetics is currently feasible. The reason for this is inherent in the fact that any electrode reaction involves as a competing-rate process the transport of the electroreactive (electrooxidizable or electroreducible) species from the bulk of the electrolyte to the electrode interface. The rate of the transport process depends on the diffusion coefficient of the electroreactive species, which is necessarily small for macromolecules. Consequently, any currents resulting from the electrooxidation-reduction of iron in hemoproteins are bound to be diffusion controlled, and thus, nonilluminating as far as electron transfer kinetics are concerned [diffusion-controlled polarograms of cytochrome c have indeed been recently described (29)].

On the other hand, rates of oxidation by ferricyanide of divalent iron in hemoglobin, myoglobin, and cytochrome c have been measured (30, 31). Rates of cross-reactions of this type, *viz.*

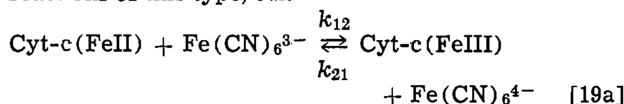

$$\text{Cyt-c(FeII)} + \text{Fe(CN)}_6^{3-} \underset{k_{21}}{\overset{k_{12}}{\rightleftarrows}} \text{Cyt-c(FeIII)} + \text{Fe(CN)}_6^{4-} \qquad [19a]$$

[2] The value of this rate constant is not of central interest in the context of the principal emphasis of the present paper. Its determination depended on Eq. [14]-[15], using assignments tabulated by Nicholson (23) and Saveant and co-workers (22) as a function of χ_P whose experimental values as a function of v were taken from Fig. 3 and similar experimental data.

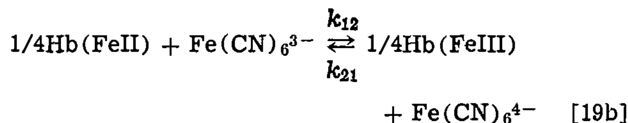

$$1/4\text{Hb(FeII)} + \text{Fe(CN)}_6^{3-} \underset{k_{21}}{\overset{k_{12}}{\rightleftarrows}} 1/4\text{Hb(FeIII)} + \text{Fe(CN)}_6^{4-} \quad [19b]$$

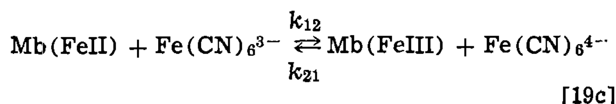

$$\text{Mb(FeII)} + \text{Fe(CN)}_6^{3-} \underset{k_{21}}{\overset{k_{12}}{\rightleftarrows}} \text{Mb(FeIII)} + \text{Fe(CN)}_6^{4-} \quad [19c]$$

can be correlated via the Marcus theory (11) with the kinetics of the isotopic electron self-exchange of the two redox couples involved, *viz.*

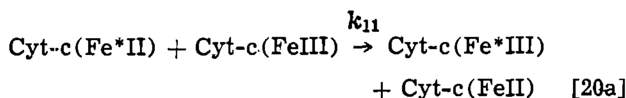

$$\text{Cyt-c(Fe*II)} + \text{Cyt-c(FeIII)} \xrightarrow{k_{11}} \text{Cyt-c(Fe*III)} + \text{Cyt-c(FeII)} \quad [20a]$$

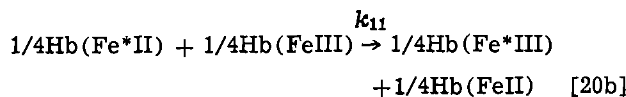

$$1/4\text{Hb(Fe*II)} + 1/4\text{Hb(FeIII)} \xrightarrow{k_{11}} 1/4\text{Hb(Fe*III)} + 1/4\text{Hb(FeII)} \quad [20b]$$

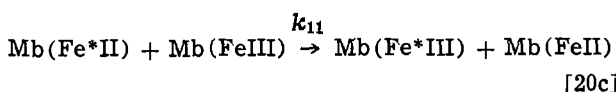

$$\text{Mb(Fe*II)} + \text{Mb(FeIII)} \xrightarrow{k_{11}} \text{Mb(Fe*III)} + \text{Mb(FeII)} \quad [20c]$$

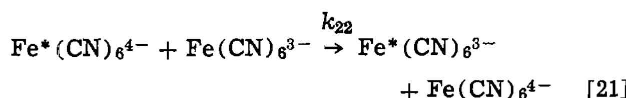

$$\text{Fe*(CN)}_6^{4-} + \text{Fe(CN)}_6^{3-} \xrightarrow{k_{22}} \text{Fe*(CN)}_6^{3-} + \text{Fe(CN)}_6^{4-} \quad [21]$$

Recently, the Marcus theory has been successful in correlating the rate constants for reaction of ferri- and ferrocytochrome c with several oxidants and reductants (32-35), including $Ru(NH_3)_6^{2+}$, $Co(phen)_3^{3+}$, $Fe(CN)_6^{3-}$, $Fe(EDTA)^{2-}$ as well as the peroxide complex of cytochrome c peroxidase.

The relationship between cross reactions as given in Eq. [19a]-[19c] and the self-exchange reaction rate constants given in Eq. [20a]-[20c] and Eq. [21] can be formulated as follows

$$k_{11} = \frac{k_{12}^2}{K_{12}k_{22}} \quad [22]$$

where K_{12} is the equilibrium constant for the cross reactions given in Eq. [19] and k_{11} is the homogeneous isotopic electron exchange reaction rate constant. When the work terms are negligible, k_{11} can be related to the standard electrochemical rate constant k^o by the following equation (11)

$$\left(\frac{k_{11}}{Z_{\text{hom}}}\right)^{1/2} = \frac{k^o}{Z_{\text{het}}} \quad [23]$$

where Z_{hom} and Z_{het} are the collision frequencies of the chemical and electrochemical reactions, respectively, (10^{11} 1 mole^{-1} sec^{-1} and 10^4 cm sec^{-1}).

Assuming, as a *pro tempore* working hypothesis, that the Marcus correlations hold for Reactions [19]-[21], Eq. [22] and [23] can be combined and rearranged to explicit k^o

$$k^o = \frac{k_{12}}{(K_{12}k_{22}10^3)^{1/2}} \quad [24]$$

If one assumes that the Marcus theory holds for a comparison between the cross reaction [19a]-[19c] on the one hand and the isotopic exchange processes [20a]-[20c] on the other hand, electron-transfer rate constants can be calculated from Eq. [24] for the hypothetical electrode reactions [25a]-[25c]

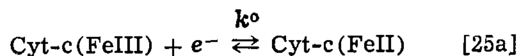

$$\text{Cyt-c(FeIII)} + e^- \overset{k^o}{\rightleftarrows} \text{Cyt-c(FeII)} \quad [25a]$$

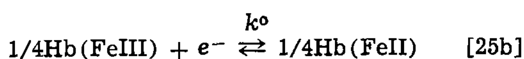

$$1/4\text{Hb(FeIII)} + e^- \overset{k^o}{\rightleftarrows} 1/4\text{Hb(FeII)} \quad [25b]$$

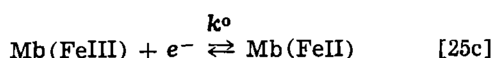

$$\text{Mb(FeIII)} + e^- \overset{k^o}{\rightleftarrows} \text{Mb(FeII)} \quad [25c]$$

An illuminating comparison of these hypothetical rate parameters of hemoproteins *vs.* their analogs determined experimentally in simpler less molecular weight heme couples is presented in Table III. Presentation of the rates in terms of k^o is equivalent to expressing the same information in terms of k_{11} (*i.e.*, via a hypothetical self-exchange rate). In a recent authoritative review aimed at inorganic chemists Wherland and Gray (35b) have indeed elected to use that alternative form of presentation. We have advisedly chosen to use the electrochemical k^o instead because it is more appropriate for an electrochemical audience. Naturally, the two types of presentation are readily interchangeable.

Equilibrium parameters K_{12} for reactions [19a]-[19c] were evaluated from relevant redox potentials available in the literature (30, 36) with the aid of the equation

$$\Delta G^o = -n\mathbf{F}\Delta E^o = RT \ln K_{12} \quad [26]$$

where ΔE^o denotes the difference in formal potentials between the couples involved in reactions [19a]-[19c].

For comparison we have also calculated the hypothetical rate constant for reaction [25a] utilizing Eq. [23] directly and the experimental self-exchange rate of horse heart cytochrome c (10^3-10^5 M^{-1} sec^{-1}) obtained by Gupta (37) using NMR techniques. Experimental self-exchange rates are not available for hemoglobin or myoglobin.

Table III reveals a surprising similarity between the ferrous-ferric electron-transfer rate parameters of simple heme compounds on the one hand, and hemoglobin and myoglobin on the other hand. This invariance is particularly impressive because the upper limit of the calculated comparable rate constants for cytochrome c is three orders of magnitude faster, *i.e.*, $k^o \simeq 1.4 \times 10^2$ cm/sec.

The rate constant assignments for Eq. [25a]-[25c] are admittedly based on a comparison of experimental measurements with values calculated from the Marcus theory which implies that all the relevant (actual and/or hypothetical) electron transfer processes (reactions [25a]-[25c]), isotopic exchange reactions (Eq. [20a]-[20c], and cross-redox reactions (Eq. [19a]-[19c]) proceeded via similar transition states. We postulate, accordingly, that all the one-electron transfer processes which are schematized in Fig. 5 proceeded through similar mechanisms regardless of whether the electron was transferred at an electrode interface, by isotopic self-exchange, or in a chemical cross reaction

Table III. Comparison of theoretical and experimental formal rate constants, k°, for the electrooxidation reduction of various heme moieties[a]

Electrode reaction	Hypothetical k^o (cm sec^{-1})	Experimental k^o (cm sec^{-1})
Cyt-cFe(III) $\overset{e}{\rightleftarrows}$ Cyt-cFe(II)	0.1-1.4 × 10^2 [b] (1-10) [c]	—
¼HbFe(III) $\overset{e}{\rightleftarrows}$ ¼HbFe(II)	0.05-0.2 [d]	—
MbFe(III) $\overset{e}{\rightleftarrows}$ MbFe(II)	0.2-0.5 [d]	—
PFe(III)-Fe(III)P $\overset{e}{\rightleftarrows}$ P-Fe(II)-Fe(III)P (aqueous, pH 10)	—	≧0.8
PFe(III) $\overset{e}{\rightleftarrows}$ PFe(II) (50% EtOH)	—	≧0.2
PFe(III)CN $\overset{e}{\rightleftarrows}$ PFe(II)CN	—	4.0 [e]

[a] The symbol P denotes the protoporphyrin IX equatorial ligand of heme.
[b] Calculated from Eq. [24] using the cytochrome c exchange rates calculated in Ref. (35) from cross reactions with $Co(phen)_3^{3+}$, $Fe(CN)_6^{3-}$ and $Fe(EDTA)^{2-}$.
[c] Calculated from Eq. [23] using the experimental self-exchange rates in Ref. (37).
[d] Calculated from Eq. [24] using k_{11} = 5-50 × 10^3 for cytochrome c (43).
[e] Ref. (7).

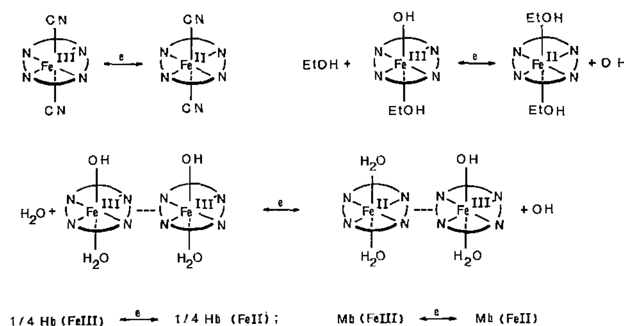

Fig. 5. Moieties exhibiting kinetically comparable electron-transfer behavior.

with another redox couple. Furthermore, the invariance of the rates in all these instances (in contradistinction to cytochrome c, *vide infra*) suggests a common "reaction path" via the porphyrin plane (which was identical in all moieties of Fig. 5) rather than through the Z orbitals which had widely different ligand coordination (cyanide, water, ethanol, hydroxyl, imidazole nitrogen). Indeed, electron transfer paths via the π bonded tetrapyrrole porphyrin plane have been suggested (32, 33, 35, 38-40). The over-all conclusion which emerges from the experimental evidence *in toto* is that (within a first approximation) the electron donor-acceptor reactivity of heme iron was the same (at least for the first electron transfer step) in all the compounds and reactions shown in Fig. 5. In other words, the behavior of heme iron was essentially invariant, irrespective as to whether the heme was monomeric (as in the presence of ethanol) or dimeric (as in aqueous solution) or imbedded in the proteinic matrices of hemoglobin or myoglobin.

On the other hand, our estimate of the electron-transfer reactivity of the heme iron in cytochrome c was 1-3 orders of magnitude faster and corresponded to an upper k^o assignment which approximated the limiting rate of 10^4 cm/sec within two orders of magnitude (41). This is in complete agreement with related conclusions (on the efficiency of cytochrome c as an electron transporter) by Urry and Eyring (42). The prosthetic group of cytochrome c differs by two cysteine linkages between the equatorial porphyrin ligand and the polypeptide chain of the protein moiety. One is tempted to speculate that involvement of sulfur atoms may provide electron-transfer paths of greatly enhanced reactivity which account for the fundamental difference between cytochrome c and the heme compounds in Fig. 5.

Acknowledgments

This work was supported by U.S. Public Health Service Research Grant HL02342 from the National Heart, Lung, and Blood Institute, National Institute of Health, and by Research Grant 794 from the North Atlantic Treaty Organization (NATO).

Manuscript submitted April 18, 1977; revised manuscript received Nov. 15, 1977.

Any discussion of this paper will appear in a Discussion Section to be published in the June 1979 JOURNAL. All discussions for the June 1979 Discussion Section should be submitted by Feb. 1, 1979.

REFERENCES

1. D. W. Urry and H. Eyring, *J. Theor. Biol.*, **8**, 198 (1965).
2. R. E. Dickerson and T. Geis, "The Structure and Action of Proteins," references therein, Harper and Row, New York (1969).
3. J. H. Wang, *Acc. Chem. Res.*, **3**, 90 (1970).
4. (a) K. M. Kadish, G. Larson, D. Lexa, and M. Momenteau, *J. Am. Chem. Soc.*, **97**, 282 (1975); (b) D. Lexa, M. Momenteau, and J. Mispelter, *Biochim. Biophys. Acta*, **338**, 151 (1974); (c) G. Cauquis and J. C. Marchon, *Bioelectrochem Bioenergetics*, **1**, 23 (1974); (d) B. A. Feinberg, M. Gross, K. M. Kadish, R. S. Marano, S. J. Pace, and J. Jordan, *Bioelectrochem. Bioenerg.*, **1**, 73 (1974).
5. K. M. Kadish and D. G. Davis, *Ann. N.Y. Acad. Sci.*, **206**, 495 (1973).
6. D. G. Davis and R. F. Martin, *J. Am. Chem. Soc.*, **88**, 1365 (1966); D. G. Davis and J. G. Montalvo, Jr., *J. Electronanal. Chem.*, **23**, 164 (1969); D. G. Davis and D. J. Orgeron, *Anal. Chem.*, **38**, 179 (1966).
7. R. F. Martin and D. G. Davis, *Biochem.*, **7**, 3906 (1968).
8. T. M. Bednarski and J. Jordan, *J. Am. Chem Soc.*, **86**, 5690 (1964); *ibid.*, **89**, 1552 (1967).
9. H. R. Gygax and J. Jordan, *Discuss. Faraday Soc.*, **45**, 427 (1968).
10. K. M. Kadish and J. Jordan, *Anal. Lett.*, **3**, 113 (1970).
11. R. A. Marcus, *Discuss. Faraday Soc.*, **45**, 7 (1968); *Ann. Rev. Phys. Chem.*, **15**, 155 (1964); *J. Phys. Chem.*, **67**, 853 (1963); *ibid.*, **43**, 679 (1965) and references cited therein.
12. G. L. Booman and W. B. Holbrook, *Anal. Chem.*, **35**, 1793 (1963); E. R. Brown, T. C. McCord, D. E. Smith, and D. D. DeFord, *Anal. Chem.*, **38**, 1119 (1966).
13. W. T. DeVries and E. VanDalen, *J. Electroanal. Chem.*, **10**, 183 (1965).
14. G. A. Philbrick Researchers Inc., "Philbrick Applications Manual," Nimrod Press Inc., Boston (1966).
15. R. Bates, "Determination of pH," 2nd ed., John Wiley & Sons, Inc., New York (1972).
16. M. L. McGlashan, *Pure Appl. Chem.*, **21**, (I), 3 (1970).
17. W. M. Latimer, "Oxidation Potentials," Prentice Hall, Inc., Englewood Cliffs, N.J. (1952).
18. R. S. Nicholson, *Anal. Chem.*, **37**, 1351 (1965).
19. R. S. Nicholson and I. Shain, *ibid.*, **36**, 706 (1964).
20. J. E. Randles, *Trans. Faraday Soc.*, **44**, 327 (1948); W. H. Reinmuth, *J. Am. Chem. Soc.*, **79**, 6538 (1957); A. Sevick, *Coll. Czech. Chem. Comm.*, **13**, 349 (1948).
21. J. M. Saveant and E. Vianello, *Electrochim. Acta.*, **12**, 629 (1967).
22. M. Mastragostino, K. Nadjo, and J. M. Saveant, *Electrochim. Acta.*, **13**, 721 (1968); M. Mastragostino and J. M. Saveant, *Electrochim. Acta.*, **13**, 751 (1968).
23. R. S. Nicholson, *Anal. Chem.*, **41**, 862 (1969).
24. R. S. Nicholson and I. Shain, *ibid.*, **37**, 178 (1965); *ibid.*, **37**, 190 (1965).
25. R. H. Wopschall and I. Shain, *ibid.*, **39**, 1514 (1967); *ibid.*, **39**, 1527 (1967); *ibid.*, **39**, 1535 (1967).
26. D. S. Polcyn and I. Shain, *ibid.*, **38**, 370 (1966); *ibid.*, **38**, 376 (1966).
27. J. M. Saveant and E. Vianello, *Electrochim. Acta.*, **8**, 905 (1963).
28. M. S. Shuman, *Anal. Chem.*, **41**, 142 (1969); *ibid.*, **42**, 521 (1970).
29. (a) S. R. Betso, M. H. Klapper, and L. B. Anderson, *J. Am. Chem. Soc.*, **94**, 8197 (1972); (b) F. Scheller, M. Jänchen, J. Lampe, H.-J. Prüme, J. Blanck, and E. Palecek, *Biochim. Biophys. Acta*, **412**, 157 (1975).
30. N. Sutin and D. R. Christman, *J. Am. Chem. Soc.*, **83**, 1773 (1961).
31. E. Antonini, M. Brunori, and J. Wyman, *J. Biochem.*, **114**, 545 (1965).
32. R. X. Ewall and L. E. Bennett, *J. Am. Chem. Soc.*, **96**, 940 (1974).
33. J. V. McArdle, H. B. Gray, C. Creutz, and N. Sutin, *ibid.*, **96**, 5737 (1974).
34. N. Sutin, in "Inorganic Biochemistry," G. Eichhorn. Editor, Chap. 19, Elsevier, Amsterdam (1973).
35. (a) J. Rawlings, S. Wherland, and H. B. Gray, *J. Am. Chem. Soc.*, **98**, 2177 (1976); (b) S. Wherland and H. B. Gray, in "Biological Aspects of Inorganic Chemistry," A. W. Addison, W. R. Cullen, D. Dolphin, and B. R. James, Editors, Chap. 10, John Wiley & Sons, New York (1977).
36. W. M. Clark, "Oxidation Reduction Potentials of Organic Systems," Williams and Wilkens, Baltimore (1960).

37. R. K. Gupta, *Biochim. Biophys. Acta.*, **292**, 291 (1973).
38. C. E. Castro, *J. Theor. Biol.*, **33**, 475 (1971).
39. E. B. Fleischer and S. K. Cheung, *J. Am. Chem. Soc.*, **98**, 8381 (1976).
40. H. L. Hodges, P. A. Holwerda, and H. B. Gray, *J. Am. Chem. Soc.*, **96**, 3132 (1974).
41. W. L. Reynolds and R. W. Lumry, "Mechanisms of Electron Transfer," The Ronald Press Co., New York (1966).
42. D. W. Urry and H. Eyring, *J. Theoret. Biol.*, **8**, 198 (1965).
43. C. F. Deck, P. King, Jr., and A. Wall, *Inorg. Chem.*, **4**, 672 (1967).

Polaromicrotribometric (PMT) and Spectroscopic (Infrared-XPS) Study of the Formation and Modifications of Films Formed on a Polarized Platinum Electrode in THF-$LiClO_4$ Medium

I. Cathodic Polarization

Jacques-Emile Dubois and Gérard Tourillon

Laboratoire de Chimie Organique Physique de l'Université Paris VII, associé au C.N.R.S., 75005 Paris, France

and Pierre-Camille Lacaze*

Université de Picardie, UER de Saint-Quentin, 02100, Saint-Quentin, France

ABSTRACT

The mechanism of formation and the changes of different deposits obtained on a Pt cathode in THF-$LiClO_4$ medium are studied by means of polaromicrotribometry (PMT). Their chemical nature is determined by infrared and x-ray induced photoelectron spectroscopy (XPS). For a polarization between −1.6 and −2.5V, a thin porous homogeneous film of lithium hydroxide occurs, which is characterized by a low friction coefficient $f = 0.7\ f_0$, where f_0 is the value in the absence of polarization. Small amounts of carbon dioxide in solution react on lithium hydroxide and convert it into lithium carbonate. This chemical change provokes a strong increase in the friction coefficient (f rises from 0.7 to 2 f_0) and is marked by the appearance of a very regular stick-slip phenomenon. Under galvanostatic control and at a weak electrolysis current, the formation of lithium hydroxide and then lithium metal is successively observed. The friction curves clearly show that Li^+ ions migrate through the porous lithium hydroxide layer and are reduced on the metal surface. When electrolysis is continued over a longer period of time the lithium hydroxide layer is coated with lithium metal. At a higher current density and at a lower water concentration, a layer of metallic lithium can be obtained in the electrode surface without the prior formation of lithium hydroxide.

The use of organic solvents and metallic electrodes in electrochemistry generally leads to a demetallization of the electrode surface, produced by the formation of organic or mineral layers (1). Such phenomena have recently been observed in hexamethylphosphoramide (HMPA) (2, 3) and their effects on electrochemical catalysis have been determined especially in the case of the reduction of quaternary ammonium salts (3). The obtention of homogeneous organic or inorganic films by an electrochemical method presents a practical value in the area of material protection and microelectronics, and knowledge of these phenomena is very important in the elucidation of organic electrochemical reactions.

In the case of an electrolytic medium composed of an organic solvent and an alkaline salt we show that some electrode reactions which can lead to irreversible changes in the surface occur in the medium. Such observations have been noted in reduction and in the case of dimethylsulfoxide (DMSO), acetonitrile, propylene carbonate, or tetrahydrofurane (THF), when a salt such as $LiClO_4$ is added to the solvent.

* Electrochemical Society Active Member.

The THF-$LiClO_4$ electrolytic medium is very often used in organic electrochemistry, and several studies have already been devoted to the reduction of Li^+ ions on a platinum electrode in this solvent (4-7). Thus, Burrows and Kirkland (4) and Dey (5) have described the behavior of Li^+ ions in the presence of water and have indicated the formation of a lithium hydroxide layer. As far as we know, however, the chemical nature of these layers has not been proved. We thus propose to study the structural modifications of the metal-solution interface in an attempt to elucidate the chemical nature and formation mechanism of the different layers.

Aside from infrared and XPS spectroscopies, we have developed a new means of analyzing the metal-solution interface, called polaromicrotribometry or PMT (8, 9). This technique, based on the measurement and recording of a friction coefficient between the electrode surface and a microslider, has proved to be particularly well adapted to the study of the formation of oxide layers (10), organic films (11, 12) and, more recently, to adsorbed layers (13, 14). This system enables one to follow *in situ* the formation and behavior

of films as a function of time, and electrical and physicochemical parameters.

Experimental

Reagents and solvents.—The THF solvent (Baker) was purified according to the following process: (*i*) The peroxides were destroyed by reaction of potassium hydroxide on the solvent over several weeks. The solvent was then distilled under atmospheric pressure. (*ii*) The distilled solvent was dried over naphthalene-sodium for 8-10 days and then redistilled as previously. (*iii*) A final distillation of the THF was carried out in the presence of $LiAlH_4$ and the middle fraction of the distilled solvent was kept under inert atmosphere.

Lithium perchlorate (Fluka grade) was dried at 100°C under vacuum for several days before being used.

All the experiments were carried out in a glove box with a strictly controlled argon atmosphere. All oxygen, carbon dioxide, and water traces were removed by trapping all these impurities with suitable filters. All the THF-$LiClO_4$ $3 \cdot 10^{-1}$M solutions were degassed for 10 min in an argon stream. The water content of the solution was around 120 ppm.

Electrodes.—Depending on the surface analysis technique, different electrode models were used.

PMT.—The PMT cell is composed of a previously described three-electrode assembly (8). The working electrode was a PTFE embedded platinum pellet (Pt Lyon-Allemand pure grade). The active surface of the electrode was a 0.6 cm² disk, polished with a 1μ diamond paste (Struers); it was rinsed by ultrasonic agitation in acetone (RP grade) and dried under nitrogen before each experiment. The reference electrode was an Ag-Ag^+ 10^{-2}M system in THF-$LiClO_4$ (7). A sintered glass tube provided electrolyte contact between the working and reference electrodes. All the potentials were measured with respect to this reference. The counterelectrode was a large surface cylindrical platinum grid centered on the working electrode.

Infrared absorption, x-ray photoelectron spectroscopy (XPS).—The working electrode used to obtain infrared and XPS spectra was composed of a rectangular glass plate on which a layer of platinum with a thickness of about 5000Å was obtained by sputtering (Balzers Model Sputron II) according to a previously described process (15).

Analysis techniques and layer characterization.—*PMT.*—The apparatus used in this work had the same characteristics as the one previously described (8, 9); the applied load on the microslider was 10g.

Multiple reflection infrared absorption spectroscopy.—We used a Perkin Elmer 225 spectrophotometer fitted with a Wilks device (Wilks Scientific Corporation, Model 49). The spectra were recorded after the infrared beam had been reflected several times between two parallel flat metallic mirrors facing each other which have been coated with the film.

Electron spectroscopy (XPS).—Spectra were recorded on an AEI ES 200 spectrometer with FRR adaptation using a Mg anticathode.

Results

PMT curves under potentiodynamic control (rate polarization 1 V/min).—Current-potential and friction-potential curves between 0 and − 1.6V show no appreciable changes. The current is negligible and the friction coefficient remains constant and has the same f_o value as in the absence of polarization (Fig. 1) (f_o = 0.17). However, between − 1.6 and − 3.5V, several electrode reactions are observed. A first current peak, whose maximum is located at − 2.3V, appears. The corresponding integrated electricity value is an increasing function of the water concentration (8000 μC/cm² for (H_2O) = $8 \cdot 10^{-3}$M). This electrode reaction is accompanied by major variations in f which rises to 1.8 f_o and then decreases and becomes constant at a value less than f_o (f = 0.7 f_o).

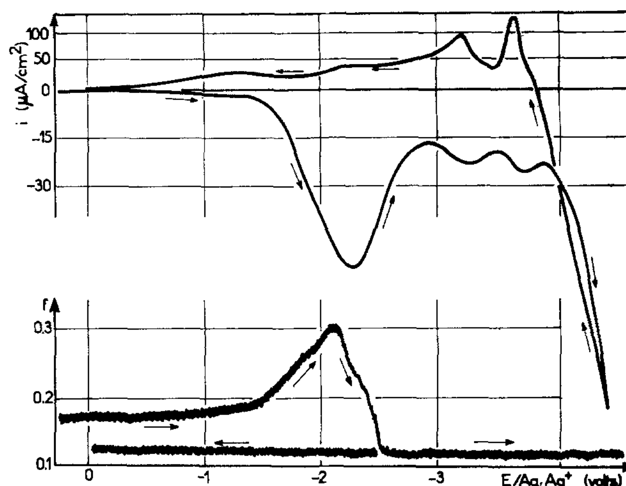

Fig. 1. Potentiodynamic and PMT curves obtained on a platinum electrode in THF-$LiClO_4$ 0.3M medium (water content, $8 \cdot 10^{-3}$M; sweep rate, 1 V/min).

Between − 3 and − 4V, the friction coefficient has the constant value 0.7 f_o, although two small current peaks are observed at − 3.25 and − 3.5V. At potentials below − 3.7V, the reduction potential of Li^+ ions is reached; the current intensity increases very rapidly, but f remains constant at 0.7 f_o. This constant value of f = 0.7 f_o is also observed in the back sweep, although several oxidation peaks appear. The height of one of them, located at − 3.6V, increases as the current intensity for the reduction of Li^+ ions increases.

PMT curves under galvanostatic control.—For anhydrous solutions (water content less than $5 \cdot 10^{-3}$M) with an applied constant current between 120 and 1500 μA/cm², the polarization of the cathode occurs at − 3.7V. The friction coefficient increases considerably and is characterized by a great irregularity whose mean value is nearly 2.5 f_o (Fig. 2). However, for hydrated solutions (H_2O = $8 \cdot 10^{-2}$M) with the same current density values as above, the potential-time curves are very different and are characterized by a first reduction wave at − 2V, followed by a second one at − 3.7V (Fig. 3).

In contrast, the friction curves are quite similar to those obtained during polarization sweeps; there is a fast increase in the friction coefficient to f = 1.3 f_o

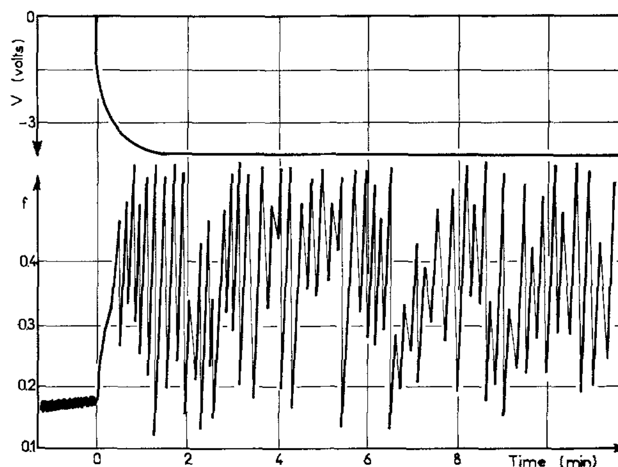

Fig. 2. Galvanostatic and PMT curves obtained on a platinum electrode in THF-$LiClO_4$ 0.3M medium (water content, less than $5 \cdot 10^{-3}$M; i = 1500 μA/cm²).

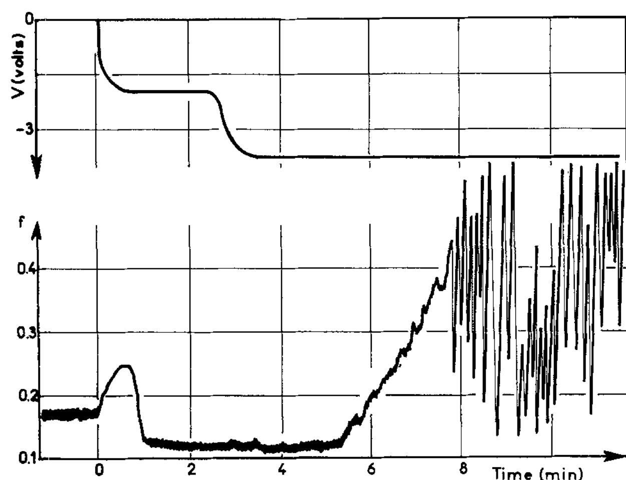

Fig. 3. Galvanostatic and PMT curves obtained on a platinum electrode in THF-$LiClO_4$ 0.3M medium (water content, $8 \cdot 10^{-2}$M; $i = 1500\ \mu A/cm^2$).

when the electrode is polarized, followed by a decrease to 0.7 f_0. This value of f remains constant for several minutes (2-3 min) and rises again to a mean value of 2.5 f_0, with very irregular variations of f. It should be noted that this new increase in the friction coefficient appears well after the electrode potential has reached −3.7V (Fig. 3).

PMT curves under potentiostatic control.—As with the potentiodynamic curves, a very fast passivating effect is observed under potentiostatic control when the platinum electrode is polarized at − 2.5V (for a water concentration of $5 \cdot 10^{-3}$M, the current density decreases from 1500 to 200 $\mu A/cm^2$ after a 3 min electrolysis) (Fig. 4). The friction curves have the same characteristics as previously: an increase in the friction coefficient of f_0 to 1.7 f_0, then a decrease to the constant value of 0.7 f_0 which, moreover, remains constant when the circuit is opened after a 10 min polarization. It is noteworthy that the decrease from 1.7 to 0.7 f_0 in the friction coefficient is also independent of the applied potential. If the polarization is interrupted when the friction has attained its maximum value (f = 1.7 f_0), it then decreases to f = 0.7 f_0 as previously observed. This transition of the friction coefficient is highly dependent on the water concentration (Fig. 5). For a water concentration of 10^{-3}M the maximum value f_M of the friction coefficient is 2 f_0; it is only 1.3 f_0 for a water content of $8 \cdot 10^{-2}$M.

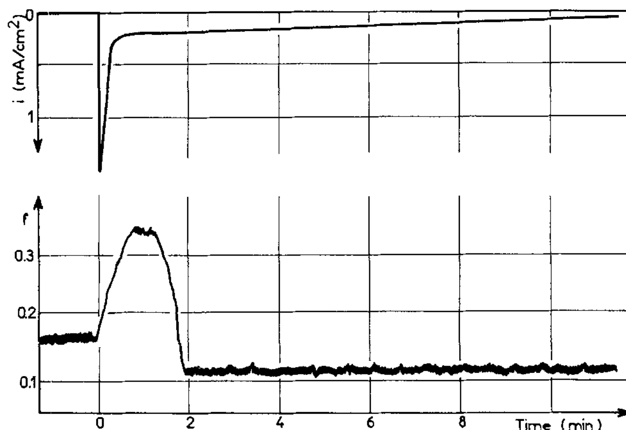

Fig. 4. Potentiostatic and PMT curves obtained on a platinum electrode in THF-$LiClO_4$ 0.3M medium (water concentration, $5 \cdot 10^{-3}$M; applied potential, −2.5V).

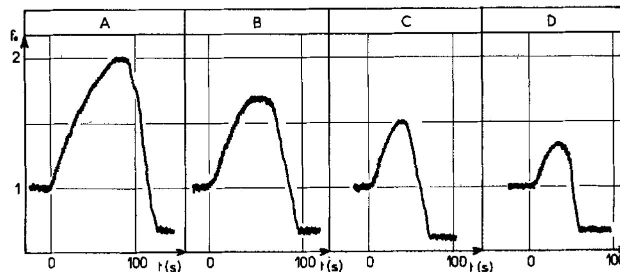

Fig. 5. Variation of the PMT curves maximum vs. the water concentration of the THF-$LiClO_4$ 0.3M medium in the case of a platinum electrode polarized at −2.5V. Water concentration: A, 10^{-3}M; B, $5 \cdot 10^{-3}$M; C, 10^{-2}M; D, $8 \cdot 10^{-2}$M.

Friction changes observed with a THF-$LiClO_4$ solution containing CO_2 traces.—Other very different friction variations are observed if the potentiostatic experiments are conducted in air or in presence of CO_2. We just showed that, when the platinum electrode is polarized at − 2.5V in a water concentration of $5 \cdot 10^{-3}$M, the friction coefficient rises to 1.7 f_0, then decreases and stays constant at 0.7 f_0. If the same experiment is operated in air, the friction coefficient remains constant for only a few minutes. There is a new increase in f whose mean value is about 2 f_0 and which is accompanied by a stick-slip phenomenon (9).

Another experiment performed with the same highly degassed solution, from which oxygen and CO_2 have been totally removed, also gives the constant friction coefficient of 0.7 f_0. If CO_2 is reintroduced into the solution by bubbling, the increase in the friction coefficient from 0.7 f_0 to a mean value of 2 f_0 is very fast (less than 30 sec) and is again accompanied by a very regular stick-slip phenomenon (Fig. 6).

Identification of layers by multiple reflection infrared spectroscopy and electron spectroscopy (XPS).—*Analysis of the layer whose friction coefficient is f = 0.7 f_0.*—A large surface thin layer platinum electrode was polarized at − 2.6V for 10 min in a THF-$LiClO_4$ solution in a very pure N_2 atmosphere. This led to the formation of a film whose friction coefficient was also 0.7 f_0.

The infrared absorption spectrum of this film is composed of several peaks located at 3580, 1580, 1000, 850, 630, 680 cm^{-1}, and of a wide one centered at 2900 cm^{-1} (Fig. 7a). This spectrum is identical to the one obtained for a layer of chemically prepared hydrated lithium hydroxide (16, 18).

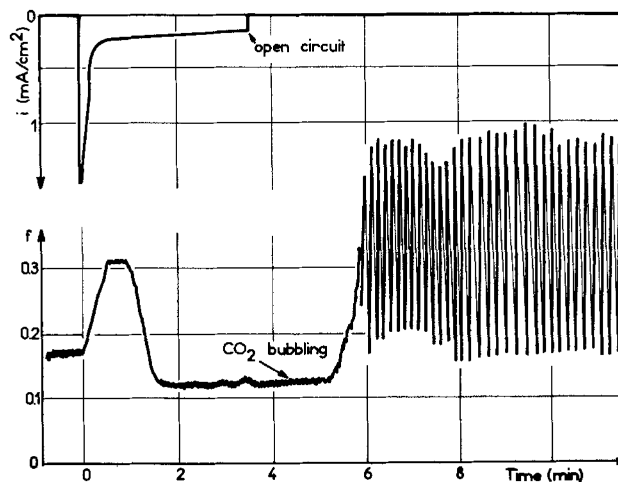

Fig. 6. PMT curves obtained on a platinum electrode after bubbling of CO_2 in THF-$LiClO_4$ 0.3M medium (the electrode is polarized at −2.5V for 3.5 min, then placed in open circuit before CO_2 bubbling; the water concentration is around $5 \cdot 10^{-3}$M).

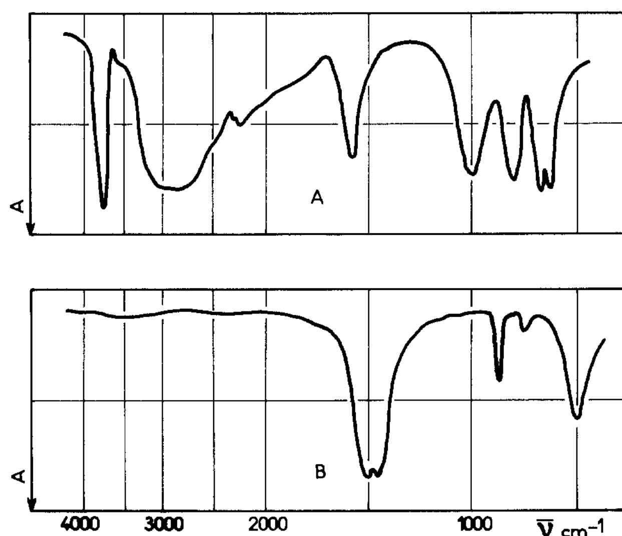

Fig. 7. Multiple reflection infrared absorption spectra obtained from thin platinum layers polarized at − 2.5V for 10 min. A. In THF-$LiClO_4$ 0.3M $H_2O \sim 5 \cdot 10^{-2}$M medium; lithium hydroxide film. B. In THF-$LiClO_4$ 0.3M saturated with CO_2, $H_2O \sim 5 \cdot 10^{-2}$M; lithium carbonate film.

The XPS spectrum composed of peaks at 285, 531.9, 74, 55.3, and 70.8 eV (Fig. 8a) confirms the hypothesis of a lithium hydroxide layer. The peak at 531.9 eV is related to O 1_S, the peaks at 74 and 70.8 eV to platinum 4 f doublet, the one at 55.3 eV to Li 1_S, and the peak at 285 eV to C 1_S, resulting from natural contamination of the samples.

Identification of the layer obtained in presence of CO_2.—The salient features of these layers are a regular stick-slip phenomenon with a dynamic friction coefficient whose mean value is $f = 2\ f_o$.

The infrared spectrum was obtained with electrode surfaces treated in the same conditions as previously except for bubbling of CO_2 in the THF-$LiClO_4$ solution. The peaks at 1510, 1450, 870, and 730 cm^{-1} (Fig. 7b) are characteristic of a lithium carbonate layer (16, 17).

The XPS spectrum is composed of the same signals as previously: 285, 531.9, 55.3, 74, and 70.8 eV with, however, a new peak at 289.8 eV corresponding to carbon 1_S of lithium carbonate (Fig. 8b). The shift in energy observed for this new peak is in total agreement with the results obtained by Siegbahn *et al.* (19) in the case of sodium carbonate.

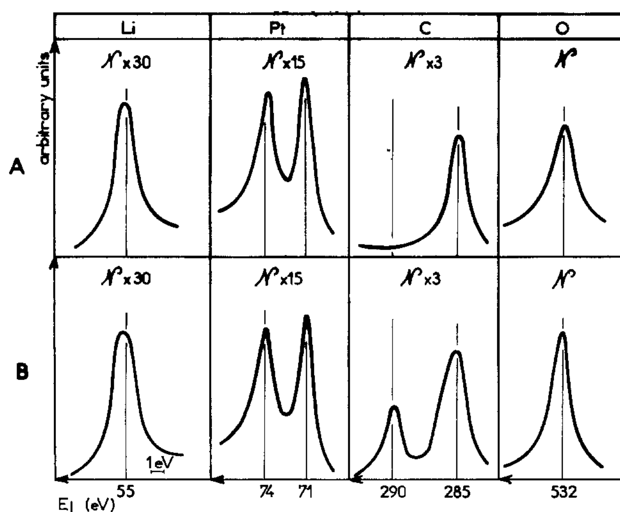

Fig. 8. XPS spectra obtained from thin platinum layers polarized at −2.5V for 10 min. A. In THF-$LiClO_4$ 0.3M, $H_2O \sim 5 \cdot 10^{-2}$M medium; lithium hydroxide film. B. In THF-$LiClO_4$ 0.3M saturated with CO_2, $H_2O \sim 5 \cdot 10^{-2}$M; lithium carbonate film.

Discussion

The results obtained by PMT and by infrared and XPS spectroscopies clearly show the formation of different layers on the platinum electrode surface. Thus, a first current peak centered at −2.3V whose intensity increases with the water concentration is observed. As proposed by Burrows and Kirkland (4), this reaction is due to water reduction and is followed by the formation of lithium hydroxide according to the diagram

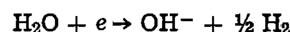

$$H_2O + e \rightarrow OH^- + \frac{1}{2} H_2$$

$$OH^- + Li^+ \rightarrow LiOH$$

The lithium hydroxide is adsorbed on the platinum surface, and the infrared and XPS spectroscopy results confirm that it is indeed a lithium hydroxide film, characterized by a low friction coefficient ($f = 0.7\ f_o$). However, it must be noticed that the friction curve obtained under potentiostatic control is composed of two distinct zones. In the first one the friction coefficient goes through a maximum value, $f_M > f_o$, whose amplitude decreases as the water concentration increases, and in the second one, f has the steady value of 0.7 f_o which is independent of the applied potential.

The first part of the friction curve cannot be attributed to adsorption of generated electrode species. With a carefully degassed solution the only generated chemical species are OH^- and H_2. Hydrogen adsorption must be set aside because we have seen that on platinum it entails a decrease in friction (10); the presence of OH^- ions in THF also has no effect on the friction coefficient, as was verified in the case of basic solutions.

It thus seems likely that this rise in the friction coefficient is related to the friction of silica on bare platinum. This result is in agreement with the fact that friction on a perfectly clean metallic surface generally entails high friction coefficients (20).

This phenomenon is very pronounced in the case of an anhydrous medium. If the water concentration is about $5 \cdot 10^{-3}$M, the friction coefficient rises from f_o to 2 f_o and remains constant for 30 to 45 sec before falling to 0.7 f_o 120 sec later. With a higher water concentration ($H_2O \simeq 10^{-2}$M) the maximum value f_M is only 1.5 f_o and the time necessary to attain the 0.7 f_o value is shorter (75 sec).

These friction variations are schematically shown in Fig. 9a. It can be supposed that at −2.5V the platinum surface is completely free of any adsorbed species; this provokes a fast rise of f along CD from f_o to f_1, where f_1 is supposed to correspond to the theoretical value of friction on bare Pt. Afterward, the OH^- ions combine with Li^+ ions to give lithium hydroxide which is adsorbed onto the Pt surface. This new deposited layer provokes a decrease in the friction coefficient from f_1 to 0.7 f_o along AB, and this latter variation is independent of the polarization.

For a very high water content, the concentration of lithium hydroxide in the neighborhood of the surface is also higher and, therefore, the film formation occurs more quickly. The decrease in friction will be quicker along A'B' parallel to AB and the maximum value f_M will be much smaller than f_1. Indeed, this is what we have qualitatively observed (Fig. 9b). Thus, the polarization applied at −2.5V temporarily cleans the surface electrode and involves an increase in the friction coefficient, followed by lithium hydroxide adsorption which causes the decrease in the friction coefficient from f_M to 0.7 f_o.

When this lithium hydroxide layer is observed with an optical microscope it appears to be porous and with a poor homogeneity. For small water concentrations, this layer is very thin and its thickness is less than 100Å. This observation is confirmed by XPS analysis

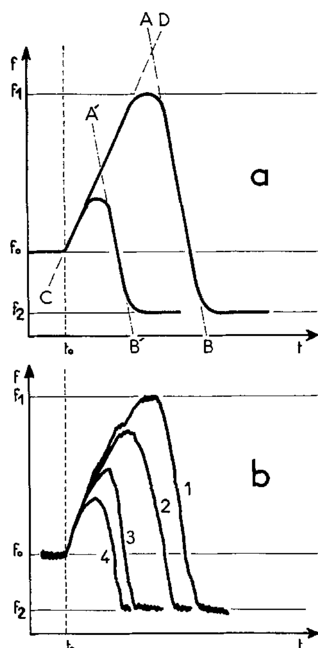

Fig. 9. Water concentration effect on the variation of the friction maximum observed after polarization at −2.5V of a platinum electrode in THF-$LiClO_4$ 0.3M medium. A. Theoretical variation. B. Experimental variation.

which shows the 70.8 and 74 eV peaks characteristic of the platinum 4f doublet.

This porosity and lack of homogeneity in the LiOH layer, which nevertheless has some passivating properties, explain the fact that for a second cathodic sweep there is again a reduction current peak which is less high than for the first sweep, but whose friction characteristics remain unchanged. They further account for the fact that all the MIM sandwich devices realized with these lithium hydroxide films are short-circuited.

This lithium hydroxide layer does not prevent the reduction of the Li^+ ions from occurring. The PMT results obtained under galvanostatic control prove that the discharge occurs through the pores of the film. Burrows and Kirkland (4) have advanced similar ideas in their study of a polarized platinum cathode in THF or propylene carbonate medium.

In the case of a very anhydrous medium (H_2O = $5 \cdot 10^{-3}$M), the application at the cathode of a constant current ($120 < i < 1500$ μA/cm^2) provokes the instantaneous formation of a metallic Li layer, which entails a high and irregular friction coefficient and the polarization of the electrode at −3.7V corresponding to the Li/Li^+ equilibrium potential (6, 7) (Fig. 2). Identical results (friction and potential) are obtained with massive Li.

However, the same experiment in a hydrated medium gives quite different results. A first potential plateau observed at −2.3V corresponds to the water reduction. As previously, the friction coefficient increases to the f_M value and then decreases to 0.7 f_o, the characteristic friction of the lithium hydroxide film. If the polarization of the cathode is continued, a second plateau appears at −3.7V, characteristic of the Li/Li^+ redox system, although the friction coefficient remains at 0.7 f_o. It is only 2 min after the potential has reached −3.7V that the friction rapidly increases again, to attain the same value as in the previous experiment (mean f value = 2 f_o).

The nonsimultaneity of the friction and the potential rises cannot be attributed to the response time of the apparatus, because it is about 1 sec (9). It seems more likely that Li^+ ions are diffusing through the lithium hydroxide layer and are reduced on the metal surface.

The hypothesis of the formation of a Li deposit on the lithium hydroxide layer must be ruled out, because in this case a rapid increase of the friction coefficient would occur. These results are quite similar to the ones we have observed in the case of a platinum electrode coated by a polymeric film which is permeable to Li^+ ions (12).

Thus it appears that the strong increase in the friction coefficient must be attributed to a Li coating of the lithium hydroxide layer, after it has been saturated by Li. Furthermore, if the electrolysis is carried out under ambient atmosphere or in the presence of CO_2 traces, the lithium hydroxide is rapidly transformed into lithium carbonate which provokes a strong increase in the friction coefficient (mean f value = 2 f_o) and a stick-slip phenomenon. These results are also confirmed by infrared and XPS analysis. Successive etchings of the layer surface by means of an Ar^+ ion beam show, moreover, that the lithium hydroxide was completely changed into lithium carbonate as is expressed by the simultaneous disappearance of XPS energy peaks for C_{1S} (carbonate) and Li 1_S.

Acknowledgment

Financial support of this research by the DRET is gratefully acknowledged.

Manuscript submitted Nov. 2, 1977; revised manuscript received March 16, 1978.

Any discussion of this paper will appear in a Discussion Section to be published in the June 1979 JOURNAL. All discussions for the June 1979 Discussion Section should be submitted by Feb. 1, 1979.

Publication costs of this article were assisted by the Laboratoire de Chimie Organique Physique.

REFERENCES

1. A. K. Vijh, "Electrochemistry of Metals and Semiconductors," Marcel Dekker, New York (1973).
2. J. E. Dubois, A. Desbene-Monvernay, Y. Robillard, and P. C. Lacaze, *Bull. Soc. Chim. Fr.*, **548** (1975).
3. J. E. Dubois, A. Desbene, and P. C. Lacaze, *J. Electroanal. Chem.*, **72**, 353 (1976).
4. B. Burrows and S. Kirkland, *This Journal*, **115**, 1164 (1968).
5. A. N. Dey, *ibid.*, **114**, 823 (1967).
6. J. Badoz-Lambling and M. Sato, *Acta. Chim.*, **32**, 191 (1962).
7. A. Caillet and G. Demange-Guerin, *J. Electroanal. Chem.*, **40**, 69 (1972).
8. J. M. Cesoron, R. Courtel, J. E. Dubois, M. Herlem, and P. C. Lacaze, *C. R. Acad. Sci.*, 266, 1667 (1968).
9. J. E. Dubois, P. C. Lacaze, R. Courtel, C. C. Hermann, and D. Maugis, *This Journal*, **122**, 1454 (1975).
10. M. Delamar, J. E. Dubois, and P. C. Lacaze, To be published.
11. J. E. Dubois, M. C. Pham, and F. Bruno, *Electrochim. Acta*, **22**, 451 (1975).
12. G. Tourillon, J. E. Dubois, and P. C. Lacaze, *This Journal*, **125**, 1262 (1978).
13. G. Tourillon, J. E. Dubois, and P. C. Lacaze, To be published.
14. M. Delamar, G. Tourillon, J. E. Dubois, and P. C. Lacaze, *J. Electroanal. Chem.*, Submitted for publication.
15. G. Tourillon, J. E. Dubois, and P. C. Lacaze, *J. Chim. Phys. Fr.*, **t 74**, No. 6, 685 (1977).
16. A. Nyquist and O. Kagel, "Infrared Spectra of Inorganic Compounds," p. 75, Academic Press, New York (1971).
17. F. A. Miller and C. H. Wilkins, *Anal. Chem.*, **24**, 1253 (1952).
18. C. N. R. Rao, "Chemical Applications of Infrared Spectroscopy," pp. 342-351, Academic Press, New York (1963).
19. U. Geluis, P. F. Heden, J. Hedman, B. J. Lindberg, R. Manne, R. Nordberg, C. Nordleng, and K. Siegbahn, *Phys. Scr.*, **2**, 70 (1970).
20. E. Rabinowicz, "Friction and Wear of Materials," p. 78, John Wiley & Sons, Inc., New York (1966).

Polaromicrotribometric (PMT) and Spectroscopic (Infrared-XPS) Study of the Formation and Modifications of Films Formed on a Polarized Platinum Electrode in THF-LiClO$_4$ Medium

II. Anodic Polarization

Gérard Tourillon and Jacques-Emile Dubois

Laboratoire de Chimie Organique Physique de l'Université Paris VII, associé au C.N.R.S., 75005 Paris, France

and Pierre-Camille Lacaze*

Université de Picardie, UER de Saint-Quentin, 02100 Saint-Quentin, France

ABSTRACT

The surface changes occurring when a platinum electrode is anodically polarized in THF-LiClO$_4$ or in THF-LiClO$_4$-9,10 diphenylanthracene (DPA) are detected and investigated by means of polaromicrotribometry (PMT). The formation of a homogeneous film on the metal surface is associated with a very small value of the friction coefficient. The thickness of this film, designated by the general symbol Pt|THF, LiClO$_4$, Ox|, may be adjusted from 100 to 5000Å. It appears as a very pure variety of polyTHF, uncontaminated by the electrolyte. Multiple-reflection infrared spectroscopy and x-ray photoelectron spectroscopy (XPS) are used to determine its structure. Its formation results from the polymerization of THF via an ionic mechanism initiated by $ClO_4{\cdot}$ or $DPA^{\cdot +}$ radicals. It only occurs if the water content is less than 250 ppm. This film has well-defined physical properties: a marked hydrophobicity, very strong adherence on the platinum surface, and great homogeneity; although it is a nonconductor out of the solution, its porous structure makes it a conductor in electrolyte solution.

The development of the technology in the area in microelectronics and, more recently, in that of integrated optics is more and more dependent on different methods of elaborating organic or mineral films (1). In the case of organic films, numerous techniques for deposition on metallic surfaces have been described. The most common methods are based on vapor deposition or sublimation (1), adsorption (2) or polymerization of an organic vapor subjected to electronic bombardment (3) or to an electric discharge (4). Electrochemical techniques can also be used for the elaboration of mineral or organic films, applicable to the previous areas. The film quality (purity, adherence, and homogeneity) depends on the chemical system chosen, on the polarization conditions, and also on the choice of the chemical medium in which the electrode reaction is occurring.

Generally speaking, it is possible to obtain an organic polymer film adsorbed on a metallic surface by oxidizing or reducing a compound which produces polymerizable radical or ionic species. The chosen reagent may either be a monomer dissolved in a solvent, or the solvent itself. The THF example belongs to this latter case, and in a previous work (5) we show that several mineral films are formed on the electrode under cathodic polarization.

The polymerization of THF by chemical (6) or electrochemical (7-10) means has already been described in the literature, but it is only related to the formation of the dissolved polymer in solution. As far as we know, no study has been devoted to the phenomena which occur on the electrode surface for an anodic polarization.

By using the PMT technique (11, 12), we have been able to show important modifications of the platinum surface in the anodic zone. These are related to the appearance of a deposit which could not be detected by analysis of the *i-E* curves alone. This first observation is confirmed by means of other analytical techniques such as multiple-reflection infrared absorption and x-ray photoelectron (XPS) spectroscopy. We have studied the mechanism by which this deposit is formed, its chemical structure, and its physical properties.

Experimental

Reagents and solvents.—THF (Baker pure grade) and the lithium perchlorate (Fluka) were purified as previously described (5). All experiments were performed in THF-LiClO$_4$ 0.3M solutions or in THF-LiClO$_4$ 0.3M diphenylanthracene (DPA) 0.03M solutions which were degassed by bubbling argon through them for 15 min. Before measurements, the water content of these solutions was about 120 ppm.

Film detection and analysis techniques.—Polaromicrotribometry (PMT).—As previously outlined for the cathodic THF study, the film formation was followed *in situ* by means of PMT. The electrolysis cell, the electrodes, and the apparatus used for friction measurements were the same as those described in the preceding work (5). The Pt working electrode was always polished with diamond paste before each experiment and rinsed in acetone.

Spectroscopic measurements.—Chemical identification of the electrode films was obtained as previously by means of x-ray photoelectron spectroscopy (XPS) and by multiple-reflection infrared spectroscopy. The same apparatuses were used under the same conditions as described in the preceding work (5).

Physical characteristics of the film.—Wettability.—The hydrophobic properties of the surface were characterized by measuring the contact angle between water and the film surface (13) from the projected image of a water drop resting on the film.

* Electrochemical Society Active Member.

Thickness.—The thickness was measured by an optical method with a Tolansky interferential device mounted on a Leitz metalloplan microscope or by the capacity of a sandwich (Pt|film|metal) device.

Capacity and conductivity.—A (Pt|film|gold) device was realized by evaporating a thin gold counterelectrode (1000Å) on the film under a vacuum of 10^{-6} Torr. Its conductivity under a-c polarization and its capacity were measured with a Wayne Kerr impedance bridge (Model B 641) at a residual pressure of 10^{-5} Torr and at constant temperature (25°C). The d-c conductivity was measured by application of Ohm's law, $V = Ri$, where V is the applied potential between the two electrodes and i is the current intensity.

Results and Discussion

PMT curves under potentiodynamic control (polarization rate 1 V/min).—In the case of a THF-$LiClO_4$ 0.3M solution, the current-potential curves obtained between 0 and +4V show two distinct zones: the first is located between 0 and +0.7V where the current intensity is small, and the second beyond +0.7V where it increases rapidly (Fig. 1). In contrast, f keeps a steady value, f_0, from 0 to +3 or +3.5V which is the value of f on the platinum electrode surface before polarization. Beyond 3 or 3.5V, f increases slightly and reaches 1.25 f_0. On the back sweep, no hysteresis is observed on the current-potential curve, but f remains constant at 1.25 f_0 from +4 to 0V.

With successive potential sweeps between 0 and +4V, the current-potential curves remain the same as with the first sweep. However, after three cyclic potential sweeps, the friction-potential curve is seriously modified: after f has increased toward 1.25 f_0, it slowly decreases to 0.2 f_0 and then remains constant, even if the electrode is in open circuit.

In the case of THF-$LiClO_4$ 0.3M solution with diphenylanthracene (DPA) 0.03M, the current-potential curves obtained between 0 and +2.5V have the same features as in the previous case. However, the appearance of a blue color near the surface is observed when the polarization reaches +1.8V. The friction coefficient stays at the constant value f_0, and it is only after three cyclic potential sweeps that f increases to 1.25 f_0 which is reached at the same time as the blue color near the electrode surface disappears. If the potential sweeps are pursued (around 10), f decreases and reaches the same constant value as that observed in THF-$LiClO_4$ ($f = 0.2 f_0$). This proves that the layer which has formed in the presence of DPA is the same as the latter one, but was obtained for smaller potentials.

PMT curves under potentiostatic control.—When the platinum electrode is polarized at +3.5V in THF-$LiClO_4$ medium, the current intensity is instantaneously 1.8 mA/cm^{-2} and remains steady at this value as long as the electrolysis continues (Fig. 2). The friction coefficient remains constant for 1 or 2 min and then increases to 1.25 f_0. After a 3 min electrolysis, it decreases slowly and stabilizes at the low value of 0.2 f_0. This value remains constant when the electrode is placed in open circuit. If the electrode is disconnected after 3 min of polarization at +3.5V where f is at a maximum, a slow decrease of f toward 0.2 f_0 is observed as in the latter case (Fig. 3).

In the case of a THF-$LiClO_4$ medium with DPA, an applied potential of 1.8V at the platinum electrode entails a current density of 1.2 mA/cm^2 and the appearance of a blue color. In contrast to the previous case, the current intensity decreases slightly and stays at 0.5 mA/cm^2 after 30 min. The time-friction curve in this case is identical to the one observed in THF-$LiClO_4$, *i.e.*, f increases to 1.25 f_0 and then decreases and stabilizes at 0.2 f_0. The initial increase of f is also accompanied by the disappearance of the blue color near the electrode surface.

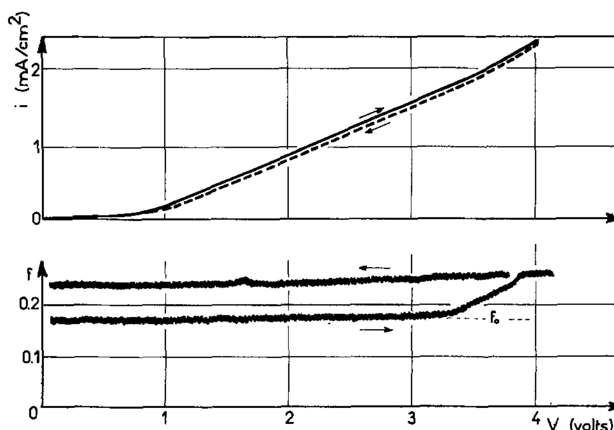

Fig. 1. Potentiodynamic and PMT curves obtained on a platinum electrode in THF-$LiClO_4$ 0.3M medium (water content, 10^{-3}M; sweep rate, 1 V/min.

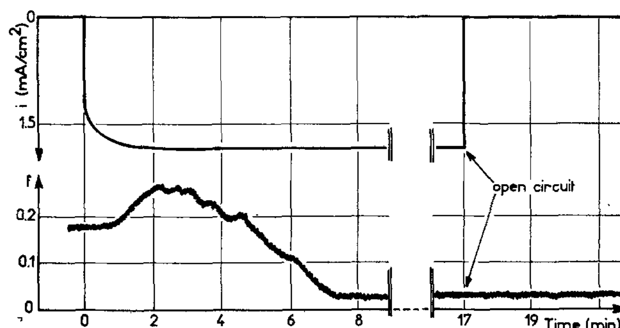

Fig. 2. Potentiostatic and PMT curves obtained on a platinum electrode in THF-$LiClO_4$ 0.3M medium (water content; 10^{-3}M; applied potential, +3.5V).

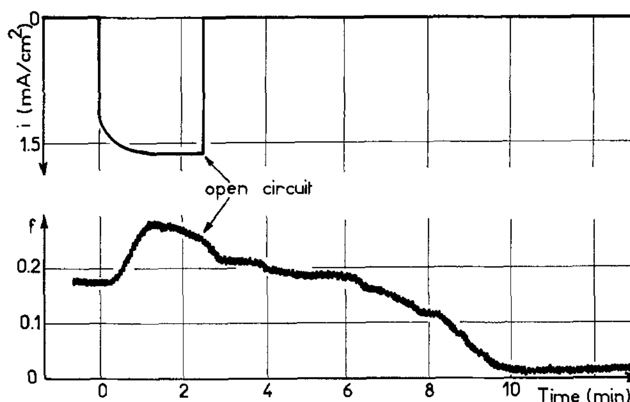

Fig. 3. PMT curves obtained in THF-$LiClO_4$ 0.3M medium in the case of a platinum electrode polarized for a short time at +3.5V and then placed in open circuit.

Film identification and formation mechanism.—Spectroscopic analysis.—The deposit characterized by the small value of the friction coefficient ($f = 0.2 f_0$) is analyzed by multiple-reflection infrared absorption and XPS spectroscopy.

The infrared spectra of the film obtained in the THF-$LiClO_4$ and THF-$LiClO_4$-DPA media are identical and correspond to the poly-THF spectra obtained in solution chemically (14). They are characterized by several absorption peaks centered at 2940, 2860, 1460, 1360, and 1110 cm^{-1}, and by a peak at 1720 cm^{-1} which is not observed in the bulk polymer spectrum (Fig. 4). The peaks located at 2940 and 2860 cm^{-1}

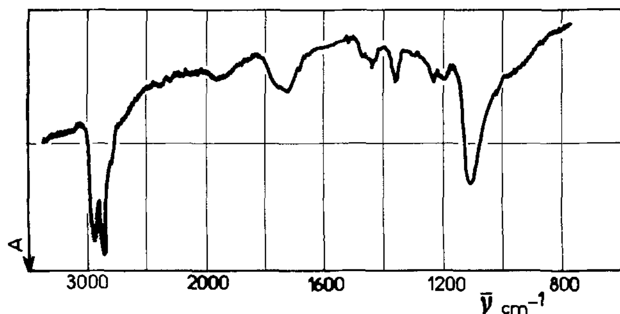

Fig. 4. Multiple-reflection infrared absorption spectrum obtained from a thin platinum layer polarized at +3.5V for 50 min in THF-LiClO$_4$ 0.3M.

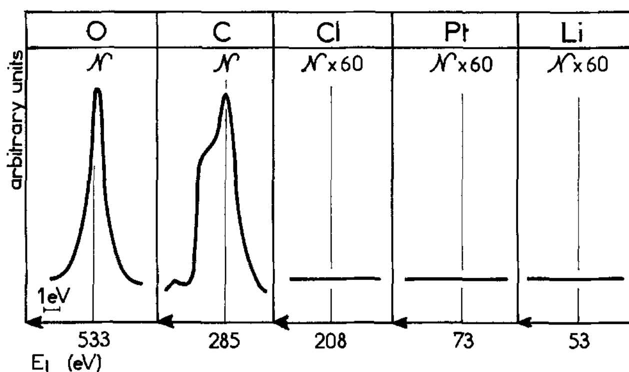

Fig. 5. XPS spectrum obtained from a thin platinum layer polarized at +3.5V for 50 min in THF-LiClO$_4$ 0.3M.

are due to stretching CH vibrations; those which are centered at 1460 and 1360 cm^{-1} are CH bending vibrations, and the one at 1110 cm^{-1} corresponds to the C—O vibration of an aliphatic ether. The peak at 1720 cm^{-1} is due to the carbonyl C=O stretching vibration.

In the case of XPS, the spectrum is composed only of peaks at 532.8, 289, 286.2, and 285 eV (Fig. 5). If we suppose that the film is made of poly-THF, two different carbons can be distinguished in the polymer formula $[O-(CH_2)_4-]_n$: one of them is bound to two neighbor carbons, the other to a carbon atom and an oxygen. Therefore, two peaks will be observed in the photoelectron energy spectrum, which are indeed the two peaks at 286.2 and 285 eV. The first one corresponds to the carbon in the α position with respect to the oxygen atom, the second one to the C—C bond. However, it should be noted that these two carbon peaks do not have the same intensity, but are in the proportion 1:1.2. The 1.2 eV energy difference between these two carbons, which was also observed by other workers (15), can be calculated by considering the electronegativity of each element.[1] The peaks located at 532.8 and 289 eV are respectively due to O_{1S} and C_{1S} of the carbonyl group.

The film appears to be very pure and uncontaminated by electrolyte elements; the analysis results are similar to those obtained in the case of bulk poly-THF.

Formation mechanism.—The results obtained by XPS, infrared, and PMT confirm the deposition on the electrode surface of a very adherent poly-THF film characterized by a very small friction coefficient. The appearance of this deposit depends on the applied potential and on the composition of the electrolytic medium.

In THF-LiClO$_4$, it is necessary to polarize the electrode at very positive potentials (+3.5V) in order to observe the film formation. In contrast, by addition of DPA to the latter solution, the same result is obtained by applying only a polarization of +1.8V.

When the polymerization is started, it can continue if the polarization is suppressed. This result clearly appears on the friction-time curves obtained in open circuit after a polarization has been applied for a short time (Fig. 3). These observations tend to prove that polymerization is initiated via electrochemical species and then proceeds via a chemical chain process which no longer depends on the electrogenerated precursors.

The film formation clearly appears to be due to the presence of radicals at the electrode level. The very positive potential of +3.5V likely involves the oxidation of perchlorate anion into $ClO_4\cdot$ radical, and that of +1.8V the oxidation of DPA to $DPA^{\cdot+}$. In this latter case, the oxidation of DPA is confirmed by the appearance of a blue color in the electrode vicinity which may be attributed to the presence of the $DPA^{\cdot+}$ radical cation. Thus it may be considered that $ClO_4\cdot$ and $DPA^{\cdot+}$ radicals initiate the THF polymerization, a very likely hypothesis as we know that DPA is very often used for cationic polymerization (18). This hypothesis is also confirmed by the work of Nakahama *et al.* (8) but is in opposition to the mechanism proposed by Dey *et al.* (10), who assume that the polymerization is initiated by the THF electrooxidation.

Nakahama *et al.* have proposed a reaction path in which $ClO_4\cdot$ radical reacts on a THF molecule and gives $HClO_4$, which in turn induces the polymerization according to the diagram

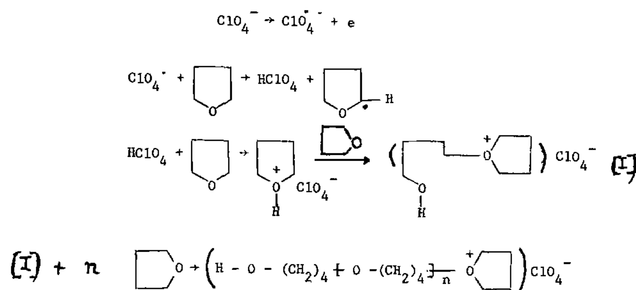

A similar mechanism may be considered in the case of THF-LiClO$_4$ with DPA. The anodic polarization produces $DPA^{\cdot+}$ radical cation which reacts on THF and gives H^+ which, as previously, initiates the polymerization. As added proof, it must be noted that in each case, after the electrode was anodically polarized, we observed a reduction peak at −0.5V, characteristic of H^+ ions. In this last case we propose the following reaction diagram

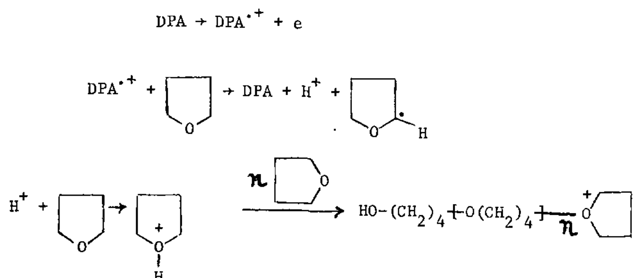

The polymerization process can fail in the presence of nucleophilic species such as water (6). Indeed, this has been observed when the water content of the solution was above 250 ppm. It is possible that water destroys the radicals which initiate the polymerization

[1] It is possible in XPS to correlate the peak energy values of an element with the partial electric charge located on this element. This partial charge, q, is calculated in the electrostatic theory by the relationship $q = Q + \Sigma I$, where Q is the charge of the element, and ΣI the added ionic partial character of the bonds attached at the element (16). According to the Pauling theory (16), for the C/O linkage. $I = 1 - e^{-0.25 (\chi_C - \chi_O)^{1/2}}$, where χ_C and χ_O are respectively the C and O electronegativities. By setting χ_C equal to 2.5 and χ_O to 3, we compute, in the case of poly-THF, a partial ionic character of 0.22 for the C—O bond and therefore a partial charge of 0.22 for the carbon which entails an energy shift between 1 and 2 eV (17).

or reacts on the cationic adduct and stops the chain propagation.

It must also be noticed that the infrared and XPS spectra reveal some aldehydic bonds which may be attributed to the polymer peroxidation by air. Such reactions have been observed with the bulk polymer in contact with air (19). These are oxidation reactions which entail a fragmentation of the chain and the formation of aldehyde fragments (19). These aldehydic groups may also originate from a secondary polymerization process between the 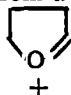 cation and the THF molecules (20, 21).

Finally, it should also be noticed that the PMT curves show two different friction coefficient values; the one observed at the beginning of the polarization is high ($f = 1.25\ f_0$), the other one is weak and independent of the potential. Up to now this observation has not been clearly explained. We think it is probably only due to a difference of friction between the first growing polymer layers and those corresponding to the thick deposit.

Physicochemical and electrical properties of Pt|THF, $LiClO_4$, Ox| films.—Physicochemical properties.—The film analysis by means of XPS shows that the film is very pure and does not contain impurities such as lithium, chlorine, and perchlorate. Moreover, it is very homogeneous, a feature not found with other electrochemically formed polymers, which are very often unhomogeneous [surface formed of small spheres (22)] or contaminated by the support electrolyte (23). An optical microscopic view of the surface at 1300 magnification does not show any defects (Fig. 6).

This film homogeneity is also revealed by the steady value of the friction coefficient at 0.2 f_0 without any irregular fluctuation. Moreover, this value is the same when the measurement is operated in the solution or outside after the film has been rinsed with acetone and dried in a stream of nitrogen.

This homogeneity is only observed with a film thickness less than 2000Å. With very thick films (1 or 2μ) obtained for a lengthy polarization (more than 120 min), the top layers are less adherent and they rearrange when the film is rinsed to give an unhomogeneous surface aspect. The film thickness is generally independent of the nature of the electrolyte but is very sensitive to small variations in water content.

These films have marked hydrophobic properties: The contact angle between the surface and a drop of water increases from 8° to 70° from bare to film-coated platinum. When heated in air between 100° and 120°C, the films are destroyed; this result must be related to the melting point of bulk poly-THF which has a similar value (19).

Fig. 6. Optical microscope view of a poly-THF film obtained after polarization of a platinum surface at +3.7V for 40 min. $THF\text{-}LiClO_4$ 0.3M, $H_2O \sim 10^{-3}$M. Magnification 1300×.

Electrical characteristics.—They are measured from (Pt|film|gold) sandwich devices. For a film thickness of 1200Å obtained after electrolysis of Pt at +3.5V in $THF\text{-}LiClO_4$ for 20 min, the device capacity is 25 **nF** · cm^{-2}, the loss ($tg\delta$) is $8 \cdot 10^{-3}$, the breakdown field is $2.5 \cdot 10^6\ V \cdot cm^{-1}$; the dielectric constant measured at 10 mV a-c with polarization at a frequency of 10^4 rad · sec^{-1} is 3. The film conductivity is very weak: under a-c polarization, $\sigma_{1000Hz}^{25°C} = 2 \cdot 10^{-9}\ \Omega \cdot cm^{-1}$; under d-c polarization, $\sigma^{25°C} = 10^{-14}\ \Omega \cdot cm^{-1}$. These latter results show that the film conductivity in solution is not electronic but is due to ion diffusion through the polymer matrix. We have indeed checked that the presence of the film on the electrode surface does not disturb the discharge of alkaline cations such as Li^+, Na^+, which migrate through the film before being reduced at the film-metal interface (24).

This film permeability to ions is probably due to the fact that the polymer chains are parallel and regularly spaced, thus having a partially crystalline character, as has been shown in the case of bulk poly-THF (25, 26). Experiments on this point are currently under way.

Conclusion

The results obtained by spectroscopic analysis and by PMT confirm the possibility of depositing an organic film in $THF\text{-}LiClO_4$ or $THF\text{-}LiClO_4$-DPA medium. This film obtained on a platinum electrode is thin, homogeneous, free of impurities, and very adherent to the surface. It has been shown with the help of PMT and electrochemical techniques that its formation is slow, initiated by radicals $ClO_4\cdot$ or $DPA^{\cdot +}$, and needs an anhydrous medium. This film is a nonconductor, but its permeability to ions makes it a conductor in solution. This latter possibility eventually could be used for doping and for making organic semiconductor films.

Acknowledgment

Financial support of this research by the DRET is gratefully acknowledged.

Manuscript submitted Nov. 2, 1977; revised manuscript received March 16, 1978.

Any discussion of this paper will appear in a Discussion Section to be published in the June 1979 JOURNAL. All discussions for the June 1979 Discussion Section should be submitted by Feb. 1, 1979.

Publication costs of this article were assisted by the Laboratoire de Chimie Organique Physique.

REFERENCES

1. S. Madorsky, *J. Polym. Sci.*, **9**, 133 (1951).
2. M. M. White, *Thin Solid Films*, **18**, 157 (1973).
3. A. M. Mearns, *ibid.*, **3**, 201 (1969).
4. M. A. Havens, M. E. Biolsi, and K. G. Mayhan, *J. Vac. Sci. Technol.*, **13**, 575 (1976).
5. J. E. Dubois, P. C. Lacaze, and G. Tourillon, *This Journal*, **125**, 1257 (1978).
6. P. Dreyfuss and M. P. Dreyfuss, *Adv. Polym. Sci.*, **4**, 528 (1967).
7. C. F. Herns, *Polym. Lett.*, **7**, 625 (1969).
8. S. Nakahama, S. Hino, and N. Yamazaki, *Polym. J.*, **2**, 56 (1971).
9. M. R. Rifi, U.S. Pat., 3, 645, 986 (1972).
10. A. N. Dey and E. J. Rudd, *This Journal*, **121**, 1294 (1974).
11. J. E. Dubois, P. C. Lacaze, R. Courtel, C. C. Hermann, and D. Maugis, *ibid.*, **122**, 1455 (1975).
12. J. M. Cesbron, R. Courtel, J. E. Dubois, M. Herlem, and P. C. Lacaze, *C. R. Acad. Sci.*, **266**, 1667 (1968).
13. J. S. Pirie and D. W. Gregory, *J. Chem. Ed.*, **50**, 682 (1973).
14. T. Saegusa, H. Imai, and J. Furukawa, *Makromol. Chem.*, **56**, 55 (1962).
15. G. Maccagnani, A. Mangini, and S. Pignatana, *Tetrahedron Lett.*, 3852 (1972).
16. L. Pauling, "The Chemical Bond," Oxford University Press, London (1967).

17. U. Geluis, P. F. Meden, J. Medman, B. J. Lindberg, R. N. Manne, R. Nordbers, G. Nordling, and K. Siegbahn, *Phys. Scr.* **2**, 70 (1970).
18. L. Turcot, A. Glasel, and B. L. Funt, *Polym. Lett.*, **12**, 687 (1974).
19. A. Davis and J. M. Golden, *Makromol. Chem.*, **81**, 38 (1965).
20. M. P. Dreyfuss, J. C Westfahl, and P. Dreyfuss, *Macromolecules*, **1**, 437 (1968).
21. A. Ledwith and C. Fitzsimmonds, in "High Polymers," Vol. XXIII, J. P. Kennedy and E. G. Törnqirst, Editors, p. 394, Interscience Publishers, New York (1968).
22. F. Bruno, Doctoral thesis, Paris (1973).
23. F. Bruno, M. C. Pham, and J. E. Dubois, *J. Chim. Phys.*, **4**, 490 (1975).
24. G. Tourillon, J. E. Dubois, and P. C. Lacaze, To be published.
25. R. E. Wetton and G. Williams, *Trans. Faraday Soc.*, **61**, 2132 (1965).
26. M. Cedari, G. Perego, and A. Mazzei, *Makromol. Chem.*, **83**, 196 (1965).

The Activation and Deactivation of Iridium Electrodes in Acid Electrolytes

J. O. Zerbino, N. R. de Tacconi, and A. J. Arvía*

Instituto de Investigaciones Fisicoquímicas Teóricas y Aplicadas, División Electroquímica, Sucursal 4, 1900 La Plata, Argentina

ABSTRACT

The electrochemical behavior of the Ir/1*M* H_2SO_4, Ir/96% H_2SO_4, and Ir/$KHSO_4$(melt) interfaces at different temperatures was investigated using potentiodynamic techiques, covering the potential range between the H_2-evolution reaction and the O_2-evolution reaction. Electrodes with different degrees of activation were employed. The surface electrooxidation is explained by a sequence of reactions involving oxo-hydroxo species and IrO_2 electroformation. The activation effect, particularly noticed with 1*M* H_2SO_4 at 25°C, is assigned to an accumulation of oxo-hydroxo species on the electrode and the occurrence of proton transfer reactions. The activation effect is practically absent in the $KHSO_4$ melt, but instead, it exhibits an aging of the electroformed oxygen-containing species, which under a complete coverage probably entails an IrO_2 monolayer. Results with 96% H_2SO_4 correspond to an intermediate situation between 1*M* H_2SO_4 and molten $KHSO_4$, depending on the temperature.

The potentiodynamic polarization of Ir electrodes in acid electrolytes using symmetric triangular potential perturbation from 0.4 to 1.4V and vice versa, reveals the electroformation and electroreduction of oxygen-containing layers (1-8). These processes apparently behave in a manner considerably different from most of the other metals of the Pt group. Under certain experimental conditions the amount of charge that the Ir surface can store in the oxide region increases during cycling. The electrode activation depends on the limits of the potential excursion, on the rate of the potential perturbation, and on the electrolyte composition (8-23).

The anodic and cathodic potentiodynamic current/potential (*I/E*) profiles of Ir either in acid aqueous electrolyte at room temperature or in molten potassium bisulfate electrolyte show very little hysteresis. Nevertheless, the oxide charge capacity increase observed in the aqueous electrolyte at room temperature is drastically reduced in the molten electrolyte (24, 25). Then, the Ir/$KHSO_4$ (melt) interface behaves more like other Pt/acid solution interfaces. This means that both the composition and the temperature should be included in the number of variables playing a part either in the activation or deactivation of the Ir electrode.

Various explanations have been advanced for the electrochemical behavior of Ir in aqueous solutions such as an expanded lattice theory for oxide growth on noble metals (5), an irreversible oxide formation with subsequent stoichiometry changes (16), oxide-filled pitting formation, and formation of a polymeric layer of oxygen-bridged hydrated oxy-hydroxo species (18, 19). These attempts, however, are only qualitative and restricted to a relatively limited range of experimental conditions. They are unable to explain that the electrode activation observed in the potential region of the oxygen-containing electrosorbed species is absent in the potential region of the hydrogen electrode reactions. The results reported so far therefore indicate the complexity of the electrochemical processes at the Ir/acid electrolyte interface and suggest the importance of attempting further research of this system under a wider range of experimental conditions with the aim of attaining a more extended mechanistic interpretation of these processes.

Experimental

The electrolysis cell system was the same one previously described (26). The working electrode consisted of an Ir wire (spectroscopically pure, Johnson, Matthey and Company) of 1.5 cm^2 apparent area. A Pt counterelectrode and a Pt/H_2 (1 atm)/electrolyte reference electrode completed the electrolysis cell arrangement. The following electrolytes were used: 1*M* H_2SO_4 (at 25°C); 96% H_2SO_4 (at 25° and 90°C); and $KHSO_4$ (melt) (at 230°C). Analytical grade reagent chemicals and triple distilled water were employed. Experiments were made under continued N_2-saturation. Two basic experimental techniques were used, namely, the triangular potential sweep (TPS) technique, either single (STPS) or repetitive (RTPS), also employing other potential/time perturbation functions, and the triangular modulated linear potential sweep technique (TMLPS), either single sweep (TMLPS) or triangular sweep (TMTPS).

The corresponding circuitry was essentially the same as in previous publications (27, 28), including a fast rise time potentiostat (Tacussel Type PIT 20-2 X, rise

* Electrochemical Society Active Member.

Key words: iridium, oxide layers, molten salts, electrode activation.

time 0.2 μsec) and an ohmic drop compensator (Tacussel Type CDCO).

Results

Types of Ir electrodes.—The electrochemical response of the Ir electrode is strongly dependent on the history of the electrode. The types of electrodes are characterized as: (*i*) clean wire electrodes "as received" previously treated with HNO_3-H_2SO_4 mixture (type I); (*ii*) electrodes potentiodynamically activated by cycling the potential between 0.0 and 1.6V (type II); (*iii*) electrodes of type II anodically deactivated at $E = 1.6V$ in 1*M* H_2SO_4 at 25°C (type III); (*iv*) electrodes of type II deactivated by heating *in vacuo* at 300°C for 2 hr (type IV); and (*v*) electrodes of type II mechanically deactivated by rubbing its surface with a filter paper or more effectively with very fine Al_2O_3 powder (type V). Activated surface electrodes (activated electrodes) mean electrodes with a high charge capacity in the potential region where the oxygen-containing species are electroformed and electroreduced. The reverse corresponds to the so-called deactivated electrode.

The rest potential of the Ir/1M H_2SO_4 interface.—The rest potential, E_r, of type I electrodes immersed in 1*M* H_2SO_4 at 25°C is *ca.* 0.85V. The E_r value is attained spontaneously both from the anodic potential side and from the cathodic potential side. They require 17 min to reach E_r from 1.3V and only 90 sec from 0.03V. Type II electrodes require about twice that time to attain E_r starting from 1.3V.

The E/I voltammograms obtained with symmetric triangular potential scans.—Electrodes of type III in 1*M* H_2SO_4 at 25°C exhibit repetitive voltammetric *E/I* displays in which the amount of charge, particularly that involved in the processes occurring in the 0.4-1.50V potential range (Fig. 1), depends on the perturbation conditions. The current peaks located in the 0-0.4V range mainly pertain to the hydrogen electrode reaction (peaks Ia, IIa, IIIa, IIc, and IIIc) while those found in the 0.4-1.6V range correspond to the electroformation and electrodesorption of oxygen-containing species on Ir (peaks IVa, Va, VIa, VIIa, VIIIa, IVc, VIc, VIIc, and VIIIc). The anodic current beyond 1.6V principally corresponds to the oxygen evolution on the oxidized surface (22, 29-31). The first TPS swept from −0.07 to 1.62V at $V = 0.15$ V/sec (Fig. 1a) involves a total apparent anodic charge density, Q_a, equal to 0.95 mC/cm² which increases to 2.7 mC/cm² beyond the 100th cycle, the Q_a/Q_c ratio remaining always very close to one. The charges required both in the hydrogen region and in the region of formation of oxygen-containing species are in agreement with previous results (22, 29).

During the RTPS an increase of the total charge in the 0.8-1.6V range is observed, but the charge change in the hydrogen electrode reaction region is relatively small. The time, *t*, required to obtain a fixed charge increase is, in principle, proportional to *V*. The number and location of the current peaks are strongly dependent on the degree of activation of the electrode surface as well as on $E_{\lambda a}$ and $E_{\lambda c}$, the anodic and cathodic potential limits (switching potentials), respectively.

Dependence of the electrode activation and deactivation on $E_{\lambda a}$ and $E_{\lambda c}$.—Type II electrodes show a relatively high degree of activation when dipped into a 1*M* H_2SO_4 solution at 25°C (Fig. 2). Under a RTPS covering the 0.060-1.4V potential range at 0.3 V/sec they exhibit a further and continued increase of activation even after a RTPS lasting 10 min (Fig. 2a). But if $E_{\lambda a}$ is decreased down to 1.25V (Fig. 2b), a net decrease of the over-all charge is observed. The deactivation process operates even after a RTPS of 90 min. In both cases no appreciable change is observed in the hydrogen electrode potential range.

A change of $E_{\lambda a}$ during the RTPS ($E_{\lambda c} = 0V$) from 1.35-0.62V and the RTPS continued for 10 min (Fig. 3a) produces a decrease of the cathodic profile and an increase of the hydrogen adatoms electrooxidation current. But the following potential excursion run again between 0.0 and 1.35V involves a charge equal to that observed during the initial sweep. A continuing RTPS during another 10 min between the latter potential limits exhibits a partial inhibition for the hydrogen adatoms electrooxidation together with an increasing electrode activation.

Electrodes of type IV previously perturbed for 60 min by RTPS in the 0.60-1.45V range show a very slow increase of the electrode activation (Fig. 3b), but when $E_{\lambda c}$ is changed to 0.18V and the RTPS continued between the new switching potentials, the first RTPS presents a small current contribution of current peaks IVa and IVc which increases during the following RTPS simultaneously with the electrode activation. The anodic charge, under the present circumstances, attains a limiting value beyond the 100th cycle. These effects are again observed as $E_{\lambda c}$ is fixed at more cathodic potentials. The characteristics of Fig. 3a and 3b are independent of the type of electrode. There are just slight modifications in the electrode activity within the corresponding range of potentials either with small

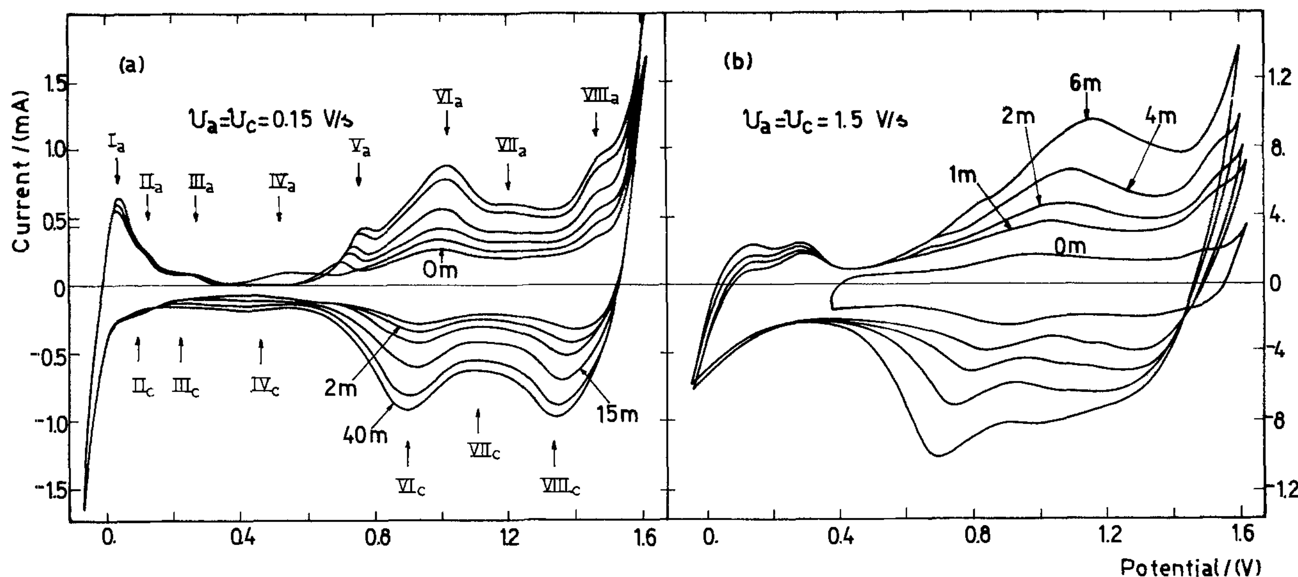

Fig. 1. E/I displays (RTPS). Influence of the perturbation time at different V. 1M H_2SO_4, 25°C, type III electrode (1.4 cm²). (a) $V = 0.15$ V/sec, 0, 2, 7, 15, 30, 40 min. (b) $V = 1.5$ V/sec, 0, 1, 2, 4, 6 min.

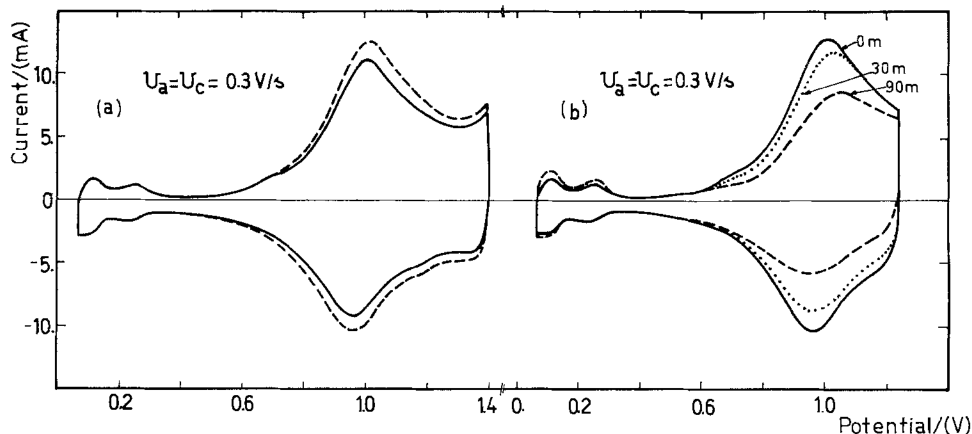

Fig. 2. *E/I* **displays (RTPS) at 0.3 V/sec. 1M H_2SO_4, 25°C, type II electrode (1.4 cm²). (a) The full trace is the initial record. The dashed line corresponds to a record after 30 min RTPS. (b)** *E/I* **displays recorded after 0, 30, and 90 min RTPS.**

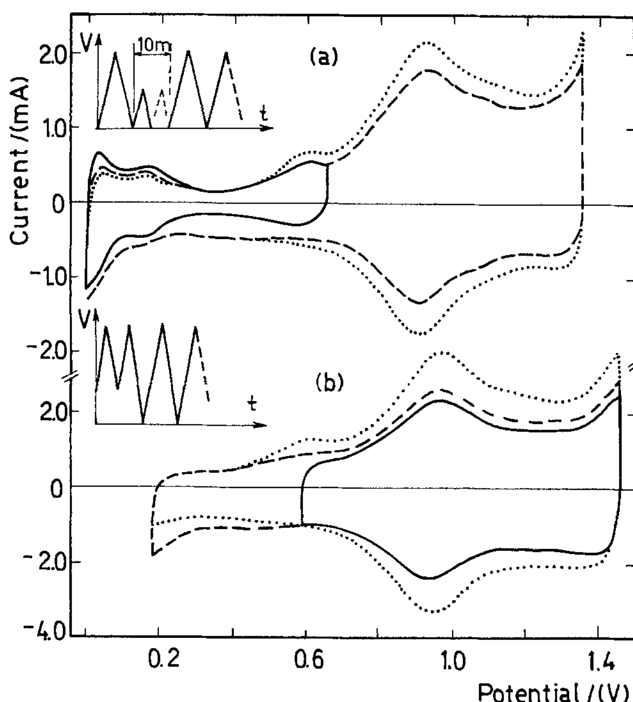

Fig. 3. (a) *E/I* **displays at 0.15 V/sec. 1M H_2SO_4, 25°C, type II electrode (1.4 cm²). The dashed trace is the initial record. The full trace is obtained after 10 min RTPS within the 0-0.65V range. The dotted trace results after another 10 min RTPS in the 0-1.35V range. (b)** *E/I* **displays at 0.3 V/sec. 1M H_2SO_4, 25°C, type IV electrode (1.5 cm²). The full trace corresponds to the first record and the dashed line to the following record after changing $E_{\lambda c}$. The dotted trace is obtained after 15 min RTPS.**

variations in the switching potentials or with the time spent during cycling.

The current peak IVa is clearly observed with an intermediate degree of the electrode activation but it is practically unnoticed with highly activated electrodes. The contribution of the anodic current VIa during the first RTPS is quite large after the previous cathodization at 0.03V for 25 min, but no increase of the activation degree is noticed.

Type I electrodes under RTPS, with $E_{\lambda a}$ stepwise either decreasing or increasing, show that in the former case there is a net decrease of the cathodic current peaks IIc and IIIc. The reverse is noticed for current peak IIa. Nevertheless, when $E_{\lambda a}$ becomes larger than 1.1V the cathodic profiles between 0 and 0.45V change appreciably. Furthermore, because there is a clear potential difference between the anodic and cathodic current peaks of the hydrogen electrode reaction at 0.150 V/sec, the latter exhibits an appreciable degree of irreversibility. On the other hand, the jump of the current at the switching potential seems to indicate that the processes related to the electroformation and electroreduction of the oxygen-containing species are quite reversible under the perturbation conditions already mentioned. When the TPS is initiated from 0.43V upward no appreciable change of charge is found either as $E_{\lambda a}$ increases stepwise from 0.53 to 1.33V or as it decreases from 1.3V downward. When the Ir electrode is under a RTPS in the 0-0.35V range at 0.150 V/sec no charge increase is observed when $E_{\lambda a}$ is afterward extended up to 1.35V.

Electrode capacitance.—The apparent electrode capacitance at 25°C obtained for type I electrodes in 1*M* H_2SO_4 is 0.39 mF/cm² at 0.350V, in good agreement with previously reported results (22, 23). This value, however, largely exceeds that of the same electrodes in the $KHSO_4$ melt which is equal to 0.09 mF/cm² at 230°C (24).

Triangular potential runs with changing $E_{\lambda a}$ using a highly activated electrode.—The runs in 1*M* H_2SO_4 at 25°C with type II electrodes of different degrees of activation depend on *V* as has been well established (22, 23). Q_a and Q_c involve two contributions, namely, that of the reactions related to the oxygen-containing species (Q_O) and that corresponding to the hydrogen adatoms (Q_H), so that $Q_a = Q_{Oa} + Q_{Ha}$ and $Q_c = Q_{Oc} + Q_{Hc}$. The *E/I* records show that for a particular *V*, $Q_a = Q_c$ (at $V = 0.3$ V/sec, $Q_a = Q_c = 11.3$ mC/cm² and at $V = 3.0$ V/sec, $Q_a = Q_c = 7.0$ mC/cm²) but $Q_{Oa} > Q_{Oc}$ while $Q_{Hc} > Q_{Ha}$. Furthermore, the *E/I* characteristics at 0.3 V/sec are more reversible in spite of more accumulation of charge than those recorded at 3.0 V/sec. Any possible distortion of the *E/I* profiles by an ohmic polarization contribution have been eliminated. Anyway, the initial slope of the cathodic scans which increases when $E_{\lambda a}$ increases, indicates that at 3 V/sec the electrochemical process exhibits some degree of irreversibility.

Electrochemical deactivation: Activation of thermally deactivated electrodes.—The E/I profiles run with type III electrodes in the 0.30-1.40V potential range at 0.150 V/sec are very similar to those recorded with type I electrodes. The two anodic current peaks at *ca.* 0.9 and 1.3V and the two cathodic ones reproduce very well after a RTPS of 10 min. When $E_{\lambda c}$ reaches 0.11V and after another RTPS of 10 min in that range of potentials the anodic current scarcely increases and finally, when $E_{\lambda c}$ is 0.010V, there is a net increase of the charge involved in the potential region exceeding 0.4V with a simultaneous definition of the current peaks related to the redox system at *ca.* 0.5V.

An electrochemical deactivation of a type II electrode is achieved after a prolonged anodic polarization. The *E/I* display obtained between 0.65 and 1.30V after polarizing at 1.625V during 10 min (i = 95 mA) involves $Q_a = Q_c = 2.2$ mC/cm², but a second anodization at the same potential for another 10 min (i =

115 mA) yields a smaller E/I display and lower charges, namely, 1.48 mC/cm^2. The second display also shows an anodic shift of both current peaks.

The potential cycling of type IV electrodes between 0.65 and 1.25V involve initial Q_a and Q_c values of the order of 0.250 mC/cm^2 with no appreciable change of the profile during 10 min but can be slowly activated by RTPS between 0.65 and 1.46V at 0.3 V/sec. After 20 min Q_a becomes 0.865 mC/cm^2 and Q_c, 0.685 mC/cm^2. The increase of Q_a is due to an accumulation of an anodic product which is only partially electroreduced during cycling within the 0.65 and 1.46V range. Then, the area remains always small but the shape of the E/I contour changes slightly. The cathodic current at $E_{\lambda c}$ decreases during cycling while the reverse occurs with the cathodic current at $E_{\lambda a}$.

A type IV electrode can be rapidly activated by running RTPS from 0.85V toward cathodic potentials down to 0.03V, then continuing upward to 1.47V, and finally following the potential cycling between the latter potential limits. If the E/I display is arbitrarily divided in two regions at 0.4V and the area between 0.4 and 1.3V is assigned to a reaction involving the oxygen-surface species, then $Q_{Oa} > Q_{Oc}$ while $Q_{Ha} < Q_{Hc}$. The charge involved in the anodic scan is, however, equal to that involved in the cathodic scan. This clearly reveals that a fraction of the oxygen-containing species anodically formed is most likely electroreduced in the hydrogen electrode reaction region since any contribution of molecular oxygen or molecular hydrogen is discarded.

Triangularly modulated linear potential scans.—Under the TMTPS perturbation conditions of Fig. 4 in 1*M* H_2SO_4 both the anodic and the cathodic excursions are quite symmetric with respect to the potential (time) axis. The E/I display within the 0-0.4V potential range contains the current peaks related to hydrogen adatoms, together with the hydrogen ion discharge current and the anodic current associated with hydrogen diffusion-controlled electrooxidation. Within the 0.4-1.4V potential range there are three anodic and three cathodic current peaks clearly distinguished which apparently pertain to three redox systems. Their kinetic behavior appears to be rather irreversible under the prevailing perturbation conditions. Another point worth noting is that during the anodic excursion (Fig. 4a), Q_a is larger than Q_c, while the reverse occurs during the cathodic excursion (Fig. 4b).

The Ir/96% H_2SO_4 interface.—RTPS runs with type I electrodes at 0.3 V/sec in the -0.34 to $+1.50$V range at 25°C exhibit poorly defined anodic and cathodic current peaks (Fig. 5), but when $E_{\lambda a}$ extends stepwise to $+1.55$V, overlapping the potential of the net evolution of oxygen, a further RTPS produces a net increase of the charge involved and a clearer definition of the anodic and cathodic current peaks related to the oxygen-containing species at *ca.* 0.6V. Simultaneously, the baseline within the -0.34 to $+0.4$V range changes downward due to the electrochemical reduction of molecular oxygen. Those current peaks are associated with a reversible over-all reaction. The increase of the current peaks at *ca.* 0.6V shows more clearly the anodic and the cathodic current contributions in the 0.8-1.4V range until the E/I profile finally comprises at least three redox couples in good agreement with the TMTPS described later. Dissolved oxygen has no appreciable influence in the potential range involving the formation of oxygen-containing species. The degree of surface activation is, however, in principle, unchanged when the electrode is potentiostated at cathodic potentials such as at -0.35V for about 1 hr. To achieve a net activation of the electrode surface the potential cycling requires, therefore, an anodic potential limit larger than 1.5V at 25°C. On the other hand, if $E_{\lambda a}$ is fixed at 1.5V and $E_{\lambda c}$ is larger than 0.15V, the RTPS produces practically no change in the voltammogram. But if $E_{\lambda a} < 1.5$V and $E_{\lambda c}$ is kept at -0.35V (Fig. 5c) a slight but steady deactivation of the electrode is noticed.

The effect of increasing $E_{\lambda a}$ during successive STPS with type II electrodes (Fig. 5b) is practically the same either for $E_{\lambda a}$ increasing or $E_{\lambda a}$ decreasing. The charge involved between 0.5 and 0.6V is related to the pseudofaradaic processes occurring in the 0.4-0.8V range. The anodic and cathodic peaks located therein correspond apparently to a single redox couple (Fig. 5c). The increase of the cathodic current between 0.8 and 1.2V when $E_{\lambda a}$ increases is related to the appearance of two anodic current peaks at 1.10 and 1.35V and two cathodic current peaks at 0.95 and 1.20V, approximately.

Finally, once the display shown in Fig. 5b is attained the following RTPS between -0.35 and $+1.37$V (Fig. 5c) exhibits a decrease of Q_a and Q_c, a large decrease of the current peak heights located at *ca.* 0.6V, and a slight decrease of those located at higher potentials. The contribution of the redox couple located at *ca.* 0.95V is also enhanced. The electrode surface becomes first increasingly active with respect to the oxygen evolution reaction but finally it turns in the reverse way. This change is also clearly reflected in the potential range where the oxygen electroreduction takes place. An over-all deactivation effect is observed. The shape of the final E/I display shown in Fig. 5c coincides with the first E/I profile depicted in Fig. 5a for a practically deactivated electrode.

The STPS E/I profiles run at 25°C, from $E_{\lambda c}$ = 0.35V to a stepwise changing $E_{\lambda a}$ (0.1V $\leq E_{\lambda a} \leq$ 1.38V), at 0.3 V/sec (Fig. 6), exhibit practically no anodic cur-

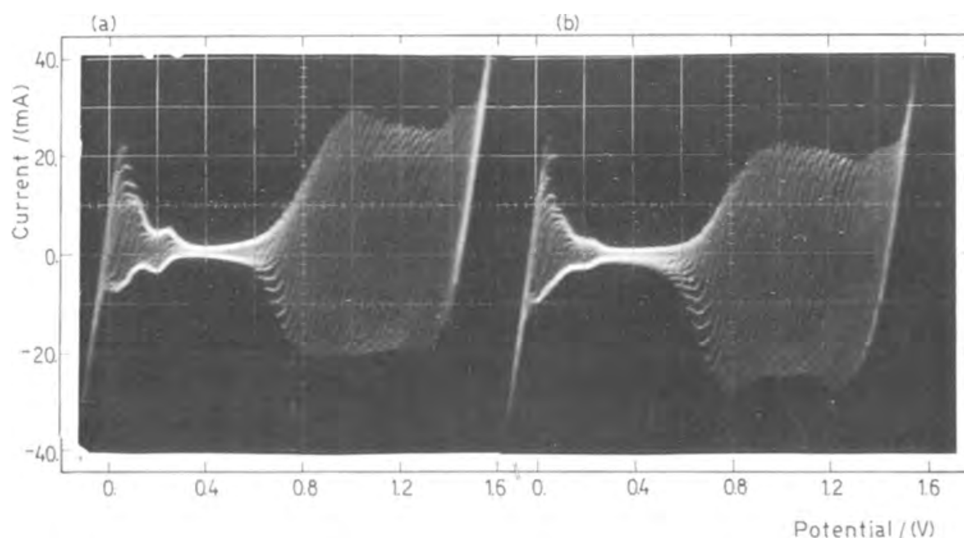

Fig. 4. TMLPS E/I displays. 1M H_2SO_4, 25°C, type I electrode (1.0 cm^2). V(guide) = 0.15 V/sec; V(modulation) = 2 V/sec; amplitude of the modulating signal = 0.18V. (a) Anodic scan. (b) Cathodic scan.

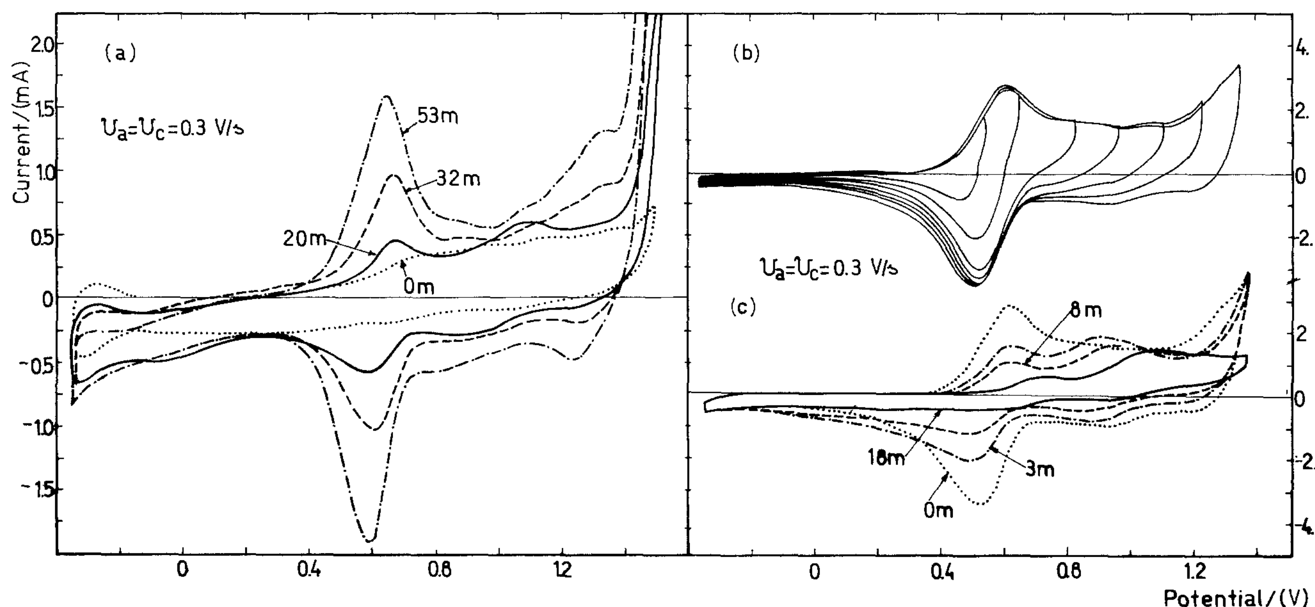

Fig. 5. *E/I* profiles (TPS). 96% H_2SO_4, 25°C, type I electrodes (1.0 cm²). (a) RTPS at 0.3 V/sec. First cycle (dotted trace). Other traces are recorded after RTPS during 20, 32, and 52 min. (b) STPS at 0.3 V/sec. $E_{\lambda a}$ stepwise changing during each cycle from 0.75-1.55V. (c) RTPS at 0.3 V/sec. Electrochemical deactivation. First cycle (dotted trace). The following profiles are recorded after RTPS during 3, 8, and 18 min.

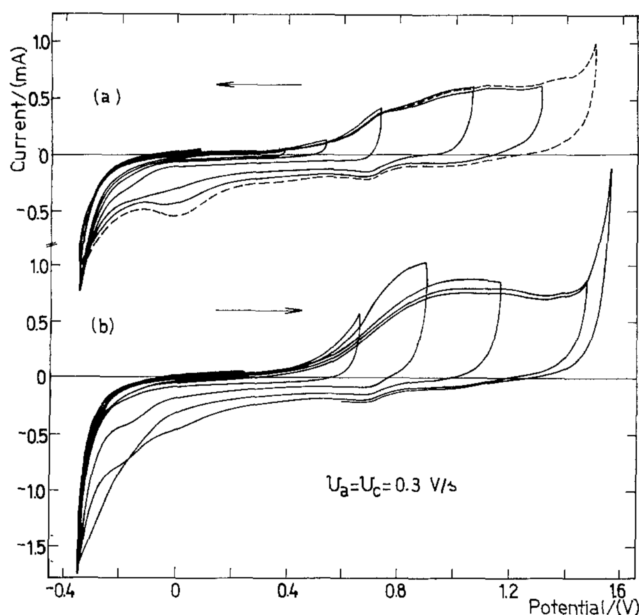

Fig. 6. *E/I* displays at 0.3 V/sec. 96% H_2SO_4, 25°C, type I electrode (1.0 cm²). (a) STPS $E_{\lambda a}$ decreasing from 1.5 to 1.0V. The dotted trace corresponds to RTPS between −0.35 and 1.5V. (b) RTPS with $E_{\lambda a}$ stepwise increasing.

rent in the −0.35 to 0.4V range but instead four humps at *ca.* 0.75, 1.0, 1.15, and 1.35V. The anodic current during the anodic scan increases when $E_{\lambda a}$ increases; the effect, however, is less obvious when $E_{\lambda a}$ moves in the decreasing direction. The cathodic potential excursion shows a cathodic limiting current at *ca.* 0.85V and two cathodic current peaks at 0.7 and 0V, the latter only being distinguished when $E_{\lambda a} > 0.9$V. This suggests that some species electroformed at high anodic potentials are electroreduced at the cathodic potential extreme. At −0.35V a net hydrogen evolution takes place. In either circumstance no hydrogen adatoms are clearly depicted in the *E/I* records, except the small couple at −0.3V (Fig. 5a). Q_a, which is of the order of 2.0 mC/cm², is always larger than Q_c. After an RTPS of 15 min the over-all charge increases slightly and simultaneously the definition of both the anodic and cathodic current peaks are appreciably improved. Most of the features just described are also observed during the TPS perturbation of the Ir/$KHSO_4$ (melt) interface as described later.

STPS *E/I* records between −0.120V and $E_{\lambda a}$, where the latter is either increased or decreased stepwise from 0.08 to 1.0V at 0.05 V/sec and 25°C (Fig. 7a and 7b), show the following features: When $E_{\lambda a} > 0.55$V, two anodic current peaks at *ca.* 0.3V and *ca.* 0.5V are recorded during the anodic potential excursion together with a hump at *ca.* 0.8V and during the cathodic scan a cathodic current peak is also observed at *ca.* 0.25V together with a hump at *ca.* 0.45V. When $0.3\text{V} \leq E_{\lambda a} \leq 0.55$V only the anodic current peak at 0.3V is seen. Finally, no current peaks are distinguished for lower $E_{\lambda a}$ values. These responses suggest that the cathodic current peak at *ca.* 0.30V comes from a product formed during the anodic potential excursion at

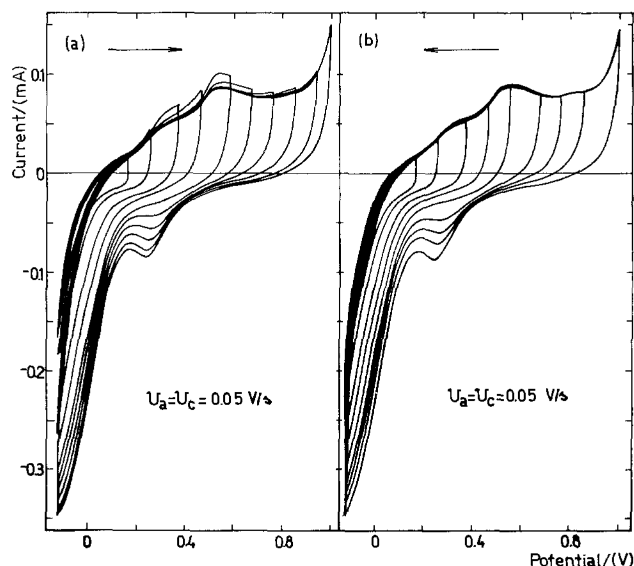

Fig. 7. *E/I* displays (STPS) at 0.05 V/sec. 96% H_2SO_4, 25°C, type I electrodes (1.0 cm²). (a) $E_{\lambda a}$ stepwise increasing. (b) $E_{\lambda a}$ stepwise decreasing.

high potentials. From the kinetic standpoint the over-all process becomes slightly more irreversible the larger the $E_{\lambda a}$ values are. Furthermore the Q_a and Q_c values confirm that some product anodically formed is electroreduced, at least in part, in the hydrogen evolution region. The resulting metal surface remains covered by some oxide species since no hydrogen adatom electrooxidation is observed.

The E/I profiles run at 90°C between −0.58 and 1.2V depend also very markedly on V (3 V/sec $\leq V \leq$ 10 V/sec) and on the charge playing a part at the cathodic potential extreme. Nevertheless the situation becomes somewhat involved as the electroreduction of the oxygen-containing species occurs at more cathodic potentials as V increases. Then, the shape of the E/I profile approaches that of a type I electrode in 96% H_2SO_4 at 25°C.

The E/I profile run between 0.09 and 1.0V involves Q_a = 0.55 mC/cm² and Q_c = 0.41 mC/cm² (Fig. 8a). When $E_{\lambda a}$ decreases the current peaks disappear and at the cathodic potential side there is a partial but systematic electroreduction of the surface species yielded by the anodic process.

The same profiles recorded after keeping a RTPS between fixed limits during 10 min (Fig. 8b) with $E_{\lambda a}$ decreasing stepwise, exhibit approximately the same features described for Fig. 8a, but there is no coincidence among the E/I lines in the potential region of the anodic current peak.

An electrode, which has attained a Q_a/Q_c ratio equal to one through RTPS between 0.09 and 1.0V, is then successively perturbed with RTPS between 0.09 and 0.2V during 5 min and is finally perturbed with three TPS between 0.09 and 1.0V (Fig. 8c), presents the following characteristics. The first of the three scans involves $Q_a > Q_c$, but the second and the third scans repeat the E/I profile as already known. The most abrupt current decrease occurs in the 0.4-0.8V potential range. This effect becomes more evident at the highest temperature and increases in going from 1M H_2SO_4 to the $KHSO_4$ melt.

Triangularly modulated triangular potential sweeps with the Ir/96% H_2SO_4.—The TMTPS at 95°C changes quite markedly with the cathodic potential limit of the base signal (Fig. 9a-b). The current peaks existing within the 0-1.2V range for the anodic excursion differ from those recorded during the cathodic excursion (Fig. 9b). Thus, the anodic excursion exhibits an anodic peak at 0.5V and two small humps at 0.8 and 1.0V with the corresponding complementary cathodic current contributions. The over-all anodic profile is somewhat symmetric with respect to the potential axis. The cathodic excursion presents an anodic envelope which is very similar to that already described for the anodic excursion but the cathodic envelope presents, in addition, a net current peak at 0.2V. The display is much more complex when it initiates from −0.4V. Then, the anodic envelope during the anodic excursion comprises a small limiting current at *ca.* −0.3V, a first hump at 0V, a second hump at 0.3V, a net current peak at 0.5V, a small one at 0.75V, another

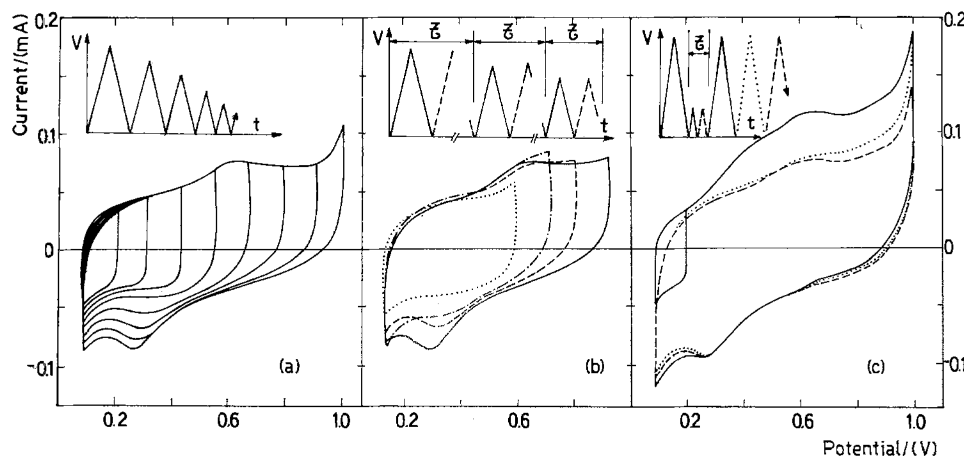

Fig. 8. E/I profiles. 96% H_2SO_4, 90°C, type I electrodes at 0.1 V/sec (1.0 cm²). (a) STPS, $E_{\lambda a}$ successively decreased from 1.0 to 0.2V. (b) RTPS. The E/I records correspond to the first TPS at the preset $E_{\lambda a}$ value but the interface is previously perturbed by a RTPS during 10 min at the preceding (higher) $E_{\lambda a}$. (c) RTPS between 0.09 and 0.2V followed by three RTPS between 0.09 and 1.0V. The full trace corresponds to the first scan, the dotted trace belongs to the second scan, and the dashed trace is the third scan.

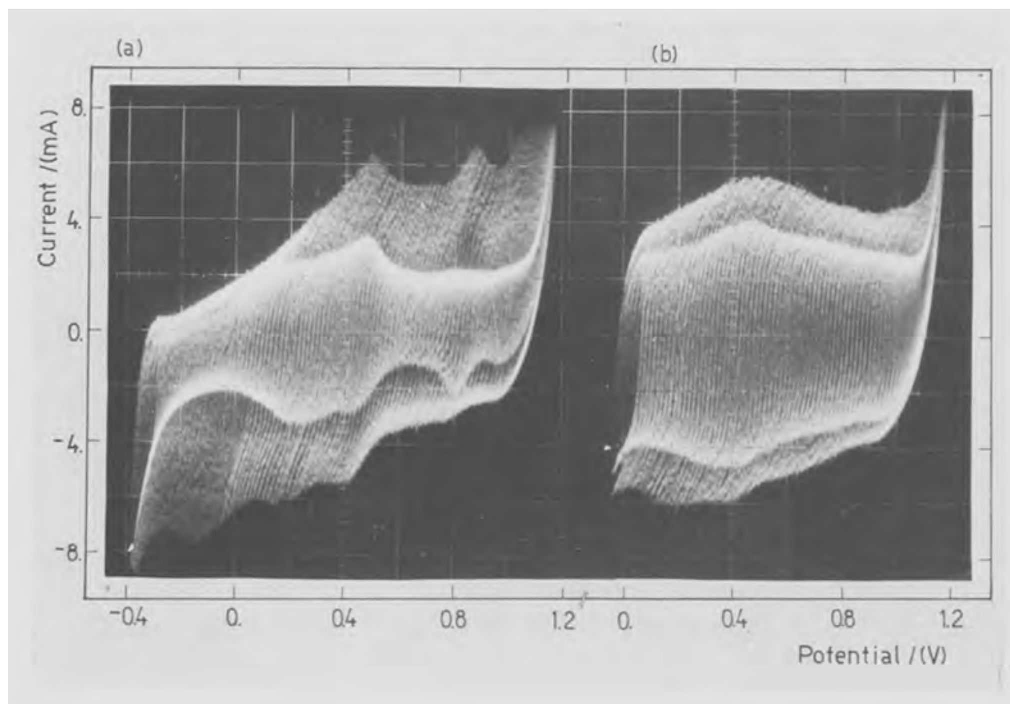

Fig. 9. TMTPS displays. 96% H_2SO_4, 95°C, type I electrode (1.0 cm²). V(guide) = 1.5 V/sec; V(modulation) = 20 V/sec; amplitude of the modulating signal = 0.12V. (a) $E_{\lambda c}$ = −0.4V and $E_{\lambda a}$ = 1.2V. (b) $E_{\lambda c}$ = −0.04V and $E_{\lambda a}$ = 1.2V.

net current peak at 0.9V, and a hump at 1.1V. The cathodic envelope contains a current peak at 0.95V, a well-defined peak at 0.8V, and two current peaks at 0.4 and 0.25V, respectively.

Now, the anodic envelope of the cathodic excursion exhibits small humps at 1.0 and 0.8V, and a current peak at *ca.* 0.5V, and the rest of details already referred to for the anodic potential excursion. The cathodic envelope contains practically the same characteristics as before although the peaks are appreciably reduced and a new wide cathodic current peak appears at −0.15V thereabouts. The current peaks at 0.3, 0.75, and 0.9V are intimately related to the high initial cathodic potential. The same occurs with current peaks at 0.8V. The current peak at −0.15V is directly produced by the high anodic potential limit reached. The anodic current involved during the cathodic excursion is largely magnified in the 0V potential region. Probably these current peaks are related to surface products yielded by the electrolyte electrooxidation at high anodic potentials.

Characteristics of activated electrodes.—An electrode that has been activated by RTPS in 1*M* H_2SO_4 and kept in the solution maintains its activation state after the circuit is open for a certain time, as confirmed by the reproducible *E/I* profile observed afterward. The same occurs if the electrode is removed from the solution and placed back into the cell. Furthermore, no deactivation occurs even after keeping the electrode for various days at open circuit. The degree of activation of the Ir electrode maintained in solution for 5 days at open circuit in a N_2 atmosphere remains practically unaltered. The activation state persists longer in 1*M* H_2SO_4 than in the concentrated acid.

The RTPS *E/I* profiles at 25° involving an $E_{\lambda a} <$ 1.24V in 1*M* H_2SO_4 and $E_{\lambda a} <$ 1.38V in concentrated H_2SO_4 produce the deactivation of an activated electrode. The deactivation is definitely more marked for the concentrated acid and under these circumstances it is even faster than that occurring under open circuit. In 1*M* H_2SO_4 the activation disappears when the electrode is placed in contact with 96% H_2SO_4. The degree of deactivation reached depends on the time elapsed in the concentrated electrolyte. But an electrode previously activated in 1*M* H_2SO_4 placed in contact for 5 min with any of several solutions (1:1 HCl; 1*M* NaOH; 65% HNO_3; 85% H_3PO_4; absolute ethyl alcohol; distilled water) remains unaltered. If an electrode is activated in concentrated H_2SO_4, it behaves as a deactivated one after potential cycling in 1*M* H_2SO_4. The reverse is also true. An electrode activated in 96% H_2SO_4, after a rinse in distilled water, behaves as a deactivated electrode when it is dipped again in the same electrolyte. The activation is newly gained by RTPS. The same electrode dipped for 5 min in one of the following media: 85% H_3PO_4; 65% HNO_3, or absolute ethyl alcohol, presents only a small deactivation.

The Ir/KHSO$_4$ (melt) interface.—The *E/I* displays obtained with STPS with decreasing $E_{\lambda a}$ (Fig. 10a) at 6 V/sec show during the anodic excursion the anodic current peak at *ca.* 0.4V while during the cathodic excursion the current peaks are seen in the 0-0.2V potential range. For $E_{\lambda a}$ of 0.3V, although a low surface coverage degree is attained, the amount of surface species anodically formed is enough to inhibit the electroformation of either hydrogen atoms or molecules. The *E/I* curves run with RTPS between −0.2 and +0.30V are appreciably distorted. They exhibit a steady decrease of the cathodic current associated with the electroreduction of the oxygen-containing surface species and an enhancement of both the cathodic and anodic current associated with the hydrogen electrode reactions. Undoubtedly, the complete electroreduction of the oxygen-containing surface species takes place at the cathodic potentials where the hydrogen electrode reactions should proceed.

The first TPS always involves a Q_a that is almost twice Q_c (Fig. 10b). After a few TPS, Q_a approaches $Q_a/Q_c = 1$ ($Q_a = Q_c = 0.4$ mC/cm^2). This suggests that for the present system there is also a partial reduction of the anodic product at the cathodic potential reached. When the interface is perturbed first with RTPS between −0.075 and +0.16V during 5 min and then with four successive RTPS up to $E_{\lambda a} = 0.52$V, the changes of the *E/I* profile at the cathodic potential extreme are less pronounced at 0.05 V/sec than at 6 V/sec. For the latter the potential range of the electroreduction of the oxygen-containing species overlaps largely the hydrogen ion discharge potential region. However, the effect at 6 V/sec (Fig. 10a) can be equally reproduced at 0.05 V/sec by maintaining the RTPS for a longer time.

Although the first TPS always involves $Q_a > Q_c$, the $Q_a = Q_c$ conditions can, however, be achieved during the second RTPS for $E_{\lambda a} > 0.550$V. Otherwise, if the runs are made by changing $E_{\lambda a}$ stepwise from

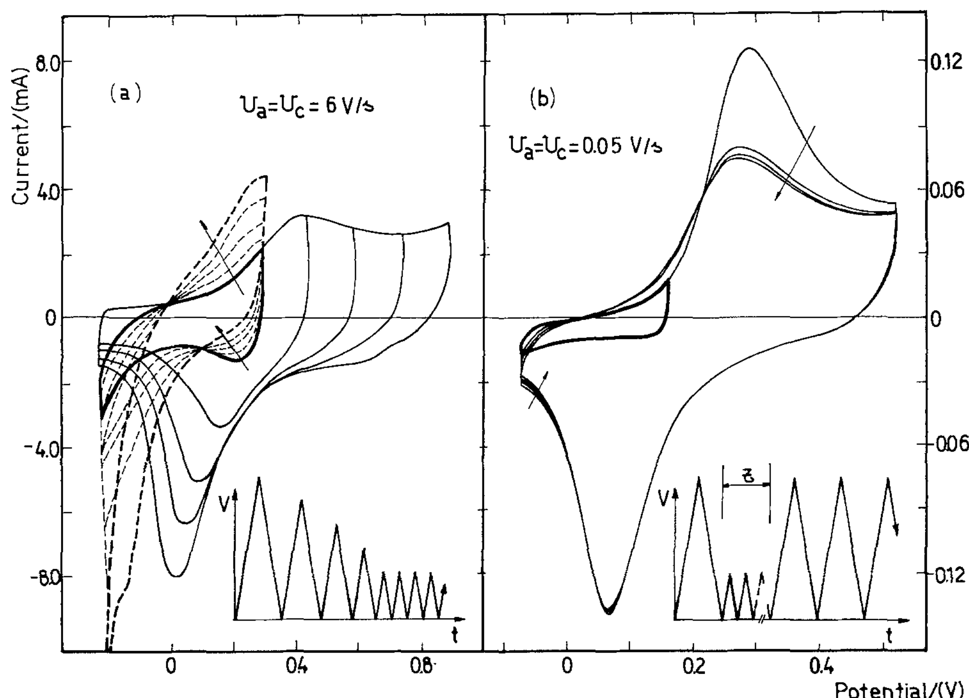

Fig. 10. *E/I* profiles. Molten $KHSO_4$, 230°C, type I electrodes (1.0 cm^2). (a) STPS at 6 V/sec, $E_{\lambda a}$ stepwise decreasing from 0.9 to 0.3V. The dashed trace corresponds to RTPS in the −0.2 to 0.3V range. (b) RTPS during 5 min in the −0.075 to 0.16V range followed by four RTPS in the −0.075 to 0.52V range.

0.16V upward, the successive scans involve anodic currents increasingly exceeding those reached for a stabilized E/I profile only until $E_{\lambda a}$ becomes equal to the anodic current peak potential. Further increases of $E_{\lambda a}$ tend to decrease gradually this effect, which finally disappears when $E_{\lambda a} > 0.55V$. The sum of the excesses of Q_a corresponding to the anodic excursion with increasing $E_{\lambda a}$ are practically equal to the Q_a change obtained between the first and the second anodic scans run between E_i and $E_{\lambda a} > 0.55V$. This feature of the Ir/$KHSO_4$ interface resembles that already described for the Ir/H_2SO_4 96% at 25° and 90°C and to a lesser extent for the Ir/1M H_2SO_4 at 25°C. The latter, however, implied the activation of the electrode.

Consider the E/I profiles in the case of an electrode which has previously attained a stable E/I profile and is perturbed with RTPS by a stepwise decreasing of $E_{\lambda a}$ (Fig. 11a). As $E_{\lambda a}$ decreases, it is quite clear that $Q_a < Q_c$ and the location of the cathodic current peak is more anodic until finally disappearing when $E_{\lambda a} \leqq$ 0.1V. However, if the E/I profiles are recorded after 5 min RTPS at each preset $E_{\lambda a}$ value (Fig. 11b), one also observes a net decrease of the anodic E/I contour. The reverse situation is seen when $E_{\lambda a}$ increases (Fig. 11c). The E/I records in this case are obtained successively after an initial RTPS from −0.075 to 0.52V followed by another 5 min of RTPS from −0.075 to 0.16V. Afterward each successive E/I record involves a stepwise increase in $E_{\lambda a}$. Now as $E_{\lambda a}$ increases there is a steady slight decrease of the anodic charge in the 0-0.2V range and a major current increase at the anodic current peak. The rate of increase of the latter diminishes for the following potential sweeps involving $E_{\lambda a}$ values larger than 0.36V. The described effect is enhanced if the RTPS at $E_{\lambda a} = +0.150V$ is prolonged for 40 min (Fig. 11d). The broadening of the anodic current peak as $E_{\lambda a}$ increases might be due to an increasing interaction. If it were due to hydrogen atom accumulation one would expect the effect to be independent of the direction of changing $E_{\lambda a}$.

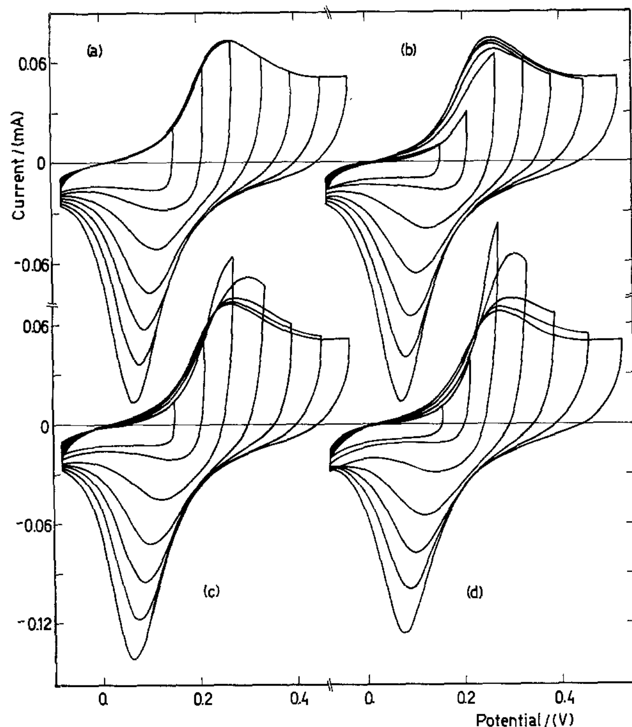

Fig. 11. *E/I* displays at 0.05 V/sec. Molten $KHSO_4$, 230°C, type I electrode (1 cm^2). (a) STPS, $E_{\lambda a}$ stepwise decreasing as in Fig. 10a. (b) The system is initially cycled (RTPS) in the −0.075 to 0.52V range to attain a Q_a/Q_c ratio equal to one. Then the amplitude is stepwise decreased but the *E/I* profile is only recorded after 5 min RTPS at each $E_{\lambda a}$. (c) The same as (b) but the amplitude is directly decreased to $E_{\lambda a} = 0.16V$ and the RTPS continued during 45 min before the following record involving the higher $E_{\lambda a}$ value. (d) The same as (c) but the RTPS lasts for 40 min.

Discussion

Preliminary considerations.—The results are strongly dependent both on the electrolyte composition and temperature. Thus, under constant perturbation conditions the activation of Ir electrodes, as measured from the increase of Q_a and Q_c during the RTPS, is more manifested in 1M H_2SO_4 acid at room temperature than either in the concentrated acid or in the $KHSO_4$ melt at higher temperatures. In the former solution the two potential limits for the activation, one located in the hydrogen adatom electrosorption region (cathodic activation limit) and the other in the region preceding the oxygen evolution (anodic activation limit), coincide with those reported earlier by other authors (22, 23). The strong dependence of the potentiodynamic E/I profiles run under RTPS on V is at the same time confirmed (9, 22, 23). Besides, two electrochemical deactivation potential limits are observed which correspond, respectively, to the potentials of the net hydrogen and oxygen evolution reactions. Nevertheless, neither the electrode activation nor its deactivation are sensitive to the hydrogen gas saturating the electrolyte. The accumulation of charge in the potential range preceding the oxygen evolution during the RTPS is apparently bound to an increase of irreversibility of the various processes either anodic or cathodic, as noticed through the shifts of the corresponding current peak potentials with cycling at constant V. Furthermore, the location of the various current peak potentials depends on V. Thus, the potential of current peak V_a, which emerges when the potential excursion extends into the hydrogen ion discharge region, becomes more positive when V increases. This same shift is noticed for the potentials of the anodic current peaks located at higher potentials. The reverse influence is found for the complementary cathodic current peaks. The anodic current peaks, however, move more rapidly with V than the cathodic ones. There is also a net shift of the anodic current peaks toward more anodic potentials as n, the number of potential cycles, increases. This is independent of $E_{\lambda c}$ and entails an apparent increasing irreversibility of the over-all anodic processes as n increases. Both $E_{\lambda c}$ and $E_{\lambda a}$ are very important in defining the changes of the E/I contour recorded under RTPS. Thus, when $E_{\lambda c}$ lies within the potential range of the hydrogen adatom it has influence on the anodic process occurring at higher potentials. On the other hand, when $E_{\lambda a}$ is about 1.4V there is an accumulation of anodic reaction products which are not readily electroreduced during the cathodic scan, not even when the hydrogen ion discharge takes place, and consequently this certainly restrains the sites for hydrogen adatoms. No clear aging effect of the anodic film is noticed for the activated electrode.

The other extreme situation is found in the case of the Ir/$KHSO_4$ (melt) interface which shows practically no activation effect, but it does exhibit a net aging of the electroformed film (24). The results corresponding to the 96% H_2SO_4 electrolyte are intermediate between those of the 1M H_2SO_4 and the $KHSO_4$ melt, depending on the temperature.

On the basis of these results the following discussion deals first with the probable reactions involved in the range of the monolayer formation and afterward the buildup of the thicker layer related to the electrode activation from the monolayer film either complete or incomplete. For the latter the amount of charge is within the order of an oxygen-monolayer thickness, the stoichiometry of the stable oxidized surface probably corresponding to an Ir/O ratio equal to 0.5 (24, 25).

The probable surface species anodically formed in the monolayer thickness film.—The following equilibria

and the corresponding standard potential ($E°$) of Ir metal/Ir oxide systems are reported (7, 22, 32)

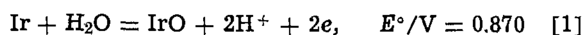

$$Ir + H_2O = IrO + 2H^+ + 2e, \quad E°/V = 0.870 \quad [1]$$

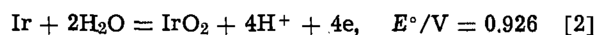

$$Ir + 2H_2O = IrO_2 + 4H^+ + 4e, \quad E°/V = 0.926 \quad [2]$$

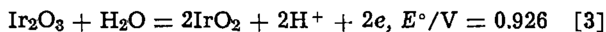

$$Ir_2O_3 + H_2O = 2IrO_2 + 2H^+ + 2e, \quad E°/V = 0.926 \quad [3]$$

Therefore, stoichiometries such as IrO and IrO_2 are, in principle, thermodynamically possible. However, taking into account that the electrochemical reaction in 1*M* H_2SO_4 and 96% H_2SO_4 at room temperature involves at least three anodic and three complementary cathodic current peaks within the potential range of the activation process, various different surface species must exist. These redox systems are clearly detected through the TMTPS experiments. Various successive processes are quite reasonably already starting from a pure Ir surface dipped into the pure acid solutions. In this case the structure of the metal/solution interface may be relatively complicated since adsorption of water, the eventual formation of hydrogen adatom and OH-species, and, to a less extent, anion adsorption are possible. During the initial anodic STPS from the hydrogen electrode potential upward, the hydrogen adatoms, if present, are first electrodesorbed. Then, on the same surface the OH-species are electrosorbed. The very initial steps can be idealized as follows

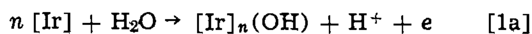

$$n\,[Ir] + H_2O \rightleftharpoons [Ir]_n(OH) + H^+ + e \quad [1a]$$

followed by

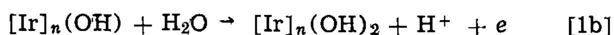

$$[Ir]_n(OH) + H_2O \rightleftharpoons [Ir]_n(OH)_2 + H^+ + e \quad [1b]$$

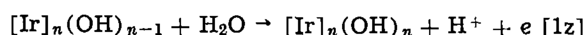

$$[Ir]_n(OH)_{n-1} + H_2O \rightleftharpoons [Ir]_n(OH)_n + H^+ + e \quad [1z]$$

where n is the number of surface sites available on the metal. Steps [1a] to [1z] involve the electrosorption of water on a surface increasingly covered by the OH-species. Step [1z] implies the ideal situation of the metal surface covered by a monolayer of electrosorbed OH-species. Following the reaction sequence, the latter undergoes a further oxidation at higher potentials which can be generalized as

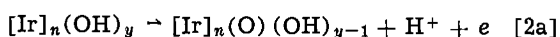

$$[Ir]_n(OH)_y \rightleftharpoons [Ir]_n(O)(OH)_{y-1} + H^+ + e \quad [2a]$$

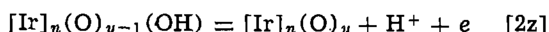

$$[Ir]_n(O)_{y-1}(OH) = [Ir]_n(O)_y + H^+ + e \quad [2z]$$

where $0 \leq y \leq n$ and again $y = n$ when the degree of surface coverage expressed in terms of the IrO stoichiometry is one. In this case the overall reaction agrees with reaction [1].

A further oxidation must be associated with a higher oxidation state of Ir which can be achieved according to

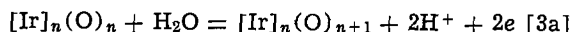

$$[Ir]_n(O)_n + H_2O = [Ir]_n(O)_{n+1} + 2H^+ + 2e \quad [3a]$$

$$[Ir]_n(O)_{(2n-1)} + H_2O = [Ir]_n(O)_{2n} + 2H^+ + 2e \quad [3z]$$

Eventually, the $(n + 1)/n$ ratio would approach 3/2 when a monolayer of Ir_2O_3 is formed. The reaction pathway [1a] to [3z] implies, in principle, that various OH- and O-containing species are possible on the Ir surface in the absence of any activation. The presence of nonstoichiometric oxides (hydrated oxides) in the anodic film has already been considered as probable (22, 23). Formally, the proposed reaction pathway resembles those earlier postulated for Pt and Au in aqueous acid solutions (33, 34) and quite reasonably can be extended to the Ir/$KHSO_4$ (melt) interface. But it fails to explain the charge increase related to the Ir activation process. It should be remarked that the advance of the process from step [1a] to step [3z] implies the oxidation of Ir and the concomitant decrease of the binding energy of the Ir atom to the bulk metal, so that when the Ir atom is completely saturated either with OH-species or O-atoms it becomes detached from the lattice, the metal undergoing electrodissolution. As a matter of fact, the anodic dissolution rate of Ir on potential cycling in 1*M* H_2SO_4 is claimed to be *ca.* 8-9 times that found for Pt under the comparable experimental conditions (20). The metal corrosion, therefore, should be considered as the initial stage yielding the formation of a multilayer anodic film, which is responsible for the electrode activation.

The charge increase at the Ir/H_2SO_4 (aq) interface.—Various interpretations have been advanced to explain this effect: (*i*) The accumulation of an oxide species, probably IrO_2, that is irreversibly electroreduced at potentials overlapping those of the hydrogen ion discharge (16). An IrO_2 covered metal surface can probably still adsorb an appreciable amount of water. (*ii*) Oxygen absorption through the surface oxide film (5). Comparing radius of Ir and oxygen-species, it is difficult to see, as already pointed out (22), how oxygen could be adsorbed or desorbed through an oxide film of *ca.* 100 atoms thickness rapidly enough to give a reversible response in the case of an activated Ir electrode. (*iii*) A possible, although unlikely, occurrence of a roughness factor that manifests preferentially in the region of the electroformation and electroreduction of the oxygen-containing species. (*iv*) Migration of hydrogen ion into the oxide layer with further electrochemical reaction in the bulk of the solid phase. In terms of hydrogen ion migration the effect should become more unnoticed when the electrode potential is positive with respect to the potential of zero charge of the metal and it becomes enhanced in the reversed situation (32). The formation of either an IrO and an IrO_2 surface or an IrO multilayer results. This explanation, in principle disregarded, seems to be more likely for the oxygen layers formed on Pt at high anodic potentials (9, 15). (*vi*) A possible dissolution of hydrogen atoms into the bulk of the metal which may react electrochemically. This is unlikely as a major contribution since the experimental data (35) which sustains the idea of Ir dissolving an appreciable amount of hydrogen is questionable because most of them were obtained with powdered metal (36). (*vii*) Finally, pitting corrosion is assumed to be a major contribution in the anodic charge increase during the RTPS (18, 19).

The various explanations briefly summarized only deal with partial aspects of the electrochemical process. Thus, the existence of potential limits for the so-called "activation state" of Ir, the influence of acid concentration and temperature, and the apparent discrepancy in charge accumulation in the hydrogen electrode reaction region in contrast with the potential region of the oxo- and hydroxo-species formation are not clearly explained.

The line of thought to develop a model for explaining the electrochemical behavior of the Ir/H_2SO_4 (aq) interface is based on the following evidence: (*i*) In H_2SO_4 (aq) the potential region of Ir activation involves at least three clear anodic current contributions, which are complemented by the corresponding cathodic currents. The pertaining redox couples exhibits a very reversible behavior which is particularly obvious in the TMTPS experiments. (*ii*) X-ray analysis of the surface products formed during the electrooxidation of Ir in 0.1*N* H_2SO_4 solutions reveals IrO_2 as the only surface compound in the 0.5-2.2V potential range (37). This compound in aqueous solutions exists as $Ir(OH)_4$, that is, $IrO_2 \cdot 2H_2O$ in agreement with the x-ray diffractometry. Compounds of this type involving polymeric films of hydrated-oxy-hydroxide species are often postulated during electrodissolution and passivation of some metals in aqueous electrolytes (38) and the electrical conduction operates through a proton transfer mechanism (39-41). On the other hand, the formation of a compound such as $Ir(OH)_4$ means that the binding forces left on Ir in relation to the metal lattice have been practically canceled out and, instead, the metal atom becomes part of a complex IrOH lattice on the surface of the metal. (*iii*) The activation effect

decreases as the dehydrating power of the electrolyte increases, the latter being related either to the acid concentration increase or to the temperature increase. Certainly the largest dehydrating effect is expected in the $KHSO_4$ (melt). (*iv*) The activation effect occurs in different acid electrolytes independently of the presence of SO_4^{-2} ions (42).

Therefore, the charge increase of the Ir/H_2SO_4 (aq) interface during the RTPS comes out from a simultaneous occurrence of steps [1a] to [3z] and proton transfer reactions related to the $Ir(OH)_4$-type species yielded by the metal electrodissolution. Hence, as steps [1a] to [1z] occur statistically, the saturation condition corresponding to the stable $Ir(OH)_4$ structural configuration should be attained in some places before achieving a full coverage of the surface by the OH-species. Therefore

$$[Ir]_n(OH)_m \rightleftharpoons [Ir]_{n-1}(OH)_{m-4} + Ir(OH)_4 \quad [4]$$

where $n \geqq m$. Reaction [4] yields simultaneously a surface species and free metal sites. When the amount of $Ir(OH)_4$ exceeds that of a monolayer, the electrochemical interface formerly defined in terms of the metal/solution plane (π_1), embraces now another plane (π_2) corresponding to the $Ir(OH)_4$/solution interface. Both planes π_1 and π_2 are, in principle, charge transfer planes, either for electron transfer or for ion transfer, and the region between them corresponds to the hydrated-oxy-hydroxide phase where the following are feasible processes

$$Ir(OH)_4 + H^+ + e \rightleftharpoons Ir(OH)_3 \cdot H_2O \quad [5a]$$

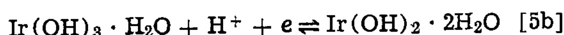

$$Ir(OH)_3 \cdot H_2O + H^+ + e \rightleftharpoons Ir(OH)_2 \cdot 2H_2O \quad [5b]$$

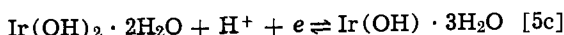

$$Ir(OH)_2 \cdot 2H_2O + H^+ + e \rightleftharpoons Ir(OH) \cdot 3H_2O \quad [5c]$$

Reactions [5a] to [5c] are deprotonation processes which take place both at π_1 and in the region between π_1 and π_2. These reactions explain the three relatively reversible redox couples appearing at the activation potential range. They occur at potentials lower than the thermodynamic threshold to form IrO_2 according to reaction [2] and involve a proton transfer process between π_1 and π_2. The possibility of a proton transfer mechanism in the film formed on Ir in aqueous H_2SO_4 has recently been proposed (22). Such a mechanism has also been considered by other authors for other metals/film systems in aqueous solutions (38-43).

The hydrogen atom electrosorption and electrodesorption must occur principally on the π_1 plane. It can be represented as three limiting possibilities

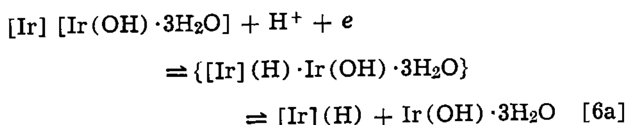

$$[Ir]\,[Ir(OH) \cdot 3H_2O] + H^+ + e \rightleftharpoons \{[Ir](H) \cdot Ir(OH) \cdot 3H_2O\} \rightleftharpoons [Ir](H) + Ir(OH) \cdot 3H_2O \quad [6a]$$

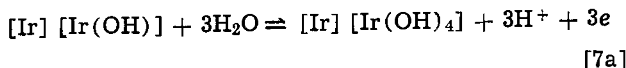

$$[Ir]\,[Ir(OH)] + 3H_2O \rightleftharpoons [Ir]\,[Ir(OH)_4] + 3H^+ + 3e \quad [7a]$$

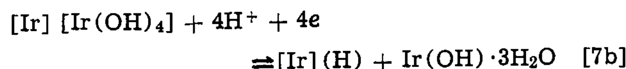

$$[Ir]\,[Ir(OH)_4] + 4H^+ + 4e \rightleftharpoons [Ir](H) + Ir(OH) \cdot 3H_2O \quad [7b]$$

and

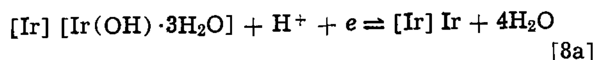

$$[Ir]\,[Ir(OH) \cdot 3H_2O] + H^+ + e \rightleftharpoons [Ir]\,Ir + 4H_2O \quad [8a]$$

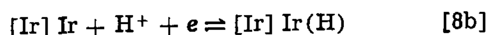

$$[Ir]\,Ir + H^+ + e \rightleftharpoons [Ir]\,Ir(H) \quad [8b]$$

Reaction [6a] implies that the reaction product of step [4], although it mainly contributes to the film, still leaves the possibility that a new metal plane becomes covered by hydrogen adatoms. Reactions [7a] and [7b] promote a thickening of the hydrated-oxy-hydroxo layer and reactions [8a] and [8b] involve a complete electroreduction of the surface without layer thickening. The energetics of these processes are probably slightly different so that the extent of the contribution of each possibility depends on the electrode potential. Reaction [7b] explains the cathodic potential limit for the electrode activation. Moreover, the amount of charge playing part in the hydrogen adatom region when no IrO_2 has been formed is confined to the adsorption capacity at the π_1 plane and it is certainly independent of the amount of hydroxo compound lying between planes π_1 and π_2. Hence, the electrode roughness factor should be actually related to the π_1 plane. The formation of either $Ir(OH)_4$ or some equivalent hydrated-oxy-hydroxo species produces the enlargement of the metal-metal bond through the introduction of a new coordinated oxygen atom. But the reduced species $Ir(OH) \cdot 3H_2O$ produced from $Ir(OH)_4$ will not begin to form the film until the potential makes possible a reaction such as [6a]. When the latter takes place it is possible the $Ir(OH) \cdot 3H_2O$ reduction and also the adsorption of a hydrogen atom interacting with an Ir atom of the second layer and the concomitant displacement of the $Ir(OH) \cdot 3H_2O$ species form the film.

On the other side when the anodic potential just exceeds that of reaction [2], the IrO_2 formation begins to take place at the π_1 plane and this process again should enhance the increase of charge. As a matter of fact the thermodynamic potential for such reaction comes close to the anodic potential limit required for activating the electrode. The complete electroreduction of the IrO_2 surface species should only be achieved at cathodic potentials of net hydrogen evolution, probably through a series of reactions such as [7b] to [8b].

On the basis of the proposed model any process which either produces a net corrosion of the metal as IrO_2 or leaves a new reduced metal surface contributes to the $Ir(OH)_4$ formation within the π_1 and π_2 planes. Therefore, the two potential limits to achieve the increasing electrode activation are related to the processes just described. Under these circumstances, the potential change of the activated electrode kept within those limits is predominantly bound to reactions [4] to [5c]. The change of the electrode activity will depend on the rate of shifts of the π_1 and π_2 planes caused by the various possible steps already discussed.

Furthermore, one reasonably admits that at the plane π_2 either a dissolution of the hydroxo species or a dehydration or both simultaneously take place. The latter is probably favored by the dehydrating power of the electrolyte.

The proposed explanation involves the net metal electrodissolution after a continuous RTPS and the formation of a relatively loosely attached layer between the π_1 and π_2 planes. This renders possible either a partial or total mechanical detachment of the layer, thus accounting for either the anodic or cathodic electrode deactivation limits. Otherwise, at high anodic potentials a change to a valence state +6 and a breaking of the film structure may occur but this is far from proved.

The activation process in concentrated H_2SO_4 exhibits a major contribution of the first redox couple to the detriment of the others. Then, the film composition may approach a predominant $Ir(OH)_2$ stoichiometry due to a competence between the film formation and the dehydration of the hydroxo-containing species by the concentrated acid. Finally, no hydrated species can exist in the molten $KHSO_4$ so that no charge increase is observed.

The reaction model also explains that a direct oxidation of the surface to IrO_2 entails the formation of a difficulty reducible surface species since the hydrogen adatom current peaks practically disappear. As earlier presumed, this indicates that a complete surface reduction can only be achieved after a drastic electroreduction at cathodic potentials exceeding by far that of the hydrogen electrode potential. This is perhaps more clearly observed in the case of the $Ir/KHSO_4$ (melt)

interface where no hydrogen adatom contributions are seen for an electrode attaining a stable E/I profile and where the potential excursions are limited to the monolayer oxygen electrosorption region. Only after a drastic electroreduction the current peaks related to the hydrogen adatoms are then recorded. The complete surface reduction would imply the electroreduction of Ir-O-Ir species or related ones which have already been assumed by other authors (23).

Finally, aging effects such as those described for monolayers of oxygen-containing species in other noble metal/acid electrolyte interfaces (26, 34) become clearly evident when there is no electrode activation interference and the charge involved in the process is of the order of one monolayer, as recently reported for the Ir/$KHSO_4$ (melt) interface (24).

Acknowledgment

This Institute (INIFTA) is sponsored by the following institutions: Universidad Nacional de La Plata, Consejo Nacional de Investigaciones Científicas y Técnicas, and Comisión de Investigaciones Científicas (Provincia de Buenos Aires). This work is partially supported by the Regional Program for the Scientific and Technological Development of the Organization of American States.

Manuscript submitted July 25, 1977; revised manuscript received March 17, 1978.

Any discussion of this paper will appear in a Discussion Section to be published in the June 1979 JOURNAL. All discussions for the June 1979 Discussion Section should be submitted by Feb. 1, 1979.

REFERENCES

1. M. W. Breiter, C. A. Knorr, and W. Volkl, *Z. Elektrochem.*, **59**, 681 (1955).
2. M. W. Breiter, K. Hoffmann, and C. A. Knorr, *ibid.*, **61**, 1168 (1957).
3. K. Franke, C. A. Knorr, and M. W. Breiter, *ibid.*, **63**, 226 (1959).
4. F. G. Will and C. A. Knorr, *ibid.*, **74**, 270 (1960).
5. W. Böld and M. W. Breiter, *Electrochim. Acta*, **5**, 169 (1961).
6. M. W. Breiter, *Z. Phys. Chem. N. F.*, **52**, 73 (1967).
7. J. P. Hoare, "The Electrochemistry of Oxygen," Interscience, New York (1968).
8. P. Stonehart, H. A. Kozlowska, and B. E. Conway, *Proc. R. Soc. London, Ser. A*, **310**, 541 (1969).
9. A. Capon and R. Parsons, *J. Electroanal. Chem. Interfacial Electrochem.*, **39**, 275 (1972).
10. A. T. Kuhn and P. M. Wright, *ibid.*, **41**, 329 (1973).
11. B. D. Kurnikov, A. I. Zhurin, V. V. Chernyi, Yu. B. Vasil'ev, and V. S. Bagotskii, *Elektrokhimiya*, **9**, 833 (1973).
12. B. D. Kurnikov and Yu. B. Vasil'ev, *ibid.*, **9**, 1203 (1973).
13. B. D. Kurnikov and Yu. B. Vasil'ev, *ibid.*, **9**, 1739 (1973).
14. B. E. Conway and S. Gottesfeld, *Trans. Faraday Soc.*, **69**, 1090 (1973).
15. G. Allen, P. M. Tucker, A. Capon, and R. Parsons, *J. Electroanal. Chem. Interfacial Electrochem.*, **50**, 335 (1974).
16. R. Woods, *ibid.*, **49**, 217 (1974).
17. B. D. Kurnikov and Yu B. Vasil'ev, *Elektrohimiya*, **10**, 77 (1974).
18. J. M. Otten and W. Visscher, *J. Electroanal. Chem. Interfacial Electrochem.*, **55**, 1 (1974).
19. J. M. Otten and W. Visscher, *ibid.*, **55**, 13 (1974).
20. D. A. J. Rand and R. Woods, *ibid.*, **55**, 375 (1974).
21. B. I. Podlovchenko, N. A. Epshtein, and A. N. Frumkin, *ibid.*, **53**, 95 (1974).
22. D. N. Buckley and L. D. Burke, *Trans. Faraday Soc.*, **71**, 1447 (1975).
23. D. N. Buckley, L. D. Burke, and J. K. Mulcahy, *ibid.*, **72**, 1896 (1976).
24. J. O. Zerbino, N. R. de Tacconi, A. J. Calandra, and A. J. Arvía, *J. Electroanal. Chem. Interfacial Electrochem.*, **77**, 379 (1977).
25. F. Colom, A. de la Plaza, and R. Gancedo, *Anal. Quim.*, **71**, 985 (1975).
26. N. R. de Tacconi, A. F. Calandra, and A. J. Arvía, *J. Electroanal. Chem. Interfacial Electrochem.*, **51**, 25 (1974).
27. J. O. Zerbino, N. R. de Tacconi, and A. J. Arvía, *ibid.*, **79**, 287 (1977).
28. J. O. Zerbino, N. R. de Tacconi, A. J. Calandra, and A. J. Arvía, *This Journal*, **124**, 475 (1977).
29. M. Bonnemay, G. Bronoel, and M. Haim, *Compt. Rend. C*, **277**, 903 (1973).
30. A. Damjanovic, A. Dey, and J. O'M. Bockris, *This Journal*, **113**, 739 (1966).
31. A. Damjanovic and M. K. Y. Wong, *ibid.*, **114**, 592 (1967).
32. J. F. Llopis and F. Colom, "The Electrochemistry of the Elements," Vol. VI, A. J. Bard, Editor, chap. 5, p. 221, Marcel Dekker, New York (1976).
33. H. A. Kozlowska, B. E. Conway, and W. B. A. Sharp, *J. Electroanal. Chem. Interfacial Electrochem.*, **43**, 9 (1973).
34. C. M. Ferro, A. J. Calandra, and A. J. Arvía, *ibid.*, **57**, 267 (1974).
35. D. P. Smith, "Hydrogen in Metals," The University of Chicago Press, Chicago (1947).
36. W. Mueller, J. P. Blackledge, and G. G. Libowitz, "Metal Hydrides," p. 633, Academic Press, New York-London (1968).
37. C. C. Schubert, C. L. Page, and B. Ralph, *Electrochim. Acta*, **18**, 33 (1973).
38. D. Gallizzioli, F. Tantardini, and S. Trasatti, *J. Appl. Electrochem.*, **4**, 57 (1974).
39. J. P. Gabano, J. Seguret, and J. F. Laurent, *This Journal*, **117**, 147 (1970).
40. K. R. Newby and A. B. Scott, *ibid.*, **117**, 152 (1970).
41. D. M. Mac Arthur, *ibid.*, **117**, 729 (1970).
42. J. O. Zerbino and A. J. Arvía, In preparation.
43. J. Vilche and A. J. Arvía, *Corros. Sci.*, In press.

The Theoretical Energy Conversion Efficiency of a High Temperature Fuel Cell Based on a Mixed Conductor

D. S. Tannhauser

Department of Physics, Technion—Israel Institute of Technology, Haifa, Israel

ABSTRACT

We have calculated the voltage *vs.* current characteristic and the energy conversion efficiency of a fuel cell based on a mixed ionic-electronic conductor. The transport equations for the electrolyte are solved exactly and the material parameters which determine the shape of the characteristic are determined. The equations are then applied to the special case of doped ceria, which becomes a mixed conductor only at low oxygen pressures. We then show that for the purpose of efficiency calculations, the finite but small ratio of ionic to electronic mobility valid for ceria can be safely taken as zero, and we compare the resulting simple equations with the equivalent circuit approach to a fuel cell. The characteristic is found to be curved instead of being a straight line and for typical operating conditions the best energy conversion efficiency is, for the transport theory approach, 50% higher than for the equivalent circuit one. We conclude from the calculated new values of conversion efficiency that the equivalent circuit underestimates the conversion efficiency of a mixed conductor seriously and that doped ceria as a solid electrolyte is a more serious contender to doped zirconia than believed up to now.

A very important factor in judging the economic performance of a fuel cell is its energy conversion efficiency, η, defined as (power delivered to the load)/(rate of conversion of chemical energy). A fuel cell based on a purely ionic conductor and operating under a very light load can have an efficiency close to 100%. This, however, is not an economical way of using the fuel cell because it implies a very small current density. For a fuel cell based on a mixed ionic-electronic conductor, η will never be 100% because of the internal short by the electronic current. However the efficiency of a purely ionic conductor under actual working conditions will also be much less than 100%, and we need, therefore, a detailed analysis to judge the relative suitability of a given purely ionic conductor *vs.* a given mixed conductor. It may well happen that in spite of a slightly smaller η the mixed conductor will be more suitable because its internal resistance is smaller or because it has less electrode problems.

The calculation should start from the experimentally determined material properties of the mixed conductor and result in the maximum obtainable energy conversion efficiency under given external conditions. Takahashi (1) has done such a calculation but his analysis is based on averaged material properties which lead to a simple equivalent circuit and to a linear current-voltage characteristic of the fuel cell. A more reliable calculation of the efficiency should start from the transport relations for ions and electrons in the material, this has never been done. A similar physical problem is that of migration of ions and electrons during oxidation of a metal under the influence of an electric field, an approximate solution is given by Kroeger (2). The approximations used by Kroeger, when applied to a fuel cell material, lead to a linear dependence of current on voltage, *i.e.*, to the equivalent circuit used by Takahashi.

The purpose of this paper is to present a detailed calculation of the maximum theoretical energy conversion efficiency for a fuel cell based on a mixed conductor and working under given external conditions. The result of this calculation, which starts from the transport equations, is of interest because it defines an upper limit which can be reached, given the right technology. It serves a similar purpose as the theoretical energy conversion efficiency of a silicon solar cell, in both cases the reason why the theoretical limit is not easily reached is connected with the electrodes which collect the current.

We shall not do the calculation in the most general form but shall base our terminology and the application of our results on the properties of doped CeO_2 (3). This material is a competitor to doped ZrO_2, the material on which most of the development of high temperature fuel cells has been concentrated. Doped zirconia is a purely ionic conductor at any oxygen pressure of interest in fuel cells, but because of its relatively low conductivity it has to be used near 1000°C to get a reasonable current density. Doped ceria has a somewhat higher conductivity and can therefore be used near 800°C, it also seems to have less aging and polarization problems than doped zirconia. Its one disadvantage is that it becomes a mixed ionic-electronic conductor at the low oxygen pressures which prevail on the fuel side of a fuel cell.

After defining the system mathematically we first solve the set of transport equations. Among our assumptions is that of electrical neutrality, but we arrive at a solution with a small space charge. We show in Appendix A that for the material properties of doped ceria the space charge is so small that the approximation of neutrality is justified. We then apply the general solution to doped ceria, where the electronic conductivity at the cathode can be neglected, and calculate for this material the characteristic and maximum efficiency. In the last section we compare the calculated efficiency with that obtained from the equivalent circuit solution, and find that η for the transport model is considerably larger. We conclude that the equivalent circuit does not represent the system very well and specifically that doped ceria should be considerably more suitable as a fuel cell material than believed up to now.

In our analysis we assume that the power delivered by the fuel cell is limited by bulk properties and not by electrode or surface reactions.

The results of this paper can be applied, with slight modifications, to fuel cells based on mixed conductors other than doped ceria.

Description and Defining Equations of the System

In this and the next section we calculate the relationship between the load current, j_L, the electronic loss current, j_e, and the load voltage, E_L, of a fuel

Key words: fuel cell, transport theory, energy conversion, cerium dioxide.

cell made of a solid electrolyte which becomes a mixed ionic-electronic conductor at low oxygen pressure. From the $j_L(E_L)$ and $j_e(E_L)$ curves we then find the energy conversion efficiency. We base our terminology on doped CeO_2, the calculation however is quite general.

The electrolyte, a membrane of doped CeO_2, is typically at 800°C and extends from $x = 0$ to $x = l$ (see Fig. 1a). The oxygen partial pressure is $p_{O_2}{}^{I}$ (normally about 10^{-20} atm as in $H_2/H_2O = 10/1$) at $x = 0$ and $p_{O_2}{}^{II}$ (normally 0.21 atm) at $x = l$. The electrolyte is doped substitutionally with a lower valent metal ion, which we take for definiteness to be Ca^{2+}, in the range $[Ca_{Ce}''] = 10\%$ molar concentration. This doping creates oxygen vacancies, $V_O^{\cdot\cdot}$, with an effective double positive charge, in addition to those which already exist in the undoped material. These charged vacancies conduct the ionic current. At $x = 0$ and at $x = l$ there are electrodes and we assume that the electrode-electrolyte interface presents a negligible resistance to the transfer of electrons or ions, *i.e.*, that the reaction

$$2e + V_O^{\cdot\cdot} + \tfrac{1}{2}\, O_2(\text{gas}) \leftrightarrow \text{zero} \qquad [1]$$

is in equilibrium near each of the electrodes. Therefore, even when current flows, the concentration of electrons, n, and of vacancies, $[V_O^{\cdot\cdot}]$, obeys near $x = 0$ the equation

$$(n^I)^2[V_O^{\cdot\cdot}]^I(p_{O_2}{}^I)^{1/2} = K_O(T) \qquad [2]$$

while near $x = l$

$$(n^{II})^2[V_O^{\cdot\cdot}]^{II}(p_{O_2}{}^{II})^{1/2} = K_O(T) \qquad [2a]$$

$K_O(T)$ is the equilibrium constant of reaction [1] at temperature T. Equations [2] and [2a], together with the condition of local neutrality

$$2[V_O^{\cdot\cdot}] = 2[Ca_{Ce}''] + n \qquad [3]$$

determine n and $[V_O^{\cdot\cdot}]$ near each of the electrodes, these concentrations will subsequently serve as boundary conditions. In doped ceria the value of n^I is such that the electronic conductivity at $x = 0$ competes with the ionic conductivity. The validity of the neutrality condition [3] will be discussed in Appendix A.

An expression for the load voltage may now be derived. For convenience we use the formalism of electrochemical potentials, for the electrons these are $(\tilde{\mu}_e{}^I)$ and $\tilde{\mu}_e{}^{II}$ in the two electrodes. The load voltage is given by

$$-qE_L = \tilde{\mu}_e{}^I - \tilde{\mu}_e{}^{II} \qquad [4]$$

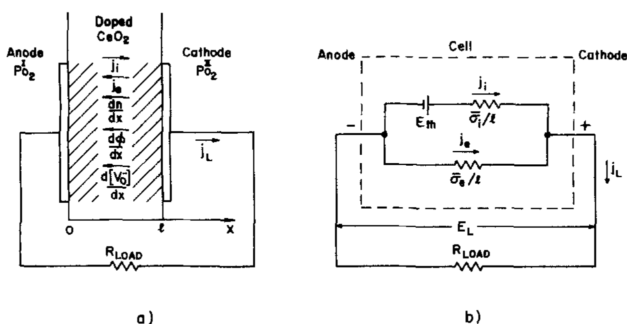

Fig. 1. (a) Schematic cross section of a fuel cell based on doped ceria. The directions of the electric currents and of the gradients correspond to normal operation of the cell. The thickness l is typically 1 mm. The electronic current is seen to be negative. The ratio $p_{O_2}{}^{II}/p_{O_2}{}^{I}$ is typically 10^{20}. (b) Equivalent circuit of a fuel cell with mixed conductivity. E_{th} is the theoretical open-circuit voltage of the ideal fuel cell. $\bar{\sigma}_i$ and $\bar{\sigma}_e$ are specific ionic and electronic conductivities. The current directions are drawn for all currents positive, as defined after Eq. [10].

The electrochemical potential $\tilde{\mu}_e$ is the same in the electrode and in the outer layer of electrolyte next to it, since we assumed nonblocking electrodes. For electrons $\tilde{\mu}_e = \mu_e - q\phi$, Eq. [4] is therefore equivalent to

$$-qE_L = (\mu_e{}^{II} - \mu_e{}^{I}) - q(\phi^{II} - \phi^{I}) \qquad [5]$$

Here μ_e is the chemical potential and ϕ the electrical potential in the electrolyte, and q is the elementary charge, defined positive.

We can calculate $\Delta\mu_e$ for the electrolyte from $\mu_e = kT \ln n + \text{const.}$ which gives

$$\mu_e{}^{II} - \mu_e{}^{I} = kT \ln \frac{n^{II}}{n^{I}} \qquad [6]$$

The ratio n^{II}/n^{I} is determined by Eq. [2] and [3] and, in order to calculate $E_L(j_L)$, we are left with the problem of expressing $(\phi^{II} - \phi^{I})$ in terms of the load current j_L.

To do this we have to solve the set of coupled transport equations for the ionic current density j_i and for the electronic current density j_e. These are

$$j_i = -2qD_i \frac{d[V_O^{\cdot\cdot}]}{dx} - 2qv_i[V_O^{\cdot\cdot}] \frac{d\phi}{dx} \qquad [7]$$

and

$$j_e = qD_e \frac{dn}{dx} - qv_e n \frac{d\phi}{dx} \qquad [8]$$

Here D_i is the diffusion coefficient of vacancies and v_i their mobility; D_e is the diffusion coefficient of electrons and v_e their mobility. The mobilities and diffusion constants are connected through the Einstein relations

$$D_i = \frac{kT}{2q} v_i \qquad [9]$$

$$D_e = \frac{kT}{q} v_e \qquad [9a]$$

and we assume that the mobilities do not depend on the defect concentrations. The currents in Eq. [7] and [8] are electric, not particle, currents. As usual the field currents flow in the direction of decreasing ϕ while the diffusion currents flow toward low concentrations for the positive vacancies and toward high concentrations for electrons. Particle conservation demands that both j_e and j_i are independent of x. The current per unit area delivered by the fuel cell to the load is given by

$$j_L = j_i + j_e \qquad [10]$$

We define the direction from the anode to the cathode as positive and shall see later that j_e is negative under normal operating conditions, and therefore, $j_L < j_i$. In Fig. 1a we show the directions under normal operating conditions of the various currents and gradients introduced above.

Calculation of Cell Characteristic and Efficiency

We first derive a differential equation for the dependence of n on x. Substitution of [9] and [10] into [7] gives

$$j_L = j_e - kTv_i \frac{d[V_O^{\cdot\cdot}]}{dx} - 2qv_i[V_O^{\cdot\cdot}] \frac{d\phi}{dx} \qquad [11]$$

Equation [3] leads to $2d[V_O^{\cdot\cdot}]/dx = dn/dx$, and Eq. [8] together with [9a] to

$$q \frac{d\phi}{dx} = -\frac{j_e}{v_e n} + \frac{kT}{n} \frac{dn}{dx} \qquad [12]$$

Substitution into Eq. [11] gives

$$j_L = j_e - \frac{kTv_i}{2}\frac{dn}{dx} - 2kTv_i\frac{[V_O^{\cdot\cdot}]}{n}\frac{dn}{dx} + 2\frac{[V_O^{\cdot\cdot}]}{n}\frac{v_i}{v_e}j_e \quad [13]$$

We substitute now Eq. [3] and get the following differential equation

$$\left(A + \frac{3}{4}Cn\right)\frac{dn}{dx} - (1+D)n - B = 0 \quad [14]$$

where we have defined

$$C \equiv \frac{2kTv_i}{j_e - j_L}, \quad A \equiv [Ca_{Ce}'']C,$$

$$D \equiv \frac{v_i}{v_e}\frac{j_e}{j_e - j_L}, \quad B \equiv 2[Ca_{Ce}'']D$$

To calculate $(\phi^{II} - \phi^{I})$ we start from Eq. [12], which can be written

$$\left[q\frac{d\phi}{dn} - \frac{kT}{n}\right]\frac{dn}{dx} = -\frac{j_e}{v_e n} \quad [15]$$

We substitute dn/dx from Eq. [14] and get after some algebra

$$q\frac{d\phi}{dx} = kT\frac{1 - \frac{1}{2}D}{B + (1+D)n} \quad [16]$$

Integration gives

$$q(\phi^{II} - \phi^{I}) = kT\frac{1 - \frac{1}{2}D}{1+D}\ln\frac{B + (1+D)n^{II}}{B + (1+D)n^{I}} \quad [17]$$

and we write this in terms of the material properties in the form

$$\Delta\phi = \frac{kT}{q}\frac{\frac{v_i}{2v_e} - y}{\frac{v_i}{v_e} + y}\ln\frac{1 + \left(\frac{v_i}{v_e} + y\right)\frac{\sigma_e^{I}}{\sigma_i^{\circ}}}{1 + \left(\frac{v_i}{v_e} + y\right)\frac{\sigma_e^{II}}{\sigma_i^{\circ}}} \quad [18]$$

Here we have defined

$$\Delta\phi \equiv \phi^{II} - \phi^{I}, \quad y \equiv \frac{j_e - j_L}{j_e}, \quad \sigma_e \equiv qv_e n,$$

$$\sigma_i^{\circ} \equiv 2qv_i[Ca_{Ce}'']$$

From Eq. [5], [6], and [18] we can now calculate $E_L(y)$

$$E_L(y) = \frac{kT}{q}\ln\frac{n^{I}}{n^{II}} + \Delta\phi(y) \quad [19]$$

The characteristic of the fuel cell, $E_L(j_L)$, will subsequently be described parametrically by $E_L(y)$ and $j_L(y)$.

For later use in this paper we note that Eq. [19] can be written

$$E_L = E_{th} + \frac{kT}{2q}\ln\frac{1 + (\sigma_e^{II}v_i/\sigma_i^{\circ}v_e)}{1 + (\sigma_e^{I}v_i/\sigma_i^{\circ}v_e)} + \Delta\phi \quad [20]$$

Here E_{th} is the theoretical open-circuit voltage of the ideal fuel cell, which is in our case

$$E_{th} = \frac{kT}{4q}\ln\frac{p_{O_2}^{II}}{p_{O_2}^{I}} \quad [21]$$

To derive Eq. [20] we add and subtract E_{th} to Eq. [19] and use the relation

$$n^2 p_{O_2}^{1/2} = \frac{K_O}{[Ca_{Ce}''] + \frac{n}{2}} \quad [22]$$

which is derived from Eq. [2] and [3]. This gives

$$E_L = E_{th} + \frac{kT}{2q}\ln\frac{2[Ca_{Ce}''] + n^{II}}{2[Ca_{Ce}''] + n^{I}} + \Delta\phi \quad [23]$$

which is easily converted to [20].

In order to calculate $E_L(j_L)$ we still need an expression for $j_L(y)$. Integration of Eq. [14] and use of the boundary values for n leads to

$$l = \frac{3}{4}\frac{C}{1+D}(n^{II} - n^{I}) + A\frac{1 - \frac{1}{2}D}{(1+D)^2}\ln\frac{B + (1+D)n^{II}}{B + (1+D)n^{I}} \quad [24]$$

or

$$l = \frac{1}{1+D}\left\{\frac{3}{4}C(n^{II} - n^{I}) + Aq\frac{(\phi^{II} - \phi^{I})}{kT}\right\} \quad [25]$$

This converts easily to

$$j_e = \frac{\sigma_i^{\circ}\Delta\phi}{l\left(\frac{v_i}{v_e} + y\right)}\left\{1 + \frac{3}{2}\frac{\sigma_e^{II} - \sigma_e^{I}}{\sigma_i^{\circ}}\frac{v_i}{v_e}\frac{kT}{q\Delta\phi}\right\} \quad [26]$$

Equations [18] and [26] permit calculation of $\Delta\phi$, and j_e as a function of the parameters σ_i°/l, v_i/v_e, $\sigma_e^{II}/\sigma_i^{\circ}$, $\sigma_e^{I}/\sigma_i^{\circ}$, T, and the dummy variable y. Note that $j_e \leq 0$. The numerical relation $j_L(y)$ is now described by Eq. [26] and $j_L = (1 - y)j_e$.

We would like to show now that the shape of the characteristic $E_L(j_L)$ is determined only by four parameters. We normalize the load voltage E_L by division by E_{th} and get from Eq. [18] and [20]

$$\frac{E_L}{E_{th}} = \frac{f\left(\frac{v_i}{v_e}, \frac{\sigma_e^{II}}{\sigma_i^{\circ}}, \frac{\sigma_e^{I}}{\sigma_i^{\circ}}, y\right)}{\ln(p_{O_2}^{II}/p_{O_2}^{I})} \quad [27]$$

For given values of the three material parameters and $p_{O_2}^{II}/p_{O_2}^{I}$, E_L equals zero at a certain y_o; this y_o determines the short-circuit current, $j_{s.c.}$. It follows then from Eq. [18], [26], and the relation $j_L = (1 - y)j_e$ that

$$\frac{j_L}{j_{s.c.}} = \frac{g\left(\frac{v_i}{v_e}, \frac{\sigma_e^{II}}{\sigma_i^{\circ}}, \frac{\sigma_e^{I}}{\sigma_i^{\circ}}, y\right)}{g\left(\frac{v_i}{v_e}, \frac{\sigma_e^{II}}{\sigma_i^{\circ}}, \frac{\sigma_e^{I}}{\sigma_i^{\circ}}, y_o\right)} \quad [28]$$

The relation between the normalized values E_L/E_{th} and $j_L/j_{s.c.}$ depends, therefore, only on the three material parameters and on $p_{O_2}^{II}/p_{O_2}^{I}$ but not explicitly on the temperature. The same is true for the relation between E_L/E_{th} and $j_e/j_{s.c.}$.

With these relations we are ready now to calculate the energy conversion efficiency η, which is of central interest in this work. The value of η, which is defined as (power delivered to the load)/(rate of conversion of chemical energy) is given by

$$\eta = \frac{E_L j_L}{E_{th} j_i} = \frac{E_L j_L}{E_{th}(j_L - j_e)} = \frac{y-1}{y}\frac{E_L}{E_{th}} \quad [29]$$

Equation [29] implies that η_{max}, the maximum fuel conversion efficiency for a given material, also depends only on the three material parameters and on the ratio $p_{O_2}^{II}/p_{O_2}^{I}$.

Up to this point the calculation is exact, except for the use of the neutrality condition which is discussed in Appendix A.

The open-circuit voltage calculated from Eq. [18] and [19] with $y = 1$ agrees with that calculated by Wagner (4) from more general thermodynamic considerations. This is shown in Appendix B.

Application to Doped Ceria

We now calculate the characteristic and efficiency for doped ceria used under the conditions described earlier. We note that for this system the ratio $\sigma_e^{II}/\sigma_i^\circ$ is about 10^{-4} and $\sigma_e^I/\sigma_i^\circ$ is of order 1. The ionic conductivity of $(CeO_2)_{0.90}(La_2O_3)_{0.10}$ at 800°C is $\sigma_i = 10^{-1}\ \Omega^{-1}\ cm^{-1}$ (1, 5), which corresponds to $v_i = 1.2 \times 10^{-4}$ cm²/V-sec, and v_e at 800°C is reported to be about 3×10^{-3} cm²/V-sec (6). For doped ceria the mobility ratio is therefore about 0.04.

We can neglect therefore all the terms containing σ_e^{II} in Eq. [18], [20], and [26] and get with the help of the relation $j_L = (1 - y)j_e$

$$\Delta\phi = \frac{kT}{q}\,\frac{\dfrac{v_i}{2v_e} - y}{\dfrac{v_i}{v_e} + y}\ln\left[1 + \left(\frac{v_i}{v_e} + y\right)\frac{\sigma_e^I}{\sigma_i^\circ}\right] \quad [30]$$

$$E_L = E_{th} - \frac{kT}{2q}\ln\left(1 + \frac{\sigma_e^I v_i}{\sigma_i^\circ v_e}\right) + \Delta\phi \quad [31]$$

and

$$j_L = \frac{\sigma_i^\circ\Delta\phi(1-y)}{l\left(\dfrac{v_i}{v_e} + y\right)}\left(1 - \frac{3}{2}\frac{\sigma_e^I}{\sigma_i^\circ}\frac{v_i}{v_e}\frac{kT}{q\Delta\phi}\right) \quad [32]$$

The shape of the characteristic $E_L(j_L)$ is now determined by the two material parameters v_i/v_e and $\sigma_e^I/\sigma_i^\circ$ and by the ratio $p_{O_2}^{II}/p_{O_2}^I$ and is expressed by the above equations in terms of the parameter y. The conversion efficiency η is calculated from Eq. [29] and is maximized by varying y.

In Fig. 2 we have plotted the characteristics for various mobility ratios and in Fig. 3 the maximum conversion efficiency η_{max} *vs.* $\sigma_e^I/\sigma_i^\circ$, again for various mobility ratios. We see from Fig. 2 that at $\sigma_e^I/\sigma_i^\circ = 5$ the characteristic calculated for $v_i/v_e << 1$ describes the behavior of doped ceria still quite well. Figure 3 shows that even at $\sigma_e^I/\sigma_i^\circ = 15$, corresponding to $\eta_{max} = 0.5$, the characteristic for $v_i/v_e << 1$ can be safely used to calculate η_{max}. This value of η_{max} is about the limit where the fuel cell stops being of interest. We shall therefore base the continuation of our discussion and the comparison with the equivalent circuit on $v_i/v_e << 1$, this simplifies the equations considerably.

Comparison with Equivalent Circuit

In this section we compare the characteristic calculated with $v_i/v_e << 1$ with that calculated by Takahashi (1), who used an equivalent circuit to describe the fuel cell. The use of such a circuit actually goes back to Jost, see, for instance, Kroeger (2). To make the comparison meaningful we assume that we have measured σ_i° by measuring the conductivity of the material in air, and we have also measured the total conductivity at $p_{O_2}^I$. We calculate the characteristic and η_{max} by both methods.

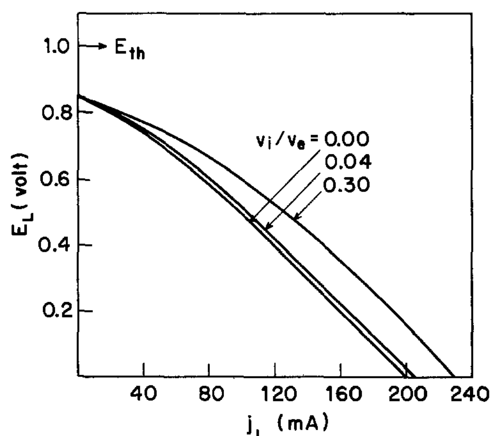

Fig. 2. Transport theory characteristic of a fuel cell made of doped ceria for various ratios of ionic to electronic mobility. The calculation is based on the following parameters: $T = 735$°C, $p_{O_2}^{II}/p_{O_2}^I = 10^{20}$, $\sigma_i^\circ/l = 0.2\ \Omega^{-1}\ cm^{-2}$, and $\sigma_e^I/\sigma_i^\circ = 5$. $E_{th} = 1$V under these conditions.

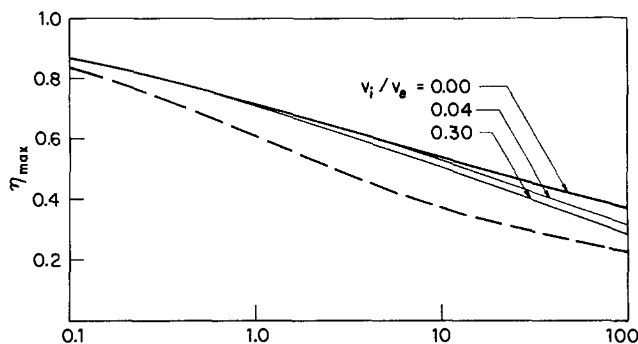

Fig. 3. Maximum fuel conversion efficiency vs. $\sigma_e^I/\sigma_i^\circ$ for a fuel cell based on doped ceria. The thick full line is calculated from transport theory with $v_i << v_e$, the two thin lines correspond to two finite values of v_i/v_e. The dashed line follows from the equivalent circuit approach. $p_{O_2}^{II}/p_{O_2}^I$ is taken as 10^{20}.

In order to facilitate the comparison, we now assume that $v_i\sigma_e^I/v_e\sigma_i^\circ = n^I/[Ca_{Ce}''] << 1$. This permits us immediately to neglect the second term in Eq. [31]. We have seen in Fig. 3 that the practical limit of use of fuel cells made from doped ceria is $\sigma_e^I/\sigma_i^\circ \cong 10$ so that even with $v_i/v_e = 0.04$ this assumption is almost always very good. It implies, together with Eq. [6] and the fact that $n(x) < n^I$, that $[V_O^{\cdot\cdot}] \simeq [Ca_{Ce}'']$ throughout the electrolyte, and therefore that $\sigma_i(x) = \sigma_i^\circ$. From the total conductivity at the anode we can then calculate the ratio $\sigma_e^I/\sigma_i^\circ$, which we need in Eq. [30] to [32].

The open-circuit voltage expected from the fuel cell may now be calculated under the simplifying conditions assumed above. This then is used to set up the equivalent circuit.

Under normal operating conditions $y \geq 1$ and we can, therefore, neglect the term v_i/v_e in Eq. [30] and [32]. Furthermore, it is easy to show that the second term in the parenthesis of Eq. [32] is of order v_i/v_e and can, therefore, also be neglected. Equations [30] to [32] now simplify further to

$$\Delta\phi = -\frac{kT}{q}\ln\left[1 + y\frac{\sigma_e^I}{\sigma_i^\circ}\right] \quad [33]$$

$$E_L = E_{th} + \Delta\phi \quad [34]$$

$$j_L = \frac{\sigma_i^\circ\Delta\phi(1-y)}{ly} \quad [35]$$

and the open-circuit voltage is

$$E_{o.c.} = E_{th} - \frac{kT}{q}\ln\left[1 + \frac{\sigma_e^I}{\sigma_i^\circ}\right] \quad [36]$$

We introduce now the transport fraction defined by $t_i \equiv \sigma_i/(\sigma_i + \sigma_e)$ and get

$$E_{o.c.} = \frac{kT}{4q}\left(\ln\frac{p_{O_2}^{II}}{p_{O_2}^I} + 4\ln t_i^I\right) \quad [37]$$

With the further definition $\overline{t_i} \equiv E_{o.c.}/E_{th}$ this leads to the following relation between the average transport fraction $\overline{t_i}$ and the transport fraction at the anode, t_i^I

$$\overline{t_i} = 1 + \frac{4\ln t_i^I}{\ln(p_{O_2}^{II}/p_{O_2}^I)} \quad [38]$$

The equivalent circuit used by Takahashi (1) is of the form shown in Fig. 1b. In Takahashi's notation E_{th} is, as before, the open-circuit voltage of the ideal fuel cell, $\overline{\sigma_i}/l$ is the ionic conductance per unit area of the electrolyte, and $\overline{\sigma_e}/l$ is the electronic one.

The characteristic of this circuit is

$$j_L = \frac{\overline{\sigma_i}}{l}(E_{th} - E_L) - \frac{\overline{\sigma_e}}{l}E_L \quad [39]$$

and its open-circuit voltage is, therefore, $E_{o.c.} = E_{th}\overline{\sigma_i}/(\overline{\sigma_i} + \overline{\sigma_e})$. Since the equivalent circuit should give the same $E_{o.c.}$ as the exact theory we have to take

$$\frac{\overline{\sigma_i}}{\overline{\sigma_i} + \overline{\sigma_e}} = \overline{t_i} \quad [40]$$

where $\overline{t_i}$ is given by Eq. [38].

The characteristic $j_L(E_L)$ (Eq. [39]) is evidently a straight line, and so is the relation $j_e(E_L)$

$$j_e = -\frac{\overline{\sigma_e}}{l}E_L \quad [41]$$

In Fig. 4 we plot these lines and compare them with the corresponding lines for the transport model calculated with the same values of open-circuit voltage $E_{o.c.}$ and short-circuit current $j_{s.c.}$. Since the calculations of η which follow rely only on the ratio j_L/j_e it is not really essential to choose the same $j_{s.c.}$ for both models, but it facilitates the graphical comparison.

We see from Fig. 4 that at any particular value of E_L, j_L comes out slightly larger in the transport model, and that j_e, which determines the internal loss current of the fuel cell, is considerably smaller. Since the fuel conversion efficiency is determined by the ratio j_L/j_e (see Eq. [29]), the transport model predicts a larger value for this efficiency than the equivalent circuit model. The values of η_{max} are 0.59 and 0.44 for the parameters of Fig. 4.

To make the comparison quantitative we use in the case of the equivalent circuit an equation for η_{max} derived by Takahashi (1)

$$\eta_{max} = \frac{1 - (1 - \overline{t_i})^{1/2}}{1 + (1 - \overline{t_i})^{1/2}} \quad [42]$$

The dashed line in Fig. 3 describes this equation, $\overline{t_i}$ is connected with the abscissa scale, $\sigma_e^I/\sigma_i^\circ$, through Eq. [39] and the relation $t_i^I = \sigma_i^\circ/(\sigma_i^\circ + \sigma_e^I)$.

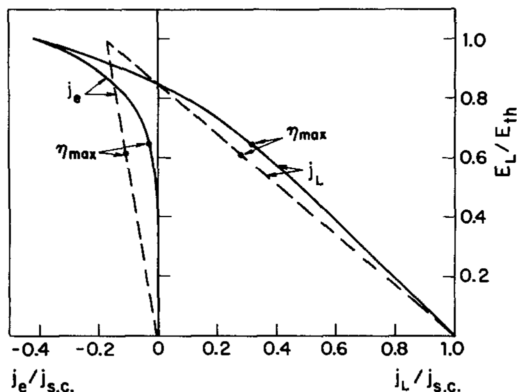

Fig. 4. Load current j_L and electronic loss current j_e against output voltage E_L of a fuel cell made of doped ceria. The scales are normalized by division with $j_{s.c.}$ and with E_{th}, respectively. The full lines are calculated from transport theory with $v_i << v_e$; the dashed lines follow from an equivalent circuit approach. The current values at η_{max} are shown for both models. η_{max} is 0.59 for the transport model vs. 0.44 for the equivalent circuit. The conductivity ratio at the anode is taken as $\sigma_e^I/\sigma_i^\circ = 5$ ($t_i^I = 0.166$) and the ratio $p_{O_2}^{II}/p_{O_2}^I$ is 10^{20}. Negative values of j_L imply an outside current source.

It is seen from Fig. 3 and 4 that the equivalent circuit is not a good approximation to the fuel cell under load. The maximum efficiency predicted by the transport calculation is, for typical operating conditions of a ceria fuel cell, about 50% higher than that predicted by the equivalent circuit. The main reason for the difference is that in the transport model the electronic current decreases very much faster with decreasing E_L than predicted by the equivalent circuit.

Since for doped ceria used at 800°C in H_2O/H_2 = 10/1, $\sigma_e^I/\sigma_i^\circ$ is approximately 9, and Fig. 3 gives then η_{max} = 55%, we expect that this material will now be considered more seriously than before as an electrolyte in fuel cells.

Acknowledgment

Thanks are due to N. Klein and I. Riess for their helpful remarks concerning this paper. This work was supported by a grant from the National Council of Research and Development, Israel, and the KFA, Jülich, Germany.

Manuscript submitted Dec. 7, 1977; revised manuscript received March 17, 1978.

Any discussion of this paper will appear in a Discussion Section to be published in the June 1979 JOURNAL. All discussions for the June 1979 Discussion Section should be submitted by Feb. 1, 1979.

APPENDIX A

In the process of solution of our equations we assumed the validity of the local neutrality Eq. [3] throughout the electrolyte. This assumption is not quite exact, since the solution which it generates implies a small space charge. We really should have used Poisson's equation in the form

$$2[V_O^{\cdot\cdot}] - 2[Ca_{Ce}''] - n = \delta(x) = -\frac{\epsilon_0}{q}\frac{d^2\phi}{dx^2} \quad [A\text{-}1]$$

this however leads to the extremely complicated differential equations.

We now show that the approximation of local neutrality is justified, *i.e.*, that the space charge δ is negligible.

In Eq. [11] we substituted $2d[V_O^{\cdot\cdot}]/dx = dn/dx$, *i.e.*, we assumed that $d\delta/dx << dn/dx$. In Eq. [13] we substituted $2[V_O^{\cdot\cdot}] = 2[Ca_{Ce}''] + n$, this is justified if $\delta << n$. δ is given by $\delta = -(\epsilon_0/q)d^2\phi/dx^2$ and we calculate an upper limit for δ as follows

$$\frac{d\phi}{dx} = \frac{d\phi}{dn}\frac{dn}{dx} = \frac{kT}{q}\frac{1 - \frac{1}{2}D}{A + \frac{3}{4}Cn} \quad [A\text{-}2]$$

(see Eq. [15] + [17])

$$\frac{d^2\phi}{dx^2} = \left(\frac{d}{dn}\frac{d\phi}{dx}\right)\frac{dn}{dx}$$

$$= -\frac{3}{4}\frac{kT(1 - \frac{1}{2}D)}{q(A + \frac{3}{4}Cn)^2}\frac{[B + (1 + D)n]}{(A + \frac{3}{4}Cn)} \quad [A\text{-}3]$$

We use $D << 1$ and get

$$\frac{d^2\phi}{dx^2} = \frac{3}{16}\frac{j_i^2}{qkTv_i^2}\frac{\left(2\frac{v_i}{v_e}\frac{1}{y}[Ca_{Ce}''] + n\right)}{([Ca_{Ce}''] + \frac{3}{4}n)^3} \quad [A\text{-}4]$$

We use now $n << [Ca_{Ce}'']$ in the denominator and substitute $[Ca_{Ce}'']$ for the parenthesis in the nominator, which is a very rough upper limit. This gives

$$\frac{d^2\phi}{dx^2} < \frac{3}{16}\frac{j_i^2}{qkTv_i^2[Ca_{Ce}'']} \quad [A\text{-}5]$$

Substitution of the following values typical for CeO_2 under normal operating conditions

$j_i = 0.2\ A/cm^2$, $v_i = 10^{-4}\ cm^2/V\text{-sec}$,

$kT = 0.1$ eV, $[Ca_{Ce}''] = 2 \times 10^{21}\ cm^{-3}$

gives

$\delta < 10^8$ (charge carriers)/cm^3

Since n varies from $\sim 10^{21}$ at the anode to 10^{16} at the cathode, we get $\delta < 10^{-8}n$.

A similar calculation gives $d\delta/dx < 10^{-12}\, dn/dx$. Our assumptions are, therefore, justified by the solution.

APPENDIX B

We now show that the open-circuit voltage $E_{o.c.}$ calculated from Eq. [19] with $y = 1$ agrees with $E_{o.c.}$ calculated from the general equation derived by Wagner (4) without the use of the neutrality condition

$$E_{o.c.} = \frac{kT}{4q} \int_{p_{O_2}{}^{I}}^{p_{O_2}{}^{II}} t_i(p_{O_2})\, d \ln p_{O_2} \quad \text{[B-1]}$$

We substitute in Eq. [B-1]

$$t_i \equiv \frac{\sigma_i}{\sigma_i + \sigma_e} = \frac{(2[\text{Ca}_{\text{Ce}}''] + n)v_i}{(2[\text{Ca}_{\text{Ce}}''] + n)v_i + nv_e} \quad \text{[B-2]}$$

and

$$\ln p_{O_2} = \ln K_o - 4 \ln n - 2 \ln \left([\text{Ca}_{\text{Ce}}''] + \frac{n}{2} \right) \quad \text{[B-3]}$$

(see Eq. [22]). The result of the integration is

$$E_{o.c.} = \frac{kT}{q} \ln \frac{n^{I}}{n^{II}} + \frac{kT}{q} \frac{\dfrac{v_i}{2v_e} - 1}{\dfrac{v_i}{2v_e} + 1} \ln \frac{\sigma_i{}^{I} + \sigma_e{}^{I}}{\sigma_i{}^{II} + \sigma_e{}^{II}} \quad \text{[B-4]}$$

This agrees with Eq. [19], since $\sigma_i = \sigma_i{}^{o} + \sigma_e(v_i/v_e)$. In Eq. [B-2] and [B-3] we have used the neutrality condition $2[V_O{}^{\cdot\cdot}] = 2[\text{Ca}_{\text{Ce}}''] + n$, so the agreement is perhaps not surprising.

APPENDIX C

We collect here some additional mathematical relations which illustrate the main text.

(*i*) In the case of the section on Comparison with Equivalent Circuit we get from Eq. [34] and [35] the following rather intuitive expression for E_L

$$E_L = E_{th} - j_i \frac{l}{\sigma_i{}^{o}} \quad \text{[C-1]}$$

which agrees with the equivalent circuit model if we set $\sigma_i{}^{o} = \overline{\sigma_i}$.

(*ii*) From Eq. [33] to [35] one can derive an explicit expression for j_L (E_L)

$$j_L = \frac{\sigma_i{}^{o}}{l}(E_{th} - E_L) - \frac{\sigma_e{}^{I}(E_{th} - E_L)}{l\left[\exp \dfrac{q(E_{th} - E_L)}{kT} - 1\right]} \quad \text{[C-2]}$$

This should be compared with Eq. [39] for the equivalent circuit. For $\sigma_e = 0$ both models give, of course, the same straight line.

(*iii*) For the equivalent circuit we get from Eq. [39] $j_{s.c.} = E_{th}\overline{\sigma_i}/l$. For the transport model we have to a very good approximation $j_{s.c.} = E_{th}\sigma_i{}^{o}/l$ (see Eq. [C-2]. In order to get for both models not only the same $E_{o.c.}$ but also the same $j_{s.c.}$, we set $\overline{\sigma_i}$ equal to $\sigma_i{}^{o}$. It is easy to show that once we have done this both approaches give for $j_L = 0$ $j_e = (\overline{t_i} - 1)E_{th}\overline{\sigma_i}/l$. This intersection point of the two models can be seen in Fig. 4. Furthermore, both models give $j_e = j_L$ when $E_L = E_{th}$. This last condition happens, of course, only when a negative load current is impressed on the cell from an outside current source.

(*iv*) A useful way to illustrate the calculation is to plot η_{max} for the two models *vs.* $p_{O_2}{}^{I}$, the oxygen pressure at the anode. As material parameter we take here $p_{O_2}{}^{*}$, the oxygen pressure where $\sigma_e/\sigma_i = 1$. This oxygen pressure is often called the limit of the ionic domain.

In Fig. 5 we have plotted η_{max} for representative values of $p_{O_2}{}^{*}$ and compared again with the equivalent circuit calculation, where $\overline{t_i}$ was calculated from the following equation, first derived by Schmalzried (7)

$$\overline{t_i} = \frac{\ln[(p_{O_2}{}^{*})^{1/4} + (p_{O_2}{}^{II})^{1/4}] - \ln[(p_{O_2}{}^{*})^{1/4} + (p_{O_2}{}^{I})^{1/4}]}{1/4[\ln p_{O_2}{}^{II} - \ln p_{O_2}{}^{I}]} \quad \text{[C-3]}$$

We see from the figure that the oxygen pressure at

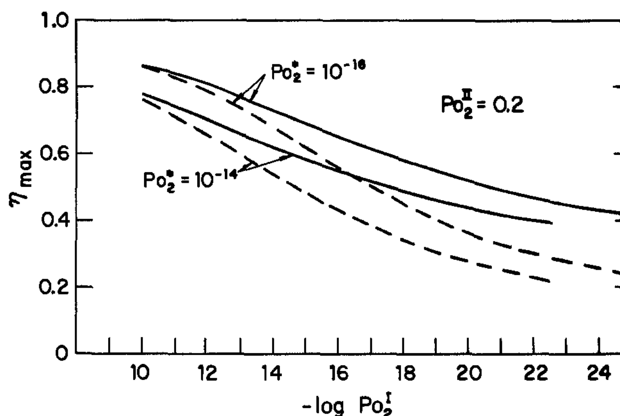

Fig. 5. Maximum fuel conversion efficiency vs. oxygen pressure at the anode for a fuel cell based on doped ceria. The oxygen pressure at the cathode is taken as 0.2 atm and $p_{O_2}{}^{*}$ is the oxygen pressure at which the ionic transport number, t_i, equals 0.5. The full lines are calculated from transport theory with $v_i << v_e$, the dashed lines are calculated from an equivalent circuit approach.

which $\eta_{max} = 0.5$ is for the transport model four orders of magnitude lower than for the equivalent circuit.

LIST OF SYMBOLS

A, B, C, D	constants defined after Eq. [14]
$[\text{Ca}_{\text{Ce}}'']$	concentration of Ca^{2+} ions on Ce^{4+} sites
D_e	diffusion coefficient of electrons
D_i	diffusion coefficient of ions
E_L	voltage of fuel cell under load
$E_{o.c.}$	open-circuit voltage of fuel cell
E_{th}	theoretical open-circuit voltage of fuel cell
j_e	electronic current density
j_i	ionic current density
j_L	load current per unit area of fuel cell
$j_{s.c.}$	short-circuit current per unit area of fuel cell
l	thickness of electrolyte
$K_o(T)$	equilibrium constant in Eq. [2]
n	concentration of electrons
p_{O_2}	partial pressure of oxygen
$p_{O_2}{}^{*}$	oxygen pressure at which $t_i = 0.5$
q	absolute value of electronic charge
T	temperature
t_i	transport fraction of ions
$\overline{t_i}$	average of t_i, defined after Eq. [37]
$[V_O{}^{\cdot\cdot}]$	concentration of vacancies on oxygen sites
v_e	mobility of electrons
v_i	mobility of vacancies
x	dimension through electrolyte
y	ratio $(j_e - j_L)/j_e$
σ_e	electronic conductivity
σ_i	ionic conductivity
$\sigma_i{}^{o}$	ionic conductivity for zero electron concentration
$\overline{\sigma_i}$	average ionic conductivity in the equivalent circuit model
$\overline{\sigma_e}$	average electronic conductivity in the equivalent circuit model
η	energy conversion efficiency
$\tilde{\mu}_e$	electrochemical potential for electrons
μ_e	chemical potential for electrons
ϕ	electrical potential
I, II	(superscripts) refer to the immediate neighborhood of anode and cathode, respectively

REFERENCES

1. T. Takahashi, in "Physics of Electrolytes," Vol. 2, J. Hladik, Editor, pp. 989-1047, Academic Press, New York (1972).
2. F. A. Kroeger, "The Chemistry of Imperfect Crystals," p. 852, North Holland (1964).
3. H. L. Tuller and A. S. Nowick, *This Journal*, **122**, 255 (1975).
4. C. Wagner, *Z. Phys. Chem. Abt. B*, **21**, 25 (1933).
5. D. S. Tannhauser, To be published.
6. R. N. Blumenthal and R. K. Sharma, *J. Solid State Chem.*, **13**, 360 (1975).
7. H. Schmalzried, *Z. Elektrochem.*, **66**, 572 (1962).

SOLID-STATE SCIENCE
—AND TECHNOLOGY

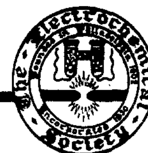

AUGUST
1978

The Effect of NaCl(g) on the Oxidation of NiAl

J. G. Smeggil* and N. S. Bornstein

United Technologies Research Center, East Hartford, Connecticut 06108

ABSTRACT

NaCl is ingested into operating gas turbines. The effect of this salt on the high temperature surface stability properties of turbine hardware is not well understood. The involvement of NaCl(g)[1] in the high temperature oxidation of NiAl, a principal component in many high temperature environmental coatings, is herein examined. The results of this work indicate that NaCl(g) present in an oxidizing atmosphere affects the formation of Al_2O_3 whiskers on a dense Al_2O_3 layer. Such whisker growth, attributed to vapor transport processes through an otherwise dense Al_2O_3 scale. increases the aluminum depletion of the NiAl substrate.

Materials for hot-section gas turbine applications must be strong enough to physically support the mechanical loads impressed upon them without failing, and they must also exhibit sufficient surface stability to the hot combustion gases. In current high temperature superalloys, it is frequently difficult to simultaneously obtain sufficient strength and surface stability characteristics. The present solution to this problem, therefore, involves the use of high strength materials which are subsequently coated to impart sufficient high temperature oxidation and corrosion resistance.

Currently used coatings involve either the simple aluminides or one of the many MCrAl(Y) chemistries or a combination of the two. A critical component in these coatings is the cubic β-NiAl or -CoAl formed in the nickel- or cobalt-based systems, respectively (1).

The presence of the β phase in such coating compositions is principally responsible for the formation of an adherent Al_2O_3 scale, thus accounting for the ability of such coatings to afford suitable surface protection (1).

In service, these aluminide coatings are believed to degrade by the depletion of aluminum from the coating layer as a result of both high temperature exposure and thermal cycling (1-3). This effect is manifested in two ways. Initially, aluminum in the coating forms a protective alumina scale, however, the spallation of this film on thermal cycling and its replenishment eventually depletes the coating composition of aluminum at the gas-oxide interface. In the second place, aluminum diffuses from the coating into the substrate. Therefore the coating loses protective efficiency from both gas-coating and substrate-coating interactions.

Both the air and fuel which enter the gas turbine can contain minute quantities of impurities such as sea salt. Sodium chloride is the principal constituent of sea salt crystals which can be carried far inland by prevailing winds. Depending on wind conditions, the concentration of sea salt in the air can vary from less than one tenth to more than 5 ppm (4, 5).

Bessen and Fryxell have shown that the compressors of gas turbine engines are effective physical separators of the chloride and sulfate components of sea salt (6). They reported constant levels of Na_2SO_4, ~0.1 mg/cm², present on all stages of the compressors of an LM-2500 engine which had been operated for over 7000 hr. NaCl, on the other hand, was found to vary from 0.1 mg/cm² at the first stage of compressor to ~0.02 mg/cm² at the seventh stage. After this stage and through the sixteenth stage, no meaningful chloride levels were detected, *i.e.*, < 0.01 mg/cm². Furthermore, their surveys of the high pressure turbine components from several engines failed to reveal the presence of any condensed chlorides.

The deposited salts present on the compressor components can periodically shed. The composition of the salt entering the burner will be dependent upon the compressor location from which it was shed. The condensed salt particles shed from compressor sections in passing through the burner can (*i*) react within the burner; (*ii*) vaporize; or (*iii*) impact the turbine components as particulate matter. The high vapor pressure of NaCl, *e.g.*, 0.35 Torr at 800°C, would be expected to lead to its rapid removal (7). This would account for the virtual absence of chlorides in deposits found on turbine surfaces (6).

Although some NaCl ingested into the turbine burner section may be converted to Na_2SO_4, equilibrium thermodynamic calculations indicate that for gas turbines operating under conditions favoring Na_2SO_4-induced hot corrosion attack, the engine hot section environment is relatively rich in the contaminant gases NaCl, HCl, and NaOH (8).

Intensive work by many investigators has shown that condensed NaCl or NaCl-Na_2SO_4 mixtures can be very corrosive (9-25). Additionally, several investigations have shown that gaseous NaCl is not innocuous. Hancock, using a vibrational technique, has reported that NaCl(g) adversely affects isothermal oxide scale adherence with respect to elements, simple alloys, and superalloys (9, 10, 11b). Stearns *et al.* (26) and Fryburg *et al.* (27) have reported enhanced rates of chromium transport loss for certain materials oxidized in an atmosphere containing NaCl(g), however, none of the studies involving gaseous NaCl report how the observed results manifest themselves microstructurally.

The work reported here is primarily a microstructural study of the effects of NaCl vapor on the oxidation behavior of NiAl, an alumina former. The levels of NaCl vapor examined range from 100 to less than 1 ppm. The latter level approximates the concentration of NaCl vapor anticipated to be found in the combustor and high pressure turbine sections of marinized or industrial gas turbines.

* Electrochemical Society Active Member.

Key words: alloys, coatings, whiskers, corrosion.

[1] In this report the bracketed c implies the phase is present in the condensed state, solid, or liquid. The bracketed g similarly refers to the gaseous state.

Experimental Procedures

The NiAl alloy was prepared by rf melting the desired nominal composition in an argon atmosphere and pouring the melt into an alumina mold. The ingot was then heat-treated in a hydrogen atmosphere at 1350°C for two days. Subsequent chemical analysis of a section of the ingot was found to contain 31.06 ± 0.09 weight percent Al. The annealed ingot was found to be single phase by metallographic examination.

Sample specimens cut from the ingot measured approximately 2.5 × 1.0 × 2.0 cm. These samples were then ground to 600 grit SiC. A platinum wire was welded on one end for sample support. The samples, prior to insertion into the experimental apparatus, were washed and degreased; the final rinse was given with absolute ethanol. The air used in these experiments was taken from the laboratory service strip. The water content of this air was brought to a constant level by passage over anhydrous calcium sulfate (Drierite). The air flow rate for all the experiments was 300 sccm as determined from a calibrated flow meter, and the flow velocity was 0.18 cm/sec.

All oxidation experiments were conducted using an Ainsworth Type RV-AU-1 balance which is readable to 0.01 mg and reproducible to ±0.03 mg. The specimens were introduced into a quartz tube (2.5 in. OD) which was within a heated furnace. The temperature inside the three-zone Marshall furnace was maintained to within ± 5°C by a Leeds and Northrup proportional controller series 60.

The NaCl vapors were generated from condensed NaCl in a platinum crucible fixtured to a movable pedestal in the oxidation tube. The temperature of the crucible was measured by a thermocouple fixtured into a quartz tube and lying immediately adjacent to the NaCl-containing platinum crucible. The NaCl used here was an ultrapure grade obtained from Alfa-Ventron. The data of Ewing and Stern (7) were used to calculate NaCl vapor pressures and gas-phase compositions. Thus the temperatures of the NaCl-containing Pt crucible and the "anticipated" nominal gas phase compositions used here were 802°C, 1000 ppm; 710°C, 100 ppm; 630°C, 10 ppm; and 566°C, 1 ppm. However, recognizing that equilibrium may not have been established between NaCl in the condensed and vapor states, the actual NaCl partial pressure was determined from the difference in weights of platinum crucible before and after each experiment. From these calculations, it was found that the empirical vapor pressures were lower than those expected by a factor of about 10 at the three higher temperatures used here, *i.e.*, 802°, 630°, and 710°C. However, good agreement was observed at the lowest temperature, 566°C. Accordingly, the empirical (as opposed to theoretical) gas-phase compositions for atmospheres involving NaCl vapor are herein cited. The weight change data for samples exposed to NaCl vapors at concentrations above 10 ppm were corrected for condensation of NaCl onto the Pt suspension wire. No correction was made for samples oxidized in atmospheres with NaCl vapors at concentrations of less than 10 ppm.

Subsequent to oxidation, selected samples were examined by optical metallography, scanning electron microscopy (SEM), and transmission electron microscopy techniques. Examination of the oxidized coupons by x-ray diffraction techniques indicated only the presence of the β-NiAl structure because the Al_2O_3 scale was so thin.

Experimental Results

Oxidation (NaCl-free air).—Thermogravimetric studies.—NiAl is a classical alumina former, and the rate of weight gain for NiAl oxidized in pure air at 900° and 1050°C is shown in Fig. 1 and 2, respectively. These data are in agreement with data reported by Pettit (28).

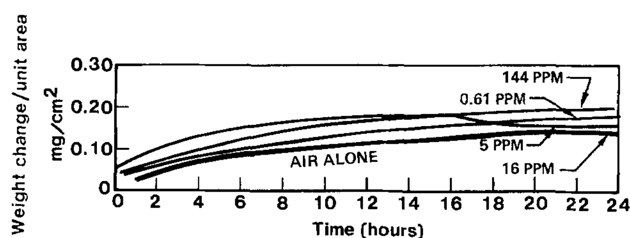

Fig. 1. Thermogravimetric data for NiAl oxidized in air with and without NaCl vapors present at 900°C.

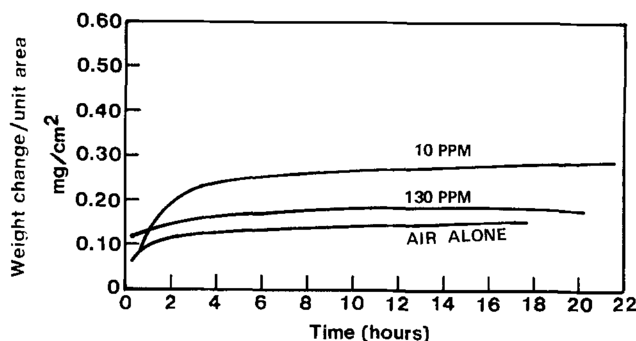

Fig. 2. Thermogravimetric data for NiAl oxidized in air with and without NaCl vapors present at 1050°C.

SEM studies.—During 1050°C oxidation, an adherent dense Al_2O_3 layer is formed, Fig. 3. Occasionally an area of the NiAl substrate can be seen where the Al_2O_3 oxide layer locally spalled on cooling to room temperature, Fig. 4. Such rupturing did not occur isothermally since the substrate would have attempted to reform a protective oxide scale and no indication of any such healing oxide scale was observed. The undulations of the NiAl substrate seen where the scale has locally spalled derive from the final polish (600 grit SiC) used to prepare the specimens. The sample oxidized in air at 900°C also formed a dense Al_2O_3 layer similar to that exhibited by the sample oxidized at 1050°C.

Oxidation (NaCl-containing air).—Thermogravimetric studies.—The thermogravimetric data for samples oxidized at 900° and 1050°C in atmospheres containing approximately 1-140 ppm NaCl is also shown in Fig. 1 and 2, respectively. On the basis of the experi-

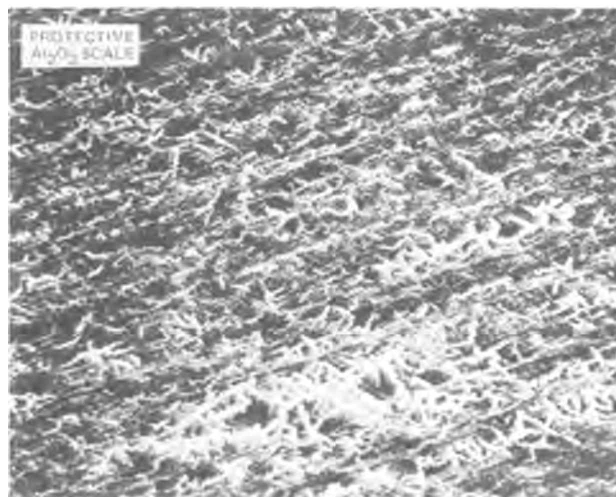

Fig. 3. NiAl oxidized in air at 1050°C for 24 hr

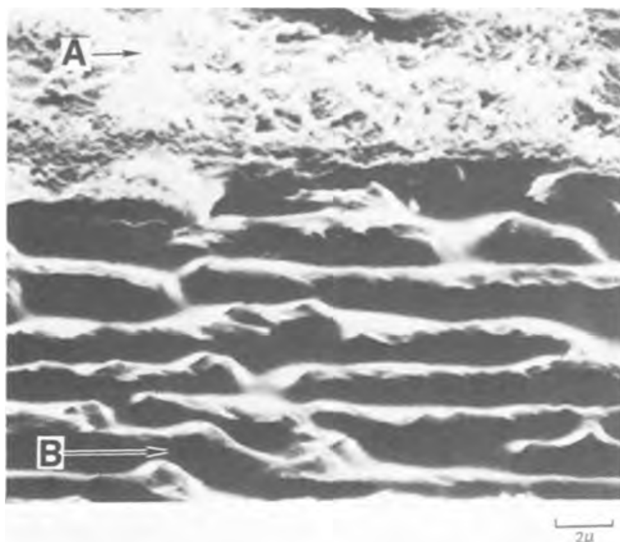

Fig. 4. NiAl oxidized in air at 1050°C for 24 hr showing a break in the compact oxide layer. A, protective Al_2O_3 scale; B, NiAl substrate.

mental techniques used here, no significance is attached to the differences in the thermogravimetric data between samples exposed to pure air and those exposed to NaCl-containing air atmospheres. However, this does not indicate that NaCl vapors are innocuous. The effect of NaCl vapor on the weight gain data is further discussed in the following section.

SEM studies.—In the presence of NaCl vapors, marked differences are seen in the morphologies of the Al_2O_3 oxide scales formed on NiAl. At 1050°C whiskers were formed on the surface of samples of NiAl exposed to 10 and 130 ppm NaCl, Fig. 5. Subsequently these whiskers were shown by transmission electron microscopy techniques to be α-Al_2O_3. No dramatic differences are seen in the whiskers grown with two different NaCl vapor concentrations (10 and 130 ppm) except that the higher NaCl level produces whiskers which are more blade-like while the lower level results in more needle-like Al_2O_3 crystals. EDAX techniques indicated only the presence of alumina in these fibers. Even though they were extensively sought for, neither sodium nor chlorine (above background levels) were detected either in the whiskers growing on the surface, in the NiAl substrate, or at the gas-oxide interface of the dense Al_2O_3 layer. The Al_2O_3 whiskers grew from the dense Al_2O_3 layer which, in turn, formed on the NiAl substrate, Fig. 6.

The surface of the sample oxidized for 24 hr at 900°C in the presence of 16 ppm NaCl is shown in Fig. 7. The dense oxide layer has extensively spalled upon cooling. The spallation did not occur at temperatures during oxidation because there is no evidence of oxide reformation in any of the spalled areas. Furthermore, this type of spallation was not observed in the samples oxidized in air alone at 900°C.

In an attempt to determine if very low levels of NaCl had a similar effect on the oxidizing substrate, an NiAl sample was oxidized at 900°C in an atmosphere containing 0.61 ppm NaCl. The general surface of the oxidized sample, Fig. 8, appears as if at temperature the oxide scale were in the continual process of locally forming, breaking, and then reforming. In some areas of the surface, Al_2O_3 whiskers, as seen earlier, *cf*. Fig. 5, abound. In other areas, the compact Al_2O_3 oxide scale has spalled and was in various stages of reforming and healing when the experiment was terminated, Fig. 9-11.

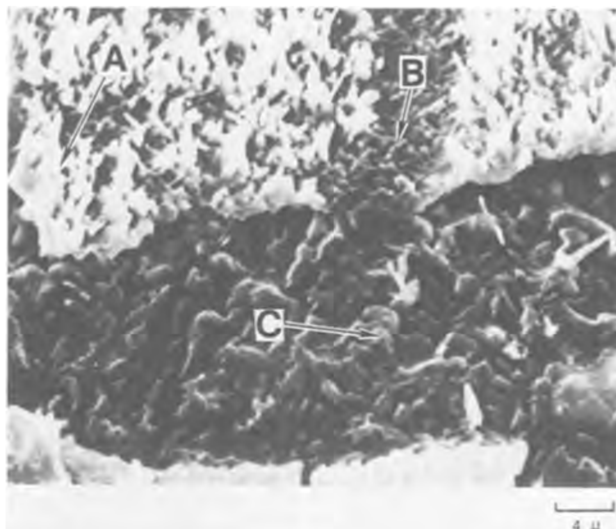

Fig. 6. α-Al_2O_3 fibers growing from dense Al_2O_3 found on NiAl oxidized at 1050°C for 24 hr. A, Al_2O_3 whiskers; B, protective Al_2O_3 scale; C, NiAl.

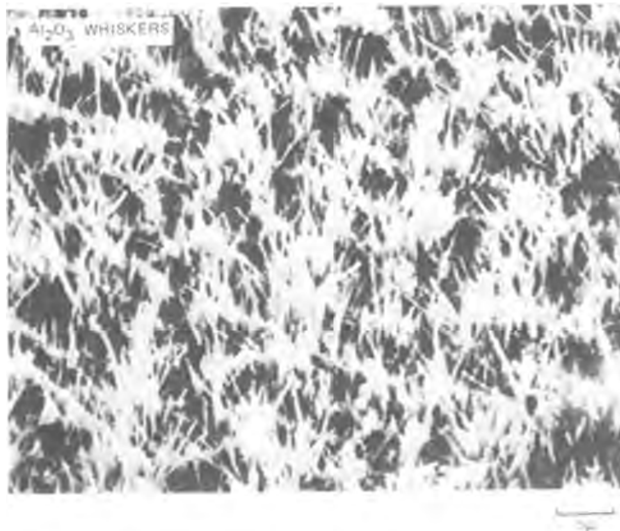

Fig. 5. Surface of NiAl oxidized at 1050°C for 24 hr with 10 ppm NaCl vapor present.

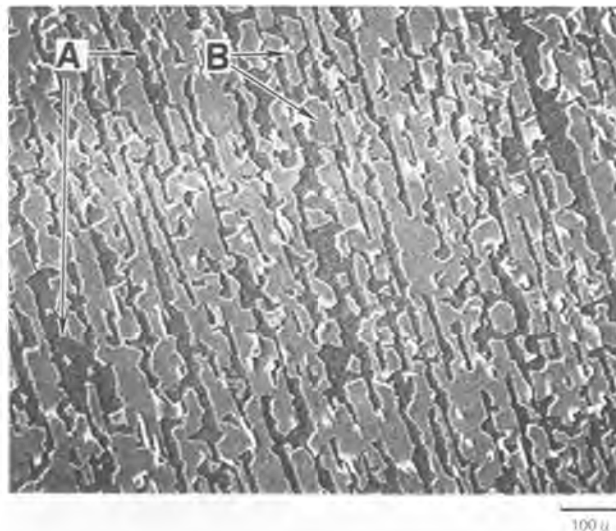

Fig. 7. NiAl oxidized for 24 hr at 900°C in air containing 16 ppm NaCl(g). A, NiAl; B, protective Al_2O_3 scale.

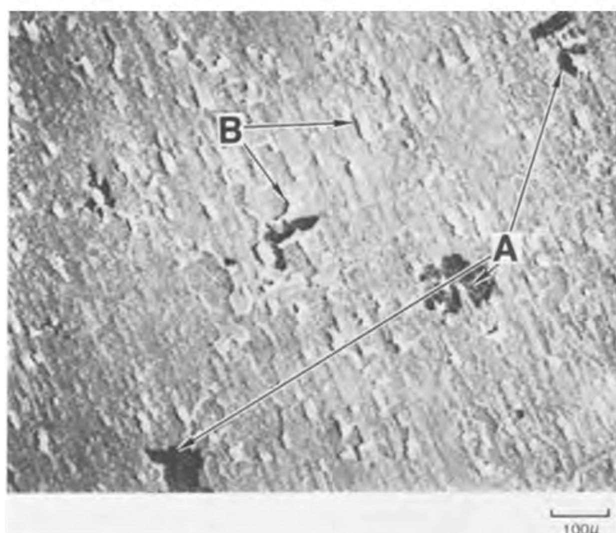

Fig. 8. NiAl oxidized at 900°C for 24 hr in air with 0.61 ppm NaCl vapor present. A, overturned dense oxide layer; B, spalling protective oxide scale.

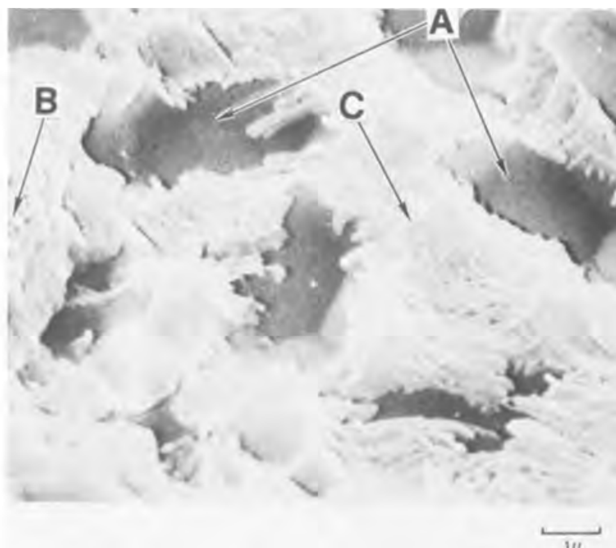

Fig. 10. NiAl oxidized at 900°C for 24 hr in air with 0.61 ppm NaCl(g) showing Al_2O_3 scale reforming over spalled oxide region. A, NiAl; B, original protective Al_2O_3 scale; C, reforming protective Al_2O_3 scale.

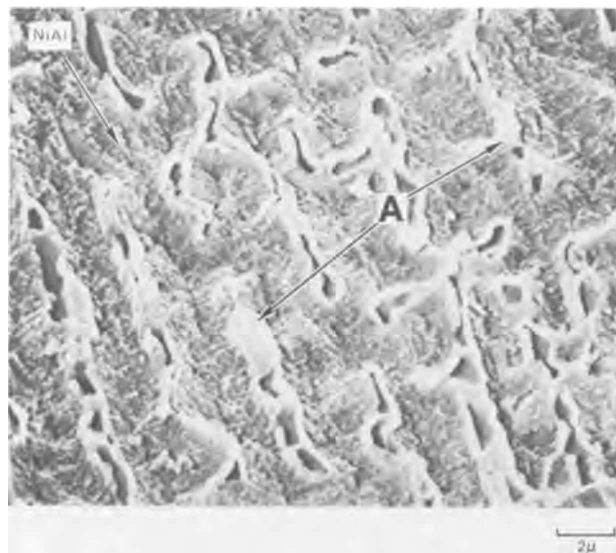

Fig. 9. NiAl oxidized at 900°C for 24 hr in air with 0.61 ppm NaCl vapor showing a region where the compact Al_2O_3 oxide spalled. A, remains of spalled dense Al_2O_3 layer.

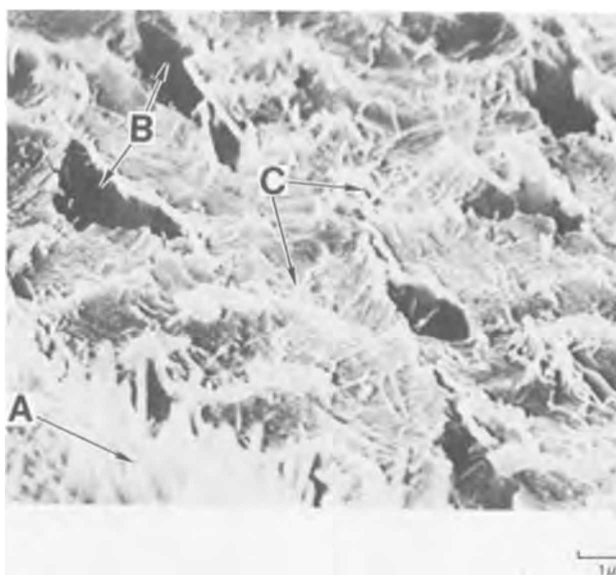

Fig. 11. NiAl oxidized at 900°C for 24 hr in air with 0.61 ppm NaCl showing Al_2O_3 reforming over spalled oxide region. A, original Al_2O_3 scale; B, pegs from spalled oxide; C, protective Al_2O_3 scale reformed over spalled oxide region.

The black appearing regions in Fig. 12, *cf.* Fig. 8, represent areas where the oxide scale has broken and fallen back to the compact oxide surface showing the side of the oxide scale which was initially attached to the substrate metal, Fig. 13. By comparison, Fig. 13 shows that Al_2O_3 whiskers are growing from the inverted base (or original surface) of a similar spalled Al_2O_3 oxide layer. The sample shown in Fig. 13, however, had been oxidized at 1050°C in air containing 128 ppm HCl, not NaCl (29). The EDAX technique applied to the sample oxidized in an HCl-air atmosphere indicated no chloride in the fibrous Al_2O_3 growths either on the original surface or on the upturned sections. Furthermore, no chloride was detected at the surface of the exposed substrate.

Additionally fine Al_2O_3 fibers have formed on the blackened surface, Fig. 14. This result suggests that the compact oxide spalled at temperature and that spallation occurred long enough before the experiment was terminated to allow for the Al_2O_3 fibrous growth to occur.

Furthermore, examination of the base of the overturned oxide in regions where Al_2O_3 growths were not present indicated the presence of both Na and Cl, Fig. 15. Regions of the overturned dense oxide surfaces examined by EDAX techniques where Al_2O_3 whiskers are not present are the only areas where Na and/or Cl have been detected in samples oxidized in NaCl-bearing atmospheres. The detection of Na and Cl on such overturned surfaces was not limited to the particular area of the spalled surface shown here. Such an analysis was typical of numerous separate overturned oxide surfaces. However this appearance of Na and Cl only on this kind of surface is difficult to understand. Questions arise such as: Why it was observed there and not on the original surface of the oxidizing sample; and How it could have survived any period of time at that site without vaporizing since at 900°C the partial pressure of NaCl is approximately 2.5 mm (7)? Thus it seems that the Na and Cl found here may be incorporated at reduced activities (but not necessarily as NaCl) into the dense Al_2O_3 layer itself. Similar effects involving isothermal dense alumina scale spal-

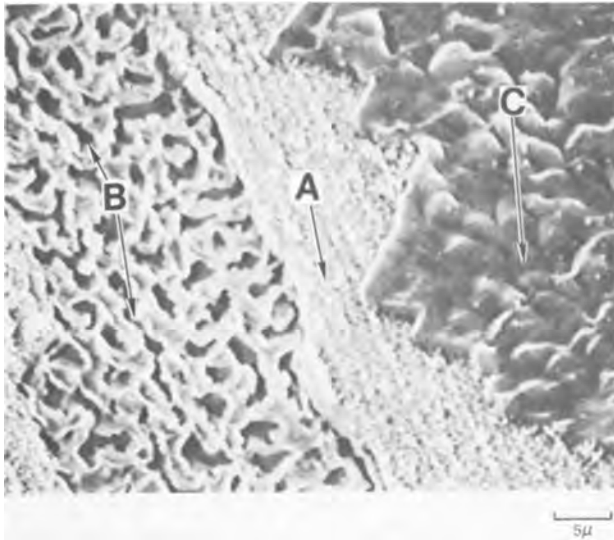

Fig. 12. NiAl oxidized at 900°C for 24 hr with 0.61 ppm NaCl(g) showing regions with: A, adherent-scale and Al_2O_3 fibers growing on it; B, NiAl substrate on which a protective oxide scale is reforming; C, overturned spalled oxide.

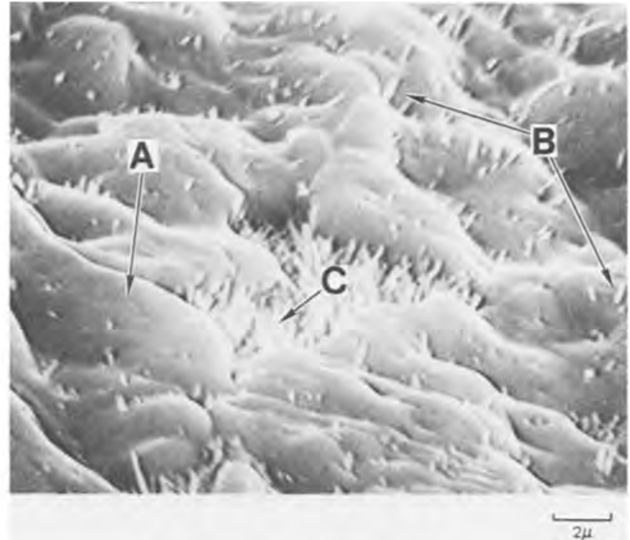

Fig. 14. Al_2O_3 fibers growing from the upturned side of the spalled Al_2O_3 segment. A, base of overturned oxide; B, Al_2O_3 whiskers growing on surface of overturned oxide; C, hole in overturned oxide showing Al_2O_3 whiskers from the surface of the scale below.

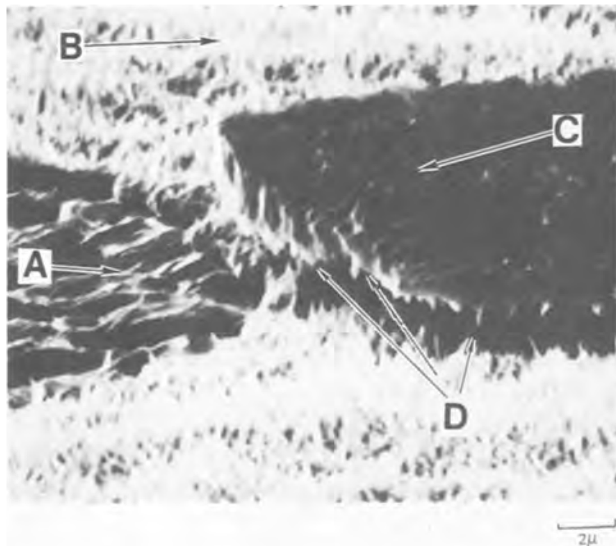

Fig. 13. NiAl oxidized at 1050°C for 24 hr in air with 128 ppm HCl showing a region of the spalled overturned oxide. Note the Al_2O_3 fibers growing from the original surface of the spalled oxide segment. A, NiAl; B, Al_2O_3; C, spalled protective oxide surface originally attached to the NiAl substrate; D, Al_2O_3 whiskers growing on the original surface of overturned oxide.

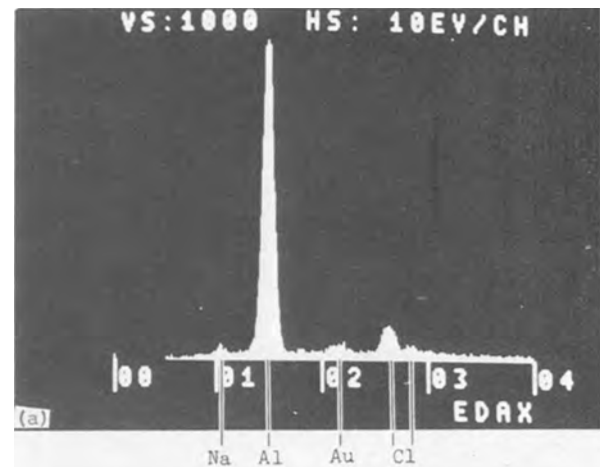

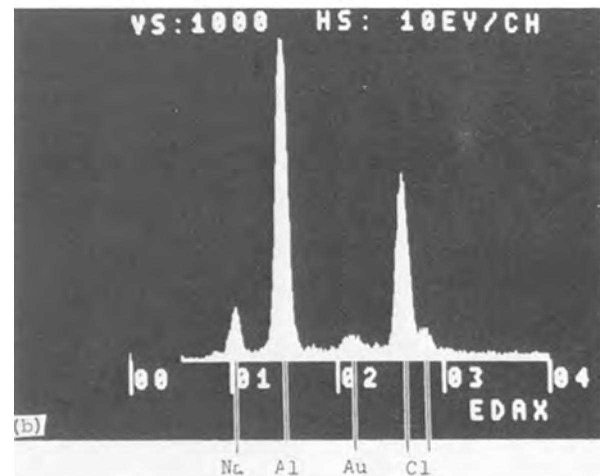

Fig. 15. Investigation of the oxide surface adjacent to the substrate. (a) EDAX of white crystals showing high Al (Al_2O_3) and low Na and Cl peaks; and (b) EDAX of the dense black scale showing high Na and Cl levels (samples Au-coated to prevent surface charging).

lation have been observed by SEM techniques for other NiAl samples oxidized at 900°C in atmospheres containing < 1 ppm NaCl(g).

Experiments were conducted to determine if the alumina in the Al_2O_3 whiskers in the work reported herein derived from a rearrangement of the surface Al_2O_3 at the gas-oxide surface or from aluminum at the metal-oxide interface. Both impure (a Coor's alumina crucible of ordinary commercial quality) and high purity dense (99.5% from Western Gold and Platinum Company) alumina were exposed to both pure air and to air containing NaCl vapors. The concentrations of NaCl examined were in the range of 100-200 ppm, at a temperature of 1050°C for 24 hr. Subsequently both samples were examined by SEM techniques. In all cases whiskers were not observed. Thus, the aluminum source for the Al_2O_3 whiskers does not lie at the surface of the oxidizing NiAl coupons. The Al_2O_3 whiskers are not forming simply in response to a drive to lower the free energy of the surface Al_2O_3 layer. The inability to grow Al_2O_3

whiskers on Al_2O_3 substrates under the "mild" experimental conditions used here is in full agreement with literature reports describing the preparation of such whiskers where substantially higher temperatures (~1300°C) and more vigorous atmospheres are required (30, 31).

Occasionally a citation is observed in the literature briefly mentioning observing a few Al_2O_3 whiskers which formed on oxide scales in the course of an oxidation study, *e.g.*, Kuenzly and Douglass (32). Because such whisker growth is not concomitantly associated with a large difference in the thermogravimetric weight change data, their presence is largely ignored. Sodium chloride is anticipated to be a ubiquitous contaminant at low levels unless precautions are taken to exclude it from the experimental environment. The fact that such whiskers have not been observed more frequently likely results from two factors. In the first place, equipment used for oxidation experiments is frequently kept very clean. This itself would tend to minimize the concentration of NaCl which would cause such effects. In the second place, oxidation studies generally emphasize optical metallography as a tool to examine oxide-substrate interfaces. Although metallographic techniques can be used to see whiskers under favorable circumstances, it is really not the optimum instrument for examining features such as the Al_2O_3 blades discussed here.

Discussion

The results of these experiments show that gaseous products interact with oxidizing NiAl. A product of this interaction is Al_2O_3 whiskers which form on the dense Al_2O_3 scale. These whiskers are not observed unless the environment contains gaseous NaCl.

A number of mechanisms involving the Al_2O_3 fiber growth effects observed here can be speculated on. Potential growth mechanisms can involve compact oxide growth stresses or chemical transport processes. Chemical vapor transport processes might result from reactions involving either Al_2O_3(c) alone or Al_2O_3(c) with the gas-phase corrodent, NaCl(g). In turn, NaCl(g) could react with Al_2O_3 either directly as NaCl or indirectly as its hydrolysis products, NaOH and HCl. These possibilities are discussed further.

Kuenzly and Douglass (32) have suggested that Al_2O_3 whiskers, observed in oxidation experiments involving Ni_3Al specimens, grew by a cation-diffusion mechanism resulting from growth stresses in the compact oxide scale. If this is the case in the work discussed here, then it might be expected that if oxide scale growth stresses and cation, *i.e.*, Al^{+3}, diffusion through Al_2O_3 were the dominant factors in Al_2O_3 whisker growth, Al_2O_3 whisker growth should have occurred independently of the presence or in the absence of NaCl(g) in the oxidizing atmosphere. Furthermore, differences in NaCl(g) concentrations should have no effect on whisker morphology. However, differences, though subtle, in Al_2O_3 whisker morphology are seen for samples oxidized at the same temperature and with different levels of NaCl(g) in the oxidizing atmosphere. Thus, this mechanism does not explain the effects reported here.

With respect to the possible chemical vapor transport processes, a conceptual reaction for the Al_2O_3 fiber growth might involve the disproportionation-vaporization of Al_2O_3(c)

$$Al_2O_3(c) = AlO(g) + AlO_2(g) \quad [1]$$

However, the blank experiments involving dense Al_2O_3 failed to show any whisker growth. This result is readily anticipated since at 1300°C the calculated K_p for the above reaction is approximately 10^{-43} (33). Therefore, a disproportionation-vaporization mechanism is again not applicable.

Another chemical-transport process could involve the reaction of HCl(g) with Al_2O_3. The HCl vapors for such reactions could be intentionally present in the oxidizing atmosphere or derive from the hydrolysis of NaCl, *i.e.*,

$$NaCl(g) + H_2O(g) = NaOH(g) + HCl(g) \quad [2]$$

The HCl(g) present would then diffuse through the dense Al_2O_3 scale formed on the oxidizing NiAl sample. At the metal-oxide layer interface, the HCl could react either with the Al_2O_3 scale itself or with the aluminum in the substrate. Examples of the former equilibria are

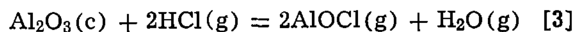

$$Al_2O_3(c) + 2HCl(g) = 2AlOCl(g) + H_2O(g) \quad [3]$$

and

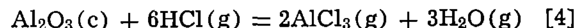

$$Al_2O_3(c) + 6HCl(g) = 2AlCl_3(g) + 3H_2O(g) \quad [4]$$

The free energy values for these reactions at 1300°K are positive and quite large, *i.e.*, 142 and 77 kcal for reaction [3] and [4], respectively (33). Similarly, the reaction involving the substrate can be represented by

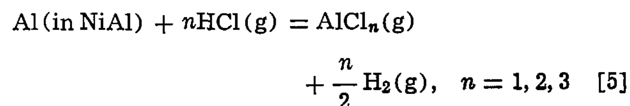

$$Al(\text{in NiAl}) + nHCl(g) = AlCl_n(g) + \frac{n}{2}H_2(g), \quad n = 1, 2, 3 \quad [5]$$

The free energies for these reactions at 1300°K are −13, −27, and −50 kcal for the formation of the monochloride, dichloride, and trichloride, respectively, (33).

Thus, if the dense Al_2O_3 oxide layer can keep the oxygen potential sufficiently low at the metal-oxide interface and if the HCl and aluminum halides and oxyhalides can diffuse through the dense Al_2O_3 scale, then Al_2O_3 whiskers could form from the appropriate disproportionation reactions. Such a mechanism would not allow for easy "short circuit" diffusion of aluminum halide gaseous species through cracks in the protective Al_2O_3 scale, because if HCl and the appropriate aluminum vapor species can diffuse through such cracks, so could oxygen. Such oxygen would then interact with the transporting aluminum vapor species forming Al_2O_3 which would be expected to plug up such easy diffusion paths. Grain boundary diffusion would not be precluded by such a model as long as the diffusivity of the oxygen was much less than that for the responsible halogen and aluminum-halogen vapor species.

A mechanism such as this would suggest extensive and virtually continuous dense oxide scale rupture, spallation, and reformation at constant temperature. As more and more material was removed from the scale-metal interface, the oxide scale would become locally nonadherent. Cracks then would locally develop in the scale because of heterogeneous dense scale growth kinetics. Gross oxidation of the substrate immediately below the locally spalled area would then proceed rapidly as a protective scale tried to reform. This type of behavior was seen here for NiAl oxidized at 900°C in an atmosphere containing 0.61 ppm NaCl(g).

The transport of aluminum to form Al_2O_3 blades has been described in terms of a cycle involving aluminum chloride or aluminum-oxychloride vapor species derived from HCl vapors. Stearns *et al.* (26) and Fryburg *et al.* (27) have observed the gaseous species $(NaCl)_{1,2,3}$ CrO_3, $(NaOH)_{1,2}$ CrO_3, $(NaCl)_{1,2}$ $(MoO_3)_3$, and (NaOH) MoO_3. These vapor species may be viewed as volatile complexes of NaCl (or its hydrolysis product NaOH) and a metal oxide. If similar but as yet unidentified species exist in case of alumina, the over-all interpretation of the transport effect suggested above in the case of HCl remains the same while the specifics, *e.g.*, the vapor species responsible for transport, will obviously differ. Alternatively, it might be speculated that only the chloride component of the NaCl species diffuses through the dense alumina scale

to form volatile aluminum chloride species at the substrate-protective scale interface. However such an explanation alone would not account for the sodium found at the base of the dense alumina scale, *cf.* Fig. 15.

On the basis of the surface structures seen for NiAl samples exposed to slowly moving oxidizing atmospheres containing NaCl vapors, the thermogravimetric data for such samples should not yield net weight losses. The aluminum removed from the alloy by such vapor processes is partially redeposited on the outer surface of the oxide layer. However, in a rapidly moving gas stream, the fine Al_2O_3 whiskers would not be expected to form on the substrate surface. Rather the chemical species responsible for their growth would be swept down the turbulent gas stream. Accordingly, examination of turbine hardware would only fortuitously be expected to show the presence of such Al_2O_3 fibers.

Furthermore, from empirical observations of the factors leading to Al_2O_3 whisker formation, the higher the temperature the more effective will be the diffusivity of pertinent vapor species through the dense Al_2O_3 oxide layer and so aluminum will be increasingly more rapidly removed from below the dense Al_2O_3 scale. Again, NaCl for such processes need not be reformed in the chemical cycle. In the 1 ppm NaCl-air composition range, the NaCl(g) should be lost to and gained from the atmosphere of a marine or industrial gas turbine, in the absence of an unidentified chloride sink, at approximately equal rates (4). Although these experiments dealt strictly with NiAl, similar NaCl(g) effects are expected with other coating and alloy compositions which are also Al_2O_3 formers.

The description here of aluminum transport effects has been admittedly both speculative and qualitative because of our present lack of knowledge of specific factors controlling this effect. The precise nature (composition and properties) of the pertinent chemical species and the diffusion mechanism(s) responsible for transport through an otherwise dense alumina scale are unknown.

Summary and Conclusions

NaCl has been known to be an effective corrodent in the liquid phase with and without condensed Na_2SO_4 (9-25). However, the work presented herein has shown NaCl vapor present at low concentrations substantially modifies the high temperature oxidation behavior of the alumina former NiAl. The role of NaCl vapor in the oxidation of NiAl is two-fold. In the first place aluminum is removed from a dense protective Al_2O_3 scale and redeposited on the surface of the scale as Al_2O_3 whiskers. Secondly, the NaCl vapor effects isothermal protective Al_2O_3 scale spallation. Such effects are contrary to those reported for Na_2SO_4 which, to be an effective corrodent, must be present in the condensed phase (34).

The interaction of NaCl(g) with NiAl is not expected to be unique and likely occurs with other alumina-forming coating and substrate compositions.

Thermodynamic and kinetic treatments of oxidation phenomena in actual turbine atmospheres should, in order to be accurate, take NaCl(g) effects into account. The presence of NaCl(g) in the tenths of a ppm range in turbine atmospheres is anticipated to be virtually ubiquitous resulting from either fuel or atmosphere contamination. The effects of NaCl(g) in the absence of condensed Na_2SO_4 will contribute to the high temperature degradation of alumina-forming protective coatings used in gas turbines.

Acknowledgments

The author acknowledges helpful discussions with Mr. C. A. Stearns and Drs. F. J. Kohl and G. C. Fryburg of NASA-Lewis Research Center, Cleveland, Ohio, and Dr. R. A. Pike of the United Technologies Research Center, East Hartford, Connecticut. Also, thanks go to efforts of Messrs. R. Brown, L. Jackman, and G. McCarthy for assistance in conducting the experiments presented herein.

This work was supported by NASA-Lewis Research Center, Contract No. NAS3-20039.

Manuscript submitted Aug. 1, 1977; revised manuscript received March 27, 1978. This was Paper 36 presented at the Philadelphia, Pennsylvania, Meeting of the Society, May 8-13, 1977.

Any discussion of this paper will appear in a Discussion Section to be published in the June 1979 JOURNAL. All discussions for the June 1979 Discussion Section should be submitted by Feb. 1, 1979.

Publication costs of this article were assisted by United Technologies Research Center.

REFERENCES

1. S. J. Grisaffe, "The Superalloys," C. T. Sims and W. C. Hagel, Editors, p. 341 John Wiley & Sons, New York (1972).
2. "High Temperature Oxidation-Resistant Coatings," National Academy of Science, Washington, D.C. (1970).
3. G. W. Goward, D. H. Boone, and C. S. Giggins, *Trans. ASM*, **60**, 228 (1967).
4. H. F. G. Condé, Paper presented at the Gas Turbine Materials Conference Proceedings, Materials Advisory Group/U.S. Army Materiel Command in cooperation with the National Assoc. of Corrosion Engineers, Washington, D.C. (1972).
5. C. G. McGrath, *Trans. Inst. Mar. Eng.*, **88**, 145 (1976).
6. I. I. Bessen and R. E. Fryxell, "Proceedings of the 1974 Gas Turbine Materials in the Marine Environment Conference," MCIC Report 75-27, p. 219, Castine, Maine (1974).
7. C. T. Ewing and K. H. Stern, *J. Phys. Chem.*, **78**, 1998 (1974).
8. F. J. Kohl, C. A. Stearns, and G. C. Fryburg, in "Metal-Slag-Gas Reactions and Processes," Z. A. Foroulis and W. W. Smeltzer, Editors, p. 649, The Electrochemical Society, Softbound Symposium Series, Princeton, N.J. (1975).
9. R. C. Hurst, J. B. Johnson, M. Davies, and P. Hancock, in "Deposition and Corrosion in Gas Turbines," A. B. Hart and A. J. B. Cutler, Editors, p. 143, John Wiley & Sons, New York (1973).
10. P. Hancock, R. C. Hurst, and A. R. Sollars, in "Chemical Metallurgy of Iron and Steel," p. 413, Iron and Steel Institute, London (1973).
11. (a) J. F. G. Condé and B. A. Waltham, in "Proceedings of the 1974 Gas Turbine Materials in the Marine Environment Conference," J. W. Fairbanks and I. Machlin, Editors, p. 73, MCIC 75-27, Washington, D.C. (1975); (b) P. Hancock, *ibid.*, p. 225.
12. H. T. Shirley, *J. Iron Steel Inst.*, **182**, 144 (1956).
13. H. W. Pickering, F. H. Beck, and M. G. Fontana, *Trans. ASM.*, **53**, 793 (1961).
14. A. U. Seybolt, *Oxid. Metals*, **2**, 119 (1970).
15. A. U. Seybolt, *ibid.*, **2**, 161 (1970).
16. P. A. Alexander, in "The Mechanism of Hot Corrosion by Fuel Impurities," H. R. Johnson and D. J. Littler, Editors, p. 571, Butterworths, London (1971).
17. F. Mansfeld, N. E. Paton, and W. M. Robertson, *Met. Trans.*, **4**, 321 (1973).
18. D. M. Johnson, D. P. Whittle, and J. Stringer, *Corros. Sci.*, **15**, 721 (1975).
19. P. Hancock, "Corrosion of Alloys in High Temperatures in Atmospheres Consisting of Fuel Combustion Products and Associated Impurities—A Critical Review," Her Majesty's Stationary Office, London (1968).
20. H. Lewis and R. A. Smith, Corrosion of High-Temperature Nickel-Base Alloys by Sulphate-Chloride Mixtures," p. 202, First International Congress on Metal Corrosion, Butterworths, London (1961).
21. T. J. Raqzavich and F. S. Pettit, Contract No. N00173-76-C-0146, Second Quarterly Report, Naval Research Laboratories, Washington, D.C. (1976).
22. E. J. Felten and F. S. Pettit, Contract No. N00173-76-C-0146, Third Quarterly Report, Naval Research Laboratories, Washington, D.C. (1976).

23. R. H. Barkalow and F. S. Pettit, Contract No. N00173-76-C-0146, Fourth Quarterly Report, Naval Research Laboratories, Washington, D.C. (1976).
24. R. L. Jones, Naval Research Laboratory LTR Report 6170859, Washington, D.C. (1975).
25. R. L. Jones, K. H. Stern, and S. T. Gadowski, Paper to be published in Proceedings of the 1976 Gas Turbine Materials in the Marine Environment Conference, Bath, England, MCIC (1976).
26. C. A. Stearns, F. J. Kohl, and G. C. Fryburg, in "Properties of High Temperature Alloys," Z. A. Foroulis and F. S. Pettit, Editors, p. 655 The Electrochemical Society Softbound Symposium Series, Princeton, N.J. (1976).
27. G. C. Fryburg, R. A. Miller, F. J. Kohl, and C. A. Stearns, Paper 32 presented at the Philadelphia, Pennsylvania, Meeting of the Society, May 8-13, 1977.
28. F. S. Pettit, *Trans. MS-AIME*, **239**, 1296 (1967).
29. J. G. Smeggil and N. S. Bornstein, Unpublished research.
30. S. Minagowa, *J. Am. Ceram. Soc.*, **55**, 77 (1972).
31. "Whisker Technology," A. P. Levitt, Editor, Wiley-Interscience, New York (1970).
32. J. D. Kuenzly and D. L. Douglass, *Oxid. Met.*, **8**, 139 (1974).
33. JANAF Tables, Dow Chemical Co., Midland, Mich.
34. M. A. DeCrescente and N. S. Bornstein, *Corrosion (Houston)*, **24**, 127 (1968).

Chromate Passivation Protection of Zn- and Al-Zn-Coated Steel Sheet Against Wet-Storage Stain

H. E. Townsend and J. C. Zoccola

Bethlehem Steel Corporation, Homer Research Laboratories, Bethlehem, Pennsylvania 18016

ABSTRACT

The results of laboratory wet-pack tests show that chromate-passivation treatments provide temporary protection for both Zn- and Al-Zn-coated steel sheet against wet-storage staining. Compared with Zn coatings, the Al-Zn coating requires about half as much chromium deposited on the surface to achieve a given level of protection. Also, chromate passivation of the Al-Zn coating is consistently more effective and less sensitive to application conditions than chromate passivation of zinc coatings. Unlike the dark-colored aluminum-rich corrosion products (mostly aluminum hydroxide) that form on unpassivated Al-Zn-coated sheet, the corrosion products that eventually form at long exposure times on passivated Al-Zn-coated sheets are richer in zinc and lighter in color.

Zinc coatings are widely used to protect steel from atmospheric corrosion (1). The protective qualities of the zinc coatings on galvanized steel result from the formation of a protective layer of insoluble basic zinc carbonate that forms on the surface of the zinc coating during bold exposure (2). However, in the absence of air and in the presence of moisture, zinc coatings corrode with the formation of a relatively nonprotective zinc hydroxide, often called "white rust" (1, 3). These conditions can occur during shipment or storage of galvanized steel if water is allowed to enter the capillary channels that form when sheets are coiled or stacked. The resulting phenomenon, referred to as "wet storage staining," usually produces only superficial attack of the coating and thus is objectionable only in terms of esthetics. In extreme cases, however, significant amounts of coating may be consumed, thus reducing the longevity of the product upon subsequent exposure to the atmosphere (4).

Passivation of Zn-coated steel in chromate solutions provides temporary protection against wet-storage staining. Many types of chromate passivation treatment have been described (1, 5, 6). Chromate passivation produces a thin film on the surface of the sheet that contains hexavalent and trivalent chromium compounds. Most investigators believe that the trivalent chromium present as chromium hydroxide or zinc chromate acts as a protective barrier, whereas the soluble hexavalent portion of the film serves to repair the barrier at areas of localized breakdown.

An Al-Zn-alloy [weight percent (w/o) 55 Al-43.4 Zn and 1.6 Si] coating that is at least 2-4 times more resistant to atmospheric corrosion than zinc coatings of equivalent thickness has been developed for steel sheet by Bethlehem Steel Corporation (7). The coated product is currently being marketed in the U.S. under the name Galvalume sheet steel. Like Zn, the Al-Zn-alloy coating is subject to wet-storage staining, but the corrosion product on unpassivated sheet is characteristically black. The experimental program described in this paper demonstrated that chromate passivation is effective in preventing corrosion, *i.e.*, "black staining," on the Al-Zn-coated sheet during shipment and storage.

Key words: coatings, corrosion, inhibitors, products, testing.

Experimental

Zn- and Al-Zn-alloy-coated steel sheets produced without chromate passivation on a continuous hot-dip production facility were chromate-treated in the laboratory after solvent-vapor degreasing. Chromate-treatment consisted of preheating the coated sheet in air to the temperature of the chromate bath, immersion in the chromate solution for times that were varied in the range 1-5 sec, removal of excess solution by passing the treated sheet through rubber squeegee rolls, and drying in air at 165°F. Temperatures of the chromate bath were varied in the range 120°-180°F. Chromate baths were prepared from a proprietary mixture available as Iridite 9L6.[1] This mixture is described by its supplier as a fluoboric acid-activated chromate passivation treatment comprised of approximately 10% hexavalent chromium, 8% fluoride compounds, and 1.6% boron compounds. For our experiments, the mixture was diluted with distilled water to produce solutions with hexavalent chromium concentrations which were varied in the range 1.3-7.7 g/liter and with pH 2-3.

The amounts of chromium deposited on the passivated sheet were determined by stripping the film and analyzing the stripping solution by use of either colorimetry or atomic absorption. Water-soluble chromium was determined by partially stripping the film in boil-

[1] Trademark of the Richardson Company, Des Plaines, Illinois.

ing distilled water. Total chromium was determined by stripping the entire film in a dilute solution of phosphoric and sulfuric acid.

Total chromium deposited on the strip was found to increase systematically with increasing solution concentration, solution temperature, or immersion time. Thus it was possible to control the amount of chromium deposited in several ways through selection of different combinations of these parameters.

Resistance to wet-storage staining was determined in laboratory pack tests conducted as follows. The surfaces of 8 × 10 × 0.02 in. sheets were wetted with distilled water and the sheets were placed in stacks to simulate severely corrosive (complete wetness) storage conditions. Each stack comprised 50 sheets and had a 25 lb weight placed on top to assure uniformity of spacing between sheets from top to bottom. Once each week, the stacks were opened for visual evaluation of degree of stain, then wetted and stacked again. Visual ratings are based on a scale of 0-10, where 0 corresponds to 100% of the surface area stained and 10 to no staining. The nonlinear scale (Table I) is defined in order to emphasize differences when only small amounts of staining have occurred. We consider a ranking of 6 or more to represent acceptable performance in the wet-pack test.

Corrosion products formed on Al-Zn-coated sheet were analyzed by several techniques, including x-ray diffraction (XRD), secondary ion mass spectrometry (SIMS), and energy-dispersive x-ray fluorescence (EDXRF).

Results and Discussion

Wet-pack test results.—The results of wet-pack tests on the Zn-coated sheets after 4 weeks exposure, Fig. 1, show that the level of protection increases rapidly with increasing amounts of chromium applied up to about 8 $\mu g/in.^2$. With further increases in chromium above 8 $\mu g/in.^2$, the degree of protection does not increase as quickly and there is considerable variability in the results. We observed that for a given amount of chromium above 8 $\mu g/in.^2$ satisfactory results (*i.e.*, a rating of 6 or more) were obtained only when the sheets were treated in hotter ($T \geq 150°F$) and more concentrated (hexavalent chromium ≥ 4.1 g/liter) solutions. Longer contact times to produce equivalent chromium levels in cooler, less concentrated solutions did not provide satisfactory passivation. Thus above 8 $\mu g/in.^2$ the protection is dependent more on application conditions than on chromium level for galvanized sheet.

Four-week wet-pack test results for Al-Zn-coated sheet, Fig. 2, show increasing protection with increasing chromium until complete protection is achieved at about 4 $\mu g/in.^2$, a value roughly half that required to reach satisfactory behavior for the Zn-coated sheet. Above the 4 $\mu g/in.^2$ level, complete protection against wet-storage stain was achieved by chromate passivation of the Al-Zn-coated sheet, regardless of application conditions such as solution temperature and concentration. Thus, chromate passivation of Al-Zn coatings is consistently more effective and less sensitive to application conditions than chromate passivation of zinc coatings.

Typical time dependence for wet-pack corrosion of chromate-treated sheets, Fig. 3, shows that the protec-

Table I. Wet storage stain rating

Rating	Percent of total area with stain
10	0
9	<1
8	1
7	2
6	4
5	6
4	10
3	20
2	40
1	60
0	100

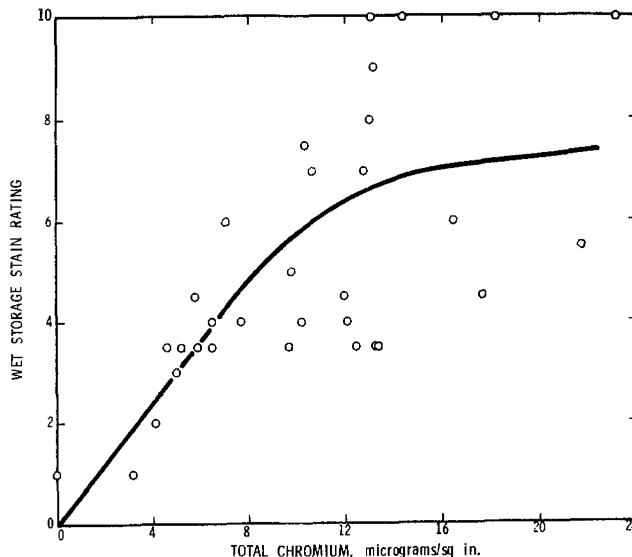

Fig. 1. Effect of total chromium on the resistance of a Zn-coated steel sheet to wet-storage stain in a four-week test.

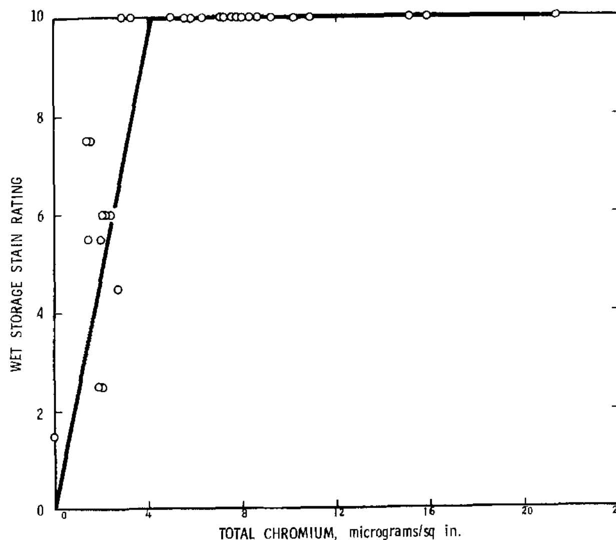

Fig. 2. Effect of total chromium on the resistance of an Al-Zn-coated steel sheet to wet-storage stain in a four-week test.

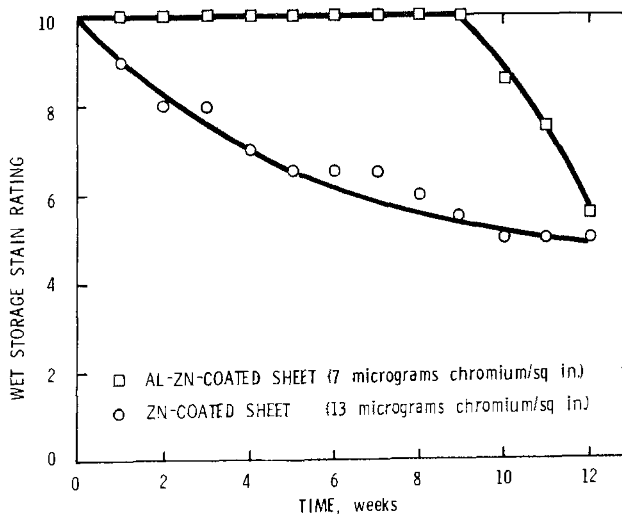

Fig. 3. Typical time dependence of storage staining for a chromate-treated steel sheet.

tion afforded by chromate passivation diminishes with longer exposure time. Compared to unpassivated sheet, which within a few days in the wet-pack test exhibits

severe storage stain ratings (of 3 or less), the protection imparted by chromate (ratings of 6 or more) lasts for several weeks.

Soluble chromium content of passivation films.—The film that forms on a chromate-passivated sheet contains varying amounts of water-soluble and water-insoluble chromium compounds. We observed that the water-soluble fraction decreases slowly with time as the film ages. The relative amounts of water-soluble and total (water-soluble plus water-insoluble) present in the film two weeks after application are shown in Fig. 4. We note that soluble chromium is not observed in the passivation film until the total chromium exceeds 4 and 8 $\mu g/in.^2$ for Zn- and Al-Zn-coated sheet, respectively. Above these levels, the amounts of water-soluble chromium increase with increasing total chromium. The coincidence of these values with those required for attainment of satisfactory behavior in the wet-pack tests suggests that availability of water-soluble chromium for film repair is needed to achieve the higher levels of protection.

Analysis of corrosion products on Al-Zn-coated sheet.—Corrosion products formed on the surface of an unpassivated Al-Zn-coated sheet in the wet-pack test are generally black in color. Another study previously reported that the dark corrosion product is comprised of beta-$Al(OH)_3$ (bayerite) (8). Our XRD analysis of the dark corrosion product found evidence of beta-$Al(OH)_3$ and also trace amounts of alpha-$Al(OH)_3$ (gibbsite). Although gibbsite is the most commonly occurring mineral form of $Al(OH)_3$, its presence in corrosion products is regarded as unusual (9). By use of SIMS and EDXRF, we also found the presence of small amounts of zinc in the black corrosion product.

Analyses of the light-colored corrosion products that eventually form on the passivated Al-Zn-coated sheet at long exposure times indicates a much higher content of zinc. In view of the fact that the Al-Zn coating is a two-phase structure comprised of about 80 volume percent aluminum-rich cored dendrites with zinc-rich alloy occupying the interdendritic regions (7), this result suggests that chromate passivation is more effective on the aluminum-rich portion of the coating. Thus, the zinc-containing portions of the passivated sheet are the first to be attacked at longer exposure times and light-colored zinc corrosion products are formed. Conversely, the dark color associated with aluminum corrosion products that form on unpassivated sheet is avoided.

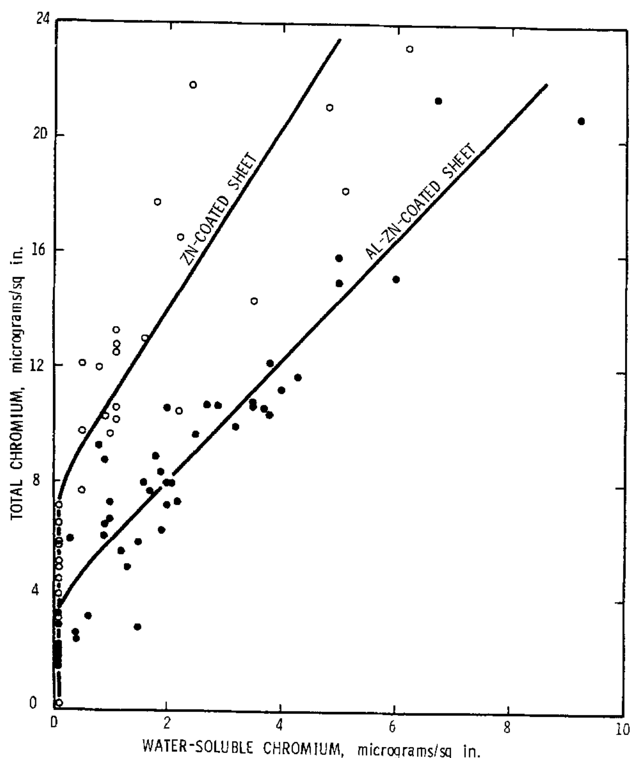

Fig. 4. Relationship of water-soluble chromium to total chromium on Zn and Al-Zn-coated steel sheet (film aged for 2 weeks prior to analysis).

Summary

1. For both the Zn- and Al-Zn-coated sheet steel, chromate passivation provides several weeks protection against wet storage staining.

2. Compared with Zn coatings, Al-Zn coatings require about half as much chromium to achieve this level of protection.

3. Chromate passivation of Al-Zn coatings is consistently more effective and less sensitive to application conditions than chromate passivation of zinc coatings.

4. Corrosion products formed on the Al-Zn-coated sheet under wet-pack conditions are black and aluminum-rich on unpassivated sheet but are light-colored and zinc-rich on passivated sheet.

Acknowledgments

The authors are indebted to the management of Bethlehem Steel Corporation for permission to publish these results, the management of the Research Department (D. J. Blickwede, J. W. Frame, E. H. Mayer, and J. B. Horton) for stimulation and support of this work, technical editor B. S. Mikofsky for help in writing this manuscript, F. H. Ruch for wet-chemical analysis, K. F. Watterson for SIMS analyses, R. W. Hinton and E. S. Erickson for x-ray analyses, and E. L. Gehman and D. H. VanBilliard for technical assistance.

Manuscript submitted Oct. 20, 1977; revised manuscript received Jan. 3, 1978. This was Paper 123 presented at the Atlanta, Georgia, Meeting of the Society, Oct. 9-14, 1977.

Any discussion of this paper will appear in a Discussion Section to be published in the June 1979 JOURNAL. All discussions for the June 1979 Discussion Section should be submitted by Feb. 1, 1979.

Publication costs of this article were assisted by Bethlehem Steel Corporation.

REFERENCES

1. R. M. Burns and W. W. Bradley, "Protective Coatings for Metals," Reinhold Publishing, New York (1967).
2. C. J. Slunder and W. K. Boyd, "Zinc: Its Corrosion Resistance," Zinc Institute, New York (1971).
3. A. R. Cook, *Anti-Corros. Methods Mater.*, **23**, No. 3, 5 (1976).
4. C. E. Bird and F. J. Strauss, *Mater. Perform.*, **15**, No. 11, 27 (1976).
5. H. Geduld, *Met. Finish.*, **74**, No. 6, 46 (1976).
6. L. F. G. Williams, *Surf. Technol.*, **5**, 105 (1977).
7. J. C. Zoccola, H. E. Townsend, A. R. Borzillo, and J. B. Horton, in "Atmospheric Factors Affecting the Corrosion of Engineering Materials, STP646," ASTM, Philadelphia (1978).
8. T. Watanabe, E. Tarumi, and S. Tsuda, *Corros. Eng.*, **25**, 561 (1976).
9. H. P. Godard, W. B. Jepson, M. R. Rothwell, and R. L. Kane, "The Corrosion of Light Metals," John Wiley & Sons, New York (1967).

High Dose Ion Implantation into Photoresist

Y. Okuyama, T. Hashimoto, and T. Koguchi

Nippon Electric Company, Limited, IC Division, Kawasaki, Japan

ABSTRACT

The characteristics of heavily ion-implanted photoresist films were studied in relation to types of photoresist, ion species, accelerating energies, and dose levels. By high energy, high dose ion implantation it was observed that the optical transmission of the resist film was exceedingly decreased and the resist becomes more mechanically, thermally, and chemically resistant. Several experimental data indicated that these results are due to the change of photoresist to disordered graphite. As an application of this ion-implanted resist, a new photomask fabrication process is developed.

Photoresist films are commonly used as a mask against ion implantation in MOS integrated circuits production. For practical applications at present, the implantation dose ranges from 10^{11} to 10^{14} ions/cm^2 (1, 2). In this dose level, the photoresist films are easily removed after ion implantation. As the dose level increases, however, they cannot be stripped off completely by chemical strippers, hot nitric acids, or hot sulfuric acids; the chemical durability and hardness of the resist films are increased. The scratch resistance and thermal durability are also increased and the optical transmission is decreased. This paper describes (*i*) the characteristics of high energy and high dose ion-implanted resist films; (*ii*) the reason for such a drastic change in the characteristics by heavy ion implantation; and (*iii*) the application of these characteristics to a new photomask fabrication method (3).

Experiments and Results

Photoresist films (Shipley's AZ-1350, Tokyo Oka Kogyo's OMR-83 or OSR) with thickness of 0.2 ~ 1 μm were spin coated on silicon wafers or on glass substrates. The name and structure of the base polymers and sensitizers of these photoresists are shown in Table I. The photoresist was then patterned through the steps of prebaking, exposure, development, and postbaking. An argon ($^{40}Ar^+$), phosphorus ($^{31}P^+$), or boron ($^{11}B^+$) ion beam with an energy of 20 ~ 180 keV and a current density of 0.16 ~ 1.25 μA/cm^2 was implanted into the resist film at the dose level of 10^{14} ~ 10^{16} ions/cm^2. Estimated ion ranges in the unreacted resists are shown in Table II (4-6). The original characteristics of the photoresist film changed drastically by this treatment (7),

Figure 1 shows the infrared light absorption peak of the negative photoresist layer (OMR-83, 8000Å), which was $^{11}B^+$ ion implanted to a dose level of 3×10^{14} ions/cm^2 at various accelerating energies. There is an absorption peak at a wave number of 2800 cm^{-1} which corresponds to the C-H bonds in the resist. The peak decreases as an accelerating energy increases. But, it is clear from Fig. 1 that ion beam density has no effect on the destruction of the C-H bonds.

Figure 2 shows the optical transmission variation of the positive photoresist layer (AZ-1350, 4300Å), which was $^{31}P^+$ ion implanted at 120 keV with a dose level of 10^{15} ~ 10^{16} ions/cm^2. The optical transmission in an ultraviolet ray and in visible light zones was decreased greatly with increasing dose level. Corresponding to the increase of dose level, the color of the resist layer changed from brown to black. The tendency of these two results shown in Fig. 1 and 2 was observed with any types of photoresist, positive or negative, and with any ion species, *e.g.*, $^{31}P^+$, $^{40}Ar^+$, $^{11}B^+$, or $^{49}BF_2^+$. The efficiency in changing the characteristics of photoresist film was found to depend on the ion species; it was ranked in the order of $^{40}Ar^+ > {}^{31}P^+ > {}^{11}B^+$ in our experiments. On this basis, the following experiments were conducted, using AZ-1350 as the positive photoresist, OSR as the negative photoresist, and $^{40}Ar^+$ as the ion species. Figure 3 shows the chemical

Key words: polymers, integrated circuits, dissociation.

Table I. Base polymers and sensitizers of photoresists

OMR-83	Base polymer cyclized polyisoprene (I)	SG 0.99
	Sensitizer: bis-azide (II)	
OSR	Base polymer poly(-vinyloxethyl cinnamate) (III)	SG 1.19
AZ-1350	Base polymer cresol novolac resin (IV)	SG 1.22
	Sensitizer naphthoquinone-1,2-diazide-5-sulfonic ester (V)	

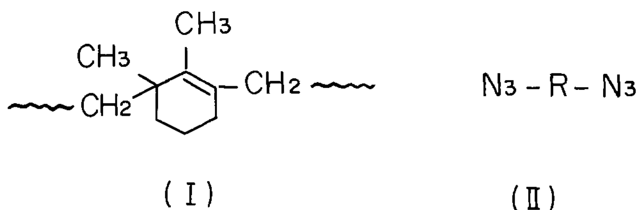

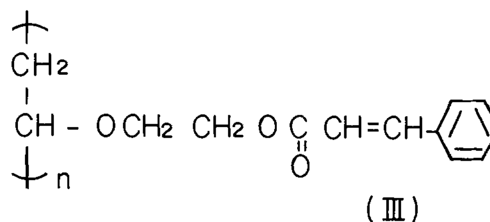

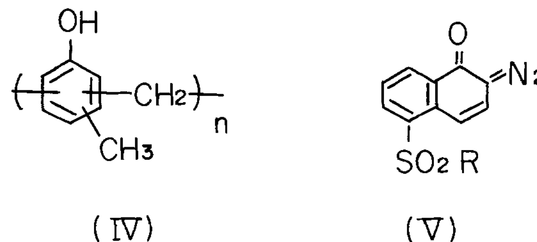

Table II. Estimated projected ion ranges in the unimplanted photoresists

Ion species	Ar⁺				P⁺		B⁺	
Energy (keV)	50	100	150	200	50	150	50	150
OMR-83	650	1300	2000	2700	790	2500	2600	7200
OSR	540	1100	1700	2300	650	2100	2200	6000
AZ-1350	530	1100	1600	2200	640	2000	2100	5800

(Unit Å)

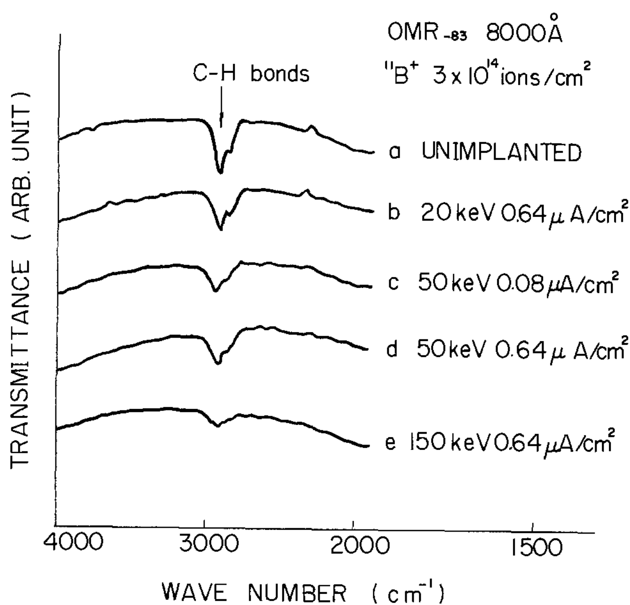

Fig. 1. The variation of infrared light absorption peak of negative photoresist by ion implantation.

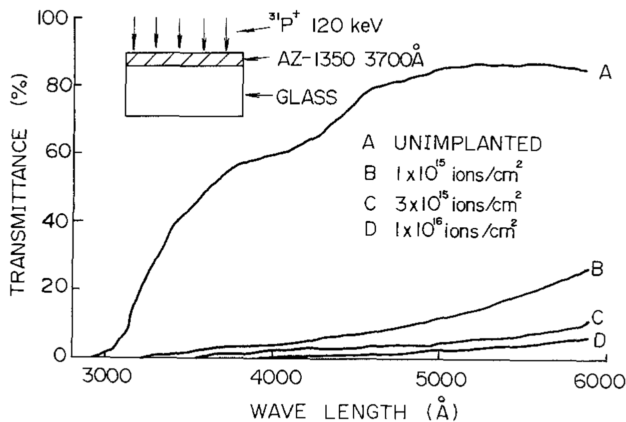

Fig. 2. Optical transmission variation of the negative photoresist layer with $^{31}P^+$ ion implanted at 120 keV. The photoresist becomes opaque to ultraviolet and visible light by the ion implantation.

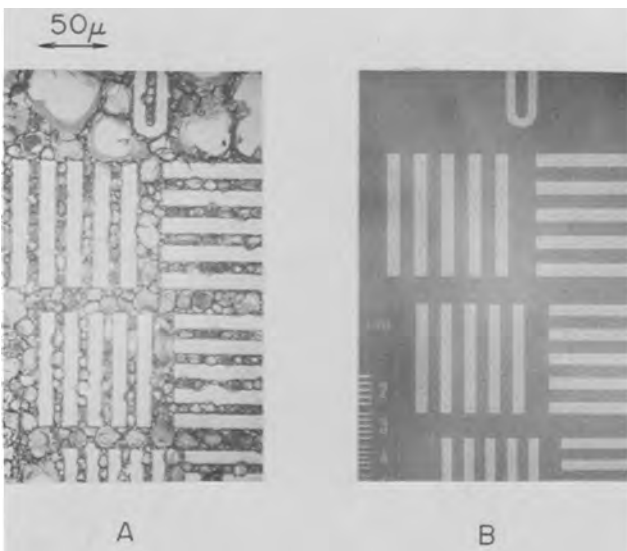

Fig. 3. The chemical durability of negative photoresist (OSR) against 49% hydrofluoric acid. (A) Unimplanted, dipped for 5 min in HF; (B) implanted ($^{40}Ar^+$, 170 keV, 1 × 10^{16} ions/cm^2), dipped for 1 hr in HF.

durability against 49% (hydrofluoric acid). The negative photoresist layer (OSR of 4000Å initial thickness) could not endure for less than a few minutes in the solution, while the $^{40}Ar^+$ ion-implanted resist with a dose of 10^{16} ions/cm^2 at 170 keV endured for more than 1 hr in the same solution.

Figure 4 also shows the chemical durability against hot nitric acid and hot sulfuric acid. The manufacturing conditions of the sample for this test were the same as shown in Fig. 3, except that a transparent glass was used as a substrate. At first the initial transmission was measured to be 0.5% at a wavelength of 405 nm. Then the sample was subjected to a series of HNO_3-H_2SO_4 cleaning; in which the following cycle was repeated: (*i*) dipping the sample in 75% HNO_3 at 90°C for 2 min; (*ii*) dipping the sample in 85% H_2SO_4 at 120°C for 2 min; (*iii*) dipping the sample in 75% HNO_3 at 90°C for 2 min. After five cycles of this chemical treatment, no variation was observed in the transmission at 405 nm wavelength.

Figure 5 shows the optical density variation (at a wavelength of 405 nm) of the photoresist layers on a transparent glass substrate at increasing doses and at constant accelerating energy. The initial photoresist thickness for this evaluation was 4300 and 3000Å for AZ-1350 and OSR, respectively. The optical density increases in proportion to the logarithm of the dose level.

Figure 6 shows the optical density variation (at a wavelength of 405 nm) of photoresist layers, having the same initial thickness as the preceding evaluation in Fig. 5 with a constant dose and with increasing accelerating energies. Figure 6 shows that optical density increases linearly with increasing accelerating energies. From the two experiments shown in Fig. 5 and 6 it may be concluded that the optical density increases as a function of the total energy which is effectively conveyed to the photoresist layer from the implanted ions.

Figure 7 shows the variation of the photoresist thickness before and after ion implantation (150 keV, 10^{16} ions/cm^2). It is evident from Fig. 7 that the initial photoresist thicknesses are decreased by about half as a result of the ion implantation. Figure 8 shows the etching rate of the photoresist film by O_2 gas plasma. The etching rate of unimplanted photoresist was about 1500 Å/min, and it decreased as dose level increased; about 300 Å/min at a dose level of 10^{15} ions/cm^2 and about 200 Å/min at 10^{16} ions/cm^2.

Figure 9 shows the variation of pattern width by ion implantation to the positive photoresist (AZ-1350,

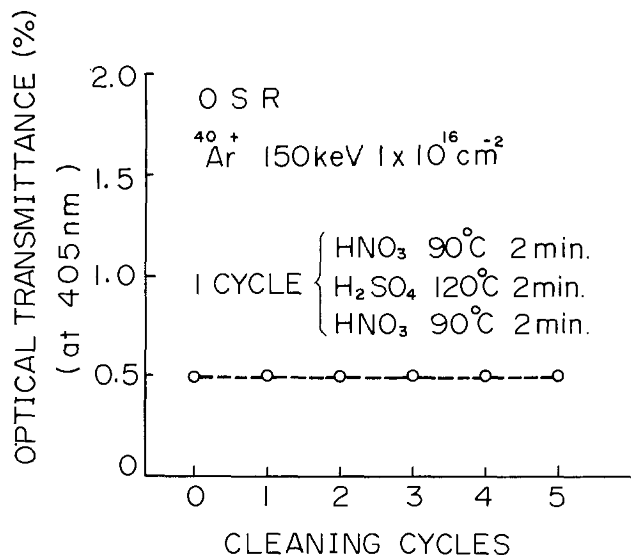

Fig. 4. Chemical durability against hot HNO_3-H_2SO_4. The resist on a transparent glass substrate was ion implanted and its optical transmission was measured after each cleaning cycle.

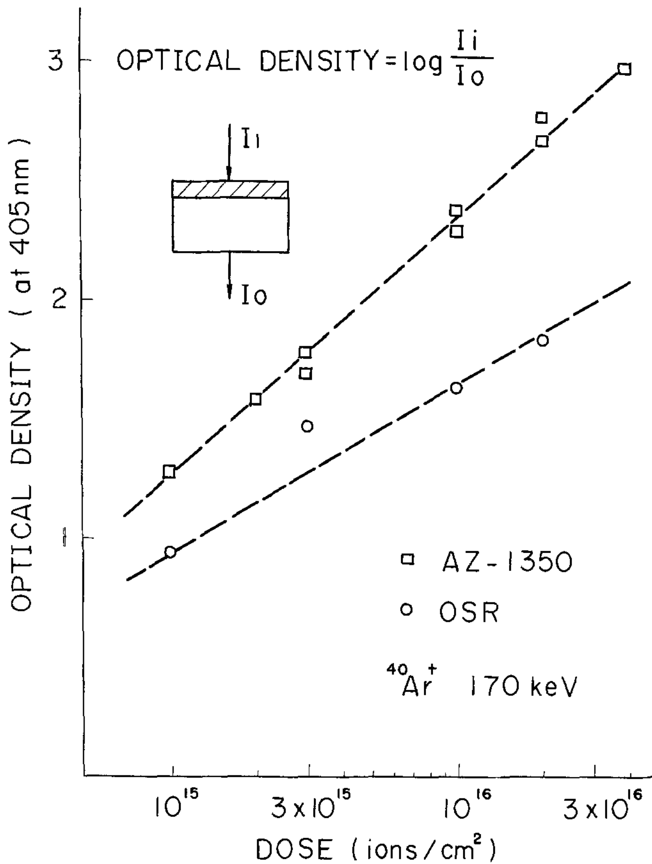

Fig. 5. Optical density variation as a function of dose. The initial photoresist thickness was 4300 and 3000Å for AZ-1350 and OSR, respectively.

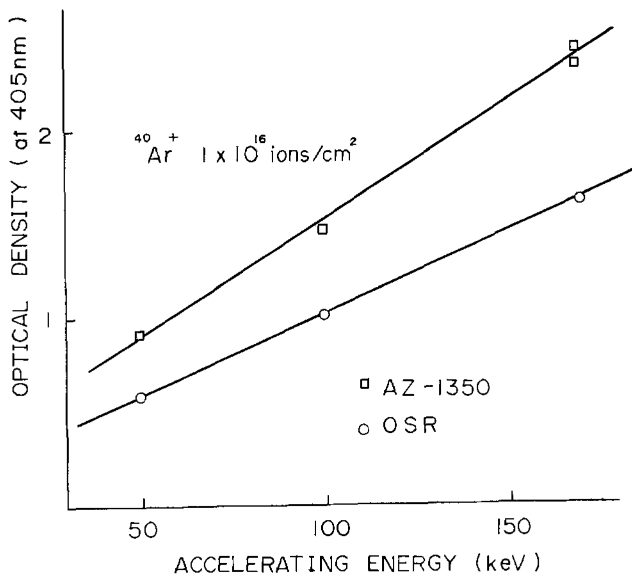

Fig. 6. Optical density variation as a function of accelerating energy.

4300Å as initial thickness). The variation of the pattern width before and after ion implantation (170 keV 10^{16} ions/cm^2) is within ± 0.2 μm, which is within permissible measuremental error. Therefore it may possibly be concluded that no measurable variation occurred in the pattern width of photoresist by the ion implantation.

Figure 10 shows the scratch-resistance variation of the photoresist layers by ion implantation at a constant accelerating energy and at increasing dose levels. The initial photoresist thickness of AZ-1350 and OSR was 4300 and 3000Å, respectively. The scratch resistance was expressed by the weight at which a sapphire needle could scratch the sample surface. A sapphire needle of 0.6 mm diam was positioned straight above the sample surface and then lowered downward with a weight. For comparison, the scratch resistance of chromium-oxide (Cr_xO_y) by the same measurement method was also shown in this chart. The figure shows that the scratch resistance for AZ-1350 and OSR increases to the level of chromium oxide as the dose level is increased. However in case the initial thickness is thick enough, *i.e.*, more than 1 μm, the scratch resistance stays very weak even after the ion implantation of the same conditions as mentioned above. This is a result of the insufficient ion range and the ion implantation did not harden the bottom of the resist.

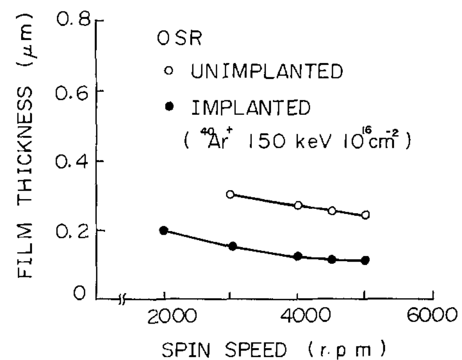

Fig. 7. Variation of the film thickness before and after ion implantation.

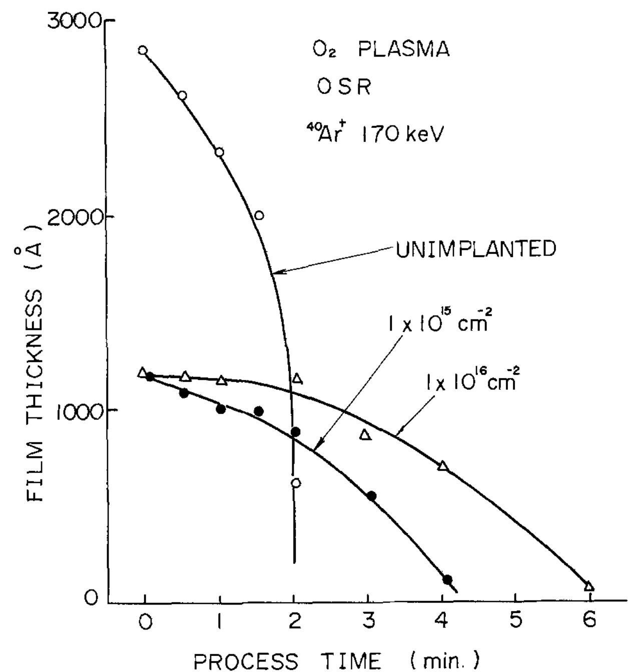

Fig. 8. Film thickness as a function of time in oxygen gas plasma

Figure 11 shows the thermal durability of the photoresist layer in dry O_2 atmosphere. The photoresist (OSR, 2600Å as initial thickness) was patterned on a silicon substrate in this case. Argon ions were implanted into the sample at 170 keV to a dose level of $10^{15} \sim 10^{16}$ ions/cm^2. The photoresist film thickness was decreased to 1200Å by this implantation. Then the sample was exposed to dry O_2 atmosphere in a variable temperature furnace for 15 min. After each heat-treatment the film thickness was measured by a Talystep. Figure 11 shows that the thermal durability of the resist films gradually increases with increasing dose levels.

Figure 12 shows the same evaluation as in Fig. 11 in dry N_2 atmosphere. The thermal durability of unim-

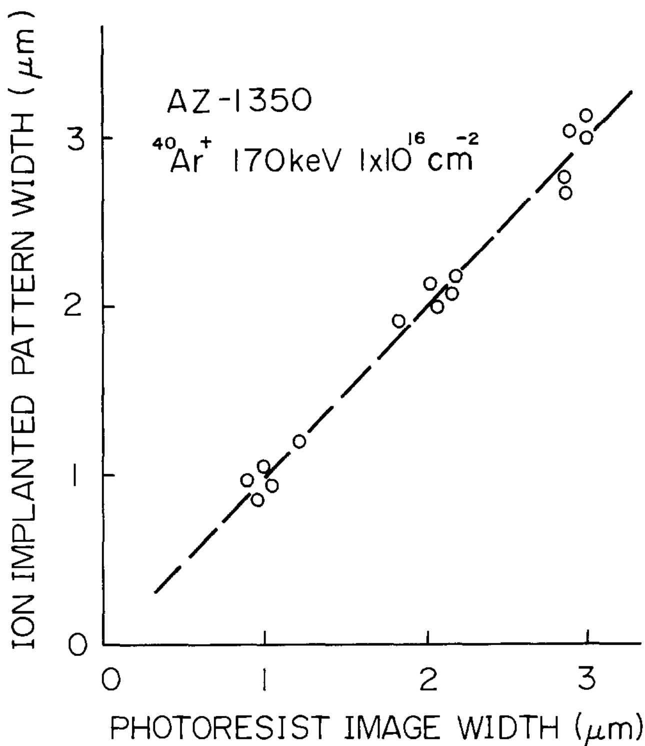

Fig. 9. The variation of pattern width before and after ion implantation.

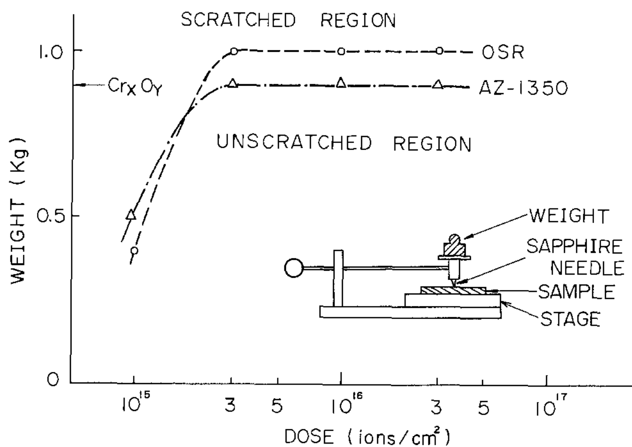

Fig. 10. The scratch resistance variation as a function of dose. The thickness of unimplanted photoresist was 4300Å (AZ-1350) and 3000Å (OSR), and $^{40}Ar^+$ was implanted at 170 keV.

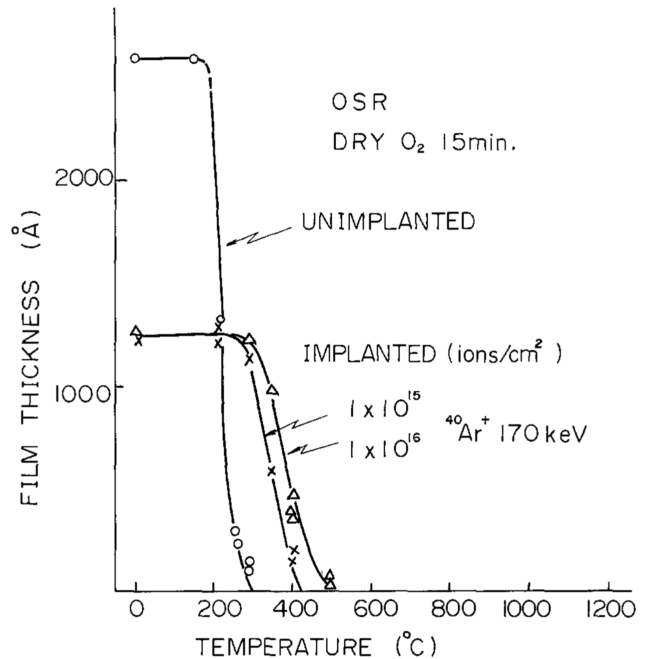

Fig. 11. Thermal durability of the photoresist film in dry O_2 atmosphere.

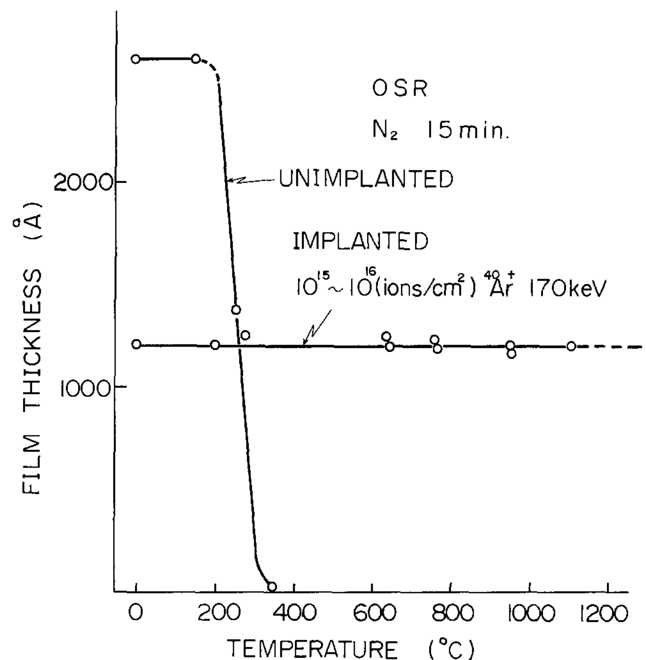

Fig. 12. Thermal durability of the photoresist film in N_2 atmosphere.

planted photoresist layer was very weak and the film thickness was decreased exceedingly at a certain temperature between 250° and 350°C. In contrast, the film thicknesses of ion-implanted photoresist did not decrease even at 1100°C, but after heat-treatment of more than 600°C, it was observed that the film became fragile and was easily scratched by a pincette. This result indicates that some change in quality occurred during the heat-treatment.

Graphitization by Ion Implantation

In our experimental activity, we noticed three phenomena which characterized high dose ion-implanted photoresist layers; (*i*) the color changed to brown or black according to the dose level; (*ii*) the thermal, physical, and chemical resistances were greatly improved; and (*iii*) the only way to strip the film off from the substrate was to combine it with oxygen. As these characteristics resemble those of graphite (disordered), we deduced that these phenomena by ion implantation were a result of graphitization.

In order to confirm this assumption, the ion-implanted photoresist was subjected to infrared absorption spectrum analysis and gas chromatographic analysis. Figure 13 shows the infrared light absorption spectrum of the photoresist layer before and after ion implantation. The ion-implanted photoresist was scraped off from the surface of silicon wafers using a diamond point and then it was collected for evaluation. The major absorption peaks of the unimplanted photoresist correspond to certain organic radicals, *e.g.*, $-CH_3$, $-C_6H_3$, and $-C{=}O$, which characterize the base polymer of the photoresist. They decreased by the ion implantation and finally they disappeared completely as shown in the figure at a dose level of 10^{16} ions/cm². This phenomenon suggests that the photoresist layer was converted from organic to inorganic material by the ion implantation and that the reaction

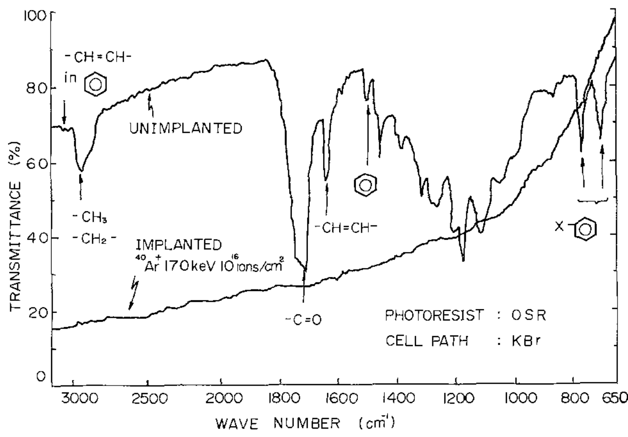

Fig. 13. Infrared light absorption spectrum of the photoresist layer before and after ion implantation.

had more to do with the base polymer than with the photoactive sensitizers.

Figure 14 shows the result of gas-chromatographic analyses for the resist layer before and after ion implantation. The sample preparation was the same as in the case of Fig. 13. The analyses were performed under the following conditions: thermal decomposition temperature, 720°C; column, molecular sieve, 50°C; carrier gas, He 0.8 kg/cm^2; detector, FID. The large peak for the unimplanted resist is due to poly (-vinyloxyethylcinnamate) (the composition of OSR). This peak became negligibly small by the ion implantation. For comparison, pure graphite (disorder) was subjected to the same analysis described above. A small peak appeared after the same retention time as in the case of OSR. Because of this resemblance of the peaks, we concluded that the ion-implanted resist was changed to nearly the same material as disordered graphite. This chemical change of photoresist, *i.e.*, graphitization, was supposed to be caused either by thermal or by mechanical effect of the ion implantation. The former possibility, however, was excluded because of the following two reasons: (*i*) Ion beam density (heat-generation rate) has no effect on the change of photoresist layer (Fig. 1); (*ii*) Unimplanted resist evaporates even in an inactive gas atmosphere at a certain temperature between 250° and 350°C (Fig. 12). Therefore we attributed the graphitization of photoresist to the mechanical bombardment effect by ions. According to this model, incident ions break the chemical bonds within photoresist, and successively scatter hydrogen and oxygen atoms away from the major radicals of the resist. As a result, the resist becomes relatively richer in carbon.

Application to a New Photomask

As one of the most profitable applications of ion-implanted resist, a new photomask manufacturing process is explained in detail.

In Fig. 15(A) a conventional process for making a photomask is described. A film of metal or metal oxide, *e.g.*, chromium oxide, is evaporated to a thickness of 1000-5000Å on the surface of a transparent glass substrate. Photoresist is patterned by using a conventional photolithographic technique. Then the film of metal or metal oxide is etched selectively using photoresist as a protective mask against an etching solution. Finally, the photoresist is removed and a conventional hard-type photomask is obtained.

Figure 15(B) shows a new photomask manufacturing process. At first, photoresist is patterned on a transparent glass substrate by using a conventional photolithographic technique. Then the entire top surface of the glass substrate is implanted with some suitable ions, such as $^{31}P^+$, $^{40}Ar^+$, etc. By this treatment ion-implanted photoresist becomes opaque to ultraviolet light. On the other hand, the glass substrate remains transparent to ultraviolet and to visible light. As a result, a high quality photomask can be readily obtained. In order to obtain a hard-type photomask by this method, it is necessary that the initial thickness of photoresist be less than 4000Å, accelerating energy be more than 120 keV, and the dose level be more than 3×10^{15} ions/cm^2. A requirement of increased optical density is easily achieved by thickening the photoresist and increasing the accelerating energy.

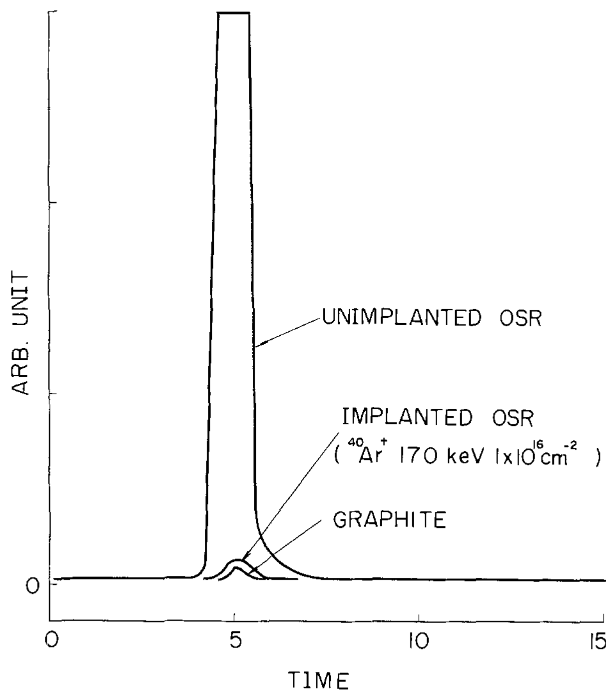

Fig. 14. Gas-chromatographic analysis of the photoresist layer before and after ion implantation.

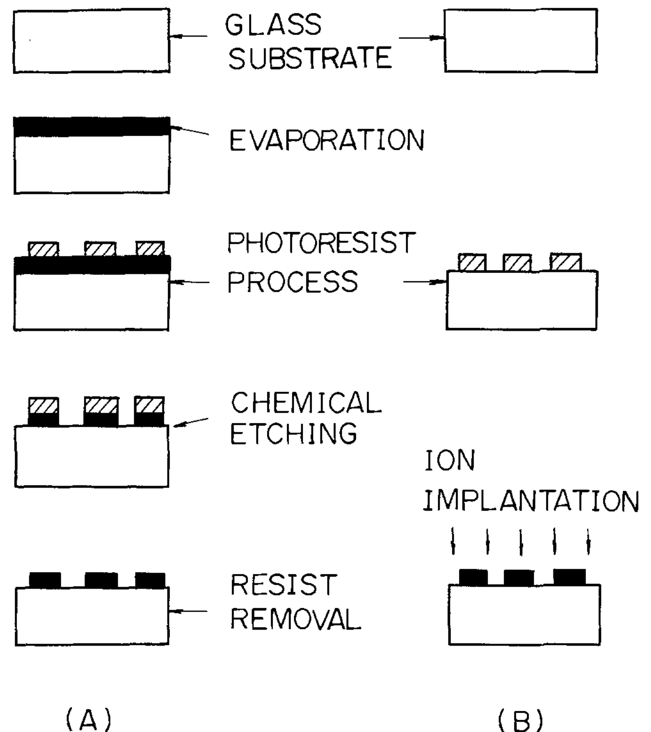

Fig. 15. Comparison of (A) conventional and (B) new process for photomask production.

This new process has completely eliminated the etching process. Accordingly, so-called "over-etching" will not appear at all. Therefore, the dimensional accuracy of photomask patterns is much improved. In addition, the production cost of photomask can be decreased due to the process simplicity.

Summary

The characteristics of heavily ion-implanted photoresist films are studied. Optical density increases in proportion to accelerating energy and to the logarithm of dose level. Other properties such as chemical durability, thermal resistance, scratch resistance, and adherence to a substrate are also improved greatly. No conventional stripping method can effectively remove the resist from the substrate except a forced recombination of the resist with oxygen. Moreover, no variation of the resist pattern is caused by ion implantation. Visible and ultraviolet light spectrometric and gas chromatographic experiments indicate that these characteristics are due to the change of photoresist to disordered graphite. By using ion-implanted resist as the dark portion of a photomask, economical yet excellent photomasks are successfully obtained.

Acknowledgments

The authors wish to thank Messrs. H. Tajima, H. Okabayashi, K. Uda, T. Igarashi, and T. Tashiro for preparing samples and for their assistance in ion implantation, and also Mr. H. Tsunemitsu for useful discussions and the reviewing of this paper. The authors also would like to thank Dr. M. Kamoshida, Messrs. K. Shimakura, K. Takahata, and K. Yamamoto, Drs. T. Yanagawa, Y. Miura, and T. Okada, and Mr. K. Sato for their encouragement.

Manuscript submitted July 25, 1977; revised manuscript received April 3, 1978.

Any discussion of this paper will appear in a Discussion Section to be published in the June 1979 JOURNAL. All discussions for the June 1979 Discussion Section should be submitted by Feb. 1, 1979.

Publication costs of this article were assisted by Nippon Electric Company, Limited.

REFERENCES

1. M. R. MacPherson, *Appl. Phys. Lett.*, **18**, 502 (1971).
2. J. R. Edwards and G. Marr, *IEEE Trans. Electron Devices*, **ED-20**, 283 (1973).
3. T. Hashimoto, T. Koguchi, Y. Okuyama, K. Yamamoto, K. Takahata, M. Kamoshida, and T. Yanagawa, 1976 IEDM Tech. Dig., 198 (1976).
4. J. F. Gibbons, W. S. Johnson and S. W. Mylroie, "Projected Range Statistics," 2nd ed, Dowden, Hutchinson, and Ross, Inc. Stroudsburg, Pa. (1975).
5. G. Baccarani and K. A. Pickar, *Solid-State Electron.*, **15**, 239 (1972).
6. Y. Okuyama and M. Kamoshida, *Denki Kagaku*, **41**, 482 (1973).
7. Y. Iida, H. Okabayashi, and K. Suzuki, *Jpn. J. Appl. Phys.*, **16**, 1313 (1977).

Deposition of Fluorine-Doped Silica Layers from a $SiCl_4/SiF_4/O_2$ Gas Mixture by the Plasma-CVD Method

D. Küppers, J. Koenings, and H. Wilson

Philips GmbH Forschungslaboratorium Aachen, 5100 Aachen, Germany

ABSTRACT

Silica layers doped with fluorine have been deposited inside a quartz glass tube from a $SiCl_4/SiF_4/O_2$ gas mixture. The oxidation reaction was initiated by a nonisothermal microwave plasma maintained at pressures of about 10 Torr and wall temperatures in the region of 1000°-1100°C. From the experiments it was found that fluorine was incorporated in the silica deposit, producing layers with a lower refractive index than that of pure silica. Although the reaction to form SiO_2 from a SiF_4/O_2 gas mixture is different from that with $SiCl_4/O_2$, the efficiency of the deposition reaction with $SiCl_4/SiF_4/O_2$ is comparable to that with $SiCl_4/O_2$.

Various techniques for the fabrication of low loss optical fibers have been described (1-3). To date, one of the most promising procedures utilizes a local reaction zone to deposit glassy layers of varying refractive indexes on the inner surface of a silica tube. To yield homogeneous deposition over a considerable length, the reaction zone must be moved to and fro. In a subsequent step the tube is collapsed to a rod called the preform, and a fiber is drawn (Fig. 1).

In order to guide light, the fiber core must have a refractive index slightly higher than that of the pure silica and, therefore, the deposit has to be doped. Hitherto the dopants most used have been GeO_2, P_2O_5, and B_2O_3, because they introduce negligible absorption losses in the wavelength region of interest, *viz.*, 0.8-1.3 μm. While nearly all dopants increase the refractive index of silica, the addition of B_2O_3 decreases it.

Commonly used dopants have been found to give rise to some unfavorable properties, such as: (*i*) the small change in refractive index on increasing the dopant concentration (B_2O_3); (*ii*) the quenching dependent nature of the change in the refractive index of silica on doping (B_2O_3); (*iii*) the formation of large stresses on doping (GeO_2); (*iv*) the depletion of the dopants from surface adjacent layers on collapsing of the tube to a rod (P_2O_5, GeO_2); and (*v*) the large decrease of the softening point of the glass when doped with the oxide (B_2O_3, P_2O_5).

Key words: doping, glass, plasma chemistry.

Recently it has been pointed out that doping with fluorine might be very attractive (4) since all these disadvantages are avoided. However, the application of the so-called modified chemical vapor deposition (MCVD) to fluorine containing gases gave rise to serious problems. Here, thermal reactions in the gas phase led to soot particles which fused into a compact layer at about 1400°-1600°C. It was found that the total deposition rate of fluorine-doped silica decreased remarkably, the more silicon tetrafluoride present in the gas phase (5). Further it would be desirable to incorporate more fluorine into the deposit in order to obtain a greater variation of the refractive index. The

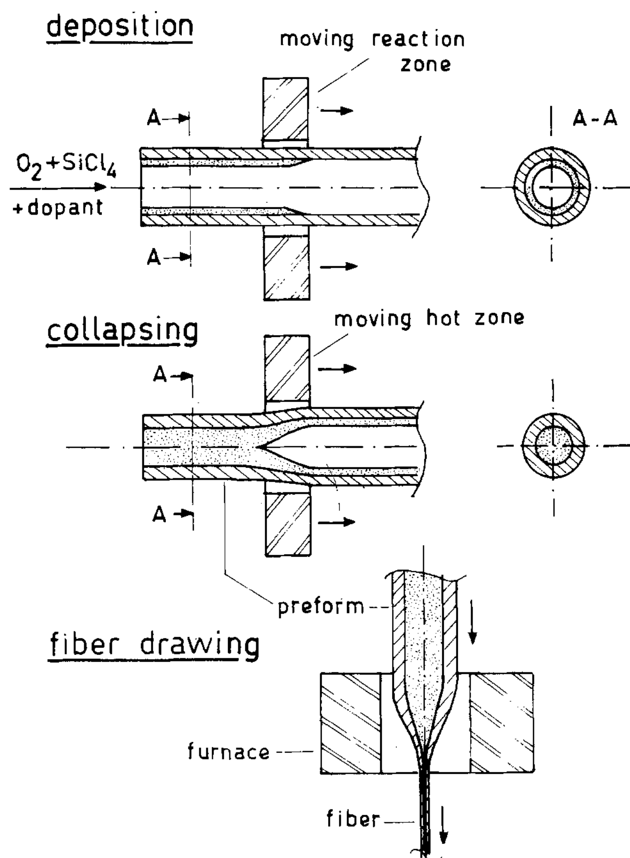

Fig. 1. Preparation steps in the optical fiber production route

core region of an optical fiber usually has a refractive index about 1% higher than the cladding glass. This implies that a fluorine content of at least 3 atomic percent (a/o) should be present (5, 6).

The plasma-activated CVD process (PCVD) had previously been applied successfully to the deposition of pure silica from a gas phase of composition $SiCl_4/O_2$ (7) and for deposition of doped silica from $SiCl_4/GeCl_4/O_2$ (3) for the preparation of optical fibers (8). The question arose whether it is also capable of fabricating fluorine-doped fibers.

From earlier work (9) it was known that oxyfluorides were formed by a SiF_4/O_2 nonisothermal plasma at temperatures of about 100°C and at pressures of about 0.8 Torr. Polymers were obtained of the approximate composition $(SiO_{1.5}F)_n$. The refractive index of the polymers was found to be less than 1.4, considerably lower than that of pure silica. In our plasma experiments the conditions normally differ from those mentioned above in that the total pressure is in the 1-30 Torr region and that the substrate temperature is typically 1000°-1200°C.

Experimental

The experimental setup consisted of a gas-supply system, a reactor, and a pumping system. The gas-supply system was made of stainless steel tubing and connectors. Mass flow controllers for $SiCl_4$, SiF_4, and O_2 allowed gas flow measuring and control. Prior to the measurements the gas supply system was checked for leakage, which was found to be less than 10^{-9} Torr · liter/sec. The $SiCl_4$ of electronic grade was obtained from Wacker Chemie. Oxygen of 99.998% purity (H_2O < 2 ppm) was used. The SiF_4 was obtained from Matheson and had the impurity specification of 0.3% air and 0.04% sulfur dioxide.

The reactor is shown schematically in Fig. 2. It consists of a silica tube with inner and outer diameters of $\phi_{id} = 8$ mm and $\phi_{od} = 10$ mm, respectively, a furnace

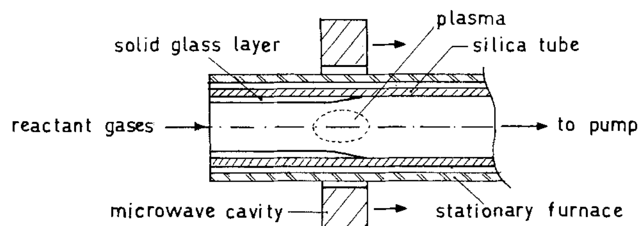

Fig. 2. Microwave reactor set up for the inside coating of a quartz tube.

and a microwave cavity. The furnace heats the tube to a temperature T_f of about 1100°C. The microwave plasma is maintained with the aid of a microwave cavity which is connected to a power supply capable of delivering $E_m = 200$ W at 2.45 GHz. The water-cooled cavity together with the furnace is mounted on a slide and can be moved rapidly to and fro. For mechanical reasons the maximum speed in our experiments was 17 cm/sec and the deposition length was 30 cm.

A sorption pump filled with a synthetic zeolite and cooled by liquid nitrogen was used to maintain an oil- and water-free atmosphere. Typical gas flows during the experiments were $Q_{O_2} = 100$ sccm, $Q_{SiCl_4} = 9\text{-}25$ sccm, and $Q_{SiF_4} = 0\text{-}5$ sccm, while the pressure in the reaction zone was normally between 10 and 20 Torr, as indicated by a capacitance manometer.

Results and Discussion

Microwave reactor stationary.—In the first experiments the reactor was held stationary and constant gas mixtures were supplied for a certain period of time. The results are discussed by means of Fig. 3. The upper photograph shows the results of an experiment in which oxygen together with silicon tetrachloride enters the tube from the left. The detailed experimental data are given in the legend to the figures. The result has been discussed earlier in detail (7). Silica is deposited in a small zone about 10 mm long, shifted in the direction of the incoming gas flow and 45 mm from the middle of the resonator cavity, which is indicated by a mark. The deposit is transparent and free from cracks.

The photograph in the middle is from an experiment in which silicon tetrachloride was replaced by silicon tetrafluoride at a lower flow rate. The other experi-

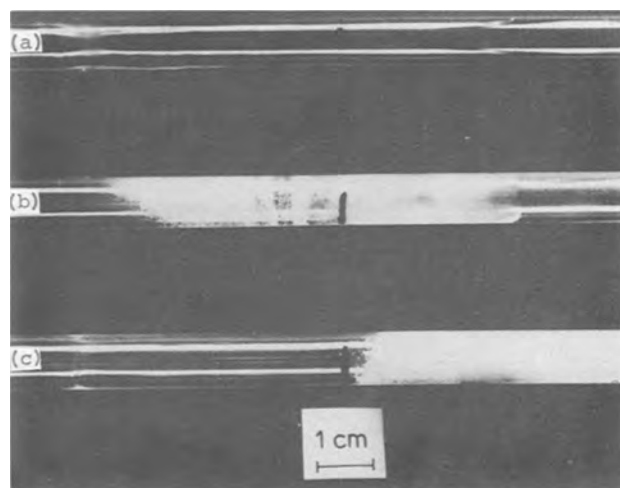

Fig. 3. Stationary deposition experiments, with the experimental conditions: $\phi_{od} = 10$ mm, $\phi_{id} = 8$ mm; $T_f = 1100$°C, $p = 8$ Torr, $E_m = 170$W. (a) $Q_{SiCl_4} = 9$ sccm, $Q_{O_2} = 110$ sccm; (b) $Q_{SiF_4} = 4$ sccm, $Q_{O_2} = 110$ sccm; (c) $Q_{SiCl_4} = 9$ sccm, $Q_{SiF_4} = 4$ sccm, $Q_{O_2} = 110$ sccm.

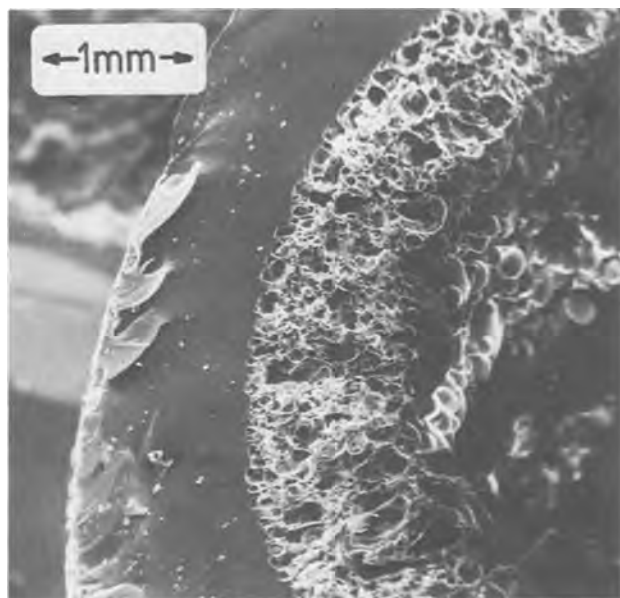

Fig. 4. SEM photograph of the opaque part of the deposit

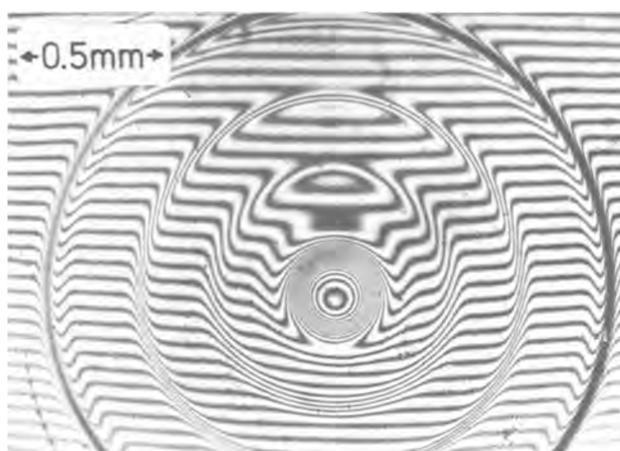

Fig. 5. Michelson interference micrograph of a preform core showing the decrease of refractive index with increasing fluorine content in the gas phase. (Wavelength, 550 nm; sample thickness, 200 μm).

mental conditions remained unchanged. Now the deposit was milky and opaque, it extended over a length of about ten times the inner diameter of the tube and it was approximately symmetrical about the middle of the resonator cavity.

The result of the third experiment, which is a combination of the former two, is given in the lower photograph. It is not a simple superposition of the two preceding photographs. The local deposit of silica appears at the same position as in the first experiment followed by a region which is transparent to the middle of the resonator. Thereafter the deposit is opaque again and even more extended than the deposit from SiF_4 alone. Figure 4 shows the consistency of the deposit in the opaque areas. It has a granular appearance and looks as though it was sintered from small spherical particles.

From these experiments it is clear that the deposition reaction from SiF_4/O_2 and $SiF_4/SiCl_4/O_2$ gas mixtures differs from that occurring with $SiCl_4/O_2$. No measurements characterizing the plasma itself have been carried out and therefore no detailed description of the processes occurring in the gas phase can be given. One may speculate, however, that the different gas-phase compositions lead to different species in the plasmas and also to different deposition kinetics.

Microwave reactor moving.—The experiment in which the deposition was studied from a mixture of $SiCl_4$ and SiF_4 was repeated with the reaction zone moving to and fro along the tube. About 1000 layers were deposited over a length of 30 cm. During the deposition the flow ratio of $SiF_4/SiCl_4$ was maintained at four increasing levels. The resulting deposit looked uniform and transparent apart from an opaque layer downstream from the main layer. This result is not to be expected from considerations of the static experiments. It is reminiscent of the case of a $SiCl_4/GeCl_4/O_2$ gas-phase composition (3) where it was found that the deposition profiles of SiO_2 and GeO_2 did not coincide in the static experiments. Instead they led to a partial separation of both oxides. When a multilayer structure was formed by moving the reactor rapidly to and fro to make the individual layers less than 1 μm thick, the separation was no longer detectable either in the collapsing behavior or in the optical properties of the preform. By analogy it is assumed that in the case of fluorine doping the multilayer structure also leads to a seemingly homogeneous layer when the individual layers are thin enough.

After deposition of the fluorine-containing layers, the tube was collapsed to a rod, with the core consisting of the deposited material. Slices were cut from the rod and viewed by Michelson interference microscopy. Figure 5 shows the resulting interference pattern. It is obvious that fluorine has been incorporated during deposition, leading to a remarkable decrease in refractive index. The influence of the flow ratio changes can be seen very clearly. Each of the steps consists of some hundreds of layers corresponding to the number of passes of the reaction zone. The increase in the refractive index at the center, as indicated by the concentric rings, reflects the fact that fluorine evaporates from the layers near the surface during collapsing. This is very similar to what happens with GeO_2 as the dopant. In practice, this effect is not of importance for the fabrication of optical fibers, since, in contrast to most other dopant materials, fluorine-rich layers must first be deposited, followed by layers containing less fluorine. This is a direct consequence of the fact that the refractive index of silica is lowered when fluorine is used as the dopant material.

Figures 6 and 7 give the results of two experimental runs, (x) and (·),[1] where the $SiF_4/SiCl_4$ ratio was changed, although the volumetric flow $Q_{SiX_4} = Q_{SiCl_4} + Q_{SiF_4}$ remained constant. In Fig. 6 the decrease in the refractive index is plotted *vs.* the ratio $q = Q_{SiF_4}/Q_{SiX_4}$. The greatest change in refractive index obtained under these experimental conditions is $\Delta n_{max} = -2.1 \times 10^{-2}$, corresponding to a change of 1.5% relative to pure silica. A first attempt with 50 mole percent (m/o) SiF_4 in the gas phase to get even greater changes in refractive index failed. Although the layer was of good appearance after deposition, bubbles developed on collapsing of the tube into a rod. It is thought that this is due to fluorine being released in the deposit at high temperatures. Analogously to the case of chlorine doping (4), we found that the curve is sensitive to changes in the deposition temperature.

The two experiments were made with two different microwave cavities. The cavity which gave the curve indicated by crosses ($\times$) had an inner length of 30 mm with a hole in the side walls of 30 mm diam which was off the cavity axis. The other cavity, with data designated by dots (·), had an inner length of 10 mm with a hole of 15 mm diam on the axis of the cavity.

The efficiency of the deposition process with $SiCl_4$ partially substituted by SiF_4 has been studied. The total volume of silica deposited per unit time dV_{SiO_2}/dt is given by

[1] With different microwave cavities as described later.

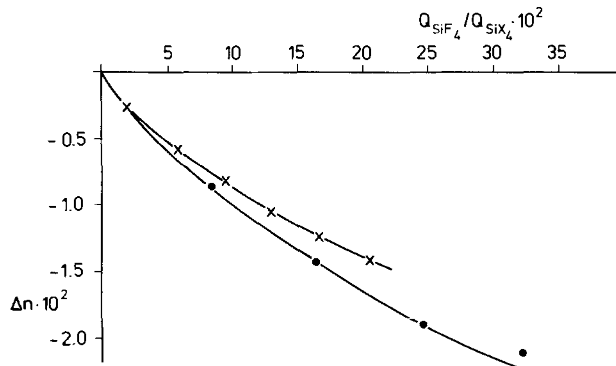

Fig. 6. Change of refractive index with increasing silicon tetrafluoride content in the gas phase for two separate runs, $Q_{SiX_4} = 10$ sccm.

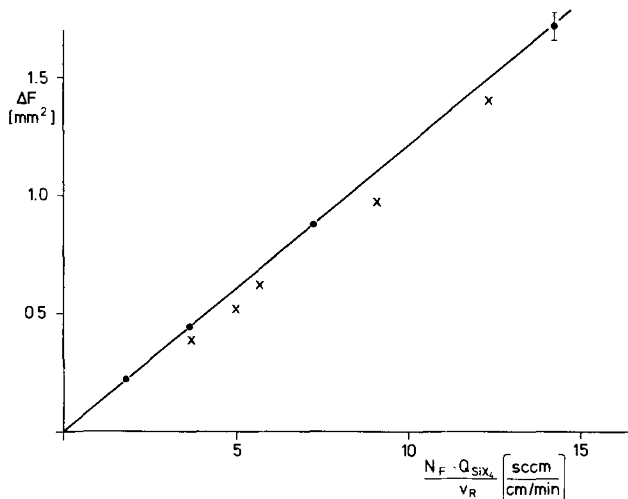

Fig. 7. Cross section of the rings as obtained for an increasing number of individual layers: $Q_{SiX_4} = 10$ sccm, $v_R = 2$ m/min (x), and $V_R = 3.5$ m/min (·).

$$dV_{SiO_2}/dt = \frac{f \cdot L}{t} = \Delta F/N_F \times v_R \quad [1]$$

where L is length of the deposition zone, f is cross-section area of one layer, t is time for one pass, v_R is the reaction zone velocity, N_F is the number of layers, and ΔF is the cross-section area of N_F successive layers, $\Delta F = N_F \times f$.

The maximum volume of SiO_2 that can be deposited if all SiF_4 and $SiCl_4$ is converted into SiO_2 is given by the formula

$$dV_{SiO_2}/dt = (Q_{SiX_4} \times M_{SiO_2})/(R \times T \times \rho_{SiO_2}) \quad [2]$$

where M_{SiO_2} = molecular weight of silica, R = gas constant per mole, $T = 273°K$, and $\rho_{SiO_2} = 2.201$ g/cm^3, the mass density of silica.

In Eq. [2] the influence of the incorporation of fluorine on the density of the deposit has been neglected. From Eq. [1] and [2] we get

$$\Delta F = M_{SiO_2}/(R \times T \times \rho_{SiO_2}) \times (N_F \times Q_{SiX_4})/v_R \quad [3]$$

From photographs similar to that of Fig. 5 ΔF can be obtained by measuring the radius of each ring. The number of layers N_F in each area is known from the experiments. Thus the theoretical curve of Eq. [3] for complete reaction can be calculated and is given in Fig. 7 as the full curve together with the measured values of two experimental runs.

There is no drastic decrease in the efficiency of the over-all reaction when SiF_4 is added to the gas flow, in contrast to the results of the MCVD process (6). In Fig. 7 it can be seen that the cavity with the greater field strength (·) gives complete reaction within experimental error. The other cavity (×) reflects a slightly lower yield.

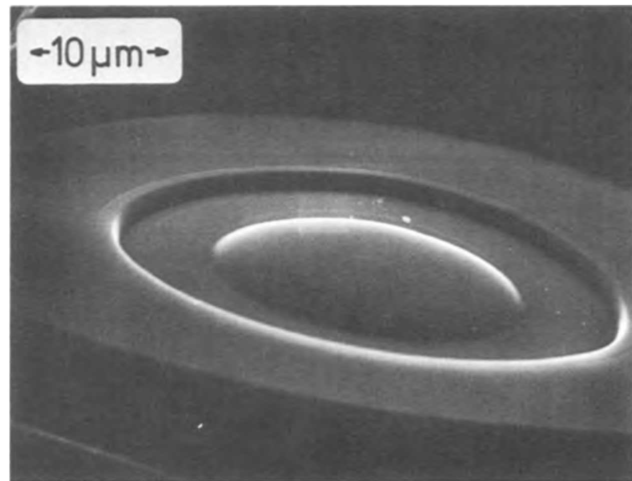

Fig. 8. Etch relief of a fluorine-doped graded index fiber

A graded index preform was prepared by coating the inner surface of a quartz tube with 400 layers of pure silica, followed by 1070 silica layers with constant fluorine concentration, and finally by 820 layers with decreasing fluorine content. The total flow of silica halides was up to 30 sccm in these experiments. After the collapsing of the tube into a rod, a fiber was drawn. Figure 8 shows a cross section of the fiber etched in HF solution. The fluorine-doped areas of the fiber are clearly visible due to the greater etch rate.

First fibers drawn from preforms prepared by the method described above show a minimum total loss of about 5 dB/km at 1050 nm wavelength. This indicates that the fluorine-doped layers are of good optical quality.

Summary

Highly transparent, thick glass layers doped with fluorine have been obtained by means of the plasma-activated CVD method. Although the stationary experiments gave nonuniform layers, good results were obtained when the reaction zone was moved repeatedly over some length of the substrate tube.

The over-all efficiency of the deposition process is not greatly influenced when silicon tetrafluoride is added to silicon tetrachloride. Under the experimental conditions applied, the greatest change in refractive index is found to be $\Delta n = -0.021$ with respect to pure silica.

Manuscript submitted Dec. 6, 1977; revised manuscript received March 17, 1978.

Any discussion of this paper will appear in a Discussion Section to be published in the June 1979 JOURNAL. All discussions for the June 1979 Discussion Section should be submitted by Feb. 1, 1979.

Publication costs of this article were assisted by Philips GmbH Forschungslaboratorium Aachen.

REFERENCES

1. P. C. Schultz, *Bull. Am. Ceram. Soc.*, **52**, 383 (1973).
2. J. B. McChesney, P. B. O'Connor, F. V. DiMarcello, J. R. Simpson, and P. D. Lazay, in "Proceedings of the 10th International Glass Congress," p. 40, The Ceramic Society of Japan, Kyoto (1974).
3. D. Küppers, J. Koenings, and H. Wilson, *This Journal*, **123**, 1079 (1976).
4. A. Mühlich, K. Rau, F. Simmat, and N. Treber, "1st European Conference Optical Fiber Comm.," IEE, London, September 1975.

5. K. Abe, "2nd European Conference Optical Fiber Comm.," p. 59, IEE, Paris, (1976).
6. K. Rau, A. Mühlich, and N. Treber, "Topical Meeting on Optical Fiber Transm.," p. TuC4, IEEE, Williamsburg (1977).
7. J. Koenings, D. Küppers, H. Lydtin, and H. Wilson, "5th International Conference on CVD," p. 270, The Electrochemical Society, London (1975).
8. D. Küppers, H. Lydtin, and L. Rehder, Ger. Pat. 24 44 100.
9. D. R. Secrist and J. D. Mackenzie, *Polym. Lett.*, **4**, 537 (1966).

Room Temperature Instabilities of p-Channel Silicon Gate MOS Transistors

Haruo Nakayama, Yoshihiro Osada, and Masahiro Shindo

Mitsubishi Electric Corporation, Kita-Itami Works, 4-1 Mizuhara, Itami, Hyogo, Japan

ABSTRACT

New unusual phenomena such as a rapid negative shift of a threshold voltage due to positive bias treatment, a time-dependent increase of a junction leakage current, and a fast recovery of a breakdown voltage after walk-out are observed on specially processed p-channel silicon gate MOS transistors. Furthermore the charge decay in specially processed FAMOS devices is found to be very fast compared with that in correctly processed devices. Process conditions inducing the instability are investigated and it is found out that 400°-500°C heat-treatment with a trace of ethyl alcohol or acetone after metallization induces the instability if a gate oxide contains a large quantity of boron. The activation energy of the mobile species which cause the threshold voltage shift is found to be 0.54 eV. A new model to explain these phenomena is proposed.

A room temperature instability of p-channel silicon gate MOS devices has been reported by Faggin *et al.* (1) and by Shimakura *et al.* (2). This instability appears as a rapid negative shift of a threshold voltage when positive bias is applied on a gate electrode even at room temperature. A breakdown voltage degradation (1) and an increased junction leakage current (2) have also been reported. The instability is observed only on silicon gate devices the gate oxide of which contains a large quantity of boron diffused from a boron-doped polysilicon electrode. Therefore, the existence of boron in the gate oxide must be an important factor of the instability. This alone, however, does not induce the instability, as is seen from the fact that correctly processed p-channel silicon gate devices are stable. Therefore, there must be other factors. Faggin *et al.* have reported that the instability occurs when devices are "prealloyed," that is, annealed at 500°C before metal mask so that aluminum covers the entire device. Shimakura *et al.*, on the contrary, observed the instability on the devices which were not "prealloyed." According to Shimakura *et al.*, the other factor of the instability is boron drive-in ambients.

In our work, process conditions inducing the instability are investigated and it is found out that a 400°-500°C heat-treatment after definition of aluminum, with a trace of ethyl alcohol or acetone attached to the wafers, induces the instability. Neither "prealloy" nor boron drive-in ambients are the major factor of the instability. Furthermore, various electrical characteristics of unstable devices are investigated in detail. And besides the threshold voltage shift, new unusual phenomena are observed on unstable devices: a time-dependent increase of a junction leakage current, a fast recovery of a breakdown voltage after walk-out, and a fast charge decay in FAMOS devices. Finally a new model to explain the instability is proposed.

Process Conditions Inducing the Instability

N-type (111) silicon wafers of 4-6 Ωcm resistivity were used. A 1200Å gate oxide was grown in a dry O_2 ambient at 1100°C. A 4000Å polysilicon film was deposited and defined by photolithographic technique. Boron predeposition was carried out for 20 min with B_2H_6 as a source gas, temperature being changed over a range from 950° to 1030°C. Subsequent boron drive-in was carried out in dry N_2 at 1100°C, in dry O_2 at 1100°C, or in H_2O at 950°C. As a result of boron-diffusion processes, source regions and drain regions were formed and gate electrodes were heavily doped with boron. The parameters of boron diffusion processes were decided in order to get a wide range of the boron concentration in the gate oxide. A 8000Å oxide was deposited and contact holes were defined. An aluminum film was evaporated, defined, and then alloyed in dry N_2 at 500°C. Finally, the wafers were subjected to 400°C heat-treatment in H_2 to reduce surface-state densities. Some wafers were dipped in ethyl alcohol prior to metallization. Some wafers were "prealloyed" for 10 min at 500°C in dry N_2 immediately after aluminum evaporation, that is, before definition of aluminum. The flow of sample preparation is illustrated in Fig. 1.

Table I summarizes the experimental parameters and threshold voltage shifts, ΔV_{th}, which were measured after 1 min BT treatment of $V_g = +20V$ at room temperature. Threshold voltage shifts were not uniform within a wafer, therefore the averages of 10 transistors are shown in Table I. It can be seen that ethyl alcohol attached to the wafer prior to metallization plays an important role. Negative shifts of threshold voltages were observed on all the samples treated with ethyl alcohol (Flows A and B), while the samples not treated with ethyl alcohol (Flows C and D) were all stable. Boron diffusion parameters were not the major factor of the instability. "Prealloy" did not induce the instability either.

In the second experiment, all the samples were fabricated without ethyl alcohol dip (Flow D), and therefore no threshold voltage shift was observed at the final stage of the usual wafer process. After the ΔV_{th} measurement, the samples were dipped in ethyl alcohol, acetone, toluene, trichloroethylene, freon, or deionized water, and baked for 30 min at temperatures

Key words: threshold voltage shift, junction leakage, walk-out, alumina silica catalyst.

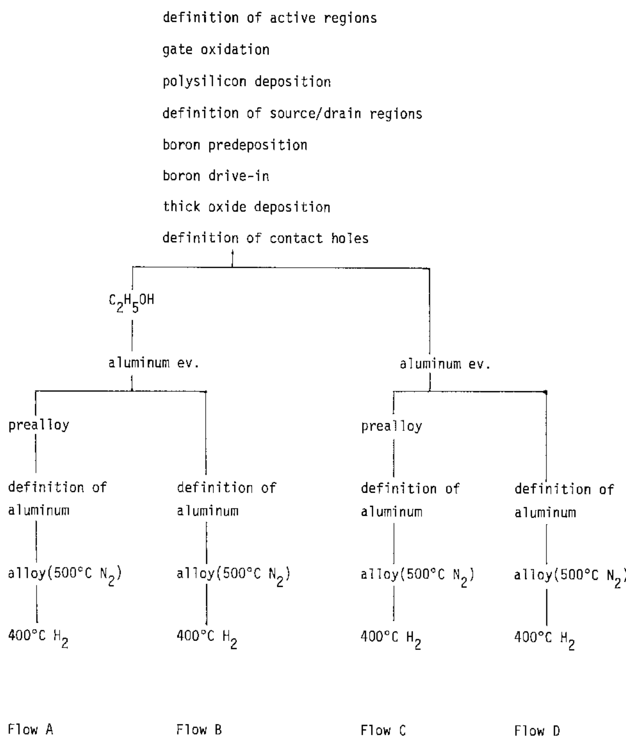

Fig. 1. Flow of sample preparation

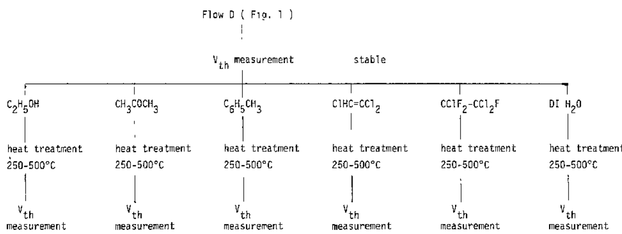

Fig. 2. Flow of sample preparation after usual wafer process

of 250°-500°C, and ΔV_{th} were measured again (Fig. 2). The experimental results are shown in Fig. 3, in which ΔV_{th} after 1 min BT treatment ($V_g = +20V$, room temperature) are plotted against the baking temperature. It can be seen that ethyl alcohol and acetone induce the instability at temperatures above 400°C. It is deduced, therefore, that in the case of the first experiment shown in Fig. 4 the instability was induced during the 500°C alloying step. Toluene, trichloroethylene, freon, and deionized water did not induce the instability over the experimented temperature range.

Alkali ion contaminations in ethyl alcohol or in acetone may be suspected to induce the instability, but this is not the case; ethyl alcohol dip performed prior to important processes such as gate oxidation, boron predeposition, and boron drive-in did not induce the instability.

In short, 400°-500°C heat-treatment after metallization induces the instability if the gate oxide contains a large quantity of boron and if ethyl alcohol or acetone is attached to the wafer. The mechanism is discussed later.

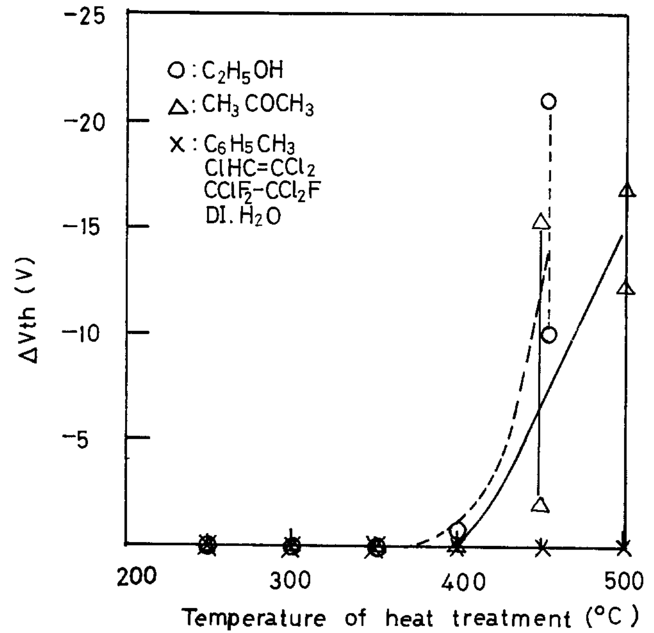

Fig. 3. Generation of the V_{th} drift instability due to heat-treatment with some kinds of chemicals attached to the wafer (Fig. 2).

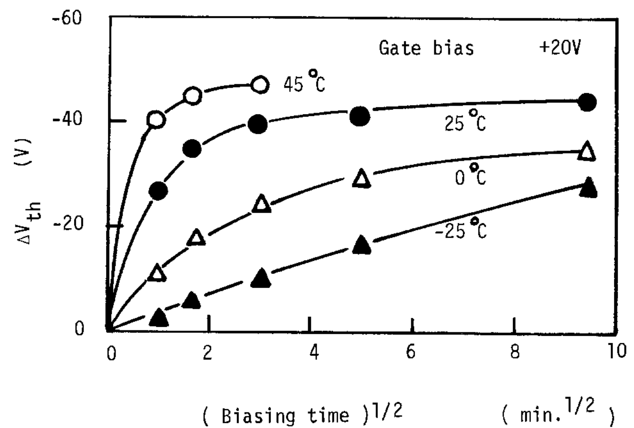

Fig. 4. Typical V_{th} shifts due to positive bias treatment

Table I. Process conditions and V_{th} shifts due to 1 min bias treatment of +20V at room temperature

Process conditions: Boron predeposition	Process conditions: Boron drive-in	Flow of sample preparation (Fig. 1)	V_{th} shifts $\overline{\Delta V_{th}}$* (V)		
950°C 20 min	1100°C N_2 30 min	B	−4.5	−10.2	−13.7
(ρ_{sP^+} ~ 60 Ω/□)	1100°C N_2 30 min	D	0.0	0.0	0.0
1000°C 20 min	1100°C N_2 30 min	A	−0.2	−0.8	−8.1
(ρ_{sP^+} ~ 30 Ω/□)	1100°C N_2 30 min	B	−1.0	−4.9	−22.7
	1100°C N_2 30 min	C	0.0	0.0	0.0
	1100°C N_2 30 min	D	0.0	0.0	0.0
	1100°C N_2 60 min	D	0.0	0.0	0.0
	1100°C O_2 30 min	D	0.0	0.0	0.0
	950°C H_2O 20 min +	C	0.0	0.0	0.0
	1100°C N_2 30 min	D	0.0	0.0	0.0
1030°C 20 min (ρ_{sP^+} ~ 20 Ω/□)	1100°C N_2 60 min	D	0.0	0.0	0.0

* Each $\overline{\Delta V_{th}}$ is the average ΔV_{th} of 10 transistors in a wafer (Three wafers for each process conditions).

Electrical Characteristics

Some interesting characteristics were observed on "unstable" MOS devices. The sample preparation conditions were as follows; boron predeposition at 1030°C for 20 min, boron drive-in at 1100°C in dry N_2 for 30 min, and ethyl alcohol dip prior to metallization (Flow B).

Threshold voltage shift.—The dependence of a threshold voltage shift, ΔV_{th}, on a biasing time and a temperature is shown in Fig. 4 for an applied gate bias of +20V. A large negative shift of a threshold voltage is observed. This shift is attributed to the change in the positive charge distribution in a gate oxide; positive charges move to the SiO_2/Si interface during positive bias treatment. The activation energy for the diffusion coefficient of the positive charge is calculated to be 0.54 eV.

Threshold voltage shifts were not uniform even within a wafer. An example is shown in Fig. 5, in which a large variation of ΔV_{th} is seen and contour lines can be drawn. This large variation of ΔV_{th} cannot be attributed to the variation of the boron concentration in a gate oxide, for the boron concentration was rather uniform within a wafer. The distribution of ΔV_{th} seems to be related to evaporation of liquid, probably ethyl alcohol.

Time-dependent increase of a junction-leakage current.—A drain-junction leakage current was measured with a gate electrode grounded. Figure 6 shows the experimental results. A reverse bias of −15V was applied to a drain and the leakage current was observed to increase rapidly. The rate of the increase depends on temperature. In the case of a measurement at 100°C, the leakage current after 10 min became two orders as much as the initial value. Then suddenly, the drain bias, V_d, was changed to −1V, and the leakage current was observed to decay to its saturation value for V_d = −1V.

The mechanism of this increase of a junction leakage current is considered to be as follows. Since the gate electrode is grounded and a negative bias is applied to the drain, the electric field in the gate oxide moves the positive charges to the vicinity of the drain. These positive charges in the vicinity of the drain enhance the electric field across the junction and increase the leakage current. The junction leakage current I_R is given by

$$I_R = MI_{Ro}$$

where M is a multiplication factor (3)

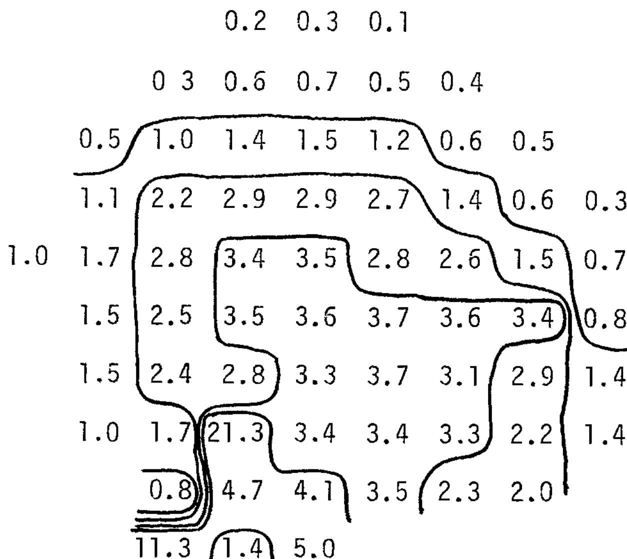

Fig. 5. Distribution of V_{th} shifts within a wafer due to 1 min bias treatment of +20V at room temperature.

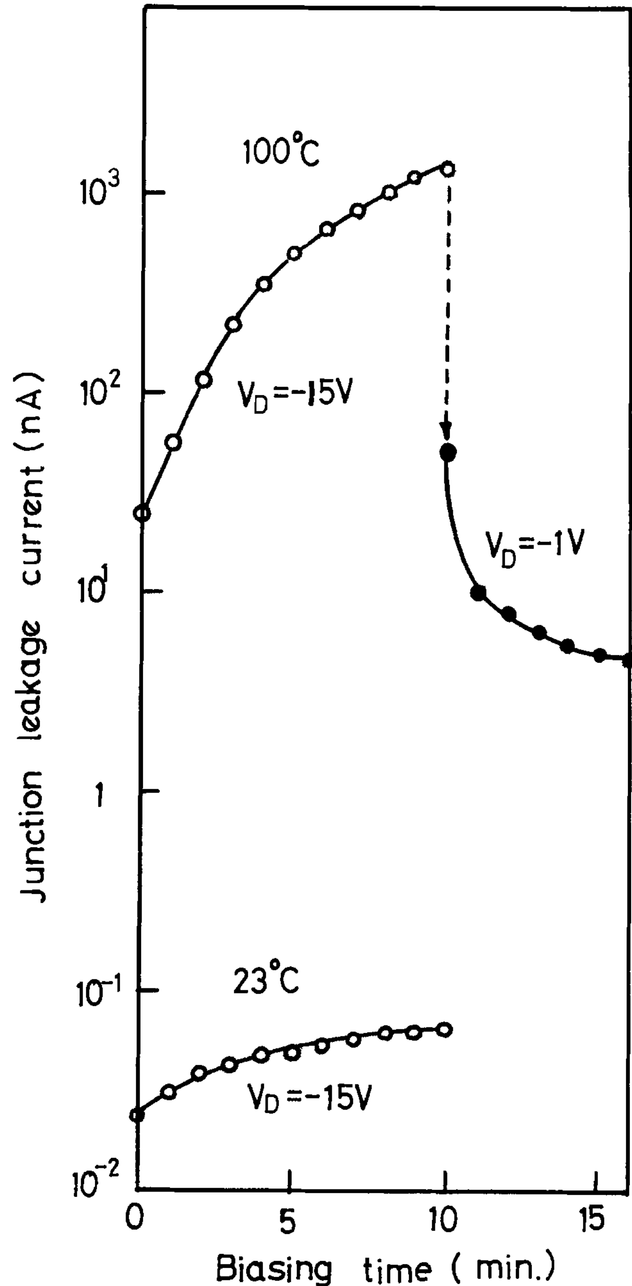

Fig. 6. Increase and decay of a junction leakage current observed on an "unstable" device.

$$M = \frac{1}{1 - (E/E_B)^n}$$

where E is the electric field across the junction; E_B is the electric field across the junction which induces an avalanche breakdown; and n is 3 ~ 6. If E is not negligible compared to E_B, as is the case of the experiment shown in Fig. 6, a small increase of E causes a large increase of a leakage current.

The mechanism proposed above was verified experimentally as is shown in Fig. 7. A reverse bias of −15V was applied to a drain of a "stable" MOS device and the dependence of the leakage current on a gate bias was investigated. A strong dependence can be seen for positive gate biases; the leakage current with a gate bias of +20V is two orders as much as that with the gate grounded. This positive gate bias simulates the effect of the positive charges near the drain of "unstable" gate-grounded devices because both enhance the electric field across the drain junction. This phenomenon is considered to correspond to a junction breakdown voltage degradation reported by Faggin *et al.* (1).

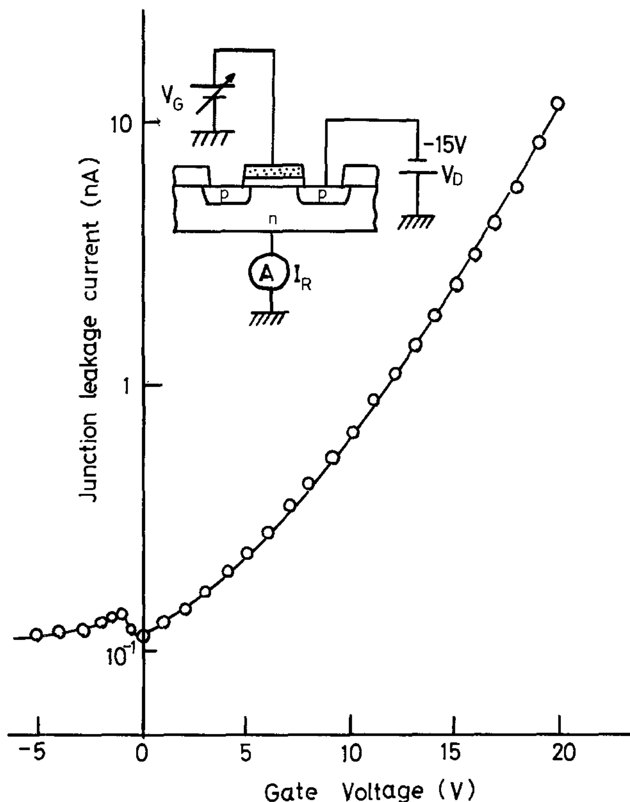

Fig. 7. Effect of a gate bias on a junction leakage current of a "stable" device.

Fast recovery of a breakdown voltage after walk-out.—It is well known that a junction breakdown voltage, V_B, shifts to a higher value when a high voltage enough for an avalanche breakdown is applied to a drain. This phenomenon is called walk-out. In the case of a p-channel MOS transistor, walk-out is considered to be caused by an injection of hot electrons, which are generated during avalanche, into the gate oxide near the drain (4). After avalanche has ceased, V_B will remain at its high value initially but after a long period of time it will recover to its initial value, V_{Bo}. This recovery is considered as a consequence of the escape of the trapped electrons. This recovery characteristic was studied for "unstable" MOS transistors as well as "stable" devices.

Breakdown voltages were measured with the gate electrodes grounded. Initial breakdown voltages, V_{Bo}, were -30V for all samples. Then walk-out was carried out with the gates grounded, a reverse bias of -50V being applied to the drain electrodes for 1 min. As a consequence of walk-out, breakdown voltages became -50V. In other words, the breakdown voltage shifts immediately after walk-out, $\Delta V_B(0)$, were 20V. In the next step, the samples were stored at temperatures of 100°-200°C for time t. Then breakdown voltages were measured again. In Fig. 8 $\Delta V_B(t)/\Delta V_B(0)$ are plotted against storage time t for various temperatures. Here $\Delta V_B(t)$ are the differences between the initial V_{Bo} and V_B after high temperature storage. The recovery of walk-out is described by

$$\Delta V_B(t)/\Delta V_B(0) \propto t^{-\lambda}$$

where λ is a function of temperature and varies for different devices (5). From Fig. 8 it is found that the recovery is extremely fast for "unstable" devices. This means that trapped electrons escape much faster in "unstable" devices than in "stable" devices.

Charge decay in p-channel FAMOS devices.—In a p-channel FAMOS device, the electrons transported from substrate across a gate oxide by an avalanche injection are stored in a floating polysilicon gate and induce a channel between a source and a drain. The storage of electrons in the floating gate needs no power supply, therefore a FAMOS device is a kind of a nonvolatile memory.

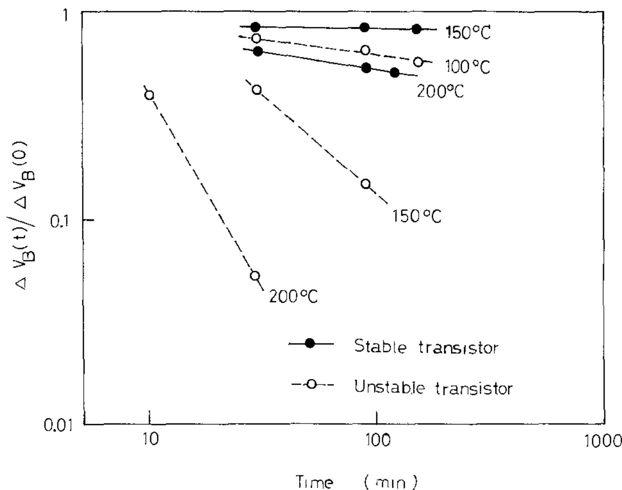

Fig. 8. Recovery of a junction breakdown voltage after walk-out

The retention characteristics were studied for correctly processed FAMOS devices and for FAMOS devices treated with ethyl alcohol (6). The memory retention time τ_{ret} depends on temperature exponentially

$$\tau_{ret} \propto \exp(\Delta E/kT)$$

In the case of correctly processed FAMOS devices, $\tau_{ret}(250°C)$ is an order of 10^6 sec and ΔE is 2.8 ~ 3.2 eV, therefore, the electrons will be stored for more than 10 years at a temperature lower than 150°C. On the other hand, the retention capability of FAMOS devices treated with ethyl alcohol was found to be very poor; $\tau_{ret}(250°C)$ is 10^3 ~ 10^5 sec and ΔE is 0.8-2.2 eV.

Mechanism of the Instability

This instability is considered to be due to positive charges which move fast in a gate oxide. In Faggin's model, H^+ ions are generated during prealloy and these H^+ ions are the moving species. One of the reasons is the agreement of the diffusion constants as shown in Fig. 9, which is cited from Fig. 11 of the Ref.

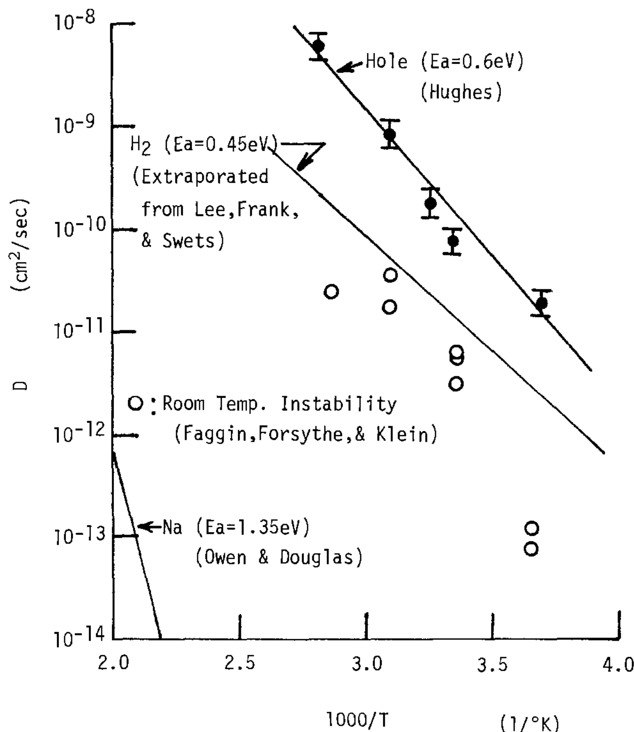

Fig. 9. Temperature dependence of diffusion constants

(1). But this model cannot explain the reason the instability appears only on p-channel silicon gate MOS devices. An explanation proposed by Shimakura *et al.* is based on an assumption that H^+ ions move much faster in a boron-doped oxide than in a nondoped oxide. According to their model, the amount of a threshold voltage shift depends on the thickness of a boron-doped oxide layer which is formed in the upper region of a gate oxide during the boron drive-in process. But our experimental results showed no dependency on the boron diffusion conditions, which must be related to the thickness of the boron-doped oxide layer, as shown in Table I.

An alternative model, which is based on our experimental results, is as follows. H^+ ions or H atoms are generated from ethyl alcohol at temperatures of 400°-500°C.

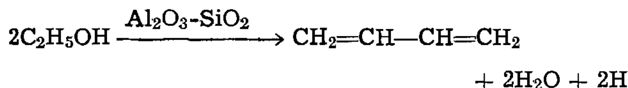

$$2C_2H_5OH \xrightarrow{Al_2O_3\text{-}SiO_2} CH_2{=}CH{-}CH{=}CH_2 + 2H_2O + 2H$$

Al_2O_3-SiO_2 is known to be an effective catalyst of the chemical reaction and considered to exist at the Al/SiO_2 interface (Fig. 10). The hydrogen generated must be in a reactive form to induce the instability, because our experiment showed that heat-treatment at 400°C in an H_2 ambient does not induce the instability if the sample is processed correctly (Flows C and D of Fig. 1). The reactive hydrogen diffuses to a gate oxide which contains a large quantity of boron. Boron is a kind of network former, and a rearrangement of the SiO_2 network may take place with the aid of reactive hydrogens, and hole traps may be generated as illustrated in Fig. 10. Holes which are initially located near the poly-Si/SiO_2 interface drift to the SiO_2/Si interface by positive bias and induce the instability. The amount of a threshold voltage shift depends on the number of hole traps in the gate oxide, which in turn depends on the amount of hydrogen generated from ethyl alcohol or acetone.

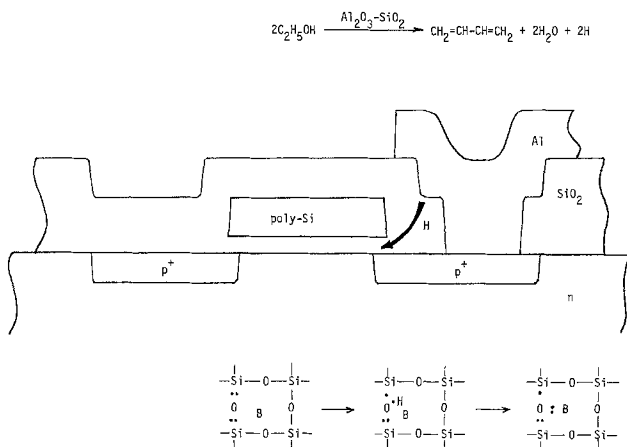

Fig. 10. Proposed model for the generation of hole traps

The mobility of hole in an oxide film has been measured by R. C. Hughes and found to follow $\mu = 20 \exp(-0.6 \text{ eV}/kT)$ cm/Vsec. The diffusion constant D can be calculated from μ using Einstein's relation

$$D = kT\mu/q$$

and it is plotted in Fig. 9. Fairly good agreement is recognized.

Summary

A room temperature instability has been found to occur if the following conditions are satisfied: (*i*) a large quantity of boron is contained in the gate oxide; (*ii*) a trace of ethyl alcohol or acetone is attached to the wafer; and (*iii*) heat-treatment of 400°-500°C. The latter two suggest the chemical reaction that hydrogen is generated from ethyl alcohol or acetone with Al_2O_3-SiO_2 catalyst. To explain why the first condition is necessary, a new model has been proposed; that is, hole traps are generated in a boron-containing gate oxide with the aid of hydrogen and holes are the moving species of the instability.

New unusual phenomena are observed on the unstable devices besides the already reported V_{th} drift. A junction leakage current increases with time. A junction breakdown voltage after walk-out recovers to its initial value much faster than stable devices. The charge decay of p-channel FAMOS devices is very fast. All these phenomena are related to charge transport in a gate oxide.

Acknowledgments

The authors wish to acknowledge helpful discussion with Tomoichi Ishikawa, Katsuhiko Hasegawa, Tatsuya Enomoto, Masanobu Tosa, and Dr. Taiji Oku.

Manuscript submitted Sept. 6, 1977; revised manuscript received March 30, 1978. This was Paper 89 presented at the Philadelphia, Pennsylvania, Meeting of the Society, May 8-13, 1977.

Any discussion of this paper will appear in a Discussion Section to be published in the June 1979 JOURNAL. All discussions for the June 1979 Discussion Section should be submitted by Feb. 1, 1979.

Publication costs of this article were assisted by Mitsubishi Electric Corporation.

REFERENCES

1. F. Faggin, D. D. Forsythe, and T. Klein, in "Proceedings of the 8th Annual Reliability Physical Conference (1970).
2. K. Shimakura, T. Suzuki, and Y. Yadoiwa, *Solid-State Electron.*, **18**, 991 (1975).
3. A. S. Grove, "Physics and Technology of Semiconductor Devices," p. 194, John Wiley & Sons, Inc., New York.
4. H. Hara, Y. Okamoto, and H. Ohnuma, *Jpn. J. Appl. Phys.*, **9**, 1103 (1970).
5. R. W. Gurtler, *IEEE Trans.*, **ED-15**, 980 (1968).
6. Y. Kuramitsu, H. Matsumoto, Y. Nakao, H. Nakayama, and H. Harima, in "Proceedings of the 10th Symposium on Semiconductors and IC Technology," Tokyo, 6 (1976).
7. R. C. Hughes, *Appl. Phys. Lett.*, **26**, 436 (1975).

Concentration Dependence of a Diffusion Coefficient at Phosphorus Diffusion in Germanium

Satoru Matsumoto and Tatsuya Niimi

Department of Electrical Engineering, Keio University, Hiyoshi, Yokohama 223, Japan

ABSTRACT

Phosphorus diffusion into germanium is carried out at 600°-750°C by using red phosphorus powder as a diffusion source. Source temperatures are maintained at 240° and 430°C, corresponding to low and high surface concentrations, respectively. At low surface concentration, C_s 3-7 $\times$ 10^{18} cm^{-3} ($C_s \sim n_i$, n_i; intrinsic carrier concentration at the diffusion temperature), concentration profiles agree well with the erfc curves, showing the behavior of Fick's law. While at high surface concentration, C_s 5-8 $\times$ 10^{19} cm^{-3} ($C_s > n_i$), profiles deviate from the erfc curves. Diffusion coefficients depend both on the local and surface concentrations, representing the same result as that of phosphorus diffusion into silicon.

There is little information regarding diffusions of group III and V elements into germanium. As for phosphorus diffusion into germanium, three researches by Dunlap (1), Meer *et al.* (2), and Lehovec *et al.* (3) have been reported. It is not clear in these experiments, however, except in those by Lehovec *et al.* whether diffusions were carried out under low surface concentration or under high surface concentration. The precise concentration profiles of phosphorus were not given in those reports. Moreover, the concentration dependence of the diffusion coefficient of phosphorus in germanium has not been reported yet.

In this article, in order to investigate the concentration dependence of the diffusion coefficient of phosphorus in germanium, diffusions are carried out both at low and high surface concentrations and the diffusion coefficients of phosphorus are determined for the respective cases. Furthermore, the mechanism of the phosphorus diffusion in germanium is discussed by comparison with the phosphorus diffusion in silicon.

Experimental procedure.—Substrates used were (111) oriented p-type germanium single crystals of resistivity 1.9-2.7 $\Omega \cdot cm$ and of thickness 200 μm. They were chemically polished by etching with CP-4A solution. Phosphorus diffusions into germanium were carried out from the vapor phase with red phosphorus powders as a diffusion source. Red phosphorus powders were placed at one end of a vacuum-sealed quartz tube and a germanium substrate on the other end. The range of the diffusion temperature was from 600° to 750°C. In order to carry out phosphorus diffusions under conditions of low and high surface concentrations, the source temperatures of red phosphorus were held at 240° and 430°C, respectively. The technique with the anodic oxidation and sheet resistivity measurement was used to determine the concentration of phosphorus in germanium. The anodic oxidation was done in the solution of *N*-methylacetamide ($CH_3CONHCH_3$) and 0.04*N* potassium nitrate (KNO_3). The thickness of germanium dioxide (GeO_2) formed by the anodic oxidation was controlled by the oxidizing time. GeO_2 on the substrate was washed by deionized water and sheet resistivity was measured by the four-point probe method at each step. The thickness of the removed thin layer by one step was previously determined by the repetition of the anodic oxidation of a dummy sample. Phosphorus concentrations at various depths from the surface were determined by using the relation between resistivity and impurity concentration (4).

Results and Discussion

Figure 1 shows a typical concentration profile of phosphorus, which was obtained at a source temperature of 240°C and a diffusion temperature of 700°C. In the diffusion temperature range of the present work, 600°-750°C, the values of the surface concentration of phosphorus obtained at the source temperature of 240°C are 3-7 $\times$ 10^{18} cm^{-3}. The values of the intrinsic carrier concentration n_i corresponding to this diffusion temperature range are 3-7 $\times$ 10^{18} cm^{-3} (5). Therefore, at the source temperature of 240°C, diffusions are carried out under condition of low surface concentration. A full line in Fig. 1 is a theoretical curve (erfc), showing a good agreement with the measured points. From this result, Fick's law is obeyed under condition of low surface concentration. At low surface concentration, concentration profiles obtained at other diffusion temperatures also agree well with the erfc curves.

Figure 2 shows typical concentration profiles of phosphorus which were obtained at a source temperature of 430°C and a diffusion temperature of 700°C for 2 and 10 hr. In the case of a source temperature

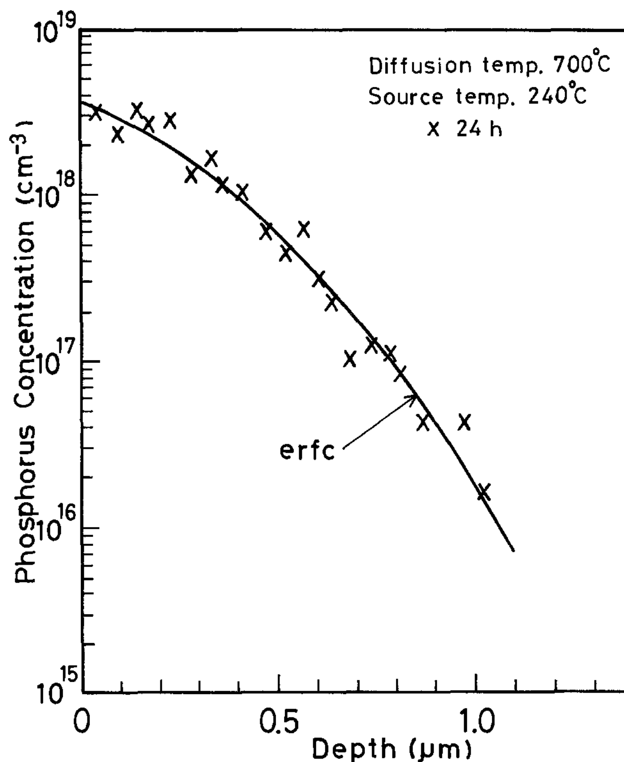

Fig. 1. Concentration profile of phosphorus in germanium. A full line is a theoretical curve (erfc).

Key words: vapor phase phosphorus diffusion, germanium, concentration-dependent diffusion coefficient.

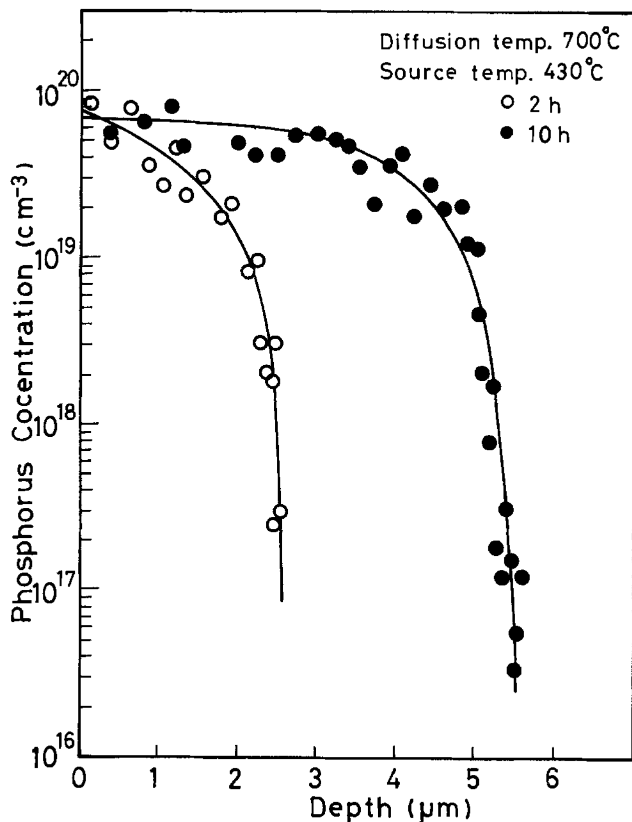

Fig. 2. Concentration profiles of phosphorus in germanium

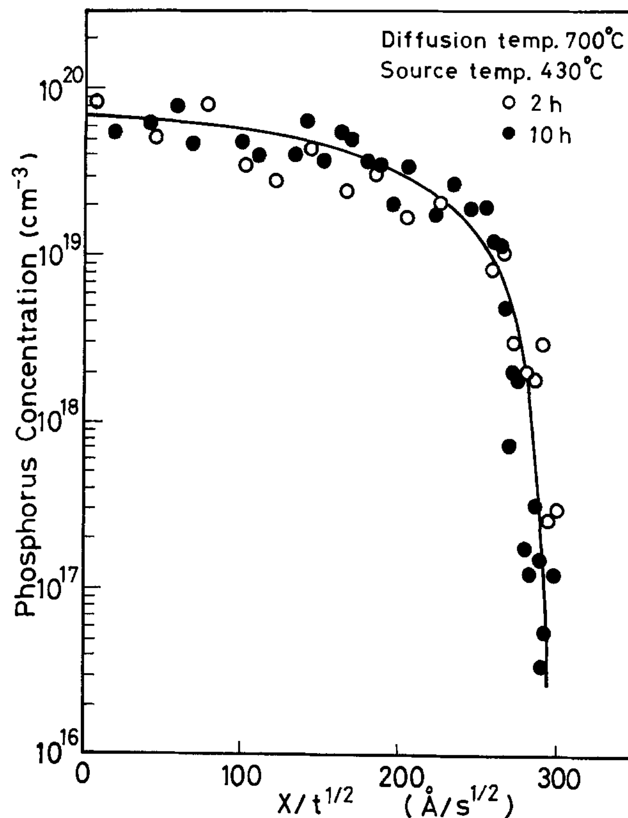

Fig. 3. Concentration profile of phosphorus as a function of $x/t^{1/2}$, which is obtained from Fig. 2.

such as this, the values of the surface concentration are 5-8 $\times$ 10^{19} cm^{-3} at the diffusion temperature range of the present work. The surface concentrations are much larger than n_i's at the diffusion temperatures. Therefore, in the case of 430°C, diffusions are carried out under condition of high surface concentration. Unlike the profile at low surface concentration, the concentration profiles in Fig. 2 do not agree with the erfc curves. For the diffusions at high surface concentration, the concentration profiles at other diffusion temperatures also do not agree with the erfc curves. Since the diffusion coefficients cannot be determined with ease in such case, Boltzmann-Matano analysis (6) can be used to determine them. In Fig. 3, phosphorus concentrations in Fig. 2 are plotted as a function of $x/t^{1/2}$, where x is the depth and t is the diffusion time. As shown in Fig. 3, phosphorus concentrations are a function of $x/t^{1/2}$ only, and then the applying condition of the analysis is satisfied. For the other diffusion temperatures in addition to 700°C, this applying condition is also satisfied.

The diffusion coefficients calculated by Boltzmann-Matano analysis are shown in Fig. 4 as a function of the local phosphorus concentration for respective diffusion temperatures. Diffusion coefficients are nearly constant at lower phosphorus concentration but increase rapidly with the phosphorus concentration for every diffusion temperature. Diffusion coefficients at the concentration of 1 $\times$ 10^{17} cm^{-3} where no local concentration dependence of the diffusion coefficient is seen in Fig. 4, D_h's are tentatively chosen. D_h's are plotted in Fig. 5 as a function of the reciprocal of absolute diffusion temperatures. Diffusion coefficients, D_l, which are obtained under conditions of low surface concentration, are also shown in Fig. 5. D_l and D_h are expressed by the following equations

$$D_l = 3.3 \times 10^2 \exp(-3.1\ \mathrm{eV}/kT)\ \mathrm{cm^2/sec} \quad [1]$$

$$D_h = 1.0 \times 10^{-2} \exp(-2.1\ \mathrm{eV}/kT)\ \mathrm{cm^2/sec} \quad [2]$$

Equation [1] is determined by the present results, including the data by Lehovec *et al.* (3). It should be noted that the diffusion coefficients in Fig. 4 are larger

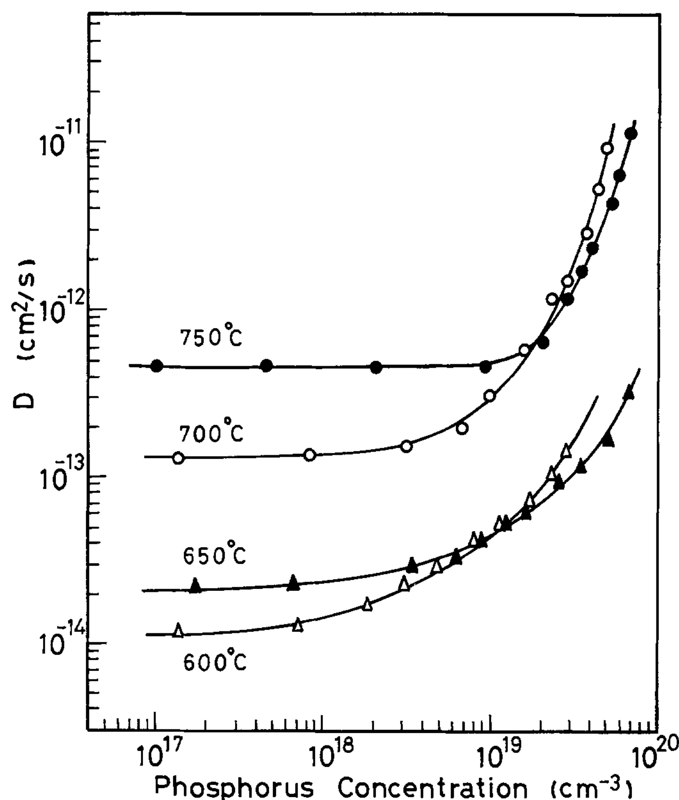

Fig. 4. Diffusion coefficient *vs.* phosphorus concentration for diffusions at source temperature 430°C, with diffusion temperature as a parameter.

than D_l not only at higher phosphorus concentration but also at lower ones. Results by Dunlap (1) and Meer *et al.* (2) are also shown in the figure, though their experimental conditions were not clear.

After diffusion, the layer with a thickness of 20-30μm was lapped from the surface to investigate the influence of the thermal treatment of the sample. The change in conductivity type was not seen through the diffusion. Little change was observed in resistivity through the diffusion with the high surface concentration, though a little change was observed at the low surface concentration. Therefore, the influence of the thermal treatment of the sample was negligibly small.

The theoretical curve in Fig. 1 is based on a constant surface concentration throughout the diffusion. It is well known that the surface barrier is present at the surface of germanium for impurity diffusion from the vapor phase (7) though. It is, however, confirmed that the diffusion times used in the present work are long enough to establish the state of equilibrium at the surface. It is shown in Fig. 2 that the surface concentration does not change with the diffusion times.

From the results of Fig. 4 and 5, it is found that the diffusion coefficients in germanium depend not only on the local concentration but also on the surface concentration. This is the same result as that of phosphorus diffusion into silicon. The present result seems to indicate that the diffusion mechanism of phosphorus in germanium is the same as that of phosphorus in silicon. Recently, a model on the basis of E center (phosphorus-vacancy pair) diffusion has been proposed to explain the dependence of the diffusion coefficient of phosphorus in silicon on the local and the surface concentrations (8). Although the presence of E centers is not identified in germanium, it is inferred that E centers may control the phosphorus diffusion in germanium. Furthermore, it has been made clear that the local concentration dependence of the diffusion coefficient of phosphorus in silicon is attributed to the diffusion-induced strain (9). The remarkable increase of the diffusion coefficient at the higher concentration in Fig. 4 is also considered to be due to the strain effect by the difference of the covalent radii of germanium and phosphorus.

It is well known that at phosphorus diffusion in silicon with high surface concentration, a kink is found in the concentration profile at relatively low diffusion temperatures (below approximately 1000°C) (8). The kink is, however, not found in the concentration profile in the present work. On the other hand, a diffusion "tail" was reported by Lehovec *et al.* (3). It is, however, considered that this tail has no relation with the mechanism of the kink formation in silicon because it was observed at very low concentration region and at low surface concentration unlike the case in silicon. Further investigation must be required to decide whether the kink formation is peculiar to phosphorus diffusion into silicon.

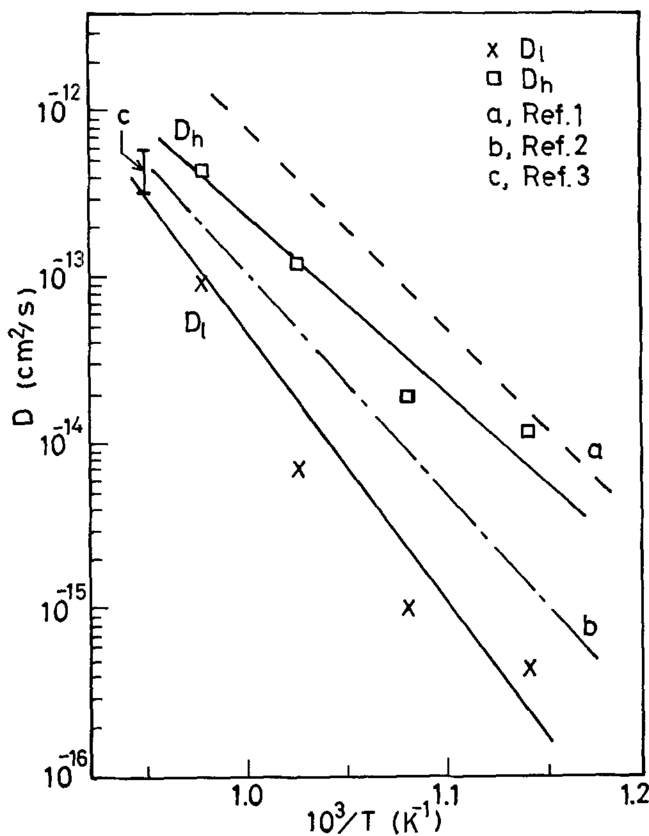

Fig. 5. Diffusion coefficient vs. reciprocal absolute temperature. D_l (×) are obtained at source temperature 240°C and D_h (□) at 430°C.

Summary

Phosphorus diffusion into germanium is performed under conditions of low and high surface concentrations. At low surface concentration Fick's law is obeyed, while at high surface concentration, concentration profiles deviate from the erfc curves. Diffusion coefficients in this case depend both on the local and on the surface concentrations. This result is the same one as that of phosphorus diffusion into silicon, indicating that phosphorus in germanium diffuses via the diffusion of E centers.

Acknowledgments

The authors wish to express their gratitude to the Sakkokai Foundation for financial support of this work. They also wish to thank Messrs. Y. Enomoto and H. Tajima for their help during the experiments.

Manuscript submitted Sept. 13, 1977; revised manuscript received March 7, 1978.

Any discussion of this paper will appear in a Discussion Section to be published in the June 1979 JOURNAL. All discussions for the June 1979 Discussion Section should be submitted by Feb. 1, 1979.

Publication costs of this article were assisted by Keio University.

REFERENCES

1. W. C. Dunlap, *Phys. Rev.*, **94**, 1531 (1954).
2. W. Meer and D. Pommerrenig, *Z. Angew. Phys.*, **123**, 369 (1969).
3. K. Lehovec and C. Pihl, *This Journal*, **108**, 552 (1961).
4. S. M. Sze, "Physics of Semiconductor Devices," p. 43, Wiley-Interscience, New York (1969).
5. F. J. Morin and J. P. Maita, *Phys. Rev.*, **94**, 1525 (1954).
6. C. Matano, *Jpn. Phys.*, **8**, 109 (1933).
7. F. M. Smits and R. C. Miller, *Phys. Rev.*, **104**, 1242 (1956).
8. M. Yoshida, E. Arai, H. Nakamura, and Y. Terunuma, *J. Appl. Phys.*, **45**, 1498 (1974).
9. S. Matsumoto and T. Niimi, Paper 353 presented at The Electrochemical Society Meeting, Atlanta, Georgia, Oct. 9-14, 1977.

Growth of $Ga_yIn_{1-y}As/InP$ Heterostructures by Molecular Beam Epitaxy

B. I. Miller* and J. H. McFee*

Bell Laboratories, Holmdel, New Jersey 07733

ABSTRACT

Lattice-matched layers of $Ga_yIn_{1-y}As$ ($y = 0.47$) have been grown at 510°C on (100) InP substrates by molecular beam epitaxy. Epitaxial layers of highly uniform composition were achieved by mixing Ga and In together in a single source, Reproducible flux control was achieved by careful use of a quadrupole mass analyzer. In addition, the morphology, reflection electron diffraction, and electrical properties of $Ga_yIn_{1-y}As$ epitaxial layers were studied as function of y. When $y \simeq 0.47$ the epitaxial layers exhibit mirror-smooth, featureless morphology devoid of misfit dislocation-induced crosshatching. Such crosshatching becomes prominent when $y = 0.41$ and $y = 0.50$. Further, those epitaxial layers which are under tensile stress ($y > 0.47$) tend to exhibit cracking when thermally cycled. The best unintentionally doped epitaxial layers had $N_d - N_a \simeq 2 \times 10^{17}$ cm^{-3} and $\mu_{77} = 6500$ cm^2/Vsec. $InP/Ga_{0.47}In_{0.53}As/InP$ double heterostructures have also been fabricated and made to lase at 77°K under optical excitation conditions. These lasers have a threshold of 6.2 kW/cm^2 and an output wavelength of about 1.425 μm.

Recently there has been a great deal of interest in sources and detectors in the 1.5-1.0 μm range for possible application to optical fiber communications. In this wavelength range the optical fibers exhibit less loss (1, 2) and zero dispersion (3). LED's and lasers have been made covering this wavelength range using the double heterostructure (DH) GaInAs/InP (4, 5) GaInAs/GaInP (6), GaInPAs/InP (7-9), and AlGaAsSb/GaSb (10, 11) systems. All these double heterostructure devices were grown either by liquid-phase epitaxy (LPE) or vapor-phase epitaxy (VPE). To our knowledge no such DH devices in this range have been fabricated by molecular beam epitaxy (MBE). The unique capabilities of MBE, such as allowing abrupt atomically smooth interfaces and the ability to use masks, make it attractive as a method of growth for these systems. A further advantage of MBE is the ability to grow lattice-matched heterostructure alloy systems which are difficult or impossible to grow by LPE or VPE. An example of such a system is $(Al_xGa_{1-x})_{0.47}In_{0.53}As/InP$ where an exact lattice match is possible over a wavelength range from 1.44 to 0.85 μm at 300°K.[1] The first step in growing epitaxial layers in this attractive alloy system by MBE is to successfully grow the lattice matched ternary system $Ga_{0.47}In_{0.53}As/InP$. The growth of lattice-matched $Ga_{0.47}In_{0.53}As$ onto InP requires that the flux ratio of Ga/In be precisely controlled, whereas in the case of binary or even AlGaAs compounds this problem does not exist. We have developed a technique for precise flux control which allows us to grow such lattice-matched layers reproducibly. Also, by evaporating Ga and In from a single source, $Ga_yIn_{1-y}As$ epitaxial layers of highly uniform composition have been grown. These advances have permitted a systematic study of the morphology and electrical properties of $Ga_yIn_{1-y}As$ grown on InP as a function of the degree of lattice mismatch. Finally, $InP/Ga_{0.47}In_{0.53}As/InP$ lattice-matched double heterostructures have been grown which exhibit lasing under optical pumping at 77°K.

Experimental

The MBE system and its use in growing homoepitaxial layers of InP has been described previously (14). In the present work, GaInAs layers were grown epitaxially on (100) and $(\bar{1}\bar{1}\bar{1})$ InP substrates which were cut from single-crystal boules grown by Buehler using the liquid-encapsulated Czochralski (LEC) method described by Bachmann *et al.* (15, 16). In most growth runs Sn-doped ($n \sim 10^{18}$ cm^{-3} and also Fe-doped semi-insulating substrates were mounted side by side on the sample block. The semi-insulating substrates were included so that the electrical properties of the epitaxial layers could be measured. A typical substrate size is 1 cm^2.

The substrates were indium-soldered to a molybdenum sample block and chemically polished to a mirror finish on a dextilose paper lap saturated with weak bromine-methanol solution. The sample block is then promptly loaded into the MBE system which is pumped and mildly baked (150°C) overnight to a typical base pressure of 1×10^{-9} Torr or less. In the morning the sample block (which had remained at ambient overnight) is heated to 365°C and the substrates are sputter etched for about 5 min in 5×10^{-5} Torr of argon at 3 kV and about 5 μA/cm^2 current density. Following this sputter cleaning the samples are annealed at 365°C for at least 1 hr behind a shutter which shields the substrates from the direct source fluxes. During the annealing period the Ga, In, and As [2] source ovens are brought to operating temperature and fluxes adjusted to the desired values. The source fluxes are monitored by a UTI Model 100C quadrupole mass analyzer which is situated so that it has direct line of sight to the source ovens at all times. A chopper wheel is placed between the source ovens and mass-analyzer ionizer cage and synchronous detection is used to enhance the signal-to-noise ratio of the mass analyzer. Epitaxial layer growth is initiated by raising the sample temperature to 510°C (typical for GaInAs) and then opening the sample shutter.

Initially we attempted to grow $Ga_yIn_{1-y}As$ of lattice-matched composition ($y \simeq 0.47$) by using separate Ga and In sources. This method gave erratic results which we believe were due to spatial nonuniformity in the composition of the epitaxial layers. For example, the GaInAs layers exhibited significant variations in photoluminescent efficiency and line shape over the surface of the layers. Also, the surfaces were not smooth but rather had complicated morphologies not typical of good epitaxy. Compositional analysis of

* Electrochemical Society Active Member.

Key words: epitaxy, semiconductors, mobility, photoluminescence, lasers.

[1] This wavelength range was determined by using the bandgaps corresponding to the end points of $Ga_{0.47}In_{0.53}As$ and $Al_{0.47}In_{0.53}As$, which lattice-match InP. For $Ga_{0.47}In_{0.53}As$ we used the results of Baliga *et al.* (12), and for $Al_{0.47}In_{0.53}As$ we used the results of Lorenz and Onton (13).

[2] The Ga used was 99.9999% pure and obtained from Alusuisse, Fort Lee, New Jersey. The In and As were 99.9999% pure and supplied by Kawecki Berylco, Incorporated.

these $Ga_yIn_{1-y}As$ layers using a scanning electron microscope (SEM) equipped to perform energy dispersive x-ray spectroscopy (EDS) disclosed variations in y as large as 10% between positions separated by only 5 mm. The sources in this case were open cylindrical crucibles situated 6.5 cm distant from the substrates. Actual investigation of the angular distribution of flux by evaporating Ga and In onto glass slides mounted on the sample block confirmed that the observed nonuniformities in the GaInAs layers could easily be explained in terms of the angular distribution of flux from the two separate sources. The situation can be improved by moving the two sources closer together and/or by increasing the source-to-substrate distance, but either of these options can be pursued to only a limited extent. Moreover, there is another serious disadvantage in the case of separate Ga and In sources: A small change in the melt configuration or temperature of one source oven during a growth run can change the Ga/In flux ratio significantly and cause a compositional gradient in the direction of film thickness. Both of the foregoing disadvantages are virtually eliminated by use of a common source containing a homogenous Ga-In mixture. The Ga/In flux ratio will then be exactly the same in all directions and will be independent of the melt configuration. Also, a change in the single source oven temperature will cause only a second-order change in the Ga/In flux ratio.

For all of the foregoing reasons we found it advantageous to change over to a single source crucible in which Ga and In are premixed in proper proportion to achieve the desired film composition. Through use of this technique, and by careful use of the mass analyzer to monitor the Ga/In flux ratio, we have been able to grow GaInAs layers of precisely controlled and highly uniform composition. For a typical source temperature near 800°C (corresponding to a growth rate $\simeq 1$ μm/hr) the evaporation rate of In is more than an order of magnitude greater than that of Ga. A calculation based on tabulated evaporation rates shows, and experiment verifies, that a mass ratio $M_{Ga}/M_{In} \simeq 10$ in the crucible yields the approximately equal Ga and In fluxes required for a lattice matched composition in the growing layer. The vapor pressure of Ga varies slightly more rapidly with temperature than does the vapor pressure of In. Thus, raising the temperature of the single source will increase the Ga/In flux ratio, and vice versa. Changing the source temperature is a convenient way to make fine adjustments in the GaInAs film composition to achieve precise lattice match. The range of adjustment is eventually limited by the much larger changes produced in the growth rate. For example, at a source temperature of 800°C the Ga/In flux ratio increases by ~0.5%/°C while the individual Ga and In fluxes increase at a rate of ~3%/°C.

The required 10:1 M_{Ga}/M_{In} mixture means that only a relatively small amount of In will be present in the single source. Thus, if the source volume is small, In depletion in the source during film growth will lead to a nonuniformity in the film composition. Our standard oven crucibles hold about 1.5 cm^3 of charge. In this case, for a growth rate of 0.8 μm/hr the Ga/In flux ratio is observed to increase 2.5%/hr due to In depletion. For an initially lattice-matched $Ga_yIn_{1-y}As$ film this increase means that y would vary from 0.470 to 0.476 from bottom to top of a 2 μm thick film. However, even this small amount of change in the Ga/In ratio can be compensated by reducing the source temperature gradually, as explained above. Also, of course, the effects of In depletion could be made negligible by substantially increasing the source volume.

In order to grow ternary layers of precise composition, a reliable means of measuring the Ga/In flux ratio before and during growth is almost a necessity. The UTI mass analyzer can serve this purpose provided it is properly used. During growth of a GaInAs layer a background pressure of order 10^{-6} Torr of As is present in our MBE system. The presence of this much As has several effects on the performance of the mass analyzer when used in the Faraday Cup mode without the electron multiplier. Firstly, the basic sensitivity of the analyzer for any given mass number is increased, but the magnitude of the increase is a function of mass number. Thus if the Ga ($M = 69$) and In ($M = 115$) fluxes are measured with the analyzer, the current ratio i_{69}/i_{115} obtained will be a function of the As background pressure. Secondly, we have observed occasional abrupt changes in the basic sensitivity of the analyzer which take place without apparent cause. Fortunately, these abrupt sensitivity changes appear to be independent of mass number and do not alter the current ratio i_{69}/i_{115}. Finally, we find that setting the mass analyzer to read the As (M = 150 or M = 75) flux will cause the basic sensitivity to change drastically. Following a reading of the As flux the basic sensitivity gradually relaxes toward its original value over a period of about 1 hr. Thus, when precise Ga/In flux measurements are desired, As flux readings must be avoided.

In order to demonstrate that the mass analyzer can be reliably calibrated in terms of the Ga/In ratio in the epitaxial layer, a series of five $Ga_yIn_{1-y}As$ epitaxial layers were grown on InP substraes as listed in Table I. Each layer was grown on a separate day's run. The $Ga_yIn_{1-y}As$ layer composition was changed from decidedly In rich in the first run (071877), through approximately lattice-matched composition (072577), to decidedly Ga rich in the final growth run (072977). In all of these runs the Ga and In were mixed together in a single source and the y values given in Table I for each grown layer were measured with the SEM equipped to do compositional analysis via EDS. Each y value is the average of repeated readings made at two different points (separated by ~1 cm) on each sample. These average values typically agree to within 1%, which demonstrates the improved spatial uniformity of the GaInAs layers grown from a common Ga-In source. Indeed, the spatial uniformity of composition may be better than these figures indicate because the relative error in the EDS measurements is estimated to be 1%. The i_{69}/i_{115} values in Table I represent an average of many readings taken with the mass analyzer during the growth of each GaInAs layer. In all growth runs listed in Table I the As background pressure was maintained at or near 6.0×10^{-7} Torr to eliminate the effect of a changing As background on the measured current ratio. The accuracy of the current ratios given is estimated to be about 2%.

It is most revealing to plot $y/1-y$ for the five runs listed in Table I *vs.* the corresponding i_{69}/i_{115} ratio as measured by the mass analyzer. This is done in Fig. 1. If the mass analyzer is linearly indicating the Ga/In flux ratio, one would expect a simple linear relationship between $y/1-y$ and i_{69}/i_{115}. From Fig. 1 it appears that $y/1-y$ is, within experimental error, a linear function of i_{69}/i_{115}. The straight line drawn in Fig. 1 is the best least squares linear approximation to the data, and has slope = 2.0. The vertical error bars correspond to the 1% uncertainty in the y values as measured with the SEM. If it is assumed that the mass analyzer behaves linearly, a "theoretical" value for the constant relating $y/1-y$ and the i_{69}/i_{115} current

Table I. Summary of mass analyzer and SEM data on $Ga_yIn_{1-y}As$ growth runs

Sample grown	i_{69}/i_{115}	y (SEM)	$y/1-y$
071877	0.30	0.39	0.64
072777	0.36	0.414	0.706
072577	0.41	0.46	0.85
072177	0.50	0.50	1.0
072977	0.75	0.59	1.44

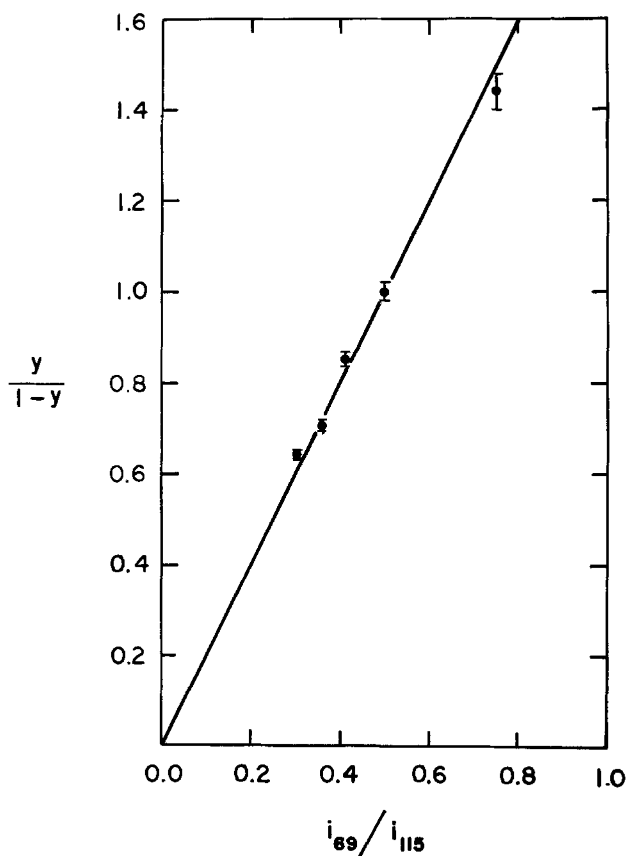

Fig. 1. Ga/In ratio, $y/1 - y$ in $Ga_yIn_{1-y}As$ epitaxial layers (as measured by SEM) *vs.* mass analyzer current ratio, i_{69}/i_{115}, recorded during layer growth.

ratio can be calculated from the ionization efficiency (I) and quadrupole transmission (T) data given for $M = 69$ and $M = 115$ in the UTI 100C instruction manual. The relative masses and isotopic abundances of $M = 69$ and $M = 115$ also come into this calculation. We further assume unity sticking coefficients for Ga and In, and get the result $y/1 - y = 1.5 \times i_{69}/i_{115}$. This calculated slope of 1.5 is surprisingly close to the experimental slope of 2.0 (Fig. 1) when one considers the substantial uncertainties in the I and T data and, particularly, when one recalls that the mass analyzer operates in an ambient of 6×10^{-7} Torr of As which, as we have noted, significantly alters its basic sensitivity.

In summary, then, Fig. 1 gives a calibration of our mass analyzer. If we are careful to reproduce the conditions under which the data of Fig. 1 were obtained, namely the same As ambient and a single source for Ga + In, we can use Fig. 1 to determine the mass analyzer current ratio which corresponds to any desired value of y. When this i_{69}/i_{115} ratio is maintained throughout the growth period, the composition of the resulting $Ga_yIn_{1-y}As$ layer will be within about 1% of the desired value. In this way lattice-matched GaInAs can be grown reproducibly.

Results

$Ga_yIn_{1-y}As$ grown on InP.—In order to demonstrate how the degree of lattice mismatch affects the various epitaxial film parameters such as morphology, surface structure (as revealed by reflection electron diffraction), carrier concentration, etc., the series of five epitaxial layers listed in Table I was investigated in some detail.

Morphology.—The resulting morphology is shown in Fig. 2. The polished substrate is also shown for reference. When $y = 0.39$ and $y = 0.41$ there appears a strong crosshatching, stronger for the larger lattice mismatch. This type of crosshatching has been observed in other lattice-mismatched epitaxial systems (17) and is believed to be associated with arrays of misfit dislocations. In Fig. 2, where $y = 0.46$, there is essentially a lattice match ($y = 0.468$ according to Vegard's law) and the morphology of the grown layer is nearly indistinguishable from the substrate. There

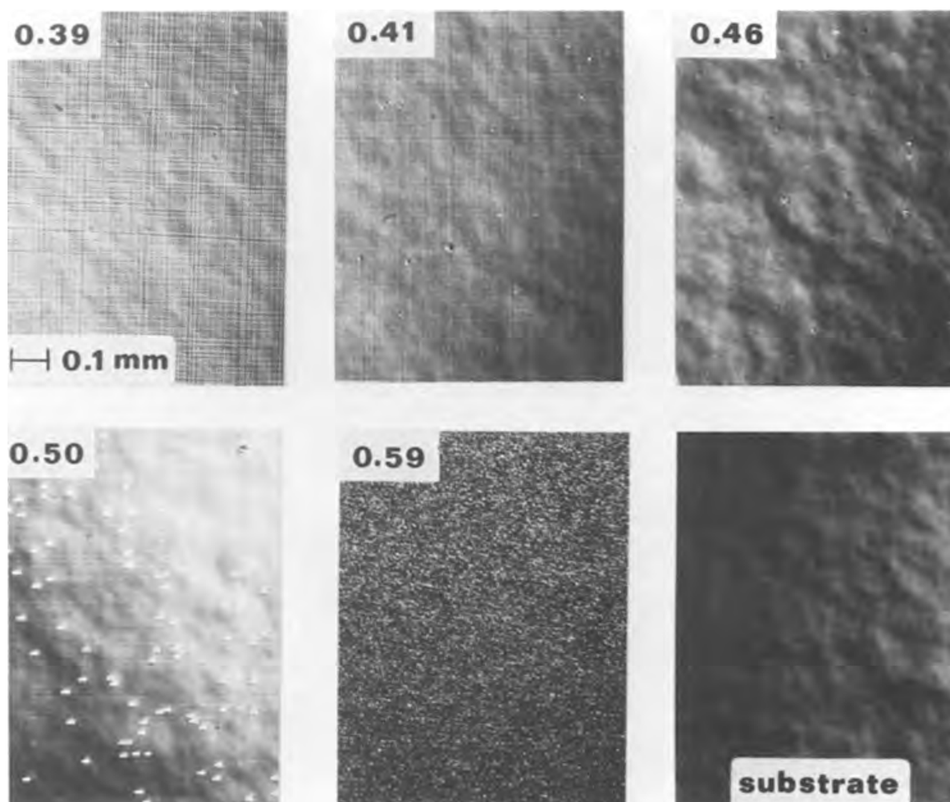

Fig. 2. Nomarski interference-contrast photographs of (100) $Ga_yIn_{1-y}As$ epitaxial layer surfaces, showing effect of lattice mismatch on surface morphology. Measured composition, y, given at upper left of each photograph. The Nomarski photograph of a polished InP substrate also shown for reference.

appear to be a few defects scattered about whose density is roughly $\sim 10^4/cm^{-2}$. This suggests that these defects may be related to or generated by dislocations, since the dislocation count in the LEC-grown InP crystals used for substrates is typically $\sim 10^4$ (15).

When $y = 0.50$, the crosshatching appears as before. It is interesting to note here that when $y = 0.39$ and $y = 0.41$ the GaInAs layer is under compression since its lattice constant is larger than the InP substrate. When $y = 0.50$ and $y = 0.59$, however, the epitaxial layer is under tension and, in fact, when $y = 0.59$ the layer has so much tension that it becomes very rough and fragmented. Examination of this latter surface with an SEM shows a grain size $\sim$ 1-2 μm, rather than a continuum as for the other surfaces.

Reflection electron diffraction (RED).—Figure 3 shows the RED patterns taken from these five surfaces. In Fig. 3 the RED pattern from the polished InP substrate is shown for reference. In this case the electron beam is along the $(\bar{1}\bar{1}0)$ azimuth and a typical C(2 $\times$ 8) pattern (18) is seen. The arrows point to the streaks corresponding to the bulk lattice spacing, and the one-half order lines corresponding to the surface reconstruction can also be distinctly observed. When there is a lattice match ($y = 0.46$), a similar pattern can be seen, with the major streak spacing corresponding to the bulk lattice spacing of $Ga_{0.46}In_{0.54}As$. However, in this case we notice that the one-half order lines are not quite as distinct as in the case of the InP substrate, but are somewhat fuzzy and broadened. This may reflect the lack of order in our crystal, as this is a mixed III-V alloy system. Locally there is a large degree of disorder in the crystal due to the difference in lattice constants between InAs (19) and GaAs (20). When this same $Ga_{0.46}In_{0.54}As$ layer is subsequently covered by a top layer of InP, the RED pattern recovers and often becomes sharper than the pattern from the substrate. For InP, of course, there is no disorder. It is interesting to note that in the AlGaAs system this degree of disorder does not occur since AlAs and GaAs have very nearly the same lattice constant.

The RED patterns coming from the lattice mismatched samples show the lack of lattice perfection in their spotty, less streaked character, and also the almost complete lack of the one-half order lines. The $y = 0.59$ layer shows almost no RED pattern at all indicating the granular nature of this film.

Cross sections.—The cleaved cross section of the five samples of Table I are shown in Fig. 4 in the same sequence as before. The cleaved cross section of the lattice-matched epitaxial layer ($y = 0.46$) appears to be as strain-free and smooth as a homoepitaxial layer. The epitaxial layers shown for $y = 0.39$ and $y = 0.41$, although lattice mismatched and under compression, also show little evidence of lattice strain. For the slight mismatch where $y = 0.41$ the cross section is as smooth as when $y = 0.46$, while for the greater mismatch ($y = 0.39$) the slight roughness is an indication of some lattice strain. When $y = 0.50$ the epitaxial layer is under tension, the cleaved cross section is considerably rougher, and the epitaxial surface itself is also rough. Yet the magnitude of the lattice mismatch is less than when $y = 0.41$ where the cleave is featureless. When $y = 0.59$ the epitaxial layer is under

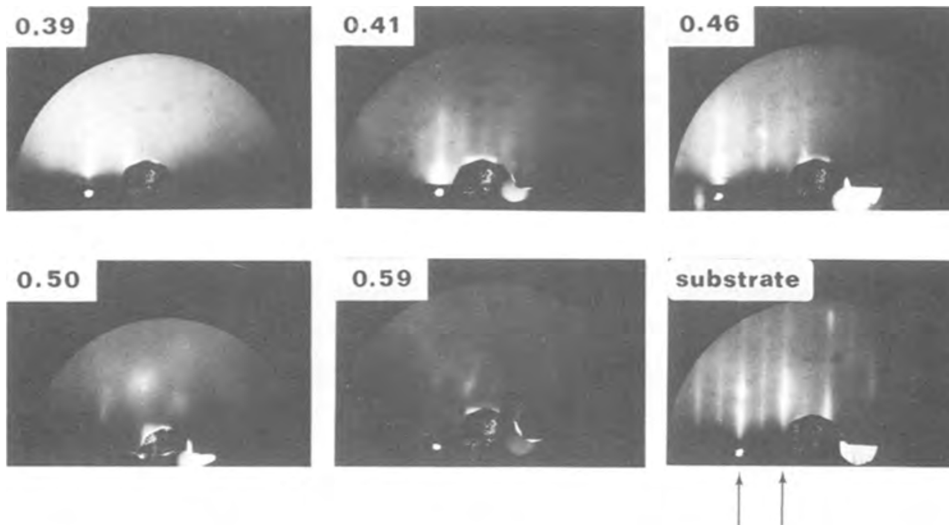

Fig. 3. Reflection electron diffraction (RED) patterns (3 keV) obtained from the $Ga_yIn_{1-y}As$ epitaxial layers of Fig. 2. Primary beam direction is along $(\bar{1}\bar{1}0)$ azimuth. The corresponding RED pattern obtained from a polished (100) InP substrate is shown for reference.

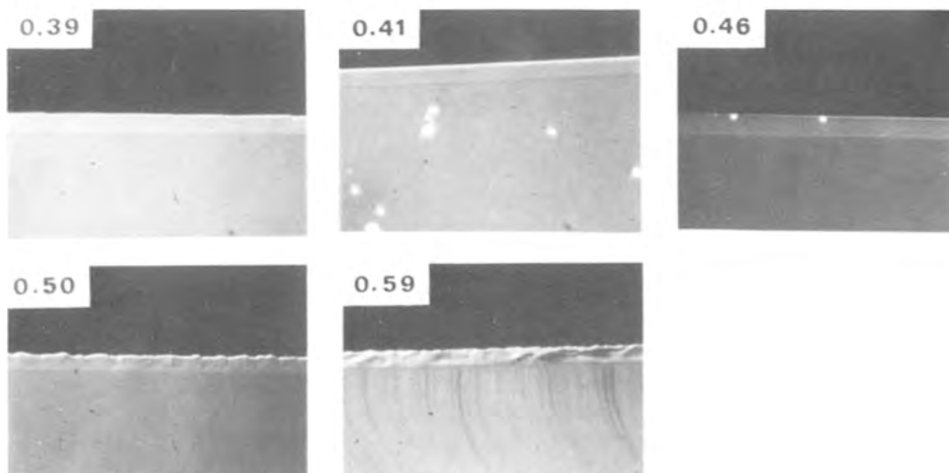

Fig. 4. Cleaved cross section of $Ga_yIn_{1-y}As$ epitaxial layers of Fig. 2. The layers, approximately 2 μm thick, are grown on (100) InP substrates.

much greater tension than when $y = 0.50$. This is reflected in the great roughness of the cleave and epitaxial surface. In general, it appears that the epitaxial layer will tolerate a lattice mismatch in the direction of compression ($y < 0.47$) much more readily than tension ($y > 0.47$). These findings have also been observed by others (17, 4).

It should be noted that those epitaxial layers which are under tension tend to crack and peel upon temperature cycling from 300° to 77°K and back, while those under compression do not.

Scattered light.—The film smoothness during growth is monitored by observing the nonspecular scattered light coming from the epitaxial surface which is illuminated by a He-Ne laser beam. In Fig. 5 the nonspecular scattered laser light output is plotted *vs.* growth time for some of the samples shown in Fig. 2 to 4. At time $t = 0$ min, just before initiating epitaxial growth, the scattered light comes from the uncoated substrate. All three curves are plotted unnormalized and thus at $t = 0$ the scattered light is a measure of the reproducibility of the substrate smoothness from run to run. Curve 3 corresponds to the lattice-matched epitaxial layer ($y = 0.46$) and remains relatively unchanged during the growth period. The $y = 0.41$ epitaxial layer, the layer under slight compression, has a curve (not shown) similar to 3. Curve 2 corresponds to the $y = 0.39$ epitaxial layer and increases by almost two orders of magnitude during the growth and curve 1 corresponding to the $y = 0.59$ epitaxial layer increases by over three orders of magnitude. The scattered light curve from the $y = 0.50$ epitaxial layer (not shown) lies somewhere between curves 1 and 2, having their same general shape.

The most noteworthy feature of these curves besides their sensitivity to lattice match is the initial dip in the scattered light at the onset of growth. This dip in light output lasts for approximately 5-15 min. Assuming an average growth rate of 0.75 μ/hr, the dip corresponds to a 600-1900Å thick layer or 120-360 monolayers. It appears that the dip is caused by the accommodation to the substrate of the epitaxial layer, which is under strain but smoother than the substrate. After a certain thickness the epitaxial layer can no longer accommodate itself to the substrate, and the strain is relieved by dislocations which cause the crosshatching and surface roughness seen in Fig. 2. Even the "lattice-matched" layer $y = 0.46$ (curve 3) shows a slight increase of scattered light after the initial dip, however, the final scattered light intensity is about the same as that coming initially from the substrate. The slight drop in the scattered light output in curves 1 or 2 during the latter part of the run may be due to a specular component of the scattering coming from the crosshatching and from surface faceting. As the run progresses these surface features may change with time and cause more or less specular scattering. In many instances the scattered light does not change at all during the latter half of the run.

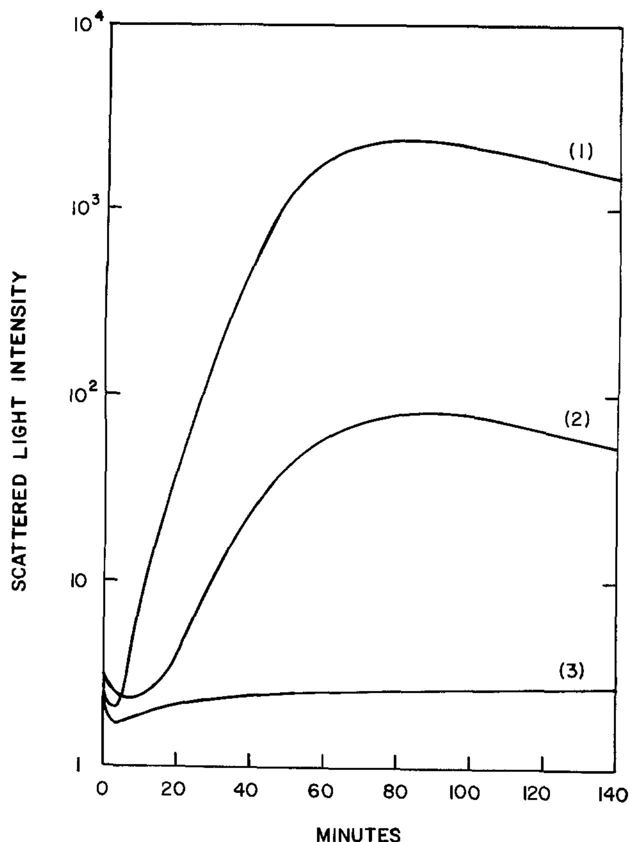

Fig. 5. Time evolution of nonspecular scattered laser light from surface of the growing epitaxial layer for some of the samples shown in Fig. 2-4. Growth starts at 0 min. Curve 1, $Ga_{0.59}In_{0.41}As$ on InP; Curve 2, $Ga_{0.39}In_{0.61}As$ on InP; curve 3, $Ga_{0.46}In_{0.54}As$ on InP.

Electrical properties.—Table II is a summary of the electrical properties of the various $Ga_yIn_{1-y}As$ layers grown on InP. The first five samples correspond to the same growth runs referred to in Fig. 1-5. All these layers were grown unintentionally doped. The purest material grown to date is n-type with $n = 2 \times 10^{17}$, $\mu = 5300$ at 300°K, and $n = 1.8 \times 10^{17}$, $\mu = 6500$ at 77°K. The mobility of $Ga_{0.75}In_{0.25}As$ grown by vapor phase epitaxy on GaAs has been reported by Glicksman *et al.* (21) to be 5950 at 300°K and 17,700 at 77°K, for $n = 10^{15}$. At the impurity levels reported in Table II one would expect the mobility to be dominated by impurity scattering as the following considerations show. Glicksman *et al.* (21) write the mobility of $Ga_yIn_{1-y}As$ as

$$1/\mu = 1/\mu_{ph} + 1/\mu_d + 1/\mu_I \quad [1]$$

where μ_{ph} is the phonon contribution to mobility, μ_d the disorder contribution arising from the alloy composition y, and μ_I the impurity contribution coming from both ionized donors and acceptors and the number of free electrons. Both μ_I and μ_{ph} are implicitly dependent only upon the alloy composition y, through the effective mass (m^*) variation with y. In addition to its implicit dependence on m^*, μm_d varies as $[y(1-y)]^{-1}$. For $y = 0.47$ we find, using formulas given in Ref. (21), that at room temperature $\mu_{ph} =$ 13,200 and $\mu_d =$ 41,000. For our best sample (041377, see Table II) $\mu = 5300$ so that from Eq. [1], $\mu_I =$ 11,300. Similarly at 77°K, $\mu_{ph} =$ 310,000 and $\mu_d =$ 80,000; thus using the 77°K mobility of $\mu = 6500$, we get $\mu_I = 7700$ for this sample.

From these considerations it is obvious that in the samples listed in Table II the major contribution to the mobility comes from impurity scattering. Any variation of mobility with alloy composition would not be expected to play a significant role at these impurity levels. In fact, this is borne out by comparing the mo-

Table II. Electrical properties of $Ga_yIn_{1-y}As$ epitaxial layers

Sample	y	300°K n (cm^{-3})	300°K μ (cm^2/Vsec)	77°K n (cm^{-3})	77°K μ (cm^2/Vsec)
071877	0.39	4.8×10^{18}	3500	4.8×10^{18}	4000
072777	0.41	5.2×10^{18}	3200	5.2×10^{18}	3700
072577	0.46	4.7×10^{18}	3100	4.7×10^{18}	3500
072177	0.50	1.4×10^{18}	230*	2.4×10^{18}	140*
072977	0.59	6.2×10^{18}	410*	6.4×10^{18}	440*
041177	~0.42	3.4×10^{17}	5000	3.3×10^{17}	6000
041377	~0.42	2.0×10^{17}	5300	1.8×10^{17}	6500

* Sample cracked after immersion in liquid nitrogen.

bilities in Table II for the first five samples, which have similar carrier concentrations, where y ranges from 0.39 to 0.59. The mobilities are essentially the same except for those samples under tension ($y > 0.47$) where cracking had occurred while undergoing a 77°K temperature cycle prior to the Hall test. The carrier concentrations even for the purest samples is rather high, $\geq 2 \times 10^{17}$. The fact that there is virtually no carrier freezeout from 300° to 77°K implies that the impurities are coming from shallow donors and we estimate that any deep impurities are contributing $\sim 10^{16}$ donors or less. It is interesting to note that on $(\overline{111})$ oriented samples grown simultaneously along with the (100) samples shown in Table II, n is generally 2-5 times greater. At present, we have made no systematic effort to reduce the carrier concentration.

Double heterostructure.—In order to test the optical quality and potential application for LED's and heterostructure lasers, a lattice-matched $InP/Ga_yIn_{1-y}As/InP$ double heterostructure was grown for optical pumping purposes. It is common practice to grow a buffer layer between the substrate and the active layer. In this case the buffer layer would be InP grown on the InP substrate followed by the $Ga_yIn_{1-y}As$ active layer. We have grown such buffer layers but have found that prior to changeover from InP to GaInAs growth, the small background pressure ($\lesssim 10^{-7}$ Torr) coming from the shuttered As source was sufficient to cause InAsP growth because of the much greater sticking coefficient of As compared to P. In order to avoid this, the InP growth must be terminated prior to the heating of the As source. This requires that the freshly grown InP surface be exposed to the ambient background behind the sample shutter for ~15 min while the As oven is heated and stabilized. For this reason some of the advantages of growing a buffer layer are negated.[3] In the present case, in order to minimize complications in growing, the buffer layer was omitted and the substrate served as one of the cladding layers. Only the $Ga_yIn_{1-y}As$ layer and top InP layer were grown by MBE. The resulting morphology was mirror smooth as seen in Fig. 6. The cross section of the double heterostructure is shown in Fig. 7. The active layer thickness of 1 μm was chosen as a compromise between the maximum optical absorption of the Nd:YAG (1.06 μm) pump and the optimum carrier confinement. The wafer of Fig. 6 was cleaved into bars of various cross sections, typically 400-800 μm spacing between Fabry-Perot faces. A Nd:YAG laser (either cm or Q-switched) was focused normal to the surface of the cleaved bar. The pump light was able to penetrate the InP ($\lambda^{gap} = 9000$Å) cladding layer and optically excite the $Ga_{0.47}In_{0.53}As$ layer. The beam was focused through cylindrical optics and had a cross section of 3 × 0.3 mm. The pumping configuration was such that the 3 mm dimension of the beam lay perpendicular to the Fabry-Perot faces. In this way the beam can be centered on the bar with very uniform excitation along the direction of lasing. At low excitation the pump was operated cw, but at the higher power necessary for lasing, the pump was Q-switched, putting out 0.25 μsec wide pulses at a repetition rate of ~500 Hz. The resulting signal was passed through a ½ m Jarrall-Ash spectrometer, detected with a Ge detector (cooled for cw measurements) and amplified and integrated by a boxcar integrator.

[3] Possibly a better isolated As source, where the background As pressure is $<10^{-8}$ Torr when shuttered, would allow a more rapid changeover (<1 min).

Fig. 6. Lattice-matched, MBE-grown $InP/Ga_{0.47}In_{0.53}As/InP$ double heterostructure. Mirror-smooth InP cladding layer is shown.

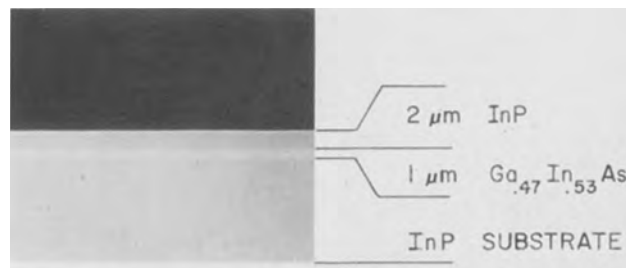

Fig. 7. Cleaved cross section of the lattice-matched $InP/Ga_{0.47}In_{0.53}As/InP$ double heterostructure shown in Fig. 6.

At low cw excitation the resulting photoluminescence of the $Ga_{0.47}In_{0.53}As$ layer at 77°K is as shown in Fig. 8. The peak is at 1.368 μm (0.907 eV) and a

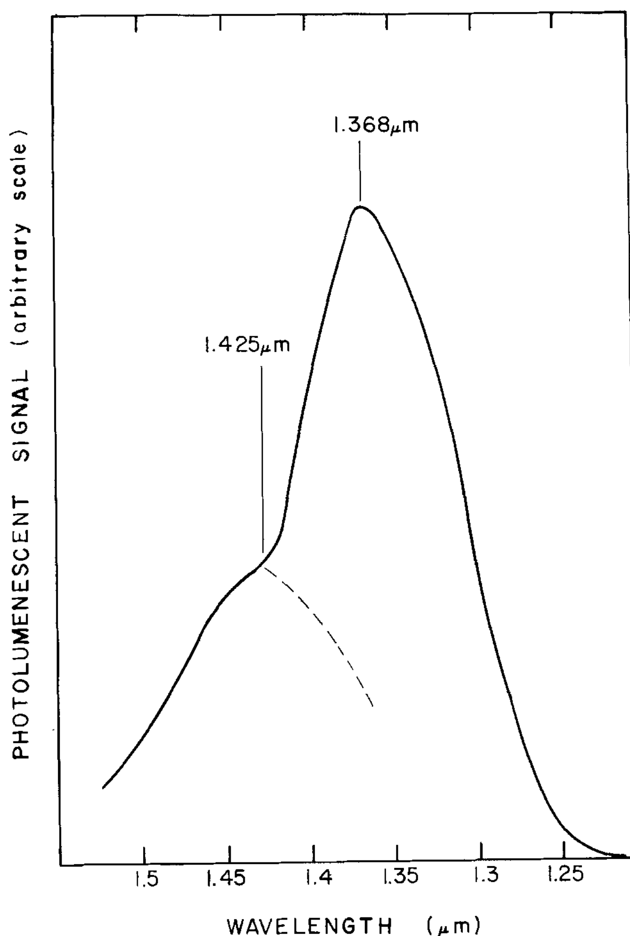

Fig. 8. Photoluminescent spectrum of $Ga_{0.47}In_{0.53}As$ layer of the double heterostructure shown in Fig. 6 and 7. The GaInAs layer was excited through the InP cladding layer by means of a Nd:YAG (1.06 μm wavelength) laser.

shoulder appears at 1.425 μm (0.870 eV). The half-width is rather broad, $\Delta E/E \simeq 0.084$, typical of most of these GaInAs layers. The half-width varies from $\Delta E/E = 0.047$ to $\Delta E/E = 0.15$ and roughly correlates with the carrier concentration of the ternary layer. All samples grown from the single Ga-In source show little spatial variation of the photoluminescence over the epitaxial surface ~1 cm². For comparison, in bulk GaSb ($p \sim 10^{17}$-10^{18}) at 77°K the photoluminescent peak occurs at 1.57 μm and $\Delta E/E = 0.030$. Also the photoluminescent peak height for the $y = 0.46$ epitaxial layer is about the same as for the bulk GaSb. If one assumes a linear relation for E_g *vs.* y in the $Ga_yIn_{1-y}As$ (22) system and takes the bandgaps of GaAs (23) and InAs (24) at 77°K for end points, one gets the relation between alloy composition and badgap that

$$E_g = 0.410 + 1.094y \qquad [2]$$

Assuming the 1.368 μm photoluminescent peak is coming from a band-to-band transition, then from Eq. [2] we derive $y = 0.455$ in agreement with the SEM microprobe which gives $y = 0.45$ for this sample. This fairly close lattice match is also confirmed by the smoothness of the cleaved cross section (Fig. 7) and smooth surface morphology (Fig 6).

A shoulder appears at 1.425 μm in the photoluminescence spectrum of Fig. 8. This represents a level ~40 mV deep. This kind of level is quite common in GaAs at 30 mV (25) and in InP at 40 mV (26), and is usually associated with an acceptor such as Zn.

Under high power pulse conditions at 77°K the double heterostructure bar lases with the spectrum shown in Fig. 9. Three peaks appear at 1.420, 1.428, and at 1.437 μm approximately 85Å apart. It is interesting to note that the lasing peaks coincide with the broad shoulder at 1.425 μm in Fig. 8, corresponding to the 40 meV acceptor level. The widths of the peaks are limited by the resolution of the spectrometer, which in this case is 16Å. The peaks are not exactly evenly spaced nor are they quite symmetrical; the reason for this, we believe, is that the lasing is very unstable due to the inherent instability of the Q-switched Nd:YAG laser and also because of vibrations which displace the beam along the bar causing different areas of the bar to lase in a random fashion. By sitting on the 1.428 μm line we were able to plot the laser power out *vs.* pump power (Fig. 10). Above 6 kW/cm² lasing occurs and the power output rises rapidly. By extrapolating the power output to zero power (dotted line in Fig. 10) we can get a measure of the threshold which in this case is ~6.2 kW/cm². Although it is difficult to compare this threshold directly to a GaAs/AlGaAs DH laser, a typical optically pumped threshold reported in the literature (27) for this system is ~10^4 W/cm² at 300°K. It appears then that this material may hold some promise for LED's and lasers.

Discussion

We have shown that it is possible to grow lattice-matched ternary layers of GaInAs on InP substrates by MBE at substrate temperatures of 510°C. Layers having a high degree of spatial uniformity of composition result from premixing the Ga and In in a single source. The mass analyzer has been successfully used to accurately monitor the Ga/In flux ratio and thereby achieve the desired lattice-matched composition reproducibly. Typically, we are able to grow a

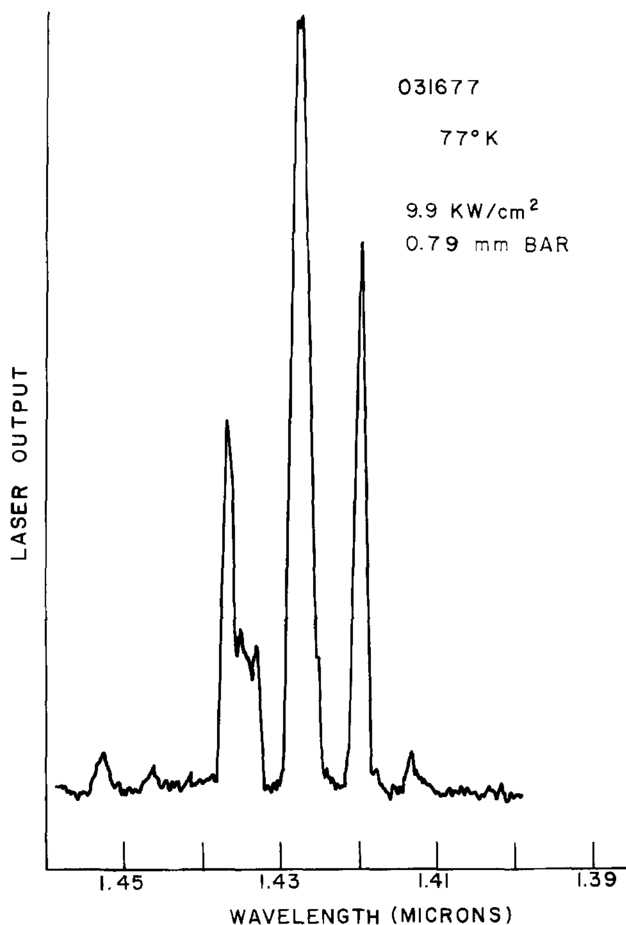

Fig. 9. Lasing spectrum at 77°K of a bar (0.79 mm between cleaved Fabry-Perot faces) cut from the $InP/Ga_{0.47}In_{0.53}As/InP$ double heterostructure of Fig. 6. The high intensity (9.9 kW/cm²) pump power at 1.06 μm was provided by a Q-switched Nd:YAG laser.

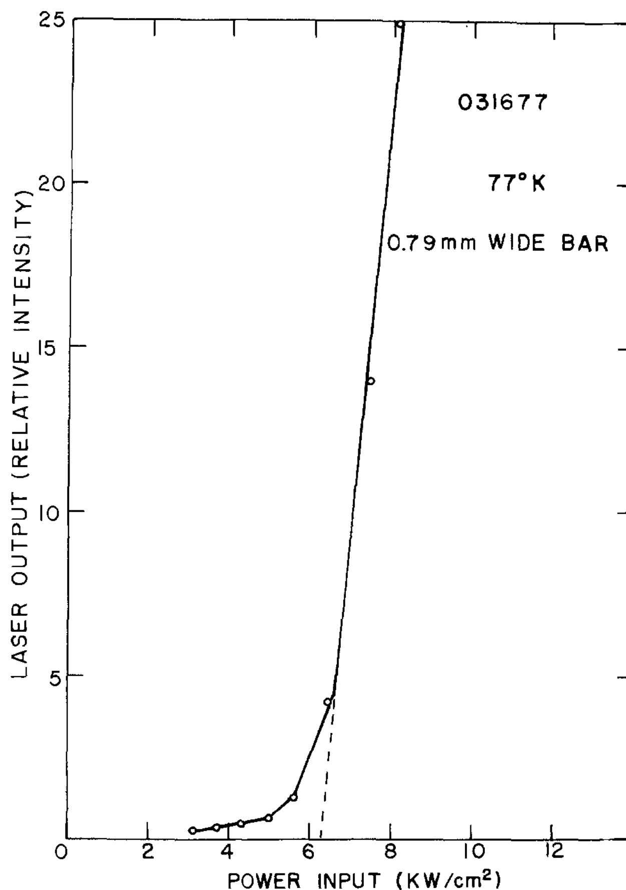

Fig. 10. Laser output power at 1.482 μm wavelength vs. pump power for laser bar of Fig. 9. Extrapolation (dotted line) yields a threshold pump power of 6.2 kW/cm.

$Ga_yIn_{1-y}As$ layer where $y = 0.47 \pm 0.005$. For comparison, the lattice mismatch between $Al_{0.3}Ga_{0.7}As$ and GaAs, the composition most commonly used for laser and LED's, is about 0.04%. Since the lattice constants of GaAs and InAs differ by 7%, a 0.04% mismatch in the $Ga_yIn_{1-y}As/InP$ system implies that $y = 0.47 \pm 0.006$. Thus we are able to obtain the same degree of lattice-match as is commonly achieved in the AlGaAs/GaAs system.

We have also demonstrated the dependence of the morphology of the $Ga_yIn_{1-y}As$ epitaxial layers on deviations from the lattice-matched composition. For example (100) layers for which $y = 0.41$ and $y = 0.50$ are covered with the crosshatching known to be associated with arrays of misfit dislocations. Furthermore, those layers having $y > 0.47$ are under tensile stress because their lattice constants are smaller than that of the InP substrate, and these layers tend to be discontinuous or develop cracks. When $y < 0.47$, the epitaxial layers are under compression and do not exhibit these deleterious effects. For these reasons it is desirable to aim for the In-rich side of the lattice-matched composition, *i.e.*, $y = 0.46$-0.47.

Except for those layers which exhibited cracking or discontinuous morphology, the electrical properties (carrier concentration and mobility) showed little correlation with composition y. The high carrier concentration ($n > 10^{17}$ cm^{-3}) found in our unintentionally doped GaInAs layers is due to the presence of shallow donors which probably come from contaminants in the Ga-In source. Prolonged degassing of this source might be beneficial in this respect; a prolonged bake-out of the In source oven in the case of MBE-grown InP resulted in decreasing the carrier concentration of the unintentionally doped layer from $n \sim 3 \times 10^{16}$ cm^{-3} to $n \sim 5 \times 10^{15}$ cm^{-3}, and increasing the mobility from $\mu_{77} \sim 8000$ to $\mu_{77} \sim 20,000$ cm^2/Vsec.

Double heterostructures were made by growing a cladding layer of InP on top of the lattice-matched GaInAs epitaxial layer. Such a structure was optically pumped and found to lase at a pump level of 6.2 kW/cm^2. This threshold pump power is comparable to that reported for AlGaAs/GaAs DH lasers. Thus our InP/GaInAs/InP double heterostructure appears to be a promising candidate for long-wavelength LED's or injection lasers. Work toward this goal is in progress.

Acknowledgments

We gratefully acknowledge the encouragement and support of P. K. Tien. We wish to thank R. J. Martin for fabrication of the DH lasers and for expert technical assistance, Steven Forman for analysis of the photoluminescence data and for Hall and resistivity measurements on the epitaxial layers, and E. Buehler for providing the InP substrate material used in this work.

Note added in proof.—We now know that our photoluminescent spectra were significantly shifted toward shorter wavelengths by band filling (Burstein Shift). This effect is enhanced in GaInAs, as compared to GaAs, because of a smaller electron-effective mass. Thus our carrier concentration, $n \sim 10^{18}$ cm^{-3}, gives considerable band filling. As a result, our attempts to relate the peak position of the GaInAs photoluminescent spectra to film composition are not valid.

Manuscript submitted Dec. 6, 1977; revised manuscript received March 15, 1978.

Any discussion of this paper will appear in a Discussion Section to be published in the June 1979 JOURNAL. All discussions for the June 1979 Discussion Section should be submitted by Feb. 1, 1979.

Publication costs of this article were assisted by Bell Laboratories.

REFERENCES

1. H. Osanai, T. Shioda, T. Moriyama, S. Araki, M. Horiguchi, T. Izawa, and H. Takata, *Electron. Lett.*, **12**, 549 (1976).
2. M. Kawachi, A. Kawana, and T. Miyashita, *Electron. Lett.*, **13**, 442 (1977).
3. L. G. Cohen and Chinlon Lin, *Appl. Opt.*, **16**, 3136 (1977).
4. H. Nagai and Y. Noguchi, *Appl. Phys. Lett.*, **29**, 740 (1976).
5. S. B. Hyder, G. A. Antypas, J. S. Escher, and P. E. Gregory, *ibid.*, **31**, 551 (1977).
6. C. J. Nuese, G. H. Olsen, M. Ettenberg, J. J. Gannon, and T. J. Zamerowski, *ibid.*, **29**, 807 (1976).
7. J. J. Hsieh and C. C. Shen, *ibid.*, **30**, 429 (1977).
8. J. J. Hsieh, J. A. Rossi, and J. P. Donnelly, *ibid.*, **28**, 709 (1976).
9. T. P. Pearsall, B. I. Miller, R. J. Capik, and K. J. Bachmann, *ibid.*, **28**, 499 (1976).
10. R. E. Nahory and M. A. Pollack, *ibid.*, **27**, 562 (1975).
11. R. E. Nahory, M. A. Pollack, E. D. Beebe, J. C. DeWinter, and R. W. Dixon, *ibid.*, **28**, 19 (1976).
12. B. J. Baliga, R. Bhat, and S. K. Ghandi, *J. Appl. Phys.*, **46**, 4608 (1975).
13. M. R. Lorenz and A. Onten, in "Proceedings of the 10th International Conference on the Physics of Semiconductors," Cambridge, Mass., S. P. Keller, T. C. Hensel, and F. Stern, Editors, p. 444, U.S. Atomic Energy Commission, Washington, D.C. (1970).
14. J. H. McFee, B. I. Miller, and K. J. Bachmann, *This Journal*, **124**, 259 (1977).
15. K. J. Bachmann, E. Buehler, J. L. Shay, and A. R. Strnad, *J. Electron. Mater.*, **4**, 389 (1975).
16. K. J. Bachmann, E. Buehler, J. L. Shay, and D. L. Malm, in "Proceedings of the 5th International Symposium on GaAs and Related Compounds," p. 121, Institute of Physics, London, Bristol (1975).
17. G. H. Olsen, *J. Cryst. Growth*, **31**, 223 (1975).
18. A. Cho, *J. Appl. Phys.*, **42**, 2074 (1971).
19. G. Giesecke and H. Pfister, *Acta. Crystallogr.*, **11**, 369 (1958).
20. C. M. H. Driscoll, A. F. W. Willoughby, J. B. Mullin, and B. W. Straughan," Gallium Arsenide and Related Compounds. 1974," p. 275, Institute of Physics, London (1975).
21. M. Glicksman, R. E. Enstrom, S. A. Mittleman, and J. R. Appert. *Phys. Rev., B*, **9**, 1621 (1974).
22. B. J. Baliga, R. Bhat, and S. K. Ghandi, *J. Appl. Phys.*, **46**, 4608 (1975).
23. C. D. Thurmond, *This Journal*, **122**, 1133 (1975).
24. J. R. Dixon and J. M. Ellis, *Phys. Rev.*, **123**, 1560 (1961).
25. D. E. Hill, *J. Appl. Phys.*, **41**, 1815 (1970).
26. E. W. Williams, W. Elder, M. G. Astles, M. Webb, J. B. Mullin, B. Straughan, and B. Tufton, *This Journal*, **120**, 1741 (1973).
27. W. D. Johnston, Jr. and B. I. Miller, *Appl. Phys. Lett.*, **23**, 192 (1973).

Evaluation of S- and Se-Implanted GaAs by Contactless Mobility Measurement

B. Molnar* and T. A. Kennedy

Naval Research Laboratory, Washington, D.C. 20375

ABSTRACT

Implantation of S and Se into GaAs has been studied with a novel contactless mobility measurement. The method, in which the mobility is obtained from a microwave measurement of the conducting layer's magnetoconductivity, is described in detail. Comparisons with Hall mobility are provided. Evaluation of different GaAs substrate material is described. A wide range of implantation and annealing conditions for S and Se in GaAs have been explored. S implantation of $5 \times 10^{12}/cm^2$ with a 850°C, 20 min anneal is found to produce FET quality layers.

As ion-implanted GaAs FET's (1-3) approach the quality of those made by epitaxial growth, ion implantation is being used more to produce semiconductor devices. The implantation-processing steps must be optimized and tightly controlled in order to produce uniform, high quality layers. In order to assure the quality of particular processing steps, layer characterization must be carried out. In the present work, a new characterization technique (4, 5) has been used to study the implantation of S and Se into GaAs.

Since carrier mobility directly affects FET transconductance and high frequency cutoff, a mobility measurement provides a relevant characterization. The traditional resistivity and Hall method provides two parameters, the sheet resistivity and the Hall mobility, but the measurement requires alloyed contacts. Problems associated with contacts have led to investigation of various noncontacting (6-8) methods. In the present work, the implanted layer mobility is obtained from a microwave measurement of the magnetoconductivity. Since contacts are not necessary, the method is rapid and nondestructive.

Employing the mobility characterization, a variety of GaAs implantation parameters have been evaluated. Choice of qualified substrates and Se implantation have been examined. A full study of dose and annealing for S implantation has been carried out and recommendations are provided for optimization of the parameters.

Experimental

Mobility determination.—The microwave mobility measurement was made in an 11 GHz reflection microwave spectrometer employing an IMPATT diode source (see Fig. 1). The samples were placed a quarter wavelength from the short. The microwave power reflected from the shorted waveguide section is monitored and recorded on the y axis of an X-Y recorder. The d-c magnetic field was provided by the NRL 14 Tesla Bitter solenoids with the x axis derived from the magnetic field. The orientations of the magnetic field and the microwave E field with respect to the sample are shown in the insert in Fig. 1.

The results of the microwave measurement, the reflected microwave power as a function of magnetic field B for thin n-type layers on semi-insulating GaAs, are shown in Fig. 2. The change in detected power for each sample relative to the empty waveguide was small. When the sample produces only a small perturbation on the fields in the waveguide, the detector output is linearly proportional to the free-carrier power absorption. The free-carrier power absorption is directly proportional to σV, where σ is the semiconductor conductivity and V is the volume. In two-layer structures the conductivities add linearly. However, in the semi-insulating substrate, the conductivity is negligible. Therefore, the measurement represents only the contribution of the conductive n-type layers. One condition, however, must be satisfied. The skin depth at the operating frequency has to be large compared to

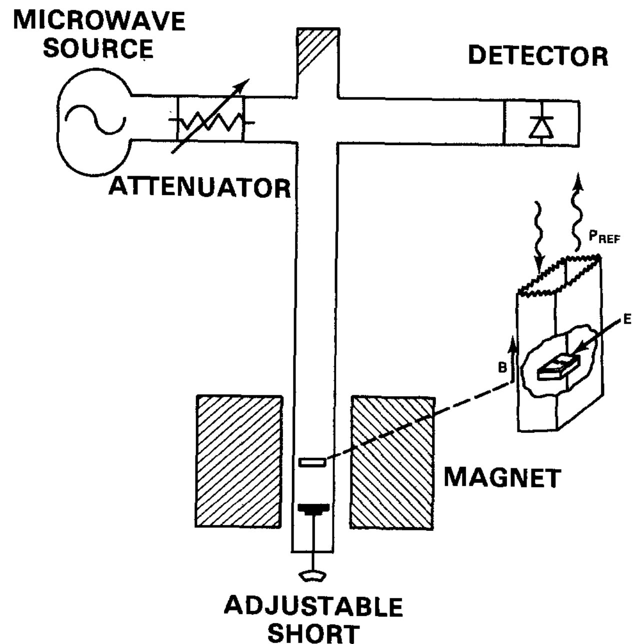

Fig. 1. Diagram of the microwave mobility-measurement apparatus

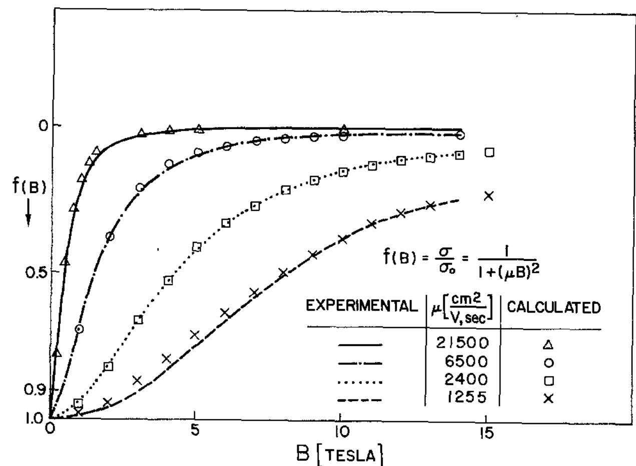

Fig. 2. The magnetic field-dependent part of the reflected power for four thin n-type layers on semi-insulating GaAs. The curves are normalized for comparison to the theoretical expression $f(B) = 1/[1 + (\mu B)^2]$.

* Electrochemical Society Active Member.

Key words: semiconductor, microwave, GaAs substrate.

the thickness of the layers. This condition is always satisfied in implanted layers for FET's.

The mobility of the free electrons is determined from the magnetic field B dependence of the conductivity σ. Since the frequency-scattering time product, $\omega\tau$, is much less than one at 11 GHz, the simple Drude theory conductivity in a magnetic field B can be approximated by the expression

$$\sigma(B) = \frac{\sigma(0)}{1 + \Omega^2\tau^2} \qquad \Omega = \frac{eB}{m^*}$$

where $\sigma(0)$ is the zero magnetic field conductivity, m^* is the effective mass, e is the magnitude of the electronic charge, and Ω is the Larmor frequency. Note that (in MKS units) $\Omega\tau = \mu B$ where μ is the electron mobility. The Drude theory describes the change of conductivity with $\sigma(B)/\sigma(0)$ equal to 1/2 when the mobility times magnetic field B is equal to 1. The inverse of B at the half-power point, therefore, gives the mobility of the free carriers. The microwave mobility values in Fig. 2 have been determined in the way described above. The experimental curves are well described by the simple $1/[1 + (\mu B)^2]$ formula. Some deviation, however, is present for the low mobility case. At low mobilities, the asymptotic value determination, and therefore, the half-power point determination, is hindered by the available magnetic field. The 14 Tesla magnet limits this technique to mobilities greater than 1000 cm^2/Vsec.

While it is not necessary to know the exact relationship between the microwave mobility and the Hall mobility in order to use the microwave measurements for studying processing parameters, the relationship must be known in order to compare our results with the Hall mobilities reported by other workers. Therefore, experimental comparisons of the microwave and the Hall mobilities on two sets of samples have been made. For one set, the GaAs samples were subjected to identical implantation and annealing treatments. The Hall mobility and the microwave mobility were measured for each sample. The reproducibility on a single sample of either mobility measurement is about 2.5%. The average microwave mobility is 20% smaller than the average Hall mobility with standard deviations for each around 13%.

A comparison between the Hall mobility and the microwave mobility on some thin epitaxially grown layers with a wide range of doping levels is shown in Fig. 3. The doping concentration of the n-type layers varied between $1 \times 10^{14}/cm^3$ and $1 \times 10^{17}/cm^3$ and the thickness varied between 0.2 and 10.0 μm. For convenient reference, the Hall mobility as a function of impurity concentration in n-type GaAs from Sze and Irvin (9) is also shown. The microwave mobility follows the same type of concentration dependence as the

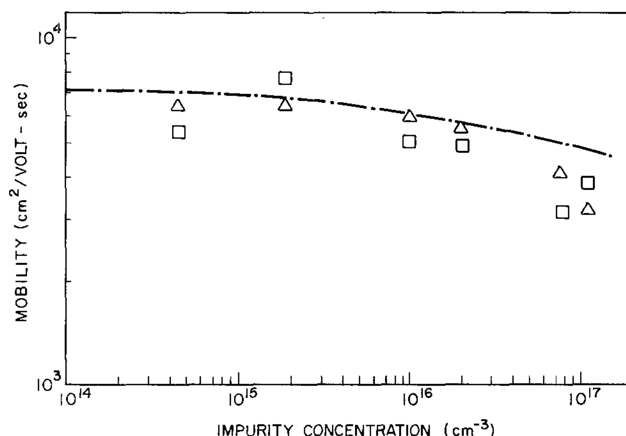

Fig. 3. The mobilities of a set of epitaxial layers on GaAs as measured by microwave (△) and Hall (□) measurement at 300°K *vs.* impurity concentration. The curve is the bulk mobility *vs.* concentration for GaAs (9).

Hall mobility. However, differences of up to 20% are found. Differences between the two mobilities arise from differences in the effect of low and high magnetic fields on the important electronic scattering processes, effects of sample geometry, and effects of sample inhomogeneities, such as doping gradients. Thus, relating the microwave mobility to the Hall mobility by a simply proportionality factor is only possible under tightly controlled conditions. In most cases, the mobilities measured by the two methods are fairly close.

Implantation procedure.—GaAs slices with (100) surfaces were cut from different, often Cr-doped, semi-insulating ingots. The wafers were chemical-mechanically polished. Each wafer was cleaved into several 5×5 mm^2 samples, which were etched in 5 H_2SO_4:1 H_2O_2:1 H_2O solution. Immediately after etching the samples were implanted with S^+ or Se^+ ions. The implanted samples were then coated with approximately 1500Å of Si_3N_4 using either plasma or reactive-sputtering deposition and annealed between 600° and 900°C in forming gas. The implantation process produced a submicron thick n-type layer on a 0.3-0.5 mm semi-insulating GaAs substrate. After annealing the microwave mobilities were determined either with or without the Si_3N_4 encapsulating layers.

Results

The microwave mobility has been used as a control parameter for the evaluation of the influence of substrate, implantation, and annealing conditions on GaAs FET-type n-channel layers.

The influence of the semi-insulating substrate on the implanted layer mobilities is shown in Table 1. Three different Cr-doped semi-insulating ingots were tested. The wafers were implanted at room temperature with $1 \times 10^{13}/cm^2$ 120 keV S^+ ions, and were annealed at 900°C for 60 min with a Si_3N_4 cap. Since all conditions except the starting wafers were identical, the large difference in the microwave mobilities originates from the different semi-insulating substrates.

A complete understanding of the influence of the starting semi-insulating GaAs substrate on the sulfur implantation has not yet been achieved. Eisen (10) observed little variation in the carrier concentration and mobility when he used different semi-insulating GaAs substrates. On the other hand, Stolte (11) did find significant substrate dependence. Kellner (3) has shown that the electrical activation of sulfur depends critically on the substrate material. Lower mobility may indicate an excessive carrier concentration which might come from the pile-up of the implanted sulfur at the surface during annealing (12). When processing is identical, the critical factor controlling the sulfur redistribution should be related to the presence of residual impurities in the GaAs substrates. Stolte (11) correlated the excess carriers with the amount of Cr and Si found in the substrates. The result of a high resolution chemical spectroscopy on our starting material is also shown in Table I. As in the case of Stolte, the decreased mobilities correlate with increased concentrations of Si and Cr.

The microwave mobility has been used for examination of the influence of other implantation-processing steps, such as the dose level, ion type, annealing time, and annealing temperature. As an example of these experiments, the influence of the annealing tempera-

Table I. Mobilities of S-implanted layers on different semi-insulating GaAs substrates

Substrates	1	2	3
Microwave mobility (cm^2/Vsec)	3400	2400	1000
Emission spectroscopy impurity		In ppm (wt)	
Si	0.01	0.02	0.05
Cr	0.04	0.57	0.40
Mg	0.008	0.014	0.04
Cu	0.004	0.02	0.03

Table II. The influence of annealing temperature on the mobility of sulfur-implanted layers

Annealing temperature (°C)	620	700	800	900
Microwave mobility (cm^2/Vsec)	3100	3400	3800	4000

ture on S-implanted layers is shown in Table II. Mobilities less than those shown in Table II were found when samples were annealed at less than 600°C. The mobility increases with temperature up to 900°C.

These observed microwave mobilities represent good values for implants in Cr doped semi-insulating substrates. Such substrate material contains up to $5 \times 10^{15}/cm^3$ Cr atoms as well as around $10^{16}/cm^3$ oxygen and carbon atoms (13). Therefore, it is not surprising that the mobilities are not greater than 4000 cm^2/Vsec. The mobility *vs.* annealing temperature on sulfur-implanted MESFET structures has previously been examined (3) by van der Pauw measurements. The present findings are in agreement with their results. For short anneals, one expects the mobility to increase with annealing temperature, indicating that the damage is being removed. Such behavior has been observed by Sanbury (14), who examined the isochronal annealing behavior of n-type dopant of GaAs. He found that the 600°C anneal greatly increased both the mobility and the carrier concentration and that both increase slowly above 600°C.

The diffusion which occurs during the high temperature anneal must also be considered. Thus, the influence of the annealing time was studied. At 800°C, by increasing the annealing time from 20 to 120 min, the mobility increased from 3800 to 4200 cm^2/Vsec. The diffusion of sulfur leads to a decreased carrier concentration level which could account for the increased mobility found at longer anneal time. Such diffusion of the implanted sulfur has contributed to the high mobilities on sulfur-implanted Gunn devices (15). However, as far as FET devices are concerned, the doping level and the layer thickness cannot be allowed to change by diffusion.

The microwave mobility *vs.* Se concentration is illustrated in Fig. 4. Double implantation has been used in order to achieve a flat selenium concentration. The implantations were carried out at 260°C with 480 and 160 keV Se^+ ions with fluences necessary to achieve the indicated concentrations. The samples were capped

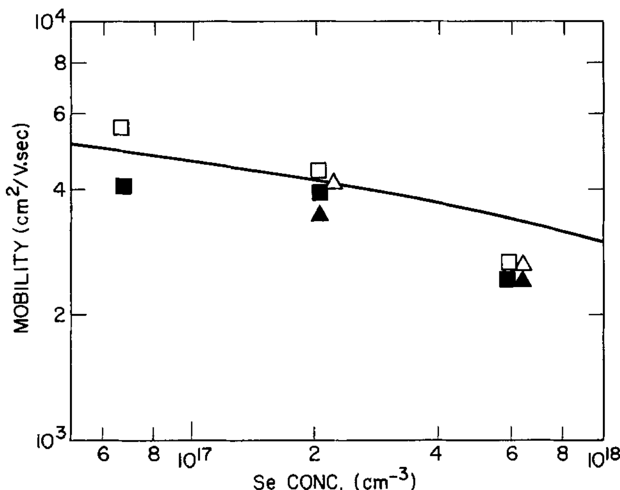

Fig. 4. The microwave mobilities for different concentrations on implanted Se. The triangle and square signs indicate two starting materials. The solid points were obtained at 300°K, while the unfilled points were measured at 77°K. The curve is the bulk mobility (9).

with Si_3N_4 and were annealed at 800°C for 30 min. The two different semi-insulating substrates introduced only slight differences. We see that the implanted samples' microwave mobilities compare favorably with Sze-Irvin (9) Hall mobilities except at higher carrier concentrations. But such an effect is in line with the increased compensation from radiation damage, which should be present at increased doses. Note also that the presence of compensation is more pronounced at 77°K where the impurity scattering is dominant.

Conclusions

We have shown that the microwave mobility is a valuable parameter for rapid, contactless evaluation and control of many implantation processing steps. Evaluation of starting wafers has been described. Optimization of the processing parameters for sulfur-implanted layers for FET's structures leads to the conclusion that at around $5 \times 10^{12}/cm^2$ dose level an anneal at 850°C for about 20 min is optimal. Different encapsulation procedures, which are observed to affect the mobility, are now under investigation using the contactless mobility technique.

Acknowledgments

We wish to thank the members of the NRL High Magnetic Field Facility for their assistance and C. A. Stolte of Hewlett-Packard Corporation for the emission spectroscopy.

This work is sponsored in part by the Naval Electronic Systems Command.

Manuscript submitted Nov. 30, 1977; revised manuscript received March 15, 1978. This was Paper 95 presented at the Philadelphia, Pennsylvania, Meeting of the Society, May 8-13, 1977.

Any discussion of this paper will appear in a Discussion Section to be published in the June 1979 JOURNAL. All discussions for the June 1979 Discussion Section should be submitted by Feb. 1, 1979.

Publication costs of this article were assisted by the Naval Research Laboratory.

REFERENCES

1. R. G. Hunsberger and N. Hirsch, *Solid-State Electron.*, **18**, 349 (1975).
2. B. M. Welch, F. H. Eisen, and J. A. Higgins, *J. Appl. Phys.*, **45**, 3685 (1974).
3. W. Kellner, H. Kniepkamp, D. Ristow, M. Heinsle, and H. Broffka, *Solid-State Electron.*, **20**, 459 (1977).
4. P. Stallhofer, Thesis, T. U. Munchen (1975).
5. J. E. Stannard, T. A. Kennedy, and B. D. McCombe, *J. Vac. Sci. Technol.*, **13**, 869 (1976).
6. G. L. Miller, D. A. H. Robinson, and J. D. Wiley, *Rev. Sci. Instrum.*, **47**, 799 (1976).
7. T. S. Benedict and W. Shockley, *Phys. Rev.*, **89**, 1152 (1953).
8. C. A. Bryant and J. B. Gunn, *Rev. Sci. Instrum.*, **36**, 1614 (1965).
9. S. M. Sze and J. C. Irvin, *Solid-State Electron.*, **11**, 599 (1968).
10. F. H. Eisen, B. M. Welch, K. Gamo, T. Inada, H. Mueller, M. A. Nicolet, and J. W. Mayer, in "Application of Ion Beams to Materials, 1976," G. Carter, J. S. Colligon and W. A. Grant, Editors, p. 64, Inst. Phys. Conf. Ser. 28 (1976).
11. C. A. Stolte, "Technical Digest International Electron Devices Meeting," p. 585, IEEE, New York (1975).
12. F. H. Eisen and B. M. Welch, in "Ion Implantation in Semiconductors and Other Materials," F. Chernow, J. A. Borders, and O. K. Brice, Editors, p. 97, Plenum Press, New York (1977).
13. P. F. Lindquist, *J. Appl. Phys.*, **48**, 1262 (1977).
14. J. D. Sanbury and J. F. Gibbons, *Radiat. Effect*, **6**, 269 (1970).
15. T. Mizutani, T. Honda, H. Yamazaki, and M. Fujimoto, *Solid-State Electron.*, **20**, 443 (1977).

The Fabrication of High Precision Nozzles by the Anisotropic Etching of (100) Silicon

E. Bassous* and E. F. Baran

IBM Thomas J. Watson Research Center, Yorktown Heights, New York 10598

ABSTRACT

Arrays of nozzles of uniform size ($\simeq 25 \times 25\ \mu m^2$) and spacing ($\simeq$0.3 mm) suitable for high quality and high speed ink-jet printing have been fabricated by the anisotropic etching of holes through (100) Si wafers using conventional Si-processing techniques. The etchant used is a mixture of pyrocatechol, ethylene diamine, and water. The nozzles are well-defined truncated, square pyramidal cavities bounded by 4 convergent {111} planes. The square orifice, side W_O, is given by $W_O = W_B - \sqrt{2}\, t_{Si}$, where W_B is the side of the square base and t_{Si} the wafer thickness. Successful fabrication of these silicon microstructures requires the application of well-controlled patterning and etching processes and the selection of a uniform, defect-free, accurately oriented single crystal substrate.

Arrays of nozzles of uniform size and spacing are required to generate drops of ink with uniform characteristics for high speed and high resolution ink-jet printing using binary, deflected, electrostatically charged ink jets (1-5). In ink-jet printing, fine jets of conductive ink are formed by forcing the pressurized ink through an array of nozzles; the jets break up into uniform streams of droplets by vibrating the nozzle array at a fixed frequency by means of a piezoelectric transducer. In one method of printing, unwanted drops are selectively charged and deflected electrostatically from the main streams, and the uncharged drops are allowed to strike the paper to form the required characters (1, 6).

Arrays of nozzles with square orifices of potential usefulness in ink-jet printing have been fabricated by etching holes through single crystal silicon wafers of (100) orientation (4-5, 7) using an anisotropic (crystallographically preferential) etching solution containing pyrocatechol, ethylene diamine, and water

* Electrochemical Society Active Member.

Key words: silicon nozzles, nozzle fabrication, 3-D microstructures, ink-jet printing, anisotropic etching.

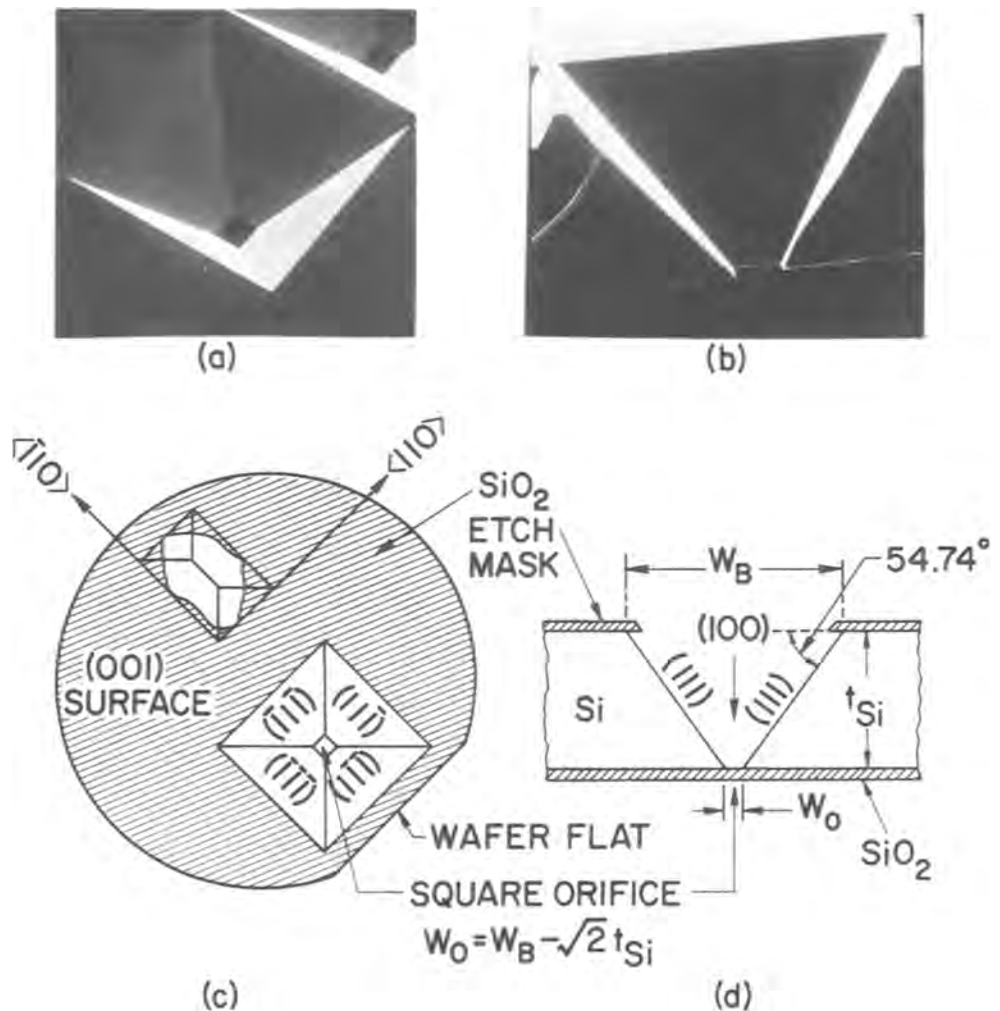

Fig. 1. Anisotropic etching of holes in single crystal silicon of (100) orientation. (a) SEM photomicrograph of a nozzle etched through a silicon wafer 200 μm thick; (b) SEM photomicrograph of a cross section through the nozzle shown in (a); (c) Self-limiting {111} etch planes define the side walls of holes etched through openings in the surface masking film (SiO_2). The sides of the rectangular holes at the surface are parallel to the [110] directions; (d) Cross section through a nozzle showing the relationship between base hole side W_B, orifice side W_O, and Si wafer thickness t_{Si}.

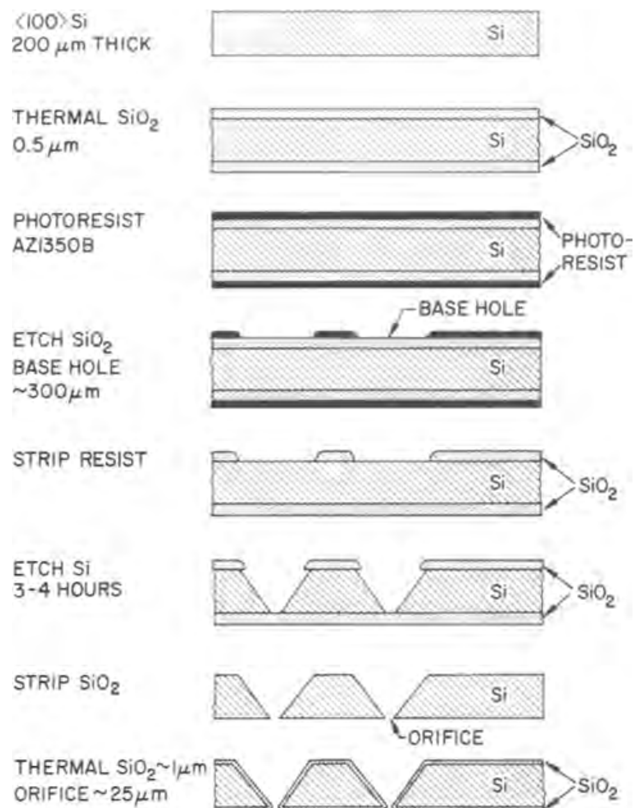

Fig. 2. Sequence of steps in the fabrication of silicon nozzle arrays using conventional photolithographic techniques and anisotropic etching of the silicon substrate.

(8-12). Each nozzle in the array is a truncated square pyramidal cavity bounded by 4 convergent {111} planes and 2 {100} surface planes as shown in Fig. 1. The high degree of symmetry exhibited by these three-dimensional microstructures results from the crystallographic perfection of the starting wafer and the well-controlled, high etch rate of the {100} planes relative to the {111} planes.

The size and shape of the holes etched in single crystal Si depend on the geometry and orientation of the openings in the surface masking film, *e.g.*, SiO_2, the duration of etching, and the wafer thickness. As shown in Fig. 1, a small opening forms a cavity with a rectangular base hole on the Si surface which encloses the original opening in the SiO_2 film. The sides of the rectangle represent the intersections of the {111} planes with the (100) surface plane and are parallel to the <110> direction. Because the etch rate of {111} planes is very low, cavities and nozzles bounded only by exposed {111} planes are self-limiting and thus do not change significantly in size or shape even after prolonged etching.

In a perfect crystal the angle between the {111} planes and the (100) surface is 54.74° (Fig. 1). Assuming no misorientation of the Si wafer, the side dimen-

Fig. 3. SEM photomicrograph of an 8 nozzle array etched in silicon. The array is 0.25 cm long, the base hole 290 × 290 μm^2, the orifice 28 × 28 μm^2, wafer thickness 185 μm, and the center-to-center spacing is 305 μm.

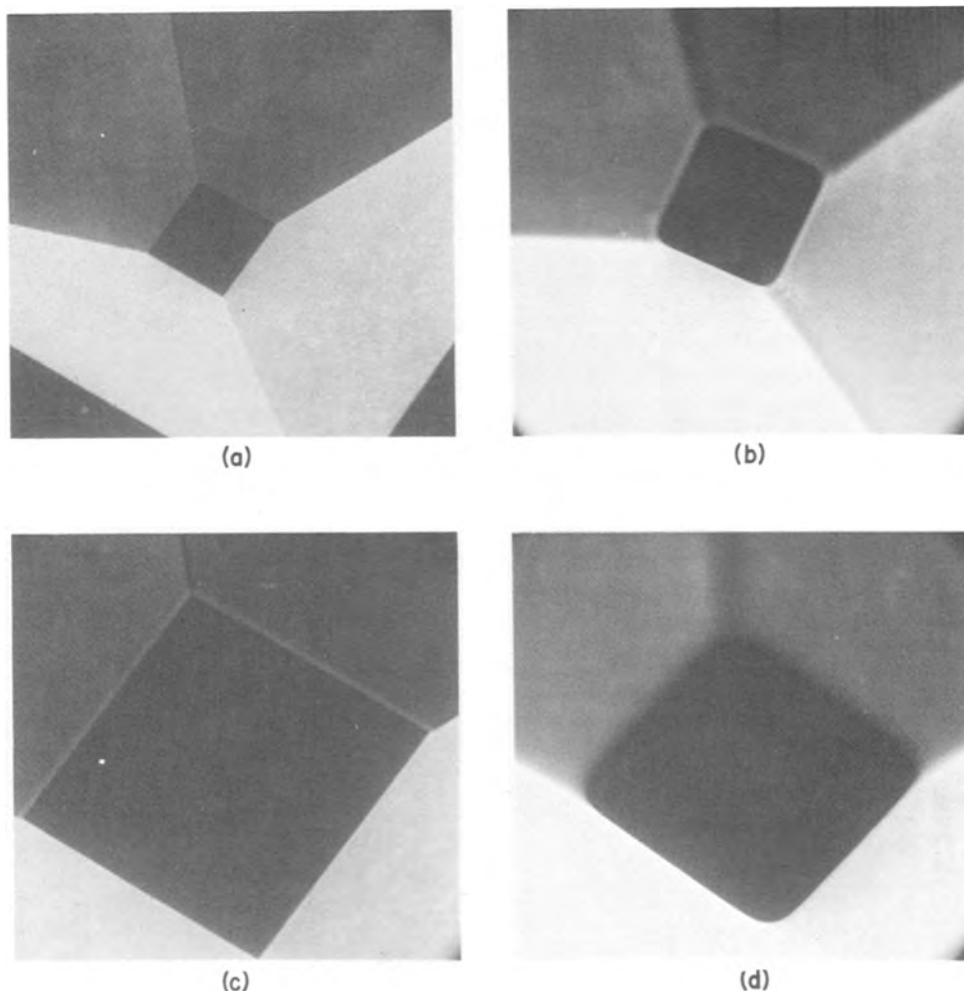

Fig. 4. SEM photomicrographs of uncoated Si nozzle orifices 30 × 30 μm^2. The knife edge corners of the orifice in (a) and (c) can be rounded by successive thermal oxidation and stripping. Rounding shown in (b) and (d) is obtained after growing 5 μm SiO_2.

sion W_O of the square orifice which results after etching through a wafer of thickness t_{Si} is given by the expression $W_O = W_B - \sqrt{2}\, t_{Si}$, where W_B is the side of the square-base hole etched in the Si surface. The processing conditions and the results obtained in fabricating uniform nozzle arrays in (100) Si are described below.

Experimental

The fabrication of Si nozzle arrays is carried out using conventional Si-processing techniques. The sequence of steps in the process are shown in Fig. 2. Czochralski-grown, p- or n-type Si wafers 32 mm diam, 200 μm thick, (100) orientation, chem-mechanically polished on both sides are cleaned in ammonia peroxide and acid peroxide solutions, then thermally oxidized in steam to form an SiO_2 film 0.5 μm thick. Photoresist is applied to both surfaces of the wafers and using standard photolithographic methods, arrays of square openings are defined and etched in the SiO_2 film on one side of the wafers. The wafers are then etched in an aqueous solution containing 4 mole percent (m/o) pyrocatechol $C_6H_4(OH)_2$, (P), 46.4 m/o ethylene diamine $NH_2(CH_2)_2NH_2$ (ED), and 49.6 m/o water. The P-ED solution is used at its boiling point 118° ± 1°C in a quartz flask fitted with a condenser to maintain the composition constant and N_2 gas is bubbled through the solution to prevent it from oxidation. The total etching time required is 3-4 hr based on an average etching rate of ~50 μm/hr on the (100) plane. Etching is stopped when orifices appear on the opposite side of the wafers. After cleaning, the oxide is etched off, and the wafers are oxidized in steam to form a uniform coating of thermal SiO_2 on the nozzle surfaces.

Results and Discussion

Arrays of silicon nozzles possessing uniform physical characteristics suitable for ink-jet printing were fabricated reproducibly by the above procedure. An array of 8 identical nozzles with square orifices ~ 25 × 25 μm^2 on 0.3 mm centers and with smooth well-defined defect-free surfaces is shown in Fig. 3. Structural symmetry and uniformity as well as the absence of visible defects in the nozzles are necessary requirements for high quality printing at high speed. Surface irregularities or contaminants and variations in orifice dimensions alter the flow characteristics of the streams of droplets generated across an array, resulting in a degradation of printing performance (4). The tapered geometry of each nozzle is a useful feature which permits by means of a simple microscopic examination to determine the suitability of an array of nozzles for printing purposes. Due to the brittle properties of single crystal silicon and the small size of the orifices, the nozzles are subject to chipping and clogging if they are poorly handled. By treating these structures in the same way as microelectronic devices they can be processed and tested with relative ease. Ink-jet printing experiments are performed by mounting an array of nozzles on a printhead, forcing ink under pressure (~2 atm) through each nozzle, and simultaneously vibrating the printhead at high frequency (~100 kHz) by means of a piezoelectric crystal. To protect the silicon from attack by the corrosive inks a layer of SiO_2 ~1 μm thick is thermally grown on the nozzles. The square orifice has sharp knife-edge corners and edges which are susceptible to structural damage from stress concentrations resulting from the induced oscillations and the pressurized ink in the printhead. To overcome this potential problem, rounding of the orifice corners and edges was attempted by a technique which uses repeated thermal oxidation and oxide-stripping cycles. In each cycle a thickness of silicon is removed equivalent to ~44% of the thermally grown SiO_2 thickness. Since thermal oxidation is a surface diffusion process, rounding of corners and edges occurs symmetrically and uniformly in each nozzle across an array. Figure 4 shows the rounding obtained after growing a

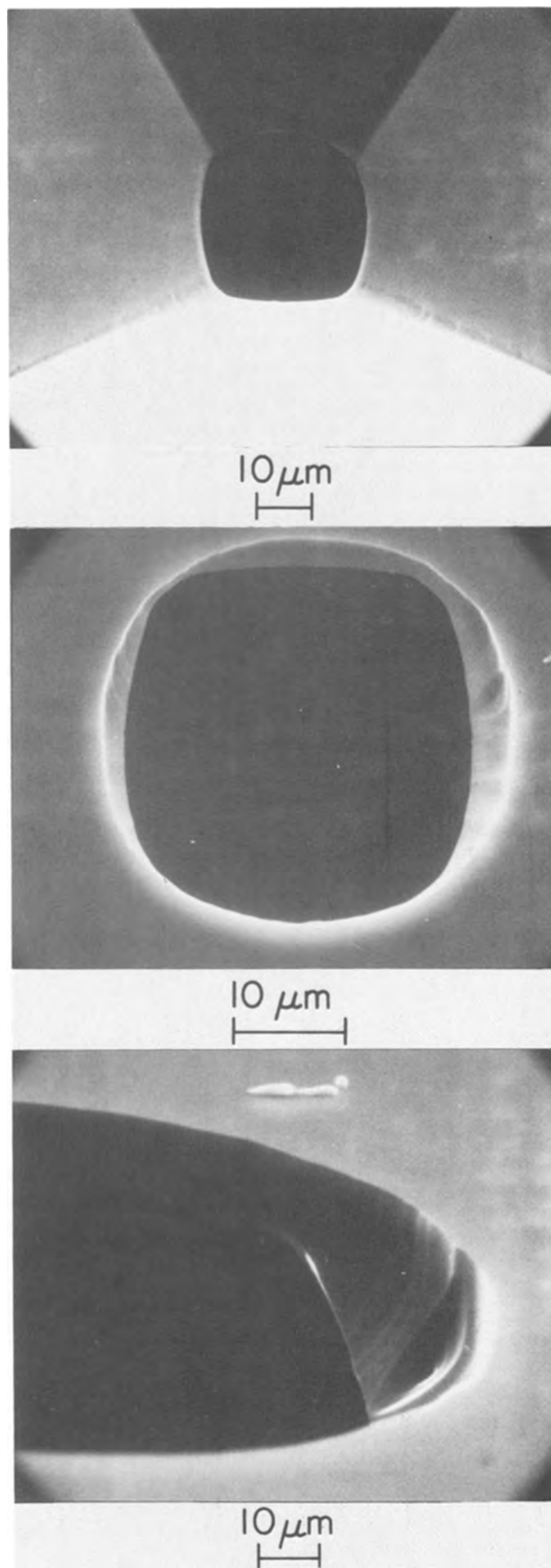

Fig. 5. SEM photomicrographs of an uncoated Si nozzle which was rounded by etching ~ 5 μm Si in a mixture of HF, HNO_3, and HAc. (Upper) nozzle viewed from the base hole side: (middle) nozzle viewed from the orifice side; (lower) edge of orifice showing nonsymmetrical etching.

total of 5 μm thermal SiO_2 in steam at 1000°C in 5 successive oxidation and stripping cycles. This technique causes orifice dimensions to increase incrementally with each cycle and therefore allows orifice area to be controlled with a high degree of precision. An etching method for rounding nozzles using a mixture of HF, HNO_3 and acetic acid was also attempted. This method yielded a geometry which was not as symmetrical and uniform as the oxidation and stripping technique. Figure 5 shows SEM photomicrographs of a nozzle which was rounded by etching ~5 μm of Si from the (100) Si surface. The lack of symmetry is mostly due to the differential etch rate of the various Si planes exposed to the etchant and to the nonuniform flow of etchant through the nozzles during the etching process. Under similar operating conditions, the performance of square and rounded nozzles is identical provided the orifice areas are equal (4).

The successful fabrication of arrays of nozzles with predictable dimensions is accomplished by selecting an appropriate substrate, defining and aligning the array pattern accurately on the wafer surface, and controlling the anisotropic etching conditions. Orifice dimensions are determined by the size of the base hole W_B and wafer thickness only. In practice, the required base hole for a wafer of a given thickness is obtained by controlling the underetching U of the cavity formed in the Si surface (Fig. 6). This is a critical factor in the fabrication of microstructures which require prolonged etching in anisotropic etchants. The underetching shown in Fig. 6, given by $U = R_{(111)}t/\sin\theta$ where $R_{(111)}$ is the etch rate of the {111} planes and t the etching time, is the minimum which can be achieved under ideal processing conditions. Factors which contribute to variations in underetching and hence to variations in orifice dimensions are discussed below.

Substrate.—The orientation of the {100} surface planes and the <110> flat are critical and should be accurate within ± 1° in order to control the symmetry, size, and relative alignment of the arrays of nozzles. Wafer orientation, though critical, is seldom a problem in practice because a precision $\leq \pm 1°$ is routinely obtained in commercially available wafers. The variation in wafer thickness (t_{Si}) affects orifice size uniformity for the same base hole dimensions. A change Δt_{Si} across an array results in $\sqrt{2}\,\Delta t_{Si}$ variation in the orifice side dimension W_O (Fig. 1). Defects originating at the Si surfaces, due, for example, to poor polishing or cleaning, induce pinholes in the surface masking film (SiO_2) which result in characteristic square etch pits in the Si surface. These defects are distinguishable from process-induced defects in the SiO_2 by the formation of both square and rectangular etch pits in the Si surface as shown in Fig. 7. Any small defect at the Si-SiO_2 interface located on the perimeter of the etched-base hole causes enlargement or merging of adjacent holes (Fig. 7).

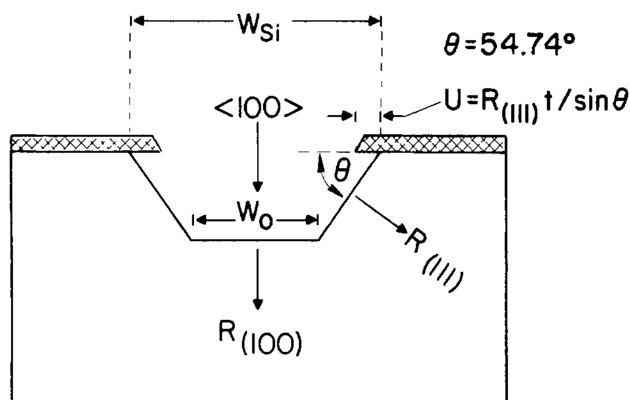

Fig. 6. Nozzle dimensions are critically dependent on control of the underetching U below the edge of the surface etch mask. Under ideal conditions $U = R_{(111)}\ t/\sin\theta$, where $R_{(111)}$ is the etch rate of the {111} planes, and t the etching time.

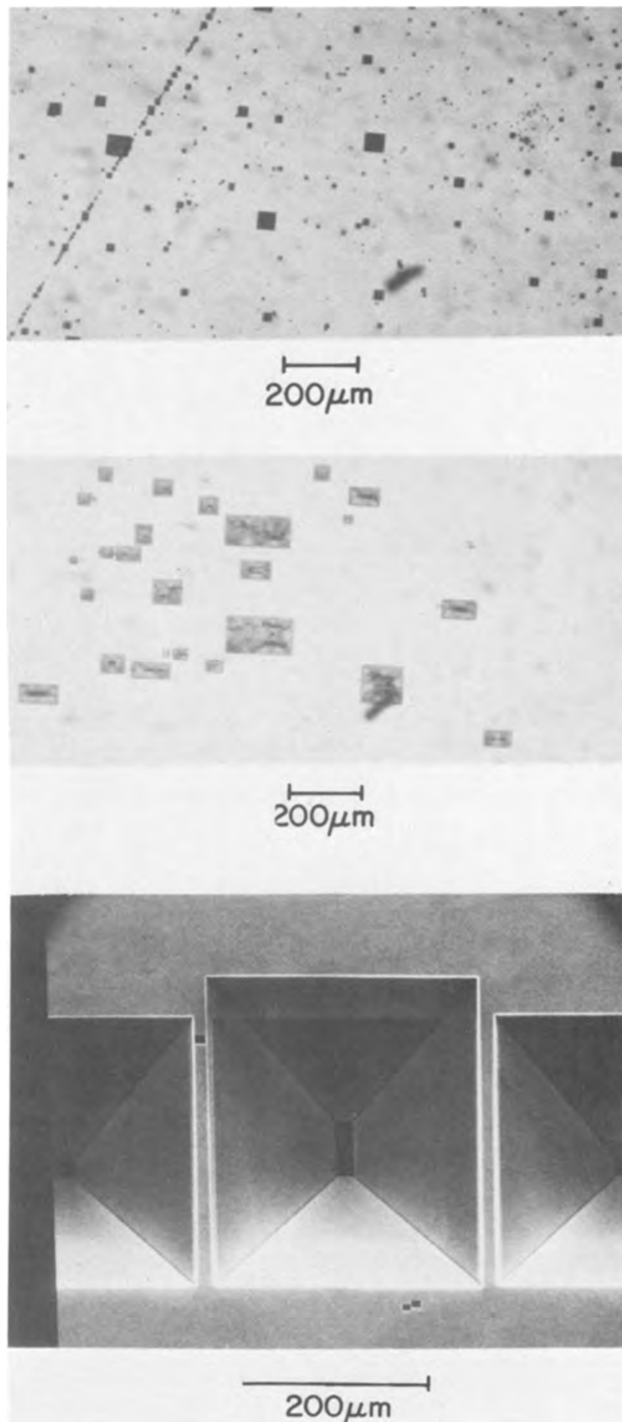

Fig. 7. Characteristic square and rectangular etch pits on Si surfaces after anisotropic etching in pyrocatechol-ethylene diamine-water mixture using thermal SiO_2 as the surface etch mask. Upper photomicrograph: square etch pits result from pinholes in the SiO_2 induced by defects in the Si surface. Middle photomicrograph: rectangular etch pits result from process-induced defects in the SiO_2. Lower SEM photomicrograph: defect on the perimeter of the base hole leads to an enlargement of the nozzle.

Pattern definition.—A square opening, side W, in the surface masking film produces minimum underetching if it is precisely aligned parallel to the <110> direction (Fig. 1). A misalignment $\theta°$ results in an increase to $W' = W(\sin\theta + \cos\theta)$ which reaches a maximum at $\theta = 45°$ as shown in Fig. 8.

Small circular openings in the SiO_2 surface film form octagonal base holes which eventually became a square pyramidal cavities after prolonged anisotropic etching of the substrate. A circular opening and an ac-

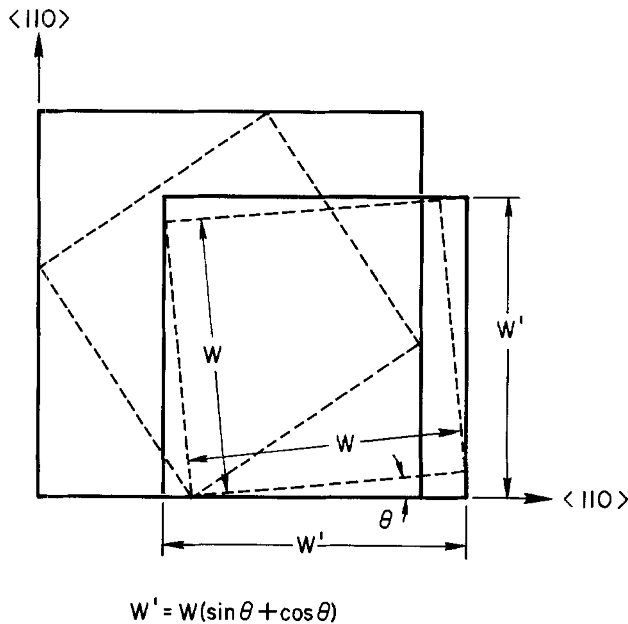

Fig. 8. The size of an etched hole (solid lines) increases in proportion to the misalignment of the original square opening (dashed lines) in the surface-masking film and reaches a maximum at $\theta = 45°$.

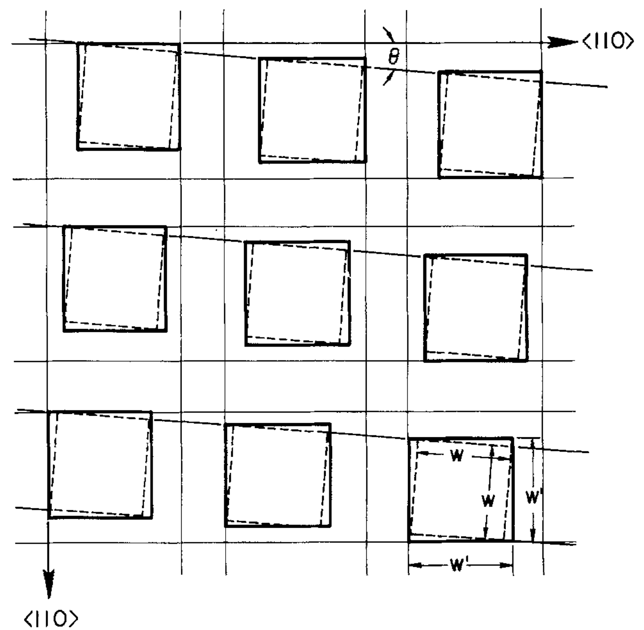

Fig. 10. Staggered square-etched holes (solid lines) resulting from a misalignment of an array of square openings (dashed lines) along the vertical and horizontal [110] directions.

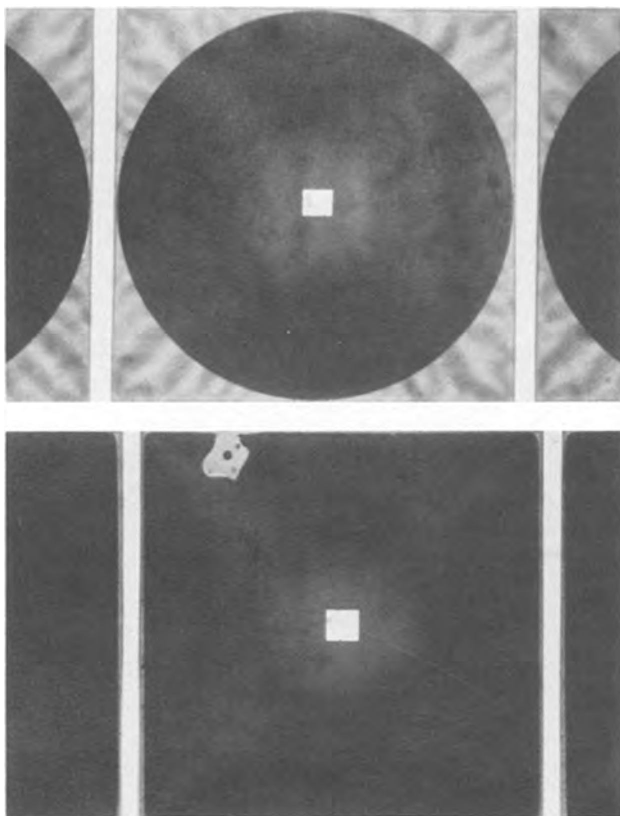

Fig. 9. Photomicrographs of nozzles formed in (100) Si by etching through circular and square openings in the surface-masking film (SiO_2). The nozzles are identical if the side of the square is accurately aligned ond equal to the diameter of the circular opening.

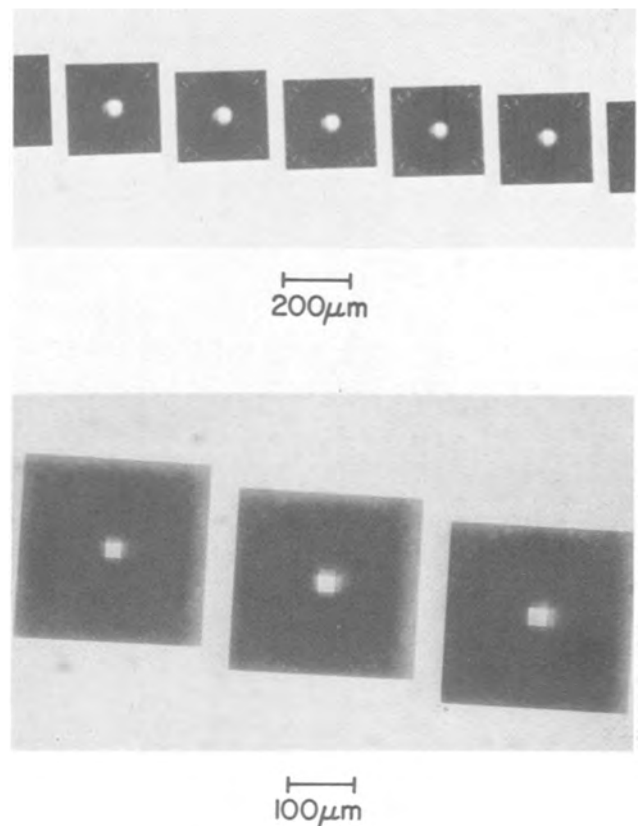

Fig. 11. Photomicrographs of a single array of nozzles etched through an Si wafer showing the staggered orifices resulting from misalignment of the array relative to the <110> direction.

curately aligned square opening form identical nozzles when the side of the square and the diameter of the circle are equal (Fig. 9). Small openings of any geometry form nozzles which are staggered in the vertical and horizontal directions if the arrays are not accurately aligned parallel to the <110> direction (Fig. 10 and 11).

Anisotropic etching.—Solutions of KOH (13-17), P-ED (8-12), and hydrazine N_2H_4 (18-20) are commonly used anisotropic etchants for single crystal silicon. Of the 3 etchants, KOH is the most stable and the most convenient to use; however, it attacks SiO_2 at a rapid rate especially at defect sites, and thus SiO_2 films cannot be used as etch masks in the fabrication of Si

devices which require prolonged etching in KOH. Despite the fact that other masking films could be used with KOH, *e.g.*, Au, they are not as practical as thermally grown SiO_2 films for the fabrication of precision nozzles. P-ED and N_2H_4 solutions attack SiO_2 at a very low and comparable etch rate, but N_2H_4 tends to etch (100) Si nonuniformly by forming pyramidal-shaped crystalline hillocks (13-15) on {100} surfaces in deeply etched cavities. Hillock formation also occurs with the P-ED etch composition used by Finne and Klein (8), particularly at temperatures below 110°C. In a solution containing 4 m/o (P), 46.4 m/o (ED), and 49.6 m/o water, used at its boiling point 118° ± 1°C, hillock formation is inhibited and (100) Si is etched at a high, uniform, and reproducible etch rate

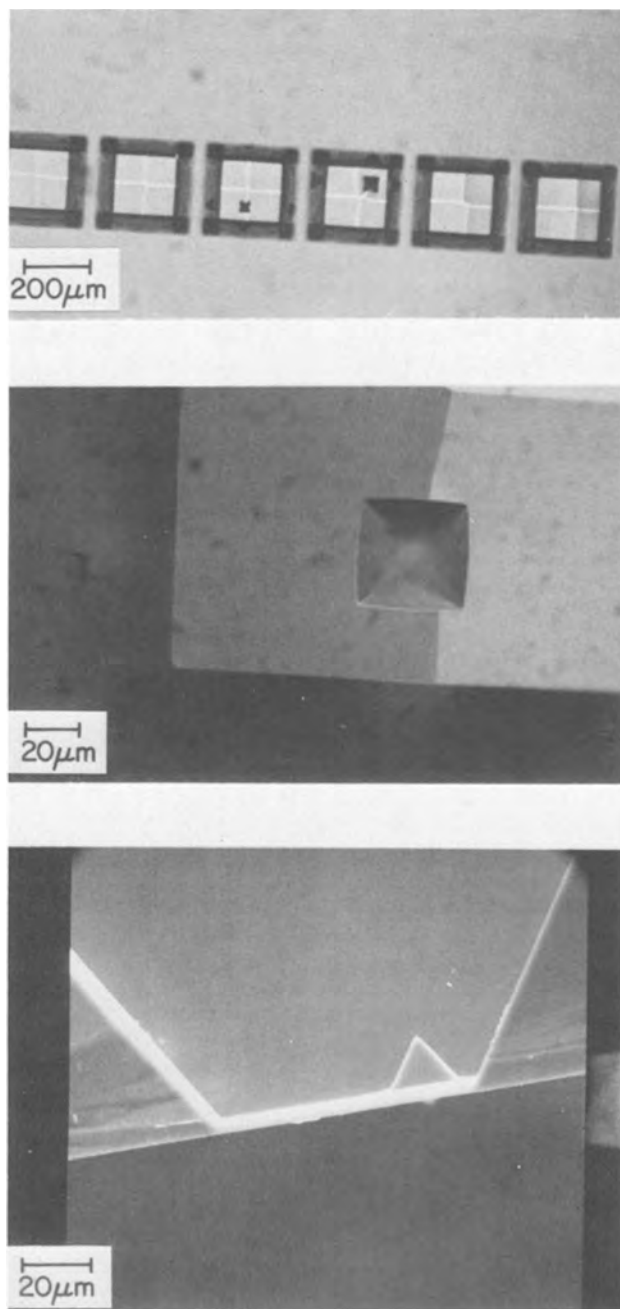

Fig. 12. Pyramidal-shaped crystalline hillocks formed on anisotropically etched {100} surfaces. Upper, array etched 30 μm deep, showing single hillocks in 2 holes; middle, magnified image of a single hillock; lower, SEM photomicrograph of a cross section through a partially etched nozzle with a hillock on the (100) plane. The hillock is a mesa with side walls parallel to the convergent {111} crystal planes of the nozzle.

with an anisotropic etch rate ratio $R_{(100)}/R_{(111)} = 50/1$. Solutions containing higher concentrations of (ED) at 110°-118°C are equally effective in preventing hillocks on {100} surfaces. Hillocks are structures bounded by 4 {111} planes (Fig. 12) which etch very slowly in P-ED and often cause a partial or total blockage of nozzles during the fabrication process (Fig. 13). The hillocks tend to form readily on poorly cleaned surfaces and in etchants containing excessive amounts of dissolved silicon; thus it is likely that they result from local masking by contaminants or from reaction products of the etching process (8). Although P-ED solutions etch (100) Si uniformly, chem-mechanically polished surfaces tend to develop a fine wavy texture which becomes coarser as etching progresses (Fig. 14). As the surfaces remain clean and specular throughout the etching reaction their topography does not affect the nozzle fabrication process. A similar etching behavior has been observed with KOH (13, 16) and N_2H_4 (19).

The average etch rate of the (100) plane in the P-ED etchant of the given composition at 118° ± 1°C is ≃ 50 μm/hr based on measurements of the total etching time required to etch nozzles through 200 μm thick wafers. The etch rate of the {111} plane is ≃ 1 μm/hr determined from measurements of the oxide overhang or "underetching" of the base hole in the Si surface.

For consistently good etching results the Si surface should be highly polished and free from contaminants such as photoresist and oxide residues. Prior to anisotropic etching, the substrates are etched in buffered HF to ensure complete removal of the native oxide on the Si surface. Similarly, wafers are etched in buffered HF after removal from P-ED solution to dissolve the deposit which forms on etched surfaces. P-ED solutions are stable in the absence of oxygen and oxidizing agents and can be used over periods of 2-3 weeks provided the amount of dissolved silicon is small. A solution containing a large concentration of silicon forms a heavy white precipitate of a pyrocatechol-silicon complex (8) when it is cooled to room temperature. Such solutions are generally not suitable for making precision structures which require etching of deep cavities.

Conclusions

Silicon nozzle arrays with uniform orifice dimensions suitable for ink-jet printing applications have been fabricated reproducibly by the anisotropic etching of

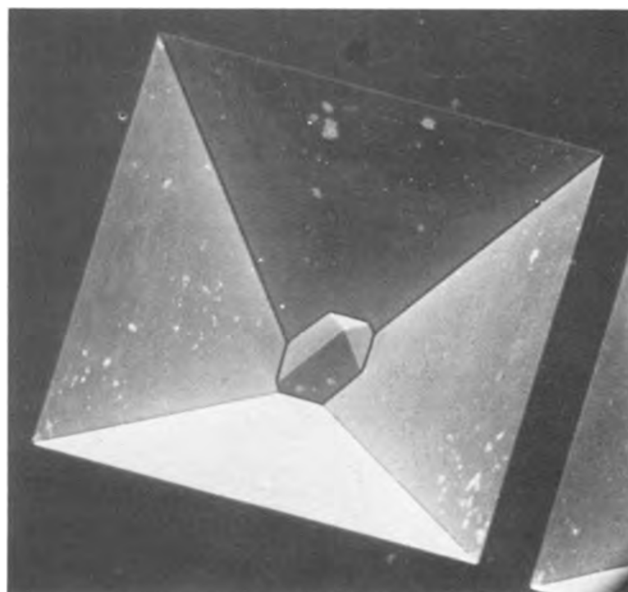

Fig. 13. SEM photomicrograph of a nozzle with the orifice totally blocked as a result of poor etching conditions. Base hole is 300 × 300 μm^2.

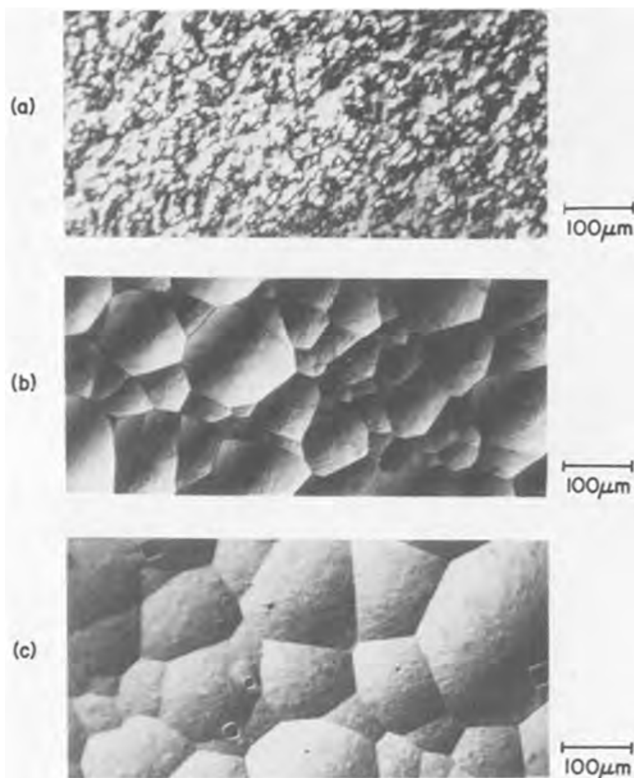

Fig. 14. Photomicrographs using phase-contrast illumination (Nomarski) of {100} Si surfaces before and after anisotropic etching. (a) Original unetched chemically polished back surface of a wafer; (b) same surface after etching 25 µm of Si; (c) same surface after etching 65 µm of Si. Chem-mechanically polished wafers also yield wavy textured surfaces after anisotropic etching.

holes through Si wafers of (100) orientation using standard Si-processing methods. The successful fabrication of these novel three-dimensional microstructures which require unusually long etching times is strongly dependent on the crystallographic perfection and the physical uniformity of the silicon wafer and on the control exercised in the patterning and etching processes. A key factor in the fabrication process is the use of an anisotropic etching solution containing pyrocatechol 4 m/o ethylene diamine 46.4 m/o, and water 49.6 m/o, at its boiling point 118° ± 1°C.

Acknowledgments

We wish to thank A. Reisman, H. N. Yu, C. M. Osburn, L. Kuhn, and H. H. Taub for many helpful discussions and support. The technical assistance of H. F. Lazzari, J. Wilson, J. A. Kucza, V. Maniscalco, M. J. Smyth, A. Cramer, and E. J. Petrillo is gratefully acknowledged.

Manuscript submitted Nov. 7, 1977; revised manuscript received March 10, 1978.

Any discussion of this paper will appear in a Discussion Section to be published in the June 1979 JOURNAL. All discussions for the June 1979 Discussion Section should be submitted by Feb. 1, 1979.

Publication costs of this article were assisted by IBM Corporation.

REFERENCES

1. R. G. Sweet, *Rev. Sci. Instrum.*, **36**, 131 (1965).
2. R. G. Sweet, U.S. Pat. 3,596,275 (1971).
3. *IBM J. Res. Dev.*, Special Issue on Ink Jet Printing, 21 (1977).
4. E. Bassous, H. H. Taub, and L. Kuhn, *Appl. Phys. Lett.*, **31**, 135 (1977).
5. E. Bassous and E. Baran, Paper 363 presented at The Electrochemical Society Meeting, Atlanta, Georgia, Oct. 9-14, 1977.
6. F. J. Kamphoefner, *IEEE Trans. Electron Devices*, **ED-19**, 584 (1972).
7. E. Bassous, L. Kuhn, A. Reisman, and H. H. Taub, U.S. Pat. 4,007,464 (1977).
8. R. M. Finne and D. L. Klein, *This Journal*, **114**, 965 (1967).
9. J. C. Greenwood, *ibid.*, **116**, 1325 (1969).
10. A. Bohg, *ibid.*, **118**, 401 (1971).
11. T. O. Sedgwick, A. N. Broers, and B. J. Agule, *ibid.*, **120**, 1769 (1972).
12. C. J. Schmidt, P. V. Lenzo, and E. G. Spencer, *J. Appl. Phys.*, **46**, 4080 (1975).
13. J. B. Price, in "Semiconductor Silicon 1973," H. R. Huff and R. R. Burgers, Editors, p. 339, The Electrochemical Society Softbound Symposium Series, Princeton, N.J. (1973).
14. D. L. Kendall, *Appl. Phys. Lett*, **26**, 195 (1975).
15. W. T. Tsang, C. C. Tseng, and S. Wang. *Appl. Opt.*, **14**, 1200 (1975).
16. D. F. Weirauch, *J. Appl. Phys.*, **46**, 1478 (1975).
17. A. I. Stoller, *RCA Rev.*, **31**, 271 (1970).
18. D. B. Lee, *J. Appl. Phys.*, **40**, 4569 (1969).
19. M. J. Declercq, L. Gerzberg, and J. D. Meindl, *This Journal*, **122**, 545 (1975).
20. M. J. Declercq, *IEEE J. Solid-State Circuits*, **SC-10**, 191 (1975).

Determination of Electron Affinity of In_2O_3 from Its Heterojunction Photovoltaic Properties

Edward Y. Wang and Lan Hsu

Department of Electrical and Computer Engineering, Wayne State University, Detroit, Michigan 48202

ABSTRACT

In_2O_3-Si, In_2O_3-Ge, In_2O_3-GaAs, and In_2O_3-InP heterojunction solar cells have been fabricated and their photovoltaic properties have been investigated. All devices show rectifying and photovoltaic effects. The experimental results can be explained by a simple heterojunction energy band diagram. In order to match the experimentally observed polarities of the open-circuit voltage and short-circuit current of these heterojunction solar cells, the electron affinity of In_2O_3 materials is determined to be 4.45 eV. The substrate-resistivity dependence of open-circuit voltage is consistent with the energy band diagram using the electron affinity value of 4.45 eV for In_2O_3.

The formation of heterojunctions between conducting glasses, silicon (1-3), and other materials (4) has previously been reported. The current-transport mechanism of In_2O_3-Si heterojunction solar cells has generally been explained by a simple heterojunction model or by a metal insulator-semiconductor model. In both models, the value of the electron affinity of the oxide semiconductor is one of the most important factors in determining the photovoltaic properties. Very few studies, however, have been reported (5-7) on the properties of In_2O_3: its electron affinity was uncertain and its estimated value was about 4.31 eV, 0.3 eV greater than that of Si (1).

In this paper, we report the first successful formation of In_2O_3-Ge, In_2O_3-GaAs, and In_2O_3-InP heterojunctions through the chemical vapor deposition method. These heterojunction cells show the photovoltaic effects. Based on the simple heterojunction energy band diagram, an electron affinity of 4.45 eV was obtained for In_2O_3 in order to match the experimentally observed polarities of the open-circuit voltage and the short-circuit current of these heterojunction solar cells. Built-in potential values from constructed heterojunction energy band diagrams agree with experimental V_b values from capacitance and current-voltage measurements. Results on photovoltaic cells using various substrate resistivities of Si and Ge materials are also consistent with the energy band diagram using electron affinity value of 4.45 eV for In_2O_3.

Experimental

Cell fabrication.—Mechanically polished semiconductor wafers, p- and n-type Si, Ge, GaAs, and n-type InP, were used in this experiment. Wafers were cleaned with diluted HF, acetone, and methanol solutions. The deposition of thin film In_2O_3 was carried out by hydrolysis of $InCl_3$. $InCl_3$ powder was formed by boiling indium wire (99.999%) in concentrated HCl solution. The reaction took place upstream from a boat, containing a melted $InCl_3$ powder source placed in the zone close to the inlet. The semiconductor substrate was placed on a holder in the center zone of the furnaces (about 500°-550°C) with helium or oxygen bubbled through deionized water as the carrier gas to form the In_2O_3/semiconductor heterojunction cells. In the indium-oxygen system, In_2O_3 is the only stable crystalline-oxide phase (8). The temperature of the optimum heterojunction formation was different for various substrate materials. It was 500°C for Si and Ge; 450°C for GaAs and InP. The front contact to the In_2O_3 layer was made with aluminum evaporated through a finger mask. For back contacts, In-Ag was applied for p-GaAs, n-GaAs, and p-Ge; Sn-Ag for n-InP and n-Ge. For better ohmic contacts, cells were sintered at 500°C for 8 min.

Results.—Photovoltaic properties.—Figure 1 shows the current-voltage characteristics on a linear scale both in the dark and under illumination for the (n-p) In_2O_3-Si heterojunction solar cell. Under air mass zero (AM0) illumination, a short-circuit current (J_{sc}) of 22 mA/cm², open-circuit voltage (V_{oc}) of 0.34V and fill factor (FF) of 45% are obtained. Its simple heterojunction energy band is also shown in Fig. 1. Under illumination, the polarities of V_{oc} and I_{sc} (negative for the In_2O_3 side and positive for the Si side) are in accordance with the direction of the energy-band bending. Obviously, the construction of a heterojunction energy band diagram depends on the Fermi level E_F. We take the Fermi level of In_2O_3 in equilibrium to be 0.05 eV below its conduction band. This is supposed by the experimental evidence of ohmic-tunneling behavior for In_2O_3 depositing on 0.0003 Ω-cm p-type germanium substrate and rectify-

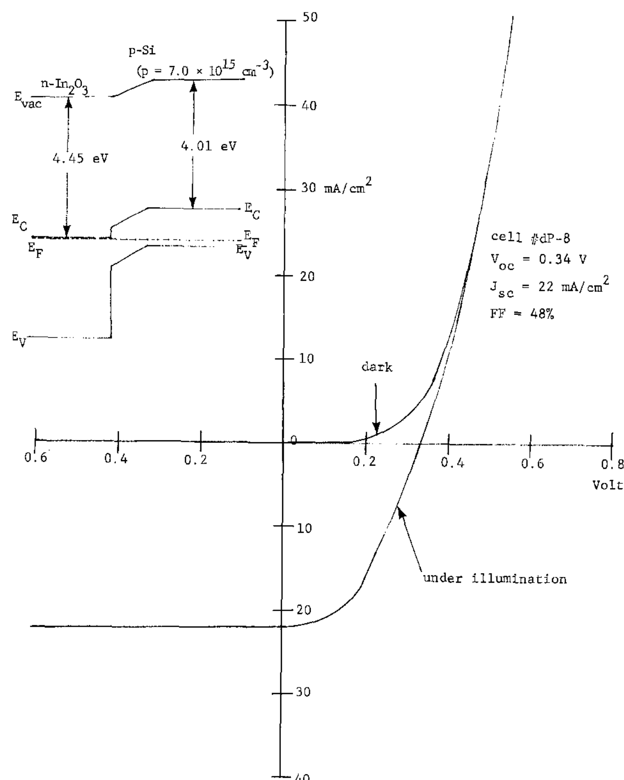

Fig. 1. Current-voltage characteristics for the (n-p) In_2O_3-Si heterojunction solar cell in the dark and under illumination (AM0).

Key words: heterojunction solar cell, indium oxide, electron affinity.

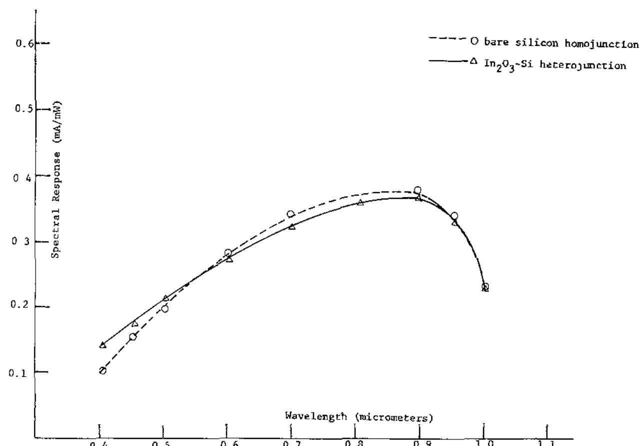

Fig. 2. Spectral response of (n-p) In_2O_3-Si heterojunction and Si homojunction solar cell.

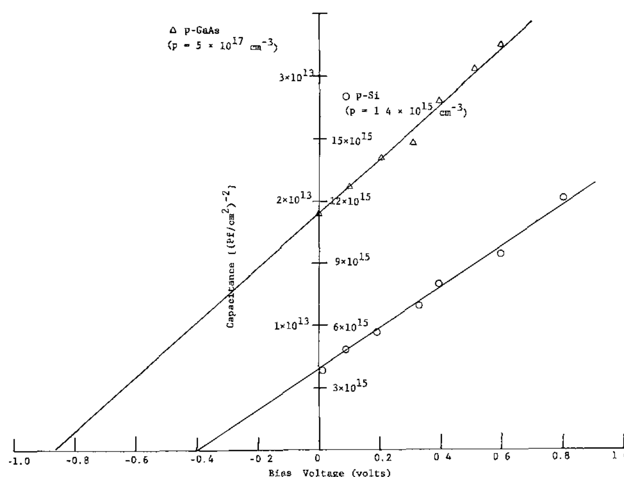

Fig. 3. $1/C^2$ vs. bias voltage plot of (n-p) In_2O_3-Si and (n-p) In_2O_3-GaAs heterojunction cells.

ing behavior for 0.004 p-type silicon substrate. Also, conductivity measurements on In_2O_3 thin film deposited on glass slides indicates that the In_2O_3 film is a heavily doped, near degenerate, n-type semiconductor.

The spectral response of a typical (n-p) In_2O_3-Si heterojunction solar cell under AM0 condition is shown in Fig. 2. The maximum sensitivity occurs near a wavelength of 0.9 μm. The spectral response of the bare 3 Ω-cm silicon homojunction cell fabricated in the normal diffusion process is superimposed on the same plot for comparison. There is a clear increase of the spectral response in the short wavelength region for heterojunction solar cells. The junction depth of the homojunction is about 0.2 μm for silicon homojunction cell. For a heterojunction, the In_2O_3 is transparent and junction begins at the interface of the In_2O_3 and the semiconductor. The decrease of spectral response in the long wavelength region is probably due to the difference of the minority carrier lifetime in the base material. Results on other heterojunction solar cells including both (n-p) and (n-n) In_2O_3-semiconductor heterojunction devices are summarized in Table I.

Capacitance measurements.—Figure 3 shows the capacitance results for some of the typical (n-p)In_2O_3-Si and In_2O_3-GaAs solar cells. The capacitance results seem to fit the straight lines of the C^{-2} *vs.* V plot. Built-in potential V_b is 0.4V for an (n-p)In_2O_3-Si heterojunction (1.4 × 10^{15} cm^{-3} Si substrate) and 0.86V for an (n-p)In_2O_3-GaAs heterojunction (5 × 10^{17} cm^{-3} GaAs substrate). It was difficult to apply the capacitance measurement technique to the capacitance of the In_2O_3-Ge heterojunction solar cell because of its high junction leakage current. Values of built-in potential deduced from the heterojunction energy band diagram listed in Table I are also in good agreement with the values through the linear extrapolation of the *I-V* characteristics at high forward current and capacitance measurements.

Resistivity dependence of V_{oc}.—The bending direction of heterojunction energy band is dependent on the electron affinity of semiconductors and the Fermi level (E_f) in the base materials. For example, as the E_f-E_v increase, we expect a change of polarity for V_{oc} and I_{sc} in the p-type substrate. Therefore, 10, 3, 1, and 0.004 Ω-cm p-type silicon were used to fabricate the (n-p)In_2O_3-Si heterojunction solar cells. Their open-circuit voltages (V_{oc}) increase in accordance with the decrease of resistivity value. Tables II and III show the results for (n-p) and

Table II. Resistivity dependence of V_{oc} for p-type germanium material

p-type Ge resistivity (Ω-cm)	Built-in voltage from heterojunction band diagram V_b (mV)	Polarities w.r.t substrate	Experimental V_{oc} (mV)	J_{sc} (mA/cm^2)	J_o (A/cm^2)	R_s (Ω)
37	15	+	+2.7	+0.3	1.8 × 10^{-3}	11
20.5	15	−	−0.538	−0.8	2 × 10^{-3}	6
10	50	−	−4.52	−1.6	4 × 10^{-3}	3
1	100	−	−5.58	−3	1.52 × 10^{-2}	1.7
0.1	170	−	−9.0	−2.1	2 × 10^{-2}	4.1
0.0003	200			Tunneling		

Table III. Resistivity dependence of V_{oc} for n-type germanium material

n-type Ge resistivity (Ω-cm)	Built-in voltage from heterojunction band diagram, V_b (mV)	Polarities w.r.t. substrate	Experimental V_{oc} (mV)	J_{sc} (mA/cm^2)	R_s (Ω)	J_o (A/cm^2)
10	70	+	4	0.7	8.4	9 × 10^{-3}
3	100	+	5.7	3.6	11	9.4 × 10^{-3}
0.1	200	+	10	2.3	12	8.5 × 10^{-3}

Table I. Summary of results for In_2O_3/semiconductor heterojunction solar cells

Heterojunction	Substrate impurity concentration (cm^{-3})	Polarity of V_{co}, I_{sc} w.r.t. substrate	Experimental J_{sc}, V_{oc}, obtained (~ AM0 condition) J_{sc} (mA/cm^2)	V_{oc} (mV)	Built-in voltage from heterojunction energy band diagram, V_b (mV)	Built-in voltage from *I-V* characteristics, V_b (mV)
(n-p)In_2O_3/GaAs	5 × 10^{17}	−	6.17	84	850	500*
(n-n)In_2O_3/GaAs	8.7 × 10^{14}	+	1.2	82	320	280
(n-p)In_2O_3/Ge	1 × 10^{15}	−	3.0	5.5	80	75
(n-n)In_2O_3/Ge	1.5 × 10^{15}	+	3.6	5.7	120	120
(n-n)In_2O_3/InP	3 × 10^{16}	+	0.6	18	60	80
(n-p)In_2O_3/Si	7 × 10^{15}	−	22.0	340	430	430
(n-n)In_2O_3/Si	2.1 × 10^{15}	+	1.5	100	220	210

Operating temperature = 300°K.
The In_2O_3 film was formed by the CVD method and all devices had good rectifying characteristics.
Electron affinity values are 4.01 eV for Si; 4.13 eV for Ge; 4.07 for GaAs; and 4.38 eV for InP (9).
* The energy band diagram indicates that an inversion layer might exist at the interface as the device behaves like a homojunction. However, direct comparison may not be valid.

(n-n)In_2O_3-Ge heterojunction solar cells with substrates of various resistivities. There is a clear polarity change of V_{oc} and I_{sc} between 37 Ω-cm and 20 Ω-cm p-type Ge substrates. The heterojunction energy band diagram, which was constructed by using the In_2O_3 electron affinity value of 4.45 eV, fits this result reasonably well.

Discussion and Conclusion

According to the (n-p) heterojunction energy band diagram in Fig. 4, under the illumination conditions, the electron-hole pairs created by the photons will be separated by the built-in electric field. A negative voltage with respect to the semiconductor substrate will exist at the (n-p) heterojunction barrier. Either electrons from the semiconductor side will flow downhill to the conduction band of In_2O_3, or there will be thermionic emission of holes from the valence band of the semiconductor substrate into the interface state where they recombine with the electrons from the conduction band of In_2O_3 to give the observed short-circuit current. Those interface states exist uniformly between the interface of In_2O_3 and the semiconductor substrate. The electrons at the interface states are supplied by the nearby conduction band of In_2O_3 because of their proximity to the interface states. There is very little band bending on the In_2O_3 side because of the high electron concentration in In_2O_3. The experimental observations in this paper also confirm this finding. For (n-n) heterojunction devices (Fig. 5), the dark current is mainly due to the majority carriers; however, the main factor leading to the short-circuit current has to be the recombination of electrons from the conduction band of In_2O_3, with holes from the semiconductor substrate at the interface states. If the holes at the interface states recombine with the electrons in semiconductor side, it will be a loss mechanism and contributes no short-circuit current. The other loss mechanism is probably due to the recombination process in the depletion region.

All In_2O_3-semiconductor heterojunction solar cells show photovoltaic effects and rectifying characteristics except the 0.0003 Ω-cm germanium substrate material. The results of V_{oc} and I_{sc} are inferior to those of homojunction devices. The limiting factors

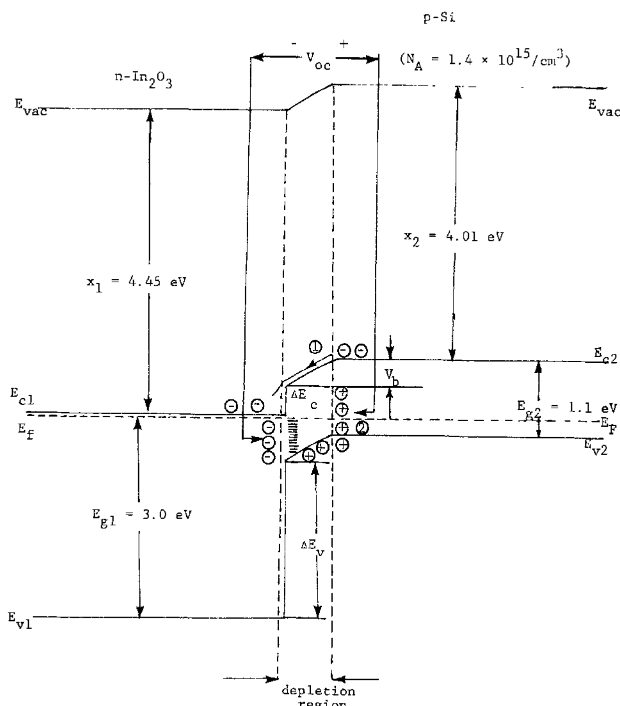

Fig. 4. Energy band diagram of an n-p heterojunction showing possible processes contributing to the generation of photocurrent.

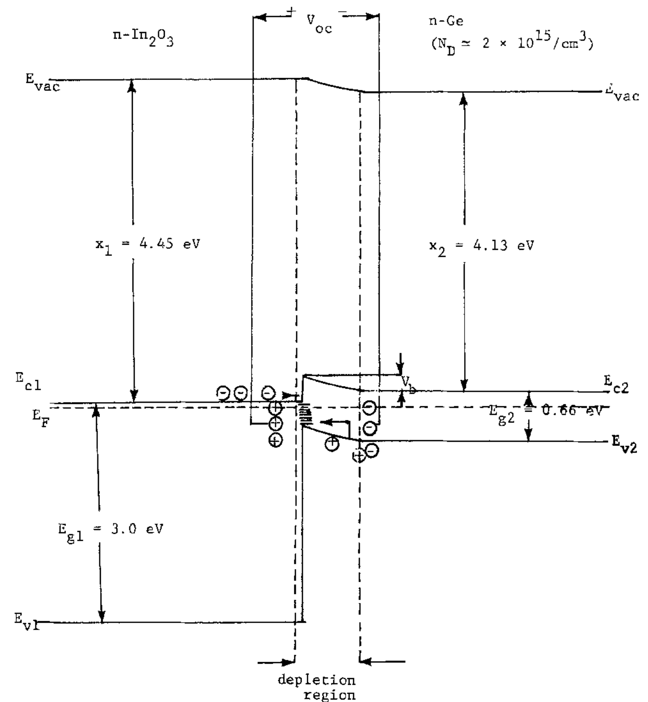

Fig. 5. Energy band diagram of an n-n heterojunction with possible processes contributing to the generation of photocurrent.

are high series resistance (R_s) and junction leakage current. In this work, no attempt is made to optimize the energy conversion efficiency of solar cell. The main objective is to determine the electron affinity of In_2O_3 based on the polarities of V_{oc} and I_{sc} from the In_2O_3-semiconductor heterojunction energy band diagrams.

In conclusion, we have successfully determined the electron affinity value of In_2O_3 from its photovoltaic properties. In addition, we believe that we have reported for the first time the success of In_2O_3-Ge, In_2O_3-GaAs, and In_2O_3-InP heterojunction formation by the chemical vapor deposition method. Based on the determined electron affinity value of In_2O_3, we can construct the heterojunction energy band at equilibrium. From this, we have successfully explained: (*i*) that the observed polarities of V_{oc} and I_{sc} of the heterojunction devices are consistent with the band bending in the energy band diagram; (*ii*) that the built-in potentials are in good agreement with those deduced from the capacitance-voltage and the current-voltage results; and (*iii*) that the semiconductor substrate resistivity dependence of the V_{oc} results is consistent with heterojunction energy band diagram.

Manuscript submitted June 23, 1977; revised manuscript received Feb. 24, 1978.

Any discussion of this paper will appear in a Discussion Section to be published in the June 1979 JOURNAL. All discussions for the June 1979 Discussion Section should be submitted by Feb. 1, 1979.

Publication costs of this article were assisted by Wayne State University.

REFERENCES

1. S. W. Lai, L. Franz, G. Grant, R. L. Anderson, J. K. Clifton, and J. V. Masi, in "11th IEEE Photovoltaic Spec. Conf.," p. 398, IEEE, Scottsdale, Ariz. (1975).
2. R. L. Anderson, *Appl. Phys. Lett.*, **27**, 691 (1975).
3. J. B. Dubow, D. E. Burk, and J. R. Sites, in "12th IEEE Photovoltaic Spec. Conf.," p. 971, Baton Rouge, La. (1976).

4. E. Y. Wang, and R. N. Legge, in "12th IEEE Photovoltaic Spec. Conf.," p. 967, Baton Rouge, La. (1976).
5. J. H. W. Dewit, *J. Solid-State Chem.*, **8**, 1142, (1973).
6. R. L. Weiher, *J. Appl. Phys.*, **33**, No. 9, 2834 (1962).
7. E. Staritzky, *Anal. Chem.*, **28**, No. 4, 553 (1956).
8. R. P. Elliot, "Constitution of Binary Alloys," p. 546, McGraw-Hill, New York (1965).
9. A. G. Milnes and D. L. Feucht, "Heterojunctions and Metal-Semiconductor Junctions," p. 8, Academic Press, New York (1972).

Color-Band Generation during the High Dose Ion Implantation of Silicon Wafers

D. G. Beanland

Royal Melbourne Institute of Technology, Australia

and D. J. Chivers

Chemistry Division, AERE Harwell, England

ABSTRACT

Color-bands may be observed on silicon wafers following high dose ion implantation. The implantation conditions which give rise to color band generation are described. The temperature variations occurring across the wafer during implantation are shown to be of primary importance in generating color bands. The colors observed result from interference effects when light is reflected from subsurface interfaces of amorphous and crystalline silicon; the surface layer may be amorphous or crystalline silicon. The depth and nature of the surface layer determines the color observed. The depth-color relationship for these layers is discussed together with the variation of color-bands with implantation conditions. Experimental results show that the color-bands are evidence of damage nonuniformity across the wafer. This damage nonuniformity may also be evident after high temperature annealing.

Color-bands on ion-implanted silicon wafers were first reported by Freeman *et al.* (1) who used high beam currents while studying sheet resistance uniformity for high dose implantations. They also showed that the colored regions were associated with crystalline surface layers and the effect was due to variations in temperature across the wafer during high current implantations. Csepregi *et al.* (2) qualitatively associated the thickness of the surface crystalline layers with visual color changes. Seidel *et al.* (3) quantitatively correlated thickness measurements of the surface crystalline layer with "optical-thicknesses" derived from peaks in the visible optical reflectance spectrum. They also correlated thicknesses of thicker (mostly buried) amorphous layers with peaks in the near infrared reflectance spectrum. Their interpretation is based primarily on the fact that amorphous and crystalline silicon have different indexes of refraction and absorption.

In the present work it is pointed out that visible interference colors may also be generated when the amorphous layer is continuous to the surface. A more general model has been developed to explain this (4). The color-bands are only evident on implanted specimens when the conditions during implantation are not identical at all points on the specimen. Electrostatically scanned wafers experience the same thermal conditions at all points during implantation and consequently will not exhibit color-bands unless a thermal gradient is established by nonuniform cooling (3) or as a result of nonuniform doping. Similarly, color-bands are not produced on wafers bonded to a constant temperature heat-sink.

To enable high dose implants to be completed within a reasonable time, high beam currents are commonly utilized, but the beam heating then becomes significant (5). The temperature rise of the wafer can be reduced by increasing the scan area if a mechanical scanning technique is employed. This approach has an associated advantage of improved dose uniformity. However, the resulting temperature changes cause sections of the wafers to be implanted at different temperatures with a consequent damage nonuniformity across the wafer.

The color-bands of a typical wafer are shown schematically in Fig. 1; however, many variants on this form are possible, as is explained later. In most cases a sharply defined color-band is evident (region 2, Fig. 1). It is obviously a region of the wafer in which the conditions for amorphous zone generation are par-

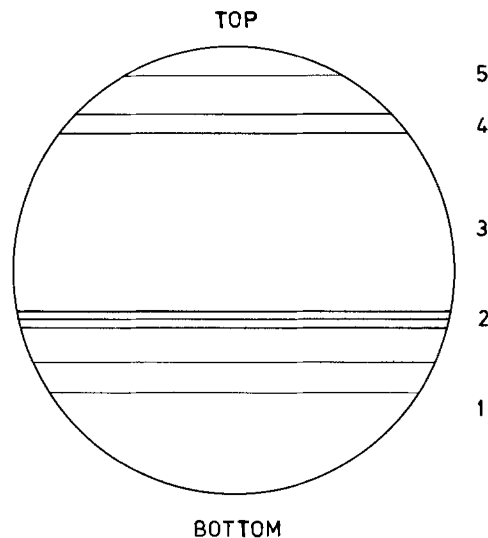

Fig. 1. Schematic diagram of color-bands formed on a silicon wafer implanted to high dose with mechanical scanning.

ticularly sensitive to temperature changes for the implantation parameters employed.

The damage created by implantation into silicon and described by the color-bands is the result of the disordering processes caused by the deposition of the energy of the incident ions and the dynamic annealing which occurs during the implantation process. The annealing is strongly dependent on the implantation temperature (6). This effect can be considered as a shift of the amorphous threshold as a function of implantation temperature. Nelson and Mazey (7) demonstrated for 60 keV Ne^+ implants that the amorphous threshold, as determined by the "milkiness" criterion, rose from approximately 1×10^{14} cm^{-2} at 20°C to approximately 4×10^{15} at 200°C. Morehead and Crowder (8) showed a similar variation for the amorphous thresholds of B^+, P^+, and Sb^+ implants, as determined by EPR data. They also proposed a model for this behavior.

Experimental Conditions

The silicon wafers were 5 cm diam and of <111> orientation. All were implanted in the Mk IV Harwell-Lintott isotope separator (9) which uses double-axis mechanical scanning (10) to scan the wafers through the stationary 3 cm high line focus ion beam. The wafers move with a horizontal stroke of 17 cm and then drop a small distance, as determined for the beam current and the total dose required, before again sweeping through the beam.

A number of analysis techniques were used to analyze the color-bands formed during high dose implantation. The conditions used are presented with the results in the following section. The details of the implantation conditions for the various wafers discussed in this paper are presented in Table I, together with the maximum temperature calculated to have been reached by the wafer during implantation. It should be noted that the examples discussed throughout this paper are related to the particular scanning system employed. The data and discussion can be applied to other scanning systems only if the relevant implantation conditions are carefully noted.

Results and Discussion

Temperature variation during implantation.—The ion-beam power density, which determines the temperature rise of the wafer, has been defined as the irradiance (1)

$$\text{Irradiance} = \frac{I \cdot E}{A}$$

where I is the beam current, E is the energy of the incident ions, and A is area scanned by the beam.

Freeman *et al.* (1) measured the temperature rise of silicon targets implanted at various irradiances and showed that the wafer has an effective average emissivity, ϵ, of approximately 0.45. The relationship they obtained between temperature rise and irradiance is shown in Fig. 2. It assumes that the entire target area is being scanned. The heat loss from the silicon is almost entirely by radiation. Parry (11) has shown the back surface to be a less efficient radiator than the front surface but has obtained a similar average emissivity for a silicon wafer mounted on a plate by a clamping mechanism without the use of a thermal bonding agent. The equilibrium temperature rise of the wafer thus varies as the fourth root of the irradiance

$$T_w - T_a = \left(\frac{\text{Irradiance}}{2\epsilon\sigma}\right)^{1/4}$$

where T_w is the wafer temperature, T_a is the ambient temperature, σ is the Stephan-Boltzmann constant, and 2ϵ is the effective total emissivity, assuming heat conduction from the wafer to the holder to be negligible (11).

The equilibrium temperature rise-irradiance relationship of Fig. 2 assumes that the ion beam is scanning the entire area of the target specimen. In the Mk IV Harwell-Lintott separator, a 3 cm high beam is used to progressively scan across a 5 cm diam silicon wafer. The percentage area of the target being scanned by the ion beam is thus a function of the relative location of the ion beam centerline and the wafer. It increases to a maximum when the ion beam is scanning the center of the wafer; the relationship is shown in Fig. 3. The beam power transmitted to the wafer is proportional to the area of the wafer being scanned. The heat deposited into the wafer is conducted through it with a time constant of approximately 20 sec (11). Heat dissipation only occurs by radiation from the entire surface area, since conduction to the mounting plate is negligible. If it is assumed that the lateral conduction time constant is negligible compared to the total time taken by the implantation cycle, the "equilibrium" temperature rise as a function of the ion beam centerline position can be calculated as a percentage of the temperature predicted in Fig. 2 when complete scanning of the wafer occurs. The result is shown in Fig. 4. Each horizontal strip on the wafer has a unique temperature-time profile as the scan proceeds across it. Strips at the bottom are initially at a low temperature with an increasing temperature during implantation, strips at the center have high and relatively consistent temperatures during implantation, while strips at the top of the wafer have an initially high temperature which decreases as the implantation cycle is concluded. This temperature variation during implantation is shown in Fig. 5 for some points on the wafer. These results, however, assume that implantation has proceeded sufficiently slowly for lateral heat conduction to maintain a uniform temperature across the wafer and that the wafer has negligible thermal capacity, so that cooling is equally efficient. It is known that wafer cooling has an appreciable time constant and this effect has been estimated to determine the more realistic temperature variation curves of Fig. 6.

Table I. Implantation conditions

Ion species	Ion energy (keV)	Dose (cm^{-2})	Beam current (μA)	Irradiance (W/m^2)	Maximum temperature during implantation (°C)
P	40	2×10^{16}	500	3900	220
P	60	1×10^{16}	660	7800	290
P	80	1×10^{16}	500	7800	290
P	118	1×10^{16}	340	7800	290
P	154	1×10^{16}	260	7800	290
Ne	80	1×10^{16}	500	7800	290
P	80	2×10^{15}	500	7800	<290

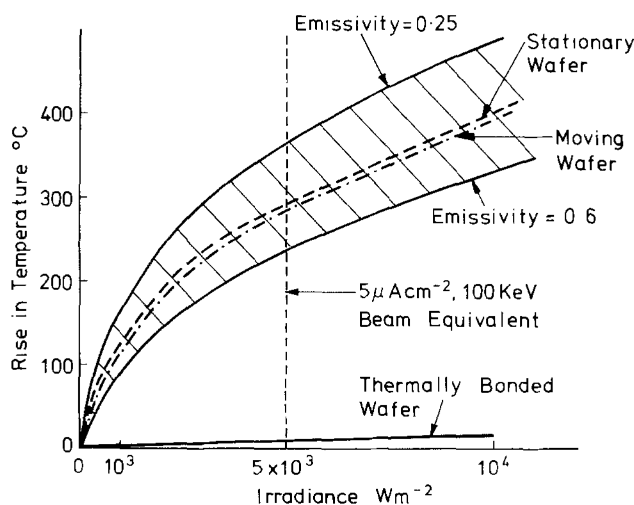

Fig. 2. Equilibrium temperature rise as a function of irradiance [after Freeman *et al.* (1)].

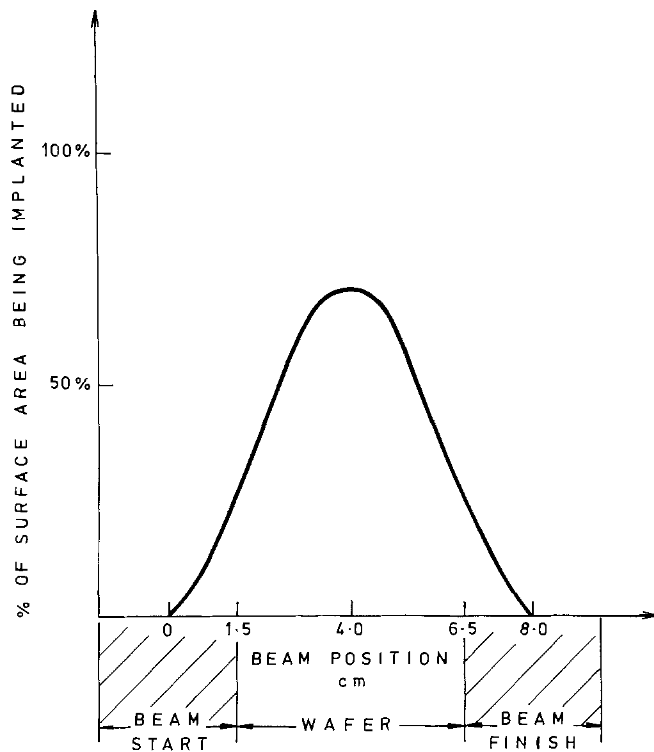

Fig. 3. Percentage of wafer implanted as a function of ion beam centerline position.

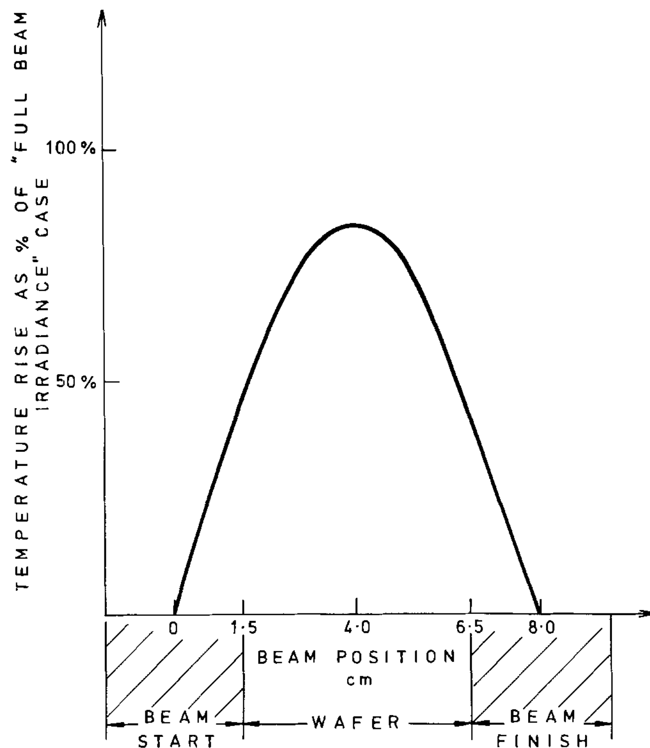

Fig. 4. "Equilibrium" temperature rise as a function of ion beam centerline position.

The thermal conditions of a wafer scanned by such a mechanical scanning system are thus seen to vary in a complex manner during implantation when beam heating is significant. Each horizontal strip of the wafer has a unique thermal behavior during implantation. The temperatures attained, in addition to being determined by the ion beam irradiance, are also modified by the efficiency of the thermal contact with the mounting, the duration of the implantation cycle, and the efficiency of radiation to the surroundings.

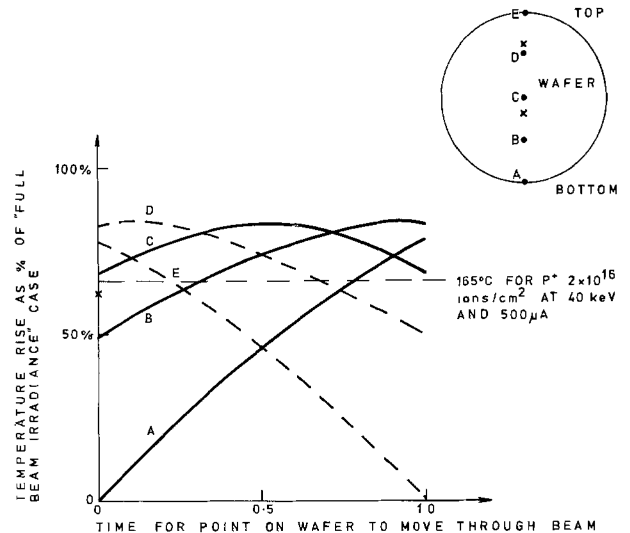

Fig. 5. Temperature variation of horizontal strips across the wafer during implantation with no thermal capacitance.

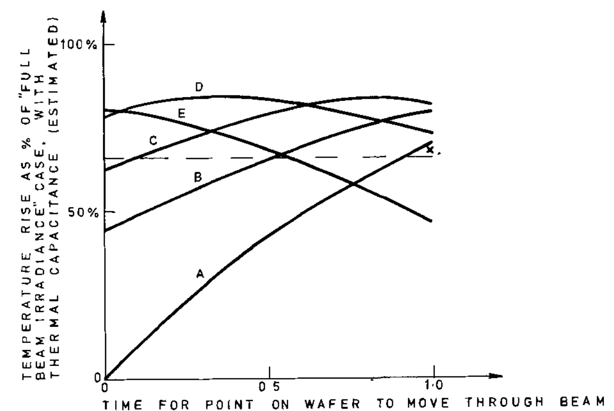

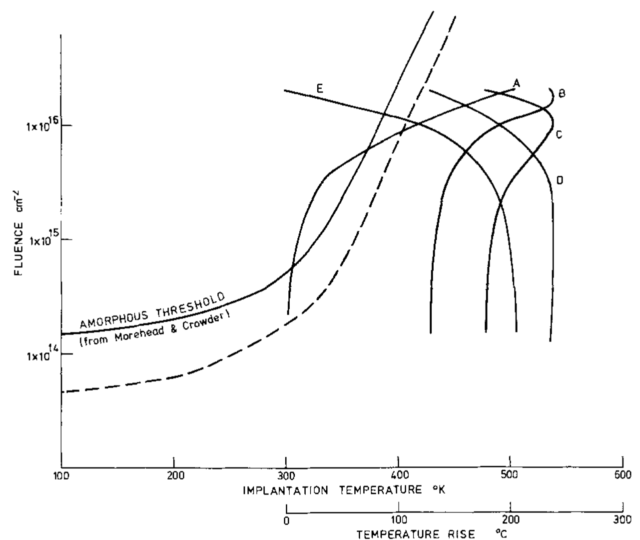

Fig. 6 (top). Temperature variation of horizontal strips across the wafer during implantation with estimated thermal capacitance.

Fig. 7 (bottom). Fluence variation as a function of implantation temperature (with no thermal capacitance).

Generation of amorphous regions during varying temperature implantation.—As was noted earlier, the amorphous threshold increases with implantation temperature because the dynamic annealing process becomes more efficient. The amorphous threshold is not, however, a concept which is readily applicable to implantation at varying temperatures. A more general concept of an amorphizing fluence, ϕ_{am}, is required to

account for the varying temperatures during the implantation cycle.

The effective amorphizing fluence, which is a function of the implantation temperature-time cycle, is less than the actual fluence because of the temperature-time dependent dynamic annealing

$$\phi_{am}(\theta, t) = \int_0^\phi \{1 - k(\phi, \theta, t)\}\, d\phi$$

where ϕ = fluence, t = time, and θ = temperature.

In addition, the amorphous threshold should be related to a volumetric disorder density rather than a surface fluence. Since, at the present time. inadequate data exists to enable a more adequate consideration to be made, a simplified discussion based on amorphous threshold variation is presented. It must, however, be noted that it only represents an approximation to the more complex actual situation.

In the Mk IV Harwell-Lintott separator the beam current density is approximately constant along the height of the line focus beam. Therefore, as the sweep proceeds the fluence, ϕ, increases αt. Since the θ-t relationship has already been established (see Fig. 5) the θ-ϕ relationship can be readily derived for the various horizontal strips of the wafer. These are plotted for points A-E in Fig. 7 using a logarithmic scale for the fluence. The numerical scale is for a 2×10^{16} cm^{-2}, 40 keV P^+ implant at 500 μA. Also plotted in Fig. 7 is the variation of amorphous threshold with implantation temperature for 280 keV P^+ implants using the EPR data of Morehead and Crowder (8), who predicted that for temperatures above 430°K the P^+ implants will not be amorphous at any dose. Even though this data cannot be expected to predict the "milkiness" threshold accurately, it exhibits the expected relationship with temperature.

Although the approach of Fig. 7 is approximate, some interesting trends are indicated. For implants which commence at low temperatures, *i.e.*, point A at the bottom of the wafer, it is relatively easy to generate an amorphous layer. (An amorphous layer is certainly generated when a ϕ-t cycle crosses the amorphous threshold curve from a lower temperature. An amorphous layer will be generated at a dose lower than that predicted by the amorphous threshold curve because of the integrated effect of the damage as the implantation proceeds.) For a point such as B an amorphous layer may be established if the integrated damage, as the temperature increases, is sufficiently high. The damage occurring before the temperature increases significantly is the determining factor. For point C on the wafer the temperature is too high, when it is implanted, for an amorphous layer to be created. Amorphousness could be created at D, but it is unlikely as it approaches the amorphous threshold curve with much less damage than a constant temperature implant, since the majority of the damage has been generated at high temperature. It is, however, likely that amorphousness is created at point E as the wafer cools.

The steepness of the amorphous threshold variation with temperature can be seen to be of fundamental importance in determining the generation of amorphous regions of varying thickness across a wafer implanted with the conditions just considered. The amorphous layer generation is primarily determined by the behavior of the wafer during its lowest temperature phases of the implantation process.

Typical color-bands.—The color-bands observed on the silicon wafers after implantation have infinite variations because the depth of the amorphous-crystalline silicon interface which determines the color (see section on Interference colors) and the position of the bands is also effected by all the implantation parameters (see section on Variation of color-bands). They do, however, exhibit a general form, as shown in Fig. 1, which is now explained.

The bottom of the wafer, being implanted first at a low, but rising, temperature, is likely to generate a deep amorphous layer extending to the surface. The depth of the amorphous layer is reduced in the successive horizontal strips of the wafer which are implanted at progressively higher temperatures. This corresponds to region 1 in Fig. 1. The colors are relatively diffuse and change to indicate layers of reducing depth.

This is usually followed by a narrow brightly colored band (region 2). For low voltage implants this corresponds to a region of rapid reduction of amorphous layer thickness. In this case, region 3 may either have a thin amorphous layer or be heavily damaged but crystalline silicon, depending on the implant conditions. In this region, the implant temperature is high but relatively constant and relatively uniform colors are likely when a thin amorphous layer results.

For high voltage implants, which have a peak energy deposition density some distance below the surface, region 2 is a narrow, more brightly colored band in which the order of colors is reversed. It is the region in which the amorphous layer is buried below a layer of crystalline silicon. The colors are brighter because of the greater optical transparency of crystalline silicon. The color order is reversed because the depth at which the colors are generated now increases as the implantation temperature is increased. For such implants region 3 is then crystalline silicon.

Regions 4 and 5 may not be evident if insufficient cooling of the wafer occurs. When they are evident, region 4 is a bright band; it is less distinct than region 2 because it has been formed on cooling and the amorphous-silicon interface is apparently less abrupt. Region 5 is similar to region 1, exhibiting diffuse colors arising from deep amorphous layers continuous to the surface.

Experimental evaluation of "color-band" wafers.—In this section, experiments conducted on the wafers to determine the properties of the color-band regions of the wafers are discussed. The discussion has been mainly restricted to experiments relating to the 40 keV P^+ implant to 2×10^{16} cm^{-2} at 500 μA, although observations have been made on wafers implanted under many different conditions.

Sheet resistance.—The sheet resistance (R_s) variation across the diameter of the P^+ implanted wafer, in a direction normal to the color-bands, was measured using the four-point probe technique following 30 min isochronal anneals at temperatures to 1100°C. The results are shown in Fig. 8, together with the color-bands on the "as implanted" wafer. A large sheet resistance variation exists across the wafer after implantation, due to the amorphous layers being of greater depth in the high R_s regions at the top and bottom of the wafer. This variation is maintained throughout the annealing cycle, but is reduced to a maximum variation of 14% after annealing to 1100°C. The central section of the wafer, which was implanted at approximately 200°C, exhibits the lowest sheet resistance after each annealing cycle.

It should also be noted that the sheet resistance annealing characteristics vary dramatically at different parts of the wafer. The annealing characteristics for points A, B, and C (as denoted in Fig. 8), are shown in Fig. 9. Curve D was obtained on a wafer implanted with the same implantation parameters, but with the temperature increasing from room temperature to 220°C during implantation. Also included in Fig. 9. is the result of Shannon *et al.* (12) obtained following room temperature implantation. It will be seen that the room temperature implant anneals more efficiently during the epitaxial regrowth phase at approximately 600°C, but that the implant at approximately 200°C is much more efficient than the implants which are undertaken over a range of temperatures from room temperature to 200°C. It is considered that under

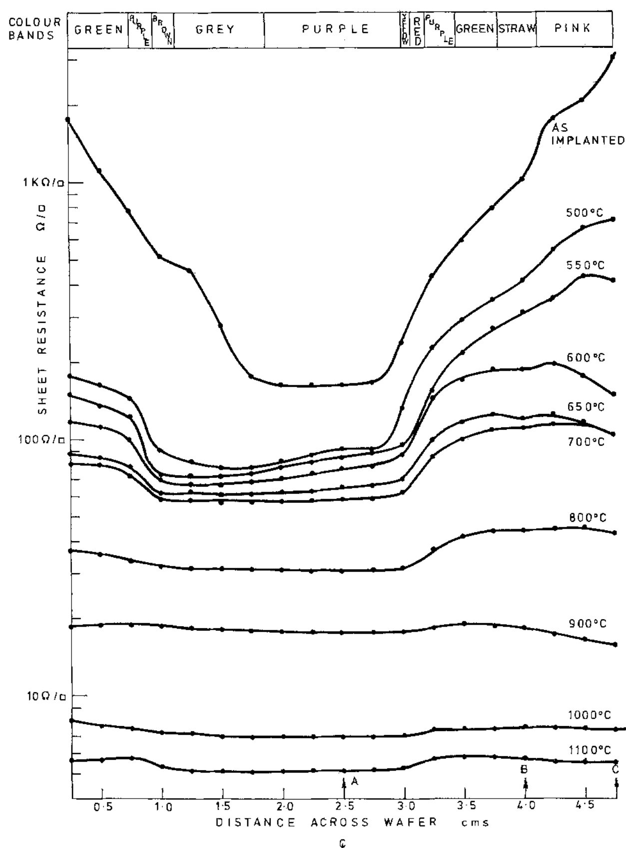

Fig. 8. Sheet resistance profiles across wafer implanted with 2 × 10^{16} cm^{-2} P^+ at 40 keV, 500 μA and isochronally annealed. Bottom of wafer at the right.

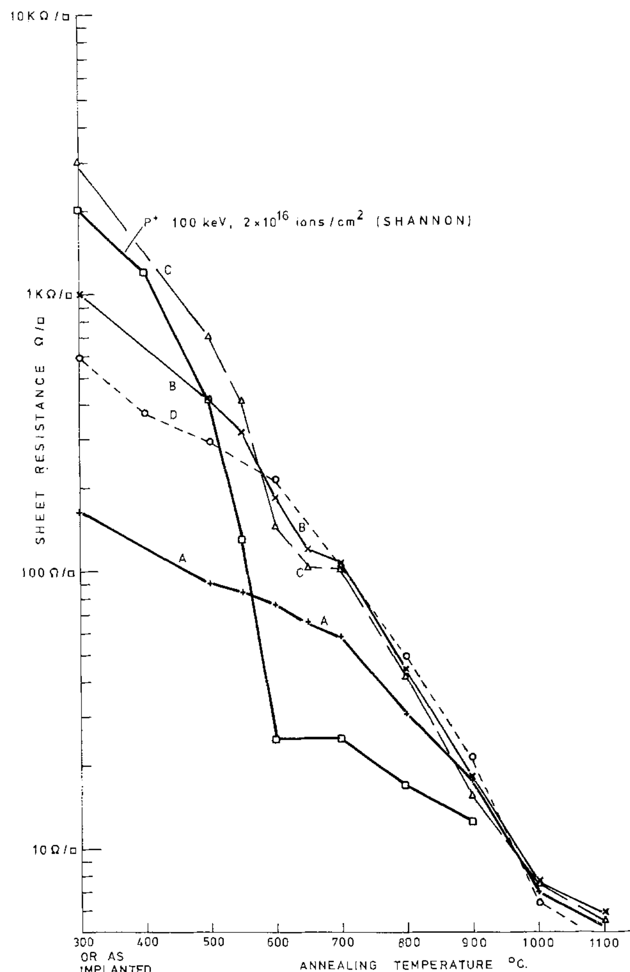

Fig. 9. Isochronal anneal characteristics of sheet resistance for 40 keV P^+ implant to 2 × 10^{16} cm^{-2} at 500 μA with varying implant temperature conditions.

such conditions (curves B, C, and D) the dynamic annealing, which reduces the depth of the amorphous layer, permits disorder, generated during the low temperature phase of the implantation process to remain in the deep subamorphous layers.

Anodization and stripping.—Areas of the color-banded P^+ wafer were oxidized using a calibrated anodization facility. The oxide was removed with a buffered HF solution and the depth of silicon removed confirmed by optical interferometry. In the stripped region the color-bands moved since they then were generated by a thinner surface layer. By this method the colors generated by thinner surface regions were confirmed and for particular differences in depth the color changes were observed (refer to section on Interference colors).

Scanning electron microscopy.—The electron channeling patterns (ECP's) (13) generated by the surface layers of the color-banded specimens were observed in the SEM after implantation. The clarity of the channeling patterns gives a qualitative indication of the crystal quality in the 500Å surface layer.

In Fig. 10 the ECP's from various positions on a color-banded wafer implanted with 1 × 10^{16} cm^{-2}, 80 keV Ne^+ at 500 μA are shown. The section of the wafer implanted first is at the top. It will be seen that the crystal quality of the surface layers changes abruptly within a distance of 0.5 cm across the wafer. At position 1, the amorphousness extends to the surface. At position 2, there is a thin surface crystalline region above a buried amorphous layer. This is also true at position 3, but the surface crystalline layer is thicker. The ECP obtained from position 4 is of much better quality. In this region there is no surface coloration and no buried amorphous layer. Since the wafer was not annealed the ECP quality from the crystalline silicon is limited by the disorder generated in the implanted layer.

Transmission electron microscopy.—Specimens from different regions of the 2 × 10^{16} cm^{-2} 40 keV P^+ at 500 μA implanted wafers were examined by TEM. The specimens were ultrasonically cut from implanted wafers, annealed at 800°C for 30 min in a vacuum, and then jet thinned (14) from the back. The defect structure resulting in different regions of the color-banded wafers showed considerable variation. The micrographs of Fig. 11 enable a comparison of the damage in specimens near the bottom and the center of the wafer. The specimen from a "pink" region near the bottom of the wafer had been implanted with increasing temperature and a thick amorphous layer continuous to the surface formed. The micrograph showed a dense dislocation network with extensive twinning. The specimen from the "purple" central region had been implanted at a relatively uniform and high temperature and a very thin amorphous layer formed. The resulting dislocation structure is much less dense with less twinning. This is consistent with the sheet resistance observations reported in section on Sheet resistance which showed this latter region to have a much lower sheet resistance after annealing at 800°C.

Rutherford backscattering analysis.—The Rutherford backscattering (RBS) channeling technique was applied to various points on the 2 × 10^{16} cm^{-2} 40 keV P^+ at 500 μA implanted wafer. During analysis a 2.9 MeV He^+ beam was used in a <111> direction. The thickness of the damaged layer on the surface of the Si was examined at various points on the wafer. In each case the damage depth observed was approximately 2000Å. It is evident that the damage below the amorphous layer was too large to permit the amorphous layer thickness to be measured with this

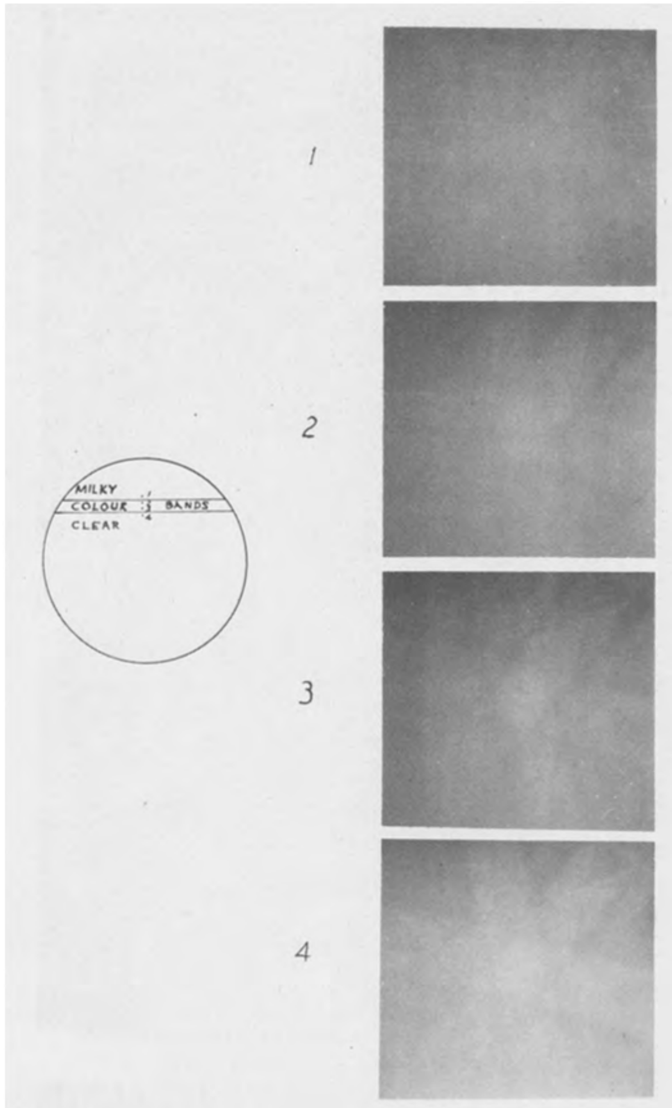

Fig. 10. Electron channeling patterns from various regions of a color-banded wafer implanted with 1 $\times$ 10^{16} cm^{-2} 80 keV, Ne^+ at 500 μA. Section of wafer implanted first is at the top.

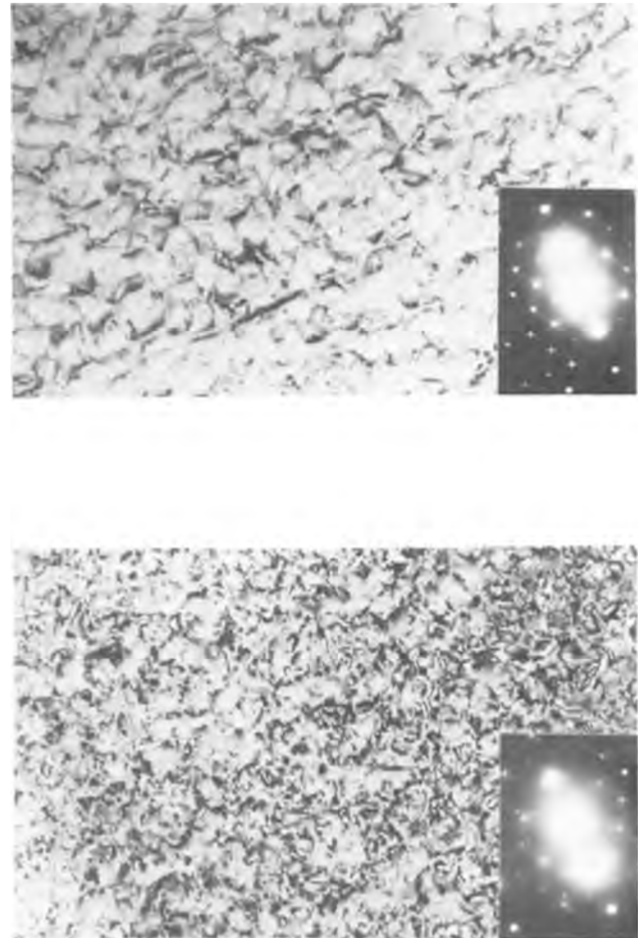

Fig. 11. Transmission electron micrographs of 2 $\times$ 10^{16} cm^{-2}, 40 keV P^+ at 500 μA implanted into Si and annealed for 30 min at 800°C. Upper specimen was from the bottom of wafer and lower specimen was from the center.

technique at this dose of P^+ ions since RBS cannot distinguish between amorphous and heavily damaged regions (15). (An identical region with 300Å removed by anodic stripping indicated a depth of approximately 1700Å.)

RBS measurements were also undertaken on a wafer with less damage. The disorder produced at various points on a color-banded wafer implanted to 2 $\times$ 10^{15} cm^{-2} with 80 keV P^+ at 500 μA was measured. A 2.0 MeV He^+ beam was directed in the <111> direction to four points each spaced at a distance of 1 mm from the previous point, as shown in Fig. 12. The RBS spectra are also given in Fig. 12. The "clear" region can be seen to have very little disorder. The "blue" and "purple" bands are confirmed to have buried amorphous layers beneath a surface crystalline region, while the "green" region has a deep amorphous layer which is continuous to the surface. The RBS measurements of the crystalline layer depth are 500 and 375Å for the "blue" and "purple" regions. These thicknesses can be compared to the approximate depth predicted on the basis of interference colors (section on Interference colors), of 410 and 340Å, respectively. The depth of the amorphous layer in the "green" region is 1375Å by RBS as compared to 1200Å by interference color prediction. The agreement is quite reasonable, in each case, considering the approximations involved.

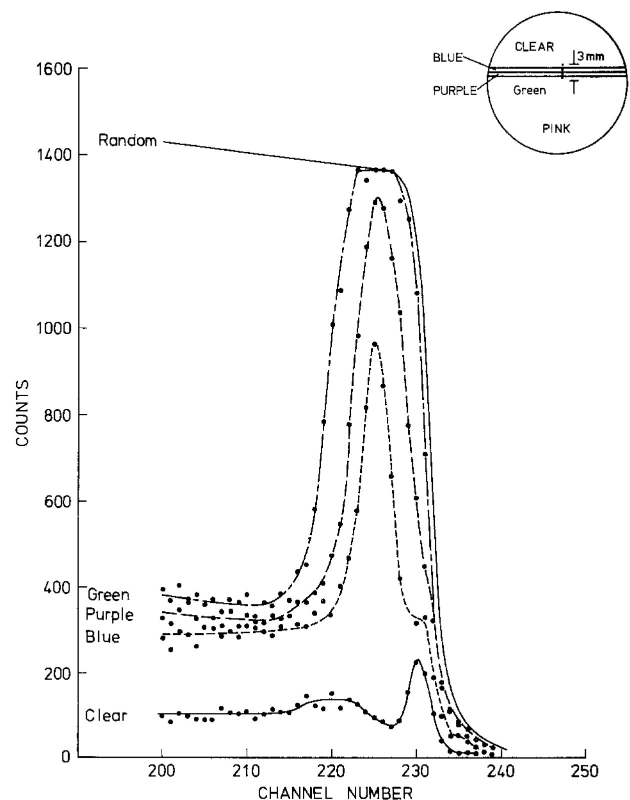

Fig. 12. Rutherford backscattering data for areas of color-banded wafer implanted with 2 $\times$ 10^{15} cm^{-2}, 80 keV P^+ at 500 μA.

Ellipsometry.—The method of ellipsometry (16) was used to study the properties of the various regions of the color-banded wafers. Ellipsometry can be used to measure the refractive index and thickness of uniform absorbing layers on a substrate of known optical constants. Unfortunately, implanted layers do not have uniform optical properties and the substrate properties are also modified by the implantation process. In addition, a thin oxide layer is formed on the surface of the wafer. Complete analysis of the layers is possible if the multiple-angle-of-incidence method of Adams and Bashara (17) is used.

Single angle measurements only were taken and, although accurate depth determinations cannot be made for the reasons stated above, it is possible to identify, because of the entirely different results, when the amorphous layer is buried and when it is continuous to the surface. Also the results obtained for regions of various colors are consistent with large changes of thickness occurring in the surface layer.

Surface height measurements.—The change of surface height of the silicon wafer in the region of various color-bands was measured using a surface profilometer on a masked 2 × 10^{16} cm^{-2}, 40 keV P^+ at 500 μA implant. The increase in surface height was of the order of 25Å and no significant changes, correlated with the color-bands, were observed.

Color changes during annealing.—The color-bands disappear after annealing to 650°C. At this temperature the epitaxial recrystallization of the amorphous region is known to be complete (7). The color-bands are observed to move as the amorphous layer anneals in the temperature range 400°-650°C. The color movement is consistent with the epitaxial regrowth, of amorphous layers continuous to the surface, occurring from the crystalline substrate. The annealing of the buried amorphous layer shows a color shift in the direction of increasing surface layer depth, *i.e.*, the crystalline surface layer grows into the amorphous layer. The colors may also brighten considerably during annealing.

Interference colors as a function of depth.—The observed colors result from the interference of light reflected from the surface with that reflected from the subsurface interface at which the refractive index change occurs. The particular wavelength attenuated, λ, is dependent on the depth of the surface layer, *d*, and is given by (18)

$$\lambda = \frac{4 - n}{2k - 1} d$$

where $k = 0, 1, 2, 3, \ldots$, and n = refractive index of surface layer.

Since the interference is subtractive, the color observed is the complement of the wavelength attenuated. Using $n = 3.865 - j\ 0.14$ for crystalline silicon and $n = 4.25 - j\ 0.45$ for amorphous silicon, which are consistent with experimental results which have been reported by other workers (17, 19, 20), the colors likely to be observed have been calculated for both amorphous and crystalline silicon surface layers of various depths; they are given in Fig. 13. These depths must be considered approximate because the damage variation throughout the surface layers can cause the optical constants of the layers to be nonuniform and phase shifts (3) can result in an error of approximately 25% for the first-order colored layers.

Color assessment is also somewhat subjective and depends on the light source. It is also affected by the absorption of the surface layer, particularly for amorphous surface layers. The colors associated with surface crystalline layers are usually brighter and more distinct. It is difficult to assess the order of the interference color; colors up to fourth order have been observed. However, if an approximate damage profile is known, the depth of the damage peak is a convenient reference point for wafers which show color-bands in addition to having a "clear" crystalline region on the wafer. The color at the interface between the color-band and the "clear" silicon represents the depth of the damage peak. Also the region at the bottom of the wafer, which is implanted cold, can be used as a reference point by utilizing the theoretical damage profile in conjunction with room temperature data of the amorphous threshold.

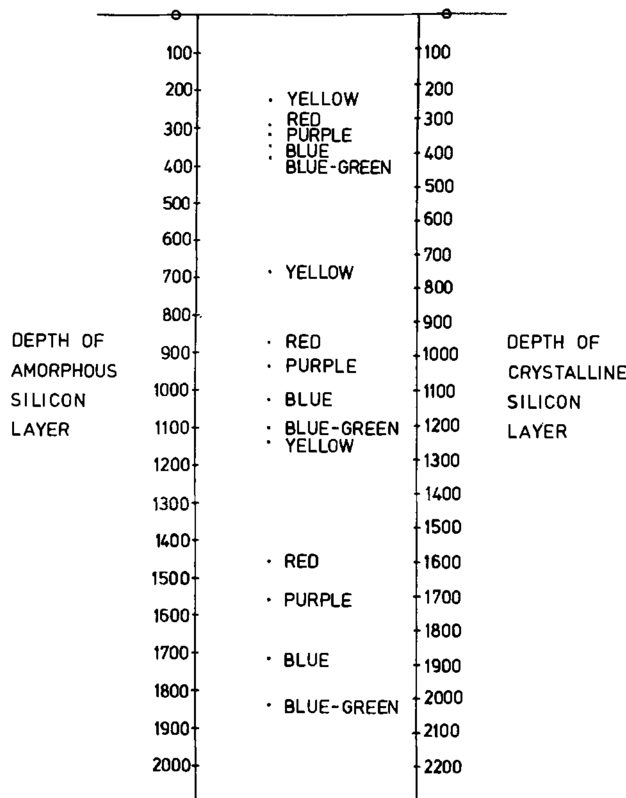

Fig. 13. Interference colors as a function of depth for amorphous and crystalline silicon surface layers (1st and 2nd and 3rd order).

For P^+ implants at various voltages the depth of the peak of the damage profile can be determined from the color-band table (Fig. 13) and compared to the calculated damage profile peak (21). The results are compared in Table II. The agreement is very good considering the limitations discussed above.

Variation of color-bands with implant conditions.—The color-bands observed on silicon wafers are a function of the implantation temperature and the total energy deposition function. The implantation temperature is a function of the ion energy, the ion beam current, the scan cycle used in the implantation process, and the radiative and conductive cooling of the wafer. The total energy deposition function is dependent on the ion energy, the ion dose, and the ion species. With so many variables there are obviously many possible variations of color-bands. Some brief general comments are now given to describe the variations which have been observed over a wide range of conditions.

The range of colors observed on a particular wafer is determined primarily by the depth scale of the damage profile, *i.e.*, by the ion species and its energy. The posi-

Table II. Comparison of damage peak depths determined by color-bands, with calculated values

Ion energy (keV)	Color at damage peak	Approx. depth of damage peak from color-band (Å)	Calculated depth of damage peak (Å)
40	(Peak not observed)	—	220
60	Yellow	240	280
80	Blue	390	440
118	Red	950	800
154	Light blue	1150	1140

tion of the color-bands is determined primarily by the temperature rise of the wafer. The implantation temperature is more critical than the peak damage density, as can be seen from Fig. 7. The temperature rise at the beginning of the implantation process is particularly important for high dose implants, as is the final temperature at the end of the implantation cycle. Wafers with the same maximum temperature, but a different rate of rise of temperature will consequently produce different color-bands.

The variation of the amorphous threshold as a function of temperature is an important parameter which relates to the color-band position for different ion species. For a species such as B^+, which will not produce amorphous silicon if the implantation temperature rises more than approximately 20°C, color-bands will only arise when the temperature rise during implantation is very small. For many species a maximum temperature rise of approximately 200°-250°C will generate bright color-bands as this temperature will produce crystalline silicon irrespective of dose. Color-bands are only generated when the thermal behavior varies across the wafer during the implantation cycle.

Conclusions

The observation of the color-bands formed during the implantation of silicon wafers to high doses, with conditions which result in significant temperature rises, can quickly provide useful information about amorphous layer formation. It is possible to tell whether the amorphous layer is continuous to the surface or buried and to obtain an approximate estimate of the depth of the surface layer which will be amorphous or crystalline silicon, respectively. A knowledge of the temperature variations undertaken by each section of the wafer during implantation, for the particular scanning system employed, is advantageous in assisting such interpretation.

Temperature rises during implantation of 200°C or more from room temperature will generate color-bands on high dose implants of medium mass ions if the thermal behavior varies across the wafer. Mechanical scanning systems, which are often used for high dose implants because they reduce the temperature rise of wafers implanted with high beam currents, are likely to generate color-bands. The color-bands indicate a damage nonuniformity across the wafer, and, even after annealing to high temperatures, an electrical activity nonuniformity may result. For applications where a high degree of implant uniformity is required across the wafer, care should be taken to avoid implant conditions which generate color-banded wafers. If R_s measurements are made on such a wafer, or TEM specimens examined, the experimental results can vary considerably depending on the area of the wafer examined.

Baker and Ogden (22) discussed such a case where nonuniformity of crystal imperfections was observed in the epitaxial layers grown on a substrate implanted with 150 keV As^+ to 1×10^{16} cm^{-2} at 1 mA and annealed at 1200°C for 2 hr. The implanted wafers exhibited color-bands and the density of defects observed was greater in the implanted regions which produced the thicker amorphous layers.

Consideration should be given to the development of ion implantation scanning systems which are suitable for high dose, high dose rate implants and result in uniformly low disorder.

Although the generation of color-bands can be adequately explained, the prediction of their location on a wafer is difficult without much better information on the generation of amorphous regions in silicon under conditions of varying temperatures. It is, however, much easier to predict the implant conditions which will result in their generation.

Acknowledgments

One of the authors (D.G.B) wishes to acknowledge the cooperation and assistance of Harwell Research Laboratories where this work was undertaken. The encouragement and advice of Dr. J. Stephen, Prof. J. H. Freeman, and G. A. Gard is thankfully acknowledged, together with the assistance of Dr. G. Dearnaley, Dr. K. V. Anand, Dr. M. Nicholas, Dr. B. J. Smith, M. Wilkins, E. Wittam, and R. Fuller during various phases of the experimental measurements.

Manuscript submitted Aug. 5, 1977; revised manuscript received March 21, 1978.

Any discussion of this paper will appear in a Discussion Section to be published in the June 1979 JOURNAL. All discussions for the June 1979 Discussion Section should be submitted by Feb. 1, 1979.

Publication costs of this article were assisted by the Royal Melbourne Institute of Technology.

REFERENCES

1. J. H. Freeman, D. J. Chivers, G. A. Gard, G. W. Hinder, B. J. Smith, and J. Stephen, in "Ion Implantation in Semiconductors," S. Namba, Editor p. 555, Plenum Press, New York (1975); and A.E.R.E. Report R-7796 (1974).
2. L. Csepregi, E. F. Kennedy, S. S. Lau, J. W. Mayer, and T. W. Sigmon, *Appl. Phys. Lett.*, **29**, 645 (1976).
3. T. E. Seidel, G. A. Pasteur, and J. C. C. Tsai, *ibid.*, **29**, 648 (1976).
4. D. G. Beanland, *Rad. Effects*, **33**, 219 (1977).
5. G. Dearnaley, J. H. Freeman, R. S. Nelson, and J. Stephen, "Ion Implantation," North Holland, Amsterdam (1973).
6. S. T. Picraux and F. L. Vook, *Rad. Effects*, **11**, 179 (1971).
7. R. S. Nelson and D. J. Mazey, *Can. J. Phys.*, **46**, 689 (1968).
8. F. F. Morehead and B. L. Crowder, *Rad. Effects*, **6**, 27 (1970).
9. J. H. Freeman, in Proceedings of International Mass Spectrometry Conference, Kyoto, Japan, 1969; and A.E.R.E. Report R-6254 (1969).
10. J. H. Freeman, L. R. Caldecourt, K. C. W. Done, and R. J. Francis, in Proceedings of Conference on Ion Implantation, Reading, Peter Peregrinus, Stevenage, England (1970); and A.E.R.E. Report R-6496 (1970).
11. P. D. Parry, *J. Vac. Sci. Technol.*, **13**, 623 (1976).
12. J. M. Shannon, R. A. Ford, and G. A. Gard, *Rad. Effects*, 6, 217 (1970).
13. S. M. Davidson and G. R. Booker, *ibid.*, **6**, 33 (1970).
14. G. R. Booker and R. Stickler, *Br. J. Appl. Phys.*, **13**, 446 (1962).
15. J. W. Mayer, L. Eriksson, and J. A. Davies, "Ion Implantation in Semiconductors," Academic Press, New York (1970).
16. R. J. Archer, *J. Opt. Soc. Am.*, **52**, 970 (1962).
17. J. R. Adams and N. M. Bashara, *Surf. Sci.*, **49**, 441 (1975).
18. R. W. Ditchburn, "Light," Blackie, London (1963).
19. E. C. Baranova, V. M. Gusev, Yu. V. Martynenki, and I. B. Hailbullin, *Rad. Effects*, **25**, 157 (1975).
20. M. H. Brodsky, R. S. Title, K. Weiser, and G. G. Pettit, *Phys. Rev. B*, **1**, 2632 (1970).
21. M. D. Matthews, A.E.R.E. Report R-7805 (1974).
22. J. F. C. Baker and R. Ogden, *J. Mater. Sci.*, **10**, 1259 (1975).

Structure of Porous Silicon Layer and Heat-Treatment Effect

Takashi Unagami and Masahiro Seki

Nippon Telegraph and Telephone Public Corporation, Musashino Electrical Communication Laboratory, Musashino-shi, Tokyo, 180, Japan

ABSTRACT

The structure of an as-grown and heat-treated porous silicon layer (PSL) and silicon epitaxial growth on PSL are investigated. Many micropores are formed inside of PSL and zig-zag in the thickness direction. The crystalline structure of PSL is single crystal, but there is a polycrystal silicon on the surface and lattice strain exists. The structure of PSL is changed by high temperature heat-treatment. At 1000°C, PSL is a mosaic crystal. Above 1070°C, PSL is a single crystal. After heat-treatment, PSL remains porous and both the pore distribution and the pore size are changed. The surface roughness and the pore size become large with rising heat-treatment temperature. From the experimental results of silicon epitaxial growth on PSL it is found that good epitaxial layers grow on PSL.

The anodic reaction of silicon in hydrofluoric acid solution was investigated by Uhlir (1) and Turner (2). They found that a porous silicon layer (PSL) is formed by anodization below the critical current density. PSL is very chemically reactive and consists of silicon with a small amount of fluorine, hydrogen, and oxygen (3, 4). Recently Watanabe *et al.* noticed that PSL can be oxidized much more easily than silicon single crystal and suggested the application of oxidized PSL to dielectric isolation in integrated circuits (5).

The authors carried out silicon epitaxial growth on PSL and found that epitaxial layers of good quality grow on PSL. The quality of the epitaxial growth layer strongly depends on the surface morphology and the crystalline structure of the substrate. In order to investigate the epitaxial growth on PSL, the structure of PSL used as a substrate of epitaxial growth needs to be known. In this paper, the dependence of the structures of as-grown and heat-treated PSL on both the heat-treatment condition and the PSL formation condition and the result of silicon epitaxial growth on PSL are described.

Experimental

Formation of PSL.—Silicon wafers were anodized in 50% hydrofluoric acid solution with the equipment shown in Fig. 1. Silicon wafers were cut from (111) oriented p-type single crystal grown by the Czochralski method (boron doped). The wafer surfaces were metallographically polished, cleaned, and etched. Etch pit density of each wafer was less than 500/cm^2. Before anodization, aluminum alloy layers were formed on the back of silicon wafers as the low resistivity contact layer in order to make the anodic current distribution uniform. The wafer was coated with acid-proof wax to prevent current flow from the aluminum alloy layer to hydrofluoric acid solution and to perform anodic reaction selectively on the wafer's surface. Bubbles are produced on the surface of PSL, so an ultrasonic oscillator source was used to prevent the sticking of bubbles at the PSL surface.

Observation of PSL structure.—The surface morphology of as-grown and heat-treated PSL was observed by the scanning electron microscope (SEM). The inner structure of PSL was investigated by the observation of thin PSL with the transmission electron microscope (TEM) and the observation of the cleaved thin film of PSL was made using SEM. The crystalline structure of PSL was examined by reflection electron diffraction (ed) and x-ray diffraction.

Preparation of the PSL thin film for TEM and SEM observation.—Thin films of PSL were formed in order to investigate the inside structure of PSL, in particular, the distribution of pores in PSL. A fabrication process is shown in Fig. 2. The p$^-$ type layer in (a)

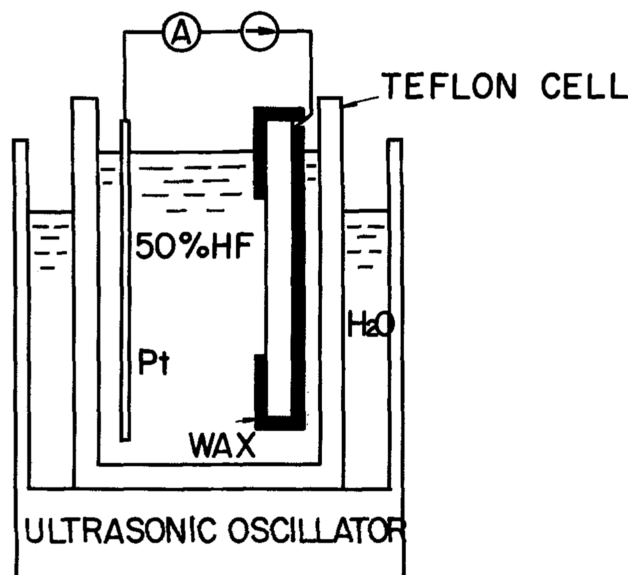

Fig. 1. The equipment for anodization in hydrofluoric acid solution.

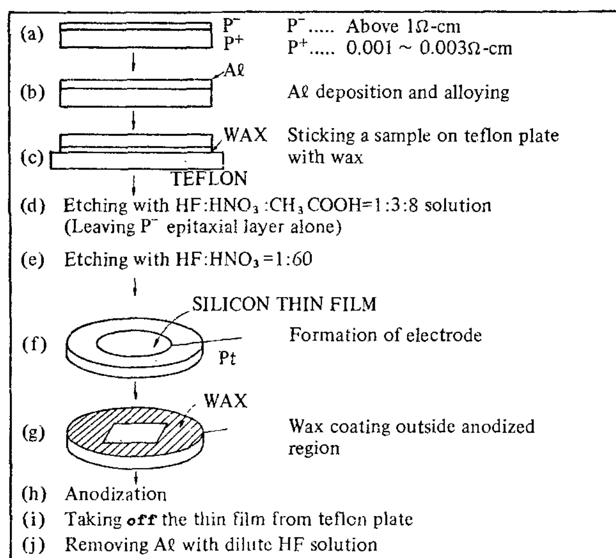

Fig. 2. Fabrication process for the thin film of PSL

Key words: porous silicon, film structure, heat-treatment.

is an epitaxial layer whose thickness is 0.6 μm. In (b), 300Å aluminum is deposited and then alloyed. ~100Å aluminum alloy layer is formed on the p^- type epitaxial layer. After that, thick aluminum is additionally evaporated in vacuum. The $HF:HNO_3:CH_3COOH = 1:3:8$ solution in (e) is the solution which has selectivity of etching rate against impurity concentration in silicon crystal (6). Thereby this solution can leave the p^- layer alone. p^- layer is etched further in $HF:HNO_3 = 1:60$ solution in order to be about 0.4 μm in thickness. In final process, this thin p^- layer is anodized in hydrofluoric acid solution. In the case of forming the thin film of PSL to observe the cleaved cross section, p type substrate was used instead of p^- on p^+ wafer, and the etching processing (d) was omitted.

Results and Discussion

PSL region.—A cross-sectional view of PSL is shown in Fig. 3. The sample was angle lapped with a plane inclined from the surface and slightly etched in an etchant ($HF:HNO_3 = 1:60$ solution). The region of PSL is observed to be black and the boundary of PSL and the silicon substrate region is clearly revealed. The PSL thickness is determined by this angle-lapping method. The surface step between the surface of PSL and that of the unreacted region is shown in Fig. 4. An interference microscope was used to observe it. The surface step does not appear; that is, PSL keeps the original surface contour.

Structure of PSL.—Some investigations about the structure of PSL have been reported (5, 7-9). However, those observations were not directed toward investigation of the detailed structure of PSL. In this section, the results of the detailed structure of PSL observed by TEM and SEM as well as the crystalline structure of PSL are reported. Figure 5 shows ED

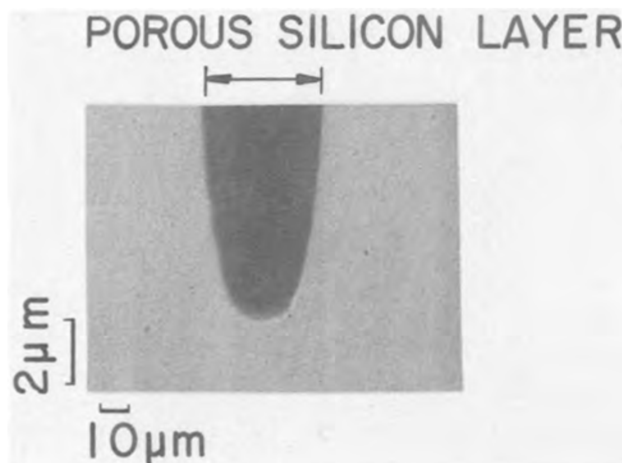

Fig. 3. Cross-sectional view of PSL observed by angle lapping

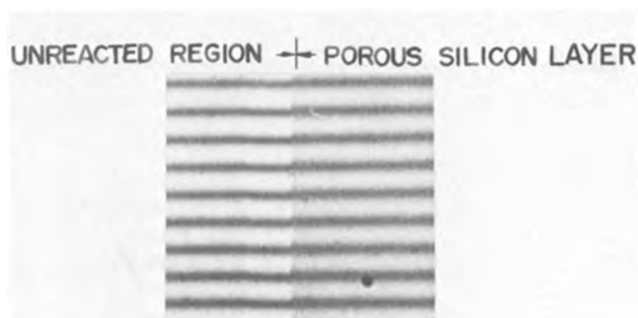

Fig. 4. Interference micrograph of the surface after anodization

and x-ray diffraction patterns of PSL. Figure 5(a) is the ED pattern of the PSL surface immediately after anodization. PSL was 15 μm in thickness and formed at 100 mA/cm² in anodic current density. Figure 5(b) is the x-ray diffraction pattern of PSL which is about 60 μm in thickness. Both Kikuchi's line and ring pattern are observed in ED pattern. However in the x-ray diffraction pattern, only the peak of the (111) plane is observed. The breadth of the x-ray diffraction line becomes broad in comparison with bulk single silicon. In the case of PSL in another orientation of single silicon crystal, the x-ray diffraction pattern shows only the peak of its orientation and the breadth of line also becomes broad. X-ray line broadening seems to be caused by the strain in PSL from the following three results: (*i*) The existence of the strain in PSL is confirmed by x-ray topograph observation (Lang method) (10); (*ii*) The transmission ED of PSL thin film does not show the pattern of mosaic structure but shows the pattern of single crystal structure; (*iii*) No grains which have the size (about 0.13 μm) equivalent to the broadening of the half-peak breadth of x-ray line can be observed in a transmission electron micrograph of PSL thin film given in the following paragraph. Consequently, PSL is thought to be a single crystal from the results of x-ray diffraction, but polycrystal silicon is observed only on the surface of PSL by ED.

Figure 6 shows the surface feature of PSL observed by SEM. Figure 6(a) indicates the surface immediately after anodization, and Fig. 6(b) indicates the surface which was etched in $HF:HNO_3 = 1:300$ solution for 4 sec. The surface immediately after anodization, as shown in Fig. 6(a), has microunevenness, but pores cannot be observed. In the case of Fig. 6(b), many pores of some 10-300Å appear below the surface. These pores are disorderly located and have various shapes. The inside structure of PSL was examined by TEM observation of PSL thin film which was prepared by the method shown in Fig. 2. The anodic current density and the reaction time were 30 mA/cm² and 10 sec, respectively. The results of observing an ~0.4 μm thick PSL film in the bright

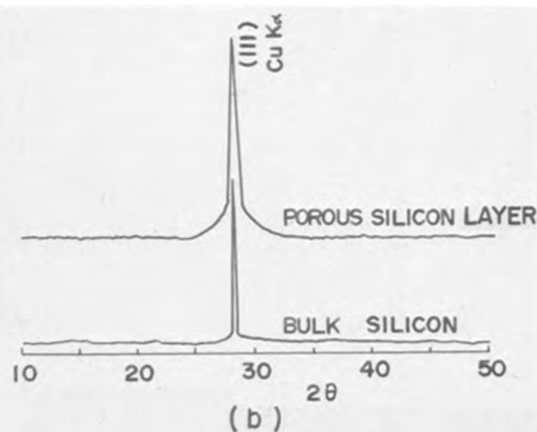

Fig. 5. Electron and x-ray diffraction pattern of PSL formed in (111) single crystal silicon.

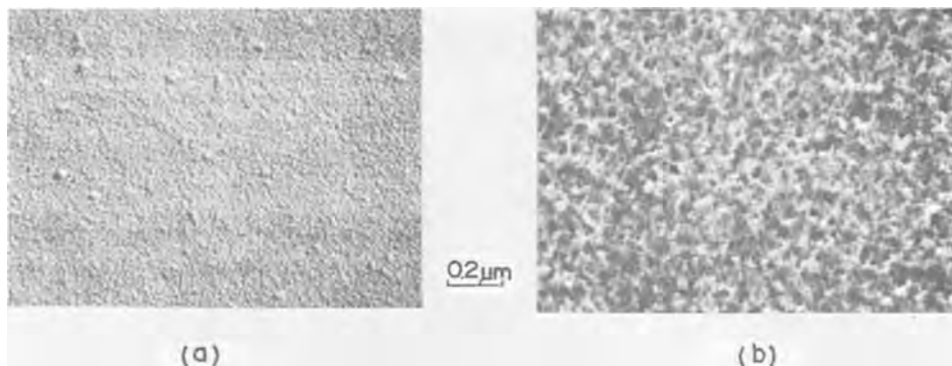

Fig. 6. Scanning electron micrograph of the surface of PSL. (a) Immediately after anodization; (b) after slightly etching.

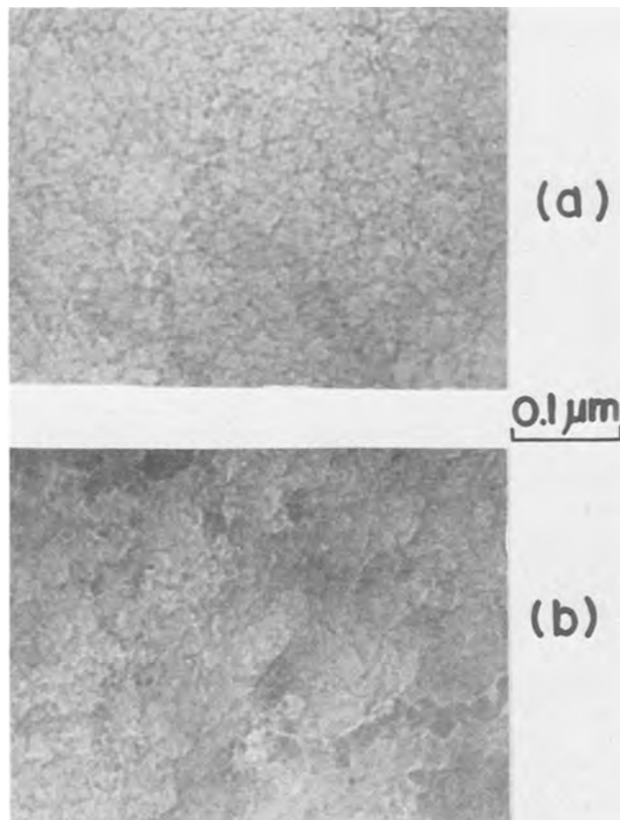

Fig. 7. Transmission electron micrograph of the thin film of PSL. (a) Vertical view; (b) tilted view at 40°.

field image by TEM is shown in Fig. 7. Figure 7(a) indicates transmission image of PSL observed vertically. Figure 7(b) is the transmission image of PSL observed with tilted illumination at 40°. The bright and dark-striped image is observed, but the image does not have the regular pattern. The contrast of brightness and darkness in Fig. 7(b) is more intense than that in Fig. 7(a). The irregularity of the pattern becomes increased with increasing the tilt angle of observation. As shown in Fig. 6(b), there are many pores in PSL. However, definite image corresponding to these pores is not observed in transmission micrograph. As a result, it can be said that the pores distribute at random in PSL and the pores are not formed straight, that is, the pores are formed zig-zag in the thickness direction of PSL. This result is quite different from that of aluminum anodic oxide film. In the case of aluminum anodic oxide film, a definite (bright and dark) image corresponding to straight pores formed by anodization was observed (11).

To prevent the structure of PSL from changing by chemical and mechanical treatment, the samples were prepared by cleavage of PSL thin films. PSL was roughly cleaved when silicon substrate under PSL was thicker than PSL. PSL has the same crystalline structure as silicon substrate (see Fig. 5), but the cleavage direction of PSL becomes different from that of silicon substrate. PSL is cleaved toward the thickness direction, that is, the cleavage plane of PSL is perpendicular to the surface. In order to prevent PSL from being cleaved roughly, the sample, in which the unreacted region of silicon substrate was sufficiently thinner than PSL, was prepared by the method shown in Fig. 2. PSL was about 17 μm thick and the unreacted region under PSL was about 3 μm thick. The cleaved cross section of PSL observed by SEM is shown in Fig. 8. As shown in Fig. 8(a), the cross section of PSL is uniform from the surface to the boundary between PSL and the silicon substrate. It means that the anodization is achieved uniformly toward the thickness direction. In Fig. 8(b) the vertical striations corresponding to the straight pores, which are perpendicular to the silicon substrate, can be observed near the boundary between PSL and the silicon substrate. But no straight striations continuing from the surface of PSL to the boundary can be observed by the enlarged cross section of PSL as shown in Fig. 8(c).

From the investigation of structures of PSL, the obtained results are following. PSL is formed uniformly in the thickness direction, so it can be said that silicon is dissolved uniformly by anodization toward the thickness direction. PSL is a single crystal and is cleaved perpendicularly, and it seems that silicon is dissolved locally and vertically in PSL for

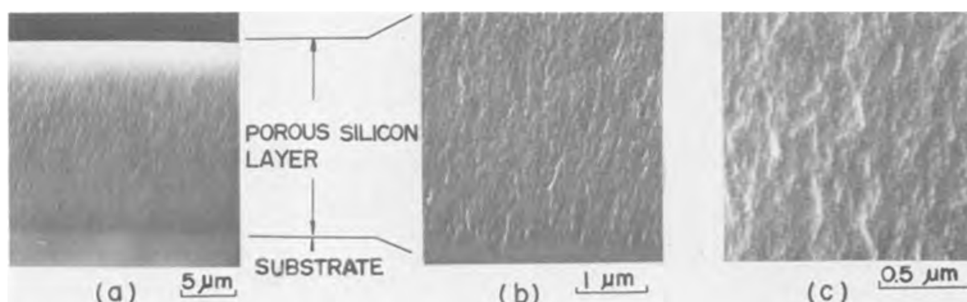

Fig. 8. Scanning electron micrograph of cleaved cross section of PSL. (a) Total view; (b) view at the boundary between PSL and the silicon substrate; (c) enlarged cross-sectional view of PSL.

the most part. Pores are not formed straight, that is, they are formed zig-zag and the pore distribution is irregular.

Changes of PSL by heat-treatment.—In the case of epitaxial growth, PSL is heated at high temperature. It is therefore important to investigate the changes of the distribution of pores and crystalline structure of PSL. These changes were observed by SEM and ED. Heat-treatment was performed in a hydrogen atmosphere. Hydrogen gas was purified by passing through a paladium filter because PSL is very susceptible to oxidation. Figure 9 shows the heat-treatment conditions, scanning electromicrographs, and ED patterns of heat-treated PSL. The silicon substrates were 0.2-0.4 Ω-cm in resistivity. PSL was 4 μm in thickness. The anodic current density and the reaction time were 30 mA/cm^2 and 140 sec, respectively. On the surface of PSL heat-treated at 1000°C little pits and cracks are observed. The crystalline structure is a mosaic pattern. By the heat-treatment above 1070°C, the crystalline structure of PSL is changed to a single crystal. But on the surface of PSL, large pits begin to appear. As shown in Fig. 9, the surface roughness becomes violent with the rise in heat-treatment temperature. Figure 10 shows the cross section of heat-treated PSL which was prepared by cleavage of PSL heat-treated at 1070°C. It can be seen that there are pores inside corresponding to pits observed on the surface.

The migration of silicon in PSL occurs by high temperature heat-treatment, so the crystalline structure becomes a single crystal and the distribution of pores is changed. Heat-treated PSL has larger pores than as-grown PSL. Heat-treated PSL has the third dimensional mesh structure which consists of single crystal grains associated with neighbors.

In order to investigate the dependence of pore distribution of heat-treated PSL on both the anodic current density and the substrate resistivity, the surface of heat-treated PSL was observed by SEM (Fig. 11). The temperature of heat-treatment was 1070°C and PSL was 4 μm in thickness. The surface roughness becomes larger both at high resistivity region and at high anodic current density. This tendency seems to depend on the change of the silicon density in PSL (9).

Silicon epitaxial growth of PSL (12).—From the results mentioned above, for the purpose of epitaxial growth of good quality on PSL, PSL needs to be recrystallized by the heat-treatment above 1070°C and it is profitable to use a low resistivity silicon substrate. Therefore, a p-type (111) single silicon wafer, which was 0.004-0.15 Ω-cm in resistivity, was used as a silicon substrate for anodization. The anodic current density and the anodic reaction time were 50 mA/cm^2 and 60 sec, respectively. Epitaxial silicon was grown at 1170°C by the commonly used thermal decomposition of $SiCl_4$ with hydrogen. The growth rate of epitaxial silicon was 0.4 μm/min and the nondoped epitaxial layer was grown to be about 5 μm in thickness. Figure 12 shows the surface morphology and the crystalline structure of silicon epitaxial layer grown on PSL. The surface morphology was obtained from observation of shadowed carbon replicas by TEM. It is clear that the surface is flat and the crystalline structure observed by ED is single crystal. Figure 13 shows the cross section of this sample. The cross section was obtained by angle lapping and etched for several seconds in HF:HNO_3 = 1:60 solution. Three layers can be observed, these being an epitaxial layer, PSL, and silicon substrate. Observation of etch pits by Sirtl etching makes it clear that stacking faults are very few. From these results, it is revealed that silicon epitaxial layer of good quality can be grown on PSL.

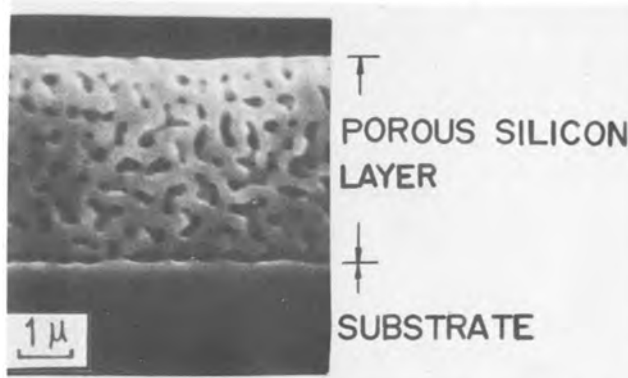

Fig. 10. Scanning electron micrograph of the cleaved cross section of PSL heat-treated at 1070°C.

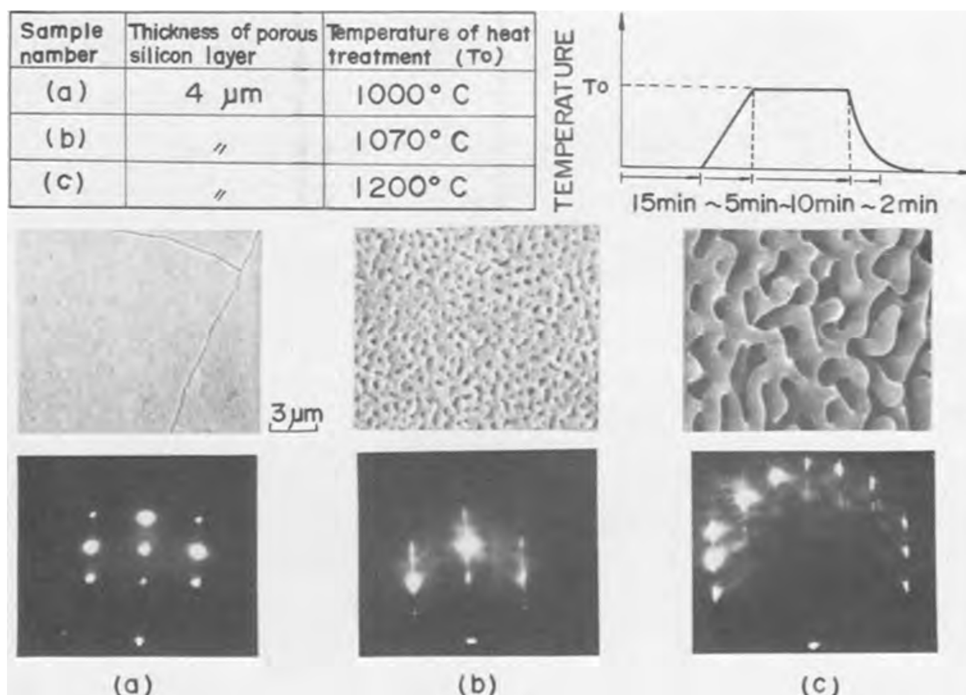

Sample number	Thickness of porous silicon layer	Temperature of heat treatment (To)
(a)	4 μm	1000° C
(b)	〃	1070° C
(c)	〃	1200° C

Fig. 9. Heat-treatment condition, scanning electron micrograph, and electron diffraction pattern of heat-treated PSL.

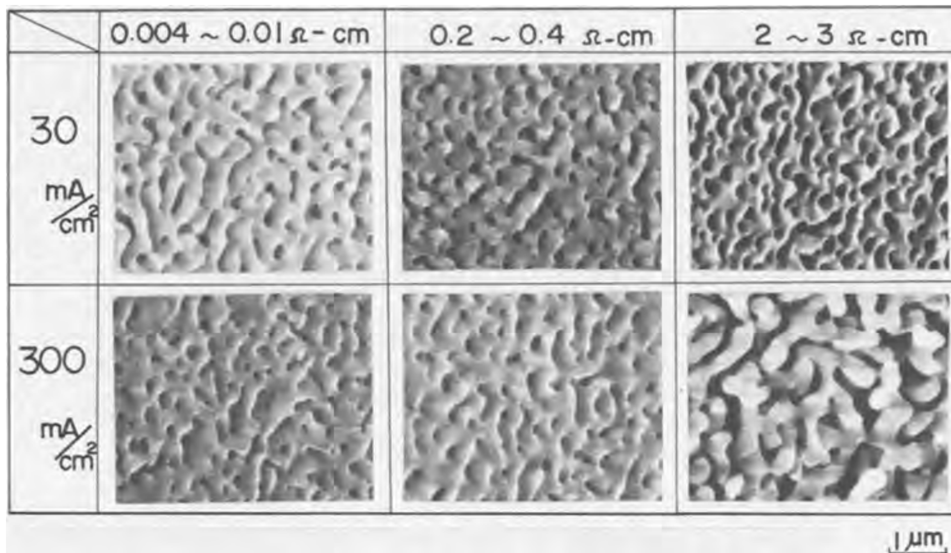

Fig. 11. Dependence of the surface roughness of heat-treated PSL on both the resistivity of the silicon substrate and the anodic current density.

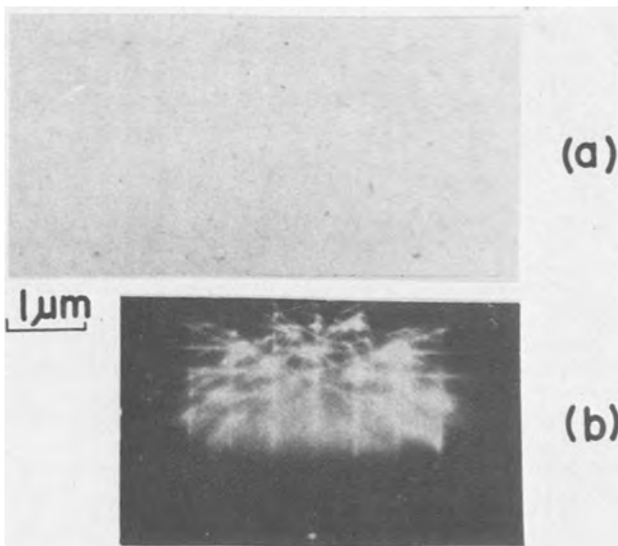

Fig. 12. Electron micrograph (a) and electron diffraction pattern (b) of silicon epitaxial layer grown on PSL.

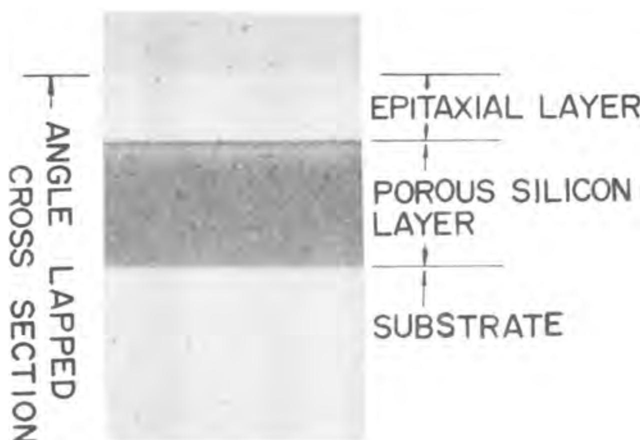

Fig. 13. Cross-sectional view of the sample of silicon epitaxial layer grown on PSL observed by angle lapping.

Conclusions

The structures of PSL formed by anodization and the change by high temperature heat-treatment were investigated by SEM, TEM, ED, and x-ray diffraction. PSL is formed uniformly in the thickness direction. Pores cannot be observed on the surface by SEM, but many pores are observed inside. These pores are formed zig-zag in the thickness direction. The cleavage plane of PSL is perpendicular to the surface, so silicon dissolution by anodization seems to be performed vertically in the silicon substrate. The crystalline structure of PSL is a single crystal, but there is a polycrystal silicon on the surface and the strain exists in PSL.

High temperature heat-treatment modifies the microstructure of PSL. Silicon migrates during the heat-treatment, changing the pore size and distribution of the pores. After heat-treatment at a temperature greater than 1070°C, PSL is single crystalline and porous. The surface roughness and pore size increase with heat-treatment temperature.

For the purpose of growing single crystalline silicon on PSL, PSL needs to be a single crystal. In the method of epitaxial growth, which includes heat-treatment above 1070°C, PSL is recrystallized to be a single crystal when silicon epitaxial growth is performed. So single crystalline silicon can be grown on PSL. But in spite of the rough surface of heat-treated PSL, the surface of the epitaxial layer is flat as shown in Fig. 12. This is a very interesting phenomenon, but the reason is not clear now. So it is expected that the reason becomes clear in the future by the investigation of silicon epitaxial growth mechanism.

Acknowledgments

The authors are grateful to H. Araki for his encouragement during the course of this work, and also to H. Takaoka, S. Hirota, and Y. Kobayashi for useful discussions.

Manuscript submitted Dec. 12, 1977; revised manuscript received March 20, 1978.

Any discussion of this paper will appear in a Discussion Section to be published in the June 1979 JOURNAL. All discussions for the June 1979 Discussion Section should be submitted by Feb. 1, 1979.

Publication costs of this article were assisted by Nippon Telegraph and Telephone Public Corporation.

REFERENCES

1. A. Uhlir, *Bell Syst. Tech. J.*, **35**, 333 (1956).
2. D. R. Turner, *This Journal*, **105**, 402 (1958).
3. D. R. Turner, in "The Surface Chemistry of Metals and Semiconductors," H. C. Gatos, Editor, p. 285, John Wiley & Sons, New York (1960).
4. K. H. Beckmann, *Surf. Sci.*, **3**, 314 (1965).
5. Y. Watanabe, Y. Arita, T. Yokoyama, and Y. Igarashi, *This Journal*, **122**, 1351 (1975).
6. Y. Sumitomo, T. Yasui, H. Nakatsuka, T. Oohashi, H. Tsutsumi, and H. Muraoka, Paper 25 pre-

sented at The Electrochemical Society Meeting, Houston, Texas, May 7-11, 1972.
7. M. M. Koltun, *Russ. J. Phys. Chem.*, **38**, 381 (1964).
8. M. J. J. Theunissen, *This Journal*, **119**, 351 (1972).
9. Y. Arita and Y. Sunohara, *ibid.*, **124**, 285 (1977).
10. H. Takaoka, Private communication.
11. F. Keller, M. S. Hunter, and D. L. Robinson, *This Journal*, **100**, 411 (1953).
12. M. Seki and T. Unagami, Paper submitted to *Rev. Elec. Commun. Lab.*

Electrochromism in Anodically Formed Tungsten Oxide Films

A. Di Paola, F. Di Quarto, and C. Sunseri
Istituto di Ingegneria Chimica, University of Palermo, Italy

ABSTRACT

By anodization of tungsten in acid solutions, oxide films were obtained whose composition depended on the working temperature. In particular, the composition of the films was WO_3 at 25° and 50°C, but $WO_3 \cdot H_2O$ at 70°C. Studies of electrochromism in these films seem to show that the electrocoloration occurs with different mechanisms according to the oxide chemical composition. For WO_3 films the coloration is due to a simultaneous injection of electrons and H^+ ions with formation of hydrogen tungsten bronzes H_xWO_3. For $W_3 \cdot H_2O$ films the coloration could occur as a result of the injection of electrons and oxygen ion vacancies with formation of blue oxide hydrate $WO_{3-x} \cdot H_2O$.

The phenomenon of electrochromism in WO_3 films is under active investigation because of its potential use for passive alphanumeric displays.

Electrochromism in WO_3 films was first reported by Deb (1). A reversible blue coloration was generated at the cathodic area on applying a d-c electric field across an evaporated WO_3 film. Deb has proposed (2) that the coloration occurred as a result of the formation of F or F^+ color centers in oxygen ion vacancies. Chang *et al.* (3) have attributed the blue color to the formation of reduced oxides of general formula WO_{3-x} according to the electrochemical reaction

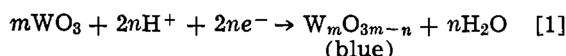

$$mWO_3 + 2nH^+ + 2ne^- \rightarrow W_mO_{3m-n} + nH_2O \quad \text{(blue)} \qquad [1]$$

Other authors (4-8) have suggested the formation of hydrogen tungsten bronzes by double injection of protons and electrons

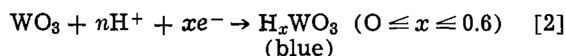

$$WO_3 + nH^+ + xe^- \rightarrow H_xWO_3 \quad (O \leq x \leq 0.6) \quad \text{(blue)} \qquad [2]$$

In this hypothesis the phenomenon of coloration was explained by Faughnan *et al.* (8) as an intervalence transfer absorption

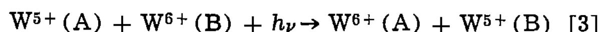

$$W^{5+}(A) + W^{6+}(B) + h\nu \rightarrow W^{6+}(A) + W^{5+}(B) \qquad [3]$$

Recent studies (9-11) have confirmed the model proposed by Faughnan and co-workers.

In almost all previous investigations, the WO_3 films were prepared by evaporation of WO_3 onto transparent substrates (generally quartz or glass). The films were amorphous and with an unknown water content.

Although all the authors have recognized the importance of the water presence, only Hurditch (12) has studied the dependence of the coloration phenomenon on the water content of the films. For the case of hydrated oxides represented as $WO_3 \cdot aq$, Hurditch has proposed the formation of blue hydrogen tungsten bronzes of general formula $WO_{3-m}(OH)_m \cdot aq$. The H_2O molecules provide H^+ ions which are reduced at the cathode giving rise to active hydrogen atoms, which form a reduced tungsten blue phase

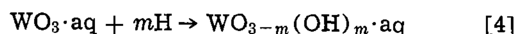

$$WO_3 \cdot aq + mH \rightarrow WO_{3-m}(OH)_m \cdot aq \qquad [4]$$

This tungsten blue phase does not correspond to any of the phases studied by Glemser *et al.* (13, 14), who have obtained blue tungsten compounds by reduction of WO_3, $WO_3 \cdot H_2O$, and $WO_3 \cdot 2H_2O$ by means of nascent hydrogen.

Key words: tungsten oxide films, electrochromism, hydrogen tungsten bronzes, blue tungsten oxide hydrates.

In this paper we report some results on the electrochromism of anodically formed tungsten oxide films. The experimental results indicate that different coloration mechanisms can occur, depending on the oxide chemical composition.

Experimental

The electrodes were obtained from spectrographically pure tungsten sheets 0.1 mm thick. They were electropolished in 15% NaOH at room temperature, rinsed with distilled water, and dried in a nitrogen stream. The anodization was performed at three different temperatures (25°, 50°, 70°C) but always at the same constant current density of 8 mA cm^{-2}. The current was supplied by a Keithley Model 227 constant current generator.

After the oxidation the electrodes were either submitted to x-ray analysis or inserted into an electrochemical cell containing H_2SO_4 1*N* at room temperature to investigate the coloration process. Nitrogen was bubbled through the solution before and during the experiments. The auxiliary electrode was Pt. The electrode potential was measured with respect to a Hg/Hg_2SO_4 (1*N* H_2SO_4) reference electrode with a Keithley Model 610 C electrometer. Cyclic voltammetry measurements were carried out with a Amel Model 557 potentiostat and a Systron-Donner Model 410 function generator. All potentials reported are referred to the standard hydrogen electrode at 25°C.

Direct x-ray diffraction patterns of the films on the tungsten sample were obtained using a Philips Model PW 1130 generator and PW Model 1050 goniometer. Copper $K\alpha$ radiation was used and the scanning rate of 2θ 1°/min. Measured d spacings were compared with the ASTM index values. The data reported by Glemser *et al.* (13, 14) were used mainly for the identification of the hydrated oxides.

Results and Discussion

Oxide film formation.—In previous works (15, 16) it has been shown that the temperature and the electrolyte composition strongly influence the anodic behavior of tungsten in acid solutions.

1*N* H_2SO_4 solutions were used for the anodization at 50° and 70°C. 1*N* HNO_3 solutions were preferred at 25°C, since a poor mechanical stability of the layers was observed in H_2SO_4 solutions at high potentials (15).

Figure 1 shows the influence of temperature on the anodic charging curves at constant C.D. During the first instants of anodization, the shape of the curves is the same for every temperature investigated. With the increase of time all curves reach a maximum.

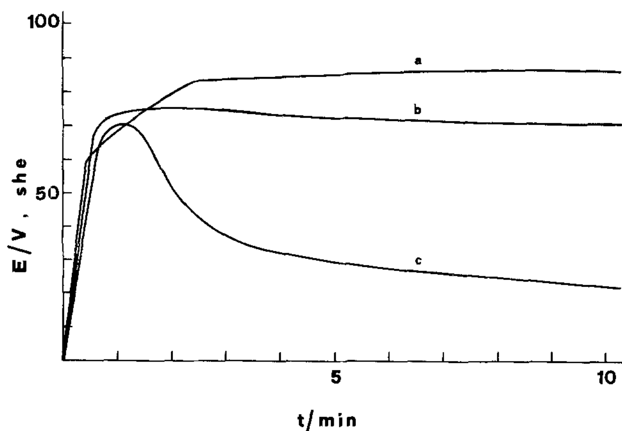

Fig. 1. Effect of temperature on anodic-charging curves at 8 mA cm^{-2} (pen recorded): (a) 1N HNO_3 at 25°C; (b) 1N H_2SO_4 at 50°C; (c) 1N H_2SO_4 at 70°C.

However, while at 25° and 50°C the electrode potential remains practically constant thereafter, at 70°C it decreases until a quasisteady-state value is obtained. This last value is about 50V smaller than the maximum. In any case by increasing the anodization time the oxide films thicken. This oxide growth indicates that a corrosion process is operating with formation of a thicker porous layer outside a barrier layer. This process depends on the temperature and the electrolyte composition (17). The times of anodization were selected so as to produce comparable thickness and weight of the films.

At the end of the experiments, at 25° and 50°C, the electrodes were normally covered by a whitish-gray oxide film, while a yellow-green film was obtained at 70°C. All the oxide layer have shown a good adherence to the metallic substrate.

X-ray analysis of the oxidation products.—Recent investigations (17) have shown that the temperature plays a fundamental role in determining the chemical composition and the morphology of the oxide layers.

Figures 2a, 3a, and 4a, show the x-ray diffraction patterns of the films obtained at different temperatures. The experimental data were compared with the ASTM and Glemser *et al.* (14) d spacings, which are reported in the Tables I and II.

Both at 25° and 50°C the composition of the anodic films is mainly WO_3. At 25°C the diffraction pattern shows two peaks for 2θ values near 13° and 27° which could be attributed to the simultaneous presence of $WO_3 \cdot 2H_2O$.

The whitish-gray color of the electrodes does not seem due to the presence of white $WO_3 \cdot 2H_2O$ (18) but to the morphology of the layers. In fact whitish films often do not show peaks characteristic of $WO_3 \cdot 2H_2O$.

At 70°C the diffraction data have shown that the composition of the films is $WO_3 \cdot H_2O$. Also at this temperature there are sometimes very weak reflections of the dihydrate phase.

In conclusion, by means of the x-ray analysis the following aspects can be emphasized: (*i*) in every electrolyte solution and for working temperatures up to 50°C the oxide film is mostly composed of WO_3[1]; (*ii*) the increase of temperature above 50°C causes the formation of $WO_3 \cdot H_2O$. This compound is practically the only phase present above 70°C and for 1N H_2SO_4 solutions. $WO_3 \cdot 2H_2O$ can be found in the films, especially in those formed at 25°C.

Coloration of the films.—The coloration process of the anodic oxide films was studied by cathodic polarization of the specimens at different current densities. The shape of the potential/time curves was similar for any chemical composition of the starting films.

[1] On the basis of the available data one cannot definitely exclude the presence of H_2O, though at very low levels, in these films.

Also the final value of the potential was practically equal for all electrodes at the same C.D. In any case the final process was hydrogen evolution as evidenced by gas bubble generation at the electrode.

During the cathodic reduction the electrode surface became more and more blue with the increase of the injected charge. Colored electrodes exposed to air showed a different rate of bleaching depending on their chemical composition. Generally, reduced hydrated oxides bleached faster.

In Fig. 5 and 6 the cyclic voltammetry measurements of WO_3 and $WO_3 \cdot H_2O$ are reported. The voltammograms show significant differences both in the anodic and cathodic portions. In the cathodic curve two peaks were observed. For WO_3 electrodes, the former (more anodic) can be attributed to the formation of hydrogen tungsten bronzes (7); the latter is obviously due to the hydrogen evolution process.

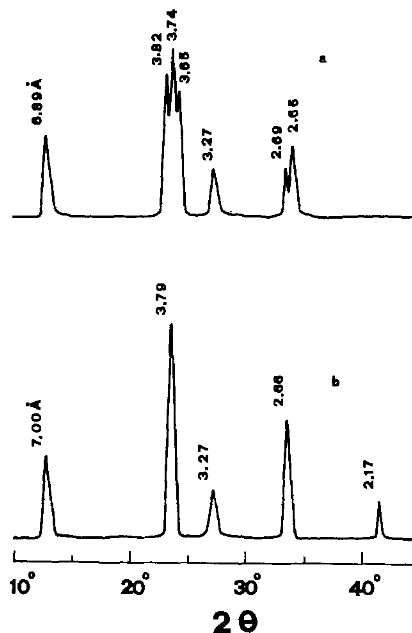

Fig. 2. X-ray diffraction patterns: (a) film obtained by oxidation in 1N HNO_3 at 25°C for 10 min; (b) the same film after reduction in 1N H_2SO_4 at 25°C.

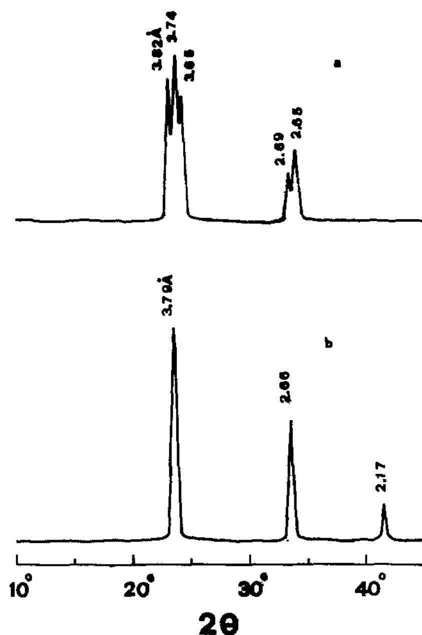

Fig. 3. X-ray diffraction patterns: (a) film obtained by oxidation in 1N H_2SO_4 at 50°C for 15 min; (b) the same film after reduction in 1N H_2SO_4 at 25°C.

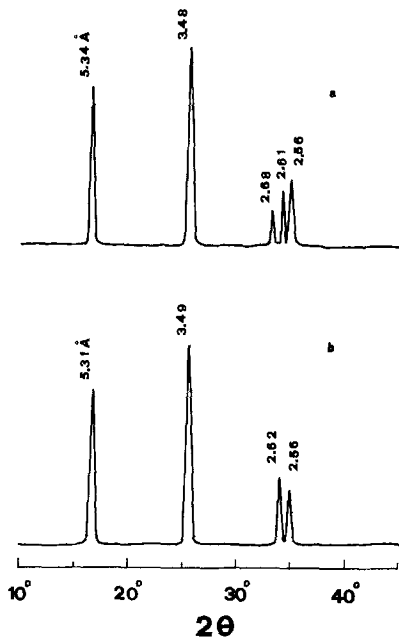

Fig. 4. X-ray diffraction patterns: (a) film obtained by oxidation in 1N H_2SO_4 at 70°C for 60 min; (b) the same film after reduction in 1N H_2SO_4 at 25°C.

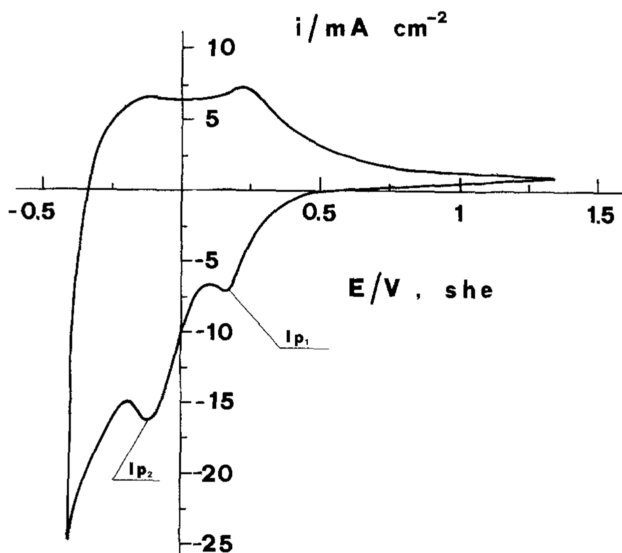

Fig. 5. Cyclic voltammetry measurement of a WO_3 film in 1N H_2SO_4 at 25°C, sweep rate 210 mV min^{-1}.

For $WO_3 \cdot H_2O$ electrodes both peaks were found at more anodic potential values. In this case, the former could be attributed to the formation of a reduced hydrate tungsten oxide (see below).

The voltammograms were not significantly modified by repetitive cycling. The different bleaching rate of the electrodes was evident also during the cyclic voltammetry measurements. Electrodes obtained by reducing WO_3 were pale blue even at the end of the anodic sweep when the electrode potential

Table I. ASTM d spacings for WO_3 and hydrogen tungsten bronzes

WO_3 d (A)	I	$H_{0.33}WO_3$ d (A)	I	$H_{0.5}WO_3$ d (A)	I
3.83	100	3.79	80	3.68	50
3.76	95	2.69	80	2.63	50
3.64	100	2.19	10	2.16	10
3.41	5	1.91	20	1.87	30
3.34	50	1.87	10	1.68	100
3.11	50	1.69	100	1.53	80
3.08	50	1.68	20		
2.68	75	1.55	100		
2.66	60				
2.62	90				

Table II. Glemser et al. d-spacings for hydrated tungsten oxides (14)

$WO_3 \cdot H_2O$ d (A)	I	$WO_{2.88} \cdot H_2O$ d (A)	I	$WO_3 \cdot 2H_2O$ d (A)	I	$WO_{2.88} \cdot 2H_2O$ d (A)	I
5.34	70	5.27	70	6.80	100	6.70	100
3.80	20	3.77	30	3.67	80	3.67	80
3.48	100	3.48	100	3.37	30	3.37	40
2.92	30	2.90	10	3.21	100	3.23	100
2.70	30	—	—	3.00	10	—	—
2.62	50	2.63	70	2.58	50	2.61	60
2.56	70	2.56	50	2.51	30	2.49	40
2.37	30	2.34	50	2.43	20	2.43	30
2.31	40	2.27	10	2.27	10	2.29	20

value was about 1.4V. This color was maintained even though an anodic potential of 5V was applied for a few seconds. Instead, electrodes obtained by reducing $WO_3 \cdot H_2O$ were completely bleached already about 1V.

The relative heights of the two peaks of cathodic current show further differences. In fact for WO_3 electrodes the ratio $I_{p2} - I_{p1}/I_{p1}$ is about 1.25, while for $WO_3 \cdot H_2O$ this ratio is one.

X-ray analysis of the reduction products.—After the coloration process the electrodes were rinsed with distilled water, dried rapidly in a nitrogen stream, and immediately submitted to x-ray analysis.

Figures 2b, 3b, and 4b show the x-ray diffraction patterns of the electrodes after cathodic reduction. When the composition of the formed film was WO_3, the reduction products were hydrogen tungsten bronzes, whose hydrogen content changed with change of the charge injected during the cathodic polarization. For bronzes with a high hydrogen content ($x > 0.1$), the diffraction patterns proved difficult to index (see Table I) as already reported by Chevrier *et al.* (7).

Instead, sharp peaks attributable to $H_{0.1}WO_3$ were exhibited by the patterns of the same electrodes analyzed after waiting a time sufficient for a partial reoxidation to air (see Table III). $H_{0.1}WO_3$ was also the composition of the films at the end of the anodic sweep in the cyclic voltammetry measurements of WO_3 electrodes.

For cathodic reduction of $WO_3 \cdot H_2O$ films, a "tungsten-blue" phase was obtained whose diffraction pattern could be interpreted in terms of the reduced oxide hydrate $WO_{2.88} \cdot H_2O$. It was the only phase found also after a prolonged cathodic polarization at constant C.D. The attribution was made by comparison of the d spacings with the index values (see Table II) reported by Glemser *et al.* (14). This conclusion was supported by the diffraction patterns of the electrodes reoxidized to air. In fact these last d spacings matched those obtained by Glemser (14) for reoxidized $WO_3 \cdot H_2O$.

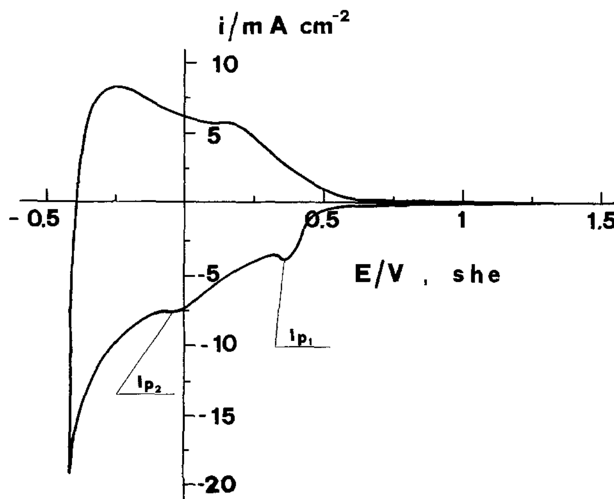

Fig. 6. Cyclic voltammetry measurement of a $WO_3 \cdot H_2O$ film in 1N H_2SO_4 at 25°C, sweep rate 210 mV min^{-1}.

Table III. X-ray diffraction data

(a) film obtained in 1N HNO_3 at 25°C; (b) the same film after cathodic reduction in 1N H_2SO_4; (c) the (b) film after partial reoxidation to air.

Experimental values a		b		ASTM values c		$H_{0.1}WO_3$	
d (A)	I	d (A)	I	d (A)	I	d (A)	I
6.89	m	7.00	m	6.93	s	—	—
3.82	s	3.79	vs	3.84	s	3.84	60
3.74	vs	3.27	m	3.67	vs	3.64	100
3.65	s	2.66	s	3.25	w	—	—
3.27	w	2.17	m	3.09	w	3.11	10
3.13	vw	1.90	w	2.67	s	2.67	60
3.10	vw	1.87	vw	2.60	m	2.61	20
2.69	w	1.69	m	2.16	w	2.16	10
2.65	m	1.55	m	2.00	vw	2.00	10
				1.85	w	1.84	40

Intensity key: vs = very strong, s = strong, m = medium, w = weak, vw = very weak.

Reduced dihydrate oxides were obtained for cathodic reduction of $WO_3 \cdot 2H_2O$ in those specimens where this species was present. Mention should be made that the same reduction products were obtained by reducing the films with indium in 20% H_2SO_4 solution (19).

Conclusions

By anodization of tungsten at various temperatures, different oxide films are obtained which exhibit the electrochromism effect as WO_3 evaporated films. The coloration occurs whatever is the composition of the starting oxide, but the bleaching seems reversible only for the hydrate oxides.

Two different mechanisms can be suggested for the coloration process of tungsten oxide films according to their chemical composition. The most direct evidence is given by the x-ray analysis and the cyclic voltammetry measurements. In fact, different reduction products and different cathodic processes are obtained depending on the starting oxide film. For WO_3 anodic films the coloration can be attributed to the formation of blue hydrogen tungsten bronzes of formula H_xWO_3, as a result of a diffusion of H^+ ions from the electrolyte into the WO_3 lattice and a simultaneous injection of electrons from the oxide-metal interface (8-11).

Otherwise, for anodic-hydrated oxide films of formula $WO_3 \cdot H_2O$ or $WO_3 \cdot 2H_2O$, the coloration could occur as a result of the injection and trapping of electrons in oxygen ion vacancies $O\square^{\cdot\cdot}$ (where the square indicates a vacancy and the dots the number of positive charges).

These vacancies are likely originated by the reaction of H^+ ions in the electrolyte with the oxide surface

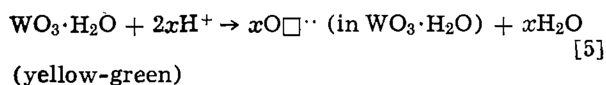

$$WO_3 \cdot H_2O + 2xH^+ \rightarrow xO\square^{\cdot\cdot} \text{ (in } WO_3 \cdot H_2O) + xH_2O \quad [5]$$
(yellow-green)

Then the vacancies $O\square^{\cdot\cdot}$ diffuse in the bulk of the oxide layer and capture the electrons injected from the oxide-metal interface according to the reaction

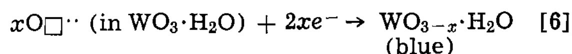

$$xO\square^{\cdot\cdot} \text{ (in } WO_3 \cdot H_2O) + 2xe^- \rightarrow \underset{\text{(blue)}}{WO_{3-x} \cdot H_2O} \quad [6]$$

The over-all reaction is

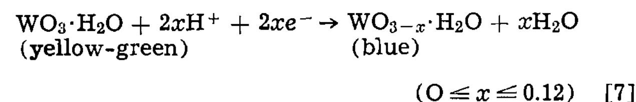

$$\underset{\text{(yellow-green)}}{WO_3 \cdot H_2O + 2xH^+ + 2xe^-} \rightarrow \underset{\text{(blue)}}{WO_{3-x} \cdot H_2O} + xH_2O$$
$$(0 \leq x \leq 0.12) \quad [7]$$

In conclusion, two different mechanisms of coloration seem possible in tungsten oxide films depending on their starting composition.

For anhydrous oxides of formula WO_3 the appearance of color centers is due to the formation of the H_xWO_3 phase (with $x \leq 0.6$), while for hydrate oxides of formula $WO_3 \cdot H_2O$, F or F^+ centers in oxygen ion vacancies are involved. In $WO_3 \cdot H_2O$ oxides the presence of H_2O in the WO_3 matrix likely hinders the diffusion of H^+ ions into the otherwise "open" crystal structure of WO_3, and therefore the coloration takes place with formation of blue $WO_{3-x} \cdot H_2O$.

This interpretation is in agreement with the hypothesis reported by Witzke (10), who found that already blue WO_{3-y} films, which therefore contain large densities of oxygen vacancies, may be colored to a deeper blue according to the reaction

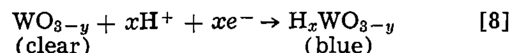

$$\underset{\text{(clear)}}{WO_{3-y}} + xH^+ + xe^- \rightarrow \underset{\text{(blue)}}{H_xWO_{3-y}} \quad [8]$$

A diffusion of the H^+ ions from the electrolyte with formation of hydrogen tungsten bronzes of formula H_xWO_{3-y} seems so possible also for anhydrous oxides substoichiometric but not for hydrated oxides. The experimental evidence is consistent with this interpretation, but further work seems necessary to verify the validity of this model. In view of technological applications, the anodic $WO_3 \cdot H_2O$ films could be a new interesting material for display devices.

Manuscript submitted June 23, 1977; revised manuscript received April 3, 1978.

Any discussion of this paper will appear in a Discussion Section to be published in the June 1979 JOURNAL. All discussions for the June 1979 Discussion Section should be submitted by Feb. 1, 1979.

Publication costs of this article were assisted by the University of Palermo.

REFERENCES

1. S. K. Deb, *Appl. Opt. Suppl.*, **3**, 192 (1969).
2. S. K. Deb, *Phil. Mag.*, **27**, 801 (1973).
3. I. F. Chang, B. L. Gilbert, and T. I. Sun, *This Journal*, **122**, 955 (1975).
4. B. S. Hobbs and A. C. C. Tseung, *Nature (London)*, **222**, 556 (1969).
5. B. S. Hobbs and A. C. C. Tseung, *This Journal*, **119**, 580 (1972).
6. G. Siclet, J. Chevrier, J. Lenoir, and C. Eyraud, *C. R. Acad. Sci., Ser. C*, **277**, 227 (1973).
7. J. Chevrier and G. Siclet, *Bull. Soc. Chim. Fr.*, 1037 (1976).
8. B. W. Faughnan, R. S. Crandall, and P. M. Heyman, *RCA Rev.*, **36**, 177 (1975).
9. H. N. Hersh, W. E. Kramer, and J. H. McGee, *Appl. Phys. Lett.*, **27**, 646 (1975).
10. H. Witzke, Paper 423 presented at The Electrochemical Society Meeting, Washington, D.C., May 2-7, 1976.
11. M. L. Hitchman, Paper 202 presented at the 27th Meeting, Zürich (1976).
12. R. Hurditch, *Electron. Lett.*, **11**, 142 (1975).
13. O. Glemser and C. Naumann, *Z. Anorg. Chem.*, **265**, 288 (1951).
14. O. Glemser, J. Weidelt, and F. Freund, *Z. Anorg. Chem.*, **332**, 299 (1964).
15. A. Di Paola, F. Di Quarto, and G. Serravalle, *J. Less-Common Met.* **42**, 315 (1975).
16. A. Di Paola, F. Di Quarto, and G. Serravalle, *Gazz. Chim. Ital.*, **106**, 277 (1976).
17. A. Di Paola, F. Di Quarto, and C. Sunseri, Unpublished results.
18. N. Stolica, *Werkst. Korros.*, **27**, 85 (1976).
19. R. S. Crandall and B. W. Faughnan, *Appl. Phys. Lett.*, **26**, 120 (1975).

The Defect Structure of Pure and Doped ZnSe

A. K. Ray*,[1] and F. A. Kröger*

Department of Materials Science, University of Southern California, Los Angeles, California 90007

ABSTRACT

Measurements of Hall effect and Zn self-diffusion on single crsytals of ZnSe doped with various amounts of Al or As were performed at 800°, 900°, and 1000°C when the crystals were in equilibrium with atmospheres of well-defined zinc pressures; Hall effect measurements were also performed on crystals cooled after high temperature equilibration. Analysis of the results leads to the conclusion that Schottky disorder is the main type of atomic disorder. Values of the parameters for various equilibrium constants are determined.

ZnSe has potential as a material for electroluminescent diodes and windows for high power infrared lasers. Knowledge of the high temperature defect structure is important for predicting the properties of materials made under different preparative conditions. A considerable amount of work has been devoted to the determination of the position of energy levels of various defects in the forbidden gap. Some levels are unambiguously assigned to certain foreign defects, while others are attributed to native defects, the exact nature of which (vacancies or interstitials, state of ionization) is not known. So far efforts to reach an understanding of the defect structure of ZnSe have been limited. High temperature Hall effect and conductivity measurements (1, 2) and self-diffusion measurements (3) were interpreted differently and no single model has emerged on the basis of which all the observations on ZnSe can be explained. In this investigation we attempt to determine the defect structure of ZnSe by high temperature measurements of the Hall effect and zinc tracer self-diffusion for Al- and As-doped ZnSe crystals. Measurements of the electron concentration at room temperature on ZnSe crystals quenched from high temperature after equilibration with atmospheres with well-defined zinc pressures provide information on the processes taking place during cooling.

Al substituting for Zn acts as a single donor with a level close to the conduction band. Solubilities of 2×10^{19} cm^{-3} (4) and 1.5×10^{20} cm^{-3} (5), reached by in-diffusion, have been reported. In the latter case the samples are degenerate. Implantation also gives rise to large Al concentrations (6). Often the electron concentration is a small fraction (10%) of the Al concentration as a result of self-compensation with formation of $(Al_{Zn}V_{Zn})'$ (4, 7). The largest electron concentrations are found after annealing in zinc vapor (8, 9). As substituting for Se acts as a single acceptor (10, 11) with an As_{Se}' acceptor level at $E_v + 0.5$ eV (12). Another level caused by As is found at $E_v + 0.22$ eV; the nature of the center responsible for this level is not known (12). As_{Se}' is believed to be involved in luminescence at 1.67 eV (11) and 2.328 eV (12). Whereas the latter fits the level at $E_v + 0.5$ eV, the former does not.

Samples and Experimental Procedures

Crystal boules of ZnSe grown from melts containing 3, 10, 30, or 300 ppm Al or 50 ppm As were obtained from the Eagle Picher Company. Plates of $10 \times 10 \times 1$ mm were cut from the boules for the electrical measurements and blocks of $10 \times 8 \times 1.5$ mm for the diffusion experiments. The samples are referred to as sample No. 1, 2, 3, 4 in sequence of Al content; ZnSe:As is sample No. 5. After cutting, the samples were etched for 5 min in a boiling aqueous solution of NaOH and were then rinsed with deionized water. Measurements of Hall effect and resistivity were performed at temperatures from 800° to 1000°C in an apparauts as described by Hershman and Kröger (13) which allowed establishment of well-defined zinc pressures. The van der Pauw method (14) was used with a magnetic field of 0.35 Weber/m² (= 3.5 kilogauss) and d-c currents ranging from 0.5 to 50 mA depending on the resistivity of the sample. Ohmic contacts were "written" on the etched crystal surface with the aid of an indium wire dipped in a (In, Hg) alloy; the crystals were then heated for 2-3 min to 300°C in a hydrogen atmosphere and then cooled to room temperature (15). Electron concentrations were calculated from $[e'] = (Rq)^{-1}$, R being the Hall constant and q the electronic charge.

For zinc tracer diffusion measurements, Zn^{65}, γ, 1.12 MeV tracer was obtained from the New England Nuclear Corporation in the form of $ZnCl_2$ in 0.5*N* HCl. The tracer was dissolved in normal zinc by the procedure described for Cd by Kumar and Kröger (16). After diffusion anneal, tracer penetration profiles were determined by the procedure reported by Kumar and Kröger (16).

Experimental Results

High temperature Hall measurements.—Figures 1, 2, 3, and 4 show the variation with p_{Zn} of high temperature resistivity and electron concentration of samples 1, 2, 3, and 4, respectively. For samples 1, 2, and 3, containing the lowest amounts of Al, the electron concentration and resistivity were independent of p_{Zn} at high zinc pressures. Under these conditions the electron concentration was also independent of temperature. Electron concentration was proportional to $p_{Zn}^{1/2}$ and resistivity to $p_{Zn}^{-1/2}$ at low zinc pressures. For

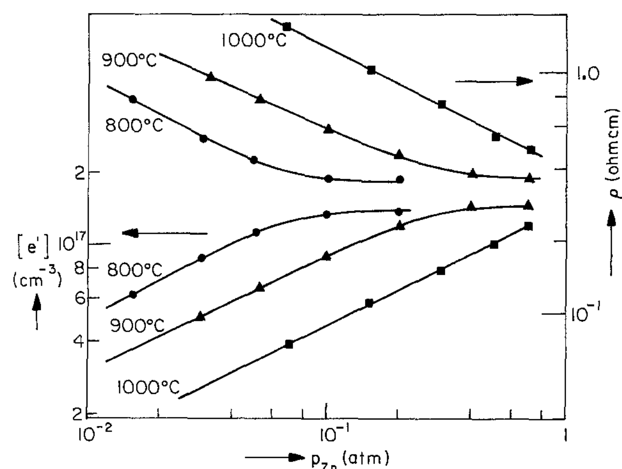

Fig. 1. Resistivity (ρ) and electron concentration of sample 1 as a function of p_{Zn} at 800°, 900°, and 1000°C.

* Electrochemical Society Active Member.
[1] Present address: IBM Thomas J. Watson Research Center, Yorktown Heights, New York 10598.

Key words: ZnSe:Al, ZnSe:As, Hall effect, self-diffusion.

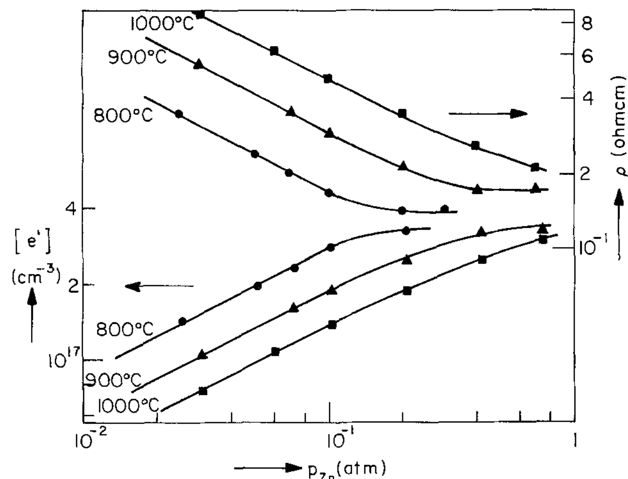

Fig. 2. Resistivity (ρ) and electron concentration of sample 2 as a function of p_{Zn} at 800°, 900°, and 1000°C.

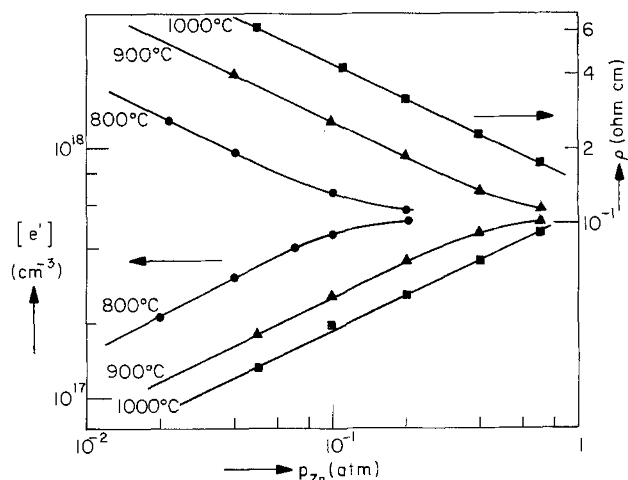

Fig. 3. Resistivity (ρ) and electron concentration of sample 3 as a function of p_{Zn} at 800°, 900°, and 1000°C.

sample 4, containing a large concentration of Al, electron concentration varied as $p_{Zn}^{1/2}$ and resistivity as $p_{Zn}^{-1/2}$ over the entire zinc pressure range investigated. In all ZnSe:Al samples electron concentration decreased and resistivity increased with increase in temperature. Electron concentration in the low p_{Zn} region was found to be proportional to the square root of Al added in the melts from which crystals were grown. The activation energy of electron concentration in this region was −0.5 eV.

Figure 5 shows the variation of high temperature resistivity and electron concentration of ZnSe:As (sample 5) as a function of p_{Zn}. At all temperatures the electron concentration is proportional to $p_{Zn}^{1/2}$ and resistivity to $p_{Zn}^{-1/2}$ in the zinc pressure range investigated. Different from what was found for ZnSe:Al, the electron concentration increased and resistivity decreased with increase in temperature. The activation energy of electron concentration was 0.9 eV. At a given temperature and p_{Zn} the electron concentration of the ZnSe:As sample was less than that of the ZnSe:Al samples. For all samples, the accuracy of the p_{Zn} exponents is ± 0.03.

Room temperature Hall measurements.—Figures 6 and 7 show room temperature electron concentrations of ZnSe:Al samples when quenched from 800° and 900°C, respectively. At high p_{Zn}, room temperature electron concentrations are the same as those at high temperature. At medium p_{Zn}, the electron concentration follows a $p_{Zn}^{1/2}$ law over a fairly wide zinc pressure range. For each sample there is a critical p_{Zn} at which there is a sharp cutoff of the electron concentration. Crystals quenched after equilibration at p_{Zn} lower than $p_{Zn,\,cutoff}$ have a high resistivity at room temperature.

ZnSe:As crystals always have a high resistivity at room temperature, independent of p_{Zn} and temperature at which they have been equilibrated.

Diffusion experiments.—Zinc tracer diffusion coefficients measured in ZnSe:Al crystals at 900°C and $p_{Zn} = 10^{-2}$ atm are shown in Fig. 8. D_{Zn}^* is seen to be proportional to [Al] for medium and high Al concentrations. Figure 9 shows D_{Zn}^* of samples 4 and 5 as a function of temperature at $p_{Zn} = 10^{-2}$ atm. The diffusion coefficients of Zn are represented by

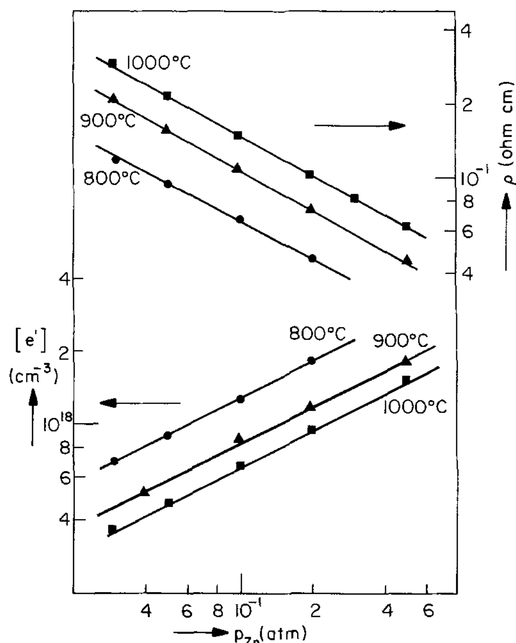

Fig. 4. Resistivity (ρ) and electron concentration of sample 4 as a function of p_{Zn} at 800°, 900°, and 1000°C.

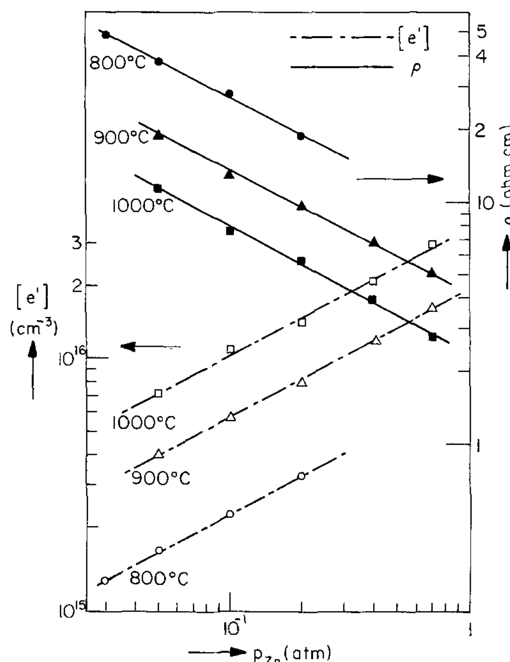

Fig. 5. Resistivity (ρ) and electron concentration of ZnSe:As as a function of p_{Zn} at 800°, 900°, and 1000°C.

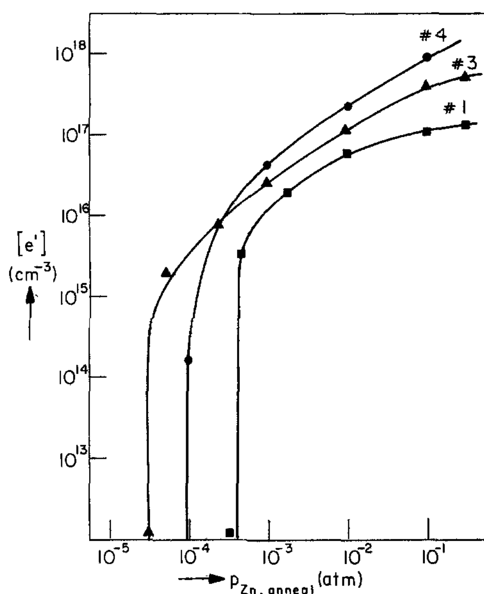

Fig. 6. Room temperature electron concentration in samples 1, 3, and 4 cooled after equilibration at 800°C.

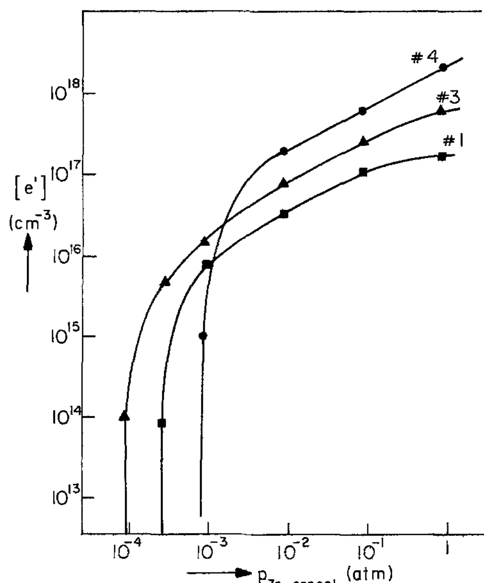

Fig. 7. Room temperature electron concentration in samples 1, 3, and 4 cooled after equilibration at 900°C.

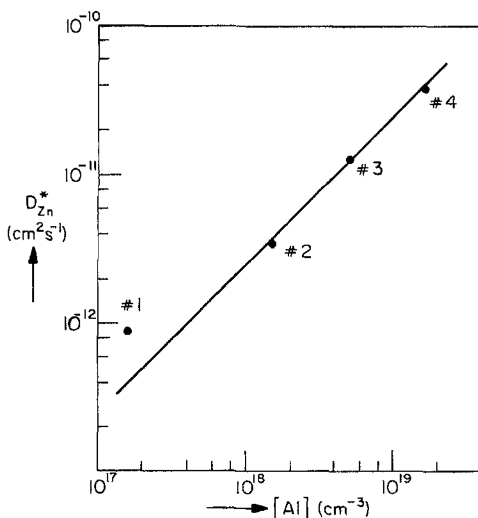

Fig. 8. Zinc tracer diffusion coefficients at 900° as a function of [Al] in the crystals. $p_{Zn} = 10^{-2}$ atm.

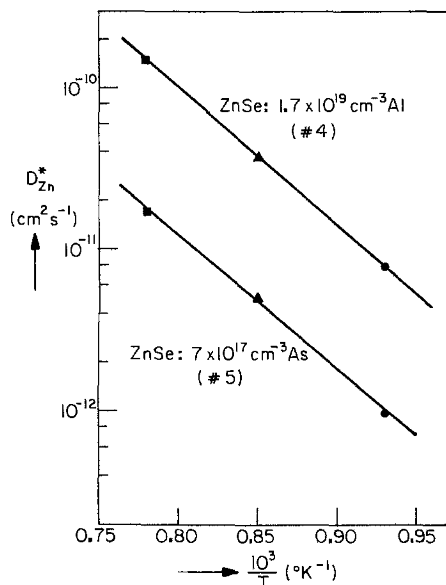

Fig. 9. Temperature dependence of zinc tracer diffusion coefficients for ZnS: 1.7 × 10^{19} cm^{-3} Al and ZnSe: 7 × 10^{17} cm^{-3} As.

$$(D_{Zn}^*)_{Al} = 8.4 \times 10^{-4} \exp - (1.70 \pm 0.05\ eV/kT)\ cm^2\ sec^{-1} \quad [1]$$

$$(D_{Zn}^*)_{As} = 5.0 \times 10^{-5} \exp - (1.65 \pm 0.05\ eV/kT)\ cm^2\ sec^{-1} \quad [2]$$

Discussion

High temperature Hall effect measurements.—ZnSe: Al.—All our observations on ZnSe:Al can be explained with the aid of defect chemistry, which consists of ionization and incorporation reactions and the corresponding mass action relations combined with the neutrality relation

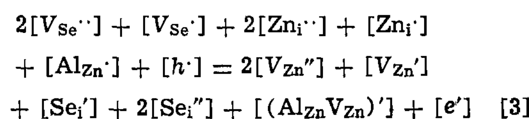

$$2[V_{Se}^{\cdot\cdot}] + [V_{Se}^{\cdot}] + 2[Zn_i^{\cdot\cdot}] + [Zn_i^{\cdot}] + [Al_{Zn}^{\cdot}] + [h^{\cdot}] = 2[V_{Zn}''] + [V_{Zn}'] + [Se_i'] + 2[Se_i''] + [(Al_{Zn}V_{Zn})'] + [e'] \quad [3]$$

and the aluminum balance relation

$$[Al]_{total} = [Al_{Zn}^{\times}] + [Al_{Zn}^{\cdot}] + [(Al_{Zn}V_{Zn})'] + [(Al_{Zn}V_{Zn})^{\times}] \quad [4]$$

The symbols used here follow the convention proposed by Kröger and Vink, on-line symbols indicating species (atoms or vacancies, V), subscripts indicating the site occupied by the species (an interstitial site being indicated by i), while superscripts dot (·), dash ('), and multiplication sign (×) indicate positive, negative, or zero effective charges with the electronic charge $|q|$ as the unit. Square brackets indicate concentrations in numbers per cubic centimeter.

When the neutrality and mass balance relations are approximated by their dominant members (17) the concentrations of all species can be expressed as $[Al]^m p_{Zn}^n$ where m and n can be integers or simple fractions. In principle 36 neutrality approximations can be made from Eq. [3]. Only 11 of those need to be considered as a possibility for ZnSe doped with Al. Schottky disorder will be assumed to be the dominant disorder process in ZnSe. The justification of this assumption is given later. Defect concentrations for various neutrality and Al balance approximations are shown in Table I. By comparing experimental results with the expressions in Table I, it is found that at low zinc pressures all Al-doped ZnSe crystals are in range 8 whereas at high zinc pressures samples 1, 2, and 3 are in range 10 but sample 4 is still in range 8. The

Table I. Defect concentrations as $\propto [Al]^m p_{Zn}^n$ for various approximations in the neutrality and mass balance relations

Range	Defects	m	n
1	$[V_{Zn}''] \approx [V_{Se}^{\cdot\cdot}]$	0	0
	$[Al_{Zn}^{\cdot}] \approx [Al]$	1	0
	$[e']$	0	1/2
	$[h^{\cdot}]$	0	−1/2
	$[V_{Zn}']$	0	−1/2
	$[V_{Se}^{\cdot}]$	0	1/2
2	$[V_{Se}^{\cdot}] \approx [e']$	0	1/2
	$[Al_{Zn}^{\cdot}] \approx [Al]$	1	0
	$[V_{Se}^{\cdot\cdot}]$	0	0
	$[V_{Zn}'']$	0	0
	$[h^{\cdot}]$	0	−1/2
	$[V_{Zn}']$	0	−1/2
3	$2[V_{Se}^{\cdot\cdot}] \approx [e']$	0	1/3
	$[Al_{Zn}^{\cdot}] \approx [Al]$	1	0
	$[h^{\cdot}]$	0	−1/3
	$[V_{Zn}'']$	0	−1/3
	$[V_{Zn}']$	0	−2/3
	$[V_{Se}^{\cdot}]$	0	2/3
4	$[V_{Zn}'] \approx [h^{\cdot}]$	0	−1/2
	$[Al_{Zn}^{\cdot}] \approx [Al]$	1	0
	$[e']$	0	1/2
	$[V_{Zn}'']$	0	0
	$[V_{Se}^{\cdot\cdot}]$	0	0
	$[V_{Se}^{\cdot}]$	0	1/2
5	$2[V_{Zn}''] \approx [h^{\cdot}]$	0	−1/3
	$[Al_{Zn}^{\cdot}] \approx [Al]$	1	0
	$[e']$	0	1/3
	$[V_{Se}^{\cdot\cdot}]$	0	1/3
	$[V_{Zn}']$	0	−2/3
	$[V_{Se}^{\cdot}]$	0	2/3
6	$[V_{Zn}'] \approx 2[V_{Se}^{\cdot\cdot}]$	0	−1/3
	$[Al_{Zn}^{\cdot}] \approx [Al]$	1	0
	$[V_{Zn}'']$	0	1/3
	$[e']$	0	2/3
	$[h^{\cdot}]$	0	−2/3
	$[V_{Se}^{\cdot}]$	0	1/3
7	$[V_{Se}^{\cdot}] \approx 2[V_{Zn}'']$	0	1/3
	$[Al_{Zn}^{\cdot}] \approx [Al]$	1	0
	$[e']$	0	2/3
	$[h^{\cdot}]$	0	−2/3
	$[V_{Se}^{\cdot\cdot}]$	0	−1/3
	$[V_{Zn}']$	0	−1/3
8	$[Al_{Zn}^{\cdot}] \approx 2[V_{Zn}''] \approx [Al]$	1	0
	$[e']$	1/2	1/2
	$[h^{\cdot}]$	−1/2	−1/2
	$[V_{Zn}']$	1/2	−1/2
	$[V_{Se}^{\cdot}]$	−1/2	1/2
	$[V_{Se}^{\cdot\cdot}]$	−1	0
9	$[Al_{Zn}^{\cdot}] \approx [(Al_{Zn}V_{Zn})'] \approx \frac{1}{2}[Al]$	1	0
	$[V_{Zn}'']$	0	0
	$[e']$	0	1/2
	$[h^{\cdot}]$	0	−1/2
	$[V_{Zn}']$	0	−1/2
	$[V_{Se}^{\cdot}]$	0	1/2
	$[V_{Se}^{\cdot\cdot}]$	0	0
10	$[Al_{Zn}^{\cdot}] \approx [e'] \approx [Al]$	1	0
	$[h^{\cdot}]$	−1	0
	$[V_{Zn}'']$	2	−1
	$[V_{Se}^{\cdot\cdot}]$	−2	1
	$[V_{Zn}']$	1	−1
	$[V_{Se}^{\cdot}]$	−1	1
11	$[Al_{Zn}^{\cdot}] \approx [V_{Zn}'] \approx [Al]$	1	0
	$[e']$	1	1
	$[h^{\cdot}]$	−1	−1
	$[V_{Se}^{\cdot}]$	−1	0
	$[V_{Zn}'']$	2	1
	$[V_{Se}^{\cdot\cdot}]$	−2	−1

neutrality conditions 1, 2, and 9 which would also give $[e'] \propto p_{Zn}^{1/2}$ are rejected because for them the electron concentrations are independent of Al concentration. Electron concentration at any p_{Zn} can be determined by considering the incorporation reaction

$$V_{Zn}'' + Zn(g) \rightleftarrows Zn_{Zn}^{\times} + 2e'; \; K_{ZnV} \quad [5]$$

$$[e'] = K_{ZnV}^{1/2} \, [V_{Zn}'']^{1/2} \, p_{Zn}^{1/2} \quad [6]$$

In range 8, the neutrality condition is

$$[Al_{Zn}^{\cdot}] = 2[V_{Zn}''] \quad \text{and} \quad [Al_{Zn}^{\cdot}] = [Al]_{total}$$

therefore

$$[e']_{Al,8} = 2^{-1/2} \, K_{ZnV}^{1/2} \, [Al]^{1/2} \, p_{Zn}^{1/2} \quad [7]$$

In range 10, the electron concentration is given by

$$[e'] = [Al]_{total} \quad [8]$$

The zinc pressure at which transfer from range 8 to range 10 takes place is found by equating the expressions for $[e']$ in the two regions

$$p_{Zn(8,10)} = \frac{2[Al]}{K_{ZnV}} \quad [9]$$

Therefore at a given temperature, transfer from range 8 to range 10 takes place at a value of p_{Zn} that is the higher, the higher the Al concentration. This explains why sample 4 was never in range 10. The Al concentration in ZnSe can be found from the electron concentration if the sample is in the range where $[Al_{Zn}^{\cdot}] = [e']$. In this manner sample 1 was found to contain 1.6×10^{17} Al cm^{-3}. Aluminum concentrations of samples 2, 3, and 4 were computed from the electron concentration in range 8 using [7] and were found to be 5.2×10^{17}, 1.5×10^{18}, and 1.7×10^{19} cm^{-3} Al, respectively. Comparison with the corresponding Al contents of the melt shows that the distribution constant $k_{Al} = [Al]_{ZnSe}/[Al]_l = 0.44 \pm 0.03$. Spectrographic analysis of sample 4 gave an Al concentration of 1.44×10^{19} cm^{-3} close to the value mentioned above, thus supporting the assumptions underlying the estimate. The Al concentrations of other samples were below the detection limit of the spectrographical analysis. The constant K_{ZnV} in [7] as $f(T)$ was determined from the temperature dependence of the electron concentration of a ZnSe:Al sample at a particular p_{Zn}. It can be represented by

$$K_{ZnV} = 4.65 \times 10^{13} \exp{(1.0 \text{ eV}/kT)} \text{ atm}^{-1} \text{ cm}^{-3} \quad [10]$$

ZnSe:As.—Sample 5 showed $[e'] \propto p_{Zn}^{1/2}$ in the entire zinc pressure range investigated. It is *a priori* uncertain whether this sample is acceptor dominated or shows intrinsic behavior because of compensation Let us first consider the last possibility. In this case the defect structure of the sample in the zinc pressure range investigated would correspond to range 1 or 2 of Table I. If the sample would be in range 1, then $[e']$ is given by

$$[e'] = K_{ZnV}^{1/2} \, K_S''^{1/4} \, p_{Zn}^{1/2} \quad [11]$$

Here K_S'' is the equilibrium constant of Schottky disorder

$$O \rightleftarrows V_{Zn}'' + V_S''; \quad K_S'' = [V_{Zn}''][V_S^{\cdot\cdot}] \quad [12]$$

The measured activation energy for the electron concentration in sample 5 was 0.9 eV. With $K_{ZnV} = K_{ZnV^{\circ}} \exp{(-H_{ZnV}/kT)}$ and $K_S'' = K_S^{\circ} \exp{(-H_S''/kT)}$ then according to Eq. [11], $\frac{1}{2} H_{ZnV} + \frac{1}{4} H_S'' = 0.9$ eV. Or, with $H_{ZnV} = -1.0$ eV, $H_S'' = 5.6$ eV. As we shall see, such a high value of H_S'' is unacceptable.

If the defect structure of sample 5 would correspond to range 2, then the room temperature electron concentration of crystals quenched to room temperature after annealing at high temperature with different p_{Zn} should be almost equal to that at high temperature because the $V_{Se}^{\times}$ level is only 0.008-0.02 eV below the conduction band (18-20). This was not observed for sample 5: It had almost no free carriers after cooling. Therefore, it must be concluded that the sample is acceptor dominated, As being the acceptor.

Our experimental results indicate that As is not incorporated according to $[As_{Se}'] = [V_{Se}^{\cdot}]$, because in that case $[e']$ would be proportional to p_{Zn}. On the other hand, incorporation of As as $[As]_{total} = [As_{Se}'] = 2[V_{Se}^{\cdot\cdot}]$ leads to the observed dependence $[e'] \propto p_{Zn}^{1/2}$. Substituting $[V_{Zn}'']$ in Eq. [6] by $[V_{Zn}''] = K_S''/[V_{Se}^{\cdot\cdot}] = 2K_S''/[As_{Se}']$, we get

$$[e']_{As} = 2^{1/2} \, K_{ZnV}^{1/2} \, K_S''^{1/2} \, [As_{Se}']^{-1/2} \, p_{Zn}^{1/2} \quad [13]$$

Hence $\frac{1}{2} H_{ZnV} + \frac{1}{2} H_S'' = 0.9$ eV, the observed activation energy. We found earlier $H_{ZnV} = -1.0$ eV; therefore, $H_S'' = 2.8$ eV, an acceptable value.

If $[As_{Se}']$ would be known, it would also be possible to determine $K_S^{\circ\prime\prime}$. Unfortunately the As content of the sample was below the detection limit by spectro-

graphic analysis. It is possible, however, to estimate the As concentration indirectly by comparing our results with those obtained by Smith (1). This author measured the high temperature electron concentration in ZnSe crystals containing 10^{17} to 3×10^{18} cm^{-3} electrically active impurities and found an activation energy of 0.8 ± 0.1 eV, almost the same as that found by us for sample 5. He also found that crystals quenched after a high temperature anneal had a high resistivity, again similar to what we found for sample 5. This suggests that Smith's sample was not undoped (as believed by him) but acceptor dominated with an acceptor concentration $\approx 10^{18}$ cm^{-3}. The electron concentrations found by us were two times larger than those of Smith's sample, indicating a four times smaller acceptor concentration in our sample. We shall assume sample 5 to contain 7×10^{17} cm^{-3} As. Since the melt from which the crystal was grown contained 50 ppm or 2.2×10^{18} cm^{-3} As, this corresponds to $k_{As} = [As]/[As]_l = 0.32$. We can now compute $K_S''^{\circ}$. Rather than do this using Eq. [13] which tends to add the errors in $[e']$ and K_{ZnV}, we calculate K_S'' from

$$K_S'' = \frac{[Al_{Zn}^{\cdot}]\,[As_{Se}']}{4[e']_{Al}^2/[e']_{As}^2} \qquad [14]$$

an expression obtained by combining [7] and [13]. Here $[e']_{Al}$ and $[e']_{As}$ are values of the electron concentration in Al- and As-doped samples at the same temperature and zinc pressure. $[e']_{Al}/[e']_{As}$ values for each ZnSe:Al crystal at one temperature were computed at different zinc pressures. The average value was used in the calculation of K_S''. Each ZnSe:Al sample yields values of K_S'' at various temperatures. In Fig. 10 values of $K_S''^{1/2}$ obtained in this manner are plotted against $1/T$. K_S'' is found to obey the relation

$$K_S'' = 4.84 \times 10^{44} \exp\{-(2.9 \pm 0.1)\ \text{eV}/kT\}\ \text{cm}^{-6}$$

$$= 1 \times \exp\{-(2.9 \pm 0.1)\ \text{eV}/kT\}\ \text{site}\ fr^2 \qquad [15]$$

Electron concentrations at room temperature.—ZnSe:Al.—At high temperatures electrons are minority species compared to atomic defects. It will be assumed that during cooling from the annealing temperature to room temperature, atomic defects are frozen in, but that electron and hole equilibria are maintained, excess of electrons over holes remaining free or changing the charge of atomic defects. At high p_{Zn}, room temperature electron concentrations are the same

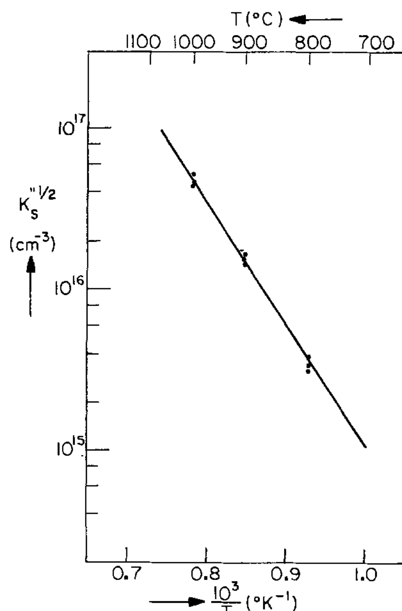

Fig. 10. Temperature dependence of $K_S''^{1/2}$

as those at high temperatures. This indicates that $Al_{Zn}^{\times}$ is a shallow donor, consistent with the observation of Aven and Segall (19) who found $E_d \approx 0$. It also shows that precipitation of donors does not occur. The cutoff in electron concentration at low p_{Zn} can be due to recombination with holes or to trapping of electrons at V_{Zn}' or some transition metal impurity which gives rise to a deep acceptor level inside the bandgap.

If the cutoff in electron concentration is caused by recombination with holes, the p_{Zn} at which this takes place is given by the condition $[e'] = [h^{\cdot}] = K_i^{1/2}$ at high temperature, K_i being the equilibrium constant of intrinsic electronic disorder. Using Eq. [7] this zinc pressure is given by

$$p_{Zn([e']=[h^{\cdot}])} = 2K_i/(K_{ZnV}[Al]) \qquad [16]$$

Thus the zinc pressure at which the cutoff in electron concentration takes place should vary inversely with [Al]. If at high temperature $[V_{Zn}'] > [e']$, electrons would be trapped by V_{Zn}' centers at room temperature, transforming these centers to V_{Zn}'' centers. The zinc pressure at which the cutoff in electron concentration takes place is given by the condition $[V_{Zn}'] = [e']$ at high temperature. Using

$$V_{Zn}'' \rightleftarrows V_{Zn}' + e'; \quad \frac{[V_{Zn}']\,[e']}{[V_{Zn}'']} = K_{a2}' \qquad [17]$$

we find

$$p_{Zn,\text{cutoff}} = K_{a2}'/K_{ZnV} \qquad [18]$$

i.e., the cutoff should be a material constant, independent of [Al]. As seen in Fig. 6 and 7, $p_{Zn,\text{cutoff}}$ follows neither relation [16] nor [18]. Apparently the third possibility, trapping at transition metal impurities has to be invoked. In samples with small Al concentration, $[V_{Zn}']$ may be lower than the transition metal impurity concentration and the cutoff in electron concentration takes place by trapping of electrons at the impurities. Only in the sample with the highest Al concentration the cutoff may be caused by trapping of electrons at V_{Zn}'. Since K_{ZnV} is known, the temperature dependence of $p_{Zn,\text{cutoff}}$ for this sample gives us K_{a2}' as $f(T)$. Interpreting the results in terms of

$$K_{a2}' = 4(2\pi m_e^* kT/h^2)^{3/2} \exp(-E_{a2}'\ \text{eV}/kT)\ \text{cm}^{-3} \qquad [19]$$

with $m_e^* = 0.1m$ (21) gives $E_{a2}' = 1.1$ eV, *i.e.*, the V_{Zn}'' level is 1.1 eV below the conduction band. Calculation of the ratio $[V_{Zn}']/[e']$ at $p_{Zn,\text{cutoff}}$ for sample 4 from $[V_{Zn}']/[e'] = K_{a2}'/(K_{ZnV}\,p_{Zn})$ gives values in the range 0.63-0.66 (*i.e.*, close to 1), thus indicating the validity of our model. In this sample 4, the cutoff in electron concentration does not take place due to recombination with holes because the calculated electron concentration for sample 4 at 900°C and $p_{Zn,\text{cutoff}}$ is 7.8×10^{16} cm^{-3}. Equating this with $K_i^{1/2}$ would make $K_i^{1/2}$ greater than $K_S''^{1/2}$ which is inconsistent with the experimental results.

ZnSe:As.—Arsenic-doped ZnSe crystals, when quenched from high temperature, had a high resistivity at room temperature which was independent of p_{Zn} and the equilibration temperature from which the crystals were quenched. Smith (1) also found that the electron concentration dropped from 10^{16} cm^{-3} at 1000°C to 10^{10} cm^{-3} or less at room temperature. This is due to the fact that at high temperature $[e'] \ll [V_{Se}^{\cdot\cdot}]$: During quenching electrons are trapped at some $V_{Se}^{\cdot\cdot}$ centers. If the $V_{Se}^{\cdot}$ level is fairly deep the electron concentration at room temperature would be very low. We can estimate the $V_{Se}^{\cdot}$ level position from Smith's results. Let us assume the acceptor concentration of Smith's sample was 3×10^{18} cm^{-3}, *i.e.*, $[V_{Se}^{\cdot\cdot}] = 1.5 \times 10^{18}$ cm^{-3}

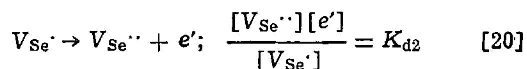

$$V_{Se}^{\cdot} \rightarrow V_{Se}^{\cdot\cdot} + e'; \quad \frac{[V_{Se}^{\cdot\cdot}][e']}{[V_{Se}^{\cdot}]} = K_{d2} \qquad [20]$$

$$[V_{Se}^{\cdot}]_{1000^\circ C} = \frac{[V_{Se}^{\cdot\cdot}]_{1000^\circ C}[e']_{1000^\circ C}}{(K_{d2})_{1000^\circ C}} = \frac{1.5 \times 10^{18} \times 10^{16}}{(K_{d2})_{1000^\circ C}} \quad [21]$$

$$[V_{Se}^{\cdot}]_{27^\circ C} = \frac{[V_{Se}^{\cdot\cdot}]_{27^\circ C}[e']_{27^\circ C}}{(K_{d2})_{27^\circ C}}$$

With

$$[V_{Se}^{\cdot\cdot}]_{27^\circ C} = [V_{Se}^{\cdot\cdot}]_{1000^\circ C} - [e']_{1000^\circ C} = 1.5 \times 10^{18}\ \text{cm}^{-3}$$

and

$$[e']_{27^\circ C} = 10^{10}\ \text{cm}^{-3}$$

$$[V_{Se}^{\cdot}]_{27^\circ C} = \frac{1.5 \times 10^{28}}{(K_{d2})_{27^\circ C}} \quad [22]$$

But also

$$[V_{Se}^{\cdot}]_{27^\circ C} = [V_{Se}^{\cdot}]_{1000^\circ C} + [e']_{1000^\circ C} = [V_{Se}^{\cdot}]_{1000^\circ C} + 10^{16} \ldots \quad [23]$$

Combining Eq. [21]-[23] we get

$$\frac{1.5 \times 10^{28}}{(K_{d2})_{27^\circ C}} = \frac{1.5 \times 10^{34}}{(K_{d2})_{1000^\circ C}} + 10^{16} \quad [24]$$

Analytical solution of [24] with $K_{d2} = (2\pi m_e^* kT/h^2)^{3/2} \exp(-E_{d2}/kT)$ and $m_e^* = 0.1m$ (21) gives $E_{d2} = 0.4$ eV.

The major type of atomic disorder.—At this point it is necessary to justify the arbitrary choice of Schottky over Frenkel disorder as the main disorder mechanism.

H_S'', the enthalpy of Schottky disorder with formation of doubly charged defects, is related to the corresponding enthalpy for formation of neutral defects, $H_S^{\times}$, through (22)

$$H_S^{\times} = H_S'' + 2E_i - E_d - E_{d2} - E_a - E_{a2} \quad [25]$$

E_i being the width of the bandgap, E_d and E_{d2} the first and second ionization energy of $V_{Se}^{\times}$, and E_a and E_{a2} the first and second ionization energy of $V_{Zn}^{\times}$. E_d is of the order of 0.01 eV (18-20). Values reported for E_{d2} vary widely (23, 24); we shall use $E_{d2} = 0.4$ eV as found in the previous section. Values reported for E_a vary from 0.5 to 0.75 eV (18, 24). We shall use $E_a = 0.65$ eV and for E_{a2} we shall take $E_{a2} = E_i - E_{a2}' = 2.7$ (25) $- 1.1 = 1.6$ eV (with E_{a2}' as determined in the previous section. Then $H_S^{\times} = 2.9 + 2 \times 2.7 - 2.66 \approx 5.6$ eV. Van Vechten (26) calculated $H_S^{\times} = 6.18$ eV. According to this author his values are $\approx 12\%$ too high, giving 5.4 eV as the corrected value. A second estimate for $H_S^{\times}$ is obtained from $H_S^{\times} \leqq H_{atom}$, H_{atom} being the enthalpy of atomization of ZnSe (27). Combining H_{ZnSe}, the heat of sublimation of ZnSe with formation of Zn(g) and Se_2(g) (28), with H_D, the heat of dissociation of Se_2(g) (29) we find

$$H_{atom} = H_{ZnSe} + \tfrac{1}{2} H_D = 3.75 + 1.71 = 5.46\ \text{eV}$$

Thus the observed $H_S^{\times}$ is larger than, but close to, both estimates of H_{atom}. If Frenkel disorder would be the dominant type of atomic disorder, with $H_F'' < H_S''$, our results, interpreted on the basis of this disorder, would give $H_F^{\times} = 5.6$ eV with $H_S^{\times} > 5.6$ eV, making the discrepancy with the estimated $H_S^{\times}$ even larger. Therefore, it may be concluded that Schottky disorder is the major type of atomic disorder, the small discrepancy between $H_S^{\times}$ and H_{atom} probably being caused by errors in the energy level positions used in Eq. [25].

Diffusion.—In general, tracer diffusion of zinc is the sum of contributions by the zinc defects V_{Zn} and Zn_i in various states of ionization. Under the conditions of our experiments, *i.e.*, $p_{Zn} = 10^{-2}$ atm, our electrical measurements show that $[V_{Zn}''] >> [V_{Zn}']$ and $[V_{Zn}^{\times}]$ in ZnSe:Al and $[Zn_i^{\cdot\cdot}] >> [Zn_i^{\cdot}]$ and $[Zn_i^{\times}]$ in ZnSe:As. On the other hand, the linear relation between D_{Zn}^* as f[Al] shown in Fig. 8 indicates that only one species is involved: $[V_{Zn}''] >> [Zn_i^{\cdot\cdot}]$ and

$$(D_{Zn}^*)_{Al} = f_V D_V [V_{Zn}''] = f_V D_V [Al_{Zn}^{\cdot}]/2 \quad [26]$$

f_V being the correlation constant and D_V the diffusion constant of V_{Zn}''. For ZnSe:As where $[As_{Se}'] \approx 2[V_{Se}^{\cdot\cdot}]$

$$(D_{Zn}^*)_{As} = f_i D_i [Zn_i^{\cdot\cdot}] + f_V D_V [V_{Zn}''] \quad [27]$$

f_i being the correlation constant and D_i the diffusion constant of $Zn_i^{\cdot\cdot}$. But $[V_{Zn}'']_{As} = r[V_{Zn}'']_{Al}$ with $r = 4K_S''/[Al_{Zn}^{\cdot}]\ [As_{Se}']$ and thus

$$(D_{Zn}^*)_{As} = f_i D_i [Zn_i^{\cdot\cdot}] + r(D_{Zn}^*)_{Al} \quad [28]$$

As seen from [14], $r = ([e'']_{As}/[e']_{Al})^2$; its value was determined earlier. With this value and the value of $(D_{Zn}^*)_{Al}$ we find that the second term in [28] is equal to 1.5×10^{-15} cm^2 sec^{-1} $<< (D_{Zn}^*)_{As} = 5 \times 10^{-12}$ cm^2 sec^{-1}. Thus

$$(D_{Zn}^*)_{As} \approx f_i D_i [Zn_i^{\cdot\cdot}] = f_i D_i (K_F''/K_S'')[As_{Se}']/2 \quad [29]$$

Since both $[Al_{Zn}^{\cdot}] \approx [Al]_{total}$ and $[As_{Se}'] \approx [As]_{total}$ are known, Eq. [26] and [29] combined with [1] and [2] give

$$f_V D_V = 2.17 \exp - \{1.70 \pm 0.05\}\ \text{eV}/kT\ \text{cm}^2\ \text{sec}^{-1} \quad [30]$$

$$f_i D_i K_F''/K_S'' = 3.14 \exp\{-1.65 \pm 0.05)\}\ \text{eV}/kT\ \text{cm}^2\ \text{sec}^{-1} \quad [31]$$

Since the two enthalpies are approximately equal

$$H_V = H_i + H_F'' - H_S'' = 1.65\ \text{eV} \quad [32]$$

where H_V and H_i are the enthalpy of migration of V_{Zn}'' and $Zn_i^{\cdot\cdot}$. Since $H_F'' > H_S''$ (required to make Frenkel disorder less important than Schottky disorder) $H_V > H_i$. D_{Zn}^* of undoped ZnSe measured at a p_{Zn} such that $[V_{Zn}''] = [V_{Se}^{\cdot\cdot}] = K_S''^{1/2}$ is given by

$$D_{Zn}^* = f_V D_V [V_{Zn}''] + f_i D_i [Zn_i^{\cdot\cdot}] = \left(f_V D_V + \frac{f_i D_i K_F''}{K_S''}\right) K_S''^{1/2} \quad [33]$$

Taking the activation energies for D_V and $D_i K_F''/K_S''$ to be equal at 1.65 ± 0.05 eV, leaving preexponentials unchanged

$$D_{Zn}^* = 5.3 \exp\{-(3.1 \pm 0.1\ \text{eV}/kT\}\ \text{cm}^2\ \text{sec}^{-1} \quad [34]$$

This is almost exactly the expression

$$D_{Zn}^* = 9.8 \exp\{-3.0\ \text{eV}/kT\}\ \text{cm}^2\ \text{sec}^{-1} \quad [35]$$

found by Henneberg and Stevenson (3) for crystals containing 2.9-10 $\times 10^{16}$ cm^{-3} Al and 1-25 $\times 10^{16}$ cm^{-3} Cu. Apparently these crystals were exactly compensated.

Defect isotherms for ZnSe, ZnSe:Al, and ZnSe:As.—Expressions for the various equilibrium constants are summarized in Table II. Values calculated at 800°, 900°, and 1000°C are given in Table III. Approximate defect

Table II. Expressions for various defect constants

$K_S'' = [V_{Zn}''][V_{Se}^{\cdot\cdot}] = 4.84 \times 10^{44} \exp\{-(2.9 \pm 0.1)\ \text{eV}/kT\}\ \text{cm}^{-6}$

$K_{ZnV} = [e']^2/([V_{Zn}'']p_{Zn}) = 4.65 \times 10^{13} \exp 1.0\ \text{eV}/kT\ \text{atm}^{-1}\ \text{cm}^{-3}$

$K_{d2} = [e'][V_{Se}^{\cdot\cdot}]/[V_{Se}^{\cdot}] = 2.42 \times 10^{15}\ (m_e^*/m)^{3/2} T^{3/2} \exp(-0.4\ \text{eV}/kT)\ \text{cm}^{-3}$

$K_{a2}' = [e'][V_{Zn}']/[V_{Zn}''] = 9.7 \times 10^{15}\ (m_e^*/m)^{3/2} T^{3/2} \exp(-1.1\ \text{eV}/kT)\ \text{cm}^{-3}$

$K_i = [e'][h^{\cdot}] = 1 \times 10^{35} \left(\frac{m_e^* m_h^*}{m^2}\right)^{3/2} T^3 \exp(-2.8\ \text{eV}/kT)\ \text{cm}^{-6}$

$m_e^* = 0.1m$ (21)

$m_h^* = 0.6m$ (21)

$E_i = (2.8\text{-}7.2 \times 10^{-4}T)$ eV (25)

$K_P = 5.45 \times 10^{-22} \exp(\leqq 0.45\ \text{eV}/kT)$

Table III. Values of various constants at 800°, 900°, and 1000°C

Temp (°C)	K_{ZnV} (atm^{-1} cm^{-3})	K_{d2} (cm^{-3})	K_{a2}' (cm^{-3})	$K_S''^{1/2}$ (cm^{-3})	$K_i^{1/2}$ (cm^{-3})
800	2.3×10^{18}	3.65×10^{16}	7.3×10^{13}	3.3×10^{15}	3.6×10^{14}
900	9.2×10^{17}	5.97×10^{16}	2.3×10^{14}	1.3×10^{16}	1.5×10^{15}
1000	4.25×10^{17}	9.0×10^{16}	6.1×10^{14}	4.0×10^{16}	5.0×10^{15}

isotherms for ZnSe, ZnSe: 1.6×10^{17} cm^{-3} Al and ZnSe: 7×10^{17} cm^{-3} As at 800°C are shown in Fig. 11, 12, and 13. The fact that both the electrical measurements and the diffusion measurements do not indicate the presence of pairs $(Al_{Zn}V_{Zn})'$ at $[Al] = 1.7 \times 10^{19}$ cm^{-3} at 800°C indicates that $[(Al_{Zn}V_{Zn})'] = K_P[Al_{Zn}^{\cdot}]$ $[V_{Zn}''] < 10^{19}$ cm^{-3} or the pairing constant $K_P < 6.92 \times 10^{-20}$ cm^3. If H_P is the enthalpy of pairing, $K_P = K_P^{\circ} \exp(H_P/kT)$ with $K_P^{\circ} = Z/N = 12/2.2 \times 10^{22}$ $cm^{-3} = 5.45 \times 10^{-22}$ cm^3. Here Z is the number of nearest neighbor metal sites and N is the number of molecules ZnSe per cubic centimeter. Then $-H_P \leq 0.45$ eV. With the relative dielectric constant $\epsilon_r = 8.1$ (21) and $r_{Al\text{-}V} = r_{Zn\text{-}Zn} = 8.01$Å, $(H_P)_{coulomb} = -2q^2/4\pi\epsilon_r r_{Al\text{-}V} = -0.44$ eV. Thus practically no pairs will be formed at high temperature; pairs at room temperature must have largely been formed during cooling (4, 7). On the basis of Fig. 11, the expected room temperature electron concentration for undoped ZnSe equilibrated at 800°C with molten zinc is $\approx 10^{16}$ cm^{-3}. Values reported for undoped ZnSe after the so-called zinc extraction process (to remove impurities such as copper) are indeed in the range $0.6\text{-}2 \times 10^{16}$ cm^{-3} (19, 21).

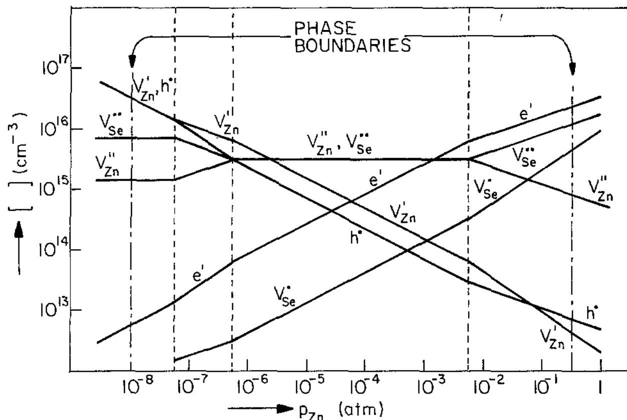

Fig. 11. Defect isotherms for undoped ZnSe at 800°C

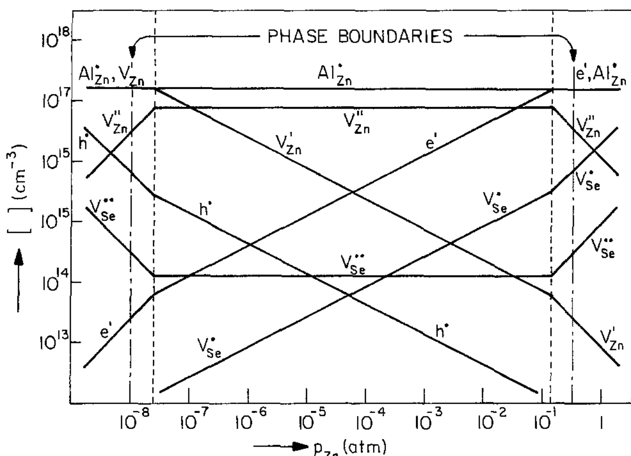

Fig. 12. Defect isotherms for ZnSe: 1.6×10^{17} cm^{-3} Al at 800°C

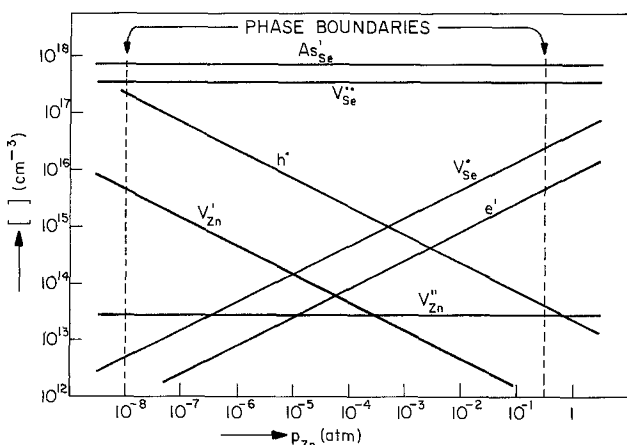

Fig. 13. Defect isotherms for ZnSe: 7×10^{17} cm^{-3} As at 800°C

Figure 11 also indicates that it should be possible to make undoped ZnSe p-type by annealing in a Se_2 atmosphere. It would, however, be a poor hole conductor, the V_{Zn}' level being far from the valence band. Similarly with the help of Fig. 12 we can explain that at high p_{Zn} the room temperature electron concentration must be the same as that at high temperature, but at p_{Zn} below $p_{Zn,cutoff}$ (*i.e.*, where $[V_{Zn}'] = [e']$ at high temperature) ZnSe:Al will have a high resistivity at room temperature. ZnSe:As will have a high resistivity at room temperature at all p_{Zn} because $V_{Se}^{\cdot}$, $As_{Se}^{\times}$, and V_{Zn}' levels are all deep, even though there is a transition from n to p type at the relatively large p_{Zn} where $[e'] = [h^{\cdot}]$ at high temperature.

Summary

Measurements of the Hall effect, resistivity, and zinc self-diffusion of crystals of ZnSe doped with Al or As at high temperatures, where the crystals are in equilibrium with zinc vapor, and of the Hall effect of crystals cooled after equilibration are used to determine the defect structure of pure and doped ZnSe. Schottky disorder with doubly charged defects dominates the defect structure of undoped ZnSe at medium zinc pressures. Table II gives parameters of various equilibrium constants determined in the analyses, with the aid of which properties of crystals equilibrated under various conditions can be predicted.

Acknowledgment

This work was supported by the United States Defense Advanced Research Projects Agency under Contract No. F 19628-75-C-0080 and by the Joint Services Electronics Program through the Air Force Office of Scientific Research (AFSC) under Contract No. F 44620-76-C-0061.

Manuscript submitted Oct. 31, 1977; revised manuscript received March 20, 1978.

Any discussion of this paper will appear in a Discussion Section to be published in the June 1979 JOURNAL. All discussions for the June 1979 Discussion Section should be submitted by Feb. 1, 1979.

REFERENCES

1. F. T. J. Smith, *Solid State Commun.*, **7**, 1757 (1969).
2. T. Nirk, M. Noges, and J. Varvas, *Phys. Status Solidi A*, **10**, K27 (1972).
3. M. M. Henneberg and D. A. Stevenson, *Phys. Status Solidi B*, **48**, 255 (1971).
4. M. Aven and R. E. Halsted, *Phys. Rev.*, **137**, A228 (1965).
5. M. Aven and B. Segall, *ibid.*, **130**, 81 (1963).
6. B. K. Shin, Y. S. Park, and D. C. Look, *Appl. Phys. Lett.*, **24**, 435 (1974).
7. M. Aven and J. Z. Devine, *J. Lumin.*, **7**, 195 (1973).
8. Y. Fukuda and M. Fukai, *J. Phys. Soc. Jpn.*, **23**, 602 (1967).
9. B. V. Dutt, O. K. Kim, and W. G. Spitzer, *J. Appl. Phys.*, **48**, 2110 (1977).
10. R. K. Watts, W. C. Holton, and M. de Wit, *Phys. Rev. B*, **3**, 404 (1971).

11. A. R. Reinberg, W. C. Holton, M. de Wit, and R. K. Watts, *ibid.*, 3, 410 (1973).
12. D. Etienne and G. Bougnot, *Mater. Res. Bull.*, **10**, 1365 (1975).
13. G. H. Hershman and F. A. Kröger, *J. Solid State Chem.*, 2, 483 (1970).
14. L. J. Vander Pauw, *Philips Tech. Rev.*, **20**, 220 (1959).
15. M. Aven, Private communication.
16. V. Kumar and F. A. Kröger, *J. Solid State Chem.*, **3**, 387 (1971).
17. G. Brouwer, *Philips Res. Rep.*, **9**, 366 (1954).
18. G. B. Stringfellow and R. H. Bube, *Phys. Rev.*, **171**, 903 (1968).
19. M. Aven and B. Segall, *ibid.*, **130**, 81 (1963).
20. G. Jones and J. Woods, *J. Phys. D*, **9**, 799 (1976).
21. M. Aven, R. E. Marple, and B. Segall, *J. Appl. Phys.*, **32**, 2261 (1961).
22. F. A. Kröger, "The Chemistry of Imperfect Crystals," Vol. 2, p. 240, North Holland Publishing Co., Amsterdam, Oxford (1974).
23. A. M. Gurwitsch, *Isv. Akad. Nauk. SSSR*, **40**, 1904 (1976).
24. P. W. Yu and Y. S. Park, *Appl. Phys. Lett.*, **27**, 74 (1975).
25. R. H. Bube, *Phys. Rev.*, **98**, 431 (1955).
26. J. A. Van Vechten, *This Journal*, **122**, 419 (1975).
27. F. A. Kröger, "The Chemistry of Imperfect Crystals," Vol. 2, p. 292, North Holland Publishing Co., Amsterdam, Oxford (1974).
28. W. J. Wosten and M. G. Geers, *J. Phys. Chem.*, **66**, 1252 (1962).
29. K. P. Haber, in American Institute of Physics Handbook, 3rd ed., p. 7-181, McGraw Hill Book Co., New York (1972).

The Defect Structure of ZnSe:Ga

A. K. Ray*,[1] and F. A. Kröger*

Department of Materials Science, University of Southern California, Los Angeles, California 90007

ABSTRACT

Hall effect and resistivity measurements on single crystal samples of ZnSe doped with various amounts of gallium were performed both at high temperature while the crystals were in equilibrium with atmospheres of known zinc pressures and after cooling to room temperature. At high temperatures, gallium present at a low concentration behaves as aluminum and acts as a single donor. At high concentrations and high zinc pressures, the donor efficiency is strongly reduced. This reduction is attributed to the precipitation of a fraction of the gallium as GaSe. Cooled crystals with low Ga concentrations show a similar behavior, the only difference being a sharp reduction in electron concentration at low p_{Zn} when $[V_{Zn}'] \gtrsim [e']$. At high Ga concentrations and high zinc pressures, black precipitates are formed near the surface during cooling. In addition, changes take place in the ZnSe phase which strongly reduce the electron concentration. These changes are believed to consist of the transfer of Ga from Zn to Se sites with formation of centers acting as multiple acceptors and electron traps.

Trivalent metal atoms substituting for zinc in ZnSe are expected to act as donors. Such a behavior was actually found for Al: at high zinc pressures free electrons are formed with $[e'] \approx [Al_{Zn}^{\cdot}]$, at low zinc pressures self-compensation occurs, with $2[V_{Zn}''] \approx [Al_{Zn}^{\cdot}]$ (1-4). A different behavior was reported for Ga, In, and Tl: Samples doped with Ga were found to contain fewer free electrons than undoped samples prepared under the same conditions (5). Ga_{Zn}, In_{Zn}, and Tl_{Zn} are believed to be deep donors as opposed to Al_{Zn} which is a shallow donor (6). ZnSe: 5×10^{19} Ga/cm^3 grown from (Ga(l) had $\rho = 250 \pm 50$ Ω cm and was thus heavily compensated (7). With increasing concentration of Ga or In, electronic conductivity decreases and the Fermi level drops to $E_c - 0.2$ eV (8). Heating of Ga-doped crystals in zinc vapor leads to the formation of black precipitates (8). N-type conductivity with 2×10^{16} to 5×10^{17} electrons/cm^3 was found for ZnSe equilibrated with dilute (Zn, Ga) alloys (9). P-type conductivity was found in the surface of an iodine donor-doped crystal after in-diffusion of Ga or In from a molten (Ga, Zn) or (In, Zn) alloy at 560°C followed by a 30 min anneal of crystal plus alloy in a closed capsule at 950°C (10, 11). The p-type behavior was attributed to the tendency of Ga, In, and Tl to form monovalent positive ions which were believed to be the acceptors, divalent ions being donors (and trivalent ions ionized donors) (10). This explanation can, however, not be correct. Since Ga_{Zn}' contains one electron more than $Ga_{Zn}^{\times}$, the energy level of Ga_{Zn}' must be above the level of $Ga_{Zn}^{\times}$. Since the latter is a donor level close to the conduction band at $E_c - 0.028$ eV (12), the Ga_{Zn}' level must be even higher and thus cannot give rise to appreciable hole conduction.

In the present paper we report on an investigation of the semiconductor properties of ZnSe: Ga, both at high temperatures where the crystals are in equilibrium with atmospheres of well-defined zinc pressure and at low temperatures after high temperature equilibration.

Experimental

Single crystals of ZnSe grown from melts containing, respectively, 1.6×10^{18}, 4.8×10^{18}, 1.6×10^{20}, and 1.6×10^{21} Ga cm^{-3} were obtained from the Eagle Picher Company. Electrical analysis of the first two crystals assuming Ga to be a single donor gives for the Ga content of these crystals 5×10^{17} and 2.0×10^{18} Ga cm^{-3}. Spectrographic analysis of the last two, using the other ones as a standard, yielded values of 5.2×10^{19} and 6×10^{20} Ga cm^{-3} indicating a distribution coefficient $k = c_s/c_l = 0.3 \pm 0.05$. Samples of $10 \times 10 \times 1$ mm were cut from the crystals for measurement of Hall effect and resistivity by the van der Pauw technique (13). High temperature measurements with the crystals in equilibrium with atmospheres of known zinc

* Electrochemical Society Active Member.
[1] Present address: IBM Thomas J. Watson Research Center, Yorktown Heights, New York 10598.

Key words: Hall effect, resistivity, precipitates.

pressures were performed in an apparatus described earlier (14). Room temperature measurements on crystals cooled after equilibration with a known p_{Zn} at temperatures from 800°-1000°C were performed in air. Electron concentrations were calculated from the Hall constant R by the formula $c_e = (Rq)^{-1}$, q being the electronic charge.

Experimental Results

Figure 1 shows values of $[e']$ and ρ for ZnSe: 5×10^{17} Ga cm^{-3} as a function of p_{Zn} at 800°, 900°, and 1000°C. Similar results were obtained for ZnSe: 2×10^{18} Ga cm^{-3}. Figures 2, 3, and 4 show the p_{Zn} dependence of samples with different amounts of gallium at 800°, 900°, and 1000°C, respectively. Figure 5 shows $[e']$ as a function of gallium concentration for samples annealed under $p_{Zn} = 2 \times 10^{-2}$ atm at 900° and 1000°C. Figure 6 shows the corresponding behavior of $[e']$ for $p_{Zn} = 0.7$ atm. Both figures show for comparison data for ZnSe: Al. Crystals quenched after annealing at high temperatures at low zinc pressures were orange to red in color, the density of the coloration increasing with [Ga]. Samples with $[Ga] \geq 2 \times 10^{18}$ cm^{-3} quenched after annealing at high p_{Zn} were

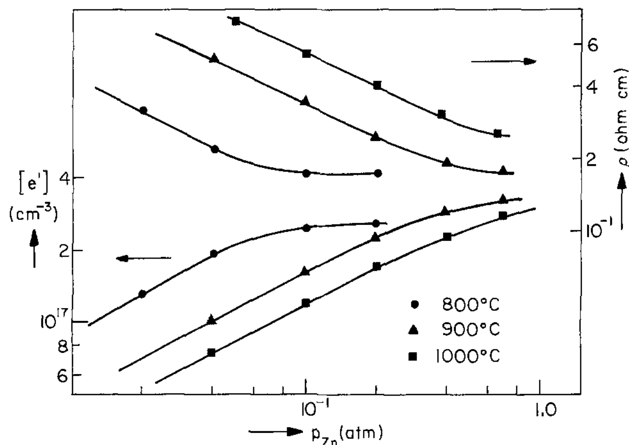

Fig. 1. High temperature resistivity (ρ) and electron concentration of ZnSe: 5×10^{17} Ga cm^{-3} as a function of p_{Zn}.

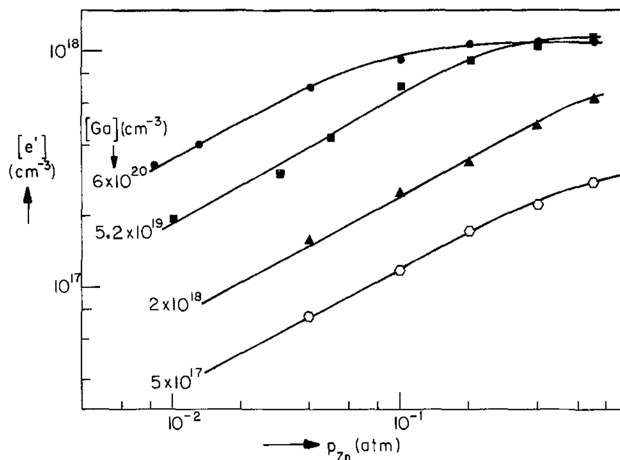

Fig. 4. Electron concentrations in different ZnSe:Ga crystals as a function of p_{Zn} at 1000°C.

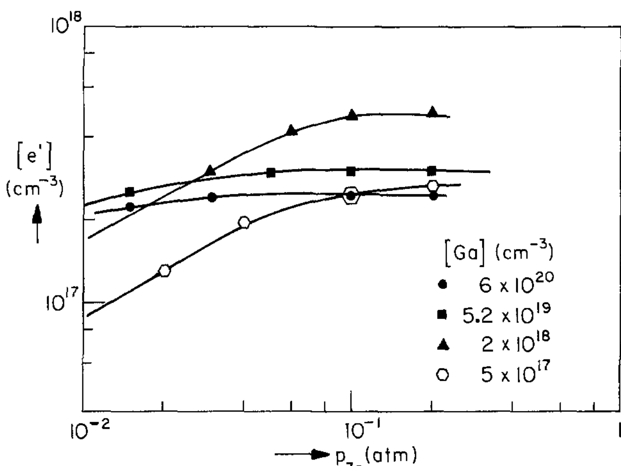

Fig. 2. Electron concentrations in different ZnSe:Ga crystals as a function of p_{Zn} at 800°C.

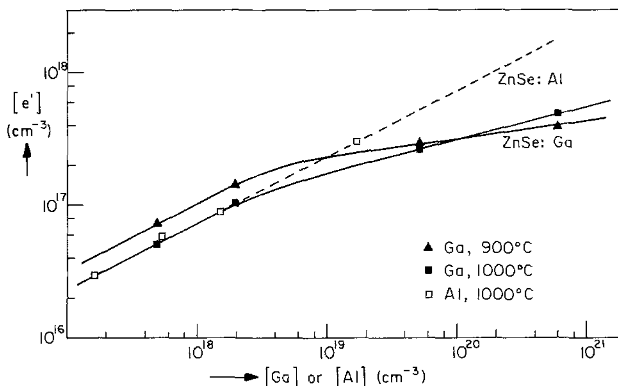

Fig. 5. Electron concentrations as a function of dopant concentration in ZnSe:Ga at 900° and 1000°C (solid lines) and in ZnSe:Al at 1000°C (dashed line); all at $p_{Zn} = 2 \times 10^{-2}$ atm.

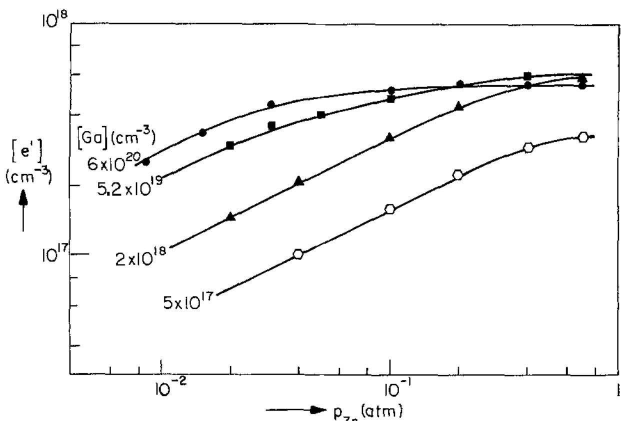

Fig. 3. Electron concentrations in different ZnSe:Ga crystals as a function of p_{Zn} at 900°C.

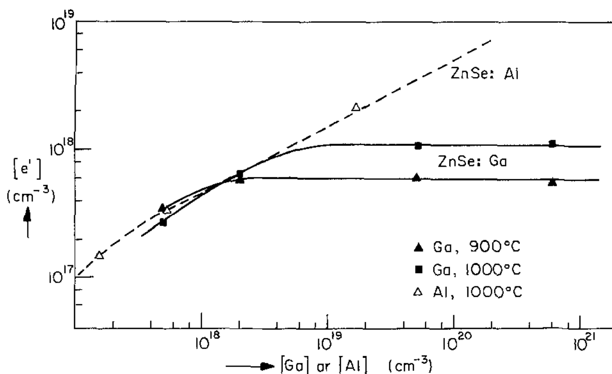

Fig. 6. Electron concentration as a function of dopant in ZnSe:Ga at 900° and 1000°C (solid lines) and in ZnS:Al at 1000°C (dashed line); all at $p_{Zn} = 0.7$ atm.

black; only the sample with 5×10^7 Ga cm^{-3} remained yellow. Inspection of the samples showed the black coloration to be limited to a surface layer that is the thicker the higher $p_{Zn_{anneal}}$, [Ga], and T_{anneal}.

The two most strongly doped samples quenched after annealing at 1000°C, $p_{Zn} = 2.25$ atm were black throughout. For a particular T_{anneal}, the lowest p_{Zn} at which blackening occurs decreases with increasing [Ga]. Observation under an optical microscope in transmission of a black sample, thinned by jet polishing with 40 HCl-10 H_2O_2-1H_2O showed the presence of black star-shaped precipitates, 5-8 μm in size (Fig. 7); similar precipitates were reported in Ref. (8). The precipitates were not visible in reflection. Attempts to determine the nature of the precipitates by electron microscopy failed, probably because the etchant used to thin the samples etched away the precipitates. Whereas it is clear that the blackening is due to the presence of dark precipitates, the facts that the precipitates are generally restricted to surface layers and are only formed after annealing at high p_{Zn} suggest that the precipitates are not present during the high temperature anneal, but are formed during cooling. Since the degree of blackening depends on [Ga], the precipitates almost certainly contain gallium. Their probable nature is discussed later.

Electron concentrations in crystals quenched after annealing at various temperatures and p_{Zn} are shown in Fig. 8-10 (as a function of p_{Zn}) and Fig. 11 (as a function of [Ga]). For samples that were blackened after quenching, the electron concentration determined from the Hall effect measured at room temperature was a function of the thickness of the sample and depended on whether the black surface layer was or was not removed. In Fig. 8-10, points of such samples measured without removal of the black surface layer are connected by dashed lines. Points given in Fig. 11 are the results of measurements after removal of the black surface layer (if any).

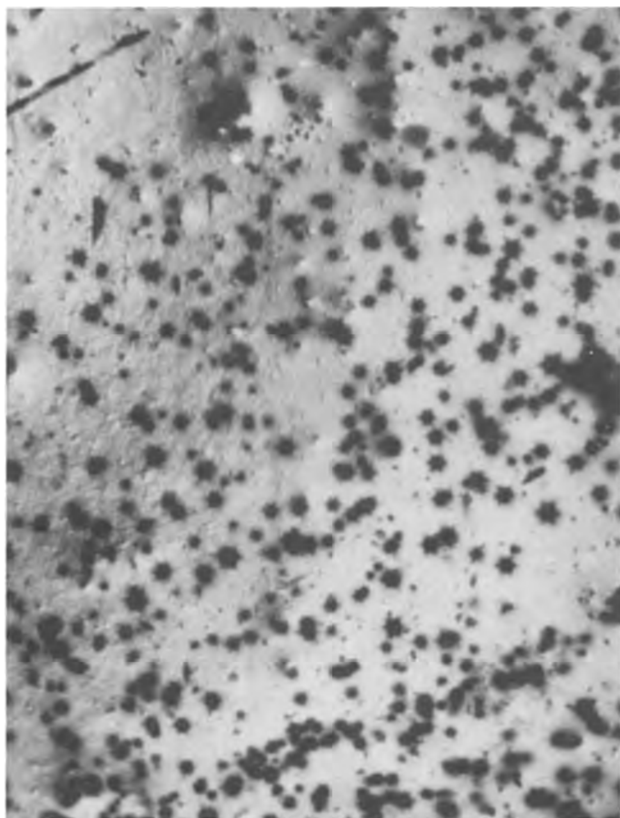

Fig. 7. Optical micrograph in transmission (magnification 200×) of ZnSe: 5.2 × 10^{19} Ga cm^{-3} cooled after an anneal at 1000°C, $p_{Zn} = 2$ atm.

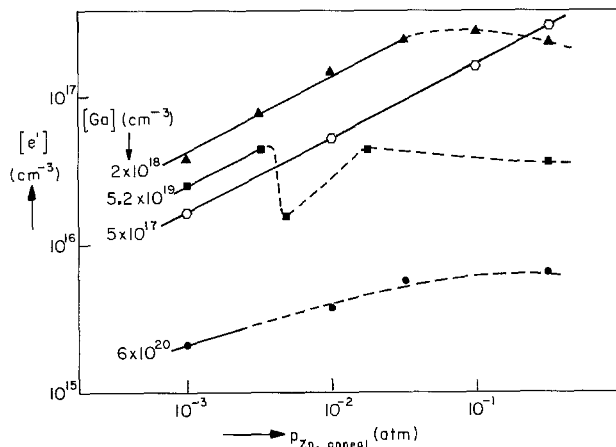

Fig. 8. Electron concentration at room temperature in ZnSe:Ga crystals cooled after annealing under different p_{Zn} at 800°C; solid lines, homogeneous crystals; dashed lines, partly blackened crystals.

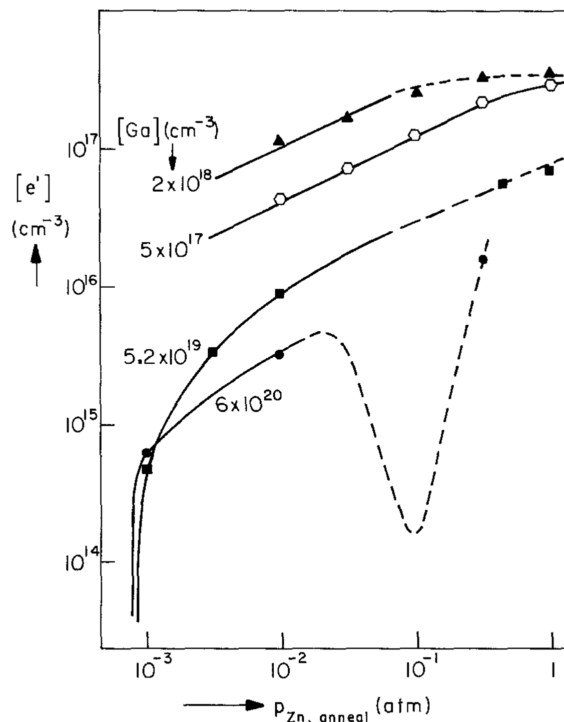

Fig. 9. Electron concentrations at room temperatures in ZnSe:Ga crystals cooled after annealing under different p_{Zn} at 900°C. Solid lines, homogeneous crystals; dashed lines, partly blackened crystals.

Discussion

High temperature results.—Inspection of Fig. 1 and 2 shows that at low p_{Zn} and small [Ga], $[e'] \propto p_{Zn}^{1/2}$; [e'] approaches a constant level that is almost equal to [Ga] at high p_{Zn}. Note the negative temperature dependence of [e'] at low p_{Zn}. The behavior is similar to that observed for ZnSe:Al (1). Interpretation of the results at low p_{Zn} on this basis, assuming Ga_{Zn} to be a single donor with

$$[Ga]_{total} = [Ga_{Zn}^{\cdot}] = 2[V_{Zn}''] \quad [1]$$

leads to

$$[e'] = 2^{-1/2} K_{ZnV}^{1/2} [Ga_{Zn}^{\cdot}]^{1/2} p_{Zn}^{1/2} \quad [2]$$

Here K_{ZnV} is the equilibrium constant of the reaction

$$V_{Zn}'' + Zn(g) \rightleftarrows Zn_{Zn}^{\times} + 2e' \quad [3]$$

$$K_{ZnV} = [e']^2/[V_{Zn}''] p_{Zn} \quad [4]$$

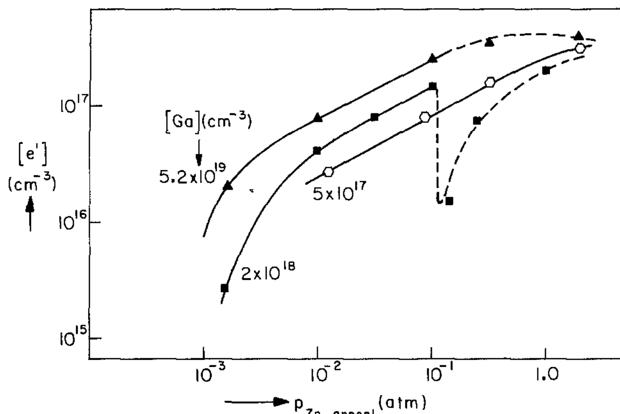

Fig. 10. Electron concentrations at room temperatures in ZnSe:Ga crystals cooled after annealing under different p_{Zn} at 1000°C. Solid lines, homogeneous crystals; dashed lines, partly blackened crystals.

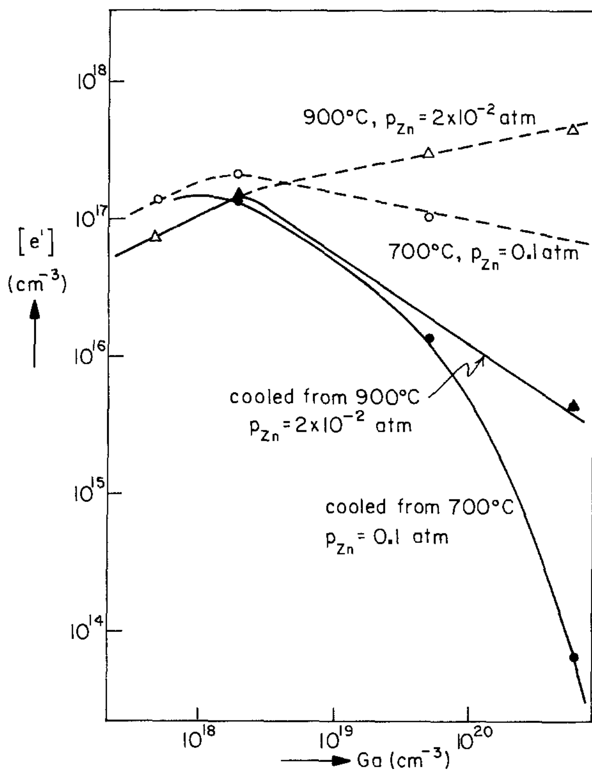

Fig. 11. Electron concentrations in ZnSe:Ga crystals annealed at $p_{Zn} = 2 \times 10^{-2}$ atm, 900°C or $p_{Zn} = 10^{-1}$ atm, 700°C at temperature (dashed lines) and after cooling (solid lines).

Use of the value of K_{ZnV} as determined in Ref. (1) in Eq. [2] leads to Ga contents of the weakly doped samples of 5×10^{17} and 2×10^{18} Ga cm^{-3} as mentioned earlier.

At higher gallium concentrations at $T_{anneal} = 800°C$, [e'] is almost independent of [Ga] and p_{Zn} (Fig. 2). At higher T_{anneal} the p_{Zn} dependence is restored (Fig. 3 and 4), but a decreased dependence of [e'] on [Ga] at high [Ga] still pertains for $T_{anneal} = 900°C$ (Fig. 3).

Similarity in behavior of Ga and Al at low [Ga] and low p_{Zn} is also seen in Fig. 5, Eq. [2] being satisfied. At high p_{Zn}, $[e'] \approx [Ga]$ at small [Ga], but $[e'] < [Ga]$ at large [Ga] (Fig. 6). At low p_{Zn} and $[Ga] \geqq 10^{19}$ cm^{-3}, $[e'] \propto [Ga]^m$ with $m = 0.15$ to 0.22 (Fig. 5). At large p_{Zn}, [e'] is independent of [Ga], but dependent on temperature (Fig. 6).

These facts strongly suggest that part of the Ga precipitates at a relatively low annealing temperature (800°C), less at medium annealing temperature (900°C), and less again at the highest annealing temperature (1000°C); precipitation, if occurring, occurs above a certain critical value of p_{Zn} which decreases with increasing [Ga]. As we shall see, the observations can, in fact, be explained on this basis if Ga_{Zn} is assumed to be a single donor, the precipitated phase being GaSe. Figure 12 shows a schematic isothermal phase diagram in which it is assumed that of the compounds of the Ga-Se system, GaSe (red) and Ga_2Se (black) can coexist with ZnSe; in addition ZnSe can coexist with $ZnGa_2Se_4$ and with alloys (Ga, Zn) which are molten at the temperatures of our experiments. Coexistence with Ga_2Se is questionable for two reasons: Although the existence of this compound was reported by Klemm and von Vogel (15) and Rustamov *et al.* (16), a different compound (Ga_3Se_2) was found by Terhell and Lieth (17) while Susuki and Mori (18) found no compound at all between GaSe and Ga. The second reason is that, even if Ga_2Se exists, coexistence with ZnSe may not be possible. In this case the tie lines between Ga_2Se and ZnSe have to be replaced by tie lines GaSe(Ga,Zn), *i.e.*, from GaSe to point a in Fig. 12. Various three-phase regions (triangles in Fig. 12), valid for the tie lines as drawn, are marked with the type of coexisting condensed phases. With modified tie lines the two upper three-phase regions change to ZnSe + GaSe + $(Ga\text{-}Zn)_{1,a}$ and GaSe + Ga_2Se + $(Ga\text{-}Zn)_{1,a'}$.

The activities of Zn and Se in ZnSe are variable because of ZnSe(s) → Zn(g) + ½ Se_2(g), giving

$$p_{Zn}p_{Se_2}^{1/2} = K_{ZnSe} \quad [5]$$

When another condensed phase is present, a similar relation exists for the components of that phase; *e.g.*, for GaSe

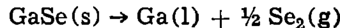

$$GaSe(s) \rightarrow Ga(l) + \tfrac{1}{2}Se_2(g)$$

or

$$a_{Ga}p_{Se_2}^{1/2} = K_{GaSe} \quad [6]$$

If ZnSe and GaSe coexist, both [5] and [6] have to be satisfied and thus

$$a_{Ga} = K_{GaSe}K_{ZnSe}^{-1}p_{Zn} \quad [7]$$

i.e., there is a relation between a_{Ga} and p_{Zn}. Similarly, for coexistence of ZnSe with $ZnGa_2Se_4$ or Ga_2Se

$$a_{Ga}^2 = K_{ZnGa_2Se_4}K_{ZnSe}^{-4}p_{Zn}^3 \quad [8]$$

$$a_{Ga}^2 = K_{Ga_2Se}K_{ZnSe}^{-1}p_{Zn} \quad [9]$$

A relation similar to [8] would be obtained if Ga_2Se_3 rather than $ZnGa_2Se_4$ would occur as the phase coexisting with ZnSe.

If the constants K_{ZnSe}, $K_{Ga_2Se_3}$, $K_{ZnGa_2Se_4}$, K_{GaSe}, and K_{Ga_2Se} were known, it would be possible to construct a diagram with log a_{Ga} and log p_{Zn} as ordinates consisting of single-phase regions and regions of coexistence of two and three condensed phases. In the absence of such detailed knowledge it is only possible to draw a schematical figure. Figure 13 shows such a figure. In this figure single phase regions are areas:

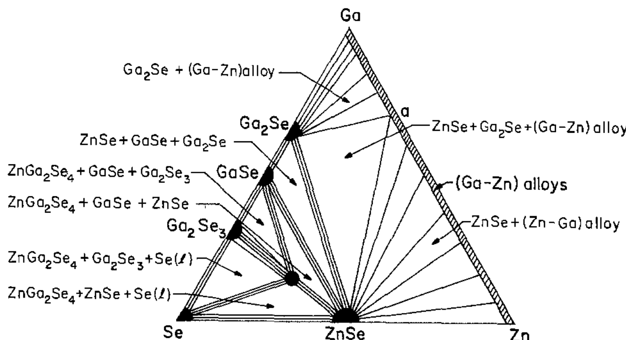

Fig. 12. Schematic isotherm of the Ga-Zn-Se system

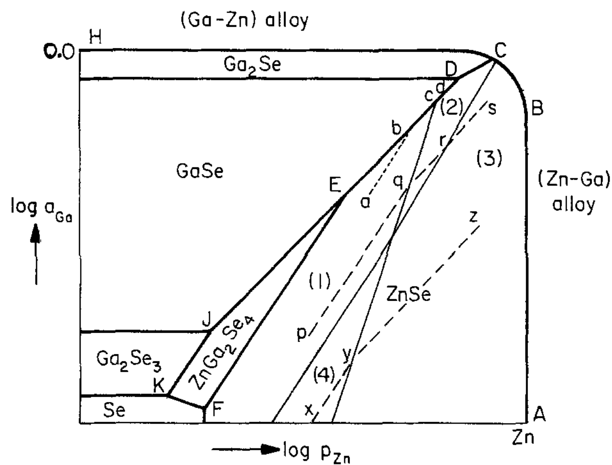

Fig. 13. a_{Ga} vs. p_{Zn} isothermal phase diagram of the system Ga-Zn-Se showing phase boundaries (heavy solid lines), range boundaries (thin solid lines), and lines of constant [Ga] (dashed lines). At the top $a_{Ga} = 1$, $\log a_{Ga} = 0$.

A B C D E F is the ZnSe area; areas to the left of CD, DE, EF, and FSe are, respectively, the areas of Ga_2Se, GaSe, $ZnGa_2Se_4$, and Se. Owing to the low solubility of Se in $(Ga, Zn)_l$, the liquid alloy phase is represented by a line A B C H. Lines separating neighboring areas represent coexistence of two condensed phases. Meeting points of phase boundaries represent coexistence of three condensed phases (corresponding to the triangles of Fig. 12). Thus, point E represents coexistence of ZnSe, $ZnGa_2Se_4$, and GaSe. If the defect structure consists of various ranges dominated by different approximations to the neutrality condition and/or mass balance, range boundaries are represented by straight lines inside the single phase areas; 1, 2, 3, and 4 indicate such ranges for ZnSe; for the characterization of these ranges see Table I. Isotherms for constant gallium concentration are represented by straight, dashed lines inside the single-phase fields. The lines change slope when a range boundary or a phase boundary is reached, *i.e.*, when a second phase is formed. The former give a gradual, the latter a sharp change of slope. The lines xyz, pqr, and abc correspond to increasing gallium concentrations. As is shown below, abc corresponds to the experimental specimens.

As shown earlier, at low gallium concentrations and low p_{Zn}, the behavior is described by Eq. [1] and [2]; this corresponds to region 4 in Fig. 13. At higher p_{Zn} the neutrality and Ga balance change to $[Ga]_{total} \approx [Ga_{Zn}^{\cdot}] \approx [e']$ (region 3 in Fig. 13). The concentration of $Ga_{Zn}^{\cdot}$ in ZnSe is related to the activity of gallium as measured in an outer phase by

$$Ga_{outside} + Zn_{Zn}^{\times} \rightleftarrows Ga_{Zn}^{\cdot} + e' + Zn(g) \quad [10]$$

or

$$[Ga_{Zn}^{\cdot}][e'] \propto a_{Ga} p_{Zn}^{-1} \quad [11]$$

Thus in region 3

$$[Ga_{Zn}^{\cdot}] = [e'] \propto a_{Ga}^{1/2} p_{Zn}^{-1/2} \quad [12]$$

Elimination of $[e']$ from [11] and [4] gives

$$[Ga_{Zn}^{\cdot}]^2 [V_{Zn}''] \propto a_{Ga}^2 p_{Zn}^{-3} \quad [13]$$

Thus in region 4

$$[Ga_{Zn}^{\cdot}] = 2[V_{Zn}''] \propto a_{Ga}^{2/3} p_{Zn}^{-1} \quad [14]$$

Table I. Characterization of the defect structures in the various ZnSe regions of Fig. 13

Region	Neutrality condition	$[Ga]_{total}$
1	$[Ga_{Zn}^{\cdot}] = 2[V_{Zn}'']$	$1/2[(2Ga_{Zn}V_{Zn})^{\times}]$
2	$[Ga_{Zn}^{\cdot}] = [e']$	$1/2[(2Ga_{Zn}V_{Zn})^{\times}]$
3	$[Ga_{Zn}^{\cdot}] = [e']$	$[Ga_{Zn}^{\cdot}]$
4	$[Ga_{Zn}^{\cdot}] = 2[V_{Zn}'']$	$[Ga_{Zn}^{\cdot}]$

At the boundary between regions 3 and 4 both [12] and [14] hold, *i.e.*

$$(a_{Ga})_{3,4} \propto p_{Zn}^3 \quad [15]$$

Isotherms for $[Ga_{Zn}^{\cdot}] = [Ga]_{total}$ = constant follow the path xyz in Fig. 13 as defined by [14] and [12]; point y shifts to higher p_{Zn} for higher gallium concentrations.

In region 4 associates $(Ga_{Zn}V_{Zn})'$ and $(2Ga_{Zn}V_{Zn})^{\times}$ increase their concentrations with increasing gallium concentration. The properties of ZnSe:Ga at high gallium concentration can be explained if the triplet becomes the dominant Ga species before the pair (the pair gives a dependence on p_{Zn} that is not in agreement with experiment). This leads to a new region 1 dominated by

$$[Ga]_{total} = \tfrac{1}{2}[(2Ga_{Zn}V_{Zn})^{\times}] \quad [16]$$

and

$$[Ga_{Zn}^{\cdot}] = 2[V_{Zn}''] \quad [17]$$

It is easily shown that both the boundary 1, 4, and the isotherm path ab inside region 1 satisfy $a_{Ga} \propto p_{Zn}^{3/2}$, *i.e.*, both are parallel to xy, FE, and JK. This means that it is impossible to move from 4 into 1 or from 1 into the $ZnGa_2Se_4$ region by increasing p_{Zn}; it can only be done by increasing $[Ga]_{total}$. On the other hand ab intersects the phase boundary ZnSe-GaSe with increasing p_{Zn} at point b; beyond b the phase boundary bcd is followed. For intermediate Ga concentrations (path pq in region 1) a change in the neutrality condition to [12] occurs before the phase boundary is reached. A new region 2 governed by Eq. [16] and [12] is reached in which $a_{Ga} \propto p_{Zn}$. With increasing p_{Zn} the system follows the path pqrs (a transition from 2 to 3 occurring at point r. Defect isotherms along path abcd are shown in Fig. 14. Three ranges occur: I ≡ ab, II ≡ bc, and III ≡ cd. Since $2Ga_{Zn}^{\cdot} + V_{Zn}'' \rightarrow (2Ga_{Zn}V_{Zn})^{\times}$ with

$$\frac{[(2Ga_{Zn}V_{Zn})^{\times}]}{[Ga_{Zn}^{\cdot}]^2 [V_{Zn}'']} = K_T \quad [18]$$

in range I (as in the whole of region 1)

$$[Ga_{Zn}^{\cdot}] = 2[V_{Zn}''] = [Ga]_{total}^{1/3} K_T^{-1/3}$$

and

$$[e'] \propto [V_{Zn}'']^{1/2}/[V_{Zn}^{\times}]^{1/2} \propto [Ga]_{total}^{1/6} p_{Zn}^{1/2} \quad [19]$$

In range II, where GaSe is present as a second phase

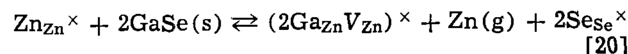

$$Zn_{Zn}^{\times} + 2GaSe(s) \rightleftarrows (2Ga_{Zn}V_{Zn})^{\times} + Zn(g) + 2Se_{Se}^{\times} \quad [20]$$

and thus

$$[2(Ga_{Zn}V_{Zn})^{\times}] \propto a_{GaSe}^2 p_{Zn}^{-1} \quad [21]$$

which for $a_{GaSe} = 1$ is independent of $[Ga]_{total}$

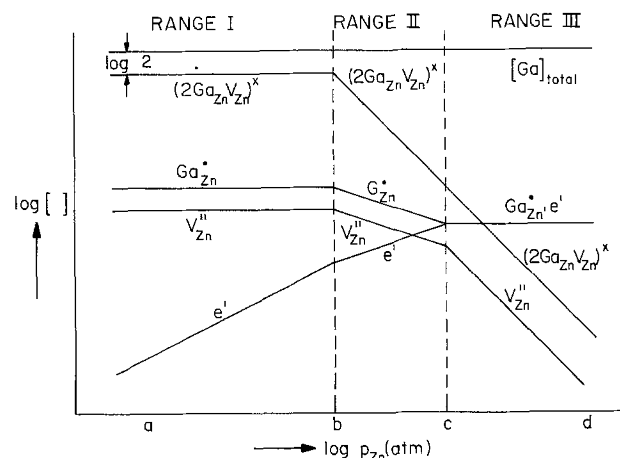

Fig. 14. Defect isotherms corresponding to the path abcd in Fig. 13 (schematical) of ZnSe:Ga with large [Ga] at 900°C.

$$[Ga_{Zn}^{\cdot}] = 2[V_{Zn}''] = 2^{1/3}K_T^{-1/3}p_{Zn}^{-1/3}$$

and

$$[e'] \propto p_{Zn}^{1/3} \quad [22]$$

independent of $[Ga]_{total}$. In range III [21] still holds. From [18] and [21], $[Ga_{Zn}^{\cdot}]^2[V_{Zn}''] \propto p_{Zn}^{-1}$. With $[e']^2 \propto [V_{Zn}'']/[V_{Zn}^{\times}]$ and $[V_{Zn}^{\times}] \propto p_{Zn}^{-1}$, $[Ga_{Zn}^{\cdot}] \approx [e']$ = constant, independent of both $[Ga]_{total}$ and p_{Zn}.

Ranges I, II, and III show the behavior observed in Fig. 2-6 for ZnSe with higher Ga contents and, therefore, may be accepted as the defect model for such crystals. As can easily be verified, the region boundary 1, 2 has the same slope as the boundary 3, 4, while the boundary 2, 3 has $(a_{Ga})_{2,3} \propto p_{Zn}^{5/3}$. Table I summarizes the characterizations of regions 1 to 4 in Fig. 13. It is conceivable that with increasing [Ga], the pair $(Ga_{Zn}V_{Zn})'$ becomes dominant before the triplet $(2Ga_{Zn}\ V_{Zn})^{\times}$. In that case a region 5 dominated by $[(Ga_{Zn}V_{Zn})'] \approx [Ga_{Zn}^{\cdot}]$ will occur between regions 1 and 4 with boundaries 1, 5 and 4, 5 parallel to the present boundary 1, 4. Since no experimental evidence for such a region was obtained, it was not introduced.

Interpretation of low temperature results.—Precipitate formation.—Formation of black precipitates at high [Ga] and high p_{Zn} during cooling can be explained on the basis of a phase diagram such as Fig. 13, but drawn for the lower temperature at which precipitation occurs. Figure 13 was drawn with the assumption that coexistence of ZnSe and Ga_2Se is possible. If this is indeed the case, the precipitates can be either Ga_2Se (which is black) (15) or (Ga, Zn) alloy. If coexistence with Ga_2Se is not possible the boundary CD in Fig. 13 would be missing, and the only possible black second phase would be (Ga, Zn) alloy. Both phase boundaries DC and CBA have the property that they can be crossed with increasing p_{Zn} (or with increase of Zn incorporation during cooling) as required for the formation of precipitates. GaSe is not considered as a possible black precipitate because of its red color. Although the color might possibly darken with deviation from stoichiometry, the model fitting the electrical properties discussed earlier requires formation of almost invisible precipitates at zinc pressures that are lower than those required for blackening to occur. These precipitates are believed to be GaSe, the black precipitates being Ga_2Se or a (Ga,Zn) alloy. Precipitation of an alloy (In, Cd) was previously proposed for CdTe:In (19).

Electrical properties.—Comparison of the electron concentrations in cooled crystals with those in the same samples at high temperatures (*e.g.*, Fig. 8 and 2, Fig. 9 and 3, Fig. 10 and 4) shows that in the two samples with the lowest Ga content the electron concentrations are approximately the same as long as $p_{Zn\ anneal} > p_{Zn,\ cutoff}$ (10^{-3} atm in Fig. 10). Such a cutoff occurs in all donor doped II-VI compounds and is well understood. It is due to trapping of electrons at the empty V_{Zn}'' level and occurs when $[e'] \leq [V_{Zn}']$. In the samples with the largest Ga content there is a marked reduction in the electron concentration on cooling, the concentrations in the cooled crystals being even smaller than those in the samples with less gallium. This is also evident from Fig. 11. Since the points of Fig. 11 were measured after removal of the black surface layer, the reduction in electron concentration of the samples with large gallium concentrations cannot be due to formation of the black precipitates. Although formation of less conspicuous red (15, 20, 21) precipitates of GaSe is possible and is even likely, since such precipitates were already assumed to be formed at high temperatures, reduction of the electron concentration in this manner can be ruled out by the fact that the largest concentration reduction (to $\simeq 10^{14}\ e'\ cm^{-3}$) was found for the crystal with the largest gallium concentration after an anneal at high p_{Zn} at the lowest temperature of anneal, 700°C. Once precipitation occurs there should no longer be a dependence on gallium concentration. Evidently processes other than participation must occur in the crystals during cooling. The decrease of $[e']$ with increasing [Ga] observed at 700°C at $p_{Zn} = 0.1$ atm (Fig. 11) indicates that these processes occur to a certain extent even at the annealing temperature.

One possibility is the transfer of Ga from zinc sites where it is a donor to selenium sites where it is a multiple acceptor

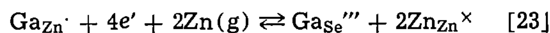

$$Ga_{Zn}^{\cdot} + 4e' + 2Zn(g) \rightleftarrows Ga_{Se}''' + 2Zn_{Zn}^{\times} \quad [23]$$

The high charge of Ga_{Se}''' makes pairing with Ga_{Zn} likely

$$Ga_{Zn}^{\cdot} + Ga_{Se}''' \rightleftarrows (Ga_{Zn}Ga_{Se})'' \quad [24]$$

or, combining [23] and [24]

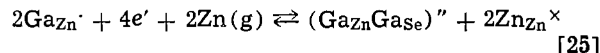

$$2Ga_{Zn}^{\cdot} + 4e' + 2Zn(g) \rightleftarrows (Ga_{Zn}Ga_{Se})'' + 2Zn_{Zn}^{\times} \quad [25]$$

$$[(Ga_{Zn}Ga_{Se})''] = K_{Ga}''[Ga_{Zn}^{\cdot}]^2[e']^4 p_{Zn}^2 \quad [26]$$

For a neutrality condition $2[(Ga_{Zn}Ga_{Se})''] \approx [Ga_{Zn}^{\cdot}]$ and a Ga balance $[Ga]_{total} = [Ga_{Zn}^{\cdot}] + 2[(Ga_{Zn}Ga_{Se})''] = 2[Ga_{Zn}^{\cdot}]$, the equilibrium electron concentration is given by

$$[e'] = K_{Ga}''^{-1/4}[Ga]_{total}^{-1/4}p_{Zn}^{-1/2} \quad [27]$$

showing that the electron concentration decreases with increasing gallium concentration and zinc pressure. Since Zn(g) is involved, this process involves interaction between crystal and atmosphere and depends on diffusion of Zn from the crystal surface to the interior (or of Se in the opposite direction). Nevertheless, the process may occur at $T < T_{anneal}$. Similar reactions and mass action relations can be formulated for Ga_{Se}'' and $(Ga_{Zn}G_{Se})'$, with 3 rather than 4 electrons as in Eq. [23] and [25]. This leads to

$$[(Ga_{Zn}Ga_{Se})'] = K_{Ga}'[Ga_{Zn}^{\cdot}][e']^3 p_{Zn}^2 \quad [28]$$

which combined with [27] and the Ga balance gives

$$[(Ga_{Zn}Ga_{Se})'] = \tfrac{1}{2}K_{Ga}'K_{Ga}''^{-3/4}[Ga]_{total}^{1/4}p_{Zn}^{1/2} \quad [29]$$

$(Ga_{Zn}Ga_{Se})'$ must be expected to be a deep electron trap and may be responsible for the loss of electrons beyond that corresponding to [27]. Such trapping is indicated by the observation of a large activation energy of conduction in the samples with a low electron concentration (8).

Summary

Measurements of Hall effect and resistivity were performed for ZnSe crystals doped with various amounts of gallium, both at high temperature when the crystals were in equilibrium with zinc vapors of known pressures and on crystals cooled after the high temperature equilibration. Crystals with low Ga concentrations behave as ZnSe:Al, $Ga_{Zn}^{\times}$ acting as a single donor. Strongly doped crystals annealed at high zinc pressures show a different behavior. At high temperatures this is explained by formation of GaSe precipitates. At low temperatures both the formation of black precipitates of Ga_2Se or (Ga, Zn) alloy and processes inside the ZnSe phase are involved. Transfer of Ga from Zn to Se sites with formation of multiple acceptors Ga_{Se}''' and clusters $(Ga_{Zn}Ga_{Se})''$ and $(Ga_{Zn}Ga_{Zn})'$ acting as electron traps is proposed as a possible mechanism.

Acknowledgments

This work was supported by the United States Defence Advanced Research Projects Agency under Contract No. F 19628-75-C-0080 and by the Joint Services Electronics Program through the Air Force Office of Scientific Research (AFSC) under Contract No. F 44620-76-C-0061.

Manuscript submitted Oct. 31, 1977; revised manuscript received March 20, 1978.

Any discussion of this paper will appear in a Discussion Section to be published in the June 1979 JOURNAL. All discussions for the June 1979 Discussion Section should be submitted by Feb. 1, 1979.

REFERENCES

1. A. K. Ray and F. A. Kröger, *This Journal*, **125**, 1348 (1978).
2. B. V. Dutt, O. K. Kim, and W. G. Spitzer, *J. Appl. Phys.*, **48**, 2110 (1977).
3. Y. Fukuda and M. Fukai, *J. Phys. Soc. Jpn.*, **23**, 902 (1967).
4. M. Aven and R. E. Halsted, *Phys. Rev. A*, **137**, 228 (1965).
5. M. Aven, D. T. F. Marple, and B. Segall, *J. Appl. Phys. Suppl.*, **32**, 2261 (1961).
6. A. Räuber and J. Schneider, *Phys. Status Solidi*, **18**, 125 (1966).
7. P. Wagner and M. R. Lorenz, *J. Phys. Chem. Solids*, **27**, 1749 (1966).
8. G. Jones and J. Woods, *J. Phys. D*, **9**, 799 (1976).
9. D. D. Nedeoglo, *Phys. Status Solidi B*, **80**, 369 (1977).
10. R. J. Robinson and Z. K. Kun, *Appl. Phys. Lett.*, **27**, 74 (1975).
11. Z. K. Kun and R. J. Robinson, *J. Electron. Mater.*, **5**, 23 (1976).
12. J. L. Merz, H. Kukimoto, K. Nassau, and J. W. Shiever, *Phys. Rev. B*, **6**, 545 (1972).
13. L. J. van der Pauw, *Philips Tech. Rev.*, **20**, 220 (1959).
14. G. H. Hershman and F. A. Kröger, *J. Solid State Chem.*, **2**, 483 (1970).
15. W. Klemm and H. H. von Vogel, *Z. Anorg. Allgem. Chem.*, **219**, 45 (1934).
16. P. G. Rustamov, B. K. Babaeva, and N. P. Luzhnaya, *Izv. Akad. Nauk SSSR, Neorg. Mater.*, **1**, 843 (1965).
17. J. C. J. M. Terhell and R. M. Lieth, *Phys. Status Solidi A*, **10**, 529 (1972).
18. H. Suzuki and R. Mori, *Jpn. J. Appl. Phys. Soc.*, **13**, 417 (1973).
19. F. Selim, V. Swaminathan, and F. A. Kröger, *Phys. Status Solidi A*, **29**, 465 (1975).
20. E. L. Lind and R. H. Bube, *Bull. Am. Phys. Soc. (II)*, **4**, 134 (1959).
21. R. Le Toulhec, M. Balkanski, J. M. Besson, and A. Kuhn, *Phys. Lett. A*, **55**, 245 (1975).

Technical Note

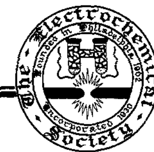

The Possibility of Black Zinc Oxide as Spectrally Selective Coating for Low Temperature Solar Collectors

M. van der Leij

Department of Applied Physics, Delft University of Technology, Delft, The Netherlands

The utilization of solar energy for space heating requires, especially at higher latitudes where a sea climate dominates, solar collectors with high efficiency. That means that for a flat absorber plate in the first instance the total solar absorptivity (α) should be near one and secondly the infrared total emissivity (ϵ) should be near zero. Such a surface is called spectrally selective. A more detailed description about this can be found in the paper of Mattox and Sowell (1). The solar spectrum concerned at higher latitudes is mostly confined in the wavelength region 0.3-2.4 μm, while the thermal radiation spectrum has its maximum intensity at about 9 μm for a black body at 60°C and extends from about 2 μm to infinity. The smallest overlap of these two spectra is at about 2.2 μm, this is also called the cutoff wavelength. It is often convenient, in researching spectrally selective surfaces, to work with spectral reflectivities instead of spectral absorptivities. The relation between the directional spectral absorptivity or emissivity and the directional hemispherical spectral reflectivity (ρ) at temperature T is, following Kirchhoff's law (2), briefly given by

$$\alpha(\lambda, T) = \epsilon(\lambda, T) = 1 - \rho(\lambda, T)$$

in which λ is the wavelength in μm.

The ideal spectrally selective reflectivity curve is shown in Fig. 1. A simple spectrally selective absorber consists of a metal substrate covered with a thin semiconductor film. This semiconductor must then have a high absorptivity for wavelengths shorter than 2.2 μm and a high transmissivity for wavelengths longer than 2.2 μm. The mechanism concerned was earlier described by Christie (3). An example of such a semiconductor is metal oxide, but only certain types of metal oxides will have suitable spectrally selective properties. The chemical compound and, therefore, the optical and electrical properties are strongly determined by the way these oxides are produced. In other words, the process parameters and the working circumstances are of great importance. In this paper the effect of different process parameters as well as the effect of aging tests on the solar absorptivity and the thermal emissivity are discussed.

Key words: solar, absorptivity, emissivity, durability, anodic.

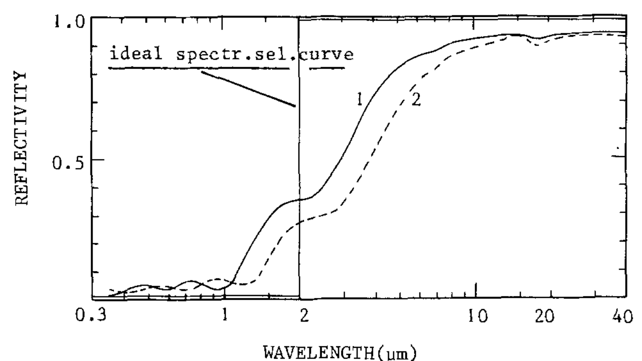

Fig. 1. Near-normal hemispherical spectral reflectivity of zinc oxide on leaf-zinc prepared by anodic treatment of the substrate in a solution containing 30 g/l NaOH and 20 g/l $NaNO_3$ at 40°C bath temperature, with current density of 20 (a.c.) A/dm^2 during 1 min (curve 1) and 3 min (curve 2).

Table I. Effect of different process parameters on the normal total solar absorptivity α_n and the normal total thermal emissivity ϵ_n for 60°C

Sample number	NaOH (g/l)	$NaNO_3$ (g/l)	$NaClO_2$ (g/l)	Bath temp. (°C)	Current density (A/dm^2)	Voltage (V)	Process time (min)	α_n	ϵ_n (60°C)
1	30	20	—	40	20	2.2-1.6 VAC	1	0.92	0.10
2	30	20	—	40	20	2.2-1.6 VAC	3	0.94	0.13
3	30	20	—	60	20	2.2-1.6 VAC	1	0.82	0.21
4	30	20	—	40	40	2.2-1.6 VAC	1	0.94	0.13
5	10	20	—	40	20	5-4 VAC	1	0.94	0.08
6	10	20	—	40	20	5-4 VAC	1.5	0.96	0.16
7	30	20	5	40	20	3 VAC	1	0.96	0.12
8	30	20	—	40	20	5 VDC	1	0.93	0.17

Experimental Techniques

Optical measurements.—In the solar spectrum (here from 0.35 to 2.5 μm) an integrating sphere according to Saftwat's design (4) attached to a spectrophotometer has been used to measure the near-normal hemispherical spectral reflectivity in steps of 0.05 or 0.1 μm, depending whether the intensity of the solar energy is high or low. The coating of the inner wall of the sphere consists of $BaSO_4$. The reliability and reproducibility were first checked with some reference standard samples as Minnesota 101-C10-3M Nextel velvet black coat paint, vacuum-evaporated gold film, diffuse white standard ceramic material No. 22614 from Zeiss, and a pressed-pure $BaSO_4$ powder. In the thermal radiation spectrum (from 2.5 to 40 μm) a Beckman Acculab VI infrared spectrophotometer has been available to measure the near-normal specular spectral reflectivity. A vacuum-evaporated gold film has always been used as a reference.

The connection between the two reflectivity curves at 2.5 μm was rather close because our surfaces always have mirrorlike appearance in the visible region so that the near-normal specular reflectivity can be considered as near-normal hemispherical reflectivity. The normal total solar absorptivity, α_n, was calculated by numerical integration of the normal spectral absorptivity multiplied by the normalized spectral distribution of solar energy. Here a standard direct spectral solar energy distribution of Moon (5) for air mass 2 (in accordance with a zenith angle of 60°) was taken as a weight factor. The integration boundaries are 0.3 and 2.2 μm. The same procedure was carried out on calculation of the normal total emissivity ϵ_n, only here the black body radiation function at temperature of 60°C was taken as a weight factor. The total experimental and numerical relative error of α_n was less than 2%; that of ϵ_n was about 10%.

Preparation techniques.—The basic materials for the anodic treatments are commercial leaf-zinc (1.5% Pb + Si) and plate steel 37 (0.12%C). All the samples have a diameter of 28 mm and a thickness of 2 mm. These samples were initially ground with grit 400 and 600, then polished with 3 μm diamond paste, and finally polished after with 1 μm diamond paste until a mirrorlike surface appeared. The root mean square roughness measured was less than 0.5 μm. The chemical and electrochemical treatments of the samples were done by the Dutch Organization of Applied Scientific Research (T.N.O.) at Apeldoorn, The Netherlands.

After polishing, the steel samples received a 2 min hot anodic and a cold cathodic pretreatment (TNO recipes). In between they were rinsed in cold tap water and dipped in 50% hydrochloric acid solution. The final pretreatment consisted of rinsing the steel samples in cold tap water and dipping them in a 10% sulfuric acid solution. The clean steel samples now were electroplated with bright zinc for about ½ hr in an electrolyte containing: 75 g/l zinc cyanide, 125 g/l sodium cyanide, 85 g/l sodium hydroxide, 2 g/l TNO organic brightener, at pH > 13, temperature of 25°C, and with a current density of 4 A/dm^2. A zinc anode was used. There was no stirring in the bath. The zinc thickness is approximately 20 μm. The pretreatment of the leaf-zinc samples consisted only of degreasing with calcium hydroxide, dipping in 1% sulfuric acid solution and, rinsing in cold tap water. All the zinc substrates received an a-c (50 Hz) anodic treatment in solutions with NaOH and $NaOH_3$ as used by Encheva (6). The concentration of the bath components, the bath temperature, and the current density were chosen such as to obtain the best corrosion resistance as reported extensively by Encheva (6), namely: 20-30 g/l NaOH, 15-20 g/l $NaNO_3$, 25°-40°C bath temperature, 10-140 A/dm^2, treatment time of 8-15 min, and coating thickness of 4-6 μm. As far as the last two requirements are concerned, they are hard to fulfill because thick coatings usually have high emissivities, which are not suitable as spectrally selective coatings. Our process times are mostly near 1 min.

In Table I all the different process parameters used are summarized. In this table the zinc oxide coatings on bright zinc-electroplated steel are not included. It concerns samples prepared on the same way as No. 5 and 8. It was not our intention in the first instance to optimize zinc oxide coatings by varying all the parameters involved, but we are interested in the effect of some process parameters on the spectral selectivity, taking into account the corrosion resistance recommendations as reported by Encheva (6). In a few cases these recommendations were not wholly followed, see No. 3, 5, 6, and 8 in Table I. The purpose of these deviations was to examine the effect of gas evolution, higher a-c voltage, and the use of d-c voltage, respectively, on the radiation properties α_n and ϵ_n. In one case (No. 7 in Table I) 5 g/l $NaClO_2$ were added. This was done because, following Pushpavanam's (7) suggestion, the coating would have a deep black color and would have high corrosion and abrasion resistance. After the anodizing process all the samples were washed in a stream of cold tap water and then rinsed after in hot deionized water.

Temperature and ultraviolet aging.—Some of the samples (see Table II) were exposed to air heating at 80°C for two weeks and at 180°C for one week at a stretch. 80°C was chosen because these surfaces are supposed to work beneath this temperature, while 180°C is the maximum temperature of a stagnating flat plate collector which must be avoided anyhow.

The same samples were also exposed to a u.v. radiation test of 120 W/m^2 for about 72 hr. The aim of these tests was to get a rough idea about the

Table II. Effect of heating and u.v. tests on α_n and ϵ_n (60°C)

Sample number	α_n Before test	ϵ_n Before test	α_n After 80°C, 2 weeks	ϵ_n After 80°C, 2 weeks	α_n After 180°C, 1 week	ϵ_n After 180°C, 1 week	α_n After u.v., 72 hr	ϵ_n After u.v., 72 hr
1	0.92	0.10	0.91	0.10	0.84	0.09	0.91	0.10
4	0.94	0.13	0.93	0.13	0.87	0.10	0.94	0.13
5	0.94	0.08	0.94	0.08	0.93	0.07	0.94	0.08
5a*	0.95	0.08	0.92	0.12	0.88	0.47	0.92	0.13
7	0.96	0.12	0.96	0.12	0.95	0.11	0.96	0.12
8	0.93	0.17	0.93	0.17	0.92	0.14	0.93	0.16
8a*	0.93	0.17	0.92	0.16	0.89	0.13	0.93	0.15

* On bright zinc-plated steel 37.

stability of the radiation properties α_n and ϵ_n for the short term.

Results and Discussion

The normal hemispherical spectral reflectivity curves of zinc oxide on leaf-zinc samples of number 1-8 are presented in Fig. 1-4. In Table I the process parameters are given with the normal total solar absorptivity α_n and normal total thermal emissivity ϵ_n values concerned. Zinc oxide coatings on zinc-plated steel produced in the same way as No. 5 and 8 are not included in the figures as well as in Table I, because the optical properties are not different from No. 5 and 8, respectively. In Table II the effect of short-term heating and u.v. tests on α_n and ϵ_n of some surfaces is shown including those (No. 5a and 8a) with a zinc-electroplated substrate.

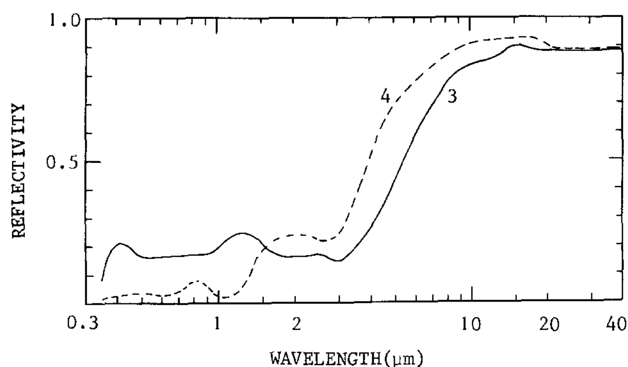

Fig. 2. Near normal hemispherical spectral reflectivity of zinc oxide on leaf-zinc prepared by anodic treatment of the substrate in a bath with 30 g/l NaOH and 20 g/l $NaNO_3$ for 1 min with 20 (a.c.) A/dm^2 at 60°C (curve 3) and with 40 (a.c.) A/dm^2 at 40°C (curve 4).

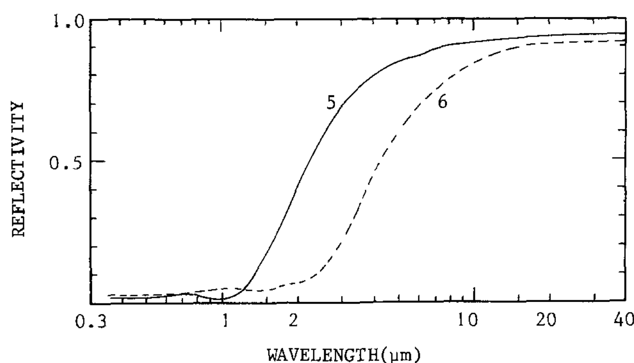

Fig. 3. Near normal hemispherical spectral reflectivity of zinc oxide on leaf-zinc produced by treating the substrate anodically in an electrolyte with 10 g/l NaOH and 20 g/l $NaNO_3$ at 40°C with 20 (a.c.) A/dm^2 and for a process time of 1 min (curve 5) and 1.5 min (curve 6).

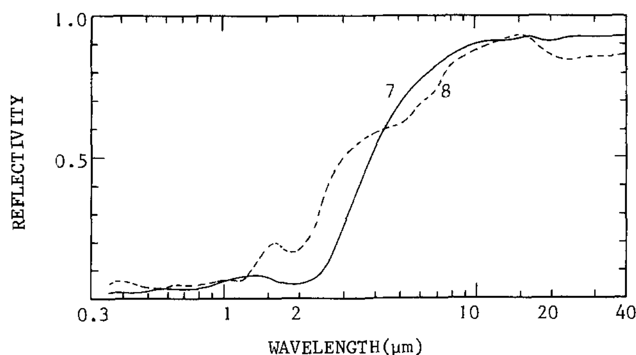

Fig. 4. Near normal hemispherical spectral reflectivity of zinc oxide on leaf-zinc produced by anodic treatment of the substrate in a solution with 30 g/l and 20 g/l $NaNO_3$ at 40°C with 20 (d.c.) A/dm^2 for 1 min (curve 8); for curve 7, 5 g/l $NaClO_2$ was added and an a-c current density of 20 A/dm^2 was used.

In general most of the zinc oxide coatings investigated here have a black color and mirrorlike appearance. Unfortunately the blackness is not uniform; some of the surfaces show tiny white dots sparsely spread, perhaps white zinc oxide or zinc which was not affected by the anodic treatment.

The black color is, according to the literature (7, 8), due to nonstoichiometric effects. Usually an excess of zinc has been found (7-9), but here we have found in our zinc oxide coatings a deficit of zinc. (Analysis was carried out with a MeV-Van de Graaff-accelerator.) Sample No. 5 reveals an atomic ratio of zinc/oxygen of 0.86 and sample No. 8 a ratio of 0.95.

Each sample or set of samples will be discussed successively from the standpoint of spectral selectivity and corrosion resistance (6, 7).

Sample No. 1 and 2, Table I, Fig. 1.—The spectrally selective property is not bad in the first instance. Because of corrosion resistance longer treatment times are desirable, but this was not possible due to adhesion problems.

Sample No. 3, Table I, Fig. 2.—It has been found that a higher bath temperature seems to damage the surface too much, resulting in a poor spectral selectivity.

Sample No. 4, Table I, Fig. 2.—This surface has nearly the same optical properties as surface No. 2, as can be expected. In practice, however, high current densities are usually not attractive.

Sample No. 5, Table I, Fig. 3.—Reflectivity curve No. 5 approaches the ideal spectral selective curve (Fig. 1) best. The coating thickness is 0.38 μm. A thicker coating was obtained by a little longer treatment time (No. 6), but then the normal total emissivity raised very strongly. Besides this, following Encheva's corrosion test results, the concentration of NaOH is rather low and therefore high corrosion resistance can not be assured.

Sample No. 7, Table I, Fig. 4.—The addition of 5 g/l $NaClO_2$ to the electrolyte, as suggested by Pushpavanam (7), resulted as expected in a deep black coating with good spectrally selective properties. A treatment time of 40 sec yielded a normal total emissivity of 0.10. The expectation is that a treatment time of 1.5 min will give an ϵ_n of 0.15. This value is still acceptable for low temperature solar collectors. For corrosion resistance it is better to have the thickest coating as possible.

Sample No. 8, Table I, Fig. 4.—In Fig. 4 we see that a d-c current reveals a capricious form of the spectral reflectivity curve with poor α_n and ϵ_n values. The thickness of this coating is 0.46 μm.

If we consider the short term heating and u.v. test results, we may say in general that the low temperature aging as well as the u.v. aging have not changed the radiation quantities α_n and ϵ_n very much. This is in contrast with the 180°C test, after which different results have been obtained: the anodized zinc-plated steel sample of No. 5a shows the largest change in α_n and ϵ_n, while the corresponding sample No. 5 with leaf-zinc as a substrate and also sample No. 7 show the smallest change. The cause of these different results has not yet been understood.

Conclusion

The best spectrally selective surface, taking into account corrosion resistance considerations and thermal and u.v. stability, seems to be zinc oxide on polished leaf-zinc prepared by anodic treatment of the substrates in a solution containing 30 g/l NaOH, 20 g/l $NaNO_3$, and 5 g/l $NaClO_2$ at 40°C bath temperature with 20 (a.c.) A/dm^2 for 1 min or slightly longer treatment time. Before applying this oxide even in

low temperature collectors, long-term durability tests should be carried out first.

Acknowledgment

The author wishes to thank Ir. C. A. Boose of Apeldoorn T.N.O. for the preparation of the samples and Dr. L. W. Wiqqers of F.O.M. Institute in Amsterdam for the chemical analyses of some of the surfaces with a MeV-Van de Graaff-accelerator.

Manuscript submitted May 6, 1977; revised manuscript received March 21, 1978.

Any discussion of this paper will appear in a Discussion Section to be published in the June 1979 JOURNAL. All discussions for the June 1979 Discussion Section should be submitted by Feb. 1, 1979.

Publication costs of this article were assisted by the Delft University of Technology.

REFERENCES

1. D. M. Mattox and R. R. Sowell, *J. Vac. Sci. Technol.*, **11**, 793 (1974).
2. R. Siegel and J. R. Howell, "Thermal Radiation Heat Transfer," McGraw Hill, New York (1972).
3. E. A. Christie, Paper No. 7/81 presented at the I.S.E.S. Congress in Melbourne, Australia (1970).
4. H. H. Safwat, Ph.D. Dissertation, West Virginia University, West Virginia (1968).
5. P. Moon, *J. Franklin Inst.*, **230**, 583 (1940).
6. M. A. Encheva, *J. Appl. Chem. USSR*, **45**, 318 (1972).
7. M. Pushpavanam and B. A. Shenoi, *Electroplat. Met. Finish.*, **27**, 9 (1974).
8. K. Huber, *This Journal*, **100**, 376 (1953).
9. Z. M. Jarzebski, "Oxide Semiconductors," Pergamon Press, New York (1973).

JOURNAL OF THE ELECTROCHEMICAL SOCIETY

REVIEWS AND NEWS

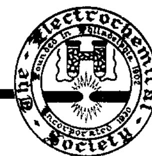

MAY
1978

Heinz Gerischer—Palladium Medalist

Charles W. Tobias[1]

The Palladium Medal of the Society, established in 1951, is given for distinguished contributions to the field of electrochemical science and corrosion. What this award is designed to recognize was clearly demonstrated already in 1951 by the selection of Carl Wagner as the first medalist. The 13th recipient of this award, Professor Heinz Gerischer, follows a list of eminent scientists: Wagner, Furman, Evans, Bonhoeffer, Frumkin, Uhlig, Hackerman, Delahaye, Hoar, Brewer, Levich, and Pourbaix. A commendable lack of chauvinism has been evident in the selection of the medalists: eight of the 13 recipients were foreign nationals.

Heinz Gerischer's career started out under what one could call less than auspicious circumstances. A series of nearly miraculous turn of events are responsible for his having been admitted at all, in 1938, to any university in Germany. No sooner did he complete his first year as a student in chemistry in Leipzig, then in 1939 he had to join the German army, only to be ejected as a half-aryan in 1941. Allowed to return to continue his studies in Leipzig, obviously a serious mistake on the part of Nazi authorities, he obtained his chemistry diploma in 1943. Then, with another forced interruption during war time in "Arbeitsdienst," he stayed on as a researcher in Karl-Friedrich Bonhoeffer's laboratory.

In 1946, after obtaining his doctorate, he followed Bonhoeffer to the University of Berlin. According to Gerischer, Bonhoeffer, a great scientist and an exceptional human being, was perhaps the greatest single influence in his life. At a time when all intellectual and human values crumbled Bonhoeffer saved not only human lives, he was among the few who succeeded in maintaining a thin thread of continuity in the great tradition of science in Germany.

In 1949, during the blockade of Berlin, Gerischer again followed his mentor, this time to Gottingen, where Bonhoeffer was named the director of the newly created Max Planck Institute für Physikalische Chemie.

During the five years Gerischer spent in Gottingen he developed a definite interest in an academic career. As a consequence of the somewhat rigid structure of the German academic scene, he had to move on to work toward his habilitation to achieve the status of a dozent. In 1954 he joined the Max Planck Institute für Metallforschung in Stuttgart, heading a small department of corrosion science. In Stuttgart Gerischer enjoyed a considerable degree of freedom in the selection of research topics and in accepting students working on their doctoral dissertations. In 1955 he became a dozent at the University of Stuttgart and began to lecture there, and in 1960 he was advanced to full membership of the Max Planck Gesellschaft. Soon thereafter, in 1962, he accepted an invitation to the Technische Hochschule in Munich as a Professor Extraordinarius.

Seven years later, in 1969, after he had advanced in academic rank, and following service in various important academic administrative positions, he accepted an invitation to become the director of the Fritz Haber Institute of the Max Planck Gesellschaft in Berlin. Since 1970 he resides in the director's villa on Faradayweg and heads an institution of great renown, one that was directed earlier by Fritz Haber, under whose guidance Bonhoeffer obtained his doctorate. The series of events that led to Gerischer's directorship of this famed institution involved many improbable turns, many near miracles. It is indeed fortunate for Germany and for science that today a man of Gerischer's intellectual caliber and integrity occupies this very influential post.

Gerischer's early work addressed various problems in the area of kinetics and mechanisms of electrode processes. Numerous papers originating from the 1950's and early 1960's concern the elucidation of mechanisms of anodic and cathodic reactions involving simple and complex ions, others pertain to corrosion and electrocatalysis. His papers on electrode reactions of complex ions and on electrocrystallization processes are examples of the best work published on these subjects in the fifties and sixties.

Gerischer made important contributions to the development of new experimental techniques for the investigation of fast electrode reactions. Among these the potential-step and current-step methods, and the invention of the double-pulse method deserves particular mention. He designed and employed a special flow cell for the study of fast homogeneous reactions and also developed a temperature step method for similar purposes.

These earlier investigations were based on classical concepts, macroscopic treatments of electrode phenomena, in which Gerischer's contributions were particularly significant through the introduction of new experimental techniques, resulting in important improvements in the accuracy with which kinetic parameters could be obtained.

Already during his student days in Leipzig, Gerischer, after reading Gurney's book, "Ions in Solutions," thought of the desirability of employing electronic energy levels to the description of electrode reactions. However it was only in the mid-fifties, after he came across Brattain and Garrett's work involving the first electrochemical experiments with germanium, that he realized the opportunity offered by semiconductors for the application of electronic states in the interpretation of electrode reactions. His first paper on the anodic dissolution of n- and p-type germanium, coauthored with his student Fritz Beck, was published in 1957, and some 70 papers concerning semiconductor electrodes have followed since. When Gerischer moved to Munich, his nascent interest in photoelectrochemistry received a strong boost by the long tradition in spectroscopy and photochemistry in the institute he joined. Here he

[1] Introductory remarks by C. W. Tobias, Department of Chemical Engineering, University of California, Berkeley, on the occasion of the presentation of the Palladium Medal Award to Heinz Gerischer on October 11, 1977, at the Atlanta Meeting of the Society.

began to use semiconductor and insulator electrodes to study the reactions of excited molecules, especially of dyes. Finally, in Berlin he extended his work to include photoreactions at metal electrodes, specifically photoelectron emission into electrolytes and photooxidation of electrolyte components.

Thus, Gerischer is realizing the dream he had as a student in Leipzig; the analysis of electrode reaction mechanisms from an atomistic point of view, using atomic and electronic energy schemes. Many of you already know that his work established the foundations on which some of the present, very exciting developments in the area of photogalvanic cells are based.

It is evident that the recipient of the Palladium Medal of 1977 has covered in his research activities a large part of electrochemical science, and that he has made significant contributions to a number of disciplines represented in the various Divisions of this Society. To the surprise of no one his nomination to the Palladium award was cosponsored by an unprecedented large number of Divisions of the Society.

In concluding my introduction of the Palladium Medalist I only want to add a brief personal note. I studied Professor Gerischer's papers far before I met him in the early sixties. In subsequent years I have seen him on many occasions, and had the opportunity for close interaction with him during his stay as a visiting scientist in the Lawrence Radiation Laboratory in 1967-1968. This personal knowledge of the man allows me to say that Professor Gerischer's great talent and fine contributions to science are matched by his qualities as a human being.

For this reason it is with the greatest of pleasure that I present to you Professor Heinz Gerischer, the Palladium Medalist of 1977.

Electrochemistry of the Excited Electronic State

Heinz Gerischer[2]

Since the Palladium Medal of The Electrochemical Society is one of the greatest honors an electrochemist can be awarded with, I feel very pleased and honored to be the thirteenth recipient of this medal. I want to express my sincere thanks to you, Mr. President, as the representative of the society and particularly to you, Charles, for your so very kind and friendly introduction. You have mentioned therein how decisive my personal contact with K. F. Bonhoeffer was for my life, scientifically and otherwise. It was 20 years ago that this medal was awarded to him, but he tragically passed away before he received the message. Now, I am standing here in his succession being strongly reminded of his unforgettable personality. This is a very personal reason for me to acknowledge this medal particularly highly and to be so especially touched at this occasion.

I would not be standing in this place if I should not have found, over the years, the cooperation of a number of highly talented co-workers. Most of my contributions to various fields of electrochemistry have been made possible by their enthusiasm and their devotion to research. Without mentioning individual names, I wish to express my gratitude to all of them for their personal contributions.

The subject of my lecture has little to do with the problems which I have studied 10-20 years ago. Although it was apparently my contributions to these areas—according to the published appreciation—which should be acknowledged by this award, I have deliberately chosen a different subject for my presentation. This not only corresponds to my more recent interests, it also demonstrates that electrochemistry is still widening its objectives and far from being exhausted although it has a very long history.

Most of the electrochemistry work is still done in the dark and the electrochemists hope to enlighten themselves to understand the complicated systems with which they have to deal. However, more than a century ago, Becquerel had already illuminated the electrodes of Galvanic cells and detected photovoltaic effects (1). This created great excitement among the then very small and exclusive scientific community, but it certainly did not promote the understanding of electrochemistry. On the contrary, the speculations about such photoelectrochemical phenomena contributed to the fact that some parts of electrochemistry, especially the nonthermodynamic ones, appeared to the scientists of neighboring fields for a long period of time as quite obscure.

This situation has changed since the time when electrochemists could profit from the development of solid-state physics and photochemistry and have learned to combine these experiences with their classical electrochemical knowledge. This has demonstrated once more that electrochemistry is an interdisciplinary science and that a competent electrochemist must be alert to developments in various fields. We know today that all these photoelectrochemical effects are caused by the generation of excited electronic states, and my intention is to explain in this lecture the basic phenomena which are due to the presence of excited electronic states. I am especially pleased that I can address this lecture to a society which has combined in its development so closely the interests of electrochemists and solid-state physicists. The topic I will discuss today demonstrates forcibly how necessary it is to connect these two fields.

Reactivity in the Excited State

Electron transfer between a donor and an acceptor is one of the most common of electrochemical reactions. In Galvanic cells the donor or the acceptor is the electrode. It is obvious that this type of electrochemical reaction must be affected by electronic excitation. Figure 1 shows in a very simple picture how electronic excitation influences electron transfer processes.

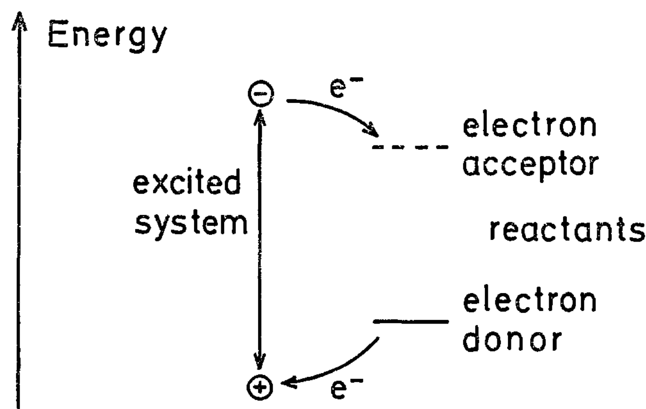

Fig. 1. Energy scheme for electron transfer between excited system and electron donor or acceptor.

[2] Palladium Medal Address delivered October 11, 1977, at the Atlanta, Georgia, Meeting of The Electrochemical Society. The medal was struck from palladium supplied by the International Nickel Company, 67 Wall Street, New York, New York 10005.

Electron transfer occurs between an occupied and a vacant electronic quantum state. Light absorption changes the distribution of electrons over the available electronic energy levels. As a consequence, electrons at higher energy levels are created simultaneously with vacant electronic states at low energies. The electrons of the high energy levels can be transferred to electron acceptors in this energy range. The vacant electronic states at low energy levels can be filled by electron donors with electronic energies in this region as is indicated in Fig. 1. We see immediately that, in electrochemical language, cathodic redox processes will be accelerated by light absorption and also anodic redox reactions will be enhanced. If the excitation energy is large enough, redox processes will become possible which cannot occur in the dark.

There are other possibilities of generating excited electronic states, for example, the application of very high electric fields to solids. We shall, however, limit our discussion with one exception to the generation of excited states by light absorption only.

What happens in an electrochemical system after light absorption depends both on the light absorber, which can be the electrode or one component of a redox couple, and on the reaction partner, which can be a redox couple or an electrode. In Fig. 2 three typical cases are shown which we shall later discuss in more detail. The excited molecule corresponds to the excitation of a redox system, and a possible consequence is, as we see, electron transfer in two opposite directions in contact with an electrode. In case of an electronic excitation in the electrode we shall distinguish between a metal and a semiconductor electrode. At both types of electrodes, cathodic and anodic electron-transfer processes can be induced by light absorption as is indicated in this figure. We shall discuss this in more detail later.

The other type of electrochemical reaction which occurs at interfaces is ion transfer. How electronic excitation affects an ion transfer process is much less obvious than for electron transfer. One can, however, expect that ion-transfer reactions also can be accelerated by electronic excitation. The reasons are given in Fig. 3. Ion transfer at the interface between an electrode and electrolyte must involve an energy barrier. If the initial state of this process is electronically excited, the energy of this state will be increased. How much depends on the localization of the excitation energy. The influence on the transition state will be much smaller, and there is no influence on the final state. Figure 3 shows schematically that the activation energy for the ion-transfer process will be reduced by electronic excitation, and in some cases, as we shall later discuss, this effect even controls the possibility of ion transfer.

We will make a brief estimation of how large these effects might be. It must be taken into consideration that excited electronic states have a limited lifetime.

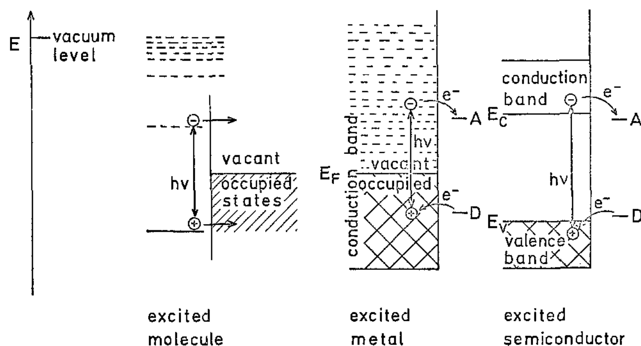

Fig. 2. Energy scheme for electron transfer between excited molecule and metal, excited metal, or excited semiconductor and redox couples.

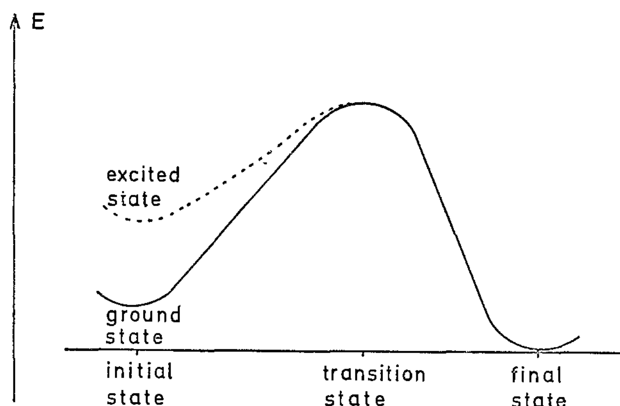

Fig. 3. Influence of electronic excitation on ion transfer reaction

The efficiency will therefore depend on the relation between the lifetime of the excited state and the time needed for completing the electrochemical reaction. Table I gives some characteristic time constants for electron transfer, ion transfer, and the lifetimes of excited states.

It is obvious that the chance to see the effect of electronic excitation is much larger for an electron-transfer process than for ion transfer, because electron transfer is so much faster. On the other hand, the efficiency of electronic excitation in metal electrodes will be very low because of the extremely short lifetime of excited states in metals. This is quite different for semiconductors and insulators where we therefore can expect to find very pronounced effects. In the following we shall discuss a typical case for every kind of excitation.

Excited Molecules as Redox Reactants

To understand the action of an excited molecule as an electron donor or electron acceptor we must get some idea of the redox potential of an excited redox system (2). This depends clearly on whether the reduced or the oxidized component of the redox system is excited. For this discussion we shall use the so-called absolute scale of redox potentials which is closely related to the electronic energy level system of solid-state physics (3, 4). The relation between the electrochemical redox scale and this absolute scale is given in the definitions and the energy scheme shown in Fig. 4. A comparison of the two scales is shown in Fig. 5.[3]

What happens with the redox potentials of a molecule in the excited state is shown in the following two figures. Figure 6 describes this in a very simplified molecular orbital picture. We consider a molecule in its singlet state and assume that the lowest vacant molecular orbital is the acceptor orbital for the reduction of this molecule while the highest occupied orbital is the donor orbital. By electronic excitation to the lowest excited singlet state an electron will be promoted from the donor orbital to the acceptor orbital. We see that the situation is just inverted now. The previous donor orbital becomes an acceptor orbital while the previous acceptor orbital has become the donor orbital. This means that the redox potential

[3] It should be mentioned that the position of the NHE, located in this picture at E_{NHE} = −4.5 eV, is still open to discussion (31, 32).

Table I. Comparison between reaction time and lifetime

Electron transfer		10^{-12}-10^{-14} sec
Ion transfer		10^{-10}-10^{-12} sec
Molecules	Excited singlets	10^{-8} 10^{-12} sec
	Excited triplets	10^{-3}-10^{-10} sec
Metals	Excited electrons	10^{-14}-10^{-15} sec
Semiconductors and insulators	Excited electrons or holes	10^{2}-10^{-13} sec

Conventional and Absolute Scale of Redox Potentials

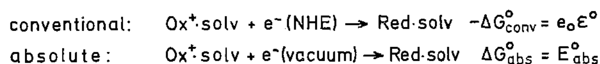

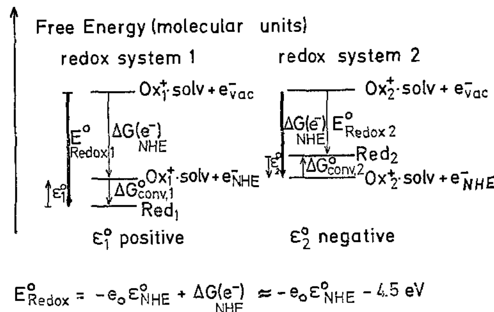

$$E^{o}_{Redox} = -e_o \varepsilon^{o}_{NHE} + \Delta G(e^-)_{NHE} \approx -e_o \varepsilon^{o}_{NHE} - 4.5 \text{ eV}$$

Fig. 4. Conventional and absolute scale of redox potentials derived from the free-energy changes in the corresponding redox reactions.

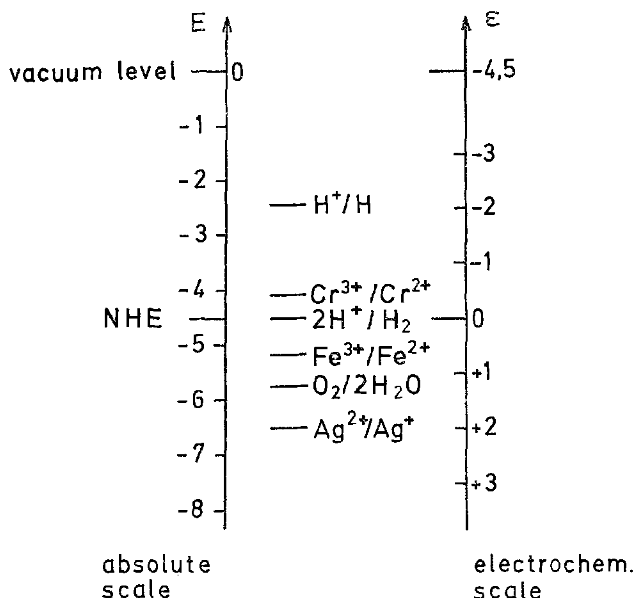

Fig. 5. Comparison of conventional and absolute scale of redox potentials.

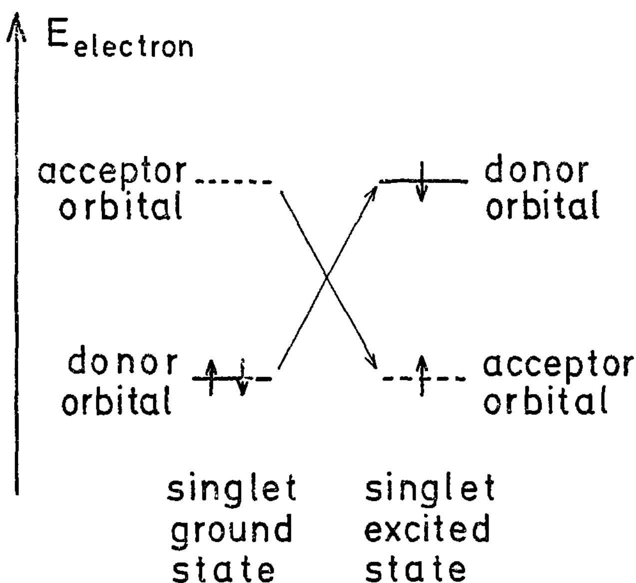

Fig. 6. Energy position of redox orbitals of a molecule in the ground state and the excited state according to simplest M O-picture.

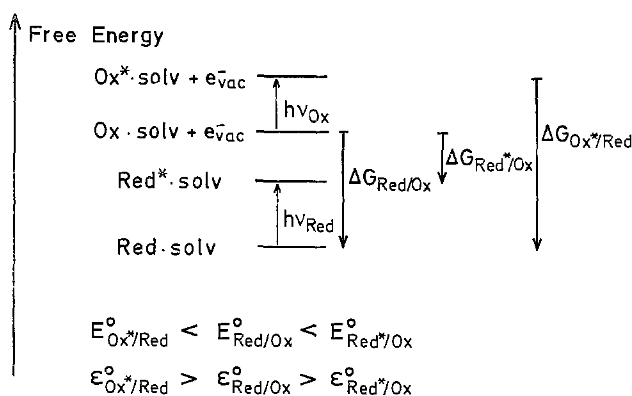

$$E^{o}_{Ox^*/Red} < E^{o}_{Red/Ox} < E^{o}_{Red^*/Ox}$$

$$\varepsilon^{o}_{Ox^*/Red} > \varepsilon^{o}_{Red/Ox} > \varepsilon^{o}_{Red^*/Ox}$$

Fig. 7. Shift of redox potentials by electronic excitation of the reduced or the oxidized species of a redox couple derived from the free-energy changes.

of an excited molecule is shifted in two directions. Its reductive power has been increased simultaneously with its oxidative power. Figure 7 shows this more concretely in a free energy scale for a redox system with two components where either the reduced species is excited or the oxidized species. This picture demonstrates that the shift of the redox potential between the reaction in the ground state and in the excited state is just given by the stored excitation energy in the molecule. If the reduced component is excited, the free energy for electron abstraction is reduced by this amount and the redox potential is shifted in the negative direction in the conventional electrochemical scale while excitation of the oxidized component increases the energy gained by electron addition, this meaning that the redox potential of the system is shifted in the positive direction of the conventional electrochemical scale.

What happens when such an electronic excitation occurs exactly at the interface between the electrolyte and an electrode? The various possibilities are shown in Fig. 8 where metals, semiconductors, or insulators are assumed as the electrode material (5, 6). The positions of the electronic energy levels in the excited molecule are represented again in the simplified molecular orbital picture. The figure shows that in contact with a metal in a situation where no dark reaction is possible, electron transfer in both directions will be opened after excitation of the molecule. This means that no external current can be observed in such cases since both processes will compensate each other. This is a mechanism of energy quenching by mutual electron exchange. Even if one of these processes should be faster than the other, the reverse process will occur in the dark as a consecutive reaction. The chance that such photocurrents can be found at metal electrodes is, therefore, very dim. Only in cases where a very fast chemical reaction follows one of the electron-transfer steps which prevents the reverse process can photocurrents be observed in such systems. If photoeffects are found, they are usually caused either by the existence of nonmetallic surface layers on the electrode or by photochemical reactions in the electrolyte which generate species with a different redox potential which can either be oxidized or reduced at the electrode during their lifetime.

The attractive cases involve contact between an excited molecule and a semiconductor as shown in (b) and (c) of Fig. 8. What happens in such a case depends on the relative position between the energy bands and the redox orbitals of the excited molecules. In case (b) electron injection into the conduction band is possible and can be observed as an anodic photocurrent. In case (c) electron extraction from the valence band equivalent to hole injection will occur, and a cathodic photocurrent is found. Case (d) shows a system

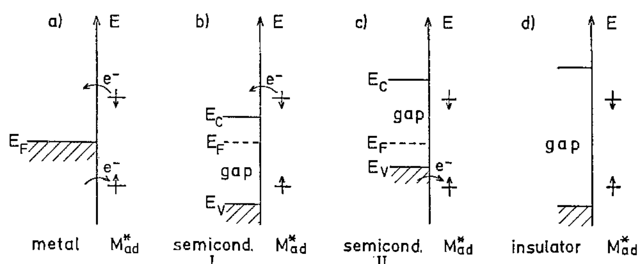

Fig. 8. Typical situations for electron transfer between an excited molecule and various solids.

where the bandgap is too wide to permit any kind of electron transfer.

In this picture we have not yet discussed another possibility of energy quenching which is very efficient at a contact with metals, that is, energy transfer. This is found whenever the absorption spectrum of the electrode overlaps the fluorescence spectrum of the excited molecule (7, 8). To avoid this, the bandgap of the semiconductor must exceed the energy stored in the molecule after excitation. This is another reason why photocurrents at metal electrodes are usually not caused by direct electron transfer in the excited state.

Figures 9 and 10 give examples of cases (b) and (c) of Fig. 8. Figure 9 shows a comparison between the absorption spectrum of a dye molecule in solution and the action spectrum of the photocurrents if this dye is brought into contact with a ZnO electrode which is suitably polarized to collect all injected charge carriers (9). This requires an anodic bias in case of electron injection, as found at the ZnO electrode. Figure 10 shows hole injection by the same excited dye molecule at a p-type GaP-electrode (10) where we have the situation of Fig. 9(c). Since the bandgap

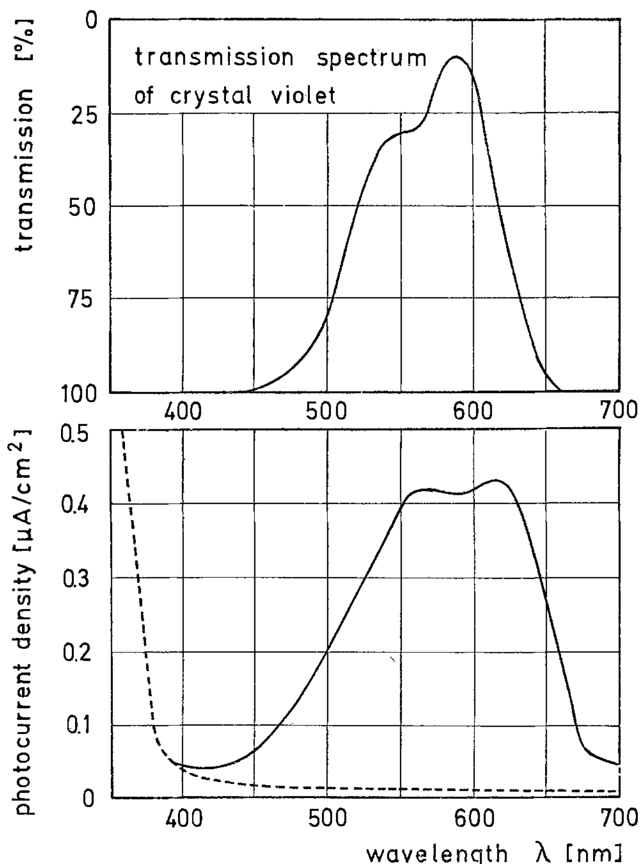

Fig. 9. Photocurrent spectrum for electron injection from crystal-violet into a ZnO electrode in comparison with absorption spectrum of the dye in solution.

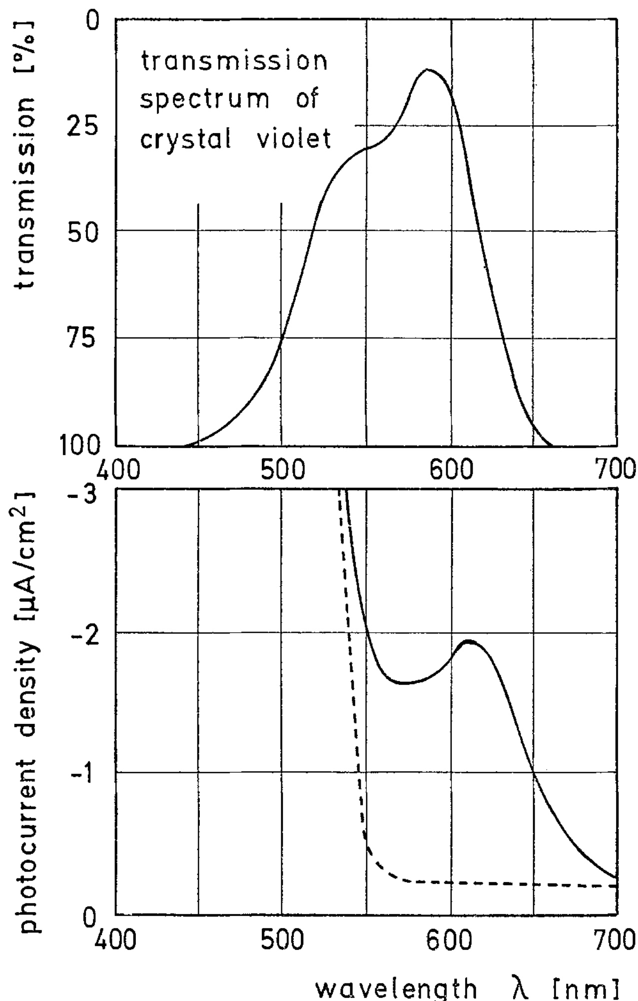

Fig. 10. Photocurrent spectrum for hole injection from crystal-violet into a GaP electrode in comparison with absorption spectrum of the dye in solution.

of GaP is not wide enough, only the long range part of the dye absorption spectrum can be used for this kind of sensitization.

Such experiments provide sensitive tests of models for the spectral sensitization of solid materials (11), which has long found wide technical application in photography. This demonstrates again the close relationship of electrochemistry and solid-state physics.

Electronically Excited Metals

Now we consider electronic excitation in metals. Although we have stated earlier in the paper that we should not expect large effects due to the short lifetime of excited states in a metal, we are all aware that photoemission from metals into vacuum is a process well known for a long time. The reason that there is any chance to observe an effect of electronic excitation despite the short lifetime is the fact that electrons have an enormous velocity and therefore a chance to reach the surface in a very short time after excitation. Photoemission from a solid into vacuum is limited by the height of the energy barrier for leaving the solid material. For a metal in contact with the electrolyte the situation is not different. Only the shape of the energy barrier and its height are modified. In case of an aqueous electrolyte there is some interaction between the free electrons and the solvent which reduces the energy barrier. In addition to this, the electric potential drop in the electrical double layer at the interface influences the barrier height drastically and gives the means to alter it systematically.

Photoelectron emission into electrolytes has been studied in recent years quite intensively by the Russian School (12, 13), centered in the Institute of the Academy of Sciences which was headed by the late Professor Frumkin, after it had been started by the pioneering work of Barker (14). Some recent investigations in our institute, mainly done by J. K. Sass, have demonstrated that this technique is especially useful for studying the excitation and emission mechanism of electrons from solids in energy ranges which are not accessible to experiments *in vacuo* (15, 16).

Figure 11 shows the modification of the threshold for photoelectron emission by the presence of a condensed medium like an aqueous solution. The magnitude of the photocurrent depends on the quantum energy of the light, on the electrode material, and on the electrode potential. Two typical results are shown in Fig. 12 for a gold electrode. One sees, however, that not only cathodic photocurrents can be observed but also anodic ones (17). It can be concluded that the anodic photocurrents mean the oxidation of water by vacant electronic states at deep energy levels. These are excited holes in the metal.

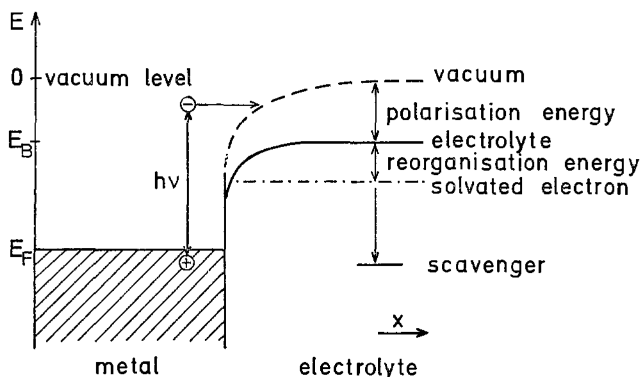

Fig. 11. Energy barrier for photoelectron emission from a metal into an electrolyte in comparison to the barrier against vacuum.

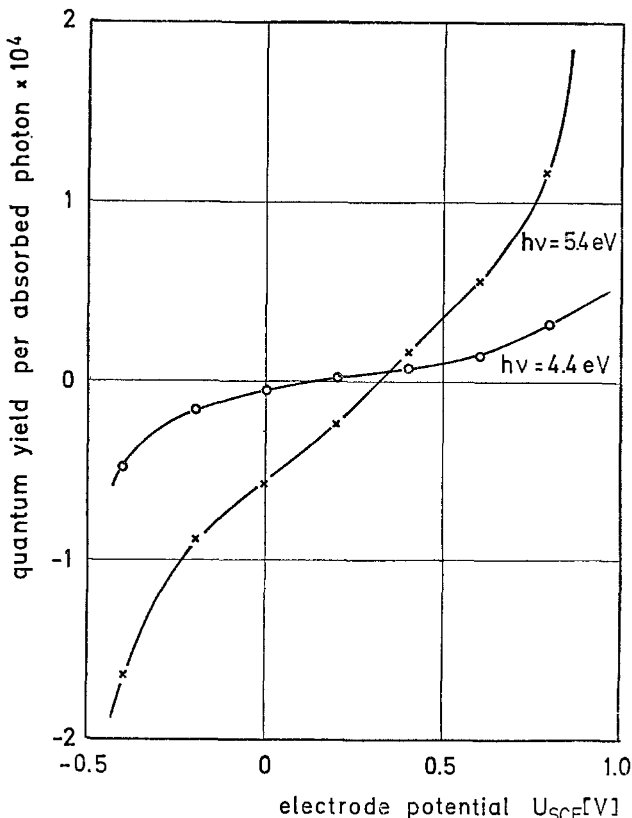

Fig. 12. Photocurrent-potential curves for a gold electrode in 1M H_2SO_4 for two different light energies.

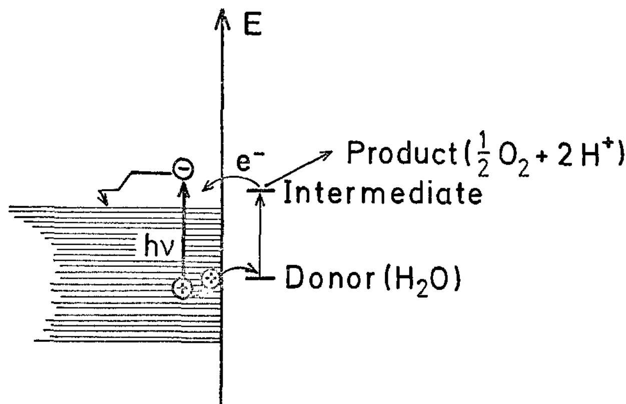

Fig. 13. Water oxidation by excited holes at the metal-electrolyte contact in terms of energy levels.

Figure 13 shows the mechanism of this reaction which ends in molecular oxygen. The potential dependence of the cathodic and anodic photocurrents clearly indicates that there is an energy threshold for both processes, photoelectron emission and water oxidation, which varies with the applied potential. If we assume that the potential drop between the electrode and the electrolyte is located exclusively in the Helmholtz double layer, a variation of the electrode potential means that the Fermi level, relative to the energy levels in solution, is shifted up or down by the applied voltage, and both thresholds are shifted in parallel, but in opposite direction. This is shown in Fig. 14.

Photoelectron emission studies at single crystal faces demonstrate that the crystal orientation plays an important role for the quantum yield. One knows from thermodynamics that the energy threshold between the bulk of a metal and the electrolyte is the same for any face at a given electrode potential. Nevertheless, photoemission quantum yield varies drastically with orientation as shown in Fig. 15 (18). This effect is most pronounced if polarized light is used (19). One

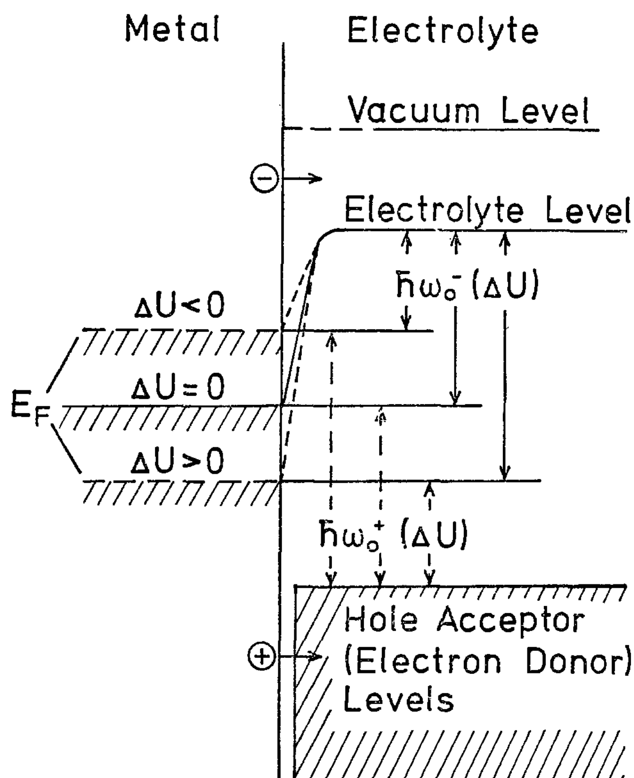

Fig. 14. Variation of the energy thresholds for photoelectron emission and photohole oxidation by the electrode potential.

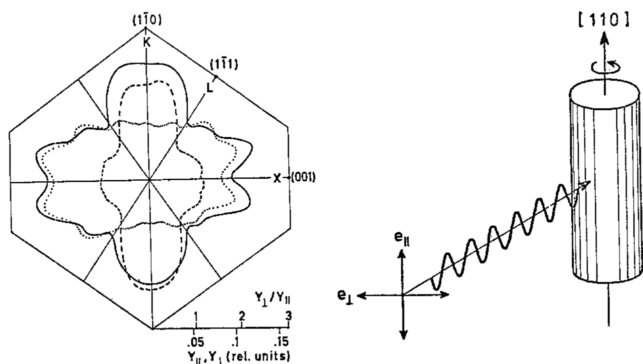

Fig. 15. Variation of the photoemission yields ($Y_{\perp}$ (———), $Y_{\parallel}$ (· · ·), and the ratio $Y_{\perp}/Y_{\parallel}$ (– – –) with crystallographic orientation on the single crystal cylinder surface for $h\nu = 3.45$ eV. A schematic illustration of the experimental geometry is shown on the right-hand side of the figure.

sees in Fig. 15 considerable differences in the efficiency for the two modes of polarization. This can be understood by correlating the different excitation conditions with the band structure of a metal. The momenta of the excited electrons and the chance to pass the barrier depend on crystalline direction.

As mentioned at the beginning of the paper, one should expect also that ion transfer should be accelerated by electronic excitation. There is, however, to my knowledge only one case where this effect has been observed at a metal electrode in the absence of a surface coverage with an oxide layer or other surface compound (20). This case is shown in Fig. 16. The gold electrode tends to dissolve in the presence of halide ions in a narrow range of electrode potentials just before an oxide layer is formed on the surface. The figure shows that in this range the dissolution rate is somewhat enhanced by illumination. The mechanism of this phenomenon, however, is still somewhat obscure and needs further studies.

Electronic Excitation in Semiconductors

As we expect from our estimation earlier in the paper, semiconductors show much more pronounced photoeffects than metals if light is absorbed beneath the surface. Quantum yields close to 1 can be obtained if the light is absorbed exclusively in a space-charge layer underneath the surface where a high enough electric field provides full separation of the electron hole pairs generated by light absorption. Such a situation can be reached at n- or p-type semiconductors by applying a suitable voltage which creates a depletion layer of large enough depth (21, 22), as is shown in Fig. 17. If electron donors or acceptors are present, the minority carriers reaching the surface will undergo redox reactions with these components of a redox couple. This will create a photovoltage of opposite sign to the initially present voltage across the space charge layer as is indicated in Fig. 17. Such photovoltages are the driving force for any kind of photoelectrolysis as in photoelectrochemical solar cells based on light absorption in semiconductors.

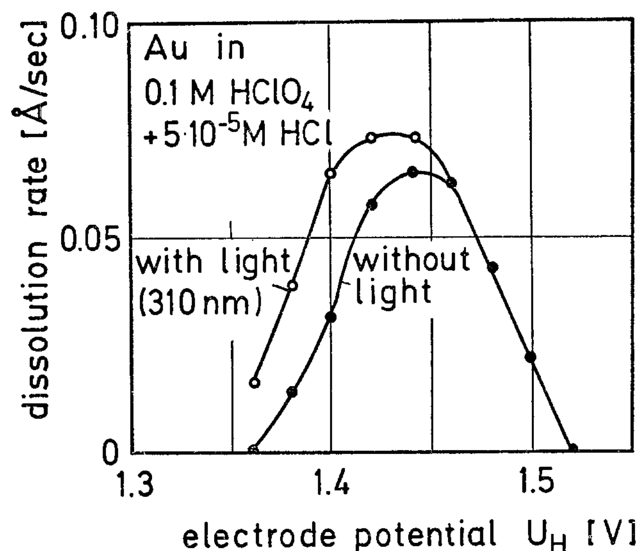

Fig. 16. Influence of illumination on the dissolution rate of gold in chloride-containing electrolyte.

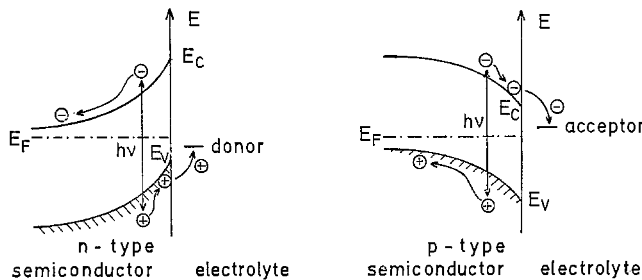

Fig. 17. Electron hole pair separation in illuminated depletion layer of a semiconductor.

If no suitable components of a redox couple are present the minority carriers will accumulate in the surface and the chance for ion-transfer reactions is enhanced (23). In most semiconductors the accumulation of holes means the weakening of bonding states and the preformation of a cationic state in the surface (24). Such cationic states react easily with nucleophilic reagents from the electrolyte and form reaction products which can be soluble in the form of ions or may be deposited as another compound on the surface.

The accumulation of electrons in the surface also usually results in the weakening of the surface bonds by the occupation of antibonding or nonbonding states. The consequence is a preformation of an anionic state in the surrace which easily can react with electrophilic components of the electrolyte. Decomposition of the semiconductor is the result. Table II summarizes a number of such reactions.

The quantum yield of all these photoreactions by excitation of the semiconductor depends on the penetration depth of the light and the extension of the space charge layer. The penetration depth of the light decreases drastically as the photon energy approaches the bandgap energy. The extension of the space-charge layer increases with applied voltage. These two effects are clearly shown in Fig. 18 for an n-type ZnO-electrode, where the photocurrents are compared at equal light intensities for different wave lengths and at different voltages. If one measures the photocurrent at a given voltage, the action spectrum of the semiconductor is revealed in the photocurrents. Some examples are given in Fig. 19 for two n-type and one p-type material.

These large effects of photoexcitation in semiconductors have in recent years found great interest for the purpose of solar light to energy conversion (25-27). In such systems the sensitivity of semiconductors to decomposition reactions in contact with electro-

Table II

Anodic oxidation
$CdS + 2h^+ + aq \rightarrow Cd^{2+} \cdot aq + S$
$ZnO + 2h^+ + aq \rightarrow Zn^{2+} \cdot aq + \frac{1}{2} O_2$
$GaAs + 6h^+ + aq \rightarrow Ga^{3+} \cdot aq + AsO_2^- \cdot aq + 4H^+ \cdot aq$
Cathodic reduction
$CdS + 2e^- + aq \rightarrow Cd + S^{2-} \cdot aq$
$ZnO + 2e^- + aq \rightarrow Zn + 2OH^- \cdot aq$
$Cu_2O + 2e^- + aq \rightarrow 2Cu + 2OH^- \cdot aq$

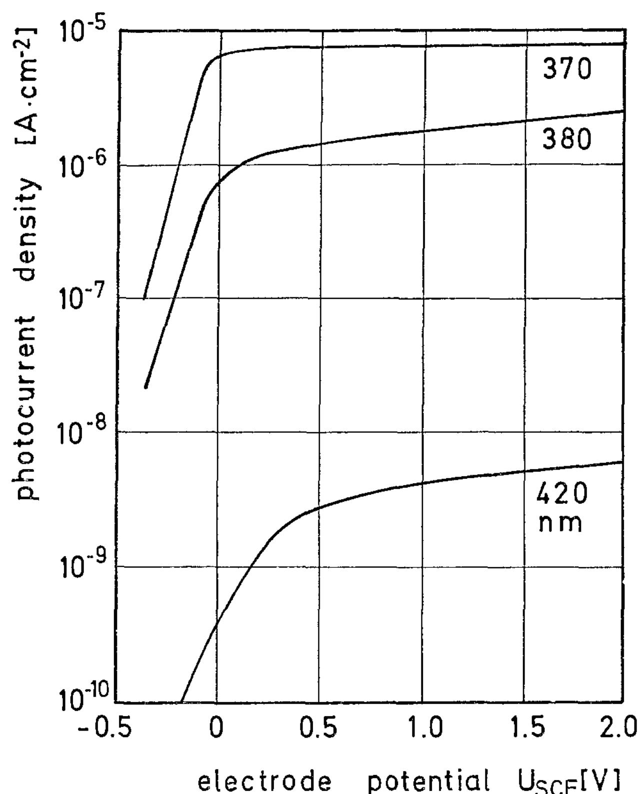

Fig. 18. Photocurrent-potential curves for ZnO electrodes at illumination with light of different penetration depth.

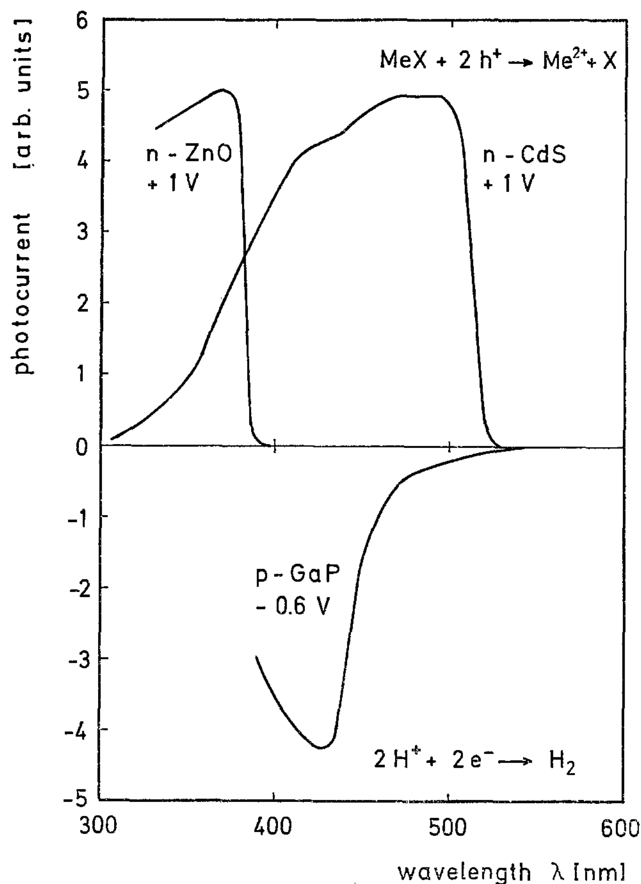

Fig. 19. Photocurrent spectra for n- and p-type semiconductors in saturation range.

lytes is the largest obstacle (28) Many research groups are working hard to overcome these difficulties and to develop devices by which either hydrogen or electric power can be generated in a photoelectrochemical cell.

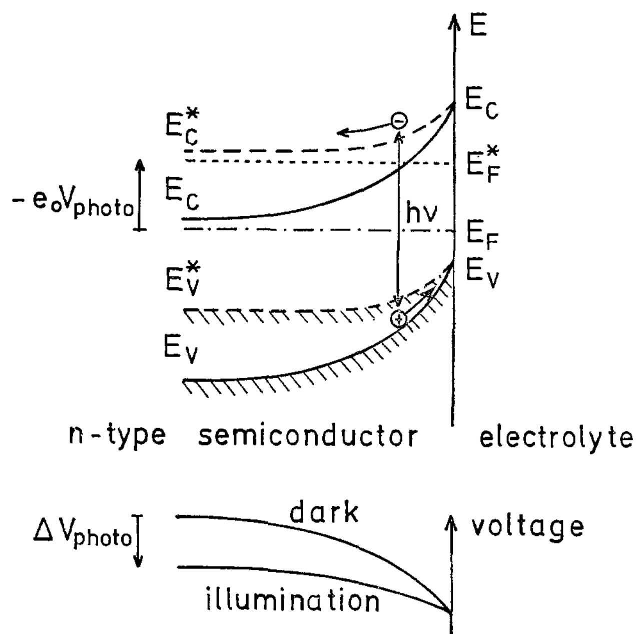

Fig. 20. Generation of a photovoltage in illuminated Schottky barrier.

The common bases of all these devices is the fact that semiconductor/electrolyte contacts form a Schottky barrier if the electrolyte contains a suitable redox system. Illumination of this Schottky barrier generates a photovoltage which acts as the driving force for electrolysis. As shown in Fig. 20, the source of the power and the mechanism of light to electrical energy conversion is the same as in photovoltaic solid-state devices. Therefore, semiconductor/electrolyte systems are subject to the same limitations in energy conversion efficiency as are the usual solid-state devices. The advantage of the electrochemical systems is the fact that this type of Schottky barrier can be formed very easily and without any problems with regard to the epitaxial conditions to avoid lattice misfit at the contact between two solids. The price one pays, however, is a susceptibility of the material to decomposition. The future will show whether technically reliable and efficient devices can be built on this principle.

Generation of Excited States by Electrolysis

Finally, we discuss somewhat the inverse of the processes discussed earlier, *i.e.*, the electrolytic generation of excited states. I shall not include the generation of excited states in homogeneous electrolytes which leads to luminescence and where the reaction partner can be generated by electrolysis. The discussion shall be restricted to the direct generation of excited states by electrode reactions.

Again, this can only be observed at semiconductors since the signal which indicates the generation of an excited electron state is light emission. How this is accomplished at the semiconductor electrode is shown in Fig. 21. If conditions can be found where the redox system injects minority carriers into the surface, they will recombine with the majority carriers. This is often a radiative process. Figure 21 shows this schematically for electron injection into a p-type semiconductor and hole injection into an n-type. In Fig. 22 are given the spectra of the emitted light from various electrodes where the conditions of Fig. 21 were met (29). These spectra for various n-type semiconductors show that the emitted light not only stems from band-to-band recombination, but sometimes contains light with smaller energy. It can be assumed that this light comes from recombination via surface states according to a mechanism which is shown in Fig. 23. Similar results have been obtained by electron injection into

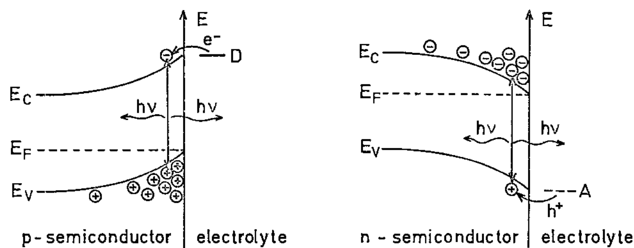

Fig. 21. Generation of luminescence by injection of minority carriers from redox systems into accumulation layer at the semiconductor/electrolyte contact.

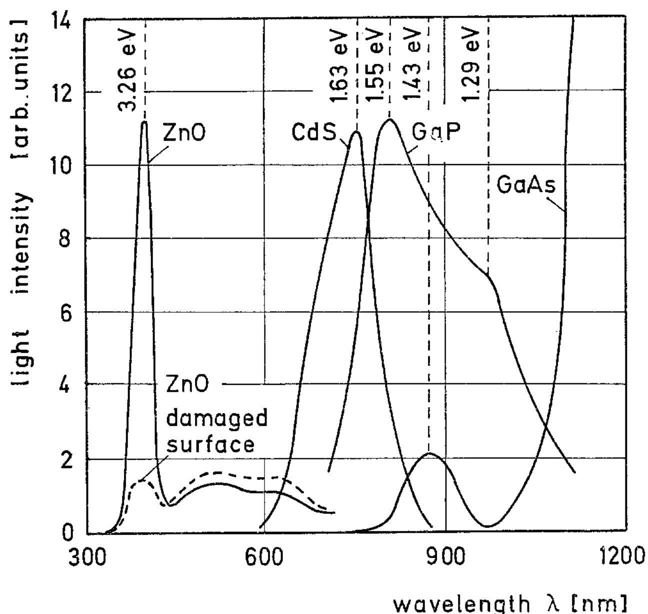

Fig. 22. Luminescence spectra of n-type semiconductors with hole injection by the radical SO_4^- with high oxidation potential.

p-type GaP (30). Such experiments can be very useful for elucidating the mechanism of electrochemical reactions at semiconductors and also for characterizing the electronic situation at a semiconductor electrolyte contact.

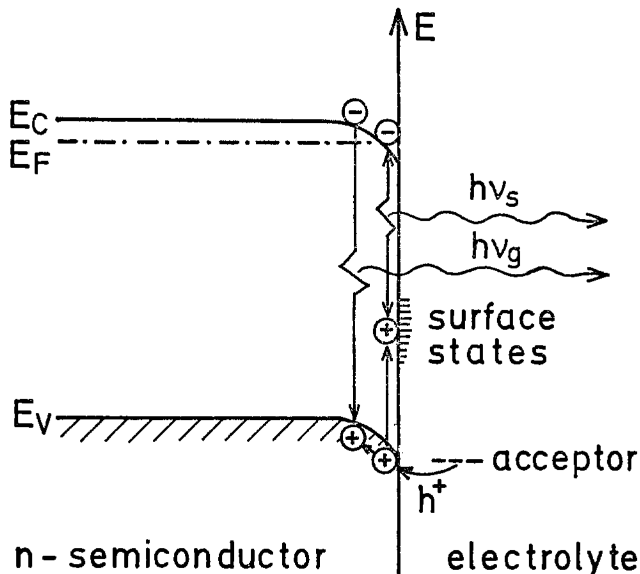

Fig. 23. Energy terms for luminescence by recombination from band-to-band or via surface states.

Summary

I have treated in my brief review only the simplest cases. As usual, the problems are in reality much more complicated and many questions are still open to discussion. There are many more applications of electronic excitation as a sensitive tool for studying the mechanism of electrode reactions or the properties of surface layers formed in an electrochemical process. I hope that the few examples given have demonstrated that the study of excited electronic states in electrochemistry is an exciting subject and I am convinced that many more electrochemists will be fascinated by this field in years to come. I am sure that this subject will contribute further to improving the understanding between electrochemists and solid-state physicists.

Acknowledgments

Those of my former and present co-workers who have made possible the contributions from my laboratory to the field which I have discussed in this lecture are portrayed in my last picture. I wish to express my appreciation.

Fig. 24. Co-workers of Heinz Gerischer.

REFERENCES

1. E. Becquerel, *C.R. hebd. Séances Acad. Sci.*, **9**, 58, 145, 561, 711 (1839).
2. H. Gerischer, *Faraday Discuss.*, **58**, 219 (1974).
3. F. Lohmann, *Z. Naturforschung*, **22a**, 813 (1967).
4. S. Trasatti, in "Advances in Electrochemistry and Electrochemical Engineering," H. Gerischer and C. W. Tobias, Editors, **10**, 213 John Wiley & Sons, New York (1977).
5. H. Gerischer, *Photochem. Photobiol.*, **16**, 243 (1972).
6. H. Gerischer, *Isr. J. Chem.*, **14**, 138 (1975).
7. Th. Förster, *Ann. Physik*, **2**, 55 (1948).
8. H. Kuhn, *J. Chem. Phys.*, **53**, 101 (1970).
9. H. Tributsch and H. Gerischer, *Ber. Bunsenges. Phys. Chem.*, **73**, 251, 850 (1969).
10. R. Memming and H. Tributsch, *J. Phys. Chem.*, **75**, 562 (1971).
11. H. Gerischer and F. Willig, "Topics in Current Chemistry," **61**, p. 31, Springer Verlag, Berlin-Heidelberg New York (1976).
12. Yu. V. Pleskov and Z. A. Rotenberg, *J. Electroanal. Chem.*, **20**, 1 (1969).
13. A. M. Brodsky and Yu. V. Pleskov, "Progress in Surface Science," Vol. 2, part 1, Pergamon Press, Oxford (1972).
14. G. C. Barker, A. W. Gardner, and D. S. Sammon, *This Journal*, **113**, 1182 (1966).
15. J. K. Sass, *Surf. Sci.*, **51**, 199 (1975).
16. J. K. Sass, E. Meyer, and H. Gerischer, *Ber. Bunsenges. Phys. Chem.*, **79**, 1077 (1975).
17. H. Gerischer, E. Meyer, and J. K. Sass, *ibid.*, **76**, 1191 (1972).
18. J. K. Sass and H. J. Lewerenz, Submitted to *J. Phys.*
19. J. K. Sass, H. Laucht, and S. Stucki, in "Proceedings of the International Symposium on Photoemission," Noordwijk, The Netherlands, R. F. Willis *et al.*, Editors, p. 83, European Space Agency, Paris (1976).
20. H. Gerischer, E. Meyer, and J. K. Sass, *Werkst. Korros.*, **25**, 235 (1974).
21. V. A. Myamlin and Yu. V. Pleskov, "Electrochemistry of Semiconductors," Plenum Press, New York (1962).
22. H. Gerischer, in "Physical Chemistry," Vol. IX A, H. Eyring, D. Henderson, and W. Jost, Editors, Academic Press, New York (1970).
23. H. Gerischer and F. Beck, *Z. Phys. Chem.*, **23**, 113 (1960).
24. H. Gerischer and W. Mindt, *Electrochim. Acta*, **13**, 1329 (1968).
25. A. Fujishima and K. Honda, *Nature (London)*, **238**, 37 (1972).
26. H. Gerischer, *J. Electroanal. Chem.*, **58**, 263 (1975).
27. "Proceedings of the Conference on Semiconductor-Liquid Junction Solar Cells," The Electrochemical Society, Princeton, N.J. (1977).
28. H. Gerischer, *J. Electroanal. Chem.*, In press.
29. B. Pettinger, H.-R. Schöppel, and H. Gerischer, *Ber. Bunsenges. Phys. Chem.*, **80**, 845 (1976).
30. R. Memming, *This Journal*, **116**, 785 (1969).
31. S. Trasatti, "Advances in Electrochemistry and Electrochemical Engineering," Vol. 10 H. Gerischer and Ch. W. Tobias, Editors, p. 213, J. Wiley & Sons, New York (1977).
32. R. Gomer and G. Tryson, *J. Chem. Phys.*, **66**, 4413 (1977).

JOURNAL OF THE ELECTROCHEMICAL SOCIETY

REVIEWS AND NEWS

JUNE 1978

Process and Equipment Developments in Electrothermics and Metallurgy over the Last Twenty-Five Years

R. Bakish*

Bakish Materials Corporation, Englewood, New Jersey 02631
and Fairleigh Dickinson University, Teaneck, New Jersey 07666

The Electrothermics and Metallurgy Division of The Electrochemical Society has a relatively broad mission in the subject matter which it considers as its province, and in the past 25 years much has transpired here. Reference is made to the period 1952-1977, the first year of which coincides with this writer's graduation as a metallurgist from Columbia University. Progress in these areas has had a major influence in much that is related to materials and materials processing today.

Let us begin by examining the scope of interests of the Division by considering the definition of the scope of its mission. By definition metallurgy is the science and art of extracting metals from their ores, refining them, and preparing them for use, while electrothermics in its broadest connotation is the use of electrical energy for heat generation and the application of this heat to a wide range of metal and nonmetal processing operations.

A thorough examination and review of all developments which took place in the last 25 years and which have had impact upon our Division will exceed the scope of this article. The writer instead will concentrate on the more important events of the period which affected materials processing technology of interest to our Division. He will also make passing reference to evolutionary changes in this technology and to areas which, though in most general terms fall within the definition of our Division's mission, have never been made part of its activities.

Perhaps the single most important development affecting activities of our Division in the period is the fact that vacuum and vacuum processes have become virtually an inseparable component in the preparation of an important number of materials today. To quote Winkler (1) of Balzers: "Almost all metals in the periodic table nowadays belong to the vacuum metals and are thus produced by vacuum methods, or to those that undergo vacuum processes at some stage in their manufacture."

Today by a wide variety of pumping schemes we can readily produce vacuums from 10 to 10^{-10} Torr. Much of the tremendous growth and advances of vacuum technology are both a product and fallout of effort to meet the needs of both the nuclear energy and aerospace fields, the latter triggered by that eventful October 4, 1957, when the Russian Sputnik appeared in the sky. Requirements of these two important domains of national scientific and engineering thrusts made possible the development of capabilities for the generation of vacuum on an industrial scale unheard of in the past. By virtue of this tremendous growth in scope and scale, costs have come to levels deemed well acceptable to the economics of the prevailing industrial climate, and as a consequence vacuum has made tremendous inroads in all kinds of industrial operations and is an integral part of the materials processing and industrial scene.

* Electrochemical Society Active Member.

Extractive Metallurgy, Materials Purification, and Crystal Growth

The advances in vacuum technology have played an important role and influenced the field of extractive metallurgy in this period. They made it possible to effect major, though really only evolutionary, advances (2) in the carbothermic and metallothermic reduction processes for V, Nb, Ta, Cr, Mo, W, Mg, Ti, Sm, Eu, La, Ce, and Ca. Not only metal production has benefited here, benefits were also derived in the production of a variety of carbides of these metals.

Advances of vacuum technology have played an equally important role in the area of metals refining as manifested in a number of ways. There was major growth in distillation techniques for metal purification on metals produced in large tonnage. For example in the case of lead almost the total world production (3) is subjected to the so-called vacuum dezincing process. An intermediate product in the refining of lead bullion, the so-called reichshaum (silver crust), is also processed by distillation (4) to separate such noble metals as Ag and Au which lead readily collects. Distillation processes for production of commercial purity indium and cadmium as well as the rare earth, alkali, and alkaline earth metals have equally benefited from the advances of vacuum technology.

The beginning of the 25 year period being considered here saw also the first paper (5) on the subject of zone melting, a technique which revolutionized the concept of realistic material purity attainable by those working in or with materials. I am now talking of production on much smaller scale than materials just mentioned. Perhaps the most significant initial application of Pfann's discovery was its application to the refining of germanium (6), the first important solid-state device material. This led to explosive adoption of the technique, where today its application is first and foremost for purification of silicon, and then for other materials for solid-state devices. Subsequent to this we saw its application for the purification of many metals. Work for purification of ionic compounds with activities directed to the alkali halides followed, though this work was by no means limited to these compounds.

In 1957, through utilization of electron beams by Calverley and his associates (7), the zone-melting technique was also adopted for the refining of the refractory metals and for single crystal growing. This was of considerable importance because of the role these metals were to play in the aerospace industry and in the conquest of space. While it will be discussed later, one should mention here that electron beams, through evaporative purification in cold-mold drip-melting techniques, also made important advances in the purification of refractory metals on a large industrial scale. Another matter to be discussed briefly later is the problem of vacuum and related processes for the purification and refining of steels for the pur-

pose of property beneficiation. It should also be stated that in the mid-1960's organic compounds joined the list of materials available in ultrapure condition, as a result of purification by zone-refining techniques.

In addition to making solid-state devices possible, this new generation of materials obtained through application of the new refining technique, *i.e.*, zone refining, has helped improve our understanding of materials on one hand and also established new uses for some of these materials. Ultrapure materials have shown properties differing from those of the very same materials of lesser purity. In metals, for example, plastic deformation studies revealed as expected much lower values for critical resolved shear stresses. In some organics (8) odors believed to be typical of certain compounds were established to be actually due to the presence of trace impurities within the compounds. In other cases of organic compounds, some believed to be by their nature self-oxidizing in air actually were stable after zone refining. Many other such examples (9) showing major changes in the properties of zone refined materials could be referred to.

Zone-melting techniques have actually had broader applications than simply for the purification of material. This technique has also been adopted to the so-called zone-leveling process, a method that makes it possible for us to distribute uniformly throughout the volume any trace impurities left.

Of much importance to the semiconductor industry were also the ideas of Dash (10-12) which led to the growth of essentially dislocation-free crystals. These ideas have been widely adapted to industrial crystal growing techniques and by integrated circuit materials manufacturers. By virtue of the considerable competitive importance of growing dislocation-free crystals to those in device manufacture, not all facts here have reached the literature. While single crystal growing techniques proceeded by many years the period which we are looking at, one must state that the most important advances with far-reaching commercial implications were made in this period.

When in 1955 the Bell System licensed electronic companies to manufacture the most elementary of the solid-state devices, the point contact transistor, the licensing agreement brought blueprints and instructions for a germanium single crystal growing installation. I became familiar with the Sprague system built under this license in 1955 and 1956. This company was growing 2-2.5 cm diam crystals using induction heating for the melting of the germanium in a carbon vessel. Both the growing crystal and the melt were contained under inert atmosphere. We were aware of dislocations and were suspicious that they could lead to problems in the simple devices which Sprague, like most other companies in the field, manufactured at that time. Yet in 1956 and 1957 we were a long way from a thorough understanding of the role of imperfections in electronic devices. Today silicon rather than germanium dominates the semiconductor industry and the bulk of commercial or captive silicon crystal growers produce 7.5 cm diam silicon crystals. Some can grow up to 10 cm and for that matter larger diameter crystals, but with the larger diameters a host of problems are encountered including those brought by the economics of this time. The crystals produced often reached 10 kg in weight and up to 1m in length; not only can we grow crystals of such size, but as indicated we can grow crystals with controlled dislocation distributions, grow these crystals virtually dislocation-free, and grow them with almost no impurities. The highest documented purity ever reached in any material (2×10^{10} defects/cm^3) was reported in 1974 by Hall of GE for germanium (13). We not only grow elemental single crystals from the melt today, but also crystals of compounds of elements with important divergence in their vapor pressures, and of controlled stoichiometry, problems also resolved in this period. Today we have readily available commercial crystal growers capable of growing crystals from notably low pressure ambients up to inert atmosphere environments with pressures reaching 150 atm (see Fig. 1 and 2). Units of this type, of units powered by diverse heat sources, produce single crystals of virtually any elemental or compound material and at almost any purity level.

We should add that these 25 years also saw the development of a single crystal growing industry, an industry producing a tremendous variety of materials in single crystal form. Crystals are made for: solid-state devices including IC's, transducers, fundamental studies of any type, and optical elements with properties tailored for a wide diversity of applications. We also produce organic crystals with large interatomic spacings for focusing and deflection of x-rays and, last but not least, crystals for decorative and jewelry uses. All these crystals are not grown from the melt, though the largest part probably are. The single crystal industry of the 1970's utilizes diverse techniques which, among others, grow crystals from the melt by vapor condensation (expitaxial layers), in the solid state, by the hydrothermic, and by the Verneuil processes. Because of its diversity and nonrelated final application of its products, it is difficult to place a dollar value on the total product of this industry, but it is quite considerable.

New Heat Sources and New Processes

Another major development which has had profound effect upon materials-processing technology has been the discovery and perfection of new heat sources to be used either in conjunction with the now more readily available vacuum environment or without it. These heat sources have led to the development of numerous new processes and these in turn have become an integral part of our industrial scene.

In the pages to follow I would like to look at two of these heat sources and the innovative processes and systems which they brought into our technology. I will illustrate my discussion with an occasional example of

Fig. 1. Single crystal silicon growing furnace, 75 mm diam capacity. Courtesy: Ham Company.

Fig. 2. "Melbourne" gallium phosphide single crystal growing system capable of maximum working pressure of 150 atm. Courtesy: Dr. J. Barret, Cambridge-Iman Company.

systems which embody these processes coming out of the manufacturers' lines today.

The electron beam, which is a collimated beam of highly accelerated electrons, has unusual characteristics which have made it a powerful tool for a diverse range of applications. These beams, which in principle had been proposed for some of these applications long before the period which we are considering, are best suited to vacuum operations. The now readily available vacuum made possible the development of a whole new technology, "The Electron Beam Technology." This is a technology with far-reaching consequences which encompasses a broad spectrum of applications. Our Division has closely monitored progress here since 1964 (14), and will again be taking pulse of the situation in May 1978 in Seattle. I would like to refer to the more important achievements in the areas where electron beams have made major contributions and give some reasons for the level of developments here.

Though in principle the first application of electron beams for metal melting and purification was proposed in 1907 (15), electron beams did not really begin to make a real contribution here until 1957 when their successful application to metal purification was realized by the then newly established Temescal Metallurgical Corporation. This was a company devoted to exploitation of electron beams as heat sources for metal processing. Shortly after this modest beginning the writer had a 2 cm Ta ingot processed by an early Temescal electron beam furnace in 1958 for subsequent rolling to capacitor foil. Electron beams in melting, refining, and welding have since moved far (16-19). Their success in the first two fields is a consequence of their ability to efficiently melt any metal including tungsten without contamination in a cold-walled ingot mold which permits evaporative removal of virtually all impurities as already mentioned. Electron beams today are responsible for most of the tonnage of reactive and refractory metals and alloys reaching the field. Typical analyses from various sources for several electron beam processed materials are given in Table I (20-24). This today is a mature process which truly developed in the period in review, but a process which, by virtue of costs and other competitive processes, has not made inroads in the processing of ferrous metals which still remains the largest tonnage in the metallurgical field. Nevertheless, it has captured virtually all the reactive and refractory metal and alloy-processing business, as well as a very small tonnage fraction in the production of specialty steels for corrosion resistance, tool, die, and bearing applications. Some of the steel work has been carried out in hybrid vacuum induction/electron beam installations.

A diversity of gun types and configurations exist, and installations which initially were capable of only melting a few pounds have developed into systems capable of melting ingots of several tons. Specifically for a long time the simple Temescal-developed transverse guns competed with the von Ardenne-developed, LEW-built, axially deflected, differentially pumped, sophisticated electron optical system. The relatively inexpensive Temescal type guns made important contributions to the state of the art because of their cost-effective performance at low power levels. To this writer it appears that they also had restraining effects on the over-all U.S. industrial development at the upper power levels because of inherent instability of systems based on these guns at high power levels. For reliable and stable performance at the high ambient pressures typical of electron beam melting installations the differentially pumped guns certainly have excelled in the past and continue to do so. In fact they have displaced the unsophisticated electron guns from melting installations where such conditions prevail. I believe that the hybrid 6 MW Airco/Temescal steel-refining installation for production of E-Brite stainless steel in Berkeley, which is now out of commission, could probably have continued to produce today. It would have produced in a much more trouble-free fashion and more efficiently had its multitude (over 20) of transverse electron guns which powered its cold-wall refining trough, been powered by programmed, axial deflection, differentially pumped guns. To appreciate what has happened here one need only look at a 1200 kW installation available as a standard product today, see Fig. 3.

With the energy pinch and the EPA's continued tightening of environmental standards, the writer sees a new potential for the highly efficient and extremely clean electron beam melting and refining installations. As a matter of fact, plans for electron beam furnaces capable of producing 30 and 150 ton ingots are in the making (25).

Electron beams were responsible indirectly for a major advance in our understanding of refractory metals by making it possible to grow refractory metal single crystals as already mentioned. While used on a routine basis today virtually without notice, these systems and the work done with them were in the headlines of many a meeting where metallurgists and solid-state physicists gathered in the mid-sixties.

The evaporation area is another area where electron beams played and continue to play a most important role. Today their applications span the gamut from thin film components and related production activities through major installations for coating for corrosion protection; from items as down to earth as aluminum-coated steel strip used in the manufacture of sardine cans (see Fig. 4) to as sophisticated an application as coated components for gas turbines and jet engines. A number of installations using electron beam evaporation for R-C circuit manufacture have been produced. These systems actually utilize electron beams both for

Table I. Typical analysis of EB-processed metals

Impurities* (%)

Metal processed	Reference source	Al	B	C	Cd	Cr	Fe	H	Mg	Mn	Mo	Number of passes
Nb	15	<0.002	<0.0001	<0.003	0.002	0.007	<0.01	—	<0.002	<0.002	0.002	2
Hf	16	0.0025	—	—	—	—	0.005	—	—	—	—	1
Ti	17	—	—	0.04	—	—	0.15	0.0006	—	—	—	NA
Cu	18	—	—	—	—	—	0.0007	—	—	—	—	NA
W	19	—	—	0.04	—	—	0.0001	0.02	—	—	—	NA
Ta** Extra high purity		—	—	0.0025	—	—	0.001	0.0002	—	—	0.0005	NA
Ta** Select quality		—	—	0.0025	—	—	0.001	0.0001	—	—	0.007	NA

Metal processed	Reference source	Ni	N_2	O	Pb	Si	Ta	Ti	V	W	Zn	Zr	Number of passes
Nb	15	0.005	0.002	0.0052	<0.005	<0.01	0.078	<0.015	0.002	0.0287	<0.002	—	2
Hf	16	0.0029	0.0027	0.04	—	0.007	—	0.001	—	—	—	—	1
Ti	17	0.008	—	0.005	—	—	—	—	—	—	—	—	NA
Cu	18	0.0007	—	0.0001	0.0007	—	—	—	—	—	—	ND	NA
W	19	—	—	0.0008	0.018	0.0017	—	—	—	—	ND	—	NA
Ta** Extra high purity		—	0.002	0.006	—	0.0005	99.96 typical 99.93 minimum	—	—	0.005	—	0.0005	NA
Ta** Select quality		—	0.0025	0.010	—	0.001	99.92 typical 99.85 minimum	—	—	0.007	—	0.0005	NA

* A dash at the site of an element analysis indicates that no analysis of that particular element was reported in the reference.
** Kawecki Berylco Industries, Incorporated.

Fig. 3. 1200 kW electron beam melting system. Courtesy: Dr. Schiller, Institute M. von Ardenne.

Fig. 4. Strip-coating installation. Courtesy: Dr. S. Schiller, Institute M. von Ardenne.

evaporation of the resistance film and thermal machining, an alternate electron beam application, for trimming of these circuits.

Thermal electron beam machining then is another area where electron beams have made major contributions. It has, however, had a relatively slow growth. Since its original entry in 1959 as a commercial electron beam machine, these have been used for drilling of jeweled bearings, drilling of breathable jet engine blades, for drilling of plastics, and even for cutting of green ceramics. The electron beam thermal machining system of today is a major piece of capital equipment with costs approaching $300,000 and we can perhaps count a world population of only 20 units, if indeed that many. An example of such a machine produced by Steigerwald Strahltechnik can be seen in Fig. 5.

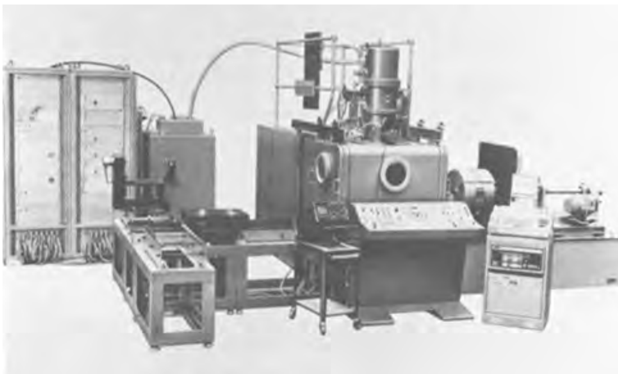

Fig. 5. Micro machining installation. Courtesy: Mr. Jack Drew, Steigerwald Strahltechnic-Farrel Corporation.

Perhaps the most consequential contribution of thermal electron beams to today's technology and affecting the widest possible number of people has been their application in welding. The electron beam (EB) welding process was invented independently in 1957 and almost simultaneously by Stohr (26) at the Saclay laboratories of the French Atomic Energy Commission, and by France and Wayman (27) at the General Electric Company, Hanford, Washington. Both inventions arose from efforts fostered by the needs of the atomic power field in the mid-fifties. The ensuing years have seen tremendous growth in acceptance of EB welding, substantial broadening of its capabilities, and the development of most sophisticated systems. Today the simple work-accelerated electron beam welders of Stohr and Wayman's time have been replaced by work-accelerated welding systems which operate, depending on the ultimate application, in three ranges of pressure, *i.e.*, 1 atm., 10^{-2} and 10^{-4} Torr, and below. These are the so called IAEBW, the commercial or soft-vacuum process and the hard-vacuum process. The simple manual control systems of yesterday have been replaced by sophisticated NC, fully programable installations capable of high production rates and outstanding quality of welding operations. The early producers and sucessors of the important pioneering entries in electron beam equipment are very much still part of the manufacturing scene today. Sciaky, Leybold-Heraeus (as successor of Zeiss) and Hamilton Standard and Steigerwald Strahltechnik very much dominate the scene with large welding systems, while the Torvac-EBTEC alliance has taken the lead in the small systems field. Despite the high initial capital cost of electron beam welding equipment, there is no segment of the metal processing industries where the process has not made major inroads by virtue of its performance capability, speed of welding, and cost effectiveness—this despite the high initial capital investment. Examples illustrating the status today are seen in Fig. 6, 7, and 8.

Perhaps the most exciting and sophisticated electron beam application which emerged in the period is that which uses the electron beam as an ionizing radiation source rather than as a heat source. Reference is made to the technique called electron beam lithography, which has all but revolutionized production of IC's. The "crown jewels" of this revolution are systems of the type developed by IBM (28), Bell Laboratories (29), and the commercial version of the EBES produced by its two licensees, Extrion and ETEC, to name a few (see Fig. 9, 10, and 11). These systems are capable either of manufacturing masks for IC production, or of actually producing individual IC's on silicon chips. The integrated circuit which has changed the face of the free world's electronic industry continues to shrink in size, improve in reliability and decrease in cost. The electron beam systems referred to above have made readily possible the generation of 1-2 μm device structural details. I believe that machines with the

Fig. 6. A multistation CV electron beam welding system for the manufacture of automotive transmissions. Fully computer controlled (cabinet at the right). Courtesy: Dr. S. Solomon, Sciaky Brothers.

Fig. 7. Electron beam welder, 150 kV. Courtesy: Mr. R. Samuelson, Leybold-Heraeus.

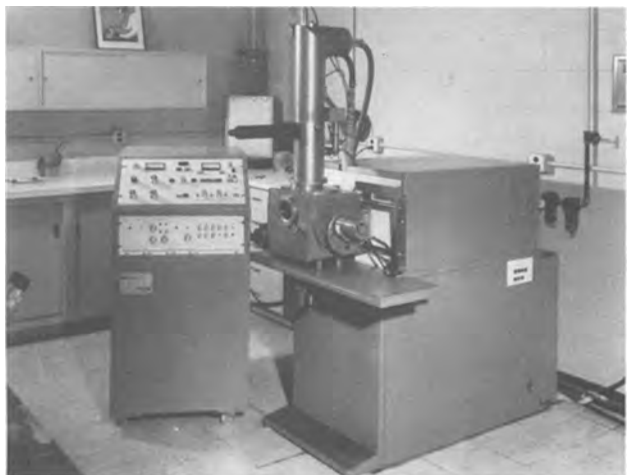

Fig. 8. Small components electron beam welder, 60 kV. Courtesy: Mr. L. Derose, EBTEC Corporation.

capability to produce 0.1 μm details are not really that far in the future and are certainly present in research hardware at hand in the laboratories of the leaders of

Fig. 9. Vector scan—electron beam lithography system. Courtesy: Dr. P. Chang, IBM Corporation, Yorktown Heights.

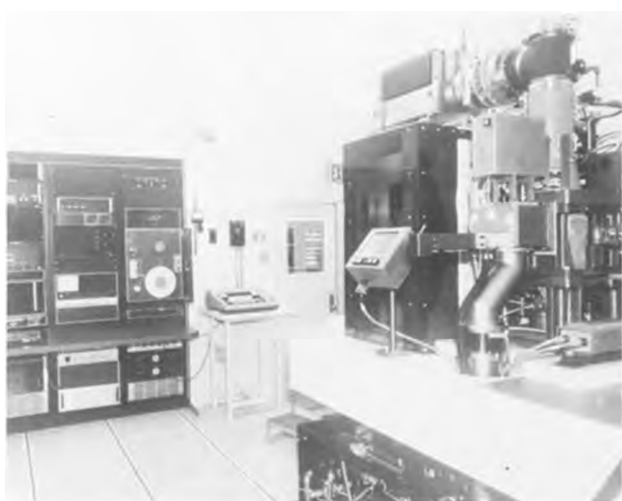

Fig. 10. EBES electron beam lithography system. Courtesy: Dr. D. Herriot, Bell Telephone Laboratory.

Fig. 11. EBMG 20 electron beam lithography system. Courtesy: Dr. A. A. Witkower, Varian Extrion.

the industry. When one talks of an electron beam microfabrication system, a 2 million dollar price tag is well in the range of reality. In closing my discussion on electron beam technology I wish to remind readers of the continued publication of our Society's proceedings (14) in this field and those of conferences jointly sponsored by the American Vacuum Society and the IEEE (30).

Perhaps one of the most exciting inventions to be made in the last 25 years is that of the laser. It was actually independently proposed by a number of investigators (31-37). Last October (1977) the U.S. Patent and Trademark Office, however, granted a patent to R. Gordon Gould dealing with the fundamental technology of lasers. This patent is being issued 18 years after Gould's invention. If it survives in a likely court challenge, it will confirm Gould as one of the laser's primary inventors—a distinction long denied to him by the fame of others. Today the developments emanating from laser work have had far-reaching repercussions in the world of science and technology. The laser by now is a firmly established measuring tool, and it has contributed much to spectroscopy as it has to holography. Strides with the laser in the communications field have been made but their full potential in this field has yet to be developed.

The laser is also an important heat source with distinctive characteristics, and it is its application as a materials processing tool that is of particular interest to us. The finely collimated laser beam is capable of producing effects similar to those of the electron gun even though by a much different mechanism. The greatest plus of the laser in comparison to the electron beam is the fact that it does not need vacuum for its operation. Thus, despite the fact that the laser is at best only about 10% efficient when contrasted with the better than 95% conversion efficiency of the electron beam, it does offer unique capabilities, and it is a most powerful material-processing tool. The primary applications here have been in welding, machining, and, more recently, heat-treating. Let us look at welding first because we have had the largest growth here. From initial work with pulsed ruby and neodymium glass lasers with output of 100-200W, we have moved today to the readily available multikilowatt lasers with the upper power limit of commercially available lasers for welding being 25 kW. Virtually all of these high power lasers in welding are operating in the continuous duty mode, and in most cases they are CO_2 lasers (38). From simple manually controlled lasers, we have gone to NC installations for reliably high rate part processing. This growth of power capability has seen the relatively limited upper thickness capability of 0.005-0.010 in. bypassed with today's lasers welding materials exceeding 1.00 in. in thickness. Many of the laser welding installations of today use inert gas assist for joining of some materials. The laser in a welding system is but the power source and much effort has been invested in the system design and system control to develop the capabilities of the systems which we have on the market today (see Fig. 12). Often welding system designers acquire the laser from a laser man-

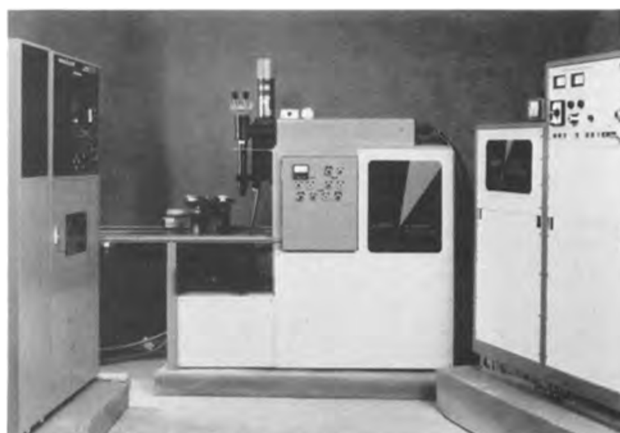

Fig. 12. NC-controlled laser welding system. Courtesy: Mr. L. Derose, EBTEC Corporation.

ufacturer, but they are the sellers of the integrated system. The acceptance of the laser as a welding tool also has led to expanded use in many industries including aerospace, electronics, and automotive.

The capability of the laser to ablate materials has led to its adoption as a machining tool. Today we have extensive laser machining applications including: extensive thin film applications in resistor trimming, jewel-bearing drilling, cutting of quartz tubing, cutting of metallic materials including titanium and super-alloys (these are often performed with an oxygen assist), cutting of materials for the packaging and the garment industries, and many more.

A third quite interesting and recently developed materials-processing application for lasers has been the area of heat-treating of materials, specifically highly localized heat-treating. It takes advantage of phase-transformation responsiveness of some alloys to the rapid heat cycles which lasers can produce. Essentially we are talking of the performance of a task equivalent to the case-hardening produced by more conventional approaches. In this case the laser technique permits local or selected-area heat-treating. One can also carry out surface alloying by depositing materials on the surface of parts to be alloyed and then performing laser-assisted local-diffusion treatments.

The laser as a heat source has also made important inroads in surgery and specially opthalmic surgery and of course the laser is intimately tied to fusion research and will most likely trigger most, if not all, fusion reactions of the future. Last but not least, the laser has tremendous potential for destruction, these applications of course being in the province of the military. There has been a virtual torrent of publications in the laser field and numerous references on all possible aspects of lasers can be found. A few of general utility are suggested here (39-41).

Our Division has usually stayed away from covering steel-processing activities of any sort, but as these are related to much already referenced in the paper, a brief reference to this area of materials processing is made here. Production difficulties with the manufacture of large forgings in the mid-fifties and the realization that high gas content was one of the main causes for these problems acted as catalysts for much of the developments that affected specialty steel processing. The introduction of the now more readily obtainable vacuum for the processing of these steels was one of the first developments which led to a variety of processes. Many of them have been well publicized while specific details of others have remained in the realm of "company confidential." While new installations based on these developments have been built in the U.S., it is believed that much larger investments in this area have been made by overseas manufacturers including those in Japan, France, and Germany. The Electrochemical Society's interest in this area is evidenced by the 1975 symposium (42) on metal-slag-gas reactions.

In addition to various degassing schemes for the specialty steels, the vacuum-arc process and the vacuum-induction process which combine both the melting and degassing operation have made important strides. Today installations exceeding 100 tons capacity have become available as standard industrial products. Another high quality steel-processing technique, the so-called electroslag remelting, became so identified in the mid-fifties by the Soviets (43). While the writer has not investigated the origins of the process, there is considerable evidence that processes of refining steel under a slag blanket with an electric arc as the power source were practiced in the U.S. under different names since the forties, this of course being the essence of the electroslag processing as defined today. It is quite conclusively demonstrated, however, that with the introduction of the term "electroslag melting" by the Soviets in the mid-fifties, a new phase in the development of this steel-refining process was initiated.

In 1963 the writer visited the Paton Institute for Electrowelding in Kiev and inspected what was considered one of the early electroslag remelting installations in the Soviet Union. Today we have reached and exceeded 100 tons size capacity electroslag (ESR) installations. These are presently manufactured by a number of companies both in the U.S. and abroad. A 165 ton furnace produced by Leybold-Heraeus is illustrated in Fig. 13. Electroslag remelting has seen an acceptance and steady growth by virtue of its ability to produce a high quality, cost-effective product with competitive properties meeting a diversity of ultimate applications. The electroslag process appears to have surpassed the growth rates of vacuum arc and vacuum induction for the specialty steel processing in the Soviet Union and has also achieved major industrial significance in the U.S. where two comprehensive reviews of the process have just appeared in print (44, 44a).

In 1960, among other activities, the writer became involved in what at the time was referred to as vapor phase metallurgy, the technique of producing metallic materials through the decomposition of inorganic or organometallic compounds. This technique was used then as now either to prepare very pure metals, metal coatings, or diverse free-standing metal shapes (45-48). The subject, which has since been renamed chemical vapor deposition or CVD, has been another important area of activities of the Electrothermics and Metallurgy Division with a number of meetings held under its auspices since 1955 (49-54). Its application to the electronics field was reviewed in some detail a few years ago by Tietjen (55).

Although the electric arc has been used industrially since the turn of the century, and for welding since about the time of World War I, only in the 1960's was this energy source used extensively for deposition of metallic and refractory compound coatings. In the plasma-arc spray process, powdered material is fed, together with a gas, through an electric arc where it is heated sufficiently to cause melting and then to be deposited on a cool substrate. Electrons from the arc cause substantial ionization of the gas atoms, and the resultant state is referred to as a plasma, although 100% ionization does not occur. Such plasma-arc sprayed coatings have been applied as thermal barriers, solid lubricants, corrosion- or abrasion-resistant surfaces, ablative layers, or for spray forming; but few of these are yet important commercially. Plasma spraying competes with both oxygas flame spraying and detona-

Fig. 13. 165 ton electro slag remelting installation. Courtesy: Dr. W. Dietrich, Leybold-Heraeus, and Stahlwerke, Rochling Burbach, GmbH.

tion coating, not usually on an economic basis but wherever the quality of the deposit, the diverse range of materials that can be sprayed, the feasibility of large scale application, and the suitability of plasma arc spraying to both metallic and nonmetallic substrates give it unique advantage over the other processes. Fisher (56) has provided a recent review.

The combination of vacuum and heat sources has led to the development of another important area of concern to our Division which can be referred to as thin film technology. This technology plays a key role in diverse segments of industry today, but has developed to its greatest level of sophistication in the electronics industry. In the last 25 years and most importantly in the last 15 years, we have seen this industry adopt evaporation approaches for material deposition in large scale manufacturing operations, and of recent date diverse sputtering approaches are gaining ground here relative to the former type. Table II (57) shows a comparison between electron beam evaporation and high rate sputtering (15 kW sources) for thin film deposition. Table III (57) shows the types of variation that are encountered in these processes and the reasons for those variations. Thornton (58) discusses the application of the sputtering process to thick film growth.

When small amounts of material are to be evaporated one can either use direct wire evaporation or foil evaporant containers. Special ceramics or ceramic-coated vessels become containers as the scale of applications grows. Of greatest importance for assuring deposit purity and prevention of contamination of the melt is the nature of the liquid metal container. Depending on the material to be evaporated and final use of the film, we can find as the container: refractory metals, oxides, boron, nitrides, and carbon. These are selected in order to assure no or minimum reaction of the evaporant with the container. The container can be either water cooled or heated, the latter used when higher rates are needed. Resistance heating and electron beams of diverse configuration have become the backbone of evaporation processes with each specific material and ultimate application determining the selection of the heat source.

Perhaps one of the earliest large scale commercial evaporative applications was the metallization of paper with zinc, and then mylar with aluminum for the manufacture of film capacitors. In the electronics industry the next thrust was brought about by requirements in manufacture of passive microcomponents, specifically resistors and capacitors. A steady growth in the application of thin films in the areas of active components has occurred in the last five years with both magnetic and semiconductor devices participating. The electronics applications are but one of the areas within what is referred to as thin film technology (59). We must also mention here the widest variety of thin films for the coating of optical lenses for diverse applications and including all types of optical filters. From here we can go to thin films in glass panels in simple or thermopane configuration for both decorative and functional uses. Last but not least, we come upon thin films for corrosion protection in specialized situations. When corrosion and oxidation resistance are the main reason for application of these coatings, much thicker coatings are often used (micrometers rather than angstoms).

Table II. Comparison of parameters for electron beam evaporation and high rate sputtering

Parameters	Electron beam evaporation	High rate sputtering
Deposition materials	Very restricted	Somewhat restricted
Condensation rate	Equal magnitude	
Evaporation rate/ sputter rate	$a_v = 1$ $a_v{}^* = 5\text{-}10a_v$	$a_s = 0.2\text{-}0.5a_v$
Particle source characteristic	Small area source	Large area linear source
Energy utilization	Less favorable with hr-sputtering	
Material utilization	Equal magnitude	
Uninterrupted operating time	Comparable in case of eb-evaporator with feed and hr-sputtering source	
Mean particle energy on substrate	0.1-0.2 eV	0.2-10 eV
Thermal load on substrate	0.1 Wcm^{-2}	0.2-1 Wcm^{-2}
Irradiation of substrate by	X-rays, (electrons)	Photons, low energy electrons, ions (low)
Residual gas effects	Higher in case of sputtering	
Impurity sources	Crucible reactions*	Sputtering of source components
Adaptability to substrate fixture	Favorable with hr-sputtering	
Extending feasibilities of basic processes	Generally by additional equipment	Generally by parameter selection
Instrumental expenditure source and power supply process control extended process variants	Referred to equal power: low in case of hr-sputtering	

* Hot crucible evaporation.

Table III. (57) Process variations of evaporating and sputtering techniques

Processing variants	Goal	Basic process: Evaporation	Basic process: Sputtering
High vacuum deposition	Avoidance of residual gas interactions	Internal HV or UHV evaporation	With ring-gap sources mean-free path $>h$ (the distance between source and substrate) working pressure $p = 5 \times 10^{-2}$ Pa or 1×10^{-4} Torr
Gas-scattering deposition	Particle scattering step coverage	Pressure plating (PP) (inert gas inlet)	Internal sputtering in inert gas
Reactive decomposition		Reactive evaporation (RE) (reactive gas inlet)	Internal
Electron-activated or plasma-activated reactive deposition	Chemical reaction	Activated reactive evaporation (ARE) (reactive gas inlet and electron or plasma generation)	Reactive sputtering in reactive gas
Ion-aided deposition, intermediate	Activated condensation	Ion plating (IP) (gas inlet and ion generation)	Internal bias sputtering
		Plasma plating Plasma pretreatment and EB-evaporation	

I wish to close my discussion on sources and processes by referring briefly to ion implantation. For a long time high temperature diffusion treatments were the only means available to the manufacturers for composition modification of semiconductor materials in device production. These diffusion treatments which by their very nature necessitate high temperature led to substantial control difficulties, high costs, and often low yields. This was a situation ripe for a take-over by a superior technique. But not only were the difficulties of the existing techniques favorable to the advent of a new technique, the requirements evolving from the very direction of development of solid-state devices and integrated circuitry, *i.e.*, much tighter specifications, higher frequencies, and in general ever increasing demands from this circuitry could be better served with the new technique of ion implantation.

Ion implantation then had a ready stage for its development and growth. Yet initial costs and limits on early implantation equipment capabilities (in particular the slow rates of material processing) led to slower than expected progress in adopting this technique. Nevertheless ion implantation is here to stay and is slowly but irreversibly replacing the gaseous diffusion process as a manufacturing tool for both individual and integrated solid-state devices.

I believe that ion implantation will eventually lead to complete displacement of gaseous diffusion for a number of reasons. If we consider composition uniformity we are capable of reducing variation from $\pm$ 15% to better than $\pm$ 1%. Ion implantation permits a much better lateral spread for most practical purposes and there is virtually no contamination from it. We have by far superior delineation techniques and, of course as we already mentioned, it is a clean vacuum operation against an operation in an alien high temperature environment. We can also implant a considerable variety of impurities with relative ease. Today cost of an ion implantation system depending on type is up to 2-3 times higher than a comparable diffusion system. While this cost differential is still important today, its importance will decrease in the future as the requirements of IC's and devices become such that diffusion techniques would no longer be capable of meeting them. A commercial ion implantation system, vintage 1977, is seen in Fig. 14. Progress in ion implantation has been recorded in both monographs (60-62), conference proceedings (63-66), and review articles (67).

Summary

The writer has attempted to convey an impression of what has happened in the last 25 years in the areas delineated within the mission of the Electrothermics and Metallurgy Division of the Society. He also brought into the discussion items related to these, even though they have not been considered in the customary proceedings of the Division. It was felt that bringing these into the discussion will help round up the impression of the happenings here. Under no circumstances should this be considered as a thorough reveiw of the subject. The author also wishes to express sincere thanks to the companies which provided the illustrations.

Fig. 14. The model 200-20 A2 ion implantation system with way flow end station. Courtesy: Dr. A. Witkower, Varian Extrion.

REFERENCES

1. "Vacuum Metallurgy," J. Kruger, O. Winkler, and R. Bakish, Editors, p. i, Elsevier Publishing Co., Amsterdam, The Netherlands (1971).
2. *Ibid.*, pp. 145-321.
3. *Ibid.*, p. 222.
4. V. F. Le Ferrer, *Trans AIME*, **209**, 1459 (1957).
5. W. G. Pfann, *Trans. AIME*, **194**, 747 (1952).
6. W. G. Pfann and K. M. Olsen, *Phys. Rev.*, **89**, **322** (1953).
7. A. Calverley, M. Davis, and R. F. Lever, *J. Sci. Instrum.*, **34**, 142 (1953).
8. J. H. Beymon and R. A. Sounders, *Brit. Appl. Phys.*, **11**, 128 (1960).
9. H. Schildknecht, "Zoonenschmelzen," Verlag Chemie, Weinheim/Bergstrasse, Germany (1964).
10. W. C. Dash, *J. Appl. Phys.*, **29**, 736 (1958).
11. W. C. Dash, *ibid.*, **30**, 459 (1959).
12. W. C. Dash, *ibid.*, **31**, 736 (1960).
13. R. N. Hall, "Proceedings 12th International Conference on Physics of Semiconductors," p. 363, Stuttgart, July 1974.
14. "Proceedings of Conference on Electron and Ion Beam Science and Technology," R. Bakish, Editor, The Electrochemical Society, Inc., Princeton, N.J. (1974-1976).
15. M. von Pirani, U.S. Pat. 848,600 (1907).
16. R. Bakish and S. S. White, "Handbook on Electron Beam Welding," J. Wiley & Sons, New York (1962).
17. "Proceedings of the French Atomic Energy Commission Colloquium," M. Rapin and H. Bordes, Editors, p. 852 France (1971).
18. S. Schiller, V. Heisig, and S. Panzer, "Electron Beam Technology," VEB Verlag Technik, Berlin, DDR (1976).
19. "Electron Beam Melting and Welding Technology," B. Paton, Editor, p. 767 (1974).
20. D. J. Maykuth and R. I. Jaffee in "Columbium Metallurgy," D. L. Douglas and F. W. Kunz, Editors, p. 223, Interscience, New York (1961).
21. D. S. Fairgrieve and J. W. Fortner, "Production and Purification of Hafnium" *J. Met.*, **12**, 25 (1960).
22. C. B. Ditmar and S. Abkowitz, in "Trans. Vacuum Metals Conference, New York, 1957," R. F. Bunshah, Editor, p. 109, New York University Press, New York (1960).
23. Private communication.
24. "Nickel," Paton Institute for Electrowelding, Kiev, USSR (1965).
25. Private communication.
26. J. A. Stohr, "Fuel Element Conference," Book 1, pp. 9-17, TID 7546, Paris, USAEC (1957); also *Nucl. Power Tokyo*, **272**, (1958).
27. W. L. Wayman and W. S. Steinkamp, GE Co. Rep. H.W.-55667 (1958); also *Weld. J.*, **21**, 49 (1958).
28. T. H. P. Chang, A. D. Willson, A. J. Speth, and C. H. Ting, in Proceedings of the 7th International Conference on Electron and Ion Beams in Science and Technology, R. Bakish, Editor, The Electrochemical Society, Princeton, N.J. (1976).
29. D. S. Alles, F. R. Ashley, A. M. Johnson, and R. L. Townsend, *ibid.*
30. "Proceedings of Symposia on Electron, Ion, and Photon Beam Technology," IEEE and AVS, publishers (1965-1977).
31. J. Weber, *Trans. IRE PGED*, **53**, 1 (1953).
32. N. G. Basov and A. M. Prokhorov, *Zh. Experim. Tekn. Fiz.*, **28**, 249 (1955).
33. J. P. Gordon, H. J. Ziegler, and C. H. Townes, *Phys. Rev.*, **95**, 282 (1954).
34. J. P. Gordon, H. J. Ziegler, and C. H. Townes, *ibid.*, **99**, 1264 (1955).
35. A. L. Schawlow and C. H. Townes, *ibid.*, **112**, 1940 (1956).
36. T. H. Maiman, *Nature* (*London*), **187**, **4736**, **493** (1960).
37. A. Javan, W. R. Bennett, Jr., and D. R. Herriot, *Phys. Rev. Lett.*, **6**, 106 (1961).
38. W. W. Duddley, "CO_2 Laser," p. 427, Academic

Press, New York (1976).
39. R. Brown, "Lasers," Business Books Ltd., London (1969).
40. H. J. Beesley, "Lasers and Their Applications. Taylor Francis Ltd., London (1971); also Halsted Press, Div. of Wiley, London (1976).
41. F. T. Arecci and E. O. Schultz-Dubois "Laser Handbook," North Holland Publishing Co., Amsterdam (1972).
42. "Metal-Slag Gas Reactions and Processes," Z. A. Foroulis and W. W. Smeltzer, Editors, The Electrochemical Society, Princeton, N.J. (1975).
43. B. E. Paton and B. I. Medovar, "Electroslag Furnaces," Nailovaya Dumka, Kiev, USSR, (1976).
44. NMAB Rep., **324**, (1976).
44a. R. H. Natziger, "The Electroslag Melting Process," Bureau of Mines, PB-**263**, **219** (1976).
45. M. Badiali, R. Bakish, and N. Kirshenbaum, in "Proceedings of the 1961 Dresden Symposia on Ultra Pure Materials," p. 148, Akademie Verlag, Berlin (1963).
46. R. Bakish, C. A. Gellar, and I. Marinow, *J. Met.*, **14**, 770 (1962).
47. M. Badiali, N. Kirschenbaum, and R. Bakish, *Trans. AIME*, **32**, 227 (1963).
48. R. Bakish, "Vapor Phase Metallurgy," International Science and Technology, pp. 54-60, New York (1963).
49. "Vapor Plating, Proceedings of the 1st International Conference," C. F. Powell, I. E. Campbell, and B. W. Gonser, Editors (1955).
50. Chemical Vapor Deposition, 2nd International Conference, J. M. Blocher, Jr. and J. C. Withers, Editors, The Electrochemical Society Softbound Symposium Series, Princeton, N.J. (1970).
51. Chemical Vapor Deposition, 3rd International Conference, F. A. Galski, Editor, The Electrochemical Society Softbound Symposium Series, Princeton, N.J. (1972).
52. Chemical Vapor Deposition, 4th International Conference, G. F. Wakefield and J. M. Blocher, Jr., Editors, p. 595, The Electrochemical Society Softbound Symposium Series (1973).
53. Chemical Vapor Deposition, 5th International Conference, J. M. Blocher, Jr., H. E. Hinterman, and L. H. Hall, Editors, p. 848, The Electrochemical Society Softbound Symposium Series, Princeton, N.J. (1975).
54. Chemical Vapor Deposition, 6th International Conference, L. F. Donaghey, P. Rai-Choudhury, and R. N. Tauber, Editors, p. 581, The Electrochemical Society Softbound Symposium Series, Princeton, N.J. (1977).
55. J. J. Tietjen, *Ann. Rev. Mater. Sci.*, **3**, 317 (1973).
56. I. A. Fisher, *Int. Metall. Rev.*, **17**, 117 (1972).
57. S. Schiller, U. Heisig, and K. Goedecke, in "Proceedings of the 2nd International Conference on Metallurgical Coating," San Francisco (1977).
58. J. A. Thornton, *Ann. Rev. Mater. Sci.*, **7**, 239 (1977).
59. L. I. Maissel and R. Glang, Editors, "Handbook of Thin Film Technology," McGraw Hill, New York, p. 1216 (1970).
60. J. W. Mayer, L. Eriksson, and J. A. Davies, "Ion Implantation in Semiconductors (Silicon and Germanium)," Academic Press, New York (1970).
61. G. Dearnaley, J. H. Freeman, R. S. Nelson, and J. Stephen, "Ion Implantation," Amsterdam, North Holland (1973).
62. R. G. Wilson and G. R. Brewer, "Ion Beams with Application to Ion Implantation," J. Wiley & Sons (1973).
63. "Ion Implantation in Semiconductors, Proceedings of the 1st International Conference," Thousand Oaks, Calif., Gordon and Breach, London (1970).
64. "Ion Implantation in Semiconductors, Proceedings of the 2nd International Conference," Garmisch-Partenkirchen, Springer-Verlag, Berlin (1971).
65. "Proceedings of the 3rd International Conference on Ion Implantation in Semiconductors, B. L. Crowder, Editor, Yorktown Heights, New York, Plenum Press, New York (1973).
66. "Ion Implantation in Semiconductors, Proceedings of the 4th International Conference," Warwick University (1976).
67. G. Dearnaley, *Ann. Rev. Mater. Sci.*, **4**, 93 (1974).

Progress in Electroanalytical Chemistry 1952-1977

H. A. Laitinen*

Department of Chemistry, University of Florida, Gainesville, Florida 32611

Even though electroanalytical chemistry was not covered in the series of technical reviews published in 1952, the present article will cover events only during the past 25 years. The early history was covered in 1971 by Kolthoff (1). The subject has gradually broadened from analytical measurements and titrations based upon electrode potential, conductance, and coulombic charge to include a diversity of measurements based upon interaction between charge transfer, mass transport, and heterogeneous and homogeneous chemical processes preceding or following charge transfer. A classification and systematic nomenclature of electroanalytical methods was suggested by Delahay, Laitinen, and Charlot (2). Three main categories are recognized: those for which electrode reactions, if any, need not be considered; methods involving only double layer phenomena at zero faradaic current; and methods involving faradaic electrode reactions. These three categories will be considered in turn.

Methods for Which Electrode Reactions, If Any, Need Not Be Considered

Conductance measurements and conductometric titrations have seen relatively few analytical applications during the past 25 years. Early in this period, there was a flurry of activity in the area of high frequency titrimetry, in which a combination of dielectric constant changes and conductance changes gives rise to changes in electrical characteristics of a high frequency oscillator. These methods have not found wide application, evidently because simpler alternative methods are usually available. Direct monitoring of dielectric constant changes to detect traces of polar materials in nonpolar solvents does find occasional application.

Methods Involving Double Layer Phenomena at Zero Faradaic Current

Under carefully controlled conditions, the differential capacity of the double layer can be related to surface excess. Limited examples of analytical application to adsorption, especially at mercury electrodes, are available. Similarly, interfacial tension, a closely related quantity, can in principle be used for analysis, although only in limited cases because of the lack of specificity.

The term "tensammetry" was introduced by Breyer and Hacobian to the measurements of pseudocapacitance corresponding to the adsorption and desorption of organic substances at a dropping mercury electrode without the passage of faradaic current. Such measurements are often useful as a diagnostic test in the study of electrode processes but have found limited use in analysis.

* Electrochemical Society Active Member.

Methods Involving Faradaic Electrode Reactions

Potentiometry at zero current.—By the beginning of our review period, 1952, classical potentiometry had long since reached a state of maturity. The glass electrode had largely replaced other *p*H electrodes, and had been widely used in nonaqueous as well as aqueous solutions for acid-base titrations.

The most important advances during the past 25 years have been in the area of ion-selective electrodes, which have been reviewed by Buck (3). These fall into several classes (4).

Glass electrodes.—They have been developed with varying degrees of selectivity for various univalent cations: H^+, Na^+, K^+, NH_4^+. In particular, glasses responding to Na^+ in preference to K^+, and to a lesser degree, the reverse, are available (5).

Solid-state electrodes.—Although the principles of using silver halide membranes for halide ion activity measurements had been demonstrated as early as 1937 (6), the modern era was stimulated by the work of Pungor and associates in the 1960's (7). Their electrodes consisted of particles of an insoluble solid imbedded in an inert matrix such as silicone rubber. More recent versions have emphasized silver sulfide without a binder as an ionically conductive membrane responsive to silver ion and sulfide ion. Composite membranes incorporating other heavy metal sulfides (*e.g.*, CdS, PbS, CuS) into a silver sulfide membrane have been found responsive to the corresponding heavy metal ions. Other composite structures involve silver halides with silver sulfide and selenite. Still another form that has seen limited application consists of an insoluble film directly on a metal surface.

The outstandingly successful solid-state electrode is the doped LaF_3 single crystal fluoride ion electrode described by Frant and Ross (8). This electrode responds specifically to fluoride ion activity over a wide range, and has found many thermodynamic as well as analytical applications.

Liquid membrane electrodes.—A family of electrodes consisting of a liquid organic membrane has emerged in several forms. The liquid itself may be selective to a given species of cation or anion through reaction and extraction, or it may serve as a solvent for a selective reagent. The liquid may be contained in a suitable structure to contact two solutions, or it may be placed in direct contact with an electronic conductor such as a metal or graphite. A commercial form uses graphite impregnated with polytetrafluoroethylene.

By selecting appropriate combinations of selective reagent and solvent, a large variety of membranes responsive to cations, anions, and neutral species is possible. Electrodes of this type are actively being studied, and new varieties continue to be reported.

Gas-sensing electrodes.—Glass electrodes have long been used as indirect sensors of CO_2 and NH_3 through their *p*H-dependent equilibria in water. More recently, such electrodes have been rendered truly responsive to gas tension through the interposition of hydrophobic membranes permeable to the gas. In addition, this arrangement permits measurements in complex systems such as biological fluids by preventing access of macromolecular and colloidal species to the surface. An important gas-sensing electrode operating on an entirely different principle (amperometric) is discussed below.

Enzyme electrodes.—Incorporation of an enzyme onto a membrane coupled with a suitable ion-selective or gas-sensing membrane permits the monitoring of a substrate through its generation or consumption of a detectable species such as H^+, CO_2, or NH_3. Conversely, enzyme concentrations in solution can be monitored by using a fixed concentration of substrate. An extension of the use of specific biochemical interactions is represented by the use of a silver sulfide sensor for sensing proteins, and indirectly for monitoring antibody-antigen reactions (9).

Methods based on transitory electrode phenomena.—*Polarography.*—By 1952, the beginning of our review period, classical polarography was well established as an analytical method for many inorganic, organic, and biochemical species. Several current-limiting processes were recognized (diffusion, migration, convection, charge transfer, reaction kinetics, adsorption) at the dropping mercury electrode, and some, such as diffusion or purely kinetically limited currents, could be treated in an adequate way theoretically. It remained for Koutecky (10) to derive the mathematical solution of the interaction between diffusion and reaction kinetics for the case of the dropping mercury electrode. This treatment permitted a quantitative interpretation of irreversible polarographic waves, in which charge-transfer rate controls the current at the foot of the wave and diffusion at the plateau. It also permitted a calculation of rate constants of homogeneous reactions coupled with charge transfer reactions under partial diffusion control. The 1954 book by Delahay (11) was a milestone in acquainting electroanalytical chemists generally with this treatment as well as several other techniques to be discussed below.

During the 1950's, the instrumentation group at Oak Ridge National Laboratory, headed by D. J. Fisher and M. T. Kelley, made several refinements in polarographic instrumentation. These included a precision drop timer, a three-electrode measurement system, a means of measuring instantaneous currents, and circuits for registering first and second derivatives of current-voltage curves as a function of potential (12).

Various modifications of classical polarography have appeared over the years. In "Tast" polarography, the instantaneous current is measured relatively late in drop life to minimize the nonfaradaic charging current, which decreases during drop growth, and to maximize diffusion or kinetic-controlled currents, which increase during drop life.

Superimposing periodic potential changes on a gradually increasing applied potential leads to several types of modified polarography. The simplest form, in which a small sinusoidal voltage signal is applied and the rectified a-c component is recorded, has been exploited especially by Breyer and his co-workers (13). Later modifications include the measurement of current at second and higher harmonics of the applied frequency to minimize charging currents, and the use of phase-sensitive amplifiers for the same purpose. A typical modern minicomputer controlled circuit has been described by Glover and Smith (14). The square wave polarograph of Barker (15) has largely been supplanted by the pulse polarograph (16) in which a single voltage pulse is applied at some instant in drop life, and the current measurement is made relatively late during the pulse to allow charging current transients to decay. The original Barker circuit (16) was greatly simplified by Parry and Osteryoung (17). A commercial instrument introduced by Princeton Applied Research Corporation, operating both in the direct and derivative modes, has done much to popularize the applications of pulse polarography. An automated version operated by means of a microprocessor is also available.

Little analytical application has been made of several types of polarographic methods involving a-c techniques, such as faradaic rectification (low and high levels, depending upon the magnitude of the a-c signal), radio-frequency polarography, intermodulation polarography, and polarography with complex plane analysis of cell impedances. These techniques have primarily found use in the study of electrode reaction mechanisms. A summary is available in several reviews (18-20).

Chronopotentiometry.—The concept of transition time, marking the instant of attaining zero surface concentration under diffusion-controlled constant current electrolysis, dates back to Sand in 1901. Some

mechanistic studies had been made with the technique in the 1930's and 1940's. However, the modern era dates back only to 1953, when Gierst and Juliard (21) applied the technique to a dropping mercury electrode under conditions such that the current pulse was applied relatively late in drop life, and of sufficient magnitude to yield transition times of 1-100 msec. In that same year, Berzins and Delahay (22) presented the theory of the method as applied to several types of electrode processes. The present name was suggested by Delahay and Mamantov (23) and in an adjoining paper Reilley and co-workers (24) described several experimental studies. The method received a flurry of attention during the late 1950's and early 1960's. Reinmuth (25) listed criteria for various kinetic schemes, based upon measurement of potential-time transients and transition times. The popularity of the method, both for theoretical and practical studies, has waned more recently because of some inherent problems. Of these, two merit special mention. First, there is the problem of adequate correction for charging current, which limits the accuracy of transition time measurements. Second, the influence of adsorbed reactants, which becomes relatively more important at short transition times, is dependent upon the sequence of events, *i.e.*, whether the adsorbed reactant is reduced first, last, or continuously during the electrolysis. For certain applications, *e.g.*, the estimation of diffusion coefficients in molten salts, and the use of current reversal technique to distinguish between soluble or insoluble reaction products, chronopotentiometry still merits consideration because of its inherent simplicity.

Linear sweep voltammetry (single scan and cyclic).—The technique of applying a single linear voltage sweep to a dropping mercury electrode relatively late in the formation period of the drop and observing the current-time trace with a cathode ray tube was introduced in 1947 by Randles (26). A related technique, consisting of a triangular voltage-time signal applied continuously during the formation of mercury drops, was independently introduced by Sevcik (27). Both authors gave theoretical interpretations of the current-time relationship for reversible processes. The book of Delahay (11), describing both reversible and totally irreversible processes, greatly stimulated research into this technique. One of the earlier applications to trace analysis was the technique of anodic stripping using a stationary hanging mercury drop for the deposition of one or more metals at a constant cathodic potential, followed by a linear scan anodic stripping cycle. In recent years this technique has been applied in the form of thin-film mercury coatings, usually on graphite, with a greatly increased sensitivity due to the use of electrodes of larger area (30). By using exceedingly thin films, the diffusion rate of amalgamated metals can be increased to the point that quantitative anodic dissolution occurs, and the method can also be applied in a coulometric mode by measuring peak area rather than height. Commercial apparatus permitting anodic stripping to be operated in the derivative as well as direct mode has stimulated applications of the technique to trace analysis.

A landmark paper was that of Nicholson and Shain (31), who presented a comprehensive theory of linear scan voltammetry, both single scan and cyclic, as applied to reversible and irreversible charge transfer, including those coupled with preceding or following chemical reactions. This paper greatly stimulated applications of the technique, which has become accepted by organic and physical chemists as a diagnostic tool, as well as an analytical method.

Christie and Osteryoung (32) presented a theory of staircase voltammetry to replace linear sweep voltammetry for stripping analysis using the thin film mercury electrode. They concluded that the decrease in faradaic sensitivity is more than compensated by the decrease in charging current. The theoretical expectation was verified by Osteryoung and co-workers (33), who concluded that the method is similar in sensitivity to that of differential pulse stripping, but is much faster. Both techniques were applied to trace metal determinations in the 0.1-10 μg/l concentration range.

Thin-layer electrochemistry.—Anson (34), in studying the chronopotentiometry of iron (III) at platinum electrodes, found that the redox behavior persisted even after electrodes that had been soaked in acidic iron (III) solutions were rinsed and immersed in acid solutions containing no iron (III). He at first believed he was observing the behavior of adsorbed iron (III), but later concluded that the redox behavior was due to a thin film of solution trapped in a faulty seal of the platinum into glass.

Later work by Christensen and Anson (35) using uniform thin films of solution established the technique as a form of constant current coulometry on a time scale of the order of a few seconds. Hubbard and Anson (36) devised improved electrodes and Reilley and co-workers (37) carried out electrochemical studies using controlled potential as well as controlled current. By measuring transition times at sufficiently high current densities, diffusion coefficients can be estimated without a knowledge of the solution concentration or electrode area if the thickness of the solution layer is first evaluated. The status of this subject was reviewed by Hubbard (38) in 1973. A more recent development is the optically transparent thin-layer cell of Heineman and co-workers (39) which was used to measure formal potentials of enzyme systems by controlling the ratio of oxidized to reduced forms by applying a potential and monitoring the corresponding concentration ratio optically.

Chronocoulometry.—The technique of chronocoulometry involves the determination of coulombic charge, Q, as a function of time under specified conditions of potential change. The first version as described by Osteryoung, Lauer, and Anson (40) involved application of a linear voltage scan. Because the shape of the current time transient depends upon charge transfer rate except for reversible systems under pure diffusion control, the applicability of this method proved to be quite limited. By using a potential step of relatively large magnitude, Christie *et al.* (41) showed that even for irreversible systems the intercept of a plot of Q *vs.* $t^{1/2}$ (which is linear for diffusion-controlled processes) allowed the detection of surface films or adsorbed layers. Still another refinement by Anson (42) was the introduction of a double potential step method, in which the potential was returned to its initial state after a definite time τ. In this way, any effect of double layer charging could be eliminated because the initial and final states of the double layer should be the same. The method permits an evaluation of adsorbed reactant by extrapolation to eliminate the diffusion controlled reduction and reoxidation of reactant. It is, however, limited to reversible charge-transfer processes.

Semiintegral and semidifferential electroanalysis.—In 1972, Oldham (43) introduced a technique called semiintegral electroanalysis which has the property of being independent of the form of the applied voltage-time signal, provided that the electrode, during an excursion of potential in a time interval τ, proceeds from a condition of no reaction to a condition of complete concentration polarization, under semiinfinite diffusion control. Thus, the method in principle is insensitive to imperfections in the shape of the applied signal, as, for example, a finite rise time in a potential-step method. The method involves a mathematical device called the semiintegral of the current-time function, intermediate between the current itself and its time integral, the coulombic charge. A plot of the semiintegral, M, *vs.* E is termed a neopolarogram. Shapes of neopolarograms have been theoretically and experimentally examined for reversible and irreversible processes by Goto and Oldham (44).

A related technique, semidifferential electroanalysis, generated by semidifferentiation of the current, produces a quantity *e* which is the time derivative of M. The plot of *e vs.* potential has the same relationship to a neopolarogram as a derivative polarogram has to a classical polarogram, and is therefore called a derivative neopolarogram (45). The characteristics of this technique in qualitative and quantitative analysis, using a stationary hanging drop electrode and a ramped voltage-time signal, have been described (45).

Steady-State Processes

Voltammetry and amperometric titrations.—Earlier versions of voltammetry with stationary electrodes in unstirred solutions have largely fallen into disuse because of the slowness with which steady-state mass transport is attained, and because of the sensitivity of the steady-state condition to disturbances such as vibration. Nevertheless, Blaedel and Jenkins (46) noted that with glassy carbon electrodes steady-state voltammetry has the distinct advantage of smaller residual currents as compared with scanning voltammetry because of the slow adjustment of surface states to changes of potential. Blaedel and Iverson (47) have recently studied steady-state voltammetry using tubular electrodes. By using pulsed flow at constant potential, the response time was shortened considerably and sensitivity in the micromolar concentration range was achieved.

Steady-state voltammetry with rotated wire microelectrodes were at first interpreted in terms of a simple Nernst diffusion layer model. Later work showed that, owing to complications such as turbulent flow, such electrodes are not favorable for mechanistic studies. Nevertheless, many analytical applications, especially amperometric titrations, continue to be made (48), because of the inherent simplicity and sensitivity of the method. All classes of reactions, *i.e.*, acid-base, precipitation, complexation, and redox, operated in the classical volumetric mode as well as by coulometric generation of reagents are represented in titrations involving single indicator electrodes as well as in biamperometric titrations (49). The latter is the ultimate in simplicity, because only a pair of polarized electrodes, without a salt bridge or reference electrode, needs to be used.

By attaching a membrane to the electrode surface, the disturbing effects of convection can be eliminated, but the nature of the diffusion process is altered (50). A fundamentally different membrane system is the lyophobic gas-diffusion membrane, introduced in 1956 by Clark (51) for sensing oxygen amperometrically. Because oxygen diffuses across the membrane in the gas phase, its diffusion rate is not affected by the viscosity of the solution, and the response is truly an oxygen tension independent of salt effects upon solubility. A great many applications are being made, for example, in clinical chemistry and oceanography.

The rotating-disk electrode, described theoretically by Levich in 1942, was experimentally studied by several investigators, especially in the U.S.S.R., in the 1940's. The book of Delahay (11) stimulated applications to analytical chemistry. Among the earlier publications in the analytical literature are papers by Adams and co-workers (52) and by Azim and Riddiford (53) in 1962. The rotating ring-disk electrode, introduced by the Frumkin school in the U.S.S.R., has been studied extensively by Bruckenstein and co-workers. Albery and Bruckenstein (54) refined the calculation of the collection efficiency at the ring for soluble species generated at the disk. The rotating-disk electrode is of analytical importance because the limiting current can be accurately related to hydrodynamic quantities (55). The effective diffusion layer thickness has a known relationship to rotation speed, so calibration need not be done on a purely empirical basis.

Hydrodynamic modulation of rotating-disk electrodes as a means of avoiding interfering currents that are mass transport-independent was suggested by Miller and Bruckenstein (56). The ring-disk electrode is primarily useful in mechanistic studies and is not discussed further.

Hydrodynamic techniques have proven to be useful in monitoring effluents from chromatographic columns. Johnson and Larochelle (57) have reviewed past designs of flow-through cells, operating both in the amperometric and coulometric modes. Blaedel, Olson, and Sharma (58) confirmed the theoretical Levich equation for convective-diffusional mass transport under conditions of negligible consumption of electroactive species, and Blaedel and Boyer (59) applied a tubular platinum electrode at concentrations down to $10^{-8}M$.

Coulometry.—Steady-state coulometry, both in the controlled-potential and controlled-current modes, was well established as an electroanalytical method by 1952, the beginning of the present survey. Many applications continue to be reported (60), generally as adaptations of well-established principles to new situations. Monitoring of chromatographic column effluents by coulometric determination using flow-through cells is an active field of application. An example is the packed tubular platinum electrode which was shown to operate at 100% electrolytic efficiency for copper(II) and iron(III) in microgram quantities (57). Thin-layer electrochemistry has already been mentioned above as a form of coulometry on a short-time scale.

Another modern form of coulometry is represented by the measurement of peak areas rather than peak heights in anodic (or cathodic) stripping voltammetry. This version of stripping analysis has already been mentioned above in connection with thin mercury film electrodes operated under slow scan rate so that quantitative electrolysis can occur. The method is so sensitive for solid deposits that fractional monolayers can readily be detected. In fact, Andrews and Johnson (61) reported quantitative results for stripping selenium from a rotating gold-disk electrode only when less than a monolayer equivalent layer had been deposited. Laitinen and Watkins (62) were clearly able to distinguish fractional monolayers of PbO_2 on a substrate of conductive SnO_2 and to determine the total PbO_2 by cathodic stripping coulometry.

Spectroelectrochemistry

Many spectroscopic techniques have been applied to the examination of electrode surfaces. Strictly speaking, these are not electroanalytical techniques and therefore will not be covered in this review, but mention may be made of ellipsometry, infrared absorption, x-ray photoelectron spectroscopy (XPS or ESCA), ultraviolet photoelectron spectroscopy (UPS), Auger electron spectroscopy (AES), low energy electron diffraction (LEED), and scanning electron microscopy (SEM), which are primarily aimed at the study of electrode surfaces and thin films on them. Similarly, electrochemiluminescence has received considerable attention from electroanalytical chemists, but the technique is rarely, if ever, used for analytical purposes as such, and is not discussed further.

The use of spectrophotometric techniques to study species generated at the electrode or products of their reaction in solution represents analysis at least in an enlarged if not in the traditional sense. The use of optically transparent electrodes coupled with u.v.-visible spectrophotometry has been an established technique since 1964 (63). The subject has been more recently reviewed by Kuwana and Winograd (64). By using rapid scanning spectrophotometry, it is possible to follow the kinetics of homogeneous reactions following the charge-transfer step. The use of thin-layer optically transparent electrodes has already been mentioned (39).

An elegant application of laser-Raman spectroscopy was described by Van Duyne and co-workers (65). Taking advantage of the resonance Raman effect, they

were able to procure vibrational information about species generated electrochemically during a short voltage pulse. Using double laser beams, the technique has recntly been extended to include electronically excited states.

Electron spin resonance has become well established as a technique to determine radicals generated at electrodes. A review by Kastening (66) in 1974 summarized experimental techniques and results. Kinetic experiments using ESR coupled with constant current pulses have been described by Goldberg and Bard (67). A new coaxial cavity ESR cell using a helical gold-wire working electrode surrounding an auxiliary electrode and Luggin capillary reference electrode probe has been described (68) as being especially advantageous for solutions of high resistivity using potential sweep and pulse experiments.

REFERENCES

1. I. M. Kolthoff, *This Journal*, **118**, 5C (1971).
2. P. Delahay, H. A. Laitinen, and G. Charlot, *Anal. Chem.*, **32**, 103A (1960).
3. R. P. Buck, *ibid.*, **44**, 270R (1972); *ibid.*, **46**, 28R (1974); *ibid.*, **48**, 23R (1976).
4. NBS Special Pub. 314, R. A. Durst, Editor, U.S. Government Printing office, Washington, D.C. (1969).
5. "Glass Electrode for Hydrogen and Other Cations," G. Eisenman, Editor, Marcel Dekker, Inc., New York (1967).
6. I. M. Kolthoff and H. L. Sanders, *J. Am. Chem. Soc.*, **59**, 416 (1937).
7. E. Pungor, *Anal. Chem.*, **39**, 29A (1967).
8. M. S. Frant and J. W. Ross, *Science*, **154**, 3756 (1966).
9. P. W. Alexander and G. A. Rechnitz, *Anal. Chem.*, **46**, 250 (1974); *ibid.*, **46**, 860 (1974); *ibid.*, **46**, 1253 (1974).
10. J. Koutecky, *Chem. Listy*, **47**, 323 (1953).
11. P. Delahay, "New Instrumental Methods in Electrochemistry," Interscience Publishers Inc., New York (1954).
12. H. C. Jones, W. L. Belew, R. W. Stelzner, T. R. Mueller, and D. J. Fisher, *Anal. Chem.*, **41**, 772 (1969).
13. B. Breyer and H. H. Bauer, "Alternating Current Polarography and Tensammetry," Wiley-Interscience, New York (1963).
14. D. E. Glover and D. E. Smith, *Anal. Chem.*, **44**, 1040 (1972).
15. G. C. Barker, *Anal. Chim. Acta*, **18**, 118 (1958).
16. G. C. Barker and A. W. Gardner, *Z. Anal. Chem.*, **175**, 79 (1960).
17. E. P. Parry and R. A. Osteryoung, *Anal. Chem.*, **36**, 1366 (1964); *ibid.*, **36**, 1634 (1965).
18. D. K. Roe, *ibid.*, **44**, 85R (1972); *ibid.*, **46**, 8R (1974).
19. D. R. Roe and P. Egginmann. *ibid.*, **48**, 9R (1976).
20. P. T. Kissinger, *ibid.*, **46**, 15R (1972); *ibid.*, **48**, 17R (1976).
21. L. Gierst and A. Juliard, *J. Phys. Chem.*, **57**, 701 (1953).
22. P. Delahay and T. Berzins, *J. Am. Chem. Soc.*, **75**, 2486 (1955); *ibid.*, **75**, 4205 (1955).
23. P. Delahay and G. Mamantov, *Anal. Chem.*, **27**, 478 (1955).
24. C. N. Reilley, G. W. Everett, and R. H. Johns, *ibid.*, **27**, 483 (1955).
25. W. H. Reinmuth, *ibid.*, **32**, 1514 (1960); *ibid.*, **33**, 322 (1961).
26. J. E. B. Randles, *Trans. Faraday Soc.*, **44**, 322 (1947); *ibid.*, **44**, 327 (1947).
27. A. Sevcik, *Coll. Czech. Chem. Comm.*, **13**, 349 (1948).
28. F. D. DeMars and I. Shain, *Anal. Chem.*, **29**, 1825 (1957).
29. W. Kemula and Z. Kublik, *Anal. Chim. Acta*, **18**, 104 (1958).
30. D. K. Roe and J. E. A. Toni, *Anal. Chem.*, **37**, 1503 (1965).
31. R. S. Nicholson and I. Shain, *ibid.*, **36**, 706 (1964).
32. J. H. Christie and R. A. Osteryoung, *ibid.*, **48**, 869 (1976).
33. U. Eisner, J. A. Turner, and R. A. Osteryoung, *ibid.*, **48**, 1608 (1976).
34. F. C. Anson, *ibid.*, **33**, 1498 (1961); *ibid.*, **33**, 1838 (1961).
35. C. R. Christensen and F. C. Anson, *ibid.*, **35**, 205 (1963); *ibid.*, **36**, 495 (1964).
36. A. T. Hubbard and F. C. Anson, *ibid.*, **36**, 723 (1964).
37. C. N. Reilley *et al.*, *ibid.*, **37**, 1312 (1965); *ibid.*, **37**, 1317 (1965).
38. A. T. Hubbard, *Crit. Rev. Anal. Chem.*, **3**, 201 (1973).
39. W. R. Heineman, B. J. Norris, and J. F. Goelz, *Anal. Chem.*, **47**, 79 (1975); *ibid.*, **47**, 1364 (1975).
40. R. A. Osteryoung, G. Lauer, and F. C. Anson, *ibid.*, **34**, 1833 (1962).
41. J. H. Christie, R. A. Osteryoung, G. Lauer, and F. C. Anson, *ibid.*, **35**, 1979 (1963).
42. F. C. Anson, *ibid.*, **38**, 54 (1966).
43. K. B. Oldham, *ibid.*, **44**, 196 (1972); *ibid.*, **45**, 39 (1973).
44. M. Goto and K. B. Oldham, *ibid.*, **45**, 2043 (1973).
45. P. Dalrymple-Alford, M. Goto, and K. B. Oldham, *ibid.*, **49**, 1390 (1977).
46. W. J. Blaedel and R. A. Jenkins, *ibid.*, **46**, 1952 (1974).
47. W. J. Blaedel and D. G. Iverson, *ibid.*, **48**, 1563 (1977).
48. J. T. Stock, "Amperometric Titration," Wiley-Interscience, New York (1965).
49. J. T. Stock, *Anal. Chem.*, **44**, 1R (1972); *ibid.*, **46**, 1R (1974); *ibid.*, **48**, 1R (1976).
50. R. C. Bowers and A. M. Wilson, *J. Am. Chem. Soc.*, **80**, 2968 (1958); *ibid.*, **81**, 1840 (1959).
51. L. C. Clark, *Trans. Am. Soc. Artif. Intern. Organs*, **2**, 41 (1956).
52. Z. Galus, C. Olson, H. Y. Lee, and R. N. Adams, *Anal. Chem.*, **34**, 164 (1962).
53. S. Azim and A. C. Riddiford, *ibid.*, **34**, 1023 (1962).
54. W. J. Albery and S. Bruckenstein, *Trans. Faraday Soc.*, **62**, 1946 (1966).
55. R. N. Adams, "Electrochemistry at Solid Electrode," Marcel Dekker, New York (1969).
56. B. Miller and S. Bruckenstein, *Anal. Chem.*, **46**, 2026 (1974).
57. D. C. Johnson and J. Larochelle, *Talanta*, **20**, 959 (1973).
58. W. J. Blaedel, C. L. Olson, and R. L. Sharma, *Anal. Chem.*, **35**, 2100 (1963).
59. W. J. Blaedel and S. L. Boyer, *ibid.*, **43**, 1538 (1971).
60. D. G. Davis, *ibid.*, **46**, 21R (1974).
61. R. W. Andrews and D. C. Johnson, *ibid.*, **47**, 294 (1975).
62. H. A. Laitinen and N. H. Watkins, *ibid.*, **47**, 1352 (1975).
63. T. Kuwana, R. K. Darlington, and D. W. Leedy, *ibid.*, **36**, 2023 (1964).
64. T. Kuwana and N. Winograd, *J. Electroanal. Chem., Interfacial Electrochem.*, **7**, 1, (1974).
65. D. L. Jeanmaire, M. R. Suchanski, and R. P. Van Duyne, *J. Am. Chem. Soc.*, **97**, 1699 (1975).
66. B. Kastening, "Electroanalytical Chemistry," 2nd edition, H. W. Nürnberg, Editor, p. 421, Wiley-Interscience, New York (1974).
67. J. B. Goldberg and A. J. Bard, *J. Phys. Chem.*, **78**, 290 (1974).
68. R. D. Allendoerfer, G. A. Martinchek, and S. Bruckenstein, *Anal. Chem.*, **47**, 890 (1975).

JOURNAL OF THE ELECTROCHEMICAL SOCIETY

REVIEWS AND NEWS

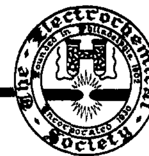

JULY 1978

75th Anniversary Review Series
Primary Batteries 1951-1976

R. J. Brodd,* A. Kozawa,* and K. V. Kordesch*
Union Carbide Corporation, Battery Products Division, Parma, Ohio 44130

The past twenty-five years have seen many changes in primary batteries. Although the Leclanché cell celebrated its 100th Anniversary in 1966, it is still the main commercial primary cell. Table I shows the growth of dry batteries over the past 25 years. The growth rate is 8-12% per year, depending on the year and country (U.S.A., Japan, and Western Europe). Total dry cell production in Japan is roughly 1/3 the total production of that in the U.S.A., and the total production in Western Europe (West Germany, France, Great Britain, Switzerland, etc.) is roughly the same as that in the U.S.A. Dry cell consumption is about 8-15 cells per person annually in the U.S.A., Japan, and Western Europe in recent years. The steady growth of the dry cell industry is mainly due to the increase of electronic or electrical devices using dry cells.

The key to this growth has been the advent of low cost consumer devices such as watches, transistor radios, tape recorders, and calculators which require small portable power sources. Table II shows production figures of several devices using primary cells in Japan from 1956-1976. This figure is a good indicator of the worldwide trend regarding devices using primary cells.

Growth has been due in part to new systems which have increased ability to store and deliver energy. New battery systems which have been established commercially are: (*i*) zinc chloride, (*ii*) alkaline MnO_2-Zn (high-rate), and (*iii*) silver-zinc (miniature).

Many other systems have been developed, but they have reached only limited commercial production. Some of the more publicized systems in this group include: (*i*) lithium-iodine (charge-transfer complex), (*ii*) lithium-sulfur dioxide, (*iii*) lithium-CF_x, (*iv*) lithium-MnO_2, (*v*) Ca-$CaCrO_4$ thermal battery, (*vi*) magnesium-MnO_2, (*vii*) divalent silver-zinc, (*viii*) lithium-oxyhalide ($SOCl_2$ and SO_2Cl_2), and (*ix*) lithium-Ag_2CrO_4.

While growth has emphasized smaller size and higher energy density, two large-size systems, the Zn-CuO and Zn-air box cells, have decreased or almost disappeared from the commercial market.

In addition to the systems listed above, many new anode and cathode combinations and battery-related fundamental discoveries have been reported in the literature. At the risk of omitting an important future system, only those systems for which significant published information exists are discussed below. Several excellent books and symposium volumes which review the status of primary batteries have been published recently (1-5). The reader is referred to these references for more detailed discussions of specific battery systems.

Zinc-MnO_2 Batteries

From 1920 to 1950, flashlights using C and D size cells were the major devices using dry cells. Today, many other devices such as tape recorders, hand-held calculators, electric clocks, and radios are being used.

* Electrochemical Society Active Member.

Table I. Growth* of dry battery industry
(Unit: million dollars) Reference (6-8)

	1950	1960	1970	1977
U.S.A.	95	153	400 (e)	600 (e)
Japan	—	43	105	200 (e)

* Approximate value of dry batteries shipped from manufacturers.
(e): estimated values.

Table II. Production of devices using dry cells in Japan
(Unit: million units) Reference (8)

	1956	1966	1976
1. Battery operated toys	20	20	45
2. Hand held calculators	—	—	40
3. Tape recorders	1	6	27
4. Dry cell operated clocks	0.3	1.6	18
5. Flashlights	10	21	13
6. Transistor radios	2	25	9

Because of this, many new smaller cells (the AA, AAA, and N sizes) are becoming popular.

Table III summarizes Zn-MnO_2 cells on the market today. The Leclanché (or type I) in Table III is the traditional regular cell which was introduced in the late 1860's. It is still the least expensive of the battery systems. The heavy-duty Leclanché, zinc chloride, and alkaline cells (types II, III, and IV) are the cells which were developed after 1950 in Japan and are now being produced in large quantities. Type II cells were produced earlier in the United States. The major changes in the cell's design are shown in Fig. 1. In 1977, about 70% of the total cell production in Japan was of types II, III, and IV. In the United States, about 50% of cell production was made up of new types of cells; percentage-wise, more alkaline cells are used in the U.S. than in Japan. One important raw material which is common in the three new cells is EMD (electrolytic manganese dioxide). EMD is made by electrolysis of $MnSO_4$ in a near-boiling solution.

Table III. Four types of MnO_2-Zn cells on the market today
(See the performance shown in Fig. 1, 2, and 3)

Type I:	A natural MnO_2 ore* cell using a starch paste separator, NH_4Cl electrolyte and zinc can. (Production started in late 1800's.) Example: Eveready 950, Ray-O-Vac *1D*.
Type II:	An EMD** cell using a starch paste separator, NH_4Cl electrolyte containing some $ZnCl_2$, and a zinc can. (A large production started in Japan around 1960-1963.) Example: Hi-Top in Japan.
Type III:	An EMD** cell using a coated paper separator liner in a zinc can, and $ZnCl_2$ electrolyte usually containing some NH_4Cl. (A large scale production started around 1970.) Example: Eveready 1250, Ray-O-Vac 6D.
Type IV:	Alkaline MnO_2-Zn cell using KOH electrolyte and a gelled zinc powder as anode and a mixture of graphite and EMD as a cathode molded in a steel can. Examples: Eveready E95, Ray-O-Vac 813, Mallory Duracell.

* Cells I, II, and III use a mixture of acetylene black and MnO_2 powder as the cathode.
** EMD = Electrolytic manganese dioxide made by electrolysis of $MnSO_4$ solution.

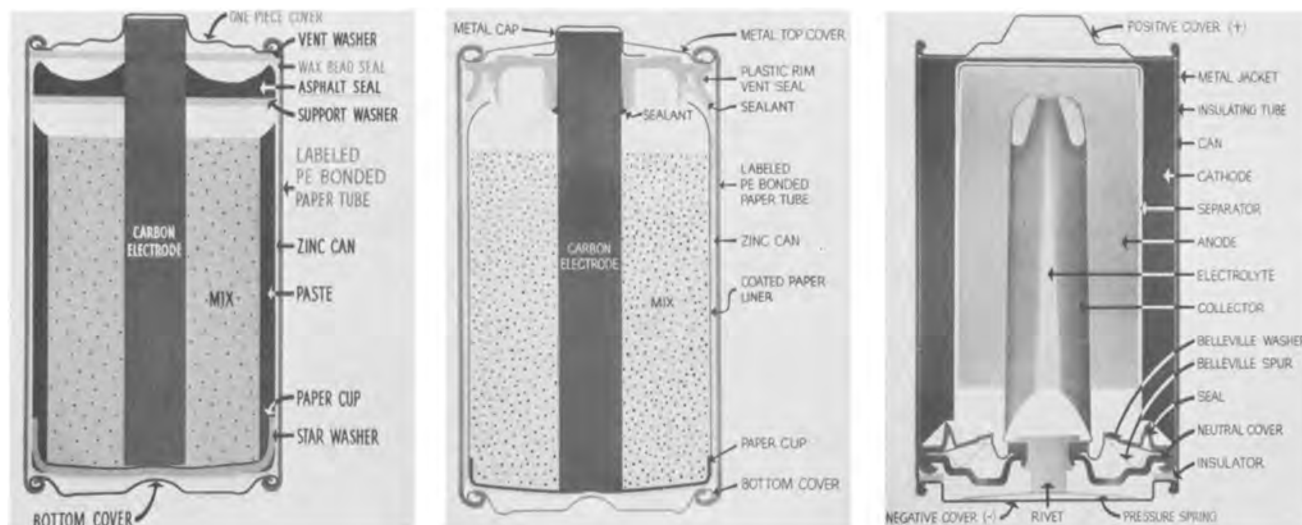

Fig. 1a. Schematic presentation of the progress in cell design, type I and II since late 1800. (A bobbin cathode cell using asphalt seal, paste separator and natural MnO_2 ore.); b. Type III since around 1970. (A paper lined $ZnCl_2$ electrolyte cell using plastic seal and EMD.); c. Type IV since around 1960. (An alkaline KOH electrolyte cell using plastic seal and EMD).

In the traditional Leclanché cells, natural MnO_2 ore (MnO_2 content: 70-75%) is used in the bobbin cathode. In the new cells mostly EMD (MnO_2 content: 91-93%) is used in the cathode. A large-scale EMD production started around 1960 in Japan (in two plants having a capacity of 500 tons/month). Because of the use of EMD, the new cells (types II, III, and IV in Table III) have a discharge capacity of two to five times greater than that of the regular cell (type I in Table III), as noted in Fig. 2-4. Details of the new cells have been described elsewhere (9-12). Therefore, only the main technical features of each type are pointed out here.

The heavy-duty Leclanché (or type II cell) has the same cell structure as the regular (type I) cell but uses EMD in the cathode rather than natural MnO_2 ore as well as a more oxidation-resistant chemically treated starch (10). The chemically treated starch withstands the low pH concentrated zinc solution. In

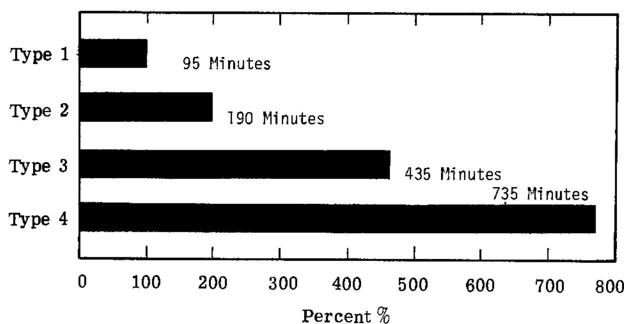

Fig. 2. Discharge capacity of D-size cells at 2.25Ω continuous discharge to 0.9V.

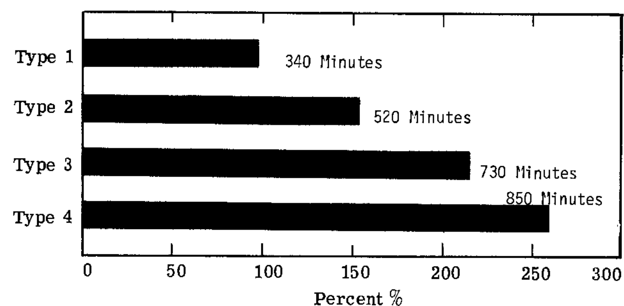

Fig. 3. Discharge capacity of D-size cells at 2.25Ω LIF test to 0.9V. (LIF test: 5 min discharge every hour for 8 hr period per day.)

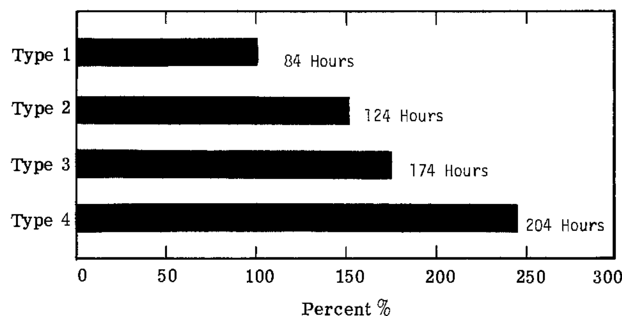

Fig. 4. Discharge capacity of D-size cells at 25Ω test (4 hr per day to 0.90V.)

this cell, the solution produced on discharge near the zinc anode has a very low pH of 0-1, and the starch-gel layer hydrolyzes and becomes liquid. This combination enhances the tendency to leak through the perforation of the zinc can.

The zinc chloride (type III) cell uses, in place of the starch gel layer, a paper separator which is coated either with a cross-linked starch (10-14) mixed with a binder (15) such as polyvinyl alcohol, hydroxyethyl cellulose, vinyl acetate, etc., or with a cross-linked polymer such as polyacrylamide (16). Since the paper is much thinner than the starch layer, the cell contains about 10% more capacity than the type II cell. Another significant difference is the use of $ZnCl_2$ solution (about 28-30%) as the electrolyte. In NH_4Cl electrolyte cells, when the cell is discharged, particularly at a continuous high rate, an electrolyte solution called "spew" is pushed into the upper space of the cell. By using $ZnCl_2$ electrolyte, the cell leakage is considerably reduced because the solution produced on discharge is absorbed in the cathode and does not enter the top space of the cell (15).

The alkaline (or type IV) cell is the so-called alkaline manganese cell. Union Carbide introduced this in 1959, and its construction differs considerably from the "Crown" cell described by Herbert (17, 18). The cell uses concentrated KOH electrolyte and, with about 10.4 A-hr of EMD (for a D cell) based on the one-electron reaction, $MnO_2 + H_2O + e \rightarrow MnOOH + OH$. This type of cell is excellent for high rate discharge applications. Also, the reliability is greater and leakage is far less than for the other cells.

It is most convenient to compare the cell performance of the various cells in the D size (R20 cell in IEC designation). Since the cells are used in various ways (low rate, high rate intermittent, and high rate continuous), three types of discharge tests (2.25Ω continu-

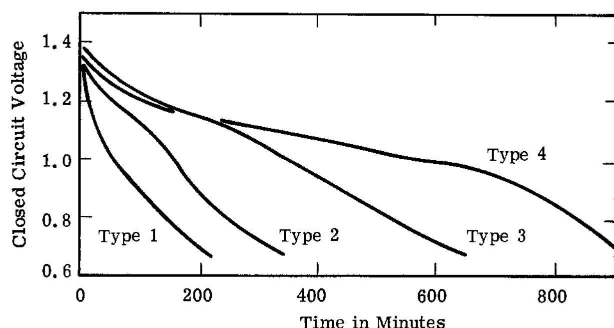

Fig. 5. Discharge curves of D-size cells on 2.25Ω continuous test at 21°C.

ous, 2.25Ω intermittent, and 25Ω) to a cutoff voltage of 0.90V are presented in Fig. 2-4, and the relative value (%) was calculated based on the discharge capacity of type I cells (100%). Figure 5 shows typical discharge curves for the four cell types on a continuous discharge test. It can be seen from the data in the above figures that really significant progress has occurred in the past 25 years. Since the size and shape of dry cells have remained the same since the late 1800's (for example, a D size cell is 3.5 cm in diam and 5.8 cm in height), such great technical progress has not been recognized by the general public. Major recent progress in dry cells in Japan has been summarized by Watanabe (13).

As mentioned earlier, the material responsible for the remarkable improvements of the cell capacity is EMD. Its production process and properties have been described in detail (11). It is, however, worth mentioning a few key properties. Today's EMD is very pure (most of the metallic impurities are of the order of less than a few ppm) and the average particle size is 10-15 μm and the net MnO_2 is 91-93% (7-9% being water). The particles have numerous micropores of diameter 40-50Å and the BET surface area is 40-60 m^2/g depending on the preparation conditions. Electrochemical polarization of EMD is much less than that of natural MnO_2 ore as shown in Fig. 6. CMD is a MnO_2 produced by a chemical process for dry cell use. CMD is equivalent or superior to EMD in certain types of cells. The total MnO_2 used for dry cells in the world is about 350,000 tons per year (1976). Of this amount about 60,000 tons are EMD and about 20,000 tons are CMD. The increase in the EMD production for Japan is shown in Fig. 7.

Significant progress in understanding the reduction processes of MnO_2 has been made. Kozawa *et al.* (19-21) have shown that the electron-proton mechanism is the major discharge reaction particularly in KOH electrolyte. The results show that γ-MnO_2 (EMD) which is most important for dry cells is a homogeneous phase solid redox system as Brenet (22) and Vosburg (23) proposed in the 1950's. The theory and the experimental results on the discharge mechanism of MnO_2 were summarized recently by Kozawa (11, 24). Miyaski (25) and Leger and Brodd (26) have reported heterolyte formation relating to the crystal structure of the MnO_2. The discharge process beyond MnOOH (Mn^{+3}) in KOH electrolyte is not well established and it was restudied by McBreen (27, 28).

Despite the numerous previous studies of MnO_2, many unsolved problems on MnO_2 remain, particularly concerning the intrinsic activity and the surface and the pore structure. The Battery Division and the Cleveland Section of the Electrochemical Society established the I.C. Sample Office in 1971 in order to promote the study of the characteristics of MnO_2. Currently 12 different MnO_2 samples are kept and distributed upon request. It is extremely difficult to reproduce exactly the same MnO_2 material even when the conditions described in the literature are followed closely. Therefore, the use of common samples for studies is not only

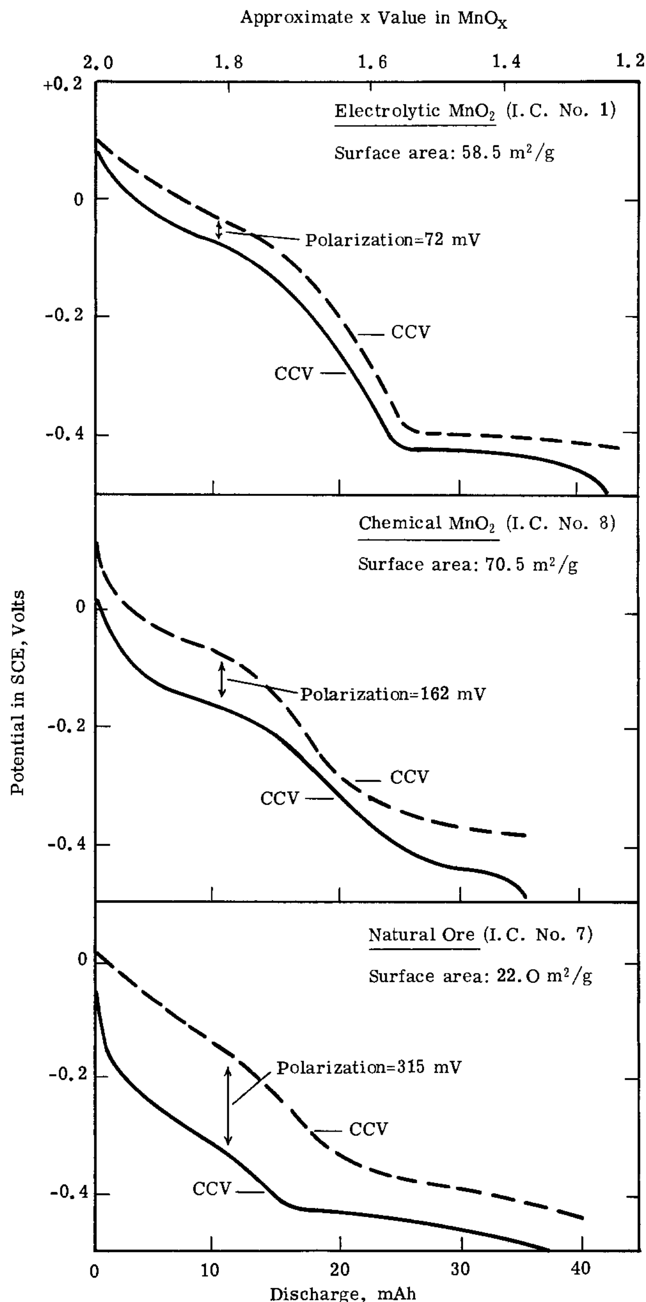

Fig. 6. Open-circuit voltage (OCV) and closed-circuit voltage (CCV) of three types of MnO_2 in 9M KOH.

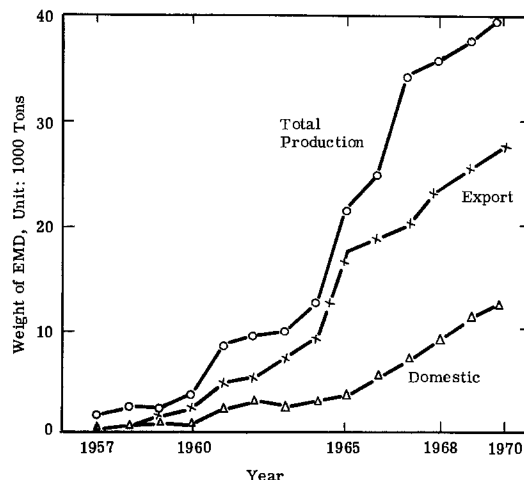

Fig. 7. Production and export and domestic consumption of electrolytic manganese dioxide (EMD) in Japan.

convenient but almost essential in order to compare results from one laboratory to those of another. The proceedings of a symposium on MnO_2 held in Cleveland in 1975 was printed (5).

Mercury and Silver Miniature Cells

The mercury cell is essentially unchanged in construction concept since its introduction in the 1940's. Of course, many new sizes have since been introduced. Ruetschi (29) reported that the reaction proceeds through a soluble intermediate

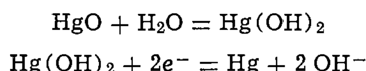

$$HgO + H_2O = Hg(OH)_2$$

$$Hg(OH)_2 + 2e^- = Hg + 2\ OH^-$$

The species $Hg(OH)_2$ rather than $HHgO_2^-$ is postulated because of an apparent lack of dependence of HgO solubility on the OH^- concentration.

The mercury cell discharges at a constant voltage of 1.35V (1.4-1.35, if MnO_2 is added to the cathode). For many applications, a higher voltage discharge is desirable. To satisfy this need, the $Zn/KOH/Ag_2O$ cell system was developed and introduced by Union Carbide in 1961. The cell has a similar design to that of the present mercury cell, except that Ag_2O is used instead of HgO in the cathode. Figure 8 shows a typical construction. The silver cell discharges at a constant 1.65-1.5V, depending on current drain. It can handle pulses upward to 50 mA/cm^2. The coulombic capacity is about 10% lower than the equivalent size mercury cell.

Divalent silver oxide (AgO) has higher energy density and essentially twice the coulombic capacity/gram of Ag_2O. AgO is metastable and should, thermodynamically, spontaneously decompose with oxygen evolution. As a result, it has not been suitable for use in sealed cells because

$$2AgO \rightarrow Ag_2O + \tfrac{1}{2}\ O_2$$

Considerable effort has been expended to render AgO stable for use in sealed miniature cells. This effort consummated in 1976 when ESB introduced the divalent silver cell. Cells being marketed contain both Ag_2O and AgO and provide about a 20% increase in capacity over monovalent Ag-Zn cells.

The rate of AgO decomposition can be reduced by the presence (and adsorption) of small amounts of impurities or additives. Cahan (30) showed that PbO additions reduced significantly the decomposition rate. Amlie and Ruetschi (31) found Cd and Zn additions decreased the decomposition rate. Tvarusko (32) reported that Ni and Co additives increase the rate of decomposition while Cd, Zn, Al, and Pb decrease the rate of decomposition. He also found that stability depended on the mode of preparation of AgO. Davis (33) has reported the beneficial effect of gold additives. A common thread underlying these studies is the thought that stability results from a protective coating of Ag_2O on the surface of the AgO particle.

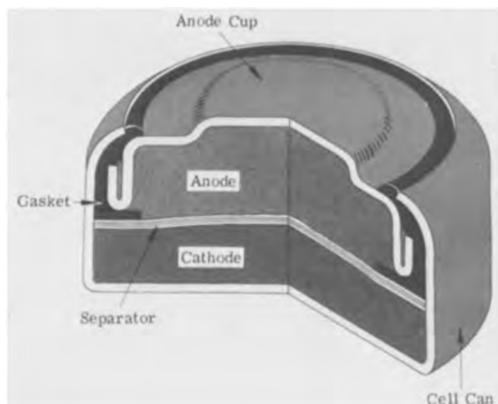

Fig. 8. Schematic of HgO-Zn and Ag_2O-Zn miniature cells

AgO has a monoclinic crystal habit with four AgO in the unit cell (34). There are two nonequivalent silver sites which are postulated to be Ag^+ and Ag^{+3}. The dual valency accounts for the observed diamagnetism and unusually high conductivity. The so-called divalent silver oxide is really a combination of Ag^+ and Ag^{+3} although the formula is still written AgO.

AgO normally discharges with a two-step discharge. Certain applications require substantially constant voltage discharge. Krebs (35) has reported a technique for stabilization of AgO which results in discharge at the constant Ag_2O voltage (monovalent voltage) but with the coulombic capacity essentially that of AgO. Dawson (36) disclosed a construction in which the monovalent oxide provides the contact to the current collector and isolates the AgO from the collector and the electrolyte. During discharge an exchange takes place to regenerate the monovalent material

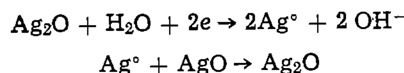

$$Ag_2O + H_2O + 2e \rightarrow 2Ag^\circ + 2\ OH^-$$

$$Ag^\circ + AgO \rightarrow Ag_2O$$

Thus the cell discharges at the monovalent voltage but the exchange permits utilization of coulombic capacity of AgO. The isolation of AgO can be obtained by reducing the surface of the AgO particles chemically or electrochemically.

Organic Depolarizers

Organic cathode materials or depolarizers have been studied for possible replacement of MnO_2 in primary batteries. Because of their low operating potential, magnesium anodes have been used to give an acceptable unit cell voltage. Of all the depolarizers metadinitrobenzene (MDB) has been the most extensively studied (37, 38). Figure 9 shows a comparison of the performance of MDB with MnO_2. The results are typical of most organic depolarizers. To high voltage cutoff (1.1V) the performance is poor but to the lower cutoff (0.65V) the organic depolarizers give excellent service compared to MnO_2. Best performance has been obtained with high surface area carbons and $MgClO_4$ electrolyte (39, 40). Andre and Reilly (41) reported that catalysts influenced the reaction path and efficiency in practical cells with acetylene black conductor. With V_2O_5 and Fe_2O_3 catalyst, the principal products are *m*-nitroaniline and *m*-nitrophenylhydroxylamine, respectively. Other products form depending on the current drain, pH, etc.

Workers at American Cyanamid (41-43) identified several high voltage organic depolarizers based on benzofuroxan oxide and azodicarbonamides which do not require the use of a magnesium anode to obtain

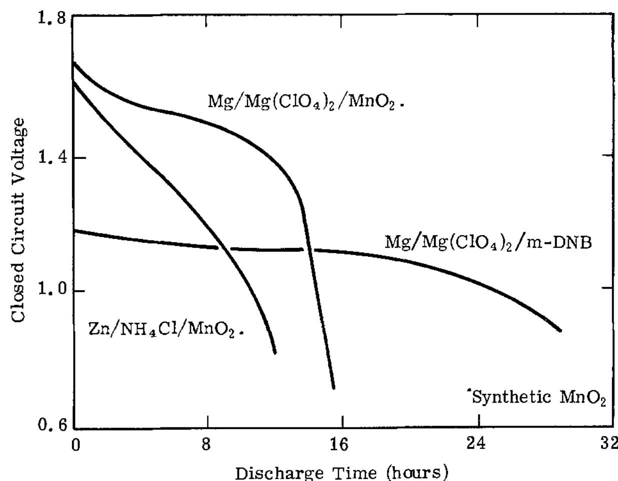

Fig. 9. Discharge curves of magnesium and zinc A-size cells on 16-2/3Ω test. Discharge curves for dry cells tested at 70°F (A cells), 16-2/3Ω drain. m-DNB represents *meta*-dinitrobenzene. Reference (40), with permission from PSC Publication Committee.

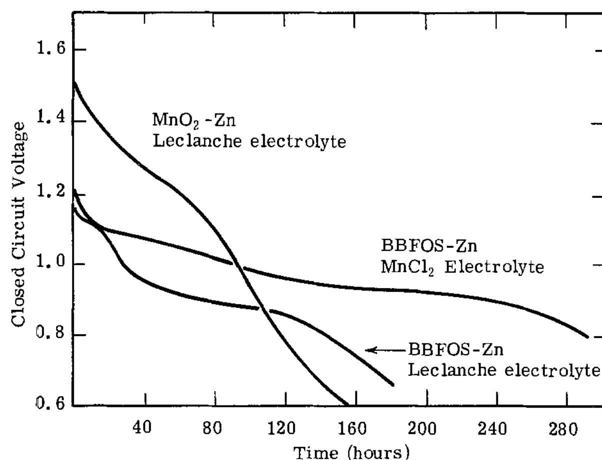

Fig. 10. Discharge curves through 150Ω of AA size cells comparing standard MnO_2 cathods cells with BBFOS organic depolarizer in two electrolytes. Reference (42).

a satisfactory cell emf. A comparison of the performance is shown in Fig. 10 for similar cell constructions with zinc anodes. Longer service to low cutoff voltages was obtained when the electrolyte contained $MnCl_2$ (42). Because benzofuroxans have limited solubility, modification of the structure such as BBFOS (5, 5′ sulfonyl bisbenzofurazan 3, 3′ dioxide) is preferred for its low solubility. Unlike MDB, catalysts have no effect on the performance of BBFOS.

Another series of compounds azobisdicarbonamides, also have as good activity as cathodes. Substitution improves their chemical and thermal stability as well as lowers the solubility. The compound 1,1′azobis(N-n-butyl formamide) gave the best performance (43). This compound also exhibits rechargeability. Cells made with the reduced product, biurea, have excellent stability and can be stored for prolonged periods, then charged for use (44).

Magnesium and Aluminum

Magnesium batteries $Mg/MgClO_4/MnO_2$ (40, 45, 46) have been produced for the military since 1971. The use of perchlorate electrolyte reduces the delay over the older $MgBr_2$ electrolyte. $BaCrO_4$ inhibitor is usually added to reduce wasteful corrosion. Figure 11 shows typical construction. Once put into service, the batteries must be used to exhaustion. This controlled application circumvents the difficulties of commercial application, *e.g.*, voltage delay (less than 1 sec), excess H_2 evolution on discharge, and very poor intermittent service. Magnesium anodes have also found considerable application in seawater batteries with $CuCl_2$ or AgCl cathodes (47).

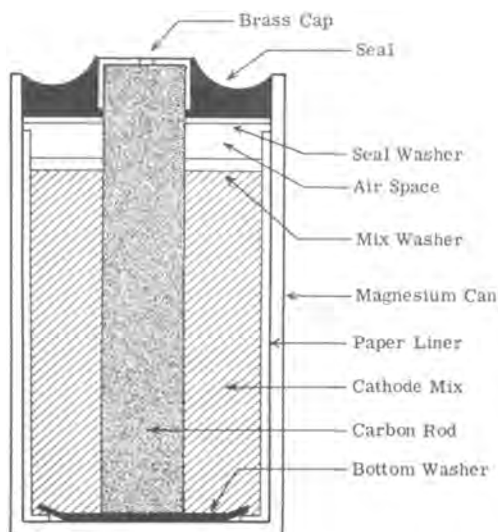

Fig. 11. Cross-section view, $Mg/Mg(ClO_4)_2/MnO_2$ dry cell. With permission from PSC Publication Committee.

Aluminum has not proved to be a satisfactory anode for aqueous electrolyte batteries (48). Aluminum can compete with Zn and Mg only on continuous discharge. The protective film which stabilizes aluminum in the environment contributes to its failure as a battery material. The anode shows delay characteristics. The activation of the cell destroys the passive film and leads to poor intermittent service, excessive H_2 evolution, and rapid perforation on discharge (49). Alcoa has developed a two-layer zinc alloy anode which minimizes but does not solve the problems (50). Other alloys, electrolytes, and inhibitors have been reported, but none fully solve the aluminum anode problem areas.

Reserve Batteries

Thermal batteries are reserve batteries which are activated by heating from a pyrotechnic device. On reaching the melting point of the electrolyte (usually KCl-LiCl eutectic, mp 352°C), the cell is ready to deliver current. The activation time is 0.5 sec or less. Thermal batteries find application mainly in military ordnance devices. Goodrich and Evans (51) reviewed the early work up to 1952. Other reviews have also appeared (52-54). The first thermal batteries of Ca-WO_3 were produced about 1948. The early cells were of the "cup" or closed-cell design in which the cathode faces both sides of the anode and the entire cell is enclosed into a can construction.

McKee (55) described the Ca-$CaCrO_4$ system which gave better high rate performance than the Ca-WO_3 battery. However, the self-discharge reaction of the $CaCrO_4$ cathode accelerates with temperature and, above 600°C, can lead to thermal runaway conditions. This is thought to be due to the increased solubility of the salt with increased temperature. Other thermal batteries of the cup type included Ca-K_2CrO_4 and Ca-V_2O_5 in which the V_2O_5 and boric acid formed a glaze coating on the cathode (56). Heat pads of Zr-$BaCrO_4$ were used in the cup batteries. The problems of the cup or closed-cell construction include short activated stand (5 min or less), and intricate battery design (intercell connections, etc.). Also, the heat pad can induce thermal shocks which damage battery operation.

Workers in the United States and England developed a bipolar construction shown in Fig. 12 which has been used in subsequent thermal battery designs (57-59). The cells are constructed with three layers or pellets: a heat pellet, a combination depolarizer-electrolyte-binder (DEB) pellet, and a calcium anode on an ion collector.

A kaolin or powdered silica binder holds the electrolyte in place to reduce shorting and to permit operation in high spin applications (60). The KCl-LiCl eutectic is the electrolyte for most cells, although LiBi-KBr has been used in some instances. The heat pellet of powdered iron and potassium perchlorate has excess iron to serve as the intercell connector after performing its heating function. The pellets are stacked one on top of each other, heat pad, anode, DEB tablet, heat pad, etc, to give the bipolar construction which

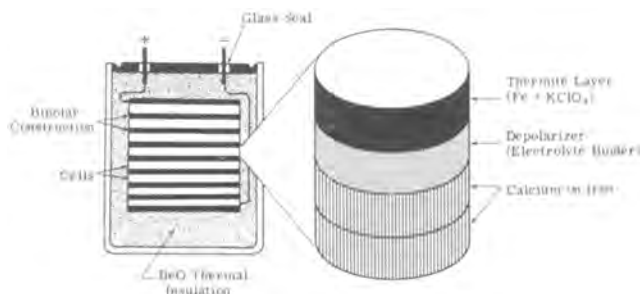

Fig. 12. Cross-section of typical thermal battery. Reference (58)

is efficient and simple to construct. A BeO sleeve or container is used as an electrical insulator, but it has good thermal conductivity to maintain heat balance. The heat pad is usually activated with an electrical match. Typical construction is shown in Fig. 12. The original pellet or open-cell construction was applied to the Mg-V_2O_5 system, but the Ca-$CaCrO_4$ system gives better performance. Goldman and Smith (61) demonstrated that the pellet construction gave superior performance to that of the cup construction for the same chemical combination. They also reported that the depolarizer with best performance was $CaCrO_4$. Thow (59) showed that the open-cell construction gave faster activation.

The chemistry of calcium has several features which can lead to poor cell performance. The calcium anode reacts with the lithium electrolyte to form the alloy, $CaLi_2$. The alloy tends to collect at the edges of the anode and leads to intermittent shorts and electrical noise, especially in spin applications. It is thought that the formation of the alloy may contribute to good anode performance. It is reported that acetic acid treatment reduced alloy formation (62). Chromate in the electrolyte can also form a protective anode film. Calcium chloride formed by anode reaction forms an insoluble double salt $CaCl_2 \cdot KCl$, mp 575°C. This compound can precipitate and prematurely passivate the calcium anode. In spite of these problems the calcium anode is preferred because of its high electrode potential, excellent energy density, and high discharge rate capability.

Longer lived thermal batteries have been reported (63) as has the use of other cathode reactants, *e.g.*, Fe_2O_3, CuO (64, 65). Ammonia and SO_2 reserve batteries have also been developed for use in military ordnance devices (54). Other systems with good storage and activated life include Cd/HgO (66-68) and solid electrolyte cells discussed below.

Solid Electrolyte

The interest in solid electrolytes with high conductivity was stimulated by the discovery of the super ionic conductor silver rubidium iodide by Bradley and Green (69) and Owens and Argue (70). Solid electrolyte cells offer the advantages of low shelf discharge rates and thus long shelf life, wide temperature range of operation, absence of leakage, and ease of miniaturization. Table IV lists several properties of solid electrolyte systems which have been developed. The silver-based electrolytes have the disadvantage of low energy density and low voltage but can have good high rate performance. The lithium iodide and β-Al_2O_3 cell systems based on lithium or sodium conduction, respectively, have high unit cell voltages and high energy density but are relatively poor conductors at room temperature. They perform satisfactorily where low currents and long life are required, such as in heart pacers. The incorporation of Al_2O_3 in the Li-PbI_2PbS cell is an example of the improvement of the conductivity by inclusion of an inert material to enhance surface conductivity (76). Several of the iodine cathode systems use a charge-transfer complex to enhance cathode activity (73, 77). The LiI cells have the disadvantage of increased internal resistance as the discharge progresses. The lithium iodide forms at the interface between lithium and the iodine cathode. Thus the contact develops a thin layer of LiI electrolyte which also serves as the separator. It is sufficiently thin so that the poor LiI conductivity does not contribute significant voltage loss at the current drains of normal operation (*e.g.*, 10-100 μA).

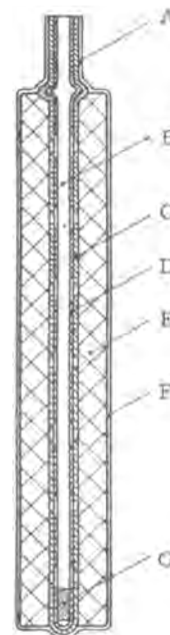

Fig. 13. Cross-section of the air electrode designed by Siller (Pertrix, 1961), Reference (85). A, electrode seal; B, air-access space; C, conductive foil with holes; D, aluminum foil; E, carbon plates; F, cellulose acetate film; G, paper spacer.

When low steady drains over extremely long periods, *e.g.*, 10 years, are required, atomic batteries greatly exceed the capabilities of chemical systems. Atomic batteries convert the heat from radioactive decay, *e.g.*, Pu^{238}, Po^{210}, etc., by use of thermoelectric converters. The cells are very rugged and can withstand incineration at about 1300°C for 2 hr or direct impact from a 0.44 magnum pistol without rupture. Systems have been developed for long lived pacemaker applications and for power in remote areas (81, 82).

Zinc-Air Cells

A strong effort was made at the Pertrix, A.G. (now Varta Batterie, A. G.) to improve the neutral electrolyte cells by substituting manganese chloride and magnesium chloride for the usual ammonium and zinc chloride electrolytes (83). Siller attempted to adapt the vapor pressure of the solution to the relative humidity ranges of the ambient. Siller also used thin carbon plates for large cells to improve the current output. Figure 13 shows the air electrode as manufactured in 1961 (84, 85).

The alkaline cells with thin-walled, molded-type air cathodes shown in Fig. 14 and 15 were manufactured

Table IV. Performance of solid electrolyte battery systems

System	$Ag/Ag_4RbI_5/R_4NI_3$	$Ag/4AgI/KCN/$perylene-I_2	$Li/LiI,Al_2O_3,LiOH/PbI_2,PbS$	$Li/LiI/I_2$	$Na,Hg/\beta$-Al_2O_3/Br_2
OCV	0.66	0.64	1.9	2.8	3.77
W-hr/in.^{3}	0.6-1.2	~0.6-1.2	3.4-8.0	4.1	3.9-5.4
Typical currents obtainable	10^{-3}-10^{-5}A cont. 100 mA pulse	10^{-3}-10^{-5}A cont. 1A pulse	10^{-4}-10^{-5}A	10^{-4}-10^{-5}A	10^{-3}-10^{-5}A
Electrode conductivity at room temp., $(\Omega$-cm$)^{-1}$	0.21	0.14	10^{-5}	10^{-7}	10^{-2}-10^{-3}
Storage life, years	10	10	—	8	—
Reference	(71)	(72-74)	(75, 76)	(77-79)	(80)
Developed by	Gould	Union Carbide	Mallory	Catalyst Research	General Electric

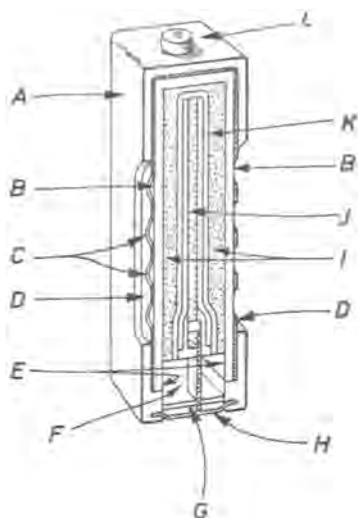

Fig. 14. The Eveready 1005 zinc-air cell (1952). A, housing; B, carbon electrode; C, air holes; D, metal plates; E, carbon layer; F, air space; G, inner seal; H, negative contact; I, electrolyte; J, zinc electrode; K, separator; L, positive seal.

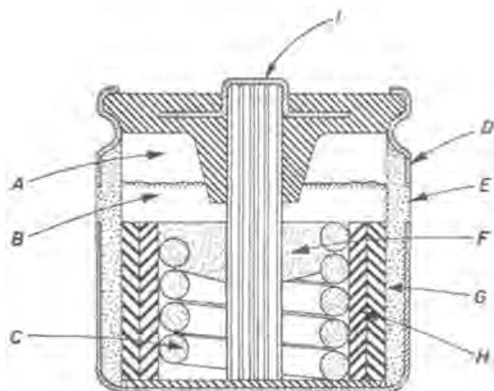

Fig. 15. The Eveready 1002E zinc-air cell (1955), A, air space; B, electrolyte paste; C, wound wire zinc; D, steel case; E, air hole; F, zinc powder; G, carbon electrode; H, separator.

in the early 1950's (86-88) as hearing aid cells. These cells reached energy densities of 200 W-hr/kg, which was more than any primary cell of previous aqueous types. Like the neutral electrolyte cells in Europe which had far lower current densities, they became obsolete when the current demanded by radios and other portable electronic devices rapidly dropped into the low milliampere range with the advent of the transistor.

The designs shown in all three air cell figures have one common feature: the use of thin plates with improved oxygen-transport capabilities. The high ampere-hour capacities were achieved because most of the remaining cell volume was occupied by the anode and the electrolyte. The neutral salt electrolyte cells manufactured by Pertrix, A.G. used solid zinc anodes, while the alkaline cells made by Union Carbide Corporation used large surface powder zinc anodes and wire coils along with gelled sodium hydroxide. Earlier, large box air cells using liquid NaOH were improved by the addition of calcium hydroxide (89) which reduced the electrolyte requirement from 9 to 4 ml/A-hr. The small hearing aid cells described in Fig. 14 and 15 reduced this value to less than 1 ml/A-hr. Both cells were sealed in plastic which was opened before use.

Figure 16 shows a D-size cell which was manufactured in 1951 by the Austrian firm W. I. F. (88) and was based on utilization of the spinel-catalyzed carbon electrodes invented a few years earlier by Marko and Kordesch (90). This cell could deliver 200 mA continuously for 75 hr and more than equaled the output

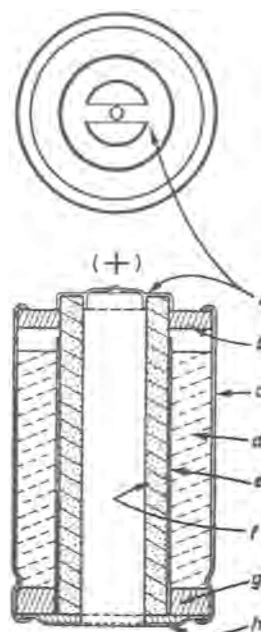

Fig. 16. The D-size zinc-air cell of W. I. F. (1951). a, Metal cap; b, spacer; c, steel can; d, electrolyte paste with zinc particles; e, separator; f, carbon tube; g, spacer; h, bottom contact.

of a (R-20) mercuric oxide cell. The electrolyte used was potassium hydroxide gelled with sodium carboxymethylcellulose, and zinc was distributed in the form of very small leaflets (less than 0.05 mm thick) which were produced by breaking up amalgamated zinc foil. A reserve cell of this type but with the carbon tube as the outside shell gave 500 mA current and had a capacity of 18 A-hr. However, this cell suffered from carbon dioxide pickup as well as drying out or wetting up after the seal was broken. The cell was soon abandoned. Even so, the design of the modern alkaline MnO_2-zinc cell with its outside cathodic sleeve is strongly related to the above-mentioned outside carbon-air cell.

Even though no commercial interest developed for the small zinc-air cells for use in portable devices, the unexcelled capacity of these cells was attractive for military applications and several versions (mostly reserve-type) of thin plate cells were produced using air electrodes from fuel cell technology (91, 92). A mechanically rechargeable zinc-air battery was developed by Leesona-Moos Laboratories for the U.S. Army Electronics Command (93). This "bicell" construction, shown in Fig. 17, was capable of delivering up to 160 W-hr/kg. For "recharging," the zinc plates were renewed, and one set of cathodes permitted up to 50 refillings. An air-blower was incorporated to sustain high rates and to provide air cooling. The anode packages, which were activated with water, contained powder zinc and dry KOH. A similar battery was developed by Energy Conversion, Limited, in England.

Several large air cells have been constructed. General Motors built an experimental vehicle in 1969 which included a 20 kW mechanically rechargeable zinc-air battery (94). The sodium-amalgam/(carbon) oxygen cell gained recognition as a high power, high voltage system, and considerable effort went into its technical realization by the M. W. Kellogg Company (95) in the mid-1950's.

Realizing that aluminum-air is a galvanic element with theoretically 7900 W-hr/kg metal consumed, many attempts were made to reduce such a system to practice. Zaromb Research Corporation (96) reported in 1967 that a 2 kW system with provisions for the exchange of the spent alkaline electrolyte was feasible.

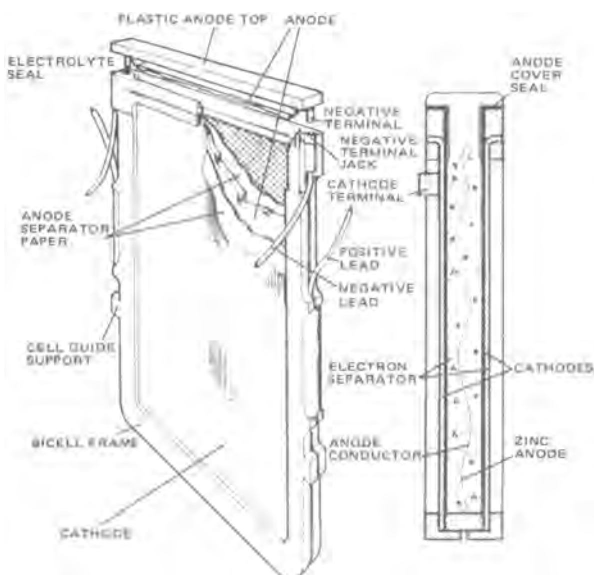

Fig. 17. Zinc-air bicell construction (Leesona Moos, 1968)

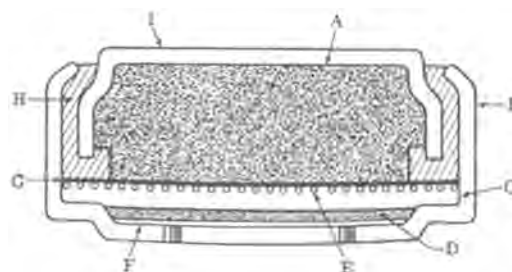

Fig. 18. Schematic of zinc-air miniature cell. Courtesy of Gould, Incorporated. A, Zinc powder; B, cathode casing; C, cathode; D, porous Teflon; E, current collector; F, absorbent material; G, separator; H, gasket.

Magnesium-air systems operate with neutral electrolytes. However, the achieved current densities are low (97). An air-sodium amalgam cell combined with a molten salt-liquid sodium "supply" half-cell to operate at temperatures above 100°C was proposed by Atomics International (98).

In recent years, there have been attempts to revive small size air-zinc primary cells. An experimental high capacity zinc-air D-size cell produced by Energy Conversion Limited, England, is pictured in a 1972 air cell review by Gregory (99). The capacity was claimed to be 22 A-hr. The air cathode is on the outside (Teflon-coated and screen protected), and the powder zinc anode is in the center of the cell. In all likelihood, the "old problems" encountered with alkaline cells once again manifest themselves. A powerful air cell needs the thin electrode with good diffusion properties, but if this is achieved then the cell suffers from exposure to air. For this reason, it is understandable why another recent attempt to build a nonreserve-type high power alkaline zinc-air cell (100) achieved no real breakthrough in technology despite excellent packaging prior to self storage.

The Russian Krona cell version of small alkaline zinc-air cells constitutes a compromise. The carbon electrode is kept rather thick (2-3 mm) and serves as a barrier to protect the zinc from air access. In addition, MnO_2 is added to the carbon to provide peak power capabilities for a short period, while the recharging action of the air electrode is utilized to regenerate the MnO_2.

Recently, miniature cell applications for hearing aids were found for the hybrid zinc-air MnO_2 (alkaline) primary system. The approach at Gould (101) is to restrict air access to the minimum needed to provide the average current (in the order of mA and μA) and thereby minimize the exchange of CO_2 and water vapor. These cells are claimed to have about twice the ampere-hour capacity of corresponding mercuric oxide-zinc cells. A cross section of a Gould No. 675 cell is shown in Fig. 18. Air access is limited through the use of very small holes. Activated (open) shelf life is quoted to be satisfactory in the hearing aid as well as for calculator and watch applications.

Lithium Batteries

Nonaqueous cell systems have received increasing attention during the past 25 years, starting with the use of liquid ammonia for reserve cells (54). Since lithium has the highest potential on the emf scale, it is one of the highest available energy anode systems. Its low equivalent weight makes lithium batteries very lightweight and enhances their aerospace and military applications. The lightness of weight, together with good low temperature operation, was responsible for much of the early interest. For most earth-based applications, the volume energy density is more important. In this case, the low density of lithium detracts from the energy density of lithium battery systems. Of the lithium battery systems listed in Table V, only the lithium-$SOCl_2$ system has clearly superior volume energy density over those of the commercial silver and mercury aqueous systems shown in Table VI. The real advantages for lithium batteries are in their excellent storage life, their ability to operate over a wide temperature range, and, in some cases, in their high unit cell voltage. Eichinger and Basenhard (102, 103) have surveyed the large literature of lithium battery reactions. The better-known systems are discussed below.

The early SO_2 batteries were developed as reserve batteries for the military, in which the SO_2 served only as the ionizing solvent base for the electrolyte (54). In the early 1960's, a group at American Cyanamid observed an emf generated by SO_2 in an electrolysis cell. This discovery led directly to the development of lithium-SO_2 cells where the SO_2 served a dual purpose: as the ionizing solvent for the electrolyte and as the cathode reactant (104-106). This new concept of a liquid cathode cell led to higher energy density through greater efficiency of utilization of the cathode material. A solvent, *e.g.*, acetonitrile, propylene carbonate, is sometimes added to lower the vapor pressure of SO_2 to help control the lithium-passivation problem, and to provide a conductive solution for greater SO_2 efficiency. The preferred solute is LiBr.

One would expect lithium and SO_2 to react spontaneously in the cell. The formation of a thin protective film of SO_2 reduction product (LiS_2O_4?) on the sur-

Table V. Primary cell systems (nonaqueous base)

	Nominal voltage	Nominal W-hr/in.³	Comments
Li-SO_2	2.9	8.0	Military, safety
Li-CuO	1.6	10.0	C-Zn replacement
Li-CF_x	2.8	10.0	High unit cell voltage
Li-CuS	2.0	8.0	Low rate
Li-Ag_2CrO_4	3.3	10.0	Pacemakers
Li-I_2	2.8	4.1	Pacemakers
Li-$SOCl_2$	3.5	15.0	Safety, high rate
Li-V_2O_5	3.4	11.0	Electronic
Li-MoO_3	2.9	10.0	Electronic

Table VI. Primary cell systems (aqueous base)

	Nominal voltage	Nominal W-hr/in.³	Comments
Leclanché	1.5	2.5	Low cost
Zinc chloride	1.5	2.6	Medium cost, higher rate
Alkaline	1.5	2.7	High rate, low leakage
Magnesium	1.7	4.1	High rate continuous
Mercury	1.35	9.5	High energy density
Silver	1.6	8.8	High energy density
Divalent silver	1.6	10.0	Leakage, stability
Zinc-Air	1.4	12.0	Shelf problems

face of the lithium electrode inhibits the internal self-discharge. This film is responsible for the observed voltage delay during cell discharge, but it also provides the protection for good shelf life of the cell.

Power Conversion, Incorporated first marketed the Li-SO_2 cells in 1972. Typical discharge characteristics and cell construction are shown in Fig. 19 and 20. Lithium passivation effects are noted during the initial portions of the discharge. The cells exhibit good performance, especially at low temperatures. This is due to the good transport properties of the SO_2 electrolyte and the extended surface area electrode construction. Figure 21 shows the performance of Li-SO_2 compared with present commercial and military batteries as a function of temperature. The good performance at low temperature is especially attractive for military applications. Safety is still an unresolved problem area (110).

The discovery of oxyhalides, thionyl chloride, and sulfuryl chloride as liquid cathodes represents another recent advance in battery technology (111-113). The lithium cells with oxyhalide cathode reactant have been reported to deliver 18 W-hr/in.^{3}; this is significantly better that any other lithium battery. As with the Li-SO_2 cell, the soluble cathode construction results in increased efficiency in cell performance.

The oxyhalide cell construction for high rate cells is very similar to that of the Li/SO_2 in Fig. 19. Typical cell performance of the high energy construction is shown in Fig. 22. Film formation in lithium, mainly

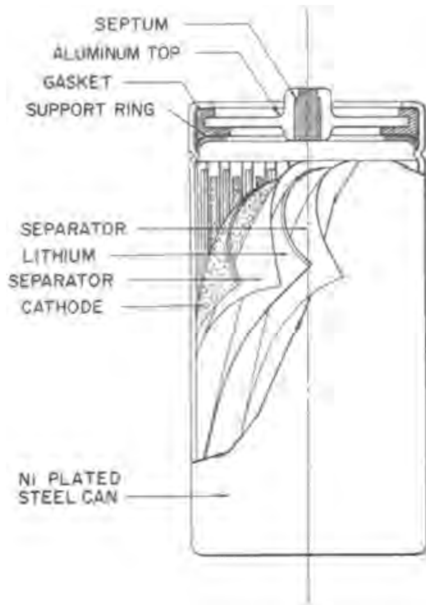

Fig. 19. Schematic diagram of cell. Reference (107). Courtesy of P. R. Mallory & Company, Incorporated.

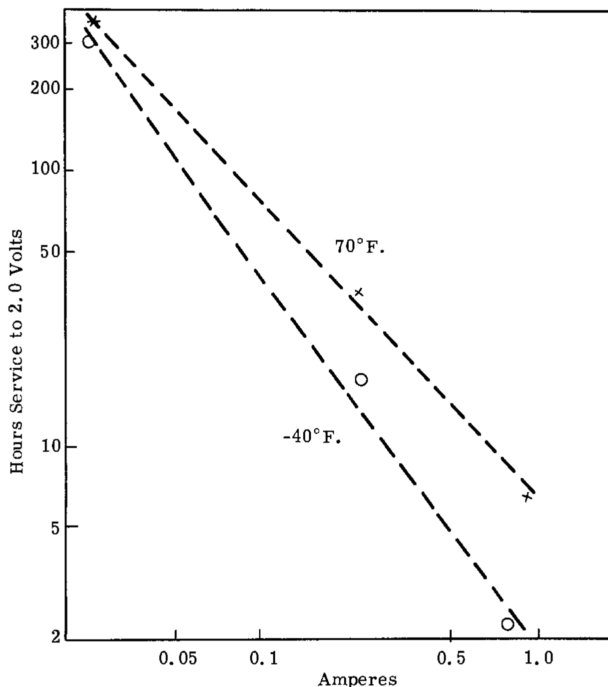

Fig. 20. Lithium-sulfur dioxide system, D cells, service vs. current from —40° to 70°F. Reference (108).

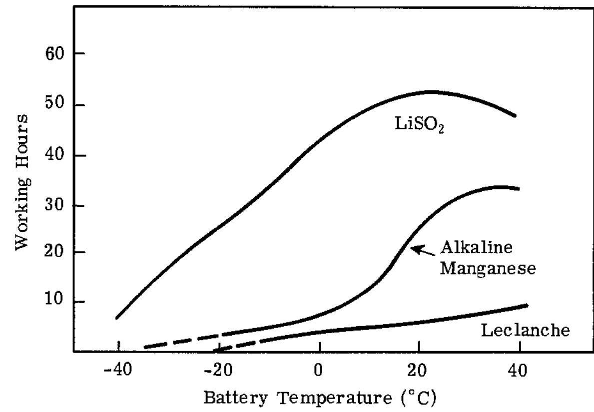

Fig. 21. SEM-52N. Working hours with various battery systems. With permission from Reference (109). Copyright by Academic Press, Incorporated (London) Limited.

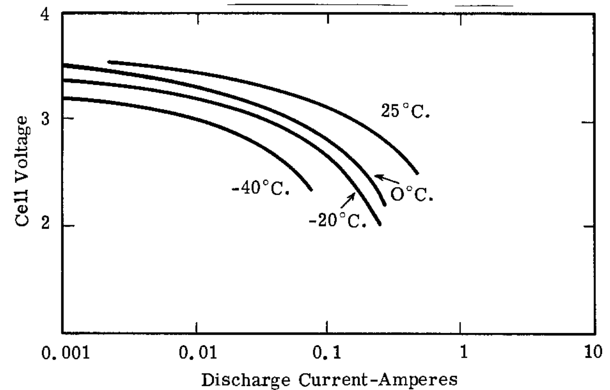

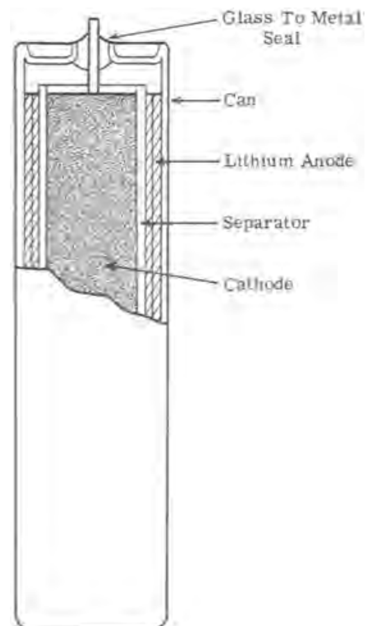

Fig. 22a. Voltage-current characteristics of AA cells. High energy type cell with thionyl chloride electrolytic solution. With permission from Ref. (115). Copyright by Academic Press, Incorporated (London) Limited; b. Schematic of high energy cell construction. Reference (114). Courtesy of GTE Laboratories, Incorporated.

LiCl, during open-circuit stand results in a severe voltage delay in some cases (116, 117). The film from self-discharge reaction effectively blocks the surfaces. Various techniques have been reported to eliminate this problem, including purification of the electrolyte and protective plastic film on the lithium (118-120). The ionizing solute is $LiAlCl_4$. A wide spectrum has been reported of cell sizes which range from 40 mA-hr button cells to several thousand ampere-hour high current power supplies. Larger cells have some unresolved safety problems, and Mallory has reported on thermal runaway conditions (121-122).

Two types of lithium anode-nonaqueous cells, Li-CF_x (123, 124, 126) and Li-MnO_2 (125), were developed in Japan and were introduced commercially in 1973 and 1976, respectively. Polycarbonmonofluoride (or CF_x), having an x value close to 1.0, is usually used. The advantage of using CF_x is that the material does not dissolve in the organic electrolyte and also produces carbon (a conductive material) upon discharge: $CF_x + xe^- \rightarrow C + xF^-$.

Six types of Li-CF_x cells are being offered, with capabilities ranging from 500 to 5000 mA-hr. A small cylindrical cell (BR-435 cell, shown in Fig. 23), 4 mm diam $\times$ 30 mm long, is the most popular, and about 4 million such cells were produced in 1977. The BR-435 cell is being used mostly to power a light-emitting diode to illuminate fishing floats in Japan. Figure 24 shows a comparison of the discharge capacity of C-size cells against regular MnO_2-Zn type cells. The Li-CF_x cell has a closed-circuit voltage of 2.8V, and its energy density is 4 to 5 times greater than that of the Leclanché cells. Figure 25 shows that the cell voltage during the discharge depends on the temperature.

Li-MnO_2 cells are being offered in sizes from 30 to 5000 mA-hr capacity (125). Among these cells, a thin (2.8 mm thick) coin-type cell is in limited commercial production, mainly for hand-held calculators. The typical discharge curves of the thin coin-type cell (LF-½W) are shown in Fig. 26. Manganese dioxide used for Li-MnO_2 cells is electrolytic MnO_2 which is properly heat-treated in order to remove the water and to modify the crystal structure. Figure 27 shows the effect of heat-treatment on the MnO_2 reactant. It was confirmed by x-ray study (128) that the MnO_2 lattice expands when it is discharged. This is believed to be due to Li^+ ion penetration into the MnO_2 lattice, similar to the proton penetration (20) in the case of discharge of γ-MnO_2 in aqueous solution. This was supported from the cell voltage by the shape of the

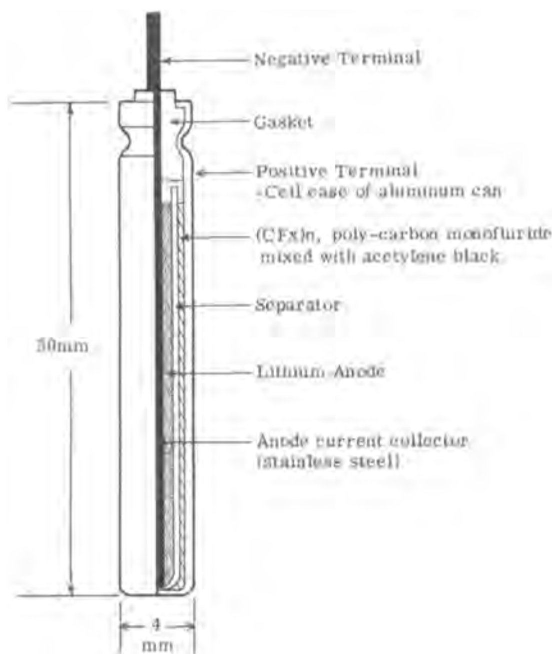

Fig. 23. Li-CF_x Matsushita. Reference (124).

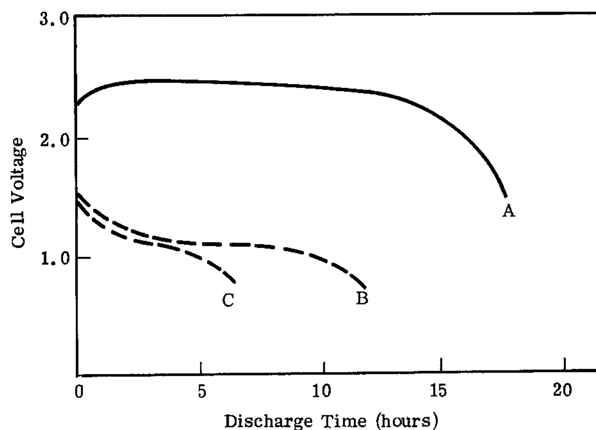

Fig. 24. Comparison of C-size cells. A, Li-CF_x cell (8Ω continuous discharge); B, alkaline MnO_2-Zn cell (4Ω continuous discharge); C, Leclanché type MnO_2-Zn cell (4Ω intermittent discharge). With permission from Reference (123). Copyright by Academic Press, Incorporated (London) Limited.

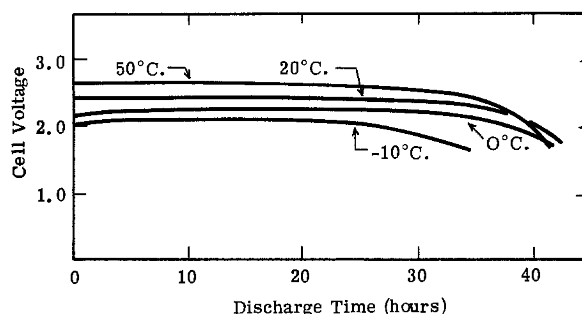

Fig. 25. Discharge of BR 435 cell through 2.5KΩ. Reference (124)

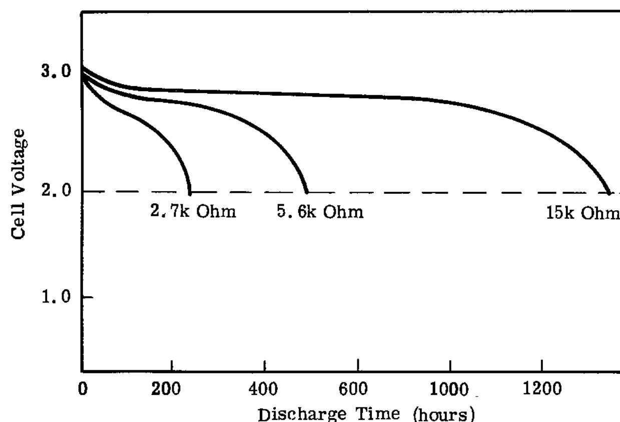

Fig. 26. Discharge curves of Sanyo pressed type cell (LF-½W) with various loads. Reference (125).

discharge curve. The cell voltage is calculated based on the following reaction: $2Li + 2MnO_2 = Mn_2O_2 + Li_2O$; the expected voltage is only 2.69 ($= E°$). Actual cell voltage is 3.0-3.4V. To explain this, Ikeda *et al.* (127) assumed that Li^+ ion incorporation into the MnO_2 lattice is similar to the familiar manganite and hetaerolyte reactions in aqueous media.

A low drain Li/Ag_2CrO_4 cell system has been developed by SAFT (129). Cell construction is very similar to that of the miniature silver-zinc in Fig. 8. They report excellent stability with the organic $LiClO_4$ electrolyte. The cells deliver their initial fresh capacity after 4-years' storage at 45°C. The cells are suitable for electronic applications requiring low steady currents, and at pacemaker drains the cells deliver current at a steady 3.0V for 6-8 years.

Lehmann *et al.* (130) have reported a low cost Li/CuO cylindrical cell of nonspiral construction. Figure 28 depicts typical cell performance with a comparison

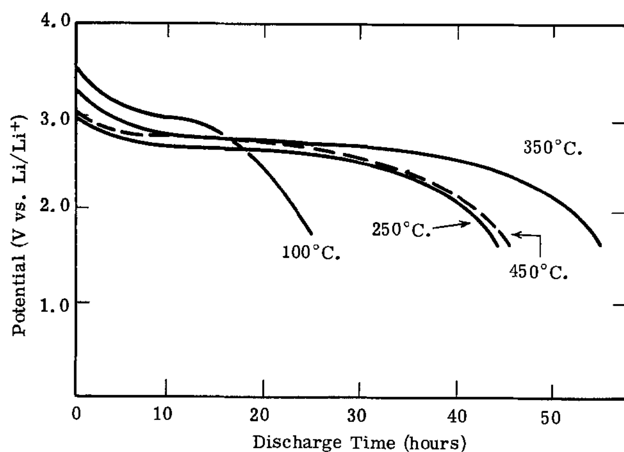

Fig. 27. Discharge characteristics of MnO_2 heat-treated at various temperatures. The current density was 1.2 mA/cm^2. Reference (127).

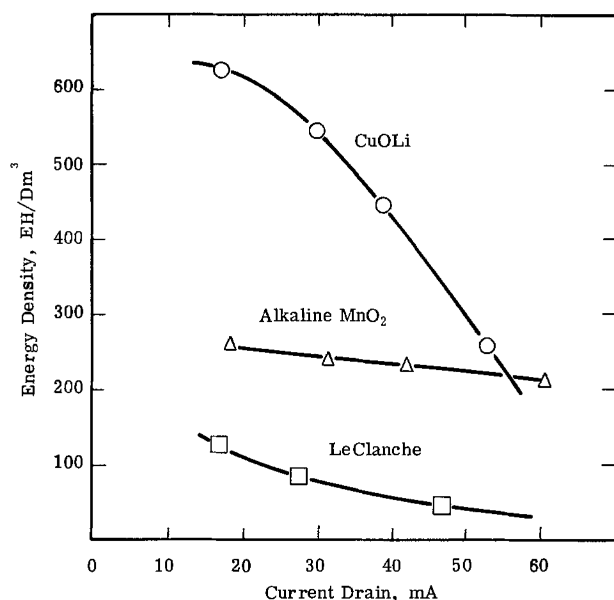

Fig. 28. Energy density of AA size cells under continuous loads. With permission from Reference (130). Copyright by Academic Press Incorporated (London) Limited.

to Leclanché and alkaline cell systems. Although the cell has a thermodynamic voltage of 2.4V, it discharges at 1.4-1.0V depending on current drain. The system has good storage properties and delivers 95-100% of its original capacity after six months and has no measurable loss after 3 weeks at 70°C.

Other lithium cell systems in advanced states of development include Li/CuS, Li/MoO_3, and Li/V_2O_5 (131-133).

REFERENCES

1. G. W. Heise and N. C. Cahoon, Editors, "Primary Batteries," Vol. 1, John Wiley & Sons, Inc., New York (1971).
2. N. C. Cahoon and G. W. Heise, Editors, "Primary Batteries," Vol. 2, John Wiley & Sons, Inc., New York (1976).
3. K. V. Kordesch, Editor, "Batteries," Marcel Dekker, New York (1974).
4. R. Jasinski, "High Energy Batteries," Marcel Dekker, New York (1963).
5. "Proceedings of the Manganese Dioxide Symposium," Vol. 1, A. Kozawa and R. J. Brodd, Editors, I. C. Sample Office, Cleveland, Ohio (1975).
6. "100 Years of Japan Dry Battery Industry," *Trade Time*, No. 289 (special issue) p. 13 (May 20, 1977).
7. A. Kozawa and T. Takahashi, *Dry Battery*, No. 509, p. 11 (Nov. 5, 1968).
8. T. Takahashi, *ibid.*, No. 664, p. 21 (June 15, 1977).
9. N. C. Cahoon, in "Primary Batteries," Vol. 2, N. C. Cahoon and G. W. Heise, Editors, Chap, 1, John Wiley & Sons, Inc., New York (1976).
10. T. Takeda, S. Hosoi, and M. Ueyama, Japanese Pat. 37-5208 (1962).
11. A. Kozawa, in "Batteries," K. V. Kordesch, Editor, chap. 3, Marcel Dekker, New York (1974).
12. R. Huber, *ibid.*, chap. 1.
13. J. Watanabe, R. Furumi, and A. Ohta, in "Proceedings of the Manganese Dioxide Symposium," Vol. 1, A. Kozawa and R. J. Brodd, Editors, pp. 435-451, I. C. Sample Office, Cleveland, Ohio (1975).
14. Y. Uetani, T. Togo, and T. Iwamaru, in *ibid.*, pp. 183-201.
15. Y. Uetani, R. Ikeba, M. Sugihara, K. Kashiwaya, and K. Hisatomi, Jpn. Pat. 52-9814 (1977).
16. C. Davis, U.S. Pat. 3,905,851 (1975).
17. W. S. Herbert, *This Journal*, **99**, 190C (1952).
18. H. P. Keating, in "Proceedings of Southern California-Nevada Section, Advances in Battery Technology Symposium," Vol. 4, p. 115, The Electrochemical Society, Princeton, N.J. (1968).
19. A. Kozawa and J. F. Yeager, *This Journal*, **112**, 959 (1965).
20. A. Kozawa and R. A. Powers, *ibid.*, **113**, 870 (1966).
21. A. Kozawa and R. A. Powers, *Electrochem. Technol.*, **5**, 535 (1967).
22. J. P. Brenet, in "Proceedings of 8th CITCE, Madrid (1956)," p. 394, Butterworth Scientific Publ., Kent, England (1959).
23. W. C. Vosburgh, *This Journal*, **106**, 839 (1959).
24. A. Kozawa and R. A. Powers, *J. Chem. Educ.*, **49**, 587 (1972).
25. K. Miyazaki, in "Power Sources 3," D. H. Collins, Editor, p. 670, Orial Press, Newcastle upon Tyne, England (1970).
26. V. Z. Leger and R. J. Brodd, at 10th International Power Sources Conference 1976, Preprint.
27. J. McBreen, *Electrochim. Acta*, **20**, 221 (1975).
28. J. McBreen, in "Proceedings of the Manganese Dioxide Symposium," Vol. 1, A. Kozawa and R. J. Brodd, Editors, p. 97, I. C. Sample Office, Cleveland, Ohio (1975).
29. P. Ruetschi, in "Power Sources 4," D. H. Collins, Editor, Oriel Press, New Castle upon Tyne, England (1973).
30. B. Cahan, U.S. Pat. 3,017,448 (1962).
31. R. F. Amlie and P. Ruetschi, *This Journal*, **108**, 813 (1961).
32. A. Tvarusko, *ibid.*, **116**, 1070 (1969).
33. S. M. Davis, U.S. Pat. 3,853,623 (1974).
34. V. Scatturin, P. L. Bellon, and A. Salkind, *This Journal*, **108**, 819 (1960).
35. L. A. Soto-Krebs, U.S. Pat. 3,615,858 and U.S. Pat. 3,655,450 (1972).
36. R. J. Dawson, U.S. Pat. 3,484,295 (1969).
37. J. S. Dereska in "Primary Batteries," Vol. 2, N. C. Cahoon and G. W. Heise. Editors, chap. 4, John Wiley & Sons, Inc., New York (1976).
38 J. B. Doe and D. B. Wood, in Proceedings of 22nd Power Sources Conference, 1968, p. 97.
39. S. J. Bartosh and J. C. Pawlak, U.S. Pat. 3,025,336 (1962).
40. J. J. Murphy and D. B. Wood, in Proceedings of 21st Power Sources Conference, 1967, p. 100.
41. A. L. Andre and T. A. Reilly, in Proceedings of 22nd Power Sources Conference, 1968, p. 91.
42. J. T. Shaw, J. D. Vorhies, and S. M. Davis, U.S. Pat. 3,260,621 (1966).
43. S. M. Davis, C. M. Kraebel, and R. A. Parent, U.S. Pat. 3,357,865 (1967).
44. S. M. Davis, C. M. Kraebel, and R. A. Parent, U.S. Pat. 3,481,792 (1969).
45. J. L. Robinson, in "Primary Batteries," Vol. 2, N. C. Cahoon and G. W. Heise, Editors, chap. 2, John Wiley & Sons, Inc., New York (1976).
46. G. S. Lozier, U.S. Pat. 2,993,946 (1961); Proceedings of 16th Power Sources Conference, 1962, p. 134.
47. D. J. Doan, in "Primary Batteries," Vol. 2, N. C. Cahoon and G. W. Heise, Editors, chap. 7, John Wiley & Sons, Inc., New York (1976).
48. J. J. Stokes Jr. and D. Belitskus, in *ibid.*, chap. 3.
49. D. Belitskus, *This Journal*, **119**, 295 (1972).
50. J. J. Stokes Jr., U.S. Pat. 2,796,456 (1957); *Electrochem. Technol.*, **6**, 36 (1968).

51. R. B. Goodrich and R. C. Evans, *This Journal,* **99,** 207 (1952).
52. B. H. Van Donelen and R. D. Werhle, in Proceedings of 9th IECEC, 1974, p. 665.
53. F. Tepper, in *ibid.,* p. 671.
54. C. W. Jennings, in "Primary Batteries," Vol. 2, N. C. Cahoon and G. W. Heise, Editors, p. 263, John Wiley & Sons, Inc., New York (1976).
55. E. S. McKee, in Proceedings of 10th Power Sources Conference, 1956, p. 26.
56. R. T. Mead, in Proceedings of 23rd Power Sources Conference p. 137 (1969).
57. N. C. Nielsen and E. Williams, in Proceedings of 23rd Power Sources Conference, 1969, p. 140.
58. D. M. Bush, in Proceedings of 25th Power Sources Conference, p. 24 (1972).
59. D. H. Thow in, "Power Sources 3," D. H. Collins, Editor, p. 579, Oriel Press, New Castle upon Tyne, England (1971).
60. K. P. Grothaus, in Proceedings of 26th Power Sources Conference, 1974, p. 141.
61. H. Goldsmith and J. T. Smith, *Electrochem. Technol.,* **6,** 16 (1968).
62. R. P. Clarke and E. R. Grothaus, *This Journal,* **118** 1680 (1971).
63. D. M. Bush and A. Baldwin, in "Power Sources 5," D. H. Collins, Editor, p. 581, Academic Press, New York (1975).
64. S. M. Selis, L. P. McGinnis, E. S. McKee, and J. T. Smith, *This Journal,* **110,** 469 (1963).
65. L. H. Thaller, *ibid.,* **113,** 212 (1967); *ibid.,* **115,** 116 (1968).
66. M. G. Klein and K. Eisenberg, *Electrochem. Technol.,* **3,** 58 (1965).
67. R. F. Thornton, in Proceedings of 26th Power Sources Conference, 1974, p. 169.
68. M. Eisenberg, in Proceedings of 4th IECEC, 1969, p. 330.
69. J. N. Bradley and P. D. Green, *Trans. Faraday Soc.,* **62,** 2069 (1966); *ibid.,* **63,** 424 (1967).
70. B. B. Owens and G. R. Argue, *Science,* **157,** 308 (1967).
71. "The Gould Battery Handbook," G. A. Mueller, Editor, pp. 135-140, Gould Inc., Mendota Heights, Minn. (1973).
72. G. W. Mellors and D. V. Louzos, *This Journal,* **118,** 846 (1971).
73. G. W. Mellors, D. V. Louzos, and J. A. vanLier, *ibid.,* **118,** 850 (1971).
74. D. V. Louzos, W. G. Darland, and G. W. Mellors, *ibid.,* **120,** 1151 (1973).
75. C. C. Liang, in Proceedings of 7th IECEC, 1971, p. 673.
76. C. C. Liang, *This Journal,* **123,** 453 (1976).
77. W. Greatbatch, in IEEE *Trans. Biomedical Eng.,* **bme-18,** 317 (1971).
78. K. Fester, in 7th Annual AAMI Meeting, April 1972.
79. R. T. Mead and W. Greatbatch, U.S. Pat. 3,937,635 (1976).
80. F. G. Will and S. P. Mitoff, *This Journal,* **122,** 457 (1975).
81. M. Alais, R. Berger, R. Boucher, K. A. Gasper, and P. Lamens, *Nuclear Technol.,* **26,** 307 (1975).
82. G. H. Ogburn, in Proceedings of 14th Power Sources Conference, 1960, p. 12.
83. B. Siller, German Pat. 967,773 (1942).
84. B. Siller, German Pat. 1,187,696 (1961).
85. A. G. Varta, "Luftsauerstoffelemente," Varta Fachbuchreihe, Vol. 5, by B. Siller, Dusseldorf, VDI-Verlag Gmbh, 1968.
86. P. A. Marsal and R. P. Fox, U.S. Pat. 2,597,116 (1952).
87. E. A. Schumacher and R. J. Bennett, U.S. Pat. 2,597,119 (1952).
88. E. A. Schumacher, in Proceedings of 10th Annual Battery R&D Conference, Power Sources Division, Ft. Monmouth, N.J., 1956, pp. 14-19.
89. G. W. Heise and E. A. Schumacher, U.S. Pat. 2,180,995 (1939).
90. A. Marko and K. Kordesch, Austrian Pat. 169,-782 (1950); later U.S. Pat. 2,615,932 (1952).
91. K. V. Kordesch, in "Fuel Cells," W. Mitchell, Jr., Editor, pp. 329-370, Academic Press, New York, (1963).
92. M. B. Clark, W. G. Darland, and K. V. Kordesch, *Electrochem. Technol.,* **3,** 166 (1965).
93. S. M. Chodosh, B. Jagid, and E. Katsoulis, in "Power Sources 2," D. H. Collins, Editor, p. 423, Pergamon Press, London (1968).
94. R. R. Witherspoon, Automotive Engineers Conference, Society of Automotive Engineers, Detroit, 1969, Paper No. 690204.
95. E. Yeager, in "Fuel Cells," W. Mitchell, Jr., Editor, pp. 300-327, Academic Press, New York (1963).
96. S. Zaromb, in "Power Systems for Electric Vehicles," U.S. Public Health Service Publication No. 999-AP-36, pp. 255-267 (1967).
97. C. E. Kent, USAECOM 21st Annual Power Sources Conference Proceedings, May 1967, Redbank, N.J., PSC Publications Committee, pp. 106-109.
98. L. A. Heredy, H. L. Recht, and D. E. McKenzie, in "Power Systems for Electric Vehicles," U.S. Public Health Service Publication No. 999-AP-36, pp. 245-253 (1967).
99. D. P. Gregory, "Metal-Air Batteries," Mills and Boon, London (1972).
100. R. E. Biddick, J. W. Cretzmeyer, and D. L. Douglas, in "Power Sources 5," D. H. Collins, Editor, pp. 411-429, Academic Press, New York (1975).
101. J. W. Cretzmeyer, H. R. Espig, and R. S. Melrose, 10th International Power Sources Conference, 1976, Preprint.
102. J. O. Besenhard and G. Eichinger, *J. Electroanal. Chem.,* **68,** 1 (1976).
103. G. Eichinger and J. O. Besenhard, *ibid.,* **72,** 1 (1976).
104. A. Y. Fraioli, U.S. Pat. 3,475,226 (1969).
105. D. L. Maricle and J. P. Mohns, U.S. Pat. 3,567,515 (1971).
106. D. L. Maricle and A. K. Hoffman, U.S. Pat. 3,578,-500 (1971).
107. P. Bro, R. Holmes, N. Marincic, and H. Taylor, in "Power Sources 5," D. H. Collins, Editor, p. 703, Academic Press, New York (1975).
108. E. S. Brooks, in Proceedings of 7th Intersociety Energy Commission and Engineering Conference, 1973, p. 71.
109. E. D. Widman, in Proceedings of 10th International Power Sources Conference, 1976, Preprint.
110. H. Taylor and B. McDonald, in Proceedings of 27th Power Sources Conference, 1976, p. 66.
111. G. E. Blomgren and M. L. Kronenberg, Ger. OLS 2,262,276 (1973).
112. J. J. Auborn, K. W. French, S. I. Lieberman, V. K. Shaw, and A. Heller, *This Journal,* **120,** 1613 (1973).
113. W. K. Behl, J. S. Christopulos, M. Ramirez, and S. Gilman, *ibid.,* **120,** 1619 (1973).
114. J. J. Auborn and N. Marincic, in "Power Sources 5," D. H. Collins, Editor, p. 683, Academic Press, New York (1975).
115. A. N. Dey and P. Bro, in Proceedings of 10th International Power Sources Conference, 1976, Preprint.
116. A. N. Dey and C. T. Schlaikjer, in Proceedings of 26th Power Sources Conference, p. 47 (1974).
117. A. N. Dey, *Electrochim. Acta,* **21,** 377 (1976).
118. K. French, P. Cuker, C. Persiani, and J. Auborn, *This Journal,* **121,** 1045 (1974).
119. T. Kalnoki-Kis, U.S. Pat. 3,993,501 (1976).
120. J. R. Driscol, G. Holleck, and D. E. Toland, in Proceedings of 27th Power Sources Conference, 1976, p. 28.
121. A. N. Dey, in Proceedings of 27th Power Sources Conference, 1976, p. 42.
122. A. N. Dey, *Electrochim. Acta,* **21,** 855 (1976).
123. M. Fukuda and T. Iijima, in "Power Sources 5," D. H. Collins. Editor, p. 713, Academic Press, New York (1975).
124. M. Fukuda and T. Iijima, *Denki Kagaku,* **44,** 543 (1976).
125. H. Ikeda, S. Ueno, T. Saito, S. Nakaido, and H. Tamura, *ibid.,* **45,** 314, 391 (1977).
126. N. Watanabe and M. Fukuda, U.S. Pat. 3,536,532 (1970); *ibid.,* 3,700,502 (1972).
127. H. Ikeda, T. Saito, and H. Tamura, in "Proceedings of the Manganese Dioxide Symposium," Vol. 1, A. Kozawa and R. J. Brodd, Editors, p. 384, I. C. Sample Office, Cleveland, Ohio (1975).
128. A. Kozawa and R. A. Powers, *This Journal,* **113,** 870 (1966).
129. G. H. Lehmann, T. Rassinoux, G. Gerbier, and J. P. Gabano, in "Power Sources 4," D. H. Collins, Editor, p. 493, Oriel Press Ltd., Newcastle

upon Tyne, England (1973).
130. G. Lehmann, G. Gerbier, A. Brych, and J. P. Gabano, in "Power Sources 5," D. H. Collins, Editor, p. 695, Academic Press, New York (1975).
131. J. P. Gabano, V. Dechenaux, G. Gerbier, and J. Jammet, *This Journal*, **119**, 459 (1972).
132. D. Linden, N. Wilburn, and E. Brooks, in "Power Sources 4," D. H. Collins, Editor, p. 483, Oriel Press Ltd., Newcastle upon Tyne, England (1973).
133. S. C. Levy, in Proceedings of 27th Power Sources Conference, 1976, p. 52.

Reports on Electrochemical Society Summer Fellowship Awards

During the summer of 1977 the following graduate students received $1000 each, representing the three Summer Fellowship Awards of The Electrochemical Society.

Mr. Paul A. Kohl, University of Texas, Austin, Texas, was awarded the Edward Weston Fellowship.

Mr. Paul D. Tyma, Michigan State University, was designated as the recipient of the Colin Garfield Fink Fellowship.

Mr. Harold C. Faulkner III, University of California, Riverside, California, received the Joseph W. Richards Fellowship.

The Summer Fellowshp Awards are made "without regard to sex, citizenship, race, or financial need, to a fellow or teaching assistant pursuing work between the degrees of B.S. and Ph.D. on a subject in a field of interest to The Electrochemical Society." They are intended to cover a period during which the recipient has no financial support for the continuance of his or her work.

The Edward Weston Summer Fellowship Report

Mr. Kohl's report is given below.

The Photoelectrochemical Behavior of Semiconducting n- and p-GaAs and InP Electrodes in Acetonitrile Solutions

Semiconductor electrodes have recently shown promise as a means of electrochemically converting light energy into chemical and/or electrical energy. Since the photoassisted oxidation of water into hydrogen and oxygen on n-TiO_2 was suggested (1), an increasing amount of research has been aimed at utilizing smaller bandgap semiconductors which absorb a greater fraction of the solar spectrum than TiO_2 and extend the concepts of electron transfer in semiconductors to new systems such as different solvents, photocatalysis, and solution kinetics.

The semiconductor-solution interface (2) is analogous to a semiconductor-metal junction where light of energy greater than the bandgap (E_g) can promote electrons from the valence band (VB) to the conduction band (CB) as shown in Fig. 1. Photogenerated minority carriers (electrons in p-type semiconductor or holes in n-type semiconductor) can be forced to the solution interface and be consumed by electroactive species in solution with the gross work available given by $|E_{fermi} - E_{redox}|$. However, key factors in the utilization of semiconductor electrodes in electrochemical cells are knowledge of the relative location of the energy levels in the semiconductor and solution and an understanding of the role surface states or intermediate levels within the bandgap play in charge-transfer processes.

In this work, the electrochemical behavior of the small bandgap semiconductors n- and p-GaAs (E_g = 1.35 eV) and InP (E_g = 1.27 eV) was investigated in acetonitrile (ACN) solutions which contained various one-electron Nernstian redox couples. The use of ACN not only allows the use of a larger working potential range (5V) than water (1.23V) and a greater number of reversible redox couples, but also the rate of dissolution of the semiconductor (Eq. [1], [2]), which readily occurs in aqueous solutions at potentials where holes are forced to the interface, is decreased because of the poor solvation of the products of dissolution

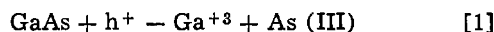

$$GaAs + h^+ - Ga^{+3} + As\ (III) \quad [1]$$

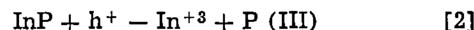

$$InP + h^+ - In^{+3} + P\ (III) \quad [2]$$

where h^+ represents a hole in the VB of the semiconductor

The cyclic voltammetric current-voltage curves (3) suggest three main conclusions in this work. The first is that the dissolution of the semiconductors (Eq. [1], [2]) is decreased and does not occur until the electrode potential is more positive than observed in aqueous solutions. This enables electroactive solution species to compete more favorably with dissolution for photogenerated holes in the n-type semiconductors over a wider potential range.

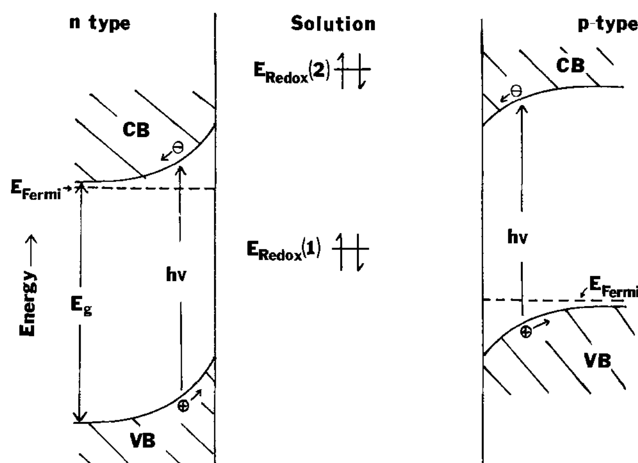

Fig. 1. Energy level representation of an n-type and p-type semiconductor in contact with a solution containing a redox couple located within the bandgap [E_{redox} (1)], and negative of the CB edge [E_{redox} (2)]. CB and VB are the conduction and valence bands, respectively, E_{fermi} is the Fermi level, and E_g is the bandgap.

Secondly, redox couples lying within the bandgap region (Fig. 1) seem to follow previously proposed models for electron transfer via intermediate levels within the bandgap region (4, 5). Reduction of solution species lying below the midgap region occurred at potentials near the middle of the gap through the intermediate level. Photoassisted reductions (on p-type material) and oxidations (on the n-type materials) were observed with underpotentials (negative overpotentials due to the utilization of light energy) up to 700 mV. The magnitude of the underpotential appeared to be limited by the position of the intermediate level, $|E_{\text{flatband}} - E_{\text{intermediate band}}|$. That is, the underpotential observed upon photooxidation was limited by the potential of the reduction of oxidized species (or back reaction).

The third and most unique result was the photoassisted electron transfer observed with redox couples located negative of the CB edge. Ideally, degeneracy and metal-like behavior is observed as seen with n-ZnO, n-CdS (4), and n-TiO_2 (5). Photooxidations (within-GaAs) are observed at potentials more negative than observed with a Pt disk electrode, and photoreductions are observed (on p-GaAs and InP) at potential more positive than Pt similar to that observed with redox couples located within E_g. Reasonable evidence for the formation of surface layers which produce a photovoltage when illuminated analogous to a semiconductor-metal junction exists. Thus, the potential range of photoassisted electron transfer is at least twice the size of the bandgap while a 1.35 eV or larger photon can be used.

The simplest illustration of photoassisted electron transfer and its possible uses is in regenerative photoelectrochemical cells such as

n-GaAs |0.01*M* BQ, 0.01*M* $BQ^{\bar{\cdot}}$, 0.1*M* TBAP (ACN) | Pt

where BQ is p-benzoquinone and TBAP is the supporting electrolyte tetra-n-butylammonium perchlorate. Upon irradiation of the n-GaAs, the radical anion is oxidized to BQ and BQ is reduced to $BQ^{\bar{\cdot}}$ at the Pt electrode. The driving force and current in the external circuit are produced by light of energy greater than the bandgap. An open-circuit photovoltage of 700 mV was measured and when the GaAs was irradiated with 96 $\mu W/cm^2$ of 600 nm light, the maximum power was produced at 28 $\mu A/cm^2$ and 0.4V, yielding a 12% conversion of light to electricity. While the intensity was corrected for solution absorption, no attempts were made to optimize the cell concentrations or intensities to the maximum power.

The electrochemical behavior was also found to be very dependent on the condition and pretreatment of the semiconductor surfaces. The density and position of the intermediate levels within the bandgap which can provide a mechanism for the back reaction and thus a recombination or quenching of photogenerated minority carriers in the semiconductor can be changed by chemical pretreatments.

In general, nonaqueous investigations of the mechanism of electron transfer at the semiconductor surface can be used as a basis to predict the behavior of other photoassisted reactions for possible photocatalytic synthetic work, photoelectrochemical cells, upconversion of light (6), or behavior in other solvents.

Acknowledgments

The support of The Electrochemical Society through the Edward Weston Fellowship and consultations of Professor Allen J. Bard are gratefully acknowledged.

REFERENCES

1. A. Fujishima and K. Honda, *Nature (London)*, **238**, 37 (1972).
2. H. Gerischer, in "Physical Chemistry: An Advanced Treatise," Vol. 9A, H. Eyring, D. Henerson, and W. Jost, Editors, Academic Press, New York (1970); H. Gerischer, *Adv. Electrochem. Electrochem. Eng.*, **1**, 139 (1961).
3. Paper presented at The Electrochemical Society Meeting, Seattle, Washington, May 21-26 (1978).
4. P. A. Kohl and A. J. Bard, *J. Am. Chem. Soc.*, **99**, 7531 (1977).
5. S. N. Frank and A. J. Bard, *ibid.*, **97**, 7427 (1975).
6. J. D. Luttmer and A. J. Bard, Unpublished results.

The Colin Garfield Fink Summer Fellowship Report

Mr. Tyma's report is given below.

Determination of Kinetic Parameters from Polarographic Data Obtained at Short-Sampling Times

An over-all objective of our research efforts is to correlate electrochemical reactivities with the structure of both the reactants and the interphasial region. Studying rate responses to systematic changes in solution composition can lead, for example, to determining whether the activated state prior to electron transfer leaves the inner coordination sphere of the reactant unchanged (outer-sphere mechanism) or whether the reaction proceeds *via* an intermediate which involves specific interactions between reactant ligands and the electrode surface (inner-sphere mechanism) (1). Such experiments can also provide information concerning the position of the reaction site for electron transfer (2). In the case of a liquid metal electrode, one can characterize the interphasial structure; therefore, rate responses to changes in the structure of the interface brought about by variations in solution composition can be monitored. This process can then be turned around so that these "kinetic probes" yield information about interphasial structure from rate data for solid electrodes for which the former is not readily accessible.

The simplest method of polarographic data analysis to extract the electrochemical rate constants as a function of overpotential is to record the ratio of the current measured at a time *t* following drop birth to the current measured at time *t* when the reaction is completely diffusion-controlled and to use the Koutecky treatment of irreversible polarographic waves (3). There are, however, two types of systems for which this approach will not succeed. Because it is necessary to correct voltammetric data of limited precision for diffusion polarization at potentials beyond the foot of the wave, a natural limit of about 10^{-2} cm/sec is imposed upon rate constants determined in this manner *via* conventional polarography; polarograms of faster systems appear reversible. Furthermore, systems which give maxima are not amenable to this technique. The theory of Koutecky predicts that the upper limit to rate constants ascertained by the polarographic method should increase an order of magnitude for each hundredfold decrease in the time at which the currents are measured (3). Moreover, it may be possible to outrun maxima if the phenomena leading to their occurrence develop in the later stages of drop-life. Cover and Connery have shown (4) that maxima can be reduced or eliminated from polarographic concentration determinations by measuring the current at the end of the life of a drop which is forcibly dislodged from the capillary at frequencies as high as 210 Hz. For natural drop-times down to 1.25 sec and forced drop-times as low as 160 msec it has been demonstrated that the Ilkovic equation is applicable (5). The purpose of the present study is to develop instrumentation suitable for determining under what conditions the Koutecky theory can be applied to the polarographic data obtained at times shortly after the birth of the drop.

Two general approaches to this technique have evolved. The first, and by far the more common, is to

Secondly, redox couples lying within the bandgap region (Fig. 1) seem to follow previously proposed models for electron transfer via intermediate levels within the bandgap region (4, 5). Reduction of solution species lying below the midgap region occurred at potentials near the middle of the gap through the intermediate level. Photoassisted reductions (on p-type material) and oxidations (on the n-type materials) were observed with underpotentials (negative overpotentials due to the utilization of light energy) up to 700 mV. The magnitude of the underpotential appeared to be limited by the position of the intermediate level, $|E_{\text{flatband}} - E_{\text{intermediate band}}|$. That is, the underpotential observed upon photooxidation was limited by the potential of the reduction of oxidized species (or back reaction).

The third and most unique result was the photoassisted electron transfer observed with redox couples located negative of the CB edge. Ideally, degeneracy and metal-like behavior is observed as seen with n-ZnO, n-CdS (4), and n-TiO_2 (5). Photooxidations (within-GaAs) are observed at potentials more negative than observed with a Pt disk electrode, and photoreductions are observed (on p-GaAs and InP) at potential more positive than Pt similar to that observed with redox couples located within E_g. Reasonable evidence for the formation of surface layers which produce a photovoltage when illuminated analogous to a semiconductor-metal junction exists. Thus, the potential range of photoassisted electron transfer is at least twice the size of the bandgap while a 1.35 eV or larger photon can be used.

The simplest illustration of photoassisted electron transfer and its possible uses is in regenerative photoelectrochemical cells such as

n-GaAs |0.01*M* BQ, 0.01*M* $BQ^{\overline{\cdot}}$, 0.1*M* TBAP (ACN) | Pt

where BQ is p-benzoquinone and TBAP is the supporting electrolyte tetra-n-butylammonium perchlorate. Upon irradiation of the n-GaAs, the radical anion is oxidized to BQ and BQ is reduced to $BQ^{\overline{\cdot}}$ at the Pt electrode. The driving force and current in the external circuit are produced by light of energy greater than the bandgap. An open-circuit photovoltage of 700 mV was measured and when the GaAs was irradiated with 96 $\mu W/cm^2$ of 600 nm light, the maximum power was produced at 28 $\mu A/cm^2$ and 0.4V, yielding a 12% conversion of light to electricity. While the intensity was corrected for solution absorption, no attempts were made to optimize the cell concentrations or intensities to the maximum power.

The electrochemical behavior was also found to be very dependent on the condition and pretreatment of the semiconductor surfaces. The density and position of the intermediate levels within the bandgap which can provide a mechanism for the back reaction and thus a recombination or quenching of photogenerated minority carriers in the semiconductor can be changed by chemical pretreatments.

In general, nonaqueous investigations of the mechanism of electron transfer at the semiconductor surface can be used as a basis to predict the behavior of other photoassisted reactions for possible photocatalytic synthetic work, photoelectrochemical cells, upconversion of light (6), or behavior in other solvents.

Acknowledgments

The support of The Electrochemical Society through the Edward Weston Fellowship and consultations of Professor Allen J. Bard are gratefully acknowledged.

REFERENCES

1. A. Fujishima and K. Honda, *Nature (London)*, **238**, 37 (1972).
2. H. Gerischer, in "Physical Chemistry: An Advanced Treatise," Vol. 9A, H. Eyring, D. Henerson, and W. Jost, Editors, Academic Press, New York (1970); H. Gerischer, *Adv. Electrochem. Electrochem. Eng.*, **1**, 139 (1961).
3. Paper presented at The Electrochemical Society Meeting, Seattle, Washington, May 21-26 (1978).
4. P. A. Kohl and A. J. Bard, *J. Am. Chem. Soc.*, **99**, 7531 (1977).
5. S. N. Frank and A. J. Bard, *ibid.*, **97**, 7427 (1975).
6. J. D. Luttmer and A. J. Bard, Unpublished results.

The Colin Garfield Fink Summer Fellowship Report

Mr. Tyma's report is given below.

Determination of Kinetic Parameters from Polarographic Data Obtained at Short-Sampling Times

An over-all objective of our research efforts is to correlate electrochemical reactivities with the structure of both the reactants and the interphasial region. Studying rate responses to systematic changes in solution composition can lead, for example, to determining whether the activated state prior to electron transfer leaves the inner coordination sphere of the reactant unchanged (outer-sphere mechanism) or whether the reaction proceeds *via* an intermediate which involves specific interactions between reactant ligands and the electrode surface (inner-sphere mechanism) (1). Such experiments can also provide information concerning the position of the reaction site for electron transfer (2). In the case of a liquid metal electrode, one can characterize the interphasial structure; therefore, rate responses to changes in the structure of the interface brought about by variations in solution composition can be monitored. This process can then be turned around so that these "kinetic probes" yield information about interphasial structure from rate data for solid electrodes for which the former is not readily accessible.

The simplest method of polarographic data analysis to extract the electrochemical rate constants as a function of overpotential is to record the ratio of the current measured at a time *t* following drop birth to the current measured at time *t* when the reaction is completely diffusion-controlled and to use the Koutecky treatment of irreversible polarographic waves (3). There are, however, two types of systems for which this approach will not succeed. Because it is necessary to correct voltammetric data of limited precision for diffusion polarization at potentials beyond the foot of the wave, a natural limit of about 10^{-2} cm/sec is imposed upon rate constants determined in this manner *via* conventional polarography; polarograms of faster systems appear reversible. Furthermore, systems which give maxima are not amenable to this technique. The theory of Koutecky predicts that the upper limit to rate constants ascertained by the polarographic method should increase an order of magnitude for each hundredfold decrease in the time at which the currents are measured (3). Moreover, it may be possible to outrun maxima if the phenomena leading to their occurrence develop in the later stages of drop-life. Cover and Connery have shown (4) that maxima can be reduced or eliminated from polarographic concentration determinations by measuring the current at the end of the life of a drop which is forcibly dislodged from the capillary at frequencies as high as 210 Hz. For natural drop-times down to 1.25 sec and forced drop-times as low as 160 msec it has been demonstrated that the Ilkovic equation is applicable (5). The purpose of the present study is to develop instrumentation suitable for determining under what conditions the Koutecky theory can be applied to the polarographic data obtained at times shortly after the birth of the drop.

Two general approaches to this technique have evolved. The first, and by far the more common, is to

record the current throughout the entire drop and to obtain the value at a desired time by knocking off the drop at that time through suitable mechanical means. Since the maximum current for each drop occurs prior to the forced drop-fall, the envelope of the polarogram constitutes the current-voltage curve at the specified time. However, since the capillary is in motion just after the drop is knocked off, convection in the vicinity of the electrode is enhanced and the current increased early in the drop-life. This enhancement becomes relatively larger as the forced drop-time is decreased, and the frequency-response requirements of the recording system correspondingly become more stringent. What remains to be determined is whether there is a significant difference between kinetic parameters measured by that approach and those obtained by the second method, which is to use currents sampled at short times following the natural birth of the drop.

Since the accoutrements for the former technique are familiar and readily assembled, attention was focused on the development of the latter. A programmable sample-and-hold system was constructed for use with a Princeton Applied Research (PAR) Model 174 Polarographic Analyzer and a Hewlett-Packard Model 7045 XY Recorder; a schematic representation is shown in Fig. 1 and 2. Rather than being used to drive the Y axis of the recorder directly, the output of the potentiostat's current-to-voltage converter is applied to the analog input of the sample-and-hold amplifier (Fig. 2) whose output, which normally tracks its input, is connected to the recorder. At the appropriate time following the birth of the drop, an $\overline{\text{ENABLE}}$ negative-going logic pulse triggers two monostables with periods of 100 and 600 msec. The latter causes the sample-and-hold amplifier to hold its current value and activates the Y axis servo, which is normally disengaged to minimize unnecessary pen travel. After the delay provided by the former, a third monostable is triggered, momentarily dropping the pen to plot the measurement and resetting the delay logic. At the heart of the timing circuitry (Fig. 1) is a Mostek MK5009 time-base chip which divides a 1 MHz master oscillator frequency by the number of decades selected by a binary-coded decimal (BCD) thumbwheel switch or remote frequency-selection lines which may be driven by a computer interface. At the beginning of each measurement cycle, a two-digit BCD counter is loaded from switches or remote lines with the number of scaled oscillator pulses necessary to achieve the desired time delay between the detection of drop-fall and the sampling of the cell current. Once a detector pulse is received, the counters count down to zero and an $\overline{\text{ENABLE}}$ pulse is generated.

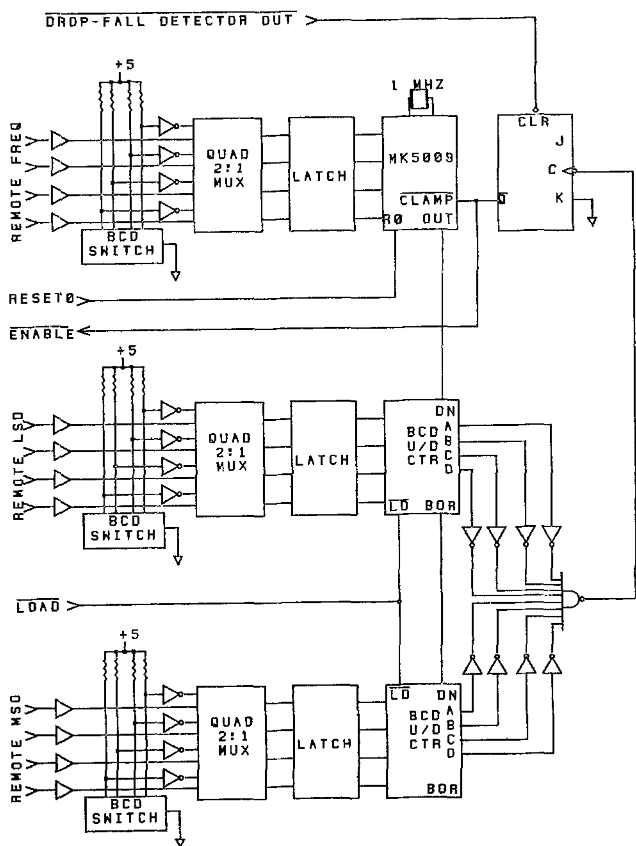

Fig. 1. Programmable timing circuit. Multiplexer (MUX) is 74157, latch is 7475, and BCD counter is 74192.

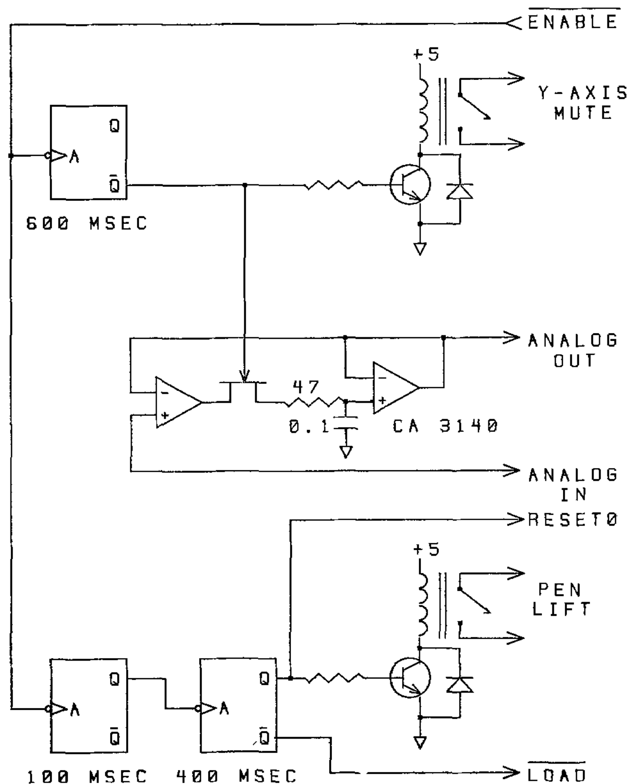

Fig. 2. Sample-and-hold sequencer. Monostables are 74121, and capacitor is a low-leakage type (polystyrene).

In order to synchronize the current-sampling with drop-fall, some sort of detection system is required. While many approaches have been taken on this aspect of the problem [see, for example, the citations in Ref. (6)], we initially chose the optical method of Hahn and Enke (6) based upon its lack of interaction with the potentiostat circuitry and simplicity of implementation; Fig. 3 presents a schematic diagram. The sudden change in light scattered up the capillary when the drop falls is converted to an electrical signal which is differentiated and amplified to provide a detector pulse which is compatible with transistor-transistor logic. Preliminary measurements produced rate constants which decreased monotonically as the sampling time increased and which were inconsistent with previously reported values (7), and efforts were undertaken to determine if systematic errors were introduced by any portion of the measurement system.

Upon closer scrutiny it was found that the signal produced by the drop-fall detector occurred no less than 80 msec following the fall of the drop. What appeared to be the source of the delay was that the original designers did not reckon with the inversion produced in the comparator stage of the level shifter [amplifier A4 in Fig. 2 of Ref. (6)]. The desired negative-going logic transition occurred only as the result of noise in the differentiator output on the trailing edge of its output spike. Once this level-inversion discrepancy was rectified, however, a nonreproducible 20 msec delay remained. Since one of our design goals was the capa-

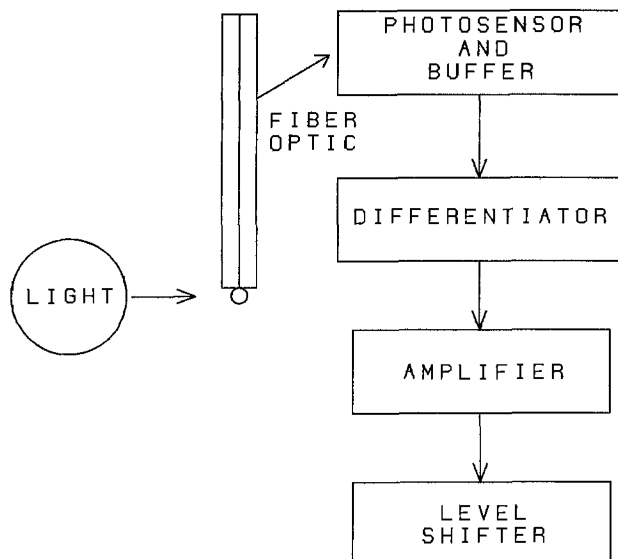

Fig. 3. Optical drop-fall detector [full details in Ref. (6)]

bility to sample currents after 50 msec, this performance remained unacceptable.

To meet this goal, it is necessary that the detector error be less than 1 msec. For it to be capable of this, however, it must have preferential frequency response in the 1-10 kHz region. Examination of the original passive components of the differentiator (6) showed that they limit frequency response to between 0.16 and 3 kHz (unity-gain limits), with maximum gain at 22.5 Hz and gain in excess of 10 at the archetypal noise frequencies 60 and 120 Hz. Even with more appropriate passive components, however, insufficient signal amplitude was present in the necessary frequency range; efforts to remove sources of stray light by optical shielding and to increase the gain of the amplification stage proved equally unsuccessful. Because the light is attenuated appreciably by the fiber optic system, even with the recommended polishing of the capillary groove and fiber optic ends, we tried attaching a more sensitive photodarlington transistor (2N5777) directly to the capillary groove with the die facing the Hg drop. The buffer amplifier in the detector was replaced by a current-to-voltage converter (10 μA/V); the a-c component of a typical differentiated output is shown in Fig. 4. While the signal-to-noise ratio would undoubtedly be increased if the current-to-voltage conversion were performed directly at the phototransistor, the necessary mounting considerations vitiate such an undertaking. Furthermore, inspection of Fig. 4 will reveal that the rise time of the differentiator spike produced by the fall of the drop is approximately 20 msec. This result is not surprising in view of the fact that the drop continues to reflect light after detachment until it falls below the light path, and a 20 msec delay corresponds to the time required for a 2 mm displacement of a freely falling object.

The inevitable conclusion is that the optical detection system is inappropriate for this or any other application where inaccuracies of 20 msec cannot be tolerated. It is still useful in systems such as its original utilization (8) where a precise albeit inaccurate time delay following the birth of the drop is all that is required. Subsequent measurements were made with an a-c tuned amplifier-based detection system to be described elsewhere (9). Features of the detector include a self-contained strobable oscillator and a response time of less than 150 μsec.

The large number and time-consuming nature of the experiments and data analysis required for the satisfactory scrutiny of this problem makes it an excellent candidate for automation. To place this and other DME studies under on-line control, a laboratory microcomputer based upon the Digital Equipment Corporation LSI-11 microprocessor[1] was constructed from commercially available modules and those of our own design, including a versatile, indirectly addressing digital interface which substantially reduces the number of ports required on the computer bus to service numerous digital devices (9).

Typical time-resolved polarograms of 2 m*M* $Cr(H_2O)_6^{3+}$ in 1*M* $NaClO_4$ at *p*H 4 and 24°±1°C with an Hg flow-rate *m* of 17.0 mg/sec are shown in Fig. 5. Kinetic parameters extracted from these data are less disparate from reported values (7) than those obtained above; a systematic decrease in calculated rate constant, although smaller than before, still occurs as the sampling time increases.

An important advantage of measurements at short sampling times is illustrated in the limiting current region. According to Koutecky theory (3), the currents at the top of the $Cr(H_2O)_6^{3+}$ wave due to $Cr(H_2O)_6^{3+}$ reduction vary as $t^{1/6}$ (diffusion-controlled), whereas those in the same region which result from proton reduction depend on $t^{2/3}$ (kinetically controlled). As the sampling time approaches zero (below 1 sec), the contribution from the kinetically controlled succeeding wave should become smaller relative to that from the wave which is diffusion-controlled, and this is borne out experimentally. The theory's assertion that the limiting current follows the Ilkovic equation does not work, however, at the large Hg flow rates necessary to make the area sufficiently large to assure reasonable signal-to-noise ratio at the shortest sampling times. In Fig. 6 plots are presented of limiting

[1] Trademark of Digital Equipment Corporation, Maynard, Massachusetts 01754.

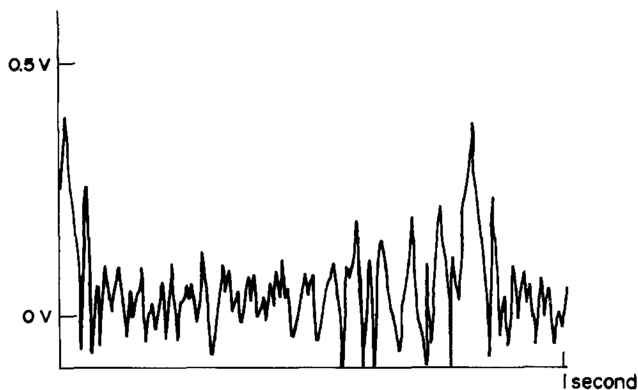

Fig. 4. Differentiated representation of photodarlington current

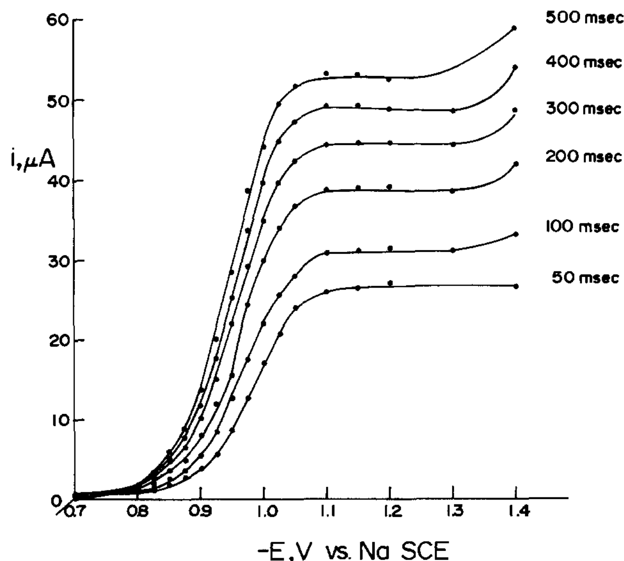

Fig. 5. Time-resolved polarograms of 2 m*M* $Cr(H_2O)_6^{3+}$ in 1*M* $NaClO_4$ at *p*H 4 and 24° ± 1°C; *m* = 17.0 mg/sec.

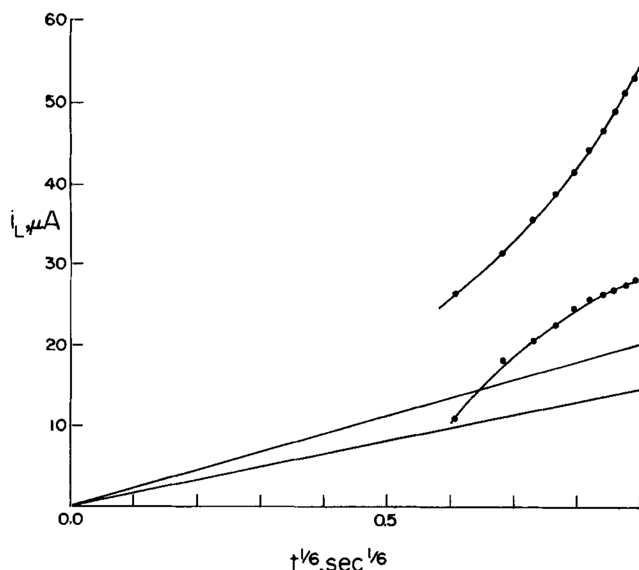

Fig. 6. Comparison of Ilkovic equation predictions (lines) and experimental results (curves). The upper line and curve are for $m = 17.0$ mg/sec, the lower ones for $m = 10.3$ mg/sec.

currents *vs.* $t^{1/6}$. The upper curve and line are the experimental data and theoretical prediction, respectively, for 2 m*M* $Cr(H_2O)_6^{3+}$ reduction for an Hg flowrate of 17.0 mg/sec; and the lower ones are for a flowrate of 10.3 mg/sec. That the limiting currents are substantially larger than what the Ilkovic equation predicts is reasonable when one considers that in the derivation of the Ilkovic equation one assumes that the mercury surface velocity has only radial components (10). However, it has been shown that Hg drops in 1*M* KCl solutions have appreciable tangential motion between −0.5 and −1.5V *vs.* SCE (11). This additional convection in the entrained solution enhances the current over and above that due to the convective diffusion phenomena which lead to the Ilkovic equation. Since Bond has demonstrated that under some conditions of natural drop fall at comparable flowrates the limiting current is less than that predicted by the Ilkovic equation (5), it should therefore be possible to determine the appropriate combination of flow-rate and drop-time where Ilkovic behavior should be observed. Further studies are in progress.

Acknowledgment

The author would like to thank The Electrochemical Society for support provided by the Colin Garfield Fink Fellowship.

REFERENCES

1. M. J. Weaver and F. C. Anson, *Inorg. Chem.*, **15**, 1871 (1976).
2. M. J. Weaver and T. L. Satterberg, *J. Phys. Chem.*, **81**, 1772 (1977).
3. J. Koutecky, *Coll. Czech. Chem. Commun.*, **18**, 311 (1953).
4. R. E. Cover and J. G. Connery, *Anal. Chem.*, **41**, 918 (1969).
5. A. M. Bond and R. J. O'Halloran, *J. Phys. Chem.*, **77**, 915 (1973).
6. B. K. Hahn and C. G. Enke, *Anal. Chem.*, **46**, 802 (1974).
7. M. J. Weaver and F. C. Anson, *J. Electroanal. Chem.*, **65**, 711 (1975).
8. B. K. Hahn, Ph.D. Thesis, Michigan State University, East Lansing, Mich. (1974).
9. P. D. Tyma, To be published.
10. V. G. Levich, "Physicochemical Hydrodynamics," p. 538, Prentice-Hall Inc., Englewood Cliffs, N.J. (1962).
11. T. A. Kryukova and B. N. Kabanov, *Zh. Fiz. Khim.*, **20**, 1179 (1946).

The Joseph W. Richards Fellowship

Mr. Faulkner III's report with his professor Dr. DeHayes is given below.

Electrochemical Studies of Oxo- and Sulfido-Bridged Molybdenum (V) Dimers

Dimeric molybdenum (V) complexes with cysteine (1), dithiocarbamate (2), and EDTA (3) ligands have been studied as reaction models for molybdenum-containing enzymes. EPR evidence indicates that the ligand field surrounding the molybdenum atoms at the active sites of these enzymes contains sulfur donors (4, 5). X-ray structural analyses have been performed on several dithiocarbamate complexes in which the terminal ligands bound to molybdenum and the bridging ligands between the molybdenums have been both oxygen and sulfur (6-10). Electrochemical studies in aprotic solvents have been performed on two diethyldithiocarbamate compounds (2) and aqueous studies have been carried out on both the EDTA and cysteine complexes of molybdenum (V) (1, 3). In addition, infrared studies have been made of di-μ-oxo-bis[N,N-dialkyldithiocarbamatooxomolybdenum (V)] and μ-oxo-μ-sulfido-bis[N,N-dialkyldithiocarbamatooxomolybdenum (V)] with the intent to observe and assign the bands due to the bridging oxygen and sulfur ligands (11). The present study summarizes the results of a systematic investigation of the influence of a sulfur *vs.* an oxygen ligand field on molybdenum (V) dialkyldithiocarbamate compounds. The groups that have been included in the investigation are

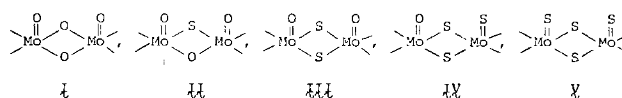

with diethyldithiocarbamate (dedtc) and di-n-butyldithiocarbamate (nbudtc) as the ligands.

Although infrared spectroscopy has been a major tool for the characterization of the compounds, the effects of the systematic substitution of sulfur for oxygen have been observed by cyclic voltammetry and u.v.-vis. spectroscopy for solutions of the compounds in dimethylformamide (DMF) and dimethylacetamide (DMA).

Experimental

Preparation of the complexes.—μ-Oxo-μ-sulfido-bis [N,N-di-n-butyldithiocarbamatooxomolybdenum (V)] and di-μ-sulfido-bis[N,N-di-n-butyldithiocarbamatooxomolybdenum (V)].—"Sulfurized molybdenum di-n-butyldithiocarbamate" was prepared according to the literature (12). TLC of the product exhibited two spots. 0.3g of this product yielded two bands on a dry-packed column (described below). After rotary evaporation of the solvent at 30°C and recrystallization the first band exhibited infrared peaks at 967, 955, 478, and 338 cm^{-1} [corresponding to $Mo_2O_2S_2(nbudtc)_2$], and the second band had peaks at 970, 951, 711, 513, 460, and 350 cm^{-1} [corresponding to $Mo_2O_3S(nbudtc)_2$].

Di-μ-sulfido-{[N,N-di-n-butyldithiocarbamatooxomolybdenum (V)]-[N,N-di-n-butyldithiocarbamatosulfidomolybdenum (V)]} and di-μ-sulfido-bis-[N,N-di-n-butyldithiocarbamatosulfidomolybdenum (V)].—10g of the "sulfurized molybdenum di-n-butyldithiocarbamato" was added to 8g of P_4S_{10} in 100 ml of xylene. The mixture was stirred for 15 hr at room temperature and then refluxed for an additional 2.5 hr. The xylene was removed by rotary evaporation. TLC of the product exhibited three spots. 1g of the product was eluted with benzene from a slurry-packed column (described below) to yield two bands. After rotary evaporation of the solvent and recrystallization the first band exhib-

ited peaks at 549, 533, 467, and 335 cm^{-1} [corresponding to $Mo_2S_4(nbudtc)_2$] and the second band exhibited peaks at 960, 538, 470, and 333 cm^{-1} [corresponding to $Mo_2OS_3(nbudtc)_2$].

Di-μ-oxo-bis-[N,N-diethyldithiocarbamatooxomolybdenum (V)].—The procedure used was a modification of that of Newton and Corbin (13). Under a nitrogen atmosphere, 4g of $MoCl_5$ (1.5×10^{-2} moles was dissolved in 25 ml H_2O. A solution of 1g of sodium diethyldithiocarbamate (5.8×10^{-3} moles) in 10 ml H_2O was then slowly added. The purple precipitate was refluxed for 2 hr, at which time it had changed to a brown color. The brown precipitate was isolated by vacuum filtration in air. Attempts at the synthesis of $Mo_2O_4(dedtc)_2$ with a 1:1 mixture of molybdenum pentachloride and sodium diethyldithiocarbamate as described by Newton and Corbin (13) yielded mainly $Mo_2O_3(dedtc)_4$. When the ratio was increased to 2:1 (molybdenum pentachloride to sodium diethyldithiocarbamate) the pure dioxobridged compound was obtained. The infrared spectrum of this compound is given in Table I and Fig. 1. The data agree well with that of Newton and McDonald (11).

Di-μ-sulfido-bis[N,N-diethyldithiocarbamatooxomolybdenum (V)] and di-μ-sulfido-{[N,N-diethyldithiocarbamatooxomolybdenum (V)]-[N,N-diethyldithiocarbamatosulfidomolybdenum (V)]}.—1g of $Mo_2O_3(dedtc)_4$ (13) was added to 50 ml $CHCl_3$. H_2S was bubbled through the solution for 20 min. The precipitate was then isolated and gave two spots upon TLC. 0.3g of this product was then added to the column. Elution with benzene dichloromethane solvent gave two bands. The infrared spectrum for the material in the first band had peaks at 955, 541, 470, and 335 cm^{-1} [corresponding to $Mo_2OS_3(dedtc)_2$] while the peaks for the second band were at 967, 953, 479, and 338 cm^{-1} [corresponding to $Mo_2O_2S_2(dedtc)_2$].

All of the compounds were recrystallized by slow evaporation of a CH_2Cl_2 solution except $Mo_2O_4(dedtc)_2$, which was recrystallized by adding petroleum ether (30°-60° bp) to a CH_2Cl_2 solution.

Materials and measurements.—TLC plates were prepared with EM Silica Gel A and spread to 0.25 mm thickness. The column used for separations measured 6.6 × 71.8 cm and was dry-packed with EM Silica Gel 60 except for the separation of $Mo_2OS_3(nbudtc)_2$ and $Mo_2S_4(nbudtc)_2$. For these latter EM Silica Gel 60 was slurry packed with benzene into the column and the mixture of complexes introduced as a solution. In the other separations the compound was rotary evaporated into a sample of silica gel that weighed 25-50 times more than the sample. This was then introduced at the top of the column prior to elution. In the case of $Mo_2S_4(nbudtc)_2$ and $Mo_2OS_3(nbudtc)_2$ the solvents were benzene and methanol for both the column and TLC separations. In all other cases the best solvent was found to be a 5:2 (vol:vol) mixture of benzene and CH_2Cl_2.

The electrochemical experiments were carried out with a PAR Model 173 Potentiostat/Galvanostat, Model 174 Digital Coulometer, and Model 175 Universal Programmer. A three-electrode system was utilized in all cases. The reference electrode was an Ag-AgCl electrode in aqueous tetramethylammonium chloride

Table I. Infrared bands

Complex	νMo-O_t (cm^{-1})	νMo-S_t (cm^{-1})	νMo-O_b (cm^{-1})	νMo-S_b (cm^{-1})
$Mo_2O_4(dedtc)_2$	973vs, 956s		730m, 709w, 472m	
$Mo_2O_2S_2(dedtc)_2$	967s, 953s			479m, 338m
$Mo_2OS_3(dedtc)_2$	955s	541s		470m, 335m
$Mo_2O_3S(nbudtc)_2$	970s, 951s		711m, 513m	460m, 350w
$Mo_2O_2S_2(nbudtc)_3$	967s, 955s			478m, 338m
$Mo_2OS_3(nbudtc)_2$	960s	538s		470m, 333m
$Mo_2S_4(nbudtc)_2$		549s, 533m		467m, 335s

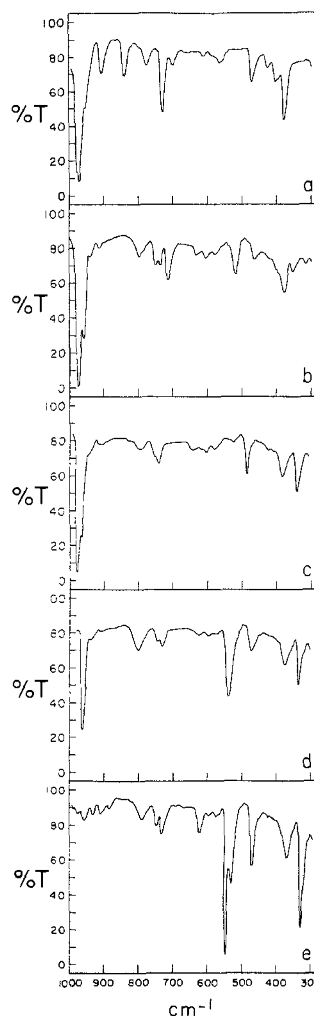

Fig. 1. Infrared spectra of 0.3% KBr disks of, (a) $Mo_2O_4(dedtc)_2$; (b) $Mo_2O_3S(nbudtc)_2$; (c) $Mo_2O_2S_2(nbudtc)_2$; (d) $Mo_2OS_3(nbudtc)_2$; (e) $Mo_2S_4(nbudtc)_2$.

(0.00V *vs.* SCE) in a capillary tube with a cracked-glass bead junction for contact with the solution. The auxiliary electrode was a Pt flag electrode, while the working electrode was a Beckman Pt inlay electrode for cyclic voltammetry and a Pt gauze electrode for coulometry. The supporting electrolyte, tetraethylammonium perchlorate, was synthesized and purified by established methods (14).

Cyclic voltammetric and coulometric studies of all the compounds were carried out in DMF and DMA. The electrochemical behavior was identical in both solvents with the exception of the $Mo_2O_4(dedtc)_2$ complex which seemed to decompose in DMA. Attempts were made to use DMSO and acetonitrile as solvents, but the compounds decomposed in DMSO and were too insoluble in acetonitrile to get reliable data. Reversibility of the first cathodic peaks was also determined as a function of scan rate.

Transfers of reduced species to airtight spectrometer cells were made inside a Vacuum Atmospheres Corporation Dry-Lab glove box. U.V.-vis. spectra were recorded on a Cary Model 14 spectrophotometer in quartz cells that ranged from 0.01 to 1.0 cm in path length. EPR spectra were recorded on a Varian Model 4500 X-band spectrometer by use of a Varian V-4548 solution cell. Infrared spectra were recorded with either a Perkin-Elmer 621 or Perkin-Elmer 283 spectrometer. All spectra were run as 0.3% KBr pellets. Dimethylformamide (DMF) was purified by refluxing 2 liters over 200g P_2O_5 for two days, followed by distillation at a pressure between 8-12 Torr. Dimethylacetamide (DMA) was purified by the same procedure.

Results

Infrared.—Two bands are obtained when "sulfurized molybdenum di-n-butyldithiocarbamate" is eluted from the column. The infrared spectrum of the first band displays a sharp doublet at 967 and 955 cm^{-1} and also contains stretches at 478 and 338 cm^{-1}. The spectrum from the second band also has a well-resolved doublet at 970 and 951 cm^{-1} as well as stretches at 711, 513, 460, and 350 cm^{-1}, with the stretches at 711 and 513 cm^{-1} not being observed in the spectrum of the first band. These two compounds are identified as $Mo_2O_2S_2(nbudtc)_2$ and $Mo_2O_3S(nbudtc)_2$.

The product of the reaction between P_4S_{10} and "sulfurized molybdenum di-n-butyldithiocarbamate" has three components. The first band eluted displays a finely resolved doublet at 549 and 533 cm^{-1} besides stretches at 467 and 335 cm^{-1}. The second band eluted has two strong singlet peaks at 960 and 538 cm^{-1} besides two stretches at 470 and 333 cm^{-1}. Finally, the third band eluted exhibits the same infrared spectrum as the first band of "sulfurized molybdenum di-n-butyldithiocarbamate." These three components are identified as $Mo_2S_4(nbudtc)_2$, $Mo_2OS_3(nbudtc)_2$, and $Mo_2O_2S_2(nbudtc)_2$.

The product of the reaction between H_2S and Mo_2O_3 (dedtc)$_4$ has two components. An infrared spectrum of the first compound has two strong stretches at 955 and 541 cm^{-1} besides the two stretches at 470 and 335 cm^{-1}. A spectrum of the second band exhibits four stretches, besides those associated with the ligand, a sharp doublet at 967 and 953 cm^{-1}, and stretches at 479 and 338 cm^{-1}. These two compounds are identified as $Mo_2OS_3(dedtc)_2$ and $Mo_2O_2S_2(dedtc)_4$.

Finally, the compound $Mo_2O_4(dedtc)_3$ prepared by a modified procedure (13) exhibited five stretches in the infrared spectrum not related to the ligand. The first two are a well-resolved doublet at 973 and 956 cm^{-1}, and the other three are at 730, 709, and 472 cm^{-1}. The infrared spectral data are displayed in Table I and Fig. 1.

U.v.-vis. spectra.—$Mo_2O_4(dedtc)_2$ exhibited a featureless u.v.-visible spectrum with a single peak at 268 nm ($\epsilon = 3.12 \times 10^4$). For compounds with the core structure, Mo_2O_3S and $Mo_2O_2S_2$, shoulders were exhibited at 370 and 350 nm, as well as peaks at 280 and 250 nm in DMF. The Mo_2OS_3 core exhibited peaks at 397 nm ($\epsilon = 3.37 \times 10^3$) and 260 nm ($\epsilon = 3.85 \times 10^4$ for $Mo_2O_2S_3(dedtc)_2$) while $Mo_2S_4(nbudtc)_2$ exhibits peaks at 441 nm ($\epsilon = 5.20 \times 10^3$) and 293 nm ($\epsilon = 4.33 \times 10^4$).

Electrochemistry.—Initial reduction scans showed all the compounds to be electroactive, but none of them exhibited peaks on an initial oxidation scan. A summary of the electrochemical results is contained in Table II.

Except for $Mo_2O_4(dedtc)_2$ and $Mo_2S_4(nbudtc)_2$, an oxidation peak is exhibited 80-150 mV more anodic than the reduction peak following reversal of the scan direction, *i.e.*, the reductions are quasireversible. Two compounds exhibit this reoxidation peak at scan rates slower than 100 mV/sec and they are $Mo_2O_2S_2(nbudtc)_2$ and $Mo_2O_2S_2(dedtc)_2$. $Mo_2S_4(nbudtc)_2$ behaves reversibly at scan rates of 200 mV/sec while the reduction peak for $Mo_2O_4(dedtc)_2$ seems to be totally irreversible, since there is no reoxidation peak exhibited at any scan rate. The first reduction peak for all the complexes is a one-electron reduction, except for $Mo_2O_4(dedtc)_2$ which is a two-electron reduction as shown by the coulometry and peak height data.

Two compounds exhibited a prominent second reduction peak in the voltammograms; $Mo_2O_2S_2(dedtc)_2$ displays a peak at −1.62V *vs.* SCE while $Mo_2O_2S_2$ (nbudtc)$_2$ displays a peak at −1.67V *vs.* SCE, which is shown to be a two-electron reduction by coulometric and peak-height data. $Mo_2OS_3(dedtc)_2$ has a second reduction peak at −1.72V *vs.* SCE, while Mo_2O_3S (nbudtc)$_2$ has a second reduction peak at −1.78V *vs.* SCE, and $Mo_2OS_3(nbudtc)_2$ has one at −1.75V *vs.* SCE. $Mo_2S_4(nbudtc)_2$ definitely exhibits a second, quasireversible reduction peak at −1.52 V *vs.* SCE but $Mo_2O_4(dedtc)_2$ exhibits no distinct reduction peaks following the one at −1.41V *vs.* SCE.

Coulometry performed at a potential just negative of the first cathodic peak indicated that the compounds are reduced by one electron. There is no evidence of the reverse oxidation peak for any of the complexes and all of the second reduction peaks exhibited by the compounds in the voltammograms prior to coulometry have disappeared. The color of the solutions after reduction by one electron per molecule is dark red, and u.v.-vis. spectra were featureless. Attempts were made, using both lithium amalgam and sodium amalgam, to chemically reduce the compounds on a larger scale in the hope of isolating the reduction product. However, the voltammetry of the chemically reduced product did not reproduce the voltammetry of the electrochemically reduced product. For all the complexes, except $Mo_2O_4(dedtc)_2$, initial anodic scans on the solutions after coulometry yield three peaks, one at +0.09V due to ligand oxidation, and small broad peaks at +0.65 and +0.90V. Coulometry at the potential of the ligand oxidation peak regenerates some of the starting material, while coulometry at +1.00V regenerates up to 60-80% of the starting material.

$Mo_2O_4(dedtc)_2$ is reduced by two electrons. An anodic scan of the reduced solution shows peaks at −0.24, +0.10 (due to ligand), +0.42, and a small broad peak at +0.80V. Coulometry at a potential just positive of the first oxidation peak yields about 25% regeneration of the starting material while oxidation at a potential just positive of the ligand peak yields about 50% regeneration of the starting complex.

The electrochemical data are displayed in Table II and Fig. 2.

Table II. Electrochemical data

Complex	$E_{p,c}$[a]	$E_{p,a}$[a]	n[a]
$Mo_2O_4(dedtc)_2$	−1.41		2
$Mo_2O_3S(nbudtc)_2$	−1.40	−1.30	1
$Mo_2O_2S_2(dedtc)_2$	−1.32	−1.22	1
$Mo_2O_2S_2(nbudtc)_2$	−1.33	−1.23	1
$Mo_2OS_3(dedtc)_2$[b]	−1.00	−0.88	1
$Mo_2OS_3(nbudtc)_2$	−0.98	−0.87	1
$Mo_2S_4(nbudtc)_2$	−0.89	−0.83	1
$Mo_2S_4(nbudtc)_2$[c]	−1.52	−1.44	1

[a] $E_{p,c}$ cathodic peak potential. $E_{p,a}$ anodic peak potential at 200 mV/sec, n is the number of electrons per dimeric molecule after coulometry for the first reduction peak.
[b] Scan rate is 500 mV sec.
[c] Second reversible peak which is observed for $Mo_2S_4(nbudtc)_2$ before coulometry.

Discussion

Infrared spectra.—All the complexes in this study exhibit either C_S or C_{2V} symmetry, and these symmetry groups have been used to predict the number of expected infrared active bands. In all cases two terminal oxygen- or sulfur-molybdenum stretches are predicted to be infrared active, with an additional three or four infrared-active bridge stretches also expected.

$Mo_2O_4(dedtc)_2$ has C_{2V} symmetry, requiring two terminal and three bridge stretches. These are all observed and are in good agreement with those reported by Newton and McDonald (11). There is a lowering of symmetry to C_S in going from the Mo_2O_4 unit to the $Mo_2O_2(\mu\text{-}O)(\mu\text{-}S)$ unit. For this complex four bridge bands are predicted as well as the two terminal stretch bands. The four bridge bands are observed at 711, 513, 460, and 350 cm^{-1}, in good agreement with the results of Newton and McDonald (11). The $Mo_2O_2(\mu\text{-}S)_2$ unit exhibits C_{2V} symmetry, again requiring two terminal stretches and three bridge stretches. Only two bridge stretches are observed, however, the third

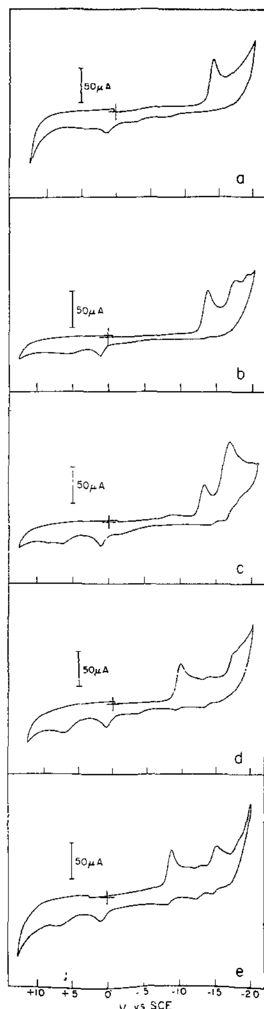

Fig. 2. Cyclic voltammograms at 200 mV/sec of 1 mF solutions of: (a) $Mo_2O_4(dedtc)_2$; (b) $Mo_2O_3S(nbudtc)_2$; (c) $Mo_2O_2S_2(nbudtc)_2$; (d) $Mo_2OS_3(nbudtc)_2$; (e) $Mo_2S_4(nbudtc)_2$.

one possibly coming below 300 cm^{-1} which is the limit of our spectra. The bridge stretches for $Mo_2O_4(dedtc)_2$, appearing at 730, 709, and 472 cm^{-1}, while those for $Mo_2O_2(\mu\text{-}S)_2$ appear at 478 and 338 cm^{-1}. Comparing these to the bridge bands observed for $Mo_2(\mu\text{-}O)(\mu\text{-}S)(nbudtc)_2$, it appears that the 711 and 513 cm^{-1} bands are associated mainly with the oxygen bridge atom, and that the bands at 460 and 350 cm^{-1} are associated mainly with the sulfur bridge atom, again in good agreement with Newton and McDonald (11). In all of the complexes so far the terminal molybdenum-oxygen stretch has been a doublet at approximately 970 and 955 cm^{-1}. The next unit of the series, $MoOS_3$, however, has a new terminal atom as well as a descent in symmetry to C_S. Two terminal stretching bands are required and observed, one at 960 cm^{-1} for the terminal molybdenum oxygen stretch, and one at 540 cm^{-1} for the terminal molybdenum sulfur stretch. Of the four predicted bridge stretches only two are observed, at 470 and 334 cm^{-1}, again presumably because two stretches may be of lower energy than can be observed in a KBr medium. The final complex in the series $Mo_2S_4(nbudtc)_2$ is C_{2V}. The two terminal stretches are represented by a doublet at 549 and 533 cm^{-1}. Only two bridge stretches, at 467 and 335 cm^{-1}, of the three required are observed.

Electrochemistry.—$Mo_2O_4(dedtc)_2$ is reduced by a two-electron process, in agreement with results published previously (2). The reduced species has lost one or more ligand molecules as evidenced by the presence of a ligand oxidation peak in the cyclic voltammograms after coulometry. The peak at +0.42V corresponds to the oxidation of $Mo^{IV}O(dedtc)_2$ (2). This implies that at least some of the binuclear molybdenum core has decomposed into a monomeric species which has then combined with free ligand to form $Mo^{IV}O(dedtc)_2$. This accounts for only 10% of the molybdenum in solution, however. Two possibilities exist for the oxidation peak at −0.24V. Either it is the oxidation of $[Mo^{IV}{}_2O_4(dedtc)_2]^{2-}$ to the starting material $Mo_2O_4(dedtc)_2$, or it is the oxidation of a species due to the decomposition of reduced $Mo_2O_4(dedtc)_2$. In this case after the decomposition product is oxidized it must somehow regenerate starting material, possibly by reaction with free ligand in solution. Oxidation at a potential positive of the ligand oxidation peak produces tetraalkylthiuramdisulfide (15). Regeneration of starting material after ligand oxidation is probably due to oxidative addition of the tetraalkylthiuramdisulfide to the major reduction product of $Mo_2O_4(dedtc)_2$.

Substitution of one sulfur into the Mo_2O_4 core causes a significant change in the electrochemical behavior. Although the reduction potential is not changed dramatically, the first reduction peak is only a one-electron process and it has become quasireversible. Introduction of the second sulfur atom into the bridge position causes a further change in the electrochemistry. The one-electron reduction product of this $Mo_2O_2S_2$ core is the most stable reduction product of all the complexes studied. Even at 50 mV/sec, it still exhibits a quasireversible reoxidation peak. The complex also appears to be capable of a further two-electron irreversible reduction, probably to a molybdenum (IV)-molybdenum (III) dimer which then decomposes. When these complexes are reduced by controlled potential coulometry, both the first and second reduction peaks disappear and a voltammogram for the resulting solution has three oxidation peaks in a positive scan.

Introduction of a sulfur into a terminal position of the binuclear molecules causes a further anodic shift in the potential of the first reduction peak to −0.99V. There is a second reduction peak observed at −1.75V which is also observed for $Mo_2O_3S(nbudtc)_2$, which is the size of the initial reduction peak. Because both of these compounds decompose at a much faster rate than the $Mo_2O_2S_2$ compounds, this peak at −1.75V may be a two-electron reduction of $Mo_2O_3S(dtc)_2^-$ and $Mo_2OS_3(dtc)^-$.

$Mo_2S_4(nbudtc)_2$ exhibits the most positive first-reduction potential and in this case it is reversible at a scan rate of 200 mV/sec. Also a second quasireversible one-electron reduction is observed at −1.52V (see Table II). In this case the first peak probably is due to reduction to $(Mo^VMo^{IV}S_4(nbudtc)_2)^-$ and the second peak is due to reduction to the dianion $(Mo^{IV}{}_2S_4(nbudtc)_2)^{-2}$. Coulometry after the first reduction peak causes the disappearance of both the first and second reduction peaks. A voltammogram on the resulting solution exhibits three oxidation peaks on an anodic scan which are discussed below.

On all complexes with sulfur substituted into the Mo_2O_4 core, coulometry after the first reduction peak yields a solution which is dark red. For the solutions containing the reduction products coulometry at a potential just positive of the ligand oxidation yields about 50% regeneration of the starting material. This probably is due to oxidative addition of tetraalkylthiuramdisulfide to the major reduction product. Since coulometry at +1.00V can regenerate 60-80% of the starting material, the peaks at +0.65 and +0.90V may be minor products of the decomposition which when oxidized produce starting material.

The sulfur-substituted core units do not appear to be broken up into monomeric units because the initial reduction does not exhibit catalytic behavior, even during coulometry, and no signal is observed by EPR. Further substantiation is provided by the fact that the reaction of coulometrically reduced product yields

only the original starting material and not a mixture of products.

U.V.-vis. spectra.—Perkins and Brown (16, 17) have shown that the $Mo_2O_2S_2$ core has more delocalization than the Mo_2O_4 core as well as a smaller formal positive charge on the molybdenum. This has been attributed to sulfur "d" orbitals allowing more delocalization in the $Mo_2O_2S_2$ unit than can be achieved in Mo_2O_4. The electrochemical data substantiate these results because $Mo_2O_2S_2(dedtc)_2$ is more easily reduced than $Mo_2O_4(dedtc)_2$. Introduction of additional sulfur into the terminal position appears to reduce the energy of the lowest unoccupied molecular orbital still further. This is consistent with the anodic shift in reduction potential of the Mo_2S_4 and Mo_2OS_3 cores with respect to the $Mo_2O_2S_2$ core [44 and 34 mV, respectively (see Table I]. Also the energy of the first electronic transition is lowered for those compounds that exhibit distinct peaks in the visual region specifically 397 nm for Mo_2OS_3 and 441 nm for Mo_2S_4.

The chromatographic elution of the compounds also is in accord with the reduction of the formal charge on the molybdenum upon replacement of oxygen by sulfur. The compound which elutes first is $Mo_2S_4(dtc)_2$, followed by Mo_2OS_3, $Mo_2O_2S_2$, and Mo_2O_3S. Apparently the more oxygens present the more polar the compound, with even the bridge oxygens having a significant effect.

Conclusions

The data in this paper indicate that there is little coupling between molybdenum terminal atom stretches and molybdenum bridge atom stretches as demonstrated by the constancy of the frequency of the infrared bands. Even when the bridge atoms are different, the bridge stretches appear almost independent of each other as can be seen by comparison of the infrared bands for $Mo_2O_4(dedtc)_2$, $Mo_2O_3S(nbudtc)_2$, $Mo_2O_2S_2(nbudtc)_2$, and $Mo_2O_2S_2(dedtc)_2$. These observations make it possible to determine both the number and the position of different atoms in binuclear molybdenum (V) compounds. The presence of two bridging sulfur atoms between the molybdenum (V) ions appear to be a requirement (at least in this system) for fast electron transfer with no subsequent decomposition of the complex. Additionally it is clear that binuclear molybdenum (V) complexes in an environment consisting mainly of sulfur donors can undergo reversible one-electron transfer reactions and that completely surrounding the molybdenum atoms with sulfur donors allows a binuclear molecule to undergo two consecutive one-electron transfers without appreciable decomposition. We conclude that an oxygen ligand field most likely could not support fast enzymatic redox reactions, and that the ligand field around the molybdenum atoms in redox enzymes, therefore most likely contains all sulfur donors.

Acknowledgment

This work was supported by a Cottrell Research Grant from the Research Corporation, by the Petroleum Research Fund administered by the American Chemical Society, by an Intramural Research Grant from the University of California, and by the J. W. Richards Fellowship from The Electrochemical Society.

REFERENCES

1. V. R. Ott aend F. A. Schultz, *Electroanal. Interfacial Electrochem.*, **61**, 81 (1975).
2. L. J. DeHayes, H. C. Faulkner, W. H. Doub, Jr., and D. T. Sawyer, *Inorg. Chem.*, **14**, 2110 (1975).
3. V. R. Ott and F. A. Schultz, *Electroanal. Interfacial Electrochem.*, **59**, 47 (1975).
4. R. C. Bray, in "Proceedings of the Climax Second International Conference on the Chemistry and Uses of Molybdenum," P. C. H. Mitchell and A. Seaman, Editors, p. 271, Climax Molybdenum Co. Ltd., London (1977).
5. L. S. Merriwether, W. F. Marzloff, and W. C. Hodgson, *Nature (London)*, **212**, 465 (1966).
6. L. Ricard, C. Martin, R. Wiest, and R. Weiss, *Inorg. Chem.*, **14**, 2300 (1975).
7. J. Dirand-Colin, L. Ricard, and R. Weiss, *Inorg. Chim. Acta.*, **18**, L21 (1976).
8. R. Winograd, B. Spivack, and Z. Dori, *Cryst. Struc. Comm.*, **5**, 373 (1976).
9. A. Spivack, Z. Dori, and E. I. Steiffel, *Inorg. Nucl. Chem. Lett.*, **11**, 501 (1975).
10. L. J. DeHayes, H. C. Faulkner, and R. M. Wing, To be published.
11. W. E. Newton and J. W. McDonald, in "Proceedings of the Climax Second International Conference on the Chemistry and Uses of Molybdenum," P. C. H. Mitchell and A. Seaman, Editors, p. 25, Climax Molybdenum Co. Ltd., London (1977).
12. H. H. Farmer, U.S. Pat. 3,355,702 (1967).
13. W. E. Newton, J. L. Corbin, D. C. Bravard, J. E. Searles, and J. W. McDonald, *Inorg. Chem.*, **13**, 1100 (1974).
14. H. O. House, E. Feug, and N. P. Peet, *J. Org. Chem.*, **36**, 2371 (1971).
15. G. Couquis and D. Lachenal, *J. Electroanal. Interfacial. Chem.*, **43**, 205 (1973).
16. D. H. Brown and P. G. Perkins, *Rev. Roum. Chim.*, **20**, 515 (1975).
17. D. H. Brown, P. G. Perkins, and J. J. Stewart, *J. C. S. Dalton*, 1105 (1972).

JOURNAL OF THE ELECTROCHEMICAL SOCIETY

REVIEWS AND NEWS

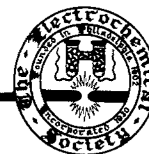

AUGUST
1978

Secondary Batteries: 1952-1977

A. J. Salkind,* D. T. Ferrell, Jr., and A. J. Hedges

ESB Technology Company, Yardley, Pennsylvania 19067

In the 25 years since the Society's 50th anniversary review, there have been many changes in the designs, manufacturing processes, and markets for secondary batteries. Some developments which were promising and disclosed in the Golden anniversary review in 1952 have been successful, while others failed. This paper will review briefly the major changes that have occurred and current research and development efforts that may lead to future progress in secondary batteries.

Review of the Industry

The secondary battery industry has grown greatly in the past 25 years; however, it is still dominated by the automotive starting, lighting, and ignition (SLI) battery. A major impetus for this growth has been the increase in popularity of internal combustion engine-powered automobiles and trucks. This is effectively illustrated in Table I which shows for the United States and for the free market countries of the world the growth in motor vehicle registrations and SLI battery shipments. These figures, in millions of units, are indicated in lines A and B. The dollar values of all major secondary battery shipments are shown in the subsequent lines. The data in Table I are based on the best available information from various sources; however, in some cases, the data had to be interpolated or estimated. The data are useful to illustrate trends and there are several interesting observations based on Table I. SLI battery shipment growth closely parallels the growth in vehicle registration and seems to have leveled off at about one battery annually for 2.2 to 2.4 vehicles registered. There has been a significant development since 1952 of consumer (nonautomotive) applications for secondary batteries; principally, small maintenance-free units for hand and garden tools, personal care products, calculators, and lighting devices. While inflation has contributed significantly to the dollar growth, normalization to constant dollars would still show substantial increase in shipments as evidenced by the SLI unit growth. Perhaps surprising to some is the indication that worldwide, alkaline secondary batteries have maintained a rather steady 8 to 10% of the total secondary battery business. This relatively constant market share, even with the development of new applications, reflects the limiting effect of the higher cost of the alkaline systems on market penetration.

* Electrochemical Society Active Member.

Product and Process Changes, 1952-1977

From an over-all viewpoint, the general thrusts of the secondary battery industry can be summarized as follows:

Research—The research thrust has been largely devoted to the application of modern scientific methods and instrumentation for a better understanding of the reaction mechanisms which control performance and life.

Development—The development effort has been aimed at improvements in performance per unit weight and volume, reduction of maintenance, improved charge acceptance, and use of new materials.

Manufacturing—New and improved processes and equipment have permitted increased productivity through mechanization and automation. Recently, much attention has been paid to changing manufactur-

Table I. Estimated growth of the secondary battery business in U.S. and worldwide (free market countries)

(All values in millions)

	U. S.				Worldwide incl. U. S.			
Calendar year	1952	1960	1969	1976	1952	1960	1969	1976
	Units	Units	Units	Units	Units	Units	Units	Units
A. Motor vehicle registration	53	74	105	134	75	122	220	322
B. Lead-acid, SLI	28	34	47	60	35	54	90	143
Ratio A/B	1.9	2.2	2.2	2.2	2.1	2.3	2.4	2.3
	Dollars	Dollars	Dollars	Dollars	Dollars	Dollars	Dollars	Dollars
C. Lead-acid, SLI	260	330	510	1040	320	520	1040	2750
D. Lead-acid, other								
Industrial	60	70	105	200	100	140	300	710
Consumer	0	<1	3	10	0	1	8	18
E. Nickel-cadmium								
Industrial	6	12	16	30	30	45	80	150
Consumer	0	5	20	60	2	20	50	140
F. Others Ni-Fe, Ag-Zn, Ni-Zn	8	18	24	28	16	24	33	60
G. Total value	334	436	678	1368	468	750	1511	3828

ing processing to minimize personnel and facility environmental problems.

The extent of what has been achieved is best understood by considering each of the secondary battery systems in production today.

Lead-acid system.—The published research activities in the lead-acid system up to 1970 are covered in detail in an excellent review article by Burbank, Simon, and Willihnganz (1). They point out a number of challenging questions that remain unanswered and to which the answers, unfortunately, are still being sought today. Auger, SEM, x-ray microprobe, and other modern techniques are beginning to delineate definite areas of attack for resolution of some of the questions; however, today many important questions remain unanswered. Typically, but in no way complete, the questions are:

1. The exact nature of the interface between positive active material and the grid, and the influence of grid composition, additives, etc., on the interface and the changes which occur when cycling.
2. How to improve active material utilization beyond the 25-35% typically experienced in commercial batteries and maintain or increase cycle life.
3. How to maintain particle morphology in positive active material to maximize performance and life.
4. The mechanism of expander action in the negative active material.

While these and other questions still occupy the scientist today, the last 25 years have seen significant changes in the product. Basically, the products described in the Society's 1952 review articles still exist today; however, most of them have undergone dramatic changes which are in some cases apparent and in other cases perhaps invisible but nevertheless equally as impressive.

Starting, lighting, ignition.—The 1952 review article by Willihnganz (2) indicates the typical SLI battery was 6V with a 20 hr discharge rating of about 100 A-hr. The average battery weighed about 40 lb (18 kg) and had a density of about 138 lb/ft³ (2.2 kg/liter). The battery was made in a hard rubber container with a soft asphalt cover seal. The grid alloys were high antimonial alloys (above 6% Sb), specific gravity of the electrolyte was 1.285, and there was a 50% or better chance that the separators were treated wood. The charger in the car of the period was a rotating generator which did not charge the battery below an engine rpm that was considerably above the idle speed.

A comparison of the features of the typical 1952 SLI battery with the ones found in the 1977 product is illustrated in Table II. Significant is the change during the period from rubber container and cover to battery cases that usually consist of thermoplastic polypropylene. Use of this material permits the container and cover to be heat-sealed together with a permanently bonded seam, eliminating most of the problems associated with the former asphalt compound sealing method.

Table II. SLI batteries: 1952-1977

Component or characteristic	1952	1977
Container	Rubber	Polypropylene
Cover	Rubber	Polypropylene
Seal	Asphalt	Heat-sealed
Intercell connector	Over cover	Thru-partition
Voltage	6V	12V
Specific gravity	1.285	1.260
Separators	Wood Treated paper Microporous rubber	Treated paper Microporous rubber Microporous plastic
Grid alloys	>6% Sb	<4% Sb or calcium
Weight	40 lb (18 kg)	35 lb (15 kg)
Density	138 lb/ft³ (2.2 kg/liter)	118 lb/ft³ (1.9 kg/liter)
Watering interval	7-30 days	6 months to several years
Charger	Generator	Alternator
Capacity (20 hr rate)	100 A-hr	48 A-hr*

* The 20 hr discharge rating which was in use in 1952 is no longer used for SLI batteries and the value shown for 1977 is for comparative purposes.

The use of polypropylene also allows the introduction of distinctive colors into SLI packaging to make the one-time, so-called "small black box" a far more attractive product and adding a new dimension to its marketability. The change, too, from exposed over-the-cover intercell connectors to concealed through-partition connectors, as well as the repositioning of terminal posts from the top to the side of the battery in late models of the period, also enhanced product appearance while reducing safety hazards that previously existed.

Perhaps most significant is the recent (1974) introduction of the maintenance-free (MF) SLI battery which theoretically requires no addition of water throughout its service life. Water loss in standard SLI batteries generally is the result of electrolysis during charging. Manufacturers of MF/SLI batteries have practically eliminated water loss by changes in the alloys used in the grids.

One approach is the use of a lead-calcium alloy grid (usually below 0.08% calcium), which not only results in lower self-discharge rates but also in an increase in the hydrogen evolution potential of the negative electrode. As a consequence, at the usual voltage regulator setting less current is available to decompose the water content of the electrolyte.

Water loss in standard SLI batteries also can be directly related to the buildup of antimony deposits on the sponge lead of negative plates during operation. Another approach to the MF/SLI battery is a reduction of the antimony content of grid alloys. Lowering the antimony content from 4-6% to 2-3% has cut the water loss drastically.

Another major development adopted nearly universally throughout the SLI battery industry during the 25-year period is the "dry charge" process. Basically, this involves the use of negative plates in which, after formation, the water content is reduced to a minimum without a corresponding increase in the oxygen content of the plates.

Since batteries can be stored for an extensive period in a dry charge condition without detrimental effect and then easily activated by the addition of standard electrolyte to the cells followed by a brief charging period, the process greatly simplifies the shipping and, in particular, the warehousing of SLI batteries.

The recently developed MF/SLI battery, however, now offers economic as well as practical advantage over the dry charge variety. Because of its much lower self-discharge rate, the MF/SLI battery can be shipped as well as stored in a wet, activated state for a relatively long time. This eliminates the cost of the dry charge process during manufacture and also the chore of adding acid electrolyte at the point of sale, an often unpleasant job not without danger.

One of the developments associated with the introduction of the MF/SLI battery has been the investigation of techniques for producing grids other than by the traditional casting method. At least one manufacturer is in large scale production using grids manufactured by expanding thin, continuously cast, lead-calcium alloy sheet. Techniques such as this offer the opportunity for continuous production of plates and significant reduction in the weight of the grid.

Industrial.—Lead-acid industrial storage batteries, which basically are larger, with stronger, better quality construction than SLI batteries, fall into three general application categories. Comprising about 55% of the industrial lead-acid market are the motive power types that propel material handling lift trucks, tractors, and motorized hand trucks; mining railcars, tractors, and specialized types of self-propelled mining vehi-

cles; industrial power sweepers and floor scrubbers; some electric street vans, buses, and autos (mostly experimental); and to a limited extent, golf carts and personnel carriers (the majority in service use automotive-type batteries).

Highlighting technological improvements in motive power batteries during the period is the development of improved sealing methods for cell covers and containers. Traditional in the industry has been the use of hard rubber cell covers and containers sealed together with an asphalt-like compound. Since this asphalt seal could be adversely affected by hot and cold ambient temperatures, internal cell stresses during battery operation, and physical shocks to which the vehicle was subjected, the leakage of acid electrolyte, with subsequent damage to both battery and vehicle, was not uncommon.

The first step in improvement of the sealing method came with the introduction of an epoxy sealant in the mid-1960's which proved to be an effective means of bonding cell cover and container together. It was, however, a time-consuming process in manufacturing. This was followed in the early 1970's by introduction of the faster, far more simplified (from the standpoint of manufacturing) heat bonded seal made possible by the use of thermoplastic polypropylene cell covers and containers.

The period also saw the phasing out of slotted plastic tubes in tubular-positive plate battery types. These have been replaced entirely by tubes made of woven glass fiber and synthetic polymer which are stronger, less costly, and offer greater porosity.

Another major application for lead-acid industrial batteries (approximately 30% of the market) is in stationary service: telecommunications systems; electric utilities, operating circuit breakers, switches, alarms, and other power distribution controls; emergency lighting, and fire, security, and similar standby power systems; and uninterruptible power systems (UPS) which have come into wide use in the past decade, providing precise a-c power to back up real-time computers and other critical processing and control equipment. Additionally, railroads use stationary-type lead-acid batteries for signals and track controls, in passenger car power systems for air conditioning and lighting, and to supplement axle-generator systems on caboose cars for lighting and communications. During the period, the use of tempered glass jars for stationary battery cell containers virtually ceased. These have been replaced by lighter, more durable and less costly units made from polystyrene, polycarbonate, and similar materials.

Another major application category for lead-acid industrial batteries is that of diesel locomotive engine starting. These rail diesel cranking batteries and similar units used for various engine starting chores in industry account for approximately 7% of the lead-acid industrial market. The so-called "unitized" container was brought out during the period for diesel locomotive batteries. Normally, such a battery consists of 32 cells in eight 4-cell hard rubber monoblock containers. The unitized container, however, holds 16 cells so that only two of these are required to make up a battery, greatly reducing handling and maintenance work. When first introduced in the late 1960's the unitized container consisted of a steel tray, usually with a plastic insulation coating, with hard rubber cell containers. This was followed by polypropylene trays and tray covers as well as cell covers and containers, the latter being heat-sealed.

Also in the railroad field, the period witnessed the debut of the lead-acid rapid transit battery to replace the waning nickel-iron-alkaline battery (see below) which at one time was used virtually 100% on rapid transit lines in the United States. To withstand the rigors of this service, the lead-acid rapid transit battery, introduced in 1975, utilizes a container made of polycarbonate and incorporates other features for additional physical strength.

Not to be overlooked is a miscellaneous group of lead-acid industrial batteries that include those for such applications as submarine service, miners' cap lamps, and reserve power in marine service. The demand for submarine batteries declined during the period with the diminishing use of diesel-battery boats; batteries, however, with smaller numbers of cells still are a necessity in nuclear submarines for reactor start-up and emergency power.

Lead-acid industrial batteries are available with three different positive plate configurations: tubular and pasted flat plate designs used in motive power, stationary and diesel cranking batteries, and Planté designs, characterized by active material areas that are formed from pure lead, found primarily in stationary-type batteries. Flat plate batteries additionally are classified as to whether the grids are cast from lead-antimony or lead-calcium alloys. The latter, however, are used mostly in stationary industrial batteries because of the inability of calcium alloy grids to withstand the rigors of the deep discharging associated with motive power and cranking service. It should be pointed out that the trend in recent years has been away from Planté-type batteries in stationary service, because of their higher initial cost, in favor of calcium-alloy units. Small maintenance-free lead-calcium alloy batteries have been available since the mid-1960's for emergency lighting and similar applications.

All of the above lead-acid batteries, including the SLI types, are prismatic in structure with flat, parallel plates. A new configuration, the "round cell," was developed for the telephone industry around the beginning of the present decade. Designed for a goal of trouble-free long life, this unique battery design features grids cast of pure lead in a shallow, conical shape which are stacked as finished positive and negative plates one above the other vertically in a cylindrical cell container.

Consumer.—Nonexistent in the marketplace 25 years ago, lead-acid consumer or "sealed" batteries have grown in United States sales from less than $1 million in 1960 to more than $10 million by the end of 1977. The worldwide sales of sealed lead-acid batteries reached a total exceeding $18 million by that year.

Sealed lead-acid batteries come in two general configurations, prismatically shaped units with parallel plate construction, ranging in capacity from 1 to 30 A-hr, and cylindrically shaped units, similar in physical appearance to several of the more popular dry cell types, having spirally wound grids and capacities ranging from 1 to 5 A-hr.

Although sealed lead-acid batteries can be operated in any position without danger of leakage, the term sealed is really a misnomer. The electrolyte is either in a gel form or as an aqueous solution absorbed in the plates and in highly porous separators. The batteries also make use of chargers that incorporate voltage-limiting circuitry to reduce water decomposition to a minimum. Too, the batteries have a one-way venting system that releases any gases that might possibly form only when a predetermined pressure is exceeded.

The grids employed in sealed lead-acid batteries generally are of lead-calcium alloy. Some cylindrical types, though, use grids of pure lead and have an internal design that successfully contributes to the recombination of any gases which might evolve. Sealed lead-acid batteries are used as power sources in emergency lighting equipment, cordless television sets, portable instruments and tools, and alarm and security systems.

In many respects the electrolyte retaining (ER) and charge retaining (CR) types of batteries reviewed in 1952 were the predecessors to today's sealed lead-acid batteries. Interestingly, usage of both ER and CR types declined during most of the last 25 years; however, in recent years there has been a resurgence of sales of the CR type for use with solar photovoltaic energy conversion systems.

Nickel-cadmium system.—Although nickel-cadmium batteries represent only slightly over 7% of the value of all secondary batteries produced in the noncommunist world, they comprise, nevertheless, a significant market. Nickel-cadmium battery sales in 1977 totaled more than $300 million or approximately 82% of the total value of all alkaline secondary batteries produced. The total world figure for nickel-cadmium batteries probably is as high as $600 million since they are known to be manufactured in large quantities in China (People's Republic), the U.S.S.R., and in other communist areas from which no confirming market data are presently obtainable.

Nickel-cadmium secondary batteries are available in a wide variety of electrode and cell design types as well as sizes. Most familiar, since its introduction at the beginning of the century, is the nickel-cadmium couple with its active materials contained in thin perforated, nickel-plated steel pockets. A modification of this is the use of perforated, nickel-plated steel tubes (actually the Edison-type positive with active materials consisting of metallic nickel flake and nickel hydrate) with standard pocket negatives.

Another electrode design is the sintered type that makes use of metal wire screens or perforated metal sheets which have sintered metal powder applied to the surfaces. Still another technique is to combine the active material with a conductive substance, such as carbon, and a plastic to serve as a binder. This mixture, after being heated or made fluid by addition of a solvent, is pressed into or pasted on a conductive grid. A more recent development is to make the plates by electrodepositing the active material on a conductive sheet or metallic fiber.

In addition to the variety of electrode structures, nickel-cadmium batteries are made with so-called "flooded and vented" cells and with "starved and sealed" cells, the latter containing only enough electrolyte to maintain the plates and separators in a saturated condition. Besides the conventional steel cell containers, nickel-cadmium batteries also are made with plastic containers, consisting of such materials as polyvinyl chloride, nylon polyamide, polystyrene, polyethylene, and polypropylene. Metal cell containers generally are used for batteries subject to the internal stresses of deep cycling operations or mechanical abuse.

In addition to prismatic cell configurations, nickel-cadmium batteries also are available in some of the familiar dry cell configurations, such as "AA," "C," and "D" shapes and sizes. These are sealed types having sintered plates that are spirally wound for insertion in the cylindrical containers. Nickel-cadmium batteries, additionally, are made in a button cell configuration to power cameras, calculators, and other electronic devices. These are generally made with electrodes consisting of pressed powder pellets.

The nickel-cadmium system has undergone three distinct periods in its evolution. The first period covered roughly the first 50 years of the present century and is the era of the nickel-cadmium battery as developed by Waldemar Jungner and his associates. This battery is constructed nearly entirely of nickel-plated steel with pocket-type plates. It is used primarily in heavy duty industrial applications such as motive power in material handling trucks, mining vehicles, and street delivery vans (the lattter two mostly in Europe), and for railway signals, emergency lighting, standby power, and diesel engine starting.

The second period of evolution began about 1950 with the development of sintered plates which resulted in significant increases in power delivery capability and specific energy content. Sintered nickel-cadmium batteries are used in aircraft engine starting, communications, and electronics.

The early 1960's ushered in the third period of nickel-cadmium evolution with introduction of the sealed cell. This is made possible by using a surplus of uncharged active material in the negative electrodes. This eliminates hydrogen gassing and permits controlled recombination of oxygen evolving from the positive electrodes. Additionally, the amount of electrolyte in sealed cells generally is lower than that which can normally be absorbed in the electrodes and separators.

Sealed nickel-cadmium batteries, which can be charged or discharged in any position, are used for portable power tools and appliances, emergency equipment, and small-engine starting, such as the recently introduced alternator-battery equipped, gasoline-powered lawnmower for example. The sintered, sealed type is by far the most widely produced nickel-cadmium battery at the present time.

Nickel-iron-alkaline systems.—From its introduction in 1908 until the cessation of its United States production in 1974, the nickel-iron-alkaline battery waged a losing contest in the marketplace, particularly whenever it came into direct competition with the industrial lead-acid system. Conceived originally by its inventor, Thomas A. Edison, as a power source for the early, but short-lived electric auto, the nickel-iron battery eventually saw service in material handling trucks, mining tractors, and other underground work vehicles, railway car lighting and air conditioning, rapid transit cars, and in stationary applications such as emergency lighting, circuit breaker control, and railway signal systems.

The nickel-iron battery, with major cell components of nickel-plated steel, is extremely durable in construction and exhibits basically stable thermodynamic reactions, both of which contribute to its long life. However, the nickel-iron system's lower emf (1.37 vpc) and lower specific energy (<0.8 W-hr/in.^{3}) along with its high cost of manufacture, in comparison with the lead-acid system, led to its ultimate decline in usage. As a result of the depressed market for the nickl-iron battery, the sole United States supplier recently terminated its production. The battery still is being manufactured on a limited basis elsewhere, notably in West Germany, and very possibly in the U.S.S.R. and other communist nations from which accurate information is not available.

Recent interest in electric vehicles has led to investigations of new approaches to the manufacture of nickel-iron batteries in the United States and in Europe. These approaches differ sigificantly from the Edison design and are based on sintering, pressing or thin-foil techniques for producing electrodes. Still experimental these designs offer promise of good performance and life; however, the cost of manufacturing may preclude their commercialization.

Silver-zinc and silver-cadmium systems.—The silver-zinc battery is noted for its high energy density, in fact, the highest attainable of any secondary system in use today. It also has a very low internal resistance (matched only by the sintered nickel-cadmium couple) with a very flat voltage discharge characteristic which is desirable in many high-rate applications. Among its shortcomings is the fact that the silver-zinc system has a somewhat limited cycle life, capable normally of less than 200 cycles of discharge and charge with an overall activated life of no more than two years. Most significant among its shortcomings, however, is the high cost of the silver.

Since the United States government removed controls on silver bullion prices in the late 1960's, silver has risen steadily from $1.35/troy ounce to as high as $5/troy ounce. Silver has since leveled off at about $4.50/troy ounce. This high cost of the active silver material, in addition to the high cost of manufacture associated with silver-zinc batteries, because of the preponderance of manual operations resulting from low production demand, has limited application of this system almost entirely to military and aerospace programs where the emphasis is on the performance rather than the economic factor. These include space satellites, missile power, submarine and torpedo pro-

pulsion, and some types of portable military communications.

Silver-zinc cells generally are prismatic in construction with flat parallel plates, using a restricted amount of electrolyte. They also generally make use of a pressure-type vent which permits the escape of gases but prevents continuous entry of the atmosphere.

Silver-zinc cells have silver electrodes with grids or substrates made exclusively of silver in the form of expanded sheet, wire mesh, or perforated silver sheet or, in some cases, made of silver-plated copper. The silver oxide active material is applied as a slurry pasting of fine particles followed by a sintering operation, by pressing the dry material into a grid structure and then sintering, or by incorporating a plastic bonding material with the silver powder particles, pressing this to the grid structure, heating to fire off the plastic, and then sintering.

Zinc electrodes utilize a substrate of either expanded metal, screen or perforated metal either of silver, which is preferred, or of silver-plated copper. The zinc oxide active material is applied as a dry powder and pressed, as a slurry paste which is then dried and pressed, or by a electroforming process in which zinc is deposited from solution.

Typical silver-zinc cells make use of a regenerated cellulose separator (unplasticized cellophane) which, while sufficient, has not been entirely successful. The cellophane is hydrated by the caustic electrolyte and expands. This, in turn, exerts a small internal pressure that helps to restrain the zinc anode material making it less available for dissolution. Since it is hydrated, the cellophane separator also is susceptible to oxidation and degradation which can lead to short circuits between positive and negative electrodes, often made worse by dissolved silver in the electrolyte forming conductive paths through the separators or by penetration of zinc nodules or dendrites.

Several approaches have been used in efforts to extend the life of silver-zinc separators. One is the use of a regenerated cellulose which includes a fibrous material that adds to the strength of the separator. Another is to impregnate the cellulose separator material with a silver salt which helps it to resist degradation.

The requirement of the aerospace program in the late 1960's for a heat sterilizable silver-zinc cell led to the development of an improved separator material. It was found that cellophane would degrade drastically with the application of sterilization temperatures of about 250°C. The new organic-inorganic separator, taken from fuel cell technology, consists of an asbestos mat base impregnated on one side with an organic resin and on the other side with a metal oxide such as zirconia or magnesium oxide. This separator is able to resist the high heat of sterilization and offers good zinc stopping characteristics. It does, however, have a relatively high resistance per layer that limits the system to medium or low rates of discharge. The separator also is expensive to manufacture which further adds to the high cost of the silver-zinc system.

Silver-cadmium.—Historically, the silver-cadmium battery goes back to the beginning of the century when Jungner conceived such a battery to power early electric autos. He soon dropped the idea because of the high cost of silver. The system lay dormant until the late 1950's when interest was revived in the silver-cadmium system as an energy source for appliances and power tools and for scientific satellites. Two factors made the silver-cadmium system promising for these applications: its relatively high energy density and its nonmagnetic property. The latter was particularly a requirement for the satellites which were constructed of nonmagnetic components since they carried magnetometers to measure radiation and the effects of magnetic fields of energetic particles. Also, sealed batteries were required by the satellites. Today the system has a very limited use in special applications which are not expected to increase.

Silver-iron.—Recently the silver-iron secondary system has been introduced in a special telecommunications application. As with the other silver systems, the cost and life considerations are expected to limit this system to very special applications (3).

New systems—The energy crisis that became painfully apparent to the public toward the mid-1970's has spurred an unparalleled interest in the development of new, more advanced secondary battery systems. The quest centers, in particular, on systems for electric road vehicles and electric utility load leveling.

The ubiquitous lead-acid system, despite its commercial dominance and its present (and, quite possibly, foreseeable) state of development, is not ideally suited to these applications. Lead-acid batteries have a low energy density that restricts the operating range of electric road vehicles; present lead-acid designs are too costly to be economically applied to load leveling.

Nevertheless, since the lead-acid system is the only commercially available system which comes close to meeting the load leveling and electric vehicle requirements, there are major development programs based on novel approaches to improving the performance and costs of the lead-acid system for these applications. Thus the potential of the lead-acid battery for these systems cannot be ignored in view of the problem of the new systems discussed below.

Advanced systems currently under study fall into two general groups. One consists of ambient temperature systems that make use of active materials which are stable to water, such as iron, zinc, and nickel, and can be utilized with aqueous electrolytes. The other group includes systems which use alkali metals as active materials that require a nonaqueous electrolyte for room temperature operation, either based on organic solvents or molten salt or ceramic electrolytes, operating at temperatures ranging from 200° to 600°C.

Included among the aqueous electrolyte types are the nickel-zinc, nickel-iron, zinc-air (oxygen), iron-air (oxygen), nickel-hydrogen, silver-hydrogen, and zinc-chlorine systems. The status of development of these systems has been described in some detail in many recent publications. Strictly speaking, the nickel-zinc and nickel-iron systems are not "new" systems; and the recent development programs involve new approaches to resolving old problems. There are many development problems which remain to be resolved before these systems can become significant commercial products.

The metal-air systems are limited in life as a result of the deterioration of the air electrode on the charging part of the cycle. The metal-hydrogen systems seem likely to be limited to space applications until a reliable, low cost method is established for storing hydrogen at low pressure.

The most promising of the aqueous systems for electric vehicles is the nickel-zinc system; however, the tendency of the zinc electrode to densify and to form dendrites has not been solved in the conventional approaches to cell design. A novel approach to cell design which eliminates both the separator and zinc electrode problems by vibrating the zinc electrode during the charging part of the cycle has recently been described (4). The cost of any of the systems using nickel electrodes will depend markedly on developing a high performance electrode with a high ratio of active material to nickel support.

Another aqueous system of promise is the zinc-chlorine system in which the chlorine is stored as a solid in chlorine hydrate (5). Because of the need for refrigeration, separation, and circulation systems, this system appears to be of most interest in large installations such as load leveling and perhaps the larger electric vehicle systems.

The nonaqueous secondary battery systems under development are those which operate at room temperature using an electrolyte dissolved in an organic sol-

vent or which operate at elevated temperatures and use either molten salt or ceramic electrolytes.

The room temperature systems appear likely to be limited to low rate applications in view of the low conductivity of the electrolyte and do not appear to be candidates for either electric vehicles or load leveling. There are several systems under investigation using lithium anodes (6, 7).

The high temperature systems receiving significant development are the lithium-molten salt-metal sulfide system which operates at 450°C (8), the sodium-ceramic electrolyte-sulfur system which operates at 300°-350°C (9), and the sodium ceramic-molten salt-metal chloride system operating at 200°C (10). If problems of seals, life, and scale-up can be resolved and low cost manufacturing methods are developed, these systems can be candidates for the electric vehicle and load-leveling applications.

Conclusion

While the next 25 years are likely to see the introduction of one or more advanced secondary battery systems, the lead-acid battery seems likely to remain the dominant system for most, if not all, of the period.

REFERENCES

1. Burbank, Simon, and Willihnganz, in "Advances in Electrochemistry and Electrochemical Engineering," Vol. 8, Delahay and Tobias, Editors, Wiley-Interscience, New York (1971).
2. Willihnganz, *This Journal*, **99**, 234C (1952).
3. J. T. Brown, "Alkaline Batteries," Westinghouse Research and Development Center, Pittsburgh, Pa. (undated paper).
4. O. von Krusentsierna and M. Reger, SAE Paper No. 770384 (1977).
5. Energy Development Associates, EPRI Project 226-1, Report EPRI-EM-249 (September 1976).
6. M. S. Whittingham, *This Journal*, **123**, 315 (1976).
7. S. B. Brummer *et al.*, Annual Report, NSF Grant AER 75-03779 (1976).
8. P. A. Nelson *et al.*, Argonne National Laboratory, Rept. ANL-77-18 (1977).
9. (a) D. Chatterji, S. P. Mitoff, and M. W. Breiter, "Proceedings of the Symposium on Load Leveling," The Electrochemical Society Softbound Symposium Series, p. 251, Princeton, N.J. (1977). (b) F. A. Ludwig, M. Mikkor, R. W. Minck, and A. Topouzian, *ibid.*, p. 289. (c) C. Levine and J. Anand, *ibid.*, p. 292.
10. W. P. Sholette, I. S. Klein, and J. Werth, *ibid.*, p. 295.

BIBLIOGRAPHY

S. U. Falk and A. J. Salkind, "Alkaline Batteries," Wiley-Interscience, New York (1969).

H. Bode, "Lead-Acid Batteries," Wiley-Interscience, New York (1977).

J. T. Brown, "Alkaline Batteries," Symposium and Workshop on Advanced Battery Research and Design, ANL 76-8 (1976).

A. J. Salkind and E. Pearlman, "Secondary Cells—Alkaline," *Encyclopedia of Chemical Technology* (1977).

J. H. B. George, "The World Battery Industry—A Multiclient Study," Arthur D. Little, Inc. (1976).

JOURNAL OF THE ELECTROCHEMICAL SOCIETY

ELECTROCHEMICAL SCIENCE
AND TECHNOLOGY

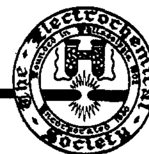

SEPTEMBER
1978

Electrodic Phenomena at the Anode of the Totally Illuminated, Thin Layer Iron-Thionine Photogalvanic Cell

D. E. Hall*

International Nickel Company, INCO Research and Development Center, Sterling Forest, Suffern, New York 10901

and P. D. Wildes and N. N. Lichtin*

Department of Chemistry, Boston University, Boston, Massachusetts 01125

ABSTRACT

Properties of Corning thin-film SnO_2 electrodes in contact with 0.005-0.5*M* solutions of sulfuric acid in aqueous solvents containing 0-50 v/o CH_3CN were characterized. Schottky-Mott plots gave flatband potentials (E_{FB}) in the range 0-0.2V *vs.* SCE and charge carrier densities in the range 4-7 $\times$ 10^{20} cm^{-3} in 0.01*M* sulfuric acid, independent of solvent composition. Standard reduction potentials *vs.* SCE in 0.01*M* acid at room temperature were calculated from equilibrium compositions to be −0.04V for $TH^+/\cdot TH_2^+$, 0.33V for $\cdot TH_2^+/TH_4^{2+}$ and 0.14V for TH^+/TH_4^{2+} in water and −0.06V for $TH^+/\cdot TH_2^+$, 0.28V for $\cdot TH_2^+/TH_4^{2+}$ and 0.11V for TH^+/TH_4^{2+} in 50 v/v/o aq. CH_3CN. Voltammetric data show that establishment of protonic equilibrium is rapid compared with cathodic reduction of TH^+ at SnO_2 in water and in 50 v/o aq. CH_3CN. In contrast, protonic equilibration between the two electron-transfer steps is slow for thionine-1-sulfonic acid. Voltammetric data show that reduction of TH^+ and oxidation of TH_4^{2+} are kinetically controlled at both SnO_2 and Pt electrodes with reversibility greater at platinum than at SnO_2. Reversibility is slightly reduced by addition of CH_3CN to the solvent. Rectification (inhibition of oxidation of TH_4^{2+}) is not severe enough to prevent the use of SnO_2 as a selective anode but may reduce efficiency of photogalvanic conversion. Weak but persistent adsorption of TH^+ on SnO_2 activates photogalvanic conversion. Adsorption of TH_4^{2+} varied considerably from sample to sample of SnO_2 and was strong in some cases. Both oxidation and reduction of the Fe^{+3}/Fe^{+2} couple are much less reversible at SnO_2 than at Pt. Rectification (inhibition of oxidation of Fe^{2+}) is pronounced. Both oxidation and reduction on SnO_2 become more reversible with increasing fraction of CH_3CN; the major effect is enhancement of oxidation of Fe^{2+} but even with 50 v/o CH_3CN the couple is much less reversible than at Pt. Implications of the data with respect to efficiency of totally illuminated thin-layer iron-thionine photogalvanic cells are discussed.

A totally illuminated, thin layer iron-thionine photogalvanic cell has been described in recent publications (1-3). It differs from many other photoelectrochemical cells, which are essentially solid-liquid junction photovoltaic cells (4), because light is absorbed by solution species, initiating a photoredox reaction which produces high energy products. The energy conversion process is reversible, in the sense that the electrode reactions reform the photoredox reactants. Thus, the cell can be operated continuously.

The photogalvanic cell anode is a large bandgap n-type semiconductor with a high charge carrier density, which is transparent to the excitation radiation. Tin oxide is commonly used (1-3, 5), although highly reduced TiO_2 thin films have also proved suitable (6). As discussed in an earlier paper (1), the two photogalvanic cell couples discharge at the semiconductor electrode at widely differing rates. Consequently, under illumination a photopotential is established with respect to a metallic cathode.

* Electrochemical Society Active Member.

Key words: photogalvanic, iron-thionine, electrodic, SnO_2.

Other means of establishing a photopotential difference between photogalvanic cell electrodes may be used. The earliest method (7, 8) involved illuminating only one electrode. The photopotential was thus a result of the difference in electrochemical potentials of the redox components at the two electrodes. A theoretical analysis for this type of cell has recently appeared (9). Gomer (10) has suggested that efficient operation of the cell should be achieved if the cell contains a membrane impermeable to one of the photochemically produced species, *e.g.*, allowing transfer of small inorganic cations but not of large dye molecules. Efficiency should be improved if a second membrane of opposite permeability is also used. However, the development of cells with suitable membranes has not been reported in the literature. Indeed, as Gomer points out, such an approach presents formidable technical problems. The selective semiconductor anode, while not without problems, is an effective and simple way to establish a potential difference in the iron-thionine cell. To date, it has produced the best energy

conversion efficiencies (1, 2) and also allows the design of simple, area-type cells.

Many aspects of thin layer cell performance can be related to the unique properties of the thin film semiconductor anode. The present paper, therefore, examines the electrodic phenomena in more detail. The electrode reactions of the thionine/leucothionine couple at SnO_2 are described. Additionally, the adsorption of dye species at the SnO_2 anode and consequent activation of thin layer cells is reported for the first time. The importance of solvent effects on the electrode reactions of thionine/leucothionine and Fe^{+2}/Fe^{+3} is discussed, and it is shown that when mixtures of acetonitrile and water are used as solvent, anode selectivity is highly dependent on the proportion of acetonitrile present in the photogalvanic cell electrolyte. Another publication currently in press reports the relationship of photostationary state solution composition and electrode phenomena to detailed current and potential measurements for iron-thionine cells and half-cells.

Experimental

Thionine was obtained as thionine acetate (99% purity, MCB) and was used without further purification or was converted to the free base form from the chloride salt and purified by recrystallization. Thionine-1-sulfonic acid was synthesized using the method of Havemann *et al.* (11). The dye content of solutions was analyzed spectroscopically. Reagent grade $FeSO_4 \cdot 7H_2O$ and $Fe_2(SO_4)_3 \cdot 9H_2O$ were used without further purification, and acetonitrile was u.v. grade, distilled in glass (Burdick and Jackson Laboratories).

Tin oxide (SnO_2) thin film electrodes on low alkali glass substrates were obtained from Corning Glass Works. These were cut to approximately 1×2 cm for electrochemical measurements. The active electrode area (≤ 1 cm^2) was obtained by masking off the remainder of the SnO_2 film with silicone rubber or pressure-fit Teflon masks. Electrical connections were made to the masked area of the electrode using conductive silver paint. Before using the SnO_2 electrodes to investigate electrode processes in the iron-thionine cell, several of them were characterized as follows. The flatband potential and charge carrier density were determined from capacitance *vs.* potential data, which were used to construct Schottky-Mott plots ($1/C^2$ *vs.* E) (12). The best straight-line fit was obtained by computer. The flatband potentials (E_{FB}) of the SnO_2 electrodes in $10^{-2}M$ H_2SO_4 varied from sample to sample, but were all near -0.1 to $-0.2V$ *vs.* SCE. This is, as expected, somewhat negative of E_{FB} values reported for SnO_2 with lower charge carrier densities (12), but positive of values recently obtained (13) for highly conducting SnO_2 films similar to those used in the present study. Charge carrier densities were mostly in the range $4\text{-}7 \times 10^{20}$ cm^{-3}. The values obtained were not greatly affected by addition of acetonitrile to the electrolyte.

The counterelectrode was a large platinum mesh and the reference electrode was a commercial saturated calomel electrode, against which all potentials are reported. The SCE was separated from the working solution compartment by a short salt bridge.

Current *vs.* potential measurements were made using a PAR Model 170 electrochemistry system. The internal resistance of the SnO_2 electrodes caused some distortion of voltammetric waves, giving erroneous results at the higher scan rates used. Accordingly, the feedback circuitry of Model 170 was used to compensate for ohmic losses where necessary in the data reported below. Photogalvanic cell short-circuit currents and open-circuit voltages were measured using the apparatus and methods described previously (1, 2). The photogalvanic cell assembly and solutions have also been described (1, 2).

Reactions of Thionine/Leucothionine at SnO_2

The equilibrium potential of the thionine/leucothionine (TH^+/TH_4^{+2}) [1] couple depends on solution pH. In acid media, the two-step reduction of thionine to leucothionine proceeds through a one-electron intermediate (semithionine, $\cdot TH_2^+$) and hydrogen ions are incorporated into the molecule. In neat water as solvent the equilibrium electrode potential fits Eq. [1] (14)

$$E_T = 0.321 - 0.09\,pH + 0.03 \log \frac{[TH^+]}{[TH_4^{+2}]} \quad [1]$$

The pH dependence has been explained in terms of the acid-base equilibria which obtain. We have found (14a) that in 50 v/v percent (v/v/o) acetonitrile/water in the pH range 1-3, $E^\circ = 0.321$ is replaced in Eq. [1] by $E^\circ = 0.29$.

The potential for each reaction step ($TH^+/\cdot TH_2^+$ and $\cdot TH_2^+/TH_4^{+2}$) can be determined if the equilibrium concentrations of TH^+, $\cdot TH_2^+$, and TH_4^{+2} are known. The case in which Fe^{+2}/Fe^{+3} is not present is considered to eliminate alternate pathways of converting one dye form to another via redox reactions with Fe^{+2}/Fe^{+3}. The equilibrium concentrations are obtained by considering the disproportionation of semithionine and the reverse process. At equilibrium, therefore

$$[\cdot TH_2^+]^2[H^+] = \frac{k_{-d}}{2k_d}[TH^+][TH_4^{+2}] \quad [2]$$

where k_d is the rate constant for disproportionation and k_{-d} is the rate constant for the reverse reaction. In aqueous sulfuric acid at $pH = 2.0$ the rate constants are $k_d = 1.0 \times 10^9$ M^{-1} sec^{-1} and $k_{-d}/[H^+] = 1.2 \pm 0.4 \times 10^3$ M^{-1} sec^{-1} (14a). In 50 v/v/o acetonitrile/water with $0.01M$ sulfuric acid, the solvent composition of recently reported photogalvanic cells (1, 2), we have found $k_d = 1.4 \times 10^8$ M^{-1} sec^{-1} and $k_{-d}/[H^+] = 7.5 \pm 2.5 \times 10^2$ M^{-1} sec^{-1} (10a). Inserting these values in Eq. [2] for an initial dye concentration of $10^{-3}M$ and 50% bleaching, the concentrations of the three dye species in water at pH 2 are $[TH_4^{2+}] = 5 \times 10^{-4}M$, $[\cdot TH_2^+] = 3.9 \times 10^{-7}M$, and $[TH_4^{2+}] = 5 \times 10^{-4}M$ while in 50 v/v/o acetonitrile/water at pH 2 $[TH^+] = 5 \times 10^{-4}M$, $[\cdot TH_2^+] = 8.2 \times 10^{-7}M$, and $[TH_4^{2+}] = 5 \times 10^{-4}M$. Thus almost all of the dye exists in either the totally oxidized or totally reduced forms.

The potentials for each of the reaction steps are

$$E_1' = E_1^{\circ\prime} + \frac{RT}{F} \ln \frac{[TH^+][H^+]}{[\cdot TH_2^+]} \quad [3]$$

$$E_2' = E_2^{\circ\prime} + \frac{RT}{F} \ln \frac{[\cdot TH_2^+][H^+]^2}{[TH_4^{+2}]} \quad [4]$$

where E_1' is the pH-dependent equilibrium potential of the first reaction step, etc. Combining [3] and [4] gives

$$E_1^{\circ\prime} - E_2^{\circ\prime} = (E_1' - E_2') + \frac{RT}{F} \ln \frac{[\cdot TH_2^+]^2[H^+]}{[TH^+][TH_4^{+2}]} \quad [5]$$

and at equilibrium, $E_1' = E_2'$. A similar treatment was used by Memming and Möllers for the quinone/hydroquinone system (15). Inserting the calculated concentrations of TH^+, $\cdot TH_2^+$, and TH_4^{2+} into Eq. [5] for the equilibrium condition at pH 2 gives $E_2^{\circ\prime} - E_1^{\circ\prime} = 0.37V$ in water and $E_2^{\circ\prime} - E_1^{\circ\prime} = 0.33V$ in 50 v/v/o acetonitrile/water. The value in water is substantially larger than an earlier estimate of 0.14V based on then-available solution kinetic data (16). The potential $E_T^{\circ\prime}$ for the TH^+/TH_4^+ couple is the average of the potentials for each step, $E_T^{\circ\prime} = (E_1^{\circ\prime} + E_2^{\circ\prime})/2$. Table I

[1] The symbol TH_3^+ has been used for leucothionine in earlier work (2) to represent a general protonated form of leucothionine in acidic media. However, in the following discussion it is necessary to consider that form of leucothionine predominating in the pH range 0-3.

Table I. Standard reduction potentials of redox states of thionine in water and in 50 v/v/o acetonitrile/water at *p*H 2 and room temperature

Redox couple	$E°'$ *vs.* SCE in water (V)	$E°'$ *vs.* SCE in 50 v/v/o CH_3CN/H_2O (V)
$E_T°'$, TH^+/TH_4^{2+}	0.142	0.110
$E_1°'$, $TH^+/\cdot TH_2^+$	−0.04	−0.06
$E_2°'$, $\cdot TH_2^+/TH_4^{2+}$	0.33	0.28

Table II. Variation of $i_{p,c}/v^{1/2}$ with sweep rate for thionine reduction at SnO_2 electrodes* in aqueous acetonitrile solutions**

v (mV sec^{-1})	$i_{p,c}/v^{1/2}$ in		
	0% CH_3CN†	20% CH_3CN†	50% CH_3CN†
10	0.81	0.79	0.82
50	0.82	0.84	0.83
200	0.90	0.85	0.83
500	1.10	0.94	0.92

* $n_D = 7.2 \times 10^{20}$ cm^{-3}, $E_{FB} = -0.16$V *vs.* SCE.
** Solutions contained $2.6 \times 10^{-5}M$ thionine acetate and 0.5*M* sulfuric acid.
† Volume percent CH_3CN in water.

summarizes values of $E_T°'$, $E_1°'$, and $E_2°'$ calculated from the data at *p*H 2. These potentials are compared to E_{FB} for SnO_2 in Fig. 1.

Protons are incorporated into the molecule during reduction, *i.e.*, the heterogeneous redox reactions involve electron transfers coupled with chemical steps. The protonations represent possible limitations in electrode reaction rate. For an ECE mechanism with a slow chemical step, for example, the function $i_{p,c}/v^{1/2}$, in which $i_{p,c}$ is the cathodic peak current and v is the potential sweep rate, decreases with increasing sweep rate (17). Table II shows that $i_{p,c}/v^{1/2}$ for thionine in acid media at SnO_2 increases with sweep rate, for reasons which are discussed below. Also the distinctive morphology of cyclic sweeps for E-slow C-E mechanisms with highly positive $\Delta E°$ was never observed, even when sweeps were extended >0.6V positive of the anodic peak. Rapid establishment of proton equilibria is also found in similar systems, *e.g.*, methylene blue (18) and quinone/hydroquinone (19).

Thus, the electrochemistry of thionine/leucothionine in protic solvents is, as expected, similar to that reported for methylene blue (18). In both cases, the reaction proceeds through an intermediate, with $E_2°'$ more positive than $E_1°'$. Under the conditions studied, $\Delta E°' = (E_2°' - E_1°')$ is considerably higher for thionine than for methylene blue (18) and hence the intermediate concentration is much lower. The proton exchanges are very rapid, so that the process can be described in terms of the E-E mechanism (20). The electron transfers for methylene blue at Pt are reversible. However, the reduction of thionine and the oxidation of leucothionine at Pt and SnO_2 electrodes are kinetically controlled. The anodic and cathodic waves are broader than reversible waves and there is a steady positive shift of $E_{p,a}$ and a negative shift of $E_{p,c}$ as the sweep rate is increased from 2 to 500 mV sec^{-1}.

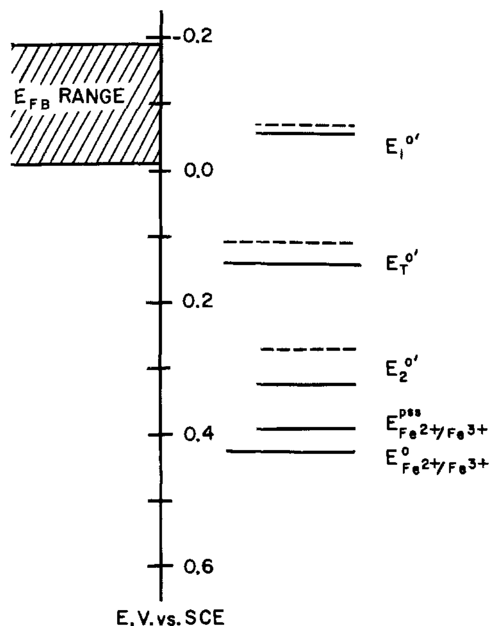

Fig. 1. Electron energy levels at the SnO_2 anode in the iron-thionine photogalvanic cell at *p*H 2. Solid lines, aqueous H_2SO_4; dashed lines, H_2SO_4, 50 v/v/o water/acetonitrile.

The voltammetry of thionine/leucothionine was examined in H_2SO_4 concentrations ranging from 5×10^{-3} to 0.5*M*, with CH_3CN present from 0 to 50 volume percent (v/o). In all cases, behavior was similar to that described above. The observed effect of changing [H_2SO_4] was a shift of the entire current-potential curve to more negative potentials with increasing *p*H, as predicted by Eq. [1]. The effects of acetonitrile are discussed below.

The thionine/leucothionine electrode reactions are less reversible at SnO_2 than at platinum, as seen from the greater shifts of $E_{p,c}$ and $E_{p,a}$ as a function of sweep rate (Table III). The potentials of dye couple reduction and oxidation waves (Fig. 2) *vs.* E_{FB} for SnO_2 are such that both processes are subject to tunneling limitations (21). Some degree of rectification is expected at SnO_2, because reduced states of the dye lie further below E_{FB} than oxidized states and, hence, overlap less favorably with the conduction band. The greater shift of $E_{p,a}$ than $E_{p,c}$ in Table III shows that the oxidation process is indeed more strongly affected by SnO_2. Since the anode reaction in the iron-thionine thin layer cell is leucothionine oxidation at SnO_2, the fact that rectification is not severe is critical to successful operation of the device. Ideally, a better match of the dye couple to the semiconductor conduction band would result in greater reversibility and the elimination of a possible efficiency loss at the photogalvanic cell anode.

The most efficient iron-thionine cells have used an aqueous sulfuric acid electrolyte with up to 50% acetonitrile by volume (1-2). Accordingly, cyclic potential sweeps were performed in aqueous H_2SO_4 containing 0, 20, and 50% acetonitrile to determine its effect on the reactions of thionine/leucothionine at SnO_2. A slight decrease in reversibility was noted as the fraction of acetonitrile was increased (Fig. 2). To determine whether the decrease in reversibility was perhaps caused by a negative E_{FB} shift associated with the presence of acetonitrile, E_{FB} was determined for SnO_2 electrodes in aqueous sulfuric acid solutions containing 0 and 50% CH_3CN. No significant shift in E_{FB} was seen. Thus, the decreased reversibility is apparently caused by the influence of CH_3CN on the properties of the dye couple.

The behavior of thionine-1-sulfonic acid illustrates the effect of poor dye reaction characteristics at SnO_2

Table III. Variation in peak potentials (mV vs. SCE) with sweep rate at SnO_2 and Pt electrodes

Sweep rate (mV sec^{-1})	Pt*		SnO_2†	
	$E_{p,c}$	$E_{p,a}$	$E_{p,c}$	$E_{p,a}$
2	207	237	—	—
10	—	—	165	260
50	—	—	150	295
100	200	245	—	—
200	193	246	135	342
500	182	250	115	365

* [TH^+] = $4.2 \times 10^{-4}M$, [H_2SO_4] = 0.5*M*, 50% CH_3CN.
† [TH^+] = $2.6 \times 10^{-5}M$, [H_2SO_4] = 0.5*M*, 50% CH_3CN.
Electrode: $E_{FB} = -0.16$V, $n_D = 7.2 \times 10^{20}$ cm^{-3}.

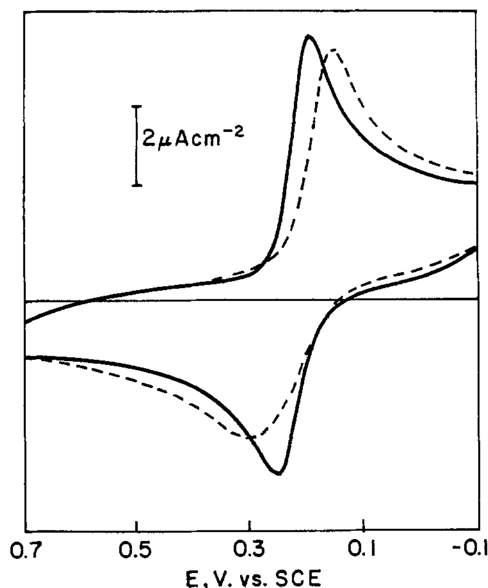

Fig. 2. Voltammetry of thionine acetate ($2.6 \times 10^{-5}M$) at SnO_2($n_D = 7.2 \times 10^{20}$ cm^{-3}, $E_{FB} = -0.16V$ vs. SCE). Sweep rate = 50 mV sec^{-1}. Solid line, aqueous 0.5M H_2SO_4; dashed line, 0.5M H_2SO_4, 50 v/v/o water/acetonitrile.

on thin layer cell performance. Although a previous investigation established that photochemical redox activity was similar to thionine (22), photogalvanic cells containing the sulfonic acid derivative produced much lower response. In identical aqueous cells ($10^{-2}M$ H_2SO_4 electrolyte), thionine produced open-circuit voltages of ~140 mV, while thionine-1-sulfonic acid gave V_{oc} ~75 mV. The difference was more pronounced in mixed solvent cells ($10^{-2}M$ H_2SO_4, 50% CH_3CN) in which V_{oc} ~150 mV for thionine and V_{oc} ~20 mV for thionine-1-sulfonic acid. Correspondingly lower short-circuit currents were also obtained with the sulfonic acid derivative in both cases. The explanation for reduced photogalvanic response is obtained from the cyclic voltammetry of thionine-1-sulfonic acid at SnO_2 (Fig. 3). The oxidation of leucothionine-1-sulfonic acid occurs via two well-separated waves, the second of which is very positive. This behavior is more pronounced in the presence of 50% CH_3CN, corresponding to the very low open-circuit voltages obtained in the mixed solvent photogalvanic cells. Peak potential shifts *vs.* sweep rate for the cathodic and first anodic waves were slightly greater than those of thionine/leucothionine. However, the positive shift of the second anodic peak was much greater, increasing as the fraction of CH_3CN in the electrolyte increased. The quantity $i_{p,c}/v^{1/2}$ decreased as the sweep rate increased, characteristic of a slow chemical step between charge transfer. Thionine-1-sulfonic acid is thus a poor candidate for the thin layer photogalvanic cell because of activation overpotential limitations.

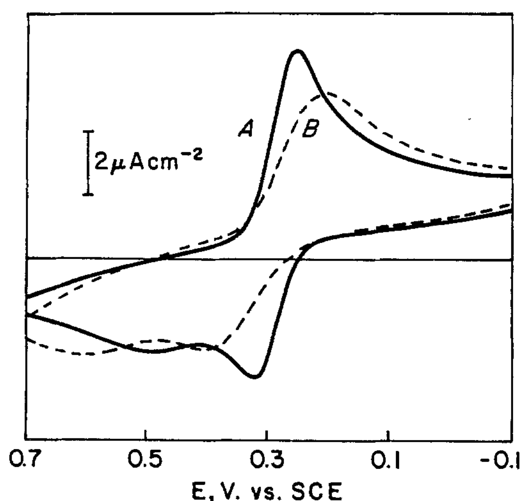

Fig. 3. Voltammetry of thionine-1-sulfonic acid ($1.1 \times 10^{-5}M$) at SnO_2. Sweep rate = 50 mV sec^{-1}. Solid line, aqueous 0.5M H_2SO_4; dashed line, 0.5M H_2SO_4, 50 v/v/o water/acetonitrile.

Reactions of Fe^{+2}/Fe^{+3} at SnO_2 in Photogalvanic Cell Electrolytes

The potentials of Fe^{+2}/Fe^{+3} in various acid electrolytes were measured by Miller (7) as part of an investigation of the limitations of the iron-thionine cell photopotential. Miller reported $E° = 0.426V$ *vs.* SCE for Fe^{+2}/Fe^{+3} in aqueous sulfuric acid. The anion concentration was reported to be not critical.

In the thin layer photogalvanic cell, the initial concentrations of Fe^{+2} and Fe^{+3} are typically 10^{-2} and $5 \times 10^{-4}M$, respectively. In a cell containing 1 mmole thionine which is 50% bleached under illumination, the photostationary state concentrations are $[Fe^{+2}]_{pss} = 9 \times 10^{-3}M$ and $[Fe^{+3}]_{pss} = 1.5 \times 10^{-3}M$. Using these concentrations, the photostationary state Fe^{+2}/Fe^{+3} potential is $E^{pss} = 0.39V$ *vs.* SCE (10a). This is very close to the 0.385V observed at the thin layer cell cathode in the photostationary state (1). A more rigorous study of the relationship between the photostationary state and half-cell potentials in the iron-thionine cell will be reported in a subsequent publication (23). The equilibrium and photostationary state potentials for Fe^{+2}/Fe^{+3} are compared to the dye couple potentials and E_{FB} for SnO_2 in Fig. 1.

A high degree of rectification for the Fe^{+2}/Fe^{+3} reactions at SnO_2 was found by Memming and Möllers (24). This was particularly true at lower SnO_2 charge carrier densities where the oxidation of Fe^{+2} was suppressed due to low tunneling probability. Raising the charge carrier density caused an increase in anodic current as the space charge layer became thinner and hence more penetrable to tunneling electrons. However, even at the highest charge carrier densities investigated (~5×10^{19} cm^{-3}) rectification was significant.

The present work with SnO_2 electrodes with high charge carrier density has shown that similar behavior is observed even at $n_D > 5 \times 10^{20}$ cm^{-3}. This result is consistent with the fact that tunneling probability changes less rapidly with n_D as the charge carrier density becomes large (21). Limiting anodic currents were eventually obtained in slow positive potential scans, but the current rise with departure from equilibrium was much more drawn out than for the cathodic process (Fig. 4, curve A). The effect of acetonitrile on the Fe^{+2}/Fe^{+3} reactions at SnO_2 is much greater than on thionine/leucothionine, and oppositely directed. A marked increase in reversibility was observed as the fraction of CH_3CN in the solvent was raised from 0 to 50% in 10% increments. Results for solutions containing 0, 20, and 40% CH_3CN are presented in Fig. 4. Both the oxidation and reduction became more reversible, but the major effect was a strong enhancement of the Fe^{+2} oxidation. A curious feature which emerged from the current-potential curves at SnO_2 electrodes with high charge carrier density was the structure of the anodic wave when CH_3CN was present. A well-defined reproducible current peak was observed to shift to more negative potentials with increasing acetonitrile content. Peak potentials are listed in Table IV. No attempt was made to explain the presence of current peaks or the wave structure in the limiting current region.

The cyclic voltammetry of Fe^{+2}/Fe^{+3} (Fig. 5) for solutions containing 0 and 50% CH_3CN also shows enhanced Fe^{+2} oxidation in the latter solvent, as seen from the large negative shift of $E_{p,a}$ and the large increase in anodic current. In addition, the ratio of

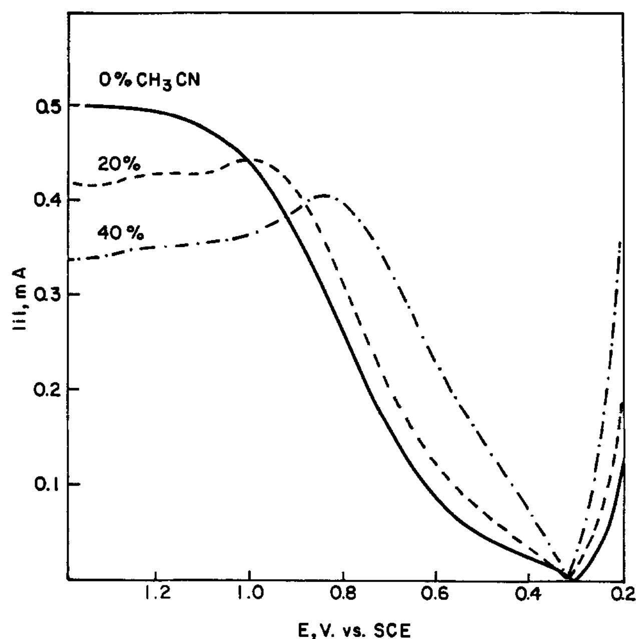

Fig. 4. Effect of fraction of acetonitrile in solvent on current vs. potential behavior of Fe^{2+}/Fe^{3+} at SnO_2. $[Fe^{+2}] = [Fe^{+3}] = 0.05M$; $[H_2SO_4] = 0.5M$; 0, 20, and 40 v/v/o acetonitrile/water. Sweep rate = 5 mV sec^{-1}.

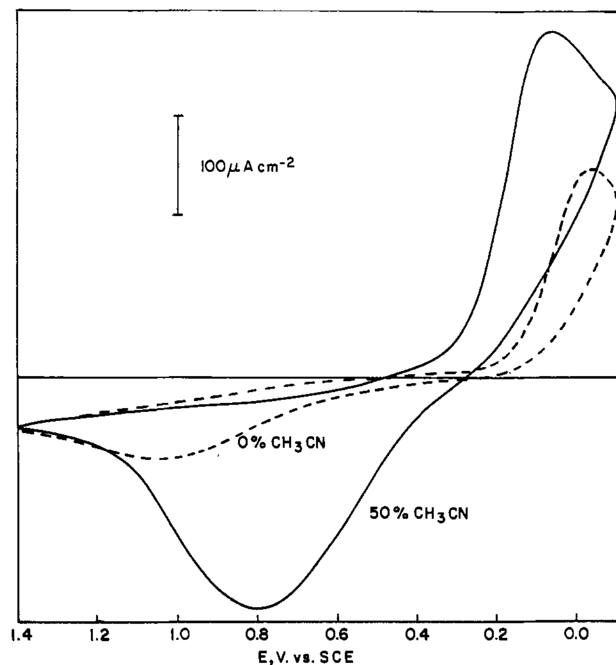

Fig. 5. Voltammetry of Fe^{2+}/Fe^{3+} at SnO_2, showing effect of fraction of acetonitrile in solvent. $[Fe^{2+}] = [Fe^{3+}] = 10^{-3}M$; $[H_2SO_4] = 0.5M$. SnO_2: $n_D = 7.4 \times 10^{20}$ cm^{-3}, $E_{FB} = -0.07V$ vs. SCE.

anodic to cathodic peak current increased as the fraction of CH_3CN in the solvent was raised. As with the slow scan current-potential curves, a smaller effect was also noted for the reduction wave. Even in 50% CH_3CN, however, the couple is much less reversible than at platinum electrodes, hence, considerable anode selectivity in the thin layer cell is still preserved.

In an earlier study, Miller (7) reported electrode activation in the iron-thionine cell, *i.e.*, prior exposure of platinum electrodes to thionine solution, increased photovoltages from those electrodes. Furthermore, the activation persisted even after the electrodes were washed and dried several times. Miller proposed that a layer of dye adsorbed on the electrode either enhanced leucothionine oxidation or suppressed the reaction of Fe^{+3}. A detailed study of dye adsorption was not made, however. It was also reported that activated electrodes were not able to generate a photopotential when exposed to an acidic solution of Fe^{+2} reducing agent.

Table IV. Peak potentials for Fe^{+2} oxidation at SnO_2

% CH_3CN	Potential of current peak (V *vs.* SCE)
0	No peak
10	1.08*
20	1.01
30	0.90
40	0.84
50	0.79

* Current was erratic near peak.
$[Fe^{+2}] = [Fe^{+3}] = 0.05M$, $[H_2SO_4] = 0.5M$.
SnO_2: $E_{FB} = -0.26V$, $n_D = 9.2 \times 10^{20}$ cm^{-3}, $A = 0.60$ cm^2.

Similar activation has been observed at SnO_2 electrodes in the iron-thionine thin layer cell. The possibility of markedly increasing the concentration of electroactive material in the vicinity of the anode, and thereby the efficiency of the thin layer cell, was pursued through a more detailed study of the adsorption of dye species at SnO_2. Evidence for the weak adsorption of thionine at SnO_2 is obtained from the increase of $i_{p,c}/v^{1/2}$ with sweep rate shown in Table II. This is consistent with thionine adsorption with a low free energy and its reduction in the same potential range as thionine from the bulk solution. The peak current function ($\alpha i_{p,c}/v^{1/2}$) is thus larger than predicted from diffusion limitations and increases with sweep rate due to the larger fraction of adsorbed dye participating in the reaction (25). The quantity of adsorbed thionine at equal bulk concentrations increases as the fraction of CH_3CN in the electrolyte is decreased, as shown in Table II by the greater increase in $i_{p,c}/v^{1/2}$. This is expected, because the addition of acetonitrile increases thionine solubility considerably.

Strong leucothionine adsorption occurred at some SnO_2 electrodes. A cathodic prewave (often poorly defined) was observed on negative potential sweeps (Fig. 6). A corresponding rise in anodic current positive of the principal oxidation wave was also observed on the reverse sweep. Adsorption peaks were greatly affected by the particular SnO_2 electrode used. Electrodes with nearly identical E_{FB} and n_D frequently showed large differences in leucothionine adsorption. The wide variation in leucothionine adsorption under thin layer cell conditions may explain the nearly two-

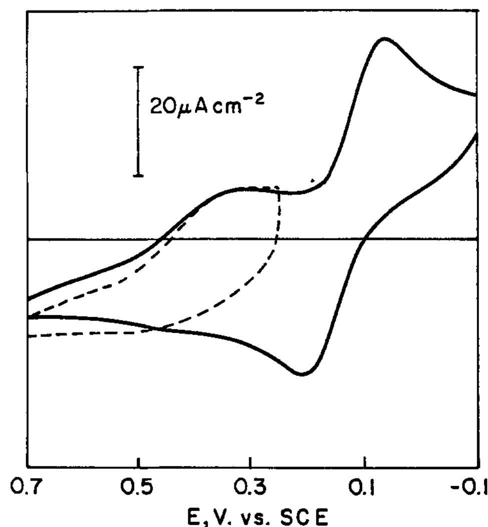

Fig. 6. Voltammetry of thionine acetate ($1.1 \times 10^{-4}M$) at SnO_2, showing strong adsorption of leucothionine. Sweep rate = 100 mV sec^{-1}. $5 \times 10^{-3}M$ H_2SO_4, 50 v/v/o water/acetonitrile.

fold variation in short-circuit current obtained from seemingly similar SnO_2 anodes (2).

Miller's observation (7) that platinum electrode activation persists is also true of SnO_2 electrodes. The adsorbed dye is very resistant to removal by water and a large portion survives washing with organic solvents such as isopropanol. This is shown in Fig. 7. After prolonged exposure to thionine solution, an SnO_2 electrode showed an increase in reversibility and peak current (curves A and B) which is characteristically obtained when a new hydrophobic SnO_2 electrode is wet by the solution (26). Part of the peak current increase can likely be ascribed to thionine adsorption. In addition, a prewave indicating strong leucothionine adsorption was obtained. The electrode was then removed from the solution, washed with isopropanol, and replaced in solution. Taken immediately following re-insertion, curve C shows that much of the adsorbed dye was retained. In a similar experiment, the washed electrode was inserted into electrolyte containing no thionine. At slow sweep rates, small reduction and oxidation waves of retained adsorbed dye were clearly seen.

The contribution of adsorbed dye to iron-thionine cell photogalvanic activity was substantiated in the following way. Three thin layer cells were constructed with new (previously unused) SnO_2 anodes. Initial measurements of V_{oc} and I_{sc} were made, exposing the SnO_2 electrodes to the photogalvanic cell solution for the minimum time necessary for steady-state outputs. The SnO_2 anodes were then removed and cleaned. One electrode was soaked in the photogalvanic solution, while a second was soaked in a similar solution containing no dye. The third electrode was soaked in distilled water. After 24 hr, the electrodes were dried and used to obtain new measurements of V_{oc} and I_{sc}. Electrodes 2 and 3 showed small ($<3\%$) increases in V_{oc} and I_{sc}, presumably due to increased wetting of the SnO_2 surface. Electrode 1, soaked in dye solution, showed much greater enhancement of photogalvanic activity. A 10% increase in V_{oc} and a 20% increase in I_{sc} were obtained.

In a second experiment, a tin oxide anode was used to make a preliminary measurement of V_{oc} and I_{sc} after prolonged exposure to photogalvanic solution (Table V). The cell was then taken apart, cleaned thoroughly with distilled water, and blotted dry. The cell was reassembled and filled with a photogalvanic blank solution, containing all components except thionine. As Table V shows, a photogalvanic response was obtained and furthermore, persisted over the course of the measurement (~5 min). The cell was then drained, dried, and filled again with blank solution. A smaller but still noticeable photogalvanic response was measured. These data are consistent with the retention of adsorbed thionine at SnO_2 reported above. Miller's observation that activated Pt electrodes were unable to generate a photogalvanic response by themselves is thus not supported by results with SnO_2 electrodes.

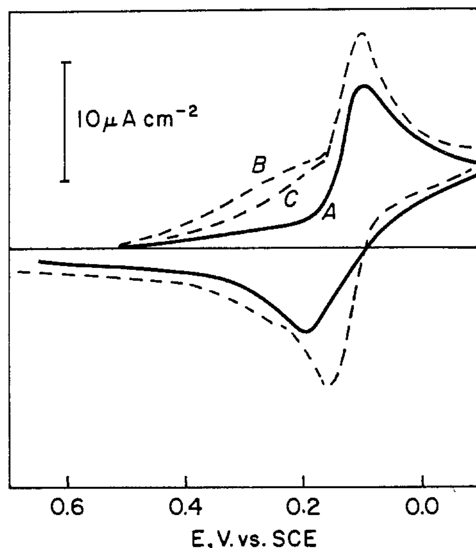

Fig. 7. Voltammetry of thionine acetate ($1.1 \times 10^{-4}M$) at SnO_2, showing activation and adsorption of leucothionine. Sweep rate = 20 mV sec^{-1}. A, New SnO_2; B, SnO_2 electrode from A, after prolonged exposure to dye solution; C, SnO_2 electrode from B, after isopropanol wash.

Table V. Output of photogalvanic cells showing influence of dye adsorption

Cell solution	V_{oc} (V)	I_{sc} (μA)
Photogalvanic*	0.102	320
Blank†	0.021	25
Blank, repeat	0.004	5

* $10^{-3}M$ thionine, $10^{-2}M$ H_2SO_4, $10^{-2}M$ $FeSO_4$, Fe^{+3} as impurity, 50 v/v/o CH_3CN.
† Photogalvanic solution without thionine.
Cell area = 5.5 cm^2. Illumination: tungsten, 35 mW cm^{-2} solar equivalent.

In several of the highest output thin layer cells, the photovoltage was established rapidly but I_{sc} rose slowly for 1-2 min or more, frequently to double the initial value. The current rise is much too slow to be ascribed to photochemical kinetics (27) and is not likely due to establishment of steady-state concentration gradients by diffusion, because most cells reached steady-state within a few seconds. It is possible that the current rise is caused by slow formation of the adsorbed dye layer at certain SnO_2 electrodes, as discussed above.

A film of adsorbed dye provides charge transfer species localized at the anode, which can be photochemically reduced and electrochemically oxidized without appreciable bulk motion. In addition, a more subtle effect is probably also present. For anodic band bending, the transition probability for tunneling depends not only on the band bending and energy positions of the donor electrons, but also on electronic coupling between the electrode surface and redox species. Thus, tunneling currents for the dye species should be enhanced relative to those for Fe^{+2}/Fe^{+3}. This factor operates in addition to those causes of selectivity which have been discussed previously (1, 2).

The use of aqueous acetonitrile in the thin layer cell may appear questionable on the basis of the results presented here. However, addition of acetonitrile prevents formation of photoinactive thionine dimers and increases the solubility of thionine, and hence the number of charge carriers in solution can be greatly increased. Enhancement of the efficiency of photochemical reduction of TH^+ by Fe^{+2} in bulk solution is also observed (27). The net result of using solvents containing CH_3CN is an increased cell efficiency arising almost entirely from greater current flow.

The most obvious factor determining the reversibility of the iron-thionine cell redox processes at SnO_2 is $E_{FB} - E_{redox}$. The redox potential difference between the dye and Fe^{+2}/Fe^{+3} couples is not large, however, and other redox couple pairs with similar potential separations and relationships to E_{FB} show smaller differences in reversibility at SnO_2 electrodes, even when n_D is much lower. The couple $Fe(CN)_6^{-4}$/$Fe(CN)_6^{-3}$, for example, has a redox potential nearly equal to Fe^{+2}/Fe^{+3} in sulfuric acid but is considerably more reversible at SnO_2 (24). The contribution of the large Fe^{+2}/Fe^{+3} rearrangement energy to the SnO_2 anode selectivity has been pointed out in previous publications (1, 2).

Acknowledgment

This research was performed under Grant No. SE/AER/72-03579 of the National Science Foundation's

Research Applied to National Needs Program. The role of Dale E. Hall in the preparation of this manuscript was made possible by the INCO Creative Research Program. This work was done at Solar Energy Conversion Unit, Exxon Research and Engineering Company, Linden, New Jersey 07036.

Manuscript received Nov. 10, 1977.

Any discussion of this paper will appear in a Discussion Section to be published in the June 1979 JOURNAL. All discussions for the June 1979 Discussion Section should be submitted by Feb. 1, 1979.

Publication costs of this article were assisted by Boston University.

REFERENCES

1. D. E. Hall, J. A. Eckert, N. N. Lichtin, and P. D. Wildes, *This Journal*, **123**, 1705 (1976).
2. D. E. Hall, W. D. K. Clark, J. A. Eckert, P. D. Wildes, and N. N. Lichtin, *Bull. Am. Ceram. Soc.*, **56**, 408 (1977).
3. W. D. K. Clark and J. A. Eckert, *Solar Energy*, **17**, 147 (1975).
4. A. Heller, K. C. Chang, and B. Miller, *This Journal*, **124**, 697 (1977).
5. D. A. Fine and A. N. Fletcher, Report NWC TP 5813, Naval Weapons Center, China Lake, Calif. (1976).
6. D. E. Hall, Unpublished results.
7. L. Miller, Flight Accessories Laboratory, Aeronautical Systems Div., Air Force Systems Command Tech. Documentary Rep. ASD-TDR-62-373, Wright-Patterson Air Force Base, Dayton, Ohio (1962).
8. a. A. E. Potter, Jr. and L. H. Thaler, *Solar Energy*, **3**, 1 (1958); b. E. Rabinowitch, *J. Chem. Phys.*, **8**, 560 (1940).
9. W. J. Albery and M. D. Archer, *This Journal*, **124**, 688 (1977).
10. R. Gomer, *Electrochim. Acta*, **20**, 13 (1975).
10a. P. D. Wildes and N. N. Lichtin, *J. Am. Chem. Soc.*, In press. A preliminary report was presented at the 174th National Meeting of the American Chemical Society, Chicago, Illinois, Aug. 28-Sept. 2, 1977. See Abstract Phys 117.
11. R. Havemann, H. Pietsch, and H. Reiche, *Z. Wiss. Phot., Photophysik Photochem.*, **58**, 3 (1964).
12. F. Möllers and R. Memming, *Ber. Bunseng. Phys. Chem.*, **76**, 469 (1972).
13. N. R. Armstrong, A. W. C. Lin, M. Fujihira, and T. Kuwana, *Anal. Chem.*, **48**, 741 (1976).
14. W. M. Clark, B. Cohen, and H. D. Gibbs, *Public Health Rpt. (U.S.)*, **40**, 1131 (1925).
15. R. Memming and F. Möllers, *Ber. Bunseng. Phys. Chem.*, **76**, 609 (1972).
16. R. Hardwick, *J. Am. Chem. Soc.*, **80**, 5667 (1958).
17. R. S. Nicholson and I. Shain, *Anal. Chem.*, **37**, 178 (1965).
18. R. A. Wopschall and I. Shain, *ibid.*, **39**, 1527 (1967).
19. B. R. Eggins and J. Q. Chambers, *This Journal*, **117**, 186 (1970).
20. D. S. Polcyn and I. Shain, *Anal. Chem.*, **38**, 370 (1966).
21. B. Pettinger, H. R. Schöppel, and H. Gerischer, *Ber. Bunseng. Phys. Chem.*, **78**, 450 (1974).
22. R. Havemann, H. Pietsch, and H. Reiche, *Z. Wiss. Phot. Photophysik Photochem.*, **58**, 8 (1964).
23. P. D. Wildes, N. N. Lichtin, and D. E. Hall, To be published.
24. R. Memming and F. Möllers, *Ber. Bunseng. Phys. Chem.*, **76**, 475 (1972).
25. R. H. Wopschall and I. Shain, *Anal. Chem.*, **39**, 1514 (1967).
26. H. Kim and H. A. Laitinen, *This Journal*, **122**, 53 (1975).
27. P. D. Wildes, N. N. Lichtin, M. Z. Hoffman, L. Andrews, and H. Linschitz, *Photochem. Photobiol.*, **25**, 21 (1977).

The Stability of the Secondary Lithium Electrode in Tetrahydrofuran-Based Electrolytes

V. R. Koch* and J. H. Young

EIC Corporation, Newton, Massachusetts 02158

ABSTRACT

The stability of tetrahydrofuran (THF)-based electrolytes toward bulk and electroplated Li has been assessed. Those electrolytes incorporating $LiAsF_6$ were least reactive to Li at elevated temperature and gave the best cycling efficiencies. These efficiencies could be further improved by aging the electrolyte at 71°C and by the addition of O_2 or N_2. Conversely, CO_2 degraded the performance of the secondary Li electrode. Small quantities of Na^+ and the variation of inert metal substrate had little, if any, effect on cycling efficiencies. Preelectrolyzing the electrolyte improved the cycling characteristics initially, but lengthy preelectrolysis resulted in electrolyte degradation. A recontact phenomenon, whereby previously isolated Li is recouped in subsequent cycles, was noted. The intervention of films is proposed to account for these observations.

Tetrahydrofuran (THF) is an aprotic cyclic ether with a variety of physical and chemical properties which favor its use in a secondary Li battery. It has, for example, a wide liquid range (−108° to +65°C at 1 atm), and low viscosity (0.461 cp at 25°C). It forms conductive solutions with Li salts, and THF itself is expected to manifest low chemical reactivity to reducing environments. With respect to the Li electrode, this last feature is of critical importance.

Aliphatic cyclic ethers like THF are very resistant to ring opening. The energy of the C—O bond is on the order of 85-91 kcal/mole, similar to that of an sp^3 C—C bond (1). While THF is routinely used as an inert solvent for dissolving metal reductions employing Li or Na (2) and reductions with $LiAlH_4$ (3), electrolytes prepared from it are known to anodically polymerize (4) and react with Li foil at elevated temperatures (5). In the latter instance, it was suggested that electrolyte reactions with Li were initiated by impurities.

The importance of eliminating (or at least minimizing) solvent impurities has been considered by Butler and co-workers (6). They determined that 1 ppm H_2O in 1 ml of solvent led to a 1000Å oxide film on 1 cm^2 of a clean Li surface; and in dimethylsulfoxide (DMSO),

* Electrochemical Society Active Member.
Key words: organic, electrolyte, lithium battery.

Li_2O appears to promote solvent reduction. Work in these laboratories with methyl acetate (MA) (7) and propylene carbonate (PC) (8, 9) has established that the cycling efficiency and open-circuit stability of the Li electrode is intimately dependent on the kinds and quantities of reactive contaminants present. Usually this reaction leads to formation of a surface film which protects the metal from further attack (10). Such films confer practical stability in a number of primary batteries. With a secondary battery, the consequence of this filming reaction is more serious: If Li is not plated smoothly, the rate of filming will be enhanced, and the effects will be very damaging. Individual Li grains can become encapsulated by (insulating) film. This "encapsulated" Li cannot be discharged. Subsequently, Li tends to plate at places where there is no such encapsulated material. This causes dendritic growth, which enhances further encapsulation, and speeds up ultimate failure.

In this paper, we assess the stability of the Li electrode in THF-based electrolytes under a variety of static and dynamic experiments. Static tests involved the incubation of Li foil with electrolytes at 71°C. Dynamic conditions were achieved by galvanostatically cycling Li to and from an inert substrate at 25°C. The effects of various supporting electrolytes, purification procedures, metal substrates, and gaseous additives on the cycling efficiency of the Li electrode are also explored herein.

Experimental

General.—All purification procedures and the electrochemical experiments themselves were conducted at room temperature under an Ar atmosphere in a Vacuum/Atmospheres Corporation dry box equipped with a Model He-493 Dri-Train. The dry box atmosphere was continuously recirculated through a column containing molecular sieves and an activated Cu gettering material (BASF catalyst R3-11) which scavenged moisture and oxygen. The quality of this atmosphere was such that an exposed 25W light bulb filament burned for 3 days on line voltage. This is qualitatively indicative of O_2 concentrations of from 1-5 ppm (11).

Ultraviolet spectra were recorded with a Perkin-Elmer 124D spectrophotometer. Sodium analyses were carried out on a Perkin-Elmer Model 460 atomic absorption spectrophotometer.

Materials.—Tetrahydrofuran (THF) (Burdick and Jackson, distilled-in-glass), lithium hexafluoroarsenate ($LiAsF_6$) (U.S. Steel Agri-Chemicals, electrochemical grade), and lithium tetrafluoroborate ($LiBF_4$) (Foote Mineral Company) were used as received. Lithium perchlorate ($LiClO_4$) (Alfa, anhydrous) was dried *in vacuo* for 2 hr at 230°C prior to use. Lithium foil (15 mil) was obtained from Foote Mineral Company, sealed under Ar.

Ar (99.99%), CO_2 (bone dry, 99.8%), N_2 (99.999%), and O_2 (99.99%) were obtained in lecture bottles from Matheson Gas Products.

Activated neutral alumina (Fisher, Brockman Activity 1) and molecular sieves (Linde, 4Å) were used as received and exposed only to the dry box atmosphere. Approximately 1g desiccant per 5 ml of electrolyte was used in each purification procedure. The first 10% eluting through a column was always discarded.

Electrolyte preparation and storage.—All electrolytes were prepared with cooling (<0°C) to minimize possible decomposition. The following abbreviations are used to represent purification procedures: A, solvent through alumina, then the Li salt added in the cold; S, solvent through molecular sieves, then the Li salt added in the cold; APA, A followed by preelectrolysis, then passage through a thin plug of alumina to remove Li fines.

Storage tests were conducted in 16 × 100 mm culture tubes (Corning C9826) equipped with Teflon-lined screw caps. Lithium foil, 5.0 × 6.35 cm, was spiral wound after which 8 ml of electrolyte was added to the tube, yielding an area/volume ratio of 8 cm^{-1}. The outer surface of Li was scratched with a glass rod and immediately immersed in the electrolyte. This insured that a source of fresh Li was available to the electrolyte at the outset of the experiment. The Li was maintained below the surface of the electrolyte by weighting it with a 2 cm length of 6 mm diam glass rod. Teflon tape was wrapped around the culture tube threads prior to capping to insure a tight seal. These tubes were stored in a Blue M bacteriological incubator thermostated at 71° ± 2°C. The average rate of weight loss from this system was found to be 3.9 mg/day over a 30-day period.

Criteria for Li-electrolyte reaction were twofold: visual signs of corrosion on the Li ribbon, and coloration of the electrolyte was noted by comparison with a tube containing fresh electrolyte. In all cases, electrolyte stored in the absence of Li remained clear and colorless over the 30-day storage period.

Electrolyte aging was accomplished at 71°C in the culture tubes described previously. The Li, of course, was omitted during storage.

Cells and electrodes.—Glass rectangular cells (10 × 40 × 60 mm, Vitro Dynamics) were used for the galvanostatic plating and stripping of Li, as shown in Fig. 1. Spacers and tops were machined from polypropylene stock. The working electrode was a 5.5 cm × 3.8 cm × 5 mil strip cut from Ni 200 sheet (Roblinger). A Ni wire lead was spot-welded to the strip. The surface of the working electrode was cleaned by treatment with methanol followed by acetone. The degreased surface was then treated with dilute HCl, rinsed with twice distilled H_2O, and dried. This procedure was also employed for other substrate metals; Al, Cd, Cu, Fe, Nb, Mo, and Zr (Alfa-Ventron); cold-rolled steel, and stainless steel (Roblinger). With the exception of a 9 cm area, the rest of the electrode was masked with Teflon tape. The Teflon was bonded to the Ni substrate by pressing the assemblage at 16,000 psig on a Carver hydraulic press for 3-4 min between plates heated to 100°C. The counterelectrode was fabricated from 15 mil Li ribbon.

The reference capillary was constructed from 4 mm OD glass tubing through which a Li strip made contact with the electrolyte (volume ≃ 17 cm^3). All potentials are quoted *vs.* Li^+/Li.

Galvanostatic preelectrolysis was conducted in a 4 oz snap-cap bottle between two 15 mil Li electrodes. Both the anode and cathode had surface areas of about 20 cm^2. An electrolyte solution was electrolyzed with stirring for 16-24 hr at current densities of either 1.5 or 3.0 mA/cm^2 (*vide infra*). At the end of preelectrolysis the cathode was covered with dendritic Li, some of which had broken off and floated to the sur-

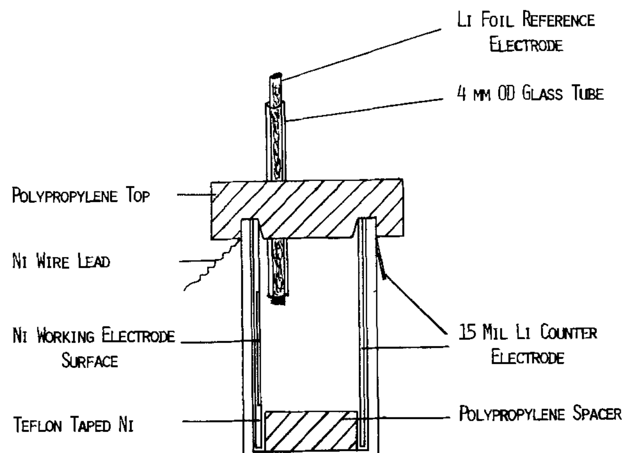

Fig. 1. Glass rectangular cell (10 × 40 × 60 mm) for coulometric cycling experiments. (Side view; not drawn to scale.)

face. The anode was smooth and uniformly brown in color. The electrolyte itself was clear and colorless.

Electrochemical instrumentation.—Chronopotentiometric plating and stripping were conducted with either a Wenking LT 73 potentiostat in the galvanostatic mode, or with a constant current power supply (constructed in-house). Long-term experiments utilized an automatic cycler (constructed in-house) which allowed plating for a given period of time, then stripped to a preset potential (+1.0V). Upon reaching this potential, stripping was terminated and the cell reverted to OCV until plating again commenced. Cycling experiments were conducted at 25° ± 2°C.

Results and Discussion

Cycling studies.—Cycling the Li electrode in a half-cell configuration mimics the charge and discharge characteristics of the negative in a secondary battery. In a given cycle, Li was plated and stripped galvanostatically. The over-all efficiency of a cycle was taken to be the ratio of charge stripped to charge plated (Q_s/Q_p). Each plate consisted of a 5 mA/cm^2 current for 225 sec, yielding a 1.125 C/cm^2 charge of Li. While ~1 C/cm^2 plates do not accurately reflect the amount of Li normally cycled in a secondary battery, they are useful in rapidly assessing the quality of a given electrolyte. Cycling of thin plates many times accelerates conditions leading to inefficiencies and failure. After a series of 1.125 C/cm^2 cycles, a final 30 C/cm^2 charge was plated and stripped.

All cycling experiments were conducted in the rectangular glass cell illustrated in Fig. 1. Typical Ni working electrode areas employed in this cell were 9 cm^2, as opposed to the 1 cm^2 area for the snap-cap vial cell used previously (7-9). It was found that for a given electrolyte, efficiency values decreased more rapidly in the vial cell than in the rectangular cell. Table I compares cycling efficiencies obtained in 1M $LiAsF_6$/MA for these two cells (12). Beyond the 6th cycle, efficiencies in the vial cell (A = 0.85 cm^2) rapidly fall off, while those in the rectangular cell (A = 9 cm^2) diminish at a more moderate rate.

Earlier work conducted in the snap-cap cell (13) revealed that edge effects played a significant role in terms of cycle inefficiencies. Thus, on going to thick (30 C/cm^2) plates most of the Li dendritic growth was found to occur along the perimeter of the Ni electrode. The perimeter to area ratio (P/A) for a 1 cm^2 Ni working electrode is 4 cm^{-1}; for a 9 cm^2 area, P/A = 1.3 cm^{-1}. Besides reducing P/A, the rectangular cell enforces the parallel placement of the Ni working and Li counterelectrodes. Carefully machined tops and spacers constrain the Ni and Li sheets flat against the walls of the glass cell. This leads to a more uniform electric field, and, therefore, a more uniform current density at any point on the working electrode surface.

The Li cycling efficiencies of three THF-based electrolytes were initially surveyed. Solutions 1M in either $LiAsF_6$, or $LiBF_4$ were prepared from THF passed through alumina (A electrolytes). As seen in

Table I. The effect of Ni working electrode area on Li cycling efficiency*

Cycle	Cycling efficiency (%) 0.85 cm^2	9.0 cm^2
1	86	86
2	95	92
3	94	92
4	95	91
5	91	90
6	82	87
7	61	85
8	36	89
9	—	87
10	—	78

* $i_p = i_s$ = 5 mA/cm^2; Q_p = 1 C/cm^2; 1M $LiAsF_6$/MA.

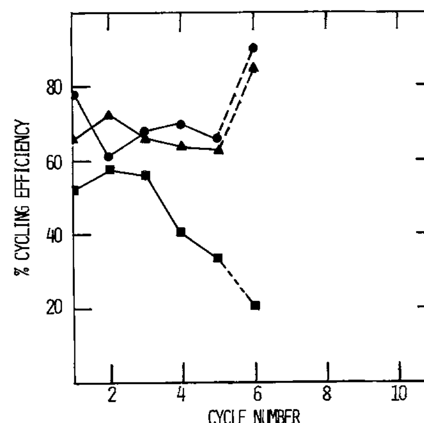

Fig. 2. Variation of efficiency with cycle number for $i_p = i_s = 5$ mA/cm^2, Q_p = 1.125 C/cm^2 (cycles 1-5); Q_p = 30 C/cm^2 (cycle 6). ●, 1M $LiAsF_6$/THF; ▲, 1M $LiClO_4$/THF; ■, 1M $LiBF_4$/THF; A— purification.

Fig. 2, somewhat higher values were achieved using the $LiAsF_6$ salt compared to those obtained with $LiClO_4$ as the supporting electrolyte. In both cases, the efficiency for the 30 C/cm^2 plates was markedly superior to that of the 1 C/cm^2 plates. Conversely, the $LiBF_4$ solution afforded very poor efficiencies. Data obtained over the first 10 cycles were reproducible to better than 5%. In parallel experiments involving $LiAsF_6$ and $LiClO_4$ electrolytes, the efficiency curves of the former salt were always higher than those of the latter.

Electrolyte storage with Li at 71°C.—The results of the cycling studies were complemented with data from static tests at 71°C. In Table II, the reactivities of THF and three THF-based electrolytes toward bulk Li are tabulated as a function of purification procedure. The first entry in each column represents the number of elapsed days after which Li corrosion was noted; the second entry in parenthesis represents the number of elapsed days at which solution coloration was detected. Corrosion invariably started on the scratched Li surface as well as on the edge of the freshly cut Li foil. All of the electrolytes yellowed with time.

We note that the static reactivity of A electrolytes toward Li roughly parallels their dynamic reactivity, as exemplified by decreasing cycling efficiencies (Fig. 2). Indeed, 1M $LiAsF_6$/THF-A is seen to be most resistant to Li-electrolyte degradation while electrolytes prepared from $LiBF_4$ are essentially insensitive to different purification procedures. While treatment with alumina helps stave off reaction with Li, electrolytes incorporating $LiClO_4$ or $LiAsF_6$ manifest a greater tendency to react when purified by the more elaborate APA procedure.

Variations of preelectrolysis time.—Earlier work (9) dealing with electrolyte purification procedures addressed itself to PC-based solutions. The effects of desiccants and preelectrolysis on the cycling efficiency of the Li electrode were noted. These efficiency values were highest and most long-lived when an alumina-

Table II. The onset of Li reaction with THF-based electrolytes at 71°C

Purification procedure	THF	Time (days) 1M $LiAsF_6$/THF	1M $LiClO_4$/THF	1M $LiBF_4$/THF
None	1 (3)*	2 (16)	1 (4)	1 (9)
S	1 (7)	1 (7)	7 (19)	—
A	4 (7)	25 (28)	9 (17)	1 (8)
APA	—	4 (7)	4 (16)	1 (8)

* Noticeable Li corrosion after 1 day; noticeable electrolyte coloration after 3 days.

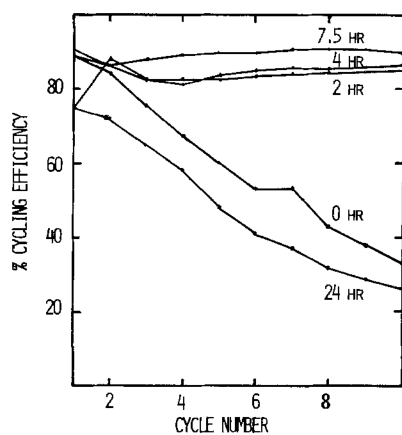

Fig. 3. Variation of efficiency with cycle number for $i_p = i_s = 5$ mA/cm^2, $Q_p = 1.125$ C/cm^2. 1M $LiAsF_6$/THF-APA aliquots taken at various preelectrolysis times.

preelectrolysis-alumina sequence was employed. In order to more fully understand the effect of preelectrolysis on electrolyte behavior, a variety of parameters was monitored as a function of preelectrolysis time. To this end, 100 ml of 1M $LiAsF_6$/THF was preelectrolyzed at our standard current density of 3 mA/cm^2. Aliquots were taken at various intervals and subjected to spectrochemical analysis as well as half-cell cycling studies. Figure 3 presents the cycling efficiency of the first ten 1.125 C/cm^2 cycles. The efficiency dramatically improved on going from no electrolysis to 2 hr of electrolysis. Small improvements are gained at 4 and 7.5 hr. The efficiency then decreased after 24 hr. On the basis of these data, subsequent preelectrolyses were run at current densities of 3 mA/cm^2 for 8 hr, or 1.5 mA/cm^2 for 16 hr. Loss of good cycling efficiency as the result of extended preelectrolysis is presumably due to electrolyte degradation. As electrolysis continues, the surface area of the cathode increases as Li dendrites build up. Dendritic growth is thought to arise from Li-impurity reactions, which proceed at a high rate, and Li-solvent reactions, which are somewhat slower (9). We believe that reaction of Li with THF itself eventually dominates on going to longer preelectrolysis times and therefore degrades the electrolyte.

Some evidence is available to support this hypothesis. Table III compares the u.v. cutoff and absorption intensity at 258 nm for electrolyte aliquots taken at several preelectrolysis times. Although the solvent cutoff limit increases only slightly after 7.5 and 24 hr, the intensity at 258 nm first decreases and then increases with time. The nature of the species absorbing in this region is unknown. However, its intensity seems to correlate with cycling efficiency, *i.e.*, higher concentrations are reflected in poorer cycling efficiencies (Fig. 3).

Since Foote Li is known to contain small amounts of Na, we sought to determine if Na^+ increased with preelectrolysis time. Duplicate samples from each aliquot were analyzed by atomic absorption spectroscopy and the results are shown in Table IV. After 2 hr of preelectrolysis, [Na^+] drops from about 8 to 5.5 ppm and remains essentially constant thereafter. Thus,

Table III. U.V. absorptions of 1M $LiAsF_6$/THF electrolyte as a function of preelectrolysis time

Time (hr)	Charge (C/cm^3)	Cutoff (nm)	Absorbance at 258 nm
0	0	210	0.09
1	2.16	210	0.09
2	4.32	210	0.03
4	8.64	210	0.04
7.5	16.20	212	0.04
24	51.84	215	0.11

Table IV. Sodium ion concentration of 1M $LiAsF_6$/THF electrolyte as a function of preelectrolysis time

Time (hr)	Charge (C/cm^3)	Sample A (ppm)	Sample B (ppm)
0	0	7.78	7.70
1	2.16	6.48	7.15
2	4.32	5.35	5.22
4	8.64	5.50	5.51
7.5	16.20	5.29	5.35
24	51.84	5.45	5.30

Na^+ is both a small and invariant contaminant in the electrolyte. Accordingly, we do not expect Na^+ to play a role in either solvent purification or electrolyte degradation on cycling.

The effect of different metal substrates on cycling efficiency.—To date, our cycling studies with the Li electrode have used Ni substrate exclusively. The following metals, representative of different groups in the Periodic Table, were surveyed: Nb, Mo, Fe, Cu, Cd, and Al. Two alloys were also tested: cold-rolled steel (CRS) and stainless steel (SS). These data are presented in Fig. 4 and compared with efficiencies achieved on Ni for 1M $LiAsF_6$/THF-APA electrolyte. Other than metals known to alloy with Li, *i.e.*, Al and Cd (14, 15), there were no dramatic changes in cycling efficiencies. In general, the efficiency plots paralleled each other, giving ~90% on the 1st cycle and between 60-73% on the 5th cycle. It would seem, therefore, that major improvements in both cycle efficiency and life must begin with the electrolyte itself.

Electrolyte aging at 71°C.—An effort was made to determine if exposure to elevated temperature would degrade $LiAsF_6$/THF electrolyte (yielding poorer cycling efficiencies). Thus, 10 ml of APA was stored in a screw-cap culture tube for 26 days at 71°C. When this electrolyte was brought into the dry box and cycled, the best results to date in this electrolyte were achieved. Figure 5 compares these data to those obtained for unstored APA electrolyte. Instead of rapidly decreasing to 50% on the 5th cycle, the cycling efficiencies of the stored APA electrolyte maintained values near 80% out to the 18th cycle. After a

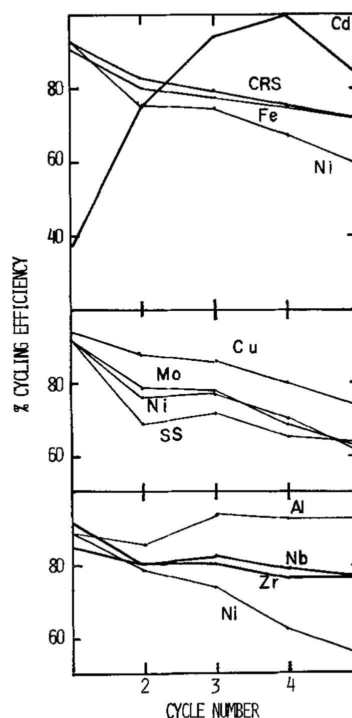

Fig. 4. Variation of efficiency with cycle number for $i_p = i_s = 5$ mA/cm^2, $Q_p = 1.125$ C/cm^2. 1M $LiAsF_6$/THF-APA at various working electrodes.

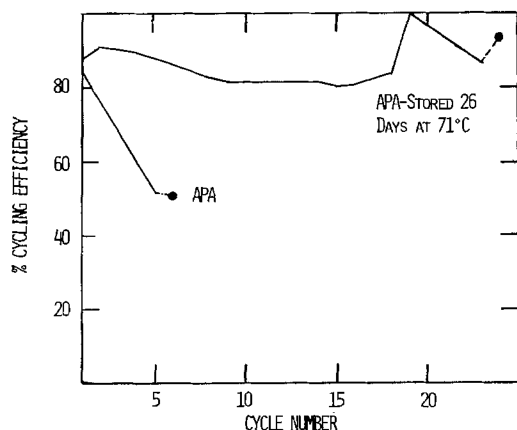

Fig. 5. Variation of efficiency with cycle number for $i_p = i_s = 5\ mA/cm^2$, $Q_p = 1.125\ C/cm^2$; $Q_p = 30\ C/cm^2$. 1M $LiAsF_6$/THF-APA.

60 min pause at OCV, the 19th cycle yielded 100% cycling efficiency. Subsequent cycles decreased in efficiency to 85% on the 23rd cycle. The 24th cycle gave a 94% efficiency for a 30 C/cm^2 plate, after which the cell was disassembled and the Ni working electrode examined. A very adherent and uniformly thin plate of residual Li remained. No gross dendritic growth was noted after a total of 54 C/cm^2 (28.6 C/cm^3) Li had been shuttled to and from the Ni. This is indeed a remarkable observation in that earlier results incorporating only 5 × 1 C/cm^2 cycles yielded highly dendritic residual Li.

A second batch of APA electrolyte was prepared and stored for 9 days at 71°C. The cycling results are shown in Fig. 6. After the 6th cycle, efficiency values remained nearly constant at 88% out to the 40th cycle. The 6th, 17th, and 26th cycles reflect slight improvements in efficiency due to pauses of 17, 15, and 30 min, respectively, between cycles. On the 41st cycle a 1.125 C/cm^2 charge of Li was plated onto the Ni, and the cell switched to OCV. After 44 min, the Li was stripped and an efficiency value of 73% was obtained. The 42nd cycle was run as usual and a 91% value was achieved. The 43rd cycle yielded the "baseline" value of 85%. On the 44th cycle 1.125 C/cm^2 was plated, and the cell switched to OCV overnight. Sixteen hours later the Li was stripped, yielding only 60% efficiency. The 45th cycle, however, gave a value of 107%! Clearly, some of the Li isolated from the Ni electrode on overnight stand was recouped on the 45th cycle. The 46th cycle gave 83%, after which the cell was disassembled and inspected. As in the earlier run with stored APA, the Ni electrode revealed compact, uniformly thin residual Li. The electrolyte solution itself was clear but very slightly tan in color, indicative of degradation products. A new Ni working electrode was inserted and a 30 C/cm^2 cycle yielded a 75% efficiency. The residual Li was dendritic in nature. Fresh

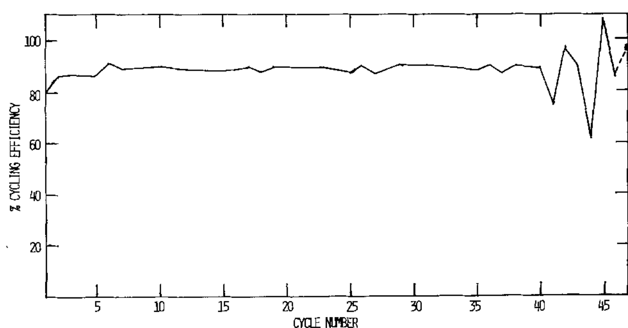

Fig. 6. Variation of efficiency with cycle number for $i_p = i_s = 5\ mA/cm^2$. $Q_p = 1.125\ C/cm^2$; $Q_p = 30\ C/cm^2$. 1M $LiAsF_6$/THF-APA stored 9 days at 71°C.

electrolyte and another new Ni electrode gave 95% efficiency on a 30 C/cm^2 cycle. This difference in cycling efficiencies clearly reflects the deleterious effect of degradation products on the Li electrode.

Lithium isolation rates calculated from the 41st and 44th cycles gave 57 $\mu A/cm^2$ over 44 min and 5 $\mu A/cm^2$ over 16 hr. These values are similar to those reported earlier for $LiAsF_6$/PC electrolytes (9) and reflect the initially rapid reaction of electrolyte with as-plated Li. The novelty of this result lies in the ability to recover some isolated Li in a subsequent cycle. This suggests a mechanism in which Li, electrochemically insulated from the Ni electrode, becomes reattached and thereby available for anodic dissolution.

Other investigators have invoked Li^+-conductive films to account for the behavior of the Li electrode in aprotic media. Dey (16) indicated that in PC the Li electrode is coated with a Li^+-conducting film composed of Li_2CO_3. More recently, Peled and Straze (17) have proposed a simple model of alkali and alkaline-earth metal/electrolyte films in terms of their ionic and electronic transport properties. A key component of these films is an insoluble metal salt, the cation of which migrates through the film on polarization. Others (18, 19) have compared corrosion and exchange currents of the Li electrode in a variety of media. They found that after initial Li-electrolyte contact, the corrosion rate became 1000 times slower than the rate at which the Li/Li^+ equilibrium was established. This implies the presence of a Li^+-conducting film which acts as a barrier to the reactive electrolyte. Finally, Besenhard (20) suggests that the conductivity of Li^+ through encapsulating films is enhanced when Li is electrodeposited in the presence of I^-. The I^- anion is presumed to be incorporated in the film thus providing high mobility for Li^+.

The effect of storage time at 71°C on cycling efficiency was assessed for APA electrolyte samples removed at 1, 3, 5, 7, 9, and 11 day intervals. The long-lived cycling efficiencies in Fig. 4 could only be reproduced when the electrolyte had been stored for 9 or more days. Electrolytes stored for shorter periods of time manifested initially higher efficiencies, which rapidly declined after the first few cycles. For example, the 5th cycle of APA-1, 3, 5, and 7 gave efficiencies of from 35-59%. The 5th cycle efficiencies of APA-9 and 11 were never less than 76%. The 71°C storage must chemically alter the electrolyte with time. Whether this alteration involves the formation of a stabilizing agent or the removal of an impurity is presently open to question.

The effect of various gases on electrolyte cycling efficiency.—Formidable efforts have been made to remove or minimize contaminants in the electrolyte. Distillation, adsorption of organic impurities on alumina, pre-electrolysis at the Li potential, and aging electrolyte in glass have dramatically improved the cycling efficiency of the Li electrode. Little attention, however, has been directed toward the presence of dissolved gases in the electrolyte. Burdick and Jackson u.v. grade THF used in all our THF-based electrolytes is packed under N_2 as received. Furthermore, when solvent is percolated through alumina, N_2, O_2, and CO_2 absorbed on the alumina particles surely dissolve into the THF. We set out to assess the effect of electrolyte perfused with Ar, CO_2, N_2, and O_2 on subsequent cycling experiments.

Gasification was achieved by passing the gas under study from a lecture bottle through an intervening Drierite column and then through a coarse glass frit immersed in electrolyte. Approximately 40 ml of electrolyte was perfused at any one time, and the gas under study was allowed to slowly bubble through the electrolyte for 5.0 min. Figure 7 presents the efficiencies of the first 10 cycles obtained in the presence of these gases. Each run was conducted on a new Ni electrode in freshly gasified electrolyte. Perfusion with Ar improved the cycle life of the Li electrode perhaps by

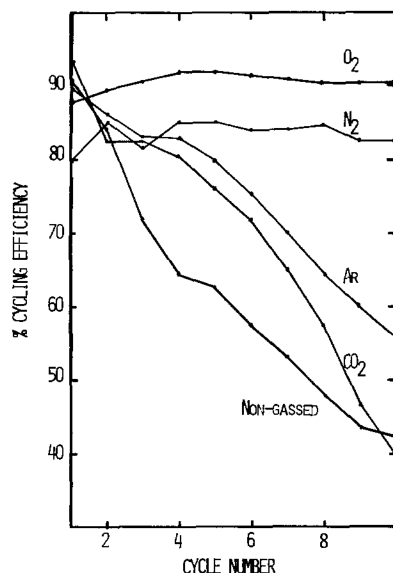

Fig. 7. Variation of efficiency with cycle number for $i_p = i_s = 5$ mA/cm², $Q_p = 1.125$ C/cm². 1M $LiAsF_6$/THF-APA perfused with various gases.

replacing other gases and/or volatile organic contaminants dissolved in the electrolyte. Oxygen and N_2 helped maintain cycle life relative to Ar while CO_2 and nongassified electrolyte did not. While dry O_2 does not readily react with Li at room temperature, dry N_2 and CO_2 form the nitride and carbonate (21). That N_2 was found to be superior to Ar is indeed surprising. We had thought that an Li_3N film would perturb the morphology of the electrodeposit so as to allow the rapid generation of dendrites. This would in turn lead to electrode failure. However, recent work with Li_3N single crystals has shown them to be pure Li-ionic conductors giving high conductivity at moderate temperatures (22). Polycrystalline Li_3N also manifests similar, though attenuated, conductivity values (22, 23). Thus the Li_3N film may partially protect Li from attack by residual impurities or THF itself, and there is some precedent for this hypothesis. Carbon dioxide in 1M $LiClO_4$/THF has been used to improve the self-discharge characteristics of Li primary cells (10). Apparently, CO_2 forms a protective (Li_2CO_3) which then allows Li^+ migration into solution on discharge. Oxygen afforded the highest cycling efficiencies over 10 cycles. While Li and O_2 are essentially inert on open circuit, protective oxide films could form as Li is plated down on Ni. Indeed, we observe that the OCV of Ni *vs.* Li in freshly oxygenated electrolyte is 300-400 mV higher than the OCV's in the other perfused electrolytes. The OCV is a mixed potential reflecting the midpoint between Li reduction and electrolyte oxidation. Thus, its shift to more positive OCV values (+2.60V → 2.95V) in the presence of O_2 suggests that O_2 can be reduced at potentials positive of Li. When Li is plated (reduced) on Ni, a concurrent reduction of O_2 to O^{-2} may occur. Subsequent reaction with freshly plated Li may then lead to a film which affords protection. If an oxide film is the source of higher cycling efficiencies and larger cycle life, its effect can only be short-lived. Li_2O cannot be electrochemically converted back to Li and O_2. Thus, after several cycles the film must ultimately perturb the Li morphology, leading to dendritic growth and subsequent electrode failure. In this regard, we note that cycling efficiencies in electrolytes perfused with O_2 and N_2 rapidly degrade beyond the 10th cycle.

Summary and Conclusions

The results of cycling and storage indicate that electrolytes incorporating $LiAsF_6$ are more stable to Li. This may be due to the high purity of this salt, or reflect a stabilizing property afforded by the AsF_6^- anion. In fact, we have found that THF and AsF_6^- react concurrently at a Li anode to form a brown coating (24). This film may provide some protection against further reaction. The storage tests also indicate that, on going to more stringent purification procedures, the reactivity of electrolyte to bulk Li increases. While some contaminants are known to degrade cycling efficiency, *e.g.*, CO_2 and organic electrolyte degradation products, others like H_2O (8), N_2, and O_2 help, albeit temporarily.

Preelectrolysis of the electrolyte improves its "inertness" with respect to the Li electrode, presumably by scavenging reactive impurities. However, continued preelectrolysis degrades the electrolyte, as evidenced by poor cycling efficiency and the appearance of contaminants in the u.v. spectrum. This suggests that impurities react with Li at a faster rate than electrolyte itself, as has been noted previously (9). Neither small Na^+ concentrations nor the use of different metal substrates have any significant effect on the cycling efficiencies of a given electrolyte. This indicates that solvent, salt, and impurities contained therein play a major role in determining the over-all reactivity of an electrolyte with Li.

Electrolyte aging at 71°C and the recontact phenomenon merit more study. Subtle changes in the electrolyte itself and in the structure of the encapsulating film dramatically affect the number of high efficiency cycles obtained. The understanding and subsequent control of these phenomena are required if a THF-based electrolyte is to be employed in a practical Li secondary battery.

The introduction of gases into the electrolyte dramatically alters the cycling efficiency. Apparently, the *in situ* generation of Li_3N and Li_2O films protects the underlying Li from parasitic electrolyte/impurity reactions. Conversely, a Li_2CO_3 film either affords no protection or seriously perturbs the plate morphology from the outset, leading to dendritic growth and rapid reaction with the electrolyte medium.

When taken together, these results point up the importance of films in ultimately determining the rate of Li/electrolyte reactivity. The specific nature of the reaction of Li with THF-based electrolytes, the kinds and distribution of products, and a mechanism accounting for their formation will be the subject of a forthcoming publication (24).

Acknowledgment

This work was supported by NSF-RANN under Grant No. AER75-03779.

Manuscript submitted Jan. 16, 1978; revised manuscript received March 29, 1978.

Any discussion of this paper will appear in a Discussion Section to be published in the June 1979 JOURNAL. All discussions for the June 1979 Discussion Section should be submitted by Feb. 1, 1979.

REFERENCES

1. J. March, in "Advanced Organic Chemistry," p. 28, McGraw-Hill, New York (1968).
2. H. O. House, in "Modern Synthetic Reactions," p. 50, W. A. Benjamin, Inc., New York (1965).
3. H. O. House, *ibid.*, p. 23.
4. A. N. Dey and E. J. Rudd, *This Journal*, **121**, 1294 (1974).
5. J. B. Doe, F. W. Dampier, K. Jefferies, P. E. Krause, N. Margalit, E. J. Merrick, and L. C. Thompson, USAF Technical Report AFAPL-TR-76-63 [AD-A004543], December 1974.
6. J. N. Butler, R. J. Jasinski, D. R. Cogley, H. L. Jones, J. C. Synott, and S. Carroll, USAF Technical Report AFCRL-70-0605, September, 1970.
7. R. D. Rauh and S. B. Brummer, *Electrochim. Acta*, **22**, 85 (1977).
8. R. D. Rauh and S. B. Brummer, *ibid.*, **22**, 75 (1977).
9. V. R. Koch and S. B. Brummer, *ibid.*, **23**, 55 (1978).
10. J. O. Besenhard and G. Eichinger, *J. Electroanal. Chem.*, **68**, 1 (1976) and references therein.

11. "Glove Box Operations Manual," p. 6, Vacuum-Atmospheres Corp., North Hollywood, Calif. (1970).
12. S. B. Brummer, F. W. Dampier, and V. R. Koch, Semiannual Report, NSF-RANN Grant No. AE-R75-03779, February 1977.
13. S. B. Brummer, R. D. Rauh, T. F. Reise, and J. H. Young, Annual Report, NSF-RANN Grant No. AER75-03779, June 1976.
14. A. N. Dey, *This Journal*, **118**, 1547 (1971).
15. R. D. Rauh, T. F. Reise, and S. B. Brummer, Abstract 2, p. 14, The Electrochemical Society Extended Abstracts, Fall Meeting, Atlanta, Ga., Oct. 9-14, 1977.
16. A. N. Dey, *Thin Solid Films*, **43**, 131 (1977).
17. E. Peled and H. Straze, *This Journal*, **124**, 1030 (1977).
18. T. V. Kuznetsova, I. A. Kedrinskii, E. G. Ivanov, and G. P. Potapova, *Soviet Electrochem.*, **12**, 1327 (1977).
19. I. A. Kedrinskii, T. V. Kuznetsova, S. V. Morozov, E. G. Ivanov, and I. G. Grudyanov, *ibid.*, **12**, 1332 (1977).
20. J. O. Besenhard, *J. Electroanal. Chem.*, **78**, 189 (1977).
21. W. A. Hart and O. F. Beumel, Jr., in "Comprehensive Inorganic Chemistry," A. F. Trotman-Dickenson, Executive Editor, pp. 336-337, Pergamon Press, Oxford (1973).
22. U. v. Alpen and G. Müller, Abstract 19, p. 55, The Electrochemical Society Extended Abstracts, Fall Meeting, Atlanta, Ga, Oct. 9-14, 1977.
23. R. A. Huggins, *Electrochimica Acta*, In press.
24. V. R. Koch, Submitted to *This Journal*.

Thermodynamic Properties of Liquid Na-Sn Alloys by emf Measurements with Beta-Alumina Electrolytes

M. Rivier and A. D. Pelton

Département de Génie Métallurgique, Ecole Polytechnique, Université de Montréal, Montréal, Québec, Canada

ABSTRACT

The thermodynamic properties of liquid Na-Sn alloys have been measured over the temperature range $250° < T < 450°C$ and over the composition range $0 < X_{Na} < 0.3$ by means of concentration cells employing beta-alumina solid electrolytes. Compositions were varied by coulometric titration over the entire range from 0 to 30% Na. Enthalpies and entropies were obtained from the temperature dependence of the emf's. The results indicate that the alloys are strongly ordered and of partial ionic character.

Although a great deal of attention has been recently accorded to beta-alumina because of its importance in the development of the sodium-sulfur battery (1, 2), the applications of this solid electrolyte for thermodynamic measurements have only begun to be explored (3-7). To a large extent this has been due to the unavailability of an inexpensive source of impermeable tubes of beta-alumina.

A new, simple, and inexpensive slip-casting technique of making impermeable crucibles and tubes of beta-alumina has recently been developed in this laboratory (8). The crucibles used in the present investigation were made by this technique.

In the present study, the emf of the cell

Na (liquid) | beta-alumina | Na-Sn (liquid alloy)

has been measured. The transport number of Na^+ ions in the beta-alumina is unity. (This fact has been verified in the present study as is discussed below.) The emf of the cell is thus given by

$$E = -\frac{RT}{\mathbf{F}} \ln a_{Na} \quad [1]$$

where a_{Na} is the activity of Na in the alloy.

The high selectivity of the beta-alumina for conduction by Na^+ ions, as well as the completely sealed cell design used in the present study, enables highly reproducible and stable emf's to be obtained. In addition, the very low resistivity of the solid electrolyte ($\sim 1\Omega$ in the present study) permits the concentration of the alloy to be varied by coulometric titration over a composition range of 30 mole percent (m/o). This is to be compared to the composition variations of fractions of 1 m/o which are the maximum obtainable by coulometric titration with conventional solid electrolytes such as stabilized zirconia.

Key words: beta-alumina, sodium-tin system, liquid alloys—thermodynamics, liquid alloys—structure, alloy concentration cells.

The Na-Sn system was chosen for this study because of the interesting thermodynamic properties of these structurally highly ordered liquid alloys and the scatter in the reported data (9-15).

Experimental

The apparatus is shown in Fig. 1. A tube of beta-alumina (1 cm diam, 5 cm long, wall thickness 0.2 mm) is joined to a Pyrex tube by a Corning KOVAR 7056 graded seal. This joint can be used under vacuum to 450°C. In order to remove all traces of water, the beta-alumina is heated for 24 hr at 150°C in a vacuum oven. The tube is then filled with high purity[1] Sn, and this inner-electrode compartment is sealed under vacuum in order to avoid any oxidation of the alloy or any losses of Na from the alloy by volatilization. The outer reference electrode compartment contains pure[1] Na which has been prefiltered through a glass frit. During the course of the subsequent experiment, high purity argon gas is circulated over the sodium.

Emf measurements are made by a TACUSSEL millivoltmeter via tungsten electrodes. The temperature is measured by a thermocouple dipping into the Na.

The selectivity of the electrolyte for Na^+ ions, as well as its very low resistivity (the apparatus in Fig. 1 has a resistance of about 1Ω at 350°C), permits the composition of the alloy to be conventiently, accurately, and rapidly altered by the passage of a measured current (coulometric titration). The constant current (maximum 500 mA) is furnished by a Koslow Scientific coulometer.

The composition of the alloy was varied in this way from 0% Na up to more than 25 m/o Na and back again. Whenever the current was interrupted to make an emf measurement, the equilibrium emf was always attained within less than 10 sec. Figure 2 shows a measured curve of emf *vs.* composition at

[1] ALFA Inorganics Company.

constant $T = 360°C$. Some of the points shown were obtained upon increasing the composition and others upon decreasing it. The points obtained as the composition was increased were within ±0.5 mV of all those obtained as the composition was decreased. Furthermore, analysis of the sample by atomic absorption after the coulometric titration showed that the composition agreed with that given by the coulometry. Finally, at low concentrations of Na, the curve of emf *vs.* log X_{Na} is linear. Thus, Faraday's law is obeyed with a transport number of Na^+ of unity.

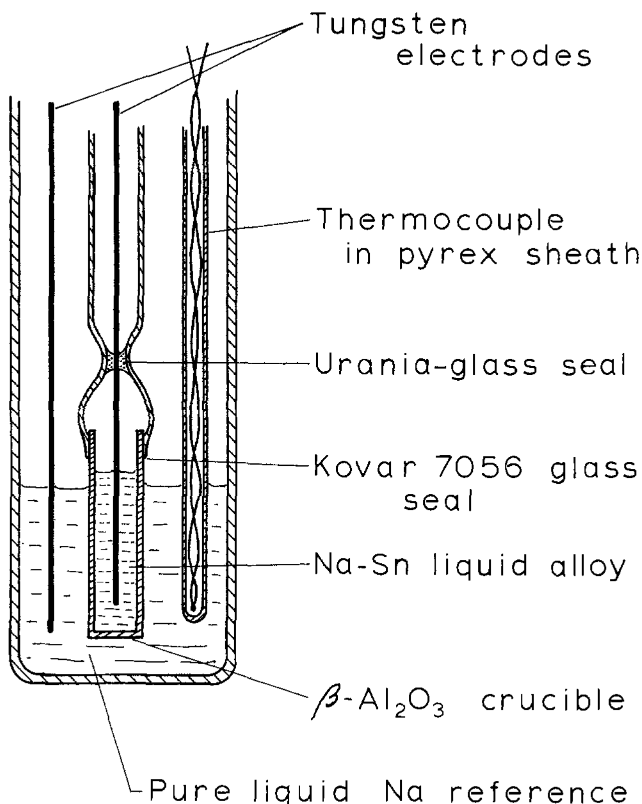

Fig. 1. Experimental apparatus

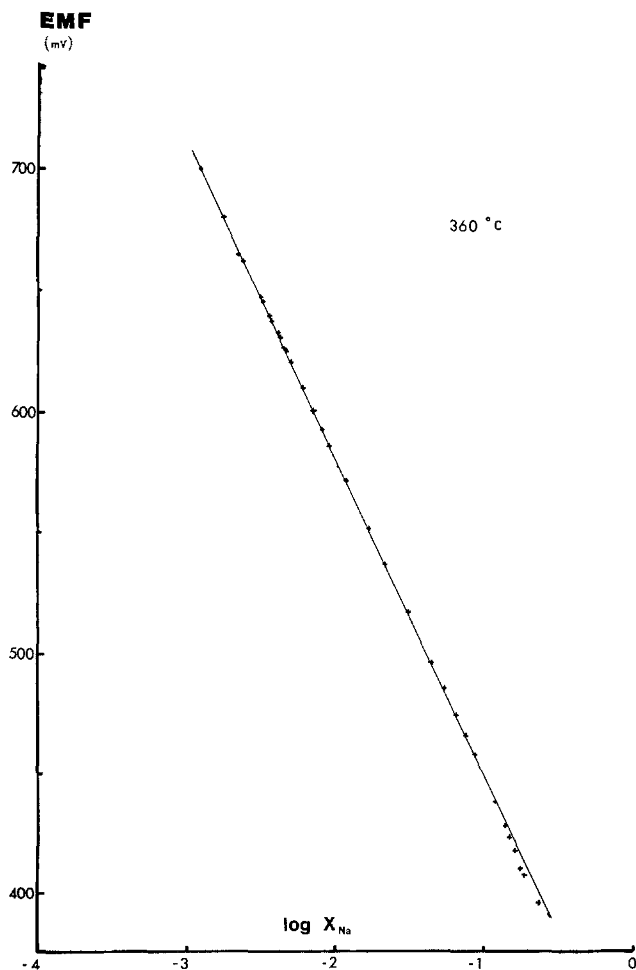

Fig. 2. Emf *vs.* log of sodium mole fraction in Na-Sn liquid alloys at 360°C. Composition varied by coulometric titration.

Three separate samples were studied over the range of temperature from 250° to 450°C and from 0% Na up to the phase boundary (20-30% Na). At all compositions and temperatures, emf's from the three samples were in agreement within ±0.5 mV.

During one week at 400°C, the emf was stable to within ±0.5 mV. This stability results from the fact that changes of composition by volatilization of the Na are prevented by sealing the inner electrode compartment near the meniscus of the alloy.

Results

Measurements were made at several compositions at 360°C. The excess free energy of Na, g_{Na}^E, at 360°C, calculated from the measured emf via the equation

$$g_{Na}^E = RT \ln a_{Na} - RT \ln X_{Na} = -\mathbf{F}E - RT \ln X_{Na} \quad [2]$$

(where X_{Na} is the mole fraction of Na in the alloy) is plotted in Fig. 3. Points shown are from all three samples.

At several composition, emf's were measured as a function of temperature over the range 250°-450°C. The curves of E *vs.* T deviated very slightly from linearity, thus indicating a slight temperature dependence of the entropy. However, for the temperature range 250°-450°C it was not deemed possible to determine the curvature with any precision. Hence, points obtained during both heating and cooling were fitted to straight lines by least squares regression. The resultant entropy and enthalpy values are thus "averages" for this temperature range. The equations of E *vs.* T and the root-mean-square deviations are listed in Table I, in which data obtained from all three samples are shown. Partial enthalpies, Δh_{Na}, and partial entropies, Δs_{Na}, of mixing of Na, calculated from the temperature dependence of the emf, are plotted in Fig. 4 and 5. The excess entropy of Na

$$s_{Na}^E = \Delta s_{Na} + R \ln X_{Na} \quad [3]$$

is plotted in Fig. 6.

Error limits may be estimated from the reproducibility (~ ±0.5 mV) and the temperature range (~200°C) of the measurements. The error in dE/dT is thus ~ ±2(0.5)/200 = 0.005 mV/K. The lower limits for random errors are thus ~0.5**F** or ±50J for

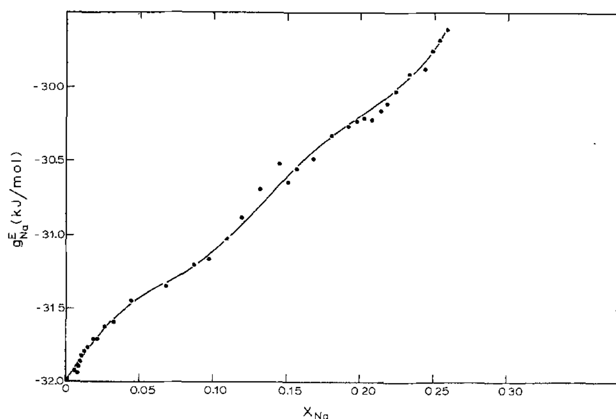

Fig. 3. Partial excess free energy of sodium in liquid Na-Sn alloys at 360°C calculated via Eq. [2] from experimental measurements. Curve is given by Eq. [10].

Table I. Least squares linear fits of emf vs. temperature for range 250° < T < 450°C

X_{Na}	E (mV) = $A + BT$		rms deviation (mV)
	$A = -\Delta h_{Na}/F$	$B = \Delta s_{Na}/F$	
0.0327	447.31	0.105	0.080
0.0445	447.72	0.076	0.001
0.0679	451.21	0.032	0.107
0.0869	459.87	−0.005	0.205
0.0962	452.05	−0.002	0.006
0.1097	452.29	−0.016	0.004
0.1196	446.73	−0.017	0.051
0.1326	448.47	−0.032	0.990
0.1452	430.71	−0.014	0.094
0.1513	455.89	−0.056	0.379
0.1574	448.16	−0.048	0.265
0.1693	459.66	−0.074	0.535
0.1808	449.13	−0.065	0.420
0.1921	458.92	−0.087	0.753
0.1976	458.43	−0.089	0.308
0.2030	463.72	−0.100	0.486
0.2084	469.16	−0.111	0.159
0.2136	470.44	−0.116	0.342
0.2240	469.41	−0.121	0.275
0.2341	471.79	−0.130	0.451
0.2439	480.86	−0.149	0.327
0.2488	476.81	−0.146	0.219
0.2535	474.98	−0.146	0.148
0.2582	474.27	−0.148	0.176

g_{Na}^E, 0.005**F** or ±0.5 J/K for s_{Na}^E, and $(50 + 0.5T)$ or ±650J for Δh_{Na}.

Discussion

A direct comparison of the present results with those of other workers (9-15) is difficult because of the widely different ranges of temperature and composition studied. Figure 4 shows the curve of Δs_{Na} calculated by Morachevskii and Lantratov (15) from the temperature dependence of the emf's of electrochemical cells containing Na-glass membranes for a

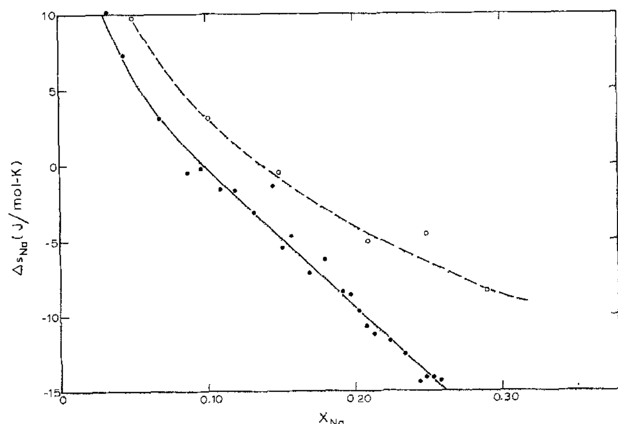

Fig. 4. Partial entropy of mixing of sodium in liquid Na-Sn alloys calculated from temperature dependence of emf's. —●—●— Present study; —○—○— Ref. (15), 600°C.

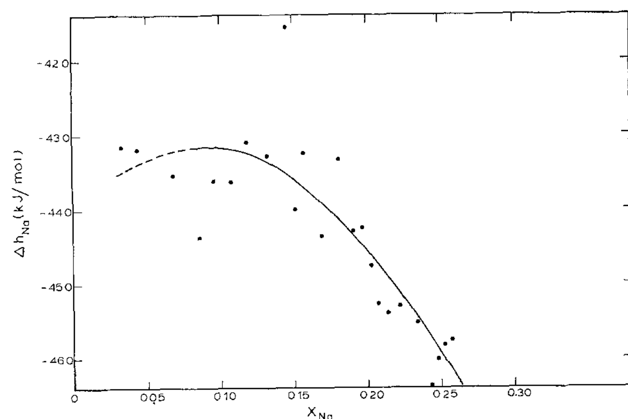

Fig. 5. Partial enthalpy of mixing of sodium in liquid Na-Sn alloys calculated from temperature dependence of emf's. Curve is given by Eq. [4]).

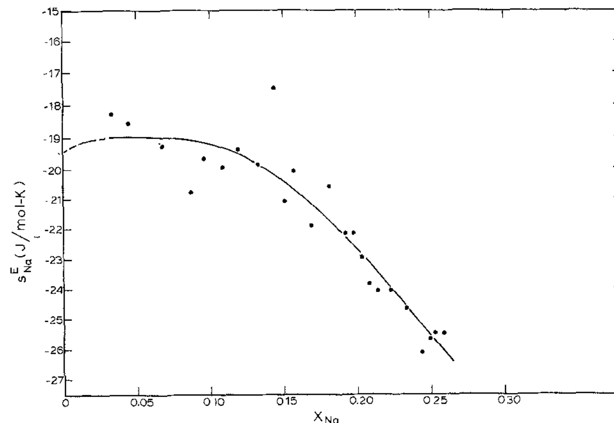

Fig. 6. Partial excess entropy of sodium in liquid Na-Sn alloys calculated from temperature dependence of emf's and Eq. [3]. Curve is given by Eq. [5].

range of temperatures around 600°C. The curve is in qualitative agreement with the present results. As suggested by Bartlett and Crowther (12), the discrepancy may be due to attack on the Na-glass electrolytes, however, the difference could also be explained by a temperature dependence of the entropy.

The excess free energy, g_{Na}^E, and enthalpy, Δh_{Na}, of Na are both quite negative, indicating that the liquid alloys are very stable. The excess entropies are also very negative—so negative, in fact, that the partial entropy of mixing in Fig. 4 is negative for $X_{Na} > 0.1$. This indicates that the structure of these liquid alloys is highly ordered. Further information can be obtained from an examination of the partial properties of Sn and the integral properties of mixing which may be calculated from integration of the Gibbs-Duhem equation. To this end, the curves in Fig. 3, 5, and 6 were first fitted to analytical expressions. For the curves of Δh_{Na} and s_{Na}^E in Fig. 5 and 6, three coefficient equations were used. The equations obtained by least squares regression analysis of the experimental points are

$$\Delta h_{Na} = -77.282 + X_{Sn}^2(123.702 - 90.689\, X_{Sn}) \text{ kJ/mole} \quad [4]$$

$$s_{Na}^E = -82.429 + X_{Sn}^2(215.962 - 153.162\, X_{Sn}) \text{ J/mole-K} \quad [5]$$

Application of the Gibbs-Duhem equation then gives the following expressions for Δh_{Sn} and s_{Sn}^E which are plotted in Fig. 7

$$\Delta h_{Sn} = X_{Na}^2(78.358 - 90.689\, X_{Sn}) \text{ kJ/mole} \quad [6]$$

$$s_{Sn}^E = X_{Na}^2(139.381 - 153.162\, X_{Sn}) \text{ J/mole-K} \quad [7]$$

The curve for Δs_{Na} drawn in Fig. 4 was calculated by combining Eq. [3] and [5]. Figure 8 shows the integral molar entropy of mixing

$$\Delta s = -R(X_{Na} \ln X_{Na} + X_{Sn} \ln X_{Sn}) + (X_{Na}s_{Na}^E + X_{Sn}s_{Sn}^E) \quad [8]$$

where s_{Na}^E and s_{Sn}^E are given by Eq. [5] and [7]. Also shown in Fig. 8 is the integral enthalpy of mixing

$$\Delta h = X_{Na}\Delta h_{Na} + X_{Sn}\Delta h_{Sn} \quad [9]$$

where Δh_{Na} and Δh_{Sn} are given by Eq. [4] and [6].

For the curve of g_{Na} in Fig. 3, the precision of the results merits a 7-coefficient expansion. For an ordinary power series expansion with this many terms, about 13 significant figures would have to be retained in each coefficient in order to avoid round-off errors. This problem can be avoided through the use of an orthogonal series. The curve drawn in Fig. 3 is represented by the following 7-coefficient Legendre orthogonal expansion

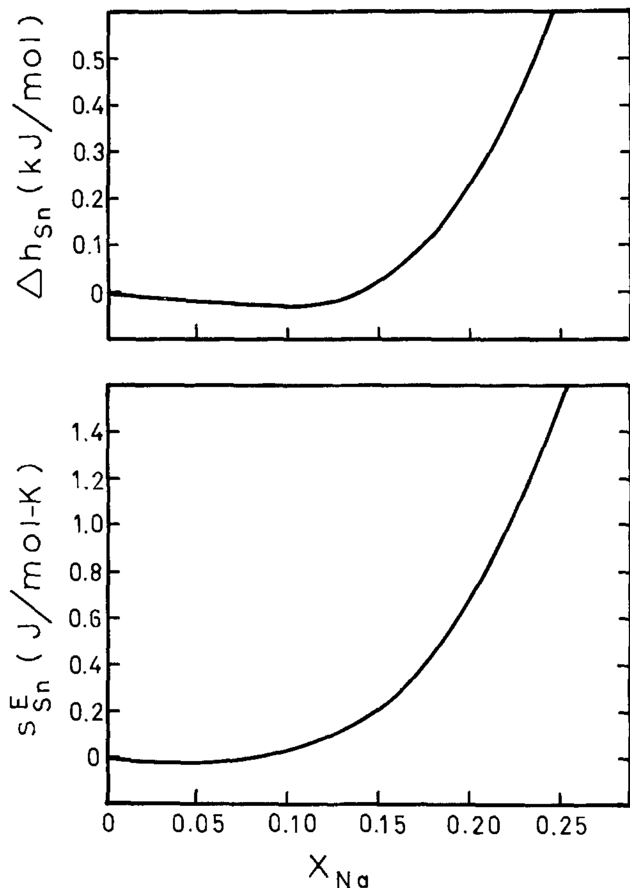

Fig. 7. Partial enthalpy of mixing and excess entropy of Sn in liquid Na-Sn alloys calculated by integration of the Gibbs-Duhem equation.

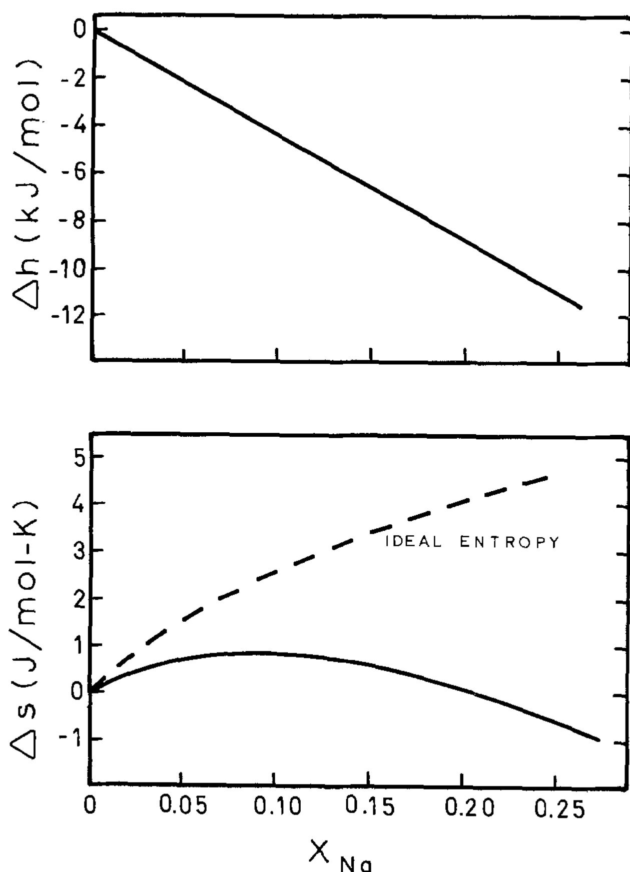

Fig. 8. Integral molar enthalpy and entropy of mixing in liquid Na-Sn alloys calculated by integration of the Gibbs-Duhem equation.

$$g_{Na}{}^{E} = X_{Sn}{}^{2} \sum_{n=0}^{6} a_n P_n(X_{Sn}) \qquad [10]$$

where the coefficients a_n are given in Table II and where $P_n(X_{Sn})$ is the nth orthogonal Legendre polynomial. The first few terms in the series are

$$a_nP_n(X_{Sn}) = a_0 + a_1(2X_{Sn} - 1) + a_2(6X_{Sn}{}^2 - 6X_{Sn} + 1) + a_3(20X_{Sn}{}^3 - 30X_{Sn}{}^2 + 12X_{Sn} - 1) + \ldots \qquad [11]$$

The general recursion relationship is

$$P_n(x) = \frac{(2n-1)(2x-1)}{n} P_{n-1}(x) - \frac{(n-1)}{n} P_{n-2}(x) \qquad [12]$$

The advantages of orthogonal Legendre series for representing thermodynamic solution properties have been discussed (16).

Integration of the Gibbs-Duhem equation then gives the following expansion for $g_{Sn}{}^{E}$

$$g_{Sn}{}^{E} = X_{Na}{}^{2} \sum_{n=0}^{6} b_n P_n(X_{Sn}) \qquad [13]$$

where the coefficients b_n are listed in Table II.

The integral enthalpy of mixing in Fig. 8 is nearly a straight line. The partial enthalpy of mixing of Sn in Fig. 7 is nearly zero (and even becomes very slightly positive at higher concentration of Na). The entropy of mixing in Fig. 8 deviates very negatively from ideality. Both the enthalpy and entropy are thus indicative of the formation of a liquid "compound" or "complex." That is, structural or electronic ordering is indicated.

Studies of binary alloy systems formed between two components with largely different electronegativities show that there may be electron transfer from one component to the other to form partially ionic species. Wagner (17) first suggested such behavior for molten Mg-Bi alloys. In this system there is an inflection point in $g_{Mg}{}^{E}$ near the composition Mg_3Bi_2 (18) as well as a deep minimum in the electrical conductivity near this same composition (19). Recent studies (20, 21) of the Cs-Au system have shown that at the 50-50 composition, the liquid "compound" CsAu has a very strong ionic character. The system Li-Pb exhibits a minimum in electrical conductivity and in molar volume (22, 23), and an inflection in $g_{Li}{}^{E}$ (24) near the composition Li_4Pb.

The ionic character, IC, of an alloy can be estimated using the empirical criterion of Pauling

$$IC = 1 - \exp(-0.25\, d^2) \qquad [14]$$

where d is the difference in electronegativities of the two metals. For Mg-Bi, Cs-Au, and Li-Pb, ionic characters of 11, 51, and 15%, respectively, are calculated. For Na-Sn, an ionic character of 18% is predicted. From the valencies of Na and Sn it would be expected that the anomalies would occur near the composition Na_4Sn which, however, is not within the range of the present study.

Table II. Coefficients of Legendre series expansions (Eq. [10] and [13]) for $g_{Na}{}^{E}$ and $g_{Sn}{}^{E}$ (kJ/mole)

n	a_n	b_n
0	7167	−32
1	−16872	−541
2	16871	1791
3	−10531	−2377
4	4241	1710
5	−1017	−671
6	110	110

In this model, then, the negative enthalpy of mixing results from the localization of electrons which occurs progressively as Na is added to molten Sn. This occurs approximately linearly with added Na, such that $\Delta h_{Na} \approx$ constant and $\Delta h_{Sn} \approx 0$ as observed. The negative deviations in entropy would result from short-range structural ordering (a preference of Na to have Sn as nearest neighbor and vice-versa as in an ionic melt) or from electronic ordering as the density of free electrons is decreased as Na is added. At low Na concentrations it would be expected that the decrease in free-electron density would occur approximately linearly with added Na. Hence, the electronic ordering would, at low Na concentrations, give $s_{Na}^E \approx$ constant and $s_{Sn}^E \approx 0$ as observed (Fig. 7 and 8). At higher concentrations of Na, localization of electrons on Sn atoms begins to occur. Electrons can then exist in localized bound states or in free-electron gas states. A positive entropy contribution arises from the distribution of the electrons between these two states, thus accounting for the positive values of s_{Sn}^E at higher Na concentrations observed in Fig. 7. Short-range structural ordering, on the other hand, would be expected to give negative values of s_{Sn}^E at all compositions. Hence, the results suggest that electronic ordering is occurring in these alloys.

A useful function for examining the thermodynamic behavior of melts is the stability function

$$\psi = 1 + \frac{X_{Na}X_{Sn}}{RT} \frac{d^2g^E}{dX_{Sn}^2} \quad [15]$$

which, as has been discussed by Darken (25), gives an indication of the stability of the melt and passes through maxima at compositions of particular stability (compositions where g^E has an inflection point). For example, ψ passes through sharp maxima at the approximate compositions Mg_3Bi_2 (18) and Li_4Pb (24) in the Mg-Bi and Li-Pb systems.

The stability function plotted in Fig. 9 was calculated for the Na-Sn system at 360°C from the Legendre series expansion for g_{Na}^E. As expected, ψ is very positive, and increases rapidly with X_{Na} at higher values of X_{Na}.

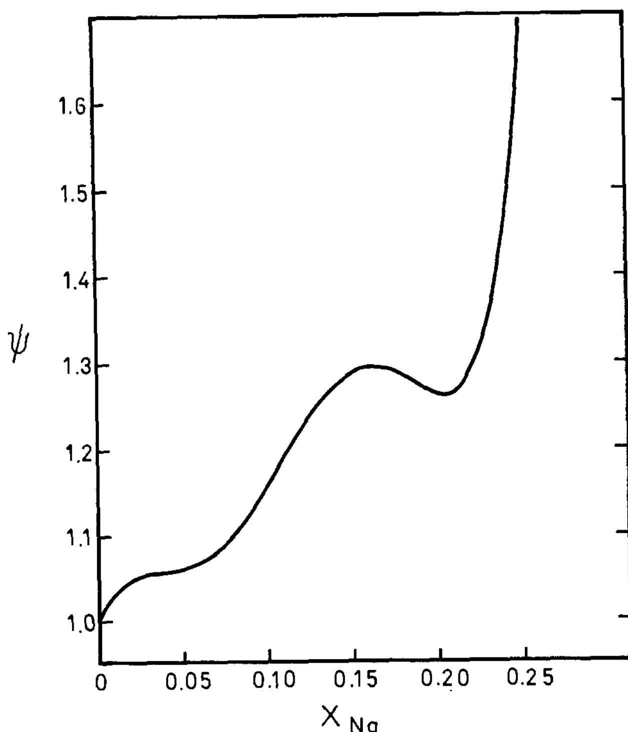

Fig. 9. Stability function $\psi = 1 + X_{Na}X_{Sn}/RT\ d^2g^E/dX_{Sn}^2$ at 360°C.

What is more interesting, however, is the small maximum in ψ observed around $X_{Na} = 0.16$, corresponding to the inflection point in the curve of Fig. 3. Resolution here is near the limit of precision of the measurements. The maximum in Fig. 9 occurs near the composition $NaSn_5(X_{Na} = 0.167)$ or $NaSn_6(X_{Na} = 0.143)$. There exists a solid intermetallic phase with the composition $NaSn_6$. It may be that in the liquid state short-range ordering at specific compositions is also energetically favored.

Conclusions

The beta-alumina solid electrolytes, which were fabricated in this laboratory in the form of impermeable tubes by a new slip-casting technique (8), have been shown to have a transport number of Na^+ ions equal to unity. This solid electrolyte works very well in a liquid sodium alloy concentration cell. Emf's are very stable and reproducible. The fact that impermeable tubes of the electrolyte are available permits the use of a sealed electrode compartment. This prevents Na losses by volatilization and contributes to the high stability and reproducibility of the measurements. The cells were sealed by a Pyrex-to-beta-alumina seal which is limited to temperatures below about 450°C. Aluminosilicate joints with much higher melting points are currently being developed, as are methods of fabrication of longer tubes of beta-alumina.

The very low resistivity and high selectivity for Na^+ ions of the beta-alumina permits the concentration of the alloy to be conveniently changed over a wide concentration range by the method of coulometric titration. Thus, one experimental cell can be used to study the entire composition and temperature range.

For the liquid Na-Sn alloys, the enthalpy of mixing and the excess free energy and excess entropy are all very negative, indicating a very stable ordered melt. The partial enthalpy of mixing and partial excess entropy of Sn, Δh_{Sn} and s_{Sn}^E, are very small and slightly positive. The results are interpreted in terms of a model of electron transfer from Na to Sn. Finally, a small maximum in the stability function is observed near $X_{Sn} = 0.16$, indicating short-range ordering near this composition.

Acknowledgments

The authors wish to thank Mr. Alain Dubreuil for his help and suggestions. Special thanks are also due to Mr. G. Sarfi for his expert assistance with the glass blowing, and to Dr. M. Gauthier for his understanding, and to Dr. M.-L. Saboungi for a critical reading of the manuscript. Financial assistance from the National Research Council of Canada and from a Cottrell grant from Research Corporation are gratefully acknowledged. One of the authors (M.R.) was supported by a France-Quebec graduate fellowship.

Manuscript submitted Aug. 3, 1977; revised manuscript received March 29, 1978.

Any discussion of this paper will appear in a Discussion Section to be published in the June 1979 JOURNAL. All discussions for the June 1979 Discussion Section should be submitted by Feb. 1, 1979.

REFERENCES

1. S. A. Weiner, "Ford Motor Co. Reports on Sodium-Sulfur Battery," Ford Motor Co., Dearborn, Mich.
2. R. R. Sayano and M. L. McClanahan, Rep. ECOM 74 0587-F, TRW Systems Group (1975).
3. L. Hsueh and D. N. Bennion, *This Journal*, **118**, 1128 (1971).
4. N. S. Choudhury, *ibid.*, **120**, 1664 (1973).
5. W. W. Liang and J. F. Elliott, *ibid.*, **123**, 617 (1976).
6. J. Lam and P. S. Nicholson, *Ceram. Bull.*, **55**, 286 (1976).
7. D. J. Fray and B. Savory, *J. Chem. Thermo.*, **7**, 485 (1975).

8. M. Rivier and A. D. Pelton, *Ceram. Bull.*, **57**, 183 (1978).
9. K. Hauffe and A. L. Vierk, *Z. Elektrochem.*, **53**, 151 (1949).
10. Y. K. Delimarsky and A. Kolorin, *Zh. Fiz. Khim.*, **28**, 1169 (1954).
11. H. E. Bartlett, A. J. Neethling, and P. Crowther, *J. Chem. Thermo.*, **2**, 583 (1970).
12. H. E. Bartlett and P. Crowther, *Electrochim. Acta*, **15**, 681 (1970).
13. P. Hubberstey and A. W. Castelman, *This Journal*, **119**, 967 (1972).
14. R. Hultgren, R. L. Orr, P. D. Anderson, and K. K. Kelley, "Selected Values of Thermodynamic Properties of Metals and Alloys," Wiley, New York (1963).
15. A. G. Morachevskii and M. F. Lantratov, *J. Gen. Chem. USSR (Engl. Transl.)*, **29**, 2075 (1959).
16. C. W. Bale and A. D. Pelton, *Metall. Trans.*, **5**, 2323 (1974).
17. C. Wagner, "Thermodynamics of Alloys," Addison-Wesley, Reading, Mass. (1952).
18. K. Hauffe and C. Wagner, *Z. Elektrochem.*, **46**, 160 (1940).
19. B. R. Ilschner and C. Wagner, *Acta Metall.*, **6**, 712 (1958).
20. H. Hoshino, R. W. Schmultzler, and F. Hensel, *Phys., Lett.*, **51A**, 7 (1975).
21. R. W. Schmultzler, H. Hoshino, R. Fisher, and F. Hensel, *Ber. Bunsenges. Phys. Chem.*, **80**, 107 (1976).
22. J. E. Enderby, *J. Phys. (Paris)*, **35**, C4-309 (1974); V. T. Nguyen and J. E. Enderby, *Phil. Mag.*, **35**, 1013 (1977).
23. H. Ruppersberg and W. Speicher, *Z. Naturforsch.*, **31a**, 47 (1976).
24. M-L. Saboungi, J. Marr, and M. Blander, *J. Chem. Phys.*, In press.
25. L. S. Darken, *Trans. TMS-AIME*, **239**, 80 (1967).

Occurrence of Salt Films during Repassivation of Newly Generated Metal Surfaces

Richard Alkire* and Daniel Ernsberger

Department of Chemical Engineering and Materials Research Laboratory, University of Illinois, Urbana, Illinois 61801

and Theodore R. Beck*

Electrochemical Technology Corporation, Seattle, Washington 98107

ABSTRACT

A mathematical model is developed to describe the processes by which transient appearance of salt films occurs during initial stages of corrosion of oxide-free metal surfaces. The model describes transport-controlled processes which lead to supersaturation by anodic dissolution, to precipitation of a salt film, and eventually to dissolution of the salt film after oxide passivation of the substrate material. Experimental observations on iron repassivation in $6N$ H_2SO_4 were used to test predictions of the model. Measurements of the lifetime of the salt film on the iron surface were in agreement with the model predictions; measurements of the extent of supersaturation prior to precipitation and of the moment of precipitation were in agreement with previous studies. In applying the model to predict the behavior of titanium in $3N$ HCl, calculations indicated that salt films of 20-100Å would be expected to form and then disappear within the time period of 10^{-5}-10^{-3} sec after generation of the oxide-free surface; during this period of time, the anodic dissolution rate of titanium would be expected to exceed 150 A/cm² if the salt film hypothesis is valid. The model presented here should be useful in guiding future experimental work into critical regions of parameter space.

During stress corrosion cracking, virgin metal surfaces are created and a sequence of electrochemical processes then takes place. In aqueous solutions, these processes would include metal dissolution, formation of a passive oxide film, and hydrogen ion reduction. While conducting fundamental investigations on repassivation processes, it has been found that, for some metals, the initial metal dissolution rate is so high that a salt film precipitates prior to oxide passivation. The investigation reported here uses a mathematical model to clarify conditions under which salt films may play a role in repassivation processes.

The awareness of salt films during metal passivation is not new. In 1927, Müller (1) reported observations on the existence of salt films during the passivation of iron and nickel. His work on these and other metals inspired a large number of investigations (2) which have continued for several decades (3). Various interpretations of passivation processes were reviewed by Hoar (4) in a work of broad scope and, more recently, by Galvele (5). Vetter and Strehblow (6) and Isaacs (7) have recently given persuasive evidence that pitting processes are closely related to the formation of salt layers at the interface.

For iron dissolution in sulfuric acid, the formation of a ferrous salt film was described by Serra and Feliú (8) who concluded that supersaturation of the electrolyte occurred prior to precipitation. Schwabe (9) indicated that a primary salt layer was a necessary precursor in the passivation of iron in sulfuric acid. More recently, Abakumova and Milyutin (10) suggested that the salt film creates conditions under which subsequent passivation by oxide films can occur.

For nickel passivation in sulfuric acid, early studies by Turner (11) and by Landsberg and Hollnagel (12) supported the view that pH changes occur in addition to accumulation of nickel ions in the anolyte. A number of authors (13-18) have used continuous mechanical scraping to study broader aspects of repassivation phenomena on bare surfaces of iron, nickel, chromium, gallium, and titanium. These studies, however, did not

* Electrochemical Society Active Member.

lend themselves to quantitative analysis because of the distribution of residence times exhibited by the continuously abraded rotating anode. An improved technique was developed by Ambrose and Kruger (19) who used triboellipsometry to investigate repassivation of freshly abraded titanium surfaces in NaCl; they concluded that the first monolayer of oxide was completed about 40 msec after cessation of abrasion. Using a different method to generate bare metal surface, *i.e.*, rapid fracture, Beck (20) showed that repassivation of titanium begins within 1 msec following fracture; the sequence of likely events following fracture would in this situation include formation and collapse of a cavitation bubble, charging of the electrical double layer, anodic dissolution of the bare metal (accompanied by hydrogen reduction), and eventually formation of a protective oxide film. Beck postulated that transient salt films were responsible for the primary passivation of bare titanium surfaces.

Salt films can also occur during the dissolution of nonpassivating metals (1). Lorenz (21) used unsteady-state experiments at constant current to demonstrate that supersaturation occurred prior to salt film precipitation; investigating several metals, he found that precipitation occurred with anolyte concentrations ranging between 1.4 and 5.0 times the saturation concentration. In a similar manner, Beck (22) reexamined the earlier data of Müller (1) and calculated supersaturation levels in the range of 1-5 times the saturation concentration for a variety of metal/salt systems. Alkire *et al.* (23) carried out dissolution experiments on artificial copper pits and observed precipitation when the anolyte concentration exceeded 2.2 times the saturation value.

Whereas the foregoing investigations were mostly carried out under diffusion-controlled transport, salt films have also been reported in the presence of convection past the anode. Ross *et al.* (24) studied anodic behavior of iron and steel in flowing sulfuric and hydrochloric acids and found that mass transfer behavior at high current densities was complex owing to a surface layer of ferrous precipitates. Kolotyrkin *et al.* (25) describe various salt film effects which accompany iron corrosion in phosphate solutions. Chin (26) reported precipitation on nonprotective anodic films during controlled mass transfer studies on electrochemical machining systems. Landolt and co-workers (27) studied the role of convective mass transfer on high rate iron and nickel dissolution under nonpassivating conditions and have emphasized the role of salt precipitation layers on system behavior.

The literature cited above indicates clearly that salt films play a major role in many transient repassivation processes as well as in both transient and steady-state nonpassivating processes. Accordingly, it seems reasonable that a more quantitative treatment of salt film precipitation phenomena under both diffusive and convective transport situations would be useful for the clarification of fundamental aspects of many anodic dissolution processes.

The purpose of this investigation is to develop a mathematical model for the formation and disappearance of salt films during early stages of diffusion-controlled metal passivation. An original objective was to determine whether primary passivation of titanium within 1 msec (20) could be attributed to formation of a salt film. As will be shown below, the model developed for this purpose predicts that the salt film, if formed on titanium, would develop and then disappear in the time period of about 10^{-5}-10^{-3} sec after formation of the bare surface. However, present experimental methods are unable to provide direct verification within this time scale. Therefore an additional objective of this work has been to test the theoretical model against experimental observations on metals which passivate more slowly than titanium. Experimental results on iron in 6*N* H_2SO_4, reported elsewhere (28), provided a convenient set of data for testing the mathematical model.

Experimental

The experimental procedures used in the investigation of iron repassivation (28) are summarized briefly here. Cylindrical and rectangular anodes of high purity iron were cast in epoxy resin so that only the end was exposed to electrolysis. Prior to study, the metal was recessed by 1-2 mm below the resin surface by means of anodic dissolution in chloride media. By recessing the anodic surface, the current distribution is nearly uniform over the recessed surface, and one-dimensional transport equations can thereby be used. The anode was positioned facing upward in the cell in order to minimize natural convection effects.

Experiments were performed in 6*N* H_2SO_4 containing various concentrations of ferrous sulfate. A potentiostatic power supply was programmed to apply a step change in electrode potential. Prior to the step change, the potential was held in the active region at low anodic current (−0.47V *vs.* SCE) under which conditions there is no surface film. Following the step change, the potential was held constant in a region where the metal eventually passivated (+0.4 to +1.0V *vs.* SCE). Current transients were recorded with a storage oscilloscope while simultaneously viewing the surface with a 60× binocular microscope.

Theoretical Model

The model developed below is designed to deal with diffusion-controlled salt film phenomena which might occur at bare metal surfaces exposed to electrolyte under an applied potential. The model is therefore capable of being used to inquire whether the proposed existence of salt films is consistent with experimental observations, as in the case of titanium investigated below.

The model does not deal specifically with the method by which bare metal is generated, common methods being abrasion, shearing or fracturing, stretching, and electrochemical reduction. Only anodic processes are taken into account; although it is clear that simultaneous cathodic processes occur during repassivation, it is assumed that such cathodic processes would not influence the course of the anodic processes other than by providing additional current for oxidation over and above the measured anodic current. Thus, for example, the model would not apply to situations where copious hydrogen evolution would stir the electrolyte and thereby influence diffusion processes which accompany anodic dissolution.

Following a sudden appearance of oxide-free metal, the sequence of events which is to be described by the model is:

1. Rapid metal dissolution under *IR*-limited constant current conditions causes an increase in metal salt concentration near the corroding surface.
2. Nucleation occurs on the surface of an adherent salt film which then grows by continued precipitation from the supersaturated electrolyte and also by continued anodic dissolution of the metal.
3. Growth of the salt layer is accompanied by a rapid decrease in the anodic current. Formation of a passive oxide layer occurs under the salt layer. (The precipitated salt layer is assumed to have an equilibrium quantity of water of hydration which is thereby available for oxide formation.) The region of supersaturated electrolyte becomes dissipated, and the salt film thereby attains a maximum thickness.
4. The salt film begins to dissolve, eventually to disappear altogether, leaving only the passive oxide film on the metal surface.

The period of time up to the instant of precipitation is denoted as stage I, and the period of time during which the salt film exists on the surface as stage II.

The experimental studies were designed to simplify the mathematical treatment as much as seemed rea-

sonable while still preserving the salient features of the corroding system. The assumptions which have been made are: (*i*) Only one electrochemical reaction is taken into account, *i.e.*, anodic metal dissolution; (*ii*) diffusion of the reaction product away from the surface obeys semi-infinite one-dimensional diffusion without migration or convection effects; (*iii*) the diffusion coefficient is constant; (*iv*) the anodic dissolution rate is constant prior to salt film precipitation, and decreases thereafter according to the empirical relation given by Eq. [9]; (*v*) precipitation of the salt films occurs onto the electrode surface and not homogeneously in the electrolyte phase. Concerning migration effects, Serra and Feliú (8) have provided strong evidence that proton and anion diffusion effects are negligible in iron passivation in sulfuric acid. Assumption (*iv*) implies that the current needed to form the passive film is negligible.

The diffusion of metal ions in the presence of excess supporting electrolyte obeys Fick's second law

$$\frac{\partial c}{\partial t} = D\frac{\partial^2 c}{\partial y^2} \qquad [1]$$

Because the side conditions on Eq. [1] during stage I are different from those during stage II, it is convenient to discuss these stages separately.

Diffusion during stage I.—At the instant of generation of fresh surface, it is assumed that the electrolyte composition is uniform. The anodic dissolution process commences with a constant rate. The side conditions on Eq. [1] are therefore

$$\begin{aligned} c(\infty, t) &= c_b \\ c(y, 0) &= c_b \\ \frac{\partial c}{\partial y}(0, t) &= -\frac{i}{n\mathbf{F}D} \end{aligned} \qquad [2]$$

The well-known analytical solution of Eq. [1] and [2] is given by Carslaw and Jaeger (29)

$$c(y,t) = c_b + \frac{2i}{n\mathbf{F}}\sqrt{\frac{t}{\pi D}}\exp\left(-\frac{y^2}{4Dt}\right) - \frac{iy}{n\mathbf{F}D}\,\mathrm{erfc}\left(\frac{y}{\sqrt{4Dt}}\right) \qquad [3]$$

Stage I continues up to the moment of precipitation, denoted by t^*, at which time the concentration at the electrode surface is denoted by $c^s{}_{\mathrm{pptn}}$. At the instant of precipitation, Eq. [3] shows that

$$c^s{}_{\mathrm{pptn}} = c(0, t^*) = c_b + \frac{2i}{n\mathbf{F}}\sqrt{\frac{t^*}{\pi D}} \qquad [4]$$

Diffusion during stage II.—Following the instant of precipitation, the concentration distribution in the electrolyte is given by Eq. [3] except at the surface, where the precipitated salt film is in equilibrium with saturated solution. For stage II, the side conditions on Eq. [1] are therefore

$$\begin{aligned} c(\infty, t) &= c_b \\ c(y, t^*) &= c_b + \frac{2i}{n\mathbf{F}}\sqrt{\frac{t^*}{\pi D}}\exp\left(-\frac{y^2}{4Dt^*}\right) - \frac{iy}{n\mathbf{F}D}\,\mathrm{erfc}\left(\frac{y}{\sqrt{4Dt^*}}\right) \\ c(0, t > t^*) &= c_{\mathrm{sat}} \end{aligned} \qquad [5]$$

The analytical solution of Eq. [1] subject to side conditions of Eq. [5] is given in Carslaw and Jaeger (30)

$$c(y,t) = c_{\mathrm{sat}}\left[1 + \frac{1}{\sqrt{4\pi Dt}}\int_0^\infty f(y')\left(\exp\frac{-(y-y')^2}{4Dt} - \exp\frac{-(y+y')^2}{4Dt}\right)\right]dy' \qquad [6]$$

where

$$f(y') = -1 + \frac{c_b}{c_{\mathrm{sat}}} + \frac{2i}{n\mathbf{F}c_{\mathrm{sat}}}\sqrt{\frac{t}{\pi D}}\exp\left(-\frac{y'^2}{4Dt}\right) - \frac{iy}{n\mathbf{F}c_{\mathrm{sat}}D}\,\mathrm{erfc}\left(\frac{y'}{\sqrt{4Dt}}\right) \qquad [7]$$

Equations [3] and [6] provide a complete history of the concentration profile in the solution during stages I and II.

Salt film existence during stage II.—During stage II, a salt film appears on the metal surface. Growth of the salt film occurs via two routes by which metal ions arrive at the surface: (*i*) anodic oxidation of the metal by electrochemical reaction, and (*ii*) diffusion from supersaturated solution near the metal surface. The thickness of the salt film is therefore

$$d(t) = m\int_{t^*}^{t}\left(\frac{i(t)}{n\mathbf{F}} - D\frac{\partial c}{\partial y}\bigg|_{y=0}\right)dt \qquad [8]$$

The anodic reaction rate during stage II was experimentally observed (28) to decrease according to $(\mathrm{time})^{-s}$ where s has a constant value during the initial stages of decrease, that is

$$i\,(t > t^*) = i|_{t=t^*}\left(\frac{t}{t^*}\right)^{-s} \qquad [9]$$

Equation [8] has two terms within the integral, the first of which is always positive (anodic film growth) but which decreases in the course of time. The second term is initially positive (film growth by precipitation) but changes sign during the course of stage II (film dissolution). Because the film dissolution rate can eventually exceed the anodic formation rate, the salt film thins and eventually disappears.

Although the mathematical model takes specific account only of the salt film, it is tacitly presumed that additional passivation processes also occur during the existence of the salt film to such extent that, by the time the salt film dissolves, the surface is sufficiently passive that large anodic dissolution currents would not be observed. A mathematical treatment of the growth of oxide films would require consideration of the potential distribution in addition to the mass transfer aspects treated here.

Method of solution.—Equation [8] was integrated by a numerical procedure. It was found necessary to use different methods of integration over various ranges of time in order to avoid overflow and underflow difficulties.

$0 < t/t^* < 10^{-6}$: The complementary error function in Eq. [7] was approximated by

$$\mathrm{erfc}\left(\frac{x}{2}\right) \simeq 1 - \frac{x}{\sqrt{\pi}}$$

$10^{-6} < t/t^* < 1$: The derivative term in Eq. [8] was first rearranged with use of Leibnitz' rule, and the resulting integral (which extends to infinity) was evaluated with use of twelve-point Gauss-Laguerre quadrature. Equation [8] was then integrated with use of the trapezoidal rule.

$t/t^* > 1$: Equation [8] was integrated with use of the trapezoidal rule. The Leibnitz' integral, which extends to infinity, was truncated when the area of the final trapezoid was less than 0.01% of the accrued value of the integral.

Table I. Physical properties of systems under study

Property	Iron system	Ref	Titanium system
n, g-equiv./g-mole	2		3
ρ_{soln}, g/cm^3	1.294	(31)	
c_{sat}, g-mole/liter	0 971	(32)	4†
D, cm^2/sec	5.5×10^{-6}	(33-35)	10^{-5}†
Crystal	$FeSO_4 \cdot 7H_2O$	(31)	$TiCl_3$
ρ_{xtl}, g/cm^3	1.898	(36)	2.64
m, cm^3/g-mole	146.0*		58.5†
c_{acid}, g-equiv./liter	6N H_2SO_4		3N HCl
Electrode area, cm^2	0.5		0.5

* Calculated.
† Estimated.

Comparison of Experiments with Theory

Investigations were conducted with two different systems: iron in 6N H_2SO_4 and titanium in 3N HCl. In the iron system, the purpose of the investigation was to test model predictions in a system for which the parameters are reasonably well known. In the titanium system, the purpose was to predict conditions under which salt films might be expected and to compare those conditions with experimental observations reported to date. The parameters of both systems are listed in Table I.

Iron system.—Since the passive film on iron is reducible, oxide-free metal surfaces were obtained by controlling the metal potential at values at or slightly cathodic to its rest potential (−0.46V *vs.* SCE). The process of repair following rupture was simulated by suddenly changing the control potential from the above value to a more anodic potential (between +0.4 and +1.0V *vs.* SCE) at which passivity is eventually gained. A typical current-time response following a potential step to +0.5V *vs.* SCE is shown in Fig. 1. The current rapidly increased to a plateau level and then decreased. Light green crystals were first observed growing inward from the edges of the specimen at the time indicated by t^* on Fig. 1. Crystal growth continued inward until the sharp drop in current shown. At +0.4V, the entire iron surface became covered with green crystals; at +1.0V, approximately 20% of the surface was covered with green crystals at the time of the sharp drop in current. No other changes were visible until the crystals dissolved at t_p.

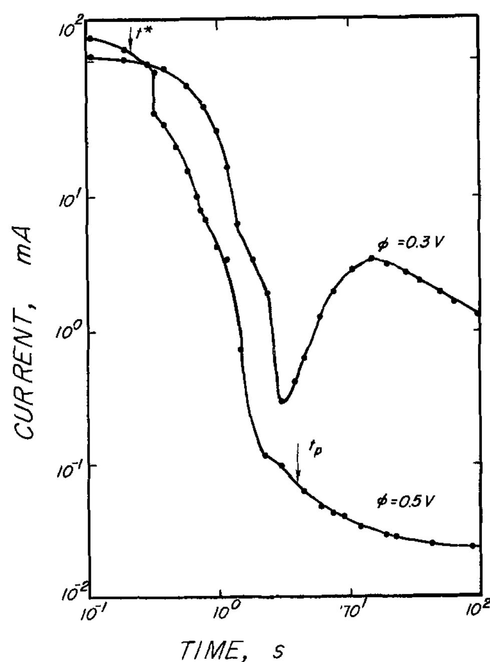

Fig. 1. Current decay curves for zone-refined iron in 6N H_2SO_4 at potentials below and above passivation potentials (anode area = 0.050 cm^2).

A transient current curve for a potential step to +0.3V, just below the passivation potential, is also shown in Fig. 1. For this condition a salt film forms but does not redissolve. The minimum in current for the +0.3V curve corresponds to a visible change in the salt crystal morphology. Flushing the pit with a jet of electrolyte for a period of 10 sec or longer reactivates the pit and repeats the sequence at +0.3V but has no effect at +0.5V. In the latter case the passive oxide film has formed.

The time during which lateral growth or dissolution of crystals occurred may be compared to the time constant characteristic of diffusion processes in the lateral direction, D/r^2. For pits of about 0.2 cm diam and for $D = 5.5 \times 10^{-6}$ cm^2/sec, one finds a time constant of roughly 10^4 sec. Since this time constant is much greater than the time during which repassivation events occur, it is proper to claim that the one-dimensional diffusion equation can be applied locally along the surface. That is, although the model does not account for crystal growth processes, it is still appropriate to compare the average time to film formation and average time to film dissolution to predictions based on a one-dimensional model.

In Fig. 1, the plateau region is identified as stage I. The plateau current density is taken to be i in Eq. [5], and the time at which the current decreases sharply is taken to be t^* in Eq. [5]. With these values, the supersaturation ratio at the moment of precipitation has been calculated with use of Eq. [8]. Figure 2 gives results for various magnitudes of potential jump and for various solutions. Each data point represents the average of about four separate measurements; measurements agreed among each other to within 2% of the value displayed. It is seen that the supersaturation ratio is slightly lower for the saturated solutions and for the larger potential jumps (higher plateau currents). These data support the interpretation that the initial plateau region in Fig. 1 corresponds to stage I.

Figure 3 gives the time at which dissolution of the salt film was observed in experiments on two unsaturated solutions. The initial plateau current was determined from the initial plateau region of the oscilloscope trace (see Fig. 1), and the dissolution process was observed with a microscope during the course of the experiment. It was difficult to see the surface salt as clearly at the highest current densities. Disappearance of the salt film did not occur uniformly over the surface at a particular instant. The salt film was observed to disappear from various parts of the surface over a range of time. In Fig. 3, each data point corresponds to the average of the beginning and the end of that time period; the vertical lines indicate the range of times over which disappearance was observed. Each data point is the average of about four separate experimental observations. In Fig. 3, it is seen that dis-

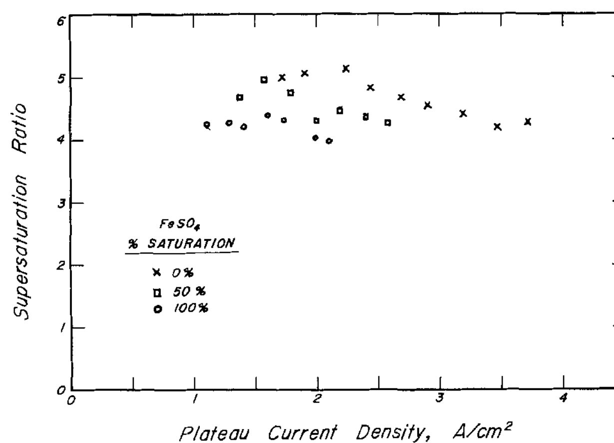

Fig. 2. Evidence for supersaturation processes during iron passivation in 6N H_2SO_4 containing various amounts of ferrous sulfate.

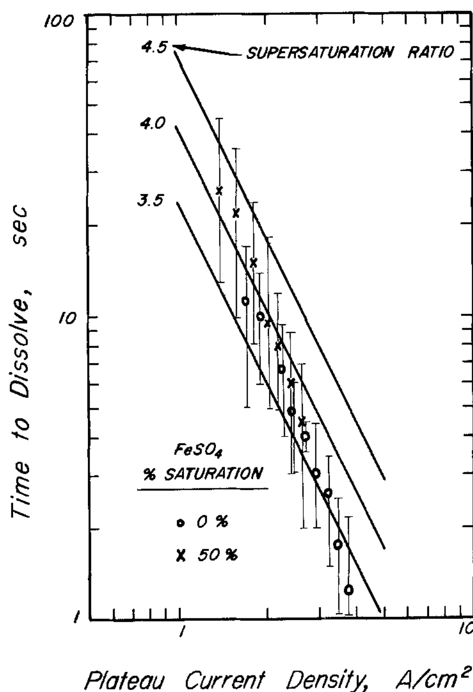

Fig. 3. Duration of existence of salt films during iron passivation in 6N H_2SO_4; solid lines give theoretical results with $s = 4$.

solution behavior in both solutions is correlated with use of the plateau current density.

In order to compare the data in Fig. 3 with calculations, it is necessary to specify the parameter s which appears in Eq. [9], and the parameter η which is proportional to the supersaturation ratio. For the iron system, the current decreased approximately at t^{-4} after the initial plateau period (28) as seen in Fig. 1. Calculations were therefore carried out with $s = 4$ and with various values of c^s_{pptn}/c_{sat} (supersaturation ratio): 3.5, 4.0, and 4.5. Calculated results are shown by the three diagonal solid lines in Fig. 3. By comparison with average experimental values (symbols) it is seen that data fall into a range of supersaturation ratios between 3.3 and 4.3, about 15% lower than the range found previously in Fig. 2. The data in Fig. 3 exhibit lower supersaturation ratios at larger values of plateau current density, in agreement with the trends seen in Fig. 2.

The theoretical model was also used to calculate the maximum salt film thickness which would be expected during stage II of dissolution in the iron system. Results are given in Fig. 4 for $s = 4$ and various supersaturation ratios. The maximum film thickness was found to vary inversely with the plateau current density. For the supersaturation ratios reported here (3.5-5.0) and for the observed range of plateau current densities (1.4-3.8 A/cm²), it was found that the maximum film thickness would be expected to be between 2 and 25 μm. The difficulties in observing films at the higher current densities may therefore be owing to the thinness of the film being less than the wavelength of light.

Titanium system.—The iron system is well poised for comparison between experimental data and theoretical calculations because the parameters which characterize the system are reasonably well known. On the other hand, making theoretical calculations for the titanium system is less satisfying since many of the system parameters are unknown. However, as indicated by the introductory remarks, it is nevertheless possible to estimate the range of several important parameters from experimental studies to date. The purpose of conducting theoretical calculations on the titanium system is, therefore, to determine whether or not, within reasonable constraints, it is possible for a salt film to form during initial moments of corrosion following generation of a virgin surface.

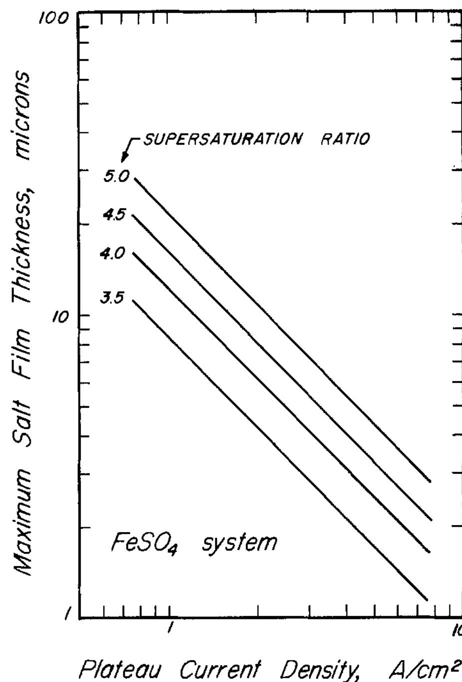

Fig. 4. Calculated results for iron system under study, with $s = 4$

In order to carry out theoretical calculations, it is necessary to specify the initial plateau current density, the supersaturation ratio at the moment of precipitation, and the parameter s in Eq. [9]. For the titanium system, rapid fraction experiments (20) have suggested that the initial anodic current density may be as high as 10^1-10^3 A/cm²; current decay was observed to begin at about 1 msec after fracture, and to decrease initially as t^{-2}. Because the supersaturation ratio had not been reported independently, calculations were carried out for various ratios between 1.0 and 3.0. Other values of parameters in the titanium system were given in Table I. Calculated results are given in Table II for $s = 2$, $10^2 < i < 10^3$, and $1.0 < c^s_{pptn}/c_{sat} < 2.82$.

Table II. Predicted behavior for titanium system for $s = 2$ and a range of parameter values

c^s_{pptn}/c_{sat}	100 A/cm²	200 A/cm²	500 A/cm²	1000 A/cm²
Part I: Time to salt film formation in milliseconds				
1.02	1.1	0.27	0.04	0.01
1.07	1.2	0.30	0.05	0.01
1.13	1.3	0.34	0.05	0.01
1.24	1.5	0.41	0.06	0.02
1.35	1.9	0.48	0.08	0.02
1.47	2.3	0.57	0.09	0.02
1.69	3.0	0.75	0.12	0.03
2.03	4.3	1.1	0.17	0.04
2.26	5.4	1.3	0.21	0.05
2:48	6.5	1.6	0.26	0.06
2.82	8.4	2.1	0.34	0.08
Part II: Time to salt film dissolution in milliseconds				
1.02	1.5	0.38	0.06	0.02
1.07	2.2	0.56	0.09	0.02
1.13	3.0	0.74	0.12	0.03
1.24	4.4	1.11	0.18	0.04
1.35	6.8	1.7	0.27	0.07
1.47	10.5	2.6	0.42	0.10
1.69	19	4.7	0.75	0.19
2.03	43	10.8	1.7	0.43
2.26	63	16	2.5	0.63
2.48	107	27	4.3	1.1
2.82	195	49	7.8	2.0
Part III: Maximum salt film thickness in angstroms				
1.02	26	13	5	3
1.07	104	52	21	10
1.13	206	103	41	20
1.24	473	237	94	47
1.35	819	409	153	82
1.47	1,243	621	249	124
1.69	2,331	1,165	466	233
2.03	4,572	2,286	914	457
2.26	6,475	3,238	1,295	648
2.48	8,723	4,362	1,745	872
2.82	12,743	6,371	2,547	1,274

In the body of Part I of Table II, the time is given at which a salt film would form for each combination of supersaturation ratio and initial current density indicated. Since it is known that the initial current plateau does not persist for more than 1 msec, certain regions of parameter space clearly do not conform to experimental observations; these regions lie below the solid line drawn between entries in Part I. In Part II of Table II, the time at which dissolution is complete is listed for the various combinations of parameter values indicated. The ellipsometric measurements of Ambrose and Kruger (19) imply that if a salt film existed, it must already have disappeared within the 10 msec needed to initiate ellipsometric observations, since these authors did not observe salt films. The region below the solid line drawn in Part II corresponds to regions of parameter space which do not conform to the Ambrose and Kruger observation. Finally, Part III of Table II lists the maximum film thickness which may be expected for the different parameter values. Coulometric measurements during repassivation have indicated (20) that if a salt film exists, its thickness would range between 20 and 100Å. As seen in Part III of Table II, this criterion is by far the most stringent since it blocks out all but a narrow band of parameter space, contained between the solid lines.

By comparing the three parts of Table II, the view emerges that if salt films indeed form during the initial moments of titanium corrosion, then the initial plateau current density would exceed 150 A/cm², the supersaturation ratio would lie between about 1.1 and 1.3, and dissolution of the salt film would be complete within 0.03 to 1.0 msec following generation.

Discussion: Theoretical Model

A limiting case of behavior is encountered when all of the salt film originates by precipitation from the solution phase, that is, $s = \infty$. Pursuit of this limiting case provides a method for tabulating computer results so that users can, with simple algebra, estimate the salt film thickness and the lifetime of the film on the surface.

To achieve more general results, Eq. [8] will be cast into dimensionless form by defining

$$T = \frac{t - t^*}{t^*}$$

$$\theta = \frac{c}{c_{sat}}$$

$$\xi = \frac{y}{\sqrt{Dt^*}}$$

$$\delta = \frac{d}{\sqrt{Dt^*}}$$

$$M = mc_{sat}$$

By disregarding the anodic growth contribution to Eq. [8], the dimensionless form which results is

$$\frac{\delta(T)}{M} = -\int_0^T \frac{\partial\theta}{\partial\xi}(0, T)\, dT \qquad [10]$$

The right-hand side of Eq. [10] can be evaluated upon specification of the value of the parameter

$$\eta = \frac{i}{n\mathbf{F}c_{sat}}\sqrt{\frac{t^*}{D}}$$

The integration indicated by Eq. [10] has been carried out numerically, and dimensionless results are tabulated in Table III wherein the maximum value of the right-hand side of Eq. [10] is given for various values of η. As shown by the example calculation which follows, these results can be used to estimate the maximum thickness which a salt film will attain during its lifetime in any system which conforms to the model assumptions. If anodic film growth also occurs during precipitation, then the film will actually be thicker than the value computed from Table III.

Table III. Dimensionless salt film thickness and lifetime for the limiting case of $s = \infty$

η	$\frac{\delta_{max}}{M}(\eta)$	$T_p(\eta)$
0.9	0.00083099	1.0004
1.0	0.0053905	1.0263
1.2	0.035969	1.1630
1.5	0.116730	1.5842
2.0	0 30972	2.7444
2.2	0.40091	3.0932
2.5	0.54880	4.0143
3.0	0.81755	6.2089
3.2	0.93071	7.2506
3.5	1.1067	8.5007
4.0	1.4136	11.801

The dimensionless time at which the salt film dissolves completely, T_p, is that nonzero value for which

$$\int_0^{T_p} \frac{\partial\theta}{\partial\xi}(0, T)\, dT = 0 \qquad [11]$$

The integration indicated by Eq. [11] has been performed numerically for various values of η, and the resulting function $T_p(\eta)$ is tabulated in Table III. As illustrated by the following example, these results can be used to estimate the lifetime of the salt film on the surface for any system which the model describes. If anodic film growth also occurs after salt film precipitation, then the film will actually exhibit a longer lifetime than would be computed from data in Table III.

To demonstrate use of Table III, consider events for an iron system in which the electrolyte contains no iron salt ($c_b = 0$). For sake of example, suppose that experimental data indicate that the initial plateau current density is 2 A/cm² and that precipitation sets in 0.6 sec after polarization. By Eq. [4], one finds that the surface concentration at the moment of precipitation is 0.0039 gmole/cm³, or 4.0 times the saturation concentration. Also, η is found as

$$\eta = \frac{\sqrt{\pi}}{2}\frac{c^s{}_{pptn}}{c_{sat}} = 3.5$$

From Table III, find

$$\frac{\delta_{max}}{M} = 1.1067$$

where

$$d = 1.1067\,\frac{n\mathbf{F}c_s{}^2D\eta m}{i} = 2.83 \times 10^{-4}\text{ cm}, \quad \text{or } 2.83\ \mu\text{m}$$

This value may be compared with the value reported in Fig. 4 (4 μm). The difference corresponds to the effect of anodic film growth which is not considered in the limiting case under discussion.

From Table III, also find

$$T_p = 8.50$$

whence

$$t_p = (T_p + 1)\,\frac{\eta^2n^2\mathbf{F}^2c_{sat}{}^2D}{i^2} = 5.62\text{ sec}$$

This value may be compared with the experimental value reported in Fig. 3 (5-18 sec). The difference may be owing to anodic current flowing during precipitation.

Summary and Conclusions

A theoretical model has been developed to evaluate the hypothesis that salt films appear during repassivation of newly generated surfaces of certain metals. The model was tested by conducting experiments with iron in 6N H_2SO_4 under controlled ranges of system parameters. The model provided a correlation between the extent of supersaturation prior to salt precipitation,

the moment at which precipitation occurs, and the moment at which salt film dissolution occurs. The same model was then used to predict conditions under which a salt film would be expected on freshly generated titanium in 3*N* HCl, should such a film form. Comparison of calculated results with previously reported experimental observations indicates that the possible existence of salt films on titanium cannot be evaluated with data which are to date available. The investigation demonstrates how a mathematical model can be used to test hypotheses and to guide experimental work into regions of parameter space where definitive experiments can be carried out.

The model presented here does not include potential field effects or potential dependent aspects of charge-transfer or crystallization processes. To do so would require further clarification of various transport mechanisms which are incompletely understood at present.

The assumptions on which the model rests have been chosen primarily for the specific applications discussed here. The assumptions could be modified with relative ease to include additional effects such as convection, migration, hydrolysis, variable transport properties, and multiple reactions.

Acknowledgments

This investigation was supported by the National Science Foundation (NSF DMR 74-08716), by the Department of Energy (EY-76-C-02-1198) and by the Air Force Office of Scientific Research (F44620-76-C-0001).

Manuscript submitted Feb. 2, 1978; revised manuscript received April 10, 1978.

Any discussion of this paper will appear in a Discussion Section to be published in the June 1979 JOURNAL. All discussions for the June 1979 Discussion Section should be submitted by Feb. 1, 1979.

Publication costs of this article were assisted by the University of Illinois.

SYMBOLS

- c concentration of salt, gmole/cm^3
- c_b bulk concentration of salt, gmole/cm^3
- c^s_{pptn} surface concentration at moment of precipitation, gmole/cm^3
- c_{sat} saturation concentration of salt, gmole/cm^3
- d thickness of salt film, cm
- D diffusion coefficient, cm^2/sec
- $\mathbf{F}$ Faraday's constant
- i current density, A/cm^2
- m molar volume, cm^3/gmole
- M mc_{sat}, dimensionless molar volume
- n number of electrons in dissolution reaction
- s parameter defined by use in Eq. [9]
- t time, sec
- t^* duration of stage I, sec
- t_p total duration of stage I and stage II, sec
- T $(t - t^*)/t^*$, dimensionless time
- y distance variable, cm
- δ $d/\sqrt{Dt^*}$, dimensionless salt film thickness
- ξ $y/\sqrt{Dt^*}$, dimensionless distance variable
- θ c/c_{sat}, dimensionless concentration variable
- η $i\sqrt{t^*}/n\mathbf{F}c_{sat}\sqrt{D}$, dimensionless current

REFERENCES

1. W. J. Müller, "Die Bedeckungstheorie der Passivität der Metalle under ihre experimentelle Begründung," Verlag-Chemie, Berlin (1933).
2. R. Weiner and F. Halla, *Z. Elektrochem.*, **48**, 361 (1942).
3. W. Machu and A. Rägheb, *Werkst. Korros.*, **4**, 429 (1953); *ibid.*, **15**, 215 (1954); *Z. Metallk.*, **47**, 176 (1956).
4. T. P. Hoar, in "Modern Aspects of Electrochemistry," Vol. 2, J. O'M. Bockris, Editor, p. 262, Butterworths, London (1959).
5. J. R. Galvele, in Proceedings of 4th International Symposium on Passivity, Airlie, Virginia, Oct. 17-21, 1977.
6. K. J. Vetter and H. H. Strehblow, *Ber. Bunsenges. Phys. Chem.*, **74**, 1024 (1970).
7. H. S. Isaacs, *This Journal*, **120**, 1454 (1973).
8. M. Serra and M. Feliú, in "Proceedings of 6th C.I.T.C.E. Meeting," p. 360, Butterworths, London (1954).
9. K. Schwabe, *Z. Phys. Chem.*, **215**, 343 (1960).
10. Yu. P. Abakumova and N. N. Milyutin, *J. Appl. Chem. USSR*, **45**, 809 (1972).
11. D. R. Turner, *This Journal*, **98**, 434 (1951).
12. R. Landsberg and M. Hollnagel, *Z. Elektrochem.*, **58**, 680 (1954); *ibid.*, **60**, 1098 (1956).
13. K. Schwabe and G. Dietz, *Ber. Bunsenges. Phys. Chem.*, **62**, 751 (1958).
14. N. D. Tomashov, H. M. Strukov, and L. P. Vershinina, *Dokl. Akad. Nauk SSSR*, **171**, 1134 (1966); *Elektrokhimiya*, **5**, 26 (1969); N. D. Tomashov and L. P. Vershinina, *Electrochim. Acta*, **15**, 501 (1970).
15. C. M. Chen, F. H. Beck, and M. G. Fontana, *Corrosion*, **26**, 135 (1970).
16. T. I. Popova and N. A. Simonova, *Electrokhimiya*, **6**, 1125 (1970).
17. R. S. Perkins, *This Journal*, **119**, 713 (1972).
18. T. R. Beck, *Electrochim. Acta*, **18**, 807 (1973).
19. J. R. Ambrose and J. Kruger, *Corrosion*, **28**, 30 (1972); *This Journal*, **121**, 599 (1974).
20. T. R. Beck, *This Journal*, **115**, 890 (1968); *Electrochim. Acta*, **18**, 815 (1973); *Corrosion*, **30**, 408 (1974).
21. W. Lorenz, *Z. Phys. Chem. N. F.*, **20**, 95 (1959).
22. T. R. Beck, Paper 99 presented at the Electrochemical Society Meeting, Boston, Massachusetts, Oct. 7-11, 1973.
23. R. Alkire, D. Ernsberger, and D. Damon, *This Journal*, **123**, 458 (1976).
24. T. K. Ross, G. C. Wood, and J. Mahmud, *ibid.*, **113**, 334 (1966).
25. Ya. M. Kolotyrkin, Yu. A. Popov, and Yu. V. Alekseev, *Elektrokhimiya*, **8**, 1725 (1972); *ibid.*, **9**, 192 (1973); A. N. Katrevich, G. M. Florianovich and Ya. M. Kolotyrkin, *Zashch. Met.*, **10**, 369 (1974); Ya. M. Kolotyrkin, *Mendeleev Chem. J.*, **20**, 76 (1975).
26. D.-T. Chin, *This Journal*, **118**, 174 (1971).
27. M. Datta and D. Landolt, *ibid.*, **122**, 1466 (1975); H. C. Kuo and D. Landolt, *Electrochim. Acta*, **20**, 393 (1975).
28. T. R. Beck, To be published in *This Journal*.
29. H. S. Carslaw and J. C. Jaeger, "Conduction of Heat in Solids," p. 75, Oxford University Press, London (1959).
30. H. S. Carslaw and J. C. Jaeger, *ibid.*, p. 58.
31. A. P. Belopolskii, V. N. Kolycheva, and S. Shpunt, *Zh. Prikl. Khim. (Leningrad)*, **21**, 794 (1948).
32. "Solubilities," 4th ed., W. F. Linke, Editor, p. 1049, American Chemical Society, Washington, D.C. (1958).
33. D. Jahn and W. Vielstich, *This Journal*, **109**, 849 (1962).
34. L. B. Anderson and C. N. Reilley, *J. Electroanal. Chem.*, **10**, 295 (1965).
35. A.-M. Baticle, F. Perdu, and P. Vennereau, *C. R. Acad. Sci. Paris*, **264**, 12 (1967).
36. J. W. Mellor, "A Complete Treatise on Inorganic and Theoretical Chemistry," Vol. XIV, p. 242-288, Longmans Green & Co., New York (1935).

An Application of Coulostatic Method for Rapid Evaluation of Metal Corrosion Rate in Solution

Ken-ichi Kanno, Masayuki Suzuki, and Yuichi Sato

Tokyo Shibaura Electric Company, Limited,
Toshiba Research and Development Center, Saiwai-ku, Kawasaki 210, Japan

ABSTRACT

The coulostatic method was successfully applied to a rapid evaluation of metal corrosion rate in solution, where a known amount of small charge was supplied to the test piece, and the potential decay curve recorded was analyzed to obtain the corrosion rate. According to the theory developed, polarization resistances of mild steels in sulfuric acid and in distilled water were obtained, which agreed fairly well with resistances measured by usual methods. The coulostatic method developed in this study can be useful without ohmic drop correction, even in a high impedance solution. The time needed for measurement is considerably shorter, compared to the well-known linear polarization method.

The principal advantage of the polarization resistance technique (1-3) is its rapidity, compared to the weight loss method, in corrosion rate measurement. However, the measurements become markedly time dependent in the case of very low corrosion rate and the method involves a series problem in ohmic drop correction. Jones introduced a bridge circuit in order to correct the ohmic resistance of the solution (4). It is an excellent method, which we use regularly, but has several defects. For instance, it is useful only for galvanostatic measurement. It seems to be difficult, without several assisting devices, to apply the method to the solution of especially high ohmic resistance, such as distilled water or organic solvent. Further, the technique for detecting the balancing point by eliminating only the solution resistance from the polarization resistance requires a delicate, expert touch. To overcome this defect, an attempt was made to apply the coulostatic technique to the corrosion study. This was proposed by Delahay (5, 6) for the kinetic study of a usual electrode system, where redox species are in solution. In the coulostatic method, a known amount of small charge was applied to the test electrode at equilibrium state and the potential decay curve was recorded for analysis. In the present paper, the authors describe the coulostatic method applicability to a rapid metal corrosion rate evaluation from the theoretical point of view and its practical application to mild steels in 1N H_2SO_4 and in distilled water.

Theoretical

When a small amount of charge pulse is supplied to the electrical double layer of a metal test piece at a corrosion potential E_{corr}, the potential jumps to another potential E_m. It is assumed that the charging time is so short that leakage by the charge transfer reaction (corrosion reaction) can be neglected. Overvoltage η_0 of the test piece immediately after charging of the double layer is given by the equation

$$\eta_0 = E_m - E_{corr} \quad [1]$$

Assuming that the differential capacity per unit area of test piece C_d is essentially constant within a small voltage domain ($|\eta_0| < 5$ mV), the amount of charge density Δq_t consumed from time 0 to t, due to the corrosion reaction, is written by the equation

$$\Delta q_t = C_d(\eta_0 - \eta_t) \quad [2]$$

where η_t is the overvoltage at time t, namely the difference between the polarized potential and the corrosion potential. The increment of charge supplied to the electrode is consumed progressively by the corrosion reaction and the potential drifts back to its initial corrosion potential, E_{corr}. If it is assumed that the charge initially added is consumed only by the corrosion reaction of the test piece and that the concentration polarization is negligibly small in the corrosion process, the relation between overvoltage η_t and the faradaic current density I_t for discharge at time t is given by the next equation

$$I_t/I_{corr} = \exp\{(\alpha_+ n_+ \mathbf{F}\eta_t)/RT\} - \exp\{-(\alpha_- n_- \mathbf{F}\eta_t)/RT\} \quad [3]$$

where I_{corr} is corrosion current density, α_+ and α_- are transfer coefficients of anodic and cathodic reaction, and n_+ and n_- are the numbers of electrons concerning anodic and cathodic reactions, respectively. R, T, and $\mathbf{F}$ are gas constant, absolute temperature, and faradaic constant, respectively. When the absolute value of η_t is less than a few millivolts, Eq. [2] can be simplified to the following Stern-Geary equation (1-3)

$$I_t = 2.3\, I_{corr}\{(\beta_a + \beta_c)/\beta_a\beta_c\}\eta_t \quad [4]$$

where $\beta_a = 2.3\ RT/(n_+\alpha_+\mathbf{F})$, $\beta_c = 2.3\ RT/n_-\alpha_-\mathbf{F})$. The amount of charge density Δq_t defined by Eq. [2] is also expressed by using Eq. [4]

$$\Delta q_t = \int_0^t I_t dt = \int_0^t 2.3\ \{(\beta_a + \beta_c)/\beta_a\beta_c\}\eta_t \cdot I_{corr} dt \quad [5]$$

The combination of Eq. [2] and [5] yields the following differential equation

$$-C_d d\eta_t/dt = 2.3\{(\beta_a + \beta_c)/\beta_a\beta_c\}\eta_t \cdot I_{corr} \quad [6]$$

Solving Eq. [6] under the initial condition that $\eta_t = \eta_0$ at $t = 0$, the next equation is derived

$$\eta_t = \eta_0 \exp\{-2.3 I_{corr} \cdot t/(C_d K)\} \quad [7]$$

where $K = \beta_a\beta_c/(\beta_a + \beta_c)$.

Equation [7] suggests that overvoltage $\eta_t(t)$ decays exponentially with time t. Equation [7] is simplified by using polarization resistance R_p in place of $K/2.3I_{corr}$ (2)

$$\eta_t = \eta_0 \exp\{-t/(C_d R_p)\} \quad [8]$$

Polarization resistance R_p is considered to be one of the most important parameters concerning corrosion rate, which is inversely proportional to the corrosion current. If K values, namely the Tafel slopes for the anodic and the cathodic process, are known already or can be obtained by an appropriate method, corrosion current density I_{corr} is readily computed from R_p by the definition. Even if the Tafel slopes are un-

Key words: corrosion rate, rapid evaluation, coulostatic method.

known, the value of the reciprocal of R_p is useful as an indicator of the corrosion rate from a practical standpoint. Equation [8] is rewritten into a logarithmic equation

$$\log \eta_t = \log \eta_0 - t/(2.3C_dR_p) \quad [9]$$

which shows that a plot of log η_t against t is linear. By extrapolating log η_t plot to $t = 0$, η_0 can be obtained. Differential capacity C_d, which is needed in polarization resistance computation, is obtained simply from the next equation

$$C_d = \Delta q/\eta_0 \quad [10]$$

where Δq means a known amount of charge density supplied at first to the double layer of the test piece from capacitor C_1 of the equipment (see Fig. 1). Thus, polarization resistance R_p is calculated from Eq. [9] slope.

As C_d usually takes the value of 10^{-5}-10^{-4} F/cm^2, η_0 may be within 1-10 mV, if Δq is chosen as 0.1 μC/cm^2.

Experimental

Instrument.—The circuit of the instrument supplying known quantities of electric charge and recording variation of potential is shown in Fig. 1. This circuit is separated into two parts. One of them, the left side of the test cell, is composed of capacitor C_1, relay RL, battery B_1, battery B_3, and variable resistor VR_1 that acts as a source of known quantities of electric charge supply. The other is composed of battery B_2, variable resistor VR_2, operational amplifier OA, and voltage recorder D that follows potential variation of a test piece, called working electrode (WE). Before the measurement, a test piece was set with counter (CE) and reference electrodes (RE) in a test cell containing test solution. Measurement was made as follows: At first, capacitor C_1 was charged up to a certain voltage V_1, as was required to change the potential of the test piece a few millivolts from E_{corr}. Capacitor C_1 was then abruptly discharged across the cell by the action of relay RL, in order that the charge in C_1 was supplied to the test piece. In this equipment, three different capacitors are connected to a rotary switch so that the most suitable value can be selected. Capacitor C_1 is chosen sufficiently small, compared to the double layer capacity of the test piece, so that the almost whole charge stored in C_1 flows into the test piece.

The overvoltage (η_t)-time (t) curve shown in Fig. 2 was recorded with an Iwasaki SS-5003 Synchroscope, shown as D in Fig. 1. Before supplying the charge, the potential difference between WE and RE was canceled by the potentiometer composed of variable resistor VR_2 and battery B_2 in order to record only overvoltage η_t. The Teledyne Filbrick 1026 operational amplifier was used as a voltage follower.

Test pieces and other electrodes.—Commercially available mild steel plates (JIS SS41 and SB46), whose chemical compositions are given in Table I,

Table I. Compositions of mild steels tested in this work

Materials	C	Mn	S	P	Si
SS41	0.12	0.58	0.02	0.03	—
SB46	0.18	0.65	0.014	0.009	0.23

were used as test pieces. They were polished by 0.05 μm Al_2O_3 and were degreased in acetone. The surface of the specimen was coated with Parafilm (American Can Company) for an area of 9 cm^2 for SB46 and 5 cm^2 for SS41. About 10 cm^2 platinum plates, plated by platinum black, were used as counter and reference electrodes, respectively. Potential of the platinum plate as a reference electrode was sufficiently stable to observe the potential change in the test piece during measurement. A saturated calomel electrode was used for polarization curve measurement.

The solutions used in experiments were made from reagent grade chemicals with doubly distilled water. The conductance of distilled water was less than 1×10^{-6} Ω cm^{-1}. All measurements were carried out at a room temperature (28° ± 1°C) under atmospheric pressure without expelling dissolved oxygen in the solution.

Results and Discussion

Mild steel in 1N H_2SO_4.—The anodic overvoltage-time curve, resulting from the application of 5.82 μC of charge to the SB46 electrode immersed in 1N H_2SO_4 for 2 hr, is reproduced in Fig. 2. The corrosion potential E_{corr} of SB46, just before charging the double layer, is -0.5V *vs.* SCE and the end value of the potential decay curve coincided with the initial E_{corr} value. The log η_t-t plot, obtained from the potential decay curve of Fig. 2, indicates a good linearity in agreement with Eq. [9] (see Fig. 3). By extrapolating log η_t plot to $t = 0$, the value of η_0 was obtained as 3.0 mV, from which differential capacity C_d was calculated as 216 μF/cm^2. Although the value of η_0 was changed by changing the quantity of charge being supplied to the electrode the differential capacity, calculated by Eq. [10], is almost constant as long as η_0 is less than 10 mV. Polarization resistance R_p was deduced as 7.9 Ω cm^2 from the slope of log η_t plot, shown in Fig. 3, with the aid of C_d value.

For comparison, steady-state polarization curves were measured for the same test piece (Fig. 4), from which 2.8 mA/cm^2 and 50 and 128 mV were obtained as the values of I_{corr}, β_a, and β_c, respectively. From these parameters, R_p was computed as 5.6 Ω cm^2 by using the definition $R_p = K/2.3I_{corr}$, which agreed very closely with that obtained by the coulostatic method. The fact that the obtained C_d value is considerably larger, compared to that of a smooth electrode, such as mercury drop (7) (10-40 μF/cm^2), suggests an increase in the surface roughness of the test

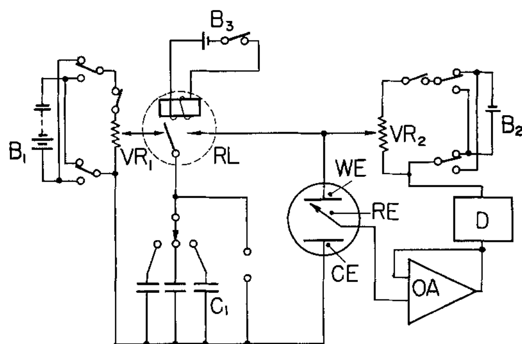

Fig. 1. Coulostat circuit. WE, test piece as working electrode; RE, reference electrode; CE, counterelectrode; OA, operational amplifier; D, voltage recorder; RL, relay; C_1, capacitor.

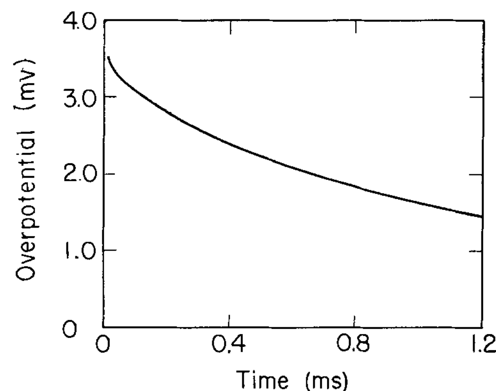

Fig. 2. Polarization potential (η_t)-time (t) curve for SB46, obtained after immersion in 1N H_2SO_4 for 2 hr. Applied charge was 5.82 μC.

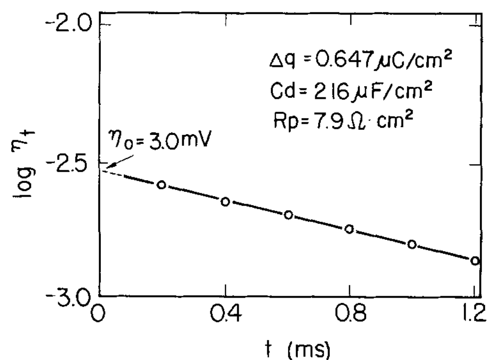

Fig. 3. Log η_t-t relationship for SB46, according to Fig. 2

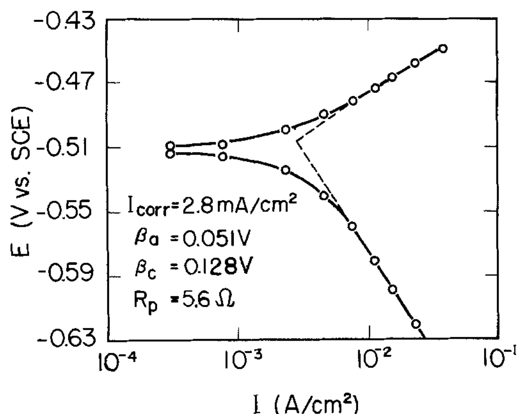

Fig. 4. Polarization curve for SB46 after immersion in 1N H_2SO_4 for 2 hr. E and I mean the potential of the test piece and faradaic current density, respectively.

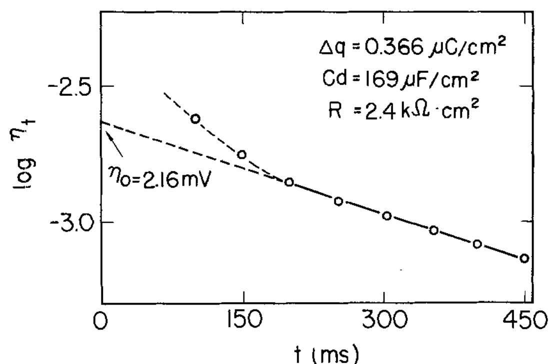

Fig. 5. Log η_t-t relationship for SS41 after immersion in distilled water for 45 hr. Charge applied was 1.83 μC.

piece due to corrosion reaction, pseudocapacitance caused by adsorption (8), and/or film formation (9).

Mild steel in distilled water.—The overvoltage-time curves for SS41 were also measured at various immersion times in distilled water. The relation between log η_t and t for the anodic process is shown in Fig. 5, which shows the case for 45 hr immersion. From Fig. 5, it is shown that the plots after about 200 msec indicate a fairly good linearity, while, at the initial stage of the decay curve, they deviate from the linear relationship. These deviations from the linear relationship may be due to the large resistance of distilled water. Since the charging process did not terminate instantaneously, due to the large resistance of the solution, it continued to proceed simultaneously with the discharge process at the initial part of the decay curve. Thus, during charging of the double layer, the overvoltage due to the ohmic drop between the reference and working electrodes was superimposed on the activation overvoltage due to the corrosion reaction which we wanted to measure. In such a case, the η_0 value was obtained by extrapolating the linear parts of the log η_t plots to $t = 0$.

The validity of this treatment and an interpretation of the deviation were confirmed by the following experiment, using the Graham-type equivalent circuit (Fig 6.) for the corrosion cell system composed of resistors, R_s', R_p', and capacitor C_d', which were solution resistance, polarization resistance, and double layer capacity, respectively. When charge Δq, stored in capacitor C_1 of the equipment, is transferred to capacitor C_d', current i, flowing through R_s', is given by

$$i = \frac{\Delta q}{R_s'C_1} \exp\left(-\frac{t}{R_s'C}\right) \quad [11]$$

where $C = C_1C_d'/C_1 + C_d'$). This equation explains that the time constant for charging capacitor C_d' becomes larger, with increasing R_s' values. For the discharging process in the equivalent circuit, the following relations also hold

$$V_t = V_0 \exp\left(-\frac{t}{C_d'R_p'}\right) \quad [12]$$

$$\Delta q = C_d'V_0 \quad [13]$$

where V_0 means the voltage difference in terminals (a and b in Fig. 6) immediately after charging the equivalent circuit by an external electricity source, V_t is voltage difference at time t, Δq is a known amount of charge stored in capacitor C_1. If a large resistor value, such as 97.7 kΩ, was used as R_s', deviation was observed, as expected, in log V_t plots of Eq. [12], while no deviation was observed in the case of $R_s' = 0$. These features are shown in Fig. 7 as plots a and b.

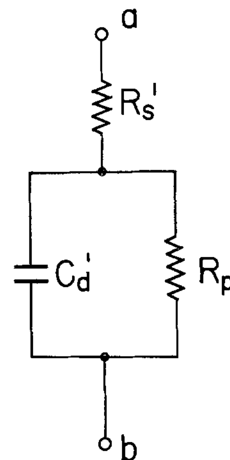

Fig. 6. Equivalent circuit for the test cell where R_s', R_p', and C_d' correspond to solution resistance, polarization resistance, and double layer capacitance, respectively.

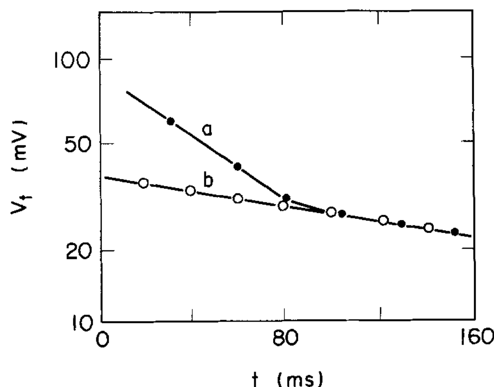

Fig. 7. Log V_t-t relationship for equivalent circuit. (a) $R_s' = 97.7$ kΩ, $R_p' = 29.5$ kΩ, $C_d' = 9.87$ μF; (b) $R_s' = 0$Ω, $R_p = 29.5$ kΩ, $C_d' = 9.87$ μF. Charge applied was 0.370 μC for both cases. Voltage values V_t were observed between terminals a and b in Fig. 6.

Table II. R_p' and C_d' data observed at various R_s' values

	Used values			Observed values			Reliability	
$\Delta q'$ (μC)	R_s' (kΩ)	R_p' (kΩ)	C_d' (μF)	V_0 (mV)	R_p' (kΩ)	C_d' (μF)	$(R_p')_{obs}/R_p$	$(C_d')_{obs}/C_d'$
0.128	0	2.94	7.40	16.3	2.95	7.87	1.003	1.064
0.370	0	1.29	7.40	48.2	1.35	7.68	1.046	1.038
0.370	0	29.5	9.87	37.4	28.4	9.90	0.963	1.003
0.370	0.509	29.5	9.87	36.9	28.9	10.0	0.980	0.993
0.370	3.00	29.5	9.87	37.1	28.8	9.98	0.976	1.011
0.370	97.7	29.5	9.87	37.0	28.7	10.0	0.973	1.013

The potential decay curve b in Fig. 7 can be regarded as being controlled by two different successive processes, indicated by $V_t = (\Delta q/C_1) \exp \{-t/(C_1R_s')\}$ and $V_t = V_0 \exp \{-t/(C_d'R_p')\}$, if $C_d' >> C_1$. The first equation corresponds to the C_1 discharging process, the second to the C_d' discharging process. As time constant $C_d'R_p'$ is from a few times to ten times larger than C_1R_s', the C_1 discharging process effect (R_s' effect) appears only at the initial part of the potential-time curve. Therefore, the latter part is controlled only by the large time constant $C_d'R_p'$, resulting in the latter part being unaffected by R_s'. In Table II, V_0 values obtained by extrapolating the linear parts of log V_t plots to $t = 0$ at various combinations of R_s', R_p', and C_d', C_d' values calculated by Eq. [13], and R_p' values calculated from the slope of log V_t plots by using Eq. [12] are tabulated in comparison with actual values of resistors and capacitors used. This table shows the observed values of C_d' and R_p' are nearly equal to the actual values used and are almost constant, even if the R_s' values are changed. From these results, it is shown that high resistance (R_s' in the equivalent circuit), in series to the leaky condenser, has virtually no effect in determining capacity C_d' and resistance R_p' values, although it delays the charging process. In an actual corrosion system with large solution resistance, the situation seems to be similar.

Thus, polarization resistances obtained in distilled water with high solution resistance seem to be correct. These values are tabulated in Table III with differential capacities at various immersion times. On the other hand, a value of 21 mdd was obtained by the weight loss method for the same test piece after 75 hr immersion. To confirm the validity of the coulostatic method, this 21 mdd (8.4 μA/cm^2) corrosion rate was transformed to an R_p value by using the following relations

$$\text{corrosion rate} = (M/n\mathbf{F}) I_{corr}$$

$$R_p = K'/I_{corr}$$

where M is atomic weight of iron, and $K' = \beta_a\beta_c/2.3(\beta_a + \beta_c)$. Constant K' used was 0.018V determined previously in this laboratory with a galvanostatic linear polarization method using Jones' circuit (4) and the corrosion rate by the weight loss method for nearly equal immersion time in distilled water. In the authors' experience, the K' value seems to be almost constant, even if the Tafel slopes changed to some extent with the immersion time. Although many combinations of β_a and β_c on the K' value of 0.018V may be possible, some reasonable combinations are 60 mV (β_a) and 134 mV (β_c) or 70 mV (β_a) and 105 mV (β_c), which are in good agreement with values reported in several papers (10-12). From this K' value (0.018V), the average R_p value was thus calculated to be 2.2 kΩ cm^2. This value seems to be in good agreement with the values tabulated in Table III, showing the usefulness of the coulostatic method.

Table III. Double layer capacity and polarization resistance for SS41 in distilled water for various immersion times $\tilde{t}$

$\tilde{t}$ (hr)	Δq (C/cm^2)	η_0 (mV)	C_d (μF/cm^2)	R_p (kΩ cm^2)
45	0.366	2.16	169	2.4
51	0.364	1.83	199	2.1
74	0.376	1.57	239	1.1

The C_d values given in Table III are also worth noting. Observed values are larger, compared to those for a smooth electrode (7), and tend to increase with increasing immersion time. Surface roughness, oxide film formation (9), adsorption of some charged species or hydrogen (8), etc., may be considered as factors that affect the C_d values. The stainless steel double layer capacity value is strongly affected by specimen pretreatment, such as pickling temperature, time, and precathodizing (8). Recently, Azzerri reported a large C_d value for mild steels covered by corrosion product layers (13). Though the physical meaning of the large C_d value is not clear at the present time, an increase in its value with increasing immersion time (Table III) may suggest that the surface roughness and the corrosion film formation of the test piece increase as the corrosion progresses.

From a practical standpoint, it is useful if the forms of corrosion are detectable, *e.g.*, general or localized. By using the coulostatic technique, it may be possible to determine whether it is general or pitting corrosion by comparing a pair of C_d and R_p values for each corrosion system. For instance, the C_d and R_p of Type 304 stainless steel in air-saturated $1N$ H_2SO_4 were 50 μF/cm^2 and 610 kΩ cm^2 after 54 hr immersion, while those of Type 304 stainless steel in 10% $FeCl_3$ solution after 19 hr were 40 μF/cm^2 and 0.14 kΩ cm^2, respectively. If the Tafel slopes in both solutions are not so different from each other, the corrosion rate is about 4000 times faster in $FeCl_3$ solution than in H_2SO_4, while the C_d values in both solutions are quite similar, and suggests that the metal surfaces are nearly equal in area, roughness, and/or state. Namely localized corrosion is expected to be occurring in $FeCl_3$ solution. In actuality, corrosion pits were observed on the test piece in $FeCl_3$ solution, while the surface, except the pits, maintained a metallic luster similar to that in H_2SO_4.

The advantage of the present method is that the overvoltage variation is measured without applying current between working and counterelectrodes. Therefore, the method is easily applicable to a high impedance solution, such as distilled water, without consideration of the ohmic drop correction. The coulostatic method is a sort of relaxation method, where measurement may be carried out within a much shorter time under more natural conditions, compared to the usual linear polarization method. To reduce the time-consuming defect of the linear polarization method, especially when measuring a low corrosion rate, Jones and Greene (14) derived a new charging curve analysis technique. In this method, however, the surface state of a specimen may change, owing to a constant current flow through the test piece surface. It is difficult to obtain a unique time constant and requiring much longer time, compared to the coulostatic method.

From the above results and discussion, it may be concluded that the coulostatic method is useful for a rapid corrosion rate evaluation for mild steel in sulfuric acid and in distilled water with high ohmic resistance. Experiments concerning other combinations of metals and solutions are in progress.

Acknowledgment

The authors wish to thank Dr. Takamura of Toshiba Laboratory for helpful discussions during the course of this study.

Manuscript submitted Sept. 23, 1977; revised manuscript received March 30, 1978.

Any discussion of this paper will appear in a Discussion Section to be published in the June 1979 JOURNAL. All discussions for the June 1979 Discussion Section should be submitted by Feb. 1, 1979.

Publication costs of this article were assisted by the Tokyo Shibaura Electric Company.

REFERENCES

1. M. Stern and A. L. Geary, *This Journal*, **104**, 56 (1957).
2. M. Stern, *Corrosion*, **14**, 440t (1958).
3. M. Stern and E. Weisert, *Proc. Am. Soc. Testing Mater.*, **59**, 1280 (1959).
4. D. A. Jones, *Corros. Sci.*, **8**, 19 (1968).
5. P. Delahay, *J. Phys. Chem.*, **66**, 2204 (1962).
6. P. Delahay and A. Aramata, *ibid.*, **66**, 2208 (1962).
7. R. Parsons, in "Modern Aspects of Electrochemistry," Vol. 1, J. O'M. Bockris, Editor, p. 103, Butterworth, London (1954).
8. J. O'M. Bockris and H. Kita, *This Journal*, **108**, 676 (1961).
9. M. Prazak, M. Lukasovaka, and B. Eremias, 25th ISE Meeting, Brighton, England, Extended Abstracts, p. 371 (1974).
10. A. C. Makrides, *This Journal*, **108**, 412 (1961).
11. S. Asakura and K. Nobe, *ibid.*, **118**, 13 (1971).
12. S. Asakura and K. Nobe, *ibid.*, **121**, 1276 (1974).
13. N. Azzerri, *J. Appl. Electrochem.*, **6**, 139 (1976).
14. D. A. Jones and N. D. Greene, *Corrosion*, **28**, 26 (1972).

Inhibition of Corrosion of Iron in Acids by Thiourea and Derivatives

K. Chandrasekhara Pillai

National Metallurgical Laboratory, Jamshedpur, Bihar, India

and R. Narayan

Department of Chemistry, Indian Institute of Technology, Madras 600 036, India

ABSTRACT

The inhibition of corrosion of iron (0.13%C) in hydrochloric acid by thiourea and its derivatives has been investigated. Inhibition is due to adsorption of the molecular species. The maximum of efficiency with low concentrations of thiourea and its N-substituted derivatives is attributed to the protonation of the inhibitor with consequent acceleration of the hydrogen evolution process. Protonation is high with the simple thiourea and increases with the concentration of the inhibitor and hydrogen ion concentration. S-substituted derivatives show an increasing efficiency with concentration and are safe inhibitors.

Thiourea (TU) has been studied as a corrosion inhibitor by several groups of workers (1-14), and the reports are conflicting. Some workers finding TU to be a cathodic or anodic inhibitor depending on the concentration of TU (1, 7, 9) while others have observed a corrosion-stimulating effect by TU (4-6, 8). Where the TU is reported to be an inhibitor, it is a general observation that the effective inhibition is restricted to a small range of concentrations, the maximum efficiency being observed with 1-3 mM concentration of TU. No clear explanation is given for this maximum in efficiency. Several derivatives of TU have also been studied periodically and reported as moderately good inhibitors (15-18). Hence it was proposed to study TU and its derivatives for their inhibition of corrosion of a particular composition of the metal, varying other parameters like pH, oxygen content, etc. The objective was to correlate the structure of the inhibitor with its inhibiting action. Thiourea, tetramethyl thiourea (TMTU), and ethylene thiourea (ETU) as representatives of N-substituted derivatives, and S-methyl isothiourea (SMTU) and S-benzylisothiourea (SBTU) as S-substituted derivatives were chosen for the study.

Experimental

Corrosion rates were followed by gravimetric measurements and also by estimation of the Fe^{2+} in solution by spectrophotometry, as the complex of O-phenanthraline or dipyrydyl. Thin 0.2 mm plates (3.5 cm^2) were immersed in 150 ml of the corroding solution. Deaeration was carried out with deoxygenated nitrogen when necessary. The electrochemical studies were mainly measurements of the rest potentials and potentiostatic polarization using a 3 electrode combination of a platinum counter, a calomel reference with suitable bridge solution, and a test electrode with approximately 1 cm^2 circular face being exposed for corrosion. The mild steel test electrode had the following composition (percentage) 0.13 C, 0.032 S, 0.14 Si, 0.025 P, 0.48 Mn. All potentials are quoted with respect to the saturated calomel electrode. Tensammetric and drop times measurements were made with a dropping mercury electrode to observe the variation of the adsorption of the inhibitors at the metal solution interface.

Key words: metals, acid, corrosion, inhibition.

Results

The inhibition efficiency of the inhibitor is calculated as $(r_1 - r_2/r_1) \times 100$ where r_1 = corrosion rate in mg cm^{-2} without inhibitor and r_2 = corrosion rate in mg cm^{-2} with inhibitor, and r_1 and r_2 are the mean of four values. The mean deviation of the reported results is ±5%.

Figures 1, 2, and 3 show the variation of the inhibition efficiency with concentration of the inhibitor in 1 MHCl, 3 MHCl, and in a solution of pH 2.5 (KCl

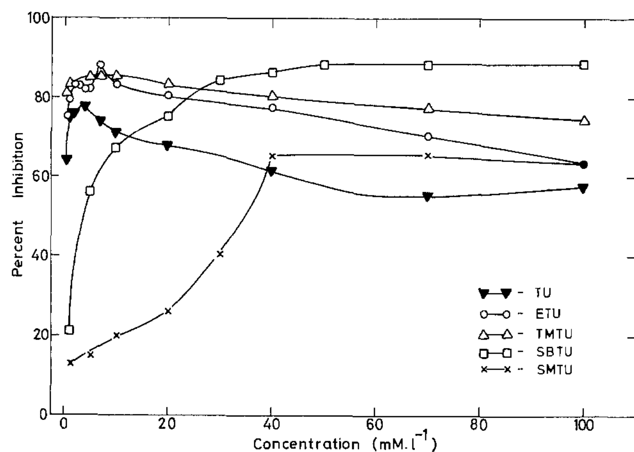

Fig. 1. Variation of inhibition efficiency with concentration of inhibitor in deaerated 1M HCl.

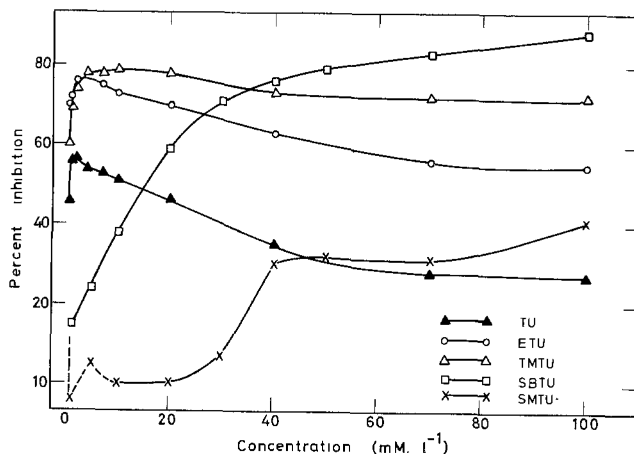

Fg. 2. Variation of inhibition efficiency of inhibitor in deaerated 3M HCl.

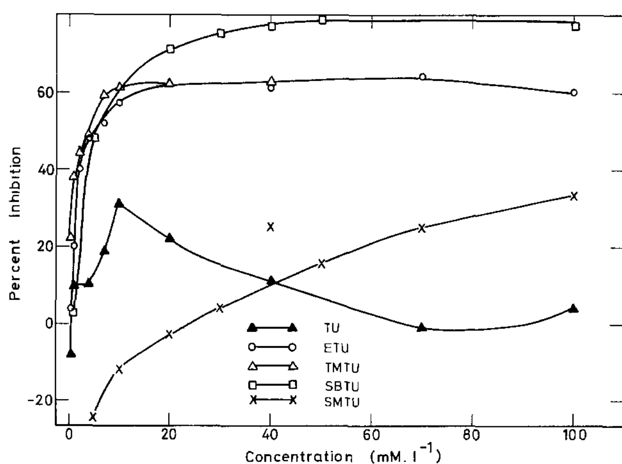

Fig. 3. Variation of inhibition efficiency in solution of pH_2

+ HCl). The efficiency goes through a maximum for TU, ETU, and TMTU while it increases continuously with concentration to a limit with SMTU and SBTU in deaerated 1M HCl and 3M HCl. TMTU shows a higher efficiency than TU and ETU at higher concentrations. The inhibition efficiencies are low in the solution of *p*H 2.5, low concentration of the inhibitors even stimulating corrosion. The sharp maximum in efficiency is observed only with TU.

The I_{corr} has been obtained from the polarization curves at the E_{corr}, which is the point of intersection of the extrapolated linear regions of the cathodic and anodic curves. Where a linear cathodic Tafel region alone could be observed this has been extrapolated and the current corresponding to the E_{rest} has been taken as the I_{corr}. The inhibition efficiency is then calculated and the variation is generally similar to those observed with the gravimetric measurements. The E log i variations in 1M HCl are shown in Fig. 4-8.

The E_{rest} potentials (Tables I-III) show an initial negative shift with increasing concentration of TU, ETU, or TMTU and then a positive shift with higher concentrations. The concentrations corresponding to the maximum negative shift are the same as those which exhibit maximum inhibition efficiencies. The E_{rest} shifts continuously to cathodic values with increasing concentrations of SBTU. The E_{corr} values are more positive than E_{rest}, but changes in E_{corr} parallel the E_{rest} changes. Similar observations are made in deaerated 3M HCl solutions. The polarization of the cathodic process increases to a maximum with increasing concentration of TU, ETU, or TMTU and subsequently decreases with higher concentrations. The changes in the Tafel slopes are shown in Tables

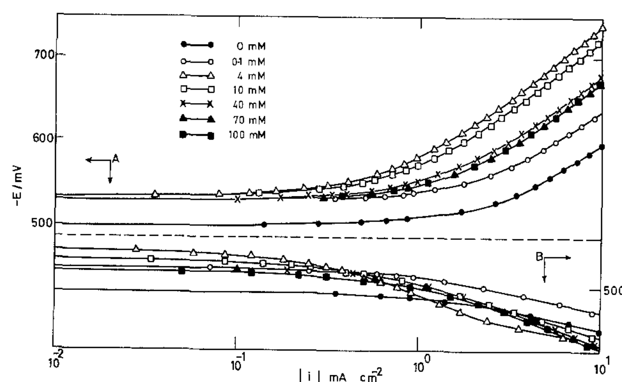

Fig. 4. Polarization curve-mild steel in deaerated 1M HCl with TU: A, cathodic; B, anodic.

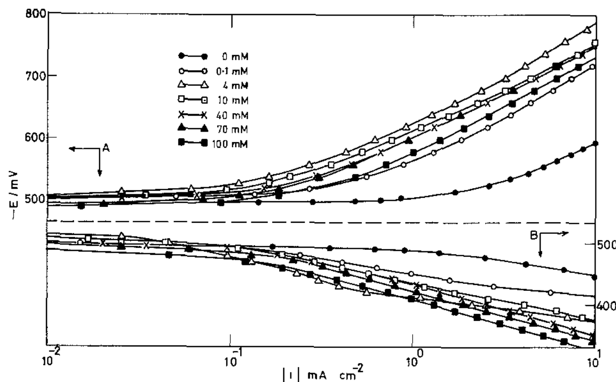

Fig. 5. Polarization curves. Mild steel in deaerated 1M HCl with TMTU: A, cathodic; B, anodic.

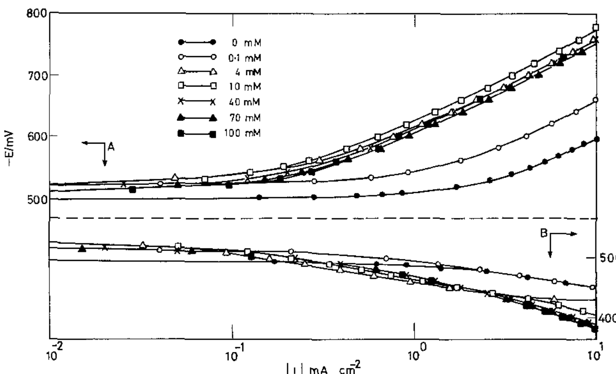

Fig. 6. Polarization curves. Mild steel in deaerated 1M HCl with ETU: A, cathodic; B, anodic.

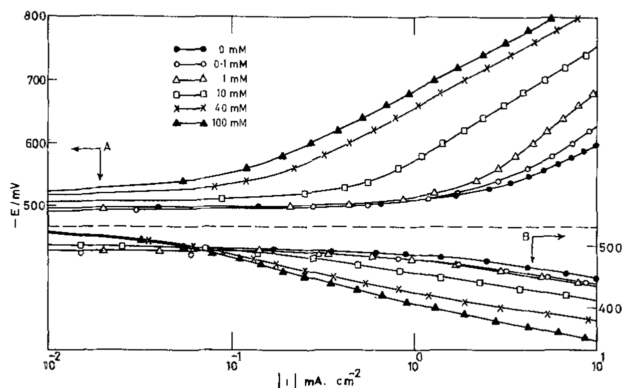

Fig. 7. Polarization curves. Mild steel in deaerated 1M HCl with SBTU: A, cathodic; B, anodic.

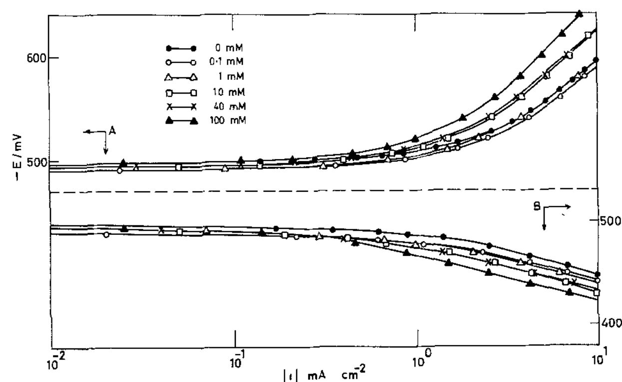

Fig. 8. Polarization curves. Mild steel in deaeroted 1M HCl with SMTU: A, cathodic; B, anodic.

I-III. The b_a or slope of the anodic Tafel region goes through a maximum with increasing concentration of TU, ETU, and TMTU. The polarization of the anodic process by TU, ETU, and TMTU is not very large. SBTU and SMTU polarize both the cathodic and anodic processes increasingly as their concentration is increased. SBTU has a greater polarizing effect than SMTU.

Table I. Electrochemical parameters—mild steel with TU in deaerated 1M HCl

TU concn. (mM · l^{-1})	$-E_{rest}$ (mV)	$-E_{corr}$ (mV)	Corrosion current (mA, cm^{-2}) I_{corr}	$-b_c$ (mV)	b_a (mV)
0.0	497	486	1.65	135	47
0.1	526	512	1.30	140	46
0.5	532	515	0.95	150	47
1.0	533	513	0.67	156	48
2.0	530	505	0.445	165	51
4.0	530	514	0.48	167	80
10.0	531	520	0.62	167	65
40.0	526	516	1.05	165	88
70.0	523	515	1.10	164	92
100.0	519	513	1.05	164	92

I_{corr} obtained at E_{corr}.

Table II. Electrochemical parameters—mild steel with ETU in deaerated 1M HCl

ETU concn. (mM · l^{-1})	$-E_{rest}$ (mV)	$-E_{corr}$ (mV)	Corrosion current (mA, cm^{-2}) I_{corr}	$-b_c$ (mV)	b_a (mV)
0.0	497	486	1.65	135	47
0.1	520	497	0.82	145	47
0.5	523	500	0.445	155	45
1.0	524	493	0.20	155	50
2.0	527	500	0.20	155	60
4.0	531	506	0.225	156	63
10.0	522	503	0.185	155	55
40.0	517	503	0.23	155	58
70.0	515	502	0.25	155	58
100.0	510	503	0.23	155	58

Table III. Electrochemical parameters—mild steel with TMTU in deaerated 1M HCl

TMTU concn. (mM · l^{-1})	$-E_{rest}$ (mV)	$-E_{corr}$ (mV)	Corrosion current (mA, cm^{-2})	$-b_c$ (mV)	b_a (mV)
0.0	497	486	1.65	135	47
0.1	501	472	0.365	172	50
0.5	508	480	0.23	150	63
1.0	511	477	0.165	150	65
2.0	515	480	0.155	150	65
4.0	507	478	0.11	150	89
10.0	505	496	0.11	150	65
40.0	503	483	0.17	150	79
100.0	489	465	0.20	150	80

Discussion

Several workers have reported the maximum in corrosion efficiency with 1-2 mM thiourea in acid solution (8, 19, 20). The inhibition is ascribed to adsorption of thiourea. The initial increase in inhibition efficiency can be associated to the increased surface coverage by the adsorbed species, which appears to be a molecular form of thiourea (8). The fall in efficiency at higher concentrations should be the result of desorption of thiourea or due to modification in the adsorbed species. Other studies have shown that thiourea is adsorbed on several metals over a wide potential and concentration range (up to even 0.5M). Desorption is unlikely with iron at the corrosion potential (−0.25V) which is only a little positive to the pzc (−0.3V).

Stimulation of corrosion by H_2S obtained from the reduction of TU (8, 20) and through a negative ψ effect (5, 25) from the presence of HS^- have been suggested while Antropov (21) showed that H_2S actually increased the inhibition efficiencies of certain thiourea derivatives. H_2S could be detected presently only on prolonged contact of the iron with the solution while the high acid concentration used reduces HS^- concentration to negligible values.

We therefore propose that adsorbed thiourea undergoing a modification accelerates the hydrogen evolution reaction (HER) and hence exerts a lower inhibition effect. Polarographic studies show that the hydrogen overvoltage on mercury is lowered considerably by the presence of even small quantities of TU, ETU, or TMTU in solutions of pH less than 4 (Table IV). Mauree and Gierst (22) had shown that TU reduces the overvoltage of several reduction processes at mercury. These could generally be accounted for by a ψ effect, but they indicated that the much greater acceleration of the HER requires a different catalytic mechanism. The kinetic parameters of the HER on iron in the present studies follows the Volmer mechanism. Thus the discharge of H_3O^+ is the rate-determining step, both with mercury and iron electrodes, and this step is catalyzed by the adsorbed TU. Protonated thiourea is inferred to be the catalyst. The proton is attached to the sulfur and hence is brought closer to the metal since the adsorption of TU is through the metal sulfur interaction. The charge

Table IV. Decomposition potential (mV) of deaerated 1M HCl in presence of TU and derivatives, at a mercury electrode

Concentration (mM · l^{-1})	TU	ETU	TMTU	SMTU	SBTU
0.0	−1120 ± 5	−1120 ± 5	−1120 ± 5	−1120 ± 5	−1120 ± 5
0.1	−1015	−940	−835		
0.5	−985	−8 0	−790		
1.0	−950	−863	−768		
5.0	−885	−790	−740		
10.0	−850	−785	−740	−1110	−1058
20.0	−815	−755	−740	−1110	−1055
40.0				−1105	−1045
60.0				−1105	−1035
100.0				−1095	−1025

transfer process can thus go through with a lower activation energy. The thiourea after adsorption may undergo protonation or may be protonated in the bulk and then adsorbed. With increasing concentration of TU in bulk, the interfacial concentration of the protonated species will increase at the cost of molecular thiourea. The former accelerates the HER while the latter inhibits the process. The two opposing effects lead to a maximum in the inhibition efficiency.

The concentration of the adsorbed thiourea and the protonated species will be higher at the mercury solution interface than with the iron solution interface for the following reasons: (*i*) the generally greater adsorption of organic compounds on mercury (23, 24); and (*ii*) the higher hydrogen overvoltage on mercury resulting in greater protonation process (23). Hence the acceleration of the HER is observed at mercury electrodes even with very small concentrations of TU.

The inhibition efficiency is a maximum with 10 mM TU in a solution of *p*H 2 with 4 mM in 1M HCl and with 2 mM in 3M HCl. The relative reduction in inhibition efficiencies are also greater in 3M HCl. These are due to the higher H_3O^+ concentrations resulting in greater protonation of TU in the more concentrated acids. However at any of the concentration studied, the concentration of molecular TU is apparently greater than that of the protonated species and net inhibition only is observed. The polarization curves show that the cathodic process is initially polarized by the molecular form. With higher concentrations, more and more of the protonated species take part in catalyzing the HER and the polarization becomes smaller.

The E_{rest} shift and cathodic polarization by ETU and TMTU are similar to those observed with TU. The polarizing effects are however greater while the accelerating effects on the HER by protonated species are much smaller. Similarly the anodic depolarizing effects are largest with TU. There are some depolarizing effects with ETU at 10 mM concentration while TMTU exerts at 20 mM or higher concentrations, a small part but a definite polarizing effect. The inhibition efficiency curve shows a clear maximum with TU while a flattening out of the curve is observed with TMTU (Fig. 1).

The drop-time potential curves which are similar in 1M HCl, 1M KCl, and in solution of *p*H 2 show that TU, ETU, and TMTU are specifically adsorbed at the mercury-solution interface. The negative shift of the pzc indicate the strong Hg-S interaction. The order of adsorption is TMTU > ETU > TU. The dipole moments calculated by the CNDO method is $\mu_{ETU} > \mu_{TU} > \mu_{TMTU}$ (Table V). The more extensive adsorption of TMTU causes a greater shift of the pzc. If this order of adsorption also holds good with iron [Antropov (26)], the inhibition effect will also increase in the order TMTU > ETU > TU. The protonation process, on the other hand, will be controlled by the electron density of the sulfur atom and availability of a proton adjacent to this atom, the latter

Table V. Dipole moments (μ) of TU, ETU, and TMTU calculated by "CNDO" method

Thiourea derivatives	$\mu_{calculated}$	Electron density on C	Electron density on N	Electron density on S	$\mu_{reported}$
TU	4.23	+0.2777	−0.1744	−0.4101	4.89[a]
ETU	5.98	+0.2853	−0.1297	−0.4101	5.51[b]
TMTU	3.69	+0.2688	−0.1209	−0.4086	

The dipole moments were computed by the "complete neglect of differential overlap (CNDO)" method proposed by Pople *et al.* (30), which is an approximate version of self-consistent Field (SCF)-LCAO-MO theory.
[a] In dioxane (28).
[b] In dioxane (29).

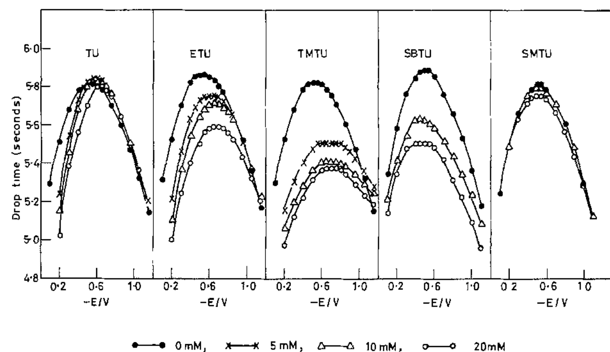

Fig. 9. Drop time-potential plots in *p*H2 solution with additives

factor being important if the protonation is a surface process. Steric factors will thus come into play. The order of protonation will be TU > ETU > TMTU. Hence TMTU with the greatest adsorption and least protonation will have the maximum inhibition efficiency, while the relative lowering in efficiency will be largest with TU.

The near-symmetrical nature of the drop-time curves (Fig. 9) and the tensammetric studies (27) shows that both SBTU and SMTU are nonspecifically adsorbed over a wide range of potentials. The small positive shifts of the pzc are due to the adsorption of positively charged isothiouronium species. The adsorption increases continuously with the concentration. Studies with urea (27) showed very little adsorption and hence the absence of metal-nitrogen interaction. Thus SBTU and SMTU are adsorbed through the sulfur. This adsorption is not high, due to the substituent present on the sulfur. SBTU is more extensively adsorbed than SMTU, due to the metal-Π electron interactions and a probable flat orientation of the aromatic ring. The substitution will also reduce protonation of the sulfur. The proton is attached to the nitrogen as these are isothioureas. Hence catalysis of the HER is not to be expected as with the other thioureas. Very little lowering of the hydrogen overvoltage is observed on mercury while the cathode processes on iron are increasingly polarized (Fig. 7 and 8). Inhibition alone is expected and found.

The mechanism of anodic dissolution in the presence of protonated thioureas, the stimulation of corrosion with very small addition ($<10^{-4}$ Ml^{-1}) of the thioureas, and the influence of oxygen on these processes are to be dealt with separately.

Conclusion

The maximum in the inhibition efficiency of thiourea and N-substituted derivatives is the result of two opposing effects—an inhibition by adsorbed molecular species and an acceleration by adsorbed protonated species. The cathode polarization by these additives is greater than anode polarization. Substitution in the parent thiourea modifies metal-sulfur interaction and protonation. Alterations in the bulkiness, solubility, and symmetry of the structure due to substitution change the adsorption characteristics. TMTU with least protonation and with maximum adsorption thus is a better inhibitor than ETU and TU. SMTU and SBTU increasingly polarize the cathode and anode process and are safe inhibitors even at high concentrations.

Manuscript submitted Aug. 19, 1977; revised manuscript received Feb. 20, 1978. This was Paper 7 presented at the Philadelphia, Pennsylvania, Meeting of the Society, May 8-13, 1977.

Any discussion of this paper will appear in a Discussion Section to be published in the June 1979 JOURNAL. All discussions for the June 1979 Discussion Section should be submitted by Feb. 1, 1979.

REFERENCES

1. T. P. Hoar, "Pittsburgh International Conference on Surface Reactions," p. 127, The Corrosion Publishing Co., Pittsburgh (1948).
2. P. H. Cardwell and L. H. Eilers, *Ind. Eng. Chem.*, **40**, 1951 (1948).
3. C. A. Marsh and H. J. Macdonald, "Pittsburgh International Conference on Surface Reactions," p. 1, The Corrosion Publishing Co., Pittsburgh (1948).
4. L. Cavallaro and G. Bolognesi, *Atti. Acad. Sci. Ferrara*, **24**, 1 (1946-1947).
5. V. A. Kuznetzov and Z. A. Iofa, *J. Phys. Chem. (USSR)*, **21**, 201 (1947).
6. J. Elze and H. Fischer, *J. Electroanal. Chem.*, **99**, 259 (1952).
7. T. P. Hoar and R. D. Holliday, *J. Appl. Chem.*, **3**, 502 (1953).
8. A. C. Makrides and N. Hackerman, *Ind. Eng. Chem.*, **47**, 1773 (1955).
9. G. Oakes and J. M. West, *Br. Corr. J.*, **4**, 66 (1969).
10. I. E. Titova and U. A. Guseva, *Zasch. Met.*, **4**, 588 (1968).
11. G. S. Parfenov, Y. Y. Ezaw, and G. P. Abrosimov, *Fiz. Khim. Mekh. Mater*, **4**, 352 (1968).
12. I. P. Anoschenko, *Zasch. Met.*, **3**, 231 (1967).
13. I. P. Anoschenko and T. Mezhdunar, *Kongr. Korras. Metal*, 203, (1966).
14. B. Donnelly, T. C. Downie, R. Grzekowiak, and D. Short, *Corros. Sci.*, **14**, 597 (1974).
15. H. Kaeshe, *Z. Elektrochem.*, **63**, 492 (1959).
16. H. Kaeshe, *Werkst. Korros.*, **10**, 622 (1959).
17. L. Cavallaro, L. Felloni, G. Trabenelli, and F. Pulidori, *Electrochim. Acta*, **8**, 521 (1963).
18. L. Cavallavo, L. Felloni, G. Trabenelli, and F. Pulidori, 2nd International Congress, Metallic Corrosion, p. 581, NACE, Houston (1966).
19. T. K. Ross and D. H. Jones, Eur. Symp. Corrosion Institution, p. 163, Annali Univ., Ferrara, N.J. (1961).
20. I. A. Ammar and S. Darwish, *Corros. Sci.*, **7**, 579 (1967).
21. L. I. Antropov, G. G. Vrzhosek, G. I. Dremove, V. P. Panesenko, and I. S. Pogrebova, *Zasch. Metal*, **6**, 440 (1970).
22. N. Meuree and L. Gierst, *Collect. Czech. Chem. Commun.*, **36**, 389 (1971).
23. L. I. Antropov, *Corros. Sci.*, **1**, 607 (1967).
24. E. Blomgren and J. Bockris, *J. Phys. Chem.*, **63**, 1475 (1955).
25. Z. A. Iofa and G. N. Tomashov, *Russ. J. Phys. Chem.*, **34**, 492 (1960).
26. L. I. Antropov, "Kinetics of Electrode Processes and Null Points of Metals," CSIR, New Delhi (1959).
27. K. Chandrasekara Pillai, Ph.D. Thesis, IIT Madras (1975).
28. W. D. Kumler and G. M. Fohlen, *J. Am. Chem. Soc.*, **64**, 1944 (1942).
29. L. Cavallaro, L. Felloni, and G. Trabanelli, European Symposium on Corrosion Inhibition, p. 111 (1961).
30. J. A. Pople and D. L. Beveridge, "Approximate Molecular Orbital Theory," McGraw Hill, New York (1970).

The Voltammetric Behavior of Some Viologens at SnO_2 Electrodes

J. Bruinink and C. G. A. Kregting

Philips Research Laboratories, Eindhoven, The Netherlands

ABSTRACT

The reduction peak of a linear potential sweep voltammogram of 1,1'-diheptyl-4,4'-dipyridinium dibromide in water, was found to be very steep with $E_p - E_{p/2} \approx 0.020$V at a scan speed less than 0.1 V/sec. This behavior was discussed on the basis of a model consisting of a reversible electron transfer and a coupled chemical reaction in analogy with reversible metal deposition. With modified viologens similar results have been obtained. The role of the coupled chemical reaction was underlined by the observed Nernstian dependence on cation and/or anion concentrations of both first and second reduction peak potential. The observed anodic peak of the first reduction step differs from the peak expected from the dissolution of a bulk deposit.

The use of viologens in redox chromic displays is well known (1-3). It has been demonstrated that with a suitable combination of viologen cation A^{2+} and anion X^-, *e.g.*, 1,1'-diheptyl-4,4'-dipyridinium dibromide, the first reduction step in water is followed by a chemical reaction causing a solid deposit on the electrode. The following reaction scheme in an aqueous solution has been proposed on the basis of polarographic and conductometric experiments (2, 3)

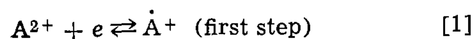

$$A^{2+} + e \rightleftarrows \dot{A}^{+} \quad \text{(first step)} \qquad [1]$$

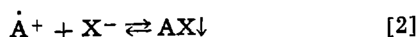

$$\dot{A}^{+} + X^{-} \rightleftarrows AX\downarrow \qquad [2]$$

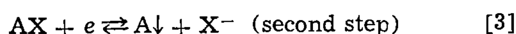

$$AX + e \rightleftarrows A\downarrow + X^{-} \quad \text{(second step)} \qquad [3]$$

The reaction product AX is deposited as a solid purple film on the electrode. The product A is also a solid deposit but with a yellowish-brown color.

Previous voltammetric measurements on tin dioxide electrodes revealed that the ratio of the charges involved in reduction and oxidation of heptyl viologen bromide is about unity for the first reduction step. Further, it was found that the first reduction step gives a very steep current peak, whereas the corresponding oxidation peak showed a very fast drop of the current after dissolution was completed (4).

The present study presents the results of some voltammetric investigations of the first reduction and oxidation steps of film-forming viologens on tin dioxide with the emphasis on 1,1'-diheptyl-4,4'-dipyridinium dibromide (HV-Br). The results are compared with a theoretical model.

Key words: deposition, nucleation, dipyridinium compound.

Theoretical

Cathodic current voltage curve.—The theory of linear potential sweep voltammetry (LSV) at solid electrodes for a reversible metal film deposition has been presented by Berzins and Delahay (5), whereas Nicholson and Shain described this theory for various other reduction schemes involving soluble reactants and products (6). When considering the redox reaction of viologens, it was necessary to extend this theory

to an electrochemical reaction with a coupled chemical reaction yielding an insoluble deposit on the electrode. In a simple approximation this can be done by considering reaction [1] as being reversible under the experimental conditions. This assumption is very reasonable, as appears from literature (7, 8). Further it is assumed that the precipitation reaction [2] proceeds fast and quantitatively thus yielding an equilibrium concentration of the monocation C_{A^+} equal to K_s/C_X (2, 9, 10), where K_s represents the solubility product of the viologen radical salt AX and C_X the anion concentration. All activity coefficients are assumed to be unity.

Semi-infinite diffusion to a plane electrode is assumed to be responsible for mass transport in the solution. For the cathodic sweep, $E = E_i - vt$, where v is the scan rate. The initial potential E_i at $t = 0$ is given by the equilibrium potential of the electrode covered with at least one monolayer of deposit

$$E_i = E_o + \frac{RT}{n\mathbf{F}} \ln (C^*_{A^{2+}} C_X/K_s) \quad [4]$$

where $C^*_{A^{2+}}$ represents the bulk concentration of A^{2+}.

The present situation is identical with that of reversible deposition of a metal film on a solid electrode, which was solved by Berzins and Delahay (5). The reduction current was given by them as

$$I = \frac{2n^{3/2}\mathbf{F}^{3/2}}{\pi^{1/2}R^{1/2}T^{1/2}} AC^*_{A^{2+}}D_{A^{2+}}{}^{1/2}V^{1/2}\Phi\left[\left(\frac{n\mathbf{F}}{RT}vt\right)^{1/2}\right] \quad [5]$$

where

$$\Phi(\alpha) = \exp(-\alpha^2) \int_0^\alpha \exp(z^2)\,dz \quad [6]$$

A is the surface area. The function Φ defined by [6] has a maximum value of 0.5410 at $\alpha = 0.9241$, as can be found in tables (11). The peak current at 25°C is then proportional to the square root of the scan rate

$$I_p = 367n^{3/2}AC^*_{A^{2+}}D_{A^{2+}}{}^{1/2}v^{1/2} \quad [7]$$

At the peak potential E_p, $vt = 0.022/n$ (V) at 25°C so that

$$E_p = E_i - 0.022/n \text{ (V)} \quad [8]$$

The concentration dependence of the first reduction peak potential of HV-Br at solid electrodes follows directly from Eq. [4] and [8], namely, at 25°C

$$E_p(1) = E_o(1) + 0.059 \log \{C^*_{A^{2+}} C_X/K_s\} - 0.022 \quad [9]$$

Further it is found that

$$E_{p/2} = E_i - 0.002/n \text{ (V)}$$

and

$$\Delta E = E_p - E_{p/2} = 0.020/n \text{ (V)} \quad [10]$$

From the simple model used it is clear that very steep reduction peaks are expected. They are shifted anodically in comparison with a reduction in which both reactant and product are soluble as follows directly from [4]. In the latter case I_p is also proportional to $v^{1/2}$, but ΔE is about $0.056/n$ (V) at 25°C (6). Deviations from this metal deposition theory such as a cathodic shift of the peak potential at increasing scan rate have been observed by Hills *et al.* (12). Their origin has been ascribed to the occurrence of nucleation effects.

These nucleation effects during electrochemical formation and growth of a metal deposit have been discussed by Fleischmann and Thirsk for the case where the depositing metal is the same as the electrode (13). An extension to nucleation and growth on inert substrates was presented by Astley, Thirsk, and Harrison (14). It was shown that if linear diffusion is the rate-controlling process in the three-dimensional growth of instantaneously formed hemispherical nuclei, the observed current-time transient due to a potentiostatic step has a dependence of the form

$$I \propto t^{1/2} \quad [11]$$

Anodic current-voltage curve.—The electrochemical dissolution of a bulk viologen radical salt deposit during the anodic sweep is considered to be a reversible oxidation process preceded by a fast chemical reaction as presented by [2] and [1]. In this case, too, the concentration of the deposit is assumed to have unit activity until complete dissolution occurs at t_{max}. With these assumptions, the dissolution can be compared with the anodic dissolution of a bulk metal deposit as discussed earlier by Nicholson (15). In the anodic case $E = E_i + vt$ in which E_i is given by [4]. The expression for the current is obtained after substitution of $\beta = -\frac{n\mathbf{F}}{RT} vt$ in [5]. The expression for the anodic current is then

$$I = -n\mathbf{F}AC^*_{A^{2+}}(\beta D_{A^{2+}})^{1/2}\exp(\beta t)\,\mathrm{erf}[(\beta t)^{1/2}] \quad [12]$$

The total charge q_o involved in the anodic dissolution is obtained by integration. As a result of this theory one obtains a rather steep anodic peak, while at $t = t_{max}$ the current drops abruptly to zero.

Experimental

The voltammetric experiments were performed with a PAR 173 potentiostat system and electronic *IR* compensation was used. A Hewlett Packard 7000 AM recorder and a Philips PM 3330 oscilloscope with a polaroid camera were used for signal monitoring. The electrode material employed was tin dioxide coated glass (10 Ω/□) made by pyrolitic decomposition of $SnCl_4$ in *n*-butylacetate using antimony as dopant.

The electrode area was 0.2 cm². All experiments were carried out in a vessel thermostated at 25°C. The electrolyte solutions were deoxygenated by passing argon through them (5 ppm O_2). The reference and counter-electrodes used were Ag/AgCl electrodes separated from the cell solution by Luggin capillary and glass frit, respectively. The 1,1′-diheptyl-4-4′-dipyridinium dibromide (HV-Br) and other dipyridinium derivatives were of the same purity as described in a previous paper (4).

Results and Discussion

Cathodic peak.—The LSV behavior of the first reduction step of HV-Br on tin dioxide is shown in Fig. 1, which is typical of this viologen at scan speeds less than 0.1 V/sec. The same figure gives theoretical values, calculated using Eq. [5]. The value of K_s used was calculated with aid of Eq. [9], while the value of the diffusion coefficient was obtained from the experimental value of I_p and Eq. [7]. It can be seen that the calculated values fit the experimental data very well, if at least one monolayer has been formed. In addition it is obvious that the voltammogram is very steep with $\Delta E \approx -0.02$V in agreement with the simple model.

An indication about monolayer completion can be deduced from Fig. 2 in which the charge involved in

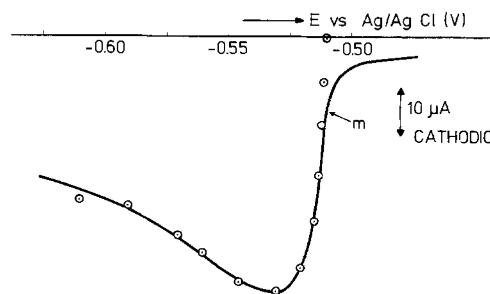

Fig. 1. Linear potential sweep voltammogram for 8.8 × 10^{-4}M diheptyl viologen dibromide in an aqueous solution of 0.3M KBr. Scan rate 0.1 V/sec. ⊙, Values calculated with $D = 6.4 \times 10^{-6}$ cm² sec^{-1} and $K_s = 6 \times 10^{-7}$. *m* indicates monolayer completion.

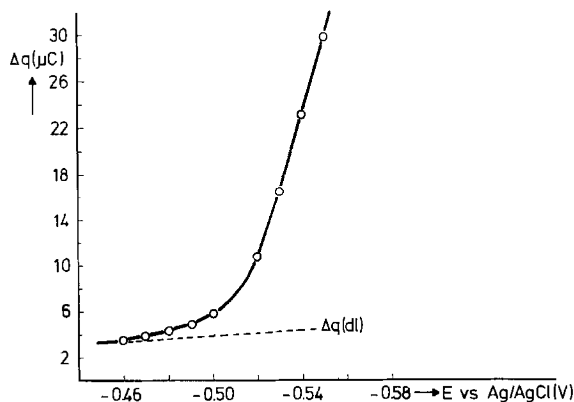

Fig. 2. Charge vs. potential of LSV for 8.8 × 10^{-4}M diheptyl viologen dibromide in an aqueous solution of 0.3M KBr. Scan rate 0.1 V/sec. Δq(d.l) is integrated charging current in 0.3M KBr. Starting point of the sweep 0V (Ag/AgCl).

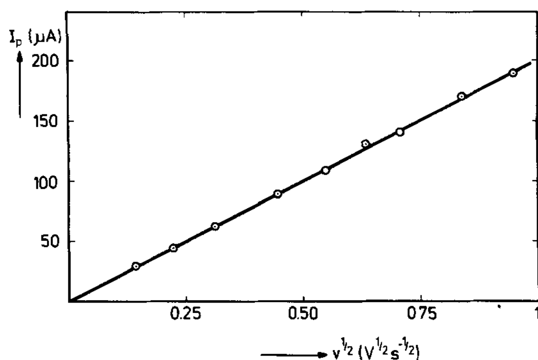

Fig. 3. I_p vs. $v^{1/2}$ plot for 10^{-3}M diheptyl viologen dibromide in an aqueous solution of 1M KBr.

film formation has been indicated. In general the predicted linear I_p — $v^{1/2}$ behavior is also found (Fig. 3). From this figure, and using the geometrical electrode surface area, a diffusion coefficient of 7.4 × 10^{-6} cm^2 sec^{-1} for the diheptyl viologen cation was calculated. In all experiments a reasonable agreement between the measured values of the diffusion coefficients was found, with values varying between 6 × 10^{-6} and 10^{-5} cm^2 sec^{-1} for HV-Br. Deviations from this ideal behavior have been observed at higher scan rates. In this respect it can be seen from Fig. 4 that the peak potential E_p varies with the scan rate if v is larger than 0.1 V/sec. In the same region (0.1 V/sec) it was found that $E_{p/2}$ was constant within the experimental error. This means that the value of ΔE varied from 0.02V at low scan speeds up to about 0.05V at 1 V/sec. Several reasons for this deviation from the simple model can be given. Since an uncompensated ohmic drop would be responsible for only a few millivolts deviation, other possibilities have

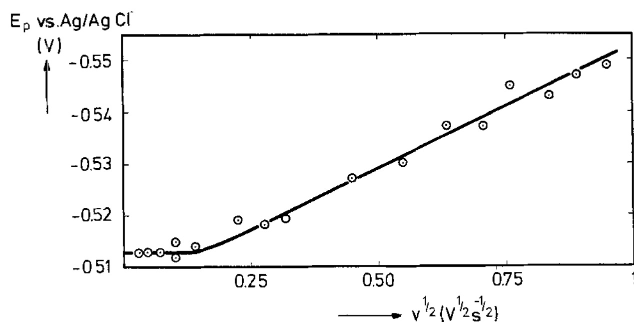

Fig. 4. Variation of the peak potential E_p with $v^{1/2}$ for 0.94 × 10^{-3}M diheptyl viologen dibromide in an aqueous solution of 1M KBr.

to be considered. Also the role of the film resistance can be neglected as followed from galvanostatic step measurements of films deposited with a charge density of 2 mC/cm^2.

A reason for the observed deviation can be the rate-determining character of the coupled chemical reaction at higher scan speed. This case is difficult to investigate since one has to make assumptions about the activity of the deposit at partial electrode coverage. Although some rate-determining role of the chemical reaction cannot be precluded, it is known that formation of a metal deposit on an inert electrode usually requires an overpotential, causing similar effects (12). Similarly, an explanation of the dependence of the peak potential on the scan rate is probably given by a rate-determining nucleation as mentioned earlier.

Nucleation phenomena during reduction.—The first stage in the electrodeposition of a heptyl-viologen bromide radical film was studied by applying a potential step to the electrode. After measuring the equilibrium potential of the radical film, the current-time dependency was determined at several small overpotentials. The results are represented in Fig. 5, which gives the $I - t^{-1/2}$ plot. At short times (milliseconds) the usual double layer charging is found (not indicated in the figure), followed by a rising part of the current which is proportional to $t^{1/2}$. After some time the usual $I - t^{1/2}$ diffusion behavior is observed as was reported in an earlier paper (16). The $I - t^{1/2}$ behavior can be observed only if small overpotentials are used and care is taken to avoid the presence of traces of radical film on the electrode. With very small amounts of radical film present, only the diffusional behavior is observed. As an explanation of the observed behavior it is proposed that a diffusion process controls the growth of nuclei formed by instantaneous three-dimensional nucleation in analogy with metal deposition. After some time overlapping of nuclei would occur and the $I - t^{-1/2}$ behavior is observed. It can also be seen from Fig. 5 that in the $I \propto t^{1/2}$ region, slopes as well as intercepts are dependent on the overpotential. An explanation of this dependence is thought to be that the number of active sites available for nucleation is potential dependent, while in addition some induction period for the formation of these sites must be considered. The cathodic shift of the peak potential (Fig. 4) at increasing scan rates might be due to these nucleation effects.

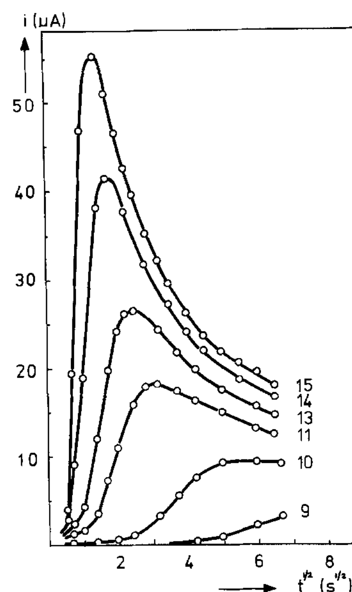

Fig. 5. Potentiostatic I — $t^{1/2}$ dependence for the deposition of diheptyl viologen radical bromide at tin dioxide. 0.01M diheptyl viologen dibromide in an aqueous solution of 0.3M KBr. Overpotentials (mV) indicated in figure.

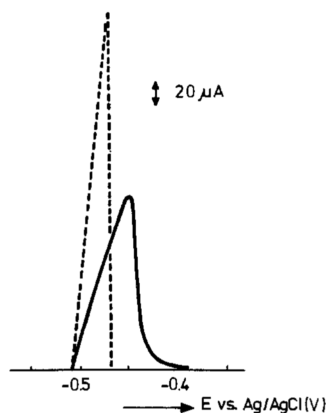

Fig. 6. Anodic peak due to the oxidation of a diheptyl viologen radical bromide film during a linear potential sweep voltammogram of 10^{-3}M diheptyl viologen dibromide in an aqueous solution of 0.3M KBr. Scan rate 0.1 V/sec. Total charge involved 0.679×10^{-4}C. Solid line, experimental curve; broken line, bulk theory. The value of the diffusion coefficient used was $D = 6 \times 10^{-6}$ cm^2/sec.

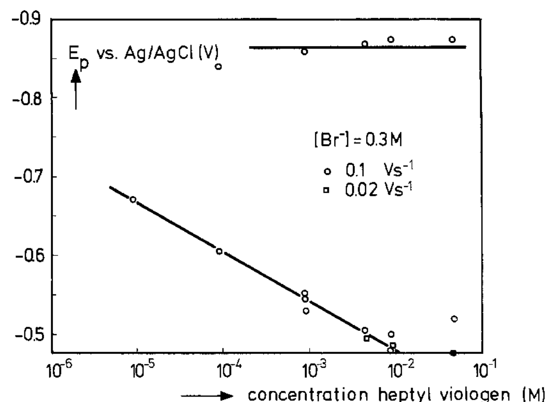

Fig. 8. Peak potentials of first and second reduction steps of HV-Br as a function of the diheptyl viologen concentration. Scan rates are indicated in the figure. The solid lines represent the Nernstian slope.

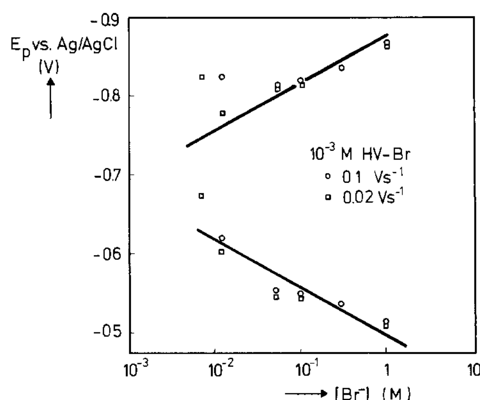

Fig. 9. Peak potentials of first and second reduction steps of HV-Br as a function of the bromide concentration. Scan rates are indicated in the figure. The solid lines represent the Nernstian slope.

Anodic peak.—The predicted dissolution behavior [12] of a bulk deposit is compared with experimental data in Fig. 6 for a diheptyl viologen radical bromide film deposited during a voltage sweep at 0.1 V/sec. It is clear that there is a considerable discrepancy between the theoretical dissolution behavior of the bulk film and the experimental curve although the current still drops very rapidly. It is likely that the observed discrepancy is due to a change in activity of the solid radical salt film just as occurs when dissolving metal films (15). With the viologen radical salt film dissolution this change in activity might be due to reorientation of the molecules as already mentioned in an earlier paper (4).

Reduction of modified viologens.—The experimental and calculated cathodic peaks of the two electron reduction of the modified viologen tetramethylen bis-[4(1-ethyl pyridin-4′-yl)pyridinium] perchlorate or ED-ClO_4 with $n = 2$ are shown in Fig. 7. The measured ΔE is about 0.013V which was found to be systematically larger than the 0.010V expected from theory. Also with this material nucleation phenomena were found comparable to those observed with heptyl viologen dibromide. Similar results were obtained with the modified viologen tetramethylen bis-[4(1-benzyl pyridin-4′-yl) pyridinium] tetrafluoroborate.

Concentration dependence of the reduction peak potentials of HV-Br.—The expression for the concentration dependence of the reduction peak potential [9] holds only at relatively low scan rates for which E_p is not much affected by nucleation effects. From Fig. 8 and 9 it can be concluded that the expected Nernstian dependence of both $C^*_{A^{2+}}$ and C_X is found experimentally. These results are in good agreement with those found at mercury electrodes (2). From the present

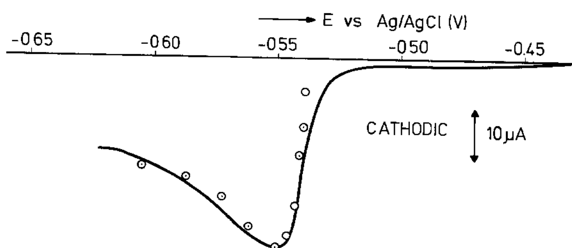

Fig. 7. Linear potential sweep voltammogram of 5×10^{-4}M of tetramethylene bis-[4(1-ethyl pyridin-4′-yl) pyridinium] perchlorate in an aqueous solution of 0.1M $NaClO_4$. Scan rate 0.02 V/sec. ⊙, Calculated with $D = 6.3 \times 10^{-6}$ cm^2/sec, $E_i = -0.539$V (Ag/AgCl), and $n = 2$.

experiment it can be concluded that the value of the solubility product of HV-Br is between 10^{-7} and 10^{-6}.

The expression for the second reduction peak potential of HV-Br is somewhat difficult to derive, since we are dealing here with the reduction of an insoluble deposit yielding an insoluble reaction product. At 25°C the equilibrium potential of the second reduction step product is equal to $E_0(2) + 0.059 \log(1/C_X)$, [see (2)], so it is expected that the second reduction step peak potential will also obey this dependence. From Fig. 8 it follows that $E_p[2]$ is indeed almost independent of $C^*_{A^{2+}}$ whereas Fig. 9 shows an anion dependence in agreement with theory. These results underline the role of the coupled chemical reaction and confirm the model proposed for the HV-Br reduction and oxidation.

Acknowledgment

Thanks are due to Mr. P. van Zanten for helpful discussions.

Manuscript submitted Nov. 1977; revised manuscript received May 6, 1978.

Any discussion of this paper will appear in a Discussion Section to be published in the June 1979 JOURNAL. All discussions for the June 1979 Discussion Section should be submitted by Feb. 1, 1979.

Publication costs of this article were assisted by Philips Research Laboratories.

REFERENCES

1. C. J. Schoot, J. J. Ponjeé, H. T. van Dam, R. A. van Doorn, and P. T. Bolwijn, *Appl. Phys. Lett.*, **23**, 64 (1973).
2. H. T. van Dam and J. J. Ponjeé, *This Journal*, **121**, 1555 (1974).

3. H. T. van Dam, *ibid.*, **123**, 1181 (1976).
4. J. Bruinink, C. G. A. Kregting, and J J. Ponjeé, *ibid.*, **124**, 1854 (1977).
5. T. Berzins and P. Delahay, *J. Am. Chem. Soc.*, **75**, 555 (1953).
6. R. S. Nicholson and I. Shain, *Anal. Chem.*, **36**, 706 (1964).
7. W. M. Schwarz, Thesis University of Wisconsin (1961).
8. R. M. Elofson and R. L. Edsberg, *Can. J. Chem.*, **35**, 646 (1957).
9. I. F. Chang, B. L. Gilbert, and T. I. Sun, *ibid.*, **122**, 955 (1975).
10. R. J. Jasinski, *This Journal*, **124**, 637 (1977).
11. W. L. Millar and A. R. Gordon, *J. Phys. Chem.*, **35**, 2785 (1931).
12. G. J. Hills, D. J. Schiffrin, and J. Thompson, *J. Electroanal. Chem.*, **19**, 657 (1974).
13. M. Fleischmann and H. R. Thirsk, in "Advances in Electrochemistry and Electrochemical Engineering," Vol. 3, P. Delahay and C. W. Tobias, Editors, Interscience, New York (1963).
14. D. J. Astley, J. A. Harrison, and H. R. Thirsk, *Trans. Faraday Soc.*, **64**, 192 (1968).
15. M. M. Nicholson, *J. Am. Chem. Soc.*, **79**, 7 (1957).
16. J. Bruining and P. V. Zanten, *This Journal*, **124**, 1232 (1977).

Syntheses with Electrogenerated Halogens

Part III. Oxidation of Primary Alcohols to Acetals of 2-Haloaldehydes

Donald A. White* and James P. Coleman*

Monsanto Company, St. Louis, Missouri 63166

ABSTRACT

Electrolysis of primary alcohols having one or more β-hydrogen atoms in the presence of anhydrous hydrogen halides affords acetals of 2-haloaldehydes.

Direct electrochemical oxidation of anhydrous primary alcohols has been investigated by several workers (1-6) and affords aldehydes (1, 4, 6), acetals (1, 3, 6), or esters (6). Indirect oxidation has been investigated less extensively. With sodium iodide as the electrolyte, formate esters are obtained from methanol and ethanol (7) and oxidation of methanol containing anhydrous hydrogen chloride has been reported to give formaldehyde (8). The oxidation of alcohols containing anhydrous hydrogen chloride is also the subject matter of the present paper. The objective of this work has been the conversion of alcohols ($RR'CHCH_2OH$) having one or more β-hydrogen atoms to the acetals of the corresponding 2-chloroaldehydes [$RR'CClCH(OCH_2CHRR')_2$]. These acetals have been obtained previously by the reaction of alcohols with chlorine (9-13). This chemical reaction proceeds satisfactorily but produces three moles of hydrogen chloride per mole of acetal (1). Disposal of or recycle of this byproduct must be arranged. On the otherhand, the indirect electrochemical reaction offers the possibility of a process which consumes hydrogen chloride and gives innocuous coproducts, hydrogen, which may be burned to water, and water itself (2).

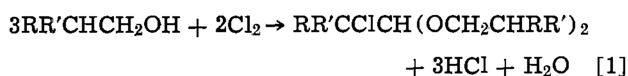

$$3RR'CHCH_2OH + 2Cl_2 \rightarrow RR'CClCH(OCH_2CHRR')_2 + 3HCl + H_2O \quad [1]$$

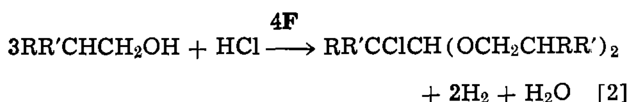

$$3RR'CHCH_2OH + HCl \xrightarrow{4F} RR'CClCH(OCH_2CHRR')_2 + 2H_2 + H_2O \quad [2]$$

Experimental

A Sorenson Model DCR 80-6B power supply (Raytheon Company, Manchester, New Hampshire), operating in its constant current mode, was used for the electrochemical reactions. The cell used was a 500 ml three-necked flask equipped with two graphite-rod (12 × 1/4 in. diam, Laboratory Supply and Equipment Company, Chevy Chase, Maryland) electrodes which were parallel and *ca.* 2 cm apart. The remaining necks were used for the attachment of a thermometer and a water-cooled condenser. The cell contents were stirred magnetically.

Anhydrous alcohols were obtained from Fisher Scientific Company, Fairlawn, New Jersey, or Mallinckrodt Chemical Works, St. Louis, Missouri, and anhydrous hydrogen halides from Matheson Gas Company, East Rutherford, New Jersey. They were used as supplied.

Reactions were followed and the product distributions (Table I) determined by observation of the NMR resonance due to the acetal proton [$RCH(OR')_2$] which could be easily observed in the acidic solutions and by GLC of neutralized (calcium carbonate) solutions. For the methanol reaction (Table I) the GLC column was a 7 ft × 1/8 in. stainless steel column packed with Porapak Q (40°-200°) and for the other reactions a similar 2 ft × 1/8 in. column packed with 5% OV101 on 100/120 Chromosorb G-HP (40°-200°). NMR spectra were recorded at 60 MHz on a Varian Model A56/60 or T60 machine.

The products from methanol oxidation (Table I, line 1) were determined by the NMR and GLC methods but were not isolated. The products from the other reactions were isolated by neutralization of the reaction mixture with excess calcium carbonate, filtration, and atmospheric-pressure distillation of the alcohol to give a mixture of the crude product and calcium chloride. This was partitioned between ether and water and the ether layer was separated, washed with water, dried over anhydrous calcium sulfate, filtered, and evaporated to give the crude product. This was distilled at atmospheric pressure (ethanol and *iso*butanol oxidations) or *in vacuo* (*n*-butanol oxidations).

The isolated haloacetals were identified via their NMR spectra, which, in the case of the ethanol oxidation products (Table I, line 2), were identical to published spectra (14). The spectra of *n*-butanol oxidation products (Table I, lines 3-7) are summarized in Table II. 2-Chloro*iso*butyraldehyde dimethyl acetal (from Table I, line 8) showed NMR bands at 1.50, 3.53, and 4.13 ppm downfield from internal $(CH_3)_4Si$ reference in $CDCl_3$ solution, due to C-methyl, O-methyl, and acetal protons, respectively.

The electrochemical reactions were carried out with the quantities shown (Table I) in the cell, which was

* Electrochemical Society Active Member.

Key words: organic, electrolysis, oxidation.

Table I. The formation of acetals via electrolysis of anhydrous alcohols in the presence of hydrogen halides

	Alcohol	(Moles)	Solvent[a]	Halide	(Moles)	Current (A)	Temp. (°C)	Electricity passed (F)	Acetals formed [mmoles (current efficiency)] Unsubs.	Monohalo	Dihalo	Selectivity to mono[b] (%)
1.[c]	CH_3OH	(8.0)		HCl	(0.98)	4.0	28	1.60	40 (5)	—	—	—
2.	C_2H_5OH	(5.0)		HCl	(1.04)	2.0	32-3	1.00	4 (1)	201 (80)	7 (4)	95
3.	*n*-C_4H_9OH	(4.0)		HCl	(0.55)	1.0	30-2	0.50	6 (2)	103 (82)	trace	95
4a.	*n*-C_4H_9OH	(4.0)		HCl	(1.10)	1.5	35-40	0.40	trace	83 (83)	4 (6)	95
4b.								0.80	trace	154 (77)	15 (11)	91
4c.								1.20	trace	204 (68)	31 (16)	84
4d.								1.68	trace	268 (64)	44 (16)	86
4e.								2 00	trace	276 (56)	51 (15)	84
4f.								2.36	trace	282 (34)	56 (10)	84
5.	*n*-C_4H_9OH	(4.0)		HCl	(2.06)	1.5	35-6	0.40	trace	76 (76)	8 (12)	90
6.	*n*-C_4H_9OH	(4.0)		HBr	(0.50)	1.0	58-60	1.00	trace	57 (23)	13 (8)	81
7.	*n*-C_4H_9OH	(1.0)	CH_2Cl_2[d]	HCl	(satd.)	0.8	38-40	0.10	trace	20 (80)	0.3 (2)	99
8.	*iso*-C_4H_9OH	(1.0)	CH_3OH[e]	HCl	(2.08)	4.0	35-40	4.0	nd[f]	610 (61)[g]	—	—

[a] Apart from excess alcohol.
[b] Monosubstituted acetal as a percentage of all three (mole basis).
[c] Methyl formate, 19 mmoles (5% curr. eff.), also formed.
[d] 200 ml.
[e] 256g, (8.0 mole).
[f] No attempt made to detect this compound.
[g] Product is the dimethyl acetal of 2-chloro*iso*butyraldehyde.

Table II. NMR spectra of $CH_3{}^ACH_2{}^BCXYCH^C(OCH_2{}^DCH_2{}^ECH_2{}^ECH_3{}^F)_2$

X	Y	Proton chemical shifts[a] H^A	H^B	X	H^C	H^D	H^E	H^F
H	Cl	1.03 t, 7	*ca.* 1.5 m	*ca.* 3.7 m	4.42 d, 5.5	*ca.* 3.7 m	*ca.* 1.5 m	0.93 t, 7
Cl	Cl	1.20 t, 7	2.18 q, 7	—	4.60 s	*ca.* 3.8 m	*ca.* 1.6 m	0.93 t, 7
H	Br	1.05 t, 7	*ca.* 1.5 m	*ca.* 3.7 m	4.53 d, 6	*ca.* 3.7 m	*ca.* 1.5 m	0.93 t, 7
Br	Br	1.23 t, 7	2.35 q, 7	—	4.62 s	*ca.* 3.8 m	*ca.* 1.5 m	0.93 t, 7

[a] Measured in $CDCl_3$ solution at 60 MHz and reported in ppm downfield from internal tetramethylsilane reference signal. Multiplicity of signals (s = singlet, d = doublet, t = triplet, q = quartet, m = multiplet) and coupling constants (Hz) are shown below the chemical shift.

partially immersed in a bath of flowing cold water. In this preliminary work current density effects were ignored, and a current which would generate an electrolyte temperature in the desired range (30°-40°) was used. Since the expected anode (chloride discharge) and cathode (proton discharge) reactions tolerate a wide range of current densities, this approach may not be unreasonable. A typical example follows.

2-Chlorobutyraldehyde dibutyl acetal.—Electrolysis (1.0A for 13.4 hr ≡ 0.5**F**) of a solution of anhydrous hydrogen chloride (20g, 0.55 mole) in *n*-butanol (296g, 4.00 mole) afforded a clear, colorless solution containing the quantities of acetals shown in Table I, line 3. Butyl butyrate was also detected by GLC but not measured. Work-up, as described above, gave a colorless oil (28.5g) which was distilled *in vacuo*. Two fractions were collected: (*i*) a colorless liquid, bp 65°-70° (0.05 mm), 12.0g; and (*ii*) a colorless liquid, bp 72°-73° (0.04 mm), 13.5g. The latter was identified by its NMR spectrum (Table II, line 1) as 2-chlorobutyraldehyde dibutyl acetal. Found: C, 60.9; H, 10.9%. Calculated for $C_{12}H_{25}ClO_2$: C, 60.6; H, 11.0%. The presence of the chlorine substituent was evident from its mass spectrum, obtained via chemical ionization, which showed parent ion peaks at *m/e* = 236 and 238 in the expected 3:1 ratio. Fraction (*i*) was the same compound containing *ca.* 10 mole percent (m/o) of butyraldehyde dibutyl acetal. This impurity was identified by combined GLC/mass spectroscopy and measured using an authentic sample prepared by acetalization of *n*-butyraldehyde with *n*-butanol in the presence of anhydrous hydrogen chloride.

A portion (2.37g, 0.01 mole) of fraction (*ii*) was stirred with a solution (0.05*M*, 200 ml, 0.01 mole) of 2,4-dinitrophenylhydrazine in concentrated aqueous hydrogen chloride for 3 hr. The orange solid formed was removed by filtration, washed with water, and dried by suction on the filter. The dry solid (1.16g) was recrystallized from cyclohexane (100 ml) to give 2-chlorobutyraldehyde 2,4-dinitrophenylhydrazone as orange needles (0.75g), mp 93°-94°, liter[15] mp 93°-94°.

Results and Discussion

The electrolysis of some typical aliphatic primary alcohols containing anhydrous hydrogen chloride has been examined using a constant current in an undivided cell with graphite electrodes. Prior to examining its higher homologs the previously reported (8) reaction of methanol was reexamined. The products were found to be methylal and methyl formate, each in *ca.* 5% current efficiency. Throughout most of the electrolysis period the green color of anodically generated chlorine was evident in the solution. Its cathodic reduction explains the low current efficiencies and the drop, from the initial theoretical value, of the rate of cathodic hydrogen evolution observed by the previous workers (8). The discrepancy in the product formed may be an artifact of the different analytical methods used—GLC and NMR in the present work and reaction with ammonia to form hexamethylenetetramine in the previously reported work (8).

In contrast to the behavior observed with methanol, solutions of anhydrous hydrogen chloride in ethanol or *n*-butanol stayed absolutely colorless on electrolysis. The desired monohaloacetals were obtained with high current efficiencies (Table I, lines 2-5). Byproducts included the unsubstituted acetal and the dichloroacetal (also traces of the trichloroacetal from ethanol). The relative importance of these byproducts depends on reaction temperature, hydrogen chloride concentration, and alcohol conversion. Low temperatures (<30°) favor the unsubstituted acetal as do low hydrogen chloride concentrations (*cf.* Table I,

lines 3, 4a, 5). The effect of conversion is a little more complex. As it increases, selectivity to the monochloroacetal decreases due to increased dichloroacetal formation (Table I, lines 4a-4c). However, a constant selectivity is reached (Table I, lines 4c-4f) which, in the example shown, is still quite high (84%). However, there is a progressive decline in current efficiency (Table I, lines 4a-4f) which makes it desirable to use fairly low conversions. The corresponding ester, ethyl acetate, or butyl butyrate is also a minor byproduct. This became the major product when concentrated (37%) aqueous hydrogen chloride was substituted for the anhydrous material.

These results are consistent with a mechanism involving the anodic generation of chlorine (Eq. [3]), which oxidizes the alcohol to the aldehyde (Eq. [4]), acid-catalyzed conversion of the aldehyde to the acetal (Eq. [5]), and chlorination of the acetal (Eq. [6]).

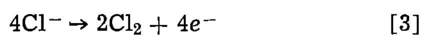

$$4Cl^- \rightarrow 2Cl_2 + 4e^- \quad [3]$$

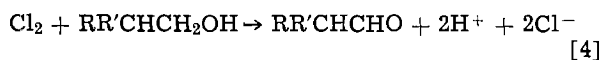

$$Cl_2 + RR'CHCH_2OH \rightarrow RR'CHCHO + 2H^+ + 2Cl^- \quad [4]$$

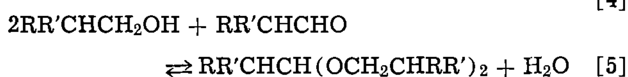

$$2RR'CHCH_2OH + RR'CHCHO \rightleftarrows RR'CHCH(OCH_2CHRR')_2 + H_2O \quad [5]$$

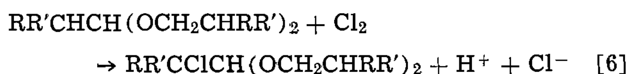

$$RR'CHCH(OCH_2CHRR')_2 + Cl_2 \rightarrow RR'CClCH(OCH_2CHRR')_2 + H^+ + Cl^- \quad [6]$$

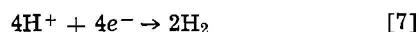

$$4H^+ + 4e^- \rightarrow 2H_2 \quad [7]$$

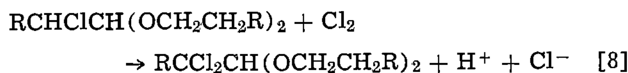

$$RCHClCH(OCH_2CH_2R)_2 + Cl_2 \rightarrow RCCl_2CH(OCH_2CH_2R)_2 + H^+ + Cl^- \quad [8]$$

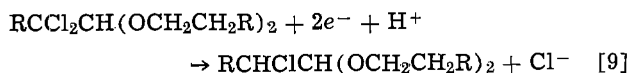

$$RCCl_2CH(OCH_2CH_2R)_2 + 2e^- + H^+ \rightarrow RCHClCH(OCH_2CH_2R)_2 + Cl^- \quad [9]$$

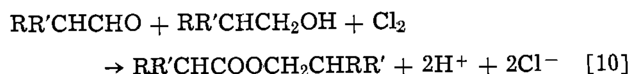

$$RR'CHCHO + RR'CHCH_2OH + Cl_2 \rightarrow RR'CHCOOCH_2CHRR' + 2H^+ + 2Cl^- \quad [10]$$

The cathodic reaction is hydrogen evolution (Eq. [7]), and the summation of these reactions [3-7] is the over-all reaction [2]. The dichloroacetal byproduct arises from further chlorination of the product (Eq. [8]). The fact that it builds up to a constant percentage of the acetal product mixture suggests that it may be cathodically reduced back to the monochloroacetal (Eq. [9]). Added water displaces equilibrium in Eq. [5] to the left. The aldehyde is then present in greater abundance and its oxidation (Eq. [10]) leads to ester formation. This becomes the major reaction when concentrated aqueous acid is used instead of the anhydrous material.

For satisfactory isolation of the acetals unreacted hydrogen chloride must be neutralized. This is conveniently done by stirring with calcium carbonate (sodium carbonate became coated with sodium chloride and was not so effective). If it is not done, the acetal is found to distill over with the solvent alcohol, even though its boiling point is much higher than that of the alcohol. In the case of ethanol, the "solvent" distilled at 77°-85° and chloroacetal (bp 157°) (13) was found in the distillate. The acetal may distill over in the form of chloroacetaldehyde (bp 85°) (13), which could be present in an acid-catalyzed equilibrium with the acetal (*cf.* Eq. [5]) and reform the acetal in the collected distillate. After neutralization, only normal, minor losses of the product into the solvent were found.

Electrolysis of *n*-butanol containing anhydrous hydrogen bromide has also been examined. In this case, bromine accumulated in the solution from the moment the current was turned on. In order to speed up the chemical reactions the temperature was allowed to rise to *ca.* 60°. In spite of this, bromine still remained in solution throughout the electrolysis period. As expected, the current efficiency was low and the product was a mixture of the bromo- and dibromoacetals (Table I, line 6).

To extend the scope of the present reaction, the possibility of using a solvent other than excess alcohol has been examined. This would permit oxidation of higher molecular weight alcohols which have low dielectric constants and may be solids at appropriate reaction temperatures. Due to the presence of anhydrous hydrogen halides, several of the usual electrochemical solvents cannot be used, *e.g.*, amines, ethers, cyclic carbonates. Both dimethylformamide and acetonitrile reacted with a mixture of anhydrous hydrogen chloride and an alcohol. Methylene chloride, however, was usable and gave results comparable with those obtained when using excess alcohol as solvent (*cf.*, Table I, lines 4a and 7). Though its volatility is useful in work-up, the low dielectric constant of methylene chloride is a disadvantage. However, methanol has a high dielectric constant and, as shown (Table I, line 1), is oxidized only with difficulty by anodically generated chlorine. This suggested its use as a solvent for the oxidation of higher alcohols to dimethyl acetals (Eq. [11]). This reaction is exemplified by the

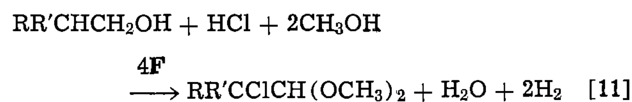

$$RR'CHCH_2OH + HCl + 2CH_3OH \xrightarrow{4F} RR'CClCH(OCH_3)_2 + H_2O + 2H_2 \quad [11]$$

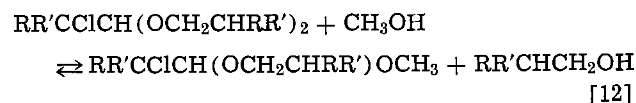

$$RR'CClCH(OCH_2CHRR')_2 + CH_3OH \rightleftarrows RR'CClCH(OCH_2CHRR')OCH_3 + RR'CHCH_2OH \quad [12]$$

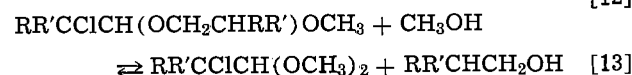

$$RR'CClCH(OCH_2CHRR')OCH_3 + CH_3OH \rightleftarrows RR'CClCH(OCH_3)_2 + RR'CHCH_2OH \quad [13]$$

oxidation of *iso*butanol (Table I, line 8). The formation of the dimethyl acetal depends primarily on the use of a large excess of methanol, but also on the acid-catalyzed equilibria Eq. [12] and [13] between the three acetals which may be formed. As the reaction progresses, consumption of the substrate alcohol will displace these equilibria to the right.

In summary, the present procedure offers a convenient route to acetals of 2-chloroaldehydes. High current efficiencies are obtained using a simple cell with inexpensive graphite electrodes. From the industrial point of view, the tendency, discussed above, of the product acetal to distill with the solvent alcohol is regrettable as it necessitates neutralization (or, perhaps, dehydration) of the reaction mixtures.

Manuscript submitted Jan. 9, 1978; revised manuscript received March 15, 1978.

Any discussion of this paper will appear in a Discussion Section to be published in the June 1979 JOURNAL. All discussions for the June 1979 Discussion Section should be submitted by Feb. 1, 1979.

Publication costs of this article were assisted by Monsanto Company.

REFERENCES

1. G. Sundholm, *J. Electroanal. Chem. Interfacial. Electrochem.*, **31**, 265 (1971).
2. G. Sundholm, *Acta Chem. Scand.*, **25**, 3188 (1971).
3. M. Finkelstein and S. D. Ross, *Tetrahedron*, **28**, 4497 (1972).
4. C. Iwakura, T. Hayashi, S. Kikkawa, and H. Tamura, *Electrochim. Acta*, **17**, 1085 (1972).
5. F. Sundholm, G. Sundholm, and K. Suontama, *Suom. Kemistilehti B*, **45**, 383 (1972); *C. A.*, **78**, 66162 (1973).
6. P. C. Scholl, S. E. Lentsch, and M. R. Van De Mark, *Tetrahedron*, **32**, 303 (1976).
7. D. A. White, *This Journal*, **124**, 1177 (1977).
8. A. P. Tomilov, Yu. D. Smirnov, and Yu. I. Rozin, *Zh. Obshch. Khim.*, **44**, 2028 (1974).
9. A. Lieben, *Ann.*, **104**, 114 (1857).
10. P. Fritsch, *ibid.*, **279**, 288 (1894).
11. F. D. Chattaway and O. G. Backeberg, *J. Chem. Soc.*, **125**, 1097 (1924).

12. P. C. Guha, P. L. N. Rao, and T. G. Verghese, *Curr. Sci.*, **12**, 82 (1943); *C. A.*, **37**, 5696 (1943).
13. P. J. De Bièvre, G. P. Van der Kelen, G. Cornille, and Z. Eeckhaut, *Bull. Soc. Chim. Belg.*, **68**, 550 (1959).
14. C. J. Pouchert and J. R. Campbell, "The Aldrich Library of NMR Spectra," Aldrich Chemical Company, Milwaukee, Wisc. (1974).
15. A. Ross and R. N. Ring, *J. Org. Chem.*, **26**, 579 (1961).

The Metal-Liquid Insulator Interface in Presence and Absence of an Applied Electric Field

Ikram Morcos*

Institute of Research of Hydro-Quebec, Varennes, Quebec, Canada J0L 2P0

ABSTRACT

The meniscus rise of different insulating liquids at a partially immersed copper rod and copper and gold plates was measured both in the absence and presence of different applied d-c voltages. Variations in contact angle in the absence of the field are qualitatively interpreted in the light of the Young and Duprée equation. Discrepancies between the experimentally observed meniscus height *vs.* voltage curves and theoretical curves calculated on the basis of an electrical-force mechanism are pointed out and a new mechanism envisaging the effect of interfacial forces is suggested.

The study of electric-field dependence of the interaction between a solid metal and an insulating liquid is complicated by the fact that the electrochemical parameters of the system are neither well defined nor accessible by presently available experimental techniques. Among the methods developed to study metal-liquid electrolyte interfaces, the meniscus-rise method (1-5) offers some promise in the study of metal-liquid insulator interfaces. The latter method has two criteria which make it attractive to use with liquid insulators notwithstanding the other problems with such systems. First, the method provides direct information on a single polarized interface which is essential for understanding the effect of electric field on the interfacial forces. Second, the meniscus height is measured by optical techniques which do not depend on the resistivity of the investigated system.

Observations on meniscus rise at high voltage electrodes date back to Faraday (6) who reported in 1836 that if two high voltages leads are dipped into a disk-containing turpentine, the liquid will rise along the positive electrode. The same phenomenon was rediscovered by Sumoto (7) who noted that the magnitude of rise and its dependence on the field direction are related to the type of liquid used The Sumoto effect was subsequently studied by Pickard (8), Middendorf and Brown (9), Krawinkel (10), and Pohl (11), and the subject has been more recently reviewed by Pickard (12).

Interpretations of the Sumoto effect have centered in the past around electrical-force mechanisms (12-15). In the present study the effect of interfacial forces, not dealt with in previous work, is considered. The study involves measurement of meniscus rise in both absence and presence of applied d-c voltage using insulating liquids of different chemical structure and test electrodes of two different geometries. In addition to its intrinsic scientific interest this problem was undertaken with two practical applications in mind. First, the data should be useful in the understanding of mechanisms of prebreakdown phenomena in transformer oils. Second, it is hoped that the measuring technique can be eventually developed into an analytical tool for detecting surface active impurities and/or degradation products.

Four insulating liquids were used in this study. These included the two alkylbenzene cable-insulants known as dodecylbenzene and decylbenzene, the transformer oil Voltesso 35 (chemical composition disclosed later), and polydimethylsiloxane which is a silicone oil known as the Dow Corning 200 fluid (electrical grade).

Both alkylbenzenes contain homologs with side chain ranging from C_9 to C_{12}. The main component, one with a side chain of C_{12} (dodecylbenzene) in one case and the other with C_{10} (decylbenzene) in the other case, constitutes only about 50% of the product. The dodecylbenzene is an electrical grade product commercially known as Chevron alkylate 21 (provided by Dussek Brothers) and is obtained by two vacuum distillations of the normal grade. The decylbenzene was provided by Pirelli Industries of Canada and was obtained from the normal grade by treating the latter product with Fuller's earth. Both the normal and electrical grades of decylbenzene but only the electrical grade of dodecylbenzene were used in this study. The dielectric constant and d-c resistivity of dodecylbenzene were 2.3 and 3.9×10^{14} Ω-cm, respectively. These alkylbenzenes are intrinsically stable compounds and impurities if present result from sources other than processes such as chemical rearrangement, degradation, or oxidation. Being good solvents for a wide variety of polar materials, these relatively low molecular weight alkylbenzenes are prone to contamination during transference from one container to another. The alkylbenzenes are produced by the Friedel-Krafts synthesis which involves the alkylation of benzene with the aliphatic chloro-derivatives of the hydrocarbons in the presence of aluminum trichloride as a catalyst.

Polydimethylsiloxane has the chemical structure $R_3SiO(R_2SiO)SiR_3$ where R is a $—CH_3$ radical. It is an extraordinarily stable product with a volume resistivity at 23°C and 500V d.c. of 1.0×10^{14} Ω-cm, dielectric constant at 23°C and 100 Hz of 2.7, and nominal viscosity at 25° of 20 centistates.

The Voltesso 35 is a mineral naphthenic-based oil in which the great majority of molecules are made up of one to three condensed cycloaliphatic and/or aromatic rings substituted with aliphatic side chains of variable lengths. Duval and Lamarre (16) studied the average molecular size distribution by liquid-solid chromatography (LSC) and gel permeation chromatography (GPC) of the Voltesso 35 oil and reported the following chemical constituents.

* Electrochemical Society Active Member.

80% saturates with 25Å average molecular size with one or more of the structures

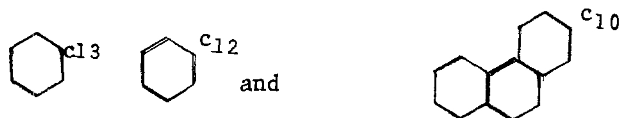

15% monoaromatics with 25Å average molecular size with one or more of the structures

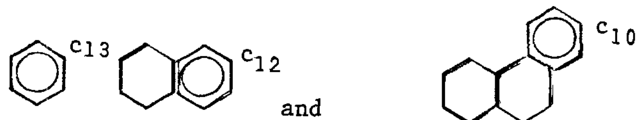

5% diaromatics and triaromatics with 19 and 12Å average molecular size, respectively, with one or more of the structures

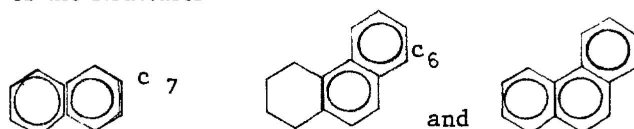

The Voltesso 35 contains a 0.08% by weight, 2,6-ditertiary butyl-p-cresol as an antioxidant. The Voltesso 35 has a volume resistivity of 10^{13} Ω-cm and a dielectric constant of 2.2. The Voltesso 35 was used without any further treatment.

Water contents are approximately 40, 30, and 110 ppm in dodecylbenzene, Voltesso 35, and polydimethylsiloxane.

Experimental Section

Experiments with each liquid were carried out with both cylindrically shaped and plate electrodes. The former electrode was in the form of a copper rod of 2.3 cm diam and the latter consisted of bright smooth 2 × 4 cm gold plate of 99.99% purity. Some experiments were also carried out with copper plates of 99.9% purity.

Surface roughness was measured by a Dekkak instrument provided by Sloan Instruments Corporation. The copper rods and plates were mechanically polished to produce a very bright surface with an average surface roughness of less than 0.1 μm. The plates were polished with aluminum oxide paste on a felt-covered wheel and the rod with a red-rouge polishing compound on a cotton-covered wheel. Prior to polishing the copper plates and rods were ground with different grade sandpapers. When the copper electrodes were not polished but chemically treated in a concentrated solution (1 part H_2O, 1 part HNO_3) of HNO_3 in water, their roughness was ~1.0 μm. Some experiments were also carried out with the latter electrodes. All electrodes were cleaned in methanol followed by drying at 110°C prior to the measurement.

Figure 1 shows a sketch diagram of the cell and type of electrodes used in the study. The measurement was made in a Teflon cell which has an ID of 12.3 cm and a height of 3.9 cm. The counterelectrode has the form of a cylindrical cage that consists of a 6 cm diam ring supported on four 4 cm long strips.

The level of the meniscus edge at the metal surface and the level of the liquid surface in the cell were measured with a cathetometer with a ± 0.001 cm sensitivity. To facilitate the measurement of the liquid surface level in the cell the latter was completely filled with the liquid until the liquid climbs forming a flat top. Before the measurement was started the electrode was lowered into and raised from the liquid several times to permit the establishment of equilibrium between the liquid vapor and the adsorption layer at the metal surface. With both gold and mechanically polished copper, the liquid meniscus forms a well-defined straight and horizontal edge with the metal surface (which is diagnostic of a surface free of macroscopic roughness or heterogeneity) and consequently its measurement could be carried out without much difficulty. In the case of chemically treated copper, however, the metal surface was observed to be covered above the proper meniscus with a liquid film which had probably resulted from the high surface roughness which by its capillary forces retains the liquid in the isolated depressions of the surface. The work with the latter electrodes was therefore discontinued.

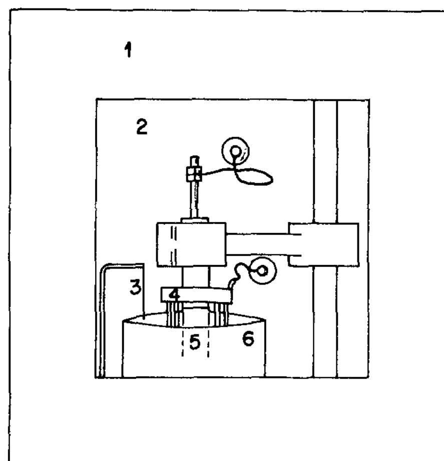

Fig. 1. Sketch diagram of cell and electrode. 1, Metal box; 2, glass window; 3, glass needle; 4, counterelectrode; 5, test electrode; 6, Teflon cell.

For the study of electric field dependence of the meniscus height, a high voltage power supply "LABTROL" provided by Universal Votronics Corporation was used. The voltage was increased in steps of 1 kV from 0 to the cathodic limit and from 0 to the anodic limit. Unless indicated otherwise, the voltage applied in each case ranged from 0 to ± 8 kV. No measurements were possible, however, at voltages higher than about 10-14 kV (depending on the liquid and polarity) because of the start of vibrations in the liquid meniscus. The equilibrium advancing meniscus height at a fixed voltage was measured after each voltage adjustment. After a series of measurements was completed between 0 and the cathodic or anodic limit, the voltage was reversed and a series of measurements for the receding meniscus height as a function of the decrease in voltage was carried out.

No attempt was made to measure the contact angle directly, but a technique used by Bascom *et al.* (17) was applied to determine whether zero and nonzero contact angles in the absence of the field remain or not as such in the presence of the electric field. This involved the use of monochromatic illumination and the same cathetometer used to measure the meniscus height. As indicated by Bascom *et al.*, a zero contact angle shows a diffuse wide zero-order fringe at the meniscus edge followed by narrow bands of higher order; a behavior that is not observed with a nonzero contact angle. This information was found to be useful in the discussion of the data as is demonstrated later.

Results and Discussion

In the absence of an externally applied voltage the meniscus height h at a partially immersed vertical plate is related to the contact angle θ by the exact equation

$$\sin \theta = 1 - (\rho g h^2 / 2\gamma_{LV}) \qquad [1]$$

where ρ and γ_{LV} are the liquid density and surface tension and g the acceleration of gravity. Equation [1] is derived (18) for an infinitely wide plate but the requirement of infinite width is experimentally satisfied if the plate width is only about 2 cm (19). There is no exact equation analogous to Eq. [1] for a partially immersed wire or rod but it has been experimentally demonstrated (20) that the meniscus height at a par-

Table I. Meniscus rise and contact angles for gold and copper in insulating liquids

Metal	Liquid	Advancing meniscus rise (cm)	Receding meniscus rise (cm)	Average contact angle (degrees)
Copper cylinder	Dodecylbenzene	0.220, 0.223	0.224, 0.220	—
Gold plate	Dodecylbenzene	0.249, 0 251	0.249, 0.251	3.8
Copper cylinder	Decylbenzene (treated with Fuller's earth)	0.214, 0.211, 0.211	0.215, 0.212	—
Copper plate	Decylbenzene (treated with Fuller's earth)	0.220	0.219	16.5
Gold plate	Decylbenzene (normal grade)	0.268		1.2
Copper plate	Decylbenzene (normal grade)	0.247, 0.246	0.248, 0.249	6.4
Copper cylinder	Voltesso 35	0.232, 0.234	0.231, 0.235	—
Copper plate	Voltesso 35	0.235, 0 241, 0.236	0.238, 0.242, 0.234	10.5
Gold plate	Voltesso 35	0.250, 0.246, 0.249	0.258, 0.238, 0.250	7.5
Copper cylinder	Polydimethylsiloxane	0.186, 0.190	0.186, 0.193	—
Gold plate	Polydimethylsiloxane	0.209, 0.208, 0.204	0.209, 0.206, 0.210	0

tially immersed glass rod increases with the increase in the diameter of the rod until it asymptotically approaches the meniscus height observed at a plate 2 cm wide. The higher the surface tension of the liquid the larger will be the rod diameter required to provide conditions approaching that of a plate (20). But even with liquids with low surface tensions from 20 to 30 dynes/cm the conditions of infinite width are not approached until the rod diameter is considerably larger than 2 cm. If the rod diameter is only 2 cm the meniscus height will be less by about 15% than the corresponding meniscus height observed at a 2 cm wide plate. Consequently, under the present experimental conditions accurate value of θ can be only obtained from h measured at a plate.

Table I shows the meniscus height and corresponding contact angle data obtained with different systems in the absence of electric field. The contact angles are calculated by means of Eq. [1] from h values measured at metal plates. Both advancing and receding data are shown. With many systems several measurements were made to test the reproducibility. Each set of measurements has been obtained with one and the same metal plate but at different levels. The data are generally reproducible and exhibit very little hysteresis. Contact-angle magnitude vary between zero and 16.5° depending on the surface tension of the liquid, its chemical composition, and probably on whether or not the surface is covered with adsorbed oxygen or other impurities left over from the polishing process. A discussion of the manner in which these factors affect contact angles is given below.

The contact angle between a solid and a liquid is determined by the Young and Duprée equation (21)

$$\gamma_{LV} \cos \theta = \gamma_{SV} - \gamma_{SL} \quad [2]$$

where γ_{SV}, γ_{SL}, and γ_{LV} are the metal/vapor, metal/liquid, and liquid/vapor interfacial tensions, and

$$\gamma_{SV} = \gamma_S - \pi \quad [3]$$

where γ_S is the metal surface tension in vacuum and π is the film pressure (22) of the adsorbed vapor film. The system will exhibit a zero or nonzero contact angle depending on whether $\gamma_{SV} - \gamma_{SL}$ is $\geqq \gamma_{LV}$ or $< \gamma_{LV}$. A nonzero contact angle probably results from the presence at the metal surface of a liquid film which converts the high energy metal surface into a low energy surface with a lower γ_{SV} (23). In the presence of such film, a zero contact angle may be established only if the liquid (such as polydimethylsiloxane) has a very low surface tension (23). On the other hand, the effect of adsorbed films on the magnitude of γ_{SV} and consequently on θ will depend on the configuration of the film (23). Zieman (23) has concluded from extensive studies that the reduction in γ_{SV} will be more if the film comprises unbranched long-chain close-packed molecules terminating with groups such as $—CH_3$, $—CF_3$, or $—CF_2H$ than if the adsorbed molecules exhibit cyclic or branched structures. The adsorption of molecules of aromatic rings with aliphatic nonbranched side chains is probably responsible in the case of Voltesso 35 and the alkylbenzenes for the nonzero contact angle.

Adsorption layers of oxygen usually exist on all metal surfaces except that of gold. Such layers are known (24) to increase contact angles. This probably explains the larger θ observed with copper than with gold.

Smaller contact angles are observed with the normal-grade decylbenzene than with the same liquid after treatment with Fuller's earth. The difference must be due to the presence in the normal-grade sample of polar impurities which adsorb at the metal surface and decrease γ_{SL}.

The experimental meniscus height *vs.* voltage curves for different insulating liquids are plotted in solid heavy lines in Fig. 2-11. In most cases there is little hysteresis between the advancing and receding meniscus height. Figures 2-3 show the results with the vacuum-distilled dodecylbenzene, Fig. 4 and 5 with Fuller's earth-treated decylbenzene, and Fig. 6 for decylbenzene without the latter treatment. Figures 2 and 4 are for the copper rod electrode and Fig. 3, 5, and 6 are for the gold and copper plate electrodes. Figure 7 is for Voltesso 35 with a copper rod and Fig. 8 and 9 are for the same liquid with copper and gold plate electrodes, respectively. Figures 10 and 11 are for polydimethysiloxane with copper rod and gold plate, respectively.

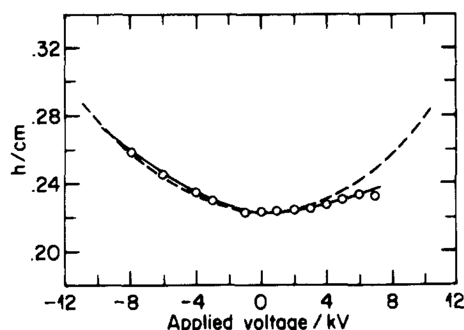

Fig. 2. Voltage dependence of meniscus height for dodecylbenzene on a copper rod. ○, Experimental advancing curve and . . . ., theoretical curve.

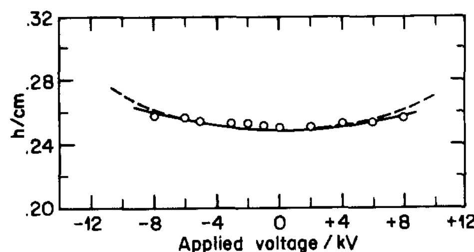

Fig. 3. Voltage dependence of meniscus height for electrical-grade dodecylbenzene on a gold plate. ○, Experimental advancing curve and - - -, theoretical curve.

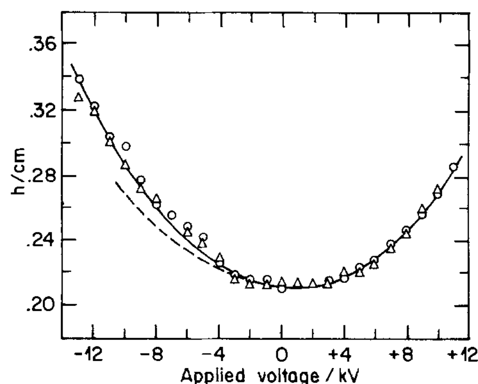

Fig. 4. Voltage dependence of meniscus height for electrical-grade decylbenzene on a copper rod. ○ and △, Experimental advancing and receding curves and - - -, theoretical curve.

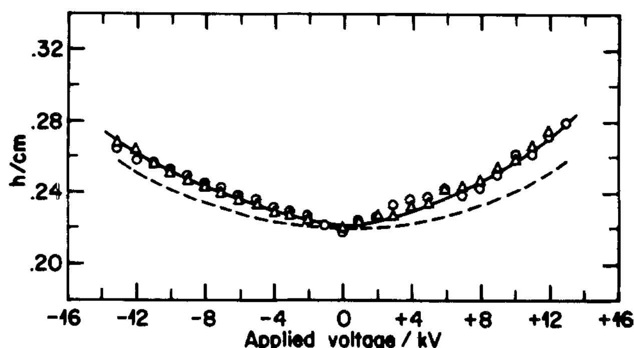

Fig. 5. Voltage dependence of meniscus height for electrical-grade decylbenzene on a copper plate. ○ and △, Experimental advancing and receding curves and - - -, theoretical curve.

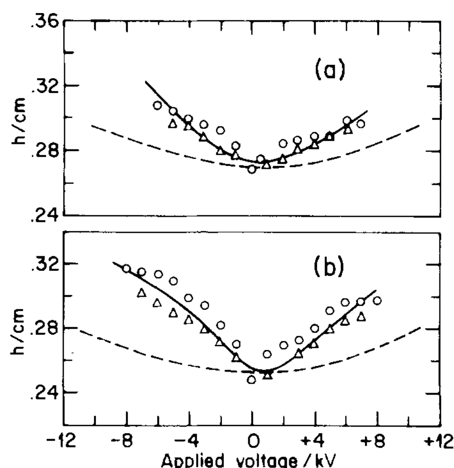

Fig. 6. Voltage dependence of meniscus height for normal-grade decylbenzene on (a) gold plate and (b) copper plate. ○ and △, Experimental advancing and receding curves and - - -, theoretical curve.

Figures 2-11 show that in the presence of electric field the meniscus height is a function of the applied voltage, the chemical composition of the insulating liquid, and the polarity of the field. With the alkylbenzene the voltage dependence of h appears to be a function of the technique applied to purify the oil before use. A smaller increase of h with voltage is observed with a dodecylbenzene sample treated with vacuum distillation than with a decylbenzene sample treated with Fuller's earth. A greater increase is observed with a decylbenzene sample not treated with Fuller's earth than with one subjected to such treatment. With the alkylbenzenes the increase in h with the applied voltage is larger with the rod than with the plate electrode. With Voltesso 35 and polydimethylsiloxane

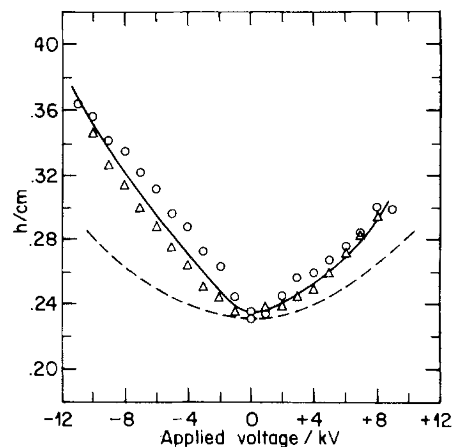

Fig. 7. Voltage dependence of meniscus height for Voltesso 35 on a copper rod. ○ and △, Experimental advancing and receding curves and - - -, theoretical curve.

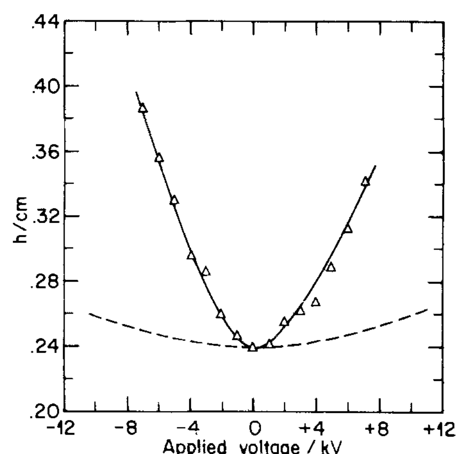

Fig. 8. Voltage dependence of meniscus height for Voltesso 35 on a copper plate. △, Experimental receding curve and - - -, theoretical curve.

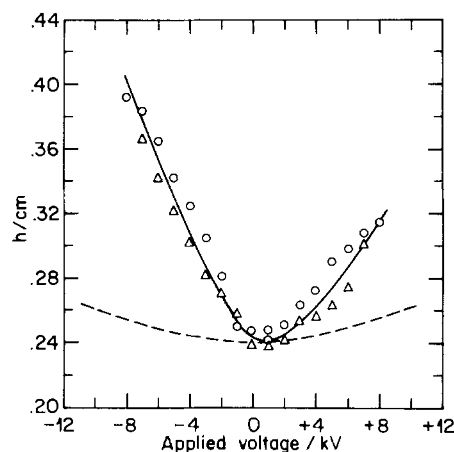

Fig. 9. Voltage dependence of meniscus height for Voltesso 35 on a gold plate. ○ and △, Experimental advancing and receding curves and - - -, theoretical curve.

h dependence on the voltage is slightly greater with the plate than with the rod.

There is experimental evidence that the change of meniscus height with the applied voltage is not accompanied by any significant change in the contact angle. The use of reflection microscopy and monochromatic illumination has indicated that the type of interference bands observed at the meniscus edge does not change with the electric field regardless of the

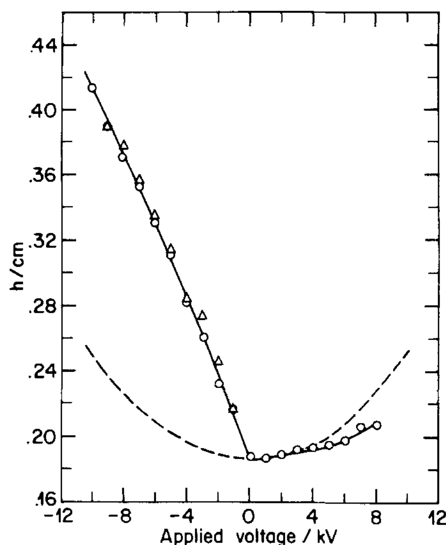

Fig. 10. Voltage dependence of meniscus height for polydimethylsiloxane on a copper rod. ○ and △, Experimental advancing and receding curves and - - -, theoretical curve.

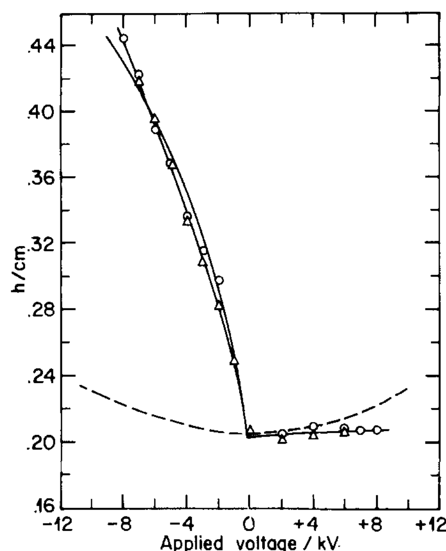

Fig. 11: Voltage dependence of meniscus height for polydimethylsiloxane on a gold plate. ○ and △, Experimental advancing and receding curves and - - -, theoretical curve.

initial value of contact angle in the absence of the field. For example, with a copper plate in Voltesso 35, the contact angle is 10.5°, in the absence of the field and the meniscus edge appears as a dark line. In the presence of the field such behavior does not change regardless of the increase in meniscus height. A gold plate in polydimethylsiloxane gives a zero contact angle in the absence of the field and the meniscus edge in both absence and presence of the field shows a diffuse wide zero order fringe followed by narrow bands of higher order.

The voltage dependence of meniscus height in the case of Voltesso 35 was found to be influenced by the time of exposure to light. This effect is negligible for a series of experiments carried out within the first few days after a fresh sample was taken from the metal-storage tank but becomes significant in a few weeks' time. Light is known to accelerate the oxidation process of the oil.

A linear variation of the current with the applied voltage was indicated (5) in the case of Voltesso 35. A similar current-voltage relationship was observed with the alkylbenzenes.

For interpreting the experimental curves of Fig. 2-11, it is appropriate to consider first the electrical-force mechanisms previously (13-15) mentioned. One may first assume that the insulating liquid is a perfect dielectric free of any space-charge zones. An electric field applied parallel to the liquid surface in the test cell will exhibit a mechanical stress directed normally to the liquid surface of the meniscus. Acting to minimize the mechanical potential energy of the system, the dielectrophoretic forces of the liquid will raise the meniscus upward. At equilibrium the vertical component of the mentioned mechanical force can be equated with the hydrostatic pressure due to the liquid head. The result (15, 25) will be

$$\Delta h = \frac{\epsilon - \epsilon_0}{2\rho g} E^2 \quad [4]$$

where Δh is the variation in meniscus height, E the field strength at the top of the meniscus, ρ the liquid density, g the acceleration of gravity, and ϵ and ϵ_0 are the permittivities of the liquid and the vapor. Theoretical plots for the variation of h with the voltage are given in dotted lines in Fig. 2-11. In each case h at a given voltage is obtained by adding Δh calculated by means of Eq. [4] to the experimentally measured h in the absence of the field. For a cylindrically shaped rod electrode E is calculated from the voltage V by means of

$$E = \frac{V}{a \ln b/a} \quad [5]$$

where a and b are the radii of the rod and coaxial cylindrical cage. For a rectangularly shaped (plate) electrode the field can be assumed to be elliptically shaped and is therefore calculated from

$$E = \frac{V}{f \ln c + d/f} \quad [6]$$

where the plate width is $2f$ and c and d are the semiaxes of the surrounding elliptically shaped outside electrode. For a cylindrically shaped outside electrode, the term $c + d$ can be approximately obtained from

$$b \sim \frac{c + d}{2} \quad [7]$$

The theoretical curves shown in Fig. 2-11 are both parabolically shaped and polarity independent. At a given E value Δh at the plate is approximately 38% its corresponding value at the rod. An examination of all the data of Fig. 2-11 shows however considerable discrepancy between the experimental and theoretical curves. The most marked discrepancy is observed with polydimethylsiloxane with which the experimental curves are strongly polarity dependent and contrary to theoretical predictions Δh is slightly higher with the plate than with the rod. A far smaller discrepancy is observed with the alkylbenzenes, where with both the vacuum-distilled dodecylbenzene and Fuller's earth-treated decylbenzene, the experimental curves are parabolically shaped and, as predicted by theory, Δh at a given voltage is greater with the rod than with the plate. However, normal-grade decylbenzene shows more deviation from theory than electric-grade decylbenzene. With Voltesso 35 the experimental curves are slightly asymmetric but as in the case of polydimethylsiloxane Δh is slightly greater with the plate than with the rod.

Pickard (8) reported a voltage dependence of meniscus height in excess of that expected on the basis of perfect-dielectric theory with a molybdenum wire cathode in acetone. This phenomenon was attributed (13) to the formation of an ionic specie charge zone with an associated potential drop near the cathode. In Pickard's view, the potential drop occurs only near the cathode because the ion responsible for its formation is a positively charged metal ion electrochemically produced by the anode. Expressed more

quantitatively, the presence of space-charge zone near the cathode means a larger E than that predicted at a given voltage by Eq. [5] or [6] and consequently a larger Δh. A larger E at the cathode reduces E at the anode which leads to a smaller Δh at the latter electrode. The interpretation provided by Pickard (13) may well be valid for the molybdenum/acetone system but it is doubtful that it can be generalized for other systems as well. First, the electrochemical mechanism suggested for producing the ions cannot explain similar phenomenon observed with other liquids such as chloroform at the anode (7) or as in the present work with Voltesso 35 at both the cathode and anode. Second, a space charge zone produced near the cathode implies that electrons are injected from the cathode but the linearly shaped current-voltage curves observed in the present work indicate that the conductance current is still ohmic in nature in the low field region (26). The explanation given by Pickard also suffers from the lack of experimental evidence that metal ions do indeed exist in the insulating liquids.

A more general mechanism based on interfacial forces may be used to explain the discrepancy between the experimental and theoretical curves of the present work. This is based on the assumption that an electric double layer probably exists between the metal surface and oriented liquid dipoles. The magnitude of dipole orientation depends on their dipole moment, the magnitude and polarity of the applied voltage, the nature of the solid substrate, and the strength of the intermolecular binding forces in the liquid. The effect of polarity should be particularly important with liquids whose molecules are naturally oriented at the phase boundary. An increase in the applied voltage will increase the potential drop across the double layer provided that the polarity of the field is favorable for the natural orientation of the dipoles. This increase in potential difference will be associated with an increase in the charge density at the metal surface (as in the case of an ideally polarizable electrode) and an increase in the orientation and polarization of the liquid molecules in the neighborhood of the liquid side of the double layer. The first effect causes a decrease in the metal/liquid interfacial tension (as indicated by the Lippmann equation) and the second causes an increase in the liquid surface tension. The increase in γ_{LV} results according to Eq. [1] in an increase in h. An increase in γ_{LV} alone should, according to Eq. [2], increase θ, but this does not take place because of the decrease in γ_{SL}.

The variation in γ_{SL} and γ_{LV} with the applied voltage should not depend on the geometry of the electrode and were it not for the conditions of infinite width required by Eq. [1], Δh caused by a change in γ_{LV} would be equal with both the rod and plate. However, as previously explained, the plate satisfies the conditions of infinite width and the rod does not and, therefore, the same increase in γ_{LV} causes a smaller Δh with the rod than with the plate.

The structural properties of polydimethylsiloxane appear to satisfy the requirements for the interfacial tension mechanism described above. First, the siloxane bond includes an appreciable polar component which is known (27) to interact with other surfaces by dipole or hydrogen bonding. Second, the molecule as a whole attains a helical conformation in which the siloxane dipole is internally compensated by another dipole of opposite polarity. The intermolecular binding forces are, therefore, particularly weak, a fact which enhances the affinity between polydimethylsiloxane molecules and other surfaces (27). This particular structure, however, probably results in strongly oriented molecules even in the absence of the field. On the basis of the present experimental data, this natural orientation is aided by the field direction at the cathode. A sterically hindered reorientatian process appears, however, to impede the formation of a double layer at the anode.

In the case of alkylbenzenes the results indicate that the double layer is formed by polar impurities rather than by any constituent of the pure liquid. Voltesso 35 has a very complex chemical nature and, therefore, it is difficult even to speculate on the nature of the species responsible for establishing the double layer.

A confirmation of the ideas suggested above would require some experimental knowledge of the potential drop across the metal/liquid interface and an independent study of the field dependence of the liquid surface tension. Unfortunately, however, the mentioned potential drop cannot be measured because reference electrodes conveniently used in electrochemical systems cannot be used in ion-free liquids. Wire probes which are occasionally used in the study of the distribution of charge carriers in insulating liquids cannot be placed with sufficient proximity from the electrode to detect the potential drop in the interfacial region. Information provided by these probes on charge distribution in the bulk have been both qualitative and subject to criticism (26). The resistivity of the insulating liquid also changes as a function of the field and, therefore, the original resistivity (in the absence of the field) cannot be used to calculate IR drops in the presence of the field. No definitive conclusions are available yet from studies of field dependence of liquid surface tensions (25, 28-30). The experimental data appear to depend on the technique applied probably because different techniques measure different parameters.

Conclusions

Contact angles between a sufficiently smooth solid metal surface and insulating liquids can be conveniently and accurately obtained from the liquid meniscus rise measured at a partially immersed plate in the liquid. Nonzero contact angles most probably result from the presence at the metal surface of a liquid film which converts the high energy metal surface into a low energy surface with a lower γ_{SV}. The liquid meniscus height at a partially immersed rod of a relatively small diameter ($\sim$2 cm) is less than the corresponding height at a plate, 2 cm wide, because the rod does not satisfy the conditions of infinite width required by Eq. [1].

Meniscus height *vs.* voltage curves measured with dodecylbenzene, decylbenzene, Voltesso 35, and polydimethylsiloxane show that the variation of h with the voltage depends on the magnitude of the voltage, the polarity, and the chemical composition of the insulating liquid. The variation of h with the voltage is not accompanied by any significant change in the contact angle. The variation of h with the voltage is discussed in the light of an electrical force mechanism and it is shown that such a mechanism can satisfactorily explain only those results obtained with vacuum-distilled dodecylbenzene. A mechanism based on the formation of a double layer between the metal surface and liquid dipoles and associated variation in γ_{SL} and γ_{LV} is suggested to explain the discrepancies between the experimental results with other liquids and theoretical predictions based on an electrical-force mechanism.

Acknowledgments

It is a pleasure to acknowledge the financial support of Hydro-Quebec Institute of Research. Acknowledgements are also due to Dr. F. Rizk for helpful discussions on electrical-force mechanisms associated with Eq. [4] and to Dr. D. Pugh, Dr. D. Couderc, and Dr. R. Malewski for useful comments.

Manuscript submitted Sept. 19, 1977; revised manuscript received March 7, 1978.

Any discussion of this paper will appear in a Discussion Section to be published in the June 1979 JOUR-

NAL. All discussions for the June 1979 Discussion Section should be submitted by Feb. 1, 1979.

Publication costs of this article were assisted by the Institute of Research of Hydro-Quebec.

REFERENCES

1. I. Morcos, *J. Chem. Phys.*, **56**, 3996 (1972).
2. I. Morcos, *J. Phys. Chem.*, **76**, 2790 (1972).
3. I. Morcos, *This Journal*, **121**, 1417 (1974).
4. I. Morcos, in "Proceedings of the Symposium on Oxide-Electrolyte Interfaces," R. S. Alwitt, Editor, p. 143, The Electrochemical Society Softbound Symposium Series, Princeton, N.J. (1973).
5. I. Morcos and F. Rizk, *IEEE Trans. Insul.*, **ei-12**, 309 (1977).
6. M. Faraday, "Experimental Researches in Electricity," Vol. 1, Sec. 1595, Richard Taylor and John Edward Taylor, Editors, London (1839).
7. I. Sumoto, *Oyo Butsuri*, **25**, 264 (1956).
8. W. F. Pickard, *J. Appl. Phys.*, **32**, 1888 (1961).
9. W. H. Middendorf and G. H. Brown, *Trans. Am. Inst. Electr. Eng.*, **77**, Part 111, 795 (1958).
10. G. H. Krawinkel, *Z. Angew. Phys.*, **11**, 305 (1959).
11. H. A. Pohl, *J. Appl. Phys.*, **29**, 1182 (1958).
12. W. F. Pickard, in "Progress in Dielectrics," Vol. 6, J. B. Birks and J. Hart, Editors, pp. 15-18, Academic Press, New York (1965).
13. W. F. Pickard, *J. Appl. Phys.*, **33**, 941 (1962).
14. J. S. Mirza, C. W. Smith, and J. H. Calderwood, "Conference on Electrical Insulation and Dielectric Phenomena," 1974 Annual Report, p. 549, National Academy of Sciences, Washington, D.C.
15. M. Abraham and R. Becker, "The Classical Theory of Electricity and Magnetism," p. 81, Hafner, New York (1950).
16. M. Duval and C. Lamarre, *IEEE Trans. Insul.*, **ei-12**, No. 5, p. 340 (1977).
17. W. D. Bascom, R. L. Cottington, and C. R. Singleterry, "Advances in Chemistry," No. 43, p. 355, American Chemical Society, Washington, D.C. (1964).
18. A. W. Neumann, *Z. Phys. Chem. (Frankfurt am Main)*, **41**, 516 (1964).
19. A. W. Neumann and W. Tanner, *J. Colloid Interface Sci.*, **34**, 1 (1970).
20. I. Morcos, *J. Electroanal. Chem. Interfacial Electrochem.*, **51**, 211 (1974).
21. T. Young, "Miscellaneous Works," Vol. 1, G. Peacock, Editor, p. 418, Murray, London (1855); A. Dupré, "Théorie Méchanique de la Chaleur," p. 352, Gauthier-Villars, Paris (1869).
22. D. H. Bangham and R. J. Razouk, *Trans. Faraday Soc.*, **33**, 1459 (1937).
23. W. A. Zieman, "Advances in Chemistry," No. 43, p. 1, American Chemical Society, Washington, D.C. (1964).
24. J. J. Bikerman, "Physical Surface," p. 259, Academic Press, New York (1970).
25. E. K. Koplikina, *Elektron. Obrab. Mater.*, **4**, 57 (1970).
26. A. A. Zaky and R. Howley, "Conduction and Breakdown in Mineral Oil," Peter Peregrinus Ltd., London (1973).
27. W. Nall, "Chemistry and Technology of Silicones," chap. 1, 6, 9, Academic Press, New York (1968).
28. G. M. Schmid, R. M. Hurd, and B. S. Snavely, Jr., *This Journal*, **109**, 852 (1962); *Science*, **135**, 791 (1961).
29. C. F. Hayes, *J. Phys. Chem.*, **79**, 1689 (1975).
30. I. S. Rezin, *Elektron. Obrab. Mater.*, **3**, 28 (1979).

Anodic Process Kinetics on the Passive Surfaces of Titanium, Nickel, and Titanium-Nickel Alloys

E. N. Paleolog, A. Z. Fedotova, O. G. Derjagina, and N. D. Tomashov

The Institute of Physical Chemistry, The USSR Academy of Sciences, Moscow, U.S.S.R.

ABSTRACT

The anodic oxidation kinetics and electrochemical properties of the passive surfaces of Ti, Ni, and Ti-Ni alloys (0.2-37.5 w/o) in 1*N* Na_2SO_4 (pH 5.6 and 10.6) solutions with and without redox couples have been investigated by electrochemical methods. Measurements have been made also on single crystals of TiO_2 (n-type) and NiO (p-type) with known electrophysical parameters. It was found that the passive surface of pure Ti and Ni electrodes having a thin-phase oxide film shows specific features of semiconductor electrodes. The electrochemical behavior of passive metal electrodes depends on the potential distribution at the passive metal/solution interface. The rate of anodic oxidation of Ti-Ni alloys is close to that of pure Ti. The solution ion oxidation reactions are greatly facilitated on the oxidized alloys as compared to Ti. To explain the results obtained a specific model of the alloy oxide layer structure has been adopted.

Today, one may consider it to be a proven fact that the starting metal passivation stage is associated with the adsorbed oxygen monolayers settling on the surface and drastically reducing the rate of electrochemical metal dissolution (1-5). The oxide layers formed during further passivation, however, produce a marked effect on the passive metal surface properties and, in many cases, determine the stability of passive metal condition.

The electrochemical properties of phase-oxide layers formed during anodic passivation have a big significance in developing commercial processes for producing controlled property surface oxide layers and in developing alloy compositions for cathodic protection or the electrolysis industry. The latter stimulates research to establish anodic oxide layer growth laws and to study anodic oxide layer structure and properties. Much attention has been focused on these problems at present with the major programs being deployed on iron, aluminum, titanium, and stainless steels (6-18).

The present work studies by electrochemical methods the growth kinetics of thin-phase oxide layers formed during anodic passivation of Ti, Ni, and Ti-Ni alloys, and also the redox reaction kinetics on these electrodes defined by the semiconductor properties of the passive surface. At the same time, measurements were made on single crystal compact oxides, *i.e.*, on TiO_2 (rutile, n-type conductance, $n = 5 \cdot 10^{18}$ cm^{-3}) and NiO (p-type, $p = 1.3 \cdot 10^{20}$ cm^{-3}), with known electrophysical parameters. The above oxides possess the properties of semiconductor electrodes and are a model to simulate the oxidized metals.

Key words: anodic oxidation kinetics, oxide films, Ti-Ni alloys.

Experimental

The measurements were made on rotating electrodes in an argon environment at 25° ± 0.1°C. Systems with one-electron transfer, *i.e.*, $Fe(CN)_6^{4-}/Fe(CN)_6^{3-}$ and Fe^{2+}/Fe^{3+}, were used as a redox system. The supporting solutions were 1*N* Na_2SO_4 with *p*H values of 5.6 for Ti and 10.6 for Ni. There was no anodic dissolution of Ti or Ni in these solutions. The electrodes were anodically oxidized in the supporting solution at a constant potential for 60-150 min, then redox substances were added to the solution and the electrode was immediately polarized in cathodic or anodic directions at a potential sweep rate of 60 V/min (Ti) or 4.8 V/min (Ni). The $Fe(CN)_6^{4-}$ or Fe^{2+} oxidizing current on Ti electrode was assessed from anodic *E*, *i* curves by the difference of the over-all anodic current (obtained in a reducing-agent solution) and the anodic current on Ti in the supporting solution.

The oxide layer increments were estimated by coulometric measurements and depending on the oxide formation potential changed in the range of 20-40Å.

Potential values are cited in relation to the NHE.

Results and Discussion

Figures 1 and 2 illustrate the potential, current density relationship for the oxidation reaction of $Fe(CN)_6^{4-}$ and Fe^{2+} on Ti and Ni passivated under different potentials.

The above processes occur on these electrodes in a radically different way. They tend to be strongly inhibited on the passive Ti electrode (the overvoltage of the $Fe(CN)_6^{4-} \rightarrow Fe(CN)_6^{3-}$ reaction is great and *E*, log *i* lines have unusually steep slopes).

The oxide formation potential shift in the positive direction increases the inhibition of the subsequent oxidizing reaction, and the *E*, log *i* line slopes become steeper. It should be noted that the *E*, log *i* curve slope for one and the same oxide film practically does not depend on whether $Fe(CN)_6^{4-}$ or Fe^{2+} is oxidized on the electrode. No oxygen is found to evolve on Ti up to ~3V.

For oxidized Ni, at the oxide layer thickness approaching that of Ti, the oxidizing anodic-reaction rate (the latter including oxygen evolution) is much greater, being close to that on Pt, and does not depend on the oxide forming conditions.

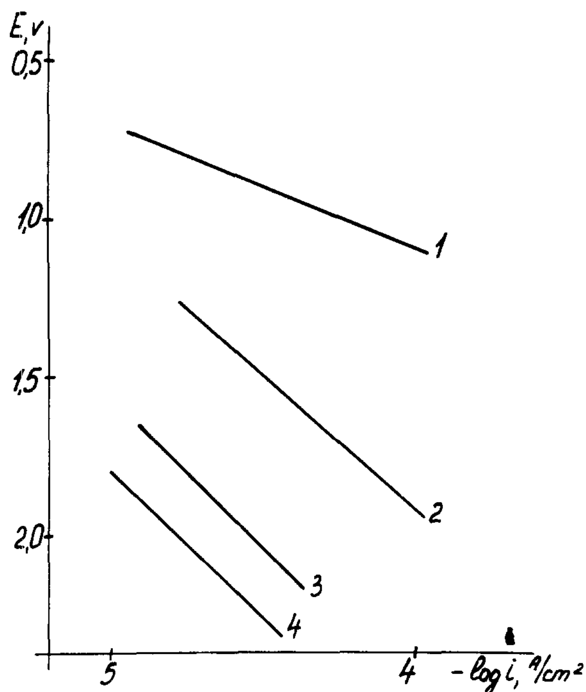

Fig. 1. Anodic *E*, log *i* plots in 1*N* Na_2SO_4 + 0.05*N* $K_3Fe(CN)_6$ + 0.05*N* $K_4Fe(CN)_6$ for Ti oxidized at curve (1) 0.25V; curve (2) 0.95V; curve (3) 1.40V; and in curve (4) 1*N* Na_2SO_4 + 0.05*N* $Fe_2(SO_4)_3$ + 0.05*N* $FeSO_4$ at 0.95V.

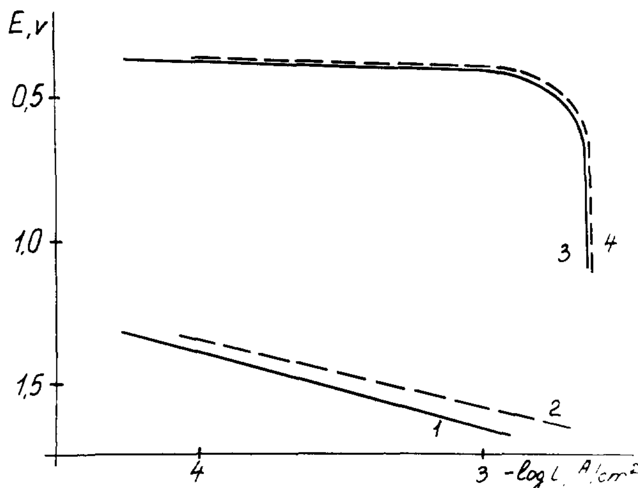

Fig. 2. Anodic *E*, log *i* plots in 1*N* Na_2SO_4 for curve (1) Ni oxidized at 0.50V; curve (2) for Pt; and in curve (3) 1*N* Na_2SO_4 + 0.005*N* $K_3Fe(CN)_6$ + 0.005*N* $K_4Fe(CN)_6$ for Ni oxidized at 0.50V; curve (4) for Pt.

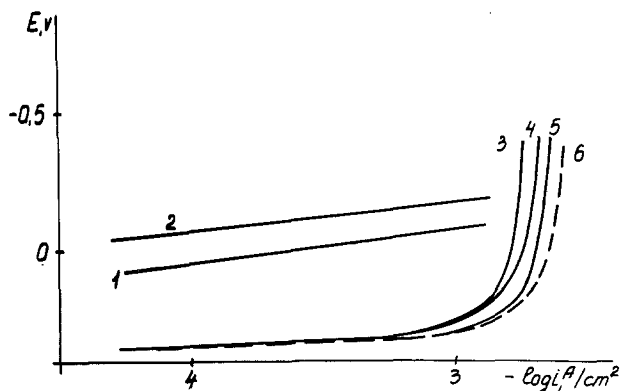

Fig. 3. Cathodic *E*, log *i* plots in 1*N* Na_2SO_4 + 0.05*N* $K_3Fe(CN)_6$ + 0.05*N* $K_4Fe(CN)_6$ for Ti oxidized at curve (1) 0.25V; curve (2) 0.95V; and in curve (3) 1*N* Na_2SO_4 + 0.005*N* $K_3Fe(CN)_6$ + 0.005*N* $K_4Fe(CN)_6$ for Ni oxidized at 0.30V; curve (4) 0.05V; curve (5) 0.70V; curve (6) for Pt.

The other relationships are observed for cathodic-reducing reactions (Fig. 3): normal *E*, log *i* curve slopes and their independence on the film-forming potential for Ti, and a marked reaction inhibition in the potential range of < 0.30V for Ni, showing the sooner, the less positive is the potential to form the film (19).

The *E*, log *i* curves shown in Fig. 4 for compact oxides point to the complete qualitative similarity of the electrochemical behavior of semiconductor (TiO_2 and NiO) and passive metal electrodes with a thin surface oxide layer.

Basing our consideration on the electron transfer theory for electrochemical reactions on semiconductors (20), we can explain the special features of redox-process kinetics on single crystal oxides, and primarily, abnormally steep *E*, log *i* curve slopes in a certain potential range in terms of potential localization in the solid phase, provided the electron exchange takes place through the conduction band for rutile[1] and valent band for NiO.

This fact finds an experimental proof in capacitance changes. Figure 5 shows that the linear relationship $1/c^2$, *E* indicating the presence of a space-charge region in the semiconductor, is valid in a broad range

[1] An indirect indication of this mechanism is the tendency to increased transfer coefficient of ferrocyanide reduction reaction (from 0.5 to 0.7) with the rise of the TiO_2-electrode polarization rate.

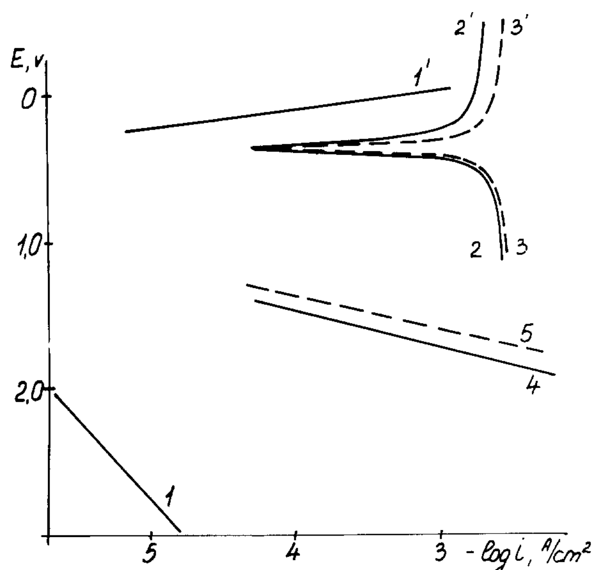

Fig. 4. Anodic and cathodic E, log i plots in curve (1.1') 1N Na_2SO_4 + 0.05N $K_3Fe(CN)_6$ + 0.05N $K_4Fe(CN)_6$ for TiO_2; curve (2.2') in 1N Na_2SO_4 + 0.005N $K_3Fe(CN)_6$ + 0.005N $K_4Fe(CN)_6$ for NiO; curve (3.3') for Pt; and curve (4) in 1N Na_2SO_4 for NiO; curve (5) for Pt.

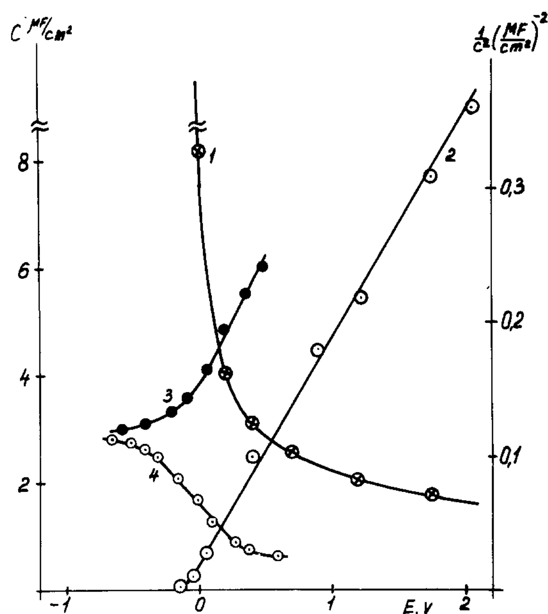

Fig. 5. The dependence of C and $1/C^2$ on potential in curves (1, 2) 1N Na_2SO_4 for TiO_2; curves (3, 4) and NiO, respectively.

of positive potentials for TiO_2 and in the potential range from about −0.35 to 0.30V for NiO, *i.e.*, at the very potentials where the redox reactions are inhibited on these electrodes.

Assuming the redox reaction mechanism for a passive metal surface and corresponding compact oxide to be the same, the distribution of the interfacial potential difference for the passive titanium electrode was estimated (20, 21) from the experimentally obtained E, log i curves slope for the oxidation reaction of $Fe(CN)_6^{4-}$ (Table I).

We can see that the potential drop part occurring in the oxide layer during anodic Ti polarization is fairly large and increases as E_f shifts in the positive direction. In the range of $Fe(CN)_6^{3-}$ reducing potentials, the main potential drop is probably concentrated in the Helmholtz layer. These data are in agreement with the results of study (22). The potential localization in the Helmholtz layer for Ni occurs at potential > 0.30V.

Table I. Estimation of interfacial potential difference distribution for TiO_2 and oxidized Ti

Electrode	pH	Oxide layer forming conditions E_f (V)	Oxide layer forming conditions t (min)	$Q_{oxid.}$ (mC/cm^2)	Potential drop part in oxide layer $\left(1 - \frac{2RT}{b_a \cdot F}\right) \cdot 100$ (%)
Ti	5.6	0.25	120	2.5	66
Ti	5.6	0.95	120	5.1	86
Ti	5.6	1.40	120	6.7	88
TiO_2	5.6	—	—	—	90

It is the different character of potential distribution that explains the differences in electrochemical properties of oxidized Ti and Ni surfaces.

To find out which of two factors—the film thickness or film nature—determines, for instance for Ti, the film/solution potential drop ratio, titanium was oxidized at two different potentials (0.25 and 0.95V) so as to maintain the amount of electricity spent for the surface oxidation (equivalent to film thickness) at a close level in both cases. The $Fe(CN)_6^{4-}$ oxidation rate at these electrodes was found to be different and the anodic E, log i slope describing potential localization in the oxide layer to be larger when the film was formed at a more positive potential (Fig. 6). Consequently, it is the oxide nature which depends on the oxide formation potential that in the given range of film thicknesses primarily controls the electrochemical properties of oxidized Ti. The more positive formation potential leads to a smaller concentration of oxygen vacancies. Since these act as electron donors, this, in turn, leads to a smaller free electron concentration, and hence, to a larger potential drop across the oxide film.

In contrast to Ti, the majority charge carriers in the surface oxide on Ni are holes. For the film formation potential shift in the positive direction (>0.30V) or during anodic polarization of electrode, the hole concentration increases, due to the increase in acceptor impurity (Ni^{3+}) concentration in the film. The latter factor decreases potential localization in the oxide layer and leads to the "metallization" of the passive nickel surface in relation to the anodic oxidation of solution ions.

Due to the different character of potential distribution for oxidized Ti and Ni electrodes, it was of interest to investigate the oxide growth kinetics on these metals. Figure 7 shows the change in the anodic

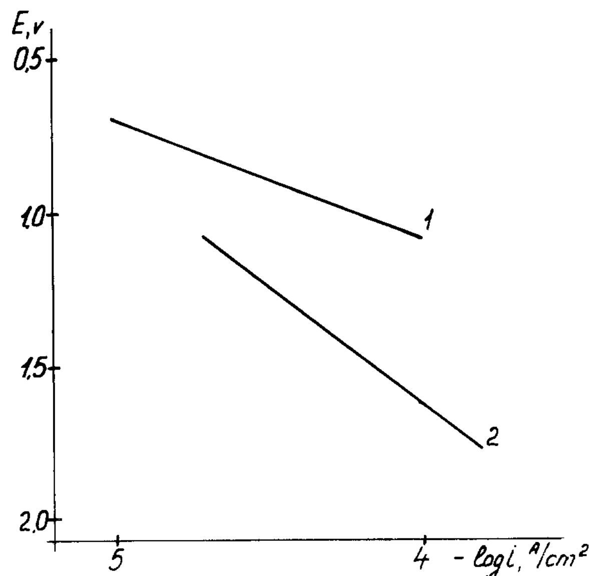

Fig. 6. Anodic E, log i plots in 1N Na_2SO_4 + 0.05N $K_3Fe(CN)_6$ + 0.05N $K_4Fe(CN)_6$ for Ti, E_f curve (1) 0.25V, $Q_{oxid.}$ 2.5 mC/cm^2; curve (2) 0.95V, $Q_{oxid.}$ 3.1 mC/cm^2.

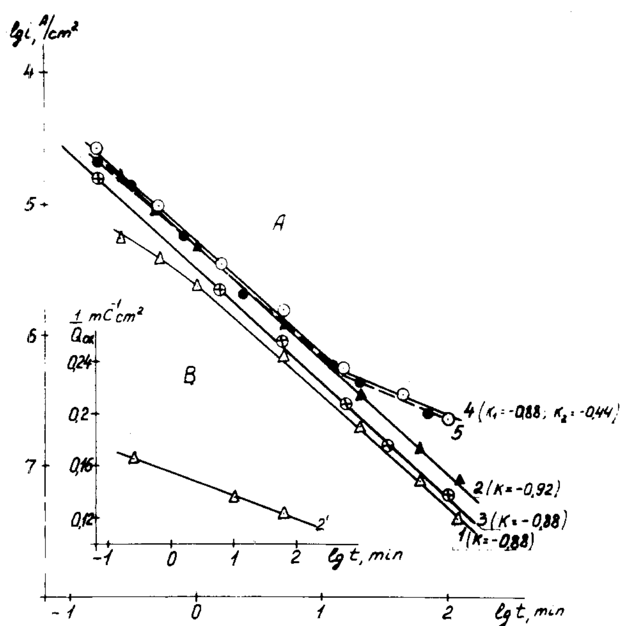

Fig. 7. A, The variation of Ti/Ni anodic oxidation current in 1N Na_2SO_4 with time: curve (1) Ti, E_f 0.25V; curve (2) 0.95V; curve (3) Ni, E_f 0.30V; curve (4) 0.70V; curve (5) 0.70V without agitation. B, $1/Q_{\text{oxid.}}$ — log t plot in 1N Na_2SO_4 for Ti E_f 0.95V curve (2′).

oxidation current of Ti and Ni surfaces in time under a constant potential in double logarithmic coordinates. The inverse logarithmic oxide film growth law, $1/Q_{\text{oxid}} = A - B \log t$, is valid for Ti oxidized in the given potential range. The latter is in agreement with the presence of electric field in the film and suggests the dominating role of ion generation and migration in the anodic surface oxidation processes (23). The time effect of Ni oxidation at film thicknesses approaching those of Ti depends on the oxide formation potential. At $E_f = 0.30$V, nickel oxidizes according to the logarithmic law.[2] For the oxidation at more positive potentials the logarithmic law is valid only during the first minutes of anodic oxidation, and then is replaced by the parabolic one, indicating the domination of free-particles diffusion in the film during its growth, since the solution agitation does not produce any effect on the oxidation rate. Oxygen evolves on the Ni electrode in the potential range >1.0V, and further thickening of the oxide film virtually stops.

Summing up the results, it is possible to conclude that the main difference in anodic behavior of oxidized Ti and Ni is caused by the difference in the interface potential drop distribution. The main potential drop for Ti under the conditions of developing anodic reactions is concentrated in the oxide layer, for oxidized Ni, in the Helmholtz layer. These differences are explained by the different nature of the majority carriers in the oxides formed and the change in their concentration when the oxide layer-forming potential is changed and, in some cases, too, in the process of anodic electrode polarization.

It was interesting to find out how the properties of the passive Ti electrode will change when it is gradually alloyed with Ni. To study this question representing also an independent interest (24-26), measurements were made on the Ti-Ni alloys containing different amounts of Ni changed from 0.2 to 37.5 w/o of Ni. The alloys were tested as annealed (600°C, 1 hr), and had a heterogeneous diphase structure (α + Ti_2Ni), excluding 37.5 Ni alloy corresponding to the monophase intermetallic compound Ti_2Ni. The test conditions were the same. The potential sweep rate during polarization measurements on the alloys was 4 V/min.

[2] We suppose that for Ni (or Ti-Ni alloys) the inverse logarithmic dependence in anodic oxidation may also be valid, but it was not specially tested.

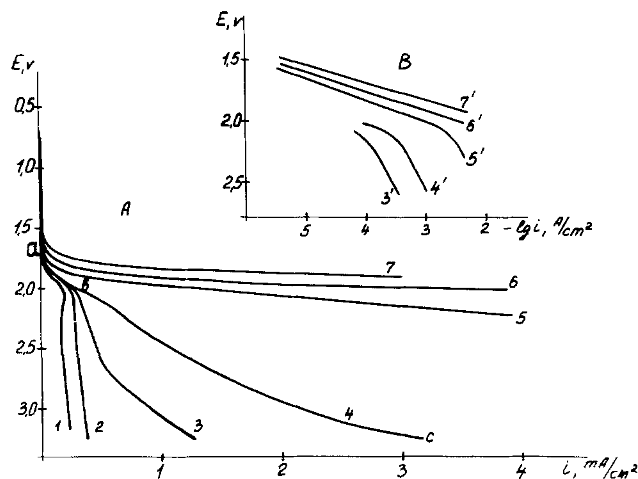

Fig. 8. Anodic polarization plots (A) and E, log i plots for the reaction of O_2 evolution (B) in 1N Na_2SO_4 for oxidized (at 0.95V) titanium curve (1) and Ti-based alloys with various nickel concentrations (w/o): curve (2) 0.2; curve (3.3′) 0.5; curve (4.4′) 1.0; curve (5.5′) 5.0; curve (6.6′) 11.0 and curve (7.7′) 37.5.

Figure 8 shows the anodic polarization curves for Ti and the alloys after film preforming at 0.95V in the supporting solution. In contrast to Ti, the oxygen-evolution reaction on Ti-Ni alloys can develop at rather significant rates, depending on Ni concentration. For the more Ni content in the alloy (5.0, 11.0, and 37.5% Ni) the O_2 evolution commences at potentials up to the secondary surface oxidation of the electrode and is rather facilitated. At low Ni concentration in the alloy (0.2, 0.5, 1.0%), oxygen evolves simultaneously with surface oxidation and the $H_2O \rightarrow O_2$ reaction is greatly inhibited in time. The O_2 evolution starting potential depends on Ni concentration in the alloy and shifts to the less positive values as Ni concentration increases. The clearest picture of the differences in the oxygen evolution kinetics on different alloys is obtained from the E, log i curves built from the over-all anodic current density/oxide growth current density difference, assuming that the oxide layer growth currents are the same for the alloys and Ti. For the Ti-0.5Ni and Ti-1.0 Ni alloys E, the log i curves slopes are rather steep and become even steeper during polarization.

For greater nickel concentration (5.0, 11.0, and 37.5%) the slopes of E, log i curves are much smaller, however, they, too, increase with the attainment of the secondary surface oxidation potential.

The results shown in Fig. 9 indicate that the $Fe(CN)_6^{4-}$ oxidation, not accompanied by the oxide film growth, is greatly facilitated as compared to the

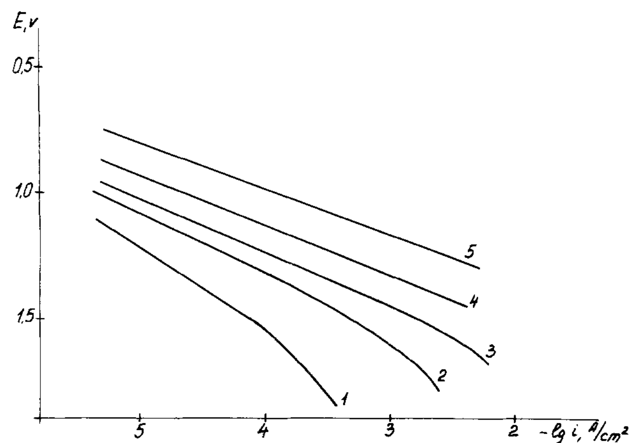

Fig. 9. Anodic E, log i plots in 1N Na_2SO_4 + 0.05N $K_3Fe(CN)_6$ + 0.05N $K_4Fe(CN)_6$ for oxidized (at 0.95V) Ti-based alloys containing Ni at: (1) 0.2; (2) 1.0; (3) 5.0; (4) 11.0; (5) 37.5%.

process of O_2 evolution, *e.g.*, on the Ti-1Ni alloy (curve 4 Fig. 9). For the less Ni content in the alloy (Ti-0.2 and Ti-0.5 Ni), this process facilitation covers only the potential range up to the secondary electrode oxidation. The overvoltage of the ferrocyanide oxidation reaction, in like manner to the overvoltage of the oxygen evolution process, depends on the Ni content in the alloy, having a tendency to diminish with the increased Ni concentration.

Figure 10 shows anodic polarization curves for pure Ti and alloys primarily oxidized at $E_f = 0.25$V. The film-forming potential shift to the less positive values makes it possible to divide the potential ranges corresponding to the oxide growth and oxygen evolution processes (sections ab and cd, respectively), thus providing additional information on the alloy surface oxidation kinetics. It follows that the secondary surface oxidation rate (Fig. 10, B) is not practically affected by the alloy composition. The dependence of the current for surface oxidation on the potential for both pure Ti and the various alloys has the same slope and, in fact, the curves virtually coincide. When plotted in double logarithmic coordinates the variation of current density with time (at a constant potential) gives a straight line with a slope close to -1. This indicates that the anodic oxide growth on Ti-Ni alloys proceeds by a law similar to that observed on pure Ti. Thus it follows that the law and the rate of anodic oxidation of the Ti-Ni alloys are identical to the oxidation of pure Ti, whereas oxidation reactions of solution ions are greatly facilitated on the alloys.

The similarity between the surface oxidation kinetics for the alloys and pure titanium suggests that in both cases a large part of the potential drop occurs through the surface oxide film.

In order to explain the results obtained, an alloy oxide layer structure model has been adopted including a provision for considerable oxide film composition variation across the film thickness. In agreement with this model Fig. 11 sketches the hypothetical changes in nickel content across the film thickness and interfacial potential drop distribution, depending on Ni concentration in the alloy at the same oxide-forming potential. The oxide zones adjacent to the metal (d_1, d_2 . . .) are assumed to be enriched in Ni, with the amount and penetration depth of the enrichment increasing with increasing Ni content in the alloy. At the film/solution interface, the film zone (d_1', d_2', . . .) is approaching TiO_2 in composition, its thickness correspondingly diminishing with the increase in Ni

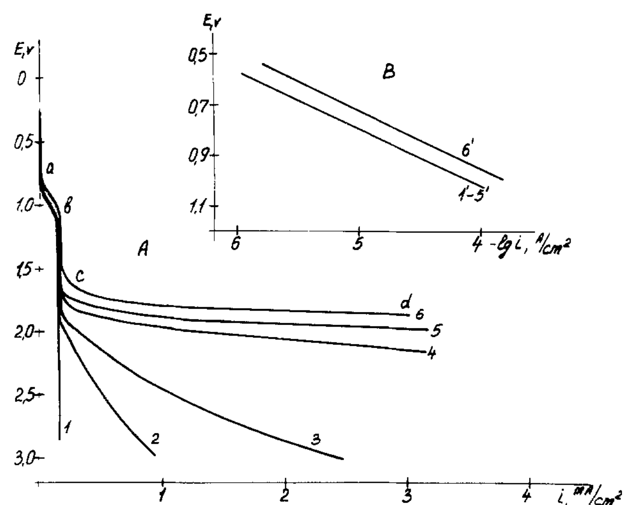

Fig. 10. A, Anodic polarization plots in 1*N* Na_2SO_4 for curve (1) preoxidized (at 0.25V) Ti; and curve (2) Ti-Ni alloys containing Ni (%) 0.5; curve (3) 1.0; curve (4) 5.0; curve (5) 11.0; and curve (6) 37.5.
B, *E*, log *i* plots for Ti and Ti-(0.2-11.0%) Ni alloys curve(1'-5') and Ti-37.5 Ni curve (6').

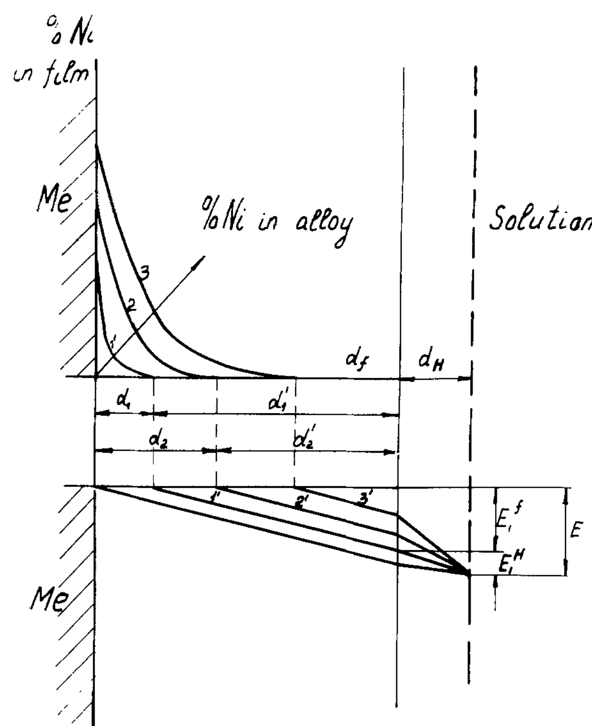

Fig. 11. Schematic presentation of Ni concentration variation across the film thickness and interfacial potential difference distribution depending on Ni concentration in the alloy (at the same E_f).

concentration in the alloy. The film composition variations across the film thickness may have resulted from the predominant Ti^{4+} ion migration as compared to that of Ni^{2+} to the outer surface during oxide formation. The outer film part composed of TiO_2 and having a thickness changing depending on the alloy composition is an energy barrier and probably determines the electrochemical properties of Ti-Ni electrodes. The facilitation of solution ions oxidation can be caused, for the more alloyed compositions, by both the increased potential drop part in the Helmholtz layer and the lowering of the outer barrier layer thickness and corresponding increase in the probability of electron tunneling through the oxide layer (27, 28). The oxide growth rate on the surface is independent of alloy composition since the electric field strength in the barrier film of varying thickness remains at a constant value (potential range up to the oxygen evolution is implied here).

Summing up the results obtained, it is possible to conclude that the passive surface of pure Ti and Ni electrodes having a thin phase oxide film possesses the peculiarities of the semiconductor electrodes. The dual electrochemical properties of the oxidized alloys are probably determined by their specific film structure.

Summary

1. The anodic oxidation kinetics and electrochemical properties of passive surfaces of titanium, nickel, and titanium/nickel-based alloys in sulfate solutions have been investigated.

The anodic oxidation of solution ions are strongly inhibited for oxidized titanium (at an oxide layer thickness of 30-50Å). The kinetics parameters of these reactions depend on the oxide layer-forming conditions. The kinetics of the oxidizing reactions for passive nickel does not practically differ from that of platinum electrode. The main potential drop under conditions of anodic polarization for Ti is concentrated in the oxide film, and for oxidized nickel, in the Helmholtz layer.

2. The rates of anodic oxidation of Ti-Ni alloys (0.2-37.5 w/o Ni) are identical to those of pure

titanium. A significant difference is observed in relation to the solution ion oxidation reactions which are greatly facilitated on the oxidized alloys as compared to Ti. The results are interpreted using an assumption that the oxide film composition on the alloy changes across the film thickness. The oxide zone adjoining metal is enriched with nickel, and the zone bordering on solution approaches TiO_2 in its composition and represents an energy barrier for the solution ion oxidation reaction. The reduction of the thickness of the outer film part with the increase of Ni content in the alloy results in a facilitated anodic solution ion oxidation on the Ti-Ni alloys with elevated nickel concentration.

Manuscript submitted Aug. 29, 1977; revised manuscript received Feb. 15, 1978.

Any discussion of this paper will appear in a Discussion Section to be published in the June 1979 JOURNAL. All discussions for the June 1979 Discussion Section should be submitted by Feb. 1, 1979.

REFERENCES

1. Ya. M. Kolotyrkin, *Zh. Vses. Khim. Ova.*, **20,** 59 (1975).
2. B. N. Kabanov, "Electrochemistry of Metals and Adsorption," Nauka, Mosikva, U.S.S.R. (1966).
3. K. Schwabe, *Zashc. Met.*, **2,** 393 (1966).
4. N. Sato, in "Passivity and its Breakdown on Iron and Iron Base Alloys," U.S.-Japan Seminar, p. 1, NACE, Washington, D.C. (1976).
5. I. Siejka, C. Cherku, and J. Yahalom, *Electrochim. Acta,* **17,** 2371 (1972).
6. A. C. Makrides, *This Journal,* **111,** 392 (1964).
7. E. N. Paleolog, A. Z. Fedotova, and V. D. Fityulina, *Electrokhimiya,* **4,** 700 (1968).
8. E. K. Oshe and I. L. Rosenfeld, *Zashc. Met.*, **5,** 524 (1969).
9. A. G. Akimov and I. L. Rosenfeld, *ibid.*, **6,** 640 (1970).
10. C. L. McBee and J. Kruger, *Electrochim. Acta,* **17,** 1337 (1972).
11. G. Okamoto, *Corr. Sci.*, **13,** 471 (1973).
12. N. D. Tomashov, Yu. S. Ruskol, and G. A. Ayuyan, *Zashc. Met.*, **10,** 515 (1974).
13. N. D. Tomashov, G. P. Chernova, Yu. S. Ruscol, and G. A. Ayuyan, *Electrochim. Acta,* **19,** 159 (1974).
14. N. Sato, T. Noda, and K. Kudo, *ibid.*, **19,** 471 (1974).
15. R. P. Frankenthal, in "Passivity and its Breakdown on Iron and Iron Base Alloys," U.S.-Japan Seminar, p. 10, NACE, Washington, D.C. (1976).
16. A. E. Yaniv, J. B. Lumsden, and R. W. Staehle, *ibid.*, p. 72.
17. H. Okada, H. Ogawa, I. Itoh, and H. Omata, *ibid.*, p. 82.
18. R. V. Moshtev, *Electrochim. Acta,* **16,** 2036 (1971).
19. O. G. Derjagina and E. N. Paleolog, *Electrokhimiya,* **4,** 700 (1968).
20. R. R. Dogonadze, A. M. Kuznetsov, and A. A. Chernenko, *Usp. Khim.*, **34,** 1779 (1965).
21. E. N. Paleolog and A. Z. Fedotova, in "New Methods of Investigation of Corrosion of Metals," p. 51, Nauka, Moskva, U.S.S.R. (1973).
22. A. G. Akimov, M. G. Astafyev, and I. L. Rosenfeld, *Electrokhimiya,* **11,** 1578 (1975).
23. F. P. Fehlner and N. F. Mott, *Oxid. Met.*, **2,** 59 (1970).
24. A. J. Sedriks, J. A. S. Green, and D. L. Novak, *Corrosion (Houston)*, **28,** 137 (1972).
25. J. A. S. Green and R. M. Latanision, *ibid.*, **29,** 386 (1973).
26. V. I. Kazarin, N. D. Tomashov, V. S. Mikheev, and V. A. Goncharenko, *Zashc. Met.*, **12,** 268 (1976).
27. J. W. Schultze and K. J. Vetter, *Electrochim. Acta,* **18,** 889 (1973).
28. A. Damjanovic, A. T. Ward, and M. O'Jea, *This Journal,* **121,** 1186 (1975).

Electrochemical-Ellipsometric Studies of Oxide Film Formed on Nickel during Oxygen Evolution

P. W. T. Lu*,[1] and S. Srinivasan*

Department of Applied Science, Brookhaven National Laboratory, Upton, New York 11973

ABSTRACT

The time variation of current density at constant potentials for oxygen evolution on metals or alloys is one of the most difficult problems needing a solution in commercial water electrolyzers. The mechanism of this phenomenon on nickel electrodes was studied in 1*N* KOH using ellipsometry to analyze the nature of anodic oxide films. Effects of electrochemical pretreatment of oxide films on the kinetics of the oxygen evolution reaction were investigated. Nickel oxide films, formed potentiostatically at 1.5V, are more active than untreated nickel for this reaction. The time variation of current density for oxgen evolution at constant potentials (above 1.56V) is essentially due to the gradual conversion of Ni^{3+} to Ni^{4+} ions in the oxide film on the surface of the electrode. The electrocatalytic activities of aged electrodes are regained by rejuvenating the electrodes at 1.5V. The rejuvenation of aged oxide films is essentially attributed to the recovery of active sites on the very top layers of the films, rather than the diminution of the film thickness. The higher the electrolyte temperature the shorter the period of time required for approaching a stable current density. In addition, with increasing temperature, there is a more significant improvement of the electrocatalytic activity by rejuvenation on aged electrodes. Tafel plots for oxygen evolution on nickel preanodized or rejuvenated at 1.5V exhibit only one linear region with $b \approx 40$ mV, while dual Tafel regions are observed on nickel prepolarized at 1.8 or 2.0V: $b \approx 40$ mV at low η and $b \approx 170$ mV at high η. In comparison with the thickness of oxide films, the chemical identity of the very top layers of oxide films plays a more significant role in determining the kinetics of the oxygen evolution reaction.

One of the significant factors contributing to the performance degradation with time in water electrolysis cells is due to the increase of overpotential for oxygen evolution with time at a constant current density, which occurs over a period of two years or even more. This phenomenon has been observed on platinum in the potential range of 1.6-2.0V (1), on iridium (2), and on nickel (3). The authors of the work on iridium (2) and nickel (3) suggested that the decay of current with time is ascribed to the continuous growth of poorly conducting oxide films, which in return retard the electron transfer. Further confirmation of this suggestion, based on the nature of the oxide film, is needed.

According to thermodynamic data (4), the insoluble oxygen-containing species of the highest oxidation state of Ni, formed in the potential region for oxygen evolution, is hydrated NiO_2. Although x-ray crystallographic studies of nickel oxide films yield no direct evidence for the presence of NiO_2 in the films (5), many authors (6-9) have found oxides with ratios of O/Ni in the range of 1.7-1.9. Thus, further oxidation of Ni beyond the oxidation number of β-NiOOH (O/Ni = 1.5) is possible. The only direct evidence to demonstrate the existence of Ni^{4+} ions has been reported by Labat and Pacault (10, 11), who investigated the alteration of the magnetic susceptibility of $Ni(OH)_2$ subjected to electrochemical oxidation and reduction. It is generally accepted that, in the potential region for oxygen evolution, a certain number of Ni^{3+} ions in the β-NiOOH lattice is further oxidized to Ni^{4+} ions, thus, resulting in a nonstoichiometric oxide film essentially composed of Ni^{3+}, Ni^{4+}, OH^-, and O^{2-} ions (9, 12). The ratio of Ni^{3+} to Ni^{4+} ions is strongly dependent on the anodization potential (9). Similar results have also been reported for Pt anodes from ESCA measurements, which show that the amount of PtO_2 in oxide films increases with the polarization potential (13).

Oxide films on nickel in alkaline solutions have been extensively studied using ellipsometry (14-16), specular reflection spectroscopy (17), and x-ray photoelectron spectroscopy (18), only in the potential region for the formation and conversion of oxides. It is of interest to examine the nature of nickel oxide films, formed at higher potentials in the oxygen evolution region, using optical techniques. A possible explanation for the lack of such investigations is that at sufficiently high potentials, the vigorous generation of oxygen bubbles on an electrode surface may interfere with the measurement of optical parameters. Recently, Vinnikov and co-workers (19) have proposed a method to carry out ellipsometric measurements on oxide films formed in the oxygen evolution reaction. In this method, a platinum electrode was maintained in a potential region for oxygen evolution (about 2.0-2.3V) for a desired period of time. Ellipsometric measurements were then taken after decreasing the potential to 1.6V, under which conditions the rate of oxygen generation was low enough so as not to influence optical readings.

In spite of the extensive studies of nickel oxide films (14-18), information on the effect of the nature of the films on the kinetics of the oxygen evolution reaction from alkaline solutions is relatively sparse (12, 20). The present paper deals with this subject as well as the mechanism of the current decay for this reaction with time by an ellipsometric examination of the nature of oxide films formed on Ni at various potentials in the oxygen evolution region. Effects of electrochemical pretreatment of oxide films on the electrode kinetics of this reaction are also elucidated. In addition, efforts are made to develop methods for reactivating oxide films for oxygen evolution on aged nickel electrodes. It was recently proposed (21) that the electrocatalytic activity for oxygen evolution on aged Ir electrodes can be regained by applying a cathodic potential scan back to 0.25V and then returning to 1.50V.

* Electrochemical Society Active Member.
[1] Present address: Westinghouse Electric Corporation, Pittsburgh, Pennsylvania 15236.
Key words: ellipsometry, oxide films, oxygen evolution, performance degradation, rejuvenation, chemical transformation, mechanism.

Experimental

Electrode preparation.—The electrode was fabricated by mounting a nickel rod of purity 99.999% into a Teflon holder. Thus, only a single face with a geometric area of ~0.33 cm^2 was exposed to the electrolyte. Prior to each measurement, the electrode was mechanically polished to a mirrorlike finish as described elsewhere (22). The oxide film on the electrode surface, arising from the polishing process, was removed with dilute HCl solution. The electrode was then rinsed thoroughly with distilled water. Since oxide films on nickel electrodes are not removed by electroreduction (16, 17), the clean electrode surface could be obtained only by repolishing after each experiment. A cylindrical electrode made of platinum gauze was employed as the counterelectrode.

Electrolyte preparation and purification.—The 1*N* KOH solution was prepared from Baker analyzed reagent grade potassium hydroxide and triply distilled water. The electrolyte was purified by anodic preelectrolysis at a current density of 2 mA/cm^2 for at least 24 hr. Before each experiment, the electrolyte within the cell (about 120 ml) was deaerated by bubbling purified nitrogen.

Electrochemical measurements.—A cylindrical cell, made by inserting a Teflon sleeve into a brass envelop, was used to carry out the combined electrochemical and ellipsometric study. The electrochemical measurements were made using a PAR Model 173 potentiostat. Electrode potentials were measured with respect to the Hg/HgO electrode with KOH of the same concentration as the measuring solution. The potentials quoted in this paper are referred to the reversible hydrogen electrode (RHE) which is −926 mV *vs.* Hg/HgO electrode as determined in a previous study (23). Tafel plots for oxygen evolution on various pretreated nickel electrodes were determined by use of the steady-state potentiostatic method. In general, current density-potential measurements were made in the direction of decreasing current for the electrodes preanodized at 1.8 or 2.0V, and in the opposite direction for those pretreated at 1.5V. In all cases, the observed currents were reasonably stable at potentials below 1.56V. At higher potentials, readings were taken after the varying rate of current density was less than 0.2%/min. Ohmic overpotentials between the working and reference electrodes were determined using an interruptor technique (24).

Ellipsometric measurements.—*In situ* optical analysis of oxide films was conducted by use of a Rudolph Model RR2000 automatic ellipsometer. The combined ellipsometric and reflectometric measurements, as described in detail in the work of Gottesfeld and Srinivasan (21), were made at an angle of incidence (Φ) of 65° using a monochromatic light of wavelength (λ) 5461Å. The three-parameter (*i.e.*, Δ, ψ, and $\delta R/R$) method of solution was employed to determine the thickness (d_f) and optical constants (n_f, k_f) of oxide films. The optical readings of the bare surface were taken by maintaining a freshly prepared electrode at −50 mV for about 5 min. The ellipsometric and reflectometric measurements on oxide films grown in the oxygen evolution region were conducted by stepping the potential to 1.5V and then passing a stream of purified nitrogen gas over electrode surfaces to remove oxygen bubbles. A computer program, based on a system for function minimization (25), was used for the quantitative analysis of optical data. The film thickness observed under a fixed condition was ascertained by measuring a separate set of optical data with a light source of wavelength 6328Å.

Results and Discussion

Effects of electrochemical pretreatment on current density-time relations at constant potentials.—The influence of preanodization of nickel electrodes at 1.5V on the kinetics of the oxygen evolution reaction is shown in Fig. 1. On polarization at 1.8V, the initial current densities for oxygen evolution on preanodized electrodes are 4-5 times larger than on the freshly prepared electrodes. (The current density, recorded after the polarization of an electrode at 1.8V for 6 min, is referred to as the initial current density.) Similar results have been reported in the recent work of Shumilova and co-workers (26), who found that thermally oxidized nickel or cobalt oxide films are more active for oxygen evolution than pure metals.

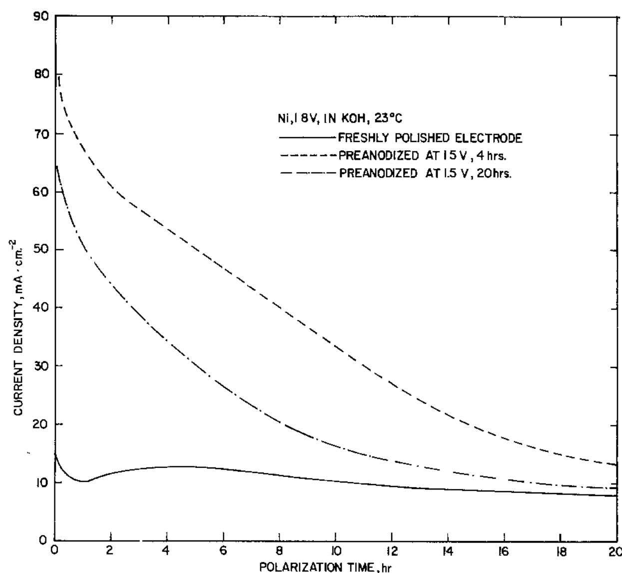

Fig. 1. Effect of preanodization at 1.5V on the current density for oxygen evolution on nickel electrodes in 1*N* KOH at 23°C.

Since oxide films on preanodized electrodes are thicker than on the freshly prepared one, it is extremely unlikely to correlate the considerable enhancement of initial current densities arising from preanodization (see Fig. 1) with film thickness. Instead, as it has been shown for the oxygen evolution reaction on iridium oxides (21) and on ruthenium oxides (27), the improvement of electrocatalytic activities for this reaction on preanodized nickel electrodes is apparently associated with the formation of the "right type of oxide." In the literature (15, 17, 28), it has been reported that preanodization of nickel at 1.5V yields oxide films essentially composed of β-NiOOH. On further oxidation at higher potentials, nonstoichiometric oxide films containing Ni^{3+} and Ni^{4+} ions are formed (6-9). The ratio of Ni^{3+} to Ni^{4+} ions in the films is dependent on the potential (9, 29) as well as the polarization time (29). Thus, the direct polarization of a freshly prepared nickel electrode at 1.8V produces an oxide film enriched in Ni^{4+} ions, which probably inhibit the oxygen evolution reaction, as discussed in a later section. Therefore, in comparison with the situation on the freshly prepared electrode, the significant increase of initial current densities on preanodized electrodes is essentially attributed to the presence of β-NiOOH, which is the so-called "right type of oxide" to activate the oxygen evolution reaction.

Further anodization of preoxidized nickel electrodes, by stepping the polarization potential from 1.5 to 1.8V, results in the gradual diminution of the concentration of Ni^{3+} ions in oxide films (9, 29). The current densities for oxygen evolution on these electrodes may thus be anticipated to decay with time, as supported by the experimental evidence shown in Fig. 1. Further, an increase of preanodization time at 1.5V causes an enhancement of the film thickness, which in turn produces an increase of resistance for the electron transfer. Consequently, as seen from Fig. 1, the performance for oxygen evolution on nickel preanodized

for 20 hr is poorer than that on the one preanodized for only 4 hr.

Despite the method of pretreatment, the oxygen evolution reaction on various electrodes exhibits approximately the same current densities after 20 hr of polarization at 1.8V (see Fig. 1). As illustrated in Fig. 2, however, the electrocatalytic activities of aged electrodes are rejuvenated by stepping the potential back to 1.5V. After maintaining aged electrodes at 1.5V for 2 hr, the initial current densities for oxygen evolution at 1.8V increase 3-7 times, but decrease with time again. The extent of improvement in electrocatalytic activities of oxide films is strongly dependent on the rejuvenation time as demonstrated in Fig. 2. Rejuvenation of an electrode at 1.5V for 12 min only doubles the initial current density. However, increasing the rejuvenation time to 2 hr results in an enhancement of about 7 times in the current density. Corresponding to the increase of rejuvenation time from 12 min to 2 hr, the period in which current densities on rejuvenated electrodes are higher than the initial current densities, increases from 2.2 to 11.5 hr.

Optical analysis of oxide films.—Figure 3 gives the variation of thickness (d_f) and optical constants (n_f, k_f) of oxide films with the electrochemical treatment applied to a nickel electrode. The complex refractive index ($\hat{n}_f$) on the bare nickel surface is 2.47-3.05i. Preanodization of the nickel electrode at 1.5V for 4 hr yields an oxide film with thickness of ~190Å and an absorption coefficient typical for semiconductors (n_f = 1.42-0.15i). It has been reported that, at $\Phi = 60°$ and $\lambda = 6328Å$, β-NiOOH film exhibits a complex refractive index of 1.6-0.117i in 5*N* KOH (15) and of 1.46-0.165i in 0.1*M* $Ni(NO_3)_2$ (30). From the observed optical constants in the present work, one confirms that the oxide film formed on nickel preanodized at 1.5V is β-NiOOH. The species β-NiOOH is a reasonably good electron conductor (20).

When this preanodized electrode is further oxidized at 1.8V for 20 hr, the film thickness increases to ~690Å with its $\hat{n}_f$ value[2] altering to 1.36-0.063i and the current density decreases from initial 79 to 13.3 mA/cm² (see Fig. 1). Further polarization of the preanodized nickel electrode results in the transformation of Ni^{3+} ions in the β-NiOOH lattice to Ni^{4+} ions (9, 12, 28). As has been pointed out by Vijh (31), the approximate relationship between the electronic conductivity (σ) and heat of formation per equivalent (ΔH_e) of intrinsic binary semiconductors may be represented by the equation

$$\sigma = \sigma_0 \exp(-\Delta H_e/kT) \quad [1]$$

where k is Boltzmann's constant, T is the absolute temperature, and σ_0 is the limiting electronic conductivity as T approaches zero. Apparently, Ni^{4+} oxide has a larger ΔH_e value than the Ni^{3+} oxide. Hence, the conversion of Ni^{3+} to Ni^{4+} ions may induce a decrease in the electronic conductivity of the oxide film and thus results in a considerable change in the k_f value of this film, as observed in the present work.

After polarization at 1.8V, the electrocatalytic activity of the aged electrode is rejuvenated by stepping its potential back to 1.5V.[3] As shown in Fig. 4, ellipsometric and reflectometric parameters remain approximately constant during the rejuvenation. After 2 hr of rejuvenation at 1.5V, the thickness of oxide film decreases slightly to ~680Å, having $\hat{n}_f$ = 1.36-0.065i. Apparently, the rejuvenation process causes no significant change in the thickness and optical constants of the oxide film. Subsequently, an increase of the potential of this rejuvenated electrode to 1.8V results in an enhancement of only ~15Å in the film thickness in the first 20 hr. However, the current density for oxygen evolution at this potential diminishes remarkably from initial 41 to 6 mA/cm² in the same period of time.

Influence of electrochemical treatment on Tafel parameters.—Tafel plots for oxygen evolution on various pretreated nickel electrodes are shown in Fig. 5. On electrodes which are preanodized at 1.8 or 2.0V, it always takes 1-2 hr to obtain a single current density with varying rate less than 0.2% per minute, particularly in the transition region between 1.56 and 1.7V. Above the potential 1.56V, Tafel plots for oxygen evolution on nickel electrodes preanodized or rejuvenated at 1.5V deviate from linear regions. For the oxygen evolution reaction on iridium in acid solution, a sharp break in the Tafel plot has been observed at 1.57V (2). Kinetics parameters for this reaction, as well as the thickness of oxide films, on various pretreated nickel electrodes are summarized in Table I.

Tafel plots for the anodic evolution of oxygen on the electrodes preanodized or rejuvenated at 1.5V exhibit only one linear region with $b \approx 40$ mV, while dual Tafel regions are observed on those preanodized at 1.8 or 2.0V: $b \approx 40$ mV at low η and $b \approx 170$ mV at high η (b and η represent the Tafel slope and oxygen overpotential, respectively). From optical analyses, the preanodization of nickel at 1.8 or 2.0V yields oxide films with low k_f (~ 0.06) values and thus poorer electronic conductivity. The films, in turn, lead to barrier-layer effects (32) on the reaction kinetics,

[2] By use of the three parameter method of solution, no difficulty was encountered in determining $\hat{n}_f$ value for a mixed oxide film containing Ni^{3+} and Ni^{4+} ions from the measured optical parameters.

[3] It may be more efficient to rejuvenate an aged electrode at less anodic potentials. However, it is found that the thickness of oxide films, grown at potentials above 1.56V, is greatly decreased when the potential is subsequently lowered below 1.35V, as shown by the significant reduction in the alteration of ellipsometric and reflectometric parameters with respect to the bare nickel surface. Also the conversion of Ni^{3+} to Ni^{2+} ions takes place below this potential (17). To eliminate the complications arising from these factors in the optical analysis of oxide films formed in the oxygen evolution region, the aged electrode is rejuvenated only at 1.5V.

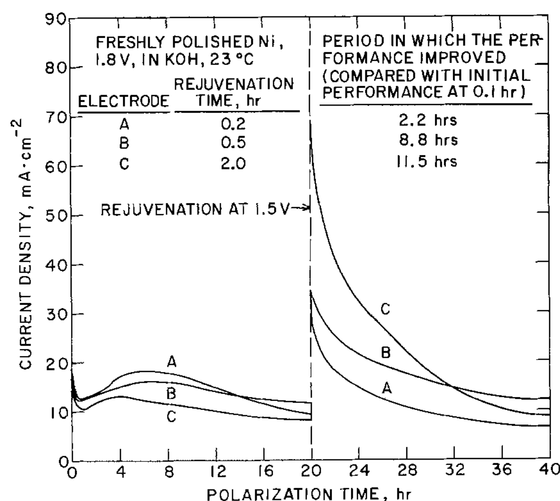

Fig. 2. The dependence of the extent of improvement in the electrocatalytic activity of oxide films for oxygen evaluation on the rejuvenation time.

Fig. 3. Variation of the thickness (d_f), refractive index (n_f) and absorption coefficient (k_f) of oxide film with anodization potential in 1*N* KOH at 23°C ($\Phi = 65°$ and $\lambda = 5461Å$).

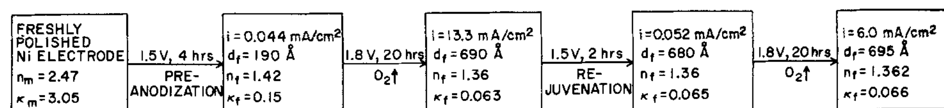

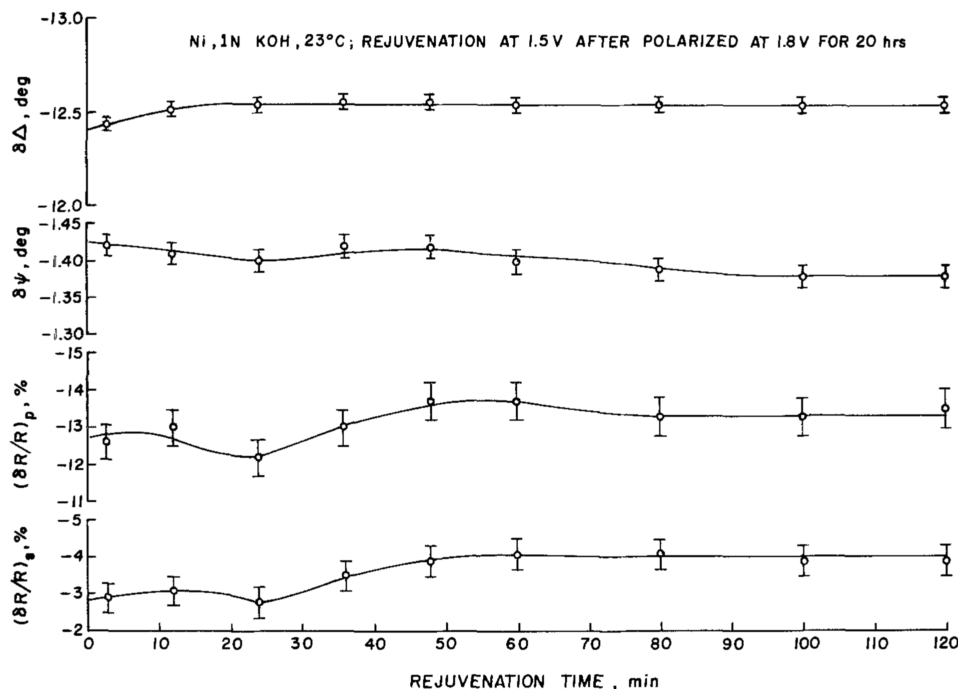

Fig. 4. Variation of ellipsometric ($\delta\Delta$, $\delta\Psi$) and reflectometric parameters [$(\delta R/R)_p$, $(\delta R/R)_s$] with the rejuvenation time.

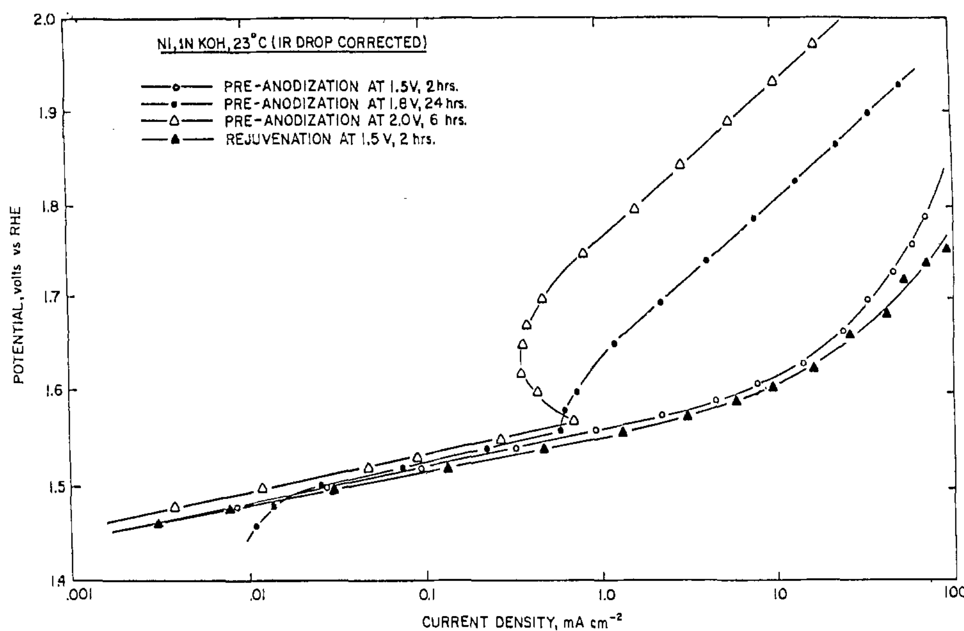

Fig. 5. Tafel plots for the oxygen evolution reaction on various pretreated nickel electrodes in 1N KOH at 23°C.

as further supported by the unusually high Tafel slopes of ~170 mV observed at high η.

In comparison with the case of pretreating nickel electrodes at 1.8V, preanodization of an electrode at a higher potential (*e.g.*, 2.0V) simply shifts the Tafel region at high η to a lower current density range in a parallel direction (see Fig. 5). Because the ratio of Ni^{3+} to Ni^{4+} ions in oxide films is dependent on the polarization potential (9, 29), the decrease in current density for oxygen evolution at high η can be attributed to the diminution of the concentration of Ni^{3+} ions in the films. Preanodization at 2.0V produces an oxide film of thickness ~1400Å,[4] which is much thicker than those formed on the electrode preanodized at 1.8V, being ~620Å in thickness. At potentials below 1.56V, however, Tafel plots for oxygen evolution on all the preanodized electrodes are in fair agreement with one another, in spite of the considerable difference in the electrode pretreatment.

As seen from Fig. 5, the Tafel plot for oxygen evolution on the rejuvenated electrode substantially coincides with that on the electrode preanodized at

[4] Actually, the electrode was first preanodized at 1.8V for 72 hr and then at 2.0V for 6 hr.

Table I. Kinetic parameters for oxygen evolution on pretreated nickel electrodes

Pretreatment	d_f, (A)	Tafel slope, b (mV) High η	Tafel slope, b (mV) Low η	Exchange c.d., i_o (A/cm²) High η	Exchange c.d., i_o (A/cm²) Low η
1. Preanodization at 1.5V, 2 hr	~230	—	39	—	3.8×10^{-12}
2. Preanodization at 1.8V, 24 hr	~620	170	43	4.2×10^{-6}	1.1×10^{-11}
3. Preanodization at 2.0V, 6 hr	~1400	167	40	6.2×10^{-7}	2.2×10^{-12}
4. Rejuvenation at 1.5V, 2 hr	~620	—	38	—	1.1×10^{-12}

1.5V. It is clear that the rejuvenation of an aged electrode causes the reappearance of the so-called "right type of oxide" in the film. Further, the film thickness on the rejuvenated electrode is much larger than that on the preanodized electrode (see Table I). However, the oxygen evolution reaction exhibits approximately equal Tafel slope and exchange current density on the two electrodes. These observations imply that the chemical nature of oxide films plays a more important role than the film thickness in the determination of the kinetic parameters for this reaction.

By intentionally extending the rejuvenation time to 12 hr, the influence of rejuvenation on Tafel plots for oxygen evolution on a nickel electrode is shown in Fig. 6. After preanodization of a freshly prepared nickel electrode at 1.8V for 4 hr, a Tafel plot for the anodic evolution of oxygen was determined. This aged electrode was then rejuvenated at 1.5V for 12 hr. Subsequently, the rejuvenated electrode was polarized at 1.8V for 20 hr, and a second Tafel plot for oxygen evolution was finally determined. The rejuvenation of a preanodized electrode results in the remarkable shift of the Tafel plot at high η to a higher current density range, in spite of the fact that the preanodization time has been increased from 4 to 20 hr. At potentials below 1.56V, however, the two Tafel plots are in excellent accordance with each other.

Effects of temperature on the rate of current decay.—The rate of the conversion of Ni^{3+} to Ni^{4+} ions in oxide films increases with increasing temperature. In general, higher oxides such as NiO_2 are less stable at higher temperature. Thus, if the time variation of currents under constant potential conditions is really associated with the further oxidation of Ni^{3+} ions. one is able to confirm this by investigating the variation of the rate of current decay with temperature.

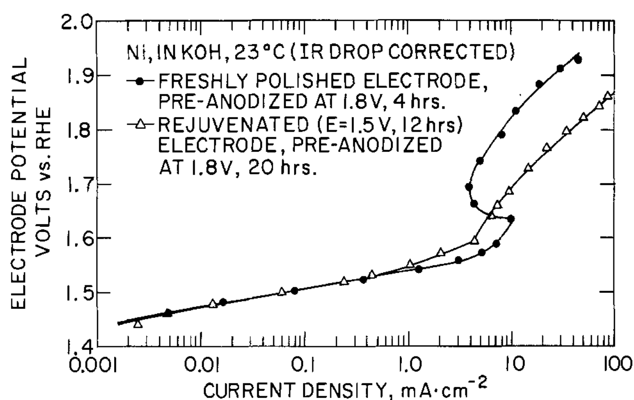

Fig. 6. Effect of rejuvenation (at 1.5V) on Tafel plots for the oxygen evolution reaction on a nickel electrode which is preanodized at 1.8V.

The initial current density varies significantly with the electrolyte temperature. With a view of comparing the rate of current decay at various temperatures, the ratios of the current density to its initial value rather than the apparent current densities, are plotted as a function of time in Fig. 7. The higher the electrolyte temperature, the shorter the period of time required for approaching a stable current. Also, the time variation of current density becomes a less serious problem at higher temperatures. For instance, after the polarization of preanodized electrodes at 1.8V for 20 hr, the current density diminishes to ~1/6 of its initial value at 23°C. Under the same conditions, however, the current density drops only about 50% at 80°C. After the rejuvenation of an aged electrode at 1.5V for 2 hr, the current density for oxygen evolution on this electrode at 1.8V regains 100% of its initial value at 80°C, but only 64% at 23°C. From these observations, it is obvious that the time variation of current for oxygen evolution is closely correlated with the chemical conversion of Ni^{3+} to Ni^{4+} ions.

Mechanism of current decay.—As has been confirmed in the present work, the preanodization of a nickel electrode at 1.5V yields β-NiOOH film, which is the "right type of oxide" providing active sites, *i.e.*, Ni^{3+} ions, for the oxygen evolution reaction. On further anodization of this electrode at potentials above 1.56V, it is assumed that some Ni^{3+} ions are converted to Ni^{4+} ions by an equation of the form

$$\beta\text{-NiOOH}_{(latt)} + OH^- \rightarrow NiO_{2(latt)} + H_2O + e^-_{(latt)} \quad [2]$$

where the formation of lattice, rather than intermediate, Ni^{4+} ions takes place in the bulk as well as on the surface layers of oxide films.

The oxygen evolution reaction occurs only at the surface of the films. For this reaction on nickel in alkaline solutions, the generally accepted mechanism (20), modified from the one suggested by Krasil'shchikov (33), involves the following steps

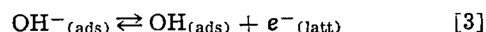

$$OH^-_{(ads)} \rightleftarrows OH_{(ads)} + e^-_{(latt)} \quad [3]$$

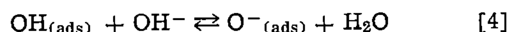

$$OH_{(ads)} + OH^- \rightleftarrows O^-_{(ads)} + H_2O \quad [4]$$

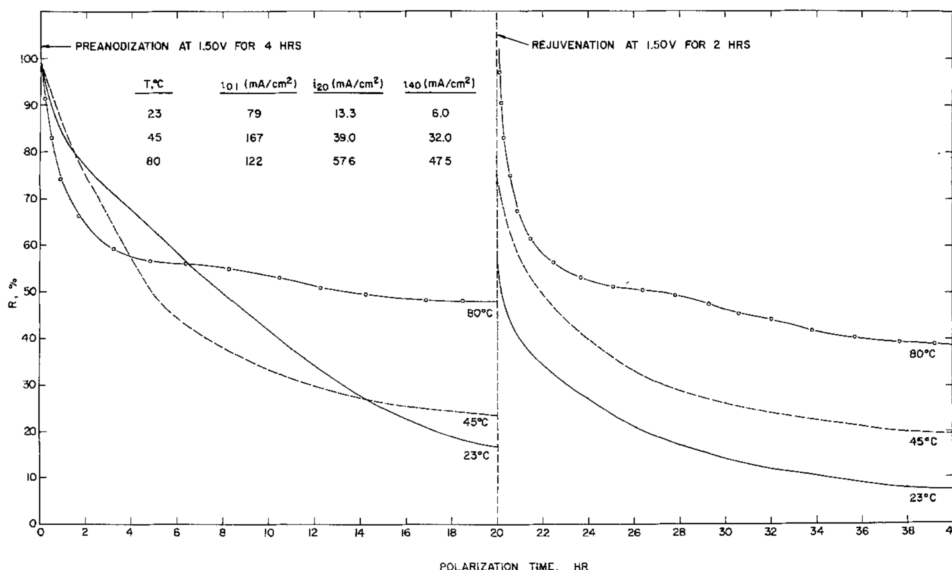

Fig. 7. Effect of temperature on the rate of current decay for the oxygen evolution reaction on preanodized and rejuvenated nickel electrodes.

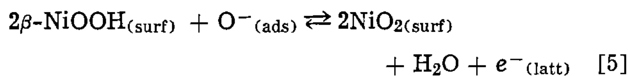

$$2\beta\text{-NiOOH}_{(surf)} + O^{-}_{(ads)} \rightleftarrows 2NiO_{2(surf)} + H_2O + e^{-}_{(latt)} \quad [5]$$

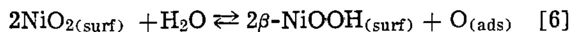

$$2NiO_{2(surf)} + H_2O \rightleftarrows 2\beta\text{-NiOOH}_{(surf)} + O_{(ads)} \quad [6]$$

$$O_{(ads)} + O_{(ads)} \rightleftarrows O_2 \quad [7]$$

Despite the pretreatment on each electrode, the observed Tafel slopes of $2RT/3\mathbf{F}$ (*i.e.*, ~40 mV, see Table I) at potentials below 1.56V support that Eq. [5] is the rate-determining step for oxygen evolution on nickel at low η. It is noted that NiO_2 formed via Eq. [5] is an intermediate species on the film surface only. According to thermodynamic data (4), the further anodization of NiO_2 to form insoluble solid species on the electrode surface is not possible. When an active species, *i.e.*, Ni^{3+} ion, on the film surface is anodized to Ni^{4+} ion, an intermediate step, similar to Eq. [5] cannot take place on the latter site and all the following steps in the over-all reaction for oxygen evolution may be completely inhibited. Thus, NiO_2, which is an intermediate in the oxygen evolution reaction, cannot function as an electrocatalyst for the over-all reaction. Therefore, the generation of each lattice Ni^{4+} ion on the film surface creates an inert site for oxygen evolution. On the other hand, the formation of lattice Ni^{4+} ions in the bulk of the oxide film, initially composed of β-NiOOH, results in a remarkable decrease in the electronic conductivity of the film itself as indicated by the significant drop of its absorption coefficient from 0.15 to 0.063 (see Fig. 3).

Figure 8 illustrates a possible mechanism for the loss and regain of electrocatalytic activities on oxide films. On further oxidation of one Ni^{3+} ion via Eq. [2], one proton migrates across the oxide-electrolyte interface accompanied by an electron transfer through the oxide-metal interface. The extent of the loss of electrocatalytic activity is dependent on the amount of protons ejected from the film into the electrolyte. Therefore, on polarization of pretreated nickel electrodes at 1.8V, the current decay with time is presumably attributed to the slow migration of protons from the oxide film into the electrolyte. In other words, the time variation of current density is essentially due to the gradual conversion of Ni^{3+} to Ni^{4+} ions in the bulk or on the surface of oxide films.

Possible reason for the rejuvenation of electrocatalytic activity.—As shown in Fig. 2, the current densities for oxygen evolution on nickel are considerably increased after rejuvenation of aged electrodes at 1.5V for different periods of time. The significant enhancement in current density, arising from the rejuvenation, is possibly ascribed to (*i*) the decrease of thickness of oxide films, and thus the diminution of resistance for the electron transfer; (*ii*) the alteration of microstructure of film surfaces, or more specifically, the increase of real surface area of oxide films; and (*iii*) the electrochemical reduction of Ni^{4+} to Ni^{3+} ion in oxide films.

During rejuvenation, the observed ellipsometric parameters are practically independent of time as shown in Fig. 4. After 2 hr of rejuvenation, the thickness of oxide film decreases slightly from ~690 to ~680Å (see Fig. 3). Furthermore, repolarization of this rejuvenated electrode at 1.8V for 20 hr results in a significant current decay, *i.e.*, from initial 41 to 6 mA/cm², but only a slight increase of ~15Å in the film thickness. Thus factor (*i*) hardly influences the current density for oxygen evolution at the potential of 1.8V.

The ellipsometric parameters, Δ and ψ, are sensitive to the variation of surface roughness of specimens (34). On rejuvenation of an aged electrode at 1.5V, these parameters remain substantially constant with time, as demonstrated in Fig. 4. Roughening of an oxide film causes an increase of real surface area and consequently results in a remarkable shift of Tafel plots for oxygen evolution on a rejuvenated electrode to a higher current density region. As shown in Fig. 6, however, intentional extension of the rejuvenation time to 12 hr causes no detectable shift of Tafel plots at low η. These observations strongly support that factor (*ii*) is unlikely to be the reason for the considerable enhancement of current density caused by the rejuvenation.

After the elimination of factors (*i*) and (*ii*) by the stated experimental evidence, chemical transformation of Ni^{4+} to Ni^{3+} ions, *i.e.*, factor (*iii*),[5] is the only possible reason for the increase of current density on rejuvenated electrodes. This transformation could induce two effects: (*i*) enhancement of active sites for oxygen evolution on the film surface; and (*ii*) increase of the electronic conductivity of the oxide film.

As demonstrated in Fig. 8, the electroreduction of Ni^{4+} to Ni^{3+} ions involves the migration of protons from the oxide-electrolyte interface onto the film surface and/or into the bulk of the film. Thus, at a constant potential, temperature and rejuvenation time are the essential factors controlling the extent of the electroreduction. Although the oxide film on the rejuvenated electrode exhibits no remarkable change in optical properties compared to that on the aged electrode (Fig. 3), the extent of improvement in the initial current density is strongly dependent on the length of rejuvenation time as well as on the temperature (see Fig. 2 and 7). Therefore, the electroreduction reaction does occur during rejuvenation in spite of the fact that no striking alteration of optical constants is detected. This peculiar phenomenon is elucidated below.

When an aged electrode is rejuvenated at such a high anodic potential (*e.g.*, 1.5V), it seems reasonable to assume that protons cannot migrate deeply through the oxide film because of the lack of sufficient field

[5] There is possibly an alternative explanation that, during rejuvenation, the lack of change in optical parameters is due to a compensating change in increased surface roughness for a decrease in film thickness. In this case, rejuvenation should arise due to decrease of film thickness. Figure 2 shows that the initial current densities on rejuvenated electrodes increase with the length of rejuvenation time. This result will then indicate that the film thickness decreases with increasing rejuvenation time. Certainly, thinning of oxide film could cause a surface roughening. However, it will be purely coincidental that, despite the length of rejuvenation time, changes in optical parameters, resulting from surface roughening, will always be equal to and thus compensate the change caused by the decrease in film thickness.

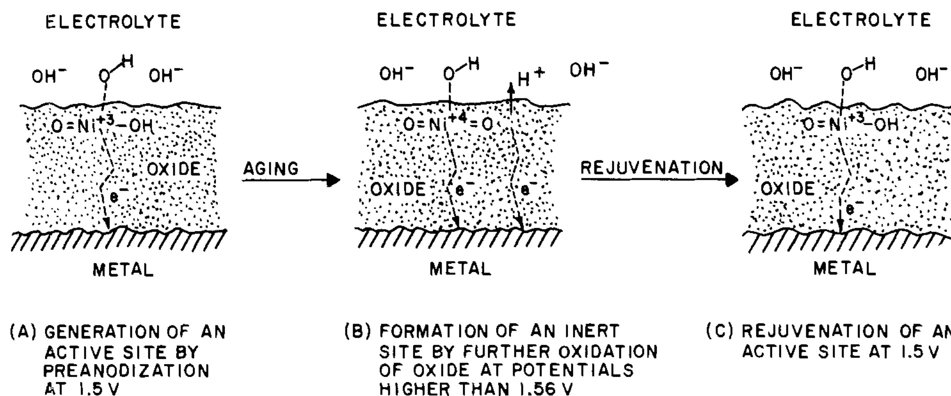

Fig. 8. Schematic illustration of deactivation and rejuvenation of active sites for oxygen evolution in the top few layers of nickel oxide films.

assistance. Thus, the electroreduction of Ni^{4+} ions possibly takes place only on the very top layers of the surface oxide. No significant change of the chemical identity in the bulk oxide is involved. The ellipsometry detects only the average properties of oxide films. Since thick films (~700Å) are present in the potential range for evolving oxygen, any possible change of optical properties in the top few layers of the films, arising from the electroreduction of Ni^{4+} ions, results in no detectable effect on the over-all film properties. Therefore, the rejuvenation of electrocatalytic activity is essentially attributed to the increase of active sites, *i.e.*, Ni^{3+} ions, on the very top layers of oxide films.

Conclusion

Nickel oxide films formed by the preanodization of the electrodes at 1.5V are more active than untreated nickel for oxygen evolution. This is essentially ascribed to the presence of the so-called "right type of oxide," *i.e.*, β-NiOOH, on the electrode surface. The β-NiOOH film with thickness of ~190Å exhibits an absorption coefficient typical for semiconductors ($\hat{n}_f$ = 1.42-0.15i). Further increase of potential on this preanodized electrode to higher values (say 1.8V) results in the gradual conversion of Ni^{3+} to Ni^{4+} ions on the surface layers of oxide films. Consequently, it causes a considerable enhancement of the film thickness and a remarkable drop in the electronic conductivity of the films, as determined using ellipsometric techniques. The time variation of current density for the oxygen evolution reaction at a constant potential above 1.56V is due to the continuous transformation of active (*i.e.*, Ni^{3+} ion) to inactive (*i.e.*, Ni^{4+} ion) sites.

From a practical point of view, the electrocatalytic activities of aged electrodes are regained by rejuvenating the electrodes at potentials below 1.56V. The rejuvenation of aged oxide films is substantially attributed to the recovery of active sites on the very top layers of the films. The time variation of current density for the oxygen evolution reaction at constant potential is less at higher temperatures. The higher the electrolyte temperature, the shorter the period of time required for approaching a stable current density and the more significant the improvement of the electrocatalytic activity of aged electrodes by rejuvenation.

Although the oxide film on the rejuvenated electrode is much thicker than that on the one preanodized at 1.5V, the Tafel plots for oxygen evolution on the two electrodes exhibit similar Tafel slopes (~40 mV) and exchange current densities (~10^{-12} A/cm^2). On the electrodes which are preanodized at 1.8 or 2.0V, dual Tafel regions are observed: $b \approx 40$ mV at low η and $b \approx 170$ mV at high η. It is concluded that the chemical nature of the top few layers of the films plays a more important role than the film thickness in the electrocatalysis of the oxygen evolution reaction on nickel. Methods to overcome the problem of performance degradation on anodes in water electrolysis cells include (*i*) increase of operating temperature to reduce the equilibrium ratio of Ni^{4+} to Ni^{3+} ions in the surface film, (*ii*) use of high surface electrodes to maintain the anode potential below the critical value of 1.56V at desired current densities, and (*iii*) introduction of a stable secondary cation into nickel oxide film (*e.g.*, $NiCo_2O_4$).

Acknowledgments

The authors wish to thank Professor B. E. Conway and Dr. S. Gottesfeld for their invaluable discussions. This work was carried out under the auspices of the United States Energy Research and Development Administration.

Manuscript submitted Oct. 10, 1977; revised manuscript received March 1, 1978. This was Paper 350 presented at the Philadelphia, Pennsylvania, Meeting of the Society, May 8-13, 1977.

Any discussion of this paper will appear in a Discussion Section to be published in the June 1979 JOURNAL. All discussions for the June 1979 Discussion Section should be submitted by Feb. 1, 1979.

Publication costs of this article were assisted by Brookhaven National Laboratory.

REFERENCES

1. J. W. Schultze, *Z. Phys. Chem., N.F.*, **73**, 29 (1970).
2. D. N. Buckley and L. D. Burke, *Faraday Trans. I*, **72**, Part II, 2431 (1977).
3. A. C. C. Tseung and S. Jasem, *Electrochim. Acta*, **22**, 31 (1977).
4. E. Deltombe, N. de Zoubov, and M. Pourbaix, "Atlas of Electrochemical Equilibrium in Aqueous Solutions," pp. 343-357, Pergamon Press, London (1966).
5. S. U. Falk, *This Journal*, **107**, 661 (1960).
6. R. W. Chairns and E. Ott, *J. Am. Chem. Soc.*, **56**, 1094 (1934).
7. O. Glemser and J. Einerhand, *Z. Elektrochem.*, **54**, 302 (1950).
8. G. W. D. Briggs and W. F. K. Wynne-Jones, *Trans. Faraday Soc.*, **52**, 1272 (1956); *Electrochim. Acta*, **7**, 241 (1962).
9. D. E. Davies and W. Barker, *Corrosion*, **20**, 47t (1964).
10. J. Labat, *Ann. Chem.*, **9**, 399 (1964).
11. P. Pacault and J. Labat, *Compt. Rend.*, **258**, 5421 (1964).
12. E. Jones and W. F. K. Wynne-Jones, *Trans. Faraday Soc.*, **52**, 1260 (1956).
13. K. S. Kim, N. Winograd, and R. E. Davis, *J. Am. Chem. Soc.*, **93**, 6296 (1971).
14. Yu. N. Chernykh and A. A. Yukoleva, *Elektrokhimiya*, **7**, 530 (1970).
15. M. A. Hopper and J. L. Ord, *This Journal*, **120**, 183 (1973).
16. W. Visscher and A. Damjanovic, Extended Abstracts, paper presented at the 27th Meeting of I.S.E., Zurich, Switzerland, September 1976.
17. J. D. E. McIntyre and D. M. Kolb, *Symp. Faraday Soc.*, **4**, 99 (1970).
18. K. S. Kim, C. D. Sell, and N. Winograd, in "Proceedings of the Symposium on Electrocatalysis," M. W. Breiter, Editor, pp. 242-257, The Electrochemical Society Softbound Symposium Series, Princeton, N.J. (1974).
19. Yu. Ya. Vinnikov, V. A. Shepelin, and V. I. Veselovskii, *Elektrokhimiya*, **9**, 649 (1973).
20. J. P. Hoare, "The Electrochemistry of Oxygen," chap. 7, Interscience, New York (1968).
21. S. Gottesfeld and S. Srinivasan, *J. Electroanal. Chem.*, **86**, 89 (1978).
22. M. H. Miles, G. Kissel, P. W. T. Lu, and S. Srinivasan, *This Journal*, **123**, 332 (1976).
23. F. Z. Fried, *Z. Phys. Chem.*, **123**, 1406 (1926).
24. K. R. Williams, "Introduction to Fuel Cells," pp. 57-63, Elsevier, New York (1966).
25. F. James and M. Roos, *Comput. Phys. Commun.*, **10**, 343 (1975).
26. V. S. Bagotzky, N. A. Shumilova, and E. I. Khrushcheva, *Electrochim. Acta*, **21**, 919 (1976).
27. W. O'Grady, C. Iwakura, J. Huang, and E. Yeager, in "Proceedings of the Symposium on Electrocatalysis," M. W. Breiter, Editor, pp. 286-302, The Electrochemical Society Softbound Symposium Series, Princeton, N.J. (1974).
28. J. L. Weininger and M. W. Breiter, *This Journal*, **110**, 484 (1963).
29. B. E. Conway and M. A. Sattar, *J. Electroanal. Chem.*, **19**, 351 (1968).
30. J. L. Ord, *Surf. Sci.*, **56**, 413 (1976).
31. A. K. Vijh, in "Oxides and Oxide Films," Vol. 2, J. W. Diggle, Editor, Marcel Dekker, New York (1973).
32. R. E. Meyer, *This Journal*, **107**, 847 (1960).
33. A. I. Krasil'shchikov, *Zh. Fiz. Khim.*, **37**, 531 (1963).
34. I. Ohlidal and F. Lukes, *Opt. Acta*, **19**, 817 (1972).

Electrogenerated Chemiluminescence

XXXIII. The Production of Excited States by Direct Heterogeneous Electron Transfer from Semiconductor Electrodes

J. D. Luttmer* and Allen J. Bard**

Department of Chemistry, The University of Texas at Austin, Austin, Texas 78712

ABSTRACT

Electrogenerated chemiluminescence (ECL) arising from direct electron transfer from semiconductor electrodes to solution species was examined. The reduction of the oxidized forms of several luminescent species [$Ru(bipy)_3^{2+}$, thianthrene, 9,10-diphenylanthracene, and rubrene] on several n-type semiconductor electrodes (CdS, ZnO, TiO_2, SiC, GaP) was investigated. Only for reduction of rubrene radical cation on n-ZnO and n-CdS was unequivocal evidence found for production of an excited state (triplet) by direct heterogeneous electron transfer at potentials where homogeneous redox processes producing excited states were not possible. Current interruption techniques were employed to study the emission decay and an unusual emission at open circuit following a cathodic potential step was found. A model for direct triplet generation based on reduction via surface states within the bandgap region and quenching of excited states by the electrode is proposed and constraints on the experimental observation of direct excited state formation are suggested.

Many examples of the electrogenerated chemiluminescence (ECL) of aromatic molecules and rare earth chelates have been reported over the last decade and several reviews have been published (1-8). Usually these studies involve generating excited states (triplets and singlets) via homogeneous electron transfer between electrogenerated oxidized and reduced forms, frequently radical anions and cations ("radical ion annihilation"), *e.g.*, for rubrene (R)

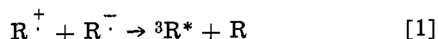

$$R^{\dot{+}} + R^{\dot{-}} \rightarrow {}^3R^* + R \quad [1]$$

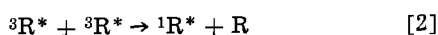

$$ {}^3R^* + {}^3R^* \rightarrow {}^1R^* + R \quad [2]$$

$$ {}^1R^* \rightarrow R + h\nu \quad [3]$$

or for $Ru(bipy)_3^{2+}$

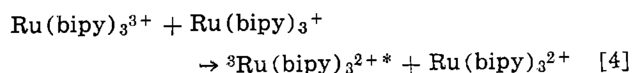

$$Ru(bipy)_3^{3+} + Ru(bipy)_3^{+} \rightarrow {}^3Ru(bipy)_3^{2+*} + Ru(bipy)_3^{2+} \quad [4]$$

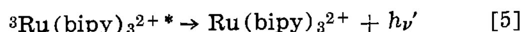

$$ {}^3Ru(bipy)_3^{2+*} \rightarrow Ru(bipy)_3^{2+} + h\nu' \quad [5]$$

Recent papers however have reported that excited states may also be formed by direct heterogeneous electron transfer at a semiconductor electrode surface (9, 10). Gleria and Memming (9) observed emission upon reduction of $Ru(bipy)_3^{3+}$ (bipy = 2,2'-bipyridine) at n-SiC and n-GaP semiconductor electrodes in H_2O or acetonitrile (ACN) solutions and proposed the reaction sequence

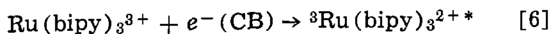

$$Ru(bipy)_3^{3+} + e^-(CB) \rightarrow {}^3Ru(bipy)_3^{2+*} \quad [6]$$

followed by [5], where $e^-(CB)$ represents an electron in the conductor band of the semiconductor. Yeh and Bard (10) reported singlet emission from rubrene produced by direct heterogeneous generation of the triplet state by reduction of $R^{\dot{+}}$ at an n-ZnO electrode followed by triplet-triplet annihilation in benzene-benzonitrile mixed solvent. *i.e.*

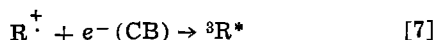

$$R^{\dot{+}} + e^-(CB) \rightarrow {}^3R^* \quad [7]$$

followed by [2] and [3]. In both studies it was proposed that the electron transferred from the conduction band to the oxidized solution species to form the excited triplet species. This is shown schematically in Fig. 1. Direct electron transfer to produce the ground state molecule should be less probable when the redox potential of the ground state molecule corresponds to an energy level within the bandgap of the semiconductor.

On a metal electrode an electron can be transferred from an isoenergetic state in the electrode to a lower orbital to produce the ground state of the molecule and no emission is expected. Moreover, excited state species are both more easily oxidized and more easily reduced at metal electrodes compared to the ground state species and metals are consequently good quenchers of excited states via electron transfer (11, 12). Quenching of excited state species by energy transfer to a metal is also well known (13). Although the direct heterogeneous production of triplet states at metal electrodes has been claimed (14), the emission observed in such cases has been attributed to a "preannihilation" type of ECL which involves reactions of impurities or electrogenerated products in the ECL solution (15, 16). Several other authors have been unable to observe evidence for the direct heterogeneous production of excited states on semiconductor

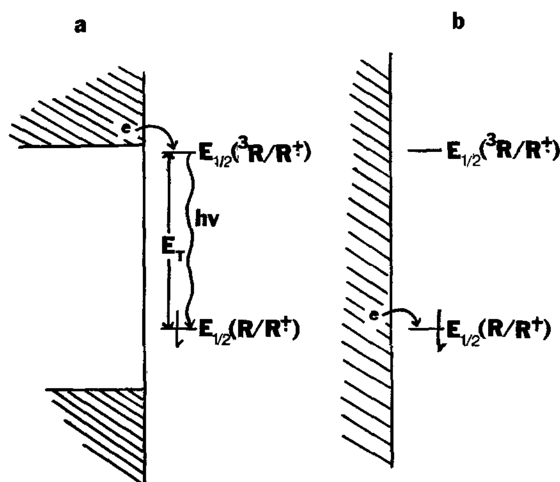

Fig. 1. Electron transfer from electrodes to oxidized solution species: (a) on a semiconductor, (b) on a metal electrode.

* Electrochemical Society Student Member.
** Electrochemical Society Active Member.

Key words: luminescence, energy transfer, organic, voltammetry.

electrodes (17, 18). Moreover, in the studies reporting the direct heterogeneous production of excited states at semiconductors a rigorous examination of the possibility of preannihilation ECL contributing to the observed emission and of the extent of ECL arising from a homogeneous electron transfer involving inadvertently generated reduced forms of the emitting species was not undertaken. We report here a more detailed study of the ECL emission mechanism in these systems and examine other possible systems for excited state production by direct heterogeneous electron transfer from semiconductor electrodes.

Experimental

Acetronitrile (ACN) (Spectro Grade, Matheson, Coleman, and Bell; MCB) was purified by repeated vacuum distillation from P_2O_5 and freeze-pump-thaw cycles to remove O_2 as described by Park and Bard (19). Benzonitrile (BZN; MCB) was fractionally distilled under partial vacuum from $CaSO_4$ and again from P_2O_5. It was then refluxed over, and fractionally distilled from, CaH_2 under high vacuum. Oxygen was removed by three freeze-pump-thaw cycles and the solution was stored over activated neutral alumina. Benzene (Spectro Grade MCB) was stored over a sodium mirror for more than one week, then was vacuum distilled, and underwent four freeze-pump-thaw cycles to remove O_2.

Tris (2,2′ bipyridyl) ruthenium (II) perchlorate, $[Ru(bipy)_3(ClO_4)_2]$ was prepared by metathesis of $Ru(bipy)_3Cl_2 \cdot 6H_2O$ (G. F. Smith) with excess $NaClO_4$ in H_2O. The crystals were washed with H_2O, recrystallized once from ethanol and twice from ACN, and dried under vacuum at 90°C for 24 hr. Thianthrene (TH) (Aldrich) was recrystallized twice from benzene and sublimed. Rubrene (R) (Aldrich) was recrystallized three times from xylene-methanol under nitrogen in subdued light and dried under vacuum at 80°C. 9,10-Diphenylanthracene (DPA) (Gold Label, Aldrich) was recrystallized from xylene-methanol, sublimed, and zone refined.

Tetra-n-butylammonium perchlorate (TBAP) (Polarographic Grade, Southwestern Analytical Chemicals) was purified by filtering a warm ethanolic solution of the electrolyte containing activated carbon and repeated recrystallization from an ethanol-water mixture. A final recrystallization was done from benzene and the crystals were dried under vacuum at 50°C for 36 hr. All samples, solvents, and electrolytes were transferred to a Vacuum Atmospheres dry box in which the solutions were prepared and the electrochemical/ECL cells were filled.

The n-type single crystal semiconductor electrodes were prepared and mounted as previously described (20, 21). Ohmic contacts were made to them by electrodepositing indium on one side and attaching a lead with silver-epoxy cement. Silicone adhesive (Dow Corning) was used to insulate the electrical contact from the electrochemical solution. A platinum foil working electrode of similar area and geometry was fabricated in a similar manner. The electrodes were polished with 0.5 μm alumina and had geometric areas of 0.3-0.5 cm^2. N-CdS (National Lead) and n-GaP (Atomergic) were etched in 11M HCl for 30 sec. N-TiO_2 (National Lead) and n-SiC[1] were etched in an HF/HNO_3 mixture for 30 sec. N-ZnO (Atomergic) was first etched in H_3PO_4 and then in concentrated HCl, each for 15 sec. The flatband potentials of these semiconductor electrodes have previously been determined from the onset of the anodic photocurrent in ACN (9, 20, 21) and are given in Table I.

The electrochemical/ECL cell was of conventional design with the reference compartment separated by a porous Vycor (Corning Glass) glass plug and the auxiliary electrode separated by dual frits of medium porosity. The auxiliary electrode consisted of a very large piece of platinum foil or wire mesh. Controlled potential waveforms for ECL and cyclic voltammetry were obtained with a PAR Model 175 programmer and Model 173/176 potentiostat. Current-time and ECL intensity-time curves were obtained with a Nicolet 1090A digital oscilloscope and recorded on a Houston 2000 X-Y recorder. An Aminco-Bowman spectrophotofluorometer was used to obtain ECL and fluorescence spectra. The ECL and fluorescence detectors used were RCA 1P28 and RCA 4832 photomultiplier tubes incorporating an RCA 3140 operational amplifier as a current follower. The intensity response of the emission detectors was adjusted, as necessary, by the selected input sensitivity of the Nicolet oscilloscope or by expansion of the digitized data in the oscilloscope. The current interrupter, fabricated with a silicon p-channel field effect transistor (Archer, No. 276-2037) driven by a Wavetek Model 114 signal generator, had a switching time of less than 3 μsec. The oxidized form of the electroactive species studied was produced by partial (25-75%) *in situ* controlled potential bulk electrolysis of the solution (about 20 min) on a large platinum foil electrode prior to the ECL studies.

[1] Courtesy of Prof. R. Memming, Phillips Research Laboratories, Hamburg, Germany.

Table I. Semiconductor electrode properties

Electrode	E_g (eV)[a]	V_{fb}[b]
n-CdS	2.45	−0.85[c]
n-ZnO	3.1	−0.76[c]
n-TiO_2	3.2	−0.8[d]
n-GaP	2.25	−1.5[c]
nSiC	3.0	−1.5[e,f]

[a] Bandgap energy.
[b] Flatband potential, *V vs.* SCE in ACN.
[c] Ref. (21).
[d] Ref. (20).
[e] Ref. (22).
[f] P. Kohl, private communication.

Results

Experimental approach.—In demonstrating direct excited state production via heterogeneous electron transfer at the electrode care must be taken to assure that the emission does not arise from the homogeneous radical ion annihilation path (Eq. [1]-[5]) or from a "preannihilation" or impurity pathway. In this latter case emission arises from the electrogeneration of a reactant from a small amount of impurity (X). For example, if X is reducible the following sequence is possible

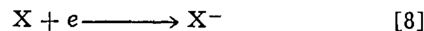

$$X + e \longrightarrow X^- \quad [8]$$

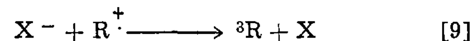

$$X^- + R^{\overset{+}{\cdot}} \longrightarrow {}^3R + X \quad [9]$$

followed by reactions [2] and [3]. Because light levels 10^{-3}-10^{-4} times below the annihilation level are detected readily, impurity concentrations at the 10^{-6}-$10^{-7}M$ level can contribute appreciable preannihilation emission. X can represent either an impurity initially present or one generated from a small amount of decomposition of $R^{\overset{+}{\cdot}}$ (or other electrogenerated reactant in the ECL annihilation reaction). The possibility of these paths was not studied in depth in the previous investigation of ECL at semiconductor electrodes (9, 10).

The approach employed to distinguish the direct route from the annihilation and preannihilation paths involved examining the electrochemical behavior and emission observed with a platinum electrode (which we assume will not show direct excited state formation), under careful potential control, with that of the semiconductor electrode. A solution containing the oxidized precursor [*e.g.*, $R^{\overset{+}{\cdot}}$ or $Ru(bipy)_3^{3+}$] was prepared and the potential of the working electrode was scanned linearly in a negative direction at 2

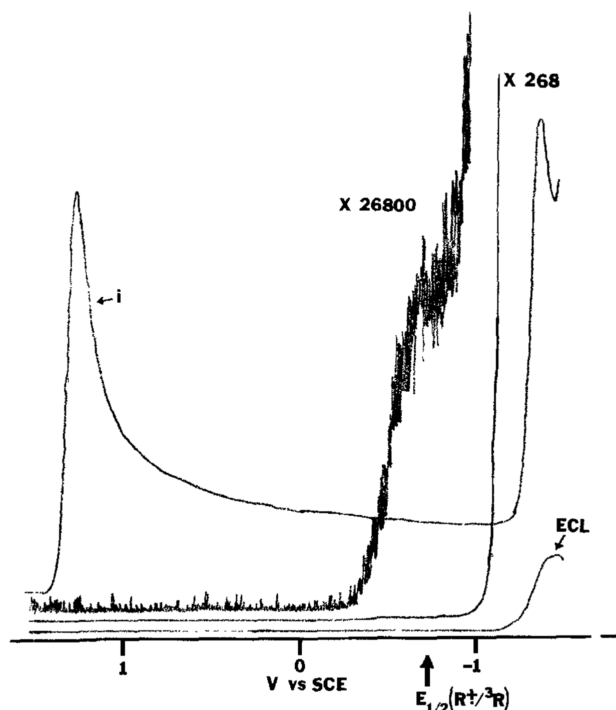

Fig. 2. ECL-potential and current-potential profiles obtained by cathodic potential scans at 2 V/sec 1.5 mmoles $Ru(bipy)_3^{3+}$ in 0.1M TBAP/ACN on platinum.

V/sec from potentials where the oxidized percursor was stable. Plots of the cathodic current (i) and the ECL intensity (I) as a function of potential (E) were thus obtained with different photomultiplier sensitivities. Typical results for a platinum electrode and $Ru(bipy)_3^{3+}$ in ACN/TBAP solution are shown in Fig. 2. The current scan shows two maxima, corresponding to the following electron transfer reactions at the electrode

$$Ru(bipy)_3^{3+} + e \rightleftharpoons Ru(bipy)_3^{2+} \ (E_p = +1.3V) \quad [10]$$

$$Ru(bipy)_3^{2+} + e \rightleftharpoons Ru(bipy)_3^{+} \ (E_p = -1.3V) \quad [11]$$

Homogeneous electron transfer between ionic species giving excited states occurs when the electrode potential becomes sufficiently negative to produce the reduced form of the ground state species; thus essentially all of the emission observed beyond $-1.0V$ *vs.* SCE in this system can be attributed to annihilation. Some residual emission is seen, however, at high sensitivities at potentials where the concentration of the electrogenerated +1 reduced species should be quite small. For example, the concentration of $Ru(bipy)_3^+$ at the electrode surface at $-1.3V$ *vs.* SCE is approximately 1.5 mmole; from the Nernst equation one calculates the concentration of $Ru(bipy)_3^+$ at the electrode surface at $-0.5V$. *vs.* SCE to be less than 2×10^{-13} mmole. This is too low to cause the residual emission observed at this potential. Thus this residual emission could not arise from homogeneous electron transfer but would necessarily arise from a preannihilation-type mechanism or conceivably, but not probably, by direct heterogeneous electron transfer at the metal electrode. Similar preannihilation emission was observed with all of the systems examined. Rigorous purification of solvent and supporting electrolyte would greatly reduce this emission but never entirely eliminate it, indicating at least some contribution to the ECL emission by impurities in the solvent and electrolyte.

Another possible approach to discriminate among the possible paths involves studying the time dependence of the ECL emission. Although attempts have been made to use the time dependence of the emission intensity during the potential step for this purpose (9, 10), the effects of possible quenching by radical ions and the complexity of the predicted annihilation results for triplet intermediates (2) suggest that unambiguous assignment by this approach may be difficult. An alternative method involves observation of the intensity decay following rapid current interruption. Qualitatively, under these conditions, the intensity would decay with the lifetime of the excited state for direct heterogeneous production. For homogeneous annihilation ECL the electrode would not reduce or oxidize the reactant ions at open circuit and the intensity decay should be governed by the rates of diffusion of the reactants.

Experimental results.—A summary of the results obtained using various compounds and semiconductor electrodes is given in Table II. For $TH^{\dot{+}}$, $DPA^{\dot{+}}$, and $Ru(bipy)_3^{3+}$, no emission which could be attributed unambiguously to direct heterogeneous production of excited states at the semiconductor electrodes was found. Either no emission was observed at potentials sufficient to produce excited states or the low levels of emission which were found at these potentials occurred at similar intensities and at the same potentials at a platinum electrode. Moreover, in these cases the decay times of the emission upon current interrup-

Table II. Summary of electrochemical and ECL data

Compound[a]	E_{T_1} (eV)	$E_{1/2}(R^{\dot{+}}/R)$[b]	$E_{1/2}(R^{\dot{+}}/^3R)$[b] (calc.)	Electrode	E_p[b,c]	Emission onset[b,d]
$Ru(bipy)_3^{3+}$	2.03[e]	1.30	−0.73	Pt	1.26	−0.5
				n-CdS	0.0	−0.6
				n-ZnO	−0.05	−0.65
				n-TiO_2	0.28	−0.6
$TH^{\dot{+}}$	2.58[f]	1.23	−1.35	Pt	1.19	−1.9
				n-SiC	−0.75[i]	−2.0
				n-GaP	−0.95[i]	−2.0
$DPA^{\dot{+}}$	1.8[g]	1.22	−0.58	Pt	1.18	−0.9
				n-ZnO	0.45	−0.9
				n-CdS	0.25	−0.9
$R^{\dot{+}}$	1.2[h]	0.94	−0.26	Pt	0.90	−0.6
				n-TiO_2	−0.15	−0.7
				n-ZnO	0.45	−0.2
				n-CdS	−0.13	−0.25

[a] ACN solutions approximately 1 mmole compound and 0.1M TBAP ($TH^{\dot{+}}$, $DPA^{\dot{+}}$, and $R^{\dot{+}}$ are radical cations of thianthrene, 9,10-diphenylanthracene, and rubrene, respectively).
[b] V *vs.* SCE.
[c] Reduction of compound. Cathodic current peak potential obtained by linear potential sweep voltammetry at 2 V/sec.
[d] Onset of ECL emission obtained with cathodic potential scans at 2 V/sec.
[e] Ref. (26).
[f] Ref. (27)
[g] Ref. (28).
[h] Ref. (29).
[i] Broad current peaks observed.

tion were much longer than those expected from the excited state lifetimes. These results suggest then that the observed emission at the semiconductor electrodes could be attributed mainly to preannihilation ECL rather than direct excited state formation. Different results were obtained upon reducing rubrene radical cation on n-CdS or n-ZnO, however. In these cases the behavior at platinum and at the semiconductors was very different and the ECL emission on current interruption showed unique and previously unobserved features. Details of these experiments are given below.

Because of the low solubility of R in ACN, ECL and electrochemical studies of R were carried out in benzonitrile (BZN) or in the mixed solvents benzene-BZN or benzene-ACN. A cyclic voltammogram of R in 0.1M TBAP/benzene-BZN is given in Fig. 3. R is reversibly oxidized and reduced in one electron transfer steps at 0.94 and −1.45V *vs.* SCE, respectively, in these solvent systems. Although phosphorescence of R has not been reported, energy transfer experiments indicate that the energy of the first triplet state is ~1.2 eV (23), approximately that of its parent molecule, naphthacene. Thus reduction of $R^{\cdot +}$ to the triplet state should occur at about −0.26V *vs.* SCE and n-TiO_2, n-ZnO, and n-CdS are suitable semiconductor electrodes to study the direct production of ^3R. Ideally the semiconductor electrodes should have a flatband potential, V_{fb}, negative of the potential needed to form the triplet, yet considerably removed from the thermodynamic potential for the reduction of R to $R^{\cdot -}$ to discriminate between reduction of $R^{\cdot +}$ to the excited triplet state and production of $R^{\cdot -}$ and annihilation ECL.

Current-potential curves for the reduction of $R^{\cdot +}$ at n-ZnO and n-CdS by linear single sweep voltammetry are given in Fig. 4. In the absence of intermediate levels or surface states within the bandgap region reduction of couples with redox potentials deep in the gap (*e.g.*, $R^{\cdot +}/R$ or $R^{\cdot +}/^3R$) should occur only at potentials near or negative of V_{fb}. However, studies of a number of redox couples in nonaqueous solutions at these semiconductors (20, 21) have shown reductions to occur significantly positive of V_{fb} at potentials characteristic of some intermediate levels or surface states. The current peak for the reduction of $R^{\cdot +}$ at about 0.5V *vs.* SCE (Fig. 4a) agrees quite well with the intermediate level proposed for n-ZnO (21). For potentials more negative than V_{fb}, the n-ZnO becomes degenerate, the electrode behavior approaches that of a metal (24) and reversible reduction of R to $R^{\cdot -}$ is observed.

The ECL intensity-potential profiles obtained during reduction of $R^{\cdot +}$ at Pt, n-CdS, and n-ZnO upon cathodic linear potential scans from potentials where $R^{\cdot +}$ is stable, well positive of the flatband potential of the semiconductor electrodes, are shown in Fig. 5. Note that reduction of $R^{\cdot +}$ on n-CdS and n-ZnO yields considerable emission at potentials positive of those where emission is observed on the platinum electrode. The potential sweep at the n-ZnO semiconductor electrode resulted in an emission peak at *ca.* −0.35V *vs.* SCE (in addition to the emission at *ca.* −1.5V due to the homogeneous ion annihilation reaction of $R^{\cdot +}$ and the $R^{\cdot -}$). Similarly, a peak at *ca.* −0.50V was obtained on the n-CdS semiconductor electrode. In both cases, the emission occurred at potentials where the triplet state is energetically just accessible yet at potentials positive of the flatband potential. This emission at rather positive potentials was quite reproducible over several hours and was found to be as large as 2-3% of the homogeneous annihilation

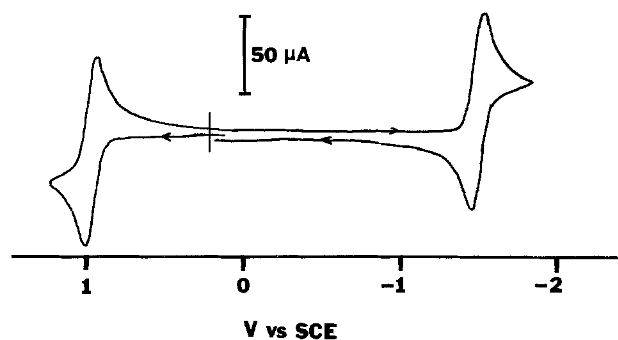

Fig. 3. Cyclic voltammogram of 1.5 mmoles R in 0.1M TBAP/benzene-BZN on platinum. Scan rate is 200 mV/sec.

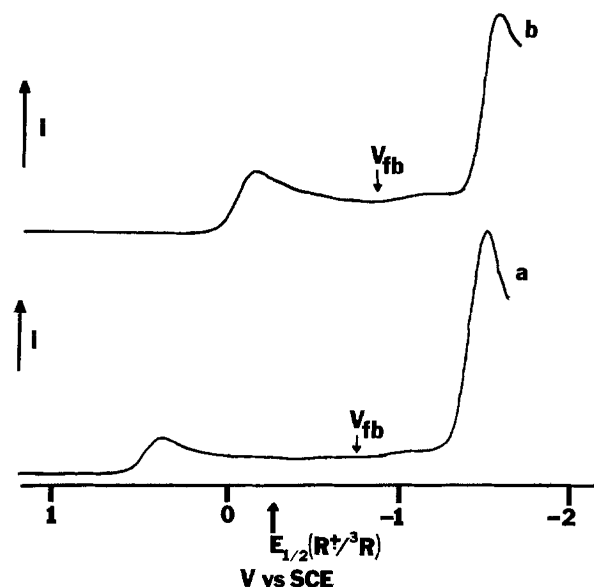

Fig. 4. Linear potential sweep voltammogram obtained with *ca.* 1 mmole $R^{\cdot +}$ in 0.1M TBAP/BZN on (a) n-ZnO, (b) n-CdS. Scan rate is 2 V/sec.

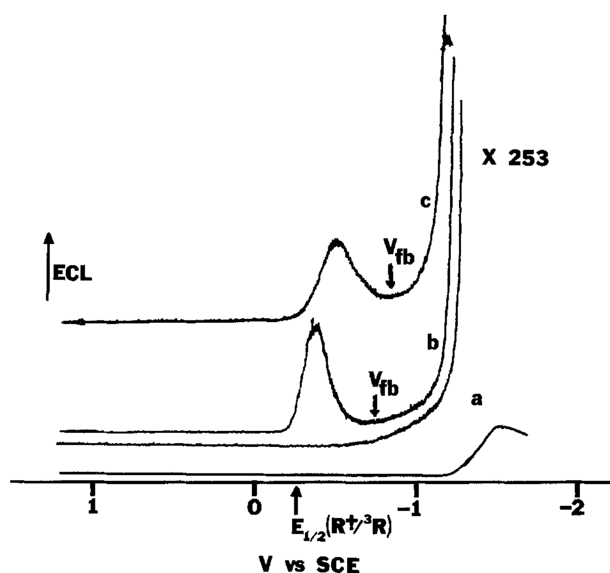

Fig. 5. ECL-potential profiles obtained with *ca.* 1 mmole $R^{\cdot +}$ in 0.1M TBAP solution at 2 V/sec. (a) Platinum electrode in benzene-ACN, (b) n-ZnO in benzene ACN, (c) n-CdS in BZN.

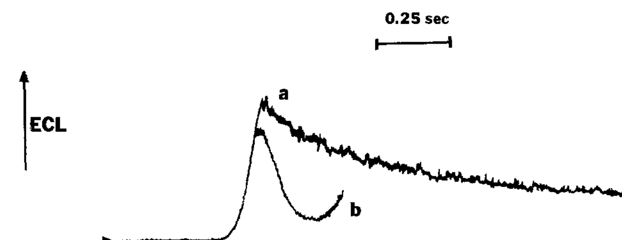

Fig. 6. ECL-time profile obtained concurrently with cathodic potential scan from 1.18V *vs.* SCE with *ca.* 1 mmole $R^{\cdot +}$ in 0.1M TBAP/BZN on n-CdS. Scan rate is 2 V/sec. (a) Potential ramp terminated at −0.5V *vs.* SCE (at curve maximum); (b) scan to −1.1V *vs.* SCE.

ECL emission produced at −1.5V under these conditions. That the peaked shape of the emission observed on the potential sweep at −0.35V (n-ZnO) and −0.50V (n-CdS) was caused by a potential, rather than a time, dependence was shown by the experiment of Fig. 6. When the potential ramp was stopped at potentials of the emission peak, the decay of the emission was rather slow (curve a). However, if the potential was scanned beyond the peak potential, the emission decayed abruptly (curve b).

To study the contribution to the emission by triplet states via triplet-triplet annihilation, the time dependence of the ECL emission was examined using a potential step excitation. Typical results obtained by stepping the potential from +1.1 to −0.7V *vs.* SCE at n-ZnO or to −0.62V at n-CdS are shown in Fig. 7. In both cases the cathodic current decay was proportional to $t^{-1/2}$, as expected for the diffusion-controlled reduction of $R^{\cdot +}$. The ECL intensity decay, however, was proportional to t^{-1}, or the square of the current, indicative of triplet generation followed by triplet-triplet annihilation (assuming a triplet lifetime controlled by quenching). Note that although a homogeneous annihilation production of ^3R could lead to a similar t^{-1} decay, the potentials employed in the step experiments preclude appreciable generation of $R^{\cdot -}$ and emission from the $R^{\cdot +}/R^{-}$ reaction route. In fact, potential steps to potentials where $R^{\cdot -}$ was generated at the semiconductor showed an emission decay with a dependence between $t^{-1/2}$ and t^{-1}.

Current interruption techniques were also informative and showed very different behavior for Pt and the semiconductor electrodes. ECL intensity time curves for a Pt electrode for potential steps of 30 msec to −1.1V (the presumed preannihilation region) are shown in Fig. 8. When the current was interrupted at the end of the step (curve a), the emission decay time was *ca.* 5 msec. In contrast, when the potential was stepped back to +0.0V after the cathodic step the emission decay was much faster (*ca.* 5 μsec) (curve b). In this case, bringing the electrode potential to positive potentials caused oxidation of the species responsible for emission and probably also ^3R; this result suggests that the emission occurs at or very near the electrode surface. Very different results were obtained upon current interruption with the semiconductor electrodes; typical results are shown in Fig. 9 and 10. When the initial potential step was to a potential, E_1, corresponding to the emission peak (Fig. 9c or 10a), the emission showed a slow decay during the peak and a decay in 0.4-3.6 msec to zero upon interruption. However, when the potential was stepped to values beyond the emission peak (but before potentials where preannihilation ECl is observed) a large peak which rapidly decays to low emission intensities during the step is

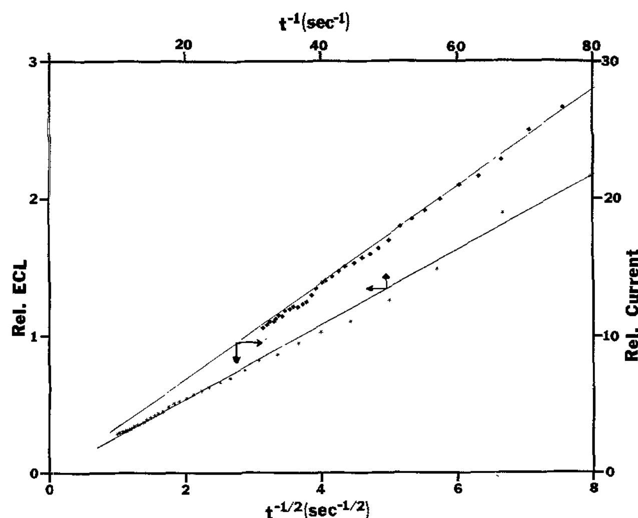

Fig. 7. ECL-time and current time profiles obtained with *ca.* 1 mmole $R^{\cdot +}$ in 0.1M TBAP/benzene-BZN by a cathodic potential step from +1.0V *vs.* SCE to −0.7V *vs.* SCE on n-ZnO. Current, ■; emission, *.

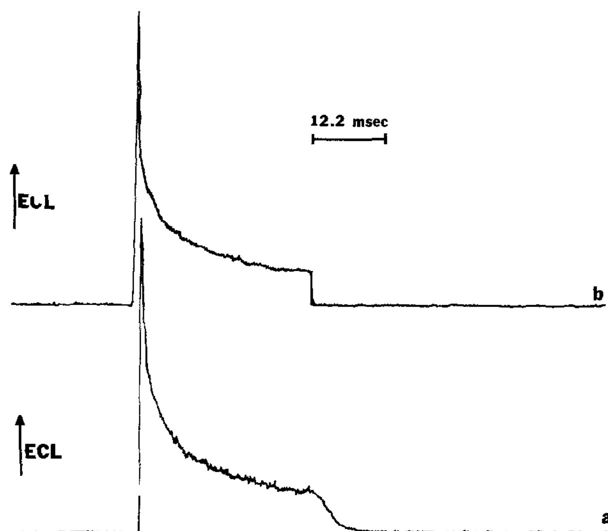

Fig. 8. ECL-time profiles obtained by cathodic potential steps to −1.1V *vs.* SCE with 1.5 mmoles $R^{\cdot +}$ in 0.1M TBAP/benzene-BZN on platinum. (a) Current interruption was employed after 30 msec. (b) Anodic potential step to 0.0V *vs.* SCE was employed after 30 msec.

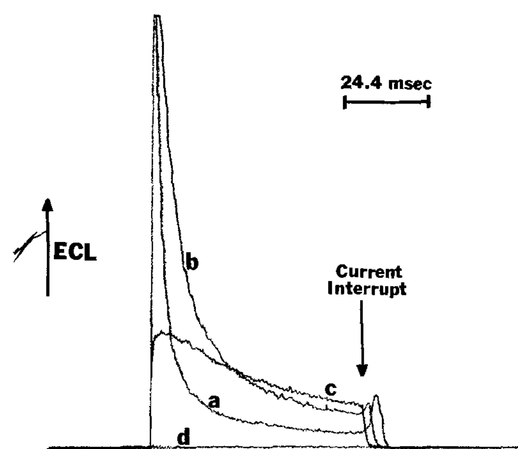

Fig. 9. ECL-time profiles obtained by cathodic potential steps n-CdS with *ca.* 1 mmole $R^{\cdot +}$ in 0.1M TBAP/BZN. Current interruption employed after 60 msec. Cathodic potential: (a) −0.92V *vs.* SCE, (b) −0.62V *vs.* SCE, (c) −0.47V *vs.* SCE, (d) −0.27V *vs.* SCE.

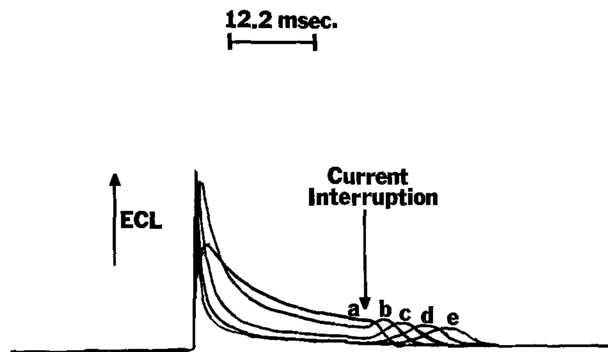

Fig. 10. ECL-time profiles obtained by cathodic potential steps on n-ZnO with $R^{+\cdot}$ in 0.1M TBAP/benzene-BZN. Current interruption was employed after 30 msec. Cathodic potential: (a) −0.3V *vs.* SCE, (b) −0.4V *vs.* SCE, (c) −0.5V *vs.* SCE, (d) −0.6V *vs.* SCE, (e) −0.7V *vs.* SCE.

observed (Fig. 9a and b, Fig. 10b-e). Upon interruption the emission decays or remains small for a time, but then a new emission peak, which occurs while the electrode is at open circuit, appears. This second, "echo" peak occurs at progressively later times after current interruption, the more negative is E_1. If, rather than using current interruption, the electrode was stepped to more positive potentials following the cathodic step, the emission would decay abruptly when the final potential was well positive of the emission peak potential (*e.g.*, 0.0V). However, when the second potential step was to a value at or near the emission peak, a second emission on the positive potential step occurred. Thus, for example, when $E_1 = -0.7$V on n-ZnO the effective decay time of emission on interruption was as long as 14 msec. However, when the potential was stepped to +1.1V, the emission decayed in about 95 μsec. Similar behavior was found with the semiconductor electrodes with triangular potential ramps (*i.e.*, cyclic voltammetry) (Fig. 11). When the scan direction was reversed following the emission peak, the emission again increased (although the cathodic current decreased on reversal) at potentials near the original emission maximum.

Discussion

The results obtained can be rationalized based on the known energetics of the rubrene system and the band structure of the semiconductors (Fig. 12). In this model there are different potential regions of the semiconductor electrode of interest. At positive potentials, just above the E° of the R^+/R couple, the number of electrons at the electrode-solution interface is small and no overlap between semiconductor levels and solution levels exists. Here no current flow or emission is observed. At somewhat more negative potentials the Fermi energy of the electrode is sufficient to populate an intermediate level or surface states, which leads to reduction of $R^{+\cdot}$ to the ground

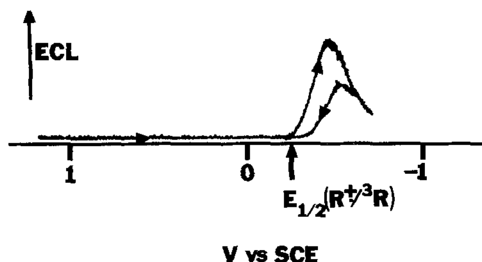

Fig. 11. ECL-potential profile obtained with concurrent cyclic voltammetry from +1.2V *vs.* SCE to −0.7V *vs.* SCE on n-CdS with *ca.* 1 mmole $R^{+\cdot}$ in 0.1M TBAP/BZN. Scan rate is 2 V/sec.

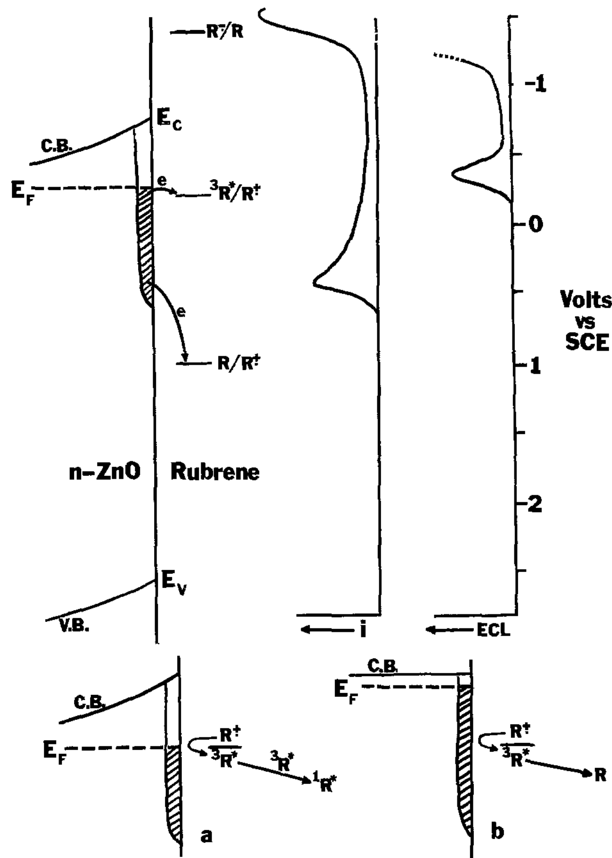

Fig. 12. Model for reduction of $R^{+\cdot}$ on n-ZnO. The current is proportional to the diffusion-limited reduction of $R^{+\cdot}$ to the ground state species and the ECL commences at potentials where $^3R^*$ is accessible (a) by electron transfer from the surface state. At more negative potentials (b) the excited states are more effectively quenched by the increased density of states at the electrode-solution interface.

state molecule, and a cathodic current is observed. The potential in this region is not sufficient to produce excited states, however. At more negative potentials the excited triplet species is thermodynamically accessible via surface states (the potential is still well positive of V_{fb}). Current continues to flow and is proportional to the flux of $R^{+\cdot}$ to the electrode. ECL emission is observed as the triplet species annihilate to yield the emitting singlet species. At still more negative potentials, however, as the surface states become more populated and the Fermi level approaches the conduction bandedge, the electrode becomes an effective quencher of the triplet states and the emission intensity increases. This explains the peak-shaped emission curve found on potential sweeps where the emission maximum occurs at potentials just at the $R^{+\cdot}/^3R$ potential. This model also explains the interruption experiments and the echo signals which appear at open circuit. Upon a potential step to potentials beyond the emission maximum the electrode is in a quenching mode and the emission decays to low levels. Upon interruption the Fermi level in the semiconductor begins to relax to that of the solution governed by the $R^{+\cdot}/R$ couple, by transfer of electrons to $R^{+\cdot}$ (coulostatic discharge). When E_F passes through the region of the $R^{+\cdot}/^3R$ potential, emission is observed. This potential drift was verified by independently monitoring the open-circuit potential of the n-ZnO electrode after a potential step to −0.93V *vs.* SCE followed by current

interruption. Thus, the time dependence of emission and the potential at open circuit monitors the rate of equilibration of the semiconductor electrode with the solution. The model further suggests that a semiconductor electrode can also act as an efficient quencher of excited states via surface or intermediate levels as well as via the conduction and valence band. The final potential region of interest is that well negative of V_{fb} where the electrode becomes degenerate. $R^{\overline{\cdot}}$ is produced and emission via annihilation ECL in the bulk solution well away from the quenching electrode surface is observed.

That ECL emission by direct heterogeneous production of excited states on semiconductor electrodes is not observed with the other systems examined can also be rationalized by this model. The critical restraints for excited state production and emission on semiconductor electrodes are (*i*) the oxidized form of the parent-emitting species must be reducible at a surface state at energies within the gap at a potential to provide sufficient energy to populate the excited state species and (*ii*) this reduction must occur at potentials well positive of the flatband potential where the electrode is not degenerate and quenching by the electrode is less favorable. Competitive reductions of the oxidized species to ground state species by surface states must also be considered in evaluating the lack of observable ECL emission by the direct heterogeneous production of excited states on semiconductor electrodes in some systems. Moreover, evidence for direct excited state production probably requires a sufficiently stable oxidized species which is reducible to a triplet state undergoing triplet-triplet annihilation to form the emitting singlet, since direct reduction to a singlet state will frequently occur at potentials negative to V_{fb} and near potentials where annihilation ECL is possible. We conclude that it will be difficult to find many examples of direct excitation although the process is possible and that the efficiency of emission via this route will be small.

We might comment on other possible explanations for the results presented here. One might suggest production of ^3R via a discrete surface level of energy, E_T, which is only rapidly filled when E_F is near this level. At more negative potentials one would have to invoke a slower filling of the level and hence decreased emission, even when $E_F > E_T$. However, this model does not agree with past results on reductions of couples with potentials located in the gap region (20, 21), with the observed reduction of R^+ to the ground state at more positive potentials, and with the lack of perturbation of the cathodic current for potential steps into this region.

A second possible explanation for the potential dependence of the emission invokes the electrogeneration of quenchers at potentials just negative of where the emission is observed. In this case, however, the quencher concentration would be expected to be large enough after the cathodic potential step to diminish significantly the emission upon a subsequent anodic pulse or sweep. This is contrary to experimental observations. Moreover, the generation of quenchers might shift the emission potential or alter the emission peak shape in separate experiments at different rubrene concentrations, but this was not observed.

The model predicts that the quenching of excited states at a semiconductor electrode should be potential dependent and this could probably be tested in photoexcitation experiments. Moreover, observation of the rate of relaxation of an electrode at open circuit following a potential step may be useful in determining the extent to which surface states mediate electron transfer at the liquid/semiconductor junction.

Acknowledgment

The authors wish to thank Professor H. Gerischer for his enlightening conversations concerning this work and Paul Kohl for the flatband potential measurements. The support of this research by the Army Research Office is gratefully acknowledged.

Manuscript submitted March 21, 1978; revised manuscript received May 1, 1978.

Any discussion of this paper will appear in a Discussion Section to be published in the June 1979 JOURNAL. All discussions for the June 1979 Discussion Section should be submitted by Feb. 1, 1979.

Publication costs of this article were assisted by The University of Texas at Austin.

REFERENCES

1. T. Kuwana, in "Electroanalytical Chemistry," Vol. 1, A. J. Bard, Editor, chap. 3, Marcel Dekker, Inc., New York (1966).
2. A. J. Bard, K. S. V. Santhanam, S. A. Cruser, and L. R. Faulkner, in "Fluorescence," G. G. Guilbault, Editor, chap. 14, Marcel Dekker, New York (1966).
3. A. Zweig, *Adv. Photochem.*, **6**, 425 (1968).
4. E. A. Chandross, *Trans. N.Y. Acad. Sci., Ser. 2*, **31**, 571 (1969).
5. D. M. Hercules, *Acc. Chem. Res.*, **2**, 301 (1969).
6. D. M. Hercules, in "Physical Methods of Organic Chemistry," 4th ed., Part II, A. Weissberger and B. Rossiter, Editors, Academic Press, New York (1977).
7. A. J. Bard and L. R. Faulkner, in "Electroanalytical Chemistry," Vol. 10, A. J. Bard, Editor, chap. 1, Marcel Dekker, Inc., New York (1977).
8. L. R. Faulkner, in *MTP Int. Rev. Sci., Phys. Chem., Ser. Two*, **9** (1976).
9. M. Gleria and R. Memming, *Z. Phys. Chem.*, **101**, 171 (1976).
10. L. S. R. Yeh and A. J. Bard, *Chem. Phys. Lett*, **44**, 339 (1976).
11. E. A. Chandross and R. E. Visco, *J. Phys. Chem.*, **72**, 378 (1968).
12. R. A. Marcus, *ibid.*, **43**, 2654 (1965).
13. (a) R. R. Chance, A. Prock, and R. Sibley, *ibid.*, **60**, 2744 (1974); (b) K. H. Drexhage, H. Kuhn, and F. P. Schäfer, *Ber. Bunsenges. Phys. Chem.*, **72**, 329 (1968).
14. (a) A. Zweig, D. L. Maricle, J. S. Brinen, and A. H. Maurer, *J. Am. Chem. Soc.*, **89**, 473 (1967); (b) D. L. Maricle and A. H. Maurer, *ibid.*, **89**, 118 (1967).
15. R. E. Visco and E. A. Chandross, *Electrochim. Acta*, **13**, 1187 (1968).
16. D. M. Hercules, R. C. Lansbury, and D. K. Roe, *J. Am. Chem. Soc.*, **88**, 4578 (1966).
17. E. W. Grabner, *Electrochim. Acta*, **20**, 7 (1975).
18. R. Lansberg, P. Janietz, and R. Dehmlow, *J. Electroanal. Chem.*, **65**, 115 (1975).
19. S. M. Park and A. J. Bard, *J. Am. Chem. Soc.*, **97**, 2978 (1975).
20. S. N. Frank and A. J. Bard, *ibid.*, **97**, 7427 (1975).
21. P. A. Kohl and A. J. Bard, *ibid.*, **99**, 7531 (1977).
22. L. R. Faulkner, *This Journal*, **124**, 1724 (1977).
23. D. K. K. Liu and L. R. Faulkner, *J. Am. Chem. Soc.*, **99**, 4594 (1977).
24. J. F. Dewald, *Bell Syst. Tech. J.*, **39**, 615 (1960).
25. J. N. Demas and G. A. Crosby, *J. Mol. Spectrosc.*, **26**, 72 (1968).
26. F. E. Lytle and D. M. Hercules, *J. Am. Chem. Soc.*, **91**, 253 (1969).
27. J. M. Bonnier and R. Jardon, *J. Chim. Phys. Physiochim. Biol.*, **68**, 428 (1971).
28. S. L. Murov, in "Handbook of Photochemistry," p. 10, Marcel Dekker, New York (1973).
29. L. R. Faulkner, H. Tachikawa, and A. J. Bard, *J. Am. Chem. Soc.*, **94**, 691 (1972).

Electrogenerated Chemiluminescence

XXXII. ECL from Energy-Deficient Aromatic Hydrocarbon Acceptor and Tetrathiafulvalene Donor Systems

William L. Wallace and Allen J. Bard*

Department of Chemistry, The University of Texas at Austin, Austin, Texas 78712

ABSTRACT

The ECL emission from energy-deficient mixed aromatic hydrocarbon (AHC) acceptor and tetrathiafulvalene (TTF) donor systems has been investigated in acetonitrile. Radical ion annihilation involving TTF radical cations and AHC radical anions was found to result entirely in acceptor fluorescence emission. Energy considerations show that AHC triplet formation followed by triplet-triplet annihilation to produce the AHC first excited singlet state is the most probable mechanism for the observed ECL. The intermediacy of exciplexes in the ECL process was not observed experimentally.

Tetrathiafulvalene (TTF) has been the subject of intense investigation for its role as a donor in highly conducting one-dimensional solid-state complexes (1-3), such as, for example, its simple salt with tetracyanoquinodimethane (TTF-TCNQ) (4). These conducting salts form a class of ground state organic charge transfer complexes. Less is known about the potential of TTF as a donor in excited state reactions such as: (*i*) the formation of excited state complexes (exciplexes) via direct photoexcitation; and (*ii*) the formation of excited states via radical ion annihilation involving electron transfer from acceptor radical anions ($A^{\overline{\cdot}}$) to donor radical cations ($D^{\dot{+}}$), electrogenerated chemiluminescence (ECL). As judged from its ionization potential (6.95 ± 0.1 eV) (5) and oxidation potential (+0.33V *vs.* SCE, 0.1*M* TEAP in acetonitrile) (6) the donor strength of TTF should be comparable to that of amines (*e.g.*, IP = 6.86 eV for triphenylamine and 7.50 eV for triethylamine) (7) which as a donor class have been observed to form exciplexes efficiently in both the photoexcitation (8-11) and ECL (12-17) modes. Many examples of ECL generation in mixed systems using amines as donors have been investigated (12-15) and on a purely speculative basis, behavior similar to that using N,N,N',N'-tetramethyl-*p*-phenylenediamine (TMPD) as a donor ($E_{p,a}$ = +0.24V *vs.* SCE, 0.1*M* TBAP in DMF) (12) might be expected for TTF.

In addition a major goal in ECL studies has been to search for donors and acceptors which form highly stable radical ions in an attempt to extend the long-term lifetime of ECL systems (18, 19). The stability of the TTF radical cation by controlled potential reversal bulk coulometry on a time scale of a few hours has previously been observed (20) which makes it considerably more stable than amine oxidation in general [TMPD (16) and tri-*p*-tolylamine (TPTA) (17) are exceptions]. The stability of mixed TTF donor-acceptor ECL systems is therefore of interest. The following work represents a survey of mixed ECL systems consisting of TTF as the donor and various aromatic hydrocarbons as acceptors in acetonitrile solution undertaken as an initial effort to characterize TTF as a donor in excited state reactions.

Experimental

Chemicals.—Rubrene (Aldrich) was dissolved in hot xylene and precipitated with cold ethanol under nitrogen in subdued light twice. $Ru(bipy)_3(ClO_4)_2$ was prepared by metathesis with excess $NaClO_4$ in a water-ethanol mixture from $Ru(bipy)_3Cl_2 \cdot 6H_2O$ purchased from G. F. Smith Chemical Company. Further purification of $Ru(bipy)_3(ClO_4)_2$ was accomplished by two recrystallizations from acetonitrile. Anthracene (Matheson, Coleman, and Bell) was recrystallized once from benzene and sublimed twice. Diphenylanthracene (DPA; Aldrich) was sublimed twice and then zone-refined. Dimethylanthracene (DMA; Aldrich, 99%) was sublimed twice under vacuum at 120°C. *Trans*-stilbene was sublimed twice before use. Tetrathiafulvalene (Aldrich) was either sublimed twice under high vacuum at 60°C or was first recrystallized once from dry, degassed hexane and then sublimed twice. No difference in experimental results was observed between the two purification procedures. Tetra-*n*-butylammonium perchlorate (TBAP) purchased from Southwestern Analytical Chemical Company was used as received after drying under vacuum at 100°C for 24 hr. Benzonitrile and acetonitrile were both purchased from Matheson, Coleman, and Bell. A previously reported procedure was used to purify benzonitrile (21). Acetonitrile was dried and degassed by three transfers from dry P_2O_5 under vacuum. The solvent was stored under vacuum or in an inert helium atmosphere. Benzene (Fisher) and tetrahydrofuran (Matheson, Coleman, and Bell) were refluxed over sodium-benzophenone and subsequently distilled and stored in an inert nitrogen or helium atmosphere.

Apparatus and procedures.—Cyclic voltammetry and ECL experiments were carried out in the controlled potential mode using a Princeton Applied Research (PAR) Model 173 potentiostat and a Model 175 universal programmer. The voltage analog output from a PAR Model 176 current follower was either recorded directly using a Houston Instrument Model 2000 X-Y recorder or monitored and subsequently recorded via a Nicolet Model 1090A digital oscilloscope. Electrochemical cells of a conventional three-electrode design were used for cyclic voltammetry and ECL and were similar to ones previously described (22, 23). Emission spectra, fluorescence, and ECL were obtained using an Aminco-Bowman spectrophotofluorometer.

Solutions were prepared under an inert helium atmosphere in a Vacuum Atmospheres Model HE-43-2 dry box. Since TTF was found to undergo photodecomposition in dry degassed solutions of acetonitrile, ECL solutions were exposed to a minimum of room light. A background cyclic voltammogram was taken of the solvent-supporting electrolyte (0.1*M* TBAP) system before each study to insure the absence of residual oxygen and electroactive trace contaminants. ECL was generated in the pulse mode (cyclic double

* Electrochemical Society Active Member.
Key words: chemiluminescence, ECL, organic free radicals.

Table I. Electrochemical parameters for various acceptors in the presence and absence of TTF

	Oxidation[a]			Reduction[a]		
Compound	E_{pa} (V)[b] ±0.02	ΔE_p (mV) ±5	i_{pc}/i_{pa} ±5%	E_{pc} (V)[b] +0.02	ΔE_p (mV) ±5	i_{pa}/i_{pc} ±5%
Anthracene	+1.22	—	—	−2.12	70	0.91
	(+1.25)	—	—	(−2.09)	(70)	(0.87)
Rubrene[c]	+0.83	110	0.99	−1.63	100	0.92
	(+0.83)	(100)	—	(−1.65)	(100)	(0.93)
DMA	+1.07	80	0.83	−2.12	70	0.93
	(+1.07)	(80)	(0.87)	(−2.14)	(80)	(0.94)
DPA	+1.17	70	0.93	−2.04	70	0.99
	(+1.17)	(70)	(0.79)	(−2.03)	(70)	(0.98)
trans-stilbene[d]	+1.43	—	—	−2.37	70	0.98
	(+1.45)	—	—	(−2.30)	(60)	(0.66)
$Ru(bipy)_3^{+2}$	+1.28	70	1.0	−1.41	70	0.90
	(+1.25)	(70)	(0.94)	(−1.46)	(70)	(0.85)

[a] Values in parenthesis are for the acceptor in the presence of TTF. Solutions contain 0.1*M* TBAP in acetonitrile unless otherwise noted. Acceptor concentrations are in the range 3.4×10^{-3}-$1.2 \times 10^{-2}M$. TTF concentrations are in the range 2.1×10^{-3}-$7.1 \times 10^{-3}M$.

[b] Cyclic voltammetric peak potentials using a Pt disk electrode in V *vs.* Ag QRE corrected to V *vs.* SCE using $E_{pa}(TTF^+/TTF) = +0.34V$ *vs.* SCE.

[c] In benzonitrile.

[d] [*Trans*-stilbene] = $8.2 \times 10^{-3}M$; [TTF] = $2.1 \times 10^{-3}M$.

potential step waveform) and in general ECL experiments were carried out on the same solutions previously characterized by cyclic voltammetry.

Results

Electrochemistry.—The electrochemical parameters listed in Table I show that except for the case of *trans*-stilbene and TTF, the interaction of donor and acceptor neutral and radical ion species on the cyclic voltammetric time scale is small. Values of E_p and ΔE_p, cyclic voltammetry peak potentials and peak separations, and i_{pc}/i_{pa} or i_{pa}/i_{pc}, peak current ratios for oxidation and reduction, respectively, were monitored for the acceptor in the presence and absence of TTF and show only slight variations. Deviations from ideal electrochemical behavior (*e.g.*, $\Delta E_p > 60$ mV) or slight shifts in values of E_p can be attributed to: (*i*) uncompensated cell resistance as in the case of using benzonitrile as a solvent; or (*ii*) the use of an unshielded Ag quasireference electrode in contact with the bulk electrochemical solution. For most of the systems examined, including *trans*-stilbene and TTF, values for ΔE_p and i_{pc}/i_{pa} for the two reversible one-electron oxidations of TTF were 70 mV and 1.00 ± 0.02, respectively, both in the absence and presence of the various acceptors. The only exception occurred for TTF in benzonitrile in which the second TTF oxidation wave overlapped with the first oxidation wave of rubrene and a large cathodic current spike was observed for dication reduction upon potential reversal. Large cathodic current spikes for the reduction of the TTF dication were frequently observed in nonpolar solvents and nonpolar solvent mixtures, such as tetrahydrofuran and benzene-acetonitrile (50:50). Unfavorable electrochemistry for TTF oxidation prevented ECL experiments in pure tetrahydrofuran. Under the experimental conditions of cell design and at a potential scan rate of 200 mV sec^{-1}, a value of 70 mV represents the peak separation expected for a reversible one-electron transfer in acetonitrile.

Examination of Table I reveals that in some cases values of i_{pa}/i_{pc} for reduction of the acceptor in the presence of TTF are significantly less than in the absence of TTF. Such behavior is represented in the extreme case by the *trans*-stilbene-TTF system in which increasing the concentration of TTF results in increasing values of i_{pc} and decreasing values of i_{pa}/i_{pc}. Limiting behavior for [TTF] > [*trans*-stilbene] is characterized by the complete absence of anodic current upon potential reversal following *trans*-stilbene reduction and by values of $i_{pc}/v^{1/2}$ which are approximately 2.8-3.0 times larger than those in the absence of TTF. A plot of $i_{pc}/v^{1/2}$ *vs.* log v was approximately linear (slight curvature was observed for extreme high and low values of v) for a solution consisting of $5.4 \times 10^{-3}M$ TTF, $1.2 \times 10^{-2}M$ *trans*-stilbene, and 0.1*M* TBAP in acetonitrile. The reaction(s) represented by these results have not been thoroughly investigated but the electrochemical data is consistent with a reaction of the *trans*-stilbene radical anion with TTF neutral as a first step forming a product which undergoes further reduction. A similar reaction may occur to a much lower degree in some of the other aromatic hydrocarbon acceptor-TTF systems.

Figures 1 and 2 illustrate the cyclic voltammograms resulting from the two extreme cases of electrochemical behavior observed in this investigation: (*i*) slightly interacting, anthracene-TTF; and (*ii*) strongly

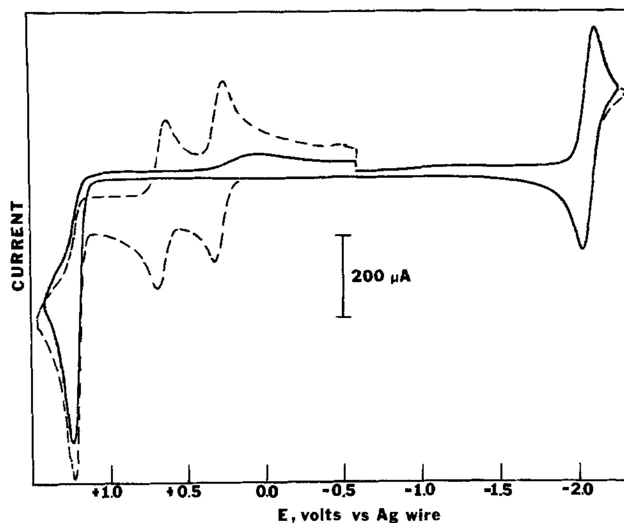

Fig. 1. First scan cyclic voltammograms of (———) $1.2 \times 10^{-2}M$ anthracene and (– – –) $1.2 \times 10^{-2}M$ anthracene and $7.1 \times 10^{-3}M$ TTF in a 0.1M TBAP-acetonitrile supporting electrolyte-solvent system using a scan rate of 200 mV sec^{-1}.

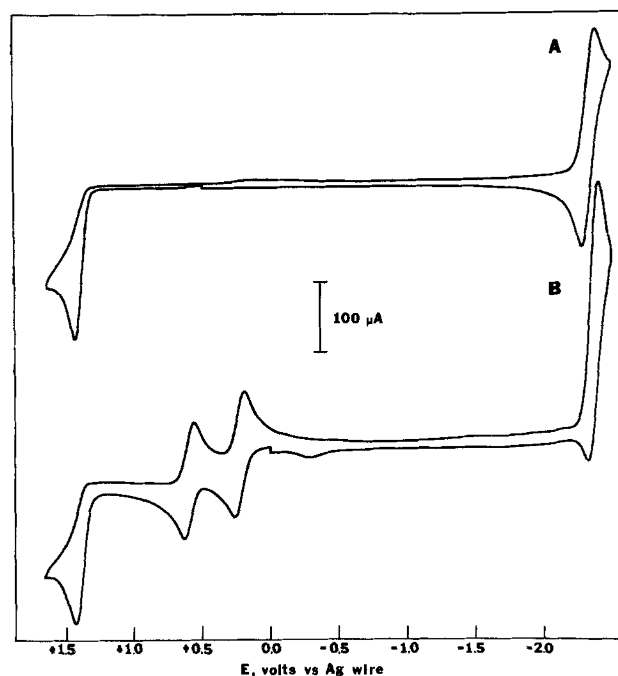

Fig. 2. First scan cyclic voltammograms of (A) $1.1 \times 10^{-2}M$ *trans*-stilbene; and (B) $1.1 \times 10^{-2}M$ *trans*-stilbene and $4.9 \times 10^{-3}M$ TTF in a 0.1M TBAP-acetonitrile supporting electrolyte-solvent system using a scan rate of 200 mV sec^{-1}.

interacting, *trans*-stilbene-TTF. In Fig. 1 and 2 a small cathodic wave in the range 0.0-+0.50V *vs.* Ag QRE is observed upon potential reversal following the anodic scan in the absence and presence of TTF. These waves can be attributed to the reduction of an oxidation product of the unstable anthracene and *trans*-stilbene radical cations. An anodic wave at −0.4V *vs.* Ag QRE found after potential reversal following *trans*-stilbene reduction is also observed for *trans*-stilbene in the presence of TTF. For all of the systems examined except *trans*-stilbene and TTF no additional product waves are observed when the applied potential limits are set to allow only the one electron oxidation of the donor (TTF) and the one electron reduction of the acceptor (AHC).

ECL.—Of the six donor-acceptor systems examined in this work, four exhibited ECL. The ECL was generated in the controlled potential mode employing a cyclic double potential step waveform alternately generating the acceptor radical anion and the donor radical cation. The ECL spectra obtained for three of the systems in Table II are shown in Fig. 3. The luminescence in all three cases can be attributed entirely to DPA, DMA, and rubrene fluorescence when reabsorption at the appropriate donor-acceptor concentrations is taken into account. In the case of DMA an additional component due to excimer emission contributes to the ECL spectrum. The observed spectral distributions, relative peak intensity ratios, and peak energies compare well with previously published ECL spectra of the isolated acceptors (12, 24, 25). The ECL spectra also essentially match the fluorescence spectra taken of the original electrochemical bulk solutions either at full concentration or diluted by a factor of 1/10 in a 1.00 cm path length fluorescence cell taken using a right angle illumination geometry. In addition fluorescence spectra of the bulk electrochemical solutions compare well in spectral distribution and peak energies with fluorescence spectra of the isolated acceptors taken in acetonitrile or other solvents (24, 26). The ECL spectrum of TTF and DMA was also taken in a relatively nonpolar acetonitrile-tetrahydrofuran (40:60) solvent mixture, and within experimental error it was identical in spectral distribution with the spectrum obtained in pure acetonitrile. A complete ECL spectrum of anthracene-TTF could not be obtained due to rapid decay of the ECL emission; however, emission was observed at a wavelength of 400 nm when the working electrode was pulsed between potential limits corresponding to the generation of $TTF^{+\cdot}$ and the anthracene radical anion.

In all cases where ECL is observed, emission is clearly the result of TTF radical cation-acceptor radical anion annihilation as the anodic potential is varied from a point where no faradaic oxidation processes occur toward more positive potentials. The onset of spectrophotofluorometric detection of ECL always corresponded to the onset of anodic current for TTF oxidation. Extending the anodic potential limit to values which cause TTF dication or acceptor radical cation formation resulted in either a rapid decrease in the peak ECL intensity as a function of potential, as in the case of DPA-TTF, or in a gradual decrease in ECL intensity, as in the case of DMA-TTF. Intensity enhancements at potentials more positive than $TTF^{+\cdot}$ production were never observed.

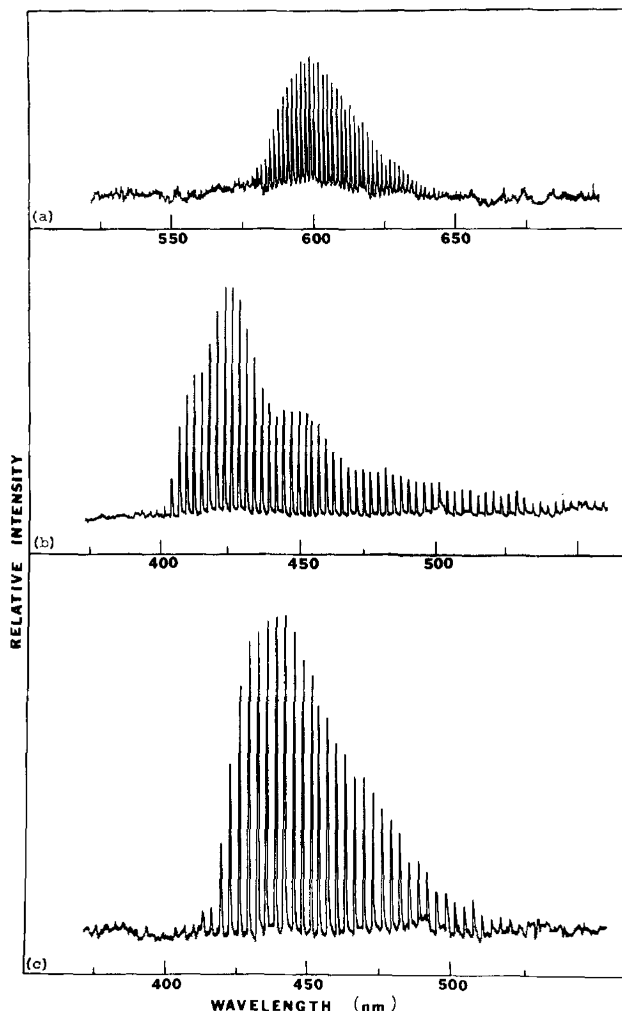

Fig. 3. ECL spectra of (a) $5.0 \times 10^{-3}M$ rubrene and $2.2 \times 10^{-3}M$ TTF, pulse width = 500 msec; (b) $2.4 \times 10^{-3}M$ DMA and $1.9 \times 10^{-3}M$ TTF, pulse width = 500 msec; and (c) $4.3 \times 10^{-3}M$ DPA and $5.9 \times 10^{-4}M$ TTF, pulse width = 500 msec; all in acetonitrile containing 0.1M TBAP; spectrophotofluorometer bandpass = 5 nm.

Peak ECL intensities for all the TTF-aromatic hydrocarbon systems monitored under continuous pulsing conditions on a time scale of a few minutes to 1 hr

Table II. Electrochemical and excited state energy parameters for TTF-acceptor ECL systems

Compound	$E_p(A^+/A)^a$ (V *vs.* SCE)	$E_p(A/A^-)^a$ (V *vs.* SCE)	$E(^1A^*)^b$ (eV)	$E(^3A^*)^d$ (eV)	$-\Delta H°$ $(A^-\ldots D^+)^f$ (eV)	ECL
Anthracene	+1.25	−2.09	3.3	1.8	2.27	Yes (unstable)
Rubrene	+0.83	−1.65	2.2	1.2	1.83	Yes
DMA	+1.07	−2.14	3.10[c]	1.80[c]	2.32	Yes
DPA	+1.17	−2.03	3.0	1.8	2.21	Yes
Trans-stilbene	+1.45	−2.30	3.8	2.0	2.48	No
$Ru(bipy)_3^{+2}$	+1.25	−1.41	—	2.04[e]	1.59	No

[a] Cyclic voltammetry peak potentials from Table I.
[b] Singlet energies from Ref. (38), unless otherwise noted.
[c] Reference (13).
[d] Triplet energies from Ref. (31) unless otherwise noted.
[e] Reference (39).
[f] Free enthalpy for radical ion annihilation in eV taking $E_{pa}(D^+/D)$ for TTF as +0.34V *vs.* SCE in acetonitrile (0.1*M* TBAP) and using $-\Delta H° = E_p(D^+/D) - E_p(A/A^-) - 0.16$, see Ref. (15).

decayed to zero intensity in a few hundred pulses or less. ECL emission in these mixed systems in acetonitrile was always observed to occur on only one pulse polarity which was usually, but not consistently, anodic. Emission could not be observed on the opposite polarity pulses except under the most sensitive spectrophotofluorometric conditions. Observation of emission only on anodic pulses might be attributed to instability of the TTF radical cation relative to that of the aromatic hydrocarbon radical anion; however, on the cyclic voltammetric time scale such instability is not observed. Only the aromatic hydrocarbon radical anions exhibited significant instability as judged by peak current ratios (see Table I). Correlated to the decrease in ECL intensity with time under continuous pulsing conditions was the buildup of a layer of colored material in the solution surrounding the working electrode. Cyclic voltammetry showed no new peaks or product waves associated with the colored material and presumably it arises from the accumulation of excess stable radical ion ($TTF^{\dot{+}}$ or $AHC^{\dot{-}}$) with time. Prolonged pulsing resulted in product formation observed as a gray precipitate of unknown composition in the TTF-DMA and TTF-DPA systems.

Discussion

Listed in Table II are the cyclic voltammetric peak potentials for the first oxidation and reduction waves of several acceptor compounds deemed suitable for study in this work. Also tabulated are the acceptor singlet and triplet energies and the enthalpies for radical ion annihilation for the reaction between the TTF radical cation and the acceptor radical anion to produce ground state products. The calculated enthalpies for radical ion annihilation are based on experimental data obtained in this work and represent the maximum excess energy available for donor or acceptor excited state production in the radical ion annihilation reaction.

Examination of the data in Table II reveals several important aspects of ECL production using TTF as a donor. Note that the cyclic voltammetry peak potentials for the first oxidation wave of all the acceptors fall well outside the first oxidation wave for TTF; therefore, no interference is to be expected from the acceptor in generating $TTF^{\dot{+}}$. In only one case (TTF-rubrene) does overlap occur between the acceptor first oxidation and TTF second oxidation waves. In addition, TTF is not reduced within the potential range available for the acetonitrile-TBAP solvent-supporting electrolyte system and therefore cannot interfere with acceptor reduction. These conditions insure that with the appropriate selection of potential limits the reaction between the donor radical cation and the acceptor radical anion may be probed exclusively.

Comparison of ΔH° values with the excited state energies listed in Table II shows that in no case is the energy release during radical ion annihilation sufficient to populate the acceptor excited singlet state; however, in most systems (the first five in Table II) the acceptor first excited triplet state may be attained. The situation for TTF is less clear since the excited state singlet and triplet energies for this molecule are not well defined. To our knowledge fluorescence and low temperature phosphorescence studies of TTF are absent in the literature. Our own fluorescence studies at room temperature show weak emission from 10^{-3} to $10^{-4}M$ deaerated acetonitrile solutions of TTF in the range 300-500 nm. The spectral distribution of this emission was dependent on excitation wavelength and irradiation time (photolysis of $10^{-4}M$ acetonitrile solution via the unfiltered output of a 450W Xe lamp) and can be attributed predominantly to impurity fluorescence. The disappearance of TTF as a function of irradiation time can be followed by absorption spectroscopy and correlates with increasingly efficient Rayleigh scattering and formation of cloudy photolysis solutions. Results of a low temperature phosphorescence study of $10^{-4}M$ TTF in methyltetrahydrofuran at 77°K were similarly inconclusive. Although phosphorescence was observed, the spectral distribution of the emission was again a function of excitation wavelength and irradiation time. It should be mentioned that the fluorescence observed in TTF solutions was too weak to contribute significantly to fluorescence spectra of mixed TTF-acceptor solutions and was never observed in ECL spectra.

Attempting to estimate the singlet energy of TTF from its absorption spectrum also presents problems. The longest wavelength low molar absorptivity coefficient band of TTF at 450 nm has been variously assigned to: (*i*) an $n \rightarrow \pi^*$ transition of the sulfur lone pair electrons (27); (*ii*) a symmetry forbidden singlet-singlet $\pi \rightarrow \pi^*$ transition of B_{1g} symmetry (28); and (*iii*) a composite of two weakly allowed spin-forbidden singlet-triplet $\pi \rightarrow \pi^*$ transitions of B_{2u} and B_{3u} symmetry (29). Self-consistent statistical exchange multiple-scattering calculations also lead to the prediction of a spectroscopically unobserved triplet state at approximately 1.7 eV (29). The discrepancy in the assignments for the low energy TTF absorption band has so far not been resolved by spectroscopic means.

If indeed the lowest lying excited singlet state in TTF can be correlated with the lowest energy absorption band (E_s = 2.58-2.8 eV), then the TTF singlet will be inaccessible in all the ECL systems examined in this study. The TTF triplet, which has been estimated to be 0.20-0.68 eV lower than the singlet by $X\alpha$-scattered wave calculations (30), could be accessible in several systems. If, however, the lowest energy TTF absorption band correlates with the lowest energy triplet, then neither the TTF singlet or triplet states could be populated in the systems examined. Population of a TTF excited state cannot be probed by ECL since no emission which could be attributed to TTF (or an impurity) was ever observed in the ECL spectra monitored in acetonitrile solution.

The observed ECL behavior for the six systems in Table II can be divided into two categories: (*i*) ECL is observed and corresponds entirely to emission from the aromatic hydrocarbon acceptor (first four systems); and (*ii*) ECL is not observed [TTF-*trans*-stilbene and TTF-Ru(bipy)$_3$(ClO$_4$)$_2$]. Of the systems in the first category the absence of emission other than acceptor fluorescence in the ECL rules out the formation of stable emitting excited state complexes (exciplexes) (although not exciplex formation itself). Exciplex emission in the long wavelength region of the TTF-DMA ECL spectrum in acetonitrile can be ruled out by the observation that within experimental error the spectral distribution is identical to that in the ECL spectra of DMA alone in acetonitrile and DMA-TTF in an acetonitrile-tetrahydrofuran (40:60) solvent mixture. An enhancement in the exciplex/monomer intensity ratio and a blue shift in exciplex emission would otherwise be expected in the less polar solvent (ϵ = 7.4 for tetrahydrofuran and ϵ = 36.7 for acetonitrile) (15). Excimer emission is considerably less affected by solvent polarity. The DMA excimer emission observed in the TTF-DMA ECL spectra is produced probably via triplet-triplet annihilation of $^3DMA^*$ as in the previously studied $DMA^{\dot{-}}/TPTA^{\dot{+}}$ (15) and $DMA^{\dot{-}}/TMPD^{\dot{+}}$ (16) systems. In addition, fluorescence studies of 10^{-3}-$10^{-4}M$ aromatic hydrocarbon solutions containing 10^{-3}-$10^{-1}M$ concentrations of TTF in acetonitrile, benzene, and tetrahydrofuran failed to produce definitive evidence for exciplex emission. Although apparent long wavelength emission was observed in solutions containing the highest TTF concentrations, reabsorption of acceptor fluorescence emission by TTF, not exciplex emission, was found to be

responsible. Both competitive absorption and reabsorption caused serious experimental difficulties in carrying out energy transfer studies in these systems.

Since the acceptor excited triplet states are accessible in all systems exhibiting ECL triplet-triplet annihilation is adequate to account for acceptor fluorescence in every case. Numerous investigations, including the study of magnetic field effects and energy deficient systems, have demonstrated the intermediacy of triplets in the ECL of rubrene (31, 32), DPA (31, 33), DMA (13, 16), and anthracene (31, 33) mixed systems. An over-all mechanism for ECL emission can be represented as follows

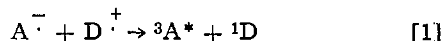

$$A^{\overset{-}{\cdot}} + D^{\overset{+}{\cdot}} \rightarrow {}^3A^* + {}^1D \quad [1]$$

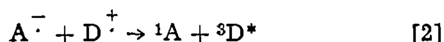

$$A^{\overset{-}{\cdot}} + D^{\overset{+}{\cdot}} \rightarrow {}^1A + {}^3D^* \quad [2]$$

$${}^3A^* + {}^3A^* \rightarrow {}^1A^* + {}^1A \rightarrow 2{}^1A + h\nu \quad [3]$$

Again note in Eq. [1] that the formation of acceptor excited singlet states can be omitted on the basis of energy considerations. Equation [2] necessarily includes the possibility of forming donor triplets; however, formation of TTF singlets cannot occur in the four systems exhibiting ECL.

The relatively rapid degradation of ECL intensity over a period of time under continuous pulsing conditions makes it amply clear that the reactions in Eq. [1]-[3] are not the only pathways available for donor-acceptor interaction. Numerous possibilities exist for chemical reactions leading to ECL degradation including: (*i*) direct interaction of neutral donor and acceptor molecules to form ground state complexes or other products; (*ii*) chemical reaction of radical ions either by first-order degradation processes or by reaction with neutral donor and acceptor molecules or other solution constituents including impurities; (*iii*) chemical reactions via radical ion annihilation; and (*iv*) photochemical reactions of donor and acceptor excited states produced by radical ion annihilation. The formation of ground state complexes incorporating TTF as a donor are well known and as previously mentioned form an important and highly studied class of conducting solid-state DA complexes. Formation of such DA complexes commonly occurs via reaction of the neutral substituents but can also occur as a radical ion reaction as, for example, in the reaction of electrogenerated $TTF^{\overset{+}{\cdot}}$ with X^- to form TTF halide salts (34, 35). Ground state complex formation by either method, however, or any other reaction between neutral donor and acceptor molecules is unsupported in the systems examined in this study by the electrochemical evidence. In addition, formation of strong DA complexes with the acceptors in this study is unlikely due to their relatively weak electron accepting ability. Furthermore, electrochemical data show that donor radical cations in the presence of neutral acceptor and acceptor radical anions in the presence of neutral donor are stable on a cyclic voltammetric time scale, with the one exception of *trans*-stilbene$^{\overset{-}{\cdot}}$ in the presence of TTF neutral. However, even though evidence for a chemical reaction cannot be observed in initial mixed donor-acceptor solutions, product formation is observed after electrochemistry, possibly indicating the contribution of radical ion reactions on a long-time scale. The possible contribution of photochemical reactions to over-all ECL degradation cannot be easily probed; however, the reactivity of TTF excited state(s) appears to be established in this and other studies (5, 36) and must be taken into account. An analysis of the products formed in the ECL systems examined in this study will be necessary to elucidate precisely the specific pathway(s) involved in the observed degradation behavior. It should be noted that in general studies defining the stabilities of radical ions on a cyclic voltammetric or even bulk coulometric time scale will not necessarily be of use in predicting the stability of ECL systems.

Of the two systems which did not exhibit ECL the TTF-*trans*-stilbene system was chosen as a possibility for exhibiting exciplex emission. Observation of exciplex emission in the ECL from *trans*-stilbene radical anion and amine radical cation annihilation has been observed (15) enhancing the possibility of observing exciplex emission using TTF as a donor. The complete absence of emission from the *trans*-stilbene-TTF system seems to rule out the formation of a stable emitting exciplex. The *trans*-stilbene triplet state is accessible in this system; however, the short triplet lifetime at room temperature in fluid solution (37) is adequate to explain the absence of stilbene fluorescence via triplet-triplet annihilation. The most compelling reason for not observing ECL is the extreme reactivity of the *trans*-stilbene radical anion in the presence of TTF. A new product-forming route is opened for the radical anion which competes with radical ion annihilation and excited state formation. As stated previously, the evidence at this point indicates a reaction of the stilbene radical anion with neutral TTF forming a further reducible product

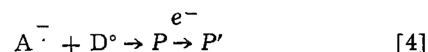

$$A^{\overset{-}{\cdot}} + D^\circ \rightarrow P \xrightarrow{e^-} P' \quad [4]$$

The $Ru(bipy)_3(ClO_4)_2$-TTF system was chosen as a test case. No ECL was expected for reaction with the TTF radical cation, although reaction with TTF^{+2} would just barely be energetic enough to produce the Ru(II) triplet state. No ECL is observed, however, pulsing between potential limits sufficiently anodic to produce $TTF^{\overset{+}{\cdot}}$, TTF^{+2}, or the Ru(III) complex. The lack of emission from the Ru(I)-Ru(III) reaction in the presence of TTF indicates that efficient quenching of either the Ru(I)-Ru(III) radical ion annihilation and/or of the Ru(II) excited triplet state takes place. A possible explanation for the lack of emission in the TTF^{+2}-Ru(I) annihilation reaction is the presence of the TTF radical cation in the solvent cage complex immediately after electron transfer leading to efficient quenching

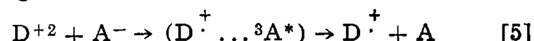

$$D^{+2} + A^- \rightarrow (D^{\overset{+}{\cdot}} \ldots {}^3A^*) \rightarrow D^{\overset{+}{\cdot}} + A \quad [5]$$

Acknowledgment

The support of this research by the Army Research Office is gratefully acknowledged.

Manuscript submitted Feb. 27, 1978; revised manuscript received April 10, 1978.

Any discussion of this paper will appear in a Discussion Section to be published in the June 1979 JOURNAL. All discussions for the June 1979 Discussion Section should be submitted by Feb. 1, 1979.

Publication costs of this article were assisted by The University of Texas at Austin.

REFERENCES

1. B. A. Scott, S. J. LaPlaca, J. B. Torrance, B. D. Silverman, and B. Welber, *J. Am. Chem. Soc.*, **99**, 6631 (1977).
2. E. M. Engler, *Chem. Technol.*, 274 (1976).
3. A. F. Garito and A. J. Heeger, *Acc. Chem. Res.*, **7**, 232 (1974).
4. J. Ferraris, D. O. Cowan, V. Walatka, Jr., and J. H. Perlstein, *J. Am. Chem. Soc.*, **95**, 948 (1973).
5. C. E. Klots, R. N. Compton, and V. F. Raaen, *J. Chem. Phys.*, **60**, 1177 (1974).
6. D. L. Coffen, J. Q. Chambers, D. R. Williams, P. E. Garrett, and N. D. Canfield, *J. Am. Chem. Soc.*, **93**, 2258 (1971).
7. J.-P. Blanchi and A. R. Watkins, *Chem. Comm.*, 265 (1974).
8. H. Knibbe, D. Rehm, and A. Weller, *Ber. Bunsenges. Physik. Chem.*, **72**, 257 (1968).
9. D. Rehm and A. Weller, *Isr. J. Chem.*, **8**, 259 (1970).

10. J. Saltiel, E. E. Townsend, B. D. Watson, P. Shannon, and S. L. Finson, *J. Am. Chem. Soc.*, **99**, 884 (1977).
11. N. C. Yang, D. M. Shold, and B. Kim, *ibid.*, **99**, 6587 (1977).
12. J. T. Maloy and A. J. Bard, *ibid.*, **93**, 5968 (1971).
13. C. P. Keszthelyi, N. E. Tokel-Takvoryan, H. Tachikawa, and A. J. Bard, *Chem. Phys. Lett.*, **23**, 219 (1973).
14. H. Tachikawa and A. J. Bard, *ibid.*, **26**, 568 (1974).
15. S. M. Park and A. J. Bard, *J. Am. Chem. Soc.*, **97**, 2978 (1975).
16. A. Weller and K. Zachariasse, *Chem. Phys. Lett.*, **10**, 197 (1971).
17. A. Weller and K. Zachariasse, *ibid.*, **10**, 424 (1971).
18. S. M. Park and A. J. Bard, *J. Electroanal. Chem.*, **77**, 137 (1977).
19. D. Laser and A. J. Bard, *This Journal*, **122**, 632 (1975).
20. M. R. Suchanski, Ph.D. Dissertation, Northwestern University, Evanston, Ill. (1977).
21. R. C. Larson and R. T. Swamoto, *J. Am. Chem. Soc.*, **82**, 3239 (1960).
22. N. E. Tokel, C. P. Keszthelyi, and A. J. Bard, *ibid.*, **94**, 4872 (1972).
23. T. H. Teherani, L. A. Tinker, and A. J. Bard, Paper submitted to *J. Electroanal. Chem.*
24. T. C. Werner, J. Chang, and D. M. Hercules, *J. Am. Chem. Soc.*, **92**, 763 (1970).
25. C. P. Keszthelyi and A. J. Bard, *This Journal*, **120**, 241 (1973).
26. C. P. Keszthelyi, N. E. Tokel-Takvoryan, and A. J. Bard, *Anal. Chem.*, **47**, 249 (1975).
27. R. Zaradnik, P. Carsky, S. Hunig, G. Kiesslich, and D. S. Scheutzow, *Int. J. Sulfur Chem., C*, **6**, 109 (1971).
28. R. Gleiter, E. Schmidt, D. O. Cowan, and J. P. Ferraris, *J. Electron Spectrosc. Relat. Phenom.*, **2**, 207 (1973).
29. B. I. Bennet and F. Herman, *Chem. Phys. Lett.*, **32**, 334 (1975).
30. P. S. Bagus and B. I. Bennet, *Int. J. Quant. Chem.*, **9**, 143 (1975).
31. L. R. Faulkner, H. Tachikawa, and A. J. Bard. *J. Am. Chem. Soc.*, **94**, 691 (1972).
32. H. Tachikawa and A. J. Bard, *Chem. Phys. Lett.*, **26**, 246 (1974).
33. L. R. Faulkner and A. J. Bard, *J. Am. Chem. Soc.*, **91**, 209 (1969).
34. J. Q. Chambers, D. C. Green, F. B. Kaufman, E. M. Engler, B. A. Scott, and R. R. Schumaker, *Anal. Chem.*, **49**, 802 (1977).
35. F. B. Kaufman, E. M. Engler, D. C. Green, and J. Q. Chambers, *J. Am. Chem. Soc.*, **98**, 1596 (1976).
36. B. A. Scott, F. B. Kaufman, and E. M. Engler, *ibid.* **98**, 4342 (1976).
37. A. Weller and K. Zachariasse, *Chem. Phys. Lett.*, **24**, 300 (1974).
38. D. J. Freed and L. R. Faulkner, *J. Am. Chem. Soc.*, **93**, 2097 (1971).
39. N. E. Tokel-Takvoryan, R. E. Hemmingway, and A. J. Bard, *ibid.*, **95**, 6582 (1973).

A Study of Anodic Dissolution of Gold in Aqueous Alkaline Cyanide

D. W. Kirk,* F. R. Foulkes,* and W. F. Graydon*

Department of Chemical Engineering and Applied Chemistry, University of Toronto, Toronto, Ontario, Canada M5S 1A4

ABSTRACT

The rate of dissolution of gold in aqueous alkaline cyanide solutions was studied as a function of potential within the range -0.9 to $+0.4$V *vs.* SCE. The dissolution rate was found to exhibit three maxima at -0.65, $+0.04$, and $+0.38$V *vs.* SCE. These maxima corresponded to three current peaks found in anodic potential sweep measurements. Data from weight loss measurements were used for the determination of the stoichiometry of the electrochemical dissolution reaction and showed that for the region -0.9 to $+0.6$V *vs.* SCE, $n = 0.85 \pm 0.01$; for the region -0.1 to $+0.15$V *vs.* SCE, $n = 0.95 \pm 0.01$; for the region $+0.2$ to $+0.38$V *vs.* SCE, $n = 1.05 \pm 0.06$. The dependence of the dissolution rate on the concentration of potassium hydroxide and potassium cyanide was determined in the two more anodic regions. At $+0.38$V *vs.* SCE the dissolution was directly proportional to the cyanide concentration and independent of hydroxide concentration. At $+0.04$V *vs.* SCE the dissolution rate was approximately linear with cyanide for low concentrations (<0.1M) and decreased with increased hydroxide concentration. At moderate hydroxide concentrations (0.1M) the dissolution rate decreased for cyanide concentrations greater than 0.2M. Several of the mechanisms suggested in the literature to account for the reactions in these two regions were shown to be incorrect in some way; instead, the following sequence was proposed

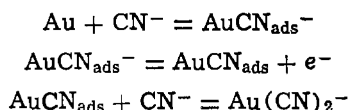

$$Au + CN^- = AuCN_{ads}^-$$

$$AuCN_{ads}^- = AuCN_{ads} + e^-$$

$$AuCN_{ads} + CN^- = Au(CN)_2^-$$

The dissolution rate was controlled by step 2 in the region of -0.1 to $+0.15$V *vs.* SCE and by step 3 in the region of $+0.2$ to $+0.38$V *vs.* SCE. The above reaction sequence appeared to account for the dissolution over the complete potential region investigated. The decrease in current between the peaks in the potential sweep measurements was discussed in terms of the formation of films which interrupt the dissolution process. At potentials anodic to $+0.38$V *vs.* SCE dissolution by the above sequence was suppressed by a gold oxidation reaction with $n > 1$.

The use of an alkaline cyanide electrolyte for gold plating was recorded in 1840 with a patent filed by Elkington (1). Since that time, this medium has been used extensively for gold electrodeposition, refining, and cyanidization. The latter remains the most important process for gold recovery (2). Despite the widespread use of alkaline cyanide, the electrochemistry of gold in this medium has not been studied extensively. Some disagreement exists in the literature concerning the nature of the complex gold dissolution process (3, 4). The potential sweep and weight loss experiments reported below were undertaken to study the electrochemical reactions of gold in alkaline cyanide, which is of interest in both the electrochemical recovery and the refining of gold.

Experimental

Solutions, prepared from analytical grade reagents and doubly distilled water, were deoxygenated by bubbling with oxygen-free nitrogen during the experiments. Pure gold foil was used for both the working and the counterelectrodes. The experimental cell is shown in Fig. 1. The working electrode, spot welded to a gold wire, was suspended 0.2 cm below the surface of the electrolyte. Two counterelectrodes set 1.25 cm to either side of the working electrode were contained in glass fritted tubes. The reference electrode was a microsaturated calomel electrode. A Luggin capillary housing the reference electrode was positioned with the 0.1 cm diam capillary tip located 0.17 cm from the electrode. This configuration has been shown to distort the current density at the point of measurement by less than 1% (5, 6). The data were

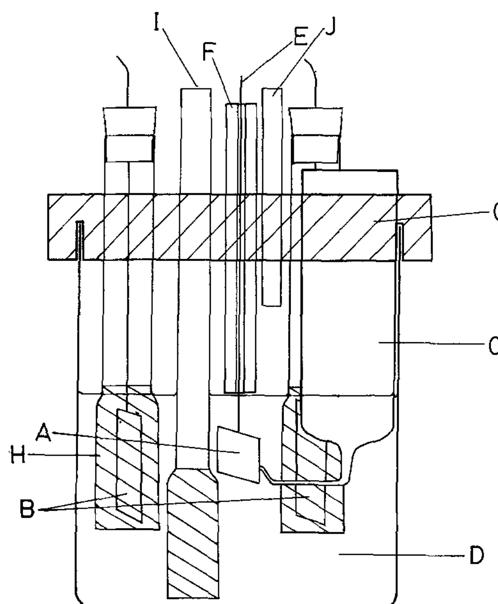

Fig. 1. Electrolytic cell. A, Working electrode; B, counterelectrode; C, reference electrode compartment; D, electrolyte; E, gold wire; F, glass capillary tube; G, Teflon cap; H, glass fritted tube; I, nitrogen inlet; J, nitrogen outlet.

* Electrochemical Society Active Member.

Key words: anode, dissolution, kinetics, metals.

not corrected for *IR* drop. The calculated maximum *IR* drops for peaks 1, 2, and 3 were 0.3, 5, and 22 mV, respectively. The absence of a visible skew at the top of peak 3 (greatest *IR* drop) indicates that the actual *IR* drops were even less than the above values.

The Pyrex beaker used to hold the electrolyte (60 cm^3) was fitted with either a machined Teflon cap or a No. 11 rubber stopper which had provisions for holding the electrodes and a glass fritted tube for nitrogen bubbling. No difference could be found in the potential sweep curves using either the rubber stopper or the Teflon cap. The solution was stirred by a magnetic stirrer located beneath the cell.

Experiments to determine the effect of stirring rate on peak height showed that the stirring rate had no effect on peak 2, whereas peaks 1 and 3 increased at higher stirring rates. With the aid of a digital tachometer it was shown that the reproducibility of the stirring rate used was such that all measured peak heights were reproducible to within less than ± 1%. The temperature of the electrolyte was found to vary less than ± 1°C during an experiment.

The electronic components consisted of a Wenking potentiostat (70TS1), voltage scan generator (VSG72), and an integrator (SS170). A Hewlett-Packard 70004Bx4 recorder was used for the potential sweep measurements.

Gold dissolution rates were determined from weight losses and electrode surface areas. Each experimental run was continued for sufficient time to allow a minimum weight loss of 200 μg, which was measured using a semimicrobalance with an accuracy of ± 10 μg. The shortest run was 1 min and the longest 2 hr. The surface area of the electrode was determined from potential scan measurements, using the linear relation between the current peak height and the square root of the voltage scan rate for the oxidation of $Fe(CN)_6^{-4}$. The relation given by Nicholson and Shain (7) is

$$\frac{i_p}{n\mathbf{F}AC_o\left(D_o\frac{n\mathbf{F}v}{RT}\right)^{1/2}} = 0.4463$$

where C_o is the concentration of $Fe(CN)_6^{-4}$ (mole · dm^{-3}), D_o is the diffusion coefficient of $Fe(CN)_6^{-4}$ ($cm^2 \cdot sec^{-1}$), i_p is the peak current (A), A is the area of the electrode (cm^2), n is the number of electrons transferred in the oxidation, v is the scan rate (V · sec^{-1}), and **F**, R, and T have their usual meanings. The electrode area was found not to change during an experimental run.

A standard pretreatment of the electrode was necessary to achieve reproducibility. The electrode was first heated to redness in air, then etched in hot aqua regia for 10 sec, washed in doubly distilled water, dried, and weighed. It was immediately given a further treatment consisting of a 5 min reduction period in the electrolyte at −1.2 V.[1] This latter procedure was found to improve the reproducibility of the weight loss and potentiodynamic measurements but did not affect the measured weight of the electrode. At the end of an experiment, the electrode was thoroughly washed in doubly distilled water, dried, and weighed.

Results and Discussion

Figure 2 shows the potentiodynamic sweep profiles for three electrolyte compositions. Within the potential range of −1.2 to +0.6V, it can be seen that there are three current peaks referred to in the figure as peak 1, peak 2, and peak 3. Three current maxima were also observed for gold in aqueous cyanide by Cathro and Koch (3) using a potentiostatic technique. Their three current maxima corresponded to the three peak regions found in our work, although the relative magnitudes of the peak current densities were different. In our work, at concentrations comparable to those used

[1] All potentials are reported *vs.* the saturated calomel electrode.

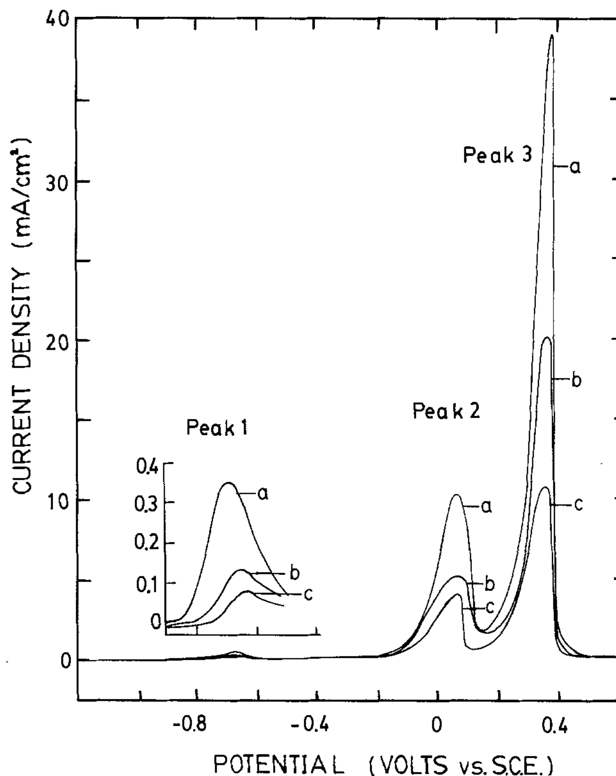

Fig. 2. Potentiodynamic anodic sweep profile in aqueous alkaline cyanide. a, 0.1M KOH + 0.2M KCN; b, 0.1M KOH + 0.1M KCN; c, 0.1M KOH + 0.05M KCN. Scan rate 1.0 mV · sec^{-1}, temperature 23.5°C.

by Cathro and Koch, peak 1 had a much smaller current density (0.096 mA · cm^{-2}) than peak 2 (5.0 mA · cm^{-2}) or peak 3 (11 mA · cm^{-2}) for the 0.05M CN^- + 0.1M KOH electrolyte. In the work of Cathro and Koch, peak 1 assumed a much greater significance relative to peaks 2 and 3, with a current maximum of 1.2 mA · cm^{-2} compared with 1.5 mA · cm^{-2} for peak 2 and 4 mA · cm^{-2} for peak 3 for a 0.038M CN^- + 0.063M KOH solution. The difference could result from the different measurement technique and the lower concentration of cyanide.

For the first peak region, Cathro and Koch proposed the following reaction scheme

$$Au + CN^- \rightleftarrows AuCN_{ads} + e^- \quad [1]$$

$$AuCN_{ads} + CN^- \rightleftarrows Au(CN)_2^- \quad [2]$$

At low surface coverage, using Tafel data, step [1] was identified by them as the rate-determining step. Anodic to the current maximum, the formation of a basic cyanide film ($Au(I)(OHCN)_x$) was considered to cause passivation. The conversion of the $Au(I)\ (OHCN)_x$ basic cyanide film to an Au(III) basic cyanide film, according to the following reaction scheme, was thought to cause peak 2

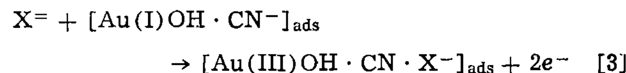

$$X^= + [Au(I)OH \cdot CN^-]_{ads} \rightarrow [Au(III)OH \cdot CN \cdot X^-]_{ads} + 2e^- \quad [3]$$

where $X^=$ is any anion except OH^-.

No reaction scheme was proposed for peak 3, but anodic to peak 3 passivation was considered to arise from the formation of a surface layer of Au_2O_3. In a more recent work, McIntyre and Peck (8) have also observed three peaks in the region of our study but did not discuss these peaks in detail.

In a study of gold reduction and oxidation in aqueous solutions, MacArthur (4) observed two peak regions for gold in alkaline cyanide electrolytes, using a cyclic voltammetric method. The first current peak was associated with the peak 1 of Cathro and Koch's

work, although the potential of the peak occurred at −0.3V rather than the −0.6V observed by both Cathro and Koch and ourselves. The reaction in the region of −0.6 to −0.3V was considered to occur via reaction scheme [1] and [2] with step [2] being the rate-determining step. An identical dissolution process had also been proposed earlier by Maja (9). The second peak observed by MacArthur, which corresponded in magnitude and potential to our peak 3 was stated to be of a complex nature, perhaps composed of two overlapping peaks. It was thought to be the result of a reaction involving either the direct oxidation of gold to a soluble species ($Au(CN)_2^-$) or the oxidation of Au to an Au(III) complex which then reacted with CN^- to give $Au(CN)_2^-$, either reaction being complicated by the formation of gold oxide which caused eventual passivation. Based on the work of Cathro and Koch, and more recently McIntyre and Peck (8), which showed three peaks, and that of MacArthur, which showed two peaks, it is not clear whether gold exhibits two or three potential regions where significant electrochemical reactions take place. In addition, the reactions corresponding with peaks 2 and 3 have not been adequately described. Therefore, experiments to measure directly the dissolution rate of gold in alkaline cyanide as a function of potential and electrolyte composition were conducted, as previously described in the experimental section. The results, weight loss per unit area per unit time ($mg \cdot m^{-2} \cdot sec^{-1}$) as a function of potential for three electrolyte compositions, are shown in Fig. 3. During the measurements, a very slight darkening of the gold surface was noted near peak 1. In the region of peak 2, a film was formed which grew darker in color as the the voltage became more anodic. This film could not be due to surface roughening, since electrode area did not vary. Attempts to measure the weight of the film in a manner similar to that made by Frankenthal and Thompson (10) in the case of gold hydroxide films in acid media were not successful, apparently because of insufficient surface product. The weight loss measured for the dissolution rate determination includes a small error (<10 μg) resulting from the weight of the film, since the film was not removed during the wash with doubly distilled water. No change in the color of the surface was noted during gold dissolution experiments in the region of peak 3.

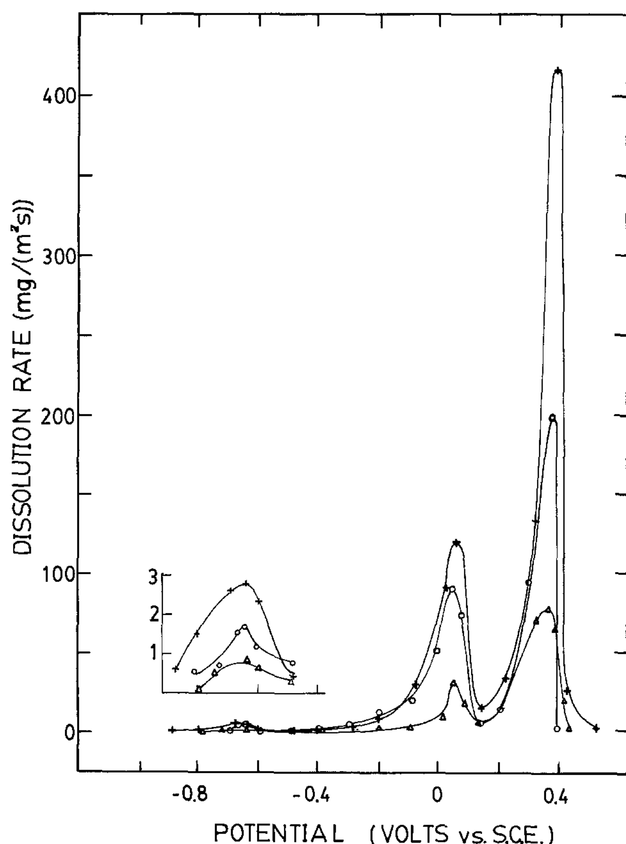

Fig. 3. Dissolution rate in aqueous alkaline cyanide. + 0.1M KOH + 0.2M KCN, ○ 0.1M KOH + 0.1M KCN, △ 0.1M KOH + 0.05M KCN. Temperature 23.5°C.

From Fig. 3 it can be seen that there are three regions of high dissolution rate and that these regions correspond, both in relative magnitude and potential range, to peaks 1, 2, and 3 found in the potential sweep measurements (Fig. 2). Thus, the current measured in the potential sweep experiments is the result of charge transfer in a gold dissolution process. In order to identify the dissolution process, the number of coulombs passed during each dissolution experiment was measured and combined with the weight loss of the electrode to give the number of Faradays per mole of gold dissolved. The results are presented in Table I as a function of potential. As can be seen from the table, the values of n range from somewhat less than 1 at potentials near −0.9V to values slightly greater than 1 at potentials near 0.3V. The averages for the regions of peak 1, peak 2, and peak 3 are 0.85, 0.95, and 1.05, respectively.

In the region of peak 1, most of the dissolution occurs by a one-electron transfer step. The n values in this region are less than 1 so that it is possible that some gold might dissolve chemically, perhaps by a reaction such as

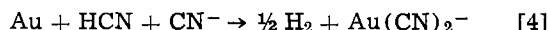

$$Au + HCN + CN^- \rightarrow \tfrac{1}{2} H_2 + Au(CN)_2^- \quad [4]$$

Free energy calculations (see Appendix) indicate that such a reaction is just barely thermodynamically possible under the prevailing experimental conditions.

In the region of peak 2, the dissolution process is clearly the result of a one-electron transfer step. Therefore, the reaction at peak 2 cannot be the conversion of a Au(I) salt to a Au(III) salt via reaction [3], as suggested by Cathro and Koch.

In the region of peak 3, the dissolution process also involves a one-electron transfer step; and, in addition, appears to show the onset of a dissolution process with $n > 1$ at more anodic potentials. Indeed, the few measurements taken at potentials greater than +0.4V indicate an $n = 3$ electron transfer reaction. Thus the dissolution occurring in the region of peak 3 is the oxidation of gold to Au(I) and not to Au(III). At

Table I. Number of Faradays (n) per mole of gold dissolved

Potential V *vs.* SCE	Number of measurements	Mean n*	
−0.90	2	0.94 ± 0.36	Peak 1 average = 0.85 ± 0.01** (−0.90 to −0.60)
−0.80	4	0.80 ± 0.6	
−0.75	4	0.89 ± 0.35	
−0.70	10	0.79 ± 0.13	
−0.68	5	0.82 ± 0.05	
−0.66	2	0.81 ± 0.72	
−0.65	17	0.85 ± 0.11	
−0.63	6	0.87 ± 0.17	
−0.60	8	0.92 ± 0.20	
−0.50	3	0.76 ± 0.5	
−0.40	7	0.94 ± 0.14	
−0.30	4	0.97 ± 0.17	
−0.20	9	0.92 ± 0.04	
−0.15	2	0.93 ± 1.52	
−0.10	6	0.91 ± 0.21	Peak 2 average = 0.95 ± 0.01** (−0.10 to +0.15)
−0.00	8	0.94 ± 0.14	
+0.05	38	0.95 ± 0.04	
+0.10	10	0.98 ± 0.04	
+0.15	2	0.95 ± 1.52	
+0.20	7	1.01 ± 0.07	Peak 3 average = 1.05 ± 0.06** (+0.20 to +0.40)
+0.25	3	1.13 ± 0.72	
+0.30	22	1.04 ± 0.05	
+0.38	10	1.07 ± 0.07	
+0.40	6	1.47 ± 0.17	
+0.50	1	3.11	
+0.60	1	2.65	
+0.80	1	3.10	

* 95% confidence limits.
** 95% confidence limits; based on method of analysis of stratified data (22).

potentials more anodic than +0.4V an oxidation process involving a three-electron transfer appears to dominate. The formation of Au(III) oxide is known to occur at anodic potentials (11-13). In acid media, the potential of Au(III) oxide formation on a polycrystalline gold surface was found to be close to +1.2V (14), which corresponds to +0.33V in 1M KOH. The form of this oxide recently has been shown (10) to be $Au(OH)_3$. This oxide peak, corresponding to the reaction

$$Au + 3\,OH^- \rightarrow Au(OH)_3 + 3e^- \quad [5]$$

can be readily seen in Fig. 4, which is a potentiodynamic sweep profile in an alkaline electrolyte with no cyanide present. Thus, at potentials anodic to peak 3, the dissolution reaction is most likely superceded and terminated by the formation of a passivating gold hydroxide layer via reaction [5], which would correspond to $n = 3$. The fact that the n values were slightly greater than 1 in the region of peak 3 may indicate that some $Au(OH)_3$ was already starting to be formed at the more positive potentials.

Peak 3.—In order to determine the effect of cyanide and hydroxide concentrations on the reaction occurring at peak 3, the dissolution rate was determined for four concentrations of cyanide, each at three concentrations of hydroxide. The results, shown in Fig. 5, clearly demonstrate that the reaction is first order with respect to cyanide concentration and independent of hydroxide concentration. Linear regression analysis yielded a correlation coefficient of 0.99 for the data. Direct oxidation, as suggested by MacArthur

$$Au + 2CN^- \rightarrow Au(CN)_2^- + e^- \quad [6]$$

must, therefore, be ruled out, because such a reaction would be expected to be second order with respect to cyanide.

In addition, the effect of diffusion on the dissolution process was studied. Figure 6 shows two anodic potential sweeps in an alkaline cyanide solution with a 1.0M KCl supporting electrolyte added to ensure diffusion control. One sweep was conducted with the electrolyte unstirred, the other with rapid stirring. It can be seen that the dissolution rate for peak 3 was enhanced by stirring; hence, in the unstirred case, the diffusion of the cyanide ion plays a significant role in the reaction rate for peak 3. The same results were obtained when KNO_3 was used as the supporting electrolyte.

Since the dissolution process involves the reaction of gold and cyanide through a one-electron transfer step and since the Au(I) cyanide complex is extremely stable ($K_{dissociation}$) $= 2.5 \times 10^{-29}$) (15), the following mechanism is proposed

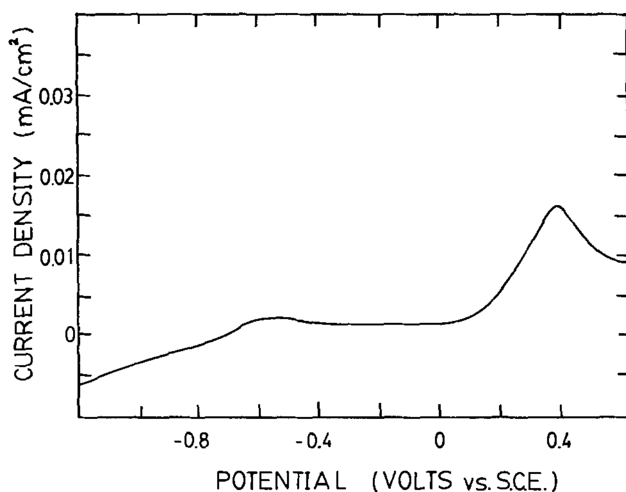

Fig. 4. Potentiodynamic anodic sweep profile in an aqueous alkaline electrolyte without cyanide. 1.0M KOH. Sweep rate 0.1 V · sec^{-1}, temperature 23.4°C.

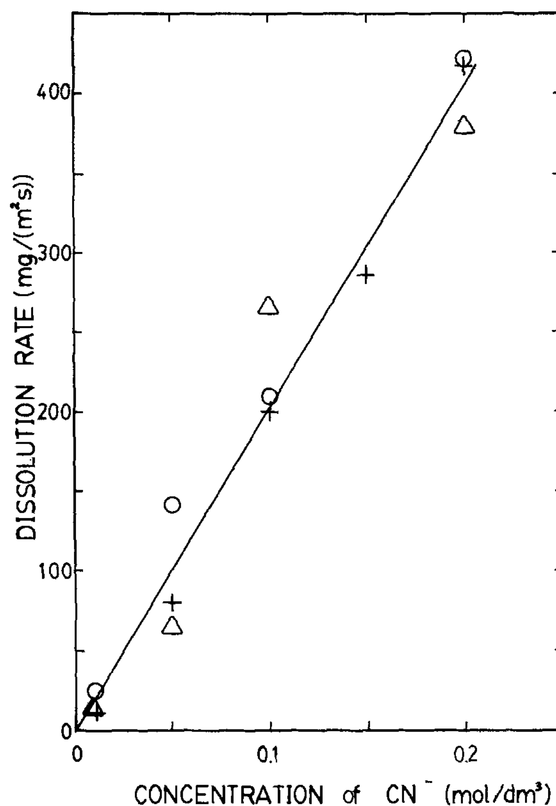

Fig. 5. Dependence of dissolution rate on cyanide and hydroxide concentration for peak 3. ○ 1.0M KOH, + 0.1M KOH, △ 0.01M KOH. Temperature 23.5°C.

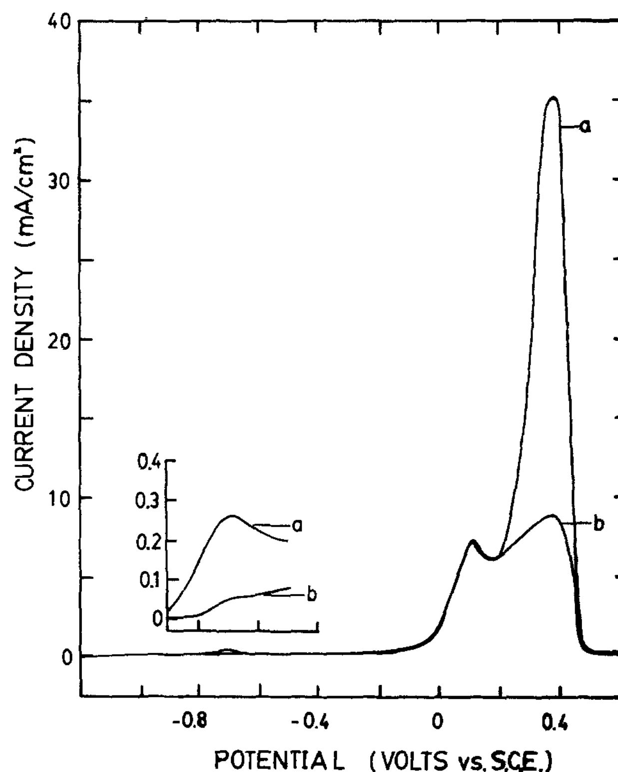

Fig. 6. Effect of stirring on reaction rate in aqueous alkaline cyanide. 0.1M KOH + 0.1M KCN + 1.0M KCl. *a*, Well stirred electrolyte; *b*, nonstirred electrolyte. Sweep rate 2 mV · sec^{-1}, temperature 23.6°C.

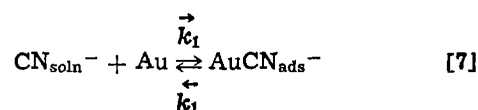

$$CN_{soln}^- + Au \underset{\overleftarrow{k_1}}{\overset{\overrightarrow{k_1}}{\rightleftarrows}} AuCN_{ads}^- \quad [7]$$

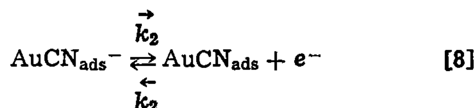

$$AuCN_{ads}^- \underset{\overleftarrow{k_2}}{\overset{\overrightarrow{k_2}}{\rightleftarrows}} AuCN_{ads} + e^- \quad [8]$$

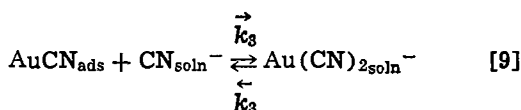

$$AuCN_{ads} + CN_{soln}^- \underset{\overleftarrow{k_3}}{\overset{\overrightarrow{k_3}}{\rightleftarrows}} Au(CN)_{2soln}^- \quad [9]$$

For each step of the reaction sequence, the dependence of the reaction rate on the bulk cyanide concentration can be calculated and is presented in Table II (see Appendix for derivations).

From Table II it can be seen that for step [7] as the rate-determining step, the reaction rate increases linearly with cyanide concentration and decreases with hydroxide concentration.

For step [8] as the rate-determining step, the reaction rate increases linearly with cyanide concentration only for low surface coverage of $AuCN_{ads}^-$. Since the surface coverage (θ') of $AuCN_{ads}^-$ should follow an adsorption isotherm, and since the reaction rate is proportional to the surface coverage, deviation of the reaction rate from linearity with cyanide concentration is expected at high cyanide concentrations. The concentration of hydroxide ion, according to

$$Au + OH^- \rightleftarrows AuOH_{ads}^- \quad [10]$$

also affects the reaction rate because of the competition for surface sites on the gold electrode (θ'' increases with $[OH^-]$).

For step [9] with low surface coverage, $(1 - \theta - \theta') \simeq 1$, and the reaction rate is second order with respect to cyanide concentration. At high surface coverage, the reaction rate is directly proportional to cyanide concentration and, since θ is high and approximately constant, there is no dependence of the reaction rate on hydroxide concentration.

In view of the above, it reasonably can be concluded that for peak 3, step [9] is the rate-determining step, since from Fig. 5 the reaction rate at peak 3 is linear with cyanide concentration and independent of hydroxide concentration. Step [9] would also account for the influence of stirring on the reaction rate at peak 3, observed in Fig. 6.

Peak 2.—The effect of cyanide and hydroxide concentration on the dissolution rate for the reaction at peak 2 was studied using six levels of cyanide and four of hydroxide. The results, shown in Fig. 7, demonstrate that at low cyanide concentrations the dissolution rate

Table II. Theoretical dependence of gold dissolution rate on cyanide concentration

Rate-determining step	
[7]	$i \simeq \overrightarrow{i_1} = \overrightarrow{k_1}[CN^-][Au] \simeq \overrightarrow{k_1}[CN^-](1 - \theta'')$
[8]	$i \simeq \overrightarrow{i_2} = \overrightarrow{k_2}\,\theta' \exp\left[\frac{\beta F \Delta\phi}{RT}\right] = \frac{\overrightarrow{k_1}\overrightarrow{k_2}[CN^-](1 - \theta - \theta'')}{\overleftarrow{k_1} + \overrightarrow{k_2}[CN^-]} \exp\left[\frac{\beta F \Delta\phi}{RT}\right]$
[9]	$i \simeq i_3 = \overrightarrow{k_3}[CN^-]\theta = \frac{\overrightarrow{k_1}\overrightarrow{k_2}k_3[CN^-]^2(1 - \theta - \theta'')}{\overleftarrow{k_1} + \overrightarrow{k_1}[CN^-]} \exp\left[\frac{F\Delta\phi}{RT}\right]$

Where θ = fractional surface coverage of $AuCN_{ads}$, θ' = fractional surface coverage of $AuCN_{ads}^-$, and θ'' = fractional surface coverage of $AuOH_{ads}^-$.

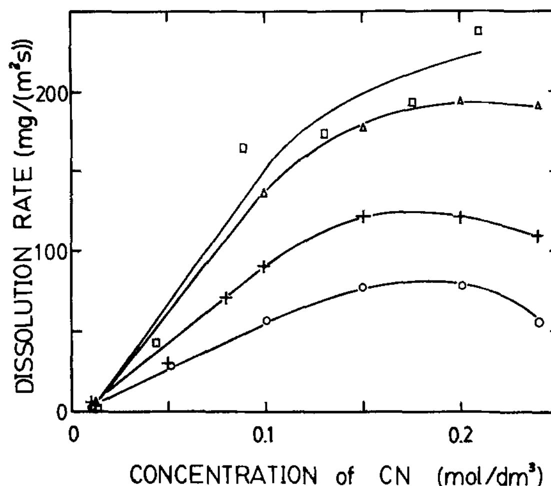

Fig. 7. Dependence of dissolution rate on cyanide and hydroxide concentration for peak 2. ○ 1.0M KOH, + 0.1M KOH, △ 0.01M KOH, □ 0.0001M KOH. Temperature 23.5°C.

is approximately linear with cyanide concentration and that the dissolution rate decreases with increasing hydroxide concentration. At moderate hydroxide concentrations, the reaction rate decreases for cyanide concentrations greater than 0.2M. In addition, the voltage scans in Fig. 6 indicate that the reaction rate is not influenced by stirring and hence is not affected by cyanide diffusion.

The reaction at peak 2 is a dissolution reaction involving a one-electron transfer step and should follow the reaction scheme [7], [8], and [9]. Although each of the steps can exhibit a reaction rate which is linear with cyanide concentration, only step [8] can account for the decrease in the reaction rate at high cyanide concentrations and for the lack of dependence of the reaction rate on the diffusion of cyanide ions. As seen from Table II, the reaction rate, if step [8] is the rate-determining step, depends on the concentration of $AuCN_{ads}^-$ on the surface and would, therefore, account for the lack of dependence of the reaction rate with stirring. At low surface coverage (θ, θ' small) the concentration of $AuCN_{ads}^-$ can be shown to be $\overrightarrow{k_1}/\overleftarrow{k_1}$ $[CN^-](1 - \theta'')$ when step [7] is in pseudoequilibrium, and thus the reaction rate is directly proportional to the cyanide concentration. An increase in hydroxide concentration causes a decrease in the reaction rate as a result of the term $(1 - \theta'')$ decreasing.

At higher cyanide and hydroxide concentrations the expression given in Table II for $\overrightarrow{i_2}$ can be shown to have a maximum if the concentration of $AuCN_{ads}$ increases with cyanide concentration. In the potential region near peak 3 the surface concentration of $AuCN_{ads}$ is known to be high (from previous discussion of peak 3); also, from the fact that surface concentrations of adsorbed species tend to follow Langmuir-type adsorption isotherms, it is reasonable to assume that the surface concentration of $AuCN_{ads}$ will increase with cyanide concentration. Therefore, at sufficiently high cyanide concentrations, the term $(1 - \theta - \theta'')$ begins to decrease and causes a lowering of the reaction rate. It is concluded that reaction [8] is the rate-determining step for peak 2.

Peak 1.—The reaction at peak 1 has been found to be a dissolution process with $n = 0.85$. The voltage scans in Fig. 6 show that the dissolution rate is affected by stirring; hence, the diffusion of the cyanide ion influences the reaction rate in the unstirred electrolyte. These data and the work of Cathro and Koch and MacArthur indicate that the electrochemical dissolution proceeds via sequence [7], [8], and [9]. Further

work is currently being conducted to identify the rate-determining step and additional processes taking place.

From the data presented, it is evident that throughout the potential range -0.9 to $+0.4$V in alkaline cyanide, gold dissolution rate are consistent with the reaction sequence [7], [8], and [9]. The rate-determining step for the dissolution process depends on potential, with step [9] controlling the reaction rate in the region of peak 3, and step [8] controlling in the region of peak 2. Despite the fact that the dissolution proceeds by the reaction sequence [7], [8], and [9] throughout the potential region investigated, the presence of the three peaks in the potentiodynamic sweep profiles (Fig. 2) as well as in the potential-dissolution rate determinations (Fig. 3) indicates that the dissolution process must be complicated by surface blockage or by the formation of a passivating surface film.

The change in color of the electrode surface observed in our work in the regions of peak 1 and peak 2 and a corresponding change in reflectance measurements of a gold surface in alkaline cyanide presented by Cathro and Koch are clear indications of film formation. The formation of simple oxides or hydroxides generally may be ruled out, because calculations made using standard electrode potentials (16) indicate that in alkaline media (1M KOH) AuOH should form at ±1.26V, AuO at $+0.302$V, $Au(OH)_3$ at $+0.382$V, and AuO_2 at $+0.682$V. These potentials generally are inconsistent with the potential regions where surface coloration was observed. There is, however, the possibility of formation of more complex species involving adsorbed hydroxide and cyanide ions, since both species can be adsorbed on a gold surface (17, 18).

The potential of zero charge for gold in alkaline solutions is known to be $\simeq 0$V (19) and independent of hydroxide concentration (20, 21). Therefore, anion electrosorption in the region of peak 1 will be relatively weak and the passivating layer need not be strongly bonded to cause interference with the dissolution reaction. At potentials near peak 2, the electrosorption of anions is much stronger and competition for surface sites between cyanide and hydroxide ions takes place. This can be seen from Fig. 7 since the reaction rate decreases with an increase in hydroxide concentration. At still more anodic potentials, the dissolution rate decreases and this decrease coincides with the formation of a dark surface film. Therefore, it would appear that this surface film is the passivating layer. Work is now being carried out to identify the surface product. At potentials near peak 3, the electrode is strongly positive, and the cyanide ion is preferentially adsorbed and, as either $AuCN_{ads}^-$ or $AuCN_{ads}$, occupies most of the available sites on the gold surface. The concentration of hydroxide has no effect on the reaction rate in this region (Fig. 5) and the dissolution is controlled by step [9], as discussed earlier. Anodic to peak 3, the formation of $Au(OH)_3$ becomes favored and the cyanide reaction is terminated.

Conclusions

1. Dissolution of gold in alkaline cyanide was found to occur via a one-electron transfer step in the potential range -0.4 to $+0.38$V *vs.* SCE. At less anodic potentials the dissolution proceeds with $n < 1$.

2. The peaks found in potentiostatic weight loss measurements and potentiodynamic sweep experiments at low sweep rates are the result of a single over-all dissolution reaction with different rate-controlling steps.

3. The reaction at peak 3 ($+0.2$ to $+0.38$V *vs.* SCE) is consistent with the sequence [7], [8], and [9] with step [9] as the rate-determining step. It cannot be the direct oxidation by reaction [6] as suggested in the literature.

4. The reaction at peak 2 (-0.1 to $+0.15$V *vs.* SCE) involves the same dissolution scheme as for peak 3, but with step [8] as the rate-determining step. It cannot be explained as the conversion of an Au(I) to an Au(III) salt as suggested by previous workers.

5. The formation of peaks in the potentiostatic weight loss measurements and potentiodynamic measurements arises because of blockage of the dissolution reaction by adsorption or the formation of passivating surface species.

6. The dissolution of gold in alkaline cyanide by the reaction sequence [7], [8], and [9] is terminated at potentials more positive than $+0.38$V (peak 3) by the formation of $Au(OH)_3$.

Acknowledgment

Financial assistance from the National Research Council of Canada is gratefully acknowledged.

Manuscript submitted Feb. 16, 1978; revised manuscript April 25, 1978.

Any discussion of this paper will appear in a Discussion Section to be published in the June 1979 JOURNAL. All discussions for the June 1979 Discussion Section should be submitted by Feb. 1, 1979.

Publication costs of this article were assisted by the University of Toronto.

APPENDIX A

Rate Equations

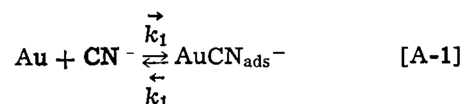

$$Au + CN^- \underset{\overleftarrow{k}_1}{\overset{\overrightarrow{k}_1}{\rightleftarrows}} AuCN_{ads}^- \qquad [A\text{-}1]$$

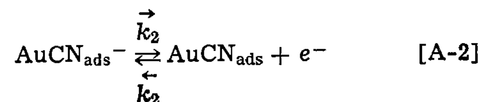

$$AuCN_{ads}^- \underset{\overleftarrow{k}_2}{\overset{\overrightarrow{k}_2}{\rightleftarrows}} AuCN_{ads} + e^- \qquad [A\text{-}2]$$

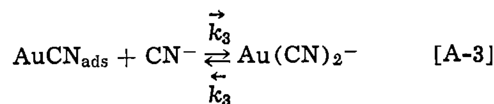

$$AuCN_{ads} + CN^- \underset{\overleftarrow{k}_3}{\overset{\overrightarrow{k}_3}{\rightleftarrows}} Au(CN)_2^- \qquad [A\text{-}3]$$

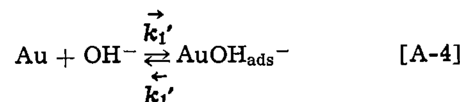

$$Au + OH^- \underset{\overleftarrow{k}_1'}{\overset{\overrightarrow{k}_1'}{\rightleftarrows}} AuOH_{ads}^- \qquad [A\text{-}4]$$

Step [A-1] is rds

$$i \simeq \overrightarrow{i}_1 = \overrightarrow{k}_1[CN^-][Au]$$

$$= \overrightarrow{k}_1[CN^-](1 - \theta - \theta' - \theta'')$$

$$i_1 \simeq \overrightarrow{k}_1[CN^-](1 - \theta'') \text{ since } \theta \simeq \theta' \simeq 0$$

rate of dissolution $\propto [CN^-]$

rate of dissolution decreases as θ'' increases

From step [A-4]

$$\overrightarrow{k}_1'(1 - \theta'' - \theta - \theta')[OH^-] = \overleftarrow{k}_1'\theta''$$

$$\theta'' = \frac{\overrightarrow{k}_1'(1 - \theta - \theta')[OH^-]}{\overleftarrow{k}_1' + \overrightarrow{k}_1'[OH^-]}$$

θ'' increases as [OH] increases

rate of dissolution decreases as $[OH^-]$ increases

Step [A-2] is rds

$$i \simeq \overrightarrow{i}_2 = \overrightarrow{k}_2\theta' \exp\left(\frac{\beta F \Delta\phi}{RT}\right)$$

step [A-1]

$$\vec{i}_1 \simeq \overleftarrow{i}_1$$

$$\vec{k}_1(1-\theta-\theta'-\theta'')[CN^-] = \overleftarrow{k}_1\theta'$$

$$\theta' = \frac{\vec{k}_1[CN^-](1-\theta-\theta'')}{\overleftarrow{k}_1 + \vec{k}_1[CN^-]}$$

$$\therefore i \simeq \vec{i}_2 = \frac{\vec{k}_1\vec{k}_2[CN^-](1-\theta-\theta'')}{\overleftarrow{k}_1 + \vec{k}_1[CN^-]} \exp\left(\frac{\beta F\Delta\phi}{RT}\right)$$

For low $[CN^-]$

$$\theta \simeq 0$$

rate of dissolution $\propto$ $[CN^-]$

rate of dissolution decreases with $[OH^-]$

For high $[CN^-]$

$$\theta \neq 0$$

$\therefore$ $(1-\theta-\theta'')$ decreases, and rate of dissolution decreases as $[CN^-]$ increases

Step [A-3] is rds

$$i \simeq \vec{i}_3 = \vec{k}_3\theta[CN^-]$$

$$\vec{i}_2 \simeq \overleftarrow{i}_2$$

$$\vec{k}_2\theta' \exp\left(\frac{\beta F\Delta\phi}{RT}\right) = \overleftarrow{k}_2\theta \exp\left(\frac{-(1-\beta)F\Delta\phi}{RT}\right)$$

$$\theta = \frac{\vec{k}_2}{\overleftarrow{k}_2} \exp\left(\frac{F\Delta\phi}{RT}\right)\theta'$$

from step [A-1]

$$\vec{i}_1 = \overleftarrow{i}_1$$

$$\theta' = \frac{\vec{k}_1[CN^-](1-\theta-\theta'')}{\overleftarrow{k}_1 + \vec{k}_1[CN^-]}$$

$$\therefore i \simeq \vec{i}_3 = \frac{\vec{k}_1 \cdot \vec{k}_2 \cdot \vec{k}_3}{\overleftarrow{k}_2} \exp\left(\frac{F\Delta\phi}{RT}\right) \frac{[CN^-]^2(1-\theta-\theta'')}{\overleftarrow{k}_1 + \vec{k}_1[CN^-]}$$

For low coverage of adsorbed intermediates

$$1-\theta-\theta'-\theta'' \simeq 1-\theta''$$

$$\vec{i}_3 = \vec{k}_3\theta[CN^-]$$

$$= \vec{k}_3 \frac{\vec{k}_1\vec{k}_2}{\overleftarrow{k}_1\overleftarrow{k}_2} \cdot \exp\left(\frac{F\Delta\phi}{RT}\right)(1-\theta'')[CN^-]^2$$

dissolution rate decreases with increase in $[OH^-]$

dissolution rate $\propto$ $[CN^-]^2$

For high coverage of adsorbed intermediates

$$\theta'' \simeq 0$$

$$\theta + \theta' \simeq 1$$

$$\vec{i}_3 = \vec{k}_3\theta[CN^-]$$

dissolution rate $\propto$ $[CN^-]$

$$\theta \simeq \text{constant}$$

dissolution rate independent of $[OH^-]$

APPENDIX B

Thermodynamic Possibility of Chemical Dissolution

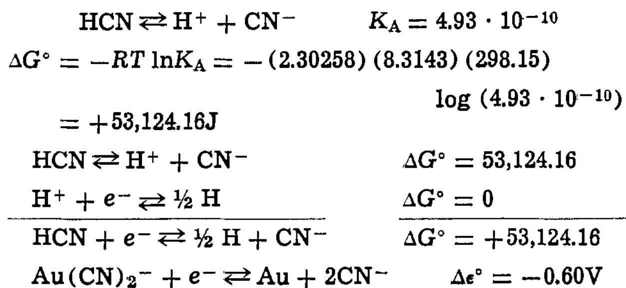

$$HCN \rightleftarrows H^+ + CN^- \qquad K_A = 4.93 \cdot 10^{-10}$$

$$\Delta G° = -RT \ln K_A = -(2.30258)(8.3143)(298.15) \log(4.93 \cdot 10^{-10})$$

$$= +53{,}124.16J$$

$HCN \rightleftarrows H^+ + CN^-$	$\Delta G° = 53{,}124.16$
$H^+ + e^- \rightleftarrows \frac{1}{2} H$	$\Delta G° = 0$
$HCN + e^- \rightleftarrows \frac{1}{2} H + CN^-$	$\Delta G° = +53{,}124.16$
$Au(CN)_2^- + e^- \rightleftarrows Au + 2CN^-$	$\Delta\epsilon° = -0.60V$

$$\therefore \Delta G° = -nF\Delta\epsilon° = -(1)(96{,}486.7)(-0.60)$$

$$= +57{,}892.02J$$

$$\therefore \text{for anodic direction, } \Delta G° = -57{,}892.02$$

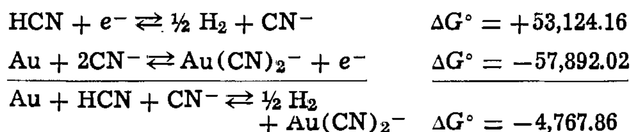

$HCN + e^- \rightleftarrows \frac{1}{2} H_2 + CN^-$	$\Delta G° = +53{,}124.16$
$Au + 2CN^- \rightleftarrows Au(CN)_2^- + e^-$	$\Delta G° = -57{,}892.02$
$Au + HCN + CN^- \rightleftarrows \frac{1}{2} H_2 + Au(CN)_2^-$	$\Delta G° = -4{,}767.86$

spontaneous reaction under standard conditions [A-5]

$$\Delta\epsilon° = -\frac{\Delta G°}{nF} = \frac{-(-4767.86)}{(1)(96{,}486.7)} = 0.049415V$$

$$\Delta\epsilon = \Delta\epsilon° - 0.59157 \log \frac{P_{H_2} \cdot a_{Au(CN)^-}}{a_{HCN} \cdot a_{CN^-}} \qquad [A\text{-}6]$$

Typical solution composition is 0.10M KOH + 0.10M KCN

Total ionic strength is $\simeq \frac{1}{2} \sum_i M_i z_i^2 = \frac{1}{2}(0.1 + 0.1 + 0.1 + 0.1) = 0.20$

Modified Debye-Hückel-Güntelberg-Davies equation (23)

$$\log \gamma_\pm = -\frac{A/z_1z_2/\sqrt{I}}{1+\sqrt{I}} + 0.1/z_1z_2/I$$

$$= \frac{-0.50841(1)\sqrt{0.2}}{1+\sqrt{0.2}} + 0.1(1)(0.2)$$

$$= -0.13711$$

$$\gamma_\pm = 0.729 \simeq \gamma_{H^+} \simeq \gamma_{CN^-} \simeq \gamma_{Au(CN)_2^-} \qquad [A\text{-}7]$$

$$\therefore \Delta\epsilon = 0.049415 - 0.059157 \log \frac{P_{H_2} \cdot [Au(CN)_2^-]}{\gamma_\pm[HCN][CN^-]} \qquad [A\text{-}8]$$

From K_A

$$[HCN][CN^-] = (4.93 \cdot 10^{-10}) \frac{[HCN]^2}{[H^+]}$$

At pH 13

$$\frac{[CN^-]}{[HCN]} = \frac{K_A}{[H^+]} = \frac{4.93 \cdot 10^{-10}}{10^{-13}} = 4.93 \cdot 10^3$$

$$\therefore [CN^-] = 4.93 \cdot 10^3 [HCN]$$

mass balance

$$[HCN] + [CN^-] = 0.10$$

$$[HCN] + 4.93 \cdot 10^3 [HCN] = 0.1$$

$$[HCN] = 2.028 \cdot 10^{-5}$$

$$\therefore [HCN][CN^-] = \frac{(4.93 \cdot 10^{-10})(2.028 \cdot 10^{-5})^2}{10^{-13}}$$

$$= 2.0276 \cdot 10^{-6} \qquad [A\text{-}9]$$

Substituting [A-7] and [A-9] in [A-8]

$$\Delta\epsilon = 0.049415 - 0.059157 \log \frac{P_{H_2} \cdot [Au(CN)_2^-]}{(0.729)(2.0276 \cdot 10^{-6})}$$

$$= -0.29549 - 0.059157 \log (P_{H_2} \cdot [Au(CN)_2^-])$$

Hydrogen will be formed at $P_{H_2} = 1$ atm, therefore the criterion for spontaneous chemical dissolution according to reaction [A-5] is that $\Delta\epsilon \leqq 0$, *i.e.*

$$\log [Au(CN)_2^-] \leqq \frac{-0.29549}{0.059157} \leqq -4.995$$

$$[Au(CN)_2^-] \leqq 1.01 \cdot 10^{-5} \text{ mole/dm}^3$$

$$\leqq 2 \text{ mg Au/dm}^3$$

The maximum dissolved gold concentration at the end of a potentiostatic dissolution run was 4 mg/dm^3, so that the concentration of $Au(CN)_2^-$ was <2 mg/dm^3 for a considerable time during a run, hence chemical dissolution was thermodynamically possible.

LIST OF SYMBOLS

- A electrode area
- C_o concentration of $Fe(CN)_6^{-4}$
- D_o diffusion coefficient of $Fe(CN)_6^{-4}$
- F the Faraday
- i_p peak current
- $\vec{k}$ rate constant of forward reaction
- $\overleftarrow{k}$ rate constant of backward reaction
- K equilibrium constant $= \vec{k}/\overleftarrow{k}$
- n number of electrons transferred in over-all reaction
- R gas constant
- T absolute temperature
- v voltage scan rate
- β anodic symmetry factor
- $\Delta\phi$ potential difference across electrode/solution interface
- θ fractional coverage of $AuCN_{ads}$
- θ' fractional coverage of $AuCN_{ads}^-$
- θ'' fractional coverage of $AuOH_{ads}^-$

REFERENCES

1. L. B. Hunt, *Gold Bull.*, 6, (1), 16 (1973).
2. M. C. Sneed, J. L. Maynard, and R. C. Brasted, "Comprehensive Inorganic Chemistry," Vol. 2, D. Van Nostrand Co. Inc., Toronto (1954).
3. K. J. Cathro and D. F. A. Koch, *This Journal*, **111**, 1416 (1964).
4. D. M. MacArthur, *ibid.*, **119**, 672 (1972).
5. E. Gileadi, E. Kirowa-Eisner, and T. Penciner, "Interfacial Electrochemistry," p. 210, Addison-Wesley Publishing Co. Ltd., Reading, Mass. (1975).
6. S. Barnartt, *This Journal*, **99**, 549 (1952); *ibid.*, **108**, 102 (1961).
7. R. S. Nicholson and I. Shain, *Anal. Chem.*, **36**, 706 (1964).
8. J. D. E. McIntyre and W. F. Peck, *This Journal*, **123**, 1800 (1976).
9. M. Maja, *Atti Accad. Sci. Torino: Cl. Sci. Fis. Mat. Nat.*, **99**, 1111 (1965).
10. R. P. Frankenthal and D. E. Thompson, *This Journal*, **123**, 799 (1976).
11. C. M. Ferro, A. J. Calandra, and A. J. Arvia, *Electroanal. Chem. Interfacial Electrochem.*, **59**, 239 (1975).
12. K. Ogura, S. Haruyama, and K. Nagasaki, *This Journal*, **118**, 531 (1971).
13. S. H. Cadle and S. Bruckenstein, *Anal. Chem.*, **46**, (1), 16 (1974).
14. D. Dickterman, J. W. Schultz, and K. J. Vetter, *Electroanal. Chem. Interfacial Electrochem.*, **55**, 429 (1974).
15. L. G. Sillén, "Stability Constants of Metal Ion Complexes," The Chemical Society, London (1964).
16. A. J. Bard, Editor, "Encyclopedia of Electrochemistry of the Elements," Vol. 4, Marcel Dekker Inc., New York (1975).
17. J. J. MacDonald and B. E. Conway, *Proc. R. Soc. London, Ser. A*, **269**, 419 (1962).
18. D. F. A. Koch and D. F. Scaife, *This Journal*, **113**, 302 (1966).
19. E. Gileadi, Editor, "Electrosorption," pp. 87-103, Plenum Press, New York (1967).
20. K. F. Lin and T. R. Beck, *This Journal*, **124**, 68C (1977).
21. V. L. Kheifats and B. S. Krasikov, *Z. Fiz. Khim.*, **31**, 1992 (1957).
22. G. W. Snedecor and W. G. Cochran, "Statistical Methods," p. 520, Iowa State University Press, Ames, Iowa (1967).
23. R. A. Robinson and R. H. Stokes, "Electrolyte Solutions," 2nd ed., pp. 231-232, Butterworths, London (1970).

An Impedance Interpretation of Small Amplitude Cyclic Voltammetry

I. Theoretical Analysis for a Resistive-Capacitive System

Digby D. Macdonald*

SRI International, Materials Research Center, Menlo Park, California 94025

ABSTRACT

The transient response of an equivalent circuit for an electrode/solution interface to a small-amplitude triangular potential excitation is derived by use of transform analysis. The response consists of both transient and steady-state contributions. The predicted steady-state response yields a hysteresis loop that is qualitatively similar to those exhibited by real systems under small-amplitude cyclic voltammetric conditions. Numerical analysis illustrates the dependence of the response on the voltage sweep rate, and the analysis of experimental data for corroding 90:10 Cu:Ni alloy in flowing seawater is described.

Small-amplitude cyclic voltammetry (SACV) (1), in which a triangular potential excitation function is imposed across an electrode/solution interface, has been used for both fundamental studies of the structure and capacitance of the double layer and for evaluating the corrosion rates of metals in condensed systems. At high voltage sweep rates, the capacitive components

* Electrochemical Society Active Member.

Key words: cyclic voltammetry, linear polarization, equivalent circuit, impedance, transform analysis.

frequently dominate the interfacial impedance, and the observed current response can be used to estimate the capacitance of the surface (1). Conversely, at low sweep rates the capacitive current is usually negligible compared with the faradaic contribution. In this case, the SACV response is principally determined by the charge-transfer (polarization) resistance of the interface.

The SACV technique is used extensively in corrosion research for estimating the polarization resistance of a metal-solution interface at the corrosion potential (2). Typically, a 10-20 mV peak-to-peak triangular excitation is imposed across a corroding interface by use of a potentiostat. The current response is then recorded over one or more cycles, and the polarization resistance is estimated from the gradient of the potential (E) *vs.* current (I) plot at the corrosion potential. The E *vs.* I plot is frequently nonlinear, but more important for the present analysis, the plot may exhibit considerable hysteresis. The nonlinear response has been discussed (2, 3), and it appears that this phenomenon can be used to obtain information on the nature of the corrosion process. On the other hand, little attention has been focused on the origin of the hysteresis, even though this property plays a central role in the interpretation of data from the closely related a-c impedance technique (1).

In this paper, the origin of the hysteresis in current *vs.* potential as observed under SACV conditions is analyzed in terms of the impedance of an equivalent electrical circuit. It is shown that the degree of hysteresis is sensitive to the potential sweep rate, and that the observed current response can be used to estimate values for the resistances and capacitances at the interface.

Impedance Operators

Provided that the amplitude of the excitation voltage is sufficiently small, the components of the impedance at a metal/solution interface can be regarded as linear; that is, the impedances of the individual components are independent of voltage. Accordingly, the interface may be represented by an equivalent electrical circuit consisting of linear components only, and the response of the system to an excitation signal $E(t)$ can be obtained by application of Eq. [1]

$$I(t) = E(t)/Z(p) \quad [1]$$

where p is the impedance operator defined as

$$p = d/dt \quad [2]$$

$$1/p = \int dt \quad [3]$$

The impedance function $Z(p)$ is chosen so that $Z(p) \times I(t)$ is equal to the voltage drop across the device in question. For instance, the drops in voltage across resistive, capacitive, and inductive components are given by

Resistive: $E(t) = RI,\ Z(p) = R$ [4]

Capacitive: $E(t) = (1/C) \int I dt,\ Z(p) = 1/pC$ [5]

Inductive: $E(t) = L(dI/dt),\ Z(p) = Lp$ [6]

Furthermore, the total voltage drop across a series combination of components is given by

$$E(t) = \sum_i E_i(t) \quad [7]$$

whereas the total current through a parallel network is

$$I(t) = \sum_i I_i(t) \quad [8]$$

Accordingly, the impedance functions for series and parallel combinations of components are given by Eq. [9] and [10], respectively

$$Z(p) = \sum_i Z_i(p) \quad [9]$$

$$1/Z(p) = Y(p) = \sum_i [1/Z(p)] = \sum_i Y_i(p) \quad [10]$$

The parameter $Y(p)$ is commonly termed the admittance function for the circuit under consideration.

Inspection of Eq. [1], [4]-[6], [9], and [10] shows that if the impedance (or admittance) operator of a complex circuit is known, then prediction of the current response to a specified excitation voltage function $E(t)$ will involve solution of one or more integral/differential equations. One of the most effective methods for handling this type of problem is by use of Laplace (or Fourier) transforms. The application of these integral transforms for predicting the transient responses of electrical circuits is known as transform analysis. Although Pilla (4) and others (1, 5, 6) have used numerical transformation techniques in the analysis of the a-c impedance characteristics and potentiostatic responses of electrochemical systems, transform analysis of either experimental data or equivalent electrical circuits does not appear to have been employed extensively in the study of SACV.

Transform Analysis

It can be shown (7) that upon transformation of Eq. [1] into Laplace space, that is

$$\overline{I}(s) = \overline{E}(s)/Z(s) \quad [11]$$

with

$$\mathcal{L}[f(t)] = \overline{f}(s) = \int_0^\infty f(t)e^{-st}dt \quad [12]$$

the impedance function $Z(s)$ has the same analytical form as $Z(p)$ with the impedance operator, p, replaced by the Laplace variable, s. This convenient property permits the straightforward derivation of an expression for the Laplace transform of the current in terms of the variable s. Inverse transformation (analytically or numerically) therefore yields the required current response in terms of real time.

By way of illustration, we consider a simple series R-C circuit. The impedance operator for this circuit is obtained from Eq. [4] and [5] as

$$Z(p) = R + 1/pC \quad [13]$$

The current response to a voltage step applied at $t = 0$ is therefore given in Laplace space as

$$\overline{I}(s) = EC/(1 + sRC) \quad [14]$$

where the Laplace transform of $E(t)$ is (8)

$$\mathcal{L}[E(t)] = E/s \quad [15]$$

Inverse transformation of Eq. [14] is straightforward by use of standard tables (8) to yield the familiar exponential decay of current with time

$$I(t) = (E/R)e^{-t/RC} \quad [16]$$

Simulated Metal/Solution Interface

The simplest general electrical equivalent circuit for a metal/solution interface is a parallel combination of a resistor (R_p) and a capacitor (C) in series with a second resistor (R_s) as shown in Fig. 1a. The resistance R_p may be identified with the charge-transfer (or polarization) resistance, whereas R_s is commonly associated with any pure resistance (*e.g.*, from the solution or low capacitive films) between the metal and the tip of the reference electrode probe. Although at first sight this equivalent circuit may appear to be unrealistically simple, it can frequently simulate the relaxation behavior of a real interface, particularly if a single relaxation process dominates the electrochemical behavior over the range of frequency of interest. In the complex plane representation of the impedance, this behavior is characterized by a single first quadrant semicircle centered on the real axis. Although other relaxation processes may exist at other frequencies, their contributions to the over-all impedance of a

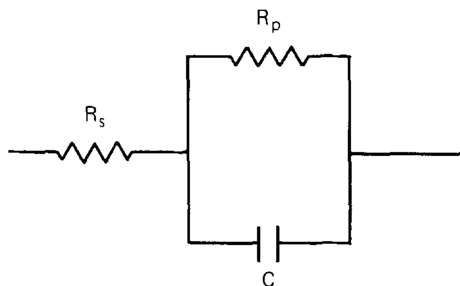

(a) EQUIVALENT CIRCUIT FOR THE METAL-SOLUTION

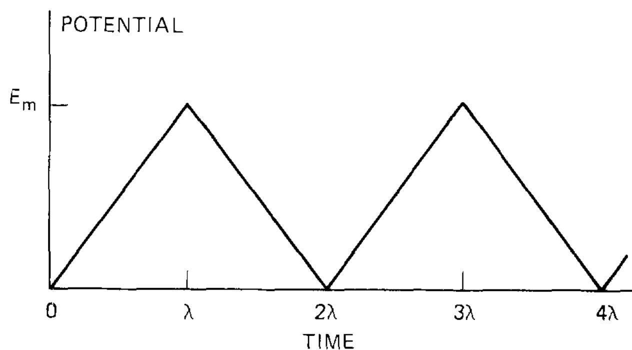

(b) TRIANGULAR VOLTAGE EXCITATION FUNCTION

Fig. 1. Equivalent circuit and voltage-excitation function for the model considered for the metal-solution interface.

series combination of elements of the type shown in Fig. 1a will be small, provided that the relaxation times are sufficiently well separated.

With these limitations in mind, the impedance of the interface under linear conditions is given by

$$Z(p) = R_s + \frac{R_p}{1 + pR_pC} \qquad [17]$$

The excitation voltage applied in the controlled potential mode across the interface is in the form of the triangle shown in Fig. 1b and is represented mathematically by Eq. [18]

$$E = \begin{cases} E_m\left[\frac{t}{\lambda} - 2n\right] & 2n\lambda < t < (2n+1)\lambda \text{ (forward sweep)} \\ E_m\left[2(n+1) - \frac{t}{\lambda}\right] & (2n+1)\lambda < t < (2n+2)\lambda \text{ (reverse sweep)} \end{cases} \qquad [18]$$

where E_m is the maximum value of the excitation voltage, λ is the time of reversal of the voltage scan, and $n = 0, 1, 2, \ldots$ is the cycle number. The Laplace transform of Eq. [18] is given in transform tables (8) as

$$\overline{E}(s) = E_m(1 - e^{-\lambda s})/\lambda s^2(1 + e^{-\lambda s}) \qquad [19]$$

Substitution of Eq. [17] and [19] into Eq. [11] with $p = s$ therefore yields the Laplace transform of the response current as

$$\overline{I}(s)/E_m = [(1 - e^{-\lambda s})/b\lambda s(1 + e^{-\lambda s})] \times \left[1/s\left(s + \frac{a}{b}\right) + R_pC/\left(s + \frac{a}{b}\right)\right] \qquad [20]$$

where

$$a = R_s + R_p \qquad [21]$$

$$b = R_sR_pC \qquad [22]$$

Inverse transformation may be accomplished by use of the convolution theorem (7, 8)

$$\mathcal{L}^{-1}[\overline{I}(s)/E_m] = \int_0^t F(x)G(t - x)dx \qquad [23]$$

where $F(x)$ and $G(t - x)$ are the inverse transformations of $f(s)$ and $g(s)$ given below

$$f(s) = (1 - e^{-\lambda s})/s(1 + e^{-\lambda s}) \qquad [24]$$

$$F(x) = \begin{cases} +1 & 2n\lambda < x < (2n+1)\lambda \\ -1 & (2n+1)\lambda < x < (2n+2)\lambda \end{cases} \qquad [25]$$

$$g(s) = 1/s\left(s + \frac{a}{b}\right) + R_pC/\left(s + \frac{a}{b}\right) \qquad [26]$$

$$G(t - x) = b/a + Ke^{ax/b} \qquad [27]$$

with

$$K = (R_pC - b/a)\, e^{-at/b} \qquad [28]$$

Substitution of Eq. [25] and [27] into Eq. [23], followed by integration over successive forward and reverse sweeps, yields

$$I^f(t) = (E_m/a\lambda)\left\{ t - 2n\lambda - (R_pC - b/a) \times \left[2\sum_{m=0}^{2n} (-1)^m e^{-a(t-m\lambda)/b} - e^{-at/b} - 1 \right]\right\} \qquad [29]$$

for the current on the forward sweep with $2n\lambda < t < (2n + 1)\lambda$, and

$$I^r(t) = (E_m/a\lambda)\left\{ 2(n+1)\lambda - t + (R_pC - b/a) \times \left[2e^{a\lambda/b}\sum_{m=0}^{2n} (-1)^m e^{-a(t-m\lambda)/b} - e^{-at/b} - 1 \right]\right\} \qquad [30]$$

for the reverse sweep with $(2n + 1)\lambda < t < (2n + 2)\lambda$. The summations contained in Eq. [29] and [30] are geometric progressions. Summation over the indicated limits therefore yields

$$I^f(t) = (E_m/a\lambda)\{t - 2n\lambda - (R_pC - b/a) \times [2e^{-at}(1 + e^{(2n+1)a\lambda/b})/(1 + e^{a\lambda/b}) - e^{-at/b} - 1]\} \qquad [31]$$

and

$$I^r(t) = (E_m/a\lambda)\{2(n+1)\lambda - t + (R_pC - b/a) \times [2e^{-(t-\lambda)a/b}(1 + e^{(2n+1)a\lambda/b})/(1 + e^{a\lambda/b}) - e^{-at/b} - 1]\} \qquad [32]$$

for the forward $[2n\lambda < t < (2n + 1)\lambda]$ and reverse $[2n + 1)\lambda < t < (2n + 2)\lambda]$ sweeps, respectively.

It is convenient to redefine the time scales so that zero time for the forward sweep coincides with $2n\lambda$ (*i.e.*, with the start of the nth forward sweep) and with $(2n + 1)\lambda$ for the reverse sweep. This is accomplished by use of the following transformations

$$t' = t - 2n\lambda \qquad [33]$$

$$t'' = t - (2n + 1)\lambda \qquad [34]$$

Thus, substitution for t in Eq. [31] and [32] using Eq. [33] and [34], respectively, yields the following expressions for the current transients for the forward and reverse sweeps

$$I^f(t') = (E_m/a\lambda)\{t' - e^{-at'/b}(R_pC - b/a) \times [2(e^{-2na\lambda/b} + e^{a\lambda/b})/(1 + e^{a\lambda/b}) - e^{-2na\lambda/b}] + (R_pC - b/a)\} \qquad [35]$$

$$I^r(t'') = (E_m/a\lambda)\{\lambda - t'' + e^{-at''/b}(R_pC - b/a) \times [2(e^{-2na\lambda/b} + e^{a\lambda/b})/(1 + e^{a\lambda/b}) - e^{-(2n+1)a\lambda/b}] - (R_pC - b/a)\} \quad [36]$$

Equations [35] and [36] demonstrate that the current response contains both steady-state and transient components. Of principal interest in this work is the steady state that is established when $na\lambda/b \to \infty$. Under these conditions $e^{-2na\lambda/b}$ and $e^{-(2n+1)a\lambda/b} \to 0$, so that Eq. [35] and [36] reduce to

$$I_{ss}^f(t') = (E_m/a\lambda)\{t' - (R_pC - b/a) \times [(2e^{a(\lambda-t')/b}/[1 + e^{a\lambda/b}]) - 1]\} \quad [37]$$

$$I_{ss}^r(t'') = (E_m/a\lambda)\{\lambda - t'' + (R_pC - b/a) \times [(2e^{a(\lambda-t'')/b}/[1 + e^{a\lambda/b}]) - 1]\} \quad [38]$$

Because SACV experiments are normally carried out with potential sweep rate as the independent variable, a further transformation of Eq. [37] and [38] is necessary. Thus, substitution of $\lambda = E_m/v$, where v is the potential sweep rate, into Eq. [37] and [38] yields

$$I_{ss}^f(t') = (v/a)\{t' - (R_pC - b/a) \times [(2e^{a(E_m-vt')/vb}/[1 + e^{aE_m/vb}]) - 1]\} \quad [39]$$

$$I_{ss}^r(t'') = (v/a)\{E_m/v - t'' + (R_pC - b/a) \times [(2e^{a(E_m-vt'')/vb}/[1 + e^{aE_m/vb}]) - 1]\} \quad [40]$$

Equations [39] and [40] therefore give the complete steady-state response of the equivalent circuit shown in Fig. 1a as a function of time and sweep rate as the independent variables.

Numerical Analysis

Equations [39] and [40] show that the steady-state response of the equivalent circuit shown in Fig. 1a to a triangular voltage excitation is a complex function of the resistances and capacitances of the circuit elements, the maximum voltage, E_m, and the voltage sweep-rate, v. The relationships given are sufficiently complex that the dependence of the response on the independent variables is best illustrated by numerical analysis; that is, the current on the forward and reverse sweeps is calculated from Eq. [39] and [40] for selected values for R_s, R_p, C, E_m, and v.

Typical steady-state current-voltage curves as a function of voltage sweep rate are shown in Fig. 2. In general, the polarization curves exhibit hysteresis between the forward and reverse sweeps, with exponential-type decays at the start of both sweep directions. The curves plotted in Fig. 2 show that the degree of hysteresis is sensitive to the voltage sweep-rate, and only at the lowest sweep-rate considered is the degree of hysteresis negligible. The amount of exponential decay at the start of both the forward and reverse sweeps depends upon the value for the series resistance R_s. Thus, if the series resistance is not present or has been compensated for by positive feedback, no exponential decay is predicted as can be shown from Eq. [39] and [40]. These calculated voltammograms are similar in both form and response to the independent variable, v, as those frequently observed for real systems (see next section).

In practice, it is possible to obtain reasonably precise data for the gradient of the current/voltage curve at the end of both the forward and reverse sweeps. Furthermore, the hysteresis current, ΔI, defined as

$$\Delta I = I_{ss}^f(t' = \lambda/2) - I_{ss}^r(t'' = \lambda/2) \quad [41]$$

is also conveniently measured from the observed current response (see Fig. 2). Differentiation of Eq. [39] and [40] with respect to t' and t'', and substitution of $t' = t'' = \lambda$, therefore yields

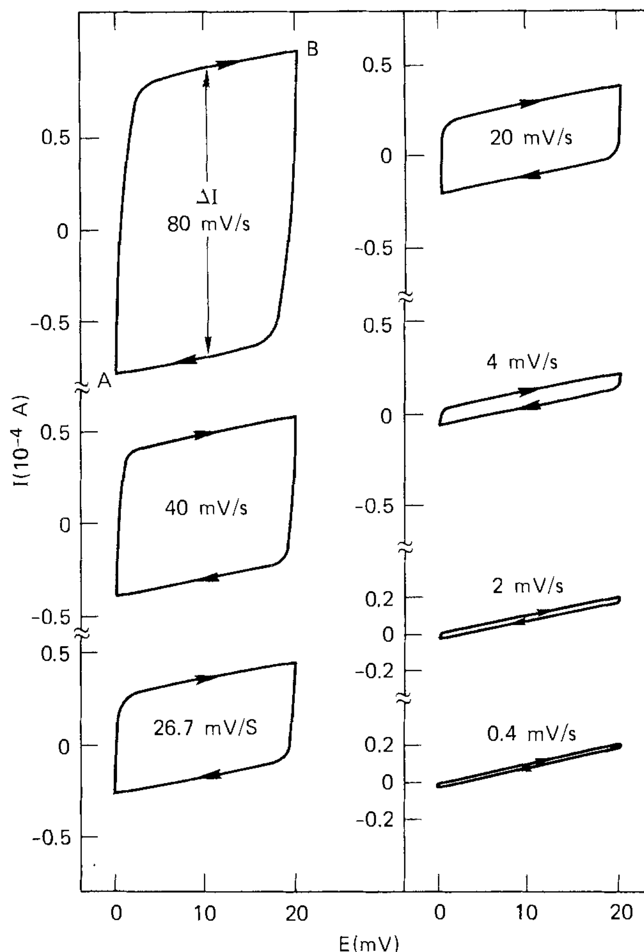

Fig. 2. Cyclic voltammograms for the electrical equivalent circuit shown in Fig. 1(a) as a function of voltage sweep rate. $R_s = 10\ \Omega$, $R_p = 1000\ \Omega$, $C = 1000\ \mu F$, $E_m = 20$ mV.

$$1/R_{app} = 1/(R_s + R_p) + 2R_p/R_s(R_s + R_p)(1 + e^{aE_m/vb}) \quad [42]$$

where the apparent polarization resistance, R_{app}, is equal to $(\partial E/\partial I_{ss})_{t=\lambda}$; that is, it is equal to the slope of the polarization curve at $t' = \lambda$ for the forward sweep and at $t'' = \lambda$ for the reverse sweep. Similarly, substitution of Eq. [39] and [40] into Eq. [41] yields the following expression for the hysteresis current

$$\Delta I = 2R_p^2C\{1 - 2e^{aE_m/2vb}/(1 + e^{aE_m/vb})\}v/(R_s + R_p)^2 \quad [43]$$

A third equation may be derived by noting that the diagonal resistance, R_d, is given by

$$1/R_d = [I_{ss}^f(t' = \lambda) - I_{ss}^r(t'' = \lambda)]/E_m \quad [44]$$

This parameter is determined experimentally as the gradient of the line joining points A and B of the voltammogram shown in Fig. 2 for a sweep rate of 80 mV/sec. Substitution of Eq. [39] and [40] into Eq. [44] therefore yields

$$1/R_d = 1/(R_s + R_p) + \{2R_p^2C(e^{aE_m/bv} - 1)/E_m(R_p + R_s)^2(e^{aE_m/bv} + 1)\}v \quad [45]$$

The variation of $1/R_{app}$ and $1/R_d$ with voltage sweep rate (or frequency $v/4E_m$) for the indicated values for R_s, R_p, C, and E_m is shown in Fig. 3. At low sweep rates, both R_{app} and R_d tend toward the total d-c resistance of the circuit, that is $R_s + R_p$. This limit is also approached at low frequency for sinusoidal excitation as used in the a-c impedance technique (1). At very high voltage sweep rates both curves approach the value for the series resistance, R_s. This expected

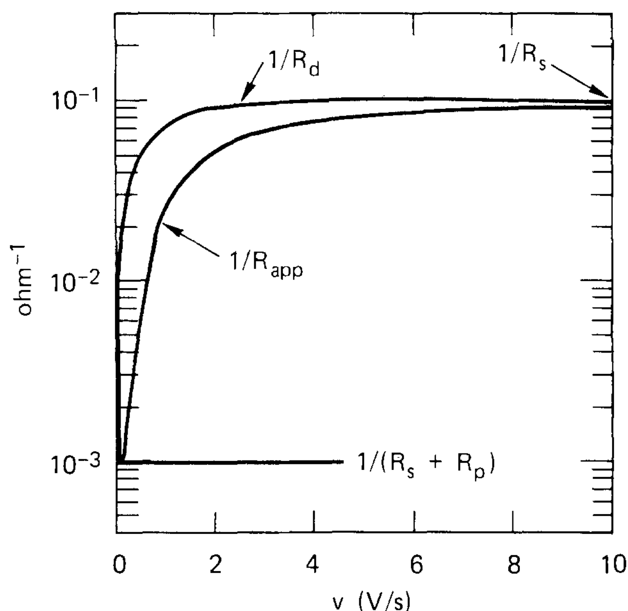

Fig. 3. Variation of $1/R_{app}$ and $1/R_d$ with voltage sweep rate for SACV. Note the two limits given by $1/R_s$ and $1/(R_s + R_p)$. $R_s = 10\ \Omega$, $R_p = 1000\ \Omega$, $C = 1000\ \mu F$, $E_m = 0.020V$.

result also parallels the well-known high frequency behavior under sinusoidal excitation (1).

The sweep rate dependence of the hysteresis current plotted in Fig. 4 shows that ΔI at first increases with v due to the increased conductance of the parallel capacitor. At higher sweep rates, however, the impedance of the interface becomes increasingly determined by the series resistance so that the hysteresis current decreases. At very low sweep rates (in the range for most linear polarization resistance measurements), ΔI is predicted to vary monotonically with v with a limiting gradient equal to $2CR_p^2/(R_p + R_s)^2$ as shown by the expanded scale plot in Fig. 4. This property is used later in this paper for the analysis of experimental data.

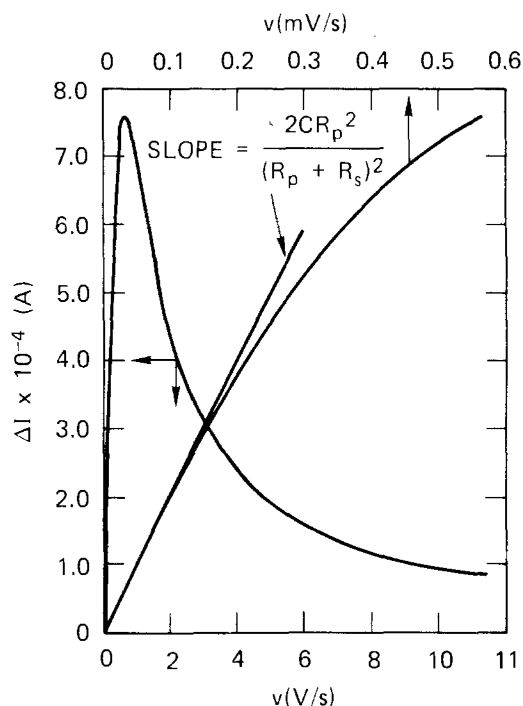

Fig. 4. Dependence of the hysteresis current (ΔI) on voltage sweep rate (v) for SACV. The arrows indicate the appropriate sweep rate axes. $R_s = 10\ \Omega$, $R_p = 1000\ \Omega$, $C = 1000\ \mu F$, $E_m = 0.020V$.

Analysis of Experimental Data

The essential features of the procedure for analyzing experimental data are illustrated by reference to the SACV's for corroding 90:10 Cu:Ni alloy in flowing seawater shown in Fig. 5. The experimental details of this work will be published in a subsequent paper (9). Comparison of these curves with those calculated theoretically (Fig. 2) shows that the responses are qualitatively similar, in that both exhibit hysteresis between the forward and reverse sweeps, and both show exponential-type relaxation phenomena at the start of the scans in both directions.

Plots of $1/R_{app}$ and $1/R_d$ against sweep rate for 90:10 Cu:Ni alloy in flowing seawater are shown in Fig. 6. These curves agree with the theoretical prediction that the plots should be approximately parabolic (Eq. [42] and [45]), and that $1/R_d$ is more dependent on sweep rate than is $1/R_{app}$. In both cases, extrapolation to zero sweep rates yields the same value of $1316 \pm 25\Omega$ for $R_s + R_p$. The dependence of the hysteresis current, ΔI, on sweep rate, is shown in Fig. 7. Again, the theoretical prediction of an approximately parabolic function that extrapolates to $\Delta I = 0$ for vanishingly small sweep rates is observed. The gradient of the ΔI *vs.* v plot at v $= 0$ is related to the values of the equivalent circuit components through Eq. [46]

$$(d\,\Delta I/dv)_{v\to 0} = 2R_p^2C/(R_p + R_s)^2 \quad [46]$$

Assuming that $R_p >> R_s$ (see below), this expression yields an interfacial capacitance of $2500 \pm 200\ \mu F$.

The validity of the values for R_p and C as determined by SACV can be assessed by comparison with data obtained by the more conventional a-c impedance technique (1). Typical impedance diagrams for 90:10

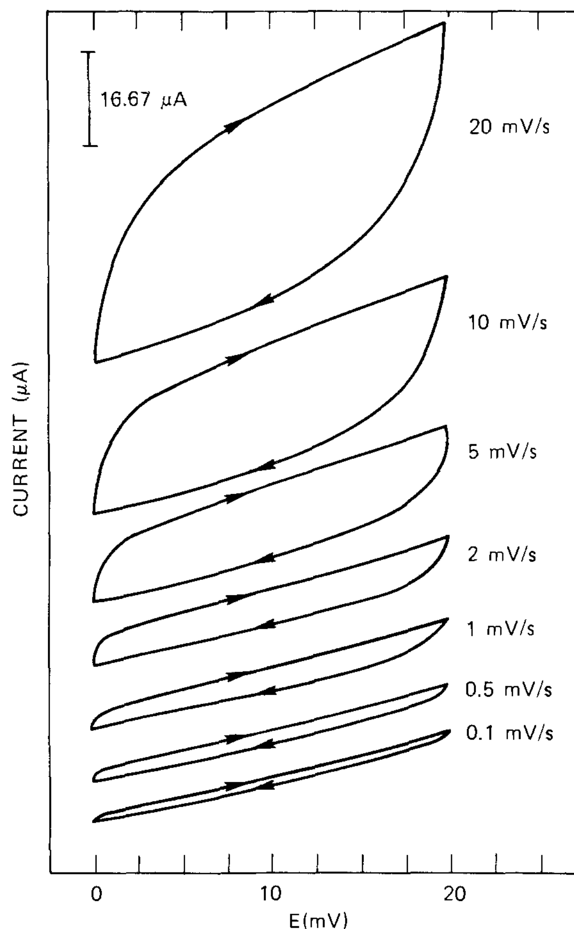

Fig. 5. Small-amplitude cyclic voltammograms for 90:10 Cu:Ni alloy in flowing seawater. Flow velocity = 1.62 m/sec; $[O_2]$ = 0.045 mg/liter; specimen area = 11.05 cm^2; T = 26°C; exposure time = 50 hr.

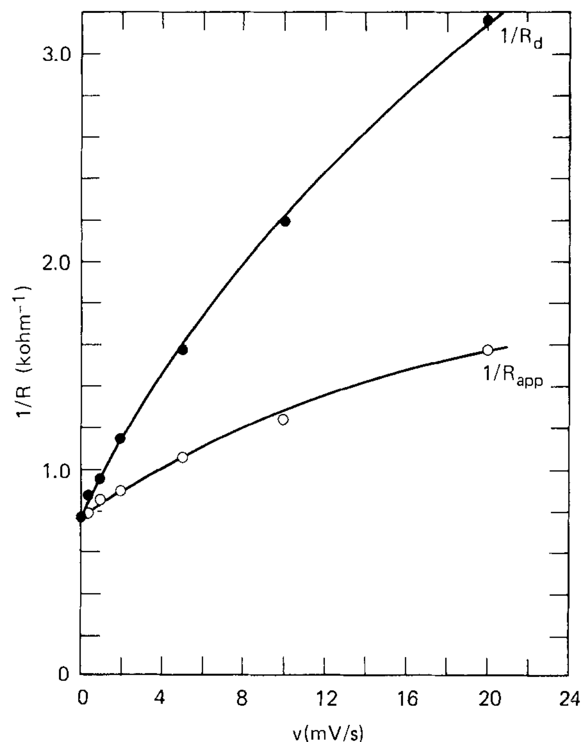

Fig. 6. Plots of Eq. [42] and [45] for 90:10 Cu:Ni alloy in flowing seawater. Experimental conditions as listed in Fig. 5.

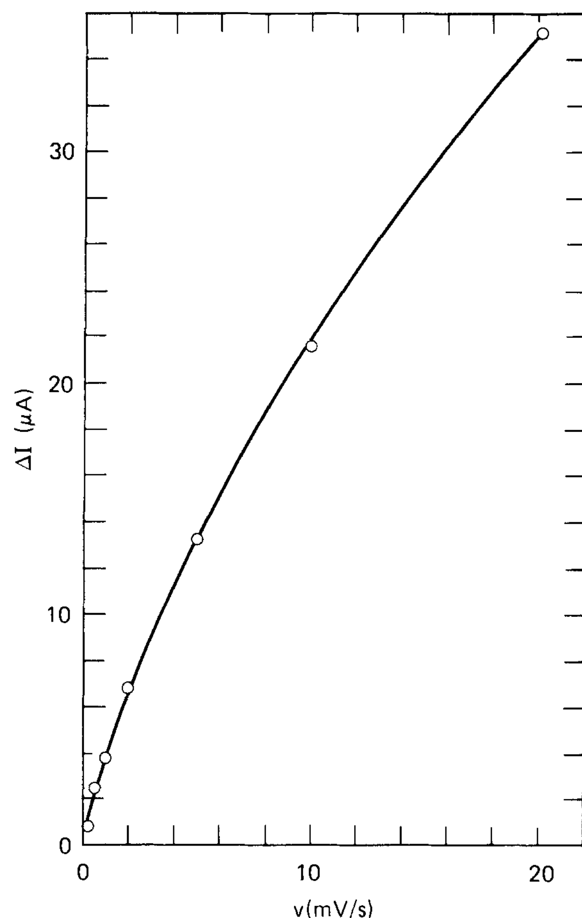

Fig. 7. Plot of Eq. [43] for 90:10 Cu:Ni alloy in flowing seawater. Experimental conditions as listed in Fig. 5.

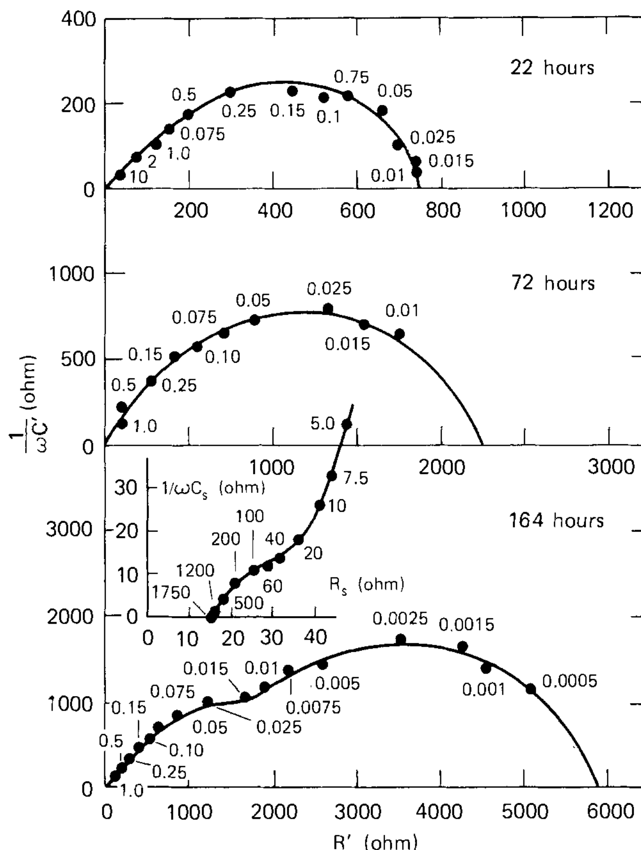

Fig. 8. Complex plane-impedance diagrams for 90:10 Cu:Ni alloy in flowing seawater as a function of exposure time. Experimental conditions as listed in Fig. 5. Numbers next to each point refer to frequency in Hz.

Cu:Ni alloy in the same experiment at three different exposure times are shown in Fig. 8. These data were obtained by analysis of the Lissajous figures generated by simultaneously imposing the sinusoidal excitation voltage and response current across the X and Y axes, respectively, of an oscilloscope (frequency > 1 Hz) or fast-response X-Y recorder (frequency < 1 Hz) (1, 9). For all three exposure times, the impedance plots take the form of distorted semicircles, or combinations of semicircles. At sufficiently low frequency, all the impedance diagrams exhibit partially resolved semicircular plots, as expected for dominance of the impedance by a single relaxation process having an equivalent circuit of the type adopted in this theoretical analysis (Fig. 1a). Other relaxation processes are evident at higher frequencies, as shown clearly by the impedance diagram for the longest exposure time. Thus, semicircles with maxima at $\sim$ 0.025 and $\sim$ 60 Hz are evident, in addition to the low frequency semicircle with its maximum at $\sim$ 0.0025 Hz. We have obtained extensive impedance data for both 90:10 and 70:30 Cu:Ni alloy in flowing seawater as a function of oxygen and sulfide concentrations. The analyses of these diagrams will be presented in a later publication (9).

In all three cases shown in Fig. 8, the impedance plots extrapolate at high frequency to very small values for the real component R', as expected for small values for the series resistance, R_s. The low frequency intercept with the real axis is equal to the impedance of the d-c path; that is, equal to $R_s + R_p$. Furthermore, the frequency (ω) at which the semicircle is at a maximum is given by

$$\omega = 1/R_pC \qquad [47]$$

Thus, substitution for R_p in Eq. [47] using the low frequency intercept with the real axis permits an estimate to be made of the interfacial capacitance.

A comparison of the values for $R_s + R_p$ and C, as derived by use of the a-c impedance and the SACV techniques is shown in Fig. 9. Excellent agreement is obtained between both experimental methods, thereby demonstrating the usefulness of SACV for investigat-

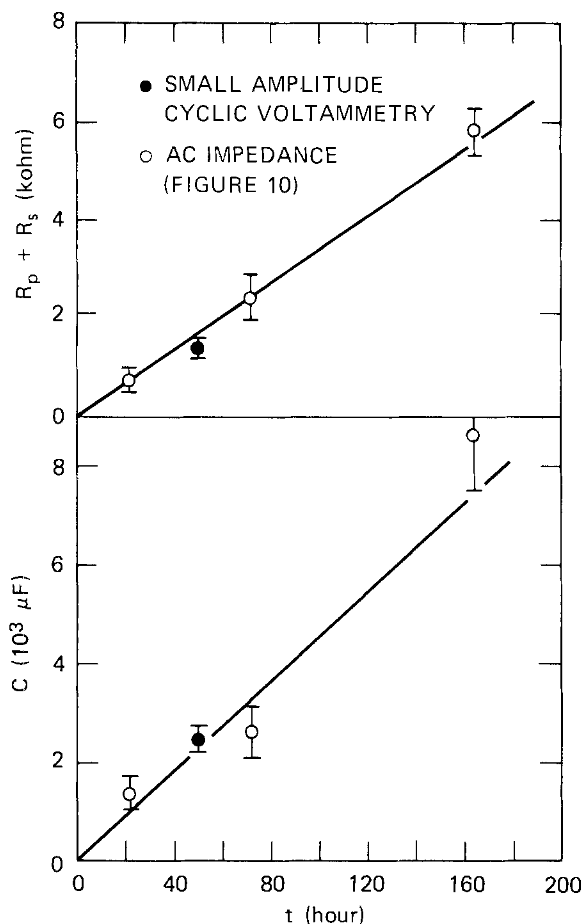

Fig. 9. Variation of $R_p + R_s$ (upper plot) and C (lower plot) with exposure time for corroding 90:10 Cu:Ni alloy in flowing seawater. Experimental conditions as listed in Fig. 5.

ing the impedance properties of a metal/solution interface. Interestingly, the capacitances measured in this work for 90:10 Cu:Ni alloy in flowing seawater are much larger than the expected double layer capacitance (200-400 μF for a specimen area of 11 cm^2) and increase with time. The observed values presumably reflect pseudocapacitance associated with the deposition of a surface film (1).

At this point it is worthwhile to comment upon the relative merits of the SACV and a-c impedance techniques for measuring corrosion rates for metals in condensed media. Although the SACV technique is used extensively in corrosion research, and indeed forms the basis of an ASTM recommended practice for measuring polarization resistance, the present work demonstrates that a full impedance interpretation of the data is very complex, even if only a single relaxation is assumed to occur at the interface. Contrariwise, the a-c impedance technique provides a powerful method for not only estimating the polarization resistance, but also for mechanistic investigations by analysis of the form of the complex plane plot (10). Nevertheless, it is likely that the SACV technique will continue to be used extensively for routine measurement of polarization resistance because of the experimental simplicity and because for many systems the SACV response at low voltage sweep is almost entirely resistive in character.

Acknowledgments

Financial support for this work by the Office of Naval Research (Contract No. N00014-77-C-0046, NR-036-116) is gratefully acknowledged. The author would like to thank Dr. C. M. Ablow for checking some of the derivations, and Drs. L. Nanis, R. L. Jones, and B. C. Syrett for helpful discussions.

Manuscript submitted Dec. 20, 1977; revised manuscript received March 31, 1978.

Any discussion of this paper will appear in a Discussion Section to be published in the June 1979 JOURNAL. All discussions for the June 1979 Discussion Section should be submitted by Feb. 1, 1979.

Publication costs of this article were assisted by SRI International.

REFERENCES

1. D. D. Macdonald, "Transient Techniques in Electrochemistry," Plenum Press, New York (1977); L. G. Austin and E. G. Gagnon, *This Journal*, **120**, 251 (1973); E. G. Gagnon, *ibid.*, **120**, 1052 (1973); *ibid.*, **121**, 512, 1444 (1974); *ibid.*, **122**, 521 (1975).
2. F. Mansfeld, *Adv. Corr. Sci. Technol.*, **6**, 163 (1976).
3. D. W. Bird, *Corr. Sci.*, **13**, 913 (1973).
4. A. A. Pilla, *This Journal*, **117**, 467 (1970).
5. M. D. Wijnen, *Recl. Trav. Chim. Pays-Bas*, **79**, 1203 (1960).
6. E. Levart and E. Poirier D'Orsay, *J. Electroanal. Chem. Interfacial Electrochem.*, **12**, 277 (1966).
7. S. Goldman, "Transformation Calculus and Electrical Transients," Prentice-Hall, Inc., New York (1950).
8. G. E. Roberts and H. Kaufman, "Table of Laplace Transforms," Saunders, Philadelphia (1966).
9. D. D. Macdonald, B. C. Syrett, and S. S. Wing, *Corrosion*, In press.
10. I. Epelboin, M. Keddam, and H. Takenouti, *J. Appl. Electrochem.*, **2**, 71 (1972).

Effect of Moisture on the Chromium (III)-Chromium (II) Electrode Reaction in Molten LiCl-KCl Eutectic

H. A. Laitinen*

Department of Chemistry, University of Florida, Gainesville, Florida 32611

Y. Yamamura

The Research Institute for Iron, Steel and Other Metals, Tohoku University, Sendai, Japan

and I. Uchida*

Department Applied Chemistry, Faculty of Engineering, Tohoku University, Sendai, Japan

ABSTRACT

The hydrolysis of chromium (III) in molten LiCl-KCl eutectic has been studied by varying the ratio of H_2O to HCl vapor pressure in equilibrium with the melt using cyclic voltammetry at a glassy carbon indicator electrode. The initial process is a reversible hydrolysis to form an electroactive species, believed to be $CrCl_5(OH)^{-3}$, followed by slower polymerization reactions culminating in the irreversible formation of an insoluble phase. Raising the temperature from 450° to 500°C causes the initial reversible hydrolysis to be less pronounced, and to increase the rate of the subsequent irreversible processes.

In view of the difficulty of completely dehydrating molten LiCl-KCl eutectic, the behavior of water is of special interest. Hydrolytic decomposition during melting according to the reaction

$$H_2O + Cl^- \rightleftharpoons HCl + OH^- \quad [1]$$

is suppressed by gaseous HCl and promoted by substances such as metal ions or acidic oxides which react with OH^- or $O^=$ ions to form soluble species or insoluble phases. Fusion of a moist salt mixture in glass or silica vessels leads to an instantaneous etching, which can be prevented by pumping off most of the water from the solid salts and fusing under dry HCl atmosphere (1). Previous studies of water in LiCl-KCl melts have been concerned with measurement of its dissociation constant (2) and with the effect of moisture on the mechanism of the cathodic reduction of chromate (3, 4). In the latter work, it was found that no etching of glass occurred in the presence of moisture if excess HCl was present.

Previous studies of the chromium (III)-chromium (II) system have included a measurement of the reversible potential (5), steady-state voltammetry (6), and cyclic voltammetry (7). In the latter study, the first reduction step was interpreted in terms of a rapid charge-transfer reaction

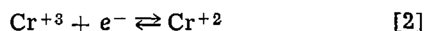

$$Cr^{+3} + e^- \rightleftharpoons Cr^{+2} \quad [2]$$

followed by a slow precipitation of $CrCl_2$

$$Cr^{+2} + 2Cl^- \rightarrow CrCl_2 \quad [3]$$

This mechanism appears implausible, in view of the fact that our previous potentiometric and voltammetric work (5, 6) had been carried out with solutions of chromium (II).

Spectrophotometric studies of $CrCl_3$ have indicated an octahedral coordination to produce $CrCl_6^{-3}$ in LiCl-KCl eutectic at temperatures of 392° and 444°C (8) and also in molten CsCl at temperatures of 650°-750°C (9). Divalent ions such as Ni(II), Co(II), Cu(II) were found to have tetrahedral coordination, corresponding to $MCl_4^=$. Gruen and McBeth (10) found that V(III) and V(II) in LiCl-KCl melts showed octahedral coordination at 400°, while at higher temperatures a transition to tetrahedral coordination took place. Accordingly, it appeared probable that the first step of electroreduction should best be written

$$CrCl_6^{-3} + e^- \rightleftharpoons CrCl_6^{-4} \quad [4]$$

and the second, slow step as the dissociation reaction

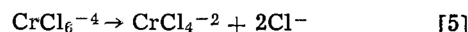

$$CrCl_6^{-4} \rightarrow CrCl_4^{-2} + 2Cl^- \quad [5]$$

The simplest hydrolysis reaction of Cr(III) may be written

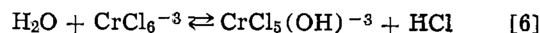

$$H_2O + CrCl_6^{-3} \rightleftharpoons CrCl_5(OH)^{-3} + HCl \quad [6]$$

By equilibrating an inert carrier gas with aqueous HCl solution, a variable ratio of p_{HCl}-p_{H_2O} could be maintained in the gas phase, and correspondingly the concentration ratio of HCl to H_2O could be varied in the solution phase.

The present investigation was carried out using cyclic voltammetry to monitor the progress of reaction [6] and subsequent polymerization reactions to produce an insoluble product.

Experimental

Reagents.—The LiCl-KCl eutectic was obtained from Anderson Physics Laboratories, Incorporated, Urbana, Illinois, where it was prepared and purified by the method outlined by Laitinen *et al.* (1).

Anhydrous $CrCl_3$ was prepared by heating $CrCl_3$ (Research Organic/Inorganic Chemical Corporation) to 650°C in a stream by CCl_4 vapor (11). The product was refined further by sublimation between 700°-750°C in an anhydrous HCl gas (12). The other chemicals were used without further purification.

Electrodes.—Platinum reference electrodes and spectroscopic grade graphite counterelectrodes were used as in previous studies (13).

Glassy carbon electrodes (Beckwith Carbon Corporation) were used as working electrodes. Rods of 3 mm (1/8 in.) diam were sealed into Pyrex by two techniques which were evaluated by measurements of double layer capacity and steady-state residual currents and by cyclic voltammetry of the purified solvent. For comparison, measurements of the same type were carried out with a platinum flag electrode having a geometrical area of about 16 mm^2. The glassy carbon

* Electrochemical Society Active Member.

Key words: chromium, molten salts, hydrolysis.

electrodes, designated as GCE-I and GCE-II, were prepared as follows.

GCE-I.—A glassy carbon rod, provided with a knotted platinum contact wire at one end, was placed in a Pyrex glass tube, closed at one end, and provided with a thin-walled section slightly larger than the carbon rod. By lowering the pressure at the open end and heating the thin-walled section to the softening point, the rod was coated with glass, taking care to avoid bubbles at the carbon-glass interface. The thin-walled section was strengthened by welding it into a commercial glass tube, again under reduced pressure, and pulling off the thick-walled tube in the flame. After cooling in an oven maintained at 160°C, the end was cut off to expose the flat circular cross section of the glassy carbon which was polished to a mirror finish using fine alumina powder on a glass plate. The electrode was stored in an oven regulated at 160° until its use in electrochemical experiments, because glassy carbon has a coefficient of thermal expansion close to that of Pyrex glass at temperatures above 100°C (14).

GCE-II.—To improve the seal between glassy carbon and Pyrex glass, the rod was first treated with a silica coating, prepared by soaking in 20% sodium silicate solution, drying in an oven at 160°C, exposing it to dry HCl gas at 200° for 30 min, washing with deionized water several times to remove NaCl, and dehydrating by heating to red heat. The rod was treated in this manner five times and then sealed into Pyrex using the same technique as described above for GCE-I.

Apparatus.—Double layer capacity measurements were made with a Wayne Kerr Universal Bridge B221 using 1000 Hz signal source. A Universal Programmer Model 175 (Princeton Applied Research Corporation) was used as a potential source, a 241 A Oscillator (Hewlett-Packard) as an a.c. sine wave source, and a Type 1232, A Tuned Amplifier and Null Detector (General Radio Company) as a zero detector were used.

Cyclic voltammetric scan waves were obtained with a Polarographic Analyzer Model 174A (Princeton Applied Research Corporation) coupled to a Universal Programmer PAR (Model 175), and the current-voltage curves were recorded on a Moseley Model 7000 AM X-Y Recorder (Hewlett-Packard).

Procedure.—All electrochemical experiments were performed at 450°C. A Hevi-Duty MK 3012-S Vertical Split Tube Furnace (Hevi-Duty Electric Company) was used. The temperature was regulated with a Wheelco Panel-Mount Capacitrol Temperature Controller (Wheelco Instrument Company). The procedures employed for cleaning glassware and handling the molten salt with special glass devices were described in detail by Johnston (15). The melt solution of Cr(III) was prepared by dissolving a known weight of anhydrous $CrCl_3$ in the molten LiCl-KCl eutectic saturated with dry HCl gas.

Moist HCl gas was prepared by passing Ar gas through a series of two gas washing bottles fitted with fritted glass dispersion tubes to assure equilibrium between aqueous HCl and carrier gas (3). Concentrations of H_2O and HCl were expressed in terms of their partial pressures in Ar gas, using tabulation of the partial pressures in equilibrium with aqueous solutions at various temperatures (16). For the three aqueous HCl concentrations, 12, 11, and 10*M*, the values of p_{H_2O}/p_{HCl} were, respectively, 0.0173, 0.0467, and 0.134 at 30°C.

After replacing the gas in the cell containing the melt with moist HCl gas by blowing at least 30 min, it was bubbled into the melt for the desired time. After termination of an electrochemical experiment, the salt was dissolved in deionized water. The volume of melt was calculated from the amount of chloride ion determined by argentometry and the density.

Research and Discussion

Evaluation of glassy carbon electrodes.—Measurements of double layer capacity revealed that GCE-I showed an apparent differential capacitance of the order of 100 ± 20 $\mu F/cm^2$ over a potential range of 0–−1.6V *vs.* 1*M* Pt(II)/Pt. At more negative potentials the capacitance gradually increased several-fold evidently because of faradaic processes. In comparison, GCE-II showed a much lower capacitance, of the order of 40 ± 10 $\mu F/cm^2$ over the same potential range, once more increasing without apparent limit at potentials more negative than −1.6V.

Cyclic voltammetry and steady-state residual current measurements likewise indicated lower blanks for GCE-II, presumably because the silica layer provided superior bonding to glass. Both types of measurements indicated a useful potential range of 0–−1.8V for GCE-II. The residual current was slightly anodic at potentials near zero *vs.* Pt, presumably because of a slow anodic oxidation of the carbon surface, in agreement with the observation of Levy and Reinhardt (7).

Cyclic voltammetry of chromium(III) in dry HCl.—Cyclic voltammetry experiments were carried out at 450°C at three concentrations of Cr(III) prepared by the addition of anhydrous $CrCl_3$ to melts saturated with HCl gas at seven voltage scan rates ranging from 1.000 to 0.010 V/sec. Typical voltammetric curves are shown in Fig. 1.

Plots of the cathodic peak current *vs.* square root of the voltage scan rate were linear through zero. The diffusion coefficients of Cr(III) calculated from the slopes of these plots ranged from 0.8 to 1.0 × 10^{-5} cm^2 sec^{-1}, somewhat larger than those reported by Levy and Reinhardt (7).

The ratios of cathodic to anodic peak currents were measured for each scan, using the empirical expression developed by Nicholson (17)

$$i_a/i_c = i_{ap}/i_{cp} + 0.485\, i_{sp}/i_{cp} + 0.086 \qquad [7]$$

when i_{ap} and i_{cp} are the measured anodic and cathodic

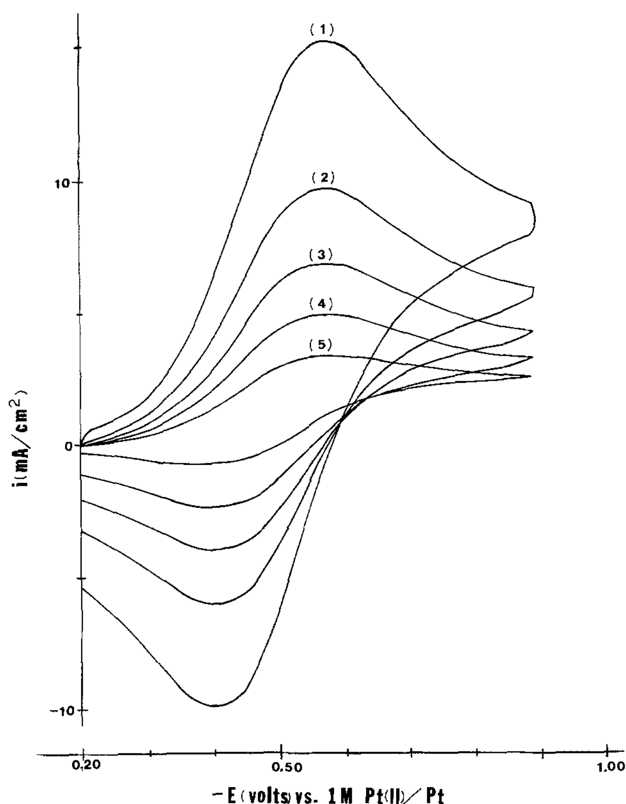

Fig. 1. Cyclic voltammograms for reduction of Cr(III) to Cr(II) in melt solution saturated HCl gas. Curve (1) Voltage scan rate of 0.500 V/sec; curve (2) 0.200 V/sec; curve (3) 0.050 V/sec; curve (4) 0.020 V/sec; curve (5) 0.010 V/sec.

peak currents and i_{sp} is the cathodic current at the switching potential. The values of i_a/i_c plotted against voltage scan rate are shown in Fig. 2. In agreement with the observations of Levy and Reinhardt (7), the ratio i_a/i_c is near unity at high scan rates ($0.10 < V < 1.00$) and decreases with decreasing scan rate at lower scan rates ($0.01 < V < 0.10$). The peak separation ΔE_p between cathodic and anodic peaks was close to the theoretical value of 140 mV, indicating a reversible charge transfer reaction. The variation of i_a/i_c indicates a relatively slow chemical step following charge transfer. This slow step was interpreted by Levy and Reinhardt in terms of the formation of "insoluble" $CrCl_2$, with a rate constant of 0.028 sec^{-1} at 500°C. In view of the spectrophotometric evidence cited above, and in view of our experience in preparing solutions of Cr(II) by electrochemical reduction of Cr(III), we prefer to write Eq. [4] and [5] to represent the electrode process in a dry melt.

Confirmation of a soluble Cr(II) species in dry melts was provided by carrying out a coulometric titration of Cr(III) by electrolytic reduction at constant current (5, 18), using a glassy carbon electrode as a cathode and interrupting the current periodically to register a potentiometric titration curve. Such a titration curve, for 26 mM Cr(III), in comparison with the theoretical curve, is shown in Fig. 3.

The two curves show close similarity during the first 2/3 of the titration, but no endpoint could be detected.

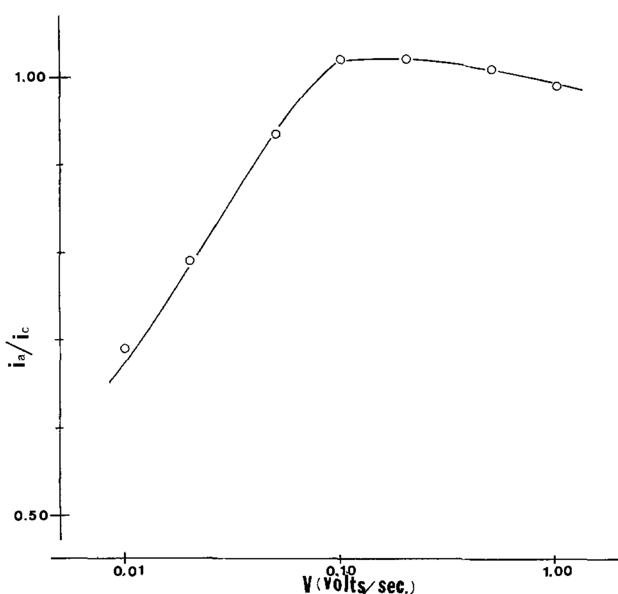

Fig. 2. Anodic to cathodic peak current ratio (i_a/i_c) vs. voltage scan rate (V) for melt solution saturated HCl gas.

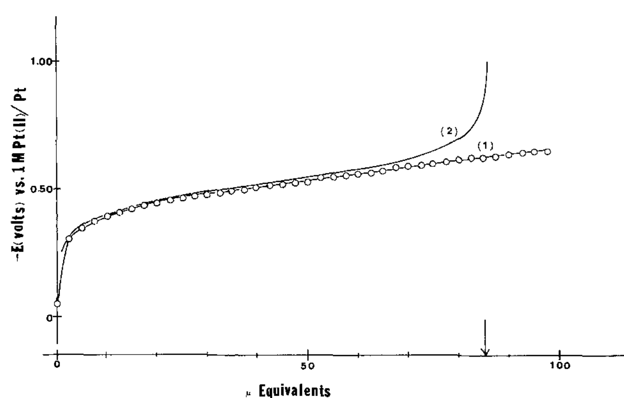

Fig. 3. Potentiometric titration curve for reduction of Cr(III) to Cr(II). Amount of Cr(III) added shown by arrow. Curve (1) Titration curve of 85.3 μequiv. Cr(III) in 3.3 ml melt solution; curve (2) Titration curve calculated theoretically.

To ensure that no hydrolysis of Cr(III) could occur, the melt was continuously stirred by a stream of HCl gas bubbles during the titration. The lack of an endpoint is no doubt due to the fact that the reduction potential of HCl is close enough to that of Cr(III) (5, 19)

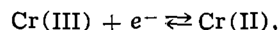

$$Cr(III) + e^- \rightleftarrows Cr(II),$$

$$E^\circ = -0.525V \text{ vs. } 1M \text{ Pt(II)/Pt} \quad [8]$$

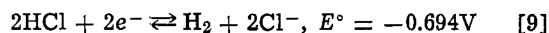

$$2HCl + 2e^- \rightleftarrows H_2 + 2Cl^-, \; E^\circ = -0.694V \quad [9]$$

so that quantitative reduction of Cr(III) could not be achieved before some HCl reduction took place. A color change corresponding to reaction [8] could be observed near the equivalence point although the potential change was obscured by mixed potential behavior.

Cyclic voltammetry of chromium(III) in moist HCl. —To determine the effect of moisture on the electrochemical behavior of the Cr(III)-Cr(II) couple, a series of cyclic voltammograms was run, varying the ratio of p_{H_2O}/p_{HCl} by equilibrating the Ar carrier gas with 12, 11, and 10*M* aqueous HCl, and using dry HCl gas as a comparison. The curves shown in Fig. 4 were run after bubbling for 20 min in each experiment. It is evident that the principal change is a marked lowering of the peak currents of both the cathodic and anodic branches.

By varying the voltage sweep rate, it was found that the cathodic peak current was proportional to the square root of sweep rate (Fig. 5), as would be expected for an essentially reversible mass-transport controlled process. We are led to the conclusion that an increasing fraction of the electroactive Cr(III) species is converted to an electrochemically inactive species by hydrolysis. We believe that the first step of hydrolysis

$$CrCl_6^{-3} + H_2O = CrCl_5(OH)^{-3} + HCl \quad [10]$$

is reversible and does not lead to an electroinactive species, but that subsequent polymerization reactions

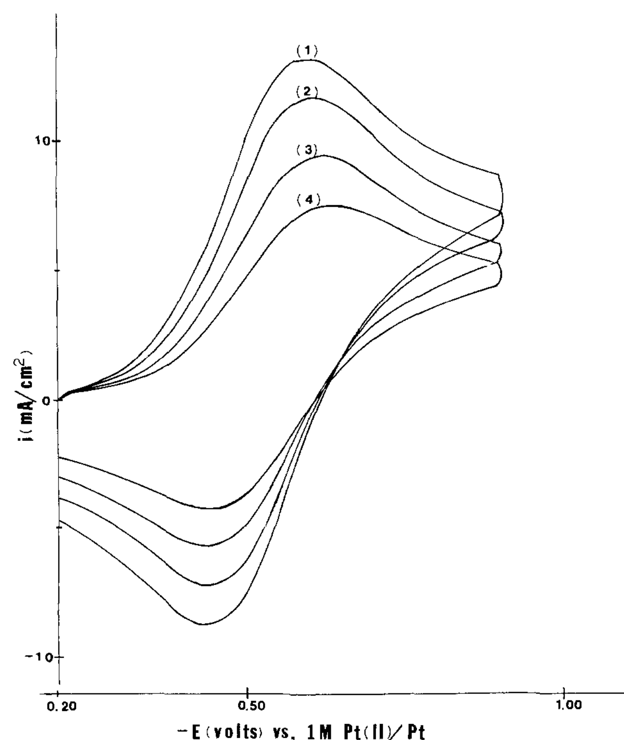

Fig. 4. Cyclic voltammograms for reduction Cr(III) to Cr(II) in melt solution equilibrated with dry HCl gas and moist HCl gas for 20 min. a) Voltage scan rate of 0.500 V/sec. Curve (1) Bubbling dry HCl gas; curve (2) bubbling moist HCl gas-I (12*M* HCl); curve (3) bubbling moist HCl gas-II (11*M* HCl) curve (4) bubbling moist HCl gas-III (10*M* HCl).

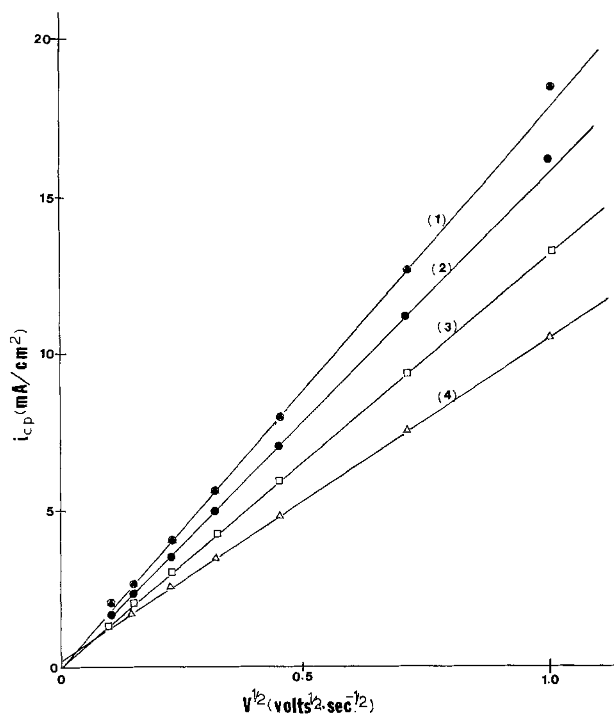

Fig. 5. Cathodic peak current (i_{cp}) vs. square root of voltage scan rate ($v^{1/2}$) for melt solution equilibrated with dry and moist HCl gases. Curve (1) Dry HCl gas; curve (2) moist HCl gas-I (12*M* HCl); curve (3) moist HCl gas-II (11*M* HCl); curve (4) moist HCl gas-III (10*M* HCl).

form bridged species such as through irreversible reactions

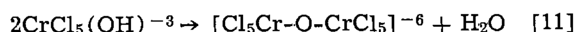

$$2CrCl_5(OH)^{-3} \rightarrow [Cl_5Cr\text{-}O\text{-}CrCl_5]^{-6} + H_2O \quad [11]$$

The final product would be an insoluble oxychloride of Cr(III).

To look for evidence for a slower charge-transfer reaction such as

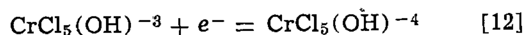

$$CrCl_5(OH)^{-3} + e^- = CrCl_5(\dot{O}H)^{-4} \quad [12]$$

in a moist solution, we calculated the charge transfer rate constant k_s as well as a first order rate constant k_f for the homogeneous chemical reaction subsequent to the primary charge transfer (reaction [4]). These parameters, calculated for four melt treatments are presented in Table I. The apparent decrease in D actually reflects a decrease in concentration, as mentioned above, whereas the changing k_s indicates a slower effective charge-transfer rate due to a greater participation of Eq. [12] as compared with Eq. [4] with increasing moisture content.

It was of interest to run a few experiments at 500°C, to allow a direct comparison with the work of Levy and Reinhardt (7) and to compare the hydrolysis effects at the two temperatures. Preliminary experiments showed a relatively rapid precipitation upon equilibration with 10*M* HCl, so this condition was omitted. The results are presented in Table II.

Comparing the two tables, we can conclude that the first hydrolysis reaction is less pronounced at 500° than at 450°C, evidently because of the lower solubility of water in relation to HCl. However, the subsequent irreversible polymerization reactions are more rapid at 500°C. This is illustrated by the effect of a short Ar flush, which results in a rapid change in calculated D and k_s due to the removal of HCl.

Table I. Calculated parameters of Cr(III) reduction in LiCl-KCl eutectic treated with dry and moist HCl gases for 20 min at 450°C

Treatment	$D \times 10^5$ (cm²/sec)	k_f (sec⁻¹)	k_s (cm/sec)
dry HCl	0.81	0.009	0.052
12*N* HCl	0.72	0.012	0.050
11*N* HCl	0.52	0.013	0.026
10*N* HCl	0.33	0.014	0.022

Table II. Calculated parameters of Cr(III) reduction in LiCl-KCl eutectic treated with dry HCl and moist HCl gas for 30 min at 500°C

	$D \times 10^5$ (cm²/sec)	k_f (sec⁻¹)	k_s (cm/sec)
dry HCl	0.92	0.021	0.098
12*N* HCl	0.85	0.018	0.022
11*N* HCl	0.85	0.014	0.095
dry Ar flush, 10 min	0.33	0.016	0.039

Comparing the data with dry HCl treatment at 500°C with those of Levy and Reinhardt, we observed a k_f value close to theirs, but larger D and k_s values. These differences imply that their experiments were done in the presence of a trace of moisture.

The polymerization reaction.—At 450°C in moist melts, it was found that a relatively rapid change in peak current and kinetic parameters occurred during the first 20 min, as described above, and that subsequent changes occurred much more slowly. These changes ultimately lead to the appearance of a solid phase, at a rate increasing with moisture content. The irreversible nature of this slow reaction was demonstrated by returning from the moist HCl to dry HCl bubbling. Instead of the voltammetric curves returning to their original heights, the peak continued to decrease in height.

A similar experiment at 500°C, in which the solution that had been flushed with dry Ar after equilibration with 11*M* HCl was treated with dry HCl gas, showed increased calculated values of D and k_s, but the recovery was not complete even after 2 hr. We conclude that the hydrolysis reactions can be reversed at higher temperature but the reverse reactions are quite slow.

Acknowledgments

This work was supported by the U.S. Army Research Office grant number DAAG 29-75-G-0092.

Manuscript submitted Jan. 16, 1978; revised manuscript received April 3, 1978.

Any discussion of this paper will appear in a Discussion Section to be published in the June 1979 JOURNAL. All discussions for the June 1979 Discussion Section should be submitted by Feb. 1, 1979.

Publication costs of this article were assisted by the University of Florida.

REFERENCES

1. H. A. Laitinen, R. Tischer, and D. K. Roe, *This Journal*, **107**, 546 (1960).
2. R. Combes, J. Vedel, and B. Tremillon, *Electrochim. Acta*, **20**, 191 (1975); R. Lysy and R. Combes, *J. Electroanal. Chem.*, **83**, 287 (1977).
3. I. Uchida and H. A. Laitinen, *This Journal*, **123**, 829 (1976).
4. K. Niki and H. A. Laitinen, *J. Inorg. Nucl. Chem.*, **37**, 91 (1975).
5. H. A. Laitinen and C. H. Liu, *J. Am. Chem. Soc.*, **80**, 1015 (1958).
6. H. A. Laitinen, C. H. Liu, and W. S. Ferguson, *Anal. Chem.*, **30**, 1266 (1958).
7. S. C. Levy and F. W. Reinhardt, *This Journal*, **122**, 200 (1975).
8. G. Harrington and B. Sundheim, *Ann. N.Y. Acad. Sci.*, **79**, 950 (1960).
9. H. C. Brookes and S. N. Flengas, *Can. J. Chem.*, **48**, 55 (1970).
10. D. M. Gruen and R. L. McBeth, *J. Phys. Chem.*, **66**, 57 (1962).
11. G. B. Heisig, B. Fawkes, and R. Hedin, "Inorganic Synthesis," Vol. 2, p. 193, McGraw-Hill, New York (1946).
12. A. B. Bury, "Inorganic Synthesis," Vol. 2, p. 150, McGraw-Hill, New York (1946).

13. W. S. Ferguson, Ph..D Thesis, University of Illinois, Urbana, Illinois (1956).
14. Beckwith Carbon Corp., Technical Leaflet.
15. R. O. Johnston, Ph.D. Thesis, University of Illinois, Urbana, Illinois (1974).
16. "International Critical Table," Vol. 3, p. 301, McGraw-Hill, New York (1928).
17. R. S. Nicholson, *Anal. Chem.*, **38**, 1406 (1966).
18. H. A. Laitinen and B. B. Bhatia, *ibid.*, **30**, 1995 (1958).
19. H. A. Laitinen and J. A. Plambeck, *J. Am. Chem. Soc.*, **87**, 1202 (1965).

The Electrochemical Behavior of Selenium and Selenium Compounds in Sodium Tetrachloroaluminate Melts

J. Robinson and R. A. Osteryoung*

Department of Chemistry, Colorado State University, Fort Collins, Colorado 80523

ABSTRACT

The electrochemistry of selenium and various selenium compounds in $AlCl_3$:NaCl melts has been investigated by a variety of techniques including pulse and cyclic voltammetry, coulometry, and the rotating-disk electrode. It was found that selenium can be reduced, in both acid and basic melts, by a single two-electron step to selenide which exists in the melt as either AlSeCl or $AlSeCl_2^-$ (or their analogous solvated species $Al_2SeCl_5^-$ and $Al_2SeCl_6^{2-}$) depending upon the acidity. The mechanism for the oxidation of selenium to Se(IV) was found to be dependent upon the melt acidity. In basic melts, selenium was first oxidized by a two-electron step to an Se(II) species and then by a further two-electron step to Se(IV). In acid melts the oxidation was a single quasireversible four-electron step. The reduction of Se(IV) to selenium was a single four-electron step at all melt acidities. The kinetics of these oxidation and reduction processes were investigated extensively. From studying $SeCl_4$ solutions, it was found that there were two Se(IV) species in the melt, $SeCl_6^{2-}$ and $SeCl_5^-$, linked by the acidity-dependent equilibrium

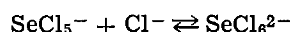

$$SeCl_5^- + Cl^- \rightleftarrows SeCl_6^{2-}$$

for which the equilibrium constant was calculated to be $6.0 \pm 1.0 \times 10^3$ on the mole fraction scale.

In recent years there has been considerable interest in the use of fused-salt media as electrolytes for high energy density batteries and fuel cells. In view of this, there have been several papers dealing with the electrochemical behavior of chalcogens and their compounds in these systems. Sulfur has been studied in a variety of these molten salts including most recently sodium tetrachloroaluminate, both in this laboratory (1) and by Mamantov and co-workers (2, 3). Studies of selenium are, however, much fewer. Bodewig and Plambeck (4) have investigated its electrochemistry in fused LiCl-KCl melts and observed that it undergoes oxidation and reduction to Se_2Cl_2 and Se^{2-}, respectively, while Shimotake and Cairns (5) have investigated a Li/Se battery using a ternary eutectic of LiF, LiCl, and LiI as the electrolyte. Recently, while screening cathode materials for use in an $AlCl_3$:NaCl battery, Marassi *et al.* (2) studied the electrochemistry of Se. They ran cyclic voltammograms on a saturated solution of Se in a 63-37 mole percent (m/o) $AlCl_3$:NaCl melt at a platinum electrode and observed a quasireversible oxidation couple close to the anodic limit of the melt and a reduction process at about 1V *vs.* an Al wire in the melt. They also observed a second, irreversible, reduction wave that appeared only on platinum electrodes. No coulometric studies were undertaken in this study; therefore, it is unknown what the reaction products were.

This latter paper appears to be the only published electrochemical study of Se in tetrachloroaluminates. There have, however, been a few studies of stabilization of low oxidation states of Se in these melts. It has been established that the large anions, $AlCl_4^-$ and $Al_2Cl_7^-$, present in acid tetrachloroaluminates are capable of stabilizing low oxidation states of metals such as Cd_2^{2+}, Sn_2^{2+}, Pb^+, and cluster cations of Te (6, 7), and recently Bjerrum *et al.* (8) identified a variety of low oxidation state species of Se such as Se_4^{2+}, Se_8^{2+}, Se_{12}^{2+}, and Se_{16}^{2+}. These were observed spectrophotometrically in mixtures of Se and $SeCl_4$ in acid tetrachloroaluminate melts and the natures of the species were found to be dependent upon the relative amounts of Se and Se(IV) present. Corbett *et al.* (9) have also studied similar systems, Se-($SeCl_4$ + $AlCl_3$) mixtures, and have identified the species Se_4^{2+} and Se_8^{2+} as being present.

Selenide anions are known to exhibit interesting chemistry in $AlCl_3$:NaCl melts. Metal oxides and chalcogenides have been observed to react with $AlCl_3$ in closed tubes at temperatures around 300°C to yield the species AlOCl (10), AlSCl (10), AlSeCl (11), and AlTeCl (12) as the products of reactions such as

$$AlCl_3 + ZnSe \rightleftarrows AlSeCl + ZnCl_2 \quad [1]$$

In a recent study in this laboratory (13), it was shown that similar reactions occur in acidic $AlCl_3$:NaCl melts where the oxide and chalcogenide ions behave as tribases reacting with the melt to yield the same species. In basic melts these anions were shown to be dibases and the product of reaction with the melt was then a species such as $AlSeCl_2^-$. The relative strengths of the tribases were found to be

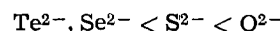

$$Te^{2-}, Se^{2-} < S^{2-} < O^{2-}$$

The papers discussed above are the only published studies of selenium and its compounds in tetrachloroaluminate melts. This paper is concerned with the electrochemistry, principally at 175°C, of these species with particular attention being given to its acidity de-

* Electrochemical Society Active Member.
Key words: fused salts, voltammetry, electrolysis, kinetics.

pendence. In order to examine this the acid-base properties of the solvent must be fully understood. The three principal equilibria linking the major species present are (14)

$$2AlCl_3(l) \rightleftarrows Al_2Cl_6(l) \quad K_o = 2.86 \times 10^7 \quad [2]$$

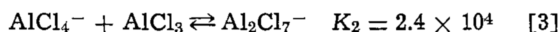

$$AlCl_4^- + AlCl_3 \rightleftarrows Al_2Cl_7^- \quad K_2 = 2.4 \times 10^4 \quad [3]$$

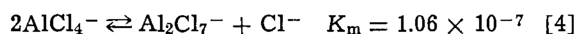

$$2AlCl_4^- \rightleftarrows Al_2Cl_7^- + Cl^- \quad K_m = 1.06 \times 10^{-7} \quad [4]$$

where K_o, K_2, K_m are the mole fraction equilibrium constants at 175°C. The dominant acid-base equilibrium is that described by Eq. [4] with Cl^- as the Lewis base and $Al_2Cl_7^-$ the Lewis acid. The pCl$^-$ of the neutral melt, 50 m/o $AlCl_3$, is 3.5 on the mole fraction scale; however, a melt of any desired acidity can be made (15) by anodizing an Al wire into the melt until the desired value, as indicated by an aluminum wire electrode, is reached.

Experimental

Melt preparation and purification.—The preparation of pure NaCl-saturated $NaAlCl_4$ melts by the preelectrolysis of a molten mixture of $AlCl_3$ (A. G. iron-free Fluka) and an excess of NaCl(A. C. S. Fisher) between two aluminum electrodes has been described elsewhere (15). After purification, a sample of the melt was filtered through a medium porosity frit to remove any excess NaCl or suspended aluminum particles and was then transferred to the small Pyrex glass experimental cell.

The melt preparation and all subsequent electrochemical experiments were performed in a dry box (Vacuum Atmospheres Company) under an argon atmosphere. This dry box was fitted with a purification system (Vacuum Atmospheres dri-train HE 193-2) that recycled the atmosphere through activated copper and molecular sieves to remove oxygen and water, respectively. The level of oxygen in the atmosphere was determined by burning a 25W tungsten lamp filament (General Electric Company) exposed to the atmosphere (16). A bulb lifetime of several days, indicating an atmosphere containing around 1 ppm of oxygen, was considered satisfactory.

Experimental cells and electrodes.—The cells were made of Pyrex glass, with a volume of approximately 75 cm^3, and had a fitted Teflon cap. This cap was drilled to facilitate the mounting of the secondary- and reference-electrode compartments, which consisted of fine porosity frits mounted on Pyrex glass tubes, the thermocouple well, and the working electrode. The working electrode compartment could readily be stirred using a glass-coated magnetic stirrer bar. The assembly was mounted in a tube furnace and the temperature was maintained within ± 1°C by a controller (Thermo-Electric Model 32422) in conjunction with a Chromel-Alumel thermocouple.

For all experiments, the reference electrode was a coiled aluminum wire (Alfa Inorganics m5N) immersed in an NaCl-saturated melt at 175°C. Throughout this paper, all potentials are referred to this electrode. The secondary electrode was also a coiled aluminum wire.

The electrodes in the voltammetric studies were either tungsten (1/8 in. diam Alfa Inorganics m3N8) or vitreous carbon (3 mm diam Atomergic Chemetals V25 or 2.5 mm diam Tokai GC 30), mounted in Pyrex glass. These were ground flat on an emery wheel and then polished to a mirror-like finish using alumina (Type B Fisher). Rotating-disk studies were carried out on a vitreous carbon disk electrode (5 mm diam Tokai GC 30) mounted and prepared in the same way as the above electrodes. This electrode was rotated by a servocontrolled motor-tachometer (Pine Instrument Company Type ASR 2), the rotation rate of which could be controlled between 50 and 10,000 rpm with an accuracy of greater than 1%.

Exhaustive controlled potential coulometry was carried out in either a tungsten crucible (Research Organic/Inorganic Chemical Corporation W120) or a vitreous carbon crucible (Atomergic Chemetals Company V25-16) used both as the cell and working electrode. Adequate mass transport was achieved by stirring with a glass-coated magnetic stirring bar and the total charge passed in these experiments was measured by a coulometer (Acromag Incorporated).

Electrochemical instrumentation.—All cyclic voltammetry and rotating-disk studies were made with a multipurpose instrument (17) constructed in this laboratory and the data were recorded on an X-Y recorder (Hewlett Packard Model 7046A). Pulse voltammetric studies were performed on a pulse polarograph (PARC Model 174), modified (18) to permit parametric studies. The melt acidity was adjusted by the anodization of an aluminum wire (Alfa Inorganics m5N) into the melt using a constant current source (Sargent Model IV coulometric current source) as has been discussed previously (13).

Chemicals.—Na_2Se (Cerac Pure, Incorporated), Na_2SeO_4, Na_2SeO_3, $SeCl_4$, and Se_2Cl_2 (Alfa Inorganics) were all used without further purification. The most readily soluble type of selenium was found to be the red amorphous form, presumably due to its structure, long chains, as compared to the ring structure of the vitreous form. This was prepared by reducing a solution of Na_2SeO_3 in 9M HCl with SO_2 (Matheson Gas Products) (25). The red precipitate was then filtered and washed, dried with diethyl ether, and finally dried under a vacuum.

Results and Discussion

A cyclic voltammogram of 1.18×10^{-3}M selenium in an NaCl saturated melt at 175°C is shown in Fig. 1. It can be seen that there is a reduction peak at 0.880V on the cathodic going sweep from the electrode rest potential. On the return sweep there is a very slight shoulder at about 0.950V followed by a peak at 1.140V; there are then two oxidation peaks close to the anodic limit of the melt, at 1.88 and 2.02V. Finally, on the return sweep there is a peak at 1.80V. Successive sweeps are identical to the first. Figure 2 is a cyclic voltammogram of a solution of sodium selenide, also in an NaCl saturated melt, showing the same features as Fig. 1. As the acidity is increased, Fig. 2b and 2c, the behavior changes significantly. The peaks previously seen at 0.880 and 1.140V in an NaCl-saturated melt move together and also in an anodic direction while the features close to the anodic limit of the melt change considerably. The cyclic voltammogram in the most acid

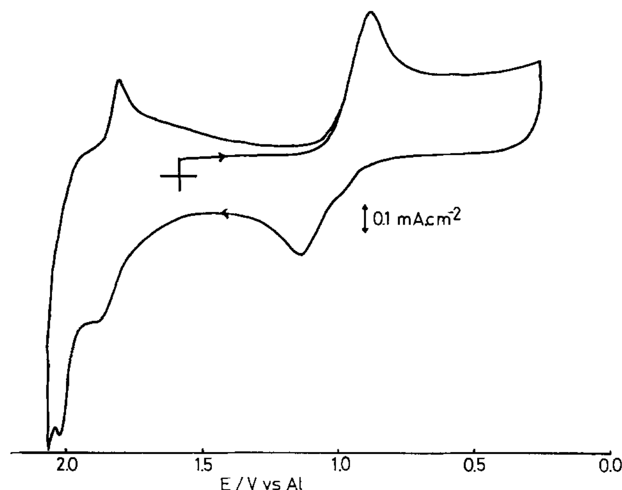

Fig. 1. Cyclic voltammogram of Se in NaCl-saturated melt (pCl = 1.9) at a glassy carbon electrode. Temperature = 175°C; sweep rate = 100 mV sec^{-1}; concentration of Se (as monomer) 1.18 mM.

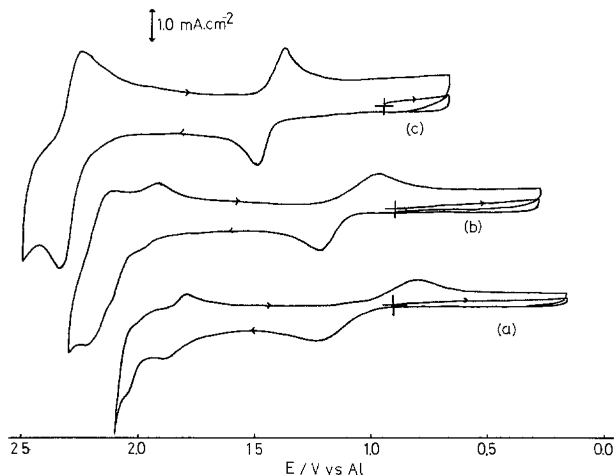

Fig. 2. Cyclic voltammogram of 3.6 mM Na_2Se at a glassy carbon electrode. Temperature = 175°C; sweep rate = 200 mV sec^{-1}. Melt pCl. (a) 1.9; (b) 2.9; and (c) 5.2.

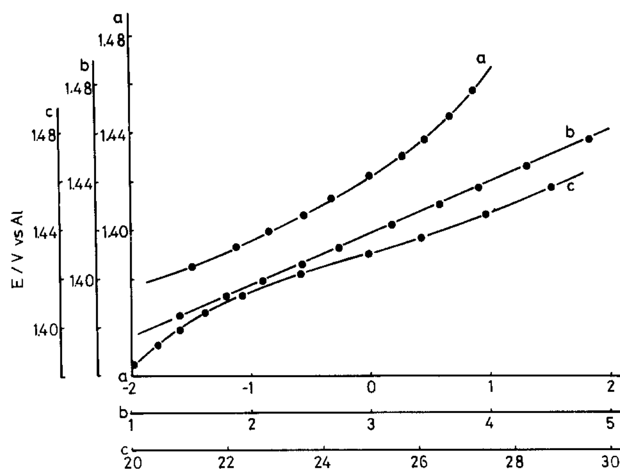

Fig. 3. Nernst plots for various Se/Se^{2-} redox couples at a pCl of 5.7 and at 175°C using a glassy carbon electrode. The units of the abscissa are (a) $\log_{10}[Se]/[Se^{2-}]$; (b) $\log_{10}[Se_2]/[Se^{2-}]^2$; and (c) $\log_{10}[Se_8]/[Se^{2-}]^8$.

melt, Fig. 2c, closely resembles that observed by Marassi *et al.* (2) for selenium on a platinum electrode in an acid melt, except that the second selenium reduction peak seen on platinum is not seen here, either for a vitreous carbon or tungsten electrode. The voltammograms shown here were all made with a vitreous carbon electrode. The behavior of a tungsten electrode was, however, very similar except that selenium, as evidenced by the shape of the cyclic voltammetric peak, appeared to adsorb strongly. For this reason all subsequent work was carried out at a vitreous carbon electrode.

To facilitate this discussion the electrochemistry of selenium is considered in two parts. The first deals with the selenium reduction, observed at 0.880V in an NaCl-saturated melt, and the subsequent oxidation of the product, which, as is shown later, is the selenide ion. The second part considers the oxidation of selenium to selenium cations and their reduction back to selenium.

The selenium-selenide couple.—Exhaustive constant potential coulometry was performed on a solution of selenium in both basic and acidic melts at a potential corresponding to the diffusion plateau of the reduction peak. It was found that for basic melts (pCl = 1.9) 2.03 ± 0.05 electrons/selenium atom were passed, while the corresponding value in an acidic melt (pCl = 6.0) was 1.99 ± 0.05. A cyclic voltammogram of the resulting solution was identical to that of a solution of sodium selenide. In the same way, sodium selenide was oxidized by a two-electron step to give a solution behaving like a solution of selenium. It can therefore be concluded that selenium is reduced by a two-electron step to selenide which itself can be oxidized back to selenium, again by a single two-electron transfer.

To obtain more information about the nature of the selenium and selenide species in the melt, the dependence of the equilibrium potential of a vitreous carbon indicator electrode on the concentrations of selenium and selenide ion present was investigated. A solution of known concentration of sodium selenide was prepared in a vitreous carbon crucible. A small amount of the selenide ion was then oxidized to selenium using the crucible as a working electrode and the rest potential of the indicator electrode was measured. The concentrations of selenium and selenide ion were readily determined from the number of coulombs passed. This procedure was repeated many times until all the selenide had been oxidized to selenium. The potential of the crucible was then changed and the selenium was reduced, in a stepwise fashion, back to selenide with equilibrium potential measurements again being made.

Figure 3 shows three attempts at fitting this data to possible redox reactions. Curve (a) corresponds to the plot for the equilibrium

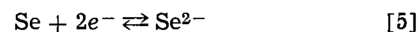

$$Se + 2e^- \rightleftarrows Se^{2-} \quad [5]$$

curve (b) to

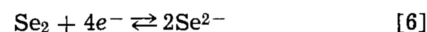

$$Se_2 + 4e^- \rightleftarrows 2Se^{2-} \quad [6]$$

and curve (c) to

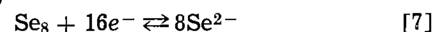

$$Se_8 + 16e^- \rightleftarrows 8Se^{2-} \quad [7]$$

It can immediately be seen that while plots (a) and (c) are curved, plot (b) is a straight line and furthermore, its slope is 22 mV which is in agreement with the value predicted, 22.3 mV at 175°C, by the Nernst equation for this process

$$E = E^\circ + 2.303 \frac{RT}{3\mathbf{F}} \log \frac{[Se_2]}{[Se^{2-}]^2} \quad [8]$$

This implies that the potential determining selenium species is the dimer Se_2, as was observed previously for the sulfur-sulfide couple (1). The above data were obtained in an acidic melt (pCl = 5.7); however, similar results, indicating the Se_2 dimer to be the potential determining species, were obtained for all the melt acidities investigated (pCl = 1.9-6.0). This is perhaps surprising in view of the fact that Se_2 is not normally stable except as a vapor at temperatures greater than 900°C. The thermodynamically stable form of selenium at 175°C is the gray form, which consists of long chains (15) between 10^3-10^4 units long. This is not, however, known to be soluble in any solvents. At room temperature there are two unstable allotropes, both of which consist of puckered Se_8 rings. These forms, which are soluble in several solvents such as CS_2, rapidly convert to the gray form on heating. Since the temperature of the melt is above this transition temperature, any Se added will rapidly convert to the gray form; the melt must then have the effect of splitting off Se_2 groups which it stabilizes. This probably explains the very slow solubilization of Se observed in this present work.

These potentiometric experiments were carried out at a range of melt acidities and it was found that the standard potential for the couple showed a very strong dependence on the pCl. This observation has been discussed in an earlier paper (13), and, as outlined in the introduction to this study, is due to the basic properties of the selenide ion. In melts more acidic than a pCl of 3.5, on the mole fraction scale, the selenide ion behaves as a tribase and reacts with the acid species in the melt, $Al_2Cl_7^-$, to form the species AlSeCl, or, more probably, the solvated species $Al_2SeCl_5^-$. Similarly, in basic melts the selenide ion behaves as a dibase and is present either as $AlSeCl_2^-$ or $Al_2SeCl_6^{2-}$. The redox reaction should therefore be written as

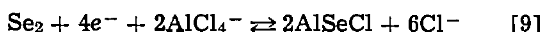

$$Se_2 + 4e^- + 2AlCl_4^- \rightleftarrows 2AlSeCl + 6Cl^- \quad [9]$$

in acid melts, and

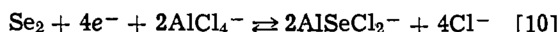

$$Se_2 + 4e^- + 2AlCl_4^- \rightleftarrows 2AlSeCl_2^- + 4Cl^- \quad [10]$$

in basic melts.

It has been shown (1) that the basic properties of the sulfide ion result in very high solubilities of metal sulfides, for example CuS, in acidic melts. Very similar behavior was observed for selenides; in a 60 m/o $AlCl_3$:NaCl melt the solubility of CuSe was found to be 0.32M. Oxides and tellurides were also found to be solubilized to the same degree, which suggests that acidic tetrachloroaluminate melts may have some application in the processing of metal ores.

The oxidation of selenide ions, or more precisely the species AlSeCl and $AlSeCl_2^-$, to selenium was investigated initially by pulse voltammetry. Figure 4 shows such a pulse voltammogram in an NaCl-saturated melt. The first wave is due to the oxidation of selenide to selenium and there is also a slight indication of waves due to the oxidation of selenium, as observed in cyclic voltammetry (Fig. 1 and 2a). These latter waves, however, are very small. The first wave, when analyzed by the method of Oldham and Parry (20), yielded a linear plot from which αn_α was calculated to be 0.59. The limiting current for the wave also showed a linear dependence on selenide ion concentration, and the diffusion coefficient of the diffusing species, probably the solvated form of $AlSeCl_2^-$, was calculated to be $2.3 \pm 0.2 \times 10^{-6}$ cm^2 sec^{-1}. While the position of the wave was strongly dependent upon the pCl of the melt, the values of αn_α and D were, despite the change in the nature of the selenide species, independent of the acidity.

Pulse voltammetry proved to be a fairly successful technique for investigating the kinetics of the oxidation process; however, the method of choice is the use of the rotating-disk electrode (RDE). Very large currents are obtained for low concentrations of electroactive material and, since the measurements are made at a steady state, there is no charging current adding to the background.

Figure 5 shows some results of a series of RDE experiments carried out on a solution of sodium selenide. These plots were obtained by sweeping the electrode potential at a rate of 2 mV sec^{-1} at various fixed rotation rates. A plot of the diffusion current, measured at a steady state, as a function of the square root of the rotation rate, $\omega^{1/2}$, is a straight line at all melt acidities, indicating that the oxidation of selenide is diffusion controlled. The diffusion current also varies linearly with the concentration of sodium selenide. From the i vs. $\omega^{1/2}$ plots, the diffusion coefficient of the selenide species is readily calculated (21) and values at a range of melt acidities are shown in Table I. These are in close agreement with the values obtained earlier from the pulse voltammetry and are independent of the melt acidity.

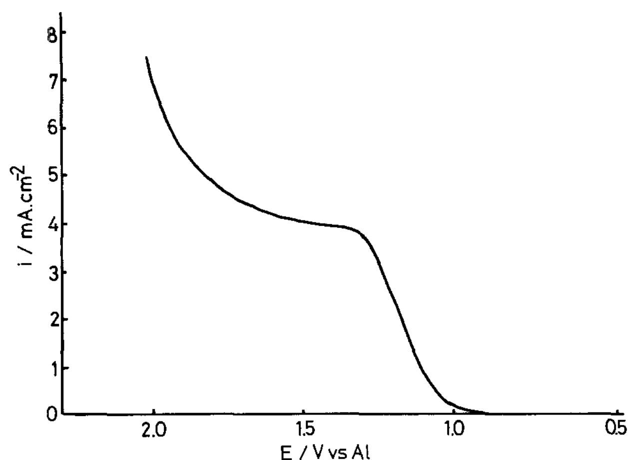

Fig. 4. Normal pulse of 5.2 mM Na_2Se at a glassy carbon electrode. Melt pCl = 1.9; pulse width 48 msec; sweep rate 5 mV sec^{-1}; temperature = 175°C.

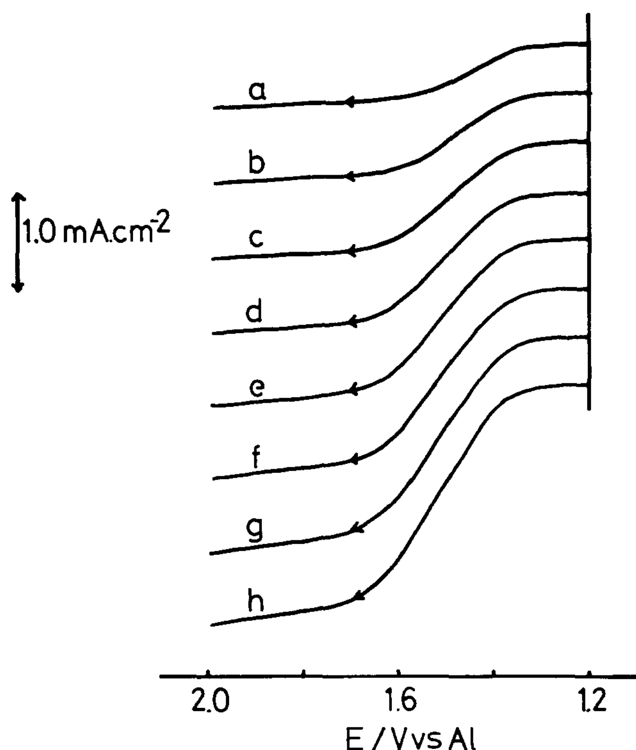

Fig. 5. RDE experiment for 2.06 mM Na_2Se at a glassy carbon electrode. Melt pCl = 4.5; rotation rates are (a) 400; (b) 900; (c) 1600; (d) 2500; (e) 3600; (f) 4900; (g) 6400; and (h) 8100 rpm; temperature = 175°C.

The rising portions of the plots in Fig. 5 are fairly drawn out; this behavior is typical of a process for which the rate is being controlled by a slow electron transfer, and the rate constant for this step can be determined (21). Figure 6 shows a kinetic plot ($1/i$ vs. $1/\omega^{1/2}$) for a sodium selenide solution under the same conditions as Fig. 5, the steady-state currents at various potentials within the rising portion of the waves being determined for a range of rotation rates. The plots are a series of parallel lines as would be expected for a slow electron-transfer step. If these lines are extrapolated to where $\omega^{-1/2}$ equals zero, that is to an infinite rotation rate, the intercept on the y-axis then corresponds to the pure kinetically controlled current since the rate of mass transfer is infinite. From these intercepts the forward rate constant can be calculated, and Fig. 7 shows a plot of $\log_{10} \vec{k}$ vs. potential. This plot is a straight line and the value of αn_α can be calculated from the slope. Knowing the value of the standard potential, E_o, from potentiometry, the standard rate constant, $k_o^\ominus$, can be determined. The values of $k_o^\ominus$ and αn_α obtained

Table I. Kinetic parameters and diffusion coefficients, obtained from RDE experiments, for oxidation of Na_2Se at 175°C

pCl[a]	$k_o^\ominus \times 10^5$ [b]	αn_α	$D \times 10^6$ [c]
1.9	4.6	0.58	1.99
2.7	6.3	0.53	1.95
3.5	8.9	0.55	2.03
4.5	7.1	0.58	2.01
6.2	17.8	0.55	2.04

[a] Mole fraction scale.
[b] cm sec^{-1}.
[c] cm^2 sec^{-1}.

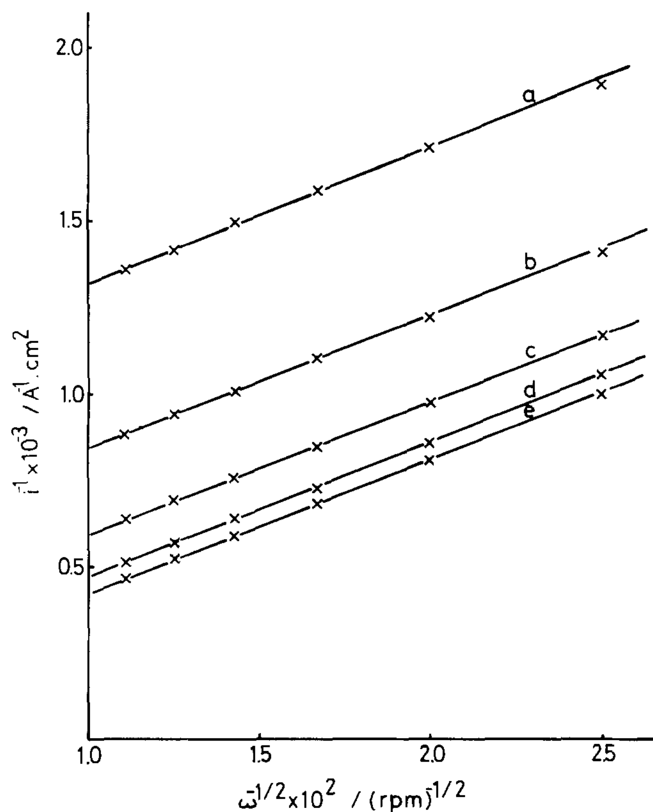

Fig. 6. Kinetic plot for 2.06 mM Na_2Se at 175°C in a melt with $pCl = 4.5$. Potentials (a) 1.5V; (b) 1.55V; (c) 1.6V; (d) 1.65V; (e) 1.7V.

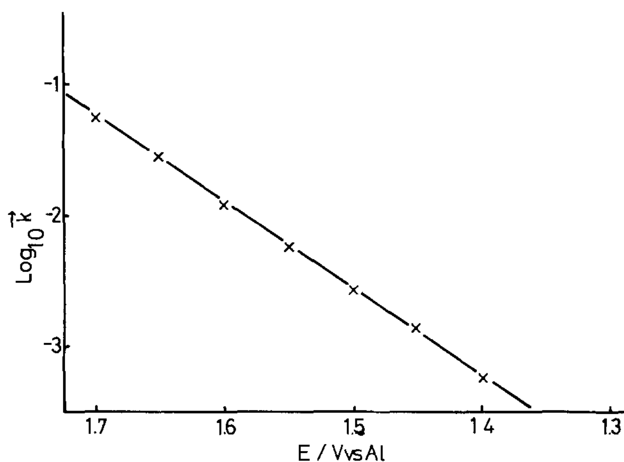

Fig. 7. Plot of the potential dependence of log $\vec{k}$ for the oxidation of Na_2Se at 175° in a melt with $pCl = 4.5$.

at various pCl's are given in Table I. The values of αn_α are independent of pCl and are in good agreement with those calculated from pulse voltammetry. The values of k_0^Θ show a slight increase with melt acidity.

It was observed earlier on the cyclic voltammograms of sodium selenide (Fig. 2) that the peaks corresponding to the reduction of selenium and the subsequent reoxidation of selenide moved closer with increasing pCl; that is, the reaction appeared to become more reversible. The RDE experiments, however, show that changing the pCl has only a slight effect on the rate of oxidation of selenide, certainly not enough to account for the apparent increase in reversibility. The observed decrease in peak separation must, therefore, be due to the increased acidity affecting the reduction of selenium. Both pulse voltammetry and RDE experiments were attempted as a means of investigating this, but no kinetic information could be obtained as selenium was found to adsorb slightly at the vitreous carbon electrode. This adsorption, which is greatest in basic solutions, can also be seen on cyclic voltammograms (Fig. 1) where the reduction peak for selenium is higher and sharper than the corresponding oxidation peak.

Interesting qualitative information was, however, obtained from the temperature dependence of the cyclic voltammetry of selenium solutions. Figures 8a, 8b, and 8c show cyclic voltammograms at 175°, 225°, and 275°C, respectively, of a selenium solution with all the potentials adjusted to the same reference electrode; an Al wire in an NaCl-saturated melt at 175°C. The melt used was of fixed composition, that of an NaCl-saturated melt at 175°C. The increase in temperature, therefore, caused a reduction in the melt acidity due to the increased dissociation of $AlCl_4^-$. These pCl changes were, however, much too small to account for the gross changes observed on the cyclic voltammograms. The selenium reduction potential changes from approximately 0.840V at 175°C to 0.985V at 225°C and to 1.090V at 275°C. The corresponding selenide oxidation potentials are 1.16, 1.13, and 1.15V. Thus, it can be seen that, within experimental error, the position of the selenide oxidation peak hardly changes with temperature, while the selenium reduction potential moves anodically 250 mV for a temperature increase of 100°C, the peak separation decreasing from 320 to 60 mV, which is close to the value for a two-electron reversible process at 75°C (54 mV). The most probable explanation for this behavior is that there is a chemical step involved in the reduction, the rate of which is greatly affected by temperature. One such possible chemical step could be the monomerization of the selenium dimer. The apparent increase in reversibility as the pCl is increased, Fig. 2a, 2b, and 2c, may also be explained by the increased rate of the same chemical step.

At this point, it should be mentioned that the nature of the slight shoulder seen at about 0.950V on an anodic going sweep of a selenium solution, Fig. 1 and 8a, is uncertain, though it may be associated with the selenium adsorption discussed earlier. It only appears on cyclic voltammograms in the most basic melts and disappears as the temperature is increased, Fig. 8b and 8c.

The electrochemical oxidation of selenium and the behavior of selenium cations.—From Fig. 1 and 2 it can be seen that the oxidation of selenium and the reduction of the products of this oxidation are fairly

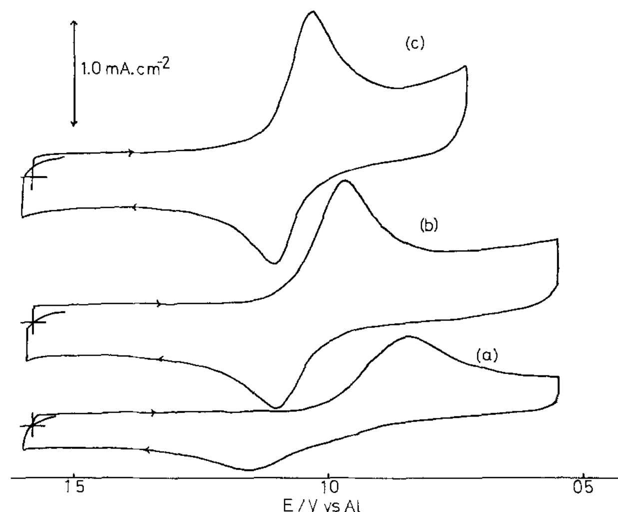

Fig. 8. Cyclic voltammogram of 1.18 mM Se (as monomer) in a basic melt (NaCl saturated at 175°C) at a glassy carbon electrode. Sweep rate = 200 mV sec^{-1}. Temperature (a) 175°C; (b) 225°C; (c) 275°C.

complex in these melts. Considering first the behavior in the most basic solutions, there are two rather poorly defined oxidation peaks for selenium at 1.88 and 2.02V with a corresponding reduction wave at 1.79V. If the potential scan is reversed after the first oxidation peak, there is still a single reduction wave at 1.79V. In order to determine the over-all stoichiometry, exhaustive coulometry was carried out on a selenium solution in a vitreous carbon crucible. If the coulometry was performed at about 1.9V in an NaCl-saturated melt (pCl = 1.9) a total of 2.03 ± 0.05 electrons/selenium atom were passed to yield an Se(II) species. Continued coulometry at about 2.05V gave a further two electrons, after correction for the background current which was rather large due to the proximity of the anodic limit of the melt. The final oxidation product, therefore, appears to be an Se(IV) species. These coulometry experiments could be carried out fairly rapidly (about 15 min each), and therefore no problem of product volatility was encountered. When potentiometric measurements were made on these couples, it was found that both the Se(IV) and Se(II) species were slowly lost from the melt, the latter being lost more rapidly. It was, therefore, not possible to make any Nernst plots. As it was found the Se(IV) was the highest oxidation state of selenium as formed $SeCl_4$ was added to the melt. A cyclic voltammogram of a solution of this showed all the same features as one of selenium or sodium selenide, and coulometry at about 1.7V showed that 4.1 ± 0.05 electrons were passed for each molecule of $SeCl_4$ added. Sodium selenite behaved in exactly the same way as $SeCl_4$, showing the high affinity of the melt for oxide ions (13). Sodium selenate, when added to the melt, first evolved chlorine and then behaved as $SeCl_4$ while Se_2Cl_2 appeared to decompose when added to the melt.

As the pCl is increased, Fig. 2b, the situation becomes more complex. The oxidation peaks formerly at 1.88 and 2.02V and the reduction peak at 1.79V are all still present but have shifted in the anodic direction and there is now a new oxidation wave at 2.19V with its corresponding reduction wave at 2.14V. As the acidity is increased further, Fig. 2c, the picture simplifies, there being a single oxidation peak and corresponding reduction peak. Coulometry at such an acidity shows that both the oxidation and reduction are four electron steps. It is therefore clear that, as in basic melts, the highest oxidation state formed is Se(IV), but the oxidation of selenium to Se(IV) now goes by a different route.

The cyclic voltammetry of an $SeCl_4$ solution of intermediate pCl, such as the pCl of Fig. 2b (pCl = 2.9) shows two reduction waves. However, if coulometry is carried out on the first wave at about 2.1V four electrons/$SeCl_4$ molecule are passed with the formation of a solution of selenium. It therefore appears that there are two Se(IV) species in the melt linked by a pCl-dependent equilibrium. This is supported by the fact that the more anodic wave grows at the expense of the other as the melt is made more acidic. The equilibrium constant for this equilibrium is calculated later from RDE results. The oxidation of selenium in very basic melts can therefore be summarized as the oxidation to Se(II) and then to an Se(IV) species followed by the subsequent four-electron reduction back to selenium. This changes in acid melts to a single quasireversible four-electron oxidation to a different Se(IV) species while at intermediate acidities both mechanisms are seen to operate.

Attempts to investigate more closely the oxidation of selenium in basic melts by either pulse voltammetry or RDE's proved fruitless. This was due in part to the proximity of the waves to the anodic limit of the melt but principally to the fact that the currents observed for these processes were very much less than would be predicted for a diffusion-controlled process. It can be concluded from this that either a very slow electron-transfer step is occurring or more probably that there are chemical steps involved in these processes. From the cyclic voltammetry it can be seen that the peaks for the Se-to-Se(II) and Se(II)-to-Se(IV) oxidations both move in an anodic direction as the acidity increases, indicating that chloride ions are involved in both these steps. It is a reasonable assumption, therefore, that both the Se(II) and Se(IV) species are chloro-complexed. It was observed that the cyclic voltammetry peak potentials for the reduction of solutions of Se(IV) and Se(II) (prepared by potentiostatic oxidation of a Se solution) were identical (1.79V at a pCl of 1.9). This suggests that the Se(II) species undergoes a chemical step prior to reduction, either a disproportionation into Se(IV) and Se or, alternatively it is a polymeric species that undergoes decomposition to Se(IV) and Se. Such a chemical step is supported by the observation that the acidification of Se(II) solution with $AlCl_3$ results in the formation of Se and Se(IV) by either a disproportionation or decomposition mechanism. Similar instability of the Se(II) ion to disproportionation is observed in fluoroacetic acid solutions (22).

In contrast to the behavior of basic melts, the oxidation of selenium in acid melts is readily studied, and Fig. 9 shows a normal pulse voltammogram at a pCl of 5.23 at three pulse widths. Plots of the diffusion current *vs.* $1/t^{1/2}$ and concentration are both linear, indicating the process to be diffusion controlled, and the diffusion coefficient of selenium was calculated to be $3.0 \pm 0.3 \times 10^{-6}$ cm^2 sec^{-1}.

The reduction of Se(IV) was studied using an RDE, and Fig. 10 shows a series of slow voltage scans, at fixed rotation rate, for three pCl values. In the most basic melt there is a very small wave followed by a much larger one, but as the acidity is increased the first wave grows at the expense of the other until in the most acid melts there is only one wave. This type of behavior is identical to that seen in the cyclic voltammetry and is attributed to there being two Se(IV) species in an acid-dependent equilibrium. At all pCl's the relative heights of the two waves are independent of the rotation rate and of the Se(IV) concentration, which indicates that the interconversion of the two species is slow and that there is no difference in the degree of polymerization between them. The diffusion current for the wave in the most acid melt varies linearly with $\omega^{1/2}$ and Se(IV) concentration, showing the reduction to be diffusion-controlled and the diffusion coefficient of the Se(IV) species was calculated to be 6.9 ± 10^{-6}

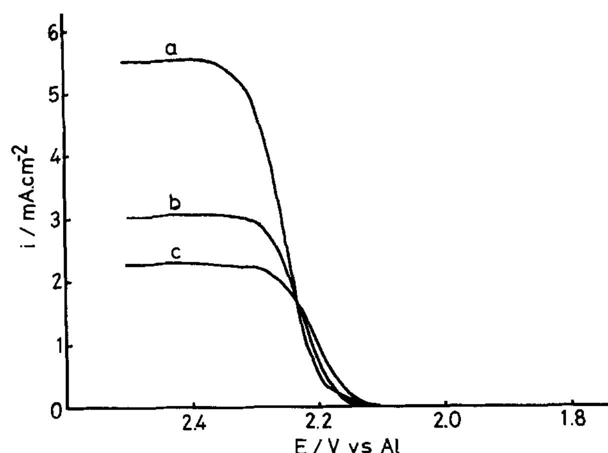

Fig. 9. Normal pulse voltammograms for the oxidation of 1.78 mM Se (as monomer) at a glassy carbon electrode in an acid melt (pCl = 5.25); temperature = 175°C. Pulse widths (a) 20 msec; (b) 50 msec; (c) 100 msec.

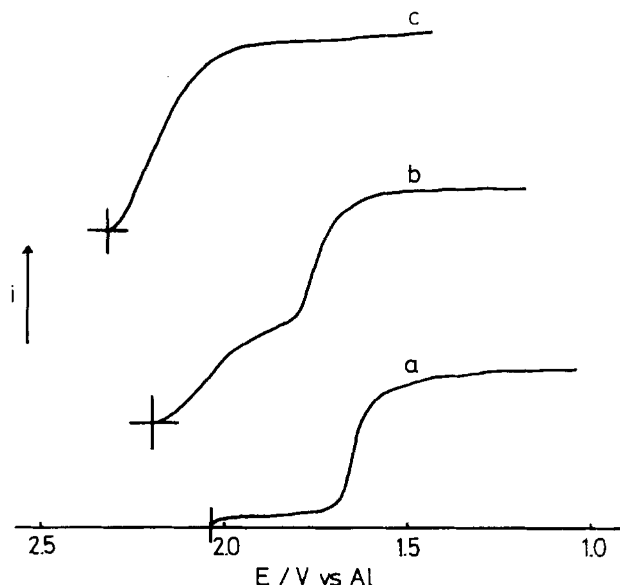

Fig. 10. RDE experiments for the reduction of Se (IV) at a glassy carbon electrode. Rotation rate = 4900 rpm; temperature = 175°C; pCl = (a) 1.9; (b) 3.5; (c) 5.8.

$cm^2\ sec^{-1}$. The reduction wave was analyzed in the same way as the oxidation of Na_2Se and αn_α was calculated to be 0.70. The standard potential for the process is not known, so k_o^Θ could not be calculated. The rate constant at the rest potential, 2.32V, was, however, determined and was found to be 4.8×10^{-4} cm sec^{-1} at a *p*Cl of 5.8. The reduction process in a basic melt was analyzed in the same way. The process was found to be diffusion controlled and by assuming that the value of *D* calculated for the acid-favored Se(IV) species did not vary with *p*Cl. The diffusion coefficient of the species favored in basic melts was found to be 1.94×10^{-6} $cm^2\ sec^{-1}$, αn_α was calculated to be 0.36, and the rate constant at the rest potential (2.04V) in an NaCl-saturated melt (*p*Cl = 1.9) was determined to be 3.8×10^{-4} cm sec^{-1}.

Knowing the diffusion coefficients for both Se(IV) species and the heights of the two waves at various *p*Cl's it was possible to fit the data to various equilibria and the one that appears to operate is shown below

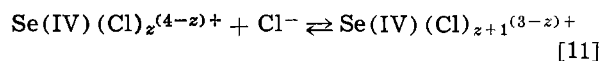

$$Se(IV)(Cl)_z{}^{(4-z)+} + Cl^- \rightleftarrows Se(IV)(Cl)_{z+1}{}^{(3-z)+} \quad [11]$$

with an equilibrium constant of $6.0 \pm 1.0 \times 10^3$ on the mole-fraction scale. From other studies in chloride-rich media (23) it was found Se(IV) is usually present as the hexachloro complex. The probable equilibrium in the present case is therefore

$$SeCl_5^- + Cl^- \rightleftarrows SeCl_6^{2-} \quad [12]$$

though comparable equilibria between $SeCl_5^-$ and $SeCl_4$ or $SeCl_5$ and $SeCl_3^+$ cannot be ruled out.

The stoichiometry of the electrochemical oxidation of selenium and reduction of selenium cations in $AlCl_3$:NaCl melts can be summarized as follows

(a) In acid melts

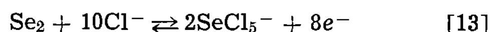

$$Se_2 + 10Cl^- \rightleftarrows 2SeCl_5^- + 8e^- \quad [13]$$

(b) In basic melts

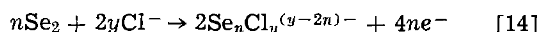

$$nSe_2 + 2yCl^- \rightarrow 2Se_nCl_y{}^{(y-2n)-} + 4ne^- \quad [14]$$

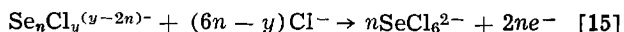

$$Se_nCl_y{}^{(y-2n)-} + (6n-y)Cl^- \rightarrow nSeCl_6^{2-} + 2ne^- \quad [15]$$

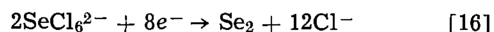

$$2SeCl_6^{2-} + 8e^- \rightarrow Se_2 + 12Cl^- \quad [16]$$

where the values of *n* and *y* are either zero or integral.

It is interesting that no evidence is found for the formation of polymeric selenium cations during the oxidation of selenium in acidic melts where they have been observed spectrophotometrically (7). This may be due to the much lower concentrations used in the present work; in this present study the solubility of selenium (as the monomer) was found to be about 3×10^{-3}M, whereas in Bjerrum's study (8) the combined Se and $SeCl_4$ concentration was 10-100 times greater than this. It is, however, possible that the species of formal oxidation state +2 formed during oxidation of Se in basic melts is polymeric, though electrochemical studies of the reduction of Te(IV) in similar melts (24) suggest that $TeCl_3^-$ and $TeCl_2$ are the predominant Te(II) species present in this case and Se(II) might be expected to behave in a similar manner.

Acknowledgment

This work was supported by the Air Force Office of Scientific Research under Grant No. AFOSR-76-2978.

Manuscript submitted Feb. 6, 1978; revised manuscript received April 7, 1978.

Any discussion of this paper will appear in a Discussion Section to be published in the June 1979 JOURNAL. All discussions for the June 1979 Discussion Section should be submitted by Feb. 1, 1979.

Publication costs of this article were assisted by Colorado State University.

REFERENCES

1. K. A. Paulsen and R. A. Osteryoung, *J. Am. Chem. Soc.*, **98**, 6866 (1976).
2. R. Marassi, G. Mamantov, and J. Q. Chambers, *Inorg. Nucl. Chem. Lett.*, **11**, 245 (1975).
3. R. Marassi, G. Mamantov, and J. Q. Chambers, *This Journal*, **123**, 1128 (1976).
4. F. G. Bodewig and J. A. Plambeck, *ibid.*, **117**, 618 (1970).
5. H. Shimotake and E. J. Cairns, Abstract 282, p. 674, The Electrochemical Society Extended Abstracts, Spring Meeting, Boston (1968).
6. T. C. F. Munday and J. D. Corbett, *Inorg. Chem.*, **5**, 1263 (1966).
7. R. Fehrmann, N. J. Bjerrum, and H. A. Andreasen, *ibid.*, **14**, 2259 (1975).
8. D. J. Prince, J. D. Corbett, and B. Garbisch, *ibid.*, **9**, 2731 (1970).
9. P. Hagenmuller, J. Rouxel, J. David, A. Colin, and B. LeNeidr, *Z. Anorg. Allg. Chem.*, **323**, 1 (1963).
10. P. Palvadeau and J. Rouxel, *Bull. Soc. Chim. Fr.*, 2698 (1967).
11. J. Rouxel and P. Palvadeau, *ibid.*, 2044 (1967).
12. J. Robinson, B. Gilbert, and R. A. Osteryoung, *Inorg. Chem.*, **16**, 3040 (1977).
13. L. G. Boxall, H. L. Jones, and R. A. Osteryoung, *This Journal*, **120**, 223 (1973).
14. L. G. Boxall, H. L. Jones, and R. A. Osteryoung, *ibid.*, **121**, 212 (1974).
15. I. D. Eubanks and F. J. Abbot, *Anal. Chem.*, **41**, 1708 (1969).
16. G. Lauer, H. Schlein, and R. A. Osteryoung, *ibid.*, **35**, 1789 (1963).
17. R. H. Abel, J. H. Christie, L. L. Jackson, J. G. Osteryoung, and R. A. Osteryoung, *Chem. Instrum.*, **7**, 123 (1976).
18. A. Eisenberg and A. V. Tobolsky, *J. Polymer Sci.*, **46**, 19 (1960).
19. K. B. Oldham and E. P. Parry, *Anal. Chem.*, **40**, 65 (1968).
20. A. C. Riddiford, in "Advances in Electrochemistry and Electrochemical Engineering," Vol. 4, P. Delahay and C. W. Tobias, Editors, p. 47, Interscience, New York (1966).
21. M. Herten, A. Thiebaut, and G. Adhan, *Ann. Lett.*, **5**, 305 (1972).
22. N. N. Greenwood and B. P. Straughan, *J. Chem. Soc. A*, 962 (1966).
23. F. W. Paulsen and N. J. Bjerrum, *J. Electroanal. Chem.*, **79**, 327 (1977).
24. K. W. Bagnall, "The Chemistry of Selenium, Tellurium and Polonium," p. 19, Elsevier, New York (1966).

Mass Transfer to an Impinging Jet Electrode

D-T. Chin* and C-H. Tsang

Department of Chemical Engineering, Clarkson College of Technology, Potsdam, New York 13676

ABSTRACT

A study has been made of mass transfer to a circular disk electrode located in the stagnation region of an impinging jet. A semiempirical solution of a convective diffusion model is presented in the form of an asymptotic series to permit an estimate of the transfer rate for $0.7 \leq Sc < \infty$. Experimental results reveal that the electrode possesses a property of "uniform accessibility" to the diffusing species if the electrode radius is less than 1 nozzle diameter for turbulent jet and ½ nozzle diameter for laminar jet. Within this region, the mass transfer is relatively independent of radial positions, and the semiempirical correlations are presented for both laminar and turbulent flows over a range of nozzle heights from 0.2 to 6 nozzle diameters. The result indicates that the impinging jet electrode is a feasible tool for electroanalytical applications. This geometry can be easily adopted in process streams and closed systems at a pressure other than the ambient atmosphere.

The impinging jet electrode is commonly used in electrochemical machining, erosion corrosion, and other industrial processes. It is composed of a submerged circular jet of electrolyte incident on a flat plate normal to the direction of flow. The electrode is a circular disk embedded on the flat plate at the stagnation point as shown in Fig. 1. This geometry is attractive because of a high mass transfer rate.

The flow characteristics of the impinging jet has been extensively studied in the past two decades. A literature survey of the subject can be found in Ref. (1). When a submerged jet collides perpendicularly with a flat plate in a stationary electrolyte, there forms four distinct flow regimes as illustrated in Fig. 1: Region I is called the potential core region in which the velocity profile of the jet changes from pipe flow to a free jet flow. As the flow discharges from the submerged nozzle, the electrolyte in the jet starts to mix with the surrounding fluid. The mixing zone grows in width along the downstream direction of the jet. This leaves a conical potential core wherein the fluid property and the velocity are relatively constant. This core length varies from 4.7 to 7.7 nozzle diameters (1). Region II is the established flow region in which the velocity profile is well developed. In this region, the centerline velocity of the jet starts to decrease; its magnitude is inversely proportional to the distance from the nozzle exit and becomes zero near the stagnation point. This region covers a distance from the apex of the potential core to a height of 1.6 ~ 2.2 nozzle diameters from the surface of the flat plate (2). Region III is the stagnation region. This is a layer of fluid, about 1.6 ~ 2.2 nozzle diameters thick and 0.6 ~ 1.4 nozzle diameters in radius, on the flat plate in which the jet is deflected from the axial direction to a radial flow. The flow in this region is of an axisymmetric inviscid irrotational type, and the thickness of the boundary layer is relatively independent of the radial position near the stagnation point (2-3). According to Homann (4), the axial and the radial velocity components in the region can be described by $v = -2az$ and $u = ar$, respectively, where a is a hydrodynamic constant. Region IV is called the wall jet region. This is a region adjacent to the flat plate at some distance from the stagnation point where the radial velocity starts to decay and the thickness of the boundary layer increases with radial positions. The flow in this region can be divided into two sublayers. They are the inner layer where the flow is influenced by the wall and the outer layer where the flow is influenced by the surrounding fluid. The maximum velocity occurs at the boundary of the two sublayers; its magnitude is inversely proportional to the radial distance from the stagnation point (5).

Heat and mass transfer from the impinging jet to the flat plate has been studied by a number of investigators (6-19). Works published before 1973 were reviewed by Livingood and Hrycak (20). Most of these studies were confined to the low Schmidt numbers of less than 2.45. The local transfer rate at the flat plate has been found to depend on the nozzle Reynolds number of the fluid, Re, the Schmidt number of the diffusing species, Sc, the dimensionless nozzle height, H/d, and the dimensionless radial position from the stagnation point, r/d. In the wall jet region (7, 9-10, 16) the transfer rate is proportional to the nozzle Reynolds number raised to a power of 0.75 and is inversely proportional to the dimensionless radial position. In the stagnation region, the mass transfer rate depends on $Re^{1/2}$ (7-8, 14-16, 18, 20). Several experiments with evaporation of naphthalene to an air jet (6, 8) and dissolution of *trans*-cinnamic acid to a water jet (7, 10-11) have found that the local mass transfer rate in the stagnation region is relatively independent of the radial position for $r/d < 1$. The evidence is supported by the analyses of Sparrow and Lee (19), and Scholtz and Trass (8), who confirmed that mass transfer rate should be constant in the neighborhood of the stagnation point. This property is similar to mass transfer to a rotating disk where the local mass transfer rate is independent of the radial position in laminar flow (21). It appears that if one limits the electrode radius to less than 1 nozzle diameter, the

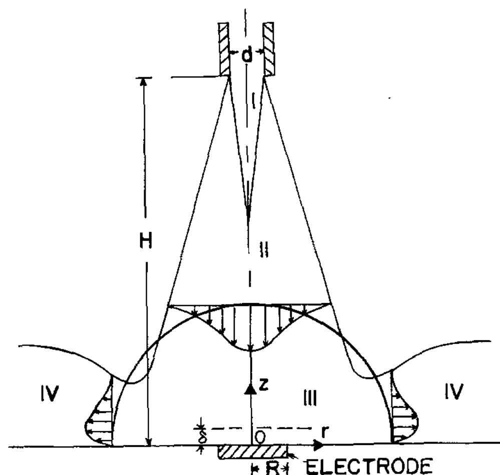

Fig. 1. The impinging jet electrode

* Electrochemical Society Active Member.

Key words: convective diffusion, limiting current, uniform accessibility.

system would possess a "uniform accessibility" to the diffusing species in the electrolyte, and a constant surface concentration could be maintained throughout the electrode. This particular feature would make the impinging jet electrode a useful tool for electroanalytical applications. It has the advantage over the rotating disk electrode that there is no mechanical movement and the electrode can be easily adopted to monitor the concentration of ionic species in a process stream.

Electrochemical study of the impinging jet has been made by Yamada and Matsuda (22) and Coeuret (23). Yamada and Matsuda measured the limiting current for the reduction of ferricyanide ions in the wall jet region. Coeuret's experiment was confined to an electrode size of $r/D = 0.5 \sim 3$; his empirical correlation basically confirmed the concept of uniform accessibility near the stagnation point.

In this study, a mathematical model is presented for mass transfer to a circular disk electrode located within the stagnation region of an impinging jet. The convective diffusion equation is solved with a perturbation method. The resulting rate equation expressed in the form of an asymptotic series of the Schmidt numbers is shown to be valid over a range of Sc from 0.7 to infinity. To determine precisely the region of uniform accessibility, a potassium ferricyanide/ferrocyanide system has been used to measure the limiting current density at the electrode for the reduction of ferricyanide ion. Mass transfer rates with both laminar and turbulent impinging jets are presented for a range of electrode radii varying from 0.02 to 6 nozzle diameters and for the nozzle heights from 0.2 to 6 nozzle diameters.

Analysis

This analysis is concerned with mass transfer to a circular disk electrode located within the stagnation of the impinging jet. Since there is a strong interaction between mass transfer and fluid flow, the latter is briefly considered here.

A mathematical solution describing the boundary layer flow in the stagnation region of a uniform flowing field incident on an infinite plate was first obtained by Homann (4). Homann's solution has been extended to the case of a uniform impinging jet by Schrader (24), who showed that there existed a boundary layer of a constant thickness having a radius of approximately 1.1 nozzle diameter in the stagnation region. The experiments with evaporation of naphthalene and dissolution of *trans*-cinnamic acid (6-11) also demonstrate that the mass transfer rate at the impinged surface is relatively uniform for $R/d < 1$. The measurements of velocity and pressure distributions (8, 25) have confirmed the existence of an inviscid flowing field just outside the boundary layer. According to Homann's axisymmetric stagnation flow (4), the radial and the vertical velocity components in this inviscid flowing field can be described by $u = ar$ and $v = -2az$, respectively. Here, the constant a is an unspecified hydrodynamic constant. For a nonuniform impinging jet (8), the radial velocity component in the inviscid flowing field becomes $u = ar + br^3 + \ldots$; however, in the neighborhood of the stagnation point, the series can be simplified to $u \sim ar$. Thus, Homann's inviscid solution is valid in the neighborhood of the stagnation point for both uniform and nonuniform impinging jets. Also, experimental evidences have indicated that Homann's solution is true whether the flow at the nozzle exit is laminar or turbulent. These different flow conditions are reflected by the different values of the hydrodynamic constant, a; they will not affect the mathematical derivation in this analysis.

Mathematical modeling.—For the simplicity of the analysis, we shall make the following assumptions: (*i*) The diffusion domain is confined to a region in which the boundary layer thickness is uniform; (*ii*) the cell diameter is large enough so that the effect of the cell wall on the flow boundary layer is negligible; (*iii*) the electrolyte flowing through the nozzle has the same physical properties as the surrounding electrolyte; (*iv*) the solution has sufficient inert salt to insure that the migration flux of the diffusing ion in the electric field can be neglected; (*v*) physical properties of the electrolyte are constant; and (*vi*) the effect of the gravitational force on the diffusion field is negligible. For a steady-state axisymmetric impinging jet, the system can be described by a cylindrical coordinate system with the origin located at the stagnation point as shown in Fig. 1. The coordinate, r, is the radial distance from the stagnation point, and z is the perpendicular distance from the electrode surface. Under the assumption of a uniform boundary layer thickness in the neighborhood of the stagnation point, there is no concentration variation in the radial direction. The steady-state convective diffusion equation for mass transfer in the diffusion domain takes the form

$$v\frac{dC}{dz} = D\frac{d^2C}{dz^2} \qquad [1]$$

with boundary conditions

$$\left.\begin{array}{ll} z = 0 & C = C_0 \\ z \to \infty & C = C_\infty \end{array}\right\} \qquad [2]$$

Here, v is the velocity component of the boundary layer flow in the z-direction; C and D are the concentration and the diffusivity of the diffusing ion.

To solve Eq. [1] and [2], v must be known. As mentioned in the foregoing paragraph, Homann's axisymmetric stagnation flow exists just outside the boundary layer in the stagnation region where the velocity components in the radial and the axial directions are given as $u = ar$ and $v = -2az$, respectively. For the flow inside the boundary layer, Homann (4) made an assumption that

$$u = ar\phi'(\eta), \qquad v = -2\sqrt{a\nu}\,\phi(\eta) \qquad [3]$$

Here, a is the unspecified hydrodynamic constant having a dimension of $\sec^{-1}$, u and v are the velocity components in the radial and axial directions, respectively; $\eta = \sqrt{a/\nu}\, z$ is a dimensionless variable; $\phi'(\eta)$ is the first derivative of a stream function $\phi(\eta)$ with respect to η; and ν is the kinematic viscosity of the electrolyte.

A dimensionless concentration may be defined as

$$\overline{C} = \frac{C - C_\infty}{C_0 - C_\infty} \qquad [4]$$

where C_∞ is the bulk concentration of the diffusion ion, and C_0 is the concentration at the electrode surface. Substituting Eq. [3]-[4] into Eq. [1]-[2], the convective diffusion equation can be reduced to a second-order ordinary differential equation

$$\frac{d^2\overline{C}}{d\eta^2} + 2\mathrm{Sc}\,\phi(\eta)\frac{d\overline{C}}{d\eta} = 0 \qquad [5]$$

with the boundary conditions

$$\left.\begin{array}{ll} \eta = 0 & \overline{C} = 1 \\ \eta \to \infty & \overline{C} = 0 \end{array}\right\} \qquad [6]$$

Here, Sc is the Schmidt number defined as $\mathrm{Sc} = \nu/D$.

To solve Eq. [5]-[6] analytically, one needs a mathematical expression for the stream function $\phi(\eta)$. Homann (4) obtained a power series solution of $\phi(\eta)$. An improved numerical solution was obtained by Froessling (26) and was tabulated in Schlichting (4). Using Froessling's results, the Taylor series expansion of the function $\phi(\eta)$ near the electrode surface, *i.e.*,

$\eta = 0$, can be found as

$$\phi(\eta) = 0.656\eta^2 - 0.16667\eta^3 + 3.6444 \times 10^{-3}\eta^6 - 3.9682 \times 10^{-4}\eta^7 + \ldots \quad [7]$$

Asymptotic solution.—The Schmidt numbers for electrochemical applications are high. In order to find a simple solution for the convective diffusion, Eq. [5]-[6], we carry out successive perturbations of the parameter, Sc. The procedures have been illustrated by Chin (27-31). Following the procedures, the concentration profile can be represented by an asymptotic series in the descending powers of Sc

$$\overline{C} = \overline{C}_0 + \frac{1}{Sc^{1/3}}\overline{C}_1 + \frac{1}{Sc^{2/3}}\overline{C}_2 + \frac{1}{Sc}\overline{C}_3 + \frac{1}{Sc^{4/3}}\overline{C}_4 + \frac{1}{Sc^{5/3}}\overline{C}_5 + \ldots \quad (\text{for } Sc >> 1) \quad [8]$$

Here, $\overline{C}_0, \ldots, \overline{C}_4$ and $\overline{C}_5$ are called the zeroth, ..., the fourth and the fifth-order concentrations, respectively. They are functions of a stretched coordinate, Z, defined as

$$Z = Sc^{1/3}\eta = Sc^{1/3}\sqrt{a/\nu}\,z \quad [9]$$

Substituting Eq. [7]-[9] into Eq. [5]-[6], and equating the terms having the like powers of Sc in the resulting equation, we have

$$\frac{d^2\overline{C}_0}{dZ^2} + 1.312Z^2\frac{d\overline{C}_0}{dZ} = 0 \quad [10]$$

$$\frac{d^2\overline{C}_1}{dZ^2} + 1.312Z^2\frac{d\overline{C}_1}{dZ} = 0.33333Z^3\frac{d\overline{C}_0}{dZ} \quad [11]$$

$$\frac{d^2\overline{C}_2}{dZ^2} + 1.312Z^2\frac{d\overline{C}_2}{dZ} = 0.33333Z^3\frac{d\overline{C}_1}{dZ} \quad [12]$$

$$\frac{d^2\overline{C}_3}{dZ^2} + 1.312Z^2\frac{d\overline{C}_3}{dZ} = 0.33333Z^3\frac{d\overline{C}_2}{dZ} \quad [13]$$

$$\frac{d^2\overline{C}_4}{dZ^2} + 1.312Z^2\frac{d\overline{C}_4}{dZ} = 0.33333Z^3\frac{d\overline{C}_3}{dZ} - 0.007288Z^6\frac{d\overline{C}_0}{dZ} \quad [14]$$

$$\frac{d^2\overline{C}_5}{dZ^2} + 1.312Z^2\frac{d\overline{C}_5}{dZ} = 0.33333Z^3\frac{d\overline{C}_4}{dZ} - 0.007288Z^6\frac{d\overline{C}_1}{dZ} + 0.00079365Z^7\frac{d\overline{C}_0}{dZ} \quad [15]$$

with the new boundary conditions

$$\left.\begin{array}{ll} Z = 0 & \overline{C}_0 = 1, \overline{C}_1 = \overline{C}_2 = \ldots = \overline{C}_5 = 0 \\ Z \to \infty & \overline{C}_0 = \overline{C}_1 = \ldots = \overline{C}_5 = 0 \end{array}\right\} \quad [16]$$

This set of simultaneous linear ordinary differential equations can be integrated to give the following solutions

$$\overline{C}_0 = 1 - 0.85002\int_0^Z e^{-0.43733Z^3}\,dZ \quad [17]$$

$$\overline{C}_1 = \int_0^Z e^{-0.43733Z^3}(-0.070835Z^4 + 0.071906)\,dZ \quad [18]$$

$$\overline{C}_2 = \int_0^Z e^{-0.43733Z^3}(-0.0029515Z^8 + 0.0059922Z^4 + 0.013913)\,dZ \quad [19]$$

$$\overline{C}_3 = \int_0^Z e^{-0.43733Z^3}(-8.1986 \times 10^{-5}Z^{12} + 2.4968 \times 10^{-4}Z^8 + 1.1594 \times 10^{-3}Z^4 + 4.879 \times 10^{-3})\,dZ \quad [20]$$

$$\overline{C}_4 = \int_0^Z e^{-0.43733Z^3}(-1.708 \times 10^{-6}Z^{16} + 6.935 \times 10^{-6}Z^{12} + 4.8309 \times 10^{-5}Z^8 + 8.85 \times 10^{-4}Z^7 + 4.0658 \times 10^{-4}Z^4 - 1.2145 \times 10^{-3})\,dZ \quad [21]$$

$$\overline{C}_5 = \int_0^Z e^{-0.43733Z^3}(-2.8467 \times 10^{-8}Z^{20} + 1.4449 \times 10^{-7}Z^{16} + 1.3419 \times 10^{-6}Z^{12} + 7.4053 \times 10^{-5}Z^{11} - 6.7386 \times 10^{-5}Z^8 - 7.4873 \times 10^{-5}Z^7 - 1.0121 \times 10^{-4}Z^4 - 1.1125 \times 10^{-3})\,dZ \quad [22]$$

Equations [17]-[22] give the concentration profile in the diffusion layer.

The local mass transfer rate, j, is related to the concentration gradient at the surface by

$$j = -D\left(\frac{\partial C}{\partial z}\right)_{z=0} = k(C_0 - C_\infty) \quad [23]$$

where k is the local mass transfer coefficient. The concentration gradient at the surface can be obtained by differentiating Eq. [8] and Eq. [17]-[22]. Since the concentration is independent of r due to the assumed uniform boundary layer thickness, the average mass transfer coefficient over the electrode surface is essentially equal to the local value of k

$$K = k = 0.85002\,D\sqrt{a/\nu}\,Sc^{1/3}g(Sc) \quad [24]$$

Here, the function $g(Sc)$ is an asymptotic series of Sc

$$g(Sc) = \left[1 - \frac{0.084593}{Sc^{1/3}} - \frac{0.016368}{Sc^{2/3}} - \frac{0.0057398}{Sc} + \frac{0.0014288}{Sc^{4/3}} + \frac{0.0013088}{Sc^{5/3}} + \ldots\right] \quad [25]$$

The Sherwood number, Sh, defined as Kd/D, can be calculated from the following equation

$$Sh = 0.85002d\sqrt{a/\nu}\,Sc^{1/3}g(Sc) \quad [26]$$

where d is the nozzle diameter. At large Sc, the function $g(Sc)$ is one and Eq. [24] can be simplified to

$$Sh = 0.85002d\sqrt{a/\nu}\,Sc^{1/3} \quad [27]$$

Comparison with numerical solutions.—By solving Eq. [5] and [6], the exact concentration profile can be expressed as

$$\overline{C} = 1 - \frac{\int_0^\eta \exp\left[-2Sc\int_0^\eta \phi(\eta)d\eta\right]d\eta}{\int_0^\infty \exp\left[-2Sc\int_0^\eta \phi(\eta)d\eta\right]d\eta} \quad [28]$$

The numerical solutions of Eq. [28] for different Schmidt numbers have been obtained with a fourth-order Runge-Kutta method and a six-points Gaussian quadrature formula on a digital computer. Figure 2 shows a comparison between the asymptotic concentration profiles calculated from Eq. [8] and [17]-[22] and the numerical concentration profiles calculated from Eq. [28]. For $Sc \geqq 2.45$, their agreement is within 8% for $\overline{C} \geqq 1.0 \times 10^{-3}$. Figure 3 is a log-log plot of $Sh/d\sqrt{a/\nu}$ *vs.* Sc for the asymptotic solution of Eq. [26] and the numerical solutions calculated from

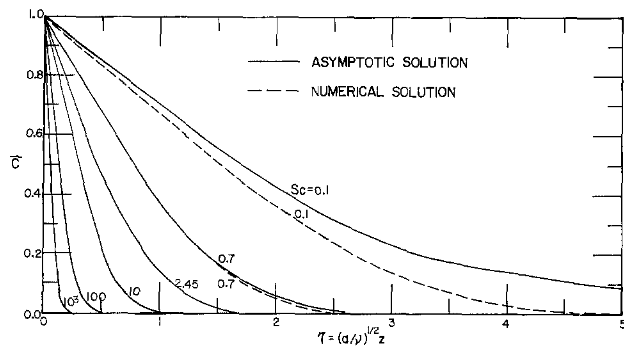

Fig. 2. Concentration distributions on the impinging jet electrode

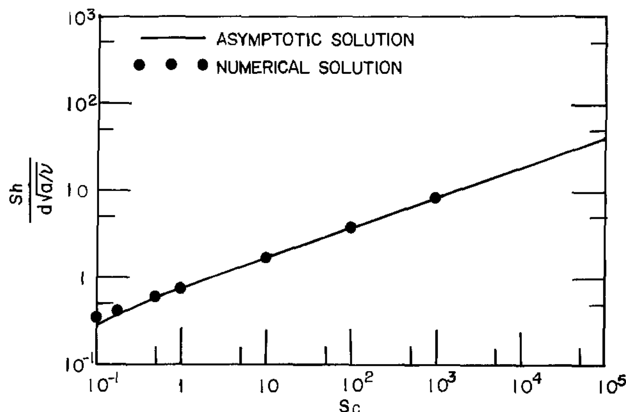

Fig. 3. Comparison for the mass transfer rate between the asymtotic and the numerical solutions.

Eq. [28]. Table I presents the numerical values for the comparison. The present asymptotic solution is based on Sc >> 1; however, at Sc = 0.7 and 1, the asymptotic solutions agree with the numerical solutions to within 0.6 and 0.3%, respectively. The slope of the curve is 1/3 at large Schmidt numbers.

Evaluation of hydrodynamic constant.—For practical application of Eq. [24]-[27], the hydrodynamic constant, a, must be known.

For a circular disk immersed perpendicularly in a uniform flow, Lamb (32) has found that the velocity component of the potential flow along an infinitely thin disk surface with radius R can be expressed as

$$u = \frac{\pi r}{8R} U' \quad [29]$$

Here, U' is the bulk velocity of the uniform flow. The hydrodynamic constant, a, for this system is essentially $\pi U'/8R$. Substituting the value of a into Eq. [24], the mass transfer rate equation becomes

$$Sh_R = \frac{KR}{D} = 0.5327 Re'^{1/2} Sc^{1/3} g(Sc) \quad [30]$$

Here, Re' is the Reynolds number defined as $U'R/\nu$. For large Schmidt numbers, g(Sc) becomes 1, and Eq. [30]

Table I. Values of $Sh/d\sqrt{a/\nu}$ at different Schmidt numbers

	$Sh/d\sqrt{a/\nu}$		
Sc	Asymptotic solution of Eq. [26]	Numerical solution of Eq. [28]	% difference
0.1	0.3061	0.3373	9.25
0.7	0.6645	0.6687	0.62
1.0	0.7616	0.7639	0.30
2.45	1.0618	1.0623	0.04
10	1.7521	1.7521	0
100	3.8703	3.8703	0
1000	8.4269	8.4269	0

agrees with the analysis of Matsuda and Yamada (33) who obtained a numerical coefficient of 0.5325.

For the case of an impinging jet, the potential flow field outside of the boundary layer depends not only on the nozzle exit flow but also on the nozzle height, H. Introducing a dimensionless hydrodynamic constant defined as

$$a^* = ad/\bar{U} \quad [31]$$

Eq. [26] becomes

$$Sh = 0.85002 Sc^{1/3} Re^{1/2} \sqrt{a^*} \cdot g(Sc) \quad [32]$$

where Re is the Reynolds number, $\bar{U}d/\nu$, based on the nozzle diameter, d, and the average nozzle exit velocity, $\bar{U}$. According to the published data, the dimensionless hydrodynamic constant, a^*, is only a function of the dimensionless nozzle height, $\bar{H}$, defined as H/d. In this study, an attempt has been made to correlate several theoretical and empirical results (2, 6, 8, 13, 17, 19) of a^* with a least squares curve fitting method. The results are tabulated in Table II for various ranges of H/d. The flow conditions at the nozzle exit, as reported in the corresponding reference, are indicated in column 4. Since this analysis is similar to that of the impinging rectangular-slot jets, the table also lists a number of correlations of a^* obtained from the slot geometry. The range of H/d for the a^*'s given in the table varies from 0.05 to ∞. Substituting these a^*'s into Eq. [32], the corresponding rate equations for mass transfer near the stagnation point are tabulated in Table III. In this way, a total of 13 equations have been obtained for various ranges of H/d; they are numbered from [III-1] to [III-13] in the last column of Table III. As it can be seen, the rate equations have a general form

$$Sh = \alpha Re^{1/2} Sc^{1/3} g(Sc) f(H/d) \quad [33]$$

where α is a constant coefficient. Figure 4 is a log-log plot of $Sh/Re^{1/2} Sc^{1/3} g(Sc)$ *vs.* H/d for the equations in Table III and the experimental data reported in Ref. (6, 8, and 23). The numbers in the figure represent the equation numbers in Table III. It is noted that there is no single equation which satisfies the measured transfer rate over the entire range of H/d. For $0.1 \leq H/d \leq 0.5$, Eq. [III-1] shows a fair agreement with the data obtained by Scholtz and Trass for the evaporation of naphthalene to a nonuniform laminar jet. For high Schmidt numbers, Coueret's electrochemical measurements with an impinging jet electrode of a radius $r/d = 1.4$, agrees fairly with the predictions of Eq. [III-2] and [III-3] at $H/d = 1.1$. However, his result with a smaller electrode of $r/d = 0.45$ is twice higher than the prediction. For $1.0 < H/d < 10$, the data of Chia *et al.* (6) at Re = 34,000 fall into the region predicted by Eq. [III-5], [III-8], and [III-9]. It seems that there is no satisfactory agreement between the correlations and the reported experimental

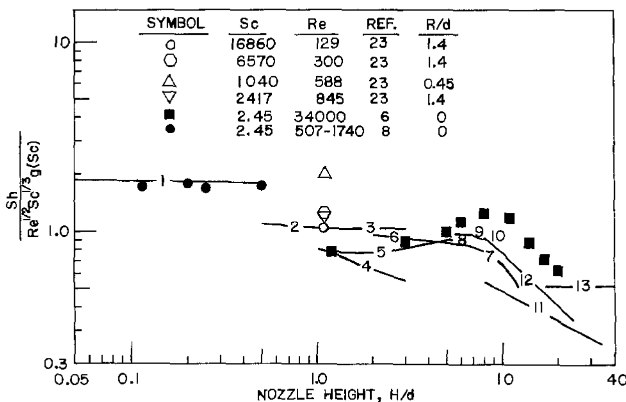

Fig. 4. Comparison between the mass transfer correlations listed in Table III and the published experimental data.

Table II. Correlations for the hydrodynamic constant, a^*

Reference	$a^{*(a)}$	Dimensionless nozzle height range	Nozzle exit flow condition	Nozzle geometry	Remarks
(8)	$a^* = 2.464 - 1.0629\bar{H} + 1.5794\bar{H}^2$	$0.05 \leq \bar{H} \leq 0.5$	Nonuniform, laminar	Circular	Theoretical
(19)	$a^* = 1.5129\bar{H}^{-0.204}$	$0.5 \leq \bar{H} \leq 1$	Nonuniform, laminar	Slot	Theoretical
(19)	$a^* = 1.5129$	$1 \leq \bar{H} \leq 3$	Nonuniform, laminar	Slot	Theoretical
(19)	$a^* = 1.5852 - 0.76385 + 0.12926\bar{H}^2$	$1 \leq \bar{H} \leq 3$	Uniform, laminar	Slot	Theoretical
(6)	$a^* = 1.038\left[\frac{1.004 - 0.03\bar{H}}{0.493 + 0.006\bar{H}}\right] \cdot f(\bar{H})^{(b)}$	$1.2 \leq \bar{H} \leq 5.5$	Turbulent	Circular	Semitheoretical
(13)	$a^* = 1.5(\bar{H})^{-0.22}$	$2 \leq \bar{H} \leq 6$	Mach No. = 0.05 $\gamma = 1.4$	Circular	Empirical
(2)	$a^* = 1.001 + 0.065749\bar{H} - 9.6249 \times 10^{-3}\bar{H}^{-2}$	$4 \leq \bar{H} \leq 12$	Turbulent	Circular	Empirical
(6)	$a^* = 1.038\left[\frac{1.35 - 0.066\bar{H}}{0.493 + 0.0066\bar{H}}\right] \cdot f(\bar{H})$	$5.5 \leq \bar{H} \leq 6.8$	Turbulent	Circular	Semitheoretical
(6)	$a^* = 1.038\left[\frac{1.35 - 0.066\bar{H}}{0.069\ (1 + \bar{H})}\right] f(\bar{H})$	$6.8 \leq \bar{H} \leq 8$	Turbulent	Circular	Semitheoretical
(6)	$a^* = 0.953\left[\frac{1.35 - 0.066\bar{H}}{0.069\ (1 + \bar{H})}\right]$	$8 \leq \bar{H} \leq 10$	Turbulent	Circular	Semitheoretical
(17)	$a^* = 7.82\bar{H}^{-1.24}$	$8 \leq \bar{H}$	Turbulent	Slot	Empirical
(6)	$a^* = 101.8\left[\frac{1}{(0.67 + \bar{H})(1 + \bar{H})}\right]$	$10 \leq \bar{H}$	Turbulent	Circular	Semitheoretical
(19)	$a^* = 0.3931$	$\bar{H} \to \infty$	Uniform, laminar	Slot	Theoretical

(a) $\bar{H}$ is the dimensionless nozzle height, H/d or H/B.
(b) $f(\bar{H}) = 0.62156 - 0.25948\bar{H} + 0.12607\bar{H}^2 - 0.019049\bar{H}^3 + 9.9051 \times 10^{-4}\bar{H}^{-4}$.

Table III. Mass transfer correlations

Sh	Dimensionless nozzle height range	Nozzle exit flow condition	Equation No.
$Sh = 1.2021Re^{1/2}Sc^{1/3}[2.464 - 1.0629\bar{H} + 1.5794\bar{H}^2]^{1/2}g(Sc)^*$	$0.05 \leq \bar{H} \leq 0.5$	Nonuniform, laminar	[III-1]
$Sh = 1.0455Re^{1/2}Sc^{1/3}\bar{H}^{-0.102}g(Sc)$	$0.5 \leq \bar{H} \leq 1$	Nonuniform, laminar	[III-2]
$Sh = 1.0455Re^{1/2}Sc^{1/3}g(Sc)$	$1 \leq \bar{H} \leq 3$	Nonuniform, laminar	[III-3]
$Sh = 0.85002Re^{1/2}Sc^{1/3}(1.5852 - 0.76385\bar{H} + 0.12926\bar{H}^2)^{1/2}g(Sc)^\dagger$	$1 \leq \bar{H} \leq 3$	Uniform, laminar	[III-4]
$Sh = 0.83414Re^{1/2}Sc^{1/3}\left[\left(\frac{1.004 - 0.03\bar{H}}{0.493 + 0.006\bar{H}}\right) f(\bar{H})\right]^{1/2} g(Sc)$	$1.2 \leq \bar{H} \leq 5.5$	Turbulent	[III-5]
$Sh = 1.0411Re^{1/2}Sc^{1/3}\bar{H}^{-0.11}g(Sc)$	$2 \leq \bar{H} \leq 6$	Mach No. = 0.05 $\gamma = 1.4$	[III-6]
$Sh = 0.85002Re^{1/2}Sc^{1/3}[1.001 + 0.065749\bar{H} - 9.6249 \times 10^{-3}\bar{H}^2]^{1/2}g(Sc)$	$4 \leq \bar{H} \leq 12$	Turbulent	[III-7]
$Sh = 0.83414Re^{1/2}Sc^{1/3}\left[\left(\frac{1.35 - 0.066\bar{H}}{0.493 + 0.006\bar{H}}\right) f(\bar{H})\right]^{1/2} g(Sc)$	$5.5 \leq \bar{H} \leq 6.8$	Turbulent	[III-8]
$Sh = 0.83414Re^{1/2}Sc^{1/3}\left[\left(\frac{1.35 - 0.066\bar{H}}{0.069\ (1 + \bar{H})}\right) f(\bar{H})\right]^{1/2} g(Sc)$	$6.8 \leq \bar{H} \leq 8$	Turbulent	[III-9]
$Sh = 0.81442Re^{1/2}Sc^{1/3}\left[\frac{1.35 - 0.066}{0.069\ (1 + \bar{H})}\right]^{1/2} g(Sc)$	$8 \leq \bar{H} \leq 10$	Turbulent	[III-10]
$Sh = 2.377Re^{1/2}Sc^{1/3}\bar{H}^{-0.62}g(Sc)$	$8 \leq \bar{H}$	Turbulent	[III-11]
$Sh = 8.5772Re^{1/2}Sc^{1/3}\left[\frac{1}{(0.67 + \bar{H})(1 + \bar{H})}\right]^{1/2} g(Sc)$	$10 \leq \bar{H}$	Turbulent	[III-12]
$Sh = 0.53294Re^{1/2}Sc^{1/3}g(Sc)$	$\bar{H} \to \infty$	Uniform laminar	[III-13]

$^* g(Sc) = 1 - \frac{0.084593}{Sc^{1/3}} - \frac{0.016368}{Sc^{2/3}} - \frac{0.0057398}{Sc} + \frac{0.0014288}{Sc^{4/3}} + \frac{0.0013088}{Sc^{5/3}} + \ldots$

† The width of the slot jet is replaced by the diameter of the circular jet.

data over the entire region of the dimensionless nozzle heights. The discrepancy is probably due to an inaccuracy in the reported dimensionless hydrodynamic constants, a^*, as well as the experimental faults. The mass transfer experiments with dissolution of a *trans*-cinnamic acid disk or evaporation of a naphthalene disk tend to roughen and deform the surface. Coueret's electrode of a radius $r/d = 1.4$ was greater than the stagnation region, and the measured mass transfer rate must be influenced by the flow in the wall jet region. It seems that more elaborate experimental work is needed to determine the hydrodynamic constant required for the transport equations.

Experimental

The purpose of the present experimental work is to determine the region of "uniform accessibility" on the impinged surface and to investigate the feasibility of the impinging jet electrode for electroanalytical applications. It also intends to further contest the rate equations listed in Table III with an electrochemical mass transfer experiment.

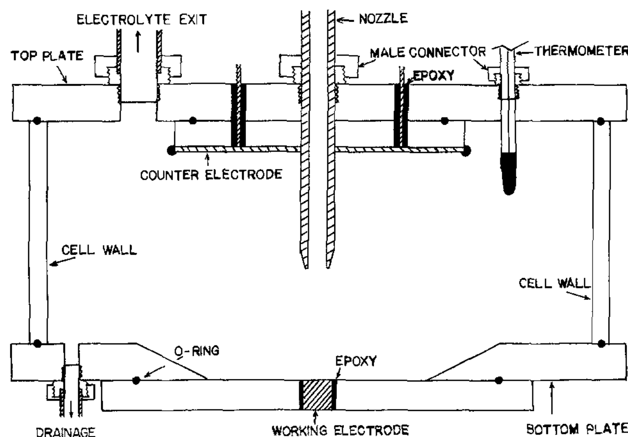

Fig. 5. The experimental cell used in this study

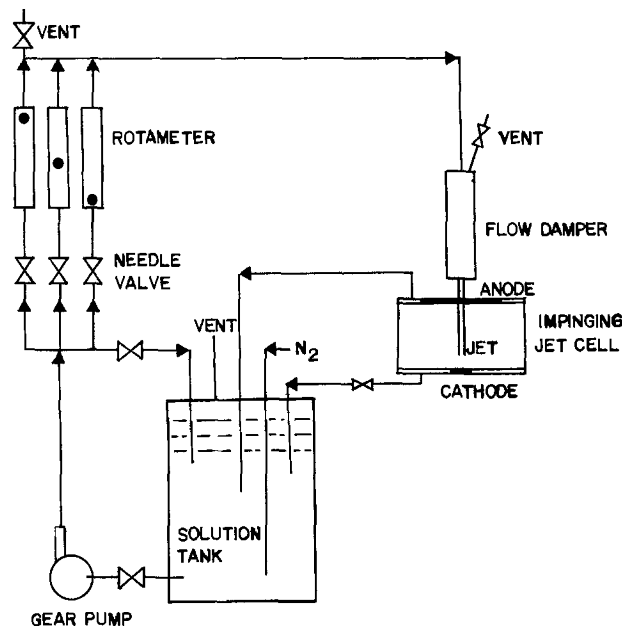

Fig. 6. The flow system used in this study

The experimental cell used is shown schematically in Fig. 5. It consisted of a section of a Plexiglas pipe, 20.3 cm ID by 7.6 cm long, and a set of Plexiglas top and bottom plates of 25.4 cm diam. They were bolted together at the circumferences of the top and the bottom plates and were sealed with O-rings.

The impinging jet electrode (or the working electrode) was located on the bottom plate; it was a circular nickel disk embedded on a replaceable Plexiglas electrode disk attached to the underside of the bottom plate as shown in Fig. 5. Eight different sizes of the impinging jet electrode were prepared; the radii of these electrodes were: 0.0127, 0.0495, 0.0787, 0.157, 0.265, 0.634, 1.27, and 1.91 cm. The electrodes with radius smaller or equal to 0.634 cm were made of either a nickel wire or a cylindrical nickel rod inserted through the central hole on the Plexiglas electrode disk and held in place with an epoxy glue. For the larger electrodes, a circular nickel foil was cemented to a shallow dent at the center of the electrode disk. The disk was then machined and smoothed until the nickel surface became flush with the Plexiglas surface. The counterelectrode was a circular nickel foil of 10.2 cm diam glued on the underside of the top plate. It had a very large surface area compared to the working electrodes to ensure that the over-all cell reaction was controlled by the reaction at the working electrode under the limiting current conditions.

The electrolyte nozzle was a Plexiglas tube inserted perpendicularly through a central hole on the top plate and held in place with a male tube connector. Two different nozzle sizes were used in the experiment; they had an inside diameter of 0.635 and 0.318 cm, respectively. Both nozzles were either 20.3 or 63.5 cm long. The nozzle height, which is the distance between the nozzle exit and the surface of the working electrode, could be adjusted by moving the nozzle tube up and down through the top plate and by tightening up the nut of the male tube connector. A micrometer depth gauge was used to measure the nozzle height when the cell was assembled.

There were two other tube connectors on the top plate. One was for accommodating a thermometer in the cell and the other was connected to an electrolyte exit tube. A small tube connector on the bottom plate was used for drainage. While in operation, the assembled cell was mounted on a sturdy bench to avoid any mechanical vibrations.

The flow system used in this experiment is shown in Fig. 6. It consisted of a solution tank, a gear pump, a set of rotameters, a flow damper, and the impinging jet cell. These components were connected together with ½-in. polypropylene tube and ½-in. nylon tube fittings. The solution tank was an 11 liter PVC tank, and an epoxy gear pump with a Hastelloy-C shaft and a Buna-N impeller was used to circulate the electrolyte. A bypass nylon needle valve and three other nylon needle valves in the upstream of three rotameters were used to control the flow rate of the electrolyte. Three Gilmont F-1500 shielded rotameters were used to measure the flow rate; they were composed of a glass tube and a glass ball to avoid the corrosion problems. The Plexiglas flow damper in the downstream of the rotameters was used to eliminate any turbulences in the electrolyte before it flowed into the impinging jet cell. The electrolyte flowed into the cell through the nozzle tube. It impinged normally on the working electrode and then returned to the storage tank via the exit on the top plate of the cell. All the components in the flow system were rigidly fastened on an aluminum rack to avoid vibrations.

The reduction of ferricyanide ion at the working electrode was used for the limiting current measurement. The solution used was composed of 0.01M potassium ferricyanide, 0.01M potassium ferrocyanide, and 1.0M sodium hydroxide. An iodimetric titration method was used to determine the ferricyanide concentration. An Ostward viscometer was used to determine the viscosity of the electrolyte. The density of the electrolyte was measured with a specific gravity bottle and the diffusivity of ferricyanide ion was determined with a rotating disk electrode. The typical properties of the solution with 9.774×10^{-4}M ferricyanide ion at 23°C were as follows:

density: 1.042 g/ml
viscosity: 1.06 cp
diffusivity of ferricyanide ion: 6.54×10^{-6} cm^2/sec
Stokes-Einstein parameter: $D\mu/T = 2.34 \times 10^{-10}$ cm^{2}poise/sec°K

The above Stokes-Einstein parameter agreed with the measurement by Gordon *et al.* (34), who obtained a value of $2.36 \pm 0.05 \times 10^{-10}$ cm^{2}poise/sec°K.

To obtain reproducible limiting current data, the working and the counterelectrodes were polished with 600 grade emery paper before the run. They were further degreased in methanol and cathodically activated in a 5% NaOH solution for 15-30 min before putting into the impinging jet cell. The solution was bubbled with nitrogen gas for at least 2 hr to remove any dissolved oxygen before the experiment. During the run, a nitrogen atmosphere was maintained in the storage tank. A Lambda LT-2095 d-c power supply was used as a d-c source for the cell reaction. The applied potential drop across the cell was controlled by a 10-turn potentiometer. The cell current for the reduction of ferricyanide ion at the working electrode

was obtained by measuring the voltage drop across a standard resistor with a Hewlett-Packard 3476A digital multimeter. To obtain the limiting current at a specific flow rate, a complete curve of cell current *vs.* cell voltage was measured by increasing the applied voltage across the cell. As the applied voltage increased, the current flowing through the cell first increased, then leveled off to form a plateau, and finally increased sharply. The current plateau was taken as the limiting current for the reduction of ferricyanide ion. The present system had a negligible background current and a wide limiting current region which existed over the cell voltages varying from 0.3 to 1.2V. All the runs were made at a constant room temperature of 23° ± 1°C. The details of the experimental setup and procedures are given in Ref. (35).

Results and Discussion

Uniform accessibility.—To determine the region of "uniform accessibility" at the impinging jet electrode, the limiting current density for the reduction of ferricyanide ion was measured as a function of electrode radius. The results for $H/d = 1$ are presented in Fig. 7 for four different nozzle Reynolds numbers. The curves represent the typical behavior observed in this study. The results with other nozzle heights exhibited the same characteristics. It is seen that for each curve there is a region where the limiting current density was relatively constant. This uniform mass transfer region varies from $R/d = 0.1$ to 1.0 for turbulent jets and from 0.1 to 0.5 for laminar jets; within this region, the variation in the limiting current density for different electrode sizes was less than ±10% of the average value. At the radial positions greater than the uniform accessible region, the limiting current density started to decrease with increasing electrode radius. A surprise feature revealed by this study is the nonuniformity in mass transfer for $R/d < 0.1$. Each curve reached a maximum value at the stagnation point as represented by the smallest electrode with $R/d = 0.02$. It (except at Re = 1210) also exhibited a minimum at $R/d = 0.078$. This particular behavior has not been reported in any previously published literature. The high mass transfer rate at the smallest electrode ($R = 0.0127$ cm) can probably be attributed to the mass transfer enhancement of the edge effect. The fact that it might be located slightly away from the centerline of the impinging jet, because of mechanical misalignments in the cell assembly, could also contribute to the higher rate at the smallest electrode (36). However, the result of a minimum mass transfer rate for the electrode with $R/d = 0.078$ cannot be explained. This minimum did not occur for all the nozzle heights tested; it gradually disappeared with increasing nozzle distance. At $H/d = 6$, the limiting current density for this electrode became consistently higher than that in the uniform accessible region. Since there have not been any published data showing the variation of mass transfer rate for $R/d < 0.1$, this problem will be left to future studies.

Effect of nozzle flow rates.—The limiting current densities at the eight working electrodes were measured for five different nozzle heights over a range of the nozzle Reynolds numbers from 500 to 16,000. This covered the laminar, the transitional, and the turbulent flow conditions in the impinging jet. Since the limiting current density for the reduction of ferricyanide ion is related to the average mass transfer coefficient by $i_{\lim} = KFC_\infty$, according to Eq. [32] a plot of $i_{\lim}$ *vs.* $\sqrt{Re}$ should result in a straight line passing through the origin with a slope equal to $0.85\, FDC_\infty Sc^{1/3} a^{*1/2}/d$. Figure 8 is the typical of such a plot obtained with a 0.635 cm diam nozzle at $H/d = 1.0$. Also shown in the figure are two vertical lines which separate the nozzle flow into the laminar and the turbulent flow regimes. The behavior of the data points can be classified into three categories according to whether the electrode radius was smaller, within, or greater than the uniform accessible region shown in Fig. 7:

(*i*) For R/d less than 0.1, the typical behavior can be represented by the limiting current at $R/d = 0.02$. For this electrode, a straight line passing through the origin can be drawn through the data points located in the transitional and the turbulent regimes. The laminar data at the lower end of the Reynolds numbers can also be correlated with a straight line through the origin; however, its slope is greater than that at the higher Reynolds numbers.

(*ii*) For the electrode radii located within the uniform accessible region, the data points for three different size electrodes ($R/d = 0.124$, 0.247, and 0.417) fall together as a single curve. An attempt has

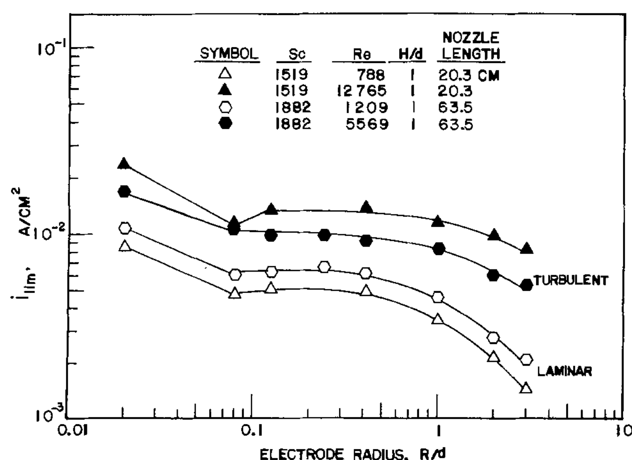

Fig. 7. Variation of the limiting current density with the dimensionless electrode radius.

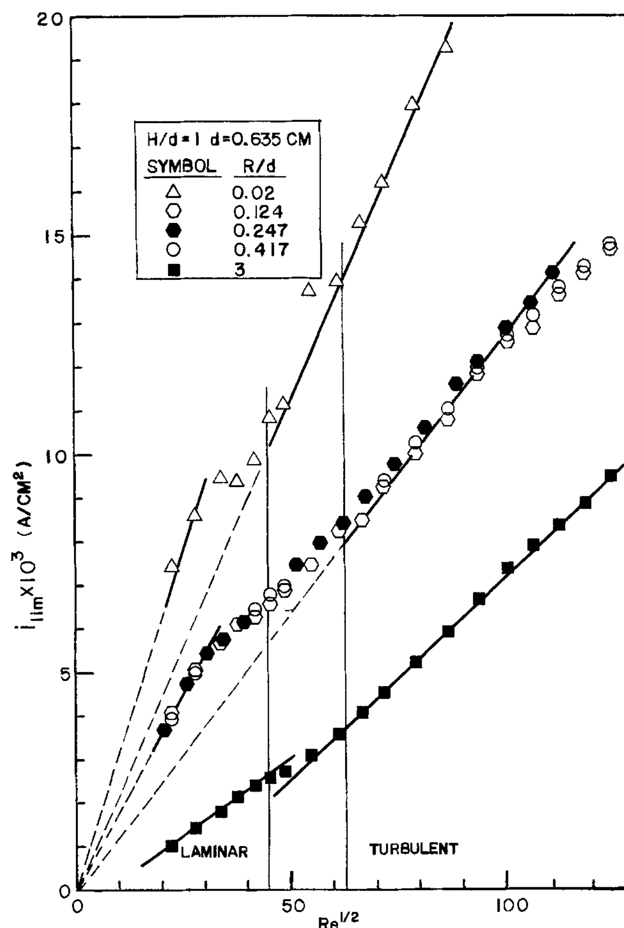

Fig. 8. Typical behavior of the limiting current density vs. the square root of the nozzle Reynolds numbers.

also been made to correlate these data with a straight line passing through the origin at the lower and the higher ends of the Reynolds numbers. It is seen that there is an excellent correlation for the data in the laminar region. The turbulent data can be correlated to within ±10% with a straight line passing through the origin. Again, the slope of the straight line in the laminar region is greater than that in the turbulent region. At the moment we do not have any suitable explanation of this phenomenon. Probably it was caused by a difference in behavior of the hydrodynamic constant, a^*, between the laminar and the turbulent impinging jets.

(*iii*) For the electrodes whose radii are greater than the outer limit of the uniform accessible region ($R/d \approx 0.5$ for laminar jet and 1.0 for turbulent jet), the limiting current density started to decrease with increasing electrode radius. The behavior in this region can be typically represented by the data obtained with $R/d = 3.0$. For this electrode, the data points in the laminar and the turbulent regimes can also be correlated with two separate straight lines; however, they cannot be extrapolated to the point of origin as shown in Fig. 8.

During the measurements, the limiting current was found to fluctuate. For the smallest electrode, the fluctuation was ±2% of the average limiting current in the laminar flow regime, ±5% in the turbulent region, and was ±20% in the transitional regime. The fluctuations decreased with increasing electrode sizes. The reproducibility for the smallest electrode with $R/d = 0.02$ was about ±8%. For the larger electrodes, the reproducibility of the limiting current measurement was better than ±3%.

To further contest the one-half power dependence of the mass transfer rate on the nozzle Reynolds numbers, the limiting current densities were converted to the Sherwood number, Kd/D, and the results were plotted against the Reynolds number in a log-log scale. Two such plots for $H/d = 1.0$ with two different nozzle sizes (one with a 0.318 cm diam nozzle and the other with a 0.635 cm diam nozzle) are given in Fig. 9 and 10, respectively. Again, the general feature of the data depends on the electrode sizes. For the smallest electrode and the electrodes located within the uniform accessible region, the data can be represented

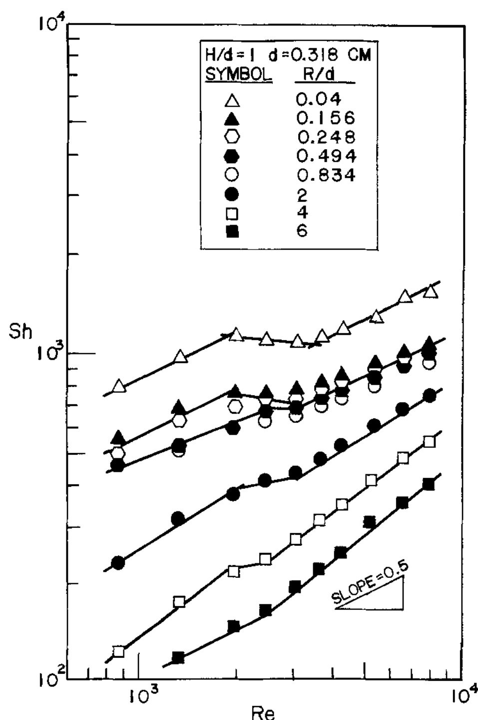

Fig. 9. Sh vs. Re for a 0.318 cm diam nozzle

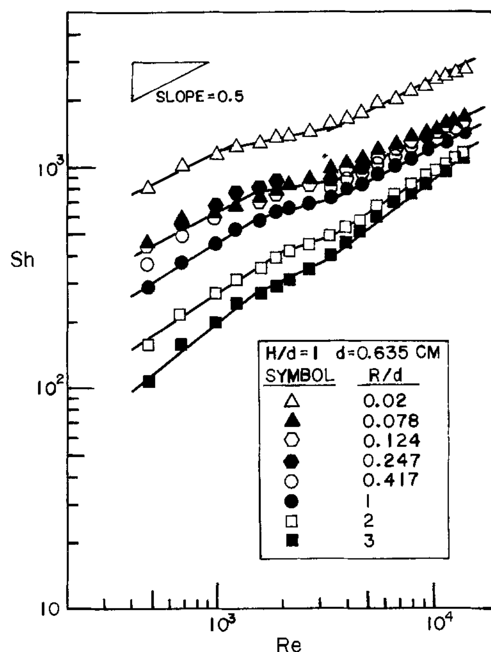

Fig. 10. Sh vs. Re for a 0.635 cm diam nozzle

by the three straight-line segments. The two breakpoints at the intersections of the segments correspond more or less to the point of instability (Re ~ 1500) and the transitional Reynolds number (Re ~ 3500) of pipe flow. The slopes of the straight lines in both laminar and turbulent flow were approximately equal to one-half. This result agrees with those of Scholtz and Trass (8), Giralt and Trass (7), and Belove *et al.* (14). These authors found that the one-half power dependence on the Reynolds number was true for both laminar and turbulent jets. The data points for different size electrodes located within the uniform accessible region ($0.1 < R/d < 0.5$ for laminar flow and $0.1 < R/d < 1$ for turbulent flow) have a tendency to merge together even though there is still a slight variation with the radial position. In general, these data could be correlated to within ±10% with a straight line of slope one-half.

For the electrodes with R/d greater than the uniform accessible region, there is a strong dependence of the Sherwood number on the dimensionless radius. For each electrode, the data points can also be correlated with three separate linear segments representing laminar, transitional, and turbulent flows. However, the slopes in the laminar and the turbulent regimes are greater than one-half. Also the break points become less distinguished and the width of the transitional regime seems to diminish with increasing electrode radius. For $R/d = 6$, for instance, the transitional regime completely disappeared, and the flow seemed to change directly from laminar to turbulent flow. An attempt has been made to correlate the data in this region with the following empirical equation

$$\mathrm{Sh} = l\mathrm{Re}^m \mathrm{Sc}^{1/3} \quad [34]$$

where the proportional constant, l, and the exponent, m, depend upon the electrode sizes. The results of a least squares curve fitting for Re greater than 4000 and H/d between 0.2 and 6 are listed in Table IV. It is

Table IV. Summary of the least squares curve fittings for the data with $R/d \geq 2$, $\mathrm{Re} \geq 4000$, and $0.2 \leq H/d \leq 6$

Empirical equation: $\mathrm{Sh} = l\,\mathrm{Re}^m\,\mathrm{Sc}^{1/3}$

R/d	l	m
2	0.342	0.59
3	0.133	0.68
4	0.0635	0.73
6	0.0316	0.77

seen that the value of l decreases with increasing R/d. On the other hand, the exponent m increases asymptotically with R/d; the values at $R/d = 4$ and 6 are seen to agree with the work of Yamada and Matsuda (22), who obtained an exponent of 0.75 for mass transfer in the wall jet region. This result clearly demonstrates that the wall jet region begins approximately at $R/d = 4$. Between $R/d = 1$ and 4, there is an intermediate region, where the turbulent impinging jet changes from the stagnation flow to the wall jet flow.

Mass transfer correlation for the uniform accessible region.—To compare the experimental data with the predictions of the equations listed in Table III, the values of $Sh/Re^{1/2}Sc^{1/3}$ were calculated for the electrodes located in the uniform accessible region for both laminar and turbulent jets. The results are plotted in Fig. 11 against the dimensionless nozzle height, H/d. Each data point represents the average value of several electrodes in the uniform accessible region over a range of Reynolds numbers indicated in the figure. Two different nozzle diameters and two different nozzle lengths were used to collect the data. Also plotted in the figure are the 13 equations listed in Table III. They are represented by the thin curves and identified by the corresponding equation numbers. It is seen that the present experimental results fall into the general area predicted by the equations. The agreement is poor for most equations. Only Eq. [III-1] is close to the laminar data; however, the prediction is at least 20% higher than the experimental value. For the turbulent data there is a satisfactory agreement between the data points and those predicted by Eq. [III-2] and [III-3] even though they were based on an analysis of a nonuniform rectangular laminar jet (19).

The data in Fig. 11 can be correlated in the form of Eq. [33]. A least squares curve fitting of the results gives the following equations:

(*i*) for the laminar data ($Re < 2000$, and $0.1 < R/d < 0.5$)

$$Sh = 1.51 Re^{1/2} Sc^{1/3} g(Sc) (H/d)^{-0.054} \quad [35]$$

(*ii*) for the turbulent data ($4000 < Re < 16{,}000$ and $0.1 < R/d < 1$)

$$Sh = 1.12 Re^{1/2} Sc^{1/3} g(Sc) (H/d)^{-0.057} \quad [36]$$

where the asymptotic series $g(Sc)$ is given by Eq. [25]. Equations [35] and [36] are plotted in Fig. 11 as the thick solid lines; the standard deviation of these correlations from the experimental data is ±10%. It should be noted that these equations are valid for $0.2 \leq H/d \leq 6$.

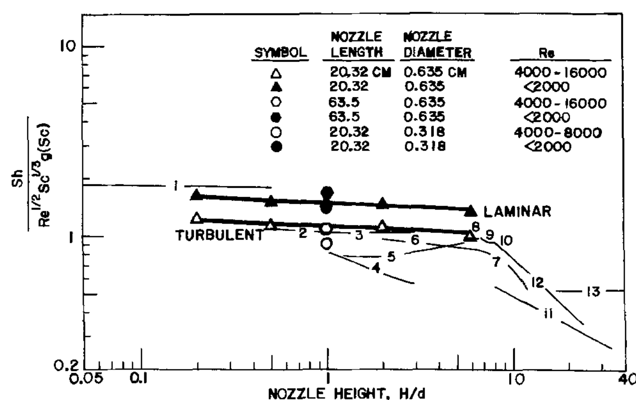

Fig. 11. Mass transfer rate as a function of the dimensionless nozzle height. For comparison the equations listed in Table III are also plotted as the thin curves; they are identified by the corresponding equation numbers. The thick solid lines are the least squares correlations of the present experimental results, Eq [35]-[36].

Electrochemical applications.—This result has proved that the impinging jet electrode is a feasible tool for electrochemical applications because of the existence of a uniform accessible region. This geometry can be adopted for the process streams and the closed systems requiring a pressure other than the ambient atmosphere. Since the electrode can be used for both laminar and turbulent flows, the upper limit in kinetic measurement is determined only by the pump size. At a nozzle Reynolds number of 10^8, for instance, Eq. [36] indicates that a first-order rate constant on the order of 1 cm/sec can be determined with the impinging jet. This is about one order of magnitude higher than the rotating disk electrode. It is suggested that a cell with a fixed ratio of nozzle height to nozzle diameter, H/d, be constructed, and the radius of the electrode be limited to less than 1 nozzle diameter. A convenient choice for the electrode size is $R/d = 0.5$, for which the nonuniform central core of $R/d < 0.1$ constitutes less than 4% of the total surface area; this is an acceptable error for most experimental work. In view of the complexity of mass transfer at the impinging jet electrode, the semiempirical equation in the form of Eq. [33] should be used for any kinetic, diffusivity, and concentration measurements. For a cell with fixed H/d and R/d ratios, the quantity $\alpha f(H/d)$ in Eq. [33] becomes a simple empirical cell constant which may be calibrated with a known redox reaction such as the reduction of ferricyanide to ferrocyanide ions. The present results of Eq. [35] and [36] can be used as a guideline to check the accuracy of the calibrations.

Conclusions

A theoretical and experimental study has been made of mass transfer to a circular disk electrode located within the stagnation region of an impinging jet. Using the method of perturbation, an asymptotic series is presented for the Schmidt number corrections over the range of Sc from 0.7 to ∞. The maximum deviation of the asymptotic series from the numerical solution is less than 0.7%. It is found that the electrode possesses a "uniform accessibility" to the diffusing ions within a range of dimensionless electrode radius, r/d, from 0.1 to 1.0 for turbulent nozzle flow and from 0.1 to 0.5 for laminar nozzle flow. Within this uniform accessible region the mass transfer rate is relatively independent of the electrode size, and the semiempirical correlations are presented in both laminar and turbulent flow regimes for $0.2 \leq H/d \leq 6$. Beyond the uniform accessible region, the mass transfer rate decreases with the radial position, and the wall jet region is found to begin approximately at $R/d = 4$.

Manuscript submitted March 21, 1978; revised manuscript received May 1, 1978.

Any discussion of this paper will appear in a Discussion Section to be published in the June 1979 JOURNAL. All discussions for the June 1979 Discussion Section should be submitted by Feb. 1, 1979.

LIST OF SYMBOLS

a — a hydrodynamic constant, sec^{-1}
a^* — dimensionless hydrodynamic constant, defined as $ad/\bar{U}$
C — concentration of the diffusing ion, g-mole/cm^3 or kg-mole/m^3
C_0 — concentration of the diffusion ion at the electrode surface, g-mole/cm^3 or kg-mole/m^3
C_∞ — bulk concentration of the diffusing ion, g-mole/cm^3 or kg-mole/m^3
$\bar{C}$ — dimensionless concentration of the diffusing ion
$\bar{C}_0 \ldots \bar{C}_5$ — the zeroth order, ..., 5th order concentration, dimensionless
D — diffusivity of the diffusing ion, cm^2/sec or m^2/sec
d — diameter of the circular nozzle or the width of the rectangular slot nozzle, cm or m

F	Faraday constant, 96,487 C/g equiv.
$f(H/d)$	an empirical function of H/d, see Eq. [33]
g(Sc)	a series expression of Sc given by Eq. [27]
H	nozzle height, cm or m
$\overline{H}$	dimensionless nozzle height, H/d
i_{lim}	limiting current density, A/cm^2 or A/m^2
j	local mass transfer flux at the electrode surface, g-mole/cm^2 sec or kg-mole/m^2 sec
K	average mass transfer coefficient, cm/sec or m/sec
k	local mass transfer coefficient, cm/sec or m/sec
n	number of electrons transferred in the electrode reaction, g-equiv./g-mole
R	radius of the disk electrode, cm or m
r	radial coordinate measured from the stagnation point, cm or m
$\overline{U}$	average velocity at the nozzle exit, cm/sec or m/sec
U'	bulk velocity of the uniform flow, cm/sec or m/sec
u	velocity component in the radial direction, cm/sec or m/sec
v	velocity component in the axial direction, cm/sec or m/sec
Z	a stretched coordinate for the diffusion boundary layer defined as $Sc^{1/3}$ η or Sc^{3} $\sqrt{a/\nu}\, z$, dimensionless
z	a coordinate perpendicular to the electrode surface, cm or m

Greek letters

α	an empirical constant in Eq. [33], dimensionless
γ	the adiabatic exponent in Table I, dimensionless
δ	boundary layer thickness in Fig. 1, cm or m
η	a dimensionless variable defined as $\sqrt{a/\nu}\, z$
μ	viscosity of the electrolyte, poise or Pa · sec
ν	kinematic viscosity of the electrolyte, cm^2/sec or m^2/sec
ϕ	stream function, dimensionless

Dimensionless groups

Re	Reynolds number, $d\overline{U}/\nu$
Re'	Reynolds number, RU'/ν
Sc	Schmidt number, ν/D
Sh	Sherwood number, Kd/D or kd/D
Sh_R	Sherwood number, KR/D

REFERENCES

1. J. W. Gauntner, J. N. B. Livingood, and P. Hrycak, NASA TN D5652 (1970).
2. I. Tani and Y. Komatsu, in "Proceedings of the 11th International Congress of Applied Mechanics," H. Gortler, Editor, pp. 672-676, Springer-Verlag (1966).
3. T. Strand, AIAA Paper No. 64-424 (1964).
4. F. Homann, *ZAMN*, **16**, 153 (1936); *Forschg. Ing-Wes*, **7**, 1 (1936); also see H. Schlichting, "Boundary Layer Theory," pp. 78-83, McGraw-Hill, New York (1960).
5. M. B. Glauert, *J. Fluid Mech.*, **1**, 6 (1956).
6. C. J. Chia, F. Giralt, and O. Trass, *Ind. Eng. Chem. Fundam.*, **16**, 28 (1977).
7. F. Giralt and O. Trass, *Can. J. Chem. Eng.*, **53**, 505 (1975); *ibid.*, **54**, 148 (1976).
8. M. T. Scholtz and O. Trass, *AIChE J.*, **16**, 82 (1970).
9. M. T. Scholtz and O. Trass, *ibid.*, **9**, 548 (1964).
10. D. A. Dawson and O. Trass, *Can. J. Chem. Eng.*, **44**, 121 (1966).
11. V. V. Rao and O. Trass, *ibid.*, **42**, 95 (1964).
12. K. P. Perry, *Proc. Inst. Mech. Eng.*, **168**, 775 (1954).
13. P. M. Brdlik and V. K. Savin, *Inzh-Fiz. Zh.*, **10**, 423 (1966).
14. I. A. Belov and V. S. Terpigorev, *ibid.*, **17**, 1106 (1969).
15. A. A. Andreev, V. N. Dakhno, V. M. Savin, and B. N. Yudaev, *ibid.*, **18**, 631 (1972).
16. C. D. Donaldson, R. S. Snedeker, and D. P. Margolis, *J. Fluid Mech.*, **45**, 477 (1971).
17. M. Kumada and I. Mabuchi, *Bull. JSME*, **13**, 77 (1970).
18. M. Kumada, I. Mabuchi, and K. Oyakawa, *ibid.*, **15**, 1246 (1972).
19. E. M. Sparrow and L. Lee, *Trans. ASME, Ser. C*, **97**, 191 (1972).
20. J. N. B. Livingood and P. Hrycak, NASA TM X-2778 (1973).
21. V. G. Levich, "Physicochemical Hydrodynamics," Prentice-Hall, Englewood Cliffs, N.J. (1962).
22. J. Yamada and H. Matsuda, *J. Electroanal. Chem.*, **44**, 189 (1973).
23. F. Coeuret, *Chem. Eng. Sci.*, **30**, 1257 (1975).
24. H. Schrader, *Ver. Dtsch. Ing.*, **B27**, 484 (1961).
25. P. Hrycak, D. T. Lee, J. W. Gauntner, and J. N. B. Livingood, NASA TN D-5692 (1970).
26. N. Froessling, *Lunds Univ. Avd.*, **2**, 35 (1940).
27. D-T. Chin, *This Journal*, **118**, 1434 (1971).
28. D-T. Chin, *ibid.*, **119**, 1049 (1972).
29. D-T. Chin, *ibid*, **120**, 628 (1973).
30. D-T. Chin, *ibid.*, **122**, 643 (1975).
31. D-T. Chin, K. Viswanathan, and R. Gutowski, *ibid.*, **124**, 713 (1977).
32. H. Lamb, "Hydrodynamics," Cambridge University Press, p. 144 (1932).
33. H. Matsuda and J. Yamada, *J. Electroanal. Chem.*, **30**, 261 (1971).
34. S. L. Gordon, J. S. Newman, and C. W. Tobias, *Ber. Bunsenges.*, **70**, 414 (1966).
35. C-H. Tsang, M.S. Thesis, Clarkson College of Technology (1978).
36. D-T. Chin and M. Litt, *This Journal*, **119**, 1338 (1972).

Reversibility and Growth Behavior of Surface Oxide Films at Ruthenium Electrodes

S. Hadzi-Jordanov,[1] H. Angerstein-Kozlowska, M. Vuković,[2] and B. E. Conway

Chemistry Department, University of Ottawa, Ottawa, Ontario, Canada K1N 6N5

ABSTRACT

Experiments are described in which the nature of surface oxidation processes at Ru electrodes are investigated and compared with those of other noble metals. Surface oxidation of Ru is much more irreversible than at Pt, Au, or Rh and the oxide formed in sweeps taken to 1.4V can only be reduced in the H region, usually with some coevolution of H_2. However, surface oxidation already begins at potentials in, or close to, the H region; this behavior is somewhat similar to that of Pt in alkaline solutions. Upon repeated cycling into the oxide region up to 1.4V E_H, a new state of the oxidized Ru surface is generated which exhibits remarkable reversibility of the *i-V* profile in anodic and cathodic sweeps taken to any potential in the range 1.4V. This effect is associated with a reversible redox process in the oxide film, probably between Ru(IV) and Ru(III), but reduction back to the metallic surface does not occur as it does in the initial sweeps. The behavior is somewhat similar to that previously observed with Ir. Time-dependent growth of the oxide film at Ru is observed, as at other noble metals, and the direct logarithmic law applies. Similarities to the surface oxidation behavior of other noble metals, especially iridium, are pointed out and depend on anion adsorption.

Ruthenium is of current interest as an electrocatalyst material, especially in combination with an oxidized Ti substrate, as an anode material for Cl_2 evolution (1-3). From an electrochemical point of view, this metal has, however, been less well characterized than most other noble-metal materials, especially with regard to the state of adsorbed H at its surface near the reversible H_2/H^+ potential and the nature of surface oxidation processes that occur at more positive potentials. In the case of Pt, Rh, Ir, and Au, the general surface oxidation characteristics were studied in some detail by Breiter *et al.* in a number of papers (4-6) using the potentiodynamic sweep method of Will and Knorr (7), and by Vetter and Berndt (8), and Schultze and Vetter (9), using galvanostatic conditions. Apart from the literature quoted in an earlier preliminary communication on Ru (10), relatively little work has been carried out on the surface oxidation behavior of Ru. An extended abstract (11) of a paper presented at the same meeting as that at which the present paper was given, reports comparisons between the properties and electrochemical behavior of oxide films on Ru and Ir and confirms the main features of the results given in our preliminary communication (10) in 1975.

In the previous short communication (10) we showed (*i*) that a region of H deposition and re-ionization could be distinguished at Ru electrodes, (*ii*) that a region of surface oxidation occurred over a broad potential range, and (*iii*) that the processes of formation and reduction of surface oxide showed much more hysteresis than at Ir (12), Pt (13), Rh (13), or Au (14), depending on the positive potential limit in the anodic sweep (13) in cyclic voltammetry experiments.

It is the purpose of this paper to give an account of further work [cf. (10)] that has been carried out in order to characterize more fully the formation and reduction of thin oxide films at Ru electrodes and to relate the observed behavior in a general way to that of Pt, Ir, and Au.

Experimental

Method.—Cyclic voltammetry experiments were carried out by well-known procedures. Anodic and cathodic sweeps at various rates could be applied to the electrode in a repetitive mode or individually after holding the potential for a controlled time [cf. (13)] at a particular value.

In the cyclic voltammetry experiments, it is found to be useful to take the potential successively to a series of increasing or decreasing values in the anodic or cathodic sweeps and thus generate a family of *i-V* profiles which illustrate the progressive changes of properties of the electrode, or oxidized electrode, surface in relation to the reversibility of the processes involved, as was done previously (13, 15) at Pt.

All experiments were conducted in solution bubbled with O_2-free N_2 as described previously (16).

Electrode preparation.—Most experiments were conducted at ruthenized Pt or Au, or a ruthenized Ru electrode prepared by the electroplating of the substrate metal from a recrystallized ammonium ruthenichloride solution. The Ru layer was electrodeposited at *ca.* 100 mA initial apparent current density at 300°K until an average Ru loading of *ca.* 5×10^3 atoms Ru per substrate Pt, Au, or Ru atom was obtained, as described previously (10). Some experiments were conducted on the ground and polished surface of a 2.5 mm diam $\times$ 2 cm long zone-refined Ru rod supplied by Research Organic and Inorganic Chemical Corporation, Sun Valley, California. The behavior of an electroplated layer on the Ru itself was not different from that on Pt or Au.

The real/apparent area ratio of the electroplated electrodes was initially *ca.* 100 after plating but in some experiments (see below) the real areas became diminished due to electrode dissolution upon cycling. Exact real areas cannot, however, be electrochemically determined, *e.g.*, through electrodeposited H accommodation measurements, as at Pt, due to the appreciable absorption of H that occurs simultaneously with H adsorption as described elsewhere (10, 17).

In other experiments, a chemically formed Ru electrode was prepared by painting a strong solution of $(NH_4)_2RuCl_6$ on a cleaned glass tube and firing it, in air, at *ca.* 723°K. A Pt contact had previously been sealed into the side of the tube.

Solutions.—0.1 or 1*N* aq. H_2SO_4 (B.D.H. Aristar grade) solutions, made up in pyro-distilled water (18), were employed as electrolytes. The cell was periodically washed with pure H_2SO_4 and then with the pyro-distilled water.

[1] Present address: Faculty of Technology and Metallurgy, University of Skopje, Skopje, Yugoslavia.
[2] Present address: Ruder Bošković Institute, Zagreb, Yugoslavia.
Key words: metals, electrode, charge, adsorption.

Potential scales and reference electrodes.—Measured potentials were referred to an H_2/Pt (reference) electrode in the same solution as that used for the working electrode and are referred to as E_H in the text which follows.

Currents and current densities.—Owing to the problem of defining real areas of electrodes in the case of Ru by H accommodation, because of H absorption [as we (17) and others (19) have found previously], it will not be possible to give real current densities on most of the graphs in this paper. Similar problems arise in evaluations of charges per unit area. However, for convenience and possible comparison with other published data, current densities and charges are recorded per geometric square centimeter of substrate electrode or the initial geometric area of an electrode. The time dependence of electrode areas upon anodic/cathodic cycling, mentioned above, is a further complicating aspect of this question.

Results and Discussion

Processes in the H region at ruthenium.—In previous papers (10, 17), it was demonstrated that a potential range (0.05-0.2V E_H) exists at Ru electrodes over which processes of H deposition and ionization arise, as at Pt, Rh, and Ir. In order to be able to describe and interpret the surface oxidation behavior which is observed at more positive potentials, it is first necessary to recapitulate briefly the conclusions (10, 17) regarding the H processes at Ru since at Ru, unlike Pt, there can be appreciable overlap between the processes of surface oxide formation and reduction with those of H ionization and deposition, respectively; also appreciable absorption as well as adsorption of H occurs.

Several aspects of the behavior at Ru indicate that the processes in the H region do not correspond simply to underpotential deposition of H in a series of four or five multiple states below monolayer coverage, as at polycrystalline Pt (20). The situation is complicated on the cathodic side by overlap with irreversible surface-oxide reduction processes in or near the H deposition region and facile H_2 evolution, and on the anodic side by H_2 reoxidation and reformation of a surface oxide species already at low positive potentials (17), 0.2 ~ 0.3V E_H.

A number of characteristics of the process in the H region indicated that H deposition and sorption into Ru, as well as adsorption onto its surface, occurs. H diffusion into Ru, as at Pd, is, *e.g.*, mentioned in early literature (21), and was demonstrated in a previous paper (17) by (*i*) cyclic voltammetry experiments where currents in the H region were shown to be dependent on square root of sweep-rate, *s*, rather than on its first power as for a surface process, *e.g.*, at Pt. Similar conclusions were reached by Bagotskii and co-workers (19); and (*ii*) by microcurrent-efficiency measurements for H_2 evolution at bulk Ru electrodes. These results indicate that a substantial fraction, if not all, of the H deposition/ionization charge measured in the H region at Ru electrodes is to be associated with H absorbed into the metal near its surface.

The general current-potential profile for formation and reduction of surface oxide at Ru.—Figure 1a shows

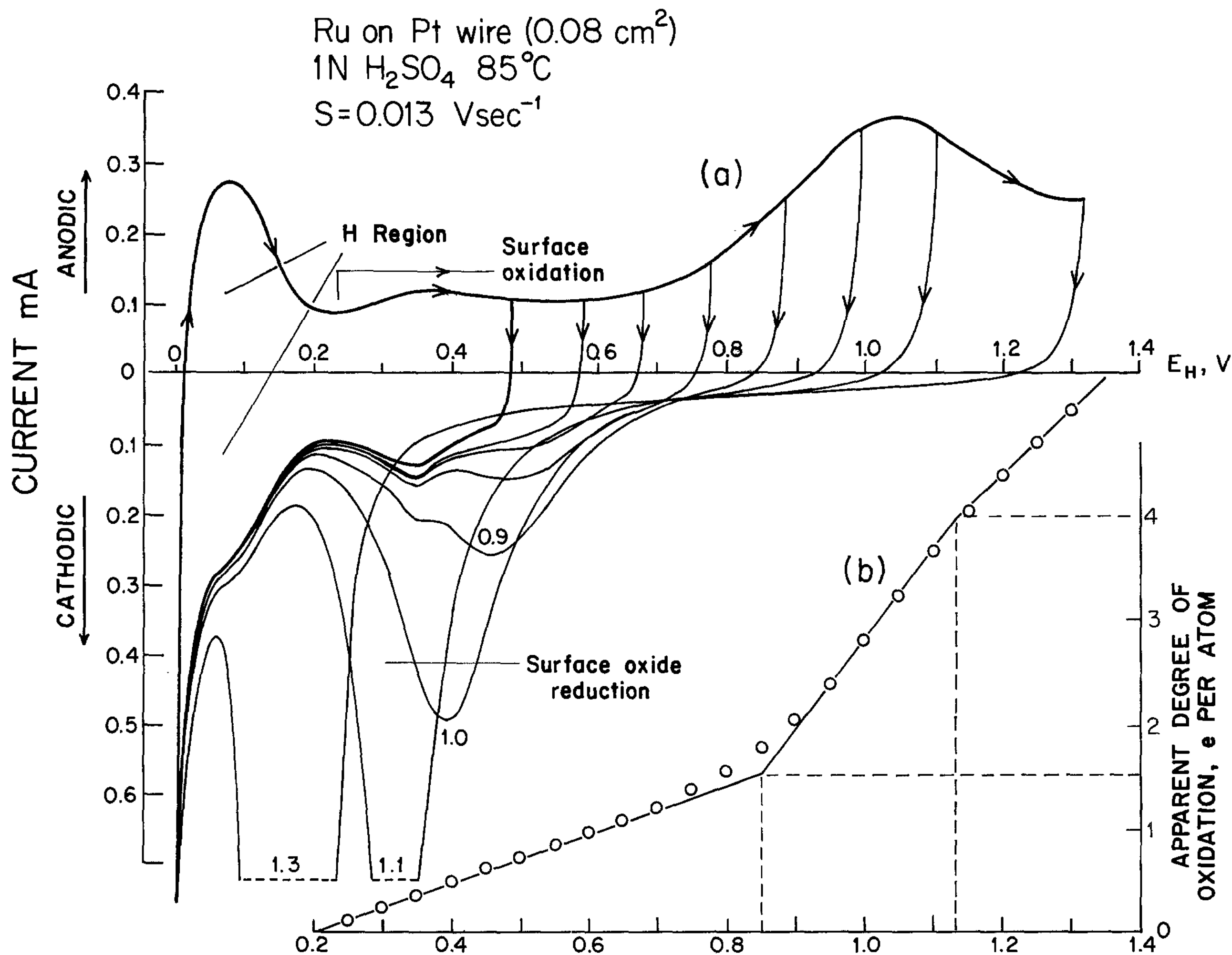

Fig. 1. (a) Cathodic and anodic potentiodynamic *i-V* profiles taken up to various potentials at ruthenized Pt, showing the H region and the progressive irreversibility between formation and reduction of surface oxide. Sweep-rate 13 mV sec^{-1}; 0.5M H_2SO_4; 358°K. Figures on cathodic curves indicate positive potential limit of previous anodic sweep. (b) Inset shows charge vs. potential profile obtained by integration of the *i-V* curves giving apparent degree of surface oxidation in e per atom.

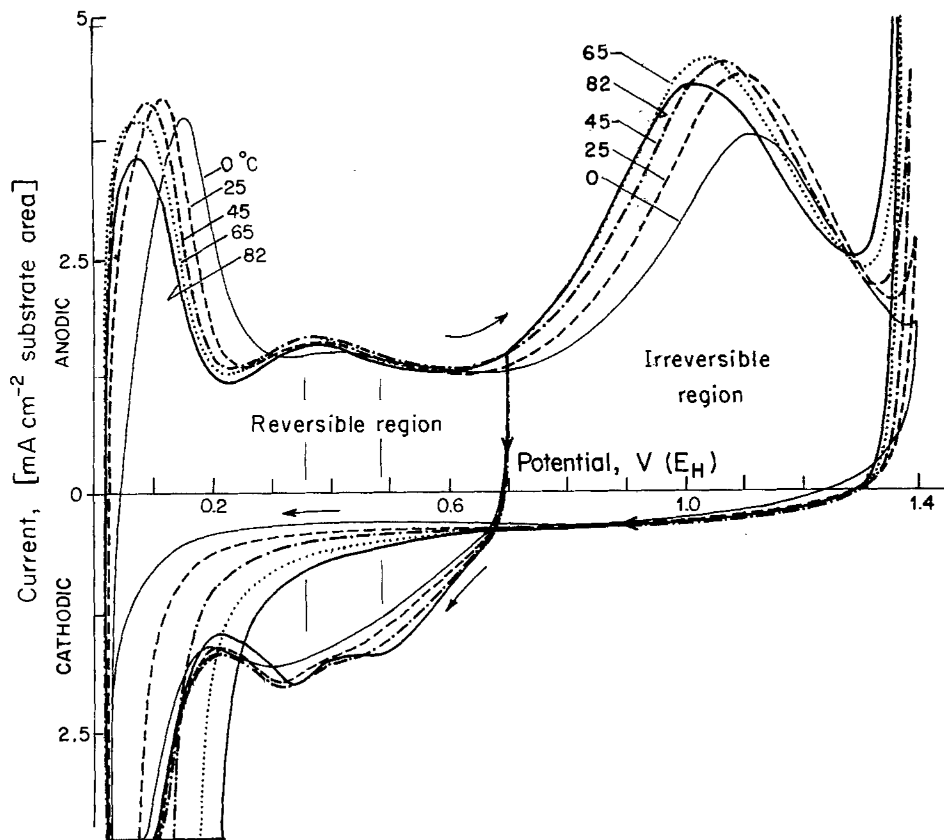

Fig. 2. Comparison of a series of potentiodynamic i-V curves for ruthenized Pt in 1N aq. H_2SO_4 taken over a range of 0.05-1.4 and 0.05-0.7 E_H, illustrating the region of almost reversible oxide formation and reduction if the anodic potential limit is < 0.8V. Temperatures 273°, 298°, 318°, and 355°K; sweep rate 13 mV sec^{-1}.

the general behavior of Ru surfaces subjected to a small number of anodic and cathodic sweeps. The characteristic features to be emphasized are (*i*) the early onset of surface oxidation, overlapping with the H region as mentioned above; (*ii*) a more or less reversible behavior in the processes of formation and reduction of the surface oxide when the extent of oxidation of the Ru surface is small (Fig. 2) [cf. the behavior of Pt (15)], (*iii*) development of a stage of higher oxidation of the Ru surface beyond 0.8V E_H (Fig. 1), and (*iv*) increasing hysteresis, much more than at Pt, Pd, Rh, or Au, between the processes of surface oxide formation and reduction when the potential of Ru has been taken above *ca.* 0.6V E_H and especially in the range 1.1 ~ 1.4V E_H (Fig. 1).

From current-potential profiles, such as those in Fig. 1a, the integrated charge for surface oxidation can be obtained as a function of potential as shown in Fig. 1b. Similar data at four temperatures are shown in Fig. 3. The second main region has a slope twice that of the first, suggesting that an oxide film involving twice the valence change of Ru compared with that in the first region is involved.

The true extents of surface oxidation per square centimeter up to any given potential cannot be reliably evaluated, as they can at Pt, owing to the uncertainty (10, 17) of the significance of the charge measured in the H region on account of substantial H absorption mentioned earlier. However, relative estimates, based on a fast sweep in the H region, are shown in the inset of Fig. 1 (marked b). The apparent degree of surface oxidation attained at 1.4V would then correspond nominally to "RuO_2" but this should be taken only as an approximate figure, not reliable to better than 30%.

From various i-V profiles similar to Fig. 1a but taken on a more sensitive current scale, it appears that the region between *ca.* 0.2 and 0.65V E_H corresponds to at least two broadly overlapping stages of surface oxidation, which are resolvable with difficulty below 0.65V in the anodic and cathodic sweeps. This region is evidently comprised of at least two-non-Langmuir peaks [cf. (22, 23)] for the initial stages

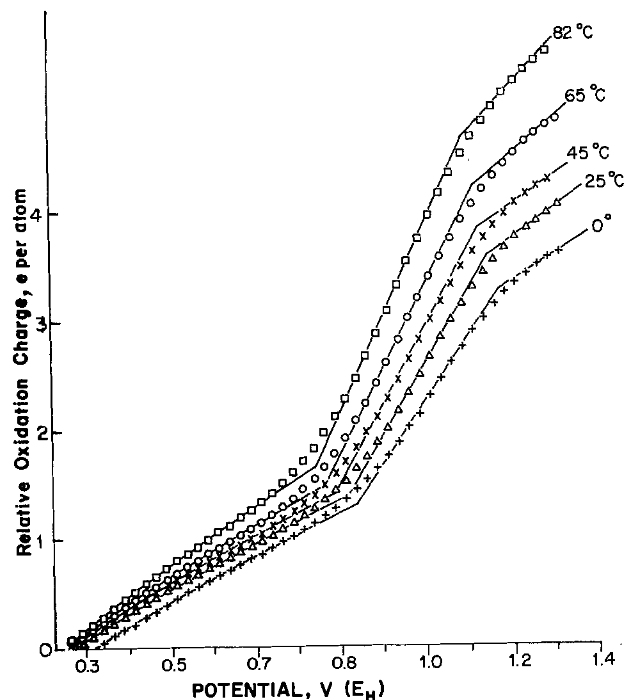

Fig. 3. Charges for surface oxide formation beyond 0.25V E_H showing the two or three principal stages of oxidation (the first region is probably resolvable into two overlapping components; see Fig. 1a and 2).

of surface oxidation of Ru, but these stages are better resolved in the cathodic sweeps (Fig. 1a).

Irreversibility in formation and reduction of the oxide film at Ru.—The hysteresis observed between the i-V profiles of Fig. 1a for the anodic and cathodic sweeps increases with the positive potential limit in the anodic sweep, as it does at other noble metals (7, 13), but the effect is much greater than at Pt or Au.

From Fig. 1 it is evident that the surface oxide formed when the potential of a Ru electrode is taken progressively to values > 0.8V E_H in the anodic sweep is only incompletely reduced in the cathodic sweep. In fact, in repetitive sweeps between 0.05 and 1.4V, the surface oxide formed is never reduced so that the full currents for its reformation are not required on a following anodic sweep. Then an unstructured i-V profile, of the kind reported in earlier work[3] (10, 24), over a 1.4V range at pure bulk Ru is observed. In a restricted range cycling experiment (0.05-0.7V E_H) on bulk Ru, the H region can be resolved after some cycling.

The slow process of reduction of surface oxide formed at appreciable positive potentials (1.1-1.4V E_H) can be followed by bringing the sweep back in a cathodic direction to the H region (to 0.05V E_H) and then holding the potential constant. During this potential-hold, the current can then be recorded as a function of time; it corresponds to slow reduction of the oxide film formed on the previous anodic sweep. In fact, the oxide film reduction is only completed in the H region or with H_2 evolution as at some other metals, *e.g.*, in the reduction of NiO, and the experimental behavior observed is shown in Fig. 4a and b.

Figure 4a shows the current-potential and current-time responses of a ruthenized Pt wire in 1*N* H_2SO_4 to the potential program shown in the inset of Fig. 4a: The potential of the electrode is swept at 0.1 V sec^{-1} to 0.7, 1.0, or 1.35V and then returned to 0.05V at which it is then held constant. The subsequent current-time transient is then recorded as shown to the right of the zero of time on the X axis of Fig. 4a.

After oxidation of the Ru to 0.7 or 1.0V, the cathodic sweep already shows a normal peak corresponding to oxide film reduction. Then the following cathodic current-time transients at 0.05V E_H are almost identical and extend over *ca.* 25 sec. However, when the electrode has been oxidized to ≳ 1.35V, there is almost no main oxide film reduction peak on the cathodic sweep and the reduction occurs on the cathodic current-time transient. This exhibits a maximum which may correspond to a nucleation-controlled reduction of the oxide film with codeposition of H.

In Fig. 4b, the results of a somewhat different but related experiment are shown. For this case, the potential program is as shown below the X axis. The potential is swept from 0.05 to 1.5V and then held for 0, 10, or 100 sec in successive experiments at that potential. The potential is then returned to 0.05V in a cathodic sweep at 0.1 V sec^{-1}, held at 0.05V, and then the cathodic current-time transient is recorded as shown to the right of the 0 on the X axis of Fig. 4b. Longer anodic holding (0 → 10 → 100 sec) produces a longer delay in the cathodic current-time transient corresponding to slower reduction of the oxide film in the H region. After 100 sec holding at 1.5V, the oxide film requires about 90 sec to become fully reduced. Hence, in repetitive sweeps between 0.05 and 1.35 ~ 1.5V, the oxide film is only incompletely reduced in the cathodic sweeps, unless very low sweep rates (<0.01 V sec^{-1}) are employed.

The reversibility of the process of formation and reduction of the oxide is illustrated in another way by the ratios, Q_A/Q_C, of charges Q measured in the anodic (A) and the cathodic (C) sweep, respectively. Q_A/Q_C remains almost equal to unity (Fig. 5) up to a potential of *ca.* 0.8V. If the sweep is taken beyond this potential, then $Q_A/Q_C > 1$ as seen in that figure. The effect is due mainly to incomplete reduction of the oxide in the cathodic sweep but also significantly to some dissolution (see below) of Ru toward the positive end of each anodic sweep.

Induction of a reversible process in oxide film formation and reduction upon multiple cycling.—Very interesting behavior arises at Ru after many (~25-50)

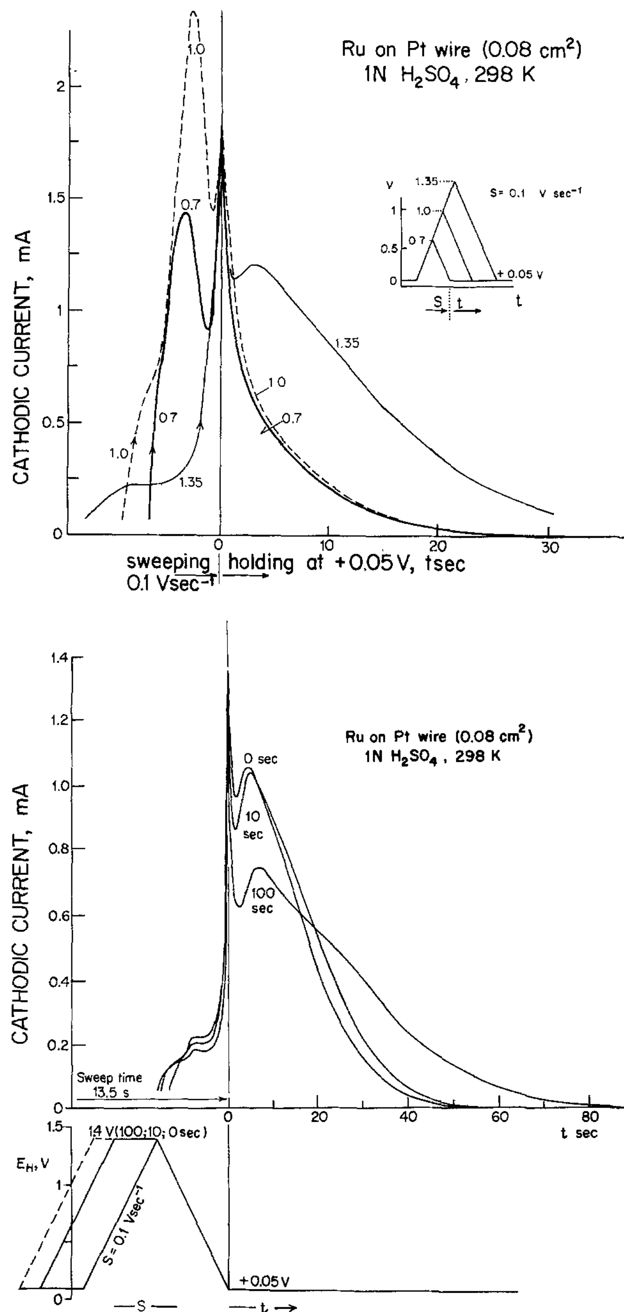

Fig. 4. Current-time transients for potentiostatic completion of reduction of oxide films on Ru after an anodic potentiodynamic sweep: (a, top) for sweeps to 0.7, 1.0, and 1.35V; (b, bottom) for sweeps to 1.4V with 0, 10, and 100 sec holding.

anodic/cathodic cycles up to 1.4V E_H. Initially, the behavior is as in Fig. 1 with much hysteresis between the processes of formation and reduction of the oxide; unless the potential is held at *ca.* 0.05V at the end of the cathodic cycle, the oxide formed in the previous anodic sweep will not be completely reduced, as was indicated with respect to Fig. 1, 2, and 4a and b.

However, upon repeated cycling, the behavior shown in Fig. 6 develops where, at any potential in the sweep, an almost reversible behavior is observed (25) as the direction of the sweep is changed. This is characterized by a sudden change of direction of current, from anodic to cathodic, at a magnitude almost the same as that on the immediately previous anodic sweep. The kinetic relaxation characteristics [cf. (26)] are then those of an almost reversible process, like the behavior of H at Pt (20, 26) or of the initial stage of surface oxidation of Pt (15), especially in alkaline solution. The changed state of the surface is initiated when sweeps are taken beyond

[3] In a paper just published by Trasatti *et al.* (48), similar behavior is found.

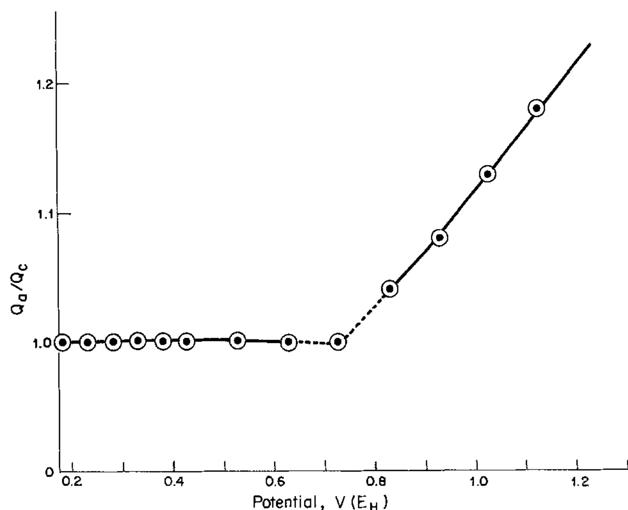

Fig. 5. Values of Q_A/Q_C as a function of the reversal potential in the anodic sweep at ruthenized Pt. Sweep rate 18 mV sec^{-1}. (Compare oxidation charge isotherms of Fig. 3.)

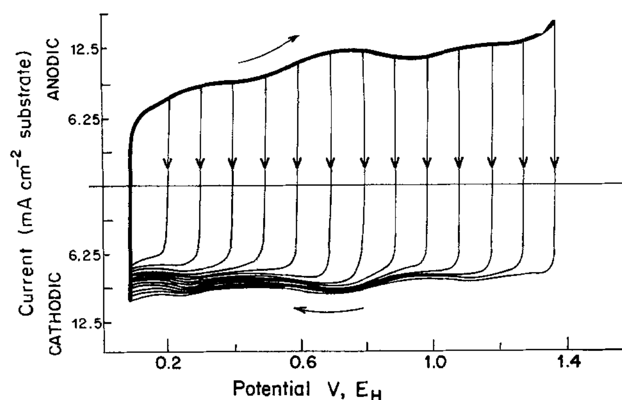

Fig. 6. Behavior of a Ru electrode in anodic and cathodic sweeps taken to various potentials after repetitive cycling ($\geqq$ 50 cycles); (note development of almost reversible cathodic and anodic sweep behavior but absence of reduction peaks or H deposition region shown in Fig. 1a). Sweep-rate 200 mV sec^{-1}.

the 0.8V potential where the higher stage of oxidation sets in (Fig. 3).

During repetitive cycling at a ruthenized electrode, some material is lost by dissolution (see below). This results in some diminution of currents at a given sweep rate but coupling with the effect mentioned above, gives *i-V* profiles (Fig. 6) with much increased reversibility at any potential. An electrode which has reached this state of surface conditioning no longer exhibits (Fig. 6) a resolvable region of H deposition and ionization, as it did initially (Fig. 1). This is because cycling to 1.4V produces the irreversibly oxidized surface that is not reduced in the H region in cathodic sweeps. At Ir, ellipsometric experiments (27) show that the oxide film which is similarly generated upon cycling (12) and which exhibits (12, 13) reversible redox behavior like oxidized Ru, is also not reducible to Ir metal in the H region [cf. (11)].

We have suggested (25) that the remarkable reversibility within the *i-V* profile at any potential, as demonstrated by Fig. 6, is due to establishment of an oxide film in which a rapid redox process,[4] *e.g.*, formally $2RuO_2 + 2H^+ + 2e \rightleftharpoons Ru_2O_3 + H_2O$, can occur with kinetic facility. This process is probably, in reality, more complex involving Ru-O-Ru bridges (28, 29) dependent on the valence state of Ru and on protonation (30, 31). The special state of the surface is only generated, however, by repetitive cycling without reduction of the anodically generated oxide back to the metal at the end of each cathodic sweep. In this respect, the behavior is similar to that of Ir in the experiments of Visscher (12) and of Rand and Woods (32), where an oxide film grows on cycling and exhibits remarkably reversible behavior as noted first by Stonehart, Kozlowska, and Conway (13). Even at Pt, somewhat similar effects of cycling have been reported (33).

Presumably, in the state of oxidation generated by cycling, there is a mixed valency [Ru(III) and Ru(IV)] oxide on the Ru surface at all potentials but the Ru(III)/Ru(IV) ratio, which characterizes the oxide film, evidently depends in a continuous way on the potential of the electrode. In this respect, the surface-oxide redox behavior is analogous to the titration behavior of a polyelectrolyte or ion-exchange resin where the ionizable groups, although having the same individual *p*K values, give rise to a broad titration curve over a wide *p*H range without the inflections characteristic of titration of di- or tribasic acids. The reason for this behavior is that interaction effects destroy the individuality of the *p*K value. Similarly, in a redox system involving two or more charged (ionic) states, interaction effects will broaden the electrode potential degree of oxidation (reduction) relation. Addressing an oxide redox system with a linear potential sweep is analogous to effecting a redox titration of the surface oxide material. We suggest that this is what is observed in Fig. 6, where the individual stages of surface-oxide formation and reduction, which are resolved in initial sweeps (Fig. 1a), are no longer observable in the multiply repeated *i-V* profile.

It is interesting that a similar state of reversibly reducible/oxidizable oxide can be generated on the surface of Ru by thermally forming a Ru film on glass in air at *ca.* 450°C from $(NH_4)_3RuCl_6$. The behavior of this kind of film is illustrated in Fig. 7 and is to be compared with that generated on cycling the nonthermally formed film (Fig. 6).

Film growth behavior.—At the noble metals, holding the potential at a value where surface oxidation can occur results in growth of the oxide film and/or change in the state of oxidation of the metal in the film. The growth is conveniently measured by the charge, Q_C, recovered in a slow cathodic sweep. Q_C is usually (34, 35) a direct logarithmic function of the duration, *t*, of the growth period, although direct and inverse log laws of film growth are sometimes

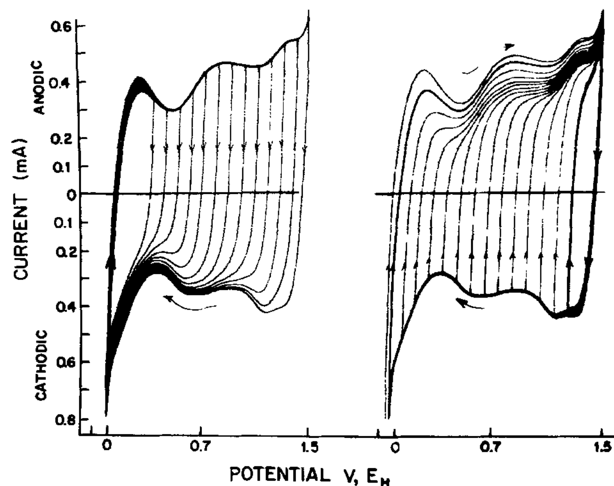

Fig. 7. Reversible anodic/cathodic *i-V* profiles for a Ru film (presumably oxidized) formed by thermal decomposition of $(NH_4)_3RuCl_6$ on glass in air at 450°C. (Compare Fig. 6.) Sweep-rate 200 mV sec^{-1}.

[4] The species shown in this reaction are intended only to represent the probable well-known valence states involved [Ru(IV) and Ru(III)]. The formulas probably do not correspond to bulk compounds for the case of the thin films.

difficult to distinguish unless data over a wide range of time is available. The initial oxidation, *e.g.*, of Pt, in an anodic sweep is a fast process as indicated by the large value of its reversibility parameter, s_0 (36, 37); [s_0 is the maximum value of sweep rate, s, up to which a surface process remains reversible, *i.e.*, peak potentials for electrodeposition of O-species, or of H, remain independent of s. When $s > s_0$, Tafel-type behavior arises, viz., peak potentials are displaced logarithmically in s, see Ref. (23) and (34)]. The growth process, logarithmic in t, is associated with a slow rearrangement of the film in a step following the initial deposition of OH/O species, by place-exchange (38-40) between Pt and OH or O species. The continuing deposition of OH and O species is made possible at the holding potential by the rearrangement process, as discussed in more detail below.

At Ru, very similar behavior to that at Pt (34) is observed; both at the bulk Ru rod (Fig. 9) and at ruthenized Pt (Fig. 9), the oxide film growth is logarithmic in time (except at short times), with a slope $dQ_C/d \log t$ which increases with the holding potential E_A, as shown in the inset of Fig. 9; also Q_C, measured after a given holding time (100 sec), is almost linear in E_A (inset of Fig. 8). Results for two temperatures are shown in Fig. 8.

An interesting characteristic of the growth process, found first at Pt (41), is that if the potential is held for a short time (1 ~ 100 sec, for example) during the anodic sweep, and then the sweep is continued, the resulting i-V profile will fall on the fast continuous-sweep profile determined previously, after an interval in the potential scan, dependent on the time of holding during the sweep. This behavior is also found for Ru as shown in Fig. 10a and b for various holding potentials. Figures 10a and b show that this behavior commences at Ru already at quite low potentials, *ca.* 0.35V E_H.

The behavior of Ru shown in Fig. 10a and b appears to be a general feature of initial stages of oxide film growth at noble metals as it is also found at Au, Pd, and Rh as well as at Pt (41). The following pro-

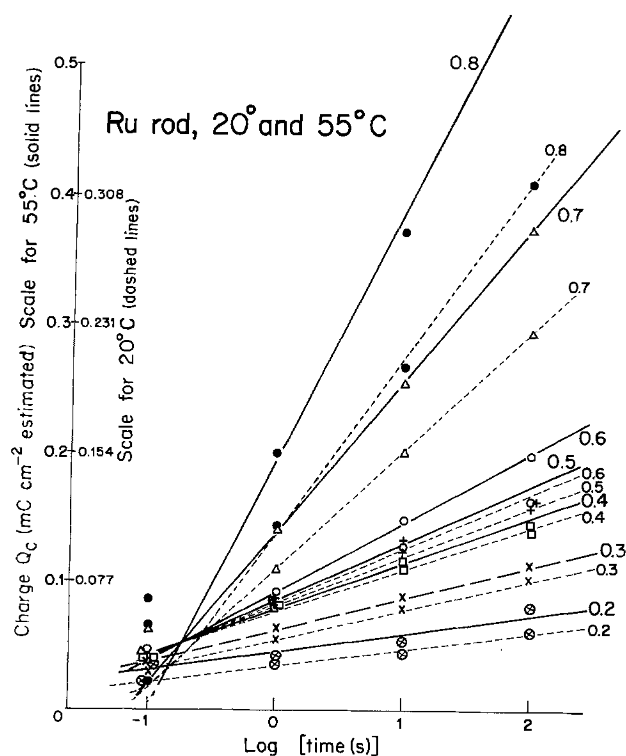

Fig. 8. Plots of increase of degree of surface oxidation (measured as cathodic charge Q_C for reduction of the anodically formed film) of a Ru rod electrode at 293° and 328°K as a function of the log of the growth time.

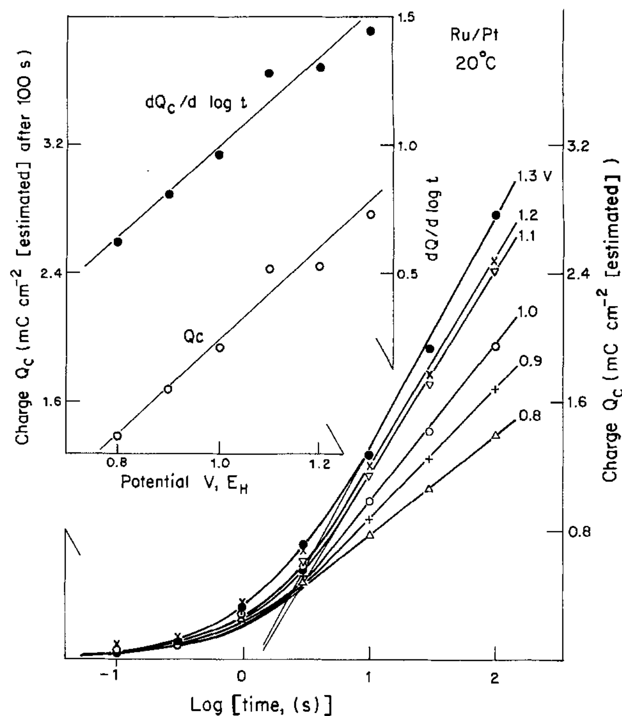

Fig. 9. As in Fig. 8, but for ruthenized Pt at 293°K. Inset shows other functions of Q_C.

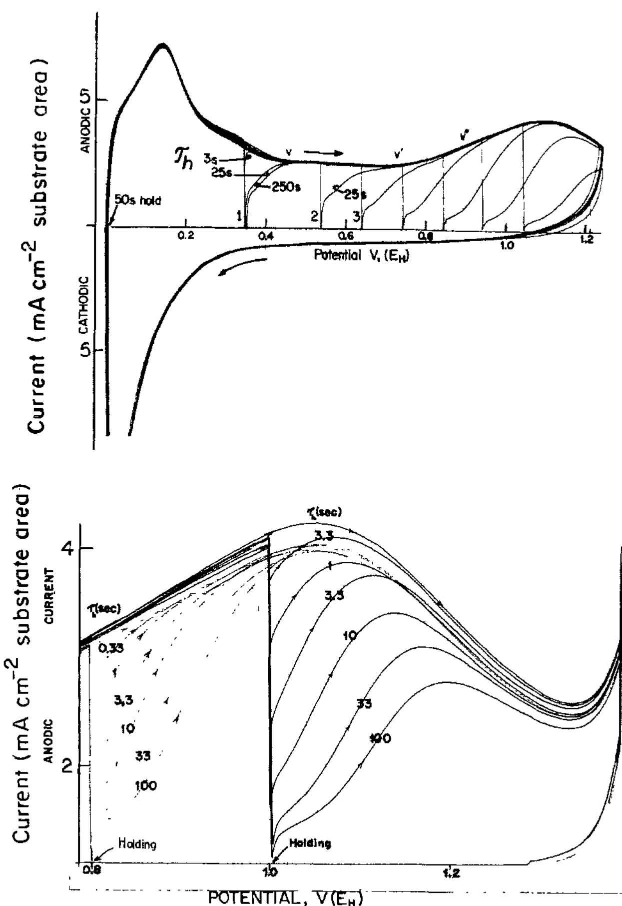

Fig. 10. (a, top) Anodic i-V profiles for a ruthenized Pt electrode with and without holding at various potentials for the indicated times τ_h during the potential sweep. (b, bottom) As in 10a, but at higher potentials of 0.80 and 1.0V.

posal for the origin of this behavior can be made. Although of a tentative nature, it provides a basis for understanding a number of features of the initial stages of oxidation of Ru and other metals, and the irreversibility between oxide film formation and re-

duction processes which is notable characteristic of films formed at coverages $\theta > ca.$ 0.15.

In a fast anodic sweep, rapid (high s_o) underpotential deposition of OH and O species first occurs[5] on noble metal surfaces and at low extents of oxidation, *e.g.*, $\theta \leq ca.$ 0.75, the coverage θ at any potential in a fast sweep over this range of surface oxidation is a reproducible function of that potential. Relatively successful attempts have been made to represent this behavior by an additive combination of two or three electrochemical isotherms of the form [1], *e.g.*, at Pt (23, 40)

$$\theta/(1-\theta) = K \exp(-g\theta)\cdot C \exp VF/RT \quad [1]$$

where g is an interaction parameter, V the potential, and C the reactant concentration, *e.g.* of OH^- or H_2O. Usually, for electrodeposited OH and O films with $\theta_{OH/O} < 0.75$, the isotherms contain repulsive terms, *i.e.* $g > 0$ [cf. Ref. (23, 42)], so that occupancy of the surface by OH and O species is spread over a wider range of potentials than in the Langmuir case ($g = 0$). Usually, distinguishable multiple states of adsorption (*i.e.*, ranges of θ with different K values) can be resolved below monolayer coverage, as at Pt (15), and probably also here with Ru.

As potential and time progress in the anodic sweep, it has been proposed (40) that a relatively slow process of place-exchange between metal atoms and OH/O species in the surface occurs. This is directly indicated by the results of Arvia (43) on open-circuit time-effects in the change of state of oxide films at Pt and by effects of holding the potential constant in the film formation region, followed by cathodic reduction (13, 15).

As the place-exchange process progresses, repulsive interactions existing between the initially electrodeposited OH/O species in the developing monolayer (due to the "MOH" or "MO" surface dipoles) can become locally relieved due to MOH or M-O dipole inversion, so that further deposition of OH or O can occur at a potential below that which would be defined by a $\theta \sim V$ relation such as Eq. [1] for deposition of OH or O species in a regular monolayer on the metal surface. Thus a greater coverage can be attained by holding at some potential E_h in the sweep in the surface oxidation potential region than the equivalent coverage attained in a continuous sweep. Coupled desorption of previously adsorbed anions occurs as the film growth continues.

Eventually, (see Fig. 10a and b) as the continued sweep, after holding at a potential E_h, progresses to sufficiently high potentials E_s in the sweep s, the same coverage and state of the surface is reached after holding as in the regular continuous sweep. This is because the same state of surface oxidation is achieved by holding the potential at E_h for a time τ_h as in a continuous sweep up to the potential E_s, where $E_s > E_h$ to an extent dependent on τ_h (see Fig. 10a and b).

That the same degree of surface oxidation is attained when this condition obtains, is indicated experimentally [cf. (41)] by the fact that the cathodic i-V profile following the anodic sweep is identical for the continuous sweep as for the sweep with intermediate holding at E_h for time τ_h provided that the anodic i-V curve for the continued sweep, after holding, has reached a potential where the i-V profile coalesces with that for the continuous sweep, *e.g.*, at points V, V', V" in Fig. 10a for Ru oxidation.

These results lead to the conclusion, as at Pt, that a given extent of oxide film growth at Ru can be achieved in a "holding" experiment at a potential E_h, as in a continuous sweep to higher potentials, $E_s > E_h$, where the field for continuing oxidation by place-exchange at E_s is larger than that at E_h in the holding experiment. During the holding time, τ_h, the growth of the film is logarithmic in τ_h as described earlier.

Some place-exchange always occurs, of course, in a continuous sweep due to lateral interaction and field effects; the extent of this naturally depends on the sweep rate. The holding effects are hence best observed when $\tau_h >> \Delta t$ where $\Delta t = \Delta V/s$ is the time interval in a sweep at rate s for traversal of a potential excursion ΔV in the surface oxidation region.

Unlike the behavior of Pt or Au in acid solution, however, the growth of surface oxide at Ru commences already at potentials around 0.2 $\sim$ 0.3V E_H. This is apparent in Fig. 10a as well as in the logarithmic plots in Fig. 8.

In order to investigate the growth of the surface oxide film at low potentials, the effect of holding the potential in the range 0.4-0.2V E_H was investigated at a ruthenized Pt electrode that had been subjected only to a few initial conditioning cycles, as for the electrode which gave the results in Fig. 1a. The behavior is shown in the oscilloscope photographs of Fig. 11. Even at these low potentials, the extent of surface oxidation of Ru increases with τ_h as indicated on the successive cathodic i-V profiles of Fig. 11.

Bagotskii *et al.* (19) observed a cathodic peak at 0.27V similar to those in Fig. 11, but attributed it to deposition of H which became sorbed into the Ru.[6] Since the charge under these i-V profiles increases with increasing τ_h at 0.45V E_H (*i.e.*, at a potential where adsorbed or absorbed H would be readily oxidized) it seems that the observed cathodic current peak must be assigned to growth of surface oxide in the early stages of development of the oxide film at Ru rather than to H deposition. This is confirmed by the observation (Fig. 11) that there is constancy of the anodic i-V profiles following the cathodic sweeps after various holding times at 0.45V. This seems to support the conclusion that the cathodic process at these potentials is surface oxide reduction since if the cathodic currents and the current during holding were associated with H deposition in a sorbed state, then more H should be available for the following anodic sweep, which is not the case. This question has been dealt with in more detail elsewhere (17) in a paper on the state of electrodeposited H at Ru.

Relation to surface oxidation behavior of other noble metals.—While the oxidation behavior of Ru surfaces is in some respects unusual, it is useful to point out some of the features which are basically similar to those for other metals. The hysteresis between forma-

[6] Other evidence, *e.g.*, the sweep-rate dependence of the anodic peak current in the H region, does indicate (17) H diffusion from the bulk of Ru. However, such evidence is not obtained from the cathodic sweep behavior at 0.27V.

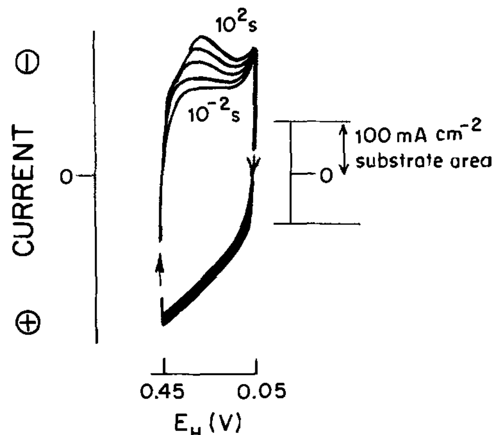

Fig. 11. Oscilloscope i-V profiles for cathodic sweeps from 0.45V E_H after various holding times τ_h from 10^{-2} to 10^2 sec. Anodic and cathodic sweep rates 20 V sec^{-1}.

[5] This reaction itself is found kinetically to be highly reversible (15). However, as shown elsewhere (34), the over-all process of surface oxidation of Pt always exhibits hysteresis due to transformation of the "PtOH" species into a place-exchanged oxide film. This is equivalent to an irreversible chemical step following the reversible electrodeposition process of OH or O species (37).

tion and reduction of surface oxide in initial sweeps is greater than at Pt, Rh, or Au but similar to that at Pd. It increases, as at most metals (13), with increasing potential in the anodic sweep, *i.e.*, with increasing extent of surface oxidation and consequently greater place-exchange (13, 15). Almost reversible surface oxidation of Ru in aq. H_2SO_4, we have shown, already commences at, or close to, the H region. While this is different from the behavior of Pt in acid (15), it is similar to that of Pt in alkaline (NaOH) solution where a reversible region of surface oxidation is already observable at *ca.* 0.4V E_H. This is illustrated for comparison in Fig. 12 for fast anodic and cathodic sweeps at Pt in NaOH solution. Under these conditions, the H region is moved to appreciably more positive potentials in the anodic sweep and to appreciably more negative ones in the cathodic sweep due to irreversibility of H ionization and deposition processes in alkaline solution (36). The surface oxidation and reduction processes are more reversible in alkaline than in acid, so are observed in a well-resolved way as seen in Fig. 12.

The difference between the acid and alkaline solution behavior is due in part to the lack of anion adsorption in the latter case because the potential of surface oxidation (relative to the H_2 electrode potential for the same solution) is much less positive with respect to the potential of zero charge than in acid solution (44). Thus, in acid media, it is known that SO_4^{2-} concentration has a substantial effect at Pt and especially at Au on the potential for onset of surface oxidation. This is because, in the deposition of OH species in the initial stages of surface oxidation of Pt and Au, previously adsorbed anions must be displaced. At Ru, SO_4^{2-} anion adsorption is evidently less competitive with regard to surface oxidation. Despite conclusions (45) that Cl^- does not depress oxygen adsorption at Ru very much, we find that in strong Cl^- solutions (5M NaCl), anion adsorption effects at Ru become more comparable to those at Pt with SO_4^{2-}; then the H region becomes displaced cathodically and the initial surface oxidation region anodically [as is well known at Pt (44)], so that a "double-layer" charging region with a smaller and more normal capacitance becomes revealed in the potentiodynamic *i-V* profile which then is seen to be more similar to that at Pt in aq. H_2SO_4 where strong SO_4^{2-} adsorption prevails. These results illustrate the importance of anion adsorption in determining the shapes of the *i-V* profiles for H deposition and surface oxidation at noble metals, as shown in the early work of Breiter (46).

In other respects, *e.g.*, effects of cycling, Ru behaves somewhat like Ir, as we have shown above and as was noted by Rand, Woods, and Michell at the 1977 Spring Electrochemical Society meeting (11).

Dissolution accompanying surface oxide formation and reduction.—The stability of oxidized Ru surfaces is of interest in relation to the performance of continuous anodic reactions, *e.g.*, Cl_2 evolution, at such electrodes. A number of experiments were conducted at oxidized bulk Ru rod electrodes in order to evaluate rates of dissolution in 1*N* aq. H_2SO_4 and NaCl solutions under steady-state and cyclic anodic polarization. Weight losses were determined directly by withdrawing the electrode periodically from the cell, washing and drying it, and then recording weight changes by means of a microbalance.

The experiments on extents of dissolution were conducted in two ways: (*i*) by cycling the electrode for various numbers of cycles up to various anodic potentials E_a = 0.7, 0.9, 1.1, and 1.3V E_H and recording the losses of weight after 5, 10, 15, 20, 25, and 30 cycles as shown in Fig. 13a, and (*ii*) by establishing an anodic current in the range 6-16 mA and following weight changes, if any, over a period of 4 hr. None was observed (Fig. 13b). The same electrode was then subjected to anodic/cathodic cycling over the range 0.05-1.3V E_H at 16 mV sec^{-1} for 55 min. During this time, a substantial loss of weight occurred as shown in Fig. 13b. The electrode was then returned to a continuous anodic polarization mode at 8-14 mA. The rate of weight loss was then much diminished in comparison with that in the cyclic mode but significant further weight loss did occur over the next 5 hr (Fig. 13b) and more than in the first 4 hr prior to cycling.

After the period of intermediate cycling (Fig. 13b), a change of state of the electrode had evidently taken place, as described earlier. The electrocatalytic properties for anodic reactions are then found to be changed although the real area of the material is, in the short term, not diminished by more than 5%.

It is to be concluded that the stability of a Ru electrode in acid is much less under cyclic polarization conditions than under continuous anodic current operation. This is probably due to the repetitive reorganiza-

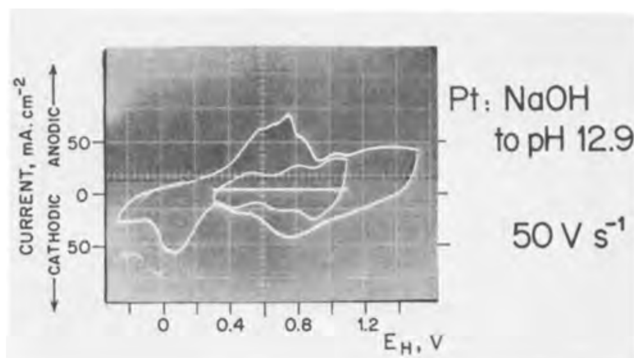

Fig. 12. Resolution of reversible regions of Pt surface oxide formation and reduction near the H region for alkaline solution conditions by displacement of the H oxidation and deposition profiles at a high sweep rate. 1*N* NaOH at 298°K. Sweep rate 50 V sec^{-1}. Outer profiles for full potential range with displaced H region. Inner profiles for the same sweep rate, but over a restricted potential range revealing regions of reversible surface oxide formation and reduction at low anodic potentials.

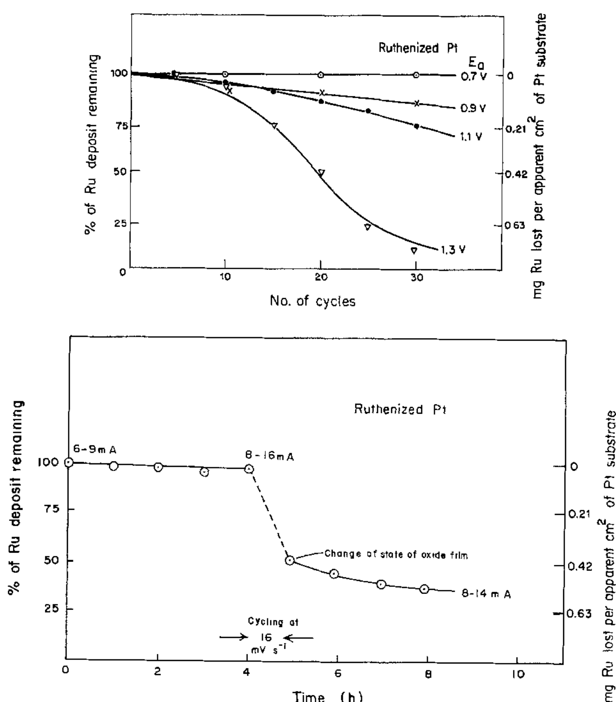

Fig. 13. (a, top) Relative and absolute extents of dissolution of Ru from a ruthenized Pt electrode by cycling to various potentials E_a in the anodic sweep. (b, bottom) Relative and absolute extents of dissolution of Ru from a ruthenized Pt electrode under steady-state and cyclic anodic polarization conditions.

tion of the surface which accompanies cyclic polarization and is associated with the place-exchange processes referred to earlier and with possible accompanying deprotonation and reprotonation (31). Generally, it seems that dissolution depends on: (*i*) the positive potential in the anodic sweep (Fig. 13a); (*ii*) the number of sweep cycles to which the electrode has been subjected (Fig. 13b), and (*iii*) whether the electrode has been polarized only in continuous anodic current mode or otherwise in a cyclic regime (Fig. 13b).

The dissolution is found to be quite appreciable, especially during an anodic/cathodic cyclic treatment, when the anodic potential limit exceeds 0.8V. This is the potential at which a higher state of surface oxidation begins to arise (see Fig. 1b and 3). The effect of Cl^- ion is to enhance the dissolution rate in comparison with that in aq. H_2SO_4 alone. On account of the dissolution which occurs on repetitive cycling, a Ru rod electrode will become "autoruthenized" and will suffer significant increase in real area. On the other hand, a ruthenized Pt electrode progressively loses Ru by dissolution under such conditions, with a decrease of real area, as mentioned earlier.

The extents of dissolution are substantially greater than those which are found at Pt (47) and Ir (32). In alkaline solution, electrochemical oxidation leads directly to dissolution of Ru as solution-soluble ruthenate which can be easily observed on account of its dark red color.

These results emphasize the importance of stabilizing RuO_2 electrode materials by combination, *e.g.*, with a TiO_2/Ti substrate.

Conclusions

Studies on the formation and reduction of surface oxide on Ru lead to the following conclusion: (*i*) At low potentials (0.2-0.4V E_H) initial stages of surface oxidation arise which are almost reversible and overlap with the process of H (absorbed and adsorbed) ionization. (*ii*) Beyond *ca.* 0.8V, a higher state of oxidation of the surface arises and its formation and reduction is progressively more irreversible the more positive is the potential. Formation of oxide at 1.3-1.4V results in a film that is only slowly reducible in the H region. (*iii*) Repetitive cycling to $\geq$ 1.3V causes an irreversible transformation of the behavior of the surface oxide to a state in which the film apparently undergoes a remarkable redox process over a wide range of potentials yet is not reducible back to the metallic state. The role of a Ru(III)/Ru(IV) redox couple in the oxide film is suggested. (*iv*) Appreciable anodic dissolution of Ru occurs on cycling over a potential range >0.7V from 0.05V E_H, especially to higher positive potentials. Dissolution on steady-state anodic polarization is much less rapid. (*v*) In the presence of strongly adsorbed anions, *e.g.*, Cl^-, the current-potential profiles for Ru become more like those of Pt in aq. H_2SO_4. (*vi*) The over-all behavior of Ru is more like that of Ir than that of Pt or Rh, although some important similarities to the latter metals are apparent.

Acknowledgments

Grateful acknowledgment is made to Hooker Chemicals and Plastics Corporation, Niagara Falls, New York for support of this work. Helpful discussions with Drs. Emery, Pouli, Stephens, and Tilak of Hooker have been much appreciated.

Manuscript submitted July 12, 1977; revised manuscript received April 17, 1978. This was Paper 336 presented at the Philadelphia, Pennsylvania, Meeting of the Society, May 8-13, 1977.

Any discussion of this paper will appear in a Discussion Section to be published in the June 1979 JOURNAL. All discussions for the June 1979 Discussion Section should be submitted by Feb. 1, 1979.

REFERENCES

1. A. T. Kuhn and P. M. Wright, *J. Electroanal. Chem.*, **41**, 329 (1973); see also O. De Nora, *Chem. Ing. Tech.*, **42**, 222 (1970).
2. D. Galizzioli, F. Tantardini, and S. Trasatti, *J. Appl. Electrochem.*, **4**, 57 (1974).
3. G. Faita and G. Fiori, *ibid.*, **2**, 31 (1972).
4. M. W. Breiter, C. A. Knorr, and W. Volkl, *Z. Elektrochem.*, **59**, 68 (1955).
5. M. W. Breiter, H. Kammermaier, and C. A. Knorr, *ibid.*, **60**, 37, 119 (1956).
6. W. Böld and M. W. Breiter, *Electrochim. Acta*, **5**, 145 (1961).
7. F. G. Will and C. A. Knorr, *Z. Elektrochem.*, **64**, 258 (1960).
8. K. J. Vetter and D. Berndt, *ibid.*, **62**, 378 (1958).
9. K. J. Vetter and J. W. Schultze, *Ber. Bunsenges. Phys. Chem.*, **76**, 920, 927 (1972); *J. Electroanal. Chem.*, **34**, 131, 141 (1972).
10. S. Hadži-Jordanov, H. Angerstein-Kozlowska, and B. E. Conway, *ibid.*, **60**, 359 (1975).
11. D. A. J. Rand, R. Woods, and D. Michell, Abstract 338, p. 866, The Electrochemical Society Extended Abstracts, Spring Meeting, Philadelphia, Pennsylvania, May 8-13, 1977.
12. J. M. Otten and W. Visscher, *J. Electroanal. Chem.*, **55**, 1, 13 (1974).
13. P. Stonehart, H. A. Kozlowska, and B. E. Conway, *Proc. R. Soc. London, Ser. A*, **310**, 541 (1969).
14. B. E. Conway, L. Laliberté, S. Gottesfeld, and H. Angerstein-Kozlowska, in "Oxide-Electrolyte Interfaces," R. S. Alwitt, Editor, p. 181, The Electrochemical Society Softbound Symposium Series, Princeton, N.J. (1972).
15. H. Angerstein-Kozlowska, B. E. Conway, and W. B. A. Sharp, *J. Electroanal. Chem.*, **43**, 9 (1973).
16. J. J. MacDonald and B. E. Conway, *Proc. R. Soc., London, Ser. A*, **269**, 419 (1962).
17. S. Hadži-Jordanov, H. Angerstein-Kozlowska, M. Vukovič, and B. E. Conway, *J. Phys. Chem.*, **81**, 2271 (1977).
18. B. E. Conway, H. Angerstein-Kozlowska, and E. Criddle, *Anal. Chem.*, **45**, 1331 (1973).
19. E. K. Tuseeva, A. M. Skundin, and V. S. Bagotskii, *Electrokhimiya*, **9**, 1541 (1973).
20. H. Angerstein-Kozlowska, W. B. A. Sharp, and B. E. Conway, in "Electrocatalysis," M. W. Breiter, Editor, p. 94, The Electrochemical Society Softbound Symposium Series, Princeton, N.J. (1974).
21. See B. Smith-Hopkins, Chapters in "The Chemistry of the Less Familiar Elements," Stripes Publishing Co., Ill. (1942).
22. B. E. Conway, E. Gileadi, and M. Dzieciuch, *Electrochim. Acta*, **8**, 143 (1963).
23. H. Angerstein-Kozlowska, J. Klinger, and B. E. Conway, *J. Electroanal, Chem.*, **75**, 45 (1977).
24. W. O.'Grady, C. Iwakura, J. Huang, and E. Yeager, in "Electrocatalysis," M. W. Breiter, Editor, p. 286, The Electrochemical Society Softbound Symposium Series, Princeton, N.J. (1974); see also K. Kinoshita and P. N. Ross, *J. Electroanal. Chem.*, **78**, 313 (1977).
25. S. Hadži-Jordanov, H. Angerstein-Kozlowska, M. Vukovič, and B. E. Conway, in "Electrode Materials and Process for Energy Conservation and Storage," J. D. McIntyre, S. Srinivasan, and F. G. Will, Editors, p. 183, The Electrochemical Society Softbound Symposium Series, Princeton, N. J. (1978); this phenomenon was first described in an annual research report to Hooker Chemicals and Plastic Corp., December 1976.
26. B. E. Conway, H. Angerstein-Kozlowska, F. C. Ho, B. MacDougall, J. Klinger, and S. Gottesfeld, *Faraday Discuss. Chem. Soc.*, **56**, 199 (1973).
27. S. Gottesfeld and S. Srinivasan, *J. Electroanal. Chem.*, **86**, 89 (1978).
28. W. P. Griffin, "The Chemistry of the Rarer Platinum Metals," chap. 4, Interscience, London (1967).
29. J. Dunwitz and L. E. Orgel, *J. Chem. Soc.*, **1953**, 2594.
30. L. D. Burke, J. K. Mucahy, and S. Venkatesan, *J. Electroanal. Chem.*, **81**, 339 (1977); *ibid.*, **73**, 207 (1976).
31. J. McBreen, in "Power Sources," Vol. 5, D. H. Col-

lins, Editor, p. 525, Academic Press, London (1975).
32. D. A. J. Rand and R. Woods, *J. Electroanal. Chem.*, **55**, 375 (1974).
33. W. Visscher and M. Bleilevens, *Electrochim. Acta*, **19**, 387 (1974).
34. D. Gilroy and B. E. Conway, *Can. J. Chem.*, **46**, 875 (1968); see also *J. Electroanal. Chem.*, **71**, 257 (1976).
35. A. Damjanovič, A. T. Ward, B. Ulrick, and M. O'Jea, *This Journal*, **122**, 593 (1975).
36. H. Angerstein-Kozlowska and B. E. Conway, *J. Electroanal. Chem.*, In press.
37. For review, see B. E. Conway, H. Angerstein-Kozlowska, and F. C. Ho, *J. Vac. Sci. Technol.*, **14**, 351 (1977).
38. A. H. Lanyon and B. M. W. Trapnell, *Proc. R. Soc. London, Ser. A*, **227**, 387 (1955).
39. A. K. Reddy, M. Genshaw, and J. O'M. Bockris, *J. Chem. Phys.*, **48**, 671 (1968).
40. B. V. Tilak, B. E. Conway, and H. Angerstein-Kozlowska, *J. Electroanal. Chem.*, **48**, 1 (1973).
41. S. Gottesfeld and B. E. Conway, *J. Chem. Soc., Faraday Trans. I*, **69**, 1090 (1973).
42. B. E. Conway and E. Gileadi, *Trans. Faraday Soc.*, **58**, 2493 (1962).
43. N. R. de Tacconi, A. J. Calandra, and A. J. Arvia, *J. Electroanal. Chem.*, **51**, 25 (1974).
44. A. N. Frumkin and O. A. Petrii, *Electrochim. Acta*, **15**, 391 (1970).
45. T. N. Stoyanovskaya and G. D. Vovschenko, *Vest. Moscow Univ., Sev. II, Khim.*, **17**, 30 (1962).
46. M. W. Breiter, *Electrochim. Acta*, **8**, 925 (1963).
47. D. A. J. Rand and R. Woods, *J. Electroanal. Chem.*, **47**, 353 (1973).
48. G. Lodi, E. Sivieri, S. Trasatti, and A. de Battisti, *J. Appl. Electrochem.*, **8**, 135 (1978).

Technical Notes

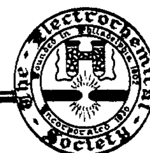

STEM/EDAX Analysis of the Cell Walls in Porous Anodic Films Formed on Aluminum

G. E. Thompson, R. C. Furneaux, and G. C. Wood

Corrosion and Protection Centre, University of Manchester, Institute of Science and Technology, Manchester M60 1QD, England

and R. Hutchings

Department of Physical Metallurgy and Science of Materials, University of Birmingham, Birmingham B15 2TT, England

Recently, ultramicrotomy (1) and ion beam thinning of films (2), allied with transmission electron microscopy and secondary ion mass spectrometry (SIMS) (3), have provided greater resolution of film morphology and composition. Furthermore, the completeness of the apparently neat but simple explanation of steady-state porous film formation involving field-assisted dissolution (4,5) has now been questioned and an additional mechanism involving direct loss of Al^{3+} ions to solution proposed (6). A model of film growth has been developed (7) which considers solid-state growth of relatively pure alumina at the metal/oxide interface, together with the deposition of microcrystalline, acid anion-incorporated film material at the film/solution interface. This outer layer of film material is derived from impure, colloidal alumina which results from the ejection of Al^{3+} ions, not consumed in solid-state film formation, at the film/solution interface. The two types of film material (distinguished by acid anion incorporation) have been detected by SIMS for barrier (3) and porous films (8). Cell boundary bands, possibly depicting the relatively pure alumina region, have been observed by transmission electron microscopy of ion beam thinned porous anodic films formed in oxalic and phosphoric acids (2). The purpose of this note is to distinguish further between the relatively pure alumina boundary bands and the outer, pore-adjacent acid anion-incorporated material [observed using conventional transmission and scanning transmission microscopy (STEM) allied with energy dispersive x-ray analysis (EDAX)].

Key words: anion, anode, x-rays, sputtering.

The porous anodic films were formed for 10 min on electropolished aluminum at a constant voltage of 150V in vigorously stirred 0.4M phosphoric acid. The films were stripped from the substrate in the usual manner (5) and ion beam thinned from both sides until a suitable thickness for transmission electron microscopy was achieved. The films were generally examined in a Philips 301 electron microscope and analyzed in a Philips 400 electron microscope with scanning transmission and energy dispersive x-ray analysis facilities.

The conventional transmission electron micrograph of the ion beam thinned film shows a distorted cell pattern and the pore section shapes appear to follow the irregular cell morphology (Fig. 1). The cell boundary bands are readily apparent from the onset of examination but become more sharply defined with exposure to the electron beam. With continued exposure to the electron beam, remarkable changes in the film material substructure are observed and are probably related to a drying out process, sintering, or agglomeration and crystallization in the electron microscope (2). The micrograph illustrated in Fig. 1 was taken as soon as possible to avoid the changes discussed above, but some change in appearance is likely since the specimen was exposed, under the vacuum, to the electron beam.

For STEM analysis a nominal probe diameter of 25 nm was selected in order to optimize spatial resolution and count rate for x-ray analysis. The x-ray spectrum from the cell material remote from the cell boundary band and that from an area associated with the junc-

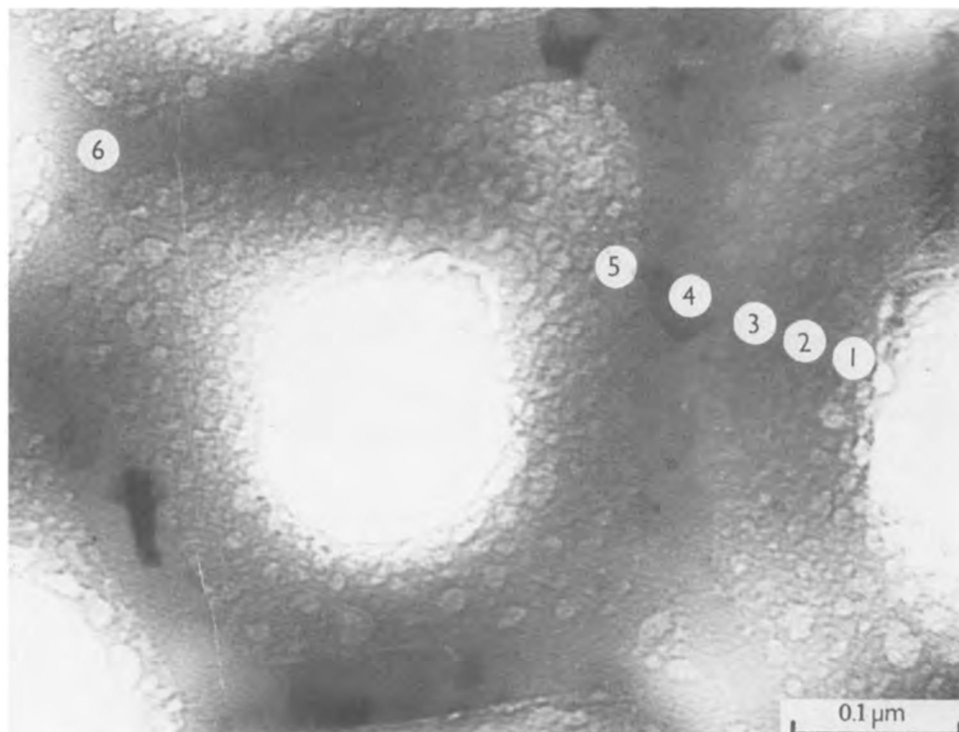

Fig. 1. Transmission electron micrograph of the ion beam thinned film, formed for 10 min on aluminum at 150V in phosphoric acid at 20°C, showing the cell boundary bands and the typical probe areas employed for STEM/EDAX analysis.

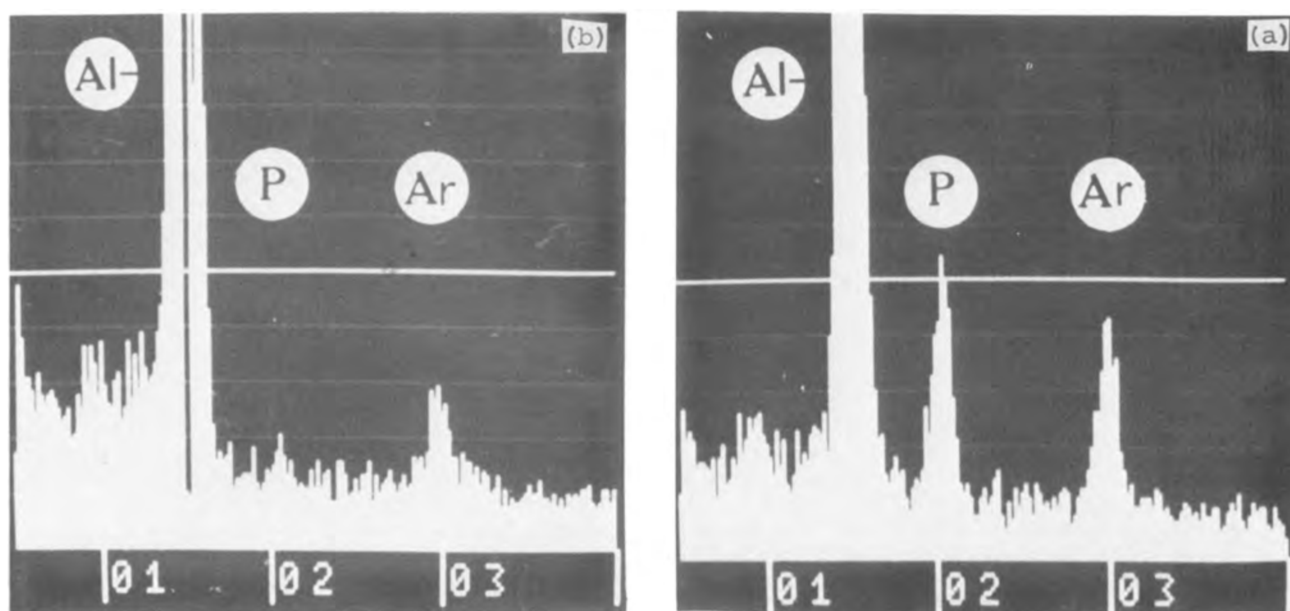

Fig. 2. Typical x-ray spectra (a) for the film material away from the cell boundary band and (b) for the film material associated with the cell boundary band.

tion of the cell boundary bands are displayed in Fig. 2a and 2b, respectively. The energy-dispersive analysis shows aluminum, phosphorus and argon, a much larger phosphorus yield being detected in the cell material away from the cell boundary bands than that associated with the cell boundary bands.

A similar analysis was carried out on several microareas of the cell material between two pores, and the results are shown in Table I. Position 1 represents an area adjacent to one pore and positions 2-5 represent successive probe areas moving inwards from the pore. The probe positions are shown with respect to a comparable pore in the conventional transmission electron micrograph of Fig. 1. X-ray spectra obtained from positions 2 and 6 are shown in Fig. 2a and 2b, respectively. The results indicate that the P/Al ratio decreases as the probe area moves inwards from the pore to the cell boundary band and increases beyond the cell boundary band. The cell boundary band is located between the probe positions 3 and 5.

The detection of a low phosphorus yield within the cell boundary band may be genuine or may be due to x-ray source overlap into the adjacent anion-incorporated material. The distribution of phosphate may

Table I. Comparison of the x-ray counts for aluminum, phosphorus, and argon

Position	Aluminum	Phosphorus	P/Al ratio × 10^3	Argon	Ar/Al ratio × 10^3
1	2,232	207	93	364	163
2	4,951	359	73	368	74
3	7,811	395	51	325	41
4	10,902	149	14	236	22
5	11,206	318	28	175	16
6	11,385	37	3	265	23

also be shifted during ion beam thinning and associated heating of the anodic film.

Argon and silicon were detected for probe areas very close to the pores. Argon ion beams were employed for ion beam thinning and so the detection of argon may be anticipated; silicon may arise from contamination from vacuum greases during ion beam thinning or from the glassware during specimen preparation.

The Ar/Al ratio decreases as the probe area moves inwards from the pore to the cell boundary band (as does the P/Al ratio). This variation is thought to reflect the degree of "openness" of the film across the cell material. The film material adjacent to the pore (formed originally by deposition of impure colloidal alumina) and in contact with the aggressive electrolyte is more hydrated than the film material comprising the cell boundary band (formed originally by ionic migration through an existing film). Thus, as the probe area moves inwards the compactness of the cell material increases in addition to the compositional changes, with respect to acid anion-incorporation recorded.

The results of the present investigation confirm that the cell boundary bands are composed of relatively pure alumina, whereas the cell material adjacent to the bands contains incorporated phosphate species from the anodizing electrolyte. These direct results are in general agreement with the work of Takahashi and Nagayama (9), who determined the distribution of the phosphate species indirectly by dissolution in sulfuric acid of the porous anodic film formed in phosphoric acid.

Acknowledgments

The authors thank the Science Research Council and Howson-Algraphy Limited for financial support of the work and the Department of Physical Metallurgy and Science of Materials, University of Birmingham, for provision of time on the Philips EM 400 with STEM and EDAX facilities.

Manuscript submitted Dec. 21, 1977; revised manuscript received April 18, 1978. This was Paper 186 presented at the Seattle, Washington, Meeting of the Society, May 21-26, 1978.

Any discussion of this paper will appear in a Discussion Section to be published in the June 1979 JOURNAL. All discussions for the June 1979 Discussion Section should be submitted by Feb. 1, 1979.

REFERENCES

1. R. C. Furneaux, G. E. Thompson, and G. C. Wood, *Corros. Sci.*, In press.
2. G. E. Thompson, R. C. Furneaux, and G. C. Wood, *ibid.*, **18**, 481 (1978).
3. M. F. Abd Rabbo, J. A. Richardson, and G. C. Wood, *ibid*, **16**, 689 (1976).
4. T. P. Hoar and N. F. Mott, *J. Phys. Chem. Solids*, **9**, 97 (1959).
5. J. P. O'Sullivan and G. C. Wood, *Proc. R. Soc. London, Ser. A*, **317**, 511 (1970).
6. J. Siejka and C. Ortega, *This Journal*, **6**, 883 (1977).
7. G. E. Thompson, R. C. Furneaux, G. C. Wood, J. A. Richardson, and J. S. Goode, *Nature (London)*, **272**, 433 (1978).
8. G. E. Thompson, R. C. Furneaux, G. C. Wood, J. A. Richardson, and M. F. Abd Rabbo, To be published.
9. H. Takahashi and M. Nagayama, *J. Chem. Soc. Jpn.*, 453 (1974); Proceedings of U.S.A.-Japan Seminar on Passivity and Its Breakdown on Iron and Iron Base Alloys, NACE, p. 56 (1976).

Corrosion of the Ruthenium Oxide Catalyst at the Anode of a Solid Polymer Electrolyte Cell

J. L. Weininger* and R. R. Russell

General Electric Company, Corporate Research and Development, Schenectady, New York 12301

New and significant developments in ion-exchange technology have been reported recently in a symposium on fluorocarbon ion exchange membranes (1). Nafion[R,1] membranes have also found application as the solid polymer electrolyte (SPE) in fuel (2) and electrolysis cells (3). Clearly, prospects for hydrogen production by electrolysis of water will be enhanced if the cost of the electrocatalysts and their loading in the electrode structures can be reduced (4). For this reason, it is of interest to study the behavior of the electrocatalyst, especially at the anode. As an example, in electrolysis iridium anodes experienced slow corrosion during oxygen evolution (5). Similar behavior of a ruthenium oxide (RuO_x) anode in an SPE cell prompted the present work, in which the electrode and electrolyte structure was examined by electron microscopy and other analytical techniques.

Structure of the Electrocatalyst and SPE Cell

The structures of the electrocatalysts and of the electrode/SPE interface were examined by microscopic means, especially electron microscopy, and by energy dispersive analysis (EDA) and optical microscopy.

Figure 1 is a micrograph of the SPE cell, which consists of a 0.010 in. thick Nafion[R] membrane, covered respectively by a RuO_x powdered anode and Pt cathode. The figure represents the cross section of a microtomed, approximately 2000Å thin, sample of a SPE cell at the end of life test. Folds in the sample on the cathode side and the torn appearance of the RuO_x catalyst (anode) are artifacts of sample preparation. Important observations, which were further explored in electron microscopy, are: (*i*) A sublayer "skin," about 10 μm into the SPE from the electrode interface. This skin has no particles or foreign inclusions; (*ii*) Beyond this sublayer, particles appear at the anode side. Those closest to the interface are largest. They decrease in number as well as size as they go into the interior of the membrane (see electron microscopy below); (*iii*) Some catalyst is torn away from the interface, but there is no smearing so that the subsurface particles are real, not artifacts. These features as well as a porosity in the surface layer of the SPE are brought out by electron microscopy.

Electron Microscopy

In the preparation of the SPE cell, catalysts produced by the Adams method (6) were used in combination with the Nafion[R] membrane as a Pt cathode and a RuO_x anode. Samples of the cells were examined at the start and end of the life test. The latter corresponded to the time at which the oxygen overvoltage had increased approximately 10%. A standard

* Electrochemical Society Active Member.

Key words: ion exchange membrane, electrocatalyst, electrolysis, electron microscopy.

[1] Sulfonated perfluoro polyethylene (du Pont).

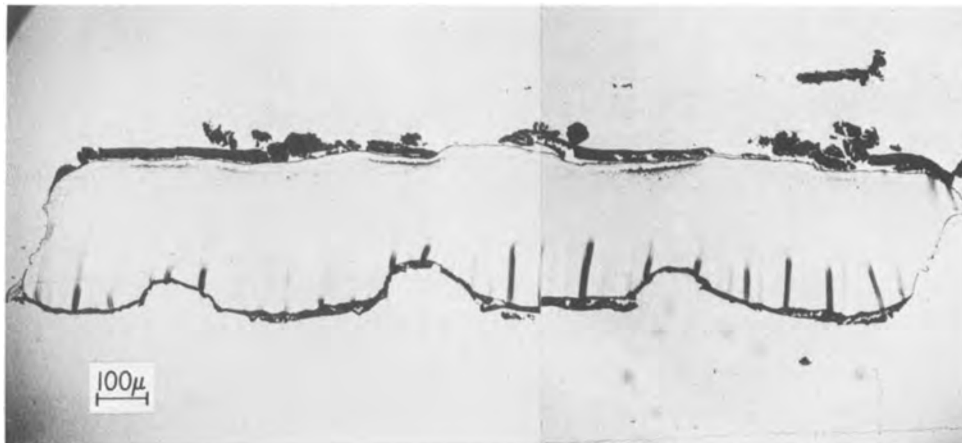

Fig. 1. Optical micrograph of SPE cell. Top electrode, RuO_x; bottom electrode, Pt black.

procedure utilizing ultramicrotomy for preparing electron microscopic samples was used (7).

The SPE/electrode interface of a new cell is shown in Fig. 2. The membrane immediately below the interface is free of foreign particles but contains pores which are 1 μm in diameter or smaller. Although the total porosity may be only 1-5%, the pores are numerous. They were seen on all samples, new and old, and at both sides. At the anode side the location of the pores corresponded to the site of the later formation of particles in the SPE (Fig. 3).

All further electron micrographs of SPE cell components deal with used cells. Thus, in the used SPE cell (Fig. 3) there are foreign inclusions at the anode side, starting at a distance of about 2 μm from the interface. Particles appear at that distance, becoming progressively smaller and fewer for a distance of about 22 μm into the interior of the membrane. Structural details of the particles are shown in Fig. 4. The largest ones, 1 μm in diameter, are agglomerates of smaller entities.

Many more electron micrographs of the SPE cell could be shown, but for the purpose of this report it may suffice to show the overview of the cathode (Fig. 5) and details of the Pt catalyst/cathode (Fig. 6) and RuO_x catalyst/anode (Fig. 7). Note that there is a difference in magnification between Fig. 6 and 7 of 165,000 and 15,000 times, respectively, with the Pt hav-

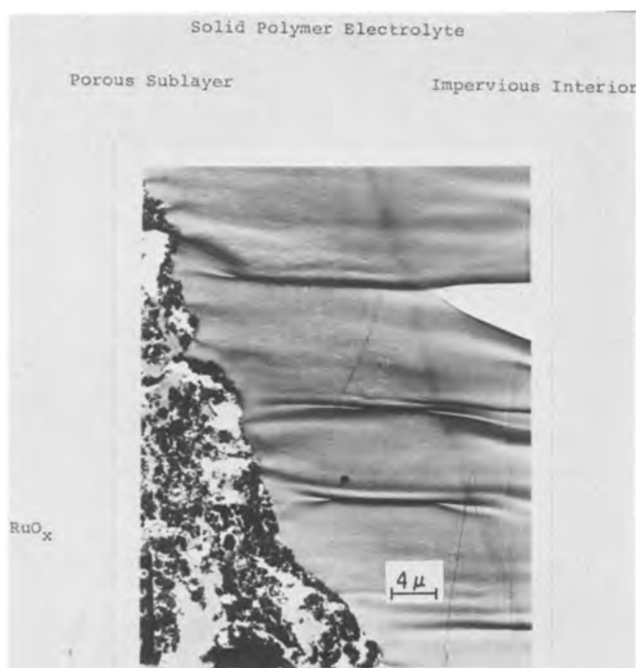

Fig. 2. Electron micrograph of a new SPE cell, RuO_x/SPE interface. Note the porosity in the 15-20 μm surface layer of the membrane.

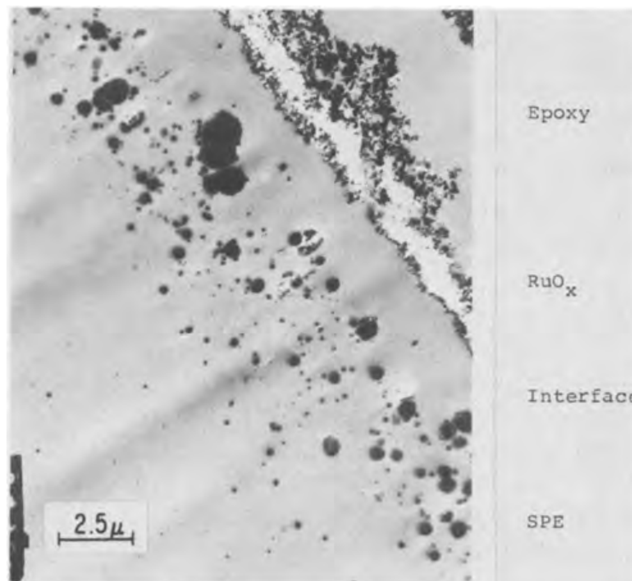

Fig. 3. Electron micrograph of an SPE cell. Interface of RuO_x electrode and SPE. Note inclusions in membrane.

ing such fine structure that the smallest discernible Pt grain has a dimension of approximately 10Å. That this is the case for a sample at the end of life test proves that no SPE deterioration occurs at the cathode. This deterioration is due to the increasing oxygen overvoltage at the anode, which in turn can be traced to corrosion and subsequent sintering of the RuO_x structure. As for sintering, the RuO_x electrode of Fig. 7 shows several large rhombohedral crystals as well as fine particle structure down to about 150Å. A comparison with the original powder, prepared by the Adams method, indicates that some of the fine particles are identical with those of the original preparation (Fig. 8), but on the average there is some increase in size in the old sample and there are also more of the rhombohedral, large particles, all of which may be the result of sintering.

Energy Dispersive Analysis

In EDA, an electron beam hits a sample and produces x-rays which are converted to voltage pulses in a detector. As in the case of transmission electron microscopy (TEM), many combined SEM views and EDA measurements were obtained on the SPE samples. Figures 9 and 10 are characteristic of these, the former being an SEM of the anode area, the latter giving the fluorescence spectrum from particles 1 and 2 in Fig. 9. There are 1 μm large inclusions in the membrane. The spectra (Fig. 10) show peaks only for Ru and Cu, the latter arising from the copper grid which supports the SPE sample in the microscope. The Ru

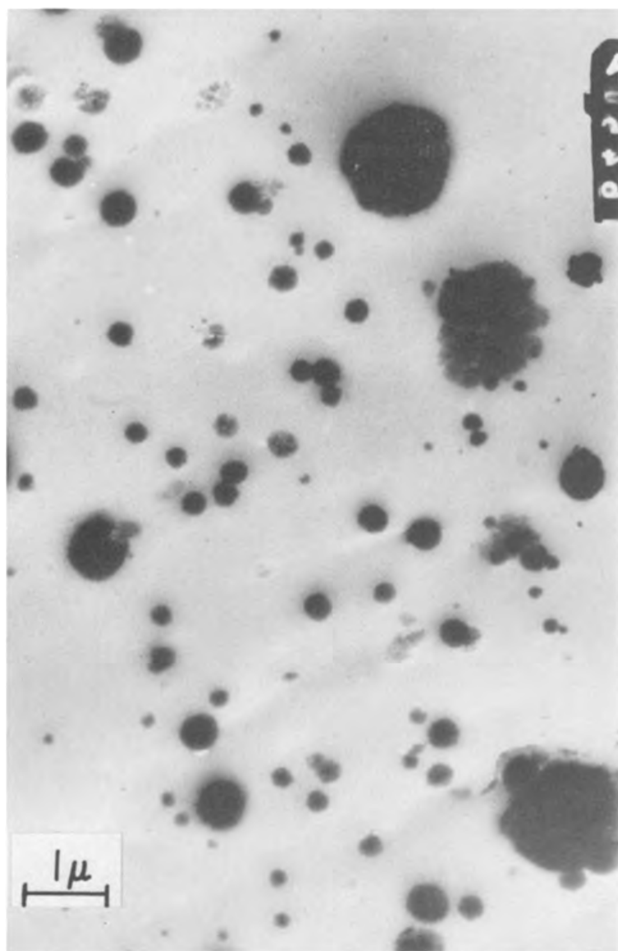

Fig. 4. Electron micrograph of inclusions close to the SPE/electrode interface.

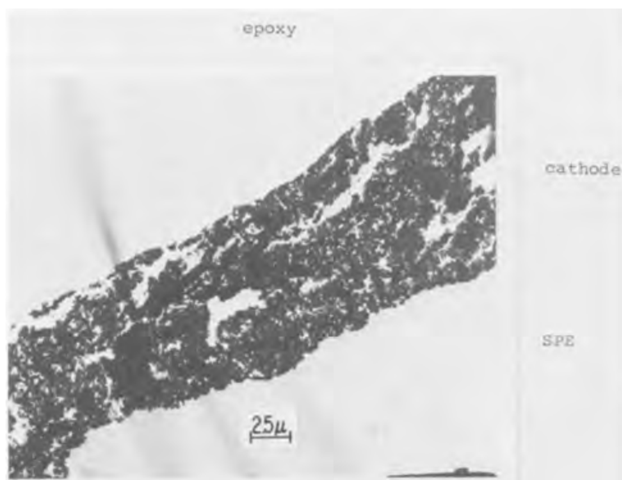

Fig. 5. Electron microgroph of o Pt cathode.

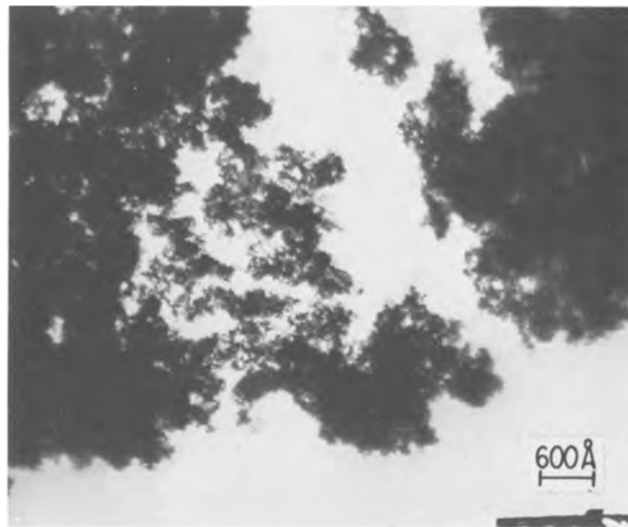

Fig. 6. Electron micrograph of a Pt cathode.

Fig. 7. Electron micrograph of RuO_x catalyst.

spectra are identical to the spectrum coming directly from the electrocatalyst. It could arise either from Ru particles or, more likely, from a Ru oxide or salt. The possibility of the presence of RuO_x particles in the membrane cannot be excluded by EDA analysis.

Other EDA observations were: (*i*) In the old cell, the Ru spots were clearly identified by short x-ray counts; (*ii*) Longer counts over larger areas show with greater instrumental sensitivity the presence of trace amounts of Ca, Si, Mg, Al, Fe, Ti, S, and Cl near the Ru particles and in the bulk of the membrane. Their sources are not visible either in SEM or TEM and must be assumed to be part of the ion-exchange polymer; (*iii*) In contrast to the above, a new SPE cell shows neither multivalent ions nor Ru particles in its membrane.

Summary of Experimental Observations

New cell. —(*i*) The new membrane has a clear appearance, without impurities, but there is a surface region, about 20 μm wide, which differs in texture and porosity from the bulk of the membrane; (*ii*) The porosity is estimated to be about 1%, with pore sizes ranging up to 1500Å, average pore size about 100Å; (*iii*) There are a few large rhombohedral particles in the RuO_x catalyst prepared by the Adams procedure.

Old cell.—(*i*) The new and old SPE cathode and its Pt catalyst appeared to be identical, including the remaining surface layer porosity; (*ii*) On the anode side, the RuO_x particle size, on the average, appeared to be slightly increased over its original condition, roughly 150-100Å; (*iii*) Ru-containing particles appear in the membrane at a distance of 2-8 μm from the interface. The subsurface area is clear of Ru; (*iv*) Beyond the

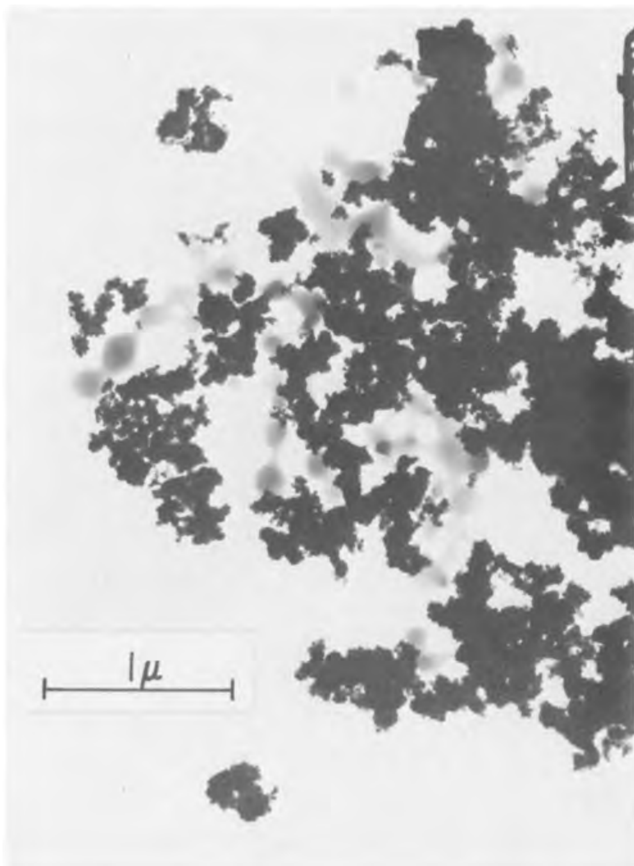

Fig. 8. Electron micrograph of RuO_x powder before use in SPE.

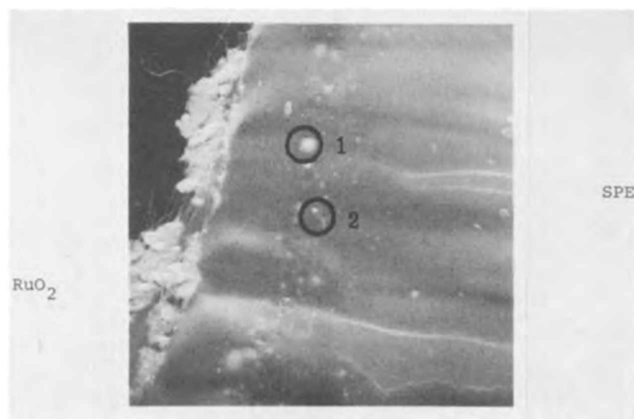

Fig. 9. Scanning electron micrograph of the RuO_x cathode/SPE interface; 7600 times. Note location of particles 1 and 2.

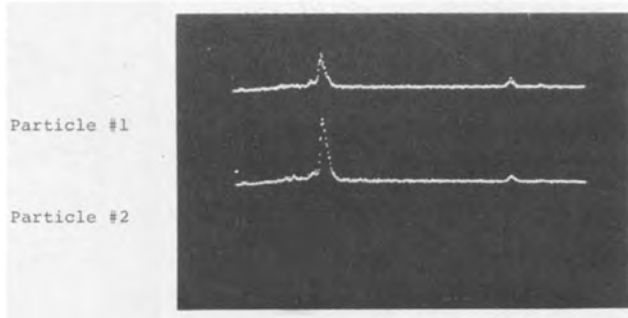

Fig. 10. X-ray spectra from particles 1 and 2, identified as Ru

subsurface region the Ru particles are located in the membrane with a rapidly decreasing distribution, in terms of size and number, toward the interior of the membrane; (*v*) Other multivalent metals (Ca, Mg, Al, Si, Fe, and Ti) and nonmetals (S and Cl) also appear in a qualitatively homogeneous distribution in the membrane.

Interpretation of Observations

A speculative interpretation, consistent with the above observations, is based on regular ion-exchange processes plus the corrosion of the RuO_x catalyst, as follows: (*i*) The membrane interacts with contaminant cations (other than H^+) and retains them to some extent particularly multivalent ions, by exchange with H^+ ions at counter-ion sites; (*ii*) By contrast, Ru dissolves slightly under the acidic conditions of the anode, produced by the electrode reaction

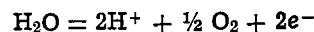

$$H_2O = 2H^+ + \frac{1}{2} O_2 + 2e^-$$

Ru precipitates on the catalyst particles or finds its way, either in ionic form or by electrophoretic action, into the membrane where it is also precipitated and deposited; (*iii*) Ru^{+x} ions which may be complexed, even to the negative ionic form, back-diffuse from the cathode, either dissolved in the swollen membrane or in cracks or gas passages. The latter are exemplified by the porous structure of the membrane adjacent to the electrodes. These gas passages can facilitate access of hydrogen gas from the cathode to the diffusing Ru^{+x} species in the water-filled pores. These pores are in the region where large and most numerous Ru particles are located. They must be distinguished from the "capillaries" of the ion exchange membrane, with sizes of the order of 10Å, which are the site of the electrolyte in the membrane; (*iv*) Once Ru is nucleated at a pore wall, the reaction

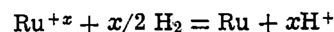

$$Ru^{+x} + x/2\ H_2 = Ru + xH^+$$

will proceed autocatalytically, leading to the observed large particles. These inclusions are similar to the calcium precipitates in Nafion[R] membranes used in electrolysis of brine which contains calcium impurity (8); (*v*) RuO_x is known to corrode in acid (9). Although the rate of this process may be very small, elevated temperature should increase it. There also exists a pH gradient from greater acidity at the RuO_x particle reaction site to lesser acidity in the membrane. If the solubility of the Ru-containing species is an inverse function of pH, it will come out of solution at a line parallel to the electrode/SPE interface, where the concentration exceeds its solubility. At that place and time, reduction processes may also take place.

Thus, the deterioration of the RuO_x catalyst is due to corrosion and sintering. The Ru particles in the membrane, per se, may not be deleterious but point up the corrosion process. More or less uniform deposition of other metal ions, in a distribution dictated by the electroneutrality of the membrane, will increase the *iR* drop in the SPE, hence lead to poorer cell performance.

Acknowledgments

We wish to thank S. Hayashi and S. Alessi for the SEM and optical microscopy of the SPE cells. Valuable discussions with M. W. Breiter, W. T. Grubb, and L. W. Niedrach are also acknowledged.

Manuscript submitted Jan 19, 1978; revised manuscript received April 24, 1978.

Any discussion of this paper will appear in a Discussion Section to be published in the June 1979 JOURNAL. All discussions for the June 1979 Discussion Section should be submitted by Feb. 1, 1979.

Publication costs of this article were assisted by General Electric Company.

REFERENCES

1. Abstracts 436-443 pp. 1135-1150, The Electrochemical Society Extended Abstracts, Fall Meeting, Atlanta, Georgia, Oct. 9-14, 1977.
2. "Fuel Cells and Fuel Batteries," Chap. 14, H. A. Liebhafsky and E. J. Cairns, Editors, John Wiley & Sons, New York (1968).

3. W. A. Titterington and J. F. Austin, Abstract 233, p. 576, The Electrochemical Society Extended Abstracts, Fall Meeting, New York, New York, Oct. 13-17, 1974.
4. S. Srinivasan and F. J. Salzano, *Int. J. Hydrogen Energy*, **2**, 53 (1977).
5. D. N. Buckley and L. D. Burke, *J. Chem. Soc. Faraday*, **76**, (II), 2431 (1977).
6. R. Adams and R. L. Schriner, *J. Am. Chem. Soc.*, **45**, 2171 (1923).
7. "Techniques for Electron Microscopy," Chap. 8, A. M. Glauert and R. Phillips, Editors, D. H. Kay, F. A. Davis Co., Philadelphia (1965).
8. C. J. Molnar and M. M. Dorio, Abstract 442, p. 1147, The Electrochemical Society Extended Abstracts, Fall Meeting, Atlanta, Georgia, Oct. 9-14, 1977.
9. M. M. Pecherskii, V. V. Gorodetskii, V. M. Pulina, and V. V. Losev, *Elektrokhimiya*, **12**, 1445 (1976).

JOURNAL OF THE ELECTROCHEMICAL SOCIETY

SOLID-STATE SCIENCE
AND TECHNOLOGY

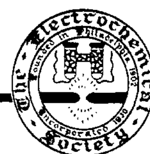

SEPTEMBER
1978

SEAT: Simulated Environment Accelerated Test

Newton Schwartz*[,1] and D. D. Bacon

Bell Laboratories, Murray Hill, New Jersey 07974

ABSTRACT

The guidelines are established for conducting an accelerated environmental test at 75% RH and 85°C with a set of multiple known pollutants from the atmosphere. The conditions for such a test are based on atmospheric upper limits (AUL) based on measured pollutants and meteorological conditions in the continental U.S. The actual concentration of the test pollutant is increased above the AUL by considering the temperature dependence of the adsorption of each pollutant. The latter is approximated at 75% RH to be similar to the temperature dependence of the solubility of each specific gas in water.

Many forms of tests are utilized to evaluate the long-term reliability of electronic materials or devices or subsystems (labeled M/D/S in this paper). Conventionally when these tests have been chemically or corrosion oriented, they have relied mainly on elevated temperature and high humidity, with the test at 85°C and 85% RH being the prime example for many device studies (1).

In recent years, chemically oriented testing has started to include individual or combinations of chemical gases to evaluate the sensitivity of the M/D/S to known environmental pollutants. Such testing for electronic M/D/S had earlier been concentrated on films, starting with the dynamic testing with about 1 ppm chlorine at low relative humidities in the temperature range of 100°-300°C (2). Static testing in sealed bulbs with water and a pollutant also has been used extensively (3). A British Post Office test for contacts is based on the dynamic SO_2 test to simulate London smog conditions (4). More recently, other tests (5, 6) have been developed using multiple pollutants in flow systems while simultaneously controlling the humidity and with the temperature being in the range of 25°-60°C. The latter workers (6), in particular, have observed that synergistic effects exist in the tarnishing of silver and copper when SO_2, NO_2, and Cl_2 are added to the active H_2S agent. Experiments of this sort have also been a part of a long term program (7), which has also concentrated on the study of aerosols (8), on which the adsorption of pollutants may be predominant. More recently, dynamic single pollutant testing at 85°C and 85% RH on thin and thick films has been performed (9, 10) utilizing the permeation tube technique for generating low concentration pollutants (6).

Table I lists some of the conditions used in previous studies (5, 6) in tests primarily oriented to metallic contact performance. In many of these studies it is not completely clear what guidelines determined the particular set of conditions used or how stated acceleration factors (6) were obtained.

The present paper is meant to state the conditions and general equipment design for a multiple pollutant environmental test for M/D/S. The philosophy of such a test, called SEAT (simulated environment accelerated test), and the assumptions on which the testing conditions are based are given.

* Electrochemical Society Active Member.
[1] Temporary address: c/o Pacific Telephone and Telegraph Company, San Francisco, California 94105.

Key words: corrosion, pollutants.

Normal Ambient Conditions

In order to realistically establish test conditions, it is first necessary to evaluate the average environment that the M/D/S will be exposed to in a 10-30 year life interval. The test is intended to simulate the design life and not temporary exposure to excessive adverse conditions. Considerable effort, therefore, has been involved in establishing normal AUL (*i.e.*, atmospheric upper limits) for a variety of atmospheric pollutants (10). Table IIA lists these AUL values as well as the stable components of the atmosphere. These values may change with time as various measures to change the environment become effective, but they represent the best evaluation at the present time of the maximum average concentration of these pollutants that the M/D/S will be exposed to in a 10-30 year life. These AUL are based on outdoor measurements but good reasons exist, in many instances, to expect these to reflect indoor air quality (10).

Table I. Conditions for some multiple gas tests and industrial requirements

	IBM test (5) (estimated)	Battelle test (6)	
Temperature, °C	25 +	30-60	
RH, %	70-95	90	
Time	?	?	
Pollutant (ppb)			
Hydrocarbons	19,000		
H_3S	300	200	200
SO_2	1,600	200	200
$(NO)_x$			
NO_2	700	200	200
NO	1,700		
CO	63,000		
Cl_2	50		50
NH_3	X		
O_3			
Particulates, $\mu g/m^3$	None	None	None
Nitrates in particulates, $\mu g/m^3$	None	None	None
Type of test	Urban, business	Industrial Medium	Severe
Acceleration factor		(30-40)X	

Table II. Stable and pollutant components of the atmosphere

		A Atmospheric upper limits 23.3°C 75% RH	B Atmospheric upper limits 85°C 75% RH
A. Stable	N_2	78.1% (vol)	76.7%
	O_2	20.9%	22.3%
	Ar	0.9%	0.88%
	CO_2	0.033%	0.065%
	CH_4	2000 ppb	3500 ppb
	H_2	500 ppb	540 ppb
	N_2O	500 ppb	1900 ppb
B. Pollutants		ppb	ppb
	NMH*	1400	1700
	CO	2000	2500
	SO_2	70	340
	NO_2	72	[1500
	NO	70	100]
	O_3	45	120
	Aldehydes	20	—
	NH_3	15	35
	H_2S	10	30
	Cl_2	3	8
C. Particulates		185 $\mu g/m^3$	—

* NMH AUL is 3100 $\mu g/m^3$, but this has been converted to ppb by assuming it is primarily C_4 hydrocarbons.

Accelerated Testing

Temperature.—The best known factor associated with the acceleration of almost all fundamental chemical reactions is temperature, which is characterized by the Arrhenius function

$$k_p = P' e^{-\Delta E/kT} \quad [1]$$

where k_p is the rate constant of the process, P' is the preexponential, ΔE is activation energy, k is the Boltzmann constant, and T is the absolute temperature,

There may be hesitancy in basing acceleration on a rise in temperature alone (*i.e.*, utilizing Eq. [1]), because the basic mechanism may change over large temperature intervals or P' may be temperature dependent. However, if these latter two factors can be eliminated, then Eq. [1] represents the best description of the change in rate of a process with respect to temperature.

Table IIA lists 23.3°C as the AUL for temperature. Since much M/D/S testing has already been performed at 85°C (1), an arbitrary "small" temperature acceleration interval is to be contrasted with some "large" intervals of 75°-225°C that have been used in some earlier tests (2, 3).

It is instructive to try to relate the significance of a positive or negative result in an 85°C test to the basic activation energy of the degradation process, the length of the test, the time dependence of the degradation process, and the predicted life at 23.3°C. A degradation process, P, can be considered which starts as some virgin state, P_o, at time equal to zero, t_0, and ends up at some failed state, P_f, at some later time, t_f. Equation [2] gives a general equation for this process

$$P_f - P_o = k_p \pi (\overline{C}_i)_s^{n_i} (\overline{C}_{H_2O})_s \int_{t_0}^{t_f} f'(t) \quad [2a]$$

$$= A_o \pi (\overline{C}_i)_s^{n_i} (\overline{C}_{H_2O})_s \, e^{-\Delta E/kT} \int_{t_0}^{t_f} f'(t) \quad [2b]$$

where A_o = temperature independent preexponential; $(\overline{C}_i)_s^{n_i}$ = product of the average concentration of individual pollutants adsorbed in the surface, each raised to some chemical reaction order; $(\overline{C}_{H_2O})_s$ = similar function for the adsorbed water on the surface; and $\int_{t_0}^{t_f} f'(t)$ = unknown time dependence of the process.

In order to use temperature acceleration as a significant tool, it is imperative that the factors $(\overline{C}_i)_s^{n_i}$ and $(\overline{C}_{H_2O})_s$ remain constant as the temperature is raised. If these factors change markedly, as they surely will because of the heats of adsorption associated with the process, then there is no clear way to evaluate the acceleration factor, which is difficult under any circumstances. The temperature dependence of $(\overline{C}_i)_s^{n_i}$ and $(\overline{C}_{H_2O})_s$ is discussed in the next section.

In many diffusion, corrosion, and oxidation processes between a gas and solid phase, the time dependence[2] of the reaction may be either directly proportional to time (associated with spalling of the separating grown phase) or proportional to the logarithm of time (associated with the separation of charge in the separating phase). Other time dependences can exist, but these will be considered as examples in attempting to evaluate the significance of a result on an 85°C test. Equation [2b][3] will be used with these different time dependencies, where the design life will be assumed to be 20 years, and where the test time at any elevated temperature will be 200 to 1000 hr. With these assumptions, the results in Table III are calculated. Table III indicates that it takes a 10,000+ hour test at 85°C to eliminate processes down to 0.4 eV for a linear time dependence.

It is obvious from this simple analysis that an 85°C-200 hr test is most effective for a (log t) process, since there are not many degradative processes with activation energies below about 0.1 eV. Table IV lists some typical activation energies for a variety of processes.

This discussion indicates that for important M/D/S intended for final manufacture and use, some effort should be devoted to determining the time dependence and activation energies of the failure process. In a general test at 85°C, however, the absence of a failure in test times of 200-1000 hr has a high probability of eliminating processes with activation energies of 0.5 eV or higher.

SEAT assumption I: Temperature will be used as the acceleration factor. The temperature interval will be relatively "small" in order to encompass the same mechanism.

Testing time.—In the previous section, it was stated that 200-1000 hr is a reasonable test time, and these

[2] The time dependence discussed here is the integrated function

$$f(t) = \int_{t_o}^{t_f} f'(t)$$

[3] For the present calculations, the concentration factors are presumed to be constant with a change in temperature.

Table III. Activation energies of the degradation process eliminated for 20 year life at 23.3°C in tests at 85°C

Time dependence of process	Activation energies, eV			
	200 hr test	1000 hr test	5000 hr test	10,000 hr test
t	≥1.0	≥0.8	≥0.54	≥0.44
$t^{1/2}$	≥0.5	≥0.4	—	—
log t	≥0.12	—	—	—

Table IV. Activation energies for different processes*

Process	ΔE, eV
Diffusion limited corrosion (solution)	0.1-0.2
Grain boundary diffusion	0.25-0.50
Hopping transport on dry surfaces	1-2
Electron transfer at surfaces	0.7-1.5
Oxidation of metals	0.75-2
Bulk diffusion	1-3

* Values not to be taken too literally; obtained by discussion with various individuals knowledgeable in the field.

times are to be contrasted to "short" intervals (*i.e.*, 20-60 min) and "long" intervals (*i.e.*, year). The latter time is more suitable for a product which has a definite commitment to manufacture, but it is impossibly long during the active development of a M/D/S. For such activities, there is a strong pressure for immediate information and "short" times are considered. Degradation can be accomplished under these latter conditions only by applying excessive elevated temperatures, fields, or pollutants. Under these conditions there may be a serious danger of studying degradation processes which normally might not be pertinent during the design life of the M/D/S. Moreover, in reliability testing, there is the well-known phenomenon of very early failures, perhaps associated with manufacturing sports, followed by a slower fallout due to various slow failure mechanisms. In "short" time testing, there may be a tendency to detect only the early fallout, without being able to detect the later failures.

Times of the order of 200-1000 hr are an arbitrary compromise to the above "short" and "long" times. However, if the information portrayed in Table III is considered, there is a definite relationship, for such "intermediate" test times, of the absence or presence of a failure to the activation energy of the process. If some prior- or post-insight is available on the process involved, then some qualitative judgments can be made on the reliability of the M/D/S, based on 200-1000 hr testing.

SEAT assumption II: A reasonable time for an accelerated test is 200-1000 hr.

Humidity.—It is well established that humidity is an aggressive agent in corrosion processes and accelerates most degradation at a given temperature. This property is associated with the adsorbed layer on surfaces, which acts as a medium for electrolytic and electrochemical processes.

In Eq. [2], the surface water factor is given as $(\bar{C}_{H_2O})_s$, which might be expressed as the weight of the adsorbed layer per unit area of exposed surface. In any general test, where many different materials might be exposed, this factor is specific for the individual material mechanism. In order to establish absolute reliability criteria for a particular M/D/S, then the entire mechanism has to be determined, and the temperature dependence of the adsorption isotherms must be considered. These same comments apply to the pollutant concentration factors, $\pi(\bar{C}_i)_s^{n_i}$, of Eq. [2].

Another semiquantitative approach is utilized in this study in order to establish a general test for a wide variety of M/D/S. In this approach, an attempt is made to hold the surface concentration of these species relatively constant as the temperature is raised to accelerate the process. In order to achieve such a minimization of the change in chemical surface concentrations with a rise in temperature, it is necessary to introduce some other simplifying assumptions.

An illustration of the dependence of the adsorbed water surface concentration on electroplated gold with respect to the gas phase pressure and temperature is given in Fig. 1 (11). The weight of the water adsorbed is determined by the shift in frequency of a quartz crystal balance (Fig. 1, left-hand side), which can be converted directly into a mass gain (Fig. 1, right-hand side); if a density of about 1 is assumed for the adsorbed water, then a nominal thickness can be determined (Fig. 1, right-hand side). The dashed vertical line indicates how the water surface concentration varies with temperature with an arbitrary choice of pressure of 10 Torr. With a change in temperature from 15.5° to 39°C, the surface concentration decreases by a factor of ~7. This change in surface concentration is equivalent to an enthalpy change of about 0.6 eV/mole, which is probably composed of a small adsorption energy and a much larger heat of condensation of water when the results are analyzed

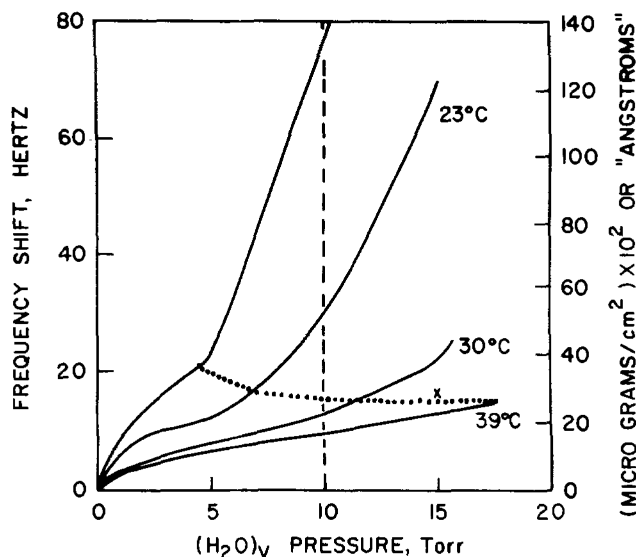

Fig. 1. Adsorption of water vapor on electroplated gold (11)

according to the BET equation (11). Any failure process, as defined in Eq. [2b] and linearly dependent in $(\bar{C}_{H_2O})_s$, with a real activation energy, E, of about 1 eV, would demonstrate an apparent activation energy of 0.4 eV when investigated near the test temperature of about 85°C if the process were investigated at a constant water vapor pressure of 10 Torr.

It is instructive to consider how these numbers might affect the extrapolation of failure data from higher temperature accelerated testing. Assume that the desired failure rate is 1% in 20 years[4] at the AUL temperature and humidity of 23.5°C and 75% RH, respectively, and that the actual E in Eq. [2b] is 1 eV. For the same surface coverage of water at the test temperature of 85°C, the calculated expected failure rate in 200 hr would be 1.1×10^{-3}%. The actual failure rate would be lowered to a value of 1.9×10^{-5}%, since the water surface coverage would be decreased by a factor of 1.76×10^{-2} because of the 0.6 eV/mole enthalpy change. This observed failure rate when combined with the 0.4 eV/mole activation energy would lead to a predicted time of 300 years to achieve the desired 1% failure rate. If such a result did not lead to a change of design, then the M/D/S would have the expected reliability in service, with no safety margin. If due to economic penalties for such a conservative design, the M/D/S were altered to give an extrapolated failure rate of 1% in 40 years, then the M/D/S will eventually be underdesigned from a reliability viewpoint.

The immediate above discussion is only illustrative, since most accelerated testing is done at constant relative humidity. The minimization of the error, due to varying surface water concentration as the temperature is raised when tests are performed at constant relative humidity, is demonstrated in Fig. 1 by the approximately horizontal dotted line. This line is calculated for a RH of 32% and indicates that the water concentration changes by only 40% in the same temperature interval that resulted in a 700% change at a constant pressure of 10 Torr.

This sort of result might indicate that the sorbed water layer has something "liquid-like" about its structure since the relative constancy in its concentration as a function of temperature depends on the equilibrium liquid water vapor pressure. This possible assumption is verified to some extent by the "thickness" axis of Fig. 1, which indicates on gold at 23°C (*i.e.*, the AUL) and 15 Torr (*i.e.*, ~70% RH, close to the AUL) that the water layer has a nominal thickness of 120Å or about 40 monolayers. This water may

[4] This assumes a $f(t)$ which is linear.

be condensed in pores or at hygroscopic impurities, but these may also act as "liquid water sinks" for corrosion processes.

SEAT assumption III: Accelerated testing will be done at a constant relative humidity and from Table II, this value will be 75% RH.

Gas phase pollutant concentrations (single additions).—The same considerations about adsorption energies discussed for water in the previous section apply to the adsorption of pollutant gases to account for the $\pi(\bar{C}_i)_s^{n_i}$ term in Eq. [2]. It will be assumed, considering the possible "liquid-like" character of the adsorbed water, that the solubilities of gases in water can be used to make corrections as the temperature is raised.

SEAT assumption IV: Pollutant gas pressures at any test temperature will be increased over the AUL by a factor proportional to the decrease in solubility of that gas in water.

It is assumed that, as the surface concentration of the adsorbed pollutant decreases as the temperature is raised, the decrease can be compensated for by an appropriate increase in gas phase pressure, similar to the Henry's law pressure dependence of the solubility of gases in liquids (12). Moreover, the magnitude of the pressure compensation as a function of temperature can be estimated from the known temperature dependence of the solubility of that gas in water. This procedure will minimize the error associated with a change of temperature but will not correct for it absolutely. Again in any critical application, specific studies will have to be performed to evaluate these factors.

The application of SEAT assumption IV will be illustrated first with the stable components of air: nitrogen (78.1%), oxygen (20.9%), argon (0.93%), carbon dioxide (0.033%), methane (2000 ppb), hydrogen (500 ppb), and nitrous oxide (500 ppb) (13).

The solubilities of all of these gases are given in terms of Henry's law (14)

$$K_a^{T_i} = P_a^{T_i}/X_a^{T_i} \quad [3]$$

where $K_a^{T_i}$ is the Henry's law constant for a particular gas at a given temperature, T_i; $P_a^{T_i}$ is the partial pressure of the gas at T_i; and $X_a^{T_i}$ is the mole fraction of the dissolved gas at T_i. For illustrative purposes, T will be taken as 23.3°C (296.5°K) the AUL, while T_i will be any elevated temperature. SEAT assumption IV requires that at any elevated temperature $X_a^{T_i}$ will remain constant relative to its value at T, so that

$$P_a^{T_i} = P_a^T \frac{K_a^{T_i}}{K_a^T} \quad [4]$$

where P_a^T is the value of the AUL at 23.3°C, $P_a^{T_i}$ is the increase in temperature and $K_a^{T_i}/K_a^T$ ratio of Henry's law constants to be used as correction factors.

These ratios of Henry's law constants are given in Fig. 2 for all of the relatively stable components of air and in Fig. 3 for all of the pollutants in air. The slopes of this ratio should be proportional to the heat of solution according to Eq. [5]

$$\log \frac{K_a^{T_i}}{K_a^T} = -\frac{\Delta H_s}{2.303R}\left[\frac{1}{T_i} - \frac{1}{T}\right] \quad [5]$$

Because of the expected dependency of Eq. [5], Fig. 2 and 3 are plotted as semilogarithmic with respect to the reciprocal absolute temperature, although the upper ordinate is given in degrees centigrade. The solid vertical line gives the results for the assumed test temperature of 85°C, and all values start at one at the AUL of 23.3°C.[5] The values at 85°C are used to calculate, according to Eq. [4], the test temperature values given in Table IIB. Figures 2 and 3 show a high degree of nonlinearity, indicating that the heat of solution is not constant over this temperature range.

[5] The dotted lines in Fig. 2 and 3 are extrapolations of known data given by the solid lines at lower temperatures.

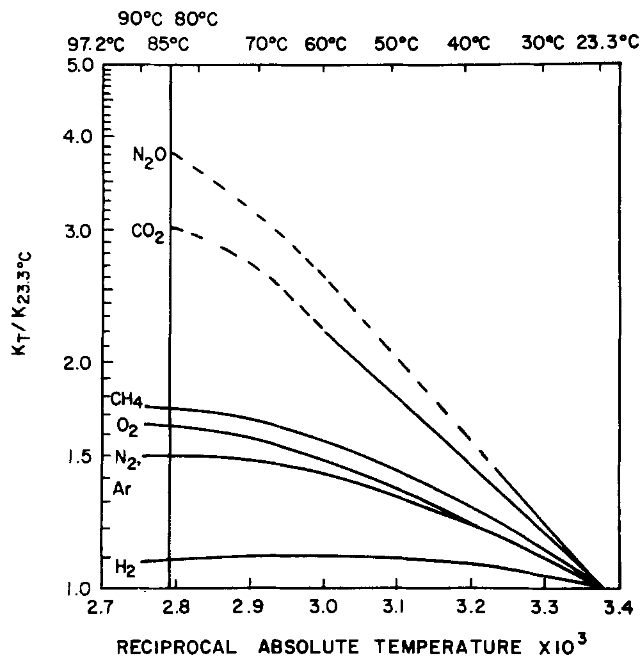

Fig. 2. Ratios of Henry's law constants for the solubilities in water of the stable components of air as a function of temperature.

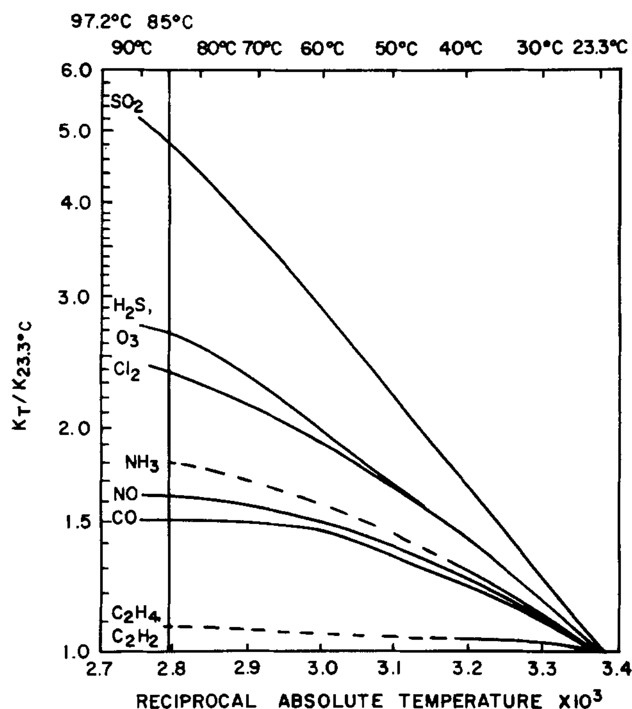

Fig. 3. Ratios of Henry's law constants for the solubilities in water of the pollutants in air as a function of temperature.

In Fig. 2, the pressure correction factor at 85°C is rather insignificant for H_2 (*i.e.*, 1.08), moderate for CH_4, N_2, Ar, and O_2 (*i.e.*, ~1.6), and rather large for N_2O and CO_2 (*i.e.*, ~3.5). For trace gases, Fig. 3, the corrections for NH_3, NO, CO, C_2H_4,[6] and C_2H_2[6] are small to moderate while those for Cl_2, O_3, H_2S, and SO_2 in particular, are quite large.

In general, the temperature dependence of these gas solubilities are related to simple heats of solution where not too strong interactions exist with water, although some heat of reaction occurs for SO_2 and Cl_2 due to the formation of acids. NO_2 represents a

[6] These were chosen as perhaps being typical of NMHC (non-methane hydrocarbons).

special case since no tabulated solubility data exist because of the formation of nitric acid. Many studies (15) indicate that in flow systems the solubility of NO_2 in water is kinetically slow, presumed to be associated with the need to form the dimer, N_2O_4. At the parts per billion levels of the NO_2 AUL, it can be calculated that N_2O_4 does not exist and NO_2 conceivably may be very slow to dissolve in water. Another report (16) exists, however, which indicates that although at moderate concentrations the solution of NO_2 is slow and incomplete, there is a tendency for NO_2 to dissolve more completely at low partial pressures. In this paper we assume that the latter observation is pertinent and that the equilibrium reactions take place at the AUL.

The reaction (17) when NO_2 dissolves in water is given by Eq. [6], and the equilibrium constant by Eq. [7]

$$3NO_{2(g)} + H_2O_{(l)} \rightarrow 2HNO_{3(aq)} + NO_{(g)} \qquad [6]$$

$$K_{T_i} = [HNO_3]_{T_i}^2 \frac{(P_{NO})_{T_i}}{(P_{NO_2})_{T_i}^3} \qquad [7a]$$

$$[HNO_3]_{T_i}^2 = K_{T_i}\,(P_{NO_2})_{T_i}^3/(P_{NO})_{T_i} \qquad [7b]$$

The left-hand side of Eq. [7b] is a function of the partial pressures of both NO_2 and NO, and, making the same assumption as previously that the concentration of the species in solution (or adsorbed) must remain constant as the temperature is raised, then Eq. [8] results

$$\frac{(P_{NO_2})_{T_i}^3}{(P_{NO})_{T_i}} = \frac{(P_{NO_2})_T^3}{(P_{NO})_T}\frac{K_T}{K_{T_i}} \qquad [8]$$

where T is the value at the AUL, T_i is any elevated test temperature, and $(P_{NO_2})_T$ and $(P_{NO})_T$ are the AUL values.

The ratio K_T/K_{T_i} can be evaluated from the usual Eq. [9]

$$\log\frac{K_{T_i}}{K_T} = \frac{-\Delta H^\circ}{2.303R}\left[\frac{1}{T_i} - \frac{1}{T}\right] \qquad [9]$$

where the enthalpy, ΔH°, is calculated from the standard heats of formation (18), and the value of $-31{,}000$ kcal (*i.e.*, -1.34 eV) is calculated for this reaction.

Values of the partial pressure of NO_2 to be used at any elevated temperature can be calculated using Eq. [8] and [9], but only for given values of the partial pressure of NO at the test temperature. Figure 4 shows the value of NO_2 to be used at different temperatures for three fixed values of NO: 70 (AUL), 100, and 200 ppb. It is assumed that the middle value of 100 ppb of NO will be easy to control at any test temperature, and for this concentration the partial pressure of NO_2 at 85°C is about 1700 ppb. This is the largest correction for all the pollutants listed in Table IIB, since the AUL for NO_2 is only 72 ppb.

Gas phase pollutant concentrations (multiple additions).—The above discussion represents semiquantitative corrections for the addition of single gaseous components, or at most pairs of components such as NO_2/NO. There are various complications to be considered when multiple additions are made. Some illustrations are:

(*i*) Catalytic conversion of SO_2 in the presence of NO_2

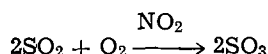

$$2SO_2 + O_2 \xrightarrow{NO_2} 2SO_3$$

(*ii*) Catalytic disappearance of O_3 with H_2O or NO

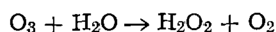

$$O_3 + H_2O \rightarrow H_2O_2 + O_2$$

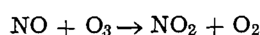

$$NO + O_3 \rightarrow NO_2 + O_2$$

(*iii*) Neutralization reactions

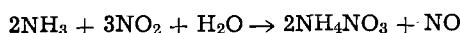

$$2NH_3 + 3NO_2 + H_2O \rightarrow 2NH_4NO_3 + NO$$

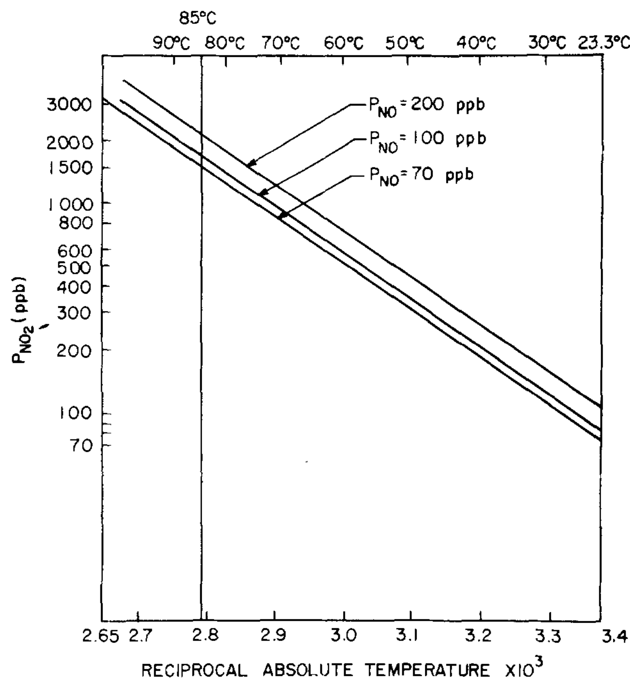

Fig. 4. Calculated partial pressure of NO_2 to be used at various test temperature for fixed NO partial pressures.

All of these chemical reactions, and others, can potentially change the temperature dependence associated with elevated temperature testing. However, these represent such a sophisticated degree of analysis and specification that no consideration will be attempted until future experiments indicate the degree to which they exist.

Initially all of these tests will be performed in the dark to avoid photochemical complications. Eventually, however, they can easily be performed in the presence of visible and ultraviolet light.

Operation of the System

The basic control factors associated with a SEAT facility are temperature, humidity, and pollutant concentrations.

Temperature and humidity.—It was desired to have a relatively large facility to allow the simultaneous testing of large numbers of M/D/S, and in common with another test (6), a commercial temperature-humidity cabinet was chosen. A single pass temperature-humidity oven (Fig. 5) was quite appropriate, since the air stream is first humidified over a heated water pan, then heated to the test temperature, then passed into the test chamber, and then exhausted. The air does not recirculate, and the pollutants can be added just before entering the test chamber.

Due to the corrosive nature of some of the potential pollutants, a Teflon box is therefore utilized inside of the test chamber. To get the most efficient evaporative cooling of the wet and dry bulb thermometer, air flows in the range of 100 to 200 slpm were used. Such high gas flows are also desirable since a previous study (19) showed that the tarnishing of metals in H_2S is dependent on the cube root of the gas flow.

Pollutant concentral control.—Permeation tube rates (6, 7, 9, 10) are not quite high enough for total flow rates of 100-200 slpm, and it was decided to use 0.75% of the pollutant in nitrogen in standard gas tanks at 700-2400 psi. Such a concentration can be made quite accurately by a gas supplier and is high enough that possible reactions with the walls of the tank represent an insignificant change in concentration.

In order to accurately meter multiple gases in the range of 0.2-20 sccm each, a gas blender consisting of electronic mass flow controllers was selected.

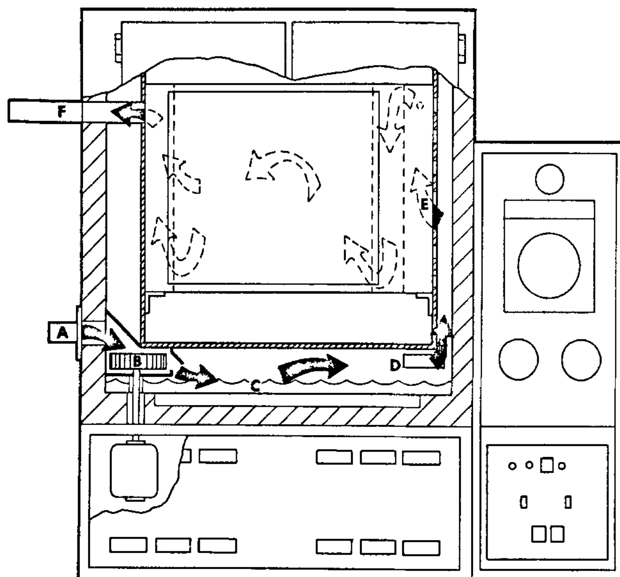

Fig. 5. Over-all diagram of Teflon box in humidity oven. Arrows show single pass air flow from inlet (A), pass blower motor (B), oven humidity tray (C), oven dry bulb heaters (D) into Teflon box (E), and out exhaust (F).

SO_2-air dilution characteristics.—The SEAT system was operated with an original source in the tank of 4.9% SO_2/nitrogen and at various flow rates of clean air. The concentration of SO_2 in the Teflon box was measured by extraction with a pump and then optically analyzed.[7] The solid curve in Fig. 6 shows the SO_2 concentration as a function of the clean air flow rate, while the dashed line is the calculated concentration based on the known SO_2 concentration and known gas flow rates. At very high air flow rates, the calculated and measured concentrations are identical, but at flow rates below about 120 slpm they depart markedly. This data can be interpreted to mean that at the selected operating condition of 100 slpm, the actual dilution air consists of about 80% of added clean air and about 20% of ambient air. This latter factor is of no great concern since this ambient air has been measured to have a low particulate content and very low SO_2 and NO_2 levels compared to the levels controlled within the SEAT system.

SO_2 concentration at different humidities.—Figure 7 shows the concentration of SO_2 inside of the Teflon box at different flow rates of the 4.9% SO_2/N_2 mixture

[7] SO_2 Pulsed Fluorescence Optical Monitor, Thermoelectron Corporation, Waltham, Massachusetts.

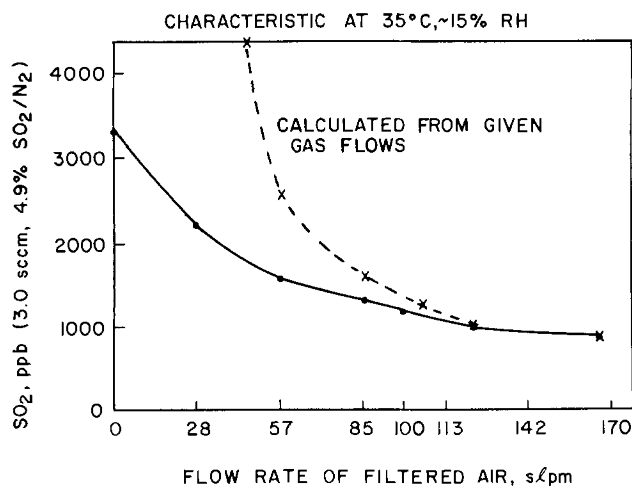

Fig. 6. Measured SO_2 concentration in SEAT facility as a function of the air flow rate.

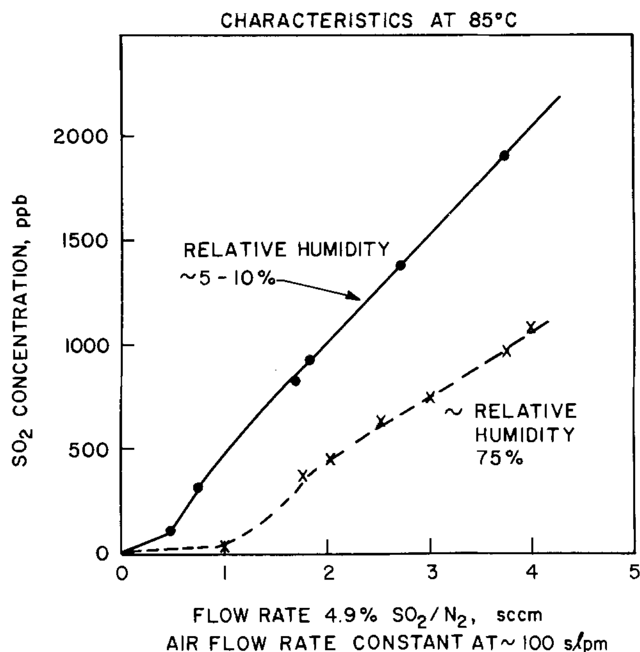

Fig. 7. Measured SO_2 concentration in SEAT facility at 85°C with and without water, as a function of the SO_2/N_2 flow rate.

with a constant flow rate of 100 slpm of air. The solid curve is for measurements at 85°C with no water in the humidifying tray, and the relative humidity was about 5-10%. The concentrations of SO_2 are essentially linear, as expected, with SO_2 flow rate; an essentially identical line was obtained for measurements at about 30°C.

A major difference appears when the same set of measurements was made in the presence of moisture (*i.e.*, dashed line, Fig. 7, 85°C, 75% RH). The same flow rate of SO_2 yields gas phase concentrations which are from 10 to 30% of the values measured in the absence of moisture. In order to protect the optical SO_2 monitor from moisture, a condenser is put in to trap out the water from the air sample. Some SO_2 is known to condense with the moisture and it is likely that this is a major cause of the discrepancy. Further tests must be made to obtain SO_2 concentrations. These over-all effects demonstrate concretely that pollutant monitors are necessary in such a system to accurately define the conditions of the test.

There are many mechanisms that can be proposed for the net equilibrium decrease of SO_2 with the addition of moisture such as a reaction to form SO_3 or a reaction with the Teflon walls or trapping in the condensate. Further characterization of this process will be deferred to another paper when more analyses have been taken.

Summary

What has been described in this paper are the general principles and assumptions underlying a proposed test of M/D/S with respect to their life of 10 to 30 years in an average high polluted environment. Other tests will have to be utilized to evaluate short time exposure to aggravated conditions of temperature, humidity, and specific high pollutant levels.

It is recognized that many subsystems and systems are not designed to survive at 85°C test for even 216 hr (9 days) at 75% RH. It is possible that these systems will require another sort of test where more moderate temperature acceleration is utilized, but compensated for with some pollutant concentration acceleration. Future work in the proposed SEAT system may provide the guidelines for establishing such a test.

It is also recognized that many *ad hoc* assumptions have been utilized in establishing the guidelines for a SEAT program. Some tests in the past have been ini-

tiated, where subsequent users were not quite aware of what guidelines determined the conditions and what assumptions were implicit in the test. This paper, at a minimum, is a source of such statements with respect to the SEAT mode of testing.

Acknowledgments

The author wishes to acknowledge very helpful discussions with C. D. Thurmond, P. A. Turner, A. T. English, and P. C. Milner of Bell Laboratories.

Manuscript submitted Jan. 6, 1978; revised manuscript received April 17, 1978. This was Paper 101 presented at the Atlanta, Georgia, Meeting of the Society, Oct. 9-14, 1977.

Any discussion of this paper will appear in a Discussion Section to be published in the June 1979 JOURNAL. All discussions for the June 1979 Discussion Section should be submitted by Feb. 1, 1979.

Publication costs of this article were assisted by Bell Laboratories.

REFERENCES

1. D. S. Peck and C. H. Zierdt, Jr., *IEEE* Reliability *Phys.*, **1975**, 146.
2. A. T. English and P. A. Turner, *J. Electron. Mater.*, **1**, 1 (1972).
3. J. Speight, *Thin Solid Films*, **15**, 325 (1973).
4. P. F. Preston, *Trans. Inst. Metal Finishing*, **50**, 125 (1972).
5. H. Frankel and W. Knsolving, IEEE Reliability Conference, Las Vegas, Nevada, April 7-10, 1970.
6. W. H. Abbott, *IEEE Trans. Parts, Hybrids, Packaging*, **php-10**, 24 (1974).
7. T. E. Graedel and J. P. Franey, *Int. Wires Cable Symp.*, **1976**, 63.
8. T. E. Graedel, J. P. Franey, and R. E. Schwab, *Proc. Holm. Contact Sem*, **1976**, 47.
9. N. L. Sbar, *IEEE Trans, Parts, Hybrids, Packaging*, **php-12**, 176 (1976).
10. T. E. Graedel and N. Schwartz, *Mater. Performance*, (August 1977).
11. J. G. Thomas, III and S. P. Sharma, *J. Vac. Sci. Technol.*, **13**, 549 (1976); *ibid.*, **14**, 825 (1977).
12. International Critical Tables, Vol. III, p. 255, McGraw-Hill Book Co. Inc., New York (1928).
13. R. C. Weast, Editor, "Handbook of Chemistry and Physics," 56th Ed, p. F-206, CRC Press, Cleveland, Ohio (1975-1976).
14. F. D. Rossini, D. D. Wagman, W. H. Evans, S. Levine, and I. Jaffe, *Nat. Bur. Stds. Circ. 500*, p. 255, U.S. Govt. Printing Office, Washington, D.C. (1952); Gmelins Handbook Der Anorganische Chemie: Chlorine, System No. 6, p. 375 (1968); Ozone, System No. 3, p. 300, (1960); Verlag Chemie GMBH Weinheim/Bergstr.
15. J. W. Chen, Thesis, University of Illinois, Urbana, Ill. (1959), "Nitrogen Dioxide and Dinitrogen Tetroxide Simultaneous Reactions with Water," University Microfilms, Ann Arbor, Mich.
16. M. T. Borok, *Zh. Prikl. Khim.*, **35**, 99 (1962); C. A. **57**, 6682d.
17. J. J. Carberry, *Chem. Eng. Sci.*, **9**, 189 (1959).
18. F. D. Rossini, D. D. Wagman, W. H. Evans, S. Levine, and I. Jaffe, *Nat. Bur. Stds. Circ. 500*, U.S. Govt. Printing Office, Washington, D.C. (1952).
19. J. A. Lorenzen, *Proc. Inst. Environ. Sci.*, **1971**, 110.

Selective Site Laser Excitation and ESR Studies of Nd^{3+} Ions in $Ca_5(PO_4)_3F$

F. M. Ryan,* R. W. Warren, R. H. Hopkins, and J. Murphy*

Westinghouse Research and Development Center, Pittsburgh, Pennsylvania 15235

ABSTRACT

Single crystals of $Ca_5(PO_4)_3F$ activated with Nd^{3+} were studied by high resolution selective site laser spectroscopy. The optical properties of Nd^{3+} ions located at various inequivalent sites were correlated with Nd^{3+} site symmetries obtained from electron spin resonance (ESR) measurements and also with the polarizations predicted by group theory. Two types of Nd^{3+} sites were observed with C_3 site symmetry, two with C_{1h}, and one with no symmetry. Models for these centers are proposed, and the effect of growth conditions on the distribution of Nd^{3+} among these various sites is discussed.

Calcium fluorophosphate is of interest because of its use as a fluorescent lamp phosphor and as a laser host. In its phosphor application it is activated with Sb^{3+} and for laser applications it is activated with Nd^{3+}. There are two inequivalent Ca^{2+} sites in the structure, denoted Ca(I) and Ca(II). The Ca(I) site is axially symmetric, C_3, with each calcium ion surrounded by six oxygen nearest neighbors forming a slightly twisted triangular prism. Three Ca(II) sites form an equilateral triangle centered on an F^- ion with reflection symmetry C_{1h} (C_s) perpendicular to the crystalline C axis. Sb^{3+} and Nd^{3+} substitute for Ca^{2+} in the apatite lattice with charge compensation required to preserve neutrality. The two calcium sites and the variety of possible compensation models make the analysis of the optical properties of trivalent activator ions in this structure very difficult. The most useful technique for determining site symmetries of activator ions is electron spin resonance (ESR), which unfortunately is useful only in studying paramagnetic ions like Nd^{3+}, although in certain cases the location of the nonparamagnetic ion Sb^{3+} can be deduced from its superhyperfine interaction with nearby paramagnetic defects of known configuration (1). However, Nd^{3+} and Sb^{3+} probably form the same types of centers so that identification of Nd^{3+} centers should by analogy yield information on Sb^{3+} centers.

In earlier work Ohlmann *et al.* (2) suggested that Nd^{3+} ions occupy only Ca(II) sites in calcium fluorophosphate because no strongly polarized fluorescent or excitation transitions were observed. Group theory predicts 100% polarization for many of the transitions of Nd^{3+} located on a site of symmetry C_3 while none of the transitions of Nd^{3+} on a site of symmetry C_{1h} (C_s) would be strongly polarized. The crystals studied in that work were grown from stoichiometric melts and the neodymium was introduced as Nd_2O_3. Eaglet *et al.* (3) conducted x-ray structure and optical investigations on crystals pulled from stoichiometric melts. They concluded that almost all of the neodymium would locate on Ca(II) sites with a compensating oxygen replacing an adjoining fluorine

* Electrochemical Society Active Member.

ion. If neodymium was introduced as NdF_3, however, they indicated that both Ca(I) and Ca(II) sites were likely to be occupied. However, no evidence was given to support these conclusions. Daraseliya *et al.* (4) observed the ESR spectrum of Nd^{3+} located on a site of C_{1h} (C_s) symmetry. Growth conditions of the crystals were not stated in their paper. Kaplyanskii and Kuzminov (5) performed piezospectroscopic measurements on crystals pulled from stoichiometric melts with neodymium added as Nd_2O_3. They also concluded that the neodymium preferentially located on a Ca(II) site with the probable method of compensation being an oxygen substituting for an adjacent fluorine.

Since these earlier studies were completed a useful new tool has been developed for studying the optical properties of ions in crystals containing multiple sites, the technique of selective site excitation with a tunable laser (6). In this paper we have combined selective site laser spectroscopy with ESR to identify the site symmetries and optical properties of Nd^{3+} in calcium fluorophosphate crystals and also the effect of melt composition on the distribution of Nd^{3+} among these sites.

Experimental Details

Crystal preparation.—The single crystals of Nd^{3+}-activated $Ca_5(PO_4)_3F$ for this work were pulled from the melt by a technique reported previously (7). Nd^{3+} was introduced as Nd_2O_3 and crystals were grown from melts with both stoichiometric and nonstoichiometric composition. The crystals studied are listed in Table I which indicates the Nd melt doping and melt stoichiometry; the Nd^{3+} incorporated into the crystals was approximately half that added to the melt.

The melts were made by combining various properties of Luminescent Grade CaF_2, $CaHPO_4$, and $CaCO_3$. The $CaCO_3$ is equivalent to CaO since CO_2 evolves during melting. Variations in melt stoichiometry may be expressed as excesses or deficiencies of CaF_2, CaO, or $CaHPO_4$. In previous work (1, 8-11) it was found that crystals pulled from stoichiometric melts are deficient in fluorine, producing large numbers of fluorine vacancies which are occupied by various configurations of electrons and substitutional oxygen ions. The concentration of substitutional oxygen ions can be greatly reduced by growing crystals from melts deficient in CaO; the number of fluorine vacancies is increased when the melts are deficient in CaF_2 (9). It was not possible to study an extended series of crystals in which only one parameter had been changed at a time (*e.g.,* Nd^{3+} concentration and stoichiometry) because of the crystals available, many contained Nd^{3+} concentrations too high to permit the separation of individual centers by ESR.

The crystals were oriented by Laue photography, cut, and optically polished. ESR and optical measurements were performed on the same piece of crystal for each boule.

ESR.—The ESR measurements were performed with a conventional x-band apparatus. To achieve adequate resolution measurements were performed at both 77° and 4.3°K. The apparatus was constructed to allow rotations of the crystals relative to the external magnetic field. This permitted a precise determination of the symmetry of each neodymium site in the crystal. No details of the ESR spectra are shown because they are not important to this work.

Selective site laser excitation.—Selective site laser excitation permits unraveling the optical properties of ions located on each of a number of inequivalent crystallographic sites (6). The composite optical spectrum of these inequivalent ions is normally very complex and the separation into the individual components quite difficult. The selective site laser technique uses a tunable dye laser as an excitation source to excite the luminescence of the ions. The energy emitted in the narrow line-width of the dye laser is very large compared to that of more conventional excitation sources, so that the signal/noise ratio is greatly enhanced, and ultrahigh resolution excitation spectroscopy becomes possible. In previous work (6) the ion studied was Er^{3+} and the fluorescent emissions of Er^{3+} at various sites were resolvable, allowing the individual excitation spectra to be easily obtained. The comparatively broad ($\sim$1 nm) linewidth of Nd^{3+} in calcium fluorophosphate leads to a more confusing overlap of the fluorescent emissions of the various site contributions. By obtaining a series of excitation spectra when viewing at various portions of the fluorescence envelope, and by varying the polarization of the excitation source and the fluorescence detector, it was still possible to sort out the individual site contributions.

The experimental arrangement used in performing our selective site excitation is shown on Fig. 1. A 1 MW Molectron Model U-V 1000 pulsed nitrogen laser is used as a u.v. excitation source for a tunable dye laser. The nitrogen laser produces 10 nsec long pulses at a repetition rate of 50 Hz to allow rapid scanning of the dye laser output for obtaining excitation spectra. The tunable dye laser used was a Molectron Model DL-20 which produced an output tunable between 570 and 590 nm of approximately 25 kW peak, consisting of 7 nsec long pulses. The FWHM resolution of the dye laser output was 0.01 nm and Rhodamine 6G was used as the dye. The output of the tunable laser passes through a polarizer to the crystal which is immersed directly in the refrigerant in the optical cryostat. The measurements were performed at 77°K in order to sharpen the optical spectra as an aid in separating the spectra of the various inequivalent neodymium sites. Further cooling of the crystal to 1.8°K gave no measurable improvement over 77°K.

The infrared Nd^{3+} fluorescence passes through an *IR* polarizer to a 0.25m Jarrell-Ash monochromator. An S-1 photomultiplier cooled to 77°K was used as a detector and coupled to a Princeton Applied Research Box Car Integrator to increase the signal/noise ratio of the fluorescence pulses. Due to the relatively slow decay time of the Nd^{3+} centers ($\sim$0.25 msec) gate widths in the order of 1 msec or longer were required. All of the Nd^{3+} centers studied had approximately identical decay times so that no site discrimination by decay times was possible.

The Site Symmetry Dependence of the Transitions of Nd^{3+} in $Ca_5(PO_4)_3F$

A partial energy level diagram of Nd^{3+} is shown on Fig. 2. Nd^{3+} has three 4f electrons which form a $^4I_{9/2}$ ground state. The fluorescence studied in this

Table I. A description of the crystals studied and the distribution of Nd^{3+} ions among various inequivalent sites as determined by ESR

Crystal	Growth conditions	ESR concentrations				
		Nd(I)	Nd(II)	Nd(III)	Nd(IV)	Nd(V)
0.01% Nd	Stoichiometric				Med.	
0.005% Nd	10% CaO def.	Large	Med.	Med.		Small
0.1% Nd	2% def. CaF_2		Large	V. large	V. large	Small

EXPERIMENTAL ARRANGEMENT

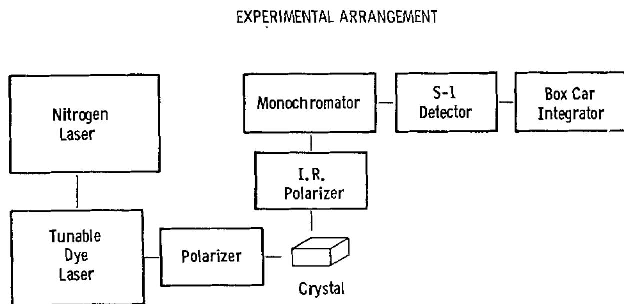

Fig. 1. The experimental arrangement used to perform selective site laser excitation.

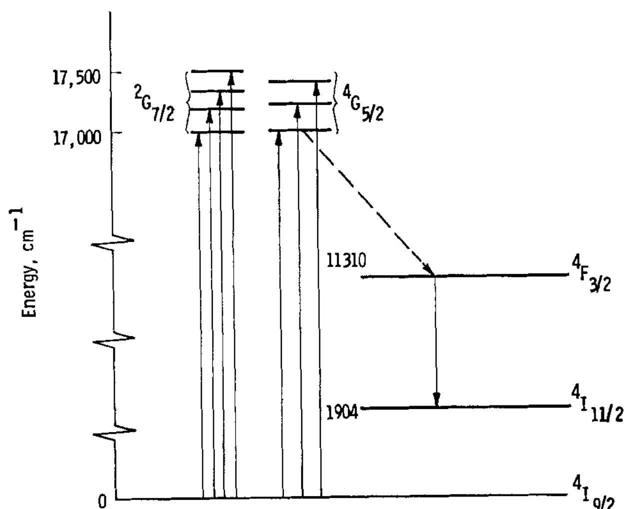

Fig. 2. A partial energy level diagram for Nd^{3+}

Ca (I) SITE, DOUBLE GROUP C_3

	E	C_3	C_3^2	R	RC_3	RC_3^2	Basis Functions
A_1	1	1	1	1	1	1	z
E	1	w	w^2	1	w	w^2	x+iy
	1	w^2	w	1	w^2	w	x−iy
D 1/2	1	$-w^2$	−w	−1	w^2	w	$e^{i\Phi/2}, e^{-5i\Phi/2}, e^{+7i\Phi/2}, \cdots$
	1	−w	$-w^2$	−1	w	w^2	$e^{-i\Phi/2}, e^{5i\Phi/2}, e^{-7i\Phi/2}, \cdots$
S	1	−1	−1	−1	1	1	$e^{\pm 3i\Phi/2}, e^{\pm 9i\Phi/2}, \cdots$

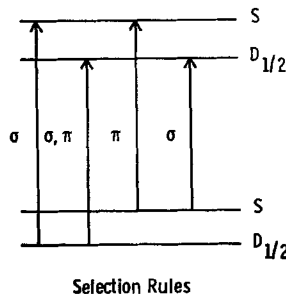

Fig. 3. The character table for transitions involving Nd^{3+} ions located on sites of C_3 symmetry.

Ca II SITE, DOUBLE GROUP C 1h

	E	σ_h	R	$R\sigma_h$	Basis Fcns.
A_1	1	1	1	1	(x, y)
A_2	1	−1	1	−1	z
D 1/2	1	i	−1	−i	$e^{i\Phi/2}, e^{-3i\Phi/2}, e^{5i\Phi/2}, \cdots$
	1	−i	−1	i	$e^{-i\Phi/2}, e^{3i\Phi/2}, e^{-5i\Phi/2}, \cdots$

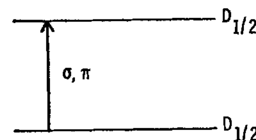

SELECTION RULES

Fig. 4. The character table for transitions involving Nd^{3+} ions located on sites of C_{1h} symmetry.

work is at 1.06 μm and is an electric dipole transition from the $^4F_{3/2}$ level to the $^4I_{11/2}$ level (2). This is also the laser transition for Nd^{3+}. Fluorescence excitation was between 17,000 and 17,500 cm^{-1}, the useful range of the dye Rhodamine 6G. Nd^{3+} has four $^2G_{7/2}$ and three $^4G_{5/2}$ levels in this energy range. Transitions from the ground state $^4I_{9/2}$ levels to the $^2G_{7/2}$ are spin forbidden so that to first order only the three transitions to the $^4G_{5/2}$ levels should be observable in the excitation spectra for each inequivalent Nd^{3+}.

The selection rules for the allowed electric dipole transitions in the Ca(I) and Ca(II) sites are determined from the character tables in Fig. 3 and 4. Since the higher symmetry (C_3) of the Ca(I) site leads to a table with more structure, it will be instructive to analyze the consequences of C_3 symmetry after which the properties of the Ca(II) table will be self-evident.

The symmetry operations E, C_3, C_3^2, R, RC_3, RC_3^2 are the transformations performed on the crystalline axes that leave the environment of the Nd^{3+} ion unchanged. The origin of coordinates is taken to be at the Nd^{3+} center. E is the identity operation and amounts to no operation at all. Its presence is required in order that the group be complete. C_3 and C_3^2 represent rotations through 120° and 240°, respectively, about the crystalline C axis. The operation R represents a rotation through 360° about the C axis. Its effect is the same as the identity operation when one is dealing with the transformation properties of (*i*) the states of systems with an even number of electrons, *e.g.*, Pr^{3+} and Eu^{3+}, or (*ii*) the operators that represent the interaction energies between systems, *e.g.*, electron-photon, electron-crystalline field. On the other hand, for the states of a system with an odd number of electrons, R changes the sign of the state function. Therefore, whenever one is dealing with an odd electron system, such as Nd^{3+}, the operation R must be included in the point group.

The eigenstates of any system must transform as one of the representations of the group of operations that leave it invariant. The functions with which we are concerned are (*i*) the three components of the electric dipole moment of Nd^{3+} ion since that is what couples to the electric field through an interaction of the form

$$-e\mathrm{E}\cdot r = -e(\mathrm{E}_x x + \mathrm{E}_y y + \mathrm{E}_z z) = -e\{(\mathrm{E}_x + i\mathrm{E}_y)(x - iy) + (\mathrm{E}_x - i\mathrm{E}_y)(x + iy) + \mathrm{E}_z z\} \quad [1]$$

where plane polarized and circular polarized descriptions of the interaction are given; and (*ii*) the angular momentum wave functions of the Nd^{3+} ion which are various linear combinations of functions of the form $e^{im\phi}$, m being the component of the total angular momentum along the C axis. The quantum mechanical expression for the transition probability includes a factor of the form

$$|\langle\psi_f|H'|\psi_i\rangle|^2 \quad [2]$$

where $H' = -e\mathrm{E}\cdot r$ and ψ_i and ψ_f are the initial and final Nd^{3+} wave functions.

Since the transition probability is just a number, its value cannot depend on any transformation of the crystal that leaves the crystal in exactly the same condition. If we carry out all of the symmetry operations on the functions contained in the matrix element, some piece of it must remain unchanged, otherwise the transition described by that matrix element is zero. There is always one representation of a group that is invariant under all of the operations and it is conventionally labeled A_1 (Γ_1 in some circles).

The previous paragraph requires that the matrix element remain unchanged under all symmetry operations. Therefore

$$<Op\psi_f|Op(-eE\cdot r)|Op\psi_i> = <\psi_f|-eE\cdot r|\psi_i> \quad [3]$$

where Op is any symmetry operation. But the character table in Fig. 3 tells what happens to the states of Nd^{3+} for all Op's.

For all states that have z components of angular momentum given by $m = 1/2 \pm 3n$, $n = 0, 1, 2, 3$, etc., the effect of the symmetry operators in Fig. 3 are

$$Ee^{im\phi} = e^{im\phi}$$

$$C_3e^{im\phi} = e^{im(\phi+2\pi/3)} = e^{i\pi/3}e^{im\phi} = -w^2e^{im\phi}$$

$$C_3^2e^{im\phi} = e^{im(\phi-2\pi/3)} = e^{-i\pi/3}e^{im\phi} = -we^{im\phi}$$

$$Re^{im\phi} = e^{im(\phi+2\pi)} = e^{i\pi}e^{im\phi} = -e^{im\phi}, \text{ etc.} \quad [4]$$

where

$$w = e^{2\pi i/e}$$

Therefore the states with $m = 1/2 \pm 3n$ transform as the first row of the representation $D_{1/2}$ in Fig. 3.

The Hermitian conjugate states, *i.e.*, those with $m = -1/2 \pm 3n$ can be shown by the same procedure as in Eq. [4] to transform as the second row of $D_{1/2}$. Those states that have $m = \pm (3/2 + 3m)$ transform as the representation S in Fig. 3.

Using the table in this way we derive the selection rules illustrated in Fig. 3 and 4 for Nd^{3+} in Ca(I) (C_3) sites and Ca(II) (C_s) sites, respectively. The set of equations corresponding to Eq. [3] with $\psi_i = e^{i\phi/2}(D1/2)$, $\psi_f = e^{3i\phi/2}(S)$ coupled together by $(E_x - iE_y)(x + iy)$

$$E: \quad <e^{3i\phi/2}|x + iy|e^{i\phi/2}> = <e^{3i\phi/2}|x + iy|e^{i\phi/2}>$$

$$C_3: <-e^{3i\phi/2}|w(x + iy)|-w^2e^{i\phi/2}> = <e^{3i\phi/2}|x + iy|e^{i\phi/2}>$$

$$C_3^2: <-e^{3i\phi/2}|w^2(x + iy)|-we^{i\phi/2}> = <e^{i\phi/2}|x + iy|e^{i\phi/2}>$$

$$R: \quad <-e^{3i\phi/2}|x + iy|-e^{i\phi/2}> = <e^{3i\phi/2}|x + iy|e^{i\phi/2}>$$

$$RC_3: \quad <e^{3i\phi/2}|w(x + iy)|\, w^2e^{i\phi/2}> = <e^{3i\phi/2}|x + iy|e^{i\phi/2}>$$

$$RC_3^2: \quad <e^{3i\phi/2}|w^2(x + iy)|we^{i\phi/2}> = <e^{3i\phi/2}|x + iy|e^{i\phi/2}>$$

Every operation leaves the matrix unchanged and therefore the transition is allowed from $e^{i/2\phi}$ to $e^{3/2i\phi}$ with a right circular polarized photon traveling parallel to the C axis.

It is not necessary to write out the transformations as indicated, we can get the answer by multiplying the corresponding table entries for the three quantities in the matrix element being careful to use the complex conjugate of the final states representation. If the product of the representations carried out in this way contains the A_1 representation, the transition is allowed, if not it is forbidden.

The result of this group theoretical treatment is, therefore, the following. A Nd^{3+} ion located on a Ca(I) site will exhibit some strongly polarized transitions such as the unmixed σ($\perp$ to C axis) and π($\|$ to C) transitions shown on Fig. 3. Charge compensation for the Ca(I) Nd^{3+} ion which is located on the trigonal axis will not alter the site symmetry or polarization. A Nd^{3+} ion located on a Ca(II) site will exhibit the polarized transitions shown on Fig. 4.

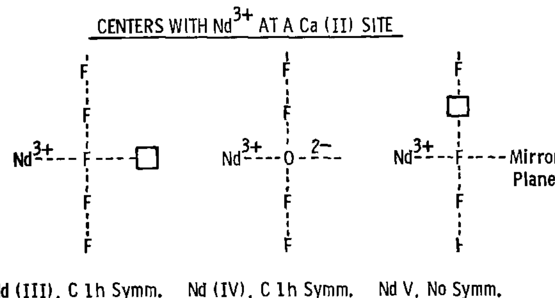

Fig. 5. Proposed models for Nd^{3+} centers located substitutionally at a Ca(II) site.

A Nd^{3+} center formed with charge compensation for the Ca(II) Nd^{3+} located out of the reflection plane (thus destroying the C_{1h} (C_s) symmetry) would also be unpolarized and would be undistinguishable from an $C_{1h}Nd^{3+}$ center from polarization measurements.

Experimental Results and Discussion

The relative ESR concentrations of the various Nd^{3+} centers observed in our crystals are listed in Table I. In the "stoichiometric melt" sample only one Nd^{3+} center was observed in ESR, labeled the Nd(IV) center. It has C_{1h} symmetry which means that it consists of a Nd^{3+} ion replacing a Ca(II) ion presumably with charge compensation, (O^{2-} replacing F^-) located in the reflection plane. The most probable model for this center is shown on Fig. 5. The corresponding fluorescence and excitation spectra of the Nd(IV) center are shown on Fig. 6 and 7 and show the lack of strong polarization expected for a C_{1h} symmetry Nd^{3+} center. What is not expected in the excitation spectrum of Nd(IV) on Fig. 7 is the appearance of at least five energy levels between 17,000 and 17,500 cm whereas only three are expected for a single type of Nd^{3+} center (see Fig. 2). All of the crystals we studied showed such "extra" energy levels with as many as 20 levels observed in one case. One explanation for these "extra" lines could be that we are observing spin forbidden transitions to the $^2G_{7/2}$ levels. An excitation spectrum does not weigh heavily against weak absorptions as does an optical

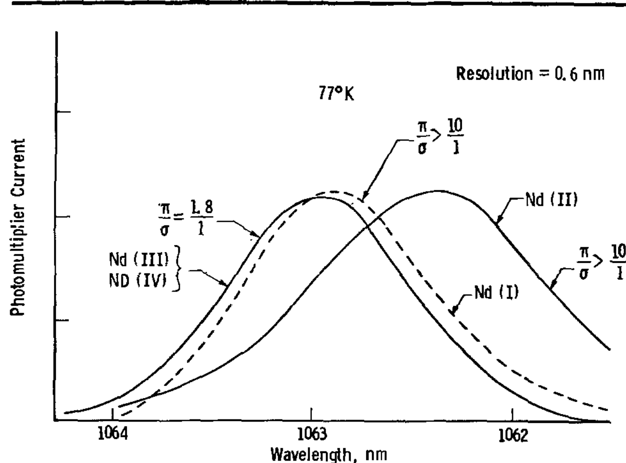

Fig. 6. The fluorescence envelopes of the Nd(I), Nd(II), Nd(III), and Nd(IV) centers.

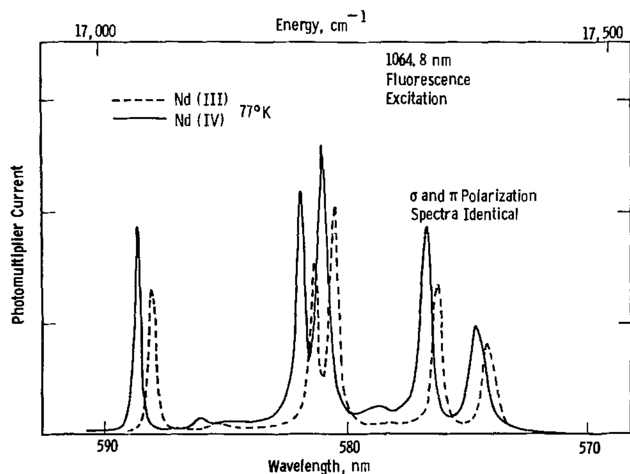

Fig. 7. The fluorescence excitation spectra of the Nd(III) and Nd(IV) centers.

absorption measurement. Unfortunately, our signal/noise did not permit optical absorption data to be taken as a check of this point. However, a more probable explanation for these "extra" lines is that while ESR is capable of identifying only one C_{1h} type of Nd^{3+} center in the "stoichiometric melt" crystal, selective laser excitation shows that indeed more than one related type of Nd(IV) center exists. We have been unable to sort out the excitation levels of each of these centers due to the broad 1 nm fluorescence envelope of Nd^{3+}. Excitation into each of the five energy levels on Fig. 7 yielded fluorescence envelopes indistinguishable from one another. In this respect an ion exhibiting much sharper fluorescence, such as Er^{3+}, is a more suitable candidate for a selective laser excitation experiment than Nd^{3+} and ambiguities of this type should not arise.

In the "10% CaO deficient" sample the Nd(IV) center was no longer observed in ESR or optically. In its place ESR displayed four distinct types of Nd^{3+} centers labeled Nd(I), Nd(II), Nd(III), and Nd(V). Selective laser excitation resolved three sets of Nd^{3+} centers which we have correlated with the Nd(I), Nd(II), and Nd(III) centers seen in ESR. It has been observed if one grows $Ca_5(PO_4)_3F$ crystals from a melt deficient in CaO that oxygen no longer locates substitutionally for fluorine vacancies (9). The disappearance in this crystal of the Nd(IV) center (attributed to a Nd^{3+} substitutional for a Ca(II) with an adjacent oxygen compensator) is consistent with this observation. In its place ESR shows a different type of C_{1h} center labeled Nd(III). As this center possesses reflection symmetry the charge compensator for the Nd^{3+} must either be very distant from the Nd^{3+} or located in the reflection plane (such as an adjacent Ca(II) vacancy as suggested in Fig. 5). The fluorescence envelope of the Nd(III) center is shown on Fig. 6. It is indistinguishable from the Nd(IV) center and is not strongly polarized, typical of a C_{1h} neodymium center. The excitation spectrum of the Nd(III) center is shown on Fig. 7. It is very similar in appearance to the Nd(IV) spectrum but is displaced slightly to higher energy.

In addition to this C_{1h} type of Nd^{3+} center, two distinct types of Nd^{3+} centers of C_3 symmetry are observed, labeled Nd(I) and Nd(II). Models for these centers are shown on Fig. 8 and involve the substitution of Nd^{3+} for a Ca(I) on the 3-fold rotation axis (C_3) with various types of on-axis charge compensation. In Fig. 8 the Nd(II) center is pictured as one for which charge compensation is achieved by an adjacent Ca(I) vacancy while the Nd(I) has more distant charge compensation. Justification for the assignment of "distant compensation" for the Nd(I) center and "nearby compensation" for the

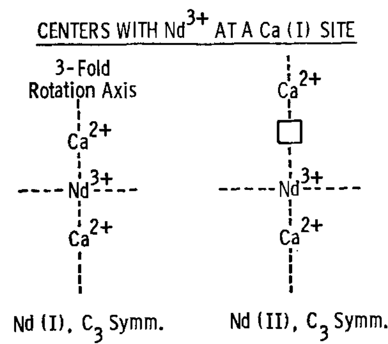

Fig. 8. Proposed models for Nd^{3+} centers located substitutionally at a Ca(I) site.

Nd(II) center will be given in the discussion of the "2% CaF_2 deficient" crystal. The correlation between the centers labeled Nd(I) and Nd(II) in ESR and the corresponding optical properties is exact as the absence of the Nd(I) center and presence of the Nd(II) in the "2% CaF_2 deficient" crystal permitted on unambiguous assignment.

The fluorescent emissions of the Nd(I) and Nd(II) centers are shown on Fig. 6 and their respective excitation spectra on Fig. 9 and 10. Both fluorescences are highly polarized parallel to the crystal C axis. In the absence of crystalline imperfections and if perfect alignment had been achieved it is likely that 100% fluorescence polarization would have been observed for these C_3 centers. The excitation spectra of both centers show some strongly polarized transitions as well as some that are relatively unpolarized,

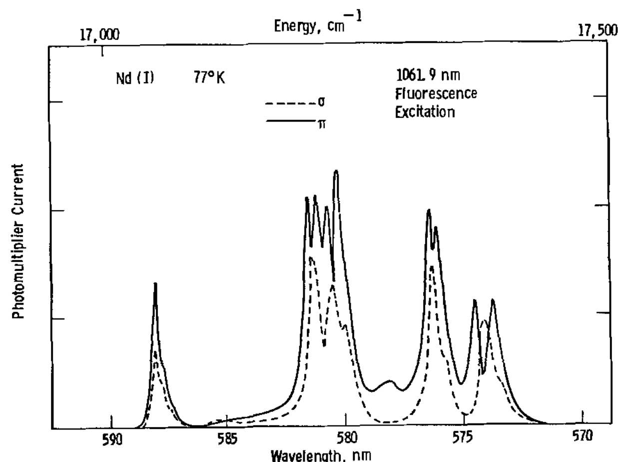

Fig. 9. The fluorescence excitation spectra of the Nd(I) center

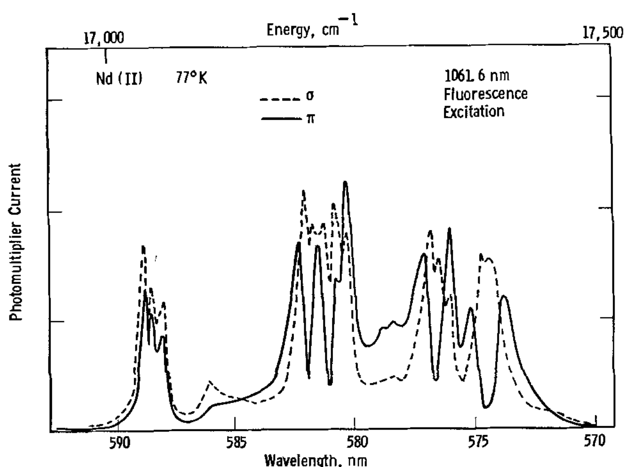

Fig. 10. The fluorescence excitation spectra of the Nd(II) center

exactly what one would expect for Nd^{3+} in C_3 symmetry. Both spectra are very complex, again indicating that the centers we have labeled Nd(I) and Nd(II) are in fact two families of Nd^{3+} centers involving a variety of similar but distinct axial compensation mechanisms.

The final type of center seen in ESR in the CaO deficient crystal has no symmetry and is labeled Nd(V). A typical model for such a center is shown in Fig. 5 where an (unspecified) charge compensator for Nd^{3+} is located nearby and out of the reflection plane, destroying the C_{1h} symmetry. We have been unable to separate the optical spectra of this center probably because (*i*) it is present in relatively low concentrations and (*ii*) it would exhibit unpolarized spectra very similar to the C_{1h} centers.

The third crystal studied was grown from a melt deficient in CaF_2 and containing a high neodymium concentration. One would expect several modifications to occur in the distribution of Nd^{3+} among the various possible sites in such a crystal. One would expect again to observe the Nd(IV) center, since oxygen compensation centers are no longer discriminated against as they were in the CaO deficient crystal. At this higher concentration of Nd^{3+} and of calcium vacancies one would also expect that centers such as the Nd(I) center might disappear as the higher Nd^{3+} concentration would decrease the average Nd-Nd and Nd-Ca vacancy separation and decrease the probability of forming isolated Nd^{3+} centers with accompanying distant Ca vacancy compensation. The disappearance that we do observe of the Nd(I) center in this crystal and the accompanying increase in Nd(II) is in fact the best argument for the relative assignment of models between the Nd(I) and Nd(II) centers previously given. The optical properties of the Nd(II), Nd(III), and Nd(IV) centers were obtained by selective laser excitation in this crystal and were identical to their counterparts observed in the other crystals. Consistent with the ESR measurement, no Nd(I) was observed. For reasons mentioned previously, no Nd(V) could be identified optically.

Conclusions

When calcium fluorophosphate crystals are grown from stoichiometric melts containing low Nd_2O_3 concentrations ($\sim$0.01%), the neodymium locates on the Ca(II) site and forms a center that preserves the local C_{1h} site symmetry. We label this the Nd(IV) center. The most likely model for this center involves Nd on the Ca(II) site and a charge compensating oxygen located on the adjacent fluorine site in the reflection plane. This center has been observed in ESR and its optical excitation and fluorescence spectra were obtained. The Nd^{3+} transitions of this center are essentially unpolarized, in agreement with the selection rules expected for this C_{1h} site. This model is consistent with the assignments given in previous work (2-5).

If crystals are pulled from a melt deficient in CaO, formation of the Nd(IV) center is suppressed and four new types of Nd^{3+} centers are observed in ESR: the Nd(III) center which has C_{1h} symmetry but differs from the Nd(IV) center, the Nd(V) center which has no symmetry, and two centers with C_3 symmetry, the Nd(I) and Nd(II). Probable models for the centers are: Nd(III), a Nd^{3+} ion substitutional for a Ca(II) with an adjacent Ca(II) vacancy in the reflection plane, Nd(V), a Nd^{3+} ion substitutional for a Ca(II) with nearby charge compensation located out of the reflection plane, Nd(I), a Nd^{3+} ion substitutional for a Ca(I) with a distant on axis charge compensating Ca(I) vacancy, and Nd(II), a Nd^{3+} ion substitutional for a Ca(I) with an adjacent charge compensating Ca(I) vacancy. The excitation and fluorescence spectra of the Nd(I), Nd(II), and Nd(III) centers were obtained and the Nd(I) and Nd(II) centers exhibit strongly polarized transitions as expected for Nd^{3+} in a C_3 site. No optical spectra could be obtained for the Nd(V) center.

When a crystal is pulled from a melt which is deficient in CaF_2 and contains a much higher Nd^{3+} concentration ($\sim$0.1%), the formation of the Nd(I) center is suppressed as Nd(I) type centers are converted to the Nd(II) type.

The effect of the growth conditions on the Nd^{3+} distribution occurred in a very predictable fashion in our crystals. A deficiency of oxygen makes oxygen compensation for Nd^{3+} more difficult, and high concentrations of Nd^{3+} reduces the concentration of isolated centers involving distant compensation. Although the electronic configurations of Sb^{3+} and Nd^{3+} are different it is very likely that analogous Sb^{3+} centers would be formed in $Ca_5(PO_4)_3F$ under similar growth conditions.

Manuscript received March 6, 1978. This was Paper 133 presented at the Philadelphia, Pennsylvania, Meeting of the Society, May 8-13, 1977.

Any discussion of this paper will appear in a Discussion Section to be published in the June 1979 JOURNAL. All discussions for the June 1979 Discussion Section should be submitted by Feb. 1, 1979.

Publication costs of this article were assisted by Westinghouse Research and Development Center.

REFERENCES

1. R. W. Warren, F. M. Ryan, R. H. Hopkins, and J. Van Broekhoven, *This Journal*, **122**, 752 (1975).
2. R. C. Ohlmann, K. B. Steinbruegge, and R. Mazelsky, *Appl. Opt.*, 7, 905 (1968).
3. R. D. Eaglet, L. G. DeShazer, G. A. Keig, and D. E. Witter, Paper 17-2 presented at the 6th International Quantum Electronics Conference, Kyoto, Japan (1970).
4. D. M. Daraseliya, G. V. Maksimov, and A. A. Manenkov, J.E.T.P. *Lett.*, **10**, 229 (1969).
5. A. A. Kaplyanskii and E. G. Kuyminov, *Opt. Spectrosc.*, **29**, 376 (1970).
6. D. R. Tallant and J. C. Wright, *J. Chem. Phys.*, **63**, 2074 (1975).
7. R. Mazelsky, R. C. Ohlmann, and K. B. Steinbruegge, *This Journal*, **115**, 68 (1968).
8. F. M. Ryan, R. C. Ohlmann, J. Murphy, R. Mazelsky, G. R. Wagner, and R. W. Warren, *Phys. Rev. B*, **2**, 2341 (1970).
9. R. W. Warren, *ibid.*, **6**, 4679 (1972).
10. B. Segall, G. W. Ludwig, H. H. Woodbury, and P. D. Johnson, *Phys. Rev.*, **128**, 76 (1962).
11. W. W. Piper, L. C. Kravitz, and R. K. Swank, *Phys. Rev. A*, **138**, 1802 (1965).

Grain Growth Mechanism of Heavily Phosphorus-Implanted Polycrystalline Silicon

Yasuo Wada and Shigeru Nishimatsu*

Hitachi Limited, Central Research Laboratory, Kokubunji, Tokyo 185, Japan

ABSTRACT

Grain growth phenomena of heavily phosphorus-implanted polycrystalline silicon films owing to high temperature annealing are investigated by transmission electron microscope. Phosphorus doping in excess of 4×10^{20} cm^{-3} is found to enhance grain growth. This growth is broken down into primary and secondary recrystallization. Isochronal annealing reveals the activation energies for these as 2.4 and 1.0 eV, respectively. The driving force of the primary recrystallization is found to be the interface energy. Therefore, the elementary process behind the primary recrystallization is attributed to silicon diffusion across the grain boundary region.

Polycrystalline silicon (poly Si) is commonly used as gate materials of MOS LSI's (1). In particular, recent progress in fine pattern lithographic technology has made it indispensable to control the pattern definition as well as to lower the resistivity of the material.

However, these two requirements have been found to be paradoxical. This is because lower resistivity, which requires heavy impurity doping, inevitably brings about an increase in poly Si grain diameter and degrades the delineation. Although variation of poly Si gate length arising from grain growth is less than 10% in today's MOS LSI's (2), it might become more than 40% in the coming submicron gate MOS LSI's (3). Therefore, from the process design viewpoint, it is necessary to quantitatively make clear the impurity-doping effect on the growth phenomena.

Grain growth phenomena owing to high temperature (above 1200°C) annealing of thick poly Si film (about 100 μm) for solar cell usage (4) as well as sintering phenomena of poly Si at more than 1200°C for high temperature material (5) have been reported. They showed that the final grain size is about the same as the film thickness or the final material density depends on the initial poly Si grain size.

On the contrary, concerning thin poly Si film, only the dependence of poly Si diameter on the growth conditions (6) and the crystalline state dependence of poly Si resistivity (7) have been reported. The impurity doping effect of grain growth or the growth mechanism itself have yet to be clarified.

This paper quantitatively reports the grain growth phenomena of heavily phosphorus-doped poly Si as functions of doping concentration, annealing conditions, and film thickness. It also aims to propose a possible growth mechanism of poly Si grains.

Experimental Procedure

Poly Si deposition and doping.—A 0.4 μm thick poly Si layer was deposited by thermal decomposition of silane (SiH_4) at 630°C onto a 0.6 μm thick SiO_2 layer, thermally grown on a p-type (100) oriented 10 Ω-cm silicon wafer. Phosphorus ions were implanted at a 50 keV accelerating energy to a dose of between 1×10^{15} and 5×10^{16} cm^{-3} in order to dope quantitatively at low temperature. Radiation damage arising from the heavy doping had no effect on the grain growth phenomena, as is shown in the experiment. The target-heating effect is experimentally ascertained to be less than 100°C since the dose rate was in the order of 0.1 W/cm^2 under these implantation conditions (8).

Doping concentration was defined as (dose/poly Si thickness); therefore, a 1×10^{15} cm^{-2} dose refers to a 2.5×10^{19} cm^{-3} doping concentration, etc.

Annealing in a dry N_2 atmosphere was carried out between 500° and 1200°C to a duration of between 20 min and 64 hr. Impurity outdiffusion was negligible since the sheet-carrier number measured by Hall effect was unchanged under these experimental conditions.

Transmission electron microscope sample preparation and grain diameter measurement.—Transmission electron microscope (TEM; Hitachi HU-12A Type) observation was used to measure grain diameter and to estimate the crystalline state of poly Si. The samples provided for TEM observation were prepared as follows: (*i*) The 400 μm thick silicon substrate was etched from the back side to the 0.6 μm thick oxide layer with $HF:HNO_3 = 1:3$ solution; and (*ii*) Samples were immersed in a dilute HF solution to remove the oxide layer.

The finished sample diameter ranged from 0.1 to 1 mm, and was ladled out by copper mesh for observation. The accelerating voltage of the TEM was 100 kV, and magnification was between 2000 and 20,000 times.

Mean grain diameter $\bar{r}$ was calculated from the following equation (9)

$$\bar{r}' = 1.5 \times l/(n \times m) \quad [1]$$

where, m is the micrograph magnification, l is the line length on the micrograph, n is the number of grains crossed by the line, and 1.5 is the parameter assuming sphere grains.

Brief Explanation of Crystallization Phenomena

Recrystallization phenomena are classified into three stages; nucleation, primary recrystallization, and secondary recrystallization. This paper describes the possible grain growth mechanism of primary recrystallization. Therefore, prior to stating the experimental results, the mechanism of primary recrystallization is briefly explained here (11, 12).

The primary recrystallization mechanism can be classified into three types:

(*i*) In strain-induced growth, the main driving force of growth is the stored strain energy (by cold-work ion implantation or by such effects) within the crystal. The growth follows the equation

$$\bar{r} = k_1 \cdot t \quad [2]$$

which indicates that linear growth on annealing time is expected.

(*ii*) In interface energy-induced growth, the main driving force is the interface energy. The growth follows the equation:

$$\bar{r} = k_2 \cdot t^{1/2} \quad [3]$$

which indicates that grain growth corresponds to the square root of annealing time.

* Electrochemical Society Active Member.
Key words: ion implantation, recrystallization, polycrystalline silicon.

(*iii*) With the impurity drug effect, although the main driving force of growth is the interface energy, impurity included in the grain boundary retards growth. The growth follows the equation

$$\bar{r} = k_3 \cdot t^{1/3} \quad [4]$$

Therefore, the mechanism can be determined by measuring the annealing time dependence of grain growth.

Experimental Results

Doping concentration dependence of grain growth.—Doping concentration dependence of grain growth was examined first. Annealing temperature was 1000°C and annealing time was 20 min. Phosphorus concentration was between 1.2×10^{19} and 7.5×10^{20} cm^{-3}. Some typical TEM micrographs are shown in Fig. 1. These results indicate that grain growth is superlinearly enhanced with impurity concentration. This is contrary to the well-known impurity doping effect on growth phenomena of metals, where "impurity drug" effect is normally observed (10).

The grains were mostly inclined to (110) orientation detected by electron diffraction measurements. This tendency was enhanced with higher annealing temperature. Phosphorus solid solubility in silicon has been reported by Trumbore (11), Kooi (12), and Sunami (13), and is schematically shown in Fig. 2. They indicate that at 1000°C, the solid solubility is around 1×10^{21} cm^{-3}, therefore, these experiments were performed well within the single phase solid solution.

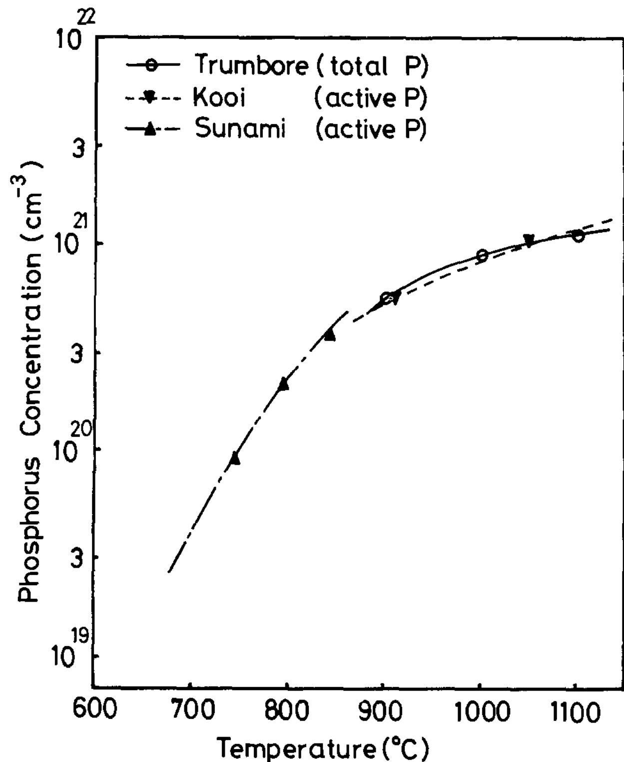

Fig. 2. Solid solubility of phosphorus in silicon; ——— Trumbore (11), - - - - Kooi (12), —·— Sunami (13).

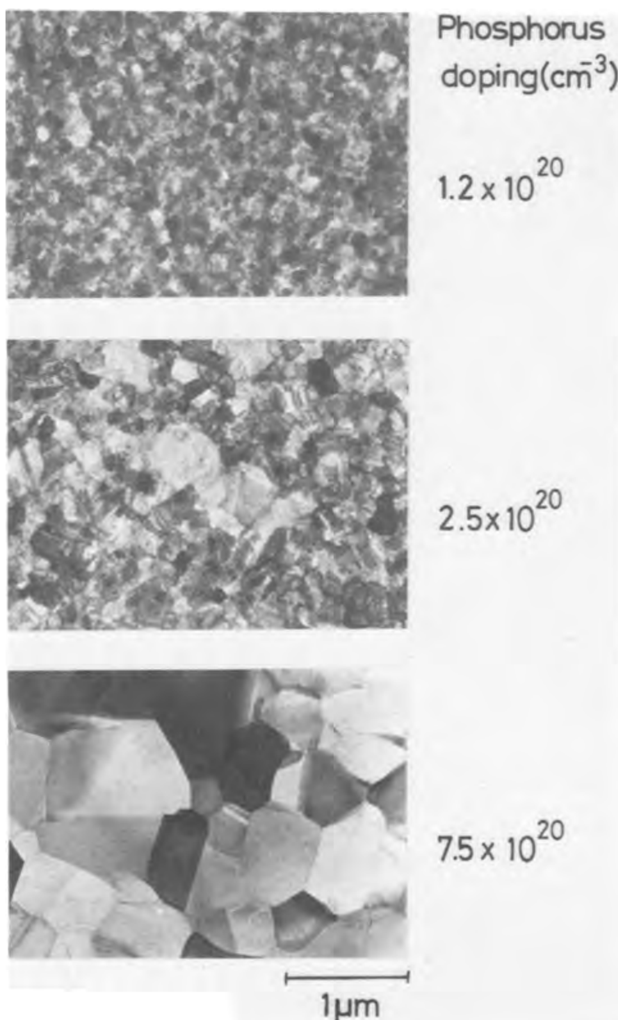

Fig. 1. TEM micrograph of 0.4 μm thick poly Si grains; phosphorus doping concentration is a parameter. Annealed at 1000°C for 20 min.

Annealing temperature dependence of grain growth.—Poly Si doped with 7.5×10^{20} cm^{-3} phosphorus was isochronally annealed for 20 min between 500° and 1100°C. Resulting TEM micrographs between 800° and 1100°C are shown in Fig. 3. Below 700°C, no grain growth was observed as the 800°C case. These results indicate a drastic increase in grain diameter between 800° and 900°C. They also show that there are two stages of grain growth above 1000°C. These, as in the case of metal, are called primary and secondary recrystallization. The former is a growth from initially less than 0.1 μm grains to about 0.8 μm in mean diameter. The latter is a growth of particular grains to more than 2 μm diam, as shown at the right of the 1100°C case in Fig. 3.

Mean grain diameter was calculated using Eq. [1], and the temperature dependence is shown in Fig. 4. The activation energy of primary recrystallization between 800° and 900°C was 2.4 eV, and the secondary recrystallization above 1000°C was 1.0 eV. The horizontal line below 800°C denotes that the mean grain diameter is the same as the as-deposited film in this temperature range. The horizontal line above 1000°C represents the termination of primary recrystallization.

Annealing time dependence of grain growth.—Poly Si doped with 7.5×10^{20} cm^{-3} phosphorus was isothermally annealed for between 20 min and 30 hr at 700°, 800°, and 1100°C. The resulting TEM micrographs are shown in Fig. 5. These results indicate that in both 700° and 1100°C cases, no additional growth as in the 20 min case was observed for longer annealing durations. On the contrary, the 800°C isothermal annealing caused a marked increase in grain diameter, which is classified as primary recrystallization. The mean grain diameter $\bar{r}$ is shown to depend on the square root of annealing time, as depicted in Fig. 5. This indicates that the relationship cited in Eq. [3] stands in these experimental conditions. An 850°C isothermal annealing also showed grain growth following Eq. [3]. These results clearly show that the main driving force of the primary grain growth phenomenon is the interface energy of

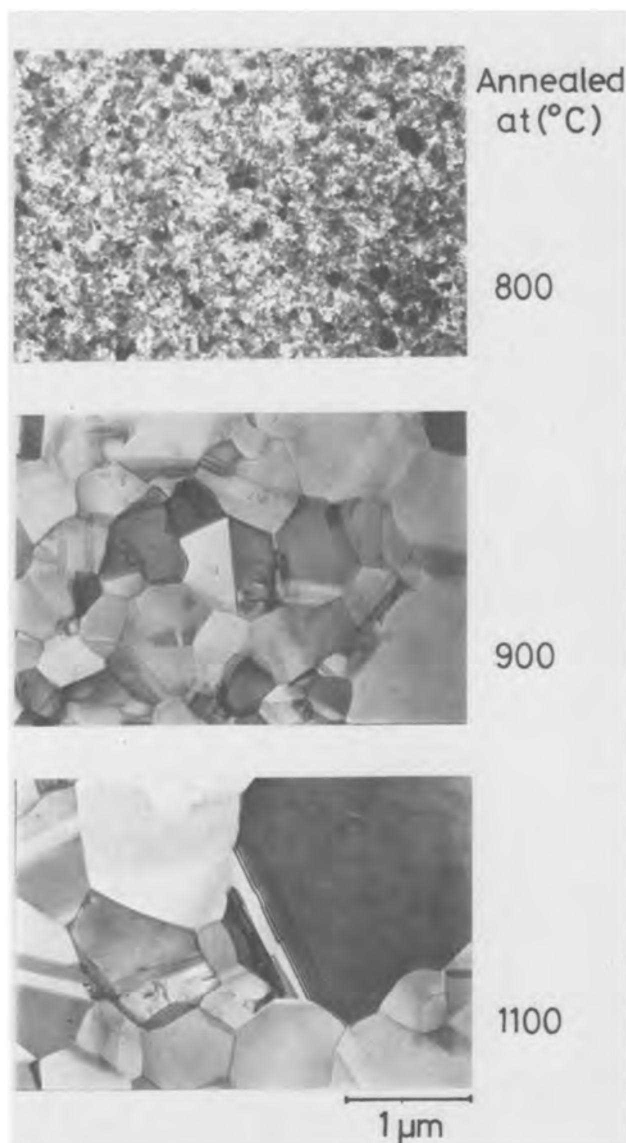

Fig. 3. TEM micrograph of 0.4 μm thick poly Si grains; annealing temperature is a parameter. The phosphorus-doping concentration is 7.5 $\times$ 10^{20} cm^{-3} and it is annealed for 20 min at each temperature.

the grains, not strain energy stored in the thin film nor radiation damage arising from heavy ion implantation (14). Thus, radiation damage is effectively removed in the initial stage of heat-treatment and does not contribute to the grain growth. The results also suggest that the elementary process of primary grain growth can be silicon diffusion across the grain boundary region (14, 15) (single boundary migration).

Although 1 μm thick samples were also examined under the same experimental conditions, almost the same results were obtained. This indicates that poly Si thickness between 0.4 and 1.0 μm has little, if any, effect on the grain boundary energy.

In addition to phosphorus, the arsenic- or boron-doping effect on the poly Si was also examined. Almost the same phenomena were observed on these three impurity dopings.

Discussion

Impurity-concentration dependence of grain growth.—The impurity-concentration dependence of primary grain growth phenomena are discussed first. As mentioned, impurity doping generally decreases the grain growth rate, and is called "impurity drug" in the metal cases (10). In our experiments, contrary to the cases

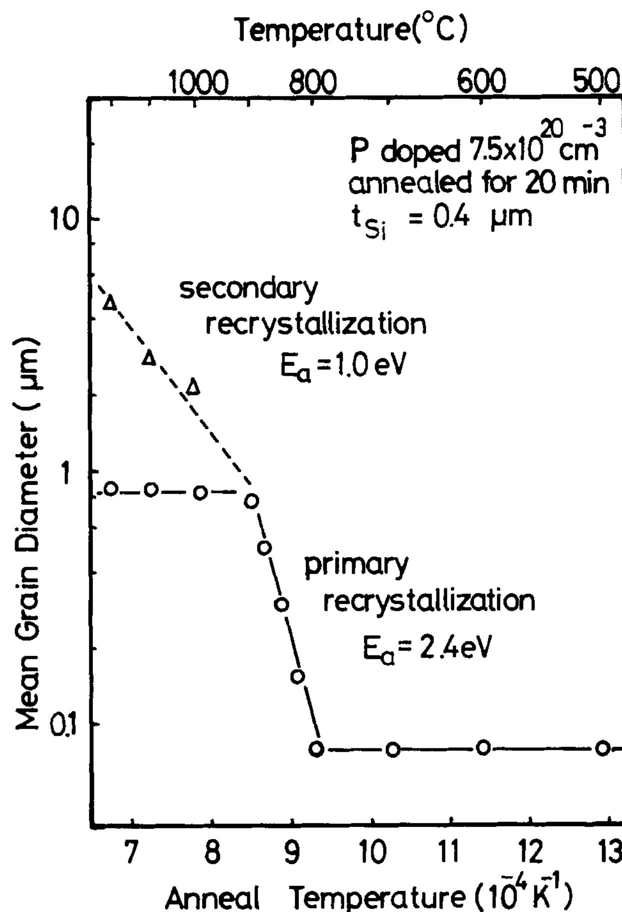

Fig. 4. Annealing-temperature dependence of the mean grain diameter derived from the results shown in Fig. 3.

of metals, impurity doping extremely enhances grain growth. There are two possible reasons for the marked increase in grain diameter, depending on impurity concentration.

One possible reason is the "liquid phase growth" (16), in which low temperature eutectic liquid phase appears in the grain boundary region. However, the Si-P phase diagram (17) shows no low temperature eutectic below 1100°C. In addition, the TEM micrograph depicted in Fig. 1 indicates no such trace of liquid phase. Therefore, this kind of growth mechanism cannot be valid in these experiments.

Another possible reason is the diffusion-enhanced growth, in which an increase in diffusion coefficient enhances grain growth. An impurity concentration-dependent diffusion coefficient has been reported on As (18) and P (19) in silicon, as well as a silicon self-diffusion coefficient under heavily As- or P-doped conditions (20). These results are shown in Fig. 6. They indicate that more than 4 $\times$ 10^{20} cm^{-3} impurity doping greatly enhances the diffusion coefficient. As will be shown later, the silicon self-diffusion coefficient has relations with a grain boundary diffusion coefficient, which in turn is related to grain growth. Therefore, impurity concentration dependence of grain growth is also shown in Fig. 6 by a solid line. A good coincidence with the diffusion-coefficient enhancement was obtained. These results indicate that the origin of grain-growth enhancement is the silicon self-diffusion coefficient enhancement with impurity concentration.

Grain boundary migration rate of primary recrystallization.—The grain boundary migration rate is calculated and compared with the experimentally obtained results to support the aforementioned single boundary migration mechanism.

The grain boundary migration rate was derived from the experimentally obtained results, shown in Fig. 3 and 5. Assuming the relationship in Eq. [3] is valid be-

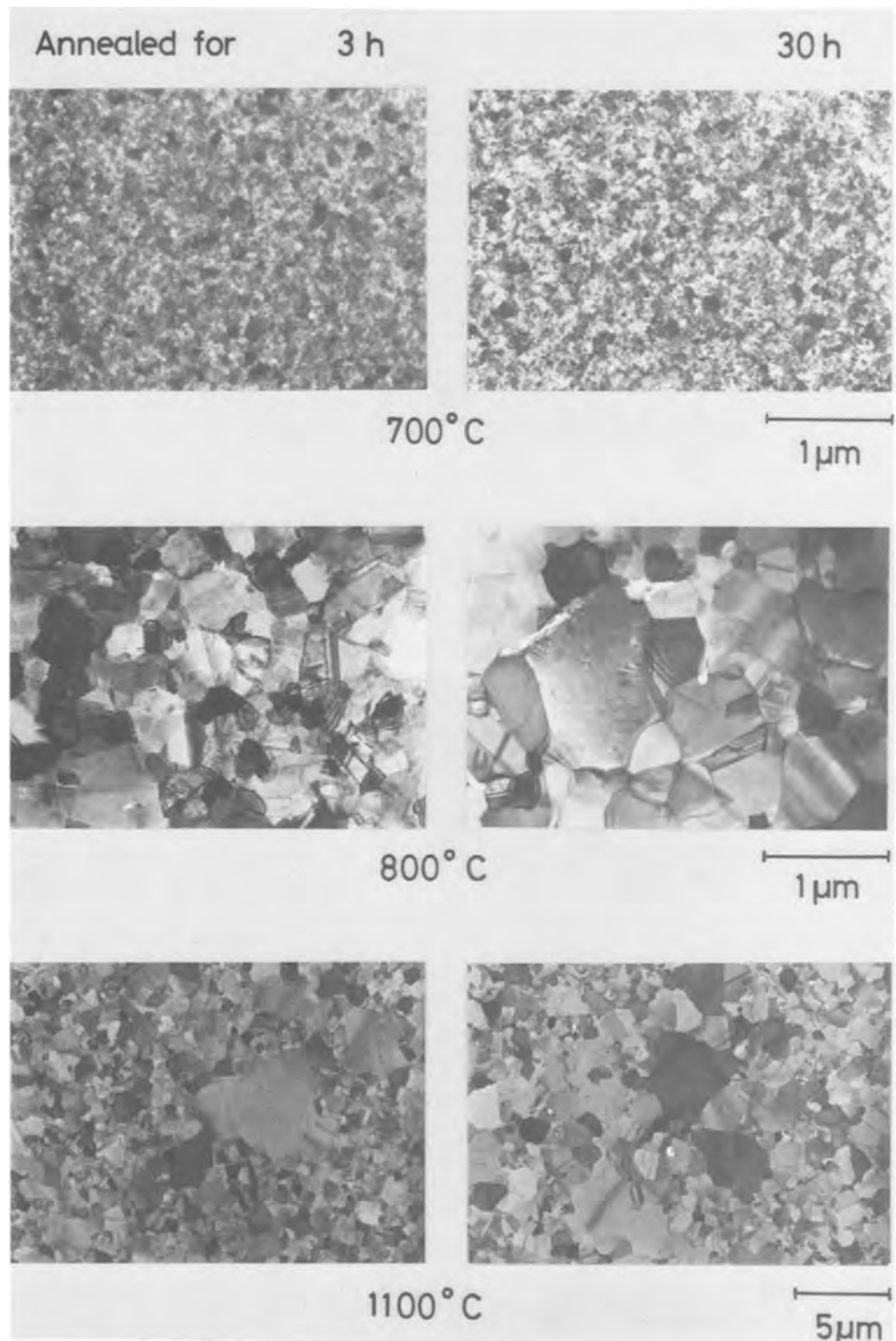

Fig. 5. TEM micrograph of 0.4 μm thick grains; annealing time is a parameter. The phosphorus-doping concentration is 7.5 × 10^20^ cm^−3^ and annealing temperatures are 700°, 800°, and 1100°C.

tween 800° and 900°C, as shown in Fig. 7, the results listed in Table I are obtained. The temperature dependence is shown in Fig. 8, in which both 0.3 and 0.5 μm cases showed the same dependence.

Assuming the migration of grain boundary is attributed to silicon diffusion across the grain boundary, the grain boundary migration rate was calculated and compared with the experimental results. According to Turnbull's equation (14)

$$G = M \cdot F \quad [6]$$

where notations and values are listed in Table II. Grain boundary mobility is expressed as follows

$$M = D_g/kT \quad [7]$$

Driving force is derived from the following equation

$$F = \lambda\sigma/\nu \cdot N_A \quad [8]$$

In these equations the only unknown parameter is the grain boundary diffusion coefficient D_g. Assuming single boundary migration, D_g can be replaced by the grain-boundary silicon diffusion coefficient D_b. D_b is expressed by D_s and D_p through the equation (21)

$$D_p = (D_p - (1 - \alpha) D_s)/\alpha \quad [9]$$

Assuming D_p is proportional to D_s through the equation

$$D_p = kD_s \quad [10]$$

the experimentally obtained grain boundary migration rate was fitted with the calculated results, with k in Eq. [10] as a parameter. The mean grain diameter used in the calculation was 0.3 and 0.5 μm, and the results

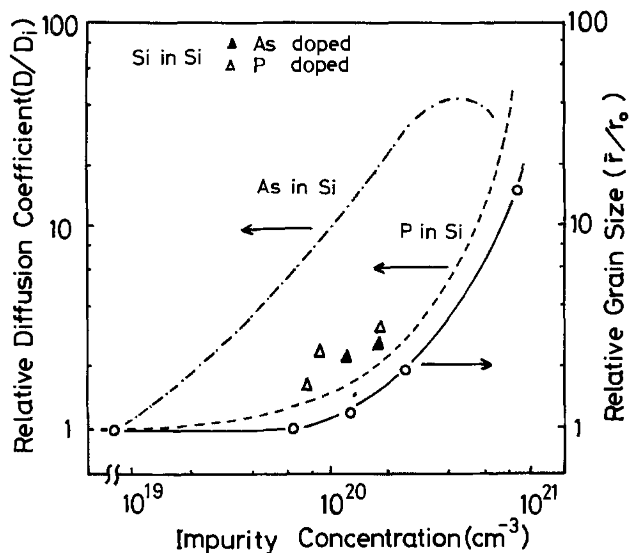

Fig. 6. Impurity concentration dependence of diffusion coefficients and grain growth. Diffusion coefficient: —·— As in Si (18), - - - P in Si (19), and Si in Si (▲ As-doped, △ P-doped) (20) —— grain growth.

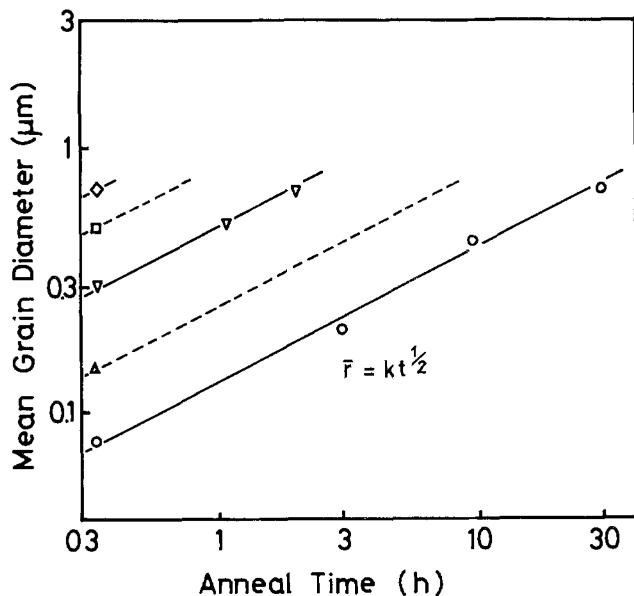

Fig. 7. Annealing time dependence of the mean grain diameter; derived results shown in Fig. 4. Phosphorus-doping concentration is 7.5 × 10^{20} cm^{-3}. ○ 800°, △ 825°, ▽ 850°, □ 875°, and ◇ 900°C.

are shown in Table I. Almost the same k values were obtained in this temperature range. That is, if the diffusion coefficient in single crystal is about two orders of magnitude smaller than that in polycrystal, quantitative agreement is obtained between experiment and calculation. This D_p-D_s relationship is reported including the impurity concentration effect (22).

The results shown here indicate that the doping-concentration dependence, annealing-temperature dependence, and annealing-time dependence of primary recrystallization can be explained by the single boundary migration mechanism. That is, the elementary process of the poly Si grain growth is attributed to silicon diffusion across the grain boundary region.

Table I. Experimental results of grain boundary migration rate and the fitting parameter in the D_p-D_s relationship

Temperature (°C)	Grain boundary migration rate (μm/hr)		Fitting k in $D_p = kD_s$
	($\bar{r}$ = 0.3 μm)	($\bar{r}$ = 0.5 μm)	
800	0.03	0.016	3 × 10^2
825	0.12	0.060	3 × 10^2
850	0.50	0.25	3 × 10^2
875	1.30	0.79	2 × 10^2
900	2.60	1.65	1.3 × 10^2

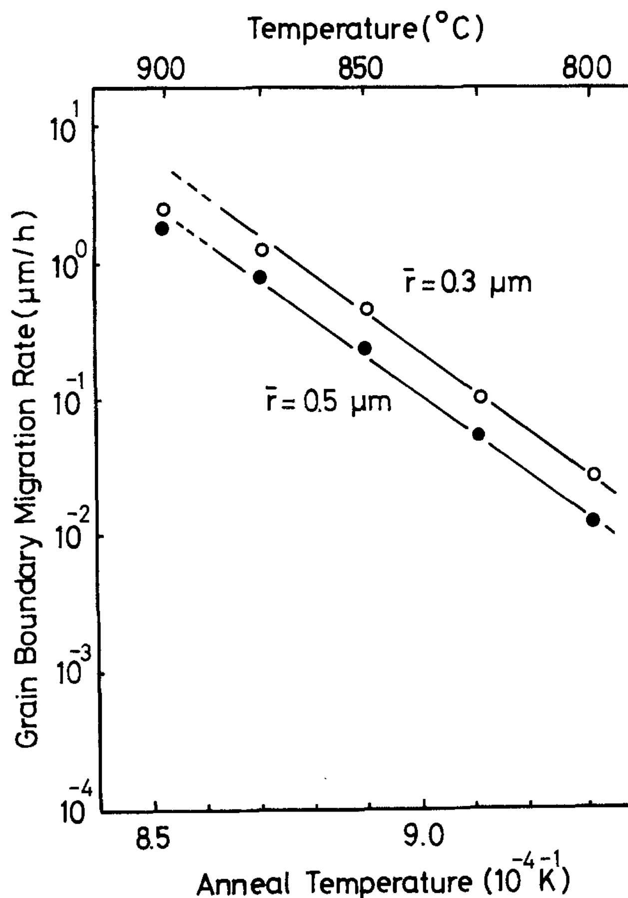

Fig. 8. Temperature dependence of grain boundary migration rate. ○, 0.3 μm; and ●, 0.5 μm mean grain diameter.

Table II. Notations and values used in the calculation

Symbol	Meaning	Value	Reference
G	Grain boundary migration rate		
M	Grain boundary mobility		(16)
F	Driving force		
D_g	Grain boundary diffusion coefficient		
D_b	Silicon self-diffusion coefficient across the grain boundary		(19)
D_s	Silicon self-diffusion coefficient in single crystal	1 × 10^{15} cm^2 sec^{-1}	(18)
D_p	Silicon self-diffusion coefficient in polycrystal	10^2 D_s	(21)
V	Silicon atomic volume	2 × 10^{-23} cm^3	
$\bar{r}$	Mean grain diameter	0.3 μm	Experiment
N_A	Avogadro's number	6 × 10^{23} $mole^{-1}$	
λ	Boundary width	0.5 nm	(20)
σ	Silicon surface energy	1.4 N_A/m^2	(22)
α	Volume fraction of grain boundary	10^{-4}	(20)
ν	Jump frequency of atom		
k	Boltzmann's constant	1.38 × 10^{-23} N_A mK^{-1}	
T	Temperature	1273°K	Experiment

Termination of primary recrystallization.—As shown in Fig. 4, the primary grain growth terminated when the 0.4 μm thick poly Si layer was singly crystallized throughout the thickness and the mean grain diameter reached around 0.8 μm. Although thickness (d_{Si}) dependent final grain size ($\bar{r}_f$) has been reported (23)

$$\bar{r}_f = k_f d_{Si} \quad [11]$$

the results obtained here showed no such evidence between 0.4 and 1.0 μm. This indicated a faster vertical grain growth than horizontal growth. The growth termination is explained by the disappearance of driving force, when three grain boundaries meet at a certain point at 120° (14). Nevertheless, it was not clarified yet why the mean final grain diameter was 0.8 μm.

Secondary recrystallization.—The final grain diameter of secondary recrystallization was found to depend only on annealing temperature between 900° and 1200°C. In addition, the poly Si thickness between 0.4 and 1.0 μm had no effect on the final grain diameter. Therefore, the activation energy of the secondary recrystallization of 1.0 eV shown in Fig. 4 can be temperature-dependent on interface energy. Notwithstanding, these peculiar phenomena were not clarified quantitatively in this report.

Although it has been reported that the final grain diameter is almost the same as the film thickness (4), it was more than 10 times as large in our experiment. The largest grain obtained was around 20 μm in diameter, which was annealed at 1200°C. This indicates the latent possibility of realizing thin single crystal films on amorphous substrates. This might lead to a new era of coming high density LSI's.

Summary

Grain growth phenomena of heavily phosphorus-doped poly Si were investigated as functions of doping concentration, annealing temperature, annealing time, and poly Si thickness. The results obtained are summarized as follows.

1. Grain growth was superlinearly dependent on phosphorus-doping concentration and was shown to be almost proportional to the dependence of silicon diffusion coefficient on phosphorus concentration.

2. Isochronal annealing revealed that the recrystallization phenomena are broken down into two stages. These, as in the case of metal, are called primary and secondary recrystallization. The former is the growth to about 0.8 μm grain diam, while the latter is the growth of particular grains to much larger diameter. The obtained activation energies were 2.4 and 1.0 eV, respectively.

3. Isothermal annealing of 7.5×10^{20} cm^{-3} phosphorus-doped poly Si showed that the driving force of the primary grain growth is the interface energy and that the elementary growth process is attributed to silicon self-diffusion across the grain boundary region.

4. The secondary recrystallization showed irregular behavior, and could not be explained in this report.

Acknowledgments

The authors wish to express their thanks to Prof. Kozuo Fueki and Dr. Koichi Kitazawa of Tokyo University for their valuable discussions. Dr. Takashi Tokuyama is very much appreciated for his valuable discussions and continuous encouragement. They also wish to express their thanks to Dr. Fumio Nagata for taking TEM micrographs, as well as to Hiroo Usui and Masami Ozawa for their experimental assistance.

Manuscript submitted Feb. 9, 1978; revised manuscript received March 30, 1978. This was Paper 299 presented at the Seattle, Washington, Meeting of the Society, May 21-26, 1978.

Any discussion of this paper will appear in a Discussion Section to be published in the June 1979 JOURNAL. All discussions for the June 1979 Discussion Section should be submitted by Feb. 1, 1979.

Publication costs of this article were assisted by Hitachi Limited.

REFERENCES

1. F. Faggin and T. Klein, *Solid-State Electron.*, **13**, 1125 (1970).
2. H. N. Yu, H. N. Yu, R. H. Dennard, T. H. P. Chang, C. M. Osburn, V. Dilonardo, and H. E. Luhn, *J. Vac. Sci. Technol.*, **12**, 1927 (1975); O. Minato, T. Sasaki, R. Hori, M. Kubo, N. Hashimoto, and H. Yoshimora, *Dig. Tech. Papers*, 9th Conference of Solid State Devices, Tokyo (1977).
3. T. H. P. Chang, in "Proceedings of the 8th Conference on Solid State Devices," Tokyo (1976).
4. C. D. Ouwens and H. Heijligers, *Appl. Phys. Lett.*, **26**, 569 (1975).
5. C. Grescovich and J. H. Rosolowski, *J. Am. Ceram. Soc.*, **59**, 336 (1976).
6. T. I. Kamins and T. R. Cass, *Thin Solid Films*, **16**, 147 (1973); R. M. Anderson, *This Journal*, **120**, 1540 (1973).
7. J. Y. W. Seto, *J. Appl. Phys.*, **47**, 5167 (1976).
8. Y. Wada, H. Usui, and M. Ashikawa, *Jpn. J. Appl. Phys.*, **14**, 1351 (1975).
9. F. C. Hull and W. J. Howk, *J. Metals*, **5**, 565 (1953).
10. K. Lucke and K. Detert, *Acta Metall.* **5**, 628 (1957).
11. F. A. Trumbore, *Bell Syst. Tech. J.*, **39**, 205 (1960).
12. E. Kooi, *This Journal*, **111**, 1383 (1964).
13. H. Sunami, *ibid.*, **125**, 892 (1978).
14. "Grain Boundary Structure and Properties," C. A. Chadwick and D. A. Smith, Editors, Academic Press, London (1976).
15. D. Turnbull, *Trans. AIME*, 661 (1951).
16. "Sintering and Related Phenomena," G. G. Kuczynski, Editors, Gordon and Breech, New York (1967).
17. B. Giessen and R. Vogel, *Z. Metallk.*, **50**, 274 (1959).
18. R. K. Jain and R. J. Van Overstraeten, *This Journal*, **122**, 552 (1975).
19. E. Tannenbaum, *Solid-State Electron.*, **2**, 123 (1961).
20. J. M. Fairfield and B. J. Masters, *J. Appl. Phys.*, **38**, 3148 (1967).
21. E. W. Hart, *Acta Metall.*, **5**, 597 (1957).
22. H. M. O'bryan and F. V. Dimarcello, *J. Am. Ceram. Soc.*, **53**, 413 (1970).
23. Yu. S. Avraamov, *Sov. Phys. Doklady*, **10**, 1104 (1966).

Zinc Ion Implantation as a Predeposition Process in Gallium Arsenide

M. C. Boissy and D. Diguet

RTC La Radiotechnique Compelec, BP 6025 14001 Caen, France

ABSTRACT

Ion implantation of zinc into n-type GaAs substrates at room temperature is used as a process of predepositing a solid source from which impurities may be thermally diffused during a postannealing treatment at high temperature (830° or 900°C). The implantation is performed through a Si_3N_4 layer (about 700Å thick) deposited on the crystal surface, in order to prevent the dissociation of the lattice and the out-diffusion of doping atoms. Due to this fact, the total implanted dose is shared between the superficial nitride layer and the semiconductor. High doses are used around 10^{15}-5×10^{15} ions implanted in the substrate per square centimeter to give rise to a deep junction depth ($\sim$10 μm) required for electroluminescence. Such a deep junction is easily obtained by using a high total dose (10^{16} cm^{-2}) and a high dose inside the GaAs substrate (5×10^{15} cm^{-2}). This paper intends to point out that a high junction depth may also be performed with a high total dose (10^{16} cm^{-2}) and a weak amount of ions implanted in the semiconductor (10^{15} cm^{-2}) which comes from the use of a weak implantation energy. This very case is found favorable to good quality doped material. Diodes obtained by this process exhibit good electrical characteristics; evidence of the quality of the resulting p-n junction. Finally, this method leads to light emission efficiency about 1.5 times greater than the standard vapor-phase diffusion, which proves both the efficient injection of minority carriers and the good quality of the implanted and annealed material.

Ion implantation used for doping of semiconductors is an attractive method compared to vapor-phase diffusion, particularily as far as the control, the reproducibility, and the purity of the dopant are concerned. However, ion implantation of p-type impurities in III-V compounds does not give very satisfactory results (presence of a semi-insulating layer between the p-type region and the n-type region, p-n junction with a low light-emission efficiency) when the subsequent annealing is carried out at a low temperature or when the protection of the surface is inefficient (1-6). Indeed radiation damage such as lattice disorder or vacancies which occurs during ion implantation is more difficult to anneal in III-V compounds than in silicon. This fact arises from the values of the binding energies of crystal lattice with regard to those of the defect generation energies. Thus the initial electronic quality is not completely recovered after a thermal treatment: the forbidden bandgap of the implanted material contains a large amount of deep energy levels (1) which have influence both on electrical properties (free carrier concentration and mobility) and on optical properties (photon absorption and light-emission efficiency).

This paper deals with the use of zinc ion implantation as a means of "predepositing" p-type dopant atoms in GaAs, this process being completed by a subsequent annealing at high temperature. In this method the heat-treatment at 800° or 900°C allows both a more efficient annealing of defects and the activation of the thermal diffusion of impurities from the solid source created by the implantation. The implantation is performed through a dielectric layer deposited onto the surface of the material in order to prevent the superficial dissociation of the crystal and the out-diffusion of the dopant during implantation or annealing.

Experimental

Sample preparation.—The GaAs substrates were obtained from ingots grown by the gradient freeze method with silicon-doping concentration ranging from 2×10^{17} to 10^{18} cm^{-3} and with a dislocation density of around 10^3-10^4 cm^{-2}. Substrate wafers about 500 μm thick were lapped and subsequently chemically polished. Their surfaces were oriented in the (100) plane. These surfaces were then coated with a layer of Si_3N_4 about 700Å thick obtained by chemical vapor deposition at 750°C from a SiH_4-NH_3 reaction. This surface protection was carried out before implantation to avoid out-diffusion of implanted dopant during Si_3N_4 deposition. Si_3N_4 was chosen in preference to SiO_2 because it has been shown that out-diffusion of gallium can occur from the substrate through silicon oxide (7) and that such a generation of gallium vacancies induces a substitutional diffusion mechanism of dopant atoms near the SiO_2-GaAs interface, thus reducing the zinc diffusivity in the semiconductor.

Implantation.—Implantation was performed with singly ionized 100-150 keV zinc ions into substrates held at room temperature with a misorientation of 7° to avoid channeling. The implantation energy was calculated using data given by LSS theory (8) in order to obtain the desired penetration depth in the material, taking into account the thickness of the superficial dielectric layer. The ion dose has been varied in the range 10^{13}-10^{16} cm^{-2}.

Assuming that the implantation profile is approximately gaussian (8) the distribution of the dopant between the nitride layer and the semiconductor may occur in three different ways, as shown on Fig. 1: (a) most of the dose is implanted in the GaAs substrate, (b) the maximum of the gaussian curve is located at the dielectric/material interface; (c) most of the dose is contained in the nitride layer. Samples with these three configurations were investigated.

Heat-treatment.—Following implantation, samples were annealed in a nitrogen atmosphere at 830° or 900°C. The properties of the resulting p-doped region were first investigated on a stained cleavage plane.

Device preparation.—Then the dielectric layer was removed with a CF_4 plasma: An ohmic contact pattern was deposited on the implanted layer by evaporation of Au + 1% Be through a metallic mask. The resulting metallic dots were 400 μm in diameter. Tin evaporation was performed on the back face to ensure the n^+-type

Key words: semiconductor, diodes, electroluminescence, ion implantation, diffusion.

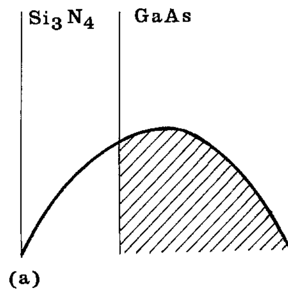

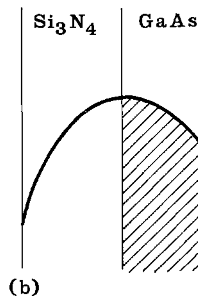

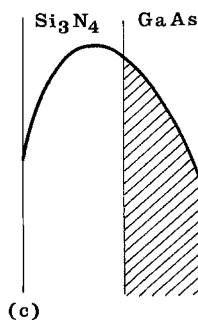

Fig. 1. Distribution of the implanted dose between the Si_3N_4 overlayer and the GaAs substrate (hatching represents the same dose implanted in the 3 substrates).

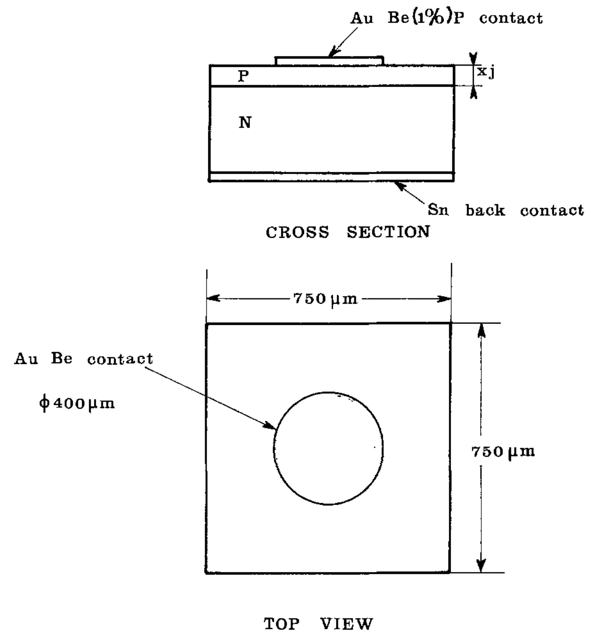

Fig. 2. Device structure

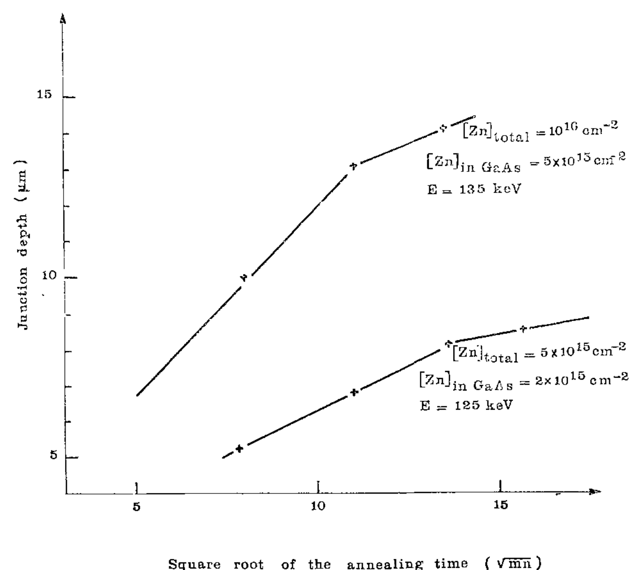

Fig. 3. Junction depth as a function of annealing time (annealing temperature, 900°C).

ohmic contacts. The processed samples were diamond scribed and diced in order to obtain 750 μm square chips which were then soldered onto TO 18 headers. Finally, a gold wire was bonded on the top metallization (Fig. 2). This simple but rapid process was chosen in order to allow fast assessment of the p-n junction properties during the optimization phase of each parameter. The analysis of the devices was carried out by assessment of the electrical (current-voltage) and optical (light emission power) characteristics.

Results

In the case of GaAs electroluminescent diodes, most of the radiative recombination takes place in the p layer. Therefore, in order to obtain the best efficiency, its thickness has to be greater than the electron minority carrier diffusion length Le. In practice for the usual p-type doping level ($p \sim 10^{19}$ cm^{-3}), Le is about 5 μm so that the junction depth xj has to be of that order of magnitude. When the p-n junction is obtained by normal zinc vapor-phase diffusion techniques, it is experimentally shown that the optimized xj is as great as 10 μm (9). Therefore, optimization of implantation conditions (dose and energy) and post annealing treatments (temperature and duration) were carried out with this aim.

Two annealing temperatures were used: 830° and 900°C. Figure 3 exhibits the evolution of the junction depth with annealing duration. This curve, in its first part, shows the expected proportionality of xj with the square root of the annealing time. Then the slope of the curve decreases for longer annealing times due to the depletion of the finite zinc source created by the implantation. So for given implantation parameters, the annealing condition can be adjusted to obtain the desired p-type region thickness.

In addition, the junction depth strongly depends on implantation conditions. Firstly, the influence of the ion-implanted dose is presented in Fig. 4. We have represented the variations of the junction depth with the zinc dose implanted in the semiconductor. In this figure the points refer to experiments carried out in the same configuration: for each sample the implantation energy is chosen so that the total dose is equally shared between the nitride layer and the GaAs substrate. In these conditions the junction depth quickly increases beyond a threshold when the dose implanted in the substrate increases, for constant annealing treatment. The thermal diffusion of impurities is slight when the dose incorporated in the material is less than 10^{15} ions cm^{-2}; the junction depth is too shallow to give an efficient light-emitting diode. This is the reason why

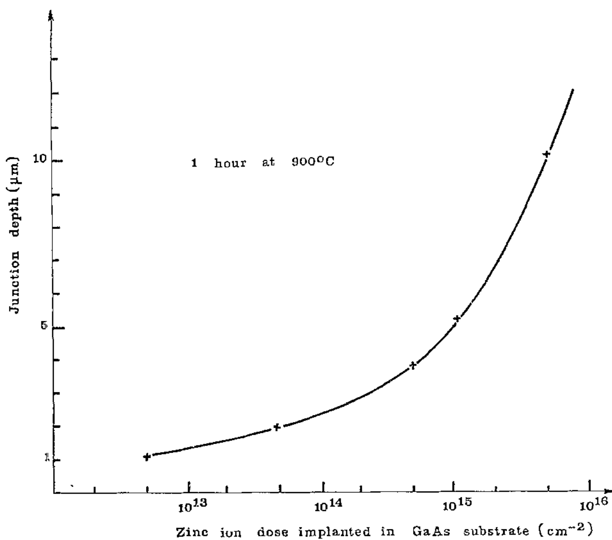

Fig. 4. Influence of the dose implanted in the substrate on the junction depth after annealing [the implantation energy is such that (Zn in GaAs = (Zn) total/2].

high doses are used for the following study, *i.e.*, 10^{15}-5×10^{15} zinc ions cm^{-2} implanted inside GaAs substrates.

Within this reduced range of values, differences can be noticed as far as the shape of the diffusion front is concerned. Thus Fig. 5 compares two samples in which the junction line is located at the same depth and results from two implantations carried out with the same total dose but with doses implanted in the semiconductor differing with a ratio of five. (The annealing conditions were chosen so that they induced about the same junction depth in the range of the optimized depth for electroluminescence). The junction lines thus obtained are straight for 10^{15} ions cm^{-2} implanted in the GaAs (Fig. 5a) but wavy and distributed for the higher doses (Fig. 5b). In the latter case the introduction of a large amount of doping atoms in the semiconductor at a few hundred angstroms from its surface induces perceptable disorder and stresses which affect the diffusion mechanisms initiated there.

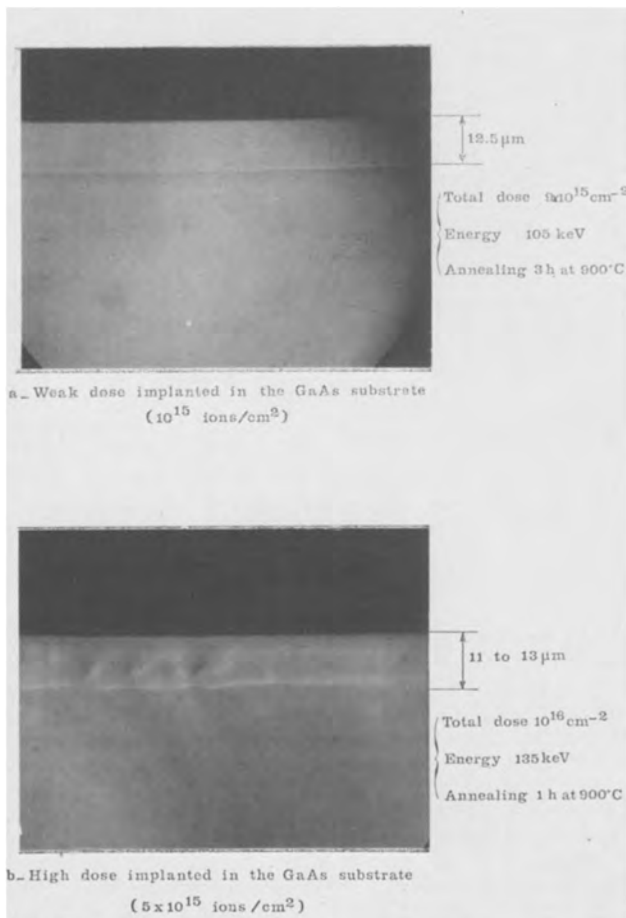

Fig. 5. The shape of the diffusion front

The influence of the dose implanted in the semiconductor itself being thus clarified, this parameter is fixed and the others are now reviewed. Data are summarized in Table I for samples processed under the same conditions: Si_3N_4 thickness (~ 600Å); implanted dose in the semiconductor (10^{15} cm^{-2}); annealing temperature and duration (3 hr at 900°C), except for the configuration of the sharing of the dose between the nitride and the semiconductor as shown in the first column of the table.

These three different configurations in which the dose implanted in the substrate is kept constant are performed by varying the value of the implantation energy and so the value of the total dose too. Indeed when one of the three parameters of implantation, total dose, dose implanted in the semiconductor, energy, is fixed, the two others are interacting. Thus, with a constant dose in GaAs, a high implantation energy implies a small total dose and inversely.

In this way the table shows that zinc diffusivity strongly increases when the implantation energy decreases and consequently the total dose increases. It can be concluded that, for a given dose implanted into the semiconductor, the diffusion coefficient is somewhat higher when the majority of the dose is located in the Si_3N_4 overlayer. Two interpretations of this behavior can be proposed.

Firstly, when the nitride layer contains a large concentration of dopants, the out-diffusion of zinc is less probable from the substrate to the dielectric than from the dielectric to the substrate and all the zinc atoms introduced in the semiconductor diffuse inside the substrate.

Besides, it is known that implantation defects are mostly generated at the start of the ion penetration into the crystal and then are found in the first part of the implantation profile (10, 11). Thus, radiation defects will be confined within the nitride layer when most of the dose is implanted in this overlayer. Thus the concentration of defects in GaAs which could trap zinc atoms in the vicinity of the semiconductor surface

Table I. Influence of the configuration of implantation (sharing of the total dose) on the zinc diffusivity after annealing

Implantation profile	Total implanted dose (cm^{-2})	Dose implanted in GaAs (cm^{-2})	Implantation energy (keV)	Junction depth (µm)
	1.4×10^{15}	10^{15}	155	2
	2×10^{15}	10^{15}	125	3.5
	9×10^{15}	10^{15}	105	13

Annealing 3 hr at 900°C.

is lowered and the concentration of zinc diffusing-in is increased.

The analysis of properties of the implanted p-type regions is also carried out by measurement of the zinc concentration profile after annealing, using a colorimetry method (12). This method consists of an electrolytic etching of the doped material introducing the zinc in solution; a colored complex of zinc is then formed which is analyzed by optical absorption. A typical measured zinc profile is given in Fig. 6. It can be seen that high zinc concentrations are present close to the surface (2×10^{19} cm^{-3}) and that the zinc concentration profile is gradual. Just such a profile gives rise to a good light-emission efficiency since it favors the injection of minority carriers. Indeed it induces a high concentration of majority carriers, to which the injection efficiency is directly proportional (13, 14).

Although the device geometry is not yet optimized, electrical measurements give satisfactory results, the characteristics being similar to that of standard light-emitting diodes. The forward current-voltage characteristics are compared in Fig. 7 with that of a vapor phase diffused device with the same structure. It should be noticed for these two kinds of devices that the variation of the current with the applied bias follows the law $I = I_{SC} \exp(qV/2\,kT)$, evidence of the predominance of space-charge recombination mechanisms. This fact proves that the junction obtained by this predeposition process is a p-n junction, unlike the p-i-n structures obtained by several authors (1-6). Hunsperger (4) attributed the existence of the intermediate semi-insulating layer to the generation of localized defects, such as arsenic vacancies, produced by ion bombardment and to their diffusion inside the lattice during annealing. During the diffusion these localized defects associate with substrate dopants to form more stable complexes. Therefore strong electrical compensation is present when the concentration of defects equals the substrate impurity concentration. In our case, it can be supposed that the nitride layer through which ion implantation is carried out prevents superficial dissociation.

Finally the light power emitted by the devices at a current of 500 mA is measured. As shown in Fig. 8, light power up to 10 mW/A is thus obtained corresponding to an external quantum efficiency about 0.7%. This figure also proves that the optimum value for the junction depth xj is around 10 μm, evidence of the high minority carrier diffusion lengths coming from the good quality of the diffused material. When comparing devices produced under different implantation conditions but having the same xj value, higher efficiencies are found for diodes in which most of the dose was implanted in the nitride layer. Indeed as the substrate contains a smaller amount of implanted ions than when the total dose is equally shared between the dielectric and the material, it is less disturbed by stresses and localized defects.

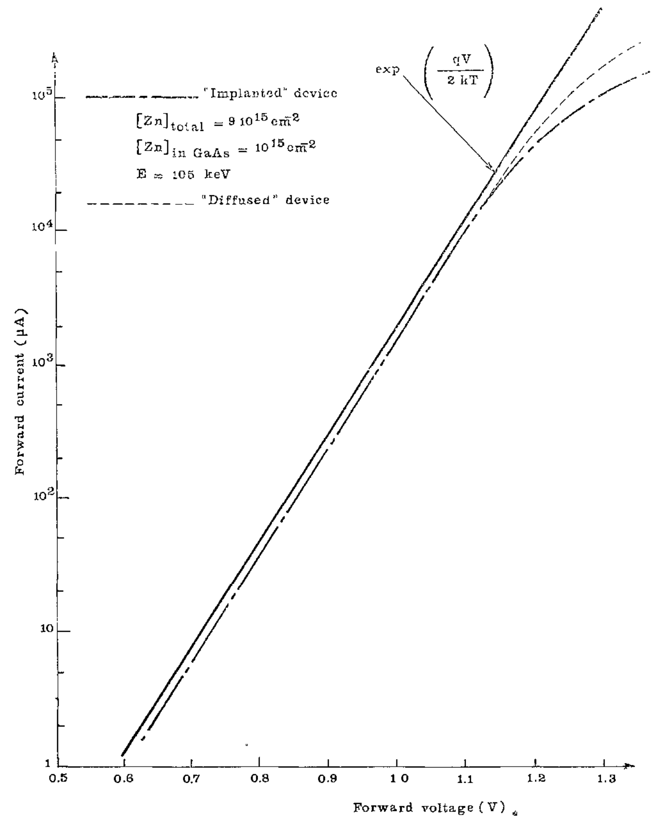

Fig. 7. Forward current-voltage characteristics

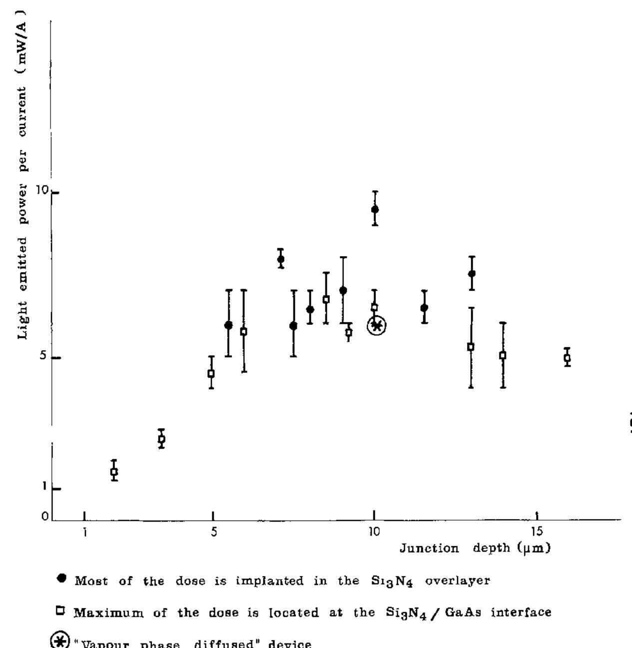

Fig. 8. Light-emission efficiency vs. junction depth

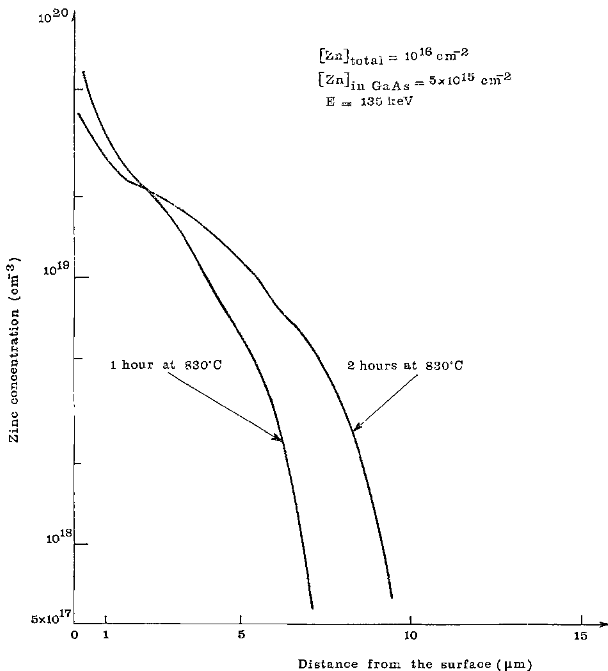

Fig. 6. Zinc concentration profile after annealing

To prove interest of this method of doping, its results are compared with those of the vapor phase thermal diffusion. For that purpose, a 3 μm-thick layer was chemically removed after implantation from part of a sample, the other part of which was processed as described previously. This first piece was then diffused with the vapor phase diffusion process, the heat-treatment conditions being approximately the same as for postimplantation annealing. So the results of both the treatments may be compared on the same material for a constant junction depth. The light-emitting power is found to be 1.5 times greater for the "implanted" diode than for the "diffused" diode. The higher efficiency of the "implanted" device is thought to be due to a better minority carrier injection coming from the gradual shape of zinc concentration profile.

Discussion

In summary, the junction depth observed after annealing is firstly determined by the amount of zinc atoms implanted within the semiconductor itself, as proved by Fig. 4. This behavior is consistent with the well-known dependence of the diffusion coefficient on the impurity concentration during zinc diffusion in III-V compounds.

Then, for a given dose in the semiconductor, the penetration depth of ions during implantation is found to play an important role since it induces the sharing of the total implanted dose between the nitride layer and the semiconductor, which has a strong influence upon the diffusivity of the doping impurities during annealing. Thus, to obtain a high diffusion depth ($\sim$ 10 μm) after annealing, high total dose (10^{16} cm^{-2}) and high implantation energy ($\geqq$ 155 keV) can be used; in such a case the deep diffusion is mainly due to the high amount of zinc atoms contained inside the substrate ($\sim 5 \cdot 10^{15}$ cm^{-2}). But, as shown in Table I, a deep junction may also be performed with a high total dose and a weak energy and this very case is favorable to good quality doped material (see photos on Fig. 5) and consequently to efficient electroluminescent devices (Fig. 8).

In conclusion, the main advantages of ion implantation, *i.e.*, the control and the reproducibility of doping, are shown to be kept in this method of predeposition. Moreover, other advantages are induced by performing the implantation through a dielectric layer, which plays a multiple role: it avoids the out-diffusion of doping atoms during the postannealing; it prevents superficial dissociation and especially generation of arsenic vacancies so that the junction formed after heat-treatment is a p-n junction with high injection efficiency; it allows most of the radiation defects to be confined within this layer by implanting most of dose there.

Due to this last point, this sharing of the dose between the dielectric and the substrate appears to be attractive for several reasons: with a constant dose implanted in the substrate, deep diffusion is easier; with a constant total dose, the diffused region is of better quality and the concentration profile is gradual.

We shall proceed with the extension of the method to other III-V's such as GaP, GaAlAs, GaAsP, and the optimization of the device processing by localizing the implanted surfaces.

Acknowledgments

The authors would like to express their thanks to M. Garcia from Leti, Grenoble, for carrying out the implantations.

They are also indebted to R. Chanu for his very capable technical assistance, to J. Lebailly for enlightening discussions, and to G. Kerr for reading the manuscript.

This work was sponsored by DGRST.

Manuscript submitted Aug. 22, 1977; revised manuscript received April 5, 1978.

Any discussion of this paper will appear in a Discussion Section to be published in the June 1979 JOURNAL. All discussions for the June 1979 Discussion Section should be submitted by Feb. 1, 1979.

Publication costs of this article were assisted by RTC La Radiotechnique Compelec.

REFERENCES

1. R. G. Hunsperger, O. J. Marsh, and C. A. Mead, *Appl. Phys. Lett.*, **13**, 295 (1968).
2. R. G. Hunsperger and O. J. Marsh, *This Journal*, **116**, 488 (1969).
3. P. E. Roughan and K. E. Manchester, *This Journal*, **116**, 278 (1969).
4. R. G. Hunsperger and O. J. Marsh, *Metal. Trans.*, **1**, 603 (1970).
5. T. Itoh and Y. Kushiro, in "Proceedings of the 2nd Conference on Ion Implantation, Garmisch, Partenkirchen (1971).
6. P. N. Favennec, Thesis, Rennes, France (1973).
7. A. S. Grove, O. Leistiko, and C. T. Sah, *J. Phys. Chem. Solids*, **25**, 985 (1964).
8. J. Lindhard, M. Sharff, and H. E. Schiott, *Mat. Fys. Meld. Dan. Vid. Selsk*, **33**, 1 (1963).
9. R. J. Archer and D. Kerps, in Proceedings of the 1st International Conference on GaAs, Reading, Pa. (1966).
10. P. V. Pavlov, D. I. Tetel'baum, E. I. Zorin, and V. I. Alekseer, *Sov. Phys. Sol. State*, **8**, 2141 (1967).
11. B. L. Crowder and R. S. Title, in Proceedings of the 1st International Conference on Ion Implantation, Thousand Oaks, Calif. (1970).
12. E. Haroutiounian, Private communication.
13. W. Shockley, *Bell Syst. Tech. J.*, **28**, 435 (1949).
14. C. T. Sah, R. N. Noyce, and W. Shockley, *Proc. IRE*, **45**, 1228 (1957).

A New Etching Solution System, H_3PO_4-H_2O_2-H_2O, for GaAs and Its Kinetics

Yoshifumi Mori and Naozo Watanabe

Sony Corporation Research Center, 174 Fujitsuka-cho, Hodogaya-ku, Yokohama 240, Japan

ABSTRACT

A new solution system consisting of H_3PO_4, H_2O_2, and H_2O was found useful for etching GaAs wafers. This solution system can be divided into four regions a-d, according to etching characteristics. The boundaries between the regions are given by a mole ratio $(m \cdot r)$ of H_2O_2 to H_3PO_4 of about 2.3 and a mole fraction $(m \cdot f)$ of H_2O of about 0.9 at room temperature. Rate-limiting processes are: a, adsorption of H_2O_2 $(m \cdot r \lesssim 2.3,\ m \cdot f \gtrsim 0.9)$; b, diffusion of H_2O_2 $(m \cdot r \lesssim 2.3,\ m \cdot f \lesssim 0.9)$; c, dissolution of oxidized products $(m \cdot r \gtrsim 2.3,\ m \cdot f \lesssim 0.9)$; and d, adsorption of H_3PO_4 $(m \cdot r \gtrsim 2.3,\ m \cdot f \gtrsim 0.9)$. Solutions in region a have a reproducible etching rate of 0.01-0.1 μm/min, which is useful for MESFET processing. Crystallographic etching is also available with solutions in region c.

In the fabrication of microwave GaAs devices with sufficient reliability and reproducibility, the thickness of the active layer must be controlled. Depth profiles of impurity concentrations and mobility must be measured accurately to correlate device characteristics with material properties. An etching technology using electrochemical reactions such as an anodic oxidation, followed by dissolving the oxide (1-3) or an anodic dissolution (4) has been proven a useful way for accurate GaAs dissolution. An etching technology using chemical reactions with sufficient accuracy and reproducibility however, has not yet been established.

GaAs field-effect transistors are usually fabricated by a lift-off and self-align techniques (5) in which the gate regions of the active layer are etched accurately through windows in protective masks. For this purpose, the chemical etching is more favorable technology than the electrochemical etching because the former way does not need ohmic contacts. However, in the selective etching through windows in protective masks, an anomaly of etching rate such as enhanced etching rate near the edge of the masks (6) is undesirable.

We have found that etching rates of less than 0.1 μm/min without this anomaly are reproducibly attainable using a new solution consisting of H_3PO_4, H_2O_2, and H_2O within a specific composition range. The etching rate is reproducible to within an accuracy of several tens of angstroms.

There is a specific composition range in which the etching rate depends strongly on crystallographic orientation. We report in this paper the etching characteristics of GaAs in this new solution and its etching kinetics.

Experimental

The solution was prepared by mixing 85 weight percent (w/o) H_3PO_4, 30 w/o H_2O_2, and deionized water. The etching studies were generally performed on Te-doped n-type (100), (110), (111)A, and (111)B-oriented GaAs wafers with net donor concentration of $\sim 10^{18}$ cm^{-3}. Etching rate was not affected by all kinds of dopants and by conductivities of wafers. Photoresist AZ-1350 and sputtered SiO_2 films were used as masks for selective etching. Etching was carried out in a temperature range of 0°-40°C without stirring and illumination with temperature control of ±0.5°C. The etched depth was measured from a step height between etched and unetched surfaces using an interference microscope.

Key words: etching, gallium arsenic, phosphoric acid, kinetics.

Results

Composition dependence of etching rate.—Figure 1 is a ternary diagram of the experimental results on a (100) surface obtained at 30°C. The basic components in the three corners in this figure correspond to H_2O, 85 w/o H_3PO_4, and 30 w/o H_2O_2. Concentrations are expressed by volume percent. The numbers within the triangle of the figure refer to etching rates in μm/min. For a given H_2O content, a maximum rate of etching is attained for a mole ratio of H_2O_2 to H_3PO_4 $(m \cdot r)$ of about 2.3. The ternary diagram of the etching rate can roughly be divided into four regions a, b, c, and d corresponding to specific etching characteristics. The etched depth depends linearly on etching time for various surface orientations in regions a, c, and d, as shown in Fig. 2. The rate in region b, on the other hand, depends roughly linearly on the square root of etching time. The etching rate in region b is considered to be limited by the diffusion of H_2O_2 in the solution. The increase in the viscosity for increasing the H_3PO_4 concentration supports this mechanism (1, 2). Figure 3 shows the dependence of the etching rate on the con-

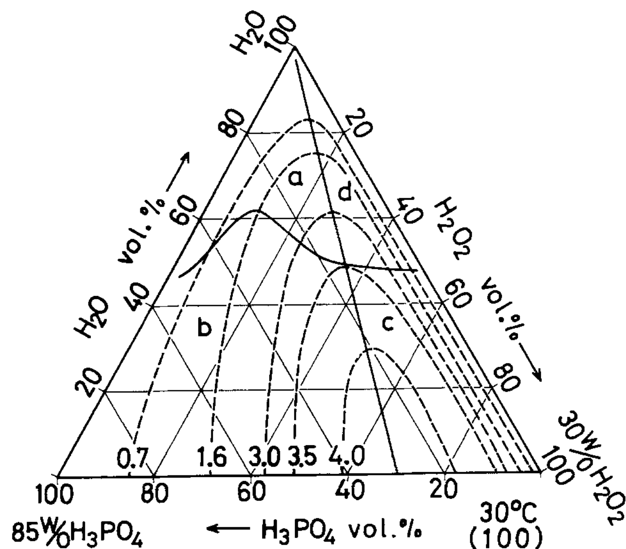

Fig. 1. Dashed lines are constant etching rate contours on (100) surface as a function of the composition of the solution. The numbers represent etching rates in μm/min obtained at 30°C. Solid lines divide ternary diagram in 4 regions: a, b, c, and d.

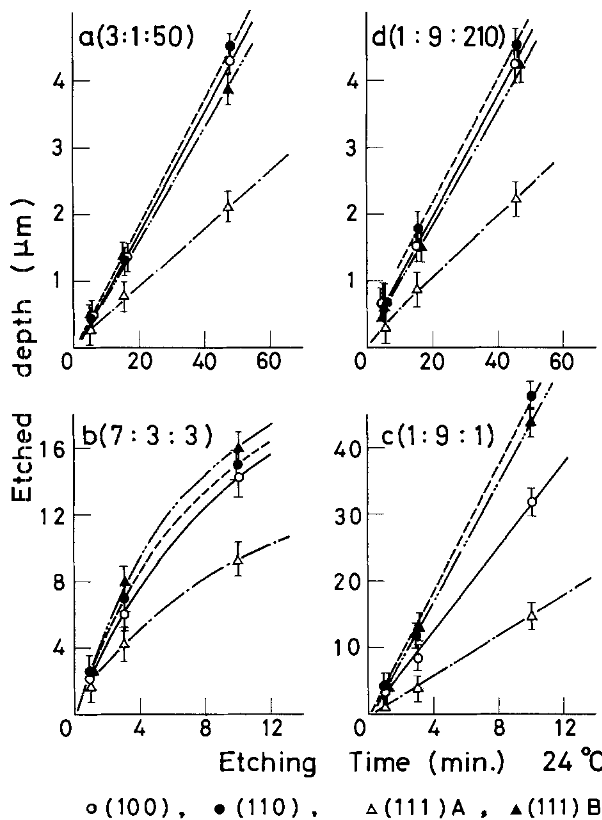

Fig. 2. Relation between etched depth and etching time for various surfaces. Composition of each region is expressed by volume ratio of 85 w/o H_3PO_4 to 30 w/o H_2O_2 to H_2O.

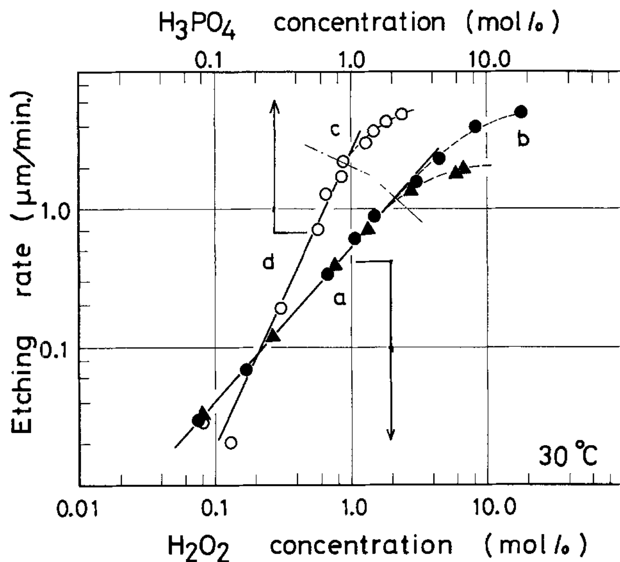

Fig. 3. Composition dependence of etching rate on the concentration of H_2O_2 for regions a and b and of H_3PO_4 for regions c and d. Open circles correspond to $[H_2O_2/H_3PO_4]$ mole ratio $(m \cdot r) = 9.1$ and closed circles and triangles correspond to 1.02 and 0.43, respectively. Concentrations are expressed by mole percent.

centrations of minority reactants, H_2O_2 and H_3PO_4, in solutions obtained on the (100) surface, *i.e.*, regions a and b, and c and d, respectively. Concentrations are expressed by mole percent. The abscissa is scaled by the percentages of minority reactants, that is, H_2O_2 in regions a and b, and H_3PO_4 in regions c and d.

Data in region a lie on an identical straight line for two series of solution having different $m \cdot r$'s, but they differ in region b. This fact indicates that the etching rate in region a is determined by and is proportional to H_2O_2 (minority reactant) concentration. A flat-bottomed hole is always obtained. In region d, the rate is proportional to the square of H_3PO_4 concentration. The etched surface frequently becomes cloudy due to formation of an oxidized film with small pits. The rate tends to saturate in region c. V-shaped and reverse mesa-shaped holes are clearly observed, as will be shown later.

Temperature dependence of the etching rate.—Temperature dependences of the etching rate for various surface orientations in each region are shown in Fig. 4. Values of activation energies are also given in the figure. The activation energy is the same in regions a and d and takes a value of about 10 kcal/mole, independent of surface orientation. In regions b and c, however, it depends on the surface orientation. These results suggest that the rate-determining process is different in each region, as is discussed later.

Slow and reproducible etching.—Stable etching is attainable using the solution in region a. The etching rate in this region is independent of H_3PO_4 concentration and of etching time. The activation energy is independent of surface orientation. Figure 5 shows changes of etching rates on repeated use of etching solutions. Vertical scales refer to the etching rate normalized to the initial rate. In the H_2SO_4-H_2O_2-H_2O system, the etching rate was not stable after about 100 min from its preparation. It sometimes increased by 50% of the initial value and then decreased gradually afterward. Fluctuation of the etching rate for repeated use is the largest in this system. The rate decreased gradually in the KOH-H_2O_2-H_2O system. Etching was not attainable after a storage time of a few months in H_2SO_4 and KOH systems. In the H_3PO_4-H_2O_2-H_2O system, on the other hand, a slow etching rate with excellent reproducibility was maintained over several months. In the H_2SO_4 system, heat evolves upon mixing the reactants and water. The solution is essentially unstable. Bubbles are generated by decomposition of H_2O_2 on the surface of a GaAs wafer while etching in the KOH system. The concentration of H_2O_2 changes with repeated use. The mixing of reactants is nonexothermic in the H_3PO_4 system. H_2O_2 is not exces-

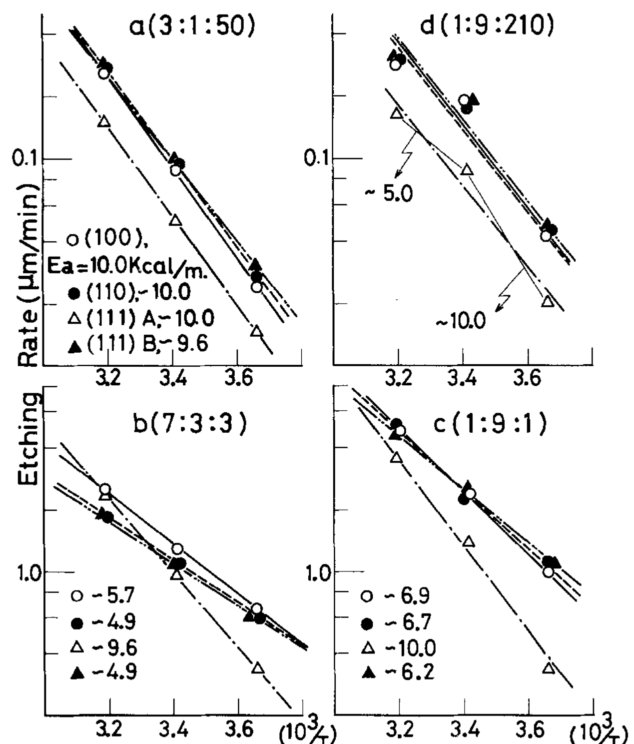

Fig. 4. Temperature dependence of etching rate on various surface orientations.

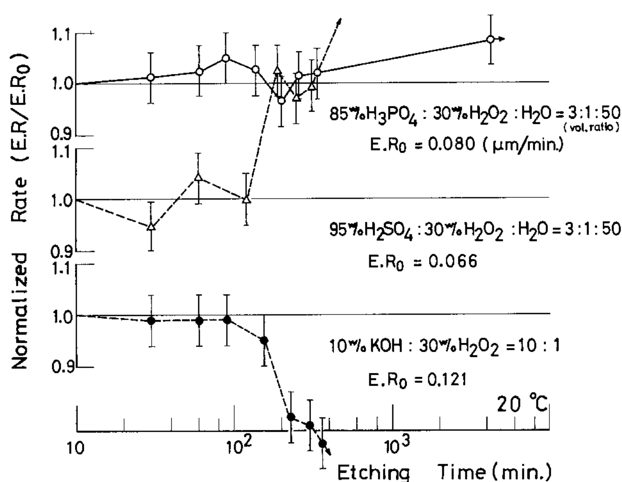

Fig. 5. Change of etching rates on repeated use of etching solutions obtained at 20°C. Every time etching was done for 5 min.

sively consumed in the etching reaction (no bubbles were observed). This is one reason why the H_3PO_4 system is the most stable of the three solutions.

Crystallographic etching.—The ratios of etching rates on the (111)B to (111)A surfaces as a function of H_2O_2 concentration at three different temperatures are shown in Fig. 6. Temperature dependence of this ratio is larger for larger H_2O_2 concentrations. This is a result of the difference in the temperature dependences of the etching rate for different surface orientations in each region (see Fig. 4). Crystallographic etching can be performed by control of temperature and of solution composition in region c. Figure 7 shows pictures of the $(0\bar{1}\bar{1})$ cleavage plane of the selectively etched (100) surface using a photoresist mask (AZ-1350). The upper pictures are for the case where $m{\cdot}r$ is 3.05 and the mole fraction of H_2O ($m{\cdot}f$) is 0.89. The lower pictures are for the cases of 9.15 and 0.83, respectively. Correlation between the etched shape and the etched depth in the case of $(01\bar{1})$ cleavage plane can be seen in Fig. 8. The etching temperature and etching time (t) are given in each photograph.

Discussion

We formulated a rate equation for GaAs etching to determine a rate-limiting process in each region. The etching process was assumed to consist of the following five steps: (i) adsorption of m molecules of H_2O_2 on an active center; (ii) formation of oxidized products; (iii) adsorption of n molecules of H_3PO_4 on oxidized product; (iv) dissolution of oxidized products; and (v) desorption of dissolved complex into solution.

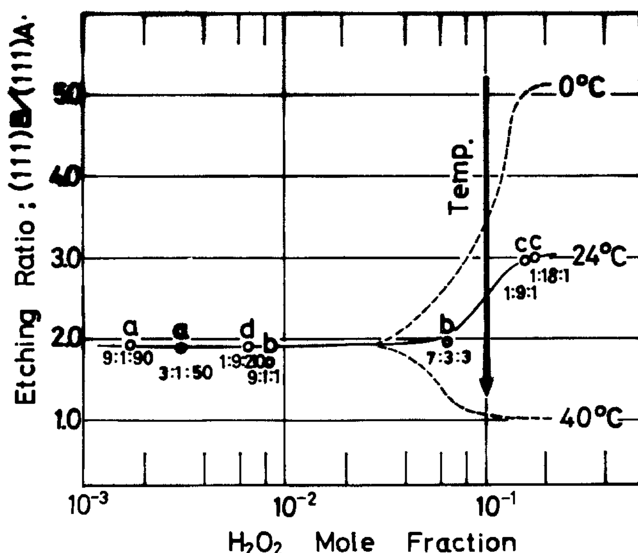

Fig. 6. Ratio of etching rate on (111)B to (111)A surface as a function of mole fraction of H_2O_2. Volume ratios of 85 w/o H_3PO_4, 30 w/o H_2O_2 to H_2O are shown in the figure.

The reaction processes are assumed to proceed at specific active centers on a GaAs surface. The active centers are in different states as the reaction proceeds through the above-mentioned five steps. The total number of active centers in these states is assumed to be constant. Solving the simultaneous rate equations for the five reaction steps, the etching rate, R, under a steady state is obtained as follows

$$1/R = 1/k_1[H_2O_2]^m + 1/k_2[H_3PO_4]^n + 1/k_3 \quad [1]$$

where k_1 and k_2 are rate coefficients for the steps (i) and (iii), and $1/k_3$ is the summation of inverse rate coefficients of each of the other steps. These parameters include temperature, activation energy, partition functions of the activated species, and the reaction frequency factor. For diluted solutions, the k_3 term can be neglected. Exponents m and n can be determined from experimental data of the concentration dependence of etching rate, as was shown in Fig. 3

$$m \simeq 1.0$$

$$n \simeq 2.0$$

Equation [1] is then reduced to the following simple relation

$$R \simeq \frac{[H_2O_2][H_3PO_4]^2}{[H_2O_2]/k_2 + [H_3PO_4]^2/k_1} \quad [2]$$

This equation corresponds to the case where the adsorption steps of reactants, (i) and (iii), are rate limiting. Equation [2] is reduced to the relation, $R \simeq k_1[H_2O_2]$, when $[H_2O_2] << [H_3PO_4]$. This corresponds to the rate equation for the H_2O_2 adsorption process. R is equal to $k_2[H_3PO_4]^2$ when $[H_2O_2] >> [H_3PO_4]$, which corresponds to the rate of H_3PO_4 adsorption. The H_3PO_4 adsorption is bimolecular.

Curve fitting was carried out using Eq. [2], which is shown in Fig. 9. Concentrations in this ternary diagram are expressed by mole percent. Solid and dashed lines represent calculated and experimental results. The calculated results in most parts of regions a, d, and a part of region c agree well with the experimental results. The etching rate in these regions can be considered to be limited by the adsorption processes. Agreement is not good in region b and in the concentrated portion of region c. The rate-limiting process in region b was presumed to be the diffusion of H_2O_2 in the solution. Therefore, the disagreement is a natural consequence. Disagreement in region c may be caused by the contribution of other surface reaction processes such as dissolution of oxidized products. It was concluded that the rate-limiting processes in regions a to d are the adsorption of H_2O_2 on the active centers of GaAs surface, diffusion of H_2O_2 in solution, dissolution of oxidized products, and the adsorption of H_3PO_4 on the oxidized products, respectively. The results are summarized in Table I.

A general concept for GaAs etching is given through the above study. The etching rate is determined by effective densities of reactants and of active centers on the GaAs surface, when the rate-limiting process is the adsorption of a reactant in diluted solutions. The temperature dependence of the etching rate on various surface orientations must be equal. In concentrated solutions, the rate-limiting process is the formation and/or dissolution of oxidized products. The etching rate is affected by the surface activities of GaAs. Temperature dependence of etching rate is different on various orientations.

Summary

A newly found solution, which consists of H_3PO_4, H_2O_2, and H_2O, is presented as a GaAs etchant. This

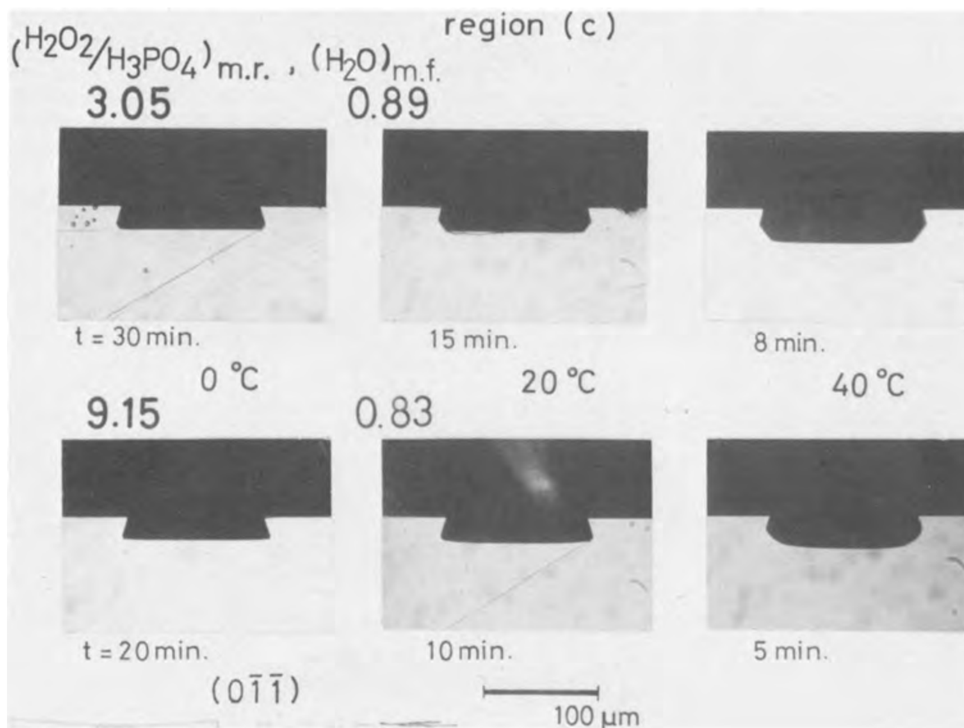

Fig. 7. Pictures of (01̄1̄) cleavage plane of selectively etched (100) surface in the solution in region c.

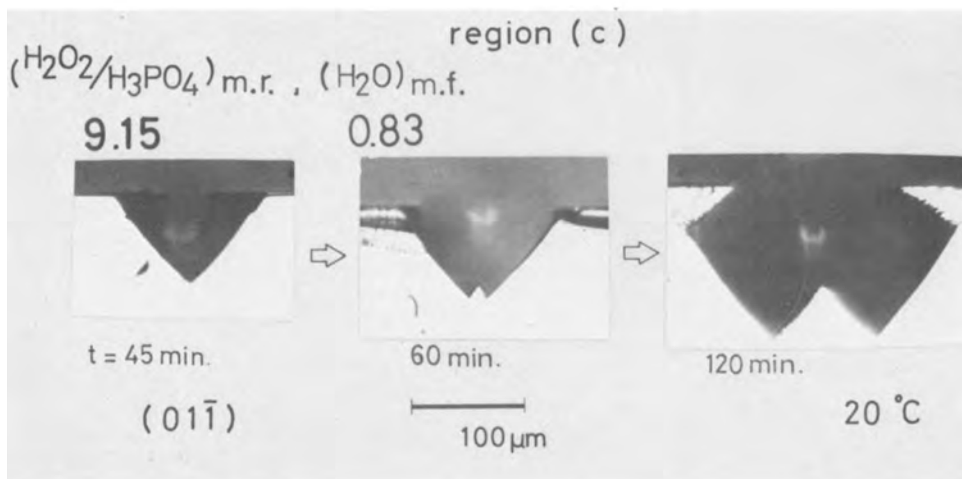

Fig. 8. Correlation between the etched shape and etched depth. Pictures are (011̄) cleavage plane.

solution system was divided into four regions a-d. The boundaries between the regions are given by a mole ratio of H_2O_2 to H_3PO_4 ($m{\cdot}r$) of about 2.3 and a mole fraction of H_2O ($m{\cdot}f$) of about 0.9 at room temperature. The activation energy in diluted solutions: regions a, $m{\cdot}r \lesssim 2.3$ and $m{\cdot}f \gtrsim 0.9$; and d, $m{\cdot}r \gtrsim 2.3$ and $m{\cdot}f \gtrsim 0.9$, is independent of crystallographic orientation. The rate-limiting process is determined as the adsorption of minority reactant in a solution, that is H_2O_2 in region a and H_3PO_4 in region d. We confirmed that the solutions in region a were useful for slow, stable, and accurate GaAs etching.

The rate-limiting process is the surface reaction, such as dissolution of oxidized products in concentrated solutions: in region c, $m{\cdot}r \gtrsim 2.3$ and $m{\cdot}f \lesssim 0.9$. A solution composition in this region c is useful for crystallographic etching. The etching rate is affected by the surface activities.

Table I. Summary of the experiments in Fig. 7 and 8

Region	a	b	c	d
H_2O_2/H_3PO_4 Mole ratio	$\lesssim 2.3$	$\lesssim 2.3$	$\gtrsim 2.3$	$\gtrsim 2.3$
H_2O Mole frac.	$\gtrsim 0.9$	$\lesssim 0.9$	$\lesssim 0.9$	$\gtrsim 0.9$
Depth *vs.* time	$\propto t$	$\propto t^{1/2}$	$\propto t$	$\propto t$
Ea (surf. orient.)	Ind.	Dep.	Dep.	Ind.
Rate-limiting process	H_2O_2 adsorption	H_2O_2 diffusion	Surface reaction	H_3PO_4 adsorption
Useful for	Accurate reproducible slow etch	Sub. surface treatment	Preferential etching	—

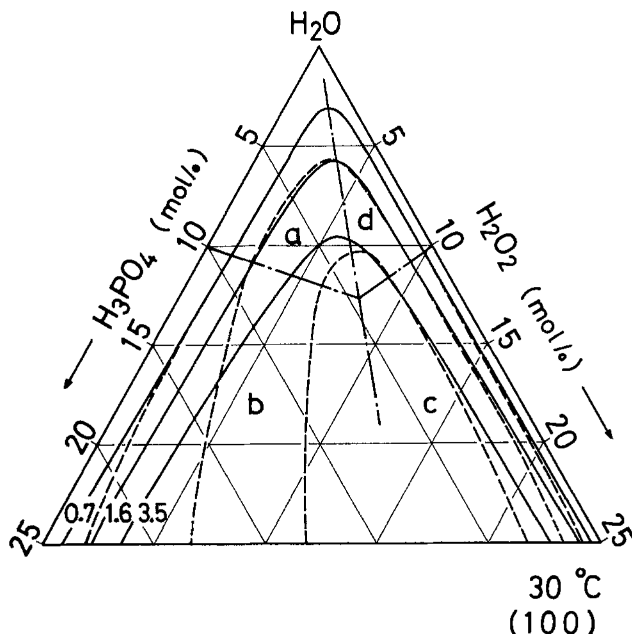

Fig. 9. Comparison between the calculated (solid lines) and the experimental (dashed lines) results on etching rate as a function of composition of solution. Compositions are expressed by mole percent. (Curve fitting was carried out using Eq. [2].)

Acknowledgment

We wish to thank Miss I. Sugawara for her assistance throughout these experiments. We also express our appreciation to Mr. T. Yamada, Dr. K. Morizane, and Messrs. M. Inoue and H. Kawai for their valuable discussion.

Manuscript submitted Sept. 12, 1977; revised manuscript received April 3, 1978. This was Paper 90 presented at the Philadelphia, Pennsylvania, Meeting of the Society, May 8-13, 1977.

Any discussion of this paper will appear in a Discussion Section to be published in the June 1979 JOURNAL. All discussions for the June 1979 Discussion Section should be submitted by Feb. 1, 1979.

Publication costs of this article were assisted by Sony Corporation.

REFERENCES

1. R. A. Logan, B. Schwartz, and W. J. Sundburg, *This Journal*, **120**, 1385 (1973).
2. D. L. Rode, B. Schwartz, and J. V. DiLorenzo, *Solid-State Electron.*, **17**, 1119 (1974).
3. J. C. Verplanke and R. P. Tijburg, *This Journal*, **124**, 802 (1977).
4. T. Ambridge and M. M. Faktor, *Inst. Phys. Conf.*, **Ser. 24**, 320 (1975).
5. C. A. Liechti, *IEEE Trans. Microwave Theory Tech.*, **mtt-24**, 279 (1976).
6. D. W. Shaw, *This Journal*, **113**, 958 (1966).
7. S. Iida and K. Ito, *ibid.*, **118**, 768 (1971).

Improved Theoretical Predictions for the Steam Oxidation of Silicon at any Elevation

Don L. Kendall,* Marcelo García C., and Mariano Aceves

Instituto Nacional de Astrofísica, Optica y Electrónica, Puebla, Puebla, Mexico

ABSTRACT

The steam oxidation of {111} Si at an altitude of 2160m is studied between 800° and 1200°C. The oxidation time to obtain a given thickness is shown to be 30% longer than that required near sea level. The data are in general agreement with the theoretical formulation of Deal and Grove (1) who showed that the oxide thickness X in μm could be related to the time of oxidation t in minutes by the expression $X^2 + AX = Bt$ for oxidation in steam. It is found that this expression is valid over a wide range of temperature and pressure for values of $A = 6.2 \times 10^{-6} \exp(1.16 \text{ eV/kT})$ and $B = 6.7(P/760) \exp(-0.776 \text{ eV/kT})$, where A is in μm, B is in μm^2/min, and P is in Torr. These values lead to thickness corrections of about 10% at 900°C and 6% at 1000°C as compared to the original formulation of Deal and Grove.

The work of Deal and Grove (1) on the oxidation of silicon in dry and wet oxygen is widely accepted as the standard at atmospheric pressure at sea level, namely 760 Torr. We have repeated these experiments over a wide range of temperatures for steam oxidation at an altitude of 2160m where the atmospheric pressure is only 586 Torr.

As expected, the same type of behavior is observed in these experiments as in those of Deal and Grove; namely the thickness is proportional to time at short times and to the square root of time at long times. However, by obtaining data over a wide range of temperatures, we show that the mathematical predictions of Deal and Grove are not precise enough to allow extrapolation to temperatures below about 1050°C.

In view of the importance of obtaining precise thickness estimates over a wide range of temperatures, for example, for computer-aided process simulations, we have calculated new activation energies and pre-exponentials for the steam oxidation of silicon. By suitable adjustment of the pre-exponentials, these expressions can be used at any altitude and with any value of atmospheric pressure.

Key words: silicon, steam oxidation, reduced pressure, process control.

Experimental

Chemically polished silicon slices grown by the Czochralski method were used in these experiments. They were n-type, the resistivity was 5 Ω-cm, and the orientation was {111}.

The silicon slices were placed horizontally on a quartz boat during the oxidation. Steam was provided to the slices by boiling deionized water. Condensation in the connecting tubing was avoided by wrapping the tubing with heating tape. The laboratory is in Tonantzintla, Puebla, near the city of Puebla, Mexico, where the altitude is approximately 2160m. The atmospheric pressure at this altitude is 586 Torr.

The day-to-day variation in pressure was typically 1-3 Torr, which is too small to be of significance in these experiments. The boiling point of water at this altitude is 92.9°C.

Incidentally, in this work no distinction is made between steam oxidation and oxidation in wet oxygen, since Deal and Grove found little difference in their data whether oxygen or argon was bubbled through 95°C water, therefore implying that the oxidizing species is water. In addition, they found that their data after suitable adjustment to 760 Torr was in good agreement with the data of Flint (2), using atmospheric steam oxidation.

The oxide thicknesses were estimated by comparing the colors of the films to the color descriptions given by Burger and Donovan (3). This method is precise to about 0.005-0.02 μm, depending on which range of thickness is being studied. It should be noted that the data of Deal and Grove should be more accurate than ours at thicknesses below 0.3 μm. They used an interferometric method and hence their data below 0.2 μm are believed to be accurate to about 0.0025 μm. We have assumed that their stated oxidation times are also reasonably precise. The latter comment regarding oxidation time is not trivial at times between 2 and 10 min. However, such times can be meaningful if a low mass boat is used, or better yet if the slices are inserted into the furnace without a boat.

Before concluding this discussion, the assumptions inherent in the determination of thickness by the colorimetric method should be discussed. The colorimetric method depends heavily on the color descriptions of Ref. (3). The present work also depends on the refractive index and the density of the oxide film remaining constant to within at least 1% for steam oxidations between 800° and 1200°C. The water content in the SiO_2 films might be thought to vary measurably over such a temperature range and therefore the density and refractive index also. However, Hetherington and Jack (4) show that neither parameter suffers large changes for considerable variations in water content. For example, they found the density of "wet" vitreous SiO_2 (containing almost $10^{20}/cm^3$ of water) to be 2.197 and for "dry" vitreous SiO_2 (with less than $10^{18}/cm^3$ water) to be 2.203. Furthermore, they found the refractive index at a wavelength of 0.5893 μm to be 1.4584 in wet SiO_2 and 1.4582 in dry SiO_2. In any case, Moulson and Roberts (5) showed that the solubility of water in vitreous SiO_2 was essentially constant over the temperature range 900° to 1200°C.

The data of Fig. 1 were obtained by careful comparison between samples oxidized at various temperatures and times. In analyzing the data we have made use of both our data and the data of Deal and Grove. The latter data was taken at a pressure of 640 instead of the 586 Torr typical of our altitude, so we have increased their oxidation times by the factor 640/586. In addition, we have taken the liberty of adjusting the 920°C data of Deal and Grove to 900°C so we could make direct comparison with our data. These adjustments were made using our theoretical curves at 900° and 920°C. In the section to follow an additional set of oxidation experiments at 898°C is described in which oxide thicknesses were measured using both interferometric and colorimetric methods.

Discussion

The theory of Deal and Grove for the oxidation of silicon is well described in their article (1) and we will only summarize the points relevant to this work. They establish that the oxide growth proceeds from the oxide-silicon interface rather than the oxide-vapor interface, and hence is dependent on the diffusion of an oxidizing species through the growing oxide film. In the presence of pure dry oxygen, the diffusing species is evidently the molecule O_2. This model is supported by the similarity between the the temperature dependence of 1.24 eV for the rate constant in the parabolic region and the literature value (5) of 1.17 eV for the activation energy for the diffusion of oxygen in fused silica.

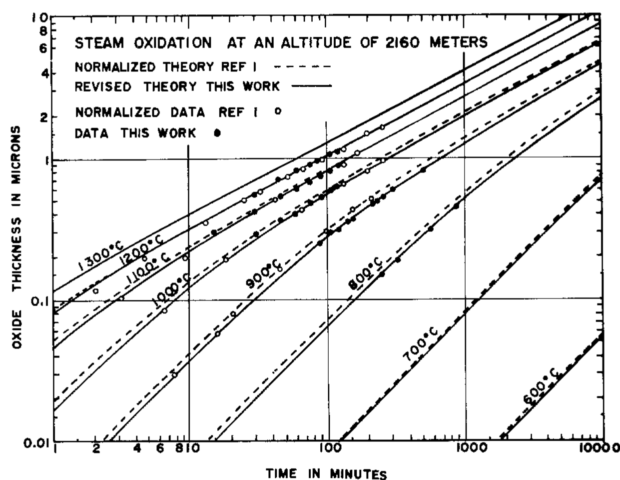

Fig. 1. Combined steam oxidation data of this work at an altitude of 2160m and that of Deal and Grove adjusted to the equivalent pressure of 586 Torr along with the revised theoretical formulation for oxide thickness as a function of oxidation time at various temperatures. The 920°C data of Deal and Grove has also been adjusted to 900°C for purposes of comparison.

Similarly, during steam oxidation, Deal and Grove found that the parabolic (diffusion limited) rate constant had a temperature dependence of 0.707 eV. The literature value (5) of 0.794 eV for the activation energy of diffusion of H_2O through fused silica is not inconsistent with this value. In this work the parabolic constant gives an activation energy of 0.776 eV. This close agreement with the diffusion data for water in SiO_2 gives even stronger support to such a model.

The general expression found by Deal and Grove for the steam oxidation of silicon is

$$X^2 + Ax = Bt \quad [1]$$

where X is the oxide thickness, t is the time of oxidation, and A and B are constants that depend on temperature. At small values of X and t, this reduces to the linear expression

$$X = (B/A)t \quad [2]$$

At large values of X and t, Eq. [1] becomes quadratic, namely

$$X^2 = Bt \quad [3]$$

In addition, the model suggests that A is independent of partial pressure of the oxidizing species and that B is directly proportional to the partial pressure. Note that Bt appears as a simple product in Eq. [1]. Thus at a given temperature, if the pressure is reduced, the constant B is reduced proportionally. Further, in order to obtain an equivalent value of X at the reduced pressure, one must increase t proportionally so that the product Bt remains constant. This is obvious in the linear Eq. [2] above, but can also be shown to be true for Eq. [1] and [3]. As an example of this behavior, one can calculate the time to grow a given thickness oxide in Tonantzintla, Puebla in Mexico, as compared to the time required at sea level. The time is increased by the reciprocal ratio of the atmospheric pressures, namely 760/586 = 1.297, in agreement with the observation that it must be 30% larger to grow a given thickness at the higher altitude. As a corrollary, one can predict the times required to grow equivalent thicknesses at sea level from the data of Fig. 1 by merely shifting all of the

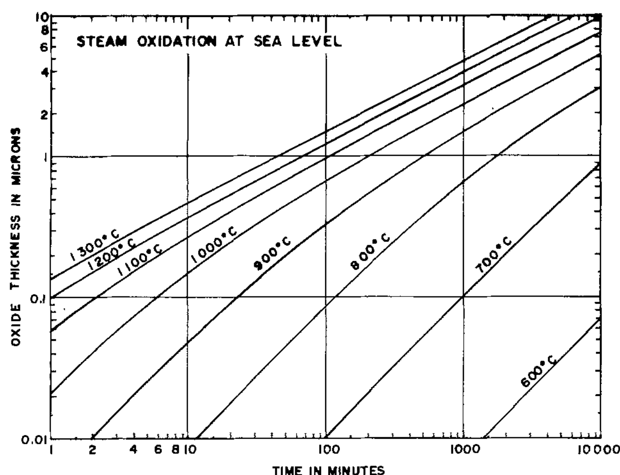

Fig. 2. The expected thickness of an oxide film on silicon grown in steam at sea level at various temperatures using the revised theoretical predictions of this work.

curves to shorter times by the factor of 1.297. This is done in Fig. 2 for purposes of reference for those working at or near sea level.

We have done a least squares analysis on the combined data of this work and that of Deal and Grove. To find the value of A and B at a given temperature, Eq. [1] can be rewritten in the form

$$X = B(t/X) - A \quad [4]$$

Thus in a graph of X *vs.* t/X, B is the slope of a straight line and $-A$ is the intercept with the X axis. The constant B is typically more precise than A since small variations in the slope B cause relatively large variations in the intercept $-A$. In order to fit the combined data over the wide temperature range of 800° to 1200°C we have chosen to exclude the 920°C data of Deal and Grove. We will explain this later. We also found it necessary to give double weight to the data points of Deal and Grove at short times at the temperatures of 1000°, 1100°, and 1200°C. Thus we give double weight to the data points at each of these temperatures when the oxide thicknesses are 0.2 μm or less. As discussed earlier, due to the interference method of measurement used by Deal and Grove, these data points should be quite accurate. In addition, however, these data points are critical in the determination of the constant A. The data at longer times do a credible job of determining the parabolic rate constant B, but it is the data at short times that gives the additional precision to the slope B needed to give an accurate value for the intercept $-A$. It should also be noted that the data in the parabolic region (long times), in addition to being less precise on average, are heavily over-represented at these three temperatures as compared to the data for shorter oxidation times.

Using the above method of weighting in a standard least squares analysis program, the values of A and B shown in Table I were determined at various temperatures. A further least squares analysis of the logarithms of these constants as a function of T^{-1}

Table I. Rate constants for the steam oxidation of silicon at an atmospheric pressure of 586 Torr. The calculated values of A and B are from Eq. [5] and [6], where A is in μm and B is in μm²/min

T (°C)	A (exp.)	A (calc.)	B (exp.)	B (calc.)
800	1.8254	1.7617	0.00118	0.00118
900	0.6025	0.6042	0.00235	0.00241
1000	0.2372	0.2451	0.00455	0.00440
1100	0.1025	0.1134	0.00723	0.00736
1200	0.0645	0.0583	0.01146	0.01149

using single weighting gave the following values for A and B at a pressure of 586 Torr

$$A = 6.2 \times 10^{-6} \exp(1.16\ \text{eV}/kT) \quad [5]$$

$$B = 5.2 \exp(-0.776\ \text{eV}/kT) \quad [6]$$

where A has units of μm and B has units of μm²/min. In this analysis the values of the correlation coefficient r were 0.998 for A and 0.9997 for B. These values are very close to unity, therefore showing that the logarithmic dependence of both A and B on T^{-1} is quite certain, with the precision of B being especially high on such a scale.

For purposes of comparison, the values chosen by Deal and Grove (1) (after adjustment to a pressure of 586 Torr) are shown as A^1 and B^1 below

$$A^1 = 2.4 \times 10^{-6} \exp(1.258\ \text{eV}/kT) \quad [7]$$

$$B^1 = 4.0 \exp(-0.707\ \text{eV}/kT) \quad [8]$$

Thus the activation energies for A and B in the revision, Eq. [5] and [6], differ by 8-9% from those of Ref. (1). However, the activation energy for the revised linear constant B/A of 1.936 eV is in good agreement with the value 1.965 eV obtained by Deal and Grove.

Finally, using the formulation of this work in Eq. [1], a general expression for the oxide thickness at any value of atmospheric pressure (or vapor pressure of water) can be obtained from Eq. [5] and [6] using the following expressions for A and B

$$A = 6.2 \times 10^{-6} \exp(1.16\ \text{eV}/kT) \quad [9]$$

$$B = 6.7(P/760) \exp(-0.776\ \text{eV}/kT) \quad [10]$$

where P is the atmospheric pressure in Torr (if the water is allowed to reach the boiling point) or is the vapor pressure of the water at the control temperature of the water, and A and B have the same units as before.

The theoretical curves shown in Fig. 1 were calculated using Eq. [1] with the parameters A and B calculated from Eq. [5] and [6]. They are seen to be in very good agreement with the experimental data of this work at all temperatures, as well as with the data of Deal and Grove at 1000°, 1100°, and 1200°C. The data of Deal and Grove in the range of 900°C are in poor agreement with these predictions, as well as with our data. Taking all of the above into account, we are led to the conclusion that the great majority of the experimental data in both sets of work is correct. However, the five upper data points of Deal and Grove at 920°C (adjusted here to 900°C) evidently suffered from some experimental problem. For example, the furnace temperature may have been inadvertently about 10°C too high. However, this is perhaps less likely than another temperature-control problem, namely the control of the water temperature at 95°C. If during these five runs, the water temperature were allowed to reach 100°C, the vapor pressure of the water in the oxidation furnace would be raised from 640 to 760 Torr. As discussed earlier, such a change in vapor pressure can be accounted for by shifting the data points to longer times by the ratio of 760/640 = 1.19. Such a shift brings these points almost exactly into line with our data. However, it is important to note that the revision in the parameters suggested here does not rest on the experimental data in one narrow temperature range. The revised theoretical predictions are also in much better agreement with both sets of data at all thickness values at 1000° and 1100°C, as well as the new data at 800° and 900°C. The 800°C data are especially valuable in establishing the linear constant B/A which is important for extrapolation to lower temperatures. On the other hand, the 900°C data are crucial to establishing both the temperature dependence of the constant B in the quadratic range of behavior, and that of B/A in the linear range.

Table II. Predicted oxide thicknesses after 100 min compared to the original formulation of Deal and Grove (at 586 Torr). The values also apply to 130 min at 760 Torr

T (°C)	X (this work) (μm)	X^1 (Deal and Grove) (μm)	$(X - X^1)/X$ (%)
700	0.00790	0.00828	−4.8
800	0.0646	0.071	−9.9
900	0.274	0.302	−10.2
1000	0.552	0.585	−6.0
1100	0.803	0.825	−2.7
1200	1.044	1.045	−0.1
1300	1.286	1.261	+2.0

The difference between the values of oxide thickness predicted by the two formulations at a time of 100 min at various temperatures is shown in Table II. For this particular period of oxidation, the maximum difference between the two formulations is about 10% and it occurs between 800° and 900°C. Deal (6) has also recently observed variations of the order of 10% between the experimental results and the earlier predictions at 900°C. It will be appreciated that the differences between the two predictions are not trivial in the semiconductor device fabrication business.

Finally, as a check on the accuracy of the predictions above, and as confirmation of some of the color descriptions in Ref. 3, it was decided to make independent measurements of the thicknesses obtained in the critical range of 900°C, since this is where the data of Deal and Grove are believed to be the least precise. This was done using both the optical-interference method of Tolansky (7) and the colorimetric method. In these experiments, windows of 200 μm width were opened in the oxides using standard photolithographic methods. These slices were then coated with an opaque layer of silver (approximately 0.3 μm). A thin microscope slide was then coated with a semitransparent film of silver until the transmission was reduced to 10-15%. This microscope slide was then placed in contact with the previously silvered slice which contained the etched windows. The combination was viewed by reflected light from a beam-expanded He-Ne laser projected through a vertical illuminator of a metallurgical microscope. When the slide was suitably adjusted on the slice surface, the interference fringes could be made approximately perpendicular to the etched windows. The photographic width of the fringes was typically λ/100 under these conditions and the center of the fringe could easily be located with a precision of about λ/500, or about 0.0012 μm. However, due to local flatness variations on these slices, the oxide thickness measurements are estimated to be precise to only about 0.0025-0.0050 μm.

The results of these experiments, along with estimates based on color, as well as predictions based on Eq. [1], [9], and [10], are shown in Table III along with the error between the predicted and measured thicknesses. The agreement between the interferometric and colorimetric methods is very good. Furthermore, the measured values are also in excellent agreement with the predicted values. On the basis of these results, as well as similar interference measurements made at 800° and 1100°C, we expect that the predicted thicknesses using Eq. [1], [9], and [10] should be precise to at least 3% over a wide range of temperatures (800°-1300°C), times, and atmospheric pressures and/or water vapor pressures.

Table III. Thickness measurements of films grown at 898°C using interference method ($X_{int.}$), colorimetry (X_{color}), and thickness calculated ($X_{calc.}$) from Eq. [1], [9], and [10] for a pressure of 586 Torr. Colorimetry is used only above 0.2 μm. The error calculations make use of $X_{int.}$ except for the 520 min sample, for which no interference measurement was made

Time (min)	$X_{int.}$ (μm)	X_{color} (μm)	$X_{calc.}$ (μm)	$\Delta X/X_{calc.}$ (%)
10	0.0365	—	0.0368	−0.8
30	0.101	—	0.100	+1.0
60	0.170	—	0.180	−5.6
120	0.316	0.31	0.310	+1.9
240	0.520	0.51	0.510	+2.0
520	—	0.84	0.848	−0.9
557	0.878	0.88	0.886	−0.9

Conclusion

In this work, the general behavior of the theory of Deal and Grove for the oxidation of silicon has been very well substantiated. The predicted pressure dependence was found to explain the 30% increase in time required to grow a given oxide thickness at an altitude of 2160m. The extensive data taken at 800° and 900°C were used to make important corrections to the original theoretical parameters of Deal and Grove. For Si of {111} orientation, these corrections lead to thickness predictions that differ by 6-10% at 1000° and 900°C, respectively, as compared to the original formulation of Deal and Grove. Similar corrections must be made in laboratories nearer sea level.

Acknowledgments

The authors would like to express their appreciation to Dr. Jorge Agraz and Ramón Nuño Z. for starting this work, and to Consejo Nacional de Ciencia y Tecnologia (CONACYT) of Mexico for supporting it. Thanks are also due Dr. David Stevenson of Stanford University for numerous helpful suggestions during the writing of the manuscript.

Manuscript submitted Oct. 20, 1977; revised manuscript received May 5, 1978.

Any discussion of this paper will appear in a Discussion Section to be published in the June 1979 JOURNAL. All discussions for the June 1979 Discussion Section should be submitted by Feb. 1, 1979.

REFERENCES

1. B. E. Deal and A. S. Grove, J. *Appl. Phys.*, **36**, 3770 (1965).
2. P. S. Flint, Abstract 94, p. 222, The Electrochemical Society Extended Abstracts, Spring Meeting, Los Angeles, Calif., May 6-10, 1962.
3. R. M. Burger and R. P. Donovan, "Fundamentals of Silicon Integrated Device Technology," Vol. I, Prentice-Hall, Englewood Cliffs, N.J. (1967).
4. G. Hetherington and K. H. Jack, *Phys. Chem. Glass*, **3**, 129 (1962).
5. A. J. Moulson and J. P. Roberts, *Trans. Faraday Soc.*, **57**, 1208 (1961).
6. B. E. Deal, Private communication, Fairchild Semiconductor.
7. S. Tolansky, "Multiple Beam Interferometry," Oxford Press, London (1948).

Implanted As Redistribution during Annealing in Oxidizing Ambient

Kunio Nakamura and Mototaka Kamoshida

Nippon Electric Company, Limited, IC Division, 1753 Shimonumabe, Nakahara-ku, Kawasaki, 211 Japan

ABSTRACT

Carrier distribution in 150 keV, $10^{16}/cm^2$ $^{75}As^+$-implanted Si layer after steam oxidation in the 850°-1000°C temperature range has been measured by the spreading-resistance probe technique. When the oxidation temperature is below 1000°C, the carrier distribution shifts toward the surface at the initial stage of oxidation due to the Si-SiO_2 interface movement, and sheet resistance increases correspondingly. After the initial stage, the carrier distribution then spreads gradually, corresponding to a slowing down in the oxidation rate. In contrast, when the oxidation temperature is above 1000°C, As diffusion effects dominate, and the carrier distribution spreads into Si and sheet resistance decreases monotonically with increasing oxidation time. These behaviors have been explained by simple numerical calculations.

Implantation of As ions has been extensively used for formation of source and drain regions in short-channel MOSIC's (1) or emitter regions in shallow junction bipolar IC's (2). Generally, a subsequent annealing process is required after implantation to recover crystallinity. This annealing process is often carried out in an oxidizing atmosphere to allow the growth of a passivating oxide layer simultaneously. In regard to implanted As redistribution during oxidation, Fair and Tsai reported detailed data at temperatures above 1000°C (3), however, there is little data reported in the case where temperatures are below 1000°C. Muller *et al.* only reported backscattering data after steam oxidation at 850°C (4).

Kudoh *et al.* recently developed a simple method for profiling the impurities within a shallow p-n junction by spreading-resistance probe technique (5). In the present study, this newly developed technique has been applied to obtain carrier distributions in $^{75}As^+$-implanted layers after steam oxidations at temperatures below 1000°C and thus to provide processing data for short-channel MOS or shallow junction bipolar IC's.

Experimental Procedure

Polished p-type silicon wafers oriented nearly in the <100> direction with 1.4Ω cm resistivity were used as starting materials. Arsenic ($^{75}As^+$) implantations were performed at 150 keV with a dose of $1 \times 10^{16}/cm^2$. The wafers were initially at room temperature. Thermal oxidations were performed in steam at 850°, 900°, 950°, and 1000°C for time periods ranging from 15 min to 8 hr. The thicknesses of the oxides formed on the implanted layers were determined by ellipsometry measurements. Carrier distributions after oxidation were measured using the spreading-resistance probe technique (5). Irvin's curve was used to convert the resistivity into the carrier concentration (6). Sheet resistances were also measured after removal of the oxide layers by using the four-point probe technique.

Results and Discussion

Figure 1 shows thickness of SiO_2 formed on the $^{75}As^+$-implanted layer during steam oxidation as a function of oxidation time at each temperature. Curves are plotted in log-log scale. It is evident that oxide growth can be divided into two stages. At the initial stage of oxidation, the slope of each growth curve is steeper than 0.5. The slopes become larger and also the periods of the initial stage increase at lower temperatures. After a certain period, oxide growth reaches the second stage, where diffusion effects dominate and growth is governed by parabolic law.

Key words: arsenic ion implantation, arsenic redistribution during oxidation, profile measurement, spreading-resistance probe.

Figure 2 shows the carrier distribution measured by the spreading-resistance probe technique after oxidation at 850°, 900°, 950°, and 1000°C. Figure 2(A) shows the carrier distribution after oxidation at 850°C. The calculated As distribution just after implantation is also shown in this figure, assuming a Gaussian distribution using projected range and projected standard deviation reported by Gibbons *et al.* (7). After 15 min oxidation, the carrier distribution spreads about 500Å. This might be due to the enhanced diffusion caused by ion-implantation-induced damage or the effect of As-diffusion tail (8). After this initial stage, the carrier distribution becomes shallower with increasing oxidation time. Diffusion effects of As can be almost neglected at 850°C; therefore, As distribution shifts toward the surface due to the Si-SiO_2 interface move-

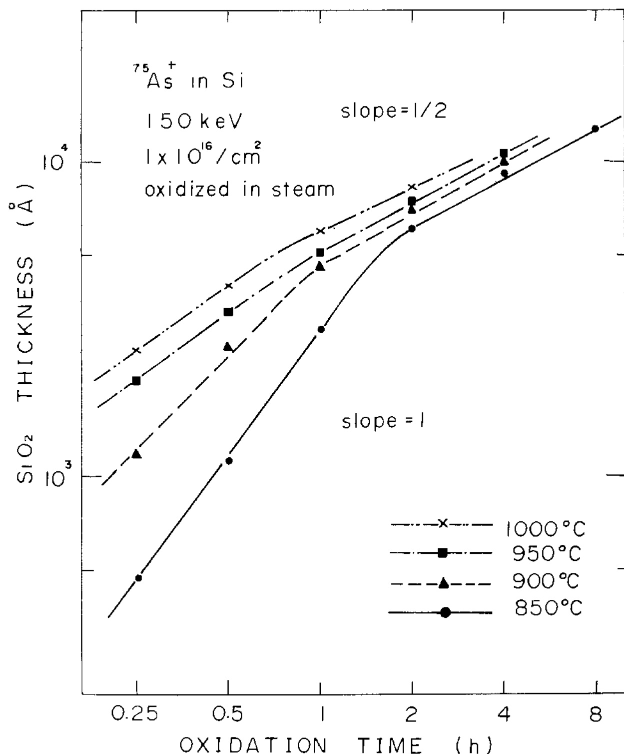

Fig. 1. Thickness of SiO_2 formed on the $^{75}As^+$-implanted layer during steam oxidation at 850°, 900°, 950°, and 1000°C as a function of oxidation time.

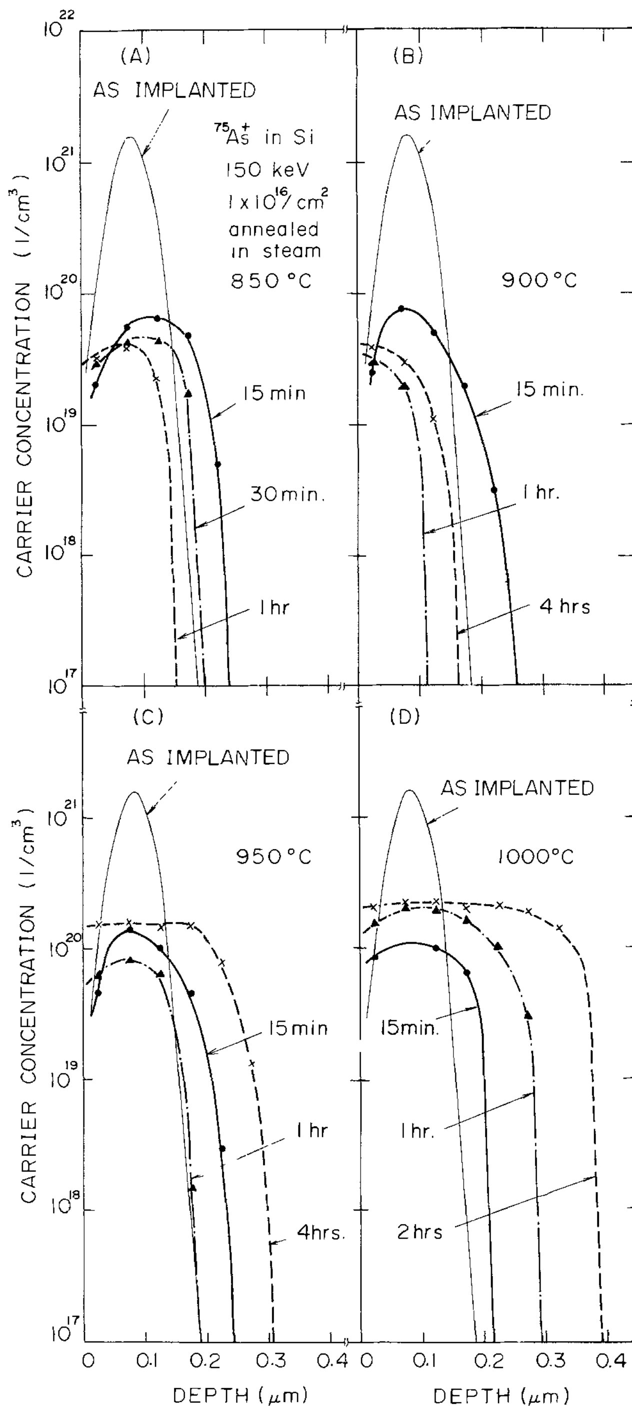

Fig. 2. Carrier distribution measured on the $^{75}As^+$-implanted layer using the spreading-resistance probe technique after oxidation at (A) 850°; (B) 900°; (C) 950°; and (D) 1000°C.

ment. In fact, during steam oxidation for between 15 and 30 min, the carrier distribution shifts toward the surface by about 800Å, which corresponds to the thickness of Si consumed during oxidation. After oxidation for 2 hr, the carriers seem to disappear according to spreading-resistance probe measurement. However, if one takes into account the fact that the segregation coefficient of As at $Si-SiO_2$ interface is quite large (3), this apparent As disappearance is not due to As segregation into the growing SiO_2 film, but to As pileup at the $Si-SiO_2$ interface. Muller *et al.* reported that the pileup region is about 200Å thick and As in this region is highly unsubstitutional (4). Therefore, the As in the pileup region is undetectable by spreading-resistance probe measurement since the pileup region depth is shallower than the 250Å resolution which corresponds to the minimum probe pitch.

At 850°C, the slope of the oxide growth curve is more than 1 as shown in Fig. 1. This might be due to the fact that interface reaction is enhanced with time by the accumulation of As in the $Si-SiO_2$ interface as described above.

Figure 2(B) shows carrier distribution after oxidation at 900°C. The carrier distribution shifts toward the surface for oxidation time up to 1 hr and then spreads gradually into the silicon substrate. From the data in Fig. 1, one can determine that oxide growth rate at 900°C slows down after 1 hr. Therefore, the gradual spread in carrier distribution after 1 hr is due to the fact that As diffusion velocity exceeds the $Si-SiO_2$ interface moving velocity.

Figure 2(C) shows carrier distribution after oxidation at 950°C. The behavior of carrier distribution after oxidation can be explained qualitatively according to the same reasons as were pertinent for Fig. 2(B).

Figure 2(D) shows carrier distribution after oxidation at 1000°C. The diffusion of As is prominent even for short oxidation time. The carrier distribution spreads deeper monotonically with increasing oxidation time. Carrier distribution after oxidation for 2 hr shows a typical feature of As-diffused layer with an abrupt p-n junction. The maximum carrier concentration measured here is about $3 \times 10^{20}/cm^3$, which agrees with the result reported by Fair and Tsai (3).

Figure 3 shows junction depth obtained from carrier distribution measurement as a function of oxidation time. For oxidation temperatures below 950°C, the junction depth decreases during the initial oxidation stage and thereafter increases gradually with time in periods corresponding to the slowing down of the oxidation rate. On the other hand, above 1000°C, junction depth increases monotonically with increasing oxidation time.

Figure 4 shows sheet resistance as a function of oxidation time. The results in this figure closely correspond to the results described above. Below 950°C, sheet resistance increases with increasing oxidation time, corresponding to the decrease in junction depth, and it reaches a maximum value when junction depth reaches a minimum. Thereafter, the sheet resistance decreases gradually. On the other hand, above 1000°C, the sheet resistance decreases monotonically with oxidation time, corresponding to the monotonic increase in junction depth.

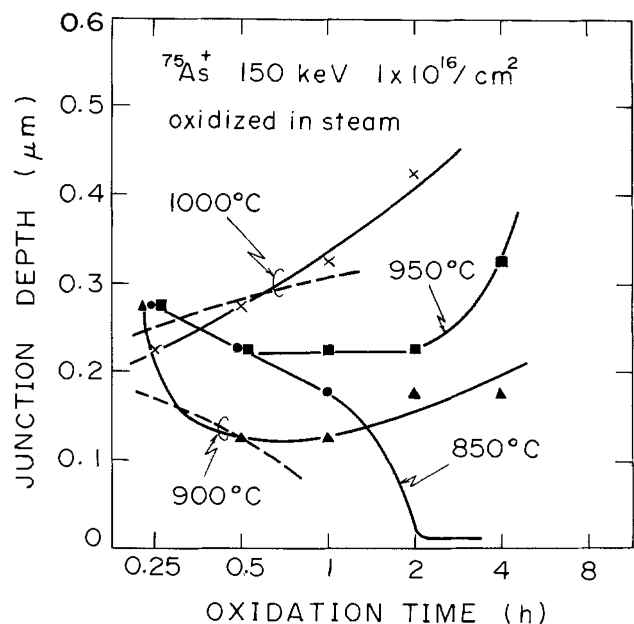

Fig. 3. Measured (solid line) and calculated (dashed line) junction depth as a function of oxidation time at 850°, 900°, 950°, and 1000°C.

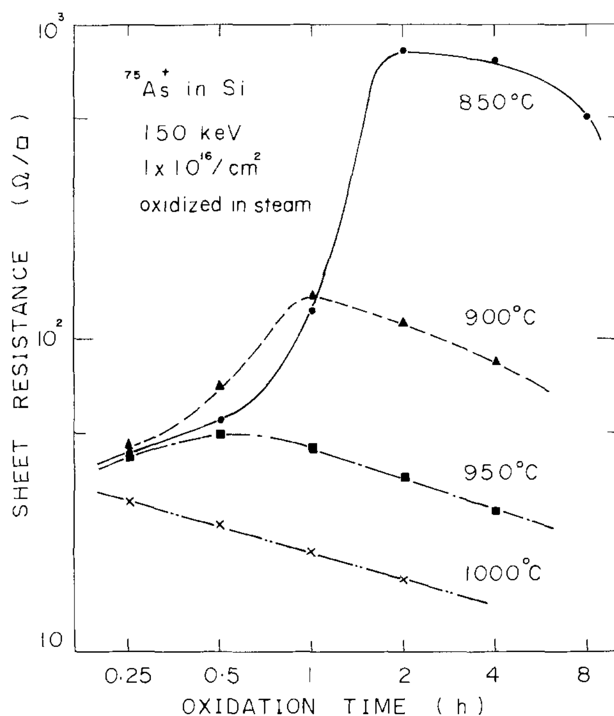

Fig. 4. Sheet resistance on the $^{75}As^+$-implanted layer after oxidation at 850°, 900°, 950°, and 1000°C as a function of oxidation time.

Results described above show that As carrier-distribution behavior depends on relative speed of As diffusion and $Si\text{-}SiO_2$ interface movement. To discuss the above results more quantitatively, diffusion equations were solved numerically. The diffusion equation in oxidizing ambient is expressed (9)

$$\frac{\partial}{\partial t} N(x,t) = \frac{\partial}{\partial x}\left[D \frac{\partial}{\partial x} N(x,t)\right] + \alpha \frac{dX}{dt} \frac{\partial}{\partial x} N(x,t)$$

and boundary condition is

$$D \frac{\partial}{\partial x} N(x,t)|_{x=0} = \left(\frac{1}{m} - \alpha\right) \frac{dX}{dt} N(0,t)$$

where the origin of the χ axis is the moving $Si\text{-}SiO_2$ interface, $N(x,t)$ is impurity concentration, D is diffusion coefficient, α is the ratio of the consumed Si thickness to the SiO_2 thickness during oxidation ($\alpha = 0.45$), X is the SiO_2 thickness, and m is the segregation coefficient. It is well known that the As diffusion coefficient depends on its concentration (3). In the present case, however, effective As diffusion coefficient data obtained from junction depth measurement by Murase *et al.* was used to simplify the calculation (10). In addition, the oxide growth rate was approximated by linear growth rate during oxidation, *i.e.*, dX/dt is constant. Their values were taken from the oxide growth curves in Fig. 1. The segregation coefficient obtained by Fair and Tsai ($m = 800$) was used (3). Initial As distribution was assumed to be Gaussian, using projected range and projected standard deviation reported by Gibbons *et al.* (7). The use of a Gaussian approximation does not necessarily give a precise profile where diffusional broadening does not wash out details of the initial profile. In the present case, junction depths calculated on the Gaussian approximation (no oxidation and no appreciable diffusion) are 0.22 μm, while including third-moment corrections yields 0.28 μm. The results, however, are qualitatively the same even if one takes into account third-moment corrections in the initial profile. Therefore, a Gaussian approximation was used for simplicity of the calculation. Calculations were performed by sectioning time and depth axes into equal intervals and by using a simple finite-difference method.

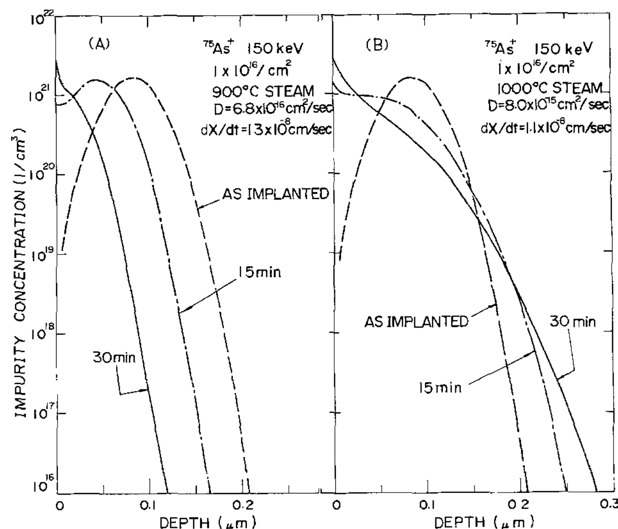

Fig. 5. Calculated distribution of As after initial oxidation stage at (A) 900°; and (B) 1000°C.

Figure 5(A) shows the calculated distribution after initial oxidation stage at 900°C. Values of the parameters used in the calculation are shown in the figure. It is evident that diffusion effect is almost negligible at this temperature, and As distribution shifts toward the surface due to the $Si\text{-}SiO_2$ interface movement during oxidation.

Figure 5(B) shows the calculated results at 1000°C. In contrast to the case of oxidation at 900°C, the diffusion effect can be observed. In both cases, As pileup at the $Si\text{-}SiO_2$ interface occurs. This is due to the fact that the As segregation coefficient is extremely high, and supports the speculation described in Fig. 2. Junction depth obtained from this calculation is shown in Fig. 3. Although good agreement was not obtained due to the rough approximation used, a general tendency in the initial stage of oxidation is evident.

Conclusions

Arsenic ions were implanted into Si and subsequent annealing was performed in an oxidizing ambient. The carrier distributions were measured by the newly developed spreading-resistance probe technique. When oxidation temperature is below 1000°C, As carrier distribution becomes shallower during the initial oxidation stage because the $Si\text{-}SiO_2$ interface moving speed is faster than the As diffusion speed. Thus, sheet resistance increases with increasing oxidation time. After this initial stage, the oxide growth rate slows down and As carrier distribution spreads. Sheet resistance then decreases correspondingly. On the other hand, when the temperature is above 1000°C, diffusion effects dominate and carrier distribution spreads into the substrate. Therefore, sheet resistance decreases with increasing oxidation time. These behaviors have been explained by simple numerical calculations. Above results provide information to design the As profile more precisely for shallow junction formation.

Acknowledgments

The authors wish to thank Drs. S. Tsuneki, M. Nakamura, and T. Okada for their continuous encouragement. The help by H. Muta and H. Okabayashi in ion implantation was invaluable.

Manuscript submitted Jan. 30, 1978; revised manuscript received May 1, 1978.

Any discussion of this paper will appear in a Discussion Section to be published in the June 1979 JOURNAL All discussions for the June 1979 Discussion Section should be submitted by Feb. 1, 1979.

Publication costs of this article were assisted by Nippon Electric Company, Limited.

REFERENCES

1. H. N. Yu, R. H. Dennard, T. H. P. Chang, C. M. Osburn, V. Dilonardo, and H. E. Luhn, *J. Vac. Sci. Technol.*, **12**, 1297 (1975).
2. R. S. Payne, R. J. Scavuzzo, K. H. Olson, J. M. Nacci, and R. A. Moline, *IEEE Trans.*, **ed-21**, 273 (1974).
3. R. B. Fair and J. C. C. Tsai, *This Journal*, **122**, 1689 (1975).
4. H. Muller, J. Gyulai, W. K. Chu, J. W. Mayer, and T. W. Sigmon, *ibid.*, **122**, 1234 (1975).
5. O. Kudoh, K. Uda, Y. Ikushima, and M. Kamoshida, *ibid.*, **123**, 1751 (1976).
6. J. C. Irvin, *Bell Syst. Tech. J.*, **37**, 711 (1958).
7. J. F. Gibbons, W. S. Johnson, and S. W. Mylroie, "Projected Range Statistics," Wiley, New York (1975).
8. F. N. Schwettmann, *Appl. Phys. Lett.*, **22**, 570 (1973).
9. T. Kato and Y. Nishi, *Jpn. J. Appl. Phys.* **3**, 377 (1964).
10. K. Murase, K. Saito, and H. Harada, in "Symposium on Ion Implantation," p. 35, The Institute of Physical and Chemical Research, Japan (1977) (Unpublished).

Analytic Study of the Si-B Phase When B_2O_3 Is Diffused in Si

E. Dominguez, E. Lora-Tamayo, and B. Blanchard

Research Semiconductor Laboratory, C.I.F.L. Torres Quevedo, C.S.I.C., Madrid-,6 Spain

and J. Bellanato

Instituto de Optica, C.S.I.C., Madrid-6, Spain

ABSTRACT

An investigation of the Si_xB_y compound formed when silicon is doped from B_2O_3 in the 950°-1100°C temperature range has been carried out. Depending on the composition, four main regions have been analyzed by different techniques: ionic analysis, x-ray diffraction, microsonde, electron diffraction, and infrared spectroscopy. Results showed that the Si-B phase crsytallizes on the cubic system with a 6.20Å parameter and the composition closely resembles SiB_5.

It is well known that the diffusion of impurities in silicon depends on the gas composition in the reactor, temperature, time of the diffusion, and on the initial resistivity of the sample.

Various authors have studied the diffusion of boron into silicon in an attempt to find an analytic law for the diffusion profile at temperatures ranging from 950° to 1200°C (1-7). Arai *et al.* (8) studied the interface reactions of B_2O_3-Si system and reported that the compound produced in the glass-silicon interface for high boron doping was SiB_4 and/or SiB_6, these compounds having been previously described in the literature (9-14). Recently, Moore *et al.* (15, 16), using standard B_2H_6 gas source, have investigated the distribution of B in SiO_2/Si with Auger electron spectroscopy. These authors found that the resulting film consisted of ~100Å B_2O_3 layer on a B-doped SiO_2 region separated from B-doped Si by a Si-B phase and this phase formed already at short deposition times, reaching a maximum B concentration of $(4 \pm 2) \times 10^{22}$ cm^{-3}. The width of the phase increased and grew into a lamellar structure, with the number and amplitude of lamellae depending on deposition time. Kiewit *et al.* (17) also investigated boron glass layers formed on silicon at high diffusion temperatures (1150°C). These authors also found an HF insoluble layer which was characterized as a Si-B phase according to Busen *et al.* (18) and by use of Auger electron spectroscopy they obtained the boron, silicon, and oxygen profiles.

In this paper we discuss the results of a study of the Si-B compound produced in the SiO_2/Si interface at 900°-1100°C by using B_2O_3 as diffusion source. In this study ionic analysis, x-ray diffraction, EDAX microsonde, electron diffraction, and infrared techniques were used in order to determine the structure and chemical composition of the compound.

Key words: B_2O_3-Si system, Si-B compounds, SiB_5, borosilicates, boron diffusion.

Experimental

Silicon used in this study was n-type and (111) surface oriented into which boron had been diffused. Samples were in the form of circular slices of 300 μm thickness and 37 mm diam.

Boron depositions were made in a ±0.5°C planar controlled furnace in the 900°-1100°C temperature range. The B_2O_3 diffusion source was of high purity (99.999) and was in an ultrapure (99.999) diffusion alumina boat at the same temperature as the silicon sample. In order to eliminate the oxygen in the reactor, a 10^{-3} mm Hg vacuum was pulled before the diffusion boat with the samples was introduced. The gas flow used was N_2 (99.999) with a water vapor content less than 5 ppm and an O_2 content less than 1 ppm. The flow rate was 0.7 liter/min.

The chemical composition measurement was made by means of ion analysis, where the primary beam consisted of Ar^+ ions with an energy of 5.5 keV and a current density of 1 μA/mm. The bombarded area was 1.5 mm diam and the analyzed one was 60 μm. Oxygen gas was introduced during the process to saturate the surface. Analyses were made by measuring the electric intensity of the B^{+11}, Si^{+30}, and O^{+17} ions.

In order to analyze the silicon on the different zones, an EDAX energy-dispersive x-ray analysis system attached to a Philips scanning electron microscope PSEM 500 was used. The sample was placed parallel to the incident beam which had a 3 keV energy.

The crystalline structure analysis was carried out with a Philips PW 1050 diffractometer using Ni-filtered Cu_α radiation (40 kV, 10 mA). In order to see a

possible structural difference between the substrate and the intermediate layer, transmission electron diffraction was also performed.

Transmission infrared measurements were made in pressed KBr disks using a Perkin-Elmer spectrophotometer, Model 457. The reflectivity curves were taken using a 30° fixed angle of incidence specular reflectance attachment. Some measurements were also made with an attenuated total reflectance (ATR) accessory.

Discussion and Results

In Fig. 1-3 and on a semilogarithmic scale, the boron and silicon concentrations *vs.* thickness are shown for three different samples studied by ionic analysis. Temperatures were 960°, 1000°, and 1100°C and the diffusion times 1200, 2350, and 345 min, respectively.

In Fig. 4 and for the 345 min, 1100°C diffused sample, the collected O^{+17} ionic intensity is plotted *vs.* depth on a semilogarithmic scale.

From the above graphics the existence of four main regions is deduced:

I $SiO_2 + B_2O_3$

II $Si_xB_yO_z$

III Si_uB_v

IV $Si + B$

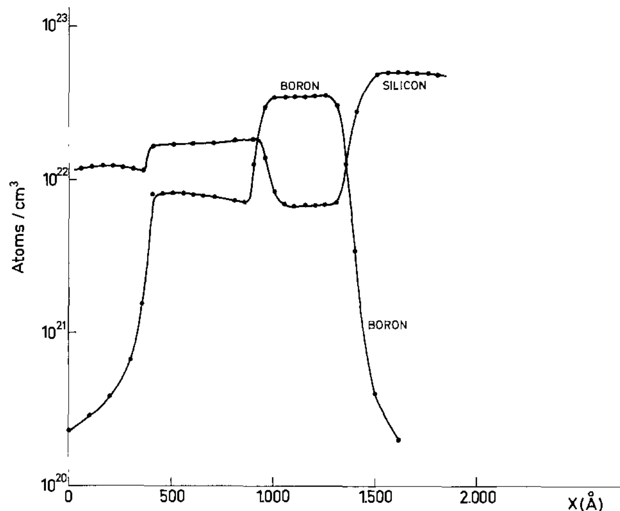

Fig. 1. Measured boron- and silicon-doping profiles in (111) surface-oriented silicon wafer after boron diffusion at 960°C for 1200 min.

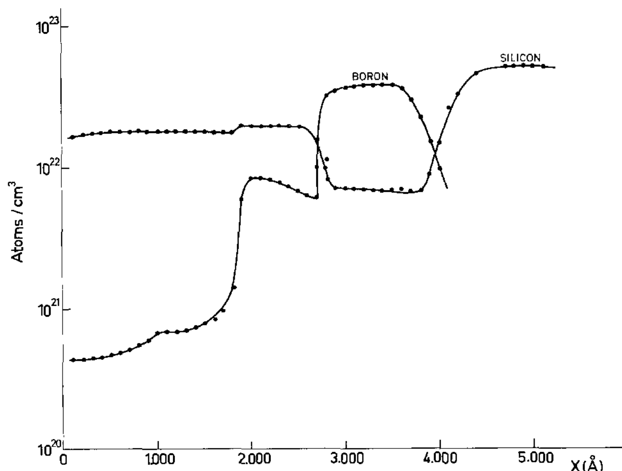

Fig. 2. Measured boron- and silicon-doping profiles in (111) surface-oriented silicon wafer after boron diffusion at 1000°C for 2350 min.

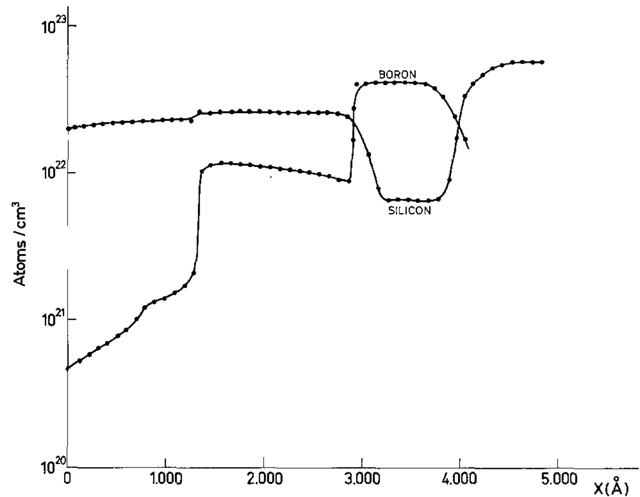

Fig. 3. Measured boron- and silicon-doping profiles in (111) surface-oriented silicon wafer after boron diffusion at 1100°C for 345 min.

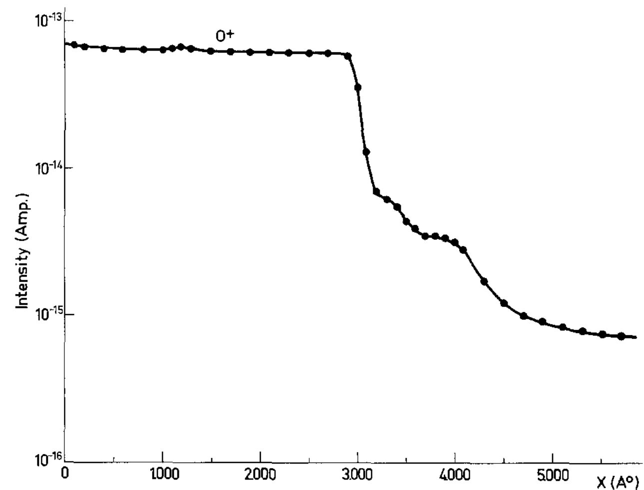

Fig. 4. O^{+17} ion intensity profile for the 345 min 1100°C diffused sample.

Table I shows the results obtained by means of the EDAX microsonde technique for three different zones, the first one comprising I and II obtained from ionic analysis. Silicon composition of zone III approximately corresponds to SiB_5.

Figure 5 shows the x-ray diffraction diagrams for three samples: a) Oxidized (111) surface-oriented sample. A wide band due to the SiO_2 is observed at $d(Å) = 10.8$; b) Boron diffused (in $N_2 + O_2$ atmosphere) (111) surface-oriented sample. Characteristic bands of the Si-B compound at $d(Å) = 6.10$ and $d(Å) = 6.20$ appear on the diagram; c) Boron diffused in N_2 atmosphere (100) surface-oriented sample. A peak at $d(Å) = 6.20$ is observed. The band decreasing is attributed to epitaxy in the (100) direction.

The Si-B layer insoluble in a HCl + HF mixture was studied by electron diffraction. Both the electron diffraction diagram and surface state micrograph are given in Fig. 6. Results reveal the existence of a crystalline compound where the growth has been rather homogeneous.

Table I. Percent silicon concentration *vs.* pure silicon

Sample	I + II	III	IV
S_1	88-42	35	*ca.* 100
S_2	88-42	36	*ca.* 100
S_3	88-42	35	*ca.* 100

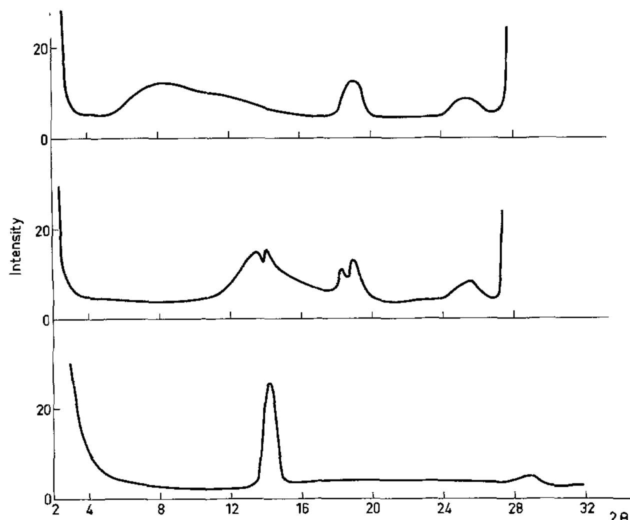

Fig. 5. X-ray diffraction diagrams. a) Oxidized in O_2 (111) surface-oriented sample; b) boron-diffused (in $N_2 + O_2$ atmosphere) (111) surface-oriented sample; c) boron-diffused in N_2 atmosphere (100) surface-oriented sample.

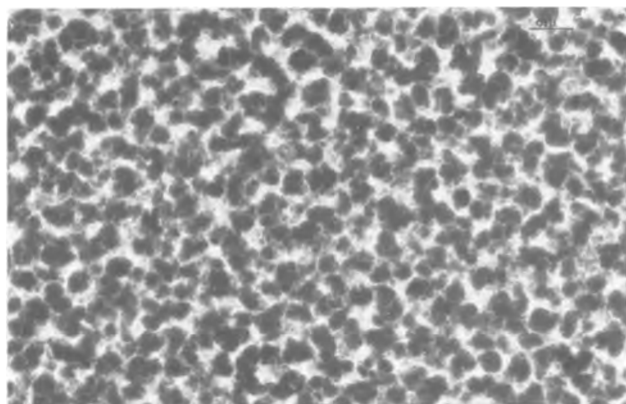

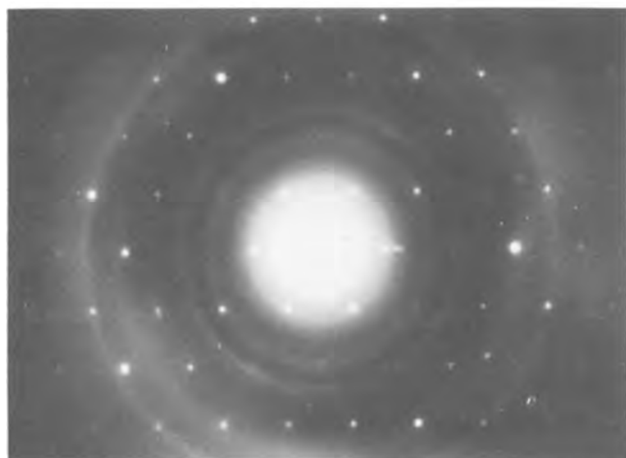

Fig. 6. Electron diffraction diagram and micrograph of Si-B compound.

Table II shows the crystallographic data corresponding to the diffraction diagram.

By use of the method given by Jamard *et al.* (19) the data of Table II are interpreted in terms of the Si-B phase having a cubic structure of 6.20Å parameter in agreement with the x-ray diffraction results. On the other hand, the x-ray and electron diffraction values measured in the present work do not coincide with the data of the literature for SiB_4 or SiB_6 (9-14).

The above results were confirmed by infrared spectroscopy as follows. Figure 7 shows the infrared absorption spectrum of powder obtained by light scraping from samples previously submitted to boron diffusion in nitrogen atmosphere for 20 hr. A complex absorption band is observed in the 9 μm region (1100 cm^{-1}) with maxima at 8.7 μm (1150 cm^{-1}), 9.1 μm (1100 cm^{-1}) and 9.35 μm (1070 cm^{-1}) which are related with Si-O vibrations. A second band centered at 7.25 μm (1380 cm^{-1}) points out to the existence of B-O bonds. A weaker band at 10.87 μm (920 cm^{-1}) might be due to Si-O-B bonds according to data of literature (20). Finally, the shoulder at 8.33 μm is attributed to O-H deformation vibrations of B-OH groups. Although the predominant bands of spectrum of Fig. 7 can be related with the compounds of the first and second layer as revealed by microsonde results, it must be borne in mind that the infrared spectrum of the insoluble compound produced in the B_2O_3-Si interface in our experiments must be similar to the spectrum of SiB_6 reported in the literature (21) and the characteristic bands could be overlapped by the stronger B-O and Si-O bands.

Table II. Crystallographic data for Si-B compound

d_{hkl} (A)	I	hkl
3.464	s	111
2.070	m	300
1.510	m	322
1.429	m	331
1.209	w	431
1.031	w	532
0.885	w	632

Abbreviations: s, strong; m, medium; w, weak.

The reflectance curves for oxidized (26 hr, 900°C), and oxidized (4 hr, 90°C) and boron-diffused (48 hr, 900°C, N_2 atmosphere) samples are given in Fig. 8. In the first case the characteristic peaks of SiO_2 (22) are observed. In the second case changes arise in the 7.27 μm (1375 cm^{-1}) region related with the presence of B-O bonds and at 10.75 μm (930 cm^{-1}) attributed to Si-O-B bonds. With increasing boron deposition time a peak at 7.97 μm (1255 cm^{-1}) and a shoulder at 8.6 μm (1165 cm^{-1}) are observed in the reflectance spectra, these new peaks corresponding to the Si-B phase.

When the boron diffusion takes place in the presence of oxygen ($N_2 + O_2$ atmosphere) the SiO_2 bands may be predominant and an additional absorption at 11.36 μm (800 cm^{-1}) has been observed in some cases probably due to some interaction between B_2O_3 and SiO_2 compounds. These results confirm the conclusion of other authors (8) that the growth rate of the Si-B compound is depressed as the oxygen concentration in the atmosphere increases according to the reaction

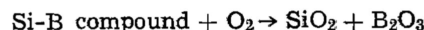

$$\text{Si-B compound} + O_2 \rightarrow SiO_2 + B_2O_3$$

However, at higher diffusion temperatures (1000°C) in N_2 (94%) + O_2 (6%) atmosphere a great propor-

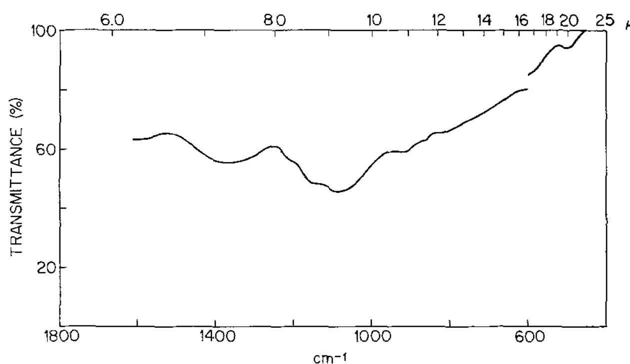

Fig. 7. IR spectrum of powder obtained by light scraping of boron-diffused sample (900°C for 20 hr, N_2 atmosphere).

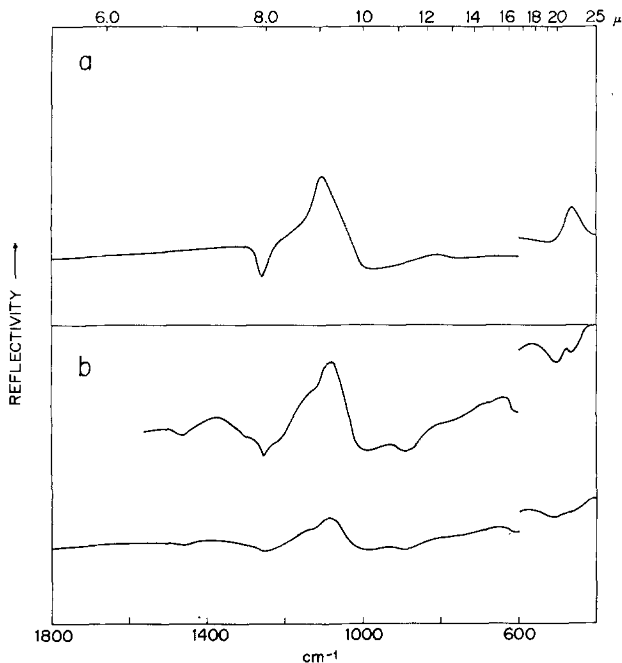

Fig. 8. Reflectance curves. a) Oxidized sample (at 900°C for 26 hr); b) heat-treated sample at 900°C, first in wet N_2 for 4 hr, and after that submitted to boron diffusion in N_2 for 48 hr.

tion of the Si-B phase was observed at 15 hr diffusion time.

Figure 9 gives the reflectance curves of two samples diffused in a N_2 atmosphere at 900°C for 48 and 90 hr, respectively, and for another boron-diffused sample after two days treatment with HF (48%). The peaks at 7.97 μm (1255 cm^{-1}), 8.55 μm (1170 cm^{-1}) are related to the Si-B phase. Another peak or inflection at 8.93-9.01 μm (1120-1110 cm^{-1}) is attributed to SiO_2.

The spectra of samples with low diffusion times show bands at 7.1 μm (1400 cm^{-1}), 8.2 μm (1220 cm^{-1}), 9.5 μm (1050 cm^{-1}), and 10.99 μm (910 cm^{-1}) related to B-O, Si-B, Si-O, and Si-O-B vibrations, respectively, according to the above results.

Conclusion

From the above experimental results it is concluded that when B_2O_3 is diffused into silicon in an N_2 atmosphere the compound produced at the B_2O_3-Si interface at 900°-1100°C is neither SiB_6 nor SiB_4 but most probably resembles SiB_5 composition.

Manuscript submitted May 3, 1977; revised manuscript received April 7, 1978.

Any discussion of this paper will appear in a Discussion Section to be published in the June 1979 JOURNAL. All discussions for the June 1979 Discussion Section should be submitted by Feb. 1, 1979.

Publication costs of this article were assisted by C.I.F.L. Torres Quevedo.

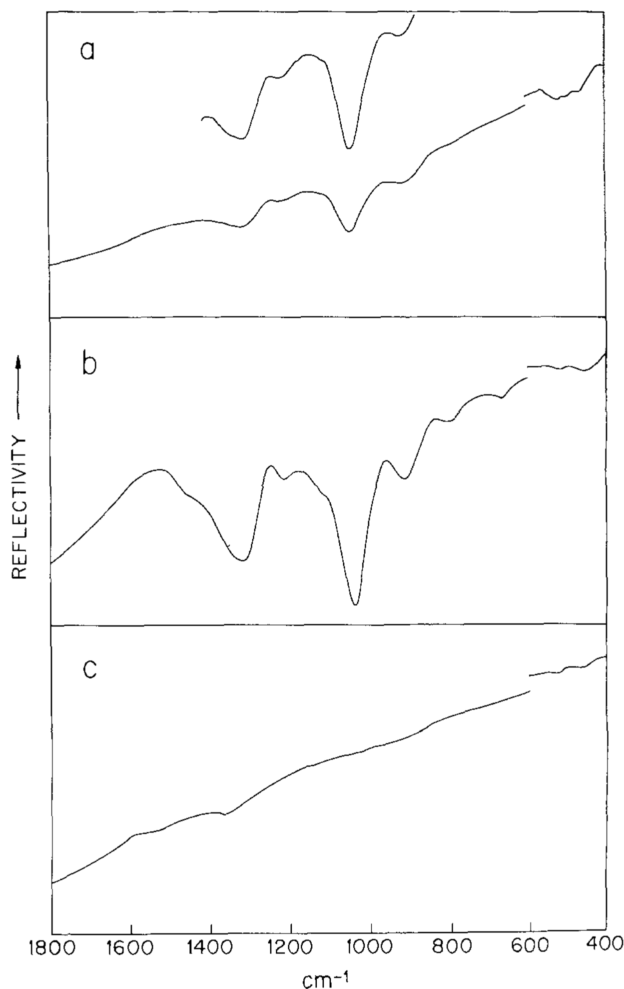

Fig. 9. Reflectance curves. a) Boron-diffused sample, in N_2 at 900°C for 48 hr; b) *ibid.* for 90 hr; c) boron-diffused sample after 48 hr treatment with HF (48%).

REFERENCES

1. G. D. Watkins, *Phys. Rev.*, **155**, 802 (1967).
2. G. L. Vick and K. M. Whittle, *This Journal*, **116**, 1142 (1969).
3. N. D. Thai, *Solid-State Electron.*, **13**, 165 (1970); *J. Appl. Phys.*, **41**, 2859 (1970).
4. W. K. Tsang, *This Journal*, **115**, 291 (1970).
5. D. M. Brown and P. R. Kennicott, *ibid.*, **118**, 293 (1971).
6. S. M. Hu, in "Atomic Diffusion in Semiconductors," Chap. 5, D. Show, Editor. Plenum Press, London and New York (1973).
7. G. Masetti, P. Negrini, and S. Solimi, *Alta Freq.*, **42**, 356 E (1973).
8. E. Arai, H. Nakamura, and Y. Terunuma, *ibid.*, **120**, 980 (1973).
9. R. F. Adamsky, *Acta Crystallogr.*, **11**, 44 (1958).
10. C. F. Cline, *This Journal*, **106**, 322 (1959).
11. C. F. Cline and D. E. Sands, *Nature (London)*, **185**, 456 (1960).
12. C. Brosset and B. Magnusson, *ibid.*, **187**, 54 (1960).
13. H. F. Rizzo and L. R. Bidwell, *J. Am. Ceram. Soc.*, **43**, 550 (1960).
14. V. I. Matkovich, *Acta Crystallogr.*, **13**, 679 (1960).
15. G. Moore, H. Guckel, and M. G. Lagally, *J. Vac. Sci. Technol.*, **14**, 70 (1977).
16. G. Moore, S. Larsen, H. Guckel, and M. G. Lagally, Abstract 88, p. 246, The Electrochemical Society Extended Abstracts Spring Meeting, Philadelphia, Pennsylvania (1977).
17. D. A. Kiewit, H. H. Busta, and J. D. Bucci, Abstract 86, p. 240, The Electrochemical Society Extended Abstracts, Spring Meeting, Philadelphia, Pennsylvania (1977).
18. K. M. Busen, W. A. Fitzgibbons, and W. K. Tang, *This Journal*, **115**, 291 (1968).
19. C. Jamard, D. Taupin, and A. Guinierd, *Bull. Soc. Fr. Mineral. Cristallogr.*, **79**, 312 (1966).
20. R. Brückner and J. Fernández Navarro, *Glastech. Ber.*, **39**, 283 (1966).
21. R. A. Niquist and R. O. Kagel, "Spectra of Inorganic Compounds (3800-45 cm^{-1})," Academic Press, New York and London (1971).
22. C. H. Perry and J. D. Wrigley, Jr., *Appl. Opt.*, **6**, 586 (1967).

Chemical Vapor Deposition of Silicon Nitride

Encapsulant Layers for Annealing Gallium Arsenide

Taroh Inada, Tatsuya Ohkubo, and Shinobu Sawada

College of Engineering, Hosei University, Kajinocho, Koganei, Tokyo 184, Japan

Tohru Hara*

Matsushita Research Institute Tokyo, Incorporated, Ikuta, Tama-ku, Kawasaki 214, Japan

and Masato Nakajima

Matsushita Electric Industrial Company, Limited, Central Research Laboratory, Moriguchi, Osaka 570, Japan

ABSTRACT

Noncrystalline Si_3N_4 layers are grown at low temperatures by the chemical reaction of silane and ammonia, and at extremely high deposition rates (120Å/sec) which is 50 times higher than the usual deposition rates. Correlations between growth conditions and layer properties are studied. The growth conditions for obtaining the most suitable encapsulant layers for the annealing of ion-implanted GaAs are: gas feed rates of silane, ammonia, and nitrogen carrier gas of 5, 200, and 1500 ml/min, respectively, and a growth temperature of 700°C. Layers formed under these conditions have a refractive index of 1.95 and an etch rate of 500 Å/min in 50% HF solution. These values are nearly equal to that of conventional Si_3N_4 layers deposited at lower deposition rates. Auger electron spectroscopic analysis shows an oxygen concentration below the detection limit (<0.1 atom percent) and a uniform Si/N ratio along the thickness direction. Out-diffusion of Ga and As into the layer does not occur on 900°C annealing. No cracks are formed when thin Si_3N_4 layers, less than 1200Å thick, are deposited on GaAs substrates. These layers are useful as encapsulant films for the annealing of GaAs.

Chemical vapor deposited noncrystalline Si_3N_4 layers have been extensively applied to silicon devices for surface passivation, diffusion masking, and MNOS devices, because of their chemical stability. Recently, Si_3N_4 layers have been frequently used as an encapsulant film for the annealing of ion-implanted GaAs (1-4).

In ion-implanted GaAs, annealing at above 800°C is necessary to eliminate radiation damage and to achieve high electrical activation of implanted species. Therefore, good encapsulant layers are required. An effective encapsulant should reduce thermal decomposition of the GaAs surface and the out-diffusion of Ga, As, and implanted species during high temperature annealing. However, encapsulation effects on GaAs annealing are significantly affected by layer quality and deposition conditions, as reported previously (1-4).

As there is a relatively large difference in thermal expansion coefficient between Si_3N_4 (2.6×10^{-6} °K^{-1}) (5) and GaAs (6.9×10^{-6} °K^{-1}) (6), a large strain is formed at the Si_3N_4-GaAs interface. Therefore, cracking and lifting of the Si_3N_4 film occurred when the film was annealed at temperatures above 800°C (7). Although GaAs decomposition increases at temperatures above 600°C (8, 9), the decomposition can be reduced by shortening the high temperature exposure of GaAs surfaces before deposition. To meet these requirements, the deposition of thin Si_3N_4 layers must be carried out at high temperatures with extremely high deposition rates. The heating of substrates up to the deposition temperature within an extremely short time is also important.

Recently, Donnelly *et al.* have reported on high rate deposition of Si_3N_4 (2, 10). They have demonstrated that this layer is a good encapsulant film for the annealing of ion-implanted GaAs. However, detailed features of growth conditions and layer properties have not been reported. It is well known that the properties of Si_3N_4 can be varied over a wide range depending on the deposition technique and conditions. Therefore, optimum growth conditions for obtaining good encapsulant layers must be established.

This paper describes the growth conditions of high deposition rate Si_3N_4. The properties of layers deposited under different conditions are also described.

* Electrochemical Society Active Member.

Key words: silicon nitride, chemical vapor deposition, gallium arsenide, ion implantation, encapsulation film.

Results and Discussion

Deposition.—Silicon nitride films were deposited on GaAs wafers using the chemical reaction between NH_3 and SiH_4. A cold wall type vertical reactor with 150 mm diam was manufactured using stainless steel. Special care was taken to eliminate slow leaks in the gas tubing system and reaction chamber by using stainless steel fittings. Chemomechanically polished GaAs substrates were cleaned with organic solvents and dipped in 35% HCl to remove residual surface oxides just prior to deposition.

After GaAs substrates of 10 × 10 mm were placed on the graphite strip heater in the reactor chamber, the reactor system was evacuated to mid-10^{-5} Torr in order to prevent oxide layer depositions. The substrates were then heated to 200°C in N_2 gas flow. This preheating procedure permits shortening the substrate heating time prior to deposition and prevents the predeposition of oxide layers (10). Reactant gases, SiH_4 and NH_3, were introduced into the reactor together with the N_2 carrier gas. High purity NH_3 gas (99.999%) was used to obtain oxygen-free Si_3N_4 layers. Then the substrate was heated rapidly from 200°C to a predetermined deposition temperature, for instance 700°C, within 5 sec by increasing the heater current. As a result, the deposition of the Si_3N_4 layer occurred at an extremely high growth rate. Silane flow rate was constant at 5 ml/min throughout this experiment, while the NH_3 and N_2 gas feed rates were varied. When deposition was carried out at the gas feed rates of SiH_4 = 5 ml/min, NH_3 = 200 ml/min, and N_2 = 1500 ml/min,

we denoted the ratio as $SiH_4:NH_3:N_2 = 1:40:300$, for simplicity. The thickness of Si_3N_4 layers deposited at different deposition times was measured using an ellipsometer.

The layer thickness variation with deposition time is shown in Fig. 1, where deposition was made at 700°C with gas feed rate ratio of $SiH_4:NH_3:N_2 = 1:40:300$. This figure shows that the layer thickness increases linearly with time and that deposition rate is nearly constant at 120 Å/sec in the range studied here (<30 sec). This deposition rate is much higher than that of conventional Si_3N_4 grown at higher temperatures (>800°C) and lower gas feed rates (11-13). High deposition rate Si_3N_4 is abbreviated as HR Si_3N_4 in the following discussion.

Depositions were carried out at various temperatures ranging from 500° to 800°C, where the gas feed ratio of $SiH_4:NH_3:N_2$ was fixed at 1:40:300, and the layer thickness was fixed at around 1000Å. The deposition rate is shown as a function of deposition temperature, T, in Fig. 2. As seen in this figure, the deposition rate of HR Si_3N_4 increases markedly with increasing T and becomes relatively temperature insensitive at temperatures above 700°C. Temperature variations at below 700°C suggest that the chemical reaction is a rate-limiting process and the deposition rate follows an exponential law. The apparent activation energy of the growth is about 10.6 kcal/mole, which is smaller than the value of 17 kcal/mole reported for conventional Si_3N_4 growth (12). Above 700°C mass transfer process is dominant as shown in Fig. 3, where NH_3 to SiH_4 feed ratios of 30, 40, and 50 are used. The deposition rate decreases sharply with increasing N_2 flow rate, for instance, from 250 Å/sec at a N_2 flow rate of 250 ml/min to 70 Å/sec at 2250 ml/min. Similar tendencies are seen for different NH_3 to SiH_4 ratios. It is clear from these results that high rate deposition should be attained if the N_2 flow rate is lowered and the SiH_4 feed rate is increased. However, layer thickness uniformity within the wafer improves significantly at higher N_2 flow rates, the best uniformity (within 12%) was attained at a N_2 flow rate of 1500 ml/min with a gas feed ratio of $SiH_4:NH_3:N_2 = 1:40:300$, and deposition temperature of 700°C. In this case, a deposition rate of around 120 Å/sec was obtained. This value is about 50 times higher than that for conventional Si_3N_4 layers.

Layer properties.—Evaluation of layer properties for HR Si_3N_4 grown under different conditions was carried out to obtain desired encapsulant layers. Refractive indexes of the layers deposited at different temperatures were measured with an ellipsometer. The refractive index as a function of deposition temperature is shown in Fig. 4 for deposits at a gas feed ratio of $SiH_4:NH_3:N_2 = 1:40:300$. The refractive index is nearly constant for depositions at above 600°C and increases slowly with decreasing deposition temperature below 600°C. Reduction of the refractive index

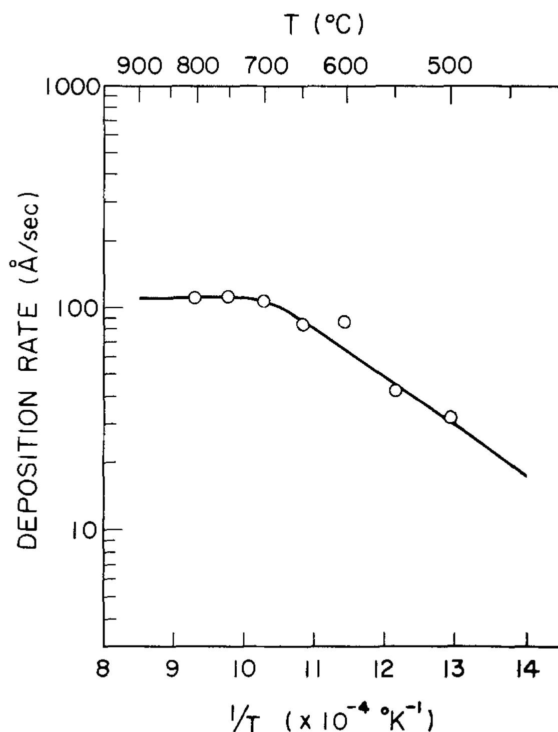

Fig. 2. Deposition rate of HR Si_3N_4 as a function of deposition temperature. Gas feed ratio, $SiH_4:NH_3:N_2 = 1:40:300$.

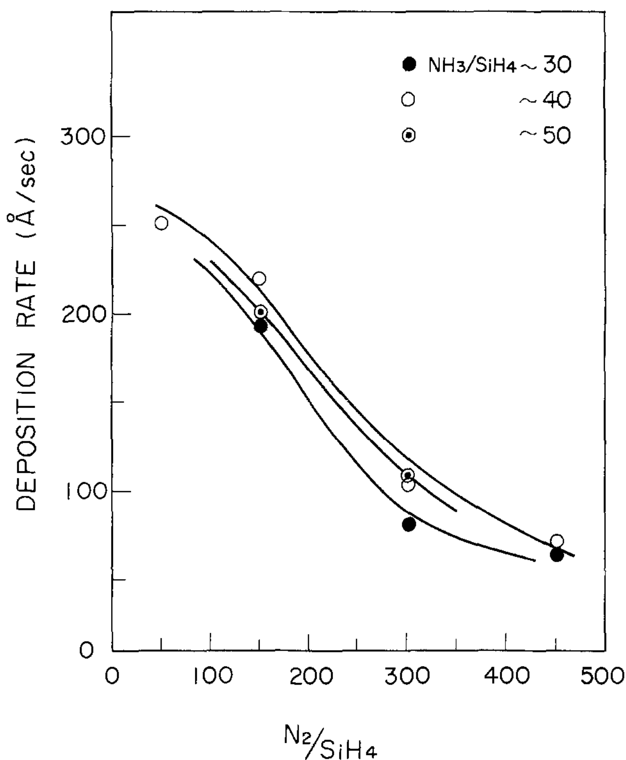

Fig. 3. Deposition rate of HR Si_3N_4 as a function of N_2 carrier gas at different NH_3/SiH_4 ratios where deposition temperature was 700°C.

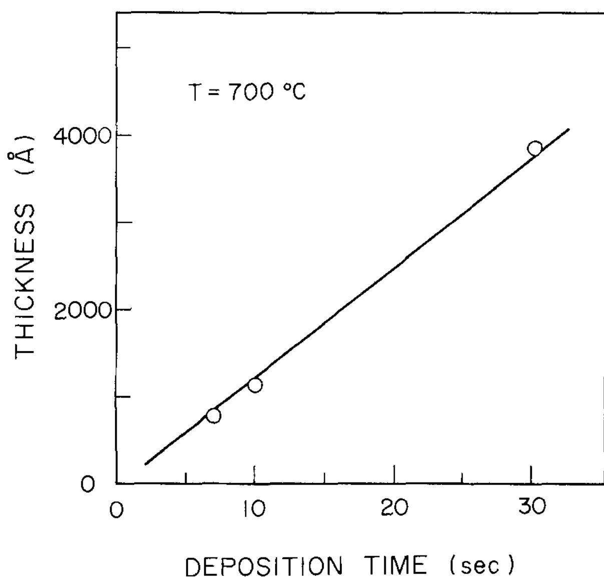

Fig. 1. Thickness variation of Si_3N_4 layers with deposition time, where the deposition was made at gas feed ratio of $SiH_4:NH_3:N_2 = 1:40:300$, and a deposition temperature of 700°C.

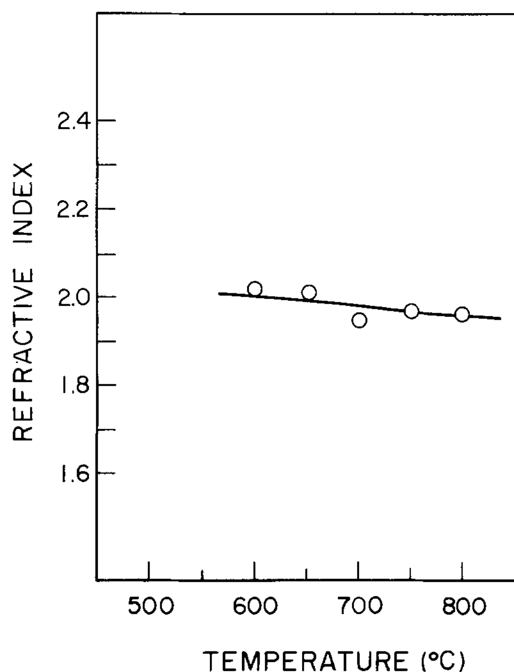

Fig. 4. Refractive index of HR Si_3N_4 as a function of deposition temperature. Gas feed ratio, SiH_4:NH_3:N_2 = 1:40:300.

by the incorporation of oxygen in the film has been demonstrated (14), although the refractive index is affected with deposition parameters such as temperature and NH_3 to SiH_4 ratio. The refractive index of 1.95 for HR Si_3N_4 grown at 700°C is nearly equal to that of conventional Si_3N_4 (15).

The etch rates of the deposited layer were measured by dipping specimens into 50% HF solution at 20°C without stirring. The layers could be removed completely from GaAs surface in this manner. The etch rates of layers deposited at a gas feed ratio of SiH_4:NH_3:N_2 = 1:40:300 are plotted in Fig. 5 as a function of deposition temperature, *T*. The etch rate decreases drastically with increasing *T* and becomes constant at about 500 Å/min for temperatures above 600°C.

Chu *et al.* (12) have reported that the etch rate of conventional Si_3N_4 deposited at 800°C is approximately 700 Å/min. As shown in Fig. 5, the etch rate of HR Si_3N_4 deposited at and above 600°C is around

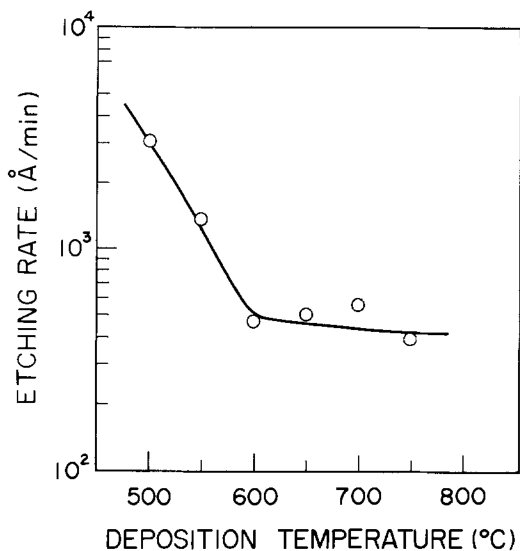

Fig. 5. Etch rate of HR Si_3N_4 in 50% HF at 20°C as a function of deposition temperature. Gas feed ratio, SiH_4:NH_3:N_2 = 1:40:300.

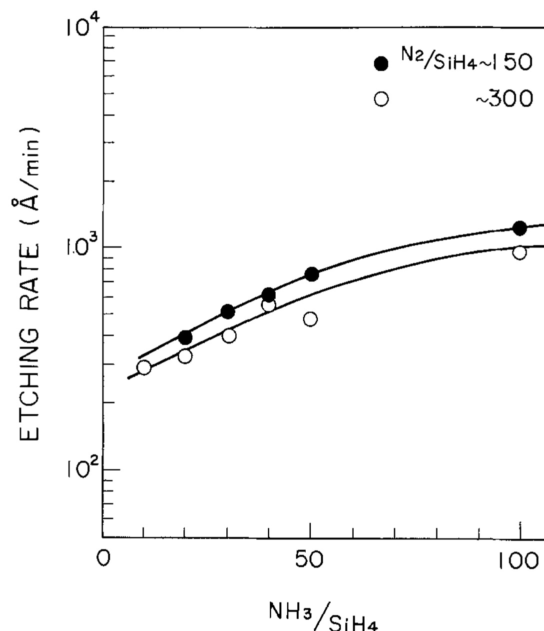

Fig. 6. Etch rate of HR Si_3N_4 layers in 50% HF at 20°C as a function of NH_3/SiH_4 ratios where deposition temperature was 700°C.

500 Å/min. The etch rates of layers deposited at different NH_3/SiH_4 ratios are shown in Fig. 6. The etch rates decrease gradually with decreasing NH_3 concentration.

Typical infrared absorption spectra are given in Fig. 7, where curves A and B are for 1000Å thick layers grown on Si substrates at a gas feed ratio of SiH_4:NH_3:N_2 = 1:40:300 and 1:40:50, respectively. The main Si-N absorption appears at around 12 μm as observed in conventional Si_3N_4 layers (14). Infrared absorption study of other layers indicates that the magnitude of this absorption is independent of both deposition temperature and gas feed ratios in the range studied here. Although the N-H absorption band at 2.97 μm was not found in layers typical of conditions shown for curve A, this band appeared in layers grown with extremely high NH_3 concentrations, as shown in curve B.

The absorption coefficient as a function of the mole fraction of NH_3 to total gas is shown in Fig. 8, where the 2.97 μm band grows rapidly with increasing NH_3 fractions in the range above 30%. The absorption peaks at 4.6 μm due to Si-H bonds, which have been reported for glow discharge Si_3N_4 (16), were not detected. Since the Si-O band at 9.2 μm was not

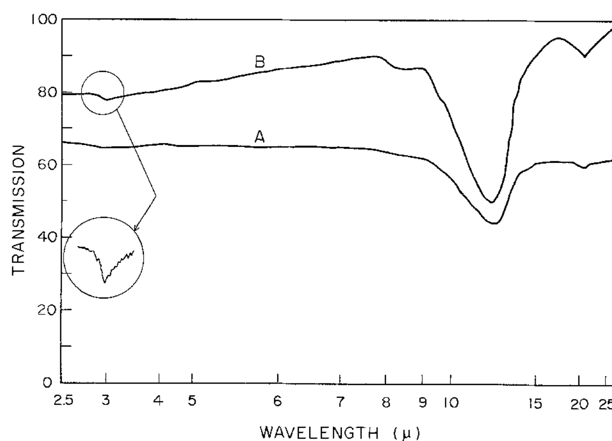

Fig. 7. Infrared absorption spectra of HR Si_3N_4 deposited at 700°C. Gas feed ratio, SiH_4:NH_3:N_2 = 1:40:300 (curve A) and 1:40:50 (curve B).

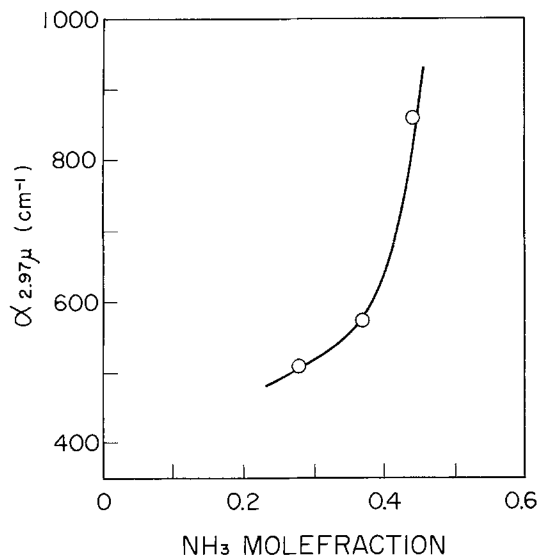

Fig. 8. Percent absorption at 2.97 μm (N-H bonds) of HR Si_3N_4 as a function of ammonia mole fraction, ($NH_3/SiH_4 + NH_3 + N_2$), where deposition was made at 700°C.

observed, these layers are regarded as low in oxygen concentration.

Auger electron spectroscopic analysis of HR Si_3N_4 was performed using a JEOL type JAMP-3, where measurement was made at $E = 5$ keV and $I = 10^{-7}$A. Depth profiles of N, Si, and O in as-deposited layers show that the distribution profile of the N/Si composition ratio was uniform along thickness direction, and that the oxygen concentration is below the detection limit (<0.1 atom percent) (17). The layer examined was deposited at 700°C and at a gas feed ratio of SiH_4:NH_3:N_2 = 1:40:300. However, trace amounts of oxygen were detected at the Si_3N_4-GaAs interface, although residual surface oxide layers were removed from the GaAs surface before growth. The origin of this oxygen is not clear at this time.

Gyulai *et al.* (18) using the MeV He ion backscattering method, have shown that out-diffusion of Ga into encapsulant Si_3N_4 film occurs when a sample is heated to 750°C. The amount of out-diffusion from the substrate seems to be affected by layer quality, for instance, growth conditions and oxygen concentration in the Si_3N_4 layer (19). The layer was annealed at 900°C for 15 min in a N_2 gas flow. Distribution profiles of N, Si, and O were then examined by Auger electron spectroscopy. Neither Ga nor As atoms diffused into the HR Si_3N_4 layer during 900°C annealing, because the oxygen concentration is below the detection limit, as shown in Fig. 9. An oxygen peak is observed at the GaAs-Si_3N_4 interface as seen in the as-deposited layers (17).

Doo *et al.* (11, 13) and others (12) have reported that cracks are often observed in as-deposited thick Si_3N_4 layers grown on Si substrates and that crack density increases with increasing growth rates. There is a much larger difference in thermal expansion coefficients between Si_3N_4 (5) and GaAs (6) compared with the Si_3N_4-Si interface. Therefore, cracks should form more easily on the Si_3N_4 layers deposited on GaAs. In order to obtain good encapsulant layers for annealing of ion-implanted GaAs, the conditions under which cracks do not appear even for annealing at 900°C must be established. To establish these conditions, layers with different thicknesses were deposited. No cracks were found in as-deposited HR Si_3N_4 layers when the layer thickness was in the range between 500 and 4000Å. Pin holes disappeared in the layer thicker than 800Å. These layers were annealed at 900°C for 15 min. A scanning electron microscope photograph of a 1100Å thick annealed Si_3N_4 layer is shown in Fig. 10. No cracks are seen in this layer.

After Si_3N_4 films were removed using an HF solution, the GaAs surface was examined by SEM. There were no cracks or damage when the thickness of the HR Si_3N_4 layer was below 1200Å. However, when thicker layers were deposited, for instance > 1500Å, cracks were formed during this annealing process. Typical cracks, which appeared on GaAs surfaces when annealing was carried out using 3000Å thick encapsulant layers, are shown in Fig. 11. It should be noted that the cracks on the GaAs seem to run along the cleaved surface. It is concluded that the HR Si_3N_4 layer thickness should be less than 1200Å for annealing GaAs.

This study on refractive index, etch rate, and Auger electron spectroscopy indicates that the HR Si_3N_4 is a good encapsulant layer and low in oxygen concentration.

Peak carrier concentrations of 4.5×10^{18} cm^{-3} have been obtained using this layer as an encapsulant film for the annealing of Si ion-implanted GaAs (17). Detailed features of the electrical properties of ion-implanted GaAs annealed with an HR Si_3N_4 encapsulant will be reported in the near future.

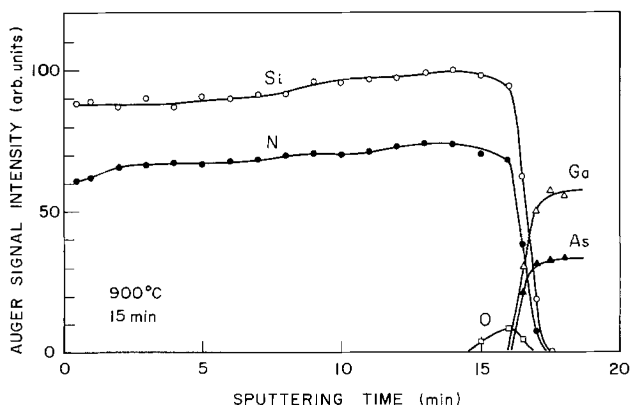

Fig. 9. Auger electron in-depth profiles of annealed HR Si_3N_4 layers deposited on GaAs substrates, where annealing was carried out at 900°C for 15 min.

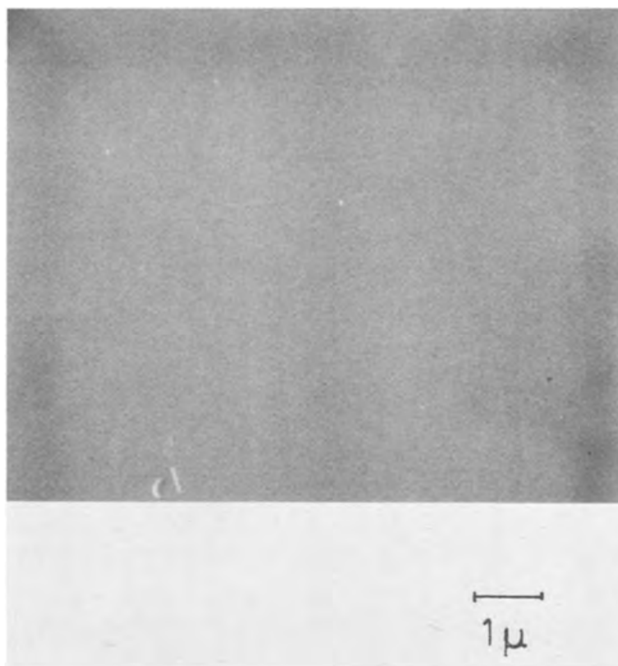

Fig. 10. Scanning electron microscope photographs of a 1100Å thick HR Si_3N_4 layer, which was deposited on a GaAs substrate and annealed at 900°C for 15 min.

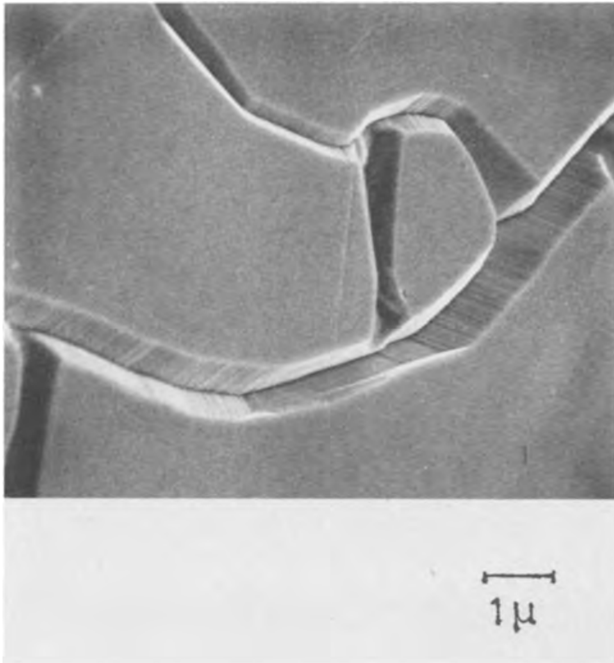

Fig. 11. Scanning electron microscope photograph of surface cracks formed on GaAs substrates under the following annealing procedure: 3000Å thick Si_3N_4 layers were deposited on GaAs. After annealing at 900°C for 15 min in N_2 flow, Si_3N_4 layers were removed by etching from GaAs surface. Cracks were formed on the GaAs surface.

Conclusion

Deposition conditions of high deposition rate Si_3N_4 were studied. From results of layer property evaluation, it is clear that good encapsulant layers for annealing GaAs can be grown by the chemical reaction of SiH_4 and NH_3 in N_2 gas flow under the following conditions: growth temperature 700°C; gas feed rates of SiH_4 5 ml/min, NH_3 200 ml/min, and N_2 carrier gas 1500 ml/min. In this case, the deposition rate was 120 Å/sec and about 50 times larger than that of conventional Si_3N_4. Properties of layers deposited at these conditions were an etch rate in 50% HF of 500 Å/min and a refractive index of 1.95. High deposition rate layers were essentially free from oxygen contamination and out-diffusion of Ga and As into the encapsulant layers did not occur during the annealing at 900°C with the layers deposited on GaAs substrates. No cracks were formed during 900°C annealing when thin layers, below 1200Å, were deposited. Pin holes could be eliminated when thick layers, above 800Å, were deposited. From these results, it can be concluded that the HR Si_3N_4 layers with around 1000Å thick are promising encapsulant films for the annealing of ion-implanted GaAs.

Acknowledgment

The authors would like to thank M. Kitahara of Hosei University for his invaluable technical assistance. They also are indebted to F. Kanauchi of Japan Spectroscopic Company Limited for the infrared absorption measurements.

Manuscript submitted Feb. 2, 1978; revised manuscript received April 11, 1978.

Any discussion of this paper will appear in a Discussion Section to be published in the June 1979 JOURNAL. All discussions for the June 1979 Discussion Section should be submitted by Feb. 1, 1979.

Publication costs of this article were assisted by Matsushita Research Institute Tokyo, Incorporated.

REFERENCES

1. P. L. F. Hemment, B. J. Sealy, and K. G. Stephens, in "Ion Implantation in Semiconductors and Other Materials," S. Namba, Editor, p. 27, Plenum, New York (1975).
2. J. P. Donnelly, W. T. Lindley, and C. E. Hurwitz, *Appl. Phys. Lett.*, **27**, 41 (1975).
3. K. Gamo, T. Inada, S. Krekeler, J. W. Mayer, F. H. Eisen, and B. M. Welch, *Solid-State Electron.*, **20**, 213 (1977).
4. A. Lidow, J. F. Gibbons, and T. Magee, *Appl. Phys. Lett.*, **31**, 158 (1977).
5. P. J. Burkhardt and R. F. Marvel, *This Journal*, **116**, 864 (1969).
6. E. D. Pierron, D. L. Parker, and J. B. McNeely, *J. Appl. Phys.*, **38**, 4669 (1967).
7. T. Inada, H. Miwa, T. Ohkubo, and S. Kato, Unpublished data.
8. G. J. Russell, H. K. Ip, and D. Haneman, *J. Appl. Phys.*, **37**, 3328 (1966).
9. S. T. Picraux, in "Ion Implantation in Semiconductors and Other Materials," B. Crowder, Editor, p. 641, Plenum, New York (1973).
10. J. P. Donnelly, in "Gallium Arsenide and Related Compounds," L. Eastman, Editor, p. 336, St. Louis (1976).
11. V. Y. Doo, D. R. Nichols, and G. A. Silvey, *This Journal*, **113**, 1279 (1966).
12. T. L. Chu, C. H. Lee, and G. A. Gruber, *ibid.*, **114**, 717 (1967).
13. V. Y. Doo, D. R. Kerr, and D. R. Nichols, *ibid.*, **115**, 61 (1968).
14. P. H. Holloway and H. J. Stein, *ibid.*, **123**, 723 (1976).
15. S. M. Hu, *ibid.*, **113**, 693 (1966).
16. E. A. Taft, *ibid.*, **118**, 1341 (1971).
17. T. Inada, H. Miwa, S. Kato, E. Kobayashi, M. Mihara, and T. Hara, *J. Appl. Phys.*, **49**, No. 9 (1978).
18. J. Gyulai, J. W. Mayer, I. V. Mitchell, and V. Rodriquez, *Appl. Phys. Lett.*, **17**, 332 (1970).
19. K. V. Vaidyanathan, M. J. Helix, D. J. Wolford, B. G. Streetman, R. J. Blattner, and C. A. Evans, Jr., *This Journal*, **124**, 1781 (1977).

Diffusion Properties of Cadmium in Indium Antimonide

A. Kolodny and J. Shappir

Faculty of Electrical Engineering, Technion-Israel Institute of Technology, Haifa, Israel

ABSTRACT

Diffusion profiles of cadmium in indium antimonide were measured by a modified C-V technique and were found to exhibit anomalous behavior, as commonly found in III-V compounds. The general shape of the diffusion profile on a logarithmic scale is characterized by a concave region close to the surface followed by a steep front. The steep front is explained by the interstitial-substitutional diffusion mechanism. The concave region is theoretically shown to be related to a decrease of the diffusion coefficient near the surface. This decrease is assumed to be the result of the surface proximity rather than the result of a nonmonotonic concentration dependence of the diffusion coefficient. This surface effect is physically explained by an extension of the interstitial-substitutional model. Computer simulations based on this model give profiles similar to those experimentally measured.

Cadmium diffusion profiles in n-type indium antimonide exhibit a steep front near the p-n junction and a concave region (when plotted on a logarithmic scale) near the surface (1, 2). Such anomalous diffusion is commonly found in III-V compounds (3) and has been reported for zinc in GaAs (3, 4), InP (1), and InAs (1), phosphorus in GaAs (5), and other diffusion systems.

The basic interstitial-substitutional diffusion mechanism (6), which is usually invoked to interpret the steep front of the profiles, does not explain the concave region in the profiles, because it leads to profiles which are convex with a steep front. The concentration dependence of the diffusion coefficient, obtained from experimental profiles by applying the Boltzmann-Matano analysis (3), is nonmonotonic, exhibiting a maximum at intermediate diffusant concentrations (4, 5). Furthermore, the behavior near this maximum varies with diffusion time. This result, which is clearly unphysical, contradicts the monotonic dependence of the diffusion coefficient on the diffusant concentration as predicted by the interstitial-substitutional model. Consequently, the validity of the Boltzmann-Matano analysis for this type of diffusion has been doubted by some authors (4, 5), since the profiles cannot be expressed in terms of a single variable $x/\sqrt{t}$ (diffusion depth divided by the square root of diffusion time). The concave region in the profiles, which causes a peak in the results of a Boltzmann-Matano analysis, is assumed to be related to a surface effect on diffusion. A qualitative explanation of this phenomenon, relating it to a nonequilibrium of vacancies, has been given by Tuck (3).

The anomalous behavior described above was observed on a cadmium diffusion profile which was measured by means of a "graded *C-V*" technique described in the experimental section.

In the theoretical section, we present a generalization of the Boltzmann-Matano formula for the case of a diffusion coefficient dependent upon depth, diffusant concentration, and diffusion time. By means of this formula, phenomenological conclusions about the behavior of the diffusion coefficient are reached, showing that it decreases near the surface. Numerical results showing good qualitative agreement with experiment are presented, and suggestions are made about the physical reasons for the phenomenon.

Graded *C-V* Profiling Method

The profile of electrically active cadmium diffused into the InSb was found from *C-V* measurements on MOS capacitors in several depths along the profile. This "graded *C-V*" technique is preferable to the well-known radiotracer and resistivity methods because it eliminates the necessity for removal of successive thin layers. The method is based on gradual immersion of a long diffused sample in an etching solution so that the surface becomes a slightly slopy plane, along with which the impurity concentration is gradually changing. The surface type is changed from p to n where the wedge crosses the junction plane. A thin insulating layer is deposited on the sample, and a series of small electrodes are placed upon it to form MOS capacitors as shown schematically in Fig. 1.

From *C-V* measurements on a MOS capacitor at high frequency, the type of impurities in the crystal below it may be determined, and their concentration may be calculated from the ratio of minimum-to-maximum capacitance. Similar methods have been used for shallow implanted layers, but in those, the varying bias voltage controls the measurement depth, and the derivative dC/dV of the measured curve is required to obtain the profile (7). In our experimental process, cadmium was diffused for several hours at 400°C into samples of tellurium-doped InSb with donor concentration of about 10^{15} cm^{-3}, cut along <111> plane and polished on the In face. After the diffusion, a slice about 2.5 cm long was gradually etched, so that a height difference of about 2 μm was obtained. A narrow strip along the sample had been protected by photoresist before the etching so that a step was formed, and the distance from every point on the wedged surface to the original surface could be determined by measuring the step height. A 1000Å pyrolitic SiO_2 layer was then deposited on the sample, and a series of 0.6 mm diam capacitors were formed on it by Cr-Au evaporation. *C-V* curves of these capacitors at 1 MHz were measured at 77°K.

The measured capacitance is equivalent to that of three capacitors in series: oxide capacitance C_{ox}, depletion capacitance C_{dep}, and the p-n junction capacitance C_j. The junction area is almost equal to the area of the whole sample, so that C_j is large and thus may be neglected. One is left with the simple structure of a MOS capacitor at high frequency, and the ionized

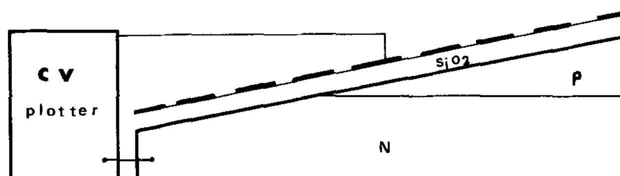

Fig. 1. Schematic setup for measurement of a diffusion profile by the graded *C-V* method. The impurity concentration below each MOS capacitor is found from the *C-V* curve.

Key words: Boltzmann-Matano analysis, C-V profiling method, concave diffusion profiles, interstitial-substitutional mechanism.

impurity concentration N_o may be readily obtained from the value of C_{min}/C_{ox} which is a function of the oxide thickness and substrate doping level, by solving

$$\frac{N_o}{\phi_F} = \frac{4C_{ox}^2}{q\epsilon_{InSb}\epsilon_o A^2} \left[\frac{\frac{C_{min}}{C_{ox}}}{1 - \frac{C_{min}}{C_{ox}}} \right]^2 \quad [1]$$

C_{min} is the minimum of the C-V curve, ϕ_F is the Fermi potential, A is the capacitor area, and the other symbols have their usual meaning.

The accuracy of the graded C-V method is determined by the following factors: (*i*) Variation of impurity concentration in the depletion region; (*ii*) variation of impurity concentration along the sloped surface under the metal electrode; (*iii*) minority-carrier generation by background illumination; (*iv*) magnification of capacitance-measurement error as $C_{min}/C_{ox} \rightarrow 1$ (see Eq. [1]; (*v*) inhomogeneity of the slope-etched surface; (*vi*) errors in the etching depth measurement.

For impurity densities above 5×10^{16} cm^{-3}, the depletion layer width is less than 0.1 μm, so that the impurity concentration may be assumed to be constant throughout the depletion layer. Making a moderate slope on a long substrate eliminates the effect of concentration variation under the metal electrode. The effect of background illumination was found to be negligible from C-V measurements on an n-type substrate with a known impurity concentration.

The minimum detectable change in capacitance is obtained for impurity concentrations below 10^{19} cm^{-3}. It may thus be concluded that the graded C-V method is applicable for measurements of diffusion profiles in InSb for the range of impurity concentrations 5×10^{16} cm$^{-3} \leq N \leq 10^{19}$ cm^{-3}.

Application of the graded C-V method to our cadmium-diffusion process gave the profile shown in Fig. 2. The measured profile of active cadmium impurities is very similar to profiles measured by radiotracer methods. Hence, the results may be analyzed assuming that all the cadmium atoms are ionized. The surface concentration was too high to be measured by this technique, so the initial part of the profile may be extrapolated to the maximum solid solubility which is in the range of 4×10^{19}-2.5×10^{21} cm^{-3} (8, 9). The spread of the measured values is believed to be mainly due to the nonuniformity of the etched surface, which was observed visually.

Inspection of the resulting profile motivated an investigation of the mathematical properties of the diffusion equation corresponding to such a diffusion profile. The treatment is given in the next section.

Analysis of Diffusion Profiles

We assume that the diffusion process obeys Fick's law with an effective diffusion coefficient, D, which accounts for the detailed transport mechanism. For fixed temperature, surface concentration, and vapor pressures, D may depend on the diffusant concentration C, the distance to the surface x, and the time t. The diffusion equation is

$$\frac{\partial C}{\partial t} = \frac{\partial}{\partial x} \left[D(C, x, t) \frac{\partial C}{\partial x} \right] \quad [2]$$

The initial conditions are $C(x) = 0$ for $x > 0$, and the boundary conditions (constant source diffusion) are

$$\left. \begin{aligned} C(\mathrm{o}, t) &= C_o \\ C(\infty, t) &= 0 \end{aligned} \right\} \quad [3]$$

It is usually assumed in the literature that D is a function of C only.

These are the conditions for application of the standard Boltzmann-Matano analysis, which gives the

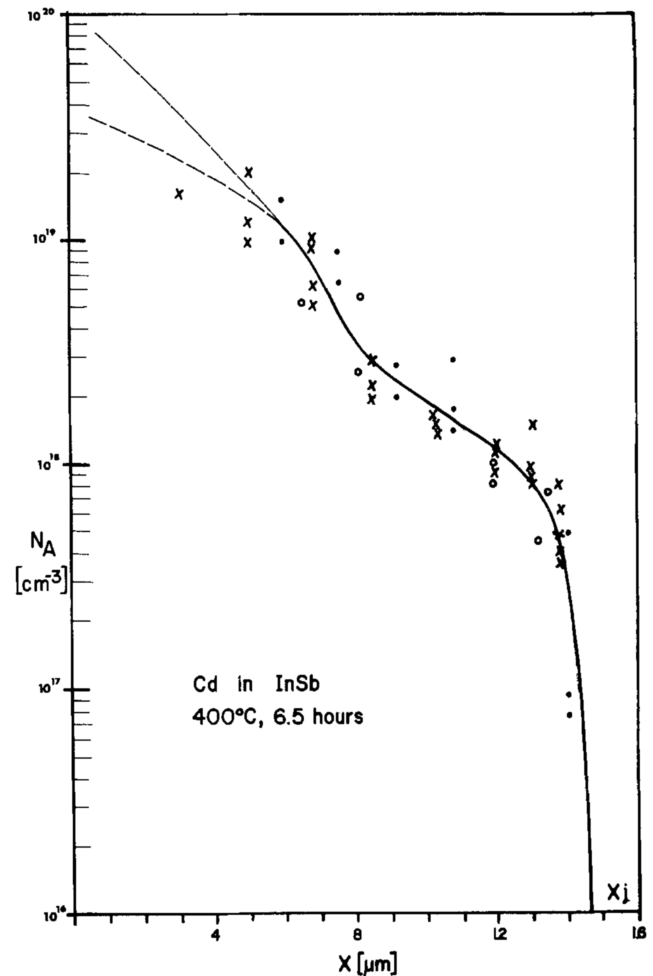

Fig. 2. Diffusion profile of Cd in InSb, measured by the graded C-V method. Experimental points represent several capacitors on three samples. The surface concentration was too high to be measured by this technique.

value $D(C_1)$ at any concentration C_1 on an experimentally-measured profile $C(x)$ as (5)

$$D(C_1) = -\frac{1}{2t_1} \left(\frac{dx}{dC} \right)_{C_1} \int_0^{C_1} x dC \quad [4]$$

where t_1 is the diffusion time used in the experiment.

Functions $D(C)$ that were obtained by applying Eq. [10] on profiles measured by us and by others (1, 9), are given in Fig. 3. Functions of similar behavior were calculated in GaAs for Zn (4) and P (5). The increase in $D(C)$ with increasing C at the low concentrations range is a consequence of the steepness of the experimental profile at the diffusion front and is physically explainable by the interstitial-substitutional diffusion mechanism (7).

The peak in $D(C)$ at intermediate concentrations reflects the existence of a concave region in the profiles. The fact that the peak of $D(C)$ is time-dependent (4) leads to the conclusion that the validity of the results is in doubt. The peak in $D(C)$ is physically unfeasible: it is the outcome of applying Eq. [4] near the surface, and probably is not representative of bulk diffusion (5). In fact, the diffusion depth of such profiles, plotted *vs.* square root of diffusion time, is not a straight line through the origin (4), indicating that a diffusion coefficient which depends only on the diffusant concentration as in Eq. [2] does not represent the actual diffusion process. It is reasonable to assume that in the actual process there is a dependence of D on x which is responsible for special behavior near the surface, and our previous assumption that a concentration dependence may account for it led us to an unphysical result.

In a more general case, $D(C)$ in Eq. [2] may be replaced by a function $D(x, C, t)$, dependent on depth, diffusant concentration, and diffusion time.

Following the steps for derivation of the Boltzmann-Matano formula (3) without any restricting conditions on D, we obtain

$$D(x_1, \hat{C}_1, t_1) = -\frac{1}{2t_1} \frac{\int_0^{\hat{C}_1} x dC}{\left.\frac{\partial \hat{C}}{\partial x}\right|_{C=\hat{C}_1}} \quad [5]$$

where $\hat{C}(x, t_1)$ is a known profile at a certain time t_1.

This is a generalization of the Boltzmann-Matano formula, giving the local value of D in a single point of a three-dimensional space. If D depends only on C, all the information about $D(C)$ may be extracted from a single experimental profile by means of Eq. [5], but an infinite number of profiles is required for doing so in the general case. Hence, Eq. [5] is not very useful without further assumptions.

With the aid of Eq. [5] we can now prove that a concave region of the diffusion profiles on a logarithmic scale indicates that D is increasing in that region from the surface toward the bulk.

The fact that the profile is concave may be expressed by (see Fig. 4)

$$-\frac{\partial}{\partial x} (\ln C)|_{x_1} > -\frac{\partial}{\partial x} (\ln C)|_{x_2} \quad [6]$$

where (x_1, C_1) and (x_2, C_2) are two points on the profile, and $x_1 < x_2$.

By Eq. [5], the ratio of the values of D in these points is

$$\frac{D_1}{D_2} = \frac{\left.\frac{\partial C}{\partial x}\right|_{x_2}}{\left.\frac{\partial C}{\partial x}\right|_{x_1}} \cdot \frac{\int_0^{C_1} x dC}{\int_0^{C_2} x dC}$$

$$= \frac{\left.\frac{\partial C}{\partial x}\right|_{x_2}}{\left.\frac{\partial C}{\partial x}\right|_{x_1}} \left[1 + \frac{\int_{C_2}^{C_1} x dC}{\int_0^{C_2} x dC}\right]$$

$$< \frac{\left.\frac{\partial C}{\partial x}\right|_{x_2}}{\left.\frac{\partial C}{\partial x}\right|_{x_1}} \left[1 + \frac{(C_1 - C_2)x_2}{C_2 x_2}\right]$$

$$= \frac{\left.\frac{\partial C}{\partial x}\right|_{x_2}}{\left.\frac{\partial C}{\partial x}\right|_{x_1}} \cdot \frac{C_1}{C_2} = \frac{\frac{\partial}{\partial x} (\ln C)|_{x_2}}{\frac{\partial}{\partial x} (\ln C)|_{x_1}} \quad [7]$$

From inequality [6] it follows that

$$\frac{\frac{\partial}{\partial x} (\ln C)|_{x_2}}{\frac{\partial}{\partial x} (\ln C)|_{x_1}} < 1 \quad [8]$$

and by substituting Eq. [8] in Eq. [7] we have

$$\frac{D_1}{D_2} < 1 \quad [9]$$

Discussion

By inspection of diffusion profiles having a concave region near the surface and a steep front, in light of the previous section it may be concluded that: (*i*) Deep in the bulk (where the cadmium concentration is low), the local diffusion coefficient is decreasing along the x direction, causing a profile with a steep front; (*ii*) Near the surface, the local diffusion coefficient is increasing along the x direction, causing a concave region in the profile.

It is physically reasonable to relate the first phenomenon to a concentration dependence of D (6), and the second to the variable x (*i.e.*, to an effect of the surface proximity on D). Ignoring any possible variations of the model in time, the behavior of D may be explained qualitatively by a family of curves as shown in Fig. 5, describing a function $D(x, C)$ that increases with C and increases with x for small values of x. If we mark a decreasing series of concentrations (representing a diffusion profile) on the curves, we get a distribution $D(x)$ with a maximum somewhere below the surface. A plot of this distribution *vs.* C will exhibit the same properties as the curves in Fig. 3. This explains the existence of a maximum in the $D(C)$

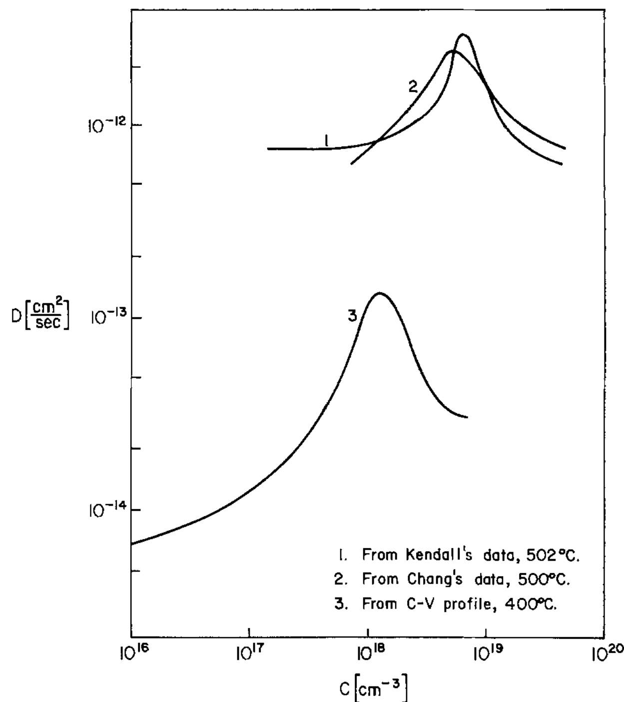

Fig. 3. Concentration dependence of the diffusion coefficient resulting from Boltzmann-Matano analysis of experimentally measured Cd profiles in InSb.

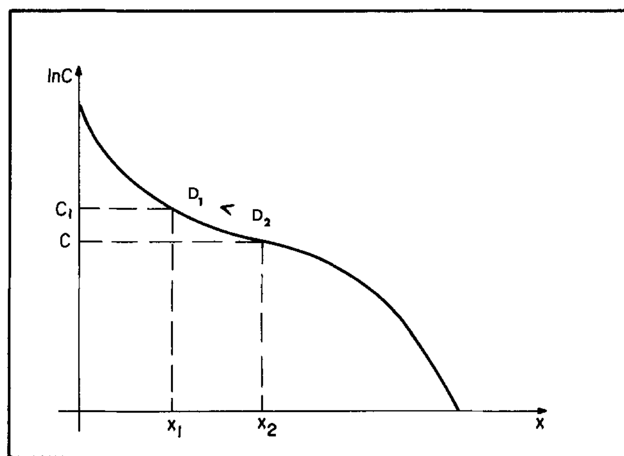

Fig. 4. Two points in the concave region of a diffusion profile. The diffusion coefficient increases with increasing depth in this region.

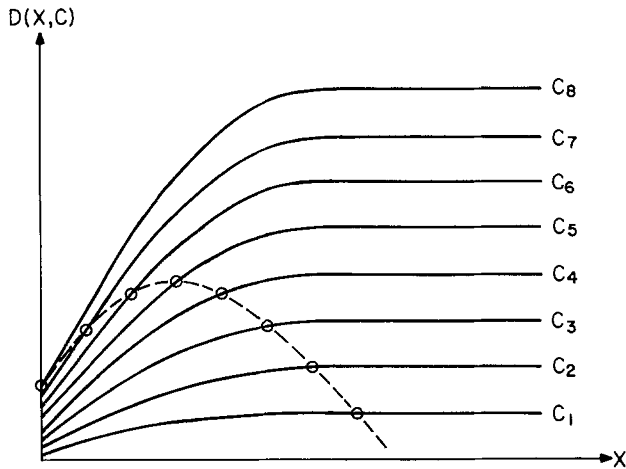

Fig. 5. Curves representing a diffusion coefficient $D(x, C)$ which increases with C and increases with x near the surface. By plotting $D(x)$ along a diffusion profile a peak is obtained.

curve calculated by the standard Boltzmann-Matano method.

The concentration dependence of D is usually explained by the interstitial-substitutional diffusion mechanism with charged interstitial species (6, 3). Another mechanism, based on charged vacancies, has also been proposed for diffusion of Cd in InSb (9). The dependence on x may be explained by an extention of the interstitial-substitutional model.

Following the derivation of the standard interstitial substitutional model (3, 6), it may be shown that

$$D(C) = K\frac{D_i}{C_v}C^n \qquad [10]$$

where D_i is the interstitial diffusion coefficient, C_v is the vacancy concentration, n depends on the interstitial charge, and K is a constant. In the derivation of Eq. [10], C_v was assumed to be constant throughout the sample. Now, if we assume that the surface supplies vacancies to the bulk during the diffusion process, so that the vacancy concentration C_v is decreasing from the surface towards the bulk, D might be expressed in an extended form of Eq. [10]

$$D(x, C, t) = KD_i\frac{C^n}{C_v(x, t)} \qquad [11]$$

In Eq. [11], $C_v(x, t)$ is the vacancy profile which diffuses simultaneously with the cadmium. Each of the curves depicted in Fig. 5 is proportional to the reciprocal of the vacancy profile. Our assumption about the vacancies implies that the interstitial-to-substitutional ratio increases along the x direction near the surface, causing a corresponding increase in diffusion coefficient. Since the incoming vacancies are consumed by interstitials going substitutional, it is reasonable to make a first-order assumption that a stationary vacancy profile is established, thus obtaining a model which does not depend on time. Numerical experiments with the model also support this assumption.

A computer routine for solving a general quasilinear parabolic partial differential equation, of which Eq. [2] is a special case, has been written, such that all the coefficients are parameters and may depend on x, C, and t. The program is based on a stable three-time-level method described by Mitchell (10), and uses Richardson's extrapolation for automatic stepsize control. Computational experiments with that program actually served as motivation for a part of the theory described above. Figure 6 shows theoretical profiles obtained for a diffusion coefficient of the form (10) where n was chosen to equal 1, and $C_v(x, t)$ was arbitrarily assumed to be of the form $1 + K_1 \cdot \exp(-x/L)$, where L is a "vacancy diffusion length" and K_1 is a constant. A qualitative agreement with experiment was clearly obtained: the profiles have a steep front (caused by C^n) and a concave section appears after a certain diffusion time. An exact quantitative agreement with experiment in InSb could not be obtained, due to lack of data, so that n could not be picked optimally, and it was impossible to fit the function C_v exactly.

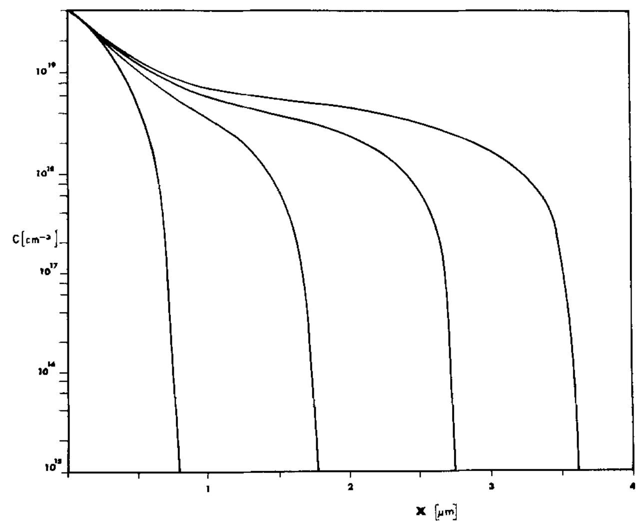

Fig. 6. Diffusion profiles calculated by the computer using the $D(x, C)$ model, for $t = 3, 6, 9, \ldots$ hr.

Figure 7 shows diffusion depth vs. $\sqrt{t}$, as obtained from the computer results. The junction depth is observed to grow slowly in the initial stage, then continues in a straight line that does not cross the origin.

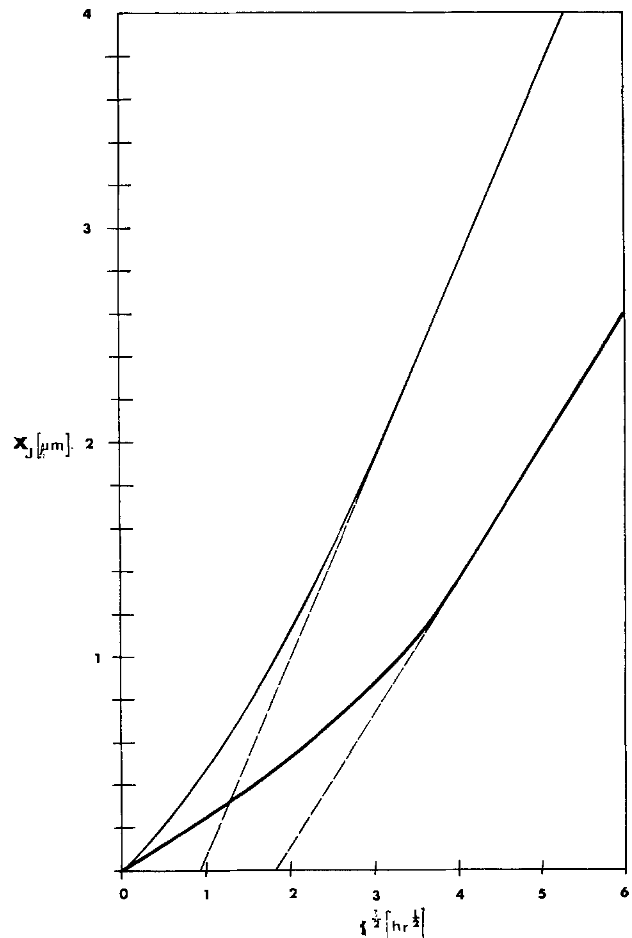

Fig. 7. Diffusion depth vs. square root of diffusion time, calculated using the $D(x, C)$ model for two different parameter sets.

Experimental results of exactly the same nature were published by Ting and Pearson (4) for zinc in GaAs.

Conclusions

A generalization of the Boltzmann-Matano analysis for diffusion profiles has been presented. As a corollary, it has been shown that a concave region in constant-source diffusion profiles (on a semilogarithmic scale) indicates that the diffusion coefficient is increasing in that region toward the bulk. By analysis and synthesis of constant-source diffusion profiles, it has been shown that the outstanding properties of diffusion of various impurities in III-V compounds may be characterized by a nonlinear diffusion coefficient which depends both on the diffusant concentration and the distance from the surface. Time dependence of the diffusion coefficient seems to be negligible. Such a diffusion coefficient may represent an interstitial-substitutional diffusion mechanism with a surface-effect that reduces the diffusion constant at small depths. An extension of the interstitial-substitutional model, assuming an enhanced vacancy concentration near the surface, has been suggested to explain this effect. The model has been implemented on a computer, and theoretical profiles that have been produced show a good qualitative agreement to experiment in shape and time dependence of the diffusion depth.

Acknowledgments

The authors are indebted to Prof. I. Blech for helpful discussions and comments on the manuscript. Some aspects of the problem have been the subject of fruitful discussions with Prof. K. Weiser, Prof. J. Steinberg, and Dr. E. Segall.

Manuscript submitted Aug. 10, 1977; revised manuscript received Nov. 28, 1977.

Any discussion of this paper will appear in a Discussion Section to be published in the June 1979 JOURNAL. All discussions for the June 1979 Discussion Section should be submitted by Feb. 1, 1979.

REFERENCES

1. L. L. Chang, *Solid-State Electron.*, **10**, 539 (1967).
2. C. K. Kim, Ph.D. Thesis, Stanford University, Stanford, Calif. (1974).
3. B. Tuck, "Introduction to Diffusion in Semiconductors," Peter Peregrinus, Stevenage (1974).
4. C. H. Ting and G. L. Pearson, *This Journal*, **118**, 1454 (1977).
5. G. C. Jain, D. K. Sadana and B. K. Das, *Solid-State Electron.*, **19**, 731 (1976).
6. L. R. Weisberg and J. Blanc, *Phys. Rev.*, **131**, 1548 (1963).
7. J. Verjans and R. J. Van Overstraeten, *Solid State Electron.*, **18**, 911 (1975).
8. B. I. Boltaks and V. I. Sokolov, *Sov. Phys.-Solid State*, **5**, 785 (1963).
9. D. L. Kendall, in "Semiconductors and Semimetals," Vol. 4, R. K. Willardson and A. C. Beer, Editors, p. 163, Academic Press, New York (1968).
10. A. R. Mitchell, "Computational Methods in Partial Differential Equations," p. 95, John Wiley & Sons, New York (1969).

Kinetics of Tungsten Deposition by the Reaction of WF_6 and Hydrogen

W. A. Bryant*

Westinghouse Electric Corporation, Research and Development Center, Pittsburgh, Pennsylvania 15235

ABSTRACT

Experimental rate data from a number of investigations on the chemical vapor deposition of tungsten by the hydrogen reduction of WF_6 were analyzed to determine the reaction mechanisms which controlled the process under experimental conditions in which mass transport limitiation was absent. Rate-controlling mechanisms were identified by comparing reaction orders obtained from the experimental data with those obtained from rate equations derived for each possible rate-controlling step. Where the reactant stream was expected to remain streamlined and only slightly heated through contact with the tungsten substrate, the rate-controlling mechanism was determined to be the dissociation of H_2 molecules adsorbed on the substrate. The activation energy for this process step was 67,000 J/mole. The reaction orders with respect to WF_6 and H_2 were zero and one-half, respectively. With experimental conditions more conducive to gas stream turbulence and stream heating, deposition rate was controlled by homogeneous gas phase reactions also having an activation energy of about 67,000 J/mole. The reaction order for this mechanism was 2 with respect to both reactants.

Although a considerable amount of work has been reported on the kinetics of tungsten deposition by the H_2 reduction of WF_6 according to the over-all reaction

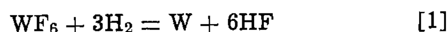

$$WF_6 + 3H_2 = W + 6HF \quad [1]$$

the rate-controlling mechanism(s) is still not completely understood. Carlton and Oxley (1) have demonstrated that the rate of tungsten deposition from WF_6 could be predicted within the regime of mass transport control. Later investigations further established that mass transport is rate controlling in this system at relatively high temperature-high pressure combinations (2, 3).

At lower temperature-pressure combinations, other processes control the deposition rate. However, the identity of the processes has not been firmly established. Haskell (4) concluded that a model based on HF desorption from the tungsten substrate was able to describe the rate data of Holman and Huegel (5). Some support for this mechanism was provided by other correlations (2) of rate data (6), however, that analysis did not provide a strong enough test of the data correlations to completely rule out other rate-controlling mechanisms. Cheung (7) has shown

* Electrochemical Society Active Member.

that a model based on the dissociation of hydrogen adsorbed on the tungsten substrate was able to explain both his data and that of Holman and Huegel. Huegel *et al.* (8), using their results of experiments in which small amounts of HCl were added to the reactant stream to serve as a deposition retardant, concluded that the Cheung model rather than the one of Haskell best described their results. Brecher's analysis (9) of the data of Berkeley *et al.* (10) did not provide identification of a rate-controlling mechanism since the analysis combined data obtained both from the regime of substrate surface process control and mass transport control.

It was the purpose of the present work to critically examine all available rate data obtained under controlled conditions for this chemical vapor deposition reaction and to definitively establish the rate-controlling mechanism(s) outside the regime of mass transport control.

Procedure

Mass transport control of a chemical vapor deposition reaction is favored by relatively high pressure and temperature and relatively low reactant flow rate. Thus correlations between these parameters and tungsten deposition rates were used to establish the boundaries separating mass transport controlled and nonmass transport controlled regimes. Only data from the latter regime were further analyzed to determine rate control mechanisms. These data included those in which the reactants were diluted with either argon or HF. [The work of Huegel *et al.* demonstrated that the influence of HF was one of dilution rather than substrate surface poisoning.]

Plots were made of deposition rate as a function of the reciprocal of substrate temperature for essentially constant pressure and gas composition and with reactant flow rates great enough as to not significantly affect deposition rate. In the region of maximum slope the deposition rate varies exponentially with temperature. However, as the extent of mass transport control becomes significant at higher temperature, the slope decreases. At the highest temperatures, the slope eventually corresponds to square root dependence on temperature as dictated by boundary layer theory. Figures 1 through 3 are examples of this type of data plot.

From Fig. 1 only the data of Berkeley *et al.*, corresponding to H_2/WF_6 of 3 and 4 and a temperature

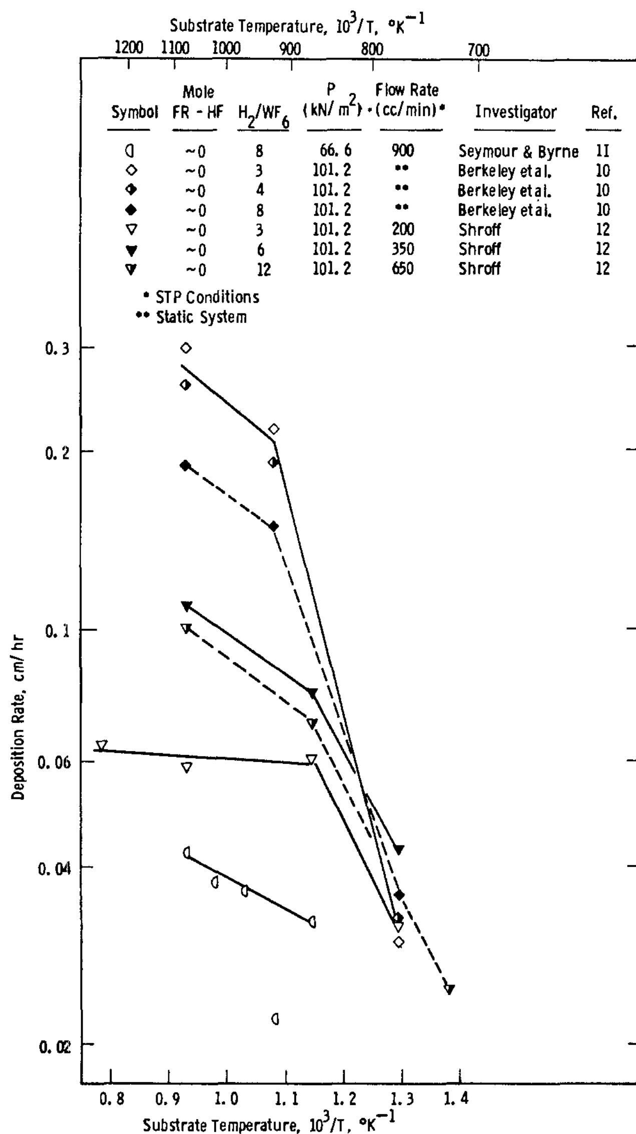

Fig. 1. Temperature dependence of tungsten deposition rate for high pressure (66.6-101.2 kN/m²).

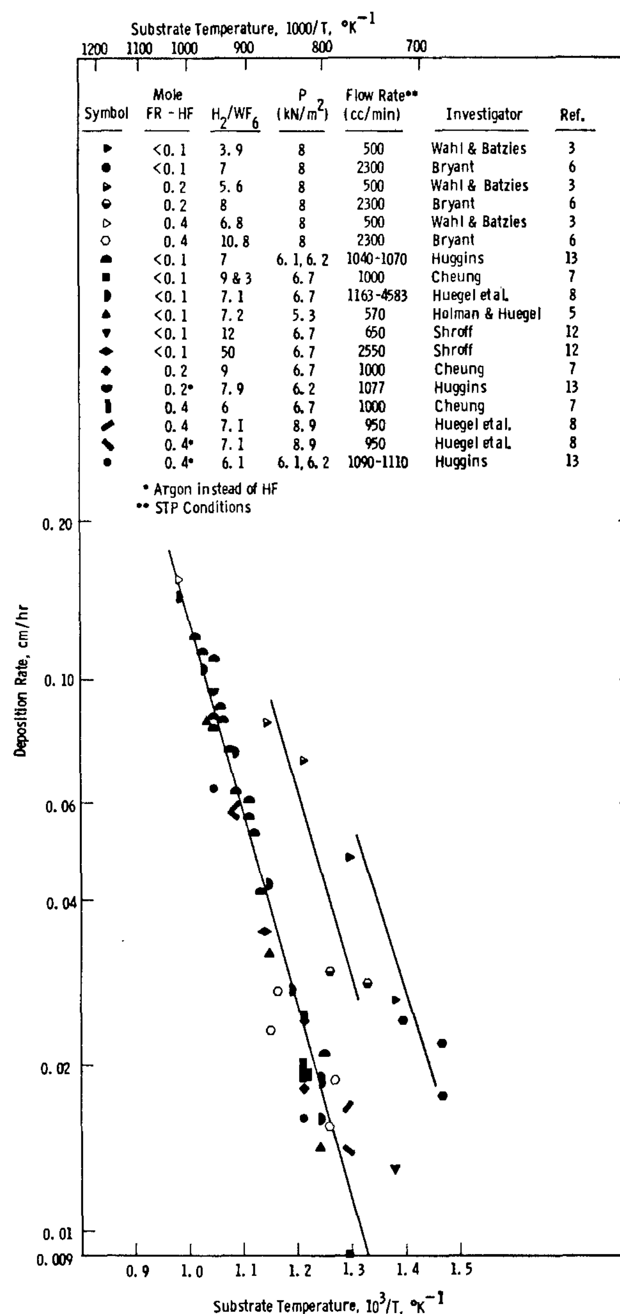

Fig. 2. Temperature dependence of tungsten deposition rate for various levels of dilution and for intermediate pressures (5.3-8.9 kN/m²).

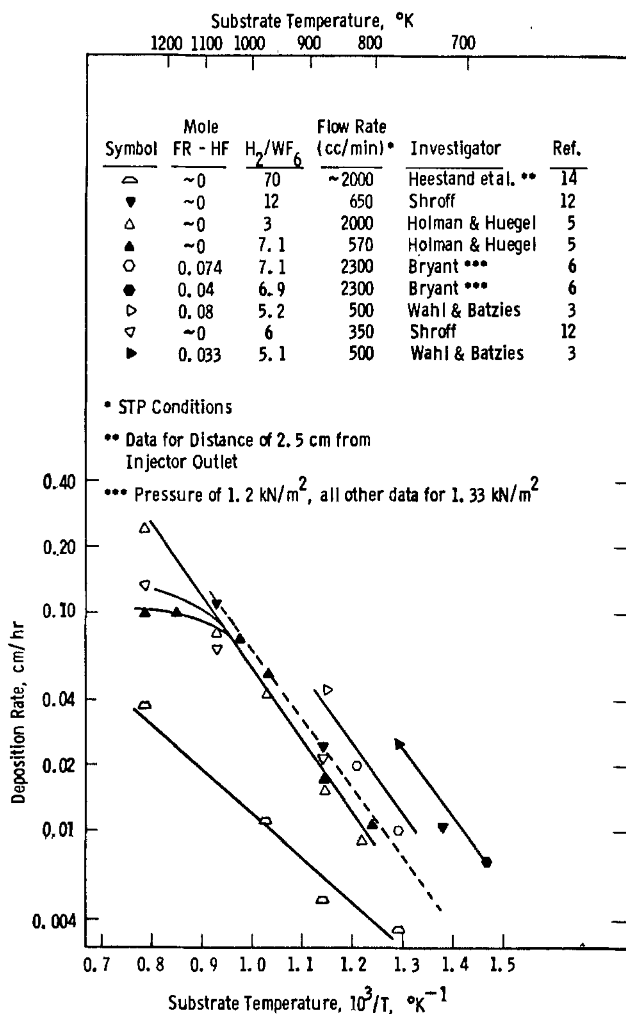

Fig. 3. Temperature dependence of tungsten deposition rate for little or no HF dilution and for low pressures (1.2-1.33 kN/m²).

of 773°K, were considered to be free of significant mass transport control. All the Fig. 2 data were judged to have been little influenced by mass transport. The data of Heestand *et al.* (14) in Fig. 3 were felt to have been obtained under conditions of excessive control by mass transport. All data for temperatures greater than 873°K were not considered further (even though some of them were undoubtedly associated with insignificant mass transport resistance) since they were too few in number to warrant the effort involved in their analysis.

Plots of deposition rate as a function of pressure (for example, Fig. 4) were constructed from data taken at essentially constant temperature and gas composition and at sufficient flow rate to minimize, as much as possible, resistance from mass transport. In these plots the onset of significant mass transport control was taken to be the pressure at which the deposition rate became essentially pressure independent. Therefore to eliminate data influenced by mass transport control, all data for pressures greater than 20 kN/m² were eliminated from further analysis. The data point of Berkeley *et al.* was not eliminated since it was previously accepted by the analysis of Fig. 1.

The onset of significant mass transport control was also indicated by a pronounced dependence of deposition rate on flow rate as the flow rate was reduced and the other parameters were held essentially constant. This criterion is in keeping with film theory (or boundary layer theory) since, as flow decreases, film thickness increases to an eventual value at which diffusion through the film completely controls the rate of deposition. In determining the cutoff point for onset of significant mass transport resistance, it

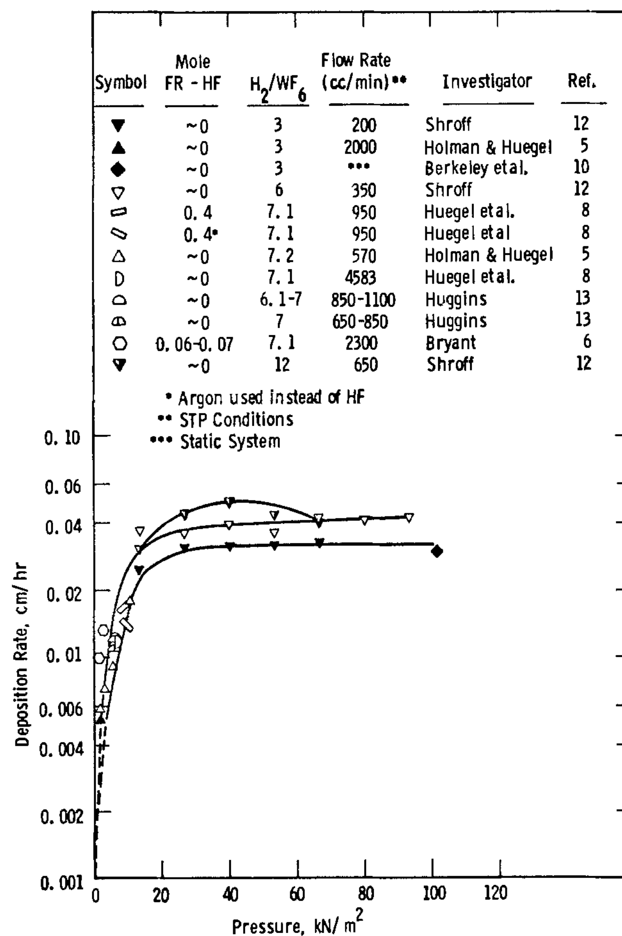

Fig. 4. Pressure dependence of tungsten deposition rate at 773°K for various gas compositions and flow rates.

was necessary that, as much as possible, each investigator's data be analyzed separately. This precaution was taken since, as observed by Chin (15), differences in experimental setups could be sufficient to influence the data. This influence was most noticeable in evaluation of flow rate data. In each curve of Fig. 5, for example, the data point corresponding to the lowest flow rate of Huggins (13) was considered

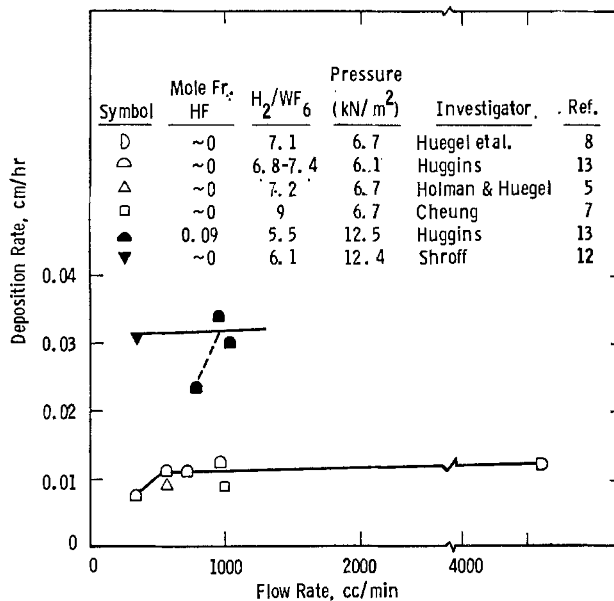

Fig. 5. Flow rate dependence of tungsten deposition rate. Data are for 773°K.

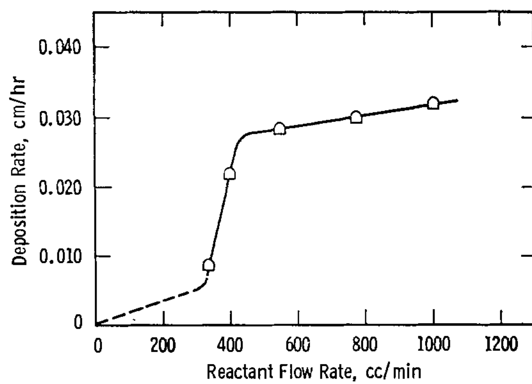

Fig. 6. Flow rate dependence of tungsten deposition rate using data of Huggins for 853°K, pressure of 6.1 kN/m² and H_2/WF_6 of 7.

to involve partial mass transport control even though in one case (nominal 12.5 kN/m² pressure) a data point of another investigator, at lower flow was not eliminated from further evaluation.

Even with the precautions taken, it is doubtful that the influence of mass transport on deposition rate was completely eliminated for data selected for further analysis. In Fig. 6 are plotted tungsten deposition data obtained under conditions which are fairly typical of those corresponding to the data of the present study. Flow rates between about 300 and 500 cm³/min define the region of mass transport control. Below 300 cm³/min convective transport effects are appreciable. Flow rates greater than about 500 cm³/min are required to essentially eliminate mass transport resistance for the subject conditions. A condition of zero transport resistance is reached only where no dependence of deposition rate on flow is indicated. However, since this dependence is asymptotic, only the use of intolerably high flow rates would eliminate this resistance altogether.

Other data, in addition to those given in Fig. 1-5, were used in the kinetic analysis. Some of these were obtained by interpolation or extrapolation. Where this was necessary, only data from a single investigator were used and extrapolations were made only to lower pressure or temperature.

HF mole fractions in the gas stream were calculated from weight change data for the investigations of Huggins (13), Wahl and Batzies (3), and Bryant (6). Since the substrate surface areas for the remaining investigations were no greater than the least of the above, it was assumed that the amount of HF formed was also no greater. Thus in many cases an assumption of essentially no HF formation was warranted. Where this assumption was not warranted and the HF concentration could not be calculated because of insufficient information, the corresponding kinetic data were not included in the study.

Deposition rate data obtained in fluidized bed systems [Oxley *et al.* (16) and Sump and Howard (17)] were also eliminated since, with the attendant very high substrate surface area and WF_6 utilization, different processes can control within different portions of the bed. [It is for this reason that Oxley *et al.* (16) determined an over-all activation energy of 30,600 J/mole for their process rather than either a much smaller value associated with mass transport (2) or a much larger value associated with the absence of mass transport (3, 5, 13, 18, 19)].

Using only the rate data found to be essentially without influence from mass transport, reaction orders with respect to each reactant were determined from log-log plots of deposition rate as a function of partial pressure of the reactant for three levels of temperature (773°, 823°, and 873°K). Care was taken to hold essentially constant the partial pressure of the other reactant and the temperature.

By comparing the experimentally determined reaction orders with respect to both reactants to those determined from Langmuir-Hinshelwood type rate equations for various possible rate-controlling mechanisms (Table I), the actual rate-controlling mechanisms were identified. Details of the procedure used to formulate these rate equations are given in Appendix A.

Results

In both Fig. 2 and 3 it was noted that for the condition of little or no presence of diluent (HF or A) the deposition rate was greater for comparable deposition parameters for the data of both Wahl and Batzies and Bryant. This suggested a reaction mechanism for these data which was different from the one for the data of the remaining investigators. This

Table I. Rate equations and reaction orders derived for study of kinetics of tungsten formation by chemical vapor deposition

Kinetic step	Rate equation: Full expression	Rate equation: Simplified form	Reaction order with respect to reactant: Hydrogen	Reaction order with respect to reactant: WF_6
1. WF_6 adsorption	$R = \dfrac{K_r p_{ai} M/\rho_w}{\left[1 + \dfrac{K_a p_{ci}^6}{K_{eq} p_{bi}^3} + (K_b p_{bi})^{1/2} + K_c p_{ci}\right]}$	$R = K_r p_{ai}$	0	1
2. H_2 adsorption	$R = \dfrac{K_r p_{bi} M/\rho_w}{\left[1 + K_a p_{ai} + \left(\dfrac{K_b p_{ci}^2}{K_r p_{bi}^{1/2} M/\rho_w}\right) + K_c p_{ci}\right]^2}$	$R = K_r p_{bi}$	1	0
3. H_2 dissociation	$R = \dfrac{K_r p_{bi}^{1/2} M/\rho_w}{\left[1 + K_a p_{ai} + \left(\dfrac{K_b p_{ci}^2}{K_{eq}^{1/3} p_{ai}^{1/3}}\right)^{1/2} + K_c p_{ci}\right]^2}$	$R = K_r p_{bi}^{1/2}$	1/2	0
4. Chemical reaction	$R = \dfrac{K_r K_a K_b \left[p_{ai} p_{bi}^3 - \dfrac{p_{ci}^6}{K_{eq}}\right] M/\rho_w}{[1 + K_a p_{ai} + (K_b p_{bi})^{1/2} + K_c p_{ci}]^n}$	$R = K_r' p_{ai} p_{bi}^3$	3	1
5. HF desorption	$R = \dfrac{K_r[(K_{eq} p_{ai} p_{bi}^3)^{1/6} - p_{ci}] M/\rho_w}{[1 + K_a p_{ai} + (K_b p_{bi})^{1/2} + K_c (K_{eq} p_{ai} p_{bi}^3)^{1/6}]^n}$	$R = K_r'' p_{ai}^{1/6} p_{bi}^{1/2}$	1/2	1/6
6. Homogeneous reaction a	$R = K_r \left[p_{ai}^2 p_{bi}^2 - \dfrac{p_{di}}{K_{eq}}\right] M/\rho_w$	$R = K_r p_{ai}^2 p_{bi}^2$	2	2
6. Homogeneous reaction b	$R = K_r \left[p_{ai}^2 p_{bi}^2 - \dfrac{P_{ci}^2 p_{di}}{K_{eq}}\right] M/\rho_w$	$R = K_r p_{ai}^2 p_{bi}^2$	2	2
6. Homogeneous reaction c	$R = K_r \left[p_{ai}^2 p_{bi} - \dfrac{p_{di}}{K_{eq}}\right] M/\rho_w$	$R = K_r p_{ai}^2 p_{bi}$	1	2

same segregation was found in the plots of experimental data for determination of reaction order with respect to each reactant (Fig. 7 through 12) where the data have also been grouped by partial pressure of the other reactant, *i.e.*, partial pressure of the reactant whose order is not being determined.

The reaction orders determined from the experimental data are listed in Table II. Reaction orders other than 2 could have been assigned to the data of Wahl-Batzies and Bryant. However the value adopted is most compatible with the findings of Huggins (13) whose work provided experimental evidence for reactions [2] and [3]. Comparison of these values with those obtained from the derived rate equations (Table I) indicate that the deposition data of Wahl-Batzies and Bryant represent control by a homogeneous reaction, specifically one of the following

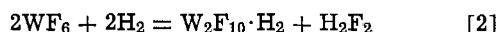

$$2WF_6 + 2H_2 = W_2F_{10}\cdot H_2 + H_2F_2 \quad [2]$$

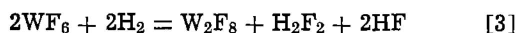

$$2WF_6 + 2H_2 = W_2F_8 + H_2F_2 + 2HF \quad [3]$$

From this comparison it is further indicated that the deposition data of the other investigators represent deposition control by H_2 dissociation on the tungsten surface.

Further evidence for the existence of two rate-controlling mechanisms in the nontransport controlled regime was provided by data concerning the influence on deposition rate of diluents added to the reactant stream (Fig. 2). The deposition rates of both Wahl and Batzies and Bryant were strongly influenced by the presence of diluent. This is the result to be expected for a homogeneous, gas-phase process since the concentration dependence of the deposition rate was large, as shown by a value of 2 for the reaction order with respect to each reactant. In contrast, the deposition rate at constant temperature for the controlling substrate surface reaction would be expected to be only slightly dependent on the reactants' partial pressures at the substrate. This conclusion follows from the determination of low reaction orders for the mechanism of H_2 dissociation.

The influence of HF on the rate of deposition controlled by the homogeneous process is one of dilution only. With the combined partial pressures of the reactants held nearly constant, the deposition rate was independent of HF concentration in the gas stream (Fig. 13).

An activation energy of 67,000 J/mole was determined for both the homogeneous, gas-phase process and the dissociation of H_2.

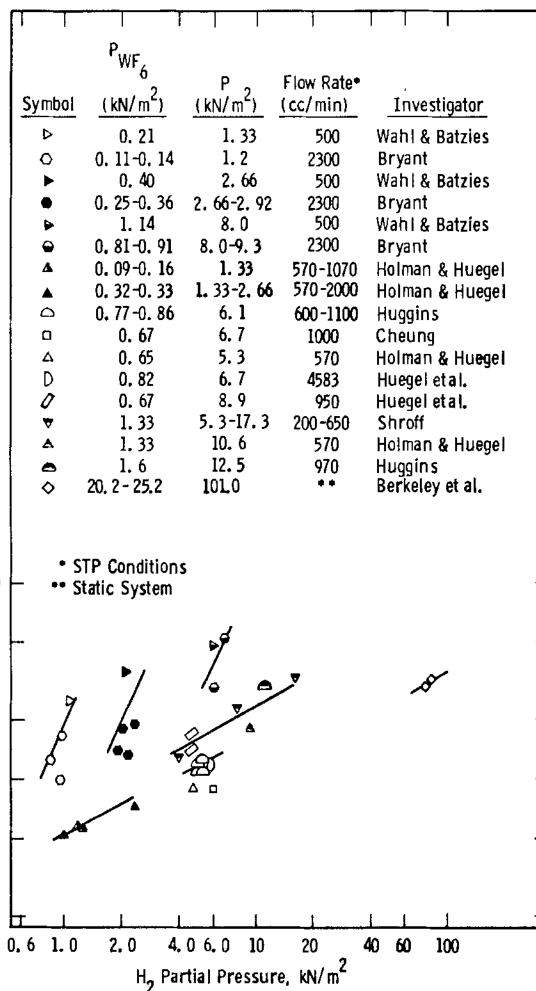

Fig. 8. Plots to determine reaction order with respect to hydrogen at 773°K.

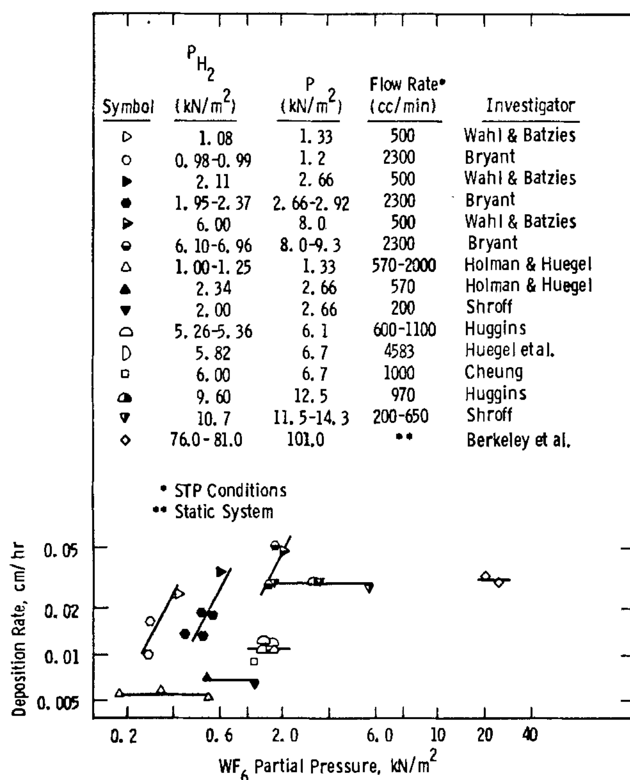

Fig. 7. Plots to determine reaction order with respect to WF_6 at 773°K.

Discussion

Identification of the rate-controlling surface reaction as H_2 dissociation agrees with the earlier result of Cheung. Further evidence supporting this mechanism as rate controlling is provided by the activation energy of 67,000 J/mole determined from the appropriate data of Fig. 1 through 3. The dissociation is

Table II. Experimentally determined reaction orders

Deposition temperature (°K)	Experimental reaction order with respect to reactant: HH, S, C, H, $\overline{H}$, Be* H_2	HH, S, C, H, $\overline{H}$, Be* WF_6	WB, B* H_2	WB, B* WF_6
773	½	0	2	2
823	½	0	2	2
873	½	0	2	2

* HH = Holman and Huegel, S = Shroff, C = Cheung, H = Huegel *et al.*, $\overline{H}$ = Huggins, Be = Berkeley *et al.*, WB = Wahl and Batzies, B = Bryant.

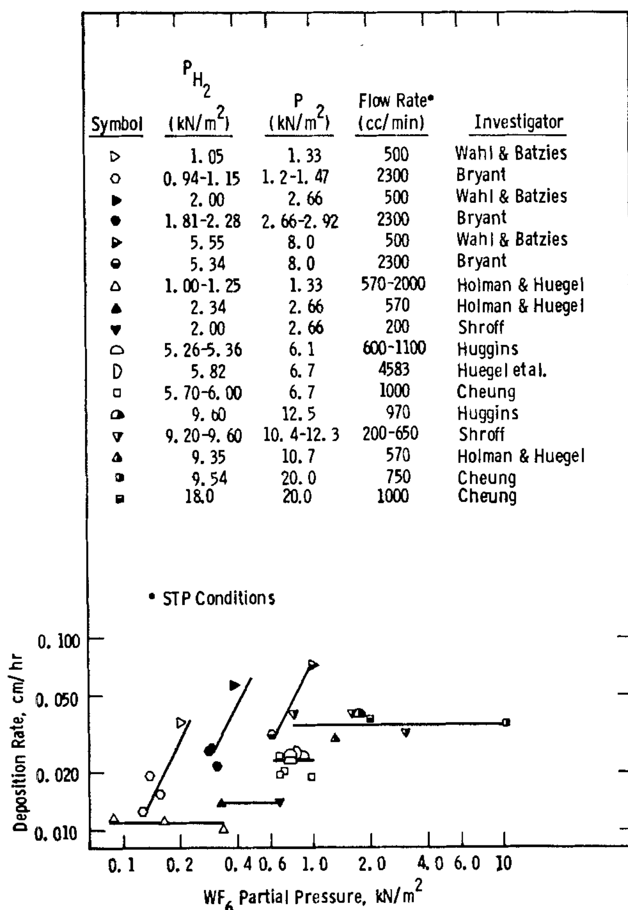

Fig. 9. Plots to determine reaction order with respect to WF_6 at 823°K.

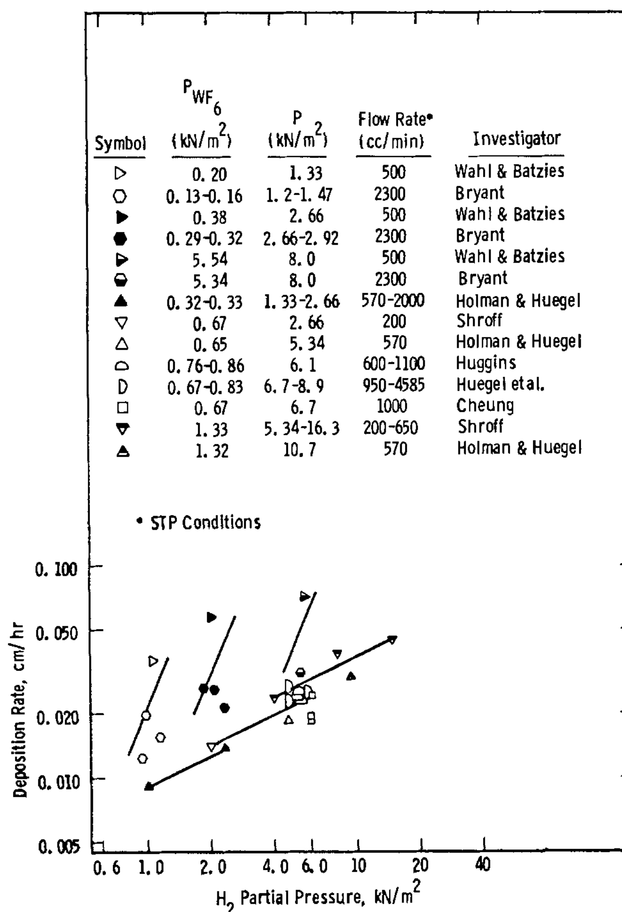

Fig. 10. Plots to determine reaction order with respect to hydrogen at 823°K.

completed by the jumping of one of the H atoms to a neighboring lattice site (7). The reported values for H_2 surface diffusion on tungsten are also 67,000 J/mole (20, 21).

The activation energy for the H_2 dissociation mechanism is in good agreement with the separate values for surface processes obtained by Holman and Huegel (67,000 J/mole), Shim and Byrne (18) (67,000 J/mole), Haskell and Byrne (19) (63,000 J/mole), and Huggins (65,400 J/mole).

A mechanism of homogeneous reaction finds support in the observations of both Huggins and Wahl and Batzies. The former found the compound W_2F_9 condensed in the cold trap of his experimental setup. A combination of the two tungsten-bearing molecules formed by reactions [2] and [3] would yield a product having the same ratio of fluorine to tungsten. The latter investigators observed, at low pressures of about 1.0 kN/m² or less, a strong dependence of growth rate on pressure (R proportional to $P^{1.8}$ to R proportional to $P^{3.3}$). [At higher pressures this dependence is less owing to effects produced by partial mass transport control (22)]. From the results of the present work, the exponent was 0.5 for rate control by the surface process. Mass transport control would also be expected to exhibit a much lower dependence of deposition rate on pressure.

It is suggested that the gas phase reactions do not stop with the formation of monomers, but instead proceed to form particles larger in size than the thermodynamically stable size. According to the theory of homogeneous gas-phase nucleation (23), the rate of formation of critical-sized nuclei, given by Eq. [4], is an exponential function of temperature

$$J = \frac{\alpha \Pi r^{*2} P C}{(2 \Pi m k T)^{1/2}} e^{-\Delta F^*/kT} \quad [4]$$

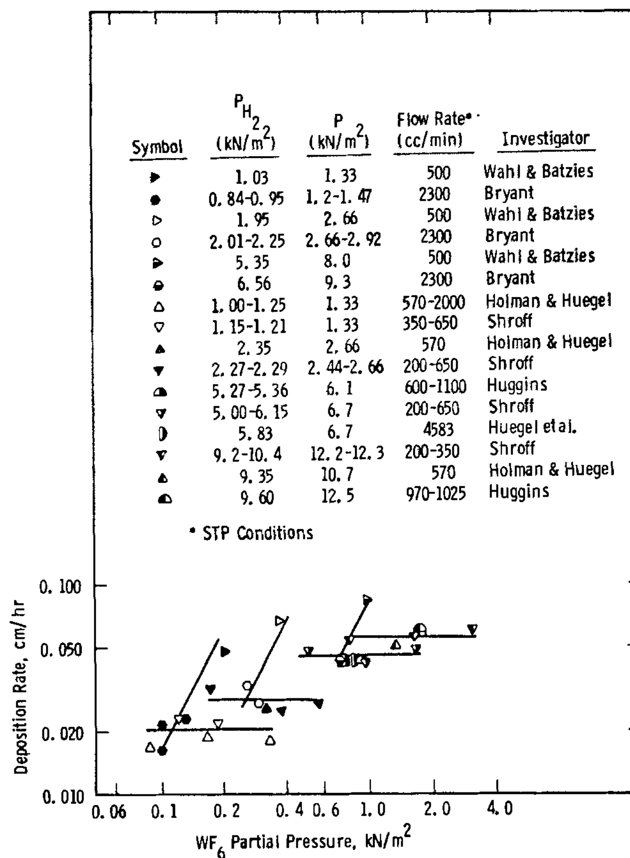

Fig. 11. Plots to determine reaction order with respect to WF_6 at 873°K.

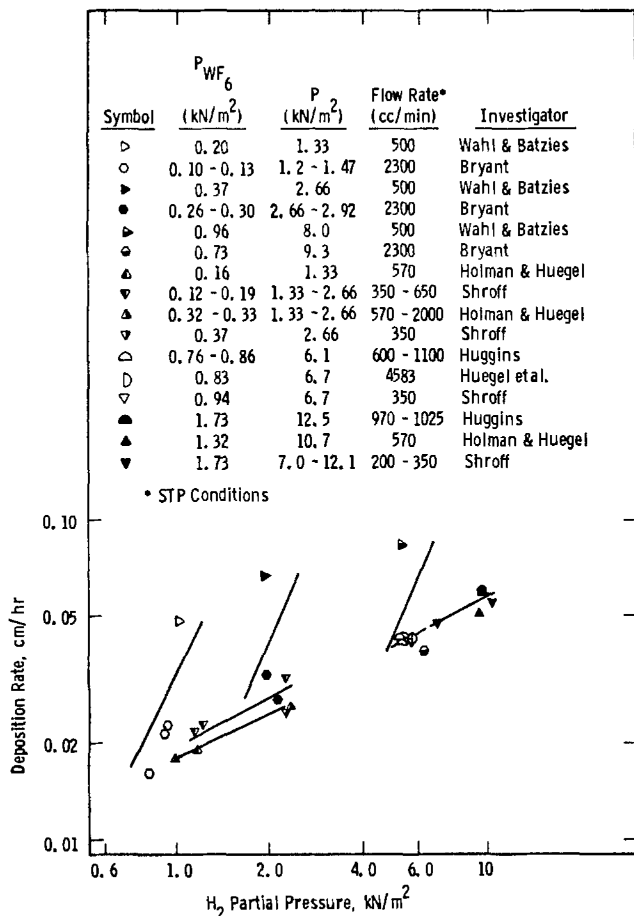

Fig. 12. Plots to determine reaction order with respect to hydrogen at 873°K.

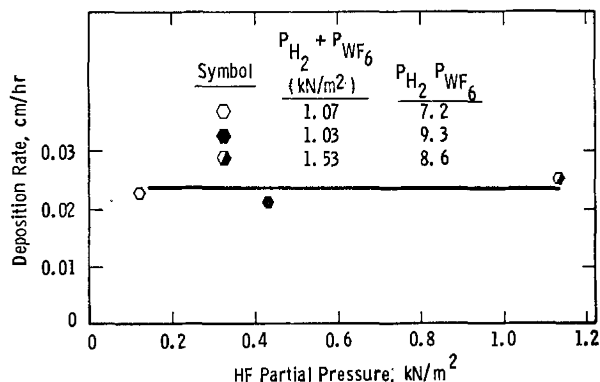

Fig. 13. HF partial pressure dependence of tungsten deposition rate for process control by homogeneous gas-phase reaction. Data are for 873°K and flow rate of 2300 cm^3/min [Ref. (6)].

It was this form of temperature dependence that was found in the present work for the data of Wahl and Batzies, and Bryant, rather than the $T^{1/2}$ dependence which would have been found if only monomers had been formed according to the collision frequency suggested by kinetic gas theory (24).

Further support for the Wahl and Batzies, and Bryant, data conforming to control by homogeneous reaction is provided by the observed linear dependence of deposition rate on the concentration of HF diluent (Fig. 14). This same linear dependence is found in relation [4] where the concentration term occurs to the first power.

Under seemingly very similar experimental conditions two modes of reaction rate control were found to occur outside the regime of mass transport control. Two conditions would favor homogeneous reaction

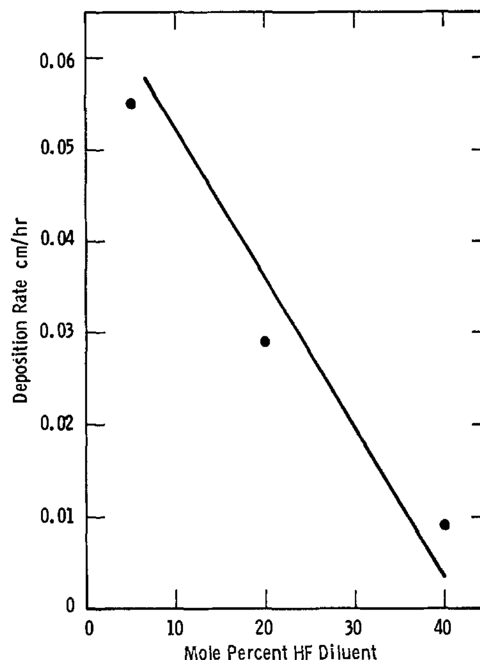

Fig. 14. Influence of HF dilution on deposition rate for the data of Wahl and Batzies, and Bryant (Data were taken from Fig. 2 for a temperature of 770°K. A value of 5 mole percent was assigned to the data corresponding to 10 mole percent diluent or less.)

over heterogeneous reaction control. Higher gas temperature and greater turbulence of the gas would both favor a homogeneous process, the former by increasing the equilibrium concentration of critical-sized nuclei and the latter by increasing the frequency of interparticle collisions.

To see if any of the experimental investigations could have produced a relatively higher gas temperature, the relative heat transfer rates for each investigator's experimental setup were calculated for representative experimental conditions by the procedure of Appendix B. The heat transfer data (Table III) show that a higher gas temperature would be expected for the work of the present author and thus reaction in the gas phase would be more favored in that experimental setup.

The second condition favoring a homogeneous process (increased molecular collisions resulting from gas turbulence) would be expected for the experimental arrangement of Wahl and Batzies where the linear velocity of the gas stream was, relatively, very high (Table III). Impingement of the stream on the flat substrate disk would produce little streamlined flow past the substrate whose diameter (2 cm) was greater than the diameter of the reactant gas nozzle (0.65 cm) located only 1.5 cm from the substrates. The stream velocities of the experimental arrange-

Table III. Data used in the analysis to determine conditions favorable to homogeneous reaction

Investigator	Relative heat transfer rate	Linear gas velocity (cm/sec)	Reference
Berkeley *et al.*	4.4	~0*	(10)
Huggins	20.5	131	(13)
Holman and Huegel	21.7	66	(5)
Cheung	15.3	116	(7)
Huegel *et al.*	26.4	110	(8)
Shroff	13.6	164	(12)
Wahl and Batzies	9.7	1060	(3)
Bryant	173.0	86	(6)

* Static system.

ments conducive to surface process control were much lower. Additionally, more streamlined flow would be expected for these arrangements since the substrate dimension normal to the gas flow direction was small relative to the stream diameter.

The deposition rates observed for the homogeneous process (in the absence of dilution) were greater than those found for the heterogeneous process under identical experimental conditions. It is suggested that residual mass transport resistance was lessened for the two investigations involving the homogeneous process. The greater degree of gas turbulence in the work of Wahl and Batzies would decrease the reactive film thickness as would the greater gas temperature determined for the work of Bryant.

The activation energy found for the homogeneous, gas-phase process of 67,000 J/mole is not in agreement with the value of 56,000 J/mole obtained by Wahl and Batzies for their data. This discrepancy is possibly the result of these authors' failure to account for the effect of HF dilution on deposition rate.

Conclusions

Under experimental conditions of minimal influence by mass transport control, the deposition of tungsten by the H_2 reduction of WF_6 is controlled either by the dissociation of H_2 on the substrate or by homogeneous, gas-phase reactions. The degree of gas stream turbulence and heating determines which of the two processes is rate controlling. An activation energy of 67,000 J/mole was found for each process.

Manuscript submitted July 27, 1977; revised manuscript received March 23, 1978.

Any discussion of this paper will appear in a Discussion Section to be published in the June 1979 JOURNAL. All discussions for the June 1979 Discussion Section should be submitted by Feb. 1, 1979.

Publication costs of this article were assisted by Westinghouse Electric Corporation.

APPENDIX A

Formulation of Rate Equations

The method of Yang and Hougen (25) was used to formulate rate equations for each possible step in the over-all reaction sequence. This methodology is based on Langmuir-Hinshelwood models for competitive adsorption by reactants. Many of the reaction steps suggested by Yang and Hougen were eliminated from further consideration by the knowledge that WF_6 would be expected to strongly adsorb on tungsten (26, 27) (the deposit substrate after the first few minutes of deposition) and that hydrogen would be readily atomically adsorbed (28).

The following reactions remained as possible rate-controlling steps. All but the last are surface processes.

1. Adsorption of WF_6
2. Adsorption of H_2
3. Dissociation of H_2
4. Chemical reaction between WF_6 and H_2
5. Desorption of HF
6. Homogeneous, gas-phase reactions as follows[1]

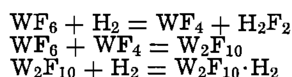

$$WF_6 + H_2 = WF_4 + H_2F_2$$
$$WF_6 + WF_4 = W_2F_{10}$$
$$W_2F_{10} + H_2 = W_2F_{10}\cdot H_2$$

a. $$2WF_6 + 2H_2 = W_2F_{10}\cdot H_2 + H_2F_2 \qquad [A\text{-}1]^2$$

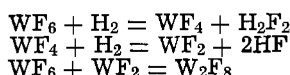

$$WF_6 + H_2 = WF_4 + H_2F_2$$
$$WF_4 + H_2 = WF_2 + 2HF$$
$$WF_6 + WF_2 = W_2F_8$$

b. $$2WF_6 + 2H_2 = H_2F_2 + 2HF + W_2F_8 \qquad [A\text{-}2]^3$$

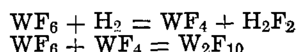

$$WF_6 + H_2 = WF_4 + H_2F_2$$
$$WF_6 + WF_4 = W_2F_{10}$$

c. $$2WF_6 + H_2 = H_2F_{10} + H_2F_2 \qquad [A\text{-}3]$$

[1] These reactions have been suggested by Huggins.
[2] Equation [A-1] is the same as Eq. [2].
[3] Equation [A-2] is the same as Eq. [3].

As shown by Yang and Hougen the net rate of a reaction can be written in the form

$$\text{rate} = \frac{(\text{kinetic term})\,(\text{potential term})}{(\text{adsorption term})^n} \qquad [A\text{-}4]$$

where n equals the number of substrate surface sites involved in the reaction. For the purpose of illustration, the rate equation for HF desorption was developed as follows, with the subscripts a, b, and c used to designate respectively the gases WF_6, H_2, and HF.

The kinetic term includes factors for the total number of active surface sites, the number of adjacent sites, an effectiveness factor, and a rate constant. These separate terms were combined into a single reaction rate constant K_r.

The potential term is the difference between the actual surface concentration (activity) and the equilibrium activity of HF gas. With these interfacial activities replaced by partial pressure values and by employing the definition of the equilibrium constant, the potential term was written as

$$(\text{potential term}) = [(K_{eq}P_{ai}P_{bi}^3)^{1/6} - P_{ci}] \qquad [A\text{-}5]$$

The general term for adsorption (all reactants and products adsorbed under equilibrium conditions and without dissociation) is given by the reaction

$$(\text{adsorption term}) = [1 + K_aP_{ai} + K_bP_{bi} + K_cP_{ci}]^n \qquad [A\text{-}6]$$

Again the equilibrium value of P_{ci} was placed in terms of the partial pressures of the reactants. Replacement in the general adsorption term was made from Table III of the subject reference to account for the dissociation of H_2. A value of unity was assigned to the exponent n according to the instructions of Table IV of the subject reference.

By making the appropriate substitutions into Eq. [A-4] and multiplying by a term consisting of the molecular weight of tungsten divided by its density, the final rate equation for the deposition rate, R (in centimeters per hour), as controlled by HF desorption was obtained

$$R = \frac{Kr[(K_{eq}P_{ai}P_{bi}^3)^{1/6} - P_{ci}]M/\rho_w}{1 + K_aP_{ai} + (K_bP_{bi})^{1/2} + K_c(K_{eq}P_{ai}P_{bi}^3)^{1/6}} \qquad [A\text{-}7]$$

The remaining rate equations were derived in similar manner. Considerable simplification was permitted by the very large value of the equilibrium constant and by the assumption of low surface coverage (and hence low adsorption constant values) by the gases.

The assumption of low surface coverage was justified in the following manner. The reported very rapid adsorption of hydrogen on tungsten (25) suggests low surface coverage by hydrogen. Because of its similarity to oxygen adsorption (27), WF_6 adsorption is expected to be essentially nonactivated (26). Thus surface coverage by WF_6 would also be expected to be slight.

APPENDIX B

Relative Heat Transfer Rates for Various Experimental Investigations

The conditions representing those most frequently used in the various experimental investigations were a H_2 to WF_6 ratio of 6.0, a substrate temperature of 823°K, a system pressure of 6.7 kN/m^2 and a stream-substrate interface concentration of HF of 5%. These conditions and the most commonly used reactant flow rates (Table IV) were employed in the calculations.

The relative rate of steady heat flow was calculated from the relation

$$q = hA\Delta T = \frac{k}{d}N_{Nu}A\Delta T \qquad [B\text{-}1]$$

Upon reaching the vicinity of the substrate, the gas stream in each experimental system would be expected to be at about the same temperature. Therefore the temperature gradient, ΔT, was assumed con-

Table IV. Information used to calculate the relative rates of heat transfer from substrate to gas stream

Investigator	System-flow geometry	Heat flow equation (Nusselt number)	Heat flow equation reference	Substrate area (cm²)	Substrate dimension (cm)	Gas flow rate (cm³/min)	Flow tube diameter (cm)
Berkeley *et al.*	Vertical cylindrical substrate, free convection only	$N_{Nu} = 0.59\ N_{Gr}^{0.25}\ N_{Sc}^{0.25}$	31	5.05	0.32	~0*	N.A.
Huggins	Forced and free convection past a single sphere	$N_{Nu} = 2.0 + 0.569\ N_{Gr}^{0.25}\ N_{Sc}^{0.25} + 0.347\ (N_{Re}\ N_{Sc}^{0.5})^{0.62}$	32	5.05	1.27	975	2.54
Holman and Huegel Cheung Huegel *et al.*	Parallel forced and free convection normal to a horizontal cylinder	$N_{Nu} = N_{Sc}^{0.33}\ [0.50 + 0.49\ (N_{Re} + N_{Gr}^{0.5})^{0.52}]$	22	12.65 3.17 12.65	1.27 0.32 1.27	570 1000 950	3.18 3.18 3.18
Bryant	Forced and free convection within a horizontal tube	$N_{Nu} = 1.27\ [N_{Re}\ N_{Sc}\ (d/L)]^{0.5}$	33	118.4	4.88	2300	4.88
Wahl and Batzies Shroff**	Downward jet flow onto a horizontal, flat plate	$N_{Nu} = 0.034\ D^{0.9}\ N_{Re}^{0.64}\ N_{Pr}^{0.33}\ e^{-0.037(t/D)}$†	35	5.53 0.85	2.00 1.04	500 350	0.65 5±1

* Static system.
** Experimental arrangement described in Ref. (34).
† This equation is recommended by the authors (35) for Reynolds numbers greater than 1600. However Nusselt numbers calculated from it for both the Wahl and Batzies and the Shroff data, for respective Reynolds numbers of 110 and 161, are in good agreement with the values determined by Gardon and Akfirat (36) for the same system-flow geometry and comparable Reynolds numbers.
N.A. Not applicable.

stant. The thermal conductivity of the gas mixture, k, was not calculated since it would be constant and only relative values for the heat transfer rates were desired.

With each value of the substrate surface area, A, and characteristic system dimension, d, known (Table IV), it remained to calculate the Nusselt number for each system. The equations for determining Nusselt numbers are also given in Table IV. In several instances it was necessary to adapt the appropriate equation from a corresponding mass flow equation by making use of the Chilton-Colburn analogy (29). A constant value of 0.73 was assigned to the Schmidt number on the basis that a narrow range of values, centering about this value, exists for a great number of gases. Based on information from the literature (30), a value of 0.65 was assumed for the Prandtl number.

LIST OF SYMBOLS

R	tungsten deposition rate, cm/hr
K_r	reaction rate constant, moles/hr
K_{eq}	equilibrium constant for deposition reaction
p	partial pressure, kN/m²
M	molecular weight of tungsten, g/mole
ρ_W	density of tungsten, g/cm³
K	adsorption constant, $(kN/m^2)^{-1}$
$K'(K'')$	combined forms of over-all rate constant, variable units
n	integer corresponding to number of surface sites involved in surface reaction
N_{Nu}	Nusselt number, hd/k
N_{Sc}	Schmidt number, $\mu/\rho\ \overline{D}_{eff}$
N_{Re}	Reynolds number, $dV\rho/\mu_f$
N_{Gr}	Grashof number, $d^3\rho_f{}^2 g\Delta\rho/\mu_f{}^2\rho_b$
N_{Pr}	Prandtl number, $Cp\ \mu/k$
d	characteristic dimension of system, cm
L	length or effective length of substrate, cm
V	linear velocity, cm/sec
μ	viscosity, g/cm·sec
$\overline{D}_{eff}$	over-all effective binary diffusivity for gases, cm²/sec
g	gravitational constant, 1.27×10^{10} cm/hr²
$\Delta\rho$	$\rho_b - \rho_i$, g/cm³
k	thermal conductivity, cal/sec·°K·cm
Q	activation energy, J/mole
h	heat transfer coefficient, cal/sec·°K·cm²
ρ	density of gas, g/cm³
A	area of substrate, cm²
T	temperature, °K
D	nozzle diameter, mm
t	nozzle to plate distance, mm
q	rate of heat flow, cal/sec
Cp	specific heat at constant pressure, cal/g·°K
J	rate of formation of nuclei of critical size, number/cm³·sec
α	condensation coefficient, dimensionless
γ^*	radius of nucleus of critical size, cm
P	vapor pressure, g/cm·sec²
C	monomer concentration, number/cm³
m	molecular mass, g
ΔF^*	free energy of formation of nucleus of critical size
k	Boltzmann's constant

Subscripts

a	WF_6
b	hydrogen
c	HF
d	H_2F_2
i	value taken at gas stream-substrate interface
b	value taken in bulk gas stream
f	value taken in film adjacent to substrate

REFERENCES

1. H. E. Carlton and J. H. Oxley, *AIChE J.*, **13**, 571 (1967).
2. W. A. Bryant and G. H. Meier, *This Journal*, **120**, 559 (1973).
3. G. Wahl and P. Batzies, in "Chemical Vapor Deposition Fourth International Conference," G. F. Wakefield and J. M. Blocher, Jr., Editors, p. 425, The Electrochemical Society Softbound Symposium Series, Princeton, N.J. (1973).

4. R. W. Haskell, in "Chemical Vapor Deposition, Second International Conference," J. M. Blocher, Jr. and J. C. Withers, Editors, p. 63, The Electrochemical Society Softbound Symposium Series, Princeton, N.J. (1970).
5. W. R. Holman and F. J. Huegel, in "Proceedings of the Conference on Chemical Vapor Deposition of Refractory Metals, Alloys and Compounds," A. C. Schaffhauser, Editor, p. 127, The American Nuclear Society, Hinsdale, Ill. (1967).
6. W. A. Bryant, M.S. Thesis, Materials Department, University of Pittsburgh, Pittsburgh, Pa. (1971).
7. H. Cheung, in "The Third International Conference on Chemical Vapor Deposition," F. A. Glaski, Editor, p. 136, The American Nuclear Society, Hinsdale, Ill. (1972).
8. F. J. Huegel, E. Fung, H. Cheung, and W. R. Holman, in *ibid.*, p. 145.
9. L. E. Brecher, in "Chemical Vapor Deposition, Second International Conference," J. M. Blocher, Jr. and J. C. Withers, Editors, p. 37, The Electrochemical Society Softbound Symposium Series, Princeton, N.J. (1970).
10. J. F. Berkeley, A. Brenner, and W. E. Reid, Jr., *This Journal*, **114**, 561 (1967).
11. W. C. Seymour and J. G. Byrne, in "Chemical Vapor Deposition, Fifth International Conference," J. M. Blocher, Jr., H. E. Hintermann, and L. H. Hall, Editors, p. 815, The Electrochemical Society Softbound Symposium Series, Princeton, N.J. (1975).
12. A. M. Shroff, in "The Third International Conference on Chemical Vapor Deposition," F. A. Glaski, Editor, p. 69, The American Nuclear Society, Hinsdale, Ill. (1972).
13. H. W. Huggins, Ph.D. Thesis, Metallurgy Department, University of Utah, Salt Lake City, Utah (1971).
14. R. L. Heestand, J. I. Federer, and C. F. Leitten, Jr., Report ORNL-3662, Oak Ridge National Laboratory, Oak Ridge, Tenn. (August 1964).
15. J. Chin, in "The Third International Conference on Chemical Vapor Deposition," F. A. Glaski, Editor, p. 164, The American Nuclear Society, Hinsdale, Ill. (1972).
16. J. H. Oxley, E. A. Beidler, J. M. Blocher, Jr., C. J. Lyons, R. S. Park, and J. H. Pearson, in "Metals for the Space Age—Proceedings of the Fifth Plansee Seminar," F. Benesovsky, Editor, p. 278, Springer-Verlag, Wien (1965).
17. K. R. Sump and B. D. Howard, in "Chemical Vapor Deposition, Second International Conference," J. M. Blocher, Jr. and J. C. Withers, Editors, p. 521, The Electrochemical Society Softbound Symposium Series, Princeton, N.J. (1970).
18. H. S. Shim and J. G. Byrne, *J. Crystal Growth*, **13/14**, 23 (1972).
19. R. W. Haskell and J. G. Byrne, in "Treatise on Materials Science and Technology," H. Herman, Editor, p. 298, Academic Press, New York (1972).
20. G. Ehrlich, in "Metal Surfaces," p. 236, American Society for Metals, Metals Park, Ohio (1963).
21. R. Gomer, R. Wortman, and R. Lundy, *J. Chem. Phys.*, **26**, 1147 (1957).
22. H. E. Carlton and J. H. Oxley, *AIChE J.*, **13**, 86 (1967).
23. J. P. Hirth and G. M. Pound, "Condensation and Evaporation—Nucleation and Growth Kinetics," p. 18, The MacMillan Co., New York (1963).
24. W. J. Moore, "Physical Chemistry," 2nd ed., p. 548, Prentice-Hall, New York (1955).
25. K. H. Yang and O. A. Hougen, "*Chem. Eng. Prog.*, **46**, 146 (1950).
26. D. O. Hayward and B. M. W. Trapnell, "Chemisorption," 2nd ed., p. 144, Butterworths, London (1964).
27. M. Metlay and G. E. Kimball, *J. Chem. Phys.*, **16**, 779 (1948).
28. D. O. Hayward and B. M. W. Trapnell, "Chemisorption," 2nd ed., p. 75, Butterworths, London (1964).
29. T. H. Chilton and A. P. Colburn, *Ind. Eng. Chem.*, **26**, 1183 (1934).
30. R. B. Bird, W. E. Stewart, and E. N. Lightfoot, "Transport Phenomena," p. 256, John Wiley & Sons, Inc., New York (1960).
31. W. H. McAdams, "Heat Transmission," 3rd ed., p. 172, McGraw-Hill Book Co., New York (1954).
32. R. L. Steinberger and R. E. Treybal, *AIChE J.*, **6**, 227 (1960).
33. R. L. Pigford, "Chemical Engineering Progress Symposium Series," **51**, No. 17, 79 (1955).
34. A. M. Shroff in "High Temperature Materials, Sixth Plansee Seminar," F. Benesovsky, Editor, p. 854, Springer-Verlag, Wien (1969).
35. V. A. Smirnov, G. E. Verevochkin, and P. M. Brdlick, *Int. J. Heat Mass Transfer*, **2**, 1 (1961).
36. R. Gardon and J. C. Akfirat, *ibid.*, **8**, 1261 (1965).

Thermodynamics of the Gaseous Zirconium Iodides

P. D. Kleinschmidt, D. Cubicciotti,* and D. L. Hildenbrand

SRI International, Menlo Park, California 94025

ABSTRACT

The gaseous zirconium iodides ZrI_4, ZrI_3, ZrI_2, and ZrI, generated by the reaction of HI(g) with Zr(s) at elevated temperatures, were identified and characterized thermochemically by Knudsen cell mass spectrometry. Gaseous ZrI_4 was the major reaction product up to about 1300°K; above this temperature, atomic I became the major product, with minor amounts of the lower Zr iodides appearing as the temperature was progressively raised. From an analysis of equilibrium data, the following enthalpies of formation were deduced; $\Delta Hf°_{298}(ZrI_3, g) = -30.8 \pm 1.5$ kcal/mole, $\Delta Hf°_{298}(ZrI_2, g) = 32.6 \pm 4.0$ kcal/mole, and $\Delta Hf°_{298}(ZrI, g) = 96.3 \pm 2.8$ kcal/ mole. Individual bond dissociation energies evaluated from the enthalpy data are close to the average value in ZrI_4. The new thermochemical data are consistent with observations on the iodide process for refining impure zirconium whereas earlier estimates are not.

Information about the chemistry of the gaseous iodides of zirconium can have an important bearing on the technology of the metal. The iodide process for refining zirconium (1) is based on vapor transport of the gaseous iodides, and iodine-induced stress corrosion cracking (SCC) of zirconium alloys has been thought (2) to involve gaseous iodide transport of zirconium. Understanding of the mechanisms of those processes has been hindered for lack of reliable data on the stabilities of the vapor species. Prior to the present work, experimental thermochemical data were available only for the tetraiodide, ZrI_4. To our knowl-

* Electrochemical Society Active Member.

Key words: mass spectrometry, inorganic, equilibrium, enthalpy.

edge, none of the other gaseous iodides had been identified by a spectroscopic technique or had been otherwise characterized experimentally.

In the iodide process for zirconium refining, impure metal is heated to 500°-600°K in a container where it reacts with gaseous iodine species at pressures of 10^{-4}-10^{-2} atm. The gaseous zirconium iodides produced are decomposed on a heated filament at 1500°-1700°K on which purified zirconium deposits. Shapiro (1) considered the chemistry of the iodide decomposition process using the thermochemical information available at that time (almost all estimated) and found that rather than clarifying the mechanism, the analysis only confused the situation. His analysis indicated that ZrI_2 was the principal gaseous Zr-containing species. We have used literature estimates (3) to calculate the partial pressures shown in Fig. 1. Those estimates also indicate that ZrI_2 should be the principal gaseous species in an iodide process cell. However, the information in Fig. 1 is obviously in error because it indicates that decomposition of gaseous ZrI_2 should not occur below about 1700°K, whereas, in the iodide process, deposition of Zr on the hot filament occurs at temperatures above about 1300°K.

In the work described below, gaseous equilibria among the zirconium iodides were studied by high temperature mass spectrometry, and thermochemical data for ZrI, ZrI_2, and ZrI_3 were derived. Our new data on the gaseous zirconium iodides show that the estimated thermochemical values are seriously in error; a recalculation of vapor composition in the iodide cell using the new results makes the process understandable.

Experimental

The equilibrium studies on the Zr-I system were carried out by high temperature mass spectrometry, using the magnetic sector instrument and experimental technique described in previous publications (4). Effusion cell beams containing a distribution of the gaseous Zr iodides were generated by the reaction of HI(g) with elemental Zr; HI was admitted to the cell via an inlet tube in the base. A rolled strip of Zr foil was placed in the bottom of the cell, covered by a thin molybdenum partition to increase the number of reactive collisions and promote equilibration. Graphite cells were used for studies of the species ZrI_4, ZrI_3, and ZrI_2 at 1100°-1500°K, while molybdenum cells were used for the corresponding studies on Zr and ZrI at 2200°-2400°K.

All ion intensities used in the equilibrium calculations were corrected for any background contributions by noting the change in signal level resulting from misalignment of the neutral beam defining slit. Background levels were generally negligible. Ion abundances were measured by pulse counting for some of the equilibrium studies and by the standard electrometer method for the remainder. The two methods are, of course, equivalent, although each has certain advantages in a given situation. For the one Zr-I reaction studied by both methods, the derived equilibrium data were in good agreement.

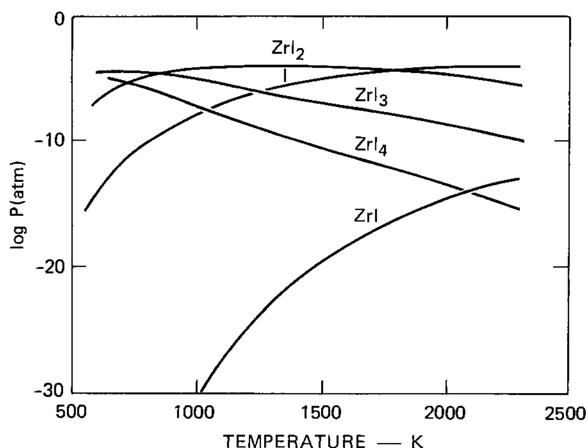

Fig. 1. Partial pressures of species in equilibrium with Zr(s) calculated from literature estimates for P(total I) $= 10^{-4}$ atm. P(total I) $=$ total iodine equivalent pressure $\equiv \Sigma np(ZrI_n) + \Sigma np(I_n)$.

In order to evaluate the absolute equilibrium constants for reactions requiring a pressure calibration, the instrument sensitivity constant was determined by using gold as a vapor pressure standard. Gold was vaporized from a graphite cell, and Au^+ abundances were observed at several temperatures, and for several ionizing energies, using both pulse counting and electrometer detection. From the abundance data and known vapor pressures (5), the sensitivity constant k in the expression

$$P = \frac{kTA^+}{\sigma} \quad [1]$$

was evaluated at several fixed values of the excess ionization energy; in this expression A^+ is the observed positive ion abundance of a species with partial pressure P at an effusion source temperature T, and with ionization cross section σ. For atomic species, values of σ were taken from the compilation by Mann (6), while values for molecular species were calculated by assuming additivity of atomic cross sections. In electrometer applications, the ion multiplier sensitivity was assumed to be mass independent, as indicated by many multiplier gain measurements with our instrument over a wide mass range. The instrument sensitivity proved to be constant over long time intervals. A subsequent check on the calibration using KCl(s) as a vapor pressure standard, monitoring the KCl(g) pressure with K^+/KCl fragment and KCl^+ parent ions, gave a KCl monomer pressure agreeing with the tabulated value (3) to within 20%. An uncertainty of about 50% is attached to the derived equilibrium constants, stemming largely from the estimated ionization cross sections.

The zirconium foil sample, obtained from Alfa/Ventron Corporation, had a minimum purity of 99.9%. Gaseous HI was taken from a Matheson commercial sample and was used without further purification.

Results

The distribution of gaseous Zr iodides in the effusion cell beam changed markedly with temperature. These species were identified from the masses, isotopic distributions, and threshold appearance potentials of the ions produced by electron impact. A summary of the appearance potentials observed for various cell temperatures, together with the neutrals inferred from the threshold values is given in Table I; these thresholds were evaluated by the vanishing current method. Only ZrI_4(g) was observed as a

Table I. Threshold appearance potentials of observed ions in the Zr-I system and the assigned neutral precursors

Ion	Appearance potential (eV)*	Neutral precursor
Zr^+	6.5 ± 0.3 (2200°K)	Zr
	18.0 ± 0.5 (1200°K)	ZrI_3
	21.5 ± 0.5 (700°K)	ZrI_4
ZrI^+	7.0 ± 0.7 (2200°K)	ZrI
	10 ± 1 (1500°K)	ZrI_2
	14.0 ± 0.5 (1200°K)	ZrI_3
	17.8 ± 0 5 (700°K)	ZrI_4
ZrI_2^+	10.3 ± 0.3 (1100°K)	ZrI_3
	14.0 ± 0.3 (700°K)	ZrI_4
ZrI_3^+	7.5 ± 0.3 (1100°K)	ZrI_3
	10.8 ± 0.3 (700°K)	ZrI_4
ZrI_4^+	9.3 ± 0.3 (700°K)	ZrI_4
I^+	10.5 ± 0.5 (1200°K)	I

* Cell temperatures at which thresholds were observed are in parentheses.

product of the $HI(g) + Zr(s)$ reaction below about 1000°K; above that temperature, ZrI_3 appeared, then $ZrI_2(g)$, and finally $ZrI(g)$ and $Zr(g)$ above 2000°K. The total pressure within the cell was kept below 10^{-4} atm, in order to maintain molecular flow conditions.

Unambiguous identification of gaseous Zr, ZrI, ZrI_3, and ZrI_4 was provided by the lowest threshold energies of the corresponding positive ions. One would expect that the ionization potential of ZrI_4, in which all of the Zr valence electrons are involved in bonding, would approach that of atomic I (10.45 eV), while those of the lower iodides, which have nonbonded Zr valence electrons, would tend toward the ionization potential of Zr (6.84 eV). The lowest threshold energies for ZrI_4^+, ZrI_3^+, and ZrI^+, which we assign to the ionization potentials of the parent neutrals, do indeed follow this pattern, corroborating the interpretation. (Ionization potentials have not been reported previously for these species.) The diiodide ZrI_2 was the least abundant of the gaseous iodides, and it was identified through observation of the fragment ion ZrI^+/ZrI_2 appearing at 10 eV.

The low abundance of ZrI_2, and of the other gaseous Zr iodides as well, compared to the considerably higher abundances of the fluorides and chlorides observed in similar studies of Zr and other metals, is a consequence of the weaker metal-iodine bonds. Quite high pressures of atomic I, approaching the molecular flow limit, were needed to generate workable Zr-I ion signals at the usual low electron energies used. It was nevertheless possible to observe all the gaseous Zr iodides and to characterize them thermochemically within certain limits. It is worth noting that there is a marked shift in the vapor phase chemistry as a result of the decrease in metal-halogen bond strength with increasing halogen atomic number. In consequence, experimental studies of the lower valent metal iodides are considerably more difficult than those of the other metal halides.

$ZrI_3(g)$.—Studies of the two reaction equilibria

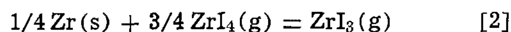

$$1/4\,Zr(s) + 3/4\,ZrI_4(g) = ZrI_3(g) \qquad [2]$$

and

$$ZrI_4(g) = ZrI_3(g) + I(g) \qquad [3]$$

were carried out over the range 1100°-1400°K using the corresponding parent ions measured at 2 eV above threshold to monitor the neutral abundances. Reaction [2] was studied in two separate experiments with different Zr samples, one with ion counting detection and one with the usual electrometer analog detection. For third law calculations, it was necessary to account for the rather extensive fragmentation of ZrI_4 and ZrI_3. Measurements of ion fragmentation showed that at an ionizing electron energy 2 eV above the respective parent and fragment ion thresholds, the total ion yield from ZrI_3 was 5.3 times that of $A(ZrI_3^+)$, while that of ZrI_4 was 2.2 times $A(ZrI_4^+)$. The ion abundance data were coupled with the fragmentation corrections, the estimated ionization cross sections, and the pressure calibration constant to yield the equilibrium constants, K_{eq}, given in Table II. At 1300°K, the I^+, ZrI_3^+, and ZrI_4^+ parent ion abundances at 2 eV above threshold were in the approximate ratio 220/1/36, respectively. In checking on the attainment of chemical equilibrium, the value of K_{eq} for reaction [2] was found to be unchanged with HI flow rate at 1305°K when the ZrI_3^+ and ZrI_4^+ signals varied by factors of 2.0 and 2.6, respectively. The good agreement in derived properties of $ZrI_3(g)$ from the data of reactions [2] and [3] is also a strong indication of equilibrium behavior.

Thermodynamic functions of the various species used in the analysis of these and other equilibria were taken from sources summarized in the Appendix. The two studies of reaction [2] yielded the third law values $\Delta H°_{298} = 32.3 \pm 1.5$ and 32.9 ± 1.5 kcal/mole, with corresponding second law values of 32.0 ± 0.6 and 30.5 ± 1.0 kcal/mole. For reaction [3], the derived second and third law values are $\Delta H°_{298} = 79.5 \pm 1.1$ and 79.8 ± 1.5 kcal/mole, respectively. The agreement between second and third law heats for reactions [2] and [3] and between the two different determinations of reaction [2] is quite good. Since the properties of $I(g)$, $Zr(s)$, and $ZrI_4(g)$ are known from other sources (3, 7) two independent determinations of the thermochemical properties of $ZrI_3(g)$ can be made. Using the average of the third law values, one derives $\Delta H_f°_{298}(ZrI_3,g) = -31.1 \pm 1.9$ kcal/mole from reaction [2] and -30.6 ± 2.1 kcal/mole from reaction [3]. A "best value" of $\Delta H_f°_{298}(ZrI_3,\ g) = -30.8 \pm 1.5$ kcal/mole is selected from the results of this research. The close accord between second and third law enthalpies shows that the estimated molecular constants and thermodynamic functions of $ZrI_3(g)$ are quite reliable.

Table II. Derived thermochemical data for the reactions

$$\tfrac{1}{4}\,Zr(s) + \tfrac{3}{4}\,ZrI_4(g) = ZrI_3(g) \quad [2]$$

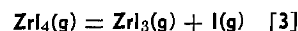

$$ZrI_4(g) = ZrI_3(g) + I(g) \quad [3]$$

T (°K)	K_{eq} [2] $\times 10^4$ $(atm)^{1/4}$	K_{eq} [3] $\times 10^8$ (atm)	$\Delta H°_{298}$ [2] (kcal/mole)	$\Delta H°_{298}$ [3] (kcal/mole)
		Series I: Electrometer		
1158	5.30	0.878	32.0*	79.4*
1159	4.39	0.644	32.5	80.2
1159	4.78	0.767	32.3	79.8
1159	4.88	0.774	32.2	79.8
1159	5.19	0.923	32.1	79.4
1240	13.2	7.09	31.9	79.8
1244	11.6	6.40	32.4	80.4
1294	17.3	23.7	32.6	80.1
1295	18.5	25.2	32.4	80.0
1330	26.6	70.2	32.3	79.5
1330	27.2	72.2	32.2	79.4
1379	43.6	173.0	32.1	80.0
1380	40.4	178.0	32.3	79.9
1394	45.4	254.0	32.3	79.7
	Avg. (Third law)		32.3 ± 1.5	79.8 ± 1.5
	Second law		32.0 ± 0.6	79.5 ± 1.1
		Series II: Pulse counting		
1124	2.48		32.8*	
1150	3.25		32.9	
1150	3.75		32.6	
1204	6.77		32.6	
1239	10.0		32.6	
1305	16.3		33.0	
1306	17.0		32.9	
1390	28.7		33.5	
	Avg. (Third law)		32.9 ± 1.5	
	Second law		30.5 ± 1.0	

* Third law enthalpies derived from information given in the Appendix.

$ZrI_2(g)$.—At temperatures slightly higher than those used in studies of reactions [2] and [3], it was possible to investigate the isomolecular reaction

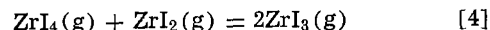

$$ZrI_4(g) + ZrI_2(g) = 2ZrI_3(g) \qquad [4]$$

using parent ZrI_4^+, and fragment ZrI_2^+/ZrI_3 and ZrI^+/ZrI_2 measured at 2.5 eV above threshold as indicators of the ZrI_4, ZrI_3, and ZrI_2 pressures. Fragment ZrI_2^+/ZrI_3 was used rather than parent ZrI_3^+ to monitor $ZrI_3(g)$, in order to gain sensitivity; there was no discernible ZrI_2^+ ion current below 10 eV, showing that there could be no parent ion contribution at the higher energies to interfere with evaluation of the ZrI_3 abundance. Likewise there was no detectable ZrI^+ current below 10 eV, eliminating any possible interference from neutral ZrI. At the selected electron energies used, the neutral procursors of ZrI_4^+, ZrI_2^+, and ZrI^+ are clearly defined as ZrI_4, ZrI_3, and ZrI_2.

At 1450°K, the ion signals ZrI_4^+, ZrI_2^+, and ZrI^+ measured at 2.5 eV above threshold were in the ratio 716/245/1. Despite the low ZrI^+/ZrI_2 signal levels, it was possible to obtain a fair degree of precision in the determination of K_{eq} for reaction [4] by using

Table III. Derived thermochemical data for the reaction

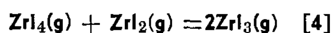
$ZrI_4(g) + ZrI_2(g) = 2ZrI_3(g)$ [4]

T (°K)	K_{eq}	$\Delta H°_{298}$ [4] (kcal/mole)
1339	48.3	−9.0*
1431	48.7	−9.6
1452	57.1	−10.2
1468	43.1	−9.5
1476	28.5	−8.4
1478	47.4	−9.8
	Avg. (Third law)	−9.4 ± 3.5
	Second law	−4.6 ± 6.8

* Third law enthalpies derived from information given in the Appendix.

ion pulse counting detection. Pulse counting is somewhat tedious at low signal levels (0.5 to 1 counts/sec) but it does provide more reproducible results than the electrometer method. Because of the low ZrI_2 signal levels, however, it was not possible to obtain meaningful second law (slope) data, and all of the derived results are based on third law analysis. Appropriate corrections for the parent-fragment ion distributions in ZrI_3 and ZrI_4 were applied. No pressure calibration was required because reaction [4] was isomolecular. The equilibrium constants and derived reaction enthalpies are summarized in Table III, leading to $\Delta H°_{928}[4] = -9.4 \pm 3.5$ kcal/mole and $\Delta H_f°_{298}(ZrI_2, g) = 32.6 \pm 4.0$ kcal/mole.

If a nonlinear structure with apex angle of 120° is assumed for ZrI_2, rather than the linear configuration adopted as noted in the Appendix, then the derived enthalpy change at 298°K for reaction [4] will be 3.2 kcal/mole more negative, and the 298°K enthalpy of formation of $ZrI_2(g)$ will be more positive by the same amount. The difference arises because the Φ function calculated for the linear form is about 2.3 cal/deg mole smaller than for the bent form at 1500°K. For a wide range of temperatures centered about the measurement temperatures, the free energies of formation of ZrI_2 calculated from $\Delta H°_{298}$ and Φ for the linear model will be the same as those calculated from the $\Delta H°_{298}$ and Φ for the bent model, within the quoted uncertainties. The present measurements give no indication of which structure is correct.

ZrI(g).—Gaseous ZrI was observed only at relatively high temperatures, above 2000°K, when a measurable level of Zr(g) was also present. Consequently, it was possible to characterize ZrI(g) through studies of the equilibrium

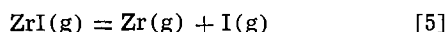
$$ZrI(g) = Zr(g) + I(g) \quad [5]$$

in the range 2200°-2400°K. Again, the ZrI^+ parent signal was relatively weak when measured a few electron volts above threshold (<count per second). Several comparisons showed that values of K_{eq} evaluated from parent ion abundances measured at 3 eV above threshold differed by less than a factor of two from those derived from 50 eV ion abundances. The comparison establishes that the use of 50 eV ionizing energies to gain additional sensitivity in the study of reaction [5] introduces no extraneous signals that would complicate the interpretation. Therefore, in the equilibrium studies of reaction [5], parent Zr^+ and ZrI^+ were measured at 50 eV, while the intense I^+ parent signal was measured at 15 eV and an accurate correction was applied to normalize all signals to 50 eV ionizing energy. At 2300°K, the Zr^+, ZrI^+, and I^+ abundances were in the approximate ratio 200/1/4.6 × 10^4. The ZrI^+ signals varied from about 1 to 20 counts/sec, while the atomic I pressure was about 5 × 10^{-5} atm under these conditions. A series of measurements at various HI flow rates and at constant temperature showed the derived equilibrium constant of reaction [5] to be independent of pressure when the I pressure was varied by a factor of 13.

Table IV. Derived thermochemical data for the reaction

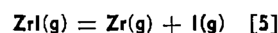
$ZrI(g) = Zr(g) + I(g)$ [5]

T (°K)	K_{eq} [5] × 10^2 (atm)	$\Delta H°_{298}$ [5] (kcal/mole)
2222	1.05	71.9*
2288	1.45	72.6
2289	1.57	72.3
2289	1.53	72.4
2289	1.38	72.9
2291	1.74	71.9
2324	1.43	73.9
2369	2.90	72.1
2405	2.61	73.8
2410	3.28	72.9
2425	4.06	72.3
2434	4.74	71.8
	Avg. (Third law)	72.6 ± 2.5
	Second law	67.9 ± 6.6

* Third law enthalpies derived from information given in the Appendix.

The equilibrium constants and derived thermochemical data for reaction [5] are summarized in Table IV. The second and third law values of $\Delta H°_{298}$ are 67.9 ± 6.6 and 72.6 ± 2.5 kcal/mole, respectively; the latter leads to $\Delta H_f°_{298}(ZrI, g) = 96.3 \pm 2.8$ kcal/mole.

The reaction thermochemistry and derived thermochemical data are summarized in Table V.

Discussion

Application to the iodide process.—The pressures of Zr-I species calculated from our experimental thermochemical data are shown in Fig. 2 for a total iodine equivalent pressure of 10^{-4} atm, typical of iodide refining process conditions. These results lead to a simple interpretation of the deposition of Zr in the iodide process, based on the thermodynamic data. At low temperatures the major gaseous species is ZrI_4, whereas at temperatures above 1300°K the major species is atomic I. Therefore, in the iodide process gaseous ZrI_4 is formed from reaction of impure Zr with iodine at low temperatures. The ZrI_4 diffuses to the hot filament and is decomposed to solid Zr and gaseous I atoms. The temperature above which deposition occurs on the hot filament is about 1300°K from the thermodynamic data in Fig. 2, in reasonable agreement with experience in the iodide process. Therefore, the data indicate that in the iodide process the only important gaseous species are ZrI_4 and I.

The effect of pressure of total iodine-containing species can be seen in Fig. 3 and 4. The major species

Table V. Summary of derived thermochemical data

Reaction	$\Delta H°_{298}$ (III)* (kcal/mole)	Derived enthalpies of formation (kcal/mole)
3/4 $ZrI_4(g)$ + 1/4 Zr(s) = $ZrI_3(g)$	32.6 ± 1.1	$\Delta H_f°_{298}(ZrI_3, g) = -31.1 \pm 1.9$
$ZrI_4(g) = ZrI_3(g) + I(g)$	79.8 ± 1.5	$\Delta H_f°_{298}(ZrI_3, g) = -30.6 \pm 2.1$
$ZrI_2(g) + ZrI_4(g) = 2ZrI_3(g)$	−9.3 ± 3.5	$\Delta H_f°_{298}(ZrI_2, g) = 32.6 \pm 4.0$
$ZrI(g) = Zr(g) + I(g)$	72.6 ± 2.5	$\Delta H_f°_{298}(ZrI, g) = 96.3 \pm 2.8$

* Third law values.

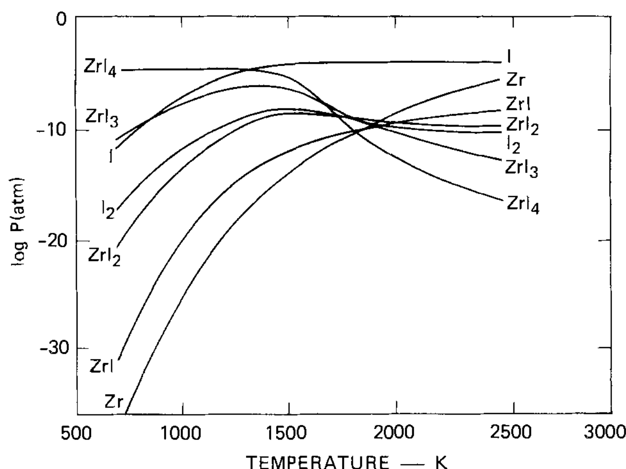

Fig. 2. Partial pressures of species in equilibrium with Zr(s) from present data for P(total I) = 10^{-4} atm. P(total I) = total iodine equivalent pressure $\equiv \Sigma np(ZrI_n) + \Sigma np(I_n)$.

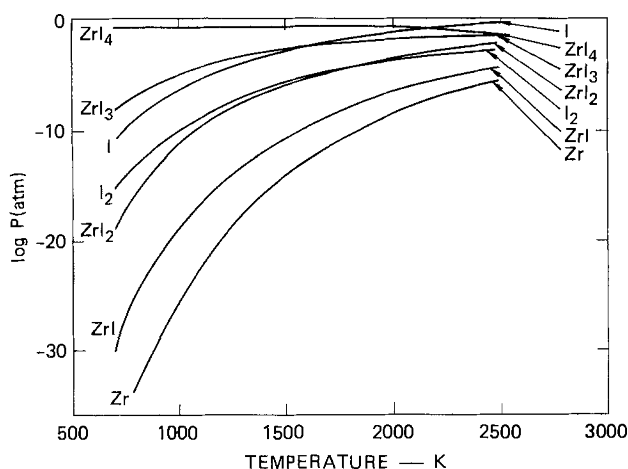

Fig. 3. Partial pressures of species in equilibrium with Zr(s) from present data for P(total I) = 1 atm. P(total I) = total iodine equivalent pressure $\equiv \Sigma np(ZrI_n) + \Sigma np(I_n)$.

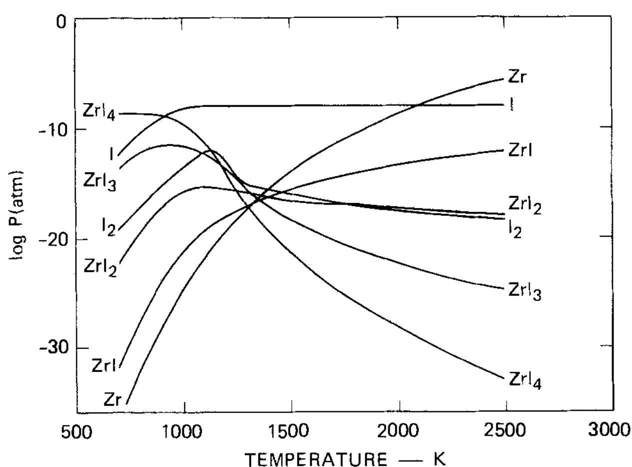

Fig. 4. Partial pressures of species in equilibrium with Zr(s) from present data for P(total I) = 10^{-8} atm. P(total I) = total iodine equivalent pressure $\equiv \Sigma np(ZrI_n) + \Sigma np(I_n)$.

under most conditions are either ZrI_4 or I. For 1 atm total iodine equivalent pressure, shown in Fig. 3, the temperature at which the ZrI_4 and I pressures cross is about 2200°K. That is, deposition of Zr would occur only at filament temperatures higher than 2200°K. For total iodine equivalent pressures of 10^{-8} atm, shown in Fig. 4, the cross-over temperature is about 900°K. Therefore as the pressure of total iodine-containing species in the system is increased, the minimum temperature for decomposition of ZrI_4 increases.

In the iodide process it has been observed (8, 9) that as the temperature of the impure zirconium was increased the rate of deposition of Zr first increased then decreased. That behavior can be related to the effect of pressure on the decomposition temperatures shown in Fig. 2-4. The initial increase in rate occurs because increasing the temperature of the impure Zr increases the partial pressure of ZrI_4 and thus its rate of arrival at the filament. As the impure Zr temperature is further increased, the fraction of the ZrI_4 arriving at the filament which is decomposed decreases, in accord with Fig. 2-4, and the decomposition rate falls off largely because that fraction decreases. Shelton (10) discussed the maximum in the rate of the process in terms of changes in the iodine diffusivity and the change in fraction decomposed is implicit in his treatment.

The composition profiles shown in Fig. 2-4 illustrate clearly the reason for the experimental difficulties in studying the lower Zr iodides alluded to earlier. The lower iodides are minor species under all practical experimental conditions, and there is no way to increase their abundances relative to ZrI_4 and I at temperatures below 2500°K.

Bond dissociation energies.—From the enthalpies of formation in Table V, one can evaluate the individual bond dissociation energies in ZrI_4 as follows: $D(I_3Zr\text{-}I)$ = 80 kcal, $D(I_2Zr\text{-}I)$ = 92 kcal, $D(IZr\text{-}I)$ = 86 kcal, and $D(Zr\text{-}I)$ = 73 kcal. These values differ only slightly from the average bond energy in ZrI_4, 83 kcal. Each of the first three bond dissociation reactions is assumed to yield an iodine atom plus a zirconium iodide molecule in which the zirconium valence electrons not used in bonding are unpaired. For ZrI_3, ZrI_2, and ZrI, these electronic configurations are those of the ground states of the gaseous ions Zr(IV), Zr(III), and Zr(II). The ground state of Zr(I), $4d^25s^2$, contains two paired and two unpaired electrons, however; the first excited state of Zr(I) in which all of the valence electrons are unpaired ($4d^35s^1$) lies 13.9 kcal above ground. Thus the comparable bond dissociation reaction for ZrI, ZrI $\rightarrow$ Zr ($4d^35s^1$) + I has an energy of 73 + 14 = 87 kcal, not greatly different from all the others.

Relevance to iodine attack and SCC of Zr.—The chemical attack of zirconium alloys by gaseous iodine at temperatures near 600°K causes pitting of the metal surface (11). Pitting probably occurs by vapor transport removal of material. The present results show (Fig. 2-4) that the predominant vapor species under those conditions is ZrI_4, which must then be the species responsible for any vapor transport of Zr. Pitting implies that some metal surface sites are more reactive so that localized removal of material is favored over uniform corrosion.

Stressed samples of zirconium alloys can also crack in iodine vapor and vapor transport has been suggested as a mechanism which maintains the sharp crack tip required for crack propagation. The validity of that mechanism has been questioned (11) because pitting, the apparently favored mode of attack would blunt the crack tip rather than sharpen it. Zirconium tetraiodide can induce the stress corrosion cracking of Zircaloys as readily as iodine (11, 12). The present work shows that the partial pressures of reduced Zr-I species are very small under conditions of ZrI_4-induced Zircaloy cracking so that the removal of zirconium by vapor transport of lower iodides is not a likely mechanism.

Thus SCC of zirconium alloys in iodine and iodides apparently occurs by mechanisms other than vapor transport.

Acknowledgment

This research was sponsored by the U.S. Department of Energy, Division of Basic Energy Sciences, under Contract No. E(04-3)-1339.

Manuscript submitted Feb. 28, 1978; revised manuscript received April 19, 1978.

Any discussion of this paper will appear in a Discussion Section to be published in the June 1979 JOURNAL. All discussions for the June 1979 Discussion Section should be submitted by Feb. 1, 1979.

Publication costs of this article were assisted by SRI International.

APPENDIX

Sources of Auxiliary Thermochemical Information

Thermodynamic functions and auxiliary thermochemical data used in the analysis of the equilibrium measurements were taken from sources listed below. The equilibrium internuclear distances in gaseous ZrI, ZrI_2, and ZrI_3 were assumed to be the same as the measured value for ZrI_4, 2.66Å. For ZrI, ZrI_2, and ZrI_3, the estimated moments of inertia (I), symmetry numbers (σ), electronic ground state statistical weights (g_0), and vibrational frequencies (ω) are listed in Table VI. Values of the Φ function (the tempered Gibbs energy function, formerly called free energy function) calculated from these spectroscopic constants are given in Table VII. The estimated uncertainties in the calculated Φ functions at the temperatures of the equilibrium measurements are ± 1, ± 2.3, and ± 1 cal/deg mole for ZrI, ZrI_2, and ZrI_3. These uncertainties are consistent with the observed agreement between second and third law heats. These uncertainties are coupled with those in the derived equilibrium constants to give the over-all estimated uncertainties attached to the third law heats.

I(g).—All data were taken from the JANAF Tables (3).

Zr(s, g).—Thermodynamic functions were taken from the JANAF Tables (3), while the enthalpy of formation of Zr(g), $\Delta H_f°_{298} = 143.4 \pm 1.2$ kcal/mole reported by Ackermann and Rauh (13), was adopted.

ZrI(g).—The vibrational frequency was estimated from the stretching frequency in ZrI_4. A $^4\Sigma$ ground state was assumed, as in ZrCl.

$ZrI_2(g)$.—A linear structure was assumed, in view of structural trends in the neighboring alkaline earths. Vibrational frequencies were estimated by analogy with those of SrI_2 and ZrI_4. The ground state was assumed to be a triplet.

$ZrI_3(g)$.—A planar symmetric structure with doublet electronic ground state was assumed. Vibrational frequencies were estimated by comparison with those of related molecules such as AsI_3.

$ZrI_4(g)$.—The thermodynamic functions, based on accurately known spectroscopic and molecular constants, were taken from the JANAF Tables (3). We have adopted the enthalpy of sublimation and enthalpy of formation of the gas, $\Delta H_f°_{298} = -84.9 \pm 1.5$ kcal/mole, given by Cubicciotti *et al.* (7).

Dates of JANAF Tables used were as follows: I(g), 6-74; Zr(s, g), 12-67; and ZrI_4(g), 6-75.

Table VI. Estimated spectroscopic constants of gaseous ZrI, ZrI_2, and ZrI_3

Molecule	$I \times 10^{39}$ (g cm²)	σ	g_0	ω_i (cm⁻¹)
ZrI	62.4	1	4	160
ZrI_2	298.0	2	3	30(2), 120, 210
ZrI_3	224.0	6	2	55(2), 60, 150,
	224.0			250(2)
	448.0			

Table VII. Calculated tempered Gibbs energy functions* (Free energy functions)

T (°K)	$\Phi°_{298}$ (cal/deg mole) ZrI	ZrI_2	ZrI_3
298	66.10	82.88	95.77
500	67.11	84.55	97.98
1000	70.62	90.40	105.73
1200	71.80	92.37	108.34
1400	72.86	94.13	110.68
1600	73.82	95.72	112.80
1800	74.68	97.16	114.72
2000	75.48	98.48	116.47
2200	76.21	99.70	118.09
2400	76.88	100.82	119.59

* $\Phi°_{298} = -(F° - H°_{298})/T$.

REFERENCES

1. Z. M. Shapiro, in "Metallurgy of Zirconium," B. Lustman and F. Kerze, Editors, chap. 5, McGraw Hill Book Co., New York (1955).
2. J. C. Wood, *J. Nucl. Mater.*, **45**, 105 (1972-1973).
3. JANAF Thermochemical Tables, NSRDS-NBS 37, U.S. Govt. Printing Office, Washington, D.C. (1971), and supplements.
4. D. L. Hildenbrand, *J. Chem. Phys.*, **48**, 3657 (1968); *ibid.*, **52**, 5751 (1970).
5. R. C. Paule and J. Mandel, NBS Spec. Publ. 260-19 (January 1970).
6. J. B. Mann, *J. Chem. Phys.*, **46**, 1646 (1967).
7. D. Cubicciotti, K. H. Lau, and M. J. Ferrante, To be published in *This Journal.*
8. H. Doring and K. Moliere, *Z. Electrochem.*, **56**, 403 (1962).
9. J. D. Fast, *Z. Anorg. Allgem. Chem.*, **239**, 145 (1938).
10. R. A. J. Shelton, *Inst. Min. Met. Trans.*, **77**, C113 (1968).
11. B. Cox and J. C. Wood, in "Corrosion Problems in Energy Conservation and Generation," C. S. Tedmon, Jr., Editor, The Electrochemical Society Softbound Symposium Series, Princeton, N.J. (1974).
12. H. Wachob and H. Nelson, NASA-Ames Research Center, Private communication.
13. R. J. Ackermann and E. G. Rauh, *J. Chem. Thermodynamics*, **4**, 521 (1972).

Investigation of Cation-Transport Processes during Anodic Oxidation of Duplex Layers of Tantalum on Niobium by the Use of Rutherford Backscattering and Nuclear Microanalysis

J. Perrière, S. Rigo, and J. Siejka*

Groupe de Physique des Solides de l'Ecole Normale Supérieure, Université Paris VII, 75221 Paris Cedex 05-France

ABSTRACT

It has been shown that, during anodic oxidation of superimposed metallic films of tantalum on niobium, a regime exists in which the growth laws of niobium substrate oxidation are the same as those found during pure niobium oxidation. Using ^{4}He Rutherford backscattering techniques we have shown that the order of cations is partially inverted in the oxide films. A pure niobium oxide region near the metal is covered by a layer in which both cations (Ta and Nb) are present. The fraction F_t of niobium atoms present in this last region was measured as a function of oxidation potential, tantalum deposit thickness, current density, and temperature. It was found that, for sufficiently high oxidation potentials, F_t is voltage independent and lies around 25%. F_t increases with increasing current density or decreasing temperature, while F_t is independent of tantalum layer thickness for thicknesses above 6 nm. Possible cation transport mechanisms corresponding to these observations are proposed and discussed.

The study of anodic oxide growth mechanisms consists in determining the moving species (metal or oxygen or both), and in elucidating their microscopic transport mechanisms. Studies of the migration of the atomic constituents of the oxide films have given rise to numerous publications (1-12). Data obtained from noble gas markers indicate that both metal and oxygen migrate during the anodic oxidation of Al (3, 5), Ta (3, 4), and Nb (3). The main difficulty in determining the microscopic transport mechanism is due to the fact that it is not possible to observe directly the movement of the constituent species during anodic oxidation since all experimental methods only give a picture of the final macroscopic situation. In order to find out how oxygen and metal move, it soon appeared that a suitable method is isotopic tracing. Thus, oxygen movements were studied by analysis of the ^{18}O distribution in duplex films obtained by successive oxidation in natural (^{16}O) and ^{18}O-enriched solutions. Results have shown that the order of oxygen atoms is on the average conserved during anodic film formation on Al (1) and on Ta (10), *i.e.*, the new oxygen atoms are incorporated at the oxide-solution interface. Isotopic tracing of metal was used in 1958 by Verkerk *et al.* (11) for Ta oxidation, but the results were not clear enough and gave rise to contradictory interpretations.

An alternative to isotopic tracing which is not always easy to carry out for studying cation movement could be the use of "substitute tracers," *i.e.*, tracer atoms whose movement with respect to the matrix is assumed to be well known. If these atoms move during anodic oxidation under the influence of electric field, with the same mechanism as the corresponding oxide constituent, they are equivalent to isotopic tracers. In the study of cation movements during oxidation of a metal M_1, this role might be played by atoms of another metal M_2 with similar properties. An oxidation of superimposed metallic films is hence carried out, in which a metal M_1 is covered by a thin film of metal M_2 (system $M_1|M_2$), and the change of cation distribution is studied after anodization. Such an approach was first used by Amsel and Samuel (1) and recently by Rigo and Siejka (12); the latter have studied cation movements during anodic oxidation of tantalum covered with a thin niobium film (Ta|Nb) and of niobium simliarly covered with tantalum (Nb|Ta). Tantalum and niobium (which are in the same column of the periodic table) are completely miscible and form the same kind of oxide with a faradaic efficiency near 100% and the ionic radii of Ta^{5+} and Nb^{5+}, and are generally listed as equal (13). It was thus initially assumed as a working hypothesis that each metal could be used with respect to the other as a practical equivalent of an "isotopic tracer." The results have shown (12) that, in the first case of (Ta|Nb), a moderate cation mixture appears in the oxide, while in the second case (Nb|Ta), a fraction of oxidized niobium atoms migrates through the oxide and fixes oxygen atoms at the oxide-solution interface. Furthermore, it was found that the cation movements seem to depend on tantalum deposit thickness (12). Differences in the anodic oxidation behavior of Ta and Nb have also been observed by Khoo *et al.* (14) in the study of the anodization of alloys. It appeared, thus, that although they are very similar in many aspects, Ta and Nb cannot be considered as equivalent to isotopic tracer for each other. This might be due, among other reasons, to the large difference in the corresponding electric fields of formation. Nevertheless, it also appeared that the study of anodization of superimposed metallic films is by itself a fruitful method to study cation migration mechanisms, shedding light on the basic transport mechanisms involved. In addition, practical applications of mixed oxide films grown in this way may be interesting in microelectronic device technology and in corrosion protection problems.

In this paper, we present results dealing with cation movements during anodic oxidation of niobium substrates covered with tantalum. The variations of the cation distribution in the oxide as a function of oxidation potential were studied for various current densities, temperatures, and tantalum layer thicknesses. A first report of these results was presented by Perrière (15).

A second purpose of this work was to elucidate the role played by the presence of tantalum at the various stages of the oxidation process of niobium. The number of tantalum atoms is always conserved during oxi-

* Electrochemical Society Active Member.
Key words: anodic oxidation, tantalum, niobium, transport mechanisms.

dation, but their depth concentration changes as a function of oxidation potential (16). Thus, the possible influence of tantalum oxide on niobium oxidation mechanism could depend on the tantalum atom distribution in the oxide. In fact, the number of niobium and tantalum atoms per unit oxide volume is practically the same in tantalum and niobium oxide. Hence, the penetration of niobium atoms in the tantalum oxide, due to cation movements, must be associated with the formation of an equivalent portion of new oxide at the oxide-solution interface. Thus the questions arise whether the microscopic transport mechanisms are conserved in tantalum oxide in spite of the penetration of niobium atoms into it, and whether they depend on niobium and tantalum atom concentration. This work was an attempt to provide at least partial answers to these questions.

Oxygen movements in these superimposed layers have been also studied. The results of these investigations are presented elsewhere (17).

Experimental

Preparation and analysis of samples.—The superimposed metallic films were tantalum layers deposited either on chemically polished bulk niobium (18), or on niobium layers deposited on aluminum. The same results were obtained (12) whatever the type of samples used. The metallic layers were obtained by d-c triode sputtering in an argon plasma at a 0.13 Pa pressure, with 2.5 kV cathode potential and a 60 mA current. The cathode diameter was 13 cm, and the cathode to substrate distance was 7 cm. Tantalum and niobium used as bulk substrates or as sputtering targets were supplied by Kawecki Berylco Industries with a 99.98% purity for tantalum and 99.9% for niobium.

As we have shown previously (12) that various electrolytes like ammonium citrate solutions, glacial acetic acid, and ammonium pentaborate solutions give the same results, we chose to use in this work aqueous solutions of ammonium pentaborate (0.5% by weight, pH kept at 9 by ammonium hydroxide additions). Such solutions do not dissolve aluminum and this insured compatibility with future work. The anodic oxidations were carried out at constant current density.

Nuclear microanalysis by the direct observation of nuclear reactions and of backscattered particles were used to study samples before and after oxidation. The experiments were carried out using the 2 MeV Van de Graaff accelerator of the laboratory.

Using nuclear microanalysis as described by Amsel *et al.* (19), the ^{16}O content of the films was obtained through the $^{16}O(d,p)^{17}O^*$ nuclear reaction. The absolute values were obtained by comparison with an oxygen reference target known to within ±3%. The preparation of such references is described in Ref. (20).

Rutherford backscattering was employed to analyze the depth distribution of cations in the superimposed films and in their anodic oxides; lateral homogeneity was assumed for the interpretation of the spectra. The basic concepts and equations related to Rutherford backscattering spectrum interpretation have been fully described (21, 22). Absolute amounts of niobium and tantalum atoms expressed in atoms/cm^2, in the deposits, and in their oxide were obtained (assuming validity of the Rutherford law), by comparison with a tantalum film containing $(525 \pm 10) \cdot 10^{15}$ at. Ta/cm^2, taken as a standard. The preparation of such standards is described in detail in Ref. (23). For convenience, the film thicknesses will also be given in nanometers, the equivalence atoms/cm^2 · thickness being practically the same for both Ta_2O_5 and Nb_2O_5, *i.e.*, 10^{15} at./cm^2 = 0.46 nm assuming the densities 8.04 and 4.74, respectively (24).

$^4He^+$ ion beams in the 1.6-1.9 MeV energy range were used according to the experiments with currents of about 80 nA on a 1 mm diam spot. The incident beam was normal to the targets and backscattered particles were detected at 165° or 150° angle by means of an Ortec silicon barrier detector of 25 mm^2 area with a 1 mm^2 diaphragm. The distance between target and detector was 59 and 50 mm, respectively, for the 165° and 150° detecting angle. With these conditions, the energy resolution (FWHM) was equal to about 14 keV and corresponds to a depth resolution of about 20 nm for tantalum and niobium oxides as calculated from Bragg's additivity rule for stopping power and using stopping power values of Ziegler and Chu (25) (see next section).

Analysis of MeV helium backscattering spectra.—As a simple initial test, the energy spectra backscattering of 1.6 MeV $^4He^+$ on a niobium sample covered by $8 \cdot 10^{16}$ tantalum atoms/cm^2 (about 15 nm assuming a density equal to 16 for tantalum) layer before oxidation (a) and after oxidation (b) were measured: They are shown on Fig. 1. The arrows Ta and Nb indicate the calculated energy values of particles backscattered by tantalum and niobium atoms located at the sample surface. In Fig. 1a, the niobium edge is shifted 20 keV with respect to its surface position. This effect is due to the energy loss in the tantalum film undergone by ^4He particles which are eventually backscattered from the niobium substrate. The tantalum peak, well separated from the niobium spectrum, is closed up against the Ta arrow, and so is the tanta-

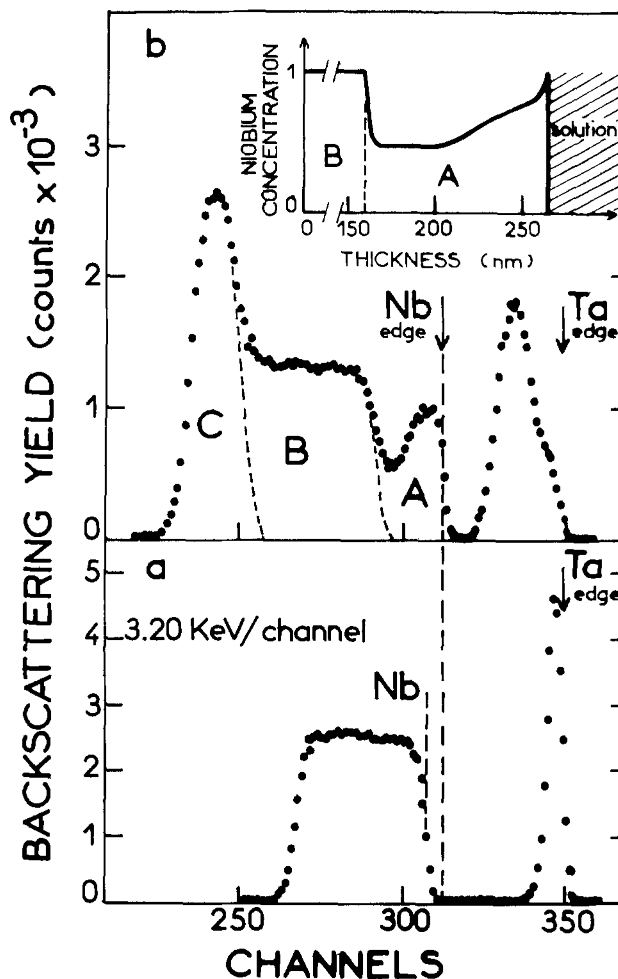

Fig. 1. Backscattering spectra of 1.6 MeV ^4He ions for a 15 nm thick tantalum film superimposed on a 120 nm thick niobium substrate on Al support. (a) Before oxidation; (b) after oxidation V = 150V; T = 23°C; i = 5 mA/cm^2. Channel 0 corresponds to E = 1.12 MeV. For the insert, see text.

lum at the surface. In Fig. 1b, the niobium edge appears at the surface energy position. Regions A and B of the niobium spectrum are related to the depth distribution of niobium atoms in the oxide; region C corresponds to unoxidized pure niobium. The tantalum spectrum is still well separated from that of the niobium; its shape is typical of tantalum atoms distributions encountered in this work. In fact, on the tantalum spectrum, a shoulder appears toward high energies; it indicates that some tantalum atoms remain in the near surface region of the oxide, mixed with niobium atoms, while the majority appears deeper in the oxide. From the spectrum, we may conclude that a niobium-rich layer is formed at the oxide surface, corresponding to the surface peak in the niobium spectrum. Thus a simple analysis of these spectra allows us to get an insight on cation movements during the anodic oxidation of this system. The atomic concentration ratio of niobium and tantalum in the two oxide mixtures is given with a good approximation (26) by $N_{Nb}/N_{Ta} = Y_{Nb}/Y_{Ta}[\sigma_{Ta}/\sigma_{Nb}]^2$ where Y_{Nb} and Y_{Ta} are the scattering yields per energy width for same energy particles before scattering (same depth), σ_{Ta} and σ_{Nb} are the elastic cross section for tantalum and niobium. Furthermore, stopping power values of niobium and tantalum oxide, as calculated from Bragg's additivity rule and Ziegler and Chu values (25), are very similar (the percentage difference is less than 4% in the 1-1.8 MeV energy range). So their differences were neglected, and we could determine a single energy-depth relationship for the tantalum and niobium oxide mixture.

The insert in Fig. 1b shows schematically the depth profile of niobium atoms in the oxide deduced from the spectrum. This niobium profile exhibits a pure niobium oxide layer (region B) covered by a tantalum and niobium oxide mixture (region A). The niobium atom concentration is constant (about 50%) in the internal part of the A region and then increases in the external part of the A region.

In this paper we present measurements of the number of niobium atoms n_A and n_B present in the parts A and B of the oxide. n_A and n_B represent, respectively, the number of niobium atoms in mixed oxide (which have crossed the inner edge of the tantalum atom distribution) and in pure niobium oxide, and we call F_t the ratio $n_A/(n_A + n_B)$. Since n_A and n_B are proportional to the areas N_A and N_B (corrected for cross section effects) of the regions A and B of the spectra, F_t can also be represented by the ratio $N_A/(N_A + N_B)$. Errors on these measurements depend on the precision with which we can establish the boundary lines between A and B, and B and C regions in the spectra. The shape of these separations was experimentally established by measuring the energy width of a niobium-niobium oxide interface. These measurements were carried out on pure niobium oxides the thicknesses of which were similar to those of A and A + B regions. So, the numbers of niobium atoms present in A and B regions were determined with an accuracy better than 5% for thick films (Nb consumption equivalent to more than 200 nm oxide) and equal to 20% for thin films (Nb consumption equivalent to less than 50 nm oxide).

Results

In order to describe and discuss our results in terms of microscopic transport mechanisms, we use the concepts of cationic events and of oxide network (27, 28). By the term of cationic events, one means the sequence of elementary jumps of one or more metallic cations which result, on the one hand in a transport of charges from their creation point to that of their recombination, and on the other hand in oxide growth. The elementary jumps can be of various types (29) such as long range (interstitial), or short range like interstitialcy, vacancy (assuming that such point defects can be defined in amorphous oxides), or Dignam lattice point defects movement (30). The term of network is meant in the sense of the continuous random network theory of amorphous media, as the spatial distribution of the atomic sites and bonds (the oxide being considered, under this concept, as mainly covalent), which is organized progressively as the oxide grows. We shall speak of "niobium or tantalum oxide networks," meaning that these two oxides may be organized in two well-defined, possibly different network types, keeping their nature even if some niobium or tantalum atoms are replaced by tantalum or niobium atoms, respectively.

Relationships between oxidation potential V and time t: $V = f(t)$.—Figure 2 shows some typical curves obtained by recording oxidation potential as a function of time during the anodic oxidation of pure niobium (curve a), of pure tantalum (curve b), and of a 15 nm thick tantalum layer superimposed on niobium substrate (curve c). All these experiments were performed at 5 mA/cm² current density and at 23°C temperature.

Three regions can be distinguished in curve c, these being regions 1 and 3 where $V = f(t)$ is linear. The slopes of these straight lines are identical to those observed for pure tantalum and pure niobium oxide growth (curves a and b). Region 2 is a transition region, between 25 and ~ 80V, where an undershoot of dV/dt is observed (see insert of Fig. 2). The intercept of the straight lines in regions 3 and 1 determine an oxidation potential V_1 which is relative to the potential drop in tantalum oxide obtained by anodization of a 15 nm thick tantalum layer. The value of the potential drop in tantalum oxide (37 nm) is 24.4V, calculated using a value of the slope of the kinetic of tantalum oxide growth equal to 1.54 nm/V [deduced from Ref. (31)]. This potential drop is in reasonable agreement with V_1 equal to about 25V.

These results confirm that tantalum oxide is formed in region 1 as expected, and strongly suggest that usual niobium oxide is formed in region 3, in spite of the presence of the tantalum oxide already formed. No clear explanation for the existence of the transition region 2 can be presented.

Oxide stoichiometry.—The total number of oxidized metallic atoms, tantalum plus niobium (the number of tantalum atoms per cm² was constant and equal to $8 \cdot 10^{16}$), as related to the number of oxygen atoms

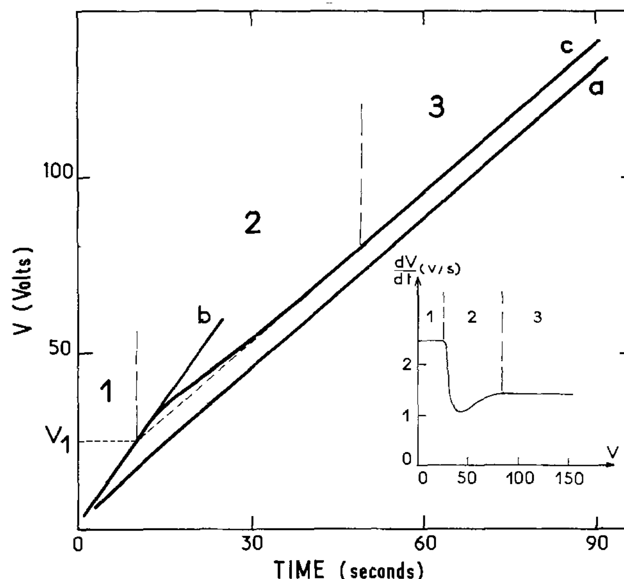

Fig. 2. Oxidation potential V as a function of time during anodic oxidation at a 5 mA/cm² current density and at a 23°C temperature for: (a) pure niobium; (b) pure tantalum; (c) 15 nm thick tantalum film on niobium substrate.

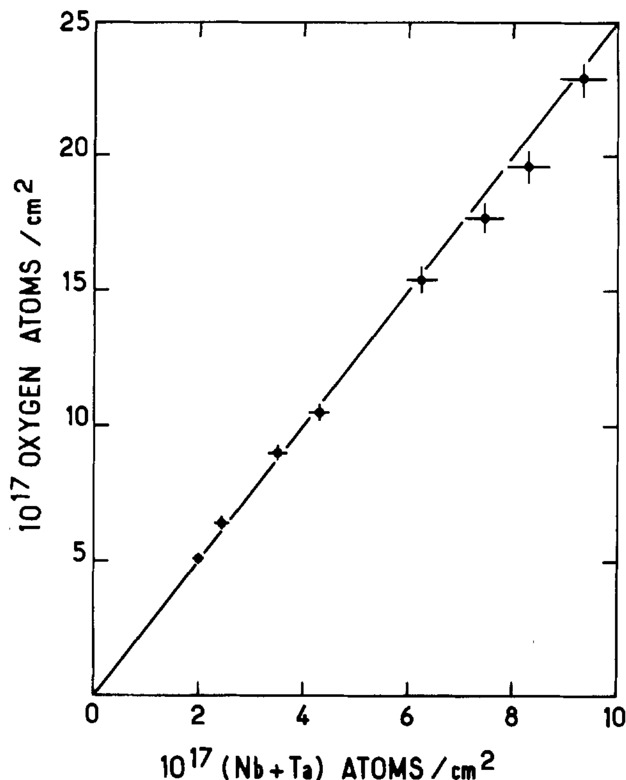

Fig. 3. Number of oxygen atoms in the oxide as a function of the total number of oxidized niobium plus tantalum atoms (the number of tantalum atoms per cm² is equal to $8 \cdot 10^{16}$ for each point). The absolute errors on each point are shown by the error bars.

fixed in the oxide for oxidation potentials lying between 60 and 220V, is presented on Fig. 3. These results were obtained using nuclear microanalysis as described above. The full line represents the theoretical curve corresponding to stoichiometric composition, *i.e.*, to the M_2O_5 formula (M for metal). Within our experimental precision (about 5%), Fig. 3 shows that for this oxidation potential range, this oxide is stoichiometric. For oxidation potentials lower than 60V, the errors on the measurements of the total number of oxidized niobium atoms increase as oxidation potential decreases; this precludes precise stoichiometry measurements in this region.

Cationic movements.—We have investigated the change of cation distribution in the oxides as a function of oxidation potential, tantalum layer thickness, and electric field.

Influence of oxidation potential.—Samples with a 15 nm thick tantalum deposit on niobium substrate were oxidized at 5 mA/cm² current density and at 23°C temperature. Oxidation potentials were chosen so that the various regimes observed in the $V = f(t)$ relationship could be studied. These oxidation potentials were chosen between 25V (total oxidation of tantalum deposit) and 220V. Figures 4 and 5 show backscattering spectra obtained on these samples. On all the spectra where the tantalum peak is well separated from the niobium spectrum, the peak area, corrected for differential cross-section effects, is constant within our experimental precision. This indicates that the number of tantalum atoms in the oxide is constant, and therefore excludes any dissolution process during oxide growth. So, even when the tantalum peak overlaps the niobium spectrum (at very high oxidation potentials), we can determine the number of oxidized niobium atoms mixed with tantalum atoms in the oxide. This is done by subtracting the tantalum peak area, obtained on the last spectrum where it is isolated, from the integral of the whole spectrum. Similar experiments were performed with double deposits on aluminum backing with a 120 nm thick niobium layer and 15 nm thick tantalum film. These latter results indicate that no appreciable dissolution of niobium occurs during anodization of superimposed layers, similarly to tantalum.

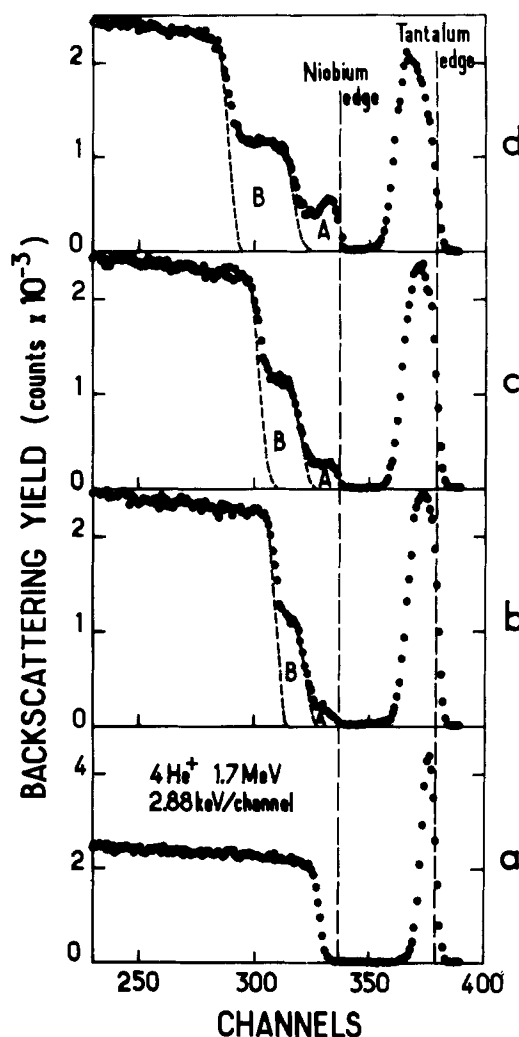

Fig. 4. Backscattering spectra of 1.7 MeV ⁴He ions for 15 nm thick tantalum film on niobium substrate: (a) before oxidation; (b) after oxidation at 23°C, $i = 5$ mA/cm², $V = 50$V; (c) 60V; (d) 80V.

The backscattering spectra are presented and discussed assuming lateral uniformity of the tantalum and niobium oxide mixture. In order to check this assumption, experiments are presently being carried out to study the lateral uniformity of tantalum distribution by using an electron probe with a resolution of about 4 μm. Preliminary results indicate that the tantalum concentration appears homogeneous with such a resolution, except in some localized defects (diameter equal to about 20 μm) with an over-all area below 1% of the whole surface.

Figure 4a represents the backscattering spectrum obtained on a sample before oxidation, and Fig. 4b, 4c, 4d, and 5 correspond to oxidized samples. Analysis of Fig. 4a shows that no mixing occurs between niobium and tantalum atoms to within 10 nm during the deposit. For an oxidation potential V equal to 25V, only the tantalum layer is oxidized. For higher oxidation potentials, the niobium substrate begins to be oxidized, and for various oxidation potentials, the changes in cation distribution appear as follows:

With 50V (Fig. 4b), a tail towards high energy appears in the niobium spectrum. It indicates a progressive penetration of niobium atoms in the tantalum

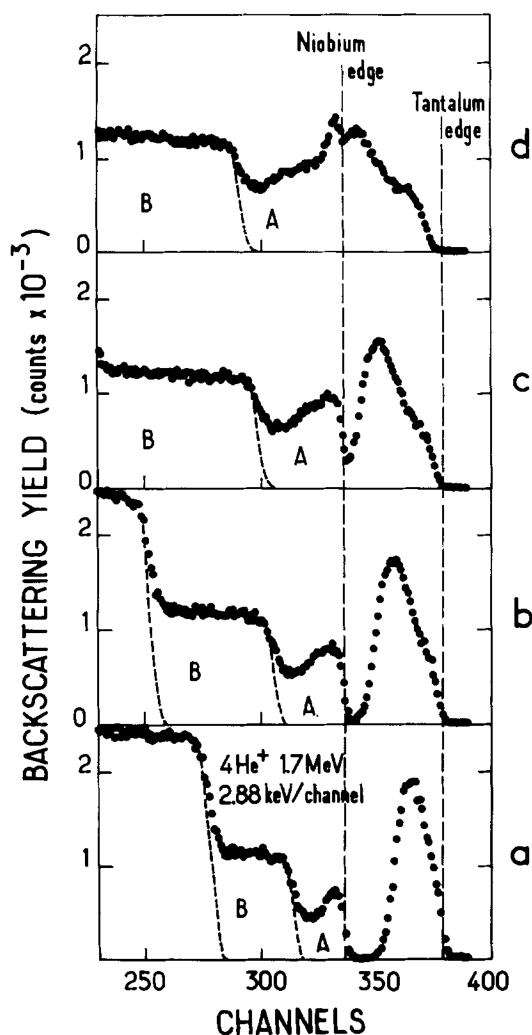

Fig. 5. Backscattering spectra of 1.7 MeV ^{4}He ions for 15 nm thick tantalum film on niobium substrate: (a) after oxidation at 23°C, i = 5 mA/cm^2, V = 100V; (b) 140V; (c) 180V; (d) 220V.

oxide network which is already formed. The presence of niobium atoms in this part of the oxide proves that niobium cations take part in cationic events, since movement of tantalum atoms against the field may be neglected.

With 60V (Fig. 4c), the niobium spectrum exhibits two clearly resolved steps. The first, corresponding to the oxide-solution interface, shows a tantalum and niobium oxide mixture over about 50 nm. In this mixture, the roughly uniform niobium concentration is about 30%. The second one corresponds to pure niobium oxide underlying the oxide mixture.

With 80V (Fig. 4d) and 100V (Fig. 5a), they correspond to the end of the transition region appearing in the $Vf(t)$ relationship (see Fig. 2). A surface peak in the niobium spectrum, and a shoulder toward high energies in tantalum spectrum begin to appear. This shows that niobium concentration increases in the near-surface region of the oxide mixture. This niobium concentration goes from 30% at 60V to about 60% for 100V oxidation potentials, and it is clearly higher than in the bulk of the oxide mixture (about 40%) where the niobium atom distribution is rather uniform.

With 120-200V (Fig. 5b-5d), oxidation potentials exist at which dV/dt is constant at the level expected for anodization of pure niobium (see Fig. 2). These spectra show that the niobium concentration first increases in the bulk of the oxide mixture: it goes from 40% to 55% as oxidation potential goes from 100 to 160V. Above, this niobium concentration remains constant within our experimental precision. The increase of the surface peak in the niobium spectrum indicates an increase of the niobium contents in the near-surface region of the oxide mixture. The tantalum spectrum is shifted towards lower energies and broadened as a function of oxidation potential, and finally, its rear edge overlaps the niobium spectrum (Fig. 5c and 5d). The shoulder on the tantalum spectrum is more and more resolved as oxidation potential increases. This fact shows that the tantalum and niobium atom ratio distribution in the surface region is steadily changing. For oxidation potentials higher than 120V, the front edge of the tantalum spectrum is shifted toward lower energies. This fact is explained by the formation of a pure niobium oxide layer at the oxide-solution interface. Its thickness increases with oxidation potential since the tantalum spectrum shift also increases, and reaches about 20 nm for a 220V oxidation potential.

In Fig. 6 we have presented schematically the depth profiles of niobium in the anodic oxides formed at 60, 100, 160, and 220V. The tantalum profile is not presented since it is the complement of that of niobium. We may distinguish a pure niobium oxide region (B) and the remainder of the oxide formed (A), *i.e.*, a tantalum-niobium oxide mixture region followed at high potentials by a pure niobium oxide region near the oxide solution interface. The sharp boundary between A and B was taken as the origin of the depth scale in Fig. 6. A region X of thickness equal to that of the oxide formed by the oxidation of the tantalum film alone has been represented on all figures by vertical dashed lines. It appears that for given potential, the niobium concentration in region X is practically constant and known with high enough relative precision (±10%). For oxidation potential higher than 160V, the niobium concentration in region X remains

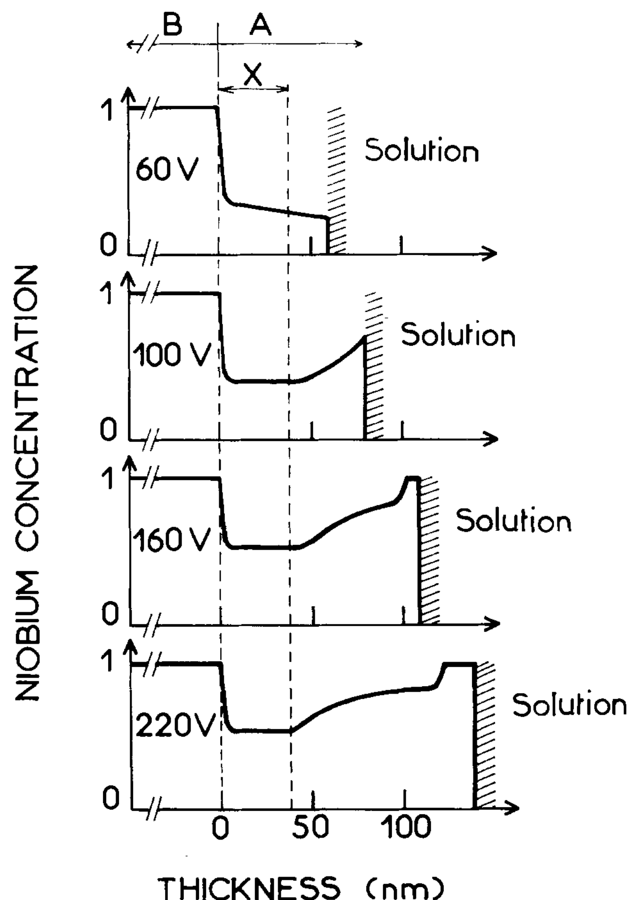

Fig. 6. Schematic representation of depth profiles of niobium for various oxidation potentials, deduced from the spectra of Fig. 4 and 5.

stationary reaching 55% ± 5%. On the other hand, the figures show that beyond region X the shape of the niobium profiles goes on changing with potential, the thickness of the mixed region as well as that of the pure surface oxide region increasing steadily.

Let us recall, as stated above, that this analysis is based on the assumption of lateral homogeneity of niobium and tantalum atoms in the oxide. As pointed out, the behavior of the niobium profile (as a function of oxidation potential) in the X region is different from that in the external part of the oxide mixture. The most likely explanation of this fact seems to be that the tantalum atoms present in the region X do not take part in cationic events for potentials higher than 160V. If we assume that these tantalum atoms have never taken part in cationic events during all the niobium substrate oxidation, one can conclude that region X can be associated to the tantalum oxide network formed during the anodic oxidation of the tantalum film alone.

From the spectra presented on Fig. 4 and 5 we have calculated F_t defined above as $F_t = n_A/(n_A + n_B)$ or $N_A/(N_A + N_B)$, *i.e.*, the fraction of oxidized niobium atoms which have crossed the inner edge of the tantalum atom distribution.

In Fig. 7, we have presented the F_t values as a function of the total number of oxidized niobium atoms n_{Nb}. For low values of n_{Nb}, the F_t measurements are not precise. It seems, however, that F_t values increase with niobium substrate consumption until about $3 \cdot 10^{17}$ Nb·at/cm^2 are oxidized (~75V of niobium oxidation). For higher oxidation potentials, the precision on F_t measurements is more satisfactory (about 10%), and F_t takes a constant value (F_t max), independent of oxidation potential and equal to 0.25 ± 0.02. Note that F_t is constant while (*i*) the distribution of tantalum and niobium atoms in the oxide mixture undergoes strong changes; and (*ii*) dV/dt is constant at the level expected for niobium anodization (see Fig. 2).

The analysis of the backscattering spectra has shown that, for oxidation potentials higher than 120V, there is a layer of pure niobium oxide at the oxide-solution interface. The thickness of this layer reaches about 20 nm for a 220V oxidation potential, while the increase, after the appearance of pure Nb_2O_5 surface layer (about 120V), of the total oxide thickness is equal to 200 nm. The pure niobium oxide layer represents then a fraction F_s equal to 0.10 ± 0.03 of the increase in total oxide thickness.

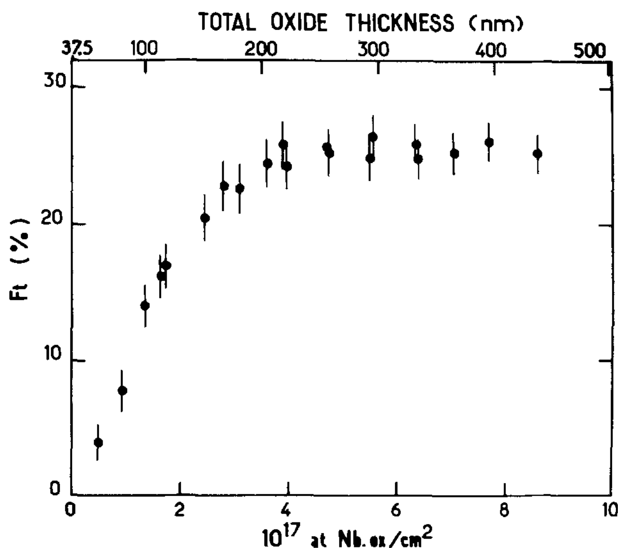

Fig. 7. Variation of F_t with niobium consumption for 15 nm thick Ta films on niobium oxidized at $T = 23°C$ and $i = 5$ mA/cm^2. The absolute errors on each point are shown by the error bars.

Note that F_s and F_t are a measure of the rate of burying of the tantalum atoms present in the surface region or in the tantalum network (region X) respectively. The difference between the values of F_s and F_t (0.10 and 0.25) is too high to be explained by measurements errors. Thus we may deduce that tantalum atoms present in the external part of the oxide mixture take part in cationic events whatever the oxidation potential.

Influence of the electric field.—F_t max was measured as a function of electric field. These experiments were performed on samples, with a 15 nm thick tantalum deposit, oxidized at 140V. During anodic oxidation of pure niobium or tantalum, an exponential-type relationship exists between the electric field, temperature, and current density. We may reasonably assume that the same relationship exists when we oxidize the niobium substrate at oxidation potentials corresponding to the linear region 3 of the $V = f(t)$ curve, regime in which dV/dt has the level expected for pure niobium anodization (see Fig. 2). Moreover, in this regime, F_t is constant and equal to F_t max (see influence of oxidation potential). Thus, the oxidation potential in these experiments (140V) was such that this regime was reached, and this was checked for each sample by recording the oxidation potential as a function of time during anodization.

Two kinds of experiments were carried out to study the influence of the electric field. The F_t max values were measured as a function of current density for constant temperature (23°C) and as a function of temperature for constant current density (5 mA/cm^2).

Figures 8 and 9 show that F_t max values increase linearly with the logarithm of current density and decrease with temperature. F_t max varies from 21 to 26% when the current density changes from 0.1 to 10 mA/cm^2 and from 23 to 27% when temperature decreases from 50° to 0°C. The relationship between F_t and current density seems to indicate that F_t is a linear function of electric field. The decrease of F_t with temperature is also likely to be due to the corresponding variation of the electric field, in the range of electric field studied in these experiments.

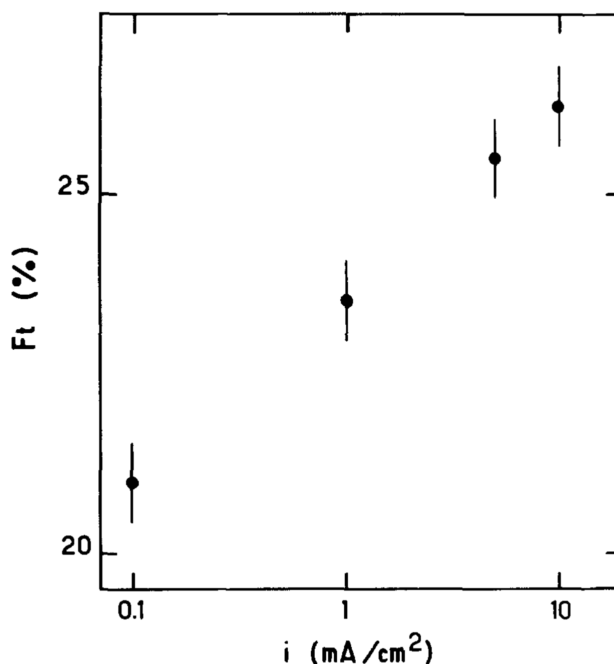

Fig. 8. Variation of F_t as a function of current density for 15 nm thick tantalum films on niobium oxidized at $T = 23°C$ and $V = 140V$. The relative errors from one point to another are shown by the error bars.

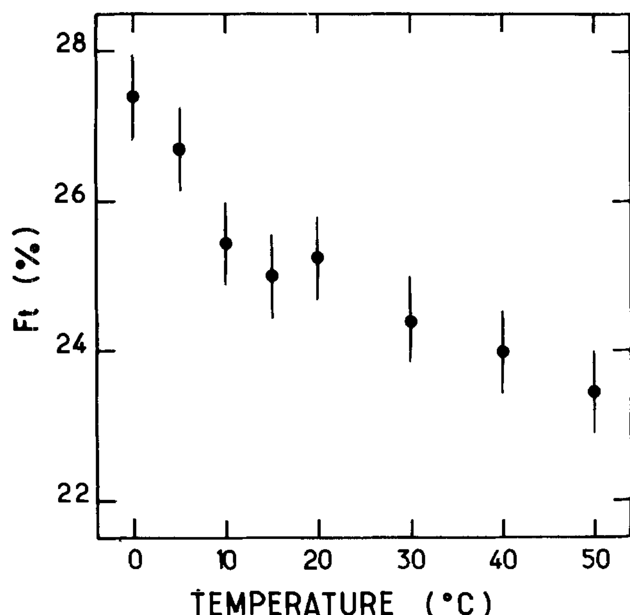

Fig. 9. Variation of F_t as a function of temperature for 15 nm thick tantalum films on niobium oxidized at $i = 5$ mA/cm^2 and $V = 140$V. The relative errors from one point to another are shown by the error bars.

Influence of tantalum deposit thickness.—Three kinds of samples were distinguished as a function of tantalum deposit thickness: (*i*) 6-40 nm. One may reasonably assume that a continuous metallic film covers the niobium substrate (32); (*ii*) (10^{14}-10^{15} at./cm^2) equivalent to the order of 0.1 nm. One may assume that anodic oxidation of this kind of samples is similar to that of pure niobium and that niobium oxide network is formed, tantalum being present as traces; and (*iii*) 1-4 nm. This is too small to ensure the presence of a continuous metallic film on the substrate (32), and too high to be considered as traces.

The experiments were carried out at a constant current density (5 mA/cm^2) and at 0°C temperature. For samples (*i*), oxidation potentials were chosen so that constant values of F_t (F_t max) as a function of oxidation potential were reached (see influence of oxidation potential). Oxidation potentials were such that the number of oxidized niobium atoms was the same for all samples (*i*). All the other samples, *i.e.*, (*ii*) and (*iii*), were oxidized at oxidation potentials where the number of oxidized niobium atoms was the same as that chosen for samples (*i*), *i.e.*, $5 \cdot 10^{17}$ at./cm^2 and in all cases, these potentials corresponded to the linear region 3 of the $V = f(t)$ curve (see Fig. 2). This was checked for each sample by recording the oxidation potential as a function of time during anodization. The results of these experiments are presented on Fig. 10.

For samples (*i*) they are expressed by the F_t max values, and for a 15 nm thick tantalum deposit a value of F_s is also presented. One can see that F_t max values are constant, equal to 27%, independently of the thickness of the tantalum deposit.

For samples (*ii*) the burying of the tantalum atoms in the oxide was determined by the shift of the position of the tantalum peak on the backscattering spectra (12). Note that this peak has a practically constant width, indicating that the tantalum atoms remain grouped to within 10 nm (limited by the depth resolution of our measurements). We can express this burying as a ratio $R = L_s/L_{Tot}$, where L_s is the oxide thickness corresponding to the energy shift of tantalum peak, and L_{Tot} is the total oxide thickness. The value of tantalum atoms burying was found equal to 10 ± 3%. Furthermore, experiments were carried out at various oxidation potentials and similar R values

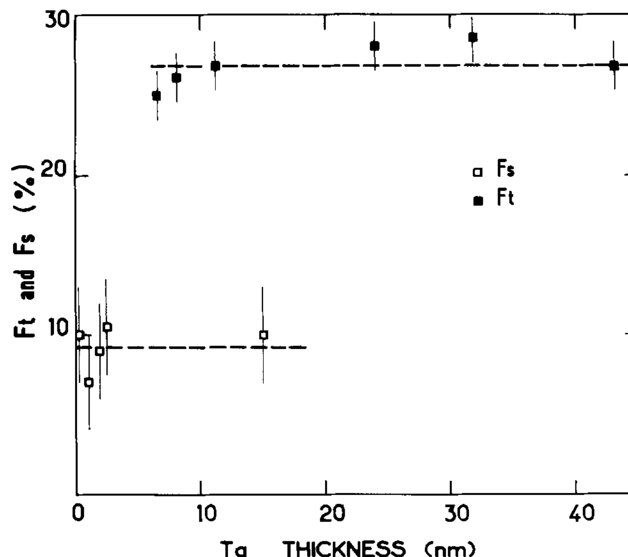

Fig. 10. Variation of F_t and F_s as a function of tantalum deposit thickness. The absolute errors on each point are shown by error bars.

were found in all cases. One can see that R has the same value as F_s for samples with a continuous tantalum deposit (15 nm).

For samples (*iii*), F_s values were measured and are presented on Fig. 10. The F_s values, so determined, appear near to that found for a 15 nm thick uniform tantalum deposit. Furthermore, one can notice that in all cases, F_s is equal to the R value defined for tantalum traces. This strongly suggests that, for a continuous tantalum film, tantalum atoms in the near surface region of the oxide move in the same way as tantalum traces in niobium oxide. Hence it is reasonable to assume that, in this case, the niobium oxide network is formed at the oxide solution interface before a pure niobium oxide layer appears there.

Discussion and Conclusion

We have shown that the anodic oxidation of a niobium substrate covered by a thin tantalum oxide takes place, for oxidation potential higher than 100V, with the same kinetics and leads to the formation of the same stoichiometric oxide (Nb_2O_5) as for pure niobium oxidation. The fraction F_t of niobium cations which crosses the inner edge of the tantalum atom distribution during anodization reaches its saturation value (25% with $i = 5$ mA/cm^2 and $T = 23$°C), for an oxidation potential equal to about 100V, and then F_t is constant for higher oxidation potentials. The F_t values increase with increasing current density and decreasing temperature.

We discuss our results using the concepts previously defined (see results); moreover we assume that the cationic events preserved their identity through the whole oxide. Let us recall that, by cationic events one means the sequence of elemetary jumps, of one or more metallic cations, which result in a transport of charge through the oxide and in oxide growth. This assumption means, thus, that the cationic events, which are initiated at the metal-oxide or oxide-solution interface (depending on the microscopic transport mechanism), result in a transport of charge to the other interface involving only the elementary jumps of metallic cations through the whole oxide. We exclude therefore *a priori*, creation of cationic events in the bulk of the oxide or the transformation of cationic events in anionic events in the bulk of the oxide.

One may notice that, with this assumption, and as any movement of tantalum or niobium atoms against the electric field may be neglected, one may write that F_t represents the minimal fraction of niobium oxide grown by cation migration. The term minimal

means that the possible movement of tantalum atoms under the influence of the electric field is not *a priori* neglected. Moreover, t_m being the transport number of niobium, since F_t is defined as the minimal fraction of niobium oxide grown by cationic movements, the relationship $F_t \leq t_m$ holds. It is interesting to compare the value of F_t with that of t_m measured during pure niobium anodization in comparable experimental conditions. According to Davies *et al.* (3) the value of t_m for niobium is equal to 27%. Let us recall that in the interpretation of our experimental results we have assumed that some tantalum atoms in region X (see Fig. 6) do not take part in cationic events. With this assumption, region X could be used as a reference frame to measure the transport number of niobium implying $F_t = t_m$. Comparison of F_t with the transport number of niobium given by Davis *et al.* (3) shows that F_t is practically equal to t_m (27%), *i.e.*, oxidation of niobium (in the presence of tantalum oxide) takes place with the same value of t_m as for pure niobium oxidation. Although the validity of this conclusion will have to be checked by other more detailed studies of the transport number of pure niobium (as a function of current density and temperature), the present work establishes that the transport number of niobium substrate covered by thin tantalum oxide is equal at least to 25% (at $i = 5$ mA/cm^2 and $T = 23°$C), assuming the preservation of cationic events.

In this work, the description of the results was based on the hypothesis of lateral uniformity of the tantalum and niobium oxide mixture, and was made by using the R, F_s, or F_t measurements. R describes the burying of tantalum traces in niobium oxide as a function of oxidation potentials. One can assume that the anodic oxidation leads in this case to the formation of practically pure niobium oxide network (Ta concentration ~0.5-5 a/o), and that we have measured the value of Ta burying in niobium oxide network in the case of isolated tantalum atoms. It was found that $R = 10 \pm 3\%$. This value is much lower than F_t (25%) and lower than the reported t_m value for pure niobium, 27% (3). This means that in this case, all tantalum atoms in the niobium oxide participate in the growth. As no movement of tantalum atoms in not growing oxide has ever been observed, we can assume that the movement of tantalum atoms is due to cationic events which take place during oxide growth. As a large spread is not observed in the tantalum distribution, we may assume that the tantalum atoms move by a neighbor-to-neighbor jump process. Hence there are two possibilities for niobium atoms: (*i*) all the movements of niobium cations are also of the neighbor-to-neighbor jump process type; or (*ii*) a fraction of niobium cations move by long-range migration (12).

(*i*) In this case, the burying of the tantalum atoms would be due to the difference between jump probabilities of tantalum (P_{Ta}) and niobium (P_{Nb}) atoms during oxide growth. We may write $P_{Ta}/P_{Nb} = (t_m - R)/t_m$, getting the value 0.6 (with $t_m = 0.25$). Let us notice that such an hypothtsis means that the order of cations would be conserved during the anodic oxidation of pure niobium and that no burying of niobium isotopic tracer would be obtained in an isotopic tracer experiment.

The F_s measurements describe the burying of the tantalum atoms in the surface layer of the mixed oxide during anodic oxidation of a niobium substrate covered by a continuous tantalum film (15 nm). It was found that the value of F_s is practically equal to R. So we can assume that these tantalum atoms take part in the ionic current in the same way as tantalum traces in niobium oxide with the same microscopic transport mechanism and that the network formed would be of the niobium type. The formation of pure niobium oxide at the oxide solution interface would be due to the fact that the jump probability P_{Ta} is smaller than P_{Nb} in this part of mixed oxide. One may conclude from these assumptions that the network formed beneath the pure surface Nb_2O_5 region is also of the niobium oxide network type although it contains more than 20% of tantalum atoms.

The F_t measurements describe the burying of the tantalum atoms present in the region X which is assumed to be the tantalum oxide network (Fig. 6). It was found that tantalum concentration (C_{Ta}) in region X is constant ($C_{Ta} = 45\%$) and independent of oxidation potential for potentials higher than 160V. This would mean that P_{Ta} is nearly zero in the tantalum oxide network for $C_{Ta} = 45\%$. However, for oxidation potentials lower than 160V ($C_{Ta} > 45\%$), some tantalum atoms take part in cationic events, *i.e.*, $P_{Ta} > 0$. One may conclude that P_{Ta}, in the tantalum network, is a function of the concentration in tantalum and niobium atoms and changes from $P_{Ta} = 1$ ($C_{Ta} = 100\%$) to $P_{Ta} = 0$ ($C_{Ta} = 45\%$). On the other hand, values of P_{Ta} higher than zero are found in the niobium network for tantalum concentrations equal to about 20% or in the case of traces. These results suggest that the jump probability of tantalum (or niobium) atoms during oxide growth depends not only on tantalum concentration but also on the type of oxide network. Note that the same results could be observed in a slightly different situation: some tantalum atoms would be rigidly locked to the network and would never participate in the cationic movements, their presence being needed to insure the stability of the tantalum oxide network; others would move freely and may be replaced by niobium atoms, the network still keeping its "tantalum network" character. In this case there would exist two different types of cationic sites in the network, in nearly equal proportions; however, this does not seem likely in an amorphous medium. As such a process would lead to a partial reversal of the order of the tantalum atoms during pure tantalum oxide growth, a precise radioactive tracer experiment could allow one to draw definite conclusions.

(*ii*) If we assume that the microscopic transport mechanism of niobium cations is not only of the neighbor-to-neighbor jump process type, the burying of the tantalum atoms would not be due to a difference in jump probabilities, but to the fact that a fraction of the cationic events are of long-range migration type (12). The progressive change in niobium profile with oxidation potential suggests that long-range migration would take place in several jumps. Hence, niobium cations could move in interstitial position, jumping over 2, 3, or more sites, the substitutional jumps of increasing length occurring with decreasing probability. Such an hypothesis should lead to an inversion of the order of cations during the anodic oxidation of pure niobium.

Although our experimental results do not permit a choice between these two possibilities, it seems to us that (*ii*) is less probable since it needs two different microscopic transport mechanisms for niobium and tantalum atoms.

Let us recall that the above discussion is based on lateral uniformity of the oxide, as suggested by preliminary results obtained by electron probe measurements (see above). However, heterogeneity of the oxide structure cannot be excluded in the dimension range lower than our experimental resolution (~4 μm). For example, tantalum oxide could form some islands of microscopic dimensions. The cationic events would pass round them, involving only the niobium atoms. Our present results do not allow us to rule out completely nonuniformity effects.

Acknowledgments

The authors wish to thank Dr. G. Amsel for his numerous comments and suggestions during this work and for his help in writing this paper. The technical assistance of Messrs. J. P. Enard and A. Laurent was much appreciated. The authors are grateful to Dr. C.

Bahezre of the "Laboratoire de Physique des Matériaux" (C.N.R.S. Bellevue) who has carried out the preliminary experiments with the electron probe, and to E. d'Artemare, E. Girard, and M. Vidal for their help in the use of the nuclear microanalysis facility of our laboratory.

This work was supported by the Centre National de la Recherche Scientifique (RCP No. 157).

Manuscript submitted July 18, 1977; revised manuscript received Feb, 28, 1978. This was Paper 129 presented at the Toronto, Canada, Meeting of the Society, May 11-16, 1975.

Any discussion of this paper will appear in a Discussion Section to be published in the June 1979 JOURNAL. All discussions for the June 1979 Discussion Section should be submitted by Feb. 1, 1979.

REFERENCES

1. G. Amsel and D. Samuel, *J. Phys. Chem. Solid*, **23**, 1707 (1962).
2. J. A. Davies, J. P. S. Pringle, R. L. Graham, and F. Brown, *This Journal*, **109**, 999 (1962).
3. J. A. Davies, B. Domeij, J. P. S. Pringle, and F. Brown *ibid.*, **112**, 675 (1965).
4. J. P. S. Pringle, *ibid.*, **120**, 398 (1973).
5. F. Brown and W. D. Mackintosh, *ibid.*, **120**, 1096 (1973).
6. W. D. Mackintosh, F. Brown, and H. H. Plattner *ibid.*, **121**, 1281 (1974).
7. J. J. Randall, Jr., W. J. Bernard, and R. R. Wilkinson, *Electrochim. Acta*, **10**, 183 (1965).
8. P. J. Silverman and N. Schwartz, *This Journal*, **121**, 550 (1974).
9. R. L. Ruth and N. Schwartz, *ibid.*, **123**, 1860 (1976).
10. J. P. S. Pringle, *ibid.*, **120**, 1391 (1973).
11. B. Verkerk, P. Winkel, and D. G. de Groot, *Philips Res. Rep.*, **13**, 506 (1958).
12. S. Rigo and J. Siejka, *Solid State Comm.*, **15**, 259 (1974).
13. L. Young, "Anodic Oxide Films," p. 186, Academic Press, London and New York (1961).
14. S. W. Khoo, G. C. Wood, and D. P. Whittle, *Electrochim. Acta*, **16**, 1703 (1971).
15. J. Perrière, Thesis, Université Paris VII, Paris (1974).
16. J. Perrière, S. Rigo, and J. Siejka, in Proceedings of Electrochemical Society Meeting in Toronto, Canada, Vol. 75-1, p. 224, May 1975.
17. J. Perrière, S. Rigo, and J. Siejka, Paper presented at The Electrochemical Society Meeting, Seattle, Washington, May 21-26, 1978.
18. C. Cherki, *Electrochim. Acta*, **16**, 1727 (1971).
19. G. Amsel, J. P. Nadai, E. d'Artemarre, D. David, E. Girard, and J. Moulin, *Nucl. Instr. Methods*, **92**, 481 (1971).
20. G. Amsel, J. P. Nadai, C. Ortega, S. Rigo, and J. Siejka, *Nucl. Instr. Methods*, in press.
21. W. K. Chu, J. W. Mayer, M. A. Nicolet, T. M. Buck, G. Amsel, and F. Eisen, *Thin Solid Films*, **17**, 1 (1973).
22. "New Uses of Ion Accelerator," p. 75, J. F. Ziegler, Editor, Plenum Press, New York and London (1975).
23. S. Rigo, C. Cohen, A. L'Hoir, and E. Backelandt, *Nucl. Instr. Methods*, in press.
24. A. J. Schrijner and A. Middelhoek, *This Journal*, **111**, 1167 (1964).
25. J. F. Ziegler and W. K. Chu, *Atom. Data Nucl. Atom. Data Tables*, **13**, 463 (1974).
26. J. A. Borders and S. T. Picraux; *Proc. IEEE*, **62**, 1224 (1974).
27. G. Amsel, M. Croset, and J. Siejka, in Proceedings of The Electrochemical Society Meeting, Vol. 75-1, p. 227, Toronto, Canada, May 1975.
28. G. Amsel, M. Croset, and J. Siejka, To be submitted to *This Journal*.
29. P. Kofstad, "Nonstoichiometry, Diffusion and Electrical Conductivity in Binary Metals Oxide," p. 71-73, Wiley-Interscience, New York (1972).
30. M. J. Dignam, in "Oxides and Oxide Films," Vol. 1, J. W. Diggle, Editor, p. 192, Marcel Dekker, Inc., New York (1973).
31. J. Siejka, J. P. Nadai, and G. Amsel, *This Journal*, **118**, 727 (1971).
32. W. D. Westwood, N. Waterhouse, and P. S. Wilcox, "Tantalum Thin Films," p. 83, Academic Press, London (1975).

Technical Notes

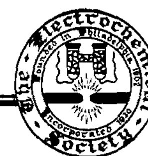

Silicon Nitride Chemical Vapor Deposition in a Hot-Wall Diffusion System

Robert Ginsburgh, David L. Heald, and Richard C. Neville

Department of Electrical Engineering and Computer Science, University of California, Santa Barbara, California 93106

The use of vapor-deposited silicon nitride films has been an essential part of the fabrication process for several types of integrated circuits for a number of years (1-3). Hot-wall silicon nitride vapor deposition systems have emerged as a means of meeting the increasing throughput requirements of semiconductor manufacturers.

Generally, hot-wall-type systems utilize a diffusion furnace or similar apparatus. The carrier reactant gases are heated and chemical reactions initiated prior to their reaching the wafers located in the hot zone. Significant variations in film growth rates and in structure can be expected for small changes in operating parameters such as gas species concentration, flow rates, wafer location, temperature, etc. However, the temperature control of a modern diffusion furnace is very precise with temperature variations of less than ¼°C over periods of months. Therefore, in any given system, temperature is the easiest parameter to control. The objectives of the study then were a characterization of silicon nitride film growth rates and properties as a function of gas parameter variations for fixed temperature operations at atmospheric pressures.

Key words: CVD, diffusion, circuits.

Equipment and Procedure

The hot-wall diffusion furnace used in this series of experiments was a single zone, Lindberg Heavy Duty model with 2 in. diam quartz tube. The furnace was set at 875°C and profiled (see Fig. 1). All experiments

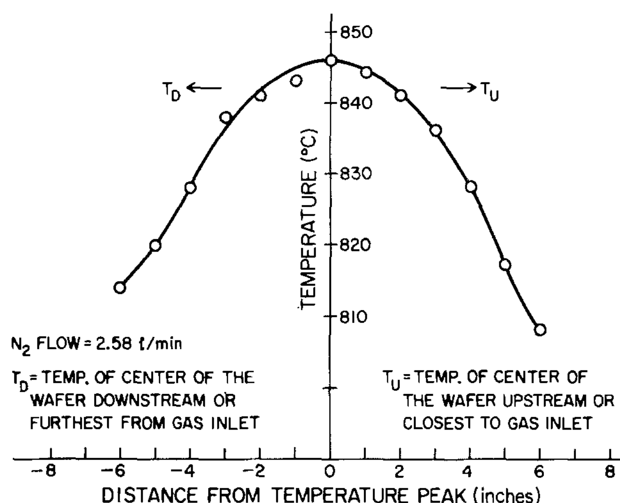

Fig. 1. Temperature profile of Si_3N_4 diffusion furnace with a 6 in. quartz boat centered at the peak temperature.

were conducted with two 1 in. diam <111> polished silicon wafers laid flat (polished side up) on a 1.5 × 6 in. quartz boat. A wafer was placed at each end of the boat on the center line. The boat was placed in the furnace at the thermal and physical center. The maximum temperature gradient across a wafer was determined to be 1.4°C. All furnace operations included a 5 min warm up period. Gas flow rates through the furnace were monitored and controlled using Brooks flowmeters. Nitrogen was obtained from the boil off of liquid nitrogen and the silane and ammonia were electronic grade.

The refractive index of the films grown on the silicon test wafers was determined using an Applied Materials ellipsometer, and the film thicknesses were determined both optically and mechanically. The optical technique used monochromatic light (Sodium-D) and involved counting interference fringes at steps between grown film areas and portions of the silicon slice from which the film had been removed. The mechanical method used a Sloan Corporation DekTak. Film thicknesses as measured by the two methods were within ±5%.

Experimental Results

Based on a number of earlier experimental runs, not reported on here, a set of flow rates for the silane ($SiHy_4$), ammonia (NH_3), and the carrier gas (N_2) which produced "satisfactory" silicon nitride films existed in our laboratory. These values were selected as a starting point. The time of growth in the furnace was then varied, with the results as shown in Fig. 2. The refractive indexes of all films were between 1.90 and 1.95. The data of Fig. 2, when linearly extrapolated to zero thickness, indicate an approximate nucleation period, before growth, of between 15 sec (for upstream wafers) and ½ min (for downstream wafers). Here upstream refers to those wafers between the gas inlet and the furnace center.

The growth period was then fixed at 5 min, and the flow rate of the carrier gas (N_2) was varied while maintaining the SiH_4 and NH_3 flow rates constant. These data are presented in Fig. 3. Note that for upstream wafers a maximum exists in the film thickness as a function of a nitrogen flow rate, and that the growth rate for wafers closest to the gas inlet is much higher than that for wafers downstream. The refractive index of all films grown in this portion of the investigation lay between 1.85 and 1.95.

The next experiment, as shown in Fig. 4, held the growth time, nitrogen flow rate, and ammonia flow rate fixed, as specified. The silane flow rate was varied so as to vary the ammonia-to-silane ratio. The data for the upstream wafers indicate that the process has

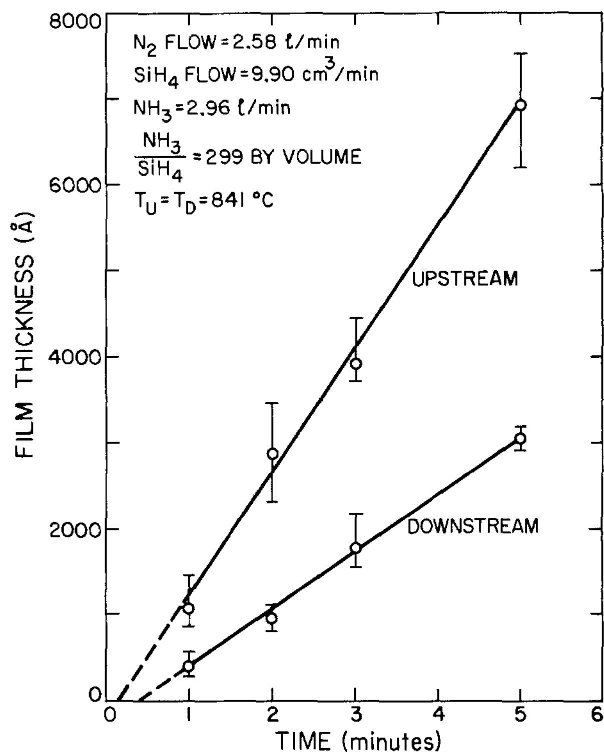

Fig. 2. Silicon nitride film thickness *vs.* time. Bars on data points indicate degree of uncertainty of data. Circles indicate average data.

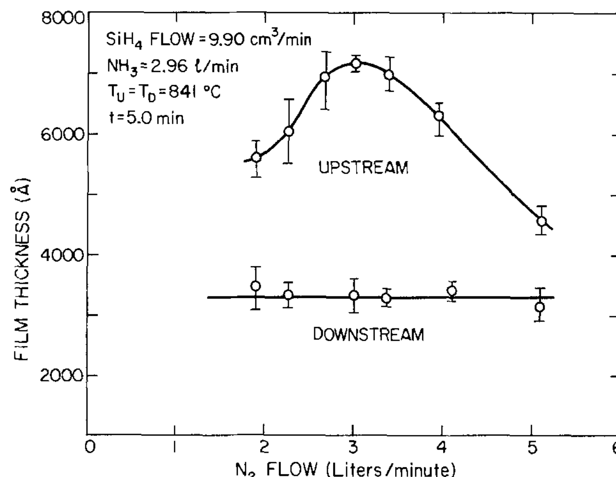

Fig. 3. Film thickness *vs.* nitrogen flow rate. Bars on data points indicate degree of uncertainty of data. Circles indicate average data.

several "type" reactions. For low ammonia-to-silane ratios, the growth rate is high. At intermediate ratios (region II) the growth rate is stable over a wide range (3/1) of flow ratios. This is attributed to a combination of the availability of the required chemical constituents at the wafer surface and the rate at which their reaction and the subsequent "siting" of the silicon nitride on the surface of wafer is carried out. In region III the ammonia-to-silane ratio is in excess of 300 and the reaction decreases, owing to a deficiency of silane. The data for the downstream wafers indicates that the process in this region remains in a "silane deficient condition" reaction for all silane: ammonia ratios. In regions I and II the bulk of the silane is reacting upstream, the silane reaction gradually shifting towards the downstream end as an increasing percentage of the silane is swept past the upstream wafer before it can react. In region III the entire tube is "silane deficient" and thus cannot support rapid silicon nitride growth.

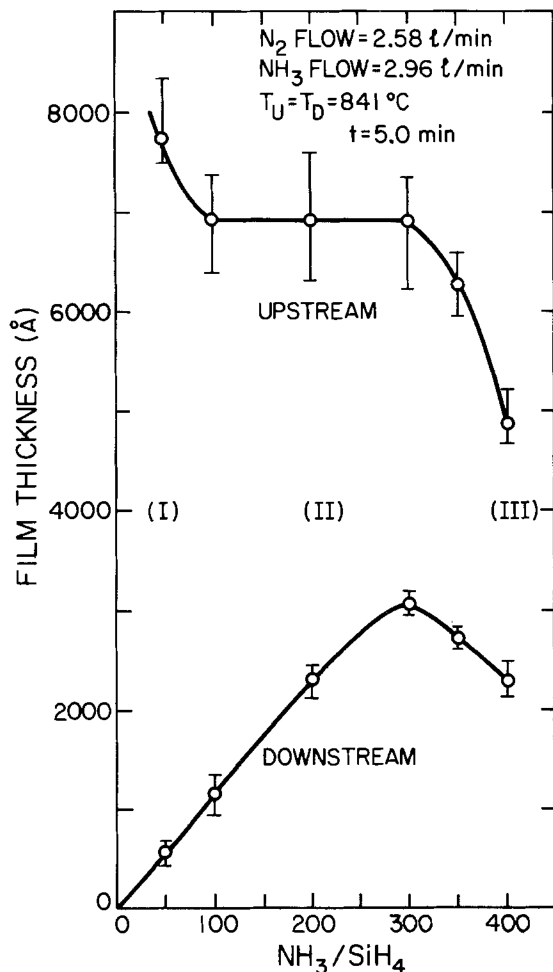

Fig. 4. Film thickness vs. ammonia:silane ratio. Bars on data points indicate degree of uncertainty of data. Circles indicate average data.

Refractive index measurements on all films were between 1.86 and 1.95 for this phase of the experiments.

The final growth rate variations, as shown in Fig. 5, involved fixing the carrier gas (N_2) flow rate, the ammonia-to-silane flow ratio (NH_3/SiH_4), and varying the total volume of ammonia and silane. Again the growth period was 5 min. The refractive index of all films was checked and found to vary between 1.90 and 1.95.

A major use for silicon nitride in semiconductor processing is as a mask against silicon oxide growth. Representative silicon nitride films from this collection of experiment, of thickness 750, 1000, and 2000Å, were placed in an oxidation furnace. An oxidation, employing oxygen saturated with water vapor at 95°C, was carried out at 950°C for a period of 6 hr. After stripping the silicon nitride film in hot phosphoric-acid, no sign of an oxide on any of the silicon wafers was detected, either optically or chemically.

Discussion and Conclusions

As stated previously, excellent agreement (within ±5%) was found for silicon nitride film thickness measurements made both mechanically and optically. In addition, the variation in uniformity of the deposited film across any individual wafer was within ±3% in all cases. However, the variation in film thickness from run to run for wafers in the same location and under measurably identical conditions was within ±15%, in-

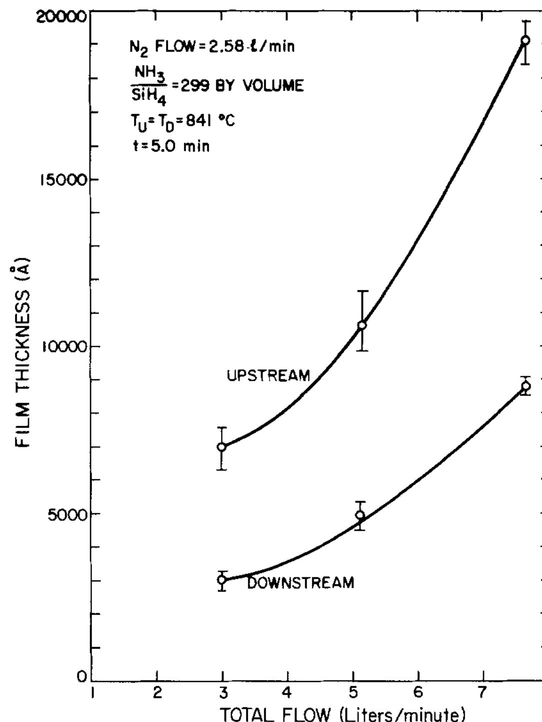

Fig. 5. Film thickness vs. total gas flow. Bars on data points indicate degree of uncertainty of data. Circles indicate average data.

dicating system instabilities. An attempt was made to correlate film thickness to chemical etch rate, employing a chemical etch of hot phosphoric acid. No correlation in etch rate for any of the samples was obtained even for samples grown under the "same" conditions. Since the etch rate of the silicon nitride films depends strongly on the structure of the film, and since the film structure depends on minute variations in gas flow patterns as well as gas composition, the results suggest that the films may possess significant difference in structure and composition.

Analysis of the refractive index measurement data revealed small variations of the index within individual wafers but significant variations among wafers of the same run and of different runs. Due to these variations it is likely that the films have considerably different structural properties. The slices closest to the gas inlets tend to have higher film growth rates and a wider range of film thickness for any given set of conditions. This is indicative of a strong "deficiency mechanism" in which most of the silane has prereacted prior to reaching downstream wafers. Even though individual film characteristics vary, hot-wall process silicon nitride films as thin as 750Å are effective in blocking oxidation of the underlying silicon surface for periods in excess of 6 hr at 950° in wet ambients.

Manuscript submitted Sept. 7, 1977; revised manuscript received Feb. 21, 1978.

Any discussion of this paper will appear in a Discussion Section to be published in the June 1979 JOURNAL. All discussions for the June 1979 Discussion Section should be submitted by Feb. 1, 1979.

Publication costs of this article were assisted by the University of California.

REFERENCES

1. Forbes, *IEEE J.S.S.C.*, **8**, 228 (1973).
2. Henderson *et al.*, *ibid.*, **10**, 94 (1975).
3. Dingwall and Stricker, *ibid.*, **10**, 299 (1975).

Surface Morphology of GaAs Layers Grown by Electroepitaxy and Thermal LPE

Y. Imamura,[1] L. Jastrzebski, and H. C. Gatos*

Department of Materials Science and Engineering, Massachusetts Institute of Technology, Cambridge, Massachusetts 02139

It was found that terraces commonly present on GaAs layers grown by standard (thermal) LPE were not present on layers grown by electroepitaxy. A comparison of the surface morphology obtained by the two methods was based on layers of the same thickness grown in the same apparatus, with the same average growth rates, on substrates having the same orientation (and electrical properties) and from solutions equilibrated at the same temperature. Growth in thermal LPE is induced by a temperature decrease; in electroepitaxy growth is initiated and sustained by passing electric current across the growth interface while the temperature of the growth system is maintained constant (1).

In electroepitaxy the growth process is controlled by electromigration of solute toward the growth interface and the contribution of the Peltier effect is negligible when appreciable convection in the solution is not present (2). Since the origin and nature of supersaturation in thermal LPE and in electroepitaxy are different, a comparision of the surface morphology of layers obtained by the two methods could elucidate the dependence of surface morphology on parameters of the growth process. The comparison is confined to epitaxial layers with the commonly used (100) crystallographic orientation.

Electroepitaxial growth was carried out in a standard LPE apparatus modified to permit controlled flow of electric current across the growth interface (3). Semi-insulating Cr-doped substrates were used. They were prepared by a standard procedure described elsewhere (4); their orientation was (100) within less than 0.1°. A uniform electrical contact on one side of each substrate was made employing a thin layer of Ga (3). The growth area was 0.5 cm^2. Interference of convection in the solution with the growth process was eliminated as described elsewhere (3). Consistent with the criteria for electromigration-controlled growth (2), the microscopic growth rate was found to be the same in experiments carried out at the same current density but employing substrates with a large difference in thickness (*i.e.*, 250 and 2500 μm).

The surface morphology of a 10 μm thick, Ge-doped ($p \simeq 2 \times 10^{18}/\text{cm}^3$) layer, grown in 11 min on a 450 μm thick substrate at 900°C from a solution with a height of 1 cm at a current density of 20 A/cm^2 is shown in Fig. 1. The layer exhibits no terracing (Fig. 1a) commonly encountered on layers grown by thermal LPE (5-8). The only detectable defects on the layer of Fig. 1a are small pits of very low density. As seen from the interferogram in Fig. 1b, that layer is flat.

A number of parameters which might affect the surface morphology were studied, such as thermal gradients in the solution, thickness of the epitaxial layer, solution height, and current density. Only one parameter was varied at a time; the other parameters, unless otherwise specified, were as indicated for the growth of the layer shown in Fig. 1. Thus, the vertical thermal gradient in the solution was varied from 0.3° to 2.7°C/cm, by varying the thickness of the substrate from 250 to 2500 μm for a current density of 10 A/cm^2 (cooling at the interface increases with substrate thickness) (9). Prior to current flow the vertical thermal gradient in the solution was less than 0.15°C/cm and the horizontal less than 0.1°C/cm. Growth was initiated either after the substrate and the solution, equilibrated at 900°C, were brought into contact (as in the case of the layer shown in Fig. 1) or after the solution, thermally equilibrated at 901.5°C (over a dummy substrate), was brought into contact with the substrate which was equilibrated at 900°C (in this case the substrate was partially backmelted). The thickness of the grown layers was varied from 8 to 70 μm. The solution height was varied from 1 to 1.4 cm. Finally, the current density was varied from 5 to 50 A/cm^2, corresponding to a growth rate variation from 0.4 to 4.5 μm/min.

The surface morphology of the layers grown under all of the above experimental conditions was essen-

Fig. 1a. Nomarski interference contrast photomicrograph of the surface of a GaAs layer 10 μm thick, grown at 900°C under 20 A/cm^2; (290 times).

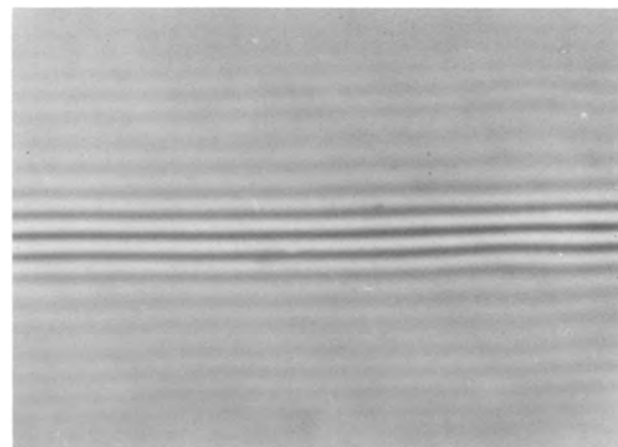

Fig. 1b. Interferogram of the same area as Fig. 1a taken by using an interference attachment to the microscope.

* Electrochemical Society Active Member.

[1] Present address: Nippon Telegraph and Telephone Public Corporation, Electrical Communication Laboratories, Tokyo, Japan.

Key words: surface morphology, GaAs, electroepitaxy, LPE.

tially indistinguishable from the surface morphology of the layer shown in Fig. 1. The occasional appearance of defects such as dishes or hillocks were invariably related to defects in the electrical contact of the substrate (3). It is, thus, concluded that, over a broad spectrum of growth conditions, GaAs layers grown by electromigration-controlled electroepitaxy are flat and exhibit no terracing or other morphological defects.

For the growth of layers by thermal LPE, the same apparatus, experimental conditions, and procedures were used as for electroepitaxial growth. After equilibration at 900°C the temperature was decreased at a controlled rate so that the average growth rates were comparable to those obtained by electroepitaxy. The surface morphology of a layer grown from 900°C by lowering the temperature is shown in Fig. 2. The layer, as the one shown in Fig. 1, is Ge-doped ($p \simeq 2 \times 10^{18}/cm^3$), 9 μm thick, and was grown in 10 min from a solution with a height of 1 cm, on a 450 μm thick substrate cut from the same wafer used for substrate of the layer shown in Fig. 1. It is seen that the surface of the layer shown in Fig. 2a exhibits terracing and is not flat as shown in the interferogram in Fig. 2a.

As in electroepitaxy, a number of parameters were varied in studying the surface morphology of layers grown by thermal LPE. Thus, layers were grown on partially melted substrates and on substrates which were not backmelted (as in the case of the layer shown in Fig. 2). The thickness of the grown layers was varied from 9 to 70 μm and the solution height from 1 to 1.4 cm. Finally, the growth rate was varied from 0.3 to 4 μm/min. The surfaces of all layers exhibited terracing similar to that shown in Fig. 2a; small (but not systematic) variations in the spacing of the terraces were observed among some layers.

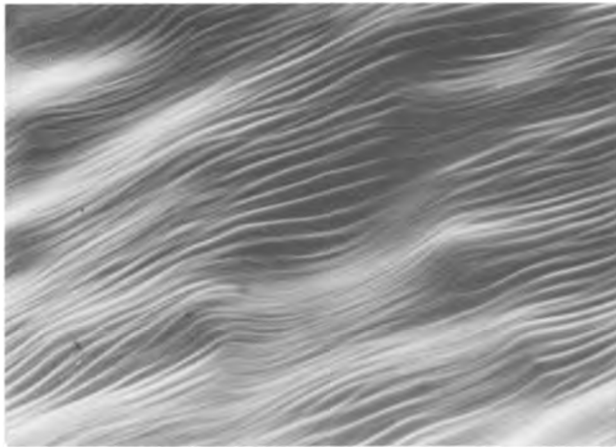

Fig. 2a. Nomarski interference contrast photomicrograph of the surface of GaAs layer 9 μm thick, grown by temperature decrease (thermal LPE); orientation of substrate was identical to that of substrate used for layer shown in Fig. 1 (growth conditions given in text); (290 times).

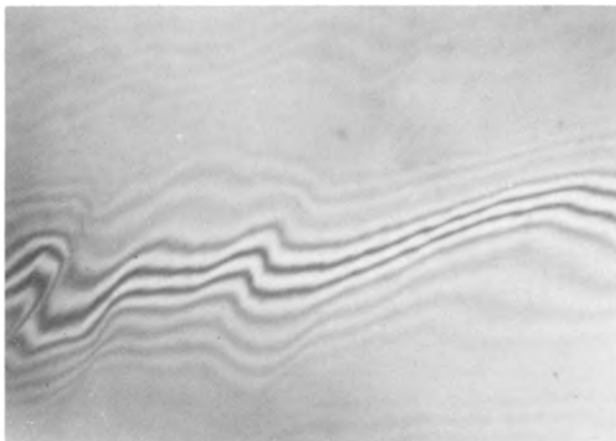

Fig. 2b. Interferogram of the same area shown in Fig. 2a

In view of the above results, the pronounced differences in the surface morphology of the layers grown by electroepitaxy and of those grown by thermal LPE cannot be attributed to specific growth conditions. Rather they must be associated with fundamental differences in the growth mechanisms involved in the two growth methods. Since quantitative models of nucleation and growth have not been established for these methods, the present results are considered in the light of some general features characterizing the methods.

In electroepitaxy supersaturation takes place in the immediate vicinity of the growth interface and growth is controlled by the rate of transfer of solute, under an electric field, to the interface (electromigration-control); the contribution of the Peltier effect is negligible (2). In fact, for a given temperature, the growth rate is directly proportional to the current density (*i.e.*, to the electric field). Under these conditions growth must take place under nearly equilibrium (isothermal) conditions and interface instabilities due to constitutional supercooling cannot occur. On the other hand, in thermal LPE supersaturation is induced throughout the solution and nucleation takes place not only on the substrate but, to some extent, also on the walls of the solution container. Unless special precautions are taken (10), random nucleation, fluctuations in solute concentration, and/or temperature gradients and constitutional supercooling are potential causes of nonuniform growth leading to terraced surface morphology.

In conclusion, in electromigration-controlled electroepitaxy, the steady-state and uniform transfer of solute to the growth interface under isothermal conditions leads to uniform growth and flat terrace-free surface morphology.

Acknowledgments

The authors are indebted to the National Science Foundation for financial support and to Dr. J. Lagowski and Professor A. F. Witt for valuable discussions.

Manuscript submitted March 27, 1978; revised manuscript received April 27, 1978.

Any discussion of this paper will appear in a Discussion Section to be published in the June 1979 JOURNAL. All discussions for the June 1979 Discussion Section should be submitted by Feb. 1, 1979.

Publication costs of this article were assisted by the Massachusetts Institute of Technology.

REFERENCES

1. M. Kumagawa, A. F. Witt, M. Lichtensteiger, and H. C. Gatos, *This Journal*, **120**, 583 (1973).
2. L. Jastrzebski, J. Lagowski, H. C. Gatos, and A. F. Witt, Submitted to *J. Appl. Phys.*
3. L. Jastrzebski, Y. Imamura, and H. C. Gatos, *This Journal*, **125**, 1140 (1978).
4. H. Morkoc and L. F Eastman, *ibid.*, **123**, 906 (1976).
5. D. J. Lawrence and L. F. Eastman, *J. Mater. Sci.*, **6**, 1 (1976).
6. B. L. Mattes and R. K. Route, *J. Cryst. Growth*, **27**, 133 (1974).
7. R. C. Peters, in "Proceedings of the 4th International Symposium on GaAs and Related Compounds," Boulder, Colo., p. 55, Institute of Physics, London and Bristol.
8. J. T. Longo, J. S. Harris, E. R. Gertner, and J. C. Chu, *J. Cryst. Growth*, **15**, 107 (1972).
9. E. K. Stefanakos, A. Abdul-Fadl, and M. D. Workman, *J. Appl. Phys.*, **46**, 3002 (1975).
10. M. Mihara, N. Toyoda, and T. Hara, *Appl. Phys. Lett.*, **27**, 131 (1975).

JOURNAL OF THE ELECTROCHEMICAL SOCIETY

ELECTROCHEMICAL SCIENCE
— AND TECHNOLOGY

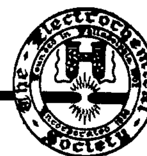

OCTOBER
1978

Dynamic X-Ray Diffraction

R. R. Chianelli, J. C. Scanlon, and B. M. L. Rao*

Exxon Research and Engineering Company, Linden, New Jersey 07036

ABSTRACT

The discharge of a TiS_2 electrode in an ambient temperature Li/TiS_2 organic electrolyte cell has been investigated by dynamic x-ray diffraction. The new technique involves a continuous *in situ* measurement of x-ray diffraction simultaneous with electrochemical polarization. The investigation has provided additional information on electrolithiation of TiS_2. These include: (*i*) the onset of changes in 101 peak position right from the start of discharge, (*ii*) correspondence of x in Li_xTiS_2 to state-of-charge from coulombic balance; and (*iii*) details of changes in the c axis during discharge, especially during the first 30% of discharge capacity. The results are discussed along with the cell design, operational details, and merits and limitations of the technique.

X-ray diffraction is a well-known technique for the analysis of composition and structure of electroactive solids used in batteries. Most of the previous work involves isolating the electrode from the environment before and after electrochemical polarization and subjecting the sample to x-ray analysis. In so doing, there is always the possibility that some details may be lost during the isolation of the electrode from the electrochemical environment and/or during the treatments needed for preparation of the sample for x-ray diffraction. This limitation could be overcome if *in situ* x-ray diffraction analysis could be carried out on electrodes in an operating cell. This would also have the advantage of gaining insight into intermediates and/or products formed during the dynamic conditions of current flow.

In this report, we have developed procedures for *in situ* x-ray diffraction of electrodes in an operating cell. We have termed the new technique dynamic x-ray diffraction (DXD) to signify x-ray diffraction measurements under dynamic conditions in which changes in micro- or macrocrystallinity, stoichiometry or composition of the electroactive material occur due to electrochemical polarization.

Recently there has been growing interest in intercalation compounds as positive active materials for lithium-nonaqueous electrolyte cells. In this context, TiS_2 has been the subject of intense investigation on physical, chemical, and electrochemical (1-6) properties. In an effort to gain further insight into the intercalation mechanism of lithium in TiS_2, we have undertaken the dynamic x-ray diffraction studies. The experimental set-up, cell design, and the technique is general enough to be applicable to similar investigations on other systems.

Experimental

Setup and operation.—The experimental setup consisted of an x-ray diffraction unit operating in conjunction with an electrochemical polarization circuit, as shown in Fig. 1. Copper-K_α radiation from a Phillips powder diffractometer was collimated onto the test electrode of an electrochemical cell mounted in a specially designed sample holder. The diffracted wave was received by x-ray electronics and analyzed in the usual manner. For the dynamic measurement the test cell was rotated to continuously scan between predetermined Bragg angles $2\theta_1$ and $2\theta_2$, back and forth, while carrying out the electrochemical measurement. Thus the changes in the position and intensity of the peaks followed as a function of coulombs of electrochemical change identified the changes in nature and concentration of the species undergoing the electrochemical reaction.

Specific materials and procedures.—The dynamic x-ray diffraction of a TiS_2 electrode in a cathode limiting Li/TiS_2 cell was investigated. In a typical experiment, the 100, 002, and 101 peaks of TiS_2 were scanned. These three peaks provided (7) a convenient check on the "a" and "c" lattice parameter as a function of state of charge during the electrochemical polarization of the cell. The scanning was performed in a 15 min/cycle at a rate of 1°/min in an automatic repeat sequence starting from 28° ($2\theta_1$) until 35° ($2\theta_2$).

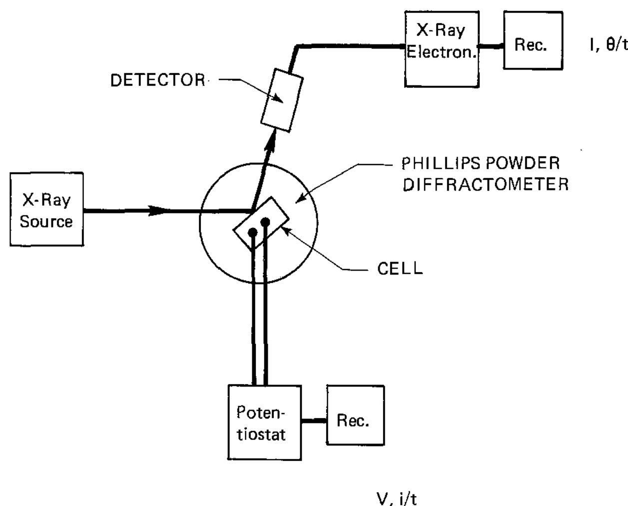

Fig. 1. Experimental arrangement

* Electrochemical Society Active Member.

Key words: lithium anode, TiS_2 cathode, organic electrolyte, *in situ* x-ray diffraction.

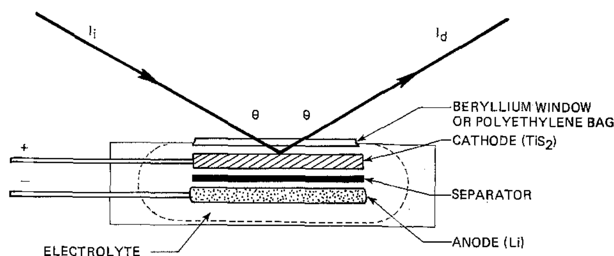

Fig. 2. Schematic of x-ray diffraction cell

Figure 2 gives a schematic representation of the Li/TiS_2 cell used in parallel plate configuration. The anode was 200 mA-hr lithium foil and the cathode was a pasted-plate TiS_2 electrode of 80-160 mA-hr loaded on 5 cm^2 nickel grid. The TiS_2 used was prepared from the elements and the electrodes contained 10 w/o polytetrafluoroethylene binder. The cells contained 65% porous fiber glass separator (0.0375 cm thick) and 0.5-1.0 ml 2M $LiClO_4$ in dioxolane electrolyte. The cell casing was either a polyethylene bag or an aluminum and polytetrafluoroethylene casing, as described later. The cells were assembled in a helium dry box and then mounted in a specially designed cell holder that would enable alignment of the test electrode in the optical path of x-ray in the diffractometer.

In the case of the polyethylene bag cell, the x-ray radiation impinged on the TiS_2 electrode by penetrating polyethylene film (0.005 cm) and the surrounding electrolyte, both of which are noncrystalline. With this cell, the polyethylene film contributes intense scattering in the region 15°-28° (2θ), making observation of the Bragg peaks difficult. However, preliminary experiments did permit observation of the 101 reflection as a function of electrochemical state of charge.

To overcome these difficulties, a second cell was designed (Fig. 3) with a beryllium x-ray window which permitted TiS_2 Bragg peaks to be analyzed with greater precision than the polyethylene bag cell. In this design, the Li/TiS_2 was an integral part of the cell holder. The cell holder comprised an aluminum (bottom) and polytetrafluoroethylene (top) casing which housed the electroactive elements, *i.e.*, Li/TiS_2 cell, and contained an electrolyte fill port. The top and the bottom were held under compression with an EPR gasket and set screw assembly, as shown: The polytetrafluoroethylene top had cemented to it a 50 μm thick beryllium window that is transparent to x-ray beam in the region of 10°-35° 2θ. We recognize that although the sharp beryllium metal peaks did not interfere with TiS_2 lines in this experiment, there might be a problem in other investigations based on this technique. Appropriate modification of x-ray window is recommended in such cases.

It is to be noted that at high discharge rates, nonuniform discharge may occur. The relationship between dynamic x-ray data and the electrochemical discharge may then represent quasi-equilibrium under this condition.

Prevention of electrolyte leakage from the cell, alignment of the test electrode in the optical path of the x-ray beam, and proper shielding of the dynamic x-ray arrangement to prevent radiation leakage to avoid hazards to the operating personnel needed special attention in these studies.

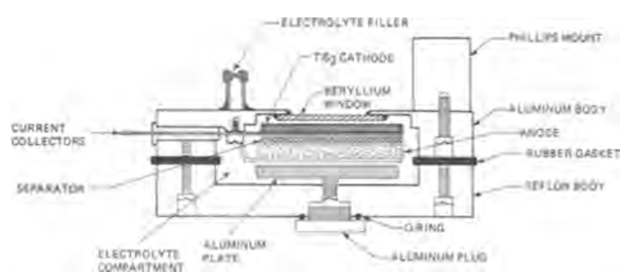

Fig. 3. Schematic of x-ray diffraction cell with beryllium window

Results and Discussion

The depth of penetration of CuK_α radiation is assessed to be ~ 50 μm of the 700 μm thick TiS_2 electrode used in test cell. Thus, the changes in Bragg peak position and intensity observed during the dynamic x-ray diffraction measurements reflected the changes in the composition and crystal structure occurring in ~10% depth in thickness as measured from the position away from the lithium electrode, *i.e.*, back side of the electrode. The x-ray spectra taken prior to switching on of the electrochemical circuit served as internal standard for the calibration of the cell.

Figure 4 represents the 101, 002, and 100 Bragg peaks of a TiS_2 electrode as measured before and after discharge of a positive limiting Li/TiS_2 cell at 1 mA/cm^2. The observed continuous variation of lattice spacings as x in Li_xTiS_2 changes from 0 to 1 during the chemical reaction (1)

$$x\text{Li}^+ + \text{TiS}_2 + xe \rightarrow \text{Li}_x\text{TiS}_2, \quad 0 \geqq x \leqq 1$$

is represented in Fig. 5. Data in Fig. 5 indicate that 002 has the greatest variation with state-of-charge of TiS_2 and 100 the least. The 101 has intermediate variation, but is the most intense line and provided greater ease of measurement. Consequently, all analyses of the results are presented with reference to varia-

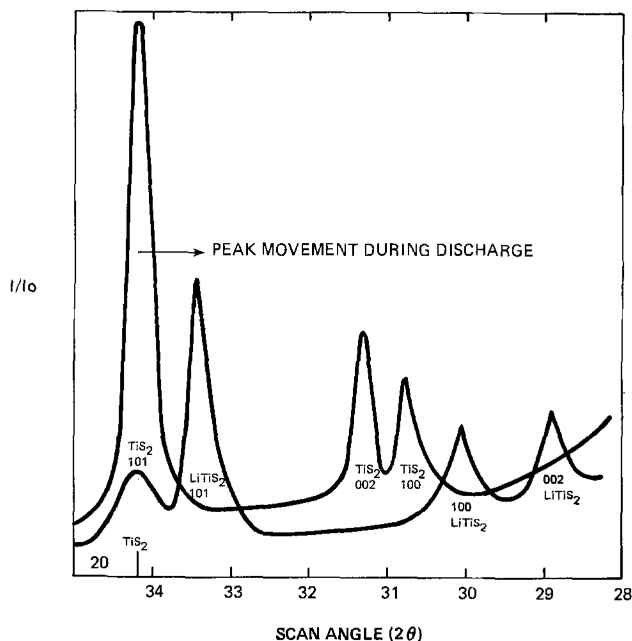

Fig. 4. Movement of Bragg peaks observed during discharge of TiS_2 to form $LiTiS_2$.

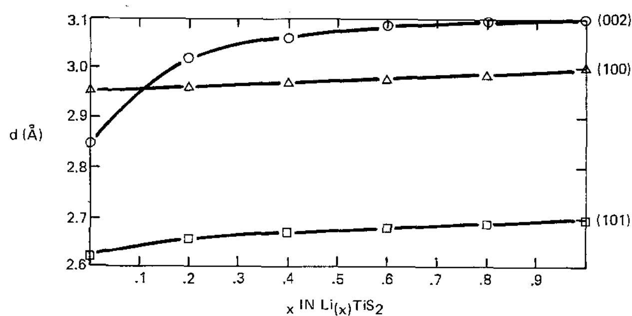

Fig. 5. Variation of 002, 001, and 101 Bragg peaks as a function of x in Li_xTiS_2 ($0 \geqq x \leqq 1$).

tions in the 101 line from 2.62A for TiS_2 to 2.69A for $LiTiS_2$.

Figure 6, curve a, illustrates the discharge data for a TiS_2 electrode of 156 mA-hr and 4.83 cm^2 area at 1 mA/cm^2. Figure 6, curve b, is a plot of the position of the 101 line measured during the discharge. The test electrode exhibited 90% depth of discharge with an open-circuit voltage of 1.84V after 10 hr of rest following discharge. The position of the 101 line was determined by measuring the relative distance between the position of the 101 line on the up θ scan, and the same line on the down θ scan, as indicated in Fig. 7. This technique permitted the determination of relative line shifts with an accuracy of 0.0015A. Thus, each point in the curve of c axis expansion *vs.* x in Li_xTiS_2, indicated by the percentage depth of discharge in Fig. 6, consists of an average of two points which are approximately 3-4° 2θ apart.

Figure 8 gives the details of the variation of 101 peak as a function of depth of discharge. The 101 line

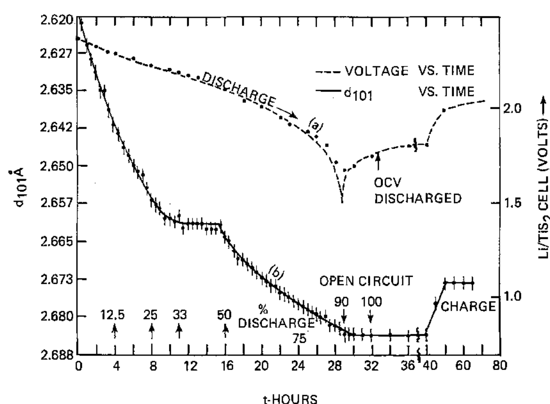

Fig. 6. Comparison of variations in Li/TiS_2 cell voltage with movement of Bragg peaks (d 101) observed during dynamic x-ray diffraction.

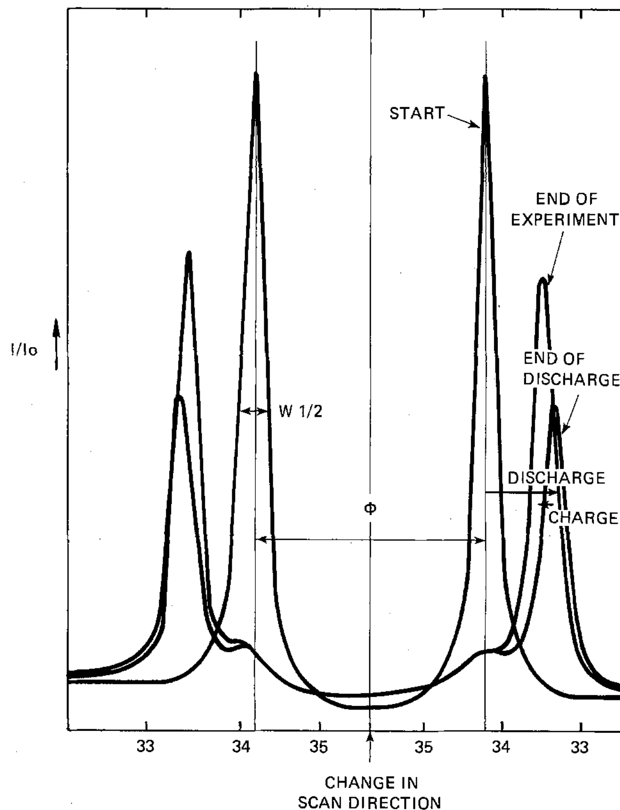

Fig. 7. Dynamic x-ray diffraction scan data used in analysis

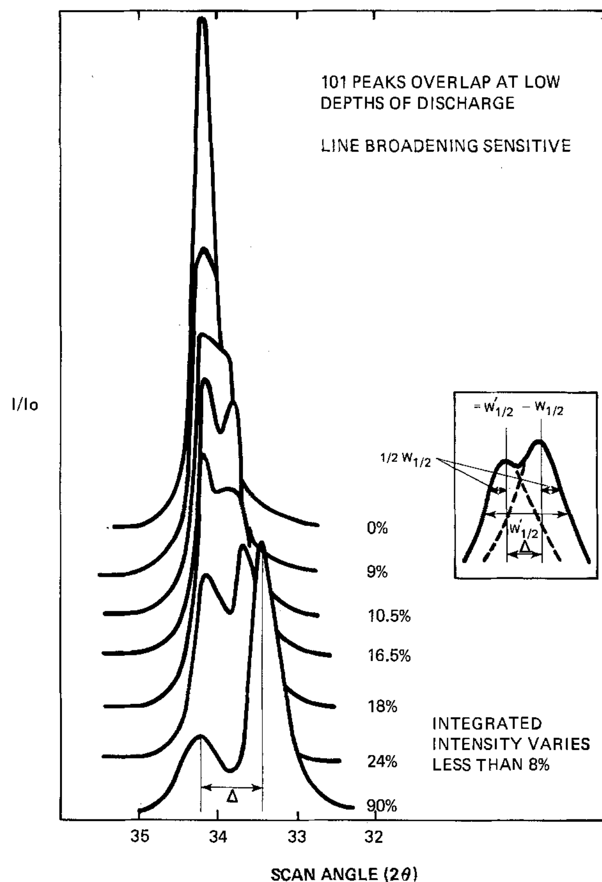

Fig. 8. Variation of Bragg peaks as a function of depth of discharge of TiS_2.

position reflects a change in composition of the test electrode as soon as discharge began. As crystallites of Li_xTiS_2 are nucleated, their contribution to the 101 line begins, resulting in an apparent decrease in intensity and line broadening until splitting of the peaks is noticeable at ~15% depth of discharge. Only after this splitting could the previously described method for determining 101 position be used. Determination of the line position *vs.* state-of-discharge at low depths of discharge was possible from the continuous scan data by measuring the half-height width (W' ½) of combined peaks (*i.e.*, resolved + unresolved) and applying the formula

$$2\theta_{101}(Li_xTiS_2) = 2\theta_{101}(TiS_2) - \Delta, \quad \Delta = (W'\,½ - W\,½)$$

where W ½ is the half-height width of the resolved TiS_2 or Li_xTiS_2 peak, as exemplified in Fig. 7.

One can see from Fig. 9 that up to $x = 0.3$, *i.e.*, 30% depth of discharge, the variation in c-axis expansion is approximately linear. The point of inflection in the region of 12-18% may be attributed to lithium ordering an effect recently reported (9).

Throughout the experiments, the width of the 101 line for a given x in Li_xTiS_2 did not change, but the intensity of the peak decreased. This decrease cannot be explained by calculating the intensity of the 101 line for various compositions in Li_xTiS_2. Because of the low scattering power of lithium atoms, no more than 10% variation is expected in the intensity of the 101 line, whereas a decrease of more than 50% is observed, as seen in Fig. 10(a). Experiments indicated that upon standing on open circuit for 10 hr, this intensity is regained almost to the original value, as indicated in Fig. 10(b). We propose that the observed intensity loss during the discharge is due to intercalated layers which are wrinkled or bent, and therefore do not contribute to the intensity of Bragg peaks. This effect occurs in TiS_2 crystals during chemical lithiation with n-butyl lithium, and has been previously re-

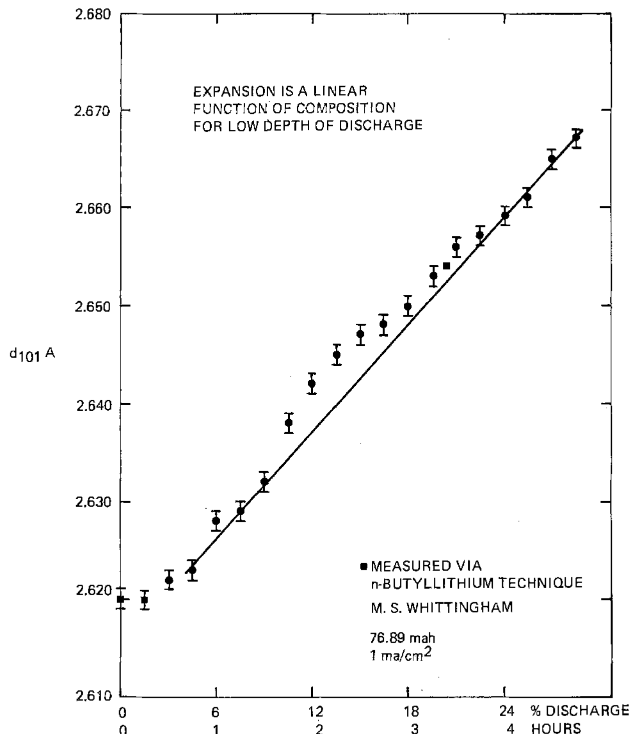

Fig. 9. Lattice expansion data for low depths of discharge

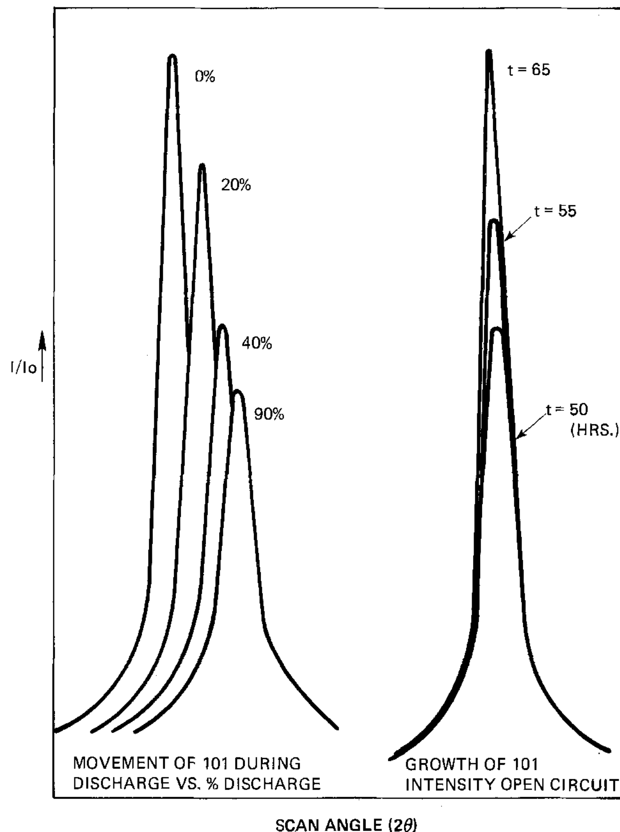

Fig. 10. Movement of 101 Bragg peaks of TiS_2 and growth of 101 peak intensity on open-circuit stand.

ported (8). Upon standing on open circuit, the stressed TiS_2 layers anneal and realign themselves, causing the intensity to be regained.

The charge used for the discharge of the TiS_2 electrode corresponded reasonably well to that expected from an estimate of the electrode composition determined by the x-ray spectrograph presented in Fig. 6. The data indicated that approximately 10 w/o of TiS_2 is left undischarged at the end of the experiment. Unavailability of this material for discharge may be traced to electrode configuration, and is also associated with the technique of preparation, a feature that is commonly encountered in battery electrodes.

A striking feature of the variation of the 101 line position is the pronounced plateau which begins at ¼ discharge and ends at about ½ discharge, as seen in Fig. 6. We believe this to be due to lithium ordering in the TiS_2 layers, and will be discussed in detail in a future publication (9).

Conclusions

The dynamic x-ray diffraction technique is an effective and sensitive method for studying bulk morphology and stoichiometry in solid electrodes. It permits accurate measurement of topochemical structural changes which take place during electrochemical polarization.

The TiS_2 cathode undergoes structural disordering during discharge and shows lattice parameter anomalies which are thought to be due to lithium atom ordering.

Manuscript submitted Dec. 27, 1977; revised manuscript received May 5, 1978. This was Paper 69 presented at the Las Vegas, Nevada, Meeting of the Society, Oct. 17-22, 1976.

Publication costs of this article were assisted by Exxon Research and Engineering Company.

REFERENCES

1. M. S. Whittingham, U.S. Pat. 4,009,052, Feb. 22, 1977; *Science*, **192** 1126 (1976); *J. Chem. Soc. Chem. Comm.*, 328 (1974); *This Journal*, **123**, 315 (1976).
2. G. L. Holleck and J. R. Drisocol, ECOM Contract DAAB07-74-C0072 (1974); *Electrochim. Acta*, **22**, 647 (1977).
3. G. L. Holleck, F. S. Shuker, and S. B. Brummer, Paper 52 presented at the New York, New York, Meeting of the Society, Oct. 13-17, 1974; Proceedings of the 10th IECEC, Newark, Del. (1975).
4. L. H. Gaines, R. W. Francis, G. H. Newman, and B. M. L. Rao, Proceedings of the 11th IECEC (1976).
5. D. A. Winn and B. C. H. Steele, *Mater. Sci. Bull.*, **11**, 551 (1976).
6. J. Broadhead, Paper 20(a) presented at the 8th International Power Sources Symposium, Brighton, England, Sept. 25-28, 1972.
7. M. S. Whittingham and F. R. Gamble, *Mater. Res. Bull.*, **10**, 363 (1975).
8. R. R. Chianelli, *J. Crystal Growth*, **34**, (2), 239 (1976).
9. A. H. Thompson, To be published.

Solubility Products of Metal Sulfides in Molten Salts:

Measurements and Calculations for Iron Sulfide (FeS) in the LiCl-KCl Eutectic Composition

Marie-Louise Saboungi,* Jane J. Marr, and Milton Blander*

Argonne National Laboratory, Chemical Engineering Division, Argonne, Illinois 60439

ABSTRACT

An electrochemical titration technique is used to determine the solubilities of Li_2S and the solubility products of FeS in the molten LiCl-KCl eutectic composition in the temperature range from 673° to 773°K. The solubility products of FeS are, on an ion fraction basis, $K_{SP} = 0.44 \times 10^{-12}$, 2.3×10^{-12}, and 1.3×10^{-11} at 673°, 723°, and 773°K, respectively. These values are in good agreement with values calculated *a priori* from an exact thermodynamic cycle; at 723°K, we deduce a value of -38.36 kcal $mole^{-1}$ (or -160.50 kJ $mole^{-1}$) for $RT \ln K_{SP}$, as compared with an experimentally derived value of -38.50 kcal $mole^{-1}$ (or -161.11 kJ $mole^{-1}$). During the operation of the cells at relatively high sulfide compositions, the complex phases Li_2FeS_2 ($\equiv$X phase) and $LiK_6Fe_{24}S_{26}Cl$ ($\equiv$J phase) are formed, as established by x-ray and metallographic analyses. A discussion of their chemical stability in the electrolyte in the temperature range of this study is presented. A moderate change in the activities of LiCl and KCl can influence the formation of the J phase.

In the development and testing of high temperature batteries utilizing iron disulfide (FeS_2) as electrodes and the molten LiCl-KCl eutectic as the electrolyte, some problems have been encountered in cells that have been subjected to extensive charging and discharging cycles (1), namely, lithium sulfide (Li_2S) and iron particles are deposited in the separator, which may lead to a loss of performance or even to cell failure. The mechanism of the formation of the deposits is not yet well understood; one of the hypotheses relates this effect to chemical transport through dissolution in the electrolyte. However, it should be noted that such deposits do not occur in cells having iron monosulfide (FeS) as the active electrode material. To resolve these problems, determinations of the solubilities of Li_2S, FeS, and FeS_2 in the LiCl-KCl eutectic are needed.

We report on an experimental and theoretical investigation of the solubilities of Li_2S and FeS in the molten LiCl-KCl eutectic in the temperature range of operation of the battery (T = 673°-773°K). The experimental method used was an electrochemical titration based on the following reaction

$$Li_2S + FeCl_2 \rightarrow FeS(\downarrow) + 2LiCl \quad [1]$$

During our experimental study, we found that the above reaction is not the only chemical reaction occurring in the solution. More complex sulfide phases (designated as J and X phases) were formed identical to those identified in engineering-scale cells (2, 3). The thermodynamics of FeS, as well as those of X phase ($\equiv Li_2FeS_2$) and J phase ($\equiv LiK_6Fe_{24}S_{26}Cl$), are derived from our data. The solubility product of FeS in the molten LiCl-KCl eutectic is evaluated from the electromotive force measurements (emf) under two different assumptions. In the first, reaction [1] is supposed to occur with no solid solutions involving FeS. In the second, the probable existence of a limited solid solution (4) in the Li_2S-FeS system is taken into consideration; consequently, the precipitate would no longer be FeS but a solid solution of FeS and Li_2S. We find that the solubility product does not vary significantly with either hypothesis. Finally, an exact calculation of the solubility product of FeS is made *a priori*. The value obtained is in good agreement with experiment.

Experimental

Materials.—Anhydrous purified LiCl-KCl eutectic was supplied in 200g ampuls by the Anderson Physics Laboratory, Champaign, Illinois. Lithium sulfide was provided by Eagle-Picher as unsintered powder. Its lithium and sulfur contents determined by chemical analysis were 30.33 (theoretical 30.21) and 69.57 (theoretical 69.79) in weight percent (w/o), respectively; a spectrochemical analysis showed less than 0.4 w/o impurities. Silver chloride of 99.9% typical purity was purchased from Cerac. Finally, anhydrous iron chloride ($FeCl_2$) was prepared on request by the Anderson Physics Laboratory by synthesis from 99.999% purity iron. The slugs were fused in quartz vials sealed under argon. A typical chemical analysis gave 44.44 w/o of Fe^{2+} (theoretical, 44.06 w/o), 44.54 w/o of total Fe (theoretical, 44.06 w/o), and 55.84 w/o of Cl (theoretical 55.94 w/o). At first, after opening a vial, $FeCl_2$ was used without further purification. The remaining $FeCl_2$ was slowly doubly sublimed under vacuum at about T = 773°K to remove Fe^{3+} and any trace of possible contamination by moisture. The distilled product was sealed in fused silica tubes until used.

Experimental procedure.—The cell used in this investigation can be schematized as follows

$$Ag|AgCl\text{-}LiCl\text{-}KCl||LiCl\text{-}KCl(eut)\text{-}FeCl_2\text{-}Li_2S|Fe \quad [2]$$

An outer high purity alumina crucible contained the electrolyte, the eutectic LiCl-KCl, to which were added known amounts of $FeCl_2$ and Li_2S. Alumina proved to be resistant to corrosion by Li_2S provided that no traces of water were present in the melt. The reference electrode consisted of a high purity silver wire (>99.9999%) immersed in a dilute solution [8.4×10^{-3} mole per cent (m/o)] of silver chloride in the LiCl-KCl eutectic melt. The AgCl-LiCl-KCl solution was contained in a Pyrex tube with asbestos fibers sealed in at the bottom. The diaphragm was made by shrinking the Pyrex tubing (½ in. OD) on to a very few asbestos fiber bundles. Electrolytic contact between the Ag electrode and the outside melt was effected through the wetting of the interstices between the fibers by the salt whereas the diffusion of dissolved AgCl was insignificant. The Pyrex tubing was con-

* Electrochemical Society Active Member.

Key words: thermodynamic properties, lithium-sulfur batteries, electrochemical titration, solubilities, solubility products.

tained in a high purity porous beryllia cup to avoid any possible attack and decrepitation of the Pyrex in contact with the sulfides. Results of chemical and spectrochemical analyses showed no evidence of silver leaking from the reference electrode.

The second electrode consisted of an iron rod (1/8 in. diam). Prior to use, the metal was filed in an inert atmosphere in order to remove any oxide coating present on the surface. Both electrodes were connected to a digital voltmeter (input resistance greater than $10^{10}\Omega$) by tantalum leads.[1] For each run, the temperature was held constant within a degree and was measured with a stainless steel (s.s.)-sheathed calibrated (Pt-Pt 10% Rh) thermocouple. The melt was constantly stirred at a uniform speed using a s.s. stirrer. The stirring was extremely important to insure complete and relatively fast dissolution of all added chemicals. Finally the emf's and the temperature were continuously recorded.

Due to the dissimilarities of the electrode materials, a thermoelectric voltage was created. In order to obtain the true electrochemical voltage, the measured voltage of cell [2] should be corrected by subtracting the thermoelectric voltage at the temperature of the experiments (−2.57 mV at $T = 673°K$, −3.03 mV at $T = 723°K$, and −3.55 mV at $T = 773°K$).

The cells were operated by making successive additions of $FeCl_2$ and Li_2S. When only $FeCl_2$ was the solute, the equilibration of the cell with respect to temperature and voltage was rapidly attained, usually in less than 5 min (or 300 sec). Upon addition of Li_2S, solid FeS precipitated and the equilibration of the cells required several hours [as much as 12 hr (43,200 sec)], particularly near the equivalence point. An increase in the temperature by about 50°-100°K helped in achieving faster equilibration. The emf's measured were steady and stable to less than 1 mV for overnight observation periods. The thermal reversibility of cell [2] was checked by temperature cycling. All the operations were carried out inside a glove box filled with helium purified by passage through molecular sieves. The levels of oxygen and water were monitored constantly; there was always less than 1 ppm water and oxygen in the helium.

Results

In all that follows, unless specified differently, the true electrochemical voltage corrected for the thermoelectric potential of cell [2] is reported.

Dilute solutions of $FeCl_2$ in LiCl-KCl eutectic.—Each experiment was initiated by checking the behavior of the iron electrode since the silver-silver chloride electrode has proved to be reversible (5, 6). Tests of the Nernst law were carried out at constant temperature. For dilute solutions of $FeCl_2$ in the LiCl-KCl eutectic, the emf's vary with composition according to the relation

$$E = E°_2 - \frac{RT}{2\mathbf{F}} \ln a_{FeCl_2} \quad [3]$$

where E is the true electrochemical voltage of cell [2]; R, the gas constant; $\mathbf{F}$, the Faraday constant; a_{FeCl_2}, the activity of iron chloride in solution; and $E°_2$, the limiting potential of $FeCl_2$ in the LiCl-KCl eutectic melt *vs.* the silver-silver chloride electrode. In Fig. 1, some typical emf's as read (without the thermoelectric effect correction) are plotted as a function of the ion fraction of Fe^{++} in solution together with the calculated Nernst slopes: $2.3026\ RT/2\mathbf{F}$ where the 2 in the denominator takes into consideration the two-electron process. For each temperature, a least squares fit of the data leads to slopes in excellent agreement with the theoretical slopes (Table I). At $T = 723°K$, combining our value for $E°_2$ with that of the standard formation potential of AgCl in the LiCl-KCl eutectic

[1] The connections Ag-Ta and Fe-Ta were made outside of the crucible, at glove box temperature.

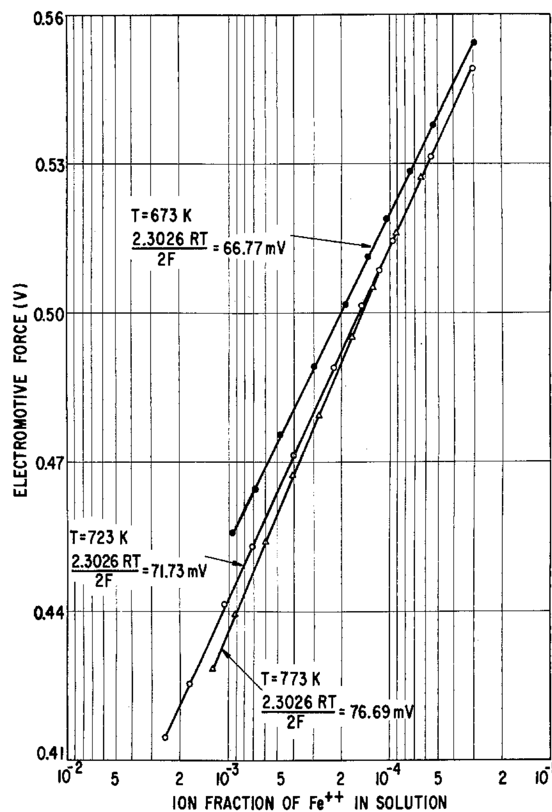

Fig. 1. Electromotive forces of the cell:

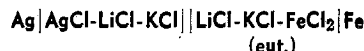
Ag|AgCl-LiCl-KCl||LiCl-KCl-$FeCl_2$|Fe (eut.)

for dilute concentrations of $FeCl_2$ at $T = 673°$, 723°, and 773°K. The slopes of the lines are equal to the calculated Nernst slopes: 66.77, 71.73, and 76.69 mV.

as obtained by Laitinen and co-workers (5, 6) and making the appropriate correction for the concentration of AgCl in the reference electrode and the thermoelectric effect, we calculate 1.382V for the standard formation potential of $FeCl_2$ in the LiCl-KCl eutectic melt. This value is in reasonable agreement with that of 1.387V as measured by Laitinen and Liu (6). The difference of 5 mV can easily be ascribed to uncertainties related to the composition of silver chloride in our reference electrode combined with uncertainties in the measurements of Laitinen and Liu (6).

Titration of $FeCl_2$ with Li_2S.—After reaching the desired composition of $FeCl_2$ in the molten LiCl-KCl eutectic, successive additions of Li_2S were made to precipitate sulfides. Around the equivalence point ($X_{Fe} = X_S$ where X_i refers to the total ionic fraction of the ith ion added to the solution), the emf's increase steeply with the concentration of Li_2S. Beyond the equivalence composition ($X_S > X_{Fe}$), the emf's keep increasing but not as steeply. Finally, when the solution is saturated with Li_2S, the emf's reach a final plateau with a constant voltage.

For each temperature, at least three independent experiments were carried out with either a different or the same initial concentrations of iron chloride. In Fig.

Table I. Least squares fitted equation of the true electrochemical voltage of cell [2] for dilute $FeCl_2$ and no Li_2S: $E = E°_2 - m \log X_{Fe^{++}}$

T (°K)	m (theor.) = $\frac{2.3026\ RT}{2\mathbf{F}}$ (mV)	m (exp.) (mV)	$E°_2$ (mV)
673	66.77	66.43 ± 0.13	256.66 ± 0.50
723	71.73	71.18 ± 0.18	231.58 ± 0.67
773	76.69	76.95 ± 0.22	209.09 ± 1.85

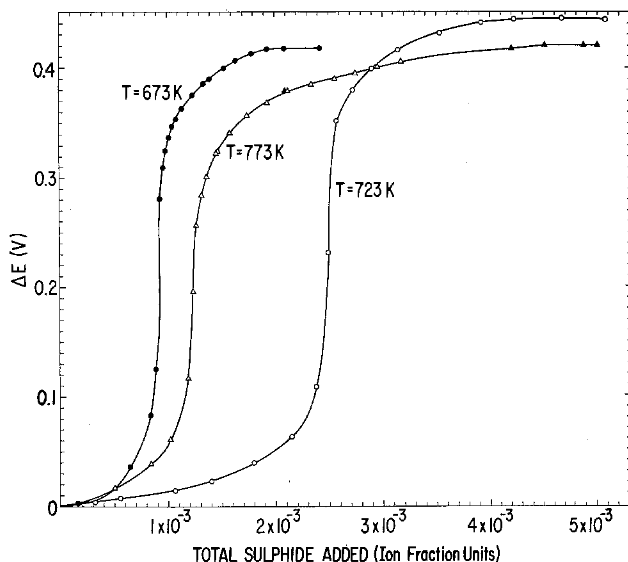

Fig. 2. Variations of the difference between the emf's of cell [2] with and without Li_2S with the total amount of added sulfides, X_S. The two symbols (△, ▲) at $T = 773°K$ refer to results collected from two different experiments. The initial concentrations of $FeCl_2$ are 9.274×10^{-4}, 2.413×10^{-3}, and 1.236×10^{-3} at $T =$ 673°, 723°, and 773°K, respectively. (Note: Saturation was not achieved in the measurements shown at 723°K.)

2, the differences in the emf's emf of cell [2]) − emf of cell [2] with $X_S = 0$) are plotted *vs.* the total sulfide added; the three titration curves shown at 673°, 723°, and 773°K are typical of those from 18 separate experiments. At $T = 773°K$, data collected in two independent experiments with the same initial $FeCl_2$ concentration are plotted to show the reproducibility of the measurements (Fig. 2). In Table II are listed some of the data measured at 673°, 723°, and 773°K.

In order to identify the black precipitate which was formed, separate samples were prepared by the following method. Carefully weighed amounts of the eutectic, $FeCl_2$, and Li_2S were melted and vigorously stirred for several days. They were rapidly cooled and submitted to x-ray and metallographic analysis. Three different phases were reported depending on the temperature and the composition of the solution. Well before the solution became saturated with Li_2S, FeS was the only precipitate to be identified in the temperature range of this study. Therefore, reaction [1] occurs and FeS is formed chemically. As the solution approaches saturation, two other sulfide phases designated by J and X, were identified.

Table II. Values of the difference between the emf's of cell [2] at a concentration of added sulfides, X_S, and the emf's of cell [2] for $X_S = 0$

$T = 673°K$; initial $X_{Fe} = 9.274 \times 10^{-4}$		$T = 723°K$; initial $X_{Fe} = 2.413 \times 10^{-3}$		$T = 773°K$; initial $X_{Fe} = 1.236 \times 10^{-3}$	
10^4 X_S	ΔE (mV)	10^4 X_S	ΔE (mV)	10^4 X_S	ΔE (mV)
1.622	2.14	0.5514	0.38	1.576	4.58
3.835	5.89	3.204	4.22	4.993	17.16
6.374	36.02	6.539	8.38	8.425	38.80
8.382	82.61	10.57	14.16	10.26	60.86
8.817	125.26	14.07	23.44	11.87	116.43
9.270	279.30	18.18	40.42	12.34	196.63
9.554	309.91	21.56	62.99	12.70	256.78
9.847	324.30	23.86	109.01	13.14	283.98
10.17	336.71	24.91	232.40	13.64	300.89
10.48	343.71	25.76	351.86	14.61	323.96
10.91	352.55	27.30	379.31	15.81	341.56
11.39	363.16	29.10	399.29	17.43	357.01
12.38	375.86	31.57	416.09	19.32	368.86
13.45	385.65	35.46	431.64	21.09	374.62
14.04	388.99	39.31	440.76	21.36	378.42
15.32	399.28	42.37	443.61	23.47	384.52
16.42	406.25	46.75	444.35	25.58	389.76
17.90	412.53	50.80	444.40	27.50	394.86
19.32	417.21			29.82	402.54
20.92	417.25			30.49	402.93
				32.77	405.96
				42.15	416.55
				45.17	419.83
				48.70	420.54
				49.85	420.68

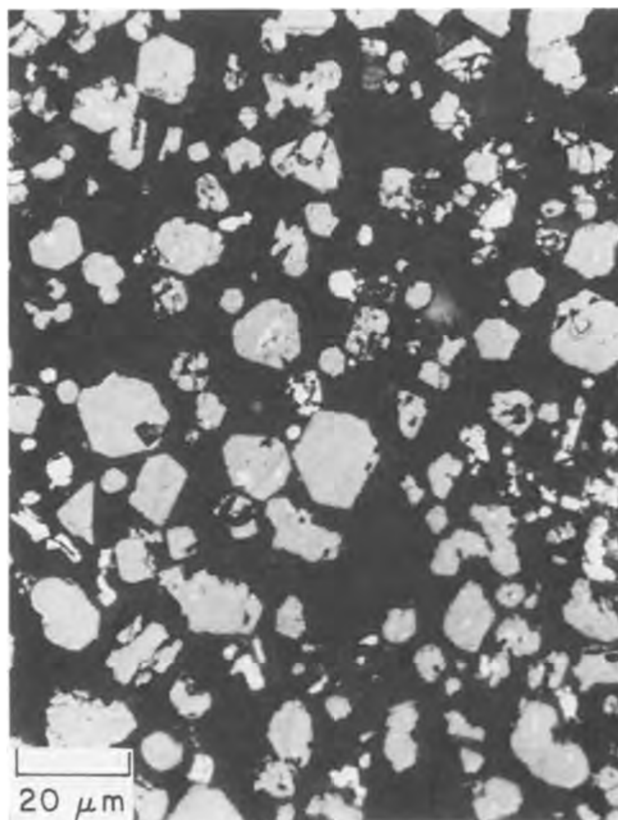

Fig. 3. Typical polished section of material collected at $T = 673°K$ showing the euhedral crystals of the J phase. (Courtesy L. Fuchs.)

The J phase refers to the mineral djerfisherite with a composition tentatively described as $LiK_6Fe_{24}S_{26}Cl$.[2] A typical polished section of this material is shown in Fig. 3. A possible reaction occurring in the solution is

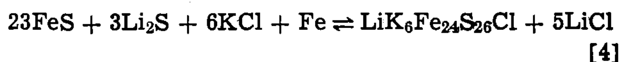

$$23FeS + 3Li_2S + 6KCl + Fe \rightleftharpoons LiK_6Fe_{24}S_{26}Cl + 5LiCl \quad [4]$$

This complex compound which forms on the iron sulfide electrode in the engineering-scale cells is highly undesirable since it slows the kinetics of the cell reaction to a considerable extent (2). As expected, it has been found that if the electrolyte is replaced by another molten salt mixture such as LiF-LiCl, the J phase does not form.

The X phase refers to the compound Li_2FeS_2 formed in solution according to the reaction

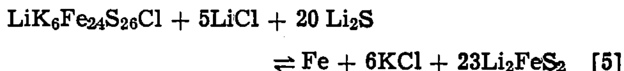

$$LiK_6Fe_{24}S_{26}Cl + 5LiCl + 20\ Li_2S \rightleftharpoons Fe + 6KCl + 23Li_2FeS_2 \quad [5]$$

A typical polished section exhibiting the X phase is given in Fig. 4.

In the temperature range of this investigation, the J phase did form as a precipitate in Li_2S-rich solutions. Except at $T = 673°K$, as the concentration of sulfide in solution increased, a conversion of J phase to X phase (Eq. [5]) occurred. According to metallographic and x-ray analyses, this conversion was noticed in essentially sulfide-saturated solutions at $T = 723°K$ or at relatively high sulfide concentrations at $T = 773°K$.

Results of metallographic and x-ray analyses of numerous samples allowed us to derive, for each tem-

[2] Differences in the analyzed composition of the mineral djerfisherite are given in Ref. (3b). The composition given in this work is commonly used for the J phase formed chemically.

Fig. 4. Typical polished section of material collected at 773°K exhibiting platelets of the X phase. (Courtesy A. E. Martin.)

perature, the concentrations of sulfide ions in solution, N_S^J and N_S^X, above which J and X phases exist respectively.[3] At $T = 673$°K, we have $N_S^J = 1.9\ (\pm 1.0) \times 10^{-4}$ (in mole fraction units); there was no evidence for the existence of X phase even in solutions in which the amount of sulfide exceeded by far the saturation limit. At $T = 723$°K, we have obtained, $N_S^J = 3.8\ (\pm 0.2) \times 10^{-4}$ and $N_S^X = 15.0\ (\pm 1.0) \times 10^{-4}$ and at $T = 773$°K, $N_S^J = 5.4\ (\pm 1.0) \times 10^{-4}$ and $N_S^X = 17.6\ (\pm 2) \times 10^{-4}$. The uncertainties are related to the interval in the composition of samples where either one phase or two coexisting phases were detected.

Finally, at relatively high concentrations of sulfides, we have noticed a progressive appearance of a red-burgundy color, which increases in intensity with the temperature. At low concentrations of sulfides, the solution has no color except for the black precipitate.

Calculations from the Data

The data collected from our titration experiments can be utilized to calculate the solubility products of FeS and the solubility of Li_2S in the LiCl-KCl eutectic solvent. In addition, with the auxiliary data on the concentrations of dissolved Li_2S where the J and X phases first form in equilibrium with FeS, we can also deduce the Gibbs free energies of formation of these phases. As will be seen, the J phase has a marginal stability so that a decrease in the activity ratio of KCl/LiCl in the solvent can prevent the formation of this undesirable phase in the battery electrode.

The solubility products of FeS.—In principle, the solubility products of FeS in the LiCl-KCl eutectic mixture, K_{SP}, can be directly derived from the titration curves such as those shown in Fig. 2. However, in this specific case, we must take into consideration the fact that FeS is not the only precipitate. Therefore, calculations of K_{SP} can be made when no other phases such as J or X are present.

If Henry's law holds for $FeCl_2$, Eq. [3] can be used to calculate, N_{Fe}, the concentration of $FeCl_2$ in solution, ($a_{FeCl_2} = N_{Fe}$). The concentrations of sulfides in solution, N_S, are given by the relation

$$N_S = X_S - r(X_{Fe} - N_{Fe}) \qquad [6]$$

where r is unity, 2 or (26/23) depending on whether the precipitating phase is FeS, X phase, or J phase, respectively. Equation [6] is valid for compositions where N_S is much larger than N_{Fe}, even if Henry's law is not accurately obeyed. (Obviously, one has $X_{Fe} = N_{Fe}$ only when no sulfide ion is present in solution.)

Near the equivalence point, the values calculated for K_{SP} are very sensitive to small uncertainties in the concentration of sulfides in solution. Beyond this point, K_{SP} is not as much affected. In most of the experiments, the experimental equivalence point did not coincide with the theoretical one, indicating a ratio of (X_S/X_{Fe}) slightly greater than unity. A possible interpretation would be the presence of small amounts of sulfide-forming impurities in the electrolyte or from the iron electrode. The measurements indicate impurity levels of 2 to 4×10^{-5} mole fraction in the melts which reacted with Li_2S to form a sulfide precipitate. The apparent impurity level increased by more than a factor of three when about 200g of fine grained iron powder prefired in a hydrogen-helium atmosphere for more than 24 hr was added to the melt. Thus, the values of N_S calculated from Eq. [6] must be corrected for the estimated amounts of impurities which are given for the three experiments listed in Table III. The impurity level was estimated from the change in the amount of sulfide necessary to achieve the theoretical equivalence point. The derived values of K_{SP} (in ion fraction units) for the three listed experiments are also reported in Table III. Our combined data lead to values of $K_{SP} = 0.44 \times 10^{-12}$, 2.3×10^{-12}, and 1.3×10^{-11} at $T = 673$°, 723°, and 773°K, respectively, with the standard Gibbs free energies of solution being 38.05, 38.50, and 38.51 kcal mole^{-1} (or 159.2, 161.1, and 161.1 kJ mole^{-1}) at these three temperatures. As will be seen, our values are in close agreement with exact theoretical predictions made *a priori* from thermodynamic considerations. The standard en-

Table III. Typical true electrochemical emf's and calculated quantities in the titration of $FeCl_2$ with Li_2S in the LiCl-KCl eutectic

$T = 673$°K, initial value $X_{Fe} = 1.126 \times 10^{-4}$, $E°_2 = 249.16$ mV*

E (mV)	$10^4 X_S$	$10^9 N_{Fe}$	$10^4 N_S$	$10^{13} K_{SP}$
762.91	1.629	20.302	0.203	4.1
785.20	1.901	9.412	0.475	4.5
824.15	3.195	2.456	1.769	4.3
Impurity level 0.30×10^{-4}				

$T = 723$°K, initial value $X_{Fe} = 0.957 \times 10^{-4}$, $E°_2 = 220.15$ mV*

E (mV)	$10^4 X_S$	$10^8 N_{Fe}$	$10^4 N_S$	$10^{12} K_{SP}$
721.31	1.432	10.346	0.216	2.2
749.89	1.820	4.134	0.603	2.5
778.75	2.609	1.637	1.393	2.3
804.50	4.390	0.716	3.173	2.3
Impurity level 0.26×10^{-4}				

$T = 773$°K, initial value $X_{Fe} = 1.233 \times 10^{-3}$, $E°_2 = 205.23$ mV*

E (mV)	$10^3 X_S$	$10^8 N_{Fe}$	$10^4 N_S$	$10^{11} K_{SP}$
729.43	1.363	14.617	0.951	1.39
752.50	1.461	7.312	1.931	1.41
770.10	1.581	4.311	3.130	1.35
785.55	1.744	2.711	4.760	1.29
Impurity level 0.35×10^{-4}				

* The differences between the values given for $E°_2$ in this Table and Table 1 are due to differences in the concentration of AgCl in the different reference electrodes used in separate experiments at the same temperature.

[3] N_S^J and N_S^X were calculated neglecting, N_{Fe}, the concentration of Fe^{++} left in solution since N_{Fe} was less than 10^{-9}. Therefore the values given for N_S^J and N_S^X are given by (X_S − 26/23 X_{Fe}) and (X_S − $2X_{Fe}$), respectively.

tropy of solution is very small, −3 cal deg^{-1} mole^{-1} (or −12J deg^{-1} mole^{-1}); the standard enthalpy of solution is 36 kcal mole^{-1} (or 151 kJ mole^{-1}). This thermodynamic behavior is similar to that observed for solutions of silver halides in molten salts, where the standard Gibbs free energies and enthalpies of solution of relatively insoluble solids are almost equal (7).

The solubility of Li_2S.—The apparent concentration of Li_2S, X_S, at which the last plateau of each titration curve begins (Fig. 2 for $T = 673°$ and 773°K), when corrected for the amount and the chemical nature of the precipitate, yields the solubility of Li_2S in the LiCl-KCl eutectic, N_S(sat). The correction depends on the temperature of the experiments. At $T = 723°$ and 773°K, it is $2X_{Fe}$ since the X phase (Eq. [5]) is the second solid phase present at saturation, while at $T =$ 673°K it is (26/23) X_{Fe} since the J phase (Eq. [4]) coexists with solid Li_2S. The results thus derived, together with those obtained by an *in situ* generation of sulfide from a nickel-nickel sulfide eutectic electrode (8) are listed in Table IV. (Note that the level of impurities as estimated in Table III was taken into account.) Although there is a difference in the absolute values, the temperature dependence of the two sets of data in Table IV is essentially the same and leads to an enthalpy of solution $\Delta H_{Li_2S} = 10.22$ kcal mole^{-1} (or 42.78 kJ mole^{-1}). Our results are in agreement with our yet unpublished measurements in a lead sulfide system saturated with Li_2S.

On the stabilities of X and J phases.—Values for the standard Gibbs free energies of formation of X and J phases can be derived from data on the solubility of Li_2S, N_S(sat), combined with data on $N_S{}^X$ and $N_S{}^J$.

The standard Gibbs free energy of formation of Li_2FeS_2, from solid Li_2S and FeS, $\Delta G°_X$ is given by

$$\Delta G°_X = \frac{\Delta G°_4 + \Delta G°_5}{23} = \frac{3}{23} RT \ln (N_S{}^J/N_S(\text{sat})) + \frac{20}{23} RT \ln (N_S{}^X/N_S(\text{sat})) \quad [7]$$

where $\Delta G°_4$ and $\Delta G°_5$ refer to the standard Gibbs free energy changes for reactions [4] and [5], respectively. We have obtained, $\Delta G°_X = -0.33$ (±0.20) kcal mole^{-1} (or −1.38 ± 0.84 kJ mole^{-1}) at $T = 723°$K and $\Delta G°_X = -0.72$ (±0.20) kcal mole^{-1} (or −3.01 ± 0.84 kJ mole^{-1}) at $T = 773°$K.

Preto and Roche [see Ref. (1), p. 58] have performed slow-scan voltametry experiments, using LiAl as a reference electrode and FeS as positive electrode. From a typical voltamogram obtained at 700°K, one can estimate the standard Gibbs free energy of formation of the X phase from the peak separation assuming that Li_2FeS_2 did form during the charging cycle, $\Delta G°_X = -0.46$ kcal mole^{-1} (or −1.93 kJ mole^{-1}).

Using the phase diagram of the Li_2S-FeS system (9) and assuming that the liquid solution is ideal (*i.e.*, $a_{FeS} = X_{Fe}X_S$ and $a_{Li_2S} = X_{Li}{}^2X_S$) we have estimated, at $T = 1158°$K, $\Delta G°_X = -1$ kcal mole^{-1} (or −4 kJ mole^{-1}). The values thus derived (cyclic voltametry and phase diagram) are in consonance with our results.

The standard Gibbs free energy of formation of the J phase, $\Delta G°_J$ may be expressed in several ways depending on the choice of the reference state. If the LiCl-KCl eutectic composition is the standard state for LiCl and KCl, $\Delta G°_J$ is then identical to the standard Gibbs free energy change for reaction [4], $\Delta G°_4$

$$\Delta G°_J = 3RT \ln \left(\frac{N_S{}^J}{N_S(\text{sat})} \right) \quad [8]$$

where Li_2S and FeS have solids for their standard states. We have calculated for $\Delta G°_J$ values of −6.2 ± 1.8 kcal mole^{-1} (or −25.9 ± 7.5 kJ mole^{-1}), −6.1 ± 0.3 kcal mole^{-1} (or −25.5 ± 1.2 kJ mole^{-1}), and −6.9 ± 0.6 kcal mole^{-1} (or −28.9 ± 2.5 kJ mole^{-1}) at $T = 673°$, 723°, and 773°K, respectively.

If we chose solids as the standard states for all reactants and products for reaction [4], we have then to account for the relative activities of LiCl and KCl; the standard Gibbs free energy of formation of the J phase, $\Delta G_J{}^*$, is given by

$$\Delta G_J{}^* = 3RT \ln \left(\frac{N_S{}^J}{N_S(\text{sat})} \right) - 5RT \ln \left(\frac{a_1}{a_1(\text{sat})} \right) + 6RT \ln \left(\frac{a_2}{a_2(\text{sat})} \right) \quad [9]$$

where a_1 and a_2 are activities of LiCl and KCl, respectively, at the eutectic composition, and a_1(sat) and a_2(sat) are those at the liquidus composition. Using activities calculated from the phase diagram and from thermodynamic data reviewed by Lumsden (10, 11), we have obtained $\Delta G_J{}^* = -5.8 \pm 1.8$ kcal mole^{-1} (or −24.3 ± 7.5 kJ mole^{-1}), −6.7 ± 0.3 kcal mole^{-1} (or −28.0 ± 1.2 kJ mole^{-1}), and −8.1 ± 0.6 kcal mole^{-1} (or −33.9 ± 2.5 kJ mole^{-1}) at $T = 673°$, 723°, and 773°K, respectively. To our knowledge, these data constitute the only thermodynamic data available on the stability of the J phase.

A consideration of the values of $\Delta G°_X$ and $\Delta G°_J$ and of the metallographic and x-ray results allows us to draw some conclusions on the relative stabilities of the X and J phases as a function of temperature and of the electrolyte composition:

1. As mentioned previously, the X phase did not form at 673°K; it is marginally stable at 723°K since $N_S{}^X/N_S(\text{sat}) \sim 1$. We can deduce that, in our cells, the X phase does not form at temperatures that are very slightly lower than 723°K.

2. In Li_2S-rich melts at temperatures of 723° and 773°K, we have obtained a conversion of the J phase to the X phase. The conversion depended on the temperature of the measurements and on the sulfide concentration in solution. From thermodynamic considerations, we can estimate that this conversion can be made to occur at lower temperatures by (*i*) altering the electrolyte composition, and (*ii*) keeping the melts at saturation with repect to sulfides. The electrolyte should be changed in such a way that the activity of LiCl is increased and that of KCl is decreased. This can be done either by enriching the LiCl-KCl mixture in LiCl or by adding a third or perhaps, if necessary, a fourth constituent. The key factors are to keep the Li_2S and LiCl activities as high and the KCl activity as low as is practical. Therefore, in the operation of high temperature lithium batteries, one can ultimately eliminate the formation of the undesirable J phase (1) and be in a regime where the X phase would form instead. From our present data and Eq. [4] and [5], we have estimated that the J phase will not form in Li_2S-saturated melts with a change in the ratio of $(a_{LiCl}{}^5/a_{KCl}{}^6)$ of a factor of 7 at 698°K and 160 at 673°K.[4]

It is important to emphasize that, in the study of the stabilities of the X and J phases, we have assumed that they are line compounds. If the stoichiometries of

Table IV. Solubility of Li_2S in LiCl-KCl eutectic (ion fraction units)

T (°K)	Soly* (Li_2S)	Soly† (Li_2S)
673	0.90×10^{-3}	0.67×10^{-3}
723	1.58×10^{-3}	1.3×10^{-3}
773	2.42×10^{-3}	(2.0×10^{-3})‡

* This work.
† Ref. (8).
‡ Extrapolated.

[4] Independent measurements of the solubility of Li_2S in the eutectic LiCl-LiF have shown that the solubility is considerably increased. Thus, if one changes the electrolyte composition, one has to be aware that the solubility of Li_2S in this new medium is consequently modified.

these phases do change significantly with temperature, our conclusions will have to be corrected.

Finally, it is worth mentioning that careful metallographic analyses combined with x-ray measurements are being undertaken to pinpoint the temperature-range and other factors which define the range of stability of the J phase (4).

Discussion

Firstly, calculations of the solubility product of FeS are carried out based on an exact thermodynamic cycle. Secondly, the presence and influence of associating species between Fe^{2+} and S^{2-}, on the solubility of FeS are examined. Thirdly, the possibility of the existence of limited solid solutions between Li_2S and FeS is considered.

A priori calculations of the solubility product of FeS.—The solubility product of FeS in the molten LiCl-KCl eutectic can be independently calculated *a priori* from thermodynamic considerations. The dissolution of FeS in the electrolyte can be written as

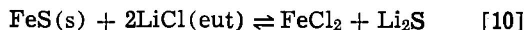

$$FeS(s) + 2LiCl(eut) \rightleftharpoons FeCl_2 + Li_2S \quad [10]$$

If one chooses as standard states, solid for FeS, liquid for LiCl, and a reference state so that the activity coefficients of $FeCl_2$ and Li_2S are unity at infinite dilution in the eutectic, the standard Gibbs free energy change for reaction [10], $\Delta G°$, is expressed as follows

$$\Delta G° = -RT \ln \left(\frac{a_{FeCl_2} a_{Li_2S}}{a_{LiCl}^2} \right)$$
$$= -RT \ln K_{SP} + 2RT \ln a_{LiCl} \quad [11]$$

The quantity $\Delta G°$ is also given by

$$\Delta G° = \Delta G_{FeCl_2}{}^* + \Delta G_{Li_2S}{}^* - \Delta G_{FeS}{}^\square - 2\Delta G_{LiCl}{}° \quad [12]$$

where the superscript * denotes the standard state defined at infinite dilution, the superscript □ denotes the solid, the superscript ° denotes the liquid, and the ΔG_i's are the standard Gibbs free energies of formation of the ith compound, at the temperature of reaction [10].

By combining our data with those of Laitinen and Pankey (5), $\Delta G_{FeCl_2}{}^*$ can be derived from the standard formation potential of $FeCl_2$ in the eutectic LiCl-KCl at 723°K. The quantity $\Delta G_{Li_2S}{}^*$ is calculated from the expression

$$\Delta G_{Li_2S}{}^* = \Delta G_{Li_2S}{}^\square - RT \ln N_S(\text{sat}) \quad [13]$$

where $\Delta G_{Li_2S}{}^\square$ is the Gibbs free energy of formation of solid Li_2S from pure liquid Li and pure sulfur in the gaseous state and under 1 atm pressure (12, 13). Similarly, $\Delta G_{LiCl}{}°$ can be derived from the standard Gibbs free energy of formation of solid LiCl as tabulated in JANAF (13) and the activity of LiCl at the liquidus composition (10, 11)

$$\Delta G_{LiCl}{}° = \Delta G_{LiCl}{}^\square - RT \ln a_{LiCl}(\text{sat}) \quad [14]$$

Finally, $\Delta G_{FeS}{}^\square$ at 723°K is calculated by extrapolating values selected by Robie and Waldbaum (14). The solubility product of FeS can be calculated *a priori* from known data combining Eq. [10]-[14]. At T = 723°K, we deduce a value of −38.36 (±3.0) kcal mole^{-1} (or −160.50 kJ mole^{-1}) for $RT \ln K_{SP}$ compared to −38.50 kcal mole^{-1} (or −161.11 kJ mole^{-1}) as derived experimentally. The good agreement between these calculations and the experiments serves as an independent confirmation of our measurements.

Influence of ionic associations.—As mentioned earlier, Eq. [6] has been derived under the assumption that Henry's law is obeyed for $FeCl_2$ and Li_2S. If this is not the case, then the solubility product is expressed as follows

$$K_{SP} = (a_{FeCl_2})(a_{Li_2S})$$
$$= N_{Fe} N_S \gamma_{FeCl_2} \gamma_{Li_2S} \quad [15]$$

where the activities, a, and the activity coefficients, γ, are defined so that the solution is ideal at infinite dilution of both solutes. Formation of associated solution species, such as the ion pair FeS or larger species, leads to deviations from Henry's law. In the event that such species exist, both γ_{FeCl_2} and γ_{Li_2S} would always be less than unity and the apparent $K_{SP} = (N_{Fe}N_S)$ would be larger than the true K_{SP} as given by Eq. [15]. In the present investigation, there is no significant difference between the true and the apparent K_{SP} since (*i*) the emf of the cell is a direct measure of a_{FeCl_2} ($= N_{Fe}\gamma_{FeCl_2}$) which was used in our calculations, and (*ii*) the calculations were made at concentrations of sulfide such that $N_S >> N_{Fe}$. Therefore, if such associated species exist, their concentrations must be much lower than N_S. Consequently, in the concentration range of this study, Li_2S should obey Henry's law closely.

The solubility of FeS cannot be unambiguously derived from the solubility product unless information is available on any significant associations between Fe^{2+} and S^{2-}. For example, if the only associated solution species is FeS with an association constant K, then the solubility of solid FeS in an equimolar solution of Fe^{2+} and S^{2-} would be $KK_{SP} + \sqrt{K_{SP}}$. For $K << K_{SP}{}^{-1/2}$ the solubility is not enhanced significantly and for $K >> K_{SP}{}^{-1/2}$ the solubility can be considerably enhanced. It seems probable that values of K would be large since both Fe^{2+} and S^{2-} are doubly charged leading to very large negative coulombic energy (in addition to possible noncoulombic energy) contribution(s) in favor of forming this ion pair. Coulomb repulsions tend to make species such as $(Fe_2S)^{2+}$ and $(FeS_2)^{2-}$ relatively unstable in this specific medium and they would tend to form only if they had some very special type of bonding that overcame the net coulomb repulsions of the two divalent ions of like charge. An experimental investigation of these considerations is being considered.

Solid solutions and solubility products.—Recent careful studies of the Li_2S-FeS binary phase diagram have indicated that limited solid solutions of Li_2S in FeS (up to 5 mole percent) might occur (4). The influence of such solid solutions on the interpretation of the present data have to be investigated.

The major effect of solid solutions would be to lower the activity of FeS by dilution, thus leading to calculated values of the apparent K_{SP} that are somewhat smaller than those of the true K_{SP}. If the solutions are dilute enough so that the Li_2S component in the solid solution obeys Henry's law and FeS Raoult's law, then one has

$$a_{FeS} = \overline{X}_{Fe}$$

and

$$\overline{X}_{Li} = 1 - \overline{X}_{Fe}$$
$$= \alpha\sqrt{N_S} \quad [16]$$

where a_{FeS} refers to the activity of FeS in the solid solution; $\overline{X}_{Fe}$ and $\overline{X}_{Li}$ are the cation fractions of Fe and Li in the solid, respectively, and α is a proportionality factor which can be calculated from the extent of the solid solution and the solubility of Li_2S. (For a maximum value of $\overline{X}_{Li} = 0.1$ at saturation with Li_2S, α would be 2.6). The true solubility product of FeS can be written as

$$K_{SP} = \frac{(a_{FeCl_2})(a_{Li_2S})}{\overline{X}_{Fe}} \quad [17]$$

where the activities of $FeCl_2$ and Li_2S are measured at saturation with the solid solutions. The activity of Li_2S can be approximated by the concentration of unassociated S^{2-} calculated from the expression

$$N_S = X_S - (X_{Fe} - N_{Fe}) \left(\frac{1 - 0.5\overline{X}_{Li}}{1 - \overline{X}_{Li}} \right) \quad [18]$$

We have computed the true solubility products of FeS

at different temperatures using Eq. [16]-[18] for a variety of possible values of α. The average values of K_{SP} increased very slightly; for example, at $T = 723°K$, this increase was less than 3%. Thus, the over-all effect of such solid solutions on the calculations of K_{SP} is negligible. Finally, the accuracy of our measurements cannot lead to a clear distinction between the effect of a small nonstoichiometry of the FeS phase or a small amount of solid solution. One must therefore, as we have, rely on the known phase diagrams of Fe — S (15) to ascertain that FeS is stoichiometric and that some solid solution with Li_2S is present (4). Until accurate measurements on the extent of solid solution are available, the small corrections to our reported values of K_{SP} cannot be attempted.

Conclusions

Values of solubility products of FeS in molten LiCl-KCl eutectic composition as measured by an emf technique are in excellent agreement with independent theoretical calculations made *a priori* based on exact thermodynamic relations. At relatively high concentrations of sulfide, phases identified as Li_2FeS_2 (X phase) at 723° and 773°K, and $LiK_6Fe_{24}S_{26}Cl$ (J phase) at 673°, 723°, and 773°K were formed in solution. These phases which occur in the full-scale engineering molten-salt batteries are shown to have marginal stabilities in the LiCl-KCl electrolyte; furthermore, the undesirable J phase can be eliminated by using an Li_2S-saturated electrolyte in which the LiCl activity is increased and the KCl activity decreased by an amount calculable from our results. The solubility of FeS in the LiCl-KCl eutectic can be determined accurately when information on the existence of associated species between Fe^{2+} and S^{2-} and their equilibrium constants becomes available.

Acknowledgments

We are indebted to A. E. Martin for the extensive metallographic analyses and all the information he generously shared with us. We are grateful to M. Roche for stimulating discussions. We also wish to acknowledge B. Tani for performing the x-ray analyses, L. Fuchs for metallographic analyses, L. Gutzman and W. Schulze for the glass-blowing, and K. Jensen and colleagues for the chemical analyses. This work was performed under the auspices of the Division of Basic Energy Sciences of the U.S. Department of Energy.

Manuscript submitted Jan. 9, 1978; revised manuscript received May 10, 1978. This was Paper 37 presented at the Atlanta, Georgia, Meeting of the Society, Oct. 9-14, 1977.

Any discussion of this paper will appear in a Discussion Section to be published in the June 1979 JOURNAL. All discussions for the June 1979 Discussion Section should be submitted by Feb. 1, 1979.

Publication costs of this article were assisted by Argonne National Laboratory.

LIST OF SYMBOLS

- T — temperature in Kelvins
- K_{SP} — solubility product (on an ion fraction basis)
- E — true electrochemical voltage of the cell (corrected for thermoelectric effect)
- $E_2°$ — limiting potential of $FeCl_2$ in the eutectic LiCl-KCl *vs.* the Ag-AgCl reference electrode
- R — the gas constant
- $\mathbf{F}$ — the Faraday constant
- a_i — the activity of the ith component
- γ_i — the activity coefficient of the ith component
- X_i — the total ionic fraction of the ith ion
- $\overline{X}_i$ — the ionic fraction of the ith ion in solid solution
- $N_S{}^J$ — concentration of sulfide ion above which the J phase exists
- $N_S{}^X$ — concentration of sulfide ion above which the X phase exists
- N_i — concentration of the ith ion in solution
- $N_S(\text{sat})$ — solubility of Li_2S in the eutectic LiCl-KCl
- $\Delta G_X°$ — standard Gibbs free energy of formation of the X phase
- $\Delta G_J°$ — standard Gibbs free energy of formation of the J phase (LiCl-KCl eutectic composition is the standard state for LiCl and KCl)
- $\Delta G_J{}^*$ — standard Gibbs free energy of formation of the J phase (solids are chosen as standard states for all reactants and products)
- $\Delta G_{FeCl_2}{}^*$, $\Delta G_{Li_2S}{}^*$ standard Gibbs free energy of formation of $FeCl_2$ and Li_2S based on a standard state defined so the activity coefficients are unity at infinite dilution
- $\Delta G_{FeS}\square$ — standard Gibbs free energy of formation of solid FeS
- $\Delta G_{LiCl}°$ — standard Gibbs free energy of formation of liquid LiCl
- $\Delta G°$ — standard Gibbs free energy change for reaction [10]
- K — association constant for the formation of FeS species in solution
- α — proportionality factor in Eq. [16], defining the relative solubilities of Li_2S in FeS and in the melt

REFERENCES

1. P. A. Nelson, N. P. Yao, R. K. Steunenberg, A. A. Chilenskas, E. C. Gay, J. E. Battles, F. Hornstra, W. E. Miller, M. F. Roche, and H. Shimotake, Progress Report, ANL 77-35, Argonne National Laboratory (1977).
2. Z. Tomczuk, A. E. Martin, and D. R. Vissers, in Progress Report, ANL-8057, Argonne National Laboratory (1973).
3. F. C. Mrazek and J. E. Battles, *This Journal*, **124**, 1556 (1977); B. Tani, *Am. Mineral.*, **62**, 819 (1977).
4. A. E. Martin, Private communication.
5. H. A. Laitinen and J. W. Pankey, *J. Am. Chem. Soc.*, **81**, 1053 (1959).
6. H. A. Laitinen and C. H. Liu, *ibid.*, **80**, 1015 (1958).
7. M. Blander and E. B. Luchsinger, *ibid.*, **86**, 319 (1964).
8. C. H. Liu, A. J. Zielen, and D. M. Gruen, *This Journal*, **120**, 67 (1973).
9. R. A. Sharma, *ibid.*, **123**, 448 (1976).
10. J. Lumsden, "Thermodynamics of Molten Salt Mixtures," Academic Press, New York (1966).
11. E. Aukrust, B. Björge, H. Flood, and T. Førland, *Ann. N.Y. Acad. Sci.*, **79**, 830 (1960).
12. K. C. Mills, "Thermodynamic Data for Inorganic Sulfides, Selenides and Tellurides," Butterworths, London (1974).
13. D. R. Stull and H. Prophet, "JANAF Thermochemical Tables," 2nd Ed., National Standard Reference Data Service, National Bureau of Standards NSRDS-NBS-37 (1971).
14. R. A. Robie and D. W. Waldbaum, Geol. Survey Bull. 1259; U.S. Government Printing Office, Washington, D.C. (1968).
15. E. M. Levin, C. R. Robbins, and H. F. McMurdie, in "Phase Diagrams for Ceramists," M. K. Reser, Editor, The American Ceramic Society, Columbus, Ohio (1964), Supplement 1975.

Primary Li/SOCl$_2$ Cells

IV. Cathode Reaction Profiles

A. N. Dey* and P. Bro

P. R. Mallory & Company Incorporated, Laboratory for Physical Science, Burlington, Massachusetts 01803

ABSTRACT

The reaction profiles of the Teflon-bonded carbon cathode of the Li/SOCl$_2$-1M LiAlCl$_4$-SOCl$_2$ inorganic electrolyte battery were determined by sectioning the discharged cathodes and analyzing for LiCl which is formed quantitatively based on the charge passed according to the reaction

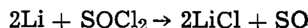

$$2Li + SOCl_2 \rightarrow 2LiCl + SO$$

The profiles show that LiCl precipitates preferentially near the cathode surface, and the interior of the cathode remains underutilized at high current density. The cathode also expands nonlinearly with the increase in the specific capacity. The longitudinal profiles of the cathodes of high rate D cells indicate that the current distribution is controlled by the electrical resistance of the cathode grid. This in turn causes the cell wall to be the hottest part of the cell on shorting.

The Li/SOCl$_2$ inorganic electrolyte system (1-4) is one of the highest energy density systems known to date. The system consists of a Li anode, a porous carbon cathode, and an LiAlCl$_4$-SOCl$_2$ electrolyte; SOCl$_2$ acts both as a solvent and as a cathode-active material. The Li anode is prevented from reacting with the SOCl$_2$ by virtue of the formation of an LiCl protective film (5) on the Li as soon as it contacts the LiAlCl$_4$-SOCl$_2$ electrolyte according to the reaction

$$2Li + SOCl_2 \rightarrow 2LiCl + SO \quad [1]$$

We proposed (6) this to be the primary cell reaction. The biradical SO is unstable and usually dimerizes and then decomposes to S + SO$_2$ according to

$$2SO \rightarrow (SO)_2 \quad [2]$$

$$(SO)_2 \rightarrow S + SO_2 \quad [3]$$

SO may undergo other possible chemical reactions to produce other byproducts (7). It was demonstrated experimentally (8) that all the Li dissolved from the anode precipitated quantitatively as LiCl on the porous carbon cathode. Furthermore, we showed (9) that the utilization of SOCl$_2$ in optimized D cells approached 100% asymptotically based on reaction [1] at low current densities. The energy densities delivered by these cells reached 20 W-hr/in.^{3} (1.24 W-hr/cm^3) and 300 W-hr/lb (661 W-hr/kg) at low current densities. At high current densities and low temperatures the energy densities were reduced significantly because of the premature passivation of the porous carbon cathode. Thus, from an energy density standpoint, the performance-limiting electrode is the porous carbon cathode. Attempts were made (9, 10) to mitigate this limitation by developing two types of D cells having a low and a high rate capability (Fig. 1). The low rate cells have shorter and thicker electrodes, thus having more active materials than the high rate cells which have longer and thinner electrodes and necessarily longer separators and current collectors which occupy space otherwise used by active materials. The object of this investigation was to determine the reaction profiles (both cross-sectional and longitudinal) of the porous carbon cathodes used in the Li/SOCl$_2$ D cells to assess its performance-limiting characteristics in some detail. The ultimate objective of these studies is to improve the porous carbon cathodes so that they may perform efficiently at high current densities, thus possibly eliminating the need of two types of cells for high and low rate applications.

* Electrochemical Society Active Member.

Key words: battery, carbon, cathode, mass transport.

Experimental

Cross-sectional reaction profiles.—The reaction profiles were determined by sectioning the porous carbon cathodes which were made by hot pressing a mixture of Shawinigan Black and Teflon on a layer of expanded Ni prewelded on a stainless steel stud. The cross-sectional view of the cathode is shown in Fig. 2. The extent of reaction in the cathode slices was determined by analyzing for LiCl which was found (8) to precipitate quantitatively based on the charge passed according to reaction [1]. The carbon cathodes were approximately 0.1 cm thick and had a diameter of 1.27 cm, which coincided with the inner diameter of the cylindrical test cell, shown in Fig. 3, to provide a relatively uniform current distribution on the cath-

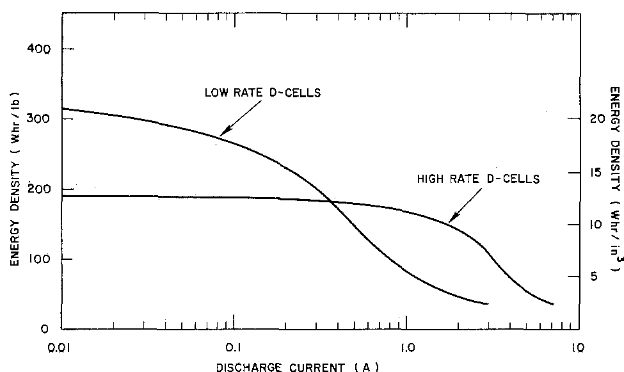

Fig. 1. Performance characteristics of the high and low rate types of Li/SOCl$_2$ D cells.

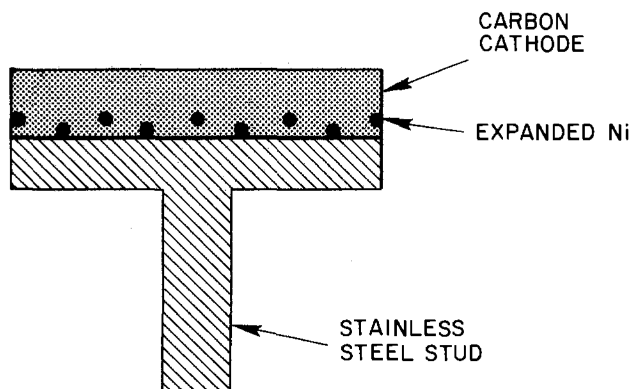

Fig. 2. Carbon cathode for reaction profile determination

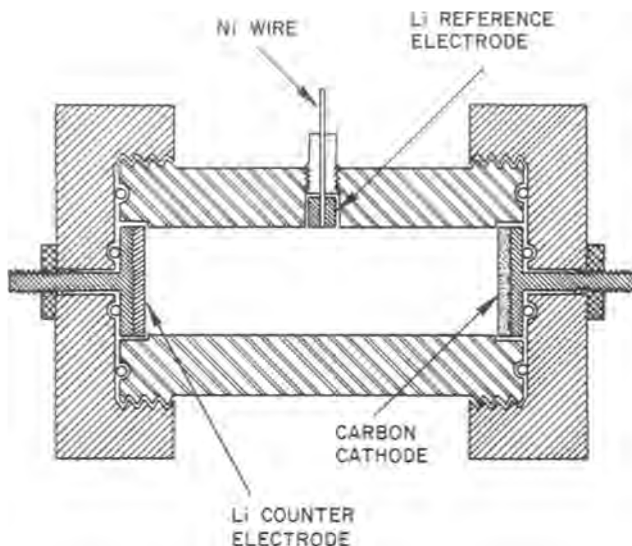

Fig. 3. The cell

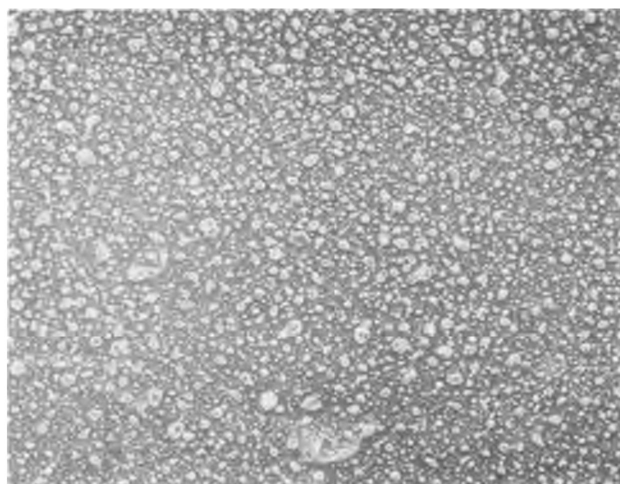
Fig. 4. SEM photograph of the cathode surface after discharge showing the LiCl precipitates (50 times).

ode. The SEM photograph (Fig. 4) of a discharged cathode surface at 50 times magnification showing the LiCl precipitation demonstrates the uniformity of current distribution. The Li counterelectrode was of the same size as the carbon cathode.

The cathodes were discharged in an excess of 1M $LiAlCl_4$ in $SOCl_2$, [the preparation and purification of which have been described elsewhere (10)] to several depths of discharge at various currents and temperatures. After the discharge, the electrodes were washed thoroughly in excess $SOCl_2$ to remove $LiAlCl_4$ and then dried under vacuum to remove $SOCl_2$. The thicknesses of the cathodes were measured before and after discharge in order to determine the cathode expansion. For analysis, a central section was cored from the cathode to eliminate edge effects on the current distribution. The central core was mounted on a microtome, as shown in Fig. 5, and the cathode was sectioned into thin slices that were leached with distilled water to recover the LiCl. The extracted LiCl was determined by analyzing the lithium in the extract by atomic absorption spectrometry. The leached cathode slices were dried and weighed.

Longitudinal reaction profiles.—The high rate Li/$SOCl_2$ D cells (10) were made by winding together Li anodes and carbon cathodes (with glass separators) having the following dimensions: carbon cathode, 20 × 1.75 in.; Li anode, 20 × 1.50 in. The wound elec-

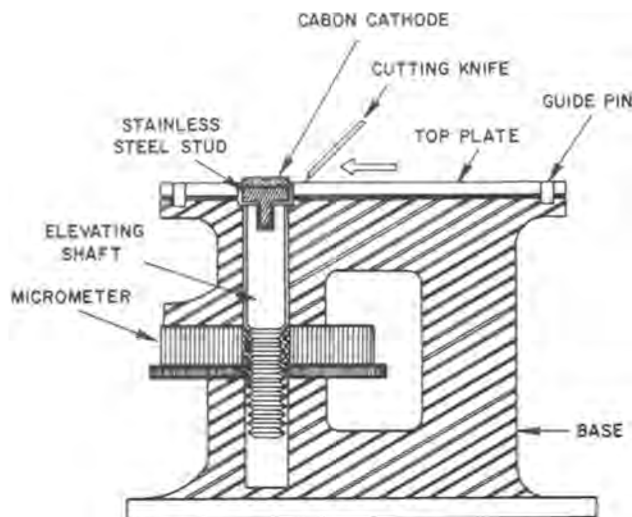

Fig. 5. Cathode-sectioning apparatus

trode assembly fit snugly into the Ni can, (OD, 1.30 in.; length, 2.38 in.). The cathode terminal in the form of an Ni tab (prewelded to the expanded Ni current collector of the porous carbon cathode) was located near the interior wall of the can and connected to the Ni can wall by welding. The Li anode was short by approximately 0.5 in. in covering the cathode on the outer wrap of the electrode assembly. The Li anode terminal in the form of a Ni tab was located at the center of the wound electrode assembly and was connected to the feedthrough of the G/M seal terminal. The longitudinal reaction profile of the cathode was determined by washing the cathode of the discharged D cell with excess $SOCl_2$ and then punching out circular disks from the cathode at various locations with respect to the tab. The LiCl content of these disks and their weights after the leaching was determined as before.

Results and Discussion

Cross-sectional reaction profile.—The histograms of the experimental results are shown in Fig. 6-9 for the various discharge conditions. The electrode depth is expressed in cumulative weights of the cathode slices starting from the electrode-electrolyte interface toward the interior of the cathode. The depth of dis-

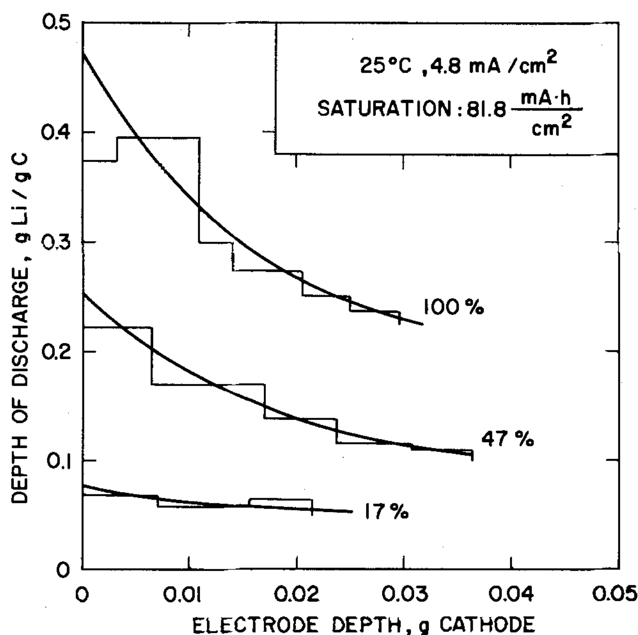

Fig. 6. Reaction profiles of the cathode discharged at 25°C, at 4.8 mA/cm².

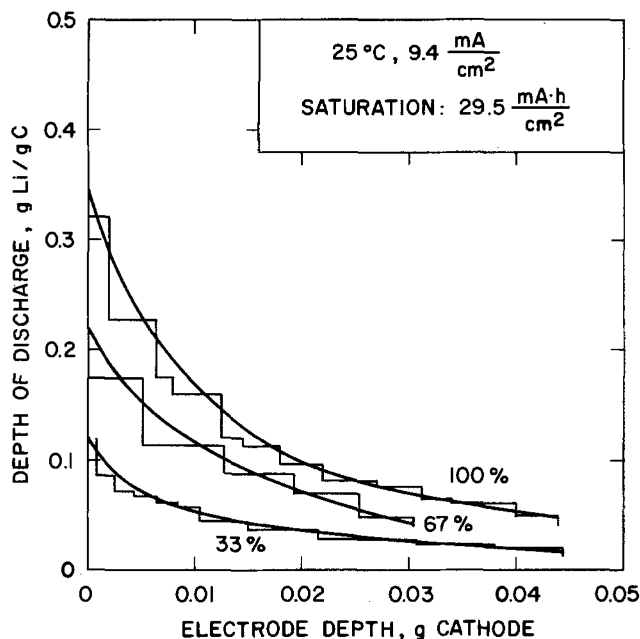

Fig. 7. Reaction profiles of the cathode discharged at 25°C, at 9.4 mA/cm^2.

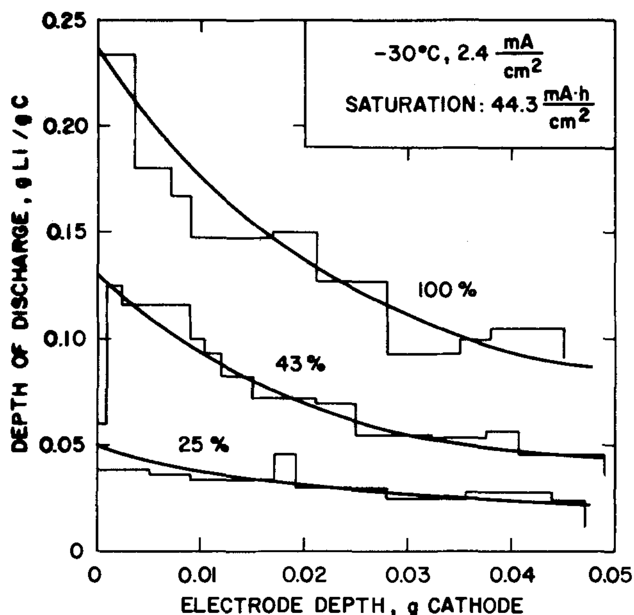

Fig. 8. Reaction profiles of the cathode discharged at —30°C, at 2.4 mA/cm^2.

charge is expressed in weight of Li (in the form of LiCl) per unit weight of the cathode slice. The smooth curves drawn through the histograms represent the reaction profiles. The reaction profiles of the cathode discharged at 25°C at a current density of 4.8 mA/cm^2 are shown in Fig. 6. The specific capacity of the fully discharged (100%) cathode was 81.8 mA-hr/cm^2 under the above condition. The reaction profiles were obtained at three different states of discharge *viz.* 17, 47, and 100%. At 17% depth of discharge, the profile is fairly flat, indicating a uniform precipitation of LiCl throughout the cathode. At higher states of discharge the profiles become nonuniform and the precipitation of LiCl occurs preferentially near the cathode-electrolyte interface. At 100% depth of discharge, the precipitation in the interior of the cathods is approximately 50% of that near the surface.

The reaction profiles of the cathode discharged at 9.4 mA/cm^2 at 25°C are shown in Fig. 7. The specific capacity of the fully discharged cathode decreased to 29.5 mA-hr/cm^2 at this higher current density. The reaction profiles become increasingly nonuniform. The precipitation of LiCl occurs primarily near the front of the cathode. The precipitation in the interior is only 14% of that near the front surface. Thus, the interior of the carbon cathodes remain underutilized at high current densities.

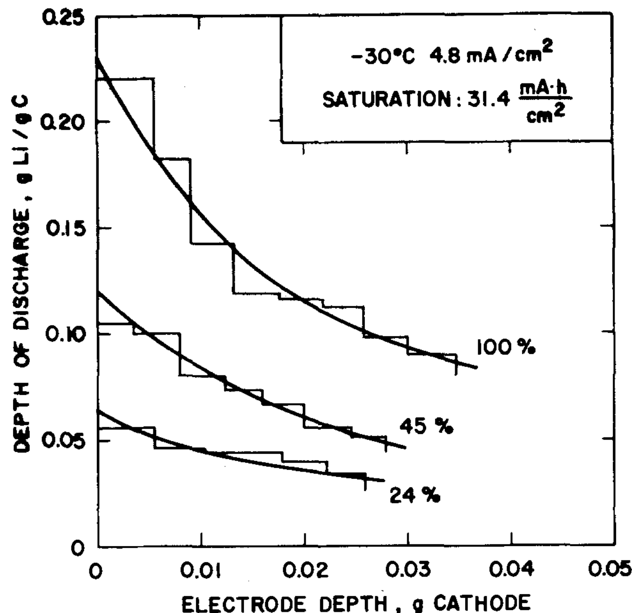

Fig. 9. Reaction profiles of the cathode discharged at —30°C, at 4.8 mA/cm^2.

The reaction profiles of the cathodes discharged at —30°C at current densities of 2.4 and 4.8 mA/cm^2 are shown in Fig. 8 and 9. The specific capacities of the fully dicharged cathodes were 44.3 and 31.4 mA-hr/cm^2 for the two current densities. The shape of the reaction profiles at 25° and —30°C at the same current density (4.8 mA/cm^2) are similar, only the specific capacities are reduced drastically at the lower temperature. Lowering of the current density to 2.4 mA/cm^2 at —30°C results in an increase of the specific capacity to 44.3 mA-hr/cm^2, although the profiles remain relatively unchanged. The cathode appears to be less efficient at low temperature.

The results suggest that the carbon cathodes are mass-transport limited, and the diffusive choking of the cathode by the precipitation of the reaction products (LiCl, S) is the likely cause of the polarization of the cathode. Therefore, the rate capability of the cathode can be improved by (*i*) increasing the porosity of the cathode to improve the mass-transport characteristics; and (*ii*) reducing the thickness of the cathode. The latter approach has been examined (9) and found to cause an energy-density penalty.

The maximum capacity predicted from the design calculations (11) of Li/$SOCl_2$ D cells having a specific electrode geometry was 11.62 A-hr, whereas the experimentally realized (9) maximum capacity of D cells having a similar electrode geometry was found to be approximately 16 A-hr. This discrepancy between the calculated and the experimental values indicates the importance of experimental characterization of the cathode in regard to the reaction profile.

Cathode expansion.—The Teflon-bonded carbon cathodes were found to expand during the discharge. The expansion of cathodes discharged under various conditions in a D cell is shown in Fig. 10. The cathode expansion depends on the specific capacity irrespective of the discharge conditions. This may be attributed to the expansion being caused by the precipitation of LiCl which is quantitatively related to the specific capacity according to the cell reaction [1]. The initial expansion of the cathode as a function of the specific ca-

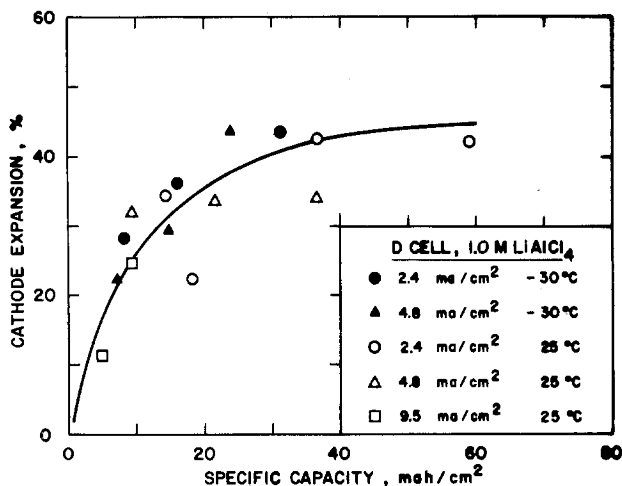

Fig. 10. Cathode expansion on discharge

pacity is rapid and levels off during the later stages of discharge. This may be attributed to the fact that the cathodes are soft and pliable during the early part of the discharge but become increasingly rigid as the precipitation of LiCl continues. Thus, the modulus of elasticity of the cathodes is dependent upon the specific capacity. It will be interesting to study the rheology of the cathode as a function of its composition.

Longitudinal reaction profile.—The longitudinal reaction profiles of a high rate D cell cathode on a 2.0A discharge at 25°C is shown in Fig. 11. The profiles were obtained at three depths of discharge, 2.5, 5.4, and 10.3 A-hr, the latest corresponding to the complete passivation of the cathode. Note that at the early stage of the discharge, most of the cell reaction occurs near the Ni tab of the cathode. This indicates that at high rates (2A) the electrical resistance of the Ni grid controls the current distribution of the cathode. It is expected that at higher currents, most of the cell reaction will be restricted to the cathode area near the tab which is welded to the cell can, and in our design this cathode area happens to be adjacent to the cell wall as shown at the top of Fig. 11. This particular longitudinal reaction profile results in an interesting internal temperature profile of the high rate D cells on shorting. The short-circuit current of these cells was approximately 20-30A. At that current, it is expected that almost all the reaction will occur right near the tab and hence near the cell wall, thus making the cell wall temperature higher than that of the cell interior. We measured the internal as well as the wall temperature of high rate D cells by means of thermocouples, as shown in Fig. 12, after externally shorting the cell. The voltage current and the temperature profiles are shown in Fig. 13. The three thermocouples located on the wall, halfway between the wall and the center, and at the center are referred to as TC-1, TC-2, and TC-3, respectively. The cell was equipped with a low pressure vent which was automatically activated at an internal pressure of 100-130 psi. We found that the cell wall temperature was substantially higher than that of the interior temperatures, as expected. This particular electrode design imparts additional safety characteristics to the cell by ensuring that the hottest point of the cell is the wall which can be cooled more easily than can the cell interior.

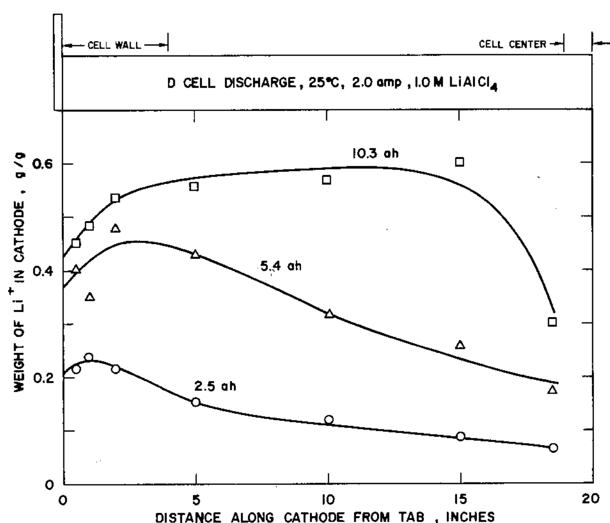

Fig. 11. Longitudinal reaction profiles of the cathode of the high rate $Li/SOCl_2$ D cell, discharged at 25°C at 2A.

Conclusions

1. Cross-sectional reaction profiles of the carbon cathodes show that mass transport through the porous carbon is the limiting feature of the cathodes. At high

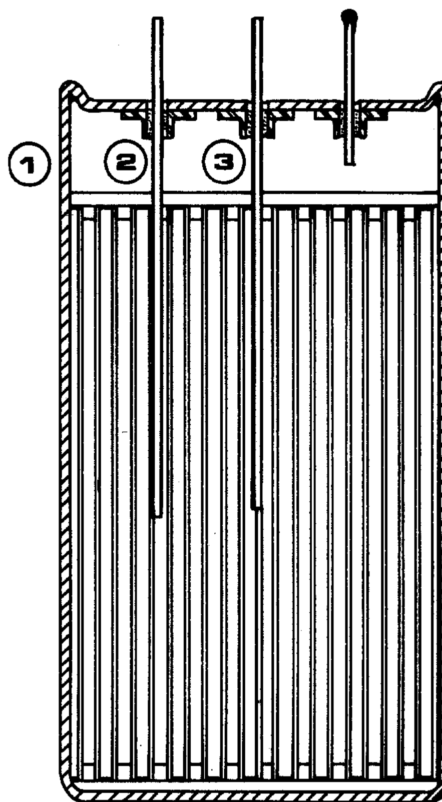

Fig. 12. Cross-sectional view of a D cell with thermocouple feedthroughs.

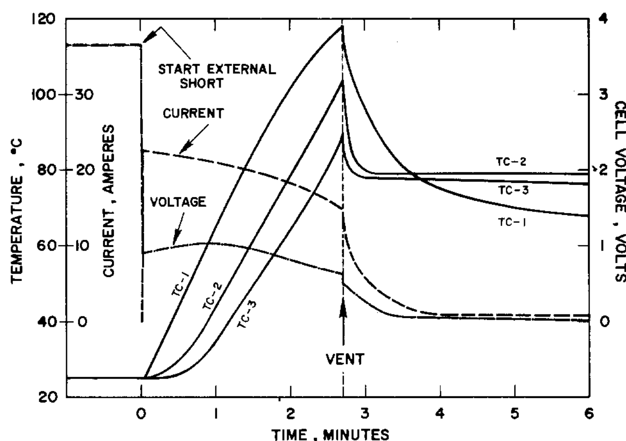

Fig. 13. Temperature profiles on shorting a high rate D cell. Wall temperature (TC-1); halfway between wall and the center (TC-2); center (TC-3).

currents the interior of the cathode remains virtually unutilized.

2. The cathodes expand nonlinearly with the specific capacity, and the expansion is independent of the current density and the discharge temperature. The expansion is rapid at first and then levels off as the cathode becomes increasingly stiff.

3. The longitudinal current distribution of the cathode is controlled by the electrical resistance of the expanded Ni grid. At high currents most of the reaction is localized near the cathode tab, thus making the cell wall the hottest part on cell shorting.

Acknowledgment

The auhors wish to thank J. Miller for experimental assistance.

Manuscript submitted Jan. 30, 1978; revised manuscript received April 21, 1978. This was Paper 23 presented at the Las Vegas, Nevada, Meeting of the Society, Oct. 17-22, 1976.

Any discussion of this paper will appear in a Discussion Section to be published in the June 1979 JOURNAL. All discussions for the June 1979 Discussion Section should be submitted by Feb. 1, 1979.

Publication costs of this article were assisted by P. R. Mallory & Company Incorporated.

REFERENCES

1. W. K. Behl, J. A. Christopulos, M. Ramirez, and S. Gilman, *This Journal*, **120**, 1619 (1973).
2. J. J. Auborn, K. W. French, S. I. Lieberman, V. K. Shah, and A. Heller, *ibid.*, **120**, 1613 (1973).
3. D. L. Maricle and J. P. Mohns, U.S. Pat. 3,567,515 (1971), G. E. Blomgren and M. L. Kronenberg, Ger. Pat. 2,262,256 (1973).
4. A. N. Dey and G. R. Schlaikjer, in "Proceedings of the 26th Power Sources Symposium," Atlantic City, N.J., April 1974.
5. A. N. Dey, *Electrochim. Acta*, **21**, 377 (1976).
6. A. N. Dey, *This Journal*, **123**, 1262 (1976).
7. A. N. Dey, *Thin Solid Films*, **43**, 131 (1977).
8. J. R. Driscoll and G. L. Holleck, Abstract 34, p. 91, The Electrochemical Society Extended Abstracts, Fall Meeting, Dallas, Texas, Oct. 5-9, 1975.
9. A. N. Dey and P. Bro, in "Power Sources 6," p. 493, D. H. Collins, Editor, Academic Press, New York (1977).
10. A. N. Dey, *Electrochim. Acta*, **21**, 855 (1976).
11. N. Marincic, *J. Appl. Electrochem.*, **6**, 51 (1976).

Rate Processes Related to the Hydrated Nickel Hydroxide Electrode in Alkaline Solutions

R. S. Schrebler Guzmán, J. R. Vilche, and A. J. Arvía*

Instituto de Investigaciones Fisicoquímicas Teóricas y Aplicadas, División Electroquímica, Sucursal 4, 1900 La Plata, Argentina

ABSTRACT

The potentiodynamic response of the Ni/alkaline aqueous solution interface in the region of the hydrated $Ni(OH)_2$ to β-NiOOH electrochemical reaction reveals that both species undergo phase transformations. The anodic product from the $Ni(OH)_2$ species involves the formation of three species energetically different which are detected during the electroreduction process. Under well-defined perturbation conditions, a reasonable set of kinetic parameters pertaining to the anodic process is obtained which is formally interpreted through a consecutive three-step mechanism of reaction involving a charge transfer, a chemical reaction, and a charge transfer and a proton transfer process. Side reactions involving water take into account the various aging processes of the reaction products.

It is well established that a nickel electrode immersed in concentrated aqueous alkaline hydroxide solutions is spontaneously covered with $Ni(OH)_2$ layers while the potential increases slowly with time (1-3). In 1*M* KOH solution the layer increases to a thickness of up to 15 atom units at open circuit during 16 hr (4, 5).

The electrochemical characteristics of nickel in alkaline solutions in the potential range preceding the O_2 evolution are related to the hydrated nickel hydroxide electrode (6-15). Its kinetics have been particularly considered in relation to the Ni-Cd battery, hence, most of the works refer to large surface area electrodes. As is well known, the reduced system consists of a variety of hydrated $Ni(OH)_2$ forms and the oxidized system is generally related to the NiOOH species. Both species exist in two structural modifications which are called α and β for the former species and γ and β for the latter (14). The α-$Ni(OH)_2$ structure is unstable on standing in an open circuit and cycling (7). In KOH solution, for a limited time, it is possible to cycle between the α-$Ni(OH)_2$ and the γ-NiOOH structure (7, 10, 11). The conversion of α-$Ni(OH)_2$ to β-$Ni(OH)_2$ has been related to the aging characteristics of the film, which correspond to the shift in potential of about 50 mV moving to higher potential as the electrode is cycled or is allowed to stay in KOH solution (7, 10).

There is evidence that the hydrated $Ni(OH)_2$ to β-NiOOH electrochemical oxidation follows a composite pattern, which still poses important unresolved questions and considerable controversy, particularly when the different authors advance explanations in terms of different stoichiometries of isolated nickel compounds (16). Apparently the amount of adsorbed oxygen on Ni changes with the ionic composition and alkali concentration (17, 18). In alkaline solution it increases on passing from LiOH to CsOH (19).

The structural changes of the $Ni(OH)_2$ species have been electrochemically observed and they were assigned to the conversion of α-$Ni(OH)_2$ into β-$Ni(OH)_2$ (7, 10, 11, 20-22). Recent reports (3, 23-25) indicate that the cathodic current peak potential recorded either with a triangular potential sweep or with trapezoidal pulses shifts toward the cathodic potential as the anodic switching potential becomes more anodic. This confirms also that the product anodically formed is partially transformed into a more stable species (24, 25). This aspect of the problem is

* Electrochemical Society Active Member.

Key words: nickel hydroxides, anodic oxidation, film formation, aging processes.

certainly not clear, and to draw definite conclusions from the kinetic response of electrochemical systems involving different amounts of active material on the electrode seems excessively optimistic. The present work refers to the potentiodynamic response of the Ni/alkaline solution interface in the potential range of the hydrated nickel hydroxide electrode under different potential perturbation conditions involving amounts of charge at most of the order of a few monolayers of reactant and product. After the systematic change of the perturbation conditions, different straightforward relationships involving the various kinetic parameters are obtained which are meaningful in terms of a relatively simple reaction pathway. The over-all electrochemical behavior of nickel in alkaline solutions is, in principle, interpreted through various film forming $Ni(OH)_2$ and NiOOH species. Although these species in bulk are apparently poor electron conductors, they appear to be good proton conductors. Therefore, the conclusions of the present work are particularly interesting for a preliminary understanding of the early stages involved in the passivity of nickel and certainly they apply to nickel electrodes as employed in alkaline batteries.

Experimental

The experimental procedure including the electrolysis cell and electrode materials are practically the same as already described in previous publications (24, 25). The following electrolyte solutions were employed: 1.00*N* KOH (solution A); 0.10*N* KOH (solution B); 0.10*N* KOH + 0.60*N* K_2SO_4 (solution C); 0.01*N* KOH + 0.66*N* K_2SO_4 (solution D). They were prepared from triply distilled water and analytical grade (Merck) reagents. Experiments were made under N_2 gas saturation at 25°C using repetitive triangular potential scans (RTPS) and other different potential/time perturbation functions which are indicated for each particular run. The latter were programmed to normalize the average structure of the reactants at the electrode surface in order to derive from each run comparable kinetic data.

After a certain number of RTPS at a particular potential sweep rate (v) the electrode attained a reproducible *E/I* contour. In the following text, these electrodes are referred to as "stabilized electrodes." The potentials are referred to the NHE scale.

Results

E/I characteristics obtained with triangular potential sweep perturbations.—RTPS run at $v = 0.1$ V/sec, between the switching potentials $E_{\lambda,c} = -0.96$V and $E_{\lambda,a} = 0.74$V, just exceeding the potential range of the electrochemical stability of water are shown in Fig. 1. The complex *E/I* contour is obtained using a polished electrode immersed in solution A, which was previously cathodized at $E_{\lambda,c}$ for 5 min. The initial anodic scan exhibits an anodic current peak at −0.44V (peak I), followed by an appreciable anodic current in the −0.4 to 0.4V range, and another anodic current peak (peak II) in the potential range just preceding the net oxygen evolution. The immediately returning scan presents a cathodic current peak (peak III) which, in principle, is complementary to current peak II. The following successive potential sweeps show practically no trace of current peak I and a net decrease of the anodic current in the −0.4 to 0.4V range. The first anodic scan exhibits the anodic current peak II located at potentials slightly more anodic than in the following successive cycles. Furthermore, there is a slight contour change of both current peak II and III, and, after a relatively large number of sweeps, a new cathodic shoulder (peak IV) on the left side of current peak III is definitely recorded. The stable *E/I* profile is only reached in this case after 50-60 potential scans. The reactions occurring in the potential range of current peak I concern the hydrated $Ni(OH)_2$ film formation. The corresponding kinetic and mechanistic interpretations have been considered in a previous publication (25).

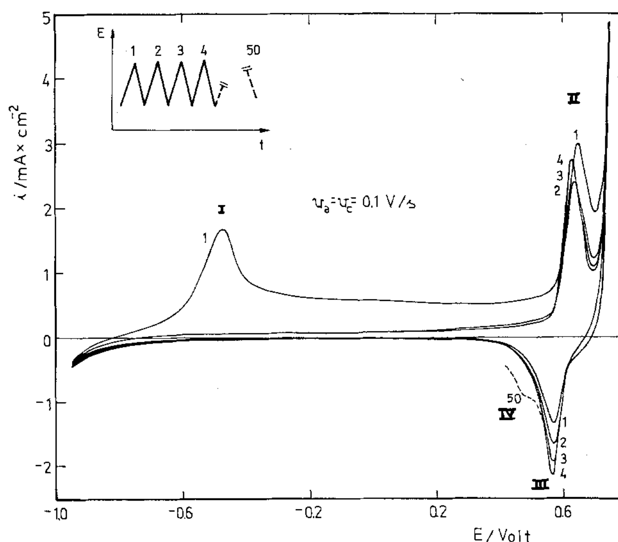

Fig. 1. Potentiodynamic displays obtained under RTPS at 0.1 V/sec. Solution A.

The passivation current recorded during the first anodic potential sweep in the −0.1 to 0.4V range fits at constant potential a linear log *i*/log v relationship (Fig. 2), with a slope equal to 1.

Current peaks II, III, and IV are better defined when $E_{\lambda,c}$ is closer to the potential of current peak II. The limiting *E/I* contours or current peaks II and III resulting after the nth RTPS between $E_{\lambda,c} = 0.34$V and $E_{\lambda,a} = 0.68$V are characterized by a high degree of symmetry as defined by the peak height to peak width at one-half of peak height (Fig. 3). Otherwise, the cathodic side of current peak III is influenced by current peak IV which, under the present conditions, actually appears as a net current plateau. The RTPS profiles run within fixed $E_{\lambda,c}$ and $E_{\lambda,a}$ yield reasonably good linear current peak height $(I_p)/v$ relationships. Once the stable *E/I* profiles are attained there is only a very small shift of the potentials of current peaks II and III on changing v. Moreover the half-wave potential of peak IV remains practically independent of v at least for $6 \leq v \leq 30$ mV/sec. The amount of charge involved on both the anodic (Q_a) (after baseline correction for the electrochemical oxygen-evolution reaction) and the cathodic scans (Q_c) decreases as v increases, approaching a charge of the order of one monolayer thickness at high v (Fig. 4). The Q_a/Q_c ratio at a constant v is practi-

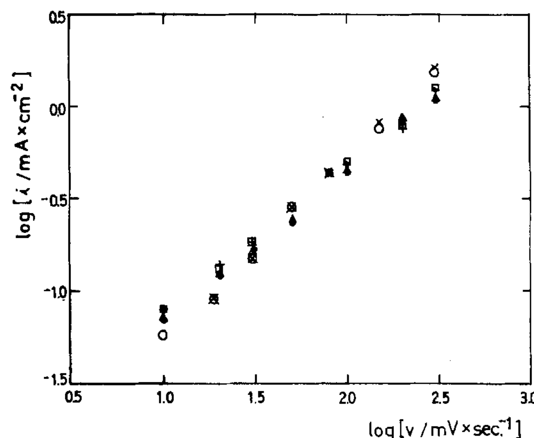

Fig. 2. Potential sweep rate dependence of the anodic current recorded during the first potential scan. Read at different fixed potentials. Solution A, −0.06V (×) and 0.04V (○); Solution C, 0.14V (□) and 0.04V (+); Solution D, 0.24V (△) and 0.14V (●).

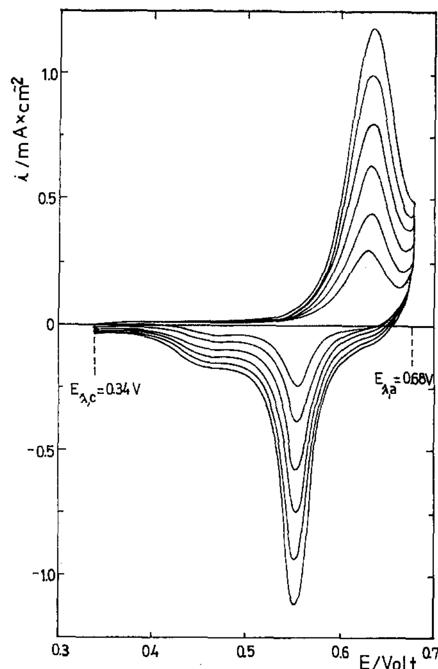

Fig. 3. E/I displays run with a stabilized electrode and symmetrical triangular potential scans at different potential sweep rates. Solution A. v = 6, 10, 15, 20, 25, and 30 mV/sec.

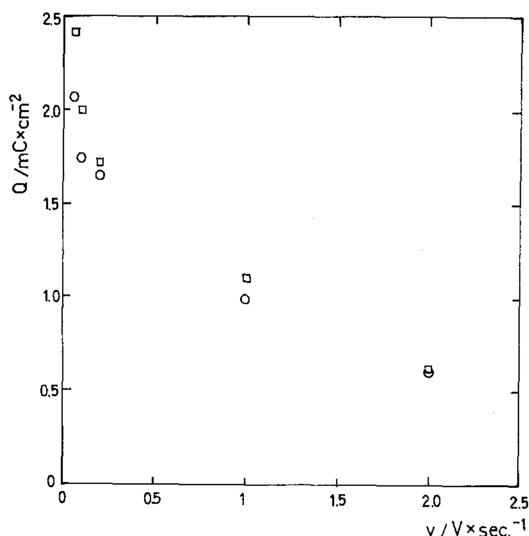

Fig. 4. Potential sweep dependence of the charge involved in the RTPS run between 0.44 and 0.79V. Solution C. (□) Anodic charge; (○) cathodic charge.

cally equal to one. The E/I profiles recorded with asymmetric repetitive triangular potential perturbations (either v_a, v_c = constant or v_c, v_a = constant), covering the potential region of current peaks II and III (Fig. 5) are influenced by the products of the reaction related to current peak III. They are probably not completely removed during the cathodic scan when $E_{\lambda,c}$ is not sufficiently cathodic. As the $E_{\lambda,c}$ becomes more anodic than the potential of current peak IV, the anodic charge decreases and simultaneously one observes that the initial part of the E/I line related to current peak II shows an appreciable depolarization as compared to that depicted in Fig. 8. On the other side, as v_a increases the contour of current peak III appears flatter and an increasing current contribution is also noticed at the anodic side of current peak III, while the corresponding current peak potential turns more anodic. The over-all effect resembles an aging-type process of the passivating species. The decrease of Q_c as v_a increases is obviously

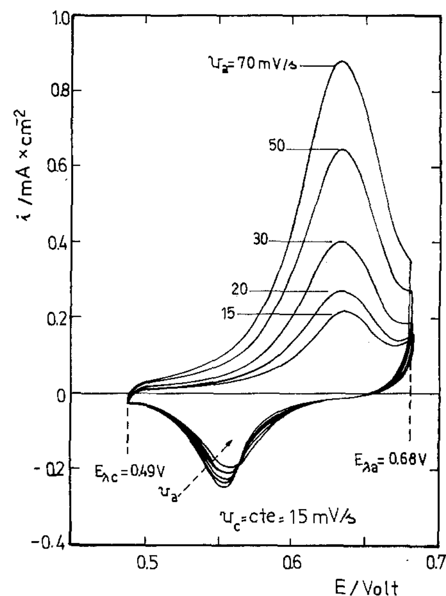

Fig. 5. Potentiodynamic E/I displays run at v_c = 0.015 V/sec and 0.015 V/sec ≤ v_a ≤ 0.070 V/sec. The dashed arrow indicates the shift of the cathodic profile as v_a increases. Solution A.

derived from the dependence of Q_a on v_a already referred to.

The shape of the stabilized electrode E/I profile depends on the $E_{\lambda,a}$ value (Fig. 6). Thus, at constant $E_{\lambda,a}$, the charge associated with current peak IV is practically constant for any potential scan. Nevertheless, it further increases as $E_{\lambda,a}$ increases because of the baseline shift of current peak III. This result indicates that the species electroreduced within the potential range of the current peak IV are those anodically produced at the lower anodic potential region of current peak II.

The E/I profile shown in Fig. 7 has been stabilized under a RTPS between $E_{\lambda,c}$ = 0.49V and $E_{\lambda,a}$ = 0.695V (E/I curve 9) covering a relatively large potential range of the O_2-evolution reaction. After the stabilized profile has been obtained the cathodic E/I profiles numbered from 1 to 8 are recorded by switching the anodic potential at different values. Thus, those cathodic scans initiated from switching potentials overlapping to a relatively larger extent the po-

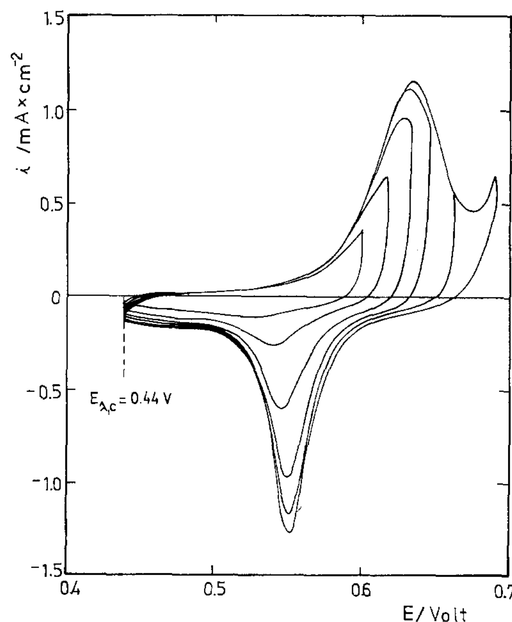

Fig. 6. Influence of the anodic potential limit on the E/I profiles recorded with triangular potential sweeps at 0.03 V/sec. Solution A.

Table I. Charges corresponding to the potentiodynamic profiles ($V = 0.02$ V/sec)

Profile number	$E_{\lambda,a}$/V	Q_a/mC $\times$ cm^{-2}	Q_c/mC $\times$ cm^{-2}	Q_a/Q_c
1	0.603	0.50	0.50	1.00
2	0.608	0.66	0.66	1.00
3	0.617	0.94	0.94	1.00
4	0.621	1.15	1.14	1.01
5	0.630	1.46	1.40	1.04
6	0.639	1.78	1.68	1.06
7	0.661	2.21	2.02	1.09

tential range of the O_2-evolution reaction imply Q_a/Q_c ratios increasing with the switching potentials values (Table I). In spite of this any surface species which might be involved in the O_2-evolution reaction produce apparently no particular change in the E/I characteristics.

An equivalent influence of $E_{\lambda,c}$ on both current peaks II and III are seen (Fig. 8). When the potential sweep covers the range between 0.675 and 0.600V, the E/I characteristics approach a highly reversible behavior as is immediately deduced from the fast response of the current to the both anodic and cathodic potential switchings. Under these circumstances only a small fraction of the total charge is periodically removed from and reformed on the surface. As $E_{\lambda,c}$ decreases, the charge fraction which is involved in the over-all process increases. Moreover, the over-all process becomes more irreversible as evidenced by the decrease of the anodic current at a given potential in the initial portion of the anodic profile. Furthermore, when $E_{\lambda,c}$ is more cathodic than the potential range of current peak IV, the potential of current peak III becomes progessively more anodic, attaining a constant value when $E_{\lambda,c} = 0.4$V. When the region of current peak IV is not included, the rest of the electrochemical reactions occurring on the covered electrode surface show a faster response to the electrical perturbation. But when those species related to current peak IV are involved in the perturbation process, their formation reaction occurs with appreciable irreversibility although this situation produces an apparent activation of the process related to current peak III.

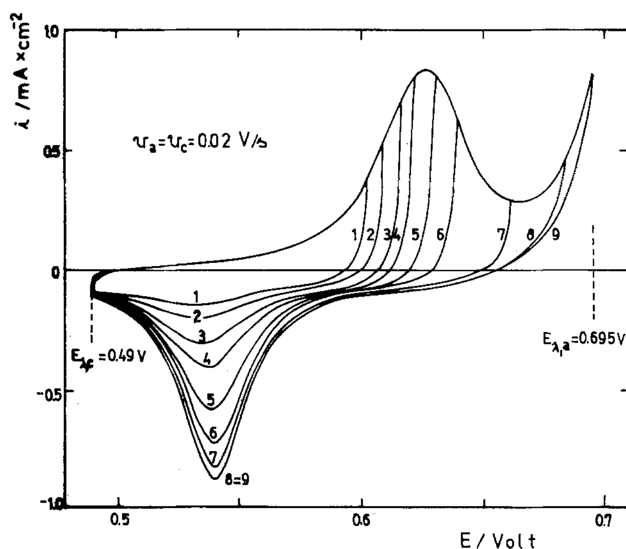

Fig. 7. Influence of the anodic switching potential on the Q_a/Q_c ratio. Each run is made from $E_{\lambda,c}$ upward after a previous RTPS at 0.02 V/sec between 0.49 and 0.695V, to attain a stable E/I profile. Solution A.

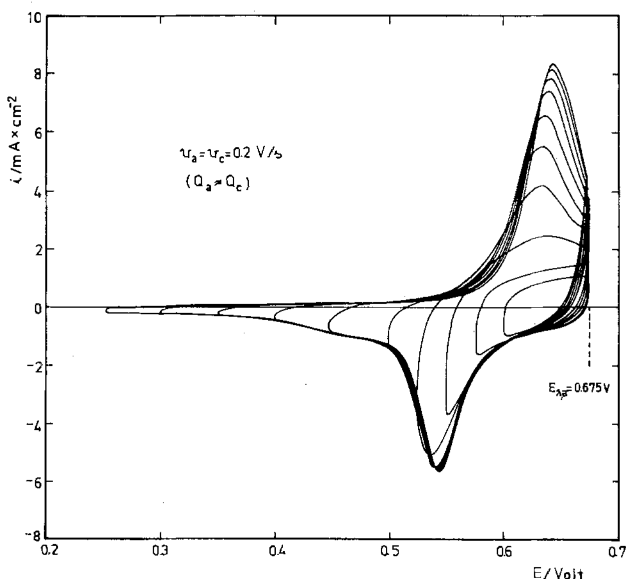

Fig. 8. Influence of the cathodic switching potential on the E/I profiles recorded with RTPS at 0.2 V/sec. Solution A.

The E/I characteristic referred to are maintained within the range $11 \leq pH \leq 14$ (Fig. 9). Under constant perturbation conditions, the potentials of current peaks II, III, and IV shift equally toward more positive potentials as the pH decreases. The charges involved in the E/I displays are practically the same in the covered range of pH although the current peaks extend over a larger potential range as the pH decreases. As a matter of fact, the relative charge contributions of current peaks III and IV in the cathodic profile change with pH. It appears as if the contribution of the former is larger as the pH of the solution decreases. This is probably related to the wider region covered by the anodic current peak. Furthermore, the contribution of the O_2-evolution reaction at $E_{\lambda,a}$ is increasingly important at lower pH.

At any pH reasonable linear log I_p/log v relationships with the slope close to 1 are obtained under the range of experimental conditions indicated in the present work (Fig. 10-13). Nevertheless, for the anodic current peak II the best straight line is obtained through the log (I_p/Q_a)/log v plot.

The potentials of current peaks II and III change linearly with log v (Fig. 14 and 15). Their corresponding slopes, as well as the remaining kinetic parameters, are assembled in Table II. The difference between the potentials of current peaks II and III, $\Delta E_p = E_{pII} - E_{pIII}$, increases linearly with v. After the extrapolation at $v \rightarrow 0$ one obtains $\Delta E_p \approx 0.080$V.

Results from complex potential/time perturbation.—The E/I profiles recorded with a stabilized electrode

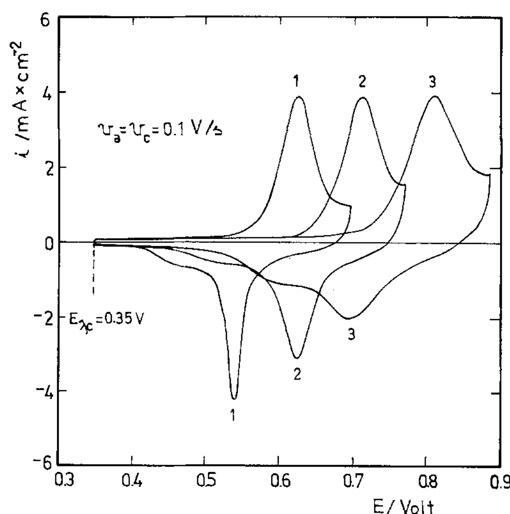

Fig. 9. Potentiodynamic E/I displays run at 0.1 V/sec with a constant $E_{\lambda,c}$ value. 1, Solution A; 2, solution C; 3, solution D.

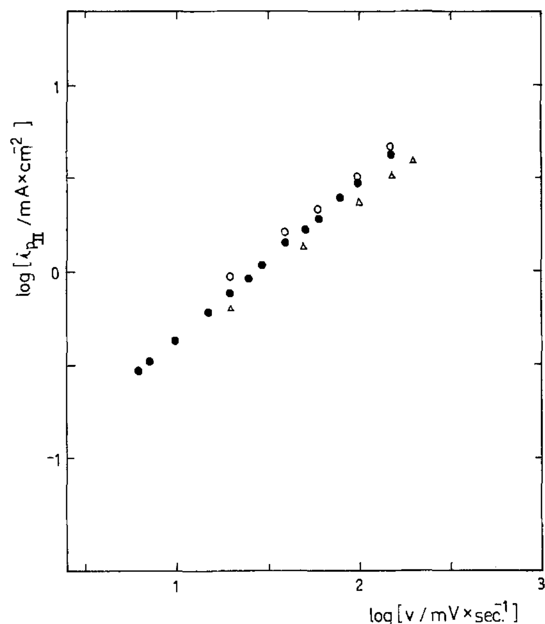

Fig. 10. Dependence of i_{pII} on v from RTPS: ●, solution A; ○, solution C; △, solution D.

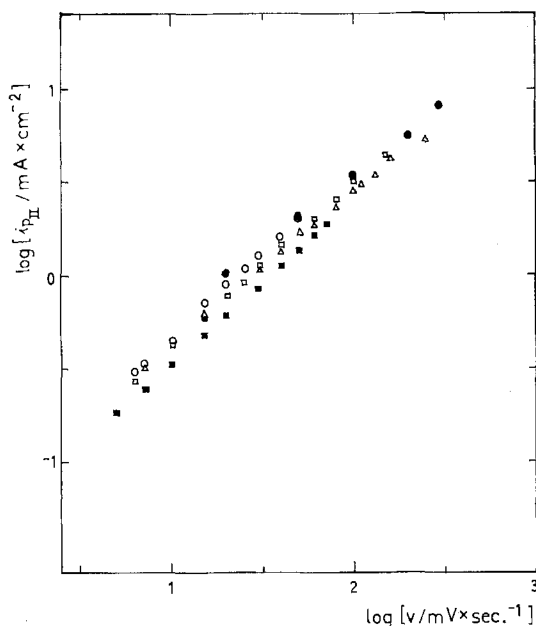

Fig. 11. Dependence of i_{pII} on v from the potentiodynamic runs between different $E_{\lambda,c}$ values and $E_{\lambda,a}$ = 0.68V. Solution A. ●, $E_{\lambda,c}$ = 0.04V; $v_a = v_c$. ○, $E_{\lambda,c}$ = 0.34V; $v_a = v_c$. □, $E_{\lambda,c}$ = 0.44V; $v_a = v_c$. △, $E_{\lambda,c}$ = 0.49V; $v_a = v_c$. ■, $E_{\lambda,c}$ = 0.49V; v_c = constant.

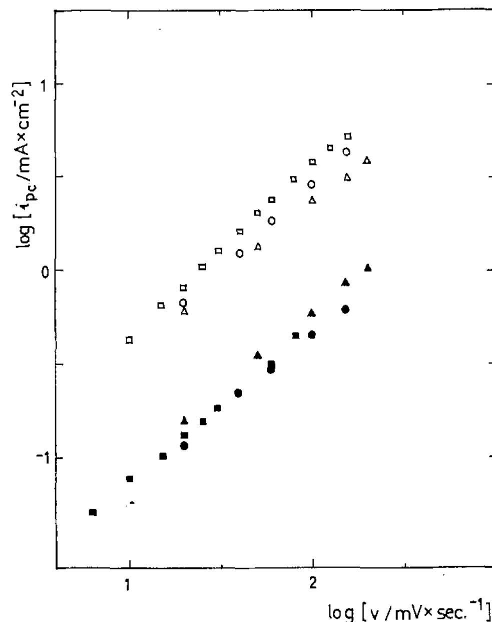

Fig. 12. Dependence of i_{pIII} (open symbols) and i_{pIV} (full symbols) on v from RTPS: □ and ■, solution A; ○ and ●, solution C; △ and ▲, solution D.

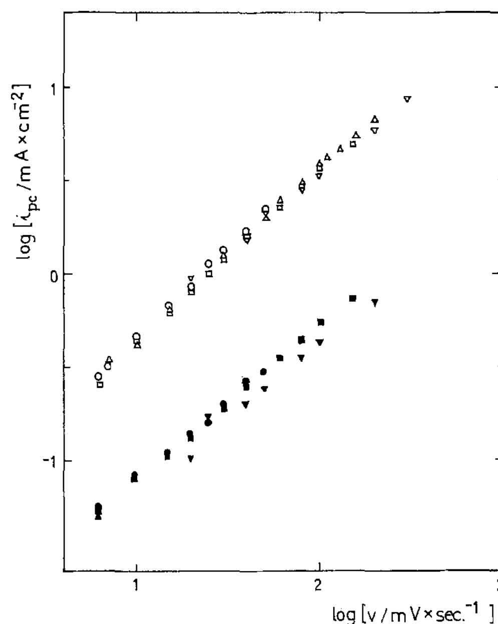

Fig. 13. Dependence of i_{pIII} (open symbols) and i_{pIV} (full symbols) on v from the RTPS run between different $E_{\lambda,c}$ values and $E_{\lambda,a}$ = 0.69V. Solution A. ▽, $E_{\lambda,c}$ = 0.04V; ○, $E_{\lambda,c}$ = 0.34V; □, $E_{\lambda,c}$ = 0.44V; △, $E_{\lambda,c}$ = 0.49V.

under the perturbation program depicted in Fig. 16 show the influence of τ, the potentiostatting time at 0.655V, a potential at which there is practically no net current flow. Under these circumstances, for the same anodic charge, as τ increases the cathodic charge remains constant but the shape of the current peak III extends over a wider potential range, its height decreasing and the corresponding current peak potential becoming more cathodic. On the other side, the current peak IV remains independent of τ, its apparent increase being only due to the changes of current peak III. These runs are indicating that during the rest time there is no appreciable chemical dissolution of the product anodically formed, but certainly the latter undergoes a chemical transformation without any likely detectable stoichiometric change through the electroreduction process.

The E/I profiles (Fig. 17) obtained with a stabilized electrode which is potentiostatted during a constant τ but at different potentials confirm that the cathodic charge of current peak IV is unaffected by the perturbation conditions. Furthermore, as $E_{\lambda,a}$ decreases, the species left on the surface after a 3 min potentiostatting are those which require the largest electroreduction potential. Therefore, from these results one deduces that at least two different species are involved in the electroreduction process occurring in the potential range of current peak III. This is also confirmed when the stabilized interface is perturbed with a fast RTPS within a range of potential where only a fraction of the surface covering species is involved in the removal and reformation processes (Fig. 18 and 19). It is clear that as τ increases and the cathodic charge remains constant (0.5 min $\leq \tau \leq$ 10 min) the cur-

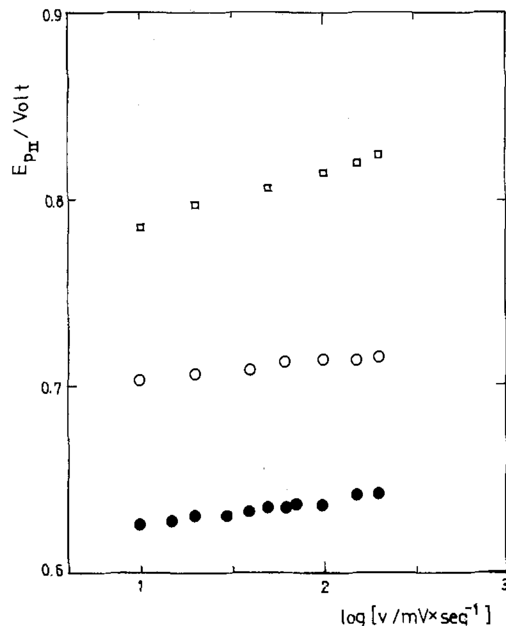

Fig. 14. Dependence of E_{pII} on v from RTPS: ●, solution A; ○, solution C; ■, solution D.

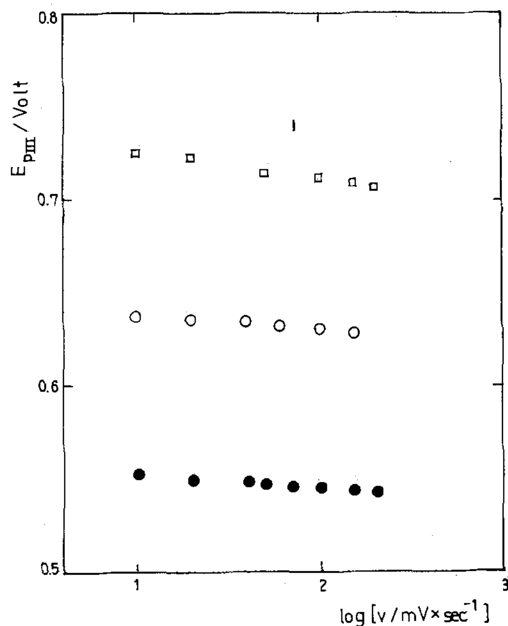

Fig. 15. Dependence of E_{pIII} on v from RTPS: ●, solution A; ○, solution C; ■, solution D.

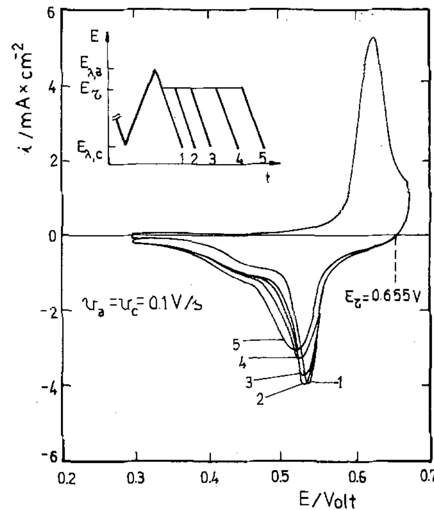

Fig. 16. E/I profiles run with RTPS including variable waiting times at E_T, after a previous cycling to obtain a stable E/I contour. Solution A. $\tau = 0$, profile 1; $\tau = 1$ min, profile 2; $\tau = 5$ min, profile 3; $\tau = 15$ min, profile 4; $\tau = 30$ min, profile 5.

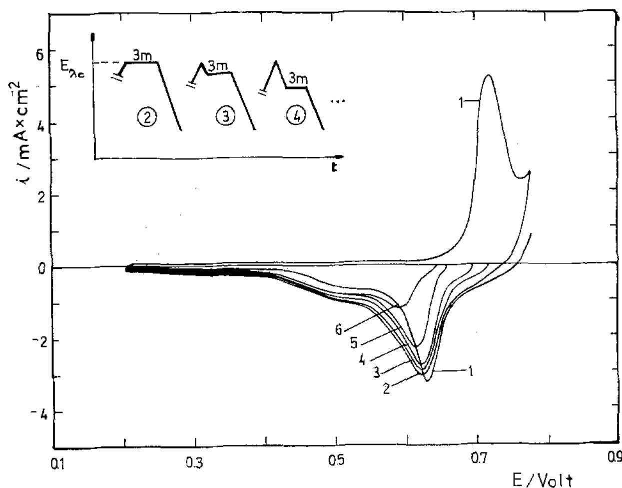

Fig. 17. Cathodic single triangular potential sweeps at 0.1 V/sec recorded after attaining the profile 1 with a RTPS and then waiting 3 min at different E_T. Solution C: $E_T = 0.78$V, profile 2; $E_T = 0.72$V, profile 3; $E_T = 0.69$V, profile 4; $E_T = 0.65$V, profile 5; $E_T = 0.64$V, profile 6.

rent peak III splits into two current peaks. The splitting of current peak III depends also on the potential limits of the past RTPS as well as the fraction of the surface covering species participating in the fast RTPS. The splitting effect is clearly established for the various solution compositions employed in the present work.

Discussion

Most of the experimental work made with the Ni/KOH interface concerns electrode structures ap-

Table II. Experimental kinetic parameters

Parameter	Solution A (mV)	Solution B (mV)	Solution C (mV)	Solution D (mV)
$\left(\frac{\partial E_{pII}}{\partial \log v}\right)$	10 ± 5	15 ± 5	10 ± 5	20 ± 10
$\left(\frac{\partial E_{pIII}}{\partial \log v}\right)$	-5 ± 5	-5 ± 5	-5 ± 5	-10 ± 10
$\left(\frac{\partial \log i_{pII}}{\partial \log v}\right)$	0.9 ± 0.1	0.8 ± 0.1	0.9 ± 0.1	0.8 ± 0.1
$\left(\frac{\partial \log i_{pIII}}{\partial \log v}\right)$	1.0 ± 0.1	0.9 ± 0.1	0.9 ± 0.1	0.9 ± 0.1
$\left(\frac{\partial \log i_{pIV}}{\partial \log v}\right)$	0.9 ± 0.1	0.8 ± 0.1	0.9 ± 0.1	0.9 ± 0.1

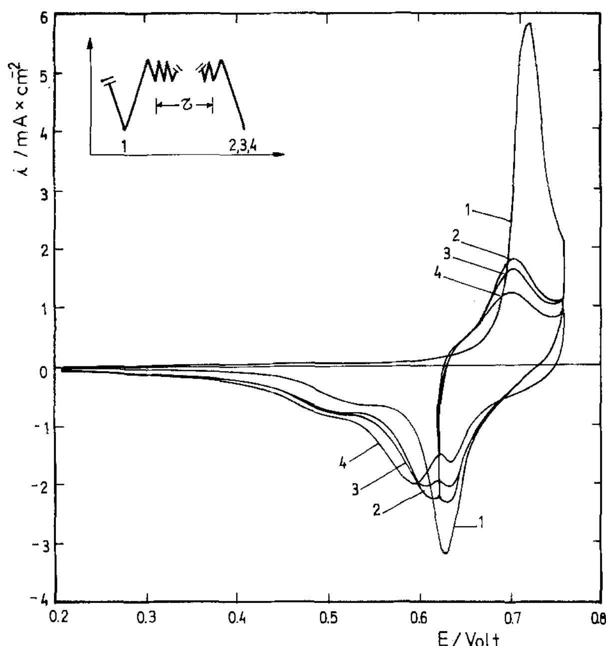

Fig. 18. Potentiodynamic *E/I* profiles run with an intermediate dynamic aging during a time τ, at 1 V/sec between 0.61 and 0.76V, as indicated in the figure. Solution C. 0.1 V/sec, profile 1; *E/I* trace obtained after a dynamic aging during $\tau = 0.5$ min, profile 2; $\tau = 2$ min, profile 3; $\tau = 10$ min, profile 4.

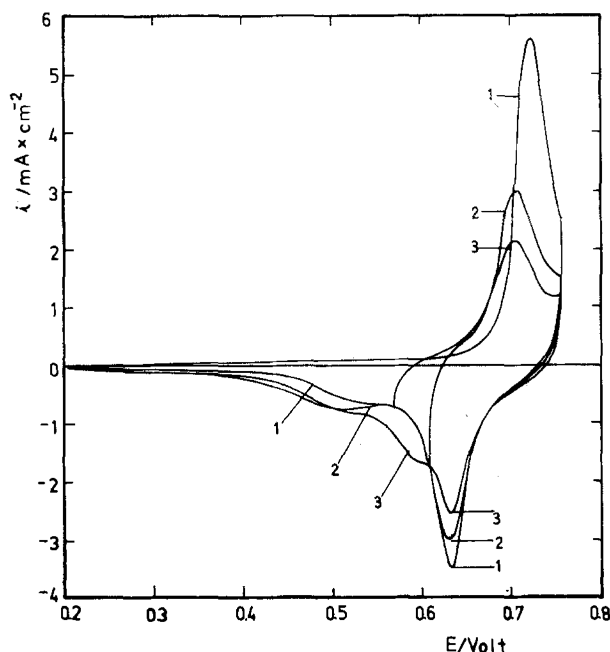

Fig. 19. Potentiodynamic *E/I* displays run with an intermediate dynamic aging at 1 V/sec during 2 min between different potential limits. Solution C. Stable *E/I* contour with RTPS at 0.1 V/sec between 0.21 and 0.76V, profile 1; *E/I* at 0.1 V/sec after the dynamic aging between 0.61 and 0.76V, profile 2; and between 0.57 and 0.76V, profile 3.

proaching the conditions prevailing in the alkaline nickel batteries. In this case, relatively large charges take part in the potentiodynamic perturbation of the interface, and, consequently, the kinetic interpretation is perhaps more complex than that resulting when charges of the order of a few monolayer thickness are involved.

The present results correspond to a surface $Ni(OH)_2$ species which is formed during relatively fast potential cycling and the charges taking part in the over-all electrochemical processes are smaller than those of previous works. In these circumstances the repetitive potentiodynamic *E/I* characteristics imply not only a single anodic *E/I* profile which just precedes the electrochemical O_2 formation but also a multiple current peak display during the reduction of the product of the anodic reaction. But the over-all reaction taking place during each periodic perturbation is completed since the Q_a/Q_c ratio is always practically one. The interpretation of the charge magnitude in terms of the actual surface area is, however, ambiguous. As a matter of fact there are two possibilities, either the metal roughness factor is one and the film thickness corresponds to a multilayer thickness or the latter is of the order of the monolayer thickness and its roughness factor changes during cycling and depends on v.

Kinetics of the anodic reaction.—Probable reaction path when the structural changes of the reactant are negligible.—Within a certain range of the perturbation variables the anodic reaction exhibits an apparent simpler response to the RTPS potentiodynamic perturbation than to the cathodic process. Consequently a set of reasonable kinetic parameters is derived for this process. Provided that the over-all anodic process under potentiodynamic conditions is expressed by the over-all reaction

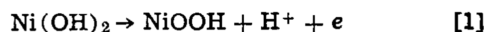

$$Ni(OH)_2 \rightarrow NiOOH + H^+ + e \quad [1]$$

a possible reaction path which may account for the kinetic behavior should imply a series of single electron transfer and chemical steps as follows. The initial stage is the proton release from the hydrated $Ni(OH)_2$ lattice on the positively charged nickel surface

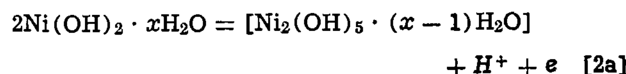

$$2Ni(OH)_2 \cdot xH_2O = [Ni_2(OH)_5 \cdot (x-1)H_2O] + H^+ + e \quad [2a]$$

The proton diffusion out of the electrochemical interface is assisted by the electrical field located there. Step [2a] involves a partially hydrated intermediate which undergoes a structural rearrangement through a chemical reaction

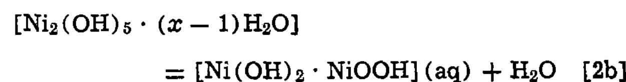

$$[Ni_2(OH)_5 \cdot (x-1)H_2O] = [Ni(OH)_2 \cdot NiOOH](aq) + H_2O \quad [2b]$$

and finally

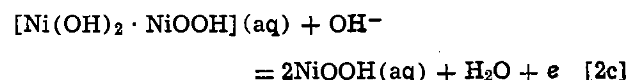

$$[Ni(OH)_2 \cdot NiOOH](aq) + OH^- = 2NiOOH(aq) + H_2O + e \quad [2c]$$

The formation of the NiOOH-species is equivalent either to the accumulation of Ni(III) species or to the creation of 3-d holes in the film (26). Whatever the case, the reaction path [2a]-[2c] implies an increasing deprotonation of the insoluble film, so that the Ni/O atomic ratio remains constant, the H/O ratio decreases, and the Ni/H ratio increases in passing from the hydrated $Ni(OH)_2$ to the NiOOH species. Ellipsometry (12, 27) and impedance measurements of the resistive layers formed during nickel anodization in 1*N* KOH (2, 28) indicate the presence of those species.

The sequence of reactions [2a]-[2c] can be analyzed either as a reversible or as an irreversible electrochemical system assuming that the same reactions hold for the cathodic processes. Thus, when one attempts to correlate the kinetic characteristics of the nickel hydroxide electrode with its fast response one finds some apparent contradictions. For a reversible conjugated electrochemical system implying a monolayer formation, the corresponding anodic and cathodic current peaks must occur at the same potential and this potential is independent of the potential sweep rate. The latter is certainly obeyed, but, in contrast, the difference between the potentials of the anodic and cathodic main current peaks as revealed by the RTPS experi-

ments is *ca.* 0.08V. Therefore, the simple three-step reversible mechanism is unsatisfactory.

Let us consider the possibility that the rate process is determined by the rate of one partial reaction. From previous stationary measurements of the nickel electrode in different alkaline solutions, step [2c] can be supposed as the rate-determining step. Then, if the reaction proceeds in only one direction, the stationary current density derived in the conventional way yields the following expression

$$i_a = k a_{Ni(OH)_2}{}^2 a_{H^+}{}^{-2} \exp\left[\frac{(1+\alpha)FE}{RT}\right] \quad [3]$$

where the a_i's are the activities of the i species at the reaction interface, k is the formal rate constant, α is the transfer coefficient assisting the reaction [2c] in the anodic direction, and E is the potential applied to the electrochemical interface.

A kinetic equation formally similar to Eq. [3] was derived from a mechanism involving Ni(IV) species and ionic nickel-oxygen surface species (16). There is, however, no firm evidence of the former species although magnetic susceptibility measurements coupled to electrochemical processes revealed the presence of Ni(IV) (26). A further oxidation in the β-NiOOH lattice may convert Ni(III) into Ni(IV), leading to the formation of very stable nonstoichiometric oxides (14, 20-22).

If Eq. [3] is valid, the corresponding potentiodynamic E/I profile related to the change of electrode coverage from the $Ni(OH)_2$ monolayer to the NiOOH monolayer derived according to the Srinivasan and Gileadi procedure (29) gives the following parameters

$$\left(\frac{\partial \ln i_p}{\partial \ln v}\right)_{pH} = 1; \qquad \left(\frac{\partial \ln i_p}{\partial \ln a_{H^+}}\right)_v = 0$$

$$\left(\frac{\partial E_p}{\partial \ln v}\right)_{pH} = \frac{RT}{(1+\alpha)F}; \qquad \left(\frac{\partial E_p}{\partial \ln a_{H^+}}\right)_v = \frac{2RT}{(1+\alpha)F}$$

Now the tentative reaction mechanism explains only three out of four kinetic parameters (Table II) leaving unclear the important one related to the apparent independence of the anodic current peak potential on the potential sweep rate. Then, the interpretation of the reaction in terms of step [2c] or any other equivalent step as the rate-determining step seems unlikely. Therefore, the sample three consecutive reaction mechanism, neither under reversible nor under irreversible conditions, is able to explain the kinetic data derived from the RTPS E/I profiles. The partial discrepancies suggest, however, that the interpretation of the over-all reaction is even more complex.

The influence of structural changes.—The experimental data revealed that the reactions related to current peaks II, III, and IV are closely connected and that the characteristics of the electrochemical processes are even more complex than earlier believed because not only the nickel hydroxide species involves structural changes (aging) as already known (14, 20-22) but also the products of its anodic oxidation undergo a similar type process.

The dependence of the experimental results on the potential perturbation conditions indicates that the anodic and cathodic processes as seen through the RTPS E/I profiles can be considered as fast reactions. But in contrast with reactions [2a]-[2c] the cathodic reactions are not exactly represented by the reverse reactions. This occurs if both reactants and products undergo structural transformations simultaneously during the electrochemical processes which alter their corresponding surface activities. Under these circumstances the over-all stoichiometry is maintained in the course of the reaction, but at least three different and fast conjugated redox couples involving proton transfer should be involved.

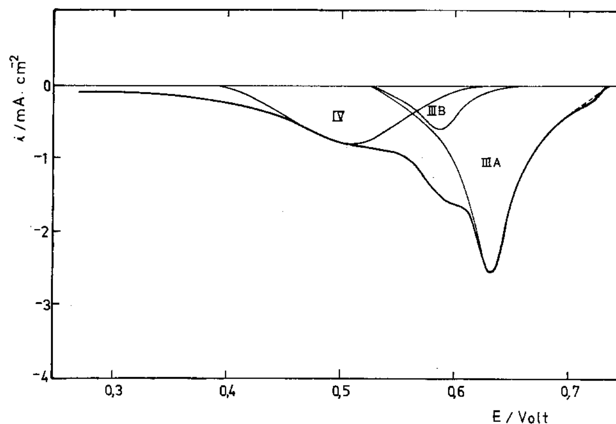

Fig. 20. Evaluation of the over-all cathodic *E/I* profile in terms of three cathodic reactants. Data correspond to profile 3 of Fig. 19.

It is clear the cathodic E/I curve can be resolved at least into three current peaks, drawn in terms of three Gaussian distribution functions (Fig. 20) with well separated current peak potentials (Table III). This is perhaps the simplest attempt for separating the contributions of the three anodically formed nickel surface species quite likely involving the same oxidation state of the metal (Ni(III)) but different energetic configurations. Each species can be assigned to a particular electroreduction process. For current peaks III-A and III-B the following reactions are tentatively proposed, without compromising any particular hydrated structure or definite configuration

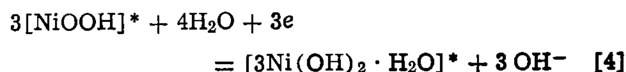

$$3[NiOOH]^* + 4H_2O + 3e = [3Ni(OH)_2 \cdot H_2O]^* + 3\,OH^- \quad [4]$$

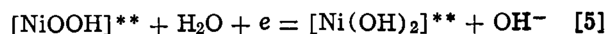

$$[NiOOH]^{**} + H_2O + e = [Ni(OH)_2]^{**} + OH^- \quad [5]$$

For current peak IV one assumes that β-NiOOH is the species more difficultly reducible out of the three

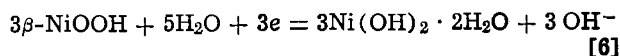

$$3\beta\text{-}NiOOH + 5H_2O + 3e = 3Ni(OH)_2 \cdot 2H_2O + 3\,OH^- \quad [6]$$

where the structure of the reaction product may be α-$Ni(OH)_2$, according to Bode (10, 11). The reactant and product involved in reaction [6] probably belong to the innermost portions of the electrode film. The extent of each reaction for a particular set of the perturbation variables is given by the corresponding cathodic charge as already indicated in Table III. The three different reactants appearing, respectively, in reactions [4], [5], and [6], two of them identified with asterisks, undergo structural changes which are represented by the following reactions

$$[NiOOH]^{**} \rightleftarrows [NiOOH]^* \rightleftarrows \beta\text{-}NiOOH \quad [7]$$

The chemical transformations of the various species schematically represented by reaction [7] probably involve structural changes related to the β-NiOOH and γ-NiOOH species discussed in the literature by different authors (13-15). These transformations, which are revealed both in the anodic and in the cathodic potentiodynamic profiles, are likely related to a change in the water content and the cation concentration in the oxy-hydroxide nickel lattice. The cation contribution to build up certain structural configurations of the lattice may involve an ionic mass transfer toward the reaction interface in an opposed electrical field.

Table III. Data derived from the cathodic current peaks

Peak number	III-A	III-B	IV
Current peak potential/V	0.630	0.585	0.510
Charge/mC × cm⁻²	1.67	0.33	0.96

Chemical reactions such as [7] should be related to the so-called aging process of the anodic reaction product.

These results can explain how three out of four transition times recorded at the four arrests of the galvanostatic E/time display the electroreduction of the oxidized nickel electrode without the assumption of dubious surface compounds (16). The fourth transition time may be related to the presence of O_2.

The anodic profile should correspond to the sum of various anodic processes, as can be deduced from potentiodynamic data previously reported (7). Therefore, the apparent independence of the potential of the anodic current peak on the potential sweep rate is difficult to interpret unless the structural transformations of the different film components at the electrode surface are taken into account. Thus, the average film composition should depend, under constant switching potentials, on the potential sweep rate. So the activity ratio of the more reactive to the more stable species increases just as the potential sweep rate does. This means that the current contribution at the cathodic side of the anodic current peak should increase accordingly so that the over-all effect is to depict an E/I profile which on the whole shifts toward the cathodic potential region. In this way if there is any shift of the current peak potential toward more anodic values as v increases, it might be either partially or totally compensated. The situation is, then, to some extent similar to that encountered in the electroreduction of oxygen-containing film monolayers on Pt (30) and Au (31).

Under the present experimental conditions the proton diffusing out of the film, as step [2a] implies, exerts no appreciable influence on the reaction rate. The reported proton diffusion coefficient in the nickel hydroxide lattice covers the range 2×10^{-7}-2×10^{-9} cm^2/sec (7, 32, 33). Therefore, this process is fast enough to be in equilibrium during the potentiodynamic sweep unless the potential perturbation is so short that the $\sqrt{Dt}$ is of the order of the layer thickness. Under the present circumstances this would require a potential sweep rate of the order of 10^3 V/sec. The situation, however, is different when thicker hydrated hydroxide films are involved. When step [2a] occurs in a multilayer it induces a proton transfer mechanism through the existing film and the proton neutralization at the solution side of the electrical double layer.

When thin films are involved under relatively fast perturbation conditions it seems rather arbitrary to assign to the ill-defined material present at the working electrodes only one particular and constant structure participating in the over-all electrochemical processes. The conclusion is that at least three anodic reaction products are formed as revealed by the three well-defined cathodic current peaks. Furthermore, depending on the number of potential sweeps there is good evidence that only two current peaks are seen during the anodic reaction under conventional triangular potential sweep perturbations, although the triangularly modulated potential sweep technique reveals the occurrence of at least three well-distinguished processes (34). Therefore, three nickel hydroxide species and three nickel oxy-hydroxide species are participating in these processes.

Crystal-structure analysis of the following pure crystalline phases has been undertaken, namely, β-$Ni(OH)_2$, α-$Ni(OH)_2$, β-NiOOH, and γ-NiOOH (11, 14). The existence of the two forms of the α-$Ni(OH)_2$ and γ-NiOOH are also reported (10, 11, 14). There is, therefore, a good correspondence between the number of species which are required for the three different electrochemical processes. The proper configuration of the species indicates that the first species to be electrooxidized is α-$Ni(OH)_2$, while the electrooxidation of β-$Ni(OH)_2$ should occur at more positive potentials. On the other hand, β-NiOOH should be elecrtoreduced at the more cathodic potentials, provided that the double cathodic current peak placed at more anodic potentials may belong to the electroreduction of the two γ-NiOOH forms. Whatever the case, caution needs to be exercised at present in assigning a particular redox system to the pairs of current peaks potentiodynamically recorded.

The suggested reaction pathway, although it must be considered without structural compromises, is more general than any of those previously discussed. As a matter of fact it contrives the idea of having a rate-controlling proton transport process as earlier suggested (7, 33), and it includes chemical side reactions to explain the aging effect of the film anodically formed.

Acknowledgments

INIFTA is sponsored by the Consejo Nacional de Investigaciones Científicas y Técnicas, the Universidad Nacional de La Plata, and the Comisión de Investigaciones Científicas (Provincia de Buenos Aires). This work is also partially sponsored by the SENID (Navy Research and Development Service of Argentina) and the Regional Program for the Scientific and Technological Development of the Organization of the American States.

Manuscript submitted Nov. 18, 1977; revised manuscript received May 10, 1978.

Any discussion of this paper will appear in a Discussion Section to be published in the June 1979 JOURNAL. All discussions for the June 1979 Discussion Section should be submitted by Feb. 1, 1979.

REFERENCES

1. G. Grube and A. Vogt, *Z. Elektrochem.*, **44**, 353 (1938).
2. Yu. N. Chernykh and A. A. Yakuvleva, *Elektrokhimiya.* **6**, 1671 (1970).
3. G. P. Samoilov, E. I. Krushcheva, N. A. Shumilova, and V. S. Bagotskii, *ibid.*, **8**, 1169 (1972).
4. J. L. Weininger and M. W. Breiter, *This Journal*, **110**, 484 (1963).
5. J. L. Weininger and M. W. Breiter, *ibid.*, **111**, 707 (1964).
6. Ku Ling-ying, N. A. Shumilova, and V. S. Bagotskii, *Elektrokhimiya*, **3**, 460 (1967).
7. D. M. MacArthur, *This Journal*, **117**, 422 (1970).
8. G. W. D. Briggs and M. Fleischmann, *Trans. Faraday Soc.*, **67**, 2397 (1971).
9. M. A. Hopper and J. L. Ord, *This Journal*, **120**, 183 (1973).
10. H. Bode, K. Dehmelt, and J. Witte, *Electrochim. Acta*, **11**, 1079 (1966).
11. H. Bode, K. Dehmelt, and J. Witte, *Z. Anorg. Allgem. Chem.*, **366**, 1 (1969).
12. Yu. N. Chernykh and A. A. Yakuvleva, *Elektrokhimiya*, **7**, 530 (1971).
13. P. C. Milner and U. B. Thomas, in "Advances in Electrochemistry and Electrochemical Engineering," Vol. 5, C. W. Tobias, Editor, p. 1, Interscience, New York (1967).
14. G. W. D. Briggs, "Electrochemistry," Vol. 4, p. 33, Specialist Periodical Reports, The Chemical Society, London (1974).
15. A. J. Arvía and D. Posadas, in "The Electrochemistry of the Elements," Vol. 3, A. J. Bard, Editor, p. 212, Marcel Dekker, New York (1975).
16. I. A. Cherepkova, V. A. Kas'yan, V. V. Sysoeva, N. N. Milyutin, and A. L. Rotinyan, *Elektrokhimiya*, **11**, 443 (1975).
17. L. D. Petriashvili, *Elektrokhim. Margantsa*, **5**, 318 (1975).
18. N. A. Balashova, G. D. Zakumbaeva, and L. A. Beketaeva, *Zashch. Met.*, **12**, 39 (1976).
19. Z. I. Kudryavtseva, V. A. Openkin, N. A. Zhochkova, E. I. Khrushcheva, and N. A. Shumilova, *Elektrokhimiya*, **11**, 1488 (1975).
20. G. W. D. Briggs, E. Jones, and W. F. K. Wynne-Jones, *Trans. Faraday Soc.*, **51**, 1433 (1955).
21. G. W. D. Briggs and W. F. K. Wynne-Jones, *ibid.*, **52**, 1272 (1956).
22. E. Jones and W. F. K. Wynne-Jones, *ibid.*, **52**, 1260 (1956).

23. G. M. Alipva, E. I. Khrushcheva, G. P. Samoilov, N. A. Shumilova, and I. E. Zimakov, *Elektrokhimiya*, **8**, 1537 (1972).
24. R. S. Schrebler Guzmán, J. R. Vilche, and A. J. Arvía, *J. Appl. Electrochem.*, In press.
25. R. S. Schrebler Guzmán, J. R. Vilche, and A. J. Arvía, *Corros. Sci.*, **18**, 441 (1978).
26. J. P. Hoare, "The Electrochemistry of Oxygen," John Wiley & Sons, Inc., New York (1968).
27. W. Visscher and A. Damjanovic, 25th ISE Meeting, Zürich (1976), Paper 138.
28. V. I. Ovcharenko, *Elektrokhimiya*, **11**, 1043 (1975).
29. S. Srinivasan and E. Gileadi, *Electrochim. Acta*, **11**, 321 (1966).
30. J. O. Zerbino, N. R. de Tacconi, A. J. Calandra, and A. J. Arvía, *This Journal*, **124**, 475 (1977).
31. C. M. Ferro, A. J. Calandra, and A. J. Arvía, *J. Electroanal. Chem.*, **57**, 267 (1974).
32. P. D. Lukovtsev and C. J. Slaidin, *Electrochim. Acta*, **6**, 17 (1962).
33. D. M. MacArthur, *This Journal*, **117**, 729 (1970).
34. J. R. Vilche and A. J. Arvía, Proceedings of 4th International Symposium on Passivity, Virginia (1977), In press.

Polarization and Corrosion in Sodium/Sulfur Cells

Roger J. Bones and Trevor L. Markin

A.E.R.E. Harwell, Materials Development Division, Didcot, Oxon, OX11 ORA, England

ABSTRACT

In a previous publication (1) we showed that stainless steel undergoes corrosion in a sodium polysulfide melt when polarized cathodically (*i.e.*, at the end of discharge in a Na/S cell). This basic electrochemical study of the sulfur/polysulfide cathode has been extended using specially designed electrochemical cells incorporating potential probes in the cathode. The apparent accumulative loss in capacity on cycling of Na/S cells is explained in terms of increasing polarization which, in turn, is related to the steel corrosion phenomenon.

The general principles of operation of sodium/sulfur cells, first developed by Kummer and Weber (2) are well known. An early favored sulfur cathode current collector, used in the form of an outer case, was stainless steel. However, it has been shown that on deep cycling, such a current collector can undergo severe corrosion during the operation of cells; also the cells in turn can suffer considerable loss of useful capacity—typically 50% in <200 cycles. In recent years workers in the U.K. have favored the central sulfur cell design (3); this circumvents the problem of cell case corrosion but the electrochemical behavior of the central cathode is similar to that of the cathode in the central Na cell. For convenience the discussions in this paper refer to a central Na cell.

The sulfur electrode itself typically consists of a sulfur/polysulfide melt distributed within a carbon felt matrix bounded on one side by the βAl_2O_3 electrolyte and on the other side by the electronic conducting current collector. There are several publications (4-6) dealing with the fundamental studies of the operation of the sulfur electrode. A relationship has also been shown to exist between cathode polarization and cell case corrosion (5) which can lead to progressive capacity loss on cycling. This paper describes an extension to the previous study; experiments have been performed to measure the electronic and sodium potentials within an actual working cathode in order to gain further insight into the factors limiting the operation of the electrode. The results are related to the corrosion phenomena observed in practical Na/S cells.

It is not possible to advance unambiguous explanations of the complete mode of operation of such a complicated electrode from these experiments alone. Rather, the results should be considered together with other studies in order to obtain a more complete picture.

Experimental

Experiments referred to previously (1) showed that when stainless steel (Type AISI 316) was immersed in sulfur or sodium polysulfide (Na_2S_5-$Na_2S_{3.6}$) a protective sulfide film formed on its surface. It was also shown that when an external potential was applied across a cathode matrix (containing $Na_2S_{3.6}$) sandwiched between two such sulfided electrodes, it was possible under certain conditions to strip off this protective film. This occurred when the particular electrode was sufficiently negatively polarized. The clean shiny metal surface remaining was rapidly resulfided on current reversal. Repeated cycling in this manner lead to progressive corrosion of the electrode and to a buildup of a crust of corrosion products adjacent to the steel electrodes, similar to that observed in the postoperative examination of tubular sodium/sulfur cells which had stainless steel cases and had suffered considerable capacity loss.

It was postulated that the imposition of an applied potential across the mixed ionic/electronic electrode matrix causes partial electrolysis of the ionically conducting molten phase, giving rise to localized sulfur/polysulfide compositions (Na/S ratios) in the vicinity of the electrodes, which can be significantly different from the bulk equilibrium composition.

In order to investigate this, the experiment was repeated using a specially constructed twin electrolyte experimental cell shown in Fig. 1.

The twin electrolyte experimental cell.—An electrochemically prepared sulfur electrode specimen was sandwiched, under compression, between two platinum gauze electrodes which were in turn strapped to two identical βAl_2O_3 tubes containing liquid sodium. The platinum electrodes could serve as both active electrodes and electron potential probes. The liquid Na/electrolyte assemblies served as similar sodium potential reference electrodes for measurement of Na potentials at the extremes of the cathode. The cell was operated at 350°C in an enclosed argon gas environment.

A range of potentials was applied across the cathode specimen between electrodes 3 and 4 in a stepwise manner. Na potential measurements were made of the melt in the vicinity of these electrodes, using a high impedance digital voltmeter, between electrodes 1 and 2 and between 4 and 3. By reference to the well-known dependence of cell OCV of Na/Na polysulfides composition shown in Fig. 2, the local Na/S ratios of the melt adjacent to the βAl_2O_3 tubes were derived.

Key words: battery, cathode, corrosion, electrode.

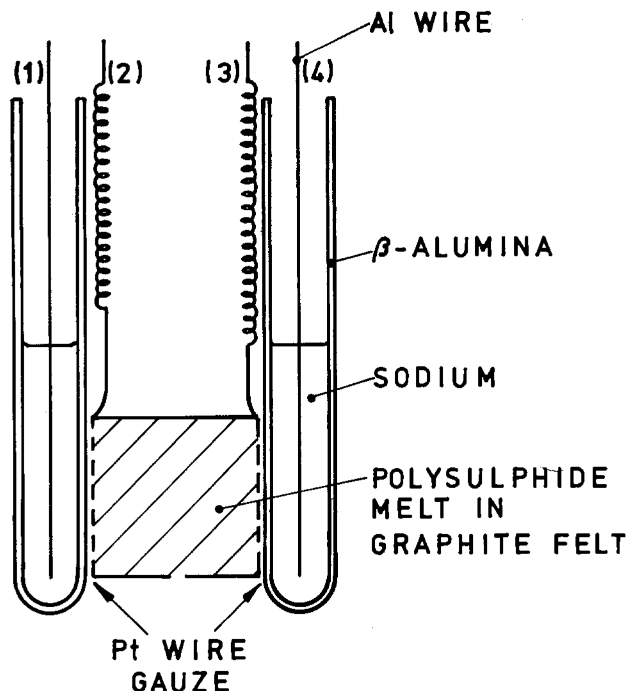

Fig. 1. Twin electrolyte experimental cell for studying the electrochemistry of the cathode melt.

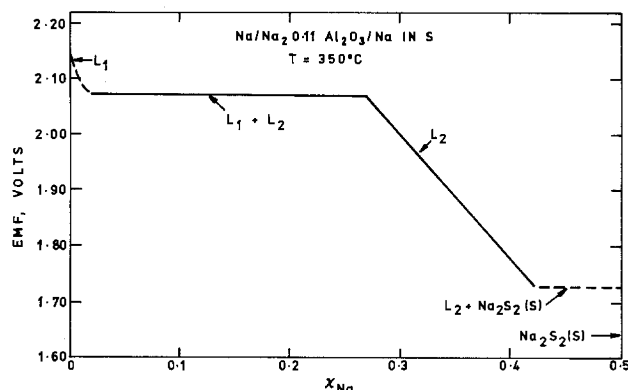

Fig. 2. Reversible emf of the Na/S cell as function of cathode composition.

Figure 3 shows the results obtained for three such experiments starting with initially different bulk Na/S melt compositions—Na_2S_4, $Na_2S_{3.45}$, and Na_2S_3. The extent of the polarization caused within the cathode matrix can be seen to increase as the applied potential IR increases. The positive electrode becomes richer in sulfur (higher OCV with respect to bulk melt equilibrium composition) whereas the negative electrode experiences a relative Na enrichment (lower OCV). Stable readings were obtained in most cases in 1-2 min, although unstable, rapidly falling values were observed at the negative electrode for values of <1.73V, indicating a rapidly increasing polarization situation.

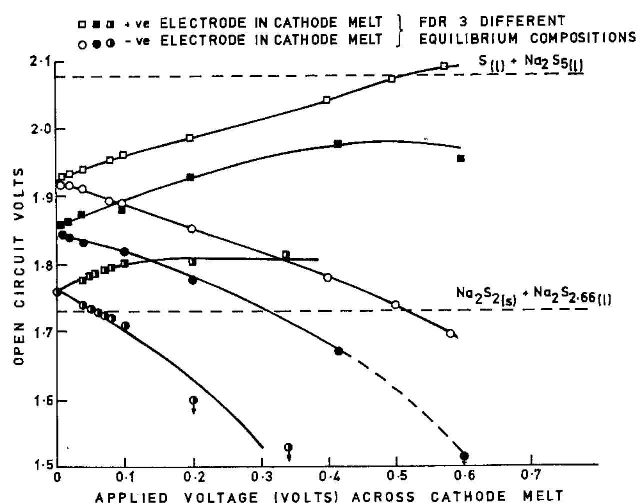

Fig. 3. OCV at positive and negative electrodes as the applied voltage across the cathode increased stepwise.

In repeat experiments, using presulfided stainless steel electrodes instead of platinum, it was found that the dark protective sulfide layer was removed when these OCV measurements of the melt at the negative electrode was less than 1.73V.

From Fig. 3 it can be seen that this occurs for example at an applied potential of 50 mV for a starting composition of Na_2S_3 (OCV = 1.78) and at an applied potential of 300 mV for an equilibrium bulk composition having an OCV of 1.85.

Thus a relationship exists between corrosion (or more exactly corrosion film stripping) of stainless steel and high imposed negative potentials. Further experiments were carried out using the same apparatus, in different modes, in order to relate this further to actual cathode behavior in a working electrode. In this series of experiments one of the Na-containing electrode tubes was used as a conventional Na electrode of a Na/S cell, transferring Na to and from the cathode matrix. The two platinum gauze electrodes were used as cathode current collector and electron potential probe, respectively, in attempts to monitor electronic potentials actually developed across a working cathode.

The later stages of a normal discharge half-cycle were studied by connecting a load between electrodes 1 and 3 and allowing the cathode specimen to complete a normal constant current discharge from an initial OCV of 1.86. During this discharge the electronic potential difference across the cathode between electrodes 2 and 3 was recorded continuously as was the change in Na potential at both the working and nonworking electrolyte surfaces. The discharge was terminated when a massive decrease in cell voltage occurred, leading to a situation when a constant current condition could no longer be maintained.

Figure 4 shows the actual voltage discharge curve between electrodes 1 and 3 simulating normal cell discharge between the sodium electrode and the cell case. The monitored Na potential close to the working electrolyte (*i.e.*, potential 1-2) showed only slight deviation from calculated equilibrium OCV values, whereas that at electrode 3 changed dramatically, indicating rapidly changing Na/S composition at the surface of electrode 3.

The potential difference monitored across the cathode 2-3 during this discharge is shown in Fig. 5 where it can be seen that over most of this range the potential drop is fairly constant (~50 mV), but this increases rapidly close to the end of discharge, leading to the low cell operating voltage. Additional platinum wire potential probes, evenly spaced across the cathode thickness, confirmed that this rapid nonohmic behavior occurred only close to the interface between the metal current collector and the cathode matrix. It is important to realize that the polarity of this developed potential is opposite to that of the cell terminals. That is to say, the cell case is negative with respect to the remainder of the cathode, even though it is the positive pole of the cell. It follows that close to the end of discharge the cell case becomes highly negatively charged with respect to the sulfur electrode. The previous applied potential experiments showed this can lead to severe progressive electrochemical corrosion (erosion) of the cell case if the extent of the polarization is not controlled.

Any change in the system which reduces the potential developed across the cathode would reduce the

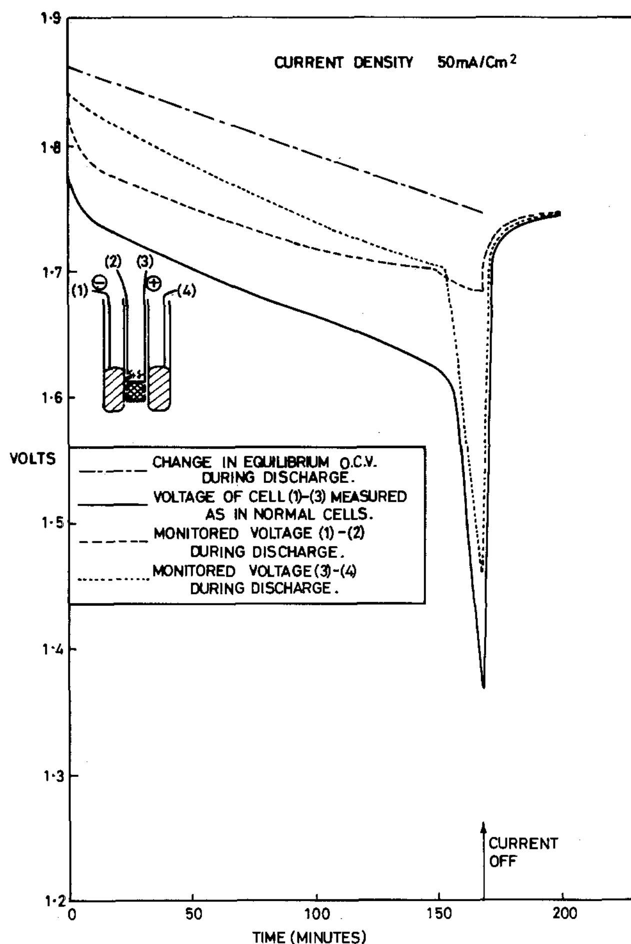

Fig. 4. Cell discharge between electrodes 1 and 3 at constant current, and sodium potentials monitored at edges of sulfur electrode.

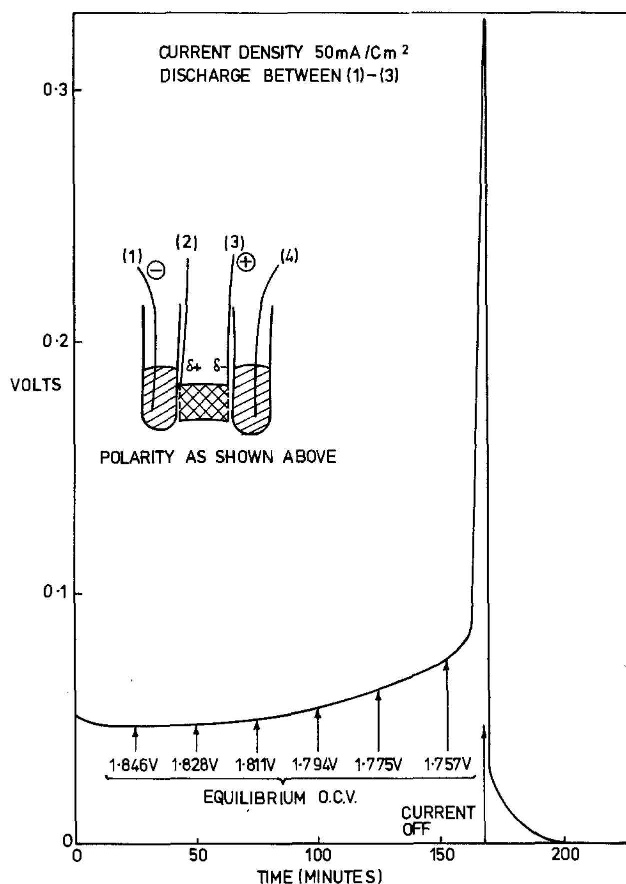

Fig. 5. Potential developed between electrodes 2 and 3 (across cathode) during cell discharge at constant current.

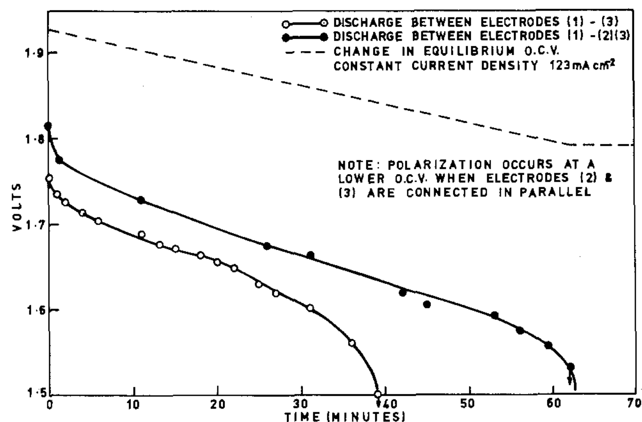

Fig. 6. Normal cell discharge 1-3, and discharging with electrodes 2-3 in parallel.

polarization and, therefore, any change within the structure of the cathode which reduces its electronic resistance R would be beneficial. The discharge experiments were repeated at different current densities, initially using electrodes 1-3 and secondly by connecting electrodes 2-3 in parallel and discharging between electrodes 1-2 and 3. One result obtained is shown in Fig. 6 for a current density of 123 mA cm^{-2}. It can be seen that the parallel coupling discharge gives a higher operating voltage on discharge than the normal electrode 1-3 discharge at the same current density. The IR voltage loss has been decreased—the cell resistance was lower due to the increased electron injection capabilities of electrode 2. The equilibrium OCV at which polarization occurred, shown by a rapid change in V, was 1.84V for normal discharge, but advantageously lower at 1.79V for the cathode with the additional current collector. The effect of coupling electrodes 2 and 3 is to reduce the potential difference across the cathode extremities to zero and to reduce significantly the internal polarization within the cathode.

If a permanent change in the cathode structure is contemplated, to reduce corrosion on discharge the effect of such a modification on the recharge must be considered.

The previous experiment was repeated for the charge half-cycle. It was found that when electrodes 2 and 3 were connected in parallel, this was not detrimental to the recharge at 50 mA cm^{-2}.

Having demonstrated practically the conditions under which polarization can be generated by applying suitable potentials across the cathode specimen and by monitoring actual potentials developed inherently in a working cathode, it was decided to use the twin electrolyte cell to study an aged cathode sample from a Na/S cell.

A radial segment was cut from a recovered cathode of a cell which had apparently lost practically all of its reversible capacity on cell cycling. The specimen was well impregnated and had a thin brown crust on the outside surface where it had been in contact with the steel cell case. The specimen was assembled into the cell between electrodes 2 and 3 with the outer surface against electrode 3 simulating the cell case.

At 350°C, under a similar compression to that employed in the cell, the OCV of the sample monitored both with reference to electrode 1 and 4 was 1.87V. By connecting an external load it was possible to discharge the cathode sample at ~100 mA cm^{-2} by using electrodes 1-2. However, a discharge current of only 3 mA was obtained when discharge was attempted between electrodes 1 and 3 and this was accompanied

by massive polarization—the potential developed across the cathode 2-3 rose rapidly to >1V.

From Fig. 3 one can see that for such massive polarization to occur on discharge with this initial composition and such a low current, the resistance R in the cathode/electrode junction must be very high. It appears that the hard outer crust (probably formed via corrosion of the can) has a very high resistance to electrons and, furthermore, its continuity prevents the carbon fibers from contacting the cell case.

This was confirmed subsequently by grinding away the hard crust from this and similar samples and replacing the cathode samples in the cell. The cathode then behaved normally when discharging with either electrode 2 or 3; it cycled readily and developed anticipated potentials of only 50-100 mV across the cathode. It appears that the high resistance to electron flow from the cell case to the cathode matrix had been interpreted as a capacity loss. In fact it has now been shown that the charge/discharge capacity of the bulk of the polysulfide cathode was far from being exhausted.

Variable compression of graphite felt.—All the previously described experiments have been carried out with a constant degree (25%) of compression of the graphite felt compared with its fully expanded state. In order to study the effect of the extent of the compression used, the compression of the graphite was varied from nil to 50% while the cell was discharged. The cell output and the potential developed across the cathode 2-3 were monitored.

The cell output improved and, as can be seen from Fig. 7, the potential across the cathode decreased as the degree of compression was increased. The 50% compression led to irreversible contraction of the graphite felt. The developed potential across the cathode seems least sensitive to degree of compression at levels of 25-33% (*i.e.*, that normally used in Na/S cells).

It can be implied that, even at optimum compression, with this cell construction one is going to be forced to tolerate potentials of >50 mV close to the end of discharge at commonly used current densities of 100 mA/cm^2. This is intrinsic to the graphite felt and is additional to potentials resulting from corrosion of the container. A current collector of lower resistance would be desirable.

Na/S cell incorporating extra potential probe.—The above experiments were repeated (and extended to study the recharge process) in a purpose-built, tubular sodium/sulfur cell. The cell (Fig. 8) incorporated an additional potential probe within the cathode consisting of a wire mesh strapped to the electrolyte tube. This probe was insulated from the cell case via a special seal.

The cell was cycled to establish stable operating characteristics. It was then subjected to several discharge cycles at different current densities during which the actual potential developed across the cathode was monitored. The results, shown in Fig. 9, confirm those obtained earlier with the small cell; over most of the range ohmic behavior is observed, but a sharp rise in cathode potential difference occurs towards the end of discharge limiting the extent of constant current discharge available.

Similar experiments on the recharge process were then carried out at a variety of current densities (Fig. 10). It should be noted that the starting OCV of the cell was different in each case. It can be seen that at charging current densities of up to 130 mA cm^{-2} the monitored potentials across the cathode are approximately ohmic throughout the entire range. There is no tendency for the potential to rise close to cell polarization on charge; in fact a slight tendency to decrease by a few millivolts is noticed. Charging the cell at 190 mA cm^{-2} caused considerable premature polarization of the cell itself, leading to nonohmic

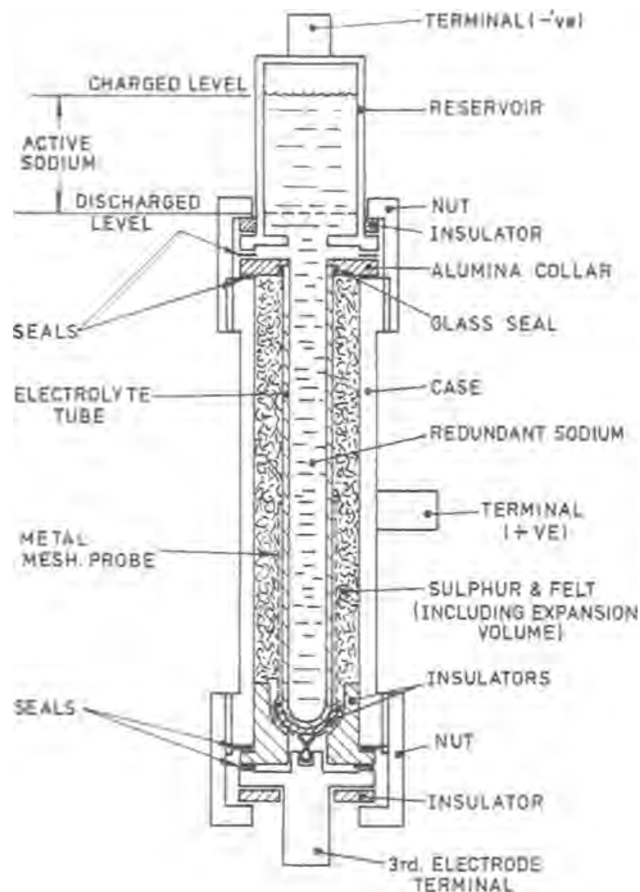

Fig. 8. Na/S cell incorporating extra cathode potential probe

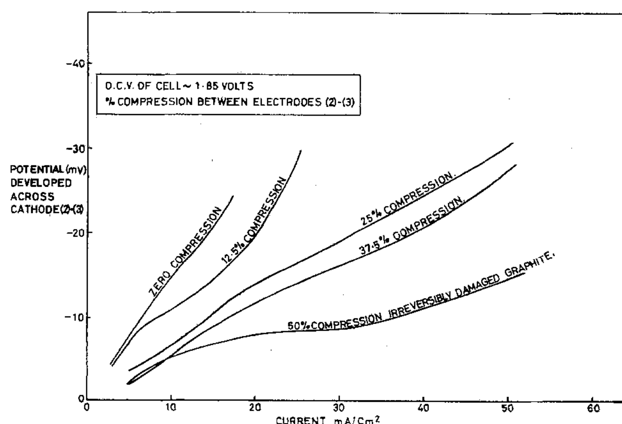

Fig. 7. Potential developed across cathode during normal discharge for varying degrees of compression of the graphite felt.

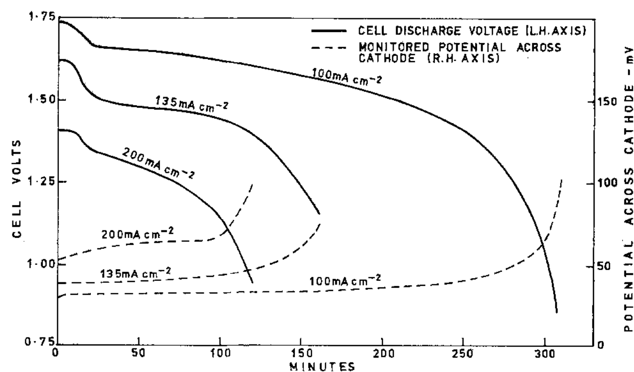

Fig. 9. Electronic potential drop across cathode and cell voltage during discharge at different current densities.

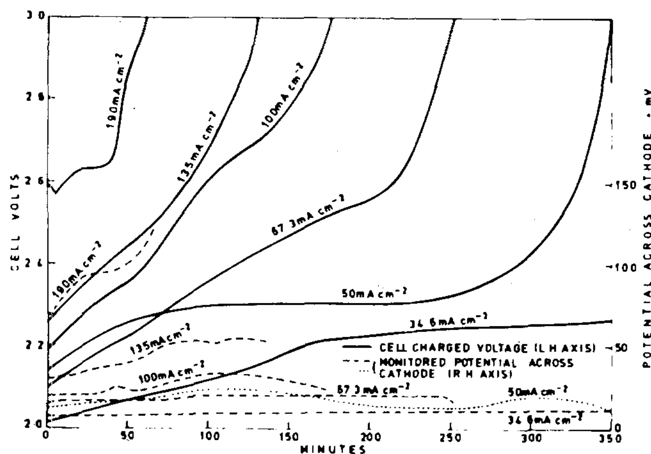

Fig. 10. Electronic potential drop across cathode and cell voltage during charge at different current densities.

behavior across the cathode. The shape of the potential curve also suggests that it is in some way directly related to the cell polarization.

For all charge current densities up to 135 mA cm^{-2}, some alternative explanation is required for the polarization often observed on charge not related to the potential as measured across the cathode. The most likely explanation for this behavior on recharge is the buildup of a sulfur insulating layer on the surface of the electrolyte.

Discussion

The onset of polarization in a working cathode has been studied in a miniature and an engineered sodium/sulfur cell. It has been shown that over the entire charge cycle and most of the discharge cycle an AISI 316 stainless steel cathode current collector forms a protective sulfide layer. Furthermore, it is only the polarization which occurs at the end of discharge that is instrumental in removal of the protective layer, a process which if repeated continuously during each cycle leads to severe thinning of the steel. For such high chromium steels as AISI 316 (17 w/o Cr) the principal protective effect arises from the formation of Cr_2S_3 and the spinel compound $FeCr_2S_4$, through which the diffusion of Fe^{++} is very much slower than either FeS or FeS_2. Since it can be shown that these chromium phases form only slowly, repeated removal of the sulfide film prevents the formation of a satisfactory barrier.

The polarization of a working cathode is primarily a function of the structure and operating conditions of the felt/melt matrix .Any change which can be made to reduce a rising potential difference across the cathode at the end of discharge will reduce the polarization and hence corrosion. Typical changes which can be made are to lower the effective resistance of the matrix, to use two or more current collectors electrically connected, to restrict the depth of discharge to, say, an OCV of 1.85 instead of Na_2S_3 (OCV 1.78), or to reduce the discharge current close to the end of the cycle. In the event of restricting the depth of discharge one would have to assess the penalty of an immediate loss in capacity initially compared with a higher initial capacity which decreased at a much faster rate. The operation of a Na/S cell in which all of the above-mentioned variables were changed favorably led to a considerably reduced capacity loss in 200 cycles from 50% to <10%.

Whether sufficient improvement can be achieved for steel to be used in an unprotected state as a cathode current collector remains to be seen. If protective coatings are found to be necessary such control of operating conditions may still be necessary if the coatings do not provide 100% protection over the entire life of the battery.

Manuscript submitted Dec. 1, 1977; revised manuscript received May 8, 1978.

Any discussion of this paper will appear in a Discussion Section to be published in the June 1979 JOURNAL. All discussions for the June 1979 Discussion Section should be submitted by Feb. 1, 1979.

REFERENCES

1. R. J. Bones, R. J. Brook, and T. L. Markin, Paper presented at the Power Sources Symposium (1974).
2. N. Weber and J. T. Kummer, Adv. Energy Conv. Eng. 913-916 ASME Conference, Florida (1967).
3. R. M. Dell, J. L. Sudworth, and I. Wynn Jones, 11th Inter-Society Energy Conversion Engineering Conference (1976).
4. J. G. Gibson, *J. Appl. Electrochem.*, **4**, 125 (1974).
5. M. P. J. Brennan, *Electrochim. Acta*, **21**, 1105 (1976).
6. Yuen-Koh KaO and P. C. Wayner, *This Journal*, **124**, 230 (1977).

The Behavior of the Zinc Electrode in Alkaline Solutions

I. The Effect of Ionic Strength at the Equilibrium Potential

T. P. Dirkse*

Calvin College, Grand Rapids, Michigan 49506

ABSTRACT

The exchange current densities of the zinc electrode in KOH solutions were determined under a variety of conditions. Special attention was given to the total ionic strength of the solutions. While the exchange current density does depend on the total ionic strength of the solution, there is no evidence that the water molecule enters directly into the electrode reaction. Instead, the ionic strength appears to influence the mobility of the reacting species and in this way modifies the exchange current density.

Previous work on the determination of the exchange current density for the zinc electrode in strongly alkaline solutions showed that this electrode process was sensitive to the ionic strength of the electrolyte (1). It was suggested at that time that his sensitivity could account for the maximum observed in the i_0 *vs.* KOH

* Electrochemical Society Active Member.
Key words: electrolyte, electrode, current density, kinetics.

concentration data. It was also suggested that this sensitivity indicates that water plays a role in the zinc-electrode processes although the role of the water could not be unequivocally determined.

The present work is a report on a further and more systematic investigation of the effect of the ionic strength of the electrolyte on the zinc-electrode processes in an effort to determine more precisely the role of the water molecule in these processes. This study is limited to the behavior of the zinc electrode near the equilibrium potential. A later report will deal with the effect of ionic strength on the zinc-electrode processes in the Tafel region.

Experimental

Stock solutions of KOH, KOH + Zn(II), and KF were prepared by using analytical grade solids and doubly distilled deionized water. The Zn(II) was introduced by dissolving ZnO in a KOH solution. These stock solutions were then used to prepare the working solutions. This was done by taking prescribed volumes of the stock solutions and quantitatively diluting them. The ionic strength of the solutions was controlled by the addition of KF or other indifferent electrolytes.

The exchange current densities were measured galvanostatically by obtaining $\eta - i$ data within 7 mV of the equilibrium potential (2). All work was carried out at room temperature, 21° ± 1°C.

Results and Discussion

The results that were obtained are shown in Fig. 1-4. At lower ionic strengths, Fig. 1, it was possible to use indifferent electrolytes other than KF, but at higher ionic strengths only KF was sufficiently soluble to obtain the desired ionic concentrations. Consequently, the ionic strength was maintained with KF. This has the added advantage that the F^- and OH^- ions are isoelectronic and thus likely have similar hydration numbers. Figures 3 and 4 show the effect of varying ionic strength at constant OH^- ion concentration: Figure 3 shows the effect on that part of the curve where i_o is increasing with increasing KOH concentration, while Fig. 4 shows the same effect on that part of the curve where i_o decreases as the KOH concentration increases.

Because the OH^- ion and the Zn(II) concentration were held constant in a given series of solutions and because the zinc electrode was 99.999% pure, a plot of log i_o *vs.* log μ should give a line whose slope is the reaction order with respect to the ionic strength. Such a plot of the data in Fig. 4 is given by the solid line on Fig. 5. The slope of this line is −1. It is tempting to ascribe this to the influence of water on

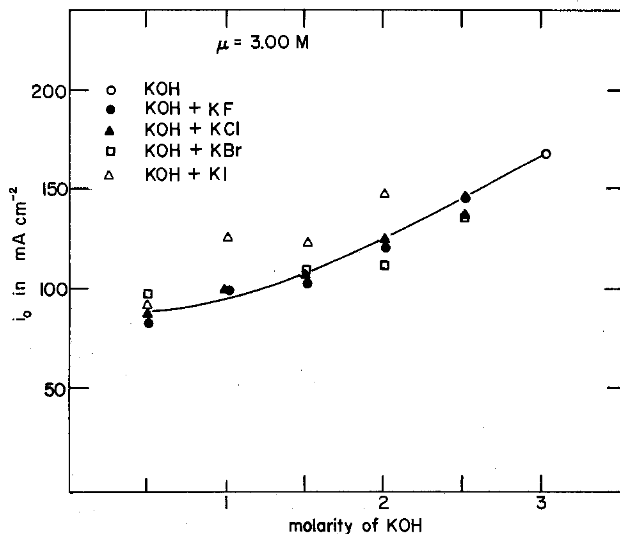

Fig. 1. Exchange-current densities of the zinc electrode in solutions of 3M total ionic strength.

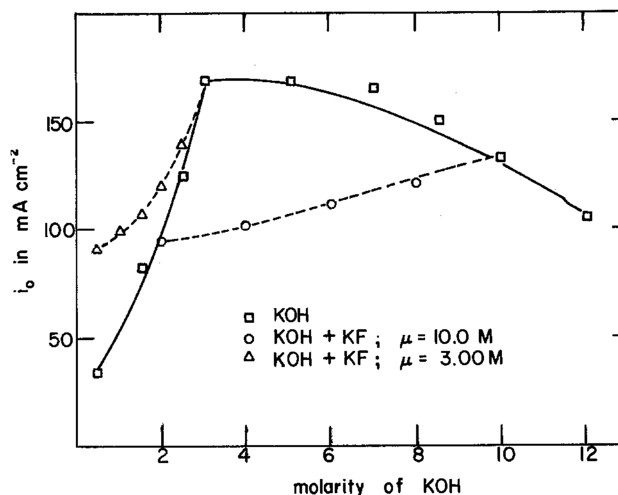

Fig. 2. Exchange-current densities of the zinc electrode as a function of OH^- ion concentration at room temperature.

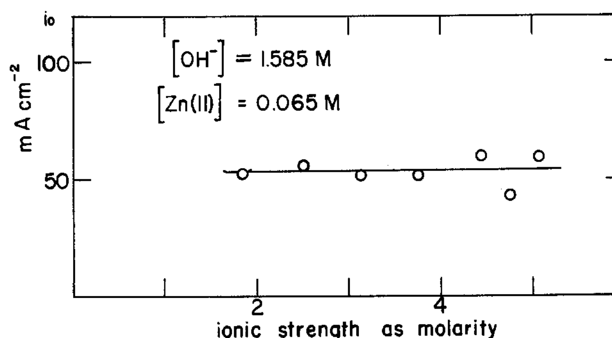

Fig. 3. Exchange-current densities of the zinc electrode as a function of total ionic strength with low OH^- ion concentration.

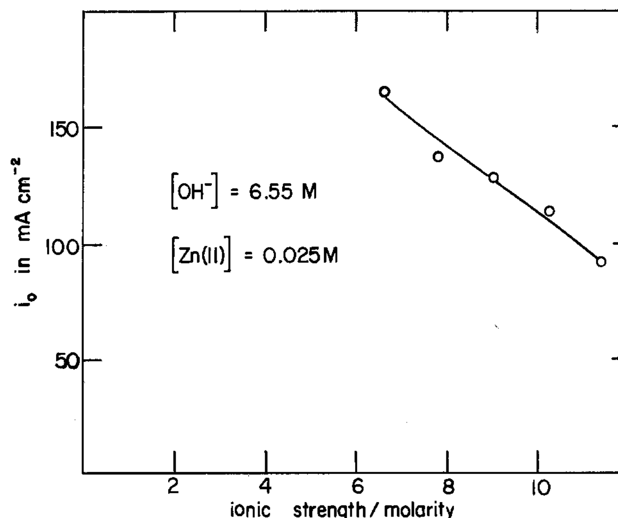

Fig. 4. Exchange-current densities of the zinc electrode as a function of total ionic strength with high OH^- ion concentration.

the electrode reaction. However, because of the uncertainty of the relationship between the ionic strength of the solution and the activity of the water, the exact significance of this result is in doubt.

An alternate way of approaching this is to assume that the activity of water is a function of the ionic strength of the solution. Then it may be possible to use the data for the activity of water in KOH solutions (3). If it assumed further that the activity of water in KOH solutions is the same as that in KOH + KF solutions having the same ionic strength then the dashed line in Fig. 5 represents the log i_o − log a_{H_2O}

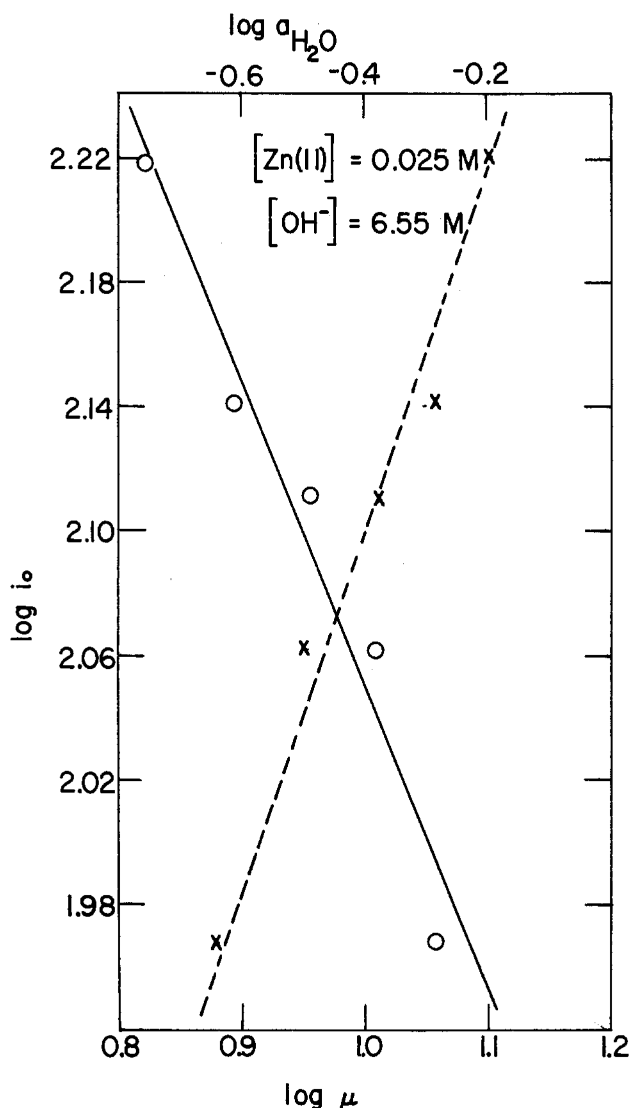

Fig. 5. Plot to determine the reaction order of the ionic strength

relationship. In this case the slope of the line is 0.54. These results indicate that the water molecule does play a role in the zinc-electrode process at equilibrium but the precise nature of this role cannot be assigned from this information.

Moreover, a log i_0 *vs.* log μ plot for the data in Fig. 3 gives a line with a slope of zero. Obviously, it is necessary to assume that the effect of ionic strength (and perhaps the role of the water molecule) depends on whether one is considering the region of ascending or descending i_0 in Fig. 2.

Solutions about 3-5M in KOH appear to be some sort of watershed so far as the characteristics of KOH solutions are concerned. In solutions less than about 3M the activity coefficients of the OH^- ion are less than one, but become larger than one at concentrations greater than 3M (3). Also, a solution that is about 3M in KOH appears to separate those solutions for which the specific conductance increases with increasing pressure and those for which the specific conductance decreases with increasing pressure (4). Lown and Thirsk account for this by suggesting that the mechanism of specific conductance is twofold: a hydrodynamic and a proton-transfer mechanism. The latter requires so-called "unbound" or "free" water molecules, *i.e.*, water molecules not dominated by proximity to an ion. As the ionic strength increases there are more ions, fewer "free" water molecules, and the proton-transfer mechanism makes a smaller contribution to the specific conductance of the electrolyte.

Using this suggestion of Lown and Thirsk for the solutions described on Fig. 1 then, as a first approximation, the amount of "free" water molecules should be the same for all the solutions because all have the same ionic strength. Then any change in the exchange current density on Fig. 1 is most likely due to the change in the concentration of the OH^- ion. Even when the total ionic strength is 10M, i_0 increases with OH^- ion concentration, Fig. 2.

The decrease in exchange current density, Fig. 4, could be attributed to a decrease in the amount of "free" water. However, if that is the cause then a decrease in i_0 should also have been observed on Fig. 3. The fact that this is not observed strongly suggests that the water molecule is not directly involved in the electrode reaction. This is further substantiated by the fact that when water was used as the electrolyte, the current flow was extremely small (less than 10^{-4} A cm^{-2} for overpotentials up to 400 mV). Further, practically no current could be obtained up to overpotentials of 235 mV in a 6.12M KF solution, indicating that neither the K^+ ion nor the F^- ion was a contributor to the exchange reaction in any of these solutions.

It appears from all this that i_0 for the zinc electrode does depend on the OH^- ion concentration and not on the water molecule directly. However, in some way the effect of changing ionic strength masks the effect of the OH^- ion concentration.

A reasonable explanation for this is suggested by the work of Lown and Thirsk (4). An increase in ionic strength causes a decrease in the amount of "free" or "unbound" water. This also means a decrease in the mobility of the OH^- ion and a decrease in the exchange current density if the OH^- ion is directly involved in the exchange reaction.

Comparing Fig. 3 and 4, it is obvious that when the OH^- ion concentration is held constant, the effect of changing ionic strength is different for solutions in which i_0 is increasing with KOH concentration, Fig. 3, than for solutions in which i_0 is decreasing with increasing KOH concentration, Fig. 4. For the solutions represented in Fig. 4 the concentration of KOH is such that there is relatively little "unbound" water and hence the effect of increasing ionic strength on decreasing the mobility of the OH^- ion is the dominant factor. On the other hand, the solutions represented on Fig. 3 are those for which the concentration of "unbound" water is larger and the effect of increasing ionic strength on the mobility of the OH^- ion is not large enough to mask the effect of the OH^- ion on the electrode process. Furthermore, as the ionic strength increases to about 4M, Fig. 3, the results become more erratic, suggesting that in this region the effect of ionic strength is beginning to make itself felt.

Conclusions

The water molecule does not take part directly in the zinc-electrode process at the equilibrium potential. The reaction does involve the OH^- ion and as the concentration of this ion increases, so does i_0. However, the ionic strength does determine the concentration of "free" water molecules in the solution and as this concentration of "free" water decreases, the mobility of the OH^- is also decreased resulting in a decreased exchange-current density. This becomes significant and increasingly dominant in KOH solutions more concentrated than about 3-5M.

As a practical matter, then, any effort to determine the role or reaction order of the species involved in the electrode reaction should give careful consideration to the ionic strengths of the electrolytes that are used. It would be well to carry out such work at constant ionic strength to minimize the effect of changing concentration of "free" or "unbound" water molecules on the mobility of any reacting species.

Acknowledgment

The work reported here was made possible by a grant from the General Electric Company.

Manuscript submitted April 17, 1978.

Any discussion of this paper will appear in a Discussion Section to be published in the June 1979 JOURNAL. All discussions for the June 1979 Discussion Section should be submitted by Feb. 1, 1979.

Publication costs of this article were assisted by Calvin College.

REFERENCES

1. T. P. Dirkse and N. A. Hampson, *J. Electroanal. Chem.*, **35**, 7 (1972).
2. T. P. Dirkse and N. A. Hampson, *Electrochim. Acta*, **17**, 135 (1972).
3. G. C. Akerlof and P. Bender, *J. Am. Chem. Soc.*, **70**, 2366 (1948).
4. D. A. Lown and H. R. Thirsk, *Trans. Faraday Soc.*, **67**, 132 (1971).

Localized Corrosion on Slip Steps of Aluminum Straining

I. A. Maier and J. R. Galvele*

Comisión Nacional de Energía Atómica, Departamento de Materiales, Av. Libertador 8250, Buenos Aires, Argentina

ABSTRACT

The initial steps of localized corrosion of aluminum strained in aggressive solutions were studied by electron microscopy of oxide replicas. Aluminum samples were strained at a constant potential in the following deaerated solutions: 1M NaCl (pH 7); 4M NaCl (pH 11); and 1M $NaNO_3$ (pH 7). No pitting was found on the aluminum strained in those solutions below the pitting potential; the slip bands showed the same substructure as that found on aluminum strained in air. At, and above, the pitting potential, pitting was found on the surface of the strained aluminum. Pitting nucleated on the whole surface in neutral NaCl solutions. In 4M NaCl solution (pH 11) and in 1M $NaNO_3$ solution pitting nucleated preferentially on the slip bands, leading to semicylindrical pits. It was also concluded that mechanical film breakdown is not a sufficient condition for pit initiation. Another process, such as localized acidification, must be assumed to explain pit initiation at pitting potential.

Pitting is a form of very localized corrosion found on corroding metal surfaces. From a mechanistic point of view, three different types of pitting have been described (1). They are: (*i*) electrochemical depassivation, which appears in neutral and alkaline solutions and is characterized by the existence of a pitting potential; (*ii*) chemical depassivation, which is observed mainly in acid solutions and in which no pitting potential is found; and (*iii*) HCl-stainless steel type, which is observed in acid solutions and which shows a pitting potential, but this potential is not affected by alloying elements as is the case with electrochemical depassivation.

The pitting initiation process in electrochemical depassivation could follow different paths, and there is no clear description yet about the detailed mechanism of pit initiation. In one line of thought (2, 3) it is considered that a very important step for pit initiation is the contamination of the oxide film by the aggressive anions. This contamination increases the conductivity of the oxide film, leading to enhanced localized dissolution (pitting). On the other hand, several authors (4-7) have suggested that the oxide film acts as an inert barrier with no effect on the mechanism of pitting. According to them pitting starts either at flaws already in the oxide film (4, 5) or at defects resulting from a continuous process of passivity breakdown and repassivation (1, 6-8).

Since the existence of such flaws or defects is questioned by some authors (2, 9), in the present work those flaws were produced by straining the metal, so as to study the changes observed on the metal surface by electron microscopy. The metal chosen was aluminum, which carries an air-formed oxide film of the order of 2.5×10^{-9}m (9). Thomas and Nutting (10) have shown that plastic deformation of annealed aluminum produces various kinds of slip bands containing slip steps at least 6×10^{-8}m high. Since the aluminum oxide film is very fragile (11), in deformation the film breaks easily, and the bare metal is exposed to the solution.

NaCl solutions and $NaNO_3$ solutions were chosen as aggressive media because aluminum shows a big difference in the rate of pit nucleation and in pit morphology in those solutions. In neutral 1M NaCl solutions pitting nucleates very easily, and the pits develop the {100} crystallographic planes (12). In 4M NaCl solution, *p*H 11, hemispherical pits have been reported (13). Hemispherical pits have also been found when aluminum is exposed in $NaNO_3$ solutions above the pitting potential (12). Pitting of aluminum in $NaNO_3$ solutions was found to develop more slowly than in neutral NaCl solutions, and it was also reported to be accelerated by straining the metal (6). The pitting potential of straining aluminum, in both solutions, was found to be equal to the pitting potential of static aluminum. From potentiostatic straining experiments Wexler and Galvele (6) concluded that semicylindrical pits should be formed on the slip steps of aluminum strained in $NaNO_3$ solutions. No direct proof of such supposition had been so far available.

During the present work no pitting was found to nucleate on aluminum strained in aggressive solutions at potentials below the pitting potential. Pits were observed only at, or above, the pitting potential. It was concluded that the mechanical breakdown of the passive film was not a sufficient condition for pit initiation, and that some electrochemical reaction should be assumed to take place at the pitting potential.

Experimental

Coupons 11.0 × 0.6 cm were cut from a 1 mm thick sheet of 99.99% aluminum. The coupons were pickled in a 10% NaOH solution, rinsed with a 10% HNO_3 solution, washed with distilled water, and dried. The coupons were annealed for 1 hr at 600°C, obtaining

* Electrochemical Society Active Member.
Key words: metals, anode, SEM, dissolution.

samples with about 1 mm diam grain size. Before being strained, the specimens were electrolytically polished for 8 hr in a 90% Butilcellosolve plus 10% perchloric acid solution, at 28V and 0°C. A metallic cell (14) internally lined with cured epoxy resin was used for the straining experiments. The joints between the parts of the cell and between the sample and the cell were sealed with silicon rubber gaskets. A platinum wire was used as a counterelectrode inside the cell, and the electrode potential was measured through a Luggin capillary.

The potential was measured against a saturated calomel electrode for the chloride-containing solutions, and against a saturated mercurous sulfate reference electrode for the $NaNO_3$ solutions. All the potentials are reported in the normal hydrogen electrode scale (NHE). The solutions were prepared with analytical-grade reagents and distilled water and were deaerated with 99.99% nitrogen. The measurements were performed at room temperature (20°C). The solutions used were neutral 1M NaCl solution, 4M NaCl solution (*p*H 11), and neutral 1M $NaNO_3$ solution. The alkalinization of the 4M NaCl solution was performed by addition of a NaOH solution. No buffers were used for these solutions.

The cell containing the sample was mounted on a straining machine and connected to a reservoir containing the test solution. Nitrogen was bubbled through the solution and the cell until deaeration was completed (about 90 min). Then the solution was let into the cell and the samples were polarized with a Tacussel PRT-20-2X potentiostat at a potential in the passive zone until the anodic current reached a quasistationary value. Then the potential was switched to the desired value and the specimen was strained at a strain rate of 5%/min and up to a total elongation of 10%.

In separate experiments the pitting potential of the samples in the different solutions was measured. The measurements were performed by increasing the potential in steps of 20 mV and recording the current until a quasistationary state was reached.

The corrosion morphology of the strained samples was studied by means of aluminum oxide replicas. The replicas were prepared (15) by anodizing the corroded samples in a 3% tartaric acid solution, partially neutralized with ammonium hydroxide, to *p*H 5.5. Good oxide replicas were obtained by anodizing the samples for 20-30 min at 28-30V. The surface of the anodized samples was scratched to obtain oxide replicas of the size of the grids for the electron microscope. The scratched samples were immersed for 1 min in a saturated mercurous chloride solution, washed with alcohol, and immersed in distilled water until the oxide replicas were detached from the metal surface. The oxide replicas were washed in a 10% HCl solution, then in distilled water, and finally in alcohol. The oxide replicas were observed either in a Philips EM 300 electron microscope or in a Hitachi HK-3AM electron microscope.

The profile of some of the corroded slip bands was measured by electron-stereomicroscopic techniques (16). By tilting the oxide replicas in the electron microscope, two pictures with a tilting angle difference of 12° were taken. These pictures were taken to a Hilger Watts SB 190 stereoscope, and from the parallax difference, the tilting angle, and the magnification, the depth profile in the pictures was calculated.

Results

Air-strained aluminum.—Figure 1 shows the electron micrograph of a sample strained to 10% elongation in air. Slip bands were found on the strained samples. The slip-line substructure of the slip bands, as described by Thomas and Nutting (10), was found on about 50% of the observed slip bands. No slip lines could be resolved on the remaining 50% of the slip bands. The absence of resolution of slip lines is probably due to the fact that the slip line separation in those bands was too small to be resolved by the oxide replica technique. By stereoscopic observation a smooth slope change is found on the sample surface across the slip band.

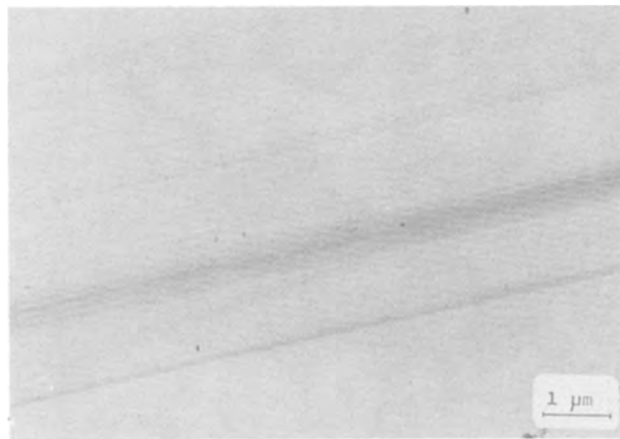

Fig. 1. Slip band substructure on aluminum strained to 10% elongation in air. Oxide replica observed by transmission electron microscopy.

Aluminum strained in pH 7, 1M NaCl solution.—The pitting potential measured for aluminum in deaerated 1M NaCl solution, *p*H 7, was found to be −0.53V. No pitting was observed on samples exposed for 5 hr at −0.70, −0.65, and −0.57V. At these three potentials the current density remained below 10^{-6} A/cm^2 during the experiments.

For the electron-microscope observations, aluminum samples were strained in the NaCl solution at the following potentials: −0.60, −0.57, −0.55, −0.53, −0.50, and −0.48V. At least two samples were strained at each potential.

The samples strained below the pitting potential showed a slip band structure similar to that found on air-strained aluminum. The main difference between the air-strained samples and the samples strained in 1M NaCl solution, below the pitting potential, was the partial disappearance of the slip line substructure, Fig. 2. While 50% of the slip bands showed slip lines on the air-strained samples, only 10% of the slip bands showed those lines on the aluminum strained in NaCl solutions below the pitting potential. One possible explanation is that the oxide film formed in NaCl solutions is thicker than the air formed film; therefore the slip line microstructure would be not so clear as in the air-strained samples. No evidence of corrosion was

Fig. 2. Slip band substructure on aluminum strained to 10% elongation in deaerated 1M NaCl solution, below the pitting potential (E = −0.55V). Oxide replica observed by transmission electron microscopy.

found on the slip bands of the samples strained in NaCl solutions below the pitting potential. No pitting was detected on the metal surface either. Besides, the stereoscopic observations gave the same profiles as those found on the air-strained samples.

At a potential 30 mV above the pitting potential some areas of the samples showed intensive pitting, as in Fig. 3. Other areas showed a disappearance of the slip lines on the slip bands, suggesting a further thickening of the oxide film. At higher potentials intense attack was observed on the slip bands and on the whole surface of the samples.

Aluminum strained in 4M NaCl solution (pH 11).—As reported by Kaesche (13), the pitting potential of aluminum in 4M NaCl solution (pH 11) is −0.56V, and the pits have a hemispherical shape. Straining experiments, most of them by duplicate, were performed at the following potentials: −0.60, −0.58, −0.56, −0.54, −0.52, and −0.50V.

Specimens strained below the pitting potential did not show localized corrosion. Beginning at the pitting potential, and up to a potential 40 mV above, the attack took the shape of hemispherical pits and was localized mainly on the slip bands (Fig. 4 and 5). At higher potentials pitting was more extensive and was localized also outside the slip bands. The pitting localization on the slip bands at potentials close to the pitting potential confirms previous observations made by Galvele *et al.* (12). According to these authors, when straining aluminum in 4M NaCl solutions (pH 11) the current density increase followed a square root law. This was interpreted as the result of nucleation of hemispherical pits on the slip bands, leading to semicylindrical pits. The microscopical observations made in the present paper confirm such supposition.

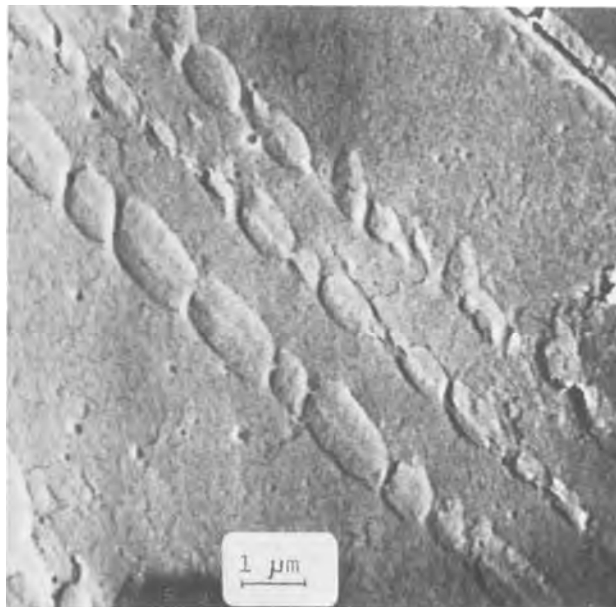

Fig. 5. Semicylindrical pits on slip bands of aluminum strained to 10% elongation in deaerated 4M NaCl solution (pH 11), above the pitting potential ($E = -0.52V$). Metallized plastic replica observed by scanning electron microscopy.

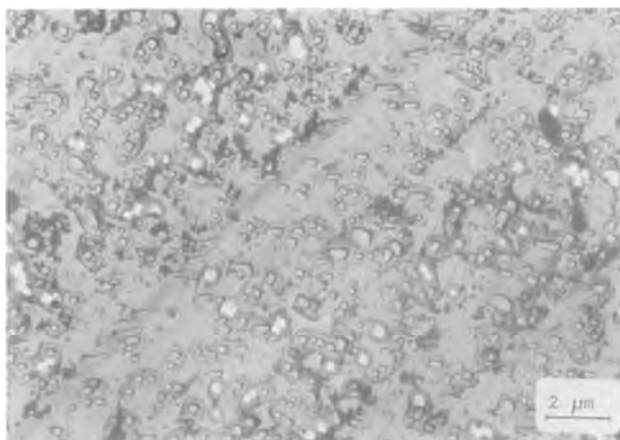

Fig. 3. Generalized pitting distribution on aluminum strained to 10% elongation in deaerated 1M NaCl solution, above the pitting potential ($E = -0.50V$). Carbon replica observed by scanning electron microscopy.

Aluminum strained in a neutral 1M $NaNO_3$ solution.—The pitting potential of aluminum in 1M $NaNO_3$ solution was found to be 1.70V, in agreement with previous publications (6). Samples exposed for 2 hr at 1.69V did not show pitting when observed under the optical microscope. There was no pitting either on samples exposed up to 5 hr at 1.0 and 1.5V. On the other hand, pitting was found on samples exposed for 2 hr at 1.71 and 1.74V.

Straining experiments were performed at least twice in neutral 1M $NaNO_3$ solutions at the following potentials: 1.69, 1.72, 1.74, 1.78, 1.79, 1.80, and 1.84V. The surface morphology of the samples strained at a potential below the pitting potential was similar to that observed on air-strained samples, Fig. 6. Above the

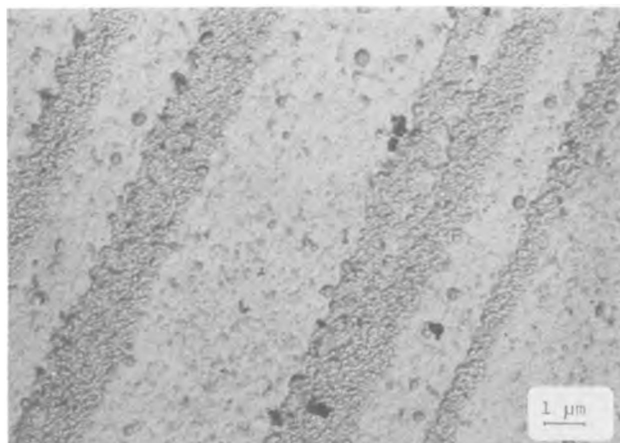

Fig. 4. Incipient hemispherical pits on slip bands of aluminum strained to 10% elongation in deaerated 4M NaCl solution (pH 11), at the pitting potential ($E = -0.56V$). Oxide replica observed by transmission electron microscopy.

Fig. 6. Slip band substructure on aluminum strained to 10% elongation in deaerated 1M $NaNO_3$ solution below the pitting potential ($E = 1.69V$). Oxide replica observed by transmission electron microscopy.

pitting potential and up to 1.80V, a disappearance of the slip steps from the slip bands was observed and incipient corrosion was detected on the slip bands. At 1.84V intensive pitting was found on the slip bands, Fig. 7, 8, and 9. No pitting was detected outside the slip bands. The extension of the pitting on the slip bands was not equal on all the bands, and three different degrees of attack could be detected. About 20% of the slip bands showed extensive, semicylindrical pits along the bands, Fig. 7 and 8. Another 20% of the slip bands showed small hemispherical pits, Fig. 9. The remaining 60% of the slip bands showed a rough surface and an absence of slip lines Fig. 9.

By stereomicrographic observation deep grooves were observed along the pitted slip bands. The semicylindrical pits appear to be the result of hemispherical pits that merge into a single semicylindrical pit after nucleating on a slip band.

Discussion and Conclusions

The present work confirms the assumptions made by Wexler and Galvele (6) that semicylindrical pits are formed on aluminum when strained in $NaNO_3$ solutions.

The present results are also relevant from the point of view of the mechanism of pitting. The straining of aluminum in NaCl solutions and in $NaNO_3$ solutions below the pitting potential produces a slip band substructure similar to that found on air-strained aluminum. Except for the effects attributed to film thickening, no other changes were found on the strained metal. No evidence of localized corrosion was found. The nucleation of pits could be seen only above the pitting potential. Above the pitting potential under conditions of easy pit nucleation, as with aluminum in NaCl solutions, pits nucleated on all the metal surface. Under conditions of difficult pit nucleation, on the other hand, as is the case with aluminum in $NaNO_3$ solutions, pits nucleated preferentially on the slip bands.

Fig. 7. Semicylindrical pits on slip bands of aluminum strained to 10% elongation in deaerated 1M $NaNO_3$ solution above the pitting potential (E = 1.84V). Oxide replica observed by transmission electron microscopy.

Fig. 8. Semicylindrical pits on slip bands of aluminum strained to 10% elongation in deaerated 1M $NaNO_3$ solution above the pitting potential (E = 1.84V). Oxide replica observed by transmission electron microscopy.

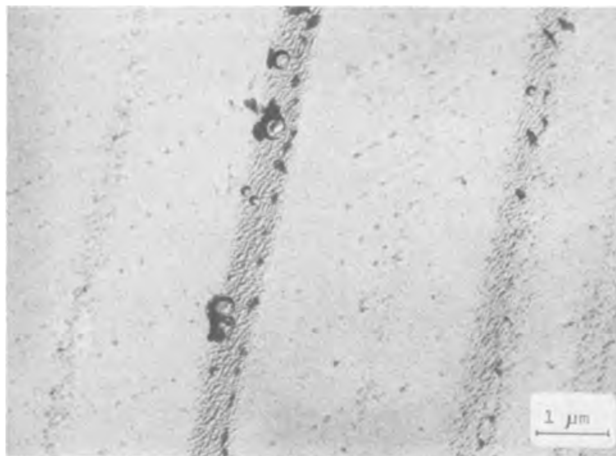

Fig. 9. Incipient hemispherical pits on slip bands of aluminum strained to 10% elongation in deaerated 1M $NaNO_3$ solution above the pitting potential (E = 1.84V). Oxide replica observed by transmission electron microscopy.

The absence of pitting on the strained metal below the pitting potential was also reported for zirconium in NaCl solutions (17, 18). It was observed that the zirconium oxide film, broken by straining below the pitting potential, was reformed by repassivation. The same conclusions were reached through surface-scratching techniques on zinc (7), cadmium (19), iron (20), and nickel (20). When the metal was scratched at a potential below the pitting potential, repassivation of the scratched surface was found. Only at potentials above the pitting potential pits were nucleated.

It is concluded that mechanical film breakdown, even in the presence of aggressive anions is not a sufficient condition for pit initiation. Assuming the presence of flaws in the film, as suggested by Wood and co-workers (4, 5), or the existence of a continuous process of film breakdown, as suggested by other authors (1, 6-8) the fact must be accepted that at the pitting potential there is some electrochemical change at the metal-solution interface that leads from repassivation to localized corrosion. As shown in other publications (1, 6, 7, 21) the conditions for pitting initiation and propagation are related to the appearance of localized acidification on the metal-solution interface. When a metal is strained below the pitting potential, no localized acidification can take place on the bare metal. In this case only repassivation will take place. At the pitting potential and above, localized acidification is formed on the bare metal surface and the repassivation process is hindered, leading to localized corrosion.

Acknowledgments

This research work has been supported by the Programa Multinacional de Metalurgia-Programa Regional de Desarrollo Científico y Tecnológico, O.E.A., and by the Servicio Naval de Investigación y Desarrolo—Programa ECOMAR.

Manuscript submitted Feb. 28, 1978; revised manuscript received May 15, 1978.

Any discussion of this paper will appear in a Discussion Section to be published in the June 1979 JOURNAL.

All discussions for the June 1979 Discussion Section should be submitted by Feb. 1, 1979.

Publication costs of this article were assisted by the Programa Multinacional de Metalurgia—O.E.A.

REFERENCES

1. J. R. Galvele, in "Fourth International Symposium on Passivity," Airlie House, Airlie, Va., Oct. 1977.
2. M. J. Pryor, in "Localized Corrosion," R. W. Stahle, B. F. Brown, J. Kruger, and A. Agrawal, Editors, p. 2, N.A.C.E., Houston (1974).
3. T. P. Hoar, D. C. Mears, and G. P. Rothwell, *Corros. Sci.*, **5**, 279 (1965).
4. J. A. Richardson and G. C. Wood, *Corros. Sci.*, **10**, 313 (1970).
5. G. C. Wood, W. H. Sutton, J. A. Richardson, T. N. K. Riley, and A. G. Malherbe, in "Localized Corrosion," R. W. Staehle, B. F. Brown, J. Kruger, and A. Agrawal, Editors, p. 526, N.A.C.E., Houston (1974).
6. S. B. De Wexler and J. R. Galvele, *This Journal*, **121**, 1271 (1974).
7. M. G. Alvarez and J. R. Galvele, *Corrosion*, **32**, 285 (1976).
8. G. Okamoto, K. Tachibana, S. Nishiyama, and T. Sugita, in "Passivity and its Breakdown on Iron and Iron Base Alloys," R. W. Staehle and H. Okada, Editors, p. 106, N.A.C.E., Houston (1976).
9. M. J. Pryor, *Corros. Sci.*, **11**, 463 (1971).
10. G. Thomas and J. Nutting, *J. Inst. Metals*, **85**, 1 (1956-1957).
11. S. I. Bubar and D. A. Vermilyea, *This Journal*, **114**, 882 (1967).
12. J. R. Galvele, S. M. De Micheli, I. L. Muller, S. B. de Wexler, and I. L. Alanis, in "Localized Corrosion," R. W. Staehle, B. F. Brown, J. Kruger, and A. Agrawal, Editors, p. 580, N.A.C.E., Houston (1974).
13. H. Kaesche, *Z. Phys. Chem.*, **34**, 87 (1962).
14. I. A. Maier, Thesis, Universidad Nacional de Buenos Aires, Buenos Aires, (1975).
15. I. S. Brammar and M. A. P. Dewey, "Specimen Preparation for Electron Metallography," Blackwell Scientific Publications, Oxford (1966).
16. A. A. Pochettino and M. Ipohorski, "Determinación de Profundidades y Espesores de Láminas Delgadas Mediante Técnicas de Estereomicroscopía Electrónica," C.N.E.A., T.E. 12/74, Buenos Aires (1972).
17. G. Cragnolino and J. R. Galvele, "Primera Reunión Latinoamericana de Electroquímica," La Plata (August 1972).
18. G. Cragnolino and J. R. Galvele, in "Fourth International Symposium on Passivity," Airlie House, Airlie, Va. Oct. 1977.
19. M. G. Alvarez and J. R. Galvele, in "II Congreso Latinoamericano de Electroquímica," Rio de Janeiro October 1974.
20. M. G. Alvarez and J. R. Galvele, In press.
21. I. L. Muller and J. R. Galvele, *Corros. Sci.*, **17**, 995 (1977).

Photopotentials on Copper and Copper Alloy Electrodes

Ugo Bertocci*

National Bureau of Standards, Metallurgy Division, Washington, D.C. 20234

ABSTRACT

The effect of white light illumination on the current-potential relationships of pure copper and of Cu-Ni and Cu-Al alloys in neutral solutions was examined, both under galvanostatic and potentiostatic conditions. The results obtained show that the photoresponse is only weakly affected by the addition of alloying elements to copper, but that it is influenced by the method of formation of the oxide film on the metal surface. Depending on whether or not the Cu_2O film was formed by reaction with a copper solution, the amplitude of the signal response could be strongly affected and the sign of the photopotential at open circuit reversed, indicating a change in the nature of the majority carriers. Polarization of the electrode can also vary the photoresponse, but its rapid following of the potential does not support the view that the structure of the oxide film is altered. Impedance measurements on electrodes under illumination and in the dark indicate that the charge-transfer reactions, rather than the resistivity of the oxide film, are affected by light.

Photopotentials have been used in corrosion research in order to obtain information on the nature and characteristics of surface films, mainly oxides, which are often formed on metals in a corrosion environment (1, 2). Such studies have been carried out under galvanostatic or potentiostatic conditions and from the variations in photoresponse, conclusions were drawn on changes in the properties of the surface film with electrode potential or as a consequence of the adsorption of corrosion inhibitors, and correlations made with changes in corrosion resistance.

The present study was undertaken to investigate the usefulness of photopotential measurements as a tool in corrosion research by studying the effects of alloy composition and different methods of producing the surface films.

In this work the materials investigated were pure copper and some copper alloys in the presence of an oxide film. Copper was chosen because information is available on its oxide films (3) and because the photosensitivity in the visible light range is such that the measurements are simplified.

* Electrochemical Society Active Member.

Key words: alloys, photovoltaic, photopotentials.

Experimental Methods

The experiments were carried out on electrodes of pure Cu and Cu alloys prepared by casting with 10 and 30 atom percent (a/o) of Ni and with 6% Al. All of these alloys are single phase. The electrodes in the form of disks 1-2 cm diam and about 1 cm thick were embedded in lucite, so as to leave only a flat circular surface exposed to the solution. Electrical contact was made through a threaded stainless steel rod in a glass tube with a Teflon gasket (4). The electrode surface was mechanically polished.

The solutions used in this work were 0.25M sodium acetate, at pH 5 and 8, the same solution plus 0.01M copper acetate with a pH adjusted to 5, and a 1:1 mixture of saturated H_3BO_3 and $Na_2B_4O_7$ with a pH close to 8. Some experiments were also carried out in a solu-

tion 0.1M both in potassium ferro- and ferricyanide plus 0.2M sodium acetate, at pH close to 8.

Measurements were taken on electrodes covered by the oxide film formed by exposure to the solution under study, or on electrodes which prior to introduction in the cell were immersed for various lengths of time in neutral (pH $\simeq$ 5) copper acetate solution. By this treatment a relatively thick layer of Cu_2O is formed by attack of the metallic copper on the part of the Cu^{++} ions in solution.

Copper acetate was chosen over other salts because the oxide film formed in this solution is more uniform and adherent than that formed in the presence of other anions (5). However, films formed in neutral copper sulfate and nitrate did not show significant differences in the light response, as shown in Fig. 1.

The light source was a tungsten-iodine lamp. The light entered the cell through a Pyrex window and traversed about 2 cm of solution before striking the electrode. The light intensity on the electrode surface was found to be approximately 150 mW/cm^2, as measured by putting a light power meter in the place of the cell. The light could be modulated by means of a rotating wheel with a slot. The frequency of rotation could reach about 50 Hz. The angular width of the slot was 12°, giving a duty cycle (time of illumination over period of rotation) of 1/30.

The cell, except for the flat window, was of conventional design, with provisions for controlling the atmosphere. Stirring was accomplished by means of a magnetic stirrer. The Pt counterelectrode was separated from the electrode compartment by a coarse glass frit. The cell was fitted with two reference electrodes, a saturated calomel electrode (SCE) which was used in most instances, and a Pt sheet electrode, employed when low impedance was necessary to prevent excessive noise pickup.

Measurements were carried out both under current and potential control. In a number of experiments, a small (a few μA/cm^2) constant a-c current was superimposed on the constant d-c current and the a-c voltage across the electrode monitored with a tracking generator. When both the real and the imaginary part of the a-c impedance were measured, a lock-in amplifier was used.

Experimental Results

Light response as a function of the method of oxide film preparation and of electrode potential.—The most important parameter in determining the photoresponse of the electrode was found to be the method of preparation of the oxide film. When the electrode was immersed in copper acetate prior to the measurements (or if the measurements were taken in copper acetate), the photopotential signal at open circuit was negative and often quite large, reaching more than 500 mV in some instances. Within the limits of current and potential in which the oxide film was not severely altered or destroyed, cathodic polarization tended to decrease the negative photopotential signal, and eventually to invert it, while anodic polarization tended to increase it.

The results obtained on a Cu alloy with 10% Ni in copper acetate are shown in Fig. 2. The two curves marked A and B shown on the cathodic side without illumination correspond to the initial values and to the steady-state condition where copper deposition has begun, and, therefore, the overvoltage decreases.

The exact value of the potential at which the sign of the photopotential is reversed is uncertain, since the light signal shows transient peaks which can be opposite to the steady-state value. Such complex transients have been reported previously (6).

The behavior of the electrode potential under illumination described here is observed on all alloys examined as well as on copper, if the electrode, after the formation of Cu_2O by reacting with copper acetate, is transferred into a neutral solution. In Fig. 1 the potential under illumination is plotted *vs.* the potential in the dark under galvanostatic conditions for a number of specimens. The open-circuit potential in this solution is close to -50 mV *vs.* SCE. The magnitude of the photopotential signal and the potential at which the signal reverses varies with the composition of the electrode and the length of time of immersion in the copper solution. This behavior, in a rough qualitative way, points to a correlation between the thickness of the oxide film and the amplitude of the signal, although this is obscured by changes in photoresponse caused by prolonged polarization of the electrode, which tends to alter the characteristics of the Cu_2O film. Nevertheless, the largest signals were observed on specimens which had been immersed for long times. Since pure copper reacted more rapidly than the alloys, short immersions produced films on Cu which exhibited large photopotentials.

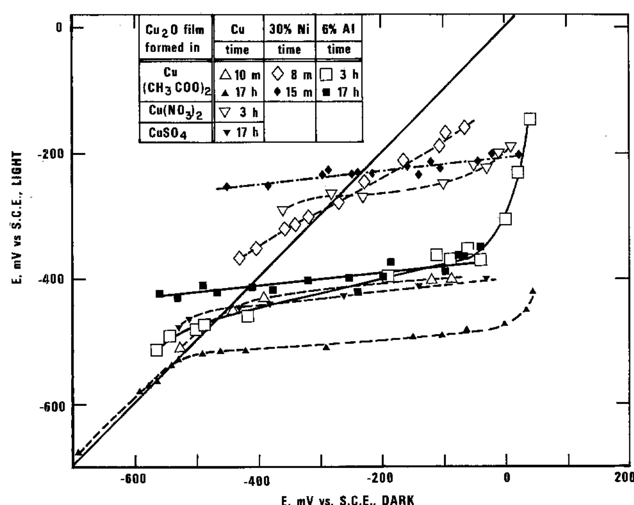

Fig. 1. Potential under illumination *vs.* potential in the dark for various electrodes with Cu_2O film formed in different copper solutions. Measurements taken in 1:1 H_3BO_3-$Na_2B_4O_7$.

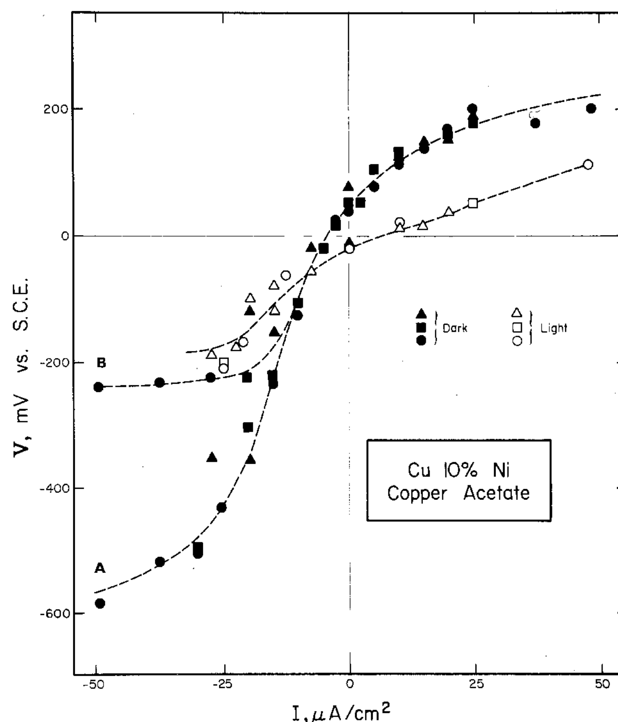

Fig. 2. Effect of light on galvanostatic current-potential curves for Cu 10% Ni in 0.05M Cu acetate. Different mark shapes correspond to different runs. Curve A, initial values. Curve B, steady state.

If the oxide film, on the contrary, is produced by exposing the metal to air or to a neutral solution not containing copper, the photoresponse is similar to that of bulk, melt-grown Cu_2O, in that it is positive at open-circuit and more cathodic potentials, with reversal to a negative signal occurring by anodic polarization. The results on bulk Cu_2O are shown in Fig. 3. The potential changes with illumination are, however, much larger on bulk Cu_2O than on film-covered metal specimens, where, typically, the signal is of the order of a few millivolts. Transient peaks, particularly in the region where signal reversal occurs, are observed on this kind of oxide also, making uncertain the determination of the potential for signal reversal.

If the experiments are carried out under potentiostatic conditions, the light current signal has, of course, a sign opposite to that of the voltage signal under galvanostatic conditions. Figure 4 shows a potentiodynamic scan on a Cu_2O-covered copper electrode in borate solution. Light produces large increases in cathodic current below the inversion point which occurs at about −400 mV. Around this value, the transients show complex shapes. On the anodic side the signal is smaller, and it is undetectable above about 600 mV.

It was found that the photoresponse could be eliminated both by reduction at very low potentials, when hydrogen evolution, or in Cu acetate solution, copper deposition occurred, or by strong anodic polarization at about + 1V *vs.* SCE. The photosensitivity, however, could be detected over a wide range of potentials, typically from −700 mV to +700 mV and, if destroyed tended to reappear within times of the order of 1 min at open circuit even before the potential had decayed back to its final open-circuit value.

Behavior in redox solution.—Measurements have been taken on some electrodes in solutions of $K_4[Fe(CN)_6]$ and $K_3[Fe(CN)_6]$, both 0.1M, plus 0.2M sodium acetate. The *p*H of the solution was 8 and the potential of a Pt electrode was about +230 mV *vs.* SCE. The purpose of the measurements was to establish the n- or p-character of the surface film from its current-potential and photoresponse behavior. Unfortunately there is a strong tendency to form layers of insoluble copper ferro- and ferricyanide, so that the reproducibility of the results is poor. Nevertheless, the behavior observed is in agreement with the assumption that the oxide film formed by reaction with copper acetate is an n-semiconductor and that formed by anodic oxidation is a p-semiconductor.

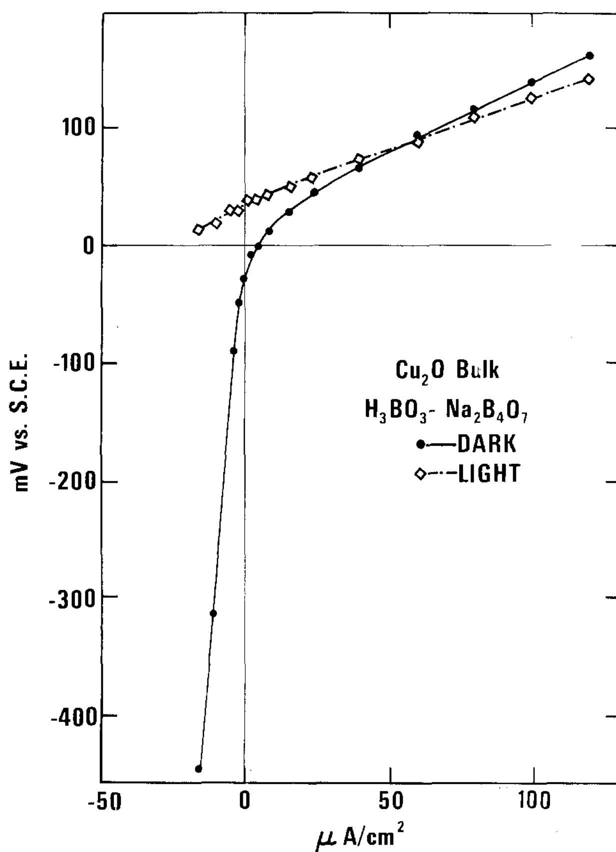

Fig. 3. Effect of light on galvanostatic current-potential curve for bulk Cu_2O in 1:1 H_3BO_3-$Na_2B_4O_7$.

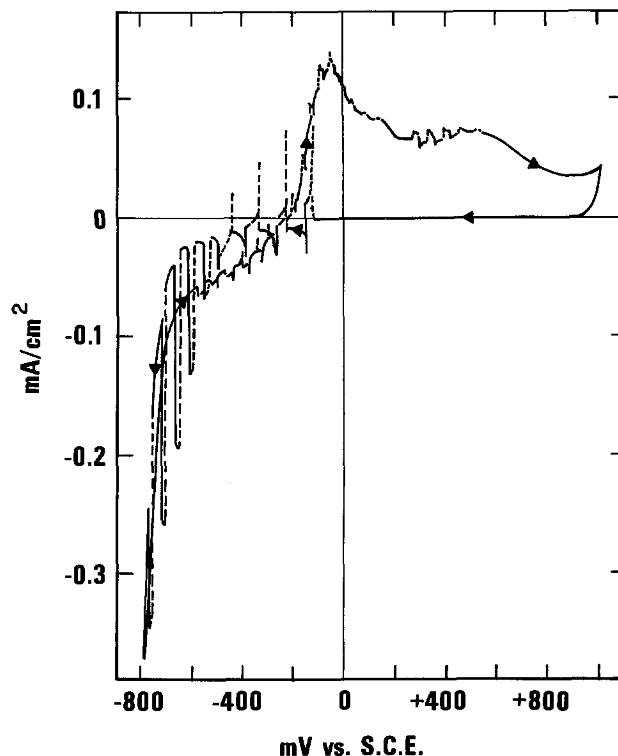

Fig. 4. Effect of light during potentiodynamic scan for Cu with Cu_2O film formed in Cu acetate. Solution, 1:1 H_3BO_3-$Na_2B_4O_7$; scan rate, 8 mV/sec; solid line, dark; dotted line, light.

Figure 5 shows a potentiodynamic scan of a 30% Ni Cu alloy which had been passivated at +700 mV *vs.* SCE in borate buffer. The anodic-cathodic dissymmetry is quite striking, pointing to a p-character in the film. Similar curves taken on pure copper and Cu-Al alloy have given rather confusing and irreproducible results, indicating a tendency for the electrode to react forming a reddish tarnish. Ferrocyanide films were detected on the electrode surface. However, the anodic branch always showed current densities five to ten times larger than the cathodic branch. The rest potential tended to be about 100 mV more negative than the equilibrium redox potential, again indicating a mixed potential.

The potentiodynamic scans of electrodes covered with Cu_2O film resembled those obtained in borate and acetate. The ferrocyanide/ferricyanide reaction did not seem to play an important role. The effect of light on one of these electrodes is shown in Fig. 6. Negative photopotentials were observed at open circuit (about +20 *vs.* SCE). The inversion of the steady-state photopotential signal occurs approximately at −250 mV, but if the initial spike is observed with an oscilloscope, the inversion occurs at about −400 mV.

A-c impedance measurements.—Cuprous oxide is a material that exhibits photoconductivity. It was interesting, therefore, to see if some of the effects observed could be attributed to a decrease in the ohmic drop in the oxide film under illumination. For this purpose, a small constant 200 Hz a-c current (of the order of 1 $\mu A/cm^2$) was passed through the cell during galvanostatic photopotential measurements, and the absolute value of the electrode impedance was recorded as a function of time. In the case of the

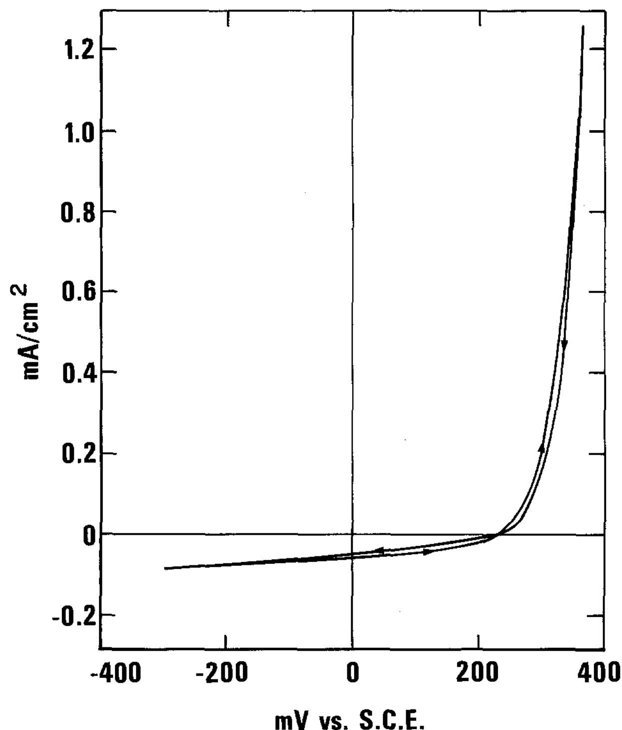

Fig. 5. Potentiodynamic scan for Cu 30% Ni in 0.1M $K_3[Fe(CN)_6]$ + 0.1M $K_4[Fe(CN)_6)]$ + 0.2M $NaCH_3COO$. Scan rate, 1.6 mV/sec. The electrode had been passivated in boric-borate solution at +700 mV *vs.* SCE.

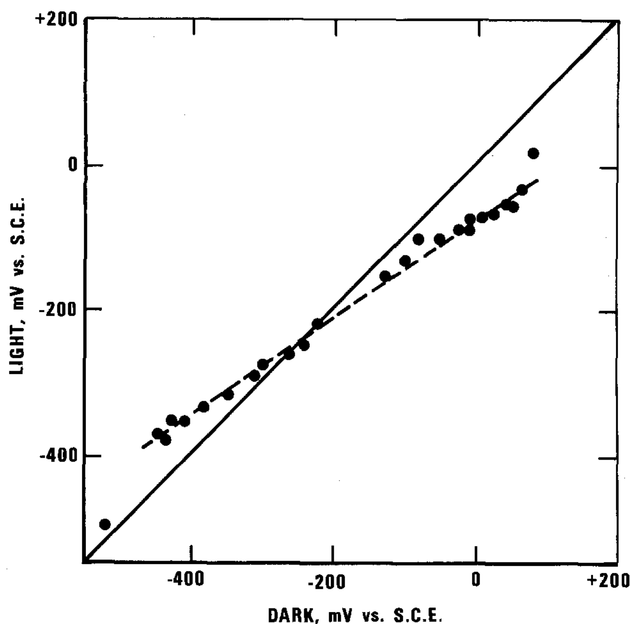

Fig. 6. Potential under illumination *vs.* potential in the dark for Cu 30% Ni with Cu_2O film formed in Cu acetate. Solution: 0.1M $K_3[Fe(CN)_6]$ + 0.1M $K_4[Fe(CN)_6]$ + 0.2M $NaCH_3COO$.

anodically produced film, the impedance was small and the decrease under illumination was hardly detectable. For the case of a film formed by reaction with Cu acetate, the effect was quite large. Figure 7 shows both a-c impedance and d-c potential for pure copper, where both light and dark transitions were quite sharp. Similar results were obtained on the other materials studied, but for the 30% Ni alloy the recovery of the dark value was much slower.

In order to establish, however, whether the impedance changes were due to a change in ohmic drop or to a decrease of charge-transfer resistance, some experiments were carried out using a phase-sensitive

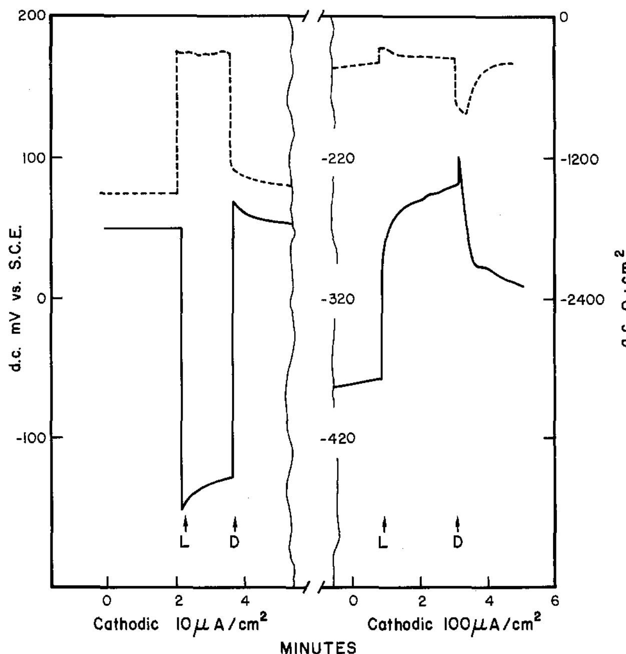

Fig. 7. Effect of light on electrode potential and on impedance at 200 Hz for Cu in 0.05M copper acetate. Solid line and left scale d-c potential; dotted line, and right scale, a-c impedance.

lock-in amplifier so as to measure both the real and imaginary part of the impedance. The measurements were done at open circuit, spanning a frequency range from about 30 KHz to as low as 5 Hz. The curves obtained in the dark and under illumination for Cu_2O covered copper in borate, and for bulk Cu_2O in copper acetate are shown in Fig. 8 and 9. The results show clearly that no change in ohmic drop resistance occurred under illumination since the high frequency limit of the real component was not affected by light. In the case of Fig. 9, for a system where the electrode is substantially in equilibrium for the Cu^+/Cu^{++} transition it appears clearly that the charge-transfer resistance decreases considerably with light, whereas the ohmic drop does not.

Discussion

The interpretation of photogalvanic effects on semiconductor electrodes has been based on the general

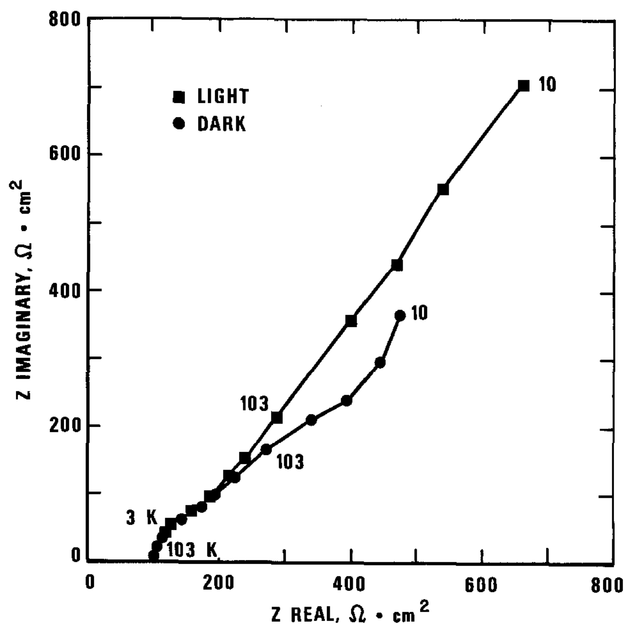

Fig. 8. Imaginary impedance *vs.* real impedance for Cu with Cu_2O film formed in Cu acetate, under illumination and in the dark. Open cirruit. Solution: 1:1 H_3BO_3-$Na_2B_4O_7$. Frequency as parameter.

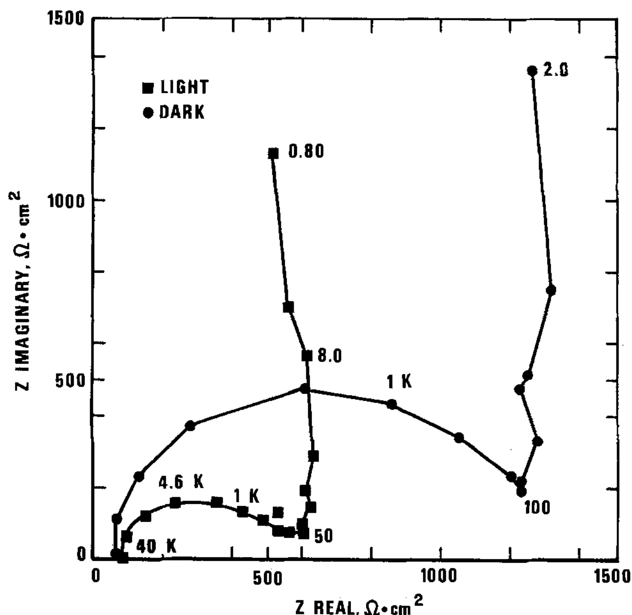

Fig. 9. Imaginary impedance vs. real impedance for bulk Cu_2O in 0.05M Cu acetate, under illumination and in the dark. Open circuit. Frequency as parameter.

treatment of semiconductor electrochemistry. The same principles, therefore, ought to be applied in the case of oxide films, although complications can be expected due to the fact that, in the case of the films, light could penetrate to the semiconductor-metal interphase, and also that the thickness of the film would be very often less than the thickness of the space-charge region in a bulk semiconductor.

The sign of the photopotential as a function of the sign of the majority carrier at or close to equilibrium can be obtained from the treatment given by Dewald (7). More recently Oshe and Rozenfeld (8, 9) have obtained the same conclusion, that is, a negative photopotential for n-semiconductor and a positive one for a p-semiconductor by assuming that, upon illumination, diffusion transport and electromigration would compensate each other and that deviations from stoichiometry in the oxide film would provide the recombination centers for the charge carriers. According to this interpretation the photopotential can become a tool for probing the composition of the oxide film.

The results presented here, as far as open-circuit conditions are concerned, confirm the usefulness of photopotential for obtaining information on the characteristics of the oxide film.

On the basis of the results presented here, it has to be concluded that alloying copper with Ni or Al, although it affects the corrosion resistance of the metal, has little influence on the semiconducting properties of the surface film. On the contrary, the method of preparation of the oxide film is much more important, as shown by the large negative potential shown by the cuprous oxide produced by reaction with Cu^{++} ions in solution. That alloying changes the photoresponse of Cu-based alloys only in minor ways is perhaps understandable, since other workers have found very small concentrations of the alloying metal in tarnish films (10).

The amplitude of the photopotential signal on these films is quite interesting since it can bring the potential of the electrode below the value of the Cu_2O/Cu equilibrium, and causes, therefore, the destruction of the oxide film under illumination. This result might have implications for the corrosion behavior of copper and copper alloys. It is, for example, known that copper can exhibit stress corrosion cracking in the dark, but not in the light (11).

The photopotential response has been used in probing the properties of the oxide film not only at open circuit, but also under polarization (2, 9). Reversal of the signal of the photopotential in these conditions, an effect already described many years ago (12), has been interpreted as caused by a change in the defect structure of the film. In light of the present results, considering how rapidly the photoresponse can be modulated by polarizing the electrode, it is very unlikely that this interpretation is correct, even if care is taken to observe the sometimes complex transients occurring when the light is switched on and off. However, as this study shows, the examination of the effect of polarization on the photosignal can give useful information on the range of stability of the semiconducting oxide and on the rate of its formation, once it has been destroyed.

Manuscript submitted Oct. 3, 1977; revised manuscript received May 4, 1978.

Any discussion of this paper will appear in a Discussion Section to be published in the June 1979 JOURNAL. All discussions for the June 1979 Discussion Section should be submitted by Feb. 1, 1979.

Publication costs of this article were assisted by the National Bureau of Standards.

REFERENCES

1. P. L. Bonora, G. P. Bolognesi, G. Trabanelli, and F. Zucchi, *Ric. Sci.*, **39**, 145 (1969); P. L. Bonora, G. P. Bolognesi, and G. Trabanelli, *Ann. Chim.*, **61**, 834 (1971); G. Trabanelli, G. Brunoro, F. Zucchi, and G. P. Bolognesi, *Ann. Univ. Ferrara, Sez. V*, **3**, 79 (1973).
2. G. Trabanelli, F. Zucchi, and G. Brunoro, *Thin Solid Films*, **13**, 131 (1972); G. Trabanelli, F. Zucchi, G. Brunoro, and V. Carassiti, *Werkst. Korr.*, **24**, 602 (1973); G. Trabanelli, F. Zucchi, G. Brunoro, and G. Gilli, *Met. Ital.*, **7/8**, 446 (1973).
3. R. F. North and M. J. Pryor, *Corr. Sci.*, **10**, 297 (1970); R. G. Blundy and M. J. Pryor, *ibid.*, **12**, 65 (1972).
4. M. Stern and A. C. Makrides, *This Journal*, **107**, 782 (1960).
5. C. E. Guthrow and G. T. Miller, *ibid.*, **113**, 415 (1966); R. W. Topham and G. T. Miller, *ibid.*, **113**, 421 (1966).
6. H. A. Arbit and K. Nobe, Report No. 62-40, Dept. of Engineering U.C.L.A. (1962); p. 461, Fig. 4.1.18, in "Encyclopedia of Electrochemistry of the Elements," Vol. II, A. J. Bard, Editor, Marcel Dekker, New York (1974).
7. J. F. Dewald, in "Semiconductors," N. B. Hannay Editor, p. 727, Reinhold, New York (1959); J. F. Dewald, in "The Surface Chemistry of Metals and Semiconductors," H. C. Gatos, Editor, p. 205, John Wiley, New York (1959).
8. E. K. Oshe and I. L. Rozenfeld, *Zashch. Met.*, **5**, 524 (1969).
9. E. K. Oshe and I. L. Rozenfeld, *Elektrokhimya*, **4**, 1200 (1968).
10. H. Gabel, J. A. Beavers, J. B. Woodhouse, and E. N. Pugh, *Corrosion (Houston)*, **32**, 253 (1976).
11. E. Escalante and J. Kruger, *This Journal*, **118**, 1062 (1971).
12. M. Theodoresco, *J. Chim. Phys.*, **31**, 433 (1934).

EMF Measurements on Electrochromic Amorphous Li_xWO_3 Films

Sarat K. Mohapatra*[,1] and Sigurd Wagner*[,2]

Bell Laboratories, Holmdel, New Jersey 07733

ABSTRACT

We report the electromotive force of cells with amorphous lithium tungsten bronze film cathodes. The cathodes were incorporated in electrochromic cells of the type Au|Li|1M $LiClO_4$ in propylene carbonate|Li_xWO_3|Au. Li-concentrations, $0 < x < 0.54$, were established by coulometric titration. Up to $x = 0.4$ the films consist of a single phase with a strongly concentration-dependent emf. A constant emf of 2.0V at $x > 0.4$ suggests the existence of an intermediate Li-WO_3 phase.

Electrochromic cells incorporating lithium tungsten bronze films are being considered for passive display applications (1). The emf measurements reported here are part of a quantitative study of the rate-determining processes and the stability of such cells. In an earlier publication the kinetics of coloration and of bleaching were presented (2). In coloration, transfer of Li^+ from the electrolyte into the WO_3 constitutes the slowest step. The over-all cycle time is determined by the rate of bleaching that depends on a space-charge limited current of Li^+ and e^- within the WO_3 film. This current is proportional to the mobility of Li^+ (μ_{Li^+} (WO_3) $= 5.3 \times 10^{-9}$ cm^2 V^{-1} sec^{-1}) which is an order of magnitude lower than μ_{H^+} (WO_3). Therefore, the coloration/bleaching cycle of Li_xWO_3-based cells takes about ten times longer than that of H_xWO_3 cells. Thus longer cycle duration appears to put Li_xWO_3 at a disadvantage to H_xWO_3. However, Li_xWO_3 is in certain respects more stable than H_xWO_3, *e.g.*, against oxidation and therefore might offer better long-term stability.

1 cm^2 WO_3 films 0.3-0.9 μm thick were electron-beam evaporated onto In_2O_3-coated glass substrates (PPG Nesatron). The film thickness at steps to the substrate was determined by interference microscopy ($\lambda = 0.589$ μm) after evaporation of a reflective Ag layer. Across samples the thickness varied by less than 7%. The electrolyte consisted of a solution of 1M $LiClO_4$ (dried at 100°C in air for 7-8 hr) in propylene carbonate (twice vacuum-distilled at 100°C and 1 Torr). The glass cell of the type employed for coloration studies was assembled in a dry box. During the experiments the space over the electrolyte was kept exacuated.

The Li concentration was adjusted in steps by coulometric titration with 50-100 mC of Li^+ apportioned by means of a Keithley 225 constant current source. After titration the external circuit was switched to a Keithley 602 electrometer for emf measurement. Steady emf values were reached within 15 min when $x < 0.4$. While the titration was always carried out at 23°C, measurements were also taken at 2° and 36°C, all temperatures being established in a water bath.

Emf and $\Delta\overline{G}_{Li}$ as a function of x are plotted in Fig. 1 for three cells at 23°C. Emf's for 2° and 36°C, respectively, lay within 5 mV of the 23°C values for each cell. The differences in the emf between the cells probably arise from different oxygen activities in the three WO_3 films (3). The standard free energy of formation $\Delta G(x\text{Li} + WO_3 = Li_xWO_3)$ obtained from a Gibbs-Duhem integration is shown in Fig. 2.

The leveling off at 2.0V of the emf for $x > 0.4$ suggests coexistence of $Li_{0.4}WO_3$ with a Li-rich WO_3 phase. This interpretation corroborates the earlier observation (2) of irreversible coloration at $x > 0.4$. While Li_xWO_3 layers are blue at $x < 0,4$, they turn

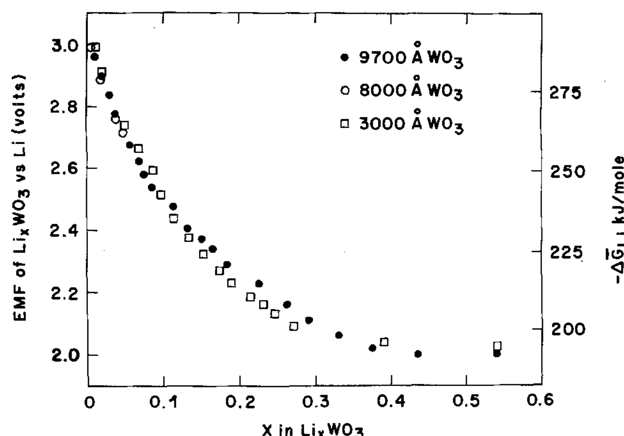

Fig. 1. Emf and $\Delta\overline{G}_{Li}$ as a function of Li content x for three cells at 23°C.

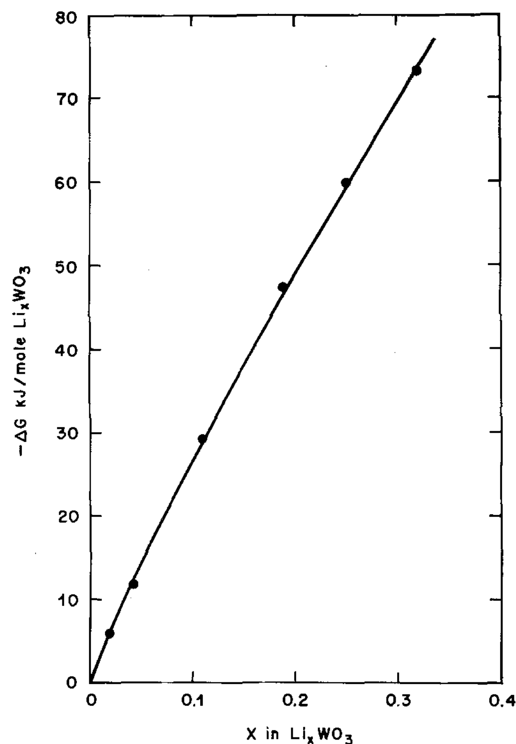

Fig. 2. $\Delta G_{Li_xWO_3}$ as a function of Li content x

* Electrochemical Society Active Member.
[1] Present address: Coulter Systems Corporation, Bedford Massachusetts 01730.
[2] Present address: Solar Energy Research Institute, Golden, Colorado 80401.

Key words: electrochromism, tungsten bronze, display.

pink at $x > 0.4$. Crystalline tungsten bronzes normally change color from blue to red with increasing alkali content (4). In the present case the shift of the principal absorption band from the infrared (700-1100 nm) to the ultraviolet (<350 nm) is so drastic that it may also be taken as indication for the formation of a new phase. The equilibration times in the two-phase region were found to be much longer than those at $x < 0.4$.

The existence of an intermediate phase constitutes one distinction between electrochromic Li_xWO_3 and H_xWO_3 films. In H_xWO_3-based cells (5) the emf varies continuously up to the highest hydrogen concentration reported, $x = 0.4$ (Fig. 3). However, amorphous $H_{0.35}WO_3$ is in equilibrium with H_2 at atmospheric pressure. Films with $x > 0.35$ are metastable against decomposition to $H_{0.35}WO_3$ and H_2 gas. Thus any intermediate phase with $x > 0.35$ will not be stable. The low stability of amorphous H_xWO_3 films is not surprising in view of the marginal stability of crystalline $H_{0.18}WO_3$ (tetragonal B phase) and $H_{0.35}WO_3$ (tetragonal A phase) (6).

A marked dependence of the emf on x distinguishes the amorphous tungsten bronze films from their crystalline counterparts. The data cannot be fitted to either a linear dependence of the partial excess free energy

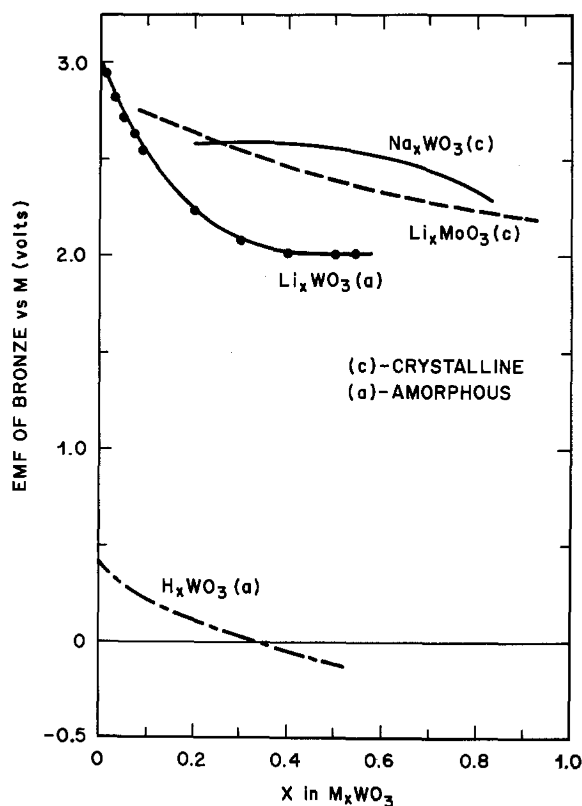

Fig. 3. Emf vs. pure component M at atmospheric pressure of amorphous H_xWO_3 [Crandall *et al.* (5)], Li_xWO_3 (this study) and crystalline Li_xMoO_3 and Na_xWO_3 [Whittingham (3)].

of Li on the mole number, x_{Li} (5), as formulated by Crandall *et al.* (5), or to the square of the mole fraction of the solvent $1/(1 + x_{Li})^2$, the well-known Bragg-Williams model. One might argue that this failure arises from improper formulation of the entropy of mixing. The linear presentation (5) assumes random distribution of one Li^+ and one electron per WO_3. As pointed out by Ramanarayanan and Worrell (7), this implies unit Li activity for the composition $LiWO_3$ which most likely is not the case. On the other hand, a mixture of Li and WO_3 in any proportion, as assumed in the quadratic formalism, disregards the filling of the cubic interstitial sites that has been observed in crystalline tungsten bronzes. In any case a simple pairwise interaction for the enthalpy is not an adequate formulation. While the question of the ideal entropy of mixing is of fundamental importance, it is of little consequence in the present case since the emf is determined by the large partial molar enthalpy of Li. The highest observed variation of the emf with temperature was 5 mV in the range from 2° to 36°C This corresponds to a partial molar entropy of Li of 14 JK^{-1} $mole^{-1}$.

Emf data for crystalline Li_xWO_3 are not available. For comparison with the emf of amorphous Li_xWO_3 films we have plotted (Fig. 3) emf's of crystalline Na_xWO_3 (3) and Li_xMoO_3 (8) as presented by Whittingham (3). The cubic "interstitial" sites in the crystalline bronzes are highly degenerate so that the emf is nearly independent of x. The marked dependence of the emf on composition for amorphous Li_xWO_3 films suggests a large spread in energy of the sites in amorphous WO_3 that accommodate Li. Only a small fraction of these sites lies at energies (emf's) as low as might be expected for crystalline Li_xWO_3, *i.e.*, ~3 eV. Our measurements also show that the partial excess entropy of Li is negligible. Therefore, the Li sites are distributed at random.

Acknowledgments

We would like to acknowledge valuable discussions with Dr. G. Beni and Professor A. Wold.

Manuscript submitted Nov. 14, 1977.

Any discussion of this paper will appear in a Discussion Section to be published in the June 1979 JOURNAL. All discussions for the June 1979 Discussion Section should be submitted by Feb. 1, 1979.

Publication costs of this article were assisted by Bell Laboratories.

REFERENCES

1. J. H. McGee, W. E. Kramer, and H. N. Hersh, *Society Inf. Disp. Int. Symp. Dig.*, **6**, 50 (1976).
2. S. K. Mohapatra, **125**, 284 (1978).
3. M. S. Whittingham, *ibid.*, **122**, 713 (1975).
4. P. G. Dickens and M. S. Whittingham, *Q. Rev. Chem. Soc.*, **22**, 30 (1968).
5. R. S. Crandall, P. J. Wojtowicz, and B. W. Faughnan, *Solid State Commun.*, **18**, 1409 (1976).
6. P. G. Dickens, J. H. Moore, and D. J. Neild, *J. Solid State Chem.*, **7**, 241 (1973).
7. T. A. Ramanarayanan and W. L. Worrell, *This Journal*, **121**, 1530 (1974).
8. L. Companella and G. Pistoia, *ibid.*, **118**, 1905 (1971).

Wettability of Some Carbon Surfaces by Molten Sulfur and Polysulfides

G. J. Janz* and R. M. Murphy

Rensselaer Polytechnic Institute, Cogswell Laboratory, Troy, New York 12181

ABSTRACT

The present communication reports a study of the wetting properties at moderately high temperatures (~350°C) using a modified wicking technique. Strong preferential wetting of bare carbon surfaces by molten sulfur is confirmed through the adhesion tension ratios and the thereby-derived contact angles. The effect of various metal oxide deposits on such properties was investigated and, specifically, the wettability of alumina-treated carbon surfaces by molten polysulfides. A technique for coating the carbon surfaces with metal oxide deposits of good adherence is reported. Some results are reported for the polysulfide transport properties of such treated carbons.

Information on the wetting properties of molten sulfur and polysulfides for carbon surfaces has followed largely from cyclic voltammetry and related techniques in the studies of the processes occurring during the charge-discharge cycling of the sulfur electrode in Na/S cells (1-5). Direct experimental investigations, based on molten salts contact angle measurements (6-8), present a number of difficulties, and with the exception of some provisional measurements for sulfur and polysulfides by Ludwig (4), have not been pursued with molten polysulfides. Capillary penetration of porous materials may also be investigated by wicking (9, 10), a technique in which the substrate is dipped into the liquid and the wetting properties are observed by the liquid rise in the porous "wick." In the present communication we report an investigation of the wetting properties of molten sulfur and polysulfides at Na/S cell operating temperatures (350°C) by this approach. The purpose was to gain insight on the relative wetting properties of these two fluids for various carbon surfaces and to investigate these with modified carbon surfaces, *e.g.*, metal oxide deposits. The preparation of a series of treated carbon surfaces was undertaken and is reported, together with the results of a series of wicking measurements with molten sulfur and polysulfides.

Experimental

Polysulfides.—Na_2S_4 (Alfa-Ventron) was used both "as received" and after toluene extraction. Last traces of toluene were removed at ~ 150°C and 10^{-2} Torr dynamic vacuum. In the latter step small amounts of sulfur sublimed (identified by mp and Raman spectra); we attribute this to the small but finite sulfur pressures reported for polysulfides (11) rather than trace impurities. Sulfur (Fisher, reagent grade) was used in the limited series of sulfur-wetting measurements. It was used "as received," except for predrying (85°C, 10^{-4} Torr dynamic vacuum). All transfers were effected in dry N_2 atmospheres.

Carbons.—Electrographitic rod (Arco Speer Grade 580) and WDF Graphite Felt (Union Carbide Corporation) were used for the wettability measurements. The pore size distributions, gained from Hg intrusion porosimetry, are summarized in Table I, together with the results for massive graphite (block) and vitreous carbon (foam) for comparison. Prior to the wetting measurements, the carbons were acid washed and baked-out at reduced pressures and elevated temperatures (~ 500°C, 10^{-3}-10^{-5} Torr dynamic vacuum).

Metal oxide deposits on carbons.—The decomposition of metal nitrates (12-15) to the oxides, *e.g.*, for a divalent salt

$$M(NO_3)_2 \rightarrow MO + 2NO_2 + \tfrac{1}{2} O_2 \quad [1]$$

offers a method for the deposition of a variety of oxides on carbon surfaces. The following procedure was therefore adopted for the surface treatment of the carbon surfaces: (*i*) Aqueous soak: The carbon specimens are immersed in aqueous solutions of metal nitrates; the soaking period is extended for a time sufficient for penetration of the porous carbons. (*ii*) Nitrate decomposition: The water is removed from the soaked carbons at reduced pressures and moderate temperatures (25°-150°C), and the temperature is increased with the specimens under dynamic vacuum until the nitrate decomposition is complete (*i.e.*, no further evolution of nitrogen oxides). The temperature range for this step must be determined for each metal nitrate; for aluminum nitrate it was in the range of 450°-600°C. (*iii*) Thermal "bake-out": The temperature of the carbon specimens is further increased under reduced pressures to well above the nitrate decomposition temperatures, and the specimens are "baked-out," *e.g.*, in the present work, 10^{-5} Torr; ~ 900°-1000°C.

The weight of the sample on completion of this procedure was noted to gain the amount of the metal oxide thus deposited. The adherence of the deposit was tested after the bake-out, using aliquots with an ultrasonic adhesion test (16).

The surfaces were characterized by scanning electron microscopy (SEM) and x-ray fluorescence. Some illustrative results for a series of alumina deposits on WDF graphite felts are in Fig. 1. The porosity of such treated surfaces was found to decrease ~20% relative to the untreated carbons (Hg intrusion porosimetry). For a series of alumina-coated samples the nature of the surface deposit was analyzed by atomic absorption spectroscopy; the results are summarized in Table II. The agreement with the weight analysis (based on complete decomposition of the nitrate to alumina) provides support for this procedure as a method for the deposition of metal oxides on carbon surfaces.

Table I. Porosity and pore spectra for various carbons

		Pore size distribution		
Sample	Porosity ϵ (%)	Median diam (μm)	Smallest diam (μm)	Diam range for 90% pore space
A*	24.25	3.5	0.005	0.02-30
B	13.62	0.8	0.004	0.02-130
C	11.64	0.02	0.005	0.01-0.05
D	17.77	0.006	<0.003	0.004-0.10

* A, graphite block; B, electrographitic rod; C, graphite felt; D, vitreous carbon foam.

* Electrochemical Society Active Member.

Key words: fused salts, battery, transport, carbon, wettability.

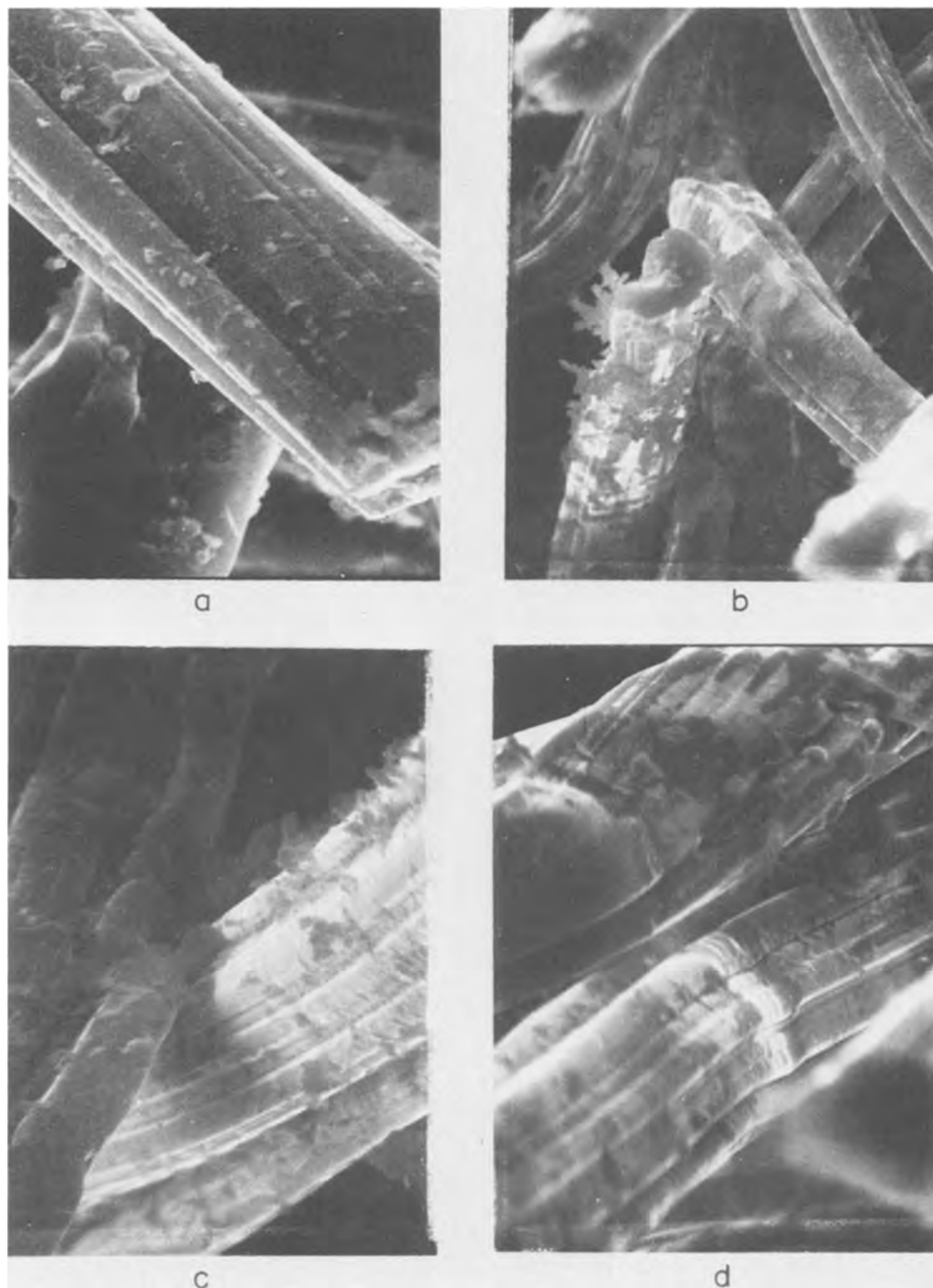

Fig. 1. Alumina-treated graphite felts—SEM photomicrographs. (a) Moderately loaded felt [4.43 w/o $Al(NO_3)_3 \cdot 9H_2O$ soak solution], 5000 times; (b) heavily loaded felt [9.27 w/o $Al(NO_3)_3 \cdot 9H_2O$ soak solution], 2000 times. Both (a) and (b) exhibit a coating of alumina, but (b) has a significant number of dendritic clusters emanating from the fiber axis. (c) Moderately loaded felt, intersection of two fibers, 5000 times; (d) heavily loaded felt, intersection of two fibers, 5000 times. X-ray fluorescence analyses at the felt fiber junctions in (c) and (d) indicate a much higher concentration of Al for (d) than for (c).

Wetting measurements.—The capillary-penetration technique was adapted for the present measurements as follows. For small carbon samples (~ 5 cm length), the experimental assembly is illustrated in Fig. 2. The under-the-pan suspension and analytical balance ensures a vertical alignment for the wicking sample and provides a sensitive detection for the contact of the wick and wicking fluid as the crucible is raised. The temperature gradient in the hot zone at 350°C was ±20° in the arrangement illustrated (Fig. 2). With molten polysulfides (*i.e.*, Na_2S_4) no difficulties were encountered due to vapor transport/condensation on the sample suspension, and the observed weight change correlated well with the amount "wicked." Owing to the high sulfur vapor pressures and consequent recondensation on the suspension, this procedure was modified with molten sulfur. For the latter, the amounts wicked were gained after the sample had been removed from the assembly. To extend the measurements to longer wicks (*e.g.*, 25-30 cm lengths), a second arrangement was used in which the wicking chamber was a sealed long-necked round-bottom flask. The sulfur (or polysulfide) was loaded through a sidearm near the lower part of the wick to minimize contact prior to the wicking measurements. Loading the wicking chamber was done under a dry Argon atmosphere. The chamber was next evacuated to 0.5 Torr and sealed off with a torch. The chamber was vertically positioned in a larger furnace already at the wicking temperatures. The temperature flat zone was ±4° at 350°C over a 32 cm length. The amounts of polysulfide

Table II. Characterization of the coated carbon surfaces

Soak solution [concentration of $Al(NO_3)_3 \cdot 9H_2O$] (w/o)	Sample weight gain (After bake-out) (w/o)	Aluminum content	
		Predicted* (w/o)	Found** (w/o)
0.92	1.26	0.67	0.78 ± 0.05
1.74	1.84	0.97	1.04 ± 0.005
4.43	6.72	3.56	4.88 ± 0.05
9.27	12.49	6.61	4.60 ± 0.05

* From weight gain, assuming surface deposit to be Al_2O_3.
** From atomic absorption spectroscopic analyses.

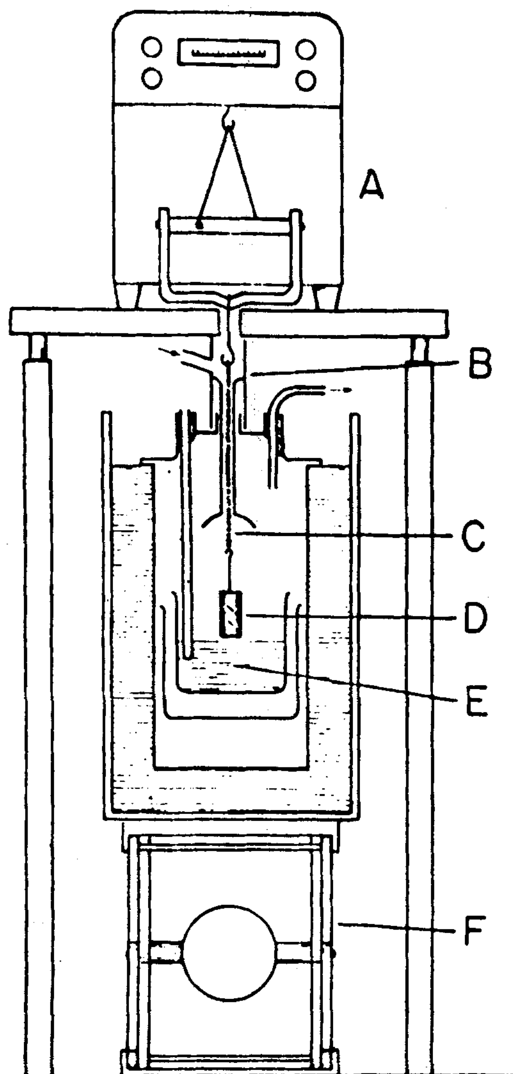

Fig. 2. Small wicking assembly. The porous wick (D) is suspended from an analytical balance (A) with a gold chain (C). The wicking liquid (E) is in a double container (for safety), and a variable height platform (F) is used to raise the liquid until contact with the wick is established. The manifold (B) enables one to maintain an inert and dry atmosphere throughout.

wicked in this series of measurements were gained by sectioning the wick for weight analysis, using a soaking technique to leach out the water soluble polysulfide.

The wetting studies undertaken were as follows: (*i*) Wettability studies of carbon surfaces (bare), with molten polysulfides and molten sulfur; (*ii*) an exploratory series of wettability studies, using a variety of metal oxide deposits on carbon surfaces (in trace amounts); (*iii*) wettability studies, with increasing amounts of metal oxide surface deposits; and (*iv*) some measurements of wettability for carbon surfaces prepared with incompletely decomposed nitrates. The nitrates of cobalt, iron (III), silver, nickel, aluminum, and mixtures (*e.g.*, Co, Al; Ni, Al; Ag, Al; and Fe, Al) were used in the exploratory series at soak solution concentrations from 0.1 to 2 M; for the later follow-up series, the studies were largely limited to alumina-treated surfaces.

Results and Discussion

The results of the wetting measurements with molten polysulfide and molten sulfur and carbon surfaces, the influence of added metal oxides on these surfaces, and the further studies with alumina-treated carbon substrates are discussed.

Carbon surfaces.—Using the electrographitic carbon (rod), a series of wetting measurements with both molten polysulfide (Na_2S_4) and molten sulfur at 350°C were undertaken to investigate the preferential sulfur wettability of such surfaces. The results of this series of measurements are in Table III, and the appearance of the specimens in Fig. 3. It is apparent that the carbon surfaces are readily wetted by molten sulfur, and that, at 350°C, molten polysulfides are relatively nonwetting. With WDF graphite felt wicks, it was observed that sulfur wicked virtually over the complete specimen length (5 cm); by contrast, the polysulfide, as shown in Fig. 3, was found not to wick to any appreciable extent. It is seen that a polysulfide residue "clings" to the porous system; this surface excess was removed mechanically with care prior to the weight analysis (Table III). Nevertheless an uncertainty is imposed on the quantitative nature of the results since it is very difficult to discriminate between a very small capillary rise and the liquid that may cling to the porous substrate (for molten polysulfides). It is of interest, nevertheless, to examine the results from viewpoints of adhesion tension and contact angle.

The adhesion tension, defined as $\gamma \cos \phi$, has been used as measure of the wettability of a substrate surface (17). Here ϕ is the contact angle and γ, the interfacial (surface) tension. The adhesion tension may be calculated from a knowledge of the equilibrium height, h_1 and the classical capillary rise equation, *viz.*

$$\gamma \cos \phi = \rho g r/2 \qquad [2]$$

where r is the average pore radius, and ρ and g are as defined conventionally. Correspondingly the volume of liquid wicked at equilibrium would be $v_e = N\pi r^2 k h_e$, where N is the number of capillaries, and k, the tortuosity factor for the wicking substrate. The equilibrium weights would be $w_e = \rho v_e$. Comparing the results for two fluids (sulfur, s; polysulfide, ps) and the same wicking material, it follows that the adhesion tension ratio is given, simply, by

$$\frac{(\gamma \cos \phi)_s}{(\gamma \cos \phi)_{ps}} = \frac{(w_e)_s}{(w_e)_{ps}} \equiv \frac{(h_e\rho)_s}{(h_e\rho)_{ps}} \qquad [3]$$

and that either measurements of the equilibrium weights or equilibrium heights may be used. In the present work the observed results (Table III) may be taken as equilibrium wicking results; the measurements were under vapor-saturated atmospheres (18, 19), and little, if any, evaporation would be expected from the liquid contents of the felts. The data in Table III show a factor of 10 difference in the weights of liquid wicked. From the adhesion tension criterion, the wettability of the carbon surface at 350°C by molten sulfur would appear as much as 10 times greater than by the molten polysulfide.

Provisional results for the contact angles, by direct observations, have been reported by Ludwig (4). Under a helium atmosphere and short-time measurements, the observed values of ϕ were 20°-30° and 100°,

Table III. Molten sulfur and polysulfide wicking at 350°C (Electrographitic carbon)

Time of wicking (min)	Amount wicked			Penetration limits	
	w (g)	V (cm³)	h (cm)	Pore diam (μm)	V/V^* (%)
Molten Na_2S_4					
30	0.0008	0.0004_4	0.43	1.9	15
60	0.0005	0.0002_7	0.35	2.8	11
90	0.0005	0.0002_7	0.22	1.7	18
120	—	—	0.55	—	—
Molten sulfur					
40	0.0084	0.0050	1.2	0.34	60
60	0.0065	0.0039	0.9	0.29	62
90	0.0066	0.0040	1.0	0.48	57
300	0.0070	0.0042	—	0.34	61

V^*, porous volume in length (h) penetrated.

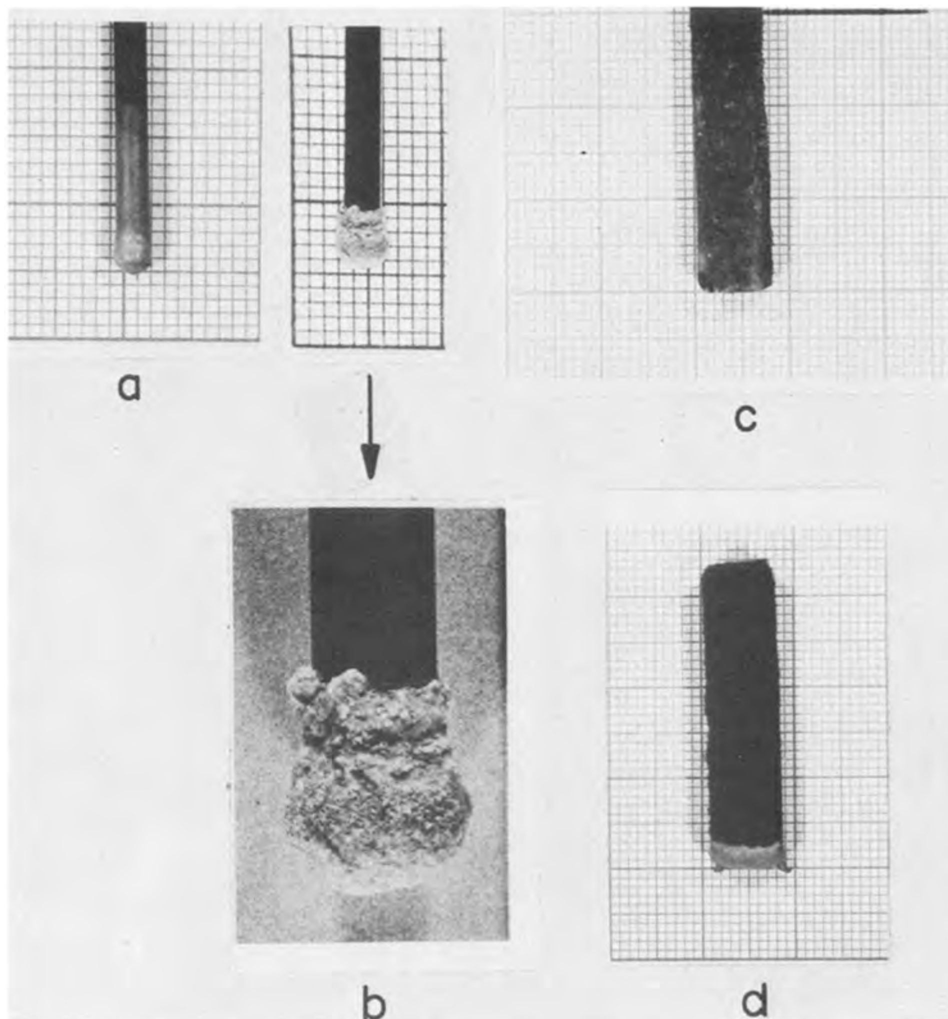

Fig. 3. Wettability of carbon surfaces at 350°C with molten sulfur and molten polysulfide. Bare electrographitic carbon (rod) contacted with (a) molten sulfur and (b) with molten polysulfide. The close-up shows a "nonwetting" globule of molten polysulfide (after solidification). Bare WDF felt wicks, after contacted with molten sulfur and polysulfide at 350°C, are shown in (c) and (d), respectively.

respectively, for molten sulfur and polysulfide at 318°C on graphite surfaces. Taking 25° as a probable value for molten sulfur, and values of the surface tensions for molten sulfur (20) and polysulfide (21) as 46 and 128 dyne cm^{-1} (at 350°C), respectively, it follows from Eq. [3] and the present wicking data (Table III), that a value of 91° is predicted for ϕ_{ps}, *i.e.*, the molten polysulfide is thus predicted to be nonwetting on bare carbon surfaces.

The difficulties of the present technique in discriminating between a very small capillary rise (for ϕ slightly less than 90°) and the liquid residue that may cling to the wick (for ϕ slightly greater than 90°) should be noted relative to the preceding calculations of adhesion tensions and contact angles. The significant result is the observation that porous carbon is much more wettable by molten sulfur than by molten polysulfide. The observations of preferential wetting of carbon graphite surfaces by molten sulfur from cyclic voltammetry and related measurements (1-5) and contact angle measurements (4) are clearly supported by the preceding observations at 350°C.

Metal oxides.—The effects of various metal oxides deposited on both the electrographitic carbon rod and WDF graphite felt were investigated with the small wicking assembly (5 cm length wicks). The amount retained by the wick (after 30-60 min contact with the molten polysulfide) relative to the amount wicked by the untreated (bare) carbon wick provides a measure of the changes in adhesion tensions. With the exception of two metal oxides, aluminum and cobalt, the various metal oxides did not markedly improve the wettability of the carbon surfaces by molten polysulfides. Some of the results for the cobalt oxide and alumina treated surfaces are in Table IV. The amount wicked is given both as weight and weight percent (w/o) (relative to the wick weights prior to the measurements). A quantitative comparison of the relative effectiveness of the various metal oxides is thus shown. It is clear that alumina (either through the thermal decomposition of the nitrate, or as a hydrosol of a dispersable form of alumina, *i.e.*, Dispal) markedly promotes the wettability of the carbon surfaces by molten polysulfides. Inspection of these specimens after the measurements showed that the polysulfide had penetrated the full 5 cm length of the felt wicks. By contrast, the bare felts showed virtually no penetration; the amount "wicked" on the bare carbons (Table IV) can be accounted for as the polysulfide retained as a pendant drop after wick detachment from the molten polysulfide.

To investigate the polysulfide transport properties of alumina-treated graphite surfaces, a series of felt

Table IV. Molten polysulfide wicking of uncoated and coated graphite felts

Surface treatment (WDF graphite felt)	Wicking conditions T (°C)	t (min)	Amount wicked g	(w/o)
1. Bare	350	30	0.1212	123*
2. Bare	350	60	0.1105	107*
3. $Al(NO_3)_3$	350	60	4.2953	1900**
4. Dispal	350	60	3.0860	1090**
5. $Co(NO_3)_2$	350	60	0.3926	290

* Bare felt: the polysulfide was attached as a pendant drop.
** The felt matrix was completely penetrated, *i.e.*, 100% "wicked."

Table V. Molten polysulfide transport by alumina-treated graphite felts

Soak solution (w/o)*	Wicking conditions		Amount of polysulfide wicked (g)					
			Distance above melt surface (cm)					Total (g)
	T (°C)	t (hr)	0-1	1-2	2-3	3-4	4-5	
4.43	350	260	0.2822	0.0093	0.0051	0.0023	0.0000	0.2989
40	350	150	0.9563	0.6331	0.5373	0.2161	0.0894	2.4322

* $Al(NO_3)_3 \cdot 9H_2O$.

wicks were prepared from increasingly more concentrated soak solutions [4-40 w/o $Al(NO_3)_3{\cdot}9H_2O$]. Because of the increasingly larger alumina loadings, the resiliency of the felt matrix is largely lost; the ultrasonic tests for adherence, however, indicated that ~90% of the surface-deposited alumina was adherent at the higher felt loadings. Inspection of the surface morphologies (see, for example, Fig. 1) showed dendritic deposits, with increasing buildups at fiber intersections as the alumina loadings were increased. The polysulfide transported as a function of wick length was gained quantitatively by weight analysis of the felts sectioned into aliquots after each measurement. The results for the limiting felt loadings ("wicked" to equilibrium conditions) are summarized in Table V. The equilibrium heights attained for the two alumina-treated felts were, respectively, 4 and 5 cm for the felts loaded with the 4.43 and 40 w/o nitrate soak solutions; inspection of the amounts wicked shows that the polysulfide transport is almost in the ratio of the soak concentrations, *i.e.*, approximately a nine-fold increase.

Some "exceptionally high" wicking heights were observed in the course of this part of the investigation, *i.e.*, 10 cm and higher, with alumina-treated felts, relatively heavily loaded (soaking concentration, ~ 20 w/o). It seemed possible that these correlated with the felts for which there had been a change in preparative procedure. Such felts had been maintained at ~350°C for the thermal decomposition of the nitrate and had not been subjected to further bake-out at higher temperatures. The studies of the thermal transformation of aluminum salts (13-15) show that $Al(NO_3)_3{\cdot}9H_2O$ decomposition to amorphous Al_2O_3 is not complete at temperatures below 500°-700°C; lower temperatures would lead to markedly different surface deposits. This was confirmed through the preparation of a series of loaded felts with 350°C as the terminal temperature and some subsequent wicking measurements. The results were as follows. With a 20 w/o soak solution, a wicking height of 10 cm was observed after 4 hr, and this had increased to 25 cm after 100 hr (350°C). Samples of this surface-treated felt, prior to wicking measurements, were found to have strong tendencies to rehydrate, *e.g.*, a continuing weight gain was observed. With further heating under dynamic vacuum (500°C, 10^{-5} Torr), both H_2O and nitrogen oxides were evolved.

The very effective transport properties of such alumina-treated felt surfaces may be undoubtedly attributed, in part, to the trace amounts of H_2O inherent with the surface deposits and the consequent species from the following chemical reactions with molten polysulfides at 350°C, but the possibility of the alumina also being in a more "reactive" morphology for polysulfide transport, *e.g.* boehmite, is not ruled out. This is being investigated further, and discussion is deferred until additional results are in hand.

Acknowledgments

The studies reported in this publication were part of a program supported at Rensselaer Polytechnic Institute by a National Science Foundation-RANN contract with Ford Motor Company for sodium-sulfur battery research. We particularly acknowledge with pleasure the discussions with F. A. Ludwig (Ford) on matters that led to the selection of metal nitrates and the long wicking techniques reported in this communication.

Manuscript submitted Feb. 27, 1978; revised manuscript received April 26, 1978.

Any discussion of this paper will appear in a Discussion Section to be published in the June 1979 JOURNAL. All discussions for the June 1979 Discussion Section should be submitted by Feb. 1, 1979.

REFERENCES

1. R. D. Armstrong, T. Dickinson, and M. Reid, *Electrochim. Acta*, **20**, 709 (1975).
2. D. A. Aikens, K. W. Fung, F. A. Ludwig, and R. P. Tischer, Abstract 386, p. 881, The Electrochemical Society Extended Abstracts, Spring Meeting, Toronto, Canada (1975).
3. R. D. Armstrong, T. Dickinson, and M. Reid, *Electrochim. Acta*, **21**, 935 (1976).
4. F. A. Ludwig, *Electrochem. Eng.*, **10**, 391 (1977) and "Advances in Electrochemistry, Chap. 5, Wiley-Interscience, N.Y.
5. M. P. J. Brennan, *Electrochim. Acta*, **22**, 279, 609 (1977).
6. A. Anundskas, K. Grjotheim, A. H. Schultz, H. Svendsen, and H. A. Øye, Paper presented at the Light Metals Conference, 106th AIME Meeting, Atlanta (1977).
7. A. Fontana and R. Winand, *J. Nucl. Mater.*, **35**, 87 (1970).
8. J. G. Eberhart, in "Proceedings Symposium and Workshop on Advanced Batteries, Research and Design," B74 ANL-76-8; NTIS, U.S. Dept. Commerce, Springfield, Va. (1976).
9. R. L. Peek and D. A. McLean, *Ind. Eng. Chem., Anal. Ed.*, **6**, 85 (1934).
10. L. S. Langston and H. R. Kunz, Paper ASME-69-HT-17, presented at the ASME-AIChE Heat Transfer Conference, Minneapolis (1969).
11. R. Tegman, *Chem. Scr.*, **2**, 221 (1972).
12. K. H. Stern, *J. Phys. Chem. Ref. Data*, **1**, No. 3, 747 (1972).
13. K. Funaki and Y. Shimizu, *Kogyo Kagaku Zasshi*, **62**, 788 (1959).
14. A. M. Kalinina and E. A. Porai-Koshito, *Dokl. Akad. Nauk. SSSR*, **114**, 365 (1957).
15. K. Nikolic and K. Velasevec, *Acta Pharm. Jugoslav.*, **10**, 131 (1960).
16. J. T. Kenney, W. P. Townsend, and J. A. Emerson, *J. Colloid Interface Sci.*, **42**, 589 (1973).
17. V. T. Crowl and W. D. S. Wooldridge, "A Method for the Measurement of Adhesion Tension of Liquids in Contact with Powders," from S.C.I. Monograph No. 25, "Wetting," p. 200 ff., Society of Chemical Industry, London (1967).
18. W. A. West and A. W. C. Menzies, *J. Phys. Chem.*, **33**, 1880 (1929).
19. R. Tegman, *Chem. Scr.*, **2**, 63 (1972); see also R. Tegman, Ph.D. Thesis, Univ. Umeå, Sweden (1974).
20. R. Fanelli, *J. Am. Chem. Soc.*, **72**, 4016 (1950).
21. B. Cleaver and A. J. Davies, *Electrochim. Acta*, **18**, 727 (1973).

Film Growth on Dilute Noble Metal Alloys

S. P. Sharma* and J. H. Thomas, III*

Bell Laboratories, Columbus, Ohio 43213

ABSTRACT

A general mathematical model for solute segregation to the surface and subsequent oxide or film development on thin (finite layer) binary noble metal alloys has been formulated. Fick's second law has been solved in a general formalism for time varying boundary conditions, thus coupling corrosion kinetics with the solute diffusion in the alloy. Closed form solutions are presented for the specific cases of linear and parabolic kinetics. Numerical results for parabolic corrosion kinetics are presented along with a procedure for determining the diffusion coefficient for the solute in the alloy if the concentration at the interface is known.

Film growth on noble metal alloys due to solute diffusion to the metal surface and subsequent reaction with a corrosive or oxidizing environment has been the subject of a number of experimental and theoretical investigations (1-7). Interest in this subject is generated primarily by the possible failure mechanisms encountered in dilute noble metal alloys due to substrate or impurity (solute) diffusion (6). For example, experiments have been performed on hard gold electroplates and analytical models developed to describe the formation of oxides of cobalt (4, 5) and copper (8) on electroplated hard gold on copper. In deriving the diffusion coefficients from experimental data, it is generally assumed that the concentration at the film-alloy interface is zero (the "infinite sink" model) (4). However, in experiments, the concentration at this interface is hardly ever measured as zero. This model may hold true in specific cases but its general validity is questionable. Tompkins and Pinnel (8) find that in the Cu-Au system, the presence of chlorine in the environment increases the amount of film formation on the surface. The rate of corrosion, therefore, plays a significant role in diffusion problems. Wagner (3) has studied noble metal alloys (*e.g.*, Au-Ni) and developed an analytical model which assumes that the alloy-film interface varies in position with film growth. Wagner's model coupled film growth kinetics for a parabolic film growth rate with the concentration gradient in an infinite thickness alloy.

In this paper, we present a mathematical analysis in which the rate of film growth has been coupled to diffusion of a solute from dilute noble metal alloys of finite thickness. The diffusion of substrate materials through the noble metal will be the subject of another paper. Our analysis employs Duhamel's (9) theorem to obtain a solution for the solute concentration for a time varying boundary condition in a general case. Closed form solutions have been obtained for parabolic and linear growth kinetics. The diffusion coefficient of the solute in the noble metal is related to the solute concentration at the interface. For the case of parabolic film growth kinetics, numerical solutions are presented. These solutions can be used to compute the solute diffusion coefficient with a knowledge of the film growth kinetics and the solute concentration at the film-alloy interface.

Model Development

The impurity diffusion from a noble metal can be be described by Fick's second law

$$\frac{\partial C}{\partial t} = D \frac{\partial^2 C}{\partial X^2} \quad [1]$$

where C and t represent concentration and time and D is the diffusion coefficient, assumed independent of concentration. It is assumed that diffusion occurs only in the thickness direction of the medium which is bounded by two planes at $X = 0$ and $X = l$ (Fig. 1).

Initially the concentration of the impurity is uniform throughout the noble metal. The initial condition therefore is

$$C(X,0) = C_B \quad [2]$$

As discussed by Goel and Bader (6), the impurity content present nearer to the metal surface at $X = l$ will diffuse out at a faster rate than that present nearer to the medium at $X = 0$. Consequently, we can assume that the concentration gradient at $X = 0$ is zero, *i.e.*

$$\frac{\partial C}{\partial X}(0,t) = 0 \quad [3]$$

As the diffusion proceeds, the impurity on the surface chemically reacts with the environment. In air or an oxygen environment, the impurity is oxidized. The film growth rate and the film thickness can be experimentally determined using Auger/ESCA depth profiling techniques or microbalance measurements. It is important to realize that the mathematical analysis presented in this paper is applicable to the particular situation of a binary alloy where solute is the only reacting specie, that is, the solvent is a noble metal.

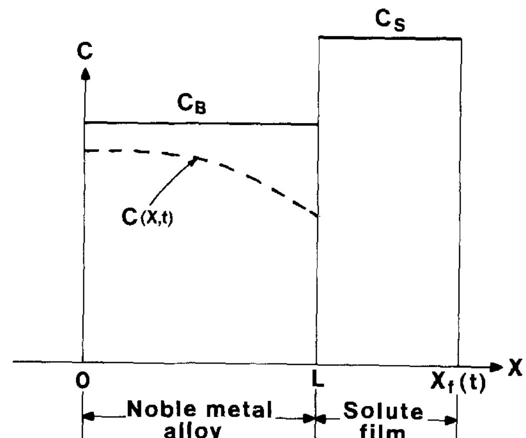

Fig. 1. Diagram of the mathematical model. C_B = bulk solute concentration, $C(X,t)$ = solute concentration at X,t for $0 \leq X \leq L$, C_S = solute concentration in the surface film, X_f = surface film thickness at t, and L = alloy thickness.

* Electrochemical Society Active Member.

Key words: diffusion, solute segregation, corrosion kinetics, oxide films.

Modern analytical techniques (ESCA/Auger, etc.) can also provide the chemical composition of the surface film. The amount of solute in the film (weight percent or atomic percent) can thus be calculated. Therefore, it is assumed in this analysis that the solute concentration in the film is known either from the stoichiometry or from other experimental measurements.

The second boundary condition needed to solve Eq. [1] is derived from the conservation of the solute (10), *i.e.*, the total amount of solute, Q, in the system remains constant

$$Q = \int_0^l C(X,t)\,dX + \int_l^{l+X_f} C(X,t)\,dX \qquad [4]$$

where X_f is the thickness of the corrosion film.

A further mathematical simplification is made by assuming the concentration of solute in the film to be a constant equal to C_s. This assumption is reasonable since the film generally is homogeneous (one phase), and, to first order, the concentration gradient effect (*e.g.*, due to diffusion of cations through the film) is small. Thus

$$Q = \int_0^l C(X,t)\,dX + \int_l^{l+X_f} C_s dX \qquad [5]$$

Using Leibniz's rule of differentiating integrals (11), for Eq. [5] and utilizing Eq. [1] and [3] we get the following boundary condition at $X = l$

$$D\frac{\partial C}{\partial X}\bigg|_{X=l} = -\frac{dX_f}{dt}C_s$$

or

$$\frac{\partial C}{\partial X}\bigg|_{X=l} = -\frac{1}{D}\left(\frac{dX_f}{dt}\right)C_s \qquad [6]$$

Equation [6] is the second boundary condition needed to solve Eq. [1]. This in fact is a time-dependent flux boundary condition at $X = l$, linking the solute flux with the film growth. Initially the growth rate is faster and therefore the impurity flux is higher. As the film growth rate reduces (film thickens), the flux at $X = l$ also reduces. This is physically a very plausible boundary condition and represents the real life diffusion processes more accurately than the infinite sink model or concentration-dependent flux conditions.

The general solution of Eq. [1] subject to initial condition [2] and boundary conditions [3] and [6] is given by Eq. [A-11] as shown in Appendix A, *i.e*,

$$C(X,t) = C_B - \frac{C_s}{D}\int_0^t \frac{\partial}{\partial t}\left\{\frac{dX_f(t-\lambda)}{dt}\right\}F(X,\lambda)\,d\lambda + \frac{C_s}{D}\cdot\frac{dX_f(o)}{dt}F(X,t) \qquad [7]$$

where F is given by Eq. [A-12] in Appendix A.

In order to use Eq. [7] for determining the concentration profiles, a simple computer program utilizing an integration subroutine has been developed. The program consists of ~30-40 instructions and is relatively simple and very inexpensive to use. The film growth rate kinetics is experimentally derived and the rate of film growth dX_f/dt is inserted into Eq. [7]. The resulting concentration profiles can be utilized to derive D and are discussed later.

Equation [7] is the most general solution applicable to any corrosion kinetics. Some of the important film growth rate laws encountered in practice are summarized in Appendix B. Closed form solutions can be obtained in specific cases and two such solutions are discussed below.

Parabolic Growth Rate Model ($X_f^2 = kt$) [8]

The boundary condition [6] in this case becomes

$$\frac{\partial C}{\partial X}\bigg|_{X=l} = -\frac{1}{D}\left(\frac{\sqrt{k}}{2\sqrt{t}}\right)C_s \qquad [9]$$

The Laplace transform of Eq. [9] is

$$\frac{\partial f}{\partial X} = \frac{-\sqrt{k}\sqrt{\pi}}{2D\sqrt{s}}C_s \qquad [10]$$

The solution to Eq. [1] in the transform space in this case is

$$f = \frac{C_B}{s} - \frac{\sqrt{k}\sqrt{\pi}}{2s\sqrt{D}}C_s\frac{\cosh gX}{\sinh gX} \qquad [11]$$

or

$$f = \frac{C_B}{s} - \frac{\sqrt{k}\sqrt{\pi}}{2\sqrt{D}\,s}C_s\sum_{n=0}^{\infty}\{e^{-g[(2n+1)l-X]} + e^{-g[(2n+1)l+X]}\} \qquad [12]$$

Taking the inverse Laplace transform of [12] yields the solution

$$C(X,t) = C_B - \frac{\sqrt{k}\sqrt{\pi}C_s}{2\sqrt{D}}\sum_{n=0}^{\infty}\left\{\operatorname{erfc}\frac{(2n+1)l-X}{2\sqrt{Dt}} + \operatorname{erfc}\frac{(2n+1)l+X}{2\sqrt{Dt}}\right\} \qquad [13]$$

where erfc is the complementary error function. The above solution converges quite rapidly except for large values of (Dt/l^2). At large values of (Dt/l^2), Eq. [7] can be used.

In situations where the value of l is so large that the system can be considered semi-infinite, a simpler solution given by Thomas (5) can be used instead. (Equation [13] reduces by suitable manipulation to his solution by using a coordinate system where $X' = l - X$ and $l \rightarrow \infty$.)

Linear Growth Rate Model ($X_f = k_1t$)

The solution in this case can be shown to be

$$C(X,t) = C_B - \frac{2k_1\sqrt{t}}{D}\sum_{n=0}^{\infty}\left\{\operatorname{ierfc}\frac{(2n+1)l-X}{2\sqrt{Dt}} + \operatorname{ierfc}\frac{(2n+1)l+X}{2\sqrt{Dt}}\right\} \qquad [14]$$

where

$$\operatorname{ierfc} X = \int_X^{\infty}\operatorname{erfc}\xi\,d\xi \qquad [15]$$

Results

Many important film growth processes encountered in practice obey the parabolic growth rate. Thomas (5) in an earlier paper has shown that Co diffusing out of gold oxidizes according to parabolic rate. Wagner (3) has shown that Ni diffusing out of Pt follows parabolic oxidation kinetics. It has been shown in the literature that a substantial number of solutes (used in noble metals) follow parabolic oxidation when they are not in solution. It may therefore be expected that even in solution, the diffusing specie may oxidize according to parabolic growth rate law. For this reason, we discuss this case in detail.

In order to understand the time development of the solution $C(x,t)$, we will first discuss a specific example as shown in Fig. 2a-c. Assume that corrosion proceeds with a rate $k = 10^{-18}$ cm²/sec for parabolic growth kinetics and $C_S/C_B = 50$. The ratio $C_S/C_B = 50$ is representative of the Co-Au system (5). Equation [13], for this case, is solved numerically for various values of k/D (3×10^{-4}, 10^{-4}, and 10^{-6}) and $C(x,t)$ is plotted for various times as a function of x/l in Fig. 2. In Fig. 2a and b, $C(l,t)$, the concentration at the interface, remains constant for times up to ~10^6 sec. As time increases, $C(l,t)$ decreases and eventually becomes zero (with a finite concentration in the alloy layer). In Fig. 2c, $k/D = 10^{-6}$, $C(l,t)$ varies continuously after 10^4 sec. For shorter times, $C(l,t)$ is also fixed at some value close to C_B for $k/D \sim 10^{-6}$.

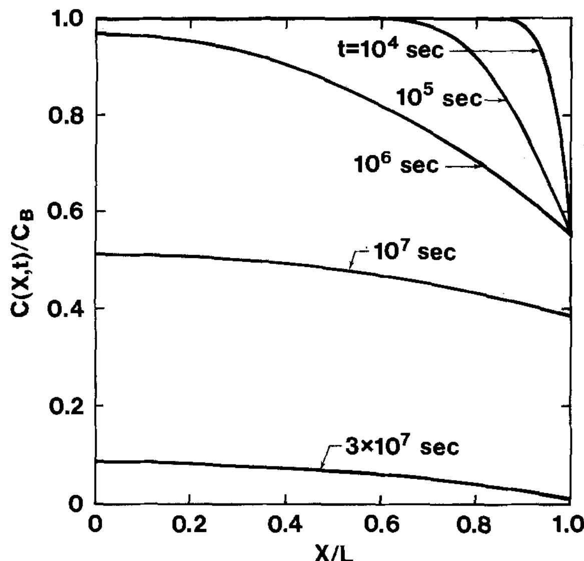

Fig. 2a. $C(X,t)$ is plotted as a function of X/l for $k/D = 10^{-4}$ for various times.

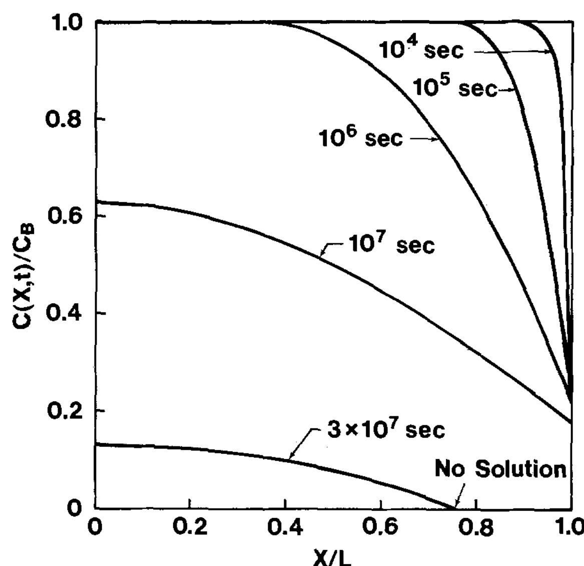

Fig. 2b. $C(X,t)$ is plotted as a function of X/l for $k/D = 3 \times 10^{-4}$ for various times.

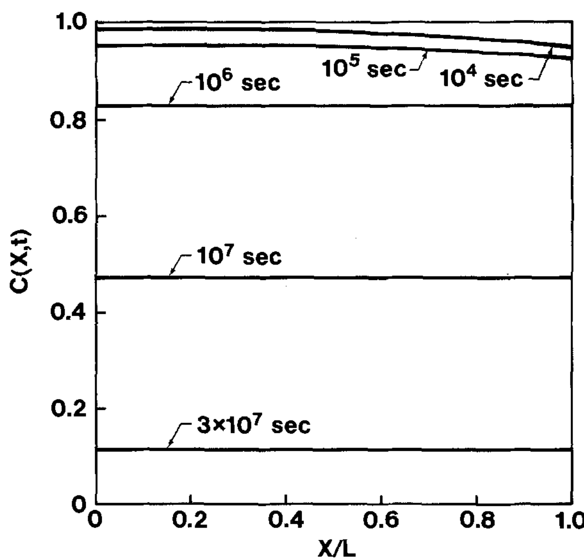

Fig. 2c. $C(X,t)$ is plotted as a function of X/l for $k/D = 10^{-6}$ for various times.

From Eq. [13], $C(x,t)$ at $x = l$ reduces to the following expression

$$C(l,t) = C_B - \sqrt{\frac{\pi k}{4D}} C_s \left\{ 1 + \sum_{n=1}^{\infty} 2 \operatorname{erfc}\left(\frac{nl}{\sqrt{Dt}}\right) \right\} \quad [16]$$

It can be shown from [16] that for $t = 0$ or $l = \infty$

$$C(l,o) = C_B - \sqrt{\frac{\pi k}{4D}} C_s \quad [17]$$

This expression is identical to the expression for $l \to \infty$ in Ref. (5). Therefore, for small times (limit $t \to 0$), the interface concentration is fixed (see Eq. [17]). This is due to the fact that the time-dependent part of Eq. [16] (erfc argument) is much smaller than unity for very large arguments. As the argument of the error function decreases (with increasing Dt), $C(l,t)$ starts decreasing as observed in Fig. 2. Physically, this is a result of finite thickness of the alloy. The error function contribution becomes significant when material (solute) from surface $x = 0$ begins to reach the surface $x = l$. Since D for $k/D = 10^{-6}$ is larger than D for $k/D = 10^{-4}$, the time at which the interface concentration begins to vary is smaller for $k/D = 10^{-6}$ (10^5 sec for $k/D = 10^{-6}$ and 10^7 sec for $k/D = 10^{-4}$). For smaller values of k/D, $C(l,t)$ is approximately equal to C_B initially, and for larger times a uniform depletion of material occurs with $C(l,t)$ decreasing continuously with time. If the diffusion coefficient is much larger than $k(>k(C_s/C_B)^2)$, there is enough time available for the diffusion of material to take place from the interior. Thus at smaller values of k/D (*e.g.*, $k/D = 10^{-6}$ in Fig. 2) no sharp concentration gradient is observed, instead a more or less uniform depletion of material from the entire thickness takes place. At some time the entire solute will be depleted. At smaller k/D values, diffusion is not rate determining. As k/D increases (10^{-4}), *i.e.*, D comparable to $k(C_s/C_B)^2$, it is seen that initially (shorter times) most of the solute material which reacts comes from near the boundary at $X = l$. With increasing time more and more solute material arrives from inside. A sharp concentration gradient exists for these higher k/D values. The concentration profile is very steep initially. As t increases the steepness of the profile decreases. Physically this is very plausible. Since k is larger, the material which arrives on the surface is quickly corroded and diffusion plays a significant role in the over-all process. It is also observed from Eq. [16] that the concentration at $X = l$ reduces with t and at a certain instant of time, $C(l,t)$ becomes zero. The condition for $C(l,t)$ to be zero is

$$\frac{C_B}{C_s} = \frac{\sqrt{\pi}\sqrt{k}}{2\sqrt{D}} \left\{ 1 + \sum_{n=1}^{\infty} 2 \operatorname{erfc} \frac{nl}{\sqrt{Dt}} \right\} \quad [18]$$

The mathematical model breaks down at this time, since the solution after this time predicts a negative concentration at the interface $X = l$, a physically impossible situation. When C becomes zero at the interface, the physical process becomes diffusion controlled and does not explicitly depend on the corrosion rate constant, k. This predicts that when the physical corrosion rate constant is measured, k will be a direct function of D as shown in Eq. [18] rather than independent of D as was the initial premise. At this time, the flux at the interface will depend only on D.

Finally, it is observed that the slope of $C(X,t)$ at the interface becomes very large for times approaching zero. This effect is a manifestation of the model used, that is, $X_f^2 = kt$. Since $dX_f/dt \propto 1/\sqrt{t}$ and when $t \to 0$, dX_f/dt (and thus $dc/dX)_{x=l}$ becomes large ($\to \infty$).

Figure 3 represents the generalized solutions, $C(X,t)$ normalized with respect to C_B (*i.e.*, $C(X,t)/C_B$) plotted as a function of X/l for various values of $l/\sqrt{kt}$ (or l/X_f) and k/D (Fig. 3a is for $C_s/C_B = 50$ and Fig. 3b is for $C_s/C_B = 10$). For a given value of l and k, the high values of l/X_f represent shorter time periods and as t increases, l/X_f decreases. Smaller

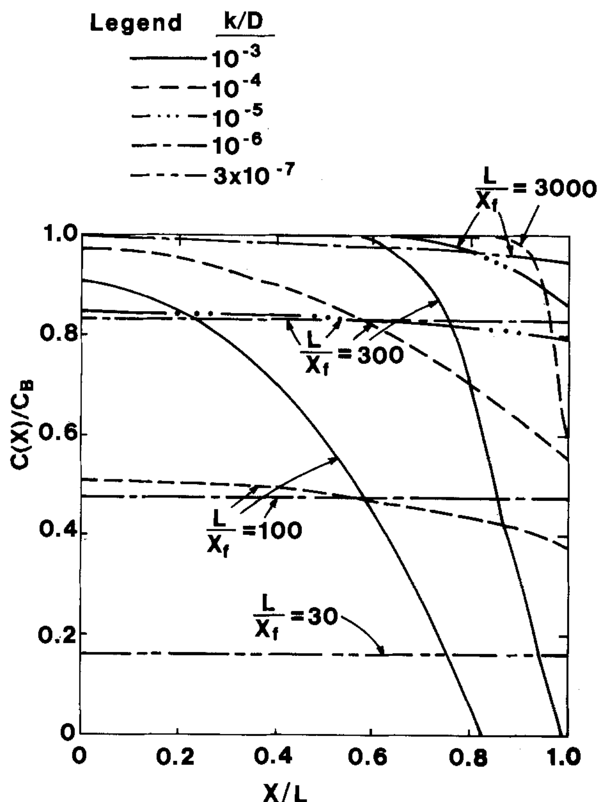

Fig. 3a. Normalized solute concentration is shown as a function of X/l with l/X_f as a parameter for $C_s/C_B = 50$.

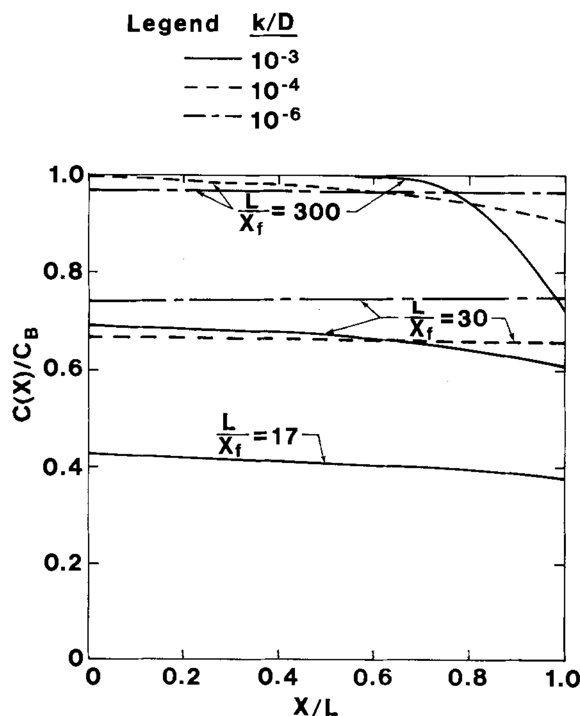

Fig. 3b. The same as Fig. 3a except $C_s/C_B = 10$. l is the alloy thickness, X_f is the solute film thickness, C_s is the solute concentration in the film, and C_B is the bulk solute concentration. For parabolic kinetics $X_f = \sqrt{kt}$.

k/D represents the situation where the oxidation rate (or film growth rate) is slow and the diffusion constant is higher. If the k value increases and/or the value of D decreases (higher k/D ratio), the system may reach a diffusion-controlled situation. The more general case is where the process is controlled by both k and D. It is seen from Fig. 3 that when $D > k(C_s/C_B)^2$, no sharp concentration gradient is observed and a more or less uniform depletion of material takes place. At higher k/D values the concentration profile is very steep initially, that is, its gradient is large as explained above. The slope of the concentration, $C(l,t)$ decreases with time. [This situation is similar to the one discussed in our specific example (Fig. 2) and need not be elaborated further.]

In actual measurements of concentration profiles by AES depth profiling, for example in the case of cobalt-hardened gold, the concentration at the interface can be measured. We believe that in most situations, film growth is not diffusion controlled and, hence, a depth profile would show nonzero concentration at the interface.

Because the concentration at the interface is most significant and can be used to determine material parameters, k, D, etc., a plot of $C(l,t)/C_B$ has been generated as a function of time. Equation [13] can be easily nondimensionalized using the following parameters which are functions of the material system constants, that is

$$(a)\ \frac{X_f}{l}\frac{C_s}{C_B} \text{ and } (b)\ \frac{k}{D}\left(\frac{C_s}{C_B}\right)^2$$

where (a) is basically $\sqrt{t}$ dependence for fixed C_s, C_B l, and k. Figure 4 shows the concentration at the interface, $C(l,t)/C_B$, as a function of X_fC_s/lC_B with $(C_s/C_B)^2\ k/D$ as a parameter. For values of $k/D \times (C_s/C_B)^2$ near unity, the ratio $C(l)/C_B$ remains constant until X_fC_s/C_Bl approaches unity then $C(l)/C_B$ rapidly goes to zero. For a specific case of $l = 3\ \mu$m, and $C_s/C_B = 50$, the concentration at $X = l$ remains constant until the film grows to 200Å. For thicknesses greater than 200Å, the concentration $C(l,t)$ goes rapidly to zero. This behavior holds true for $k/D\ (C_s/C_B)^2 > \sim 10^{-2}$. For smaller values of $k/D(C_s/C_B)^2$ (*e.g.*, 2.5×10^{-4} in Fig. 4) the $C(l,t)$ goes very slowly to zero with time (or film thickness). Figure 5 presents a plot of $C(l,t)/C_B$ as a function of $k/D(C_s/C_B)^2$ for various parameters of C_s/C_B and X_f/l and provides similar information as in Fig. 4.

Figure 6 shows a nomograph from which the parabolic rate constant, k, can be computed knowing the film thickness X_f developed in time t. Figure 6 in conjunction with Fig. 4 or Fig. 5 can be used to compute the diffusion coefficient, D, for known C_s, C_B,

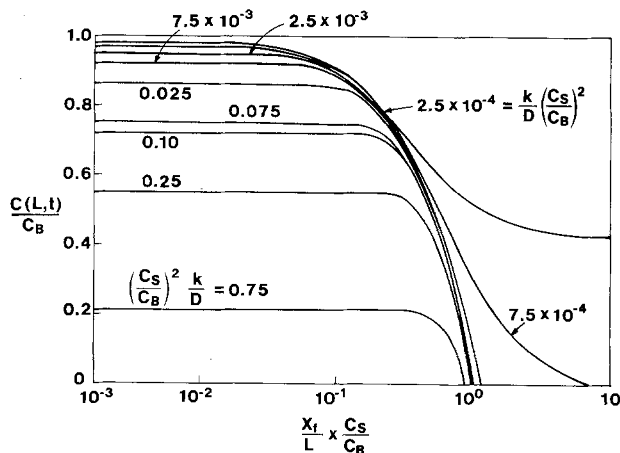

Fig. 4. Normalized solute concentration at $X = l$ is shown as a function of the nondimensional parameter $X_f/l\ C_s/C_B$ with $(C_s/C_B)^2\ k/D$, (also nondimensional) as a parameter.

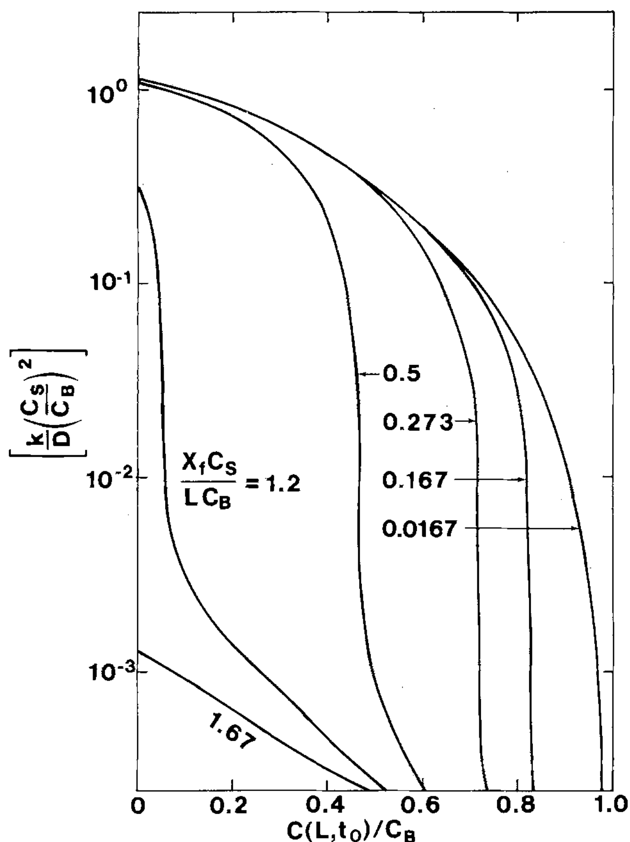

Fig. 5. This plot is similar to Fig. 4 with coordinates and parameters changed. k/D $(C_s/C_B)^2$ is shown as a function of $C(l)/C_B$ with X_f/l C_s/C_B as a parameter.

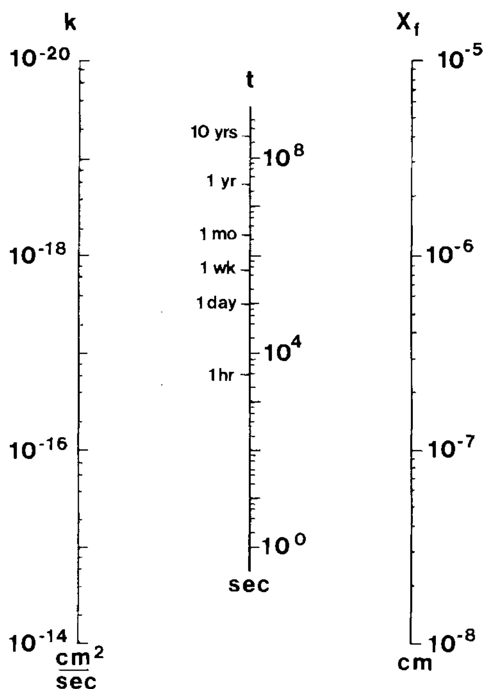

Fig. 6. This nomograph provides a means of computing the parabolic rate constant from film thickness, X_f and time, t.

$C(l)$, and film growth kinetics. Experimentally $X_f(t_o)$ and $C(l,t_o)$ are measured. The parameter $C_s/C_B(X_f/l)$ is then computed. Using Fig. 4 or 5, k/D $(C_s/C_B)^2$ is then obtained. One then computes k from Fig. 6 and proceeds to calculate D. As an example, it is assumed that $C_s/C_B = 50$, $l = 3 \times 10^{-4}$ and that a film thickness $X_f = 80$Å in 1.8×10^6 sec is produced in a certain experiment. For parabolic growth kinetics, k is found to be $\sim 5 \times 10^{-19}$ cm²/sec. If, by measurement, $C(l)/C_B$ is 0.4, the parameter X_f/l (C_s/C_B) can then be calculated as 0.134. From Fig. 5, k/D $(C_s/C_B)^2$ is found to be 0.5. The value of D is calculated to be 2.5×10^{-15} cm²/sec.

Conclusions

In calculating the solute diffusion coefficient from dilute noble metal alloys, the concentration at the alloy-film interface is often assumed to be zero (infinite sink model). Experimentally, the concentration at this interface is seldom zero. We have used a time-dependent flux boundary condition at the film-alloy interface as derived by conserving the total solute in the system. By utilizing this boundary condition, the kinetics of solute film growth has been coupled to the solute diffusion from the alloy. A general mathematical analysis has been presented for different film growth rate laws using Duhamel's theorem. Two specific closed form solutions for parabolic and linear growth rate kinetics have been derived. A method for calculating the diffusion coefficient by measuring the corrosion rate constant and the solute concentration at the film-alloy interface has been outlined for parabolic kinetics. Numerical results for the solute concentration have been presented for this case. It is observed that at low k/D values, no sharp concentration gradient occurs along the thickness of the alloy, *i.e.*, an almost uniform depletion of solute occurs in the entire thickness as a function of time. As the k/D value increases, the concentration changes sharply along the alloy thickness. At some time, $C(l) = 0$, a diffusion-controlled situation is reached. The concentration at the interface has been plotted as a function of the nondimensional parameter $(X_f/l\ C_s/C_B)$ for various values of $k/D(C_s/C_B)^2$. By knowing the concentration at the interface and other material parameters, D can be calculated. Numerical calculations have been shown as an example.

Manuscript submitted Feb. 8, 1978; revised manuscript received May 15, 1978.

Any discussion of this paper will appear in a Discussion Section to be published in the June 1979 JOURNAL. All discussions for the June 1979 Discussion Section should be submitted by Feb. 1, 1979.

Publication costs of this article were assisted by Bell Laboratories.

APPENDIX A

In order to solve Eq. [1] subject to initial condition [2] and boundary conditions [3] and [6], the Laplace transform techniques can be used. The Laplace transform of Eq. [1] with the initial condition [2] is

$$D\frac{\partial^2 f}{\partial X^2} - sf + C_B = 0 \qquad [A\text{-}1]$$

Where s is the Laplace transform variable and $f(s)$ is Laplace transform of $C(X,t)$. The solution of Eq. [A-1] is

$$f = E\cosh gx + F\sinh gx + \frac{C_B}{s} \qquad [A\text{-}2]$$

where

$$g = \sqrt{(s/D)}$$

In order to solve a general problem with time-dependent flux boundary condition, we proceed as follows (9, 13). We first solve an auxiliary problem with the following boundary condition at $X = l$

$$\frac{\partial C}{\partial X} = 1 \text{ at } X = l \qquad [A\text{-}3]$$

In transform form this boundary condition is

$$\frac{\partial f}{\partial X} = \frac{1}{s} \text{ at } X = l$$

We also take the transform of boundary condition [3], *i.e.*

$$\frac{\partial f}{\partial X} = 0 \text{ at } X = 0 \quad \text{[A-4]}$$

Utilizing Eq. [A-3] and [A-4] in Eq. [A-2], we get

$$f(s) = \frac{\cosh gx}{sg \sinh gl} + \frac{C_B}{s} \quad \text{[A-5]}$$

The solution in the time domain is obtained by taking the inverse Laplace transform of Eq. [A-5]

$$C = C_B + \frac{1}{2\pi i}\int_{\gamma - i\infty}^{\gamma + i\infty} \frac{e^{st}\cosh gx}{sg \sinh gl} ds \quad \text{[A-6]}$$

The integral, by Cauchy's theorem, is equal to $2\pi i$ times the sum of the residues at the poles of its integrand. We also assume that γ is so large that all the singularities of $f(s)$ lie to the left of the line $(\gamma - i\infty, \gamma + i\infty)$. There is a double pole at $s = 0$ and the residue at $s = 0$ is

$$\underset{s \to 0}{\text{Limit}} \frac{d}{ds} \left\{ \frac{De^{st} g \cosh gX}{\sinh gl} \right\} = \frac{Dt}{l} + \frac{3X^2 - l^2}{6l} \quad \text{[A-7]}$$

The other poles of $f(s)$ are

$$g = \frac{n\pi i}{l},\ n = 1, 2, 3, \ldots \quad \text{[A-8]}$$

and the residues at $g = n\pi i/l$ (or $s = -n^2\pi^2 D/l^2$) are

$$= (-1)^{n+1}\frac{2}{n^2\pi^2} e^{-(n^2\pi^2 Dt/l^2)} \cos\frac{n\pi X}{l} \quad \text{[A-9]}$$

The solution of Eq. [1] subject to boundary conditions [3] and [A-3] and initial condition [2] is

$$C = C_B + \frac{Dt}{l} + \frac{3X^2 - l^2}{6l} - \frac{2l}{\pi^2} \sum_{n=1}^{\infty} \frac{(-1)^n}{n^2} e^{-(n^2\pi^2 Dt/l^2)} \cos\frac{n\pi X}{l} \quad \text{[A-10]}$$

The above solution is similar to that given in Carslaw and Jaeger (13). In order to obtain the solution of the problem for time-dependent flux boundary condition [6], we use Duhamel's theorem following Churchill (9) (with the aid of convolution property) for the flux boundary conditions. The solution is

$$C(X,t) = C_B - \frac{C_s}{D}\int_0^t \frac{\partial}{\partial t}\left\{\frac{dX_f(t-\lambda)}{dt}\right\} F(X,\lambda)\, d\lambda + \frac{C_s}{D}\cdot\frac{dX_f(0)}{dt}\cdot F(X,t) \quad \text{[A-11]}$$

where $dX_f(t - \lambda)/dt$ is the time varying function of the variable $(t - \lambda)$ and $dX_f(0)/dt$ is the value of dX_f/dt at $t = 0$. The function $F(X,t)$ is the solution of the Eq. [1] with boundary conditions [3] and [A-3] but with zero initial condition and is therefore given by

$$F(X,\lambda) = \frac{D\lambda}{l} + l\left\{\frac{3X^2 - l^2}{6l^2} - \frac{2}{\pi^2} \sum_{n=1}^{\infty} \frac{(-1)^n}{n^2} e^{-(n^2\pi^2 Dt/l^2)} \cos\frac{n\pi X}{l}\right\} \quad \text{[A-12]}$$

Equation [A-11] together with [A-12] represents the solution of Eq. [1] to appropriate boundary conditions [3] and [6] and initial condition [2].

APPENDIX B

Film Growth Kinetics—Laws (14, 15)

Linear growth rate.

$$X_f = k_l t \quad \text{[B-1]}$$

where k_l is the linear growth rate constant. The rate of growth of the film in this case is constant

$$\frac{dX_f}{dt} = k_l \quad \text{[B-2]}$$

Parabolic growth rate.—The most general parabolic growth rate can be described by

$$\frac{1}{k_{p1}} X_f^2 + \frac{1}{k_{p2}} X_f = t \quad \text{[B-3]}$$

where k_{p1} and k_{p2} are the rate constants in appropriate units. The rate of growth dX_f/dt is given by

$$\frac{dX_f}{dt} = \left[\sqrt{\left(\frac{1}{k_{p2}}\right)^2 + \frac{4t}{k_{p1}}}\right]^{-1} \quad \text{[B-4]}$$

In a special case of simple parabolic growth rate we get

$$X_f^2 = kt$$

and

$$\frac{dX_f}{dt} = \frac{\sqrt{k}}{2\sqrt{t}} \quad \text{[B-5]}$$

Asymptotic growth rate.—If the film growth rate approaches some constant thickness X_c in the course of time, the growth rate law may be described by

$$X_f = X_c[1 - e^{-k_a t}] \quad \text{[B-6]}$$

Where k_a is the appropriate rate constant describing the growth characteristic. In this case

$$\frac{dX_f}{dt} = X_c k_a e^{-k_a t} \quad \text{[B-7]}$$

Logarithmic growth rate.—The film growth rate in this case is described by

$$X_f = k_n \log(at + b) \quad \text{[B-8]}$$

and

$$\frac{dX_f}{dt} = \frac{k_n a}{at + b} \quad \text{[B-9]}$$

Inverse logarithmic growth rate.—The growth rate in this case is

$$\frac{1}{X_f} = k_1 - k_2 \log t \quad \text{[B-10]}$$

and

$$\frac{dX_f}{dt} = \frac{k_2}{t(k_1 - k_2 \log t)^2} \quad \text{[B-11]}$$

In addition to above analytical expressions describing the oxidation (film growth) processes which begin at the time $t = 0$, there are many cases where experimental data reflect an over-all result for which two or more independent physical mechanisms are responsible (15). Most of these cases can be judiciously reduced to the above expressions. For example, if one of the processes is described by a linear rate and the other by parabolic

$$X_f = k_l t + \sqrt{k_p t} \quad \text{[B-12]}$$

It may be shown that the resultant curve is a skewed parabola. If there are two simultaneous parabolic processes involved in film growth, *i.e.*

$$X_f = \sqrt{k_{p3} t} + \sqrt{k_{p4} t} \quad \text{[B-13]}$$

the resultant curve is a parabola $X_f^2 = kt$, where

$$k = (\sqrt{k_{p3}} + \sqrt{k_{p4}})^2 \quad \text{[B-14]}$$

Various other situations where some process controls oxidation to certain time $t = \tau$ and at that instant another mechanism takes over, can also be reduced to above cases by suitably choosing the coordinate systems.

REFERENCES

1. K. Hauffe, "Oxidation of Metals," chap. 4.7, Plenum Press, New York (1965).
2. C. E. Birchenall, in "Oxidation of Metals and Alloys," American Society for Metals, Metals Park, Ohio (1971).
3. C. Wagner, *This Journal*, **99**, 369 (1952).
4. H. G. Tompkins, *ibid.*, **122**, 983 (1975).

5. J. H. Thomas, III, *ibid.*, **125**, 898 (1978).
6. R. P. Goel and F. E. Bader, *ibid.*, **123**, 1242 (1976).
7. C. A. Haque, Private communication.
8. H. G. Tompkins and M. R. Pinnel, *J. Appl. Phys.*, **47**, 3804 (1976).
9. See, for example, R. V. Churchill, "Operational Mathematics," pp. 212, 229-231, McGraw-Hill, New York (1958).
10. A. S. Grove, "Physics and Technology of Semiconductor Devices," chap. 3, John Wiley & Sons, Inc., New York (1967).
11. "Handbook of Mathematical Functions," M. Abramowitz and I. A. Stegun, Editors, p. 11, Dover Publishers, New York (1965).
12. J. Crank, "The Mathematics of Diffusion," Oxford University Press, London (1970).
13. H. S. Carslaw and J. C. Jaeger, "Conduction of Heat in Solids," Oxford University Press, London (1959).
14. S. R. J. Saunders, *Sci. Prog.*, **63**, 163 (1976).
15. D. I. Lainer, A. S. Bai, E. I. Slesareva, and M. I. Tsypin, "Protective Coatings of Metals," Vol. 2, p. 52, Consultants Bureau, New York (1970).

The Application of Pulsed Current Electrolysis to a Rotating-Disk Electrode System

II. Electrochemical Kinetics

K. Viswanathan* and H. Y. Cheh**

Department of Chemical Engineering and Applied Chemistry, Columbia University, New York, New York 10027

ABSTRACT

A new method which was based on a combination of pulsed electrolysis and stirring to study fast electrode reactions was developed. Theoretical expressions were derived for a first-order reversible reaction. Experimental investigation was carried out in a ferri-ferrocyanide system. Good agreement on the results was obtained between the new method and the d-c measurements.

Methods for studying fast electrode reactions can be grouped generally into two types. The first type involves the application of transient technique to an unstirred electrochemical system. Techniques such as chronopotentiometry, chronoamperometry, cyclic voltammetry, etc. all fall into this group. Theoretical analyses involve solving the diffusion equation subject to boundary conditions in accordance with the applied technique. There is a wealth of information concerning this approach in the literature in terms of research papers, review articles, and books. Major reviews on the subject include the early summary by Delahay (1) and subsequent books by Vetter (2), Adams (3), and most recently, Macdonald (4). The second type involves the application of direct current or potential to a stirred system. Theoretical analyses involve solving the convective diffusion equation under d-c boundary conditions. The rotating-disk electrode (RDE) due to its well-known mass transfer behavior, is the most prominent tool in this approach. Levich (5), Adams (3), Albery and Hitchman (6), Pleskov and Filinovskii (7), and Opekar and Beran (8) have written extensive reviews on the RDE system.

A common principle for both types of methods is that in order to study fast electrode reactions, mass transfer limitations must either be negligible or be quantitatively accounted for. The RDE system possesses both the practical advantage of effective stirring and the theoretical advantage of being a relatively simple system to analyze mathematically. A combination of the two methods, *i.e.*, the application of transient techniques to a RDE system, would in principle enable one to study quantitatively the rate of fast electrode reactions. In this paper we develop such a method by applying pulsed current electrolysis to an RDE system. Theoretical analysis on the determination of kinetic parameters is presented. Experimental investigation by using a ferri-ferrocyanide system is then reported. It is important to note here that a major advantage of pulsed current electrolysis is that the surface concentration of the reacting ion can be calculated solely from mass transfer considerations by solving the convective diffusion equation subject to Fick's first law of diffusion as a boundary condition. In other words, the surface concentration of the reacting ion depends on the transport characteristics of the system and the applied current density. It is independent of reaction kinetics.

* Electrochemical Society Student Member.
** Electrochemical Society Active Member.

Key words: pulsed electrolysis, rotating-disk electrode, kinetics.

Theoretical

The theoretical analysis is based on an RDE system with the same assumption as described in part I of our paper (9). Assume also that the following reaction may occur at the RDE

$$O + ne^- \rightleftharpoons R \quad [1]$$

where O and R represent the molecular formula of the oxidized and reduced species, respectively, and n is the number of electrons transferred during reaction. The Butler-Volmer equation is assumed to represent adequately the rate of the reaction when a pulsed current is applied

$$i_p = i_{o,\infty}\left[\frac{c_{R,i}}{c_{R,\infty}}\exp\left\{\frac{\alpha n\mathbf{F}\eta}{RT}\right\} - \frac{c_{O,i}}{c_{O,\infty}}\exp\left\{-\frac{(1-\alpha)n\mathbf{F}\eta}{RT}\right\}\right] \quad [2]$$

where i_p is the applied pulsed current density, $i_{o,\infty}$ is the exchange current density at the bulk concentration, $c_{R,i}$ and $c_{R,\infty}$ are the concentration of R at the electrode surface and in the bulk, respectively, $c_{O,i}$ and $c_{O,\infty}$ are the concentration of O at the electrode surface and in the bulk, respectively, α is the transfer coefficient, η is the overpotential, and $\mathbf{F}$, R, and T have their usual meaning.

Consider the case of applying a cathodic current and assume that the ratio, $c_{R,i}/c_{R,\infty}$, is close to unity. Equation [2] can be rewritten as

$$i_p = i_{o,\infty} \exp\left\{\frac{\alpha n F \eta}{RT}\right\}\left(1 - \frac{c_{O,i}}{c_{O,\infty}} \exp\left[-\frac{nF\eta}{RT}\right]\right) \quad [3]$$

The concentration of O at the electrode surface can be calculated by the following equation which has been derived by Cheh (10)

$$\frac{(c_{O,i} - c_{O,\infty}) nFD_O}{i_p \delta_O} = 1\text{-}2 \sum_{n=1}^{\infty} \frac{1}{\mu_n^2} \cdot \left\{ \frac{\exp[-\mu_n^2 \tau_{O,l}] - \exp[-\mu_n^2 \tau_{O,c}]}{(1 - \exp[-\mu_n^2 \tau_{O,c}])} \right\} \quad [4]$$

where

$$\mu_n = (2n - 1)\frac{\pi}{2} \quad [5]$$

$$\tau_O = D_O t / \delta_O^2 \quad [6]$$

and D_O is the diffusion coefficient and δ_O is the thickness of the Nernst diffusion layer, $\tau_{O,l}$ and $\tau_{O,c}$ are the dimensionless pulse and cycle time, all referred to species O, and t is time.

Since the RHS of Eq. [4] is equal to the ratio of the d-c cathodic limiting current density $(i_{d\text{-}c})_{l,c}$ and the pulsed cathodic limiting current density $(i_p)_{l,c}$ (9, 10) and since $(i_{d\text{-}c})_{l,c}$ is related to δ_O by Eq. [5]

$$(i_{d\text{-}c})_{l,c} = -\frac{nFD_O c_{O,\infty}}{\delta_O} \quad [7]$$

Equation [4] can be rewritten as

$$\frac{c_{O,i}}{c_{O,\infty}} = \frac{(i_p)_{l,c} - i_p}{(i_p)_{l,c}} \quad [8]$$

By substituting Eq. [8] into [3] and rearranging, one obtains

$$\ln \left\{ \frac{i_p}{\left[1 - \left(\frac{(i_p)_{l,c} - i_p}{(i_p)_{l,c}}\right) \exp\left\{-\frac{nF\eta}{RT}\right\}\right]} \right\} = \ln i_{o,\infty} + \frac{\alpha n F\eta}{RT} \quad [9]$$

Similarly, if the applied pulsed current is anodic, the following equation can be derived

$$\ln \left\{ \frac{i_p}{\left[\left(\frac{(i_p)_{l,a} - i_p}{(i_p)_{l,a}}\right) \exp\left\{\frac{nF\eta}{RT}\right\} - 1\right]} \right\} = \ln i_{o,\infty} - \frac{(1-\alpha) nF\eta}{RT} \quad [10]$$

Equation [9] and [10] are the basic equations for the analysis of kinetic parameters by the pulsed current technique.

Experimental

The same experimental setup as described in our previous paper (9) was used in this work. In order to avoid possible poisoning of Pt in ferri-ferrocyanide solution, an Au disk electrode of 0.461 cm² area was used. The electrolyte consisted of 0.01M ferricyanide, 0.01M ferrocyanide, and 0.5M K_2SO_4. K_2SO_4 instead of KCl was chosen to eliminate possible anodic dissolution of Au. All experiments were carried out at 22° ± 1°C.

The kinematic viscosity of the electrolyte was measured by an Ostwald viscometer and the value was found to be 0.00976 cm²/sec. The diffusion coefficients of the ferri- and ferrocyanide ions were obtained by d-c limiting current density measurements. The values were 6.9×10^{-6} and 5.7×10^{-6} cm²/sec, respectively.

For comparison purpose, the kinetic parameters for the ferri-ferrocyanide reaction system were first determined by using the d-c method developed by Jahn and Vielstich (11). These authors showed that the exchange current density and the transfer coefficient for the reaction could be determined from a knowledge of the intercept and slope of a 1/(applied d-c current density) *vs.* 1/(rotation speed)$^{1/2}$ plot. Experimental results are shown in Fig. 1. The exchange current density and transfer coefficient were found to be 4.3 mA/cm² and 0.5, respectively.

Pulsed experiments were carried out at rotation speeds of 400, 900, and 1600 rpm, with a pulse time of 10^{-4} sec and a cycle time of 10^{-3} sec. The overpotential of the RDE was measured as a function of the applied pulsed current density. Results are shown in Fig. 2. Equations [9] and [10] were used to calculate the

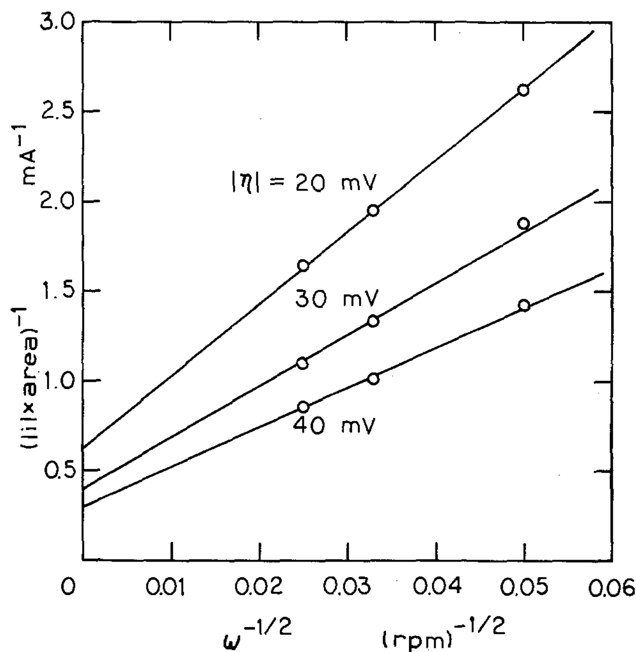

Fig. 1. Current-potential plot for the determination of kinetic parameters by the method of Jahn and Vielstich (11).

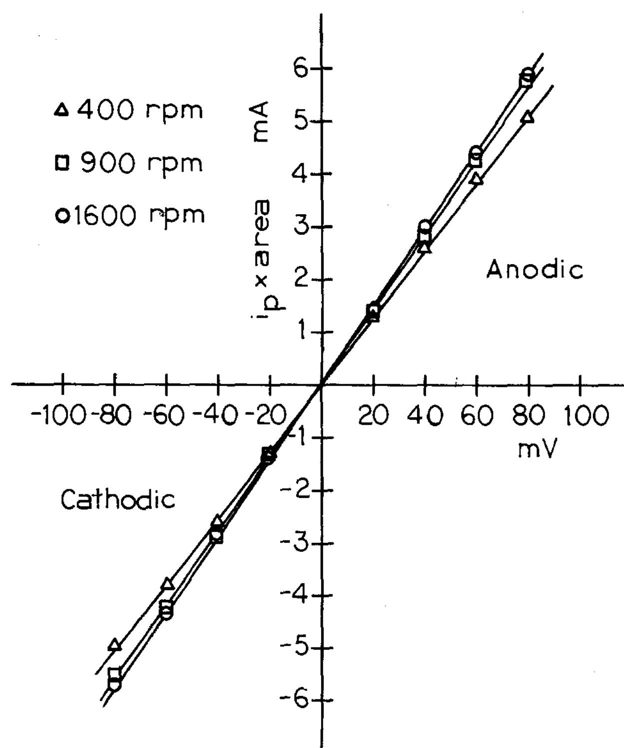

Fig. 2. Current-potential behavior of the ferri-ferrocyanide system under pulsed current conditions.

kinetic parameters. $(i_p)_{l,a}$ and $(i_p)_{l,c}$ were first calculated for the experimental conditions. The LHS of Eq. [9] and [10] were plotted as a function of overpotential. Results are shown in Fig. 3 and 4. The line in both figures was drawn so that a transfer coefficient of 0.5 would result from the slope. The exchange current density was found to be 4.3 mA/cm^2 for cathodic reduction of ferricyanide from Fig. 3, and 4.5 mA/cm^2 for anodic oxidation of ferrocyanide from Fig. 4. Comparing these results with those obtained by d-c measurements, the agreement can indeed be considered very good.

Conclusions

A new technique which is based on pulsed current electrolysis in a stirred system is developed to study fast electrode reactions. Theoretical expressions were derived for reversible first-order reaction on an RDE system. The technique was applied to determine kinetic parameters for a ferri-ferrocyanide reaction system. Good agreement was obtained between the results based on the present approach and those from d-c measurements.

The new technique is in principle capable of studying much faster reactions than the experimental system chosen for this work. This can be accomplished by a combination of applying shorter pulses with low duty cycles and increased stirring. The method can also be easily extended to reactions other than first order.

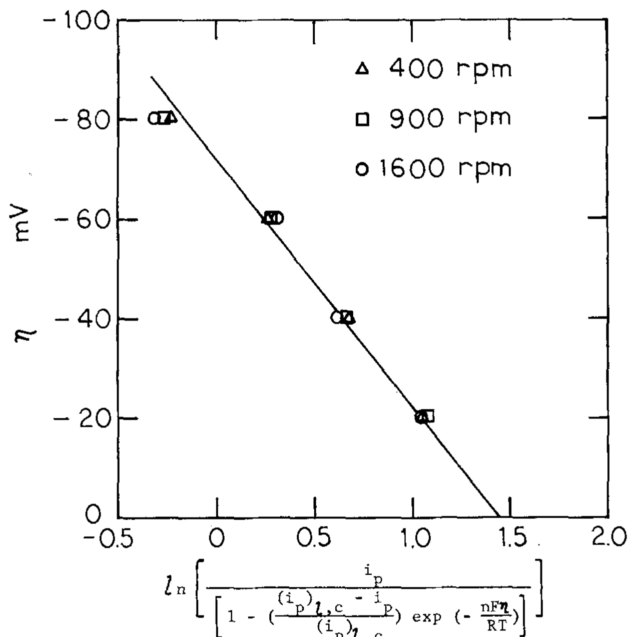

Fig. 3. Cathodic reduction of ferricyanide ion

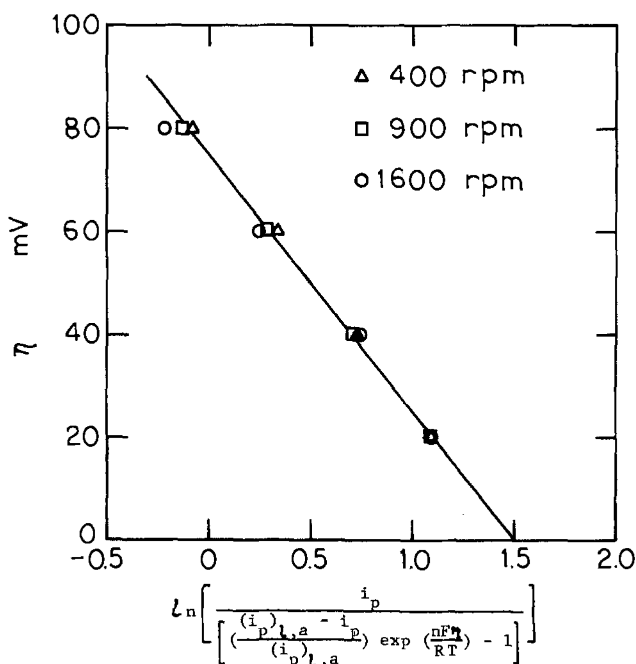

Fig. 4. Anodic oxidation of ferrocyanide ion

Acknowledgments

The authors wish to thank Drs. M. A. Farrell-Epstein and P. Duby for helpful discussion during the course of this work.

Manuscript submitted March 14, 1978; revised manuscript received May 16, 1978.

Any discussion of this paper will appear in a Discussion Section to be published in the June 1979 JOURNAL. All discussions for the June 1979 Discussion Section should be submitted by Feb. 1, 1979.

LIST OF SYMBOLS

$c_{O,i}$, $c_{O,\infty}$ concentration of oxidized species at the electrode surface and in the bulk solution, respectively
$c_{R,i}$, $c_{R,\infty}$ concentration of the reduced species at the electrode surface and in the bulk solution, respectively
D_O diffusion coefficient of the oxidized species
F Faraday's constant
i_p pulsed current density
$(i_{d\text{-}c})_{l,c}$, $(i_p)_l$ cathodic limiting current density for d-c electrolysis and for pulsed electrolysis, respectively
$(i_p)_{l,c}$, $(i_p)_{l,a}$ cathodic and anodic pulsed limiting current density, respectively
$i_{o,\infty}$ exchange current density of reaction at the bulk concentration
n number of electrons transferred in reaction
R universal gas constant
t time
T temperature
α transfer coefficient
δ_O thickness of the Nernst diffusion layer for the oxidized species
η overpotential
μ_n a constant defined in Eq. [5]
$\tau_{O,l}$, $\tau_{O,c}$ dimensionless pulsed time and cycle time for the oxidized species, respectively

REFERENCES

1. P. Delahay, "New Instrumental Methods in Electrochemistry," Wiley Interscience, New York (1954).
2. K. J. Vetter, "Electrochemical Kinetics," Academic Press, New York (1967).
3. R. N. Adams, "Electrochemistry at Solid Electrodes," Marcel Dekker, New York (1969).
4. D. D. Macdonald, "Transient Techniques in Electrochemistry," Plenum Press, New York (1977).
5. V. G. Levich, "Physicochemical Hydrodynamics," Prentice Hall, Englewood Cliffs, N.J. (1962).
6. W. J. Albery and M. L. Hitchman, "Ring-Disc Electrodes," Clarendon Press, Oxford, England (1971).
7. Yu. V. Pleskov and V. Yu. Filinovskii, "The Rotating Disc Electrode," Consultants Bureau, New York (1976).
8. F. Opekar and P. Beran, *J. Electroanal. Chem. Interfacial Electrochem.*, **69**, 1 (1976).
9. K. Viswanathan, M. A. Farrell-Epstein, and H. Y. Cheh, *This Journal*, In press.
10. H. Y. Cheh, *ibid.*, **118**, 551 (1971).
11. D. Jahn and W. Vielstich, *ibid.*, **109**, 849 (1962).

Editor's Note

By mischance, this is Part II of a two-part series and is being printed before Part I, which will appear in the November 1978 issue of the *Journal*. The *Journal* regrets very much this inadvertent transposition.

n-Heptylviologen Radical Cation Films on Transparent Oxide Electrodes

Raymond J. Jasinski*,[1]

Texas Instruments Incorporated, Dallas, Texas 75265

ABSTRACT

The cosmetic and kinetic properties of n-heptylviologen dihydrogenphosphate radical cation films deposited on transparent oxide electrodes, in particular tin oxide, are dependent upon the initial condition of the oxide-electrode surface. The implication is a strong interaction of the electrode surface with the first layer(s) of radical cation film deposited.

"Viologens" are dialkyl and diaryl 4,4' bipyridinium compounds (1). They are stable in water below pH 8-10; the water solutions are colorless, or pale yellow, depending on the substituent group. These compounds are readily synthesized in high yield, from reaction of dypiridyl and the appropriate alkyl or aryl halide (1). Other synthetic routes are also available (2-5).

Chemical and cathodic reduction of the short-chain viologens in water solutions (*e.g.*, the dimethyl and diethyl compounds) generate blue-to-violet colors which have been shown due to stable radical cations (6-8). Mild oxidation with air, for example, restores the parent dication. In 1973 it was pointed out (9) that cathodic reduction of viologens with alkyl side chains containing more than five carbon atoms resulted in deposition of colored films on the reducing electrode surfaces rather than forming soluble blue material. Furthermore, in the absence of air, these films remained adherent to the electrode surface, and on anodization yielded the parent dication.

It was also suggested that this phenomenon could be the basis for an alphanumeric display. Since that time, a number of papers and patents have discussed the use of viologens in this context. Most of these have dealt with generating viologen films onto metal electrode surfaces, and although the mechanisms involved in film growth and oxidation are not totally understood, the phenomenology appears to be relatively straightforward. Such is not the case with viologen redox reactions on transparent oxide electrodes which are of considerable importance in practical display technology.

This paper discusses properties of one viologen radical cation film (that from n-heptylviologen dihydrogenphosphate) on commercially available transparent tin oxide and on tin-doped indium oxide. The contention is made that the differences in electrode performance, vis-à-vis metal electrodes, must arise from chemical interactions of the electrode surface with the radical cation film, as well as from the higher ohmic resistance of the oxide electrode.

Experimental

The experimental techniques were substantially as described elsewhere (10), but with a few modifications. The apparatus included the following: Wenking Potentiostat, Wenking VSG 72 Scan Generator, PAR Digital Coulometer, Corning Model 101 Electrometer, TI No. 341 and Servoriter recorders, Lab Con Company glove box. The glass cell was of the standard three-compartment design; a glass frit separated the counter-electrode compartment from the working electrode; a capillary, within 1 cm of the working electrode isolated the Orion double junction reference electrode (Model 90-02-00, with 10% KNO_3 as the "outer" solution). The test cell and glove box were deaerated with nitrogen which had been passed over copper filings at 580°C.

Open-circuit ("equilibrium") potentials were recorded 7 min after depositing a nominal 3 mC/cm^2 of radical cation film at potentials positive to those required to reduce the radical cation. No attempt was made to control cell temperature precisely during these studies.

N-heptylviologen dibromide was synthesized in-house by reaction of dipyridyl and 1-bromoheptane. Recrystallization was from methanol with acetone. The dihydrogenphosphate derivatives were prepared from the bromide salt via ion exchange on Amberlite IRA-400. It was determined that the residual halide concentration was less than 5×10^{-5}M. The supporting electrolyte was molar phosphate, pH 4.

Deaerated n-heptylviologen solutions were stored in the glove box (under fluorescent lamps) with no obvious decomposition over a 12 month period. Solutions stored in air developed a pungent odor within a few days, unless contained in "actinic" glass.

The oxide electrodes (1 cm^2) studied were the commercially available "NESA," "Nesatron 20" and "Nesatron 100" from PPG Industries, as well as SnO_2 from Corning. A few measurements were made with "Electropane" from Libby-Owens-Ford. Sheet resistances for these materials were measured routinely by a two-point probe method (11), calibrated by the four-point probe method of van der Pauw (12). The cathodic limits were established by exhaustive electrolysis (13), *i.e.*, potentiostating the electrode for prolonged periods of time at the appropriate values and measuring changes in sheet resistance, usually accompanied by visible changes in the film. This technique sees" only electrode decomposition, rather than reduction of trace oxygen, hydrogen evolution, or plating of trace metal ions. Techniques for conditioning and cleaning the transparent oxide surfaces are discussed in the text.

Electrical contact to the oxide electrode was made via a direct clip to the slice, 0.5 cm above the solution level. Although poor current distribution can be expected, it was the only electrode-mounting scheme which did not perturb the electrode surface. Bonding conductive oxide-coated glasses over small apertures with epoxy did improve current distribution, however, flowing of epoxy during the sealing operation and/or simultaneous contamination of the surfaces made the technique valueless for the purposes of this work.

Surface elemental analyses were made with the PHI Model 548 Auger Spectrometer and the JEOL 3 Scanning Auger Spectrometer. The oxygen/metal ratios were calibrated by assuming that the measured signals for sputtered surfaces corresponded to a 2:1 atom ratio for tin oxide, and 3:2 for the indium oxide-based materials (14). The O/Sn calibration factors so obtained agreed to within ±2% standard deviation for 15 samples of commercial and in-house prepared tin oxide. The surface carbon contents are reported as C/metal

* Electrochemical Society Active Member.

[1] Present address: Occidental Research Corporation, Irvine, California 92713.

Key words: viologens, electrochromics, transparent electrodes, tin oxides, indium oxides.

peak height ratios, since a reasonable calibration procedure was not readily available for carbon.

Results

The bulk characteristics of the electrode materials used in this study are shown in Table I. The variations listed in sheet resistances and thicknesses are standard deviations for a minimum of 12 pieces from one shipment each. It was not possible to generate quantitative atom ratios for the dopant levels of the tin oxide samples due to the lack of fluoride and antimony standards. The dopant values listed for the Nesatron 20 samples are bulk values. The surface Sn/In ratios (*e.g.*, 0.12-0.16) were suspect due to the inevitable surface carbon contamination (see below).

Most of the electrochemical measurements were carried out with the first three materials listed because of the lower sheet resistances. The cathodic limits (at pH 4) given in the table are conservative in that all samples tested survived these potentials without change; some samples were stable at an additional -50 mV.

Films of radical cation formed on as-received electrodes were almost always "patchy" and nonuniform in appearance. The rates of cathodic decomposition and, in particular, anodic erasure of the radical cation film, were slow; 3-5 min, for example, were required to anodize completely a 3 mC/cm^2 film.

It was presumed that the nonuniformity of the film was due, at least in part, to the carbonaceous materials on the electrode surface indicated by the Auger spectra (Table II). Oxidative and extractive procedures reduced this carbon to minimal levels. Those surfaces Soxhlet-extracted 4 hr each with xylene, isopropanol, methanol, and water, as well as those surfaces treated with alcoholic caustic, subsequently yielded uniform viologen radical cation films. Films formed onto surfaces that had been subjected first to highly oxidative treatments, both wet and dry, were routinely nonuniform, being darkest around the edges and light in the center.

This relationship between carbon content and film uniformity is not particularly surprising, however the pretreatment procedure had an additional effect, that of altering the erasure kinetics. Shown in Fig. 1 are plots of the amounts of charge remaining on a tin oxide electrode surface *vs.* time after application of a constant $+100$ mV for three clean-up procedures. Each electrode had been first coated with 3 mC/cm^2 radical cation film at -525 mV and then held on open circuit

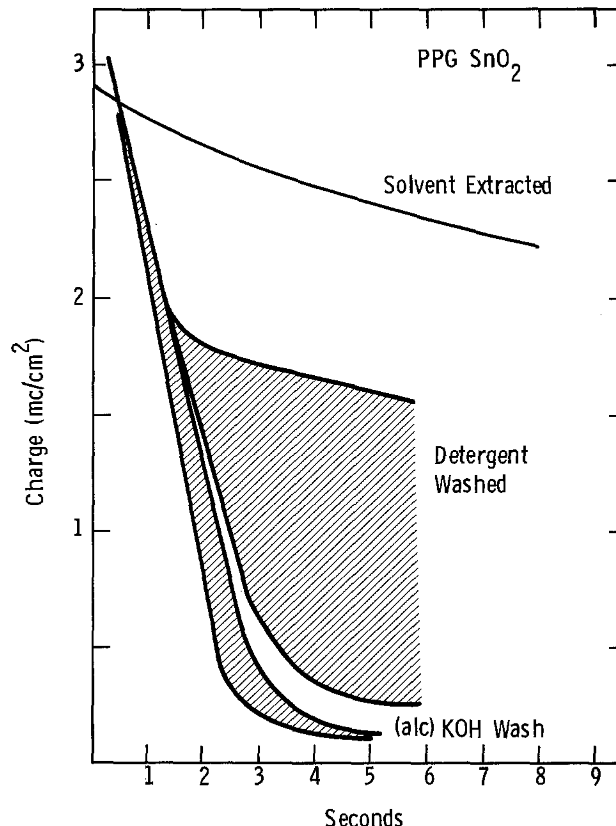

Fig. 1. Quantity of charge remaining on a PPG tin oxide sample as a function of time after application of a constant + 100 mV.

for 1 min. Obviously a uniform deposit does not correlate with fast erasure, nor did a nonuniform deposit correlate entirely with a slow erasure (the detergent-treated samples (14) were almost always nonuniform in appearance, but sometimes gave fast erasures). A rationalization of this effect is offered below after a discussion of additional phenomenology involved in film formation and erasure.

The caustic-treated and solvent-extracted samples were always wettable; the as-received samples were not. This effect has generally been ascribed to hydrolysis of the surface [*e.g.*, (14, 15)], which according to theory (19, 20) is not accompanied by an increase in O/Sn ratio.

Table I. General properties of conductive oxide electrodes

Item	C. SnO_2	NESA	Nesatron 20	N. 100	L.O.F.
Major oxide	SnO_2	SnO_2	In_2O_3	In_2O_3	In_2O_3
Dopant	Sb	F	Sn	Sn	Sn
Sn/In ratio (atom)	—	—	0.04	0.06	0.05
Oxide thickness	2300Å ± 12%	1400 ± 10%	1700 ± 12%	700 ± 20%	1100 ± 20%
Sheet resistance (Ω/□)	99 ± 13%	100 ± 18%	27 ± 10%	200 ± 10%	200
Resistivity (mΩ-cm)	2.3	1.4	0.5	1.4	2.2
Cathodic limit (mV) (pH 4)	−675	−675	−650		

Table II. Surface composition of tin oxide electrodes (via Auger analysis)

Treatment	(C/Sn) peak ratios		(O/Sn) atom ratios	
	C. SnO_2	PPG SnO_2	C. SnO_2	PPG SnO_2
As received	0.18 ± 0.4	3.0 ± 2	2.6 ± 0.1	4.2 ± 0.4
Washed in water	0.16		2.8	
Methanol	0.18 ± 0.06		2.9 ± 0.2	
$H_2PO_4^-$ buffer	0.36 ± 0.03	0.38 ± 0.16	3.3 ± 0.4	3.2 ± 0.1
NaOH	0.21	0.54	3.3	3.1
alc. KOH/buffer	0.03	0.11	3.0	2.1
Washed in H_2O/methanol, air dry				
2 hr 300°C	0.31		2.6	
400°C	0.58		2.9	
H_2O_2	0.16		3.0	
H_2O_2 + H_2SO_4	0.07	0.22	2.8	4.4
O_2 glow discharge	0.03 ± 0.02	0.53 ± 0.4	2.9	4.0 ± 0.4
Extract in (xylene/IPA/H_2O)/buffer	0.01	0.09	3.2	4.0

The measured surface O/Sn atom ratios are also given in Table II. As found by others (14), the surface ratios were always larger than the bulk atom ratios, with a ratio of nominally 2.5:1 as the lower limit, *i.e.*, when the samples had not been treated chemically and were not substantially contaminated with carbon. There is precedence in the literature [e.g., Ref. (16)] for excess surface oxygen due to compensation of bulk vacancies by adsorbed gaseous oxygen. Much, although not necessarily all, of this oxygen should be removed by pump down in the Auger chamber (17). Some oxygen is likely the result of contamination from the same source as the large amount of carbon found on the surface, particularly for the as-received PPG samples (both the carbon and oxygen signals were high and the tin signal was low). Samples simply contacted with water could be slightly "hydrated," yielding an increased oxygen signal. With one exception, both low carbon contents and increased O/Sn ratios were obtained for electrodes treated with alcoholic caustic + buffer, peroxide/sulfuric acid, and xylene extraction + buffer. This could be due to incorporation of substantial water into the tin oxide with one or more of the electrolyte constituents. (The significance of "+ buffer" is discussed below.)

An attempt was made to study the hydrolysis of the surface in a more direct fashion by correlating organosilane subsequently bonded to the surface hydroxyl groups (16) with the pretreatment procedure. As-received Corning tin oxide samples, kept from contact with bulk water, did not bond significant amounts of organosilane (specifically hydrogen triethoxysilane). Such samples soaked in buffer solution subsequently bonded considerable organosilane. Drying the surface by heating in air decreased but did not eliminate the reaction with organosilane. However samples of PPG tin oxide simply exposed to water during the glass-cutting operation bonded considerable organosilane. These samples were not visibly "wettable" (hence the surface was not hydrolyzed appreciably); the surface was contaminated with considerable carbon (Table II). Identical results were obtained with as-received Nesatron 20 and Nesatron 100 samples treated in the same manner, and these were also highly contaminated with carbonaceous material. The dry oxygen glow discharge essentially eliminated the uptake of organosilane by the Corning tin oxide and, as shown in Table II, essentially eliminated the carbon residue on the surface. The same glow discharge applied to the PPG samples decreased but did not eliminate the carbon residue on the surface. The interpretation which must be given to these results then is that the organosilane can bond to water incorporated into the surface and more incorporation takes place during extended contact with water solutions. However the organosilane can also bond to functional groups which are part of the surface contamination on the as-received samples.

Cleaned oxide electrodes were equilibrated in *p*H 4 phosphate buffer at least 12 hr before testing in viologen solution. This was a nontrivial step for the tin oxide electrodes, but was less important for the Nesatron 20. If omitted for SnO_2, the radical cation films formed nonuniformly (including this step but omitting the cleaning stage gave the same poor performance). A possibly analogous effect has been reported in the literature (15), whereby soaking the tin oxide electrode in electrolyte increased the subsequent activity for adsorption of iodide ion. The mechanism was interpreted as an increase in the hydration/ion exchange capacity of the tin oxide, a phenomenon well known with bulk cassiterite (10). Since, in the present case, surface hydroxyl groups were probably present before the equilibration, it is assumed that the dominating reaction was ion exchange. Indeed phosphorus was found on the tin oxide electrode surfaces with the scanning Auger (avoiding areas of the surface containing particulate matter). This then was the surface on which the following electrochemistry was carried out.

Shown in Fig. 2 are erasure curves for PPG tin oxide, cleaned with alcoholic caustic, onto which had been nominally deposited 1, 2, 3, 4, and 5 mC/cm^2 of radical cation film. Obviously the bulk of the film erased at a constant rate which was independent of coverage. The "tail" initiated at about 0.05 mC/cm^2. Figure 3 shows a similar plot, but with erasure potentials varied for a constant initial coverage of 3 mC/cm^2 ($\pm$ 10%). The conclusion here is that the "fast" erasure section is more potential dependent than the "tail" section. The "tail" section was less pronounced with Nesatron 20 than with the tin oxide samples.

Both the "tail" and "fast" sections were independent of the length of time after deposition and erasure of the film (between 1 and 7 min). Accumulation of color on the electrode was not observed after 10^{+3} repetitive cycles of minimal 6 sec each; the charge in the "tail" did not increase.

Cyclic voltammograms on the tin oxide electrode were of the same form as previously reported for metals (10, 13) except for the distortion due to the ohmic resistance of the electrode materials. A definite peak corresponding to deposition or removal of the "tail" section could not be distinguished from the major Faradaic processes. However, those electrode/electrolyte combinations leading to tailing on anodic erasure also lead to "drawn out" anodic peaks on cyclic voltammograms.

Shown in Table III are the cathodic peak currents observed on the three oxide electrodes, for a constant cathodic potential of −550 mV. Nesatron 20, with the lower sheet resistance, did give a higher peak current

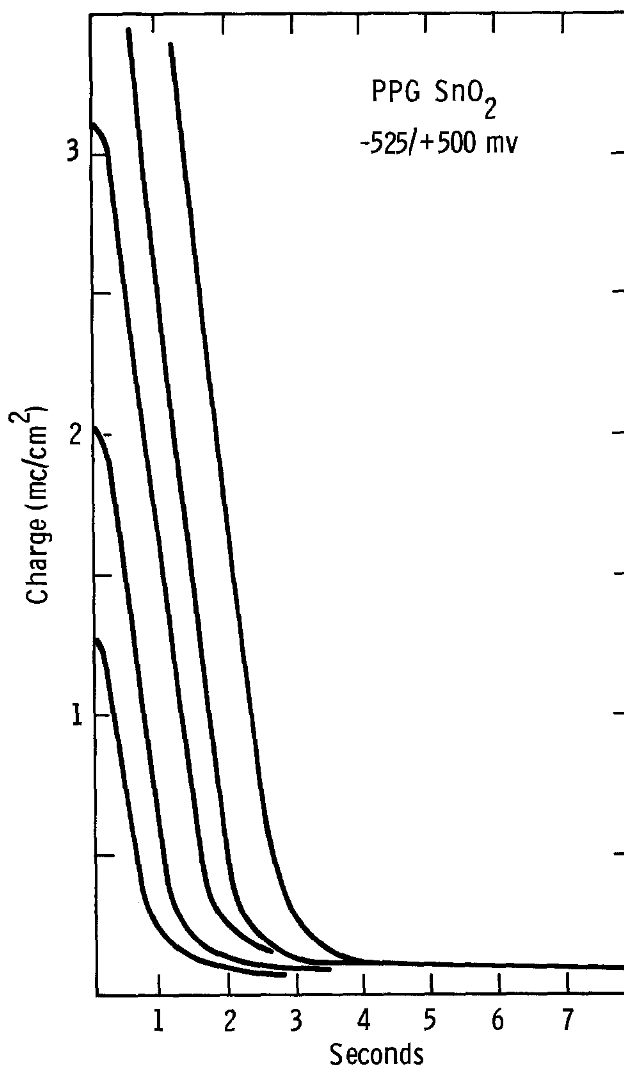

Fig. 2. Erasure curves with initial coverages of 1.3, 2, 3.1, 4.2, 5 mC/cm^2, respectively.

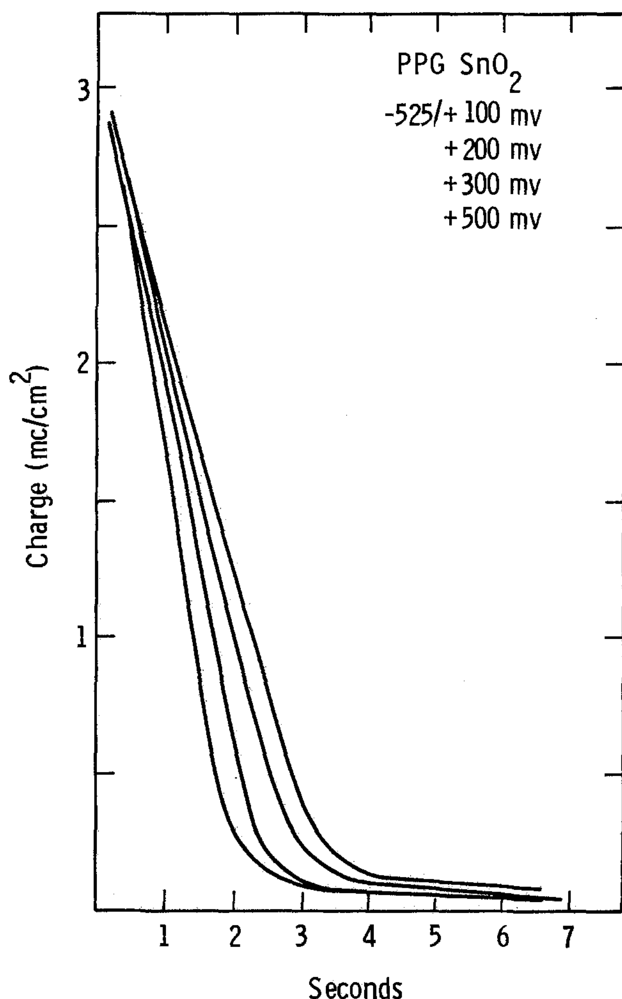

Fig. 3. Erasure plots as a function of erasure potential. The fastest erasure corresponds to the most positive potential (+ 500 mV) applied.

than the SnO_2 electrode, but not in direct proportion to the sheet resistance. For a given electrode material, however, the application of more negative potentials increased the cathodic current proportionately in the range -475--600 mV.

Discussion

The reaction sequence shown in Table IV is inferred from these results as a working model for redox processes of n-heptylviologen dihydrogenphosphate (R-V^{+2}) on transparent tin oxide electrodes.

Table III. Effect of sheet resistance

Deposition of n-heptylviologen phosphate (-550 mV)

Electrode	Sheet resistance (Ω/□)	i_{peak} (mA)
Corning SnO_2	99 ± 13%	0.36
PPG SnO_2	100 ± 18%	0.54
Nesatron 20	27 ± 10%	0.65
Gold		>3

Table IV. Viologen salts on tin oxide electrodes

Working model

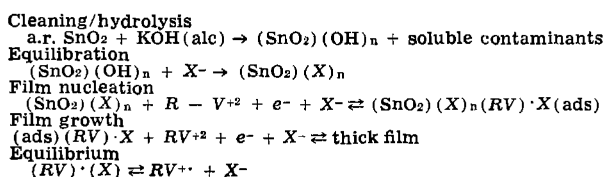
Cleaning/hydrolysis
a.r. SnO_2 + KOH(alc) → $(SnO_2)(OH)_n$ + soluble contaminants
Equilibration
$(SnO_2)(OH)_n + X^- \rightarrow (SnO_2)(X)_n$
Film nucleation
$(SnO_2)(X)_n + R - V^{+2} + e^- + X^- \rightleftarrows (SnO_2)(X)_n(RV)\cdot X(\text{ads})$
Film growth
$(\text{ads})(RV)\cdot X + RV^{+2} + e^- + X^- \rightleftarrows$ thick film
Equilibrium
$(RV)\cdot(X) \rightleftarrows RV^{+\cdot} + X^-$

The need to remove surface contaminants (step **1**) and expose conductive oxide is logical and the necessity for this step has been demonstrated herein. The simultaneous generation of surface hydroxyl groups (step 1) is consistent with the literature (15) and the wettability character of the so-treated surfaces.

It has been demonstrated that a surface equilibration with electrolyte is required before uniform radical cation films can be generated on the tin oxide electrodes. This is shown (step 2) as an ion-exchange process. Auger analysis did find phosphorus on the surface after excluding particulate residual salts from the analytical beam. Higher O/Sn ratios were also found. There is precedence in the literature for cassiterite-exchanging hydroxyl groups for dihydrogenphosphate (19). This step is apparently less important with indium oxide electrodes since uniform radical cation films could be generated and erased rapidly on nonequilibrated Nesatron 20.

The reactions of this modified oxide surface with the viologens dication (21) and/or the first layer of cathodically formed radical cation are grouped in step 3. It is this first layer which must, logically, provide for the adhesion of the subsequently deposited bulk film. The label of "nuclei" is used for this first layer on oxide electrodes to be consistent with observations on the electrodeposition of metals and metal oxides onto the same type of material [*e.g.*, Ref. (22, 23)]. It is apparent from the data presented in Fig. 2 and 3 that the last nominal 0.03 mC/cm^2 of radical cation to be anodized off the electrode surface must have different properties than the bulk of the radical cation film. This quantity of charge is consistent with that required to form nuclei from silver on tin oxide, with due allowance made for the difference in size of the viologen molecule and the silver atom.

To explain the data of Table III, *i.e.*, the less-than-expected increase in cathodic currents from oxide electrodes of lower sheet resistances, and the increase in current from increasing the overpotential applied to a given material, it is proposed (*i*) that the number of nuclei formed on an electrode surface are a function of material, pretreatment, and possibly potential; and (*ii*) only these nuclei act as electronically conducting channels for delivery of charge from the electrode to the growing film. A variation in nucleus concentration with pretreatment also would explain the erasure curves shown in Fig. 1 whereby speed was a distinct function of electrode pretreatment.

The bulk film must grow (step 4) by reduction of the dication from the solution. It is not known whether this is actually a two-stage process, *i.e.*, cathodic formation of the soluble radical cation which eventually precipitates as a salt [as has been claimed many times, *e.g.*, Ref. (9, 13)] or whether the two steps are concurrent, as implied in Table IV. As with metals, the film must be relatively nonporous since undercutting and peeling of the film are not found on anodic oxidation.

Step 5 implies an equilibrium between radical cation in the bulk film with radical cation in solution. It has been shown (10, 20) that the concentration dependences of the equilibrium potentials for such films on metals obey the Nernst equation modified for the solubility product relationship. Identical potentials were found with films on transparent oxide electrodes, so it is reasonable to assume that this equilibrium applies here as well.

Acknowledgments

The author wishes to acknowledge the assistance of Mrs. Beth Moussa and Mrs. Sarah Campbell in carrying out the electrochemical measurements as well as the participation of Mr. Carl Lentz, Dr. Gary McGuire, and Dr. Tom Shaffner in acquiring Auger data.

Manuscript submitted March 6, 1978; revised manuscript received April 24, 1978.

Any discussion of this paper will appear in a Discussion Section to be published in the June 1979 JOURNAL. All discussions for the June 1979 Discussion Section should be submitted by Feb. 1, 1979.

Publication costs of this article were assisted by Texas Instruments Incorporated.

REFERENCES

1. L. Michaelis and E. Hill, *J. Gen. Physiol.*, **16**, 859 (1933).
2. E. Kosower and J. Cotter, *J. Am. Chem. Soc.*, **86**, 5524 (1964).
3. L. Winters, A. Borror, and W. Smith, *Tetrahedron Lett.*, **24**, 2313 (1967).
4. L. Winters, N. Smith, and M. Cohen, *Chem. Commun.*, 642 (1970).
5. A. Smith, Brit. Pat. 1,119,544 (1968).
6. E. Weitz, *Angew. Chem.*, **66**, 658 (1954).
7. W. Schwartz, Ph.D. Thesis, 61-5992.
8. C. Johnson and H. Gutowsky, *J. Chem. Phys.*, **39**, 58 (1963).
9. C. Schoot, J. Ponjee, H. van Dam, R. van Doorn, and P. Bolwijn, *J. Appl. Phys.*, **23**, 64 (1973).
10. R. Jasinski, *This Journal*, **124**, 637 (1977).
11. R. Aitchison, *Aust. J. Appl. Sci.*, **5**, 10 (1954).
12. L. J. van der Pauw, *Philips Res. Rep.*, **13**, 1 (1958).
13. J. Bruinink, C. Kregting, and J. Ponjee, *This Journal*, **124**, 1854 (1977).
14. N. Armstrong, A. Lin, M. Fujihara, and T. Kuwana, *Anal. Chem.*, **48**, 741 (1976).
15. H. Yoneyama and H. Laitinen, *J. Electroanal. Chem. Interfacial Electrochem.*, **79**, 129 (1977).
16. H. Matthews and E. Kohnke, *J. Phys. Chem. Solid*, **29**, 653 (1968).
17. R. Chapman, *J. Vac. Sci. Technol.*, **12**, 723 (1975).
18. P. Moses and R. Murray, *Anal. Chem.*, **47**, 1882 (1975).
19. H. Boehm, *Discuss. Faraday Soc.*, **52**, 264 (1971).
20. H. van Dam and J. Ponjee, *This Journal*, **121**, 1555 (1974).
21. L. Pospisil, J. Kuta, and J. Volke, *J. Electroanal. Chem. Interfacial Electrochem.*, **58**, 217 (1975).
22. P. Bindra, H. Gerischer, and D. Kolb, *This Journal*, **124**, 1012 (1977).
23. H. Laitinen and N. Watkins, *ibid.*, **123**, 804 (1976).

S/Se Substitution in Polycrystalline CdSe Photoelectrodes

Photoelectrochemical Energy Conversion

David Cahen

Department of Structural Chemistry, The Weizmann Institute of Science, Rehovot, Israel

and Gary Hodes* and Joost Manassen

Plastics Research Department, The Weizmann Institute of Science, Rehovot, Israel

ABSTRACT

On the basis of x-ray photoelectron spectroscopy (XPS) studies of polycrystalline CdSe electrodes, the occurrence of S/Se substitution in these electrodes, when immersed in polysulfide solution, is verified. The substitution process is enhanced considerably when the electrode is illuminated as part of a photoelectrochemical cell. The mechanism of the S/Se exchange is discussed, as well as the consequences of such an exchange for electrode stability. The resulting presence of a thin (several tens of angstroms) layer of CdS on top of the CdSe is taken into account in constructing a rough band scheme for the system. The CdS layer is shown to influence the photovoltage and, to a lesser extent, the photocurrent obtainable from this kind of photoelectrochemical cell. Its relation to the slow deactivation of highly crystalline CdSe photoelectrodes is discussed.

Since the discovery that Cd-chalcogenide photoelectrodes can be stabilized considerably in aqueous solutions by the addition of sulfide ions to the solution (1-3), several hypotheses have been forwarded to explain this stabilization. These include the low redox potential of the $S/S^=$ redox couple, the fast kinetic behavior of the $S/S^=$ redox reaction, and the preferential absorption of sulfide ions on CdS (4), although it is quite possible that no single one of these is solely responsible and that the explanation must include a combination of these factors. An investigation of the changes occurring in Cd-chalcogenide electrodes when they are used as photoelectrodes in a photoelectrochemical cell (PEC) might shed some light on the stabilization mechanism. It is noteworthy that different degrees of stabilization have been obtained for single crystal, sintered disk, and thin layer polycrystalline electrodes (1, 3). In an earlier report we mentioned the occurrence of S/Se substitution, when CdSe is used in polysulfide (S/S^{2-}) solution as a photoelectrode (1). In this report we present results, obtained by x-ray photoelectron spectroscopy (XPS), which show the occurrence of this substitution both in the light and in the dark. Additional evidence is given which supports such a substitution and the resulting effect of it on the conversion efficiency and stability of CdSe electrodes in polysulfide solutions. The mechanism of the substitution is discussed and on the basis of these data we present a band scheme for the polysulfide electrolyte-CdS-CdSe system in which the CdS layer is considered as essentially an insulator. Therefore, in analogy to solid state MIS systems this junction can be looked upon as an EIS (electrolyte-insulator-semiconductor) one. Also, on the basis of the substitution phenomenon, we explain the difference in behavior between polycrystalline and single crystal electrodes and the short- and long-term changes in photovoltage and photocurrents obtained from such a PEC.

Experimental

XPS (ESCA) spectra were obtained on an AEI ES200 spectrometer, using Al Kα radiation (1486.3 eV, ~0.9 eV linewidth). The samples to be investigated were handled in a glove box attached to the spectrometer. Powdered samples (CdS, CdSe) were ground in the glove box, which was previously made oxygen and water free by cooling a Cu coil, situated inside the

* Electrochemical Society Active Member.

Key words: photoelectrochemistry, energy conversion, XPS, photocorrosion.

glove box, with liquid N_2 until no more condensation was observed. The freshly ground powders were then pressed into previously cleaned In foil.

The polycrystalline electrodes (5 × 16 mm) were investigated as prepared (1), although contact with air was minimized to avoid oxidation of the surface. Electrodes which had been immersed in S/S^{2-} solution were washed twice in Na_2S solution to prevent precipitation of elemental S from adsorbed electrolyte and then washed several times thoroughly in deionized water to remove adsorbed Na_2S, prior to analysis. Both wide scans [1-1000 eV binding energy (B.E.)] and narrow scans (20-40 eV) were made.

Etching of the surface was achieved using an Ar ion gun situated in the analyzing chamber at a glancing angle of 60° with respect to the substrate. The probe current was 6.6 μA for a beam voltage of 1000V. An etching time of 10 min corresponds, under these conditions, to an etched layer of 80 ± 20Å, *i.e.* 30 ± 6 atomic layers of Cd-chalcogenides (5). Pure CdS and CdSe powders (99.99% Alpha Inorganics) were used as standards. The CdS electrode consisted of a chemically vapor deposited CdS layer on In-SnO_2 conducting glass. The CdSe electrodes were prepared electrolytically on Ti-metal (1). CdSe electrodes were illuminated in a photoelectrochemical cell as described previously (1) using C/CoS counterelectrodes (6). Both sides of the Ti substrate were plated with CdSe. One side was insulated by painting with a solution of tar in benzene (which we have found to form a stable coating over long periods of time in the sulfide electrolyte), except in experiments where the two sides were compared, as in illuminated and nonilluminated sides for the XPS measurements. Illumination at ~ AM1 intensity (for higher than bandgap energy photon flux) was obtained from a conventional tungsten-iodine projector lamp, yielding short-circuit currents of 5-7 mA/cm^2 and open-circuit voltages of ~ 0.5V for samples used in XPS experiments. In these experiments samples were illuminated for 24-36 hr continuously under near short-circuit conditions. n-CdSe crystals were purchased from Cleveland Crystals Corporation (specific resistivity 1-10 Ω-cm, ~ > 10^{16} cm^{-3} donor concentration). Ohmic contact was made to the CdSe crystals by an In-Ga alloy to which a wire (Cu or Ta) was connected by silver epoxy and covered with an insulating epoxy.

XPS Results

Preliminary wide scans of the electrodes showed the presence of Cd, Se(S), C, some O, and Ti (for CdSe electrodes only). Ar^+ etching decreased the relative intensities of the Ti 2p, Cls, and Ols peaks considerably. Narrow scans were made of the S 2s, Se3s region (Fig. 1), S2p, Se3p region (Fig. 2), Se3d, Se $L_2M_{4,5}M_{4,5}$ Auger peak, S KLL Auger peak, and Cd 3d regions. The clearest evidence for the presence of S in illuminated CdSe electrodes was obtained from the Auger peak at ~ 151 eV kinetic energy (K.E.), because no Se peaks are present in this region. Because of the width of this peak no attempt was made to use it for the determination of the amount of S present; however, in a qualitative way, it proved unequivocally the increased presence (see below) of S in previously immersed and illuminated electrodes. For analysis of the relative amounts of S and Se in the samples the S2s/Se3s and S2p/Se3p peaks were used. The Cd3d peaks showed no significant change before and after illumination, which is to be expected as the peak positions of Cd3d in CdS and CdSe (both powders and electrodes) are identical (405.0 and 411.7 eV B.E.); ~ 1.40 eV FWHM). The Se $L_2M_{4,5}M_{4,5}$ Auger peak (~1307 eV K.E.) was monitored to show the (dis)appearance of Se in the electrode top layer. Again, because of the width of this peak it was used as a qualitative guide only. Figure 1 shows the region of the S2s and Se3s peaks. For comparison pure CdS is included as well. The spectrum of the nonilluminated side of a CdSe electrode after submersion is included because it shows behavior intermediate between that of an electrode prior to and after illumination. Although the S and Se peaks overlap somewhat, the strong S presence in the illuminated electrode is clear from the figure. Also the spectrum shows the presence of some S in an electrode prior to illumination. The source of this S is probably in the SeO_2 and/or H_2SO_4 used for the electrolytic preparation of the CdSe electrode (1), as this sample had not been in contact with the $S/S^=$ solution. After prolonged etching (35 min) the peak profile resembles that of an electrode prior to illumination rather closely. Even after 10 min etching a strong decrease in the S peak is observed and the peak profile is closer to that of

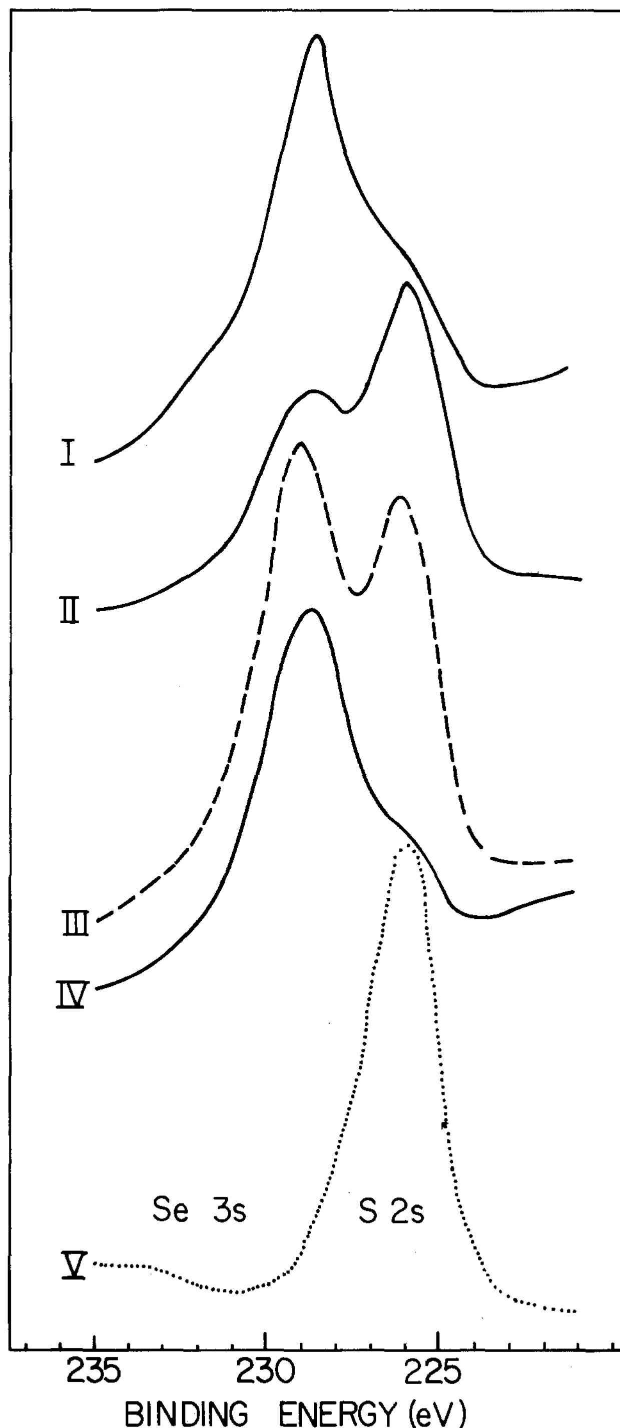

Fig. 1. Photoelectron spectra of CdSe electrodes. I, New electrode before immersion and illumination in polysulfide solution; II, same electrode after 36 hr of illumination as photoelectrode in photoelectrochemical cell (short circuit); AM1 equivalent light intensity; illuminated side; III, same as II, nonilluminated side; IV, same as II, after Ar ion sputtering for 35 (10 + 10 + 15) min; V, CdS.

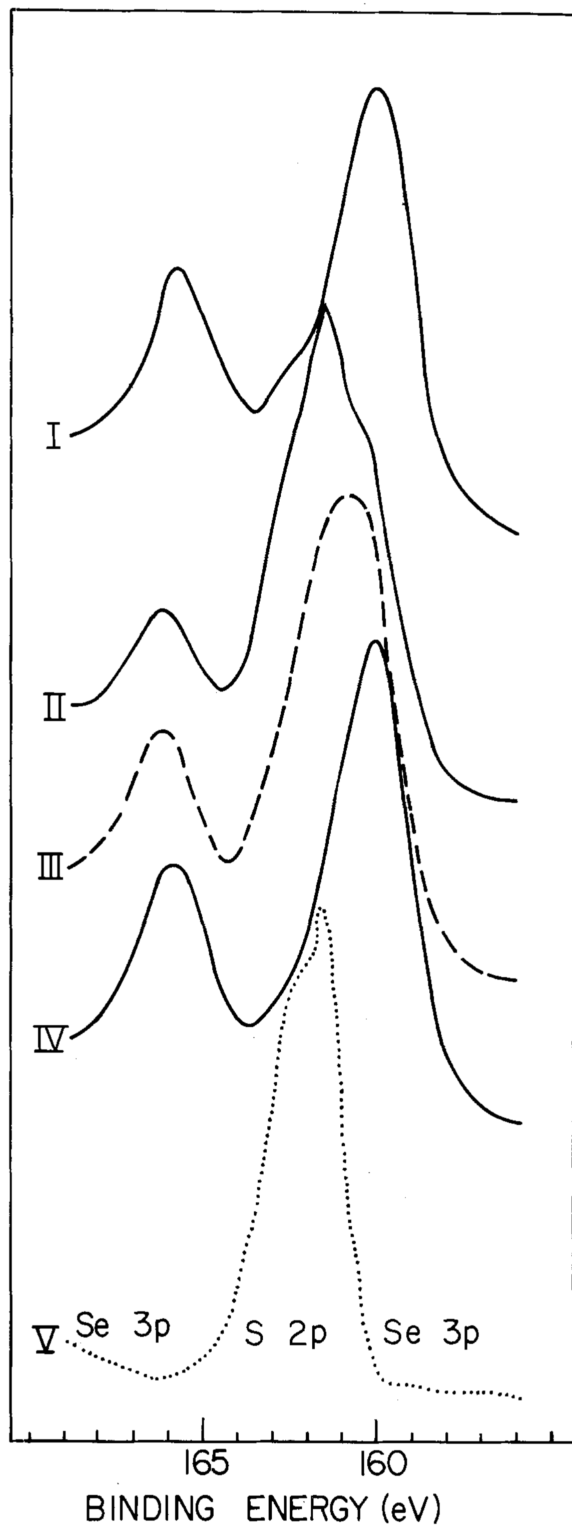

Fig. 2. As Fig. 1. Splitting of Se3p and asymmetry of S2p peaks is due to L-S coupling.

the electrode prior to illumination than to that of an illuminated one. (The continued presence of some residual S, even in nonilluminated samples, seems to argue against differential sulfur etching.) For the nonilluminated side a 10-min etching period is sufficient to make the S peak return nearly to that obtained for the electrode before illumination. Figure 2 shows the region of the S2p and Se3p peaks. The change in these peaks is parallel to that observed for the S2s/Se3s peaks. The change in relative intensity of the Se3p½ peak especially, shows the course of the S/Se substitution clearly. On the basis of the data, shown partly in Fig. 1 and 2 and those obtained for the Cd3d peaks, a rough depth profile can be obtained, using the relative intensities given in Ref. (7) for Cd3d, S2p, and Se3p. As a check on this profile, which gives the Cd/Se (Cd/S) ratio, the S2s and Se3s peaks were used to estimate the S/Se concentration ratio. In the case of overlapping peaks, manual deconvolution was used to estimate individual peak intensities. The results of these calculated estimates are shown in Fig. 3. It should be noted that the exact course of the initial decrease in the Cd/Se and S/Se ratio in the top layer is uncertain, because only points for zero and 10 min etching are used. This uncertainty in the decrease is indicated by the dashed lines in the graphs. The units used for the Cd/Se ratio were calculated using the data of Ref. (7), while in the case of the S/Se ratio arbitrary units are used.

Discussion

Exchange mechanism.—The XPS results show that a chemical exchange occurs both under illumination and in the dark. Under illumination the exchange is enhanced considerably and results in deeper penetration, *i.e.* the resulting sulfide-rich layer extends deeper into the semiconductor. It seems probable that this photoenhanced exchange occurs via hole oxidation of CdSe in the following fashion (8)

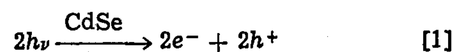

$$2h\nu \xrightarrow{\text{CdSe}} 2e^- + 2h^+ \quad [1]$$

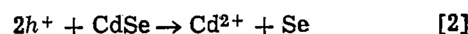

$$2h^+ + \text{CdSe} \rightarrow \text{Cd}^{2+} + \text{Se} \quad [2]$$

$$\text{Se} + \text{S}^{2-} \rightarrow \text{SSe}^{2-} \text{ (in solution)} \quad [3]$$

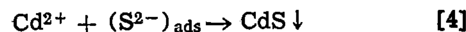

$$\text{Cd}^{2+} + (\text{S}^{2-})_{\text{ads}} \rightarrow \text{CdS}\downarrow \quad [4]$$

Thus, following oxidation of CdSe to Cd^{2+} and Se [2],

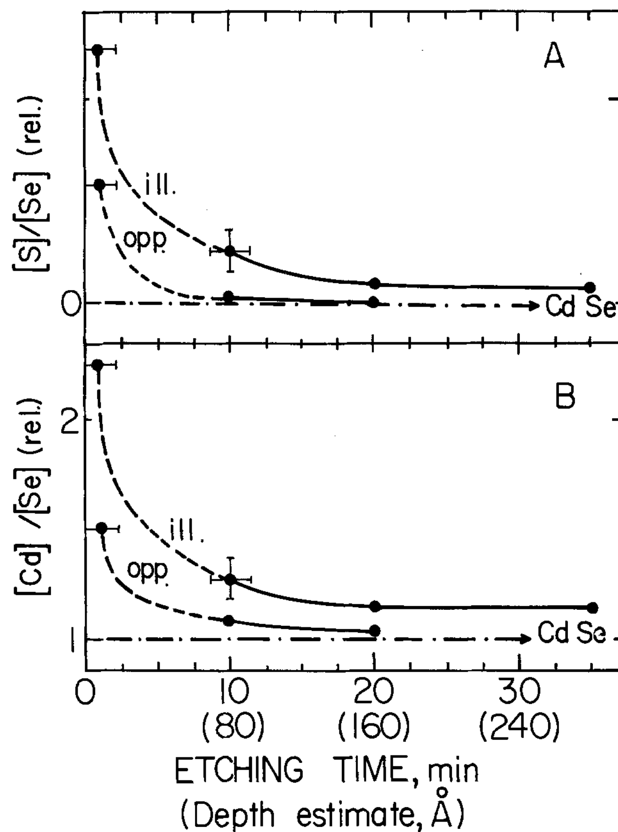

Fig. 3. Depth profile of illuminated and nonilluminated sides of CdSe photoelectrodes in photoelectrochemical cell. A, relative [S]/[Se] ratio derived from the Se3s and S2s peaks; B, [Cd]/[Se] ratio derived from the Cd3d, Se3p and S2p peaks, using the relative photoelectron signal intensities tabulated in Ref. (7). Horizontal error bars reflect the sampling depth (~ 20Å), vertical ones reflect uncertainty in peak intensities. Because of the polycrystalline nature of the surface the depth estimate in angstroms should be considered as a rough guide only. Lines labeled CdSe refer to new nonimmersed, nonilluminated CdSe electrodes.

the Se can dissolve in the sulfide-rich solution [3]. At the same time, because of the high surface concentration of sulfide ions, the Cd^{2+} ion will react to give CdS within a very short time of its formation [4]. In a way this sequence of reactions can be thought of as a reprecipitation of CdS on the CdSe surface, although not in the usual sense, *i.e.*, from the bulk solution.[1]

The presence of a polycrystalline CdS layer and the mechanism for its formation as outlined above is capable of explaining several observations, namely, (*i*) the difference in stability between single crystal and polycrystalline electrodes, (*ii*) the increase in stabilization with increase in sulfide concentration or decrease in photocurrent, (*iii*) the gradual loss of signal when a single crystalline electrode, immersed in polysulfide solution, is measured by ellipsometry, (*iv*) the increase in bias voltage dependence of the short-circuit current on single crystal electrode deactivation, and (*v*) the initial increase in photovoltage observed when immersing a clean (freshly etched) poly or single crystalline CdS electrode in polysulfide solution and illuminating it. In the following we explain these observations in more detail. From reactions [1]-[4] we expect a highly crystalline electrode of CdSe to degrade at its surface by the formation of a more polycrystalline CdS layer.[2] This then suggests a deactivation of CdSe with time, as reported by Miller *et al.* for sintered disks (3b) and single crystals [referred to in (3c)] and verified by us for single crystals. The deactivation can be dramatic indeed for electrodes with high initial (solar energy peak) efficiencies ($\sim 6\%$). Decreases to $\sim 30\%$ of the initial power output have been observed by us for single crystal electrodes in 1M [OH^-], 1M [S^{2-}], and 1M [S] solutions after a period of 7 hr, while in an electrolyte of 2M [OH^-], 2M [S^{2-}], and 2M [S], over the same period of time, the power dropped only to 80% of its initial value, and after 20 hr continuous illumination to $\sim 45\%$ ($\sim$ AM1). For our polycrystalline electrodes the deactivation is much less pronounced and proceeds very much slower if at all. For electrodes having an initial efficiency of $\sim 1\%$, complete stability, in 1M each of NaOH, Na_2S, and S, has been routinely found over many months of use in actual weather conditions. In earlier experiments, electrodes with an *initial* efficiency of 2.5-3.0% fell in efficiency by typically $\sim 15\%$ after six days under the same conditions as above, and in recent experiments, using improved techniques of preparation of the electroplated photoelectrodes, photoelectrodes with 2.5-3.0% conversion efficiencies have shown no deactivation whatever after periods up to one month of use in predominately clear sky conditions (AM2).

If we accept the hypothesis that the gradual deactivation observed for single crystal and polycrystalline sintered disk CdSe electrodes is due to a degradation of the crystallinity at tthe surface due to CdS formed, this implies a migration of cadmium (in some form) from its original lattice position. Such a migration follows from reactions [2] and [4] above, if CdS formation is not rapid enough to prevent it. Clearly an increase in S^{2-} concentration at the semiconductor surface may minimize the time free Cd^{2+} can exist, and so can a decrease in Cd^{2+} concentration. A decrease in free Cd^{2+} concentration can be obtained by working at low current densities (reaction [2] above). Miller *et al.* have indeed reported an increase in stability of sintered disk, polycrystalline CdSe electrodes with increasing S^{2-} concentration and decreasing current density (3b). The differences in stability between polycrystalline thin film, sintered disk, and single crystal electrodes can be correlated with the real surface areas of the electrodes, as they will affect the real current densities at the surface (9a). Thus, our electroplated CdSe layers, with grain size of a few microns or less (as measured by SEM techniques) will have a larger surface area than the sintered polycrystalline CdSe [with reported grain sizes of 10-20μ (3b)], or single crystals, and hence a lower local current density (for the same apparent current density) at the surface. Preliminary results from ellipsometry experiments support this hypothesis (9b). These measurements show that an initially highly polished CdSe crystal, when immersed in S/S^{2-} solution, becomes rough when illuminated and on flow of photocurrent.

Before discussing the effect of the S/Se exchange and deactivation on the open-circuit voltage and short-circuit current, we will use the XPS results to construct a rough band diagram of the system.

Band diagram.—From the depth profile (Fig. 3) and the preceding discussion it is evident that a band scheme of the $CdSe/S\text{-}S^{2-}$ semiconductor-liquid junction must take into account the presence of a sulfur-rich CdS_xSe_{1-x} layer near the surface and a surface layer which is probably pure CdS. In order to arrive at a plausible band diagram several points should be taken into consideration:

1. The thickness of the CdS layer on our CdSe electrodes is of the order of tens of angstroms (Fig. 3). While some substitution occurs even into a depth of hundreds of angstroms, the value of x in CdS_xSe_{1-x} falls sharply in the direction of the interior of the semiconductor. For simplicity's sake we shall assume an abrupt junction between a CdS layer tens of angstroms thick and the bulk CdSe. The gradual transition from CdS to CdSe will modify the band picture somewhat, but should not change its salient features (10).

2. The n-type behavior of these CdSe electrodes is due to Cd excess and/or Se vacancies. Substitution of surface layers of Se by S from polysulfide present in the electrolyte will lead to considerable compensation of previously occurring Cd excess and/or Se vacancies, because of the excess sulfur (as polysulfide) present at the surface. This means that the donor concentration, N_d, in the CdS layer would be expected to be considerably less than in the CdSe bulk. The CdS layer can then be treated as relatively electrically insulating with the Fermi level further from the conduction band than in the original CdSe.

3. The width of the space charge layer in a semiconductor is given by the equation (11) $L = (\epsilon\epsilon_0 V/qN_d)^{1/2}$ where V is the potential drop across the space charge layer in volts, N_d is the donor concentration in cm^{-3}, and the other symbols have their usual meaning. From this equation, assuming $N_d \sim 10^{16}$ cm^{-3} and with $\epsilon \sim 9$ we see that a layer of some tens of angstroms of CdS cannot support a potential drop of more than $\sim$1 mV. Because of point 2 above N_d will probably be much less than $\sim 10^{16}$ cm^{-3}, and this will reduce the maximum possible potential drop in the CdS layer even further. Therefore, the voltage drop across the CdS can be ignored compared to the hundreds of millivolts of voltage difference which exist across the CdSe space charge layer, *i.e.*, ΔV (CdS) $<< \Delta V$ (CdSe).

In view of these three points, namely that the CdS layer is very thin, relatively insulating, and unable to support a large voltage drop, we feel that it is appropriate to consider the band diagram of the $CdSe/CdS/S\text{-}S^{2-}$ system as an analogue of a metal-insulator-semiconductor (MIS) system, rather than a metal-composite abrupt isotype heterojunction system. It could be more appropriately referred to as an electro-

[1] The possibility suggested by Ellis *et al.* (2b) that the stabilization mechanism for polycrystalline and single crystal electrodes operating at different current density is different, *viz.*, rapid precipitation of CdS by reaction [4] and fast oxidation of added S_n^{2-}, respectively, does not seem to be a probable one. The presence of CdS is indeed the stabilizing factor in polysulfide solution, and chemical S/Se exchange is the cause for its formation. Stabilization will result *inter alia* from the combined effect of CdS formation and rapid kinetics for S^{2-} oxidation on the CdS surface. We see no reason why in this respect a polycrystalline electrode should behave differently from a single crystal one.

[2] Recently Gerischer has noted the possibility of destruction of a CdS single crystal photoelectrode in polysulfide solution by CdS deposition on the decomposing crystal surface, as, according to his thermodynamic arguments, the possibility for photoanodic dissolution exists (8c). Such a conclusion can be drawn also using the similar thermodynamic approach of Wrighton and Bard (8d). If we accept this possibility, it will depend on the kinetics of the system, whether in fact stability is achieved, or not. Our arguments here are concerned only with the kinetic aspects of the problem.

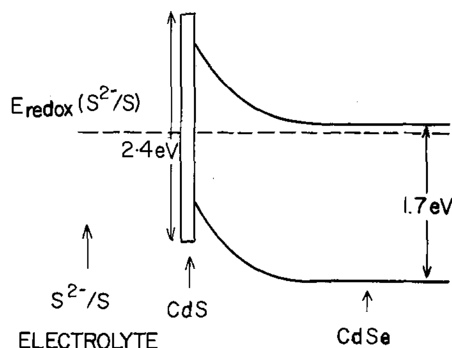

Fig. 4. Schematic idealized band scheme of polysulfide/CdS/CdSe EIS system. Because of uncertainties in the electron affinities for CdS and CdSe slight variations in the relative positions of the bandedges are possible. Presence of interface states between CdS and CdSe (due to lattice mismatch) is neglected.

lyte-insulator-semiconductor (EIS) system. A schematic of such a system is shown in Fig. 4. In this figure we have neglected interface states between CdS and CdSe, which are expected to occur because of the 4% lattice mismatch between these two chalcogenides.

From experiments with metal-semiconductor (Schottky) solar cells it is known that the presence of an insulating layer between the metal and the semiconductor can increase the photovoltage, obtainable from such a cell (12, 13). This effect is at present not fully understood. Several workers have stressed the importance of interface states between the insulator and the semiconductor in shaping the electrical field in the semiconductor (14) and in decreasing the majority carrier tunneling probability (15). Such a decrease has been explained also by considering the MIS cell as a nonequilibrium minority carrier device (16, 17). Here we shall accept the existence of the effect without further explanation and assume that similar or analogous causes can lead to an increase in photovoltage in our EIS system.

We have indeed, in a consistent way, observed increases in the photovoltage of new, or freshly etched single crystal as well as polycrystalline CdSe electrodes (18). These increases can be quite considerable (typically 20% of the initial value for polycrystalline electrodes and somewhat less for single crystal electrodes over a period of 5-10 min).

The way in which the existence of the larger bandgap CdS on top of the smaller bandgap CdSe influences the photovoltage can be considered in phenomenological terms as well. In photovoltaic cells and in photoelectrochemical cells for a given redox system, and where there is no gross deleterious chemical change at the semiconductor surface junction, materials with larger bandgaps generally yield larger photovoltages. Therefore the presence of CdS on top of CdSe can lead to a higher photovoltage than would be expected for CdSe alone as E_G (CdS) > E_G (CdSe) by ~ 0.7 eV (19). Also the photovoltage is determined by the position of the redox potential of the electrolyte with respect to the edges of the energy bands. In an n-type semiconductor the smaller $| E_{redox} - E_v \text{ (surface)} |$ the larger the photovoltage can be. In the case of chemisorbed species, which is that considered here for sulfide on CdS (4), this position should be at least partly determined by the strength of sulfide adsorption on CdS, since increased adsorption lowers the energy of the sulfide ion and thus brings it closer to the valence bandedge, E_v (surface). As the surface of a CdSe electrode in sulfide electrolyte is CdS, it will determine the adsorption properties of the sulfide ion on the electrode and, thus, can lead to an increase in photovoltage.[3]

[3] Recently Noufi *et al.* (20), reporting on CdS/CdSe solid solution photoelectrodes in polysulfide solutions, suggested that the variation in flatband potential and corresponding change in open-circuit voltage observed with change in S/Se ratio, could be brought about by changes in electron affinity or specific adsorption. From our argument it would be expected that the specific adsorption for all these systems is similar.

The last effect, which we discuss here, is the behavior of the short-circuit current upon deactivation and its changing dependence on bias voltage. The short-circuit current values which are obtainable from both single crystal and polycrystalline photoelectrodes (routinely between 10 and 15 mA/cm² for AM1 equivalent illumination) show that the current is not limited by the CdS layer, as it is impossible to create that many photons in CdS by AM1 radiation, even if we assume a quantum yield of unity, according to

$$I_{sc} = E_G \int^{\infty} A(E)\, N(E)\, d(E)$$

Here $A(E)$ is the absorption coefficient of CdS and $N(E)$ is the number of photons per unit energy in the solar spectrum. Under the same conditions, an etched CdS crystal gives a short circuit current of $\lesssim$~1 mA/cm². This low value is due mainly to absorption of light in the orange polysulfide solution. This then excludes the possibility of looking upon the system as a normal heterojunction such as the n-CdS/n-GaAs photoanode, recently investigated by Wagner and Shay (19). The possibility that the surface layer is some Cd hydroxide/oxide is rather unlikely as well, not only because in this case a much more precipitous decrease in I_{sc} (or at least some decrease, in the case of the stable polycrystalline photoelectrodes) would be expected, but also because the ESCA results do not show any evidence for it. We cannot exclude the possibility that some part of the surface is indeed Cd hydroxide/oxide, but its presence does not seem to influence the physical behavior of the electrode.

Another argument in favor of the increase in polycrystallinity (mosaicity) of the surface of illuminated photoelectrodes is found in the increasing influence of a forward bias on I_{sc}, when a single crystalline electrode deactivates. When a new or freshly etched single crystal electrode is immersed and illuminated in polysulfide solution, little increase in I_{sc} is found when a forward bias voltage V_F is applied. This indicates that recombination losses are small. Upon deactivation, I_{sc} decreases and applying V_F leads to a considerable increase in current (18). Such a behavior follows logically out of the preceding discussion. Increasing polycrystallinity leads to increasing recombination losses at newly formed grain boundaries. If now V_F is added to V_{photo} the recombination probability is decreased and thus I_{sc} increases correspondingly.

Summary

Based on a sulfide depth profile derived from x-ray photoelectron spectroscopy data, and using the analogy between the metal-semiconductor and electrolyte-semiconductor junction, we have derived a rough electron energy band picture for the CdSe/S-S⁼ junction. A possible mechanism for S/Se exchange on the surface of the CdSe electrode has also been presented. The consequences of this exchange especially for the photovoltage and electrode stability have been discussed.

Elsewhere we will deal in more detail with the short and long term behavior of the CdSe photoelectrode, polycrystalline and single crystal, especially as far as this is influenced by the presence of CdS on the surface (9, 18). Also, in collaboration with Prof. A. Bard, XPS studies similar to the ones described here, are being continued both on single crystal and polycrystalline materials, in order to obtain a more accurate picture of the S/Se substitution process.

Acknowledgments

We thank Dr. G. Sawatzky for his extensive guidance and assistance with the experimental part of this work and Ir. A. Heeres for technical assistance. D.C. thanks them and the University of Groningen for their hospitality during the performance of the XPS experiments. We thank S.O.N. and Z.W.O. for use of the Dutch National Photoelectron Spectroscopy Facility in Groningen. D.C. and G.H. thank Prof. A. Rose for help-

ful discussions. We are indebted to Dr. D. Lasar and Z. Har-Zion for their cooperation in performing the ellipsometry experiments. Part of this work was supported by Grant No. 1314 from the U.S.-Israel Binational Science Foundation to G.H. and D.C.

Manuscript submitted Dec. 30, 1977; revised manuscript received May 11, 1978.

Any discussion of this paper will appear in a Discussion Section to be published in the June 1979 JOURNAL. All discussions for the June 1979 Discussion Section should be submitted by Feb. 1, 1979.

REFERENCES

1. G. Hodes, J. Manassen, and D. Cahen, *Bull. Isr. Phys. Soc.*, **22**, 100 (1976); *Nature (London)*, **261**, 403 (1976).
2. a. A. B. Ellis, S. W. Kaiser, and M. S. Wrighton, *J. Am. Chem. Soc.*, **98**, 1635 (1976); *ibid.*, **98**, 6855 (1976); *ibid.*, **98**, 6418 (1976).
   b. A. B. Ellis, S. W. Kaiser, J. M. Bolts, and M. S. Wrighton, *ibid.*, **99**, 2839 (1977).
3. a. B. Miller and A. Heller, *Nature (London)*, **262**, 680 (1976); B. Miller and A. Heller, *This Journal*, **124**, 697 (1977).
   b. B. Miller, A. Heller, M. Robbins, S. Menezes, K. C. Chang, and J. Thomson Jr., *ibid.*, **124**, 1019 (1977).
   c. K. C. Chang, A. Heller, B. Schwartz, S. Menezes, and B. Miller, *Science*, **196**, 1097 (1977).
4. This adsorption was first reported by V. A. Tyagai in *Electrokhimiya*, **1**, 387 (1965).
5. P. W. Palmberg, *J. Vac. Sci. Technol.*, **9**, 160 (1972); M. L. Knotek, R. K. Quinn, N. R. Armstrong, and N. E. Vanderborgh, *ibid.*, **14**, 705 (1977); C. M. Garner, Y. D. Shen, J. S. Kim, G. L. Pearson, W. E. Spicer, J. S. Harris, D. D. Edwall, and R. Sahai, *ibid.*, **14**, 985 (1977).
6. G. Hodes, J. Manassen, and D. Cahen, *J. Appl. Electrochem.*, **7**, 181 (1977).
7. H. Berthou and C. K. Jørgensen, *Anal. Chem.*, **47**, 482 (1975).
8. a. H. Gerischer and W. Mindt, *Electrochim. Acta*, **13**, 1239 (1968).
   b. H. Gerischer, *J. Electroanal. Chem.*, **58**, 263 (1975).
   c. H. Gerischer, *ibid.*, **82**, 133 (1977).
   d. M. S. Wrighton and A. J. Bard, *This Journal*, **124**, 1706 (1977).
9. a. G. Hodes, D. Cahen, J. Manassen, and D. Lando, *Bull. Isr. Phys. Soc.*, **24**, 28 (1978) and to be published.
   b. Z. Har-Zion, D. Lasar, G. Hodes, J. Manassen, and D. Cahen, Unpublished results.
10. See B. L. Sharma and R. K. Purohit, "Semiconductor Heterojunctions," chap. 1. Pergamon Press, Oxford (1974).
11. A. Many, Y. Goldstein, and N. B. Grover, "Semiconductor Surfaces," chap. 4, North-Holland, Amsterdam (1965).
12. R. J. Stirn and Y. C. M. Yeh, *Appl. Phys. Lett.*, **27**, 95 (1975).
13. D. R. Lillington and W. G. Townsend, *ibid.*, **28**, 97 (1976).
14. S. J. Fonash, *J. Appl. Phys.*, **46**, 1286 (1975).
15. H. C. Card and E. S. Yang, *Appl. Phys. Lett.*, **29**, 51 (1977).
16. J. Shewchun, R. Singh, and M. A. Green, *J. Appl. Phys.*, **48**, 765 (1977); R. Singh and J. Shewchun, *Appl. Phys. Lett.*, **28**, 512 (1976).
17. R. F. McOuat and D. L. Pulfrey, *J. Appl. Phys.*, **47**, 2113 (1976); D. L. Pulfrey, *Solid State Electron.*, **20**, 455 (1977).
18. G. Hodes, J. Manassen, Y. Avigal, Y. Mirovsky, and D. Cahen, To be published.
19. J. Manassen, D. Cahen, G. Hodes, and A. Sofer, *Nature (London)*, **263**, 97 (1976). For a different application of this principle, see S. Wagner and J. L. Shay, *Appl. Phys. Lett.*, **31**, 446 (1977).
20. R. N. Noufi, P. A. Kohl, and A. J. Bard, *This Journal*, **125**, 375 (1978).

Electrode Processes of Lead Halides

Part 2: β-PbF_2

R. W. Bonne[1] and J. Schoonman*

Department of Solid State Chemistry, Physics Laboratory, State University of Utrecht, Utrecht, The Netherlands

ABSTRACT

Electrode reactions have been studied in the cell arrangements Pb|β-PbF_2|Pb and Pb|β-PbF_2|M (M = C, Pt) by means of cyclic voltammetry, scanning electron and optical microscopy, and x-ray analysis. At cathodic potentials *vs.* the reversible lead electrode lead deposit is observed, irrespective of the electrode material employed. Dependent on the oxygen content of the surrounding ambient the lead deposit can be converted partly into lead oxides, *i.e.*, PbO and Pb_2OF_2. At anodic potentials *vs.* the lead electrode, Pb reacts to form α-PbF_2, while decomposition of the lead oxides is observed. The decomposition voltage of β-PbF_2 in the cell Pb|β-PbF_2|M is well below the theoretical decomposition voltage. The decomposition is ascribed to the reaction $2PbF_2 \rightarrow PbF_4 + Pb$. X-ray analyses that support the electrode reactions are included.

In recent years the electrical properties and conduction mechanism of β-PbF_2 have attracted much attention (1-10). At elevated temperatures an unusually high temperature-independent ionic conductivity has been observed (2, 6). This has been ascribed to a liquid-like behavior of the anion sublattice (2). At low and moderate temperatures the ionic conductivity can be described by classical ionic motion theories. Intrinsic point defects are thermally generated according to the antiFrenkel mechanism (1). Kennedy *et al.* (3) verified Tubandt's finding that β-PbF_2 is a pure anion conductor. The present authors (10) have studied the conductivity of nominally pure, and AgF- and LaF_3-doped β-PbF_2 and arrived at a consistent description of the defect chemistry of β-PbF_2. Both the interstitial fluoride ions and the fluoride ion vacancies are mobile. At low and moderate temperatures the fluoride ion vacancies constitute the more mobile species.

In addition to a-c conductivity measurements, d-c polarization studies of asymmetric cells of the type $-$Pb|β-PbF_2|M+, known as Wagner polarization cells, have been reported (3, 6, 8, 11). Several authors (6,

* Electrochemical Society Active Member.
[1] Present address: Philips Research Laboratories, Eindhoven, The Netherlands.
Key words: solid electrolyte, charge, voltammetry.

8, 11) obtained plateau-type current-potential characteristics for applied d-c voltages up to 1V; these results indicate conduction by electrons. In these polarization cells graphite was used as the ionically blocking electrode. Kennedy *et al.* (3) studied the polarization behavior of this cell in the 1-1.5V range at 423°K with a vacuum-evaporated gold electrode. The slope of the reported current-potential curve, plotted at ln i *vs.* V, was about three times less than the value predicted theoretically. The electronic (presumably hole) conductivity was calculated to be less than 10^{-4}% of the total conductivity at 423°K. The observed behavior, however, was attributed to the possibility that the gold electrode was partly blocking the ionic current. The authors proposed as cell reaction

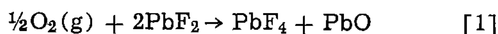

$$\tfrac{1}{2}O_2(g) + 2PbF_2 \rightarrow PbF_4 + PbO \qquad [1]$$

From the free energies of formation, Kennedy *et al.* have calculated a cell voltage of −1.59V at 423°K (3). It was very near to this voltage that the current increased dramatically.

It has been emphasized (12) that cyclic voltammetry is a useful tool in studying electrode reactions in symmetric and asymmetric all-solid cells. The electrode reactions in cells with lead chloride and lead bromide as solid electrolyte have been reported in the literature (12). Since the nature of the mobile species in β-PbF_2 is now well established, we have used cyclic voltammetry, scanning electron and optical microscopy, together with x-ray analysis to elucidate electrode reactions and their products in cells of the type Pb|β-PbF_2/Pb and Pb|β-PbF_2|M (M = C, Pt).

Experimental

A detailed description of the preparation of crystalline material of nominally pure β-PbF_2 has been given elsewhere (10). Specimens with thickness 0.2-0.5 cm and surface area 0.3-0.5 cm^2 were cut from the crystalline pieces. The polished surfaces were covered with either graphite (Aquadag) or platinum paint (Leitplatin 308) or they were covered with evaporated lead. The prepared cell systems were springloaded between two platinum disks in evacuable conductivity equipment. A potential ramp of known variable sweep rate was applied across the cell, and the current through the cell system was measured with a picoammeter (Keithley).

More details of cell preparation and a detailed description of the electrical equipment used have been reported in the literature (12). Scanning electron and optical micrographs referred to here were taken with a Stereoscan S4 scanning electron microscope and with Olympus optical microscopes. The x-ray analyses were performed on a Philips diffractometer, using Cu-Kα radiation.

Results and Discussion

Symmetric cell of the type Pb|β-PbF_2|Pb.—This cell arrangement reveals a linear behavior between the applied voltage and the measured current, the slope being equal to the frequency-independent a-c conductance, which is known to be a bulk property (9). The lead electrode is reversible at anodic and cathodic potentials, thermodynamically as well as kinetically.

Scanning electron micrographs of the lead anode demonstrate the formation of new material. The anode reaction can be represented by

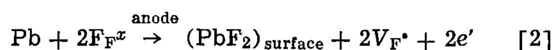

$$Pb + 2F_F^x \xrightarrow{\text{anode}} (PbF_2)_{surface} + 2V_F^{\bullet} + 2e' \qquad [2]$$

since at low and moderate temperatures fluoride ions carry the current via fluoride ion vacancies (10). Here, and throughout this paper the defect notation of Kröger is used (14).

The deposits have been studied by means of x-ray analysis. It was observed that β-PbF_2 partly converts into α-PbF_2 while the surfaces are polished prior to electrolysis. The increased intensity of the lines of α-PbF_2 in the x-ray diagram of the lead anode compared to that of the lead cathode, however, confirmed the deposit to be α-PbF_2 in accord with observations reported by Kennedy and Miles (8). A marked decrease in the intensity of the lines of metallic lead was observed on the anode side, in accord with reaction [2].

Scanning electron micrographs of the cathode surface demonstrate only a shrinkage of the crystal. The reaction

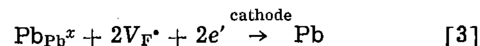

$$Pb_{Pb}^x + 2V_F^{\bullet} + 2e' \xrightarrow{\text{cathode}} Pb \qquad [3]$$

accounts for this behavior. The growth of lead dendrites from the cathode is readily observed with an optical microscope. The dentritic growth of lead occurs perpendicular to the current flow and is located in a thin region of the electrolyte at the interface electrode-electrolyte. Although similar current-potential curves and electrode reactions were observed for lead chloride and lead bromide (12), dendritic lead growth in these halides proceeds along the current flow, ultimately leading to an electrical short circuit.

Asymmetric cells of the type Pb|β-PbF_2|M (M = C, Pt).—In Fig. 1 we have gathered typical voltammograms of the cell Pb|β-PbF_2|Pt. The voltammograms were recorded in nitrogen and were strongly dependent on the electrolysis duration at cathodic potentials

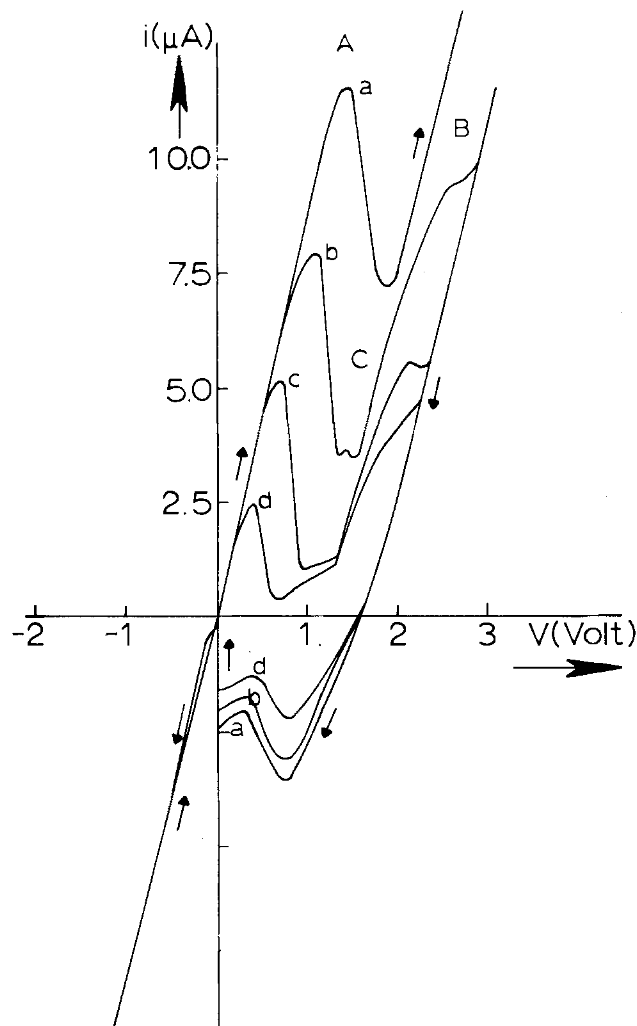

Fig. 1. Voltammograms of the cell Pb|β-PbF_2|Pt in air at 390°K for different electrolysis times. Sweep rate 83 mV sec^{-1}. Curve a, 4.0 × 10^{-4}C; curve b, 2.3 × 10^{-4}C; curve c, 1.0 × 10^{-4}C; curve d, 5.9 × 10^{-5}C. The sweep direction has been marked with arrows. For the meaning of the designations A, B, and C, see the text. The voltages indicated are measured *vs.* the reversible lead electrode.

vs. the reversible lead electrode. Analogous voltammograms were observed for cells with painted Pt or C-electrodes in nitrogen, air, and oxygen atmosphere, in the temperature range 300°-600°K. For voltages above about 2V the current varies directly with the potential, with a slope equal to the bulk conductance.

In general current-potential curves reveal two main anodic waves (A and B in Fig. 1). In several cases there is an indication of a third anodic wave (C). The waves A, B, and C appear only when the blocking electrode has been operated before at cathodic potentials (Fig. 2). The shape of the voltammogram is typical of that observed for the formation, oxidation, and reduction of reaction products (12).

According to reaction [3] a lead deposit on the blocking electrode is expected to occur during electrolysis with electrode M operating at cathodic potentials. A cell system with two reversible lead electrodes readily results. On reversing the potential, the lead deposit reacts to form α-PbF_2 (reaction [2]). Thermodynamically, the total cell reaction hardly requires any energy. The first anodic wave (A), which is also observed for lead chloride and lead bromide in identical cell arrangements (12), has been ascribed to this process. Other reactive species, however, must be responsible for the other waves, and they are to be correlated with oxidation of the reaction products formed at the blocking electrode during electrolysis at cathodic potentials.

Bonne *et al.* (12) derived a simple equation for the amount of charge transported during electrolysis and deduced an equation for the amount of charge transported in the waves. The ratio of these amounts gives the fraction x of the amount of charge transported in the wave. In Fig. 3 this inferred fraction x is plotted *vs.* the total amount of charge passed during the electrolysis at cathodic potentials. It is observed that the oxidation waves A and B account for almost all the transported charge, the major fraction being found in wave B. From these data it is concluded that a large fraction of the initial lead deposit at the blocking electrode is converted into another lead compound which acts as an electroactive compound responsible for wave B.

In Fig. 4 voltammograms recorded in a nitrogen and in an oxygen atmosphere are presented for the cell Pb|β-PbF_2|Pt. Similar voltammograms were obtained for graphite paint electrodes. A remarkable decrease in wave height is observed for the anodic wave A, when oxygen is used as ambient, while the reverse is true for the wave B. In Fig. 5 the fraction of charge transported in the wave A is plotted *vs.* the total amount of charge transported during electrolysis at cathodic potentials in nitrogen, air, and oxygen. From these observations it is evident that the freshly deposited amount of lead on the blocking electrode reacts partly with oxygen from the ambient to form an oxide. The observed waves B and C can be ascribed to the decomposition of the oxides formed on the blocking electrode. The observed voltages at

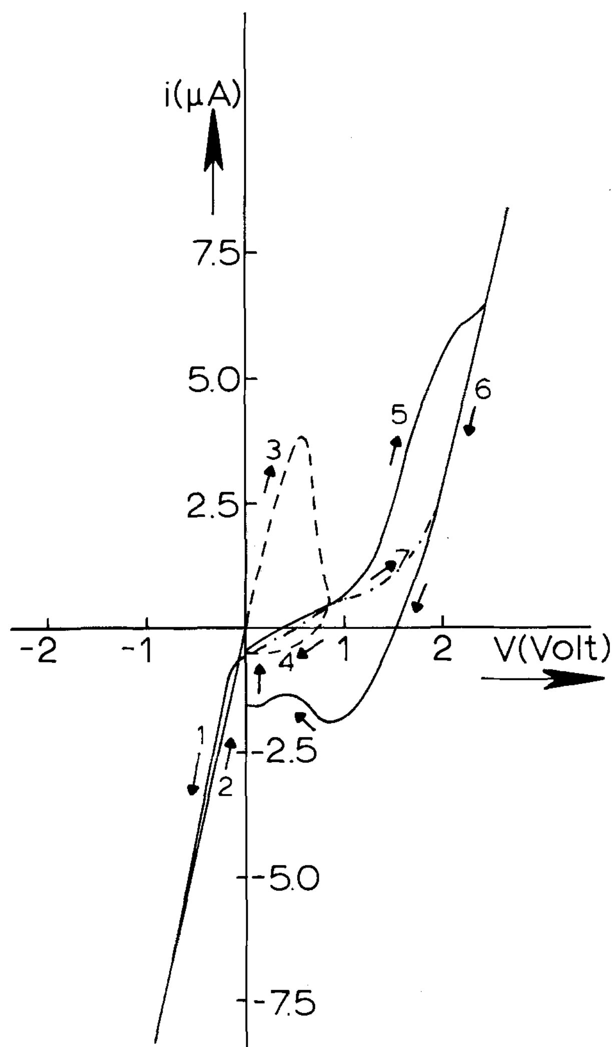

Fig. 2. Voltammograms of the cell Pb|β-PbF_2|Pt in air at 390°K. Different sweeps in the positive voltage region are shown. Their sequence is indicated by the No. 1-7. Sweep rate 83 mV sec^{-1}.

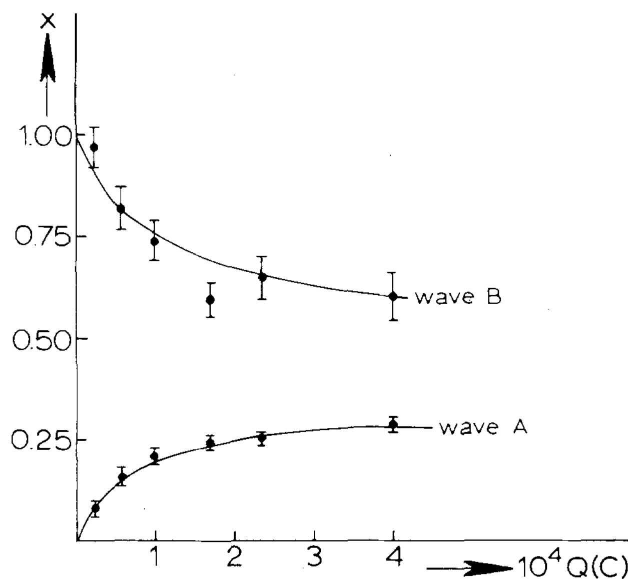

Fig. 3. The fraction x of the amount of charge transported in the wave A and B as a function of the total amount of charge passed during electrolysis of the cell + Pb|β-PbF_2| Pt — at 390°K in air.

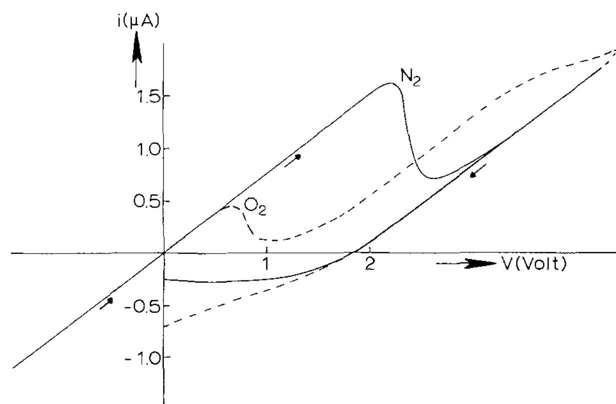

Fig. 4. The influence of the ambient on voltammograms of the cell Pb|β-PbF_2|Pt. T = 390°K, sweep rate 83 mV sec^{-1}.

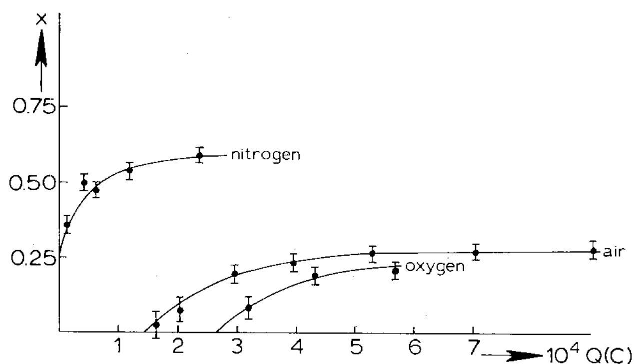

Fig. 5. The fraction x of the charge transported in wave A as a function of the total amount of charge passed during electrolysis at cathodic potentials of the cell Pb|β-PbF_2|Pt in different ambients at 390°K.

which these waves start are (1.12 ± 0.08)V, and (0.50 ± 0.15)V, respectively, at 473°K. These values are hardly dependent on temperature. The decomposition voltages of PbO_2 and PbO at 473°K are calculated to be 0.482 and 0.893V, respectively. These values are close to the voltages observed experimentally. For the anodic wave C we therefore propose the electrode reaction

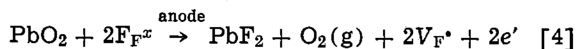

$$PbO_2 + 2F_F^x \xrightarrow{\text{anode}} PbF_2 + O_2(g) + 2V_F^{\bullet} + 2e' \quad [4]$$

whereas for the wave B the electrode reaction

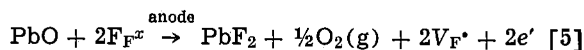

$$PbO + 2F_F^x \xrightarrow{\text{anode}} PbF_2 + \tfrac{1}{2}O_2(g) + 2V_F^{\bullet} + 2e' \quad [5]$$

is proposed. The first wave was already ascribed to reaction [2]. The minimum total cell voltage required for reaction [4] or [5] is almost equal to the decomposition voltages of the respective oxides. For PbO the observed voltage is slightly higher than the theoretical value. The experimental observations, however, do not indicate any overpotential. Kennedy and Miles (8) reported the presence of Pb_2OF_2 on the anode after electrolysis of the cell Pb|β-PbF_2|Pb. Thermodynamic data relating to this compound are not available in the literature. If wave B can be related to the reaction

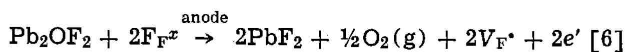

$$Pb_2OF_2 + 2F_F^x \xrightarrow{\text{anode}} 2PbF_2 + \tfrac{1}{2}O_2(g) + 2V_F^{\bullet} + 2e' \quad [6]$$

instead of reaction [5], then the formation enthalpy of Pb_2OF_2 is calculated to be about 192 kcal/mole at 473°K.

Figure 6 shows cyclic voltammograms for the cell Pb|β-PbF_2|C in air taken at a constant sweep rate in the cathodic direction, the sweep rate being varied from 167 to 8.3 mV sec^{-1} in the anodic portion. The peak currents of the waves can be expressed by (12)

$$i_p(A) = (2vxQ)^{1/2}R_b^{-1/2} \quad [7]$$

with v the sweep rate (V sec^{-1}), xQ the actual amount of charge transported in the wave, and R_b the bulk resistance. For the two main waves A and B, this square root dependence was observed. In Fig. 7 the fraction of charge transported during the wave is plotted *vs.* the sweep rate. At low sweep rates the voltammogram shows that almost all the lead deposit has been oxidized by the ambient. The oxide formation does not occur instantaneously, but only after some time has elapsed.

The observed deposition voltage of about 2V at 473°K is well below the theoretical decomposition voltage of β-PbF_2, *i.e.*, 3.082V (13). This deposition voltage is practically independent of temperature in the region 320°-450°K; it is not dependent on the electrode paint employed.

Kennedy *et al.* (3) observed a dramatic increase in current in the cell −Pb|β-PbF_2|Au+ above about 1.5V. If not all the faradaic processes were blocked, then the observed steady-state current would still contain an ionic contribution. As over-all cell reaction the authors proposed reaction [1]. Instead of the reported value of −1.59V at 423°K (3), we found by recalculation a cell voltage of −1.04V. The PbO is formed at the cathode-electrolyte interface, while PbF_4 is formed at the anode-electrolyte interface. If this reaction occurs, a rapid increase in current above 1.0V is to be expected. We expect to find not

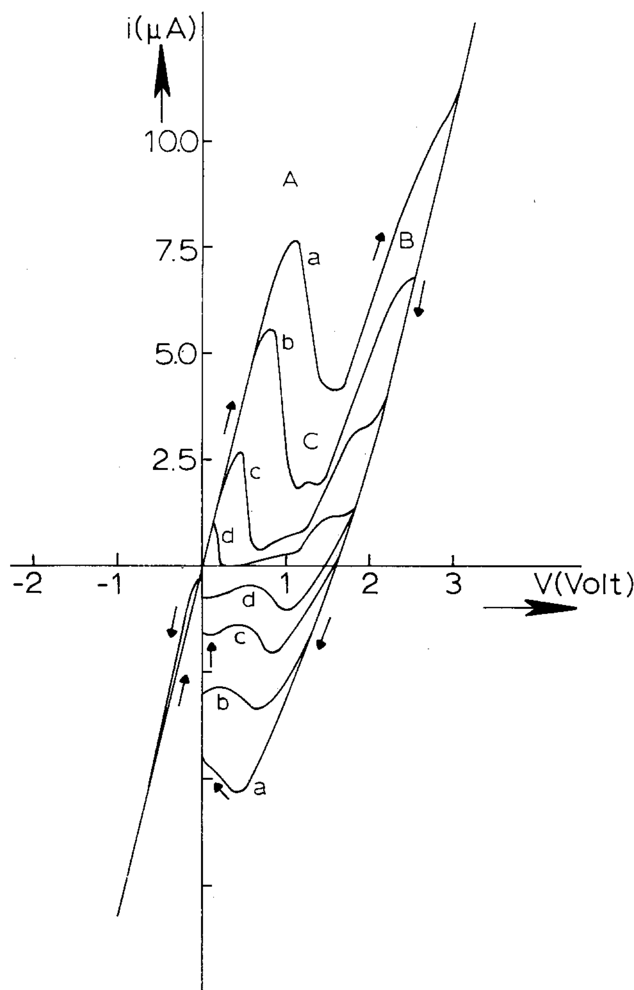

Fig. 6. Voltammograms of the cell Pb|β-PbF_2|C in air. Charge transported during electrolysis 1.0 × 10^{-4}C. Curve a, sweep rate 167 mV sec^{-1}; curve b, sweep rate 83 mV sec^{-1}; curve c, sweep rate 33 mV sec^{-1}; curve d, sweep rate 8.3 mV sec^{-1}.

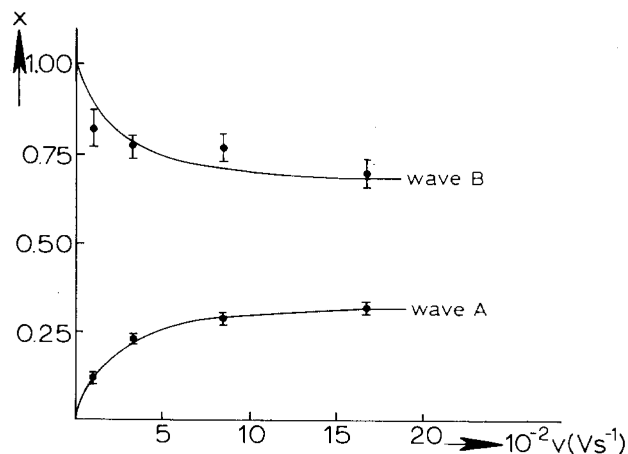

Fig. 7. The fraction x of the charge transported during the waves A and B as a function of the sweep rate for the cell Pb|β-PbF_2|Pt.

a wave but a current that varies directly with the applied voltage. In this study the wave that starts at about 1.1V is ascribed to the decomposition of PbO because the wave is clearly dependent on the amount of PbO present on the electrode surface. With an optical microscope lead dendrite formation is observed at the cathode-electrolyte interface. There is no evidence of an electrochemical reaction of oxygen with lead. From these observations cell reaction [1] is not likely for the present cell system. The slope of the current-potential curve above about 2V equals, however, the bulk conductance. The presence of a faradaic process is, therefore, established.

As total electrolysis reaction we propose the reaction

$$2PbF_2 \rightarrow PbF_4 + Pb \quad [8]$$

The cell voltage calculated from free energies of formation is -1.95 at 423°K. Lead will be deposited on the cathode-electrolyte interface, whereas PbF_4 forms at the anode-electrolyte interface.

In order to find evidence for this cell reaction x-ray analyses of the electrode surfaces were carried out after electrolysis. In this case electrolysis was performed at 2.5V on a β-PbF_2 single crystal between two platinum mesh electrodes at 493°K in air. The mesh electrodes behave in the same way as the paint electrodes. X-ray analysis of the cathode-electrolyte surface revealed the presence of β-PbF_2, α-PbF_2, Pb_2OF_2, and Pb when electrolysis times were short. After long electrolysis times the presence of PbO in the red modification was detected as well. These data indicate that the lead deposit on this electrode is oxidized into Pb_2OF_2 and PbO, and that the oxidation wave B can be related to the decomposition of Pb_2OF_2 rather than that of PbO. In the x-ray diagram of the anode-electrolyte surface the lines of α-PbO_2, β-PbF_2, α-PbF_2, and PbO (red) were observed, while, for long electrolysis times, only the lines of Pb_2O_3 were observed. The PbF_4 formed is known to react very rapidly with traces of H_2O (15). The following reaction can result

$$PbF_4 + 2H_2O(g) \rightarrow PbO_2 + 4HF(g) \quad [9]$$

especially when the crystal is removed from the conductivity cell. The PbO_2 formed is partly converted into PbO or into other lead oxides. The x-ray data therefore indicate indirectly the occurrence of the proposed cell reaction [8].

From the above results it is evident that Wagner polarization studies of cells of the type Pb|β-PbF_2|M (M = C, Pt) should at least be restricted to voltages below 1.95V, because above this voltage β-PbF_2 decomposes electrolytically.

Acknowledgments

The authors are grateful to Prof. Dr. G. Blasse for discussing the text in detail and for offering valuable criticism in the course of the preparation of the manuscript. We are indebted to Mr. J. Pieters of the Molecular Cellbiology Department of this University, who recorded the scanning electron micrographs, and to Dr. H. A. Harwig of the Inorganic Chemistry Department of this University, who kindly made available the potentiostat and optical microscopes.

Manuscript submitted July 18, 1977; revised manuscript received May 24, 1978.

Any discussion of this paper will appear in a Discussion Section to be published in the June 1979 JOURNAL. All discussions for the June 1979 Discussion Section should be submitted by Feb. 1, 1979.

REFERENCES

1. J. Schoonman, G. J. Dirksen, and G. Blasse, *J. Solid State Chem.*, **7**, 245 (1973).
2. C. E. Derrington and M. O'Keeffe, *Nature (London)*, **246**, 44 (1973).
3. J. H. Kennedy, R. C. Miles, and J. Hunter, *This Journal*, **120**, 1441 (1973).
4. J. M. Réau, J. Claverie, G. Campet, C. Déportes, D. Ravaine, J. L. Souquet, and A. Hammou, *C. R. Acad. Sci., Ser. C*, **280**, 225 (1975).
5. C. C. Liang and A. V. Joshi, *This Journal*, **122**, 466 (1975).
6. R. Benz, *Z. Phys. Chem. N.F.*, **95**, 25 (1975).
7. J. C. Gianduzzo, J. Pistré, and J. Salardenne, *Electrocomp. Sci. Technol.*, **2**, 55 (1975).
8. J. H. Kennedy and R. C. Miles, *This Journal*, **123**, 47 (1976).
9. R. W. Bonne and J. Schoonman, *Solid State Commun.*, **18**, 1005 (1976).
10. R. W. Bonne and J. Schoonman, *This Journal*, **124**, 28 (1977).
11. J. Schoonman, G. A. Korteweg, and R. W. Bonne, *Solid State Commun.*, **16**, 9 (1975).
12. R. W. Bonne, L. Boon, and J. Schoonman, *J. Electroanal. Chem.*, **89**, 7 (1978).
13. "Physics of Electrolytes," Vol. 2, J. Hladik, Editor, p. 747, Academic Press, London, (1972).
14. F. A. Kröger, "The Chemistry of Imperfect Crystals," North-Holland, Amsterdam (1964).
15. "Gmelins Handbuch der anorganischen Chemie," 8 Auflage, Blei, Teil C, p. 280, Lieferung 1, Verlag Chemie, Weinheim (1969).

Technical Note

Lithium-Boron-Silicon Alloy Lithium Electrodes

Anthony F. Sammells*,[1]

Rockwell International, Atomics International Division, Canoga Park, California 91304

Lithium/metal sulfide batteries are presently under development at the Atomics International Division of Rockwell International (1), General Motors (2), and Argonne National Laboratory (3) for their application in utility load leveling systems and electric vehicles. In recent years there have been several candidate lithium electrode materials considered for this battery system. From an energy density consideration,

* Electrochemical Society Active Member.

[1] Present address: Institute of Gas Technology, Chicago, Illinois 60616.

Key words: lithium-boron-silicon alloy, silicon migration, molten salt, secondary battery.

liquid lithium is most attractive for its low equivalent weight and high cell voltage. However, recent evidence (4) has shown that lithium can be lost by the reaction

$$\underset{\text{(melt)}}{KCl} + Li \rightarrow LiCl + \underset{\text{(melt)}}{K}$$

followed by potassium vaporization. This, together with correspondingly increased cell component corrosion and difficulties with containment of liquid lithium, has dictated that a variety of lithium alloys be investigated to avoid these problems. Binary alloys can either be formed electrochemically by charging a metal such as Bi, Pb, Sn, (5) or Al with lithium or they can be synthesized directly from the ingredients, *e.g.*, LiB (6). However, only two of the binary alloys have been found, at this time, to possess utility in secondary molten salt batteries.

The two binary lithium alloys presently under development for the lithium-metal sulfide battery include lithium-aluminum (7, 8) which has an open-circuit potential 303 mV positive to liquid lithium at 400°C and lithium-silicon (9, 10) which, in the fully charged state, has a composition approximating Li_5Si. The latter can be discharged through a series of voltage plateaus at 48, 158, 280, and 336 mV *vs.* liquid lithium at 400°C. The theoretical Faradaic capacity of Li_5Si is 2.12 A-hr/g compared to 0.8 A-hr/g for LiAl. The high capacity of Li_5Si together with excellent capacity retention over long cycling periods (11) and favorable electrochemical performance (12) has provided a strong incentive to develop this material as a lithium electrode for lithium/iron-sulfide batteries.

During the course of extended cycling tests, it has become apparent that migration of silicon to the metal substrate can occur at cell operating temperatures. This effect manifests itself by loss of capacity at the negative electrode and eventual embrittlement of the electrode structure, which can lead to electrode rupture. Silicon migration proceeds slowly at normal cell operating temperatures (425°C) but is much accelerated as the temperature approaches 550°C. Several approaches to arrest such silicon migration into the electrode substrate are being pursued at Atomics International.

This communication discusses some preliminary findings from one of these approaches, notably the use of lithium-boron-silicon ternary alloys as an active material in the electrode. The use of these alloys has been found to markedly reduce silicon attack of ferrous substrates. Thermodynamic data for one group of lithium-boron-silicon alloys are presented here together with some preliminary corrosion results.

A preliminary phase diagram for the boron-silicon system (13) indicates the existence of two compounds with the compositions B_4Si and B_6Si. The existence of the phase BSi_2 has been indicated by metallographic and microhardness data (14), but x-ray data do not appear to be conclusive at this time (15). The solubility of boron in silicon is temperature dependent but occurs by a substitutional mechanism with a silicon lattice parameter contraction from 5.430 to 5.425Å upon substitution of 1 atomic percent (a/o) boron or more as measured at room temperature.

For BSi_2 synthesized at 1310°C for 2 hr from elemental boron and silicon, the lattice parameter was observed to contract from 5.431Å for pure silicon to 5.417Å for BSi_2. Upon sectioning of the material, two phases could be seen which may possibly correspond to the alpha and beta phases of this material referred to by other workers (16).

Experimental

Chemicals.—Highly prepurified LiCl-KCl eutectic (mp 352°C) was purchased from Anderson Physics Laboratories, Incorporated, Urbana, Illinois. Silicon powder, 99.5% pure, was obtained from Atomergic Chemetals Company, Carle Place, New York. Boron metal, 5 μm amorphous type, 96% pure, was obtained from Cerac/Pure, Milwaukee, Wisconsin. Lithium metal was obtained from the Foote Mineral Division of Newmont Mining Company.

Preparation of alloys.—Lithium-containing alloys were first synthesized by the addition of silicon to molten lithium at 700°C. This molten mixture was then chill-cast to optimize the grinding procedure. Ternary alloys with compositions corresponding to BSi_2Li_4, BSi_2Li_8, BSi_2Li_{10}, and $B_{2.64}SiLi_4$ have been synthesized in this manner. The synthesis of BSi_2 was performed by thoroughly mixing boron and silicon powders, pressing these into a green slug at 15,000 psi, and heating to 1350°C under an argon atmosphere using an induction heater.

Experimental measurements and cell operations with lithium were performed in a Vacuum Atmospheres dry box equipped with a Ni-Train purifier. Concentrations of oxygen, nitrogen, and water were removed to below the parts per million level.

Apparatus.—Cell voltage measurements were made on a Sargent Recorder, Model MR. Constant current was supplied to the cell between voltage measurements by an Electronic Measurements, Model C633, constant current power supply. Temperature measurements were made with a chromel alumel thermocouple with a floating hot junction connected to a Westronics strip chart recorder. The test cell consisted of a 250 ml stainless steel beaker with appropriate electrically insulated feed-throughs to accommodate the lithium reference electrode (titanium felt metal impregnated with liquid lithium), the counterelectrode (aluminum wool), the working electrode (BSi_2Li_{10} on titanium felt), and the chromel-alumel thermocouple (not shown in Fig. 1).

Procedure.—The open-circuit temperature dependencies of the voltage plateaus of the ternary Li-B-Si alloy *vs.* liquid lithium were determined in the thermally controlled constant temperature molten salt bath. The working electrode having an initial charge state composition BSi_2Li_{10} was discharged at 5 mA/cm^2 into an aluminum wool counterelectrode. Voltage and temperature measurements were made during slow (approximately 0.2°C/min) cooling of the molten salt bath to minimize any thermal gradients between the electrodes and thermocouple. Repeated measurements using this technique gave reproducible results.

Results and Discussion

A typical *IR*-free discharge curve at 400°C for the ternary alloy having all initial stoichiometry BSi_2Li_{10} is shown in Fig. 2. As with the binary lithium-silicon alloy, the discharge occurs via five voltage plateaus. Similar discharge curves were obtained from material initially prepared in the discharged state and charged electrochemically to the same stoichiometry. BSi_2, if ground to a suitably fine powder, could be charged close to theoretical capacity. In such experiments, BSi_2 active material was contained in a honeycomb-type electrode structure shown in Fig. 3, and had a typical,

Fig. 1. Laboratory investigation cell

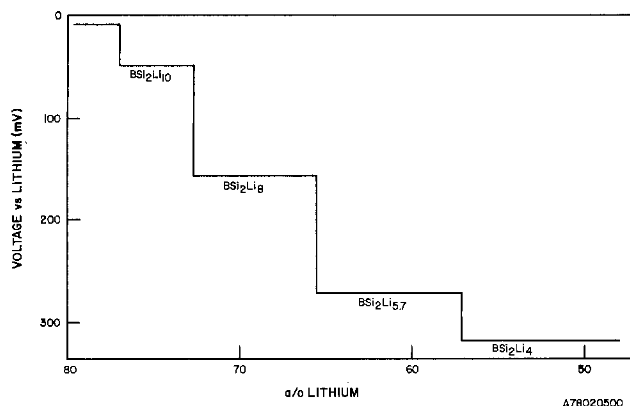

Fig. 2. *IR*-free discharge curve for BSi_2Li_{10}

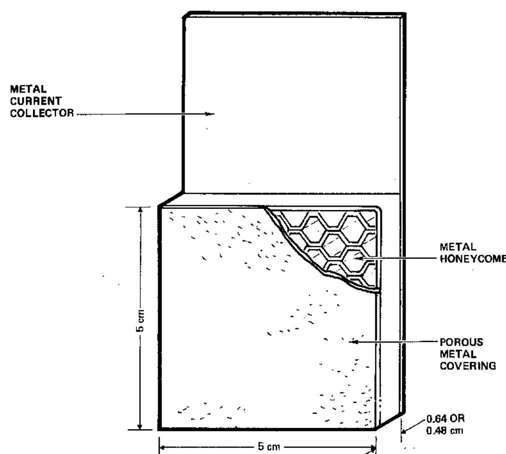

Fig. 3. Honeycomb electrode structures

average particle size of 3 μm. Particle sizes significantly larger than this exhibited a lower Faradaic capacity during charge, presumably due to the apparent unavailability of the silicon in the boron-silicon matrix. At each voltage plateau, the voltage temperature dependency was determined, typically between 650° and 730°K, from which a straight line relationship could be written, using the least squares method. The accuracy of the measurements was estimated to be ±2%. The voltage temperature dependencies and voltage plateaus at 400°C are shown in Table I. The Faradaic capacity of this ternary alloy is 1.97 A-hr/g which compares to the 2.12 A-hr/g for Li_5Si and 0.8 A-hr/g for LiAl. The voltage temperature dependencies allowed calculation of the relative partial molar entropies of lithium, $\overline{\Delta S}_{Li}$, using the thermodynamic relationship

$$\overline{\Delta S}_{Li} = n\mathbf{F}(\Delta E/\Delta T)_p \quad [1]$$

where $\overline{\Delta S}_{Li}$ = relative partial molar entropy; $\mathbf{F}$ = Faraday's constant; n = number of equivalent per mole; ΔE = voltage change; ΔT = temperature variation; and p = indicated constant pressure. After determination of $\overline{\Delta S}_{Li}$, the relative partial molar-free energy $\overline{\Delta G}_{Li}$ and enthalpy $\overline{\Delta H}_{Li}$ could be calculated from

Table I. Temperature dependency of voltage of lithium-boron-silicon alloys *vs.* lithium metal

Voltage plateau at 400°C (mV *vs.* lithium)	Temperature dependency (mV *vs.* °K)
49.79	188.9-0.2067T
156.66	270.6-0.1693T
271.44	313.5-0.0625T
318.73	350.4-0.04706T

Table II. Thermodynamic data for lithium-boron-silicon alloys at 400°C

Alloy-composition range	$\overline{\Delta S}_{Li}$ (cal/°K mole)	$\overline{\Delta G}_{Li}$ (kcal/mole)	$\overline{\Delta H}_{Li}$ (kcal/mole)
BSi_2Li_{10}-BSi_2Li_8	−9.53	−2.30	−8.71
BSi_2Li_8-$BSi_2Li_{5.7}$	−8.98	−8.31	−14.35
$BSi_2Li_{5.7}$-BSi_2Li_4	−2.45	−10.64	−12.29
BSi_2Li_4-BSi_2	−4.34	−29.4	−32.32

the relationships

$$\overline{\Delta G}_{Li} = -n\mathbf{F}E \quad [2]$$

and

$$\overline{\Delta H}_{Li} = \overline{\Delta G}_{Li} + T\,\overline{\Delta S}_{Li} \quad [3]$$

The results obtained from these calculations are shown in Table II. The composition was chosen by analogy to other metal silicides of this composition. It should be emphasized that BSi_2 is probably not a compound but a solid solution. Alloys of lower boron content (*e.g.*, BSi_4) would be expected to be equally electrochemically active.

X-ray measurements are in agreement with earlier work (15) which shows some degree of lattice parameter contraction upon substitution of boron into silicon lattice sites. This is to be expected from the 25% smaller tetrahedral covalent radii in boron when compared to silicon (17).

Accelerated 4 week tests using BSi_2Li_8 indicate that silicon migration into 1010 low carbon and 304 stainless steel electrode substrate materials can be reduced by a factor of five relative to that observed with Li_8Si_2 at 550°C in a LiCl-KCl molten salt eutectic, as determined using microprobe analysis techniques. At this time, it is difficult to determine what the corrosion-inhibiting mechanism or mechanisms might be. Whether the silicon penetration into the metal substrate electrode is reduced by the formation of a metal boride diffusion barrier or is minimized by a reduction in the activity of silicon or a combination of both is, as yet, uncertain.

Further work is in progress to determine the electrochemical and long-term corrosion-inhibiting characteristics of boron-silicon alloys in metallic honeycomb-type substrate electrodes. Such information will be used to optimize the boron to silicon ratio of the ternary alloy.

Boron presently costs around $25/lb in large quantities (2000 lb). The cost of boron per kW-hr in the lithium-iron sulfide battery will depend upon both the final alloy stoichiometry and the charge state capacity chosen for the alloy. For BSi_2, the cost penalty introduced by the boron content, assuming a final charged state composition BSi_2Li_{10}, would be around $1.80/kW-hr. It is expected that silicon migration into the negative electrode current collector structure will be inhibited to an acceptable degree by the use of lower boron containing ternary alloys and will thereby provide a cost-effective solution to achieving both an electrochemically and mechanically stable long life lithium electrode for the lithium-metal sulfide battery.

Manuscript submitted Oct. 27, 1977; revised manuscript received March 15, 1978.

Any discussion of this paper will appear in a Discussion Section to be published in the June 1979 JOURNAL. All discussions for the June 1979 Discussion Section should be submitted by Feb. 1, 1979.

Publication costs of this article were assisted by Rockwell International.

REFERENCES

1. S. Sudar and L. A. Heredy, Paper presented at the 12th IECEC, Washington, D.C., August 28- September 2, 1977.
2. J. S. Dunning, T. G. Bradley, and E. J. Zeither, Paper presented at the 11th IECEC, p. 491, September 12-17, 1976.

3. P. A. Nelson *et al.*, "Progress Report for the Period April-June 1976," ANL-76-81, Argonne National Laboratory, Argonne, Ill.
4. R. M. Seefurth and R. A. Sharma. *This Journal*, **122**, 1049 (1975).
5. E. S. Buzzelli, Abstract 14, p. 40, The Electrochemical Society Extended Abstracts, Fall Meeting, Miami Beach, Florida, Oct. 8-13, 1972.
6. S. D. James and L. E. DeVries, *This Journal*, **123**, 321 (1976).
7. N. P. Yao, L. A. Heredy, and R. C. Saunders, *ibid.*, **118**, 1039 (1971).
8. J. R. Selman, D. K. DeNuccio, D. J. Sy, and R. K. Steunenberg, *ibid.*, **124**, 1160 (1977).
9. S. Lai, *ibid.*, **123**, 1196 (1976).
10. R. A. Sharma and R. M. Seefurth, *ibid.*, **123**, 1763 (1976).
11. L. R. McCoy and L. A. Heredy, Paper presented at the 11th IECEC, p. 485, September 12-17, 1976.
12. R. M. Seefurth and R. A. Sharma, *This Journal*, **124**, 1207 (1977).
13. R. P. Elliott, "Constitution of Binary Alloys," First Suppl., p. 134, McGraw-Hill, New York (1965).
14. G. V. Samsonov and V. M. Sleptsoy, Dopovidi Akad. Navic UlG RSR 1066, (1962).
15. G. V. Samsomov and V. M. Sleptosy, *Russ. J. Inorg. Chem.*, **8**, 1047 (1963).
16. L. K. Lamikhov, *Neorg. Mater.*, **4**, 1076 (1968).
17. L. Pauling, "The Nature of the Chemical Bond," 35th ed. p. 246, Cornell University Press, Ithaca, N.Y. (1960).

ERRATA

In reference to the paper "Reactive Plasma Deposited Si-N Films for MOS-LSI Passivation," by A. K. Sinha, H. J. Levinstein, T. E. Smith, G. Quintana, and S. E. Haszko, which appeared on pp. 601-608 in the April 1978 JOURNAL, Vol. 125, No. 4, the following additional information should be noted.

The stated range of stresses in Table I is based upon data in Fig. 2-5 which indicate a value of approximately 5×10^9 dynes cm^{-2}, and upon data in Fig. 6 which indicate a stress of approximately 1×10^9 dynes cm^{-2}. The abrupt drop in stresses, shown in Fig. 6, was observed after certain modifications were made to the substrate table and the rf-tuning network. Prior to the modification, the wafer capacity on the substrate table was eight 2 in. diam Si wafers which were placed in cutouts on a stainless steel substrate table and heated by direct exposure from the quartz lamps. After the modification, the usable wafer capacity was 22 2 in. diam Si wafers which were placed on a solid aluminum plate heated by quartz lamps from underneath. At this point in time, the impedance matching network was also modified by increasing the tunable load capacitor. This greatly improved the tuning of the plasma at 1 Torr pressure. Data presented in Fig. 6-10 were taken after the above modifications—they show substantially lower tensile stresses and lower etch rates in buffered HF. The exact mechanism for these changes in film properties is not understood. However, the above observations further highlight the importance of machine-related effects in addition to the process variables discussed in the paper.

In reference to the paper "Breakdown and Efficiency of Anodic Oxide Growth on Titanium," by C. K. Dyer and J. S. L. Leach, which appeared in the July 1978 JOURNAL, Vol. 125, No. 7, pp. 1032-1038, one error should be noted. The word "interrupted" in the caption of Fig. 4, p. 1035, should be "continuous." Thus, the caption should read, "Ellipsometric film thickness during continuous anodization at 1 mA/cm^2 in 0.1M Na_2CO_3 + 0.1M $NaHCO_3$. $\lambda = 546.1$ nm, $n_f = 2.008 \pm 1\%$, $k_f = 0$. $V_B \sim 5.2V$."

SOLID-STATE SCIENCE
—AND TECHNOLOGY

OCTOBER
1978

High Temperature Reaction Kinetics of Tungsten with Sulfur Dioxide

Paul Meubus*

Applied Sciences Department, Centre de Recherche du Moyen Nord, Université du Quebec à Chicoutimi, Chicoutimi, Quebec, Canada G7H 2B1

ABSTRACT

The kinetics of reaction for the tungsten-sulfur dioxide system has been studied within the temperature range 1600°-2100°K and sulfur dioxide concentrations up to 15% in helium. The reaction rate for tungsten attack shows a maximum around 1870°K, the latter temperature being nearly independent of sulfur dioxide concentration. Experimental data lead to a reaction rate model implying a first-order reaction, becoming second order for particular conditions. Parameters defining the reaction rate equation are calculated and a $W\text{-}SO_2$ chemical reaction equation is discussed.

As part of a study of the high temperature behavior for refractory metals in adverse surroundings, the reaction for the system tungsten-sulfur dioxide has been investigated at temperatures above 1600°K. Studies of this kind are useful, for instance, in the case of tungsten electrodes in plasma industrial reactors, where corrosive gases are generated by solid-gas reactions.

Little information is available in the literature on the high temperature reactions of tungsten with sulfur dioxide. Early qualitative observation described the sulfurization of tungsten in the presence of sulfur dioxide at "red hot" temperatures (1), while oxidation of the metal is observed at higher temperatures (2). Kinetics of synthesis and structure of sulfides including tungsten sulfide are described in a recent Soviet work (3). However, the latter is related to the sulfurization of the metal by a gaseous mixture of sulfur in helium.

In view of the scarcity of information on the subject, the present work was undertaken to study the kinetics of reactions of W with SO_2 at high temperatures. In this respect, it has been shown that a maximum rate of attack does occur around 1870°K. The experiments were carried out in a reactor described in the experimental section. Mixtures of helium and up to 15% sulfur dioxide were used at various temperatures within the range 1600°-2100°K.

Experimental

The reactor used in the present study is partly shown in Fig. 1. It is made of a 6 cm long alumina or thoria tube, following the temperature to be attained, the inside diameter being 3 mm. The tube ends are connected to stainless steel lengths, tightness between the alumina and stainless steel tubes being ensured by means of Teflon O-rings. The reactor ends are provided with small quartz windows which allow a longitudinal view from the outside into the reactor. The refractory oxide tube is surrounded by a graphite electrical resistance with cooled electrical connections at both ends which also provide a thermal protection for the O-rings. The complete experimental assembly is shown in Fig. 2. Electrical current is supplied from the secondary wiring of a transformer whose primary circuit is controlled by a variac of appropriate power. The maximum power applied to the graphite heater is of the order of 6500W, with a voltage drop of about 3V across the resistance.

The reactor and heater are enclosed in a cooled vessel connected to a vacuum pump and a helium

DIFFERENTIAL REACTOR

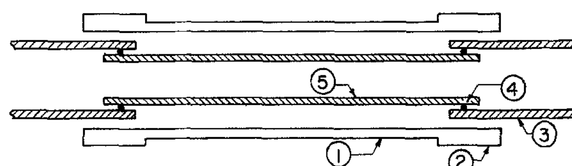

Fig. 1. Partial view of differential reactor with graphite resistance

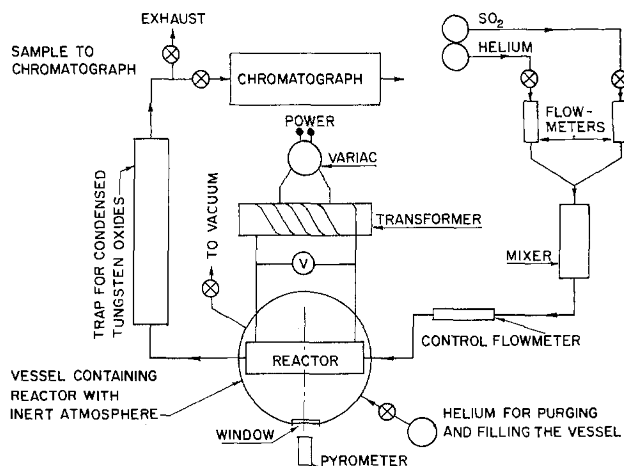

Fig. 2. Experimental layout

* Electrochemical Society Active Member.

Key words: tungsten, corrosion, sulfur dioxide, high temperature.

cylinder so that an inert atmosphere can be introduced within the vessel, thus providing an adequate protection against the graphite oxidation. The remainder of the assembly is made of conventiontal equipment consisting of a mixer for the incoming gases (helium and sulfur dioxide), a separator for products of reaction, flowmeters, etc.

In view of the temperatures to be attained in the reactor, alumina tube only was used in the course of this study. Prior to the experiments, the temperature inside the differential reactor was calibrated by means of a small piece of pure tungsten located at the required position in the refractory tube. The tungsten sample surface temperature was measured with a pyrometer (Leeds and Northrup, 1000°-6000°C) at an effective wavelength of 685 mm. The reading was corrected for blackbody deviation by means of the emission coefficient for tungsten at the considered wavelength and for the temperature obtained. The reactor inside temperature was then correlated with the temperature recorded at the middle of the outside surface of the surrounding electrical heater. The latter temperature was readily accessible during the experiments through the window provided for this purpose in the enclosing vessel, so that the inside temperature was known also from the relationship already obtained. The graphite was replaced when its electrical resistance did change. Figure 3 represents an example of the inside temperature distribution starting from the middle of the reactor.

The method of calibration used was checked by observation in the reactor of the fusion point obtained for pure alumina (FP 2323°K) which was found equal to 2300°K. Pure iron was also tested and melted at 1790°K, the theoretical FP being 1808°K. These measurements were made using a helium atmosphere. It can be shown from Fig. 3 that the temperature discrepancy is about 60°K within ±5 mm from the center of the reactor, when defined as

$$\Delta T = \frac{\int_0^5 T dx}{x} \quad [1]$$

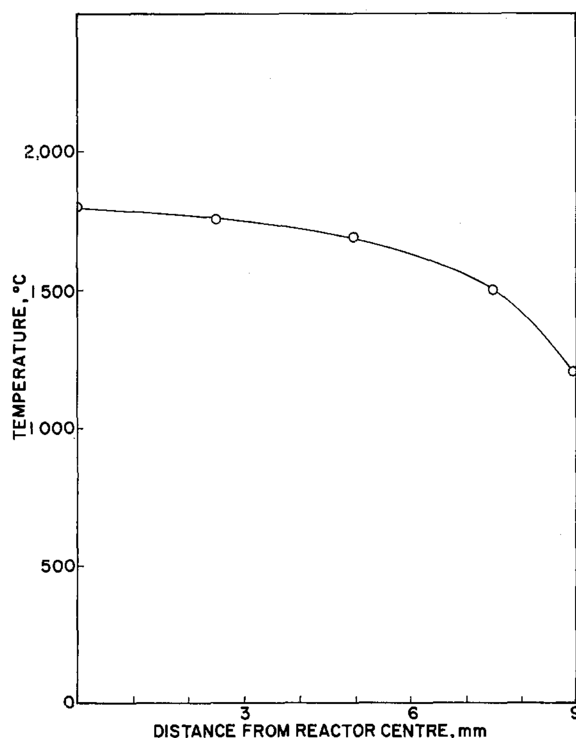

Fig. 3. Example of temperature distribution inside the differential reactor.

This situation was nearly the same for the whole temperature range used in the experiments. Equation [1] was taken into account for temperature correction and the temperature determined at the reactor center was decreased by 30°K, so that the corrected temperature did not differ by more than 30°K from the extreme temperature values as obtained from Eq. [1]. This temperature was chosen as representative of the reaction temperature. It should be noted that 5 mm on each side of the reactor center delineates the position of the tungsten samples used for the SO_2 reaction experiments.

The metal used for the rate-of-attack determination was made of 99.9% pure tungsten (Metal Werk, Plansee, AG., Reute, Tyrol) wire 0.07 cm diam, resulting in a weight of 0.0742 g/cm. The tungsten samples used for the experiments were shaped from given lengths (~2 cm) of wire in the form of small springs, the length of which was reduced down to the length of reactor available at the required operating temperature, say around 1 cm. Prior to the experiments, the tungsten samples were treated for 1 hr under an atmosphere of hydrogen at 1173°K.

The experiments were carried out at atmospheric pressure, with sulfur dioxide concentrations up to 15% in helium and temperatures ranging from 1600° to 2100°K, the choice for these temperatures being justified under the heading "Discussion." The gas velocity was chosen equal to 250 ml/min. Further increase in velocity did not affect the tungsten rate of attack, being an indication that boundary layer effects were no longer important and that pure chemical kinetics was involved. In this respect it was found that for the chosen conditions the initial sample weight did not seem to have any effect on the reaction rates observed since similar duplicate points were obtained from tungsten samples with an initial weight difference as high as 30%.

The chromatograph used for analysis of the initial gas mixture was of the Fisher Hamilton 20 type, with a sulfur dioxide and oxygen detection column 3m long and 6 mm diam, containing 10% Di-N-Decyl-phthalate on Chromosorb T(40-60 mesh). The reacted gas was analyzed for O_2 and SO_2. No attempt was made to establish an O and S balance since SO_2 and O_2 could have been absorbed with condensing WO_3 or a number of reactions could occur between the main reaction site and the cooling section of the reactor. However, it was interesting to know whether O_2 was present or not for the purpose of speculations about the main reaction with W, while the SO_2 analysis in the issuing gas was used for calculating an average pressure for SO_2 in the reactor, the issuing SO_2 gas being by all means in large excess (inlet and outlet concentrations did not differ by more than 20% in all cases). The carrier gas was helium, flowing at a rate of 40 ml/min.

The chemical inertness of the reactor was verified by carrying out blank experiments at high temperatures. The issuing gas was checked for SO_2 depletion and oxygen presence and the reactor was examined for possible alteration. No change was observed in the reaction gas composition after passage through the reactor when the highest SO_2 concentration (up to 20%) and the highest temperature (2100°K) considered for the experiments were used for the blank controls. Also, no visible alteration was found in the reactor. The sulfur dioxide used was 99.9% pure (Canadian Liquid Air).

To start a run, the hydrogen-treated tungsten sample was weighed to the nearest 0.1 mg and introduced into the reactor. By means of a three-way valve giving access to either helium or the required helium-sulfur dioxide mixture, the reactor and gas circuit were first flushed with helium and the sample was heated up to the desired experimental temperature. Connection was then established with the helium-SO_2

mixture and the reaction time was started when visible fumes evolution was observed through the small quartz windows provided at the ends of the differential reactor. The starting of visible fumes could also be predicted by calculating the time required for the reaction gas to reach the tungsten sample after opening of the three-way valve, knowing the flow rate (250 ml/min) as well as the length and diameter of the gas line. The sulfur dioxide content was then determined in the outlet gas, and after a predetermined reaction time was elapsed, the electrical power was cut off, the gas circuit was flushed, and the tungsten sample was weighed again. The average wire surface was obtained from

$$A_m = \frac{\pi l (d_1 - d_2)}{\ln \frac{d_1}{d_2}} \quad [2]$$

The average wire diameter after attack was calculated from the relationship

$$d_2 = (4P/19.3\, l\pi)^{1/2} \quad [3]$$

and the average sulfur dioxide concentration could be written

$$C_{AV} = \frac{C_{in} + C_{out}}{2} \quad [4]$$

$$p = \frac{p_{in} + p_{out}}{2} \quad [5]$$

and p_{AV} was taken as a representative value for the SO_2 partial pressure. The partial pressures p_{in} and p_{out} did not differ by more than 20% even in extreme cases of tungsten rate of attack.

The tungsten rate of attack was obtained from

$$\frac{dW}{dt} = \frac{\Delta P}{184\, A_m \Delta t} \quad [6]$$

Results and Discussion

Figure 4 shows the linearity of tungsten weight loss as a function of time for given sulfur dioxide concentrations and temperatures, no layer of reacted product being observed, at least on the macroscopic scale, in all cases covered by this study. As a result, the rate of tungsten attack in Eq. [6] could be considered constant at a given temperature for a given sulfur dioxide concentration and could be measured from the slope of lines similar to those appearing on Fig. 4. These results were observed for temperatures between 1600° and 2100°K.

Interpretation of data.—If it is assumed that the reaction rate constant for the tungsten attack by SO_2 follows the Arrhenius law behavior then one obtains

$$-\frac{dW}{dt} = e^{-E/RT}C \quad [7]$$

at constant sulfur dioxide partial pressure. In the case of Eq. [7], one can also write

$$\log\left(-\frac{dW}{dt}\right) = -0.434\frac{E}{R}\frac{1}{T} + \log C \quad [8]$$

and [7] is the equation of a straight line with slope $-0.434\, E/R$.

Figure 5 shows the tungsten rate of attack variation between 1600° and 2100°K, log $(-dW/dt)$ being represented as a function of $1/T$, and it is observed that the rate of attack is maximum around 1870°K and that on each side of the maximum the representative lines are indeed straight lines within the experimental temperature limits, showing the validity of application of Eq. [8]. In this respect, a rather small number of experimental points are required for defining the phenomena involved.

Figures 6 and 7 are derived from Fig. 5 and describe the rate of attack for tungsten as a function of sulfur dioxide partial pressure for given temperatures. They suggest a reaction rate of the kind

$$r = \frac{ap^2}{1 + bp} \quad [9]$$

being parabolic, or second order, for $bp << 1$ and becoming first order when bp is comparable to 1 or higher than 1. Exponents higher than 2 for p in Eq. [9] are not considered since reaction orders higher than 2 are very unlikely.

If a reaction rate law of the kind indicated in Eq. [9] is obtained, one may write

$$\frac{p^2}{r} = \frac{b}{a}p + \frac{1}{a} \quad [10]$$

and p^2/r is a linear function of p. Figures 8 and 9 show straight lines, representative of p^2/r variation as a function of p, for various temperatures below (Fig.

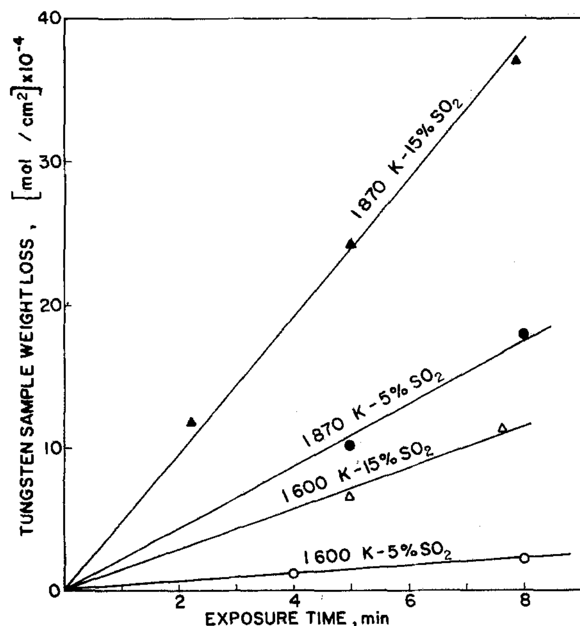

Fig. 4. Tungsten rate of attack as a function of time at given temperature and sulfur dioxide concentration.

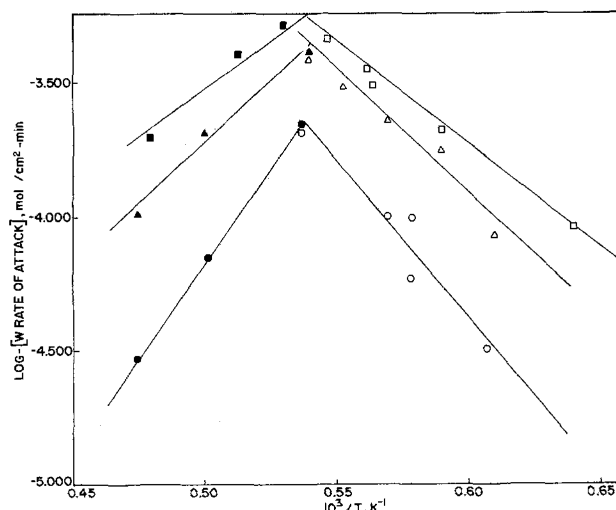

Fig. 5. Linear relationship of $\log_{10}$ [— W rate of attack] as a function of $\frac{1}{T}$. 5% SO_2, ● and ○; 10% SO_2, ▲ and △; 15% SO_2, ■ and □.

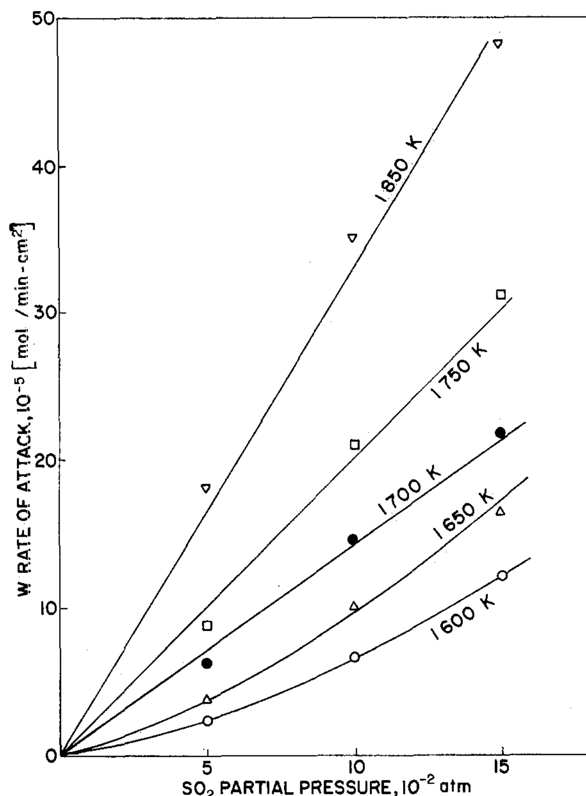

Fig. 6. Tungsten rate of attack as a function of sulfur dioxide concentration and given temperature (temperature range 1600°-1850°K).

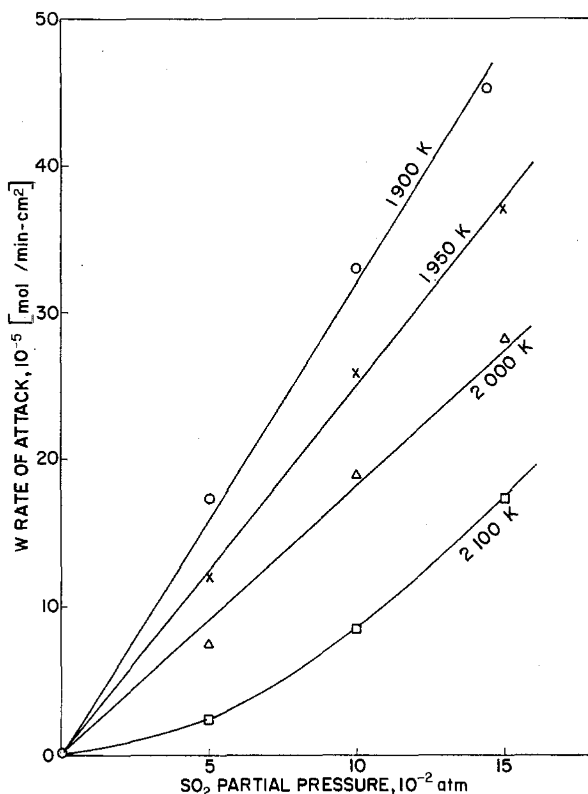

Fig. 7. Tungsten rate of attack as a function of sulfur dioxide concentration and given temperature (temperature range 1900°-2100°K).

8) and above (Fig. 9) 1870°K temperature for which a maximum rate of attack does take place. As a result, a and b may be calculated at various temperatures using the straight lines on Fig. 8 and 9. Indeed, b/a is deduced from the slope of these lines, while $1/a$ is

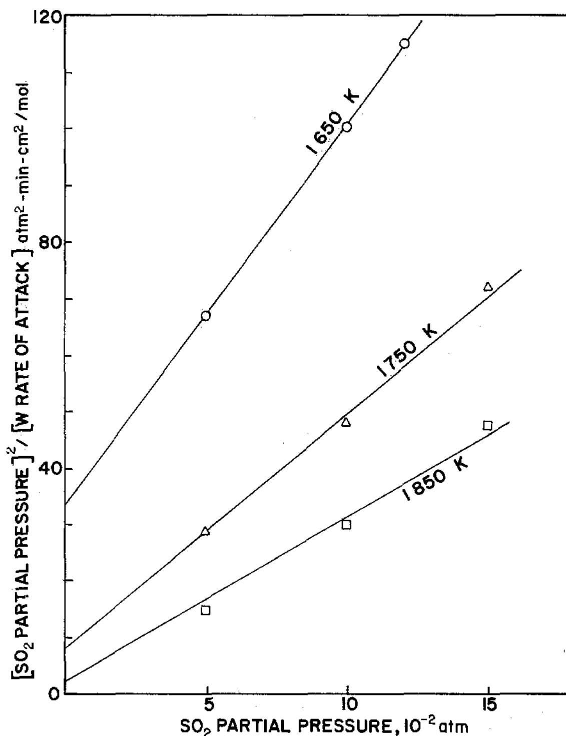

Fig. 8. Linear relationship between [sulfur dioxide partial pressure]^2/—[rate of tungsten attack] and sulfur dioxide partial pressure, for the temperature range 1600°-1870°K.

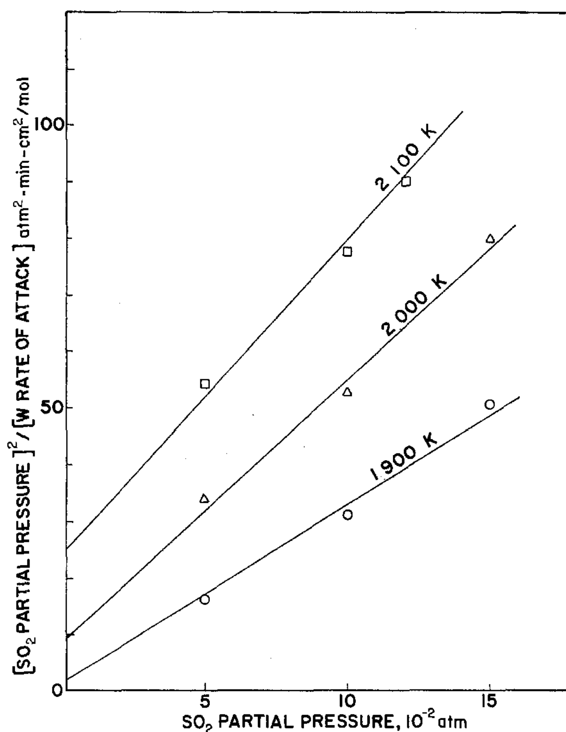

Fig. 9. Linear relationship between [sulfur dioxide partial pressure]^2/—[rate of tungsten attack] and sulfur dioxide partial pressure for the temperature range 1870°-2100°K.

the limiting value in Eq. [10] when $p \to 0$. A number of values obtained for a and b at various temperatures are shown in Table I. Using Eq. [10] and classical error calculation methods, one obtains a relative error of $\pm 15\%$ on a and $\pm 30\%$ on b, this implying 1% error on, respectively, p, t, T, and 0.5 on W.

Equation [9] implies a number of reaction steps which include a gaseous reaction with an adsorbed species, the surface reaction being the controlling step (4, 5). The resulting over-all reaction is now discussed

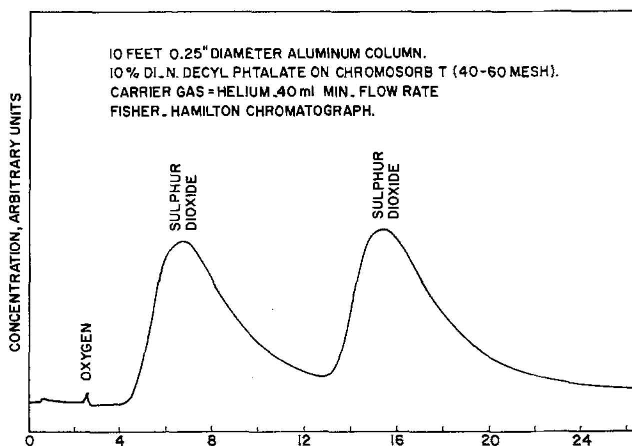

Fig. 10. Typical chromatogram for residual gases after reaction with tungsten.

in the light of experimental observations and thermodynamic constraints.

Reaction model for the system tungsten-sulfur dioxide.—Figure 10 shows an average chromatogram related to the experiments, indicating traces of oxygen and the two characteristic curves for sulfur dioxide which also appear for this gas prior to reaction. These are not due to water presence since the gases used are dried. The reaction products consisted of tungsten oxides, for which $WO_{2.9}$, in effect $W_{20}O_{58}$, was the major constituent. This dark blue oxide was identified by x-ray analysis. No tungsten oxide or sulfide was detected on the tungsten surface which, by all means,

Table I. Values of the parameters a and b at various temperatures in rate Eq. [9]. SO_2 concentration between 0 and 15%

Temperature (°K)	Parameters in rate Eq. [9] a (moles/min-cm²-atm²)	b (atm⁻¹)
1650	3.6×10^{-2}	2.3×10
1750	1.9×10^{-1}	7.3×10
1850	7.2×10^{-1}	1.9×10^{2}
1950	3.3×10^{-1}	1.1×10^{2}
2000	10^{-1}	4.8×10
2100	2.7×10^{-2}	1.8×10

did not show any visible layer, but elemental sulfur was present in the reactor tube. It is possible that free oxygen or SO_2 were absorbed during condensation of tungsten oxide vapor.

Considering the observations made and the interpretation of the experimental data which lead (Eq. [9]) to the description of a classical sequence of steps, the following model is proposed, the surface reaction being the controlling step (4, 5)

Absorption step

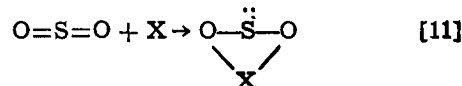

$$O{=}S{=}O + X \rightarrow O{-}\ddot{S}{-}O \text{ (bridged by X)} \quad [11]$$

Surface reaction

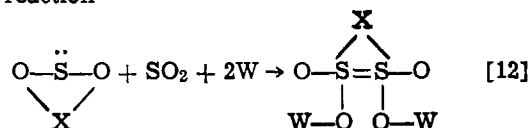

$$O{-}\ddot{S}{-}O \text{ (bridged by X)} + SO_2 + 2W \rightarrow O{-}S{=}S{-}O \text{ (S–S bridged by X; W–O, O–W)} \quad [12]$$

Desorption process

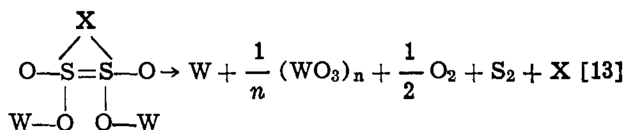

$$O{-}S{=}S{-}O \text{ (bridged by X; W–O, O–W)} \rightarrow W + \frac{1}{n}(WO_3)_n + \frac{1}{2}O_2 + S_2 + X \quad [13]$$

The over-all reaction is then

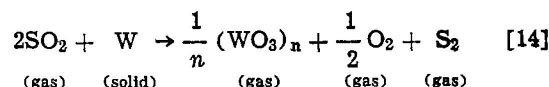

$$\underset{(gas)}{2SO_2} + \underset{(solid)}{W} \rightarrow \underset{(gas)}{\frac{1}{n}(WO_3)_n} + \underset{(gas)}{\frac{1}{2}O_2} + \underset{(gas)}{S_2} \quad [14]$$

The volatile tungsten oxide product WO_3 has been written in the more general form $(WO_3)_n$ since the species $(WO_3)_n$ with $n = 2, 3, 4$ is generated by WO_2 (solid) between 1300°-1600°K (6) and probably above. In the latter case, solid WO_3 is formed, which vaporizes and changes into $(WO_3)_{2,3}$ while vaporizing at a given temperature. The validity of Eq. [14] has been determined by means of data found in the literature for $(WO_3)_n$ (6), SO_2 (7), and S_2 (8), which are reported in Table II. The information in Table II has been used to calculate $\Delta F_T°$ for reaction [14] when the various oxides $(WO_3)_n$ are involved. The results appear in Table III together with the equilibrium constants for this reaction at various temperatures.

Table II. Thermodynamic data used in Table III

Temperature (°K)	$1/n\ \Delta F_T°$ of formation, kJ/mole $1/n\ (WO_3)_n$, gas* $(WO_3)_1$	$1/2\ (WO_3)_2$	$1/3\ (WO_3)_3$	$1/4\ (WO_3)_4$	$\Delta F_T°$ of formation, kJ/mole SO_2** (gas)	S_2** (gas)	S*** (gas)	WS_2† (solid)
1400	—	—	—	—	−261	−149	+105	−124
1523	—	—	—	—	−252	−134	+86	−114††
1600	−204	−386	−415	−417	−247	−124	+82	Decomposition of WS_2
1800	−193	−363	−385	−384	−232	−99	+59	
2100	−175	−329	−338	−334	−210††	−62††	+26	

* Ref. (6).
** Ref. (7).
*** Ref. (8).
† Ref. (9).
†† Extrapolated.

Table III. Free energy of reaction calculated for reactions [14] and [16] by means of Table II. Assumption is made of the possible presence of various $(WO_3)_n$

Free energy of reaction $\Delta F°$ for reactions [14] and [16], kJ/mole. Equilibrium constant K_{eq}

	Reaction [14] $(WO_3)_n$ (gas) $(WO_3)_1$ $\Delta F_T°$	$(WO_3)_1$ K_{eq}	$(WO_3)_2$ $\Delta F_T°$	$(WO_3)_2$ K_{eq}	$(WO_3)_3$ $\Delta F_T°$	$(WO_3)_3$ K_{eq}	$(WO_3)_4$ $\Delta F_T°$	$(WO_3)_4$ K_{eq}	Free energy of reaction for reaction [16] $\Delta F_T°$	K_{eq}
1400	—	—	—	—	—	—	—	—	+398	1.7×10^{-15}
1523	—	—	—	—	—	—	—	—	+390	5×10^{-14}
1600	+164	5×10^{-6}	−17.3	3.6	−47	33	−49	39	Decomposition of WS_2 at 1523°K. Reaction [16]	
1800	+172	1×10^{-5}	+1.30	0.9	−21	4.0	−21	4.0		
2100	+183	3×10^{-5}	+29.2	0.2	+20	0.3	+24	0.4		

From the heat of formation for the various $(WO_3)_n$ species appearing in Table II, the free energy of reaction for reaction [14] has been calculated with the assumptions of, respectively, $(WO_3)_1$, $(WO_3)_2$, $(WO_3)_3$, and $(WO_3)_4$ being present. Table III shows that the species $(WO_3)_2$, $(WO_3)_3$, and $(WO_3)_4$ are those most likely to occur at the considered temperatures. For the sake of simplicity, $n = 3$ has been retained in Eq. [14] which can then be written

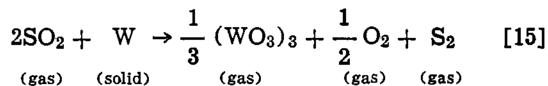

$$\underset{(gas)}{2SO_2} + \underset{(solid)}{W} \rightarrow \frac{1}{3}\underset{(gas)}{(WO_3)_3} + \frac{1}{2}\underset{(gas)}{O_2} + \underset{(gas)}{S_2} \quad [15]$$

Table II shows that the free energy of formation of S_2 from 2S is highly negative in the whole range of temperatures involved in the present study, thus ensuring the presence of the species S_2 in Eq. [14] and [15].

At first sight, the following reaction could also be responsible for tungsten attack by sulfur dioxide

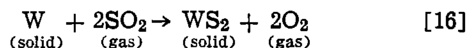

$$\underset{(solid)}{W} + \underset{(gas)}{2SO_2} \rightarrow \underset{(solid)}{WS_2} + \underset{(gas)}{2O_2} \quad [16]$$

Table III shows that this reaction is very unlikely to occur in view of the free energy of reaction found at 1400° and 1523°K, using information from Table II (9). By all means WS_2 decomposes at 1523°K (10).

Although $(WO_3)_n$ does vaporize, it could leave a solid layer of WO_3. However, if this were the case, the partial pressure of WO_3 (solid) should be the controlling step for reaction [15] at a given temperature and the rate of evolution should be independent of SO_2 concentration. This is not observed and it is concluded that the WO_3 rate of vaporization (which is possible for thermodynamic reasons) is such that no accumulation of solid oxides is possible within the experimental conditions.

Finally, in order to explain the presence of blue tungsten oxide identified as $WO_{2.9}$ by x-ray diffractometry, which was found in the cooler part of the reaction tube, the following reaction is considered

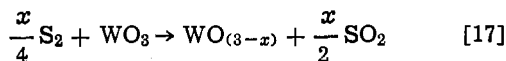

$$\frac{x}{4}S_2 + WO_3 \rightarrow WO_{(3-x)} + \frac{x}{2}SO_2 \quad [17]$$

the species $(WO_3)_n$ having receded to the state WO_3 and the reaction occurring downstream from the tungsten specimen. In the present case, $x = 0.1$ in Eq. [17].

Summarizing the development made on a possible model for the W-SO_2 reaction, the type of rate, Eq. [9], found leads to an over-all reaction Eq. [14]. The latter equation is then completed on the basis of thermodynamic considerations, thus leading to the reaction Eq. [15]. This equation also explains the experimental observations made like: (*i*) presence of sulfur and $WO_{2.9}$ in the cooler part of the reaction tube; and (*ii*) absence of a reacted layer of tungsten oxide or sulfide.

Conclusions

The kinetics of reaction for the tungsten-sulfur dioxide system has been studied within the temperature range 1600°-2100°K and sulfur dioxide concentrations up to 15% in helium. The tungsten rate of attack shows a maximum around 1870°K, this temperature being independent of sulfur dioxide concentration.

Experimental data lead to a first-order reaction rate model of the form $r = ap^2/(1 + bp)$, becoming second order when the product $bp << 1$. The parameters a and b related to the rate equation have been calculated and they have been found functions of the temperature. The rate equation leads to a W-SO_2 chemical reaction equation which has been completed on the basis of thermodynamic constraints and which explains the experimental observations made.

Acknowledgment

The financial support received from the National Research Council of Canada and the Ministry of Education of the Province of Quebec is gratefully acknowledged.

Manuscript submitted Dec. 20, 1977; revised manuscript received May 18, 1978. This was Paper 105 presented at the Atlanta, Georgia, Meeting of the Society, Oct. 9-14, 1977.

Publication costs of this article were assisted by the Université du Quebec á Chicoutimi.

LIST OF SYMBOLS

A_m	logarithmic average surface of tungsten wire exposed to sulfur dioxide attack, cm^2
a	constant in Eq. [9] and derived equations, moles/min cm^2-atm^2
b	constant in Eq. [9] and [10]
C	sulfur dioxide concentration in helium, moles fraction. Also, constant in Eq. [7] and [8], moles/cm^2-min
d_1	initial tungsten wire diameter, cm
d_2	final tungsten wire diameter, cm
e	base of naperian logarithms
$\Delta F_T°$	free energy of formation or reaction
l	length of tungsten wire exposed to attack, cm
n	coefficient of $(WO_3)_n$ in Eq. [14], under the form of $1/n$, dimensionless
p	sulfur dioxide partial pressure, atm
P	tungsten weight, g
ΔP	tungsten weight variation, g
r	tungsten rate of attack, moles/min-cm^2
R	gas constant, kJ/mole-K
t	reaction time, min
T	temperature, °K
ΔT	temperature discrepancy between center and ±5 mm from center for reactor in Eq. [1]
W	moles tungsten
x	coefficient in Eq. [17]. Also, distance from center of reaction in Eq. [1]

Subscripts

A_v	average
in	at inlet of the reactor
out	at outlet of the reactor
m	logarithmic average
n	designates the degree of polymerization for WO_3
$(1 - x)$	designates the amount of oxygen tied up to W in Eq. [17]

Abbreviations

log	log in base 10

REFERENCES

1. J. Férée, *Bull. Soc. Chim.*, 19, 213 (1898).
2. K. H. Ehrenfeld, *J. Am. Chem. Soc.*, **17**, 381 (1895).
3. M. S. Kovalchenko, V. V. Sychev, D. Z. Yurchenko, and Yu Tkorchenko, *G. Izv. Akad. Nauk SSSR*, **5**, 221 (1974).
4. J. M. Thomas and W. J. Thomas, "Introduction to the Principles of Heterogeneous Catalysis," p. 459, Academic Press, New York (1967).
5. J. M. Smith, "Chemical Engineering Kinetics," pp. 339-346, McGraw-Hill, New York (1970).
6. D. R. Stull, JANAF Thermochemical Tables, The Dow Chemical Co., Midland, Mich., June 30, March 31, 1963, Sept. 30, 1966.
7. O. Kubaschewski, E. L. L. Evans, and C. B. Alcock, "Metallurgical Thermochemistry," p. 427, 4th ed., Pergamon Press, New York (1967).
8. B. J. McBride, S. Heimel, J. G. Ehlers, and S. Gordon, "Thermodynamic Properties to 6000°K for 210 Substances Involving the first 18 Elements," p. 266, NASA, OSTI, Washington, D.C. (1963).
9. O. Kubaschewski, E. L. L. Evans, and C. B. Alcock, "Metallurgical Thermochemistry," p. 429, 4th ed., Pergamon Press, New York (1967).
10. R. C. Weast, "Handbook of Chemistry and Physics," p. B-173, 37th ed., C.R.C. press, Cleveland, Ohio (1973).

Fabrication Processes for a Silicon Substrate Package for Integrated Gallium Arsenide Laser Arrays

Michael J. Brady

IBM Thomas J. Watson Research Center, Yorktown Heights, New York 10598

ABSTRACT

Single crystal silicon substrate chips with preferentially etched V-groove structures have been fabricated to accurately hold optical fibers for efficient output coupling of integrated gallium arsenide laser arrays. In addition, the substrate contains individually addressable drive electrodes electrically isolated by reversed biased p-n junctions. This paper discusses the required fabrication and processing techniques necessary to achieve the silicon package utilizing batch-processing technology found in the manufacture of microelectronic devices.

Anisotropic etching of single crystal silicon has become a standard processing step in silicon technology (1, 4). Utilization of the preferentially etched grooves with smooth-walled topology has also been applied to the fabrication of integrated optical devices such as channel waveguides (5, 6). Recent interest in optical communications utilizing gallium arsenide light-emitting diodes and gallium arsenide-gallium aluminum arsenide double heterostructure lasers as optical sources (7) has increased due to fabrication of a high radiance and high power source. Since the output characteristics differ between an LED and a laser, various techniques have been proposed (8) to capture the highly divergent emitted beam and effectively couple it into a low numerical aperture fiber waveguide.

We present here a fabrication technique that allows precisely grooved crystalline silicon to serve as a miniature optical bench that provides highly efficient coupling of a GaAlAs laser through a lens into a fiber guide. A common glass cylindrical lens and an array of fiber lightguides are self-aligned to the optical sources' optic axis. The preferentially etched grooves provide kinematic support for both a cylindrical lens and the fiber waveguides, and allow predetermined placement of the fibers with respect to the source axis and the silicon surface. Because the etching process is self-terminating, when the characteristic V-shape is formed, grooves of different depth can be etched simultaneously into the same substrate in one fabrication step, thus allowing one to align a different diameter lens to waveguides.

In addition, individual thin film driving electrodes, consisting of titanium, palladium, and gold are evaporated on the silicon surface and photolithography delineated. To provide electrical isolation between adjacent lasers, individual p-n junctions are fabricated below the silicon surface in line with the drive electrodes. The surface topology of the silicon optical bench provides a smooth oxidation-free metallized surface for bonding of the laser arrays. The silicon bench also acts as a good thermal heat sink for the lasers, and minimizes the strain due to the closer matching of the thermal expansion coefficients between silicon and gallium arsenide. Figure 1 shows a schematic of the assembled laser array package consisting of 13 devices spaced on 200 μm centers. The lasers are fabricated from double hetrostructure material grown using standard liquid phase epitaxy techniques. The laser cavities are 575 μm long and have an active region between 0.2 and 0.3 μm and a 12 μm wide oxide stripe on the p-type side to provide current confinement and limit the active region width. Contact metallurgy on the p-side of the laser consists of 500Å of chromium and 5000Å of gold, while a gold-germanium-nickel mixture is alloyed into the n-type side. The laser is bonded to the metallurgy on the silicon substrate with indium solder. A cross section of the package in Fig. 1 is shown in Fig. 2.

Key words: optical bench, alignment grooves, optical fibers, multichannel optical links.

Processing Steps

While many steps employed in silicon device technology were utilized to fabricate the miniature optical bench several deviations were required. The specifications for the substrates, shown in Table I, were necessary to obtain precise straight walls in the <110> directions and defect-free {111} faces. The orientation flat (<110>-major flat) is required so that the photolithographic masking patterns can be aligned to the wafer with a precision of $\pm 1°$ or better in order to get the straight-wall grooves.

The fabrication steps were performed in the following sequence:

(*i*) The wafers were chemically cleaned using H_2O:H_2O_2:NH_4OH (5:1:1) and H_2O:H_2O_2:HCl (6:1:1) solutions, blown dry in oil-free N_2, and immediately

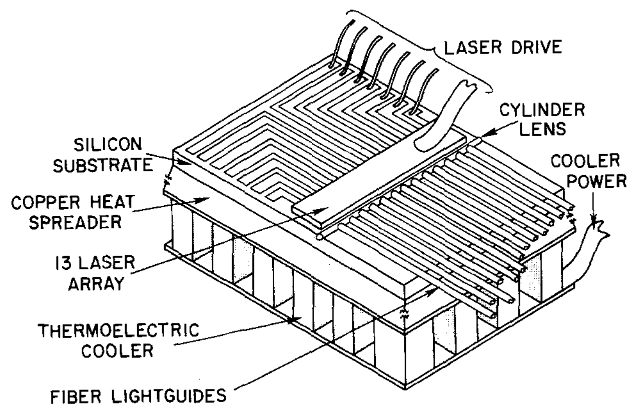

Fig. 1. Schematic of assembled substrate-laser array package with optical fibers, using a thirteen laser array as an example.

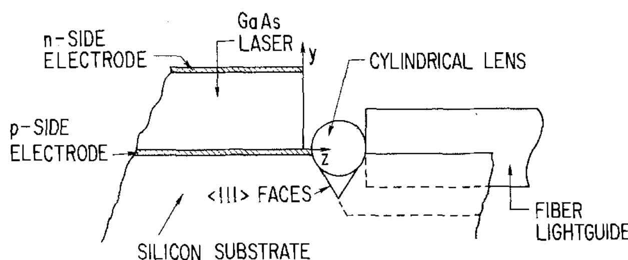

Fig. 2. Sectional view in the y-z plane showing the position of the lasers end facet (z direction) with respect to the lens groove.

Table I. Specifications required for the silicon wafers to ensure good quality optical benches

Specifications	
Single crystal silicon wafers	
Type	P
Dopant	Boron-noncompensated
Orientation	<100> Surface orientation ± 1°
Resistivity	1-2 Ω-cm ± 20%
Diameter	1.250 in. ± 0.010 in.
Thickness	Nominal 8 mils, with a thickness uniformity per wafer ± 1.0 mil
Parallelism	Within 0.5 mil
Primary flat	0.500-0.625 in. long oriented along (110) direction ± 0.5°
Secondary flat	0.250 in. long at 90° to primary flat
Dislocation density	Less than 500 per cm²
Note	Lap both sides and etch to remove damaged silicon. Chemechanically polish both sides. Periphery should be smooth, with no cracks, fractures, or sharp indents.

oxidized utilizing an open-tube steam apparatus at 1050°C to form a silicon dioxide film 1 μm thick in approximately 250 min.

(*ii*) The oxidized wafers were then coated with AZ 1350 Shipley photoresist (at 4000 RPM for 20 sec) on the front and back side, and prebaked at 70°C for 30 min. The back side protection is necessary to maintain the protective oxide layer during the isotropic etching of the windows.

(*iii*) The lens and waveguide pattern and the 75 μm junction windows (Fig. 3) were then exposed and developed. The wafers are then postbaked for 30 min at 100°C. Using the photoresist stencil, the openings are etched in the SiO_2 using buffered hydrofluoric acid at a rate of approximately 1000Å/min. The photoresist is stripped from both sides in an acetone solution that is ultrasonically agitated and the samples are then "ashed." The ashing process utilizes a plasma discharge in a Freon gas atmosphere. RF power of approximately 50W for 20 min appeared to be sufficient to remove any residual organic photoresist. At this point the samples are ready for open-tube diffusion to form the p-n junctions. A liquid n-type dopant was used, *i.e.*, phosphorous oxychloride ($POCl_3$) in a carrier gas (5500 ppm) at 870°C.

(*iv*) The junction fabrication procedure is as follows: The wafers are cleaned again using step (i). Diffused junctions are generated by depositing a blanket layer of phosphosilicate glass on the wafers, fol-

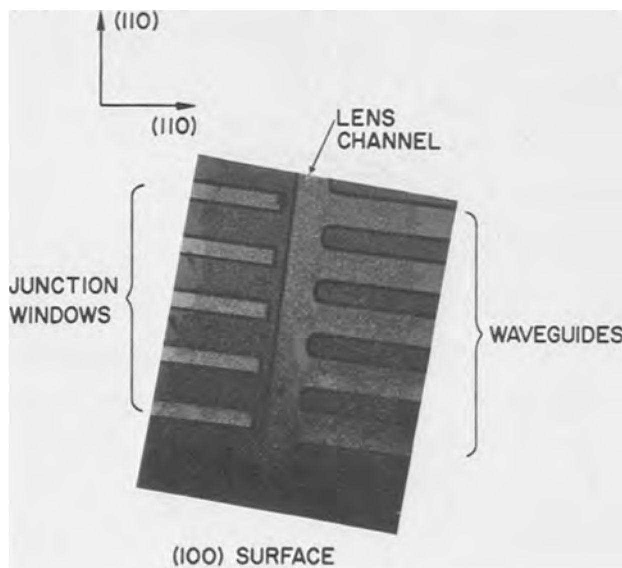

Fig. 3. Lens, waveguide, and junction patterns aligned to the {110} directions with dimensions of 125, 125, and 75 μm, respectively.

lowed by a drive-in of the phosphorous, to a depth of approximately 2 μm, in a dry oxidation atmosphere (O_2 flowing) at 1050°C for 200 min with approximately 0.3 μm of SiO_2 growing during the drive-in.

(*v*) Contact windows 50 × 550 μm are then optically positioned, centered, and photolithographly delineated in the 75 μm window and etched through the 0.3 μm layer over the N^+ diffusion area, using buffered hydrofluoric acid. This step is necessary in order to reduce the thermal resistance between the laser arrays and the heat sink, resulting in direct contact between the metal and the silicon and providing good ohmic contact. After the contact windows are opened, an additional layer of photoresist is deposited on the front surface and the resist is hardened for 30 min at 100°C. The oxide layer is then stripped from the back side by dipping in buffered HF for 15 min. The photoresist is again ultrasonically removed in an acetone solution, and after a further ashing, wafers with the freshly etched 50 × 550 μm contact regions are mounted in an electron beam evaporator and maintained at a pressure of $\leq 10^{-6}$ Torr.

(*vi*) The layered structure that was chosen for the metal electrodes was a combination of titanium, palladium, and gold. The selection of titanium was based on several parameters. Titanium has a high oxygen activity, forms a self-passivating oxide, and has a high surface bonding strength. The top layer of gold was chosen because of its high conductivity, resistance to corrosion, and ease of bonding. To prevent the gold from chemically reacting with the titanium and forming a compound, a sandwich layer of palladium was inserted to act as a diffusion barrier. Layers of titanium (500Å), palladium (1000Å), and gold (30,000Å) are blanket-evaporated on the delineated oxide pattern side. The substrate temperature during deposition of the titaninum palladium is 150°C and is lowered to 50°C for the gold layer. Deposition rates on the order of 10-12 Å/sec were used to ensure that the outer surface would be uniform, flat, and free of spikes which would affect the level of the laser arrays during the bonding process. The vacuum is broken, the wafers are inverted, and the process is repeated for the back side with the gold thickness reduced to 5000Å.

(*vii*) Using conventional photolithographic techniques and an "iron-oxide" mask, the 6 mil wide drive electrode patterns are aligned and delineated above the diffused junction windows. The alignment of the finger patterns with respect to the lens groove and the waveguides is extremely important for several reasons: Referring to Fig. 2, we see the end facet of the laser positioned in the z-direction with respect to the cylindrical lens positioned in the etched V-groove (x-direction). When the lasers are bonded to the silicon substrate, alignment is made by lining the end facets of the array to the edges of the drive electrodes. The viewing angle during positioning of the lasers is such that the highly reflecting gold surface aids in accurate placing of the array. Since coupling efficiency from the laser array to the application area depends on the laser's emission characteristics, the diameter of the lens, the core diameter of the lightguide, the indexes of refraction of the optical components, and the tolerances in component fabrication and packaging assembly, a minimum acceptable coupling efficiency of 50% was established for maximum radiance and minimum total power. This coupling efficiency (optical throughput) is measured at the outer surface of the lens. Variations in the y-direction shown in Fig. 4a and Table II indicate the sensitivity of optical throughput *vs.* vertical misalignment (Δy). Figure 4a indicates a misalignment of 5-6 μm for a 70 μm diam lens. Figure 4b indicates the second most critical alignment, the laser-to-lens spacing. The optimum position for the 70 μm diam lens is $Z_o = 12$ μm, but 50% throughput efficiency can be maintained for $Z < 37$ μm. This distance was achieved by compensating for isotropic undercutting during the 3 μm gold etch which was on the order

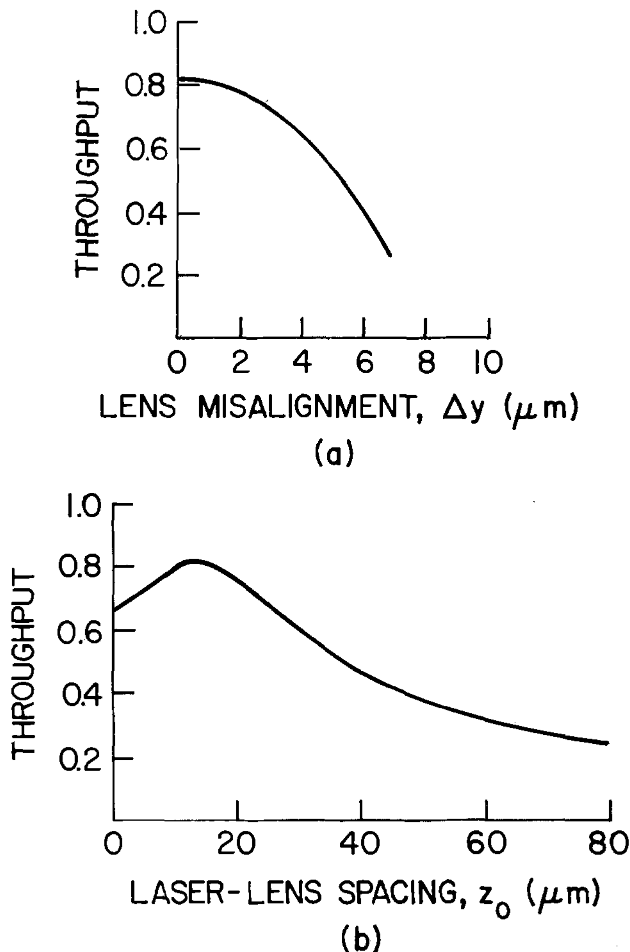

Fig. 4. (a) Variation in optical throughput as a 70 μm diam lens is shifted in the y direction with respect to lasers optic axis; (b) optical throughput as a function of the laser-to-lens distance.

of 12 μm. Positioning of the Fe_2O_3 mask with respect to the x direction, which was the most forgiving direction, was accomplished by optical alignment through a low power microscope and aligning the finger pattern with the etched SiO_2 window that forms the isolation junctions.

(*viii*) The gold and the palladium are chemically etched in an aqueous solution of KI + H_2O + I (1:1:1.5) at a temperature of 30°C. The titanium is then etched using a heated solution of H_2O + HF + H_2O_2 in a ratio of 50:1:1. Note that at this point the wafers are mounted so that the back side metallization is protected during the chemical etch back of the electrode pattern by mounting the wafers on glass disks with a low melting temperature wax. The photoresist stencil is then stripped from the wafers by flushing with acetone.

(*ix*) The 3000Å dry oxide grown during the N^+ diffusion is then removed from the lens and waveguide openings as well as the nonmetallized areas using buffered hydrofluoric acid. During this isotropic oxide etch back to expose the original silicon surface, overetching on the order of 5 min insures blanket removal of the dry oxide layer from tthe front side plus an additional 2000Å of the initial oxide layer.

Table II. Tolerance in the y direction (for 50% optical throughput) as the lens diameter changes

Lens diameter (μm)	Spot size (90% power) (μm)	y tolerance (50% thruput) (μm)
51	36	5
76	51	8
102	66	10
127	86	13

Source: λ = 0.85 μm, $w_{\perp}$ = 0.3 μm, $w_{\parallel}$ = 1.5 μm.

Recall that silicon, when exposed to the atmosphere, grows a native oxide layer on the order of 30-50Å. The initial layer of titanium, when deposited, has the ability to penetrate thin silicon dioxide layers, forming a strong surface bond. This shallow interface acted as a mask to the anisotropic etching (as explained below) and was the primary reason for growing the 0.3 μm of oxide in a dry oxidation furnace. Prior to preferential etching, the wafers are subjected to a detailed sequence of steps which have given consistently satisfactory results.

(*x*) The wafers are cleaned in solutions of trichlorethylene, acetone, and ethyl alcohol, ultrasonically, followed by a 30 min "ashing." The wafers are then placed vertically in a quartz boat, dipped in buffered HF for 10 sec, dipped into running DI water, and loaded directly into the anisotropic etching bath containing ethylene diamine, pyrocatechol, and water boiling at a constant temperature of 118°C. The etch rate for this solution is dependent upon crystallographic orientation, with the {111} faces being etched the slowest. Typical etch rate ratios of 50:30:3 μm/hr for the {100}:{110}:{111}, respectively, have been reproduced (9). Orientation dependent etching (ODE) rates of 400:1 for the {110}:{111} faces in {110} surface orientation wafers have been observed (10). Etch rates on the order of 50 μm/hr were consistently achieved. The silicon etching bath is shown in Fig. 5. Nitrogen gas was constantly bubbled through the etching solution to prevent oxidation, and a reflux apparatus was used to prevent evaporation of the chemical components. In addition, the solution is constantly stirred. The output of the system is vented through a fume hood.

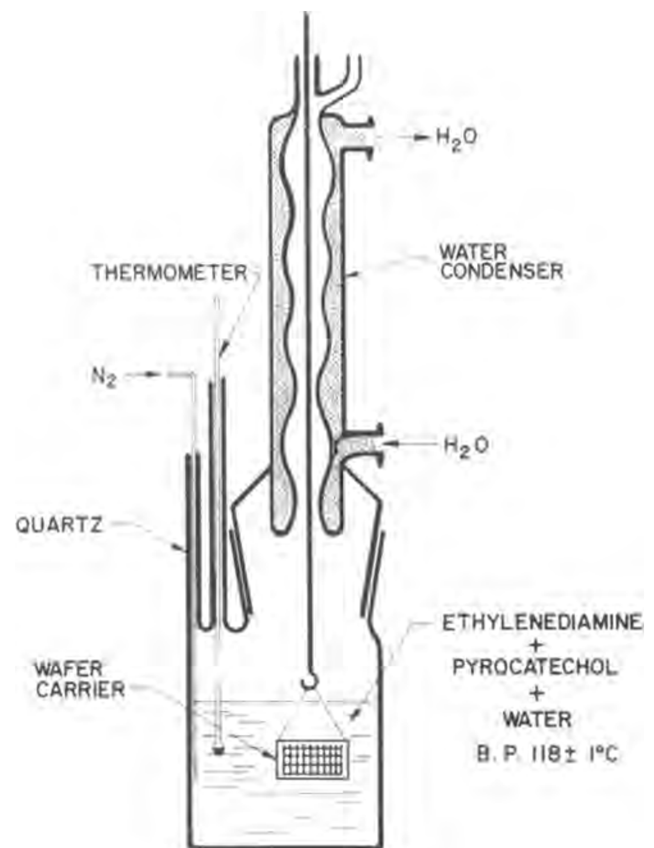

Fig. 5. Schematic of anisotropic etching bath apparatus (courtesy of E. Bassous).

(xi) Upon completion of the etching, the quartz boat is removed and rinsed in running DI water for 30 sec, then dipped in buffered HF for 10 sec, returned to running DI water, removed and blown dry in oil-free nitrogen. During the preferential etching no degradation of the metallized contact electrodes takes place. During the lens and waveguide etching in the silicon wafers, personalized chips of 250 mils square are outlined with intersecting 3 mil V-grooves. Upon completion of the etching, these intersecting V-grooves assist in cleaving of the wafer into chips. The width of the groove for the optical components is predetermined from the desired location of the optic axis with respect to the silicon surface, as shown in Fig. 6. If the center of the optical component of diameter "D" is to be a distance above the silicon surface, Eq. [1] determines the correct groove width

$$W = D \sec\theta - 2H \tan\theta \qquad [1]$$

where: H = the height of the active region of the laser source above the silicon dioxide surface, and includes all metals, as shown in Fig. 12; and $\theta = 35.3°$ for {100} surface orientation wafers.

Nominal values of H were 7 μm, which included approximately 3 μm of substrate metallurgy (titanium, palladium, and gold), 1.5-2 μm of indium bond material, and 2 μm from the p-side of the laser to the active region.

To provide mechanical support from the smooth-walled groove to the optical component, the groove depth must be greater than [$D/2H$]. Formation of the groove walls by the crystallographic {111} planes are extremely straight and smooth as shown by the SEM photo in Fig. 7. Because the etch process is self-terminating when the V-groove is formed, it is possible to fabricate lens and waveguide grooves of different depths on the same wafer. Figure 8 shows how this feature is utilized in order to align a 50 μm diam lens

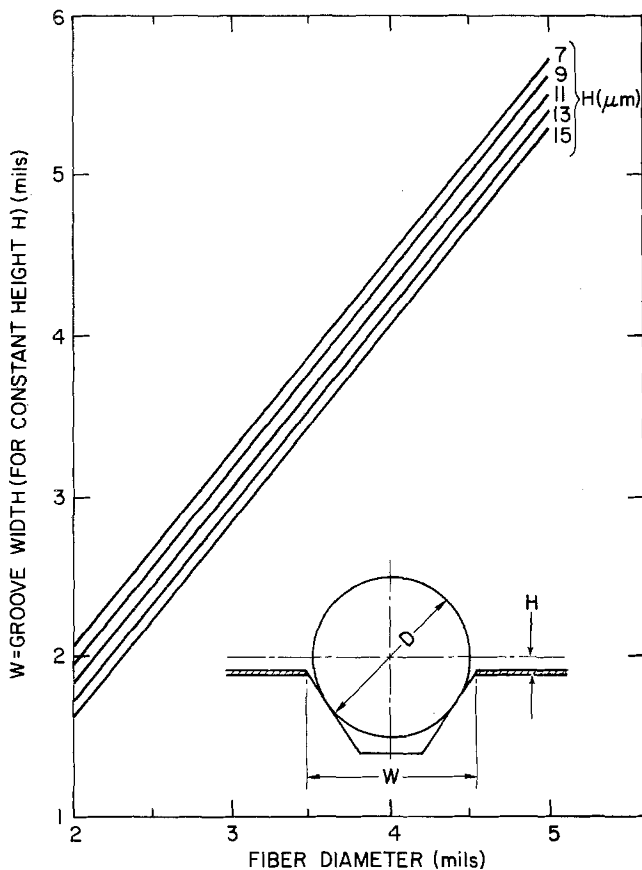

Fig. 6. Width of grooves vs. diam of fibers as a function of the height above the silicon dioxide surface.

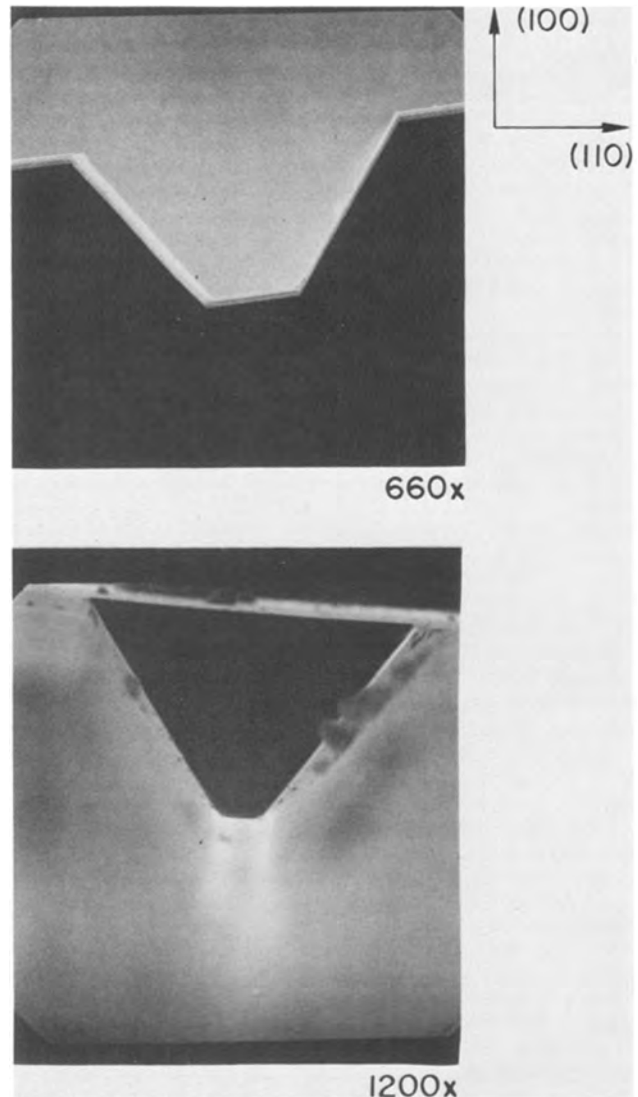

Fig. 7. SEM photograph of the <111> etched V-grooves. Top photo shows an end view of the etched groove, while the bottom photo depicts the end wall of the lens groove.

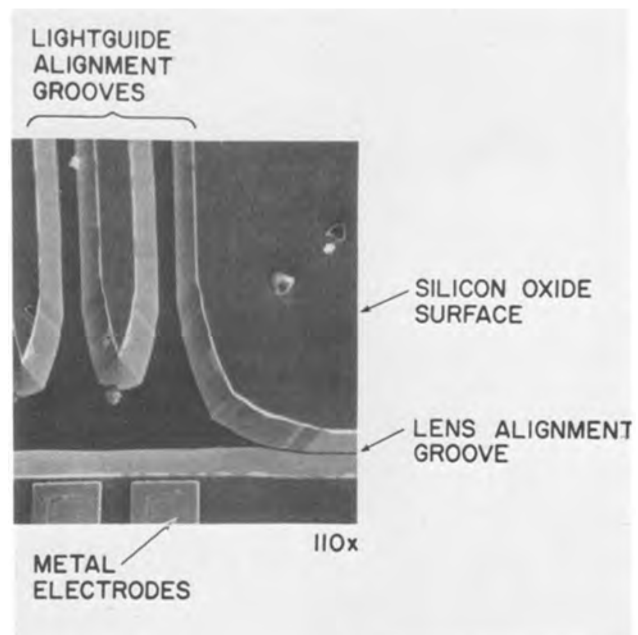

Fig. 8. Different diameter lens groove and waveguide groove etched at the same time. (Cylindrical lens diameter is 70 μm and the fiber lightguides have an outer diameter of 110 μm.)

with a 132 μm OD lightguide. Lens and waveguide fiber mounting grooves for various combinations of fibers has been accomplished, *i.e.*, 125 μm guide, 75 and 50 μm lens.

Processing Problems

Fabrication of the silicon optical bench was not without processing difficulties. Two major problem areas surfaced as the tolerances in the vertical direction became more demanding (see Table II).

The first problem developed with respect to Eq. [1]. Control over the width of the open window in the silicon is dependent on the photographic emulsion pattern width. If the emulsion mask width is generated, in our case, by a programed light table (PLT), the step and repeat process (in steps of ½ mil) can occasionally cause jogs in the pattern. These jogs or ripples in the oxide mask cause the pattern to open up to the widest dimension during anisotropic etching. An additional variation is caused by blooming of the pattern in transfer mask making as well as lateral undercutting during the silicon etching, especially in regions where perpendicular grooves intersect (Fig. 9). This undercutting is due to the exposure of the non {111} surfaces at the corners. The crystallographic planes exposed by the undercut are the {112} planes. For a groove 130 μm wide, the undercut extends about 100 μm along the groove wall so that fiber-grooved wall contact is not possible in this region. However, the fibers used are sufficiently stiff so that alignment or rigidity of the bench is not affected, since the placement of the lens fiber in the nonintersection region provides kinematic support. In the regions of nonintersecting lens and guide grooves, widths of $W = A + \delta$, (where A is the aperture command, *e.g.*, 125 μm) and δ allows for etching in the slow <111> planes and small imperfections in the silicon dioxide window. For etching depths on the order of 60-70 μm, δ had nominal values of 5-8 μm.

The second problem occurred during etching of the silicon wafer and was initially a two-part problem. Commercially available silicon wafers of standard quality for field effect transistor (FET) device fabrication which are 3.17 cm in diameter, 200 μm thick, and polished on one side exhibit a thickness variation of ± 25 μm. This would cause the grooved channel to vary along the length of the fiber some 2-3 μm. This problem was overcome by requiring both front and back wafers to be polished and plane parallel. In addition, stringent specifications were necessary to control the surface orientation to within a degree or less, *i.e.*, {100} surface $\pm < 1°$. Wafers sliced from crystals with surface orientations greater than 1° caused nonpreferential etching, and were easily observed on the {112} planes as shown in Fig. 10. The second part of the etching problem was residual crystallites. The chemical mechanism of silicon etching proposed by Finne and Klein (11) involves the oxidation of the silicon by

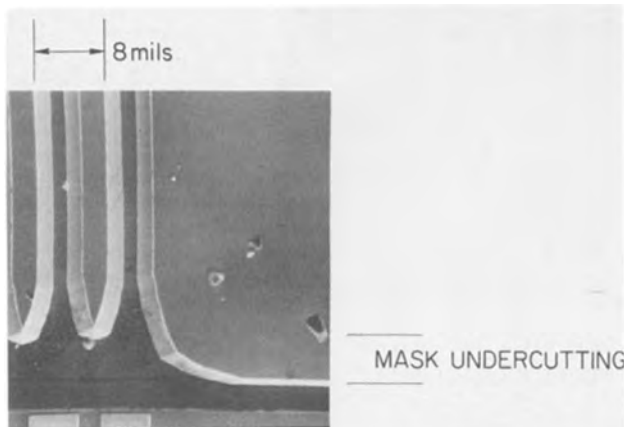

Fig. 9. Undercutting where the lens and waveguide grooves intersect.

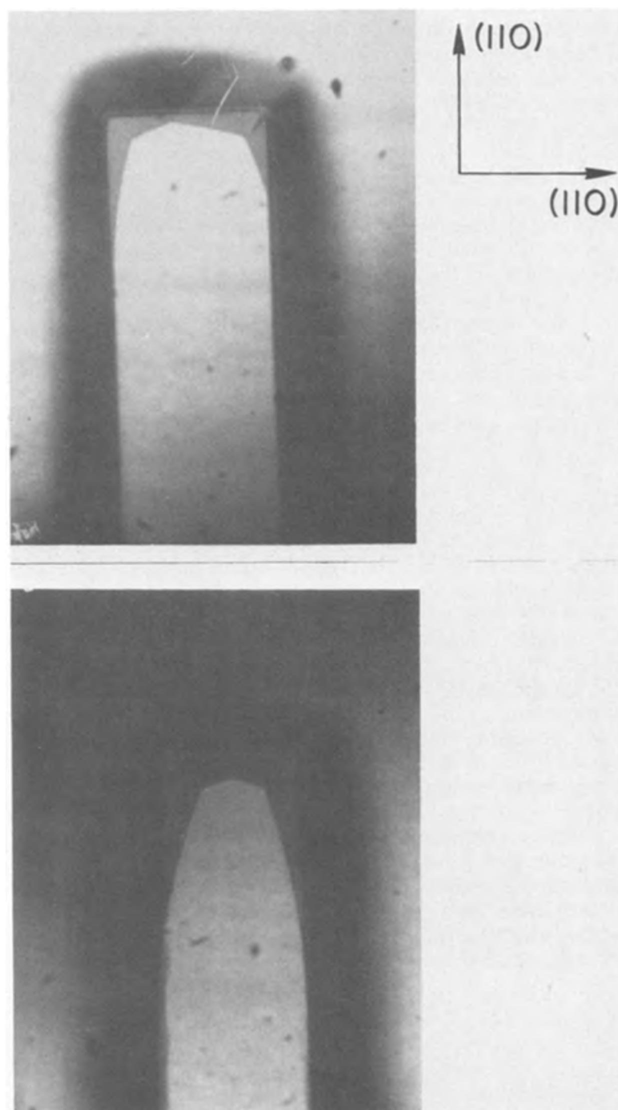

Fig. 10. (a) Misorientation of the {100} surface exposing etched asymmetric <112> planes; (b) symmetrical {112} planes on orientated {100} surface.

OH^- ions from the water present in the solution to produce hydrous silica Si $(OH)^=$ and hydrogen gas. An organo-silicon complex is then formed with the pyrocatechol C_7H_6 $(OH)_2$ which dissolves in the ethylene diamine $NH_2(CH_2)NH_2$. After extended etching periods, this solution tended to etch nonuniformly and, despite precautions to eliminate surface contaminations by ultrasonic cleaning, plasma etching, and maintaining clean room conditions, this nonuniform etching took place, causing the formation of crystallite residues on the etched {111} walls (see Fig. 11) and on the {100} surfaces. These slow etching multifaceted crystallites, which have been observed using hydrazine-water solutions (12), have been called pyrimidal hillocks. Obviously, retention of these defects along the walls would cause the fibers to be displaced in the vertical direction. A modified composition of the solution used in Ref. (11) was experimentally chosen to solve this problem and was achieved by increasing the concentration of the solvent and complexing agent in the etching solution (13).

At this point the individual 6 mm square substrate is ready for bonding of the lasers to the silicon. Figure 12 shows a cross section of the array (x-y plane) to be bonded with the indium interface between the lasers and the substrate electrodes. The bonding medium between the back side substrate metals and the copper heat sink is not shown. Detailed experimental

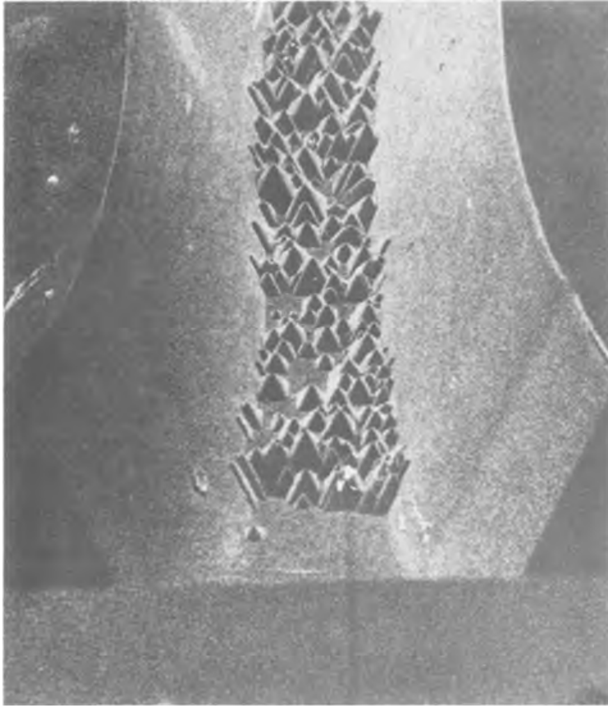

Fig. 11. SEM showing residual crystallites on the <111> walls and the <100> surface in an etched waveguide channel.

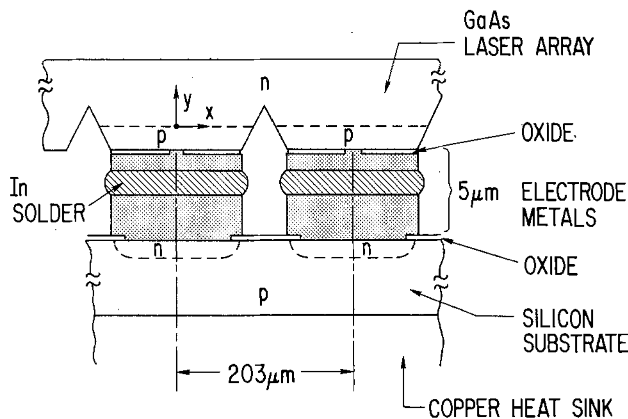

Fig. 12. Cross section of the array in the x-y plane showing position of lasers above pn junctions. Note, the vertical scale is approximately 20 times the horizontal scale.

results addressing the bonding of lasers, optical performance, and thermal characteristics of the source package and potential applications will be presented elsewhere (14-19).

Summary

We have demonstrated that fabrication of a miniature optical bench utilizing single {100} crystal silicon is a viable process for optimizing coupling efficiency of a high radiance and highly divergent optical source through a cylindrical lens and fiber waveguide. Optical throughput efficiencies on the order of 70% were achieved (17), demonstrating that this is a feasible technique which provides a low cost, rigid, mechanical support. Precise placement of a lens with respect to the optical source in both the horizontal and vertical directions is achieved by control over anisotropic etching. Individual drive electrodes on the silicon allow the lasers to be addressed. Electrical isolation between lasers is maintained by diffusing an n^+ p junction in the silicon, so when the junction laser is forward biased, the silicon junctions are reversed bias. Thermal conduction from the lasers through the metallization and silicon substrate is provided to the heat sink, and better thermal expansion matching between silicon and gallium arsenide is achieved.

Acknowledgments

I would like to thank E. G. Lean for his support and persistence throughout this work. Comments and fruitful discussions with L. D. Comerford, J. D. Crow, and R. A. Laff were instrumental in achieving the optimum sequences in the fabrication steps. I am also grateful to J. S. Harper for the optical data, J. C. Dohm for processing of the photolithographic emulsion masks, S. Ruffini for the metallization films, B. Canavello for the SEM photographs, and the Silicon Processing line for the diffusion depositions.

Manuscript submitted Dec. 12, 1977; revised manuscript received May 16, 1978.

Any discussion of this paper will appear in a Discussion Section to be published in the June 1979 JOURNAL. All discussions for the June 1979 Discussion Section should be submitted by Feb. 1, 1979.

Publication costs of this article were assisted by IBM Thomas J. Watson Research Center.

REFERENCES

1. D. B. Lee, *J. Appl. Phys.*, **40**, 4568 (1969).
2. W. K. Zwicker and S. K. Kurtz, in "Semiconductor Silicon 1973," H. R. Huff and R. R. Burgess, Editors, p. 315, The Electrochemical Society Softbound Symposium Series, Princeton, N.J. (1973).
3. J. B. Brice, *ibid.*, p. 339.
4. E. Bassous, H. N. Yu, and V. Maniscalco, *This Journal*, **123**, 1729 (1976).
5. W. T. Tsang, C. L. Tseng, and S. Wang, *Appl. Opt.*, **14**, 1200 (1975).
6. J. S. Harper and P. F. Heidrich, *Wave Electron.-2*, 369 (1976).
7. J. P. Wittke, M. Ettenberg, and H. Kressl, *RCA Rev.*, **37**, 182 (1976).
8. M. L. Dakss, *Laser Focus*, **12**, 31 (1975).
9. E. Bassous, H. H. Taub, and L. Kuhn, *Appl. Phys. Lett.*, **31**, 135 (1977).
10. D. L. Kendall, *ibid.*, **26**, 195 (1975).
11. R. M. Finne and D. L. Klein, *This Journal*, **114**, 965 (1970).
12. M. J. Declercq, *IEEE J. Solid-State Circuits*, **SC-10**, 191 (1975).
13. E. Bassous, *IBM Tech. Bull.*, **19**, 105 (1977).
14. L. D. Comerford, Private communication.
15. J. D. Crow, L. D. Comerford, J. S. Harper, M. J. Brady, and R. A. Laff, *Appl. Opt.*, **17**, 479 (1978).
16. R. A. Laff, L. D. Comerford, J. D. Crow, and M. J. Brady, *ibid.*, **17**, 778 (1978).
17. J. D. Crow, L. D. Comerford, R. A. Laff, M. J. Brady, and J. S. Harper, *Opt. Lett.*, **1**, 40 (1977).
18. B. G. Huth, J. T. Jacobs, and C. A. Bruce, Paper presented at the SPIE/SPSE Technical Symposium East, Reston, Va., March 1976, SPIE, San Diego, Calif.
19. A. G. Dewey, J. T. Jacobs, B. G. Huth, G. T. Sincerbox, G. J. Sprokel, A. Juliana, and R. W. Koepcke, Paper 9.3, presented at the S.I.D. International Symposium, Boston, April 1977, SID, San Diego, Calif.

Lateral Polysilicon p-n Diodes

M. Dutoit and F. Sollberger

Centre Electronique Horloger S.A., CH-2000 Neuchatel, Switzerland

ABSTRACT

The properties of lateral polysilicon p-n diodes as a function of doping level and temperature are discussed. Traps at grain boundaries greatly enhance charge-carrier recombination or generation and, consequently, diode current. In heavily doped diodes, an excess reverse current not accounted for by classical theories is observed. Thermal emission of charge carriers from traps followed by avalanche multiplication are proposed to explain this behavior. A current-controlled negative resistance at higher reverse bias is believed to be due to impact ionization of traps.

Integrated circuits often require high value resistors or leaky diodes. These elements can easily be implemented with lateral polysilicon diodes (1, 2). Among their advantages (3) are small size, no mandatory connection to either supply terminal, and small parasitic capacitances. In Si-gate CMOS technology they generally arise naturally without any additional process steps at the transition between the gates of p- and n-channel MOS transistors. Several years of production experience have shown that these diodes can be fabricated quite reproducibly.

p-n diodes in thin films of polycrystalline silicon were first studied by Manoliu and Kamins (4). In fine-grained films, as used in microelectronics technology, grain boundaries are expected to play a major role in determining diode properties. Compared to p-n junctions in single-crystal Si, polysilicon diodes carry much higher current densities (4-6). This increase cannot be accounted for solely on the basis of enhanced generation or recombination due to crystalline imperfections. Especially at reverse bias, heavily doped diodes carry a large excess current. At high reverse bias, a current-controlled negative resistance, not normally found in p-n junctions, is observed.

We measured the *I-V*, *I-T*, and *C-V* characteristics of p-n diodes and the influence of various process parameters. An attempt is made to explain these properties with a model derived from the work of Kamins (7) and Seto (8). They assume that the crystallites are depleted of charge carriers by traps located at their boundaries. At low doping levels, grains are completely depleted and free carrier density is very small. As the doping level increases, one reaches a critical concentration, N_t, where all traps are filled. Around N_t, free carrier density rises rapidly to approximately the same values as in single crystals. The potential barrier set up by charged traps limits mobility which is minimum near N_t. It is assumed that charge carriers cross this barrier by thermionic emission (8). An extension of this model to a p-n junction can explain some of the observed features of polysilicon diodes.

Device Processing

Standard CMOS processing (9) was simulated by growing undoped, 0.5 μm thick layers of polysilicon on thermal SiO_2 by pyrolysis of silane (0.2% SiH_4 in H_2; total gas flow, 30 l/min) at 700°C. The deposition rate was 0.05 μm/min. Average grain size, L, was about 50 nm as evaluated from TEM pictures. Next, the geometry of the devices was defined. B- and P-doped oxides deposited at 420°C were used as diffusion sources. Drive-in was carried out in N_2 at 1100°C for 45 min. Etching of contact windows, *e*-gun Al metallization, and annealing in forming gas (20% H_2 + 80% N_2) at 430°C for 1 hr completed the structure (Fig. 1a). In this case, nominal polysilicon resistivities were 100 $\Omega/\square$. The *I-V* characteristics of 10 μm wide diodes fabricated with this process are shown in Fig. 2a and 2b (uppermost curves). Diodes in polysilicon films grown by low pressure CVD had the same characteristics as those obtained with our standard process.

The influence of several polysilicon deposition variables was examined. The main effect of a change in carrier gas (N_2, Ar, or He in place of H_2) while maintaining the deposition rate, R_d constant by adjusting the flow of SiH_4 was to lower the final resistivities $\rho_s(n^+)$ and $\rho_s(p^+)$ by 10-30%. Diode reverse current, I_R increased by up to one order of magnitude. The reduction in ρ_s explains most of the change in I_R, as will be seen later. All further results concern H_2 polysilicon. In this case, ρ_s increases as R_d drops below 30 nm/min. I_R decreases with increasing R_d at a fixed deposition temperature, T_d, between 600° and 900°C. I_R varies approximately as $1/R_d$ at $T_d \leq 700°C$. The rate of change of I_R at higher T_d is lower. An increase in T_d at constant R_d decreases ρ_s and increases I_R. At this point, it is difficult to pinpoint any critical parameters, since they are generally closely interrelated. Grain size and doping level further depend on

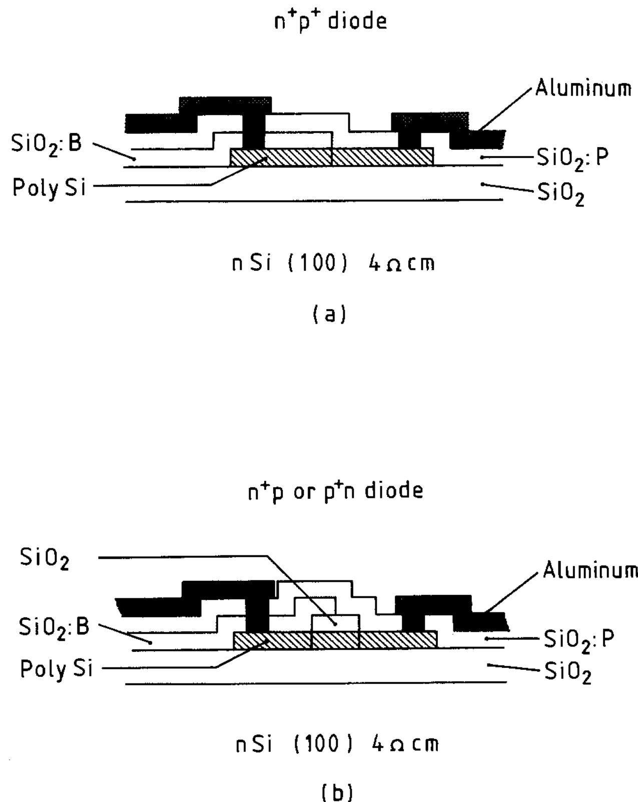

Fig. 1. Structure of (a) p^+n^+; and (b) p^+pn^+ or p^+nn^+ diodes

Key words: junction leakage, recombination-generation, grain boundaries, deep levels.

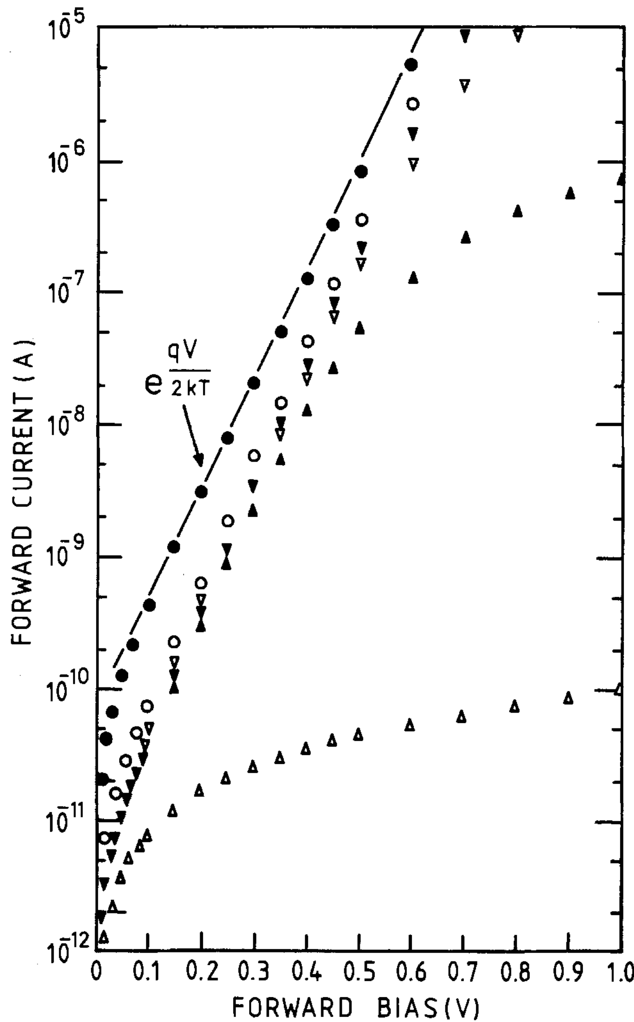

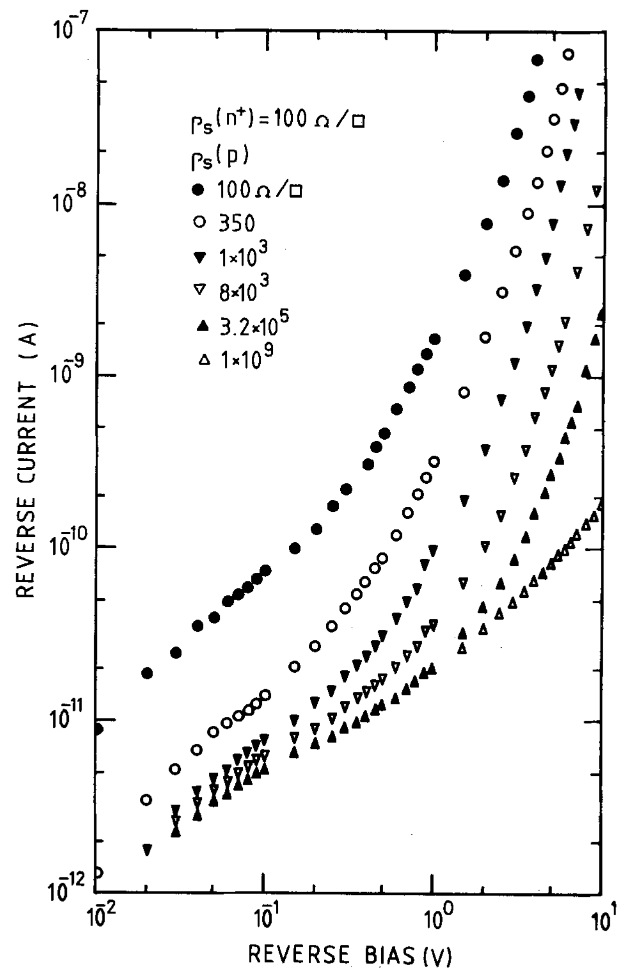

Fig. 2. (a) Forward; and (b) reverse characteristics of 10 μm wide n+p diodes

post-deposition heat-treatments. The effect of final polysilicon resistivity was studied in more detail since this parameter has a marked influence on diode properties and is easily controlled. For this purpose the structures shown in Fig. 1b were fabricated by implanting B (70 keV) or P (150 keV) into as-grown films. If doping is uniform (8), the impurity concentration N is the ratio of the implanted dose to the film thickness. This step was followed by an anneal in N_2 at 1100°C for 45 min. The 14 μm long weakly doped region was protected with a deposited SiO_2 layer. The rest of the process was unchanged. For comparison, some polysilicon films were doped during growth or with a doped oxide. No significant differences were observed (Fig. 3). The electrical properties of implanted films are accurately predicted by the model of Kamins and Seto (8). p- and n-type films have very similar properties. The parameters obtained for p-type films from fitting experimental variations of resistivity, mobility, and carrier density with doping level and temperature are trap density, $Q_t = 2 \times 10^{12}$ cm^{-2} and trap level $E_i - E_t = 0.25$ eV. These values are very close to those given in Ref. (8). The average volume density of traps is $N_t = Q_t/L = 4 \times 10^{17}$ cm^{-3}. Below 200°K, a break in the resistivity *vs.* temperature curve suggests the presence of another, shallower level in accordance with published results (10). This level has not yet been studied in detail. At low temperatures, tunneling of charge carriers through the potential barrier at grain boundaries, instead of thermionic emission, may play a role.

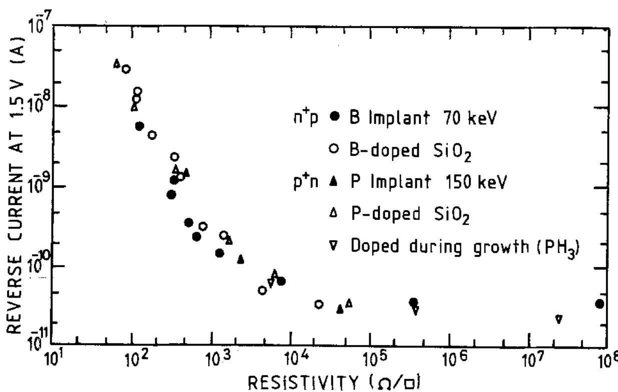

Fig. 3. Reverse current at 1.5V of 10 μm wide n+p and p+n diodes vs. resistivity of the weakly doped side.

Diode Properties

Figure 2 shows the I-V characteristics of 10 μm wide n^+p diodes with varying p-type resistivity, ρ_s. The uppermost curves represent standard n^+p^+ diodes as they are produced in CMOS technology (Fig. 1a). The other results were obtained on the devices shown in Fig. 1b.

Forward current is dominated by strong recombination, as can be inferred from its voltage dependence above 0.1V (4)

$$I_F = A \frac{qn_iW}{2\tau_o} \exp \frac{qV_F}{2kT} \quad [1]$$

where A is the junction area, q the electron charge, n_i the intrinsic carrier concentration, V_F the applied voltage, and kT the average thermal energy. The width of the space-charge region, W, is determined from

measurements of junction capacitance. The minority carrier lifetime, τ_o, determined from these results increases from 2×10^{-12} to 5×10^{-11} sec as ρ_s increases from 10^2 to 10^4 $\Omega/\square$. The generation current at 1.5V reverse bias calculated from the forward characteristics is between 10 and 100 pA. This is indeed the level measured in weakly doped diodes ($\rho_s > 10^4$ $\Omega/\square$). For lower ρ_s, I_R increases approximately as $1/\rho_s^2$ at room temperature (Fig. 3). This excess current is somewhat process dependent but insensitive to the method used to dope the p or n regions. The properties of n^+p and p^+n diodes are very similar. The reverse characteristics of heavily doped diodes depart significantly from the classical behavior of p-n junctions. I_R first increases linearly with applied bias up to a few tenths of a volt. As one approaches breakdown, the slope of the *I-V* curve gradually steepens. The breakdown voltage at 10 μA increases approximately as $\rho_s^{0.17}$ from 6V at 10^2 $\Omega/\square$ to 100V at 10^9 $\Omega/\square$. It has a positive temperature coefficient. Visible light is emitted from the junction area as reverse current approaches 1 mA. Between 2 and 5 mA, independently of ρ_s, a region of current-controlled negative resistance begins (Fig. 4). In some diodes, oscillations are observed. Diodes having been driven into this region show an irreversible increase in reverse current at low bias. A similar effect which appears at forward bias is always destructive. This behavior is similar to published results on p-i-n diodes (11, 12). Reverse current density is quite sensitive to the thickness, *t*, of the polysilicon film. It decreases by more than an order of magnitude between 0.2 and 1.2 μm, even though the average film resistivity $\rho = \rho_s t$ stays nearly constant.

The temperature dependence of the current of these diodes shows at least two thermally activated processes (Fig. 5). For standard n^+p^+ diodes the apparent activation energies near 0V are 0.2 and 0.4 eV. At sufficiently high forward bias, these two activation energies tend to decrease like $E_o - qV_F/2$, where $E_o = 0.55$ eV above 50°C and $E_o = 0.5$ eV below 50°C, independently of ρ_s (Fig. 6). This dependence is consistent with the conclusion that recombinations dominate in this range. Since in this case, $E_o = Eg/2 - |E_i - E_t|$, where Eg is the energy gap and E_i is the intrinsic Fermi level, the two levels involved are approximately 0.05 and 0.10 eV below or above E_i. The deviation from a straight line near 0V, as well as the decrease of these activation energies at reverse bias, shows that additional processes become important.

As ρ_s increases, the activation energies near 0V vary like $-\log N$ to reach limiting values near N_t that are very close to E_o (Fig. 7). Below N_t they stay

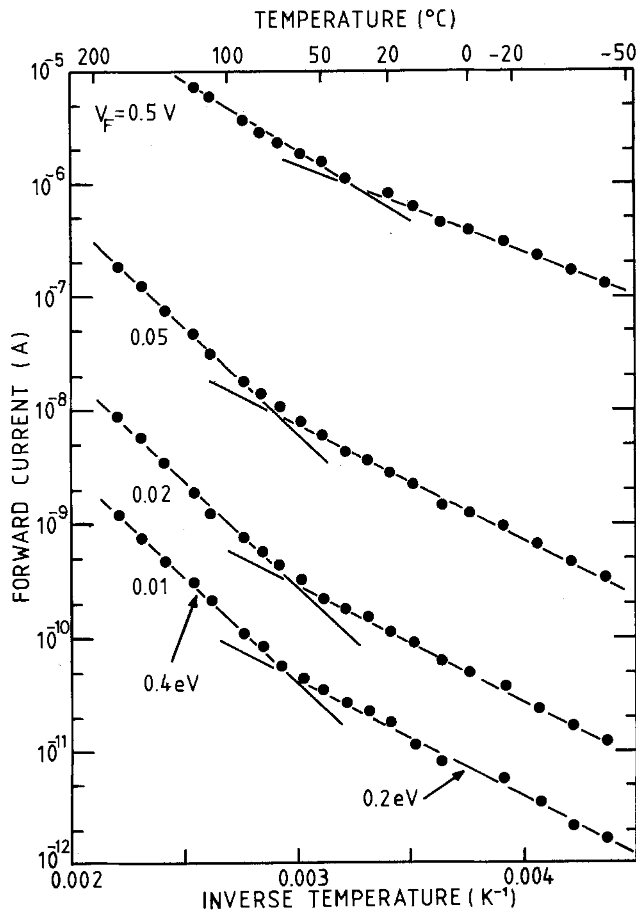

Fig. 5. Forward current of a 10 μm wide n^+p^+ diode (ρ_s = 100 $\Omega/\square$) vs. inverse temperature.

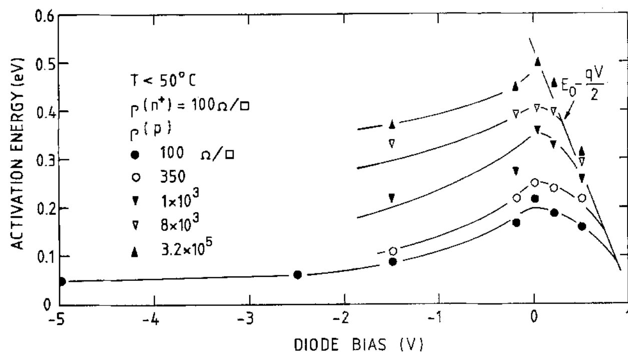

Fig. 6. Activation energy of diode current below 50°C vs. applied bias. Similar results are obtained above 50°C.

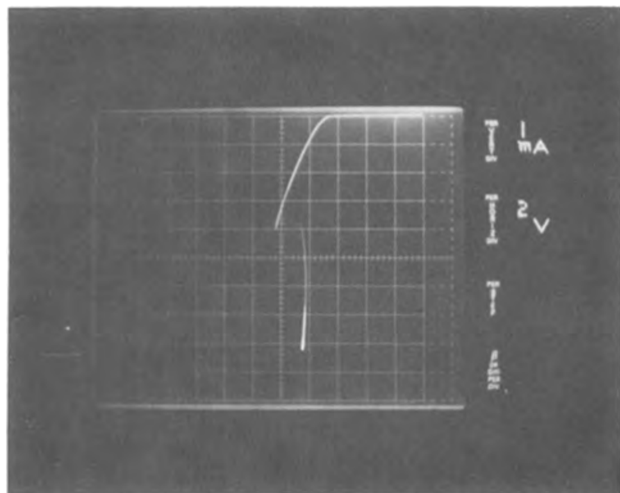

Fig. 4. Negative resistance in the reverse characteristics of a 10 μm wide n^+p^+ diode (ρ_s = 100 $\Omega/\square$).

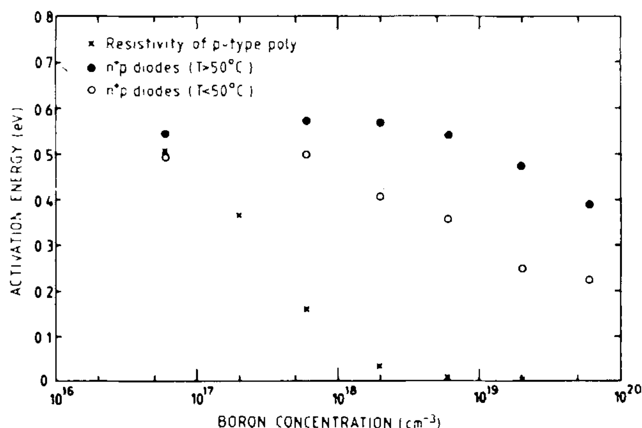

Fig. 7. Activation energies of diode current near 0V and of resistivity vs. doping concentration.

nearly constant. This confirms our earlier contention that charge-carrier generation dominates reverse current at high ρ_s. For comparison, we show the activation energy of resistivity near room temperature which falls to zero above N_t, in agreement with the model of Kamins and Seto (8).

Summarizing these measurements, an approximate expression for I_R, valid for $N > N_t$ and $T < 50°C$, can be written

$$I_R \approx \sigma_o w_d V_R \exp \frac{qV_R}{mkT} \exp \frac{-E_o + E_1 \ln \frac{N}{N_t}}{kT} \quad [2]$$

where σ_o, m, E_o, and E_1 are constants and w_d is the width of the diode. A fit to our experimental data yields $\sigma_o = 4 \times 10^{-4}\ \Omega^{-1}\ \text{cm}^{-1}$, $m = 50$, $E_o = 0.4$ eV, and $E_1 = 0.05$ eV. The value of E_o that gives the best fit is slightly different from the actual activation energy at $N = N_t$ because the voltage dependence of activation energy is not quite linear (Fig. 6). σ_o probably increases with N_t since otherwise I_R would decrease with increasing N_t, which is unlikely. As noted before, I_R does not vary linearly with polysilicon thickness.

Junction capacitance varies as $V_R^{-1/3}$ for these diodes (Fig. 8). This indicates a linearly graded doping profile, in agreement with the large lateral diffusion in polysilicon (about 5 μm in our case). The effective doping gradient determined from the slope of the curves varies from 2.6×10^{23} to 4.1×10^{22} cm^{-4} as ρ_s increases from 10^2 to 4×10^3 $\Omega/\square$. The width of the space charge region at 0V increases from 25 to 100 nm over the same range. The apparent built-in voltage is 0.1V for n^+p^+ diodes and increases with ρ_s, in contradiction with classical theories. For n^+p^+ diodes, a built-in voltage near 1V would be expected. Junction capacitance decreases slightly between 5 and 500 kHz.

Discussion

The properties of polysilicon diodes cannot be explained by simple analogy with classical p-n junctions. The enhanced rate of recombination or generation due to crystalline imperfections is not sufficient to account for all the observed features. In heavily doped diodes, reverse current is considerably higher than expected. Its voltage dependence is unusual. The width of the space-charge region and the built-in voltage are smaller than normal. Both increase at low doping.

Following Kamins and Seto, we assume that grain boundaries contribute a large density of deep levels in the bandgap. Three such levels are identified here ($|E_i - E_t| = 0.05$, 0.10, and 0.25 eV). The nearly identical properties of p- and n-type films show that holes or electrons can be trapped at grain boundaries. In a p-n junction, holes are predominantly trapped on the p side and electrons on the n side. These produce charged layers within the space charge region which screen the electric field of the junction and reduce its built-in voltage. Reverse conduction arises from thermally activated processes. We propose that thermal emission of carriers from these traps into the valence and conduction bands inside the grains is the limiting mechanism. The decrease in activation energy at low temperatures implies that multiple levels are involved. Tunneling through the barrier at grain boundaries must play a role. Avalanche multiplication probably accounts for the rapid increase in reverse current. A similar model was used to explain the characteristics of GaN MIS diodes (13). The predicted voltage and temperature dependence of current are in agreement with Eq. [2]. The negative resistance observed at high reverse bias in polysilicon diodes could be due to impact ionization of traps at grain boundaries (12), which is consistent with our model. Even though impact ionization requires a lower field than avalanche multiplication, it can start at a higher applied bias because of screening.

As the doping level decreases, fewer traps are populated and, at the same time, the field inside the junction decreases. Therefore diode current decreases until these traps merely play the role of additional recombination/generation centers. The displacement of the Fermi level with doping may explain the reduction in activation energy at high concentration.

Some experimental features are not explained by this model. In particular, the strong variation of reverse current with polysilicon thickness is still puzzling. This may indicate that surface effects need to be taken into account. Measurements on gated diodes should give more information on this point. Alternately, the variation of grain size with thickness may be important.

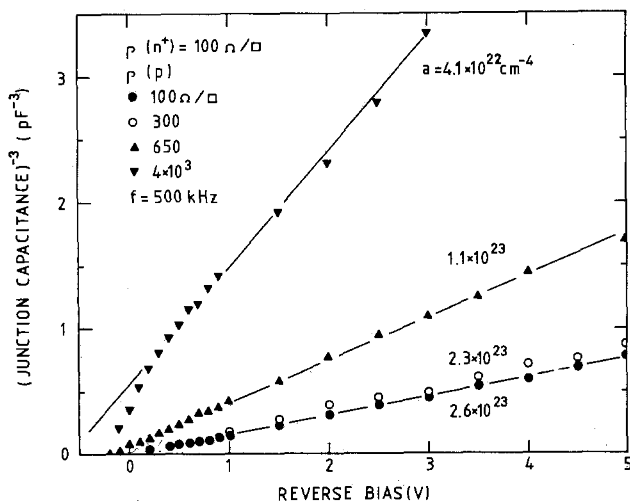

Fig. 8. Junction capacitance vs. reverse bias for 2400 μm wide n^+p diodes with ρ_s as a parameter.

Acknowledgments

Helpful discussions with B. Gerber, M. Darwish, R. Guye, and F. Leuenberger, and with A. Gnaedinger and Z. Rajgl of Faselec AG, Zurich, are gratefully acknowledged. The authors are indebted to R. Bachmann for processing the devices and to F. Mauron for his capable technical assistance.

Manuscript submitted Feb. 21, 1978; revised manuscript received May 16, 1978. This was Paper 300 presented at the Atlanta, Georgia, Meeting of the Society, Oct. 9-14, 1977.

Any discussion of this paper will appear in a Discussion Section to be published in the June 1979 JOURNAL. All discussions for the June 1979 Discussion Section should be submitted by Feb. 1, 1979.

Publication costs of this article were assisted by Centre Electronique Horloger S.A.

REFERENCES

1. H. Oguey and E. Vittoz, *IEEE J. Solid-State Circ.*, **SC-12**, 283 (1977).
2. E. Vittoz and J. Fellrath, *ibd.*, **SC-12**, 224 (1977).
3. H. Oguey and B. Gerber, U.S. Pat. 4,041,522 (1977).
4. J. Manoliu and T. I. Kamins, *Solid-State Electron.*, **15**, 1103 (1972).
5. C. Feldman and R. Plachy, *This Journal*, **121**, 685 (1974).
6. V. A. Gorohov, E. A. Matson, and C. A. Polyakov, *Thin Solid Films*, **35**, 149 (1976).
7. T. I. Kamins, *J. Appl. Phys.*, **42**, 4357 (1971).
8. J. Y. W. Seto, *ibid.*, **46**, 5247 (1975).
9. E. Vittoz, B. Gerber, and F. Leuenberger, *IEEE J. Solid-State Circ.*, **SC-7**, 100 (1972).
10. P. Rai-Choudhury and P. L. Hower, *This Journal*, **120**, 1761 (1973).
11. M. Braunstein, A. I. Braunstein, and R. Zuleeg, *Appl. Phys. Lett.*, **10**, 313 (1967).
12. J. P. Monico-García and E. Munoz-Merino, *Solid-State Electron.*, **16**, 1515 (1973).
13. A. Shintani and S. Minagawa, *J. Appl. Phys.*, **48**, 1522 (1977).

Electron Reemission Mossbauer Study of Tinplate

G. P. Huffman and G. R. Dunmyre

U. S. Steel Corporation, Research Laboratory, Monroeville, Pennsylvania 15146

ABSTRACT

Electron reemission Mossbauer (ERM) studies using the Sn^{119} Mossbauer isotope have been made on a series of tinplate samples with tin coatings ranging from 0.1 to 1.0 lb/bb (2.24 to 22.4 g/m²). With a recently developed theory of ERM spectroscopy, the ERM spectra could be analyzed to determine the thickness of the oxide (SnO_2), metallic Sn, and alloy ($FeSn_2$) layers on the tinplate samples. The resulting thicknesses were found to be in good agreement with the nominal coating weights and, for several samples, with the metal and alloy thicknesses determined by standard stripping techniques. The ERM method is shown to be very sensitive to thin tin oxide layers ranging from a few monolayers to several hundred angstroms thick.

In recent years, there has been much interest in the application of electron reemission Mossbauer (ERM) spectroscopy to the study of thin surface layers (1-8). In this technique, Mossbauer spectra are obtained by detecting the relatively low energy (typically ~1 to 20 keV) internal conversion and Auger electrons which are reemitted on deexcitation of Mossbauer nuclei following resonant absorption of recoilless Mossbauer gamma rays. Because these low energy electrons have relatively small escape distances (typically ~100-10,000Å), the bulk of the signal detected in an ERM experiment arises from the surface layers of the sample.

In a recent publication by one of the authors (7), reasonably simple analytic expressions were derived relating the ERM spectra obtained from multilayer surface films to the thicknesses of the various layers. This theory permits, for the first time, quantitative interpretation of ERM spectra; it has been initially tested and found to give reasonably accurate results in an ERM study of the oxidation of metallic Fe in oxygen at temperatures up to 500°C (8).

Although most previous ERM studies have utilized the Fe^{57} nucleus, the Sn^{119} nucleus also has excellent Mossbauer properties and is well suited to the ERM technique. The properties of Sn^{119} of most interest with regard to ERM spectroscopy have been summarized in a recent paper by Yagnik, Masak, and Collins (3). The internal conversion and Auger electrons emitted on deexcitation of the Sn^{119} nuclei have energies of 20 and 3 keV, respectively. Following resonant Mossbauer absorption of the recoilless 23.8-keV gamma rays emitted by Sn^{119m} nuclei in a suitable radioactive source, 84% of the absorbing Sn^{119} nuclei in the sample deexcite themselves by reemission of internal conversion electrons, and 89% of these internal conversion electrons are followed by Auger electrons. Therefore, for every one hundred 23.8 keV gamma rays absorbed in the sample, eighty-four 20 keV internal conversion and seventy-five 3 keV Auger electrons are reemitted. Those electrons that escape from the sample can be detected and used to obtain an ERM spectrum.

As is discussed in more detail later, the energies of these electrons are such that the bulk of the Sn^{119} ERM signal arises from approximately the top 10,000Å of the sample. This is precisely the range of most interest for tinplate with coatings of up to approximately 1 lb/bb[1] (0.1 lb/bb is equivalent to 1538Å of metallic Sn), and in the current report we summarize the results obtained by ERM studies of a fairly wide variety of tinplate samples.

Experimental Procedure

With the exception of the detection system, illustrated in Fig. 1, all aspects of the current Mossbauer experiments are the same as in conventional transmission Mossbauer spectroscopy and have been described in more detail elsewhere (9). A collimated and filtered beam of 23.8 keV gamma rays emitted by a suitable radioactive source (approximately 15 milli-Curies of Sn^{119m} in a $BaSnO_3$ matrix) is incident on the sample being investigated, which covers the rear window of a flow proportional counter; the 1 mil Pd filter serves to reduce the intensity of Sn x-rays with energies (25.0 and 25.3 keV) close to that of the Sn^{119} Mossbauer gamma rays.

When the Doppler shifted[2] energy of the incident gamma rays coincides with one of the energy separations between the various energy levels of the Sn^{119} nuclei in the absorber, resonant absorption occurs, with the absorbing nuclei being kicked into excited states. These excited Sn^{119} nuclei are deexcited 84% of the time by the internal conversion process. As noted earlier, for every one hundred 23.8 keV gamma rays resonantly absorbed, eighty-four 20 keV internal conversion and seventy-five 3 keV Auger electrons are reemitted from the absorber (3). Approximately half of these electrons are emitted in the backward direction (within the solid angle of the proportional counter window in Fig. 1); the 96% He-4% CH_4 flow gas is highly efficient for electron detection but very inefficient for detection of gamma rays and x-rays.

All tinplate samples studied in this investigation were commercial tinplate supplied by R. T. Davis and P. R. Carter of this laboratory. The tin coatings ranged from 0.1 to 1.0 lb/bb (2.4 to 22.4 g/m²). For several of the samples, independent measurements of the metallic tin and alloy layer thicknesses were made with standard stripping techniques (11).

Experimental Results

The ERM spectra of unmelted[3] tinplate samples are very similar to that of metallic tin, as illustrated in Fig. 2 which shows the spectra obtained from a metallic tin foil (top) and an unmelted 0.5 lb/bb (11.2 g/m²) tinplate sample (bottom). The labeled arrows identify the peaks arising from metallic tin (Sn) and stannic oxide (SnO_2). As discussed in a later section, the oxide layers on these samples are very thin (41Å for the metallic tin foil and 10Å for the unmelted tinplate sample). Similar oxide layers were present on all tinplate samples investigated.

After melting (reflow[4]), the tinplate samples exhibit an additional set of ERM peaks due to the alloy layer ($FeSn_2$). $FeSn_2$ is antiferromagnetic at room tempera-

Key words: surface layers, thickness determinations, SnO_2, $FeSn_2$, internal conversion.

[1] lb/bb = pounds per base box; 1 lb/bb = 22.4 g/m²

[2] The incident gamma-ray energy is Doppler modulated by vibrating the source in a controlled fashion over a small range of velocities. See Ref. (10) for a more detailed discussion.

[3] After plating, but prior to reflow, the electrodeposited tin coating is gray and nonreflective at this point.

[4] Reflow occurs for these commercially prepared tinplate samples by means of electrical resistance heating to temperatures of approximately 290-310°C, after which the strip is cooled by passage through a water bath. The resultant surface is highly reflective.

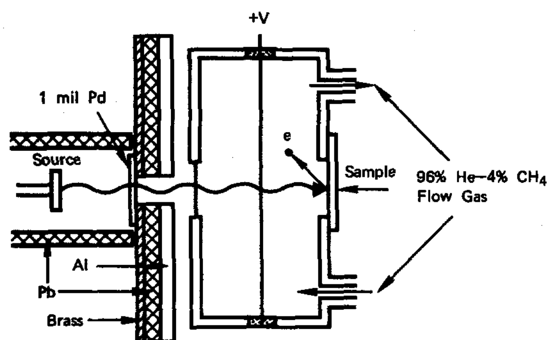

Fig. 1. Schematic diagram of the electron detection system. The dimensions of the proportional counter are approximately 10 × 4 × 4 cm.

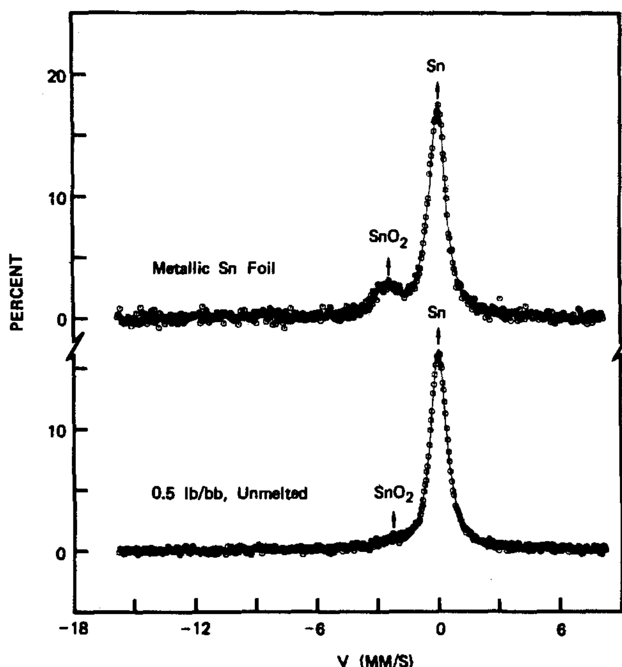

Fig. 2. ERM spectra of a metallic Sn foil (top) and an unmelted 0.5 lb/bb tinplate sample (bottom).

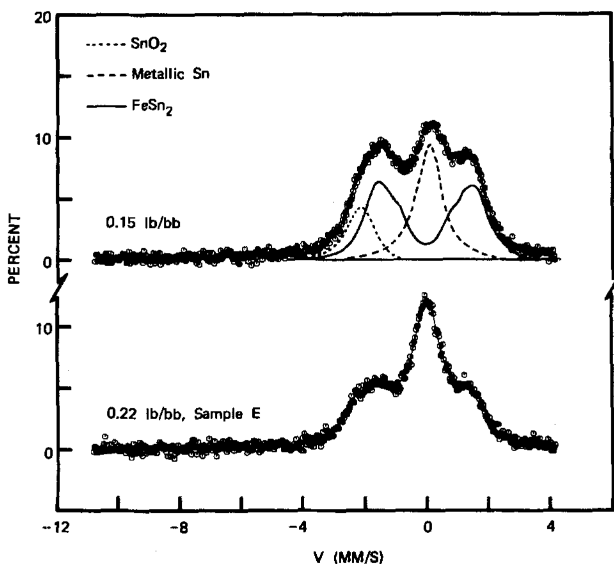

Fig. 3. ERM spectra of tinplate samples with coatings of 0.15 lb/bb (top) and 0.22 lb/bb (bottom). The approximate contributions of the oxide, metal, and alloy layers are indicated separately in the top spectrum.

ture and gives the six-peak Mossbauer pattern characteristic of magnetically ordered samples (10). Because the magnetic hyperfine field is rather small, the six peaks overlap each other considerably, as shown in the top spectrum of Fig. 3, where the spectral components arising from SnO_2, metallic Sn, and $FeSn_2$, are separately indicated. The best values of the magnetic hyperfine field, isomer shift, and quadrupole splitting for $FeSn_2$ obtained from the results found for the 12 tinplate samples studied are $H = 24.5 \pm 0.5$ kiloG, $\delta = -0.07 \pm 0.02$ mm/sec,[5] and $\epsilon \approx 0.01 \pm 0.02$ mm/sec; these values are in reasonable agreement with those obtained for bulk $FeSn_2$ (12, 13). However, the average value of the stannic oxide isomer shift for the tinplate samples was found to be -2.27 ± 0.03 mm/sec, which is somewhat more positive than the value of -2.50 mm/sec observed for SnO_2 (9). This difference in isomer shift is probably due to the incorporation of Cr into the SnO_2; the chromium originates from a chromate electrochemical treatment used industrially to retard the oxidation of the tinplate during ambient temperature storage conditions. There was no evidence of any other oxide phases, such as SnO or mixed Fe-Sn oxides. It is unlikely that such oxides could have gone undetected if they had contributed more than about 10% of the total Mossbauer signal; however, the current data cannot be regarded as conclusive with respect to the possible existence of small amounts of such phases.

ERM spectra for several tinplate samples with tin coatings ranging from 0.1 to 0.7 lb/bb (2.24 to 15.7 g/m^2) are shown in Fig. 3 and 4. As expected, the intensities of the alloy peaks decrease relative to the intensity of the metallic Sn peak with increasing tin coating weight. The experimental quantities of most interest for present considerations are the percentages of the total ERM spectrum area contributed by the oxide, metallic Sn, and alloy layers. The values of these percentages for the samples studied in this investigation are given in Table I.

Thickness Determinations

As noted earlier, a recently developed theory of ERM spectroscopy (7) permits a quantitative interpretation of ERM data. In particular, the thicknesses of thin surface layers can be determined from the percentage of the total ERM spectrum area contributed by the various layers present. The spectral area contributed by the Nth layer is

[5] All velocities and isomer shifts are measured with respect to the position of the metallic Sn peak at room temperature (β-Sn).

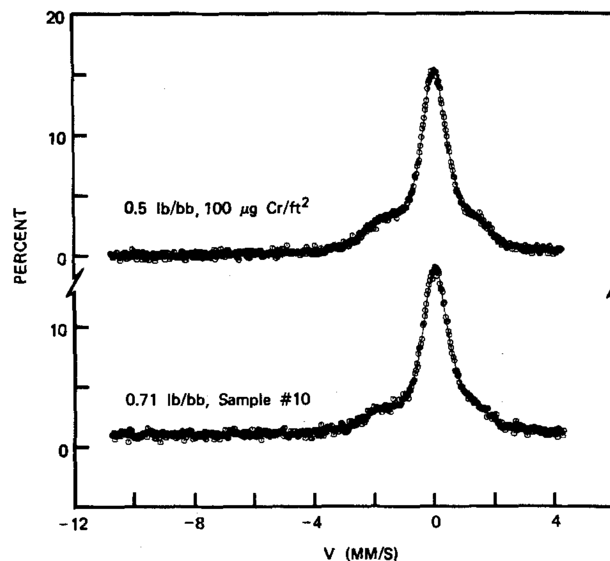

Fig. 4. ERM spectra of tinplate samples with coatings of 0.5 lb/bb (top) and 0.71 lb/bb (bottom).

Table I. ERM spectrum area percentages contributed by the oxide (P_{SnO_2}), metal (P_{Sn}), and alloy (P_{FeSn_2}) layers of various tinplate samples

Sample identification	Tin coating (lb/bb)	P_{SnO_2} (%)	P_{Sn} (%)	P_{FeSn_2} (%)
No. 89	0.15*	14.8	39.2	46.0
No. 95	0.1	15.2	43.1	41.7
No. 93	0.1	15.2	40.4	44.3
Sample E	0.22*	12.4	56.6	31.0
No. 1	0.25	10.3	56.4	33.4
No. 7	0.25	8.9	65.8	25.3
No. 5	0.25	9.7	62.2	28.1
Sample F	0.55*	3.5	82.2	14.3
700A strip	0.5	2.5	89.0	8.4
100 μ Cr/ft²	0.5	5.3	82.9	11.8
NCA, good lacquering	0.5	3.1	81.9	15.0
No. 10	0.71*	2.8	86.3	10.9

* Measured by standard stripping techniques; all other values in column 2 are nominal coating weights.

$$A_N = \sum_{j=1}^{M_N} A_{N,j} \quad [1]$$

$$= C \exp(-B_{N-1}) \sum_{j=1}^{M_N} \langle F_{N,j} \rangle \{\exp(-D_{N-1}) H(\beta_{N,j}, Y_{N,j}) + 0.89 \exp(-G_{N-1}) H(\eta_{N,j}, Y_{N,j})\} \quad [2]$$

where the Nth layer contributes M_N peaks to the ERM spectrum ($M_N = 2$[6] for SnO_2, 1 for metallic Sn, and 6 for $FeSn_2$), and $A_{N,j}$ is the area under the jth peak from layer N. Here, C is a constant (7) and the exponential functions specify the attenuation of the incident gamma rays and outgoing electrons by atomic absorption processes in layers above the Nth layer, specifically

$$B_{N-1} = \sum_{K=1}^{N-1} \mu_K Z_K \quad [3]$$

$$D_{N-1} = \sum_{K=1}^{N-1} \rho_K Z_K \quad [4]$$

and

$$G_{N-1} = \sum_{K=1}^{N-1} \gamma_K Z_K \quad [5]$$

where μ_K, ρ_K, and γ_K are the attenuation coefficients per unit length in layer K for 23.8 keV gamma rays, 20 keV electrons, and 3 keV electrons, respectively, and Z_K is the thickness of layer K. $\langle F_{N,j} \rangle$ is a more complicated exponential function which gives the attenuation of the incident gamma rays by Mossbauer absorption.

The function H specifies the maximum area contributed by the jth peak of layer N; it has the form

$$H(\beta, Y) = H_o(\beta, Y) - S(\beta, Y) \quad [6]$$

$$H_o(\beta, Y) = (1 - e^{-\beta Y})/\sqrt{\beta^2 - 1} \quad [7]$$

where S is a rapidly converging series and is $<< H_o$ [see Appendix of Ref. (7)]. The parameters $\beta_{N,j}$, $\eta_{N,j}$, and $Y_{N,j}$ to be used in Eq. [7] and [2] are given by

$$\beta_{N,j} = \frac{2(\mu_N + \rho_N)}{q_{N,j} t_o^{(N)}} + 1 \quad [8]$$

$$\eta_{N,j} = \frac{2(\mu_N + \gamma_N)}{q_{N,j} t_o^{(N)}} + 1 \quad [9]$$

and

$$Y_{N,j} = q_{N,j} t_o^{(N)} Z_N / 2 \quad [10]$$

where Z_N is the thickness of layer N, $t_o^{(N)}$ is the effective Mossbauer absorption thickness per unit length in layer N, and $q_{N,j}$ is the probability of the Mossbauer transition giving rise to the jth peak contributed by the Nth layer. The values of the various parameters used in this work are given in Tables II and III.

[6] The quadrupole splitting for SnO_2 is small (0.63 mm/sec) and the two peaks contributed by that phase appear as a single broadened peak in Fig. 2-4.

The gamma-ray attenuation coefficients (μ_N) in Table II were determined from the equations and experimental data given by Heinrich (14) and the electron attenuation coefficients (ρ_N and γ_N) from the empirical expression derived by Cosslet and Thomas (15)

$$\rho_N = \frac{1.4 \times 10^2 \times d_N}{(E)^{3/2}} (A)^{-1} \quad [11]$$

where d_N is the density of phase N and E is the electron energy in eV. $t_o^{(N)}$ is given by

$$t_o^{(N)} = f^{(N)} N_{Sn}^{(N)} a_{119} \sigma_o \quad [12]$$

where $f^{(N)}$ and $N_{Sn}^{(N)}$ are the recoilless fraction and density of Sn atoms in the Nth layer, a_{119} is the isotopic abundance of Sn^{119} (0.086) for natural tin samples, and σ_o is the maximum cross section for resonant absorption. Since the recoilless fraction of $FeSn_2$ had not previously been measured, it was necessary to estimate t_o for this phase by adjusting it to give reasonable values for the $FeSn_2$ thicknesses determined from the measured ERM area percentages for two samples with alloy layer thicknesses that had been separately determined (11) (samples 89 and E of Table I). Additionally, it should be noted that the bulk value of the recoilless fraction for SnO_2 was used. Since the recoilless fraction for the very thin SnO_2 surface layers observed is not necessarily equal to this bulk value, it is possible that some error might arise from this approximation.

It should be emphasized that the validity of using the empirical expression of Eq. [11] to derive the electron attenuation coefficients required for ERM analysis has not been adequately tested. In particular, since it was derived from electron attenuation data for pure metal films (15), its applicability to oxide phases (SnO_2) and intermetallic compounds ($FeSn_2$) is rather questionable. Nevertheless, the oxide, metal, and alloy layer thicknesses determined in this study appear to be quite reasonable for all samples investigated.

With regard to Table III, the probability values for $FeSn_2$ were determined from the relative peak intensities obtained by least squares analysis of the three ERM spectra exhibiting the largest $FeSn_2$ percentages. While the error in these probability values could be as high as 20%, this causes only a small error ($\lesssim 1\%$) in the ERM spectrum areas and percentages, as discussed elsewhere (8).

Table II. Parameter values required for ERM analysis of tinplate

Layer No. (N)	μ_N (Å⁻¹)	ρ_N (Å⁻¹)	γ_N (Å⁻¹)	$t_o^{(N)}$ (Å⁻¹)
1 (SnO_2)	0.785×10^{-6}	3.440×10^{-4}	5.921×10^{-3}	1.425×10^{-5}
2 (Metallic Sn)	1.035×10^{-6}	3.608×10^{-4}	6.211×100^{-3}	2.108×10^{-6}
3 ($FeSn_2$)	0.776×10^{-6}	2.633×10^{-4}	4.533×10^{-3}	3.001×10^{-6}

Table III. Transition probabilities ($q_{N,j}$) used in peak area equations

Phase	Type of spectrum contribution	Transition probabilities
Sn	Single peak	$q_{1,1} = 1.0$
SnO_2	Quadrupole doublet	$q_{2,1} = q_{2,2} = 0.5$
$FeSn_2$*	Six-peak magnetic	$q_{3,1} = q_{3,6} = 0.24$, $q_{3,2} = q_{3,5} = 0.18$, $q_{3,3} = q_{3,4} = 0.09$

* The transition probabilities for $FeSn_2$ are average values determined from the relative areas of the six $FeSn_2$ peaks for the 0.1 and 0.25 lb/bb tinplate samples.

Table IV. Layer thicknesses* and coating densities determined by ERM analysis

Sample identification	W_{tot} (lb/bb)	Z_{SnO_2} (A)	Z_{Sn} (A)	Z_{FeSn_2} (A)	W_{SnO_2} (lb/bb)	W_{Sn} (lb/bb)	W_{FeSn_2} (lb/bb)	W_{tot} (lb/bb)
No. 89	0.15**	35	1153	1586	0.0017	0.075	0.061	0.138
No. 95	0.1	35	1260	1420	0.0017	0.082	0.055	0.139
No. 93	0.1	32	1170	1475	0.0016	0.076	0.057	0.135
Sample E	0.22**	30	1975	1420	0.0015	0.128	0.055	0.185
No. 1	0.25	25	1971	1555	0.0012	0.128	0.060	0.189
No. 7	0.25	21	2582	1475	0.0010	0.168	0.057	0.226
No. 5	0.25	23	2316	1477	0.0011	0.151	0.057	0.209
Sample F	0.55**	9	5705	3952	0.0004	0.371	0.152	0.523
700Å strip	0.5	7	6360	2350	0.0003	0.414	0.090	0.504
NCA, 100 μg Cr/ft^2	0.5	13	5450	2449	0.0006	0.354	0.094	0.449
NCA, good lacquering	0.5	8	5576	3939	0.0004	0.363	0.151	0.514
No. 10	0.71*	7	6950	5651	0.0003	0.452	0.217	0.669

* The percentage errors in the ERM determined thicknesses are approximately 10% for the Sn and $FeSn_2$ layers and 20% for the SnO_2 layer.
** Measured by standard electrostripping technique; all other values in column 2 are nominal coating densities.

The ERM spectrum area percentages are given by

$$P_N = \frac{100 A_N}{\sum_K A_K} = \frac{100 \sum_{j=1}^{M_N} A_{N,j}}{\sum_K \sum_{l=1}^{M_K} A_{K,l}} \qquad [13]$$

where the sum over K extends over the three layers present, SnO_2, metallic Sn, and $FeSn_2$. The area percentages are determined experimentally (Table I), and substitution of Eq. [2] into Eq. [13] then gives three equations that can be solved for the three layer thicknesses, Z_{SnO_2}, Z_{Sn}, and Z_{FeSn_2}.[7] The solution of these three nonlinear equations is accomplished by using a computer program (ZNLAY), described in Ref. (8). The results are shown in Table IV. Column 2 gives either the nominal tin coating density or the value determined by electrostripping techniques (11), and columns 3 through 5 give the ERM-determined thicknesses of the oxide, metallic Sn, and alloy layers in angstroms. These thicknesses may be converted to more familiar units (lb/bb) by using the readily obtained relations

$$W_{SnO_2} = 0.489 \times 10^{-4} Z_{SnO_2} \qquad [14]$$

$$W_{Sn} = 0.650 \times 10^{-4} Z_{Sn} \qquad [15]$$

$$W_{FeSn_2} = 0.384 \times 10^{-4} Z_{FeSn_2} \qquad [16]$$

Equations [14], [15], and [16] give the coating densities in lb/bb of Sn contained in the oxide, metallic Sn, and alloy layers, respectively, with the thicknesses in angstroms. These values and the resulting total tin coating densities are shown in columns 6 through 9. As discussed above, there are a number of possible inaccuracies in some of the parameters used in this analysis of the ERM data; nevertheless, the ERM determined thicknesses and coating densities are seen to be in reasonable agreement with the values in column 2.

Discussion

Since the current report is primarily a survey study, it is useful at this point to discuss some possible future applications of ERM spectroscopy in the area of tinplate research.

Thickness determinations.—Most of the ERM spectra obtained in this study required 10-20 hr of accumulation time to attain reasonable counting statistics. This is clearly a much longer time than required by standard methods of metallic Sn and alloy thickness determination. However, the ERM technique does have the advantage of being nondestructive and might serve as a useful check in any cases where standard methods give results that are questionable for some reason. Additionally, it is worth noting that the current data were obtained using a relatively weak Sn^{119m} source and a constant acceleration Mossbauer spectrometer which scans all velocities simultaneously. By increasing the source strength by a factor of 4 or 5 and using a constant-velocity spectrometer to allow data accumulation only at the velocities where the metallic Sn and alloy layers given their maximum reemission percentages ($v_{Sn} \simeq 0$ mm/sec, $v_{FeSn_2} \simeq 1.5$ mm/sec; see Fig. 3 and 4), the time for ERM thickness determinations could be cut to perhaps 15-30 min.

Oxidation and corrosion studies.—One of the more interesting aspects of the current work is the high sensitivity of ERM spectroscopy to very thin surface layers of tin oxide. For example, the spectrum area percentages measured for the SnO_2 layers on the metallic Sn and unmelted tinplate samples shown in Fig. 2 indicate SnO_2 thicknesses of only 41 and 10Å, respectively, for these two samples. This high sensitivity arises because the recoilless fraction of SnO_2 is 9 times greater than that of metallic Sn (16) ($f_{SnO_2} = 0.45$, $f_{Sn} = 0.05$, at room temperature).

To further illustrate this point, we have used Eq. [13] and [2] to calculate the expected ERM spectrum area percentages for thin layers of SnO_2 over an "infinite"[8] metallic-Sn substrate. The results are tabulated in Table V and displayed graphically in Fig. 5, where the percentage of the ERM spectrum area contributed by SnO_2 (P_{SnO_2}) is plotted against the thickness of the SnO_2 layer (Z_{SnO_2}). It is seen that an SnO_2 layer only 270Å thick will contribute fully 50% of the

[7] The advantage of working with the percentages of the total spectrum area contributed by each phase rather than with the areas themselves is that the constant C in Eq. [2] is thereby eliminated; as discussed in Ref. (7), C involves a background component (arising principally from nonresonant photoelectrons) which is difficult to estimate.

[8] Because of the relatively small penetration range of the 20 keV conversion electrons, any layer thicker than about 20,000Å is effectively infinite to this measuring technique.

Table V. Calculated ERM spectrum area percentages contributed by SnO_2 (P_{SnO_2}) and Sn(P_{Sn}) for SnO_2 layers on a metallic Sn substrate

Z_{SnO_2} (A)	P_{SnO_2} (%)	P_{Sn} (%)
5	2.15	97.85
10	4.19	95.81
25	9.74	90.26
50	17.46	82.54
75	23.74	76.26
100	28.97	71.03
150	37.21	62.79
200	43.46	56.54
300	52.46	47.54
400	58.79	41.21
500	63.60	36.40
600	67.42	32.58
700	70.58	29.42
800	73.24	26.76
900	75.51	24.49
1000	77.49	22.51
1250	81.45	18.55
1500	84.44	15.56
1750	86.76	13.24
2000	88.61	11.39
2500	91.36	8.64
3000	93.28	6.72
4000	95.74	4.26
5000	97.20	2.81

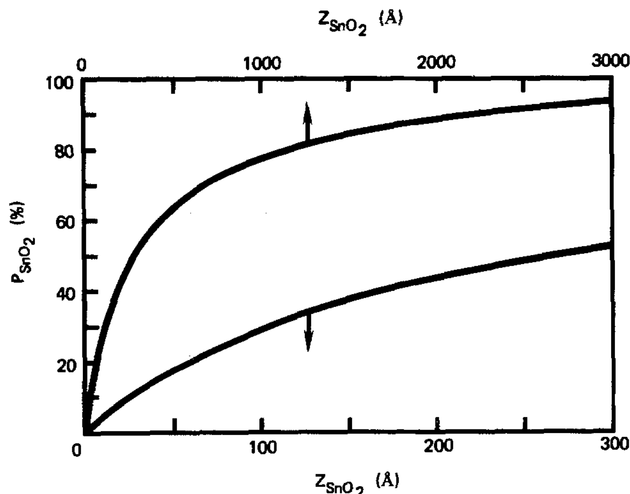

Fig. 5. ERM spectrum area percentage contributed by SnO_2 as a function of the SnO_2 layer thickness over a thick metallic Sn substrate.

spectrum area, and that oxide layers only a few monolayers thick (~5-20Å) can be detected and studied by this method. As noted earlier, the precision with which the recoilless fraction of very thin layers of SnO_2 matches that of bulk SnO_2 is not known. This could alter our estimates slightly but is not expected to cause any large variation from the behavior shown in Fig. 5. ERM spectroscopy should, therefore, be an excellent technique for oxidation and corrosion studies of metallic Sn.

Summary and Conclusions

ERM spectroscopy has been shown to be a useful new method of studying the thin stannic oxide, metallic Sn, and alloy ($FeSn_2$) layers on tinplate. With a recently developed theory of ERM spectroscopy (7), the ERM data can be analyzed to determine the thicknesses of these three layers. Although such thickness determinations are currently relatively time consuming compared to more standard methods it seems possible that experimental improvements outlined herein might significantly reduce the time required for ERM analysis of tinplate.

Probably the most interesting aspect of the current work is the observed high sensitivity of ERM spectroscopy to very thin tin oxide layers. Oxide layers ranging from a few monolayers to several hundred angstroms thick are readily observed and we know of no other technique for oxidation and corrosion studies involving Sn which combines this high sensitivity to very thin layers with the capability of conclusively identifying the tin oxide compounds which are present.

Acknowledgment

The authors gratefully acknowledge the assistance of R. T. Davis and P. R. Carter of this laboratory in providing samples and supplementary thickness measurements and for critical reviews of this report.

Manuscript submitted Dec. 19, 1977; revised manuscript received May 23, 1978.

Any discussion of this paper will appear in a Discussion Section to be published in the June 1979 JOURNAL. All discussions for the June 1979 Discussion Section should be submitted by Feb. 1, 1979.

Publication costs of this article were assisted by U.S. Steel Corporation.

REFERENCES

1. J. J. Spijkerman, "Mossbauer Effect Methodology," Vol. 7, I. J. Gruverman, Editor, p. 85, Plenum Press, New York (1971).
2. K. R. Swanson and J. J. Spijkerman, *J. Appl. Phys.*, **41**, 3155 (1970).
3. C. M. Yagnik, R. A. Mazak, and R. L. Collins, *Nucl. Instrum. Methods*, **114**, 1 (1974).
4. L. J. Swartzendruber and L. H. Bennet, *Scripta Met.*, **6**, 737 (1972).
5. G. W. Simmons, E. Kellerman, and H. Leidheiser, Jr., *Corrosion*, **29**, 227 (1973).
6. U. Baverstam, J. Ekdahl, Ch. Boh. B. Ringstrom, V. Stefansson, and D. Liljequist, *Nucl. Instrum. Methods*, **115**, 373 (1974).
7. G. P. Huffman, *ibid.*, **137**, 267 (1976).
8. G. P. Huffman and H. H. Podgurski, *Oxidation Metals*, **10**, 377 (1976).
9. G. P. Huffman and H. H. Podgurski, *Acta Met.*, **21**, 449 (1973).
10. G. K. Wertheim, "Mossbauer Effect: Principles and Applications," Academic Press, New York (1964).
11. These data were supplied by P. R. Carter.
12. V. I. Nikolaev, Yu. I. Scherbina, and S. S. Yakimov, *J. Exptl. Theoret. Phys. (USSR)*, **45**, 1277 (1963).
13. G. Trumpy, E. Both, C. Djega-Mariadassou, and P. Lecocq, *Phys. Rev. B.*, **2**, 3477 (1970).
14. K. F. J. Heinrich, in "The Electron Microprobe," T. D. McKinley, K. F. J. Heinrich, and D. B. Wittry, Editors, pp. 296-377, John Wiley & Sons, New York (1966).
15. V. E. Cosslett and R. N. Thomas, *Brit. J. Appl. Phys.*, **15**, 883 1964.
16. A. Biran, A. Yarom, P. A. Montano, and H. Shechter, *Nucl. Instrum. Methods*, **98**, 41 (1972).

Threshold Voltage Degradation of MNOS FET Devices

P. K. Chaudhari[*,1]

IBM Systems Product Division, Essex Junction, Vermont 05452

ABSTRACT

A film of Si_3N_4 deposited on thermally grown SiO_2 was studied to determine the effect that charge accumulation at the deposited film SiO_2 interface has on threshold voltage stability. V_T shifts under bias and temperature result from this charge accumulation at the nitride-oxide interface. In addition to this charge buildup-related shift, the second mechanism causing the enhanced shift in V_T is found to occur on long-time, bias-temperature stress. This second mechanism is proportional to the square root of biasing time and is exponentially dependent on temperature. The activation energy is found to be 0.36 ± 0.04 eV. Positive ionic drift is suggested as the mechanism causing this enhanced ΔV_T.

Metal-insulator-semiconductor (MIS) structures consisting of a film deposited on thermally grown SiO_2 have the inherent property of accumulating charge at the deposited film-SiO_2 interface. This charge buildup, which occurs due to different rates of current transport in the two dielectrics (1), presents a serious long-term reliability problem because of its effect on threshold voltage stability of devices. MIS structures consisting of a film of Si_3N_4 deposited on thermally grown SiO_2 were studied to determine the effect of charge accumulation on threshold voltage stability. Voltage shifts were studied as functions of bias, temperature, and stress duration. In this paper, we first describe the fabrication of MNOS FET devices and provide details of measurements. Threshold voltage degradation is next analyzed in terms of the charge accumulation at the insulator-insulator interface as a function of time. A model for threshold voltage degradation enhancement consistent with observed data is presented followed by some conclusions.

Experiment

Experimental MNOS FET devices were fabricated using p-type 1-2 Ω-cm silicon wafers. First, source and drain regions were formed using an arsenosilicate glass source as a dopant (2). After cleaning, the gate oxide was grown. Immediately following thermal oxidation, silicon nitride was deposited on the SiO_2 by decomposition of silane in ammonia.

Aluminum was the gate metal. After aluminum evaporation, the devices were treated with a forming gas anneal at 723°K for 2-5 min. Conventional photolithography was used throughout the fabrication. The high frequency (1 MHz) MNOS C-B technique was used to measure the maximum capacitance, C_{max}, with a control wafer. The equivalent gate dielectric thickness, t_{neq}, was determined from

$$t_{neq} = t_n + t_{ox}\epsilon_n/\epsilon_{ox} = \epsilon_n\epsilon_0 A_c/C_{max} \qquad [1]$$

where t_{ox} is the oxide thickness, t_n is the nitride thickness, ϵ_{ox} and ϵ_n are the dielectric constants of the oxide and nitride, respectively, and A_c is the capacitor area. Mobile ion contamination, checked with a control wafer by the high temperature quasistatic technique (3), was found to be consistently less than 5×10^{10} cm^{-2}.

The aging experiments were performed in the following manner. The gate bias was applied with respect to the commonly interconnected substrate, source, and drain. After a given period at the elevated temperature, the devices were cooled to room temperature with the bias applied. Measurements were made of drain junction leakage, gate-to-substrate leakage, and drain current at a drain voltage of +10V. The MNOS FET device threshold voltage was calculated by a least squares fit to the linear portion of the curve of the square root of the drain current as a function of gate voltage. A data listing was developed showing drain junction leakage current, gate leakage current, and threshold voltage shift, ΔV_{th}, from the initial value on each device throughout each experiment. After each test period, the median ΔV_{th} was calculated. The parameter that exhibited a consistent long-term drift problem was the threshold voltage.

The results presented in the next section deal with the time dependence of the median of the threshold voltage shift.

Results and Discussion

Figures 1 and 2 show the time, temperature, and voltage dependence of ΔV_T for metal-nitride-oxide-silicon devices plotted on a semilog scale. Each data point represents a median value obtained from a sample of 20-30 devices. The deviations from the median are shown as error bars in this and subsequent figures. In general, a maximum of 15-20% spread was observed in all these measured values. The enhanced shift above about 400 hr (Fig. 1) is discussed later.

Such a logarithmic behavior has also been observed by Rossel, Martinot, and Serhal (4) for MOSFET's. The V_T stability data of Fig. 1 and 2 cannot be explained by mobile ion motion or by slow surface-states

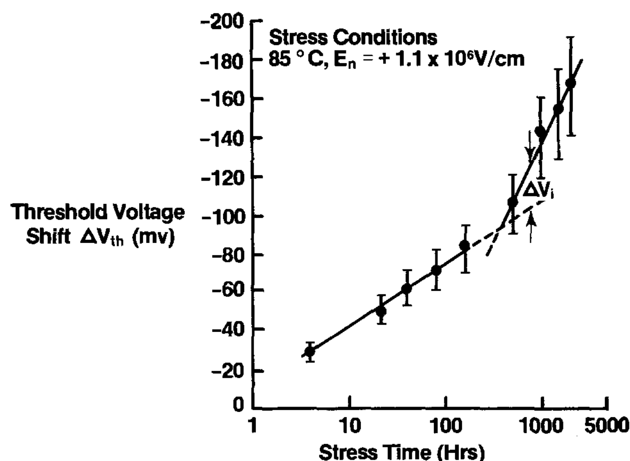

Fig. 1. Threshold voltage shift as a function of time: $T = 358°K$, and $E_n = 1.1 \times 10^6$ V/cm.

* Electrochemical Society Active Member.
[1] Present address: IBM Corporation, Poughkeepsie, New York 12602.

Key words: MNOS FET device, threshold voltage stability, dual dielectrics.

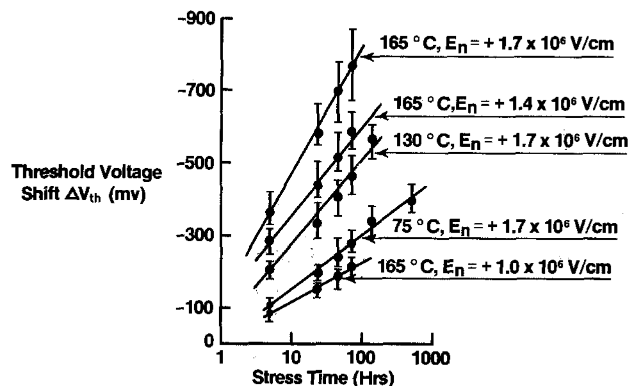

Fig. 2. Threshold voltage shift as functions of time, bias, and temperature.

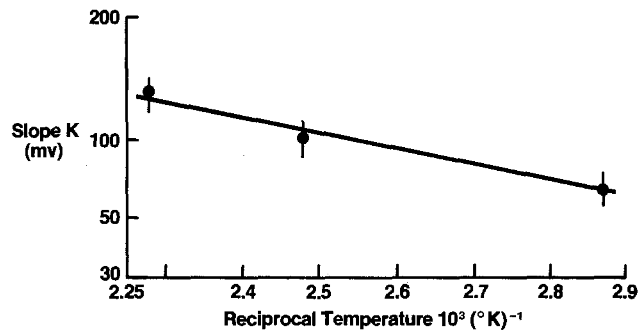

Fig. 4. Slope K as a function of reciprocal temperature. The field is 1.70×10^6 V/cm.

trapping. The mobile ion density is less than 5×10^{10} cm^{-2}. This density can produce a maximum ΔV_T of ~75 mV for the devices with $t_{neq} = 1000$Å gate dielectric. V_T shifts have been observed which are much larger than 75 mV. Slow surface-state trapping produces a positive V_T shift under positive stress and a negative V_T shift for negative stress. However, experimental data is of the opposite polarity, *i.e.*, $\Delta V_T < 0$ for positive stress. Therefore slow-state trapping cannot produce the observed V_T shifts. Charge buildup at the Si_3N_4-SiO_2 interface occurs as a result of different rates of current transported in the two dielectrics (1). This accumulation of the charge density Q_I at the insulator-insulator interface shifts the threshold voltage V_T when the device is biased because $J_n \neq J_{ox}$. This dual dielectric model predicts that a positive stress produces a negative ΔV_T and vice versa. This observation is found in our samples. For our samples, $J_n << J_{ox}$. Hence a large amount of charge accumulation will accumulate at the oxide-nitride interface, and ΔV_T will not show a saturation as is seen in Fig. 1 and 2. Therefore qualitative agreement between the experimental data and the model gives good evidence that the dual dielectric instability is the cause of the V_T shifts in MNOS FET devices. A detailed knowledge of the oxide and nitride conductivity *vs.* field relation, the various barrier heights, and the trap distributions throughout the nitride-oxide insulator is necessary to predict the time, temperature, and voltage dependence of the V_T shifts. For practical purposes, the results of this investigation can be combined into a single phenomenological expression

$$\Delta V_T = K \ln t/t_o \quad [2]$$

where K is a function of temperature and voltage and is expressed as (see Fig. 3 and 4)

$$K = K_o \exp\left[-\frac{\phi}{kT} + \beta E_n^{1/2}\right] \quad [3]$$

with $\phi = 0.65 \pm 0.05$ eV and K_o includes various incident constants.

Threshold Voltage Shift Enhancement

It is seen in Fig. 1 that beyond about 400 hr the shift in the threshold voltage increases faster than that observed below 400 hr. The results suggest that another mechanism seems to be operative in addition to the above-mentioned interfacial trapping mechanism. To establish the contribution of this second mechanism to the total threshold voltage shift ΔV_T, we will further assume that these two mechanisms are independent of each other. Under these two assumptions, the second mechanism can be identified as described below. The initial shift (below 400 hr) is extrapolated beyond 400 hr as shown dotted in Fig. 1. The difference between the extrapolated line and the observed data ΔV_i, also shown in Fig. 1, is then the contribution due to the second mechanism which causes the enhanced threshold voltage shift. Consistent with the experimental data analysis discussed below, we can now characterize the second mechanism and establish its physical model. Data of Fig. 5 indicate that with the positive bias and temperature (B-T) stress, the enhancement in V_{th} shift is negative.

Surface-state trapping produces a positive threshold voltage shift under positive stress and a negative V_{th} shift for negative stress. However, the experimental data is of the opposite polarity, *i.e.*, $\Delta V_{th} > 0$ for negative stress and vice versa, and therefore surface-state trapping cannot produce the observed V_{th} shifts. Secondly, from Fig. 5, important features of this degradation to be noted are that (*i*) the onset of ΔV_i occurs after some stress time; (*ii*) the onset is very sensitive to the temperature of stress; while (*iii*) it is almost independent of the stress voltage. Figure 6 shows the time dependence of ΔV_i with temperature as a parameter. It is clear that ΔV_i follows a $t^{0.5}$ behavior quite

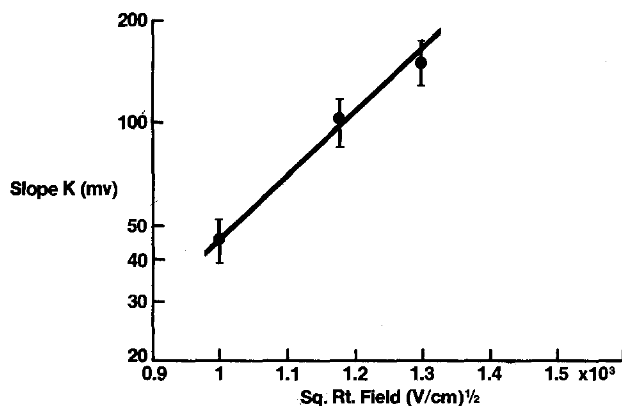

Fig. 3. Slope K derived from ΔV_{th} *vs.* ln t graph as a function of field at 438°K.

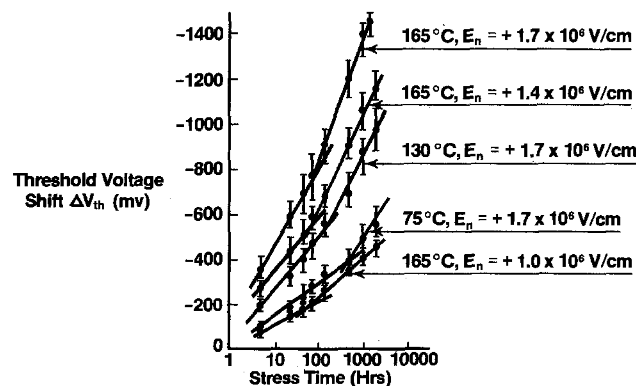

Fig. 5. Total threshold voltage shift as functions of time, bias, and temperature.

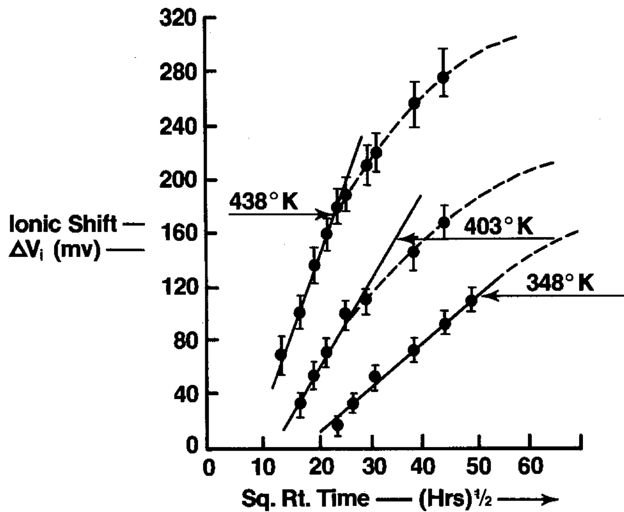

Fig. 6. Ionic component ΔV_i as a function of the square root of time.

well with the tendency to saturate. Note further that the saturation value is different for different temperatures. A plot of the slope $\Delta V_i \times t^{-0.5}$ obtained from Fig. 6 as a function of the reciprocal temperature is shown in Fig. 7, with an activation energy of 0.18 $\pm$ 0.02 eV. Therefore, the time and temperature dependence of the second mechanism can be represented by the empirical relation

$$\Delta V_i \sim t^{0.5} \exp(-H/kT), \text{ with } H = 0.18 \pm 0.02 \text{ eV} \quad [4]$$

Snow *et al.* (5) reported a ΔV_{FB} *vs.* $t^{0.5}$ dependence, and it was later verified by Singh *et al.* (6), of Na^+ transport through thermally grown SiO_2 films, deliberately contaminated in aqueous NaCl solutions. Eldridge and Kerr (7) have also reported such a time-dependent instability in sodium-contaminated PSG-SiO_2 films. This time dependence can be attributed also to the temperature- and field-induced emission of ions from trapping centers located near the metal-nitride interface. As shown by Hofstein (8), who computed the effect of small Gaussian distributed spreads in the activation energy for ion emission from such traps in MOS structures, the quantity of the drifted ions is closely proportional to $t^{0.5}$. The results thus conform to an enhanced V_T shift model based on the emission of positive ions from Si_3N_4 layer into the SiO_2 film. In addition, when all the device leads were shorted at stress temperature, subsequent measurement of the V_T shift indicated that after about 6 hr the threshold voltage shift followed the dotted line (see Fig. 1) which is the differential conductivity dominant mechanism. This observation verifies the fact that positive ions responsible for the ΔV_i are driven away from the SiO_2-Si interface (5).

The transport process is a thermally activated process with an activation energy $H = 0.18 \pm 0.02$ eV (see Fig. 7). If the transport of ions from the Si_3N_4-SiO_2 interface is assumed to be the diffusion dominant mechanism, the activation energy of the diffusion coefficient D can be determined as follows.

From simple diffusion kinetics, the diffusion coefficient is given by

$$D = t_n^2/t \quad [5]$$

Combining Eq. [3] and [4], we get

$$D \sim t_n^2 \exp(-2H/kT) \quad [6]$$

Therefore, from Fig. 7 and Eq. [6], the diffusion coefficient activation energy is determined to be 0.36 $\pm$ 0.04 eV. This value is about the same as that reported for hydrogen ions (protons) in SiO_2 (9, 10). The activation energy for Na^+ in SiO_2 is about 1.0 eV (5, 7). Secondly, the mobile ion contamination in the devices studied here was consistently less than 5×10^{10} cm^{-2}, which would cause ΔV_i max to be about 50 mV, which is not consistent with the data (see Fig. 1). Furthermore, if the ionic source is finite, then, for a fixed bias, the saturation value for different temperatures should be the same (5). But the value ΔV_i sat. is, as seen in Fig. 6, found to be different for different temperatures, indicating that the source of ions is not due to extraneous contamination, but is an inherent property of Si_3N_4 films. The supporting evidence for this conclusion is cited below. Si_3N_4 deposition with the components NH_3, H_2 used here, invariably results in Si-H, N-H traps (11, 12) as well as free hydrogen (12, 13). These traps are most likely to be concentrated at the two interfaces, Si_3N_4-SiO_2 and metal-Si_3N_4. Under B-T stress, these traps could release protons or H_2^+, thereby causing the observed enhancement in the threshold voltage shift. However, the role played by Na cannot be ruled out as well. Figure 8 shows schematically the proposed model for this ionic shift which conforms to the above discussion.

Conclusions

A study was made of the threshold voltage shifts in double layer insulator MNOS FET devices after bias-temperature treatment. The threshold voltage shifts encountered under positive bias can be explained by the existing dual dielectric instability model effect. The enhanced threshold voltage shifts observed can be explained only if, in addition to the dual dielectric instability model, a positive ion motion through the insulator is assumed. The positively charged ions initially located close to the metal-nitride interface are transported to the Si_3N_4-SiO_2 interface and are subsequently swept to the SiO_2-Si interface with an activation energy determined to be 0.36 $\pm$ 0.04 eV. In agreement with the experimental results, the source of these ions is proposed mainly to be hydrogen, the presence of which is inherent due to the Si_3N_4 process.

Although the large threshold voltage shifts described here are not necessarily typical of MNOS structures,

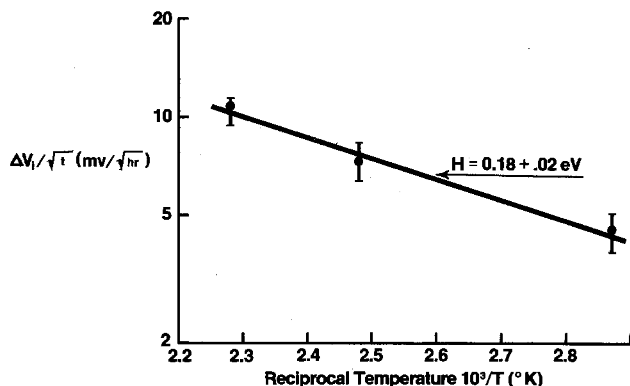

Fig. 7. $\Delta V_i \times t^{-0.5}$ as a function of reciprocal temperature

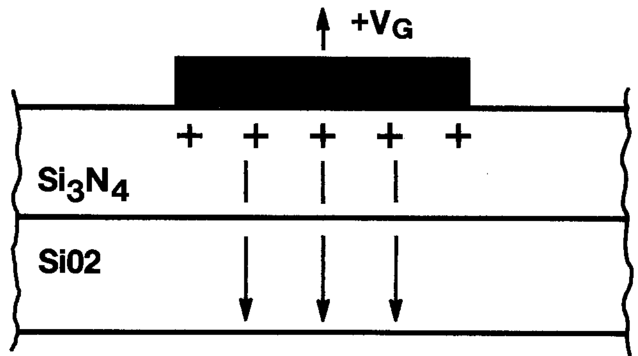

Fig. 8. Schematic representation of the enhanced threshold voltage shift model.

the data represents the kind of instability that can occur. Analysis of this data has led to the characterization of the responsible mechanisms presented here, and thereby provided a model from which insights can be obtained regarding appropriate process changes for enhancement of device reliability.

Acknowledgments

The author is grateful to Bernard Laflam for making many measurements. He also thanks Arup Bhattacharyya, Wendell Noble, and Robert Dockerty for many helpful discussions. Special thanks go to Joseph Franz and Nick Patrin for critically reviewing the manuscript.

Manuscript submitted Sept. 22, 1977; revised manuscript received May 11, 1978. This was presented in part as Paper 43 presented at the San Francisco, California, Meeting of the Society, May 12-17, 1974, and as Paper 123 presented at the Dallas, Texas, Meeting of the Society, Oct. 5-9, 1975.

Any discussion of this paper will appear in a Discussion Section to be published in the June 1979 JOURNAL. All discussions for the June 1979 Discussion Section should be submitted by Feb. 1, 1979.

Publication costs of this article were assisted by IBM Corporation.

REFERENCES

1. D. F. Bentchkowsky and M. Lenzlinger, *J. Appl. Phys.*, **40**, 3307 (1969).
2. P. K. Chaudhari, W. J. Frey, and R. M. Quinn, Abstract 80, p. 201, The Electrochemical Society Extended Abstracts, Spring Meeting, Chicago, Illinois, May 13-18, 1973.
3. M. Kuhn, *Solid-State Electron.*, **13**, 873 (1970).
4. P. Rossel, H. Martinot, and A. Serhal, *ibid.*, **13**, 257 (1970).
5. E. H. Snow, A. S. Grove, B. E. Deal, and C. T. Sah, *J. Appl. Phys.*, **36**, 1664 (1965).
6. B. R. Singh, S. S. Rai, and R. S. Srivastava, *Phys. Status Solid (A) Appl. Res.*, **13**, 51 (1972).
7. J. M. Eldridge and D. R. Kerr, *This Journal*, **118**, 986 (1971).
8. S. R. Hofstein, *IEEE Trans. Electron. Devices*, **ed-14**, 749 (1967).
9. A. E. Owen and R. W. Douglas, *J. Soc. Glass Technol.*, **43**, 159 (1959).
10. E. H. Nicollian, C. N. Berglund, P. F. Schmidt, and J. M. Andrews, *J. Appl. Phys.*, **42**, 5654 (1971).
11. M. Rands and J. Roberts, *This Journal*, **120**, 406 (1973).
12. H. J. Stein and H. A. R. Wagner, Paper presented at the First IEEE Non-Volatile Semiconductor Memory (NVFM) Workshop, Vail, Colorado, Aug. 17, 1976.
13. Y. Watanabe, *Jpn. J. Appl. Phys.*, **7**, 960 (1968).

Semiconducting Oxide Oxygen Electrodes

A. C. C. Tseung*

Department of Chemistry, The City University, London ECIV 4PB, United Kingdom

ABSTRACT

Traditional oxygen electrocatalysts do not dissociatively chemisorb oxygen, resulting in electrochemical irreversibility. The joint pseudo-splitting/peroxide mechanism suggests that the main requirement is for the oxygen molecule to be chemisorbed side on: O–O. This condition will be satisfied by paramagnetic oxides, such as high surface area lithiated nickel oxide and $La_{0.5}Sr_{0.5}CoO_3$ perovskite oxide. Such electrodes exhibit steady and reproducible open-circuit potentials which are very near the theoretical values and the variation with oxygen partial pressure follows the Nernst equation for a four-electron process. The current density at constant polarization is directly proportional to the square root of oxygen partial pressure. Homomolecular oxygen studies confirmed that oxygen is dissociatively chemisorbed on such oxides and there is a good correlation between the activation energies for the isotopic exchange and electrochemical reduction of oxygen, suggesting a similar mechanism is involved in each case.

The cathodic reduction of oxygen in alkaline solution

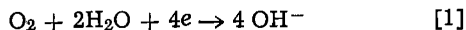

$$O_2 + 2H_2O + 4e \rightarrow 4\,OH^- \quad [1]$$

presents one of the challenging problems in electrochemistry. The standard reduction potential is

$$E^\circ = -0.401V \text{ vs. NHE} \quad [2]$$

resulting in a theoretical H_2/O_2 full cell potential of 1.229V at 25°C. This potential has seldom been achieved in practice and most oxygen electrocatalysts exhibit open-circuit potentials between 0.1 and 0.2V below the reversible value. Rotating ring disk measurements (1) have shown that the oxygen reduction does not go through a direct four-electron process but normally takes place via a HO_2^- intermediate

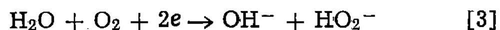

$$H_2O + O_2 + 2e \rightarrow OH^- + HO_2^- \quad [3]$$

This results in a drastic reduction of the open-circuit potential and over-all efficiency. On most catalysts other than carbon, HO_2^- can be further reduced either electrochemically by

$$HO_2^- + H_2O + 2e \rightarrow 3\,OH^- \quad [4]$$

or by direct chemical decomposition of HO_2^-

$$2HO_2^- \rightarrow O_2 + 2\,OH^- \quad [5]$$

Thus three possible routes are available for improving the kinetics of the oxygen reduction process:

(*i*) To speed up the rate of electrochemical reduction of HO_2^-. This is not likely to be fruitful since $HO_2^- \rightarrow 3\,OH^-$ is known to be highly irreversible.

(*ii*) To speed up the rate of chemical decomposition of HO_2^-. This approach has been tackled empirically by many industrial establishments, *e.g.*, the use of spinel oxides and Ag supported on carbon, with some degree of success. Theoretical and experimental studies on the system cobalt iron oxide/graphite by Goldstein and Tseung (2) showed that in order to achieve reversible oxygen electrode potentials, the $[HO_2^-]$ would have to be reduced to 6×10^{-18}M; this would require the peroxide decomposition catalyst to have a rate con-

* Electrochemical Society Active Member.

Key words: oxygen reduction, semiconducting oxides, paramagnetic behavior.

stant of 4×10^6 sec^{-1} g^{-1}. However, the most active cobalt-iron oxide tested, $Co_{2.4}Fe_{0.5}O_4$, the rate constant for peroxide decomposition is only 0.243 sec^{-1} g^{-1}. Pt-black and Ag-black catalysts are only marginally better. Consequently, several orders of magnitude increase in catalyst activity is required to achieve open-circuit potential close to the reversible oxygen potential.

(*iii*) To induce the oxygen reduction process to go directly, by passing the HO_2^- intermediate. Isotopic studies by Davies, Clark, Yeager, and Hovorka (3) showed conclusively that the O = O bond of the oxygen molecule remains unbroken on conversion to peroxide. Thus, the key to the solution of the oxygen electrode problem may lie in the electrocatalyst's ability to dissociatively chemisorb oxygen. If this condition is fulfilled, no HO_2^- intermediate can be formed and the oxygen reduction will go directly to hydroxyl ion via a four-electron process. This approach should be far more rewarding than the first two routes.

The Joint Pseudosplitting-Peroxide Mechanism

The direct splitting of the O = O bond requires 117°K cal/mole. Evans (4) proposed that O_2 molecules are adsorbed "side-on"; O–O, without dissociation, on surfaces covered by adsorbed anions, such as OH^-. The O_2 molecules enter into hydrogen-bonding with OH^- ions and this bonding spreads across the OH^- layer. At certain specific sites, *e.g.*, "kink" sites, there will be discontinuities in the OH^- "carpet" so that for steric reasons, the OH^- ions will be more likely to enter into hydrogen bonding with nearby H_2O molecules of the electrolyte. At this point the O = O bond is effectively broken (pseudo-split). One consequence of such proton-switching is that the activation energy for bond rupture is lowered considerably. Proton-switching is a process which occurs easily, *e.g.*, in the rapid neutralization of acid with alkali or of the great mobility in solution of such species as OH^- or H_3O^+. The four stages of pseudo-splitting are shown in Fig. 1. Goldstein and Tseung (5) proposed that since the reduction of oxygen on most electrocatalysts goes via the peroxide intermediate, it is necessary to consider the case when the oxygen molecule is chemisorbed "end on": O || O. In such cases, the pseudo-splitting process will lead to the formation of HO_2^- as well as OH^- (Fig. 2). It is therefore suggested that a necessary condition for dissociative chemisorption of oxygen is for the oxygen molecule to be adsorbed "side-on" on the electrocatalyst surface.

The Importance of Semiconducting Oxides

Apart from the exceptional cases of selected precious metals at high overpotentials, the oxygen reduction on nonnoble metal alloys or compounds takes place on oxide-covered surfaces. Since it is difficult to control or study the properties of oxide films, it is more convenient and practical to study oxygen reduction on specially prepared oxides. The conductivity of most transition metal oxides can be significantly improved by doping with suitable oxides whose cation is of lower valency than the cation in the host oxide (6). If doped oxide powders are used as Teflon-bonded electrodes supported on metal screens, then the likely ohmic drop due to the use of semiconducting oxide is given by (7)

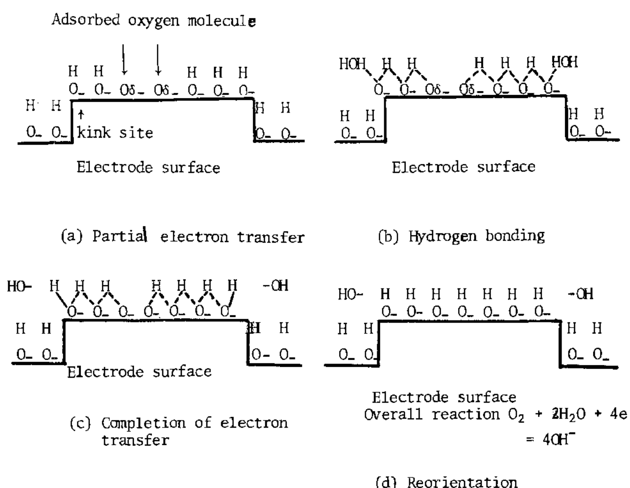

Fig. 1. Stages in pseudo-splitting

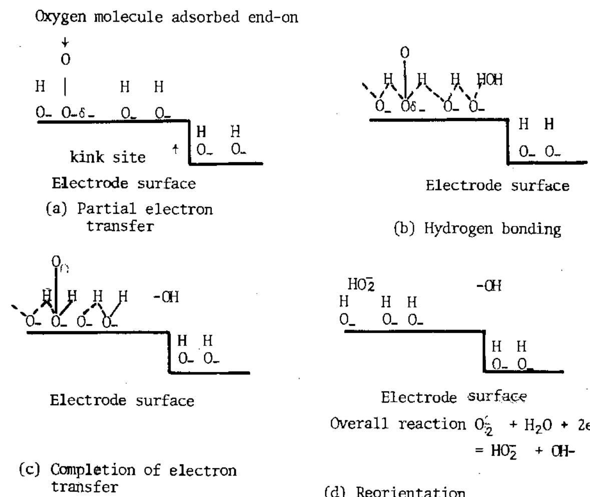

Fig. 2. Stages in the peroxide mechanism

$$IR = \rho \frac{iL^2}{16t}$$

Where I is the total current, amp; R is the total resistance of the electrode, Ω; i, current density, A/cm²; L, length of each side of the square hole in the metal mesh, cm; ρ, resistivity of the catalyst/Teflon layer, Ω cm; t, thickness of catalyst/Teflon layer, cm. Taking the typical case of Teflon-bonded porous electrode supported on 100 mesh metal screen, L is 0.04 cm and t is 0.025 cm. Hence if the catalyst/Teflon layer has a resistivity of 100 Ω cm and operating at 0.5 A/cm², the IR loss will be about 0.2V, which is just acceptable. In actual practice, taking into account the increased resistivity due to the presence of Teflon particles and contact resistance between the catalyst powder, the maximum allowable bulk resistivity of semiconducting oxide used for such applications is limited to 10-15 Ω cm.

Relationship Between the Mode of Oxygen Chemisorption and Magnetic Properties of Semiconducting Oxides

The oxygen molecule is paramagnetic. It has two unpaired electrons with parallel spins in antibonding π orbitals. Therefore, electrons transferred at, or subsequent to, bond-rupture, from the catalyst to the adsorbed oxygen species, must similarly be of parallel spin. This immediately suggests the use of paramagnetic or ferromagnetic oxides. On the other hand, antiferromagnetic compounds, in which cations are arranged with unpaired spins aligned on alternate (111) planes, will not be able to satisfy the above requirement. Lithiated nickel oxide has been studied in far greater detail than any other oxide since it is one of the first doped semiconducting oxides discovered by Verwey *et al.* (6).

Nickel oxide in its normal macroscopic state is antiferromagnetic. It becomes paramagnetic at the Neel point, T_N at 523°K (8). The magnetic transition is associated with a crystallographic transition from rhombohedral to cubic structure (9). Parravano and Boudart (10) found several physical anomalies near the Neel point of NiO. Its significance to catalytic activity was

briefly mentioned by other workers (11-13). Both Keier (14) and Charman, Dell, and Teele (15) noticed that a definite change of mechanism of O_2 chemisorption took place near 250°C. Winter (16), however, was the first to suggest that the change in the mechanism of O_2 chemisorption was attributable to the magnetic transition. He assumed that the chemisorption took place predominantly at exposed edges of magnetic domains. Below T_N, magnetostriction prevents the formation of two Ni^{+++} as adjacent nearest neighbors so that adsorption occurs as O_2^-. Above T_N, the restriction is removed and O_2 can be adsorbed as 2 O^-. Therefore, it would be interesting to observe changes in the electrochemical behavior on passing through the Neel point and, if the changes are favorable, to find methods of reducing the Neel point, or prepare other compounds with lower T_N, which will hopefully exhibit reversibility to O_2 reduction at lower temperatures.

Electrochemical Reduction of Oxygen on Lithiated Nickel Oxide Electrodes

Tseung, Hobbs, and Tantram (17) studied the electrochemical reduction of oxygen on lithiated nickel oxide at 150° and 220°C and found that there was a six-fold improvement in performance at 220°C. The open-circuit potential changed from 1.10 to 1.16V, very close to the theoretical open-circuit potential (75% KOH, 220°C, $E° = 1.17V$). Doping with lithium (18) is known to lower T_N by about 20°C. (Neel point of NiO single crystal is ~250°C). It is, therefore, suggested that oxygen is being dissociatively chemisorbed above the Neel point, thus by-passing the formation of peroxide intermediate, leading to reversible behavior and improved performance.

Richardson and Milligan (19) found a remarkable variation of magnetic susceptibility with specific surface area. As the mean particle size diameter decreased to below 200Å, the magnetic susceptibility curve developed a large peak, the position of which on the temperature axis was so dependent on the particle size diameter that for some powders, values of T_N below room temperature were observed. Cohen *et al.* (20) as well as Kawada and Kawai (21) confirmed the above results and showed that NiO powders with a mean particle size diameter of 130Å exhibited paramagnetism at room temperature. Bevan and Tseung (22) investigated the properties of high surface area lithiated NiO (180 M^2/g) prepared by the Technier method (23) and found that electrodes prepared from such powders exhibited reversible behavior at 150°C instead of 220°C found earlier for low surface area lihiated NiO samples (1-2 M^2/g). The steady-state polarization curves in 75 weight percent KOH are fundamentally different from those obtained previously for any oxygen reduction catalyst: the curve is linear over the whole potential range (Fig. 3). At a given polarization, the current density varies directly with $\sqrt{p_{O_2}}$. The variation of OCV with oxygen partial pressure is also interesting. The slopes in each case are almost exactly equal to $RT/4F \times 1/2.303$ per pressure decade, which suggests very strongly a four-electron over-all reaction. In addition, after cathodic polarization, the electrode potential returned to its original value in less than a minute. A plot of current density *vs.* $1/T$ gave a perfect straight line plot between 140°-250°C indicating that there is no change in mechanism (Fig. 4). The electrode exhibits irreversibility at temperatures below 140°C, even though the Neel point of the sample should be at room temperature (mean particle diameter 49.9Å). Though the mean particle diameter is small, electron microscopic examination confirmed the presence of particles whose diameter is greater than the critical particle diameter suggested by Richardson and Milligan (50 M^2/g, ~ 180Å particle). These large crystallites would be expected to show the normal antiferromagnetic behavior of massive nickel oxide, *i.e.*, Neel point 220°-250°C. These particles will not be able to dissociatively chemisorb oxygen below their Neel point and hence the reduction of oxygen on such particles will involve the production of HO_2^-, giving rise to a mixed potential and irreversible behavior, especially when the temperature is significantly lowered.

Sr-Doped $LaCoO_3$ Perovskite Oxides

The work on lithiated NiO has shown that it is necessary to use semiconducting oxides which are paramagnetic at room temperature, regardless of particle size. The Neel temperatures of the oxides of first row transition metals with rock-salt structure increase in the order Mn, Fe, Co, NiO. Unfortunately, all the oxides other than NiO are not sufficiently corrosion resistant in hot, concentrated KOH to merit consideration. Therefore, attention was concentrated on the perovskite oxides, such as Sr-doped $LaCoO_3$, which has a Neel point at 90°K (24). The Sr doping of $LaCoO_3$ increases the specific conductivity by increasing the number of Co^{3+}/Co^{4+} couples. In addition, the number of trivalent cobalt ions in the high spin state is increased (four unpaired spins per ion). Tseung and Bevan (25) prepared a series of $Sr_xLa_{1-x}CoO_3$ samples by freeze-drying (38 M^2/g). These oxides are corrosion resistant even at 220°C, 75% KOH and the resistivity of the powder is 0.1-1 Ω cm.

Of all the electrodes tested, only $La_{0.5}SrO_{0.5}CoO_3$ that had been leached at 220°C, 75% KOH overnight to remove unreacted free oxides, had open-circuit potential (OCV) approaching the theoretical value. Table I shows the observed value as a function of P_{O_2} at 25°C,

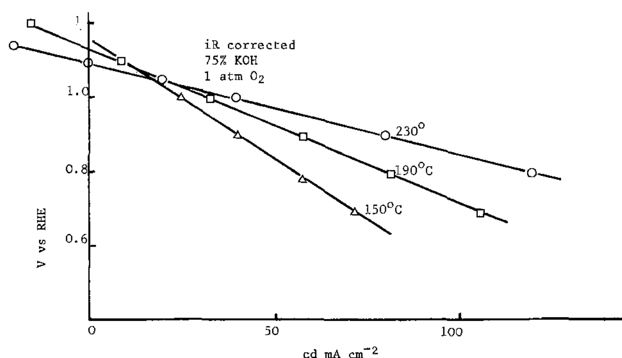

Fig. 3. V-i curves for lithiated NiO (180 M^2/g)

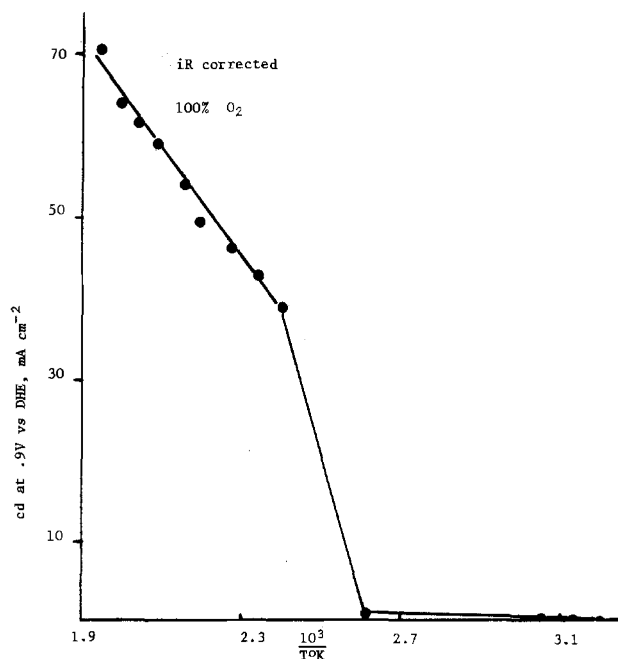

Fig. 4. CD vs. 1/T lithiated NiO (180 M^2/g)

Table I. Variation of OCV of $La_{0.5}Sr_{0.5}CoO_3$ with P_O

Po (%)	OCV *vs.* RHE (mV)	Calculated OVC *vs.* RHE (mV)	Observed shift (mV)	Calculated shift ($RT/4F$) ln P_{O_2} (mV)
100	1250	1247	0	0
21	1240	1237	10	10
14	1238	1234	12	13
5	1233	1228	17	19

45% KOH electrolyte. This shows that the electrode obeys the Nernst equation for a four-electron process and that there is an excellent agreement with calculated values.

Figure 5 shows the current-potential curve of various leached Sr-doped $LaCoO_3$ electrodes as well as a Pt Teflon-bonded electrode at 25°C. It is worth noting that the Sr-doped $LaCoO_3$ electrodes, apart from showing the theoretical OCV, do not change the slope of the current-potential curve on changing from the cathodic to anodic mode or vice versa, again confirming that they are truly reversible. On the other hand, $LaCoO_3$- and Pt-black are not reversible. By plotting the current density at 900 mV *vs.* DHE as a function of temperature, a linear relationship is obtained (Fig. 6). The performance of $La_{0.5}Sr_{0.5}CoO_3$ surpasses that of Pt-black at 170°C.

At first, it was thought that the performance was controlled by the number of "active sites" at the surface which could associate with the absorbed oxygen molecules. At higher temperatures, the lattice expands and the interaction between cations in the bulk and between the bulk and surface cation is reduced. Thus the magnetic susceptibility decreases and the number of active sites is increased. However, recent "oxygen stripping" measurements by Yeung and Tseung (26) showed that the oxygen coverage is independent of temperature and the oxygen coverage is low, about 2-3% of the perovskite oxide surface. A comparison of the steady-state performance and potentiostatic pulse performance of $Nd_{0.5}Sr_{0.5}CoO_3$ and $La_{0.5}Sr_{0.5}CoO_3$ electrodes revealed significant differences in performance,

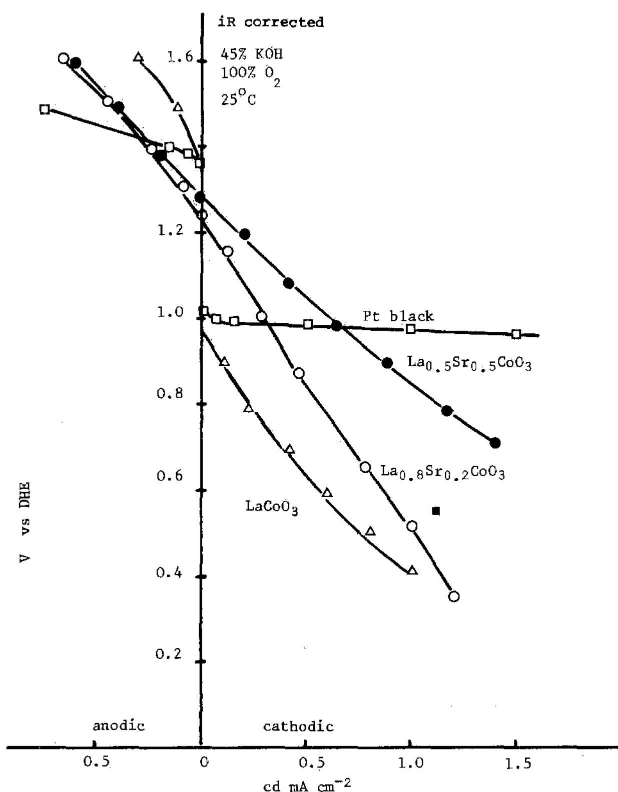

Fig. 5. *V-i* curves for Pt-black and $Sr_xLa_{1-x}CoO_3$ electrodes

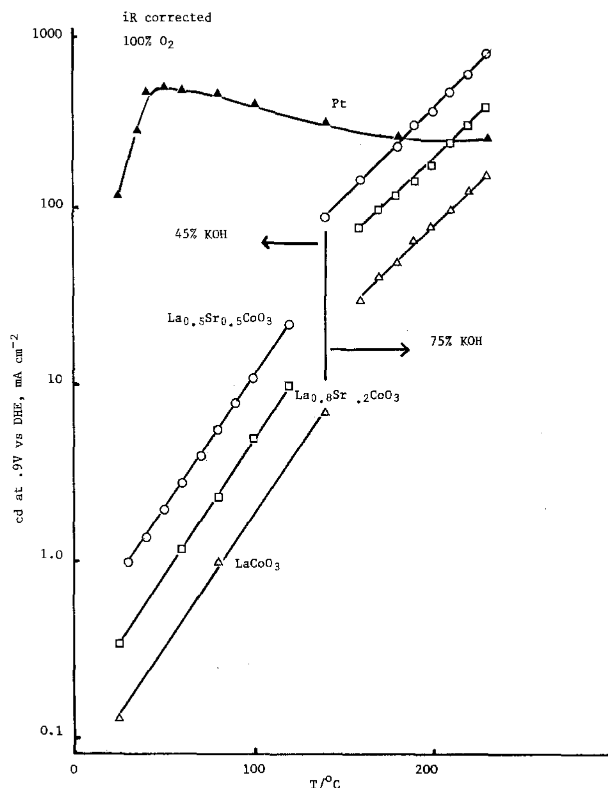

Fig. 6. *CD vs.* temperature

not accountable by mass transfer effects within the Teflon-bonded porous electrodes. The recent results suggest that the rate of oxygen chemisorption might be the controlling factor and further mechanistic investigations in this direction should be very fruitful.

Direct Evidence of Dissociative Oxygen Chemisorption

Up to now, all the electrochemical studies showed that there is a good correlation between the mode of oxygen chemisorption and the magnetic properties of lithiated nickel oxide and $La_{0.5}Sr_{0.5}CoO_3$. Hibbert and Tseung (27), by studying the rate of homomolecular exchange between $^{16}O_2$ and $^{18}O_2$, proved conclusively that oxygen can be dissociatively chemisorbed above the Neel point of lithiated nickel oxide and $La_{0.5}Sr_{0.5}CoO_3$. In addition there is close correlation between the activation energy for the dissociative oxygen chemisorption and electrochemical oxygen reduction, suggesting a similar mechanism is involved in each case.

Suggestions for Future Work

All the evidence obtained during the last ten years points to the importance of magnetic behavior of semiconducting oxides in determining the mode of oxygen chemisorption and, hence, more effort should be devoted to other paramagnetic oxides which satisfy other essential requirements such as specific conductivity and corrosion resistance. Furthermore, there is an urgent need to involve solid-state chemists and physicists to study the nature of the active sites in the paramagnetic oxides and the fundamental factors governing the rate of dissociative oxygen chemisorption (28).

Manuscript submitted Feb. 8, 1978; revised manuscript received May 5, 1978.

Any discussion of this paper will appear in a Discussion Section to be published in the June 1979 JOURNAL. All discussions for the June 1979 Discussion Section should be submitted by Feb. 1, 1979.

REFERENCES

1. Gu Lin-in, N. A. Shumilova, and V. S. Bagotsky, *Electrokhimiya*, 3, 460 (1967).
2. J. R. Goldstein and A. C. C. Tseung, *J. Phys. Chem.*, 76, 3646 (1972).

3. M. Davies, M. Clark, E. Yeager, and F. Hovorka, *This Journal*, **106**, 56 (1959).
4. U. R. Evans, "The Corrosion and Oxidation of Metals," First Supplementary Volume, E. Arnold (1968).
5. J. R. Goldstein and A. C. C. Tseung, *Nature*, **222**, 869 (1969).
6. E. J. W. Verwey and J. H. de Boer, *Recl. Trav. Chim. Pay-Bas*, **115**, 1156 (1959).
7. A. C. C. Tseung, Unpublished results.
8. M. Foex, *Compt. Rend.*, **227**, 193 (1948).
9. H. P. Rooksby, *Acta Crystallog*, **1**, 226 (1948).
10. G. Parravano and M. Boudart, *Adv. Catallogr.*, **7**, 66 (1955).
11. A. Cimino, E. Molinari, and G. Romeo, *Z. Phys. Chem. (Leipzig)*, **83**, 333 (1951).
12. D. Mehandjiev and G. Bliznakov, in Proceedings of Third International Congress on Catalysts, Amsterdam, 1965, p. 781.
13. A. Bielanski and J. Haber, *Z. Phys. Chem. (Leipzig)*, **24**, 345 (1960).
14. N. P. Keier, *Kinet. Katal.* **1**, 221 (1960).
15. H. B. Charman, R. M. Dell, and S. S. Teale, *Trans. Faraday Soc.*, **59**, 453 (1963).
16. E. R. S. Winter, *J. Catal.*, **6**, 35 (1966).
17. A. C. C. Tseung, B. S. Hobbs, and A. D. S. Tantram, *Electrochim. Acta*, **15**, 473 (1970).
18. M. Perakis, J. Wuchner, and G. Parravano, *Compt. Rend.*, **248**, 2306 (1959).
19. J. T. Richardson and W. O. Milligan, *Phys. Rev.*, **102**, 1289 (1956).
20. J. Cohen, K. M. Creer, R. Pauthenet, and K. G. Strivastava, *J. Phys. Soc., Jpn.*, **17**, (Suppl. B-1), 685 (1962).
21. T. Kawada and N. Kawai, *ibid.*, 691.
22. H. L. Bevan and A. C. C. Tseung, *Electrochim. Acta*, **9**, 201 (1974).
23. S. J. Teichner, *Adv. Catal.*, **20**, 167 (1969).
24. R. R. Heikes, R. C. Miller, and R. Mazelsky, *Physica*, **30**, 1600 (1964).
25. A. C. C. Tseung and H. L. Bevan, *Electroanal. Chem. Interfacial Electrochem.*, **45**, 429 (1973).
26. K. L. K. Yeung and A. C. C. Tseung, *This Journal*, **125**, 878 (1978).
27. D. B. Hibbert and A. C. C. Tseung, *ibid.*, **125**, 74 (1978).
28. T. Wolfram, F. J. Morin, and R. Hurst, National Bureau of Standards Special Publication 455, Proceedings of Workshop held at NBS, Gaithersburg, Md., 1976, p. 21.

Quenched-In Bulk Defects and Interface States in MOS Structures Measured by Transient Capacitance Spectroscopy

K. L. Wang*

General Electric Corporate Research and Development, Schenectady, New York 12301

ABSTRACT

The induced defects and interface states in MOS structures as a result of high temperature oxidation are investigated using a transient capacitance technique. Samples after dry oxidation at 1000 C were slowly cooled down to 700°C before pulling out. The densities of traps and interface states were shown to be two to five times lower for the slowly cooled samples than that for the fast cooled ones. The major bulk traps are at $E_c - 0.26$ and $E_c - 0.49$ eV, while the major interface state distribution resides at $E_c - 0.6$ eV. The carrier generation both in the bulk and at the interface is shown to be reduced on slow cooling. The results suggest that the interface states and the bulk traps are the consequence of quenched-in impurities.

The origins of defect states and interface states after a high temperature annealing is a subject of current interests and controversies (1-5). Their effects on the device degradation have been demonstrated. The oxidation-induced stacking faults in some cases have been demonstrated to be responsible for the minority carried generations (dark current in MOS capacitors and charge coupled devices, CCD, and other MOS related devices), while others are not (6, 7). The residual interface states on hydrogen annealing can result in surface generation and recombination. The origins of these interface states are considered as a result of the dangling bonds still present after the hydrogen bond coordination at the interface (8, 9). Others attributed to the effects of oxygen-induced phenomena (10, 11).

The purpose of this paper is to demonstrate that the induced-defect and interface-state densities can be further reduced by slow cooling. The "quenched-in" defects and interface states were measured using a highly sensitive transient capacitance technique (12-14). The effects of these states on carrier generations and gate-controlled diode reverse current characteristics are reported. It is concluded that the residual bulk traps and the interface-state densities may be the consequence of quench-in impurities and stress-induced phenomena and may be reduced through proper fabrication procedures.

* Electrochemical Society Active Member.

Key words: transient capacitance, deep level defects, MOS, interface states.

Experiments

Sample preparations.—Test P-channel FET's were fabricated using a standard Al-gate process (on N-type substrate, $N_D = 1.5 \times 10^{15}$ cm^{-3}). The material used is commercial 4 Ω-cm crystals. The gate oxidation was carried out at 1000°C in dry oxygen followed by He annealing for 1 hr. After the He annealing, type A samples were cooled rapidly by pulling the samples out within a few seconds. Type B samples were cooled very slowly by shutting the furnace down until the sample temperature reached 700°C; the sample was then pulled out of the furnace. The cooling rate is about 0.5°C/min.

Transient capacitance spectroscopy.—The transient capacitance spectra were obtained as described elsewhere (12-14). For the fast cooled samples, the spectra of electron and hole emissions under different pulsing conditions were obtained. From the electron trap spectra when pulsing the gate bias from -6 to $+2$V,

the bulk trap emission and the interface-state emission (a continuous distribution) were calculated. The population of the interface states depends on the gate bias applied. All the interface states throughout the bandgap are populated when biased at +2V and entirely depopulated while at −6V. Thus, when pulsing from −6 to 2V, not only the emission for the interface states above the midgap, but also the emission from some of those states below the midgap can be detected; one obtains the distribution of densities of states (with some of bulk trap interference) from E_C to E_C −0.65 eV showing in the upper curve of Fig. 1. The details as of how to obtain the energy scale can be referred to elsewhere (2, 14). The bulk trap interference can be subtracted when their densities are measured. For convenient comparison purposes, the contributions of the bulk traps are left unsubtracted. The maximum peak signal of the surface-state densities occurs at E_c −0.6 eV. In the interface-state measurements, the bulk trap signal can be minimized by using a small gate bias (2). The doping density ($N_D = 1.5 \times 10^{15}$ cm^{-3}) and the depletion depth under various bias conditions used for calculating the densities of the states can be obtained from the depletion *C-V* curve. Similarly, in the hole trap measurements, one obtains the densities of states from the valence band up to the midgap. In the hole trap measurements, however, the signal mostly comes from the emission of the interface states. Thus, the bulk hole trap interference is small. The lower curve in Fig. 1 shows the interface-state density of slowly cooled samples for later comparison purpose.

When pulsing the gate from −6 to −4V, the interface states throughout the bandgap are depleted all the time. As a result, only the bulk trap emission is detected. Under this condition two distinct peaks, E_1 at E_c −0.26 and E_2 at E_c −0.49 eV, are obtained and illustrated in the upper curve of Fig. 2. Their corresponding capture cross sections are 9×10^{-17} and 3×10^{-16} cm^2, respectively. The energy was determined under the bias condition to avoid the interference from the interface-state signal. In the hole trap measurement, since the space charge depth in inversion cannot be altered by selecting the bias condition, the bulk traps cannot be unambiguously measured. Thus, only the electron bulk traps are illustrated in Fig. 2.

For the slowly cooled samples (type B), the densities of interface and bulk states are calculated similarly, as illustrated in the lower curves of Fig. 1 and 2, respectively. A reduction of the densities of states for the slowly cooled samples are clearly shown in the figures.

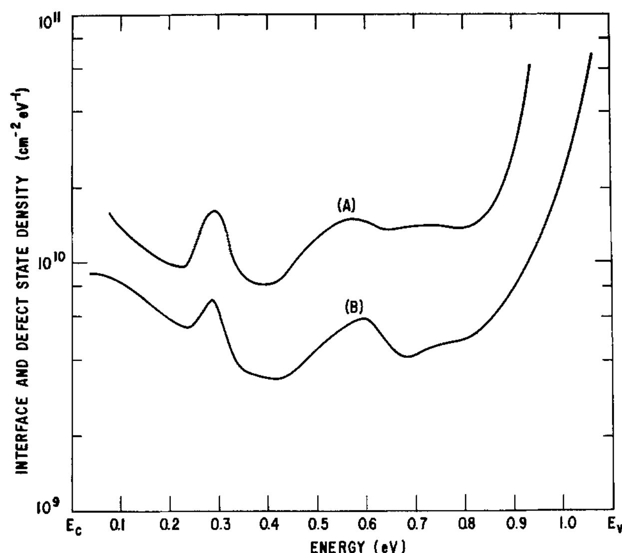

Fig. 1. The upper curve shows the interface state and the bulk trap density in the region from 1.3 μm to the surface for fast cooled samples. The lower curve shows the same density of state distribution for slowly cooled samples.

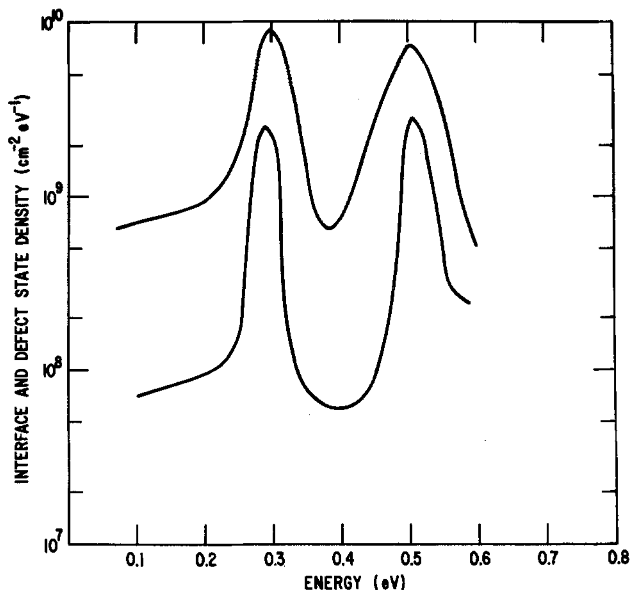

Fig. 2. The upper and lower curves illustrate the bulk traps in the region from 1.3 to 0.5 μm for fast cooled and slowly cooled samples, respectively.

For samples slowly cooled to 700°C when subjecting to a second 1000°C treatment, lower interface-state and bulk trap densities were observed as compared to those for the fast cooled ones. This suggests that the bulk trap and interface states observed bear no relations to the oxidation process per se. It should be noted that the oxygen content in the region of interest (*i.e.*, the space charge depth of 4 μm) is about 2×10^{17} cm^{-3} after the oxidation. This oxygen content depends on the oxidation temperature only, regardless of whether Czochralski material or float zone material is used (15).

Surface generation and bulk carrier lifetime.—To study the interface-state effects to the carrier generation under the gate, the gate-control diode measurements (16) were carried out in the same structures as those used in measuring the transient capacitances. The difference of the surface generation currents for the cases when the surface is depleted and when inverted is obtained as a function of temperatures. The A-type samples (fast cooled) have a higher over-all surface recombination velocity than the slowly cooled samples (B type). The Arrhenius plots of the surface current density for both sample A and B are illustrated in Fig. 3 showing almost identical activation energy, 0.68 and 0.67 eV, respectively. The surface generation current in terms of the surface recombination velocity S_o is

$$J_s \cong S_o(N_v N_c)^{1/2} \exp - (E_g/2 + \Delta E)kT \quad [1]$$

where N_c and N_v represent the densities of states of the conduction and valence bands, respectively. Usually the interface states near the midgap predominate for the surface generation for a uniform distribution (17). The ΔE is a slight deviation to indicate the small increase of activation energy to effectively take the nonuniform interface-state distribution into account. The activation energy appears to suggest that there are high densities of states at below the midgap. It should be stated that the activation energy obtained does not represent the dominant interface-state peak since the generation current is an integral of weighted average. The average is weighted more heavily near the midgap with the exponentials of energy levels in the Hall-Shockley-Read kinetics.

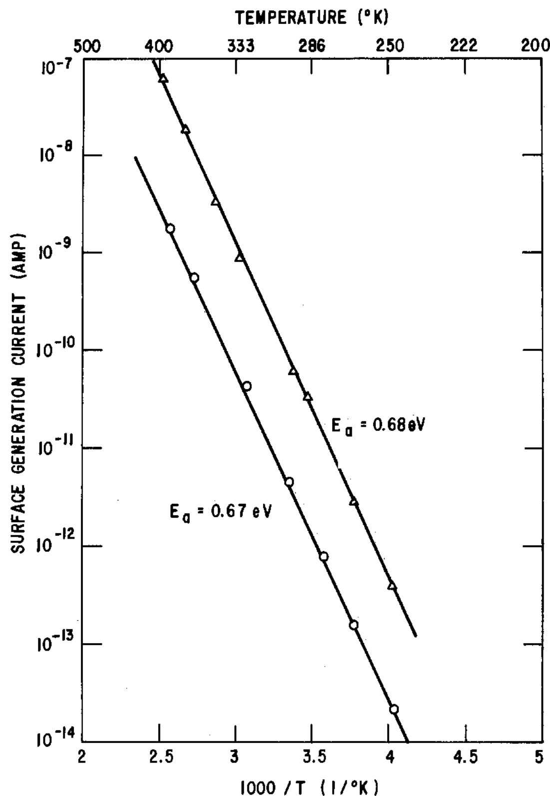

Fig. 3. Surface generation current vs. 1/T. The slowly cooled samples give an activation energy of 0.67 eV, while the fast cooled ones yield 0.68 eV.

The bulk trap effects can be best demonstrated in C-t studies or the Zerbst study (the MOS capacitance vs. the relaxation time from deep depletion to inversion) (18-20). The carrier lifetime was obtained from the slope of $d/dt\ (C_o/C^2)$ vs. (C_F/C^{-1}), where C_o is the oxide capacitance and C_F is the final inversion capacitance. As illustrated in Fig. 4 the carrier lifetime of the slowly cooled samples is longer than that of the fast cooled ones. The surface recombination velocity data in depletion are 0.9-0.2 cm/sec and 0.05-0.02 cm/sec, respectively, for fast and slowly cooled samples. These data are widely scattered in a large range. From the gate-controlled diode experiments, the depletion surface recombination velocity can also be obtained and they are 0.25 and 0.01 cm/sec for the respective samples. The surface recombination velocity near inversion obtained from the intercepts of the Zerbst plots are 6×10^{-3} and 5×10^{-4} cm/sec for fast and slowly cooled samples, respectively. They represent edge surface recombination effects. Because of the small surface recombination velocity for these samples, the surface generation in the depletion region near the circumferential edge of MOS capacitors does not have a significant effect on the values of obtained bulk carrier lifetime (20). In order to determine as to which defect levels control the carrier lifetime, the Zerbst plots and carrier lifetimes were obtained at different temperatures. The Arrhenius plots of the carrier lifetime, illustrated in Fig. 5, show that a different energy level controls the carrier lifetime in different temperature ranges: for relatively low temperatures the activation energy being $E_c - 0.51$ V and for high temperatures the activation energy being $E_c - 0.26$ eV. These activation energies agree with those of the electron emission levels at $E_c - 0.49$ and -0.29 eV as determined from the previously described transient capacitance measurements. The minority carrier lifetime for a two-level system can be expressed as

$$\frac{1}{\tau} = \frac{1}{\tau_1} + \frac{1}{\tau_2}$$

or

$$\frac{1}{\tau} = \sigma_1 N_{t1} \langle v \rangle \exp - (E_1 - E_i)/kT + \sigma_2 N_{t2} \langle v \rangle \exp - (E_2 - E_i)/kT \quad [2]$$

where σ_1 and σ_2 are the capture cross sections for the two levels at $E_c - E_1$ and $E_c - E_2$, respectively; N_{t1} and N_{t2} are the corresponding concentration of defects.

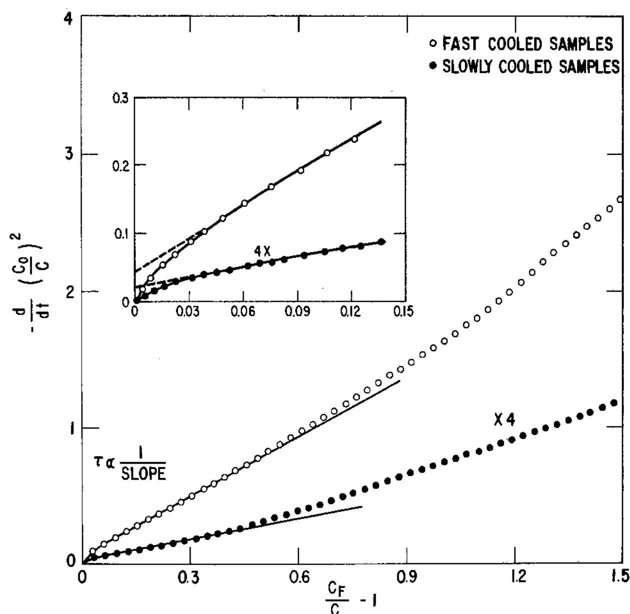

Fig. 4. The Zerbst plots obtained from capacitance vs. time taken from deep depletion to inversion of MOS capacitors. The minority carrier lifetimes for the fast cooled samples (A) and the slowly cooled samples (B) are 44 and 360 μsec, respectively. The inset shows the magnified view of the intercepts which correspond to the surface recombination velocity.

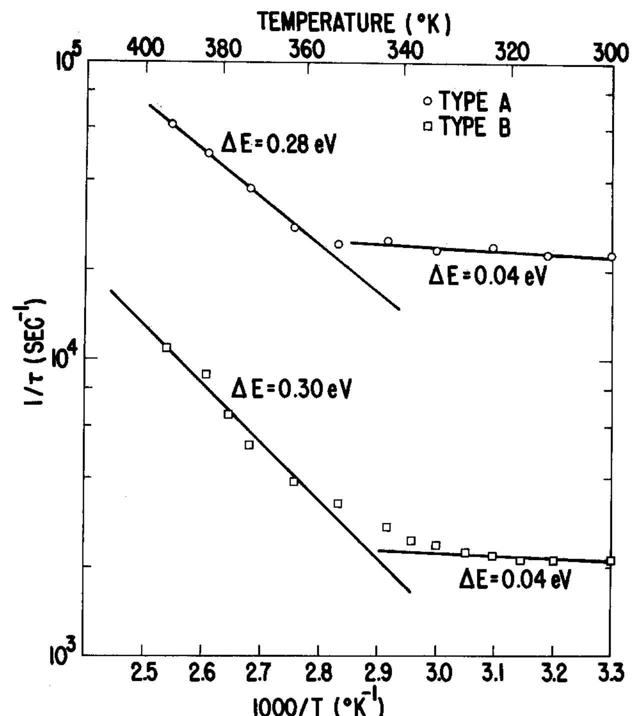

Fig. 5. Reciprocal of minority carrier lifetime vs. 1000/T. The activation energies at low and high temperatures are $E_t - E_i = 0.04$ eV, and $E_t - E_i = 0.29$ eV, respectively, for both kinds of samples. The corresponding energies as measured from the conduction band are $E_c - E_t = 0.51$ and 0.26 eV, respectively.

It is obvious from Eq. [2] that the level near the midgap controls the carrier generation at lower temperatures.

Discussion

The higher bulk trap concentration for the fast cooled samples suggests that these traps are the results of dissolved impurities in the interstitial sites when quenched, *i.e.*, some of them do not have time to precipitate. For example, a recent study for P-type samples by Lee *et al.* (1) shows that upon quenching from high temperatures they observed interstitial Fe° at E_v +0.40 eV in their EPR study. A similar quench study shows defect centers at E_v +0.45 eV and E_v +0.48 eV (5). Collins and Carlson (21) have observed E_c −0.55 eV in Fe-doped material, which is close to the present measured level at E_c −0.49 eV. The present study, however, does not reveal E_v +0.40 eV in the bulk. Furthermore, the defect concentrations measured in the present study are much lower than those of others. This may be in part owing to the result of an anneal carried out at 400°C in H_2 in the present investigation (used for practical MOS device fabrications to reduce interface-state densities). Owing to the lack of comprehensive deep level data, the precise configuration of these defects cannot be identified. It is likely that these presently observed levels are not simple Fe° interstitials but rather are complexes of impurity interstitials.

Similarly the larger interface-state densities for the fast cooled samples imply that the process-induced interface states reported here and by others likely resulted from dissolved impurities. Upon quenching, the dissolved impurities are frozen-in as active centers. Stacking faults may develop as impurities precipitate. The stress induced upon quench can enhance the precipitation of the impurities. The viscosity measurement in oxidized silicon by EerNisse (4) supports that such stress and the consequent strains near the interface are present. Another type of stress in the case of fast cooling has been demonstrated to reveal slips and dislocations and wafer warpage (22). In addition, active stacking faults have been shown to be electrically active responsible for short carrier lifetime using electron beam-induced current mode. The reduction of stacking fault length via HCl gettering during the oxidation process has been demonstrated and the improvement of carrier lifetime has also been reported (23, 24).[1] By slow cooling the strain is likely reduced and, in addition, the dissolved impurities can migrate to other regions to form precipitates.

Thus, the samples after the hydrogen anneal may intrinsically have lower interface-state densities than the values reported to date. In other words, the hydrogen bond coordination may be more effective than what we observed.

The presence of the strains owing to the viscous flow in the $Si\text{-}SiO_2$ structures suggests that all the processing should be carried out below 965°C (4). Moreover, the solid solubility would limit the dissolved impurity level as the processing temperatures are reduced. However such a processing is often too time consuming to be practical. Thus it is suggested to fabricate devices at convenient temperatures and then slowly cool samples down to 700°C, particular for the last high temperature process. By this procedure, the dissolved impurities can precipitate and form inactive complexes. Therefore the bulk traps and interface states can be reduced. The formation of such precipitation depends on the diffusivity of impurities and the strain formation time which, in turn, depends on the cooling rate. For fast diffusers, the cooling rate of the strain formation for $Si\text{-}SiO_2$ structure after the oxidation is a determining factor and estimated to be $1 \sim 2$°C/sec at 965°C (4, 25).

[1] Our recent experiment shows that the activation enthalpy of carrier lifetime improvement, 2.1 eV, suggests that the gettering of Fe may be responsible for it.

Conclusion

In conclusion, the present study has two implications. (*i*) Through a slow cooling from high temperature (1000°C), low bulk trap and interface-states densities can be obtained; and thus the minority carrier generations in MOS structures can be reduced. (*ii*) In addition to the improvement with hydrogen annealing, the interface-state densities can be still further reduced through proper procedures such as slow cooling. This suggests that the reported residual interface-state densities, to date, upon hydrogen anneal may be in part due to the impurities precipitated at near the interface and the hydrogen anneal could be still more effective. The interface-state densities may be further reduced if material impurity and processing induced contaminants are reduced.

Acknowledgments

The author would like to acknowledge the help of P. Pacini and R. Reihl for device fabrication and G. W. Ludwig for the suggestions for the manuscript.

Manuscript submitted Jan. 9, 1978; revised manuscript received May 9, 1978.

Any discussion of this paper will appear in a Discussion Section to be published in the June 1979 JOURNAL. All discussions for the June 1979 Discussion Section should be submitted by Feb. 1, 1979.

Publication costs of this article were assisted by General Electric Corporate Research and Development.

REFERENCES

1. Y. H. Lee, R. L. Kleinhenz, and J. W. Corbett, *Appl. Phys. Lett.*, **31**, 142 (1977).
2. K. L. Wang, in "Semiconductor Silicon 1977," H. R. Huff and E. Sirtl, Editors, p. 404, The Electrochemical Society Softbound Symposium Series, Princeton, N. J. (1977).
3. L. C. Kimerlin, Private communications.
4. E. P. EerNisse, *Appl. Phys. Lett.*, **30**, 290 (1977).
5. J. D. Gerson, L. J. Cheng, and J. W. Corbett, Private communications.
6. R. B. Marcus, M. Robinson, T. T. Sheng, S. E. Haszko, and S. P. Murarka, *This Journal*, **124**, 425 (1977).
7. H. Shiraki, *Jpn. J. Appl. Phys.*, **15**, 1 (1976); S. Mahajan, G. A. Rozgonyi, and D. Brasen, *J. Appl. Phys.*, **30**, 73 (1977).
8. H. Deuling, E. Klausmann, and A. Goetzberger, *Solid-State Electron.*, **15**, 559 (1972).
9. B. E. Deal, *This Journal*, **121**, 198C (1974).
10. W. Fahrnen and A. Goetzberger, in Proceedings of the 2nd International Conference on Ion Implantation in Semi-Conductors, I. Ruge and J. Graul, Editors, p. 373, Springer Verlag, Berlin (1971).
11. A. Goetzberger, E. Klausmann, and M. J. Schulz, in *CRC Rev. Solid State Sciences*, No. 1, (1976).
12. K. L. Wang and A. O. Evwaraye, *J. Appl. Phys.*, **47**, 4574 (1976).
13. K. L. Wang, *Appl. Phys. Lett.*, **29**, 700 (1976).
14. D. V. Lang, *J. Appl. Phys.*, **45**, 3014 (1974).
15. S. M. Hsu, *Appl. Phys. Lett.*, **31**, 53 (1977).
16. A. S. Grove and D. J. Fitzgerald, *Solid-State Electron.*, **9**, 783 (1968).
17. D. J. Fitzgerald and A. S. Grove, *Surface Sci.*, **9**, 347 (1968).
18. M. Zerbst, *Z. Angew. Phys.*, **22**, 30 (1966).
19. D. K. Schroder and J. Guldberg, *Solid-State Electron.*, **14**, 1285 (1971).
20. D. K. Schroder and H. C. Nathanson, *IEEE Trans. Electron Devices*, **ed-19**, 1018 (1972).
21. C. B. Collins and R. O. Carlson, *Phys. Rev.*, **108**, 1409 (1957).
22. A. W. Fisher and G. L. Schnable, *ibid.*, **123**, 434 (1976).
23. H. Shiraki, *Jpn. J. Appl. Phys.*, **15**, 1 (1976).
24. R. S. Ronen and P. H. Robinson, *This Journal*, **119**, 747 (1972).
25. W. Nowack, "Thermoelasticity," p. 549, Pergamon Press (1962).

Gallium Arsenide Films on Tungsten/Graphite Substrates

Shirley S. Chu,* T. L. Chu,* H. T. Yang, and K. H. Hong

Southern Methodist University, Dallas, Texas 75275

ABSTRACT

Gallium arsenide films have been deposited on tungsten/graphite substrates by the reaction of gallium, hydrogen chloride, and arsine in a hydrogen flow system. The effects of substrate temperature and reactant composition on the deposition rate and structural and electrical properties of gallium arsenide films have been investigated, Preliminary work on thin film gallium arsenide solar cells has also been carried out.

The current interest in the terrestrial utilization of solar energy by photovoltaic converters has stimulated considerable research and development efforts in low cost photovoltaic materials and devices. At present, single crystalline silicon solar cells are the best known photovoltaic converters; however, solar cells from some compound semiconductors have distinct advantages. For example, gallium arsenide solar cells have a higher theoretical conversion efficiency than silicon solar cells and can also operate at higher temperatures (1). In addition, gallium arsenide has high optical absorption coefficients near the bandedge, and solar radiation with energy in excess of the energy gap is essentially all absorbed within a few micrometers of the surface. The conversion efficiency of single crystalline gallium arsenide solar cells has been improved substantially during the past few years: the recently reported AM1 efficiencies are about 22% for cells with a gallium aluminum arsenide window and 15% for MIS-type cells (2, 3). Although the cost of single crystalline gallium arsenide is excessive, the use of a thin gallium arsenide film on a suitable substrate could provide a reasonable conversion efficiency and reduce substantially the cost per unit of power.

In the thin film approach, the selection of the substrate is an important consideration. The substrate must be compatible with gallium arsenide in chemical, electrical, and mechanical properties. Graphite is chemically inert toward gallium arsenide under the usual deposition conditions, and several types of graphite have a thermal expansion coefficient similar to that of gallium arsenide. However, the gallium arsenide/graphite interface has been found to exhibit a high electrical resistance, and a tungsten interlayer may be used to reduce the interface resistance to a tolerable level. In this work, gallium arsenide films have been deposited on tungsten/graphite substrates by the reaction of gallium, hydrogen chloride, and arsine in a gas flow system. The microstructure, crystallographic, and electrical properties of gallium arsenide films deposited over a wide range of conditions have been studied, and preliminary work on MIS type solar cells has been carried out. The experimental procedures and results are discussed in this paper.

Deposition of Gallium Arsenide Films

The chemical vapor deposition technique has been used extensively for the homoepitaxial growth of gallium arsenide in various device applications, and the thickness of and dopant concentration in gallium arsenide films can be accurately controlled. A number of chemical reactions have been used for the deposition of gallium arsenide films, including HCl-Ga-As (4), $AsCl_3$-H_2-Ga (5), HCl-Ga-AsH_3 (6), $GaCl_3$-H_2-As (7), and $(CH_3)_3$ Ga-AsH_3 (8). The reaction between gallium, hydrogen chloride, and arsine was selected in this work for convenience. In this process, gallium is maintained in a high temperature zone and the substrate is placed in a lower temperature zone of the deposition system. The chemical reactions are (*i*) the formation of gallium monochloride from gallium and hydrogen chloride in the high temperature zone; and (*ii*) the formation of gallium arsenide from gallium monochloride and arsine on the substrate surface in the lower temperature zone.

The apparatus used for the deposition of gallium arsenide films is shown schematically in Fig. 1. It consists of two parts: a gas flow control system and a fused silica reaction tube. Hydrogen purified by diffusion through a palladium-silver alloy was used as a diluent for the reactant mixture and as a carrier for zinc, the p-type dopant. The flow of various gases such as hydrogen, hydrogen chloride, and the hydrogen-hydrogen sulfide mixture (the n-type dopant) was directed by appropriate valves and measured by flowmeters. The reaction tube was of 55 mm ID and was held in a four-zone resistance-heated furnace with each zone separately heated and controlled; this arrangement allows sufficient flexibility in obtaining the desired temperature profile in the gallium and the substrate zones. A gallium container and the substrate were placed in the appropriate temperature zones of the reaction tube prior to the deposition process.

To evaluate the capability of the gallium arsenide deposition system, single crystalline gallium arsenide slices with main faces of a {100} orientation were first used as substrates for the deposition process. The substrates were etched with a 3:1:1 H_2SO_4:H_2O_2:H_2O solution at about 80°C for 2 min to remove the mechanical damage on the surface and were further etched *in situ* with a hydrogen-hydrogen chloride mixture prior to the deposition process. The temperatures of gallium and the substrate were 880°-890°C and 720°-750°C, respectively. Using hydrogen, hydrogen chloride, and arsine at flow rates of 1-2 l/min, 5-15 ml/min, and 15-45 ml/min, respectively, gallium arsenide films were deposited at rates of 0.5-1 μm/min. They were found to be single crystalline and epitaxial with respect to the substrates by metallographic examinations. The gallium arsenide films deposited without intentional doping were n-type, and those deposited on p-type substrates were used for the measurement of Hall mobility and resistivity at room temperature by

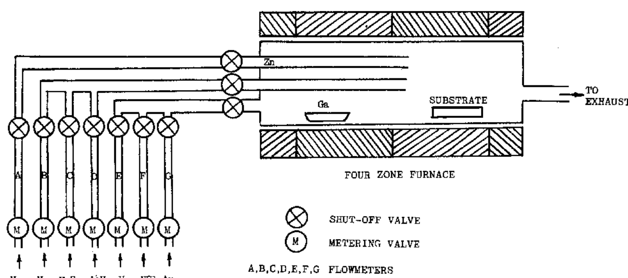

Fig. 1. Schematic diagram of the apparatus for the deposition of gallium arsenide films.

* Electrochemical Society Active Member.

Key words: chemical vapor deposition, gallium arsenide, graphite, solar cells.

the van der Pauw method. Four contacts were made by alloying indium dots to the periphery of the specimen surface at 500°C in a hydrogen atmosphere or by using a gallium-indium alloy annealed at 400°C. The resistivity of typical epitaxial film is 9 Ω-cm at room temperature, and its Hall mobility is 6470 cm^2/V-sec. Neglecting the difference between the Hall mobility and drift mobility, the net carrier concentration is then approximately 1.1×10^{14}. These properties of epitaxial gallium arsenide films are very similar to those reported in the literature, indicating that the gallium arsenide deposition system is satisfactory.

The tungsten/graphite substrates used for the deposition of gallium arsenide films were prepared by depositing a tungsten film of about 5 μm thickness on grade DFP-2 or TAR-2 graphite supplied by Poco Graphite Incorporated. The linear thermal expansion coefficient of these two types of graphite, about 7.5×10^{-6}°C^{-1}, is similar to that of gallium arsenide, 6.8×10^{-6}°C^{-1}. The deposition of tungsten was carried out by the thermal reduction of tungsten hexafluoride with hydrogen using a conventional horizontal reactor. Graphite slices of 3.5 × 3.5 cm area were supported on a graphite susceptor in a fused silica tube of 55 mm ID, and the graphite susceptor was heated externally by an rf generator. Prior to the deposition process, graphite was first heated in hydrogen at 1100°-1200°C to remove the surface contaminations. The deposition rate of tungsten is determined by the substrate temperature and the composition and flow rate of the reactant mixture. Using hydrogen containing 1.5×10^{-2}% tungsten hexafluoride at a flow rate of 20 l/min, the deposition rate of tungsten at 500°C is approximately 1 μm/min. The deposited tungsten films are polycrystalline with an average crystallite size of 1-2 μm and exhibit a strong {100} preferred orientation.

The important process parameters in the deposition of gallium arsenide films are the temperatures of the gallium source and the substrate, and the composition and flow rate of the reactant mixture. A series of experiments were carried out to study the effects of these parameters on the structural and electrical properties of gallium arsenide films on tungsten/graphite substrates. In these experiments, the temperature of gallium, the flow rate of hydrogen, and the flow rate of hydrogen chloride were fixed at 880°-890°C, 1 l/min and 45 ml/min, respectively, and the substrate temperature and the AsH_3/HCl molar ratio were varied in the ranges of 725°-825°C and 0.5-2, respectively.

The thickness of deposited gallium arsenide films was determined by direct measurement on vertical cross-sectioned surfaces in order to determine the average deposition rate. The effect of the reactant composition on the deposition rate of gallium arsenide was pronounced only at the lowest temperature used, 725°C. At 725°C, the average deposition rate was found to increase with increasing AsH_3/HCl molar ratio; it increased from 1.2 to 1.5 μm/min as the AsH_3/HCl molar ratio was increased from 0.5 to 2. At 750°C and above, the average deposition rate is essentially independent of the AsH_3/HCl molar ratio in the range of 0.5-2. These results indicate that the deposition process is surface reaction-controlled at 725°C, and that the reaction rate is not rate limiting at 750°C and higher. At a given reactant composition, the average deposition rate of gallium arsenide peaks at about 750°C, 1.5 μm/min, and decreases with increasing temperature, about 1.2 μm/min at 800°C, for example. The lower deposition rate of gallium arsenide at higher temperatures is related to the thermochemistry of the reaction and is well established (9).

Structural Properties of Gallium Arsenide Films

Gallium arsenide films deposited on tungsten/graphite substrates are all polycrystalline, and the as-deposited surfaces were examined with optical and scanning electron microscopes to determine their microstructure. At substrate temperatures of 725° and 750°C, the average crystallite size in gallium arsenide films increases with increasing arsine concentration in the reactant mixture. For example, the average crystallite size in films deposited at 725°C increased from about 5 to more than 10 μm as the AsH_3/HCl molar ratio was increased from 0.5 to 2. Figures 2A and 2B show the surface of gallium arsenide films deposited on tungsten/graphite substrates at 725°C using AsH_3/HCl molar ratios of 0.5 and 2, respectively, where the effect of AsH_3/HCl molar ratio is apparent. At higher substrate temperatures the AsH_3/HCl molar ratio has no appreciable effects on the crystallite size. At a given AsH_3/HCl molar ratio, the substrate temperature has a pronounced effect on the crystallite size in gallium arsenide films. At a low AsH_3/HCl molar ratio, 0.5-1, the average crystallite size increases with increasing substrate temperature, reaching a maximum at 750°-775°C, and decreases at higher temperatures. Figures 3A and 3B show the surface of gallium arsenide films deposited on tungsten/graphite substrates using a molar ratio of 0.5 at 775° and 825°C, respectively. A comparison of Fig. 2A, 3A, and 3B shows clearly the effect of substrate temperature on crystallite size in

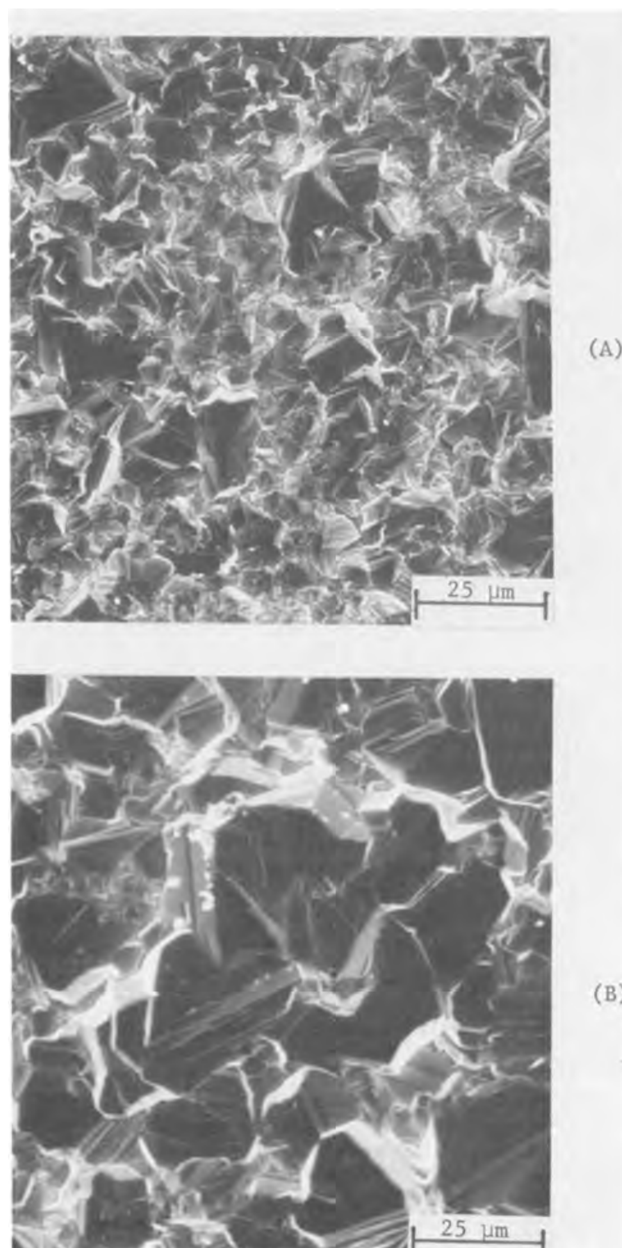

Fig. 2. Scanning electron micrographs of gallium arsenide films deposited on tungsten/graphite substrates at 725°C using AsH_3/HCl molar ratios of (A) 0.5; and (B) 2.

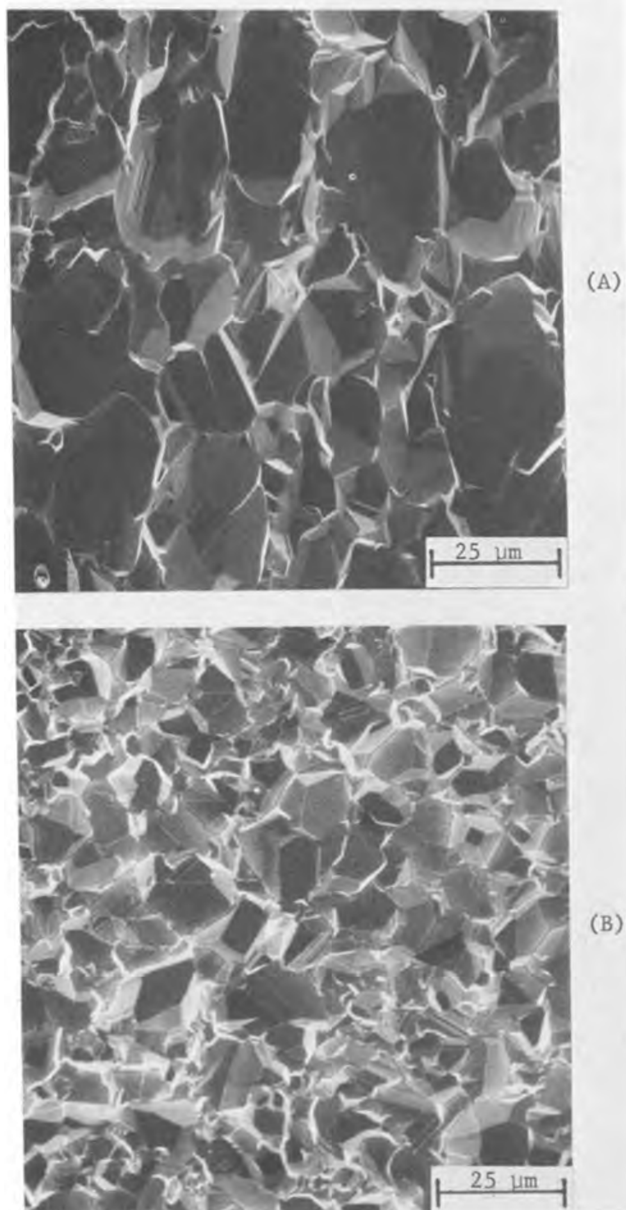

Fig. 3. Scanning electron micrographs of gallium arsenide films deposited on tungsten/graphite substrate using an AsH_3/HCl molar ratio of 0.5 (A) at 775°C; and (B)825°C.

gallium arsenide films deposited at low AsH_3/HCl molar ratios. At high AsH_3/HCl molar ratios, 2, for example, the average crystallite size is essentially independent of temperature in the range 725°775°C and decreases at higher temperatures. The crystallites in all films are of random shape and exhibit no well-developed faces.

The crystallographic properties of gallium arsenide films deposited on tungsten/graphite substrates were examined by the x-ray diffraction technique using a General Electric Model XRD-6 diffractometer with CuKα radiation. Polycrystalline gallium arsenide powder of random orientations is known to show three strong diffraction peaks associated with {111}, {220}, and {311} reflections with 2θ values of 27.3°, 45.3°, and 53.8° and relative intensities of 100, 35, and 35 (9). The diffraction spectra of the gallium arsenide films were obtained by scanning 2θ in the range of 20°-60°. When the gallium arsenide film was deposited at 725°C, the relative intensities of {111}, {220}, and {311} were found to depend strongly on the AsH_3/HCl molar ratio in the reactant mixture. Figures 4A and 4B show the diffraction spectra of gallium arsenide films deposited by using AsH_3/HCl molar ratios of 0.5 and 2, respectively. While the film deposited with a low AsH_3/HCl molar ratio shows a strong {110} preferred orientation, that deposited at a high AsH_3/HCl molar ratio shows a {111} preferred orientation. At higher substrate temperatures, no significant preferred orientations were observed, and the deposited films are essentially polycrystalline. Figure 4C shows the diffraction spectrum of a gallium arsenide film deposited at 775°C. The lack of preferred orientations in gallium arsenide films deposited at high temperatures is presumably due to local chemical transport associated with the chemical reversibility of the deposition reaction.

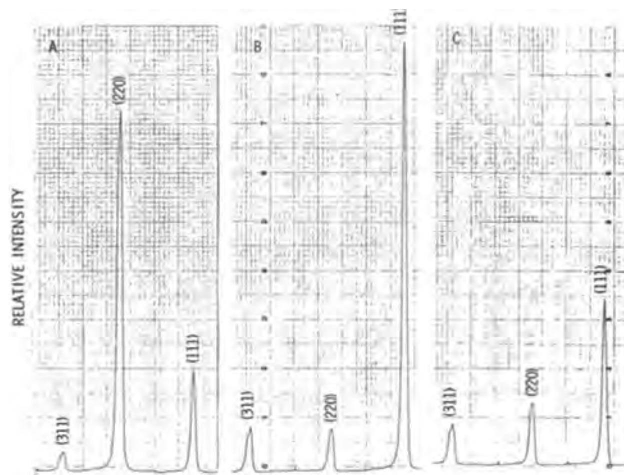

Fig. 4. X-ray diffraction spectra of gallium arsenide films deposited on tungsten/graphite substrates (A) at 725°C and an AsH_3/HCl molar ratio of 0.5; (B) at 725°C and an AsH_3/HCl molar ratio of 2; and (C) at 775°C and an AsH_3/HCl molar ratio of 2.

Carrier Concentration in Gallium Arsenide Films

Gallium arsenide films deposited on tungsten/graphite substrates without intentional doping are all n-type. The carrier concentrations in these films were determined at room temperature by the differential capacitance method. An array of sixteen silver dots of about 0.5 mm diam, 6-7 mm apart were evaporated onto each gallium arsenide film through a metal mask. The capacitance of these Schottky barriers was measured as a function of the reverse bias, and the dopant concentration in the gallium arsenide film under each Schottky barrier was calculated from the specific differential capacitance. The average dopant concentration and its standard deviation in each gallium arsenide film was then deduced from the dopant concentrations calculated from the sixteen Schottky barriers. The results are shown in Table I (no meaningful data were obtained for gallium arsenide films deposited on tungsten/graphite at 725°C because of the nonohmic interface). The carrier concentration in each gallium arsenide film is generally uniform within 50%. At a substrate temperature of 750°C, the carrier concentration is essentially independent of the reactant composition. At higher temperatures, however, the carrier concentration increases with decreasing AsH_3/HCl molar ratio.

While the carrier concentration in undoped homoepitaxial gallium arsenide films is approximately 10^{14} cm^{-3}, the carrier concentration in gallium arsenide films on tungsten/graphite substrates is two to three

Table I. Carrier concentration in gallium arsenide films ($\times 10^{-16}$)

AsH_3/HCl Temp., °C	0.5	1.0	1.5	2.0
750	7.8 ± 2	13 ± 6.5	11 ± 1.4	9 ± 0.9
775	7.5 ± 2	5.3 ± 1.8	3.8 ± 0.7	2.3 ± 0.2
800	30 ± 14	12 ± 1.7	8 ± 1.4	7.2 ± 1.6

orders of magnitude higher. This high carrier concentration could be due to the incorporation of tungsten or impurities in tungsten into gallium arsenide films, and gallium arsenide films deposited on substrates with tungsten coating on both sides have higher carrier concentrations.

Minority Carrier Diffusion Length

The minority carrier diffusion length in gallium arsenide films deposited on tungsten/graphite substrates was measured by a photoresponse technique (10). The apparatus consists of a source of monochromatic light, a light detector with known spectral response, and a lock-in amplifier for measuring the photoresponse. A Schottky barrier solar cell was made on the gallium arsenide film under test by evaporating a silver or gold film of 60-70Å thickness and a metal grid contact. The spectral response of the cell was measured at 7000 and 7500Å. The ratio of the measured responses is related to the minority carrier diffusion length in the gallium arsenide film. By comparing this ratio with the ratios calculated as a function of diffusion length for materials of the same dopant concentration, the diffusion length in the gallium arsenide film can be deduced. Most of the gallium arsenide films were found to have a diffusion length of 0.2-0.4 μm.

Solar Cell Characteristics

Preliminary work has been carried out to prepare Schottky barrier solar cells from gallium arsenide films deposited on tungsten/graphite substrates. They were n-type with a net carrier concentration of about 10^{17} cm^{-3}. A gold film of 60-70Å thickness was evaporated onto the surface of the gallium arsenide film under a pressure of less than 10^{-6} Torr. The silver grid contact was also formed by evaporation through a mask. Because of the large surface area of gallium arsenide films, a thin oxide interlayer is probably present.

The current-voltage characteristics of several solar cells were measured at room temperature under illumination with ELH quartz-halogen lamps calibrated with a standard silicon cell at AM1 conditions. Conversion efficiencies of up to 3% have been obtained. An example is shown in Fig. 5, where the characteristics of a solar cell of about 8 cm^2 area are reproduced. The open-circuit voltage, short-circuit current density, and fill factor are 456 mV, 10.4 mA/cm^2, and 59%, respectively, corresponding to an AM1 efficiency of about 2.8%. This efficiency can be increased substantially by the optimization of the gallium arsenide film and the solar cell configuration and the application of antireflecting coatings.

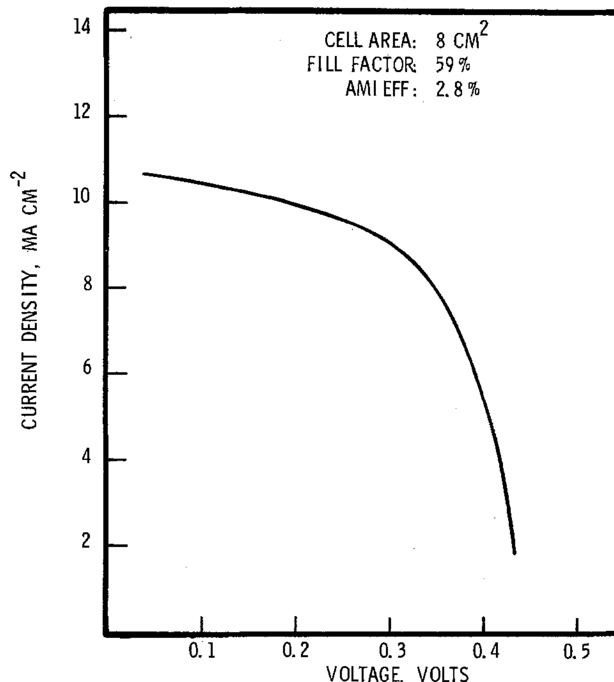

Fig. 5. Current-voltage characteristics of a thin film gallium arsenide Schottky barrier solar cell under illumination with ELH quartz-halogen lamps equivalent to AM1 conditions.

Summary and Conclusions

Tungsten-coated graphite is a suitable substrate for the deposition of gallium arsenide films by the reaction of gallium, hydrogen chloride, and arsine. The structural properties of and the carrier concentration in the gallium arsenide films are affected by the substrate temperature and reactant composition. Films deposited at 775°C using a high AsH_3/HCl molar ratio have relatively large crystallites (about 15 μm), however, the crystallites are random shaped and exhibit no strong preferred orientation. Gallium arsenide films on tungsten/graphite substrates appear to be promising for the fabrication of solar cells; the fabrication technique is simple and involves no wet chemical processing.

Manuscript submitted Sept. 19, 1977; revised manuscript received May 23, 1978. This was Paper 101 presented at the Philadelphia, Pennsylvania, Meeting of the Society, May 8-13, 1977.

Any discussion of this paper will appear in a Discussion Section to be published in the June 1979 JOURNAL. All discussions for the June 1979 Discussion Section should be submitted by Feb. 1, 1979.

Publication costs of this article were assisted by Southern Methodist University.

REFERENCES

1. J. J. Loferski, *J. Appl. Phys.*, **27**, 777 (1956).
2. J. M. Woodall and H. J. Hovel, *Appl. Phys. Lett.*, **30**, 492 (1977).
3. R. J. Stirn and Y. M. Yeh, *IEEE Trans. Electron Devices*, **ed-24**, 476 (1977).
4. S. W. Ing and H. T. Minden, *This Journal*, **109**, 995 (1962).
5. J. R. Knight, D. Effer, and P. R. Evans, *Solid-State Electron.*, **8**, 178 (1965).
6. J. J. Tietjen and J. A. Amick, *This Journal*, **113**, 724 (1966).
7. M. Rubenstein and E. Myers, *ibid.*, **113**, 365 (1966).
8. P. Rai-Choudhury, *ibid.*, **116**, 1745 (1969).
9. D. W. Shaw, *ibid.*, **115**, 405 (1968).
10. G. Giesecke and H. Pfister, *Acta Cryst.*, **11**, 369 (1958).
11. H. J. Hovel, in Conf. Record, 12th IEEE Photovoltaic Specialists Conf., p. 913, Baton Rouge, Louisiana, Nov. 1976.

Spreading Resistance Measurements on Gallium Arsenide

G. Queirolo

SGS/ATES Componenti Elettronici S.p.A., Castelletto di Settimo Milanese, Milano, Italy

ABSTRACT

Spreading resistance measurements were performed on p- and n-type gallium arsenide slices and Zn-diffused GaAs. In a very short time the method gives information on starting material resistivity and resistivity inhomogeneities and makes it possible to obtain carrier concentration profiles of diffused layers which are in a fairly good agreement with the ones obtained with incremental sheet resistivity and Hall measurements. Concentrations in excess of $\sim 5 \times 10^{17}$ (n-type) and $\sim 1 \times 10^{17}$ (p-type) can be routinely measured.

Spreading resistance measurement is a well-known and accepted method for the evaluation of diffused or epitaxial silicon layers (1); it is, in fact, currently used in production plants to measure the resistivity and the thickness of multiple epitaxial silicon layers, and as unique feedback for the control of dopant flows in epitaxial reactors.

Very few results are so far reported on spreading resistance measurements on gallium arsenide (2). Due to the high contact resistance, the carrier concentration of GaAs slices and/or dopant profiles in diffused layers are evaluated with the van der Pauw method (3) which requires the fabrication of 4Ω contact at the edge of the sample and a very time-consuming measurement schedule. Successful spreading resistance evaluation of GaAs was recently reported by the author (4); the method is now routinely used in SGS/ATES as a process monitor in the production of diffused LED.

Experimental Techniques and Results

Sample preparation and SR measurements.—The spreading resistance (SR) was measured on a commercial two-point probe system (Automatic Spreading Resistance Probe ASR-100B) with 5 mV supply between the two preconditioned tungsten-osmium probes with 40g load.

Careful sample preparation is necessary to obtain reproducible quantitative SR values on gallium arsenide: Our results show that the sample surface must be as uniformly damaged as possible, and the thin oxide film which grows on GaAs at room temperature must be removed.

Several different grain-size aluminum oxide powders and the polishing and angle lapping processes were studied. Finally, two sizes of Al_2O_3 were selected, *viz.* 0.3 μm and 5.0 μm. The abrasive was diluted with DI water at a concentration of ~200 g/liter and the sample, mounted on a bevel mount of the ASR-100B, was lapped with a 12 in. Lapmaster machine equipped with a glass plate and a slurry recirculating system. Enough lapping compound was used to avoid direct contact with the glass plate which would result in scratches or other disuniformity in surface finish.

The reproducibility of the SR values was studied in detail for the two abrasives: five p-type GaAs samples, Zn doped with a concentration ranging from 1×10^{17} to 4×10^{19} cm^{-3} were measured after several lapping steps, with or without removing the thin layer of oxide. Some typical results for p-type GaAs, $N_A = 3.5 \times 10^{18}$ cm^{-3} are reported in Fig. 1a and 1b: the R_S values increase after aging in air at room temperature and decrease at or below the original value after a 2 ft ÷ 4 min etch in HCl:H_2O 1:1 solution or a 5 min etch in straight (40%) HF. The oxide thickness was measured by means of Auger electron spectrometry, and was found to be greater for aged than for etched samples (about 50 and 15Å, respectively).

This result explains why the scattering of the experimental points is much greater for aged than for etched samples, as reported in Fig. 2a and 2b. From the same figure it is also evident that the uniformity of the R_S measurements on a given sample is much better for samples lapped with 0.3 μm abrasive. The R_S mean value is nevertheless more reproducible for coarser abrasive, as indicated from bars in the calibration curves of Fig. 3 and 4, possibly due to the failure to obtain a reproducible mechanical damage for the

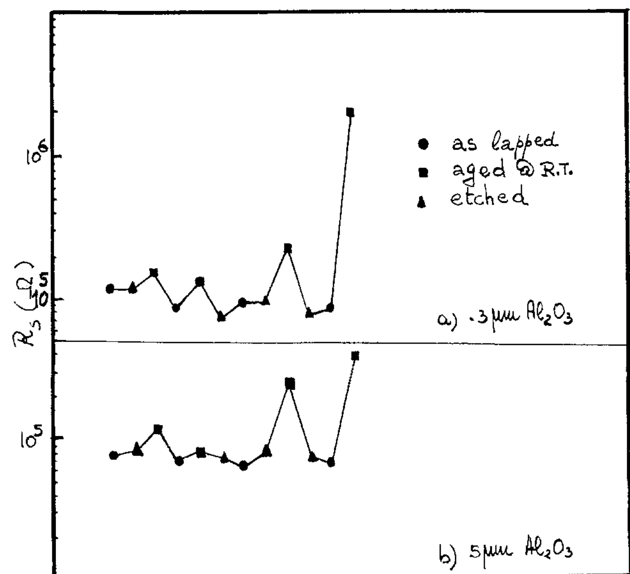

Fig. 1. Spreading resistance value for p-type GaAs, $N_A = 3.5 \times 10^{18}$ cm^{-3}, after various treatments.

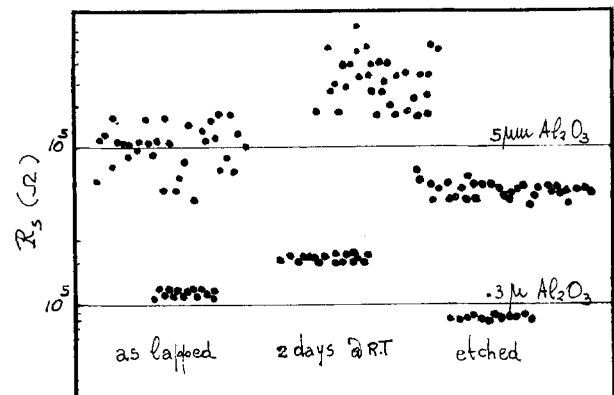

Fig. 2. Scattering of R_S values for a lapped, aged, and etched (5 min HCl:H_2O 1:1) sample ($N_A = 3.5 \times 10^{18}$ cm^{-3}).

Key words: spreading resistance, gallium arsenide, diffusion profiles, dopant concentration uniformity, contact resistance.

finer abrasive unless particular care is taken (*e.g.*, absence of scratches, scratches not detectable by visual observation, but only in SEM in cathodoluminescence mode) (5).

The metal-semiconductor contact.—A GaAs sample (n-type, Si doped at 2.9×10^{18} atoms/cm^3, horizontally Bridgman grown) was soldered to a bevel mount with a GaIn alloy and angle lapped. The value of the resistance offered by a single probe was measured as a function of the applied voltage between +50 and −50 mV, and a linear relationship was found. The $R_{s\pm}$ values obtained with the standard ±5 mV bias are the same for the two probes, and exactly half of the values of R_s are measured between the two probes.

The value of R_s is given by (6)

$$R_s = k(\rho/2a) + 2R_c \quad \text{(2 probes configuration)} \qquad [1]$$

where ρ is the sample resistivity, a is the contact radius, k is a constant not very different from unity which is a function of the nature of the sample, and R_c is the "true" contact resistance.

The first term of Eq. [1] is expected to be approximatively the same for two semiconductors of the same resistivity, apart from small variations on the constant k and the contact radius a. Nevertheless, our results show that for the same ρ and sample preparation process, the R_s value is from 3 to 6 orders of magnitude greater for GaAs than for silicon, depending on the conductivity type and the actual value of resistivity. Moreover, for silicon the contact resistance R_c is very low, and we can write

$$R_s(\text{Si}) \simeq k(\rho/2a); \quad R_c(\text{Si}) << k(\rho/2a)$$

On the contrary, for gallium arsenide

$$R_s(\text{GaAs}) >> R_s(\text{Si}) \simeq k(\rho/2a)$$

and

$$R_s(\text{GaAs}) \simeq 2R_c(\text{GaAs}) \qquad [2]$$

Hence the measure of the spreading resistance R_s on GaAs is actually a measure of the contact resistance, which is, in turn, a function of the carrier concentration (7). Separation of contact resistance from the spreading resistance was attempted using the a-c method of Wagner and Besocke (8), but no result was obtained, possibly due to the very small contact capacitance. The mechanical damage and the high pressure on the contact (9) lower the RC to a measurable value, but any damage inhomogeneities will be reflected in R_s measurements, which will be more reproducible on samples lapped with 5 μm abrasive due to more reproducible mechanical damage. Moreover, we can expect a dramatic increase of R_s value if the native oxide is not removed before the measurement.

On the basis of this result, routine work is done with the coarser abrasive, while the finer abrasive is used only when a good spatial resolution is required as in profiling thin diffused layers.

To convert R_s data to carrier concentration data, calibration curves were generated by measuring both p- and n-type GaAs slices of known resistivity with the two surface finishes studied in this work. Results are shown in Fig. 3 (p-type, 0.3 μm abrasive), Fig. 4 (p-type, 5 μm abrasive), and Fig. 5 (n-type, 0.3 μm and 5 μm abrasive, curves a and b, respectively). Note that the finer abrasive gives lower R_s values than the coarser one on n-type samples, whereas the reverse is true on p-type samples. It is difficult to explain this result due to the state-of-the-art of spreading resistance measurements, especially on GaAs, but it may be that the acceptor or donor center, the dislocation that is known to be in silicon, can be taken into account. These curves make it possible to extract quantitative information from the spreading resistance measurements, as reported in the application section below.

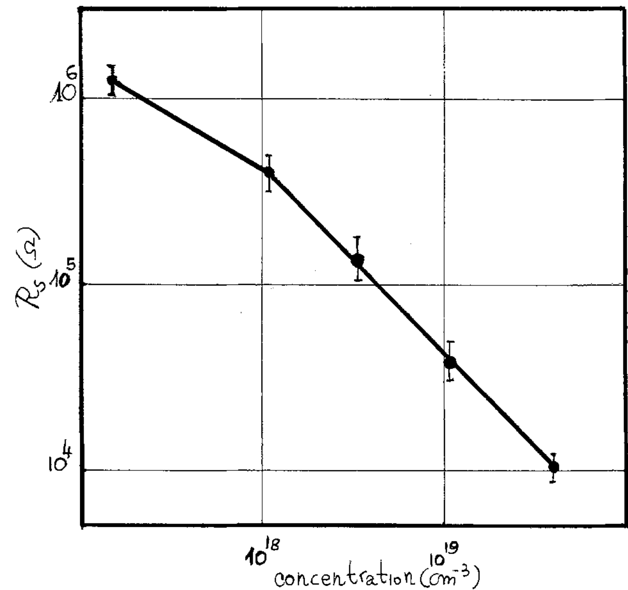

Fig. 3. Calibration curve (R_s vs N_A) for p-type GaAs lapped with 0.3 μm Al_2O_3.

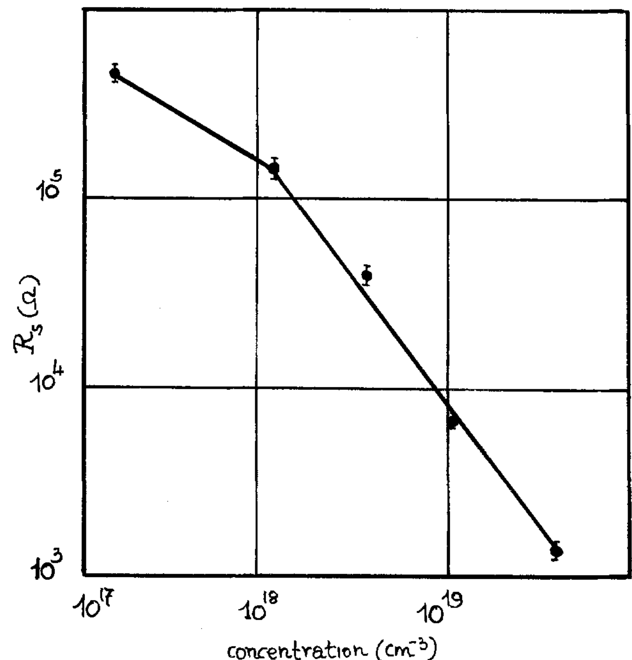

Fig. 4. Calibration curve (R_s v N_A) for p-type GaAs, lapped with 5 μm Al_2O_3.

Applications

Starting material uniformity.—The resistivity uniformity of a few GaAs slices was tested by scanning the probes across the surface. Two kinds of disuniformity were found which are described in Fig. 6.

(*i*) In some slices, a step variation on R_s values was found (Fig. 6a). This was also detected measuring the plasma resonance frequency in far IR reflectance experiments, but, of course, with much less spatial resolution.

(*ii*) Starting from the upper edge of the slice, which is also the free surface of the growing crystal, we often found an increase of a factor of ~2 in the R_s value (Fig. 6b), possibly due to some As evaporation. In this case the edge-correction factor cannot explain the result, due to the very high spatial resolution of the method (see also the following section) and the width of the transition region (~5 mm).

Concentration profiles.—For low contact resistance the spreading resistance value R_s is given by Eq. [1]

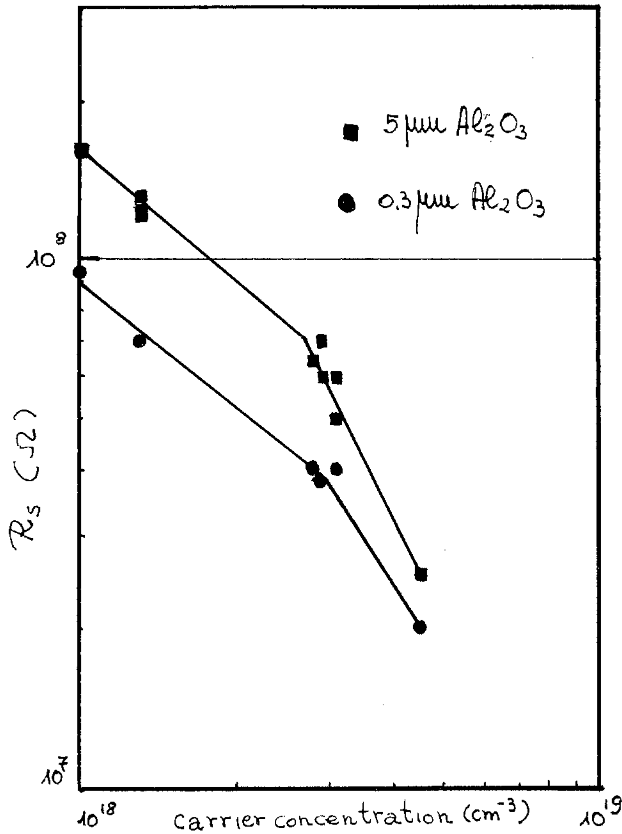

Fig. 5. Calibration curve (R_s vs N_D) for n-type GaAs

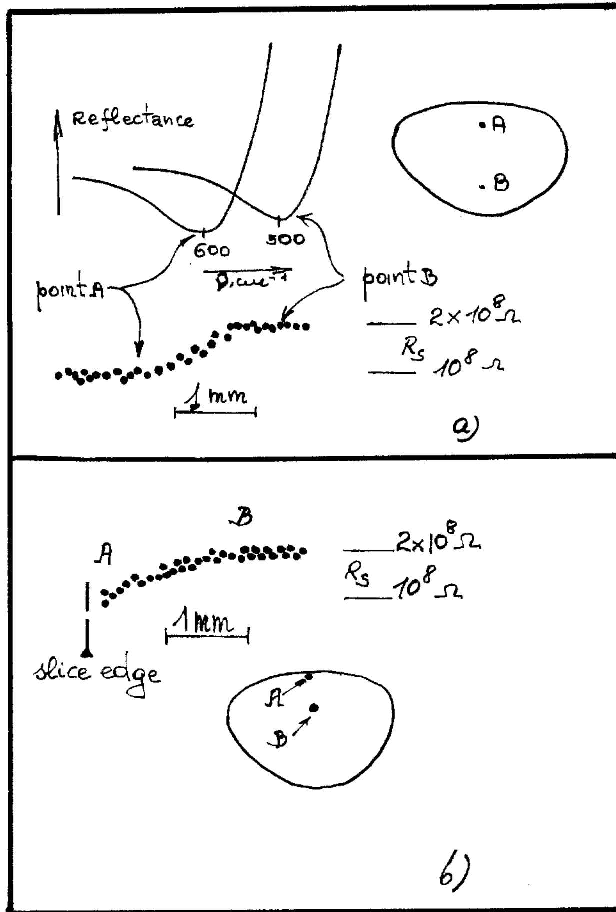

Fig. 6. Doping inhomogeneities on an n-type GaAs slice ($N_D \simeq 1.5 \times 10^{18}$).

only in the semi-infinite approximation, *i.e.*, when the sample thickness is much greater than the contact radius (6). It is necessary to apply some correction to the raw R_s data if a conducting or insulating boundary is present at a distance of less than 10 μm; in particular an R_s profile in a silicon-diffused or epitaxial layer will be distorted near the junction.

This effect should not be observed in gallium arsenide if the theory of the probe-semiconductor contact given here is correct. This was tested by evaluating a $p^+ - \nu$ double layer grown by LPE on an n-type GaAs substrate. The resulting profile shown in Fig. 7, is very flat on the doped epitaxial layer, and the transition to the high resistivity layer is very abrupt.

Figure 8 reports the R_s profile on a multiple layer epitaxial structure on which the bars indicate the position of the interfaces as determined after the bevel staining. Also in this case the R_s value is noticeably constant on a given epi layer with an abrupt transition between two layers.

This is a very interesting result because it allows us to deduce concentration profiles directly from spreading resistance data and calibration curves. A few examples of R_s and concentration profiles determined from R_s data and calibration curves in Zn-diffused GaAs are shown in Fig. 9 ($ZnAs_2$ source) and Fig. 10 (ZnGaAs source).

In Fig. 11 a profile obtained from R_s data is compared with the concentration profile obtained from the values of ρ_s (x) measured with the van der Pauw

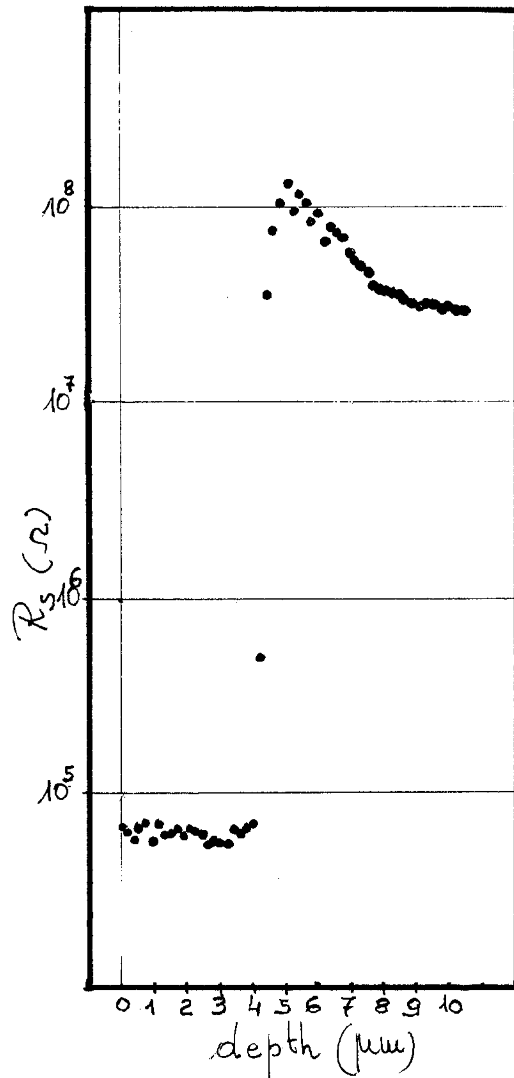

Fig. 7. R_s profile through a double epitaxial layer, grown by LPE. Note the very abrupt transition between the p-type and the undoped layer. Lapped with 0.3 μm Al_2O_3.

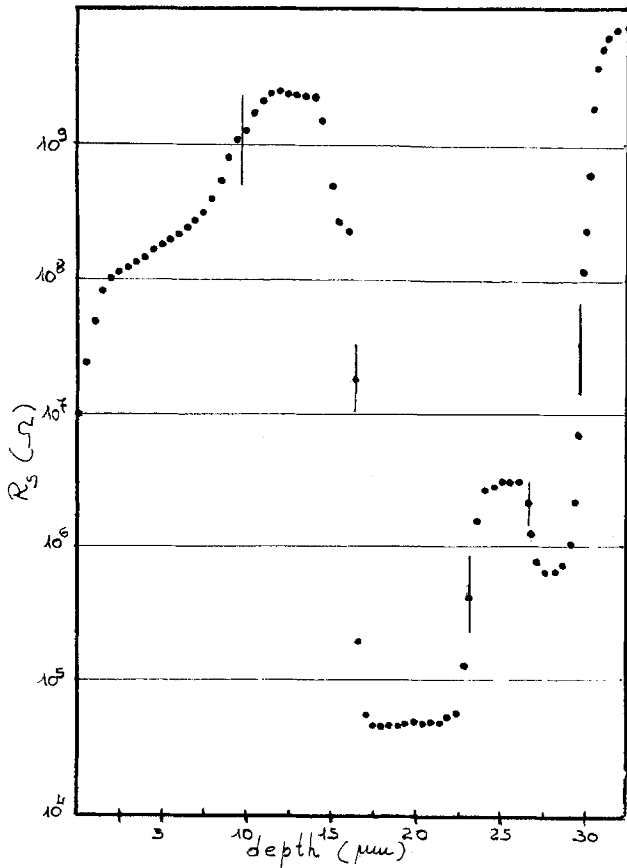

Fig. 8. Multiple epitaxial layer grown by LPE. The bars indicated the junction position, as delineated with a chemical etch. Lapped with 0.3 μm Al_2O_3.

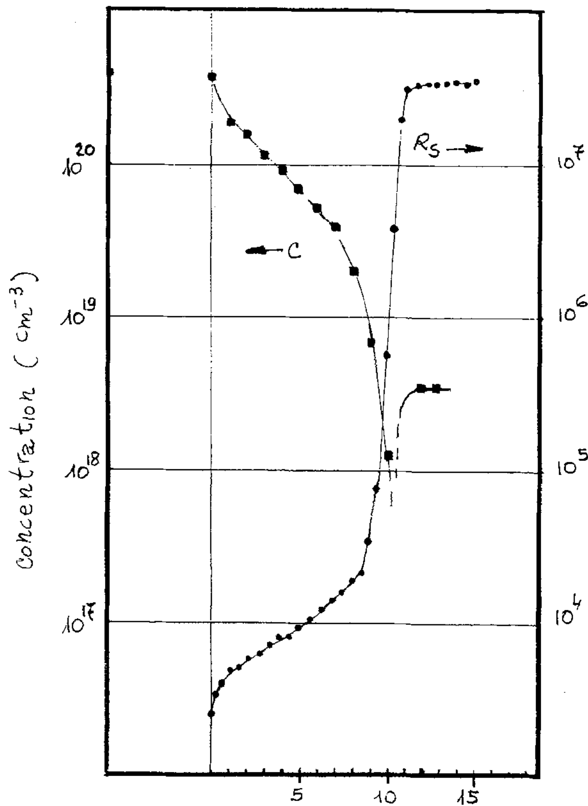

Fig. 9. R_s and concentration profiles for a Zn-diffused GaAs slice (1hr in a 850°C closed tube, $GaAs_2$ source). Lapped with 0.3 μm Al_2O_3.

method. The two curves were normalized to the same junction depth. The error bars are the same as the

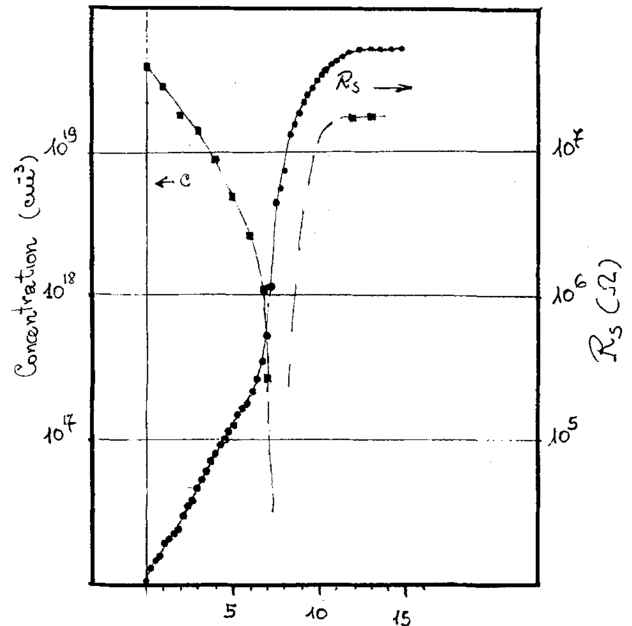

Fig. 10. R_s and concentration profiles for a Zn-diffused GaAs slice (1 hr in a 850°C closed tube, GaAsZn source). Lapped with 0.3 μm Al_2O_3.

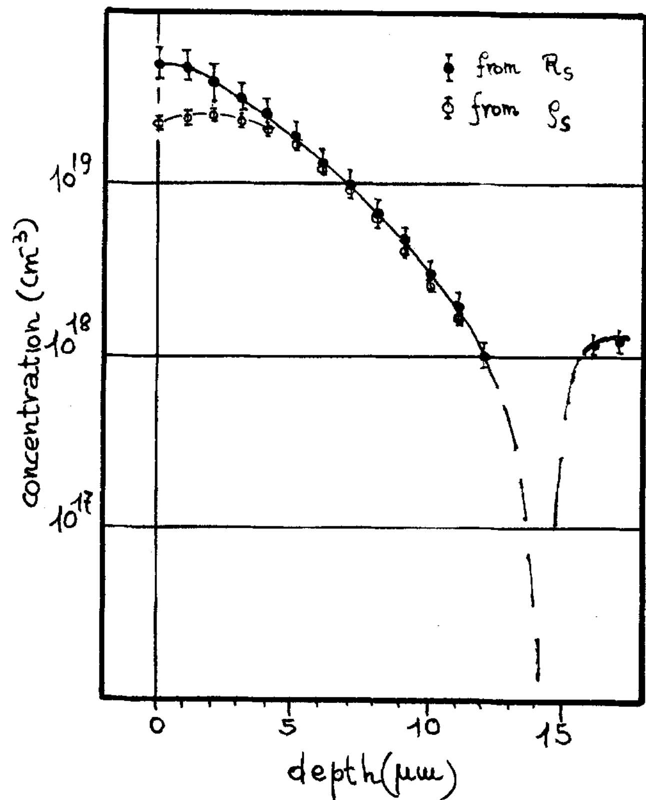

Fig. 11. Concentration profile of a Zn-diffused GaAs slice, as obtained from spreading resistance data (0.3 μm Al_2O_3, full circles) and from incremental sheet resistance measurements (open circles).

calibration curve of Fig. 3 for the R_s-derived profile and were estimated from experimental accuracies for ρ_s-derived profiles. At the moment it is not clear why the first points in the latter profile are lower.

The agreement between the two profiles is quite good and it makes it possible to establish a correlation with the diodes' performances. Other work on this subject is in progress and will be reported in a future article.

Conclusions

We have shown that spreading resistance measurements can be successfully performed not only in sili-

con, but also in gallium arsenide. Information on substrate resistivity, inhomogeneities in substrate resistivity, junction depth and concentration profiles in diffused layers, and thickness and resistivity of epitaxial layers can be obtained in a very short time.

The probe material used (tungsten-osmium alloy) was the one adopted for measurement on silicon, and probably it is not the best one for R_s measurements on GaAs. It is possible, therefore, that further improvement will be obtained with a more suitable probe material and/or pressure on the probes and other surface preparation.

Manuscript submitted April 10, 1978; revised manuscript received May 30, 1978.

Any discussion of this paper will appear in a Discussion Section to be published in the June 1979 JOURNAL. All discussions for the June 1979 Discussion Section should be submitted by Feb. 1, 1979.

Publication costs of this article were assisted by SGS/ATES Componenti Elettronici S.p.A.

Note Added in Proof

In a recent paper (10) R. C. Goodfellow *et al.* report their results on SR measurements on GaAs, using a tungsten carbide probe drawn along a bevelled sample. They too believe that the contact resistance is responsible for the measured R_s, the value of which is of the same order of magnitude found in an experiment.

REFERENCES

1. For a comprehensive review on SR measurements, see Spreading Resistance Symposium, NBS S.P. 400-10, Dec. 1974.
2. G. J. Sprokel, *IBM J. Res. Develop.*, **15**, 265 (1971).
3. L. J. van der Pauw, *Philips Res. Rep.*, **13**, 1 (1958).
4. G. Queirolo, Memoria n. 45, "Atti della LXXVIII Riunione Annuale AEI" (1977).
5. M. Cocito, F. Gorgellino, and D. Soldani, Memoria n. 53, "Atto della LXXVIII Riunione Annuale AEI" (1977).
6. B. L. Morris, P. M. Langer, and J. C. White, Jr., in "Spreading Resistance Symposium," p. 73 (1974).
7. See, for instance, O. Ishihara *et al.*, *Jpn. J. Appl. Phys.*, **15**, 1411 (1976).
8. H. P. Wagner and K. H. Besocke, *J. Appl. Phys.*, **40**, 2916 (1969).
9. V. Kamar, S. Ram, and R. Parshad, *Ind. J. Pure Appl. Phys.*, **15**, 176 (1977).
10. R. C. Goodfellow, A. C. Carter, R. Davis, and C. Hill, *Electron. Lett.*, **14**, 328 (1978).

Propane Gas Detector Using SnO_2 Doped with Nb, V, Ti, or Mo

Masayoshi Nitta, Shinji Kanefusa, and Miyoshi Haradome

The Physical Science Laboratories, Nihon University at Narashino, 7-24-1 Narashinodai, Funabashi 274 Japan

ABSTRACT

The propane gas concentration *vs.* its detection voltage characteristics have been investigated on SnO_2 doped with several transition metals. Doping with Nb, V, Ti, or Mo gives rise to a quite different behavior from the so-called Freundlich curve; that is, an inflection anomaly on the curve of the characteristics is found. The inflection point shifts toward lower gas concentration with increasing applied voltage. A remarkable jump of detection voltage observed for Nb-doped samples is also described.

A number of metal oxides have long been exploited extensively in connection with their applications to various gas-detection devices (1-3).

Recently, many attempts have been made to detect various kinds of gas involved in air by using sintered or powdered metal-oxide semiconductors (4). Among them, propane is one of the most important gases to be detected in order to prevent gas accidents. Detectors using stannic oxides have been developed for this purpose (5). Commercially available SnO_2 detectors, however, have a problem of unreliable detection. This results from the change in the detection voltage *vs.* gas concentration characteristics, depending on the humidity and ambient temperature. The detection voltage as a function of gas concentration, which is expressed by the Freundlich equation (6), tends to saturate over the range from 0.2 to 0.5% of the gas concentration. This is exactly the range of propane concentration of 0.2-0.4% to be detected for the practical use.[1] The instability of the characteristics in this region is reflected sensitively on the reliability of the detectors.

This paper describes the results of our study in an attempt to obtain an unsaturated portion on the voltage-concentration curve, especially at the gas concentration of 0.2-0.5%.

It has been found that the gas detectors of SnO_2 doped with the transition metals of Nb, V, Ti, or Mo show a different behavior from the Freundlich relation, and hence more reliable detection of leakage propane gas is expected.

Key words: sensor, semiconductor, surface, gas detection.

[1] The concentrations between 0.2-0.4% correspond to standard levels decided by the Society of Safety of High Pressure Gas Engineering: 1/10-1/5 of the lower explosion limit of propane gas.

Experimental

Stannic oxides mixed with 1 weight percent (w/o) of $PdCl_2$ and $Mg(NO_3)_2$, respectively, were used as host materials. The powders, to which Nb (max 20 w/o) were added, were presintered in air for 1-24 hr at 600°-800°C. These powders were dispersed uniformly in alcohol, painted between the electrodes on the 96% alumina substrate, and then sintered at 800°C for 1 hr. The same preparation procedure was used for V, Ti, or Mo-doped samples. The electrode was a thick film conductor (Pt-Au) which was previously prefired on the substrate at the distance of 0.5 mm. Commercial propane was used as a detective gas. As shown in Fig. 1, propane gas was introduced into a chamber at a constant flow rate through a controller. The gas concentration in the chamber was kept constant during the measurement using a stirring fan. The sample was heated by a heater of a thick film resistor at 280°C. Temperature and humidity in the chamber were kept at 25°C and 50-60% RH, respectively. A pick-up resistor (R_p) was connected in series to the sample. The value of R_p was adjusted so as to give one tenth of the resistivity of the sample before exposing to gas.

Results and Discussion

Figure 2 shows the change in resistivity as a function of propane concentration measured at 30V ap-

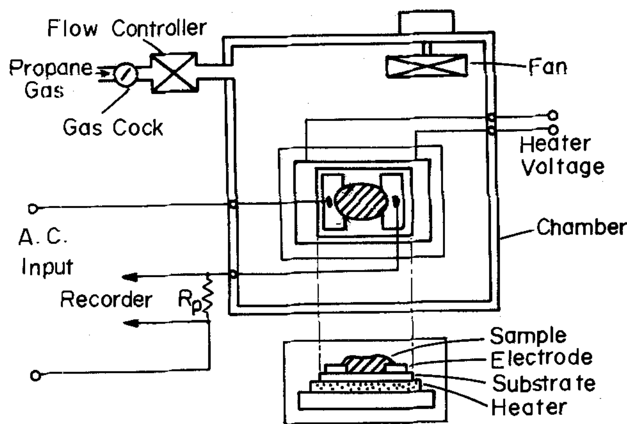

Fig. 1. A schematic diagram of an experimental system

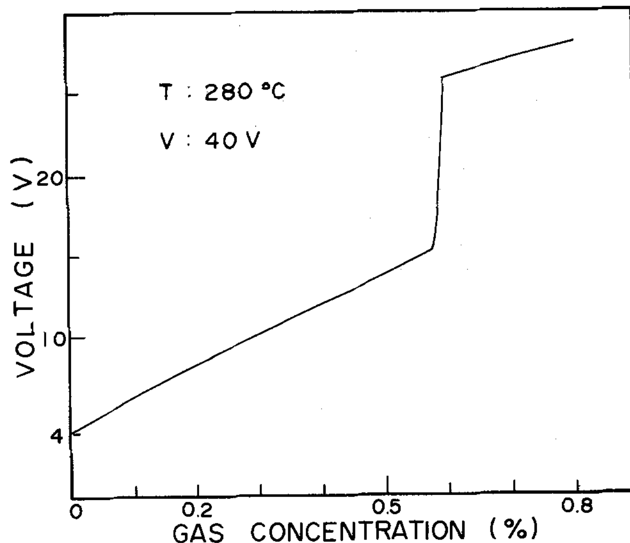

Fig. 3. Detection voltage as a function of propane concentration by a sample doped with 9 w/o Nb.

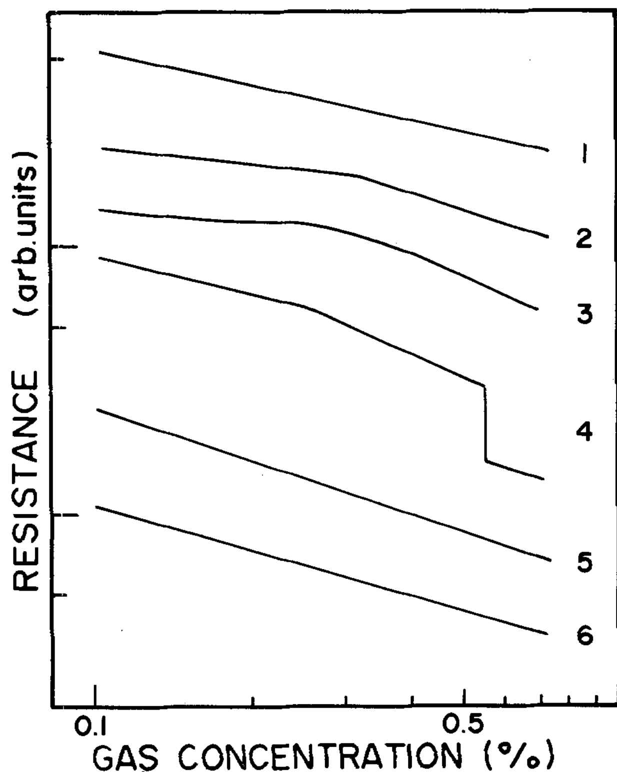

Fig. 2. Resistivity dependence on the gas concentration at applied voltage of 30V for different doping levels of Nb; 1, 20 w/o; 2, 17 w/o; 3, 15 w/o; 4, 9 w/o; 5, 7 w/o; and 6, 5 w/o.

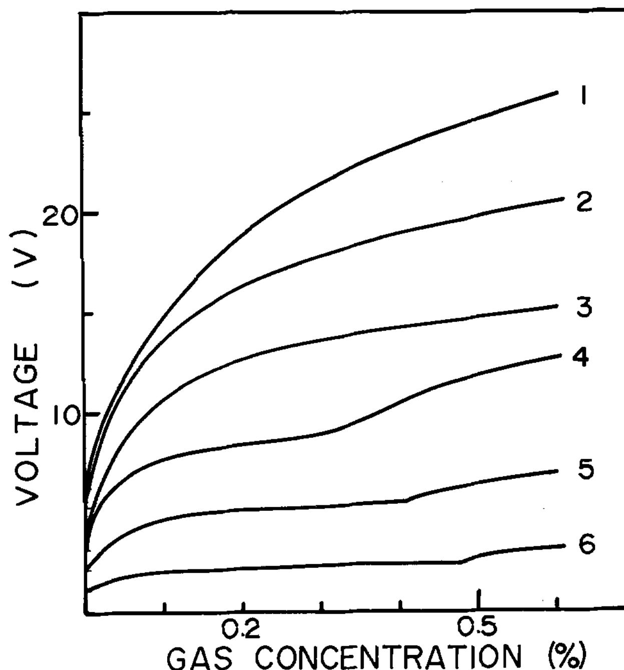

Fig. 4. Detection voltage as a function of gas concentration at various applied voltages for 15 w/o Nb-doped sample. Applied voltages are 1, 60V; 2, 50V; 3, 40V; 4, 30V; 5, 20V; and 6, 10V.

plied to the sample with various contents of Nb at 280°C. Electrical resistance of these samples decreases with increasing gas concentration. The relations for the sample with Nb of more than 20 w/o and less than 7 w/o are straight lines satisfying the Freundlich equation. For the samples with 9-17 w/o Nb, however, inflection point appears on these lines. A remarkable fact for the sample doped with 9 w/o Nb is that an abrupt change in electrical resistance occurs in addition to the inflection mentioned above. A detection voltage characteristic of this sample is shown in Fig. 3. The voltage increases abruptly from 13 to 25V at about 0.6% gas concentration as shown in the figure. Figure 4 shows the voltage as a function of the gas concentration at different applied voltages for the sample with 15 w/o Nb. The inflection is found to shift toward lower gas concentration with increasing applied voltage, and finally disappears above 40V. Thus, the occurrence of the inflection on the property depends on the Nb concentration and applied voltage. This is summarized in Table I. For the sample doped with 5 w/o Nb, the inflection anomaly is observable below 20V. For the higher concentration of Nb the

Table I. The conditions of applied voltages and Nb concentrations for the inflection anomaly to be observed. Symbols O and X indicate "yes" or "no" for the presence of the anomaly, respectively.

Nb concentration (w/o)	Applied voltage (V)						
	5	10	20	30	40	50	60
5	O	O	X	X	X	X	X
7	O	O	X	X	X	X	X
10	O	O	O	X	X	X	X
13	O	O	O	X	X	X	X
14	X	O	O	X	X	X	X
15	X	O	O	O	X	X	X
17	X	X	X	O	O	O	X
20	X	X	X	X	X	X	X

higher applied voltage is necessary to observe this anomaly. In the region marked by X in Table I, the voltage characteristics are almost of the Freundlich type. For the sample doped with 5-13 w/o Nb, however, the step phenomena as shown in Fig. 3 are observed at higher applied voltage.

For the sample doped with V, Ti, or Mo, similar inflection properties were also observed. For the sample doped with vanadium, the condition to create this phenomenon is critical. That is, it is observed only at the applied voltage between 20-30V and only for the sample doped with 15 w/o, while it is not for the sample doped with titanium or molybdenum. Figure 5 shows the gas concentration of the inflection point as a function of applied voltage. This point shifts to lower gas concentration with increasing applied voltage and also with the concentration of dopants. The shaded parts in the figure show the disappearance of the inflection phenomenon.

In Fig. 6 are shown the V-I characteristics of the Nb-doped sample (15 w/o) at the sample temperature of 280°C for different gas concentrations. Applied voltage below 20V does not have much effect on the self-heating of the sample. Therefore, the inflection phenomena observed at 10V of applied voltage in Fig. 4 are not due to the self-heating of the sample. Figure 7 shows the experimental results of the sample doped with 15 w/o Nb when the applied voltage is 20V. The variation of electrical resistance is plotted by heating the sample from 100° to 320°C at a constant heating rate of 0.14°C/sec. For the sample which showed anomaly of gas detection property, the resistance spectrum in this temperature range consists of two major minima, indicating that the lower temperature minimum is notable to the anomaly. This minimum strongly depends on the environmental gas concentration and applied voltage. From the above-mentioned facts, one can assume that the tail of the lower temperature minimum will affect the gas detection characteristics at certain gas concentration when the sample temperature is kept at the shaded region in Fig. 7. The remarkable step phenomenon found for the Nb-doped sample was not observed for the sample doped with V, Ti, or Mo within the present experimental conditions.

Let us discuss how the propane detectors of the anomalous properties can improve the reliability of the detection. Figure 8(A) shows the typical property of a Freundlich-type detector (properties of the host material) and Fig. 8(B) shows the same of the present detector which is of nonFreundlich type, in which is involved 5 w/o Ti. The detective accuracy is compared on the basis of the ±10% fluctuations of the voltage as indicated by dotted lines in Fig. 8 which would correspond to merciless circumstances like wide-range fluctuation of the ambient temperature and humidity. As an example, the accuracy is examined on the gas detector which gives an alarm when the gas concentration reaches 0.25%. As shown in Fig. 8, the errors of gas concentration at a setting voltage (V_o) for the detector of Freundlich type and nonFreundlich type are about ±0.1 and ±0.03%, respectively. Thus, one can see that our new propane gas detector is much superior to the widely used ones.

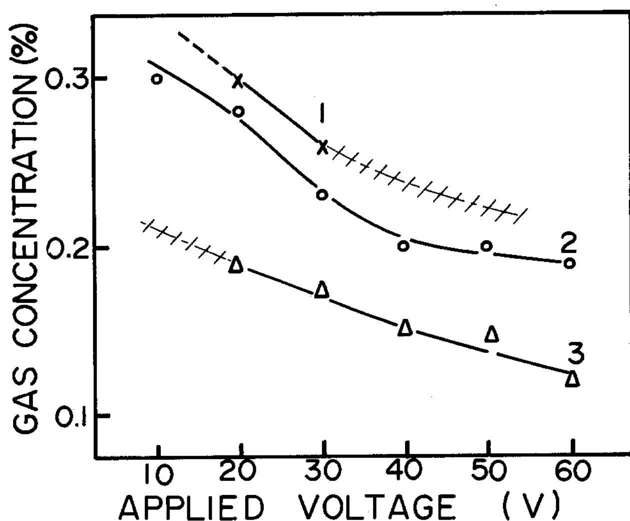

Fig. 5. The relations between the applied voltage and the gas concentrations which give the inflection at different doping levels of Mo; 1, 1 w/o; 2, 5 w/o; and 3, 10 w/o.

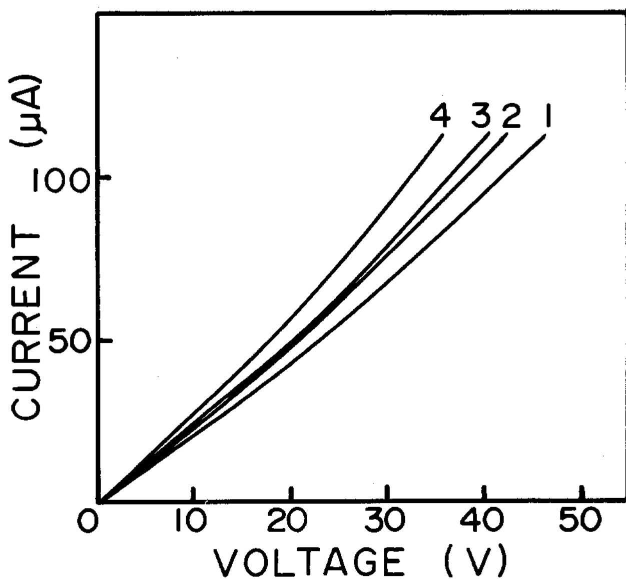

Fig. 6. V-I characteristics for the sample doped with 15 w/o Nb for different gas concentrations: 1, 0%; 2, 0.1%; 3, 0.4%; and 4, 0.6%.

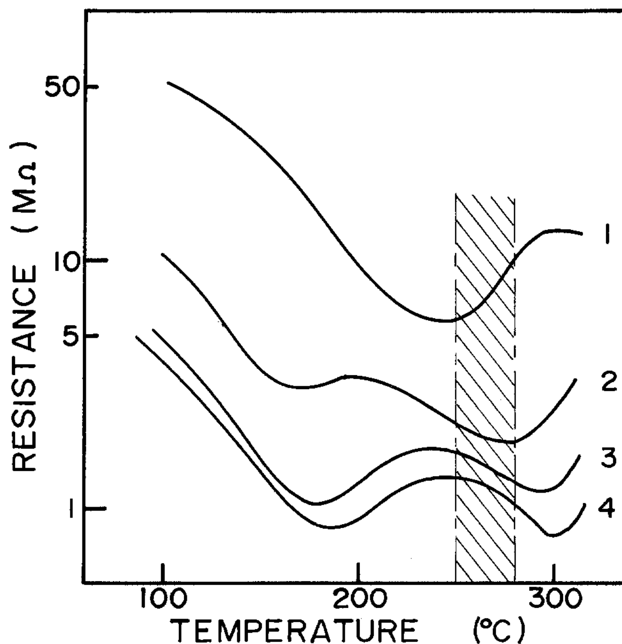

Fig. 7. Temperature dependence of the resistance for the sample doped with 15 w/o Nb for different gas concentrations: 1, 0%; 2, 0.24%; 3, 0.49%; and 4, 0.81%. The shaded regions correspond to adequate temperatures to observe the inflection phenomena in gas-detection properties.

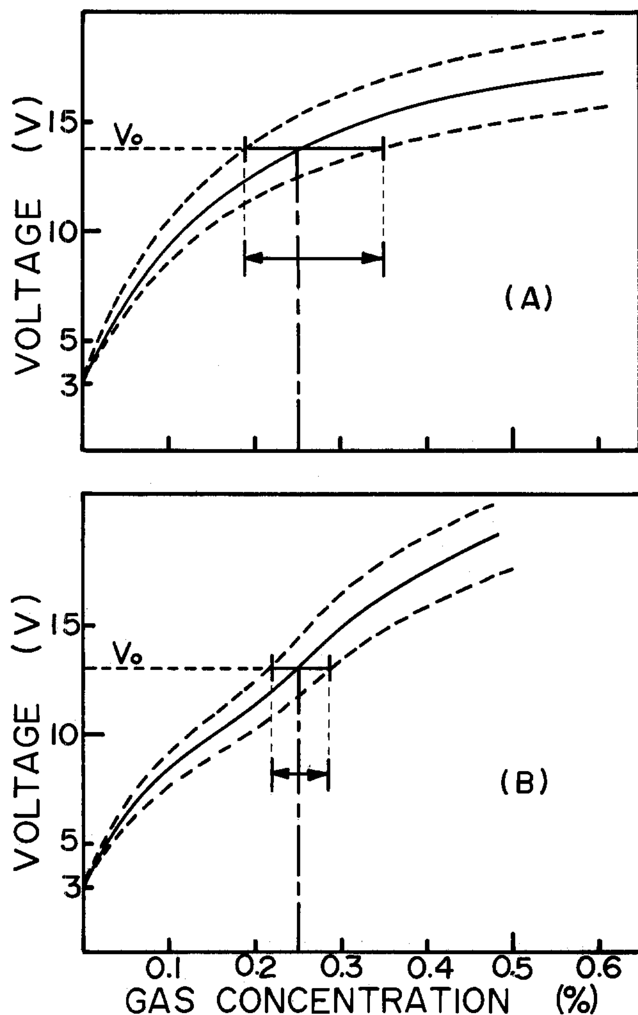

Fig. 8. The comparison of detective accuracy. (A) shows the results of a usual gas detector and (B) shows the one of our detectors. V_O indicates the point to give an alarm for the leakage of propane gas.

Conclusions

The resistance as a function of propane gas concentration for the sample of SnO_2 doped with Nb is quite different from the so-called Freundlich curve; that is, an inflection on the curve of resistance change is found in the gas concentrations of 0.3-0.5%. The similar phenomena are also observed for the samples doped with V, Ti, or Mo. The gas concentration of this inflection point depends on the applied voltage and the concentration of dopants.

From the results of the temperature dependence of resistance, it has been found that the minimum located in the lower temperature region is closely related to the observed inflection anomaly.

It has been expected that more reliable propane-gas detectors can be developed by utilizing this inflection property.

Manuscript submitted Dec. 19, 1977; revised manuscript received May 26, 1978.

Any discussion of this paper will appear in a Discussion Section to be published in the June 1979 JOURNAL. All discussions for the June 1979 Discussion Section should be submitted by Feb. 1, 1979.

Publication costs of this article were assisted by Nihon University at Narashino.

REFERENCES

1. R. D. Williams and S. K. Sikdar, *J. Catal.*, **38**, 147 (1975).
2. P. J. Shaver, *Appl. Phys. Lett.*, **11**, 255 (1967).
3. E. M. Logothetis, K. Park, A. H. Meitzler, and K. R. Laud, *Appl. Phys. Lett.*, **26**, 209 (1975).
4. T. Seiyama, A. Kato, K. Fujiishi, and M. Nagatani, *Anal. Chem.*, **34**, 1502 (1962).
5. N. Taguchi, Jpn. Pat. S47-38840.
6. N. H. Turner, *J. Catal.*, **36**, 262 (1975).

Defect Formation during High Pressure, Low Temperature Steam Oxidation of Silicon

L. E. Katz*

Bell Laboratories, Allentown, Pennsylvania 18103

and L. C. Kimerling*

Bell Laboratories, Murray Hill, New Jersey 07974

ABSTRACT

A series of experiments have been carried out to characterize the perfection of silicon wafers oxidized in an accelerated manner at 700°C and 20 atm steam. All experiments were performed using 3 in. diam wafers. High pressure steam oxidations of (100) and (111) oriented silicon, both n and p type, resulted in suppression of oxidation-induced stacking faults for all thicknesses studied (up to 5 μm oxide). Some wafers were subjected to normal 1 atm steam oxidations to produce stacking faults and subsequently steam oxidized at high pressure to study the behavior of these preexisting stacking faults. Results showed some shrinkage, but less than might be expected based solely on the consumption of silicon. Capacitance transient measurements have been made on the high pressure steam-oxidized samples and compared to wafers treated at higher temperatures at 1 atm. The defect-state concentration after high pressure steam oxidation was found to be nearly identical to the preoxidation condition.

Thermal oxidation of silicon typically produces stacking faults lying on (111) planes. These faults are extrinsic in nature and are bounded by Frank partial dislocations (1). The presence of such faults in a p-n junction can result in degraded electrical performance (2, 3). More recently, it has been observed that the formation of the stacking faults can be suppressed during oxidation. The important parameters are temperature and time of oxidation, ambient, and HCl concentration (4-8). Other important parameters are orientation and conductivity type (9, 10). It has also been observed that oxidation-induced stacking faults from previous processing can be dissolved, provided the processing conditions fall into the "retrogrowth" region (4).

While the above-mentioned parameters can be properly chosen to prevent stacking fault formation, the device processing requirements may conflict witn those conditions. Specifically, the temperature must be very high or very low (4-8) to avoid the defect formation. While addition of HCl to dry oxidations can shift the defect curves to somewhat lower temperatures, the avoidance of oxidation-induced stacking faults may be possible only in the initial oxidation where temperature is unimportant.

Since the length of the oxidation-induced stacking fault is greater at higher temperatures than at lower temperatures for the same oxide thickness, oxidizing the silicon at low temperatures in an accelerated manner should reduce the size or completely suppress such defects. Tsubouchi *et al.* (11) have recently reported a reduction in oxidation-induced stacking fault formation in the temperature range 950°-1100°C by using steam oxidation at 6.3 atm.

It is the purpose of this work to examine defect formation during high pressure steam (20 atm) and low temperature (700°C) oxidation of silicon.

Experimental

A steam oxidation apparatus capable of oxidizing 3 in. diam silicon wafers at 20 atm and 700°C has been built. The system is a flow-through type and will be described in a separate publication (12).

* Electrochemical Society Active Member.
Key words: defects, high pressure steam oxidation, silicon, stacking faults.

Silicon crystals of (100) and (111) orientations and n and p type were grown by the Czochralski technique. Wafers from these crystals were oxidized for various times at 700°C and 20 atm. Wafer doping levels were generally below $10^{16}/cm^3$. Oxide thickness ranged up to 5.5 μm. Generally wafers were stripped of oxide and Secco etched (13) followed by interference contrast microscopy examination.

Two groups of samples were studied. The first group consisted of virgin substrates which were examined for defect formation following the high pressure oxidation. The second group consisted of (100) n-type wafers which had received an 1100°C 1 atm steam oxidation to grow stacking faults approximately 34 μm in length. These wafers were then oxidized in the high pressure system and examined for size change of the stacking faults.

On some samples the oxide was stripped, and a Schottky barrier structure was fabricated for electrical evaluation of the underlying silicon. Ti and Au-Pd alloy metallizations were used for p and n materials, respectively. Capacitance transient (14) and SEM charge collection (15) measurements were performed on the resulting structure. The sample temperature did not rise above 60°C during fabrication of the test structure.

The detection limit for stacking faults is ~1 μm using the above techniques.

Results

Substrates of (100) and (111) n- and p-type silicon were oxidized at 700°C and 20 atm steam for various times to grow oxides which were in the 0.5-5.5 μm range. Wafers were Secco etched following removal of the oxide and compared to a control group of Secco etched wafers which had not be subjected to the oxidation. In all cases, using interference contrast microscopy, there was no difference in etching behavior between the oxidized wafers and the nonoxidized wafers. Both groups showed a level of hillock and saucer pit defects in $\sim 10^3/cm^2$ range. The important observation was that oxidation-induced stacking faults were not observed.

To study size change of stacking faults, lightly doped (100) n-type wafers were oxidized at 1100°C at 1 atm in steam to intentionally grow oxidation-induced stacking faults.

It has previously been established (16) that most of the surface-nucleated, oxidation-induced stacking faults will be in the same size range, whereas a size distribution will exist for the bulk faults. We observed similar results. The average oxidation-induced stacking fault size was approximately 34 μm for our 1100°C oxidation. An additional distribution of stacking faults (representing ~5% of the stacking faults) was observed which averaged 2-3 times the 34 μm length.

These wafers, with existing oxidation-induced stacking faults were steam oxidized at 700°C and 20 atm to form 1.6 and 4.2 μm thick oxides. Etching results showed little change in size of the stacking faults for the 1.6 μm oxide samples and some small shrinkage (as much as 20%) for the thicker oxide samples.

An additional group of wafers was oxidized at 1 atm and 1100°C to grow stacking faults which averaged 5 μm in length. This would project a stacking fault depth of approximately 1-1½ μm. The wafers were then steam oxidized in our high pressure system at the same temperature and pressure as previous samples. Oxide thickness for these wafers was ~5.5 μm. Such an oxidation should be sufficient to consume the already existing stacking faults if they do not grow during the high pressure oxidation. Results showed the original 5 μm stacking faults to shrink to 2.5 μm faults following the high pressure steam oxidation. A repeat experiment gave identical results.

Figure 1 depicts defect state spectra observed in the bulk silicon following three different oxidation treatments. The physical process under observation is electron emission from defect states as the Schottky barrier junction bias is repetitively pulsed from −10V to zero bias. The resulting train of junction capacitance transients is monitored through a lock-in amplifier which is tuned to a given emission time constant (12 msec). As the sample temperature is scanned, a peak is observed in the spectrum when the emission behavior of a particular defect passes through the fixed time constant window.

Both the wet and dry oxidation treatments at 1 atm introduce deep states in the 10^{11}-10^{12} cm^{-3} concentration range. The energy positions and capture cross sections given in Table I, indicate these defect states

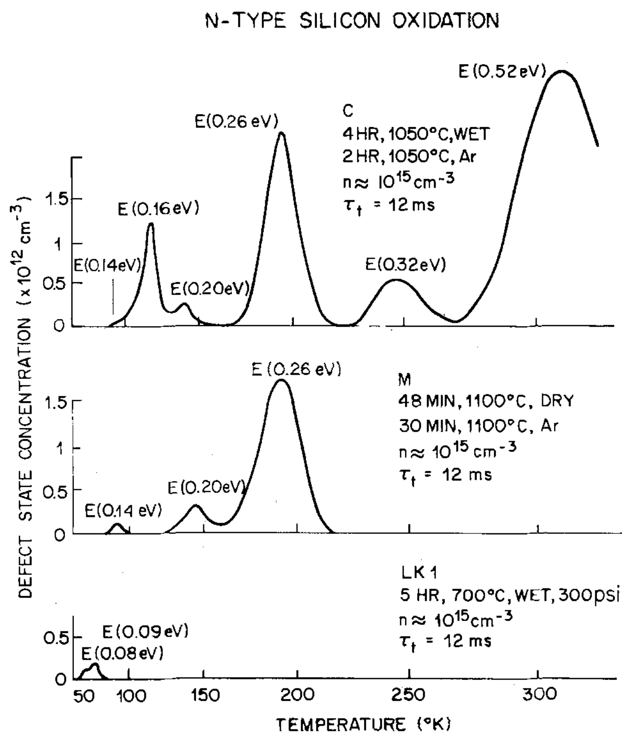

Fig. 1. Typical defect state spectrum following oxidation of n-type silicon.

Table I. Capacitance transient data

Process	$T_{1.8}$ (°K)*	E(eV)**	σ(cm^2)†	N(cm^{-3})‡
1050°C, 4 hr, H_2O + 1050°C, 2 hr, Ar	91	E(0.14)	3×10^{-15}	2.0×10^{11}
	113	E(0.16)	6×10^{-17}	1.3×10^{12}
	135	E(0.20)	$>2 \times 10^{-15}$	2.6×10^{11}
	179	E(0.26)	$>2 \times 10^{-15}$	2.5×10^{12}
	234	E(0.32)	2×10^{-16}	8.6×10^{11}
	289	E(0.52)	2×10^{-16}	3.0×10^{12}
1100°C, 48 min O_2 + 1100°C, 30 min, Ar	91	E(0.14)	3×10^{-15}	2.0×10^{11}
	135	E(0.20)	$>2 \times 10^{-15}$	3.0×10^{11}
	179	E(0.26)	$>2 \times 10^{-15}$	1.8×10^{12}
700°C, O_2, 20 atm steam	59, 60	E(0.08), E(0.09)	2×10^{-16}	2.0×10^{11}

* $T_{1.8}$(°K) refers to the deep level transient spectroscopy peak position for an emission time constant of 1.8 msec.
** E(eV) is the activation energy for electron emission of the conduction band.
† σ(cm^2) is the electron capture cross section.
‡ N(cm^{-3}) is the defect state density.

are effective generation-recombination centers. The origin of these states is as yet unidentified. Variations in relative concentrations have been observed from run to run and furnace to furnace, independent of sample origin, which suggests that stray contamination is being detected. Float zone and Czochralski samples gave similar results. The defects are not purely interface related because they exhibit a uniform concentration beyond 5 μm in depth.

The high pressure steam oxidation introduces no new states; only a pair of shallow states in the 10^{11} cm^{-3} concentration range are present. This pair of states, E (0.08 eV) and E (0.09 eV), and concentration range is typical of as-received silicon which has undergone a ~700°C heat-treatment to remove oxygen-related donor states. These states are probably derived from oxygen associates. No states representative of contamination effects have been observed. This result follows from the low diffusivities and solubilities at 700°C.

Figure 2 shows typical SEM charge collection micrographs (EBIC) taken on the same Schottky diode structures. White features indicate reduced charge collection and, hence, defects which act as recombination centers. Both wet and dry oxidations are similar showing both stacking faults and dislocations characteristic of the thermal cycling. Complimentary etching studies reveal that both bulk and surface faults are present. Only a very few dislocation-related features are evident in the high pressure steam oxidized material.

This result is consistent with prior observations of bulk, heat-treated, Czochralski silicon (17). Below 700°C no defects are observed in SEM-CCM. Above 1000°C bulk stacking faults are seen.

Discussion

Virgin substrates.—Results presented above show that oxidation-induced stacking faults were not observed in silicon wafers steam oxidized at 700°C and 20 atm for 0.5-5.0 μm thick oxides. Murarka (18) has described the length of oxidation-induced stacking faults in (100) silicon as

$$L = K' p_{O_2}{}^m t^n \exp(-Q/kT) \quad [1]$$

where K' is a constant, p_{O_2} is the partial pressure of oxygen in the oxidizing ambient, m and n are number exponents, t is the oxidation time, Q is the activation energy, and T is the temperature of oxidation.

For the case of steam oxidation it is necessary to replace p_{O_2} term with a term representing the partial pressure of the oxidizing species. This term will be proportional to the steam pressure. To determine the accuracy of Eq. [1] for 1 atm steam oxidation we have calculated stacking fault lengths using the data of Hashimoto *et al.* (19) at 1000°C for (100) silicon. Good

Fig. 2. Charge collection micrograph of oxidized silicon. Bounding partials of stacking faults visible in (a) and (b). (a) 4 hr, wet, 1050°C, <100>: $L \simeq 17$ µm. (b) 48 min, dry, 1100°C, <100>: $L \simeq 5$ µm. (c) 5 hr, wet, 700°C, 20 atm, <100>: typical of clustered oxygen defects.

agreement is obtained; *i.e.*, ~7 µm calculated *vs.* ~6 µm experimental for a 5 hr oxidation.

The value of K' as a function of temperature has been determined by Murarka (20). Extrapolating Murarka's (18) K' data to 700°C and choosing values of $n \sim 0.75$, $m \sim 0.20$, and a Q value which was experimentally determined (18) as 2.3 eV independent of temperature in the 1050°-1150°C range, it is possible to estimate the length of oxidation-induced stacking faults which might be expected at 700°C assuming the extrapolated values are valid for high pressure steam. The pressure dependence of Q is negligibly small. Based on Eq. [1] as modified for steam, we arrive at a value of 0.07 µm for a 30 hr oxidation corresponding to ~4 µm oxide for (100) silicon. Similarly a value of L equal to 0.01 µm is calculated for an oxidation of 3 hr corresponding to a ~0.70 µm oxide for (100) silicon.

Experimentally n increases with decreasing temperature whereas, theoretically, it is independent of temperature (18). Choice of a value of 1 for n would increase the above calculated values by a factor of ~20. On the other hand, choice of the theoretical value (18) for Q of ~2.7 would decrease the L values by two orders of magnitude. Using reasonable estimates for n, Q, K', and the above-mentioned model, the size of any oxidation-induced stacking faults which could form for our oxidation conditions approaches zero. The experimental techniques used in this study would not detect stacking faults smaller than 1 µm.

Use of the above model for the data of Tsubouchi *et al.* (11, 21) at 1000°C and 6.3 atm shows that the calculated values for the stacking fault length compare favorably with those observed experimentally. For example, we calculate for their 3 µm oxide on (100) silicon a stacking fault length ~9 µm whereas their data show a value ~7 µm.

Substrates with preexisting stacking faults.—It has been shown that the length to depth ratio of oxidation-induced stacking faults is related to the oxidation conditions (22). Typically observed length to depth values for a 1 µm oxide at 1100°C are in the range of 3-4. During thermal oxidation of silicon, stacking faults (at a temperature in the growth region) are growing both in length and depth.

It has been observed here that preexisting stacking faults ~34 µm long showed shrinkage up to ~20% when oxidized in the high pressure system. Our measured length to depth ratio prior to high pressure oxidation was 3.1 indicating a stacking fault depth of 11 µm. The group of wafers oxidized at 1100°C to grow stacking faults ~5 µm long should, therefore, show a stacking fault depth ~1.6 µm. These wafers, when subjected to a 5.5 µm oxide growth at 20 atm steam and 700°C showed stacking fault lengths ~2.5 µm even though the consumption of silicon was greater than the original stacking fault penetration. It is probable that the preexisting stacking faults are growing to some extent during high pressure steam oxidation but at a rate slower than they are being consumed. The net result is that the stacking fault size decreases during high pressure low temperature steam oxidation.

Hu (4) observed the retrogrowth of existing stacking faults at high temperatures. Murarka (20) has pointed out that retrogrowth is observed to occur at that temperature at which the self-diffusion coefficient of silicon becomes equal to the parabolic rate constant (B). The experimentally determined B values at 700°C and 20 atm steam for our system are 2.89 μm^2/hr for (111) silicon and 1.90 μm^2/hr for (100) silicon. These values are significantly higher than observed for 1 atm oxidations at 700°C (23).

Since, even for 5 µm thick oxide growth we are not able to achieve complete retrogrowth of small stacking faults, the retrogrowth temperature must be >700°C for our oxidation conditions. To calculate the retrogrowth temperature for 700°C and 20 atm, we determine the temperature at which the self-diffusion coefficient of silicon becomes equal to the parabolic rate constant quoted above. Based on this model and self-diffusion coefficient data of Peart (24), the retrogrowth temperature calculates to be ~1400°C. Use of the self-diffusion data of Mayer *et al.* (25) results in a calculated retrogrowth temperature greater than the melting point of silicon. This, of course, implies that under our high pressure low temperature operating

conditions the preexisting stacking faults will not shrink.

The observations that stacking fault formation is suppressed in virgin silicon and that preexisting stacking faults shrink somewhat suggests that under accelerated oxidation the consumption of silicon becomes important. Preexisting stacking faults grow, but at a rate slower than they are consumed.

The unique time-temperature relation (Eq. [1]) for stacking fault length indicates a growth mechanism which is reaction limited at the fault. One can, thus, determine oxidation conditions under which fault growth is balanced by silicon consumption for a defect-free oxidation step. At low temperatures, fault formation may be nucleation limited.

General.—The high pressure steam oxidation treatment retains more silicon crystal perfection than any other oxidation treatment tested. In fact, the material maintains its preoxidation character with respect to point defect states as well as line or planar defects. These results most certainly are due to the low temperature of the process. Oxygen clusters when supersaturated, but, in support of empirical models, nucleation and growth of stacking faults, do not occur. One must be aware, of course, that subsequent processing above 1000°C may nucleate stacking faults at these cluster sites.

In this respect, low oxygen float zone silicon presents distinct advantages. The oxygen content would represent only the 700°C equilibrium value. Subsequent treatment at higher temperatures would produce no bulk precipitation. In Czochralski silicon, the 700°C oxidation step presents the same perturbation to crystal perfection as the standard boule soaking step.

Conclusions

Steam oxidation of silicon at 700°C and 20 atm results in suppression of oxidation-induced stacking faults for oxides of all thickness (up to 5 μm) examined. This applies to (100), (111), n-type and p-type lightly doped wafers.

Preexisting stacking faults tend to grow during the high pressure steam oxidation treatment, however, their net length is reduced by the consumption of silicon.

Based on defect-state concentration measurements, the 700°C, 20 atm oxidation treatment maintains excellent silicon crystal perfection.

Acknowledgments

The authors appreciate the useful discussions with S. P. Murarka and thank J. L. Benton for the defect state spectroscopy data and S. P. Ferris for the charge collection micrograph.

Manuscript submitted Feb. 13, 1978; revised manuscript received May 16, 1978.

Any discussion of this paper will appear in a Discussion Section to be published in the June 1979 JOURNAL. All discussions for the June 1979 Discussion Section should be submitted by Feb. 1, 1979.

Publication costs of this article were assisted by Bell Laboratories.

REFERENCES

1. R. Jaccodine and C. M. Drum, *Appl. Phys. Lett.*, **8**, 29 (1966).
2. E. Barson, M. S. Hess, and M. M. Roy, *This Journal*, **116**, 304 (1969).
3. K. V. Ravi, C. J. Varker, and C. E. Volk, *ibid.*, **120**, 533 (1973).
4. S. M. Hu, *Appl. Phys. Lett.*, **27**, 165 (1975).
5. H. Shiraki, *Jpn. J. Appl. Phys.*, **14**, 747 (1975).
6. H. Shiraki, *ibid.*, **15**, 1 (1976).
7. H. Shibayama, H. Masaki, H. Ishikawa, and H. Hashimoto, *Appl. Phys. Lett.*, **29**, 136 (1976).
8. H. Hashimoto, H. Shibayama, and H. Ishikawa, *Fujitsu Sci. Tech. J.*, **13**, 73 (1977).
9. S. P. Murarka and G. Quintana, *J. Appl Phys.*, **48**, 46 (1977).
10. G. A. Rozgonyi and T. E. Seidel, in "Semiconductor Silicon 1977," H. R. Huff and E. Sirtl, Editors, p. 616, The Electrochemical Society Softbound Symposium Series, Princeton, N.J.
11. N. Tsubouchi, H. Miyoshi, and H. Abe, Digest of Tech. Papers, The 9th Conference on Solid State Devices, Tokyo (1977).
12. L. E. Katz and B. F. Howells, Work in progress.
13. F. Secco D'Aragona, *This Journal*, **119**, 948 (1972).
14. G. L. Miller, D. V. Lang, and L. C. Kimerling, *Ann. Rev. Mater. Sci.*, **7**, 377 (1977).
15. L. C. Kimerling, H. J. Leamy, J. L. Benton, S. D. Ferris, P. F. Freeland, and J. J. Rubin, in "Semiconductor Silicon 1977," H. R. Huff and E. Sirtl, Editors, p. 468, The Electrochemical Society, Softbound Symposium Series, Princeton, N.J.
16. G. A. Rozgonyi and R. A. Kushner, *This Journal*, **123**, 570 (1976).
17. J. R. Patel, K. A. Jackson, and H. Reiss, *J. Appl. Phys.*, **48**, 5279 (1977).
18. S. P. Murarka, *Phys. Rev. B*, **16**, 2849 (1977).
19. H. Hashimoto, H. Shibayama, and H. Ishikawa, *Fujitsu Sci., Tech. J.*, **13**, 73 (1977).
20. S. P. Murarka, *J. Appl. Phys.*, Submitted for publication.
21. N. Tsubouchi, H. Miyoshi, A. Nishimoto, and H. Abe, *Jpn. J. Appl. Phys.*, **16**, 855 (1977).
22. M. Jenkins and K. V. Ravi, Abs. 27, p. 79, The Electrochemical Society Extended Abstracts, Spring Meeting, San Francisco, California, May 13-17, 1974.
23. B. E. Deal and A. S. Grove, *J. Appl. Phys.*, **36**, 3770 (1965).
24. R. F. Peart, *Phys. Status Solidi*, **15**, K119 (1966).
25. H. J. Mayer, H. Mehrer, and K. Maier, "Radiation Effects in Semiconductors, 1976," p. 186, Institute of Physics, London.

Investigations of Diffusion and Nonstoichiometry in Cuprous Sulfide at 400°C

T. A. Ramanarayanan*

Department of Metallurgy and Materials Science, University of Pennsylvania, Philadelphia, Pennsylvania 19104

and P. D. Jose

G.S.S. Dustin-Ma P.M.B. 2031, Katsina, Kaduna, Nigeria

ABSTRACT

The chemical diffusivity of copper in chalcocite has been determined electrochemically as a function of the copper activity at 400°C, using the cell

$$Cu|CuBr|Cu_{2-\delta}S|Pt$$

A potentiostatic technique involving a CuBr solid electrolyte has been used. The diffusivity changes from a value of 7.3×10^{-3} cm²/sec when the copper activity is 0.78 to a value of 4.2×10^{-3} cm²/sec when the copper activity is 0.23. The copper to sulfur ratio in cuprous sulfide has been determined as a function of the copper activity using a coulometric titration technique. The results of the measurements are consistent with a model involving neutral copper vacancies, V_{Cu}, as the predominant defect carrier in cuprous sulfide. Using this model, a value of 1.9992 has been calculated for the Cu/S ratio in cuprous sulfide having unit activity of copper at 400°C.

Cuprous sulfide (chalcocite) is a nonstoichiometric compound which is metal deficient. The nonstoichiometry is accommodated by the creation of copper vacancies in the lattice. The crystal structure at 400°C is hexagonal (1, 2). According to x-ray investigations, at 400°C, at least half of the copper ions are randomly distributed among a large number of nearly equivalent lattice sites (3). This is in conformity with the high value of the self-diffusion coefficient of copper ions (9×10^{-6} cm²/sec at 420°C) and ionic conductivity ($0.2\ \Omega^{-1} \cdot \text{cm}^{-1}$ at 400°C) (4, 5). The disorder in the sulfur sublattice seems to be negligible in view of the large size of the sulfur ions and their extremely low diffusivity (6).

A potentiostatic electrochemical technique was used to determine the chemical diffusivity of copper in cuprous sulfide. The cell may be represented as

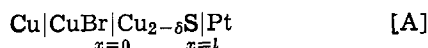

$$\underset{x=0}{Cu|CuBr|}Cu_{2-\delta}\underset{x=l}{S|}Pt \quad [A]$$

Cuprous bromide is essentially an ionic conductor between 350° and 450°C when subjected to an applied voltage of less than 300 mV (7). A fixed activity and, therefore, a fixed concentration of copper in cuprous sulfide can be established at the copper bromide/copper sulfide interface by applying a preselected voltage across cell [A] with the sulfide at positive polarity. The applied voltage is given by the expression (8, 9)

$$E_{appl} = \frac{-RT}{\mathbf{F}} \ln a_{Cu} + I\Omega \quad [1]$$

where R is the gas constant, T is the absolute temperature, $\mathbf{F}$ is the Faraday constant, a_{Cu} is the activity of Cu, I is the current in the external circuit of cell [A], and Ω is the electrolyte resistance. Equation [1] assumes that polarization effects at the electrode/electrolyte interface are negligible. According to Eq. [1], the applied voltage will fix a constant copper activity (and therefore copper concentration) in cuprous sulfide at the electrode/electrolyte interface provided the second term in Eq. [1] is small when compared to the first term. When the current, I, has dropped to zero, a uniform copper concentration is attained throughout the cuprous sulfide electrode. If the applied voltage is now quickly changed to a higher value, a new lower copper concentration will be established at the electrode/electrolyte interface of cell [A]. Copper then diffuses out of copper sulfide until the new lower copper concentration is attained throughout the copper sulfide specimen. Fick's second law for this diffusion problem may be written as

$$\frac{\partial C_{Cu}}{\partial t} = \tilde{D}_{Cu} \frac{\partial^2 C_{Cu}}{\partial x^2} \quad [2]$$

In Eq. [2], C is the concentration of copper in cuprous sulfide in moles cm^{-3}, t is the time in seconds, $\tilde{D}_{Cu}$ is the chemical diffusion coefficient of copper in cuprous sulfide, and x is the coordinate of diffusion. For the initial and boundary conditions

$$C_{Cu} = C_{Cu}', \quad 0 \leq x \leq l, \quad t = 0$$

$$C_{Cu} = C_{Cu}'', \quad x = 0, \quad t > 0$$

$$\left(\frac{\partial C_{Cu}}{\partial x} \right)_{x=l} = 0$$

the solution to Eq. [2] is (10)

$$\frac{C_{Cu}' - C_{Cu}}{C_{Cu}' - C_{Cu}''} = 1 - \frac{4}{\pi} \sum_{n=0}^{\infty} \frac{(-1)^n}{(2n+1)} \exp\left(-\frac{(2n+1)^2\pi^2\tilde{D}_{Cu}t}{4l^2}\right) \cdot \sin\frac{(2n+1)\pi x}{2l} \quad [3]$$

The magnitude of current I is related to the concentration gradient at $x = 0$ through

$$|I| = A\mathbf{F}\tilde{D}_{Cu} \left| \frac{\partial C_{Cu}}{\partial x} \right|_{x=0} \quad [4]$$

where A is the cross sectional area of the copper sulfide electrode. When the diffusion times are sufficiently long, the first term in the summation in Eq. [3] is a

* Electrochemical Society Active Member.

Key words: chemical diffusivity, nonstoichiometry, cuprous sulfide, potentiostatic technique, coulometric titration.

good approximation to the total sum. Thus, at long time

$$\left(\frac{\partial C_{Cu}}{\partial x}\right)_{x=0} = \frac{2(C_{Cu}' - C_{Cu}'')}{l} \exp - \frac{\pi^2 \tilde{D}_{Cu} t}{4l^2} \quad [5]$$

On combining Eq. [4] and [5]

$$I = 2A\tilde{D}\mathbf{F}\left(\frac{C_{Cu}' - C_{Cu}''}{l}\right) \exp - \frac{\pi^2 \tilde{D}_{Cu} t}{4l^2} \quad [6]$$

It must be emphasized that the value of the Faraday constant in Eq. [6] has units of coulombs/gram equiv. whereas in Eq. [1], it has units of cals/volt.

A coulometric titration procedure has been used to determine the activity of copper in cuprous sulfide as a function of the Cu/S ratio. When cell [A] is shorted, the cuprous sulfide sample attains the composition corresponding to equilibrium with copper. A well-defined amount of copper may now be removed from the sample by passing a current, I, through the cell for time, t. The decrease, δ', in the Cu/S ratio in cuprous sulfide with respect to the sample having unit activity of Cu is given by

$$\delta' = \frac{It}{n_s \mathbf{F}} \quad [7]$$

In Eq. [7], n_s is the number of gram atoms of sulfur in the cuprous sulfide specimen. **F** has units of coulombs/gram equiv. After passing current, I, for time, t, the cell circuit is opened and the open-circuit voltage, E, of the cell is measured until it attains a steady value. The open-circuit voltage is related to the activity of copper in cuprous sulfide through

$$E = \frac{-RT}{\mathbf{F}} \ln a_{Cu} \quad [8]$$

The experiment is repeated by passing current, I, for different time intervals and in each case measuring the final steady open-circuit cell emf.

Experimental Procedure

Chalcocite powder of 99.999% purity (obtained from Poly Research Corporation, New York), cuprous bromide of 99.95% purity, and copper powder of 99.95% purity were used in the experiments. The experimental setup used is shown in Fig. 1. It consisted of a Kanthal-wound horizontal furnace which had a constant temperature zone of about 3 in. The cell could be placed in an alumina cell holder and kept in the constant temperature zone of the furnace. The furnace temperature could be controlled at 400° ±1°C by means of a Leeds and Northrup Electromax temperature controller. Purified argon gas was used to provide the inert atmosphere; the argon was purified by first passing through anhydrous calcium chloride and then through activated copper (BASF) kept at 180° ± 10°C. A regulated power supply was used to apply selected voltages. Applied or open-circuit voltages could be measured by means of a high impedance (≈$10^{10}\Omega$) electronic voltmeter.

In cell [A], the electrode and the electrolyte materials were in the form of cylindical pellets. Copper powder was pressed into pellets of 1 cm diam and nearly 0.5 cm thickness in a die at 10-12 tsi. Cuprous bromide pellets were also prepared in a similar way, with thicknesses in the range, 0.1 to 0.3 cm. Cuprous sulfide pellets with thicknesses in the range, 0.8-2 cm and diameters of 0.5 or 1 cm were pressed at a slightly higher pressure (15 tsi). The pressed pellets had densities of 97 + % of the theoretical value.

The cell was assembed in an alumina cell holder (Fig. 1) and inserted into the furnace. Electrical contact with the electrodes was made using platinum disks. The electrodes and electrolyte could be kept in intimate contact by means of an alumina push-rod which could be tightened by means of a brass screw (Fig. 1). The system was evacuated to a pressure of 10 mTorr and refilled with purified argon successively five times. Finally, a low flow rate of a few bubbles of argon per minute was maintained. The cell was now brought to a temperature of 400°C and maintained at this value by means of the Electromax temperature controller.

A low voltage in the range, 10-30 mV, was now applied across the cell using the regulated power supply with the sulfide electrode at positive polarity. When the current in the external circuit (recorded using a Sargent recorder) had dropped to zero, the circuit was opened and the open-circuit cell voltage was measured. The open-circuit cell voltage would now be equal to the initial applied voltage. A higher voltage (higher by 20 or 30 mV) was applied across cell [A] and simultaneously the current in the circuit was recorded as a function of time. The current-time plot was analyzed to determine the chemical diffusivity of copper. A further voltage step was now given and a new current-time plot was recorded. The highest voltage applied was 130 mV. At the higher voltages, the current dropped to a finite final steady value (of a few microamperes). This could be partly due to some vaporization of sulfur from cuprous sulfide and partly due to the introduction of a small amount of positive hole conduction in the CuBr electrolyte. When this occurred, the final constant current was subtracted from the total current and the resulting current-time plot was analyzed to obtain the diffusivity. The circuit used in the experiment is given in Fig. 2.

Cell [A] was also used to determine the Cu/S ratio in cuprous sulfide as a function of the copper activity. The cell was assembled with a thin cuprous sulfide sample. A uniform initial copper activity was established in the cuprous sulfide sample by imposing a voltage of 10 mV across cell [A] with the sulfide at positive polarity. The applied voltage was now cut off and a constant current of 2 mA was passed through the cell (so as to remove copper from cuprous sulfide) for a few minutes by means of a 15V d-c source connected in series with a variable resistance. The current could be accurately determined by measuring the voltage drop across a 100Ω precision resistor included in the cell circuit (Fig. 3). The cell current was now dis-

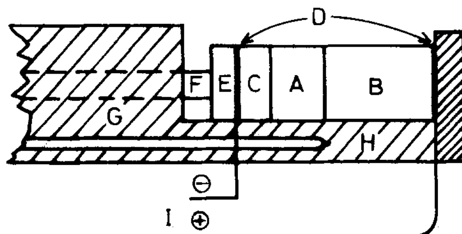

Fig. 1. Experimental setup. A, CuBr electrolyte; B, Cu_2S electrode; C, Cu electrode; D, Pt disk contacts; E, alumina disk; F, alumina push rod; G, cell holder; H, Pt-Pt(10%Rh) thermocouple; I, Pt lead wires.

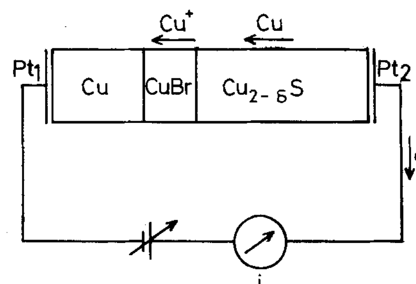

Fig. 2. Circuit for the potentiostatic single cell technique

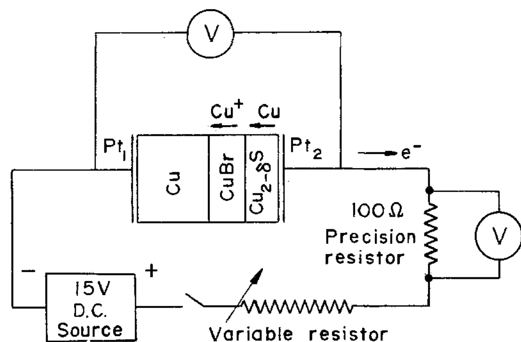

Fig. 3. Circuit used for the coulometric titration experiments

continued by opening the circuit and the final steady open-circuit cell voltage was measured. The current was imposed again and the experiment repeated. In this way, the change in the Cu/S ratio in cuprous sulfide as a function of the open-circuit cell voltage could be measured up to 200 mV.

Results and Discussion

The results reported are those obtained from five cells. Nine different cells were run, but data from four of these are considered inaccurate. Two of these cells got shorted because the CuBr pellet used was too thin. In the other two, the copper sulfide pellet was deformed because of the mechanical pressure exerted on the cell. Two typical current time plots for two sets of applied voltages (E_1 and E_2) are shown in Fig. 4. Figure 5 shows the corresponding log I *vs.* t plots. From the slopes of the straight lines in Fig. 5, the chemical diffusivity of copper can be calculated.

The chemical diffusivity values obtained from the measurements were found to depend on the ratio of the cuprous sulfide thickness to copper bromide thickness as shown in Fig. 6. The data points on Fig. 6 correspond to applied voltages of 10 and 30 mV. For each cell, at least five current-time plots were taken for each set of applied voltages. Thus each point shown on Fig. 6 is the average value obtained from five or more

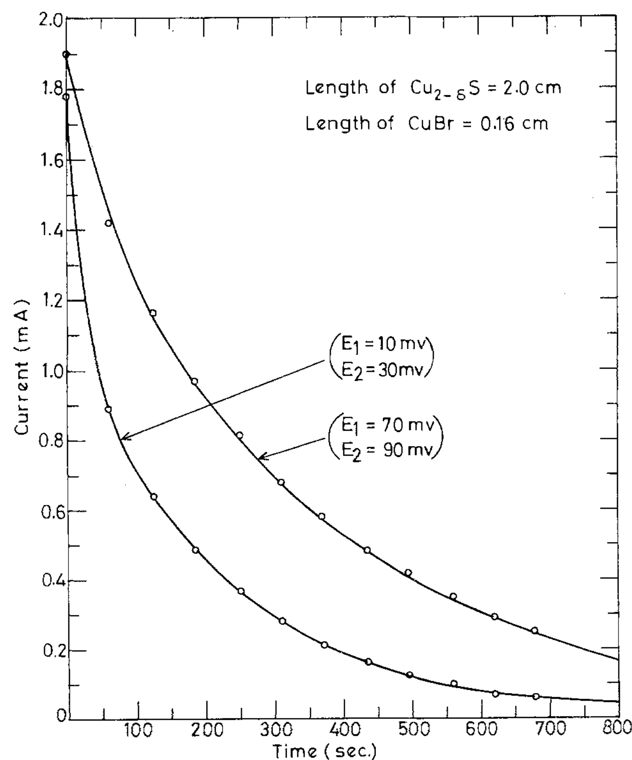

Fig. 4. Cell current *vs.* time in the potentiostatic single cell technique.

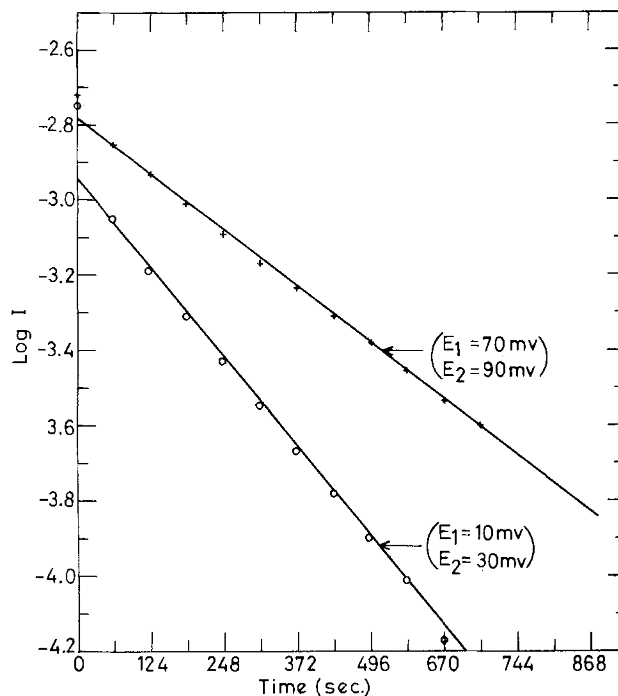

Fig. 5. Log I vs. time in the potentiostatic single cell technique

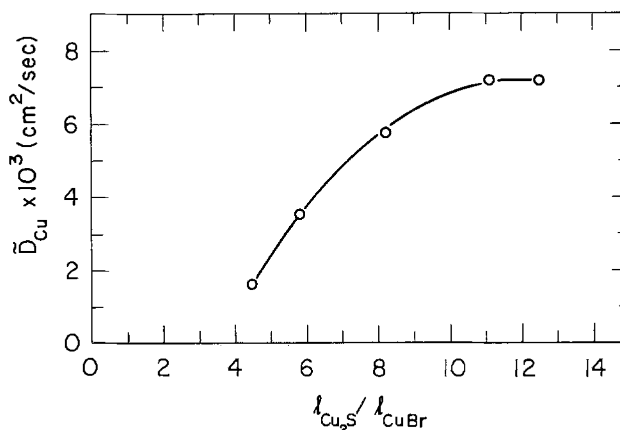

Fig. 6. Effect of the ratio of cuprous sulfide thickness to cuprous bromide thickness on the measured chemical diffusion coefficient.

current-time plots. The average uncertainty of each point is between 10 and 15%. Two of the cells, with l_{Cu_2S}/l_{CuBr} ratios of 11 and 12.5, gave identical diffusivity results. At lower ratios, the diffusivity values were lower. An electrode/electrolyte ratio of 15 was used in one cell, but this cell got shorted before too many measurements could be made. The CuBr electrolyte used in this cell had a thickness of only 0.12 cm. However, measurements at higher applied voltages were obtained with this cell before it got shorted. The diffusivity value for applied voltages of 70 and 90 mV compares well with the value obtained from the two cells which had l_{Cu_2S}/l_{CuBr} ratios of 11 and 12.5.

At l_{Cu_2S}/l_{CuBr} ratios less than 11, the diffusivity values were lower. Lower ratios correspond to larger electrolyte thicknesses and smaller electrode thicknesses. The boundary conditions used for the diffusion problem are strictly valid only if the $I\Omega$ term in Eq. [1] is zero. This ideal situation cannot be realized since there is current flow during the diffusion process. However, it is practically feasible to make the $I\Omega$ term much smaller than the first term in Eq. [1]. The identical diffusivity results obtained at electrode/electrolyte ratios of 11, 12.5, and 15 indicate that at these ratios the $I\Omega$ drop is not significant. When larger electrolyte thicknesses are used, the $I\Omega$ drop is higher.

In a typical diffusion run, the $I\Omega$ drop is largest in the first minute or two. For smaller cuprous sulfide samples, the total diffusion time is smaller (as there is less copper to be removed) and correspondingly the contribution from the $I\Omega$ drop is more significant. However, when thicker cuprous sulfide samples are used, the total diffusion time is increased and the influence of the $I\Omega$ drop on the longtime solution of the diffusion equation (Eq. [6]) is considerably reduced.

Any overvoltage built up at the Cu/CuBr interface could influence the diffusivity results especially if it is time dependent. Strictly, an overvoltage term must also be included on the right hand side of Eq. [1]. To study the overvoltages which develop at the Cu/CuBr interface, the following symmetrical cell was used

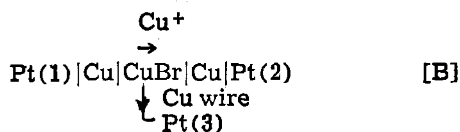

[B]

The cell was assembled and heated to a temperature of 400°C in a purified argon atmosphere. The cuprous bromide pellet which was used had a thickness of 0.5 cm. Initially, the open-circuit voltages between Pt(1) and Pt(3) and between Pt(2) and Pt(3) were measured. A very small (between 1 and 2 mV) open-circuit voltage was observed, presumably due to a small temperature gradient across the cell. A d-c polarization current in the range, 1-6 mA, was passed between Pt(1) and Pt(2) so as to transport Cu from left to right in cell [B]. The cathodic voltage between Pt(2) and Pt(3) and the anodic voltage between Pt(1) and Pt(3) were recorded as a function of time. The results are shown in Fig. 7 and 8, respectively. The cathodic voltage reaches a steady-state value in about 30 sec for all the currents used. Furthermore, the cathodic voltage is mostly the $I\Omega$ drop, the polarization being negligible. The anodic voltage reaches a steady-state value in about a minute for polarization currents ranging from 1 to 4 mA. At larger currents, the anodic voltage continues to increase with time. The magnitude of the steady-state anodic voltage shows that it

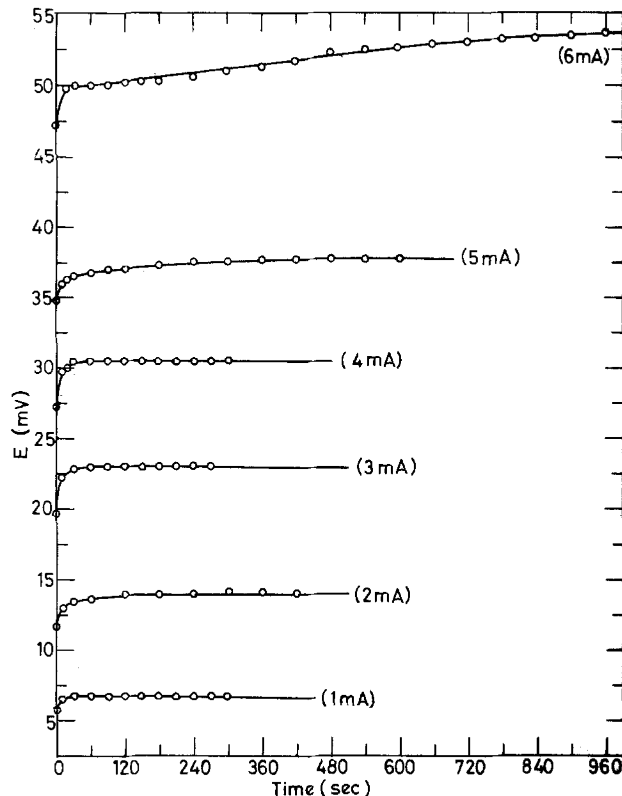

Fig. 8. Anodic voltage as a function of time in the polarization experiments with cell [B].

contains a steady-state overvoltage term in addition to the $I\Omega$ drop. This could be due to void formation at the anode when copper atoms are removed (11). All diffusivity values reported here were obtained using Cu as the cathode. The cathodic voltages in the diffusion experiments should be lower than those shown in Fig. 7 since the thickness of the CuBr electrolyte used in the polarization experiments was large (0.5 cm).

The chemical diffusivity values are plotted as a function of copper activity in Fig. 9. The diffusivity values plotted are the average of the results from the cells with l_{Cu_2S}/l_{CuBr} ratios of 11 and 12.5. The chemical diffusivity is found to increase with increase in the activity of copper.

Equation [6] indicates that the intercept at $t = 0$ of the straight line in the log I *vs.* t plots can also be used to calculate the diffusivity. The values so calculated agreed with the diffusivity values obtained from the slopes within a factor of 1.5. In calculating diffusivity values from the intercept, one needs the value

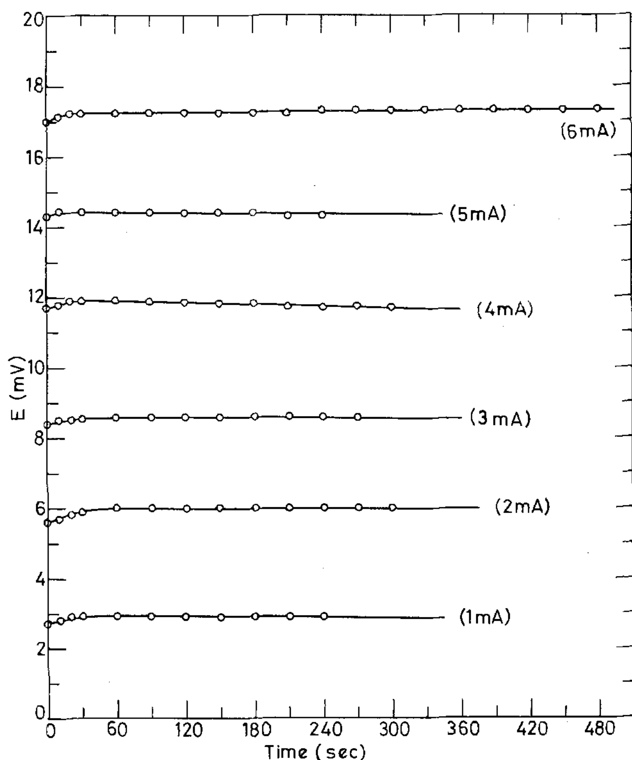

Fig. 7. Cathodic voltage as a function of time in the polarization experiments with cell [B].

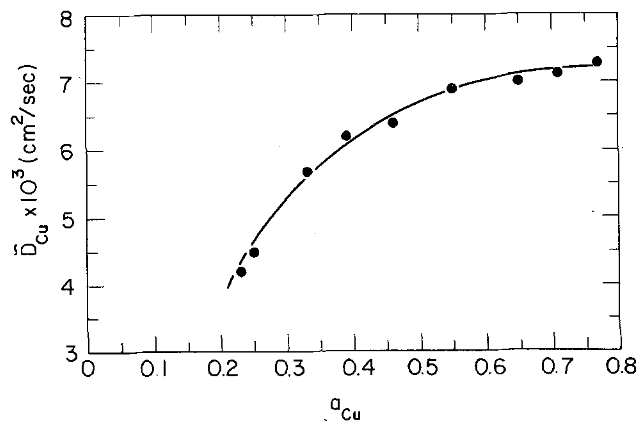

Fig. 9. Chemical diffusion coefficient as a function of copper activity.

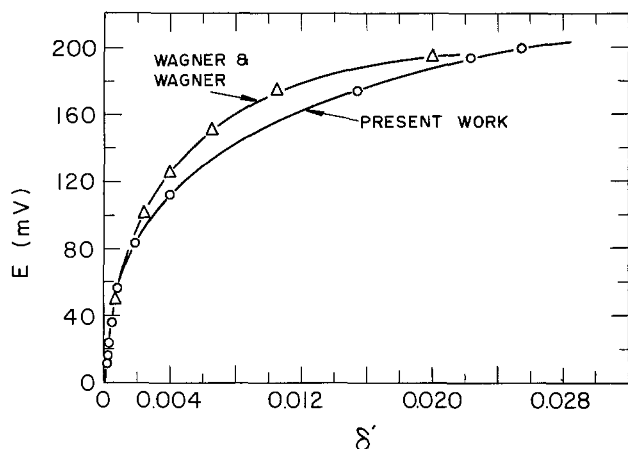

Fig. 10. The open-circuit voltage of cell [A] as a function of the deviation from stoichiometry, δ', in cuprous sulfide.

of ($C_{Cu}' - C_{Cu}''$). Reference to Fig. 10 indicates that it is difficult to pick an accurate value for this concentration difference for typical applied voltages (say 10 and 30 mV) used in the diffusion experiments. For this reason, the diffusivity values obtained from the slopes are considered more accurate and are recommended.

The results of the coulometric titration experiments are plotted in Fig. 10. Figure 10 also shows the values obtained by Wagner and Wagner (7). The agreement between the two measurements is satisfactory. In Fig. 10, δ' is the deviation in the Cu/S ratio in cuprous sulfide from the value corresponding to unit activity of copper.

The results of the coulometric titration experiments can be combined with the measured chemical diffusivity values of copper to obtain values of the self-diffusivity of copper. The chemical and self-diffusivities are related by

$$\tilde{D}_{Cu} = D_{Cu}\left(\frac{d\ln a_{Cu}}{d\ln C_{Cu}}\right) \quad [9]$$

In Eq. [9], $d\ln a_{Cu}/d\ln C_{Cu}$ is the thermodynamic factor for copper in cuprous sulfide. The thermodynamic factor can be calculated from the coulometric titration results as follows. In cuprous sulfide coexisting with metallic copper, the ratio of copper concentration to sulfur concentration is given by

$$\frac{C_{Cu}^{o}}{C_s} = 2 - \delta^* \quad [10]$$

where δ* is the copper deficit in cuprous sulfide having unit activity of copper. The concentration terms in Eq. [10] have units of moles per cubic centimeter. When the copper activity in cuprous sulfide is decreased, the copper deficit increases and one has

$$\frac{C_{Cu}}{C_s} = 2 - \delta^* - \delta' \quad [11]$$

where C_{Cu} is the copper concentration corresponding to δ'. Hence

$$\ln C_{Cu} = \ln C_s + \ln(2 - \delta^* - \delta') \quad [12]$$

$$d\ln C_{Cu} = \frac{-d\delta'}{(2 - \delta^* - \delta')} \quad [13]$$

since C_s and δ* are constants. From Eq. [8]

$$dE = \frac{-RT}{\mathbf{F}}\,d\ln a_{Cu} \quad [14]$$

Combining Eq. [13] and [14]

$$\frac{d\ln a_{Cu}}{d\ln C_{Cu}} = \frac{(2 - \delta^* - \delta')\mathbf{F}}{RT}\left(\frac{dE}{d\delta'}\right) \quad [15]$$

Combining Eq. [9] and [15]

$$\tilde{D}_{Cu} = D_{Cu}\frac{(2 - \delta^* - \delta')}{RT}\left(\frac{dE}{d\delta'}\right) \quad [16]$$

Thus using $dE/d\delta'$ values from Fig. 10, the self-diffusivity, D_{Cu}, can be calculated. Values of chemical diffusivity, self-diffusivity, and thermodynamic factor at various copper activities are presented in Table I.

Cuprous sulfide is an intrinsic semiconductor. When copper is removed from cuprous sulfide, copper vacancies are introduced into the lattice. The equilibration of a cuprous sulfide sample with an outer phase of fixed copper activity may be represented by the equilibrium

$$Cu_{Cu} = V_{Cu} + Cu \quad [17]$$

Cu_{Cu} represents a copper atom in its normal site in cuprous sulfide and V_{Cu} represents a neutral copper vacancy. The equilibrium constant for reaction [17] can be written as

$$K_{17} = [V_{Cu}]a_{Cu} \quad [18]$$

In Eq. [18], $[V_{Cu}]$ represents the concentration of copper vacancies in cuprous sulfide and a_{Cu} represents the copper activity. If the vacancy concentration in Eq. [18] is expressed as the ratio (number of copper vacancies)/(number of sulfur atoms), then

$$\delta = [V_{Cu}] \quad [19]$$

where δ is the exact copper deficit in cuprous sulfide. On combining Eq. [18] and [19]

$$\delta = K_{17} \cdot a_{Cu}^{-1} \quad [20]$$

Let δ* represent the copper deficit in cuprous sulfide when it is in equilibrium with copper. Then

$$\delta^* = K_{17} \quad [21]$$

Furthermore

$$\delta = \delta^* + \delta' \quad [22]$$

Combining Eq. [20] to [22]

$$\delta' = \delta^*[a_{Cu}^{-1} - 1] \quad [23]$$

Thus, if the removal of copper from cuprous sulfide generates neutral copper vacancies, then a plot of δ' *vs.* ($a_{Cu}^{-1} - 1$) should be a straight line passing through the origin. Furthermore, the slope should be equal to δ*. A plot of δ' *vs.* ($a_{Cu}^{-1} - 1$) is shown in Fig. 11. Our data as well as the data of Wagner and Wagner (7) are shown. The results of Wagner and Wagner would give a value of δ* = 1.9994 (from Fig. 11) whereas our data leads to a value of δ* = 1.9992.

Wagner and Wagner (7) have calculated a value for δ* in a different way using the following assumptions:

(*i*) The predominant defects in cuprous sulfide are excess electrons, electron holes, and singly ionized copper vacancies so that

$$p = n + [V_{Cu}'] \quad [24]$$

In Eq. [24] p is the concentration of holes, n is the concentration of excess electrons and $[V_{Cu}']$ is the con-

Table I. Chemical diffusivity, self-diffusivity, and thermodynamic factor at various copper activities

a_{Cu}	$\tilde{D}_{Cu} \times 10^3$	$\frac{d\ln a_{Cu}}{d\ln C_{Cu}}$	$D_{Cu} \times 10^6$
0.77	7.28	3085	2.36
0.71	7.10	3085	2.30
0.65	7.00	3085	2.27
0.55	6.90	3083	2.27
0.46	6.40	2740	2.30
0.39	6.20	1540	4.00
0.33	5.70	1027	5.55
0.25	4.50	860	5.23
0.23	4.20	690	6.08

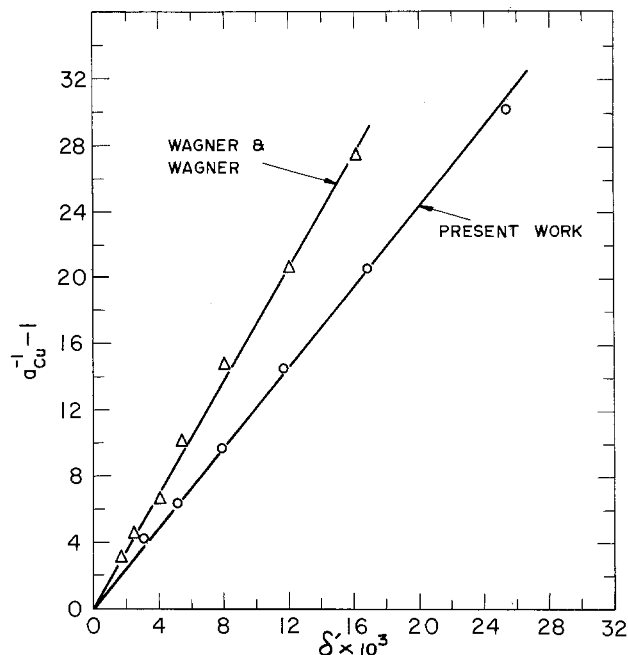

Fig. 11. Copper deficit as a function of copper activity

centration of singly ionized copper vacancies. Since $\delta = [V_{Cu}']$

$$\delta = p - n \qquad [25]$$

(*ii*) The chemical potential of copper ions, μ_{Cu^+}, is independent of the Cu/S ratio.

Their analysis leads to a value of $\delta^* = 1.9996$. The agreement between the values of δ^* obtained using two different defect models is surprisingly good. Recently, some authors have pointed out that neutral copper vacancies are the predominant defect in cuprous oxide (12, 13). According to Rau (14), in the high temperature cubic modification of cuprous sulfide ($Cu_{7-x}S_4$), neutral copper vacancy, V_{Cu}, predominates over a wide range of sulfur pressures. Thus cuprous sulfide (chalcocite) at 400°C, could have predominantly neutral copper vacancies, with some singly charged vacancies, V_{Cu}', to provide excess p-type conduction.

Acknowledgments

Helpful discussions with Professors R. A. Rapp, W. L. Worrell, and G. R. Belton are gratefully acknowledged. The facilities provided by the Department of Metallurgical Engineering, Indian Institute of Technology, Kanpur, are appreciated.

Manuscript submitted Aug. 22, 1977; revised manuscript received May 5, 1978.

Any discussion of this paper will appear in a Discussion Section to be published in the June 1979 JOURNAL. All discussions for the June 1979 Discussion Section should be submitted by Feb. 1, 1979.

REFERENCES

1. N. W. Buerger, *J. Chem. Phys.*, **7**, 1067 (1939).
2. R. Molé, *Ann. Chim.*, **9**, 145 (1954).
3. P. Rhalfs, *Z. Phys. Chem.*, **B31**, 157 (1936).
4. C. Tubandt, H. Reinhold, and W. Jost, *Z. Anorg. Allgem. Chem.*, **177**, 253 (1928).
5. E. Hirahara, *J. Phys. Soc. Jpn.*, **6**, 422 (1951).
6. H. Braune and O. Kahn, *Z. Phys. Chem.*, **112**, 270 (1924).
7. J. B. Wagner and C. Wagner, *J. Chem. Phys.*, **26**, 1602 (1957).
8. R. L. Pastorek and R. A. Rapp, *Trans. Metall. Soc. AIME*, **245**, 1711 (1969).
9. T. A. Ramanarayanan and R. A. Rapp, *Metall. Trans.*, **3**, 3239 (1972).
10. J. Crank, "The Mathematics of Diffusion," Clarendon Press, Oxford (1956).
11. D. O. Raleigh, "Fast Ion Transport in Solids," p. 477, North Holland Publishing Co., Amsterdam (1973).
12. M. O'Keeffe and J. Moore, *J. Chem. Phys.*, **36**, 3009 (1962).
13. S. Mrowec and A. Stoklosa, *Oxidation Metals*, **3**, 291 (1971).
14. H. Rau, *J. Phys. Chem. Solids*, **28**, 903 (1967).

Self-Diffusion and Na-K Exchange in β- and β''-Na-Gallate Fast Ion Conductors

L. M. Foster,* D. R. Campbell,* and G. V. Chandrashekhar

IBM Thomas J. Watson Research Center, Yorktown Heights, New York 10598

ABSTRACT

The self-diffusion coefficients for Na^+ migration in the two-dimensional, ionically conducting sodium gallates were determined as 2.0×10^{-5} and 7.6×10^{-5} cm²/sec for the β (hexagonal) and β'' (rhombohedral) phases, respectively, at 350°C. Part of the sodium of these compounds is immobile. It is proposed that this portion substitutes for Ga^{+++} in the spinel block and compensates the charge of additional sodium in the conduction plane. The correlation factor suggests a noncolinear interstitialcy diffusion model for migration of the mobile Na^+ in the β phase. The correlation factor for the β'' phase is unusually large and not explained by any present model. Activity coefficients for the Na- and K-gallates were determined in solid solutions. Na^+ and K^+ show essentially ideal behavior in the β'' structure and very nonideal behavior suggestive of ordering, in the β structure, in agreement with findings for β-Al_2O_3.

Gallium analogs of the fast ion conductors β- and β''-alumina exist and are themselves fast ion conductors (1). They exhibit many of the properties of their aluminum counterparts and, because of the relative ease of preparation, they provide an attractive new medium in which the phenomenon of exceedingly high alkali ion diffusivity can be studied. In particular, direct comparison between the β and β'' forms can be made in gallate system because pure (viz., unstabilized) monocrystals of each can be prepared (2),

* Electrochemical Society Active Member.
Key words: defects, crystallography, equilibrium, stoichiometry.

whereas in the aluminate system, the β'' form must be stabilized with magnesia or lithia (3).

β-alumina has the stoichiometric formula $Na_2O \cdot 11Al_2O_3$ (4, 5), which provides for one sodium ion per conducting plane in the unit cell. The conducting plane in the β form (space group $P6_3/mmc$) is a mirror plane, and the sodium atom has a trigonal-prismatic coordination with a triangle of three oxygen atoms of an adjacent c plane centered immediately above it, and another immediately below. A view of the β structure normal to the sodium plane is shown in Fig. 1, top. The Na is shown in the favored Beevers-Ross position (5). If occupied, the higher-energy, anti-Beevers-Ross site would have one oxygen immediately above the Na and another immediately below, in a more or less linear O-Na-O configuration.

The β'' form results from a three-fold screw rotation about the c axis (space group R3m) which removes the mirror plane and provides two possible identical sites for the sodium in tetrahedral coordination (Fig. 1, bottom).

β-Al_2O_3 contains more sodium than the stoichiometric formula provides (typically $Na_2O \cdot 9Al_2O_3$) whereas the β'' form contains still more, but presumably less than the formula $Na_2O \cdot 5.5Al_2O_3$ provides, where the two equivalent Na sites are fully occupied. A "typical" analysis of pure β''-Al_2O_3 is difficult to ascertain because unstabilized (*viz.*, no Li_2O or MgO) compositions appear to be mixures of β'' and β, and stabilized compositions have the additional complication of the presence of the second cation. Roth (6) and Roth *et al.* (3) showed by x-ray and neutron diffraction that the excess Na in β-Al_2O_3 was compensated by additional oxygen in the conduction plane (mid-oxygen positions, Fig. 1), each bonded to two aluminum ions, one immediately above and one immediately below, that had moved from their octahedral (A-1) sites into interstitial sites, leaving their octahedral sites vacant. One such oxygen would compensate the charge on two excess sodium ions. The formula $Na_2O \cdot 9Al_2O_3$ would require one new interstitial oxygen and two excess sodium ions per 9-10 unit cells.

The formula $Na_2O \cdot 5.5Al_2O_3$ for β'' also requires that the charge on the second sodium going into the conduction plane be compensated by ½ oxygen. If, on the other hand, the extra sodium were compensated by an aluminum vacancy, the formula $Na_2O \cdot 5.33Al_2O_3$ would result. This is equivalent to the ternary oxide $Na_2OMgO \cdot 5Al_2O_3$ that Bettman and Peters proposed as the prototype of the β'' form (7), except that in the latter case, two-thirds of the charge of an aluminum vacancy in the spinel block is compensated by a magnesium and the remaining third by the extra sodium in the conduction plane. Roth *et. al.* (3) found by neutron diffraction that in MgO-stabilized β''-Al_2O_3 about 38% of the aluminum in the tetrahedral (A-2) sites that are near the center of the spinel block are replaced by magnesium and the remainder of the charge is compensated by extra sodium. The increase in conductivity of the β'' over the β phase presumably reflects both this higher sodium content and the lower interstitial oxygen content of the former.

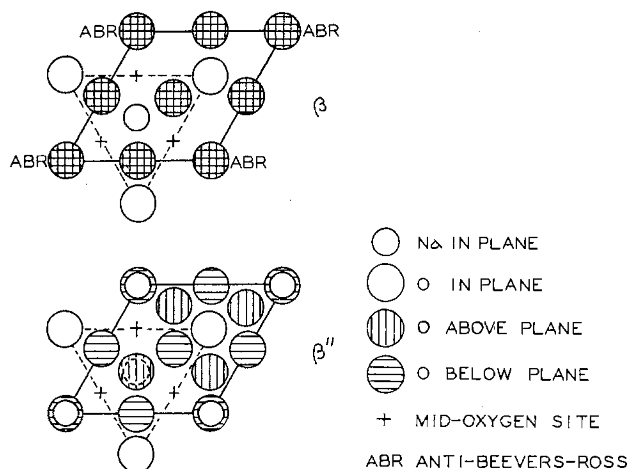

Fig. 1. Conduction plane of β- and β''-Al_2O_3

Foster and Scardefield (2) reported the growth of monocrystals of the gallium analog of β''-Al_2O_3, with the composition $Na_2O \cdot 5.7Ga_2O_3$. The β analog can now also be prepared. The ionic conductivity of these materials is considerably higher than that of their aluminum counterparts (1). Whereas at first glance this seemed to reflect the generally higher sodium content of the gallium materials, there was the complication that, in the β'' form especially, the sodium content was so high that most of the Na sites should have been full, and the disorder, which is thought to be the principal prerequisite for fast ion conductivity, should have been low. Moreover, since there was no Mg present in the β''-gallate, charge compensation for the excess sodium presumably would have had to be by additional interstitial oxygens in bridging positions where it would be expected to interfere with Na^+ migration.

Yao and Kummer (8) carried out self-diffusion and alkali ion exchange experiments in β-Al_2O_3 and obtained the diffusion coefficients and information about mixed alkali ion occupancy of the labile sites. In this paper we report similar studies with β- and β''-Na-gallate carried out in an effort to improve our understanding of the conduction process in this class of materials. We have also obtained new information about site occupancy and the alkali ion distribution.

Experimental

Self-diffusion in β- and β''-Na-gallate.—Sodium self-diffusion was followed by observing the exchange of radioactive sodium between a monocrystal of the gallate, which had been synthesized with a Na-22 tracer (2.6 yr half-life), and a melt of ordinary $NaNO_3$, at 350°C. Na-22 was obtained from the New England Nuclear Corporation as anhydrous carbonate with carrier added to a specific activity of approximately 100 μC/g.

Monocrystals of the β and β'' phases were grown in separate experiments by Na_2O vaporization from Na_2O-Ga_2O_3 melts. This procedure has been described elsewhere (2). Rectangular plates, 7-10 mm on a side and 2-3 mm thick, were employed. The ion migration was parallel to the large faces. A sufficient quantity of $NaNO_3$ was employed to contain roughly 250 times as much sodium as the crystal. Thus, once a steady state was achieved between the crystal and the melt, the equilibrium Na-22 content of the crystal would be reduced to roughly 0.4% of the original, if all of the sodium participated in the exchange. The melt was was vigorously stirred with a platinum stirrer for several minutes from the moment the crystal was dropped in, and intermittently thereafter. Approximately 0.25g samples of the melt were removed with preheated platinum scoops at timed intervals and their radioactivity compared to that of a standard.

Any radioactivity remaining in a crystal after the exchange was measured and compared to the activity before the exchange by counting with the identical geometry. The precision of this determination was limited only by counting statistics; however, it was only a relative measurement. The true composition was more difficult to ascertain. The possible variation in absolute sodium content of the two gallates as a function of growth temperature and charge composition was not known in detail and is presently under study. In general, the analytical problem with these materials is particularly severe because of the low sodium content. For example, a ±5% precision that would be considered acceptable for most analytical techniques

would give a possible range for a nominal $Na_2O \cdot 6Ga_2O_3$ composition of $Na_2O \cdot 5.70Ga_2O_3$ to $Na_2O \cdot 6.34Ga_2O_3$, which embraces a large part of the entire β''-β range. Even with the radiochemical technique, it still must be assumed that a portion of the boule that is analyzed is representative of the entire boule. From various analytical data and recent knowledge of the Na_2O-Ga_2O_3 phase diagram we assign compositions of $Na_2O \cdot 5.6 \pm 0.1Ga_2O_3$ and $Na_2O \cdot 6.8 \pm 0.1Ga_2O_3$ to the β'' and β crystals that were employed in the exchange experiments.

Na-K exchange in β- and β''-Na-gallate.—The rate of exchange of K for Na, and the equilibrium distribution of Na and K between the solids and $NaNO_3$-KNO_3 melts, were determined at 350°C.

The exchange of K for Na in the β and β'' crystals was carried out in the same manner as described above for Na-22-Na-23 exchange, but with molten KNO_3 as the liquid medium. The transfer of Na-22 to the molten salt was determined by radioactive counting, as before, and the assumption was made that the sodium was replaced one for one by K. This experiment gave information on the time that would be required to achieve equilibration of the composition of the solid crystals when in contact with melts of various $NaNO_3/KNO_3$ ratios. The results showed that a few hours would be adequate, but as a matter of convenience, the crystals were left in the melts overnight ($\simeq$16 hr).

The composition of the equilibrated crystals was determined by electron microprobe analysis with an accuracy of approximately ±5%.

Results

Self-diffusion of Na.—Figure 2 shows the extraction rate of tagged sodium from β''- and β-Na-gallate monocrystals. It is seen that after approximately 2.5 hr for β'' and 7 hr for β, the Na-22-Na-23 exchange had achieved equilibrium, even though substantial amounts of Na-22 remained in the crystals. Since this had the very important implication that part of the sodium was in immobile sites, it was essential to establish that the effect was real. Spurious observations could result from several sources. If the Na-22 stock contained a radioactive contaminant, such as Ca-45 or Sr-89, for example, which would selectively go into sites in the spinel block during synthesis of the compounds, it would not be distinguished from sodium when counting the gross activity of the crystals. This possibility was excluded by identifying the residual activity as entirely Na-22 by gamma-ray spectroscopy.

Accidental occlusion during growth of the crystal of some of the molten Na_2O-Ga_2O_3 charge would be another possible source of error, since this sodium would not be in labile sites and would not be exchangeable with the sodium of the $NaNO_3$. There would be the same end result if, in spite of visual evidence to the contrary, the samples were not monocrystals but contained some internal volume that was misoriented in such a way that the diffusion planes were blocked by c faces of the surrounding crystal. Figure 3 is an autoradiograph of the β'' crystal after the exchange. The residual activity is seen to be uniform throughout and cannot be due to a small internal volume of occluded or misoriented material. An autoradiograph of the β crystal showed a similar uniform distribution of the residual sodium.

The self-diffusion coefficients were determined in the following manner. The accumulation of Na-22 tracer in the molten salt bath is exactly equal to the loss of tracer by out-diffusion from the crystal. Following Yao and Kummer (8), the specimen can be treated as an infinitely long rectangular bar, since diffusion is confined to c planes and no concentration gradient develops along the c direction.

The loss of concentration of tracer from the sample after time t, $C(t)$, is given by

$$C(t) = C_o \frac{64}{\pi^4} \sum_{n=0}^{\infty} \sum_{m=0}^{\infty} \frac{1 - \exp\left\{-\left(\frac{\pi^2 Dt}{4}\right)\left(\frac{(2n+1)^2}{\omega^2} + \frac{(2m+1)^2}{l^2}\right)\right\}}{(2m+1)^2(2n+1)^2} \quad [1]$$

where C_o is the initial concentration, D is the diffusion constant, and ω and l are the width and length of the rectangular specimen.

The form of Eq. [1] (sums of many exponentials) is too complex to allow the determination of D by a direct method, such as least squares fit to the experimental data, and a trial and error method is employed. The procedure is to find an approximate value of D from a set of normalized curves of $C(t)/C_o$ *vs.* normalized time, Dt/ω^2. Several such curves are reproduced in Fig. 4 to provide a useful reference for others. They are labeled for different shape factors, *i.e.*, l/ω ratios. A single measurement of $C(t)/C_o$, preferably in the range of 0.4-0.6, for a sample characterized by a particular length/width ratio defines the ordinate for a point on the appropriate curve, then the diffusivity is obtained from the abscissa.

Departure from a perfect rectangular shape is taken into account by representing the sample as a stack of several smaller rectangular plates. Since diffusion occurs only out of the end faces, the contribution of each platelet to the over-all out-diffusion of tracer can be treated independent of the others.

The final curve of $C(t)/C_o$ *vs.* $\sqrt{t}$ is determined by summing the individual contributions of each platelet, weighted according to its volume fraction. The samples

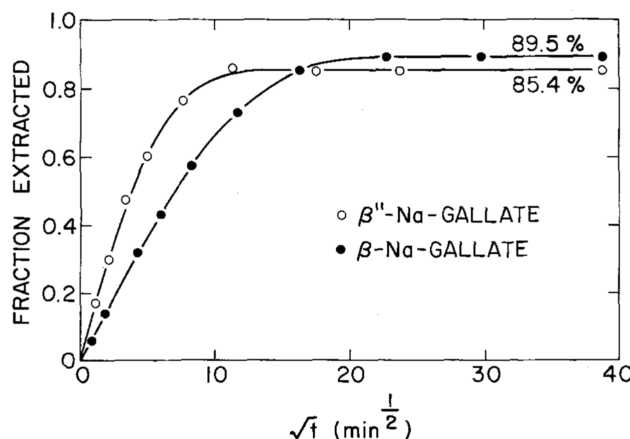

Fig. 2. Exchange of Na-22 tagged sodium with $NaNO_3$ at 350°C

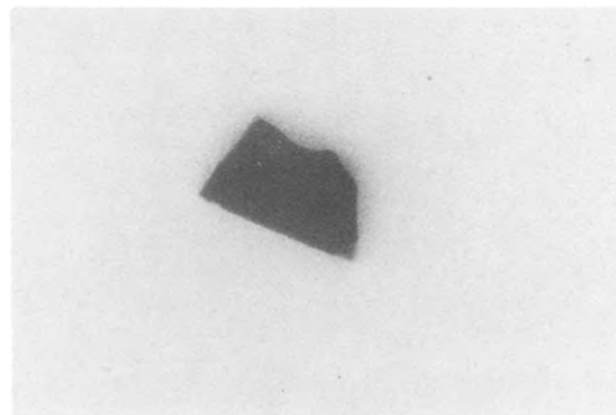

Fig. 3. Autoradiogram of residual sodium in β''-Na-gallate monocrystal.

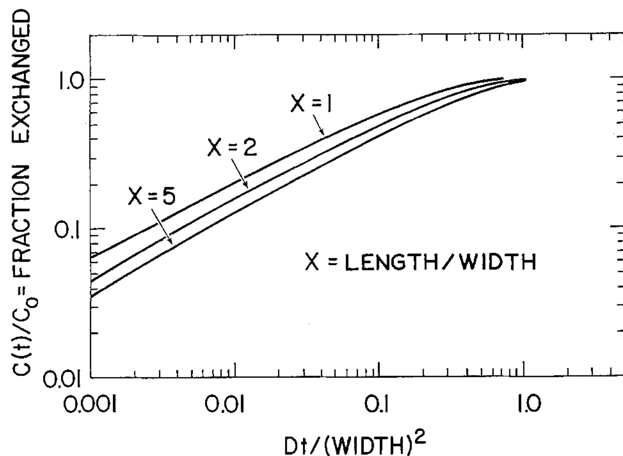

Fig. 4. Parameters for calculating D_t from out-diffusion data

were quite good and the total out-diffusion could be approximated by summing that from only two or three separate small platelets to account for deviations from perfectly rectangular shapes. The maximum error in D arising from shape irregularities is estimated as $\pm 1\%$.

To refine the calculation, several D values neighboring on the approximate one are selected and these, together with the detailed sample dimensions, are incorporated into a computer program which generates a curve of $C(t)/C_o$ *vs* $\sqrt{t}$ for each trial D. Successive refinements are made to yield a final diffusion coefficient that gives agreement between the calculated curve and experimental points to $\pm 5\%$.

Figure 5 gives the out-diffusion data for the β and β'' gallates, normalized to unity fraction exchange at long times by dividing by 0.895 for β and by 0.854 for β'' to allow for the fraction of sodium that was immobile. The solid lines are the best fits calculated by the procedure given above with the diffusion coefficients shown.

Na-K exchange in β and β'' gallate.—Figure 7 shows the equilibrium composition of β'' solid that was reached by interdiffusion of Na^+ and K^+ between monocrystals and molten $NaNO_3$-KNO_3 mixtures at 350°C. It is seen that even in the crystal that was in contact with pure KNO_3, only 85.4% of the sodium was exchanged, in agreement with the earlier Na-22-Na-23 self-diffusion result. The dashed line of Fig. 6 is the data curve, normalized to 100% replacement of the labile Na with K from a pure KNO_3 melt. Figure 7 gives similar information for β crystals.

The convex shape of the curves of Fig. 6 and 7 results from the distribution coefficient between the solid and liquid being greater for K than for Na, in-

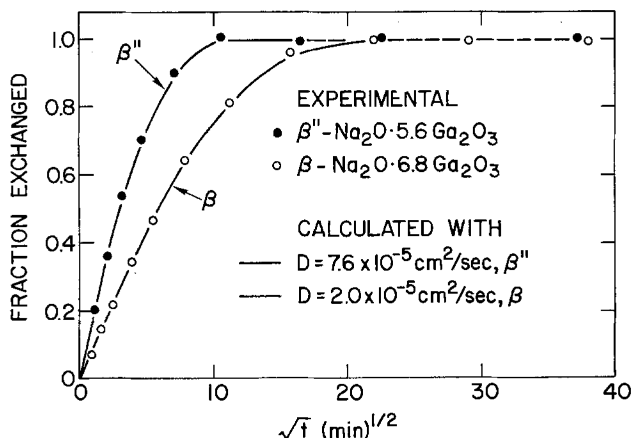

Fig. 5. Self-diffusion in β''- and β-Na-gallate monocrystals at 350°C.

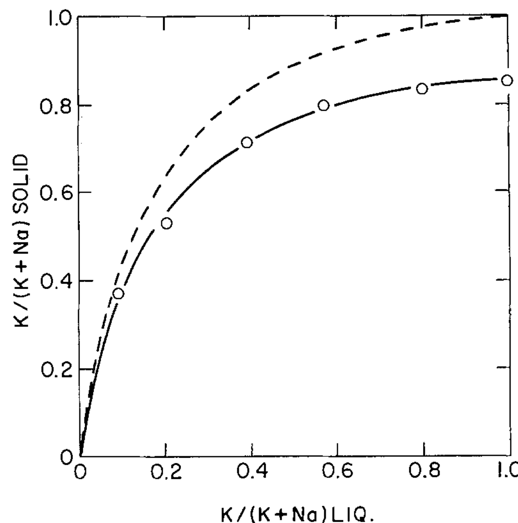

Fig. 6. Distribution of Na^+ and K^+ between B″-gallate and $NaNO_3$-KNO_3 melts at 350°C. ——— Data curve. - - - - - Normalized to K/(K+Na)solid = 1 at K/(K+Na)liq. = 1.

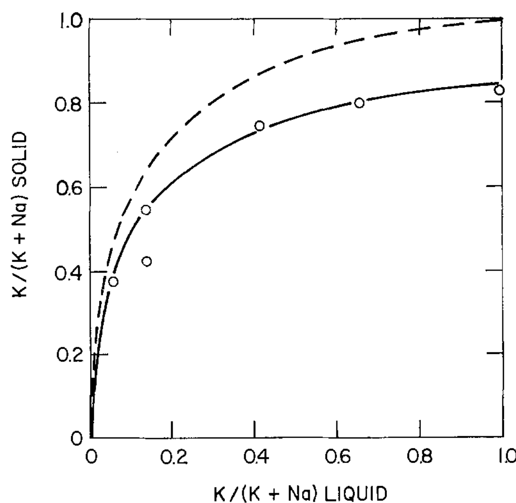

Fig. 7. Distribution of Na^+ and K^+ between β-gallate and $NaNO_3$-KNO_3 melts at 350°C. ——— Data curve. - - - - - Normalized to K/(K+Na)solid = 1 at K/(K+Na)liq. = 1.

dicating tighter binding of K in the lattice. The relative binding energies were calculated by the method of Ekedahl *et al.* (9) as employed by Yao and Kummer (8). The equilibrium is given by

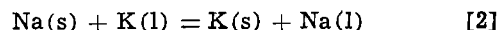

$$Na(s) + K(l) = K(s) + Na(l) \qquad [2]$$

where (s) represents the Na or K gallate crystal, and (l) represents the Na or K nitrate melt.

The equilibrium constant for [2] is

$$K_{350°C} = \{[a_{K(s)}][a_{Na(l)}]\}/\{[a_{Na(s)}][a_{K(l)}]\}$$

$$= \frac{[x_{K(s)}][\gamma_{K(s)}][x_{Na(l)}][\gamma_{(Na(l)}]}{[x_{Na(s)}][\gamma_{(Na(s)}][x_{K(l)}][\gamma_{K(l)}]} \qquad [3]$$

where x_K and x_{Na} are mole fractions, and the γ's are activity coefficients.

The activity coefficients for $NaNO_3$ and KNO_3 in their mixed melts are available in the literature, so all the terms in [3] are known except the activity coefficients for the Na and K solid gallates in solid solution. The equilibrium constant then becomes

$$K_{350°C} = Z[\gamma_{K(s)}/\gamma_{Na(s)}] \qquad [4]$$

where

$$Z = \{[x_{K(s)}][x_{Na(l)}][\gamma_{Na(l)}]\}/\{[x_{Na(s)}][x_{K(l)}][\gamma_{K(l)}]\} \qquad [5]$$

Table I. Na-K exchange results

$x_{K(l)}$	$x_{K(s)}$	$\gamma_{K(l)}$	$\gamma_{Na(l)}$	Z	log Z	$\gamma_{K(s)}$	$\gamma_{Na(s)}$	$K_{350°C}$
				For β″-Gallate				
0.090	0.406	0.713	0.962	8.400	0.924	0.977	0.990	8.29
0.203	0.640	0.752	0.916	8.122	0.910	0.990	0.977	8.23
0.391	0.828	0.814	0.854	7.847	0.895	0.997	0.960	8.15
0.571	0.915	0.870	0.807	7.731	0 888	0.999	0.950	8.13
0.799	0.972	0.937	0.857	7.550	0.878	0.999	0.943	8.00
0.993	0.999	0.994	0.720	7.612	0.881	1	0.934	8.15
								Average 8.16
				For β-Gallate				
0.060	0.470	0.699	0.977	20.25	1.306	0.783	0.874	18.14
0.140	0.647	0.731	0.940	14.90	1.173	0.894	0.738	18.05
0.413	0.870	0.821	0.846	9.84	0.993	0.986	0.542	17.90
0.657	0.950	0.900	0.785	8.50	0.929	0.998	0.466	18.20
0.993	0.999	0.998	0.723	7.74	0.889	1	0.419	18.47
								Average 18.16

From the Gibbs-Duhem relation and $dx_{K(s)} = -dx_{Na(s)}$ one obtains

$$x_{K(s)} d \ln \gamma_{K(s)} = -x_{Na(s)} d \ln \gamma_{Na(s)} \quad [6]$$

Differentiating [4] and combining with [6] gives

$$d \ln \gamma_{K(s)} = -x_{Na(s)} d \ln Z$$

$$d \ln \gamma_{Na(s)} = x_{K(s)} d \ln Z \quad [7]$$

Graphical integration of the plots of $x_{K(s)}$ and $x_{Na(s)}$ ($= 1 - x_{K(s)}$) *vs.* ln Z gives ln $\gamma_{K(s)}$ and ln $\gamma_{Na(s)}$, where the two pure alkali gallates are reference states. Table I gives the equilibria data and calculations for the β and β″ phases. The activity coefficients for $NaNO_3$ and KNO_3 in their melts are those used by Yao and Kummer (8) so that a direct comparison with their results will be possible. The consistency within the series of calculated values for the equilibrium constant is a measure of the consistency of the data. The average $K_{350°C}$ is used for calculation of the free energy change.

The standard free energy change for reaction [2] at 350°C, obtained from $\Delta G° = -RT \ln K_{350°C}$ is -2.59 kcal/mole for β″, and -3.58 kcal/mole for β. From the difference of 6.9 kcal/mole between the free energy of formation of $NaNO_3$ and KNO_3 that was employed by Yao and Kummer (8), we obtain ΔG° (K-gallate) $-$ΔG° (Na-gallate) of -9.5 kcal/mole for the β″ phase and -10.5 kcal/mole for the β.

Figure 8 shows the activity coefficients for the sodium and potassium gallates determined in the present work and the coefficients for Na- and K-β-Al_2O_3 reported by Yao and Kummer (8). No results for β″-Al_2O_3 are available because of the absence of pure crystals.

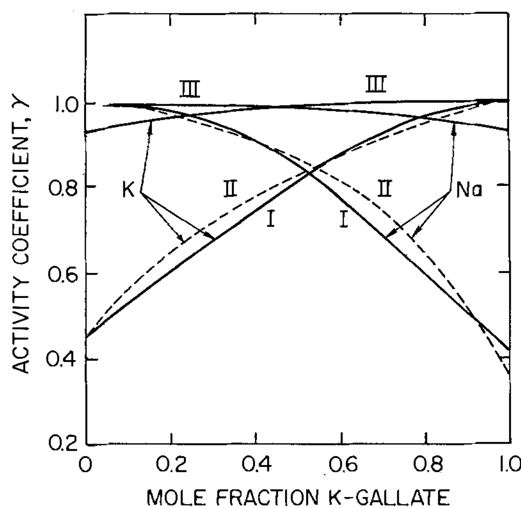

Fig. 8. Activity coefficients for Na^+ and K^+ in (Na,K)-β-gallate (I); (Na,K)-β-Al_2O_3 (II); and (Na,K)-β″-gallate (III) at 350°C.

Discussion

The self-diffusion of sodium in the sodium gallates is extremely rapid. To obtain the ionic transport from the mobility, the number of charge carriers must be known. Heretofore, it was generally assumed that all of the alkali in the class of materials typified by β-Al_2O_3 is mobile. One exception was the early work of Whittingham and Huggins (10) where it was assumed that in the β-Al_2O_3 structure only the alkali in excess of that required to completely occupy the Beevers-Ross sites should be considered "mobile" and contribute to conduction. This amounted to about 15% of the total in their case. The inference was that stoichiometric $Na_2O \cdot 11Al_2O_3$ might be a very poor (*i.e.,* normal) ionic conductor. This cannot be disproved because of the absence of a compound with the stoichiometric composition. However, it is now a commonly held view that the binding energy of sodium in the Beevers-Ross and anti-Beevers-Ross sites is not sufficiently different for a Na^+ ion to be considered immobilized in one site, particularly at elevated temperatures.

The finding that part of the sodium in the Na-gallates is immobile was new and unexpected. Whether the immobile fraction found here (14.6% for β″ and 10.5% for β) is fixed or, as is more likely, is a function of the over-all composition and the growth conditions is not yet known and is under investigation.

It is interesting to speculate on where the nonmobile sodium might be in the structures. In particular, the effect of substituting Na^+ for Ga^{+++} in the tetrahedral (A-2) sites of the spinel block will be considered. Na^+ would thus take the role of Mg^{++} in β″-Al_2O_3 (3). If in β″ and β crystals of composition $Na_2O \cdot 5.6Ga_2O_3$ and $Na_2O \cdot 6.8Ga_2O_3$, respectively, we assume that each immobile Na^+ ion substitutes for Ga^{+++}, and thereby provides charge compensation for two additional sodium ions in the conduction plane, we calculate the atom distribution given in Table II. The fraction of (A-2) gallium that is substituted for by sodium is 0.14 and 0.083 for β″ and β, respectively, compared to 0.38 of the (A-2) aluminum substituted for by magnesium in β″-Al_2O_3 (3).

It is seen that, according to this model, essentially all of the charge compensation required for the incorporation of mobile sodium beyond the $Na_2O \cdot 11Ga_2O_3$ composition is provided by sodium in the spinel block. (The very small number of additional bridging oxygens, 0.037 atoms per plane for β″ and 0.045 for β, is within the analytical error and can be disregarded.) The prototype compound for the sodium gallate then becomes $2Na_2O \cdot 5Ga_2O_3$, which would be equivalent to the $Na_2OMgO \cdot 5Al_2O_3$ suggested by Bettman and Peters as the prototype for β″-Al_2O_3 (7). $2Na_2O \cdot 5Ga_2O_3$ does not actually exist in the Na_2O-Ga_2O_3 system, which has only $Na_2OGa_2O_3$, $3Na_2O \cdot 5Ga_2O_3$, and $Na_2O \cdot 3Ga_2O_3$ as stable stoichiometric compounds.

The very high sodium contents (up to $Na_2O \cdot 5.25 Ga_2O_3$) that have been observed for β″-Na-gallate are now understandable in view of the partition of sodium between the conduction plane and spinel block.

In all studies in recent years on β-Al_2O_3 it has been assumed that all of the sodium is in the conduction plane and mobile. This had been indicated by the alkali ion exchange experiments of Yao and Kummer (8). We exchanged all of the mobile sodium of a

Table II. Atom distribution in β″- and β-Na-gallate

Composition	$Na_2O \cdot 5.6Ga_2O_3$	$Na_2O \cdot 6.8Ga_2O_3$
Fraction of immobile Na	0.146	0.105
Na in conduction plane	1.634	1.426
Na in spinel block	0.280	0.167
Ga in spinel block	10.720	10.832
O in spinel block	16.000	16.000
O in bridging positions	1.037	1.045

β-Al_2O_3 monocrystal with potassium from a KNO_3 melt at 350°C and found that no residual sodium could be detected in the crystal by an electron microprobe analysis. Although only a Czochralski-grown crystal obtained from Union Carbide was studied, and the situation might be different for crystals grown by other methods, the implication is that partition of sodium between mobile and nonmobile sites occurs only in the gallates. This possibly reflects the greater size disparity between Na and Al than between Na and Ga.

Correlation factors.—Having obtained the tracer diffusion constants for β''- and β-Na-gallate, we can determine the correlation factor, $f = D_t/D_\sigma$, from the ionic conductivity, which was reported earlier (1). Table III gives the pertinent information. The number of charge carriers, n, is taken as the sodium content of the crystals, corrected, in the case of the gallates, for the nonmobile sodium. The sodium concentration for β-Al_2O_3 was based on a $Na_2O \cdot 9Al_2O_3$ composition determined by us for the Union Carbide monocrystal. The conductivity of β-Al_2O_3 was also our value (1), which agrees well with that of Fielder *et al.* (11). The tracer diffusion constant for β-Al_2O_3 was taken from Yao and Kummer (8) on material of a different origin. The correlation factor of 0.64 for β-Al_2O_3 was calculated from the data shown. The value of 0.60 was calculated by Whittingham and Huggins from the conductivity of material similar to that employed by Yao and Kummer, but assuming that the charge carrier concentration was only the 15% sodium in excess of that required to fill the Beevers-Ross sites, as described previously. The range for f of 0.60-0.64 thus reflects the uncertainty in the data for β-Al_2O_3 and the different ways of treating it.

One calculation of the correlation factor for a two-dimensional-hexagonal lattice gives $f = 0.56$ (12). This is close to our value of 0.58 for the β-gallate and reasonably close to the lower end of the range for β-Al_2O_3. However, that calculation assumes a vacancy mechanism for diffusion. Inherent in the calculation is the assumption that the vacancies are identical and are few in number (0.001-0.01%, as typical for metals at elevated temperatures, for example), so a forward jump of an atom into a vacant site is likely to be followed by a reverse jump into the site from which it came; hence, the jump is highly correlated. This situation does not obtain in the β structure where the Beevers-Ross and anti-Beevers-Ross sites have different energies, and the vacancy concentration is large. (In the β-gallate example calculated in Table II, the vacancy concentration is 28.7%, where the Beevers-Ross and anti-Beevers-Ross sites are considered together.) Whittingham and Huggins (10) recognized this difficulty and proposed a noncolinear interstitialcy mechanism for diffusion in β-Al_2O_3, with the Beevers-Ross site as the normal site and the anti-Beevers-Ross site as the interstitial site. The complete jump path is through an angle of 120°. They calculated a correlation factor of 0.60 for the β structure, which agrees well with the 0.58 to 0.64 range observed experimentally for the β-gallate and aluminate.

The correlation factor of 0.82 for the β''-gallate is too large to be explained by any obvious diffusion mechanism. The Na^+ sites are identical and each complete jump is along a straight line. The simple vacancy mechanism might be more reasonable in this case, and an increase in the correlation factor beyond 0.56 might be attributable to the large concentration of vacancies, which in the extreme would lead to uncorrelated interstitial-like jumps with $f = 1$. Whether the observed correlation factor of 0.82 for the β'' phase could be accounted for by the vacancy content ($\simeq$18% from Table II) cannot be determined because of the lack of an accepted diffusion model. Sato and Kikuchi (13) presented a theoretical model for correlation effects in both β and β'' structures based on a "path probability" concept. Their model predicts that an ideal random walk process would give a linear dependence of f on the degree of cation site filling, terminating at $f = 0.5$ with complete site filling [or, with a more rigorous calculation, at $f = 0.33$, according to Ref. (13)] and extrapolation to $f = 1$ at zero filling. Attractive cation-cation interactions (leading to clustering) would lead to large values of f, especially at moderate to high site filling, and repulsive cation-cation interactions (leading to ordering) would lead to smaller values. The deviation from random walk behavior would be greater the lower the temperature where the interaction energies would be substantial compared to kT.

According to the model of Sato and Kikuchi, our value for f of 0.82 for the β''-gallate with approximately 82% site filling could only result from strong attractive Na^+-Na^+ interactions at low temperatures. This is contrary to their presumption that mobile cations should tend to order rather than cluster in superionic conductor lattices and, in fact, they predict that in the β'' structure f should be about 1/3. Their conclusions are more or less supported by Murch and Thorn (14) who also assume repulsive cation-cation interactions, with the principal difference being that Saito and Kikuchi assume that f_c, the charge correlation factor, is unity in the β'' structure, whereas Murch and Thorn give it nonunity values as a result of ordering, in spite of *a priori* site equivalency in the structure. Our correlation factor, f, is the Haven ratio, $H_R = f_t/f_c$, in the nomenclature of Saito and Kikuchi and Murch and Thorn.

No other diffusion measurements have been reported for β''-gallate. Correlation factors for sintered, polycrystalline, MgO and Li_2O stabilized β''-Al_2O_3 that were reported by Miles *et al.* (15) are vastly different from ours for β''-gallate monocrystals. Tentatively, we must ascribe this discrepancy either to the MgO-Li_2O stabilization of the β''-Al_2O_3 or, as they themselves suggest, to the polycrystallinity of their samples.

The great disparity between our observed correlation factor for the β''-gallate and the predictions of the various theoretical models leads us to examine our experimental procedure for possible error. The high correlation factor could result from a D_t that is too large, or a D_σ that is too small. Too large a D_t can be encountered with a material if there are unsuspected grain boundaries which, in the general case, provide highly disordered paths for rapid diffusion. A large apparent D_t could also result if the specimen has microcracks into which the "reservoir" liquid can creep and effectively shorten the path length. In β''-Na-gallate, however, diffusion through the bulk is actually easier than through crystal defects and boundaries. Moreover, it has been our experience that any microcracks in this material are invariably in the easy cleaving c planes parallel to the diffusion path. Reservoir liquid that penetrates such cracks would have no access to the conduction planes. Thus, it is difficult to visualize any circumstance that would result in a tracer diffusion constant for β''-gallate that is much too large.

It is easier to visualize ways in which the measured D_σ could be too small. The principal experimental problem in measuring the conductivity of a two-dimensional conductor is to insure that the edges of all

Table III. Transport results for gallates and β-Al_2O_3 at 350°C

	β-Gallate	β''-Gallate	β-Al_2O_3
n/cm^3	4.66×10^{21}	4.77×10^{21}	3.98×10^{21}
$\sigma(\Omega\text{-cm})^{-1}$	0.481	1.316	0.197
$D_\sigma(cm^2/sec)$	3.46×10^{-5}	9.26×10^{-5}	1.65×10^{-5}
$D_t(cm^2/sec)$	2.0×10^{-5}	7.6×10^{-5}	1.07×10^{-5}
$f = D_t/D_\sigma$	0.58	0.82	0.64 (0.60)*

* The figure in parenthesis is from Ref. (10).

the c planes are contacted, because the spreading resistance between a contacted plane and an adjacent noncontacted plane is essentially infinite. There is no way to know that contacting is complete in each instance, but a considerable number of β''-gallate crystals have now been measured, and reproducibility has been excellent. Moreover, it would be difficult to explain conductivity of this material 2 to 2.5 times higher than observed, as would be necessary to give a correlation factor that conforms to the diffusion models that were cited above.

Crystal defects such as faults or small misalignments might seriously affect charge transport in a two-dimensional conductor. However, they should affect the tracer diffusion to the same degree and have minimal effect on the correlation factor.

A more serious matter is whether the number of charge carriers, n, for electrical transport should be equated to the mobile sodium concentration when calculating D_σ from the Nernst-Einstein relation, as done in Table III, for we do not have independent information about the carrier mobility. Perhaps the most significant observation that can be made about the correlation factors at this time is that when the data for the β'' and β phases are treated in the same manner, the large difference in D_t/D_σ exists.

Na-K exchange equilibria.—The principal information obtained from the Na-K exchange equilibria is the activity coefficients of the Na- and K-gallates when present together as a mixed crystal. Although the pure compounds were taken as the standard states, the activity coefficients will reflect the interaction between the Na^+ and K^+ ions if their environment does not change when the pure compounds mix. From our understanding of these materials, that appears to be a reasonable assumption.

When two compounds mix ideally, the free energy minimization results entirely from the entropy gain in achieving a random distribution. Activity coefficients greater than unity (positive excess free energy) are usually associated with repulsive interactions between unlike species which, in the extreme, lead to phase separation. Coefficients less than unity (negative excess free energy) are usually associated with attractive interactions between unlike species which, in the extreme, lead to ordering. There can be many complicating effects, for example, association to give unlike pairs which then repulse similar unlike pairs, which can confuse the picture, but the simplest interpretation of the activity coefficients in Fig. 8 is that Na^+ and K^+ ions in β''-gallate are essentially indifferent to each other, whereas in β-gallate there is a substantial attractive interaction, which should lead to ordering. The fact that the coefficients for β-gallate agree so well with those for β-Al_2O_3 determined by Yao and Kummer (8) suggests that the principal difference is between the β and β'' structures rather than between the gallates and aluminates of the same structure. Random distribution of Na^+ and K^+ over the identical sites in the β'' lattice, and preferential occupancy of the larger Beevers-Ross sites by K^+ and the smaller anti-Beevers-Ross sites, or perhaps the mid-oxygen positions, by Na^+, in the β structure would be consistent with the trends in the activity coefficients.

Summary

1. The self-diffusion coefficients for Na^+ in β''- and β-Na-gallate are 7.6×10^{-5} and 2.0×10^{-5} cm²/sec, respectively, at 350°C.

2. Approximately 10-15% of the sodium in these compounds is nonmobile and is presumably in the spinel block. It is proposed that a Na^+ ion substitutes for a Ga^{+++} ion in the block and provides charge compensation for two additional Na^+ ions in the conduction plane.

3. The correlation factor, $f = D_t/D_\sigma$, is 0.58 for the β phase in good agreement with that determined for β-Al_2O_3, where a noncolinear interstitialcy diffusion mechanism had been proposed. A much larger value of $f = 0.82$ was found for the β'' phase, which cannot be accounted for by any proposed diffusion model.

4. Na^+ and K^+ mix nearly ideally in the β''-gallate structure, whereas in the β structure, strong interactions suggestive of ordering are encountered.

Manuscript submitted Jan. 26, 1978; revised manuscript received May 10, 1978.

Any discussion of this paper will appear in a Discussion Section to be published in the June 1979 JOURNAL. All discussions for the June 1979 Discussion Section should be submitted by Feb. 1, 1979.

Publication costs of this article were assisted by IBM Thomas J. Watson Research Center.

REFERENCES

1. G. V. Chandrashekhar and L. M. Foster, *This Journal*, **124**, 329 (1977).
2. L. M. Foster and J. E. Scardefield, *ibid.*, **124**, 434 (1977).
3. W. L. Roth, F. Reidinger, and S. J. LaPlaca, "Superionic Conductors," G. D. Mahan and W. L. Roth, Editors, p. 223, Plenum Press, New York (1976).
4. C. W. Stillwell, *J. Phys. Chem.*, **30**, 1441 (1926).
5. C. A. Beevers and M. A. Ross, *Z. Kristallogr.*, **97**, 59 (1937).
6. W. L. Roth, *J. Solid State Chem.*, **4**, 60 (1972).
7. M. Bettman and C. R. Peters, *J. Phy. Chem.*, **73**, 1774 (1969).
8. Yung-Fang Yu Yao and J. T. Kummer, *J. Inorg. Nucl. Chem.*, **29**, 2453 (1967).
9. E. Ekedahl, E. Hogfeldt, and L. G. Sillen, *Acta. Chem. Scand.*, **4**, 556 (1950).
10. M. S. Whittingham and R. A. Huggins, *This Journal*, **118**, 1 (1971).
11. W. L. Fielder, H. E. Kautz, J. S. Fordyce, and J. Singer, *ibid.*, **122**, 528 (1975).
12. K. Compaan and Y. Haven, *Trans. Faraday Soc.*, **52**, 786 (1956).
13. H. Sato and R. Kikuchi, *J. Chem. Phys.*, **55**, 677 (1971).
14. G. E. Murch and R. J. Thorn, *Philos. Mag.*, **36**, 529 (1977).
15. L. J. Miles, I. W. Jones, A. D. Le Claire, and A. H. Rowe, Abstract 166, p. 425, The Electrochemical Society Extended Abstracts, Spring Meeting, Houston, Texas, May 7-11, 1972.

The Use of 1.1.1.-Trichloroethane as an Optimized Additive to Improve the Silicon Thermal Oxidation Technology

Edmond J. Janssens,[1] and Gilbert J. Declerck*

Elektronica, Systemen, Automatisatie en Technologie, Departement Elektrotechniek, Katholieke Universiteit Leuven, B-3030 Heverlee, Belgium

ABSTRACT

Based on the pyrolysis of trichloroethene (C_2HCl_3), also referred to as TCE, and the thermodynamic analysis of its reaction products a substitute for TCE is found. It is characterized by better physical and chemical properties and behaves as an additive during silicon oxidation identical to HCl. This chlorinated hydrocarbon, 1.1.1.-trichloroethane (referred to as C33) is used for fabrication of MOS capacitors on n-type silicon to study the properties of oxides grown with this additive. Special attention is paid to the properties influencing the performance of charge coupled devices. Storage times of 500 sec, oxide defect density of 10/cm^2, and surface-state densities lower than 5×10^9/cm^2 eV are achieved. The cleaning effect on the furnace tube yields a mobile ion density lower than 2×10^9/cm^2. The fixed oxide charge on (100) material is 5×10^{10} cm^{-2}. Fabrication of CCD's with this technology proves its suitability in silicon device processing.

The superior behavior of SiO_2 grown in the presence of HCl has been described in detail (1-4). The lack of safety and special installation requirements involved with the use of HCl forced people to look for safer chlorine sources such as trichloroethene (TCE) (5) and carbon-tetrachloride (CCl_4) (8). TCE has already been proven to improve the oxide quality (4, 6-8). In the past a clear distinction between HCl oxides and Cl_2 oxides has been found (1, 8, 12, 13) and is discussed below. Moreover during recent work some similarity between Cl_2 and TCE oxides is observed:

1. From Fig. 1 one can see the same behavior in oxidation rate enhancement as a function of the additive concentration (expressed in molar ratio of additive to oxygen) for both Cl_2 and TCE as compared to the much lower increase for HCl. This difference is not fully explained by taking into account the total amount of chlorine atoms in the oxidizing ambient.
2. For oxides grown at 1000°C Osburn (4) observed a minimum oxide defect density for Cl_2 oxides at 0.5% Cl_2 and for TCE oxides at 1%. The minimum defect density for HCl oxides is much lower and occurs at 3% HCl.
3. The corrosion limit is between 2 and 3% for Cl_2 (1, 8) and 2% for TCE, while much higher concentrations of HCl, 10-20% are needed (1, 9) to introduce corrosion, dependent on substrate orientation, oxidation temperature, and time.
4. The same negative bias instability has been observed for Cl_2 and TCE oxides (10, 11).

By means of a theoretical study based on the thermodynamic equilibrium data we show in the next section the close relationship between Cl_2 and TCE oxides. Furthermore as a result of this chemical analysis, C33 (1.1.1.-trichloroethane) is proposed as a better substitute for HCl. The electrical properties of oxides grown with this additive are discussed in detail in the final section of this paper.

Chemical Analysis

In order to study the differences between HCl and TCE it was necessary to find out what reaction products are formed by heating mixtures of O_2 and HCl or TCE. Kaesche-Krischer (14) reported the combustibility of TCE in atmospheres containing at least 40% oxygen. From the low gas velocity in the furnace (about 1 cm/sec for a 1.5 liters/min flow in a 4 in. tube), compared to the burning velocity (10 cm/sec), and from the comparison of furnace temperatures (900°-1200°C) and the flame temperature (1100°C), one can conclude that there is total combustion. Because of the long transit time of the gas in the hot zone of the furnace (1 min) the combustion products will react until thermodynamic equilibrium is

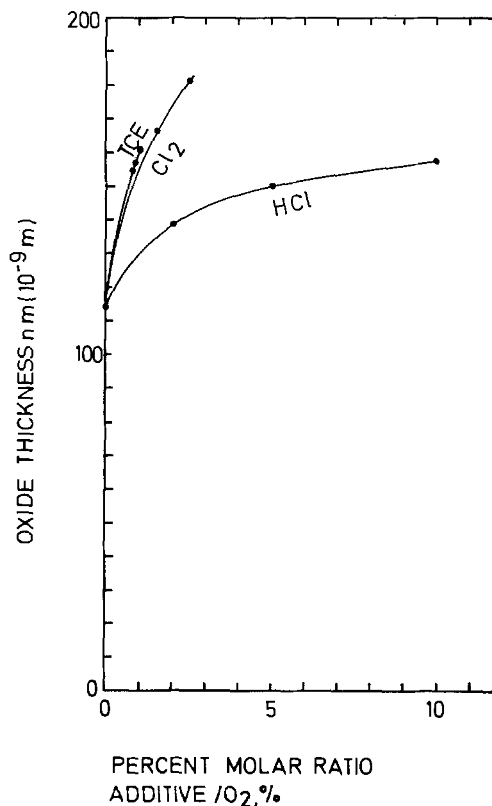

Fig. 1. The increase in oxidation rate, here shown as oxide thickness enhancement, as a function of halogen additive concentrations. The oxides are grown at 1150°C for 34 min on n-type (100) material. The HCl and Cl_2 data are from Kriegler (1).

* Electrochemical Society Active Member.
[1] Present address: Bell Telephone Manufacturing Cie, Department E.A., 2000 Antwerpen, Belgium.

Key words: MOS structure, oxide quality, halogen oxidation, minority carrier lifetime.

reached. Kaesche-Krischer proposes following over-all reaction occurring in lean mixtures

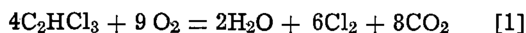

$$4C_2HCl_3 + 9\,O_2 = 2H_2O + 6Cl_2 + 8CO_2 \quad [1]$$

Between the combustion products the following reaction can occur

$$2H_2O + 2Cl_2 = 4HCl + O_2 \quad [2]$$

This should also be the equilibrium reaction occurring when HCl/O_2 mixtures are allowed to react, *e.g.*, in a heated furnace (20). A computer performed thermodynamic analysis based on free energy data (15, 16) yields the partial pressures and concentrations of the gaseous reaction products as a function of temperature and additive concentrations. These results are represented in Fig. 2a for TCE, Fig. 2b for HCl, Fig. 2c for $C_2H_3Cl_3$ (C33), and Fig. 2d for CH_2Cl_2 (dichloromethane also referred to as C22). Because the concentrations of the reaction products are directly proportional to the additive concentration only the ratio of the former to the latter is used. This is valid as long as very lean mixtures are used, additive/O_2 ratios smaller than 10%, a condition which is always satisfied in this study.

At temperatures above 600°C the free energy of formation of HCl is lower than of H_2O. In a chlorine- and oxygen-containing atmosphere at normal oxidation temperatures the hydrogen reacts to form HCl rather than H_2O. The combustion of TCE yields three chlorine atoms for every hydrogen atom and thus almost all of the hydrogen is consumed to give HCl while only trace amounts of water are formed. The excess chlorine atoms form Cl_2, as shown in Fig. 2a. The atmosphere when using TCE consists mainly of almost equal amounts of Cl_2 and HCl. This explains

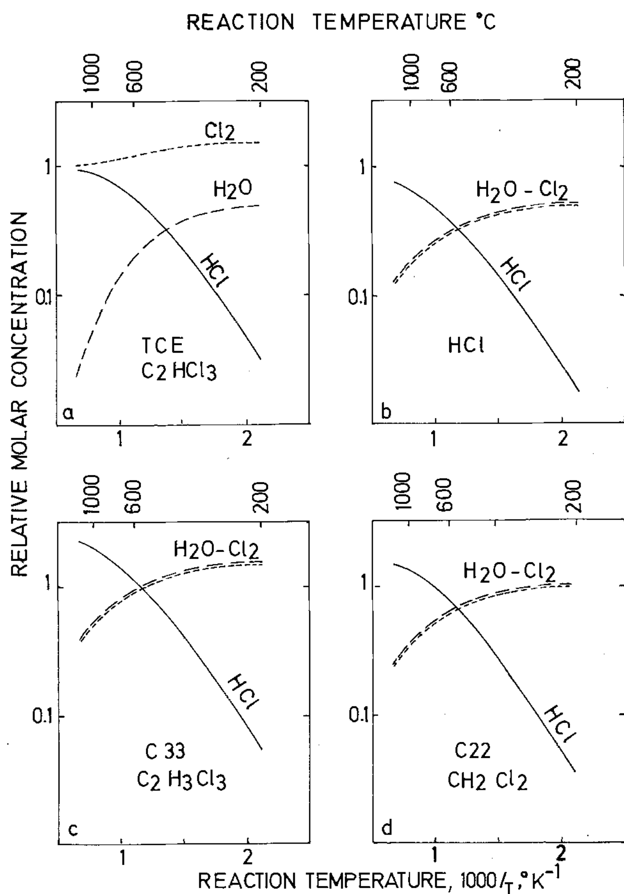

Fig. 2. The concentrations of the reaction products HCl, H_2O, and Cl_2, relative to the additive concentration are given as a function of the reaction temperature: a, the pyrolysis of TCE(C_2HCl_3): b, the pyrolysis of HCl; c, the pyrolysis of C33 ($C_2H_3Cl_3$); d, the pyrolysis of C22 (CH_2Cl_2).

the "chlorine-like" behavior of TCE. For HCl, however, an equal number of chlorine and hydrogen atoms is available, resulting at high temperature in a main quantity of HCl and a minor part of H_2O and Cl_2. In order to obtain an atmosphere in the furnace similar to HCl it is thus necessary to use an additive with an equal number of chlorine and hydrogen atoms. These additives such as $C_2H_3Cl_3$ (C33) and CH_2Cl_2 (C22) yield atmospheres as shown in Fig. 2c and 2d, respectively. They have exactly the same relative concentrations of reaction products as HCl. C33 yields three times higher and C22 yields two times higher concentrations than HCl. This unique dependence of the atmosphere on the H/Cl ratio is in agreement with the analysis of the Si-H-Cl system (17).

Our analysis is based on the assumption of thermodynamic equilibrium which is validated due to the high temperatures and the long transit time of the products through the hot zone of the furnace. The close agreement between the oxidation rate enhancement of HCl and C33 as is shown later on, confirms this.

Other reaction products with oxygen, such as HClO. ClO, and HO, are not included in the analysis because at high temperatures their free energy is too high to result in concentrations greater than 10^{-4} (18), so that they do not interfere in the comparison of the additives. Moreover different additives giving similar atmospheres will also yield the same byproducts. The carbon atoms of the additives do not intervene as long as lean mixtures are used to allow the formation of CO_2 (carbon dioxide). Although CO_2 is thermodynamically less stable than SiO_2 it is not expected to compete with oxygen in the oxidation reaction (19) also because of its lower diffusivity in SiO_2 due to its large molecular dimension. The formation of a Si-C (silicon-carbide) bond is also not likely because it is unstable in the presence of O_2 at high temperatures and will react to form SiO_2 and CO_2 (16). The carbon monoxide formed in mixtures which are too rich leads to the formation of the highly toxic phosgene ($COCl_2$) when it reaches the cold end of the furnace tube. This is a limiting factor in the safe use of every chlorinated hydrocarbon.

The choice of C33 as the optimum additive.—The conclusion from previous analysis is that the additive must have a molecular composition with the same number of chlorine and hydrogen atoms. Among the compounds satisfying this condition C33 is selected as the one with the most suitable physical and physiological properties: (*i*) boiling point of 75°C (21), it has also the suitable vapor pressure to be dissolved in a carrier gas at room temperature; (*ii*) noncorrosive; (*iii*) chemically stable; (*iv*) noninflammable in air; and (*v*) high purity semiconductor grade commercially available at low costs. In addition, C33 has improved physiological properties over TCE. The toxicity expressed by means of the TLV (threshold limit value) for C33 is 350 ppm and for TCE 100 ppm (23). It has to be distinguished from its isomer 1.1.2-trichloroethane which is highly toxic (TLV = 10 ppm). TCE is also known to cause liver and kidney injury and heart attack by repeated exposure even under the TLV value (22). TCE also suffers from instability under the influence of light by splitting off HCl.

Experimental Procedure

The experimental setup to grow C33 oxides consists of a standard resistance heated quartz tube equipped with a main N_2 and O_2 flow and with a bypass carrier gas (N_2 or O_2) which is led through a bubbler filled with C33 or TCE. The bubbler consists of two gas wash flasks put in series and held at room temperature. Weighing experiments were performed to prove that the carrier gas was saturated, within the accuracy of the measurement, for all flows used in the experiment. The amount of additive introduced

into the furnace was determined by controlling the vapor pressure of the liquid, depending on the temperature, and the gas flow through the bubbler. An extra valve is also needed between the bubbler and the furnace tube inlet to prevent C33 vapor from entering the furnace when there is no oxygen present.

The properties of the oxides are measured on MOS capacitors fabricated as follows: n-type Si-wafers, (100) oriented, 10-20 Ω-cm, were given a standard rinse (24) before oxidation at one of the following temperatures; 1000°, 1100°, 1150°, or 1200°C for different times with different concentrations of C33 or TCE. This oxidation is followed by an anneal *in situ* in N_2. Before E-beam metallization with aluminum the back side oxide is stripped in buffered HF. The MOS capacitor metal electrodes are 0.5 × 0.5 mm squares defined by photolithography. The back side metallization is followed by a low temperature anneal of 30 min at 450°C in forming gas. Other properties are tested on N-channel surface CCD's fabricated with the 3 level polysilicon gate technology (25).

Results and Discussion

Influence of C33 and TCE on the properties of the silicon dioxide film.—The increase in oxidation rate. —The use of chlorine-containing ambients enhances the oxidation. The thickness, determined ellipsometrically, of oxides grown under the same conditions (1150°C, 34 min, (100), n-type Si) but with different concentrations of additives is shown in Fig. 3. In the abscissa the equivalent HCl concentration (C33 concentration × 3) is used as a means of comparison between C33 oxides and HCl oxides.

The increase of oxidation rate is identical for C33 and HCl which confirms the assumption of total combustion made in the previous section. When using TCE the oxidation rate, as shown in Fig. 1, is much closer to that observed with Cl_2 gas. This increase in oxidation rate, cannot be explained by the influence of water vapor formed during the combustion of HCl since it occurs also in Cl_2 atmospheres according to Kriegler (1). Two other mechanisms account for the

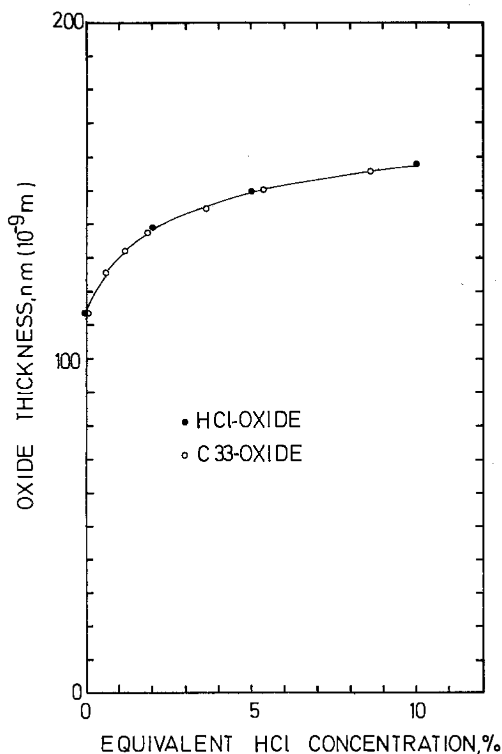

Fig. 3. The increase in oxide thickness by the use of HCl and C33 is given as a function of effective HCl concentration (C33 times 3), oxides grown at 1150°C, 34 min on n-type (100) material. The HCl oxides are from Kriegler (1).

enhanced oxidation (9, 20): (*i*) the higher diffusivity of O_2 in the presence of Cl_2 or HCl, or (*ii*) the increased reaction velocity. Chlorine acts as a catalyst on the oxidation reaction. The first step in the reaction should be the chlorination of silicon. This is a much faster reaction than the oxidation, the reaction velocity being related to the etch rate of silicon. This is about 1.5 μm/min in 0.5% HCl/H_2 at 1200°C for (111) surfaces and 3.4 μm/min for (100) surfaces (26). The oxidation reaction velocity is only 5.5 10^{-2} μm/min in 5% O_2/N_2 mixtures at 1200°C for (111) planes (27) and is slightly dependent on surface orientation. The second reaction step is the conversion into SiO_2 because of the higher thermodynamic stability of the latter. This two step reaction may proceed faster than a single step reaction. A too high chlorine concentration causes degeneration of the oxidation because the oxidation step is no longer competitive and etching of the silicon occurs.

Oxide defect density and dielectric breakdown.—The oxide defect density is one of the limiting factors in the fabrication of devices requiring large active areas. The addition of halogen during oxidation has been found to reduce this defect density (4). The improvement by the use of C33 and TCE is shown in Fig. 4. The distribution of the first self-healing breakdown and final breakdown electric fields are shown for a dry thermal oxide (referred to as DTO), a 1% C33 oxide and a 1% TCE oxide, all grown at 1000°C for 2 hr. These distributions are measured by an automated system based on a circuit similar to the one described by Osburn *et al.* (28). The thickness of the metal layer was only 30 nm to allow the self-healing breakdown to be distinguished from the final breakdown. The ramp rate was 1 MV/cm·sec.

It is observed that the maximum breakdown field as related to the intrinsic or electronic breakdown of the silicon dioxide (29) is not influenced by "chlorine" addition. More important however is the reduction of the defect density as shown in Fig. 5 where the densities averaged for several wafers are displayed. These densities are calculated according to Osburn and Ormond (30) using capacitors of three different areas, respectively, 0.072, 0.2, and 0.8 mm^2. These figures result from 1200 measurements performed over four different runs. The defect density decreases from about 150 cm^{-2} for the DTO oxide to 9 and 15 cm^{-2} for the 1% C33 and 1% TCE oxide, respectively. Occasionally C33 oxides are grown that show no defects. The increase at higher TCE concentrations, due to the higher corrosivity (4), limits the use of this additive.

Two kinds of effects are believed to explain the reduction of defects. First charged impurities, especially sodium and also interface states or oxide charges, enhance the applied field or reduce the barrier height (30). These defects are eliminated by HCl oxidation and are discussed in the following sections. A second origin of reduced dielectric breakdown is physical defects either on the silicon substrate or in the oxide film. Etching of the silicon prior to oxidation by means of HCl only reduces the defect density when subsequent oxidation is performed in a very clean ambient (29), although a strong relation is found between substrate and oxide defects (31). One of the reasons is the effect of sodium which not only acts as a charged contaminant but also as a silicon dioxide network modifier causing crystalline particulates to occur. These can be places of reduced strength and can also lead to a path of enhanced diffusion for the aluminum causing shorts during low temperature anneal (29). The formation of interface imperfections as described by Johannesson (33) during oxidation, which consists in Si-inclusions into the oxide, can also reduce the dielectric strength. This can be reduced by adding chlorine during oxidation. Physical defects resulting from the absorption at the Si-surface of airborne particulates during wafer storage or

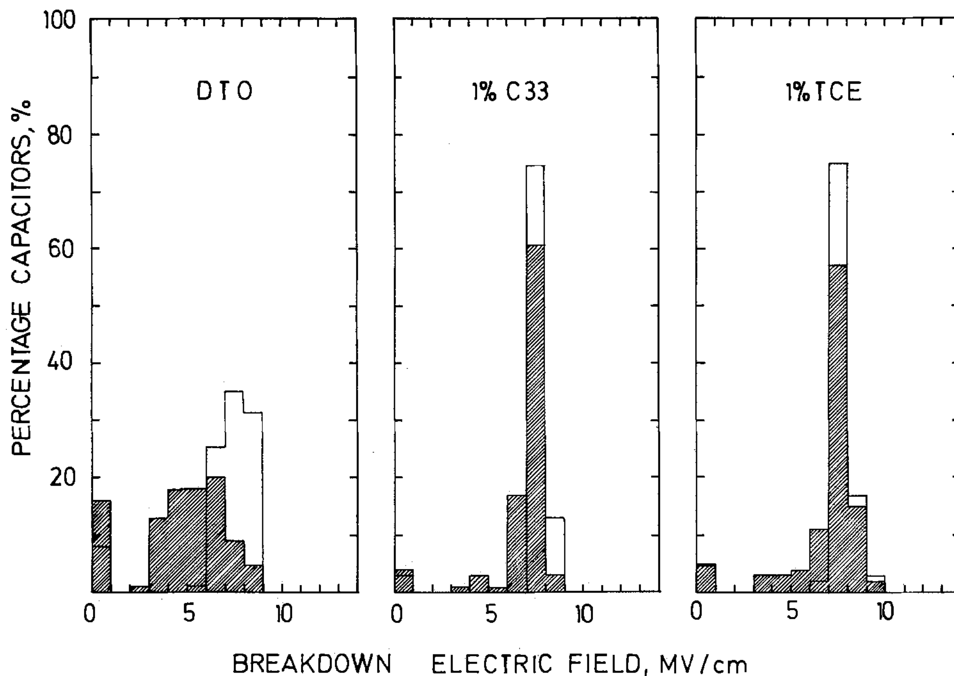

Fig. 4. The distribution of the first self-healing (shaded area) and final breakdown electric field for a dry thermal oxide (DTO), a 1% C33, and a 1% TCE oxide, all grown at 1000°C for 2 hr. The capacitor area is 0.8 mm^2. The defect density is, respectively, 120/cm^2, 9/cm^2, and 15/cm^2 due to the higher occurrence of low field breakdown observed for the DTO and the TCE oxide.

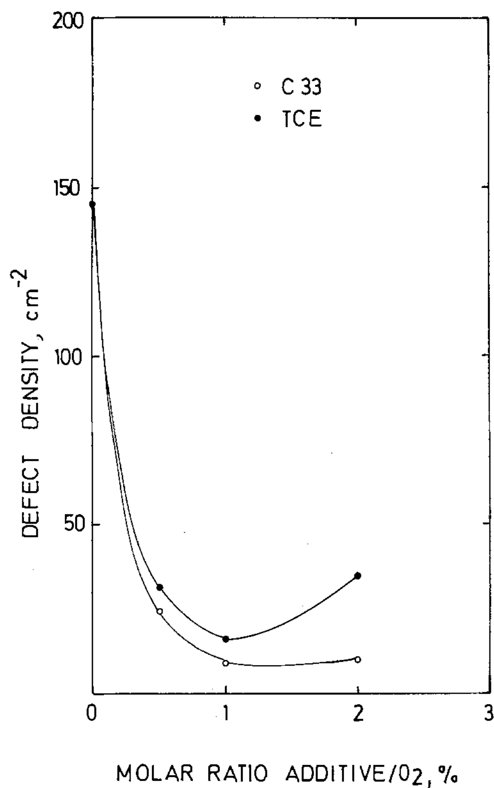

Fig. 5. The decrease of defect density as a function of additive concentration. The oxidations are the same as for Fig. 4.

drying in filtered nitrogen and residue of the cleaning solutions are found to be responsible for defects (32). Oxidation with HCl as well as H_2 high temperature treatment seems to be very effective for the desorption of these contaminants (32).

The mobile oxide charge.—This charge, mainly caused by sodium ions (34), is destructive for the reliability of MOS devices. Thus several methods have been investigated to immobilize them. Better, however, is to avoid the introduction of sodium into the oxide. Besides the metallization, the oxidation furnace has the highest contamination probability (35). C33 and TCE are effective in reducing the mobile charge during oxidation and also during previous cleaning of the furnace tubes prior to oxidation.

These experiments are performed on quartz tubes that are previously cleaned by etching them in diluted HF followed by a rinse in high purity water. Before growing the first oxide, without previous C33 or TCE cleaning, the furnace tube is flushed with N_2 for at least 3 hr. The experiments are done at 1100°C for TCE and 1200°C for C33. The wafers are oxidized in dry O_2 to yield about 90 nm thick oxide followed by a N_2 anneal *in situ*. Immediately after oxidation the oxide is covered with a silicon nitride layer to prevent any contamination from entering the oxide after oxidation. The furnace tube cleaning cycle is performed at oxidation temperatures with 0.75% TCE or 1.25% C33. After each cleaning cycle and before another oxidation, the furnace is exposed for 30 min to dry O_2 in order to avoid the effect of lingering traces of chlorine on the oxide growth. The mobile ion density is determined by applying a TVS (triangular voltage sweep) (36) at 200°C and by integrating the extra displacement current caused by the mobile ions. Independent experiments show that the oxide-nitride double layer causes no instabilities under these conditions. From Fig. 6 it is seen that

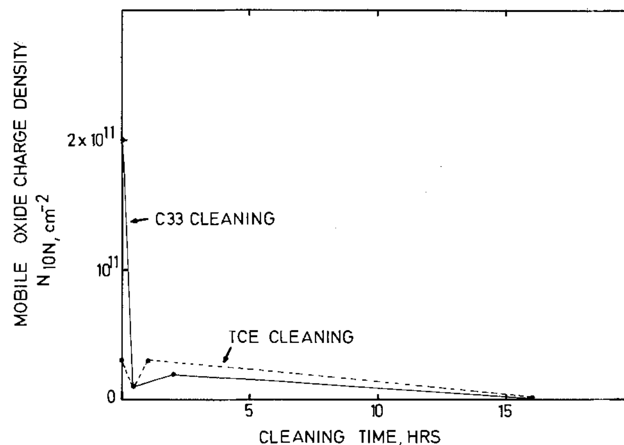

Fig. 6. The mobile ion density obtained from TVS measurements at 200°C, 200 mV/sec sweep, as a function of cleaning time with 0.75% TCE/O_2 mixture at 1100°C, or a 1.25% C33 mixture at 1200°C. The oxides are grown for 30 min at 1100°C and 14 min at 1200°C, respectively, always after a previous O_2 flow for ½ hr.

both TCE and C33 are effective in cleaning the furnace tube. The mobile ion density rapidly falls in 30 min to a low 10^{10}/cm^2 level. The increase immediately after HCl is allowed to flush the tube (37) is in agreement with Krieglers' result (12) and is explained by the higher sodium content in the atmosphere. An overnight rinse (960 min) reduces the density to the limit of detection ($2 \cdot 10^9$ ions/cm^2).

The neutralization of the mobile charge.—Oxidation in a chlorine-containing ambient leads to a neutralization capability of the oxide against mobile ions (38). From the shift in flatband voltage before and after a positive BT stress performed at 200°C with an electric field of 1 MV/cm for 20 min, the amount of unneutralized charge is calculated. The neutralization efficiency of an oxide is expressed as the ratio of the neutralized charge to the total mobile charge, the latter measured in DTO samples. This figure of merit is used to compare the TCE and C33 in Fig. 7.

The neutralization is attributed to the chlorine incorporated in the oxide and is independent of the contamination level, although the number of the neutralized ions are only a small fraction of the number of chlorine atoms in the oxide (39). Both additives show a threshold-like behavior in the dependence on additive concentration; a threshold in oxidation time is also expected as observed with HCl (12). The same threshold-like behavior is found in the chlorine content of an oxide, resulting in a close relation between the chlorine content and the neutralization efficiency (40).

The wafers are intentionally contaminated by evaporation of aluminum from a resistance-heated tungsten wire. This results in a rather good uniformity of the contamination level on samples metallized in the same run, however, large differences from run to run can occur.

The mechanism of neutralization is not well understood. It is proposed by Kriegler (41) that the mobile ions become trapped when they reach the vicinity of the chlorine, incorporated in a Si-O-Cl bond where chlorine is substitutional for oxygen. This trapping is also observed during TVS measurements (42). Results of these measurements performed at 200°C on a DTO and on a C33 oxide are represented in Fig. 8. In the DTO sample deformation of the displacement current peak occurs due to the trapping of the mobile ions at the metal-SiO_2 interface when they are swept from the metal to the silicon (39). The C33 sample, however, shows also heavy trapping when the sodium ions are at the silicon interface where the chlorine atoms are incorporated (43, 10). The sodium is not immobilized but neutralized when it reaches the interface as the flatband voltage shift is much lower for the C33

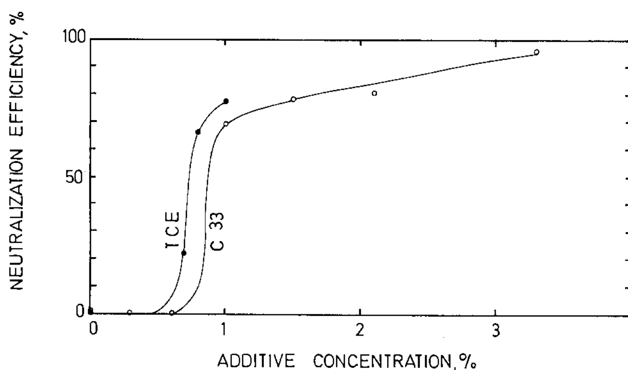

Fig. 7. The neutralization efficiency calculated from flatband shift after BT stress compared to the flatband shift with 0% additive as a function of additive concentration. The oxides are grown at 1150°C for 32 and 36 min for TCE and C33, respectively. The TCE oxide contamination level is 2×10^{12} and for the C33 oxides 4.5×10^{11} ion/cm^2.

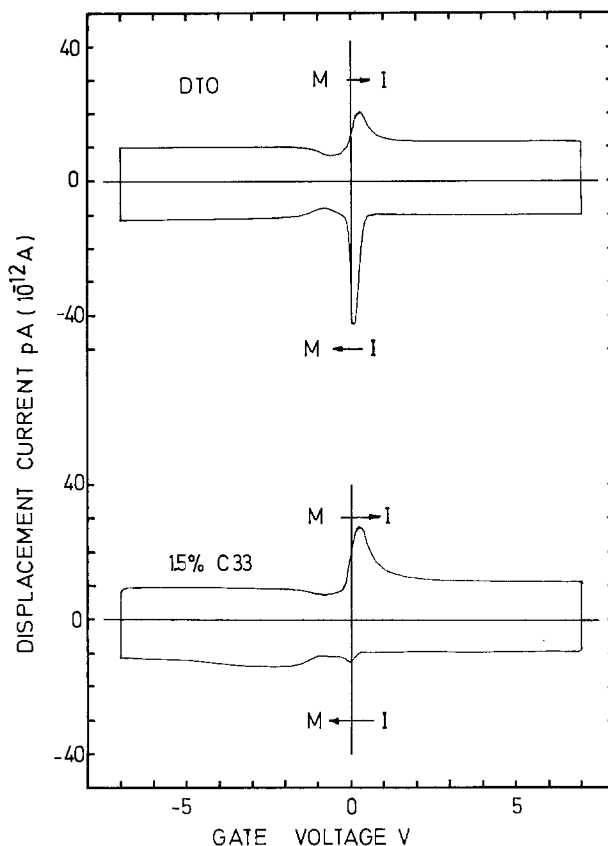

Fig. 8. TVS measurement at 200°C, 200 mV/sec sweep. Performed on a DTO (upper) and on a 1.5% C33 oxide (lower) grown at 1150°C for 36 min, showing 76% neutralization efficiency. The contamination level is 4.5×10^{11} ion/cm^2.

oxide than the DTO while integration of the displacement current yields the same total charge.

The influence of C33 and TCE on the silicon dioxide-silicon interface.—The fixed oxide charge (N_{ox}).—Samples grown in TCE/O_2 and C33/O_2 mixtures show a reduction in the fixed oxide charge (Fig. 9). This, however, is only found when the oxide charge is higher than the minimum value that can be reached by proper annealing (34). The samples referred to in Fig. 6 as C and E, grown with different TCE and C33 concentrations, respectively, have fixed oxide charge levels of about $5 \cdot 10^{10}$ charges/cm^2 as normally obtained for (100) interfacial planes by suitable processing (44). This is not influenced by the addition of chlorine species. The B and D series have a higher oxide charge decreasing with increasing chlorine concentration. From the sample A series, measured as oxidized without high temperature N_2 anneal, it is clear that the mechanism responsible for the decrease in oxide charge occurs during oxidation. A zero oxide charge as reported by Kriegler (1) has never been observed.

The origin of the fixed oxide charge is thought to be due to the oxygen deficiency and the excess ionized silicon resulting in a missing Si-O-Si bridge in the transition region near the interface (33, 34, 45).

The influence of sodium (46) is excluded because the wafers are oxidized in a sodium-free atmosphere. Moreover the samples show very low mobile ion densities even metallized. It is believed that the excess unbonded silicon ions are chlorinated because of the high reactivity of the chlorine and silicon. The analysis of the oxidation rate also supports this assumption. Consequently the oxide charge is reduced.

The interface-state density (N_{ss}).—Quasi static C-V measurements are performed on TCE and C33 oxides to obtain the interface-state density (47, 48). The samples were obtained at low temperature anneal for

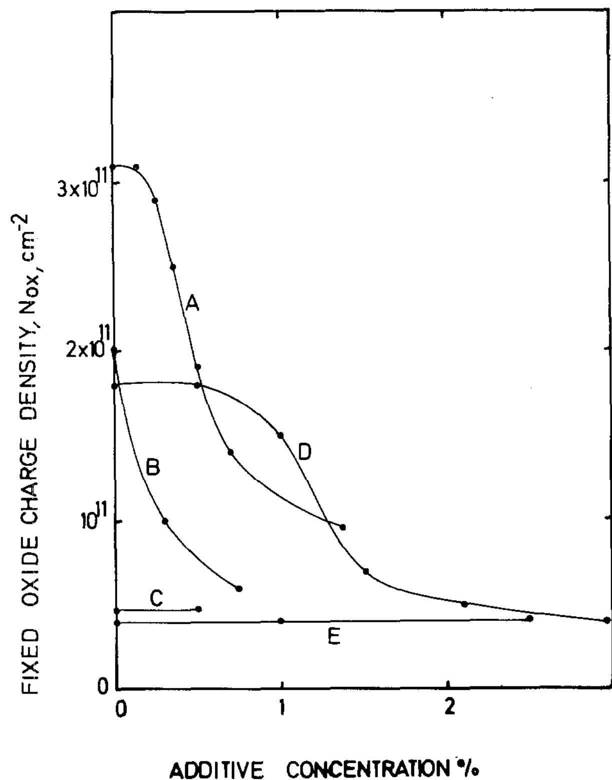

Fig. 9. The reduction in fixed oxide charge density (N_{ox}) with increasing chlorine addition. A, (TCE) 1200°C, 14 min oxidation, no anneal; B, (TCE) 1200°C, 14 min oxidation, 30 min 450°C wet N_2 anneal; C, (TCE) 1150°C, 32 min oxidation, 20 min N_2 *in situ*, 450°C, 30 min wet N_2 anneal; D, C33, 1150°C, 36 min oxidation, 5 min N_2 *in situ*, 450°C, 30 min wet N_2 anneal; E, same as D but 20 min N_2 *in situ* anneal. Sample A was measured by means of an Hg probe; B, C, D, and E after metallization.

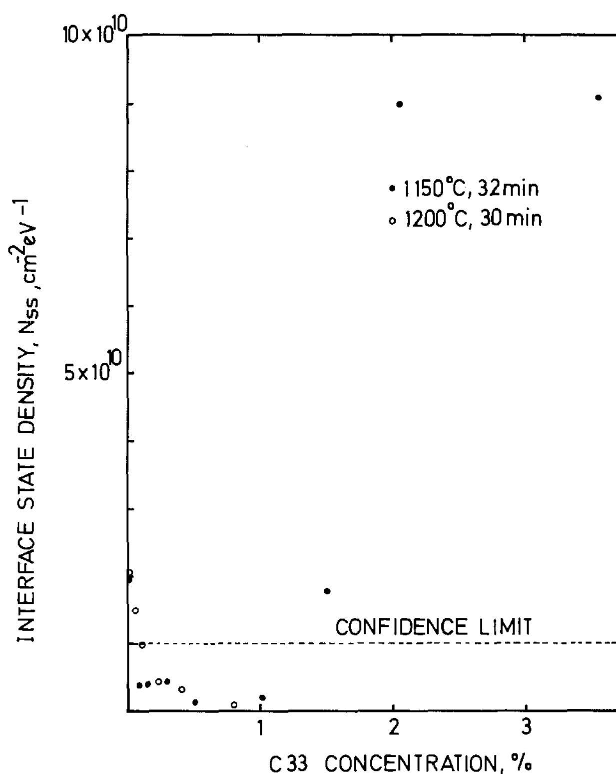

Fig. 10. The interface state density (N_{ss}) vs. C33 concentration for 1150°C, 32 min and for 1200°C, 30 min samples.

30 min in wet N_2 at 450°C after aluminum metallization. This is known as a very effective means of reducing the interface states (49). The interface-state density of oxides grown at C33 concentrations lower than 1% is beneath the limit of accuracy of the method ($10^{10}/cm^2$ eV) as shown in Fig. 10. From transfer loss experiments of charge coupled devices fabricated with the same C33 oxides as gate dielectric layer it has been found that N_{ss} is in the low $10^9/cm^2$ eV range (50). At higher C33 concentrations N_{ss} increases as has also been observed for TCE oxides (6).

According to Goetzberger the source of interface states is threefold (51), namely, chemical impurities at the interface (52), charges in the oxide, and structural imperfections such as dangling bonds. From previous sections it follows that C33 or TCE is effective in providing a clean atmosphere during oxidation minimizing the possible contamination by impurities or electrically charged ions. Also the fixed oxide charge is optimized. It is generally accepted that interface states can be annihilated by reducing ionized silicon centers at the interface during a low temperature anneal by the formation of Si-H bonds (46, 34, 53). This hydrogen can be present in the annealing atmosphere or is formed during anneal by the reaction of water vapor with the aluminum metal layer (49). The hydrogen can also be incorporated in the structure due to the previous processing step such as HCl (54), C33, or TCE oxidation. Hydrogen results from the water present in the atmosphere or from the reaction of silicon with HCl. A similar effect has been observed in oxides covered with a nitride layer formed by the reaction of SiH_4 and NH_3 (55). The higher interface-state density at higher concentrations is explained by the higher density of imperfections at the interface due to the corrosion of the silicon. The increase in imperfections is also observed during oxide defect density measurements in chlorine oxides (4).

Influence of C33 and TCE on the dark current generation.—The advantage of "chlorine" oxidation applied to CCD processing is the reduction of background dark current and dark current spikes. The dark current generation can be fully described by studying the relaxation times of MOS capacitors pulsed in deep depletion (Fig. 11a). In order to separate bulk minority carrier generation lifetime and surface generation velocity the Zerbst analysis (56) is performed on these pulsed *C-t* plots (Fig. 11b).

Care should be taken to account for the effect of surface generation at the periphery of the capacitor when making these *C-t* plots especially when very high bulk lifetimes occur, since this could lead to erroneous interpretation of the Zerbst plots (57, 58). Typical bulk generation lifetimes obtained from both Zerbst analysis and dark current CCD experiments (59) are between 0.5 and 3 msec. The surface generation velocity of an inverted surface is as low as 0.07 cm/sec raising to 1 cm/sec for the depleted surface. An optimum C33 or TCE concentration cannot be found. However a strong decrease in relaxation time is always observed at higher concentrations (1% for TCE, 2% for C33).

The thermal bulk generation is generally attributed to impurities of heavy metals (gold, copper, iron) having energy levels near the middle of the bandgap. The reduction of bulk generation is ascribed to two possible mechanisms: first the formation of volatile metal-chlorides (2, 8); second, the reduction of lattice defects, such as stacking faults, where impurities preferentially reside. A strong relation is found between stacking faults or dislocations and CCD video defects (60, 61). On the other hand, no large effect has been observed of a high temperature treatment in a mixture of HCl, H_2, and SiH_4 on the metallic content of a Si-wafer (32). Recently relaxation time experiments performed on MOS capacitors grown with HCl (62) show a strong relation between the relaxation time and crystal defects being not only large defects as stacking faults but also small etch pits whose nature is not fully understood but may be related to oxygen clusters (67). Several investigations are now undertaken that prove that the suppression of stacking faults is the predominant mechanism responsible for the lifetime

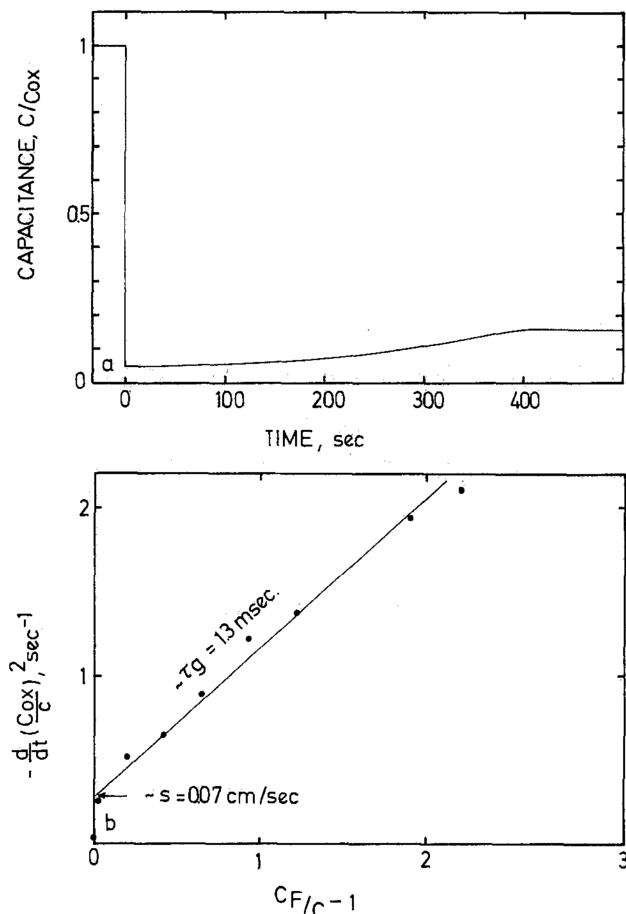

Fig. 11. a. C,t plot. b. Zerbst plot. Sample; 1150°C, 1% C33, 30 min oxidation, doping level $N_D = 1,6 \times 10^{14}/cm^3$. The Zerbst analysis yields $\tau_g = 1.3$ msec, $s = 0.07$ cm/sec, $s_o = 0.34$ cm/sec.

improvement (63). It has been proved already that HCl (64) and TCE (65) and recently also C33 (66) is effective in reducing the stacking faults. The decrease of relaxation time at higher concentrations is due to the corrosion of silicon by the chlorine resulting in a highly defective interface.

Conclusion

C33 (1.1.1.-trichloroethane) has been proved to be very effective in replacing HCl, giving oxides with identical properties. Moreover it is far less dangerous than HCl and it has also improved physical and physiological properties over TCE. The higher chlorine content of the latter tends to corrode the silicon surface during oxidation and limits the improvement on properties sensitive to interface imperfections, namely, the electric breakdown defect density, the fast interface states, and the storage times. The phenomena of neutralization of the mobile charge occur at concentrations where the structure-sensitive properties worsen, therefore, we do not recommend the use of this technology for making self-stabilizing oxides. Oxides with very low mobile ion content are achieved by the cleaning effect of C33 on the furnace tube.

The behavior of these oxides is explained by means of a very simple model. The high reaction velocity of HCl and Cl_2 with silicon compared to the oxidation reaction velocity makes silicon-chlorine bonds likely and accounts for the influence on oxidation rate, fixed oxide charge, and the neutralization capability, although the latter is not fully understood. This removal of excess silicon atoms at the interface causes lower defect density, longer relaxation times, and lower interface state densities, this also because of the hydrogen released from the reaction. The removal of contaminants especially sodium from the furnace tubes also accounts for the improved properties.

The impact of C33 oxidation on device properties as defect density, minority carrier generation lifetime, and surface-state density together with its improved physical and physiological properties makes it suitable in silicon device processing.

Acknowledgments

The authors wish to thank the staff of the ESAT laboratory for helpful discussions and technical assistance and K. Van Damme for performing the breakdown experiments. Part of this work was supported by BARCO-COBAR electronic N.V. through IWONL-Contract 2538. G. Declerck is indebted to the NFWO and E. Janssens to the IWONL for their fellowships.

Manuscript submitted Dec. 13, 1977; revised manuscript received May 16, 1978.

Any discussion of this paper will appear in a Discussion Section to be published in the June 1979 JOURNAL. All discussions for the June 1979 Discussion Section should be submitted by Feb. 1, 1979.

Publication costs of this article were assisted by the Katholieke Universiteit Leuven.

REFERENCES

1. R. J. Kriegler, Y. C. Cheng, and D. R. Colton, *This Journal*, **119**, 388 (1972).
2. P. H. Robinson and F. P. Heiman, *ibid.*, **118**, 141 (1971).
3. R. J. Kriegler, in Proceedings ISSCC, Philadelphia 1975, p. 56.
4. C. M. Osburn, *This Journal*, **121**, 809 (1974).
5. M. C. Chen and J. W. Hile, *ibid.*, **119**, 223 (1972).
6. G. J. Declerck, T. Hattori, G. A. May, J. Beaudouin, and J. D. Meindl, *ibid.*, **122**, 436 (1976).
7. E. J. Janssens and G. J. Declerck, in Proceedings ESSDER Conference, Grenoble, 1975, p. 16.
8. D. R. Young and C. M. Osburn, *This Journal*, **120**, 1578 (1973).
9. K. Hirabayashi and J. Iwamura, *ibid.*, **120**, 1595 (1973).
10. Y. J. Van der Meulen, C. M. Osburn, and J. F. Ziegler, *ibid.*, **122**, 289 (1975).
11. D. L. Heald, R. M. Das, and R. P. Khosla, *ibid.*, **123**, 302 (1976).
12. R. J. Kriegler, in "Semiconductor Silicon 1973," H. R. Huff and R. R. Burgess, Editors, p. 363, The Electrochemical Society Softbound Symposium Series, Princeton, N.J. (1973).
13. R. S. Ronen and P. H. Robinson, *This Journal*, **119**, 747 (1972).
14. B. Kaesche-Krischer, *Combust. Flame*, **6**, 183 (Sept. 1962).
15. C. E. Wicks and F. E. Block, Editors, "Thermodynamic Properties of 65 Elements, Their Oxides, Halides, Carbides and Nitrides," *Bur. Mines Bull.* 605 (1963).
16. D. R. Stull and H. Prophet, Editors, JANAF Thermochemical Tables, 2nd ed., Nat. Bur. Stand. NSRDS-NBS 37 (1971).
17. L. P. Hunt and E. Sirtl, *This Journal*, **119**, 174 (1972).
18. R. E. Tressler, J. Stach, and D. M. Metz, *ibid.*, **124**, 607 (1977).
19. W. J. Kroll, R. L. Titus, and J. B. Wagner, *ibid.*, **122**, 573 (1975).
20. Y. J. Van der Meulen and J. G. Cahill, *J. Electron. Mater.*, **3**, 371 (1974).
21. "Handbook of Chemistry and Physics," 52nd ed., R. C. Weast, Editor, The Chemical Rubber Co. (1971-1972).
22. "Handbook of Laboratory Safety," 2nd ed., Steere, Editor, The Chemical Rubber Co. (1973).
23. J. Agnew, *Solid State Technol.*, **19**, 43 (1976).
24. W. Kern and D. A. Puotinen, *RCA Rev.*, **31**, 187 (1970).
25. G. J. Declerck, K. M. De Meyer, E. J. Janssens, E. E. Laes, and J. Van der Spiegel, *IEEE J. Sci.*, **11**, 229 (1976).
26. K. E. Bean and P. S. Gleim, *Proc. IEEE*, **57**, 1469 (1969).
27. D. W. Hess and B. E. Deal, *This Journal*, **122**, 579 (1975).
28. C. M. Osburn and D. W. Ormond, *ibid.*, **119**, 591 (1972).

29. N. S. Chou and J. M. Eldridge, *ibid.*, **117**, 1287 (1970).
30. C. M. Osburn and D. W. Ormond, *ibid.*, **119**, 597 (1972).
31. A. K. Zakzouk, R. A. Stuart, and W. Eccleston, *ibid.*, **123**, 1651 (1976).
32. J. M. Green, C. M. Osburn, and T. O. Sedewick, *J. Electron. Mater.*, **3**, 579 (1974).
33. J. S. Johannessen and W. E. Spicer, *J. Appl. Phys.*, **47**, 3028 (1976).
34. B. E. Deal, *This Journal*, **121**, 198C (1974).
35. R. J. Kriegler, Proceedings 12th IEEE Rel. Phys. Symp. 1974, p. 250.
36. N. J. Chou, *This Journal*, **118**, 601 (1971).
37. S. Mayo and W. H. Evans, *ibid.*, **124**, 780 (1977).
38. R. J. Kriegler, *Appl. Phys. Lett.*, **20**, (11), 449 (1972).
39. R. J. Kriegler, A. Aitken, and J. D. Morris. Suppl. *J. Jpn. Soc. of Appl. Phys.*, 341 (March 1974).
40. A. Rohatgi, S. R. Butler, F. J. Feigl, H. W. Kraner, and K. W. Jones, *Appl. Phys. Lett.*, **30**, 104 (1977).
41. R. J. Kriegler, *Thin Solid Films*, (13), 11 (1972).
42. R. J. Kriegler and T. F. Deveny, Proceedings 11th IEEE Rel. Phys. Symp., 1973, p. 153.
43. R. L. Meek, *This Journal*, **120**, 308 (1973).
44. A. S. Grove, "Physics and Technology of Semiconductor Devices," John Wiley & Sons, Inc., New York (1967).
45. H. Goronkin, *This Journal*, **124**, 314 (1977).
46. E. Kooi, *Philips Res. Rep.*, **21**, 477 (1966).
47. R. Van Overstraeten, G. Declerck, and G. Broux, *This Journal*, **120**, 1785 (1973).
48. M. Kuhn, *Solid State Electron.*, **13**, 873 (1970).
49. P. L. Castro and B. E. Deal, *This Journal*, **118**, 280 (1971).
50. J. E. Carnes and W. F. Kosonocky, *Appl. Phys. Lett.*, **20**, (7) 261 (1972).
51. A. Goetzberger, Proceedings CCD 74 International Conference, Edinburgh, p. 47 (1974).
52. W. Fahrner and A. Goetzberger, *Appl. Phys. Lett.*, **21**, (7), 329 (1972).
53. F. Montillo and P. Balk, *This Journal*, **118**, 1963 (1971).
54. M. Severi and G. Soncini, *Electron. Lett.*, **8**, (16), 402 (1971).
55. B. E. Deal, E. L. Mackenna, and P. L. Castro, *This Journal*, **116**, 997 (1969).
56. M. Zerbst, *Z. Angew. Phys.*, **22**, 30 (1966).
57. D. K. Schroder and H. C. Nathanson, *Solid State Electron.*, **13**, 577 (1970).
58. D. K. Schroder and J. Guldberg, *ibid.*, **14**, 1285 (1971).
59. G. J. Declerck, E. J. Janssens, E. E. Laes, and J. Van der Spiegel, Paper 112 presented at The Electrochemical Society Meeting, Washington, D.C., May 2-7, 1976.
60. K. Tanikawa, Y. Ito, and H. Sei, *Appl. Phys. Lett.*, **28**, (5), 285 (1976).
61. G. J. Declerck, K. M. De Meyer, E. J. Janssens, E. E. Laes, J. Van der Spiegel, and C. L. Claeys, in Proceedings CCD 76, 3rd International Conference, Edinburgh, p. 23, (1976).
62. T. F. Unter, P. C. T. Roberts, and D. R. Lamb, *Electron. Lett.*, **13**, (4), 93 (1977).
63. E. J. Janssens and G. J. Declerck, Paper 112 presented at The Electrochemical Society Meeting, Seattle, Washington, May 21-26, 1978.
64. H. Shiraky, *Jpn. J. Appl. Phys.*, **14**, 747 (1975).
65. T. Hattori, *This Journal*, **123**, 945 (1976).
66. C. L. Claeys, E. E. Laes, G. J. Declerck, and R. J. Van Overstraeten, in "Semiconductor Silicon, 1977," R. H. Huff and E. Sirth, Editors, p. 773, The Electrochemical Society Softbound Symposium Series, Princeton, N. J. (1977).
67. S. M. Hu, *J. Vac. Sci. Technol.*, **14**, 17 (1977).

Some Aspects of Oxide Isolation Technology

P. C. Parekh

Honeywell-SSEC, Plymouth, Minnesota 55441

ABSTRACT

Generation of defects and stain profiles have been investigated in the vicinity of the oxide isolation region for the <100> oriented wafers. The variables used were SiO_2 and Si_3N_4 thicknesses at the surface and isolation oxidation temperature. It was observed that the enhancement or retardation in the epitaxial dopant diffusivity in the vicinity of the isolation region was related to the presence or the absence of defects on the <111> plane, respectively.

The impact of oxide isolation technology in the manufacture of high speed high density circuits has been significant. Earlier this type of isolation (1) was applied to bipolar memories. However, presently it is being used in all types of integrated circuits. With increasing interest in this technology, an increasing number of publications on various aspects have been released (1-8). For example recent work by Cosand and Prussin (4) have shown that defects are generated in the vicinity of the oxide isolation region if the processing conditions are not optimized. Work of Sakai *et al.* (2) and Bassous *et al.* (3) attempts to reduce "birds beak" which is a nondesirable feature of oxide isolation. Chang and Chang (6) have characterized oxide isolated structures using device parameter as the vehicle.

Three basic problems that may be experienced with oxide isolated structures are: (*i*) nonplanarity in and around the vicinity of the structure which may cause poor step coverage of metallization, (*ii*) excessive leakage and low breakdown between two regions separated by an oxide isolated region, (*iii*) leakage on devices situated in the vicinity of the oxide isolated region. Nonplanarity at the periphery of the oxide isolation opening has been discussed by Sakai *et al.* (2) and Bassous *et al.* (3). In the present work this aspect of oxide isolation technology is not discussed further.

Key words: oxidation, defects, dielectric isolation.

The work of Cosand and Prussin (4) have shown that the generation of defects was a function of processing conditions. Their work used processing conditions in a fairly narrow range. The object of the present work is to investigate stain profile and generation of defects in the vicinity of the isolation region. From these data processing conditions can be optimized to reduce isolation and active device leakage currents. The range of processing conditions comprised of varying isolation oxidation temperatures from 950° to 1150°C, Si_3N_4 thickness varying from 500 to 2500Å SiO_2 (thermally grown under Si_3N_4) thicknesses varying from 0 to 2000Å.

The tools used for the above investigations were: (*i*) Bevel and stain technique to observe stain profile at the periphery of the isolation region, and (*ii*) the wafers were (100) orientated and were cleaved along <110> directions. The cleaved portions were Sirtl

etched to delineate etch pits formed due to dislocations along the (111) plane. The pits were observed using SEM.

Experimental

The starting material was p-type wafers of (100) orientation and resistivity 8.0-13.0 Ω-cm. The wafers were cleaned and split into two halves such that n-type epitaxial layers of resistivity 0.35 Ω-cm and thicknesses 2.0 and 3.0μ were deposited. Prior to this step some wafers were processed with buried layer deposition and diffusion. However, no differences in the final results were obtained between the wafers with and without buried layer process. After the epitaxial depositions, the wafers were cleaned and thermally oxidized at 950°C with varying SiO_2 thicknesses ranging from 0 to 2000Å. The wafers were then processed through Si_3N_4 deposition performed at 800°C. The thicknesses of Si_3N_4 ranged from 500 to 2500Å. For masking purposes, 1000Å of SiO_2 was deposited at 450 C on all the wafers. An oxide isolation mask was defined and the sandwich structure of SiO_2-Si_3N_4-SiO_2 was etched. Finally, silicon in the mask opening was etched to a depth of 2.25μ using a mixure of potassium hydroxide and isopropyl alcohol as shown in Fig. 1. Here the cross sections represent two devices with epiatxial thicknesses of 2.0 and 3.0 μm. The oxidation in the isolation region was performed at temperatures of 1150°, 1050°, and 950°C. The final oxide thickness in the isolation region (henceforth called groove) in all the cases was 2.2 μm.

Subsequent to the oxidation of the grooves, the wafers were beveled and stained to observe the n-type epitaxial stain profile in the vicinity of the groove region. The method of beveling was performed using the Philtec machine. This enabled large areas of wafers to be subjected to examination. Next the wafers were cleaved along the <110> direction. The cleaved regions were Sirtl etched and subjected to SEM analysis to reveal the presence of defects in the vicinity of the groove due to the oxidation process.

Results

Table I shows a summary of the experiments performed to observe different types of stain profiles and defects generated in the viciniy of the grooves. These are, for example, shown in Fig. 2 and 3, respectively. In the former case, the dark area represents the p-type substrate while the light area represents the phosphorus-doped epitaxial region. Here the boundary between the surface and the beveled region is clearly visible. The stain profiles for the oxidation temperatures used showed the following:

1. For the oxidation temperatures of 1150° and 1050°C, there was an increase in the epitaxial thickness away from the groove region due to the diffusion of phosphorus into the substrate. For the oxidation temperature of 950°C, no significant increase in the epitaxial thickness was observed.

2. There was an enhancement in the diffusivity of the n-type epitaxial dopant under the groove region with respect to that away from the groove region for all the oxidation temperatures used. Henceforth in the article the term "enhancement" assumes that it is referenced with respect to the epitaxial thickness away from the groove region.

Table I. Types of stain profiles

Batch No.	Epi thickness (μm)	Groove oxidation temperature (°C)	Dielectric thickness		Stain profile	Defects Generated?
			SiO_2 (Å)	Si_3N_4 (Å)		
1	3.0	1150	0-2000	2500	Fig. 2	Yes
2	3 0	1150	0-2000	500	Fig. 4	No
3	2.0	1150	2000	2500	Fig. 6	Yes
4	2.0	1150	0-2000	500	Fig. 6*	No
5	2.0	1150	0	2500	Fig. 6*	Yes
6	3.0	950	0-2000	500-2500	Fig. 7	Yes
7	2.0	950	0	500-2500	Fig. 8	Yes
8	2.0	950	2000	2500	Fig. 9	Yes
9	2.0	950	2000	500	Fig. 10	Yes

* Modified stain profile.

Figure 3 shows a SEM view of the cross section of an isolation groove. As mentioned above, the wafers were cleaved along the <110> direction and Sirtl etched. The etch pits and their positioning suggests that the defects are formed on the sloping <111> plane. Henceforth in the article the meaning of the term "the generation of defects in the vicinity of the groove region" assumes that the wafers were cleaved

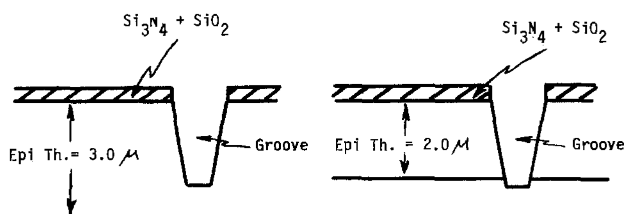

Fig. 1. Cross sections after silicon groove etching. In (a, left) epitaxial thickness > depth of groove. In (b, right) epitaxial thickness < depth of groove.

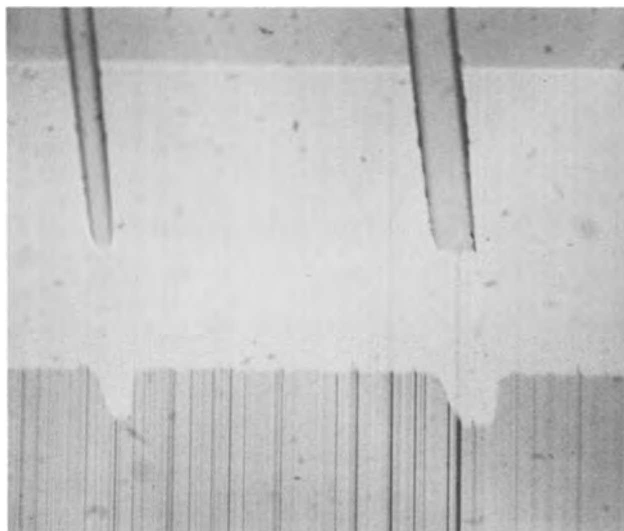

Fig. 2. Bevel and stain profiles for wafers in batch 1. SiO_2 thicknesses = 0-2000Å. Si_3N_4 thickness = 2500Å. Oxidation temperature = 1150°C. ×162.

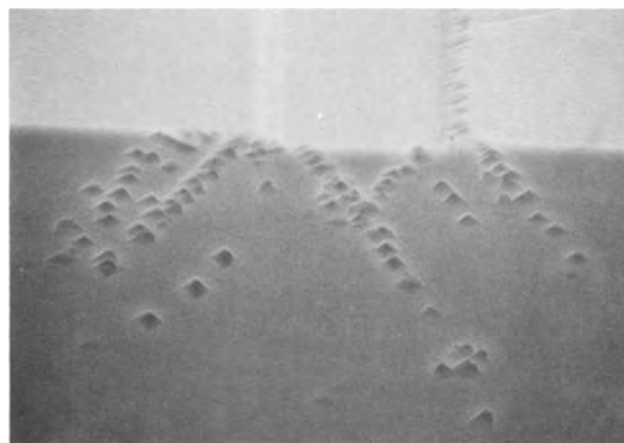

Fig. 3. SEM view of the cross section of samples in batch 1 cleaved in the <110> direction and Sirtl etched. Defects are observed on the (111) plane. ×700.

along the <110> direction and Sirtl etched. Subsequently, the cross section of the etched regions were subjected to SEM analysis and any defects present were found to lie on the (111) plane.

Groove oxidation temperature of 1150°C.—The following results were obtained and are shown in Table I:

Epitaxial thickness = 3.0 μm.—Here the interface of the epitaxial-substrate region was below the lower tip of the groove prior to the groove oxidation as shown in Fig. 1a. After the oxidation the increase in the epitaxial thickness away from the groove region was approximately 1.5 μm. Figure 2 shows typical stain profile in the vicinity of the groove for Si_3N_4 thickness of 2500Å and oxide thickness ranging from 0-2000Å. Here a significant enhancement in the diffusion coefficient of the n-type epitaxial dopant under the groove region is observed. In addition, defects were observed in the vicinity of the groove region as shown in Fig. 3. Figure 4 shows bevel and stain profile of the samples in batch 2 with Si_3N_4 and SiO_2 thicknesses of 500Å and 0-2000Å, respectively. It can be seen that there is a retardation in the diffusion coefficient of the n-type epitaxial dopant under the groove relative to that away from the groove region. Figure 5 shows that no defects were generated in the vicinity of the groove for these samples.

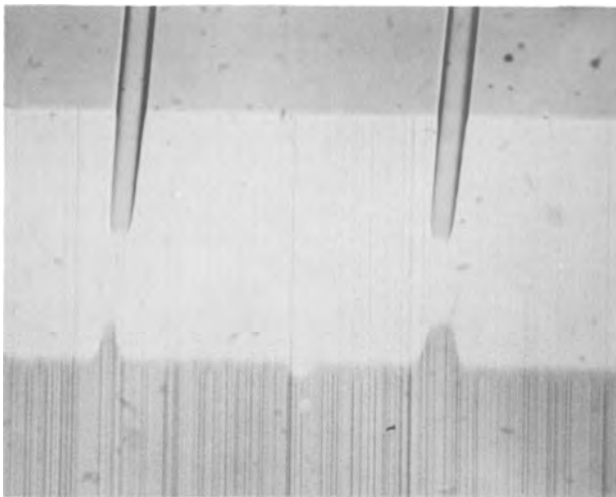

Fig. 4. Bevel and stain profile for wafers in batch 2. SiO_2 thicknesses = 0-2000Å. Si_3N_4 thickness = 500Å. Oxidation temperature = 1150°C. ×162.

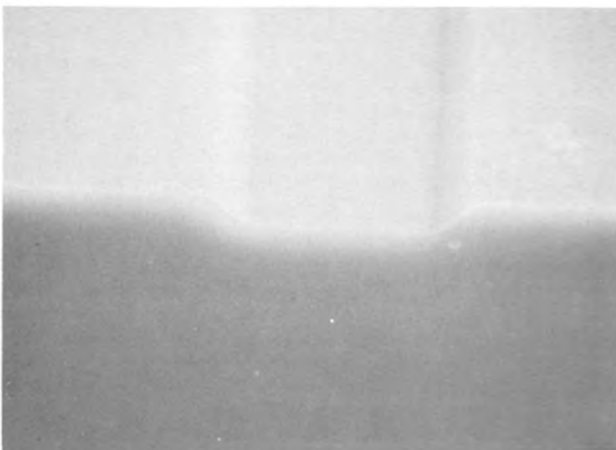

Fig. 5. SEM view of the cross section of samples in batch 2 cleaved in the <110> direction and Sirtl etched. No defects are observed on the (111) plane. ×900.

Epitaxial thickness = 2.0 μm.—Figure 1b shows that prior to the oxidation of the groove, its depth is slightly greater than the thickness of the epitaxial region. However, after the oxidation, the thickness of the epitaxial layer away from the groove region is greater than the depth of the groove. This is illustrated in Fig. 6 for wafers in batch 3 for Si_3N_4 and SiO_2 thicknesses of 2500 and 2000Å, respectively. Note that here the isolation between the two n-type regions is maintained by the continuity of the p-type region between the bottom of the groove and the substrate. During the initial phase of the oxidation of the grooves, some boron from the substrates is incorporated into the oxide. In the subsequent oxidation process, the oxide may act as a source of boron and consequently a continuity of the p-type region between the bottom of the groove and the substrate is maintained. Note that at the periphery of the groove an enhancement in the diffusion coefficient of the n-type dopant is observed. This is accompanied by the presence of defects similar to that shown in Fig. 3. For the samples in batch 4 where Si_3N_4 thickness was reduced to 500Å and SiO_2 thicknesses were allowed to range from 0-2000Å, stain profile as shown in Fig. 6 was observed but with the absence of the enhanced diffusion of the n-type dopant at the periphery of the groove. In addition no defects were observed in the vicinity of the groove region. The stain profile for the wafers in batch 5 with 2500Å Si_3N_4 and no SiO_2 under the Si_3N_4 was similar to that shown in Fig. 6 but with less enhancement at the periphery of the groove region. In addition, defects similar to that shown in Fig. 3 were observed although the density of defects was lower than shown in the figure.

Groove oxidation temperature of 950°C.—The following results were obtained and are shown in Table I:

Epitaxial thickness = 3.0 μm.—Here after the oxidation of the groove, the epitaxial thickness away from the groove region remained same as prior to the oxidation. For any combination of SiO_2 thicknesses ranging from 0-2000Å and Si_3N_4 thicknesses ranging from 500 to 2500Å, stain profile of the type shown in Fig. 7 was observed. This was also accompanied by the presence of defects in the vicinity of the groove regions.

Epitaxial thickness = 2.0 μm.—Figures 8-10 show stain profiles for samples with SiO_2 and Si_3N_4 thicknesses shown in Table I. It can be seen that on increasing the SiO_2 and Si_3N_4 thicknesses, a potential loss of isolation results between the two n-type epitaxial islands. In all the cases defects were observed in the vicinity of the groove regions.

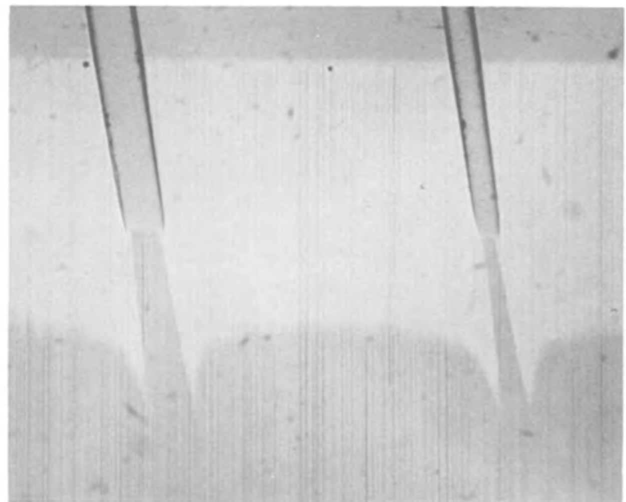

Fig. 6. Bevel and stain profiles for wafers in batch 3. SiO_2 thickness = 2000Å. Si_3N_4 thickness = 2500Å. Oxidation temperature = 1150°C. ×162.

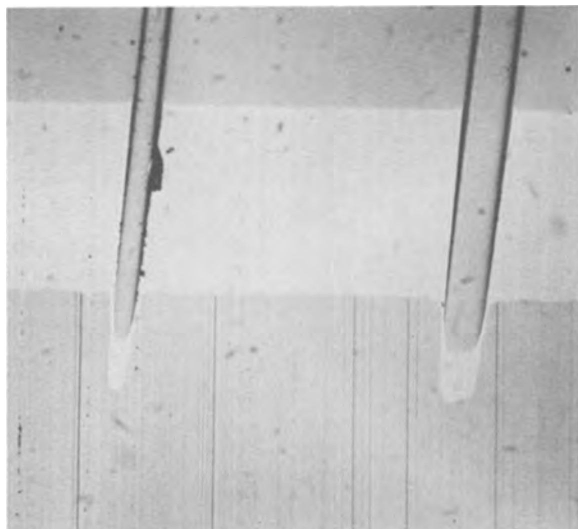

Fig. 7. Bevel and stain profiles for wafers in batch 6. SiO_2 thicknesses = 0-2000Å. Si_3N_4 thicknesses = 500-2500Å. Oxidation temperature = 950°C. ×162.

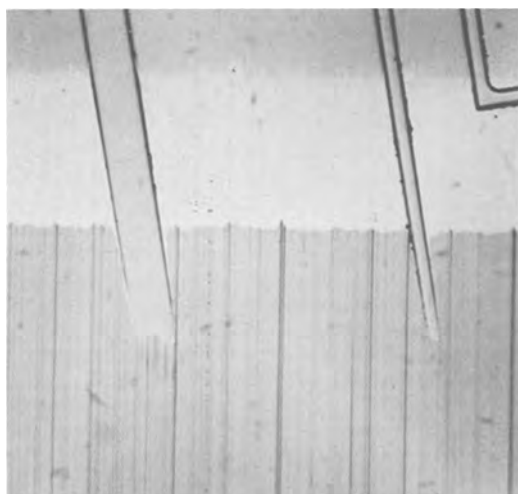

Fig. 8. Bevel and stain profiles for wafers in batch 7. SiO_2 thickness = 0Å. Si_3N_4 thicknesses = 500-2500Å. Oxidation temperature = 950°C. ×162.

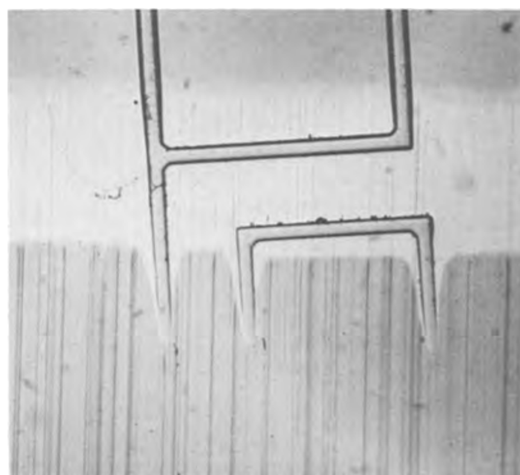

Fig. 9. Bevel and stain profiles for wafers in batch 8. SiO_2 thickness = 2000Å. Si_3N_4 thickness = 2500Å. Oxidation temperature = 950°C. ×162.

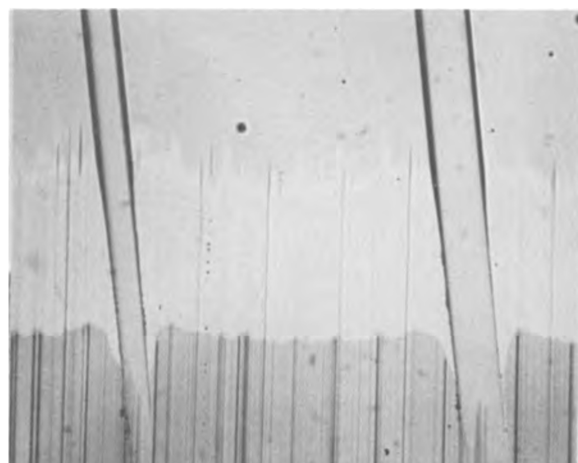

Fig. 10. Bevel and stain profiles for wafers in batch 9. SiO_2 thickness = 2000Å. Si_3N_4 thickness = 500Å. Oxidation temperature = 950°C. ×162.

Discussion

The results obtained in this work show that the enhancement or retardation of the epitaxial dopant under the groove region is a strong function of Si_3N_4/SiO_2 thicknesses. It is also interesting to observe that in the majority of the cases the enhancement was accompanied by the defects generated in the vicinity of the groove. However, in the absence of enhancement or only when retardation was present, no defects were generated.

For the oxidation temperature of 1150°C, the enhancement or retardation was a strong function of Si_3N_4 thickness and relatively insensitive to the SiO_2 thickness under the Si_3N_4. This is shown in Table I for wafers in batches 1 and 2. In the former case, irrespective of any SiO_2 thickness and Si_3N_4 thickness of 2500Å, enhancement of the n-type epitaxial dopant under the groove is observed as shown in Fig. 2. Figure 3 shows defects generated in the vicinity of the groove along the (111) plane. The generation of defects is a result of excessive stress experienced during the oxidation of the grooves. This stress is due to the thick Si_3N_4 film tending to resist the volume expansion of SiO_2 at the periphery of the groove. The enhanced diffusion observed under the groove may be a result of greater than equilibrium concentration of vacancies formed due to the generation of the defects.

The retardation of the n-type epitaxial dopant observed under the groove at the oxidation temperature of 1150°C for wafers in batch 2 is shown in Fig. 4. It must be clarified that the term retardation here implies that the n-type epitaxial dopant away from the groove diffused further into the substrate than the dopant under the groove during oxidation. Figure 5 shows the absence of defects in the vicinity of the groove for samples which experienced retardation. This can be understood by observing that the thickness of the Si_3N_4 film is only 500Å. Thus, during the oxidation of the groove, the tendency for the stress to occur at the periphery of the groove will be minimized significantly. The absence of defects, however, does not explain the decrease in the diffusivity (or retardation) of the n-type dopant under the groove. The only explanation the author can suggest is that during the oxidation, the growing oxide in the groove results in the deficiency in vacancies at the Si-SiO_2 interface. Thus vacancies from the surrounding regions such as the epitaxial-substrate interface may diffuse toward the Si-SiO_2 interface. This will result in a decrease in the diffusivity of the epitaxial dopant underneath the groove.

From Fig. 2 and 4 it can be seen that isolation between epitaxial regions on either side of the groove is

not accomplished. The primary reasons are two fold. First the depth of the groove prior to its oxidation was too shallow compared to the 3.0 μm epitaxial thickness. Second, the diffusion of the epitaxial region into the substrate is significant at 1150°C. The former objection was overcome by using vertical geometry such as shown in Fig. 1b. Here, prior to the oxidation, the depth of the groove was slightly larger than the epitaxial thickness. After the oxidation of the groove, isolation was maintained for wafers in batches 3, 4, and 5 as shown in Table I. For wafers in batch 3 with Si_3N_4 and SiO_2 thicknesses of 2500 and 2000Å, respectively, bevel and stain profiles as shown in Fig. 6 were observed. Note that here a continuity of the p-type region between the bottom of the groove and the p-type substrate is attained. In addition, it can be seen that enhancement in the diffusivity of the n-type epitaxial dopant is observed at the periphery of the groove. This was accompanied by the presence of defects in the vicinity of the groove region similar to that shown in Fig. 3. The continuity of the p-type region may be explained by the affinity of boron for SiO_2. During the initial oxidation of the groove, a significant amount of boron is incorporated into the oxide in the groove. The oxide can now act as a source of boron during the remaining phase of the oxidation. Consequently, a continuity in the p-type region is maintained between the bottom of the groove and the substrate.

Wafers in batch 4 with Si_3N_4 thickness of 500Å and SiO_2 thicknesses ranging from 0-2000Å exhibited stain profile as shown in Fig. 6 with the exception that the enhancement at the periphery of the groove was absent. In addition, no defects were generated in the vicinity of the groove region. This result is similar to that in batch 2 and was expected.

For wafers in batch 5 with no SiO_2 under 2500Å thick Si_3N_4, the enhancement at the periphery of the groove was smaller than that shown in Fig. 6. This is expected since Si_3N_4 in direct contact with silicon will reduce the volume expansion of SiO_2 at the periphery of the groove. This in turn reduces the formation of defects.

From above it can be seen that the enhancement in the diffusivity and the generation of defects was a strong function of Si_3N_4 thickness. At the lowest oxidation temperature used in the present work (950°C), enhancement was observed for all combinations of Si_3N_4/SiO_2 thicknesses. In addition, defects were observed in all cases. Cosand and Prussin (4) observed that reducing the oxidation temperature results in an increase in the viscosity of SiO_2 resulting in a large stress generated. Their work used groove oxidation temperature of 900° and 1020°C. The latter oxidation temperature generated no defects while at 900°C defects were observed.

The results for the groove oxidation temperature of 950°C are shown in Table I for wafers in batches 6 to 9. The bevel and stain profiles of these wafers showed that there was no increase in the epitaxial thickness away from the groove region after the oxidation. For wafers in batch 6 with any Si_3N_4 and SiO_2 thicknesses used, the bevel and stain profiles were similar to that shown in Fig. 7. Here a significant amount of enhancement in the diffusivity of the n-type dopant under the groove region is observed. Prior to the oxidation, the epitaxial thickness was larger than the depth of the groove. After the oxidation, the depth of the groove was larger than the epitaxial thickness since the latter did not increase during the low temperature oxidation. In spite of this, the loss in isolation that resulted is due to the enhancement in the diffusivity of the n-type dopant under the groove. The chances of maintaining isolation between the two n-type regions was greater for wafers in batches 7, 8 and 9 with epitaxial thickness of 2.0 μm. Here prior to the oxidation, the bottom tip of the groove was below the epitaxial-substrate interface. The bevel and stain profiles after the oxidation for batches 7, 8, and 9 are shown in Fig. 8, 9, and 10, respectively. Here it can be seen that a potential loss in isolation exists for wafers in batch 8 with Si_3N_4 and SiO_2 thicknesses of 2500 and 2000Å, respectively. For the same oxide thickness but using only 500Å Si_3N_4, the isolation was maintained although some enhancement at the periphery of the groove region was observed as shown in Fig. 10. For wafers in batch 7 with no SiO_2 and Si_3N_4 thicknesses ranging from 500 to 2500Å, the enhancement in the diffusivity of the n-type epitaxial dopant was minimal as shown in Fig. 8. In addition, some defects were observed in the vicinity of the groove although the density of the defects was significantly lower than those observed for wafers in batches 8 and 9. These results are somewhat similar to that observed for wafers in batch 5 which used oxidation temperature of 1150°C. It must be emphasized here that Si_3N_4 in direct contact with silicon did not always produce less enhancement than with the presence of SiO_2. Thus for batch 1 no differences were observed for oxide thickness under Si_3N_4 ranging from 0 to 2000Å. The disadvantage of using Si_3N_4 in direct contact with silicon has been well documented (7). Thus for device fabrication, a thin layer of SiO_2 between substrate and Si_3N_4 is required.

Conclusion

From the present study, the following optimum process may be recommended for oxide isolation.

1. In order to reduce defects in the vicinity of the groove region thin layers of Si_3N_4 and SiO_2 should be used.
2. The generation of defects is minimized as the groove oxidation temperature increases. However, the disadvantages in using hgh oxidation temperature is the out-diffusion of the buried layer into the epitaxial region. This can be partially offset by using a slower diffusant such as antimony instead of arsenic as the dopant for the buried layer. In addition where no buried layer is used, it is recommended that arsenic should replace phosphorus as the epitaxial dopant. The use of the former will reduce the increase in over-all epitaxial thickness after the oxidation of the groove.

Manuscript submitted Sept. 29, 1977; revised manuscript received May 2, 1978.

Any discussion of this paper will appear in a Discussion Section to be published in the June 1979 JOURNAL. All discussions for the June 1979 Discussion Section should be submitted by Feb. 1, 1979.

Publication costs of this article were assisted by Honeywell-SSEC.

REFERENCES

1. W. B. Baker, W. H. Herndon, T. A. Longo, and D. L. Pelzer, *Electronics*, **46**, 65 (1973).
2. H. Sakai, T. Yoshimi, and K. Sugawara, *This Journal*, **124**, 318 (1977).
3. E. Bassous, H. N. Yu, and V. Maniscalco, *ibid.*, **123**, 1729 (1976).
4. A. E. Cosand and S. Prossin, Abstract 109, p. 292, The Electrochemical Society Extended Abstracts, Spring Meeting, Washington, D.C. May 2-7, 1976.
5. E. Kooi, J. G. Van Lierop, and J. A. Appels, *This Journal*, **123**, 1117 (1976).
6. F. Y. Chang and A. W. Chang, Paper presented at the IEEE Conference on Electron Devices, p. 577 (1975).
7. E. Kooi, J. G. Van Lierop, W. H. C. G. Verkuijlen, and R. de Werdt, *Philips Res. Rep.*, **26**, 166 (1975).
8. K. E. Beau and W. R. Rungan, *This Journal*, **124**, 5C (1977).

Silicon Oxidation Studies: Some Aspects of the Initial Oxidation Regime

E. A. Irene

IBM Thomas J. Watson Research Center, Yorktown Heights, New York 10598

ABSTRACT

This study is concerned with the initial regime (*i.e.* up to 200Å SiO_2 thickness) of the thermal oxidation of single crystal Si. The kinetic data (SiO_2 film thickness *vs.* time of oxidation) has been generated at 780°, 893°, and 980°C in dry O_2 and H_2O-N_2 ambients and measured using an automated ellipsometer which follows the oxidation *in situ*. The data for the dry O_2 oxidation is considerably more linear than for the data produced from H_2O containing ambients which exhibit parabolic behavior. This may be attributed to a greater protectiveness for oxides grown in H_2O. Dielectric breakdown measurements show that there are fewer defects in the H_2O grown thin SiO_2 films. Transmission electron microscopy observations show that the films contain inhomogeneities which are smaller than 50Å. Therefore, the conclusion is that the pore structure is different in dry and wet grown SiO_2 films and that this microstructure is responsible for both the oxidation data and dielectric breakdown differences.

The thermal oxidation of single crystal silicon at high temperatures (800°-1000°C) in pure dry O_2, has been found to be represented adequately by a linear-parabolic film growth model (1), with an accuracy better than 10%, if the data fitted only includes film thicknesses greater than a minimum value (d_o) of several hundred angstroms (2). However, for oxidation in H_2O containing ambients (3, 4), the minimum thickness value of d_o, to be included for a good fit to the linear-parabolic model, decreases with increasing H_2O content of the oxidizing ambient. An examination of the regime of thicknesses less than d_o, shows that this thin SiO_2 region is characterized by a faster rate of oxidation than is anticipated from the rate constants for the linear-parabolic regime (1-5). One report (5) describes this region by another linear-parabolic equation with different rate constants while other authors (6, 7) assume it is the linear part of the linear-parabolic rate law. The former analysis (5) does not consider the possible curve fitting error associated with assuming a linear-parabolic initial regime and the latter authors have insufficient data to analyze for the determination of a best fit. The present study is concerned with an examination of the initial regime of oxidation (SiO_2 film thicknesses $\leqq d_o$) to determine why the initial regime for dry O_2 oxidation displays a more rapid oxidation mechanism while for H_2O oxidation $d_o \approx$ O, and the oxidation data follow the linear parabolic model throughout.

Results of the present study, indicated a decided difference between the linearity of the data for dry O_2 oxidation and oxidation in H_2O containing ambients for SiO_2 films up to 200Å thickness. The dry O_2 data are more linear. The linear-parabolic model (1) can be summarized by the integrated rate equation

$$t - t_o = \frac{1}{k_{LIN}}(d - d_o) + \frac{1}{k_{PAR}}(d^2 - d_o^2)$$

where t and d are the time of oxidation and SiO_2 film thickness, respectively, t_o and d_o represent the upper bound of the initial oxidation regime which does not conform to linear-parabolic kinetics, and k_{LIN} and k_{PAR} are the linear and parabolic rate constants, respectively. In this model, linear kinetics are the result of a surface controlled reaction while parabolic kinetics demonstrate that the oxidation is diffusion controlled. Therefore, this experimental finding suggested that wet grown SiO_2 films are more protective. Dielectric breakdown histograms support the contention that 150Å wet grown SiO_2 films have less defects than films grown in dry O_2. These results can be explained if micropores existed in the SiO_2 films. For the purpose of observing micropores in the films, transmission electron microscopy (TEM) studies were performed.

Experimental Procedures

Substrate preparation and oxidation.—The oxidation experiments were performed using an automated ellipsometer capable of measuring the SiO_2 film thickness *in situ* during oxidation. The instrument used for this study has been described in detail elsewhere (8). Basically, the ellipsometer uses a laser light source, polarizer, compensator, and a rotating analyzer-encoder. The light intensity measurement after the analyzer is automated. The ellipsometry measurements are made with the sample contained in a fused silica rf-heated reaction tube. Therefore, it is possible to collect and analyze ellipsometric data as the SiO_2 film grows without interrupting the oxidation run. The optical constants characteristic of the Si surface as a function of temperature were previously measured (8).

All substrates were <100> oriented chem-mechanically polished silicon wafers measuring 3.2 cm in diameter and 0.025 cm in thickness. All the wafers were p-type with a nominal resistivity of 2 Ω-cm. It was reported previously (3) that the resistivity type or value in the range 0.5-10 Ω-cm had no influence on the oxidation process. The wafers were cleaned as reported elsewhere (3) and an initial oxide thickness of 3-6Å SiO_2 was measured at room temperature (2).

The gases used in this study included Ar, N_2, and O_2. Both N_2 and O_2 were supplied from boil-off of liquid sources. As previously reported (2, 3) the O_2 contained trace amounts of methane (17 ppm) which at the oxidation temperature used combusts to form H_2O. This trace H_2O substantially increases the rate of oxidation (3, 4). For dry oxidations, the methane was removed by preheating the oxygen to about 1000°C, in order to combust the methane to H_2O and CO_2, and then cold trapping at −80°C to reduce the H_2O concentration to less than 1 ppm H_2O in the O_2. In order to add H_2O to N_2, the N_2 is flowed through a thoroughly cleaned fused silica vessel which contains deionized H_2O. By controlling the H_2O temperature with a variable temperature refrigeration unit, the concentration of H_2O can be adjusted to any desired level from less than 1 ppm upward. The Ar was purchased in pressurized cylinders and was the high-

* Electrochemical Society Active Member.
Key words: thin films, kinetics, SiO_2.

est purity commercially available. The moisture content was less than 0.5 ppm as measured at the furnace exit during the actual annealing experiments to be described.

In order to check on the charge levels in the SiO_2 films grown, capacitance-voltage (C-V) measurements were made on some oxides. Evaporated aluminum counterelectrodes were used as electrical contacts. The C-V measurements (1 MHz) revealed an average fixed positive charge level of less than 5×10^{10} charges/cm^2. Bias-temperature stressing (10^6 V/cm at 200°C for 15 min and subsequent cooling under bias) revealed an average mobile positive charge level of 7×10^{10} charges/cm^2. These values are characteristic of MOS quality oxides.

Dielectric breakdown measurements.—Dielectric breakdown measurements were made using a special triggering circuit configuration previously described by Osburn and Ormond (9). Essentially a linear voltage ramp is applied to the MOS sample. The voltage ramp was obtained by charging a fixed capacitor using a constant current generator; the ramp rate was then controlled by adjusting the output current from the generator. Triggering is obtained by a circuit which senses a voltage across a resistor in series with the MOS device. The series resistor must be kept at a reasonably low value (10-1000Ω) to prevent a large error in the reading of the final breakdown voltage. The electrodes used were rf evaporated Al dots of 0.127 cm diam yielding a dot area of 1.27×10^{-2} cm^2 on the SiO_2 film side and Ga-In paste on the Si side. The Al thickness was approximately 5000Å and this thickness plus the use of a small sense resistor in the circuit configuration (9) insured that the measured breakdown voltage was the final destructive breakdown. The ramp rate was the same for all measurements and about 0.5 MV/cm-sec.

The breakdown measurements were done with the Al biased negatively, *i.e.*, with the 2 Ω-cm p-type Si in accumulation. At high fields electrons are injected from the Al into the SiO_2. If electrons were trapped near the Al-SiO_2 interface, the trapped charge would alter the field across the MOS device and possibly lead to erroneous conclusions concerning histograms of the number of breakdown events *vs.* applied field. For the purpose of determining if there is sufficient trapping near the Al-SiO_2 (injecting) interface to cause the observed effects a recently described (10) technique is employed which utilizes the Fowler-Nordheim (FN) current regime. This FN technique consists of a measurement of current while applying a voltage ramp to a MOS device. The FN current regime is identified by the linearity of the plot of log I *vs.* E. The fields at which the FN conduction mechanism dominates is usually greater than 6 MV/cm for SiO_2. If trapping occurs, the FN curve is shifted to higher fields due to the trapped negative charge. Trapped charge causes field reduction, F, at the cathode according to the equation (10)

$$F = \frac{qN_t}{\epsilon_{ox}} \frac{\overline{X}}{D_{ox}}$$

where q is the electronic charge, N_t is the total trap concentration, and ϵ_{ox} is the dielectric constant for SiO_2, $\overline{X}$ is the distance of centroid of the charge from the anode, and D_{ox} is the oxide thickness. This equation shows that the effect of the charge on the field at the cathode increases as the distance to the cathode decreases. Experimentally the current through the MOS device is measured using a logarithmic picoammeter while the field is increased by means of a linear ramp. The FN regime is scanned in field from about 6-10 MV/cm and then held at 10 MV/cm for a few seconds to insure large current flow through the device; then the field is removed and the experiment repeated. If trapping occurs the FN characteristic curve is shifted to higher fields. Results of this experiment are shown below.

Capacitance-voltage measurements (1MHz) at room and LN_2 temperatures were made to determine whether charges were trapped, and/or surface states (11, 12) created, near the Si-SiO_2 interface due to the large currents which exist prior to dielectric breakdown.

Transmission electron microscopy (TEM).—Specimens of 150Å SiO_2 films were prepared by chemically etching away the Si from the Si-SiO_2 composites. The details of this procedure have been previously described (13). The TEM specimen preparation was done in four different ways, in order to eliminate possible artifacts due to a particular etchant and to decorate features of interest. Type I samples were prepared by simply etching away Si with a mixture of HF and HNO_3. This etchant also attacks SiO_2 and the successful preparation of good TEM samples with this etchant is somewhat fortuitous. When the Si-SiO_2 interface is approached, the etchant mixture is changed to a solution more dilute in HF, in order to reduce the speed of attack on the SiO_2 film. Type II samples were prepared similarly to type I except that when about 80% of the Si was removed with a HF-HNO_3 etchant, the etchant was changed to a mixture of pyrocatechol-ethylenediamine-H_2O (14). This mixture attacks Si very vigorously (20 μm/hr at 100°C) but SiO_2 very slowly (200 Å/hr). Type III films were prepared exactly as type II and when the etching was finished the samples were annealed in dry N_2 at 1000°C for 2 hr. This treatment was used to simulate an observed degradation in dielectric reliability which is reported later. Type IV samples were prepared as type II samples but before etching they were either coated with 100Å of Au by evaporation or dipped in a solution of NaCl and annealed. The Au samples were annealed for ½ hr at 800°C and the NaCl contaminated samples were heated for 1 hr at 500°C. In some cases the Au coated samples were not annealed and in other cases the Au was removed after annealing with aqua regia. It was hoped that the Au would decorate preferred diffusion paths and the NaCl would decorate weak areas by reaction.

Experimental Results

Film growth kinetics.—Figure 1 shows the experimental data for the oxidation of <100> Si in dry O_2 and H_2O-N_2 ambients for SiO_2 film thicknesses of 20-150Å. Visually these data appear to be linear. Table I shows the results of fitting the data to the linear equation

$$t = k_1 d + k_2$$

by the method of least squares (15) where t is the oxidation time and d is the SiO_2 thickness. The dry O_2 data are relatively more linear than the H_2O-N_2 data. Indeed it is known that for a 2000 ppm H_2O in N_2 ambient $d_o \approx 0$, hence the data fits the linear-parabolic equation for all values of SiO_2 film thickness (4) while for dry O_2 a best fit is not obtained when film thick-

Table I. Results of fitting the data from Fig. 1 to the linear equation, $t = k_1 d + k_2$ where t is the time (min) and d the SiO_2 film thickness (Å). D represents dry O_2 oxidation ambient and W represents 2000 ppm H_2O in N_2

Temperature (°C)	Ambient	Std dev of fit	$1/k_1$ (Å/min)	k* (Å/min)
780	D	0.86	0.56	0.57
	W	4.0	0.1	0.10
893	D	0.40	2.8	2.2
	W	1.0	0.78	0.60
980	D	0.37	8.9	7.7
	W	1.1	3.3	4.6

* k_{LIN} from the linear-parabolic model (2).
The rate constants in columns 4 and 5 are known with less than 10% total error.

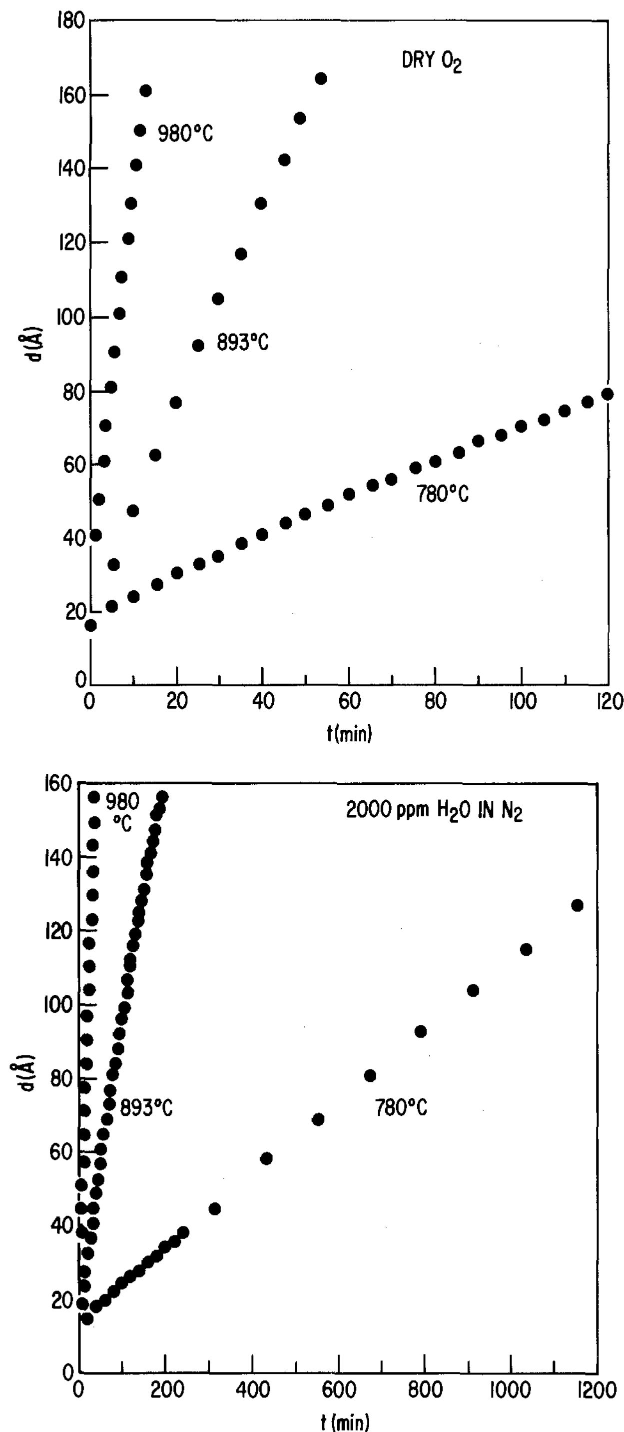

Fig. 1. SiO_2 film thickness, *d*, *vs.* time of oxidation, *t*, at 780°, 893°, and 980°C in (a, upper) dry O_2, (b, lower) 2000 ppm H_2O in N_2 as obtained from the automatic ellipsometer.

nesses less than ~200Å are included in the analysis. In keeping with the linear-parabolic model (1), the linear rate is associated with a surface controlled reaction. This plus the fact that the initial linear regime for dry O_2 displays a greater oxidation rate than the linear-parabolic mode, suggests that the SiO_2 films produced by ultra dry O_2 oxidation are less protective than films grown in an H_2O containing ambient. Enhanced protectivity for the H_2O grown 150Å films may be manifested in terms of reduced film defects. The results of dielectric breakdown measurements to be described can be interpreted in terms of film defects and will shed some light on this question of protectivity.

The difference in linearity of the oxidation data for wet and dry grown films is largest at the lower oxidation temperatures; and at the lower temperatures there is closer agreement between the slope of the straight line fitted to the data and the linear rate constant as obtained from the linear-parabolic model applied to film thicknesses up to 2000Å (2). For dry O_2 grown oxides this is understood by considering that the initial regime for dry O_2 films is not linear-parabolic and therefore agreement between k_{LIN} and k_l is not to be expected except where d_o is close to zero at the lower temperatures. For the H_2O grown films the parabolic rate constant is important even for these thin films and therefore agreement between k_{LIN} and k_l will depend on the importance of k_{PAR}.

Dielectric breakdown and trapping measurements.—The shape of the histogram of the number of dielectric breakdown events *vs.* the field at which breakdown occurs yields information relative to the defects in the SiO_2 films (9, 16). Figure 2 shows a comparison of the

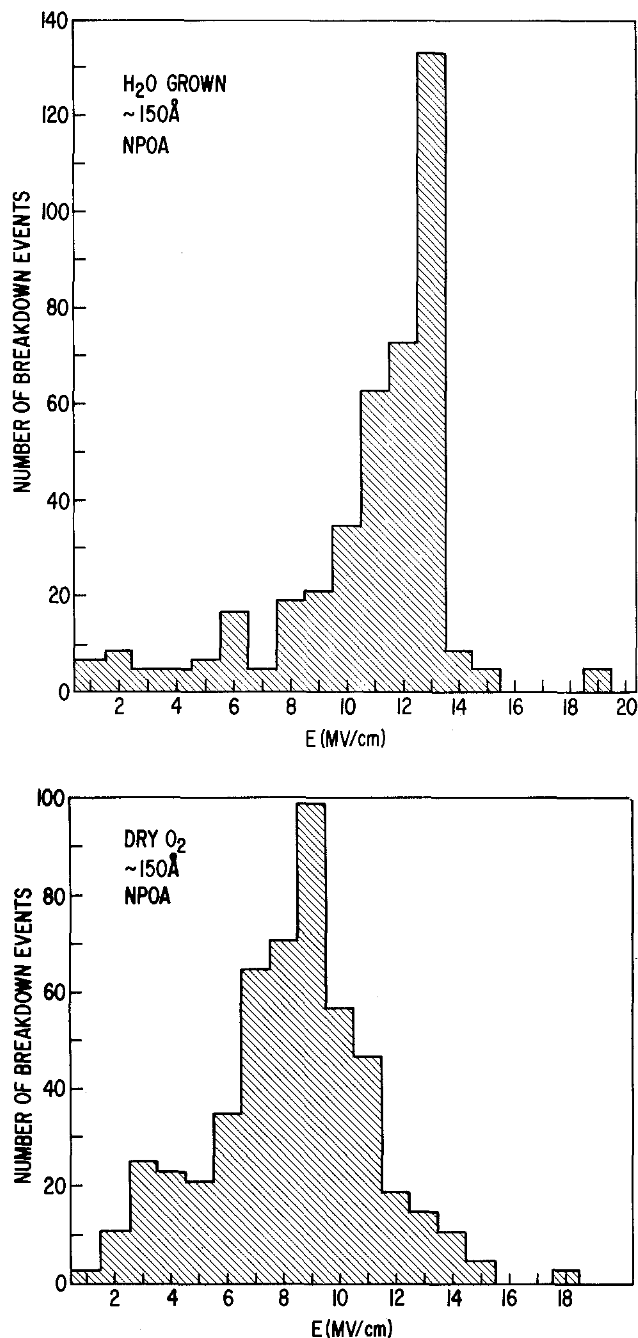

Fig. 2. A comparison of (a, upper) H_2O-N_2 and (b, lower) dry O_2 grown 150Å SiO_2 films according to the histogram of the number of destructive dielectric breakdown events *vs.* the applied electric field, *E*. Field values are calculated from the applied voltage and the ellipsometric SiO_2 thickness. NPOA means that no post oxidation annealing was performed.

histograms for 150Å SiO_2 films grown in H_2O-N_2 (Fig. 2a) and dry O_2 (Fig. 2b). It is readily seen that the maximum breakdown field for both wet and dry SiO_2 are nearly equivalent at a value of 14 MV/cm yet the shapes of the distributions are decidedly different. Theoretically, the histogram for a defect free SiO_2 film would be a delta function at the maximum breakdown field. Thickness fluctuations as well as random measuring equipment imperfections would broaden the delta function slightly, but SiO_2 film defects would cause a larger tail toward the lower fields. This type of tailing is observed in the histograms for both wet and dry grown SiO_2. However, the broadening is more severe for the dry oxides where the peak in the distribution is shifted about 2-3 MV/cm further toward low fields than for wet grown oxides and results in a distribution with a nearly Gaussian shape. The wet grown SiO_2 films have 80% of the breakdowns at fields $\geq$10 MV/cm while only 30% for dry grown films. Therefore, in view of these dielectric breakdown results the previous assertion based on the film growth kinetics that wet grown oxides are more protective seems justified.

Previously, it was reported that the effect of H_2O on the SiO_2 film oxidation kinetics is reversible (4), *i.e.*, the oxidation kinetics of an oxide growing in an H_2O containing ambient reverts to dry oxidation kinetics soon after the wet ambient is switched to a dry ambient. It is worthwhile to investigate whether the enhanced dielectric reliability of the wet grown thin SiO_2 films is coupled with the rather labile-OH in which case the enhanced dielectric integrity is easily lost or whether the enhanced reliability is due to a more stable form of OH in the SiO_2 network. Figure 3a shows that the histogram for a wet grown oxide reverts to that for a dry grown oxide after ½ hr 1000°C anneal in dry N_2. However, Fig. 3b, c, and d show that compared with the control (Fig. 3b) annealing at 1000°C in dry Ar for up to 18 hr caused only a small amount of degradation. In fact, the small amount of degradation could simply be due to sample to sample variations. In any case, the degradation in dry N_2 is unambiguously larger. Therefore, since the films were stable to the 1000°C Ar anneal, the enhanced reliability of wet grown thin oxides appears to be related to a stable form of OH in the SiO_2. The

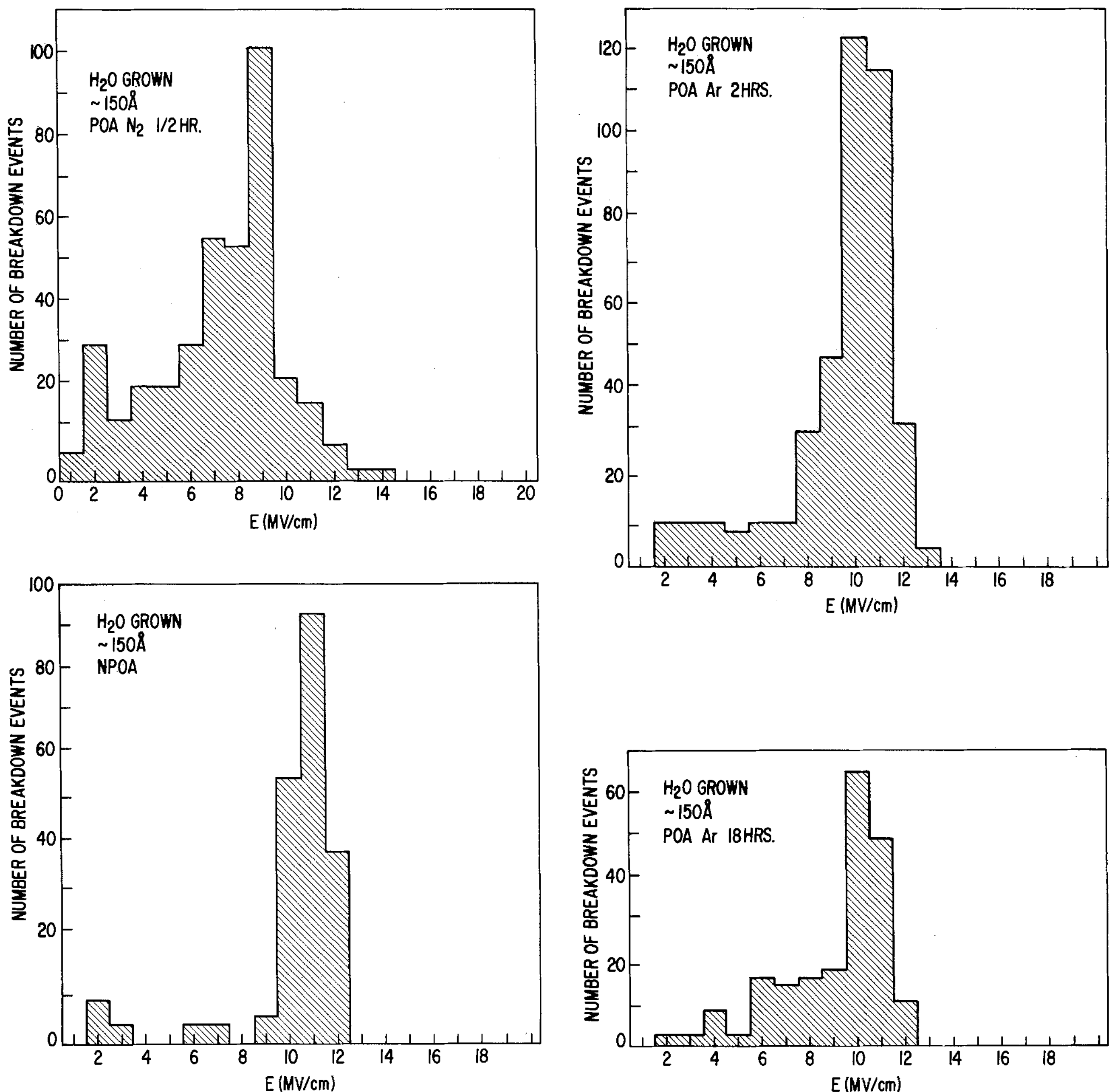

Fig. 3. A comparison of annealing H_2O-N_2 grown SiO_2 films at 1000°C in (a, upper left) N_2 for ½ hr, (b, bottom left) no anneal, (c, upper right) argon for 2 hr, (d, lower right) argon for 18 hr.

fact that there exists several forms of OH having different lability in fused silica has been reported (17). Also the reactivity of N_2 in the SiO_2-Si system in a nonoxidizing atmosphere has been reported (18) as well as the detrimental effect that the reaction of N_2 has on the dielectric reliability (19, 20). Thus, the degradation of the H_2O grown thin films is accelerated by N_2 reaction and not by the out-diffusion of labile OH.

Electron trapping and surface states.—Representative results for the electron trapping measurements by the previously described Fowler-Nordheim (FN) technique are shown in Fig. 4. The samples were ramped up to 10.5 MV/C and held there for 10 sec (i). Then the curve was retraced (re). The initial and retraced curves for a wet grown oxide (W104) differ at most by 0.5 MV/cm shift in the breakdown histogram peaks. Samples W104 and D113 displayed more than the average amount of trapping for wet and dry samples examined in this study; the average shift in the FN characteristic curve was found to be 0.2-0.3 MV/cm for both wet and dry samples with wet grown films usually exhibiting more trapping. It was sometimes difficult to find dots on dry grown SiO_2 samples which could withstand the high field for this experiment. Other than this problem however, the trapping behavior near the cathode was observed to be similar for wet and dry films and in no case was the trapping sufficient to cause the degree of electric field change necessary to explain the histograms of Fig. 2.

Capacitance-voltage (C-V) measurements at room temperature and liquid nitrogen temperature have shown that about $7.5 \times 10''$ positive charges per square centimeter are created at or near the Si-SiO_2 interface and about the same number of surface states are created by virtue of the above described FN currents. These results were the same for both dry and wet grown oxides and are in qualitative agreement with previous studies [see, for example, Ref. (21) through (24)].

Transmission electron microscopy (TEM).—Figure 5 shows representative results from type I and II samples. The results from type I, II, dry and wet samples were substantially the same. It is seen from Fig. 5 that the mode for the dissolution of the films is via attack by the etchant at selected small areas on the film surface. The differences seen between Fig. 5a and b are probably due to the time of exposure of the film to etchant. The time duration in which the sample was exposed to etchant would determine the size relationship between the final size of the hole and the original defect. This time was not controlled in this study. The nature of the defect, *i.e.*, whether a void, micropore, impurity cluster, crystallite, etc. depends on the relative reactivity of the etchant to these types of possible defects. It is clear that a void or micropore could yield the final observation, but other defects cannot be ruled out. The maximum size of the inhomogeneity must be as small or smaller than the hole found after etching. Holes which measured less than 100Å were observed, and therefore, considering the speed of the etchants, the inhomogeneities could be 50Å or less in diameter. No differences were seen upon annealing type I and II samples. Therefore, no figure for type III samples is shown.

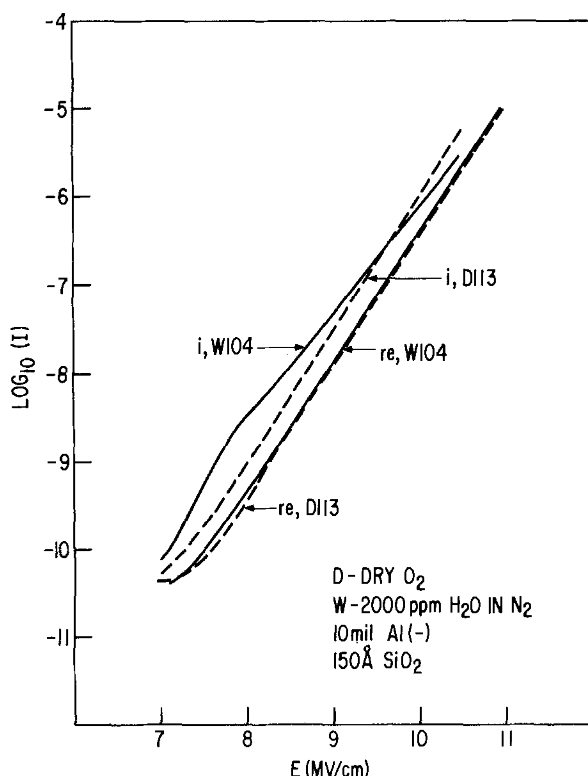

Fig. 4. A comparison of the Fowler-Nordheim conduction behavior between dry (D113) and H_2O grown (W104) SiO_2 films.

By way of explaining these results, gas permeation studies (25) have led to the assertion that pores in SiO_2 of less than 50Å diameter would explain the measured permeabilities for different gases. Another model was proposed (26) in which a nonrandom distribution of bond angles in the SiO_2 network may result in chain-like defects where $d\pi$-$p\pi$ orbital overlap between Si and O is greater than in surrounding regions. Such higher electron density regions may be more violently attacked by etchant. This latter model (26) predicts higher electrical conductivities for films which have this chain structure. However, the conduction measurements made in the present study do not show any systematic differences between wet and dry prepared 150Å SiO_2 films. Also, it is difficult to reconcile the oxidation kinetics results based on more dense localized regions.

Representative results from type IV samples are shown in Fig. 6. Figure 6a shows that less than monolayer of Au forms rod-shaped structures. A closer examination reveals that contained within the rod-like structures are smaller darker regions. Presumably these are the nuclei for the growth of the Au islands. The areal density of these nuclei ($\sim 10^{15}$ cm^{-2}) is much larger than the electrically active defect density ($<10^3$) as obtained by dielectric breakdown measurements. Figure 6b shows the results from Au decoration. Au was evaporated onto a 150Å SiO_2 film on Si. The Si was removed from a portion of the sample and then the Au was driven into the film at 800°C for ½ hr. The Au was then removed using aqua regia. The darker transparent region of Fig. 6b was caused by a piece of the film folding back to the silicon edge and then breaking off. Therefore, there is 300Å SiO_2 in the darker region. All the Au has not been removed and is seen as the nontransparent dots and islands formed by coalescence and growth. The regions where the Au has been removed appear as tunnels. However, it is known that Au reacts with SiO_2 (27) and the shape of the tunnel-like structures is similar to the shape of the Au islands. Therefore, it is believed that the tunnel-like structures are due to reaction of Au with SiO_2. Furthermore, if the Au is removed after a 300°C anneal or no anneal at all, the tunnel structures are less visible.

Figure 6c shows the result of decoration with NaCl. The NaCl nuclei appear to be located preferentially on the perimeter of holes which were produced by the etchant. Also, around the NaCl nuclei and clusters is another dark band. This is probably a region in which reaction has taken place between Na and SiO_2. The holes may have been preceded by areas which were the reaction product of NaCl and SiO_2 and this may be more vigorously attacked by the etchant. Sodium

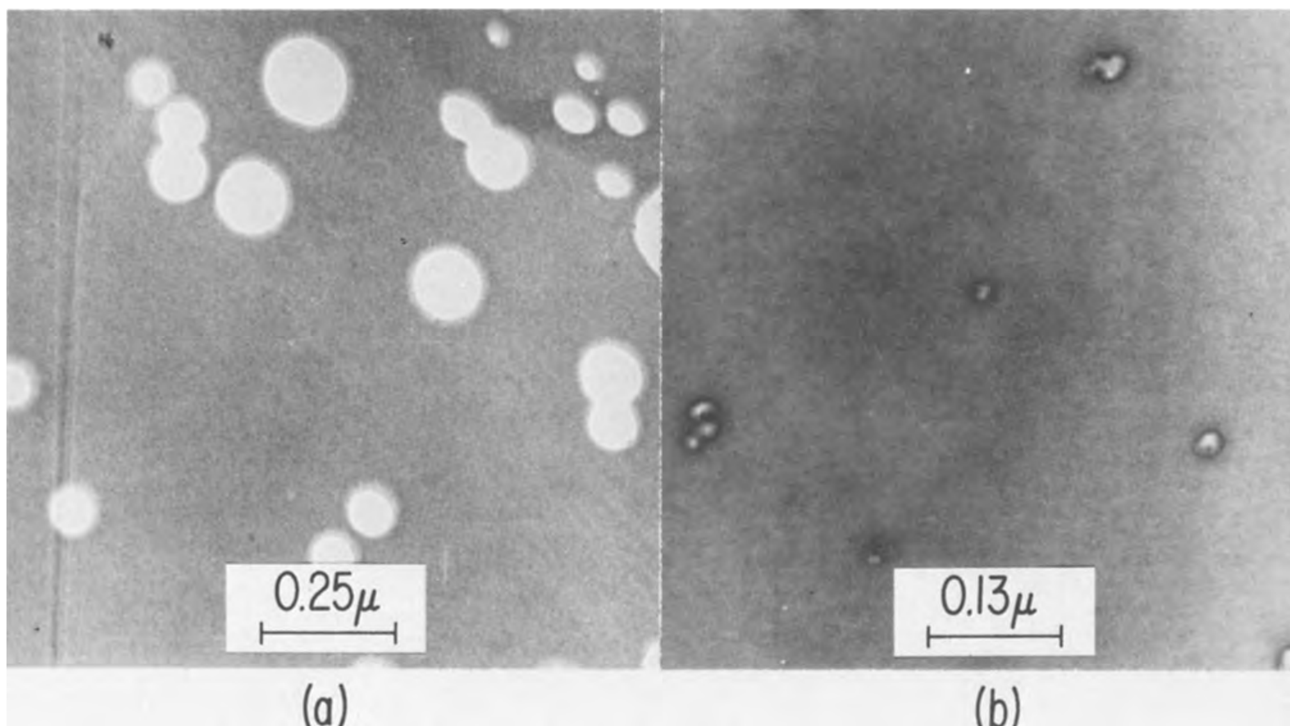

Fig. 5. Typical TEM results from 150Å SiO_2 films of type I (HF-HNO_3 etched), type II (organic etch), or type III (same as type I plus 1000°C N_2 anneal) showing holes etched through the films. Micrograph (a) shows a more advanced stage of etching than (b).

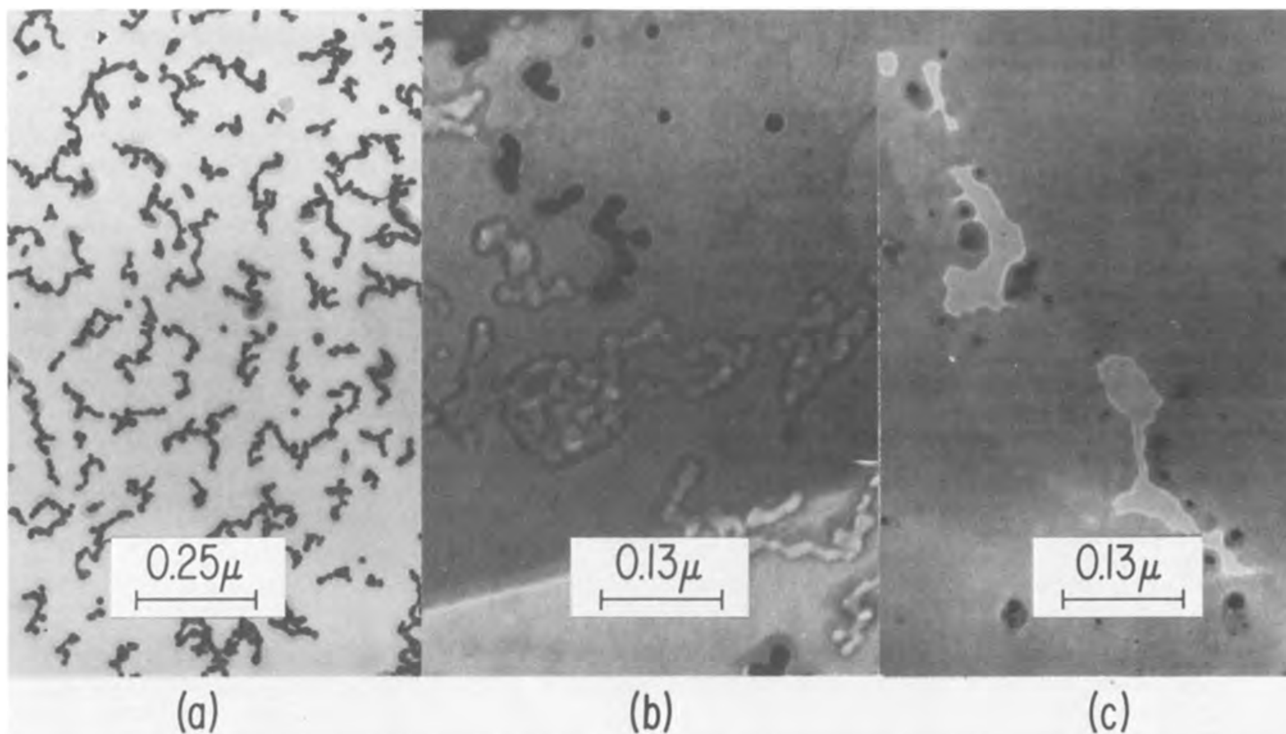

Fig. 6. Typical TEM results from Au (type IV) and NaCl (type V) decoration studies. Micrograph (a) shows Au islands as deposited on SiO_2; (b) shows the effect of annealing and then removing some of the Au; (c) shows the holes left after NaCl decoration and etching. NaCl islands are also seen as the dark spots.

silicates are usually soluble in H_2O. The shapes of the holes are irregular as compared with the circular holes which occurred without attempts at decoration.

There are several things learned from the TEM experiments. The type I and II samples strongly suggest that the films have inhomogeneities. The size of the inhomogeneities is certainly less than 100Å and probably less than 20Å which makes the resolution of the defects within the present study doubtful. The number of these inhomogeneities, assuming that they are related to the etched holes in a one to one ratio, is of the order of 10^{15} cm^{-2} which is more than 10^{12} times too large compared with the number of defects obtained from dielectric breakdown statistics. This probably means that although the type of inhomogeneity observed is part of the SiO_2 thin film structure, only a small fraction is sufficiently electrically active to cause dielectric failure. The shape of defects was not ob-

tained by decoration experiments because ambiguities arise from the reaction of the decorant with SiO_2. However, the number of nuclei of Au and NaCl is roughly the same as the number of holes observed from etching. This may mean that the decorants did indeed decorate the defects but also simultaneously obscured their shapes by reaction.

Summary and Discussion

The kinetic oxidation data suggest that the wet grown thin (~150Å) oxides are more protective than ultra dry O_2 grown films. The evidence for this is the greater linearity of the thickness-time data for the dry grown oxides as compared with wet grown films. The linearity suggests a surface reaction controlled mechanism for oxidation rather than diffusive transport of oxidant. In effect, for the case of ultra dry O_2 oxidation, the growing oxide film does not provide an effective barrier to the diffusion of oxidant. A comparison of the dielectric breakdown histograms for the wet and dry ~150Å SiO_2 films strongly supports the contention that the wet grown oxides are more protective. Annealing the wet grown oxides in dry Ar at 1000°C for long times does not cause degradation. Therefore, the enhanced dielectric reliability of the H_2O-grown films is due to a rather stable OH species. The TEM experiments offer significant evidence that SiO_2 films are not homogeneous and the size of the inhomogeneities is probably less than 50Å.

The experimental observations made in this study are consistent with the existence of micropores in the SiO_2 films, even though such small pores were not directly observed. Firstly, the presence of pores in solids is expected (28). The size and type of pore structure that a material displays is dependent on the material. Secondly, the pores would provide a "short circuit" path to the Si-SiO_2 interface for oxidant species which do not attack SiO_2 (such as O_2 related oxidant). Rapid lateral diffusion of these oxidant species would yield linear oxidation kinetics which is typical of surface controlled reactions. In addition, such pores could cause premature dielectric failure. For H_2O grown films the reactive OH attacks SiO_2 forming SiOH species. The micropores could then become partially clogged with OH groups thereby yielding parabolic oxidation kinetics and improved dielectric integrity. Thirdly, micropores are known to bind vapors tenaciously (28) in the interior of the pores thus explaining the irreversibility of the dielectric improvement even to 1000°C inert gas anneals. Further experiments would be necessary to prove the micropore model. Indirect measurements such as adsorption isotherm studies are usually performed to detect the existence and nature of pores (28, 29), particularly micropores. Only a few studies have reported the direct observation of pores smaller than ~100Å and no studies have been found in the literature by this author which show the direct (TEM, SEM), etc.) observation of micropores.

Acknowledgment

The author gratefully acknowledges D. W. Ormond for apparatus and assistance relative to the dielectric breakdown measurements, P. Solomon for assistance with the electron trapping measurements, and A. B. Fowler and D. R. Young for critically reviewing this manuscript. This research was partially supported by the Defense Advanced Research Projects Agency and monitored by the Deputy for Electronic Technology, RADC, under Contract F19628-76-C-0249.

Manuscript submitted Feb. 15, 1978; revised manuscript received May 15, 1978.

Any discussion of this paper will appear in a Discussion Section to be published in the June 1979 JOURNAL. All discussions for the June 1979 Discussion Section should be submitted by Feb. 1, 1979.

Publication costs of this article were assisted by IBM Thomas J. Watson Research Center.

REFERENCES

1. B. E. Deal and A. S. Grove, *J. Appl. Phys.*, **36**, 3770 (1965).
2. E. A. Irene and Y. J. van der Meulen, *This Journal*, **123**, 1380 (1976).
3. E. A. Irene, *ibid.*, **121**, 1613 (1974).
4. E. A. Irene and R. Ghez, *ibid.*, **126**, 1757 (1977).
5. M. A. Hopper, R. A. Clarke, and L. Young, *ibid.*, **122**, 1216 (1975).
6. A. G. Revesz and R. J. Evans, *J. Phys. Chem. Solids*, **30**, 551 (1969).
7. Y. J. van der Meulen, *This Journal*, **119**, 530 (1972).
8. Y. J. van der Meulen and N. C. Hien, *J. Opt. Soc. Am.*, **64**, 804 (1974).
9. C. M. Osburn and D. W. Ormond, *This Journal*, **119**, 591 (1972).
10. P. Solomon, *J. Appl. Phys.*, **48**, 3843 (1977).
11. P. V. Gray and D. M. Brown, *Appl. Phys. Lett.*, **8**, 31 (1966).
12. D. M. Brown and P. V. Gray, *This Journal*, **115**, 760 (1968).
13. E. A. Irene, V. J. Silvestri, and G. R. Woolhouse, *J. Electron. Mater.*, **4**, 409 (1975).
14. R. M. Finne and D. L. Klein, *This Journal*, **114**, 965 (1967).
15. H. D. Young, "Statistical Treatment of Experimental Data," chap. IV, McGraw-Hill Co., Inc., New York (1962).
16. N. J. Chou and J. M. Eldridge, *This Journal*, **117**, 1287 (1970).
17. R. W. Lee, *Phys. Chem. Glasses*, **5**, 35 (1964).
18. S. I. Raider, R. A. Gdula, and J. R. Petrak, *Appl. Phys. Lett.*, **27**, 150 (1975).
19. B. H. Vromen, *ibid.*, **27**, 152 (1975).
20. C. M. Osburn and D. W. Ormond, *This Journal*, **119**, 597 (1972).
21. C. M. Osburn and E. J. Weitzman, *ibid.*, **119**, 603 (1972).
22. M. Shatzkes, M. Av-Ron, and R. M. Anderson, *J. Appl. Phys.*, **45**, 2065 (1974).
23. M. Shatzkes and M. Av-Ron, *ibid.*, **47**, 3192 (1976).
24. C. M. Osburn and N. J. Chou, *This Journal*, **120**, 1377 (1973).
25. S. W. Ing, Jr., R. E. Morrison, and J. E. Sandor, *ibid.*, **109**, 221 (1962).
26. A. G. Revesz, *J. Non-Cryst. Solids*, **4**, 347 (1970).
27. E. I. Alessandrini, D. R. Campbell, and K. N. Tu, IBM Report RC-4844.
28. S. J. Gregg and K. S. W. Sing, in "Surface and Colloid Science," Vol. 9, E. Matijevic Editor, chap. 4, John Wiley & Sons, Inc., New York (1976).
29. I. U. P. A. C., Manual of Symbols and Terminology, Appendix 2, Part I, Colloid and Surface Chemistry, Pure and Applied Chem., **31**, 578 (1972).

Water Droplet Formation during the Life Testing of IC's in a Humid Ambient

H. Koelmans and H. J. Kretschman
Philips Research Laboratories, Eindhoven, The Netherlands

After temperature-humidity-bias (THB) life tests at 85°C and 85% relative humidity we sometimes found strong local corrosion at the tracks and/or bondpads of IC's, with indications that water droplets had been present at some time during the test. The relative humidity in the test chamber, however, was well enough under control to exclude accidental condensation of water. This failure occurred much earlier (typically within a few hundred hours) than would have been warranted by the corrosive attack as a result of electrolysis in the film of a few monolayers of water that is formed when a hydrophilic surface of, for instance, SiO_2, is exposed to a humid ambient (1). The occurrence of this type of early corrosion appeared to be strongly enhanced in the presence of a source from which ionic impurities could leach out.

These observations led to the assumption that, in the presence of ionic impurities, electrolytic transport in the thin film of adsorbed water may lead to the accumulation of electrolyte at the current-carrying electrodes to a concentration high enough to cause condensation of water droplet. The presence of Na^+ and PO_4^{3-} ions, for instance, would then lead to accumulation of NaOH at the cathode and H_3PO_4 at the anode. Water droplets formed at closely spaced tracks of opposite polarity could then bridge these tracks and induce a current spike, causing local destruction of the tracks.

In order to check this assumption we built miniature moisture chambers in which test samples could be observed under a microscope while continuously monitoring the electrolytic leakage current. The predicted chain of events, *i.e.*, droplets formation-bridging-current spiking and strong local corrosion, was indeed observed. An example is shown in Fig. 1. The sample shown is the Al metallization pattern of a PCCD on top of a silicon chip which had first been provided with 2 μm of thermal oxide and a phosphorsilicate glass film. The SEM photograph of Fig. 2 is another example of current-induced condensation. It shows droplets (or rather what remains of droplets under the vacuum conditions of the SEM) on the bonding wires of a corrosion test sample mounted on a TO_5 header, after a THB test at 85°C, 85% RH in a standard humidity chamber. The droplets appeared only on negative bonding wires and contained NaOH to such a high concentration that they did not even dry out after the sample had been withdrawn from the humidity chamber. The origin of this condensation phenomenon could be traced back in a miniature moisture chamber of the type mentioned. Some time after the application of bias, water appeared on the glass of the header (Fig. 3) and subsequently droplets climbing up cathodic bonding wires were observed. Eventually these (alkaline) droplets reached the chip and caused heavy corrosion at the Au/Al bond (Fig. 4). Examination of the glass showed that its surface had roughened during the test. Apparently the current-induced condensation in this sample is connected with a slow leaching of Na^+ ions from the glass of the header. When the headers are carefully cleaned in boiling fuming nitric acid, and then made hydrophobic wih silanes, forced condensation of water on the glass can be avoided. The mechanism responsible for the transport of electrolyte along the bonding wire remains unclear—the effect has some

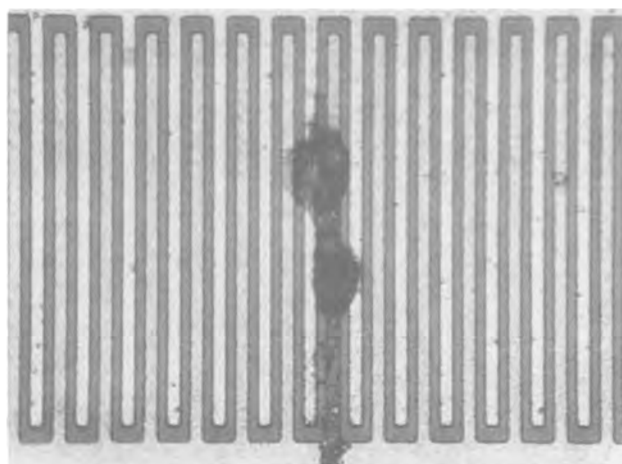

Fig. 1. Water droplets bridging electrodes of an Al interdigitated structure on PSG (7 m/o of P_2O_5). Electrode gap 6 μm: experimental conditions; bias 40V, temperature 22°C, relative humidity 88%.

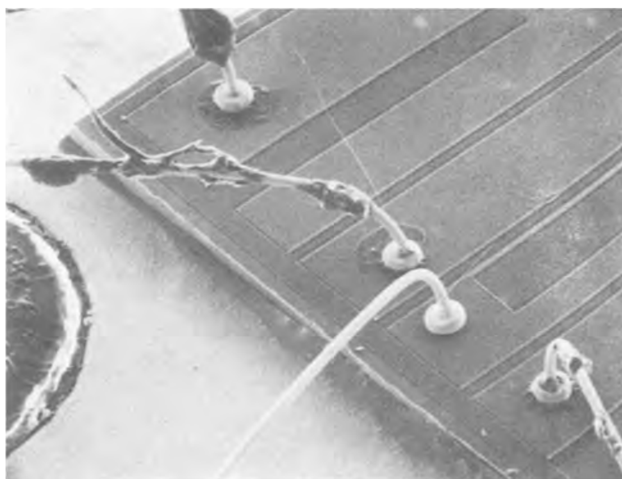

Fig. 2 SEM picture of dried-out alkaline droplets on the negative Au-bonding wires of a corrosion test sample subjected to a THB test. Bias 40V; temperature 85°C; relative humidity 85%.

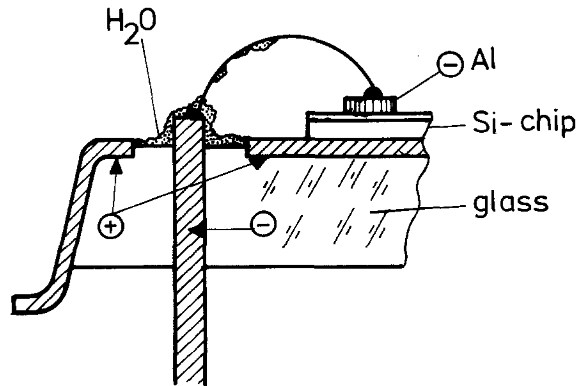

Fig. 3. Sketch of the situation at a "cathodic" pin of the header. The body of the header is connected to the anodic pins.

Fig. 4. Complete destruction of the Al at negative bond after alkaline droplets have reached the chip. Same conditions as sample of Fig. 2.

resemblance to the rise of liquids around electrodes known as the Sumoto effect (2).

Chips with the interdigital electrode pattern shown in Fig. 1 were also encapsulated in plastic and subsequently put on THB test while again monitoring the leakage current. These test samples (used without glass-over) were very suitable for this purpose because w/d, the total gap length over the gap width, was very large ($\sim$ 5000). A typical result is given in Fig. 5, for a sample on thermal SiO_2, with standard encapsulation in an epoxy DIL package.

The evolution of leakage current as a function of time can be divided into three periods. The first period is characterized by an increase in leakage current to a steady-state level (period 2). This behavior reflects the gradual penetration of moisture into the DIL package. The latter was confirmed in separate experiments on moisture absorption; the times needed for moisture saturation were found to be approximately equal to the times required for saturation of the leakage current. During the third period, violent increases in current occur. The time at which these current peaks appear and their height depend on the experimental conditions. When the steady-state current is high as a result of, for instance, a strong bias and/or the use of an impure plastic, current peaking tended to be earlier and

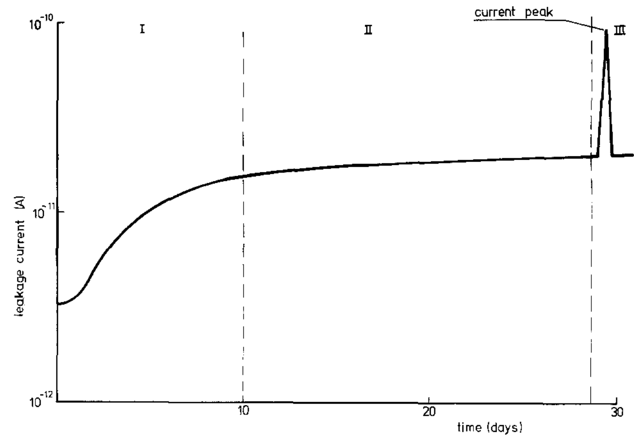

Fig. 5. The electrolytic leakage current of a test sample in epoxy as a function of time. The sample is a finely interdigitated Al electrode pattern deposited on 2 μm of thermal SiO_2. Bias 5V; temperature 85°C; relative humidity 85%. The current peaks have been simplified; their actual shape is much more complicated. The graph shows the maximum current observed and the time of duration (width at base) of the increase in current.

more violent. Under unfavorable conditions the current at maximum peak value could be 10^4 times higher than the steady-state level (period 2). Inspection of the samples after removal of the plastic in fuming HNO_3 revealed strong local corrosion when current peaks had occurred during the test. On the other hand, samples opened during period 2 hardly showed any (visible) corrosion. The behavior of the encapsulated samples with respect to current peaks coupled with strong local corrosion is very similar to that observed on bare samples. This suggests that in samples packaged in plastic too, current peaks and the accompanying local destruction of metal tracks are due to the phenomenon of forced condensation of moisture observed on bare samples. In the case of samples in plastic this could lead to the formation of voids filled with electrolyte at the interface between the plastic and the chip. In this respect it is interesting to note that void formation connected with strong local corrosion is a well-known phenomenon observed on painted steel in contact with saline water. Here the corrosion proceeds without an external bias, but still the process is electrochemical in nature, with parts of the metal surface acting as cathode and other parts acting as anode. It is also interesting to note that, similar to what we observed on IC's, the electrolyte in "cathodic" voids on steel was found to be alkaline (3).

Manuscript submitted Aug. 22, 1977; revised manuscript received March 1, 1978.

Any discussion of this paper will appear in a Discussion Section to be published in the June 1979 JOURNAL. All discussions for the June 1979 Discussion Section should be submitted by Feb. 1, 1979.

Publication costs of this article were assisted by Philips Research Laboratories.

REFERENCES

1. H. Koelmans, "12th Annual IEEE Reliability Physics Symposium," pp. 168-171, Las Vegas, Nevada, April 1974.
2. See for instance: W. F. Pickard, *Prog. Dielectr.*, **6**, 1 (1965).
3. For a review of electrochemical phenomena on painted metals see: H. Julien, *Prog. Org. Coat.*, **2**, 99 (1974).

JOURNAL OF THE ELECTROCHEMICAL SOCIETY

ACCELERATED

BRIEF COMMUNICATIONS

OCTOBER 1978

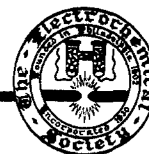

Anodic Electrodeposition of Gold from Liquid Ammonia Solutions

Towfik H. Teherani,* William J. Peer, J. J. Lagowski, and Allen J. Bard**

Department of Chemistry, The University of Texas at Austin, Austin, Texas 78712

The electroplating of metal and alloys, which is of importance in numerous applications, has always been accomplished by cathodic deposition (1-3). For example the industrially important process of gold electroplating is usually carried out by reduction of the gold(I) species from slightly acidic cyanide media. We report here the first example of anodic electrodeposition of gold by oxidation of auride ion (Au^-) in a liquid ammonia solution.

Recent results have demonstrated the formation of Au^- by reaction of gold metal with coulometrically generated solvated electrons (e_s^-) in liquid NH_3 containing 0.1 M KI at -40°C (4) or by reaction of Au with Cs metal in liquid NH_3 (5). The experimental procedures and apparatus for liquid NH_3 studies have been reported previously (6,7). A typical experiment involved the introduction of Au metal in liquid NH_3 containing excess e_s^- in a large coulometric cell. When the solution was kept at -40°C and stirred, the Au dissolved with the formation of Au^-. Alternately, the Au^- could be produced by starting with a solution of AuI in liquid NH_3. A typical cyclic voltammogram of such a solution at a Pt-electrode is shown in Fig. 1. Controlled potential electrolysis at -0.5 V resulted in the deposition of Au on the Pt working electrode. When the electrode potential was moved to the generation of e_s^- (-2.5 V), the freshly deposited gold was cathodically stripped. The cyclic voltammogram of the resulting solution after excess e_s^- was removed coulometrically, indicated the presence of an anodic wave at -2.15_0V corresponding to the oxidation of Au^- to Au^0. The electrolytic oxidation in the solution (at -2.0 V) resulted in deposition of Au on the Pt anode surface. The gold plate produced in this way was bright and could be polished to a high luster. Examination of the surface by ESCA spectroscopy showed strong bands at binding energies of 82, 85, 332, 350, and 545 eV, characteristic of metallic gold.

While it is difficult to project from these preliminary experiments whether this method of electrodeposition will be of practical use, this procedure does avoid the use of cyanide. Moreover, the oxidation of Au^- occurs with 100% current efficiency without the coevolution of hydrogen which occurs during the cathodic deposition in aqueous media. Finally liquid ammonia provides the unique opportunity to examine the course and nature of deposition of a metal both cathodically and anodically in the same medium.

Acknowledgement.--The support of this research by the National Science Foundation and the Robert A. Welch Foundation is gratefully acknowledged.

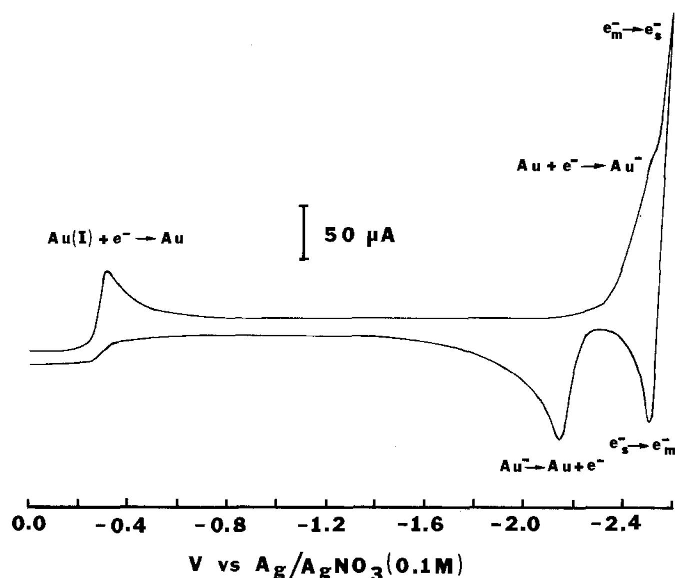

Fig. 1. Cyclic voltammogram of a 6.3 mM AuI in liquid NH_3 containing 0.1 M KI at -40°C. Scan rate 0.1 V/sec. Electrode area 0.039 cm^2.

*Electrochemical Society Student Member.
**Electrochemical Society Active Member. Key words: metals, deposition, inorganic, solvents.

REFERENCES

1. F. A. Lowenheim, Editor, "Modern Electroplating," Wiley-Interscience, New York (1974).
2. D. G. Foulke, Editor, "Electroplators Process Control Handbook," R. E. Krieger Publishing Co., New York (1975).
3. Bryan L. McKinney and Charles L. Faust, J. Electrochem. Soc., 124, 397C (1977), and references therein.
4. T. Teherani, W. Peer, J. J. Lagowski, and A. J. Bard, J. Am. Chem. Soc., (submitted).
5. W. Peer and J. J. Lagowski, J. Am. Chem. Soc., (in press).
6. W. H. Smith and A. J. Bard, J. Am. Chem. Soc., 97, 5203 (1975).
7. T. Teherani, K. Itaya, and A. J. Bard, Nouv. J. Chim., 2, (1978) (in press).

Manuscript submitted Aug. 8, 1978.

Publication costs of this article were assisted by The University of Texas at Austin.

The Corrosion of Carbon Black in Phosphoric Acid

Gary A. Gruver*

United Technologies Corporation, Power Systems Division, South Windsor, Connecticut 06074

Carbon as a material is thermodynamically unstable at phosphoric acid fuel cell cathode operating conditions. However, the kinetics of carbon corrosion are sufficiently slow so that carbon can realistically be considered for various materials applications at fuel cell operating conditions. One common use for carbon blacks in fuel cells is as a support for the (usually) noble metal catalyst required for oxygen reduction at the cathode and hydrogen oxidation at the anode. The electrochemical corrosion of various carbon blacks has been studied by several workers (1-4). Kinoshita and Bett (2) studied the corrosion of a high surface area carbon black in 96% H_3PO_4 at 135°C at several potentials and determined that two processes occurred: the formation of surface oxides and evolution of CO_2. They found that over several thousand minutes the rate of carbon corrosion decreased and that CO_2 evolution eventually became the major reaction. They speculated that while the mechanism for these processes was complex, corrosion might be controlled by mass transport of reactive species through the bulk carbon particle structure, with oxidation occurring at disorganized amorphous carbon sites inside the particle, much in the same way that Heckman and Harling (5) have observed for the gas phase oxidation of carbon blacks.

Experiments done in this laboratory indicate that the corrosion of carbon blacks in a phosphoric acid fuel cell environment does proceed in the same manner as noted by Heckman et al. for the gas phase oxidation of carbon blacks. Subscale fuel cell tests using Teflon-bonded electrodes have been performed at conditions expected to accelerate the corrosion of carbon blacks. The catalyst used in these tests was highly dispersed platinum supported on Vulcan XC-72 (Cabot Corp.). Figure 1 is a transmission electron micrograph showing the appearance of the carbon black in the catalyst before testing. Figure 2 is a transmission electron micrograph representative of the cathode catalyst after operating for 1000 hours at 191°C. The cathode was operated at an iR-free potential of 835 mV (vs a hydrogen electrode in the same electrolyte) on oxygen prehumidified with water to maintain a constant average H_3PO_4 concentration of approximately 95%. The carbon particles shown in Figure 2 do not exhibit the same uniform density throughout that appears in the untested samples in Figure 1. Detailed examination of these and other micrographs taken at higher magnifications reveals that the outer more crystalline "shell" of the carbon particles remains intact while the central portion (which is more disordered, having only short range crystallinity) has been oxidized away. These findings are in complete agreement with Heckman's observations and his "concentric crystallite model" for carbon blacks (5), and qualitatively could explain the apparently film diffusion-controlled corrosion processes noted by Kinoshita (2). Porosity in the turbostratic outer layers of the carbon particles allows access of reactive species (presumed to be H_2O) to the easily oxidizable inner portion of the particle.

As expected, no carbon corrosion was noted in the catalyst on the fuel cell anode used in this test.

*Electrochemical Society Active Member.

References

1. H. Binder, A. Kohling, K. Richter and G. Sandstede, Electrochim. Acta, 9, 255 (1964).
2. K. Kinoshita and J. Bett, Carbon, 11, 237 (1973)
3. K. Kinoshita and J. A. S. Bett, Carbon, 11, 403 (1973)
4. K. Kinoshita and J. A. S. Bett, Carbon, 12, 525 (1974)
5. F. A. Heckman and D. F. Harling, Rubber Chem. Technol., 39, 1 (1966)

Keywords: corrosion, carbon, fuel cell

Figure 1 — Untested Catalyst; Pt Supported on Vulcan XC-72

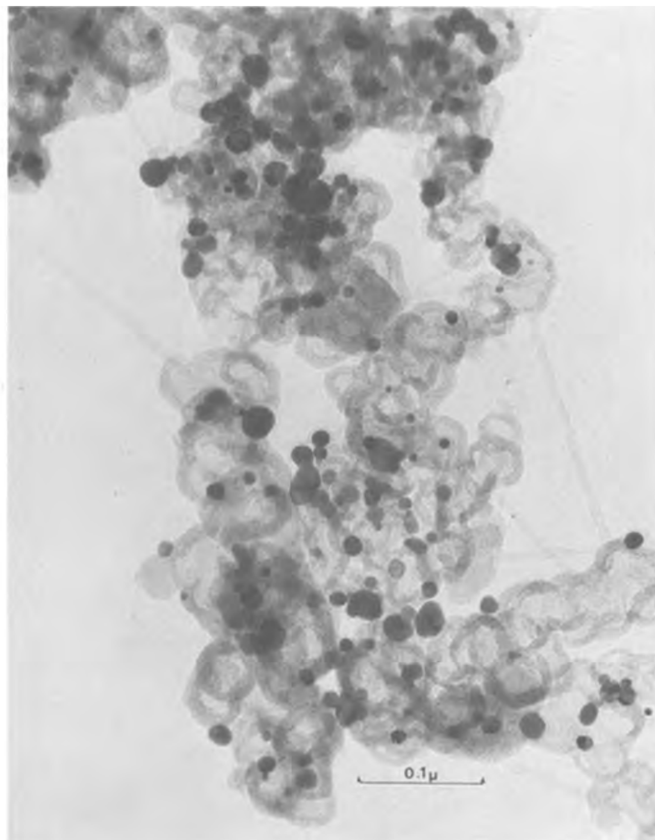

Figure 2 — Vulcan XC-72 Corroded at 191°C in 95% H_3PO_4 at a Potential of 835 mV

Manuscript submitted June 5, 1978; revised manuscript received July 31, 1978.

Publication costs of this article were assisted by United Technologies Corporation.

Low Melting-Point Compositions in Alkali Metal Metaphosphate/Fluoride Systems Applications

D. Elwell*

Center for Materials Research, Stanford University, Stanford, California 94305

Molten salt compositions of low melting point are often of interest for applications in electrochemistry or as solvents for metal oxides. This investigation was performed in order to find a phosphate-based solvent for the electrodeposition of indium phosphide at temperatures at or below 600°C.

The system Na, K/PO_3, F was investigated by Bukhalova and Mardirošova (1) and the lowest melting-point for any composition in that system was found to be 424°C. Solvents containing Li^+ are expected to have a lower viscosity because of the relatively small mass of these ions, and are therefore preferable for electrocrystallization experiments provided that the liquidus temperatures are similar to or below those of the Na, K system.

In order to accelerate the task of finding compositions of lowest melting point in the Li, Na/PO_3F and Li, K/PO_3, F systems, melts containing equal molar concentrations of the four constituents in each case were unidirectionally solidified by slow horizontal traverse of a 15 cm long crucible through a furnace. The fraction which solidified last was analyzed and a melt of the composition so determined was subjected to a further unidirectional solidification to test the accuracy of the first analysis. Atomic absorption spectrographic analysis for the alkali melts was found to be reliable to within 1% but electron microprobe analysis for F, P and O did not give reliable data, although intensities were compared with standard materials.

The Li:K ratio in the lowest-melting sample in that system was found to be 1·16(5):1 and the Li:Na ratio for the corresponding composition was 0·98(4):1. A section through the quaternary phase diagram was therefore taken with these metal ratios held constant but with the F:PO_3 ratio varied. The results are shown in Fig. 1, together with liquidus data for the corresponding section in the Na, K/PO_3, F system for comparison.

*Electrochemical Society Active Member.

Liquidus temperatures were determined by a visual polythermal method, with the samples contained in vitreous carbon crucibles in argon at atmospheric pressure. The chemicals were of reagent grade and were subjected to a preliminary dehydration at 300°C in vacuo for several hours.

Since the lower melting point materials formed glasses on solidification, it was difficult to obtain precise measurements and the ultimate test of the state of the material was the observed response of the surface to a force applied via a graphite rod of spectrographic purity. Cycling the sample through the melting temperature was used in attempts to obtain an accurate determination.

Even with this precaution, the data are reliable only to ±10°C. Supercooling was not large compared with this estimated error except in the case of the fluoride-free composition in the Na, K/PO_3, F system, for which a supercooling of 140°C was observed. A separate calibration experiment was performed and temperatures quoted are taken from the mean of two chromel/alumel thermocouples with junctions located in the region previously occupied by the crucibles containing the samples.

The Li, Na/PO_3, F system is seen to give the lowest melting temperatures, the minimum occurring at about 300°C for a composition with 20 m/o fluoride. Both the Li, Na and Li, K systems do not indicate a sharply-defined minimum but the Na,K system (1) appears to exhibit eutectic-like behavior, although the data plotted in Fig. 1 is based on intersections with rather widely-spaced isotherms.

The value of 300°C for the lowest-melting composition compares very favorably with alternative systems. The lowest melting point occurs at 580°C in the system Li, Na/P_2O_7, F (2) and at 612°C in the system Na,K/P_2O_7, F(2). However, if greater complexity can be tolerated, it should be noted that the system Li, K/PO_3, PO_4 has a minimum melting point at

340°C (3) and fluoride addition may result in compositions which melt below 300°C.

ACKNOWLEDGMENTS

The author is grateful to Dr. R. S. Feigelson for valuable comments and to Mr. F. A. Ponce for help with the measurements. Financial support was provided by the Army Research Office.

REFERENCES

1. G. A. Bukhalova and I. V. Mardirosova, Russ. J. Inorg. Chem. 11, 497 (1966).
2. V. P. Goryacheva and A. G. Bergman, Russ. J. Inorg. Chem. 12, 1167 (1967).
3. I. B. Markina and N. I. Voskresenskaya, Russ. J. Inorg. Chem. 19, 1837 (1974).

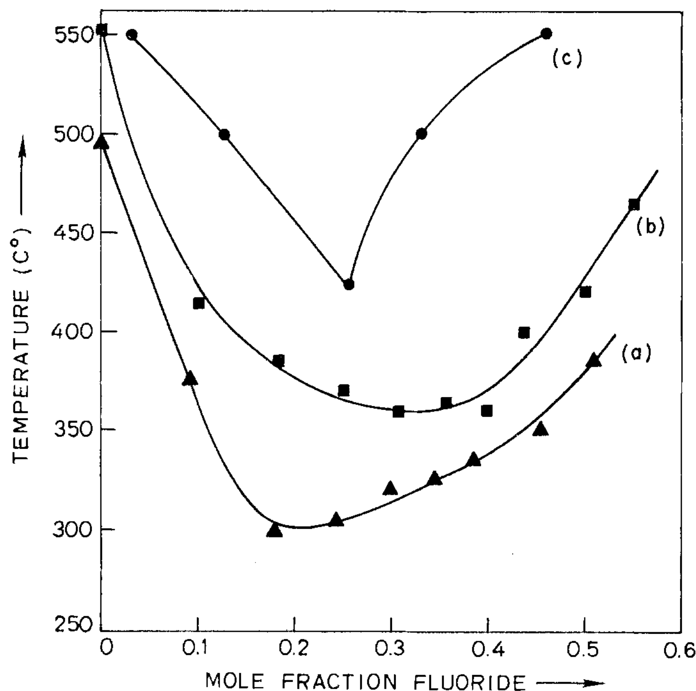

Fig. 1. Liquidus temperature of compositions

(a) $(Li_{0.496}Na_{0.504})$ (PO_3,F)

(b) $(Li_{0.538}K_{0.462})$ (PO_3,F)

(c) $(Na_{0.814}K_{0.186})$ (PO_3,F) from ref. (1).

Manuscript submitted May 22, 1978.

Publication costs of this article were assisted by Stanford University.

Oxygen Determination in SIPOS Using a Differential Thickness Measurement

A. E. Widmer and M. L. Hitchman
Laboratories RCA Limited, Zurich, Switzerland

INTRODUCTION

Semi-insulating polysilicon (SIPOS) is a thermally deposited Si film containing oxygen (SiO_x) which is used as a passivation layer for silicon devices. In order to be able to assess the electrical quality of such films it is important to be able to have a means of characterization. This can be done directly by making resistivity measurements, but it would seem desirable to have a complementary method. One possibility would be to measure the oxygen content since the electrical properties depend on this parameter (1). Normally determination of oxygen in SIPOS is done with sophisticated techniques such as electron microprobe analysis or atomic absorption. We have developed a simple, indirect method for determining the oxygen content which only requires a thermal oxidation furnace and a surface profile monitor. This method is similar to that first described by Pliskin et al. (2).

EXPERIMENTAL

Two inch diameter ($1\bar{1}02$) Czochralski-sapphire substrates polished on one side were used as test wafers. They were placed at specific positions within a stack of silicon wafers in a low pressure CVD reactor. SIPOS was deposited from a N_2O-SiH_4 mixture with the ratio of the gas flow rates (γ) being varied from 0 to 0.8. The deposition conditions were: 650°C, 100-150 mTorr, and SiH_4 flow rates between 25 and 50 $cm^3 min^{-1}$. Layers with thicknesses in the range of 0.3 to 1.8 μm were grown with most of the measurements being made on layers 0.5 μm thick.

Key words: SIPOS, oxygen determination.

After deposition a small window of about 4x4 mm was defined on each wafer with Apiezon wax. A step was etched with 1 HF : 20 HNO_3 (by volume). The layers on the rear side of the wafers were etched off completely to allow better visual control during the subsequent processing steps. The etch rate for SIPOS prepared with γ = 0.2 is about 3 μm/min. Sapphire is not attacked by the etchant. Thickness measurements were made with a surface profile monitor (Sloan, Dektak). Then the SIPOS layers were converted to SiO_2 in wet oxygen at 1100° to 1200°C. A conservative estimate of the time required for complete conversion was obtained from the time needed to oxidize a layer of silicon of the same thickness as the SIPOS layer (3). For example, for a layer 0.5 μm thick we oxidized for 150 minutes at 1200°C. The thickness of the fully oxidized SIPOS layers was measured on the previously etched steps from which the fractional increase in thickness was calculated.

RESULTS AND DISCUSSION

Fig. 1 shows a plot of fractional increase in thickness on full oxidation as a function of γ. Except at $\gamma \leq 0.05$ the reproducibility is good. The reason for the scatter at low γ is not known, although it may be associated with the transition from polycrystalline silicon at γ = 0 to amorphous material at higher values of γ. For our reactor the shape of the curve is not dependent on the SiH_4 flow input for flow rates in the range 25-50 $cm^3 min^{-1}$. Fig. 1 thus provides a simple means for process control. For example, we have had points lying below the curve corresponding to a higher γ than that expected for the gas inputs used (e.g. point X in Fig. 1). On checking the calibration of the SiH_4 mass flow controller we found it to be inaccurate due to a partial blocking as a result of

decomposition of SiH_4 to SiO_2 particles by trace amounts of oxygen. This blocking reduced the SiH_4 flow rate with the result that γ was higher than that set on the controls. The measurement of the fractional thickness increase has faithfully reflected this change in γ.

The density, ρ_x, of a SiO_x film can be written as

$$\rho_x = \frac{N(A_S + x A_O)}{F d_x} \quad [1]$$

where N is the number of SiO_x "molecules" in a layer of thickness d_x and area F and A_S and A_O are the atomic weights of Si and O respectively. The density, ρ_2, of a SiO_2 layer formed by total oxidation of SiO_x can be written similarly:

$$\rho_2 = \frac{N(A_S + 2 A_O)}{F d_2} \quad [2]$$

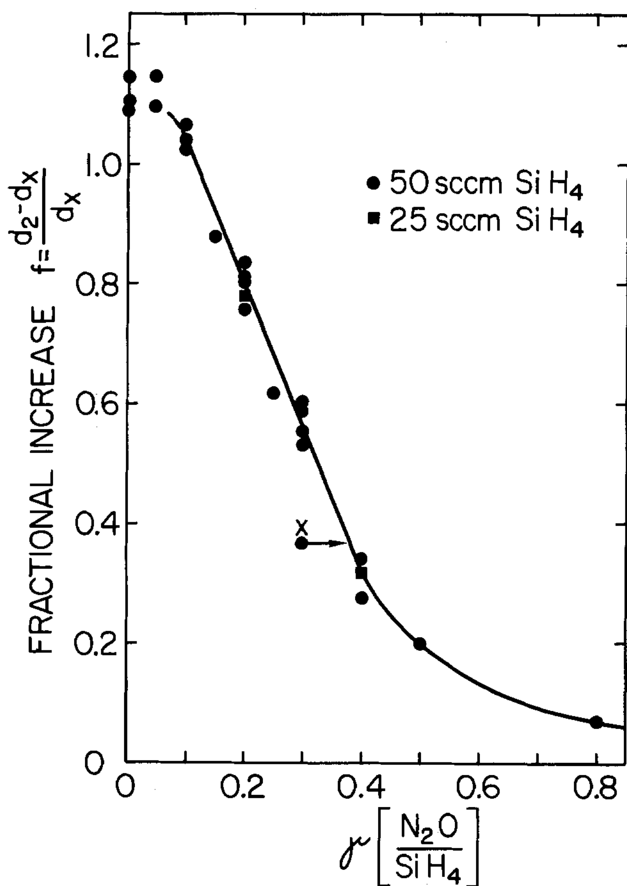

Fig. 1. Fractional thickness increase as a function of γ.

where d_2 is the oxidized layer thickness. A priori one cannot say how the density of SiO_x will vary as x changes from 0 to 2, but a linear relationship of the form

$$\rho_x = \rho_0 - \frac{x}{2}(\rho_0 - \rho_2) \quad [3]$$

where ρ_0 is the density of Si, would not seem unreasonable. However, if one takes typical values for the densities of Si and SiO_2 - approximately 2.33 and 2.2 (3), respectively - then the term $x/2\ (\rho_0 - \rho_2)$ is small compared with ρ_0 for all x in the range 0 - 2 and this suggests that one could approximate $\rho_x = \rho_2$. Making this assumption and solving eqn. [1] and [2] for the atomic fraction of oxygen gives

$$\frac{x}{1 + x} = \frac{8 - 7f}{12 - 3f} \quad [4]$$

where $f = (d_2 - d_x)/d_x$ and is the fractional thickness increase on oxidation. Fig. 2 is a plot of oxygen atomic percent, determined from the points on Fig. 1 and eqn. [4], against γ. Also plotted are values of atomic percent determined by electron microprobe analysis on some of the samples prepared in our reactor (designated reactor 1), and on samples prepared by LPCVD in a commercial reactor (designated reactor 2) at an RCA production facility. The good agreement between the determination of oxygen by the differential thickness measurement and electron probe microanalysis suggests that the assumption of $\rho_x = \rho_2$ is a reasonable one. The shape of the curves in Fig. 1 and 2 can be explained using a simple model for the growth kinetics of SIPOS (4).

CONCLUSIONS

The measurement of the thickness increase on oxidation of SIPOS to SiO_2 has been shown to be a simple method for oxygen determination and hence characterization of SIPOS. The technique requires only apparatus that is normally found in a semiconductor factory - a thermal oxidation furnace and a surface profile monitor. If the measurements are made on SIPOS grown on sapphire the oxidation needs no special control since it is self-limiting; also sharp steps can be readily etched and the sapphire test wafers can be reused. In general the results show good reproducibility and are not affected by variations in film thickness and

therefore nonuniformities. In the particular range of interest of $0.1 \leqslant \gamma \leqslant 0.4$ the variation of the fractional thickness increase with γ is linear and shows the maximum sensitivity.

ACKNOWLEDGEMENTS

J. Kane and H.P. Schweizer are thanked for preparation of the SIPOS samples, A. Oberholzer for assistance with the oxidation process and thickness measurements, and E.P. Bertin for carrying out the electron microprobe analysis.

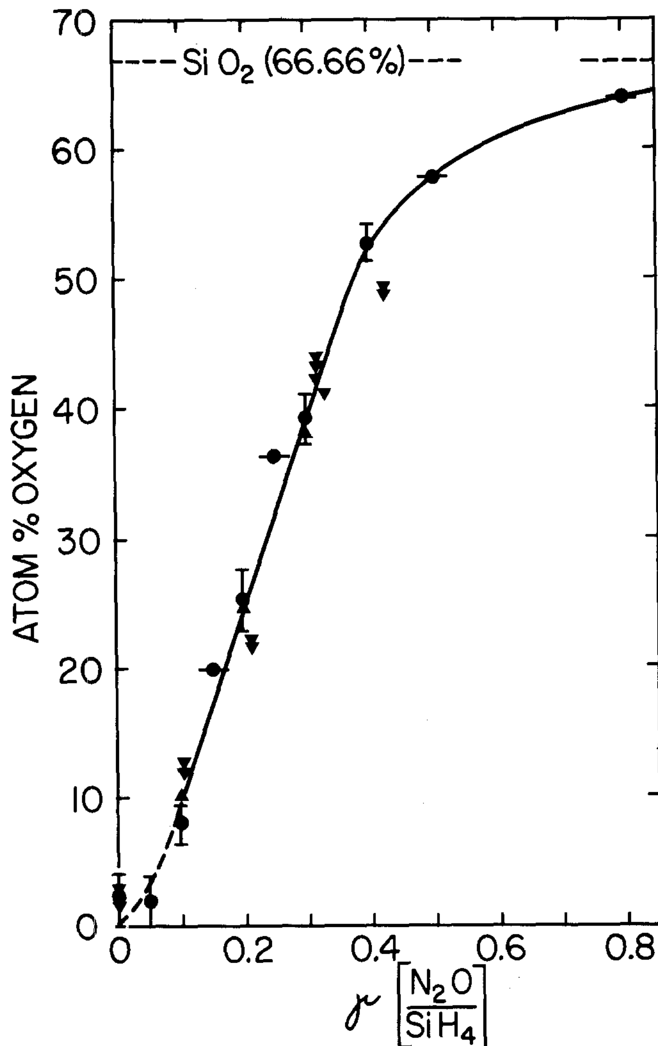

Fig. 2. Oxygen atomic percent as a function of γ.
● Range calculated from points in Fig. 1.
▲ Reactor 1 } Electron microprobe analysis
▼ Reactor 2 }

REFERENCES

(1) H. Mochizuki, T. Aoki, H. Yamoto, M. Okayama, M. Abe and T. Ando, Proc. 7th Conf. Solid State Devices, Suppl. Jap. J. Appl. Phys., 15, 41 (1976).

(2) W.A. Pliskin, P.D. Davidse, H.S. Lehman, and L.I. Maissel, IBM Journal 11, 461 (1967).

(3) H.F. Wolf, "Semiconductors", Chap. 4-2, Wiley-Interscience, New York (1971).

(4) M.L. Hitchman and A.E. Widmer, results to be published.

Manuscript submitted May 16, 1978.

Publication costs of this article were assisted by RCA Laboratories Limited.

Recovery of Shallow Junction GaAs Solar Cells Damaged by Electron Irradiation

Gilbert H. Walker* **and Edmund J. Conway**

National Aeronautics and Space Administration, Langley Research Center, Hampton, Virginia 23665

Solar cells operated in space are subject to degradation from the electron and proton radiation damage; however, it has been shown previously that for deep junction (4 μm p-GaAs layer) p-GaAlAs/p-GaAs/n-GaAs solar cells some of the electron radiation damage is removed by annealing the cells at 200°C (1). It is the purpose of this communication to show that shallow junction (0.8 μm p-GaAs layer) p-GaAlAs/p-GaAs/n-GaAs heteroface solar cells irradiated with 1 MeV electrons show a more complete recovery of short-circuit current than do the deep junction cells.

Heteroface pGaAlAs/pGaAs/n-GaAs solar cells were fabricated using the etch-back epitaxy process (2). The n-type substrates were Si doped with a carrier concentration of 1 to 2 x 10^{17} carriers/cm^3. The p-GaAlAs and the p-GaAs were Zn doped to a carrier concentration of 8 x 10^{18} carriers/cm^3. Large area back electrical contacts were Sn-Ag while the front finger contacts were Pd-Ag. The cells had no antireflection coatings nor cover glasses. The current-voltage characteristics of the illuminated cells were measured using an air mass zero solar simulator which was calibrated with a Si cell that had been standardized on a balloon flight. The spectral response of the cells was measured using an intensity calibrated spectrophotometer. Cells were irradiated in vacuum with 1-MeV electrons at fluences of 1 to 3 x 10^{14} electrons/cm^2, 1 x 10^{15} electrons/cm^2, and 1 x 10^{16} electrons/cm^2. The flux during irradiation was chosen so that the cells remained at ambient temperature. A fluence of 10^{16} 1 MeV electron/cm^2 is equivalent to the electron exposure which a solar cell with a 50 μm cover glass would encounter during 30 years in geosynchronous orbit. The current-voltage characteristics and the spectral response were again measured. The cells were annealed at 200°C in vacuum of 10^{-5} torr for 10-hour periods and their characteristics again measured after each period of annealing.

*Electrochemical Society Active Member

Key Words: Solar Cells, Radiation Damage, Annealing, Gallium Arsenide

Figure 1 shows the relative short-circuit current as a function of 1 MeV electron fluence for various annealing times. After 1 x 10^{16} electrons/cm^2 the ratio of the final short-circuit current to the initial short-circuit current (I_{SC}/I_{SC_0}) is reduced to 0.33. Annealing at 200°C for 10 hours restored the short-circuit current ratio to 0.77; after 20 hours of annealing the ratio rose to 0.82, and after 30 hours the ratio had stabilized at 0.83. Thirty-hour 200°C annealing of the cells irradiated at 10^{14} and 10^{15} 1 MeV electrons/cm^2 restored the short-circuit current to slightly greater than its original value. This increase in short-circuit current to greater than its original value after annealing (which has been seen before (1)) could be explained in terms of contact annealing or improvement in the minority carrier diffusion length.

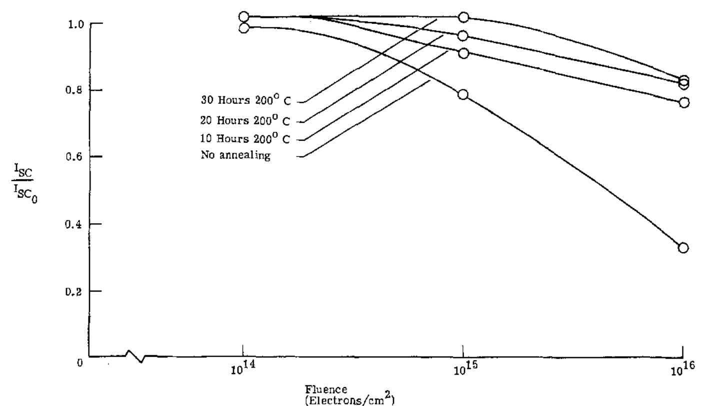

Figure 1.- Ratio of final short-circuit current to initial short-circuit current as a function of 1 MeV electron fluence for various annealing times at 200°C.

Figure 2 shows the current-voltage characteristics of a cell before irradiation and after irradiation with 1 x 10^{16} 1 MeV electrons/cm^2 at three annealing stages. The unirradiated cell, without AR coating, had a maximum power density of 15.1 mW/cm^2. Irradiation reduced the maximum power density to 29 percent of its original value; however, annealing for 10 hours at 200°C restored the maximum power density to 74 percent and after 30 hours the maximum power density stabilized at 81 percent of the original. The open circuit voltage increased from 0.82 volts before annealing to 0.875 volts after 30 hours at 200°C. The fill factor of the irradiated cell changed little with annealing.

1 MeV electron irradiation of deep junction (4 μm) GaAℓAs/GaAs solar cells produced severe degradation of the spectral response especially in the blue region of the spectrum. For the 0.8 μm cells, the spectral response after irradiation changed uniformly over the entire spectral region. Annealing for 30 hours at 200°C produced uniform recovery of the spectral response.

The improvement of the solar cell output with annealing can be correlated with an improvement of the minority carrier diffusion length over the damaged values. We believe the explanation for the improved annealing of these 0.8 μm cells as compared to the 4 μm cells (1) is due to junction location. For small junction depths, the junction effectively competes with surface and bulk recombination for minority carriers.

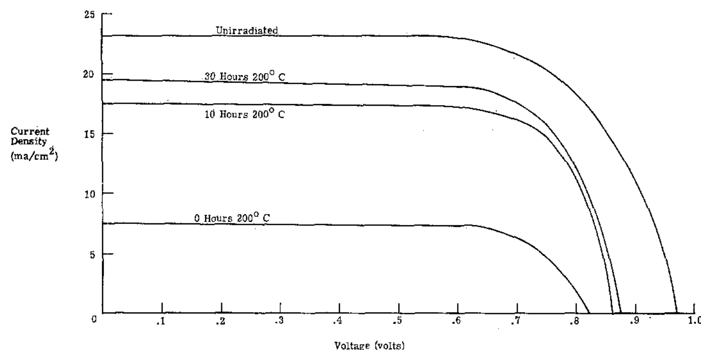

Figure 2.- Current density-voltage curves of a cell unirradiated and irradiated at 10^{16} electrons/cm^2 for various annealing times.

The recovery due to annealing of the 1 MeV electron-damaged 0.8 μm GaAℓAs/GaAs solar cells is large. Annealing can extend the useful life (defined here as more than 75 percent of maximum power) to fluences greater than 10^{16} electrons/cm^2 at 1 MeV or 30 years equivalent in geosynchronous orbit. Short periods of annealing can limit the degradation after 3 years equivalent in orbit to much smaller values. Assuming that the same type of annealing recovery occurs for cells irradiated with electrons of different energies and for cells irradiated with protons, it may be possible to periodically anneal GaAℓAs/GaAs solar cells while in space, thus significantly prolonging the life of the cells. Also, GaAℓAs/GaAs solar cells operated at high temperatures (200°C) may continually anneal radiation damage and never be degraded to any great extent.

REFERENCES

(1) G. H. Walker and E. J. Conway, this Journal, 105, 676 (1978)

(2) J. M. Woodall and H. J. Hovel, Appl. Phys. Lett. 30, 492 (1977)

ACKNOWLEDGMENT

The authors would like to thank Dr. Stanley J. Marsik of NASA Lewis Research Center for providing the irradiation facility used in these studies.

Manuscript submitted May 30, 1978.

Publication costs of this article were assisted by NASA Langley Research Center.

JOURNAL OF THE ELECTROCHEMICAL SOCIETY

ELECTROCHEMICAL SCIENCE
AND TECHNOLOGY

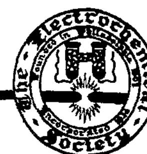

NOVEMBER
1978

Breakdown of the Passive State and Repassivation of Stainless Steels

I. L. Rosenfeld, I. S. Danilov, and R. N. Oranskaya

The Institute of Physical Chemistry, The USSR Academy of Sciences, Moscow, USSR

ABSTRACT

The mechanism of anodic dissolution and self-dissolution of stainless steels during local corrosion processes is discussed. The dissolution mechanism can be established only by determining actual velocities of metal dissolution at point anodes and their dependence on potential. In stably operating pits the actual rate of metal dissolution is potential independent. A similar relationship was found under uniform dissolution of steel in concentrated chloride solutions of low pH for the ability of steel to transform from the active to the passive state. Such an electrode dissolves at a rate similar to dissolution rates observed in the pits (50-60 mA/cm^2), and the rate is governed by diffusion kinetics. On the strength of the results, it is assumed that dissolution of steel in pits takes place by the mechanism of "salt passivity," the rate of which is controlled by the diffusion of anode reaction products through the salt film. The repassivation mechanism of steels in pits is also considered. Pits functioning in the kinetic regime repassivate easily, whereas for those operating in the diffusion regime an external effect on the system is necessary. Contrary to the point of view of some researchers an opinion is expressed that the repassivation potential does not correspond to the metal potential at the pit bottom. The repassivation potential is a variable value and, therefore, it cannot serve as a parameter characterizing the ability of steel to undergo pitting corrosion. Certain regularities of stainless steel dissolution and the causes for breakdown of the passive state are considered. Even small shifts in potential in the positive direction from the stationary one (ϕ_{cor}) can bring about activation in crevices and gaps. The corrosion resistance of stainless steels in crevices is determined essentially by their ability to resist activation in acidic chloride solutions.

The local breakdown of the passive state of stainless steels has attracted the attention of numerous researchers (1-21). Nonetheless the mechanism of the process is still obscure. In our opinion, there are questions, *e.g.*, the nature of the anodic process in point anodes, the repassivation mechanism and the nature of the repassivation potential, the mechanism of stable operation of a two-electrode system (pit-passive surface) unstable from the electrochemical point of view, the existence of the crevice corrosion potential (like that of pitting formation), etc., which are yet to be studied.

However, prior to examining these questions, we would like to draw attention to the reliability of the experimental results obtained from electrochemical kinetic studies of local corrosion processes, as well as to the conclusions drawn from them. We feel that the results of polarization measurements frequently published in the literature do not convey quantitative information on the electrochemical kinetics, because they do not reflect the true anodic dissolution rates of metal in point anodes. Moreover, false conclusions may be drawn, if the local dissolution mechanism is not taken into account. Let us illustrate this by an example. Figure 1 shows four anodic polarization curves plotted by the galvanostatic and the potentiostatic methods for Cr18Ni10Ti[1] stainless steel subjected to pitting corrosion. Curves 1 and 3 have been plotted with respect to the geometrical surface area of an electrode (just such curves are mainly published); while curves 2 and 4 have been plotted with respect to the true area[2] on which an anodic reaction occurred. It is seen that the two sets of curves have nothing in common: The true dissolution rate is potential independent, while the curves plotted without taking into account the true area of the anode indicate the presence of a quite different potential dependence of the anodic current.

From this, various conclusions may be drawn about the mechanism of the process; curves 1 and 3 suggest that the point anodes (pits) operate in the kinetic regime and the metal in them dissolves in the active part of the polarization curve, and curves 2 and 4 indicate that dissolution takes place in the passive state regime which differs from the general regime. The only difference is that the dissolution rates far exceed those noticed during normal passivation by an oxide film.

Key words: corrosion, diffusion, electron transfer kinetics, salt films.

[1] According to the USSR Standard the number after the letter indicates the average percentage of the alloying element. Thus, this steel contains 18% Cr, 10% Ni. Its total composition (weight percent) is: C $\leq$ 0.12; Si $\leq$ 0.8; Mn $\leq$ 2.0; Cr = 17-19.0; Ni = 9.0-11.0; Ti = 0.6-0.7; S $\leq$ 0.020; P $\leq$ 0.035; Fe = balance.

[2] The pits have a hemispheric shape with $\phi/h \simeq 2$ and, therefore, after determining their number and the diameter of each pit using a microscope, their surface can be calculated with sufficient accuracy. For details see Ref. (4).

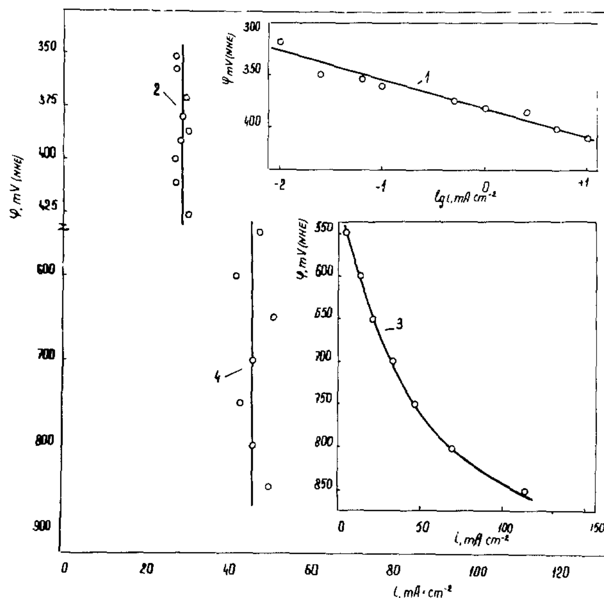

Fig. 1. Anodic polarization curves obtained for Cr18Ni10Ti stainless steel which underwent pitting corrosion in 0.1*N* NaCl. Curves 1 and 2 were obtained by the galvanostatic method; curves 3 and 4 by the potentiostatic method. Curves 2 and 4 are true polarization curves; curves 1 and 3 are imaginary plots. Polarization time was 60 min.

Dissolution rates, similar to the ones observed in pits (40-50 mA/cm^2) and the ability of steel to transform simultaneously into the passive state, are observed in concentrated acid chloride solutions with the anodic dissolution being uniform (Fig. 2a).

To understand the mechanism of steel dissolution in the passive region of potentials, we studied the anodic dissolution on the rotating disk electrode. We found that the current density in this portion of the polarization curve increases strongly as the electrolyte is agitated and that it varies according to the diffusion kinetics laws (Fig. 2b).

Taking into consideration that the studied electrolytes are similar in composition to those accumulated inside the pits and that in the considered cases one and the same relationship is observed, we can confirm that the dissolution of metal in the stably operating real pits proceeds in the diffusion regime (the same conclusion has also been drawn by authors of Ref. (7) in their studies of artificial pit model), and the steady-state (passivation) currents are determined by the properties of the electrolyte in the neighborhood of electrode surface and not by the properties of the metal surface, as suggested in Ref. (22).

Evidently, if the dissolution rate were to be determined by the properties of passivating oxide film on the electrode surface, then it could hardly be expected that the current will vary during agitation, which may increase the dissolution of the film, according to the diffusion kinetics laws.

We assume that the metal dissolution rate in a pit is controlled by the properties of the viscous salt film at the pit bottom, and, therefore, the nondependence of the dissolution current on potential can be regarded as specific "salt passsivity" when the passivating layer is in the liquid rather than in the solid phase.

In view of these facts, it is clear why pits can be easily repassivated with an insignificant potential shift in the negative direction. The true polarization curve for stainless steel, whose surface exhibits a steadily operating pit, is described by the curve ABCD (Fig. 3, plot 1). The potential across the pit bottom is close to point C; therefore, even a small potential shift in the negative direction (to C′) is sufficient to convert the steel into passive state.

These results may also explain the relationship between the repassivation potential and the time during which the pit is active and on the steel composition. The mechanism of the steady operation of the pit-passive surface system can also be explained.

As we have shown earlier (23-26), the overwhelming number of pits repassivate spontaneously fairly quickly, so that the principle "all or nothing," formulated by Frank (27, 28), is satisfied. As shown by the experimental data, the originally formed pits function in the kinetic regime (see Fig. 3, plot 2): Therefore, they are capable of spontaneous repassivation. Only those pits, which begin to operate in the diffusion regime, are able to function steadily, and some external action is needed to repassivate them.

However, as should be expected, repassivating such pits requires shifting the potential in the negative direction by an amount depending on their functioning time and, hence, on acidification of the medium and the accumulation of chloride ions inside the pits. This is obvious from the anodic potentiostatic curve which shows the anodic current *vs.* the electrode potential shift in the negative direction (Fig. 4). When the potential of an open surface is maintained at +0.55V, the corrosion current in a pit varies with time according to curve OABC. When the electrode potential is shifted

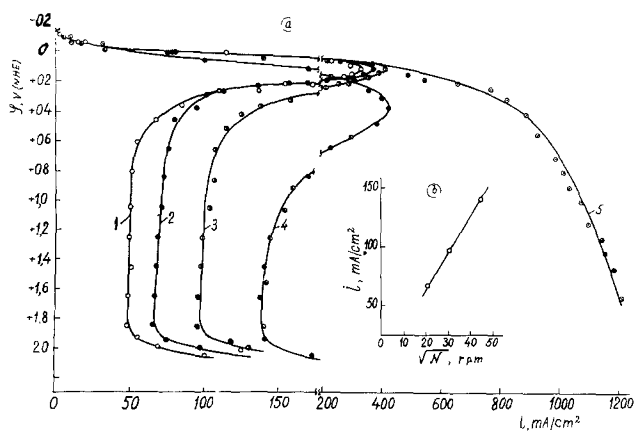

Fig. 2. Anodic polarization curves obtained with a rotating electrode of Cr18Ni10Ti stainless steel in 5*N* HCl. Curve 1 obtained without rotation; curve 2, with the electrode rotating at 421 rpm; curve 3, at 960 rpm; curve 4, at 1950 rpm; and curve 5, at 3825 rpm.

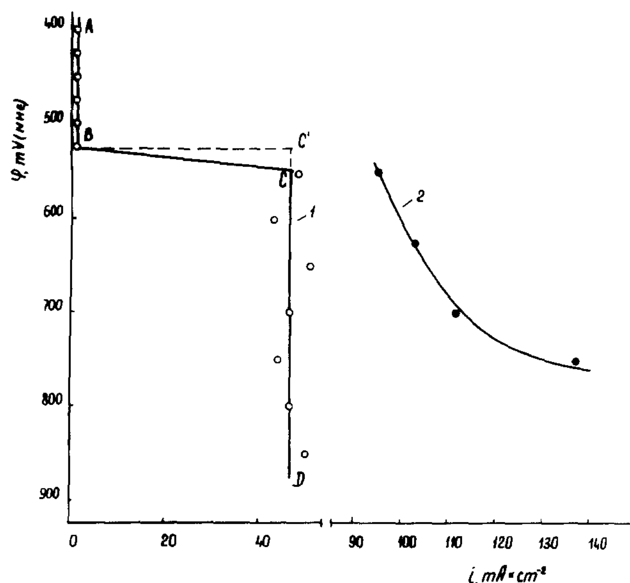

Fig. 3. True anodic polarization curves for pits operating in diffusion (curve 1) and kinetic regime (curve 2): 1, pits function steadily; 2, pits are capable of repassivating spontaneously.

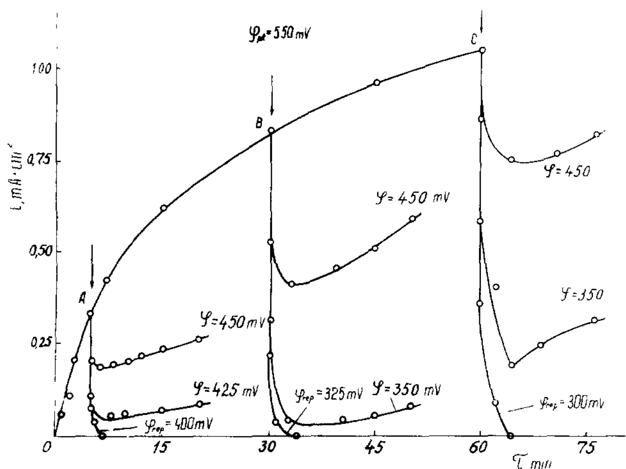

Fig. 4. Repassivation of Cr18Ni10Ti stainless steel that was pitted potentiostatically in 0.1*N* NaCl. The arrow indicates the moment of a gradual potential shift in the negative direction from the pitting-formation potential ($\phi_{pit} = +550$ mV). OABC illustrates time variation of the corrosion current; A, ϕ_{rep}; B, ϕ_{rep}; C, ϕ_{rep} indicate changes in the corrosion current with time when the potential is shifted in the negative direction.

in the negative direction (indicated by an arrow), the current first drops and thereafter begins to increase again. However, only on reaching a certain potential, which depends on the functioning time of point anodes (of pits), the system is passivated completely, and no electric current is generated by the system. It is this potential which is usually called the repassivation potential. As it appears, the longer the pit functioning time, the more negative the potential will have to be for the pit to cease functioning.

The pits also repassivate easily when they are formed under self-dissolution conditions, such as when the pitting potential is obtained by the oxidizing component of the solution. In the case of corrosion of Cr18Ni10Ti grade stainless steel in $FeNH_4(SO_4)_2 \cdot 12 H_2O + NH_4Cl$ solution, pits are formed at the steel surface fairly quickly ($\phi = +0.55$V). The potential of the steel decreases with time until it reaches a steady-state level of +0.3V; the total current of the pit-passive surface system increases to 0.36 mA/cm^2. Yet it was sufficient to shift the potential of the steel by only 25 mV in the negative direction (Fig. 5) to repassivate the surface of the pits. This may occur only in the case in which the potential of the pit-passive surface system is close to the potential at the pit bottom and when the pit operates under diffusion conditions.

We obtained direct indications that the dissolution rate of metal in a pit is determined by the composition of the electrolyte in the pit, not by the composition in the bulk of the solution. These indications were obtained in a study on the dependence of the pitting-formation potential and of the repassivation potential on the pH and the concentration of sodium chloride (Fig. 6). As is evident, the pitting-formation potential depends strongly on these factors, but the repassivation potential depends only slightly on the pH of the electrolyte and on the concentration of sodium chloride.

The pits repassivated easily also under galvanostatic polarization, which may be judged from the charging curves (Fig. 7). The pits operated steadily for 1 hr, a time period quite sufficient for the electrolyte to become highly concentrated in chloride and hydrogen ions. None-the-less, it was sufficient to reduce the anodic current density enough for the pits to repassivate. It can be seen from Fig. 7 (point E) that the repassivation time depends on the initial current density: the higher the current density, the longer the repassivation process (*i.e.*, the medium in the pit has changed to a larger extent).

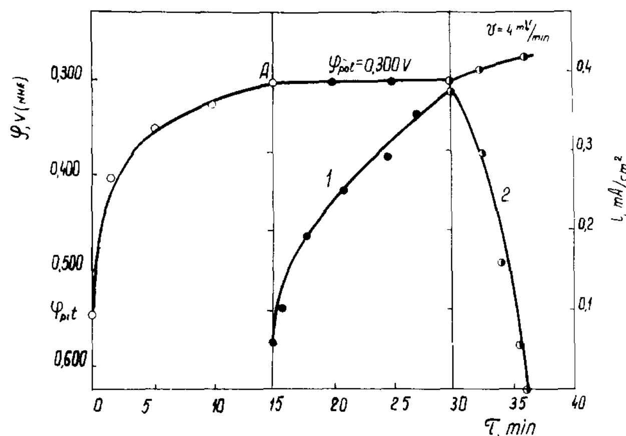

Fig. 5. Repassivation of Cr18Ni10Ti stainless steel that was pitted under self-dissolution [20 g/l $FeNH_4(SO_4)_2 \cdot 12 H_2O$ + 30 g/l NH_4Cl]: ϕ_{pit} A, indicates a change in the electrode potential with time, 1, change in the corrosion current with time at a constant potential (+0.3V); 2, a change in the corrosion current with time, as the potential is shifted in the negative direction (4 mV/min).

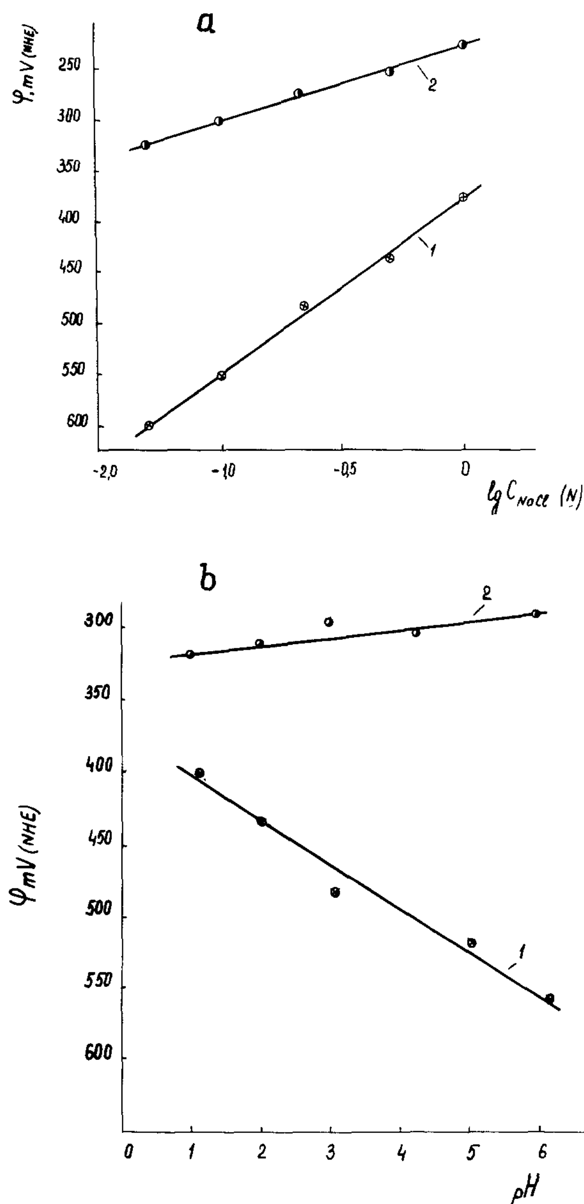

Fig. 6. Pitting-formation potential (curve 1) and repassivation potential (curve 2) vs. concentration of chloride ions (a) and pH value of electrolyte (b) for Cr18Ni10Ti stainless steel.

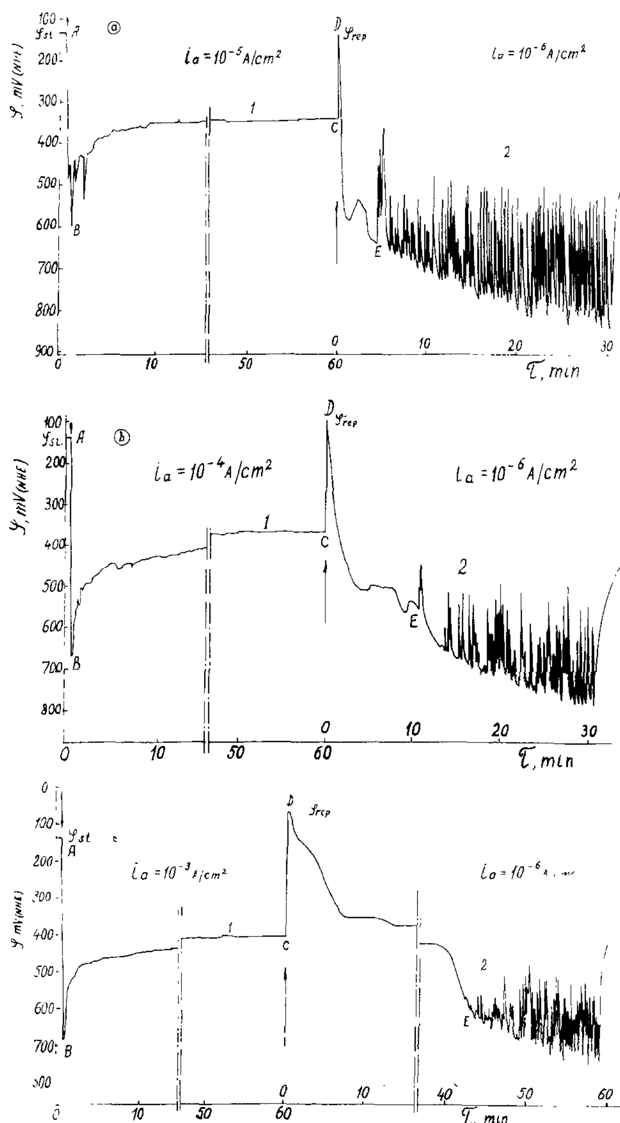

Fig. 7. Repassivation of stainless steel Cr18Ni10Ti subjected to pitting corrosion in 0.1*N* NaCl during galvanostatic polarization: point A, introduction of polarization current due to corrosion potential in the absence of pits; B, pitting-formation potential; BC, potential variation of the pit-passive surface system under conditions of stably operating pits; CD, potential shift when the polarization current is changed from its initial value up to 10^{-6} A/cm^2 (indicated by arrow CD); DE, time needed to repassivate pits; EF, potential fluctuations due to the appearance and repassivation of small, nongrowing pits.

High ability of metal in the pit to passivate is obviously a general property of the surface, independent of the polarization type. It is possible that the easy repassivation of the metal in the pits is also due to a disturbance of the equilibrium in the electrolyte when the external conditions vary.

Thus, direct proof has been obtained indicating that the steadily functioning real pit operates in the diffusion regime; hence, using the formal concepts of electrochemical kinetics as the basis, it is possible to understand why the pits repassivate so easily, when the potential is shifted in the negative direction. However, the same results suggest that the surface of the metal inside the pit possesses a surprising universal ability to passivate easily, which occurs as soon as the potential has shifted toward the values at which the stainless steel undergoing corrosion is found in the passive state. It is obvious that such an active surface is able to form passivating layers fairly easily as soon as the external effect has changed. It would be apt here to recall a phenomenon detected earlier (26), namely, that under galvanostatic polarization or self-dissolution of stainless steels, it is sufficient to switch off polarization or to extract the steel from the electrolyte, to passivate the metal in the pit.

When such an electrode was subjected to repeated polarization, the metal in earlier produced pits remained in the passive state and did not dissolve, but new pits appeared on the surface.

What is the nature of the repassivation potential and does it characterize the susceptibility of stainless steels to localized corrosion, as some authors suggest (29)? As shown above, the repassivation potential strongly depends on the pit operation time; hence, it cannot be used as the criterion of the susceptibility of stainless steels to localized corrosion processes. The pitting-formation potential is a more precise quantity, as seen in Table I. Cr18Ni10Ti stainless steel strongly differs from Cr18Ni12Mo2Ti steel in the susceptibility to pitting corrosion, the latter containing molybdenum; and this is reflected in the pitting-formation potential (+0.55V as compared with +0.825V). However, with regard to the repassivation potentials, these steels differ but slightly (in 60 min the difference amounts to only 0.050V). This is quite clear: Inasmuch as in pits a specific *p*H value is established, as well as their own concentration of chloride ions, the repassivation potential must depend but slightly on the composition of the surrounding medium, in respect to which the susceptibility of steels to localized corrosion is determined.

With regard to the repassivation potential, consider a two-electrode system with the pits as the anode and the passive surface as the cathode. Consider pitting corrosion under self-dissolution. Then from the theory of electrochemical protection, it is known that the system ceases to generate a current as its potential is shifted in the negative direction, when the potential of the system has reached the potential of the anode in the open state, *i.e.*, when there is no corrosion current through the system. From this point of view, the repassivation potential should not be identified with the potential applied to the bottom of an operating pit. Moreover, the following will have to be taken into account: When measuring the repassivation potential, the mixed potential of a complex electrode is measured, rather than the potential of the metal in a pit. Further, the question about the presence or the absence of noticeable ohmic potential drops in the system has not yet been definitely solved; hence, the nature of the repassivation potential remains obscure. The repassivation potential may coincide with that applied to the bottom of an operating pit only in the case for

Table I. Pitting-formation and repassivation potentials of stainless steels in a 0.1*N* sodium chloride solution obtained by the potentiostatic method

Grade of steel	ϕ_{st}* (V)	ϕ_{pit}** (V)	ϕ_{rep}† (V) 5 min	ϕ_{rep}† (V) 30 min	ϕ_{rep}† (V) 60 min	$\Delta\phi$‡ $\phi_{pit} - \phi_{rep}$ (V) 5 min	$\Delta\phi$‡ 30 min	$\Delta\phi$‡ 60 min
Cr13	+0.110	+0.275	+0.250	+0.175	+0.150	0.025	0.100	0.125
Cr18Ni10Ti	+0.150	+0.550	+0.400	+0.325	+0.300	0.150	0.225	0.250
Cr18Ni12Mo2Ti	+0.180	+0.825	+0.525	+0.400	+0.350	0.300	0.425	0.475

* ϕ_{st} = steady potential.
** ϕ_{pit} = pitting-formation potential.
† ϕ_{rep} = repassivation potential.

which the pit-passive surface system is polarized to the full extent (there is no ohmic drop) and when the anodic process itself occurs in the pit without any noticeable polarization. Such are the main laws governing the breakdown of the passive state and the repassivation of stainless steels when pits are formed.

The mechanism of crevice corrosion has been discussed in full detail by us (30-32) and by others (33-39). In the present paper we wish to deal only with one question; namely, whether there is a certain potential at which crevice corrosion begins to take place. Figure 8 shows how the potential of Cr13 grade stainless steel changes with time in a crevice (0.1 mm wide) in 0.1*N* sodium chloride solution, when it is in contact with Cr18Ni10Ti grade steel (the ratio of surfaces is 1:1.5) that has been immersed in the electrolyte. Already in 1.5 hr the potential of the Cr13 grade steel in the crevice reaches a value of approximately −0.3V. The potential of Cr18Ni10Ti steel also grows more negative, but the potential difference between these two steels remains the same (about 0.14V). It should be noted that the potential of the steel in the crevice first grew more positive owing to anodic polarization, whereas the potential of the steel to which the electrolyte had a free access grew more negative owing to cathodic polarization. Similar results were obtained, too, when two electrodes of the same steel (grade Cr13) contacted one another.

It is quite natural to suppose that such a strong activation of steel in the crevice should be attributed to a change in the composition of the electrolyte in the crevice. Therefore, we studied the dependence of the potential of the same steel on the *p*H at various NaCl concentrations (Fig. 9). The results obtained show that the potentials close to those in the crevice (from −0.30 to −0.32V) are observed in solutions having a *p*H value in the range from 2 to 3. At such *p*H values, NaCl concentration plays a minor role and does not exert strong influence on the potential, as is the case with neutral and weakly acid solutions. These potential values allow the approximate composition of the electrolyte, which may be stored up in the crevice, to be evaluated.

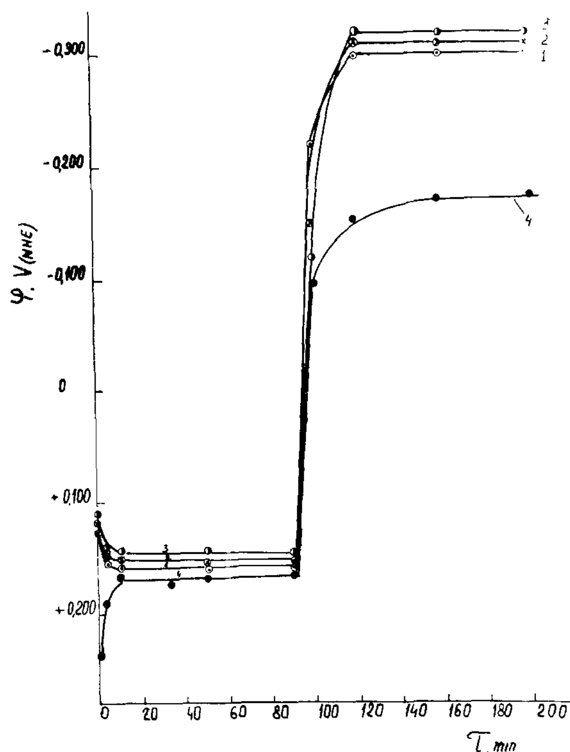

Fig. 8. Time variation of the potential of Cr13 stainless steel in a crevice (at the following depths: 1, 22 mm; 2, 44 mm; 3, 66 mm) in contact with Cr18Ni10Ti steel (open surface). The reference numeral 4 indicates the potential of Cr18Ni10Ti steels. Electrolyte: 0.1*N* NaCl.

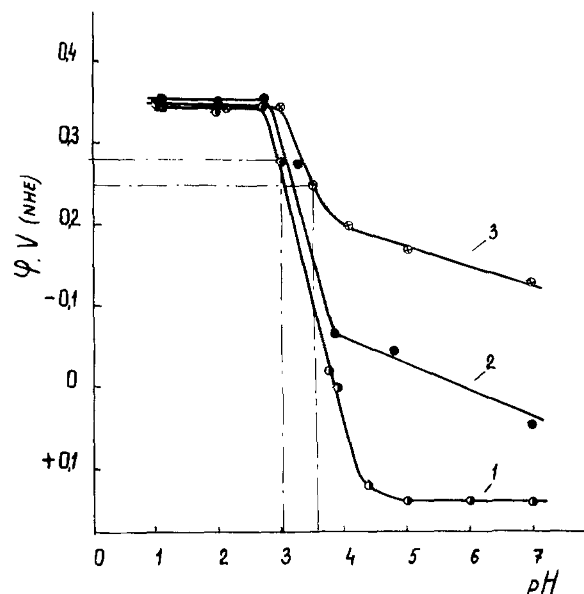

Fig. 9. Steady-state potential of chromium stainless steel (grade Cr13) vs. *p*H value of electrolyte at various concentrations of chloride ions. The reference numerals indicate: 1, 0.1*N* NaCl; 2, 1*N* NaCl; 3, 5*N* NaCl.

It is of interest to determine the extent of anodic polarization necessary for crevice corrosion to begin, that is, for the steel to be activated in the crevice over the entire surface. For this purpose, a series of anodic potentials were applied potentiostatically to the open surface of a complex electrode, and the potentials of steel within a crevice were recorded, as well as their variation with time. For Cr13 steel, even at insignificant initial potential shifts in the anodic direction within the crevice, which did not reach the pitting-formation potential (about +0.275V) for the steel, the steel in the crevice was activated with time, and its potential reached about −0.3V, that is the same value that Cr13 steel acquired when in contact with Cr18Ni10Ti steel. A difference existed only in the following: As the positive potential applied to the external electrode and, hence, to the crevice was increased, the time required for activation of the electrode in the crevice decreased (Fig. 10), whereas the current strongly increased. Hence, it may be concluded that there is no crevice corrosion potential, at least for the Cr13 steel. It is sufficient to subject such a steel in the crevice to a slight anodic polarization, and it will eventually be activated owing to variation in the electrolyte composition. The question about the susceptibility of steels to the crevice corrosion is obviously solved in respect to their sensitivity to a change in composition and character of the corrosion medium (40) (*e.g.*, the *p*H value, the concentration of sodium chloride, and temperature).

Finally, a further question remains to be discussed: Namely, how is it possible that the metal can be found in the active state within the pit or crevice and simultaneously in the passive state on the surrounding surface? As stated above, such a system is unstable from the electrochemical point of view; for in the absence of a noticeable potential difference, it should eventually be converted into either the active or the passive state.

As noted previously by us (23-26), studies of the intensity of an electric field over pits and the currents flowing from them have shown the following: As expected from the theory, the overwhelming number of pits forming on the surface repassivate spontaneously, and only a few of them (about 3-5%) function steadily; this, as shown above, is attributed to the fact

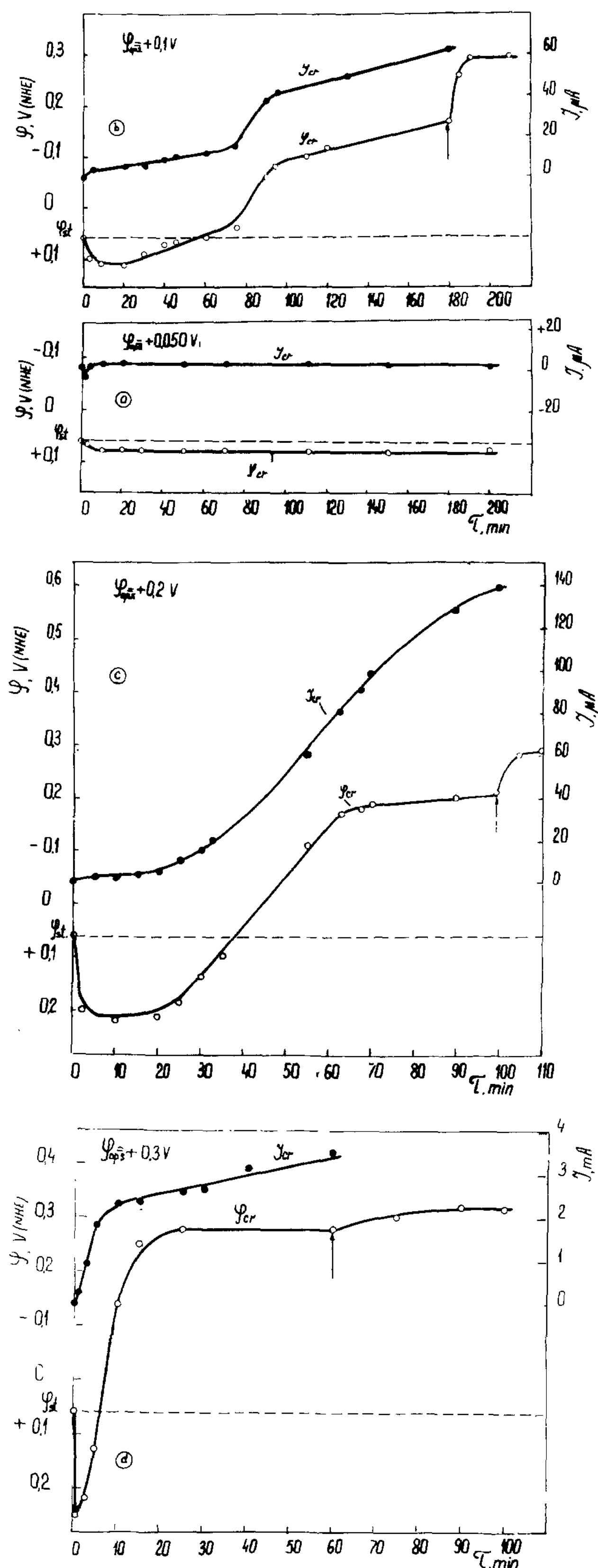

Fig. 10. Influence anodic polarization on the time variation of the potential of Cr13 chromium stainless steel in a crevice (ϕ_{cr}) and of the current (I_{cr}) at different potentials of the open surface ($\phi_{op.\ sur.}$). Electrolyte: 0.1*N* NaCl. Broken line indicates the steady-state potential before anodic polarization sets in. The arrow indicates the moment at which anodic polarization is stopped.

that they begin to operate in the diffusion regime. This is possible because localized corrosion occurs in a relatively closed volume, in which the anodic dissolution products are retained and acidify the solution by hydrolysis. Differentiation of electrochemical reactions over the surface also contribute to the concentration of activating agents in point anodes and to that of passivating agents on an open surface. Because the corrosion medium in point anodes and over the remaining portion of the electrode surface has a variable composition, even at the same potential, a part of the electrode may be in the active state, while the other part is in the passive state. That this mechanism is true is substantiated by the immediate repassivation of the system that takes place as soon as the point anodes are opened so that access of the electrolyte from the bulk has been established (25).

It is not ruled out that in the salt film at the bottom of the pit there is an ohmic potential drop that keeps the pitting-passive surface system in the stable state.

Manuscript submitted Dec. 29, 1977; revised manuscript received May 5, 1978.

Any discussion of this paper will appear in a Discussion Section to be published in the June 1979 JOURNAL. All discussions for the June 1979 Discussion Section should be submitted by Feb. 1, 1979.

REFERENCES

1. M. A. Streicher, *This Journal*, **103**, 375 (1956).
2. N. D. Greene and M. G. Fontana, *Corrosion*, **15**, 15, 32, 39 (1959).
3. Ya. M. Kolotyrkin, *Khim. Prom.*, No. 9, 38, 678 (1963); *Corrosion*, **19**, 261 (1963).
4. I. L. Rosenfeld, "Corrosion and Prevention of Metals (Localized Corrosion)," Metallurgizdat, Moscow (1970) (in Russian).
5. E. Brauns and W. Schwenk, *Werkst. Korros.*, **12**, 73 (1961).
6. N. D. Tomashov, G. P. Chernova, and O. N. Markova, "Corrosion of Metals and Alloys," p 73, Metallurgizdat, Moscow (1963) (in Russian).
7. N. D. Tomashov, G. P. Chernova, and O. N. Markova, *Zashch. Met.*, **7**, 104 (1971).
8. W. Schwenk, *Corrosion*, **20**, 129 (1964).
9. Ya. M. Kolotyrkin, G. V. Golovina, and G. M Florianovich, *Dokl. Acad. Nauk SSSR*, **148**, 1106 (1963).
10 T. P. Hoar, D. C. Mears, and P Rothwell, *Corros. Sci.*, **5**, 279 (1965).
11. G. Herbsleb and W. Schwenk, *Werkst. Korros.*, **24**, 763 (1973).
12. H. P. Leckie and H. H. Uhlig, *This Journal*, **113**, 1262 (1966).
13. W. Schwenk, *Corros. Sci.*, **3**, 1 (1963).
14 H. J. Engel and N. D. Stolica, "Korrosion 13. Diskussionstagung Lochfrasskorrosion," p. 14, Verlag Chemie, Weinheim (1960).
15. K. J. Vetter, *Ber. Bunsenges. Phys. Chem.*, **69**, 683 (1965).
16. Z. Szklarska-Smialowska and Janik-Czachor, *Br. Corros. J.*, **4**, 138 (1969).
17. Z. Szklarska-Smialowska, *Corrosion*, **27**, 223 (1971).
18. H. W. Pickering and R. P Frankenthal, *This Journal*, **112**, 761 (1965).
19. R. P. Frankenthal, *Corros. Sci.*, **8**, 491 (1968).
20. W. Schwenk, *ibid.*, **5**, 245 (1965)
21. B. E. Wilde, *Corrosion*, **28**, 283 (1972).
22. K. J. Vetter and H. H. Strehblow, "Localized Corrosion," NACE-3, p. 240 (1974).
23. I. L. Rosenfeld and I. S. Danilov, *Dokl. Acad. Nauk SSSR*, **139**, 414 (1961).
24. I. L. Rosenfeld and I. S. Danilov, *Z. Phys Chem.*, **226**, 257 (1964).
25. I. L. Rosenfeld and I. S. Danilov, *Corros. Sci.*, **7**, 129 (1967).
26. I. L. Rosenfeld and I. S. Danilov, *Zashch. Met.*, **6**, 14 (1970).
27. U. Frank, "Korrosion 13. Diskussionstagung Lochfrasskorrosion," p. 2, Verlag Chemie, Weinheim (1960).
28. U. Frank, "Institute International Congress on Metallic Corrosion," p. 197 (1961).
29. M. Pourbaix, *Corros. Sci.*, **3**, 239 (1963).
30. I. L. Rosenfeld and I. K. Marshakov, *Usp. Khim.*, **33**, 500 (1964).
31. I. L. Rosenfeld and I. K. Marshakov, *Corrosion*, **20**, 115 (1964).
32. I. L. Rosenfeld and I. K. Marshakov, *Zh. Fis. Khim.*,

30, 2724 (1956); 31, 2328 (1957); 32, 66 (1958).
33. T. J. Lennox and I. P. Peterson, *Corrosion*, 29, 406 (1973).
34. H. W. Pickering and R. P. Frankenthal, NACE, Houston, Texas, p. 261 (1974)
35. E. McCafferty, *This Journal*, 121, 1007 (1974).
36. M. Pourbaix, "Localized Corrosion MACE," p. 12 (1974).
37. J. C. Rowlands, *Br. Corros. J.*, 11, 195 (1976).
38. D. A. Jones and N. D. Greene, *Corrosion*, 25, 367 (1969).
39. E. A. Lizlovs, *This Journal*, 117, 1335 (1970).
40. M. M. Kurtepov, M. N. Fokin, V. K. Zhuravlev, and V. I. Oreshkin, "Corrosion and of Construction Alloys Protection," p. 27, "Science," Moscow (1966) (in Russian).

Anodic Oxidation of Cobalt in Neutral and Basic Solution

Norio Sato* and Toshiaki Ohtsuka

Electrochemistry Laboratory, Corrosion Research Group, Faculty of Engineering, Hokkaido University, Sapporo 060, Japan

ABSTRACT

The anodic oxidation and anodic oxide films of cobalt have been studied in borate buffer solutions in the pH range from 7 to 11. The anodic polarization curve shows the active dissolution, primary passivity, secondary passivity, tertiary passivity, and transpassivation. It is also shown that the anodic oxide film is hydrated oxide of CoO in the primary passive region, bilayered oxide CoO/Co_3O_4 in the secondary passive region, and bilayered oxide of CoO/Co_2O_3 in the tertiary passive and transpassive regions. The dissolution current of the anodic oxide film in the secondary and tertiary passive regions is much smaller than that in the primary passive region. By cathodic reduction the outer Co_2O_3 layer is first converted to Co_3O_4 and then reduced further to hydrated Co^{2+} ions before the inner CoO layer is reduced to metallic cobalt.

Early this century, it was reported that cobalt was passivated chemically in concentrated nitric acid and electrochemically in alkaline solutions (1). Later, Grube (2) found three potential arrests in galvanostatic transients of anodic oxidation of cobalt in alkaline solutions and attributed them to the formation of Co_3O_4, Co_2O_3, and CoO_2. El-Wakkad and Hickling (3) also found the three potential arrests but described them as corresponding to CoO, Co_2O_3, and CoO_2. Recently, by use of potential sweeps, Tikkanen *et al.* (4) observed three current peaks in the anodic polarization curves of cobalt in alkaline solutions and assumed the formation of CoO, Co_3O_4, and $Co(OH)_3$. Other potentiostatic studies (5-7) carried out afterward have also suggested the successive formation of cobalt oxides of different oxidation states in agreement with the thermodynamic predictions (8-9). No direct evidence, however, has been provided for the composition of anodic oxide films on cobalt, except that Leidheiser *et al.* (10-11) detected by Mössbauer spectroscopy cobalt(II) and cobalt(III) ions in the anodic oxide films.

In our previous paper (12) the thickness of anodic oxide films on cobalt has been measured by *in situ* ellipsometry in neutral borate solution. This paper deals with the anodic polarization curve and the composition of anodic oxide films on cobalt in neutral and alkaline solutions.

Experimental

The specimen was prepared from cobalt rods of 99.99% purity (Johnson-Matthey Company, Limited) into polycrystalline sheets, 0.8 mm thick and 5 or 10 cm^2 surface area. It was mechanically polished, annealed for 100 hr at 390°C in vacuum, and electropolished at 0.45 A/cm^2 in a mixture of 60% perchloric acid and pure acetic acid (5:1) at 3° ~ 5°C. The electrolytic cell was a two-compartment four-electrode cell of 50 cm^3 capacity connected with four separate solution reservoirs. It had a Luggin capillary to a saturated calomel reference electrode and two platinum counterelectrodes, one in the specimen compartment and the other in the countercompartment. The solutions, prepared from doubly distilled water and analytical grade reagents, were mixtures of 0.30 $mole/dm^3$ boric acid and 0.075 $mole/dm^3$ sodium borate solutions, and their pH was adjusted by changing the mixing ratio and, if necessary, by adding a small amount of sodium hydroxide. Before transfer into the cell, the solutions were deoxygenated practically completely by injecting purified nitrogen gas for more than 24 hr.

The specimen in the cell was first cathodically reduced at a constant current of 10 $\mu A/cm^2$ for 20 min in a borate solution of pH 8.42 to obtain the oxide-free surface, and after careful exchange of solution under nitrogen atmosphere it was anodically oxidized potentiostatically for 1 hr at a given potential in a given solution. The solution was then drawn out for chemical analysis to determine the amount of cobalt dissolution by a colorimetric nitro-R salt method sensitive to 5 $\mu g/dm^3$. The oxidation was repeated for various potentials and pH solutions starting every time from the cathodically reduced surface at pH 8.42. In some experiments the time of anodic oxidation was extended up to 24 hr and the solution was chemically analyzed for cobalt for one hour to determine the time change of cobalt dissolution at constant potential.

Cathodic reduction experiments were carried out in which the oxidized specimen, immediately after oxidation, was reduced by a constant cathodic current of 5 or 10 $\mu A/cm^2$ for different periods of time and the solution, immediately after the current was off, was taken out for chemical analysis to determine the amount of cobalt dissolved as a function of cathodic charge passed.

All measurements were performed at 20° ± 0.5°C. All electrode potentials were measured in reference to a saturated calomel electrode and converted to

* Electrochemical Society Active Member.

Key words: metals, anode, potential, passivity.

the standard hydrogen electrode potential scale E_{SHE} or the hydrogen electrode scale in the same solution $E_{HESS} = E_{NHE} + 0.058$ pH.

Results

Oxide-free reference surface.—The oxide-free surface, with which coulometric measurements were carried out, was obtained by cathodic reduction of the specimen at a constant current 10 $\mu A/cm^2$ for 20 min in a borate solution at pH 8.42. The absence of oxide films on the cathodically reduced surface appears evident from measurements of galvanostatic reduction-oxidation cycles, in which the first oxidation curve for a surface prepared by cathodic reduction of the electropolished surface was consistent with the second oxidation curve obtained after cathodic reduction of the anodically oxidized surface. This reproducible surface is suggested to be free from oxides. It has also been shown by ellipsometry that the anodic oxide films on cobalt were completely removed by cathodic reduction (12) at pH 8.42.

Anodic oxidation.—The anodic polarization curves of cobalt in borate solutions at pH 7 ~ 11 are shown in Fig. 1, where the anodic currents represent the nearly stationary values observed 1 hr after the start of potentiostatic oxidation each with the oxide-free surface. Figure 2 shows the amount of cobalt dissolved during 1 hr oxidation as a function of potential. In these two figures, the three different degrees of passivity can be distinguished; the primary passive region I extending from +0.4 to +0.8V, the secondary passive region II from +0.9 to +1.25V, and the tertiary passive region III from +1.25V to about +1.6V in the HESS potential scale referred to the hydrogen electrode in the same solution. Transpassivation appears to occur at more anodic potential. The critical potential for anodic oxygen evolution is about +1.45V (HESS), which exceeds its equilibrium potential by about 0.37V. The Tafel line for the oxygen electrode reaction in Fig. 1 gives kinetic parameters; $(\partial E/\partial \log i)_{pH} = 75$ mV and $(\partial \log i/\partial \text{pH})_E \doteqdot 1$.

The transpassive dissolution at more anodic potentials is shown in Fig. 3, where the SHE potential scale is used. It is noticed that the critical potential for transpassivation is almost independent of pH, being about +1.1V (SHE) in the pH range from 7 to 11.

To compare the anodic current with the dissolution rate of cobalt in the same scale, the anodic current after 1 hr and the dissolution current averaged for 1 hr following the initial 1 hr oxidation at constant potential are plotted as a function of potential in Fig. 4. In the passive region I, the anodic current reached the steady value within 1 hr and is equal to the dissolution current of cobalt as cobalt(II) ion. In the passive regions II and III, however, the anodic current does not reach the steady state in 1 hr. Furthermore, the anodic current in region III is larger than the dissolution current as (III) ions, indicating

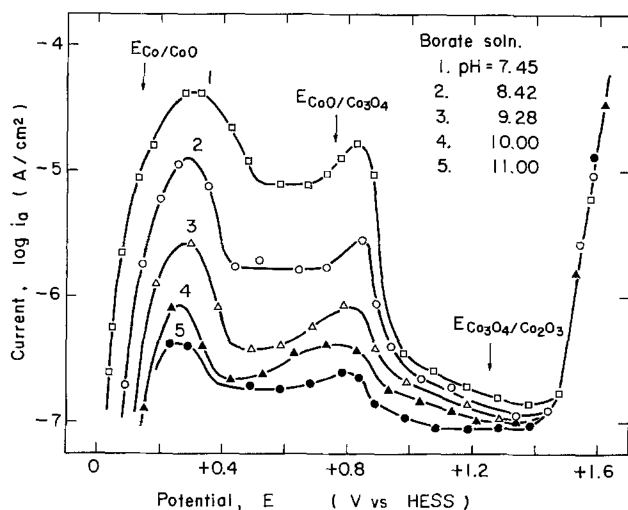

Fig. 1. Anodic current/potential curves of cobalt in borate solutions. The current is measured 1 hr after the start of potentiostatic oxidation of the oxide-free surface.

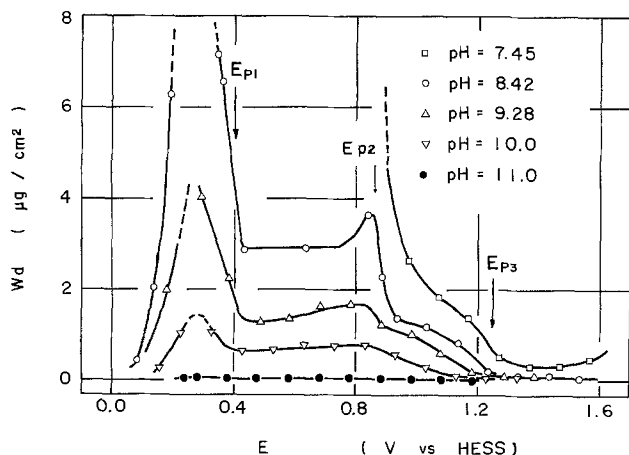

Fig. 2. Anodic 1 hr dissolution/potential curves of cobalt in borate solutions. The amount of dissolution W_d is measured for 1 hr of potentiostatic oxidation of the oxide-free surface.

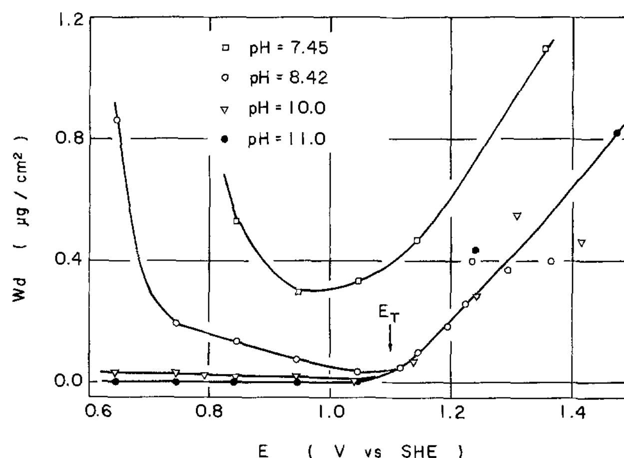

Fig. 3. Anodic 1 hr dissolution/potential curve of cobalt in passive and transpassive potential regions in borate solutions.

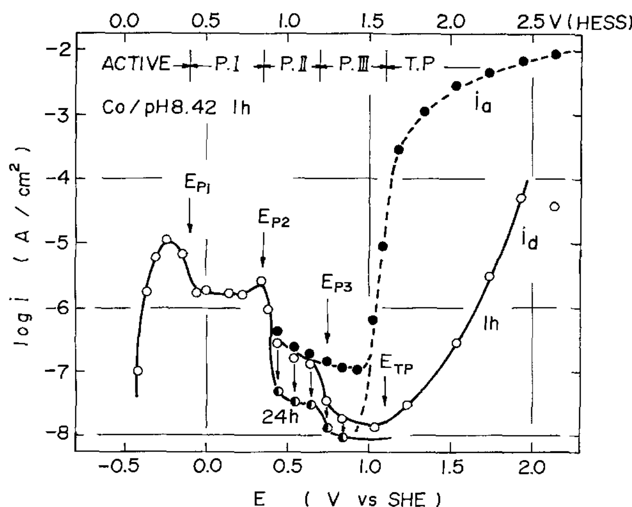

Fig. 4. Anodic current/potential and dissolution-current/potential curves of cobalt in borate solution at pH 8.42. The anodic current (●) is measured 1 hr after the start of oxidation, and the dissolution current is the average for 1 hr following first 1 hr (○) and 24 hr (◐).

that the thickening of the anodic oxide is in progress even after 1 hr. In the transpassive region, the anodic current mostly carries oxygen at more anodic potentials, and the transpassive dissolution current, though increasing with potential, takes only a diminutive part of the total anodic current. The anodic oxygen evolution current first increases with potential following a Tafel relation and then approaches a limiting current which increases with pH.

To examine how much time to take before the steady state is reached in passive regions II and III, 24 hr oxidation was carried out at constant potential. Figure 5 shows the anodic current and the cobalt dissolution current both decreasing with time of oxidation toward the steady values in 24 hr. It is evident that at the steady state the anodic current is equivalent to the cobalt dissolution rate as cobalt(II) ion in region II and as cobalt(III) ion in region III.

It has been shown in Fig. 1 and 2 that the pH dependence of cobalt dissolution is much larger in active and passive I regions than in passive regions II and III. Figure 6 shows the pH dependence of the active peak current i_{am} and of the potential-independent dissolution current i_{p1} in passive region I, leading for a pH range 7.4 ~ 9.4 to the following relations; $\log i_{am} = 0.34\text{-}0.63$ pH (A/cm²) and $\log i_{p1} = -0.44\text{-}0.63$ pH (A/cm²). In passive regions II and III, it was difficult to determine the pH dependence of the steady-state dissolution current because of the extremely small dissolution rate in this pH range.

To estimate the amount of anodic oxide formed in 1 hr, measurements were carried out of the anodic charge, Q_f, accumulated in the anodic oxide film, which could be obtained by subtracting the charge equivalent to the amount of dissolution as cobalt(II) or (III) ion from the total anodic charge passed. Figure 7 shows the anodic film charge Q_f as a function of potential. Evidently, the anodic film starts to form in the potential region of active dissolution. The amount of the anodic film charge is nearly potential independent in passive region I, but it increases with potential in passive regions II and III.

Cathodic reduction of anodic oxide films.—Figure 8 shows the galvanostatic-cathodic reduction of the anodic oxide films, where the potential decay and the amount of cobalt(II) ion dissolved from the films are plotted as a function of cathodic charge passed. In this figure, the film is formed for 1 hr at a given potential in the solution of pH 10.0 and reduced by a cathodic current of 10 μA/cm² in the solution of pH 8.42. Obviously, the anodic film formed in passive

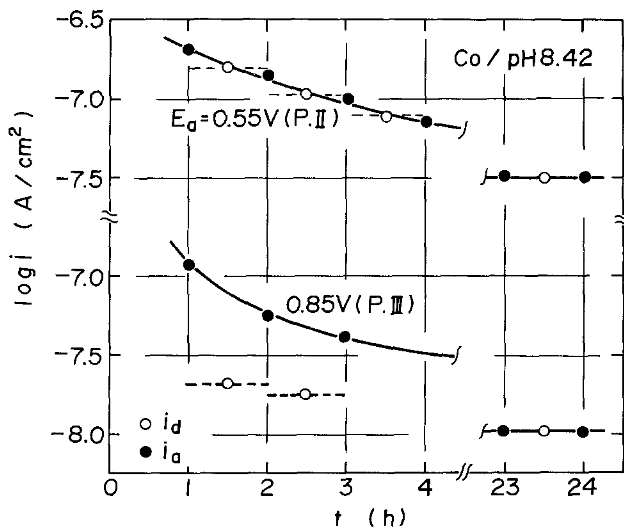

Fig. 5. Variation of anodic current i_a and dissolution current i_d with time for cobalt at constant potential in passive regions II and III in borate solution pH 8.42. The dissolution current is the average for 1 hr.

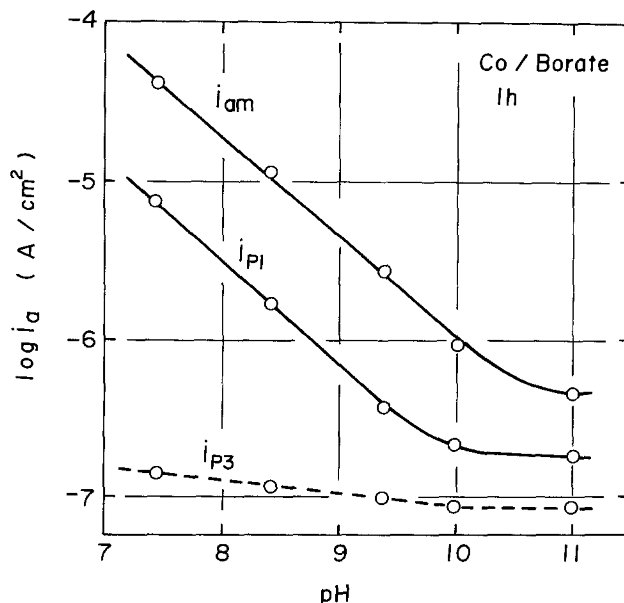

Fig. 6. Variation of active peak current i_{am}, primary passivity current i_{p1}, and tertiary passivity current i_{p3} with pH for anodic oxidation of cobalt in borate solutions. The current is measured 1 hr after the start of oxidation.

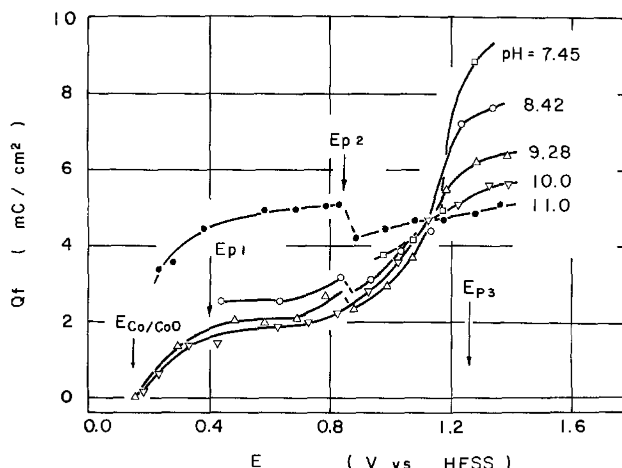

Fig. 7. Anodic film-charge/potential curves of cobalt in borate solutions. The film charge $Q_f = Q_a - Q_d$, where Q_a is the anodic charge passed for 1 hr and Q_d the charge equivalent to cobalt dissolution ($Q_d = W_d/2F$).

region I shows a rapid cathodic potential decay to an oxide reduction potential −0.55V (SHE) slightly more noble than the final potential and no cobalt(II) ion is produced in the solution during the cathodic reduction, indicating that the primary passive film of cobalt(II) oxide or hydroxide is reduced to metallic cobalt. The film formed in passive region III, however, shows a definite arrest in the potential decay and produces cobalt(II) aquo-ions in the solution during its cathodic reduction, indicating that a higher valent cobalt oxide is reduced to soluble cobalt(II) ions.

The cathodic dissolution of the film as cobalt(II) ions, which occurs only with the film formed in passive regions II and III, differs with different solution pH in which cathodic reduction is carried out. Figure 9 shows the cathodic dissolution curves in different pH solutions for the anodic oxide film formed at a constant potential in passive region III in the solution of pH 10.0. After an induction period of about 0.1 mC/cm², the amount of cobalt(II) ion dissolution increases nearly linearly with the cathodic charge passed and then gradually approaches a maximum value W_d^{max}. The broken line in Fig. 9 refers to the theoretical

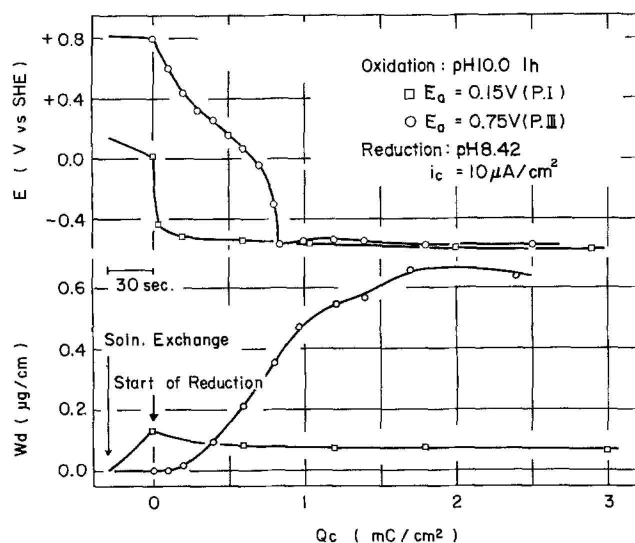

Fig. 8. Variation of potential and amount of cobalt(II) dissolution with cathodic charge passed during galvanostatic reduction of anodic oxide films formed in passive regions I and III. The film, formed potentiostatically for 1 hr in borate solution pH 10.0, is reduced by cathodic current 10 μA/cm^2 in borate solution pH 8.42.

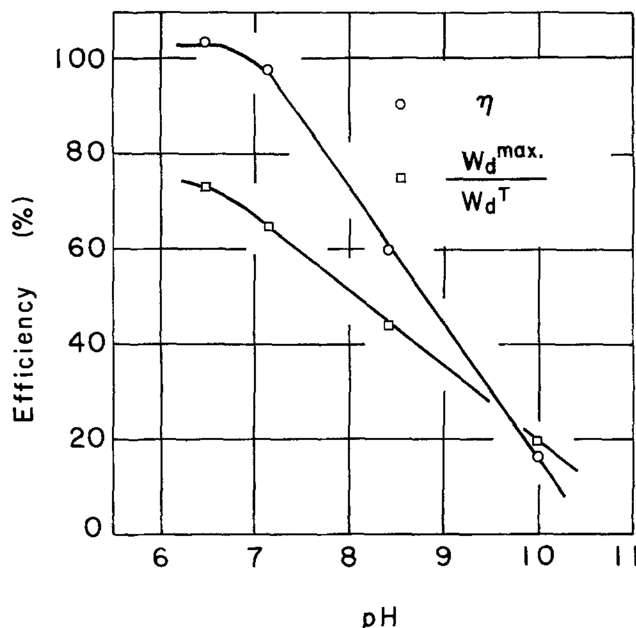

Fig. 10. Differential current efficiency η and integral efficiency W_d^{max}/W_d^T of reductive dissolution of an anodic oxide film on cobalt as a function of solution pH used for cathodic reduction.

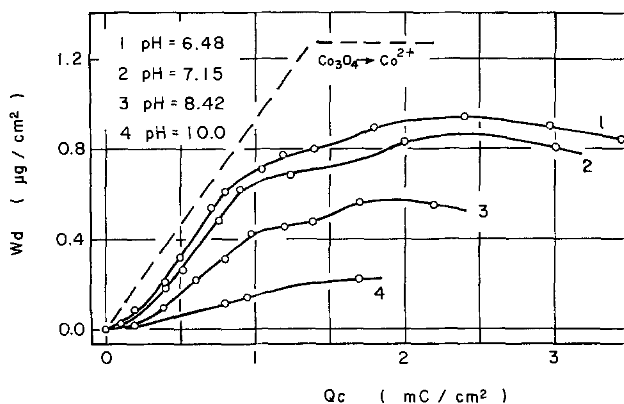

Fig. 9. Cathodic reduction curves of an anodic oxide film on cobalt in borate solutions pH 6 ~ 10. The film, formed for 1 hr at +0.75V (SHE) at pH 10, is reduced by cathodic current 10 μA/cm^2 to measure the amount of dissolution W_d as a function of cathodic charge Q_c in various solutions.

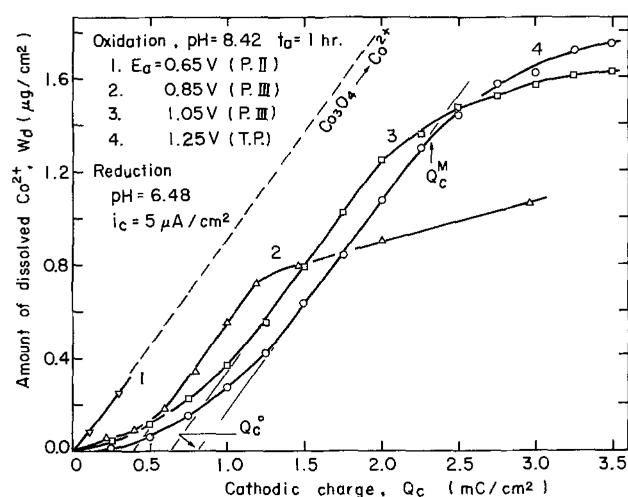

Fig. 11. Cathodic reduction curves of anodic oxide films on cobalt in passive regions II (+0.65V_{SHE}), III (+0.85V and +1.05V_{SHE}) and in transpassive region (+1.25V_{SHE}). The film, formed for 1 hr at pH 8.42, is reduced by cathodic current 5 μA/cm^2 in borate solution pH 6.48.

cathodic dissolution of stoichiometric Co_3O_4, $Co_3O_4 + 8H^+ + 2e \rightarrow 3Co^{2+} + 4H_2O$, and hence its slope can be used as a reference of differential current efficiency η for cathodic dissolution of the film. A limiting value in the broken line represents the total amount of cobalt W_d^T in the film assuming a single layer of Co_3O_4. As shown in Fig. 10, both differential current efficiency η and maximum amount of dissolved cobalt(II) ion W_d^{max} increase with decreasing pH. Notice that η reaches 100% at pH 6.48, though W_d^{max} is smaller than W_d^T even at this pH. The cathodic current density in a range 2 ~ 50 μA/cm^2 has a slight influence on W_d^{max} but produced no effect on η.

Because of the differential current efficiency η = 100%, the solution of pH 6.48 and the current density of 5 μA/cm^2 were employed as a standard cathodic reduction method to measure the composition of the anodic oxide films formed at different potentials in the solution at pH 8.42. Results are shown in Fig. 11, where the broken line again refers to the cathodic dissolution of Co_3O_4. Noticeably, the film formed at +0.65V (SHE) in passive region II dissolves along the theoretical Co_3O_4 dissolution curve without any induction charge for cathodic dissolution, indicating that at least the outer part of the film is Co_3O_4 or $Co_3O_4 \cdot nH_2O$. The film formed at +0.85, 1.05, and 1.25V (SHE) in passive region III, however, requires an induction charge Q_c^o before the cathodic dissolution occurs at the same rate as Co_3O_4, indicating that the outer part of the film is in the oxidation state higher than Co_3O_4 or contains a significant amount of cobalt ion vacancy, $Co_{3-\Delta}O_4$. Furthermore, it is found that the induction charge Q_c^o and the charge Q_c^M, beyond which the slope of the cathodic dissolution curve deviates from that of the theoretical Co_3O_4 dissolution curve, both increase with the potential of film formation. As shown below, these two charges Q_c^o and Q_c^M may be used to estimate the nonstoichiometric composition of the anodic oxide films.

Discussion

The anodic oxide film in passive region I.—As shown in Fig. 7, an anodic, prepassive oxide film begins to form at a critical potential of about +0.15-0.059 pH (V_{SHE}), where cobalt is in the active state (Fig. 1 and 2). This critical potential is close to the equilibrium potentials (13-15) for the anodic formation of CoO, α-Co(OH)$_2$, and β-Co(OH): E_{eq}(Co/CoO) =

$+0.135-0.059$ pH (V_{SHE}), $E_{eq}(Co/\alpha\text{-}Co(OH)_2) = +0.15-0.059$ pH (V_{SHE}), and $E_{eq}(Co/\beta\text{-}Co(OH)_2) = +0.08-0.059$ pH (V_{SHE}). This prepassive oxide film, which is assumed to be CoO or $Co(OH)_2$, grows to be the primary oxide film in passive region I. The fact that the galvanostatic cathodic reduction of the film formed in passive region I does not produce any detectable amount of cobalt(II) ions in the solution (Fig. 8) provides indirect evidence for a cobalt(II) oxide or hydroxide film, which is reduced to metallic cobalt at cathodic potentials.

It is also shown in Fig. 7 that the amount of anodic charge for the primary oxide film in passive region I is almost constant at $2 \sim 2.5$ mC/cm^2 in the pH range from 7 to 10, which corresponds to the thickness of $12 \sim 15$Å for a film of CoO (density $5.7 \sim 6.7$ g/cm^3) and $27 \sim 33$Å for a film of $Co(OH)_2$ (density 3.6 g/cm^3) with the roughness factor of the surface $\gamma = 1$. In the previous paper (12) the film thickness in region I has been estimated by ellipsometry to be about 25Å, which is close to the thickness calculated above for $Co(OH)_2$ rather than CoO. It thus appears that the anodic oxide film in passive region I is hydrated.

There is a slight increase in both dissolution current i_a (Fig. 1 and 2) and film charge Q_f at potentials close to the secondary passivation potential E_{p2}. This is due to the formation of a higher valence oxide, probably giving rise to the partial breakdown of the hydrated CoO film.

The anodic oxide film in passive regions II and III.—The anodic oxide films in passive regions II and III are characterized by the cathodic potential decay with two potential arrests and by their cathodic dissolution as cobalt(II) ion in the first potential arrest, which suggests a two-layered film consisting of an outer layer of higher valence oxide and an inner layer of lower oxide, probably CoO. The cathodic charge required for the first potential arrest corresponds to the reduction of a higher valence oxide layer and hence may be used as a measure of its thickness.

Figure 12 shows the cathodic charge for the first potential arrest as a function of the potential at which the anodic oxide film has been formed for 1 hr at various pH solutions. Evidently, the higher valence oxide begins to form at about +0.75V (HESS), which is consistent with the ellipsometric measurements (12). Since the higher valence oxide in passive region II has been identified as Co_3O_4 (Fig. 11), this critical potential is represented by $E_{CoO/Co_3O_4} = +0.75V-0.059$ pH (V_{SHE}), which is compared with the equilibrium potential (13), $E_{eq}(CoO/Co_3O_4) = +0.65-0.059$ pH (V_{SHE}). The secondary passivation potential, $E_{p2} = +0.85-0.059$ pH (V_{SHE}), is 0.1V more anodic than E_{CoO/Co_3O_4}, indicating that a certain thickness or coverage of the higher valence oxide layer is required for the secondary passivation to occur.

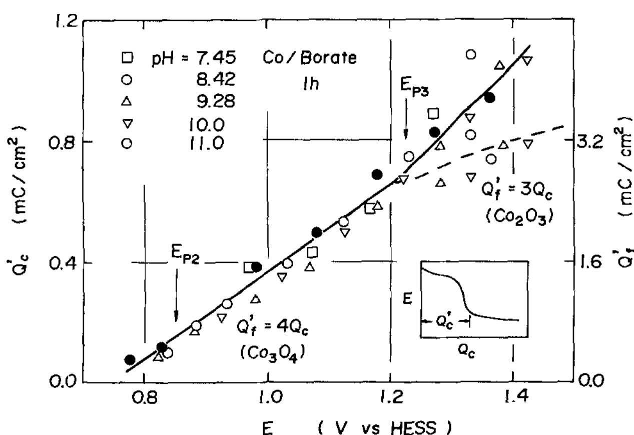

Fig. 12. Cathodic charge Q_c' for first potential arrest in cathodic reduction curves and anodic charge Q_f' for the outer layer (Co_3O_4 or Co_2O_3) as a function of potential of film formation. The film, formed for 1 hr at different pH, is reduced by cathodic current 5 μA/cm^2 in borate solution pH 6.48.

The anodic oxide film formed in passive region III exhibits an induction period in its cathodic dissolution as cobalt(II) ions (Fig. 11). This is attributed to the reduction of excess oxygen in the film

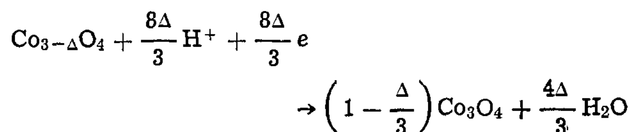

$$Co_{3-\Delta}O_4 + \frac{8\Delta}{3}H^+ + \frac{8\Delta}{3}e \rightarrow \left(1 - \frac{\Delta}{3}\right)Co_3O_4 + \frac{4\Delta}{3}H_2O$$

where Δ denotes the nonstoichiometry of Co_3O_4. It is thus assumed that the cathodic charge Q_c^o required for the induction period corresponds to the amount of nonstoichiometry Δ and that the cathodic charge Q_c^M (Fig. 11) is equivalent to the coulomb required for the dissolution of $Co_{3-\Delta}O_4$ to cobalt(II) ions. Then, the nonstoichiometry Δ may be estimated from Q_c^o and Q_c^M by use of the relation $Q_c^o/Q_c^M = 4\Delta/(3 + 3\Delta)$. Figure 13 shows Q_c^o/Q_c^M and Δ as a function of potential for the film formed at pH 8.42. The nonstoichiometry Δ is seen to change from $\Delta = 0$ to $\Delta = 0.33$ and hence the oxidation state of the film from Co_3O_4 to Co_2O_3 at about +1.2V (HESS). This potential agrees with the critical potential that separates passive region II from passive region III in the anodic dissolution curve (Fig. 2); $E_{p3} = +1.25-0.059$ pH (V_{SHE}). The corresponding equilibrium potential (13) is $E_{eq}(Co_3O_4/CoOOH) = +1.15-0.059$ pH (V_{SHE}). It has been shown in the previous paper (12) that the optical constant of the outer layer of the film also changes at this critical potential E_{p3}.

The anodic charge Q_f' for the higher valence oxide layer is estimated from the cathodic charge Q_c' required to reduce it to cobalt(II) aquo-ions, as shown in Fig. 12. The layer thickness is calculated from Q_f' by using the thickness/coulomb ratio 5.11 Å/mC for Co_3O_4 (density 6.1 g/cm^3) and 5.53 Å/mC for Co_2O_3 (density 5.2 g/cm^3). Furthermore, substraction of Q_f' from the total film charge Q_f (Fig. 7) gives the anodic charge for the inner CoO layer, which then allows the inner layer thickness to be computed. The thickness of both layers thus estimated for the anodic oxide

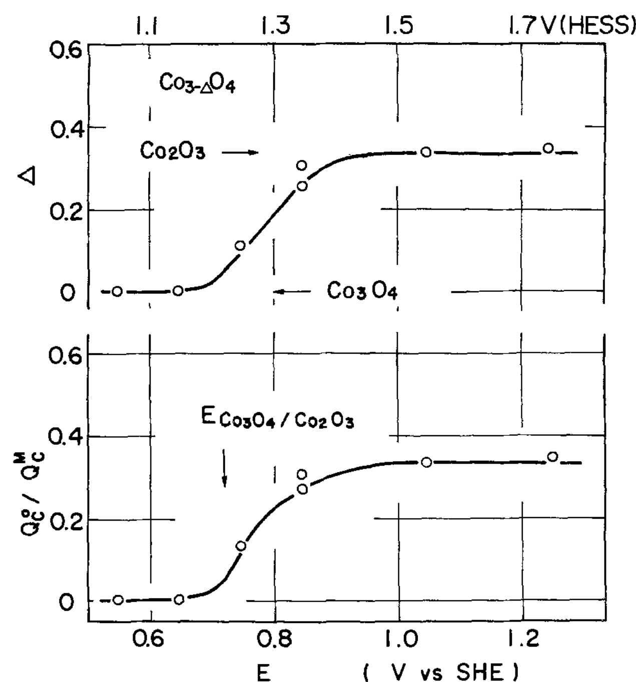

Fig. 13. Ratio Q_c^o/Q_c^M in cathodic reduction curves and nonstoichiometry Δ of the outer $Co_{3-\Delta}O_4$ layer of anodic oxide films as a function of potential of film formation.

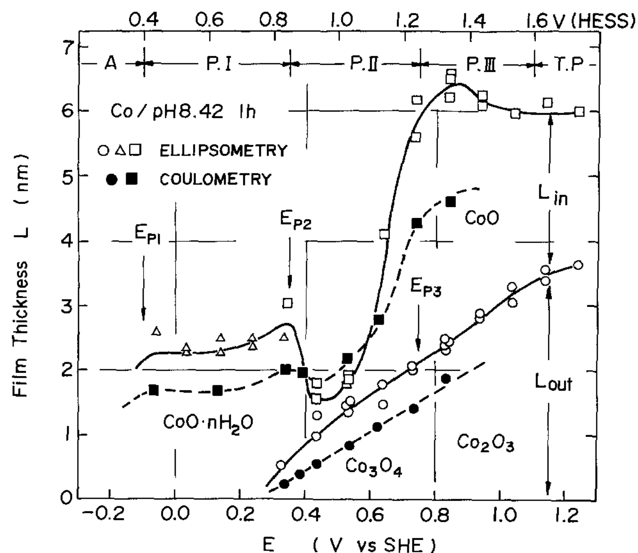

Fig. 14. Thickness/potential curves for anodic oxide films formed on cobalt for 1 hr in borate solution pH 8.42; L_{in} represents the inner CoO layer and L_{out} the outer layer.

film formed at pH 8.42 is shown in Fig. 14, where the ellipsometrically estimated thickness is also shown for comparison. Notice that the coulometric thickness estimation assumes anhydrated oxide films and hence would give a smaller thickness than expected for hydrated oxide films. The main reason for the discrepancy between the coulometric and ellipsometric thicknesses is probably the hydrated nature of the anodic oxide films.

Conclusion

1. The anodic oxidation of cobalt in borate solutions of pH 7 ~ 11 gives rise to the active dissolution, the passivation, and the transpassivation, depending on the potential.

2. The passive potential range can be divided into the three regions; the primary passivity (region I), the secondary passivity (region II), and the tertiary passivity (region III).

3. In region I, which extends from +0.4-0.059 pH (V_{SHE}) to +0.8-0.059 pH (V_{SHE}), a hydrated cobalt(II) oxide about 25Å thick is formed at pH 7 ~ 10, and the dissolution current i_{p1} nearly independent of potential decreases with increasing pH; log i_{p1}/A cm^{-2} = −0.44-0.63 pH in 1 hr oxidation.

4. In region II from +0.9-0.059 pH (V_{SHE}) to +1.3-0.059 pH (V_{SHE}), an oxide or hydrated oxide film of Co_3O_4, whose thickness increases with potential up to 15Å, is formed on the CoO film, and the dissolution current i_{p2} is much smaller than i_{p1}; log i_{p2}/A cm^{-2} = −7.5 at pH 8.42 in 24 hr oxidation. The total film thickness is estimated to increase from 15 to 50Å with potential.

5. In region III more anodic than +1.3-0.059 pH (V_{SHE}), an oxide or hydrated oxide film of Co_2O_3, whose thickness increases with potential from 15 to 35Å, is formed on the CoO film, and the dissolution current i_{p3} is smaller than i_{p2}; log i_{p3}/A cm^{-2} = −8.0 at pH 8.42 in 24 hr oxidation.

6. The transpassive dissolution begins to occur at about +1.1 (V_{SHE}) nearly independent of pH, and the anodic oxide film in the transpassive region is the same in composition as that in passive region III.

7. The anodic oxygen evolution begins to occur at +1.4-0.059 pH (V_{SHE}), irrespective of the passive and transpassive dissolution of cobalt.

8. The passive oxide films can be cathodically reduced to obtain an oxide-free cobalt surface. In borate solution at pH 6.48, the cathodic current of 5 μA/cm² reduces the outer Co_2O_3 layer to a Co_3O_4 layer, which is then reduced to Co^{2+} ions at the differential current efficiency η = 100% before the onset of the reduction of the inner CoO layer to metallic cobalt.

Manuscript submitted March 21, 1978; revised manuscript received May 30, 1978.

Any discussion of this paper will appear in a Discussion Section to be published in the June 1979 JOURNAL. All discussions for the June 1979 Discussion Section should be submitted by Feb. 1, 1979.

Publication costs of this article were assisted by Hokkaido University.

REFERENCES

1. H. G. Byers, *J. Am. Chem. Soc.*, **30**, 1718 (1908); H. G. Byers and C. W. Thing, *ibid.*, **41**, 1902 (1919).
2. G. Grube and O. Feucht, *Z. Elektrochem.*, **28**, 568 (1922); Von G. Grube, *ibid.*, **33**, 389 (1927).
3. S. E. S. El-Wakkad and A. Hickling, *Trans. Faraday Soc.*, **46**, 1820 (1950).
4. M. H. Tikkanen and T. Tuominen, in "Proceedings 3rd International Congress on Metallic Corrosion," Vol. I, p. 489, MIR, Moscow (1969).
5. R. D. Cowling and A. C. Riddiford, *Electrochim. Acta*, **14**, 981 (1969).
6. W. K. Behl and J. E. Toni, *Electroanal. Chem. Interfacial Electrochem.*, **31**, 63 (1971).
7. T. R. Jayaraman, V. K. Venkatesan, and H. V. K. Udupa, *Electrochim. Acta*, **20**, 209 (1975).
8. H. Göhr and E. Lange, *Z. Elektrochem.*, **50**, 814 (1952).
9. E. Deltombe and M. Pourbaix, in "Proceedings of 6th Meeting CITCE," p. 153, Butterworths, London (1955).
10. H. Leidheiser, Jr., G. W. Simmons, and E. Kellerman, *This Journal*, **120**, 1516 (1973).
11. G. W. Simmons, E. Kellerman, and H. Leidheiser, *ibid.*, **123**, 1276 (1976).
12. K. Kudo, N. Sato, and T. Ohtsuka, in "Proceedings of the 4th International Passivity Symposium," ECS Publication in Press (1978).
13. H. Göhr, *Electrochim. Acta*, **11**, 827 (1966).
14. W. Feitknecht and P. Shindler, *Pure Appl. Chem.*, **6**, 130 (1963).
15. K. H. Gayer and A. B. Garret, *J. Am. Chem. Soc.*, **72**, 3971 (1950).

Characteristics of Immersion-Plated Gold Deposits on Aluminum

D. J. Levy* and D. H. Ma

Lockheed Palo Alto Research Laboratory, Palo, Alto, California 94304

ABSTRACT

An alkaline $KAu(CN)_2$ bath was developed for immersion (replacement) plating of adherent gold deposits on aluminum. The deposits grow in two stages: (*i*) initial attack of the aluminum oxide film at new sites and the formation of tiny gold nodules; followed by (*ii*) growth on the nodular deposits by the addition of long, crystalline needles of gold. Deposit weight increases with the log of time, log of gold concentration, and with bath pH. Deposition rates at ambient temperature of 0.3 μm/min or more are possible. The coatings, potentially useful as electrical contacts in a moisture-free environment, were evaluated for adhesion and contact resistance.

The natural oxide film on aluminum interferes with electrical contact to the basis metal. Gold contacts plated on the aluminum will obviate this problem. While the gold-aluminum galvanic couple could lead to serious corrosion problems in the ambient terrestrial environment, the potential corrosion problems are absent in space and in controlled environments. For example, aluminum wires have been bonded to gold conductor traces in semiconductor products for many years.

The technology for plating immersion (replacement) gold deposits on chromium, copper, lead, nickel, silicon, stainless steel, and tungsten has been summarized by Parker (1), but no literature references to immersion gold deposits on aluminum were found by the present authors. Gold is commonly electroplated on aluminum, but this is accomplished by a multilayer coating system after removing the oxide film and substituting a replacement coating of zinc or tin.

This paper describes a bath for the immersion plating of gold on aluminum. The deposit morphology and the effect of bath composition on deposition at ambient temperature are discussed. Gold deposits were evaluated for adhesion and electrical contact resistance and were compared with alternate materials.

Materials and Apparatus

Test specimens.—Types 1145 and 1235 aluminum foil (10-20 μm) were used as the substrate material. Composition is shown below.

	1145	1235
Al, min. w/o	99.45	99.35
Fe + Si, max %	0.55	0.65
Cu, max %	0.05	0.06
Mn, max %	0.05	0.00

A plating fixture was used that enabled plating of a 26 mm diam spot of gold on one side of a 36 mm diam aluminum disk.

Thickness.—Thickness of the gold deposit was measured by the beta-backscatter method with a Model 28 Micro-Derm using a carbon-14 source.

Contact-resistance.—Contact resistance was measured by a Wheatstone Bridge using a Leeds & Northrup Model 5205 resistance box. A cylindrical probe 10 mm diam, weighing 4g, and plated with high purity gold was used.

Adhesion.—The 180° peel tests were made with a polyimide tape coated with a pressure-sensitive acrylic adhesive. Adhesion to steel was rated at 30 oz/in. (33 g/mm) using ASTM D 1000.

pH.—An Orion Research Model 601 Digital Ionalyzer was used with glass and Ag-AgCl electrodes.

Oxide Stripping

Activation normally consists of removing the oxide film from a metal surface prior to plating. However, aluminum is very active electrochemically and the oxide film is rapidly reformed unless the active surface is immediately protected by a replacement film (*i.e.*, zinc, tin). Surface oxides will vary in thickness and character even on the same aluminum alloy depending on the prior history of the surface. It was desirable to start with a reproducible surface condition to evaluate immersion gold plating. Therefore the existing surface oxide was stripped from test specimens prior to plating so that the surface would have a reproducible, fresh, thin, hydrous oxide film.

Both alkaline and acidic solutions were evaluated for stripping the oxide. It was found that sodium hydroxide solutions effectively strip the oxide but they also attack the aluminum metal as evidenced by excessive etching and hydrogen evolution. In comparison, nitric acid merely dissolves the oxide film and does not appreciably attack the metal. The acidic solution is also free rinsing.

The gold plate thickness (Table I) is somewhat greater after stripping with nitric acid rather than sodium hydroxide, indicating that the fresh oxide film is thinner. Adhesion is also more reliable. Electrical contact resistance was not significantly different for any of the specimens tested.

The time necessary to strip an oxide film varies with the aluminum alloy and the condition of the oxide. As a general rule, 2-5 min in 250-400 g/l [25-40 v/o (volume percent), sp gr 1.42] nitric acid at ambient (15°-25°C) temperature is sufficient (2). The effectiveness of the acid to strip oxide films is diminished as

Table I. Effect of oxide stripping before immersion gold plating (5 g/l Au)

Oxide stripping		Immersion plating		
Soln.	Min	Plating time (Min)	Au thickness (μm)	Contact resistance (Ω)
None		0.5	0	
		1	0.008	0.027
		2	0.036	0.022
NaOH	1	0.5	0.008	0.020*
		1	0.023	0.021
		2	0.041	0.024
HNO_3	5	0.5	0.013	0.026
		1	0.020	0.019
		2	0.051	0.021

* Poor adhesion.

* Electrochemical Society Active Member.

Key words: plating, deposition, pH.

concentration is increased up to 500 g/l. Use of the oxide stripper is optional and depends upon the surface condition of the aluminum being processed.

Immersion Plating

After experimenting with several gold salts and observing no substantial differences, the common gold salt potassium gold cyanide, $KAu(CN)_2$, was selected for use in the alkaline plating solution. The increase in deposit thickness with time is shown in Fig. 1. The deposit is porous and not self-limiting in thickness. Therefore rather thick deposits can be produced although the deposition rate does diminish with time. Figure 1 shows that the equivalent thickness increases with the log of time. Equivalent thickness is that of a dense, continuous gold film of the same mass per unit area.

Figure 2 shows the effect of gold concentration in the plating solution on deposit thickness after plating 2 min. The deposition rate increases directly with the log of the gold concentration. Gold content of the bath should be at least 3 g/l Au in order to achieve good adhesion of the deposit at reasonable deposition rates. Higher concentrations are entirely satisfactory but are limited as a practical matter to minimize dragout losses. An upper limit of 5 or 6 g/l gold gives a suitable broad range for process control.

The principal parameter affecting deposition rate is pH. Figure 3 shows that the deposit thickness increases exponentially with pH. The hydroxyl ion functions by dissolving the hydrous aluminum oxide film and permitting the replacement reaction to proceed. A pH of at least 11.2 enables a satisfactory deposition rate. At a pH greater than 11.8, the substrate metal is attacked excessively and the resultant hydrogen evolution disrupts adhesion of the gold deposit.

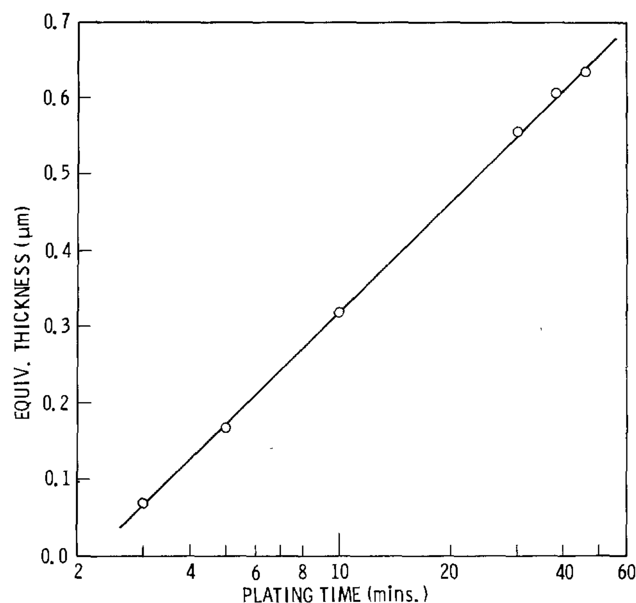

Fig. 1. Increase in gold thickness with plating time. 5 g/l gold at pH 11.8.

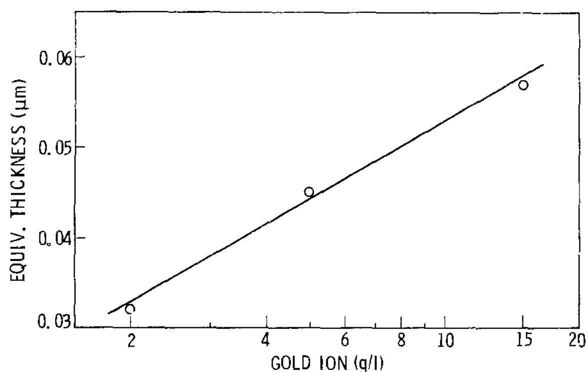

Fig. 2. Increase in deposit thickness with gold concentration. 2 min at pH 11.5.

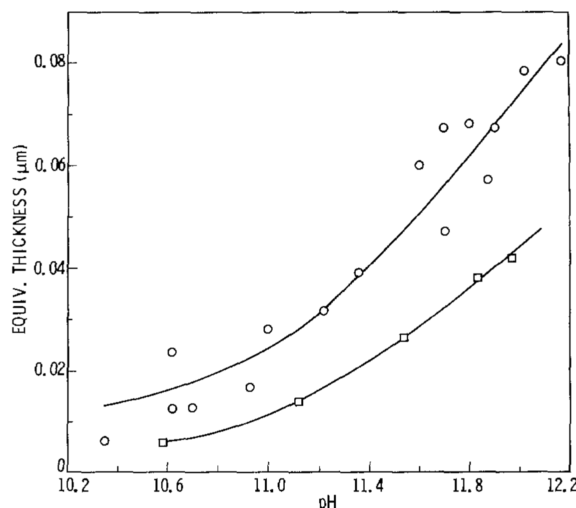

Fig. 3. Effect of pH on gold deposit thickness. 2 min plating time. 2 g/l Au, □; 5-7 g/l Au, ○.

The effect of both gold concentration and pH on average gold deposition rate can be seen in Table II. At 2 g/l Au, it was found that the gold deposits were no longer adherent when the deposition rate reached 0.10 μm/min. However, increasing the gold content to 7.0 g/l enables a deposition rate of at least 0.29 μm/min with good deposit adherence. The significant effect of pH to increase the deposition rate is also evident in the data. Average deposition rate during the plating period is listed in Table II; instantaneous rates are indicated in Fig. 1.

As the bath is used, the aluminum ion concentration will increase and eventually aluminum hydroxide will be precipitated. It is, of course, undesirable to have suspended solids present in a plating bath. A simple calculation shows that the solubility of aluminum hydroxide is only 0.06 and 0.25M at pH 11.2 and 11.8, respectively, based on the equilibrium dissociation reaction

$$Al(OH)_3 = H^+ + H_2AlO_3^- \qquad K = 4 \times 10^{-13}$$

In order to increase the bath life, a complexing agent was added. Sodium citrate was chosen because of its high solubility. A concentration of 60 g/l is very satisfactory. Addition of the citrate also increases the rate

Table II. Immersion gold deposition

Plating solution		Gold plating		
Au (g/l)	pH	(Min)	(μm)	(μm/min*)
2	10.90	1	0.01	0.01
	10.95	2	0.09	0.04
	11.52	1	0.07	0.07
	11.52	5	0.52	0.01
	11.52	10	0.83	0.01
	11.70	1	0.07	0.07
	11.74	5	0.48	0.10**
	11.78	10	1.07	0.11**
	11.82	1.1	0.13	0.12
	11.92	10	1.14	0.11**
6.1	11.36	1	0.19	0.19
	11.33	5	1.03	0.21
	11.33	10	2.00	0.20
6.8	10.98	1	0.14	0.14
	10.96	6.5	0.73	0.11
6.9	11.07	10	1.93	0.19
	11.63	10	2.52	0.25
7.0	11.60	1	0.29	0.29
	11.63	5	1.24	0.25

* Average deposition rate.
** Poor adhesion.

of gold replacement on the aluminum surface without any loss of adhesion. Furthermore, it creates a *p*H buffer system which slows the decrease in *p*H with solution use.

As the plating solution is used, free cyanide ions are released which compete with the citrate to form aluminum complexes. It was found by addition of sodium cyanide that the maximum concentration of free cyanide before the gold deposit becomes nonadherent is 6.8 g/l CN^-. In the absence of citrate, the tolerance for free cyanide is only 2.6 g/l. The plating bath was designed for convenience to be used at ambient temperature (15°-25°C) and the reaction was not studied at higher temperatures.

The principal half-reactions for the immersion plating are aluminum dissolution

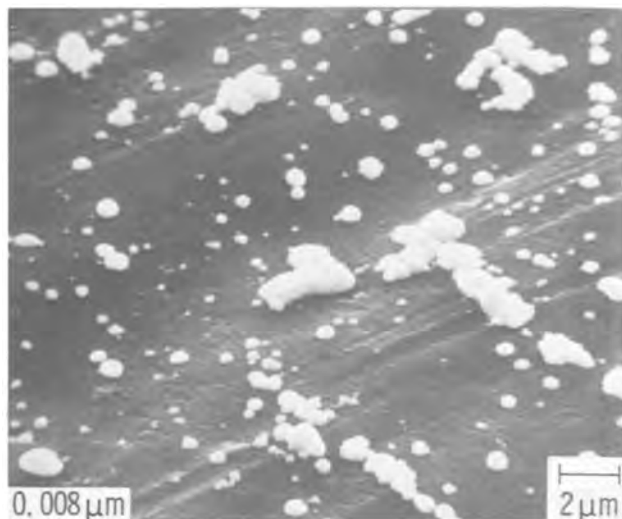

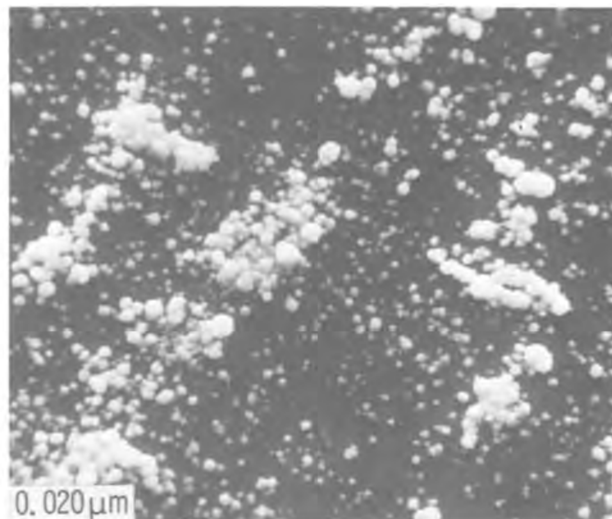

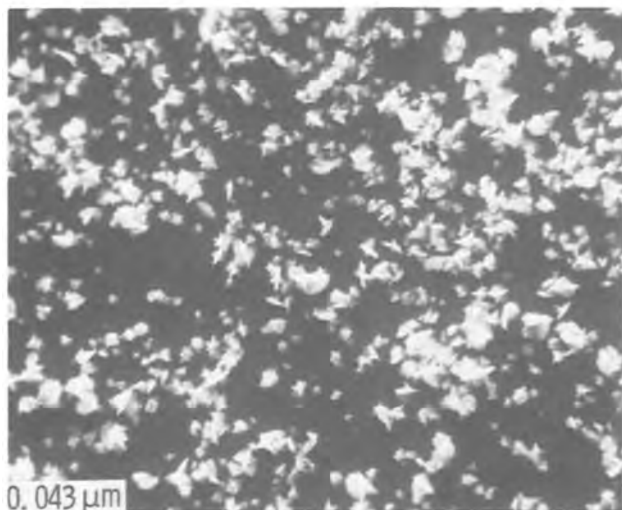

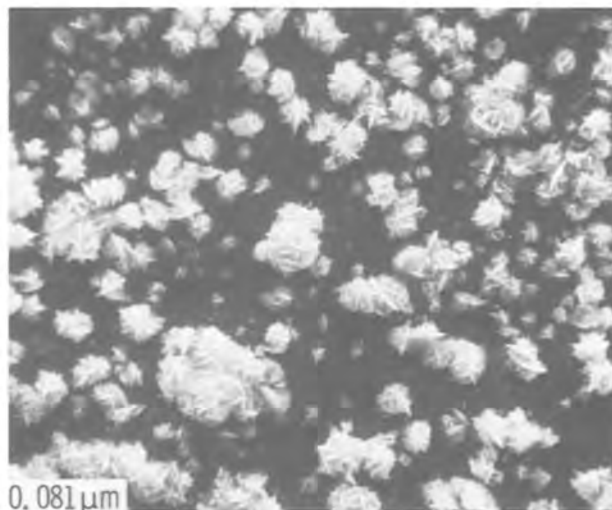

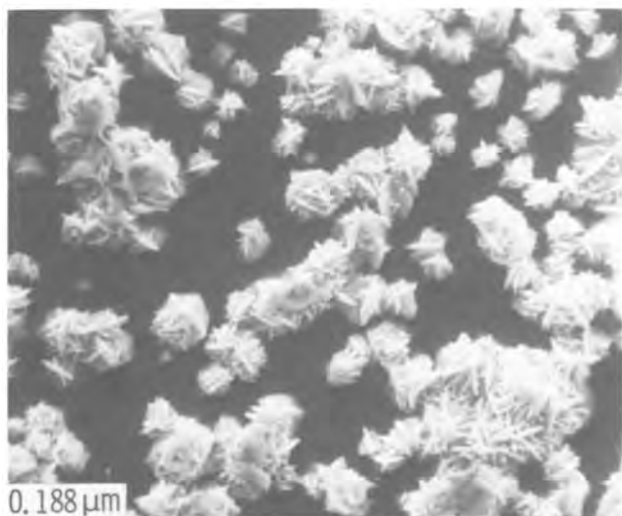

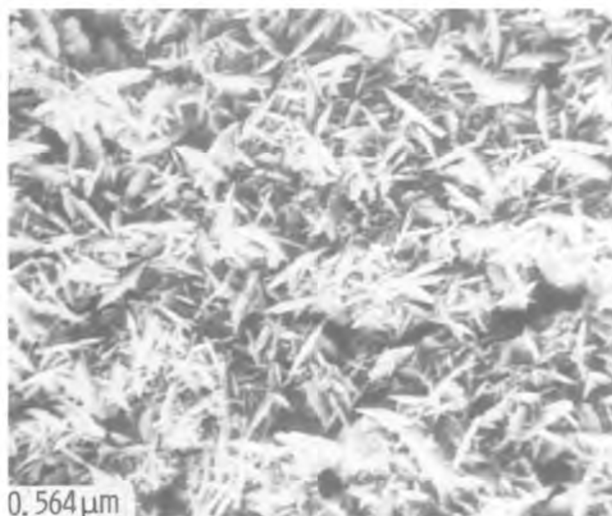

Fig. 4. Morphology of gold deposits. Original magnification 5000 times

$$Al + 4OH^- \rightarrow AlO_2^- + 2H_2O + 3e^-$$

and gold deposition

$$3Au(CN)_2^- + 3e^- \rightarrow 3Au + 6CN^-$$

Semibright to bright gold deposits are plated on 1235 Al in 1 min while a matte gold deposit forms on 1245 Al at a slower rate. However appearance differences had no effect on the measured electrical resistivity.

The suggested composition of the plating bath for immersion gold deposits on relatively pure aluminum is: potassium cyanoaurate (I), 3-5 g/l gold; sodium citrate, 30-60 g/l; pH (sodium hydroxide), 11.2-11.8; temperature, ambient (15-25°C).

Morphology

The gold deposits were examined by scanning electron microscopy. Figure 4 shows the appearance of deposits with an average thickness from 0.008 μm (0.3 μ-in.) to 0.56 μm (22 μ-in.) at 5000 times magnification. These photomicrographs reveal that a gold film of uniform thickness is not formed. Instead the alkaline plating solution attacks the oxide film on the aluminum surface only at specific sites where a tiny nodule of gold initiates. Growth takes place primarily by the formation of nodules at new sites until the amount of gold is equivalent to a film of about 0.02 μm (1 μ-in.) thickness. Further growth then takes place by the formation of long needles of crystalline gold with an aspect ratio of about 10. As the deposit grows, complete surface coverage is achieved at an equivalent thickness of 0.4 μm (15 μ-in.). At that point, some gold needles are as long as 2.5 μm.

Contact Resistance

Electrical contact resistance varies inversely with contact area and applied pressure in the region of relatively high resistance. When two test specimens are joined together in gold-gold contact by adhesive bonding around the perimeter of the gold deposit, contact pressure is essentially zero and contact resistance is found to decrease as the amount of immersion gold deposit is increased. Figure 5 shows that contact resistance is minimized at an equivalent thickness of about 0.04 μm (1.5 μ-in.). This is only 10% of the equivalent thickness required for complete coverage of gold over the aluminum surface.

Other techniques were used for creating an electrical contact on the cleaned aluminum surface, and the d-c resistance of these materials in face-to-face contact was monitored over a period of about six months in air. Comparative data is listed in Table III. The immersion gold deposit has an equivalent thickness of 0.1 μm. The brush-plated gold (electroclean, Cu strike, Ni strike, Au plate) rated high but evidently had some added electrical resistance due to the Ni strike. Most of the

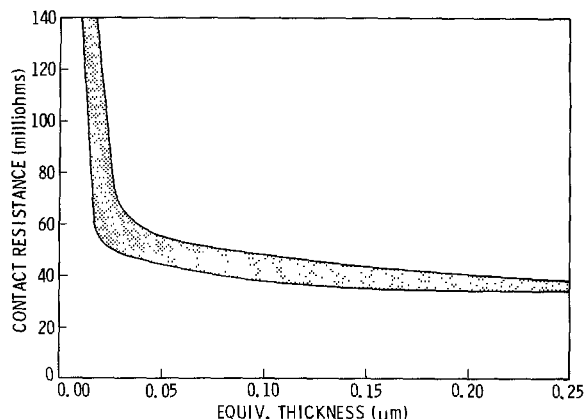

Fig. 5. Gold-gold contact resistance

Table III. Comparison of electrical contact materials

Material	Contact resistance (Ω) average	Contact resistance (Ω) range
Circuit resistance (best contact)	0.085	
Immersion gold	0.13	0.089-0.170
Silver-filled lacquer	0.22	0.128-0.344
Brush-plated gold		0.148-0.359
80% silver in polyester		0.162-0.380
70% silver in PVC		0.251-0.563
Silver-filled RTV silicone		0.137-0.984
Silver-filled contact adhesive	0.43	0.142-1.618
Silver-filled epoxy		0.598-0.982
Chrome pickle (Dow 1)		1.2-2.4
Silver-plated copper in acrylic adhesive		0.782-16*
Silver-filled silicone		1.2-14.5*
Silver in elastomer		1.1-18*
Silver-filled polyurethane		2.8-18*

* Unstable resistance.

other materials tested were electrically conductive coatings based on resins that are highly loaded with silver particles.

Summary

1. Immersion (replacement) gold coatings were deposited on relatively pure (99%) aluminum from an alkaline, cyanide gold plating bath at ambient temperature. Sodium citrate is added to prevent precipitation of aluminum hydroxide and thereby extend the bath life. Tolerance of the bath for accumulated free cyanide was also determined.
2. Metal deposition rate increases with gold content and pH of the plating bath. The maximum deposition rate before the coatings become nonadherent is proportional to the gold content. Coating thickness up to 2.5 μm and average deposition rates up to 0.3 μm/min were studied.
3. Nitric acid (250-400 g/l) at ambient temperature is effective in stripping the natural oxide on aluminum and substituting a fresh, thin, hydrous oxide film prior to plating. The use of this pretreatment is optional and dependent upon the condition of the oxide film on the aluminum surface.
4. The gold deposits are discontinuous and not limited in thickness. The alkaline plating bath penetrates the oxide film at specific sites and causes the nucleation of tiny gold nodules. Growth takes place primarily by the formation of nodules at new sites until the equivalent film thickness is about 200Å. Thereafter, the nodules grow by the formation of needle-like crystals, with an aspect ratio of about 10, until surface coverage is complete (equivalent thickness of 0.4 μm).
5. Immersion gold deposits on aluminum afford a potential means of making electrical contacts for use in environments where moisture is not present. Tests of the electrical contacts show that they exhibit a lower electrical resistance than that of a brush-plated gold or silver-filled resins.

Manuscript submitted March 20, 1978; revised manuscript received May 16, 1978. This was Paper 171 presented at the Pittsburgh, Pennsylvania, Meeting of the Society, Oct. 15-20, 1978.

Any discussion of this paper will appear in a Discussion Section to be published in the June 1979 JOURNAL. All discussions for the June 1979 Discussion Section should be submitted by Feb. 1, 1979.

Publication costs of this article were assisted by Lockheed Palo Alto Research Laboratory.

REFERENCES

1. E. A. Parker, "Gold Plating Technology," Chap. 10, F. H. Reid and W. Goldie, Editors, Electrochemical Publications Ltd., Scotland (1974).
2. H. V. Smith, *Plating Surf. Finish*, **62**, 870 (1975).

"Polymer" Inclusions in Cobalt-Hardened Electroplated Gold

Y. Okinaka,* F. B. Koch, C. Wolowodiuk, and D. R. Blessington[1]

Bell Laboratories, Murray Hill, New Jersey 07974

ABSTRACT

When cobalt-hardened electroplated gold is dissolved in either aqua regia or mercury, carbon-containing inclusions are extracted. The chemical identity of the extracts is established here by a variety of chemical and physical analyses. The indiscriminate use of the word "polymer" to refer to both the original inclusions and the extracts is inaccurate. The "polymer" separated upon dissolution of the gold in aqua regia is not an organic material but a known cobalt cyanide compound with the formula $Co_3^{II}[Co^{III}(CN)_6]_2 \cdot xH_2O$. On the other hand, the extract obtained after dissolution in mercury was shown to contain $K_3Co^{III}(CN)_6$. Based on the observation of the two different extracts and the chemistry of the plating solution, the form of the original inclusions is proposed to be either a Co(II)- or Co(III)-cyanide complex. Additional analyses on the bulk gold and on the aqua regia filtrate led to the following conclusions: (*i*) There is an additional source in the gold deposit for both cobalt and carbon apart from the cobalt cyanide complex. (*ii*) For cobalt, this additional source is the substitutional metallic form. (*iii*) For carbon, the additional source is an as yet unidentified compound probably derived from cyanide ions but containing a C:N ratio greater than one. This compound may be the source of the carbon found in the aqua regia filtrate, and it may account for the extraordinary amounts of hydrogen found in hard gold deposits. (*iv*) Some cautions are necessary in the aqua regia analyses for Co and C because of the limited solubility of "polymer."

It is well documented that hard gold deposits formed in acid cyanide baths with a cobalt salt contain significant quantities of carbon, nitrogen, hydrogen, oxygen, and potassium in addition to cobalt (1-12). Since Munier's original work (1) in which a transparent film was isolated upon dissolution of the gold in aqua regia, it has been widely believed that some "organic polymer" is codeposited in the hard gold. However, the composition of this "polymer" has never been established, nor has the chemical reaction responsible for its formation been identified. A number of speculations have been advanced in the recent literature concerning the nature of incorporated materials. For example, Raub, Knödler, and Lendvay (7) list the following species as possible inclusions: cobalt cyanides, $K_6Co_2(CN)_{10}$, salts of $Co(CN)_5H^{-3}$ and $Co(CN)_5(OH)^{-3}$, H_2O, H_2 gas, AuCN, and K-Au-CN compounds. In their Mössbauer study, Cohen, West, and Antler (13) found no significant amounts of AuCN, $KAu(CN)_2$, or $KAu(CN)_4$ in hard gold. They then suggested that the CN in hard gold is either combined with cobalt or occluded in the plate without forming well-defined gold compounds. Reid (8) speculated that the following substances may be present: $Co(CN)_2$ (or its polymer), $Co(HCN)_4$, $(CN)(NH_2)C:C(NH_2)(CN)$, or the cobalt-coordinated polymer of this substance. More recently, Eisenmann (14) proposed the hypothesis that coordination compounds of cobalt with dicyanoaurate, such as $KCo[Au(CN)_2]_3$ and $Co[Au(CN)_2]_2$, are incorporated in the deposit, and that these compounds are responsible for various properties of the hard gold. The existence of such a variety of speculations without any support of hard analytical data clearly indicates a need for a more definitive work on the subject.

A recent investigation involving two of the present authors (10) has shown that cobalt-hardened gold deposits formed in citrate-based baths contain 5-9 atom percent (a/o) hydrogen. The nuclear analysis technique used would not distinguish between elemental hydrogen (either the dissolved form or gaseous bubbles in the gold) and a chemically combined form.

A Mössbauer study recently performed by Cohen *et al.* (15) has indicated that cobalt is incorporated in two different forms: metallic (*i.e.*, substitutional) and nonmetallic, and that the nonmetallic form is not $Co(CN)_2 \cdot 2.5H_2O$, which precipitates when equivalent amounts of Co^{+2} and CN^- ions are mixed together (16).

In the present investigation, a large amount of gold was plated under controlled conditions to extract the "polymer" in a quantity sufficient to carry out repetitive quantitative chemical analyses as well as x-ray diffraction and infrared spectroscopy examinations. Since it was thought probable that aqua regia may alter the composition of the inclusions because of its strong acidity and oxidizing power, the gold was also dissolved in mercury, and the residue analyzed by both chemical and physical methods. Based on the results of these experiments, an attempt was made to deduce chemical identities of the species in the as-incorporated form and chemical reactions which occur during the dissolution processes.

Experimental

Sample preparation.—Cobalt-hardened gold deposits were plated from a bath containing a potassium citrate buffer of pH 4.0, a cobalt(II) salt, and potassium cyanoaurate(I). The concentration ranges were essentially the same as those used in previous studies (9) (8.2 g/liter of Au as $KAu(CN)_2$, 110 g/liter citric acid, 50 g/liter KOH, and 0.1 g/liter Co as $CoSO_4$). Here, however, the gold concentration was increased approximately by a factor of two in order to allow the formation of bright, hard deposits at an increased current density. The bath was operated at 65°C and at a cathode current density of 50 mA/cm². A copper sheet cathode (1.5 × 1.5 × 0.002 in. or approximately 3.8 × 3.8 × 0.005 cm) was plated in a cell which was equipped with platinum sheet anodes and a magnetic stirrer and contained 3 liters of the plating solution. The concentrations of various bath constituents were maintained within about ±5% during plating using an automatic analyzer and controller designed

* Electrochemical Society Active Member.
[1] Present address: Bausch and Lomb, Rochester, New York 14600.
Key words: gold electrodeposition, cobalt cyanides, codeposited impurities.

and constructed recently in this laboratory (17). A number of copper cathodes were plated successively with about 5g of gold on each. These plated cathodes were cut into small pieces and treated in aliquots of boiling 1:1 HNO_3 in order to dissolve away the copper completely. The complete removal of copper was confirmed by atomic absorption spectrometry.[2] The pieces of gold deposits thus obtained were thoroughly rinsed in boiling deionized water, dried at 110°C, and used in the experiments described in the subsequent sections.

Analysis techniques.—Chemical analyses were performed on the gold deposit itself as well as on residues and filtrates obtained in the aqua regia and mercury dissolution experiments described below. Potassium and cobalt in solutions were determined by atomic absorption spectrometry. In the aqua regia insoluble "polymer" residue, Co was determined by a gravimetric method involving ignition to Co_3O_4 or by the atomic absorption method after dissolution in a solution containing NaOH and NaCN. Carbon was determined either by the combustion technique[3] or by the wet persulfate method.[4] Hydrogen and nitrogen determinations were made using the standard microelemental analysis techniques.[3]

The extracts obtained after gold dissolution were also characterized by a number of physical analyses. These included (*i*) x-ray diffraction (by the Debye-Scherrer technique on extract powder contained in glass capillaries), (*ii*) infrared absorption (using a mull of the extract powders in mineral oil), and (*iii*) thermogravimetric analysis (to investigate both the reversible loss of water of hydration and the irreversible decomposition of the extract powders). The x-ray diffraction analyses were done with either Co or Cr radiation to avoid exciting cobalt fluorescent radiation from the sample. In order to check for the presence of trapped plating solution in the plated gold, the deposited foils (stripped from the copper substrate by 1:1 nitric acid) were subjected to differential scanning calorimetry.[5] By this method, the latent heat of fusion of any possible trapped solution would be detected as the temperature of the sample was cycled through the freezing point. A 10 mg sample of mercury on the reference pan provided a calibration of the observed signal in terms of millicalories from the heat of fusion.

Aqua regia extraction method.—About 20g of the gold deposit was carefully weighed and placed in a beaker containing 250 ml of 1:1 aqua regia. The contents were allowed to stand at room temperature overnight to achieve complete dissolution of the gold. After this treatment, the presence of an insoluble residue was evident on the bottom of the beaker. It was observed that a large portion of this residue retained the shape that the gold sample had before dissolution. After filtration through a preweighed, 0.2 μm, Millipore filter and thorough rinsing with water, the "polymer" had a distinct pink color. It was air-dried overnight at room temperature; at this point the weight was 40 mg. The "polymer" was then analyzed quantitatively for Co, C, H, N, Au, K, and water content. The entire plating-extraction process and analyses were repeated several times. An x-ray diffraction analysis and infrared spectroscopy were also carried out. The filtrate was diluted to 1 liter and analyzed for Co, C, and K.

Mercury extraction method.—The dissolution in mercury of the gold electrodeposits was carried out in an inert atmosphere to prevent oxidation by air of the mercury or any extracted compounds. To accomplish this, a closed, round bottomed, 50 ml flask with three ports was used. One port admitted flowing nitrogen gas, the second vented the nitrogen through a reflux tube, and the third held a thermometer. The exiting nitrogen was bubbled through water to prevent back diffusion of air. The flask, containing 5g of the gold and about 450g of mercury, was heated to 150°C in the flowing nitrogen atmosphere and held for 1 hr to insure complete dissolution. The flask was then cooled and a floating, gray powder extract was recovered from the surface of the mercury. A portion of this powder was removed with a stainless steel spatula and ground in a mortar and pestle to separate out most of the liquid mercury which was mixed in with the extract. During grinding, droplets of the liquid metal were formed and easily removed.

When the x-ray diffraction and *IR* identification of this extract indicated a water-soluble cyanide compound was present, the method of removing the extract from the surface of the mercury was modified. In this alternate extraction technique, 10 ml of water was introduced into the flask after the amalgam had cooled to room temperature. The sample was vigorously shaken to dissolve the extract and the resulting solution decanted off. This water addition procedure was repeated several more times to insure complete removal of the water-soluble component. The resulting solution was then diluted to a total volume of 100 ml and then chemically analyzed using procedures similar to those described above for the aqua regia extract.

Results and Discussion

Analysis of aqua regia extract.—Chemical analyses.—The results of quantitative analyses of the aqua regia "polymer" are listed in Table I along with calculated values for the composition of two likely compounds. An atomic absorption analysis of the "polymer" dissolved in an alkaline NaCN solution did not show the presence of K or Au. Compound (A) is $Co^{II}(CN)_2 \cdot 2H_2O$,[6] a simple pink cobalt(II) cyanide which was prepared and analyzed by Poskozim (16), while compound (B) is $Co_3^{II}[Co^{III}(CN)_6]_2 \cdot xH_2O$,[6] which was prepared and characterized by several investigators (18-20). Values ranging from 12 to 19 have been assigned to x, but a value of 16 was chosen here in agreement with Shriver and Brown (18, 19). There are three reasons why compound (B) is the more likely identification. First, the over-all composition of the "polymer" fits (B) considerably better than (A), especially for the cobalt content. Second, the reversible loss of water of hydration does not agree with that found by previous investigators (16) for (A). Finally, compound (B), hydrated cobalt(II) hexacyanocobaltate(III) is known to form upon mixing equivalent amounts of aqueous solutions of $CoSO_4$ or $CoCl_2$ and $K_3Co(CN)_6$ (18, 19) and also as an intermediate when aquo Co^{+2} ions are simply allowed to react with CN^- ions under certain conditions (20).

[6] A cobalt cyanide with the formula $Co(CN)_2 \cdot 2.5H_2O$ is also known (16). It is a gray compound, and its calculated composition does not agree with the observed values. Also, the Mössbauer spectrum of this compound did not agree with that of the "polymer" (15).

Table I. Elemental analysis of "polymer" extracted by aqua regia treatment

	% Found*	% Calculated	
		Compound (A) $Co(CN)_2 \cdot 2H_2O$	Compound (B) with $x = 16$ $Co_3[Co(CN)_6]_2 \cdot xH_2O$
Co	32.7 ± 2.1	40.10	32.92
C	17.1 ± 0.7	16.34	16.10
N	18.1 ± 0.7	19.06	18.78
H	3.0 ± 0.4	2.72	3.57
% Weight loss at 110°C	19.8 ± 0.5	9.80 (−0.8 H_2O)	20.1 (−10 H_2O)

* Averages of three determinations.

[2] If copper is not completely removed at this stage, it precipitates as part of the "polymer" giving it a greenish tinge.
[3] Schwartzkopf Microanalytical Laboratories.
[4] Total Carbon System manufactured by Oceanography International.
[5] Du Pont Differential Thermal Analyzer, Model 900.

Moreover, compound (A) is apparently unstable and easily undergoes a partial oxidation to compound (B) (20, 21). For these reasons, it is concluded that the "polymer" is a well-defined cobalt compound (B) rather than (A) or an organic compound. It should be noted, however, that an unequivocal assignment of a number to x is not possible based on the elemental analysis alone because an equally good agreement between observed and calculated values is found with $X = 13\text{-}18$. Additional evidence supporting compound (B) for the "polymer" is described in subsequent sections.

X-ray diffraction and IR analyses of "polymer".—The result of an x-ray diffraction analysis is tabulated in Table II. The excellent agreement with the ASTM values listed for $Co_3[Co(CN)_6]_2 \cdot xH_2O$ and the values obtained with this compound prepared by mixing solutions of $K_3Co(CN)_6$ and $Co(NO_3)_2$, (called "synthetic polymer" in Table II) along with the chemical analysis results described above, can be considered as a conclusive proof for the proposed structure of the "polymer." The *IR* spectra of this compound showed a sharp absorption peak at 2180 cm^{-1} and a shoulder at 2130 cm^{-1} attributable to cyanide stretching and vibrations (20).

Thermal stability and loss of water of hydration of "polymer".—In repeated drying cycles, the pink polymer was heated to 110°C in an air oven and then allowed to cool and reabsorb moisture from the atmosphere. In each cycle the color changed to a bright blue in the dried form and then back to pink again as water was reabsorbed. The change of weight in drying determined by repeated weighings was a well-defined value of 19.8 ±0.5% of the original polymer weight. This value is in good agreement with the value of 20.1% calculated if compound (B) with $x = 16$ lost ten of its water of hydration molecules.

A more complete picture of the thermal stability was obtained by the thermogravimetric analysis shown in Fig. 1. This figure shows the loss in weight of the "polymer" in two stages of dehydration: the reversible loss discussed in the previous paragraph and a second stage of dehydration which occurs in the range 150°-450°C. The diffraction patterns obtained after both stages of dehydration showed very little difference from the original pattern reported in Table II; the same cubic pattern is obtained with only an increase of the lattice constant of less than 0.1%. After dehydration at 400°C, the "polymer" was black and remained black even after reabsorbing some moisture when exposed to ambient air at room temperature. The large loss in weight seen in the temperature range 450°-525°C corresponds to decomposition. The observed weight losses seen in Fig. 1 fit the values calculated from the formula weight of the compound $Co_3^{II}[Co^{III}(CN)_6]_2 \cdot xH_2O$ very well as indicated on the figure. The weight of the residue left at 525°C (after decomposition) is somewhat greater than the weight of the cobalt present; probably this residue is a combination of cobalt and cobalt oxide formed by exposure to the air.

Table II. Diffraction patterns from polymer

"Polymer" d	"Polymer" Int.	"Synthetic polymer"* d	"Synthetic polymer"* Int.	Calculated** h,k,l	Calculated** d	$Co_3[Co(CN)_6]_2 \cdot xH_2O$† d	$Co_3[Co(CN)_6]_2 \cdot xH_2O$† Int.
5.81	30	5.84	20	111	5 82	5.90	5
5.05	100	5.05	100	200	5.03	5.10	100
3.94	20						
3.57	80	3.59	70	220	3.55	3.61	50
3.04	20			311	3.03	3.08	2
2.71	20			222	2.895	2.947	2
2.51	60	2.53	60	400	2.51	2.55	40
2.25	50	2.27	60	420	2.25	2.28	25
2.06	30	2.07	20	422	2.05	2.086	8
1.95	10			511,333	1.94	1.968	2
1.78	30	1.79	40	440	1.78	1.808	15
1.678	30	1.69	40	442,600	1.679	1.704	10
1.595	30	1.599	40	620	1.593	1.616	10
1.518	10			622	1.519	1.541	2
1.456	10			444	1.454		
1.397	20	1.404	30	640	1.397		
1.347	20	1.353	30	642	1.346		
1.225	10	1.228	30	820,644	1.222		
1.188	10			660,822	1.188		
1.076	10			664	1.074		

* Prepared by treating $K_3Co(CN)_6$ with Co^{+2}.
** Cubic, ao = 10.07A.
† ASTM 22-215, Cubic, ao = 10.22A.

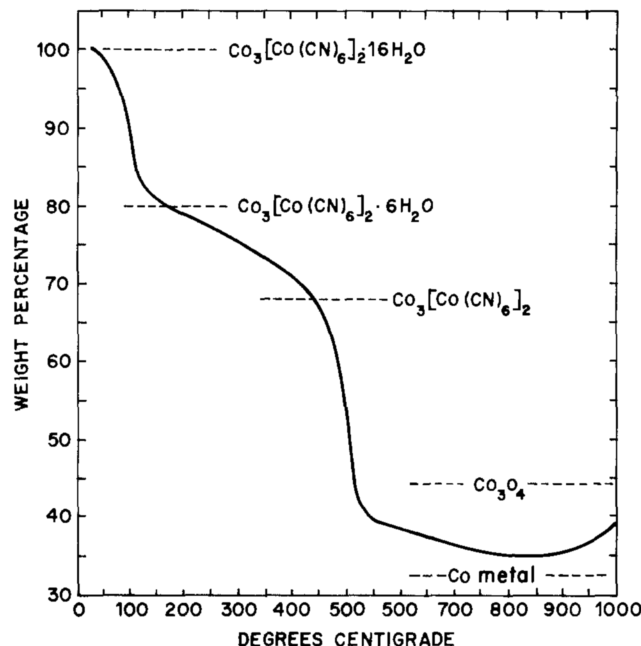

Fig. 1. Thermogravimetric analysis of "polymer"

Chemical analyses of aqua regia filtrate.—The aqua regia filtrate was analyzed for Co and C. The results are listed in Table III (first column) in weight percent (w/o) of deposit, in which the amounts of these elements found in the "polymer" are also tabulated. The sums of the amounts found in the "polymer" and in the filtrate are compared with the results of conventional deposit analyses, in which a small amount of gold deposit (<5 mg) was dissolved in 10 ml of 1:1 aqua regia and analyzed for Co by the atomic absorption method and for C by the persulfate method. Excellent agreement was obtained for both elements between the calculated sum and the total analysis result. It should be noted that this agreement can be expected only under the conditions where the "polymer" completely dissolves in aqua regia, because Co or C present in solid particles are not measured in the analytical techniques used. The solubility of the "polymer" in 1:1 aqua regia determined by the atomic absorption method was equal to 0.38 ppm as Co at room temperature. Thus, a simple calculation shows that for a deposit containing about 0.1 w/o of Co, the sample weight should not exceed about 4 mg per 10 ml of 1:1 aqua regia.

The comparison of analytical results for carbon in Table III is of great interest. The "polymer" contains only about 20% of the total carbon, the remainder being dissolved in the aqua regia. The question arises then as to the identity of the compound containing

Table III. Analysis of aqua regia filtrate, "polymer", and gold deposit for Co and C (results are expressed in weight percent of deposit)

	Filtrate	"Polymer"	Filtrate + "polymer"	Deposit
Co(%)	0.037	0.065	0.102	0.11 ± 0.02
C(%)	0.12	0.034	0.164	0.16 ± 0.01

Table IV. Molar ratios of C to N in "polymer", filtrate, and gold deposit

(Analysis results are expressed in weight percent of deposit)

	"Polymer"	Filtrate	Deposit
C(%)	0.034	0.13	0.16
N(%)	0.036	0.049*	0.085
C:N	1:0.91	1:0.32	1:0.46

* Calculated as difference since N is masked by NO_3^- in aqua regia.

the filtrate carbon. In this respect, it is of interest to compare the molar ratios of carbon to nitrogen in the "polymer," filtrate, and deposit (Table IV). The C to N ratio in cobalt-hardened gold deposits has been extensively investigated by Raub, Knödler, and Lendvay (7), who found that it ranges from 1:0.47 to 0.62. The ratio that we found, 1:0.46, is thus similar to these previously reported values. In the "polymer," the ratio found was 1:0.91 (±0.07), the deviation from 1:1 being considered as an experimental error. These values yield a C/N ratio of 1:0.32 (≃3:1) for the substance dissolved in the filtrate.[7] Thus, it appears that the filtrate soluble compound is not a simple polymer of HCN, such as $(HCN)_4$, which has been said to form at the anode in the plating bath and codeposit with gold (22). Free cyanide ions will not survive in aqua regia and gold cyanide species do not seem to exist. Further work is needed to identify this C-containing compound.

The filtrate was also analyzed for K. All K was in the filtrate, and the K content of this particular gold deposit was found to be 0.08 w/o.

Analysis of mercury extract.—The identification of the "polymer" from the aqua regia extract leaves the question as to whether the "polymer" itself is the compound incorporated in the deposit, or whether it is a product formed from other materials as a result of a reaction in aqua regia. A Mössbauer spectroscopic study carried out by Cohen *et al.* (15), showed that the spectrum of the aqua regia extracted "polymer" does not agree with that of the cobalt-containing species recorded with the gold deposit itself. Clearly, the "polymer" is a product of some chemical reaction(s) occurring during the dissolution in aqua regia. The mercury dissolution experiment was performed in the hope that the included materials might be extractable without being altered chemically.

The mercury-insoluble material which floated on the surface was analyzed chemically after extraction in water and by x-ray diffraction before the extraction. Duplicate dissolution/extraction experiments gave the following results (weight percent of the deposit): K, 0.081 ± 0.002; Co, 0.047 ± 0.001; C, 0.063 ± 0.002; and Au, 0.013 ± 0.001. These values yield the molar ratio K:Co:C:Au = 2.6:1:6.6:0.08, which is indicative of the formula $K_3Co(CN)_6$. Evidently, gold is not a major component of the water-soluble material.

[7] The contribution of the solubility of the "polymer" (0.38 ppm Co or 0.19 ppm C) is negligible as compared to 26 ppm C found in the filtrate.

Table V. Diffraction pattern from mercury extract

Observed d	Observed Int.	$K_3[Co(CN)_6]$* d	$K_3[Co(CN)_6]$* Int.
		6.63	2
		5.86	6
		5.15	20
4.05	m	4.08	100
		3.69	2
		3.33	2
3.03	w	3.04	90
2.91	w	2.92	90
2.60	w	2.61	90
2.16	vw	2.17	10
2.05	vw	2.07	50
		1.86	10
		1.84	40

* ASTM 15-586.

The x-ray diffraction lines observed are summarized in Table V. The lines could be indexed only as originating from potassium hexacyanocobaltate(III), $K_3Co(CN)_6$. Based on this result together with the chemical analysis results, it is concluded that the water-soluble cobalt compound remaining after the mercury dissolution is $K_3Co(CN)_6$.

An attempt was made to analyze the water-insoluble residue and the gold amalgam for cobalt and carbon, but difficulties were encountered in quantitatively separating the residue from mercury and in determining a small amount of cobalt in the large amount of mercury. Qualitatively, however, the results showed that the water-insoluble residue contained carbon and a trace of cobalt, while a much greater amount of cobalt was present in the mercury. It appears that the unidentified C-containing compound is largely insoluble in water, and that the mercury contains metallic cobalt in the form of a two phase mixture or an amalgam.

Relationship between aqua regia and mercury extracts.—The amount of aqua regia or mercury extracts observed is too great to result from simple physical entrapment of plating solution;[8] it must therefore result from some more active chemical process of inclusion. On the basis of the results presented in the preceding sections and the additional considerations of the chemistry of the cobalt-cyanide system described below, an attempt is made here to formulate a reaction scheme for the incorporation and extraction processes. The gold deposition reaction generates cyanide ions at the cathode surface

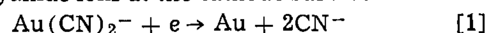

$$Au(CN)_2^- + e \rightarrow Au + 2CN^- \quad [1]$$

At the low pH(≃4) of the plating solution, the CN^- ions readily combine with H^+ to form HCN ($H^+ + CN^- \rightleftharpoons HCN$; $K = 2.5 \times 10^9$ (23)). Simple calculations show that the total cyanide ($CN^- + HCN$) concentration at the cathode surface is in great excess over the concentration of cobalt under the ordinary plating conditions. For example, taking a limiting reduction current of about 4 mA/cm^2 for 0.0045M $KAu(CN)_2$ under moderate agitation conditions (24), and for a typical bath containing 8.2g of Au/liter (≡0.042M) and a plating current of 10 mA/cm^2 with about 40% current efficiency, the surface concentration of cyanide ($CN^- + HCN$) is estimated to be 0.023M. On the other hand, the cobalt concentration at the surface must be less than the bulk concentration (100 ppm or 0.0017M). Under the conditions of high speed plating, the difference between cyanide and cobalt concentrations becomes even greater because of the higher plating current. In view of the presence of such a large excess of cyanide and the high stability of Co(II)-cyanide complexes (25), it is reasonable to assume that the aquo Co^{+2} ions originally present in the bath form anionic cyanide complexes at the cathode surface. It is also apparent from the results of a Mössbauer study (15) and the aqua regia dissolution experiment that part of the cobalt is reduced to the metallic state to form an alloy with gold, while the remainder is incorporated in the deposit in some form of cyanide compound.

Two known Co(II)-cyanide ions are $Co^{II}(CN)_4^{-2}$ and $Co^{II}(CN)_5^{-3}$ (or their hydrated forms) (26-28). Both of these ions have been shown to adsorb strongly on mercury (28). In the presence of excess cyanide $Co^{II}(CN)_5^{-3}$ is likely to be predominant. The

[8] Differential scanning calorimetry was unable to detect any latent heat of freezing from trapped plating solution in the gold deposit. Calibration with a 10 mg droplet of mercury established that a peak of 10^{-3} cal in the 100 mg sample would have been observed corresponding to an upper limit of 10^{-2} w/o trapped plating solution. The contribution of plating salts from such a small volume of solution (10^{-3}-10^{-4} w/o) is negligible compared to the amounts of extract actually observed (Tables III and IV).

$Co^{II}(CN)_6^{-4}$ ion, which appears in the older literature, apparently does not exist in aqueous solutions (21). The $Co^{II}(CN)_5^{-3}$ ion is known to undergo oxidation to $Co^{III}(CN)_6^{-3}$ when excess cyanide is present either due to dissolved oxygen or by the reaction (21)

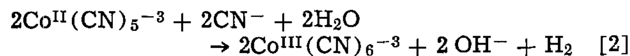

$$2Co^{II}(CN)_5^{-3} + 2CN^- + 2H_2O \rightarrow 2Co^{III}(CN)_6^{-3} + 2\,OH^- + H_2 \quad [2]$$

One may inquire when the transition from Co^{II} in the plating solution to Co^{III} in the extracts occurs. Under these circumstances, two possibilities are conceivable: (*i*) cobalt is incorporated as $Co^{II}(CN)_5^{-3}$ along with CN^- and H_2O, and it is oxidized to $Co^{III}(CN)_6^{-3}$ during the aqua regia or mercury extraction process, or (*ii*) the oxidized ion, $Co^{III}(CN)_6^{-3}$, is the incorporated species. In either case, the anions must attract cations as counterions to maintain electroneutrality, and therefore K^+ ions can be incorporated with the anions. Cohen *et al.* (15) made an attempt to identify $K_3Co^{III}(CN)_6$ in the gold deposit by Mössbauer spectroscopy, but no straightforward conclusion could be drawn because of the complex nature of the spectrum of this compound. Additional work would be necessary to distinguish the two possibilities mentioned above, but for practical purposes it is perhaps immaterial whether the cobalt is present in the divalent or trivalent form. From all of the considerations discussed above, the reactions at the gold surface and subsequent incorporation of cobalt species can be summarized as shown in the first two columns of Fig. 2. For the sake of simplicity, we shall assume in subsequent discussions that $Co^{III}(CN)_6^{-3}$ is present in the deposit.

When the deposit containing $Co^{III}(CN)_6^{-3}$ and metallic cobalt alloyed with gold is dissolved in mercury, a salt of this ion is isolated. The alloyed cobalt is probably present as a finely divided suspension in the mercury rather than a true amalgam as discussed by Hansen (29). These reactions are shown in the third column of Fig. 2.

When the deposit is dissolved in aqua regia, the metallic cobalt forms the divalent aquo cobalt ion, which combines with $Co^{III}(CN)_6^{-3}$ to produce a precipitate of $Co_3^{II}[Co^{III}(CN)_6]_2 \cdot xH_2O$, now identified as the "polymer." These reactions are depicted in the last column of Fig. 2. It should be noted that only two out of the five cobalt atoms in this compound result from the cobalt-cyanide species in the deposit, the remainder originating from the alloyed cobalt. In Table III, it was shown that the total cobalt content of the "polymer" corresponded to 0.065% of the deposit sample. Out of this, only 0.026% originated from the cyanide complex. The amount of cobalt which was present as the gold alloy is then the sum of the difference between these two values and the cobalt content found from the filtrate (0.037%, Table III). Thus, the cobalt from the alloy corresponds to

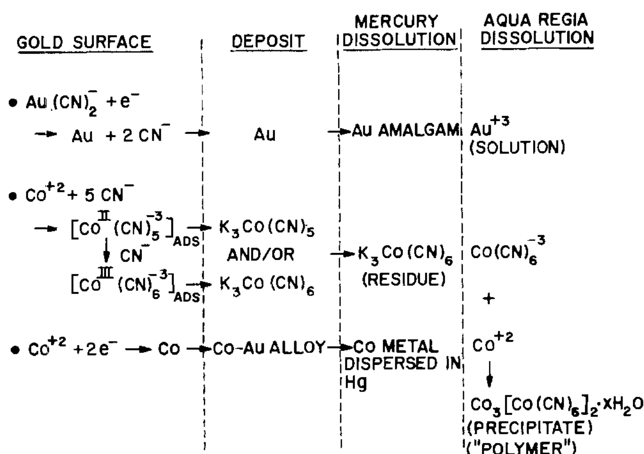

Fig. 2. Reaction paths of gold, cobalt, and cyanide

(0.065-0.026) + 0.037 = 0.076% of the deposit, and the ratio of the two types of cobalt (cyanide complex/alloy) becomes approximately equal to 1:3 in agreement with Mössbauer studies by Cohen *et al.* (15). Reid (8) reported that only about one-sixth of total cobalt is associated with this "polymer." This difference may well be due to the greatly different plating conditions used. Effects of plating conditions and bath age on the content of the two kinds of cobalt (and carbon) are currently being investigated in order to obtain understanding of the effect of the incorporated species on the properties of the deposit.

Relationship between inclusions, structure, and physical properties.—Okinaka and Nakahara (9) previously made a transmission electron microscopic (TEM) study of hard gold deposits, in which such deposits were shown to contain a large number of nonmetallic inclusions measuring about 25-70Å. In the absence of the knowledge concerning the composition of these inclusions, it was assumed that these objects represented molecules and agglomerates of the "polymer." The present study shows that the aqua regia "polymer" is a cobalt compound formed in the process of dissolving the deposit and that it does not exist in the as-plated deposit. We believe that the nonmetallic objects observed in the TEM study are perhaps molecules or agglomerates of the as-yet unidentified C-containing species, which accounts for part of the total carbon content as described in the preceding section. At present, however, the alternative that these objects are pockets of hydrogen gas has not been eliminated. More work needs to be done to identify this substance.

It is generally recognized that all hard gold deposits consist of very fine grains (100-500Å). Such fine grains result from the fact that nucleation is favored over crystal growth during the deposition process. It may be speculated that the adsorption of Co-cyanide complex on the gold surface inhibits the grain growth, bringing about the hardness of the deposit. This view is consistent with the work done by Lo and Pinnel (30) which shows that the hardening by alloying with cobalt is not sufficient to account for the observed hardness of hard gold deposits, and that the grain refining is the major factor contributing to the hardness.

Summary and Conclusions

1. Results of this investigation conclusively show that two kinds of cobalt and two kinds of carbon exist in the cobalt-hardened gold deposit. Cobalt is present partly in the form of an anionic Co(II) or Co(III)-cyanide complex in an adsorbed state and partly in the form of a gold alloy. Carbon is present partly in the above complexes and partly as an unidentified compound.

2. The so-called "polymer" isolated upon dissolution of the deposit in aqua regia has been found to be a cobalt compound with the formula $Co_3[Co(CN)_6]_2 \cdot xH_2O$, which apparently forms upon combination of the Co^{+2} ions from the alloyed cobalt and the $Co(CN)_6^{-3}$ ions. The latter may be originally in the deposit or may form from $Co^{II}(CN)_5^{-3}$ and CN^- during the dissolution process.

3. The residue obtained on dissolution of the deposit in mercury contains $K_3Co(CN)_6$.

4. In carrying out the conventional analysis of the deposit for total cobalt after dissolution in aqua regia, it is important to use a minimal amount of the gold (~4 mg in 10 ml of 1:1 aqua regia) to insure complete dissolution of cobalt because of the limited solubility of the cobalt compound.

5. Customarily, only total Co and C are analyzed with relatively small amounts of samples. Without the knowledge of the role of the two different types of each element, attempts to correlate results of the total analyses with deposit properties may be futile. More work is required to differentiate the functions of the two types of cobalt and carbon.

Acknowledgments

We are grateful to L. N. Schoenberg, R. L. Cohen, and R. Sard for discussion of the results of this study and to P. K. Gallagher for his assistance with the thermogravimetry and differential thermal analysis.

Manuscript received May 8, 1978.

Any discussion of this paper will appear in a Discussion Section to be published in the June 1979 JOURNAL. All discussions for the June 1979 Discussion Section should be submitted by Feb. 1, 1979.

Publication costs of this article were assisted by Bell Laboratories.

REFERENCES

1. G. B. Munier, *Plating*, **56**, 1151 (1969).
2. M. J. Vasile and D. L. Malm, *Anal. Chem.*, **44**, 650 (1972).
3. J. Holt and J. Stanyer, *Trans. Inst. Metal Finishing*, **50**, (1), 24 (1972).
4. L. Holt, R. J. Ellis, and J. Stanyer, *Plating*, **60**, 910 (1973).
5. L. Holt, R. J. Ellis, and J. Stanyer, *ibid.*, **60**, 918 (1973).
6. M. Antler, *ibid.*, **60**, 468 (1973).
7. Ch. J. Raub, A. Knödler, and J. Lendvay, *ibid.*, **63**, 35 (1976).
8. F. H. Reid, American Electroplaters' Society Fifth Plating in the Electronics Industry Symposium, New York, March 24-25, 1975, p. 67.
9. Y. Okinaka and S. Nakahara, *This Journal*, **123**, 1284 (1976).
10. F. B. Koch, D. R. Blessington, C. W. White, G. J. Clark, D. D. Allred, and D. R. Appleton, To be published.
11. E. Raub, Ch. J. Raub, A. Knödler, and H. P. Wiehl, *Werkst. Korro.*, **23**, 643 (1972).
12. A. Knödler, *Galvanotechnik*, **68**, 383 (1977).
13. R. L. Cohen, K. W. West, and M. Antler, *This Journal*, **124**, 342 (1977).
14. E. T. Eisenmann, *ibid.*, **124**, 1957 (1977).
15. R. L. Cohen, F. B. Koch, L. N. Schoenberg, and K. W. West, To be published.
16. P. S. Poskozim, *Inorg. Nucl. Chem. Lett.*, **5**, 933 (1969).
17. Y. Okinaka, D. W. Graham, C. Wolowodiuk, and T. M. Putvinski, *Western Electric Engineer*, **22** (2), 72 (1978).
18. D. F. Shriver and D. B. Brown, *Inorg. Chem.*, **8**, 42 (1969).
19. D. B. Brown and D. F. Shriver, *ibid.*, **8**, 37 (1969).
20. P. S. Poskozim, R. Shute, R. Taylor, and J. Wysocki, *J. Inorg. Nucl. Chem.*, **35**, 687 (1973).
21. B. M. Chadwick and A. G. Sharpe, in "Advances in Inorganic Chemistry and Radiochemistry," Vol. 8, pp. 83-176 (1966).
22. H. G. Silver, *This Journal*, **116**, 591 (1969).
23. W. N. Latimer, "Oxidation Potentials," 2nd ed., p. 137, Prentice-Hall, New York (1952).
24. H. Y. Cheh and R. Sard, *This Journal*, **118**, 1737 (1971).
25. "Stability Constants," Special Publication No. **17**, p. 109, The Chemical Society, London (1964).
26. W. P. Griffith and G. Wilkinson, *J. Chem. Soc. (London)*, 2757 (1959).
27. D. N. Hume and I. M. Kolthoff, *J. Am. Chem. Soc.*, **71**, 867 (1949).
28. H. S. Lim and F. C. Anson, *J. Electroanal. Chem.*, **31**, 297 (1971).
29. M. Hansen, "Constitution of Binary Alloys," 2nd ed., p. 477, McGraw-Hill Book Co., New York (1958).
30. C. C. Lo and M. R. Pinnel, To be published.

Fluorenone Derivatives as Electron Transport Materials

The Relationship of Electron Affinity and Electrochemistry with Photoelectric Behavior

James E. Kuder, John M. Pochan, S. Richard Turner, and DarLyn F. Hinman

Xerox Corporation, Joseph C. Wilson Center, Webster, New York 14580

ABSTRACT

Electrochemical and charge transfer studies were used to determine the electron affinities (EA) of fifteen electron acceptor compounds. The behavior of these materials as electron transport species was evaluated by the photoinduced discharge curve (PIDC) method. The relation between the PIDC results and such electrochemical information as reversibility of the charge transfer step and polarization effects is discussed and it is shown that irreversible electrochemistry correlates with deep trapping phenomena. In addition, the results are discussed in terms of a simple model which relates electron affinity to charge carrier mobility.

Electrical conduction in organic solids is a widespread phenomenon whose implications extend from biological processes to such technological applications as electrophotography. The latter, in particular, has stimulated considerable research activity, including the study of disordered amorphous systems which consist of solid solutions of hole or electron transporting materials in various binders (1-5). A key question in any of these studies is to what degree the properties of the isolated molecules are reflected in the observed electrical transport behavior of the composite solids.

Unfortunately, the answer is not straightforward, in part because of the limited degree of variation in molecular properties reported in any given study. In one such study, an apparent correlation was observed between xerographic discharge rate and the reduction potential of the guest compound in a poly(vinylcarbazole) matrix (6). Another literature example cites a qualitative trend between the electron affinity of the acceptor compound and dark decay in complexes of dibenzothiophene and various fluorenone derivatives (7). At higher electron affinities the dark decay masked any contribution of the acceptor compound to the photocurrent.

In molecularly doped systems charge transport is thought to be due primarily to hopping of holes or electrons between active sites. On a molecular basis this may be regarded as the acquiring of charge by a neutral species in the charge injecting step

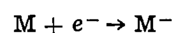

$$M + e^- \rightarrow M^-$$

and the exchange of charge between identical species

Key words polymers, photoconductivity, polarography, semiconductor, voltammetry, mobility.

in the transport step

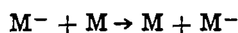

$$M^- + M \rightarrow M + M^-$$

It might also be expected that with certain molecules the process described above might lead to an unstable chemical species which affects the ultimate electrical properties of the system, *i.e.*

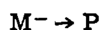

$$M^- \rightarrow P$$

where P may be a charge trapping species.

Since the steps described above are similar to those that take place in an electrochemical experiment, a correlation between the electrochemical behavior of the dopant and its observed transporting properties might be expected.

In the following, we describe the results of such a study where the electrochemical properties of a series of substituted fluorenones and other materials thought to be active electron transporting materials are compared with their transport properties in a polymeric matrix. Additionally, the electron affinities (EA) determined via electrochemistry and charge transfer spectra are correlated with a proposed theory of transport as well as the observed transport properties of the materials dispersed in a polymeric matrix.

Experimental

Synthesis.—Synthesis of new acceptor compounds are described below. Others were either commercially available or were prepared by published techniques. Melting points are uncorrected.

4,5,7-Trinitrofluorenone-2-carboxylic acid chloride.—A 200 ml round-bottomed flask was charged with 10.0g (0.028 mole) of 4,5,7-trinitrofluorenone-2-carboxylic acid prepared by the method of Sulzberg and Cotter (8). To this 150 ml of thionyl chloride were added and the stirred mixture brought to a gentle reflux for approximately 8 hr. After a couple of hours the slurry dispersed to a clear brown-yellow solution. After cooling, the thionyl chloride was removed on a rotary evaporator and the yellowish solid that resulted was recrystallized from toluene to bright yellow crystals. Washing and stirring with hot hexane changed the color to a pale yellow, presumably by destroying the toluene-TNF complex. The yield of this solid was 7.3g (69.5%) after drying at room temperature under vacuum (mp 197°-199°C). Anal. Calcd. for $C_{14}H_4N_3O_8Cl$: C, 44.50; H, 1.00; N, 11.10; Cl, 9.20. Found: C, 44.52; H, 1.23; N, 10.92; Cl, 8.90.

n-Butyl-4,5,7-trinitro-9-fluorenone-2-carboxylate.—Into a 250 ml Erlenmeyer flask were placed 10.03g (0.026 mole) of 4,5,7-trinitro-9-fluorenone-2-carboxylic acid chloride and 100 ml of tetrahydrofuran. This was stirred via a magnetic stir bar until solution was effected. Triethylamine 0.28g (0.026 mole) dissolved in 20 ml of THF was added slowly to the reddish brown solution. Some cloudiness was noted. To this solution n-butanol 2.12g (0.029 mole, 10% excess) dissolved in 20 ml of THF was added dropwise. Precipitation was noted to occur during the course of the 1.5 hr reaction time. The insoluble triethylamine hydrochloride was removed by filtration (theoretical amount 3.6g, obtained 3.3g) and the THF solution carefully evaporated, using 35°C or less temperature, on the rotary evaporator. The yellow oil formed was dissolved in 75 ml of benzene and chromatographed on a silica gel column. The first fraction, 10 ml of yellow material, was discarded. The center fraction was taken, concentrated to about 50 ml and precipitated into stirring hexane. A very light yellow powder was obtained (6.0g, 54.5% yield) (mp range 115°-130°C). NMR ($CDCl_3$) δ 0.8-2.0 (m,7H,-CH_2-CH_2-CH_3), δ 4.5(t,2H,-O-CH_2-), δ 8.8 (m,4H, aromatic). Anal. Calcd. for $C_{18}H_{13}N_3O_9$: C, 52.10; H, 3.13; N, 10.15. Found: C, 51.88; H, 2.99; N, 10.28.

n-Dodecyl-4,5,7-trinitro-9-fluorenone-2-carboxylate and ethyl-4,5,7-trinitro-9-fluorenone-2-carboxylate.—These preparations were identical to the n-butyl TNF, except dodecyl or ethyl alcohol were used. Anal. (Dodecyl): Calcd. for $C_{26}H_{29}N_3O_9$: C, 59.20; H, 5.50; N, 7.96. Found: C, 59.77; H, 5.34; N, 8.27. Anal. (Ethyl): Calcd. for $C_{16}H_9N_3O_9$: C, 49.60; H, 2.32; N, 10.85. Found: C, 49.49; H, 2.39; N, 10.79.

2,4,7-Trinitro-9-fluorenylacetate and 2,4,7-trinitro-9-fluorenyl butyrate.—The esters were prepared according to the method of Colter and Wang (9) by esterification with 9-diazo-2,4,7-trinitrofluorene. Acetic acid, 80 ml, and 9-diazo TNF 3.3g (0.01 mole) were refluxed for 2 hr. After cooling, a yellow solid was removed by filtration, rinsed with ethanol, and then recrystallized from acetone. The yield was 2.3g (69%) with a melting point of 237°-240°C.

The butyrate was prepared in a similar fashion. The crude product was recrystallized twice from carbon tetrachloride to yield a solid of mp 145°-146°C. Anal. Calcd. for $C_{17}H_{13}N_3O_8$: C, 52.71; H, 3.36; N, 10.85. Found: C, 52.95; H, 3.51; N, 10.52.

Measurements.—All electrochemical measurements were made using the PAR 170 Electrochemistry System in the three-electrode mode. Sample concentrations were $5 \times 10^{-4}M$ with $0.1M$ tetraethylammonium perchlorate (TEAP, Southwestern Analytical Chemicals) as supporting electrolyte in acetonitrile (AN, Burdick and Jackson, dried over 4A molecular sieves, then percolated through a column of Grade I neutral alumina). For d-c and a-c polarography a dropping mercury electrode (DME) was used with the following capillary characteristics: $m = 1.50$ mg/sec, $t = 4.2$ sec when measured with an open circuit at $h = 80$ cm. For cyclic voltammetry (CV) a Beckman platinum disk or hanging mercury drop served as the working electrode. Potentials are referred to the saturated calomel electrode (SCE).

Ultraviolet visible spectra for use in electron affinity correlations were recorded on mixtures of 0.1 molar N-ethylcarbazole with 0.001 molar acceptor. In cases where the acceptor compound absorbed in the visible region of the spectrum, the 0.001 molar solution was run as a reference in order that only visible charge transfer could be measured.

The electron acceptor compounds were evaluated by the photo-induced discharge curve (PIDC), see following, mode of testing (10) in a variety of matrices: LEXAN® (bisphenol A polycarbonate), polysulfone, and poly(N-vinylcarbazole) (PVK). Some of the materials could not be tested because of poor solubility characteristics. Most of the PIDC studies were conducted on solution cast films (10-15 μm thick) of the test materials on 0.5 μm amorphous Se films. In cases where strong charge transfer complexes were formed (with mixtures of acceptor in PVK) and the samples were highly colored, the materials were cast onto aluminum sheets and coated with 0.5 μm amorphous Se films. When tested in PVK, acceptor concentrations were kept constant so that effective intermolecular distances for transport were constant (2, 4).

Results and Discussion

Voltammetry.—The compounds studied are shown in Fig. 1. Their voltammetric behavior is discussed below. The compounds are divided into four groups according to structure.

The fluorenones, I-VI.—The voltammetric curves for TNF (III) shown in Fig. 2 illustrate the electrochemical response typical of these compounds. The d-c polarograms of the fluorenones show two reduction waves whose average separation is 0.30V. Both waves correspond to reversible one-electron transfer processes as evidenced by the following criteria: (*i*) The diffusion current constants I_d obtained from the d-c polarograms are in reasonable agreement with the value of 2.6 ex-

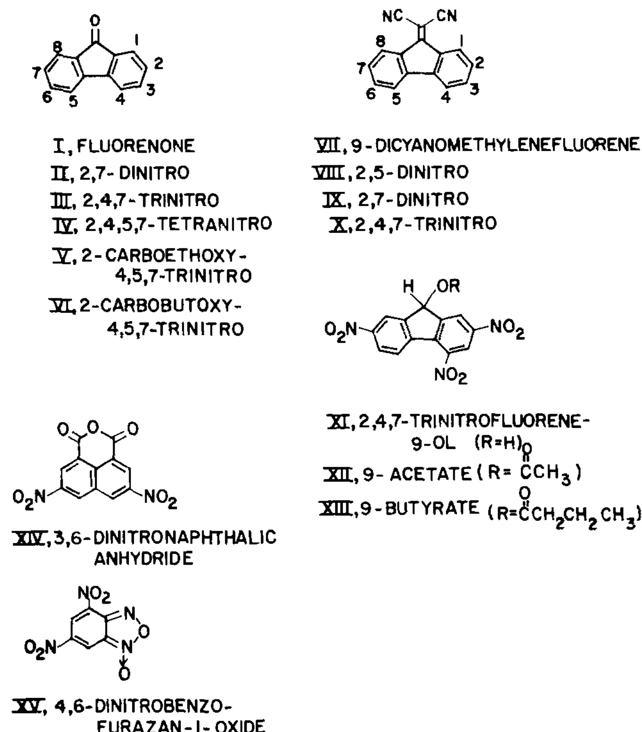

Fig. 1. Chemical structure of electron transport materials studied

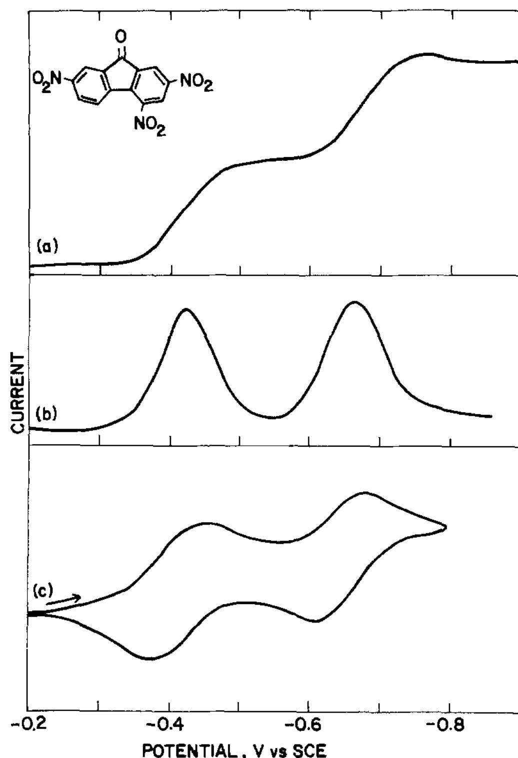

Fig. 2. Current-potential curves for 2,4,7-trinitrofluorenone: (a) d-c polargram, (b) a-c polarogram, (c) cyclic voltammogram.

pected for a one-electron process in acetonitrile (11). (*ii*) The quantity $|E_{3/4} - E_{1/4}|$ describing the slopes of the d-c wave are within 5 mV of the value 56 mV required by theory (12) for a reversible one-electron transfer. (*iii*) The peak potentials in the a-c polarograms are in good agreement with the d-c half-wave potentials and the peak half-widths are within 10 mV of the value 90 mV required by theory (13). (*iv*) The cyclic voltammograms show a reversible response, with separation of 78 mV between cathodic and anodic peak potentials, independent of scan rate (14). The reduction product formed at the working electrode has an intense color which ranges from red for fluorenone (I) to purple for compounds V and VI.

The 9-dicyanomethylenefluorenones (DCMF), VII-X.—The polarograms of these compounds also show two waves which correspond to reversible one-electron transfers as demonstrated by the criteria indicated above. For the DCMF compounds, however, the separation between the two waves averages 0.58V, *i.e.*, somewhat greater than that observed for compounds I-VI. Again, the reduction products are intensely colored, although the yellow color of the neutral species makes it difficult to describe the colors from visual observation.

The 2,4,7-trinitrofluoren-9-ols, XI-XIII.—These compounds are derived from 2,4,7-trinitrofluorenone (III) via chemical reduction of the carbonyl group. The first reduction waves of these compounds in the d-c polarograms are rather drawn out and the peaks in the a-c polarograms are broader and have lower peak currents than expected for reversible processes. The CV traces on these compounds indicate that the initial electron transfer is irreversible, although at more negative potentials (−1.14 and −1.35V) reversible reduction steps (possibly associated with the nitro groups) are seen. The cause of irreversibility is not known, but may be associated with bond cleavage at the 9-position as has been reported for other 9-substituted fluorenones (15).

3,6-Dinitronaphthalic anhydride and 4,6-dinitrobenzofurazan-1-oxide.—The d-c polarogram of the napthalic anhydride (XIV) shows two well-defined reduction waves, whose diffusion current constants indicate that each involves one electron. In the a-c polarogram the peak corresponding to the first d-c wave is preceded by a smaller peak suggestive of a nonfaradaic adsorption process.

As shown in Fig. 3, reversibility of the first reduction step depends on the nature of the working electrode. At a hanging mercury drop electrode a reversible charge transfer response is observed by CV, and the ratio of the anodic to cathodic peaks (1:17) suggests adsorption of the neutral species (16). At a platinum electrode, however, the CV response of XIV is clearly irreversible and the cathodic peak potential appears at −0.52V, some 0.2V more negative than the potential associated with reduction at a mercury electrode. Thus, there is some specific interaction of XIV with the mercury electrode, whose effect is not only to facilitate reduction relative to that observed at a platinum electrode but also to render the charge transfer process reversible.

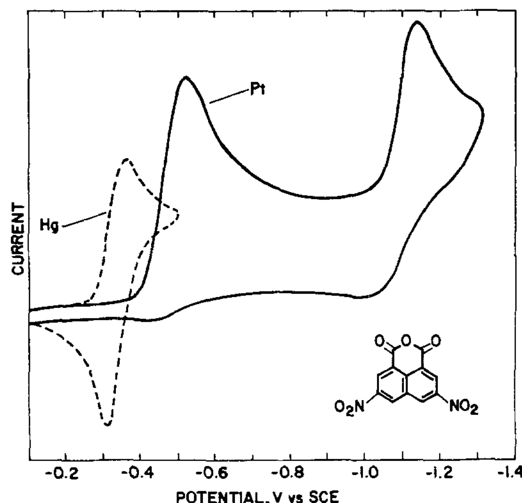

Fig. 3. Cyclic voltammograms of XIV at planar platinum electrode (solid line) and hanging mercury drop electrode (dashed line).

Table I. Voltammetric data*

Compound	D-C polarography $E_{1/2}$**	$\lvert E_{3/4} - E_{1/4}\rvert$	I_d***	CV response†
I	−1.30	0.055	3.38	Rev
	−1.78	0.070	2.33	Rev
II	−0.68	0.060	3.24	Rev
	−0.84	0.052	2.97	Rev
III	−0.42	0.060	2.83	Rev
	−0.67	0.055	2.35	Rev
IV	−0.14	0.050	2.27	Rev
	−0.42	0.060	2.34	Rev
V	−0.29	0.057	2.50	Rev
	−0.59	0.055	2.33	Rev
VI	−0.27	0.060	2.75	Rev
	−0.59	0.060	1.76	Rev
VII	−0.66	0.052	3.23	Rev
	−1.30	0.050	2.72	Rev
VIII	−0.26	0.060	2.64	Rev
	−0.80	0.053	2.48	Rev
IX	−0.25	0.060	2.73	Rev
	−0.79	0.055	2.86	Rev
X	−0.00	0.050	2.79	Rev
	−0.59	0.051	2.81	Rev
XI	−0.62	0.070	2.41	Irrev
XII	−0.56	0.065	2.38	Irrev
XIII	−0.56	0.065	1.95	Irrev
XIV	−0.35	0.047	2.38	Irrev‡
	−1.06	0.035	1.86	Irrev
XV	+0.06	0.065	1.77	Irrev

* Sample concentrations 5 × $10^{-4}M$ in AN containing 0.1M TEAP.
** Volts *vs.* SCE. The a-c peak potentials are in good agreement with the d-c half-wave potentials.
*** $I_d = i_d/\mathrm{cm}^{2/3} t^{1/6}$.
† At platinum disk electrode. Scan rate 200 mV/sec. Rev = reversible, irrev = irreversible.
‡ Reversible at hanging mercury drop electrode. At platinum the peak potential is at −0.52V.

Compound XV, the last of the series, is the most easily reduced. Based on the diffusion current constant, the reduction involves one electron. All criteria show this to be an irreversible process. For both XIV and XV irreversibility is probably associated with cleavage of heteroatom bonds following the initial electron transfer.

Effect of structure on ease of reduction.—The half-wave potentials of compounds I-XV are shown in Table I, and for the present purpose attention is drawn to the reduction potential of the first wave. In the fluorenone series (I-IV) the ease of reduction is increased by an average of 0.28V per nitro group (as shown in Fig. 4). The attachment of a carboalkoxy group (compounds V and VI relative to III) results in a positive shift of 0.14V. The replacement of the carbonyl oxygen atom by the more electronegative dicyanomethylene group (I *vs.* VII, etc.) increases ease of reduction by 0.64V. In the DCMF series (VII-X) the ease of reduction is increased by 0.22V per nitro group on the average (Fig. 4). That the effect of nitrosubstitution is greater in the fluorenone series than in the DCMF series is in agreement with the observation of Zuman (17) that substituent effects are greater as the reduction potential of the parent compound is more negative; in other words, substituent effects are greatest in systems that are most difficult to reduce.

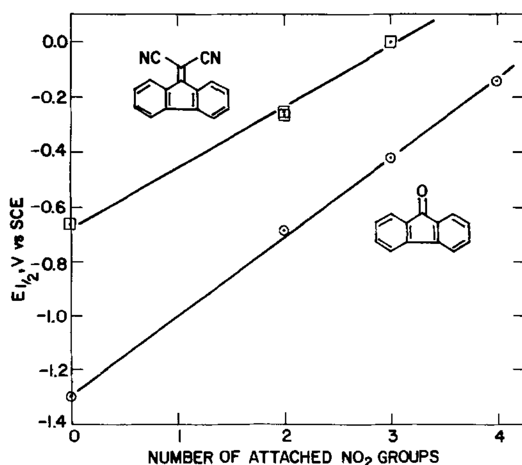

Fig. 4. Half-wave potential as a function of attached nitro groups for 9-fluorenone and 9-dicyanomethylenefluorenone.

In the fluorenol series (XI-XIII) the reduction potential is essentially unaffected by the group attached to the oxygen atom at the 9-position. Compounds XIV and XV are, of course, structurally unrelated to any others in the series, and ease of reduction could not have been predicted short of actually doing the voltammetric experiment.

Effect of solvent on half-wave potential.—In addition to the studies using AN as solvent, reduction potentials of 2,4,7-trinitrofluorenone (III) were obtained in the following solvents: propylene carbonate (PC), dimethylformamide (DMF), and dimethylsulfoxide (DMSO). In all cases two reversible one-electron reduction waves were seen. However, as shown in Table II, the measured half-wave potentials vary greatly from one solvent to another. Such solvent-induced shifts in $E_{1/2}$ have been discussed by a number of workers (18) and may include contributions from differences in liquid junction potential, ion pairing effects, and interactions of the solvent with the species undergoing the redox reaction, *i.e.*, changes in polarization.

These difficulties can be avoided in principle by referring all measurements to the reversible half-wave potential of a redox couple which does not interact with solvent and is, therefore, unaffected by a change in solvent. One such reference couple is bisbiphenylchromium (I) (BBCr), recently proposed by Duschek and Gutmann (19). The half-wave potentials of BBCr in the solvents used to study compound III are also given in Table II; relatively small shifts with solvent are seen for BBCr relative to III. The relatively large shifts in $E_{1/2}$ for III may then be assumed to be due to specific interactions of the radical anion or dianion of III with solvent or due to ion pair formation with the cation of the supporting electrolyte (20, 21). As shown in Fig. 5, changes in $E_{1/2}$ with solvent are correlated not with solvent dielectric constant (as might be expected by application of the Born equation) (22), but rather by Gutmann's donor number (23), which measures the ability of a solvent to donate electrons.

Electron affinities from half-wave potentials.—In the absence of entropy effects the free energy change for the reaction

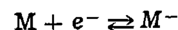

$$M + e^- \rightleftharpoons M^-$$

is given by (24, 25)

$$\Delta G = EA + \Delta\Delta G_{sol} + C$$

where $\Delta\Delta G_{sol}$ is the difference in free energies of solvation between the neutral and charged species and C is a constant dependent on the reference electrode. If the diffusion coefficients of the neutral and charged species do not differ greatly, then the half-wave potential is given by

Table II. Reduction potentials of 2,4,7-trinitrofluorenone (III) in various solvents*

Solvent	Dielectric constant**	Donor number**	$E_{1/2}$(V *vs.* SCE) First wave	$E_{1/2}$(V *vs.* SCE) Second wave	$E_{1/2}$(V *vs.* SCE) of BBCr†
AN	38.0	14.1	−0.42	−0.67	−0.73
PC	69.0	15.1	−0.42	−0.66	−0.76
DMF	36.1	26.6	−0.27	−0.53	−0.71
DMSO	45.0	29.8	−0.28	−0.50	−0.70

* Solvents dried over 4A molecular sieves prior to use. Supporting electrolyte, 0.1M TEAP.
** V. Gutmann, *Chem. Brit.*, 7, 102 (1971).
† O. Duschek and V. Gutmann, *Monatsh. Chem.*, 104, 990 (1973).

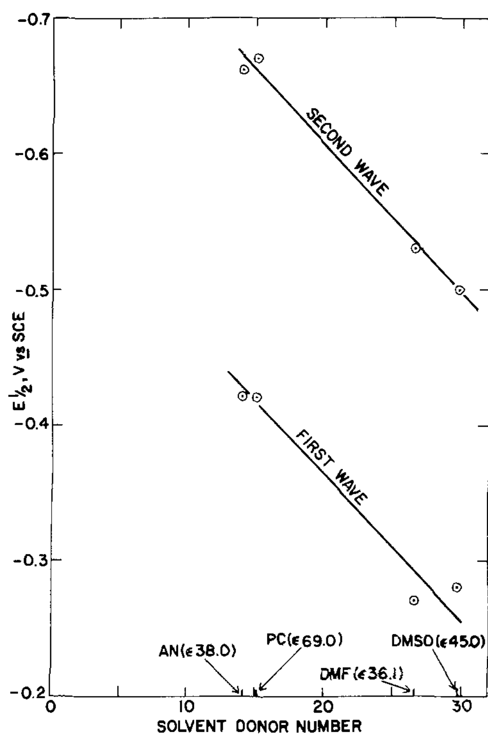

Fig. 5. Half-wave potential of 2,4,7-trinitrofluorenone as a function of solvent donor number.

$$E_{1/2} = \frac{\Delta G}{\mathbf{F}}$$

where **F** is the Faraday constant. It follows that if $\Delta\Delta G_{sol}$ is constant or varies linearly with EA then a linear relationship exists between $E_{1/2}$ and EA, which is given by (25b) and (25c) as

$$EA = E_{1/2} + 2.49 \quad [1]$$

where the value of $E_{1/2}$ is with respect to SCE and on which scale chloranil has the value $EA = 2.45$ eV. By use of the one-electron reduction potentials in Table I, the electron affinities of the compounds studied here may thus be obtained and are given in Table III. It should be pointed out that even if the assumption of constant solvation (polarization) energy is not strictly valid for the calculation of gas phase electron affinities. differences in $\Delta\Delta G_{sol}$ between compounds will, as shown above, be reflected in the half-wave potentials obtained from the solution redox measurement. Thus, while for convenience gas phase EA's are used, it is understood that such numbers are obtained from condensed phase measurements and as such are closely related to the molecule-matrix situation.

Mukherjee (26) has similarly studied compounds II-IV and VII-X and reported electron affinities which are 0.01 to 0.13 eV less than those obtained in the present study. This discrepancy may be due to his use of $LiClO_4$ as supporting electrolyte, since it is known (21) that ion pairing can cause shifts of up to 0.2V in polarographic half-wave potentials if the cation of the supporting electrolyte has a large charge to radius ratio. We also disagree with Mukherjee's claim that the second reduction wave of the DCMF compounds corresponds to the uptake of 3-4 electrons since, as was shown, for both these and the fluorenones all criteria indicate that the reduction pathway consists of two reversible one-electron steps.

Electron affinities via charge transfer spectra.—This method is essentially that of Briegleb (25) as modified by Mukherjee (27). It essentially involves measurement of the lowest energy charge transfer band of an acceptor with a donor, and referencing this transition energy to that of a known acceptor with the same donor. A specific equation is

$$h\nu_{ct}^{o} - h\nu_{ct} = EA - EA^{o} \quad [2]$$

where $h\nu_{ct}^{o}$ = energy of λ_{max}^{ct} with a standard acceptor, $h\nu_{ct}$ = energy of λ_{max}^{ct} of unknown acceptor, EA = unknown electron affinity, and EA^{o} = electron affinity of standard acceptor. Equation [2] can be changed to

$$EA - h\nu_{ct}^{o} = EA^{o} - h\nu_{ct} = K - \frac{hc}{\lambda} \quad [3]$$

This equation shows that there should be a linear relationship between EA and the wavelength of the lowest energy charge transfer band, provided that the donor material is held constant. For our correlation three known materials (III, IV, and X) have been used to generate correlation curves (EA *vs.* $1/\lambda$) with N-ethylcarbazole and the unknown materials' charge transfer λ used with these curves to obtain their EA (see Fig. 6). Interestingly, two charge transfer bands have been observed in most of the systems measured and these have been shown (28) to correspond to CT bands from the 1_{LB} and 1_{LA} energy levels of N-ethylcarbazole. Both levels have been used in our correlations and have provided similar results (Table III).

In evaluating electrical properties, it was found that many of the materials in Table III were not soluble to a sufficient level to be tested as electron transport materials. In these cases, CT spectra were not obtained.

With the exception of compound XIV, the EA obtained from CT spectra agree quite well with those from polarographic measurements. As was shown, compound XIV apparently undergoes a specific interaction with mercury, and the CV peak potential obtained at a platinum electrode probably better reflects the EA of the isolated (uncomplexed) molecule.

Table III. Electron affinities and PIDC results

Compound	Electron affinity, eV Polarography	Electron affinity, eV CT spectrum**	PDIC‡
I	1.19		ML
II	1.81		ML
III	2.07	2.03†	RM
IV	2.35	2.26†	TL-MDDTL
V	2.20	2.19	TL-RM
VI	2.22		TL-RM
VII	1.83		ML
VIII	2.23	2.26	TL
IX	2.24	2.27	TL
X	2.49	2.39†	HDDTL
XI	1.87		LDDNT
XII	1.93		LDDNT
XIII	1.93	1.86	LDDNT
XIV	2.14(1.97)*	1.96	LDDNT
XV	2.55		LDDNT

* The value in parenthesis is estimated from the CV peak potential at a platinum electrode.
** Average of both CT bands when obtained.
† Used for correlation purposes, see section on Electron affinities via charge transfer spectra.
‡ Key: ML = mobility limited, RB = reasonable mobility, TL = trap limited, HDDTL = high dark decay trap limited, and LDDNT = low dark decay no transport.

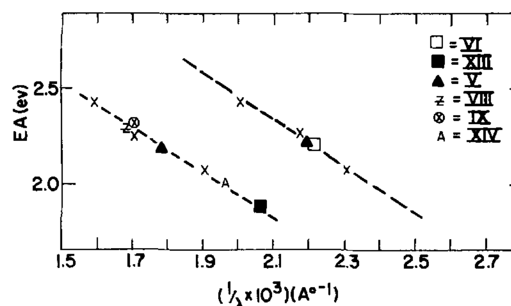

Fig. 6. Electron affinity vs. lowest energy charge transfer bands in N-ethylcarbazole/acceptor complexes. X = Standards for correlation curve.

Electrical evaluation.—Explanation of PIDC method. —The PIDC test is conducted as follows. Materials to be tested as transporting media are solvent cast onto a 0.5 μm film of amorphous selenium. These composites are then thoroughly dried in vacuo at 312°K. The films are then placed in a device which will corona charge them (either positive or negative), measure the surface voltage as a function of time, and permit illumination of the sample some time after charging. Once the sample has been charged, care must be taken to exclude any form of radiation from the sample in order that the dark decay rate (the rate at which surface voltage decays without radiation) can be measured. In the above configuration, if the material to be measured is electron transporting, the sample is corona charged positively while, if it is hole transporting, the sample is charged negatively.

The sample is capacitively charged by the corona to a charge level $q = CV$ where q is the total charge on the system, C is the capacitance of the sample, and V, the voltage generated across the sample. This is schematically shown below.

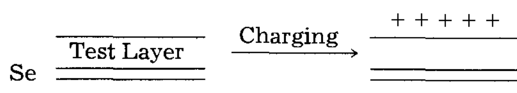

Once charged, if the sample is not conductive, it can be discharged in two ways: (*i*) photoinduction of hole/electron pairs either in the Se layer or the test layer, and (*ii*) thermal generation of hole/electron pairs in the Se layer or the test layer. The latter effect will lead to dark decay, as the thermally generated charge can lead to a reduction of the surface potential.

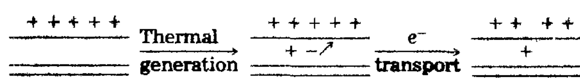

In the example shown, the coated material is an electron transport material. The surface voltage measured in the example would be 80% of the initial value. The rate of this dark decay can then be measured from the voltage/time plots. Normally, amorphous Se does not thermally generate a significant number of hole/electron pairs at room temperature (29) so that a decrease in surface voltage is due to the "dark decay" of our coated layers.

Since the photogeneration can take place in either of the layers, care must be taken to use radiative wavelength where the selenium layer is photosensitive and the organic layer is not. This requires knowing the electronic absorption spectra of the organic species and the photoresponse spectra of the amorphous Se. If these two overlap, the experimental configuration is changed so that the amorphous Se layer is on top and is made thick enough so as to allow no incident radiation to penetrate to the organic layer. If hole/electron pairs are generated in the organic layer (bulk generation), no information concerning charge trapping during transport can be obtained. If the above criteria concerning radiative absorption are met, only two other criteria need be considered; the amount of photogenerated charge and an injection barrier between the generator and transporting species. Although injection barriers have not been measured in the present systems, Mort and Emerald (30) have done so for amorphous selenium injection into PVK/TNF charge transfer complexes and found negligible injection barriers. Based on their work and the range of electron affinities being studied, negligible injection barriers are expected in the present results. In order to glean information on the transport of the charge through the sample, only enough charge need be generated in the selenium photogenerator layer to completely remove all surface charge. This would be equivalent to the capacitance charge on the sample (a so-called CV's work of charge). This charge is generated using a filtered strobe flash. If a CV's charge is generated and moves through the sample unimpeded, the sample will discharge as shown below and the surface voltage-time behavior will be described by the curve shown below.

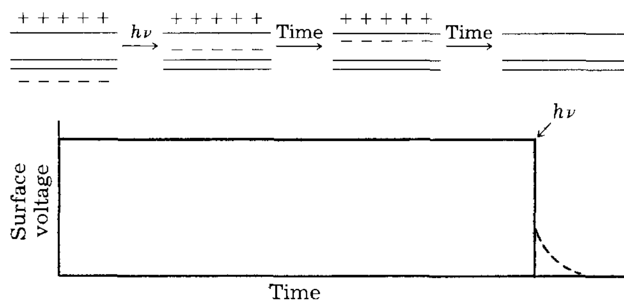

The horizontal time scale of such a measurement will depend on the transit time (the mobility of the charges moving through the sample). The voltage/time curve shown is totally idealized and will show a tailing phenomena (shown with dashes) because of space charge effects and the experimental inability to generate all charges simultaneously.

If the transporting charges encounter any molecular or morphological potential barriers, as they are traversing the sample, they can be stopped (deep traps) or slowed (shallow traps). These trapping effects cause changes in the shape of the voltage-time curves. If the transporting charges are deep trapped, a residual surface voltage V_R will remain in the time domain of the experiment.

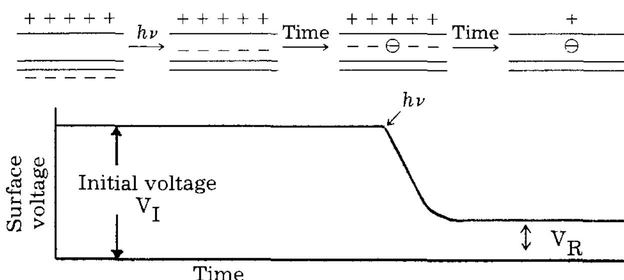

If shallow trapping occurs, the residence time of the charge in the neighborhood of the trap is short compared to the time scale of the experiment, but the "sheet" of charges generated and injected from the photogeneration layer spreads out and the voltage/time curve is not as sharp.

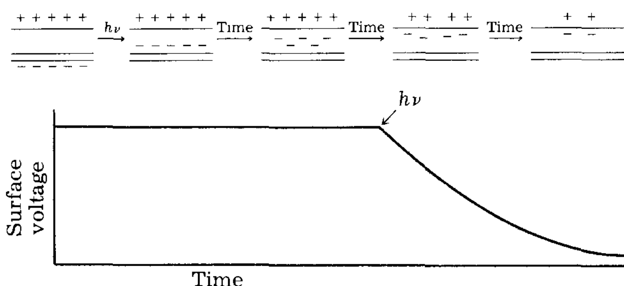

It can be seen that by analyzing the PIDC curves on the same time scale that relative mobilities, trap levels, and dark discharge rates can be obtained. In the case of the experiments below, the discharges labeled reasonable mobility were those in which the surface voltage decreased to 50% of their original value in 0.1-0.2 sec.

It should be noted in this discussion that there is no way to distinguish between shallow trapping and low mobility materials and that, in fact, the two terms may be synonymous. Within the framework of these experiments and with the trends established, we have chosen low mobility to mean low dark decay and ap-

parent trap-limited mobility. Trap-limited discharge means high dark decay and apparent trap-limited mobility. This nomenclature fits the trends established.

Discussion of PIDC results.—It is our desire to discuss, in qualitative terms, the relationship of *EA* in fluorenone derivatives to observed transport (and in some cases generation properties). Two major difficulties have been encountered in measuring the electron transport properties of these materials: (*i*) instability of the molecule/matrix systems and (*ii*) limited solubility of the molecules in the matrix polymers. An example of the former effect is shown in Fig. 7 where it is seen that aging effects of TNF in binder polymers are deleterious causing increased residuals. This was a general phenomenon. It could only be overcome by testing the molecules of interest in a PVK matrix. In PVK the PIDC's did not appear time dependent.

Limited solubility materials such as VIII and IX could not be tested as transport materials because amorphous films of high loading could not be prepared. One idea to overcome this limitation was to ball mill these insoluble materials in a solution of PVK until a uniform distribution of small particles was obtained. It was felt that this distribution with its surface charge transfer complexes of PVK/acceptor might provide adequate electron transport matrices. The concept was tested with compounds III and VIII. In both cases ballmilling 40% of III and VIII to PVK causes charge transfer complexes to be formed (solutions become highly colored). However, as seen in Fig. 8, neither materials exhibited electron transport when a CV's worth of charge was injected from overcoated amorphous Se, but both behave as bulk generating photoreceptors when used with white light. Thus, although some of the electron transport candidates might be predicted to have good transport properties (see below) their solubility limits them to bulk generation type photoreceptors.

Figure 9 is a schematic representation of various PIDC curves observed for 40% acceptor loadings of fluorene derivatives in PVK. Although there must be gradual changes between the regions defined, four different modes of transport are apparent: (*i*) mobility limited, (*ii*) "reasonable" mobility characteristics, (*iii*) trap limited, and (*iv*) high dark decay.

These definitions of mobility are qualitative in nature and depend on the time scale of measurement. For these results (see Fig. 9) reasonable mobility is defined as light-induced discharge to 50% V_o in $\sim$0.1 sec. Mobility limited is defined as low dark decay-low light-induced discharge rate (Fig. 9A); trap limited is defined as increasing dark decay (Fig. 9C) low light-induced discharge; and high dark decay trap-limited

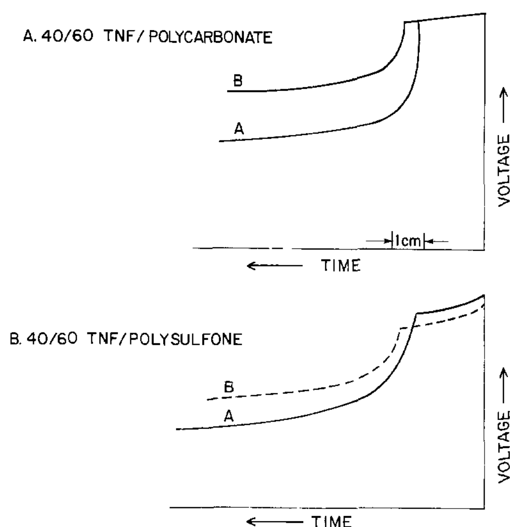

Fig. 7. PIDC of 40/60 (w/o) TNF in Lexan® and polysulfone. Horizontal scale = 10 mm/sec, vertical scale = 100 V/cm. A, Sample pumped 4½ days, 10^{-3} mm Hg, RT prior to test; B, 4 additional days stored in dark at ambient.

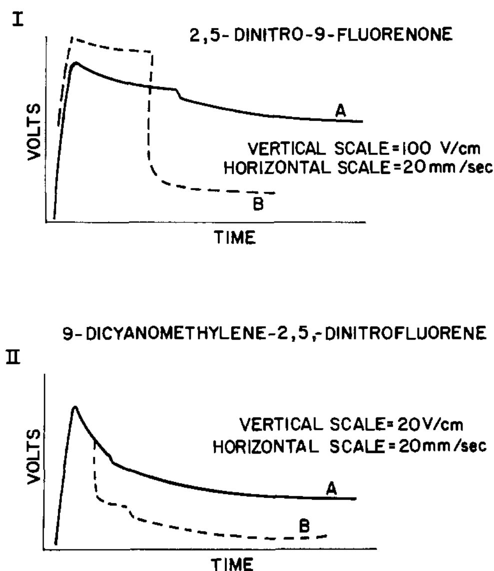

Fig. 8. PIDC of 40/60 (w/o) 2,5-dinitrofluorenone and 9-dicyanomethylene-2,5-dinitrofluorenone in PVK. Samples ball milled 24 hr in CH_2Cl_2 prior to preparation. A, Se overcoated; B, no overcoating, white strobe pulse, electron transport.

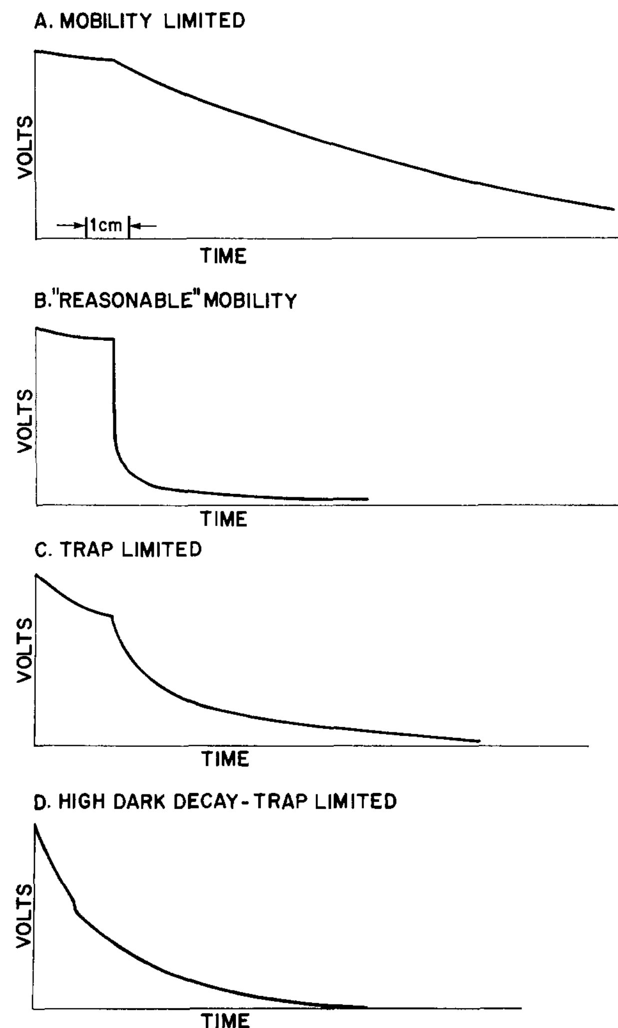

Fig. 9. Qualitative PIDC curves for PVK/acceptor mixtures. Horizontal axis = 20 mm/sec. 1 cm marker shown in A. Vertical scale dependent on dark decay. A and B, 100 V/cm, C, 50 V/cm; and D, 20 V/cm.

is defined as low charge acceptance due to dark decay and no obvious light-induced transport except the collapse of the field across amorphous Se (Fig. 9D). That trap limitations occur is seen in Fig. 8 where it is demonstrated that bulk generation (essentially trap depopulation) can discharge a sample to a much greater degree than injection from amorphous selenium.

The four regions of Fig. 9 correlate qualitatively with various ranges of *EA* values for fluorenone derivatives: the first (A) with *EA* less than ~2.0, the second (B) with $2.0 < EA < 2.2$, the third (C) with $2.2 < EA \leqq 2.4$, and the fourth (D) with $EA > 2.4$. As mentioned previously, if all *EA*'s within these regions could be tested, a gradual change in PIDC would be expected. A general increase in dark decay is also noted with increasing *EA*. These results are qualitatively described in Table III.

How are these general trends rationalized? Seki (31) has proposed a model of fluctuating hopping sites which provides a mathematical description of transport similar to that of Bagley (32) whose model is based on hopping between localized states over potential barriers. Seki (31) also included a probability factor due to tunneling or overlap of individual molecular wave functions, which has the form E^{-R/R_0}. The entire equation proposed by Seki is

$$\mu F = (\lambda_0/\tau_0)\exp(-R/R_0)\exp(-U_0/kT)\sinh(e\lambda_0F/2kT) \quad [4]$$

where μ is the mobility; F, the electric field; R, the intermolecular distance between exchange sites; τ_0, λ_0, and R_0 are constants of a specific system with units of time and characteristic distances, respectively; e is electronic charge, U_0 is the thermal barrier to transport, and kT is the thermal energy of the system. R_0 can be related to *EA* or the ionization potential (*IP*) by[1]

$$\frac{1}{R_0} = (2/\hbar)\sqrt{2mE_i} \quad [5]$$

where m is the mass of an electron and $E_i = EA$ or IP depending on whether there is hole or electron transport. An equation similar to Eq. [4] (without the R/R_0 term) can also be derived from rate theory where it is assumed that application of an electric field to a sample changes the potential well distribution (33, 34). Of importance in the above is the effect the changing *EA* or *IP* has on R_0 and its physical significance. In systems studied thus far, R_0 is of the order of an angstrom or less and thus all possible values of R are greater than R_0. On the basis of Eq. [4] and [5], it would be expected that decreasing *EA* and holding all other variables (concentration, field, etc.) constant would produce increasing electron mobility. Oppositely, increasing *EA* should result in decreasing mobility. Our results follow this in the range of $E \geqq 2.1$. It should be pointed out that the Seki equation has not been validated for a large number of materials and that experimental variables such as sample preparation, morphology, chemical structure, and inert matrix may also affect the observed transport behavior.

Materials of $EA \geqq 2.1$ eV that were tested provide discharge curves of types (B) through (D) indicating that as *EA* is increased trap-limited mobilities are observed. Trap-limited discharges were observed in compounds V and VI with extreme trapping limitations in IV, X, XIV, and XV. It is thus concluded that in the region $EA \gtrsim 2.1$ eV electron transport results for fluorenone derivatives in PVK can qualitatively be described in terms of Eq. [4] and [5]. At lower *EA* anomolies occur. On the basis of Eq. [5], the lower *EA* materials would be expected to be better electron transport materials than their high *EA* counterparts. This is not observed and the results are not unique, as Faucz (35) observed holes as the majority carrier in pure crystalline films of 9-fluorenone, a material with $EA = 1.2$ eV. There are a variety of possible reasons why the decreased electron mobility in fluorenone derivatives is seen below $EA \cong 2.1$. Impurities such as O_2 ($EA = 0.44$) (36) could interfere with transport. Injection into the low affinity materials could override other effects (Faucz observed this in 9-fluorenone, whereas mononitrofluorenone injected and transported electrons) (35). Fluorenone dispersions could be affected by the ability of the material to form charge transfer complexes with PVK, and thus, the lower *EA* materials may be dispersed differently from their high *EA* counterparts. Whatever the reason, the 9-fluorenone derivatives appear to be limited to an electron affinity region ~2.05 to 2.15 for reasonable PIDC results.

Another phenomenon noted in these studies is the increase in dark decay with increasing *EA*. Similar effects have been noted in other electron-donating systems complexed with fluorenone derivatives (37). In fact, with materials such as IV and X, dark decay was observed with no apparent electron mobility. This high dark decay occurred whether these materials were charged positively or negatively. Again, there is a variety of reasons why this increased dark decay may occur. With increased *EA* of the acceptor it may be easy for an electron to be thermally promoted from the highest occupied molecular orbital of PVK to the lowest unoccupied of the acceptor, thus creating a hole-electron pair in the media. Dark decay in this case may occur through thermally generated carrier movement. In light of our observations of trap-limited electron transport, but high dark decay, this explanation seems reasonable.

It is, of course, implicit in the preceding discussion, that if the relation between *EA* and electron mobility is valid, then it equally ought to apply to *IP* and hole mobility. Support for this approach is to be found in the work of Pfister *et al.* (4) involving xerographic discharge measurements on Lexan® doped with variously substituted derivatives of carbazole. Gibson (38) subsequently showed that the observed changes in xerographic discharge rates could be correlated with the ability of the substituents to release electrons (given by Hammett or Taft substituent constant) to the carbazole ring and thus lower the ionization potential. It should be pointed out in passing that the use of Hammett substituent constants to correlate molecular energy levels (and thus mobilities) is limited to perturbations on a given molecular framework, whereas use of redox data, such as in the present work, permits such correlations regardless of the molecular framework.

An additional consideration is the effect of the medium on the energy levels of the isolated molecule. In the condensed phase these energy levels will differ from those of the molecule in the gas phase by an amount termed the solvation (or polarization) energy. From simple theory this quantity is given by the Born equation (22)

$$\Delta G = -\frac{(ze)^2}{2r}\left(1 - \frac{1}{\epsilon}\right) \quad [6]$$

where ze is the charge acquired by the molecule, r its radius, and ϵ the dielectric constant of the surrounding medium. While this equation may be suitable for spherical ions in a continuous medium, it is not at all certain that it is applicable to planar molecules, particularly those in which heteroatoms and substituents induce a nonuniform charge distribution. Furthermore, specific solvation effects such as ion-dipole interaction, hydrogen bonding, and π bonding can effect the solvation energy to an extent beyond that esti-

[1] This equation is exact for square well potentials or the WKB approximation.

mated by considering the environment as a continuous dielectric medium.

These considerations are amply illustrated by the shifts in reduction potential of TNF (III, see Table II) which reflect the difference in solvation energies between the neutral molecule and anion formed on reduction in different solvents. As was shown, it is not dielectric constant (a macroscopic quantity) but donor number (a microscopic measure of solvating ability) which correlates the observed trend in reduction potential and thus *EA* in the condensed phase. If such effects are also operative in polymeric matrices, then the observed differences in carrier mobility when a given active transport molecule is dispersed in different binder resins could easily be explained via the donor number concept.

A final consideration involves the molecular nature of the charge transport process itself. This can be regarded as the reaction of a radical ion with a neutral molecule to give a neutral molecule and a radical ion

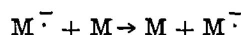

$$M^{\overline{\cdot}} + M \rightarrow M + M^{\overline{\cdot}}$$

The possibility also exists for the radical ion to undergo an irreversible chemical reaction

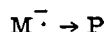

$$M^{\overline{\cdot}} \rightarrow P$$

The product of such a reaction could depend on or directly involve the surrounding medium and could easily be a compound that would act as a trap for the transport species. Thus, if the *EA* of chemical reaction product P is greater than that of molecule M, then according to the reasoning we have advanced, P will act as a trapping site. Analogous arguments, of course, hold for hole transport. When this possibility exists, the residence time of the electron at a given molecular site must be shorter than the time required for chemical reaction in order for such trap limitations not to exist.

Support of this approach is seen in the results of measurements on compounds XI-XIV. PIDC measurements on these compounds showed that although *EA* are reasonable for electron transport, none is observed. From a consideration of energy levels alone this would not have been expected since the experimental values of *EA* do not differ greatly from that of TNF. The compounds do differ from TNF, however, in that, as shown by cyclic voltammetry, each undergoes an irreversible chemical reaction coupled to the electron exchange step. It thus appears that there is a direct correlation of electrochemical stability and trap or mobility limitations in electron transport systems.

Thus, it seems that carrier mobilities and/or trap limitations can be correlated with the energy levels of the molecular species involved, but, in addition, the chemical or electrochemical reactivity of the molecules responsible for charge transport must be considered as well as their specific interactions with the host matrix.

Acknowledgments

The authors acknowledge with thanks helpful discussion with Dr. D. M. Pai as well as the technical assistance of D. Wychick. They also wish to acknowledge the typing of L. Vullo.

Manuscript submitted Dec. 16, 1977; revised manuscript received July 3, 1978.

Any discussion of this paper will appear in a Discussion Section to be published in the June 1979 JOURNAL. All discussions for the June 1979 Discussion Section should be submitted by Feb. 1, 1979.

Publication costs of this article were assisted by the Xerox Corporation.

REFERENCES

1. W. D. Gill, *J. Appl. Phys.*, **43**, 12, 5033 (1973).
2. J. Mort, G. Pfister, and S. Grammatica, *Solid State Commun.*, **18**, 693 (1976).
3. W. D. Gill, in "Proceedings of 5th International Conference on Amorphous and Liquid Semiconductors," p. 901, Garmisch-Partenkirchen, Taylor and Francis, London (1974).
4. G. Pfister, S. Grammatica, and J. Mort, *Phys. Rev. Lett.*, **37**, 20, 1360 (1976).
5. R. M. Schaffert, *IBM J. Res. Dev.*, **15**, 75 (1971).
6. J. E. Kuder, W. W. Limburg, J. M. Pochan, and D. Wychick, *J. Chem. Soc. Perkin Trans. II*, 1643 (1977).
7. V. M. Vozzhennikov, Z. V. Zvonkova, L. P. Shlyakhina, and V. V. Berezkin, *Russ. J. Phys. Chem.*, **43**, 1285 (1969).
8. T. Sulzberg and R. J. Cotter, *J. Org. Chem.*, **35**, 2762 (1970).
9. A. K. Colter and S. S. Wang, *ibid.*, **27**, 1517 (1962).
10. R. M. Schaffert, "Electrophotography," 2nd ed., John Wiley & Sons, Inc., New York (1975).
11. J. E. Kuder, D. Wychick, R. L. Miller, and M. S. Walker, *J. Phys. Chem.*, **78**, 1714 (1974).
12. J. Tomes, *Collect. Czech. Chem. Commun.*, **9**, 12 (1937).
13. A. M. Bond, *Anal. Chem.*, **44**, 315 (1972).
14. R. S. Nicholson and I. Shain, *ibid.*, **36**, 706 (1964).
15. A. Lagu, H. B. Mark, and J. R. Jezorek, *J. Org. Chem.*, **42**, 1063 (1977).
16. R. H. Wopschall and I. Shain, *Anal. Chem.*, **39**, 1514 (1967).
17. P. Zuman, "Substituent Effects in Organic Polarography," chap. 3, Plenum Press, New York (1967).
18. J. N. Butler, *Advan. Electrochem. Electrochem. Eng.*, **7**, 77 (1970) and references cited therein.
19. O. Duschek and V. Gutmann, *Monatsh. Chem.*, **104**, 990 (1973).
20. T. M. Krygowski, *J. Electroanal. Chem.*, **35**, 436 (1972).
21. M. K. Kalinowski and B. Tenderende-Guminska, *ibid.*, **55**, 277 (1974).
22. M. Born, *Z. Physik.*, **1**, 45 (1920).
23. V. Gutmann, *Chem. Brit.*, **7**, 102 (1971).
24. M. J. S. Dewar, J. A. Hashmall, and N. Trinajstic, *J. Am. Chem. Soc.*, **92**, 5555 (1970).

25a. G. Briegleb, *Angew. Chem. Internat. Ed.*, **3**, 617 (1964).

25b. E. C. M. Chen and W. E. Wentworth, *J. Chem. Phys.*, **63**, 3183 (1975).

25c. V. Kampers and O. Neilands, *Russ. Chem. Rev.*, **46**, 503 (1977).

26. T. K. Mukherjee, *Tetrahedron*, **24**, 721 (1968).
27. T. K. Mukherjee, *J. Phys. Chem.*, **71**, 2277 (1967).
28. U. Landmann, A. Ledwith, D. G. Marsh, and D. J. Williams, *Macromolecules*, **9**, 833 (1976).
29. L. B. Schein, *Phys. Rev.*, **10**, 3451 (1974).
30. J. Mort and R. L. Emerald, *J. Appl. Phys.*, **45**, 175 (1974).
31. H. Seki, in "Amorphous and Liquid Semi-conductors," J. Stuke and W. Brenig, Editors, pp. 1015-1034, Taylor and Francis Ltd., London (1974).
32. B. G. Bagley, *Solid St. Commun.*, **8**, 345 (1970).
33. N. T. Mott and E. A. Davis, "Electronic Processes in Non-Crystalline Material," Oxford Clarendon Press (1971).
34. H. Eyring, J. Walter, and G. Kimball, "Quantum Chemistry," p. 331, John Wiley & Sons, Inc., New York (1944).
35. E. C. Faucz, Private communication.
36. "Handbook of Chemistry and Physics," 49th ed., p. E-70 (1969).
37. T. K. Mukherjee, *J. Phys. Chem.*, **74**, 3006 (1970).
38. H. W. Gibson, Private communication.

Some Redox Reactions on Semiconducting Tin Oxide Electrodes in Molten LiCl-KCl Eutectic at 450°C

I. Uchida*

Department of Applied Chemistry, Faculty of Engineering, Tohoku University, Sendai, Japan

K. Niki

Department of Electrochemistry, Yokohama National University, Minami-ku, Yokohama, Japan

and H. A. Laitinen*

Department of Chemistry, University of Florida, Gainesville, Florida 32611

ABSTRACT

The electrode reactions of Eu(III)/Eu(II), Cr(III)/Cr(II), Cu(II)/Cu(I), Fe(III)/Fe(II), and Pt(IV)/Pt(II) redox couples have been studied using cyclic voltammetry at n-type semiconducting SnO_2 electrodes in molten LiCl-KCl eutectic at 450°C. The highly doped oxide electrode is a stable indicator electrode usable at anodic potentials up to chlorine evolution. The redox couples examined are reversible at the tin oxide electrode, indicating no effect of electron depletion on the electron transfer kinetics. Electron tunneling through the space charge barrier takes place more easily in the high temperature melt system. For the oxidation of Cu(I) and Pt(II), which do not show diffusion controlled current peaks, an adsorption effect due to anionic bridge formation on the oxide covered with adsorbed chloride has been suggested.

A number of electrochemical reactions in molten salt systems have been studied on metal and carbon electrodes (1). Metal electrodes, even the platinum metals, are subject to anodic dissolution in LiCl-KCl eutectic, imposing an anodic limit when they are used as indicator electrodes. Carbon is one of the inert materials usable at anodic potentials up to chlorine evolution in the melt. Previous studies on redox systems that have a more positive redox potential than that of platinum dissolution have been mostly carried out on carbon electrodes (2-4). In view of electrochemical instability of metal electrodes at anodic potentials, semiconductive oxide electrodes are of special interest.

Delarue described a group of insoluble oxides including tin oxide in molten LiCl-KCl eutectic (5). Some of them are oxide semiconductors with large bandgaps, retaining semiconductive properties at high temperatures. A single crystal of TiO_2 was used as an oxygen electrode in the melt containing O^{2-} ions, but the experiments were unsuccessful because of the soluble nature of the oxide (6). On the other hand, Sb-doped polycrystalline SnO_2 was found to be stable in the melt at 450°C, and showed a small background current until chlorine evolution took place (7).

It has been pointed out in the previous work (7) that we can use highly doped SnO_2 as a stable indicator electrode in a polarizable region which is in the electron depletion situation characterized by the Mott-Schottky equation, postulating an electron tunneling mechanism through the space charge layer. The present work was undertaken to examine the occurrence and the reversibility of redox processes at the melt-oxide interface. We selected reversible redox couples with one-electron transfer processes such as Eu(III)/Eu(II), Cr(III)/Cr(II), Cu(II)/Cu(I), and Fe(III)/Fe(II), which had been studied previously on carbon (2, 3, 8) or Pt indicator electrodes (9), but not yet on SnO_2. Some technical details for the use of SnO_2 electrodes in molten salt experiments are presented.

* Electrochemical Society Active Member.

Key words: semiconductor, molten salt, oxide electrode, electrode reaction.

Experimental

Electrodes.—Construction details of a tin oxide electrode are illustrated in Fig. 1. It was constructed from a Pyrex ground joint; the inner part was a tapered ground glass rod whose cross section (8 mm in diam) was given a mirror-like finish with fine alumina powder and coated with Sb-doped SnO_2 as described previously (7). To ensure a definite working area of the electrode, the inner part was matched precisely to the taper of the outer part. The gap between the two was filled with fine boron nitride powder; the powder suspended in isopropyl alcohol was brushed onto the oxide-coated taper of the inner part, which was twisted several times inside the outer part to spread out the boron nitride sealant. This procedure was necessary to prevent the melt from creeping into the gap. In order to make electrical contact between a lead wire and the SnO_2 film, a thin gold film was coated on a part of the oxide film with gold paste C-5040 supplied from Sumitomo Metal Mining Company. Several turns of platinum wire were wound on the gold coating.

We have tried a couple of different combinations of substrates and insulators to make melt-stable SnO_2 electrodes. A commercially available SnO_2 film, Nesa glass, was not suitable for molten salt experiments because the substrate was soda-lime glass, which was seriously attacked in the melt. Low temperature glass frits, so called solder glass, were used as an insulator, Sumitomo pastes I-9505 for Nesa Glass, and I-9004 for alumina substrate. Those compounds contained lead oxide which dissolved into the melt, and Pb(II) ions affected cyclic voltammograms when they were used in the melt. So far the combination of Pyrex substrate and boron nitride sealing was the best. However, a minor problem was encountered with this type of electrode. Creepage of the melt into the boron nitride seal could not be avoided when the electrode was left in the melt for a long time. In order to avoid this problem, experiments were finished within 2 hr, at most. A period of 1 hr was long enough to take a series of cyclic voltammograms.

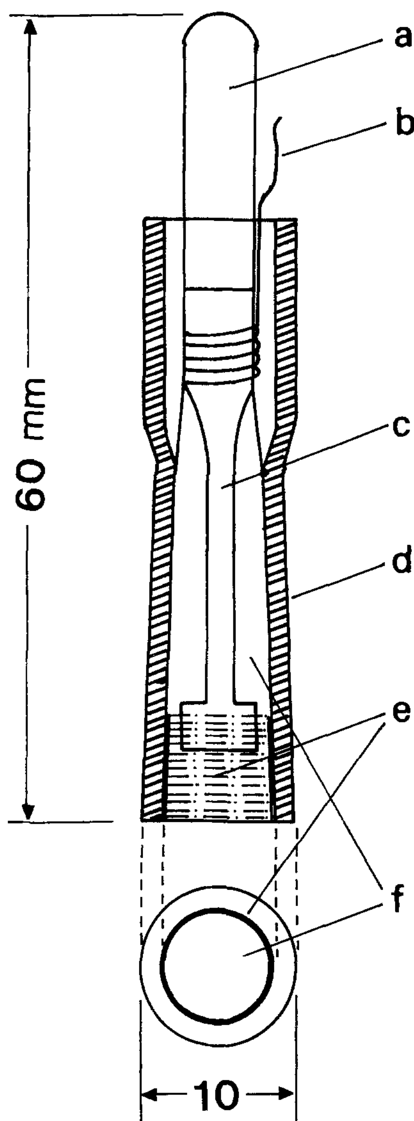

Fig. 1. Construction of a tin oxide electrode. (a) Pyrex rod; (b) platinum wire; (c) gold coating; (d) tapered ground joint; (e) boron nitride sealing; (f) tin oxide film.

The constructed electrode is demountable; the electrode is easily separated from the glass sheath after use in the melt. This is advantageous to facilitate surface conditioning of the electrode. The electrodes which had been used in the melt were sealed again with new boron nitride sealer before further experiments.

Sb-doped SnO_2 was coated onto a hot Pyrex substrate (500°C) by spraying the solution of 2.5M HCl containing 1.78M $SnCl_4$ and 0.0161M $SbCl_3$. The coating thickness was estimated as about 0.5 μm from the change in interference color, and the carrier concentration was 4.4×10^{20} cm^{-3} at room temperature, estimated from Mott-Schottky plots derived from capacitance measurements in 1*N* H_2SO_4 with an a-c bridge at frequencies from 0.7 to 4 KHz.

Glassy carbon electrodes (Beckwith Carbon Corporation) were used as working electrodes for comparison with SnO_2 electrodes. A rod of 3 mm diam was sealed into Pyrex by a technique described before (10).

Platinum reference electrodes and spectroscopic grade graphite counterelectrodes were used as in previous studies (11).

Reagents.—The LiCl-KCl eutectic was supplied from Anderson Physics Laboratories Incorporated, Urbana, Illinois.

Eu(III) and Cr(III) were added to the melt as chlorides, europium chloride (Alfa Ventron, anhydrous 99.5% pure), and chromium chloride (Alfa Ventron, sublimed, anhydrous 99% pure). Special care was needed to prevent their exposure to moisture because of their hygroscopic nature. For this purpose we designed a "powder buret" consisting of a separable type Teflon stopcock and a small glass ampul containing the chlorides. The chlorides were transferred into small ampuls (7 mm in OD and 10 cm in length) in a dry bag, and then they were sealed under an Ar atmosphere after vacuum drying. Before making an addition, one end of the ampul was cut and inserted into the opening of the stopcock. Another opening of the stopcock was connected to a long glass tube which reached the melt surface. The glass-to-Teflon fitting was so tight that the chemicals inside were not exposed to moisture. The amounts added were obtained by weighing the stopcock with the ampul before and after the addition. It was not difficult to add even 1 mg solid to the melt with fine manipulation of the stopcock.

Cu(I), Fe(II), and Pt(II) were generated by anodization of the metal wires with current densities of about 5 mA/cm^2. Currents were supplied by a Sargent coulometric current source, and the concentrations were calculated by assuming 100% current efficiency. Copper (0.64 mm in diam, m5N) and iron (0.25 mm in diam, m4N) were obtained from Alfa Ventron, Danvers, Massachusetts.

Apparatus.—Cyclic voltammograms were obtained with a Polarographic Analyzer Model-174A coupled to a Universal Programmer Model-175A (Princeton Applied Research Corporation), and the curves were recorded on a Moseley Model 7000 AM X-Y Recorder (Hewlett-Packard).

Cell impedance measurements were made with a Wayne Kerr Universal Bridge B221 equipped with a conventional polarization circuit. A 241-A Oscillator (Hewlett-Packard) as an a-c sine wave source and a Type 1232-A Tuned Amplifier and Null Detector (General Radio Company) as a zero detector were used.

Procedure.—A Pyrex container of 76 mm diam was set in a Hevi-Duty MK 3012-S Vertical Split Tube Furnace (Hevi-Duty Electric Company) regulated with a Wheelco Panel-Mount Capacitrol Temperature Controller (Wheelco Instrument Company). A Pyrex crucible and four sealing tubes with fine fritted disks were placed in the container, and about 60 ml of the melt sealed in an ampul was transferred into the cell. Two compartments of the four were small (14 mm in diam), and were occupied by the Pt(II)/Pt reference electrode and a graphite rode used as the counterelectrode. The melt solutions of the depolarizers were prepared in the large compartments of 25 mm diam. The volume of melt was calculated from the amount of chloride ion determined by argentometry and the density. Other details of experimental procedure have been given previously (2, 3). All potentials shown in this work were given with respect to the 1M Pt(II)/Pt electrode, and all experiments were carried out at 450°C under a purified argon atmosphere.

The tin oxide electrodes were subject to the following surface conditioning before experiments: the oxide surface was lightly polished with AB Alpha (0.3 μm) and AB Gamma (0.05 μm) Polishing Aluminas (Buehler Limited) on a flat disk covered with polishing cloth, and soaked in an acid mixture of H_2SO_4 and HNO_3 for 2 hr. After rinsing with distilled water and boiling in distilled water for 30 min, the electrode was assembled as shown in Fig. 1 and dried in an oven at 110°C. Finally the electrode attached to a holder was put into the cell container, where it was held for 30 min at 450°C before it came into contact with the melt.

Results and Discussion

Background current.—Current voltage traces in Fig. 2 show the background characteristics of SnO_2 with

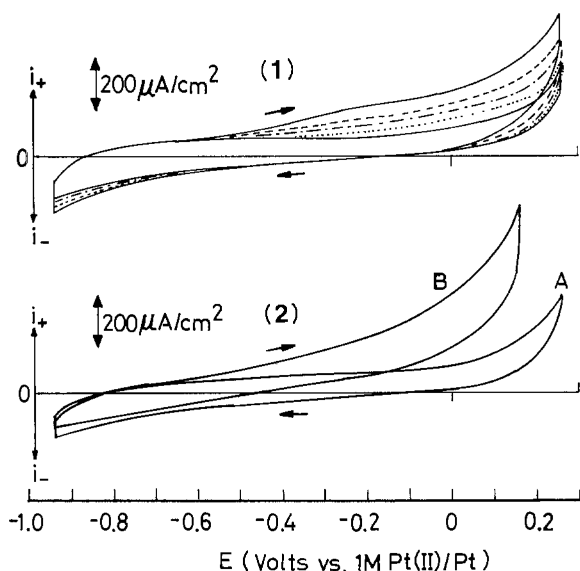

Fig. 2. Background characteristics for SnO_2 and glassy carbon electrodes with repeated potential scans (v = 100 mV/sec) in the eutectic at 450°C. (1) On SnO_2; 1st scan (——); 2nd scan (——); 3rd scan (–·–·–); 4th scan (.....); 5th scan (——). (2) Comparison of the SnO_2 with a glassy carbon electrode; (A) on SnO_2 after the 5th scan; (B) on GCE.

repeated potential scans (V = 100 mV/sec) in the melt. In the first scan, a relatively large background current was usually observed at anodic potentials, but it gradually decreased with the repetition of potential cycling (a-c treatment). After several a-c treatments the traces converged to a definitive and reproducible trace, indicating that the oxide-melt interface reached a steady state. This a-c treatment was necessary for the stabilization of electrodes.

The current increase observed at potentials more positive than −0.6V during the first few scans indicates that an irreversible oxidation process with a saturation effect takes place at the oxide-melt interface, where the specific adsorption of Cl^- ions is predominant as described elsewhere (7). The specific adsorption of Cl^- proceeds through the replacement of surface oxide groups by Cl^- ions, and then the released O^{2-} ions present at the interface can be anodically oxidized during the potential cycling

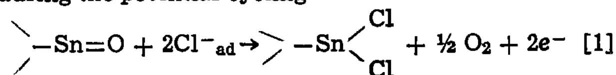

$$>\!Sn{=}O + 2Cl^-_{ad} \rightarrow\ >\!Sn\!<^{Cl}_{Cl} + \tfrac{1}{2}\,O_2 + 2e^- \quad [1]$$

According to this concept, the oxide surface subjected to a-c treatment is covered with adsorbed Cl^- ions which are strongly coupled with the surface. This is the actual condition of the electrode surface in the melt when we use it as an indicator electrode.

Figure 2 also shows that the usable anodic potential limit of the tin oxide electrode was slightly greater than that attained at a glassy carbon electrode (GCE). In comparison of SnO_2 with GCE, it was found that GCE showed a relatively large residual current at anodic potentials before chlorine evolution. This remarkable difference is due to the steep increase of the pseudocapacity at the carbon-melt interface with increasing anodic potentials because of the increased participation of adsorbed Cl^-. In contrast, the measurable capacity at the n-type oxide-melt interface is not that of the melt side, but the electrode side space charge which is smaller than that obtained at GCE and uniformly decreases with increasing anodic potentials as reported elsewhere (7).

In contrast with the amended anodic limit of SnO_2, the cathodic limit is better at GCE than at SnO_2, which undergoes cathodic decomposition at potentials beyond −1V. The available potential span of SnO_2 is about 1V.

Reduction of Eu(III) to Eu(II).—Well-defined voltammetric waves were obtained on SnO_2 at six potential scan rates ranging from 0.500 to 0.01 V/sec. Typical voltammograms are shown in Fig. 3.

The diagnostic criteria of Nicholson and Shain (12) were applied to determine the mechanism of the Eu(III)/Eu(II) reaction on SnO_2. The ratio of anodic to cathodic peak currents was measured for each scan, using the empirical expression developed by Nicholson (13)

$$i_{pa}/i_{pc} = (i_{pa})o/(i_{pc})o + 0.485\,(i_{sp})o/(i_{pc})o + 0.086 \quad [2]$$

where $(i_{pa})o$ and $(i_{pc})o$ are the measured anodic and cathodic peak currents and $(i_{sp})o$ is the cathodic current at the switching potential. The value of i_{pa}/i_{pc} plotted *vs.* scan rate are shown in Fig. 4, where the ratio is near unity over the entire scan range (0.01-0.5 V/sec). In agreement with the potentiometric study of Eu(III)/Eu(II) couple on Pt electrodes (9), the reaction on SnO_2 is a reversible diffusion-controlled process without kinetic complications.

Plots of the cathodic peak current *vs.* square root of the scan rate were linear through zero as shown in Fig. 5. The diffusion coefficient of Eu(III) in the melt at 450°C was calculated from the slope of Fig. 5; the *D*

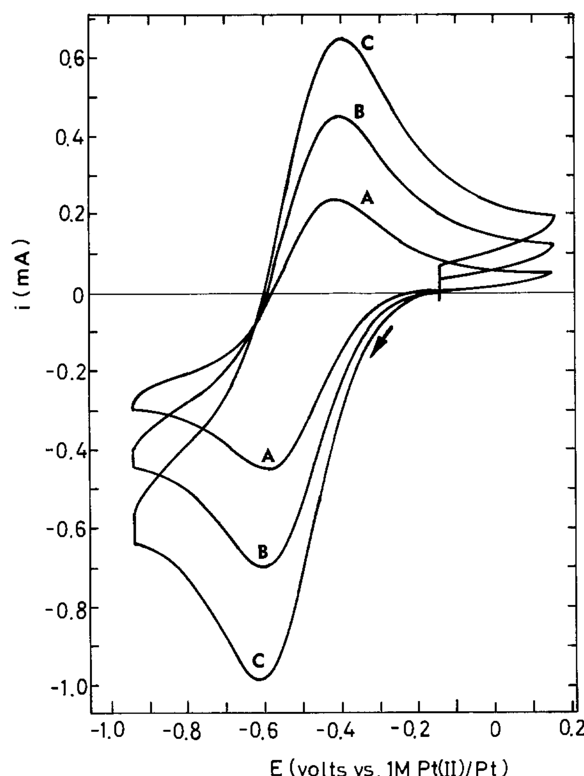

Fig. 3. Cyclic voltammograms for reduction of Eu(III) to Eu(II) in a melt solution of 11.8 mM $EuCl_3$ on SnO_2 (0.622 cm^2) at 450°C. (A) 0.020 V/sec; (B) 0.050 V/sec; (C) 0.100 V/sec.

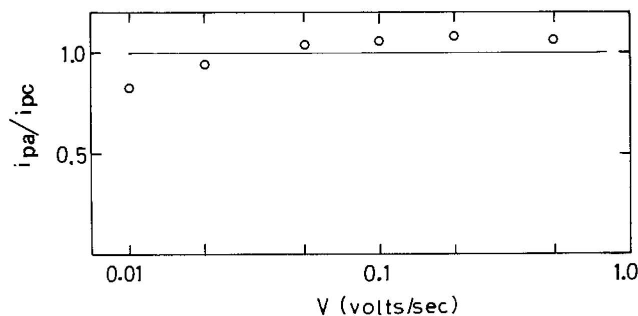

Fig. 4. Anodic-to-cathodic peak current ratio (i_{pa}/i_{pc}) vs. voltage scan rate (V) for 11.8 mM $EuCl_3$.

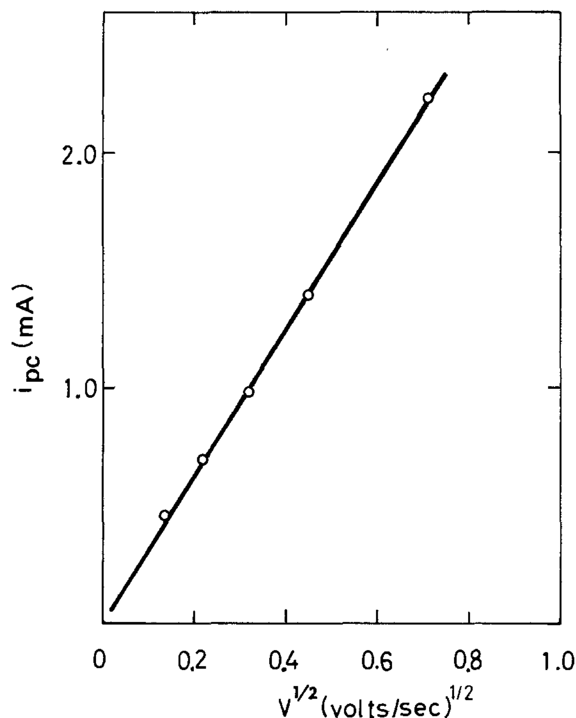

Fig. 5. Cathodic peak current (i_{pc}) vs. square root of voltage scan rate ($V^{1/2}$) for 11.8 mM $EuCl_3$.

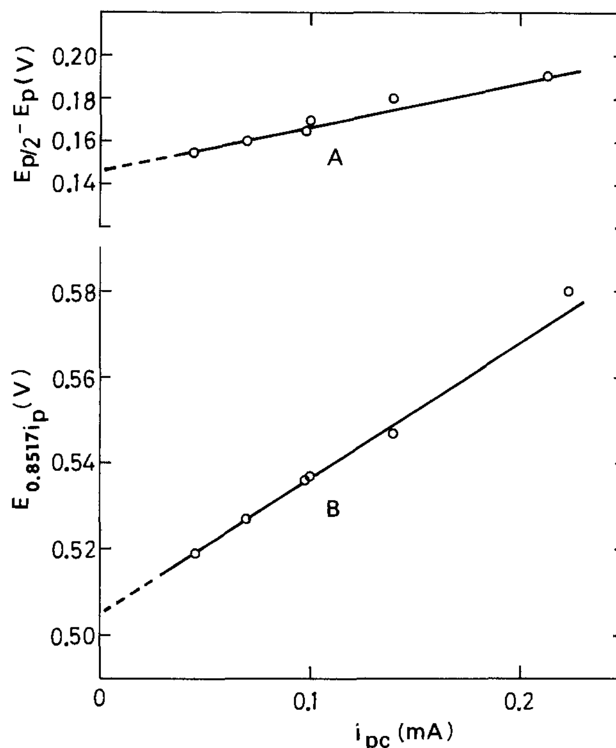

Fig. 6. Correction of *IR* effect due to electrode resistance in determination of ($E_{p/2} - E_p$) and $E_{1/2}$ for reduction of Eu(III) to Eu(II).

value was 0.61×10^{-5} cm²/sec by using the expression derived for the reversible case with $n = 1$ (12). Somewhat larger D values were obtained after various periods of standing the electrode in the melt. 2 hr after the experiments quoted in Fig. 5, an apparent 6% increase of the D value was observed. This difference is attributed to a change in the effective working area caused by penetration of the melt into the boron nitride sealer.

The most important problem in this work is the elimination of the IR drop caused by the electrode film resistance. Of the variety of methods available for correcting the resistance, a simple and reliable procedure to obtain IR-free $E_{1/2}$ and peak separation is to plot them as a function of the peak current as suggested by Kuwana *et al.* (14). Plots of observed ($E_{p/2} - E_p$) and the potentials corresponding to $0.8517 i_p$ ($E_{0.8517 i_p}$) against i_{pc} were linear, as shown in Fig. 6. The following expressions may be written for the reversible case including the IR effect

$$E_{p/2} - E_p = 2.199\, RT/n\mathbf{F} + 0.5 i_p R \quad [3]$$

$$E_{0.8517 i_p} = E_{1/2} + 0.8517 i_p R \quad [4]$$

where $2.199\, RT/n\mathbf{F}$ is $0.137/n$V at 450°C. Electrode resistance, R, is given by the slope of the line, and the IR-free $E_{1/2}$ and ($E_{p/2} - E_p$) are equal to the intercepts at $i_{pc} = 0$. The electrode resistances obtained from the slopes of (A) and (B) in Fig. 6 were 39 and 38Ω, respectively, in agreement with the values measured with an a-c bridge. The intercept of the plot (A) was 0.145V, being very close to the theoretical value with $n = 1$. The half-wave potential of the Eu(III)/Eu(II) couple was determined as $E_{1/2} = -0.504$V *vs.* 1M Pt(II)/Pt. This value is more positive by 34 mV than the standard electromotive force reported in the literature (9).

Reduction of Cr(III).—Cyclic voltammetric measurements followed by similar procedures for data analyses were carried out for the reduction of Cr(III) to Cr(II). The IR-free ($E_{p/2} - E_p$) was 0.155V, and $E_{1/2}$ was -0.529V *vs.* 1M Pt(II)/Pt, in agreement with the standard electromotive force [$E° = -0.535$V (2)]. These results indicate that the redox couple of Cr(III)/Cr(II) at SnO_2 is reversible. However, i_{pa}/i_{pc} was not unity over the whole range of scan rates ($0.01 < v < 1.00$ V/sec), and decreased with decreasing scan rate at lower scan rates between 0.1 and 0.01 V/sec, as revealed by Levy and Reinhardt (8) and the authors at GCE (10). According to the usual criteria (12), the variation of i_{pa}/i_{pc} indicates a slow chemical step following charge transfer and the reaction mechanism has been discussed in detail (8, 10).

The calculated D value of Cr(III) was 0.79×10^{-5} cm²/sec, agreeing with the D value determined at GCE (10). Strictly speaking, however, this D value was a little smaller than that obtained in a melt solution of Cr(III) saturated with dry HCl (10). As pointed out in the previous paper (10), $CrCl_6^{-3}$ in the melt easily undergoes a hydrolysis reaction with a trace of moisture, producing a less reversible species such as $CrCl_5(OH)^{-3}$ and an electro-inactive polymerized form. A greater participation of these complexes results in a smaller D value and a greater separation between $E_{p/2}$ and E_p. Unfortunately, measurements in the melt saturated with HCl were impossible because the tin oxide film chemically dissolved into the melt in the presence of HCl (15).

Oxidation of Cu(I) and Fe(II).—The standard electromotive force of the Cu(II)/Cu(I) couple is 0.061V *vs.* 1M Pt(II)/Pt, which is very close to that of the Fe(III)/Fe(II) couple, $E° = 0.086$V (2, 3). It was found that both redox couples are reversible on SnO_2, but the former oxidation process is different from the latter.

Typical cyclic voltammograms with different scan rates for the oxidation of Cu(I) are shown in Fig. 7 together with the background scan. There was no anodic peak, and only cathodic peaks were observable. Since the background current was still small at the anodic potentials, the uniform increase of anodic current could not be attributed to participation of chlorine evolution, while the location of the IR-free cathodic peak potential was -0.012V. Using the theoretical relationship between E_{pc} and $E_{1/2}$ (12), $E_{1/2} - E_{pc} = 1.109\, RT/n\mathbf{F}$, $E_{1/2}$ was estimated as $+0.057$V *vs.* 1M

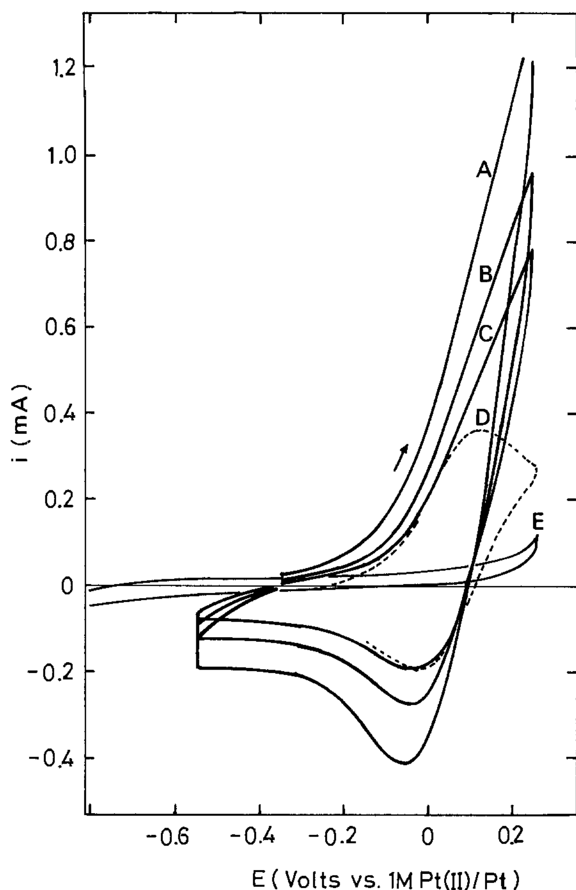

Fig. 7. Cyclic voltammograms for oxidation of Cu(I) to Cu(II) in a melt solution of 2.98 mM Cu(I) on SnO_2 (0.50 cm^2) at 450°C. (A) 0.500 V/sec; (B) 0.200 V/sec; (C) 0.100 V/sec; (D) theoretical curve for reversible one-electron transfer with $v = 0.1$ V/sec and $D - 2 \times 10^{-5}$ cm^2/sec; (E) background i-E.

Pt(II)/Pt. being very close to $E°$ of Cu(II)/Cu(I). It is obvious that the cathodic peak corresponds to rereduction of Cu(II) produced by the anodic scan.

A dotted curve in Fig. 7 is a theoretical voltammogram for a reversible one-electron transfer process with $v = 0.1$V; sec, where the D value was selected as 2×10^{-5} cm^2/sec to yield the same cathodic peak height as the observed one. The selected D value was reasonable in comparison with published data (16). The great discrepancy in the current behavior for the oxidation of Cu(I) suggests that the oxidation process is accompanied by catalytic or adsorption processes.

Similar behavior, showing no oxidation peak but a reduction peak, was observed for the oxidation of Pt(II) to Pt(IV). However, on glassy carbon electrodes De Lepinay *et al.* obtained the oxidation peak of Pt(II) in the melt at 450°C (4). Although we did not obtain the oxidation peak on SnO_2, the anodic oxidation of Pt(II) to Pt(IV) was quite evident.

In contrast with the behavior of Cu(I) and Pt(II), the oxidation peak of Fe(II) was obtained, as shown in Fig. 8, where the peaks were somewhat distorted by background currents. It was found that the anodic shoulders correspond to the diffusion-controlled current peaks with $n = 1$, if we correct for the background current.

The kinetic difference between the oxidations of Cu(I) and Fe(II) may be attributed to the different coordination structures of the ions in the melt. According to spectrophotometric studies in the melt, Cu(II) is reported to be a tetragonally distorted tetrahedral $CuCl_4^{2-}$ (17), which means a somewhat flattened structure, and Pt(II) is believed to have the D_{4h} symmetry, indicating some axial interaction between the square planar $PtCl_4^{2-}$ ion and solvent anions (18). On the other hand, Fe(II) is described as a purely tetrahedral $FeCl_4^{2-}$ in the melt at 400°C (17, 18). Unfortunately, the coordination of Cu(I) in the melt is still unknown. However, in concentrated aqueous HCl solutions (~12M) the Raman spectrum of Cu(I) suggests that the predominant species is a trigonal $CuCl_3^{2-}$ (19). From chronopotentiometric measurements of diffusion coefficients of univalent ions [Cu(I), Ag(I) and Au(I)] with different ionic radii (16), it was noted that the univalent cations are probably uncomplexed in the melt because the D values decrease as the ionic radii increase, while bivalent ions [Fe(II) and Ni(II)] are complexed because of lack of the correlation between the D values and the ionic radii. It is more likely that Cu(I) in the melt is $CuCl_3^{2-}$ or a less coordinated chloro-complex rather than tetrahedral $CuCl_4^-$. Generally speaking, a chloro-complex with a more flattened structure is accessible to the electrode surface, as suggested for the adsorption of square-planar $PtCl_4^{2-}$ in the melt (20).

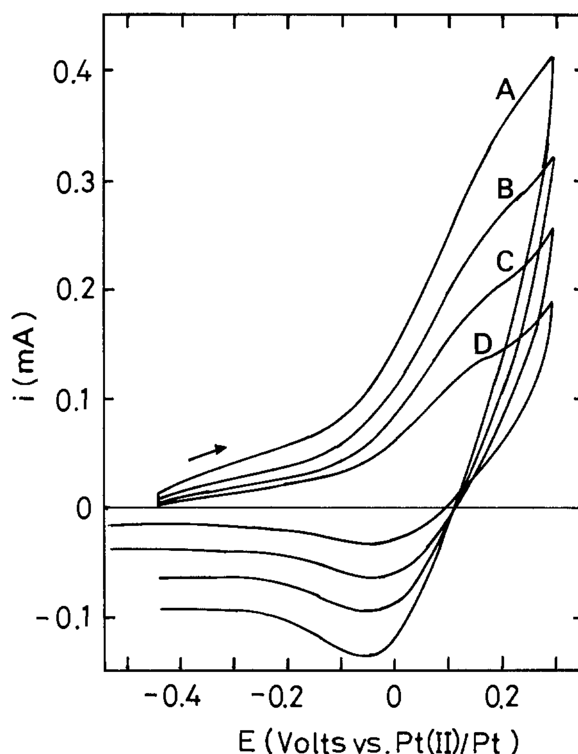

Fig. 8. Cyclic voltammograms for oxidation of Fe(II) to Fe(II) in a melt solution of 1.57 mM Fe(II) on SnO_2 (0.622 cm^2) at 450°C. (A) 0.200 V/sec; (B) 0.100 V/sec; (C) 0.050 V/sec; (D) 0.020 V/sec.

The oxide surface in the melt was drastically modified through the replacement of surface oxide groups by specifically adsorbed Cl^- ions, as shown in Eq. [1]. As for the effect of adsorption, the formation of an anionic bridge between adsorbed anions and electroactive species is a well-known phenomenon in aqueous systems in explanation of a rate-enhancing effect by specifically adsorbed anions (21). In studies on metal deposition in molten nitrate melts with halide ions, Inman *et al.* suggested anion bridging to facilitate the discharge of metal ions (22). We therefore believe that Cu(I) with the structures considered above interact with the surface chloride groups, which act as electron bridges to facilitate the oxidation. Assuming the trigonal structure, a folowing scheme may be written to produce $CuCl_4^{2-}$

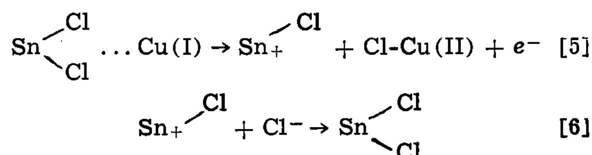

$$Sn\genfrac{}{}{0pt}{}{Cl}{Cl} \ldots Cu(I) \rightarrow Sn_{+}^{\ Cl} + Cl\text{-}Cu(II) + e^- \quad [5]$$

$$Sn_{+}^{\ Cl} + Cl^- \rightarrow Sn\genfrac{}{}{0pt}{}{Cl}{Cl} \quad [6]$$

For the case of $FeCl_4^{2-}$ with pure tetrahedral coordination, the adsorption effect does not seem to be predominant because of its steric hindrance, in contrast with the square-planar complex $PtCl_4^{2-}$, which may be suited to the formation of anionic bridges. In addition, no adsorption effects of octahedral $EuCl_6^{3-}$ and $CrCl_6^{3-}$ (17) were observed on SnO_2, because plots $i_{pc}/v^{1/2}$ *vs.* v were constant up to the scan rate of 1 V/sec. No adsorption of the latter ions on GCE was observed (8).

We therefore conclude that all the systems examined in this work undergo reversible electron-transfer processes. However, the oxidations of Cu(I) and Pt(II) involve adsorption processes via anionic bridges.

Electron transfer at the oxide-melt interface.—The Sb-doped SnO_2 is an n-type semiconductor with a large bandgap (3.8 eV) which retains semiconductive properties up to higher temperatures (> 1300°C) (23). The oxide electrodes used for the voltammetric studies were highly doped specimens with a doping level of 4.4×10^{20} cm^{-3}, which was determined by capacity measurements in 1N H_2SO_4 at room temperature. According to the previous study (7), the interfacial capacities measured in the melt at an SnO_2 electrode with the same order of doping level obeyed the Mott-Schottky relationship as well as in aqueous solutions, and the flatband potential (E_{fb}) of the oxide at 450°C was estimated as -1.29V *vs.* 1M Pt(II)/Pt. The carrier concentration at 450°C was larger than that observed at room temperature.

The potential range in this study is more positive than E_{fb}, the redox couples being located at lower energy levels far removed from the edge of the conduction band. According to the semiconductor-liquid junction theory (24), the electron concentration near the electrode surface is depleted at the potentials where the space charge barrier is present at the surface. Since an electron transfer usually occurs via the conduction or the valence band, it has to be taken into account how much the energy states in the semiconductor overlap with the energy levels of the redox couples in the melt. The overlapping is determined by the position of the redox potential relative to the E_{fb}. For the couples under study, the overlapping of the corresponding energy levels seems to be quite small and consequently the exchange current is expected to be low on the tin oxide electrode.

In spite of this prediction, however, the redox couples examined at the tin oxide electrode are reversible, indicating that the electron transfer occurs by tunneling through the space charge barrier of this highly doped oxide electrode. The electron tunneling process at SnO_2 electrodes in aqueous systems has been presented by Elliott *et al.* (25) and reexamined by Möllers and Memming (26). According to the former study, the tunneling current prevails when the carrier concentration is larger than 3×10^{19} cm^{-3}, and at 5.9×10^{20} cm^{-3} the space charge barrier is completely transparent to electrons due to tunneling. In the high temperature melt system the observed carrier concentration becomes larger than that at room temperature, and the electrode surface does not have an oriented solvation layer as in aqueous systems. This situation must be more favorable to the tunneling process. It may be emphasized that the highly doped SnO_2 electrode in the melt is a metal-like electrode in view of the highly transparent nature to electrons, while it still has a characteristic interface of the semiconductor-liquid junction, *e.g.*, lower background currents due to the smaller space charge capacities in comparison with metal-melt interfaces.

Acknowledgment

This work was supported by the U.S. Army Research Office, Grant No. DAAG 29-75-G-0092.

Manuscript submitted April 27, 1978; revised manuscript received June 28, 1978.

Any discussion of this paper will appear in a Discussion Section to be published in the June 1979 JOURNAL. All discussions for the June 1979 Discussion Section should be submitted by Feb. 1, 1979.

Publication costs of this article were assisted by the University of Florida.

REFERENCES

1. J. A. Plambeck, "Encyclopedia of Electrochemistry of the Elements," Vol. X, A. J. Bard, Editor, Marcel Dekker, New York (1976).
2. H. A. Laitinen and C. H. Liu, *J. Am. Chem. Soc.*, **80**, 1015 (1958).
3. H. A. Laitinen and J. W. Pankey, *ibid.*, **81**, 1053 (1959).
4. J. De Lepinay and M. J. Barbier, *J. Electroanal. Chem. Interfacial Electrochem.*, **45**, 419 (1973); **47**, 453 (1973).
5. G. Delarue, *J. Electroanal. Chem.*, **1**, 285 (1959).
6. K. Niki and H. A. Laitinen, Unpublished data.
7. I. Uchida, H. Asano, and S. Toshima, *J. Electroanal. Chem. Interfacial Electrochem.*, In press.
8. S. C. Levy and F. W. Reinhardt, *This Journal*, **122**, 200 (1975).
9. K. E. Johnson and J. R. Mackenzie, *ibid.*, **116**, 1697 (1969).
10. H. A. Laitinen, Y. Yamamura, and I. Uchida, *ibid.*, In press.
11. W. S. Ferguson, Ph. D. Thesis, University of Illinois, Urbana, Ill. (1956).
12. R. S. Nicholson and I. Shain, *Anal. Chem.*, **36**, 706 (1964).
13. R. S. Nicholson, *ibid.*, **38**, 1406 (1966).
14. T. Kuwana, R. K. Darlington, and D. W. Leedy, *ibid.*, **36**, 2023 (1964).
15. D. Zellmer, Ph. D. Thesis, University of Illinois, Urbana, Ill. (1969).
16. J. C. Pignet and M. J. Barbier, *Electrochim. Acta*, **17**, 1227 (1972).
17. D. M. Gruen and R. L. McBeth, *Pure Appl. Chem.*, **6**, 23 (1963).
18. K. E. Johnson and J. R. Dickinson, "Advances in Molten Salt Chemistry," Vol. 2, J. Braunstein, G. Mamantov, and G. P. Smith, Editors, p. 83, Plenum Press, New York (1973).
19. J. A. Creighton and E. R. Lippincott, *J. Chem. Soc.*, 5134 (1963).
20. A. D. Graves and D. Inman, *Nature (London)*, **208**, 481 (1965).
21. R. de Levie, *This Journal*, **118**, 185C (1971).
22. D. Inman, R. S. Sethi, and R. Spencer, *J. Electroanal. Chem. Interfacial Electrochem.*, **29**, 137 (1971).
23. H. J. van Daal, *Solid State Commun.*, **6**, 5 (1968).
24. H. Gerisher, *Adv. Electrochem. Electrochem. Eng.*, **1**, 139 (1961).
25. D. Elliott, D. L. Zellmer, and H. A. Laitinen, *This Journal*, **117**, 1343 (1970).
26. F. Möllers and R. Memming, *Ber. Bunsenges. Phys. Chem.*, **76**, 469 (1972); **76**, 475 (1972).

Laplace Plane Analysis of Skin Impedance: A Preliminary Investigation

Maria Reichmanis, Andrew A. Marino, and Robert O. Becker

Veterans Administration Hospital, Syracuse, New York 13210
and Department of Orthopedic Surgery, SUNY Upstate Medical Center, Syracuse, New York 13210

ABSTRACT

The impedance and phase angle of skin as functions of frequency were determined by Laplace plane analysis of the time domain current resulting from an external voltage perturbation. Bode plots of these functions established a passive equivalent circuit model for skin impedance which is valid over a wide range of frequencies. Typical values for the model circuit elements are given for ten human subjects.

The electrical properties of any biological tissue depend on its intrinsic structure and, for *in vivo* studies, on the functional state of the organism. For the case of human skin, the impedance can vary with the thickness and moisture content of the stratum corneum, the concentration and activity of sweat glands, localized injury, the age of the subject, and environmental factors such as temperature and humidity. Seasonal and diurnal variations have been measured: For example, the d-c resistance of skin tends to increase during sleep. Short-term fluctuations are the basis for various monitoring techniques, including the electrocardiogram, electroencephalogram, and impedance plethysmography. Changes in impedance are also associated with the psychological state of the subject (1).

Studies of the a-c impedance of biological systems, including human skin, have generally involved direct measurement of the impedance and phase angle as functions of the frequency of the applied voltage or current (2-5). Any such measurement over a wide range of frequencies tends to be cumbersome and time-consuming. Measurements with an impedance bridge have the additional disadvantage that some *a priori* assumptions must be made regarding an equivalent circuit for the skin impedance. Other reports have presented approximation methods for deriving the equivalent circuit components from the current response to a square voltage pulse input (6, 7). Burton (8) applied Bode analysis to measurements of the skin impedance and phase angle. By means of this method a passive equivalent circuit can be synthesized for any electrical "black box" from plots of its impedance and phase angle *vs.* frequency. The only assumption required is that the system consists solely of passive linear lumped circuit elements (8, 9). Even though the resulting model is not necessarily unique (8), it must represent the system accurately in the frequency range studied.

By extending this technique one step further, the entire frequency spectrum of any system can be computed by applying a Laplace transformation to the current response to an arbitrary voltage perturbation, thus eliminating the tedious process of point-by-point measurement of the impedance and phase angle.

Method

In order to obtain the impedance of a system as a function of frequency, the input voltage perturbation $V(t)$ and the resulting current $I(t)$ must be converted from the time domain (t) to the complex frequency domain (s). This may be accomplished by means of a Laplace transformation. The transform $\mathbf{F}(s)$ of a time domain function $f(t)$ is defined as

Key words: transient analysis, skin equivalent circuit, galvanic skin response, Laplace plane analysis.

$$\mathbf{F}(s) = \int_0^\infty f(t) \exp(-st)\,dt \qquad [1]$$

where $s = \sigma + j\omega$ denotes the complex frequency plane with real axis σ and imaginary axis $j\omega$ (9-11). The integration (1) can be carried out along either the real or imaginary axis of the complex frequency plane. Considering the real axis $(s = \sigma)$

$$\mathbf{F}(\sigma) = \int_0^\infty f(t) \exp(-\sigma t)\,dt, \quad \sigma > 0 \qquad [2]$$

This integral exists for any converging function $f(t)$ $\exp(-\sigma t)$. Performing real axis transformations on both $V(t)$ and $I(t)$, we can define the real axis impedance of the system as

$$Z(\sigma) = V(\sigma)/I(\sigma) \qquad [3]$$

The analogous imaginary axis Laplace transformation $(s = j\omega)$ is given by

$$\mathbf{F}(j\omega) = \int_0^\infty f(t) \exp(-j\omega t)\,dt \qquad [4]$$

equivalent to a one-sided Fourier transform. The corresponding imaginary axis impedance function is

$$Z(j\omega) = V(j\omega)/I(j\omega) \qquad [5]$$

$Z(j\omega)$ is a complex function with a real component $\mathrm{Re}Z(\omega)$ and an imaginary component $\mathrm{Im}Z(\omega)$ which define the phase angle

$$\phi(\omega) = \tan^{-1}[\mathrm{Im}Z(\omega)/\mathrm{Re}Z(\omega)] \qquad [6]$$

A FORTRAN program for both real and imaginary axis Laplace transformations has been developed by Pilla (10, 11). The input data are points defining $V(t)$, an arbitrary voltage perturbation, and $I(t)$, the current response of the system under observation from time $t = 0$ to the time at which $I(t)$ reaches its d-c limit. The program is written for a $V(t)$ which increases from zero to some final constant value and an $I(t)$ rising from zero to a single maximum before decreasing to its d-c limit. We found that the subject current matched these constraints. The output data include $Z(\sigma)$, $\mathrm{Re}Z(\omega)$, $\mathrm{Im}Z(\omega)$, and $\phi(\omega)$ as functions of frequency over any desired range. The highest attainable frequency range is proportional to the reciprocal of the smallest time after $t = 0$ at which both $V(t)$ and $I(t)$ are measurable. The Laplace

transform method of obtaining these functions is particularly advantageous in that $Z(\sigma)$ and $Z(j\omega)$ are theoretically independent of the properties of the measuring electrodes, provided that these are as nearly identical as possible (11).

Experimental Procedure

The voltage $V(t)$, a pulse with a rise time of 10 μsec, a duration of 100 μsec, and a maximum amplitude of 1V, was displayed on one channel of a Tektronix 564 dual-trace oscilloscope; the subject current $I(t)$ was displayed on the second channel (see Fig. 1). Preliminary studies indicated that a pulse duration of 100 μsec was sufficiently long to establish the d-c current limit for all subjects. The interval was set at 1000 μsec (10 times the pulse duration) throughout the study. The resulting display was adequate for photography at sweep rates slower than 0.2 μsec/cm. After the skin has been cleaned with 90% ethanol and hydrated with distilled water, two 1 cm diam carbon-impregnated conducting-rubber electrodes (modified L1DC electrodes, Ritter Company) were applied to the dorsal surfaces of the hand and upper forearm, both in areas devoid of cuts, abrasions, or pigmented moles. We found that the results obtained with these electrodes were comparable to those with metal electrodes, with the advantages of greater flexibility and ease of application. In order to study the skin in as physiological a state as possible, no electrode paste was used. The ensuing oscilloscope display of $V(t)$ and $I(t)$ was photographed for later analysis; typical curves are shown in Fig. 2. Several exposures at sweep speeds ranging from 0.5 to 10 μsec/cm were needed to obtain sufficient data for subsequent mathematical analysis. This procedure was repeated on a total of 10 volunteer subjects.

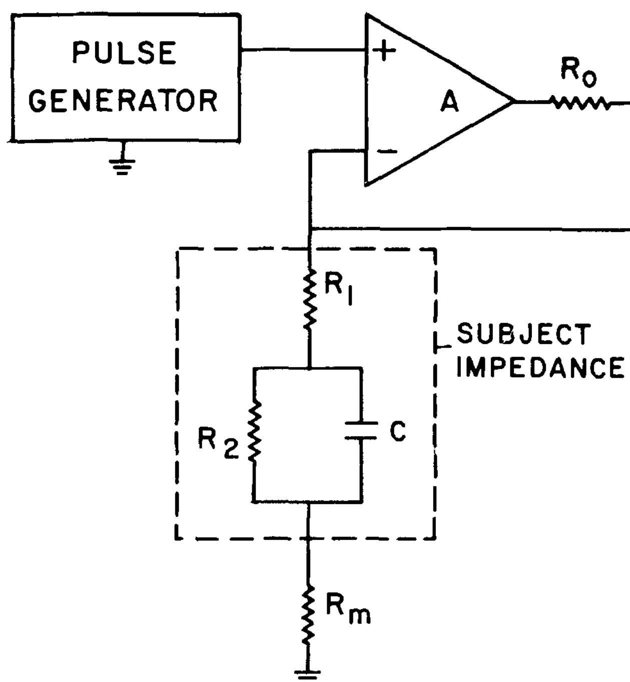

Fig. 1. Potentiostatic circuit for the study of skin impedance. The power supply consisted of a Tacussel model PRT-20-010-MOD potentiostat (A) with output impedance R_0, controlled by a model GSTP-10 pulse generator, applied to the subject. The voltage $V(t)$, a pulse with a rise time of 10 μsec and a duration of 100 μsec, was displayed on one channel of a Tektronix 564 storage oscilloscope with a 3A6 dual-trace input and 3B4 time base. The subject current response $I(t)$, proportional to the voltage across a small series resistor R_m, was displayed on the second channel. The model shown for the subject is a standard equivalent circuit for the a-c impedance of human skin (1,3,6,8).

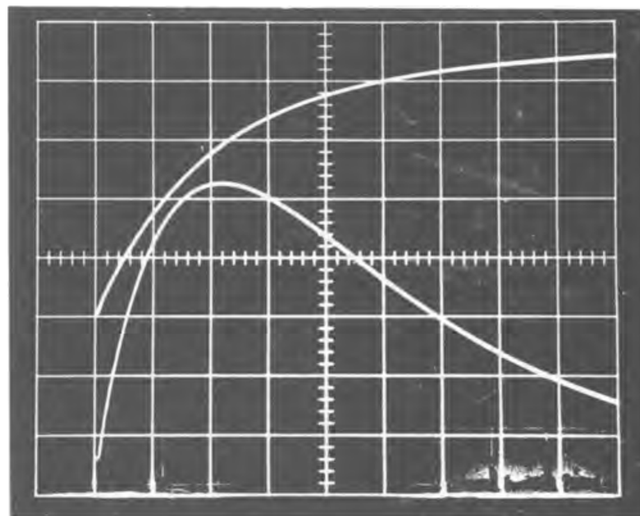

Fig. 2. Typical response curves at 2 μsec/cm. The upper trace is $V(t)$ at 0.2 V/cm; the lower trace is $I(t)$ at 5 μA/cm.

Points defining $V(t)$ and $I(t)$, taken from the photographs, were used as the input time domain data for real and imaginary axis Laplace transformations performed for each individual test by means of a FORTRAN program for numerical integration (10, 11). To attain an upper frequency limit of 1 MHz, it was necessary to record $V(t)$ and $I(t)$ from $t = 0.1$ μsec, with no more than a 10% variation in either parameter between successive data points. These conditions required 50-70 such data points per test. The output of the program included the phase angle and real and imaginary components of the impedance as functions of frequency (d-c to 1 MHz).

Results

Analysis of the frequency domain data for human skin resulting from the real and imaginary axis Laplace transformations established that all of the impedance *vs.* frequency curves were of the same form, and could be described by the real impedance function

$$Z(\sigma) = R_1 + 1/(\sigma C + 1/R_2) \quad [7]$$

This corresponds to a simple R-C circuit (see Fig. 1) found by Burton (8) to be an adequate representation of the skin impedance. Similarly, the data from the imaginary axis transformation yielded the complex impedance

$$Z(j\omega) = R_1 + 1/(1/R_2 + j\omega C) \quad [8]$$

$Z(j\omega)$ could be separated into its real and imaginary components

$$\mathrm{Re}Z(\omega) = R_1 + 1/(\omega^2 C^2 + 1/R_2^2) \quad [9]$$

and

$$\mathrm{Im}Z(\omega) = -\omega C/(\omega^2 C^2 + 1/R_2^2) \quad [10]$$

with a phase angle

$$\phi(\omega) = \tan^{-1}(\omega C/[1 + R_1(\omega^2 C^2 + 1/R_2^2)] \quad [11]$$

Once the form of the equivalent circuit was established, it was not necessary to repeat the entire analytical procedure for each individual test. When analyzing large volumes of data, the model circuit components (R_1, R_2, and C) could be derived from the appropriate low and high frequency limits of these functions (10, 11). These are listed in Table I.

Table I. Low ($R_2\omega C << 1$) and high ($R_2\omega C >> 1$) frequency limits of $Z(\sigma)$, $ReZ(\omega)$, $ImZ(\omega)$, and $\tan \phi (\omega)$

	$R_2\omega C << 1$	$R_2\omega C >> 1$
$Z(\sigma)$	$R_1 + R_2$	$R_1 + 1/\sigma C$
$ReZ(\omega)$	$R_1 + R_2$	$R_1 + 1/R_2\omega^2C^2$
$ImZ(\omega)$	$-\omega C R_2^2$	$-1/\omega C$
$\tan \phi(\omega)$	$-\omega C R_2^2/(R_1 + R_2)$	$-1/\omega C R_1$

In this case, the low frequency limit of both $Z(\sigma)$ ($\sigma CR_2 << 1$) and $ReZ(\omega)$ ($\omega CR_2 << 1$) is $R_1 + R_2$. $|ImZ(\omega)|$ *vs.* ω is a straight line through the origin with slope CR_2^2. At high frequencies ($\sigma CR_2 >> 1$; $\omega CR_2 >> 1$) $|ImZ(\omega)|$ *vs.* $1/\omega$ becomes a straight line with slope $1/C$; $Z(\sigma)$ and $ReZ(\omega)$ are lines with intercepts R_1 and slopes $1/C$. Sample curves are given in Fig. 3. All the equivalent circuit elements can be determined from the results of either transform: it is not necessary to the analysis to perform both real and imaginary axis transforms.

Values of R_1, R_2, C, and the minimum angle ϕ_{min} for all 10 subjects are listed in Table II. These results are compatible with those of earlier studies. As noted by Plutchik (4), the phase angle apparently varied much less between subjects than did the other parameters (see Table II). The equivalent circuit is valid for all anatomical locations. The actual values of the circuit elements would, however, vary with location for each individual. For example, the d-c resistance ($R_1 + R_2$) of the dorsum of the hand tends to be higher than that of the palm (1). R_2 represents the d-c resistance of the stratum corneum, probably separated by a discrete basal cell membrane from the inner tissue resistance R_1. An injury, such as a pinprick, results in a significant drop in the measured

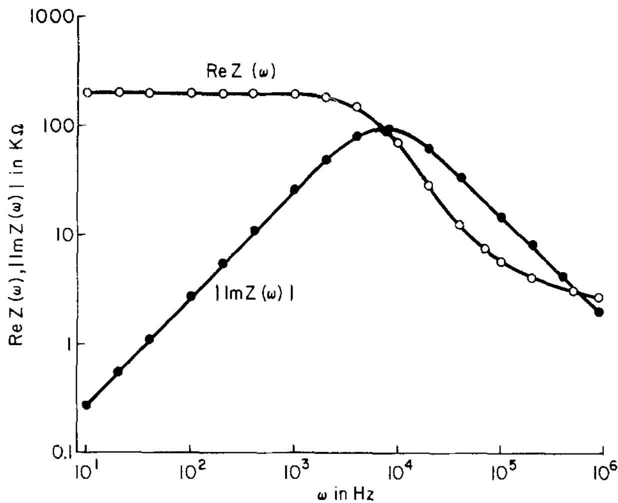

(a)

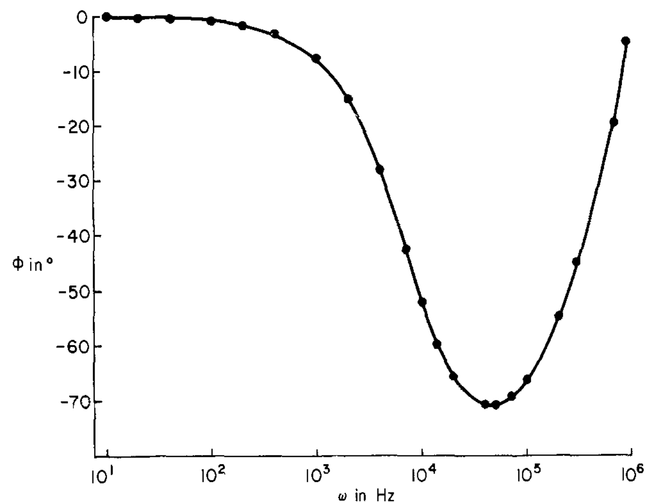

(b)

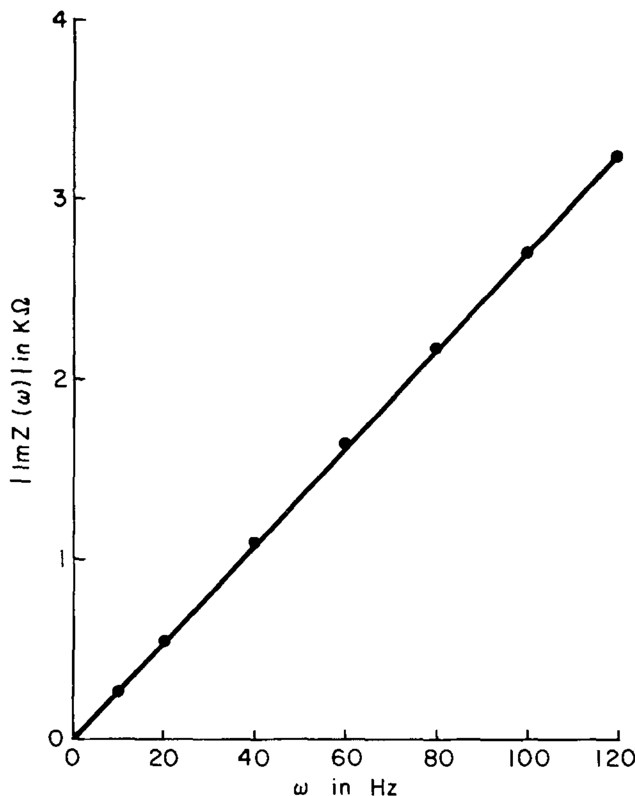

(c)

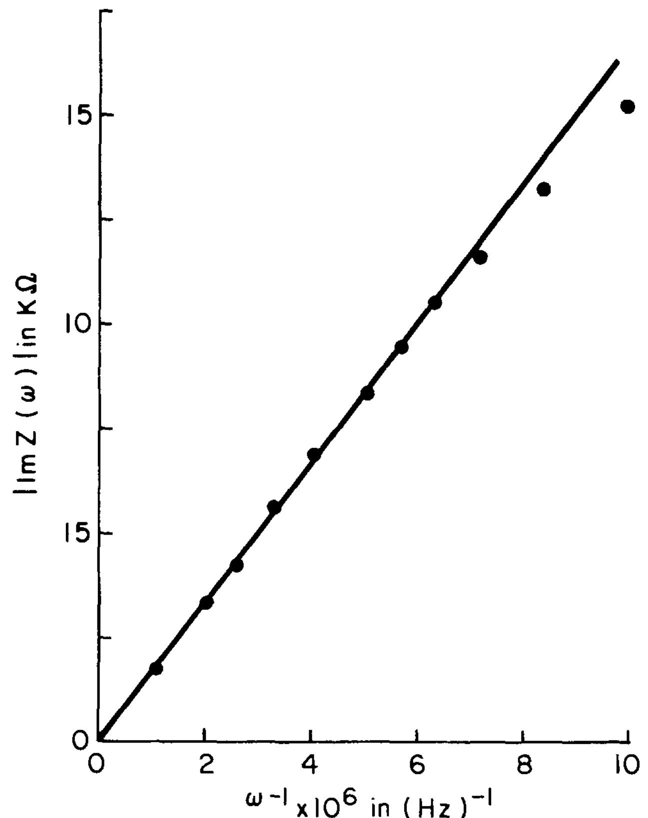

(d)

Fig. 3. Typical results of an imaginary axis Laplace transformation. (a) $ReZ(\omega)$ vs. ω and $|ImZ(\omega)|$ vs. ω; (b) $\phi(\omega)$ vs. ω; (c) $|ImZ(\omega)|$ vs. ω at low frequencies, ($R_2\omega C<<1$) has slope CR_2^2 and intercept 0; (d) $|ImZ(\omega)|$ vs. $1/\omega$ at high frequencies, ($R_2\omega C>>1$) has slope $1/C$.

Table II. Mean values of R_1, R_2, C, and ϕ_{min} for each of 10 subjects

Subject	$R_1(K\Omega)$	$R_2(K\Omega)$	$C(pf)$	ϕ_{min}(deg.)
1	17.8 ± 4.1	768 ± 299	298 ± 15.6	−72.7 ± 1.3
2	2.06 ± 0.08	159 ± 126	1730 ± 226	−75.3 ± 6.0
3	17.5 ± 0.6	292 ± 34	252 ± 2.8	−63.2 ± 1.8
4	29.9 ± 0.9	561 ± 50	165 ± 3.5	−64.6 ± 1.4
5	6.51 ± 1.80	344 ± 14	430 ± 45	−73.0 ± 7.5
6	6.19 ± 0.09	186 ± 14	720 ± 18	−69.7 ± 0.9
7	6.72 ± 0.40	224 ± 28	177 ± 15	−70.6 ± 1.7
8	212 ± 2.1	1900 ± 156	47.7 ± 0.3	−54.9 ± 1.3
9	199 ± 15	2480 ± 240	35.8 ± 4.6	−59.5 ± 0.3
10	5.89 ± 0.4	112 ± 9.9	893 ± 13	−64.8 ± 0.3

d-c resistance in that area, followed by a return to the normal level during healing. It is at present unclear whether C is a structural or merely a polarization capacitance. If the former, it could be determined by the dielectric properties of skin in conjunction with the detailed structure of the epidermis (1).

Conclusion

Data on the time domain current response of human skin to an external voltage perturbation have been subjected to a Laplace transformation, yielding the impedance and phase angle in the frequency domain. Subsequent Bode analysis of this data provided a simple equivalent circuit for skin impedance, identical to a standard model for the steady-state impedance.

This technique could be useful for the study of the frequency response of any biological system which can be described by an equivalent circuit composed of passive, linear, and lumped circuit elements. Pilla (10) has noted the desirability of automating the data-recording process for this technique. If indeed this should prove feasible, the technique of frequency domain analysis would greatly extend the study of transient responses, at present limited to monitoring of resistance or potential levels.

Acknowledgments

This study was supported by a grant from the Hendricks Research Fund (Syracuse University), Grant No. GM-21847 from the National Institute of Health, and the Veterans Administration Research Service, Project No. 0865.

Manuscript submitted March 31, 1977; revised manuscript received June 1, 1978. This was Paper 280 presented at the Philadelphia, Pennsylvania, Meeting of the Society, May 8-13, 1977.

Any discussion of this paper will appear in a Discussion Section to be published in the June 1979 JOURNAL. All discussions for the June 1979 Discussion Section should be submitted by Feb. 1, 1979.

Publication costs of this article were assisted by the Veterans Administration Research Service.

REFERENCES

1. R. Edelberg, in "Biophysical Properties of the Skin," H. R. Elden, Editor, pp. 513-550, John Wiley & Sons, New York (1971).
2. K. S. Cole, *Cold Spring Harbor Symp. Quant. Biol.*, **1**, 107 (1933).
3. S. Hozawa, *Arch. Phys.*, **219**, 111 (1928).
4. A. Plutchik and H. R. Hirsch, *Science*, **141**, 927 (1963).
5. W. G. S. Stephens, *Med. Electron, Biol. Eng.*, **1**, 389 (1963).
6. D. T. Lykken, *Psychophysiology*, **7**, 262 (1971).
7. T. Teorell, *Acta Physiol. Scand.*, **12**, 235 (1947).
8. C. E. Burton, R. M. David, W. M. Portnoy, and L. A. Akers, *Psychophysiology*, **11**, 517 (1974).
9. M. E. Van Valkenburg, "Network Analysis," 3rd ed., Prentice-Hall, Englewood Cliffs, N.J. (1974).
10. A. A. Pilla, in "Computers in Chemistry and Instrumentation," J. S. Mattson *et al.*, Editors, pp. 139-181, Marcel Dekker, New York (1972).
11. A. A. Pilla, *This Journal*, **117**, 467 (1970).

On the Normal Oxygen Potential at a Platinum-Oxygen Alloy Diaphragm Electrode

James P. Hoare*

General Motors Research Laboratories, Electrochemistry Department, Warren, Michigan 48090

ABSTRACT

Platinum foil electrodes were clamped between the compartments of a dual Teflon cell. The rest potential on the front side of the Pt diaphragm in contact with O_2-saturated 2*N* H_2SO_4 solution was observed while the back side was in contact with aerated, concentrated HNO_3. A value of 1.227V was observed on a Pt foil 0.00127 cm thick after 54 hr in contact with HNO_3 and 1.221V on a foil 0.00762 cm thick after 358 hr. This is the first time that the reversible potential has been reported on a prereduced Pt surface. The thickness effect is in agreement with the proposed model.

It has been shown (1) that the rest potential on a Pt/O_2 electrode is a mixed potential and the local cell is composed of the cathodic reduction of O_2

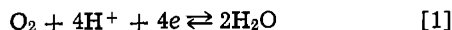

$$O_2 + 4H^+ + 4e \rightleftarrows 2H_2O \quad [1]$$

and the anodic oxidation of Pt

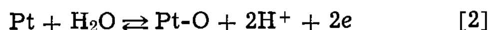

$$Pt + H_2O \rightleftarrows Pt\text{-}O + 2H^+ + 2e \quad [2]$$

Since Pt is not inert to oxygen, the establishment of the local cell prevents the potential from rising to the reversible value of 1.229V. A steady state is reached when the rate of formation of the adsorbed oxygen layer, Pt-O, by local cell action equals the rate of dissolution of oxygen in the Pt metal most likely by a place-change mechanism (2, 3)

$$Pt\text{-}Pt\text{-}O \rightleftarrows Pt\text{-}O\text{-}Pt \quad [3]$$

At this point, the coverage, θ, of the surface with adsorbed oxygen is about 0.3 and the rest potential has a value of 1.05 ± 0.01V (1). There is abundant literature (4-9) indicating that oxygen can dissolve in Pt metal.

To observe the normal oxygen potential (1.229V), it is necessary to suppress the local cell action. One way to do this is to generate a complete, conducting

* Electrochemical Society Active Member.

Key words: oxygen electrode, normal oxygen potential, platinum-oxygen alloy, rest potential, platinum diaphragm.

layer of adsorbed oxygen by oxidizing the Pt surface either thermally (10-14) or chemically (15-17). In such cases the reversible oxygen potential has been observed. However, it has not been observed on a prereduced Pt surface.

In another method, the reversible potential on a prereduced Pt electrode should be observed if the Pt metal were saturated with dissolved oxygen so that the Pt-O layer could no longer dissolve in the metal. Under these circumstances, the Pt-O layer would grow to a complete conducting layer and the rest potential would be determined by Eq. [1] alone.

It has been found (1, 4, 18-20) that significant amounts of oxygen may be dissolved in Pt which has been strongly anodized. A Pt diaphragm prereduced in H_2 was placed in contact with 1M H_2SO_4 solution on both sides in a dual Teflon cell (18). While the back side of the Pt foil was anodized, the rest potential in O_2-saturated acid solution was monitored on the front side. After an induction period, the rest potential reached a value of 1.180V, the highest potential (to my knowledge) reported in the literature on a prereduced Pt/O_2 electrode at rest.

Not only does the passivation of Pt in concentrated HNO_3 produce a complete layer of adsorbed oxygen on the Pt surface, but also it causes large amounts of oxygen to be dissolved in the bulk metal (15, 17, 20). Prompted by the reports of the behavior of hydrogen adsorption on and dissolution in Pt samples with stepped surfaces carried out by Lang, Joyner, and Somerjai (21), we proposed (20) that the HNO_3 etched the Pt surface in such a way that crystal faces favorable for the dissolution of oxygen were exposed.

In the dual Teflon cell (18), if the back side of a Pt diaphragm is exposed to air-saturated, concentrated HNO_3 while the rest potential on the front side is observed in O_2-saturated H_2SO_4 solution, it is expected, then, that rest potentials approaching the normal oxygen potential (1.229V) would be observed. This report describes the results of such an investigation.

Experimental

Four thicknesses (0.00127, 0.00254, 0.00508, and 0.00762 cm) of Pt foil (99.99% pure and about 3 cm^2 in area) were prepared and clamped between the compartments of a dual Teflon cell as described previously (18). Testing for leaks around and through the Pt diaphragm sealed with polyethylene washers, filling the cells with $2N$ H_2SO_4 solution, and purification of the system were carried out according to procedures presented in detail elsewhere (18).

After the system was preelectrolyzed for at least 48 hr, prepurified H_2 was bubbled through both compartments of the dual cell until all Pt electrodes registered 0V between one another. Then, a saturated calomel reference electrode (SCE) was inserted in the left compartment and the potential differences between the SCE and the Pt/H_2 electrodes were recorded.

The acid solution was removed from the right side with a syringe and replaced with air-saturated, concentrated HNO_3 exposed to the atmosphere. The H_2 stirring of the left side was then replaced with prepurified O_2 stirring and the rest potential of the front side of the Pt foil was followed with respect to the SCE. All potential values are recorded in this report with respect to the normal hydrogen electrode (NHE). The potential of the Pt gauze auxiliary electrode was also followed in the left-hand compartment in O_2-stirred $2N$ H_2SO_4 solution.

The partial pressure of oxygen, P_{O_2}, determinations and the potential measurement techniques have been described in detail in an earlier report (1). All measurements were obtained at ambient temperature, 24° ± 1°C. Most experiments were made on the thinnest and thickest Pt samples with shorter runs taken on the two samples of intermediate thickness to complete the thickness effect data.

Results

A plot of the rest potential on the front side of a Pt diaphragm in O_2-saturated $2N$ H_2SO_4 solution as a function of the time for which the back side was in contact with air-saturated, concentrated HNO_3 is presented in Fig. 1 for short and in Fig. 2 for extended periods of time. Also shown in Fig. 2 is a plot of the rest potential of the Pt gauze auxiliary electrodes in the left-hand compartment as a function of time, showing that these electrodes behaved in the usual way characteristically determined by the local cell (Eq. [1] and [2]).

To check on the nature of the potential-determining reaction, the rest potential is plotted in Fig. 3 as a function of P_{O_2}. A line with a slope of 0.015V is drawn on the plot to show that the data are consistent with a four-electron electrode process involving oxygen. After the rest potential had reached the reversible oxygen potential, 1.227V on the 0.00127 cm thick foil after 54 hr and 1.221V on the 0.00762 cm thick foil after 358 hr the O_2 stirring was replaced with H_2 stirring. Within 700 sec, the potential of the front side of the Pt foil and of the two Pt gauze auxiliary electrodes had reached the same potential *vs.* SCE as were observed at the beginning of the run. The three Pt potentials agreed within a millivolt. When H_2 was

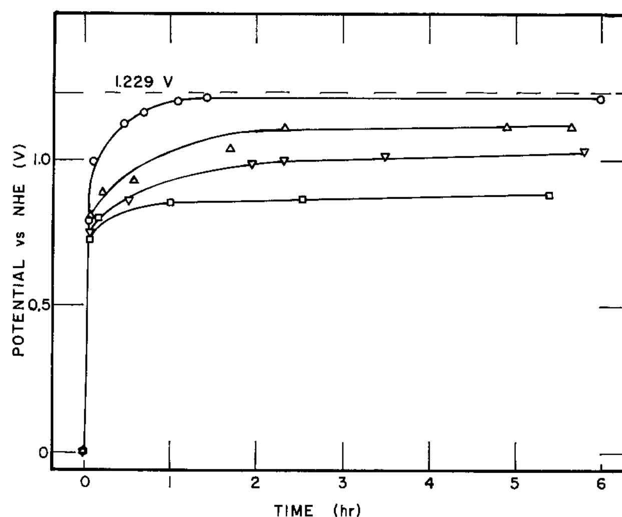

Fig. 1. Rest potential on front of Pt diaphragm in O_2-saturated $2N$ H_2SO_4 solution as a function of the time the back side of the diaphragm was in contact with air-saturated, concentrated HNO_3 for 0.00127 (circles); 0.00254 (triangles); 0.00508 (inverted triangles); and 0.00762 cm (squares) thick foil.

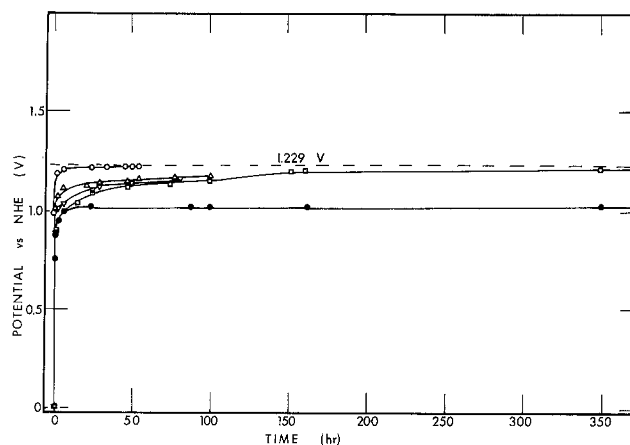

Fig. 2. Same as Fig. 1 for extended periods of time. Also shown is potential of auxiliary Pt gauze electrode (filled circles).

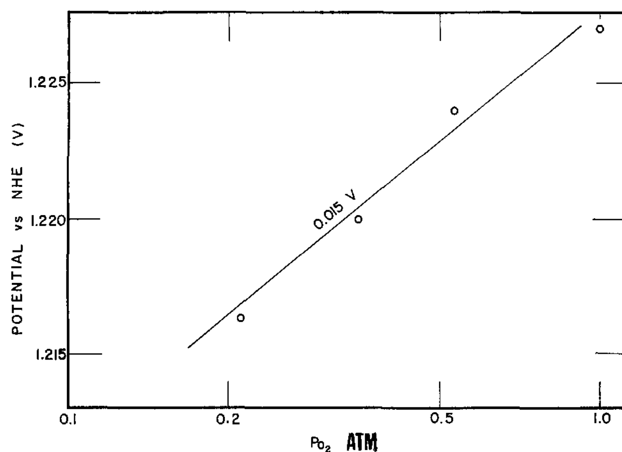

Fig. 3. A plot of the rest potential as a function of log of P_{O_2} on the front side of the Pt diaphragm electrode. A line with a slope of 0.015V is drawn on the plot to show that the data is consistent with a four-electron oxygen reaction.

replaced with O_2 stirring once more, the potential approached the reversible value at a rate similar to that shown in Fig. 2. Apparently, the H_2-saturated acid solution not only removed the adsorbed oxygen layer but also some of the dermasorbed or dissolved oxygen as well.

After the cell was dismantled, it was observed that the Pt foil in the region enclosed by the polyethylene washers was bulged toward the compartment containing the HNO_3. A similar observation was recorded in Fig. 2 of Ref. (19), where the back side of the Pt diaphragm had been strongly anodized. The Pt sample was then analyzed with x-ray photoelectron spectroscopy (XPS). From a depth profile obtained by ion-sputtering away layers of metal, dissolved oxygen was detected in the bulk metal. In passing, it was noted that nitrogen or nitrates were not detected on the surface or in the bulk metal.

Discussion

By etching the back side of the Pt diaphragm with HNO_3, it is possible to charge the Pt with dissolved oxygen to such an extent that a Pt-O alloy is formed (17, 22). Expansion of the lattice by the dissolved oxygen caused the Pt foil to buckle. Since the Pt layers next to the HNO_3 would be charged first, the lattice in these layers would expand first, causing the foil to bow toward the HNO_3 compartment of the cell in agreement with the experimental observations.

On the front side of the Pt diaphragm, the local cell (Eq. [1] and [2]) produces a partial layer of adsorbed oxygen (Pt-O). As the Pt foil becomes saturated with dissolved oxygen caused by contact with the aerated HNO_3 on the back side, the adsorbed oxygen on the front side can no longer dissolve in the Pt metal and the Pt-O layer grows. It is well known (4, 17, 23-29) that the rest potential of a Pt/O_2 electrode increases linearly with increasing coverage of the surface with dissolved oxygen. When θ approaches a monolayer, the potential approaches the reversible potential (17), 1.227V on the 0.00127 cm thick foil after 54 hr and 1.221V on the 0.00762 cm thick foil after 358 hr. To my knowledge, this is the first time that the normal oxygen potential has been observed on a prereduced Pt electrode in O_2-saturated acid solution.

From the data in Fig. 1 and 2, there is observed an effect of diaphragm thickness on the time required to approach the normal oxygen potential. The following model assists in understanding this behavior.

If S is the total number of O-penetration sites on the Pt surface on the back side of the foil, $\sigma = S/A$ where σ is the surface density of active sites and A is the surface area. Let dp/dt be the rate of penetration of O atoms per second at an active site. Then, the rate, R, at which O atoms enter the bulk metal ($cm^{-2}\ sec^{-1}$) is $R = \sigma dp/dt$. If Z is the total number of residence sites for dissolved O atoms in the bulk metal, the density of sites, ζ, is $\zeta = Z/V$ where V is the volume of the Pt foil. Assuming that the surface penetration step (Eq. [3]) is the slow step in the process, the time, t_s, required to saturate a unit of thickness of the bulk metal with dissolved oxygen atoms is

$$t_s = \frac{\zeta}{R} = \frac{\zeta}{\sigma}\frac{dt}{dp} \qquad [4]$$

To saturate the total sample requires $t_s d$ sec where d is the thickness of the diaphragm

$$t_t = t_s d = (\zeta/\sigma)(dt/dp)(d) \qquad [5]$$

Equation 4 shows that the time to saturate the Pt sample with dissolved oxygen is inversely proportional to the rate at which O atoms penetrate the metal surface, and to the ratio of the density of surface active sites to the density of bulk residence sites.

Since all of the foils were made from Pt prepared and treated in the same way, the rate of penetration of O atoms through the Pt surface should be constant from sample to sample to a first approximation. If it is assumed that a surface penetration site is a bulk residence site at the surface and that the distribution of bulk sites is uniform throughout the metal samples, then ζ and σ are also constant from sample to sample. Under these conditions, $t_t \sim d$.

According to the model presented before (18), θ approaches unity and the rest potential approaches 1.229V as the Pt sample approaches saturation with

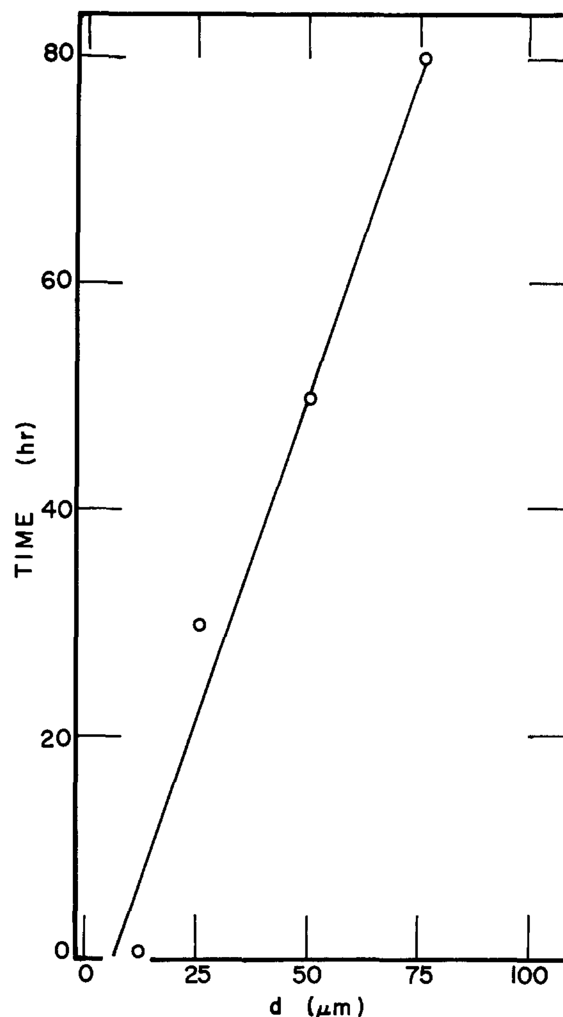

Fig. 4. Time required to reach a potential of 1.15V on the front side of the Pt diaphragm as a function of diaphragm thickness.

dissolved oxygen. Consequently, it is expected that the time required to reach a given potential increases directly with increasing foil thickness. In Fig. 4, the time required to reach 1.150V is plotted as a function of the thickness of the Pt diaphragm. These data exhibit the expected linear relationship between time and thickness. Also, after a given period of time has elapsed, the rest potential reached is inversely proportional to the diaphragm thickness as demonstrated by the linear plot of the rest potential value observed after 1 hr as a function of the reciprocal of the Pt foil thickness in Fig. 5.

What the nature of the bulk residence sites is is not clear at this time. Earlier work (20) indicates that dissolved oxygen may reside in the grain boundaries as well as in the platinum lattice. Possibly the sites in the lattice are associated with the octahedral holes in the face-centered cubic lattice. Etching the Pt surface with HNO_3 apparently exposes high index crystal faces which facilitate the passage of oxygen to the bulk residence sites after the place-change step (Eq. [3]) has taken place.

Since oxygen was found in the interior of the Pt samples from XPS depth-profile analyses, since P_{O_2} measurements of the rest potential indicate that a four-electron oxygen reaction is potential determining, and since this high rest potential can be converted to the H_2 potential by treatment with H_2-saturated acid solution and subsequently recovered by treatment with O_2-saturated acid solution again, strong support for the proposed (1, 18, 20) model of the Pt/O_2 electrode at rest is provided by these data presented in this report.

Acknowledgments

The author wishes to express his sincere gratitude to Mr. T. P. Schreiber and Dr. S. Gaarenstroom of the Analytical Chemistry Department of GM Research Laboratories for carrying out the XPS analyses on the Pt samples and to Mr. J. D. Thomas and Mr. D. W. Hardesty of the Electrochemistry Department of GM Research Laboratories for helpful discussions.

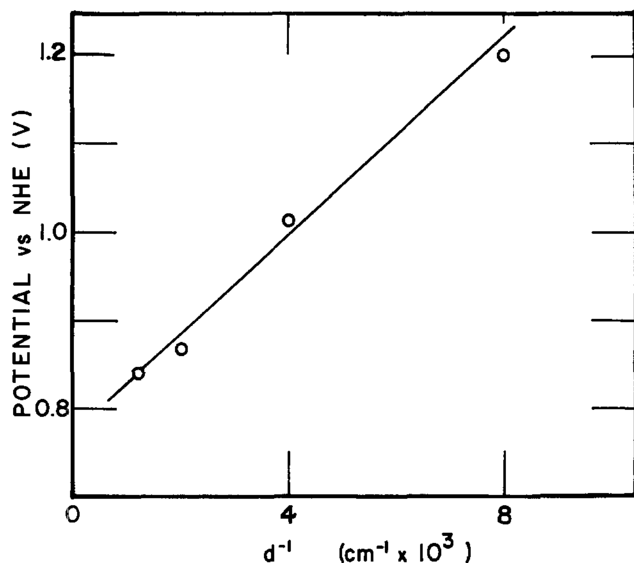

Fig. 5. Rest potential obtained on the front side of the Pt diaphragm electrode after the back side of the diaphragm had been in contact with HNO_3 for 1 hr as a function of the reciprocal of the thickness of the Pt foil.

Manuscript submitted Oct. 31, 1977. This was Paper 546 presented at the Seattle, Washington, Meeting of the Society, May 21-26, 1978.

Any discussion of this paper will appear in a Discussion Section to be published in the June 1979 JOURNAL. All discussions for the June 1979 Discussion Section should be submitted by Feb. 1, 1979.

Publication costs of this article were assisted by General Motors Research Laboratories.

REFERENCES

1. J. P. Hoare, *J. Phys. Chem.*, **79**, 2175 (1975).
2. N. Sato and M. Cohen, *This Journal*, **111**, 512 (1964).
3. B. E. Conway and S. Gottesfeld, *J. Chem. Soc., Faraday Trans. I*, **69**, 1090 (1973).
4. R. Thacker and J. P. Hoare, *J. Electroanal. Chem. Interfacial Electrochem.*, **30**, 1 (1971).
5. T. V. Kalish and R. Kh. Burshtein, *Dokl. Akad. Nauk SSSR*, **81**, 1093 (1951); **88**, 863 (1953).
6. A. D. Obrucheva, *Zh. Fiz. Khim*, **26**, 1448 (1952).
7. P. R. Nadebaum and T. Z. Fahidy, *Electrochim. Acta*, **17**, 1659 (1972).
8. J. Balej and O. Spalek, *Czech. Chem. Comm.*, **37**, 499 (1972); **38**, 29 (1973).
9. H. Shimizu, *Electrochim. Acta*, **14**, 55 (1969).
10. J. O'M. Bockris and A. K. M. S. Huq, *Proc. Roy. Soc.*, **A237**, 277 (1956).
11. W. Visscher and M. A. V. Devanathan, *J. Electroanal. Chem.*, **8**, 127 (1964).
12. N. Watanabe and M. A. V. Devanathan, *This Journal*, **111**, 615 (1964).
13. G. Bianchi and T. Muzzini, *Electrochim. Acta*, **10**, 445 (1965).
14. R. Kh. Burshtein, M. R. Tarasevich, and V. A. Bogdonovskaya, *Electrokhimya*, **8**, 1542 (1972).
15. J. P. Hoare, *This Journal*, **110**, 1019 (1963); **112**, 849 (1965).
16. R. Thacker and J. P. Hoare, *ibid.*, **113**, 862 (1966).
17. J. P. Hoare, R. Thacker, and C. R. Wiese, *J. Electroanal. Chem. Interfacial Electrochem.*, **30**, 15 (1971).
18. J. P. Hoare, *This Journal*, **121**, 872 (1974).
19. J. P. Hoare, *Electrochim. Acta*, **20**, 267 (1975).
20. J. P. Hoare, R. F. Paluch, and S. G. Meibuhr, *This Journal*, **123**, 1821 (1976).
21. B. Lang, R. W. Joyner, and G. A. Somerjai, *Surf. Sci.*, **30**, 440, 454 (1972).
22. J. P. Hoare, S. G. Meibuhr, and R. Thacker, *This Journal*, **113**, 1078 (1966).
23. V. S. Bagotskii and I. E. Yablakova, *Zh. Fiz. Khim.*, **27**, 1663 (1953); *Dokl. Akad. Nauk SSSR*, **85**, 559 (1952).
24. M. Becker and M. Breiter, *Z. Elektrochem.*, **60**, 1080 (1956).
25. T. Biegler, D. A. J. Rand, and R. Woods, *J. Electroanal. Chem. Interfacial Electrochem.*, **29**, 269 (1971).
26. A. N. Frumkin and V. V. Sobol, *Dokl. Akad. Nauk SSSR*, **141**, 917 (1961).
27. D. Gilroy and B. E. Conway, *Can. J. Chem.*, **46**, 875 (1968).
28. K. J. Vetter and D. Berndt, *Z. Elektrochem.*, **62**, 378 (1958).
29. H. Wroblowa *et al.*, *J. Electroanal. Chem. Interfacial Electrochem.*, **15**, 139 (1967).

The Application of Pulsed Current Electrolysis to a Rotating-Disk Electrode System

I. Mass Transfer

K. Viswanathan,* M. A. Farrell Epstein, and H. Y. Cheh**

Department of Chemical Engineering and Applied Chemistry, Columbia University, New York, New York 10027

ABSTRACT

A numerical solution was obtained for mass transfer to a rotating-disk electrode under pulsed current conditions. Good agreement was reached on the calculation of rate of mass transfer between the numerical solution and the solution by Cheh from a simplified diffusion model. The concept of a pulsating diffusion layer was introduced and it was shown that the thickness of the pulsating diffusion layer was a function of the pulsed current characteristics as well as the Reynolds and Schmidt numbers of the system. Experimental verification of the theoretical results was obtained by using a model ferri-ferrocyanide electrolysis.

The application of pulsed-current electrolysis to practical systems has generated a considerable amount of interest during the past several years. For instance, pulsed electrodeposition of copper, silver, and gold was reported by Cheh and co-workers (1-3). Sullivan (4) and Chen and Sautter (5) deposited cobalt under pulsed current conditions. More recently, Ibl *et al.* (6) studied the effect of pulsed electrolysis on the physical properties of electrodeposits. Pulsed electrolysis was also used in battery charging by Wagner and Williams (7) and by Bedrossian and Cheh (8).

Theoretical considerations of pulsed electrolysis were also reported in the recent literature. Cheh (9, 10) developed a simple diffusion model to calculate the rate of electrodeposition by a pulsed current and by a periodic reversal of the current. Popov *et al.* (11) studied mass transfer under pulsed potential conditions in both stirred and unstirred solutions. Wan *et al.* (12) analyzed the application of pulsed techniques to sequential electron transfer reactions.

One of the most important advantages of pulsed electrolysis is the enhancement of mass transfer during the on period of the pulse cycle. Therefore, under suitable conditions, high instantaneous current density can be obtained without the initiation of a second and perhaps undesirable reaction. Also, since mass transfer limitations can very effectively be reduced, pulsed current electrolysis can in principle be developed into a new tool to study fast electrode reactions. In order to obtain quantitative kinetic information on fast electrode reactions, it is essential that mass transfer rates be calculated exactly. An exact solution to both mass transfer and electrochemical kinetics in a stirred system under pulsed conditions is very difficult to obtain. On the other hand, the problem could be simplified considerably if the diffusion model developed by Cheh (9) can be used with confidence to account for mass transfer effects. In this paper, a rigorous theoretical calculation as well as an experimental investigation on the mass transfer rates to a rotating-disk electrode system is presented. A kinetic study of fast electrode reactions by pulsed current electrolysis is presented in a subsequent paper (see Editor's Note, p. 1775).

Theoretical

Assume that a rotating-disk electrode (RDE) is situated in an electrolyte of large extent and the electrode is rotating at a constant velocity. Both the radius of the RDE and the distance between the RDE and the counterelectrode are large as compared to the thickness of the Nernst diffusion layer. The number of coulombs passed during an experiment is assumed to be so small that the depletion of the reacting species in the solution can be neglected. An excess of supporting electrolyte is present so that electrical migration and nonfaradaic effects are negligible. Finally, the Schmidt number of the solution is orders of magnitude larger than unity so that the diffusion layer is thin as compared to the momentum boundary layer. Under these conditions, the concentration of the reacting species is governed by the following convective diffusion equation

$$\frac{\partial c}{\partial t} + v_z \frac{\partial c}{\partial z} = D \frac{\partial^2 c}{\partial z^2} \qquad [1]$$

with the following boundary conditions

$$c = c_\infty \qquad \text{at } t = 0 \text{ and all } z \qquad [2]$$

$$c = c_\infty \qquad \text{at } t > 0 \text{ and } z \to \infty \qquad [3]$$

$$-D \frac{\partial c}{\partial z} = \frac{i}{n\mathbf{F}} \qquad \text{at } t > 0 \text{ and } z = 0 \qquad [4]$$

where c is the concentration of the reacting ion, c_∞ is its concentration in the bulk of the solution, D is the diffusion coefficient of the reacting ion, $\mathbf{F}$ is Faraday's constant, i is the applied current density, n is the number of electrons transferred during reaction, t is time, v_z is the axial component of the velocity, and z is the axial coordinate extending from the electrode surface.

The form of the pulsed current is shown schematically in Fig. 1. Consequently, the pulsed current density in Eq. [4] can be expressed as

$$i = i_p \qquad \text{at } 0 < t \leq t_1, t_2 < t \leq t_3, \text{etc.} \qquad [5]$$

$$i = 0 \qquad \text{at } t_1 < t \leq t_2, t_3 < t \leq t_4, \text{etc.} \qquad [6]$$

where i_p is the pulsed current density and t_n is defined in Fig. 1. Note that one may also consider that the current is on when $t_{m-1} < t \leq t_m$ and the current is off when $t_m < t \leq t_{m+1}$ where m is an odd number.

Before one proceeds to solve Eq. [1] subject to boundary conditions, Eq. [2]-[6], it is useful to put these equations into dimensionless form. Let

$$C = \frac{c}{c_\infty}, \quad G = -\frac{i_p \delta}{n\mathbf{F}Dc_\infty}, \quad K = -\frac{v_z \delta^3}{z^2 D} \qquad [7]$$

and

$$\tau = \frac{Dt}{\delta^2}, \quad \text{and} \quad \zeta = \frac{z}{\delta} \qquad [8]$$

* Electrochemical Society Student Member.

** Electrochemical Society Active Member.

Key words: pulsed electrolysis, rotating-disk electrode, mass transfer.

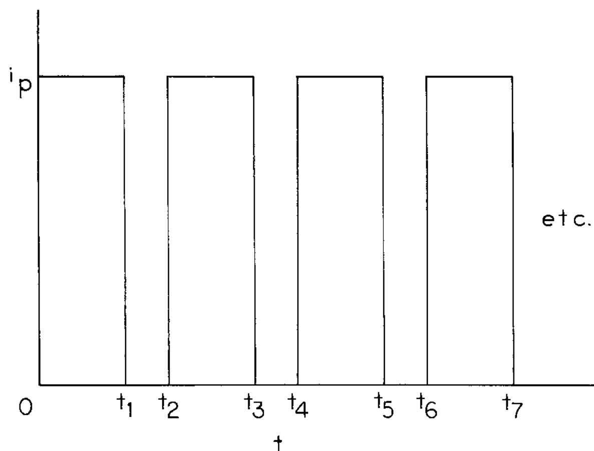

Fig. 1. Schematic diagram of a pulsed current

where δ is the Nernst diffusion layer thickness. The dimensionless equation and the boundary conditions are

$$\frac{\partial C}{\partial \tau} - K\zeta^2 \frac{\partial C}{\partial \zeta} = \frac{\partial^2 C}{\partial \zeta^2} \quad [9]$$

and

$$C = 1 \qquad \text{at } \tau = 0 \text{ and all } \zeta \quad [10]$$

$$C = 1 \qquad \text{at } \tau > 0 \text{ and } \zeta \rightarrow \infty \quad [11]$$

$$\frac{\partial C}{\partial \zeta} = G \quad \text{at } \zeta = 0 \text{ and } 0 < \tau \leq \tau_1, \tau_2 < \tau \leq \tau_3, \text{etc.} \quad [12]$$

$$\frac{\partial C}{\partial \zeta} = 0 \quad \text{at } \zeta = 0 \text{ and } \tau_1 < \tau \leq \tau_2, \tau_3 < \tau \leq \tau_4, \text{etc.} \quad [13]$$

where

$$\tau_n = \frac{Dt_n}{\delta^2} \quad [14]$$

By substituting into the definition of K the approximate velocity at small values of ζ (13)

$$v_z = -0.5102(\omega^3/\nu)^{1/2}z^2 \quad [15]$$

and the thickness of the Nernst diffusion layer at large Schmidt number (13)

$$\delta = 1.612\left(\frac{D}{\nu}\right)^{1/3}\left(\frac{\nu}{\omega}\right)^{1/2} = 1.612R\text{Sc}^{-1/3}\text{Re}^{-1/2} \quad [16]$$

where ω is the rotation speed of the electrode, ν is the kinematic viscosity of the electrolyte, R is the radius of the electrode, Sc is the Schmidt number, and Re is the Reynolds number, K is found to be a constant, 2.136, independent of the physical properties of the electrolyte as well as the rotation speed of the electrode.

An exact solution in closed form of Eq. [9] with boundary conditions, Eq. [10]-[13] is extremely difficult if not impossible. For numerical solution in terms of a series, the boundary condition Eq. [11], may be modified as follows

$$C = 1 \qquad \text{at } \tau > 0 \text{ and } \zeta = 2 \quad [17]$$

The justification of this modification was suggested by Riddiford (14). It appears that a change of the upper limit of integration from infinity to a finite value of 2 has litle effect in changing the numerical results of the solution. For instance, even at the extreme condition of performing a d-c electrolysis at limiting current density, the dimensionless concentration reaches a value exceeding 0.9995 at $\zeta = 2$.

A series solution of Eq. [9] is proposed as follows

$$C(\tau,\zeta) = \sum_{n=0}^{\infty} C_n R_n(\zeta) \exp(-\lambda_n^2 \tau) \quad [18]$$

where λ_n is the eigenvalue and C_n is the coefficient of the infinite series. The solution corresponding to $\lambda_n = 0$ satisfies the inhomogeneous part of the boundary conditions, Eq. [12] and [17]. It can be derived easily as

$$R_0 = 1 - G + G\int_0^{\zeta} \exp\left(-\frac{K\alpha^3}{3}\right) d\alpha \quad [19]$$

Note that R_0 represents physically the steady-state d-c solution.

The solution corresponding to $\lambda_n \neq 0$ is considerably more difficult to obtain. A combination of an asymptotic method and a trial-and-error method using a fourth-order Runge-Kutta technique was used to obtain the first forty series coefficients and eigenvalues. Details of the calculations are presented in the appendix and the results are shown in Table I.

From a knowledge of these coefficients and eigenvalues, the concentration of the reacting species at the electrode surface, c_i, can be calculated by

$$\frac{c_i}{c_\infty} = 1 - G + \sum_{n=1}^{\infty} C_n \exp(-\lambda_n^2 \tau) \quad [20]$$

Following the same approach by Cheh (9), the value of c_i at its periodic state and the ratio of the limiting current density under pulsed and d-c conditions can be calculated from the following equations.

During periods when the current is on, $\tau_{m-1} < \tau \leq \tau_m$

$$\frac{(c_i - c_\infty)nFD}{i_p\delta} = 1 - \sum_{n=1}^{\infty} \frac{C_n}{G} \exp[-\lambda_n^2(\tau - \tau_{m-1})] \frac{(1 - \exp[-\lambda_n^2(\tau_2 - \tau_1)])}{[1 - \exp(-\lambda_n^2 \tau_c)]} \quad [21]$$

During periods when the current is off, $\tau_m < \tau \leq \tau_{m+1}$

Table I. First forty coefficients and eigenvalues for Eq. [18]

n	Coefficients C_n/G	Eigenvalues λ_n
1	0.744020	1.435674
2	0 093243	3.160804
3	0.043258	4.578392
4	0.024912	6.000823
5	0.017566	7.468973
6	0.011433	8.969811
7	0.009296	10.490975
8	0.006356	12.024936
9	0.005717	13.567368
10	0.003981	15.115674
11	0.003870	16.668209
12	0.002700	18 223888
13	0.002799	19.781966
14	0.001937	21.341916
15	0.002124	22.903354
16	0.001448	24.465993
17	0.001671	26 029617
18	0.001118	27.594058
19	0.001352	29.159183
20	0.000884	30.724889
21	0.001119	32.291090
22	0.000714	33.857717
23	0.000944	35.424714
24	0.000586	36.992034
25	0.000808	38.559637
26	0.000488	40.127490
27	0.000701	41.695565
28	0.000411	42 263838
29	0.000615	44.832288
30	0.000349	46.400896
31	0.000544	47.969648
32	0.000300	49.538529
33	0.000486	51.107528
34	0.000259	52.676635
35	0.000437	54 245839
36	0.000225	55.815133
37	0.000395	57.384509
38	0.000197	58.953961
39	0.000360	60.523482
40	0.000173	62.093068

$$\frac{(c_l - c_\infty)nFD}{i_p\delta} = \sum_{n=1}^{\infty} \frac{C_n}{G} \exp(-\lambda_n^2(\tau - \tau_m)) \frac{[1 - \exp(-\lambda_n^2\tau_1)]}{[1 - \exp(-\lambda_n^2\tau_c)]} \quad [22]$$

and

$$\frac{(i_p)_l}{(i_{dc})_l} = \frac{1}{1 - \sum_{n=1}^{\infty} \frac{C_n}{G} \frac{[\exp(-\lambda_n^2\tau_1) - \exp(-\lambda_n^2\tau_c)]}{[1 - \exp(-\lambda_n^2\tau_c)]}} \quad [23]$$

where $(i_p)_l$ and $(i_{dc})_l$ are the limiting current densities under pulsed and d-c conditions and τ_c is the dimensionless cycle time. The ratio of the two limiting current densities as derived by Cheh (9) from a diffusion model is expressed as

$$\frac{(i_p)_l}{(i_{dc})_l} = \frac{1}{1 - 2\sum_{n=1}^{\infty} \frac{1}{\mu_n^2} \frac{[\exp(-\mu_n^2\tau_1) - \exp(-\mu_n^2\tau_c)]}{[1 - \exp(-\mu_n^2\tau_c)]}} \quad [24]$$

where

$$\mu_n = (2n - 1)\frac{\pi}{2} \quad [25]$$

A numerical comparison of the limiting-current ratios predicted by Eq. [23] and [24] is shown in Table II. The agreement between the two equations is excellent. It can therefore be concluded that the diffusion model provides an accurate calculation of the mass transfer rates. A major advantage of the simple model is that it enables one to extend the analysis to systems with kinetic hindrance, which is the subject of our subsequent paper.

Recently Ibl *et al.* (6) introduced the concept of a pulsating diffusion layer. This layer refers to a region extending from the electrode surface in which the time-dependent concentration variation is important. In accordance with the Nernst diffusion layer concept, the thickness of the pulsating diffusion layer, δ_p, can be defined by

$$i_p \equiv \frac{nFD}{\delta_p}(c_l - c_\infty) \quad [26]$$

By applying this definition to the diffusion model under a periodic state condition (9), δ_p can be calculated from

$$\frac{\delta_p}{\delta} = 1 - 2\sum_{n=1}^{\infty} \frac{1}{\mu_n^2} \exp(-\mu_n^2(\tau - \tau_{m-1})) \frac{(1 - \exp[-\mu_n^2(\tau_2 - \tau_1)])}{[1 - \exp(-\mu_n^2\tau_c)]} \quad [27]$$

Since δ is a function of the Schmidt and Reynolds numbers of the system, δ_p depends on these parameters as well as on the pulsed-current characteristics. A numerical example for the pulsating diffusion layer at $\tau_c = 0.01$ is shown in Fig. 2. The value of 0.01 for τ_c corresponds to a realistic experimental condition of the RDE system. Results clearly indicate that the thickness of the pulsating layer is a function of time during a pulse. It increases as the pulse progresses and reaches a maximum value at the end of the pulse. It also depends on the ratio of τ_1/τ_c, frequently referred to in the literature as the duty cycle (15); the shorter the duty cycle, the thinner is the pulsating diffusion layer. The maximum value of δ_p which occurs at the end of each pulse can be calculated by

$$\frac{(\delta_p)_{max}}{\delta} = 1 - 2\sum_{n=1}^{\infty} \frac{1}{\mu_n^2} \frac{[\exp(-\mu_n^2\tau_1) - \exp(-\mu_n^2\tau_c)]}{[1 - \exp(-\mu_n^2\tau_c)]} \quad [28]$$

This equation is of course the reciprocal of Eq. [24]. Numerical results of Eq. [28] are presented in Fig. 3 which clearly shows that the pulsating diffusion layer is always thinner than the corresponding d-c diffusion layer.

Experimental

The limiting current density for the reduction of a 0.01M ferricyanide in a solution also containing 0.01M ferrocyanide and 1M KCl was chosen for this study. Due to the fast kinetics of the ferri-ferrocyanide re-

Table II. Comparison between present work and Cheh's earlier results (9)

Cycle time τ_c	Duty cycle τ_1/τ_c	Ratio of pulsed limiting current density and d-c limiting current density $(i_p)_l/(i_{dc})_l$: Cheh's result Eq. [24]	Present result Eq. [23]
0.001	0.20	4.7551	4.7259
	0.40	2.4364	2.4341
	0.60	1.6439	1.6435
	0.80	1.2427	1.2426
0.005	0.20	4.4836	4.4827
	0.40	2.3621	2.3620
	0.60	1.6166	1.6166
	0.80	1.2337	1.2337
0.01	0.20	4.2996	4.2992
	0.40	2.3094	2.3093
	0.60	1.5967	1.5967
	0.80	1.2271	1.2271
0.05	0.20	3.6650	3.6648
	0.40	2.1105	2.1104
	0.60	1.5180	1.5180
	0.80	1.2000	1.2000
0.10	0.20	3.3001	3.2996
	0.40	1.9825	1.9824
	0.60	1.4639	1.4639
	0.80	1.1804	1.1804
0.50	0.20	2.3275	2.3178
	0.40	1.5778	1.5773
	0.60	1.2700	1.2734
	0.80	1.1028	1.1057
1.00	0.20	1.8750	1.8844
	0.40	1.3423	1.3643
	0.60	1.1447	1.1617
	0.80	1.0503	1.0586
5.00	0.20	1.0738	1.1046
	0.40	1.0059	1.0122
	0.60	1.0005	1.0015
	0.80	1.0000	1.0002

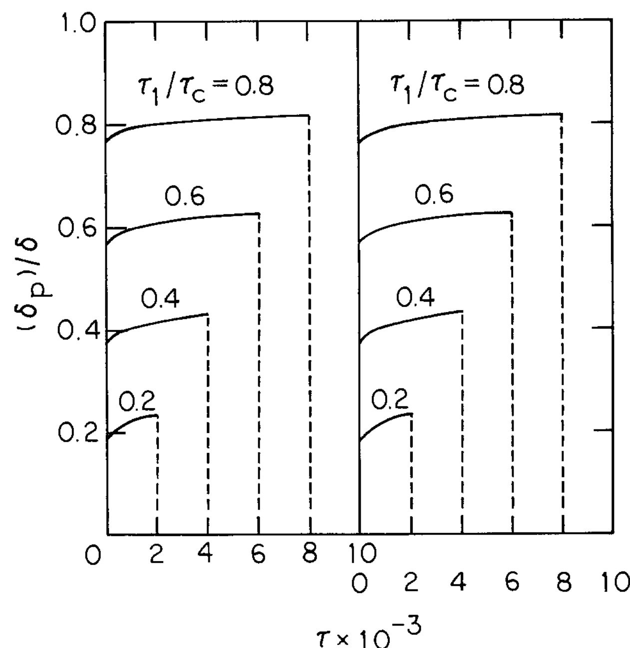

Fig. 2. The variation of pulsating diffusion layer

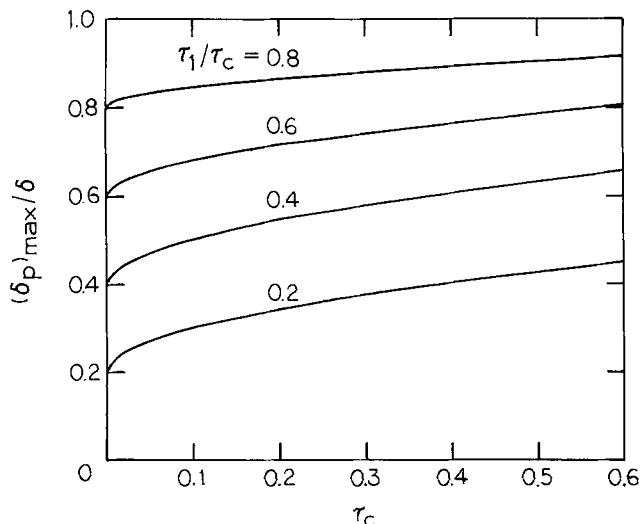

Fig. 3. The maximum variation of pulsating diffusion layer

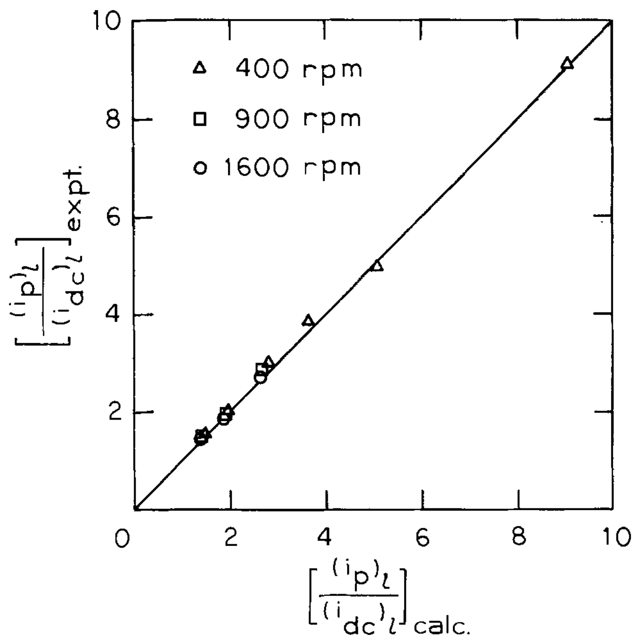

Fig. 4. Comparison of calculated and experimental results

action, the same system was also used for our subsequent kinetic study under pulsed conditions.

A Pine Instrument high speed rotator with a Pt electrode of 0.461 cm^2 area was used as the RDE. A coil of Pt was used as the counterelectrode and a Fisher Scientific saturated calomel electrode was used as the reference electrode. All experiments were carried out at room temperature which was 22° ± 1°C. The kinematic viscosity of the electrolyte was measured by using an Ostwald viscometer and the value was found to be 0.00914 cm^2/sec. The diffusion coefficient of the ferricyanide ion was measured from a d-c limiting current density *vs.* square root of rotation speed plot by using Eq. [16]. The value was found to be 7.2×10^{-6} cm^2/sec.

For pulsed current electrolysis, the current was supplied by feeding the square wave output of a Tacussel GSTP2 function generator to a Kepco PC2 power supply. The amplitude and frequency of the current pulse was determined by measuring the voltage drop across a 1000Ω standard resistor connected in series to the cell. The results were recorded on a Tektronix 5103N dual trace oscilloscope. The potential difference between the RDE and the reference electrode was recorded simultaneously on the same oscilloscope.

Experiments were carried out at rotation speeds of 400, 900, and 1600 rpm and at duty cycles and pulse periods ranging from 0.1 to 0.667 and from 0.001 to 0.006 sec, respectively. The value of τ_c varied from 0.0015 to 0.0180. Pulsed limiting current density was measured by observing the sudden jump of potential of the RDE during a gradual increase of the pulsed current density. Experimental as well as theoretical results calculated by using Eq. [23] are presented in Table III. A graphical comparison is also shown in Fig. 4. The good agreement obtained between experimental and theoretical results is evident in both displays.

Table III. Comparison between experimental and calculated results

Rotation speed (rpm)	Cycle time (sec)	Pulse time (sec)	$(i_p)_l/(i_{dc})_l$ Calculated (Eq. [23])	Experimental
400	0.001	0.0001	9.05	9.10
	0.002	0.001	1.94	2.00
	0.003	0.001	2.81	3.00
	0.003	0.002	1.47	1.52
	0.004	0.001	3.62	3.86
	0.006	0.001	5.10	4.97
900	0.002	0.001	1.91	1.95
	0.003	0.001	2.72	2.90
	0.003	0.002	1.45	1.47
1600	0.002	0.001	1.88	1.93
	0.003	0.001	2.64	2.76
	0.003	0.002	1.43	1.45

Conclusions

A numerical calculation on the mass transfer rate in pulsed current electrolysis was carried out. The results were in excellent agreement with those predicted by using a simplified diffusion model developed by Cheh. It is therefore the conclusion of the work that the diffusion model can be used to account for mass transfer effects in systems with kinetic limitations.

A quantitative analysis on the pulsating diffusion layer was made. The diminishing diffusion layer under pulsed conditions is responsible for the ability of carrying out pulsed electrolysis at high instantaneous current densities under suitable conditions.

Experimental measurements on the pulsed limiting current densities were made by using a ferri-ferrocyanide system. Good agreement was obtained between the experimental measurements and theoretical predictions.

Acknowledgment

The authors wish to thank Professor Duby for his help during the course of the experiments.

Manuscript submitted March 14, 1978; revised manuscript received May 16, 1978.

Any discussion of this paper will appear in a Discussion Section to be published in the June 1979 JOURNAL. All discussions for the June 1979 Discussion Section should be submitted by Feb. 1, 1979.

Editor's Note

By mischance, this is Part I of a two-part series, and is being printed after Part II, which appeared in the October 1978 issue of the JOURNAL, Vol. 125, No. 10, pp. 1616-1618. The JOURNAL regrets very much this inadvertent transposition.

APPENDIX

Numerical Solution of Eq. [9] for $\lambda_n \neq 0$

Substituting Eq. [18] into Eq. [9] and the homogeneous part of Eq. [12] and [17], one obtains

$$\frac{d^2R_n}{d\zeta^2} + K\zeta^2\frac{dR_n}{d\zeta} + \lambda_n{}^2R_n = 0 \quad \text{[A-1]}$$

with the boundary conditions

$$\frac{dR_n}{d\zeta} = 0 \quad \text{at} \quad \zeta = 0 \quad \text{[A-2]}$$

$$R_n = 0 \quad \text{at} \quad \zeta = 2 \quad \text{[A-3]}$$

For large values of λ_n ($n > 5$), the solution can be achieved by using an asymptotic expansion method. It is, however, convenient to first introduce the following transformation (16)

$$R_n = \psi_n(\zeta)\exp\left(-\frac{K\zeta^3}{6}\right) \quad [A\text{-}4]$$

By substituting Eq. [A-4] into Eq. [A-1]-[A-3], one obtains

$$\frac{d^2\psi_n}{d\zeta^2} + \left(\lambda_n^2 - K\zeta - \frac{K^2\zeta^4}{4}\right)\psi_n = 0 \quad [A\text{-}5]$$

with

$$\frac{d\psi_n}{d\zeta} = 0 \quad \text{at} \quad \zeta = 0 \quad [A\text{-}6]$$

$$\psi_n = 0 \quad \text{at} \quad \zeta = 2 \quad [A\text{-}7]$$

Now, one seeks an asymptotic solution of Eq. [A-5] in the following form

$$\psi_n = \psi_{n0} + \epsilon\psi_{n1} + \epsilon^2\psi_{n2} + \ldots \quad [A\text{-}8]$$

$$\lambda_n = \lambda_{n0} + \epsilon\lambda_{n1} + \epsilon^2\lambda_{n2} + \ldots \quad [A\text{-}9]$$

where

$$\epsilon = K/\lambda_{n0}^2 \quad [A\text{-}10]$$

By introducing the first three terms of Eq. [A-8] and [A-9] into Eq. [A-5], it can be shown that the following equations must be satisfied

$$\frac{d^2\psi_{n0}}{d\zeta^2} + \lambda_{n0}^2\psi_{n0} = 0 \quad [A\text{-}11]$$

$$\frac{d^2\psi_{n1}}{d\zeta^2} + \lambda_{n0}^2\psi_{n1} = \lambda_{n0}^2\psi_{n0}\zeta + \frac{K}{4}\lambda_{n0}^2\psi_{n0}\zeta^4 - 2\lambda_{n0}\lambda_{n1}\psi_{n0} \quad [A\text{-}12]$$

$$\frac{d^2\psi_{n2}}{d\zeta^2} + \lambda_{n0}^2\psi_{n2} = \lambda_{n0}^2\psi_{n1}\zeta + \frac{K}{4}\lambda_{n0}^2\psi_{n1}\zeta^4 - 2\lambda_{n0}\lambda_{n2}\psi_{n0} - 2\lambda_{n0}\lambda_{n1}\psi_{n1} - \lambda_{n1}^2\psi_{n0} \quad [A\text{-}13]$$

The boundary conditions of these equations are

$$\psi_{n0} = 1, \quad \psi_{n1} = \psi_{n2} = 0 \quad \text{at} \quad \zeta = 0 \quad [A\text{-}14]$$

$$\frac{d\psi_{n0}}{d\zeta} = \frac{d\psi_{n1}}{d\zeta} = \frac{d\psi_{n2}}{d\zeta} = 0 \quad \text{at} \quad \zeta = 0 \quad [A\text{-}15]$$

$$\psi_{n0} = \psi_{n1} = \psi_{n2} = 0 \quad \text{at} \quad \zeta = 2 \quad [A\text{-}16]$$

The solution of the above equations can be obtained easily by following standard procedures as described by Wylie (17).

The first five eigenvalues can be calculated by a trial-and-error method using a fourth-order Runge-Kutta technique (18). The coefficients in Eq. [18] can then be calculated by

$$\frac{C_n}{G} = \frac{\int_0^2 \left(1 - \int_0^\zeta \exp\left(-\frac{K\alpha^3}{3}\right)d\alpha\right)\exp\left(\frac{K\zeta^3}{6}\right)\psi_n(\zeta)d\zeta}{\int_0^2 \psi_n^2(\zeta)d\zeta} \quad [A\text{-}17]$$

LIST OF SYMBOLS

- c concentration of reacting ion
- c_i, c_∞ concentration of reacting ion at the electrode surface, and in the bulk solution, respectively
- C dimensionless concentration defined in Eq. [7]
- C_n coefficient in infinite series
- D diffusion coefficient of reacting ion
- F Faraday's constant
- G dimensionless current density defined in Eq. [7]
- i current density
- i_p pulsed current density
- $(i_{dc})_l$, $(i_p)_l$ limiting current density for d-c electrolysis and for pulsed electrolysis, respectively
- K dimensionless velocity defined in Eq. [7]
- m an odd number
- n number of electrons transferred in reaction
- R radius of RDE
- Re Reynolds number
- R_n a function of axial coordinate
- Sc Schmidt number
- t time
- t_n time periods defined in Fig. 1
- v_z axial velocity
- z axial coordinate
- α a dummy variable
- δ thickness of the Nernst diffusion layer
- δ_p thickness of the pulsating diffusion layer
- ϵ a perturbation parameter defined in Eq. [A-10]
- ζ dimensionless axial coordinate defined in Eq. [8]
- λ_n eigenvalue of series
- λ_{n0}, λ_{n1}, etc. asymptotic expansion of λn
- μ a constant defined in Eq. [25]
- ν kinematic viscosity of electrolyte
- τ dimensionless time defined in Eq. [8]
- τ_1, τ_c dimensionless pulsed time and cycle time, respectively
- ψ_n a function of axial coordinate defined in Eq. [A-4]
- ψ_{n0}, ψ_{n1}, etc. asymptotic expansion of ψ_n

REFERENCES

1. H. Y. Cheh, H. B. Linford, and C. C. Wan, *Plat. Surf. Finish.*, **64**, (5), 66 (1977).
2. H. Y. Cheh, P. C. Andricacos, and H. B. Linford, *ibid.*, **64**, (7), 42 (1977).
3. P. C. Andricacos, H. Y. Cheh, and H. B. Linford, *ibid.*, **64**, (9), 44 (1977).
4. W. Sullivan, *ibid.*, **62**, 139 (1975).
5. E. S. Chen and F. K. Sautter, *ibid.*, **63**, (9), 28 (1976).
6. N. Ibl, J. Cl. Puippe, and H. Angerer, To be published in *Surf. Technol.*
7. O. C. Wagner and D. D. Williams, Abstract **49**, p. 120, The Electrochemical Society Extended Abstracts, Fall Meeting, New York, New York, Oct. 13-17, 1974.
8. A. A. Bedrossian and H. Y. Cheh, Abstract **56**, p. 136, The Electrochemical Society Extended Abstracts, Fall Meeting, Las Vegas, Nevada, Oct. 17-22, 1976.
9. H. Y. Cheh, *This Journal*, **118**, 551 (1971).
10. H. Y. Cheh, *ibid.*, **118**, 1132 (1971).
11. K. I. Popov, D. N. Keca, S. I. Vidojkovic, B. J. Lazarevic, and V. B. Milojkovic, *J. Appl. Electrochem.*, **6**, 365 (1976).
12. C. C. Wan, H. Y. Cheh, and H. B. Linford, To be published in *J. Appl., Electrochem.*
13. V. G. Levich, "Physicochemical Hydrodynamics," Prentice-Hall, Englewood Cliffs, N.J. (1962).
14. A. C. Riddiford, *Advan. Electrochem. Electrochem. Eng.*, **4**, 47 (1966).
15. R. B. Snyder and H. Y. Cheh, *Plat. Surf. Finish.*, **62**, 786 (1975).
16. Yu. V. Pleskov and V. Yu. Filinovskii, "The Rotating Disk Electrode," Consultants Bureau, New York (1976).
17. C. R. Wylie, "Advanced Engineering Mathematics," 3rd ed., McGraw-Hill, New York (1966).
18. A. Ralson, "A First Course in Numerical Analysis," McGraw-Hill, New York (1965).

Studies of the Nickel Electrode in a Rotating Multipolar Wiper-Blade Cell

M. Farooque[1] and T. Z. Fahidy*

Department of Chemical Engineering, University of Waterloo, Waterloo, Ontario, Canada, N2L 3G1

ABSTRACT

The usefulness of nickel as the working electrode in a rotating multipolar wiper-blade cell is demonstrated by experiments related to oxygen reduction and evolution, alcohol oxidation, and anodic dissolution of nickel.

In previous publications [e.g., (1-5)] the use of a recently developed rotating multipolar wiper-blade cell to study electrochemical reactions occurring on platinum has been described. It has been shown that such a device is well suited for continuous reactivation of electrode surfaces and for maintaining relatively high mass transport rates at a properly chosen electrode rotation rate. The use of platinum, however, is a serious impediment from the viewpoint of industrial potential, which requires cheaper electrode materials.

The present study was undertaken to investigate the usefulness of nickel as an economically more attractive rotating electrode in the wiper-blade cell and this communication reports pertinent experimental results in four major areas: (*i*) oxygen reduction, (*ii*) the oxidation of ethanol, (*iii*) oxygen evolution, and (*iv*) the anodic dissolution of nickel. The experimental conditions, especially electrode pretreatment, choice of electrolyte species and concentrations, working potential and temperature (range) correspond closely to previously reported research in these areas, in order to minimize the importance of effects spurious to rotating multipolar wiper-blade cell operation. On account of their specific aspects related to these areas, experimental details are described in their respective sections rather than in a separate part of the paper, the common characteristics of the cell having already been presented in earlier communications (1, 5, 6). Although certain questions involving reaction paths and mechanisms have inevitably been faced in this work, the emphasis here is on the performance of the rotating wiper-blade electrode relative to conventional electrodes, rather than on further insights into alternative mechanistic reaction schemes. It is hoped that the results of this effort will facilitate the development of an industrial device based on the rotating wiper-blade electrode principle.

The Reduction of Oxygen on Nickel

In preliminary experiments performed in a parallel-plate cell (5), inhibition of the reduction process was found to be in agreement with previous literature where passivation was ascribed to the oxide species: Adsorbed oxygen on the electrode surface may exist at −0.15V (RHE) (7) and its strength of bonding increases with time. At potentials higher than 0.1V oxygen adsorption is possibly combined with the formation of the poorly conducting phase oxide $Ni(OH)_2$ (7, 8). The layer of oxygen adsorbed on Ni does not appreciably inhibit oxygen ionization (7), but at potentials more positive than 0.1V the rate of ionization drops sharply. In order to counteract passivation, chemical and electrochemical means of removing adsorbed oxygen and/or oxide layers have been shown successful (7, 9-11) in reestablishing high initial oxygen reduction rates.

* Electrochemical Society Active Member.

[1] Present address: Department of Chemical Engineering, University of Connecticut, Storrs, Connecticut 06268.

Key words: anodization, anodic dissolution, anodic oxidation, oxygen, ethanol.

Experiments in the rotating cell were carried out using a 0.1 mole/dm^3 KOH solution, usual in similar studies (9, 10), and specially constructed (Pt) Hg, HgO/KOH (aq) reference electrodes for determining solution potentials. Using an appropriately prepared H_2 electrode (12), the reference cell potential was found to be 0.96265V at 293°K, with a temperature coefficient of −287.8 μV/°K, in good agreement with the previous literature. Particular care was taken to minimize the misalignment of the Luggin capillaries in the working cell and the potentiostat was controlled via an average solution potential using a 3 resistor T network which also allowed biasing toward any of the compartment potentials. This arrangement also allowed comparisons of a reaction rate existing in one particular compartment under tripolar conditions with the rate in the same compartment when all compartments were operating under identical conditions. Temperature was controlled at 23°C throughout. The details of the cell construction and principles of operation have previously been described (1-6); the essentially novel feature is the rotating cylindrical nickel electrode fabricated from a Nickel 200 rod (C, 0.04; Mn, 0.25; Fe, 0.05; S, 0.005; Si, 0.06; Cu, 0.03; Ni, 99.50% composition; courtesy of INCO, Canada).

Figure 1 shows the variation of the rate of oxygen reduction with potential in the electrolyte made up of BDH quality KOH and doubly ionized water. Prior to each measurement the electrode surface was held at −0.2V for 60 sec to minimize the amount of adsorbed oxygen on its surface. The sequence of potentials was selected randomly in order to eliminate possible effects of electrode "history," hence to ensure good reproducibility. Curve 2 corresponds to decay at 120 sec after the start of the reaction, on a pretreated surface, while curve 1 shows the reduction current density observed on an oxidized surface, obtained by oxidizing nickel at 1.2V (RHE) for 2 min. In contrast, curve 3 represents reduction taking place on the continuously reactivated anode surface at a rotation rate of 0.162 rad/sec, when the cell was operated in a tripolar fashion. In so doing, the cathode potential was kept at −0.2V (with respect to the solution in the first compartment) to ensure that the oxide formed during the passage of the electrode through compartments 2 and 3 be completely reduced. The potential drop across these two compartments was maintained independently at the same desired reduction value, since (*i*) relatively large currents passed through the cell compartments due to oxide film formation and reduction, and (*ii*) the double layer charging current, especially at lower current flows, is also significant. Since the initial quick formation of oxide and double layer charging take place in the second compartment, the current flow in the third compartment is due almost exclusively to surface reactivation, except for a small contribution (about 1.3 μA/cm^2) from leakage current flow between the first and third compartments.

The beneficial effect of the electrode rotation rate on the current flow is observed best under mass trans-

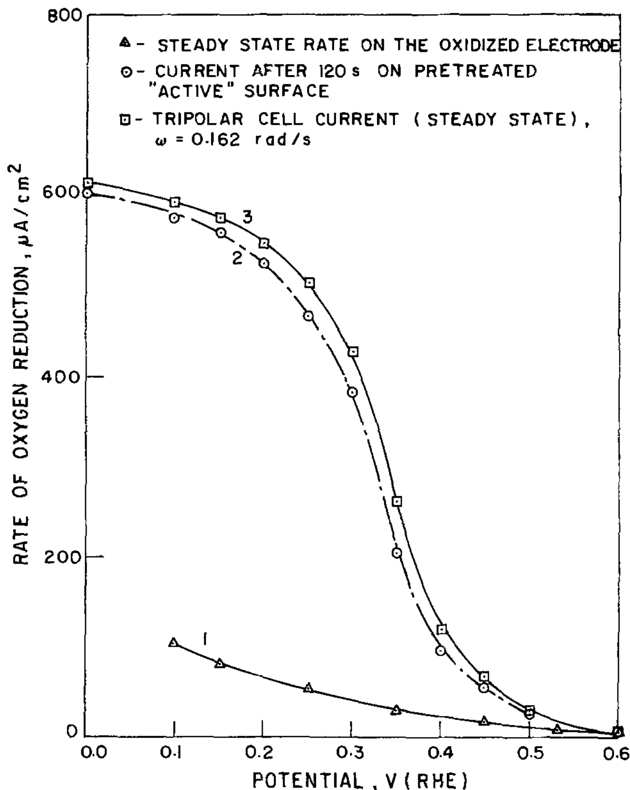

Fig. 1. The variation of oxygen-reduction current density with potential and pretreatment (electrolyte, 0.1 mole/dm^3 KOH; T = 23°C).

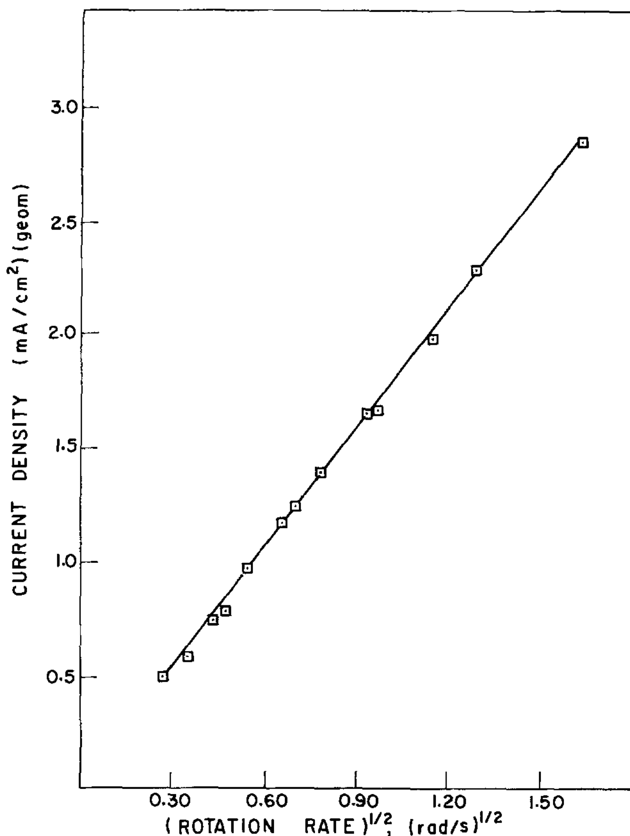

Fig. 2. The variation of oxygen-reduction current density with rotation rate in monopolar operation [electrolyte, 0.1 mole/dm^3 KOH; T = 23°C; potential = 0.1V (RHE)]. The solid line corresponds to Eq. [1].

port control. Figure 2 shows the typical linear dependence between current flow and the square root of the rotation rate, demonstrated previously (1, 6) for various reaction systems and observed here in monopolar operation, at 0.1V where O_2 reduction is mass-transport limited [pretreatment as in (7)]; the solid line represents the theoretical model (5, 13)

$$\bar{i}_L = \frac{zFDc_b}{\sqrt{t_s}}\left[\frac{1}{\sqrt{\pi D}} + \frac{1}{\psi(\sqrt{\pi\nu})}\right] \qquad [1]$$

where

$$\psi(\sqrt{\pi\nu}) \equiv \int_0^{\sqrt{\pi\nu}} \epsilon^{(y^3/6D\sqrt{\pi\nu} - y^2/4D)}dy$$

For the electrolyte used, $\nu = 8.5825 \times 10^{-3}$ cm^2/sec at 298°K and the bulk concentration of oxygen is computed as (14) $C_b = 1.175 \times 10^{-3}$ mole/dm^3 at the experimental atmospheric pressure of 98.43 kPa. The diffusion coefficient of oxygen being estimated (14) as $D = 1.815 \times 10^{-5}$ cm^2/sec, $\psi\sqrt{\pi\nu} \cong 7.71 \times 10^{-3}$ cm/sec$^{1/2}$. The magnitude of the relative error between predicted and experimental mass transport rates is less than 10%. In tripolar operation, the slope of the experimental regression line (2.4) is appreciably larger than the model-predicted slope of 1.76 in Fig. 2: It appears that the electrode rotation rate has an additional effect on surface activation and has the same role as the rate of pulsing in voltage-pulsing activation. This particular aspect of the cell is not well understood and a comprehensive analysis of the relationships involved cannot yet be given.

The Oxidation of Ethanol on Nickel

The electrooxidation of organic compounds (such as alcohols) has been the subject of numerous studies in the past and findings indicate that passivation may be ascribed to various Ni oxides whose formation depends strongly on the electrode pretreatment and oxidation potential. The positively charged Ni electrode is covered mainly by β-NiOOH in moderately alkaline solutions (15) and its discharging to $Ni(OH)_2$, studied extensively by Vertes *et al.* (15-17), is a rather complex function of time, anode potential, and electrolyte composition. Kinetic studies of the electrooxidation of alcohols (17, 18) yield rate constants two orders of magnitude apart and there is also considerable disagreement on the feasibility of reaching steady state in ethanol oxidation (18, 19). Differing oxidation mechanisms, proposed by Vertes *et al.* (15-17, 19-21), and Fleischmann *et al.* (18, 22), further indicate the incompleteness of present understanding in this area, where there is still much to learn.

The current study of ethanol oxidation on nickel may be summarized as follows. Figure 3 shows an essentially identical effect of a specific anodization procedure and tripolar operation of the rotating nickel anode, in the region of low oxidation rates. Both produce significantly higher reaction rates than conventional operation (curve 1). In a series of tests performed under various experimental conditions, the oxidation rate of ethanol was found to depend on the amount of oxide on the surface as expected from the literature: The coverage of the electrode by NiOOH increases with an increase in the potential, but at higher potentials the rate of this increase becomes smaller. Thus, the initial rate of electrooxidation of ethanol depends strongly on the anodization potential and anodization time which directly controls the amount of dischargeable oxide on the surface. Figure 4 shows the typical electrode behavior. Since oxidation starts at 1.392V, the NiOOH present on the surface is higher than the equilibrium amount corresponding to the oxidation potential; the resulting high oxidation rate gradually decreases toward a steady-state value. The decay may be characterized by the regression curve

$$i = i_2 + kQ_oe^{-kt} \qquad [2]$$

where i_2 is the steady-state component and Q_o is the initial oxide coverage of the surface, in excess

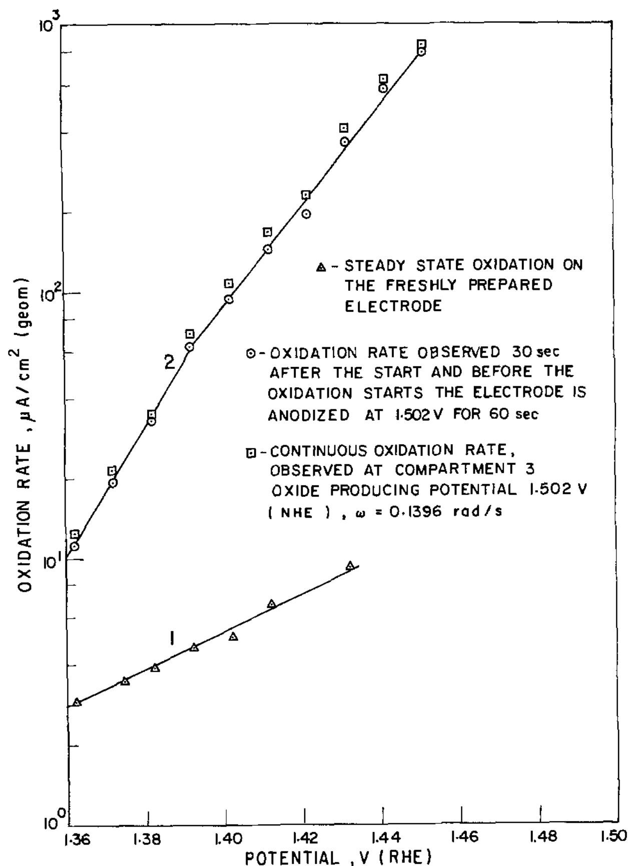

Fig. 3. The effect of electrode pretreatment on the oxidation rate of ethanol (electrolyte, 0.1 mole/dm^3 ethanol in 0.1 mole/dm^3 KOH; $T = 23°C$).

of the equilibrium value. The solid line in Fig. 4b corresponds to the experimental regression parameters of $i_2 = 48.93$ $\mu A/cm^2$, $k = 0.013614$ sec^{-1}, and $Q_o = 4.586$ mC/cm^2. It appears from Fig. 4 that the tripolar operation (where the potential of the rotating anode is kept at 1.502V in compartment 1, and in the range of 1.36-1.452V in compartments 2 and 3) maintains a continuously high oxide coverage of the surface and serves, as usual, as a continuous surface "reactivator." The experimentally observed oxidation rate, averaged over $(\tau_2 - \tau_1)$, where τ_1 is the time spent by the electrode surface in compartment 1 (before entering compartment 2) and τ_2 is the effective time during which the electrode process passes through compartments 1 and 2, varies approximately with the 0.07th power of the electrode rotation rate in the 0.08-1.1 rad/sec range, beyond which the effect of the rotation rate is essentially negligible. A similar averaging of Eq. [2] yields a 0.06th power relationship in the same range of rotation rate and the computed average current density values differ not more than -10% from the experimentally measured values.

In the region of high oxidation rates (initial current densities in the 1.0-2.0 mA/cm^2 range) decay behavior under potentiostatic conditions was found to agree with the results of Vertes *et al.* (19). While the true causes of passivation are not yet understood, two possibilities may be envisaged: (*i*) the formation of nickel-oxide-hydroxide, beyond some critical value, might inhibit the oxidation process by blocking the ethanol adsorption sites or by decreasing the surface concentration of one of the reactants, and (*ii*) with aging, the structure of the oxide may change, and the newly formed compound may have a passivating influence on the reaction rate. It may also be envisaged that the oxide gradually penetrates into the electrode surface and forms inclusions responsible for partial inactivity. At any rate, a detailed study (5) of each removal path (*i.e.*, discharge in an electrolyte; galvanostatic discharge; potentiostatic discharge; discharge by resistance loading) indicates that when the inhibiting oxide is removed from the electrode surface, the initial electrooxidation rate on the surface may be almost completely reestablished and this recovery is at relative maximum under galvanostatic reduction conditions. In this respect, the rotating tripolar wiper-blade cell offers an additional, and continuous, method for the reactivation of the rotating electrode surface when coupled with resistance shorting: This mode of operation was studied by keeping the potential of the anode surface in compartments 1 and 2 at the desired oxidation potential and shorting the portion of the anode surface in the third compartment to the outer electrode of the same compartment through a properly chosen load. Ethanol was thus oxidized in compartments 1 and 2 and the passivating

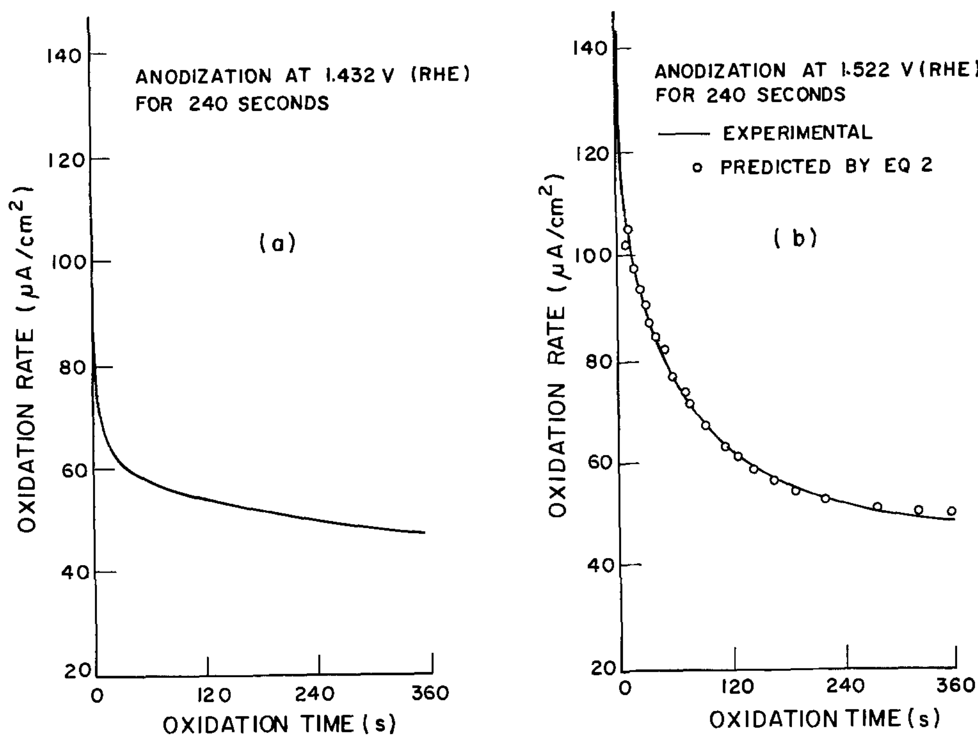

Fig. 4. The effect of anodization (anode coverage by oxide) on the oxidation rate of ethanol [electrolyte, 0.1 mole/dm^3 ethanol in 0.1 mole/dm^3 KOH; $T = 23°C$; potential $= 1.392V$ (RHE)].

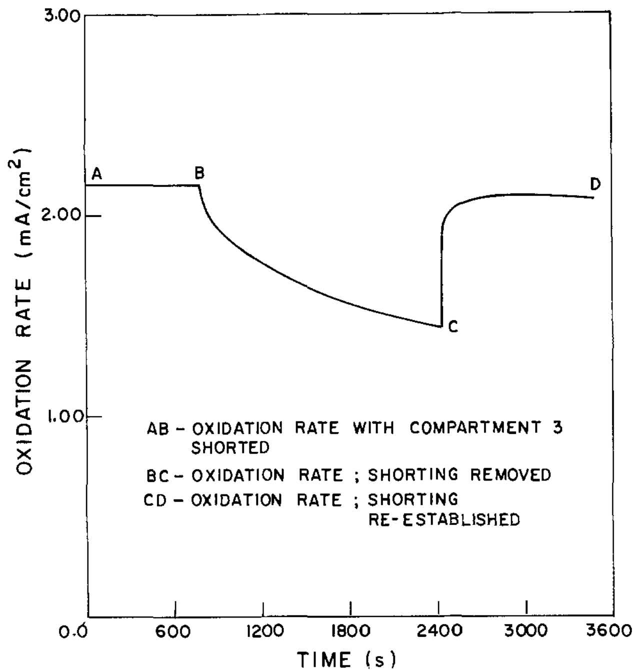

Fig. 5. The effect of shorting on the oxidation rate of ethanol [electrolyte; 0.1 mole/dm^3 ethanol in 0.1 mole/dm^3 KOH; T = 23°C; electrode rotation rate, 0.131 rad/sec; potential, 1.502V (RHE); shorting resistance, 0.976Ω].

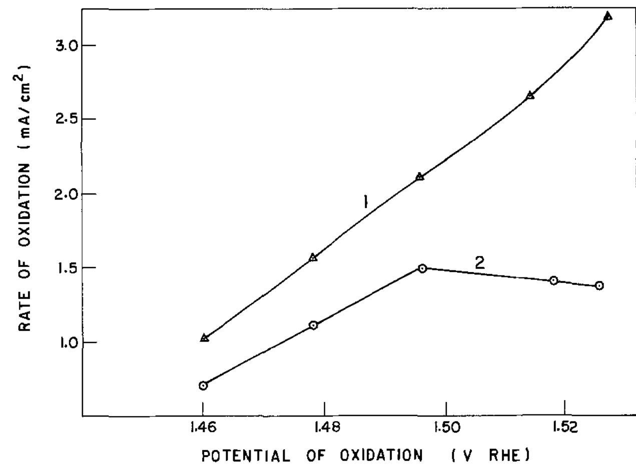

Fig. 6. The effect of oxidation potential on the rate of oxidation of ethanol in tripolar operation (curve 1) in comparison to monopolar operation (curve 2, observed at 9000 sec after start). (Electrolyte, 0.1 mole/dm^3 ethanol in 0.1 mole/dm^3 KOH; T = 23°C; electrode rotation rate, 0.131 rad/sec).

substance formed in these compartments on the anode surface was removed in the third compartment in the presence of electrode discharges. Typical results are shown in Fig. 5: In the zone designated as AB passivation is virtually absent as ethanol is continuously oxidized at a high rate, during short circuiting. At point B shorting was removed and the usual decay phenomenon is now observed until shorting was reestablished at point C, whereupon the oxidation rate, characteristic of the AB zone, is nearly fully recovered. Note also that a careful cell design may take advantage of the electrical energy produced in resistance shorting.

The oxidation rate under shorting conditions increases with the potential of oxidation at a fixed anode rotation rate (see Fig. 6); the effect of the anode rotation rate on the individual compartment reaction rates is illustrated in Fig. 7. It is seen that the related change in oxidation time on any portion of the anode surface in the first and second compartments has little effect on the rather slow decay rate (Fig. 7a); the rate of oxide reduction in the third compartment is strongly dependent on the electrode rotation rate (Fig. 7b), indicating that the latter has a positive effect on the rate of surface "rejuvenation." Note, however, that these new experimental results do not offer straightforward evidence for any of the hitherto proposed mechanisms of the oxidation reaction (such an investigation would be beyond the scope of this work) and they refer to surface-averaged phenomena; microscopic surface behavior, *i.e.*, local charge distributions, local oxide species, etc., will have to be studied in the future for a much better comprehension of what exactly happens on the electrode surface during activation and reactivation.

The Evolution of Oxygen on Nickel

The evolution of oxygen on nickel takes place on surface oxides which may exist in various oxidation states depending on the anode potential and the corresponding current density for oxygen evolution. While many studies have been reported on anodic oxygen on nickel in alkaline solutions, there is only

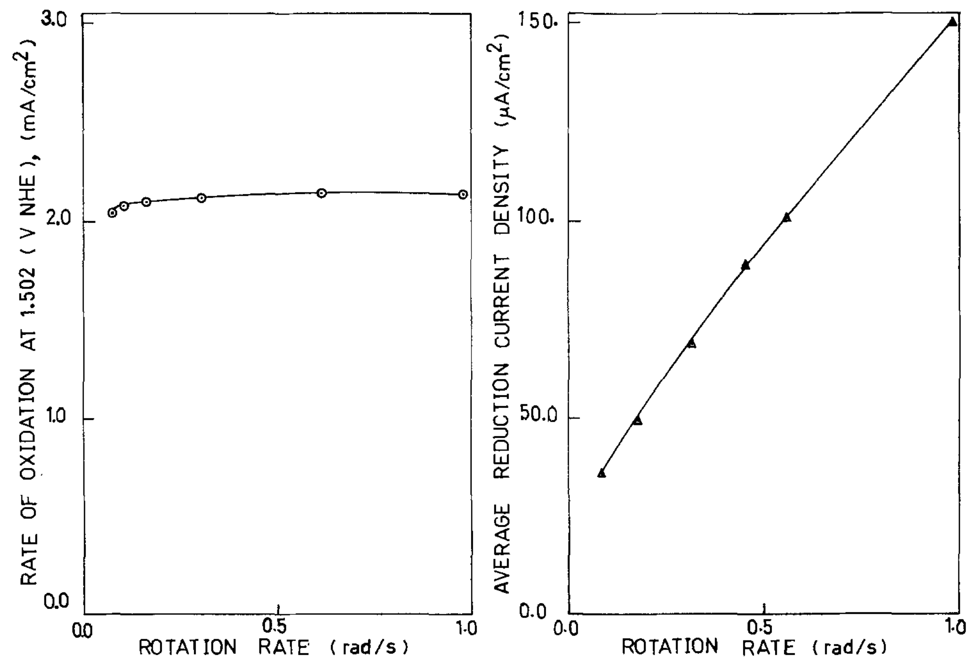

Fig. 7. The effect of electrode rotation speed on ethanol oxidation in bipolar operation: (a) activated surface, (b) compartment 3. (Electrolyte, 0.1 mole/dm^3 ethanol in 0.1 mole/dm^3 KOH; T = 23°C; shorting resistance, 0.976 Ω).

Table I. Values of the Tafel slope b reported for oxygen evolution on nickel

Authors	Electrode	Electrolyte	Current density i (A/cm^2)	Tafel slope b (mV)
Elina *et al.* (23)	Nickel	Alkaline	$>10^{-3}$	90-130
Gatman and Lukovtsev (24)	Nickel	Alkaline	$>10^{-3}$	90-130
Sato and Okamoto (25)	Nickel	Acidic	$<10^{-3}$	130-140
		Alkaline	Low current density	
Fleischmann *et al.* (22)	Nickel	KOH	$<10^{-3}$	30-40
Volchkova and Krasil'shchinkov (26)	"Bare" nickel	KOH	$<10^{-3}$	$2.3 \times RT \times 1000/3F$
	"Bare" nickel	NaOH	$<10^{-3}$	$2.3 \times 2RT \times 1000/3F$
Tsinman (27)	Electrochemically oxidized nickel	NaOH	Low current density	$(2.3 \times RT/2F)$ 1000
		KOH	Low current density	$(2.3 \times 2RT/3F)$ 1000
Thompson and Kaye (28)	Nickel	Alkaline	$>10^{-3}$	95-130
Conway *et al* (28)	Nickel	KOH	Low current density	30-42

limited agreement amongst the kinetic results of various workers, as shown in Table I. The scatter of numerical values of the Tafel slope is most likely due to the different states of the electrode surface employed or to differences in surface pretreatment, or to different thicknesses of the oxide layer. The reaction is inhibited (29) on oxidized nickel surfaces, the passivation being inversely related to temperature. A number of kinetic mechanisms have been proposed (*e.g.*, 25, 29-31) apart from the general scheme for any metal by Bockris (32). An earlier mechanism proposed by Krasil'shchinkov (33) relates distinct Tafel slope values to various rate-determining steps involving, among other species, the Ni_2O_3, Ni_2O_2, and Ni_2O_4 oxides. It appears from the literature that this oxidation process is rather complex.

Of particular importance for the current apparatus are previous observations on the existence of hysteresis between ascending and descending polarization curves (29), and on the self-passivation of oxygen evolution (29, 34); these phenomena and previous findings (5) suggest that the rotating, wiped multipolar electrode may be successfully used to increase the reaction rate at a particular potential (or in a particular potential range) via continuous surface rejuvenation.

First, polarization phenomena were studied in further detail, using the cell in a conventional monopolar manner, with the outer electrodes connected together. Since pertinent literature on oxide formation phenomena, obtained via potentiodynamic triangular sweep techniques (7, 34), indicates that adsorption of oxygen on Ni begins at about -0.15V (RHE) the rotating electrode was kept at -0.15V for 2 min, before raising its potential to the working range of 1.322-2.222V. There is some evidence that the $Ni(OH)_2$ formed in anodic polarization cannot fully be reduced by subsequent cathodic reduction even over a prolonged time period (7) and, in consequence, it is likely that the above pretreatment did not yield a fully oxide-free surface. On the other hand, it is seen from the Pourbaix diagram for Ni (35) that in a 0.1 mole/dm^3 KOH electrolyte and at -0.15V, $Ni(OH)_2$ is the only thermodynamically permissible oxide species. Thus, it is expected that although a certain portion of the hereby pretreated electrode surface has $Ni(OH)_2$ (but no other oxide species) on it, the surface is sufficiently activated to observe the pursued phenomena.

Figure 8 shows the characteristic hysteresis effect observed in anodic polarization elsewhere (29). The value of the Tafel slope was next estimated by carrying out potentiostatic oxygen evolution in the 1.432-1.507V potential range, with three replica runs in order to obtain an unbiased estimate of the experimental error variance. The electrode pretreatment was identical to that of the polarization study. The probability distribution of the Tafel slope was estimated by the conventional linear model

$$V_i = a + b \ln i_i + \epsilon_i \quad i = 1, \ldots, n \qquad [3]$$

and the statistically unbiased nonlinear model

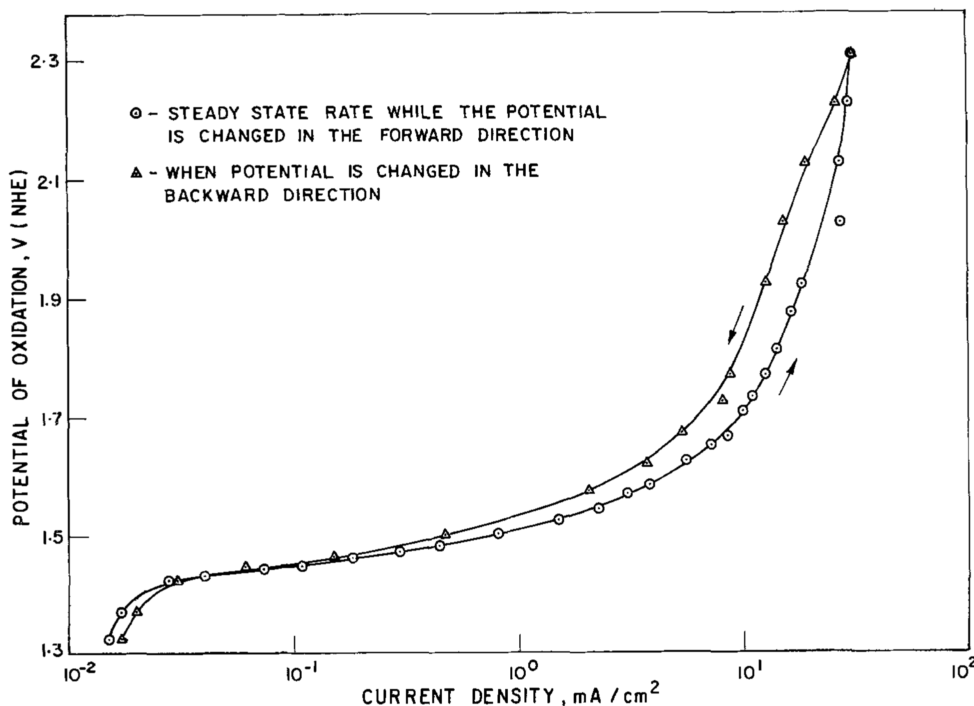

Fig. 8. Typical steady-state potentiostatic polarization curves for oxygen evolution (electrolyte, 1.0 mole/dm^3 KOH; T = 23°C).

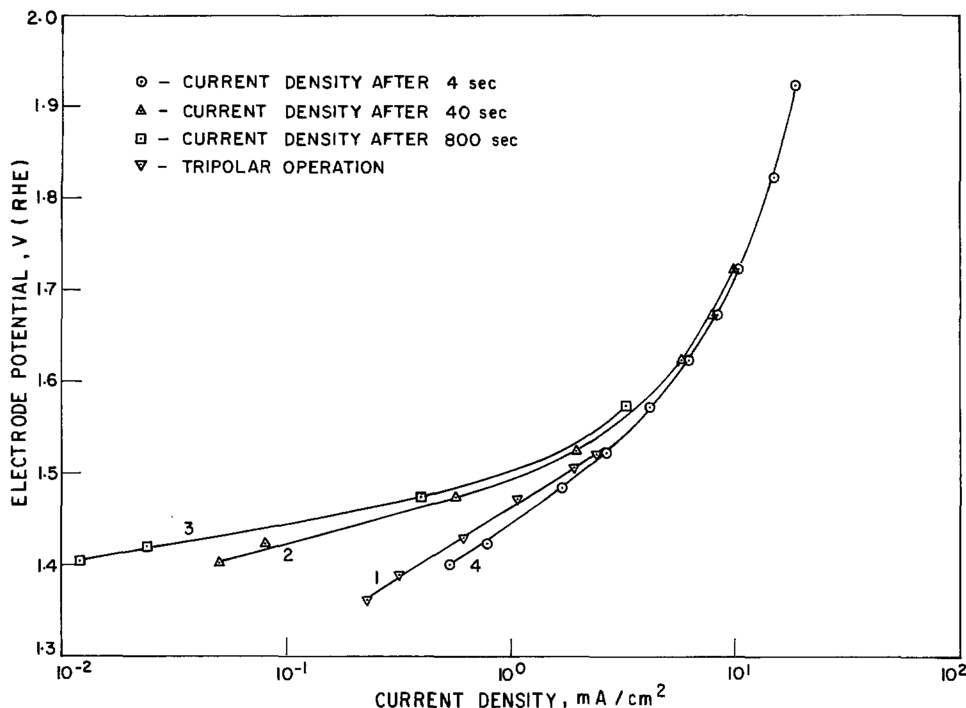

Fig. 9. Comparison of polarization curves for oxygen evolution in monopolar (curves 2, 3, 4) and tripolar (curve 1) operation.

$$i_i = a \exp(V_i/b) + \epsilon_i \quad i = 1, \ldots, n \qquad [4]$$

the experimental error variance, σ_e^2, being computed at 34 degrees of freedom. The statistically most probable value of the Tafel slope, $b = 0.0275$, obtained via Eq. [4], is somewhat different from the biased value of $b = 0.0261$ based on Eq. [3].

The usefulness of the rotating wiped electrode cell in tripolar operation is well demonstrated in Fig. 9; tripolar operation is equivalent to a continuous reduction of the oxide layer film thickness on the electrode. Curve 1 represents current flow in the third compartment, oxygen film formation being confined essentially to compartment 2; the electrode potential in compartment 1 was held at -0.15V. The contribution of oxide film growth to the current flow in the third compartment is at most 10%, this magnitude being inversely proportional to the time length of activation.

As in the case of ethanol oxidation an explanation of the experimental results in terms of mechanistic models is not yet possible. Neither the mechanism proposed by Sato (25) involving adsorbed O and OH species, nor the Krasil'shchinkov mechanism (26) involving surface reactions between various nickel oxides and atomic oxygen, nor the generalized Bockris mechanism (32) can be employed for a quantitative comparison of predicted and observed phenomena. Much more work remains to be done in this area before electrode behavior becomes fully understood.

The Anodic Dissolution of Nickel

The anodic activation phenomenon (*i.e.*, the existence of a more negative initial potential than the equilibrium value, on approaching from the oxidized state toward the free corrosion potential) for Ni has been described by several researchers (36-38) but the correct activation mechanism is not known. Gerischer (39) describes activation to (nonequilibrium) intermediate oxygen compounds formed at anodic potentials, while Oshe and Lovachev (36) to excess surface oxygen; Losev and Kabanov to oxygen penetration into the metal crystal lattice (37); Trusov *et al.* (38) to the creation of excess dissolution centers. In any event, the fact that the initial rate of nickel dissolution is much higher than the steady-state dissolution rate corresponding to the potential applied, indicates that at a given average anodic overvoltage, larger dissolution rates may be achieved by voltage pulsing techniques, such as in multipolar operation.

The experiments performed were designed with a number of important findings (38) in mind: if the nickel electrode is held at a base potential corresponding to active dissolution of the metal (0 to +100 mV RHE) and then anodic activation in the +150 to +700 mV range is carried out, when the potential is lowered again to the value of the base potential the observed current may exceed the current observed, before anodic passivation at the same base potential, up to two orders of magnitude. In Trusov's experiments the associated specific charge, 4.4×10^{-4} C/cm^2, corresponds to current flows in the 10-80 μA range; Oshe and Lovachev (36) reached current densities up to 0.3 mA/cm^2.

The experimental procedure followed closely Trusov's (38) scheme using the same electrolyte species and concentration: Fig. 10 shows the monopolar behavior of the anode in a 0.1 mole/dm^3 H_2SO_4 solution. In Fig. 10a typical fast decay is seen at +30 mV potential measured with a mercury-mercurous sulfate reference electrode at 23°C. Upon anodic activation at +330 mV for half a minute, the dissolution

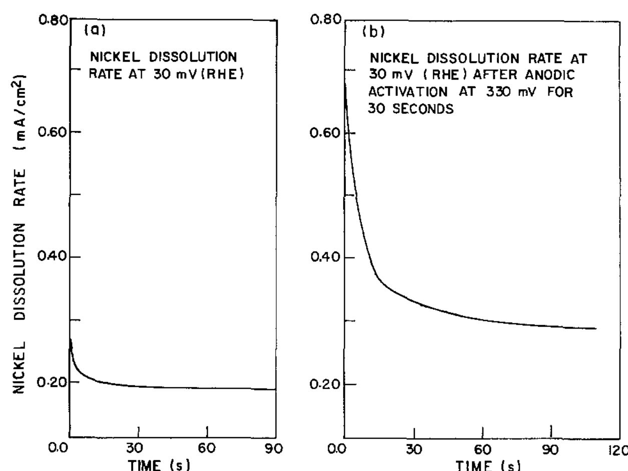

Fig. 10. Typical nickel dissolution rates in monopolar operation (electrolyte, 0.1 mole/dm^3 H_2SO_4; $T = 23°C$). (a) Potential, 30 mV (RHE); (b) potential, 30 mV (RHE) after anodic activation at 330 mV for 30 sec.

rate jumps to a rather high value, which diminishes gradually toward a steady state (Fig. 10b). The total charge density over the 0-90 sec period being computed as 17.67 mC/cm^2 (Fig. 10a) and 30.64 mC/cm^2 (Fig. 10b) by numerical integration, anodic activation under the specific conditions shown is manifest by a relative increase of about 74% in the associated flow of electric charge. A brief analysis of possible components of this flow is as follows.

Oxygen evolution at the nickel anode.—From oxygen overpotential data [Ref. (40), Table IV.8] on nickel, the computed regression line

$$\hat{\eta}_{O_2} = 1.0448 + 0.1466 \log_{10} i \, V (i\text{: A/cm}^2) \quad [6]$$

with a standard error of estimate of 7.39×10^{-3} indicates that at the observed current densities, the oxygen overpotential is in the 0.53-0.57V range and, as such, is higher than the approximate value of the passivation potential at $pH = 0$ and 25°C for Ni [0.36V, Ref. (41), Table II.7]; this value is somewhat modified for the working electrolyte with computed $pH \cong 0.96$. Thus, the contribution of oxygen evolution is negligible at the experimental conditions.

Anode reactions related to impurities in the electrolyte.—Reagent grade H_2SO_4 has at most 0.5 ppm Cu, Pb, and heavy metals; 0.2 ppm Fe and 0.5 ppm Ni in the stock solution; the working electrolyte was obtained by tenfold dilution. This effect, therefore, is likewise negligible.

Anode reactions related to impurities in the electrode.—The only metallic impurity in Ni 200 of quantitative importance and with a stronger dissolution tendency than Ni is manganese (0.25%) with an oxidation standard potential of 1.180V. From the Pourbaix diagram (35) it appears that if Mn were "free" in the nickel electrode, the $Mn \rightarrow Mn^{++} + 2e^-$ dissolution process would compute with a similar reaction involving Ni and Ni^{++}. The actual dissolution rate depending on the surface structure, etc., it does not follow that manganese in the anode would readily dissolve in the electrolyte under anodic activation. This component is expected to be quite small although probably not entirely negligible.

Hydrogen absorption or the formation of excess O_2 on the anode surface.—According to Trusov (38) this contribution is negligible, in contradiction to the statements by Oshe and Lovachev (36). There is no clear evidence that this component is of any importance.

Formation of intermediate oxygen compounds on the surface (39) or the creation of excess dissolution centers (38).—The relative largeness of the charge ratios (see above) favors the latter model where the dissolution centers represent crystallographic disruptions of the surface in the form of atoms "torn" from it. Oxygen on the surface would block such centers. Deactivation is due, according to this model, to the disappearance of dissolution centers which leads to a "self-healing" of the surface. While this model is not entirely convincing it appears that the electrode behavior in bipolar operation might be explained in its terms. In Fig. 11 monopolar and bipolar operations are compared; in the latter, the inner electrode potential was adjusted to 30 mV with respect to the solution potential in compartments 1 and 2, and the third compartment potential was maintained independently at 330 mV. It can be seen that while the anode rotation rate has essentially no effect on monopolar operation, it has a definite beneficial effect on the bipolar mode of operation, the enhancement in the dissolution rate being 2 to 3 times the monopolar rate. One might argue that the combined effect of rotating and wiping is a continuous recreation of dissolution centers, hence a continuously active reaction surface. Apart from the (yet unknown) correct reaction mechanism, the bipolar rotating cell may serve, on proper scale-up, as an improved nickel electrorefining reactor.

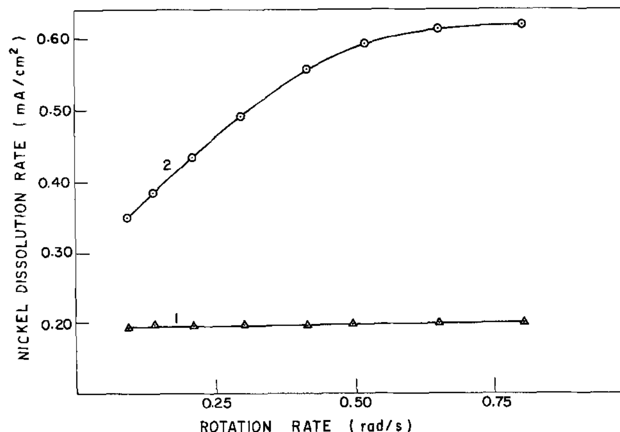

Fig. 11. The effect of rotation speed on the rate of nickel dissolution at a potential of 30 mV. Curve 1, monopolar operation; curve 2, bipolar operation. Anodization potential, 300 mV (RHE) (electrolyte, 0.1 mole/dm^3 H_2SO_4; $T = 23°C$).

Summary

The rotating multipolar, wiped electrode principle has been found useful for a nickel electrode in the following applications:

Redox reactions: As in the instance of platinum, the inhibitive effect of the oxide film can be suppressed and rates higher than those observed in conventional electrolyzers can be maintained. In contrast to Pt, enhancement on Ni, often one order of magnitude, is limited to the low current density region; the rate of enhancement increases with the electrode rotation rate.

Organic compounds which react with oxides of the electrode material can be continuously oxidized at relatively high rates in a multipolar cell and in the region of low electrooxidation current, by means of maintaining an amount of oxide, in excess of the equilibrium value, on the Ni electrode surface. In the region of high current densities, where the electrode is gradually passivated, continuous reactivation may be achieved by repeated removal (wiping) of the passivating surface.

The rotating bipolar, wiped cell is an efficient means of continuous anodic activation for electrolytic metal dissolution processes. Quantitative data concerning various other electrodes would be the subject matter of further experimental studies.

Acknowledgment

Support via the National Research Council of Canada and a Canadian Commonwealth Scholarship and Fellowship Award is acknowledged.

Manuscript submitted Feb. 13, 1978; revised manuscript received May 30, 1978.

Any discussion of this paper will appear in a Discussion Section to be published in the June 1979 JOURNAL. All discussions for the June 1979 Discussion Section should be submitted by Feb. 1, 1979.

Publication costs of this article were assisted by the University of Waterloo.

LIST OF SYMBOLS

a, b Tafel equation parameters
C_b bulk electrolyte concentration
D electrolyte diffusivity
$\mathbf{F}$ Faraday's constant
i current density; $\bar{i}$ its average value
i_L limiting current density at the rotating electrode
k rate coefficient
Q_o initial oxide coverage of electrode surface

t_S time required for an arbitrary point on the electrode surface to pass from one wiper blade to the next
ϵ_i error associated with the ith measurement
τ residence time of electrode surface in a given compartment
ν kinematic viscosity of the electrolyte
ψ integral defined in Eq. [1]

REFERENCES

1. P. R. Nadebaum and T. Z. Fahidy, *This Journal*, **122**, 1035 (1975).
2. M. Farooque and T. Z. Fahidy, *ibid.*, **124**, 836 (1977).
3. M. Farooque and T. Z. Fahidy, *ibid.*, **124**, 1191 (1977).
4. M. Farooque and T. Z. Fahidy, *ibid.*, **125**, 544 (1978).
5. M. Farooque, PhD. Thesis, University of Waterloo (1977).
6. P. R. Nadebaum, PhD. Thesis, University of Waterloo (1974).
7. Kin-Ling-Ying, N. A. Shumilova, and V. S. Bagotskii, *Elektrokhimya*, **3**, 460 (1967).
8. A. A. Rakov, T. I. Borisova, and V. B. Ershler, *Zh. Fiz. Khim.*, **22**, 1390 (1948).
9. V. S. Bagotskii and Yu. B. Vasilyev, *Electrochim. Acta*, **9**, 869 (1964).
10. N. A. Shumilova and V. S. Bagotskii, *ibid.*, **13**, 285 (1968).
11. J. Jansta and K. Micka, *Collect. Czech. Chem. Commun.*, **35**, 1650 (1970).
12. D. J. G. Ives and G. J. Janz, "Reference Electrodes—Theory and Practice," p. 403, Academic Press, New York (1961).
13. M. Farooque and T. Z. Fahidy, *Can. J. Chem. Eng.*, **55**, 355 (1977).
14. R. E. Davis, G. L. Horvath, and C. W. Tobias, *Electrochim. Acta*, **12**, 287 (1967).
15. G. Vertes, G. Horanyi, and G. Nagy, *Acta. Chim. Acad. Sci. Hung.*, **67**, 145 (1971).
16. G. Vertes, G. Horanyi, and G. Nagy, *ibid.*, **68**, 217 (1971).
17. G. Vertes, G. Horanyi, and G. Nagy, *ibid.*, **69**, 341 (1971).
18. M. Fleischmann, K. Korinek, and D. Pletcher, *J. Electroanal Chem. Interfacial Electrochem.*, **31**, 39 (1971).
19. G. Vertes and G. Horanyi, *ibid.*, **52**, 47 (1974).
20. G. Vertes, G. Horanyi, and G. Nagy, *Acta. Chim. Sci. Hung.*, **71**, 333 (1972).
21. G. Vertes, G. Horanyi, and G. Nagy, *ibid.*, **74**, 405 (1972).
22. M. Fleischmann, K. Korinek, and D. Pletcher, *J. Chem. Soc., Perkin Trans. 2*, 1396 (1972).
23. L. M. Elina, T. I. Boriskova, and Ts. I. Zalkind, *Zh. Fiz. Khim.*, **28**, 785 (1954).
24. S. A. Gatman and P. D. Lukovtsev, *Tr. Sov. Elektrokh., Izd. Akad. Nauk SSSR*, **504**, 1950 (1953).
25. N. Sato and G. Okamoto, *Electrochim. Acta*, **10**, 495 (1965).
26. L. M. Volchkova, A. I. Krasil'shchinkov, and L. G. Antonova, *Zh. Fiz. Khim.*, **23**, 441 (1949).
27. A. I. Tsinman, *ibid.*, **37**, 714 (1963).
28. K. M. Thompson and A. L. Kaye, *Trans. Electrochem. Soc.*, **60**, 229 (1931).
29. B. E. Conway, M. A. Sattar, and D. Gilroy, *Electrochim. Acta*, **14**, 677 (1969).
30. B. E. Conway and P. L. Bourgault, *Can. J. Chem.*, **37**, 292 (1959).
31. B. E. Conway and E. Gileadi, *ibid.*, **40**, 1933 (1962).
32. J. O'M. Bockris and A. K. M. S. Huq, *Proc. R. Soc. London, Ser. A*, **58**, 593 (1962).
33. A. I. Krasil'shchinkov, *Zh. Fiz. Khim.*, **37**, 273 (1963).
34. M. A. Satter and B. E. Conway, *Electrochim. Acta*, **14**, 695 (1969).
35. M. Pourbaix, "Atlas d'Equilibres Electrochimiques," Gauthiers-Villars Paris; "Atlas of Electrochemical Equilibria in Aqueous Solutions," Pergamon Press New York (1966).
36. A. I. Oshe and V. A. Lovachev, *Elektrokhimiya*, **6**, 1419 (1970).
37. V. V. Loshev and B. N. Kabanov, *Zh. Fiz. Khim.*, **28**, 842, 914 (1954).
38. G. N. Trusov and M. F. Fandeeva, *Elektrokhimya*, **8**, 1008 (1972).
39. H. Gerischer, *Z. Elektrochem.*, **63**, 500 (1959).
40. G. Milazzo, "Electrochimie," p. 1, Dunod Paris (1969).
41. J. O'M. Bockris and A. K. N. Reddy, "Modern Electrochemistry," Plenum Press, New York (1970).
42. P. M. Reilly and G. E. Blau, *Can. J. Chem. Eng.*, **52**, 289 (1974).

The Electrochemical Behavior of Te(IV) in Sodium Tetrachloroaluminate Melts

J. Robinson and R. A. Osteryoung*

Department of Chemistry, Colorado State University, Fort Collins, Colorado 80523

ABSTRACT

The electrochemistry of Te(IV) in NaCl:$AlCl_3$ melts has been investigated by a variety of techniques including cyclic and pulse voltammetry, potentiometry, controlled potential coulometry, and the use of the rotating-disk electrode. It was found that in the most basic melts at temperatures above 250°C, Te(IV) was initially reduced by a two-electron step to a soluble Te(II) species which could then be reduced further to elemental tellurium. At lower temperatures and in more acidic melts, Te(IV), which is present in the melt as the chlorocomplexed ion $TeCl_3^+$, is reduced directly to Te which undergoes a complexation reaction with Te(IV) to form Te_4^{2+}. This complexation reaction and the oxidation of Te_4^{2+} have both been extensively investigated and a mechanism for the complexation reaction involving a Te(II) intermediate is proposed.

As part of our continuing investigations into the electrochemistry of inorganic species in sodium tetrachloroaluminate melts, we have, in view of their possible use as cathode materials in molten salt battery systems (1-3), been particularly interested in the behavior of the chalcogens and their compounds. We recently reported on our studies in these solvents of sulfur (4) and selenium (5), which were shown to be reducible to the respective chalcogenide and could also be oxidized to cationic moeties. The nature of these cations was found to be highly dependent upon the composition of the melt. The present paper is con-

* Electrochemical Society Active Member.

Key words: fused salts, voltammetry, kinetics.

cerned with a similar investigation of the electrochemistry of tellurium species in the same solvent system.

In recent years Bjerrum and co-workers have reported the results of several studies, utilizing both spectrophotometric (6, 7) and potentiometric (7) techniques of unusual tellurium cations in tetrachloroaluminate melts. In particular they have reported the existence of the entities Te_2^{2+}, Te_4^{2+}, Te_6^{2+}, and Te_8^{2+}, which are stabilized by the large anions, $AlCl_4^-$ and $Al_2Cl_7^-$, present in the melt, and also Te^{2+}, which is stabilized by Cl^-. The same workers have also studied the chloro-complexes of the Te^{4+} cation in $KCl:AlCl_3$ melts (8, 9), and found there to be four species present, $TeCl_6^{2-}$, $TeCl_5^-$, $TeCl_4$, and $TeCl_3^+$, which are linked by melt acidity dependent equilibria. The solid compounds of the Te_4^{2+} cation, $Te_4(AlCl_4)_2$ and $Te_4(Al_2Cl_7)_2$, have been characterized by Corbett *et al.* (10, 11) who have also identified a tellurium cation of + 1/3 oxidation state.

Despite their possible use in battery systems, the electrochemistry of tellurium compounds does not appear to have been widely studied either in tetrachloroaluminates or any other molten salts. Bodewig and Plambeck (12) have investigated the anodization of Te into a fused LiCl:KCl eutectic and have proposed the reaction to be the oxidation of Te to Te^{2+}. Until very recently, the only study of Te in tetrachloroaluminates was a very brief one, some thirty years ago, by Verdiek and Yntema (13), however, Paulsen and Bjerrum (14) have now reported on a study of the electrochemistry of Te^{4+} in basic and neutral $KCl:AlCl_3$ melts at temperatures between 300° and 400°C. They reported that under these conditions Te^{4+}, which is chloro-complexed in the melt, was reduced reversibly to a soluble Te^{2+} species which could then be further reduced to insoluble elemental tellurium. In view of the known complexity of the redox chemistry of tellurium in these melts, and in particular its dependence upon temperature and melt composition (6, 7), the electrochemical behavior can be expected to be very different at lower temperatures and higher *p*Cl's. The work presented here is primarily concerned with the electrochemistry at lower temperatures (175°C) and over a wide range of *p*Cl's.

In order to investigate the *p*Cl dependence of the electrochemistry of the Te compounds the acid-base properties of the $AlCl_3:NaCl$ molten salt solvent system must be understood. These have been discussed previously (15) and the way the concentrations of the different species present in the melt vary with the $AlCl_3:NaCl$ ratio was shown to be fully described by the following three equilibria

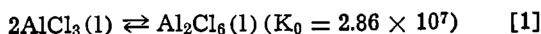

$$2AlCl_3(l) \rightleftarrows Al_2Cl_6(l)\ (K_0 = 2.86 \times 10^7) \quad [1]$$

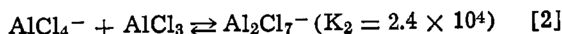

$$AlCl_4^- + AlCl_3 \rightleftarrows Al_2Cl_7^-\ (K_2 = 2.4 \times 10^4) \quad [2]$$

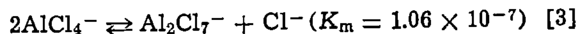

$$2AlCl_4^- \rightleftarrows Al_2Cl_7^- + Cl^-\ (K_m = 1.06 \times 10^{-7}) \quad [3]$$

where the *K* values are the mole fraction equilibrium constants. The dominant acid-base equilibrium is that described by Eq. [3] where $Al_2Cl_7^-$ is the Lewis acid and Cl^- the base. The *p*Cl (mole fraction scale) of a neutral melt, 50 mole percent (m/o) $AlCl_3$, at 175°C is 3.5; however, a melt of any desired acidity can readily be made by anodizing an Al wire into it (16) until the desired composition, as indicated by the potential of an Al indicator electrode with respect to an Al wire in a melt of known composition (15), is reached.

Experimental

The details of melt preparation and purification, electrochemical cells, electrode construction, electrochemical instrumentation and, experimental techniques have been fully described in an earlier publication (5). The $TeCl_4$ (Cerac Pure Incorporated 99.5% pure) was used as received. Throughout this work the reference electrode is an aluminum wire immersed in an NaCl-saturated melt at the temperature of the experiment separated from the bulk solution by a fine porosity glass frit.

Results and Discussion

$TeCl_4$ is readily soluble in an NaCl-saturated melt at 175°C, and Fig. 1 shows a typical cyclic voltammogram of such a solution recorded at a sweep rate of 100 mV sec^{-1}. There is a well-defined reduction peak (E_p = 1.615V) and a corresponding reoxidation wave (E_p = 1.662V). This particular voltammogram was recorded with a glassy carbon electrode; however, the behavior was identical at a tungsten electrode. Contrary to the observations of Paulsen and Bjerrum (14), no problem was ever encountered with reproducibility at a glassy carbon electrode and in view of the easier surface preparation of these carbon electrodes, they were used throughout this study. Figure 2 shows a series of normal pulse voltammograms, recorded at different pulse widths (t), of a $TeCl_4$ solution for the same conditions as in Fig. 1. The limiting plateau currents were found to be linearly dependent upon $t^{-1/2}$, indicating that within the time scale of these experiments the reduction process is diffusion controlled and a diffusion coefficient for the Te(IV) species of 4.54×10^{-6} cm^2 sec^{-1} was calculated from this data (using an n value of 4 *vide infra*). As a further test of diffusion control, the rising portions of the pulse voltammograms were analyzed. If the product of the reduction is soluble then a plot of log $(i_d - i/i)$ *vs.* E should be a straight line, whereas if the reaction product is insoluble log $(i_d - i)$ *vs.* E will be linear. Figure 3 shows such plots for a 105 msec pulse. It can immediately be seen that the log $(i_d - i)/i$ plot is linear, whereas the log $(i_d - i)$ plot is not, the product of the reaction must therefore be soluble. From the slope of the log $(i_d - i)/i$ plot, a value of $\alpha\eta_\alpha$ can be calculated and this was found to be 1.82. Log $(i_d - i)/i$ plots for the shortest pulse lengths (15 msec) begin to show a degree of nonlinearity; the reason for this effect is discussed in detail later. The reduction was also examined by differential pulse voltammetry and

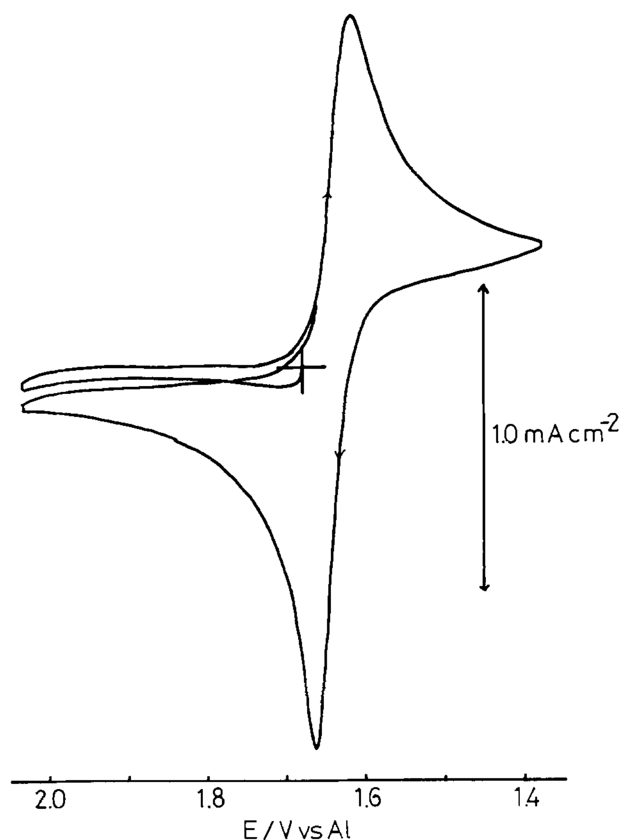

Fig. 1. A cyclic voltammogram at a glassy carbon electrode of a 1.22×10^{-3}M solution of $TeCl_4$ in an NaCl-saturated melt at 175°C. The sweep rate was 100 mV sec^{-1}.

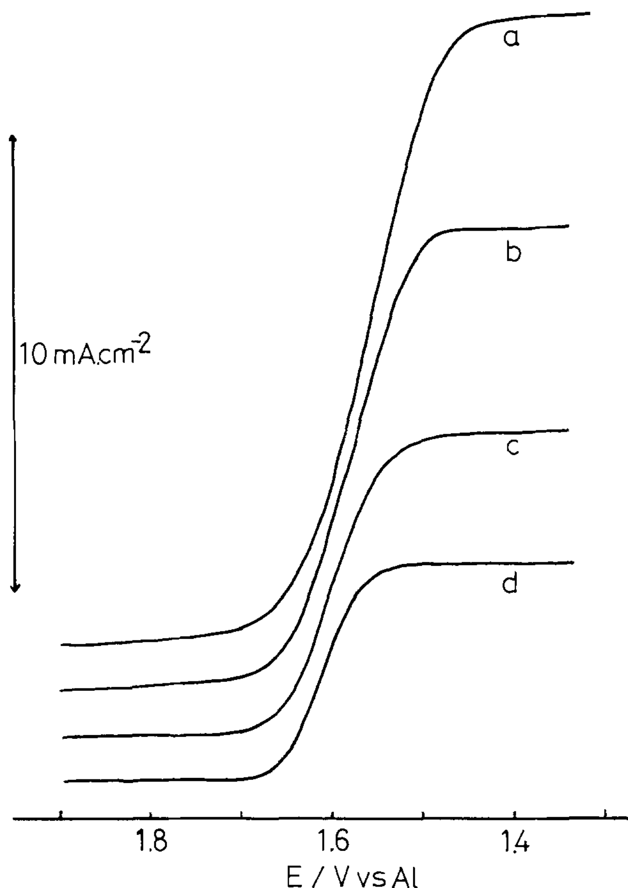

Fig. 2. Normal pulse voltammograms of a 3.55×10^{-3}M solution of $TeCl_4$ in an NaCl-saturated melt at 175°C. The sweep rate was 1 mV sec^{-1}, the delay time was 1 sec, and the pulse lengths were: (a) 15 msec; (b) 25 msec; (c) 55 msec; and (d) 105 msec.

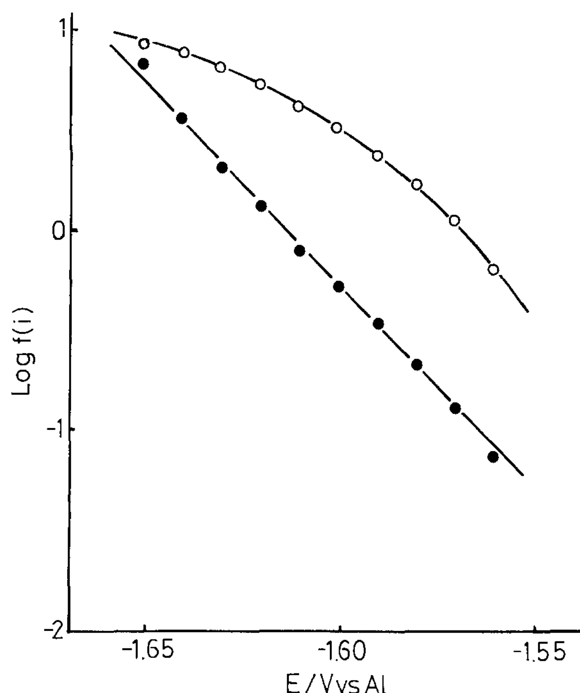

Fig. 3. A kinetic plot for a normal pulse voltammogram of a 3.55×10^{-3}M $TeCl_4$ solution in NaCl-saturated $NaAlCl_4$ melt at 175°C using a 105 msec pulse length [polarogram (d) of Fig. 2]. —○— $f(i) = (i_d - i)$; —●— $f(i) = (i_d - i)/i$.

the voltammograms for the conditions of Fig. 1 and 2 showed a single symmetrical peak. The width of this peak at half height was 39 mV for a 105 msec pulse length and increased with decreasing pulse length. This value of the peak width agrees most closely with that predicted for a reversible four-electron process (34 mV at 175°C). The increase of peak width with decreasing pulse length is indicative of the quasi-reversibility of the reduction. Exhaustive controlled potential coulometry, using a tungsten crucible as the electrode, was carried out to test this conclusion, and the number of electrons per $TeCl_4$ molecule was found to be 3.9 ± 0.1. The electrode reaction must therefore be a four-electron process. At the completion of the coulometric experiment no electroactive species were present in solution in the melt (either oxidizable or reducible) and a finely divided gray precipitate of elemental tellurium was left in the cell. This precipitation, however, only commenced at the very end of the electrolysis when very little Te(IV) was present. It therefore appears that the Te is in some way solubilized by the Te(IV). This phenomenon is discussed in detail later.

The behavior observed here is very different from that reported by Paulsen and Bjerrum (14) at similar values of melt acidity (at 175°C the pCl of an NaCl saturated melt is 1.9 on the mole fraction scale, which corresponds to a value of approximately 1.0 on the molar scale used by Paulsen and Bjerrum). The present work, however, was carried out at a significantly lower temperature. To determine the temperature effect, cyclic, normal pulse, and differential pulse voltammograms were recorded at several temperatures between 175° and 350°C. Figures 4a and 4b show typical cyclic voltammograms at 265° and 350°C, respectively, of $TeCl_4$ solutions in NaCl-saturated melts. It can immediately be seen that the four-electron reduction observed at lower temperatures (Fig. 1) splits into two distinct processes, as also does the reoxidation wave. Analogous behavior was also observed on the normal and differential pulse voltammograms. Exhaustive-controlled potential electrolysis shows that the two waves observed in the cyclic voltammetry at 350°C both correspond to two-electron processes.

These observations are in agreement with the results reported by Paulsen and Bjerrum (14), that in basic-to-neutral tetrachloroaluminate melts at high temperatures, Te(IV) is first reduced to Te(II) and then to Te. No detailed analysis of the pCl dependence of the reduction processes at these temperatures was undertaken here, as there is no reason to suppose that the behavior in $NaAlCl_4$ will be any different to that observed in $KAlCl_4$ by Paulsen and Bjerrum (14); that is that Te(IV) is present as $TeCl_6^{2-}$ and $TeCl_5^-$ while Te(II) is present as $TeCl_3^-$ and $TeCl_2$. It is interesting that the stability of the Te(II) species shows a very strong temperature, as well as acidity, dependence; *e.g.*, at a pCl of 1.9 at

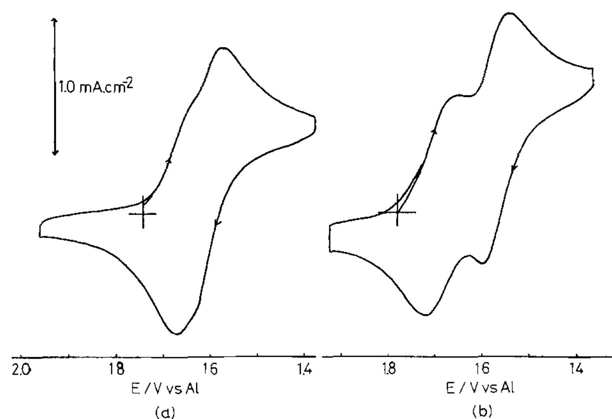

Fig. 4. Cyclic voltammograms of 2.27×10^{-3}M $TeCl_4$ solution in NaCl-saturated $NaAlCl_4$ melts recorded at 100 mV sec^{-1}. The temperatures were (a) 265°C; and (b) 350°C.

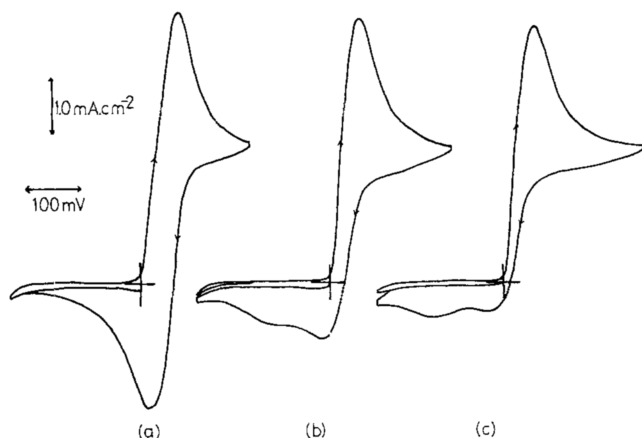

Fig. 5. Cyclic voltammograms of 8.48×10^{-3}M $TeCl_4$ solutions. The melt pCl's were (a) 2.8; (b) 3.75; and (c) 5.1, while the electrode rest potentials were (a) 1.824V; (b) 1.880V; and (c) 1.993V.

175°C the reduction (see Fig. 1) is a well-defined four-electron step, whereas at the same pCl at 350°C it was observed that the reduction showed two distinct two-electron steps.

Already it can be seen that the electrochemistry of Te(IV) in tetrachloroaluminate melts shows remarkable temperature dependence. The remaining part of this study, however, is concerned with the pCl dependence at 175°C. Figures 5a, 5b, and 5c show cyclic voltammograms, at a fixed sweep rate of 50 mV sec^{-1}, of Te(IV) solutions of increasing acidity. It can be seen that the reduction peak moves strongly in the anodic direction as the acidity increases and at the same time the reoxidation wave splits into two, the more anodic wave being broad and rather ill defined. This anodic shift in the reduction wave with increasing pCl suggests that the Te(IV) species, as expected (8, 9), is chlorocomplexed in the melt and that there is a net loss of Cl^- ions in the rate-determining step of the reduction process. At a fixed sweep rate the relative heights of the two reoxidation waves are pCl dependent, the more cathodic one being more prominent at lower pCl's, while at fixed acidity the more positive wave grows at the expense of the more negative one as the sweep rate is increased. The two oxidation waves even become apparent in the most basic melts (pCl = 1.9 at 175°C) at very high sweep rates (100V sec^{-1}). The behavior in the most acidic melts is also very interesting. At slow sweep rates the most negative reoxidation wave is fairly well defined, but on increasing the sweep rate to 1V sec^{-1} it almost disappears; however, on increasing the sweep rate further to 10V sec^{-1} or more it becomes much better defined. To explain all the above complex behavior there must be some chemical steps occurring in the over-all redox processes.

While the results from the normal pulse experiments in NaCl-saturated melt discussed earlier appeared to indicate the reduction of Te(IV) to be diffusion controlled, the results of the cyclic voltammetry do not support this hypothesis. Table I shows the sweep rate dependence of the function $i_{pc}/\nu^{1/2}$, where i_{pc} is the height of the reduction peak and ν is the sweep rate for four values of melt pCl. If the

Table I. The values of the function $i_p/\nu^{1/2}$/mA cm^{-2} $sec^{1/2}$ $V^{-1/2}$ for a 8.48×10^{-3}M $TeCl_4$ solution as a function of the sweep rate ν/V sec^{-1} at four pCl values

ν pCl	5.1	3.65	2.8	1.95
0.02	21.65	22.7	23.1	28.5
0.05	21.0	21.5	22.1	28.3
0.1	20.0	20.3	21.5	27.8
0.2	19.1	19.2	20.9	26.3
0.5	18.5	18.8	20.5	25.1

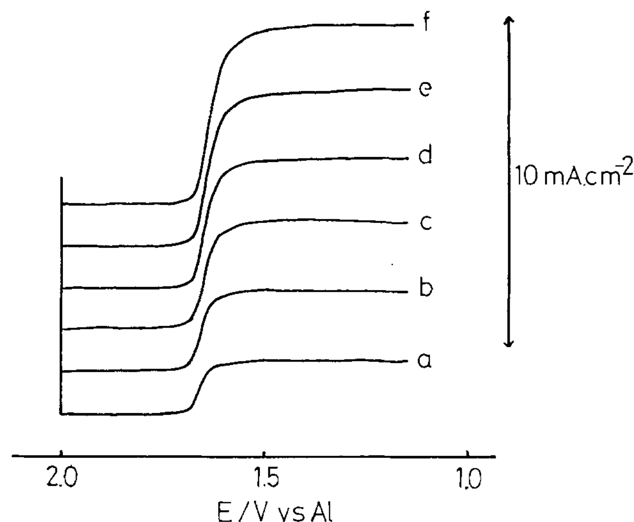

Fig. 6. RDE scans of a 1.852×10^{-3}M $TeCl_4$ solution in NaCl-saturated $NaAlCl_4$ melt. The scan rate was 2 mV sec^{-1} and the rotation rates were (a) 400 rpm; (b) 900 rpm; (c) 1600 rpm; (d) 2500 rpm; (e) 3600 rpm; and (f) 4900 rpm.

process were diffusion controlled, the value of $i_{pc}/\nu^{1/2}$ would be independent of ν. This, however, is clearly not the case here. The value of $i_{pc}/\nu^{1/2}$ decreases with increasing ν, the variation being greatest at the highest pCl's. This behavior is indicative of the presence of a preceding chemical reaction, the rate of which decreases with increasing pCl. At this point it should be mentioned that the normal pulse voltammograms cease to show linear i_{lim} *vs.* $t^{-1/2}$ dependence as the acidity is increased, the value of i_{lim} being lower than anticipated for short pulse times, again indicative of a preceding chemical step.

One of the most satisfactory techniques for investigating preceding chemical steps in electrochemical reactions is the use of the rotating-disk electrode (RDE) Figure 6 shows the results of a series of such experiments for a Te(IV) solution in a tetrachloroaluminate melt. At all the melt acidities investigated, a plot of i_{lim} *vs.* $\omega^{1/2}$ was linear, indicating a diffusion-controlled process. Furthermore when the RDE response was analyzed using a $1/i$ *vs.* $1/\omega^{1/2}$ plot (all current readings being recorded at the steady state) the behavior was typical of that for a process the rate of which is determined by a slow electron transfer, and the values of the heterogeneous rate constant and $\alpha\eta_\alpha$ could be determined (17). Table II gives the values of D, the diffusion coefficient, $\alpha\eta_\alpha$, and k_0^θ calculated for the RDE results at three different pCl's (the determination of the values of the standard electrode potential for the process, required in the determination of k_0^θ, is discussed later). The values of $\alpha\eta_\alpha$ and k_0^θ both decrease with increasing pCl, while the value of $\alpha\eta_\alpha$ at a pCl of 1.9 agrees closely with that determined from the normal pulse voltammetry as do the values of the diffusion coefficient.

The above results can be rationalized in the following manner. The Te formed by the electroreduction of Te(IV) reacts with more Te(IV) to form a complex species which must undergo a chemical reaction,

Table II. Kinetic parameters for the reduction of Te(IV) determined from RDE experiments

pCl	$\alpha\eta_\alpha$	$k_0^\theta \times 10^{3}$*	$D \times 10^{6}$**
4.5	1.27	3.98	4.69
3.8	1.37	7.9	4.71
1.9	1.80	20.0	4.69

* cm sec^{-1}.
** cm^2 sec^{-1}.

probably decomposition to Te and Te(IV), before it can be reduced further. The rate of this latter chemical reaction decreases with increasing pCl as shown by the $i_{pc}/\nu^{1/2}$ values from the cyclic voltammetry. The chemical reaction is not, however, observed at the RDE, as all the Te is swept away from the electrode before it undergoes the reaction with Te(IV). The process at the RDE, therefore, appears as a simple four-electron reduction uncomplicated by chemical steps. The two reoxidation peaks on the reverse cyclic voltammetry sweep both correspond to the oxidation of the complex but by different routes. The more cathodic one corresponds to the oxidation of Te which is formed by the decomposition of the complex, whereas at more anodic potentials the complex undergoes oxidation by a different mechanism, which, judging by the drawn-out nature of the cyclic voltammetry peak, is probably also complicated by chemical steps. At low pCl's the decomposition step is very fast and therefore the more anodic cyclic voltammetry peak is not seen except at very high sweep rates. As the pCl is increased the decomposition reaction slows down and the second peak becomes more apparent at lower sweep rates. At the highest pCl's the second oxidation mechanism becomes dominant. The reappearance in acidic melts of the more cathodic oxidation wave, corresponding to the oxidation of Te as the sweep rate is increased, does not contradict the above mechanism but is due to the fact that the reaction between Te and Te(IV) is not infinitely fast, and at these high sweep rates some of the Te has not had time to react.

The formation of the complex between Te(IV) and Te also explains the solubilization of Te in the Te(IV)-containing melts discussed earlier. It is known from spectrophotometry (6, 7) and potentiometry (7) that Te(IV) and Te form several cationic cluster complexes; however, under the conditions prevailing in the experiments described here the dominant species can be anticipated to be Te_4^{2+} (6, 7). To test this assumption a potentiometric experiment was carried out. A solution of $TeCl_4$ in a melt contained in a tungsten crucible, which also served as the working electrode, was coulometrically reduced in a stepwise manner, and the rest potential of a glassy carbon indicator electrode was measured after each step. When the reduction was nearly complete, the process was reversed and the equilibrium potential of the indicator electrode was recorded after stepwise coulometric oxidations. In this way Nernst plots were readily constructed and these are shown in Fig. 7 for a range of melt acidities. It can be seen that at large values of log $[Te^{4+}]/[Te]$, the electrode potential varies linearly with log $[Te^{4+}]/[Te]$ and the value of the slopes in this region is 22 ± 2 mV, which is in

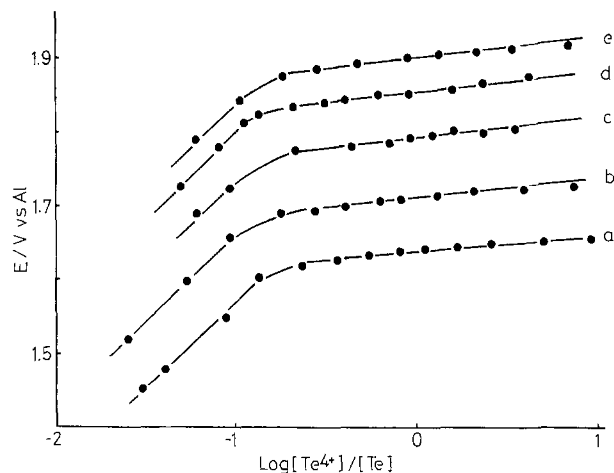

Fig. 7. Nernst plots for the Te^{4+}/Te couple. The melt pCl's were (a) 1.9; (b) 2.75; (c) 3.81; (d) 4.70; and (e) 5.29.

good agreement with the value predicted for a four-electron reduction (22.3 mV at 175°C). There is, however, a break in these plots which occurs consistently at a value of $[Te^{4+}]/[Te]$ of about 0.15 ± 0.02 which corresponds to a $[Te]:[Te^{4+}]$ ratio of 7:1. This supports the complexation reaction between Te and Te(IV) being the formation of Te_4^{2+} according to the reaction described in Eq. [4].

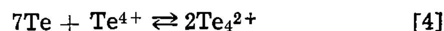

$$7Te + Te^{4+} \rightleftarrows 2Te_4^{2+} \quad [4]$$

with the equilibrium lying well to the right-hand side. At $[Te^{4+}]:[Te]$ ratios less than about 0.15, the rest potential drops sharply and also becomes unstable, possibly due to adsorption of Te on the electrode. Cyclic voltammograms under these conditions show that the concentration of Te in the melt drops sharply as the $[Te^{4+}]:[Te]$ ratio drops below 0.15, indicating the commencement of Te precipitation. Further support of the formation of Te_4^{2+} is the color of the solution which is deep violet [Bjerrum (6) reports a strong adsorption peak for Te_4^{2+} at about 18,000 cm^{-1}.] From the above Nernst plot it is possible to determine the values of the standard electrode potentials, and these are found to vary linearly with pCl as defined by Eq. [5]

$$E^\circ = (1.497 \pm 0.010) + (0.076 \pm 0.003)pCl \quad [5]$$

It is known that the process is a four-electron one; the slope observed, therefore, corresponds most closely with that predicted for $3Cl^-$ ions being lost in the over-all reaction (67 mV at 175°C). The Te(IV) must therefore be primarily present as $TeCl_3^+$, although some more highly complexed species, *e.g.*, $TeCl_4$ and $TeCl_5$, will also be present, particularly at the lowest pCl's. This is in agreement with the results of Von Barner *et al.* (8) who reported the degree of chlorocomplexation of Te(IV) in $KCl:AlCl_3$ melts for the pCl range covered here to lie between three and four. This later work was, however, carried out at a rather higher temperature (300°C).

In view of the complexity of the processes involved, the chemical steps occurring during the reduction will be very difficult to investigate. Those involved in the oxidation of Te_4^{2+} are, however, fairly readily studied at an RDE. Figure 8 shows a series of potential scans, at an RDE, for a solution of Te_4^{2+} in an NaCl-saturated melt. (This solution was prepared by the partial reduction of Te(IV), assuming Eq. [4] to lie well to the right-hand side). It can be seen that at low rotation rates only one wave is present, but as ω is increased, a second, rather drawn out one, appears at more anodic potentials, the behavior of which is analogous to the cyclic voltammetric results discussed earlier. Figure 9 shows plots of the steady-state current as a function of $\omega^{1/2}$ at 1.725V (corresponding to the plateau of the first wave) and at 2.05V (the plateau potential of the second wave). The current at 2.05V is a linear function of $\omega^{1/2}$ and a value of the diffusion coefficient of 7.7×10^{-6} cm^2 sec^{-1} was calculated from the slope of this line. The first wave is, however, only diffusion controlled at low rotation rates and the value of i becomes independent of $\omega^{1/2}$ at large values of the latter, indicating that the reaction has become kinetically controlled. The current is then given by Eq. [6]

$$i = nFkc_o^\infty \quad [6]$$

and if it is assumed that the equilibrium described in Eq. [4] lies well to the right-hand side the value of k, the pseudo-first order homogeneous rate constant, is readily calculated. This was found to be independent of the concentration of Te_4^{2+}, *i.e.*, the rate-determining reaction is first order in $[Te_4^{2+}]$, but highly dependent upon the pCl. The value of log k was found to vary linearly with pCl as described by Eq. [7]

$$\log_{10} k = (0.028 \pm 0.03) - (0.90 \pm 0.10)pCl \quad [7]$$

over the pCl range 1.9-4.0. The values at the lower end

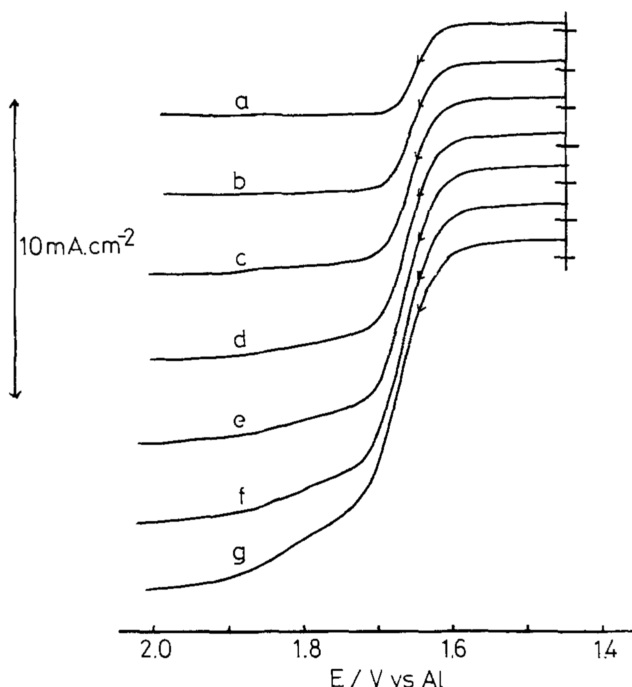

Fig. 8. RDE scans of $7.65 \times 10^{-4}M$ Te_4^{2+} in NaCl-saturated melt. The scan rate was 2 mV sec^{-1} and the rotation rates were (a) 400 rpm; (b) 900 rpm; (c) 1600 rpm; (d) 2500 rpm; (e) 3600 rpm; (f) 4900 rpm; and (g) 6400 rpm.

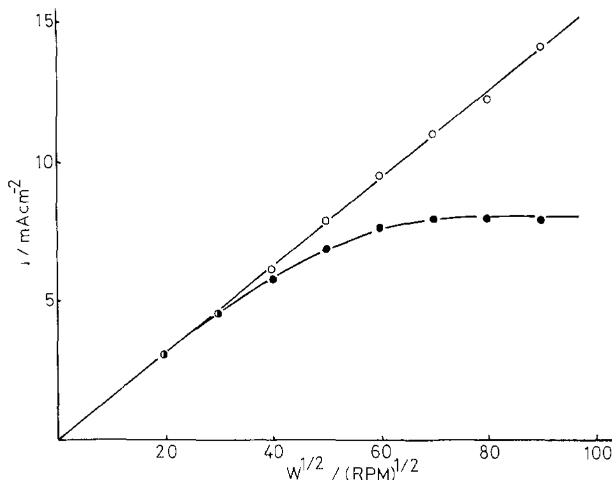

Fig. 9. Levich plots for the oxidation of $7.65 \times 10^{-4}M$ Te_4^{2+} in NaCl-saturated melt at the RDE. The currents were measured at —○—, 2.05V and —●—, 1.725V.

of the pCl range fell slightly off the line possibly because the equilibrium in Eq. [4] is not complete at these acidities. From the slope of the line the reaction must also be first order in $[Cl^-]$, and therefore the second order homogeneous rate constant for the reaction can be calculated to be 0.28 ± 0.05 liter $mole^{-1}$ sec^{-1}.

Any mechanism that is proposed for the over-all redox chemistry of Te(IV) must satisfy the above criteria that the rate-determining step in the decomposition of Te_4^{2+} is first order in $[Te_4^{2+}]$ and $[Cl^-]$ as well as the previously discussed observations that Te(IV) is present in the melt as $TeCl_3^+$ and that the stoichiometry of the reaction between Te(IV) and Te is that given in Eq. [4]. To satisfy these points it is necessary to invoke a short-lived intermediate species in the mechanism, but since the electrochemical investigation provides no clue as to the identity of such a species this precludes the proposal of a unique mechanism. One possible intermediate is a Te(II) species. This seems quite reasonable in view of the fact that such a species was observed in very basic melts at high temperatures and also because Te(II) has been observed spectrophotometrically (6) to be the first product formed when $TeCl_4$ is reduced by elemental tellurium in chloroaluminate melts. A possible mechanism for the reaction of Te with Te(IV) which satisfies all the above criteria is given below by Eq. [8] and [9]

$$TeCl_3^+ + Te \rightleftarrows 2TeCl^+ + Cl^- \quad [8]$$

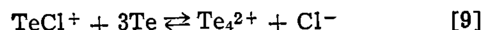

$$TeCl^+ + 3Te \rightleftarrows Te_4^{2+} + Cl^- \quad [9]$$

where the forward and backward rates of Eq. [8] are both fast and Eq. [9] is the rate-determining step. It can be seen that the decomposition of Te_4^{2+} is first order in $[Te_4^{2+}]$ and $[Cl^-]$, as required, Te(IV) is present as $TeCl_3^+$ and by adding Eq. [8] and twice Eq. [9] we get Eq. [10]

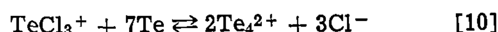

$$TeCl_3^+ + 7Te \rightleftarrows 2Te_4^{2+} + 3Cl^- \quad [10]$$

which has the required stoichiometry.

Acknowledgment

This work was supported by the Air Force Office of Scientific Research under Grant Number AFOSR-76-2978.

Manuscript submitted March 31, 1978; revised manuscript received June 6, 1978.

Any discussion of this paper will appear in a Discussion Section to be published in the June 1979 JOURNAL. All discussions for the June 1979 Discussion Section should be submitted by Feb. 1, 1979.

Publication costs of this article were assisted by Colorado State University.

REFERENCES

1. L. Redey, I. Porubszky, and I. Molner, Paper presented at the 9th International Power Sources Symposium, Brighton, England, Sept. 1974.
2. M. Shimotake and E. J. Cairns, Abstract 282, p. 674, The Electrochemical Society Extended Abstracts, Boston, Massachusetts, Meeting, May 5-9, 1978.
3. Report No. FJSRL-TR-77-0004, Air Force Systems Command, USAF, April 1977.
4. K. A. Paulsen and R. A. Osteryoung, *J. Am. Chem. Soc.*, **98**, 6866 (1976).
5. J. Robinson and R. A. Osteryoung Paper submitted to *This Journal.*
6. N. J. Bjerrum, *Inorg. Chem.*, **9**, 1965 (1970); **10**, 2578 (1971); 11, 2648 (1972).
7. R. Fehrmann, N. J. Bjerrum, and M. A. Andreasen, *ibid.*, **15**, 2187 (1976).
8. J. M. vonBarner, N. J. Bjerrum, and K. Kiens, *ibid.*, **13**, 1708 (1974).
9. F. W. Paulsen, N. J. Bjerrum, and O. R. Nielsen, *ibid.*, **13**, 2693 (1976).
10. T. W. Couch, D. A. Lokken, and J. D. Corbett, *ibid.*, **11**, 357 (1972).
11. D. J. Prince, J. D. Corbett, and B. Garbisch, *ibid.*, **9**, 2731 (1970).
12. F. G. Bodewig and J. A. Plambeck, *This Journal*, **117**, 618 (1970).
13. R. G. Verdieck and L. F. Yntema, *J. Phys. Chem.*, **48**, 268 (1944).
14. F. W. Paulsen and N. J. Bjerrum *J. Electroanal. Chem. Interfacial Electrochem.*, **79**, 327 (1977).
15. L. G. Boxall, H. L. Jones, and R. A. Osteryoung, *This Journal*, **120**, 223 (1973).
16. L. G. Boxall, H. L. Jones, and R. A. Osteryoung, *ibid.*, **121**, 212 (1974).
17. A. C. Riddiford, in "Advances in Electrochemistry and Electrochemical Engineering," Vol. 4, P. Delahay and C. W. Tobias, Editors, p. 47, Interscience, New York (1966).

Electrochemical and Surface Analytical Characterization of Titanium and Titanium Hydride Thin Film Electrode Oxidation

Rod K. Quinn*

Sandia Laboratories, Albuquerque, New Mexico 87115

and Neal R. Armstrong

Department of Chemistry, Michigan State University, East Lansing, Michigan 48824

ABSTRACT

The oxidation of the active, high energy density materials, titanium and titanium hydride, has been studied by electrochemical and electron spectroscopic techniques. The apparent thickness of the oxide was controlled by the magnitude of the applied potential across thin (200-6000Å) films of these materials. Our electrochemical measurements indicated that after irreversible oxide formation, the thin films behaved as typical semiconducting oxide electrodes. A technique of electrochemical aging is described which permits comparison with oxide thicknesses produced by thermal aging. Post mortem analysis by XPS and AES was used to characterize the extent of oxidation of the film surface. Observation of the $dN(E)/dE$ and $N(E)$ Auger spectrum (especially the $L_{III}M_{2,3}M_{4,5}$ transition) indicated that all electrode film surfaces are a mixture of TiO_2, suboxides, and the respective metallic phases (Ti or TiH_x).This observation is confirmed by the predominant XPS Ti transition. The extent of oxide growth into the films was measured by the AES/depth profiling technique and the results are comparable for the two systems to a depth of ~50Å. The results of these experiments are compared for titanium and titanium hydride and are examined with respect to a model for oxide formation and growth.

The oxidation of titanium in its various metallic and metal-oxide forms has received attention by several investigators (1-9). We have previously reported (9) on the electrochemical oxidation of titanium thin film electrodes and on the effect of oxide layer formation on the change of electrochemical reactivity. Studies of the electrochemical oxidation of the surface region (top 5-100Å) of pure titanium thin film electrodes have shown that these thin films serve as a model for the solution and solid-state oxidation of titanium and titanium hydride foil and powder surfaces. Vapor deposited thin film electrodes provide an ideal electrode surface with very high purity as well as predictable and controllable surface structure (9-12). Our surface analytical studies have indicated that freshly deposited, titanium thin film surfaces are not oxide free, but consist of a mixture of Ti metal and various titanium oxides, forming a "prepassive region" approximately 20-50Å thick. Except in ultrahigh vacuum environments, it is probably not possible to produce a fully reduced titanium surface, neither is it possible to obtain such a clean surface for even short times in contact with an electrolyte. Nevertheless, the thin film electrodes show reasonable electrochemical activity and the study of their oxidation provides a model for the passivation of fresh titanium surfaces to depths of 50Å or less.

We present here further voltammetric studies of the oxidation of titanium thin electrodes before and after electrochemical and atmospheric oxidation. The thickness of a passive oxide layer on the thin film electrodes can be estimated by straightforward voltammetric and coulometric techniques correlated to Auger and x-ray photoelectron spectroscopic measurements of these same films (9).

We further report the results of similar studies on the oxidation of titanium thin films which have been hydrided to the γ-phase stoichiometry $TiH_{1.4-1.9}$ (referred to here as TiH_x) (13). Oxidation of these films is similar to the titanium films except that a different two-phase surface composition is observed consisting of an oxide-rich outer layer (≈25-30Å thickness) and a hydride-rich bulk composition. Voltammetric and surface analytical data are presented which support this structure and quantitatively characterize the various metallic and oxide components.

We have intentionally avoided investigations of the electrochemical current/voltage regions where passivation/corrosion phenomena of titanium have normally been studied (high current densities and high overpotentials). Our main emphasis has been only on the passivation of the outer surface region of both the Ti and TiH_x films by electrochemical and atmospheric oxidation.

Experimental

Thin film preparation.—The Ti thin films were electron beam evaporated onto heated (450°C) quartz or alumina disks at a pressure of 10^{-7} Torr and a deposition rate of approximately 125 Å/min. The hydrided films were prepared in the same apparatus as the metal films. After metal deposition the films were equilibrated with purified hydrogen gas to the pressure and temperature to ensure the γ-phase TiH_x, where $x = 1.4$-1.9 (13, 14). Typical film thicknesses were 200-6000Å depending on the experimental requirements as measured by both interferometric and conductance techniques. Once deposited the electrodes were stored under dry, purified argon prior to electrochemical treatment.

Electrochemical experiments.—The electrochemical cell allowed for two potentiostat contacts for potential control and two bridge contacts for d-c conductance measurement at the working electrode (9). The auxiliary electrode was a coil of Pt wire and the reference electrode was a saturated calomel electrode, separated from the electrolyte solution by a quartz frit. All applied potentials in this paper are referenced to the saturated calomel electrode (SCE).

* Electrochemical Society Active Member.

Current and charge were recorded as a function of applied potential using a Princeton Applied Research (PAR) 173 Potentiostat/Digital Coulometer and a PAR 179 Universal Programmer. Surface conductance measurements were made with a Wheatstone bridge/amplifier circuit (15-17). The experimental arrangement allowed simultaneous recording of current, charge, and conductance as a function of applied potential. Capacitance/potential curves were recorded using a technique described previously (9). Scan rates of 5 mV/sec or less were used in all experiments.

Samples were loaded into the electrochemical cell and transported to high vacuum for surface analysis under controlled, inert (purified Ar or N_2) atmospheric conditions.

Surface analysis and data treatment.—Auger electron spectroscopy (AES) and x-ray photoelectron spectroscopy (XPS) data were obtained on a Physical Electronics 548 ESCA/Auger analysis system. Vacuum was maintained at 10^{-9} Torr or less. AES experiments were conducted using a 1 keV electron beam, 15-30 μA of current, 2 eV modulation at 17 kHz, and a lock-in amplifier time constant of 0.03 sec. Both $N(E)$ and $dN(E)/dE$ spectra were recorded directly from this instrument. XPS data were obtained using a MgKα source at 400W of power. Data were either recorded directly using the output of the photon counter or signal averaged using a Data General, Nova 800, minicomputer with 32 K core and two 1.2 million bit Diablo disks. Deconvolution of overlapping XPS peaks were accomplished using a computer routine similar to published methods (9, 18-22). The XPS spectra were computer-simulated by inputting five parameters: (*i*) the slope of the linear spectral background, (*ii*) the binding energy of each electronic component, (*iii*) the full width at half-maximum of each component, (*iv*) the peak height of each component, and (*v*) the percentage of Gaussian contribution to the slope of the spectral background. The binding energy and Gaussian contribution were evaluated using transitions from standard Ti compounds (22). The binding energy of the $Ti(2p_{3/2})$ XPS peak subtracted from the binding energy of the O(1s) XPS peak is referred to as ΔBE_1 in subsequent discussions (18, 22). Argon ion sputtering was done at 5×10^{-5} Torr with beam voltages of 1 kV and 10-20 mA of filament emission current. Under these conditions, a sputtering rate of 12.5-25 Å/min was observed in our Ti films. The ion beam was always focused so that the electron beam or x-ray source was placed well inside the sputtered area of the film surface.

Results and Discussion

Electrochemical oxidation of Ti films.—The linear sweep voltammetric (LSV) behavior of the titanium thin film electrodes in strong acid media has been previously described (9). We show in Fig. 1a typical behavior in 1*N* $HClO_4$. Anodic currents of between 30-50 $\mu A/cm^2$ were observed at bias potentials in excess of +0.5V *vs.* SCE. If the potential sweep was not interrupted, this current density was maintained up to potentials of +2.7V or greater. At greater bias potentials, a nearly exponential dependence of current with potential was observed, as would be expected for the normal corrosion/passivation reaction of titanium metal (1-6). From XPS and AES analysis data of various Ti thin film electrodes we have hypothesized that the current/potential region between the onset of current flow and the onset of the exponential current/potential dependence represents an oxidation of a region of less than 50Å thickness. This region consists of metal and titanium oxides (TiO, Ti_2O_3, etc.). A true metal/TiO_2 interface is only established at bias potentials in excess of +3.0V. Qualitatively similar LSV behavior was observed using bulk titanium metal which had been freshly etched in

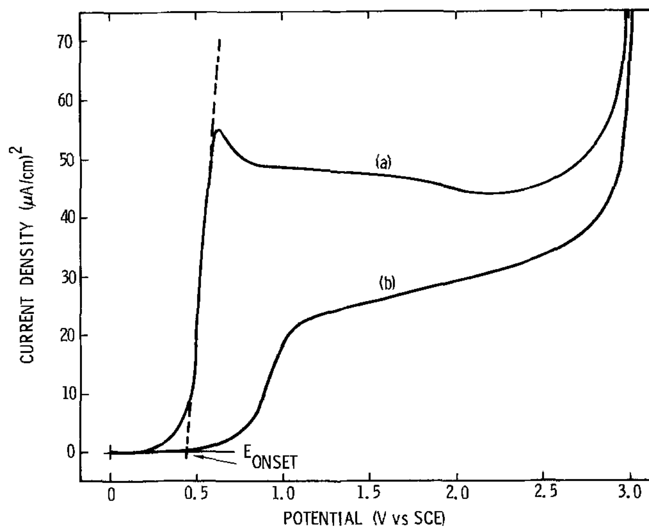

Fig. 1. (a) Typical linear sweep voltammogram (LSV) for a Ti thin film electrode in 1*N* $HClO_4$ at a sweep rate of 5 mV/sec. (b) Typical LSV for a Ti foil electrode which has been etched in HF and in boiling distilled H_2O.

HF and rinsed in distilled water (Fig. 1b). Further linear sweep and cyclic voltammetric experiments to explore the nature of the electrochemical oxidation of this surface region of the titanium thin films were therefore carried out.

We define the onset potential (E_{onset}) as the intersection of the tangent to the current/voltage curve with the potential axis, *i.e.*, where currents are first noted. E_{onset} (cf. Fig. 1a) was measured as a function of *p*H from strongly acidic to strongly basic solutions for titanium thin film electrodes (Fig. 2a). From *p*H = 0-~8, the shift in E_{onset} was −0.020V per *p*H unit, whereas for alkaline solutions, the shift was −0.080V per *p*H unit. Although the current voltage curves had the same qualitative appearance in all the solutions investigated, it is clear that the thermodynamic potential of the oxidation process is lowered by the presence of high concentrations of hydroxide. The potential at which an exponential current/potential dependence was observed also shifted cathodically with increasing *p*H to the same extent as E_{onset}. The over-all *p*H dependence for the oxidation of the surface region of the titanium film is subsequently discussed.

If the potential scan was interrupted or reversed during the voltammetric oxidation of the titanium films, the current quickly decayed to zero (Fig. 3, curve a). No current was seen until an anodic potential was applied which exceeded the previous potential limit (curves b through f in Fig. 3). This is consistent with previously reported data for aluminum passivation (1, 23). A series of such cyclic potential scans was conducted and E_{onset} for each scan recorded as a function of the total oxidative charge transferred (Q_T). Figure 3b shows that there was a linear dependence of E_{onset} with Q_T. The potential or field strength necessary to support oxidation of the surface region of the titanium thin film is clearly dependent on the total oxide thickness formed in this region. We have calculated that a monolayer conversion of titanium to TiO_2 requires approximately 1 mC/cm^2 of oxidative charge, so that an estimate of the oxide layer thickness was made in order to correlate with Q_T (Fig. 3b). The maximum thickness of 50Å is approximate since the surface region is a mixture of metal and suboxides. Using AES and XPS data (9) we estimate the thickness of the "prepassive" region to be approximately 30Å.

The slope of the tangent to the current/voltage linear region above E_{onset}, di/dE, was also monitored as a function of Q_T (Fig. 3b). As Q_T increased, di/dE

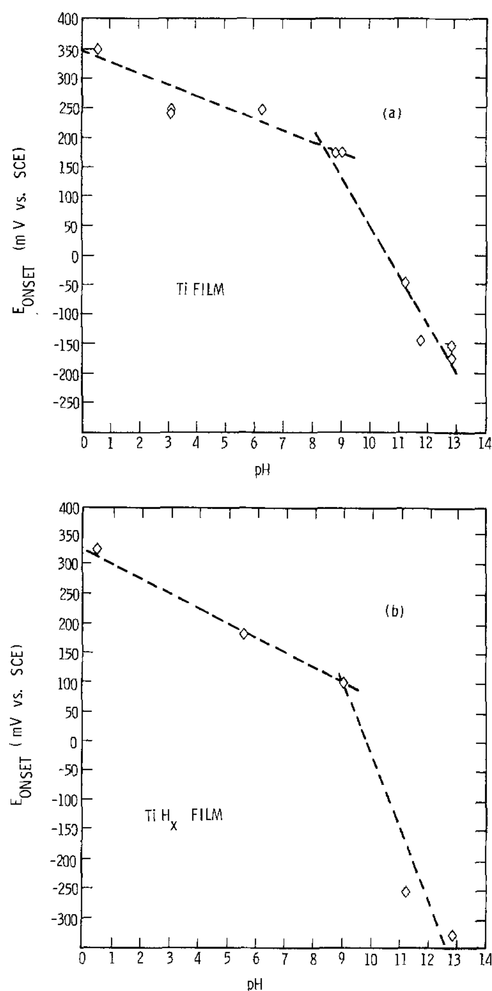

Fig. 2. E_{onset} as a function of electrolyte pH for (a) Ti thin film and (b) TiH_x thin film electrodes.

decreased sharply. The di/dE parameter may be viewed as a measure of the onset of the oxidation process with increasing potential and thus decreases as the oxide thickness (or the barrier to oxide growth) increases.

The characterization of the electrochemical growth of the surface oxide layer was also extended to the atmospheric oxidation of these titanium metal films. Figure 4a shows the voltammograms for several Ti films, heated at 150°C for times between 5 and 60 min. These conditions were chosen to accelerate atmospheric oxidation to experimentally reasonable rates. Figure 4b shows the linear increase in E_{onset} as a function of the square root of air oxidation time, while di/dE decreases almost exponentially with $t^{1/2}$. Note that the maximum current density achieved in oxidation of the surface region also decreased following air oxidation. We can conclude that the extent of

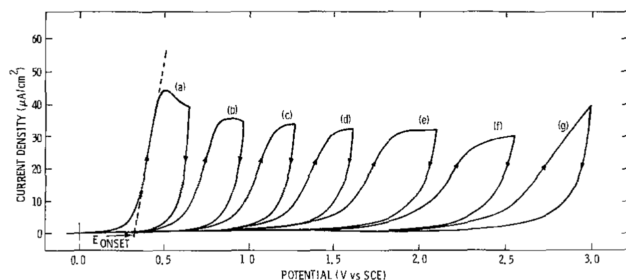

Fig. 3a. Electrochemical oxidation of fresh Ti electrode. The cyclic voltammograms are scanned to a higher applied potential limit on each successive scan. The solution used in this scan was 1*N* $HClO_4$ and the scan rate was 5 mV/sec.

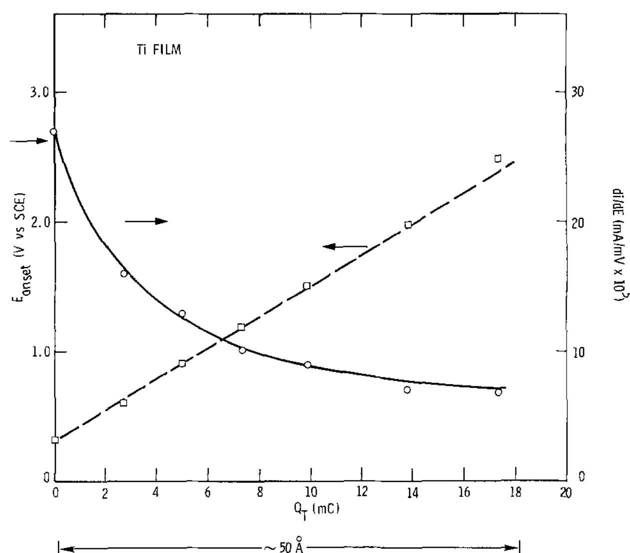

Fig. 3b. The potential at the onset of current flow (E_{onset}) and di/dE vs. the total charge (Q_T) passed at the Ti electrode of Fig. 3a.

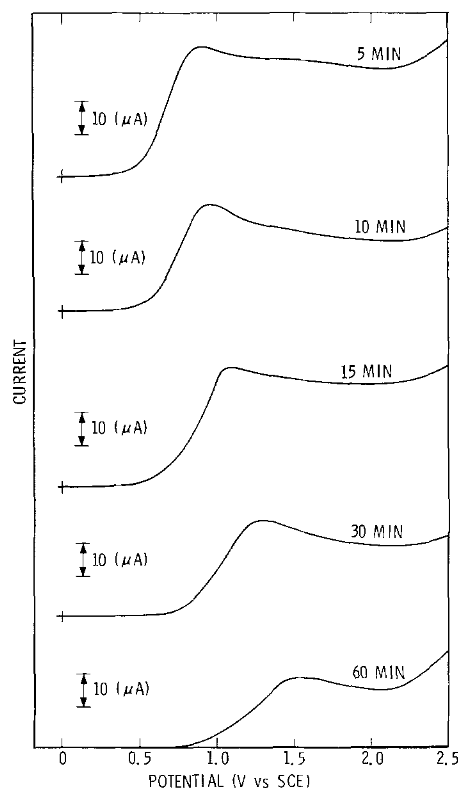

Fig. 4a. Linear sweep voltammograms for Ti electrodes heated at 150°C in air for the time specified on each voltammogram.

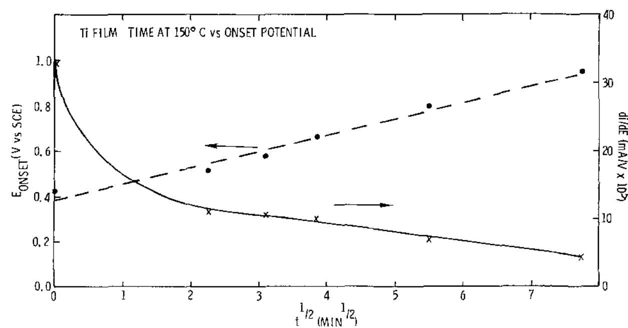

Fig. 4b. The onset potential and di/dE plotted as a function of the square root of air oxidation time at 150°C.

electrochemical oxidation, Q_T, and the time of atmospheric oxidation, $t^{1/2}$, are qualitatively equivalent. In both cases it is clear that the formation of a thin layer of surface oxide greatly inhibits further oxidation. If atmospheric oxidation was attempted at room temperature, little change in the current voltage behavior was observed for films left exposed up to several hours. However, extensive air oxidation at elevated temperatures completely oxidized the surface region of the titanium films and the current/voltage behavior of such a film showed only the exponential relationship at high applied potentials. By correlation with the electrochemical oxidation data and previous surface analysis data, it was also possible to semiquantitatively estimate the depth of the surface oxide layer formed by air oxidation (compare Fig. 3b and 4b).

Electrochemical oxidation of titanium hydride films.—The electrochemical oxidation of titanium hydride films proceeded virtually as for the titanium thin film electrodes for bias potentials up to approximately +2.0V. The linear sweep voltammetric behavior of a titanium hydride electrode in 1*N* $HClO_4$ is shown in Fig. 5. Surface conductance and differential capacitance data collected for this type of electrode were similar to the previously reported data for the titanium film electrodes (9). Surface conductance measurements indicated a linear decrease in conductance electron population during the oxidation of the surface region. The capacitance-voltage measurements showed linear $1/C^2$ *vs.* E behavior typical of an n-type semiconductor once the potential was driven past the onset potential. All of the electrochemical data for these electrodes were consistent with the oxidation of a surface region of the TiH_x film of less than 50Å thickness.

Electrochemical and atmospheric aging of the titanium hydride films also proceeded as for the titanium films. Results typical of electrochemical aging up to +2.0V are shown in Fig. 6. As the oxide layer thickness increased, the onset potential (E_{onset}) for oxidation increased and $(di/dE)_{E_{onset}}$ decreased, consistent

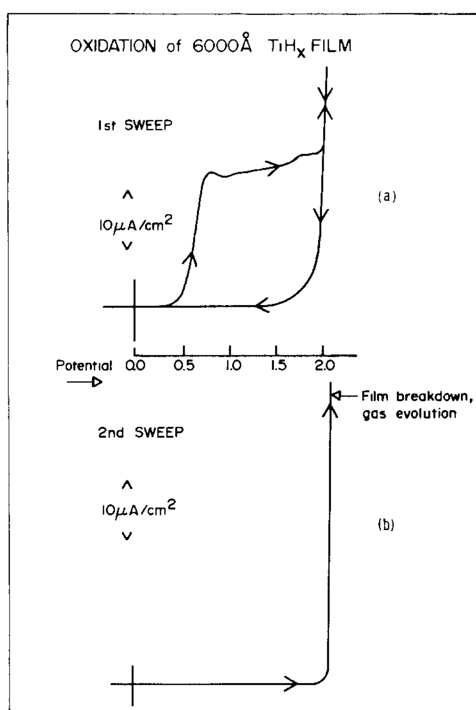

Fig. 5. (a) Cyclic voltammogram for a 6000Å TiH_x film scanned to > +2.0V and back to 0.0V *vs.* SCE in 1*N* $HClO_4$. The scan rate was 5 mV/sec. At ~ 2V the current increases from 30-50 μA/cm² to 0.5 A/cm². (b) Linear sweep voltammogram of electrode in (a) following return of bias potential to 0.0V.

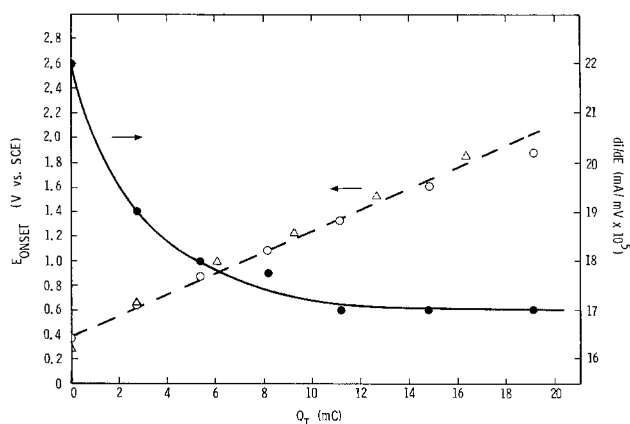

Fig. 6. The potential at the onset of current flow (E_{onset}) and the slope of the linear extrapolation of that onset ramp (di/dE) *vs.* the total charge (Q_T) passed at electrochemically oxidized TiH_x electrodes.

with an increasing energy barrier toward further oxidation. The relationship between E_{onset} and pH was also explored for the titanium hydride electrodes. Similar to the titanium films, E_{onset} shifted cathodically by 25 mV/pH unit up to pH = 7 and approximately 120 mV/pH unit for solutions with pH ≥ 7 (Fig. 2b).

The titanium hydride electrodes also showed a unique voltammetric feature which varied as a function of pH. In strong acid media the voltammetric curves for the titanium hydride electrodes were punctuated at bias potentials greater than +2.0V by a sudden increase in current density from 30-50 μA/cm² to nearly 500 mA/cm² (Fig. 5a). Concurrent with this increase in current density, gas evolution from within the electrode was observed as well as the eventual internal breakup of the titanium hydride film. If the voltammetric scan was reversed before film breakup occurred, the current density decayed to zero and no current was observed until the previous anodic potential limit was reached. At this potential large current densities were again observed (Fig. 5b). Clearly the titanium hydride electrodes possess a surface composition which produces similar electrochemical behavior to the titanium films, until the surface region is fully oxidized. Following this, a different type of oxide/metal interface is created which apparently allows direct release of the bound hydrogen in the metal lattice to form hydrogen gas. As the solution pH was increased, the potential at which film breakdown occurred, shifted toward more negative potentials. In solutions of pH ≥ 10 however, the onset of excessive current densities, gas evolution, and the breakup of the electrode were no longer observed. Current densities of 30-50 μA/cm² were observed, with some fluctuations, at bias potentials beyond 5V. No clear evidence of an exponential current/voltage behavior was observed for the oxidation of the TiH_x films in alkaline media. In the intermediate pH region between strongly acidic and strongly basic media, the TiH_x oxidation showed a tendency to decompose but at variable bias potentials above 2.0V. We believe the variability to be due to small differences in film surface morphology which affect the change in oxidation mechanism. SEM photomicrographs of the Ti and TiH_x film surfaces indicate an average defect or grain size of ~0.1 μm. Capacitance data also indicated a rather porous film surface; C(at 0.0V) = 30 ± 5 μF/cm². We feel that this surface structure will be important in determining the oxidation pathways at intermediate solution pH. It is clear that at alkaline pH, the oxidation mechanism for the titanium hydride films changes to an extent sufficient to stabilize the film in an unusual manner against gas evolution and metal degradation.

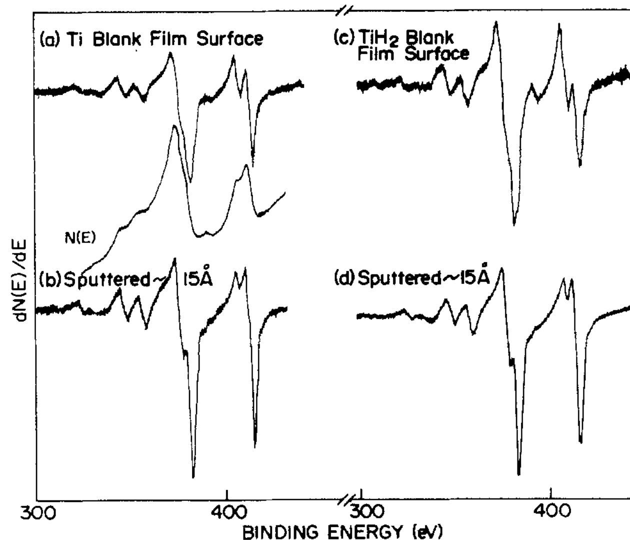

Fig. 7. High resolution Auger electron spectra of the Ti(LMM) and (LMV) peaks for (a) Ti film electrode surface; (b) that film after ion sputtering to remove approximately 15Å; (c) TiH_2 film electrode surface; and (d) that film after ion sputtering to remove approximately 15Å.

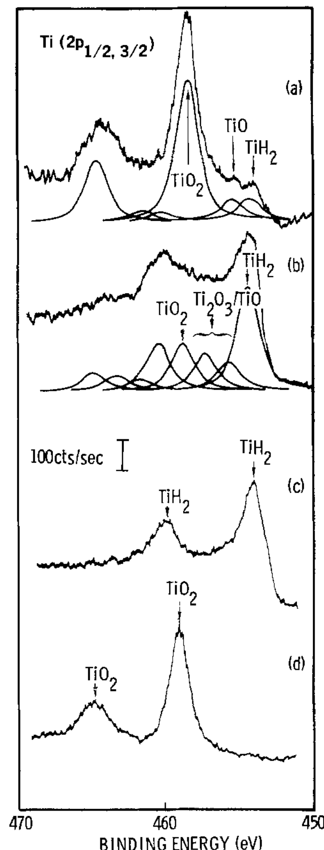

Fig. 8. The $Ti(2p_{1/2,3/2})$ XPS spectra for (a) a TiH_x blank surface; (b) that film after ion sputtering to remove approximately 20Å; (c) the same film after ion sputtering to remove approximately 60Å; and (d) the surface of TiH_x thin film electrode oxidized to 12.5 mC of charge.

Surface analysis of the TiH_x films.—AES and XPS spectra were obtained for the TiH_x film electrodes in an effort to understand the composition of the surface regions of these electrodes and to compare the surface composition to that of the pure titanium films. Figure 7 shows a series of high resolution $dN(E)/d(E)$ AES spectra of the LMM and LMV transitions of titanium and titanium hydride films as well as a typical $N(E)$ spectrum. Some difference was observed between the spectra of the Ti and TiH_x film surfaces, especially in the LMV spectral region (400-430 eV) where spectral shapes are sensitive to chemical composition of the surface (9, 24). Both types of film surfaces showed LMV spectra consistent with a partially oxidized (TiO-like) surface (9, 24-26[1]), however the TiH_x film electrode showed slightly more oxide character than the Ti film. Following ion sputtering of nearly 15Å of the surface region, the spectra became more like those expected for a lower valence form of titanium.

Oxygen-to-titanium ratios were computed from the intensities of the oxygen KLL transitions and the titanium LMM transition, according to previously discussed methods (9, 18, 22). The O/Ti intensity ratio of each film was normalized to the same ratio for a TiO_2 standard material to yield a relative atomic ratio, N_O/N_{Ti}. The TiH_x film surfaces showed a slightly substoichiometric composition, with $N_O/N_{Ti} = 1.8$. This value includes the contribution from all surface oxygen because the oxygen Auger KLL signal does not distinguish between oxide and absorbed oxygen species. The N_O/N_{Ti} surface ratios were slightly higher than those previously observed in titanium films, $N_O/N_{Ti} = 1.6\text{-}1.7$ (9). Ion sputtering of the surface lowered the N_O/N_{Ti} to *ca.* 0.3 within 20-30Å of the surface, similar to the titanium films. Electrochemically oxidized surfaces showed increased N_O/N_{Ti} values at the surface (1.9-2.0), and these values remained high following ion sputtering, depending on the extent of electrochemical oxidation.

The XPS spectra of Fig. 8 were consistent with the above AES data. The TiH_x film surface gave $Ti(2p_{1/2,3/2})$ spectra (Fig. 8a) which were composed chiefly of a TiO_2 component ($\Delta BE_1 = 71.5 \pm 0.2$ eV as for a TiO_2 standard) (18, 22). Smaller TiO ($\Delta BE_1 = 75.2 \pm 0.2$ eV) and TiH_x ($\Delta BE_1 = 76.0 \pm 0.2$ eV) components were also observed which were less than 10% of the TiO_2 concentration. This type of surface spectrum is consistent with either (*i*) a uniform surface composition consisting of TiO_2, suboxides, and titanium hydride, or (*ii*) a TiO_2 layer of less than 10Å thickness overlaying a gradient mixture of suboxides and titanium hydride. We consider the second option to be more likely, although we must consider the possibility that the titanium hydride may be a mixed oxy-hydride compound, *e.g.*, TiO_yH_x. The $Ti(2p_{1/2,3/2})$ spectra of the TiH_x film which was ion sputtered to a depth of *ca.* 15Å below the surface (Fig. 8b) showed spectral components from TiO_2 and suboxides which were nearly equal and were approximately 50% of the intensity of the TiH_x component. This observation would indicate a mixed TiO_y/TiH_x composition of the prepassive surface region. The N_O/N_{Ti} ratios computed from the XPS data [$O(1s)/Ti(2p_{3/2})$ intensity ratios normalized to TiO_2 standard] (22) showed a value of *ca.* 1.6-1.7 at the film surface and *ca.* 0.8 following ion sputtering to ~15Å below the surface. The surface N_O/T_{Ti} ratio was lower than that determined by AES because the O(1s) intensity included only oxide oxygen and not absorbed forms (OH, H_2O, etc.) (18, 22). Ion sputtering to depths of greater than 50Å yielded an XPS spectrum like that in Fig. 8c. The $Ti(2p_{1/2,3/2})$ spectrum was comprised chiefly of the titanium hydride component and the N_O/N_{Ti} ratio decreased to *ca.* 0.2. We have previously noted that the $Ti(2p_{3/2})$ binding energy for the hydrided metal is shifted to higher energies by *ca.* 1.0 eV from that of the pure metal ($\Delta BE_1 = 76.0 \pm 0.2$ eV for TiH_x *vs.* 77.0 ± 0.2 eV for Ti) (22). This chemical shift is consistent with hydrogen bound in the titanium metal in a partially anionic form, although the hydrogen does not appear to be as electronegative as oxygen in the titanium

[1] Lo *et al.* (26) have noted the presence of Ti^{3+} valence states by energy loss spectroscopy in defect-structured TiO_2 surfaces. Similar compositions are expected in the prepassive region of the titanium and titanium hydride films, cf. (9).

oxides. The electrochemical oxidation of the hydride is certainly affected by the chemical form of hydrogen in the metal lattice and the mechanism by which it is removed during oxidation (see discussion below). Following electrochemical oxidation of the TiH_x film surface ($Q_T = 12\ mC/cm^2$), the $Ti(2p_{1/2,3/2})$ XPS spectra reverted completely to that of TiO_2, $N_O/N_{Ti} = 1.9$-2.0 (Fig. 8d), confirming that the oxide interface had been extended to beyond the depth to which XPS could successfully measure a TiH_x component (~25Å).

Conclusions

The previously reported experiments (9) and those discussed here allow a more detailed understanding of the surface region of vapor deposited and clean bulk titanium and titanium hydrides. The first to be discussed is the surface composition of the titanium films. We can picture the surface of the film to consist of a gradient of metal, suboxide (or TiO_2 with oxygen defects) and stoichiometric TiO_2. A graphical illustration of this picture is shown in Fig. 9. The energy barrier for film oxidation is expressed chiefly across the stoichiometric TiO_2 phase (G_1) and the more conductive substoichiometric oxide phase (G_2); the total barrier to further oxide growth is relatively low ($G_T = G_1 + G_2$). Following electrochemical or atmospheric oxidation, the oxide layer thickness is greatly increased, the suboxide concentration diminished, and the barrier to further oxide growth is consequently increased to G_T'. The relative size of G_2' to G_1' has decreased due to the increase in thickness of the nonconductive oxide. Eventually a metal/TiO_2 interface is established. Ionic transport across the metal/metal oxide region becomes the current limiting factor and a normal corrosion/passivation mechanism is established (6).

We can picture the oxidation of the prepassive region of the Ti film electrodes in strong acid solution in a schematic fashion similar to defect-structured TiO_2 electrodes (22)

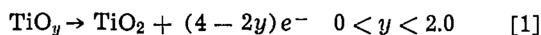

$$TiO_y \rightarrow TiO_2 + (4 - 2y)e^- \quad 0 < y < 2.0 \qquad [1]$$

[where ionic transport is not included]. In strongly

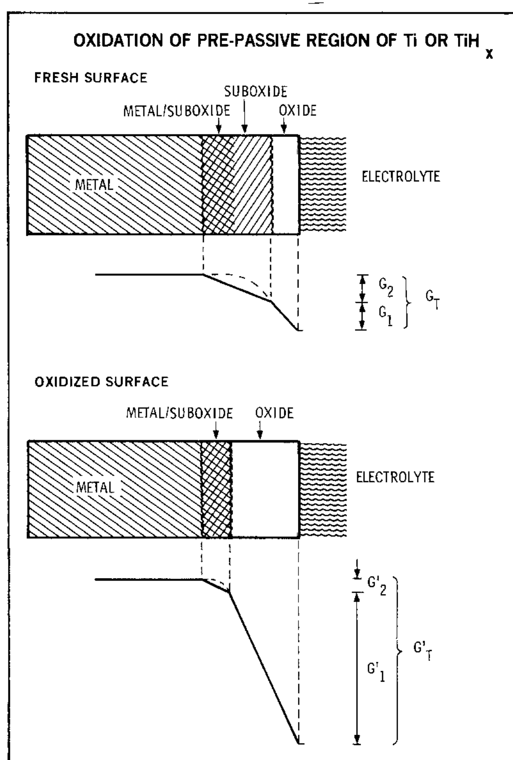

Fig. 9. Proposed model for the composition and oxidation of the "prepassive region" in Ti and TiH_x thin films.

basic solutions, the oxidation may proceed through either TiO_y or $Ti(OH)_{2y}$ reactants, *e.g.*

$$Ti(OH)_{2y} \rightarrow TiO_2/Ti(OH)_4 + (4 - 2y)e^- \qquad [2]$$

Due to the cathodic shift in onset potential with increasing pH, we feel that the latter oxidation process is more thermodynamically favorable in alkaline solutions (2). The Pourbaix diagram for the oxidation of titanium shows a strictly Nernstian relationship between equilibrium potentials of Ti/TiO_2 and *p*H (2, 27). The significance of the change in slope of E_{onset} *vs.* pH as one proceeds to more alkaline solutions remains to be investigated. The surface morphology of the titanium film will influence the surface concentration of oxidizable species, the penetrability of the electrolyte, and, therefore, the onset potential. This morphology may vary depending on the type of film or bulk titanium sample investigated and may affect the slope of E_{onset} *vs.* *p*H.

In the case of the TiH_x films, the picture of the surface composition is somewhat different. It is clear from the XPS data that the surface is still composed chiefly of TiO_2 and suboxides or defect forms of TiO_2 as well as a small amount of the hydrided metal. The type of oxide/metal gradient shown in Fig. 9 can also be envisioned for the TiH_x films. The growth of the energy barrier to oxidation as a function of oxide thickness is analogous to the Ti films. Once the prepassive region is oxidized however, one must consider the different chemistry of the TiH_x/TiO_2 interface that is formed. The oxidation of α-TiH_x (chemisorbed hydrogen from solution) proceeds by a different mechanism than for γ-TiH_x, resulting in the release of protons (2, 27)

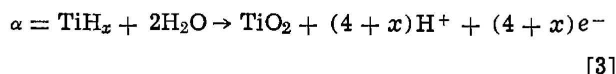

$$\alpha = TiH_x + 2H_2O \rightarrow TiO_2 + (4 + x)H^+ + (4 + x)e^- \qquad [3]$$

It is not clear that the α-phase hydride considered in the normal Pourbaix diagram has the same reactivity as the γ-phase TiH_x which is oxidized in these experiments. The XPS data clearly indicate that the hydrogen in the γ-phase hydride is at least partially anionic in nature. It is reasonable to assume that during oxidation of the γ-TiH_x, the hydrogen would be capable of capturing one electron leading to atomic H° formation and subsequently H_2

$$\gamma\text{-}TiH_x + 2H_2O \rightarrow TiO_2 + xH^\circ + 4e^- + 4H^+ \qquad [4]$$

$$xH^\circ \rightarrow x/2H_2 \qquad [5]$$

Reactions [4] and [5] constitute an interesting mechanism for the release of hydrogen from this high energy solid. In strongly acidic media, the direct oxidation of TiH_x to Ti^{+4} and H^+ is thermodynamically inhibited, and direct oxidation of TiH_x with H^+ may also occur

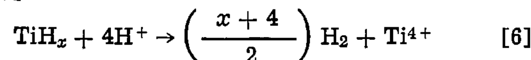

$$TiH_x + 4H^+ \rightarrow \left(\frac{x + 4}{2}\right) H_2 + Ti^{4+} \qquad [6]$$

Such a reaction has been observed for scandium hydride solids in strong acid (28). However, it appears that if the solution *p*H is sufficiently high, consumption of the released hydrogen atom will occur before H_2 gas is formed. The formation of a titanium suboxide or TiO_2 may take place at the same instant, therefore, the oxide/TiH_x interface would be propagated in the same manner as for the prepassive region of the Ti films. The current densities of 30-50 $\mu A/cm^2$ observed for the TiH_x films at applied potentials greater than 2V *vs.* SCE in alkaline solutions do not change, perhaps because of the continually reformed oxide/suboxide/metal hydride interface.

The electrochemical oxidation of both Ti and TiH_x thin films indicates the extent to which a thin, suboxide or oxide surface layer inhibits further oxidation of the bulk material. This thin oxide layer pre-

sents a large energy barrier to further oxide formation, even under high temperature atmospheric oxidation conditions. In the case of the hydrided metal, a release of bound hydrogen is possible with relatively low applied potentials, a fact which may have interesting implications for the release of energy from metal hydrides and their long-term stability in corrosive environments.

The exact mechanism for the corrosion and passivation of various titanium hydride stoichiometries is the subject of further study. Because of their technological importance, further investigation of the release of hydrogen by electrochemical oxidation of hydrided metals is clearly warranted.

Acknowledgment

The authors gratefully acknowledge the excellent technical assistance of P. G. Neiswander. The titanium and titanium hydride films were prepared by Neutron Generator Tube Laboratory, Sandia Laboratories, under the supervision of B. E. Barnaby. The generosity of Professor T. Kuwana, Ohio State University, is also acknowledged for the use of the Physical Electronics, Incorporated, Model 548 XPS/AES Analysis System. This work was supported by the U.S. Department of Energy.

Manuscript submitted March 27, 1978; revised manuscript received May 20, 1978.

Any discussion of this paper will appear in a Discussion Section to be published in the June 1979 JOURNAL. All discussions for the June 1979 Discussion Section should be submitted by Feb. 1, 1979.

Publication costs of this article were assisted by Sandia Laboratories.

REFERENCES

1. K. J. Vetter, *Electrochim. Acta*, **16**, 1923 (1971).
2. T. R. Beck, *ibid.*, **18**, 807, 815 (1973).
3. N. T. Thomas and K. Nobe, *This Journal*, **119**, 144 (1972).
4. M. J. Mandry and G. Rosenblatt, *ibid.*, **119**, 29 (1972).
5. W. Mizushima, *ibid.*, **108**, 825 (1961).
6. K. D. Allard and K. F. Heusler, *J. Electroanal. Chem. Interfacial Electrochem.*, **77**, 35 (1977).
7. E. N. Paleolog and A. Z. Fedotova, *Elektrokhimiya*, **12**, 930 (1976).
8. A. Muller and A. Benninghoven, *Surf. Sci.*, **41**, 493 (1974).
9. N. R. Armstrong and R. K. Quinn, *ibid.*, **67**, 451 (1977).
10. R. K. Quinn, N. R. Armstrong, and N. E. Vanderborgh, *J. Vac. Sci. Technol.*, **12**, 160 (1975).
11. R. K. Quinn, M. L. Knotek, N. R. Armstrong, and N. E. Vanderborgh, *This Journal*, **123**, 1794 (1976).
12. M. L. Knotek, R. K. Quinn, N. R. Armstrong, and N. E. Vanderborgh, *J. Vac. Sci. Technol.*, **14**, 705 (1977).
13. W. H. Meuller, in "Metal Hydrides," W. H. Meuller, J. P. Blackledge, and G. G. Libowitz, Editors, pp. 336-385, Academic Press, New York (1968).
14. D. R. Begeal, SC-DR-71-0789, Sandia Laboratories, Albuquerque, New Mexico.
15. M. Fujihara and T. Kuwana, *Electrochim. Acta.*, **20**, 565 (1975).
16. W. J. Anderson and W. N. Hansen, *J. Electroanal. Chem. Interfacial Electrochem.*, **43**, 329 (1973).
17. W. J. Anderson and W. N. Hansen, *This Journal*, **121**, 1570 (1974).
18. A. W. C. Lin, N. R. Armstrong, and T. Kuwana, *Anal. Chem.*, **49**, 1228 (1977).
19. K. S. Kim, N. Winograd, and R. E. Davis, *J. Am. Chem. Soc.*, **93**, 6296 (1971).
20. K. S. Kim, A. F. Gossmann, and N. Winograd, *Anal. Chem.*, **46**, 197 (1974).
21. G. C. Allen, P. M. Tucker, A. Capon, and R. Parsons, *J. Electroanal. Chem. Interfacial Electrochem.*, **50**, 335 (1974).
22. C. N. Sayers and N. R. Armstrong, *Surf. Sci.*, Submitted for publication.
23. H. H. Strehblow and C. J. Doherty, *This Journal*, **125**, 30 (1978).
24. J. S. Solomon and W. L. Baun, *Surf. Sci.*, **51**, 228 (1975).
25. H. D. Shih and F. Jona, *Appl. Phys.*, **12**, 311 (1977).
26. W. J. Lo, Y. W. Chung, and G. A. Somarjai, *Surf. Sci.*, **71**, 199 (1978).
27. M. Pourbaix, "Atlas of Electrochemical Equilibria," Pergamon Press, Oxford (1966).
28. R. K. Quinn and N. R. Armstrong, Unpublished results.

Technical Notes

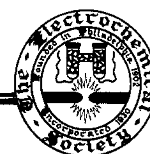

Use of Alumina as a Sheath for the Pt, CO/CO_2 | Na_2CO_3 Reference Electrode

K. Y. Kim* and O. F. Devereux*

Department of Metallurgy and Institute of Materials Science, University of Connecticut, Storrs, Connecticut 06268

The viability of electrode polarization (1) as a means for investigating corrosion phenomena in molten salts has been demonstrated (2-6). As this technique is customarily practiced (7), a current is impressed upon an electrode fashioned from the metal under study (the working electrode) using a second, inert electorde (the counterelectrode). The potential of the working electrode relative to the electrolyte is measured to within an additive constant using a third (reference) electrode and a high impedance potential-measuring device. For a given system the current passing through the working electrode is dependent upon this potential and is a measure of electrodic reactions pertaining directly to corrosion processes at the working electrode surface. Meaningful study of corrosion in molten salt systems of engineering concern requires a reference electrode that is not degraded by the system under study, permits variation of the environment of the working electrode over a meaningful range, and is itself not affected by such variation in cell environment.

* Electrochemical Society Active Member.
Key words: electrode, fused salt, polarization.

Considerable attention has been devoted to the study of electrodes for use in molten carbonates involving the electrode reactions

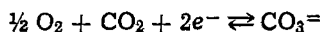

$$\frac{1}{2} O_2 + CO_2 + 2e^- \rightleftarrows CO_3^=$$

or

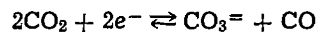

$$2CO_2 + 2e^- \rightleftarrows CO_3^= + CO$$

occurring at inert metal electrodes (8-23).

In studies in which a reference electrolyte was maintained in a separate compartment from the cell electrolyte, ionic conduction occurred via a restricted channel of the molten electrolyte (8, 17, 20) or via a solid-state process (10, 12, 16), the latter involving either a glass or a K^+-conducting porcelain. In either case a "liquid junction" potential difference may arise; this has been discussed in some detail (8, 10). The liquid junction potential is minimal if (*i*) conduction between the two electrolytes occurs via oppositely charged species whose transport numbers $\simeq$0.5; or (*ii*) conduction occurs via one or more species whose activity is the same in the two electrolytes. The use of a molten conducting path restricts use of the cell in that it precludes or renders difficult use of different pressures in the reference and test compartments, while glasses and porcelains offer very poor resistance to molten carbonate attack.

The present study was designed to test the behavior of recrystallized alumina as a container for a CO/CO_2 reference electrode for use in molten sodium carbonate. The reference electrode studied was comprised of a 20 mil (0.0508 cm) platinum wire immersed in molten sodium carbonate (Fisher Certified ACS) contained in a McDanel Type 998 alumina closed-end tube. The wire entered the electrolyte through a small diameter [¼ in. (0.635 cm) or ⅛ in. (0.318 cm) OD] alumina tube, through which a preset mixture of carbon monoxide and carbon dioxide was introduced at a flow rate of approximately 25 ml/min. Within the electrode compartment, the wire was shaped into a helix to increase the exposed electrode area. The external alumina sheath was ½ in. OD (1.27 cm), with 1/16 in. wall thickness (0.159 cm) and was immersed in the cell to a depth of about 3 cm. The depth of electrolyte inside the electrode sheath was also approximately 3 cm. The cell electrolyte was also molten sodium carbonate and was contained in an alumina crucible. The cell was housed in a vertical retort heated by a glow bar furnace with a proportioning solid-state controller. Cell temperature was measured directly by an alumina-sheathed Pt-10% Rh/Pt thermocouple immersed in the electrolyte; no discernable temperature variation occurred. Gas mixtures were derived through appropriate mixing of bottled CO (Matheson C. P. purity), CO_2 (Norwich medical grade), and a nominal 95% CO/5% CO_2 mixture (Matheson certified mixture, 95.2% CO/4.8% CO_2). Individual and total flow rates were determined with rotameter flow gauges. Initial drying of the electrolyte was accomplished by heating of the cell slowly under vacuum to test temperature. Subsequently, equilibration with the inlet gas was assumed. Equilibrium hydroxide activities have been computed for this system (24) and for low inlet moisture contents are not sufficiently high to significantly alter the carbonate activity in the melt. The accuracy to which the gas mixtures were established was dependent upon the value of P_{CO}/P_{CO_2}. For the worst case, the possible error in volumetric flow rate determination was $\simeq$20%; the cumulative errors for this case yield a maximum uncertainty in electrode potential of $\simeq$20 mV.

The current-voltage characteristic of the reference electrode was determined by impressing a potential from an external d-c power supply between two ostensibly identical reference electrodes and measuring the resulting current with a zero resistance ammeter. A typical curve, using the nominal 95% CO/5% CO_2 mixture at both electrodes at 1000°C, is shown in Fig. 1. Simple ohmic behavior was seen in all cases with observed cell resistance values falling in the range of 0.0282-0.0353 MΩ, the variation apparently reflecting differences in the immersed electrode area from one experiment to the next. Using a geometric factor of 66 cm per electrode, the apparent sheath resistivity is $\simeq$1 MΩ cm. Reported conductivity values for alumina range widely (25), from 10^{-4} to 10^{-10} Ω^{-1} cm^{-1} at 1000°C. A typical analysis for the alumina used in this study is shown in Table I. Conduction at other than very high temperatures is presumed due to impurity cations, with sodium and calcium dominating due to the very basic character of their oxides. Although diffusivity data also show considerable scatter, high temperature data for Al and O diffusion in polycrystalline alumina generally extrapolate to values of the order of 10^{-19} cm^2/sec at 1000°C (26). The data of Oishi and Kingery (27) suggest a reduction in the activation energy for these processes below approximately 1400°C, however, which would lead to somewhat higher values. In contrast, the data of Frischat (26, 28) for Na diffusion in commercial purity alumina, 95% dense, for the range 1223°-1750°C yield an extrapolated value of 5.2×10^{-11} cm^2/sec at 1000°C, and suggest a similar value for Ca diffusion. Assuming this value for both Na and Ca, and further assuming that $z_{Na} = 1$ and $z_{Ca} = 2$, using the values of Table I a resistivity of 250 MΩ cm is obtained for Type 998 alumina at 1000°C. This discrepancy is attributed to one or more of the following reasons: (*i*) A substantial increase in the Na_2O concentration within the alumina due to contact with the molten sodium carbonate; (*ii*) a change in the activation energy for Na transport with temperature, rendering invalid extrapolation of Frischat's data; or (*iii*) A simple manifestation of the tremendous variation in the reported values for diffusivity of various species and for conduction in alumina, presumably attributable to variations in method of preparation, impurity content, and/or measurement technique.

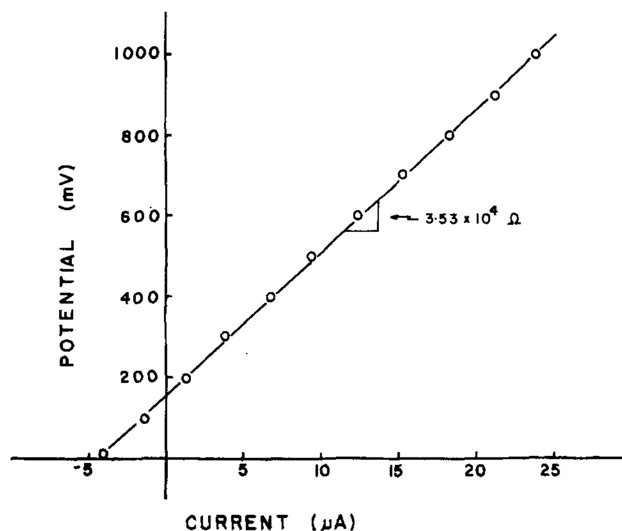

Fig. 1. Current-voltage dependence of cell comprised of two alumina-sheathed reference electrodes.

Nernstian response of the reference electrode was evaluated by maintaining the same cell configuration of two identical reference electrodes, but diluting the flow of the nominal 95% CO/5% CO_2 mixture through one of the electrodes by admixing CO or CO_2. The

Table I. Typical chemical analysis of McDanel Type 998 alumina

Al_2O_3	SiO_2	MgO	Na_2O	CaO	Fe_2O_3	Ga_2O_3	TiO_2	MnO	ZrO_2	K_2O
99.8	0.070	0.050	0.005	0.030	0.025	0.009	0.004	0.001	—	—

range of P_{CO}/P_{CO_2} employed was $0.11 < P_{CO}/P_{CO_2} < 103$, with $P_{CO} + P_{CO_2} = 1$ atm. Assuming only a negligible effect of this dilution upon the carbonate activity, the potential of this cell is expressed by

$$E = E^\circ + \frac{RT}{2F} \ln \frac{(P_{CO_2}{}^2)_r (P_{CO})_w}{(P_{CO_2}{}^2)_w (P_{CO})_r} \quad [2]$$

where E is the measured cell potential; E°, the standard cell potential; and the subscripts r and w refer to the reference (constant) electrode and working (variable) electrode, respectively. The standard cell potential is ideally zero, but nonzero values were observed when tacitly identical gas mixtures were passed through both electrodes. The magnitude of these values was typically in the range of 5-40 mV, with occasional larger values, and was reasonably consistent for a given pair of electrodes. This is within the range of error attributable to the rotameter gauges. For the purpose of evaluating Nernstian response of these electrodes, an effective E° was measured at the start of each series of experiments and subtracted from the subsequently measured potential values. Figure 2 shows such values of $(E - E^\circ)_{meas}$ compared with $(E - E^\circ)_{calc}$; Nernstian behavior is clearly demonstrated.

An additional study was performed to assess the behavior of this reference electrode in comparison to a low resistance reference electrode during an electrode polarization experiment. In this study, three electrodes were involved: The reference electrode, which was either the electrode described or a similar electrode in which a 92% ZrO_2-8% Y_2O_3 crucible [resistivity $\simeq 10\ \Omega$ cm (25)] was substituted for the Type 998 alumina tube; a nickel (Ni 200) working electrode; and a platinum counterelectrode. Although the thermodynamic state of the electrolytes was not fixed, reproducible conditions were established by bubbling oxygen through the reference and cell electrolytes. Potentiostatic polarization was accomplished via a Wenking 68 TS 3 potentiostat, with a Wenking 69 scanning potentiometer providing a potential stepping rate of 2 mV/20 sec. Figure 3 shows anodic and cathodic polarization curves obtained at 1000°C. Similar behavior is evidenced with both reference electrodes. Taking into account the expected difference in rest potential (zero current) of the nickel as measured against the

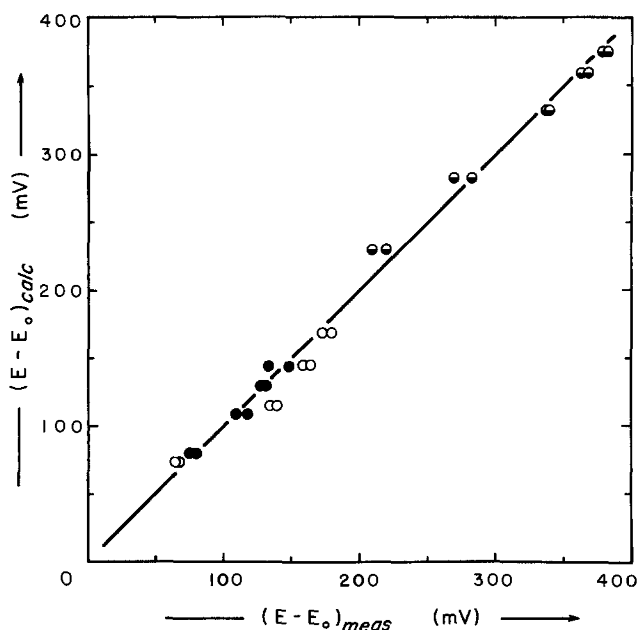

Fig. 2. Demonstration of Nernstein behavior of the alumina-sheathed electrode. ○, ◒, and ● represent different electrode pairs. Data for ○ and ◒ taken at 928°C; ●, at 957°C.

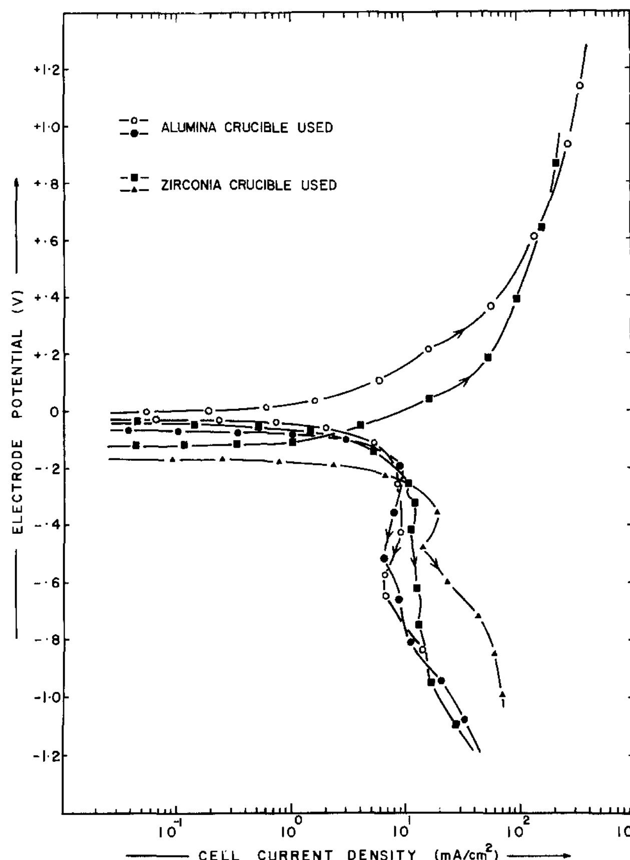

Fig. 3. Anodic and cathodic polarization behavior of Ni 200 measured against alumina-sheathed and Y_2O_3-doped ZrO_2 electrodes. All data obtained with increasing | applied potential |.

different reference electrodes, the discrepancy between the curves representing the different reference electrodes is comparable to that between curves representing different scans with the same electrode. During prolonged cathodic polarization under a CO-rich atmosphere, a slight blackening of these electrodes was observed due to the presence of cathodically reduced carbon. This is discussed in detail by Borucka (17). The Y_2O_3-doped ZrO_2 is not suitable for long term use in molten carbonates, becoming severely degraded after 50 hr exposure at 1000°C.

Acknowledgment

The authors are pleased to acknowledge the support of the Department of Energy through research contract EY-76-S-02-2960A001.

Manuscript submitted April 24, 1978; revised manuscript received July 18, 1978.

Any discussion of this paper will appear in a Discussion Section to be published in the June 1979 JOURNAL. All discussions for the June 1979 Discussion Section should be submitted by Feb. 1, 1979.

Publication costs of this article were assisted by the University of Connecticut.

REFERENCES

1. M. G. Fontana and N. D. Greene, "Corrosion Engineering," McGraw-Hill, New York (1967).
2. A. Rahmel, *Werkst. Korros.* 19, 750 (1968).
3. J. F. G. Conde and B. Wareham, in "Proceedings of the 1974 Gas Turbine Materials in the Marine Environment Conference," J. W. Fairbanks and I. Machlin, Editors, p. 73, Metals and Ceramics Information Center, Battelle-Columbus Laboratories, Columbus (1974).
4. D. A. Shores, *ibid.*, p. 555.
5. D. A. Shores, *Corrosion*, 31, 434 (1975).
6. K. Y. Kim and O. F. Devereux, Unpublished data.
7. N. D. Greene, "Experimental Electrode Kinetics,"

Rensselaer Polytechnic Institute, Troy, New York (1965).
8. H. Flood, T. Forland, and K. Motzfeldt, *Acta Chem. Scand.*, **6**, 257 (1952).
9. J. W. Tomlinson, in "Physicochemical Measurements at High Temperatures," J. O'M. Bockris, J. L. White, and J. D. MacKensie, Editors, p. 247, Butterworths, London (1959).
10. R. W. Laity, in "Reference Electrodes," D. J. G. Ives and G. J. Janz, Editors, p. 524, Academic Press, New York (1961).
11. G. J. Janz and F. Saegusa, *Electrochim. Acta*, **7**, 393 (1962).
12. G. J. Janz and A. Conte, *ibid.*, **9**, 1269 (1964).
13. A. F. Alabyshev, M. F. Lantratov, and A. G. Morachevskii, "Reference Electrodes for Fused Salts," Sigma Press, Washington (1965).
14. M. D. Ingram and G. J. Janz, *Electrochim. Acta*, **10**, 783 (1965).
15. G. J. Janz, "Molten Salts Handbook," Academic Press, pp. 265-286, New York (1967).
16. H. E. Bartlett and K. E. Johnson, *This Journal*, **114**, 457 (1967).
17. A. Borucka, *Electrochim. Acta*, **13**, 295 (1968).
18. A. Borucka and C. M. Sugiyama, *ibid.*, **13**, 1887 (1968).
19. A. Borucka and C. M. Sugiyama, *ibid.*, **14**, 871 (1969).
20. F. K. Lorenz and G. J. Janz, *This Journal*, **116**, 1061 (1969).
21. P. K. Lorenz and G. J. Janz, *Electrochim. Acta*, **15**, 1025 (1970).
22. A. Borucka, *This Journal*, **124**, 972 (1977).
23. A. Borucka and A. J. Appleby, *J. Chem. Soc., Faraday Trans.*, **73**, 1420 (1977).
24. R. A. Cooke, M.S. Thesis, University of Connecticut, Storrs (1978).
25. W. D. Kingery, H. K. Bowen, and D. R. Uhlmann, "Introduction to Ceramics," 2nd ed., p. 903, John Wiley & Sons, New York (1976).
26. J. F. Stringer, "High Temperature Corrosion of Aerospace Alloys," pp. 90-91, NATO, Neuilly-Sur-Seine, France, AGARD-AG-200 (1975).
27. Y. Oishi and W. D. Kingery, *J. Chem. Phys.*, **33**, 905 (1960).
28. G. H. Frischat, *Ber. Deut. Keram. Ges.*, **48**, 441 (1971).

Corrosion Protection of Molten Carbonate Fuel Cell Gas Seals

R. B. Swaroop,* J. W. Sim,* and K. Kinoshita*

Argonne National Laboratory, Argonne, Illinois 60439

A recent study (1) has estimated that a molten carbonate fuel cell integrated with a low BTU coal gasifier will have efficiencies (coal-to-electricity) of about 50%. The higher efficiency and the high grade heat available are advantages that the molten carbonate fuel cell has over the phosphoric acid fuel cell, which is closer to commercial realization. However, the relatively high operating temperature (~923°K) of the molten carbonate fuel cell presents severe materials problems. The metallic cell components (for example, current collectors, cell housings) of the fuel cell are susceptible to corrosion due to the molten carbonate electrolyte and the gas environment at operating temperature. In particular, the gas seal region of the anode housing is subject to extensive corrosion due to the large chemical potential gradient that arises from the fuel gas (H_2 + H_2O + carbonaceous gases) and the ambient environment (generally air) on the inside and outside of the cell, respectively. In addition, the chemical potential gradient between the fuel gas and oxidant gas (O_2 + CO_2) gives rise to corrosion in the gas seal region of the anode housing (2). The corrosion rates of metallic cell components in the gas seals of molten carbonate fuel cells must be decreased in order to increase the life of the fuel cell. A solution to the corrosion problem at the gas seal of the cell housings is described in this note.

One approach to obtain fuel cells that are free of gas leaks is to use the "wet seal" technique (3). In this technique, the wet seal is produced by contacting the electrolyte tile (*i.e.*, an electrolyte structure consisting of unconsolidated particles of $LiAlO_2$ and molten carbonate) with the cell housing, as shown schematically in Fig. 1. The electrolyte in the tile wets the metal housing (typically, Type 316 stainless steel) to form the gas seal at A. The direct contact between the molten salt and the metallic cell housing provides a leak-free gas seal, but produces an environment which leads to electrochemical corrosion in the wet seal region. Therefore, corrosion of the metallic cell housings must be prevented.

* Electrochemical Society Active Member.

Key words: wet seal, lithium aluminate, electrolyte tile, 316 stainless steel.

Two approaches were considered to minimize the corrosion of the wet seal region of the metal cell housings. In one approach various metallic cell components

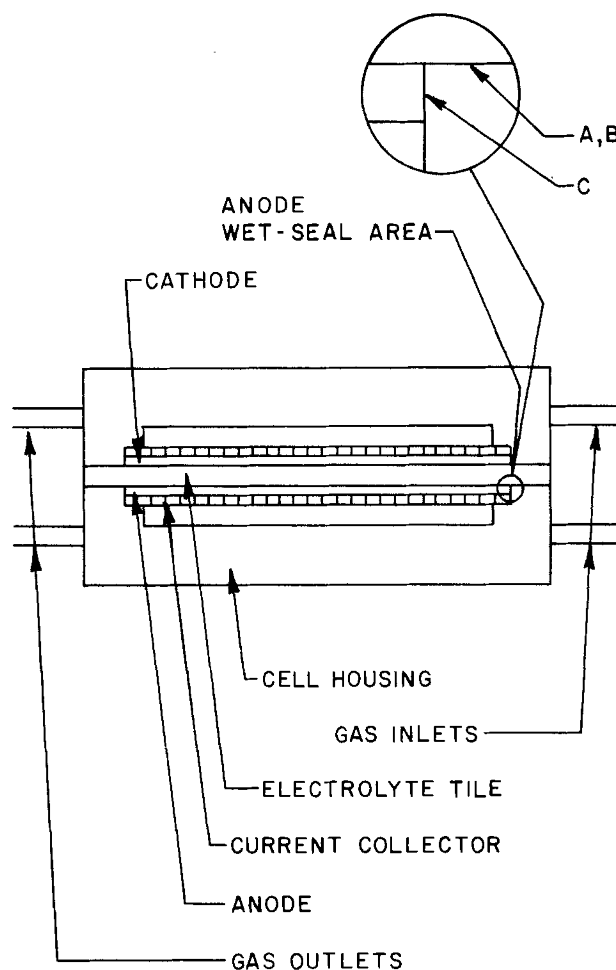

Fig. 1. Diagram of cell housings showing section examined microscopically.

that may be less susceptible to corrosion than Type 316 stainless steel, a state-of-the-art cell component, were examined. Because of the high cost of the alternative component alloys, this approach was not pursued. In the other approach aluminum metal is flame sprayed (performed at Coating Systems Technology Incorporated, North Babylon, New York) onto the seal to a thickness of ~50-70 μm, after which the housing is heated (in vacuum or in helium) to 1275°K for ~30 min to form a diffused layer between the aluminum [probably $(FeNiCr)Al_2$] and the Type 316 stainless steel substrate.

The wet seal region (A in Fig. 1) of the anode and cathode housings in fuel cells (7 cm diam) were aluminized and tested at 925°K. These fuel cells contained an electrolyte tile of 45 weight percent (w/o) $LiAlO_2$ and 55 w/o Li_2CO_3-K_2CO_3 [62 mole percent (m/o) Li_2CO_3-38 m/o K_2CO_3]. The anode gas was 80% H_2/20% CO_2 humidified with H_2O at 300°K, and the cathode gas was 30% CO_2/70% air. One of these fuel cells was operated for several periods of about 500 hr each at 925°K. After each period, the cell was disassembled and the cell housing was inspected for corrosion damage. After the anode cell housing operated in this manner for a total of 2600 hr, it was cross sectioned and examined.

A photomicrograph of a cross section through an anode housing tested for 2600 hr is shown in Fig. 2. The wet seal region consists of a coherent protective layer A (~35 μm thick) on top of an intermediate layer B (~30 μm thick) bonded to the Type 316 stainless steel housing. The aluminized layer extends to a small part of the cell housing (as shown in Fig. 2, area C) as well as to the anode wet seal directly in contact with the electrolyte tile. We believe that a few cracks evident in the protective coating have been produced because of thermal stresses. There was no evidence of corrosion of the cell housing in the areas protected by the aluminized layer, even at the bottom of the protective layer where cracks extended to the intermediate layer. The region of the cell housing which was not aluminized (as shown in Fig. 2, area C) clearly showed an extensive corrosion layer (~35 μm thick). Furthermore, close examination of Fig. 2 shows that the corrosion layer extended beneath the edge of the intermediate layer, which did not appear to have suffered corrosive attack. A few results obtained in other tests indicated that thermal cycling at rates greater than 1 cycle/500 hr does not affect the protective coating and no corrosion was evident in the wet seal area of those cell housings.

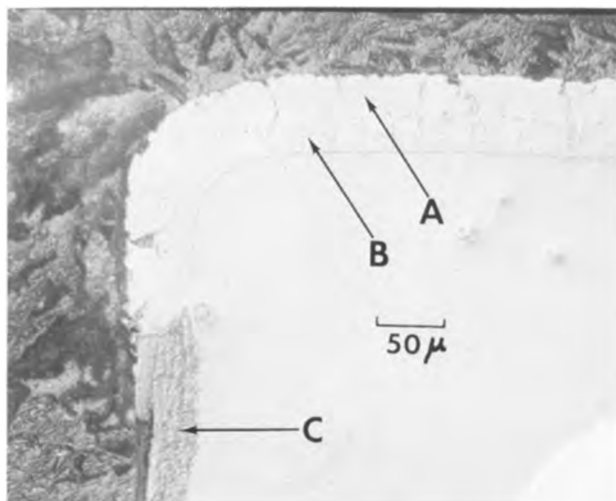

Fig. 2. Photomicrograph of section of anode housing after 2600 hr operation. A, Oxidized aluminum layer; B, diffused aluminum layer; C, Corrosion product at edge of electrode compartment (see also Fig. 1).

Scanning electron microscopy and energy-dispersive x-ray analysis SEM-EDXA) showed that the protective coating in Fig. 2 contained mainly aluminum in the top layer. The intermediate layer also showed the presence of aluminum. X-ray diffraction analysis and SEM-EDXA confirmed that the top protective coating was α-$LiAlO_2$; the intermetallic phases precipitated in the intermediate layer were suspected to be of the types: $NiAl_3$, NiAl, and/or FeAl.

These results indicate that, during initial cell operation, aluminum is converted to an oxide and then subsequently to $LiAlO_2$ by reaction with Li_2CO_3 as follows

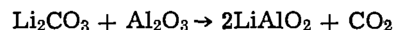

$$Li_2CO_3 + Al_2O_3 \rightarrow 2LiAlO_2 + CO_2$$

The corrosion protection to the stainless steel was provided by the $LiAlO_2$ coating. Furthermore, the coating also showed good thermal shock resistance and adherence. At 925°K, $KAlO_2$ would not be thermodynamically stable in the electrolyte tile containing 62 m/o Li_2CO_3-38 m/o K_2CO_3 (4), and would not, therefore, be present. The unprotected areas adjacent to the wet seal were corroded during cell operation as shown in Fig. 2. X-ray diffraction analysis showed that the corrosion product at C mainly consisted of $LiCrO_2$ and $LiFeO_2$ (5) that formed by the reaction of stainless steel and molten carbonate which seeped from the electrolyte tile during cell operation.

In summary, the results of this study showed that a $LiAlO_2$ coating on 316 stainless steel offers corrosion protection to metallic cell components susceptible to corrosive attack in a molten carbonate fuel cell environment, especially at the wet seal areas. Although this note described the corrosion protection of only one stainless steel, namely Type 316, we expect that other stainless steels can be protected from corrosion by the application of an aluminized layer. Based on the above experience, a further improvement for the corrosion protection of wet seals has been developed—the areas of the cell housing covered by an aluminized coating has been increased to also include the areas adjacent to the wet seal. In other words, the regions marked A, B, and C in Fig. 1 as well as the exterior of the cell housing were covered with an aluminized coating. In this manner, the formation of a corrosion layer beneath the edge of the diffuse intermediate layer (see Fig. 2) is prevented.

Acknowledgment

The authors would like to acknowledge B. S. Tani for conducting the x-ray analyses and J. P. Ackerman for many suggestions provided during the course of this study.

Manuscript submitted May 25, 1978; revised manuscript received Aug. 3, 1978.

Any discussion of this paper will appear in a Discussion Section to be published in the June 1979 JOURNAL. All discussions for the June 1979 Discussion Section should be submitted by Feb. 1, 1979.

Publication costs of this article were assisted by Argonne National Laboratory.

REFERENCES

1. J. M. King, Jr., Final Report, NASA CR 134599, FCR-0237 (1977).
2. Quarterly Status Report for period Jan. 1-March 31, 1977, Contract No. 31-109-38-3952, Institute of Gas Technology, Chicago, Ill.
3. For review of literature on the "wet seal" technique, see "Project 8984 Quarterly Status Report" for the period Oct. 1-Dec. 31, 1976, prepared by Institue of Gas Technology, Chicago, Ill. 60616.
4. G. H. J. Broers and H. J. J. Van Ballegoy, Paper presented at the 3rd International Symposium on Fuel Cells, Brussels, June 1969.
5. J. Ackerman, K. Kinoshita, J. W. Sim, R. Swaroop, and P. A. Nelson, Report No. ANL-77-79, Argonne National Laboratory, Argonne, Ill.

Analysis of Protective Oxide Films on Copper-Nickel Alloys by Auger Spectroscopy

G. E. McGuire,*[,1] A. L. Bacarella,* J. C. Griess, Jr.,* R. E. Clausing, and L. D. Hulett

Oak Ridge National Laboratory, Chemistry Division, Oak Ridge, Tennessee 37830

Alloys of copper and nickel have found extensive use in saline water environments because the corrosion resistance of such alloys is usually superior to that of copper. Some earlier work has shown that the protective film is primarily a nickel oxide (1). The previous investigation was based upon photoelectron spectroscopic results. This paper describes experiments that have been conducted to determine the surface composition, as well as the elemental depth profile of these same films using Auger electron spectroscopy (AES) and ion sputtering.

The oxide films which protect most oxidation-resistant alloys from further oxidation are so thin that they cannot be examined in section by conventional metallographic techniques. Similarly the use of the electron beam microanalyzer is limited to films thicker than 1 μm both because of its precision and because of the rather deep penetration of the high energy electron beam used to stimulate x-ray emission. Thin film analysis is now frequently obtained by use of Auger and photoelectron spectroscopy in conjunction with argon ion sputtering. It has been shown that the signal obtained by these two techniques arises from the first few (3-20) atom layers (2). It is possible to analyze the first few atom layers and then remove them by Argon ion sputtering to give a depth profile for any desired depth. These features, coupled with the well-known capabilities of Auger and photoelectron spectroscopy to do elemental analysis and to determine chemical states, make the techniques very valuable in studies of protective films on metals.

Experimental Procedure

The 70:30 cupronickel was obtained from a commercial vendor and had the following composition: 68.85% Cu, 29.93% Ni, 0.67% Fe, 0.44% Mn, 10%Zn, and 0.005% Pb. The nickel specimen was made from nickel 200 (International Nickel Company) which has a nominal composition of 99.5% Ni, 0.25% Mn, 0.15% Fe, and 0.06% C. The specimens were machined from ¼ in. rods. The 1.24M NaCl solutions used in the anodization were prepared from reagent-grade material and triply distilled water and had a pH of about 6.4. The solutions were unbuffered, and the pH's reported below are those prevailing at the termination of the polarization.

Specimens of 70:30 cupronickel were maintained potentiostatically at -0.325V *vs.* SCE and -0.360V *vs.* SCE in boiling-refluxing H_2-sparged 1.24*M* NaCl, pH $= 7.4$. Since the passivation potential (SCE) for this alloy in this solution is -0.37V ($E_p = 0.19 - 0.076$ pH) (3), the specimen should passivate. Under these conditions the current decreased from 3.1×10^{-4} to 2.2×10^{-7} A/cm^2 over a period of 224 min as a passive film formed. Other specimens were maintained potentiostatically at -0.500V and -0.450V *vs.* SCE in the boiling-refluxing H_2-sparged 1.24*M* NaCl, pH $= 8.4$. Here, the current density remained constant at 7.0×10^{-6} A/cm^2. Since the potential was below the passivation potential ($E_p = -0.448$V), no film formation was expected. However, since the potential is only slightly cathodic to the passivation potential, some film formation which may not affect the anodic dissolution may occur (3). Bockris, Reddy, and Rao (4) postulated a similar type of film on nickel in H_2SO_4 at room temperature as a precursor to the passivating film.

To obtain a specimen representative of an unoxidized 70:30 cupronickel substrate, one specimen was chemically etched in *ca.* 6*N* HCl and rinsed in triply distilled water. To check the assumption that the surface film formed on the 70:30 cupronickel is an oxide of nickel, one pure nickel specimen was anodized at -0.360V *vs.* SCE in the boiling-refluxing H_2-sparged 1.24*M* NaCl, pH $= 7.5$. The current density for this specimen decreased from 1×10^{-4} to 2×10^{-7} A/cm^2 over a period of 81 min. Another pure nickel specimen was chemically etched in a *ca.* 6*N* HCl solution and rinsed in distilled water. All specimens were rinsed in distilled water and stored dry until examined. Just prior to loading into the spectrometer, the samples were ultrasonically cleaned in absolute ethanol. Another set of samples were prepared in the same fashion at a later time to check the reproducibility of the data. A detailed description of the electrochemistry and preparation has been presented (1).

The Auger electron energy analyzer was of the cylindrical-mirror type purchased from Physical Electronics Corporation. In this design the electron gun is coaxial with the cylindrical analyzer. The electron gun was operated at 5000V with a 5 μA beam focused to a beam diameter of about 25 μm. Adequate signal and resolution were obtained with a 6 eV p-p modulation voltage, a time constant of 0.3 sec, and a scan rate of 2 eV/sec. The signal was recorded as the first derivative of the electron energy distribution, $dN(E)/dE$. The spectrum was scanned from 0 to 2000 eV.

The vacuum chamber was equipped with all metal seals and was ion pumped to a base pressure of 10^{-9} Torr. A residual gas analyzer indicated the base pressure was due to CO, Ar, CO_2, and CH_4. During sputtering the ion pump was turned off and argon added to bring the pressure to 5×10^{-5} Torr. Carbon monoxide was the major contaminant in the sputter gas and it is estimated that its pressure was 1×10^{-8} Torr or less. Sputtering with 2000 eV ions at an argon pressure of 5×10^{-5} Torr was calibrated to remove $\sim$ 50 Å/min from the sample surface. Calibration was based on sputtering through 1000Å tantalum oxide films. The sputter rate calibration for tantalum oxide is only an approximation since the sputter rate of copper, nickel, or nickel oxide will be different. The ion gun was positioned so that ion sputtering could be accomplished during the data-taking process.

There may be a tendency to overestimate the sputtering rate. When a sample undergoes ion bombardment, the central point of focus of the ion beam undergoes the greatest degree of ion etching. The rate of ion etching drops off rapidly at points away from the center of focus. Using this method, we estimated the maximum rate of removal. The Auger signal may originate from regions that have been sputtered to a range of different depths although the electron beam used for excitation is positioned at the center of the sputtered crater. Thus an Auger signal may persist even after the element is removed from the center of the sputtering region (5).

For the majority of elements, a semiquantitative Auger analysis can be made by measuring the peak-

* Electrochemical Society Active Member.
[1] Present address: Texas Instruments, Materials Characterization Laboratory, Dallas, Texas 75080.
Key words: cupronickel, Auger, corrosion, ESCA, saline water.

to-peak intensity of the Auger signal. However, Cu and Ni have a number of intense Auger transitions, several of which overlap. Pure Ni exhibits a peak at 715 eV, Cu and Ni both have peaks that appear at 775 and 850 eV, and pure Cu exhibits a peak at 920 eV. There are also overlapping Auger transitions for Cu and Ni around 61 eV. The normal mode of operation of the AES system did not permit the resolution of the overlapping Cu and Ni peaks at 775 or 850 eV. The Cu concentration was obtained by measuring the intensity of the Cu signal at 920 eV, which has no interfering lines. The contribution from Cu to the overlapping signals at 775 and 850 eV was estimated using the known ratios of the Cu peaks (6). Subtracting the Cu contribution from the total signal leaves the contribution from the Ni. The Ni peak at 715 eV was not used because the signal-to-noise ratio was not adequate.

Results and Discussion

Observations on the "unsputtered" surface.—Typical Auger spectra, obtained for the surfaces before ion sputtering was initiated, are presented in Fig. 1. The main Auger signals that appear are sulfur at 150 eV, chlorine at 181 eV, carbon at 272 eV, nitrogen at 381 eV, oxygen at 510 eV, sodium at 990 eV, and the copper and nickel transitions mentioned earlier.

The surface of the chemically etched 70:30 cupronickel specimen has approximately the Cu-to-Ni ratio expected. This sample has some oxide formation, but the ratio of Cu to Ni in the surface of the oxide has not changed substantially from that of the alloy. The 70:30 cupronickel sample anodized below the passivation potential (Fig. 1B) has a very thin oxide layer that appears to be richer in Cu than Ni. The spectrum from the 70:30 cupronickel sample (Fig. 1A), which was prepared at the passivation potential, shows an Ni signal which completely overshadows the Cu signal that is present. The O/Ni ratio is closer to that of the anodized nickel than that of the chemically etched nickel. The signal from oxygen is present on the surface of the 70:30 cupronickel and the Ni and anodized Ni are very large, but only in the case of the anodized Ni does the oxygen appear to reduce the intensity of the Ni signal. This is reasonable since this is a relatively thick oxide with possible additional adsorbed oxygen on the surface. It should be mentioned that an unknown portion of the oxygen signal on all the samples may be due to adsorbed CO, especially on the "unsputtered surface." We cannot make quantitative estimates of this effect.

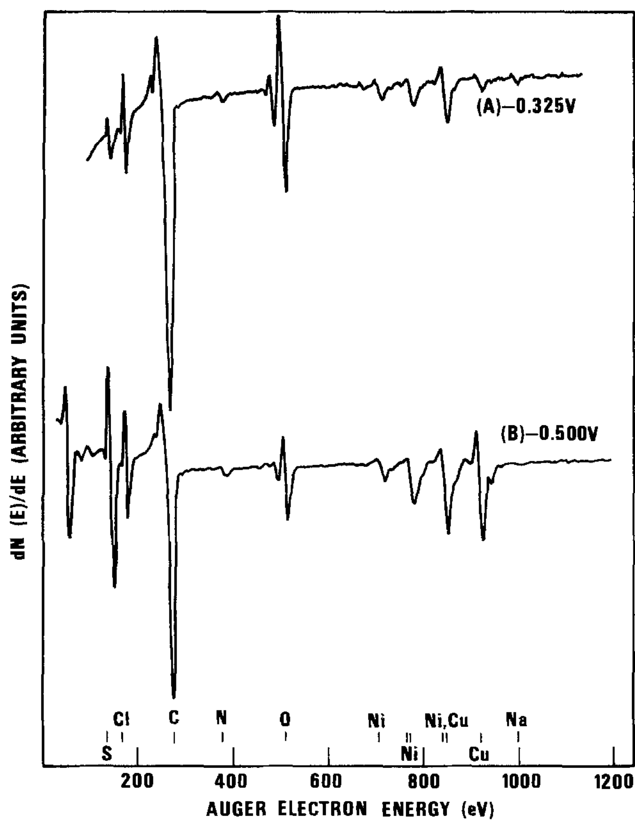

Fig. 1. Auger electron energy spectra for the Cu/Ni alloys before ion sputtering.

There is a strong carbon signal in each of the spectra. The carbon signal builds up quickly from the breakdown of CO under the influence of the electron beam (7), but the carbon layer is easily removed by argon ion sputtering. Initially, the amount of carbon present on the chemically etched samples is much greater than on the anodized samples. This may be a result of differences in the electron beam interactions with CO on the metallic and oxidized surfaces or differences in the interaction of the solvent ethanol with the surface.

Sulfur was found as an impurity on the surface of all the samples examined here. Frequently sulfur has been reported as an impurity on Cu and Ni samples (7, 8) and has been found to diffuse to the surface when samples are heated to elevated temperatures. In these samples neither anodization nor boiling reflux conditions seems to have affected the sulfur concentration at the surface layer. The concentration of sulfur seems to be approximately the same on all the samples including the chemically etched samples.

Sodium and chlorine show up probably as a result of anodizing the samples in NaCl solution. Although the samples were thoroughly cleaned, some NaCl may remain on the surface through adsorption. There is a rather strong chlorine signal, but little, if any, sodium signal. A portion of the chlorine may be appearing as $CuCl_2^-$ (9).

There is a small amount of nitrogen present on each of the samples, probably as adsorbed nitrogen. Using ion bombardment, it was possible to reduce the signals from sulfur, chlorine, nitrogen, and sodium to trace levels within a few monolayers of the surface. The signals from carbon and oxygen were more persistent, primarily because carbon and oxygen were present initially in greater amounts than the other contaminants and also because there may be some CO readsorption on the surface, even during ion bombardment.

Observations during Depth Profiling by Argon Ion Sputtering

Figure 2 presents the ratios of the Auger signal intensity of Cu_{920} to Ni_{848} as a function of the time of ion bombardment for the cupronickel alloy. Figure 3 presents the corresponding ratio of the Auger signal intensity of O_{510} to total metal signal. The ratios of

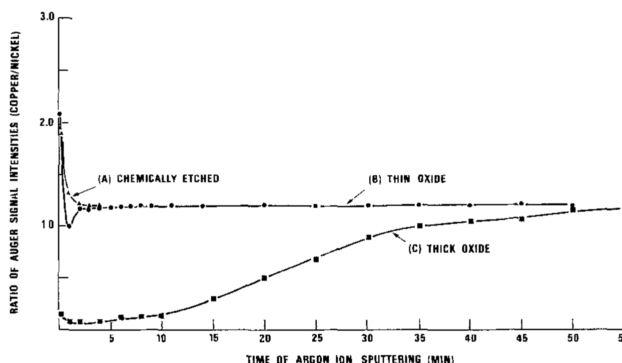

Fig. 2. Sputter profiles for Cu/Ni alloy samples showing the ratio of the Auger signal intensity from copper to that from nickel as a function of sputtering time. (A) Chemically etched; (B) thin oxide; (C) thick oxide. The sputtering rate was 50 Å/min.

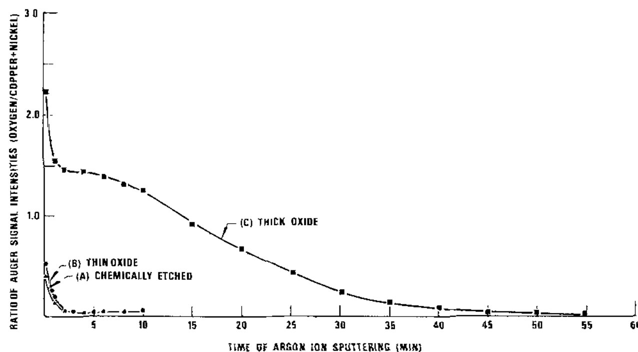

Fig. 3. Sputter profiles for Cu/Ni alloy samples showing the ratio of the Auger signal intensity from oxygen to that from nickel and copper as a function of sputtering time. (A) Chemically etched; (B) thin oxide; (C) thick oxide. The sputtering rate was 50 Å/min.

the peak heights are a better indication of the changing surface concentration than the sample Auger peak heights. Using these curves for depth profile analysis, one can observe that the chemically etched 70:30 cupronickel specimen had a very thin oxide layer that was slightly rich in Cu as compared to the bulk alloy. The oxide layer was very thin and was removed within the first few minutes of ion bombardment. With a sputtering rate calibrated at ~ 50 Å/min, the oxide film on this sample would be much less than 100Å thick.

Examination of Fig. 2B and 2C shows that the first few monolayers of each anodized cupronickel sample have a higher concentration of Cu than the region just beneath the surface layer. The ratio of Cu/Ni in samples prepared at the passivation potential (thick oxide) is below the bulk ratio, indicating that the oxide is largely a nickel oxide. The Cu/Ni ratio becomes smaller, levels off, then increases to the bulk composition as sputtering is continued. In the sample prepared below the passivation potential (thin oxide), the Cu/Ni ratio starts out above the bulk ratio, decreases below the bulk, and then quickly reaches the bulk value. The film is estimated to be less than 100Å.

The O/M ratio of the chemically etched (Fig. 3A) and thin oxide (Fig. 3B) samples reflects a thin oxide similar to the Cu/Ni curves. Figure 3C for the thick oxide shows an initial decrease in the O/M ratio which may correspond to the removal of O_2, CO, or H_2O. The O/M curve then levels off and gradually decreases over several hundred angstroms.

Nakayama *et al.* (10) and Castle (11) suggest that heating a cupronickel sample can cause Ni to migrate to the surface. Migration of Cu or Ni due to thermal effects can be ruled out in this case since the sample was not heated above about 100°C during sample preparation or examination, and self-diffusion rates for copper and nickel would be extremely small at this temperature and alloy composition even considering the possibility of faster diffusion rates along grain boundaries or near the surface (12).

It was reported previously that at anodic potentials below that required for passivation, the relative concentration of copper and nickel at the surface of the film is the same as in the bulk alloy. This suggests either the absence of a film or a film formed by uniform oxidation of the elements in the alloy (1).

Specimens of 70:30 cupronickel exposed to salt water solutions for extended periods of time are usually covered with a thin film. It has been demonstrated, using x-ray diffraction, that this film is Cu_2O, with no detectable nickel present (13). Since the present data indicate the initial films are composed primarily of nickel, the initial decrease in the cupronickel ratios in Fig. 2B and 2C may be an indication of copper oxide formation through adsorption after being hydrolyzed (9). McIntyre *et al.* (14) have presented data on the aqueous oxidation of 66% Ni, 32% Cu that would support this observation.

The oxide layers of the two nickel samples were less than 100Å thick. Initially the O/Ni ratio in the anodized Ni was greater than that of the chemically etched Ni sample, but the oxygen was sputtered away within a few minutes to what appeared to be a rather abrupt interface between the oxide layer and the pure metal underneath.

Conclusions

The use of Auger spectroscopy accompanied by argon ion sputtering has been used to identify unambiguously the surface impurities (sulfur, chlorine, carbon, oxygen, nitrogen, and sodium) on anodized and chemically etched 70:30 cupronickel samples. A very thin film was present on the outermost surface of these samples in which the Cu/Ni ratio is different than the bulk, but there is an underlying oxide layer which is very rich in nickel (below the first few atomic layers).

The underlying layer is approximately 70% nickel in the passivated sample. The sample which did not passivate also had a thin nickel-rich layer, but its oxygen content is lower and the layer is much thinner. It seems likely that this surface is not completely covered with an even, thin nickel-rich oxide but rather that patches of nickel-rich oxide and base metal coexist during anodization. The base metal would acquire a very thin oxide layer during air exposure prior to the Auger analysis, thus explaining the high initial oxygen-metal ratio and the observed profile.

The film may also be a precursor $Ni(OH)_2$ film formed in more significant quantity due to the higher pH (pH = 8.4). At this pH, the thermodynamic potential for the formation of $Ni(OH)_2$ is only 52 mV cathodic to the passivation potential.

Film formation at the passivation potential may be due to the oxidation of a precursor $Ni(OH)_2$ film to $NiO_{1.5\text{-}1.6}$ as suggested by Bockris, Reddy, and Rao (4).

The surface enrichment of Cu in the first few layers of all the cupronickel specimens may be due to surface adsorption of $CuCl_2^-$ (a corrosion product) from the anodizing solution (9).

Manuscript submitted July 18, 1978; revised manuscript received July 17, 1978.

Any discussion of this paper will appear in a Discussion Section to be published in the June 1979 JOURNAL. All discussions for the June 1979 Discussion Section should be submitted by Feb. 1, 1979.

Publication costs of this article were assisted by Oak Ridge National Laboratory.

REFERENCES

1. L. D. Hulett, A. L. Bacarella, L. LiDonnici, and J. C. Griess, *J. Electron Spectrosc.*, **1**, 169 (1972).
2. T. A. Carlson and G. E. McGuire, *ibid.*, **1**, 161 (1973).
3. J. C. Griess, A. L. Bacarella, and E. G. Bohlmann, ORNL-TM-4340, p. 58-63, 100, Oct. (1973), Oak Ridge National Laboratory, Oak Ridge, Tenn.
4. J. O'M. Bockris, A. K. N. Reddy, and B. Rao, *This Journal*, **113**, 1133 (1966).
5. R. Shubert and J. C. Tracy, *Rev. Sci. Instrum.*, **44**, 487 (1973).
6. P. W. Palmberg, G. E. Riach, R. E. Weber, and N. C. MacDonald, "Handbook of Auger Electron Spectroscopy," Physical Electronics Industries, Inc. 1972.
7. J. P. Coad, H. E. Bishop, and J. C. Riviere, *Surf. Sci.*, **21**, 253 (1970).
8. D. T. Quinto, V. S. Sandaram, and W. D. Robertson, *ibid.*, **28**, 504 (1971).
9. A. L. Bacarella and J. C. Griess, *This Journal*, **120**, 459 (1973).
10. K. Nakayama, M. Ono, and H. Shimizu, *J. Vac. Sci.*

Technol., 9, No. 2, 749 (1972).
11. J. E. Castle, *Nature Phys. Sci.*, **234**, 93 (1971).
12. A. E. Austin and N. A. Richard, *J. Appl. Phys.*, **12**, 1462 (1961).
13. R. F. North and M. J. Pryor, *Corros. Sci.*, **10**, 297 (1970).
14. N. S. McIntyre, T. E. Rummery, M. G. Cook, and D. Owen, *This Journal*, **123**, 1164 (1976).

The Electrochemical Oxidation of Hydrazine and Methylhydrazine on Gold: Application to Gas Monitoring

J. R. Stetter,* K. F. Blurton,*[,1] A. M. Valentine, and K. A. Tellefsen

Energetics Science, Incorporated, Elmsford, New York 10523

Recently (1-3), we have described a series of instruments for monitoring common pollutants, such as CO, NO, NO_2, and H_2S, in ambient air. The operating principle of these analyzers was based on the electrochemical oxidation (electroreduction for NO_2) of the gas at a catalyzed Teflon-bonded diffusion electrode (4), the potential of this sensing electrode being maintained constant at a value at which neither oxygen reduction nor electrolyte decomposition interfered with the measurement of the pollutant (essentially between 0.7 and 1.6V *vs.* RHE depending on the electrode catalyst).

In general, the desirable features of such instrumentation are signal stability, specificity (*i.e.*, the ability to measure a pollutant in the presence of other gases), precision, and ease of operation. Instrument specificity was achieved either by using selective gas filters or by optimizing the electrode catalyst and potential. The latter method was preferred since it eliminated a component from the instrument which had a finite life.

Hydrazine (H) and monomethylhydrazine (MMH) are strong reducing agents with a variety of biological effects and considerable toxicity (5), and they will be used as rocket propellants for the space shuttle. Currently, there is no instrumental technique which can satisfactorily monitor H and MMH and meet the requirements for protection of personnel during handling and storage of these chemicals (6). Therefore, since previous studies of hydrazine as fuel cell fuels (7, 8) had demonstrated the ability to electrooxidize these compounds, we decided to investigate the electrochemical technique as the basis for a hydrazine instrument (9).

In this paper, we describe the electrochemical studies which led to the development of the instrument. Gold was used as the electrode material since CO (the major interferent which cannot be selectively prefiltered) is inactive on it in the potential range of interest (10).

Experimental

The experimental cell was similar to that described previously (1). The electrolyte was either 28% H_2SO_4 solution or 23% KOH solution and these concentrations were selected such that the electrolyte vapor pressure approximated that of the average relative humidity met in practice. The cell had three electrodes. The sensing electrode was a gold-catalyzed Teflon-bonded diffusion electrode (geometric area 5 cm^2, catalyst loading 8-12 mg/cm^2) and was fabricated by applying a mixture of catalyst and Teflon suspension to a Teflon film. The reference- and counter-electrodes were platinum-catalyzed diffusion electrodes, and these were used for convenience in the cell design (3). The potential of the Pt/air reference electrode was checked against a hydrogen electrode in the same electrolyte and found to be 0.98V ± 10 mV in the acid electrolyte and 1.0V ± 10 mV in basic electrolyte. (All potentials are reported *vs.* RHE in the same electrolyte.) The potential of the sensing (working) electrode was potentiostatted *vs.* the reference electrode using an in-house designed and constructed potentiostat.

The electrochemical measurements were made using dilute mixtures (between 1 and 10 ppm by volume) of H and MMH in air (since this was the situation to be met in practice) and also in nitrogen. No difference in electrochemical cell response was noted between the air and nitrogen mixtures during these experiments.

These mixtures of H and MMH were prepared using a dynamic dilution technique (11). The neat liquid hydrazines were injected at a constant delivery rate into a glass chamber through which the diluent gas was flowed at a continuous controlled flow rate. A syringe pump (Sage Model 355) was used to deliver the liquid hydrazine from the 10 μl syringe into the 1.0 liter min^{-1} gas stream, and after mixing they were passed through a Teflon valve exhaust for sample collection.

The vapor mixtures were contained in a 50 liter Teflon bag (Cole-Parmer Company, Chicago, Illinois) prior to their introduction into the electrochemical cell. Samples of the vapor mixtures were collected from the Teflon bag during testing using an impinger filled with acid solution, and they were analyzed using a colorimetric technique (12) which was modified (13). This colorimetric technique was used as the reference standard for all H and MMH vapor mixture concentrations.

Initially, air was passed over the back (gas) side of the potentiostatted diffusion electrode, and the current generated by the electrochemical reaction was measured by determining the potential drop across a standard resistor with a recorder. Subsequently, the air/hydrazine mixture was passed over the back of the electrode at a constant flow rate and the current was measured. The difference between the currents for air and hydrazine was then recorded as the signal due to the electrochemical oxidation of hydrazine in the cell. Similarly, analyzed gas mixtures of NO/N_2, CO/air, and NO_2/N_2 were introduced into the electrochemical cell. The NO/N_2 and CO/air mixtures were obtained commercially (Airco, Incorporated) while samples containing 5 ppm of NO_2 in N_2 were prepared using high purity N_2 and thermostatted permeation tubes (Metronics Associates).

At low gas flow rates (<0.3 l/min), H and MMH interacted with the sampling system and also with the reinforced acrylic used as the electrochemical sensor endplates (gas chamber). These interactions,

* Electrochemical Society Active Member.
[1] Present address: Institute of Gas Technology, IIT Center, Chicago, Illinois 60616.

which can lead to adsorption or decomposition of the reactive vapor, cause changes in hydrazine vapor mixture concentration. They can be minimized by reducing the surface area and reactivity of the surface to which the vapor mixture is exposed prior to analysis. Therefore, for the experiments at low gas flow rates, an electrochemical cell and sampling system was fabricated from Teflon and the length of tubing used in the sampling system was kept to a minimum.

Current/potential curves for H and MMH were obtained by initially potentiostatting the sensing electrode at a constant potential (0.6V in acid electrolyte and 0.8V in alkaline electrolyte) for 24 hr. All experiments were performed at room temperature, 23°C. The current was then measured for zero air and subsequently for the test gases with a gas flow rate of 0.7 l/min through the sensor. The electrode potential was then increased stepwise and the currents at each potential were determined after potentiostatting for 24 hr.

Results and Discussion

The current resulting from oxygen reduction or evolution at the sensing electrode must be small compared with the current due to the oxidation of the test gas at practical concentrations in order to achieve accurate data on the electrooxidation of hydrazine. We have previously reported that this current is indeed small over a wide range of potentials with gold electrodes in acid electrolyte (10). However, the results in Fig. 1 show that the potential range for analyzing pollutants in alkaline electrolyte is much more restricted than in acid solution.

The current/voltage curves for H and MMH were determined with sensors containing acid and alkaline electrolyte. The data in acid electrolytes was irreproducible for both gases at all potentials, and this was probably due to the difficulty in oxidizing the protonated, $N_2H_5^+$, species. As a result, we eliminated acid as a suitable electrolyte for analyzing these low gas concentrations. The data in alkaline electrolyte were

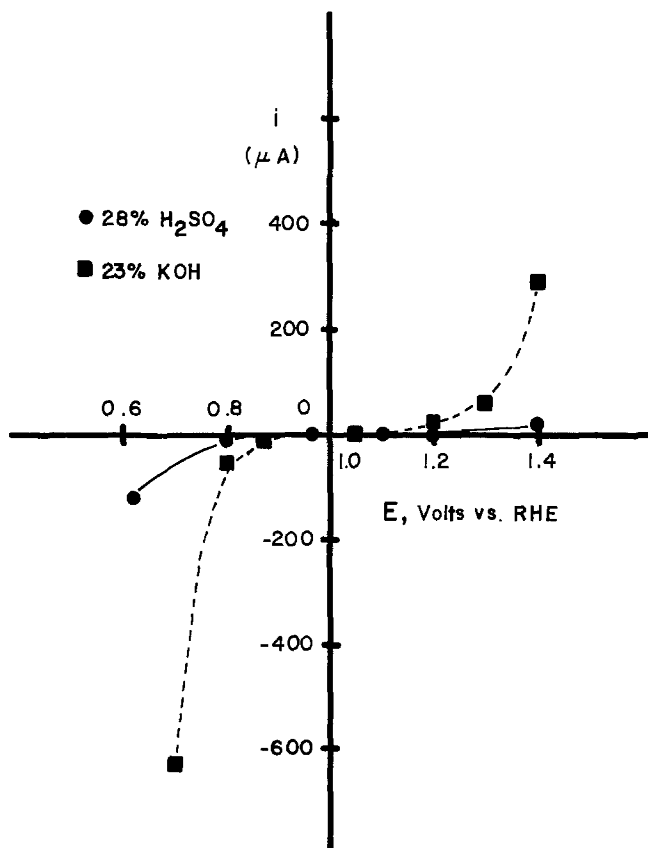

Fig. 1. Current/voltage curve on a gold electrode for zero air passing through the sensor at 0.7 l/min.

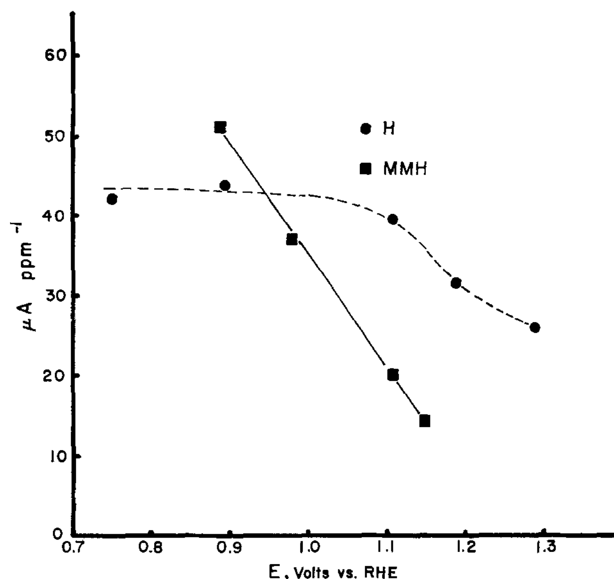

Fig. 2. Hydrazine and monomethylhydrazine oxidation currents on gold electrodes using 23% KOH electrolyte. The gas flow rate is 0.7 l/min through the sensor.

much more reproducible, and the current/potential plot shown in Fig. 2, although obtained with one cell, is similar to data obtained with three other cells. Although the cell specificity and sensitivity was enhanced by using alkaline electrolyte, problems were caused due to the absorption of CO_2 from the atmosphere by the electrolyte. This caused the cell lifetime to be limited to 600 hr of continuous use (9). However, in the instrument application, cell replacement is easily accomplished and extended use is obtained when the cell is utilized in the spot-check mode (13).

In alkaline electrolyte, both hydrazine and MMH were electrooxidized on gold at all potentials in the limited potential range where data could be obtained, and in both cases the maximum signal was obtained at the more cathodic potential. The signals for both gases were approximately 50 μA/ppm at 0.9V and decreased to approximately 20 μA/ppm at +1.2V.

In order for a practical instrument to be designed with these sensors, the instrument must also be specific to the test gas and give a minimum signal to other pollutants present in the practical situation. In this application (11, 13) the common pollutants were CO (present at common levels in the presence of vehicular traffic 10-50 ppm), NO (present in concentrations of 5 ppm due to rocket oxidant), and NO_2 (present at normal atmospheric concentration of 20-50 ppb). Figure 3 shows the current/voltage curve for these gases in the same sensor as used to obtain the data in Fig. 2. As can be seen, the currents-per-unit concentration for these potential interferences were markedly lower than that for hydrazine and MMH at potentials anodic to 0.9V. In general, the cell output increased with increasing environmental temperature (13), however this was repeatable and therefore could be compensated electronically in the instrument application.

From the current/potential results shown in Fig. 2 and 3, an instrument for the determination of hydrazine and MMH was developed (9) with the sensing electrode potential maintained at 1.1V where CO and NO are unreactive and where the signal due to NO_2 is low.

Hydrazines may undergo several charge-transfer processes at an electrode surface, and we used this electrochemical cell to determine the over-all electrochemical reactions for hydrazine and MMH at 1.1V. This technique, which we have described previously (10), is based on measuring the current at a fixed

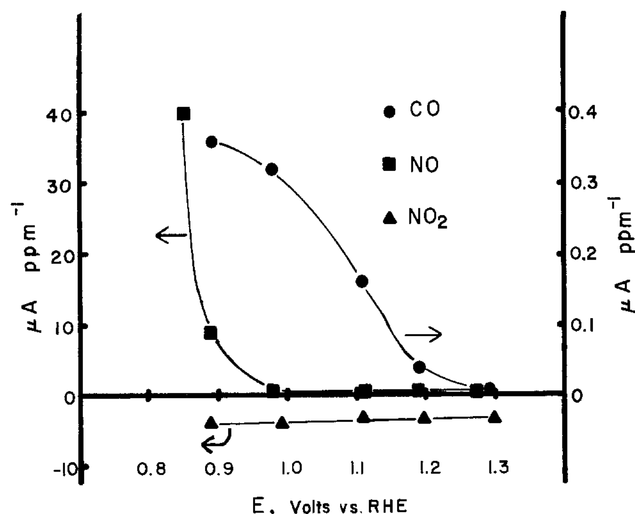

Fig. 3. CO and NO oxidation currents and NO_2 reduction current on a gold electrode using 23% KOH electrolyte. The gas flow rate is 0.7 l/min through the sensor.

potential as a function of flow rate. Less than 100% of the gas is electrochemically oxidized at high flow rates, while at low flow rates, all of the gas is oxidized. Figure 4 shows the experimentally determined current *vs.* flow rate plot for 13.8 ppm MMH and the theoretically calculated current *vs.* flow rate curve. As the flow rate is decreased, a point is reached at which all the hydrazine entering the sensor reacts, and the current (i) at this flowrate (G) is related to the electroactive gas concentration (c) by (14)

$$\lim_{G \to 0} (i/G) = zFc/V \quad [1]$$

where V is the molar volume of the electroactive gas (cm^3/mole).

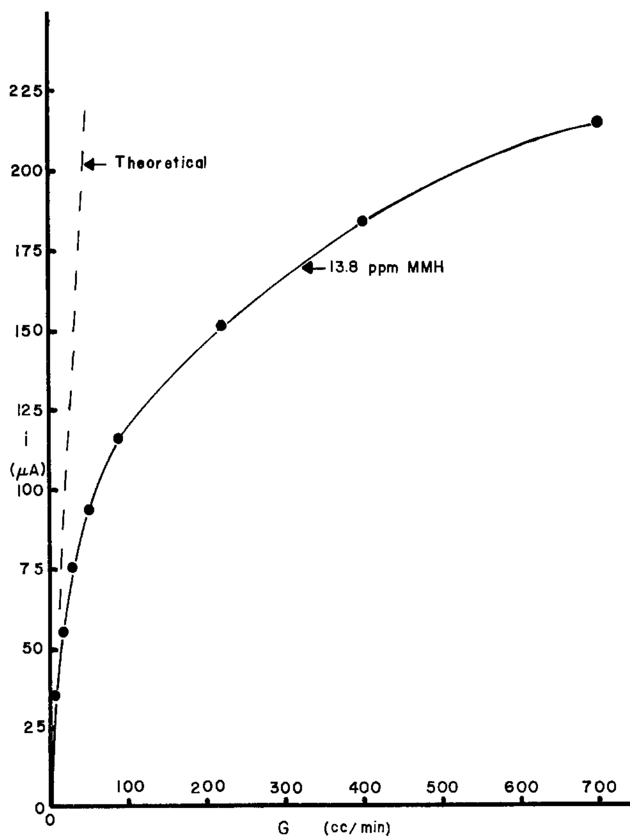

Fig. 4. Experimental and theoretical oxidation currents for 13.8 ppm monomethylhydrazine at 1.1V as a function of the gas flow rate.

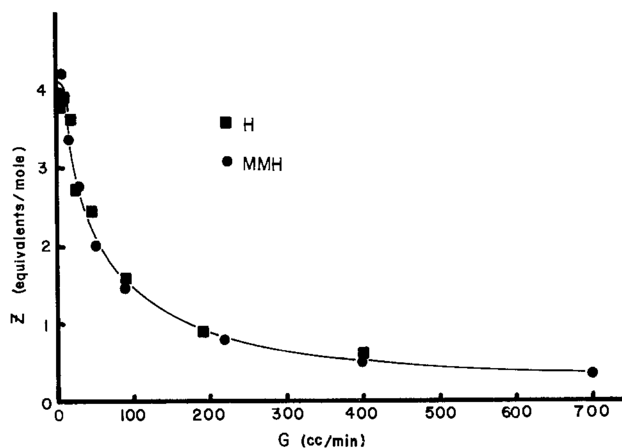

Fig. 5. Apparent values of z (calculated from Eq. [1]) for hydrazine and monomethylhydrazine oxidation at 1.1V as a function of gas flow rate.

This method was used to determine z for H and MMH oxidation using gases of known concentration using the specially fabricated Teflon cell. The apparent value of z calculated from Eq. [1] was plotted *vs.* the gas flow rate (Fig. 5). Limiting values of 4 electrons per molecule were obtained for both H and MMH oxidation. From these data, it is proposed that the over-all electrochemical process for hydrazine at 1.1V is

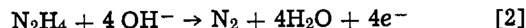

$$N_2H_4 + 4\,OH^- \rightarrow N_2 + 4H_2O + 4e^- \quad [2]$$

and for MMH is

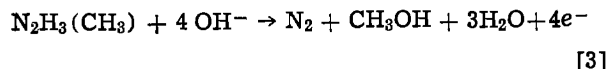

$$N_2H_3(CH_3) + 4\,OH^- \rightarrow N_2 + CH_3OH + 3H_2O + 4e^- \quad [3]$$

These over-all processes are in agreement with measurements with platinum electrodes in acid electrolyte for hydrazine (15) and monomethylhydrazine (16, 17).

Acknowledgment

This work was supported by the National Aeronautics and Space Administration under Grant No. NAS 10-8982.

Manuscript submitted April 18, 1978; revised manuscript received June 12, 1978.

Any discussion of this paper will appear in a Discussion Section to be published in the June 1979 JOURNAL. All discussions for the June 1979 Discussion Section should be submitted by Feb. 1, 1979.

Publication costs of this article were assisted by Energetics Science, Incorporated.

REFERENCES

1. K. F. Blurton and H. W. Bay, *Am. Lab.*, **6**, 50 (1974).
2. J. M. Sedlak and K. F. Blurton, *Talanta*, **23**, 811 (1976).
3. J. M. Sedlak and K. F. Blurton, *ibid.*, **23**, 445 (1976).
4. J. Giner, "Proceedings of the 21st Annual Power Sources Conference," Vol. 10, p. 10, PSC Publications Committee, Red Bank, N.J. (1967).
5. K. C. Back, V. L. Carter, and A. A. Thomas, *Aviat. Space Environ. Med.*, **49**, 591 (1978).
6. R. A. Saunders and J. T. Larkins, Naval Research Laboratory Memorandum Report 3313, Naval Research Laboratory, Washington, D.C. June (1976).
7. K. Tamura and T. Kahara, *This Journal*, **123**, 776 (1976).
8. S. G. Meibuhr and R. F. Paluch, *ibid.*, **122**, 164 (1975).
9. J. R. Stetter, Paper No. 626 presented at the Pittsburgh Conference on Analytical Chemistry and Applied Spectroscopy, March 3, 1978, Pittsburgh.
10. J. M. Sedlak and K. F. Blurton, *This Journal*, **123**, 1476 (1976).

11. J. R. Stetter, *Sci. Tech. Aerosp. Rep.*, NASA-CR-153048, July 23 (1977).
12. H. McKennis, Jr. and A. S. Yard, *Anal. Chem.*, **12**, 1960 (1954).
13. J. R. Stetter and K. Tellefsen, "A Study for Hypergolic Vapor Sensor Development," Final Report under Contract No. NAS 10-8982, November 1977, NASA, Washington, D.C.
14. H. W. Bay, K. F. Blurton, J. M. Sedlak, and A. M. Valentine, *Anal. Chem.*, **46**, 1837 (1974).
15. M. Petek and S. Bruckenstein, *J. Electroanal. Chem. Interfacial Electrochem.*, **47**, 329 (1973).
16. D. M. King and A. M. Bard, *Anal. Chem.*, **36**, 2351 (1964).
17. P. Karabinas and J. Heitbaum, *J. Electroanal. Chem.*, **76**, 235 (1977).

Solid-State Chloride-, Bromide-, or Iodide-Selective Electrodes

G. Papeschi, S. Bordi,* and M. Carlà

Istituto di Chimica Fisica, Università di Firenze, Firenze 50121, Italy

A new technique for preparing low resistance Ag/AgX (with X = Cl^-, Br^-, I^-) solid-state electrodes from a mixture of silver powder and silver halide is described.

Halide electrodes are extensively considered in the electrochemical literature either for describing preparation methods (1-3), for presenting experimental studies, or for exposing theoretical considerations.

Mention is limited here to the most promising among recent efforts directed toward the development of halide-selective electrodes.

Pungor *et al.* (4-7) and independently, Rechnitz *et al.* (8, 9), describe a halide-sensitive membrane obtained with fine particles of silver halide contained in a polymerized silicon rubber matrix. Mascini and Liberti (10) prepare a membrane pressing at 130°-150°C, a mixture of silver halide and thermoplastic polymer. The membrane of van Osch and Griepink (11) is obtained pressing the ion-sensitive material they prepare by precipitation of the silver halide-sensitive material they prepare by precipitation of the silver halide upon finely divided gold particles. Kolthoff (12) reports that chloride and bromide electrodes can be made with a membrane of fused silver chloride and silver bromide. Lately, Matsushita *et al.* (13) prepare a silver-silver chloride electrode with a twist of two silver wires coated with fused silver chloride to which they add 1% of potassium chloride. The main disadvantages (14) of the silver-fused silver chloride electrodes are the rather high resistance of silver chloride and the fact that this material exhibits large photoelectric potentials. These disadvantages have been eliminated by using membranes of a silver sulfide matrix in which the appropriate silver salt is dispersed in a very finely divided form (14, 15).

Experimental Procedure

Silver powder preparation.—Humid purified silver chloride is added to 1 g/ml KOH solution and digested for 1 hr at 90°C on a hot plate under continuous stirring. The resulting Ag_2O, still in the hot alkaline solution, is reduced with 2M glucose added dropwise until a light gray powder of silver is obtained. After a thorough washing, the powder is dried and then passed through a 5 μm mesh sieve.

Silver halide pellet preparation.—0.1M sodium chloride is slowly dropped in a slurry of 0.1M $AgNO_3$ and silver powder ($Ag:Ag^+$ ratio ranging from 5:1 to 7:10) until an excess of chloride is present. The precipitate is thoroughly washed with distilled water and dried at 110°C. A pellet is made by pressing about 1.5g of the precipitate in a KI-type pellet die with a hydraulic bench press. The compaction pressure used is 7 tons/cm^2. During the pressing procedure the pellet space is evacuated. The pellet fixed at the end of a perpex tubing is sealed with a silver wire attached to the inner face using a silver-based conducting epoxy resin. The outer face of the pellet can be shaped and smoothed with emery paper.

Procedure.—Steady-state potentials are measured *vs.* a B222 Schott double junction half-cell containing 0.1M KNO_3 in the outer chamber, using a Fluke 881 A d-c differential voltmeter. Dynamic measurements are made by the aid of Texas Instrument minicomputer Model T.I. 960 A interfaced with a 12 bit A/D converter. After use, the electrodes are rinsed with distilled water, dried with soft paper, and stored in the dark. Shortly before the measurement the electrodes have to be rinsed with water and then used directly in the test solution.

Results

Calibration curves.—Investigations on the electrode performance showed that the percentage of metallic silver in the precipitate is not critical. Electrodes employing pellets prepared from mixtures with the $Ag:Ag^+$ ratio ranging from 5:1 to 7:10 all exhibited identical behavior. Also, variations in the pressure of compaction do not significantly affect the response characteristics of the electrodes.

Stirring efficiency was not critical in order to obtain reproducible values (±0.5 mV) on repetitive measurements carried out on different days.

The AgX electrodes were tested at a fixed temperature of 25° ± 0.1°C in solutions of sodium halide at concentrations ranging from 10^{-6} to 1M for chloride, 10^{-7} to 10^{-1}M for bromide, and 10^{-7} to 10^{-1}M for iodide. The ionic strength of the halide solutions was adjusted to 0.1 with KNO_3.

In every case the electrode system was allowed to attain equilibrium as indicated by a stable (±0.01 mV) cell emf.

In Fig. 1 the electrode potential is plotted against the halide concentration and the results have been expressed in the form of an equation in the same figure.

Response time.—The response time was evaluated by submitting the electrodes to rapid changes in the halide concentration and recording the relative changes of the electrode potential *vs.* time.

The concentration was changed by addition of a measured small amount of more concentrated solution in order to increase the initial concentration. Potential electrode curves for a chloride electrode are shown in Fig. 2. The rise times measured between the 10 and 90% points are 600 msec (curve A) and 350 msec (curve B) when the chloride concentration is increased 10 and 2 times, respectively.

Because of mixing limitation, the effective electrode response time should be expected to be somewhat smaller. The noise inherent to these wide band measures is about 1 mV pp. The pass band of the measure system was limited numerically by the computer to 20 Hz.

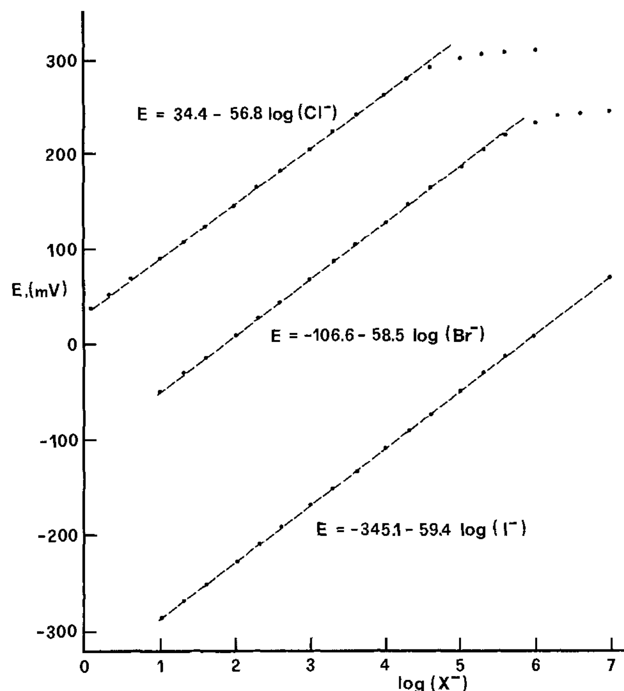

Fig. 1. Calibration curves for the halide solid-state electrode. Concentrations are molar concentrations of sodium halide. Potentials are measured *vs.* the B222 Schott half-cell at 25°C.

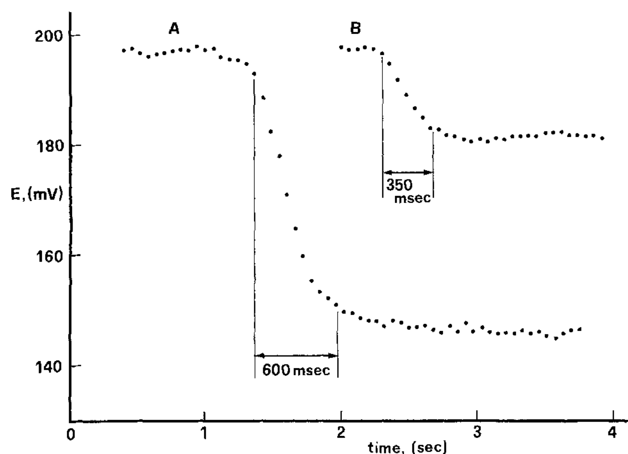

Fig. 2. Dynamic response of the Ag/AgCl electrode. Potentials (*vs.* B222 Schott half-cell at 25°C) sampled by a computer TI 960A interfaced with a 12 bit A/D converter: resolution 100 μV, band pass 20 Hz. A, Chloride concentration increase from 1.10^{-3} to 1.10^{-2}M; B, chloride concentration increase from 1.10^{-3} to 2.10^{-3}M.

Effect of pH.—The influence of pH was investigated for the chloride electrode, recording the potential of the electrode in contact with a solution containing a fixed amount of chloride ions and nitric acid to be neutralized with sodium hydroxide (Fig. 3). The measurements were started in solution containing 10^{-3}M nitric acid, 0.1M potassium nitrate, and 10^{-4}M NaCl (curve a) or 10^{-3}M NaCl (curve b). The pH was varied by means of 10^{-2} sodium hydroxide and followed by a combined glass electrode.

Thermal temperature coefficient.—The thermal temperature coefficient was measured by varying the temperature of a silver/silver chloride electrode in the cell

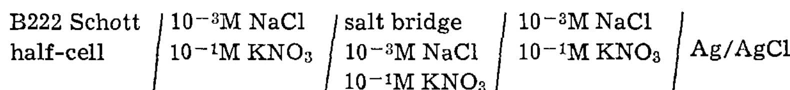

while keeping the temperature of the reference half-cell constant (25°C).

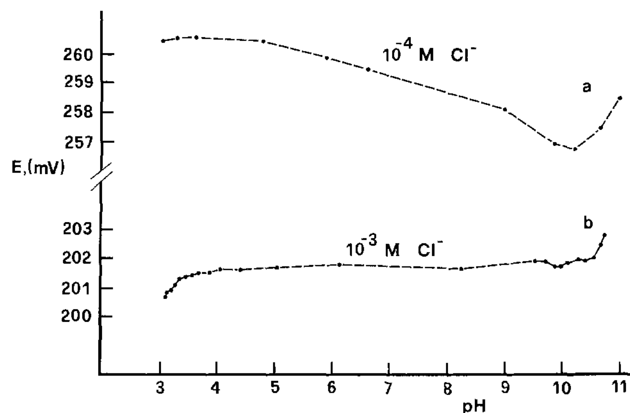

Fig. 3. Effect of pH on the potential of the silver/silver chloride electrode is NaCl solutions of various concentrations.

The electrode potential changes almost linearly with the temperature in the range 5° ÷ 40°C. Fitting experimental data with a second order polynomial yields the following equation

$$E = 184.38 + 0.876\,t - 0.00148\,t^2 \quad (E \text{ in mV}, \quad t \text{ in °C})$$

the standard deviation of experimental data around the fitted function being $\sigma = 37$V.

Conclusion

The electrodes described in this work have a number of interesting features over the conventional silver/silver halide membrane electrodes. They are rugged, yield highly reproducible results, and exhibit a very low electric resistance (0.01 Ω/cm). The ratio between the weight of silver metal and silver halide is not critical as tested when the percentage of Ag^+ in the pellet mixture ranges from 20 to 140%.

Variations of the pellet thickness (between 1 and 4 mm) do not affect the behavior of the electrode.

Moreover, this kind of electrodes has neither an inner reference aqueous solution nor a membrane. Finally, the most evident advantage is that its ion-sensitive surface, when necessary, can be easily renewed by removing the outer surface with fine emery paper.

Manuscript submitted July 25, 1977; revised manuscript received July 15, 1978.

Any discussion of this paper will appear in a Discussion Section to be published in the June 1979 JOURNAL. All discussions for the June 1979 Discussion Section should be submitted by Feb. 1, 1979.

REFERENCES

1. D. J. G. Ives and G. J. Janz, "Reference Electrodes," p. 179, Academic Press, New York and London (1961).
2. G. J. Janz and H. Taniguchi, *Chem. Rev.*, **53**, 397 (1953).
3. R. G. Bates, "Determination of pH," p. 328, John Wiley & Sons, Inc., New York (1973).
4. E. Pungor, K. Toth, and J. Havas, *J. Hung. Sci. Instr.*, **3**, 2 (1965).
5. E. Pungor, *Anal. Chem.*, **39**, 29A (1967).
6. E. Pungor and J. Havas, in "Proceedings of the Conference on Physico Chemical Methods of Analysis," p. 92. Hungarian Academy of Sciences, Budapest (1966).
7. E. Pungor, J. Havas, and K. Toth, *Acta Chim. Acad. Sci. Hung.*, **41**, 239 (1964).
8. G. A. Rechnitz, M. R. Kresz, and S. B. Zamochnick, *Anal. Chem.*, **38**, 973 (1966).
9. G. A. Rechnitz and M. R. Kresz, *ibid.*, **38**, 1786 (1966).
10. M. Mascini and A. Liberti, *Anal. Chim. Acta*, **47**,

339 (1969).
11. G. W. S. von Osch and B. Griepink, *Z. Anal. Chem.*, **273**, 271 (1975).
12. I. M. Kolthoff and H. L. Sanders, *J. Am. Chem. Soc.*, **59**, 416 (1937).
13. H. Matsushita, H. Maruyama, T. Aomi, and N. Ishikawa, *Chubu Kogyo Daygaku Kiyo*, **10A**, 117 (1974).
14. J. W. Ross, Jr., "Ion Selective Electrodes," R. A. Durst, Editor, p. 78, National Bureau of Standards, Special Publication 314, Washington D.C. (1969).
15. J. D. Czaban and G. A. Rechnitz, *Anal. Chem.*, **45**, 471 (1973).

On the Effect of Finite Rise Time of Pulse Generators on Some Relaxation Techniques for Electrode Kinetic Investigations

Z. Nagy*
Argonne National Laboratory, Chemical Engineering Division, Argonne, Illinois 60439

In previous error analyses of relaxation techniques for electrode kinetic measurements (1-5) it has always been assumed that the pulses are ideal, that is, the pulse generator has a negligibly short rise time. In practice, the rise time is often only about one order of magnitude less than the measuring time, and for short pulses the two times can even become comparable in magnitude. Equations have been derived for nonideal pulses and are presented here for the galvanostatic single- and double-pulse techniques and for the coulostatic pulse (current impulse relaxation) technique. The real pulses were approximated by pulses having a finite linear slew rate (Fig. 1) which is a good approximation for most modern pulse generators. The resulting equations are too complex to be used for simple graphical analysis of experimental data. However, they can be used for a numerical analysis of the errors resulting from the assumption of ideal pulses in the graphical data analysis. The results can be used to select the maximum rise time for an experiment or to calculate correction factors for data taken with slow pulse generators. The use of these equations is also recommended for the evaluation of kinetic parameters by computer curve fitting, which is more reliable than the graphical techniques (5, 6). In this case, the complexity of equations is not a problem and, as will be shown below, considerable errors can result if the idealized equations are used to evaluate experimental data with pulses having finite rise times.

The derivation follows the same general outline as those of Delahay *et al.* (7, 8), with two exceptions. The current pulse shapes of Fig. 1 are used, and the equations are made more general by removing a restriction of the original derivation (7), namely, that the number of electrons involved in the rate-determining step must be equal to the number of electrons transferred in the over-all reaction. The current-time relation of the pulse shown in Fig. 1b can be written as

$$i = \begin{cases} i_1 t/t_1 & ; \quad t < t_1 \\ i_1 & ; \quad t_1 < t < t_2 \\ i_1 - (i_1 - i_2)(t - t_2)/(t_3 - t_2); & \quad t_2 < t < t_3 \\ i_2 & ; \quad t_3 < t \end{cases} \quad [1]$$

and the Laplace transform of the current is [see, for example, Ref. (9)]

$$\tilde{i}(s) = \frac{i_1[1 - \exp(-st_1)]}{s^2 t_1} - \frac{(i_1 - i_2)[\exp(-st_2) - \exp(-st_3)]}{s^2(t_3 - t_2)} \quad [2]$$

The generalized overpotential-current relation can be obtained, for an over-all reaction of $O + ne = R$, by taking the diffusion overpotential from the Nernst equation

$$\eta_d = \frac{RT}{n\mathbf{F}} \ln \left[\frac{C^s_O}{C_O} \cdot \frac{C_R}{C^s_R} \right] \quad [3]$$

and the activation overpotential from the multistep version of the Butler-Volmer equation (see, for example, Ref. (10, 11)

$$i = i_o[\exp(\alpha_a \mathbf{F} \eta_a / RT) - \exp(-\alpha_c \mathbf{F} \eta_a / RT)] \quad [4]$$

with

$$\alpha_a + \alpha_c = n/\nu$$

At low overpotentials, when

$$\eta_a < \frac{RT}{\mathbf{F}} \text{ and } \frac{C^s_O}{C_O} \approx \frac{C_R}{C^s_R} \approx 1$$

these equations can be expanded to give the total

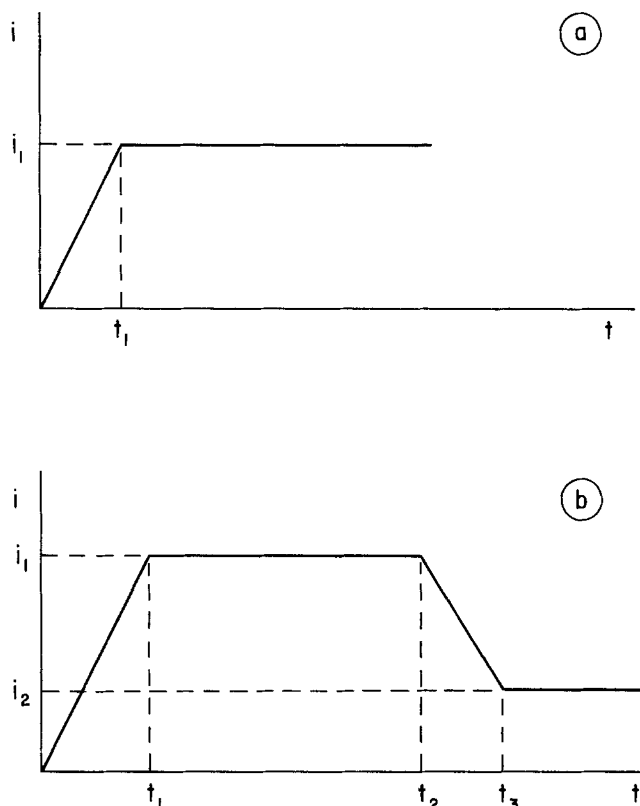

Fig. 1. Current pulse shapes: a, single pulse; b, double pulse (coulostatic with $i_2 = 0$).

* Electrochemical Society Active Member.
Key words: chronopotentiometry, kinetics, overvoltage, transients.

overpotential

$$\eta = \frac{\nu RTi}{nFi_o} + \frac{RT}{nF}\left[\frac{C^s_O}{C_O} - \frac{C^s_R}{C_R}\right] \quad [5]$$

The overpotential-time relation is then derived by solving Fick's equation for linear diffusion for the appropriate initial and boundary conditions (7, 8). Equation [6] is the final result. The same relation for idealized pulses is given in Eq. [7] for comparison

$$\eta = \frac{i_1}{ct_1}[G_2(t) - G_2(t-t_1)] - \frac{i_1 - i_2}{c(t_3 - t_2)}[G_2(t-t_2) - G_2(t-t_3)] \quad [6]$$

$$\eta = \frac{i_1}{c(b-a)}\left[\frac{b}{a^2}G_1(a,t) - \frac{a}{b^2}G_1(b,t)\right] - \frac{i_1 - i_2}{c(b-a)}\left[\frac{b}{a^2}G_1(a,t-t_3) - \frac{a}{b^2}G_1(b,t-t_3)\right] \quad [7]$$

where

$$G_2(y) = \frac{b}{a^4(b-a)}G_1(a,y) - \frac{a}{b^4(b-a)}G_1(b,y) + \frac{ab-(a+b)^2}{(ab)^2}y + \frac{4(a+b)}{3\sqrt{\pi}\,ab}y^{3/2}$$

$$G_1(x,y) = \exp(x^2y)\,\mathrm{erfc}(xy^{1/2}) + 2x(y/\pi)^{1/2} - 1$$

$$a = \frac{i_o}{2\nu nF}\left(\frac{1}{D^{1/2}_O C_O} + \frac{1}{D^{1/2}_R C_R}\right) + \left[\frac{i_o^2}{4\nu^2 n^2 F^2}\left(\frac{1}{D^{1/2}_O C_O} + \frac{1}{D^{1/2}_R C_R}\right)^2 - \frac{nFi_o}{\nu RTc}\right]^{1/2}$$

and "b" is the same as "a" except the expression in brackets is preceded by a minus sign.

Equation [7] differs from the original equation of Matsuda, Oka, and Delahay (8) by the sign convention of the current and by the appearance of the stoichiometric number (ν) in the expressions for "a" and "b." The equations are written for the galvanostatic double pulse technique; the relations for coulostatic pulse can be obtained by setting $i_2 = 0$ (in either case the equations are valid for times $t \geq t_3$). For galvanostatic single pulse measurements, the second term of the equations should be neglected and Eq. [6] is valid for times $t \geq t_1$.

The errors resulting from assuming ideal pulses in the graphical analyses of experimental data taken with real pulses were estimated as follows. Overpotential time data were generated with Eq. [6] and [7] for a series of typical values of the kinetic and double layer parameters and these "data" were then evaluated with the usual graphical techniques. It was found that the ratio of the overpotentials could be estimated by the ratio of the charge passed

$$\frac{\eta_{real}}{\eta_{ideal}} \approx \frac{Q_{real}}{Q_{ideal}} \quad [8]$$

when

$$i_c >> i_f \quad [9]$$

The approximation is good when the ratio of the sum of reaction and diffusion impedances to the double layer impedance is large, that is, at short times (usually a few microseconds). At longer times, the error is overestimated but Eq. [8] still can be used as an order-of-magnitude estimate. A brief analysis for the three relaxation techniques is given in the following.

Galvanostatic Single Pulse

The error in the overpotential will be negligible even for slow pulse generators since the graphical evaluation (7) uses data taken at long times ($\approx$50 μsec), and in this case the charge ratio of Eq. [8] is close to unity. The error in the exchange current density will then depend on the error in the double layer capacity measurement. A serious error can be made in the double layer capacity measurement and, consequently, in the calculation of the exchange current density, if it is determined from the slope of the overpotential-time curves at times $t < t_1$, using the steady current value of i_1. Rather, the capacity should be calculated using the current value at the time of the slope measurement, that is $c = i(t)/(d\eta/dt)_t$. It is assumed, of course, that condition [9] is fulfilled.

Galvanostatic Double Pulse

A heretofore unrecognized advantage of this method was found, namely, that the error in overpotential is nearly completely eliminated by the experimental adjustment of the prepulse to give $d\eta/dt = 0$ at the measuring time [independently of whether the measuring time was taken to be the end of the prepulse or at some later time, as has been recently proposed (12)]. The experimental fulfillment of the above condition assures the correct charging of the double layer capacitance independently of the shape of the prepulse, even at the extreme case when the rise and fall of the prepulse overlap. A correct exchange current density will therefore be obtained, even for real pulses, using the graphical data-evaluation technique of Matsuda, Oka, and Delahay (8). On the other hand, the double layer capacity calculated by the formula of Matsuda (13, 14) will be in error, but can be corrected using the following equation

$$\frac{c_{real}}{c_{ideal}} \approx \frac{Q_{ideal}}{Q_{real}} \quad [10]$$

Current Impulse Relaxation (Coulostatic Pulse)

A considerable error can be expected in the overpotential, since generally very short pulses are used in this method and the charge ratio of Eq. [8] will be far from unity. By application of the usual graphical data-evaluation technique (15), the double layer capacity and the exchange current density will also have the same relative error. For slow reactions (when condition [9] is strictly fulfilled) the results can be corrected by using Eq. [8]. This is, of course, equivalent to the original procedure suggested by Delahay (16). For faster reactions, especially when diffusional effects are not negligible, Eq. [6] should be used in the curvefitting programs (5, 6).

In summary, it has been shown that the neglect of the finite rise time of pulse generators can cause significant errors in the determination of the double layer capacity and the exchange current density of fast electrode systems. The only exception is the galvanostatic double pulse technique which will give the correct exchange current density even with slow pulse generators. Equations are given for computer evaluation of data taking into account the finite rise times of the measuring pulses.

Acknowledgments

This work was performed under the auspices of the Materials Science Office, Division of Basic Energy Sciences, U.S. Department of Energy.

Manuscript submitted April 28, 1978; revised manuscript received July 20, 1978.

Any discussion of this paper will appear in a Discussion Section to be published in the June 1979 JOURNAL. All discussions for the June 1979 Discussion Section should be submitted by Feb. 1, 1979.

Publication costs of this article were assisted by Argonne National Laboratory.

LIST OF SYMBOLS

- c — capacity of the double layer (F cm^{-2})
- C_j — concentration of species j in the bulk solution (mole cm^{-3})
- $C^s{}_j$ — concentration of species j at the electrode surface (mole cm^{-3})
- D — diffusion coefficient (cm^2 sec^{-1})
- F — Faraday constant
- i — current density (A cm^{-2})
- i_o — exchange current density (A cm^{-2})
- i_c — current density used to charge the double layer (A cm^{-2})
- i_f — Faradaic current density (A cm^{-2})
- $\tilde{i}$ — Laplace transform of current density
- n — total number of electrons transferred in the over-all reaction
- Q — charge passed (C cm^{-2})
- R — universal gas constant
- s — Laplace variable
- t — time (sec)
- T — absolute temperature (°K)
- α_a — anodic transfer coefficient
- α_c — cathodic transfer coefficient
- η — overpotential (V)
- ν — stoichiometric number of the reaction

REFERENCES

1. D. Inman, J. O'M. Bockris, and E. Blomgren, *J. Electroanal. Chem. Interfacial Electrochem.*, **2**, 506 (1961).
2. D. J. Kooijman, M. Sluyters-Rehbach, and J. H. Sluyters, *Electrochim. Acta*, **11**, 1197 (1966).
3. D. J. Kooijman and J. H. Sluyters, *ibid.*, **12**, 693 (1967).
4. D. J. Kooijman and J. H. Sluyters, *J. Electroanal. Chem. Interfacial Electrochem.*, **13**, 152 (1967).
5. J. M. Kudirka, P. H. Daum, and C. G. Enke, *Anal. Chem.*, **44**, 309 (1972).
6. R. F. Martin and D. G. Davis, in "Computers in Chemistry and Instrumentation," Vol. 2, Chap. 4, J. S. Mattson, H. B. Mark, and H. C. MacDonald, Editors, Marcel Dekker Inc., New York (1972).
7. T. Berzins and P. Delahay, *J. Am. Chem. Soc.*, **77**, 6448 (1955).
8. H. Matsuda, S. Oka, and P. Delahay, *J. Am. Chem. Soc.*, **81**, 5077 (1959).
9. G. Fodor, "Laplace Transforms in Engineering," pp. 158, 708, Akademiai Kiado, Budapest (1965).
10. J. O'M. Bockris and A. K. N. Reddy, "Modern Electrochemistry," Vol. II., Chap. 9, Plenum Press, New York (1970).
11. J. O'M. Bockris and Z. Nagy, *J. Chem. Ed.*, **50**, 839 (1973) and **51**, 803 (1974).
12. Z. Nagy, Abstract 544, p. 1358, The Electrochemical Society Extended Abstracts, Spring Meeting, Seattle, Washington, May 21-26, 1978.
13. H. Matsuda, Doctoral Dissertation, Tokyo University, Tokyo (1962).
14. T. Rohko, M. Kogoma, and S. Aoyagui, *J. Electroanal. Chem. Interfacial Electrochem.*, **38**, 45 (1972).
15. W. D. Weir and C. G. Enke, *J. Phys. Chem.*, **71**, 275 (1967).
16. P. Delahay, *ibid.*, **66**, 2204 (1962).

JOURNAL OF THE ELECTROCHEMICAL SOCIETY

SOLID-STATE SCIENCE
AND TECHNOLOGY

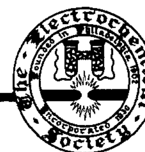

NOVEMBER
1978

Tantalum Ion Transport Number during the Anodic Oxidation of Beta-Tantalum Films

N. Schwartz*[,1] and W. M. Augustyniak

Bell Laboratories, Incorporated, Murray Hill, New Jersey 07974

ABSTRACT

In this study Rutherford backscattering has been used to determine the tantalum ion transport number during the anodic oxidation of beta-tantalum films. The required marker is the argon uniformly incorporated in tantalum during sputtering. The transport number for Ta^{+n} ions for beta-tantalum anodic oxidation is 0.25 ± 0.02 at 1 mA/cm² and 23.5°C, and there is a weak dependence on the electric field used during the oxide growth. These results are identical to that obtained for bulk alpha-(bcc)-tantalum, which may indicate that the transport number is not controlled by the crystal structure associated with the metal-oxide interface. For metal films which are anodized completely through to the substrate, there is an apparent 1% tantalum excess in the outer portion of the oxide. This effect may be associated with the argon incorporation in the oxide, or a nonequilibrium ratio of Ta/O, or a low atomic weight impurity.

Since the beginning of the utilization of anodic oxide films for electronic devices and decorative coatings (1), there has been a great interest in the unique mechanism which allows growth rates at room temperature in the range of 0.5 nm/sec up to several micrometers in thickness. The basic chemical process is the reaction of two chemical entities, the original metal and oxygen from the electrolyte, which are separated by an intervening solid film. In order for this to occur, species must be transported at very rapid rates (for a room temperature process) through the intervening film. The driving force for such rapid transport is the high electrical field utilized, which is in the range of 10^4 to 10^5 V/m. The transport is assumed to be due to charged ions through the oxide (1). In all studies of the mechanism of growth of anodic Ta_2O_5 before 1965, it was either implicitly assumed or partially demonstrated that the transported entity was the tantalum ion. This appeared theoretically satisfying because the ionic radius of the Ta^{+5} ion is considerably smaller than the O^{-2} ion, and its charge is considerably higher. Both of these properties should lead to faster transport of the metal cation. In 1965, Davies *et al.* (2) demonstrated that both ions generally participated in the transport, and the fraction of the transport attributable to the cation was generally much smaller than that associated with the anion.

Despite the expectation that the knowledge of the nature of the particular ion involved in the growth should have had a large impact on the understanding of the mechanism of growth, little further progress had been made on theoretical models for the process. Studies on tantalum, which has had a central role in the development of models because of the number of experiments associated with it, have shown it (3) to have a cation transport number of 0.243. This number is associated with growth of the oxide on bulk alpha-(bcc)-tantalum. Some studies have shown that the kinetics of oxide growth (4, 5) are slightly different for beta-tantalum (6) films compared to bulk alpha-tantalum; this has been ascribed to a variable amount of interstitial oxygen and nitrogen (5). What has not been considered is whether the transport number of the tantalum ion is different due to the change of crystal structure or the change from bulk to film material. In earlier studies on the composition of oxide films formed on Ta_xN_y (7), and either Ta_xSi_{1-x} (8) or Ta_xTi_{1-x} (9) alloy films, it was assumed that the transport number of oxide films grown on beta-tantalum was the same as alpha-tantalum. The latter two studies (8, 9) involved Rutherford backscattering (10, 11) which allows for a convenient method of determining this number without resorting to radioactive isotopes, chemical sectioning, or sputtering. This technique can easily detect the approximately 4 atom percent (a/o) argon (8, 12) incorporated uniformly in the beta-tantalum film during the sputtering process. The argon at the surface of the metal acts as the inert marker, and the position of this edge lies within the oxide film after growth. The relative position of this edge in the oxide allows the calculation of the cation transport number. The Rutherford backscattering method has been used for this purpose by MacIntosh (13) but utilizing implanted argon in bulk vanadium. This paper concerns the use of Rutherford backscattering technique to detect the position of the incorporated nonradioactive argon in anodized beta-tantalum films.

Experimental

The preparation of the beta-tantalum films, the Rutherford backscattering technique, and the general methods of analysis have been described in earlier papers (8-11). This study on beta-tantalum films differs from the earlier study (8) in that the conditions were optimized to yield a more accurate evalua-

* Electrochemical Society Active Member.
[1] Temporary address: Pacific Telephone and Telegraph, San Francisco, California 94105.

tion of the argon and tantalum spectra. The thickness of the tantalum films on fused quartz was limited to about 75 nm, so that even when the film was completely anodized, the oxide spectrum did not overlap the background silicon and oxygen spectra from the fused quartz substrate. Secondly, the 1.9 MeV $^4He^+$ bombarding time was increased such that the height of the Ta spectrum ($\sim 4.5 \times 10^5$ counts) was about five times higher than previous, while the argon counts ($\sim$1500 counts) were increased from 1.3 to 3 times background.

Three different anodizing techniques were used because the films were relatively thin and slight differences in determining the energy of the leading or back edge of the argon spectrum causes relatively large errors. Due to the energy resolution of the backscattered ion solid-state detector ($\sim$15 keV), there is some ambiguity in determining these energies; these can be quite accurately determined, however, by using the half-height energy for each edge. Some samples were anodized about half-way through at constant current to about 60V; one sample was anodized at constant current to 60V, and when the power supply was switched to constant voltage of 60V, the current decayed to a low value. Most of the samples, however, were anodized completely through at constant current to about 120V, at which time the voltage rose abruptly to a preset maximum value in the range of 130-300V as all of the tantalum was consumed. This anodization method is preferred because the determination of the transition of argon in the oxide to argon in the remaining metal film in the backscattered spectrum did not cause any difficulty. The result of the complete anodization was a transparent Ta_2O_5 film, which only in a few cases had a faint haze of isolated Ta spots; these, however, could not be detected in the backscattered spectrum. For all of the anodizations, the counterelectrode for measuring the voltage was a Pt wire placed within 3 mm of the oxide surface. The electrolyte was 0.01% aqueous citric acid; during the constant current anodization, the voltage difference between the anode and platinum wire was continuously recorded.

Results

Transport numbers.—Figure 1 shows the overlapped Rutherford backscattering spectra of a typical tantalum metal film and the same film anodized completely through. The peaks on the right are for the tantalum atoms in the metal and oxide. Since tantalum atoms are present at the surface in both films, the channel equivalent to the half-heights are identical on the leading edge (higher channels), while the channel half-heights differ on the lower channel side because the thickness of the two films are different. The lower height of the Ta/Ta_2O_5 peak[2] is due to the decreased tantalum atom density compared to the metal film.

The much smaller peaks in the 260-320 channel region are due to the argon in both films; the edges shown below 265 channels are to Si/SiO_2, O/SiO_2, and O/Ta_2O_5. The 308 channel position of the half-height for the Ar/Ta peak is that calculated for Ar at the surface of any film. The half-height position of the Ar/Ta_2O_5 at channel 298.5 indicates that the Ar is below the surface of the oxide. The thickness of the oxide where the argon is absent can be calculated from the shift of the leading edges in both samples, while the thickness of the oxide where the Ar is present can be calculated from the width of the Ar/Ta_2O_5 peak. The sum of the two gives the thickness of the complete oxide. The thickness of the complete oxide can be calculated as well from the width of the Ta/Ta_2O_5 peak.

The exact thickness of any film can be determined from the width of the peak by Eq. [1]-[3]

$$\Delta d = d_s/\rho = \Delta E/S\rho = (\Delta C)(E_c)/S\rho \quad [1]$$

Where

$$S = K_m \left(\frac{dE}{dx}\right)^{in} + \left(\frac{1}{|\cos\theta|}\right)\left(\frac{dE}{dx}\right)^{out} \quad [2]$$

and

$$(dE/dx) = \Sigma w_i (dE/dx)_i \quad [3]$$

where Δd is the thickness; ρ is the known density of the film material; d_s is the surface density in mass/unit area; ΔC is the difference in channels for the half-heights of the leading and trailing edges; E_c is the energy/channel of the detection system ($\sim$4 keV per channel); S is the scattering function where K_m is the kinematic factor; $(dE/dX)^{in}$ is the stopping power at the energy of the entering ion; θ is the angle between the entering ion beam and the detected backscattered beam (*i.e.*, 175°); and $(dE/dx)^{out}$ is the stopping power at the energy of the exiting beam. For mixtures or compounds, dE/dX can be calculated by Bragg's rule (Eq. [3]) where w_i is the weight percent of the particular component and $(dE/dX)_i$ is the stopping power for that component at a given energy.

The transport number of the Ta^{+n} ion, t_m^+, can be calculated from

$$t_m^+ = \frac{d^{Ar}{}_{Ta_2O_5}}{d^{Ar}{}_{Ar/Ta_2O_5} + d^{Ar}{}_{Ta_2O_5}} \quad [4]$$

when d_y^x is the thickness of an oxide film, where x

[2] The terminology Ta/Ta_2O_5 means that the backscattering is from Ta in Ta_2O_5.

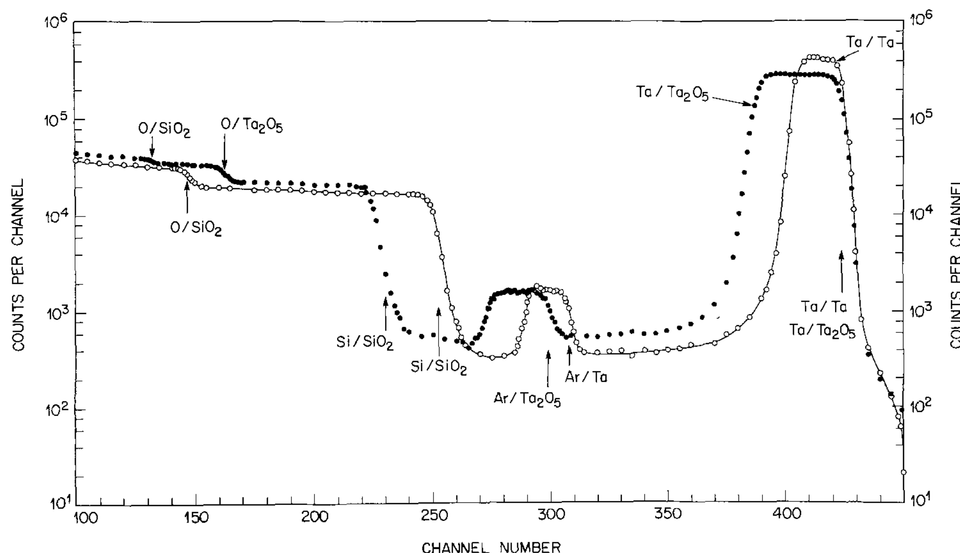

Fig. 1. Typical backscattering spectrum of sputtered beta-tantalum film (Ta) on a fused silica substrate, and an overlapped spectrum of the same film completely anodized to tantalum oxide (Ta_2O_5). The detector sensitivity is about 4×10^{-3} MeV/channel. The vertical arrows show the position of the leading half-heights for the various species (Ar or Ta) in either the Ta or Ta_2O_5 film.

means the thickness is determined from either an argon or tantalum backscattering peak, while y represents either the argon region (*i.e.*, Ar/Ta_2O_5) or argon-free region (*i.e.*, Ta_2O_5) of the oxide film.

This analysis implicitly assumes that the argon acts as a true atomic marker, which has been demonstrated by Pringle for implanted argon (3).

Equation [4] can be transformed by using Eq. [1]

$$t_m{}^+ = \frac{\Delta C^{Ar}{}_{Ta_2O_5} E_c{}^{Ar}}{S^{Ar}{}_{Ta_2O_5}\rho_{Ta_2O_5}} \Bigg/ \left[\frac{\Delta C^{Ar}{}_{Ar/Ta_2O_5} E_c{}^{Ar}}{S^{Ar}{}_{Ar/Ta_2O_5}\rho_{Ar/Ta_2O_5}} + \frac{\Delta C^{Ar}{}_{Ta_2O_5} E_c{}^{Ar}}{S^{Ar}{}_{Ta_2O_5}\rho_{Ta_2O_5}} \right] \quad [5a]$$

$$t_m{}^+ \cong \Delta C^{Ar}{}_{Ar/Ta_2O_5} / [\Delta C^{Ar}{}_{Ar/Ta_2O_5} + \Delta C^{Ar}{}_{Ta_2O_5}] \quad [5b]$$

where

$$\Delta C^{Ar}{}_{Ta_2O_5} = C_{Ta}{}^{Ar} - C^{Ar}{}_{Ta_2O_5} \quad [5c]$$

and

$$\Delta C^{Ar}{}_{Ar/Ta_2O_5} = C^{Ar}{}_{Ar/Ta_2O_5} - C^{Ar'}{}_{Ar/Ta_2O_5} \quad [5d]$$

and ($C_y{}^x$) is the half-height channel of the leading edge and $C_y{}^{x'}$ is the half-height channel of the rear edge of the appropriate peak.

In Eq. [5a], the $E_c{}^{Ar}$ cancel, and the differences in the scattering function $S_y{}^x$, and densities, ρ_y, are so slight that they cancel also. Calculations using both Eq. [5a] and [5b] give transport numbers which differ by 0.9%, while the experimental error, mainly due to the ±0.5 channel-width uncertainty in a 8.5 channel-width thickness of the argon-free Ta_2O_5 region, is ±8%. A schematic figure of the overlapped backscattered spectra from tantalum and completely anodized tantalum oxide is shown in Fig. 2. This figure shows three different possible results: anion transport only,

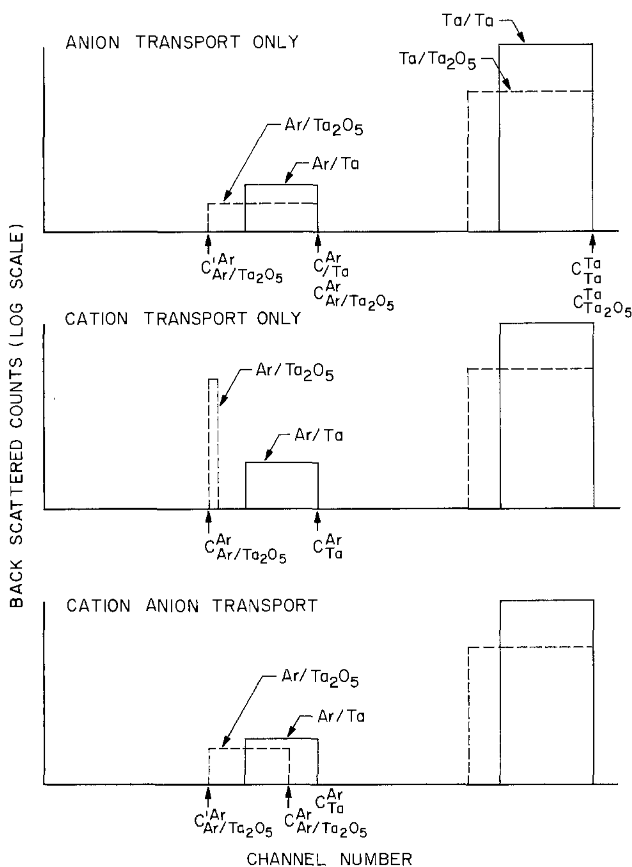

Fig. 2. Schematic backscattered spectra for the three different transport mechanisms. The solid and dashed line peaks on the right are for backscattering from tantalum atoms in the metal and oxide, respectively. The peaks in the left are for backscattering from argon atoms in Ta or Ta_2O_5.

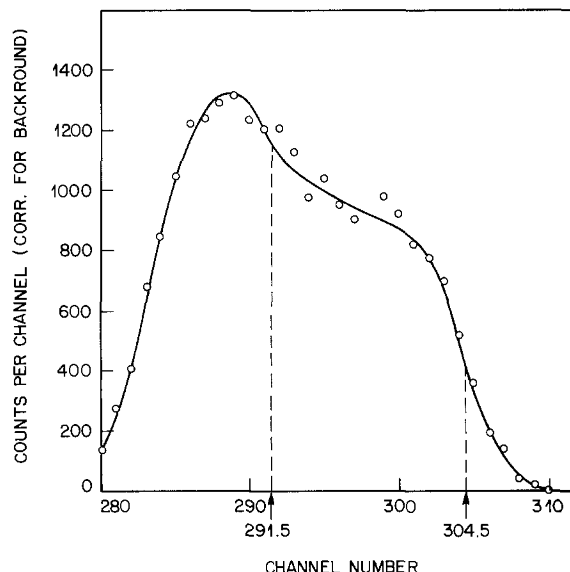

Fig. 3. Backscattered spectrum for argon in a sample which was anodized half-way through. The region from 280-292 channels is for the remaining tantalum film, while the region from 292-305 channels is for the formed oxide film. Counts corrected for background.

cation transport only, and simultaneous cation-anion transport. For the three cases, the width of the total oxide based on the argon spectrum only is: upper, the observed width of the Ar/Ta_2O_5 peak; middle, the difference, $C_{Ta}{}^{Ar} - C^{Ar}{}_{Ar/Ta_2O_5}$; and bottom, the difference, $C_{Ta}{}^{Ar} - C^{Ar'}{}_{Ar/Ta_2O_5}$. The widths of the argon-free region at the oxiae for the three cases in Fig. 2 are: top, nonexistent; middle, the difference, $C_{Ta}{}^{Ar} - C^{Ar}{}_{Ar/Ta_2O_5}$; and bottom, the difference, $C_{Ta}{}^{Ar} - C^{Ar}{}_{Ar/Ta_2O_5}$.

The basic experimental data for the calculation of transport numbers for samples anodized half-way through to only 60V is shown in Fig. 3. The open dots are the argon counts corrected for background. The high peak at channel 289 is due to the argon in the remaining tantalum film, while the lower counts above channel 290 are for argon in the oxide. The half-height channel of 304.5 at the leading edge is shifted down from the original metal film value of 308.5. The half-height channel number of the oxide at the trailing edge can be determined as was done previously (9) as equal to the point at half the value of the maximum at the tantalum metal minus the value of that of the oxide. This leads to a value of 291.5 as indicated by the left-hand dashed vertical line in Fig. 2. The decision about the value at channel 291.5 is slightly uncertain, so as indicated earlier most of the results are based primarily on samples anodized all the way through.

Table I gives the characteristics of the anodized samples, and the transport numbers obtained. Sample number 1 was analyzed in both backscattering runs

Table I. Cation transport number as a function or the type of anodization

Sample No.	Backscattering run	Anodization type: Completely ~120V	Anodization type: Partially ~60V	Anodization mode constant: $I + V$	Anodization mode constant: I	t_{m^+} transport number
1	1	√			√	0 25 ± 0.02
2	2	√			√	0.26 ± 0.02
1	3	√			√	0.25 ± 0.02
3	2		√	√		0.25 ± 0.02
4	3		√		√	0.24 ± 0.04

* All anodizations performed at 1 mA/cm² and 23.5°C.

1 and 3, and the calculated transport numbers are identical. Sample 2 is an anodized replicate of sample 3, and the results of the first three samples give a transport number of 0.25 ± 0.02. Sample 4 gives results of lower accuracy because the oxide film was much thinner. The results for samples 3 and 4 agree with the more accurate values obtained for samples 1 and 2. All of the transport numbers are in the range of 0.25 ± 0.02. This agreement indicates that during the constant voltage-soak during anodization, when approximately 25% of the oxide is grown, the transport number is the same as that obtained at constant current. During the constant voltage phase, the current density and field are dropping rapidly, which indicates that the transport of Ta^{+n} is not a strong function of current density or field.

In order to verify this last conclusion, samples were anodized all the way through for current densities which range from 10 to 0.01 mA/cm², where the exposed film area was of the order of 1 cm². Samples anodized at the low current densities had total currents of only about 50 μA; an appreciable electronic leakage current existed, however, which moreover increased as the anodization voltage increased. For these latter samples (*i.e.*, for all current densities below 0.1 mA/cm²), the current density was manually increased to maintain a relatively constant dV/dt on the recorder chart. The actual ionic current density was then calculated from the dV/dt for the given anodization compared to dV/dt for the 0.1, 1, and 5 mA/cm² anodizations, which did not have an appreciable electronic leakage. Films were also anodized at 10 mA/cm², but these resulted in a nonuniform anodic oxide color, presumably due to a nonuniform temperature rise associated with the relatively massive insulating fused-silica substrate.

The transport number as a function of current density is given in Table II. The field associated with the higher current densities was obtained from the observed voltage at the end of the anodizations divided by the oxide thickness obtained from the Rutherford backscattering data. The fields at the low current densities were estimated by an extrapolation of the above data, using Mills, Zobel, and Young's data (3) on films as an extrapolation guide.

The results in Table II indicate that there is a real but weak dependence on current density or field for the cation transport number. The significance of this important result and a comparison to other results in the literature will be discussed in the following paper (14).

Uniformity of the oxide films.—A close inspection of the spectrum for the top of the Ta/Ta_2O_5 peak shown in Fig. 1 indicates a slight concave nature, rather than an expected slight linear increase due to the increased backscattering due to the E^{-2} term (10, 11). This concavity is not observed for partially anodized films or for tantalum metal films.

The raw backscattered spectrum for tantalum in tantalum oxide from Fig. 1 was converted to a distribution of Ta atoms/cm² as a function of depth thickness by making a $(1/E)^2$ correction, as well as corrections in S for the presence or absence of Ar in different portions of the film. The distributions for Ta and Ar are shown in Fig. 4, where the normal-

Table II. Cation transport number as a function of current density and field

Sample No.	Anodization current density (mA/cm²) Actual	Anodization current density (mA/cm²) Calculated (ionic)	Field (V/cm × 10⁻⁶)	Cation transport No.
5	5	5.0	7.02	0.236
6	1	1.0	6.65	0.234
7	0.1	0.1	6.16	0.208
8	0.07	0.037 ± 0.015	5.95	0.207
9	0.01	0.011 ± 0.006	5.72	0.183

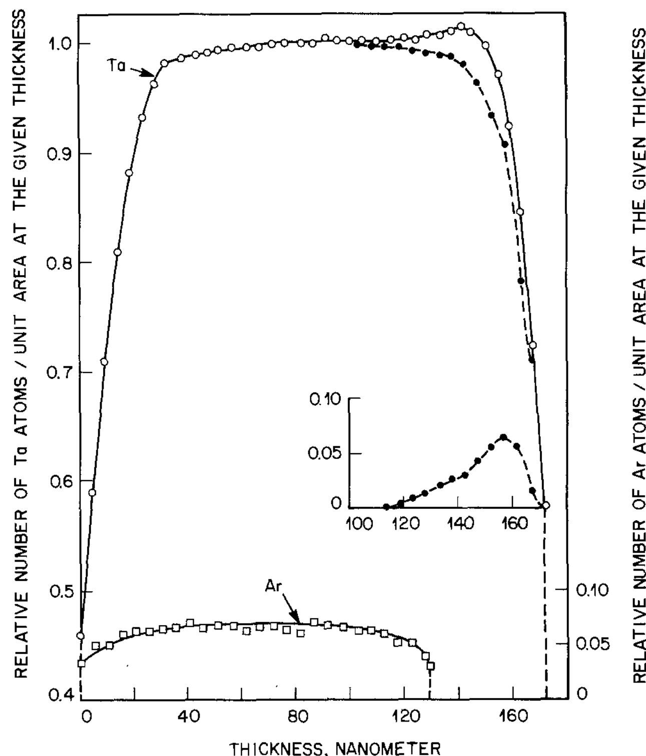

Fig. 4. Corrected tantalum (open circles) and argon (open squares) atoms/unit area as a function of oxide thickness (zero thickness is the substrate/oxide interface). These are corrected from the spectrum in Fig. 1. The upper closed circles are assumed idealized shape of the leading edge based on the corrected shaped of trailing edge. The insert is the difference, and the total "excess tantalum" is calculated from the ratio of the area under the curve in the insert to the area under the curve for the tantalum.

ization factor is the mean of the corrected counts in the region between 62 and 100 nm. The atom ratio of Ta:O:Ar for the entire film is 1/2.65/0.46, but has values of 1/2.65/0.59 for the portion of the film containing Ar, and 1/2.64/0.0 for the portion of the film containing no Ar. The Ta:O ratio is uniform to within the experimental uncertainty of ±5% in the argon-containing and argon-free portions of the film. As Fig. 4 indicates, however, the Ta atom/cm² is greater at the front[3] than at the rear portion by about 1%. The region of higher atom density is almost, but not quite, correlated with the region of the film which is argon free. This sort of deviation does not exist for the original Ta metal film as illustrated in Fig. 5, where the Ta atom density distribution is symmetrical about the middle of the film. The Ta:Ar ratio for this film is 1/0.47, identical to the ratio for the entire anodized film. The deviation for the completely anodized film is typical only for such films, since it does not exist for the partially anodized films. This is illustrated in Fig. 6, where the Ta atom distribution for sample 4 is uniform at the outer edge.

In order to obtain a semiquantitive estimate of the degree of deviation, the front part of the oxide film shown in Fig. 4 was fitted with an expected normal curve based on the shape of the curve at the rear portion of the film. This fitted curve is shown as the dashed curve, and the difference between the real and fitted curves is shown as the insert in the middle of the figure. These extra atoms, if calculated as Ta atoms, are equivalent to a 0.96% total deviation.

This "excess tantalum"[4] feature is not time dependent, since repeat backscattering analyses over a pe-

[3] The "front" edge is the oxide-electrolyte interface, while the "back" edge is the substrate-oxide interface; the "back" edge starts at zero thickness.

[4] The term "excess tantalum" is used for convenience. It could also be a "deficient tantalum" at the rear portion of the film.

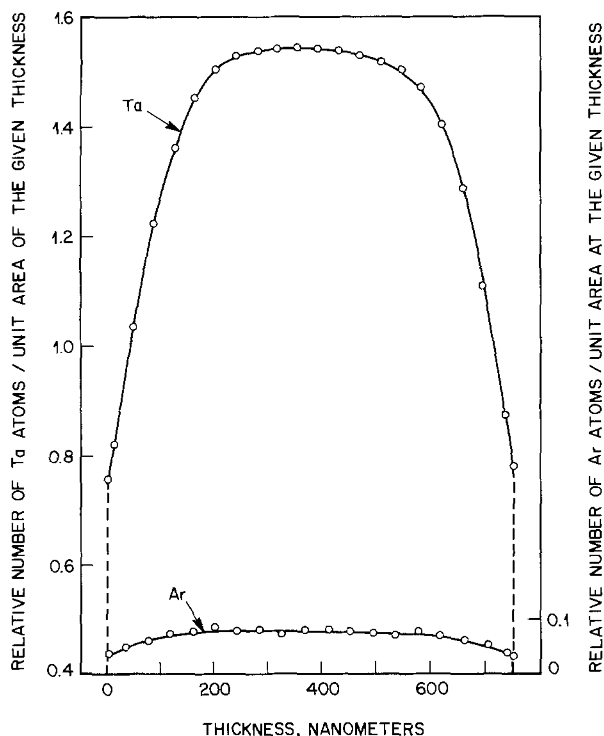

Fig. 5. Corrected tantalum and argon atoms/unit area as a function of metal thickness taken from the raw spectra of Fig. 1. The normalization is with respect to the same normalization of tantalum in tantalum oxide in Fig. 3.

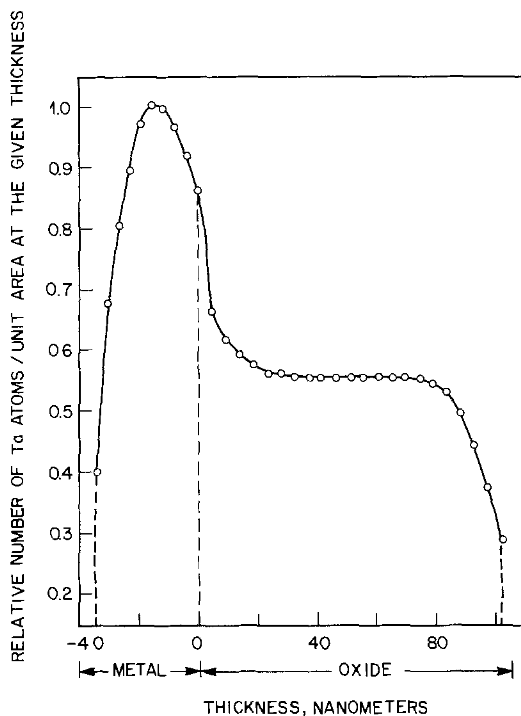

Fig. 6. Corrected tantalum atom/unit area as a function of thickness for a sample anodized partially through. The zero thickness point is taken as the metal-oxide interface, and the normalization was taken as the maximum tantalum atom density in the metal film.

riod of months showed no significant change in the spectrum. Auger analysis, with and without sputtering, showed no presence of tungsten or rhenium at the outer surface of the oxide.

To determine some parameters associated with the appearance of this "excess Ta," the samples prepared at different current densities, and samples prepared at the same current density but with different final voltage overshoots were analyzed, and the results expressed as "excess Ta," determined similar to the insert of Fig. 4. These results are summarized in Table III. No large dependence appears, but the effect appears to diminish to some extent at the higher current densities.

Table III. Dependence of "excess Ta" on current density and overvoltage, 23.5°C

Ionic current density (mA/cm^2)	Over voltage (V)	"Excess Ta" (%)
5	212	0.48
1	212	0.9
0.1	212	1.19
0.036	212	1.41
0.011	212	1.43
1	302	1.74
1	212	0.76
1	130	1.04

Discussion

The transport number for Ta^{+n} obtained for the completely anodized samples of 0.25 ± 0.02 at 1 mA/cm^2 and 23.3°C is in agreement with the results of Pringle (3) who obtained a value of 0.243 for the anodization of bulk alpha-(bcc)-tantalum. In this study, however, the original metal source is beta-tantalum which has a completely different crystal structure (6) from the bulk material. Proposals for the oxide growth mechanism are characterized as to whether they are kinetically controlled by: (*i*) metal-oxide interface; or (*ii*) oxide; or (*iii*) oxide-electrolyte interface. It has been established by Vermilyea (15) that the kinetics of oxide growth were independent of the orientation of large grain structure of bulk alpha-tantalum, and on this basis concluded that the mechanism was not oxide-metal interface controlled. Young (16) has suggested that this may not be a strong criterion because the generation of cation vacancies may cause an amorphous metal interface. Westwood (5) indicates that the growth kinetics are essentially independent of having alpha- or beta-tantalum structure. The present experiments, where a large change in crystal structure is involved, demonstrate that the cation and anion transport numbers are not controlled by the metal crystal structure.

The present results show, however, that the cation transport number has a weak positive dependency on current density or field. This is an important result which warrants detailed discussion in the subsequent paper (14).

One puzzling feature of the results is the deviation in the tantalum atom distribution in the argon-free region for the completely anodized samples. If it were due only to the difference associated with the absence or presence of argon, this feature should also be apparent in the partially anodized samples, since they have essentially the same transport number.

The effect appears to be specific to the sample preparation of converting the metal completely to oxide film. It is possible that an impurity of the order of 1% of the tantalum existed near at the substrate-metal interface or was distributed uniformly throughout the metal film. Under these circumstances, the massive spectrum of the tantalum would prevent its detection in the original metal film. If it is assumed during the anodization that the impurity has an ionic charge higher than that of Ta^{+n}, then the charge difference would provide a faster transport which would tend to concentrate the impurity at the oxide-electrolyte interface (9). The only likely components which would give such a composite spectrum are tungsten or rhenium which have melting points above tantalum and which can exist in the +6 valence state. If there is a tungsten- or rhenium-enriched oxide surface, it should have been possible to detect it with Auger spectroscopy; this experiment was per-

formed on these samples with negative results, indicating that this explanation is unlikely. Alternatively, the impurity could have a charge less than tantalum and also have an atomic mass less than tantalum. Such a small light mass impurity would have a backscattered spectrum hidden in the background and argon spectra and would be undetectable.

Another possibility is that the Ta/O ratio varies in the film, but the accuracy of the counts associated with the O/Ta_2O_5 peak is not high enough to show such small variations as a function of depth. The improved statistical accuracy associated with counting over a long period of time with respect to the tantalum peak appears to be capable of detecting such small variations. However, a Ta/O deviation would yield such nonstoichiometric films that they would be highly semiconducting and that appears not to be the case for these films.

At present, no clear explanation exists for the origin of this small nonuniformity in the tantalum atom distribution.

Summary and Conclusion

1. The transport number of Ta^{+n} ions in the growth of the anodic oxide on beta-tantalum films is 0.25 $\pm$ 0.02 at 1 mA/cm^2 and 23.2°C. This number is essentially the same as that obtained in bulk alpha-(bcc)-tantalum, which indicates that the transport number is not controlled by the crystallographic nature of the metal-oxide interface.

2. There is a weak dependence of the value of the transport number on current density or field which will be compared to other literature results and analyzed in another paper (14).

3. In metal films which are anodized completely through, there is an apparent higher tantalum atom/cm^2 at the outer portion of the oxide compared to the inner. The origin of this nonuniformity is unknown. Further experiments are required to determine the cause of this feature. However, it is important to realize that the Rutherford backscattering technique has the capability of detecting $\pm$0.5% a/o variations in some cases.

Acknowledgments

We express our appreciation to J. M. Poate who helped in the design of the backscattering experiments and in the discussion of the results, and W. Schreiber who performed the Auger analysis.

Manuscript received April 10, 1978.

Any discussion of this paper will appear in a Discussion Section to be published in the June 1979 JOURNAL. All discussions for the June 1979 Discussion Section should be submitted by Feb. 1, 1979.

Publication costs of this article were assisted by Bell Laboratories.

REFERENCES

1. L. Young, "Anodic Oxide Films," p. 13, Academic Press, New York (1961).
2. J. A. Davies, B. Domeij., J. P. S. Pringle, and F. Brown, *This Journal*, **112**, 675 (1965).
3. J. P. S. Pringle, *ibid.*, **120**, 389 (1973).
4. D. Mills, L. Young, and F. G. R. Zobel, *J. Appl. Phys.*, **37**, 1821 (1966).
5. W. D. Westwood, N. Waterhouse, and D. S. Wilcox. "Tantalum Thin Films," p. 294, Academic Press, New York (1975).
6. M. H. Read and C. Altman, *Appl. Phys. Lett.*, **7**, 51 (1965).
7. R. J. Simmons, P. T. Morzenti, D. Gerstenberg, and D. M. Smythe, *Thin Solid Films*, **23**, 75 (1974).
8. P. J. Silverman and N. Schwartz, *This Journal*, **121**, 550 (1974).
9. R. L. Ruth and N. Schwartz, *ibid.*, **123**, 1860 (1976).
10. T. M. Buck, J. M. Poate, K. A. Pickar, and C. M. Hsieh, *Surface Sci.*, **35**, 362 (1973).
11. W. K. Chu, J. W. Mayer, M. A. Nicolet, T. M. Buck, G. Amsel, and F. Eisen, *Thin Solid Films*, **17**, 1 (1973).
12. W. Guldner and R. Brown, in "Measurement Techniques for Thin Films," B. Schwartz and N. Schwartz, Editors, The Electrochemical Society, Inc., New York (1967).
13. W. D. Mackintosh and H. H. Plattner, *This Journal*, **123**, 523 (1976).
14. N. Schwartz, Submitted to *This Journal*.
15. D. A. Vermilyea, *Acta Metall.*, **103**, 690 (1956).
16. L. Young, *Can. J. Chem.*, **37**, 276 (1959).

Liquid-Phase Epitaxial Growth of Gallium-Doped Silicon

B. E. Sumner

Night Vision and Electro-Optics Laboratory, Fort Belvoir, Virginia 22060

and R. T. Foley*

The American University, Washington, D.C. 20016

ABSTRACT

A liquid-phase epitaxial technique has been used for growing layers of gallium-doped silicon on silicon. Best results were obtained from the (111) orientation and supercooling gallium melts from 600°C. The solubility of silicon in liquid gallium was determined in the growth system and showed good agreement with published data. The various growth parameters used and their effect on layer thickness, morphology, doping level, and low temperature infrared absorption are discussed. The dopant concentration in these layers was found greater than expected from the published solid solubility curves.

It is well accepted that vapor-phase epitaxy (VPE) has had a revolutionary impact on silicon device technology. It is less well known, however, that, for some applications, epitaxial growth from the liquid phase can also give excellent results. Investigations carried out in many laboratories have shown, for instance, that liquid-phase epitaxy (LPE) possesses advantages over VPE in applications demanding highly doped epitaxial films and high quality p-n junctions at the substrate-layer interface. Thus, LPE has found important applications in the growth of various III-V compound-semiconductors (1-4). Also, this technique has been used to grow low defect-density silicon layers on (111) and (100) substrates (5) as well as for growing thin silicon contact pedestals for use as ohmic contacts on planar-diffused diodes (6).

* Electrochemical Society Active Member.
Key words: silicon, liquid-phase epitaxy, growth studies, epitaxial growth, doped silicon.

With the development of charge-coupled devices in silicon, the use of doped silicon material offers an opportunity for low cost device production of monolithic infrared detector structures. Growth of doped silicon layers by LPE *vs.* VPE is quite advantageous since growth can occur at a much lower temperature making it possible to have a lower concentration of most unwanted metallic impurities.

Layers of heavily doped gallium in silicon (Si:Ga) have been needed for the fabrication of infrared detectors in the 8-14 μm spectral range. In this study, Si:Ga layers were grown on silicon by the LPE method, and their growth properties were examined. Factors which affect dopant distribution, uniformity, and growth layer morphology were investigated using secondary ion mass spectrometry (SIMS), optical microscopy, scanning electron microscopy (SEM), Auger electron spectroscopy (AES), x-ray diffraction, and infrared spectroscopy. The growth conditions found most suitable for the formation of highly doped, smooth layers were sought.

Experimental Procedure

The LPE apparatus adopted for this work was a horizontal solution-growth system similar to systems used for growth of multilayer GaAs (7). The experimental setup is shown in schematic form in Fig. 1. The graphite boat for the growth solution and the silicon substrates were mounted inside the quartz tube which was supported by stainless steel flanges. A palladium-purified hydrogen atmosphere was used for melt back-out and growth. The growth cycle involved the dissolution of silicon from the substrate by the gallium melt to solution saturation, cooling at a controlled rate for growth, and finally separation of the grown layer from the melt. The substrates were phosphorous-doped silicon (11 $\times$ 17 mm), with $n \simeq 8 \times 10^{14}$ cm^{-3} oriented to (110), (110), and (111) within 3°. Prior to growth, the substrates were chemically cleaned using a standard hydrogen peroxide method followed by a 49% hydrofluoric (HF) acid rinse to rid the surface of unwanted SiO_2. The amount of gallium used was determined from consideration of silicon-gallium solubility data, coverage area, substrate thickness, and expected dopant concentrations. In most of the growths reported in this work, 5g melts were used.

Growth Studies

A known weight of gallium was heated with a predetermined weight of silicon to various temperatures (400°-1000°C). The substrate and melt were allowed to equilibrate for several hours. The partially dissolved (etched) substrate was then pushed from the melt and the growth tube was rapidly cooled to room temperature. The silicon solubility in liquid-gallium was obtained from the difference in weight. The data obtained on the different orientations investigated [(111), (110), and (100)] were plotted and compared with the work of Keck and Broder (8). This comparison is shown in Fig. 2 and is in good agreement. The different orientations were exposed to the same growth conditions using a maximum saturation temperature of 600°C. X-ray goniometric and Laue back-reflection studies of substrates before and after layer growth report layers which were truly epitaxial with respect to the substrates. Laue back-reflection x-ray photographs of the epitaxial layers are shown in Fig. 3. The position of spots in these diagrams are indicative of orientation. Here, 3-fold, 2-fold, and 4-fold symmetry corresponded to (111), (110), and (100) orientations, respectively.

X-ray topographs of silicon surfaces of different orientations before and after growth are shown in Fig. 4. All substrate surfaces before growth were essentially featureless, whereas after growth only the (111) orientation appeared smooth and of a similar texture as the original substrate. The shadowing or line patterns in the topographs displayed here were due to improper alignment of the x-ray beam with the layer surface. Similarly, scanning electron micrographs of the same surfaces revealed different layer morphologies, as shown in Fig. 5. Oriented patterns were observed from the (100) and (110) layers while the (111) appeared essentially featureless.

The SIMS profiles of gallium in layers of different orientation are shown in Fig. 6. The (111) orientation has the highest ion count of all the layers. The (111) profile shows a high and decreasing initial gallium count near the surface, a steady increase in counts, and then a reasonable stabilization. The (110) and (100) layers show a deeper region of high initial gallium counts, a continuing decrease in counts, and then stabilization with somewhat comparable trends. The gallium profiles of the layers are strongly orientation dependent. The layers are of comparable thickness and

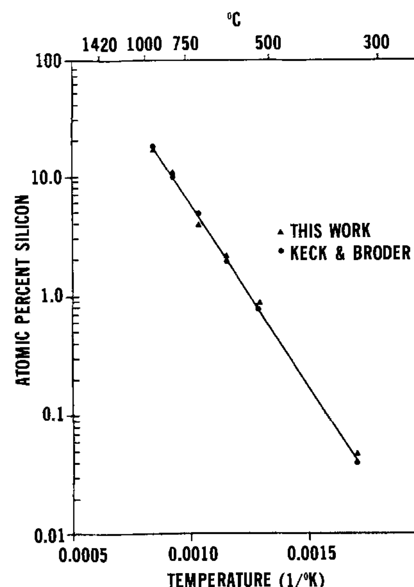

Fig. 2. Comparison of two investigations of silicon solubilities as a function of temperature in liquid gallium.

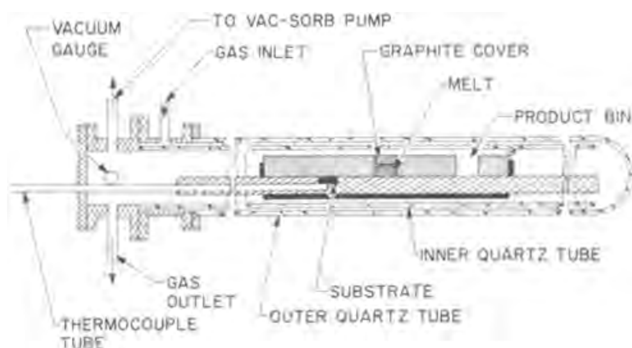

Fig. 1. Schematic of LPE growth assembly

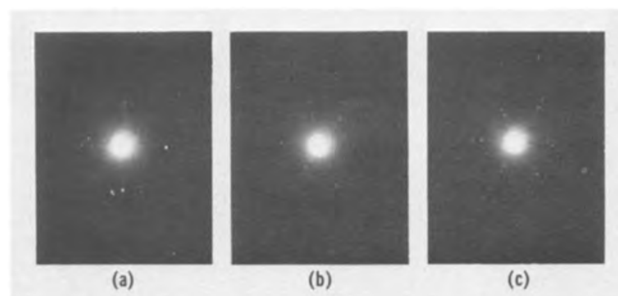

Fig. 3. Laue pattern for gallium-doped silicon on: (a) (100) silicon (4-fold symmetry); (b) (110) silicon (2-fold symmetry ; (c) (111) silicon (3-fold symmetry). Tungsten target used.

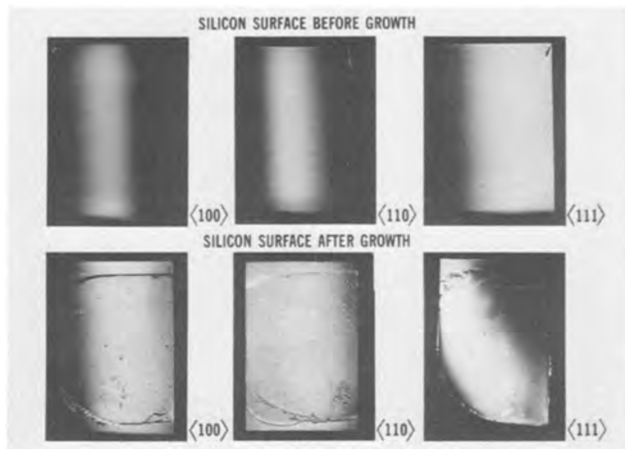

Fig. 4. X-ray topographs of silicon surfaces before and after growth.

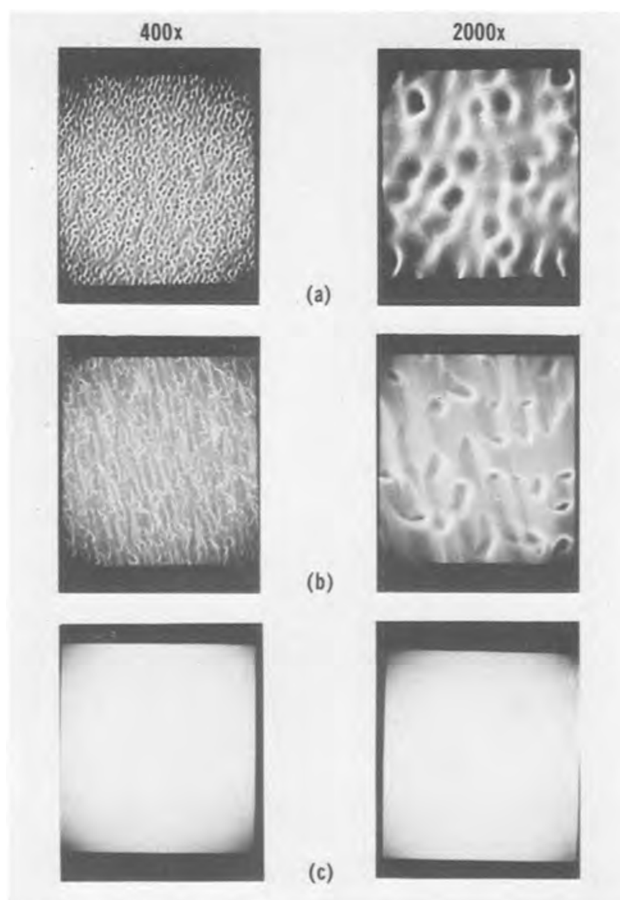

Fig. 5. Scanning electron micrographs of epitaxial layers of gallium-doped silicon from: (a) (100) silicon, (b) (110) silicon, (c) (111) silicon.

have a dependent trend in dopant concentrations toward lower values in the order (111) >> (110) > (100) after a depth of 2500Å. It has been suggested that anisotropic impurity segregation might occur in this growth process similar to that reported for germanium by Hall (9) and Dikhoff (10). The remaining studies reported in this paper were performed on (111) orientations.

The saturation temperature is defined as the temperature at which the liquid gallium is in equilibrium with solid silicon (the substrate). Layers were grown from different saturation temperatures (600°-1000°C) at a cooling rate of 15°C/min. The thickness of the layers was determined by an angle-lap and stain technique. The relationship between an average growth rate dependence of the layers with respect to the saturation temperature is shown in Fig. 7. The average growth rates were found, as expected, to increase with increasing saturation temperatures because the silicon concentration in the melt increases. Also, optical microscopic examination of the surfaces, as displayed in Fig. 8, shows increasing surface waviness and undulations with increasing saturation temperatures. It was further observed that layers grown from saturation temperatures greater than 750°C had very irregular interfaces with the substrate and poor thickness reproducibilities from run to run. Thus, the remaining studies reported here were performed at a saturation temperature of 600°C.

Layers were also grown from 600°C with varying rates of heating to the saturation temperature. A cool-

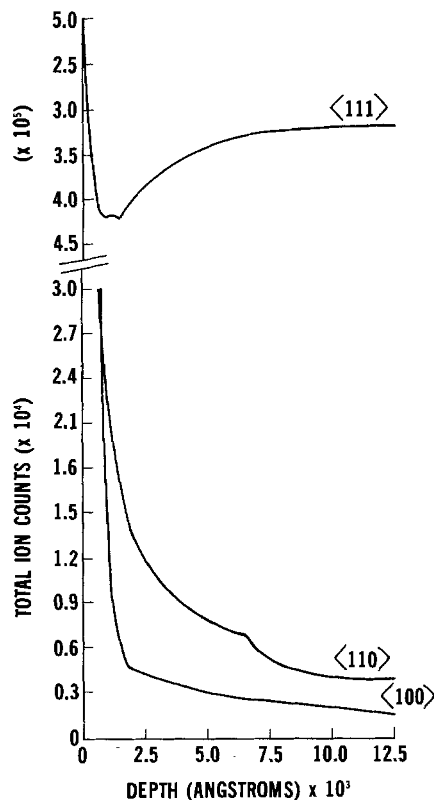

Fig. 6. SIMS profile of gallium distribution from (111), (110), and (100) silicon.

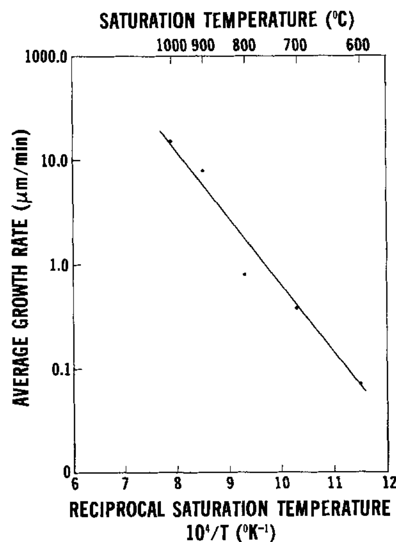

Fig. 7. The average growth rate dependence on the saturation temperature.

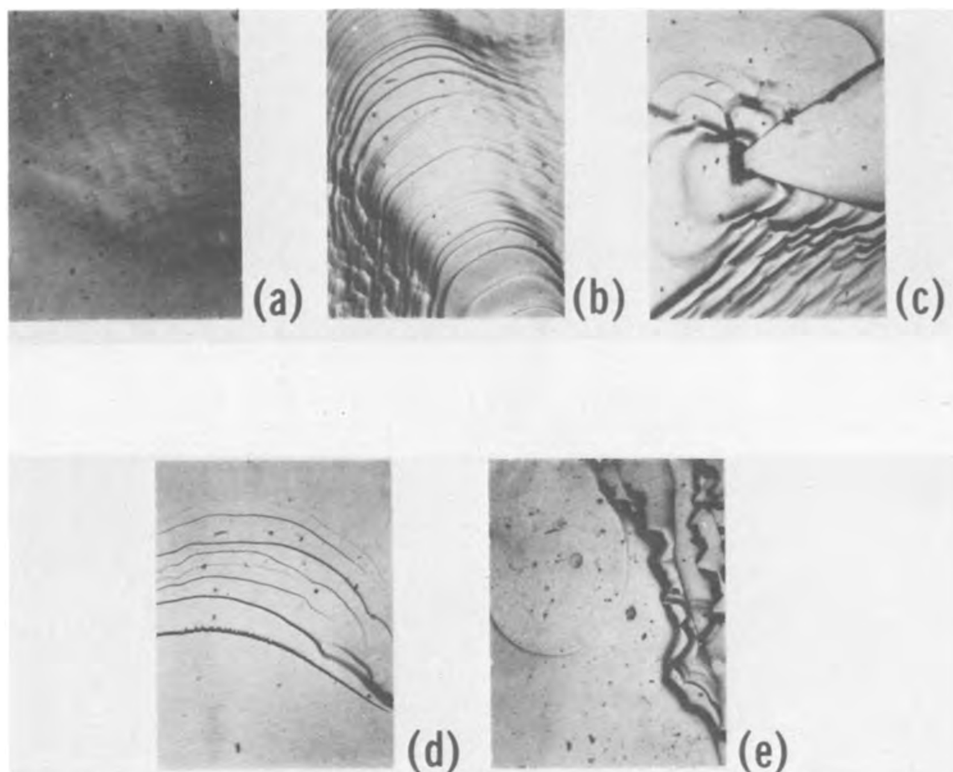

Fig. 8. Surface morphologies of gallium-doped silicon exposed to different saturation temperatures: (a) 600°C, (b) 700°C, (c) 800°C, (d) 900°C, (e) 1000°C.

ing rate of 26°C/min was chosen because no temperature programming was necessary. It was obtained by simply rolling the furnace from the growth tube for the duration of the growth. The optical micrographs of the surfaces are shown in Fig. 9. The surfaces of the slowest heating rate (0.5°C/min) show small precipitates or crystallites but no lamellar structure. The 2°C/min surface shows layer crystallites and wide lamellar structures, while the 12°C/min structure shows only the appearance of a lamellar structure.

The scanning electron micrographs, Fig. 10, of the same samples, show the characteristic features found on the various surfaces. The most significant finding is the pyramidal shapes on the surfaces which appear to vary in size and abundance with the various heating rates. However, further studies are necessary to es-

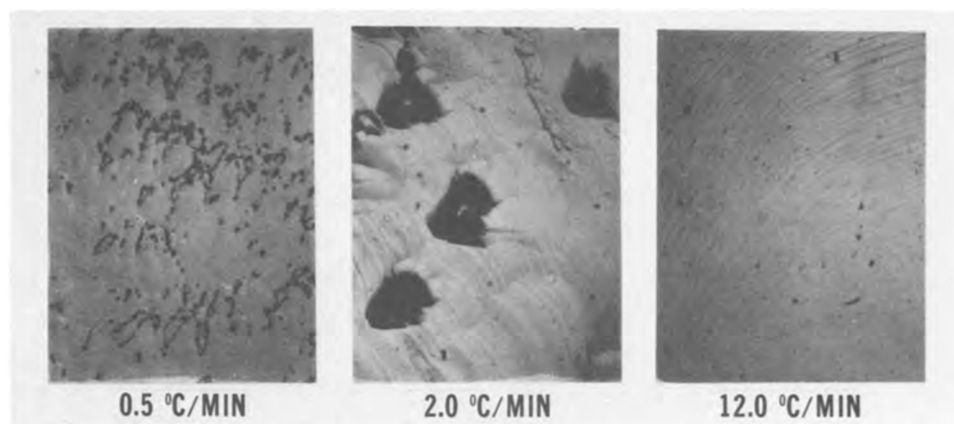

Fig. 9. Optical micrographs of gallium-doped silicon heated up to saturation temperature (600°C) at different rates. Magnification 63×.

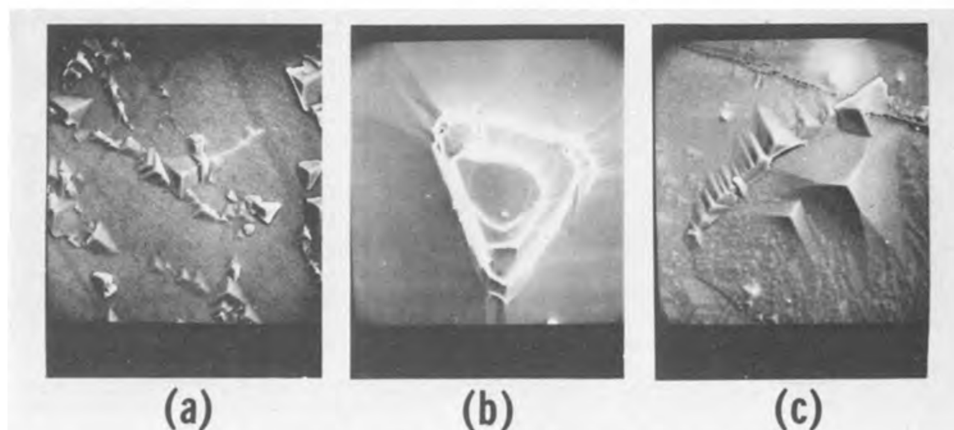

Fig. 10. Characteristic features found on surfaces of layers dissolved or heated up to saturation (600°C) at rates of: (a) 0.5°C/min, (b) 2°C/min, (c) 12°C/min.

tablish if a systematic variation exists. This type of structure also has been observed for heavily doped arsenic-silicon layers (11), where at maximum doping the epitaxial layers were completely covered with pyramids and cones.

Dopant profiles provided by SIMS are shown in Fig. 11. The layers grown using the faster rates of heating to saturation (2° and 12°C/min) exhibited a more uniform gallium distribution to the substrate. However, the 12°C/min layers repeatedly showed the highest gallium counts which implies the greater gallium concentration.

Layers were also grown from 600°C gallium melts which were not exposed to a prebake treatment and compared with layers from which the melt was baked. Auger electron spectroscopy was used to investigate the relative amounts of silicon, carbon, oxygen, and, if possible, gallium in the samples. The typical Auger sensitivity to most elements is approximately 10^{19} atoms/cm^3. The comparison is shown in Fig. 12 and indicates little if any significant difference in intensities for the various elements. The curves are slightly shifted for display purposes only. Although not shown here, the SIMS analyses showed little difference in the profiles of gallium from the surface into the layer. Thus, it was felt that the baking in H_2 before growth was not a necessary melt pretreatment.

The microscopic topography of a grown layer may reflect the stability (*i.e.*, shape) of the liquid-solid interface as well as crystallographic factors which influence attachment to the solid (12). In examining the surface morphology of decanted metallic solutions, several workers observed corrugated and cellular surface morphologies which were linked to constitutional supercooling (13-17). Andre and LeDuc (18) reported that surface irregularities in LPE-grown GaAs could be eliminated by imposing thermal gradients to eliminate constitutional supercooling conditions. Solomon and DeFevere (19) had observed ripple-like surface morphologies in LPE-grown GaP which they identified as gallium occlusions resulting from constitutional

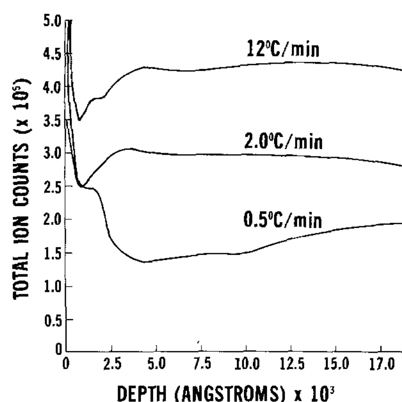

Fig. 11. SIMS profile of gallium distribution of layers heated at different rates to saturation.

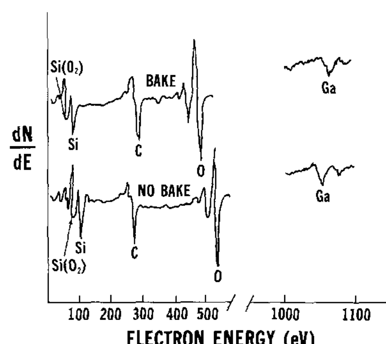

Fig. 12. Auger analysis of layers grown from baked and unbaked gallium melts.

supercooling. On the other hand, Donohue and Minden (20) interpreted this morphology in GaAs layers to result from cellular convection in the growth solution, while Peters (21) suggested surface roughness with substrate orientation.

Practically all of the layers grown in this study have shown lamellar or corrugated structure which may be tied to constitutional supercooling. A series of growth experiments were performed with hopes of shedding light on the origin of the lamellar surface morphology.

As shown by Minden (22), the liquidus temperature approaches a constant value (the interface temperature) as slower cooling rates and thinner melts are employed. Layers were grown from different weights (or volumes) of liquid gallium. The weights used were 5, 2.5, and 1g, respectively. A display of the surface structures of the layers is shown in Fig. 13 along with a surface which was only gallium etched (*i.e.*, no layer growth). Very little difference was found between the 2.5 and 1g melt but a significant difference was shown using a 5g melt. The largest weight melt showed small protrusions indicative of interface breakdown in addition to the lamellar structure. Thus, the principal lamellar structure of layers grown from 5g melts appeared to be connected with constitutional supercooling. This view was corroborated by experiments in which the substrate was melted back and no observable lamellar texture was found.

The trade-off in using a shallow melt is that of layer coverage. It was desirable for most applications and analyses to have large surface coverage. Thus, the 5g melt was used to examine the effects of cooling rates on surface morphology. The cooling rates explored were 0.8°, 2°, and 23°C/min, respectively. Scanning electron micrographs clearly displayed (Fig. 14) the surface texture with its corrugations. The smoothest surface was obtained by using the slower rate of cooling.

Burstein and co-workers examined the low temperature (4°-77°K) absorption spectra of the Group III and Group V elements, acting as acceptor or donor impurities, in silicon (23). These spectra were characterized by absorption continua which terminated at low energies with absorption edges. Below these edges in energy were found series of relatively sharp absorption lines. These spectra have been interpreted as follows: At low temperatures the hole or electrons are "frozen out" at acceptor or donor sites, respectively. A sharp absorption line indicates an optical transition from the ground state of the impurity to one of its discrete excited states. The absorption continuum indicates transitions from the ground state to an ionized state lying in either the valence or conduction band. The infrared transmission spectra obtained by Burstein are shown in Fig. 15. The concentration of carriers in the material was 1×10^{16}/cm^3. Gallium-doped silicon exhibits three prominent absorption bands at wavelengths near 18, 20, and 21 μm. These bands correspond closely to 1s-2p, 1s-3p, and 1s-4p transitions of a hydrogen-like center. The bands below 18 μm are lattice vibration bands of silicon.

The infrared spectra of LPE gallium-doped silicon on 1.35 mm thickness substrate are shown in Fig. 16. Here, the sharp lattice vibration band near 9 μm which is thought due mostly to SiO_2 absorption (24) as well as the bands near 18, 20, and 21 μm which are due to un-ionized gallium centers are absent.

The absence of structure due to Group III impurity centers in silicon was investigated by Newman (25). Newman described some studies of the discrete absorption lines of Ga as a function of the density of the impurity. He found that the spectrum was independent of concentration below 10^{16}/cm^3. However, concentrations above 10^{16}/cm^3 showed broadening of bands and by concentrations above 10^{18}/cm^3, the line structure is almost completely destroyed. He ascribes the concentration broadening of the excited levels by the overlapping of neighboring impurity centers. Thus,

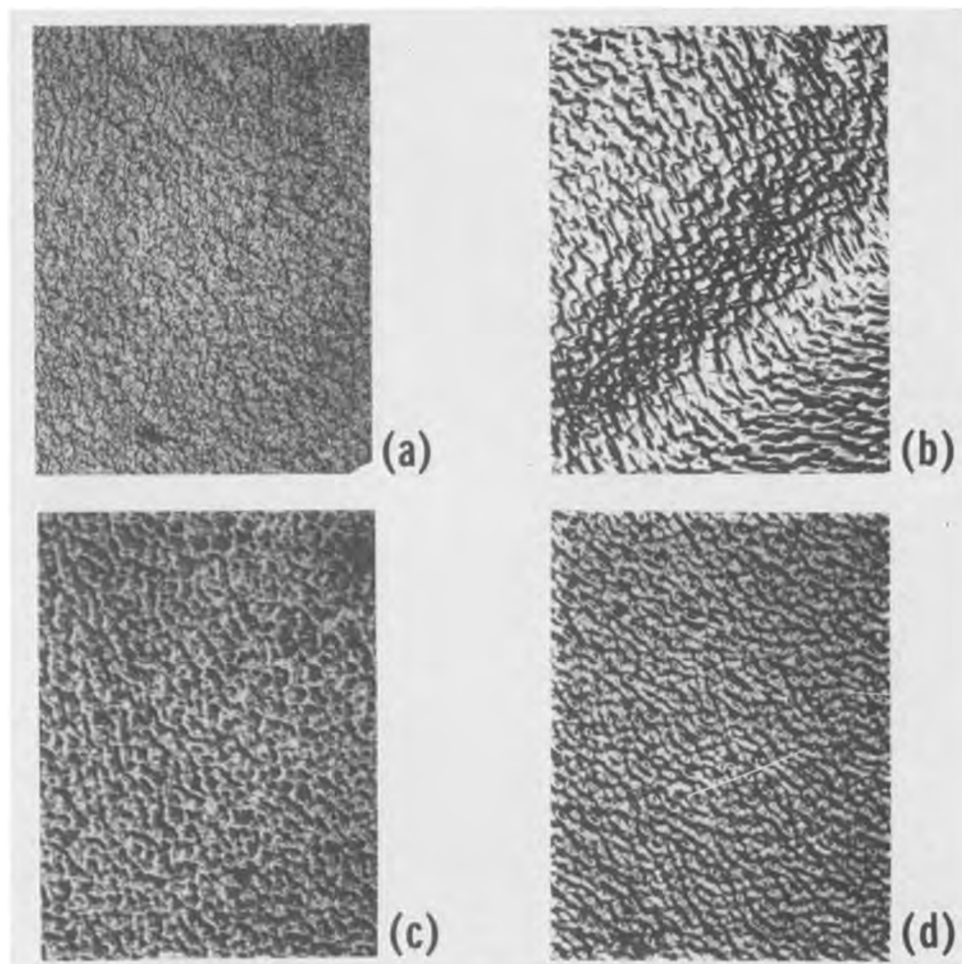

Fig. 13. Surface morphologies of (111) silicon after: (a) gallium etch (5g), (b) layer growth from 5g melt, (c) layer growth from 2.5g melt, (d) layer growth from 1g melt.

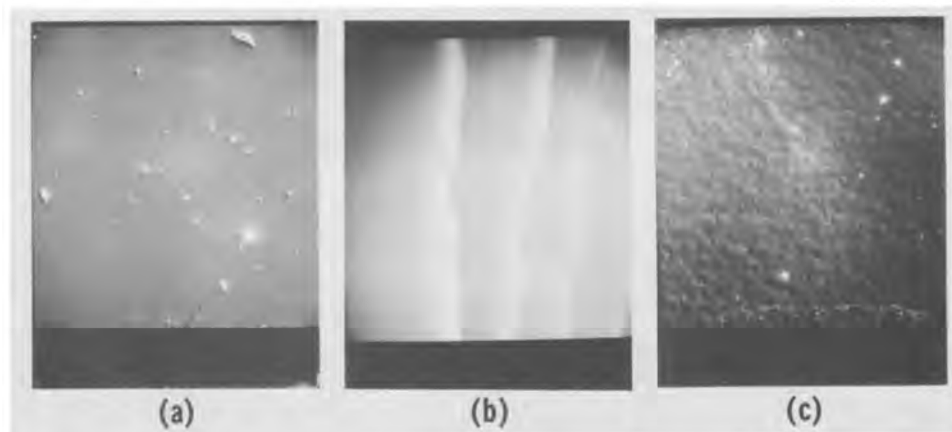

Fig. 14. Scanning electron micrographs of surfaces grown with different cooling rates: (a) 0.8°C/min, (b) 2°C/min, (c) 23°C/min. Magnification 100×.

the absence of the excitation bands in Fig. 16 between 18 and 21 μm is thought due to Ga concentrations $10^{18}/cm^3$ or greater.

Discussion

The criteria used in this investigation to judge the quality of gallium-doped silicon layers were uniformity of: (*i*) surface morphology (a smooth surface), (*ii*) substrate-layer interface, and (*iii*) dopant distribution. The best results, for large area coverage, were obtained when the growth was initiated on (111) orientations, from a saturation temperature of 600°C, and at a cooling rate of 0.8°C/min. Faster cooling rates were found to enhance irregular surface morphologies which suggested constitutional supercooling conditions. Thus, the optimum cooling rate for the growth was dictated by the speed with which silicon atoms diffuse to the growth interface since the total amount of silicon dissolved in the gallium melt is small (0.35 weight percent at 600°C).

When one calculates the distribution coefficient of gallium in silicon at 600°C and determines its concentration in the liquid phase at equilibrium, the concentration of the dopant in the solid phase can be approximated (26). Growth from saturated solutions of 600°C was expected to yield concentrations of gallium in the 10^{17} cm^{-3} range. However, higher values were suggested by SIMS profiling (using an ion-implanted standard), low temperature infrared spectroscopy, and Auger sensitivity.

The theoretical prediction of dopant concentration can be made by the following relationship (27, 28)

$$C_S = k_e C_o (1 - g)^{k_o - 1} \qquad [1]$$

and

$$k_e = \frac{k_o}{k_o + (1 - k_o) \exp\left(\frac{-fd}{D}\right)} \qquad [2]$$

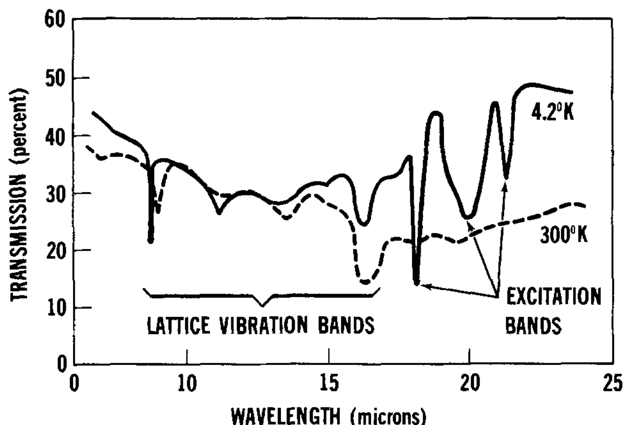

Fig. 15. Infrared transmission spectra of gallium-doped silicon (Burnstein *et al.*) at room temperature and liquid helium temperature. $n_p = 1 \times 10^{16}/cm^3$ and $t = 0.89$ mm (21).

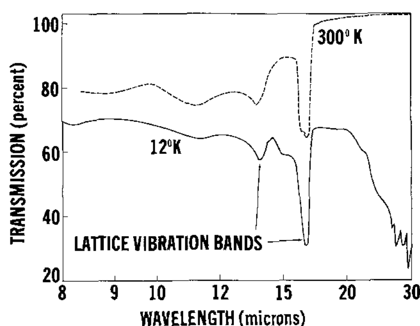

Fig. 16. Infrared transmission spectra of gallium-doped silicon grown by LPE.

where C_S is the concentration of dopant in the epitaxial layer, C_o the average concentration of dopant in the liquid, k_o the ratio of concentrations of the dopant in the solid and liquid in equilibrium with it, g the fraction of liquid that has solidified in the system, d the thickness of the boundary layer through which the solute must diffuse (1-10 mm), and D the diffusion coefficient of the dopant. The effective distribution coefficient k_e, which is defined as the ratio of the concentrations of solute in the solid that is formed to the average value for the liquid, approaches the maximum value of unity as the growth rate (f) increases and $k_e = k_o < 1$ at the very low growth rates.

It was suggested from studies of supercooling while growing that the growth kinetics could closely approximate the one in which nuclei grow rapidly laterally (29). Thus, assuming that the growth rate is infinite, the time for rearrangement of atoms will be so short that the concentration of dopant in the solid (C_s) will equal that in the liquid (C_l). Also in view of the above equations, no stirring or agitation was employed in the present growth system. This permits the incorporation of as much dopant as possible, since the mixing of liquid decreases d and effectively increases the diffusion coefficient D of the dopant (6, 27).

In addition to the effect of dopant concentration and cooling rate on nucleation of layers, impurity atoms and solvent atoms are known to greatly influence the growth morphology. In growing pure Si from a Si melt, (111) planes are the slowest growing and the most stable faces. The epitaxial growth of Si on a (111) substrate can be treated as the growth of a twin having the substrate as a twin plane. According to Wagner (30), in the twin plane having a hexagonal morphology bounded by (111) planes, the reentrant twin edge is a nucleation site for new layers on the edge of the plane, and growth occurs in a (111) direction. However, impurity or dopant atoms and solvent atoms can alter the surface energy of the substrate, thus stabilizing other crystallographic planes. This change affects the morphologies of growth from other orientations. The dopant atoms or solvent atoms act as a preferential etchant which produces a surface with well-defined pits whose facets are definite crystallographic planes. Buckley (31) gives a large number of examples of changes in crystal habit brought about by impurities of solvent atoms due to their effect on the relative growth rate of various faces. These effects have also been considered in detail by Sears (32) who proposed modification of the growth process because of impurities. Thus, it is not surprising that the orientation study in this investigation has shown preferential etching characteristics of silicon in liquid gallium.

Conclusion

The growth of heavily doped gallium in silicon by LPE has been demonstrated. This process was found to be very sensitive to cooling rate, substrate orientation, saturation temperature, and melt volume. The growth rate dependence on saturation temperature and the amount of cooling were determined. The critical parameters which give an optimum growth with respect to surface morphology and dopant distribution were obtained. Layers grown on (111) orientations from a saturation temperature of 600°C and cooled at 0.8°C/min produced the most favorable growth results. Simple solubility arguments were found in error and layers were grown with higher dopant levels than expected. Thus, this technique is thought only attractive where high dopant concentrations ($>10^{18}$ atoms/cm^3) are desirous.

Acknowledgments

The authors have benefitted from suggestions and assistance of Dr. Ward Trussell, Dr. George Hass, and Dr. Mylous O'Dell during hours of valuable discussions; Mr. John Ramsey, Mr. Gerard King, Mr. Robert Flannery, Mr. Phillip Boyd, and Dr. Randolph Longshore from their assistance with analytical tools and data interpretation; Dr. James Comas (Naval Research Laboratory) and Mr. Larry Plew (Naval Research Support Center, Crane, Indiana) for analysis and interpretation of SIMS results. The authors wish also to thank Mrs. Debrah Martin for her time and patience in the typing of this manuscript. This paper is taken from a dissertation submitted in partial fulfillment of the requirements for the Ph.D. degree in Chemistry from The American University.

Manuscript submitted March 27, 1978; revised manuscript received June 15, 1978.

Any discussion of this paper will appear in a Discussion Section to be published in the June 1979 JOURNAL. All discussions for the June 1979 Discussion Section should be submitted by Feb. 1, 1979.

Publication costs of this article were assisted by The Night Vision and Electro-optics Laboratory.

REFERENCES

1. H. Nelson, *RCA Rev.*, **24**, 603 (1963).
2. M. R. Lorenz and M. Pilkuhn, *J. Appl. Phys.*, **37**, 4094 (1966).
3. H. Rupprecht, J. M. Woodall, and G. D. Pettit, *Appl. Phys. Lett.*, **11**, 81 (1967).
4. J. M. Woodall, H. Repprecht, and W. Reuter, *This Journal*, **116**, 899 (1969).
5. L. A. D'Asaro, R. W. Landorf, and R. A. Furnange, in "Semiconductor Silicon," R. R. Haberecht and E. L. Kern, Editors, p. 233, The Electrochemical Society Softbound Symposium Series, New York (1969).
6. H. J. Kim, *This Journal*, **119**, 1394 (1972).
7. H. Nelson, U.S. Pat. 3,565,703 (1971).
8. P. H. Keck and J. Broder, *J. Phys. Rev.*, **90**, 521 (1953).
9. R. N. Hall, *J. Phys. Chem.*, **57**, 836 (1953).
10. J. A. M. Dikholf, *Solid State Electron.*, **1**, **202** (1960).
11. S. Nielson, G. J. Rich, and K. M. Fairhurst, *Microelectron. Reliab.*, **3**, 233 (1964).

12. R. H. Saul and D. D. Roccasera, J. Appl. Phys., 44, 1983 (1973).
13. J. W. Rutter and B. Chalmers, Can. J. Phys., 31, 15 (1953).
14. W. A. Tiller and J. W. Rutter, ibid., 34, 96 (1956).
15. G. S. Cole and W. C. Winegard, J. Inst. Met., 92, 332 (1964).
16. W. A. Tiller, K. A. Jackson, J. W. Rutter, and B. Chalmers, Acta. Metall., 1, (1953).
17. R. F. Sakera, J. Cryst. Growth, 3, 71 (1968).
18. E. Andre and J. M. LeDuc, Mater. Res. Bull., 3, 1 (1960).
19. R. Solomon and D. DeFevere, J. Electron. Mater., 4, 16 (1974).
20. A. Donohue and H. T. Minden, J. Cryst. Growth, 7, 221 (1970).
21. R. C. Peters, in Symposium on GaAs and Related Compounds, Boulder, Colorado, 1972 (unpublished).
22. H. T. Minden, J. Cryst. Growth, 6, 228 (1970).
23. E. Burnstein, G. Picus, B. Henvis, and R. Wallis, J. Phys. Chem. Solids, 1, 65 (1956).
24. K. Graff, E. Gallath, S. Ades, G. Goldbach, and G. Tolg, Solid-State Electron. (Great Britain), 16, 887 (1973).
25. R. Newman, Phys. Rev., 103, 103 (1956).
26. F. A. Trumbore, Bell Syst. Tech., J., 39, 205 (1960).
27. W. G. Pfann, "Zone Melting," 2nd ed., p. 259, John Wiley & Sons, Inc., New York (1966).
28. J. A. Burton, R. C. Primm. and W. P. Slichter, J. Chem. Phys., 21, 1987 (1953).
29. J. C. Brice ,"The Growth of Crystal from Liquids," North-Holland Publishing, Amsterdam (1973).
30. R. S. Wagner, Acta. Metall., 8, 57 (1960).
31. H. E. Buckley, "Crystal Growth," John Wiley & Sons, Inc., New York (1956).
32. G. W. Sears, J. Chem. Phys., 29, 979 (1958).

Selective Oxidation of Silicon in High Pressure Steam

H. Miyoshi, N. Tsubouchi, and A. Nishimoto

Computer Development Laboratories Limited, 4-1 Mizuhara, Itami, Hyogo, Japan

ABSTRACT

The selective oxidation of silicon was investigated using a high pressure oxidation apparatus at a steam pressure of 6.6 kg/cm^2 (6.4 atm) and at temperatures between 800° and 1100°C. The conversion characteristics of the silicon nitride film into silicon dioxide film in high pressure steam was analyzed on the basis of the well-known linear-parabolic relationship. The activation energy for the parabolic rate constant was found to be about 3.15 eV, which was about 5 times larger than that (0.7 eV) for silicon. On the other hand, the activation energy for the linear rate constant was about 1.25 eV which was a little smaller than that (2.03 eV) for silicon. The conventional silicon nitride film was found to be able to mask the selective oxidation even in the high pressure steam. The lateral oxidation of the silicon substrate beneath the masking nitride film occurred rapidly with decreasing oxidation temperature at the fixed pressure. The suppression of the lateral oxidation can be achieved by increasing the thickness of the masking nitride film and also by decreasing that of the oxide pad. This high pressure oxidation process was compatible with the conventional atmospheric process.

Selective oxidation of silicon substrate with the use of silicon nitride film as a mask is one of the basic process technologies in modern semiconductor integrated circuit industry. The selective oxidation technology has been applied to form thick silicon dioxide film used as an isolation layer in the integrated circuits. Conventionally, the growth of thick silicon dioxide film has been performed using wet oxidation or H_2/O_2 pyrogenic oxidation at a temperature of about 1000°C at atmospheric pressure and for a very long oxidation time. For example, the oxidation time of about 12 hr is necessary to form the silicon dioxide film of 1.5 μm thick in H_2/O_2 pyrogenic ambient at atmospheric pressure and 1000°C. The long time oxidation treatment of the silicon substrate is known to cause the degradations of some electrical characteristics of the devices of the integrated circuits (1, 2).

On the other hand, the high pressure oxidation methods (3, 4) in steam or dry oxygen ambient are known to reduce the oxidation time to a considerable extent and are expected to improve the performance of the integrated circuits. The masking capability of the silicon nitride film during the growth of thick silicon dioxide film is one of the main interests in the selective oxidation process. Further, the control of the lateral oxidation, by which the silicon substrate to be protected with the masking silicon nitride layer is oxidized, is also of interest in order to define the selective oxidation process for fabricating integrated circuits.

It is the purpose of this paper to report the masking capability of the silicon nitride film against the accelerated oxidation of silicon by using a newly developed high pressure steam oxidation system (5-7) and the control of the shape of the nitride-oxide edge, that is, the lateral oxidation of silicon beneath the mask nitride film in high pressure steam.

Key words: oxidation, silicon nitride, high pressure oxidation, selective oxidation, MOS LSI process.

Experimental

The selective oxidation of the silicon substrate with the use of a masking nitride film was performed using the newly developed high pressure oxidation system. In Fig. 1, the high pressure oxidation apparatus is schematically shown. This high pressure oxidation system is able to perform H_2/O_2 pyrogenic steam oxidation at a pressure up to 9 kg/cm^2 and an oxidation

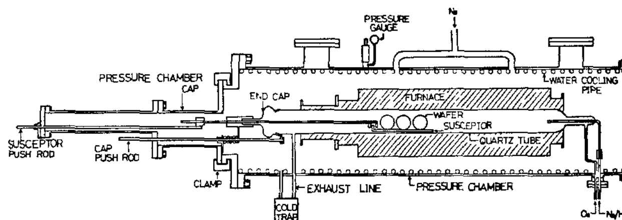

Fig. 1. Schematic diagram of the high pressure oxidation apparatus.

temperature up to 1200°C. In this high pressure oxidation system, a conventional oxidation furnace is set into a high pressure stainless steel chamber (50 cm in diameter, and 180 cm in length). A high quality quartz tube is inserted in the high pressure stainless steel chamber. High purity compressed N_2 gas for charging the stainless steel chamber and compressed O_2 gas and H_2 gas for forming the pyrogenic steam ambient are supplied from liquid N_2, liquid O_2, and compressed H_2 gas sources, respectively. In order to avoid the penetration of contaminants from the outer stainless steel chamber into the quartz tube, the total gas pressure in the quartz tube in which the substrate is oxidized is automatically controlled to be always larger than that of the outer stainless steel pressure chamber by 1 atm during oxidation. This automatic control of the pressure difference between the stainless steel pressure chamber and the quartz tube can be performed with the use of a microprocessor control system. The steam pressure inside the quartz tube can be precisely controlled by controlling mass flow ratio of H_2 gas to O_2 gas. The experiments were carried out with mass flow ratio of H_2 and O_2 being 1.76, and the total gas pressure inside the quartz tube of 7.0 kg/cm^2 (a partial pressure of H_2O should be 6.6 kg/cm^2). The details of the operation of the system have been reported elsewhere (5, 6).

The masking capability of silicon nitride is a very important factor in the selective oxidation process. Therefore, the conversion rate of silicon nitride films into silicon dioxide under the high pressure steam ambient was investigated at different oxidation temperatures. In our experiments, silicon nitride films were deposited on the surface of silicon substrate using a reduced pressure chemical vapor deposition method. The silicon nitride film is converted into silicon dioxide during high pressure oxidation. The converted nitride layer was etched in a buffered HF solution and the thickness of the remaining silicon nitride film was measured by the conventional ellipsometry technique.

In the selective oxidation experiments, a silicon dioxide layer of 300 and 500Å thick was thermally grown on the surface of (100) oriented silicon substrate (6-9 Ω·cm, p type, 2 in. in diameter). The nitride films produced from the reaction of SiH_2Cl_2 with NH_3 at 800°C in N_2 carrier gas were deposited on the silicon dioxide layer and defined by the conventional photolithography and CF_4 gas plasma etching techniques. In our experiments, the thicknesses of the underlying silicon dioxide pad and the masking silicon nitride layer were varied. Selective oxidations were performed by varying the oxidation temperature at a fixed oxidation pressure. Further, the conventional atmospheric selective oxidation was also carried out at 950°C in wet oxygen ambient as a comparison. In the selective oxidation process, the control of the shape of the oxide layer at the nitride-oxide edge, which is usually called "bird-beak," is important for the device designs. The cross-sectional view of the "bird-beak" was examined by using SEM technique.

Results and Discussion

In Fig. 2, the thicknesses of the converted silicon nitride film during the high pressure steam oxidation are shown as a function of oxidation time. In this experiment, the initial thickness of the silicon nitride film to be oxidized was 1000Å and the steam pressure in the quartz tube was kept at 6.6 kg/cm^2. The conversion behavior of silicon nitride film was measured by varying the oxidation temperature from 800° to 1000°C.

The conversion rate of silicon nitride film into silicon dioxide film increases with increasing oxidation temperature under a fixed pressure, as shown in Fig. 2. Auger electron spectroscopic (AES) measurements showed that the silicon nitride film of 1000Å thick was converted into a perfect silicon dioxide film after oxidation at a steam pressure of 6.6 kg/cm^2 and an oxidation temperature of 1000°C for 400 min.

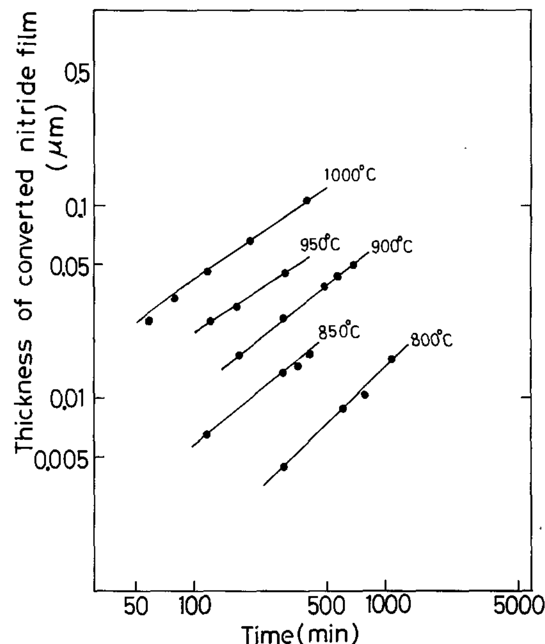

Fig. 2. Thickness of the converted silicon nitride film during the high pressure oxidation as a function of time with temperature as parameter.

The thicknesses of the silicon dioxide film converted from silicon nitride film during high pressure pyrogenic oxidation are calculated from the experimental results shown in Fig. 2 with the aid of the theoretical conversion ratio (1.95) of silicon nitride film into silicon dioxide film. The calculated thicknesses of the thermally grown silicon dioxide layer are shown in Fig. 3 as a function of oxidation time and oxidation temperature. These characteristics are very similar to the oxidation characteristics of a silicon substrate at 1 atm pressure. As is well known, the oxidation characteristics of silicon in dry and wet oxygen and steam ambient at 1 atm pressure are well described by the linear-parabolic relation (8). Thus, it can be said from Fig. 3 that the conversion characteristics will be sub-

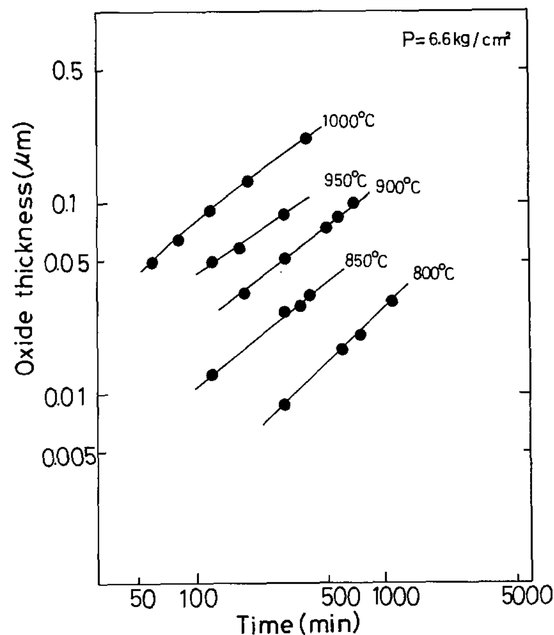

Fig. 3. Oxide thickness calculated from Fig. 2 as a function of oxidation time and oxidation temperature.

Table I. Rate constants for high pressure steam oxidation of nitride film and (100) silicon substrate at pressure of 6.6 kg/cm²

Temp (°C)	Si_3N_4			Si (100)		
	A (μm)	B (μm²/min)	B/A (μm/min)	A (μm)	B (μm²/min)	B/A (μm/min)
1000	0.23	2.3×10^{-4}	10.0×10^{-4}	0.46	2.5×10^{-3}	5.4×10^{-3}
950	0.054	0.41×10^{-4}	7.6×10^{-4}			
900	0.029	0.14×10^{-4}	4.9×10^{-4}	1.8	1.6×10^{-3}	0.92×10^{-3}
850	0.020	0.04×10^{-4}	2.0×10^{-4}			
800	0.006	0.009×10^{-4}	1.4×10^{-4}	5.2	0.8×10^{-3}	0.16×10^{-3}
E_a*	1.90 eV	3.15 eV	1.25 eV	−1.33 eV	0.7 eV	2.03 eV

* E_a = activation energy.

ject to the following linear-parabolic equation

$$t_{ox}^2 + At_{ox} = Bt \quad [1]$$

$$A = 2D_{eff}(1/k + 1/h) \quad [2]$$

and

$$B = 2D_{eff}C^*/N \quad [3]$$

where B/A is the linear rate constant, B is the parabolic rate constant, t_{ox} is the oxide thickness, t is the oxidation time, k is the reaction coefficient, h is the gas phase transport coefficient, D_{eff} is the effective diffusion coefficient, C^* is the equilibrium concentration of the oxidant in the oxide, and N is the number of oxidant molecules incorporated into a unit volume of the oxide layer.

The values of A, B, and B/A are calculated from the oxidation characteristic curves shown in Fig. 3 and summarized in Table I. The rate constants obtained from the oxidation of silicon at a steam pressure of 6.6 kg/cm² and different oxidation temperatures are tabulated in Table I. As can be seen from the table, the values of the rate constants A, B, and B/A for the oxidation of silicon nitride film are much smaller than those for silicon. The activation energy E_a for the rate constant B for the oxidation of silicon nitride film was found to be about 3.15 eV, which is about 5 times larger than that (0.7 eV) for silicon. On the other hand, the activation energy E_a for the linear rate constant B/A for the oxidation of silicon nitride film is about 1.25 eV which is a little smaller than that (2.03 eV) for silicon. The value of the activation energy E_a for the linear rate constant B/A for the oxidation of silicon at 1 atm pressure is about 1.96 eV which is comparable with that (2.03 eV) at 6.6 kg/cm². Therefore, the values of the activation energy for the constant A are 1.90 and −1.33 eV for the silicon nitride and silicon, respectively. It should be noted that the values of A decrease with decreasing temperature for the oxidation of silicon nitride which is contrary to the oxidation of silicon. This comes from the high activation energy for B in the silicon dioxide conversion of silicon nitride films. Fränz *et al.* (9) suggested that the reduction of the constant B was caused by the reduction of the equilibrium concentration of the oxidant due to the nitrogen generated during the chemical reaction at the nitride-oxide interface. On the other hand, the measurements (10) with ESCA revealed that the oxidized nitride films were apparently homogeneous and were graded, being nitrogen rich as the nitride film was approached. In the former case, C^* in Eq. [3] should be small and then B is small compared with that for the oxidation of silicon. In the latter case, the diffusion coefficient should be smaller. The experimental results did not clearly show which effect is predominant for the reduction of B. Thus the growth rate of the silicon dioxide film converted from the silicon nitride film may in any event be reduced in comparison with the oxidation of silicon. The decrease of the linear rate constant B/A in the high pressure oxidation of silicon nitride film may be caused by the decrease of the reaction constant k, because B/A is proportional to the reaction coefficient at the nitride-oxide interface.

Further, the experimental results shown in Fig. 2 show that the conventional silicon nitride film can mask the selective oxidation process at high pressure, because the silicon dioxide film of 1.5 μm thick can be thermally grown at 1000°C for 90 min in the high pressure ambient of 6.6 kg/cm².

Typical examples of the cross section of the selective oxidation structure are shown in Fig. 4a and b. In these examples, the thicknesses of the masking nitride film and the underlying silicon dioxide layer are 1000 and 500Å, respectively. The grown-up oxide layer is 1.5 μm in thickness. In Fig. 4a and b, the oxidation was performed at 1100° and 800°C under the pressure of 6.6 kg/cm². As can be seen from comparing Fig. 4a with b at lower oxidation temperature and then longer oxidation time, a deep lateral oxidation occurs and the deep area of the silicon covered with the masking silicon nitride layer is oxidized. Therefore, the profiles of so-called "bird-beak" are apparently varied by varying oxidation temperature and time.

In Fig. 5, a schematical view of the cross section of the selective oxidation structure is shown. In our experiments, the thickness t of silicon dioxide film was always 1.5 μm. In Fig. 5, X axis and Y axis are parallel and perpendicular to the surface of silicon substrate, respectively. Maximum lateral oxide thickness is labeled B. The slope profile from a point $(0, Y_0)$ to a point $(B, 0)$ was investigated. The distance H of the edge of the masking silicon nitride layer from the origin 0 is labeled "a nitride edge height."

In Fig. 6, the normalized vertical oxide thicknesses Y/Y_0 are shown as a function of normalized lateral oxide thickness X/t where t is 1.5 μm. The oxidation temperature was varied from 800° to 1100°C under fixed oxidation pressure. The shapes of the curves shown in Fig. 6 show the slope profile of so-called "bird-beak" section in selective oxidation structure. It can be seen from these curves that the gradient of the curves decreases as the oxidation temperature increases, that is, a sharper slope profile can be obtained at higher oxidation temperature. In other words, as the oxidation temperature decreases and the oxidation time becomes longer, in order to grow the film to a fixed thickness of 1.5 μm, the lateral oxidation beneath the masking silicon nitride layer is more pronounced. For example, for the oxidation at 1100°C, maximum lateral oxide thickness B is about $0.75t$ ($t = 1.5$ μm) which is 75% of the thick oxide layer t. At 950°C, B becomes the same as t. On the other hand, at 800°C, B becomes about $1.22t$, which means the lateral oxide thickness is larger than the vertical oxide thickness, and a strong lateral oxidation of silicon under the masking nitride film occurs. This might result from the deep lateral diffusion of the oxidants along the silicon surface during the long oxidation time (610 min).

In Fig. 7, a normalized maximum lateral oxide thickness B/t ($t = 1.5$ μm) and a normalized nitride edge height H/t are shown as a function of oxidation

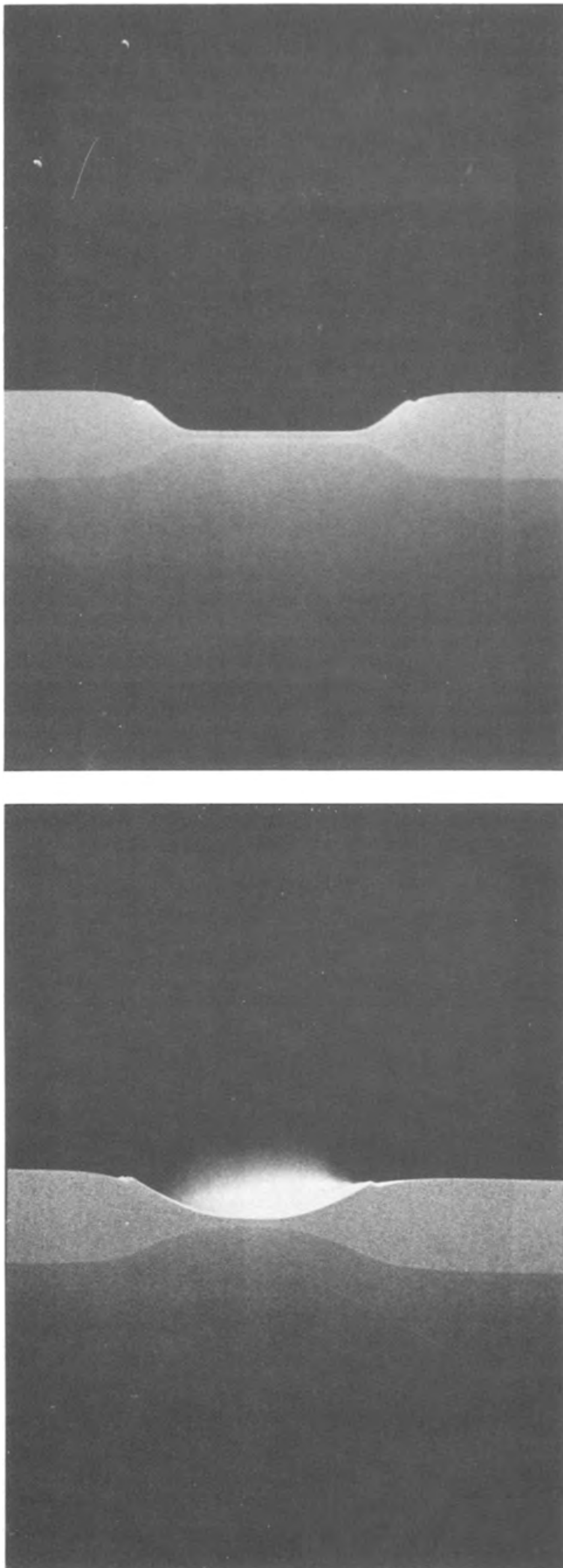

Fig. 4. Typical examples of the cross section of the selective oxidation structure showing the increase of the lateral oxidation as the oxidation temperature is decreased. In (a), the oxidation was performed at 1100°C with a pressure of 6.6 kg/cm^2 and in (b) at 800°C with 6.6 kg/cm^2.

temperature at a pressure of 6.6 kg/cm^2. Further, in Fig. 7, as a comparison, the values of B/t and H/t ob-

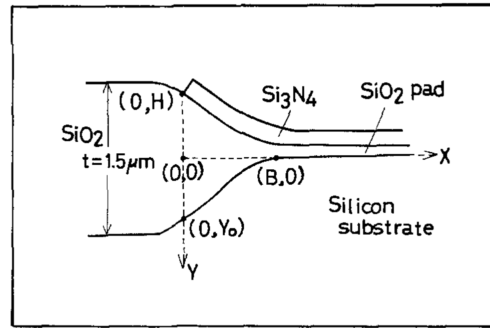

Fig. 5. Schematical view of the cross section of the selective oxidation structure.

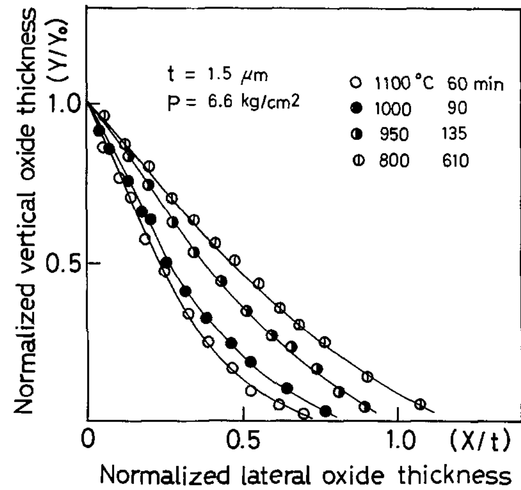

Fig. 6. Shape of the lateral oxidation as a function of the oxidation temperature. Normalized vertical oxide thicknesses Y/Y_0 are shown as a function of normalized lateral oxide thickness X/t.

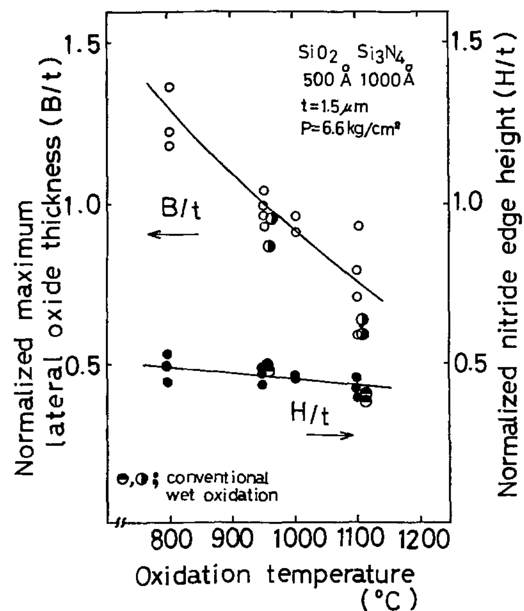

Fig. 7. Normalized maximum lateral oxide thickness B/t and normalized nitride edge height H/t as a function of oxidation temperature at the pressure of 6.6 kg/cm^2.

tained from the experiments performed by the conventional atmospheric wet oxidation are plotted. As can be seen from Fig. 7, the maximum lateral oxide thickness B decreases rapidly with increasing oxidation temperature and B/t becomes larger than 1.0 for oxidation temperatures lower than 950°C, that is, the

lateral oxidation rate is larger than the vertical oxidation rate. Further, a slight difference between the values obtained from the atmospheric oxidation and the high pressure oxidation is obtained as shown in Fig. 7. The statistically summarized experimental results showed the values of the maximum lateral oxide thickness B obtained in the conventional atmospheric oxidation were a little smaller than those obtained from high pressure oxidation. This may result from the difference of the lateral diffusion rate of the oxidant in atmospheric pressure and in high pressure. On the other hand, the nitride edge height H/t decreases gradually with increasing oxidation temperature. There is almost no significant difference in H/t between atmospheric pressure and the high pressure, as can be seen from Fig. 7.

In selective oxidation, the thicknesses of the underlying oxide layer and the masking nitride film may influence the lateral oxidation characteristics. In Fig. 8, the normalized maximum lateral oxide thicknesses B/t are shown as a function of the thickness of the underlying silicon dioxide film for different oxidation temperatures. As can be seen from Fig. 8, there is a tendency for the maximum lateral oxide thickness to increase as the thickness of the underlying silicon dioxide film is increased. This will result from the increase of the number of the incoming oxidants in the underlying oxide layer as the thickness of the oxide layer is increased.

In Fig. 9, the normalized maximum lateral oxide thickness B/t is shown as a function of the thickness of the masking silicon nitride film. In this case, the thickness of the silicon dioxide pad was 300Å. As can be seen from Fig. 9, the value of B/t decreases with increasing thickness of the masking silicon nitride film for different oxidation temperatures. Further, the normalized nitride edge height H/t is also shown in Fig. 9 as a function of the thickness of the masking silicon nitride film. The value of H/t decreases as the thickness of the silicon nitride film increases and does not strongly depend on the oxidation temperature. These tendencies of B/t and H/t are useful for showing how the lateral oxidation is decreased as the thickness of the nitride layer is increased.

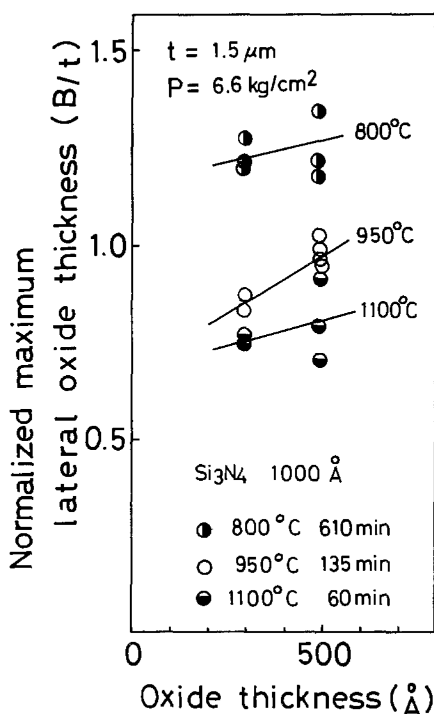

Fig. 8. Normalized maximum lateral oxide thickness as a function of the thickness of the oxide pad.

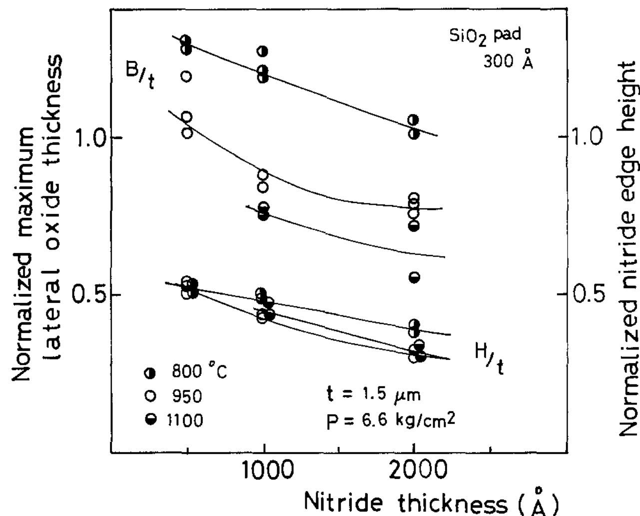

Fig. 9. Normalized maximum lateral oxide thickness and normalized nitride edge height as a function of the thickness of the masking nitride film.

The high pressure oxidation method was applied to the fabrication of a MOS Random Access Memory device with 5 μm minimum line width of the field oxide grown using the high pressure oxidation technique. The selective oxidation was performed using a 300Å dioxide pad and a masking nitride 1000Å thick. The oxidation temperatures were 950°, 900°, and 800°C. The measured electrical performances of the MOS Random Access Memory showed that the selective oxidation process with high pressure oxidation was compatible with the conventional selective oxidation process.

Summary

Selective oxidation of silicon was investigated using the new developed high pressure oxidation apparatus at a pressure of 6.6 kg/cm² and at a temperature between 800° and 1100°C. The conversion characteristics of the masking silicon nitride film into silicon dioxide film was analyzed on the basis of the linear-parabolic relation. The activation energy for the parabolic rate constant was found to be about 3.15 eV, which was about 5 times larger than that (0.7 eV) for silicon. On the other hand, that for the linear rate constant was about 1.25 eV which was smaller than that (2.03 eV) for silicon. The conventional silicon nitride film was found to mask the selective oxidation process even in this high pressure oxidation. The maximum lateral oxide thickness beneath the nitride mask decreases rapidly with increasing oxidation temperature. The thickness of the oxide pad and the masking nitride film influence the lateral oxidation characteristics. The suppression of the lateral oxidation can be achieved by increasing the thickness of the masking nitride film and decreasing the thickness of the oxide pad.

This high pressure oxidation process was found to be compatible with the conventional fabrication process for a high density MOS LSI using the selective oxidation technique.

Acknowledgment

The authors wish to thank Dr. H. Oka, Mr. H. Nakata, Dr. H. Abe, and Mr. T. Enomoto for their encouragement. They also wish to thank Mr. K. Miyake for his technical assistance.

Manuscript submitted Jan. 30, 1978; revised manuscript received June 23, 1978. This was Paper 359 presented at the Electrochemical Society Meeting, Atlanta, Georgia, Oct. 9-14, 1977.

Any discussion of this paper will appear in a Discussion Section to be published in the June 1979 JOURNAL. All discussions for the June 1979 Discussion Section should be submitted by Feb. 1, 1979.

Publication costs of this article were assisted by the Computer Development Laboratories Limited.

REFERENCES

1. C. J. Varker and K. V. Ravi, *J. Appl. Phys.*, **45**, 272 (1974).
2. Y. Hokari and H. Shiraki, *Jpn. J. Appl. Phys.*, **16**, 585 (1977).
3. R. J. Powell *et al.*, *IEEE Trans. Electron Devices*, **ed-21**, 636 (1974).
4. R. J. Zeto, C. G. Thornton, E. Hryckowian, and C. D. Bosco, *This Journal*, **122**, 1409 (1975).
5. N. Tsubouchi *et al.*, *Jpn. J. Appl. Phys.*, **16**, 1055 (1977).
6. N. Tsubouchi *et al.*, *ibid.*, **16**, 855 (1977).
7. N. Tsubouchi *et al.*, in The Proceedings of the 9th Conference on Solid State Devices, Tokyo (1977), To be published.
8. B. E. Deal and A. S. Grove, *J. Appl. Phys.*, **36**, 3770 (1965).
9. I. Fränz and W. Langheinrich, *Solid State Electron.*, **14**, 499 (1971).
10. S. I. Raider, R. Flitsch, J. A. Aboaf, and W. A. Pliskin, *This Journal*, **123**, 560 (1976).

Effects of Thin Conductive Film Mask on Ion Implantation

M. Nakatsuka, K. Tanaka, and T. Kikkawa

Nippon Electric Company, Limited, Engineering Department, Semiconductor Division,

1753, Shimonumabe, Nakahara-ku, Kawasaki City, 211 Japan

ABSTRACT

Anomalous generation of pulsive noise was observed in devices masked with SiO_2 during ion implantation in monolithic IC's. It has been found that this is not due to recoil implantation of oxygen in the SiO_2 film, but to dielectric breakdown of the SiO_2 film during ion implantation. This can be completely avoided by coating the SiO_2 mask with thin conductive films such as aluminum or polycrystalline Si just before ion implantation.

Ion implantation has come to be widely used in the processing of MOS IC's and junction FET's. In the case of bipolar IC's, however, ion implantation is confined to the restricted area of bipolar devices in spite of superior density profile controllability. One reason for this might be a development problem of high current ion implantation systems suitable for mass production. Another reason might be related to device characteristics such as noise performance of the ion implanted transistors or resistors.

This paper is an inquiry into the problem of medium dose ion implantation in bipolar devices.

Pulsive Noise Generated by Ion Implantation

For example, high value resistors are fabricated as shown in Fig. 1. In this case, $^{11}B^+$ ions are implanted into resistor area 1, while transistor area 2 is covered by SiO_2 mask 3. But in low noise IC's, there is difficulty in adopting ion implantation. We found that anomalous generation of pulsive noise with the waveform as shown in Fig. 2 is observed in transistors masked with SiO_2 during ion implantation.

Pulsive noise is also called burst noise or popcorn noise and is generated by a large number of imperfections in the crystal (1). On the other hand, most of the samples made by conventional thermal diffusion only exhibit clean noise as shown in Fig. 3. Generally, SiO_2 is used as the ion implantation mask. Therefore, either dielectric breakdown of SiO_2 caused by accumulated charge or infinitesimal knock on (recoil) implantation of oxide atoms in SiO_2 are considered to contribute to the generation of pulsive noise.

Dielectric Breakdown

As shown in Fig. 4 wafer 1 with SiO_2 pattern 3 is grounded through current integrator 2. $^{11}B^+$ or $^{31}P^+$ ions are implanted on the front surface of wafer 1. At the surface of insulating SiO_2 film, area 3, positive charges remain at the surface or at a certain penetration depth of SiO_2, inducing equal minus charges (electrons) from ground to the Si-SiO_2 interface through current integrator 2, thus raising the electric field in the insulating SiO_2 film.

Suppose that all the positive charges remain at the surface of SiO_2 with the thickness of 1 μm. Then the accumulated charge voltage of SiO_2 with the ion dose 1.5×10^{13} atoms/cm^2 of common implanted sheet resistivity of 2-3 k$\Omega/\square$ is given by the following equation

$$V = \frac{q \cdot \Phi}{\epsilon_r \cdot \epsilon_0/d} = \frac{1.6 \times 10^{-19} \times 1.5 \times 10^{13}}{3.82 \times 8.85 \times 10^{-14}/1 \times 10^{-4}} = 710\,(\text{volt})$$

Here, p-n junctions are neglected because there are always small leakage currents under certain bias voltages due to majority or minority carriers even in ideal crystal structures. This accumulated charge voltage (710V) comes near to the few kilovolts per micrometer dielectric breakdown voltage of SiO_2. It can be conjectured that local dielectric breakdown occurs and residual surface damage due to breakdown still exists after subsequent heat-treatment. In this case, dielectric breakdown could be avoided by covering the SiO_2 with a thin conductive film.

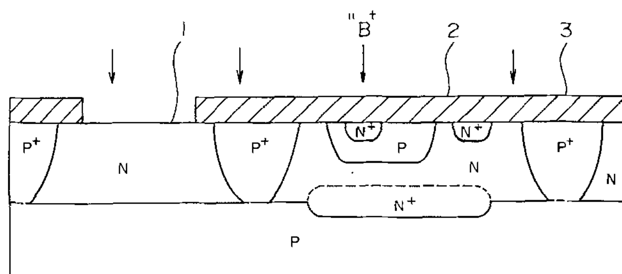

Fig. 1. Fabrication process of ion implanted resistor

Key words: insulating film mask, accumulated charge, dielectric breakdown, pulsive noise, medium dose.

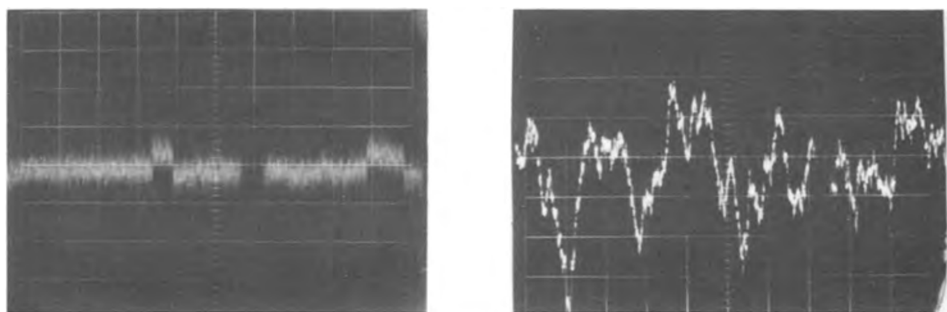

Fig. 2. (a, left) Pulsive noise waveform (horizontal: 10 msec/div). (b, right) Low frequency component of pulsive noise (horizontal: 10 msec/div).

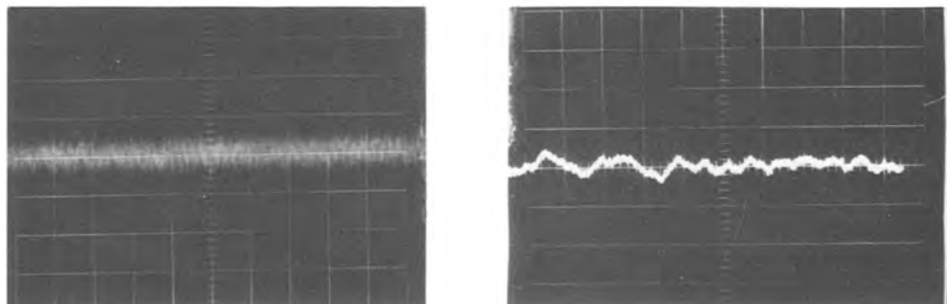

Fig. 3. (a, left) Clean noise waveform (horizontal: 10 msec/div). (b, right) Low frequency component of clean noise (horizontal: 10 msec/div).

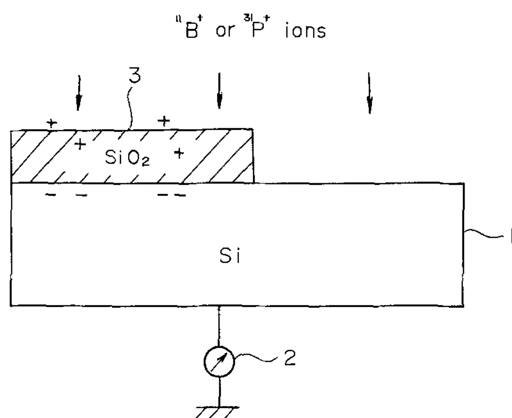

Fig. 4. Mechanism of ion implantation into SiO_2 pattern

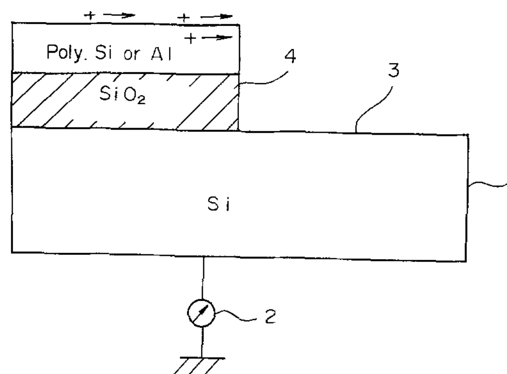

Fig. 5. Countermeasure for dielectric breakdown of SiO_2

Therefore, wafers were covered with either a 1.5 μm thick aluminum evaporated film or a nondoped polycrystalline Si film (SiH_4 at 640°C, 35 min, 0.55 μm thick) over the thermal SiO_2 film as shown in Fig. 5. The aluminum and polycrystalline Si film thickness are chosen equal to those adopted in the conventional bipolar IC's and silicon gate MOS IC's.

In this case, accumulated positive charges travel to the edges of the ion implantation mask 4 and discharge frequently, thus avoiding dielectric breakdown of the insulating SiO_2 film, as this discharge occurs in the range of a few tens of volts per micrometer at the pressure of the ion implantation vacuum chamber.

Knock on Implantation

In order to increase stopping power against incident ions, wafers were covered with chemical vapor-deposited SiO_2 film ($SiH_4 + O_2$ at 420°C, 1 atm, 8 min, 0.5 μm thick), photoresist (40 cp, OMR 83, 4000 rpm, 1 μm thick) or Scotch tape No. 56 (55 μm thick) over the conventional thermally grown SiO_2 film mask.

Experimental Results

Table I shows the processing conditions for each sample. Ion implantation was performed using $^{11}B^+$ ions with an accelerating voltage of 50 kV and doses of 1.5×10^{13} atoms/cm^2. Noise figures of 30-50 npn transistors in each group were measured as shown in Fig. 6.

Table I. Experimental data of npn transistor in bipolar IC

Wafer No.	Not implanted standard sample	Countermeasure for ion implanted sample					Data of test transistor		
		Experiment 1		Experiment 2					
		Al evap	Poly Si	CVD SiO_2	Tape	PR	Generation rate of pulsive noise (%)	Noise level median (mV rms)	h_{FE} median
1	O						8.7	8.9	555
2		O					0	9.5	374
3			O				0	9.8	316
4							31	9.2	402
5						O	20	8.8	353
6				O			41	10.0	457
7					O		24	8.8	410
8				O		O	68	14.0	384
9				O	O		30	8.0	598

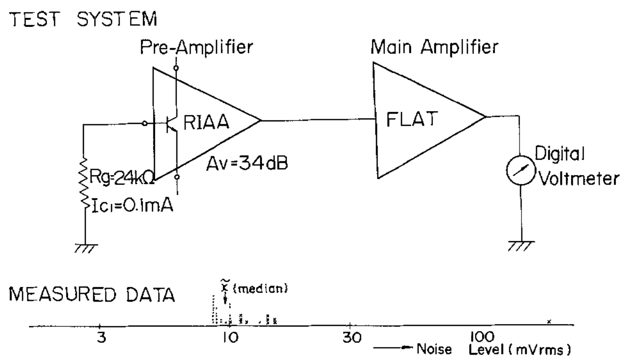

Fig. 6. Noise figure measurement for npn transistor

At first, notice wafers No. 1-4. In these cases, No. 1 is an unimplanted standard sample. Number 4 is ion implanted on to conventional thermal grown SiO_2 only. With regard to the generation of pulsive noise, less than 10% of the units in groups 1 to 3 had this characteristic, compared to over 30% in group 4. The median of noise level is almost constant as long as the generation rate of pulsive noise is below 30-50% because the level of the pulsive noise is distributed very widely as shown in the example of measured data in Fig. 6. There are no distinct tendencies in the median of h_{FE}. Therefore, a conductive film mask such as aluminum or polycrystalline Si is effective in the suppression of pulsive noise.

Then, observe wafers No. 5-9. In these cases, the generation rate of pulsive noise is over 20% in every sample. Therefore, an insulating film mask with increased stopping power against incident ions is ineffective in the suppression of pulsive noise.

In order to confirm the effect of dielectric breakdown, noise figures of bipolar IC's were measured as shown in Table II. The test system for the KC573C device is illustrated in Fig. 7. It is clear that the generation rate of pulsive noise for aluminum- or polycrystalline Si-covered samples (No. 3-6) is comparable to that for samples made by conventional thermal diffusion only (No. 1-2), while the generation rate of pulsive noise in devices fabricated without countermeasures (No. 7-8) is as large as 70%.

Discussion

Standard voltage-ramp-type dielectric strength measurement of thin SiO_2 films was carried out as shown in Fig. 8. N-type epitaxial layers grown over p-type substrates were oxidized at 1020°C in steam for 22 min (about 2400Å thick). The polarity of the applied voltage was chosen to forward bias the p-n junction. Pulse (peak) voltmeter readings indicated in Table III are about 70% of the actual breakdown voltages due to meter current I_M, when the breakdown current I_L is observed by microammeter. As shown in Table III, it is clear that ion implanted wafers with photoresist applied (No. 5-6) have the lowest break-

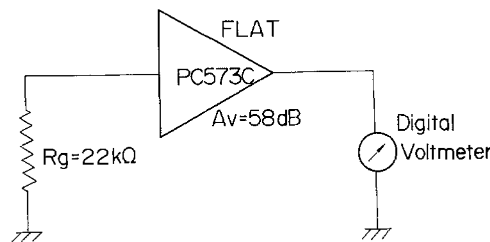

Fig. 7. Noise figure measurement for bipolar IC

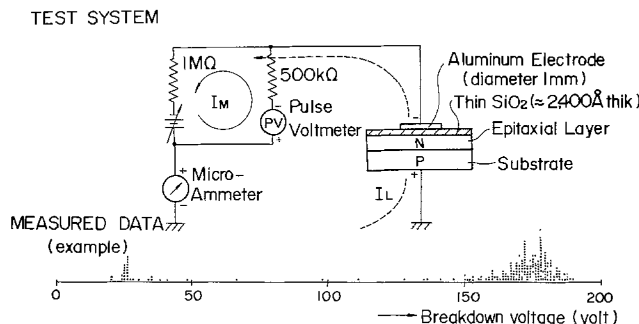

Fig. 8. Standard voltage ramp-type dielectric strength measurement of SiO_2.

down voltages, the highest standard deviation, and the highest percentage of breakdown voltage under 50V. It is concluded that the generation rate of pulsive noise during ion implantation is associated with the dielectric breakdown of SiO_2.

In order to investigate the relationship between the anomalous generation of pulsive noise and lattice defect density of the substrate surface, x-ray rocking curve checks and Sirtl etching were performed. As to the rocking curve check, peak intensity and half-width of the samples were equal to those found for bulk Si. As to Sirtl etching, there was scarcely any damage recognizable in any sample. Corresponding to these results, emitter-base or collector-base leakage current was not prominent even in the samples with the highest noise figure. It is concluded that the surface defect density is not large enough to be detected by these measurements.

The most practical way of introducing a conductive film mask is to cover the entire surface of the substrate with a very thin (for example, 50-100Å thick) aluminum film deposited as in the preparation of electron microscope samples.

Capacitance-voltage curves or surface-state density of the samples was not measured because surface states do not affect the characteristics of bipolar devices as much as that of MOS devices.

Conclusions

The mechanism of medium dose ion implantation into the insulating film mask was investigated. Accumulated charge voltage of the insulating film mask

Table II. Experimental data of KC573C

Wafer No.	Not implanted standard sample	Ion implanted sample: Countermeasure Al evap	Ion implanted sample: Countermeasure Poly Si	Ion implanted sample: No countermeasure	Data of bipolar IC: Generation rate of pulsive noise (%)	Data of bipolar IC: Noise level median (mV rms)
1	O				17.6	2.4
2	O				46.2	2.4
3		O			21.4	2.4
4		O			6.7	2.4
5			O		23.1	2.4
6			O		15.4	2.4
7				O	68.3	3.1
8				O	74.5	3.3

Table III. Dielectric breakdown voltage of SiO_2

Wafer No.	Not implanted standard sample	Countermeasure for ion implantation: Al evap	Countermeasure for ion implantation: PR	Breakdown voltage of thin SiO2: Mean value $\bar{x}$ (V)	Standard deviation σ (V)	$\sigma/\bar{x}$ (%)	Breakdown voltage under 50V (%)
1	O			164.4	33.8	20.6	4.1
2	O			155.5	42.5	27.3	7.6
3		O		171.1	38.2	22.3	6.4
4		O		158.5	46.2	29.1	9.1
5			O	152.9	49.3	32.3	12.3
6			O	149.4	51.5	34.5	14.5

rises as ion implantation proceeds and eventually leads to local dielectric breakdown of the insulating film mask. It was found that this is completely avoided by coating the insulating film mask with thin conductive film.

Acknowledgments

The authors are indebted to Mr. M. Yokozawa for the execution of x-ray rocking curve check and Sirtl etching. Also the authors are grateful to Mr. I. Sasaki for many useful suggestions and discussions.

Manuscript submitted Nov. 22, 1977; revised manuscript received May 1, 1978. This was Paper 354 presented at the Atlanta, Georgia, Meeting of the Society, Oct. 9-14, 1977.

Any discussion of this paper will appear in a Discussion Section to be published in the June 1979 JOURNAL. All discussions for the June 1979 Discussion Section should be submitted by Feb. 1, 1979.

Publication costs of this article were assisted by the Nippon Electric Company.

REFERENCE

1. S. T. Hsu, R. J. Whittier, and C. A. Mead, *Solid-State Electron.*, **13**, 1055 (1970).

Crystal Growth and Segregation under Zero Gravity: Ge

A. F. Witt,* H. C. Gatos,* M. Lichtensteiger,* and C. J. Herman

Department of Materials Science and Engineering, Massachusetts Institute of Technology, Cambridge, Massachusetts 02139

ABSTRACT

Crystal growth and segregation in space were quantitatively investigated in a Bridgman-type configuration. It was established that the segregation behavior is diffusion controlled without interference from residual gravity, G-jitter, and surface tension gradients. Radial and longitudinal segregation effects were accounted for by a lateral diffusional dopant redistribution within the diffusion boundary layer brought about by the nonplanar morphology of the growth interface.

The existing gap between theory and experiment in crystal growth and segregation is largely attributed to gravity-induced convection effects which lead to the establishment of boundary conditions significantly different from those serving as the basis of the various theories (1-5). Thus, neither ideal mixing nor complete diffusion control can be achieved in growth from the melt. Moreover, stable boundary conditions cannot be maintained because of time-dependent variations of the convection flow (6).

Attempts to eliminate convection in melts through the application of magnetic fields (7, 8) and by use of capillary dimensions have not been very successful (9). Consequently, it has not been possible to assess the validity of the existing theoretical framework, *i.e.*, to determine the relationship between the equilibrium distribution coefficient and the interface distribution coefficient, the orientation dependence of the distribution coefficient, the origin of the radial segregation effect, and other segregation anomalies (10-12).

The presently reported crystal growth experiment was conducted during the Apollo-Soyuz mission as a part of NASA's program to determine the potential of zero-gravity[1] conditions for basic research and applications in materials processing. It was designed to establish on a quantitative basis the crystal growth and segregation behavior encountered in a zero-gravity environment, to provide a further insight into the unexpected behavior of confined melts observed in the growth of InSb during the Skylab mission (13), and to assess the magnitude and effects of surface tension driven convection.

Experimental Procedure

To achieve the experimental objectives, Ga-doped germanium crystals grown on earth were partially remelted in a confined configuration and regrown in space while current pulses were applied to achieve interface demarcation (11).

Sample preparation.—The germanium crystals used for the experiment were pulled in the <111> direction by the Czochralski method from 225g melts doped with gallium to achieve an average dopant concentration of about $10^{19}/cm^3$ in the solid. The crystals were centerless ground to a diameter of 1.046 cm and cut to a length of 9.5 cm. Their diameter was reduced to 0.843 cm over a length of 2 cm from each end to permit the attachment of graphite cups which served as current contacts for interface demarcation. The crystals were subsequently etched in CP-4 (5 parts conc HNO_3 + 3HF + $3CH_3COOH$) and encapsulated into centerless ground quartz ampuls 12.7 cm long with 1.0 cm ID and 1.5 cm OD. Prior to assembly, each ampul was etched in HF, rinsed successively with distilled water, methanol, and acetone, and dried. The graphite cups were machined to make good electrical contact with the germanium crystals and were fired at 1600°C in a vacuum of 10^{-7} Torr (1.3×10^{-5} Pa) prior to attachment. A schematic diagram of the ampul is shown in Fig. 1. The ampuls were sealed in stainless steel cartridges with an argon atmospere of 40 Torr (at room temperature).

Melting and regrowth procedure.—The flight experiments (as well as ground-based tests) were carried out in a "multipurpose" gradient furnace designed originally for the Skylab mission (13). It was modified with a system of lateral heat shields to permit operation at higher temperatures with controlled heat flow along the crystal from the heat leveler region via the gradient region to the heat extractor plate (see Fig. 1).

Partial remelting of the Ge crystals in space was accomplished by raising the temperature of the heat leveler region over a period of 3.5 hr to 1120°C while

* Electrochemical Society Active Member.

[1] The actual value of gravity was of the order of 10^{-5}G. For convenience this value of G is referred to in this paper as zero.

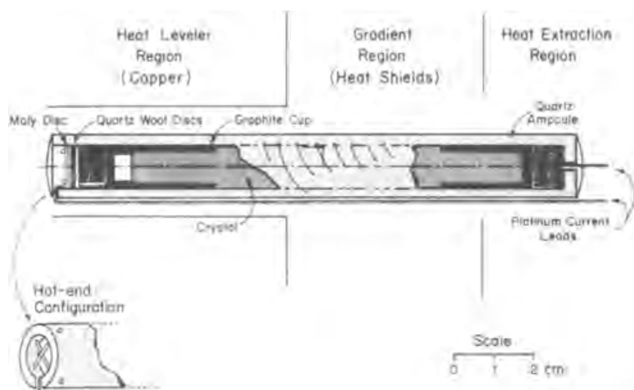

Fig. 1. Schematic representation of growth system and ampul design permitting interface demarcation through current pulsing.

maintaining the heat extractor region close to room temperature. In this thermal configuration a temperature gradient of about 50°C/cm was established in the gradient regions (Fig. 1), designed to locate the solid-melt interface at about 3.7 cm from the cold end of the crystal. To achieve thermal equilibration and to eliminate compositional inhomogeneities in the melt the temperature in the hea leveler region was maintained constant for a period of 2 hr. Regrowth was initiated by programmed reduction of the furnace power input to the heat leveler region (cooling rate 2.4°C/min), which was expected to result in a growth rate of about 5 μm/sec during the early stages of resolidification and in an increase of the growth rate to 10 μm/sec during the late stages of solidification.

Throughout thermal equilibration and controlled cool-down, current pulses of 55 msec duration and an amplitude of 15.5A were transmitted through the growth systems at a repetition rate of 0.25 Hz in order to achieve periodic demarcation of the crystal-melt interface. Following the controlled cool-down cycle (1.4 hr), the power was turned off (passive cool-down) and after 2 hr the system was subjected to forced cool-down by He injection.

A series of ground-based control experiments were carried out in an identical furnace to permit comparison of growth and segregation behavior in space and on earth. These experiments were performed in the same programmed mode as the flight experiments with the furnace positioned vertically (heat leveler up) in order to establish stabilizing vertical thermal gradients (growth took place in the upward direction). The thermal history of the growth system in space, obtained from temperature measurements in the heat leveler region and at the cold heat extractor plate, is shown in Fig. 2.

Analytical procedure.—The crystals grown were subjected to growth and segregation analyses based on procedures described elsewhere (11). For bulk analysis the regrown crystals were cut along the growth direction to obtain 0.2 cm thick slices, containing the growth axis. To permit single point spreading resistance analyses large area ohmic contacts (evaporated and micro-alloyed silver layers) were made on the back sides of the crystal segments and were pressure-bonded with conductive silver paint to brass disks. All mounted specimens were ground with 10 μm particle size abrasive, mechanically polished with Linde A alumina, and chemically polished with a modified Syton HT-30 solution (200 ml Syton, 200 ml H_2O, 5 ml H_2O_2, and 2 ml CH_3COOH). After rinsing, the samples were etched by immersion for 8 sec in a solution of equal parts of HF, H_2O_2, and CH_3COOH.

For quantitative segregation analysis, spreading resistance measurements were carried out first and subsequently the corresponding growth rates determined

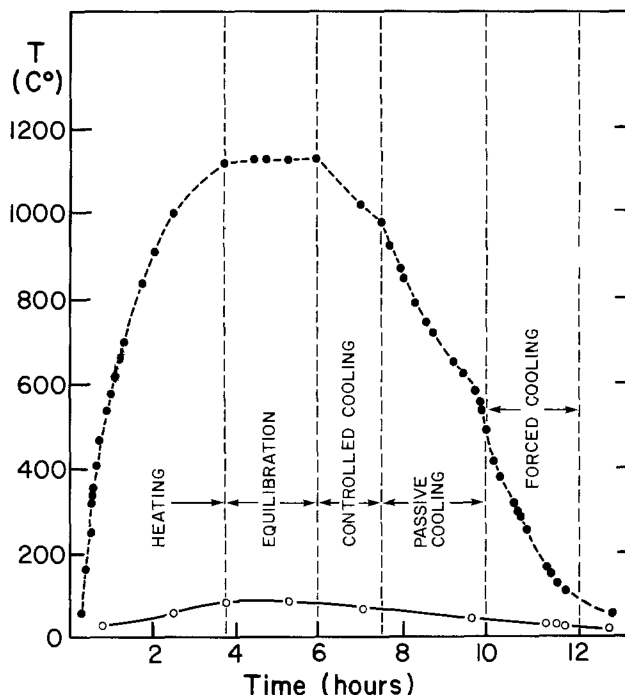

Fig. 2. Thermal cycles of growth experiment; ● temperature in heat leveler region; ○ temperature at heat extraction plate.

from demarcation spacings by interference contrast microscopy. The reproducibility of spreading resistance measurements on stabilized surfaces was better than 2%. After correcting for resistances in the external circuitry the raw spreading resistance data were reduced to normalized resistance using a quadratic progression fit. These data were converted into resistivity using an experimentally determined probe calibration factor based on measurements with samples of well-defined electrical properties. The resistivity data in turn were reduced to carrier concentration by fitting to a computer generated expression for (N_A-N_D) *vs.* ρ employing a spline cubic interpolating polynomial derived from the literature (14) and from Hall-effect data.

Experimental Results and Discussion

Surface characterization.—Each crystal regrown in space was readily removed from its quartz container (Fig. 3) suggesting that the surface morphology of the grown crystal did not conform to that of the container which exhibited microscopic irregularities. Lack of conformity of the regrown crystal with the confining quartz surface was confirmed by interference contrast microscopy. The surface of the crystal grown in space exhibited a random network of ridges (Fig. 4) ranging in height from about 1 to 5 μm. These ridges, which reduced the actual contact area between the crystal and the confining wall to a fraction of 1%, appear similar in nature to those observed on InSb

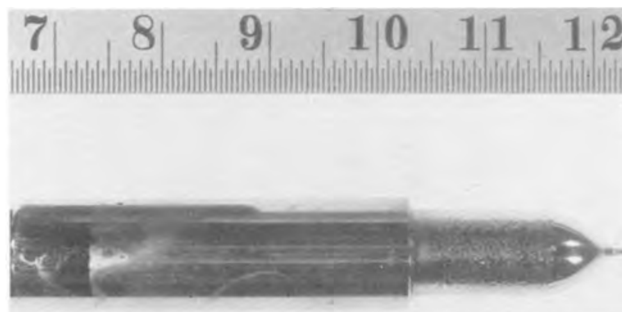

Fig. 3. Germanium crystal with <111> orientation, grown in space, after removal from quartz ampul.

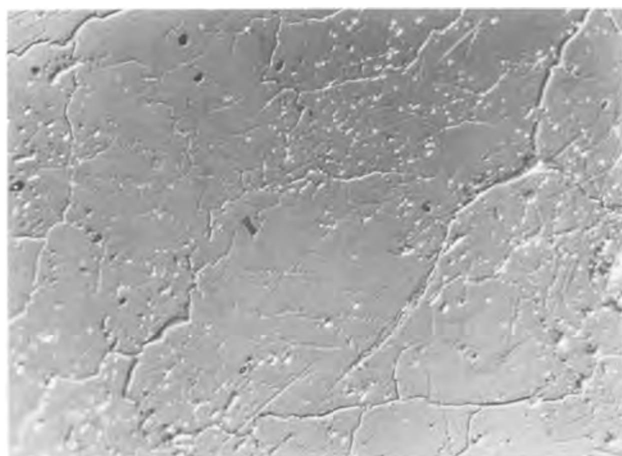

Fig. 4. Ridge patterns on the surface of the <111> germanium, grown in space.

crystals grown on Skylab (13). In view of the fact that liquid Ge expands by more than 3% on solidification it is concluded that under zero gravity conditions the germanium melt does not establish a wetting contact with the confining quartz ampuls and that the ridges observed on the regrown crystals reflect the morphological characteristics of the melt surface in the vicinity of the regrowth interface. In this respect the behavior of the germanium melt in space is fundamentally different from that encountered in ground-based experiments where wetting contact with the confining wall takes place and consequently the solidified material in all instances can be isolated only by dissolving the quartz ampuls in hydrofluoric acid.

The ridge formation, which cannot as yet be explained, could be of fundamental importance for materials processing in space, since it suggests that liquid systems may be placed in partial or complete confinement without significant contact with the confining material.

A comparison of the morphological characteristics of Ge crystals regrown on earth and in space reveals additional pronounced differences. It is found that crystals obtained from ground-based experiments invariably exhibit complete loss of single crystallinity after a growth length of about 2 cm. In contrast, single crystallinity is preserved in the peripheral region of space-grown material to the very last stages of growth in spite of internal matrix breakdown due to constitutional supercooling effects which was expected under the prevailing growth conditions (12) (Fig. 5).

Visual inspection of the space-grown crystals showed abrupt, peripherally asymmetric changes in surface morphology after about 1.5 cm of growth. The location of these morphological irregularities corresponded to the transition from the thermal gradient region to the heat leveler region within the multipurpose furnace. Bulk crystal analysis suggests that these morphological irregularities result from changes in the heat transfer characteristics of the growth system (see below).

Bulk characterization.—Etching analysis.—High resolution etching techniques were refined during ground-based testing to permit, through interference contrast microscopy, the detection of microscopic compositional fluctuations in Ge with a sensitivity of better than $\pm 0.2\%$ at dopant (Ga) levels in excess of $10^{18}/cm^3$.

The basic difference between microsegregation in the segment of the ingot grown on earth and that grown in space is apparent from the dark-field photomicrograph in Fig. 6; thus, compositional fluctuations which characterize the original seed portion grown on earth

Fig. 5. Etched cross section of the last portion of the <111> germanium crystal regrown in space. Note preservation of peripheral single crystallinity in spite of internal breakdown and phase segregation.

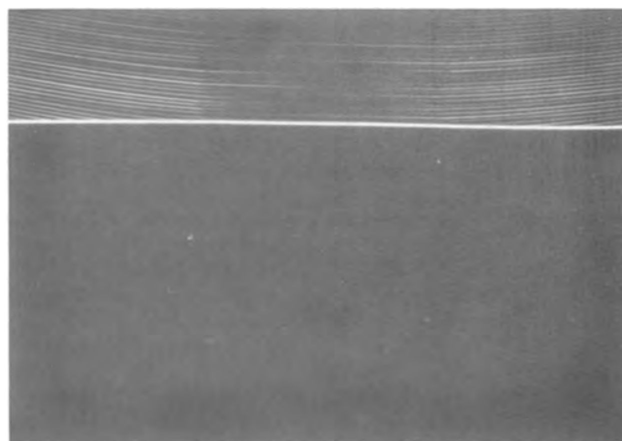

Fig. 6. Etched cross section (under dark-field illumination) of crystal grown in space; space-grown segment (bottom), in contrast to earth-grown segment (top), exhibits no compositional inhomogeneities.

(top portion) are absent in the crystal segment regrown in space (bottom portion). The pronounced demarcation of the original regrowth interface is due to the abrupt decrease in dopant incorporation associated with the initial stages of regrowth.

Details of the microsegregation behavior in the initial regrowth region were observed by interference contrast microscopy and are shown in Fig. 7. Three regions can be identified: a segment of the original seed (top of photomicrograph), a narrow growth band of about 350 μm in length with compositional fluctuations (middle), and the regrowth region exhibiting microscopic compositional homogeneity in which current-induced interface demarcation lines can be readily seen (bottom). The onset of controlled regrowth is clearly evident at the upper part of the bottom region where interface demarcations appear with gradually increasing spacing. Accordingly, the uncontrolled growth of the narrow band (middle) must

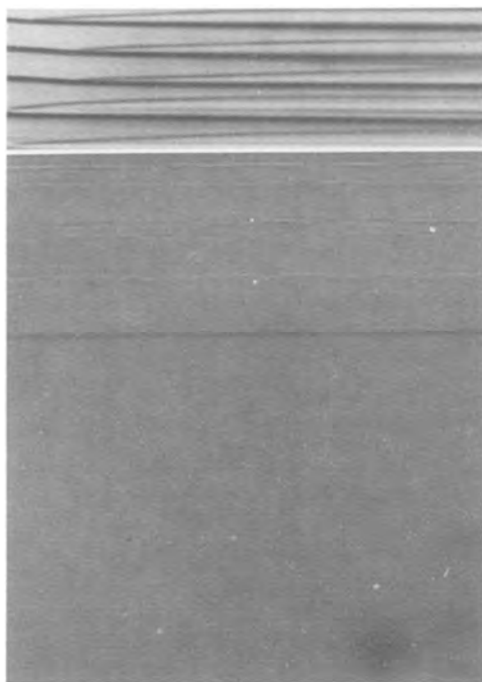

Fig. 7. Segment of Ge crystal partially regrown in space: note seed segment (top) and segment of controlled regrowth (bottom) separated by a region of uncontrolled growth and segregation.

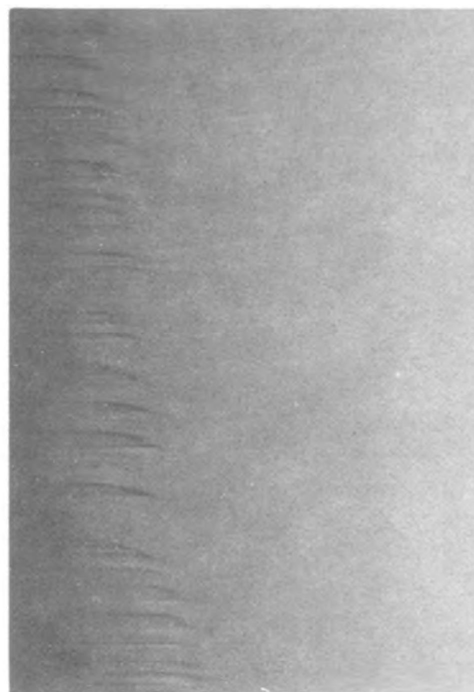

Fig. 8. Peripheral (111)-facet in the space-grown Ge crystal

have preceded the onset of controlled cool-down and, thus, took place during the thermal equilibration period. Similar narrow growth regions of apparently uncontrolled growth, ranging in length from 200 to 1000 μm, were observed also in all ground-based experiments conducted in the multipurpose furnace.

The cause of the uncontrolled growth becomes apparent on examination of the thermal history of the growth system shown in Fig. 2. It is seen that the temperature in the heat leveler region remained constant at 1120°C during thermal equilibration (2 hr) but that the temperature at the heat extraction plate increased slightly during the first hour and decreased by about 20°C during the second hour. This gradient increase associated with the temperature decrease of the heat extraction plate brought about a relocation of the growth interface toward the hot zone. Thus, the observed uncontrolled growth resulted from the thermal drift of the system during the equilibration period.

Etching analysis of the crystals regrown in space revealed that the bulk of the controlled-growth segments are free of microscopic compositional fluctuations for a length exceeding 3.0 cm. The only identifiable compositional changes were associated with peripheral (111) faceting of the growth interface which was found to extend about 0.5 mm into the bulk (Fig. 8) over the entire length of the crystal segment. Actually, these inhomogeneities within the peripheral facet region were identified as off-facet growth penetrations into the facet regions and are due to differences between the on-facet and off-facet distribution coefficient. As such they are not conventional impurity striations which are caused by variations of the growth rate and/or of the boundary layer thickness.

In the crystals regrown during ground-based testing, peripheral (111) faceting could be observed only in a few instances and at isolated locations, although the morphology of the growth interface was the same as in the space-grown crystals. Since peripheral faceting is commonly observed in nonconfined growth configurations (as in Czochralski growth) the present observation of pronounced peripheral (111) faceting in the space-grown material may be considered as indicative of virtually unconfined solidification conditions.

Compositional inhomogeneities of significant magnitude were observed in all space-grown crystals in portions formed during the late stages of growth, in which the crystal-melt interface approached and entered the graphite cup (Fig. 1). There the compositional inhomogeneities could in all instances be related, through the individual interface demarcation lines, to morphological changes of the interface caused by pronounced changes in thermal conditions. Such changes were brought about by the difference in the thermal conductivities of the confining materials (in going from quartz to graphite). The observed morphological changes resulted in interface instabilities followed by interface breakdown. Although no detailed analysis of the interface instabilities has been carried out, it is seen in Fig. 9 that their morphological characteristics conform much more to theoretical predictions than those observed in crystals grown on earth (12).

Quantitative analysis of crystal growth behavior.—The following analysis is based on data obtained from demarcation lines of the crystal-melt interface introduced at intervals of 4 sec during growth. The accuracy of the growth rate data (about ±0.1 μm/sec) is determined by the precision with which the spacings of consecutive demarcation lines could be determined by interference contrast microscopy.

The microscopic rate of growth along the growth axis for the first 2 cm of solidification in space, brought about by a constant cooling rate of 2.4°C/min in the heat leveler regions, is presented in Fig. 10. It is seen that the growth rate is transient at all times, increasing rapidly from zero to 8 μm/sec over the first 10 min and gradually approaching the value of 10 μm/sec during the ensuing growth period. No fluctuations in the growth rate are observed in any portion of the growth region (the scatter of the measurement points falls within the experimental error limits).

From growth experiments carried out in the same growth apparatus under stabilizing vertical thermal gradients on earth it was found that the microscopic growth behavior on earth is, within experimental error, the same as that observed in space. Thus, while unavoidable laminar convection in the melt on earth interferes with the segregation process (see below), it

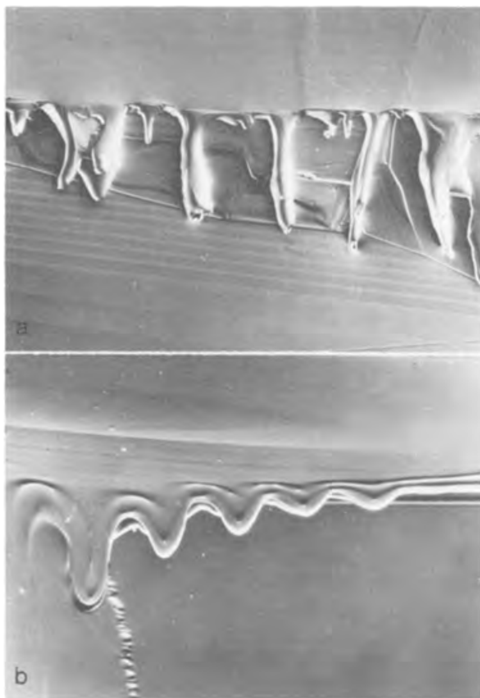

Fig. 9. Advanced stage of interface instability in germanium crystals grown (a) on earth; (b) in space.

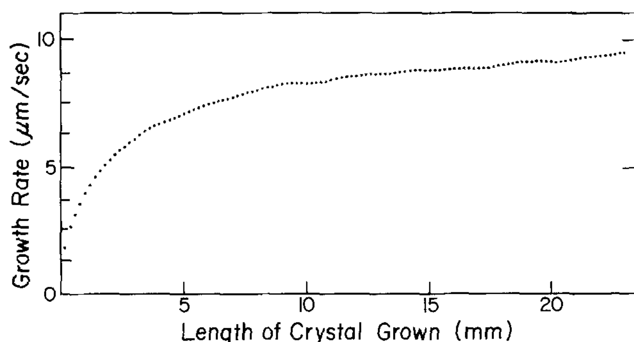

Fig. 10. Microscopic growth rate profiles along the middle of germanium crystals grown in multipurpose furnace. Profiles for growth in space and on earth are the same.

has no significant effect on the microscopic crystal growth rate.

Since the growth interface was found to be nonplanar and since its morphology changed with continuing growth (see below), it was considered necessary to determine also the microscopic growth rates on the peripheral regions of the longitudinal crystal segment (0.5 mm from the left-hand side and right-hand side edges). The growth rates at the left- and right-hand sides of the longitudinal segment are plotted as a function of distance grown in Fig. 11; distance grown is measured from a normal to the growth axis arbitrarily positioned in the uncontrolled-growth region. Thus, the plots reflect the asymmetry of the interface about the growth axis and show that the microscopic growth behavior of the two peripheral regions was different during the initial and during the late stages of growth.

The effect of the differences in the peripheral rates of growth on the morphology of the growth interface is seen in Fig. 12 where the difference of growth length ($\Delta x = x_{left} - x_{right}$) is plotted as a function of time of growth. Since the growth length (x) is measured from a normal to the growth axis, as indicated above, the Δx values reflect the deviation of the interface from a planar morphology. It is seen that originally the left-hand side of the interface was more advanced (into the melt) than the right-hand side. This asymmetry was reduced significantly during the first 500 sec of growth as a result of a larger growth rate at the right-hand side of the interface. The interface morphology remained virtually unchanged during the ensuing growth period of about 1300 sec but after 1900 sec of elapsed time a retardation of the growth rate on the right-hand side (Fig. 11) led to a significant change of the interface morphology.

The characterization of the dynamics of the interface morphology was pursued further by ascertaining the interface shape through the determination of the coordinates of up to 10 points lying on individual interface demarcation lines at varying distances from the original regrowth interface (Fig. 13). It is seen that the original melt-back interface is indeed asymmetric and that the uncontrolled growth during the equilibration period did not result in any noticeable changes in the morphology of the solid-melt interface. With the onset of controlled cool-down the interface morphology underwent rapid changes as evidenced by the shape of the demarcation lines 2 and 3 positioned 0.2 and 5 mm below the regrowth interface, respectively. At the 5 mm position the interface was concave (viewed from the melt) and nearly symmetric; it remained essentially unchanged for a total growth length of 15 mm (demarcation line 5). With continued growth (1900-3300 sec) a progressively increasing change of the interface morphology occurred (demarcation lines 6 and 7) as a result of a decrease of the growth rate on the right-hand side peripheral region of the crystal (see Fig. 11 and 12). During this change the interface apex shifted from the center of the crystal to the periphery.

The above behavior of the crystal-melt interface can be directly related to the thermal environment of the growth system. Thus, it was observed that the seed crystal was not concentrically located within the quartz ampul. Consequently the initial interface was asymmetric and on regrowth the crystal diameter increased asymmetrically, *i.e.*, by 0.5 mm at the right-hand side and 0.05 mm at the left-hand side. The establishment of the stable and nearly symmetric concave interface (with a radius of curvature of 5.6 cm) coincides with the growth of the crystal at constant diameter. The growth perturbation which commences at a distance of about 15 mm from regrowth interface

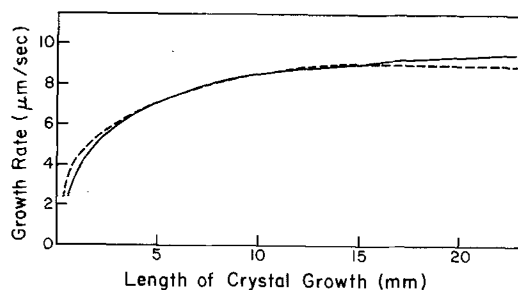

Fig. 11. Microscopic rate profiles along the periphery of germanium crystal grown in space.

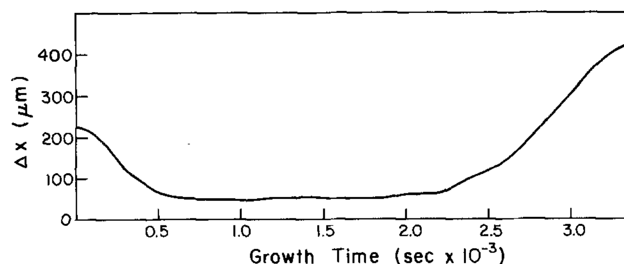

Fig. 12. Difference (Δx) in the peripheral rate of growth as a function of growth time (see text).

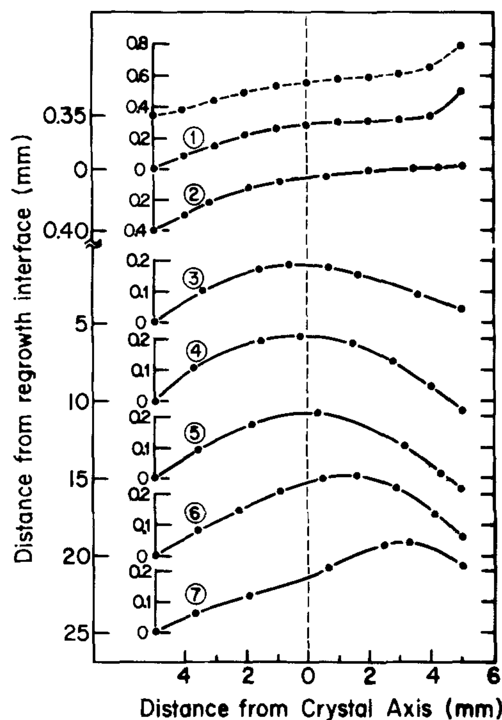

Fig. 13. Crystal-melt interface morphology determined by interface demarcation, various distances from regrowth interface denoted as ① are referenced in the text.

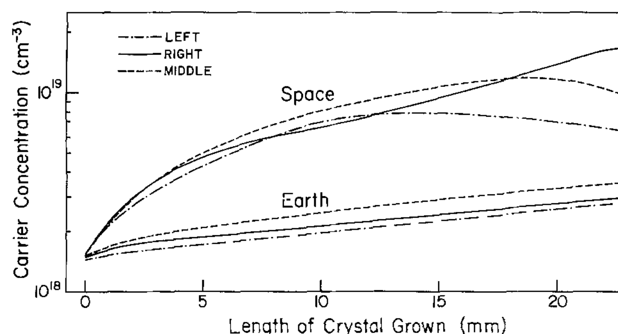

Fig. 14. Longitudinal carrier concentration (dopant) profiles in crystals grown on earth and in space.

coincides with the advancement of the interface from the gradient heating region to the heat leveler region (see Fig. 1) and reflects the changes in the radial thermal configuration within the multipurpose furnace. It is of interest to note that the changes of the interface morphology associated with the changing thermal environment are less pronounced in the ground-based growth experiments.

On the basis of the present growth analysis it is evident that within the gradient-heated region, crystal growth in space proceeded with a stable interface configuration. All observed growth perturbations are accounted for by deficiencies in the thermal characteristics of the growth apparatus.

Quantitative segregation analyses.—Before proceeding with the segregation analysis, the redistribution of Ga in the melt during the 2 hr period of thermal equilibration preceding controlled growth is considered. Taking the average temperature of the melt as 1050°C and the diffusion coefficient of Ga as 2×10^{-4} cm²/sec, the minimum diffusion distance ($\sqrt{Dt}$) of Ga is approximately 1.2 cm in the absence of convection. Accordingly all compositional inhomogeneities in the melt resulting from rotational striations and radial segregation effects in the original earth-grown crystal were eliminated prior to resolidification.

The average concentration of Ga in the earth-grown crystal increased linearly by +5.2 %/cm from the cold seed, where the Ga concentration was 1.3×10^{19}/cm³, to the hot end where the concentration was 1.88×10^{19}/cm³ as determined from Hall-effect measurements). From these data the equilibrium Ga concentration in the melt (complete homogenization), with the seed-melt interface located 3.9 cm from the cold end of the crystal, was calculated to be 1.78×10^{19}/cm³. While uncertainties in the published diffusion coefficient values of Ga in Ge melts (15) do not permit precise calculations, approximations indicate that complete homogenization was approached during the equilibration period. This conclusion is consistent with the fact that in ground-based regrowth experiments, involving crystals of the same macrosegregation profile as those used in space, the composition of the initial portions resolidified were found to have the same Ga concentration as the initial portions resolidified in space (see Fig. 14). In the ground-based experiments compositional homogenization of the melt during the 2 hr thermal equilibration must be considered as having been complete because of the presence of laminar convection which was confirmed by segregation analyses.

The macroscopic segregation behavior is discussed below. Microscopic segregation effects observed on earth and in space are presented in the Appendix.

The segregation analyses of the crystals grown on earth and in space are based on longitudinal and radial composition profiles obtained with 10 μm spatial resolution by spreading resistance scans of longitudinal crystal slices which contained the growth axis. The corresponding growth rate data were obtained as discussed above.

For a direct comparison of dopant redistribution associated with growth on earth and in space, corresponding longitudinal composition profiles are presented in Fig. 14; the microscopic growth rates were presented in Fig. 10. Since both growth experiments were carried out under identical thermal and geometrical conditions, the observed differences in composition reflect directly the effect of gravity-driven convection on segregation. It is seen that for growth on earth the longitudinal increase of the dopant concentration is small and remains essentially constant after a short initial period during which transient segregation behavior is observed. These composition profiles also indicate radially asymmetric segregation which develops during the initial growth and remains virtually unchanged. In contrast, in space, the longitudinal dopant concentration increases rapidly with transient segregation over the entire growth length; radial segregation develops less rapidly than on earth but increases with continuing growth and exhibits pronounced variations.

Segregation on earth.—All features of the composition profiles obtained from the ground-based growth experiment are consistent with convection-controlled segregation, which is amenable to quantitative analysis on the basis of the normal freezing equation (2)

$$\ln \frac{C_s}{C_L} = \ln k_{eff} + (k_{eff} - 1) \ln (1 - f)$$

where C_s is the dopant concentration in the solid for a given fraction f solidified, C_L is the dopant concentration in the melt, and k_{eff} is the effective distribution coefficient.

In view of the radially nonuniform dopant distribution (Fig. 14), transverse compositional profiles were determined at 0.5, 1.0, 1.5, and 2.0 cm from the original regrowth interface to obtain the average Ga concentration values (C_s) for four different fractions (f) of melt solidified. The plot of ln C_s/C_L *vs.* ln $(1-f)$ in Fig. 15 shows full compliance with the nor-

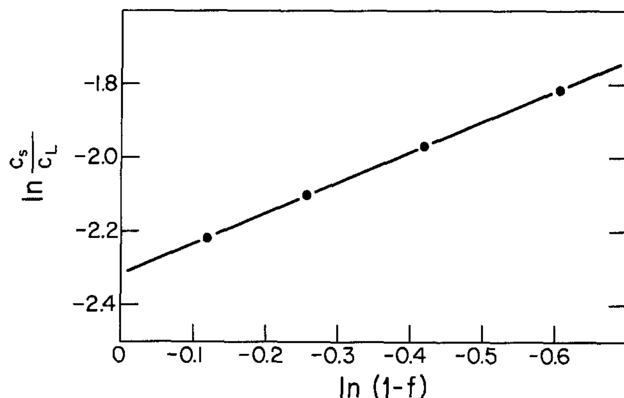

Fig. 15. Segregation analysis for crystal grown on earth

mal freezing equation and thus establishes the existence of convection-controlled segregation with a constant effective distribution coefficient ($k_{eff} = 0.099$) over the entire growth distance. Thus, on earth even under stabilizing vertical thermal gradients unavoidable radial thermal gradients constitute a driving force for the establishment of convection in the melt. The fact that the effective distribution coefficient remained constant indicates that the convective melt flow was virtually unchanged while the aspect ratio of the melt (height/diameter) changed from about 5 to 2.5.

While inadequate knowledge of the radial thermal gradients does not permit a quantitative analysis of the prevailing laminar convection, it is of interest to compare the effects of this laminar free convection on segregation with those of forced convection such as encountered during Czochralski-type growth. According to the BPS model (1) an effective distribution coefficient of 0.099 associated with an average solidification rate of 8 μm/sec requires a solute boundary layer thickness of 300 μm. Using the Cochran analysis (16) for forced convection associated with crystal rotation it is found that the mixing effect due to the laminar free convection in the ground-based experiments is equivalent to forced convection resulting from a seed rotation of 10 rpm.

Segregation in space.—A comparison of the composition profiles of the space-grown crystal (Fig. 14) with the corresponding growth rate profile (Fig. 11) shows that for the growth length in excess of 8 mm neither the radial nor the longitudinal segregation were directly controlled by the microscopic rate of growth. Thus, with a steadily increasing growth rate which was essentially the same on the left- and right-hand side, the dopant concentration in the crystal decreased on the left-hand side from $8 \times 10^{18}/cm^3$ to $6.5 \times 10^{18}/cm^3$ while at the same time it increased on the right-hand side to $1.9 \times 10^{19}/cm^3$. The observed segregation pattern is, furthermore, at variance with melt convection effects. Thus, when the equilibrium distribution coefficient is less than one (as in the present case) convective interference results invariably in a decrease of dopant accumulation within the diffusion boundary layer and, consequently, the value of the effective distribution coefficient will exceed by a small amount the value of k_0 but will remain significantly less than one as observed during growth on earth. Therefore, the observed dopant concentration increase to $1.9 \times 10^{19}/cm^3$, which corresponds to an effective distribution coefficient in excess of one, is in direct contradiction with convection effects.

The segregation behavior, while inconsistent with growth rate and convective effects, can be explained if the morphological characteristics of the crystal-melt interface are taken into consideration. Thus, for growth with diffusion-controlled segregation any deviation of the crystal-melt interface from a planar configuration is expected to result in radially nonuniform dopant incorporation since the diffusion dopant flux into the melt exhibits lateral components which lead to radial compositional variations at the curved growth interface. Accordingly, for a concave (into the crystal) interface the dopant concentration must be higher in the central than in the peripheral part of the crystal. On this basis, the radial segregation shown in Fig. 14 is consistent with the morphological characteristics of the growth interface shown in Fig. 13. Thus, at the onset of controlled regrowth (demarcation 1 in Fig. 13), in the absence of a solute boundary layer, radial segregation must be expected to be uniform. With continuing growth the interface becomes slanted to the left-hand side (demarcation 2) and the associated lateral diffusion flux to the right causes the dopant concentration to become somewhat smaller in the left-hand side of the crystal than in the center and in the right-hand side. After about 20 mm of growth (*e.g.*, demarcation lines 6 and 7) the pronounced shift of the interface apex to the right causes the concentration in the right-hand side regions to become even higher than that of the central region. At the same time the concentration in the central region begins to decrease but continues to remain higher than that on the left-hand side region.

It should be noted that the radial segregation behavior for growth on earth appears also consistent with interface morphology effects. Thus, the concave crystal-melt interface was found to be asymmetric with its apex shifted to the right-hand side of the crystal axis and the dopant concentration was found to be higher in the right-hand side peripheral region. The less pronounced and nearly constant radial segregation effect reflects decreased sensitivity of the interface morphology to thermal perturbations due to the presence of laminar convection which in turn is also responsible for the establishment of a decreased and constant boundary layer thickness.

In view of the fact that no theoretical treatment of segregation at curved interfaces has as yet been developed, it is not possible to analyze the observed radial segregation effect on a quantitative basis. However, considering the origin of radial dopant concentration gradients it appears appropriate to analyze the macrosegregation behavior by averaging the radial compositions and applying the theory for diffusion-controlled segregation as developed for plane front solidification (3). It is recognized that any such two-dimensional analysis of a three-dimensional cylindrical system is inherently limited; however, the potential error associated with the asymmetry of the growth interface is not considered major.

The averaged longitudinal composition profile of a space-grown crystal is presented together with that of an earth-grown crystal in Fig. 16. Here again the initial increase of the dopant concentration as well as its gradual approach to a steady-state value during growth in space are indicative of the absence of convective interference. When considering the various theoretical approaches to diffusion-controlled segregation (3, 17-20), it was found that for the present experimental conditions the treatment by Tiller *et al.*

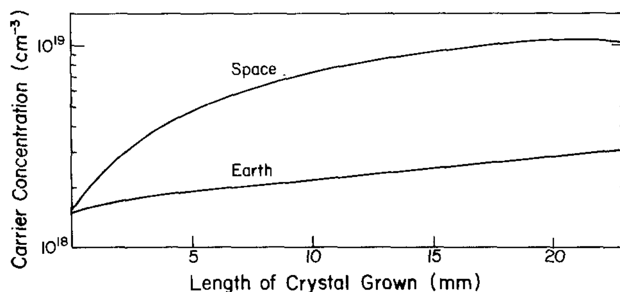

Fig. 16. Averaged longitudinal carrier concentration (dopant) profiles on crystals grown on earth and in space.

(3) can most conveniently be applied, although one of the assumed boundary conditions, *i.e.*, constant rate of growth, is not met in the present system (Fig. 10). Actually, initial growth rate transients are virtually unavoidable in directional solidification because of heat transfer considerations. To make the theory applicable, a numerical approach based on an implicit finite difference equation (21) has been used to account for the growth rate transient. These calculations yielded a compositional profile which was significantly different during the initial transient region from that obtained assuming a constant growth rate, but it was in good agreement for growth distances in excess of 1 cm.

According to theory (3), the dopant concentration (C_s) at a distance x (presently valid for $x > 1$ cm only) from the original regrowth interface is given by the expression

$$C_s = C_L \left\{ (1 - k_o) \left[1 - \exp\left(-\frac{k_o R x}{D} \right) \right] + k_o \right\}$$

The applicability of the above expression to the present segregation data was tested over the growth distance of 1-2 cm by taking the average growth rate, $R = 8.5$ μm/sec and $C_L = 1.78 \times 10^{-4}$ cm^{-3}, $k_o = 0.087$, and the generally accepted (15) value of $D = 1.9 \times 10^{-4}$ cm^2 sec^{-1}. The experimental and theoretical values of C_s, for $x = 1.0$, 1.5, and 2 cm, are presented in Table I (in the second and third column, respectively). It is seen that the agreement between theory and experiment for growth distance beyond 1 cm is remarkably good.

It should be noted that the theoretical C_s values (for $D = 1.9 \times 10^{-4}$ cm^2/sec) are consistently smaller than the corresponding experimental values, which implies that the increase in dopant concentration in Ge during growth in space is faster than predicted for diffusion-controlled segregation. If the present analytical approach is quantitatively correct, then a more accurate value for the diffusion coefficient of Ga in Ge melts is 1.7×10^{-4} cm^2/sec as seen in Table I (third column). While this conclusion may be of questionable validity in view of the difference in assumed and actual boundary conditions, it is apparent that with the appropriate theory for diffusion-controlled segregation, directional solidification experiments in space provide a means for the determination of precise diffusion coefficients which are presently unavailable.

It is recognized that the above quantitative segregation analysis is based on assumptions which require further theoretical and experimental study. However, the self-consistency of all aspects of dopant distribution in the space-grown crystal with diffusion-controlled segregation confirms the absence of any convective interference with the segregation process.

Summary

The crystal growth and segregation behavior in space were quantitatively studied by growth of Ga-doped Ge single crystals. The growth experiments in space were complemented by experiments on earth (carried out in the same system under stabilizing vertical thermal gradients) to permit a comparative analysis of gravitational effects.

Crystals grown in space exhibited a network of surface ridges which reduced the contact area with the confining quartz ampul to less than 1%. A coherent peripheral (111) growth facet, characteristic of unconfined growth, persisted over the entire growth length.

It was established that, in space, diffusion-controlled segregation prevailed with no convective interference from residual gravity, G-jitter, or surface tension gradients. Radial variations in dopant concentration were found to be a direct consequence of the nonplanar morphology of the growth interface which causes diffusion-driven dopant redistribution within the diffusion boundary layer.

Through interface demarcation thermal drift during equilibration of the system and deviations of the growth interface from planar morphology were identified; they were found to be a direct consequence of deficiencies in the thermal characteristics of the growth apparatus and demonstrate the extreme sensitivity of solidification to the thermal environment under diffusion-controlled conditions.

The present study shows that the reduced gravity environment provided in space permits the establishment of solidification conditions under which basic experimental information can be obtained which is essential for advancing our understanding of crystal growth and segregation. It is finally concluded that compositionally homogeneous materials can be achieved in space.

Table I.

x (cm)	C_s (exp) Ga · cm^{-3}	C_s (theor) Ga · cm^{-3} ($D = 1.9 \times 10^{-4}$ cm^2/sec)	C_s (theor) Ga · cm^{-3} ($D = 1.7 \times 10^{-4}$ cm^2/sec)
1.0	7.4×10^{18}	6.8×10^{18}	7.3×10^{18}
1.5	9.3×10^{18}	8.7×10^{18}	9.3×10^{18}
2.0	1.1×10^{19}	1.0×10^{19}	1.1×10^{19}

Acknowledgments

The authors wish to express their appreciation to the National Aeronautics and Space Administration and particularly to the Staff at the Marshall Space Flight Center for their uncompromising efforts, cooperation, and enthusiastic support during all stages of the experiment.

Manuscript submitted March 20, 1978; revised manscript received May 22, 1978.

Any discussion of this paper will appear in a Discussion Section to be published in the June 1979 JOURNAL. All discussions for the June 1979 Discussion Section should be submitted by Feb. 1, 1979.

Publication costs of this article were assisted by Massachusetts Institute of Technology.

APPENDIX

Microscopic Segregation Effects

Segregation associated with uncontrolled regrowth during thermal equilibration.—It was shown that uncontrolled regrowth ranging in length from 200 to 800 μm took place in all growth experiments during thermal equilibration. Attempts to determine quantitatively the growth rates of these regions through interface demarcation were unsuccessful since the spacing of demarcation lines is below optical resolution. The growth rate could, however, be estimated to be about 0.1 μm/sec from the measured time-dependent temperature change in the heat extraction system.

The compositional profiles for uncontrolled-growth regions formed on earth and in space are presented in Fig. 17. It is seen that the Ga concentration in these regions fluctuates and assumes average values of 1.85 $\times 10^{18}$ and 2.1×10^{18}/cm^2, for growth in space and on earth, respectively. It is seen further that the Ga concentration in these regions drops ultimately to 1.55×10^{18}/cm^3, which is the expected equilibrium value ($k_o C_L$) observed at the onset of controlled regrowth. Thus, it appears that during uncontrolled growth nonequilibrium segregation takes place whereby dopant accumulation to levels of 2.1 and 2.4×10^{19}/cm^3 at the crystal-melt interface raises the distribution coefficient to 0.11 and 0.12, respectively. The existence of such an accumulation layer at the growth interface is also consistent with the appearance of compositional fluctuations of up to ±3%. While the observed segregation behavior can be explained through the existence of an accumulation layer, the formation of such an accumulation layer as well as its stability over a period of about 1 hr cannot as yet be explained. Thus, diffu-

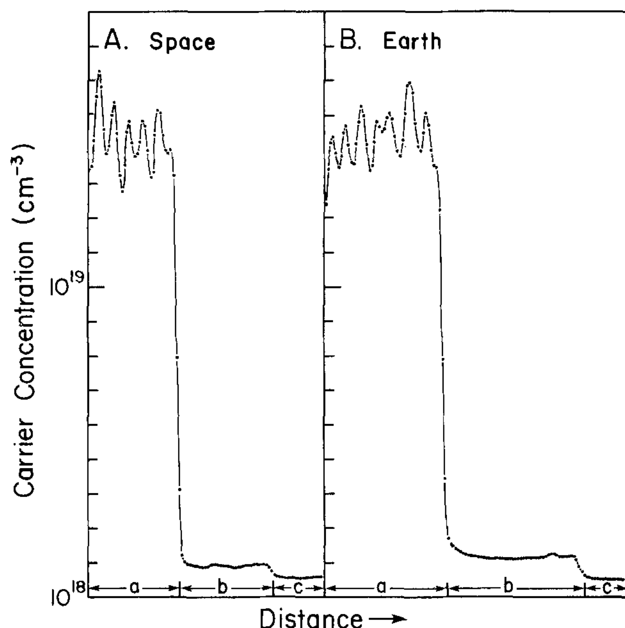

Fig. 17. Carrier concentration (dopant) profiles in uncontrolled growth regions (b) and adjacent seed (a) and controlled regrowth (c) regions of crystals grown in space and on earth.

sion from the seed crystal into the melt can neither account for the dopant accumulation at the growth interface, nor can the accumulation be attributed to electromigration effects (associated with current pulsing) since polarity reversal did not affect the composition within the uncontrolled growth region.

Facet effect.—Interference contrast microscopy of the etched Ge crystal grown in space revealed coherent peripheral (111) facet formation over the first 3 cm of regrowth, during which the growth interface was concave (as viewed from the melt). In addition, extensive central (111) faceting was observed during the later stages of growth (growth distance > 2.5 cm) as a result of changing thermal conditions. For both types of faceting the corresponding segregation behavior was quantitatively analyzed over regions where the microscopic growth rate normal to the crystal-melt interface was identical in the facet and in the adjacent off-facet region and where the facet regions were laterally expanding, *i.e.*, under conditions where the diffusion-boundary layer thickness was identical in the facet and the off-facet regions. The measurements give a ratio [k_{eff} (on-facet)/k_{eff} (off-facet)] of 0.94 indicating that the interface distribution coefficient (k_i) for facet growth differs from that for off-facet growth.

REFERENCES

1. J. A. Burton, R. C. Prim, and W. P. Slichter, *J. Chem. Phys.*, **21**, 1987 (1953).
2. W. G. Pfann, *Trans. AIME*, **194**, 747 (1952).
3. W. A. Tiller, K. A. Jackson, J. W. Rutter, and B. Chalmers, *Acta. Metall.*, **1**, 428 (1953).
4. D. T. J. Hurle and E. Jakeman, *J. Cryst. Growth*, **5**, 227 (1968).
5. C. Wagner, *J. Metals*, **6**, 154 (1954).
6. J. R. Carruthers, *J. Cryst. Growth*, **32**, 13 (1975).
7. H. P. Utech and M. C. Flemings, *J. Appl. Phys.*, **37**, 2021 (1966).
8. A. F. Witt, C. J. Herman, and H. C. Gatos, *J. Mater. Sci.*, **5**, 822 (1970).
9. F. Weinberg, *Trans. Met. Soc., AIME*, **227**, 231 (1963).
10. J. R. Carruthers, *Can. Met. Quart.*, **5**, 55 (1963).
11. A. F. Witt, M. Lichtensteiger, and H. C. Gatos, *This Journal*, **120**, 1119 (1973).
12. W. W. Mullins and R. F. Sekerka, *J. Appl. Phys.*, **35**, 44 (1964).
13. A. F. Witt, H. C. Gatos, M. Lichtensteiger, M. C. Lavine, and C. J. Herman, *This Journal*, **122**, 276 (1975).
14. H. Fritzsche, *Phys. Rev.*, **99**, 406 (1955).
15. R. L. Schmidt and J. D. Verhoeven, *Trans. Met. Soc. AIME*, **239**, 148 (1967).
16. W. G. Cochran, *Proc. Camb. Phil. Soc.*, **30**, 365 (1934).
17. V. G. Smith, W. A. Tiller, and J. W. Rutter, *Can. J. Phys.*, **33**, 723 (1955).
18. R. G. Pohl, *J. Appl. Phys.*, **25**, 1170 (1954).
19. O. W. Memelink, *Philips Res. Rep.*, **11**, 183 (1956).
20. K. F. Hulme, *Proc. Phys. Soc.*, **68B**, 393 (1955).
21. R. D. Richtmyer, "Difference Methods for Initial Value Problems," Interscience Publishers, Inc., New York (1957).

Effects of Diffusion-Induced Strain and Dislocation on Phosphorus Diffusion into Silicon

Satoru Matsumoto, Yasushi Akao, Kiyoyuki Kohiyama, and Tatsuya Niimi

Department of Electrical Engineering, Keio University, Hiyoshi, Yokohama 223, Japan

ABSTRACT

The diffusion-induced strain and dislocation effects on the diffusion of phosphorus into silicon have been investigated. When phosphorus is diffused singly, the diffusion coefficient of phosphorus increases considerably at high concentrations. While, when phosphorus and germanium are diffused simultaneously, fewer dislocations are observed and the diffusion-induced strain is compensated. In strain-compensated diffusion, concentration profiles of phosphorus agree well with the theoretical curves (erfc). It is shown that the enhancement of the diffusion coefficient of phosphorus at high concentrations is attributed to the diffusion-induced strain. Besides, dislocations retard the diffusion front by absorbing excess vacancies, showing the opposite effect of strain.

Effects of diffusion-induced dislocations on diffusion of impurities into silicon have been studied extensively by many investigators. They have reported that diffusion of phosphorus above a certain critical surface concentration or a total amount of dopant causes the generation of dislocations in the diffused region (1, 2). A generation mechanism of excess vacancies due to the climbing motion of such dislocations is proposed to explain the marked enhancement of the diffusion coefficient and emitter-push effect (3, 4). These anomalous phenomena are, how-

Key words: semiconductor, doping, diffusion.

ever, observed in the absence of dislocations (5-7). A retardation of phosphorus diffusion, which is related to the formation of dislocations, is found (8, 9). Excess vacancies generated by phosphorus diffusion are absorbed by diffusion-induced dislocations (10). The generation of dislocations is avoided by the simultaneous diffusion of tin and boron or tin and phosphorus, in spite of diffusion of high surface concentration above the critical value of boron or phosphorus (11, 12).

In this article, to make the effect of dislocations on phosphorus diffusion into silicon clearer, the dependence of the diffusion coefficient of phosphorus on the dislocation density is studied. Furthermore, phosphorus diffusions under conditions of strain compensation due to the simultaneous diffusion of phosphorus and germanium into silicon are investigated. By comparison of the respective diffusion coefficients of phosphorus, which are obtained in the single diffusion of phosphorus and in the simultaneous diffusion of phosphorus and germanium, an effect of diffusion-induced strain on phosphorus diffusion is discussed.

Experimental procedure.—The substrates used were Czochralski-grown p-type dislocation-free silicon wafers of resistivity 1 ~ 3 Ω·cm. They were (111) oriented and were mechanically and chemically polished. Diffusions of phosphorus and germanium into silicon were done with the open-tube system (13) using liquid diffusion sources of phosphorus oxychloride ($POCl_3$) and germanium tetrachloride ($GeCl_4$), respectively. The molar ratio of partial pressure of $POCl_3$ in the total gas stream for the simultaneous diffusion of phosphorus and germanium was regulated to be equal to that of the single diffusion of phosphorus, which was 0.2. The molar ratio of $GeCl_4$ in the total gas stream was also 0.2. Both temperatures of $POCl_3$ and $GeCl_4$ sources were held at 0°C. Vapor pressures of $POCl_3$ and $GeCl_4$ at 0°C are 9 and 23 mm Hg, respectively (14). Diffusions were carried out at 1100°C for 5 min-24 hr in the single diffusion and for 5-60 min in the simultaneous diffusion. The density of diffusion-induced dislocations in the single diffusion was controlled by the diffusion times, that is, the total amount of dopant.

Phosphorus concentrations in the substrate were determined by repeating the measurement of sheet resistivity and anodic oxidation in conjunction with Irvin's curve (15, 16). The average thickness of a thin layer removed by each run of anodic oxidation and HF etching was 240 ± 10Å. It was obtained by measuring the height between the original surface and the surface which was oxidized after ten times oxidation of a dummy wafer, using the interferometer (17). Junction depths were measured by the interferometer after angle lapping and chemical etching. Diffusion-induced dislocations in the surface region were observed by Sirtl etching for 15 ~ 60 sec (18). Dislocation density was determined by counting the number of etch pits at three points on wafer. Germanium concentrations in the substrate were obtained by SIMS (secondary ion mass spectroscopy).

Results

Figure 1 shows the dislocation density as a function of the diffusion time obtained for the single diffusion of phosphorus. The spread of the dislocation density in the figure for 10 and 30 min is due to nonuniformity of the dislocation density across the wafer. The dislocation density shows a tendency to saturate with the increase of the diffusion time, although the dislocation density of 8 hr or more cannot be estimated. At a diffusion time of 8 hr or more, large clusters made by dense dislocation etch pits, which have a diameter of approximately 400 μm, are observed by Sirtl etching.

To avoid the confusion of the figure, three concentration profiles of 5, 30, and 120 min are chosen for

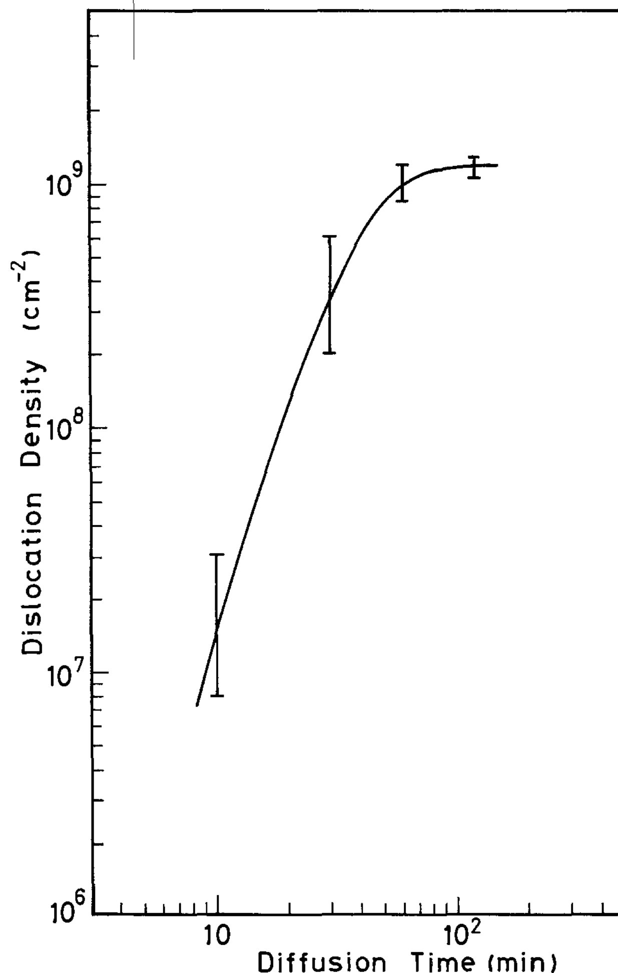

Fig. 1. Dislocation density vs. diffusion time

the single diffusion. These are illustrated as a function of $x/t^{1/2}$ in Fig. 2, where x is the depth from the surface and t is the diffusion time. Plots at the concentration of 10^{17} cm^{-3} are the data obtained by angle lapping. Junction depths obtained by anodic oxidation and by angle lapping agree well. It is found that concentration profiles of phosphorus move inside in the lower concentration region with the increase of the diffusion time. This result means that a retardation of phosphorus diffusion is seen at the diffusion front with the dislocation density. Moreover, junction depths are shown in Fig. 3 as a function of the diffusion time. The broken line in Fig. 3 has a slope of $t^{1/2}$. Junction depths obtained within 2 hr have a smaller slope than that of $t^{1/2}$, showing the retardation of phosphorus diffusion. In order to investigate the relationship between the dislocation density and the diffution coefficient, the diffusion coefficient is determined by the computer simulation from the concentration profile in Fig. 2. The computer simulation is the same method as that previously described (19). Diffusion coefficients thus obtained are shown in Fig. 4 as a function of phosphorus concentration at the points in the bulk. Irrespective of the generation of dislocations, the diffusion coefficient increases considerably with the local concentration of phosphorus above 10^{20} cm^{-3} and has a constant value at lower concentrations. It is also shown from Fig. 4 that the diffusion coefficient decreases in the lower phosphorus concentration region with the increase of the dislocation density (diffusion time).

Figures 5 and 6 show examples of Sirtl etch patterns on the surface of wafers in the single and in the simultaneous diffusions. In the single diffusion of phosphorus, no dislocations are observed for 5 min. Dislocations are, however, generated for 10 min (Fig. 5a) and slip patterns are observed for 30 min (Fig.

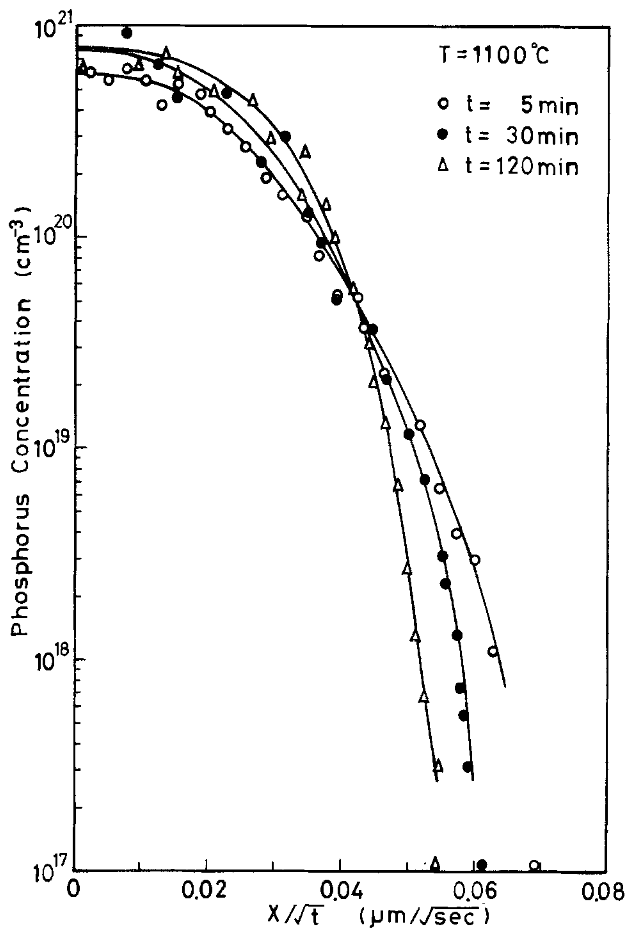

Fig. 2. Concentration profiles of phosphorus as a function of $x/t^{1/2}$ obtained from the single diffusion of phosphorus.

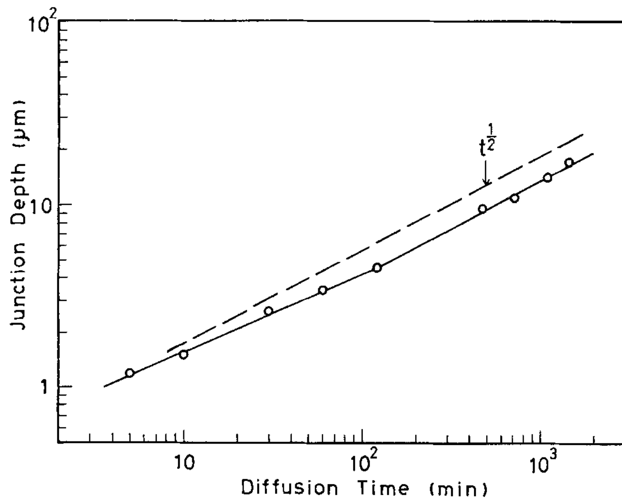

Fig. 3. Junction depth vs. diffusion time. A broken line has a slope of $t^{1/2}$.

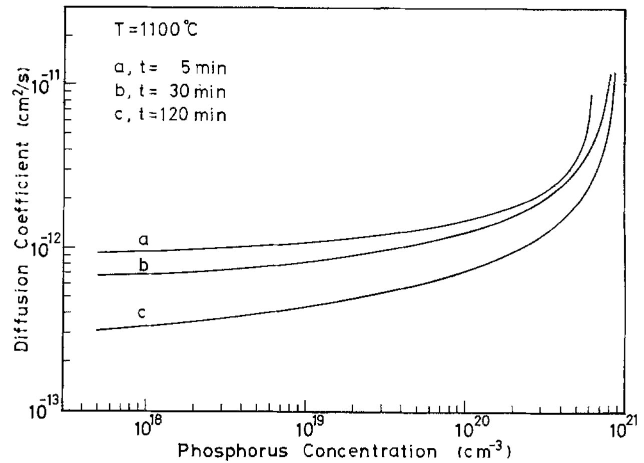

Fig. 4. Diffusion coefficient vs. phosphorus concentration with a parameter of diffusion time (dislocation density) obtained from the single diffusion of phosphorus.

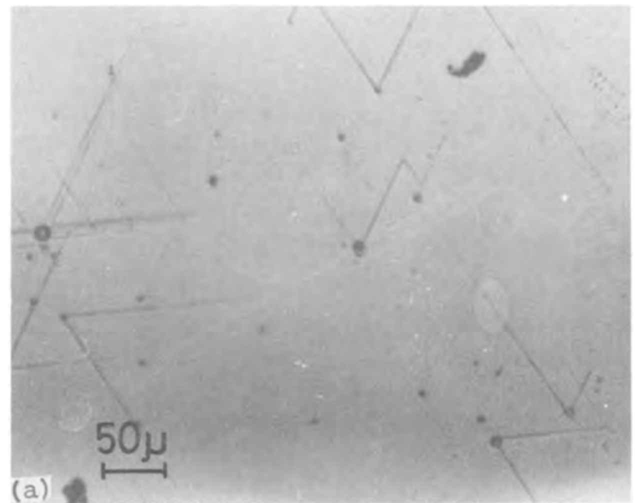

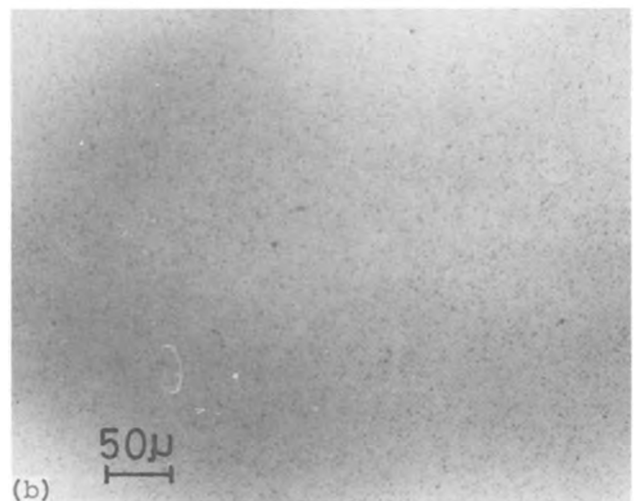

Fig. 5. Sirtl etch patterns for 10 min. (a) Single diffusion of phosphorus; (b) simultaneous diffusion of phosphorus and germanium.

6a). The dislocation densities in such cases are already shown in Fig. 1. In the simultaneous diffusion of phosphorus and germanium, no dislocations are generated for 10 min (Fig. 5b), as well as the case for 5 min. It is also seen that few dislocations are generated for 30 min (Fig. 6b). It has been reported that the sign of the lattice contraction coefficient of germanium in silicon is inverse to that of phosphorus in silicon (20). Therefore, it is considered that lattice strain produced by the incorporation of phosphorus is compensated by the simultaneous incorporation of germanium into silicon.

Figure 7 shows an example of a concentration profile of phosphorus obtained from the simultaneous diffusion for 30 min. In Fig. 7, a concentration profile of phosphorus obtained from the single diffusion for the same diffusion time is also shown. The profile of the single diffusion deviates largely from the theoretical curve (erfc) and the diffusion coefficient depends on the local concentration as described before. On

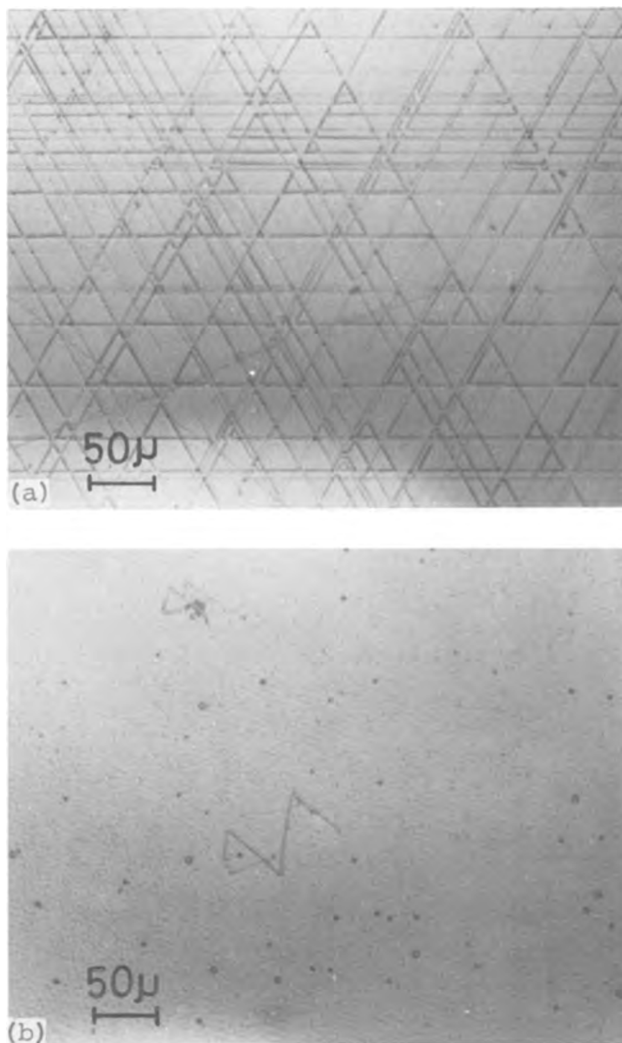

Fig. 6. Sirtl etch patterns for 30 min. (a) Single diffusion of phosphorus; (b) simultaneous diffusion of phosphorus and germanium.

the other hand, the profile of the simultaneous diffusion agrees well with the erfc curve. The value of the diffusion coefficient is given in the figure. A concentration profile of germanium (Ge^+ ion relative intensity) of the simultaneous diffusion for 30 min is shown in Fig. 8. Concentrations are measured at the surface at the depth of 0.3 and 0.6 μm. The broken curve in the figure shows the erfc curve. Concentration profiles of the simultaneous diffusion for other diffusion times (5 and 10 min) also agree well with the erfc curves, whereas the profile obtained for 60 min in the simultaneous diffusion does not agree with the erfc curve. As for this case, dislocations are observed. Thus, this disagreement is considered to be due to the reason that the lattice strain is not compensated sufficiently. Consequently, in strain-compensated diffusion, concentration profiles agree well with erfc curves and the local concentration dependence of the diffusion coefficient is not seen in spite of high surface concentration.

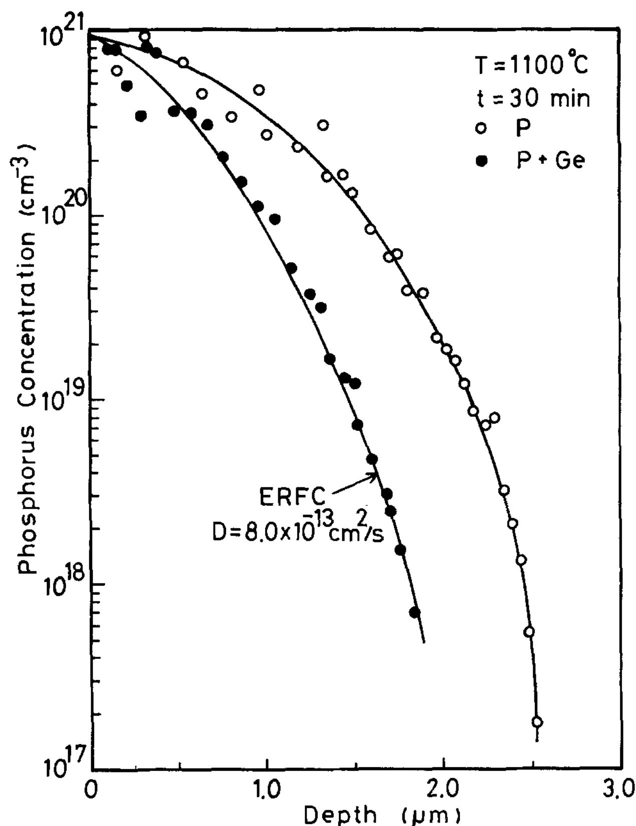

Fig. 7. Concentration profiles of phosphorus for 30 min obtained from single and simultaneous diffusions.

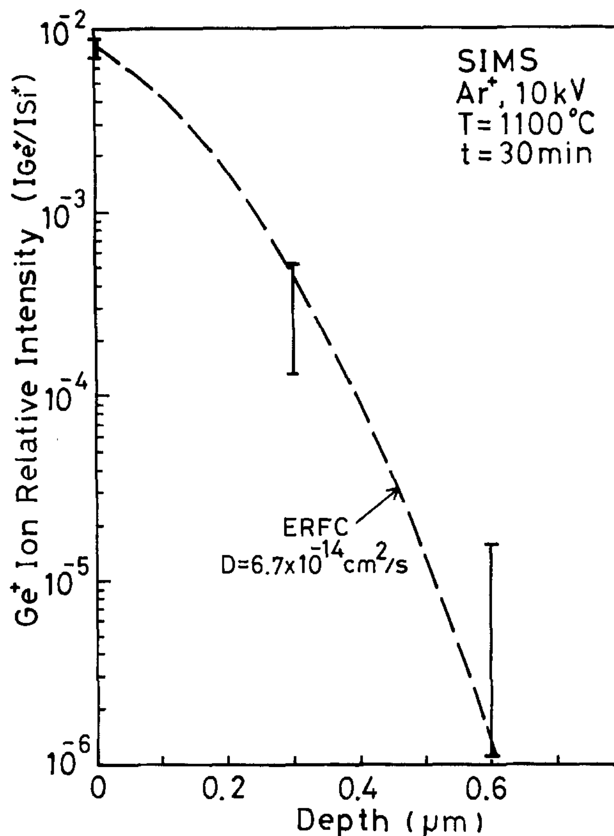

Fig. 8. Concentration profile of germanium for 30 min obtained from simultaneous diffusion.

Discussion

Enhancement of the diffusion coefficient.—Diffusion coefficients are schematically illustrated as a function of phosphorus concentration in Fig. 9 based on the result shown in Fig. 7. D_p and $D_{p \cdot Ge}$ are the diffusion coefficients of phosphorus determined from the single and the simultaneous diffusions, respectively, and D_i is the extrapolated value of the intrinsic diffusion coefficient of phosphorus at the diffusion temperature (6×10^{-14} cm^2/sec at 1100°C) (21). It is found that D_p increases considerably at high concentrations and also is larger than D_i over the whole local phosphorus concentrations. The difference between D_p and D_i consists of the two parts, that is, the difference be-

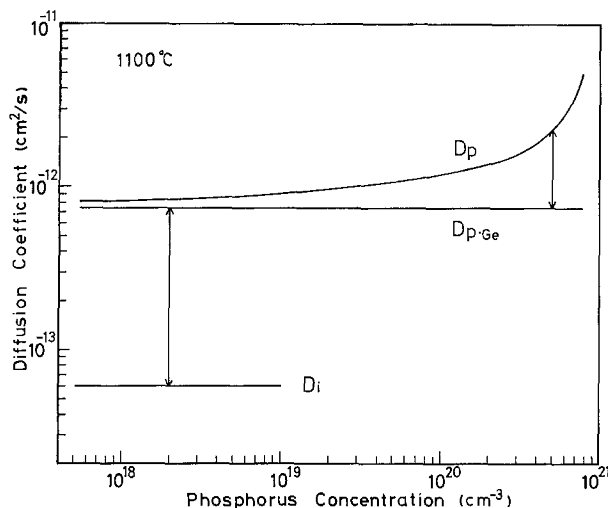

Fig. 9. Schematic illustration of diffusion coefficient as a function of phosphorus concentration.

tween D_p and $D_{p\cdot Ge}$ and the difference between $D_{p\cdot Ge}$ and D_i. That D_p or $D_{p\cdot Ge}$ are larger than D_i means excess vacancies are generated in comparison with the vacancy concentration at thermal equilibrium corresponding to D_i.

The value of D_p in the lower concentration region is nearly equal to that of $D_{p\cdot Ge}$, which is constant. Therefore, it is clear that the difference between D_p and $D_{p\cdot Ge}$, that is, the enhancement of D_p at high concentrations, is attributed to the excess vacancies generated by the strain, and this strain effect is localized. On the other hand, the generation of these excess vacancies has no relationship with dislocations since diffusion-induced dislocations were not observed for short diffusions, while the diffusion coefficient was concentration dependent (see Fig. 1 and 4). From this result, the plastic deformation model (22) based on the interaction between dislocations, which has been proposed to explain the enhancement of the diffusion coefficient of phosphorus at high concentrations, is not considered to be adequate. It is premature to establish a tangible model to explain the difference between D_p and $D_{p\cdot Ge}$. A possible mechanism of the generation of excess vacancies is, however, considered; excess vacancies are generated in order to relax the strain energy due to the incorporation of a large number of impurities (23). This is equivalent to the reduction of the formation energy of vacancy with the increase of impurity concentration, and may be localized. It has been reported, in fact, that the formation energy of vacancy decreases exponentially with the bulk impurity concentration (24). Their empirical equation for the reduction of the formation energy of vacancy is, however, not applicable for the present work.

The difference between $D_{p\cdot Ge}$ and D_i cannot be caused by the strain, because $D_{p\cdot Ge}$ is obtained under strain compensation. It can be seen that the difference is present even at lower concentration and has a dominant factor in the enhancement of the diffusion coefficient D_p. It was shown that the excess vacancies generated by high concentration diffusion of phosphorus extended deeply into the bulk to a depth of at least ~25 μm beyond the diffused region (10). Therefore, the difference between $D_{p\cdot Ge}$ and D_i is due to the presence of the excess vacancies in the deep region. Though the generation mechanism of the excess vacancies is not conclusive, it is considered that the excess vacancies are generated by the dissociation of E centers (phosphorus atom-vacancy pairs) based on the E center diffusion mechanism (6, 25).

Retardation of phosphorus diffusion.—The enhancement of the diffusion coefficient is not attributed to the climb motion of dislocations as described before. Therefore, the mechanism based on the prevention of the dislocation movement by the dislocation network may be inadequate to explain the retardation of phosphorus diffusion. Precipitations of phosphorus atoms at the dislocations may cause the retardation of phosphorus diffusion (26). However, since this effect is considered to be localized in the higher concentration region, it is difficult to manifest the result shown in Fig. 4, in which the diffusion coefficient decreases in the lower concentration region.

Previously, it was shown that excess vacancies generated by phosphorus diffusion were absorbed by diffusion-induced dislocations, using a buried layer technique (10). Therefore, it is considered that free excess vacancies, which are generated by the dissociation of E centers, would cause the enhancement of the diffusion coefficient at lower concentration, if they were not absorbed by the diffusion-induced dislocations. This being the case, retardation of phosphorus diffusion at lower concentration is observed, with this effect becoming larger with time.

Conclusions

The diffusion coefficient of phosphorus in silicon decreases in the lower concentration region with the increase of dislocations. This retardation can be related to the absorption of excess vacancies by dislocations. In the single diffusion of phosphorus, the diffusion coefficient of phosphorus increases considerably at high concentrations, while, in the simultaneous diffusion of phosphorus and geranium, fewer dislocations are observed and the diffusion-induced strain is compensated. Under strain compensation, concentration profile of phosphorus agrees well with the theoretical curve (erfc) and the diffusion coefficient of phosphorus ($D_{p\cdot Ge}$) is larger than the extrapolated value of the intrinsic diffusion coefficient (D_i) at the diffusion temperature. It is shown that the enhancement of the diffusion coefficient at high concentrations is attributed to the strain. The difference between $D_{p\cdot Ge}$ and D_i is suggested to be due to excess vacancies generated by the dissociation of E centers.

Acknowledgments

The authors wish to express their gratitude to Dr. E. Arai, Musashino Electrical Communication Laboratory, N.T. and T., for the measurement of the germanium concentration profile by SIMS.

Manuscript submitted April 10, 1978; revised manuscript received June 12, 1978. This was Paper 353 presented at the Atlanta, Georgia, Meeting of the Society, Oct. 9-14-1977.

Any discussion of this paper will appear in a Discussion Section to be published in the June 1979 JOURNAL. All discussions for the June 1979 Discussion Section should be submitted by Feb. 1, 1979.

Publication costs of this article were assisted by Keio University.

REFERENCES

1. S. Prussin, *J. Appl. Phys.*, **32**, 1876 (1961).
2. H. J. Queisser, *ibid.*, **32**, 1776 (1961).
3. T. J. Parker, *ibid.*, **38**, 3475 (1967).
4. S. M. Hu and T. H. Yeh, *ibid.*, **40**, 4615 (1969).
5. H. Nakamura, S. Ohyama, and C. Tadachi, *This Journal*, **121**, 1377 (1974).
6. M. Yoshida, E. Arai, H. Nakamura, and Y. Terunuma, *J. Appl. Phys.*, **45**, 1498 (1974).
7. S. Matsumoto and T. Niimi, *Jpn. J. Appl. Phys.*, **15**, 2077 (1976).
8. M. C. Duffy, F. Barson, J. M. Fairfield, and G. H. Schwuttke, *This Journal*, **115**, 84 (1968).
9. M. Yoshida and S. Kanamori, *Jpn. J. Appl. Phys.*, **9**, 338 (1970).
10. S. Matsumoto, E. Arai, H. Nakamura, and T. Niimi, *ibid.*, **16**, 1177 (1977).
11. T. H. Yeh and M. L. Joshi, *This Journal*, **116**, 73 (1969).

12. J. Nishizawa *et al.*, Seoul International Conference on IEEE (1970).
13. R. A. McDonald, G. G. Ehlenberger, and T. R. Huffman, *Solid-State Electron.*, **9**, 807 (1966).
14. "Handbook of Chemistry and Physics," 51st ed., D-169 The Chemical Rubber Co.
15. J. C. Irvin, *Bell Syst. Tech. J.*, **41**, 387 (1962).
16. E. Tannenbaum, *Solid-State Electron.*, **2**, 123 (1961).
17. J. C. C. Tsai, *Proc. IEEE*, **57**, 1499 (1969).
18. E. Sirtl and A. Adler, *Z. Metallkde.*, **52**, 529 (1961).
19. S. Matsumoto, E. Arai, H. Nakamura, and T. Niimi, *Jpn. J. Appl. Phys.*, **14**, 1665 (1975).
20. Y. T. Lee, N. Miyamoto, and J. Nishizawa, *This Journal*, **122**, 530 (1975).
21. R. N. Ghoshtagore, *Phys. Rev.*, **B3**, 389 (1971).
22. N. D. Thai, *Solid-State Electron.*, **13**, 165 (1970).
23. R. W. Balluffi and A. L. Ruoff, *J. Appl. Phys.*, **34**, 1634 (1963).
24. B. I. Boltaks and S. I. Budarina, *Sov. Phys. Solid State*, **11**, 330 (1969).
25. R. B. Fair and J. C. C. Tsai, *This Journal*, **124**, 1107 (1977).
26. M. L. Joshi and S. Dash, *IBM J. Res. Dev.*, **12**, 446 (1968).

Implantation and PH_3 Ambient Annealing of InP

D. Eirug Davies, W. D. Potter, and J. P. Lorenzo

Rome Air Development Center, Solid State Sciences Division, Hanscom Air Force Base, Massachusetts 01731

ABSTRACT

InP-implanted layers have been annealed using the same phosphorus ambient conditions as would be encountered during the material's vapor phase epitaxial growth. Implanted layers so annealed exhibit sheet carrier concentrations up to 5×10^{14} cm^{-2} with the n-type silicon ion and approximately 10^{14} cm^{-2} with the p-type Mg ion. No indication of outdiffusion is seen on layers that have been profiled. Though the annealing was undertaken in an epitaxial reactor, it is envisioned that a much simplified system would also suffice. The present approach provides an alternative to the more customary dielectric encapsulation whose effectiveness is often impaired by deposition variations.

It is well recognized that ion-implanted semiconductors have to be annealed in order to reduce the damage caused by the irradiation and for the implanted ions to become substitutional. In 3-5 compounds it is generally found that the annealing has to be undertaken at such high temperatures that dissociation of the surface will occur. This is normally circumvented in GaAs, the most widely implanted 3-5 compound, by encapsulating the surface with a thin dielectric film such as Si_3N_4.

Another area where thermal erosion of surfaces can cause problems is during epitaxial growth. An interface region at the initiation of the growth that is heavily compensated is frequently encountered. One of the many possible contributing factors to such an inferior initial growth is the condition of the substrate surface and any erosion that might have occurred as the substrate is brought to the growth temperature. In common with implantation annealing, it is desirable to provide a satisfactory means of preserving the surface.

Here, the annealing of implanted layers in InP has been investigated in a hydride epitaxial reactor to take advantage of conditions established for growth. The gas flow conditions normally encountered in epitaxial growth are used with one notable difference in that no HCl is provided to transport the In. Though it is customary to encapsulate surfaces for implantation annealing, other "capless" procedures have previously been reported. Immorlica *et al.* (1) have described the annealing of GaAs while embedded in a crushed mixture of GaAs and graphite, and Lee *et al.* (2) have likewise annealed unprotected GaAs wafers in an open-ended furnace with a H_2 flow over an arsenic saturated liquid Ga/GaAs solution.

Relatively little implantation has been conducted with InP. In a preceding study (3) which parallels the present PH_3 annealing to be described, it was found that useful n-type layers with sheet carrier concentrations in excess of 10^{14} cm^{-2} could be formed. Both sulfur and silicon were implanted and the layers annealed in conjunction with surface encapsulants (principally sputtered Si_3N_4). In a similar study, but employing a phosphosilicate glass, Donnelly and Hurwitz (4) have reported activation in excess of 75% for moderate dose 10^{14} cm^{-2} selenium and silicon implants. In addition, the acceptors Cd, Mg, and Be were also implanted. Mg gave sheet carrier concentrations as high as 5×10^{13} cm^{-2} from 10^{14} cm^{-2} implants. The same phosphosilicate glass was used in annealing the p-type dopants.

Key words: InP, doping, implantation.

Results

The epitaxial reactor is similar to that described by Tetjen *et al.* (5) and consists of a three temperature zone furnace. The single quartz tube is sealed and continuously purged with H_2. The implanted sample is introduced into the third temperature zone through a large orifice stopcock from a separately purgable section. The first temperature zone from where metallic gallium or indium is normally transported is not used while PH_3 and H_2 are introduced into the center mixing zone and flow over the implanted sample in the third zone. It is apparent that a much simplified system without many of the refinements required for epitaxial growth would be adequate for the purpose of implantation annealing.

A PH_3/H_2 ambient with the PH_3 content between 0.75% and 2.1% was used in an initial series of experiments for heat cycling nonimplanted InP specimens to 700°C for 10 min. Often the initial mirror polish on the surface was either not retained or masked by a surface film. Such effects could not be correlated with the amounts of phosphorus present, as the better surfaces were occasionally observed with the lowest PH_3 content. A reflection electron diffraction examination of a thicker appearing film gave a single crystal pattern with a unit cell parameter corresponding to GaP. A thinner appearing film revealed a superimposed InP pattern as well and showed the film to be of the same orientation as the InP substrate below it. A larger unit cell parameter intermediate to InP and GaP was obtained on this thinner film and it is presumed that it corresponds to InGaP. As GaAs

has also been grown in the reactor, Ga is available within the system and it appears that some deposition occurred even though no HCl was being provided for its transportation. Such difficulties have been overcome by only annealing when the reactor is dedicated for this purpose exclusively.

Figure 1 illustrates the beneficial effect of providing a PH_3 ambient while InP is being heated to 750°C for 10 min. The secondary electron emission SEM picture reveals a high density of rectangular etch pits on a sample heated in H_2 alone. These etch pits are characteristic of the <100> orientation being used. The second sample was similarly treated other than an addition of 0.4% PH_3 to the gas flow. It is apparent at the 100X magnification of Fig. 1 that the integrity of the surface is much better retained. At higher magnification (2000X) there is some trace of etch pit formation. For samples heated in gas mixtures with a PH_3 content of 1 1/3-4 1/2% no surface deterioration was visible at 100X. At 2000X an indication was again obtained that etch pits are beginning to form, but they are not well defined and possibly smaller as the PH_3 content is increased.

The first electrical evaluation was undertaken on a series of samples implanted with silicon at 1 MeV. 3×10^{14} ions cm^{-2} were introduced with the InP at RT and the postimplantation annealing was carried out at temperatures ranging from 675° to 800°C. The resulting sheet carrier concentrations and mobilities are shown in Fig. 2. 1 1/3% PH_3 was used except for two additional samples with 0.4 and 4.5% at 750°C. Only a marginal increase in N_s occurred as the PH_3 content was increased. Generally, the behavior with the necessity of annealing $\gtrsim$ 750°C and the attainment of sheet carrier concentrations $\gtrsim 10^{14}$ cm^{-2} corresponds closely to earlier results on Si_3N_4 encapsulated wafers (3).

Figure 3 shows the results from another sequence of implants that were similar to those of Fig. 2 other than the silicon dose being increased from 3×10^{14} to 1×10^{15} cm^{-2}. 1 1/3 or 4 1/2% PH_3 was used for the annealing of the various samples. Of most significance here is the fact that sheet carrier concentrations of $\sim 5 \times 10^{14}$ cm^{-2}, an order of magnitude greater than in GaAs, can be attained. Layer stripping of one of the samples indicates that peak carrier concentrations of 10^{19} cm^{-3} can be reached.

Any phosphorus loss with a vacancy gradient near the surface could have a profound influence on the distribution of implanted ions. An enhanced outdiffusion causing the dopant distribution to become asymmetric towards the surface might be anticipated. Consequently, some of the layers have been profiled and examined for such an effect.

Fig. 1. InP surface after 10 min at 750°C in (a) H_2 and; (b) H_2 + 0.4% PH_3 (secondary electron emission taken at ×100).

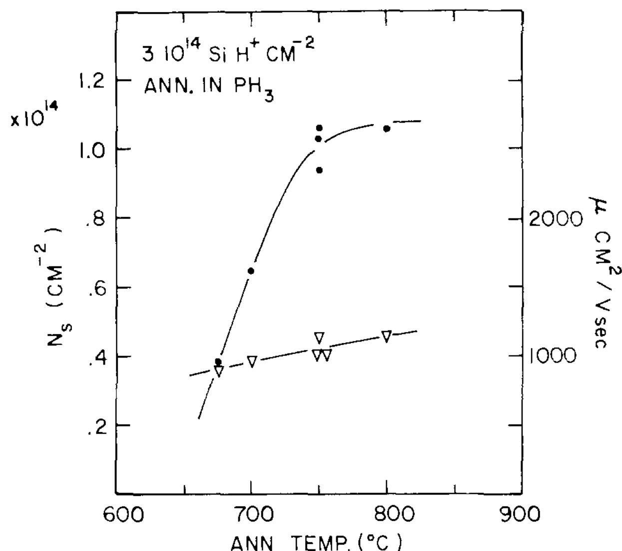

Fig. 2. The effect of annealing temperature on the electrical characteristics of 3×10^{14} Si^+ cm^{-2} implanted layers.

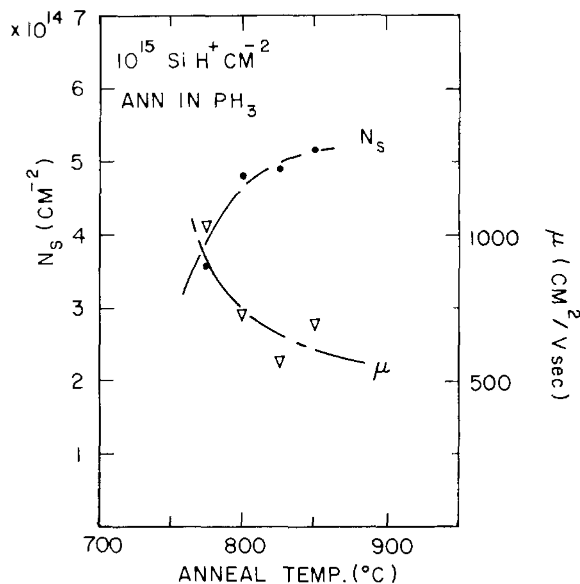

Fig. 3. The effect of annealing temperature on the electrical characteristics of 1×10^{15} Si^+ cm^{-2} implanted layers.

Figure 4 shows two profiles obtained after annealing in ambients of different phosphine to hydrogen content. The profiles were obtained through successive layer removal and Hall measurements. Anodization was used to remove the layers, and the electrolyte consists of 5% solution of citric acid combined with ethylene glycol. This has been described by Hasegawa and Hartnagel (6) in conjunction with GaAs anodization. Both of the samples shown in Fig. 4 were implanted at RT with 1 MeV silicon to 3×10^{14} cm^{-2}. For the annealing at 750°C the PH_3-to-H_2 ratio was changed from 0.4 to 4.5%. It can be seen that there is no discernable difference between the two profiles over the concentration range examined and that no outdiffusion is suggested.

Another indication of how well the InP surface is maintained on heating in low PH_3 content ambients is provided in Fig. 5 where the implantation energy has been reduced to bring the distribution closer to the surface. Doses of 4×10^{14} cm^{-2} were implanted at 200 keV and in each case the profiles are deeper than would be anticipated from LSS theory (7) (broken curve). One of these silicon-implanted layers was

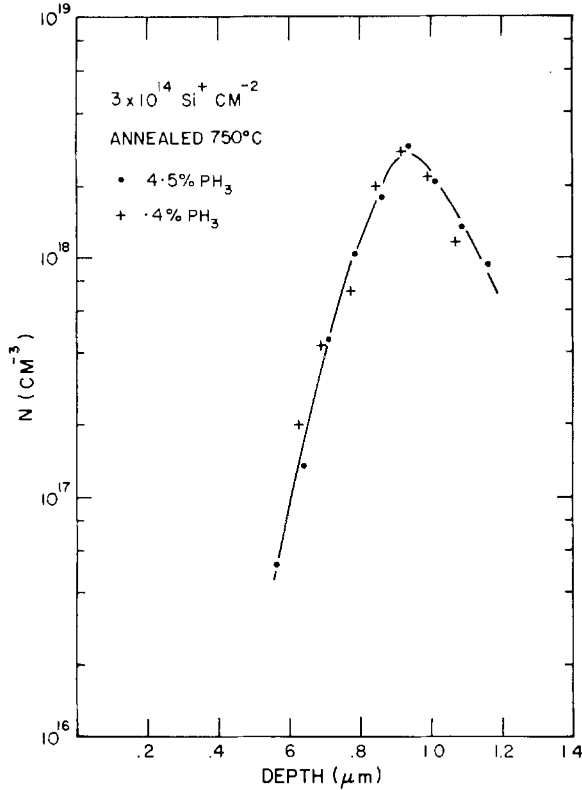

Fig. 4. The profiles of silicon-implanted layers annealed with two different phosphene ambient concentrations.

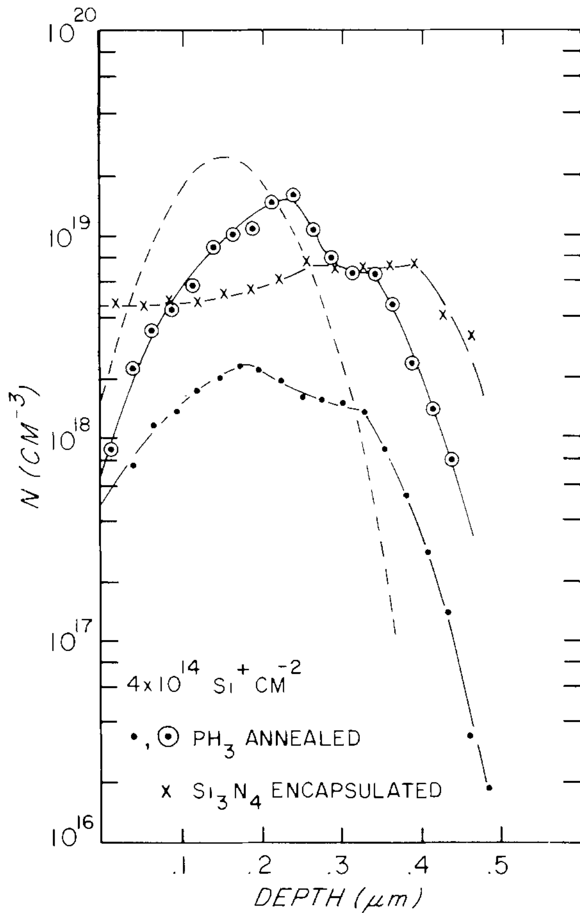

Fig. 5. Profiles of 200 keV silicon implants annealed with Si_3N_4 or under PH_3/H_2 flow. The theoretical distribution is indicated by the broken curve.

annealed at 750°C using a Si_3N_4 protective layer and it is apparent that considerable outdiffusion has occurred in this instance. The as-implanted distribution is better retained for the other two layers which were annealed at 775°C in PH_3. While the net doping within one of these layers is abnormally low, the other with a peak concentration of 1.5×10^{19} cm^{-3} illustrates that doping levels of $\gtrsim 10^{19}$ cm^{-3} are achievable through implantation in InP.

All of the above implants were conducted with the InP at room temperature. In an earlier study it was seen to be advantageous to implant at least sulfur at elevated temperatures (3). Further results concerning substrate heating, but where PH_3/H_2 rather than dielectric encapsulation is used for the post implantation annealing, are presented in Table I. Both Si^+ and S^+ have been implanted, at RT as well as at 200°C, and annealed at either 700° or 750°C. The energy of implantation is 1 MeV and the doses implanted are 3×10^{14} cm^{-2}. It will be noted that only Si^+ gives sheet carrier concentrations $\gtrsim 10^{14}$ cm^{-2} after implanting at room temperature. While there is an increase in the percentage of electrical activity on implanting hot for Si^+, it is not anywhere as pronounced as it is with S^+. However, better electron mobilities are obtained after implanting hot for both ions. This indicates more complete annealing on implanting hot, leaving fewer scattering centers to curtail the mobility.

Table I

Ion	$T_{ann.}$ (degrees)	μ_{RT}	$(N_s)_{RT}$	$\mu_{200°}$	$(N_s)_{200°}$	% activity RT; 200°C	
S^+	700	930	0.08×10^{14}	1380	1.2×10^{14}	3	40
S^+	750	1320	0.79×10^{14}	1780	1.1×10^{14}	26	37
Si^+	700	960	0.65×10^{14}	2200	0.83×10^{14}	22	28
Si^+	750	1030	1.1×10^{14}	2700	1.25×10^{14}	37	42

The behavior of p-type layers on annealing in PH_3 has also been investigated. Magnesium was implanted as an example of a p-type dopant and doses of 2×10^{14} cm^{-2} were introduced at 1 MeV. A sequence of such RT-implanted Hall samples were annealed as indicated in Fig. 6. The PH_3 in H_2 content was 4 1/2% and it can be seen that annealing to ~750°C, similar to what was previously required for silicon, is desirable. The sheet carrier concentrations of $\sim 1 \times 10^{14}$ cm^{-2} give 50% activation, a similar percentage to that

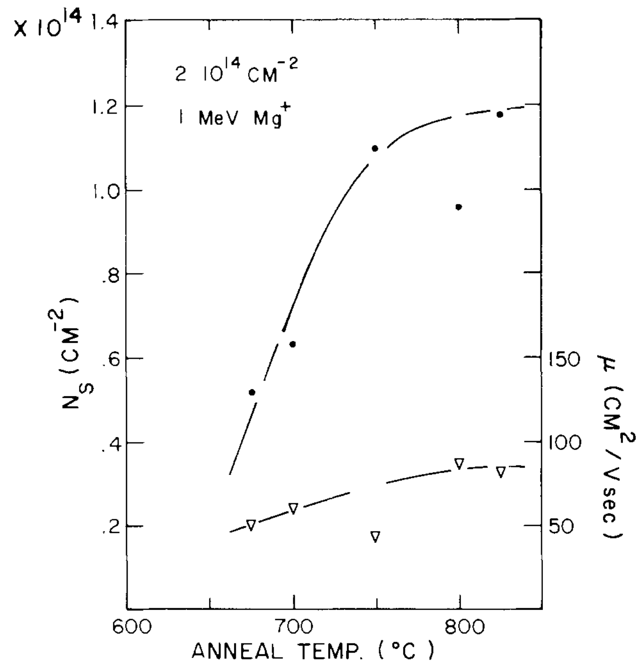

Fig. 6. Sheet carrier concentrations and mobilities for a series of magnesium implants annealed at different temperatures.

already reported for magnesium by Donnelly and Hurwitz (4).

Layers implanted with Mg to 5×10^{14} cm^{-2} and annealed as above failed to produce carrier concentrations any greater than the $\sim 10^{14}$ cm^{-2} level already indicated for the 2×10^{14} cm^{-2} implants. A similar limitation has also been seen by Donnelly and Hurwitz (4). Thus, it appears that a problem exists in attaining high p-type sheet carrier concentrations in InP.

In summary, it has been seen that a PH_3/H_2 ambient provides sufficient protection against thermal erosion on InP surfaces to make it an attractive way of annealing implanted layers without surface encapsulation. It is found that after implanting at RT, both Si and Mg layers have to be annealed to ~ 750°C. The silicon behavior is comparable to that found earlier where surface protection was afforded by sputtered Si_3N_4. While sheet carrier concentrations for the p-type dopant Mg^+ appear limited to $\sim 10^{14}$ cm^{-2}, values of $\sim 5 \times 10^{14}$ cm^{-2} are attainable with Si. It is concluded that no significant dopant outdiffusion occurs, as the profiles of the silicon-implanted layers do not exhibit any noticeable asymmetry toward the surface.

Manuscript submitted Feb. 9, 1978; revised manuscript received May 28, 1978.

Any discussion of this paper will appear in a Discussion Section to be published in the June 1979 JOURNAL. All discussions for the June 1979 Discussion Section should be submitted by Feb. 1, 1979.

Publication costs of this article were assisted by the U.S. Air Force.

REFERENCES

1. A. A. Immorlica and F. H. Eisen, *Appl. Phys. Lett.*, **29**, 94 (1976).
2. D. H. Lee, R. M. Mallon, and J. M. Whelan, in "Proceedings of the 5th International Conference on Ion Implantation in Semiconductors," p. 115, Plenum Press, New York (1976); *This Journal*, **123**, 1413 (1976).
3. D. E. Davies, J. Lorenzo, and T. Ryan, *Solid-State Electron.*, **21**, 981 (1978).
4. J. P. Donnelly and C. Hurwitz, *Appl. Phys. Lett.*, **31**, 418 (1977).
5. J. J. Tietjen and J. A. Amick, *This Journal*, **113**, 724 (1966).
6. H. Hasegawa and H. L. Hartnagel, *This Journal*, **125**, 713 (1976).
7. J. F. Gibbons, W. S. Johnson, and S. W. Mylroie, "Projected Range Statistics," Halsted Press, New York (1975).

Mechanical Stress and Electrical Properties of MNOS Devices as a Function of the Nitride Deposition Temperature

R. Hezel[1] and E. W. Hearn

IBM Data Systems Division, East Fishkill Facility, Hopewell Junction New York 12533

ABSTRACT

The mechanical stress in memory quality silicon nitride films, the lattice parameter in the silicon substrate, the index of refraction, the dielectric constant of the films, and the saturation shift of the flatband voltage under positive and negative gate voltages in MNOS devices (as a function of the nitride deposition temperature) were studied in conjunction with the fixed interface charge density after fabrication. The nitride layers were deposited by the reaction of SiH_4 and NH_3 on [111] and [100] silicon in the temperature range from 640° to 910°C. No significant dependence of the properties on deposition rate and substrate orientation was found. Index of refraction, dielectric constant, film stress, substrate lattice parameter, and the maximum shift of the flatband voltage show a common characteristic variation with deposition temperature, with a minimum between 710° and 760°C. The relationship of the structural and electrical properties is discussed.

One objective of this paper was to provide information about the stress situation present in thin oxide MNOS memory structures. Another objective was to investigate the relationship between the mechanical stress both in films and substrate and the fixed interface charge density of the as grown structures prior to any electrical stress. Similar investigations have been done for MOS structures (1, 2); however, the stress in the oxide layer is much lower than the nitride stress in MNOS structures.

Experimental data are given and correlations are attempted between the fixed interface charge density, the maximum shift of the flatband voltage under positive and negative gate voltages, the mechanical stress in the film, the effect on lattice parameter of the silicon substrate, the change in index of refraction, and the dielectric constant of the nitride films. These properties were determined as a function of deposition temperature range from 640° to 910°C. ESCA studies were included to obtain the relative oxygen content of the nitride film.

[1] Present address: Institut Fuer Werkstoffwissenschaften VI, University of Erlangen-Nuernberg, 8520 Erlangen, Germany.

Key words: silicon nitride, MNOS memory, mechanical stress, interface charges.

Sample Preparation

The silicon nitride layers were deposited in a horizontal resistance-heated reactor (hot wall) by the chemical reaction of silane and ammonia with nitrogen as the carrier gas. The NH_3/SiH_4 ratio was 1000:1 in the deposition temperature range 640°-910°C. Silicon wafers 32 mm diam [100] orientation (2Ω-cm p-type) and [111] orientation (10Ω-cm n-type), both chem-mech polished, were used as substrates. Before

the nitride deposition, the wafers were cleaned using boiling acetone and trichlorethylene NH_4OH-H_2O_2 and HCl-H_2O_2 solutions.

The nitride layers were deposited directly on the native oxide (approximately 15Å in thickness). No special oxide growth treatment was performed.

Two separate deposition series (one year apart) were made, both with [111] and [100] substrates, n- and p-type, respectively. In the first series ($T = 653°$, 765°, 828°, and 910°C), separate depositions were made for each wafer orientation, whereas in the second series ($T = 640°$, 657°, 728°, 775°, and 885°C), the films were deposited simultaneously on the [111] and [100] substrate.

The average thickness of the nitride layers was 700Å; the thinnest layer was 580Å and the thickest, 840Å. Uniformity across the wafer was better than ± 5%. Thickness and index of refraction were measured by ellipsometry at a wavelength of 5461Å.

Stress Measurements

The film stress measurements were made by measuring the substrate radius of curvature with an x-ray diffraction technique (3). The convention used for tensile and compressive films was: If the film length tends to contract and is restrained from doing so by the substrate, the film is in a state of tension. Conversely, if the film tends to expand, it will be placed under a compressive stress by the substrate.

Silicon nitride is in tension. The magnitude of the curvature is related to the film stress by (4)

$$\sigma_f = \pm \frac{t_s^2}{6t_fR} \frac{E_s}{1 - V_s}$$

where + = tension; − = compression; t_s = substrate thickness; t_f = film thickness; R = radius of curvature; E_s = Young's modulus for silicon; and V_s = Poisson's ratio for silicon.

The values of $E_s/1 - V_s$ for [100] and [111] used were 1.8×10^{12} and 2.3×10^{12} dynes/cm^2, respectively. These were obtained from calculated values in Ref. (4, 5).

Determination of the lattice spacings was made using the Bond method of the Apex unit described in Ref. (6) using the alignment procedure suggested in Ref. (7). The d spacing of the (444) planes were measured for both substrate orientations. The [111] substrates provide a symmetric orientation of the measured planes relative to the sample surface, while the [100] substrates provide an asymmetric orientation. The accuracy of this arrangement has been measured on a standard sample of [111] silicon for the (444) reflections. This value of $a_o = 5.430611 + 0.000003$Å has been reproduced over a one year time period. The deviation over the short duration of this experiment is shown by the error bars in the data plot.

The measured values of d spacing were not corrected except for temperature normalization since the standard corrections used in the Bond method are insignificant for this investigation, especially if relative values are considered.

Electrical Measurements

Standard high frequency (1 MHz) C-V measurements were performed to secure information about the charge density in the MNOS structure. The following relation was used

$$V_{FB} = \Phi_{MS} - \frac{Q_N}{\epsilon_0\epsilon_N} d_N$$

where V_{FB} is the flatband voltage, Q_N is the charge density present at the SiO_2/Si_3N_4 interface, ϵ_0 is the permittivity of free space, ϵ_N is the relative dielectric constant, and d_N is the thickness of the nitride layer. Φ_{MS} is the work function difference between the metal electrode and silicon.

The application of the simple relation above instead of the exact equation for the MNOS structure given in Ref. (8, 9) is justified by the following arguments: (*i*) According to our experiments, oxide charge and surface state density at the Si/SiO_2 interface are negligible (H_2 annealing during nitride deposition); (*ii*) The charges (of density Q_N) of the as-grown structure, prior to any electrical stress, are located at the SiO_2/Si_3N_4 interface (8, 9). (Liquid Ga-In electrodes were used instead of Al to avoid postdeposition annealing and possible stress contributions due to the metal.)

The relative dielectric constant of the silicon nitride films was calculated from the capacitance in the accumulation region of the C-V characteristic curve and the dimensions of the structures (evaporated Al-contacts were used for this determination).

In this study, $\Phi_{MS} = -0.1$V was determined experimentally for the Ga-In alloy and nSi, 10Ω cm, from the linear relationship between V_{FB} and d_N. To obtain the true Q_N values from the C-V curves, special care was taken not to apply gate voltages appreciably exceeding the flatband voltages to prevent changes in V_{FB} by charge injection into the nitride.

The charge storage window measurements were performed by recording the flatband voltage shifts under both positive and negative gate bias. Starting from the C-V curve of the as-grown MNOS structure, a positive voltage was applied to the gate for $t_p = 2$ min ($E_N = 5 \times 10^6$ V/cm), the curve shifted to V_{FB1}. Then a negative voltage of the same magnitude and time was applied, shifting the curve to V_{FB2}. Increasing the biasing time, no further shift occurred. ($V_{FB1} - V_{FB2}$) therefore represents the saturation width of the charge window for the voltage applied.

Results and Discussion

Stress data.—The stress in silicon nitride films is considered to be the sum of the thermal stress σth and the intrinsic σi. The thermal stress is directly proportional to the difference in the thermal expansion coefficients of nitride and silicon and to the difference between deposition temperature and measuring temperature (10). Stress measurements performed exactly at the deposition temperature would enable determination of the pure intrinsic stress component separately. Such measurements were performed in Ref. (10), showing that the (compressive) thermal stress σth is only a small fraction (1/10) of the (tensile) intrinsic stress in the silicon nitride films. Taking this into account, the assumption may be made that the room temperature stress is mainly due to the intrinsic stress in the nitride films.

In Fig. 1 the nitride film stress (tensile) is shown as a function of deposition temperature for both [111] and [100] substrate orientations and two different deposition series. No significant dependence on the deposition rate was found (compare series 1 and 2). The stress shows a similar dependence upon deposition temperature as the index of refraction (Fig. 2) and the dielectric constant (Fig. 3), indicating that the measured room temperature stress is a function of the structure and/or composition of the nitride films.

In Fig. 4, the d-spacing values of the (444) planes of a [100] oriented substrate are shown as a function of deposition temperature. The character of the curve for the [111] case is inverted from that of the [100] case shown in Fig. 2. The explanation for the inversion is as follows: The nitride film is in tension; this places the substrate under compression. The d values of the asymmetric planes relative to the surface in compression are decreased relative to either the unstrained case or the case of a strained [111] oriented substrate (11). The inset in Fig. 4 schematically depicts this arrangement.

The higher the tensile stress in the film, the more compressive is the stress in the substrate and the

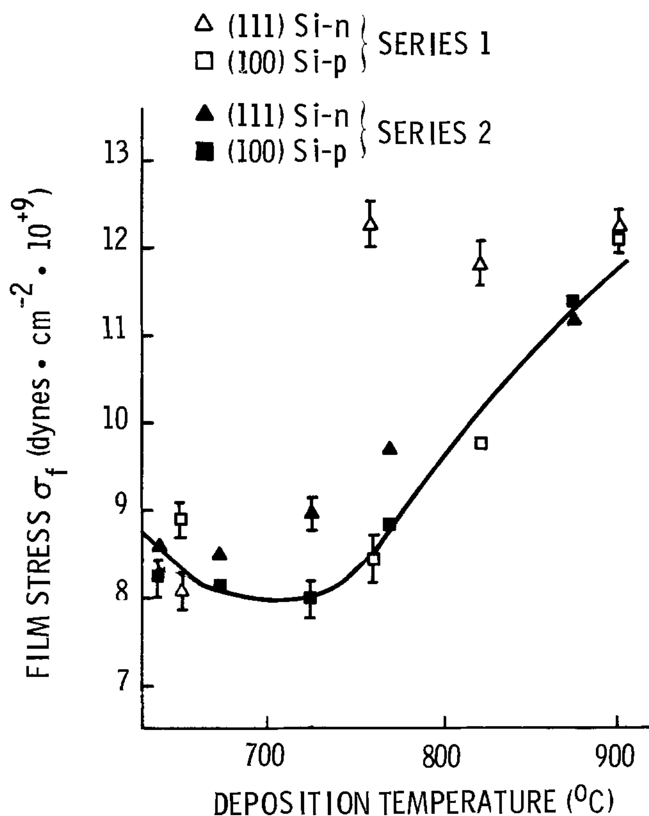

Fig. 1. Mechanical stress in silicon nitride films as a function of deposition temperature. The stress is tensile.

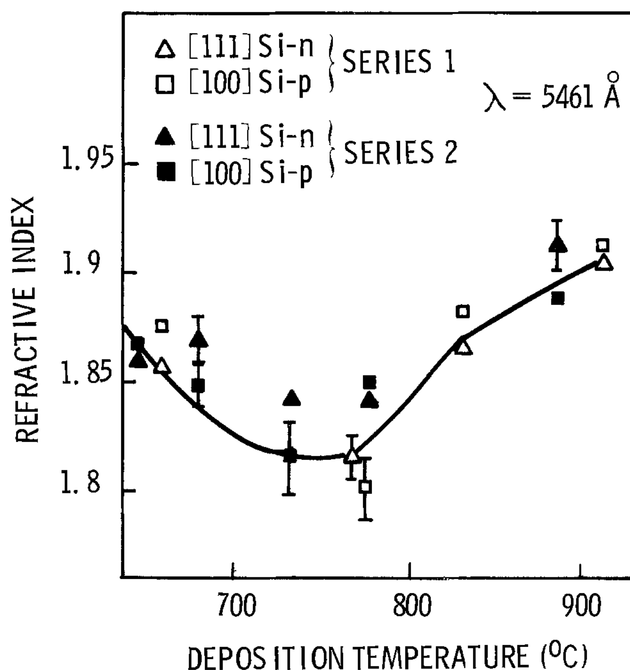

Fig. 2. Index of refraction of silicon nitride films on silicon as a function of deposition temperature.

smaller the d spacing. This is in agreement with our results (compare Fig. 1 and 2). Thus, these measurements have shown that the lattice parameter, and hence the stress introduced into the Si-substrate by the nitride film, follows a similar dependence upon deposition temperature as the stress in the film.

Finally, when one assumes the [100] and [111] orientations to have the same $E/1 - v$ value as suggested in (2), the stress *vs.* deposition temperature curves separate for both orientations, where the [111] curve is lower in value than the [100]. However,

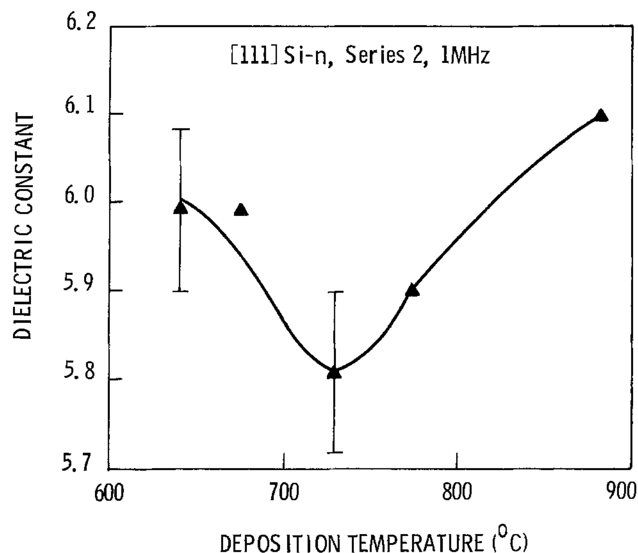

Fig. 3. Dielectric constant of silicon nitride films on silicon as a function of deposition temperature.

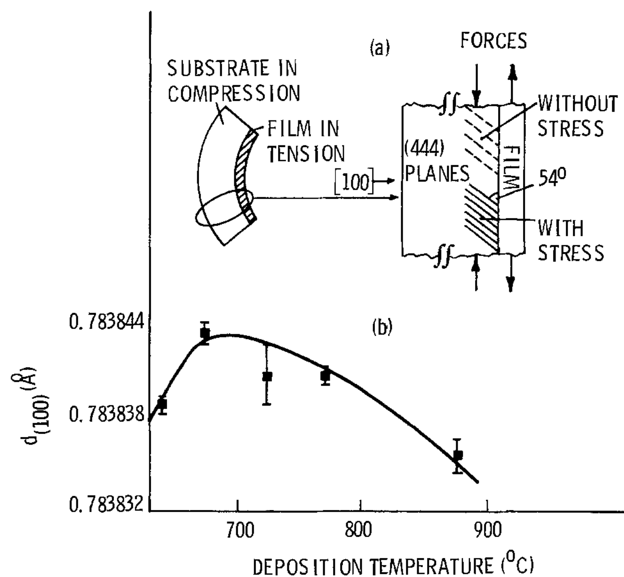

Fig. 4. (a) Schematic diagram showing the contraction of the (444) lattice planes caused by the stress in the film (high stress-low d values); (b) Interplanar spacing values of the (444) planes of a [100] Si substrate covered with silicon nitride as a function of the nitride deposition temperature.

when one uses the calculated values of Ref. (3, 4), these curves are nearly superimposed as shown in Fig. 1. The stress, then, in the film is approximately the same for both substrate orientations. However, the magnitude of the substrate warpage is dependent on the different elastic constants for each orientation.

The dependence of the film stress upon deposition temperature in the temperature region from 600° to 900°C was investigated by several authors [Ref. (10, 12-14)]. In all cases, different deposition parameters and nitride layers much thicker (2000-5000Å) than the ones actually applied in memory structures were used for the investigations. Studies reported in Ref. (10) and (13) found that the stress in the nitride film is decreasing with increasing deposition temperature, while Aboaf (12) reports an independence of the stress and deposition temperature between 500°-900°C.

Deposition Rate

In Fig. 5, the effect of deposition temperature on deposition rate is shown for the two deposition series and substrate orientations. The deposition rates as well as their temperature dependence are different for

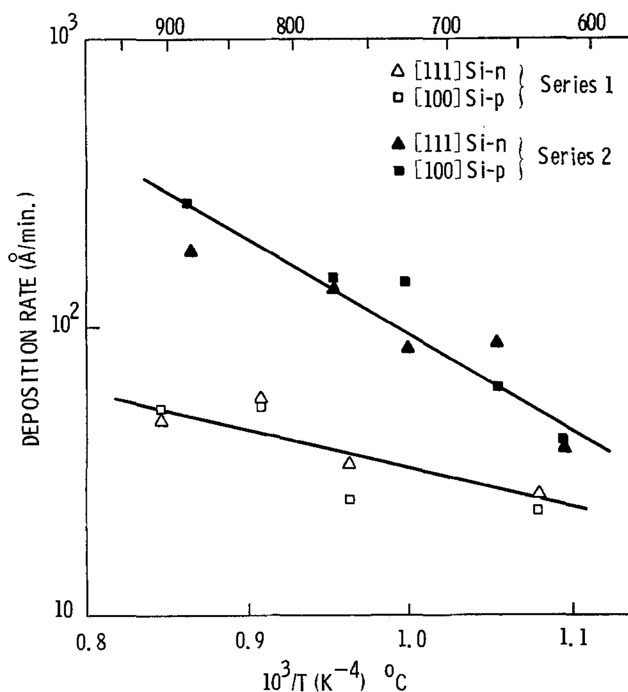

Fig. 5. Deposition rate of silicon nitride films on silicon as a function of deposition temperature.

the two series. From the log rate *vs.* $1/T$ plots, apparent activation energies were determined to be 6.1 kcal/mole for series 1, and 15 kcal/mole for series 2. The reasons for the differences are partly due to different amounts of ammonia and silane (without changing their ratio) and partly due to the properties of the hot wall deposition system itself. The deposition rate can be varied by properly positioning the wafers within the constant temperature region toward the edges of the optimal deposition zone (15). These differences make it possible to study the influence of the deposition rate on the nitride layer properties over the whole temperature range.

The independence of stress and index of refraction with respect to deposition rate points to the fact that the deposition rate in the range used here has only little or no influence upon the structure of the nitride films. This result is in agreement with Aboaf's results (12), but opposite to Irene's (13), where the stress was observed to decrease for decreasing deposition rate. The different experimental conditions may be responsible for the results cited in Ref. (13), where forming gas was used as carrier gas, the NH_3/SiH_4 ratio was much lower (150:1), the index of refraction was much higher, and layers of 2000Å and thicker were used.

Index of refraction.—Figure 2 shows the refractive index (n) as a function of deposition temperature for nitride layers deposited on [111] and [100] Si wafers. Higher values of n at low deposition temperatures pass through a minimum and finally increase to higher n values with increasing temperature. A similar behavior was found for the different deposition series and substrate orientations.

It is important to note that the n values are not dependent on the deposition rate (see series 1 and 2). They increase with increasing deposition temperature beyond the minimum. In Ref. (16), only a slight increase of n in the same temperature range was found, whereas those values published in Ref. (17) are decreasing steadily from $n = 20$ at 700°C to $n = 1.97$ at 850°C. In Ref. (17), a cold wall deposition system and a lower NH_3/SiH_4 ratio were used. Values of n in the same range between 1.8 and 1.9 were reported by Duffy and Kern (18) using similar deposition conditions as in the present work. However, most of the published values of the index refraction of silicon nitride are close to 2.0. Some possible reasons for the observed lower n values and for the deposition temperature dependence reported here are now discussed.

According to the relatively high NH_3/SiH_4 ratio, the films may possibly contain less Si compared to the stoichiometric composition Si_3N_4, resulting in lower values of n (17). The amount of Si may possibly change with deposition temperature.

As shown in Ref. (19), oxygen incorporation into the nitride films during deposition could be another reason for the variation and especially for the low values of n. Oxygen was not intentionally introduced during growth, but it is likely that our system contained enough oxygen to produce an oxy-nitride, especially by the amount of water introduced by the ammonia gas.

ESCA measurements (20) were made, and confirm that oxygen is present and varies with the deposition temperature as shown in Fig. 6. The oxygen content varies inversely with the index of refraction, as expected.

Thus, as in the case of the refractive index, the minimum in the stress-deposition temperature curve in Fig. 1 may also be attributed to the increased oxygen concentration of the nitride films deposited in the temperature range 700°-800°C. Figure 7 shows that the oxygen content is higher at the surface and decreases to a constant level after about 5 min (50Å) cf etch time.

Since an increase of n with film thickness in the range of 600-1500Å was observed in the course of the present work, the thickness has to be taken into ac-

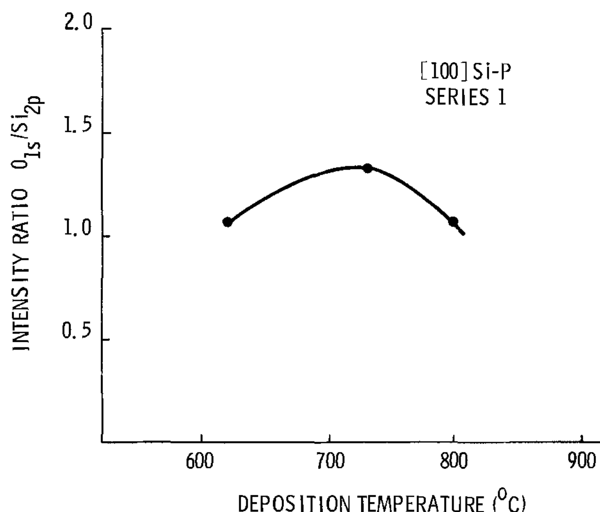

Fig. 6. ESCA data showing relative oxygen concentration vs. deposition temperature.

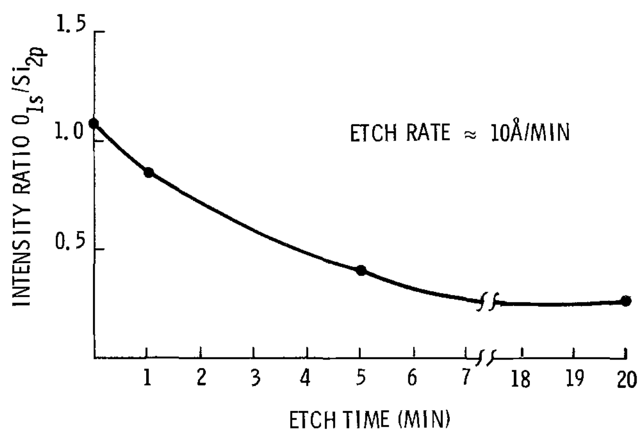

Fig. 7. ESCA data showing relative oxygen concentration vs. etch time (depth from surface).

count if comparisons are made between the n values of different authors.

The relative dielectric constant of the nitride layers was determined for the [111] oriented samples of series 2 as a function of deposition temperature, and the results are shown in Fig. 3. Uncertainties in capacitance, film thickness, and electrode area indicate an absolute error up to 3%. A behavior similar to that of the refractive index with a pronounced minimum at 730°C is obtained.

Interface Charge Density

In Fig. 8 the dependence of the interface charge density on deposition temperature is shown for the two deposition series with [111] and [100] substrate orientations. For comparison, the results reported in (16) are also given. Within a relatively narrow temperature range there is a remarkable decrease of Q_N/q with increasing deposition temperature, finally changing from positive to negative values between 800° and 900°C. Differences in the absolute values exist, but in general the dependence on deposition temperature is similar for all runs. Note especially that the results of Ref. (16) are in good agreement with those of series 2. According to series 2 but in contrast to series 1, there is no orientation dependence of the interface charge density. The results of series 2 are more reliable in this respect, since there are more data points and the depositions on the [111] and [100] substrates were made in the same run, while in series 1 separate depositions were made for the two orientations.

Stress-interface charge density relationship.—According to Fig. 1, 2, 4, and 5 the decrease in charge density at low deposition temperatures corresponds to a decrease in the refractive index, the dielectric constant, the film stress, and the stress in the substrate. In this range, the most significant change of the interface charge density occurs until that temperature at which stress and index of refraction curves reach a minimum. It may be speculated that this minimum corresponds to a turning point in the charge density *vs.* deposition temperature curve. Beyond this point, the further decrease in charge density is slowed down, finally changing from positive to negative values. Since in the temperature range beyond this possible turning point both the stress and index of refraction values increase, a different process seems to be responsible for the interface charges. Thus, the charge density *vs.* deposition temperature curve (Fig. 8) probably represents the superposition of two or even more curves, each caused by different phenomena. Therefore, a similar postulation as expressed for the case of MOS structures in Ref. (1) may also be justified for the MNOS structures that both positive and negative charges are present at the interface, their respective amounts varying with deposition temperature.

It is interesting to compare these results with the data of Stein and Wells (21), shown in Fig. 9. They measured the hydrogen bonding in silicon nitride by multiple internal reflection spectroscopy as a function of deposition temperature between 700° and 900°C. N-H bonding was observed in all films, whereas Si-H bonding decreased with increasing temperature and was not observed in films deposited at 900°C. The interface charge density (Fig. 8) is decreasing in the same temperature range and also becomes zero between 800° and 900°C, changing from positive to negative values.

Furthermore, annealing of these nitride samples above the deposition temperature in nitrogen (22) and subsequent analytical investigations by low energy electron loss spectroscy (ELS) (23) showed a similar result, namely, that with decreasing hydrogen bonding (particularly Si-H) an increase of film stress along with a simultaneous decrease of positive charges occurs. In Ref. (24), changes of several film properties upon annealing are attributed to a densification of the nitride films.

Thus, without knowing the detailed mechanism, it can be assumed that hydrogen in the nitride film (produced by the SiH_4-NH_3 reaction) is at least partly responsible for the stress and charge variation with deposition temperature.

But, similar to the Si/SiO_2 system, a definite stress-interface charge relationship cannot be established for the MNOS structures under investigation, since it is unknown whether (*i*) the changes in structure and/or composition of the film or; (*ii*) the changes in film stress, account for the interface charge density variation with deposition temperature.

Switching data.—To demonstrate the memory quality of nitride films under investigation, the saturation shift of the *C-V* curves for both positive and negative gate voltages were determined as a function of nitride

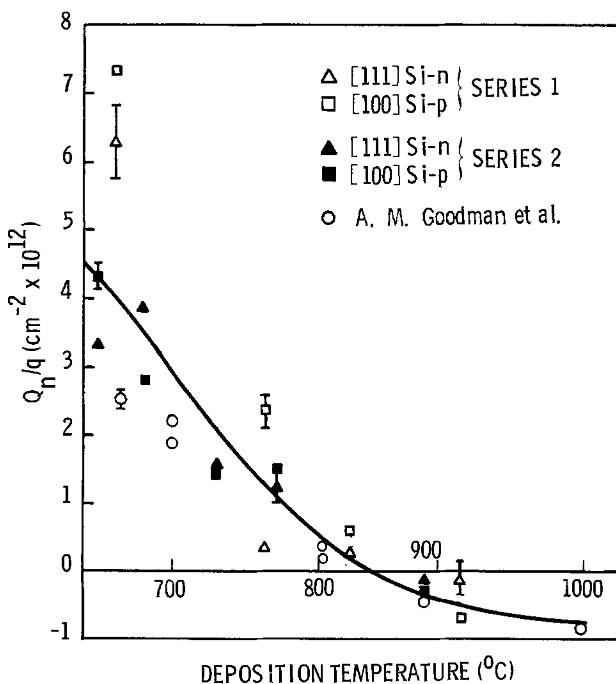

Fig. 8. Interface charge density in MNOS structures just after nitride deposition as a function of deposition temperature.

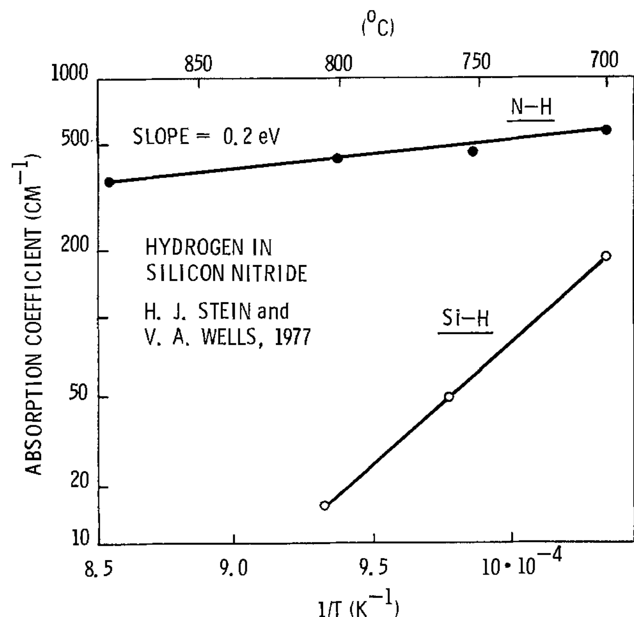

Fig. 9. Hydrogen bonding data of infrared absorption coefficient *vs.* deposition temperature.

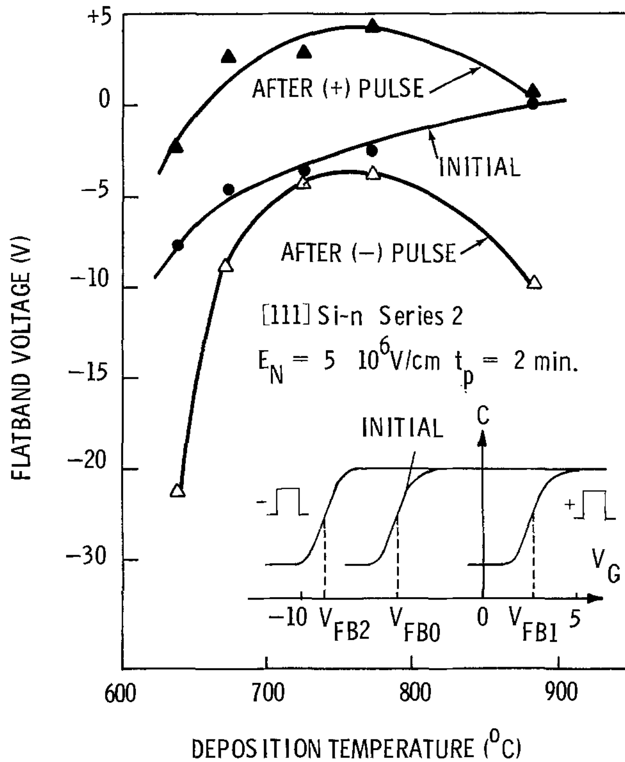

Fig. 10. Flatband voltages of the as-grown MNOS structures and after positive and negative gate voltage pulses (saturation shift as a function of the nitride deposition temperature.

deposition temperature (Fig. 10). From these curves the position of the saturation window relative to the voltage axis and relative to the initial flatband voltage can be determined. As an insert in Fig. 10, original C-V curves are shown before and after application of positive and negative voltages. No significant distortion of the curves due to fast surface states could be detected. In Fig. 11 the width of the saturation window (V_{FB1} − V_{BF2}) as determined from Fig. 10 is plotted as a function of nitride deposition temperature. The width and the position of the saturation window shows a similar dependence upon deposition temperature as the stress in film and substrate, the index of refraction, and the dielectric constant. An especially pronounced maximum/minimum was found between 740° and 760°C, slightly lower in temperature than the minimum shown in Ref. (16) for the maximum positive stored charge for negative gate voltages.

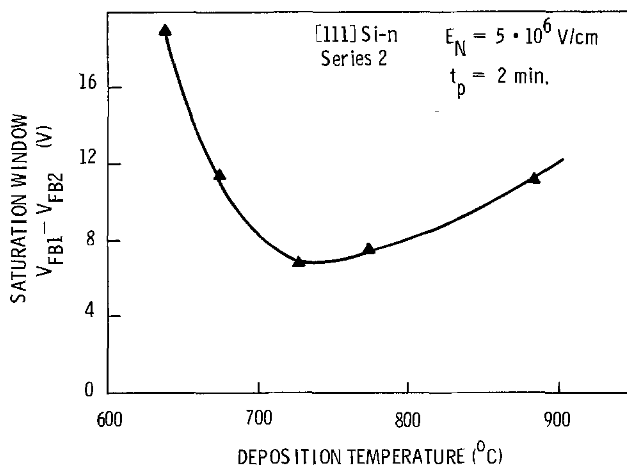

Fig. 11. Differences between the flatband voltages of MNOS devices obtained after positive and negative gate voltage pulses (see Fig. 10, "saturation window") as a function of the nitride deposition temperature.

It is well known from charge centroid studies the traps are not only present at the SiO_2/Si_3N_4 interface but are spatially distributed deep into the bulk of the nitride (25, 8). These results can be taken as another piece of evidence that the memory properties are correlated to the structure and/or composition of the nitride film.

Summary and Conclusions

Memory-quality silicon nitride films were deposited in a hot wall reactor by the reaction of silane and ammonia on [111] and [100] silicon substrates, n- and p-type, respectively. The deposition temperature ranged from 640° to 910°C and the average thickness of the nitride layers was 700Å. Index of refraction, dielectric constant, stress in the film, and the interplanar spacing in the silicon substrate together with the fixed interface charge density of the as-grown samples and the saturation shift of the flatband voltage under positive and negative gate voltages in the corresponding thin oxide MNOS structures were measured as a function of deposition parameters.

No significant dependence of these properties on the deposition rate and substrate orientation was found. Index of refraction, dielectric constant, film stress, *d* values in the substrate, and the maximum shift of the flatband voltage show a similar characteristic deposition temperature dependence with a minimum between 710° and 760°C. The variations in film stress and stress in the substrate as well as those of the switching properties are therefore very likely due to changes in structure and/or composition of the nitride films. The interface charge density *vs.* deposition temperature curve may be characterized by a sharp decrease at low temperatures, a turning point, and a lower decrease at higher temperatures, finally changing from positive to negative values between 800° and 900°C. The position of the turning point probably corresponds to the minimum of the film stress and index of refraction. It may be assumed that both positive and negative charges are present at the interface, their respective amounts changing with temperature.

No definite stress-interface charge relationship can be established for the MNOS structure since it is unknown whether structure and/or composition of the films or the film stress itself account for the interface charge density variation with deposition temperature.

Hydrogen introduced during the silane-ammonia reaction into the nitride films is assumed to strongly influence the properties of MNOS devices.

Acknowledgments

The authors are grateful to J. Ziegler for the accurate preparation of the samples at the Instiut Feur Werkstoffwissenschaften VI, University of Erlangen-Neurnberg, to E. Gorey for the ellipsometry measurements, to C. Hoogendoorn for his assistance during the course of the stress measurements, and to R. Flitsch for the ESCA measurements. Special thanks to Dr. G. H. Schwuttke for the support and encouragement of this work.

Manuscript submitted Oct. 31, 1977; revised manuscript received June 9, 1978.

Any discussion of this paper will appear in a Discussion Section to be published in the June 1979 JOURNAL. All discussions for the June 1979 Discussion Section should be submitted by Feb. 1, 1979.

Publication costs of this article were assisted by the IBM East Fishkill Facility.

REFERENCES

1. S. D. Brotherton, T. G. Read, D. R. Lamb, and A. F. Willoughby, *Solid-State Electron.*, **16**, 1367 (1973).
2. S. J. Fonash, *J. Appl. Phys.*, **44**, 4607 (1973).
3. E. W. Hearn, *Adv. X-Ray Anal.*, **20**, 2731 (1976).
4. R. Glang, R. A. Holmwood, and R. L. Rosenfeld, *Rev. Sci. Instrum.*, **36**, 7 (1965).

5. W. A. Brantley, *J. Appl. Phys.*, **44**, 534 (1973).
6. T. W. Baker, J. D. George, B. A. Bellamy, and R. Causer, *Adv. X-Ray Anal.*, **11**, 359 (1968).
7. E. S. Gruber and R. E. Black, *J. Appl. Crystallogr.*, **3**, 354 (1970).
8. H. Maes and R. J. VanOverstraten, *Appl. Phys. Lett.*, **27**, 282 (1975).
9. R. Hezel, *Siemens Forsch. Entwicklungsber.*, **1**, 153 (1972).
10. M. Tamura and H. Sunami, *Jpn. J. Appl. Phys.*, **11**, 1097 (1972).
11. B. D. Cullity, "Elements of X-ray Diffraction," Chap. 17, Addison-Wesley, Reading, Mass. (1956).
12. J. A. Aboaf, *This Journal*, **116**, 1736 (1969).
13. E. A. Irene, *J. Electron. Mater.*, **5**, 287 (1976).
14. A. K. Gaind and E. W. Hearn, *This Journal*, **125**, 139 (1978).
15. R. Hezel and F. Schwidefsky, *Siemens Forsch. Entwicklungsber.*, **1**, 297 (1972).
16. A. M. Goodman, E. C. Ross, and M. T. Duffy, *RCA Rev.*, **31**, 342 (1970).
17. C. T. Naber and G. C. Lockwood, in "Semiconductor Silicon, 1973" p. 401 H. R. Huff and R. R. Burgess, Editors, The Electrochemical Society Softbound Symposium Series, Princeton, N.J. (1973).
18. M. T. Duffy and W. Kern, *RCA Rev.*, **31**, 742 (1970).
19. P. H. Holloway and H. J. Stein, *This Journal*, **122**, 723 (1976).
20. S. I. Raider, R. Flitsch, J. A. Aboaf, and W. A. Pliskin, *ibid.*, **123**, 560 (1976).
21. H. J. Stein and V. A. Wells, Abstract 113, p. 303, The Electrochemical Society Extended Abstracts, Spring Meeting, Philadelphia, Pennsylvania, May 8-13, 1977.
22. R. Hezel and J. Ziegler, Paper HL 26 presented at the Spring Meeting of the Deutsche Physikalische Gesellschaft, Muenster, West Germany, March 1977.
23. N. Lieske and R. Hezel, To be published.
24. H. J. Stein, *J. Electron. Mater.*, **5**, 161 (1976).
25. B. H. Yun, *Appl. Phys. Lett.*, **25**, 340 (1974).

Interactions Between Cr and Pt Films: New Cr-Pt Phases

J. Baglin,* F. d'Heurle,* and S. Zirinsky

IBM Thomas J. Watson Research Center, Yorktown Heights, New York 10598

ABSTRACT

Thin film studies are frequently concerned with the characteristics of metastable alloy phases. However, the analysis of diffusion in thin film couples can lead to new contributions to the understanding of the equilibrium state. In Cr-Pt films new ordered phases Pt_3Cr and PtCr have been found. PtCr is slightly tetragonal.

Thin film deposition techniques are often used for the preparation of metastable phases, especially amorphous ones, which can be produced in bulk only by means of drastic procedures such as extremely rapid cooling (1). [The early interest in amorphous alloy films (2-4) continues to the present day when the study of amorphous Si films (5) and that of amorphous magnetic films (6) can almost be considered to constitute independent disciplines.] Evidence is presented here that by the study of diffusion between Cr and Pt films significant additions to the existing Cr-Pt equilibrium diagram could be obtained. These additions are believed to be consistent with thermodynamic requirements, with the theory of ordering transformations, and with crystallography. It may be that, at least in this one case, equilibrium conditions can be more easily reached in films than in bulk samples, where stresses could hinder certain phase transformations. The emphasis here is placed on equilibrium characteristics. Considerations about the kinetics of diffusion in Cr-Pt thin film couples have been presented elsewhere (7-9).

Experimental Procedures

For diffusion studies at low temperatures (about 500°C) the films were deposited from e-beam sources onto oxidized Si wafers at 200°C, the pressure during deposition being in the low 10^{-8} Torr range (obtained through the use of a liquid N_2 shroud surrounding the inside of the deposition chamber), at a rate of about 20 Å/sec. A few diffusion studies were carried out at high temperatures (about 1000°C) with films deposited onto sapphire wafers, at a pressure in the 10^{-7} Torr range. The films were always deposited in the sequence Cr then Pt, without breaking the vacuum. The film thicknesses were usually: Cr-1600Å, Pt-2000Å or Cr-4000Å, Pt-4800Å, for a nominal overall composition near 50 atom percent (a/o). The films were subsequently heat-treated in an atmosphere of highly purified He obtained by flowing the gas over a hot titanium bed. Most of the annealing treatments were carried out for times of 0.5, 2, 8, 32, and up to 128 hr, at temperatures from 420° to 580°C in steps of 40°C.

The films were analyzed by backscattering of 2.6 MeV He ions, and by x-ray diffraction. The standard x-ray diffractometer equipped with a Cu tube was also equipped with a post sample monochromator (bent graphite crystal) which in the present case was particularly useful in eliminating fluorescence from Cr in the samples. Computer control of the diffractometer made it possible to use long counting times when good statistics were required to reveal details of structure which could be lost in old recorder tracings. Care was exercised to check for traces of oxidation (which were not detected), and for reaction of the films with the substrates. In only one of the samples used, after 2 hr at 580°C, was any reduction of SiO_2 by Cr observed. Even in this case there was no indication of any overlap between Cr and Pt in the backscattering spectrum, so that any interference with the Cr-Pt reaction was judged to be negligible. Yet, of course, this interaction at 580°C dictated the use of sapphire substrates for any studies conducted at high temperatures.

Results

Phases formed at 400°-600°C.—A series of spectra from the backscattering experiments are presented superimposed on one another in Fig. 1. The spectra

* Electrochemical Society Active Member.

Key words: equilibrium diagram, Cr-Pt phases, ordering transformation, backscattering analysis, structure of CrPt, thin films of Cr-Pt, diffusion in Cr-Pt.

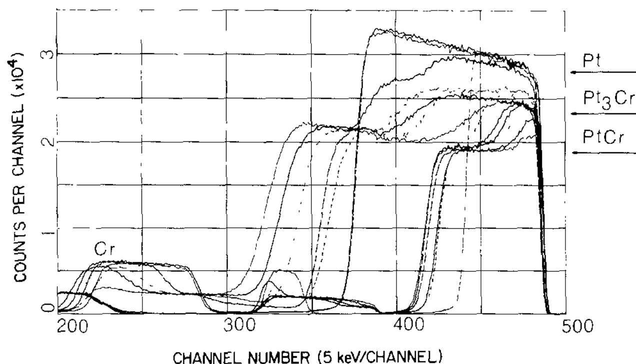

Fig. 1. Superimposed backscattering spectra for thin and thick samples (Cr: 1600, 4000Å and Pt: 2000, 4800Å) annealed for times varying from 0.5 to 32 hr at temperatures from 460° to 580°C. (Note some overlap of the Cr and Pt parts of the spectra for the annealed thick samples).

correspond to both thin and thick samples (Cr-1600Å, Pt-2000Å and Cr-4000Å, Pt-4800Å) annealed for periods ranging from 0.5 to 32 hr at temperatures from 460° to 580°C. The distinguishing feature of these overlapped spectra is the presence of discrete plateaus corresponding to specific compositions: As indicated by the arrows these are Pt_3Cr and PtCr, shown in contradistinction to the pure Pt. Similar features are shown in Fig. 2 for a thin sample annealed in similar conditions; there the discrete Cr levels are clearly shown. They correspond to concentrations of 25 and 50 a/o Cr.

The presence of two different and distinct phases, with specific compositions, in these samples is confirmed by the results of the x-ray diffraction observations. In Fig. 3 the (111) and (200) peaks for a thin sample annealed for 8 hr at 500°C are shown. Two distinct sets of peaks are evident. Their respective positions correspond to two phases with two different lattice parameters, both of which are smaller than the lattice parameter of Pt. For ease of identification the positions of the (111) and (200) diffraction peaks for Pt have been indicated on Fig. 3 by two arrows (on top of the figure). The two phases are ordered as shown by the presence of many superlattice lines which are listed in Table I for the same sample (thin, 8 hr at 500°C). While the intensities of the different lines (see Table I) varied with the heat-treatments, the lattice parameters of the two phases remained constant within the limits of experimental accuracy: ±0.002Å. Since the lattice parameters were measured at room temperature on samples annealed at elevated temperatures, the true lattice parameters must be estimated by taking into account the strains that developed during cooling as a result of the different thermal expansion coefficients of the film material and the substrates (10). For the films deposited on

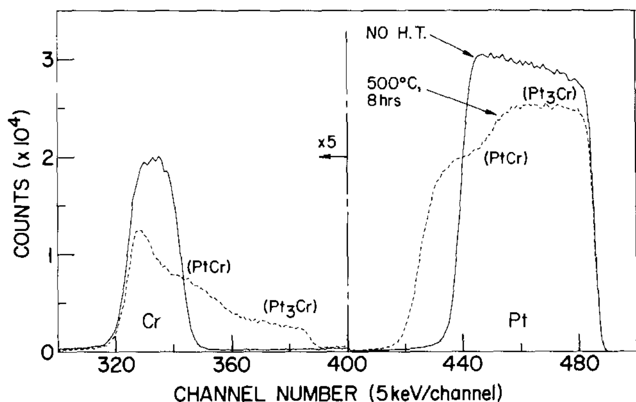

Fig. 2. Backscattering results showing discrete Cr levels. (These correspond to the Pt levels displayed in Fig. 1.)

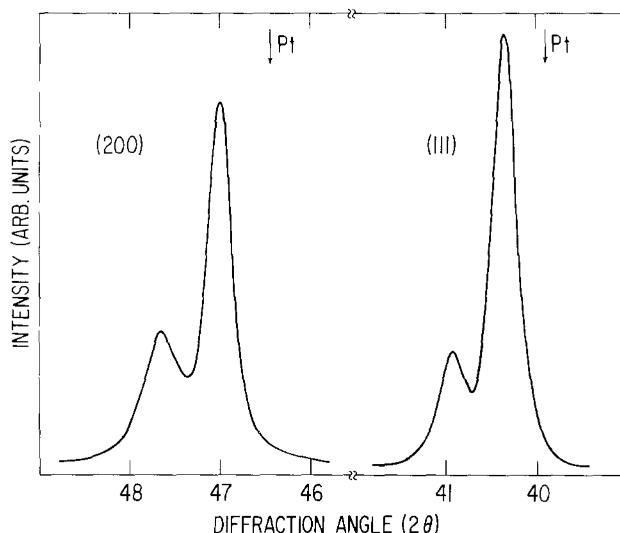

Fig. 3. The (111) and (200) diffraction peaks for $CrPt_3$ (low θ) and CrPt for a sample annealed at 500°C for 8 hr.

Si wafers, the quantities required for making the lattice parameter corrections are: the expansion coefficients of Si (3.2×10^{-6}/°C) (11), and of the Cr-Pt alloys, and the Poisson ratio for these alloys, which will be assumed to be 0.33. The expansion coefficient of the alloys is likely to be close to those of the pure metals (8.4×10^{-6}/°C and 9.1×10^{-6}/°C, respectively, for Cr and Pt) (12). For films cooled from 500°C to room temperature the correction to be added to the measured lattice parameters is about +0.010Å. Thus the final value for the lattice dimension of the two phases in Table I would be 3.877 ± 0.005 and 3.825 ± 0.005Å. The respective compositions can then be determined from the comparison of these lattice parameters with the values listed in the literature for Cr-Pt alloys. Such values (13) have been plotted in Fig. 4, where one can see that the desired compositions are very close to 25 and 50 a/o Cr.

It is to be noted that in all of these samples with an over-all composition close to 50 a/o, and annealed in a range of temperatures near 500°C, the Cr-rich

Table I. Lattice spacings d (Å) and x-ray diffraction peak intensities I for Pt_3Cr and PtCr

Phases				Peak intensities					
Pt_3Cr 1		PtCr 2		2-500*		8-500		32-460	
hkl	d	hkl	d	1	2	1	2	1	2
		100	3.81		130		400		400
110**	3.835	110**	3.835	170	170	450	450	250	250
111	3.866			1650		1125		700	
		111	3.818		450		1200		1000
200	3.860			400		300		300	
		200	3.814		150		400		400
201	3.863			10		15		10	
		201	3.817		30		100		100
112	3.859			10		10		10	
		112	3.814		30		70		70
		003	3.818	30		20		20	
		310	3.815		10		12		10
113	3.870			200		125		100	
		113	3.814		60		140		135
222	2.868			40		25		15	
		222	3.817		10		25		25
		023	3.813		***		25		10
		312	3.815		—		10		10
400	3.868			15		10		5	
		400	3.815		—		10		10
		401	3.817		—		10		10
		330	3.816		—		10		10
331	3.870			45		25		20	
		331	3.815		5		40		35
420	3.866			40		25		15	
		420	3.818		5		35		35

* 2-500 means 2 hr at 500°C.
** The spacing is exactly half-way between Pt_3Cr and PtCr indicating unresolved superimposed diffraction peaks.
*** Missing peak, too weak to be identified.

phase β, with approximately 80 a/o Cr, was generally undetectable, or was present only in very small traces. This was true in spite of the fact that the initial transformation of the film couples into CrPt and $CrPt_3$ left an excess of unreacted Cr.

Compounds formed at ~ 1000°C.—Some experiments were conducted with the films deposited on sapphire substrates and subsequently annealed in the vicinity of 1000°C. It is to be noted that the initial adhesion of the films to sapphire was extremely good. Bonding between Cr and Al_2O_3 is sufficiently strong to cause Cr atoms to adopt epitaxial positions with respect to c-axis sapphire (14). However, following heat-treatment in a range of temperature from 600° to 700°C, the films would peel off their substrates when moved from the hot to the cool zone of the annealing furnace. Films annealed above 800°C continued to adhere well to their substrates, although presumably the stresses developed in such films should be higher than in films annealed at lower temperatures. One may hypothesize that at high temperatures Cr and Al_2O_3 react sufficiently to form a good chemical bond between film and substrate, even though the extent of the reaction is too limited to allow for detection by the backscattering technique. Support for this proposition can be found in the use of Cr for the sintering of aluminum oxide powder and the report that Cr may reduce Al_2O_3 with the formation of lower Al oxides (15). Adhesion of a film on a substrate is the result of the competition between two effects: The strength of the chemical bonds across the interface and the shear stresses that develop at the interface as a result of the existence of compressive tensile stresses in the film and substrate. These latter are a strong function of temperature because of the usual difference in expansion of the film and substrate materials. The nature of the interface chemical bonds is also dependent on temperature; van der Waals type forces probably dominate for films deposited on relatively "inert" substrates at low temperature; heating may result in stronger ionic forces. The variations of adhesion with temperature due to the interplay of those two different effects will obviously be extremely dependent on the materials in question. In the case in hand, it must be presumed that at low temperatures the stresses are sufficiently weak to allow good adhesion, while at high temperatures the bonding is sufficiently strong to give the same result. At intermediate temperatures, about 700°C, apparently the stresses have increased considerably while the bonding remains limited, resulting in an over-all lack of adhesion of the Cr-Pt film to the sapphire substrates. Note that here the film stresses are functions not only of the expansion coefficients but also of the volume changes resulting from the interdiffusion of Cr and Pt.

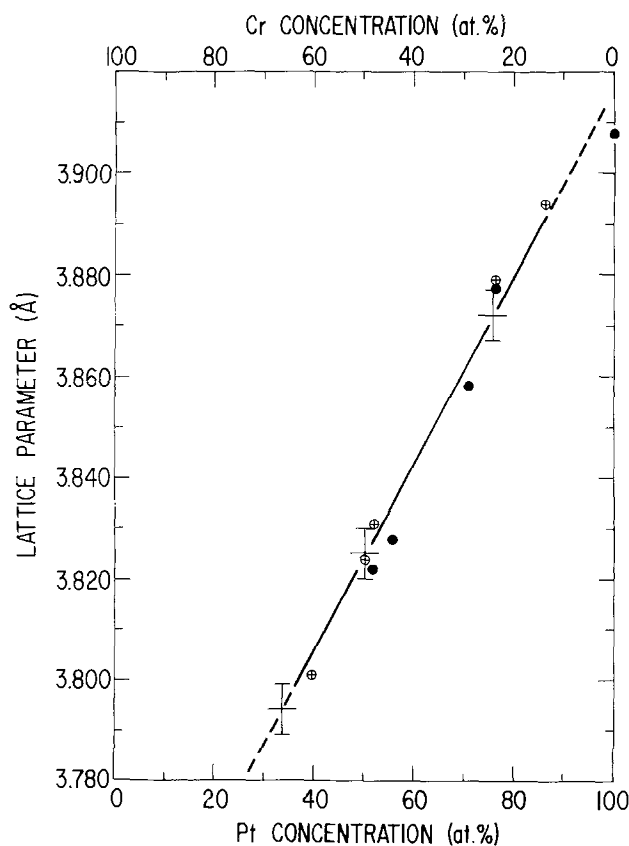

Fig. 4. The lattice parameters of Cr-Pt "solid solution" alloys according to Ref. (13). The composition of the phases considered here can be derived from the three points with error bars.

In the films annealed at high temperatures structural reorganization of the different components (Cr, Pt, and the different compound phases) prevented the clear identification of these components by backscattering experiments (as seen in Fig. 1 for films annealed at low temperatures). When the different products of the diffusion process cease to be disposed in layers, but instead tend to be distributed in parallel positions normal to the substrate, backscattering spectra can give only the over-all composition of the films but no detailed information. However, x-ray diffraction results indicate that in films annealed at high temperatures, as well as in those annealed at low temperatures, different ordered phases can be simultaneously present in the diffusion couples. CrPt and $CrPt_3$ were identifiable in a sample annealed at 1010°C. Moreover, in a sample annealed for 1 hr at 950°C, three phases were detected: PtCr with a lattice parameter of 3.815Å (uncorrected for stress), $PtCr_4$ with a lattice parameter of 4.712Å [complex cubic (13)], and a third phase with a lattice parameter of 3.784Å (face-centered-cubic, uncorrected). This third phase with a strong (111) peak, but also with a weak (210) superlattice peak (other fundamental peaks were present as well), is apparently ordered; one must ascribe to it the formula $PtCr_3$, even though its lattice parameter indicates that it is too poor in Cr to correspond to an exact stoichiometry. As previously, it is necessary here to consider the correction due to the difference in thermal expansion between film and substrate for temperatures up to 1000°C. The respective coefficients are: 10.2×10^{-6}/°C for Pt and 9.4×10^{-6}/°C for Cr (12), while for random orientation sapphire the expansion coefficient must be close to 7.6×10^{-6}/°C (15). The correction to the lattice parameter for these films is also found to be of the order of 0.010Å. Thus the lattice parameter of "Cr_3Pt" would be 3.794 ± 0.005Å, which corresponds to a composition of approximately 65 a/o Cr according to Fig. 4. Finally, the same three phases Cr_4Pt, Cr_3Pt, and CrPt were also identified in a more controlled experiment where a sample with 5400Å Cr and 2600Å Pt (72 a/o Cr) was annealed for 1 hr at 1000°C.

Detailed structural information was obtained on a sample containing 48.5 a/o Pt (analysis by backscattering) and annealed at high temperature (1 hr at 975°C) for complete homogenization. Individual diffraction peaks were scanned consecutively, the counting time being increased (for improved statistics) with decreasing maximum peak intensity. The results presented in Fig. 5 for the (100), (110), (111), (200), and (221, 003) peaks are actual peak tracings, without averaging through data points. The first three peaks (100), (110), and (111) are quite sharp, in the next peak (200, 002) one can see the anticipated splitting of the $CuK_{\alpha 1}$-$K_{\alpha 2}$ doublet on the high θ side, however, the bulge on the low θ side is unexpected for a true cubic structure, indicating a structural deformation. A more obvious evidence of structural peak splitting is visible in the (221, 003) peak. All other diffraction peaks are shown in the Appendix.

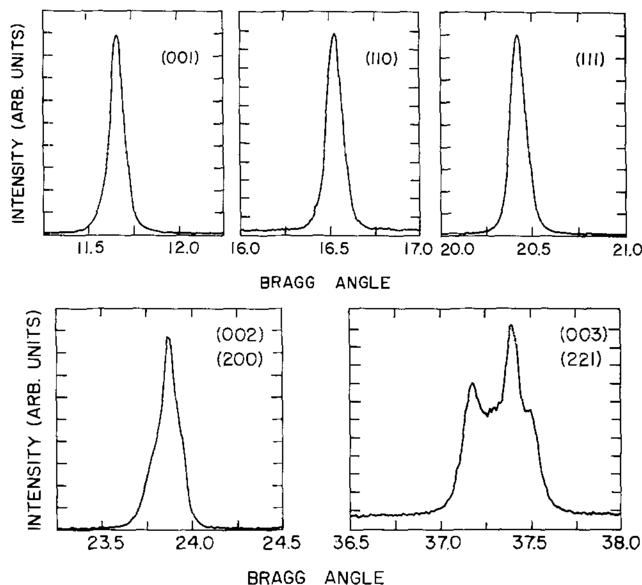

Fig. 5. Some sharp and split diffraction peaks from the CrPt phase.

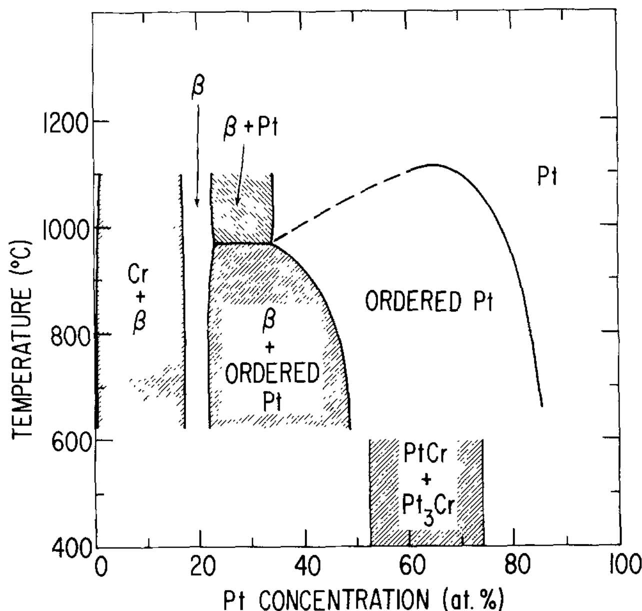

Fig. 6. The Cr-Pt equilibrium diagram. Above 600°C: as presently existing (20). Below 600°C: modifications mandated by this study.

Discussion

Dominant phases; key factors.—Ideally, at some point in the process of homogenization of a diffusion couple one should observe all of the phases in equilibrium at the temperature of annealing. Such ideal conditions are rarely encountered in actual practice, where one finds that, depending on the temperature, some phases will form in preference to others in apparent disregard of the equilibrium indications to be gathered from phase diagrams (17). The dominance of one or several phases may be due to a multiplicity of factors. Some are related to equilibrium, such as the respective free energy of formation of the different phases since, other things being equal, one would anticipate the preferential formation of that phase which has the lowest free energy. Others have their origin in kinetic considerations, such as the relative ease of diffusion of the various components in the different phases [see, for example, the analysis of phase formation in Al-Ni (18)]. Moreover, one must consider such factors as anisotropic growth rates, nucleation, and surface free energies (which in films will be related to preferred orientations), as well as stresses due to volumetric changes. Thus diffusion couples should not be expected to yield exhaustive information about equilibrium diagrams. Yet, all observations made on such couples must be consistent with equilibrium, and can deliver new information where previous results remain incomplete (19).

Equilibrium diagram; structures.—In the case at hand the equilibrium diagram is shown in Fig. 6 for the range of temperatures which is of interest. The existing part of the diagram, which is based on a recent study (20), has been drawn in the upper part, between 600° and 1100°C. It implies a continuous face-centered cubic structure from 45 a/o Pt to pure Pt, with a smooth transition (second order transformation) between the ordered and the disordered solid solutions of Cr in Pt. Such indications are not consistent with the present diffusion results.

For detailed information about ordering reactions one may turn to classical studies, which stress either statistical mechanics calculations (21) or thermodynamic relations (22), the latter being more directly relevant to the subject of this paper. In summary, these studies indicate that, as found in the Cu-Au system, the order-disorder transitions in AB_3 and AB face-centered-cubic solutions are first order reactions which mandate the presence of two phase fields in the equilibrium diagram, except at maximum ordering temperature, generally expected at the exact stoichiometric concentrations. In the AB case the matter is made more explicit since the ordered phase must have a lower crystal symmetry than the disordered face-centered-cubic solid solution, since it is impossible to conceive of a simple fcc structure with order at the 50% composition. For example CuAu is tetragonal with alternate layers of Cu and Au on the (001) planes, and CuPt is reported to be rhombohedral, with alternate layers of Cu and Pt on the (111) planes (23). Thus even if the ordered phase CrPt were found to be seemingly cubic, its true symmetry would not be cubic, but perhaps tetragonal with $c = a$.

The diffraction results obtained with the sample containing 48.5 a/o Cr indicate that CrPt is very slightly tetragonal, not rhombohedral. This judgment is largely based on the relative sharpness of the diffraction peaks (111) and (222) relative to their neighbors. Moreover if one assumes an AuCu type of structure (pseudo face-centered-tetragonal, with alternate layers of Cr and Pt atoms along the c axis) the allowed diffraction peaks would be those for which $h + k = 2n$. Then the following reflections should be sharp: (001), (110), (111), (201), (112), (310), (222), (203), (312), (401), (421), and (332); while these reflections should be broad: (200-002), (220-202), (221-003), (400-004), (114-330), (313-331), (420-402-204), and (422-242). This can be observed to conform with the experimental results (see Appendix). By least squares calculations and the use of a Nelson-Riley extrapolation the lattice parameters (uncorrected for stress) were found to be a = 3.822Å and c = 3.811Å from the d spacings for the sharp peaks. [These values, obtained with the computer-controlled diffractometer and good statistics, are to be preferred to the previously reported ones (3.825 and 3.809Å) obtained by visual reading of diffraction angles from a chart record (8)]. Even taking into account respectively the difference in atomic diameters between Cr and Pt (2.54 and 2.76Å) and the difference between Cu and Au (2.56 and 2.88Å), one can see that the c/a ratio for CrPt is much closer to 1.0 than would be anticipated on the basis of CuAu, since for this compound the lattice parameters are a = 3.960Å and c = 3.670Å.

To establish concentration boundaries for the different Cr-Pt phases referred to in this paper is beyond the scope of the present study. For the phases formed at low temperatures, in the vicinity of 500°C, experimental results indicate that the limits should

be quite narrow. The slopes of the traces corresponding to the two compounds in Fig. 1 are indicative of narrowly defined composition limits, although perhaps a case could be made for the existence of $CrPt_3$ with an excess of Pt. CrPt, on the other hand, appears to be extremely narrowly defined, regardless of the presence of both $CrPt_3$ and residual unreacted Cr. The evidence derived from the x-ray diffraction patterns points in the same direction. The lattice parameters of coexisting phases of $CrPt_3$ and CrPt indicate compositions quite close to 25 and 50 a/o Cr, leaving little freedom to extend the composition limits off stoichiometry.

One may speculate as to why the tetragonal structure of CrPt had not been reported previously. Of course, one reason is that the unit cell is almost a cube. Beyond this it is not impossible that in bulk samples stresses may considerably hinder the transformation from the cubic structure to the tetragonal one, while in films there are possibilities for stress relaxation in at least one direction. In this case the films would allow for a closer approach to chemical equilibrium than is possible with bulk samples, which leaves some ambiguity about the definition of the "equilibrium state."

Conclusions

1. Results from diffusion experiments conducted with thin films of Cr and Pt require the existence of two distinct ordered phases $CrPt_3$ and CrPt which are not shown on the presently available equilibrium diagram.

2. In a range of temperature near 500°C the limits of existence of these phases appear to be quite narrow, of the order of a few atomic percent.

3. $CrPt_3$ is ordered face-centered-cubic with a lattice parameter of 3.877 ± 0.005Å.

4. These individual phases were also detected in samples annealed at temperatures in the vicinity of 1000°C. At such temperatures an ordered phase with the presumed structure of Cr_3Pt was also observed. This phase apparently exists off stoichiometry, with a composition of approximately 65 a/o, which corresponds to the maximum "solubility limit" of Cr in Pt.

5. At least in thin film form the phase CrPt displays structural characteristics which indicate that it is ordered and tetragonal, like CuAu. This is consistent with the crystallographic requirements for an ordered phase of this composition and with the thermodynamic requirements for a first order transformation.

6. The lattice parameters of CrPt, a = 3.822Å and c = 3.811Å, indicate a very small tetragonal distortion from the cubic lattice of Pt. These values were obtained from a sample containing 48.5 a/o Cr, deposited on a sapphire substrate and annealed at 975°C. In order to obtain absolute values one would need to make careful corrections for stress effects (presumably about +0.010Å).

Acknowledgments

The authors are glad to acknowledge the considerable help received from J. Dempsey, W. Hammer, J. Angilello, A. Segmuller, and S. Laplaca in the gathering and the analysis of the data.

Manuscript submitted Feb. 27, 1978; revised manuscript received June 28, 1978. This was Paper 177 presented at the Atlanta, Georgia, meeting of the Society, Oct. 9-14, 1977.

Any discussion of this paper will appear in a Discussion Section to be published in the June 1979 JOURNAL. All discussions for the June 1979 Discussion Section should be submitted by Feb. 1, 1979.

Publication costs of this article were assisted by IBM Thomas J. Watson Research Center.

Note added in proof: The magnetic properties of the Pt-rich Cr-Pt alloys, and the effect of ordering on those alloys, are the subject of a recent article (24).

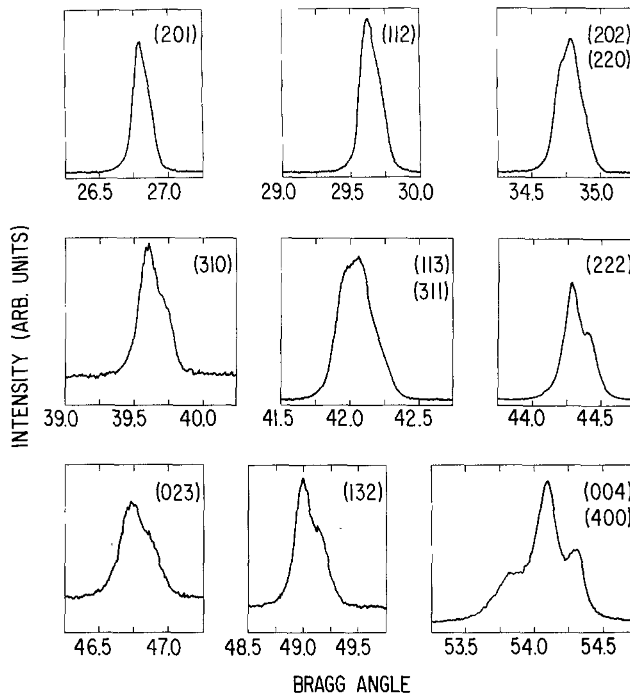

Fig. 7. Diffraction peaks of CrPt for low Bragg angles

APPENDIX

The Crystallography of CrPt

Representative details of the diffraction results obtained with CrPt have already been displayed in Fig. 5. All of the remaining evidence obtained with the same sample (48.5 a/o Cr, annealed 1 hr at 975°C) is presented in Fig. 7 for the low Bragg angles and in Fig. 8 for the high Bragg angles. Moreover the lattice spacings and peak intensities are presented in Table II. Although all of the anticipated diffraction peaks were detected (which indicates a high degree of randomness in

Table II. Lattice spacings and diffraction peak intensities for CrPt (λ = 1.54051Å)

hkl	d*	d**	I***	I/I₀‡
001	3.811	3.811	4450	100
110	2.7029	2.709	527	12
111	2.2047	2.208	3490	78
020	1.9112		2430	55
002	1.9055		—†	—
021	1.7084	1.7087	153	3
112	1.5574	1.5586	227	5
220	1.3514		200	4
022	1.3494		—	—
221	1.2737		72	2
003	1.2724		104	2
130	1.2088	1.2086	40	1
131	1.1522		261	6
113	1.1497		—	—
222	1.1023	1.1032	137	3
023	1.0579	1.0579	16	
132	1.0207	1.0208	38	1
040	0.9556		27	
004	0.9527		82	2
041	0.9269		34	1
223	0.9256		—	—
330	0.9010		7	
114	0.9008		18	
331	0.8768		64	1
133	0.8757		—	—
240	0.8547		50	1
042	0.8542		—	—
024	0.8527		58	1
241	0.8340	0.8339	16	
332	0.8145	0.8148	13	
242	0.7799	Not observed (too high θ)		
224	0.7787			

* Calculated from a = 3.82244A, c = 3.81099A.

** Determined with the Rachinger correction from the experimentally obtained peaks. The spacings listed here are for the "sharp" peaks.

*** These are experimental peak intensities not integrated intensities; for a thin film, not a powder sample with an ideally infinite depth.

† Where the intensity is indicated by a horizontal dash, the neighboring peaks could not be separated.

‡ For a true powder pattern the relative intensities are anticipated to be similar to those of CuAu.

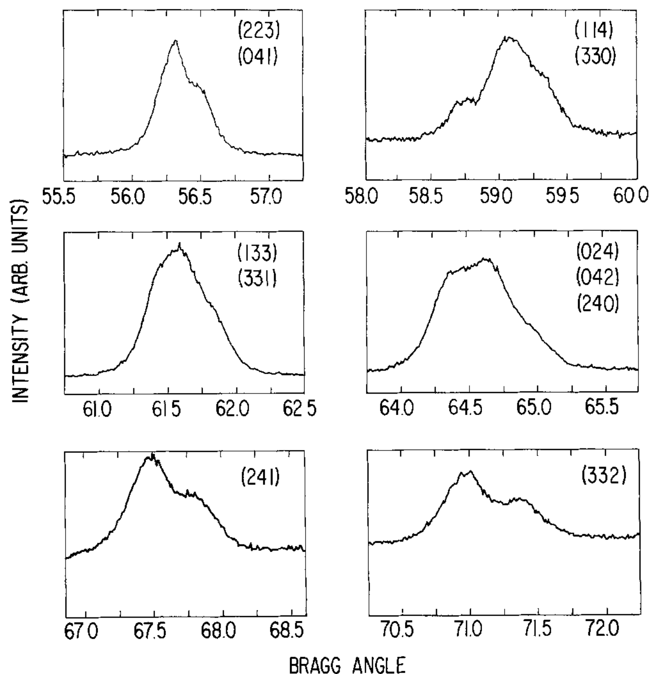

Fig. 8. Diffraction peaks of CrPt for high Bragg angles

the sample), the intensities observed cannot be considered to be valid for a truly random powder sample since, as is well known by workers in the field, thin film samples display some degree of preferred orientation almost always. Specific thin film diffraction effects are also responsible for the intensity of the (001) superlattice line being higher than the intensity of the (200-002) fundamental line.

REFERENCES

1. "Rapidly Quenched Metals, Proceedings of the 2nd International Conference on Rapidly Quenched Metals," Sec. 1, MIT Press, Cambridge, Mass. Sec. II, Elsevier Sequoia, Lausanne, 1976, N. J. Grant and B. C. Giessen, Editors.
2. E. Kneller, *J. Appl. Phys.*, **33**, 1355 (1962).
3. W. Buckel, *Z. Phys.*, **138**, 136 (1954).
4. S. Mader, H. Widmer, F. M. d'Heurle, and A. S. Nowick, *Appl. Phys. Lett.*, **3**, 201 (1963).
5. "Tetrahedrally Bonded Amorphous Semiconductors," *AIP Conf. Proc.*, **20**, (1974).
6. T. Mizoguchi, *ibid.*, **34**, 286 (1976).
7. S. Danyluk, G. E. McGuire, K. M. Koliwad, and M. C. Yang, *Thin Solid Films*, **25**, 483 (1975).
8. J. Baglin, F. d'Heurle, W. Hammer, and S. Zirinsky, in Proceedings of 7th International Vacuum Congress, Vienna, 1977, p. 2127.
9. P. Holloway, in "Thin Film Phenomena—Interfaces and Interactions," J. E. E. Baglin and J. M. Poate, Editors, The Electrochemical Society Softbound Symposium Series, Princeton, N.J. (1978).
10. F. d'Heurle, C. Aliotta, J. Angilello, V. Brusic, J. Dempsey, and D. Irmischer, *Vacuum*, **27**, 321, 1977.
11. L. Maissel, *J. Appl. Phys.*, **31**, 211 (1960).
12. C. J. Smithells, "Metals Reference Book, Vol. 3, pp. 686, 687, Plenum Press, New York (1967).
13. W. D. Pearson, "Lattice Spacings and Structures of Metals and Alloys," p. 557, Pergamon Press, New York (1958).
14. J. Baglin, J. Dempsey, F. d'Heurle, and W. Hammer, in "Thin Film Phenomena—Interfaces and Interactions," J. E. E. Baglin and J. M. Poate, Editors, The Electrochemical Society Softbound Symposium Series, Princeton, N.J. (1978).
15. P. Pascal, "Nouveau Traité de Cimie Minerale," Vol. xx, p. 547, Masson et Cie, Paris (1962).
16. W. M. Yin and R. J. Paff, *J. Appl. Phys.*, **45**, 1456 (1974).
17. S. U. Campisano, in "Thin Film Phenomena—Interfaces and Interactions," J. E. E. Baglin and J. M. Poate, Editors, The Electrochemical Society Softbound Symposium Series, Princeton, N.J. (1978).
18. A. J. Hickl and R. W. Heckel, *Met. Trans.*, **6A**, 431 (1975).
19. Y. Adda, M. Beyeler, A. Kirianenko, and F. Maurice, *Mem. Sci. Rev. Met.*, **58**, 716 (1961).
20. R. M. Waterstraat, *Met. Trans.*, **4**, 1585 (1973).
21. T. Muto and Y. Takagi, in "Solid State Physics," Vol. 1, p. 194, Academic Press, New York (1955).
22. L. Guttman, in "Solid State Physics," Vol. 3, p. 145, Academic Press, New York (1956).
23. C. S. Barrett, "Structure of Metals." p. 272, McGraw Hill Book Co., New York (1952).
24. T. Goto, *J. Phys. Soc. Jpn.*, **43**, 1848 (1977).

Transient and Steady-State Response of the Dopant System of a Silicon Epitaxial Reactor: Transfer-Function Approach

R. Reif*

Integrated Circuits Laboratory, Stanford University, Stanford, California 94305

T. I. Kamins**

Hewlett-Packard Laboratories, Palo Alto, California 94304

and K. Saraswat**

Integrated Circuits Laboratory, Stanford University, Stanford, California 94305

ABSTRACT

The transient response of the dopant system of a horizontal, silicon epitaxial reactor has been studied in order to obtain a "transfer function" relating the time variation of the dopant gas flow and the spatial variation of the dopant concentration in the epitaxial film. This transfer function should be useful in fabricating nonuniform dopant concentrations needed for desired device characteristics. The transfer function was obtained from the response of the system to both increasing and decreasing step changes in the dopant gas flow with time. The transfer-function approach was verified by experiments in which the input was an increasing step followed by a decreasing step (approximating a pulse). Pulse widths both longer than and comparable to the decay time of the system were used, and the measured profiles agreed very well with calculated profiles in all cases. The transient and steady-state responses of the dopant system were studied at different growth rates to determine the effect of growth rate on the parameters entering into the transfer function. These experiments showed the presence of two regions of operation and provide insight leading to a better understanding of the doping process.

In silicon integrated-circuit technology, three basic methods are used to introduce dopant atoms into a semiconductor: thermal diffusion, ion implantation, and epitaxy. When thermal diffusion or ion implantation is employed, the distribution of impurity atoms within the crystal can be approximated by either a "complementary error function" (erfc) or a "Gaussian" distribution. In these two cases the depth and the doping levels can be fairly well controlled, but the shape of the impurity distribution is fixed by the method of dopant introduction. In the third case the dopant atoms are incorporated during epitaxial growth, usually producing a uniform impurity distribution in the epitaxial layer. But this is not, at least in theory, the only possible distribution. In contrast with the other two methods, one should be able to obtain a desired variation of the impurity concentration as a function of position in the deposited epitaxial layer by properly varying the dopant gas flow with time during epitaxial growth. Nonuniform doping profiles can be used in specialized devices and could open up new alternatives to the integrated-circuit process engineer. One good example of a device employing a nonuniform doping profile in the epitaxial layer is illustrated in the work of Jackson and DeMassa (1) on hyperabrupt epitaxial tuning diodes.

In order to relate the spatial variation of the dopant concentration in the epitaxial layer $N(x)$ to the time variation of the dopant gas flow $f_D(t)$, the epitaxial reactor can be viewed as a "black-box" with $f_D(t)$ as the input and $N(x)$ as the output (Fig. 1). [$N(x)$ and $N(t)$ are related by the epitaxial growth rate $g = x/t$.] If the black-box behaves linearly throughout at least a limited operating range, the impulse response $h(t)$ (2) characterizing the input-output relation of the reactor can be found experimentally by studying the response of the reactor to a step change in the dopant gas flow (3, 4). By using the expression for $h(t)$ and standard linear systems techniques (2), the response $N(x)$ of the system to an arbitrary input $f_D(t)$ can readily be calculated; alternatively, the input needed for a desired dopant profile can be obtained.

While such characterization of an epitaxial reactor has not been attempted in the past, a brief literature survey indicates that the characterization of transient doping effects is promising. For example, diffusion-rate processes in catalytic reactors have been characterized by "admittance functions" analogous to a-c electrical parameters (5). In that work, the time-varying, output-gas concentrations were related to the time variations of the input gases. Other work on chemical systems has considered diffusion through a boundary layer, adsorption on a surface, and diffusion into a solid (6). Several of the same kinetic processes are important when considering dopant incorporation into epitaxial layers. Here, however, additional physicochemical processes are involved since the output is not a time-varying gas concentration, but a variation

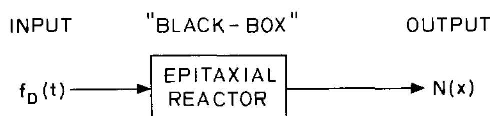

Fig. 1. Dopant system of the epitaxial reactor as a "black-box." $f_D(t)$ = time variation of the dopant gas flow, $N(X)$ = spatial variation of the dopant concentration in the epitaxial layer. $N(X)$ and $N(t)$ are related by the epitaxial growth rate $g = x/t$.

* Electrochemical Society Student Member.
** Electrochemical Society Active Member.

Key words: silicon epitaxy, arsine, silane.

of dopant concentration as a function of position in the deposited epitaxial layer.

It is worth mentioning that varying the dopant gas flow with time in a conventional reactor is not the only way of obtaining a nonuniform dopant distribution in an epitaxial layer. Using a conventional horizontal epitaxial reactor, Nihira *et al.* (7) obtained nonuniform doping profiles by changing the deposition temperature during epitaxial growth by SiH_4 pyrolysis. More recently Becker and Bean (8), using silicon molecular-beam epitaxy, obtained abrupt changes in the gallium doping level of epitaxial layers by rapidly varying the Ga oven temperature (which controls the Ga flux) during growth.

In addition to providing a method of fabricating a desired dopant profile, a transient-response study can produce basic information concerning the various mechanisms involved in the dopant incorporation process. As indicated by Kobayashi and Kobayashi (9), transient studies may reveal the importance of various mechanisms which may not be apparent in steady-state studies.

In this paper, the experiments that were carried out to obtain and verify the expression $h(t)$ characterizing the $f_D(t) - N(x)$ relation of the epitaxial reactor are described. A study of the dependence of $h(t)$ on the silicon deposition rate is also presented. The physical mechanisms involved in the dopant incorporation process will be discussed in more detail in another paper (10).

Equipment and Experimental Details

All of the experiments presented here were carried out in a commercially purchased, horizontal, rf-heated epitaxial reactor (Hugle Model HIER II) operating at atmospheric pressure. The quartz reactor tube has the dimensions 5.1 cm (height) $\times$ 8.3 cm (width) $\times$ 91.4 cm (length) and an effective cross section of 27 cm^2 above the susceptor. The silicon carbide-coated graphite susceptor is 22.8 cm long and is tilted at an angle of 2°. Dopant gases are delivered to the reactor tube through a double-dilution dopant system. Hydrogen was used as the carrier gas at a velocity of 34 cm/sec above the susceptor (at room temperature). Silane was used as the source of silicon, and arsine diluted to approximately 70 ppm in hydrogen was used as the dopant source.

Before each run, the susceptor was vapor etched with HCl and then coated with high resistivity silicon. The wafers were vapor etched with HCl before the epitaxial deposition cycle. Rotometers were used to monitor the gas flow. Temperature measurements were made during the etching and deposition cycles using a calibrated optical pyrometer and corrected for the emissivity of silicon and for absorption in the reactor tube walls. The corrected wafer surface temperatures during etching and deposition were approximately 1180° and 1050°C, respectively. The substrates were chem-mechanical polished, Czochralski-grown, silicon wafers, with (100) orientation and phosphorus doping in the 10^{15} cm^{-3} concentration range.

In the transient study, the dopant profiles in the epitaxial layers were determined by capacitance-voltage measurements on planar p-n junctions, mesa p-n junctions, and deep-depletion MOS structures (11). The epitaxial doping levels chosen in this study ($\sim 10^{15}$ cm^{-3}) correspond to the practical range of doping values of interest in semiconductor devices. In addition, they were compatible with the evaluation technique, being low enough to allow the required depth profiling and high enough to produce a relatively short Debye length (12). The p-n junctions were fabricated by diffusion of boron at 950°C for 30 min, producing a junction depth of approximately 0.6 μm. The oxides of the MOS structures were grown in wet oxygen at 950°C for 40 min and were approximately 1800Å thick. The area of each structure was 3.3×10^{-3} cm^2.

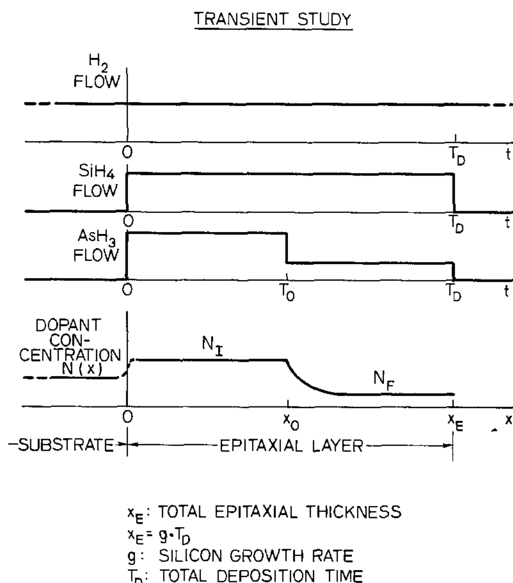

Fig. 2. Step-response experiment, showing the gas flows as functions of time and the dopant concentration as a function of the corresponding position in the epitaxial layer.

Spreading-resistance measurements were used to confirm the capacitance-voltage results. The epitaxial-layer thicknesses were determined from the size of stacking faults on the surfaces of the grown layers.

Experiments, Results and Discussion

Transfer-function determination.—Step response. This experiment allowed the study of the dopant distribution obtained when the dopant gas flow was abruptly changed during the deposition and can be easily understood with the help of Fig. 2. At time $t = 0$ the deposition cycle started, and silane and arsine were introduced into the reactor tube. The silane flow was kept constant throughout the entire deposition cycle, which ended at $t = T_D$. A silane partial pressure of 1.1×10^{-3} atm was used to obtain a growth rate of approximately 0.6 μm/min, which was used in all experiments discussed in this section. At $t = T_0$ the arsine flow was abruptly decreased by lowering the flow setting on the arsine flowmeter located nearest to the reactor tube. The arsine partial pressure was changed from approximately 6×10^{-10} to 2×10^{-10} atm, corresponding to dopant concentrations of roughly 3×10^{15} and 1×10^{15} cm^{-3} in the epitaxial layer.

The solid curve of Fig. 3 shows the measured majority carrier concentration as a function of position in the epitaxial film for a decreasing step change in the dopant gas flow during the deposition. In Fig. 3-7, which show epitaxial-layer dopant profiles, the zero of position corresponds to the Si-SiO_2 interface of the deep depletion MOS structure (see section on Equipment and Experimental Details) and is displaced from the original silicon epitaxial surface by the amount of silicon consumed during the gate oxide growth. In order to ensure that the measured profiles were not limited by the resolution of the capacitance-voltage, data-reduction technique, a theoretical capacitance-voltage curve was generated by solving Poisson's equation using an impurity profile varying more abruptly than the measured one, in a manner similar to that described in (13). The data-reduction program was then applied to this curve. The computed free carrier profile agreed very closely with the starting impurity profile, indicating that the major features observed in Fig. 3 are not artifacts of the analysis technique. Because of the low diffusivity of arsenic in silicon (14), the heat cycling during the fabrication of the MOS and p-n junction C-V structures produced a diffusion length of only 0.01 μm. Spreading-resistance

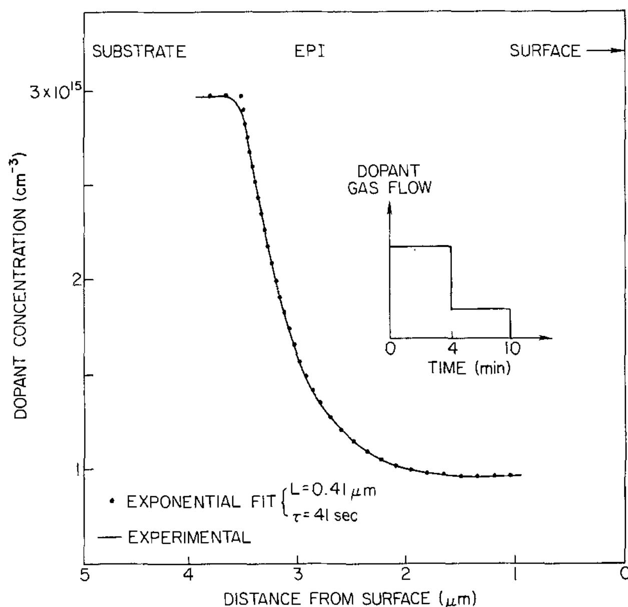

Fig. 3. Solid curve: experimentally observed majority carrier concentration as a function of distance from the surface of the epitaxial film for the decreasing step change in the dopant gas flow indicated in the inset. Dotted curve: exponential fit to the experimental profile.

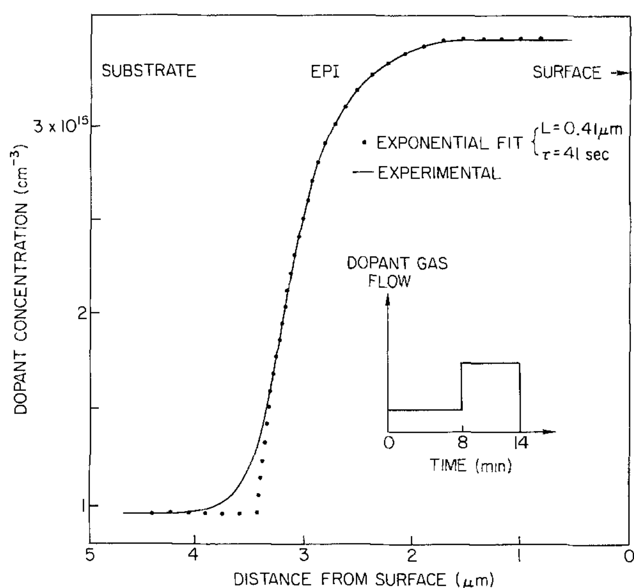

Fig. 4. Solid curve: experimental dopant profile for an increasing step change in dopant gas flow. Dotted curve: exponential fit to the experimental profile.

measurements confirmed that there was no significant difference between the dopant profiles of samples measured after epitaxial deposition and after fabrication of the complete C-V structures.

As shown by the dotted curve in Fig. 3, an excellent fit to the data can be obtained by using the expression (4, 15)

$$N(x) = N_I + (N_F - N_I) \left\{ 1 - \exp\left(-\frac{x - x_0}{L}\right) \right\} \quad \text{for } x \geqq x_0 \quad [1]$$

where, following Fig. 2, $N(x)$ is the dopant concentration at a distance x from the substrate, N_I is the initial doping level for $x < x_0$, N_F is the final doping level, L is the decay length of the exponential, and x_0 is the distance from the substrate corresponding to $t = T_0$. ($x_0 = g \cdot T_0$, where g is the epitaxial growth rate.) For this case $N_I = 3 \times 10^{15}$ cm^{-3}, $N_F = 1 \times 10^{15}$ cm^{-3}, $x_0 = 2.4$ μm, and $L = 0.41$ μm.

The response of the reactor to an increasing step change in the arsine flow is shown in Fig. 4 (solid curve). The growth conditions for this case were similar to those shown in Fig. 2, except that the flow setting of the arsine flowmeter was abruptly changed from a low value to a higher value at $t = T_0$, as shown in the inset of Fig. 4. Equation [1] also fits the measured profile reasonably well (Fig. 4, dotted curve), with the same decay length of 0.41 μm found before. However, the transition in the experimentally measured dopant profile starts more gradually than does the simple exponential function. At least a portion of this discrepancy arises since the measured free carrier profile changes less abruptly with distance than does the dopant profile. The deviation between these two profiles is caused by the lack of local space-charge neutrality resulting from the nonuniformity of the dopant profile (16). The fact that the deviation is more apparent at lower dopant concentrations (*i.e.*, it is more obvious in Fig. 4 than in Fig. 3) is consistent with this explanation. Note from Fig. 3 and 4 that the transition from one dopant concentration to the other occurs in approximately 1.2 μm, corresponding to a time of roughly 2 min.

The impulse response characterizing the input-output relation of the dopant system can be obtained from Eq. [1] to be

$$h(t) = \frac{K}{\tau} \exp\left(-\frac{t}{\tau}\right) \quad [2a]$$

or

$$H(s) = K \cdot \frac{1}{1 + s\tau} \quad [2b]$$

where $\tau \equiv L/g$ is the decay time of the dopant system; it physically corresponds to the time required to grow a thickness of epitaxial silicon equal to one decay length. From Fig. 3 and 4, τ is found to be 41 sec. K is the proportionality constant relating the dopant concentration (N) in the epitaxial layer to the dopant gas flow (f_D) for steady-state conditions: $N \equiv Kf_D$. The reciprocal of K is sometimes called the "effective segregation coefficient" (17). As shown below, Eq. [2] is useful in calculating the dopant distribution $N(x)$ in the epitaxial layer resulting from an arbitrary input $f_D(t)$ or, alternatively, the input $f_D(t)$ needed to obtain a desired profile $N(x)$.

Pulse response.—To verify Eq. [2], a series of experiments was designed in which the input to the system was an increasing step in the arsine flow followed by a decreasing step, the combination simulating a pulse. Four different pulse widths were used: 4.3, 3.0, and 1.8 min, and 48 sec.

Figure 5 shows the measured profiles for the 4.3 min and 48 sec pulses (solid curves), with the corresponding, time-varying, dopant gas flows represented in the insets. For the 4.3 min pulse (Fig. 5a) the resulting profile was a simple superposition of the profiles shown in Fig. 3 and 4 because the pulse width was much longer than the system decay time (41 sec). This was also true for the 3 min pulse. For the 48 sec pulse (Fig. 5b) the higher steady-state doping level was never reached, indicating the limits of the deposition system in responding to arbitrary changes in the dopant gas flow. In this case the pulse width (48 sec) is approximately the same as the system decay time. The doping profile corresponding to the pulse width of 1.8 min showed intermediate characteristics.

Doping profiles corresponding to the input pulses were calculated using the convolution integral (2) and Eq. [2a]

$$N(t) = \int_0^t h(t - t^*) \cdot f_D(t^*) dt^* \quad [3a]$$

After some mathematical manipulation

$$N(t) = N_L(1 - e^{-t/\tau})u(t) + (N_H - N_L)[1 - e^{-(t-T_1)/\tau}] \cdot u(t - T_1) - (N_H - N_L)[1 - e^{-(t-T_2)/\tau}]u(t - T_2) \quad [3b]$$

where N_L is the lower doping level ($\sim 1 \times 10^{15}$ cm^{-3}), N_H is the higher doping level ($\sim 3 \times 10^{15}$ cm^{-3}), $u(t)$ is the unit step function, and T_1 and T_2 represent the beginning and end of the period of high dopant gas flow.

Since the growth rate g relates time to position in the epitaxial film through $t = x/g$, the dopant concentration can be written as a function of position

$$N(x) = \underbrace{N_L(1 - e^{-x/L})u(x)}_{A} + \underbrace{(N_H - N_L)[1 - e^{-(x-x_1)/L}]u(x - x_1) - (N_H - N_L)[1 - e^{-(x-x_2)/L}]u(x - x_2)}_{B} \quad [3c]$$

where $L = g \cdot \tau$ is the decay length, and $x_1 = g \cdot T_1$ and $x_2 = g \cdot T_2$ are the distances from the substrate corresponding to the beginning and end of the period of high dopant gas flow.

In Eq. [3c], the expression labeled A corresponds to the transient at the beginning of the epitaxial deposition. This expression is not expected to be accurate because it was obtained with the assumption that the system is de-energized at $t = 0$; *i.e.*, it was obtained neglecting initial conditions such as autodoping. It also neglects the transient associated with establishing a steady-state, silicon deposition rate. Nevertheless, it may provide an estimate of the duration of the initial transient. Duchemin (18) studied experimentally and theoretically the transient effects before a steady-state doping regime is established at the beginning of the epitaxial growth, and expression A seems to agree well with his results.

The expression labeled B is plotted in Fig. 5 (dotted curves). There is good agreement between the calculated and the measured profiles; the slight discrepancies at the onset of the transitions are probably artifacts due to the absence of local space-charge neutrality (16). In another experiment where the input was an increasing ramp followed by a decreasing step, the agreement between the calculated and measured profiles was also excellent (4). Therefore, it can be concluded that the dopant system can be modeled by a transfer function over a useful operating range.

System delay.—In order to study quantitatively the time that elapses between a step change in the dopant flow and the onset of the transition in the epitaxial-layer dopant concentration, the following experiment was carried out. As shown in the inset of Fig. 6, the dopant gas input consisted of a series of two 48 sec-wide pulses separated in time by 5 min. The series of pulses provided a built-in calibration of the depth scale so that a very short delay between the change of the dopant gas flow and the onset of the transition in the dopant profile could be resolved. The dopant profile measured in the resulting epitaxial layer is also shown in Fig. 6. The distance between the two pulses was determined from the measured dopant profile, allowing a precise calculation of the growth rate. From the growth rate, the depths corresponding to the beginning and end of each pulse were then calculated and are indicated by the arrows shown in Fig. 6. As mentioned above, the zero of position in Fig. 6 corresponds to the Si-SiO_2 interface of the deep-depletion MOS structure, rather than the original silicon surface, and the displacement was accounted for in the calculations. The arrows corresponding to 6.8 and 11.8 min show that there is no appreciable delay ($\lesssim$ 4 sec) between the decrease in dopant gas flow and the onset of the change in dopant concentration in the growing epitaxial film. Since the residence time of a volume element of the flowing gas in the reactor tube is also of the order of 4 sec, the delay mentioned above may be attributed primarily to flow in the forced-convection region. The arrows corresponding to 6 and 11 min seem to indicate that the transition starts before the dopant gas flow is actually increased at the dopant flowmeter, but this apparent discrepancy is related to the lack of space-charge neutrality discussed previously.

The transfer function obtained relates the dopant distribution in the epitaxial layer to the time variation of the dopant gas flow at the flowmeter. When an abrupt change is made at the dopant flowmeter, some time is required before the dopant molar fraction in the main gas stream of the reactor tube reaches a new steady-state condition due to gas flow and intermixing. Consideration of the reactor geometry and the gas flows involved indicates that the time for the gas to be swept into the deposition region is approximately 4 sec, which is certainly short compared to the decay time of 41 sec seen in Fig. 3 and 4. In addition, it is shown in the next section that the decay time associated with the transient response is strongly dependent on the epitaxial growth rate, again indicating that gas-phase flow and intermixing in the main gas stream do not limit the transient behavior and may be neglected in the present discussion.

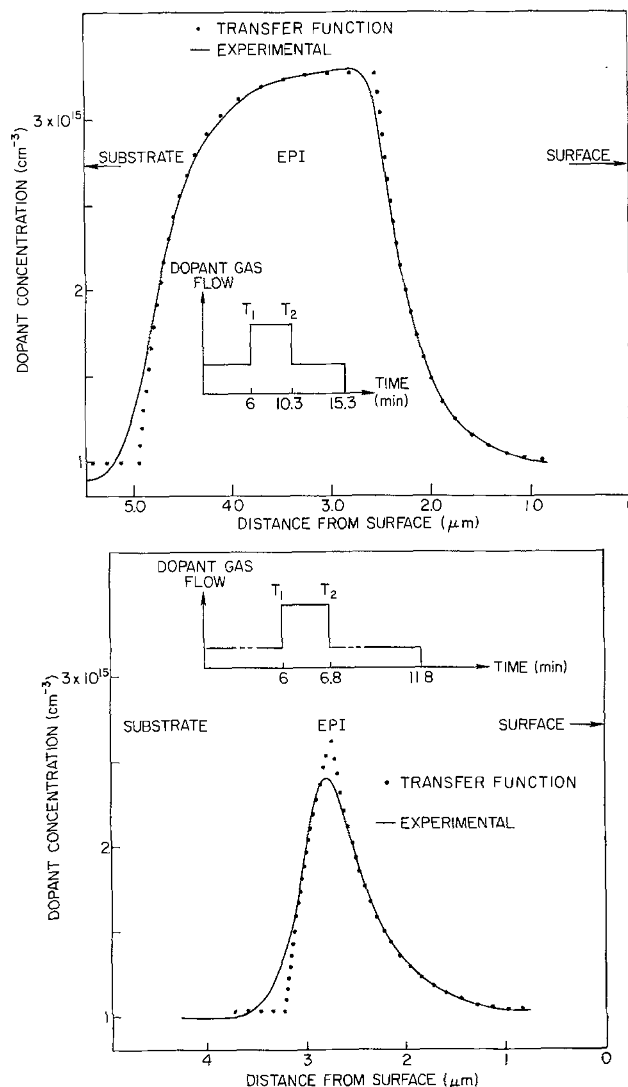

Fig. 5. Response of the reactor to pulse inputs of dopant gas. The times of high dopant gas flow were (a, upper) 4.3 min and (b, lower) 48 sec.

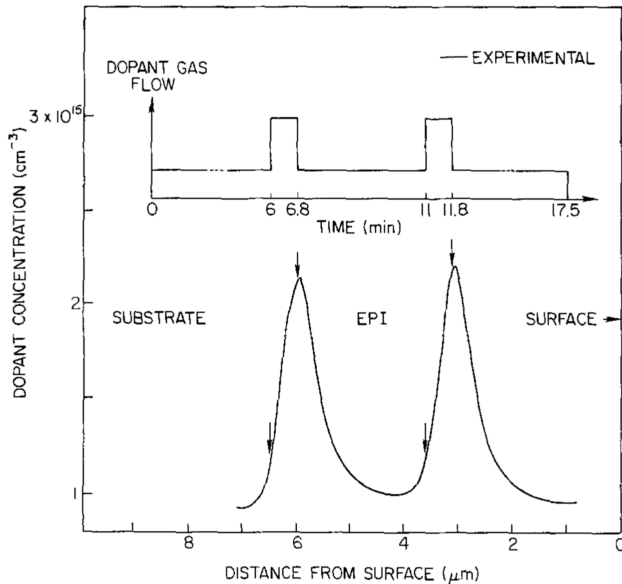

Fig. 6. Reactor response to a sequence of two pulses, each 48 sec long.

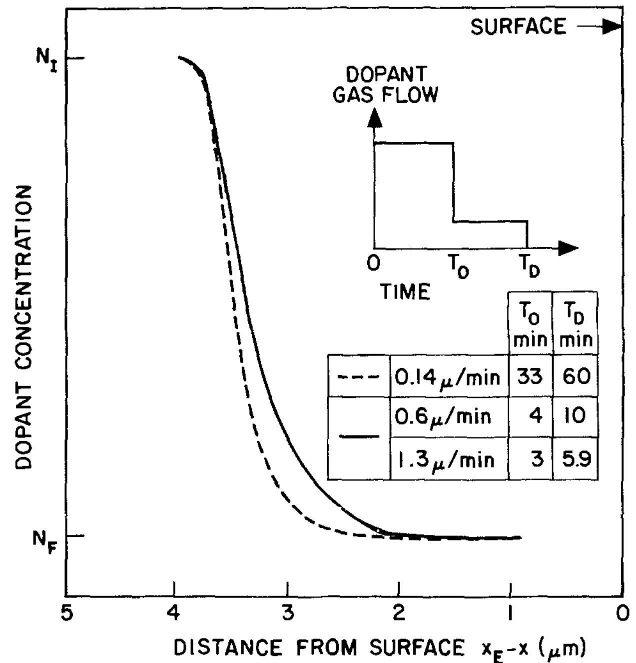

Fig. 7. Measured dopant profiles for different epitaxial growth rates.

Growth-rate dependence.—As shown above, the transfer function of the dopant system contains two basic parameters: τ, related to the transient, and K, related to steady state. To learn more about the doping process and to complete the expression for the transfer function, the growth-rate dependence of these parameters was studied.

Decay-time study.—The objective of this series of experiments was to learn how the growth rate influences the decay time τ. The input to the system was again a decreasing step, as indicated in Fig. 2, and the experiment was repeated at four different growth rates. The silane partial pressure was varied within the 10^{-4}-10^{-3} atm range to produce growth rates of 0.14, 0.32, 0.6, and 1.3 μm/min. The dopant partial pressure was simultaneously adjusted in the 10^{-10}-10^{-9} atm range to compensate for the difference in growth rate and to achieve the two doping levels of 1×10^{15} and 3×10^{15} cm^{-3} in each experiment. Equation [1] was then used to obtain the decay length and the decay time from the measured profiles.

The measured dopant profiles are shown in Fig. 7, together with a table indicating the values of T_0 and T_D in each case. These values were chosen to compensate for the different growth rate in each experiment. The impurity profiles obtained for growth rates of 0.6 and 1.3 μm/min are indistinguishable (solid curve) and differ strongly from the one obtained at 0.14 μm/min (dashed curve), which changes much more abruptly with distance. The dopant profile corresponding to 0.32 μm/min fell between the two shown in Fig. 7.

Figure 8a and b show the decay length and decay time as functions of growth rate. The dashed line in Fig. 8b corresponds to a slope of -1, which in this log-log plot indicates decay times inversely proportional to the growth rate. At 0.6 and 1.3 μm/min, the decay lengths are equal, and the decay times are proportional to g^{-1}, falling on the dashed line. At lower growth rates, the decay length decreases with decreasing growth rate, and the decay time varies less rapidly than g^{-1}, showing a tendency to become constant at very low growth rates. Expressions which fit the experimental data are found to be

$$L = \frac{K_0 \cdot g}{K_1 \cdot g + K_2} \quad [4a]$$

and

$$\tau = \frac{K_0}{K_1 \cdot g + K_2} \quad [4b]$$

where K_0, K_1, and K_2 are constants. The implications of this growth-rate dependence of the transient behavior are analyzed later, along with the results of the steady-state study to be described next.

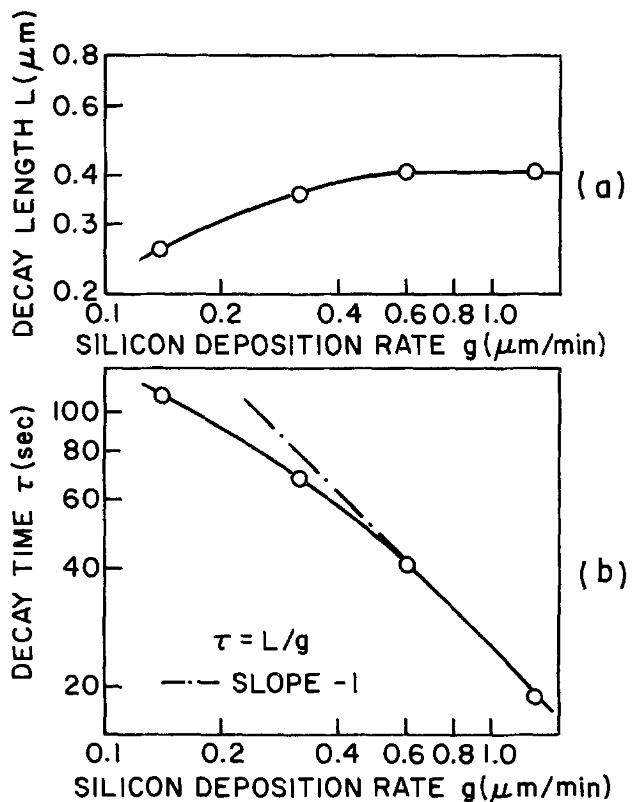

Fig. 8. (a) Decay length and (b) decay time of the transient as functions of growth rate.

Steady-state study.—The steady-state experiments involved an investigation of the effect of the silicon deposition rate on the impurity concentration of uniformly doped epitaxial layers. The arsine partial pressure was kept at 6.2×10^{-10} atm, and the silane partial pressure was varied between 2.7×10^{-4} and 2.3×10^{-3} atm to produce growth rates ranging from 0.13 to 1.2 μm/min. The substrates were boron-doped with resistivities ranging from 1 to 4 Ω-cm. The thicknesses of the epitaxial layers were between 5.5 and 8.1 μm and were measured by a groove-and-stain technique. A four-point probe was used to determine the resistivity of the layers. Carrier concentrations were obtained from Irvin's resistivity data (19) and assumed to be equal to the arsenic concentration in these lightly doped epitaxial layers.

The results of these experiments are shown in Fig. 9, where the dopant concentration of uniformly doped epitaxial layers is plotted as a function of silicon deposition rate. At growth rates greater than approximately 0.5 μm/min, the doping density becomes inversely proportional to the silicon growth rate, as indicated by a slope of -1 on this log-log plot. At lower growth rates, the doping density varies less rapidly than g^{-1} and shows a tendency to become constant at very low growth rates. Similar behavior has been observed by Shepherd for the $PCl_3/SiCl_4$ system (20), by Bloem for the PH_3/SiH_4 system (17), and more recently by Duchemin for the $B_2H_6/SiHCl_3$ and B_2H_6/SiH_2Cl_2 systems (18). The growth-rate dependence of the epitaxial-layer dopant concentration was also investigated by Rai-Choudhury and Salkovitz for the $B_2H_6/SiCl_4$ and $AsH_3/SiCl_4$ systems (21).

The data of Fig. 9 can be used to find the steady-state relation between dopant concentration and dopant gas flow used in Eq. [2]

$$N = \frac{f_D}{K_1 \cdot g + K_2} \qquad [5]$$

Equation [5] may be written in the same form as Eq. [4b]

$$K = \frac{N}{f_D} = \frac{1}{K_1 \cdot g + K_2} \qquad [6]$$

suggesting the importance of similar mechanisms in both the transient and steady-state cases, as is discussed later.

The process limiting the doping in the various regions of Fig. 9 may be localized by considering the temperature dependence of the mechanisms proposed by others on the basis of their steady-state experiments. Bloem (17) suggested that the decrease in dopant concentration with increasing epitaxial growth rate is due to a mass-transport limitation of PH_3 traversing the boundary layer. In this case, for a fixed gas-phase dopant concentration, increasing the growth rate causes the same number of dopant atoms to be incorporated in thicker silicon films, thus decreasing the epitaxial layer dopant concentration. Duchemin (18) explained the same behavior by proposing that the boron incorporation rate is limited by the gas-phase chemical decomposition of B_2H_6 above the gas-solid interface.

The temperature dependence of the As concentration in the epitaxial layer may be used to determine which of these mechanisms limits the As incorporation rate at high growth rates in the AsH_3/SiH_4 case under consideration here. If the As incorporation rate were controlled by AsH_3 mass transport across the boundary layer, the As concentration in the growing film would not change significantly with varying deposition temperature. Under normal operating conditions the deposition of Si from SiH_4 is mass-transport controlled, and the gas-phase diffusion constants of AsH_3 and SiH_4 are expected to have a similar temperature dependence. Thus, the As incorporation rate and the Si deposition rate change in the same manner, and the dopant concentration in the epitaxial layer remains relatively constant. On the other hand, if the As incorporation rate were limited by the gas-phase decomposition of AsH_3, the As concentration in the epitaxial film would increase with increasing temperature, showing an Arrhenius activation energy.

To differentiate between the possible mechanisms, the effect of the deposition temperature on the epitaxial layer As concentration was investigated. Layers were grown at 1025°, 1050°, and 1075°C with an arsine partial pressure of 6.2×10^{-10} atm and a SiH_4 partial pressure of about 2.2×10^{-3} atm, which produced a growth rate of approximately 1.2 μm/min. As indicated in Fig. 10, the As concentration in the epitaxial film decreases with increasing deposition temperature, showing a slope of approximately 30 kcal/mole. The same experiment was repeated several times, always with the same results. Since the temperature dependence does not agree with that expected from either of the mechanisms discussed above, it can be concluded that neither dopant mass transport across the boundary layer nor gas-phase chemical decomposition are dominant in the As incorporation process and that other mechanisms must limit the doping process. It is shown in another paper (10) that the experimental data in Fig. 10 can be explained by considering mechanisms occurring at the growing surface (*e.g.*, adsorption, surface chemical dissociation, site incorporation, etc.).

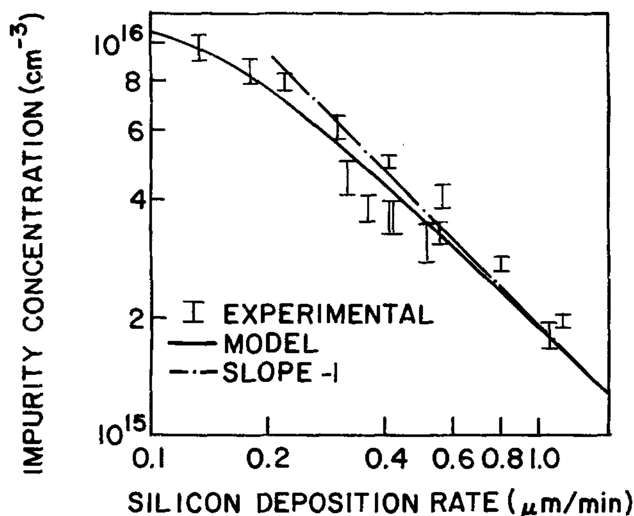

Fig. 9. Dopant concentration of uniformly doped epitaxial layers as a function of growth rate. $P_{AsH_3} = 6.2 \cdot 10^{-10}$ atm, T = 1050°C.

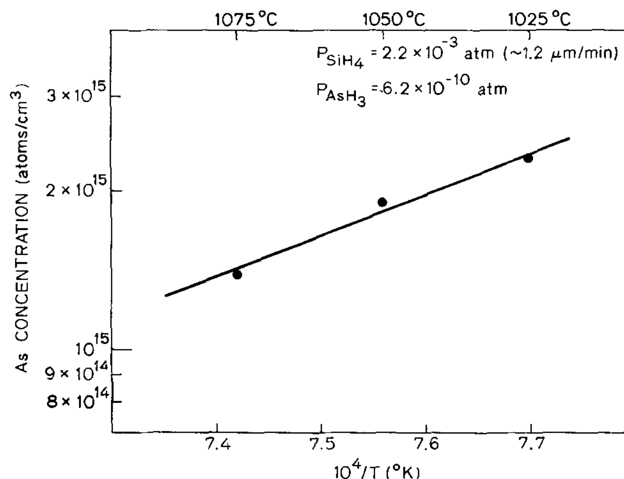

Fig. 10. Temperature dependence of As concentration in uniformly doped epitaxial layers.

Discussion.—By combining the results of the steady-state and transient experiments, some conclusions may be drawn about the mechanisms controlling the doping process.

Low growth rates ($g < 0.5$ μm/min).—Figure 9 shows that at growth rates lower than about 0.5 μm/min, the doping density in the epitaxial films varies less rapidly than g^{-1} and shows a tendency to become constant at very low growth rates. This behavior may be explained by recognizing that lowering the growth rate brings the doping process closer to equilibrium, where it becomes independent of the growth rate. In this region the dopant incorporation process is controlled by the thermodynamics of the various mechanisms entering into the over-all doping process.

High growth rates ($g \gtrsim 0.5$ μm/min).—At higher growth rates the decrease in dopant concentration seen in the steady-state experiments indicates a departure from equilibrium as a kinetic limitation begins to dominate. In this region the limiting mechanism may occur in either the gas phase or on the growing surface of the epitaxial layer. The temperature dependence of the dopant concentration seen in the steady-state experiments has been used to eliminate gas-phase processes as the limiting mechanism, suggesting the importance of surface processes. The influence of surface processes is also indicated independently by the transient experiments. If the over-all doping process were limited by gas-phase mechanisms, the decay time should be independent of the growth rate, while the decay length may be expected to be constant if surface phenomena are limiting. Since the decay length does remain constant at high growth rates, the limitation of the doping process may be attributed to mechanisms occurring at the surface. The nature of these surface mechanisms are analyzed elsewhere (10) where a physicochemical model, from which Eq. [2], [4], and [5] can be derived, is presented.

Summary and Conclusions

The transfer function of the dopant system of a horizontal epitaxial reactor was obtained experimentally by studying the response of the reactor to a step change in the dopant gas flow. This transfer function can be used to calculate the time-variation of the dopant gas flow needed to produce a desired spatial variation of the impurity concentration in an epitaxial layer. To verify the validity of the transfer-function approach, pulses of different widths were used as inputs to the system. The resulting dopant profiles were measured and compared to those calculated using the transfer function; excellent agreement was found. The system delay, defined as the time between a change in the dopant gas flow and the beginning of the resulting transition in the epitaxial dopant concentration, was studied experimentally and found to be negligible compared to the system decay time.

The expression for the transfer function contains two parameters, τ and K, related to transient and steady-state conditions, respectively. The dependence of these parameters on the epitaxial growth rate was studied, showing the presence of two regions of operation depending on the growth rate. At low growth rates ($g < 0.5$ μm/min) both the steady-state dopant concentration and the decay time of the transient tend to become constant, implying that thermodynamics control the doping process. At high growth rates ($g \gtrsim 0.5$ μm/min) the epitaxial dopant concentration and the decay time are proportional to g^{-1}, and the epitaxial dopant concentration decreases with increasing deposition temperature. This behavior is associated with a kinetic limitation on the doping process and is related to mechanisms occurring at the growing surface, rather than in the gas phase.

Acknowledgment

The authors wish to express their appreciation to Professor J. D. Meindl for his encouragement and suggestions during the course of this work. They also gratefully acknowledge J. A. Greenfield and H. G. Lee for their work on the capacitance-voltage technique and its limitations. This work was supported by the Advanced Research Projects Agency of the Department of Defense under Grant No. DAAB07-77-C-2684. One of the authors (R. Reif) gratefully acknowledges the financial support provided by the Simon Bolivar University, Caracas, Venezuela.

Manuscript submitted March 3, 1978; revised manuscript received May 8, 1978. This was Paper 350 presented at the Atlanta, Georgia, Meeting of the Society, Oct. 9-14, 1977.

Any discussion of this paper will appear in a Discussion Section to be published in the June 1979 JOURNAL. All discussions for the June 1979 Discussion Section should be submitted by Feb. 1, 1979.

Publication costs of this article were assisted by Integrated Circuits Laboratory, Stanford University.

REFERENCES

1. D. N. Jackson, Jr., and T. A. DeMassa, *Solid-State Electron.*, **20**, 485 (1977).
2. D. K. Cheng, "Analysis of Linear Systems," p. 244, Addison-Wesley Publishing Co., Reading, Mass. (1959).
3. T. I. Kamins, R. Reif, and K. C. Saraswat, Abstract 230, p. 601, The Electrochemical Society Extended Abstracts, Fall Meeting, Las Vegas, Nevada, Oct. 17-22, 1976.
4. J. D. Meindl, K. C. Saraswat, and J. D. Plummer, in "Semiconductor Silicon 1977," H. R. Huff and E. Sirtl, Editors, pp. 894-909, The Electrochemical Society Softbound Symposium Series, Princeton, N.J. (1977).
5. P. F. Deisler, Jr., and R. H. Wilhelm, *Ind. Eng. Chem.*, **45**, 1219 (1953).
6. J. B. Rosen and W. E. Winsche, *J. Chem. Phys.*, **18**, 1587 (1950).
7. H. Nihira, T. Shirasu, T. Terasaki, and J. Nishizawa, *This Journal*, **122**, 781 (1975).
8. G. E. Becker and J. C. Bean, *J. Appl. Phys.*, **48**, 3395 (1977).
9. H. Kobayashi and M. Kobayashi, *Catalysis Rev.-Sci. Eng.*, **10**, 139 (1974).
10. R. Reif, T. I. Kamins, and K. C. Saraswat, To be published in *This Journal*.
11. R. F. Pierret and D. W. Small, *Solid-State Electron.*, **18**, 79 (1975).
12. W. C. Johnson and P. T. Panousis, *IEEE Trans. Electron Devices*, **ED-18**, 965 (1971).
13. C. T. Wu, E. C. Douglas, and C. W. Mueller, *ibid.*, **ED-22**, 319 (1975).
14. R. S. Muller and T. I. Kamins, "Device Electronics for Integrated Circuits," p. 44, John Wiley & Sons, Inc., New York (1977).
15. R. Reif, T. I. Kamins, and K. C. Saraswat, Abstract 350, p. 921, The Electrochemical Society Extended Abstracts, Fall Meeting, Atlanta, Georgia, Oct. 9-14, 1977.
16. J. Lindmayer and C. Y. Wrigley, "Fundamentals of Semiconductor Devices," p. 107, Van Nostrand, New York (1965).
17. J. Bloem, in "Semiconductor Silicon 1973," H. R. Huff and R. R. Burgess, Editors, pp. 213-226, The Electrochemical Society Softbound Symposium Series, Princeton, N.J. (1973).
18. J. P. Duchemin, *Rev. Tech., Thomson-CSF*, **9**, 411 (1977).
19. R. S. Muller and T. I. Kamins, "Device Electronics for Integrated Circuits," p. 24, John Wiley & Sons, Inc., New York (1977).
20. W. H. Shepherd, *This Journal*, **115**, 541 (1968).
21. P. Rai-Choudhury and E. I. Salkovitz, *J. Cryst. Growth*, **7**, 353 (1970).

The Structure and Composition of Silicon Oxides Grown in HCl/O_2 Ambients

J. Monkowski,* R. E. Tressler,** and J. Stach**

Departments of Materials Science and Electrical Engineering, The Pennsylvania State University, University Park, Pennsylvania 16802

ABSTRACT

The structure and composition of silicon oxides thermally grown in HCl/O_2 ambients were investigated for various oxidation conditions. Oxides were grown in 6-10 v/o HCl at 1150°-1300°C for times of 15 min-6 hr. Transmission electron microscopy in conjunction with x-ray microanalysis has indicated the presence of an additional condensed phase at the oxide-silicon interface, which appears after a certain oxidation time has elapsed. Scanning electron microscopy has shown that after further oxidation, a gaseous compound accumulates at the interface, lifting the oxide from the silicon, and preferentially etching the silicon. A model of the growth mechanisms of HCl oxides, accounting for the additional phase formation, is proposed.

The improved electrical properties of silicon oxides thermally grown in the presence of chlorine have been widely documented (1-7). Recently, ellipsometry in conjunction with scanning electron microscopy (SEM) was used to observe the structure of oxides grown in HCl/O_2 mixtures, and it was found that oxides grown for a certain amount of time in a certain concentration of HCl possessed rough surfaces (8). Additionally, the conditions necessary to initiate the roughness correlated well with the conditions reported to be necessary to achieve mobile ionic sodium passivation.

In order to obtain a better understanding of the formation of the rough oxide, as well as of the origin of the roughness, oxides grown under various conditions were investigated using electron microscopy. Those conditions which were varied included the oxidation temperature, the oxidation time, and the HCl content added to the oxidizing ambient. Scanning electron microscopy was used to view the surface of the oxides, transmission electron microscopy (TEM) and scanning transmission electron microscopy (STEM) yielded information on the inner structure of the oxides, particularly at the oxide-silicon interface, and x-ray microanalysis in conjunction with STEM showed the compositional variations within the oxides.

Experimental

All oxidations were performed on (100) oriented, 2-3 Ω-cm, phosphorus-doped, 2 in. diam silicon wafers. Prior to oxidation the wafers were cleaned using an ammonium hydroxide-hydrogen peroxide solution, a hydrochloric acid-hydrogen peroxide solution, a diluted hydrofluoric acid dip, and several deionized water rinses. The oxidations were done in a resistance-heated furnace containing a fused silica tube and a mullite liner.

To ensure high temperature equilibration of the HCl/O_2 mixture, the gases first flowed through the hot zone of the furnace in a 9 mm ID fused silica tube which was located within the larger oxidation tube. At the far end of the hot zone, the gases exited the smaller tube, and flowed back through the hot zone in the oxidation tube, where the silicon wafers were oxidized.

The O_2 flow rate was kept at 1 liter/min (~23 cm/min), and the HCl flow rate was varied to obtain between 6-10 volume percent (v/o) HCl entering the furnace. The wafers were pushed into the furnace in the HCl/O_2 mixture and at the end of the oxidation period, which ranged from 15 min to 6 hr, were pulled out of the furnace in the same mixture. The oxides were grown at 1150°-1300°C.

Prior to viewing by SEM, the oxides were coated with several hundred angstroms of gold to prevent charge accumulation on the sample. Samples for the TEM were prepared by first etching the back side of the wafer with a fine jet (~0.5 mm diam) of a 9/1 solution of HNO_3/HF (9). The etching, which formed a bowl-shaped depression in the silicon, was stopped when the back side of the oxide was exposed. The sample was then flushed with deionized water, leaving a window in the silicon through which the oxide could be viewed. The procedure for preparation of the STEM samples was similar to that of the TEM samples; however, the chemical etching was stopped when several micrometers of silicon still covered the oxide. The remainder of the silicon was etched with an ion thinner to prevent preferential chemical etching of any phases present at the oxide-silicon interface.

Results and Discussion

Additional phase formaiton.—Figure 1 shows an SEM micrograph of an oxide grown in 10 v/o HCl at 1150°C for 1 hr. Bumps of approximately 1-2 μm diam uniformly cover the oxide surface. In an earlier in-

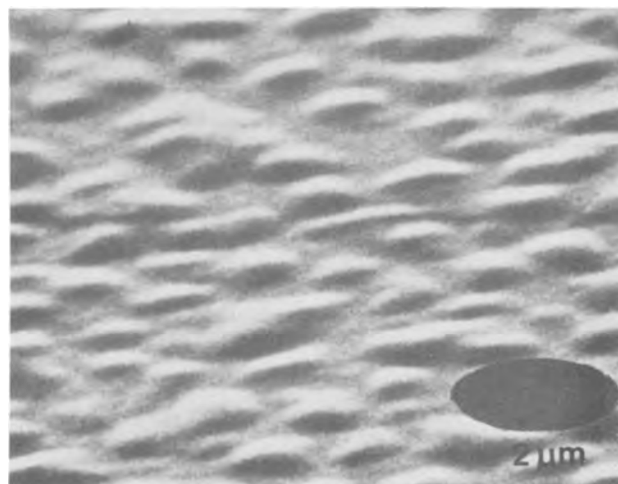

Fig. 1. SEM micrograph of oxide grown in 10 v/o HCl at 1150°C for 1hr. Sample tilted 65°.

* Electrochemical Society Student Member.
** Electrochemical Society Active Member.

Key words: silicon, HCl oxides, phase separation, sodium passivation, etching.

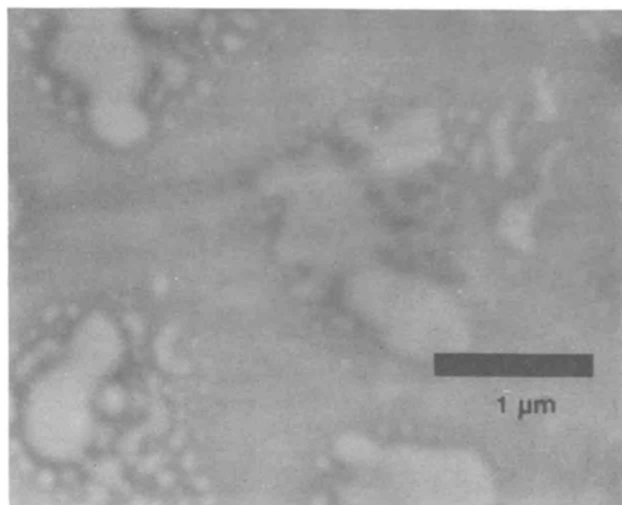

Fig. 2. TEM micrograph of oxide grown in 10 v/o HCl at 1150°C for 1 hr.

vestigation, ellipsometry was used to characterize the growth of these bumps, and it was found that the bumps increase in size as the oxidation time, the oxidation temperature, and the HCl content increase (8).

A TEM micrograph of an oxide grown under the same conditions is shown in Fig. 2. Note the inhomogeneous electron transmission indicative of an amorphous phase within amorphous phase separation. No coherent diffraction was observed, substantiating the noncrystallinity of both phases. The large, isolated regions are approximately 1-2 μm in diam, similar to the bumps seen in Fig. 1.

The additional phase regions grow as the oxidation progresses. Figure 3a shows a TEM micrograph of an oxide grown in 7 v/o HCl at 1150°C for 30 min. Figure 3b shows a similar oxide grown for 60 min. The additional phase, after a longer growth time, is more prominent and occupies a larger fraction of the area. No additional phase was observed at 15 min.

A STEM micrograph of an oxide grown in 6 v/o HCl at 1150°C for 1 hr is shown in Fig. 4. Two contamination spots from the electron beam are apparent near the center of the micrograph. An x-ray microanalysis done with the electron beam outside the additional phase regions (spot on left) yielded the spectrum shown in Fig. 5a. No counts above background (corresponding to a chlorine density of $\sim 10^{15}/cm^2$) are seen at those energies indicated by the markers, which are characteristic of chlorine. However, with the electron beam focused upon one of the additional phase regions (spot on right), the spectrum in Fig. 5b was obtained, clearly indicating the presence of a significant amount of chlorine. Oxides grown under various conditions, ranging from a 30 min oxidation performed with 2 v/o HCl at 1150°C to on oxide grown for 1 hr with 10 v/o HCl at 1300°C, yielded spectra which indicated all of the chlorine to be located within the phase-separated regions.

The chlorine concentration within a particular phase-separated region was found to be very uniform over the entire region. Profiling of a 1 μm diam region showed the chlorine to be undetectable immediately outside the region, but just inside the region the chlorine concentration was observed to sharply rise and remain constant across the entire diameter.

Rutherford backscattering (RBS) has indicated that most of the chlorine is located within several hundred angstroms of the oxide-silicon interface (7, 10, 11). Correlation of the RBS data with the x-ray analysis suggests that the additional phase is located in pancake-shaped regions of 100-300Å thickness and 1-2 μm diam which are situated at the oxide-silicon interface.

Since the majority of the chlorine is uniformly contained in the phase-separated regions, and the dimensions of the regions are known, a rough calculation can be made of the chlorine concentration within the regions.

For example, RBS has shown that for an oxide grown in 7 v/o HCl at 1150°C for 30 min (similar to the oxide shown in Fig. 3a), the chlorine content in the oxide is approximately $2 \times 10^{15}/cm^2$ (10). From TEM investigations it was ascertained that the additional phase covers roughly 10% of the interfacial area. With a thickness of about 200Å, the chlorine concentration is on the order of $10^{22}/cm^3$. This is, of course, a rough estimate, but does indeed demonstrate the relatively high chlorine concentration within the additional phase.

To substantiate the absence of voids under the oxide (which RBS is unable to do), SEM was used to look at the oxide-silicon interface in cross section. No voids were found, indicating that the additional phase is indeed contained in regions only a few hundred angstroms thick. With such a high density of chlorine, the additional phase is very probably condensed at oxidation temperatures.

Interfacial gas formation.—For the fabrication of metal-oxide-semiconductor (MOS) structures, the oxide is typically grown to a thickness of approxi-

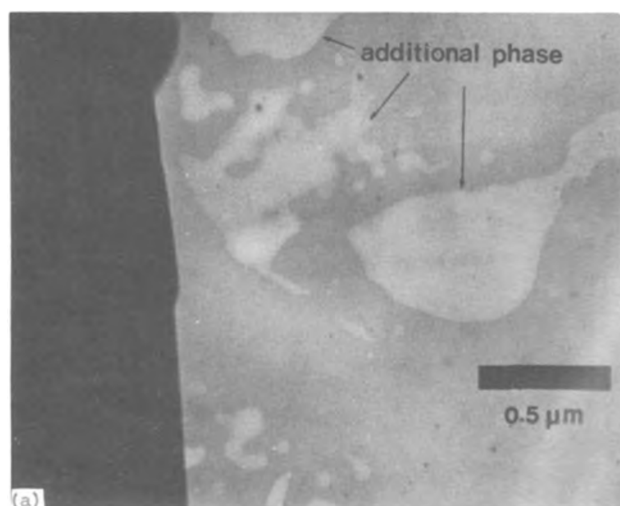

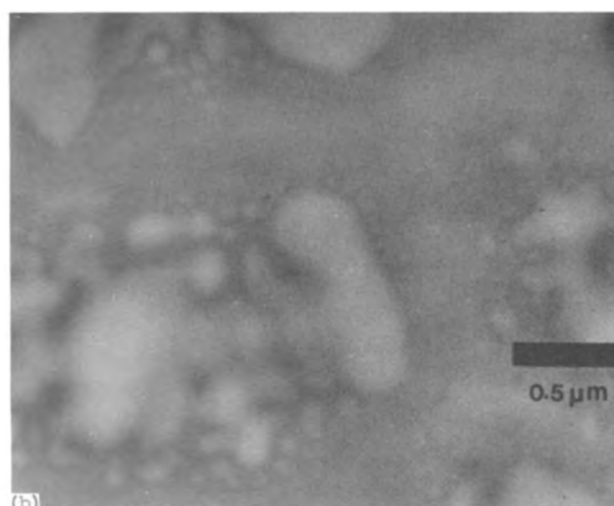

Fig. 3. TEM micrographs of oxides grown in 7 v/o HCl at 1150°C for (a) 30 min; and (b) 60 min. The dark part in (a) is part of the grid on which the sample was placed.

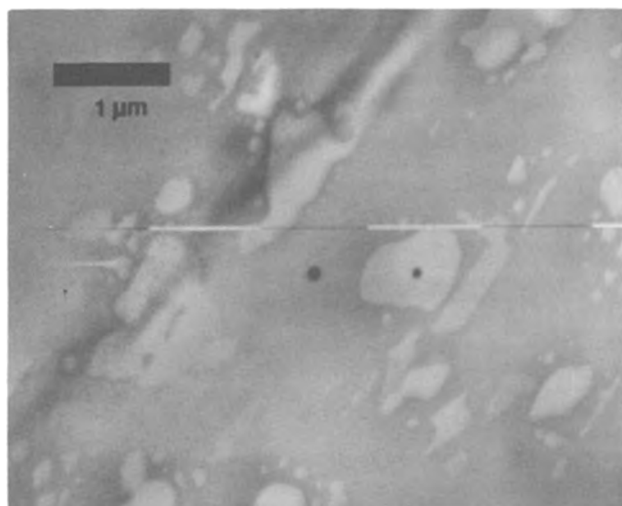

Fig. 4. STEM micrograph of oxide grown in 6 v/o HCl at 1150°C for 1 hr. The two spots are contamination from the electron beam.

mately 1000Å, which requires about a 30 min oxidation at 1150°C. However, to gain further insight into the formation of chlorinated oxides, investigations were made of oxides grown in 10 v/o HCl for oxidation times as long as 6 hr at temperatures of 1150° and 1200°C. Cross-sectional micrographs of an oxide grown for 6 hr at 1200°C (Fig. 6) clearly indicate the existence of bubbles at the oxide-silicon interface. The fine structure created by the condensed phase is seen superimposed upon the larger bubbles, and in addition, a material, perhaps the condensed phase, can be seen in several locations stretched between the oxide and the silicon. Scanning electron microscopy in conjunction with x-ray microanalysis was unable to detect any chlorine in this material; however, this is inconclusive since x-ray analysis on the SEM was unable to detect any chlorine in any of the oxides investigated.

Compressive stress in the oxide has been suggested as a possible mechanism for the lifting of the oxide (12); however, the evidence shown in Fig. 7 and 8 clearly indicates the origin of the bubbles to be the formation of a gaseous compound at the oxide-silicon interface. Figure 7 is an SEM micrograph of the oxide (shown in Fig. 6) after being etched several minutes in an $NH_4F \cdot HF$ solution. The oxide, which has weakened and collapsed, obviously has been stretched. The stretching, which is anticipated in view of the viscoelastic nature of silica at 1200°C, conclusively indicates a tensile stress in the oxide, undoubtedly caused by a gaseous pressure at the interface.

Figure 8 shows the same wafer after the oxide has been completely removed by submersion for 1 min in concentrated HF (49%). Preferential etching of the silicon, which has occurred during the prolonged oxidation at 1200°C, is obvious. The well-defined angle of the walls, the planar surfaces, and the straight edges are especially apparent in Fig. 8c.

The etching is somewhat reminiscent of that reported by Dismukes and Ulmer (13) for the etching of silicon by Cl_2. They noted steps formed in the silicon surface, as well as pits which were about 5 μm on a side. The morphology of the surface seen by Dismukes and Ulmer is not exactly as that seen in Fig. 8; however, Dismukes and Ulmer used (111) oriented wafers, whereas those of Fig. 8 are (100) oriented. Hess and McDonald (12) studied the etching of (111) oriented silicon for HCl/O_2 oxidations at 1100°C, and their SEM micrographs of the silicon surface are strikingly similar to those of Dismukes and Ulmer. Additionally, an SEM micrograph by Hess and McDonald of an oxide-silicon interface in cross section for a wafer oxidized in 1 v/o HCl at 1100°C for 16 hr shows very little lifting of the oxide. The small amount of lifting in conjunction with the substantial amount of silicon removal is an important point which will be addressed later.

Formation of a gaseous phase along with the subsequent lifting of the oxide occurs also for oxides which initially possess only the condensed, chlorine-rich phase discussed above, but which after oxidation, are annealed in N_2 at oxidation temperatures. Figure 9a shows an oxide grown in 10 v/o HCl for 1 hr at 1150°C. Figure 9b and 9c show the same oxide after being annealed 5 and 20 hr, respectively, in N_2 at 1150°C. Whereas no voids are visible under the oxide for the unannealed sample, large voids, similar to those produced by long oxidation times, are seen for the annealed samples. Transmission electron micrographs of the oxides shown in Fig. 9a-9c are shown in Fig. 2 and 10a and 10b, respectively. The development and coalescence of the gaseous phase are evident.

Kriegler has reported a decrease in passivation for oxides which have been annealed in helium at 1150° and 1200°C (6). Corresponding to this decrease in passivation, van der Meulen *et al.* have noted, using RBS, a decrease in the chlorine content of oxides after annealing in N_2 at 1100° and 1200°C (14). Consistent with these findings, x-ray microanalysis of the oxide shown in Fig. 10a has shown a significantly lower chlorine concentration than that found in the unannealed sample (Fig. 2).

Rationalization of findings.—Four phases need to be considered when discussing the microstructural development of oxides grown in HCl/O_2 ambients: silicon, silicon dioxide, the additional condensed phase,

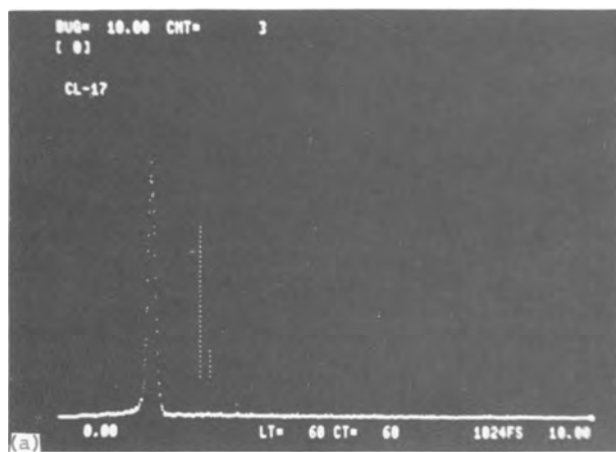

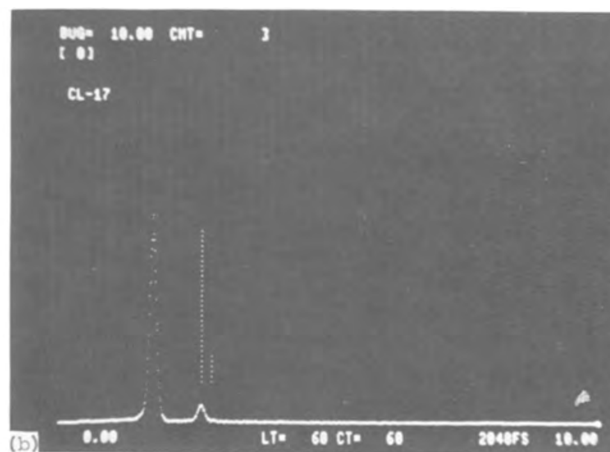

Fig. 5. X-ray fluorescence spectra of oxide grown in 6 v/o HCl at 1150°C for 1 hr (a) outside phase-separated region; and (b) inside phase-separated region.

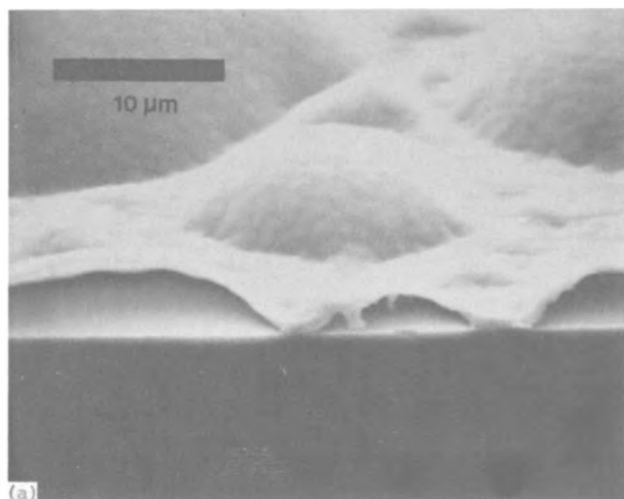

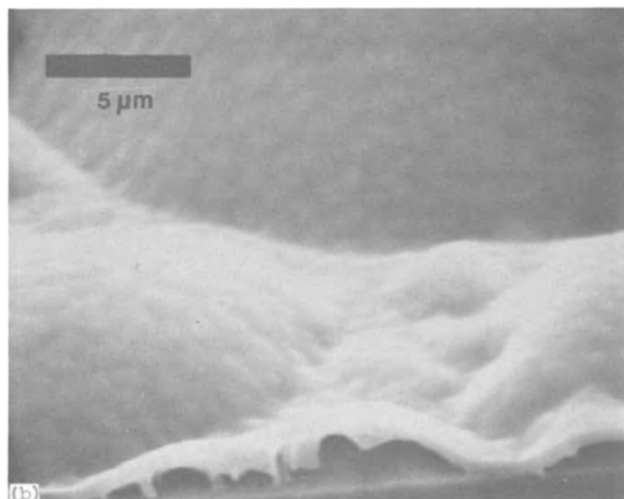

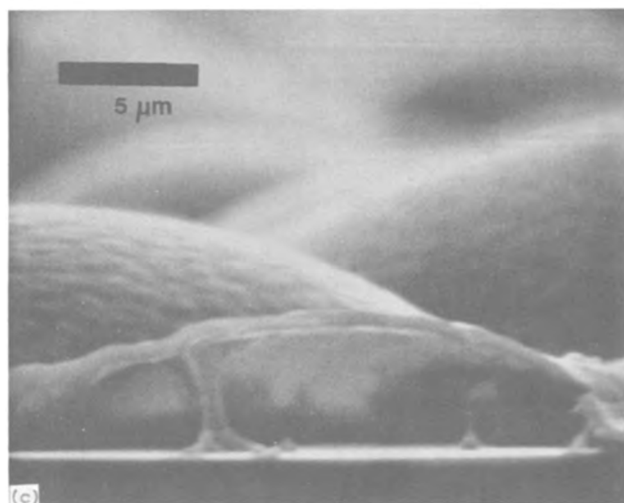

Fig. 6. Cross-sectional SEM micrographs of oxide grown in 10 v/o HCl at 1200°C for 6 hr.

and the gaseous phase at the interface. Silicon dioxide is the first reaction product to be observed for the oxidation of silicon in HCl/O_2 ambients. After a sufficient time has elapsed, the additional condensed phase is noted; for longer oxidation times, or for subsequent anneals, the gaseous phase begins to form.

In studying the simultaneous corrosion of metals by oxygen and a second oxidant (*e.g.*, S_2 or N_2), researchers have found that under the appropriate kinetic and thermodynamic conditions, the reaction products can form layers on the metal (15, 16). With the provision that the activity of each oxidant in the gaseous ambient is sufficiently high to react with the metal, that product yielding the most negative change in Gibbs free energy forms the external scale. Due to the large affinity of most metals for oxygen, this external scale is usually an oxide. If the growth rate of the more stable scale is diffusion limited (where either the metal or the oxidant diffuses through the scale), then the activity of the principal oxidant decreases as one progresses from the outer surface of the scale to the metal-scale interface. Consequently, if the second oxidant is able to diffuse in a sufficient amount from the ambient to this interface, the thermodynamic equilibria at the interface can be reversed from that at the sample surface, such that near the metal, the product of the second oxidant is the more stable. In this manner, an additional phase which is unstable in the gaseous ambient is able to form between the metal and the external scale.

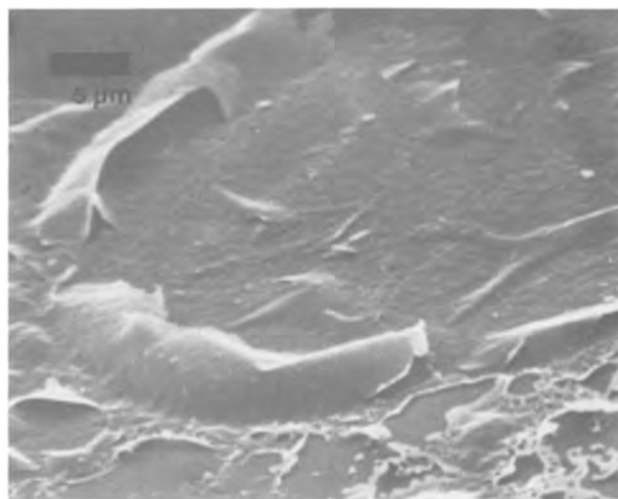

Fig. 7. SEM micrograph of oxide grown in 10 v/o HCl at 1200°C for 6 hr after partial etching in $NH_4F \cdot HF$. Sample tilted 60°.

With some modifications, the growth of HCl oxides closely resembles the model proposed above. In the HCl/O_2 ambient, oxygen is the stronger oxidant and chlorine the weaker oxidant. One apparent discrepancy, though, is the existence of three reaction products in HCl oxides. However, the condensed intermediate phase very likely contains both chlorine and oxygen, and is probably a chlorosiloxane possessing a high concentration of oxygen. Analogous to the metal sulfides or metal nitrides discussed above, this chlorosiloxane would be unstable at oxidation temperatures in large partial pressure of oxygen, and would readily oxidize to SiO_2.

That this phase contains both chlorine and oxygen, and is specifically a chlorosiloxane, is suggested by two observations. Kriegler has found that if a silicon sample is oxidized for 20 min in pure O_2 at 1150°C, and subsequently introduced into an $HCl/O_2/He$ mixture containing 15 v/o HCl and 2 v/o O_2 for an additional 20 min at the same temperature, passivation is attained (7). However, under similar conditions, if the oxide grown for 20 min is introduced into an HCl/He mixture containing 15 v/o HCl, passivation does not occur. Evidently, the chlorine cannot be incorporated into the oxide without the simultaneous presence of both chlorine and oxygen.

In addition, most of the silicon chlorides, as well as those chlorosiloxanes with an O/Cl ratio significantly below 1/2, possess boiling points (at 1 atm) far below oxidation temperatures (17). However, as the O/Cl ratio increases, the boiling points greatly increase, suggesting that the additional condensed phase is, in fact, a chlorosiloxane, rich in oxygen.

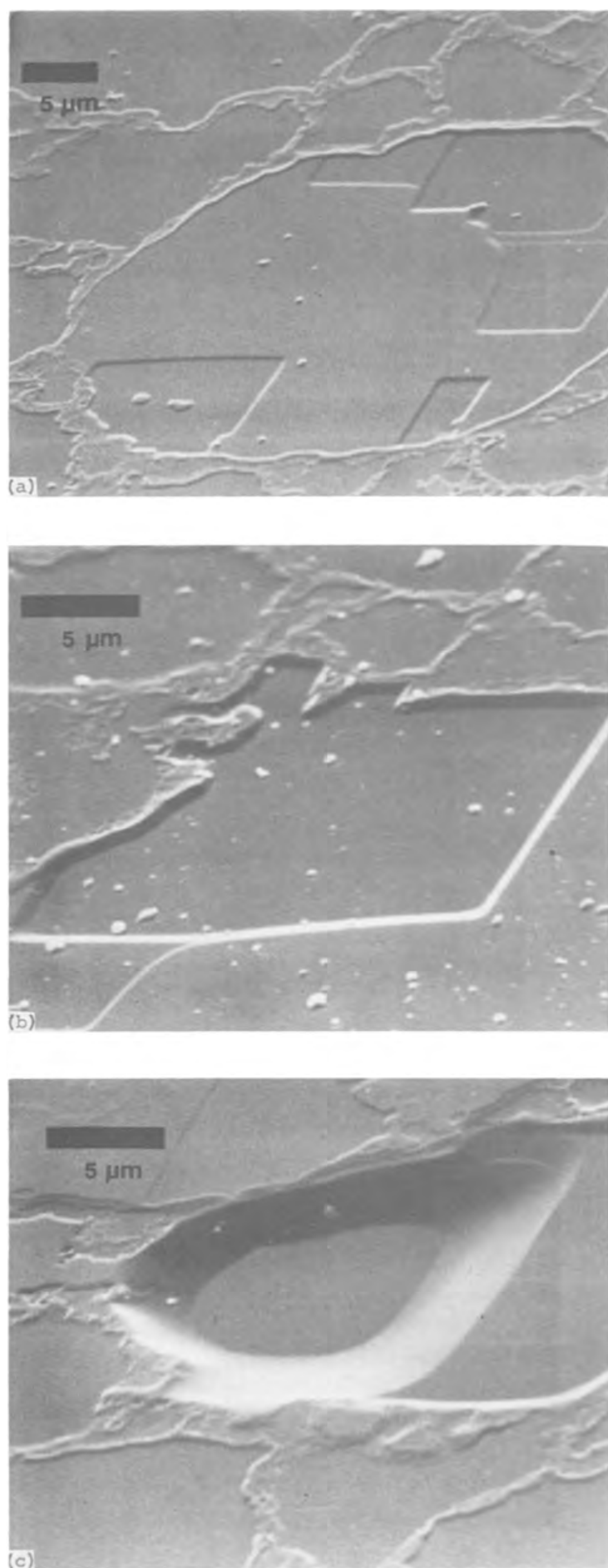

Fig. 8. SEM micrographs of silicon surface after oxidation in 10 v/o HCl at 1200°C for 6 hr with subsequent removal of oxide in concentrated HF. Samples tilted 60°.

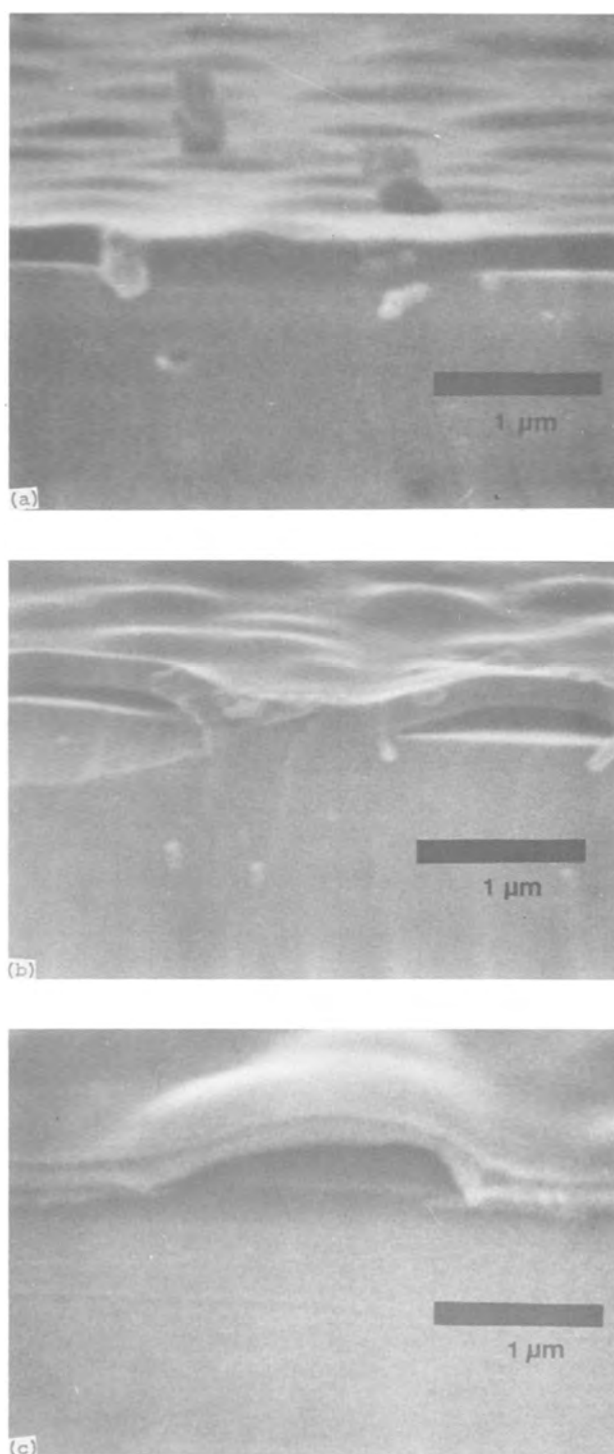

Fig. 9. Cross-sectional SEM micrographs of oxide grown in 10 v/o HCl at 1150°C for 1 hr (a) immediately after oxidation; (b) after subsequent 5 hr anneal in N_2 at 1150°C; and (c) after subsequent 20 hr anneal in N_2 at 1150°C.

If there exists yet another phase in addition to the silicon, the silica, and the additional condensed phase which is stable only in oxygen partial pressures lower than those required for the stability of the additional condensed phase, then this fourth phase would be found sandwiched between the silicon and the additional condensed phase. Such a phase may indeed exist in the form of the interfacial gas.

As discussed above, as the oxygen contents of chlorosiloxanes decrease, the compounds boil at lower temperatures. If the oxide becomes sufficiently thick to severely limit the transport of oxygen to the oxide-silicon interface, or if the oxygen at the interface is depleted by annealing in an oxygen-free ambient, gaseous chlorosiloxanes or chlorides could form. The diffusivity of the interfacial gas through the oxide may be sufficiently low such that the gas could become trapped at the interface lifting the oxide from the silicon. Ultimately, the entire oxide would separate from the silicon; such cases have been reported (12).

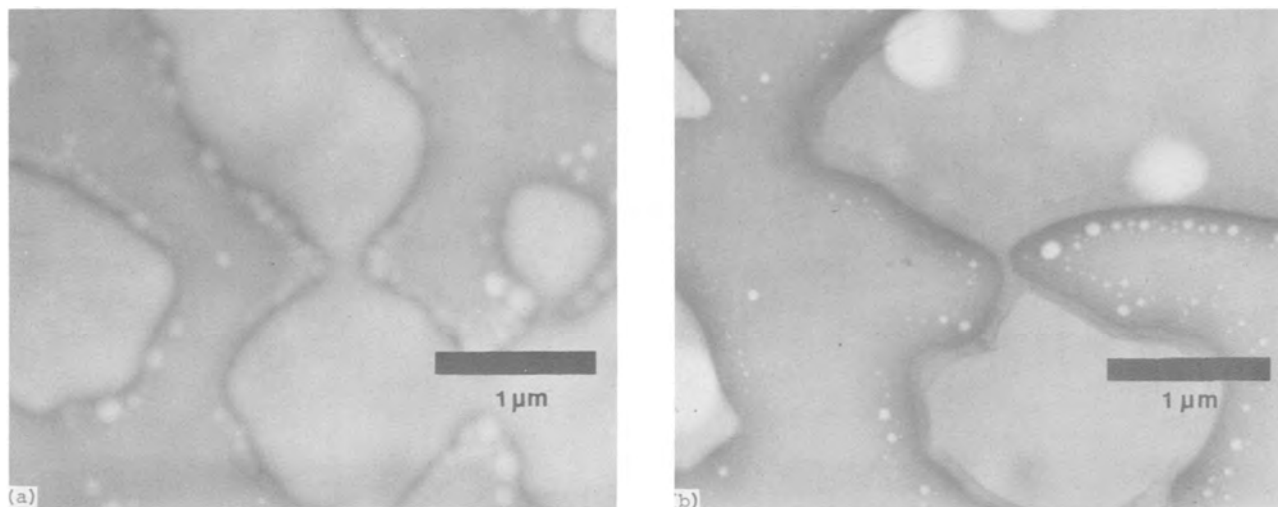

Fig. 10. TEM micrographs of oxides grown in 10 v/o HCl at 1150°C for 1 hr with subsequent (a) 5 hr anneal; and (b) 20 hr anneal in N_2 at 1150°C.

As the gas is being formed, an equilibrium is maintained between the rate of formation and the rate of escape through the oxide. As more gas is formed, the bubble under the oxide becomes larger, creating a larger pressure from the tensile stress in the oxide which increases the flux through the oxide.

The existence of this equilibrium is substantiated by a comparison of Fig. 6a-6c with the SEM micrograph, mentioned above, of an oxide grown in 1 v/o HCl for 16 hr at 1100°C, taken by Hess and McDonald. As compared to the former micrographs, the latter shows very little lifting of the oxide, but clearly indicates a substantial amount of silicon removal, suggesting a significant amount of out-diffusion of a gaseous silicon compound through the oxide. However, in contrast to the oxidations performed in 10 v/o HCl at 1200°C (Fig. 6a-6c), the rate of interfacial gas formation for the oxide studied by Hess and McDonald is significantly lower (due to the lower temperature and HCl pressure), thus requiring a much lower pressure to equalize the rates of formation and escape.

The formation and escape of a chlorine-containing gaseous compound during annealing in an oxygen-free ambient is quite consistent with the deterioration of passivation and the decrease in chlorine content discussed above. Both the passivation and chlorine content were found to decrease most rapidly at the highest annealing temperature, and, in general, were very temperature dependent in the range of temperatures investigated (1100°-1200°C). At the higher temperatures, the depletion of oxygen, the gas formation, and the out-diffusion is most rapid, thus explaining the observations.

The temperature dependence of the thermodynamic equilibria cannot be readily discussed without more information concerning the compositions of both the additional condensed phase and the gaseous phase. Moreover, depending upon the particular compositions of these phases, thermodynamic data may be unavailable in the literature, thus making any detailed calculations quite difficult.

The prediction of the kinetic behavior as a function of temperature is considerably more straightforward, particularly from a qualitative viewpoint. As the temperature increases, the diffusivities of the oxidants in the oxide, as well as the various reaction rates, increase, thus allowing the more rapid development of the chlorine-containing phases. This increase in the rate of development with increasing temperature is indeed observed (8).

Summary

Investigations using electron microscopy and x-ray analysis were done to ascertain the structure and composition of silicon oxides during their growth in HCl/O_2 ambients. Upon first introduction into the oxidizing ambient, the silicon reacts to form an SiO_2 layer. After a sufficient amount of time has elapsed, an additional condensed phase becomes apparent at the oxide-silicon interface. This phase, which contains the majority of the chlorine, remains sandwiched between the SiO_2 and the silicon as the oxide growth continues.

After an even longer growth time, an interfacial gas begins to form. The gas preferentially etches the underlying silicon, and depending upon the oxidation temperature and HCl content, the gas may significantly lift the oxide from the silicon, forming large bubbles. The gas can also be formed by annealing an oxide possessing only the additional condensed phase in an oxygen-free ambient at typical oxidation temperatures.

The formation of the two additional phases has been interpreted in terms of compounds stable at the various partial pressures (or activities) of oxygen found at the oxide-silicon interface under various oxidation and annealing conditions. When the oxide becomes thick enough to sufficiently limit the transport of oxygen to the interface, the additional condensed phase becomes stable. The evidence cited indicates the composition of this phase to be a chlorosiloxane, rich in oxygen. When the oxygen activity is further suppressed, either due to an increase in oxide thickness or a decrease in the ambient oxygen partial pressure, the gaseous compound becomes stable. By its out-diffusion through the oxide, the gas can remove substantial amounts of silicon, yielding a preferentially etched silicon surface.

Acknowledgments

The authors wish to thank S. R. Butler and D. B. Williams of Lehigh University for providing the facilities for the STEM and x-ray analysis work. All STEM micrographs and x-ray spectra were taken by D. B. Williams.

Manuscript submitted March 27, 1978; revised manuscript received June 6, 1978.

Any discussion of this paper will appear in a Discussion Section to be published in the June 1979 JOURNAL. All discussions for the June 1979 Discussion Section should be submitted by Feb. 1, 1979.

Publication costs of this article were assisted by The Pennsylvania State University.

REFERENCES

1. A. Rohatgi, S. R. Butler, F. J. Feigl, H. W. Kraner, and K. W. Jones, *Appl. Phys. Lett.*, **30**, 104 (1977).

2. C. M. Osburn, *This Journal*, **121**, 809 (1974).
3. H. Shiraki, in "Semiconductor Silicon 1977," H. R. Huff and E. Sirtl, Editors, pp. 546-558, The Electrochemical Society Softbound Symposium Series, Princeton, N.J. (1977).
4. M. Chen and J. W. Hile, *This Journal*, **119**, 223 (1972).
5. R. S. Ronen and P. H. Robinson, *ibid.*, **119**, 747 (1972).
6. R. J. Kriegler, in "Semiconductor Silicon 1973," H. R. Huff and R. R. Burgess, Editors, pp. 363-375, The Electrochemical Society Softbound Symposium Series, Princeton, N.J. (1973).
7. R. J. Kriegler, *Denki Kagaku*, **41**, 466 (1973).
8. J. Monkowski, J. Stach, and R. E. Tressler, in "Semiconductor Silicon 1977," H. R. Huff and E. Sirtl, Editors, pp. 324-331, The Electrochemical Society Softbound Symposium Series, Princeton, N.J. (1977).
9. D. J. Keast and A. D. Wilson, *J. Sci. Instrum.*, **43**, 609 (1966).
10. S. R. Butler, F. J. Feigl, A. Rohatgi, H. W. Kraner, and K. W. Jones, Abstract 77, p. 217, The Electrochemical Society Extended Abstracts, Spring Meeting, Philadelphia, Pennsylvania, May 8-13, (1977).
11. R. L. Meek, *This Journal*, **120**, 308 (1973).
12. D. W. Hess and R. C. McDonald, *Thin Solid Films*, **42**, 127 (1977).
13. J. P. Dismukes and R. Ulmer, *This Journal*, **118**, 634 (1971).
14. Y. J. van der Meulen, C. M. Osburn, and J. F. Ziegler, *This Journal*, **122**, 284 (1975).
15. R. A. Rapp, Paper presented at the United States-Japanese Seminar, Chemical Kinetics of Pyrometallurgy, The MIT-Endicott House, Aug. 29-Sept. 2, 1976.
16. F. S. Pettit, J. A. Goebel, and G. W. Goward, *Corr. Sci.*, **9**, 903 (1969).
17. "Comprehensive Inorganic Chemistry," J. C. Bailar, H. J. Emeléus, Sir R. Nyholm, and A. F. Trotman-Dickenson, Editors, pp. 1380-1381, Pergamon Press Ltd., Oxford, (1973).

Technical Notes

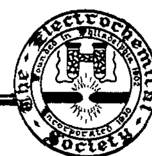

Application of Interface Demarcation to Multiphase Systems: InSb-Sb Eutectic

Douglas E. Holmes[1] and Harry C. Gatos*

Department of Materials Science and Engineering, Massachusetts Institute of Technology, Cambridge, Massachusetts 02139

The applicability of interface demarcation to the study of (directional) solidification of multiphase systems was demonstrated with the InSb-Sb eutectic. Thus, the microscopic growth rate and the interface morphology during solidification of the eutectic matrix of a nontransparent system were recorded for the first time. It is the purpose of this communication to demonstrate that parameters introduced in the theoretical models of eutectic solidification can be experimentally determined by interface demarcation.

Interface demarcation (achieved by passing current pulses of known frequency across the growth interface) has been successfully applied to the quantitative study of growth and segregation in elemental (1) and III-V compound semiconductors (2), to the study of interface breakdown due to constitutional supercooling (3), and to the study of semiconductor melt thermohydrodynamics (4). Interface demarcation should be a powerful tool for solidification studies of multiphase systems since the morphology of the solidifying interface and the microscopic growth rates are key parameters in the fundamental analysis of the solidification process (5-8). Interface demarcation has not as yet been successfully applied to the solidification of metallic phases primarily because the Peltier coefficients of metals are generally about an order of magnitude smaller than those of semiconductors; in addition, localized compositional changes brought about by current pulses at the solidification temperature should tend to fade out during cooling to room temperature since the diffusion constants in metals are typically about three orders of magnitude larger than those in semiconductors. The choice of the InSb eutectic was based on the fact that the InSb matrix is a semiconductor and its single crystal growth has been studied with interface demarcation; in addition, microstructure and x-ray (orientation) analysis have been carried out on this eutectic (9).

Cylinders of the InSb-Sb eutectic were prepared from melts (volume fraction of InSb about 0.62) confined in 5 mm diam quartz ampuls and doped with Te to a level of about $10^{19}/cm^3$ for interface demarcation (2). The melts were directionally solidified (under stabilizing thermal gradients) in a vertical stationary configuration by controlled cooling. Electrical current pulses (18 A/cm^2) of 100 msec duration were applied across the solid-melt interface at a frequency of 1 Hz. The apparatus is described in detail elsewhere (3).

The InSb-Sb cylinders were cut longitudinally along the solidification axis polished successively with Linde A, alumina, and Syton (1:1 Syton:H_2O) and preferentially etched (with 1 part acetic acid + 1 HF + 1 saturated aqueous $KMnO_4$ solution) to reveal interface demarcation lines and segregation inhomogeneities.

A typical microstructure of an InSb-Sb eutectic solidified under programmed cooling leading to relatively constant solidification rate is shown in Fig. 1. Interface demarcation lines are present in the InSb matrix but not in the Sb phase. The spacing of the demarcation lines is quite uniform, indicating a fairly uniform solidification rate of approximately 1 μm/sec. Occasional changes in the interface morphology can also be seen. The Sb phase consists of continuous and

* Electrochemical Society Active Member.
[1] Present address: Hughes Research Laboratories, Malibu, California 90265.

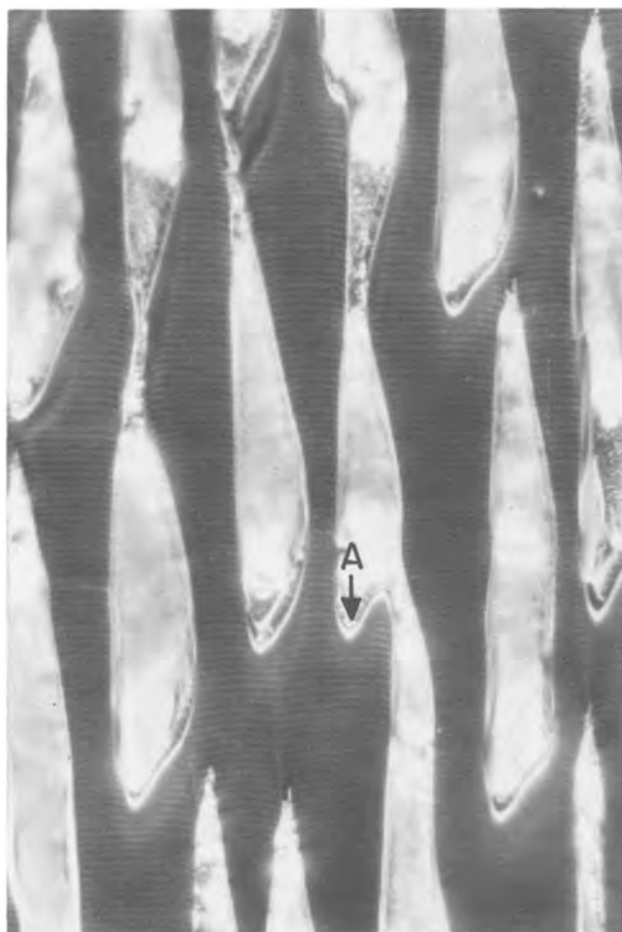

Fig. 1. InSb-Sb eutectic. Interface demarcation is present in the InSb but not in the Sb phase. The direction of solidification is from bottom to top; see text. 1300×.

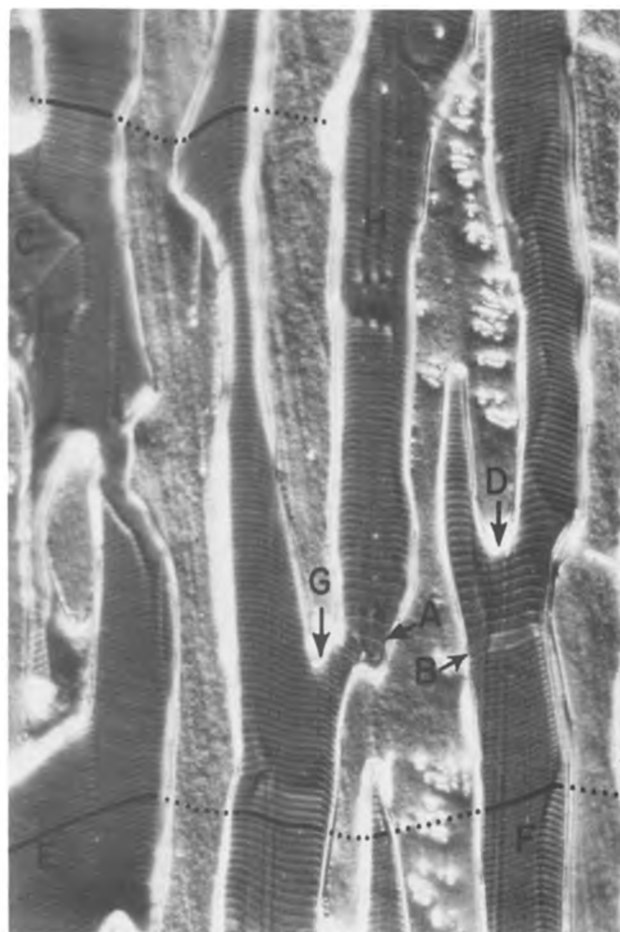

Fig. 2. InSb-Sb eutectic. Interface demarcation is present in the InSb but not in the Sb phase. The direction of solidification is from bottom to top; see text. 1300×.

discontinuous rod-type regions oriented along the solidification direction. Samples cut perpendicular to the solidification direction revealed that Sb rods have a triangular cross section as reported earlier (9) as well as cross sections of irregular shape.

A longitudinal cross section of a cylinder solidified under controlled cooling conditions is shown in Fig. 2. In this case it is seen that fluctuations in the microscopic solidification rate take place (fluctuations of the spacing of the demarcation lines) as less elaborate precautions were taken, than in the case of Fig. 1, to minimize abrupt changes in the vertical and horizontal gradients during solidification (3).

The importance of interface demarcation in studying eutectic solidification will be demonstrated by pointing out the possibilities for determining qualitatively or quantitatively parameters assumed in theoretical models. Thus, in the theories of lamellar or rod growth in eutectic solidification parameters taken into consideration are the microscopic rate of solidification, the formation and movement of faults or fault lines, the interface morphology (interface curvature) and interface instabilities (5), facet formation by one phase, interface morphology perturbations, their chronological development and wavelength (6-8). Although some of these parameters can be determined in transparent (organic) systems (5), they can only be indirectly inferred in metallic systems.

As seen in Fig. 1 and 2, the microscopic solidification rate of the matrix phase can be determined throughout solidification. The microscopic solidification rate is not constant and can be significantly different from the average solidification rate. It also exhibits local and time-independent variations. Thus, in adjacent InSb regions A and B of Fig. 2 (and most likely in the Sb rod separating these regions) the microscopic growth rate increases by more than a factor of two within 1 sec. Solidification rate variations in an individual InSb region are seen in C (Fig. 2) which appear to be associated with changes of the interface curvature as the interrod spacing undergoes adjustment under transient conditions. Faults and their movement, as discussed in Ref. (5), together with the associated interface morphology and the microscopic rate of solidification, can be observed (see, for example, region D, Fig. 2). It appears that interrod spacing is adjusted by branching of the matrix (region A in Fig. 1). A depression is first formed; by analogy with results in Ref. (5) growth of an adjacent Sb rod takes place rather than a separate Sb nucleation event.

The interface morphology of continuous regions of the matrix phase is clearly delineated by interface demarcation lines. Facet formation (planar interface) for example, is readily identified as in regions E and F of Fig. 2. These facets are inclined to the growth direction by 20°. Since InSb has a strong tendency for facet growth in the <111> direction (7), the growth direction of InSb in the present case is not the <111> (planar interface is in no instance perpendicular to the growth direction), whereas in Ref. (9) it is reported that the InSb matrix grows in the <111> direction.

Changes in interface morphology and branching of coalescence of InSb rods can be readily related. For example, in regions D and G of Fig. 2, interface instabilities (interface undulations) are seen prior to branching of InSb rods. Interface undulation with a

wavelength smaller than the rod width are seen in region H of Fig. 2. Dopant inhomogeneities parallel to the soldification direction in this region delineate undulation valleys; under quasisteady-state conditions the impurity concentration exhibits maxima and minima at undulation valleys and peaks, respectively, as a morphological instability evolves (5); similar behavior was observed in single phase material, *e.g.*, Ge (3). Interface instability with wavelengths much smaller than the width of the rod observed in the present case have not been as yet considered in the existing theoretical models. Interface instabilities with wavelengths greater than interrod spacing cannot be directly determined as the interface demarcation lines are not continuous through the Sb phase. However, the same interface demarcation line can be identified on InSb rods separated by Sb rods by counting demarcation lines of the rods from the point of their branching or merging. In this way an interface undulation can be extrapolated through the Sb phase as shown in the lower and upper parts of Fig. 2; in these cases the wavelength corresponds to more than one Sb and two InSb rods. The identification of the same demarcation line across the matrix phase could be simply achieved by interrupting the current pulses for short intervals of time (longer than the time interval between pulses). In this way, the first demarcation line after each interruption interval would serve as an absolute time reference point (10).

In summary, it was demonstrated that interface demarcation is potentially a powerful tool for the investigation of eutectic solidification. When interface demarcation is employed in conjunction with a composition profiling method, it should become possible to obtain solidification rates, interface morphology, and composition on a microscale and thus establish quantitative relationships between solidification parameters, dynamic morphological adjustments, and interface stability.

Acknowledgment

The authors are grateful to the National Science Foundation for financial support.

Manuscript submitted April 24, 1978.

Any discussion of this paper will appear in a Discussion Section to be published in the June 1979 JOURNAL. All discussions for the June 1979 Discussion Section should be submitted by Feb. 1, 1979.

Publication costs of this article were assisted by the Massachusetts Institute of Technology.

REFERENCES

1. See for example, A. Murgai, H. C. Gatos, and A. F. Witt, *This Journal*, **123**, 224 (1976).
2. A. F. Witt and H. C. Gatos, *ibid.*, **115**, 70 (1968).
3. D. E. Holmes, Ph.D. Thesis, M.I.T., June 1977.
4. K. M. Kim, A. F. Witt, M. Lichtensteiger, and H. C. Gatos, *This Journal*, **125**, 475 (1978).
5. K. A. Jackson and H. D. Hunt, *TMS-AIME*, **236**, 843, 1129 (1966).
6. D. T. J. Hurle and E. Jakeman, *J. Crystal Growth*, **3, 4**, 574 (1968).
7. W. Bardsley, J. B. Mullin, and D. T. J. Hurle, in "Solidification of Metals," Iron and Steel Institute, Publication No. 110, p. 93, London (1968).
8. H. E. Cline, *TMS-AIME*, **242**, 1613 (1968).
9. W. K. Liebmann and E. A. Miller, *J. Appl. Phys.*, **34**, 2653 (1963).
10. K. M. Kim, A. F. Witt, and H. C. Gatos, *This Journal*, **119**, 1218 (1972).

A Simple Technique for Silicon Nitride Growth

David Hackleman,[1] Yu. G. Vlasov,[2] and Richard P. Buck*

The William Rand Kenan Laboratories of Chemistry, The University of North Carolina, Chapel Hill, North Carolina 27514

The process of fabrication of ISFET's (ion-selective field effect transistors) includes formation of thin layers of the insulators SiO_2 or Si_3N_4 on silicon. Best results, at least for ISFET's used in moist environments, can be expected from insulating layers of Si_3N_4 or $SiO_2 + Si_3N_4$, rather than SiO_2. The growth of silicon nitride on silicon is usually accomplished through vapor phase epitaxial or sputtering techniques (1-3) which require use of silane mixtures or preformed nitride. Direct nitridation can also be accomplished thermally (4-6) and by glow discharge generation of atomic nitrogen to produce a thin, mixed oxy-nitride layer (5) whose growth is self-limiting. However, thermal generation of N atoms from N_2 requires temperatures of 1200°-1400°C.

Considering the negative free energy for the possible reaction

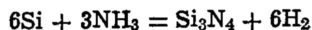

$$6Si + 3NH_3 = Si_3N_4 + 6H_2$$

it is predicted that a technique should be possible for growth of silicon nitride films on silicon using readily available anhydrous ammonia. A satisfactory procedure has been found in this laboratory when oxygen is rigorously excluded from the reaction vessel. Using a reaction chamber of the type shown in Fig. 1 and a glove bag, isolation of the silicon substrate from oxygen prior to thermal nitridation can be achieved. The experimental conditions used were 800°C for 20 hr in an anhydrous ammonia (2 cfh) atmosphere. "Chemisphere" reagent grade liquid ammonia, manufactured by Lif-o-Gen, Incorporated, was used without further purification. The substrate was first etched in HF in a helium atmosphere before transfer under helium to the reaction vessel. ESCA studies of specimens prepared by the proposed ammonia method and the sputtering method for comparison with a reference specimen heated in air (1000°C) confirm through the observed chemical shifts the creation of Si-N bonds on the surface. In Fig. 2, an ESCA spectrum of a thin,

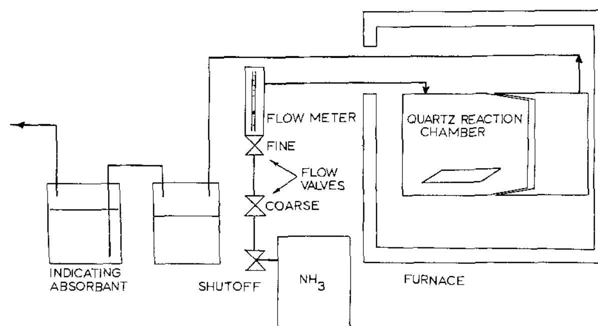

Fig. 1. Reaction apparatus

* Electrochemical Society Active Member.
[1] Present address: Hewlett-Packard Corporation, Corvallis, Oregon 97330.
[2] Permanent address: Chemistry Department, Leningrad State University, Leningrad, USSR.

Key words: silicon nitride, Si_3N_4, ISFET, ion-selective field effect transistor, chemically sensitive field effect devices.

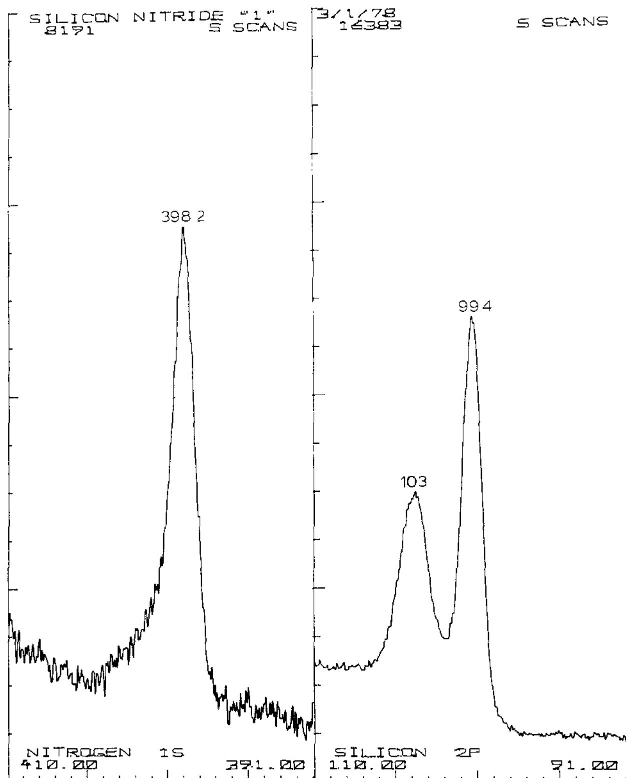

Fig. 2. ESCA of silicon nitride manufactured by this technique, ~ 25 nm thick, Si-*N* at 398 eV; *Si*-Si at 99 eV; *Si*-N at 103 eV; (Si-O is of similar chemical shift, hence the Si-*N* is the defining peak).

colorless layer, estimated 25 nm thickness grown by the ammonia process, shows the presence of N (348.21 eV) and Si (90-100 eV) in addition to expected C and O peaks. Both the oxidized Si(IV) and underlying Si-Si lattice at 99.4 eV are apparent. Figure 3 gives

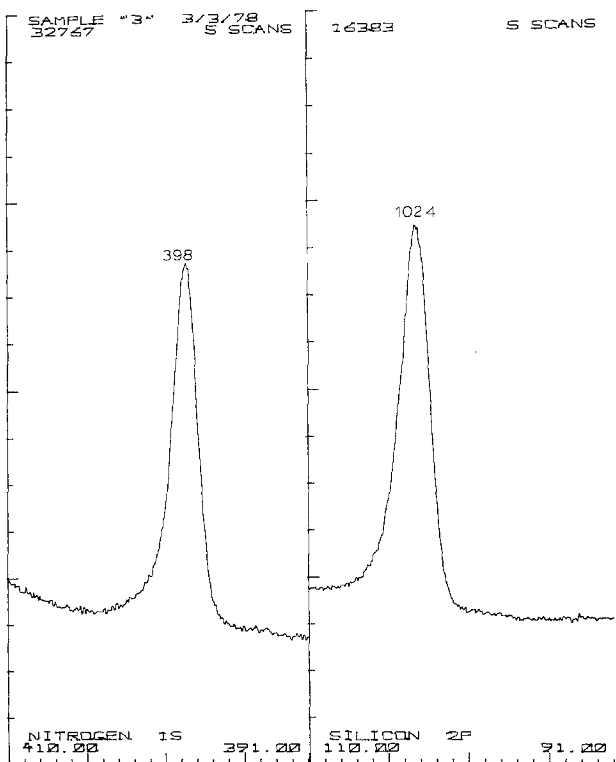

Fig. 3. ESCA of silicon nitride grown by a standard process, ~ 200-300 nm thick (8).

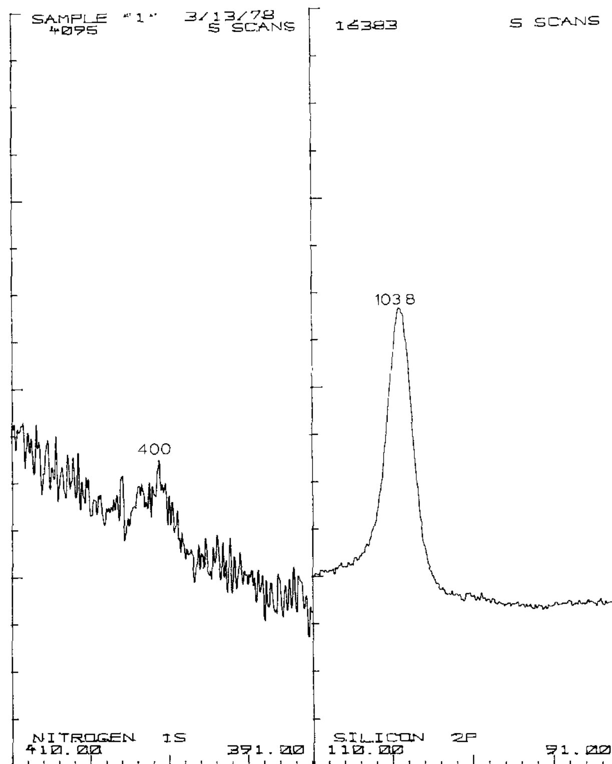

Fig. 4. ESCA of SiO_2 grown 1000°C in air for 3 hr

the results for a thick layer grown by the Si_3N_4-sputtering process. The lattice Si peak is absent. Finally, in Fig. 4 the reference specimen primarily shows a layer of SiO_2 with only a hint of N present.

This technique is simple and provides material of a quality useful for the manufacture of ISFET's. Because the nitride layer ceases to grow when it has formed a thickness great enough to inhibit diffusion of NH_3 or fragments, the process leads to a uniform layer. Further studies of the technique are worthwhile and our present accomplishments have been only briefly reported here.[3]

Acknowledgments

The authors wish to express appreciation for the use of the ESCA. They also thank its qualified operator, Dr. M. Umana of the research laboratories of Drs. Murray and Reilley of this department.

Manuscript submitted May 8, 1978; revised manuscript received July 3, 1978.

Any discussion of this paper will appear in a Discussion Section to be published in the June 1979 JOURNAL. All discussions for the June 1979 Discussion Section should be submitted by Feb. 1, 1979.

Publication costs of this article were assisted by Hewlett-Packard Corporation.

[3] The reviewer points out a nearly simultaneous study using ammonia has been reported (7).

REFERENCES

1. T. L. Chu, J. R. Szedon, and C. H. Lee, *Solid-State Electron.*, **10**, 897 (1967).
2. P. C. Parekh and J. R. Molea, *ibid.*, **16**, 954 (1973).
3. S. Mirsch and J. Bauer, *Phys. Status Solidi A*, **26**, 579 (1974).
4. S. M. Hu, *This Journal*, **113**, 693 (1966).
5. R. G. Frieser, *ibid.*, **115**, 1092 (1968).
6. T. Ito, S. Hijiya, T. Nozaki, H. Arakawa, M. Shinoda, and Y. Fukukawa, *ibid.*, **125**, 448 (1978).
7. T. Ito, T. Nozaki, H. Arakawa, and M. Shinoda, *Appl. Phys. Lett.*, **32**, 330 (1978).
8. P. Cheung, Private communication, Case Western Reserve Univ., Cleveland, Ohio.

Mass Spectrometric Detection of Intermediates in Chemical Vapor Deposition of Si_3N_4 from $SiCl_4$ and NH_3

Sin-Shong Lin

Army Materials and Mechanics Research Center, Watertown, Massachusetts 02172

Silicon nitride is known to form adhesive insulating films on silicon substrates, and thus it is an excellent material for semiconductor devices. Numerous investigations (1-4) have been made in past years to examine how the characteristics of deposit films vary with vapor compositions, temperatures, and pressures in chemical vapor deposition (CVD) processes. However none of the studies has been centered on the molecular formation processes of Si_3N_4 in the vapor phase. Although such investigation might not yield direct information concerning the production technology of semiconductor devices, nevertheless it is a fundamental process in the formation of thin film deposits.

The present study is a continuation of the previous work (5) in which many intermediate complexes leading to the formation of Si_3N_4 from SiF_4 and NH_3 were observed. The work reported here is the result obtained from the examination of vapor phase interaction of $SiCl_4$ and NH_3. While silicon tetrachloride and tetrafluoride are very similar in chemical nature, their reactivities are quite different. Consequently the difference derived from their chemical activities was observed in the molecular formation process of Si_3N_4.

The experimental setup (Fig. 1) was identical to that previously employed (5), except SiF_4 was replaced with $SiCl_4$. The $SiCl_4$ vapor was obtained from electronic grade liquid by vacuum extraction, and NH_3 was drawn from a compressed gas cylinder. The CVD reactor was made from two closed-end alumina combustion tubes and a spacer in a coaxial configuration. In order to produce an optimum condition for many complex molecular intermediates to be observed, the CVD experiments were performed in several reactor configurations at temperatures and pressures in the ranges of 800°-1200°C, and 0-80 mm Hg, respectively. The quadrupole mass filter made by Extranuclear Laboratory, Incorporated, was used and operated with ionizing electron beam at 40 eV under varying sensitivities, resolutions, and focusing conditions. Due to the difficulties inherent in the present method of sampling of the condensates through a small opening (such as orifice clogging, pressure fluctuation, and a short measurement time) it is hard to correlate systematically the characteristics of deposits with the variety and abundances of molecular intermediates. Moreover, time and resources are not available for a more extensive investigation at this time.

The identity of an ion is established from mass number and isotopic distribution. Since the chlorine atom has two major isotopes, 35 and 37, the composition of an ion could be determined from the intensities of isotopic peaks. However the presence of the isotopic peaks also complicated observed mass spectra. The majority of observed intermediate ions consisted of large numbers of atoms, and they were usually low abundant, high mass ions. With the quadrupole mass filter operating at low resolution in the high mass range, it was impossible to distinguish these weak peaks in overlapping ion spectra.

Prior to the CVD runs, mass spectra of $SiCl_4$ were taken for reference and comparison. The typical ions

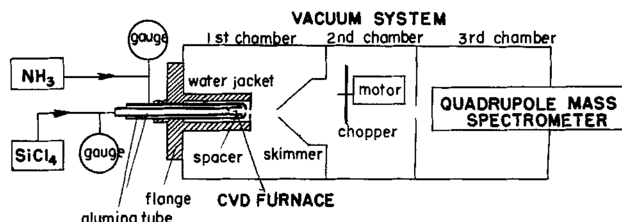

Fig. 1. Block diagram of experimental apparatus. This apparatus consisted of gas inlet lines, a miniature chemical vapor deposition furnace, and a three-stage differential pumping system. The quadrupole mass spectrometer, modulated beam mechanism, and expansion chamber are integral parts of the vacuum system.

present in these spectra are listed in Table I: The ions of $SiCl_3^+$, $SiCl^+$, $SiCl_4^+$, $SiCl_2^+$, Cl^+, and Cl_2^+ in decreasing magnitudes were observed. A trace amount of $SiCl_2F^+$ (less than 0.1%) was detected only at the introduction of the reactant. The intensity of this ion diminished with time, and was not detectable after a few runs. The mass spectra of $SiCl_4$ are very similar to those of SiF_4 (5), except there is no ion derived from the dimeric species $(SiCl_4)_2$.

The chemical reaction between $SiCl_4$ and NH_3 takes place at all temperatures as evidenced by the formation of deposits and gradual clogging of the sampling orifice. Even the mass spectra obtained at the intimate contact position of orifices [Ref. (5), Fig. 2B] where the interaction of these two gases was minimum revealed the existence of a small amount of $SiNH_2Cl_2^+$ resulting from the direct combination of the two vapors. In all CVD runs, the $SiNH_2Cl_2^+$ ion as well as ions derived from secondary collision products containing one or two Si and NH_2 groups together with HCl were always observed. However, a large number of intermediate ion species containing more than two Si atoms was detected only in some specific runs where proper conditions existed for the detection of a large scale vapor phase condensation. At the high mass end of the spectra, the resolution of the mass analyzer was lowered to compensate for the lower sensitivity of the

Table I. Ion species observed in mass spectra of $SiCl_4$

			Abundances***		
Mass*	Ion	Neutral precursor	Room temperature	T = 800°C	T = 1200°C
35	Cl	$SiCl_4$	13	9	8
63	SiCl	$SiCl_4/SiCl_3$	70	60	60
70	Cl_2	$SiCl_4/SiCl_3$	0.5	0.3	0
98	$SiCl_2$	$SiCl_4/SiCl_3$	11	15	13
107	$SiCl_2F$**	$SiCl_3F$	0.1	0	0
133	$SiCl_3$	$SiCl_4$	100	100	100
168	$SiCl_4$	$SiCl_4$	22	20	20

* Atomic weights of Si and Cl are taken as 28 and 35, respectively. Since Cl has two major isotopes 35(75.53%) and 37(24.47%), the chloride ion consists of several peaks starting from the mass number as indicated.
** Present as an impurity in $SiCl_4$ liquid, the signal is observed only at the beginning.
*** Abundances shown are not corrected for the efficiency and transmission of the mass filter.

Key words: CVD, semiconductor, films.

instrument. Consequently, the identification of these high mass, low intensity peaks could not be accomplished. Ion peaks were detected and recorded up to the limit of the mass analyzer, 900 amu, and the ion intensities were recalibrated for changes in analyzer resolution.

In Table II, the observed ion species derived from intermediate molecules existing in the CVD reaction of $SiCl_4$ and NH_3 are tabulated. The mass number shown in the first column is the position of the most abundant peak of an ion. In the high mass range, the indicated mass may not correspond to a specific ion because of two or more overlapping peaks. The compositions of the ions are indicated in the second column, and they cannot be definitely established unless the isotopic abundance agrees well with the observed peak height. Based upon the empirical fragmentation pattern (6) of chloride molecules, the neutral precursor of the fragmented ion is suggested in the third column. It is most likely (6) that gaseous chlorides predominantly produce the ions of one Cl atom less than the neutrals upon electron impact ionization. The relative abundances of these ions are shown in the last column. The intensities listed are taken directly from spectra and are not corrected for the transmission and the efficiency of the mass detector. Considering all such corrections, however, the total intensity error should not be more than one order of magnitude when comparing the abundance of ions at 100 and 10^{-5} in a relative scale.

Table II. Intermediate ion species detected in the CVD process of Si_3N_4 from $SiCl_4$ and NH_3

Mass*	Ion species**	Neutral precursor	Abundances $SiCl_3^+$ as 100†
60	$Si(NH_2)_2$	$Si(NH_2)_2Cl_2$	0.86
76	$Si(NH_2)_3$	$Si(NH_2)_3Cl$	0.26
79	$SiNH_2Cl$	$SiNH_2Cl_3$	2.85
95	$Si(NH_2)_2Cl$	$Si(NH_2)_2Cl_2$	4.85
111	$Si(NH_2)_3Cl$	$Si(NH_2)_3Cl$	0.29
114	$SiNH_2Cl_2$	$SiNH_2Cl_3$	21.4
130	$Si(NH_2)_2Cl_2$	$Si(NH_2)_2Cl_2$	0.14
133	$SiCl_3$	$SiCl_4$	100
149	$SiNH_2Cl_3$	$SiNH_2Cl_3$	1.71
176	Si_2NHCl_3	Si_2NHCl_6	0.29×10^{-2}
192	$Si_2NHNH_2Cl_3$	$Si_2NHNH_2Cl_5$	1.77
213	Si_2NHCl_4	Si_2NHCl_6	0.45
229	$Si_2NHNH_2Cl_4$	$Si_2NHNH_2Cl_5$	1.09
248	Si_2NHCl_5	Si_2NHCl_6	2.85
270	Unknown***	Unknown	4×10^{-3}
291	Unknown	Unknown	3.4
306	Unknown	Unknown	3.7
325	Unknown	Unknown	3.7
345	Unknown	Unknown	1.4
363	Unknown	Unknown	1.7
380	Unknown	Unknown	3.7
396	Unknown	Unknown	0.94
415	Unknown	Unknown	0.5
440	Unknown	Unknown	0.43
459	Unknown	Unknown	0.71
474	Unknown	Unknown	0.26
499	Unknown	Unknown	0.14
515	Unknown	Unknown	0.2
536	Unknown	Unknown	0.14
558	Unknown	Unknown	0.13
577	Unknown	Unknown	0.10
595	Unknown	Unknown	0.10
615	Unknown	Unknown	0.10
636	Unknown	Unknown	0.10
655	Unknown	Unknown	0.10
673	Unknown	Unknown	0.10
692	Unknown	Unknown	0.15
717	Unknown	Unknown	0.10
732	Unknown	Unknown	0.5×10^{-4}
748	Unknown	Unknown	0.41
770	Unknown	Unknown	0.33
785	Unknown	Unknown	0.29
803	Unknown	Unknown	0.27
826	Unknown	Unknown	0.25
850	Unknown	Unknown	0.21
868	Unknown	Unknown	0.17

* Mass number of the largest peak of an ion.

** Ions are established from mass number and isotopic distribution.

*** Due to the low resolution of the mass analyzer, the low intensity peaks above 248 amu are not identified.

† The intensity data referred to $SiCl_3^+$ as 100 are taken directly from chart 010578 where the largest number of polymeric ion peaks is observed. The CVD condition: $T = 1000°C$; $P = 18$ mm Hg; gas flows = 10 cm³/min. The reactor: Inner orifice = 0.2 mm diam; outer orifice = 0.6 mm diam; spacer = 9 mm long.

These ions, as shown in Table II, are presumably derived from molecular intermediates existing in successive stepwise reactions leading to the formation of Si_3N_4. They were observed in several sets of experiments. The abundances of these ions decrease with increasing mass numbers from the most abundant intermediate ion $SiNH_2Cl_2^+$ in order of 10% relative to $SiCl_3^+$ to the ion at 868 amu in order of 10^{-7}. The positions of these peaks are usually separated among them by units of 35, 28, 20, and 16 amu (± 1 amu due to H atom and error) corresponding to differences of Cl, Si, Cl-NH_2, and NH_2 compositions.

The over-all chemical reaction for the CVD of Si_3N_4 from $SiCl_4$ and NH_3 can be written as

$$3SiCl_4 + 4NH_3 = Si_3N_4 + 12HCl \quad [1]$$

The stepwise reactions leading to the formation of the nitride are suggested (7) to occur through a series of additive intermediates followed by the elimination of HCl such as the formation of the first intermediate

$$SiCl_4 + NH_3 = Cl_3SiCl \ldots HNH_2 = Cl_3SiNH_2 + HCl \quad [2]$$

and

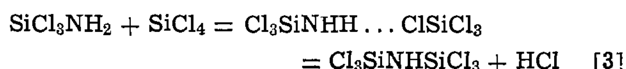

$$SiCl_3NH_2 + SiCl_4 = Cl_3SiNHH \ldots ClSiCl_3 = Cl_3SiNHSiCl_3 + HCl \quad [3]$$

or

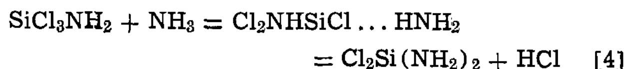

$$SiCl_3NH_2 + NH_3 = Cl_2NHSiCl \ldots HNH_2 = Cl_2Si(NH_2)_2 + HCl \quad [4]$$

After successive collisions of these intermediates and reactants, more complex intermediate molecules containing increasing numbers of N atoms should appear. This stepwise reaction generally involves the formation of a new intermediate species and the detachment of HCl from a highly unstable molecular complex. The composition of the new intermediate moves toward Si_3N_4 after numerous collisions in the vapor before striking the surface where further reactions might take place.

The experimentally observed ion species are in good agreement with the above proposed mechanism since the formation of NH and NH_2 groups are the major processes leading to Si_3N_4. The existence of the first intermediate $SiNH_2Cl_3$ confirms the first stepwise reaction [2]. The successive reaction [3] and [4] products, $Si(NH_2)_2Cl$ and Si_2NHCl_6, were supported by their fragmented ions such as $Si(NH_2)_2Cl^+$, $Si(NH_2)_2Cl_2^+$, and $Si_2NHCl_5^+$. The observation of many polymeric high mass ions in the system further indicates that a large scale vapor phase reaction and nucleation exists. Based on the variety of polymeric ion peaks possibly containing many NH_2 units, the stepwise reactions following reactions [3] and [4] seem to proceed not along some particular routes but toward all random directions of collision paths.

The most important ions derived from the first combination of two reactants are similar in the chloride and the fluoride CVD systems, but the successive collision products are quite different. In the fluoride experiment (5), only the ions derived from the first intermediate molecule $SiNH_2F_3$ were observed such as $SiNH_2F_2^+$, $SiNH_2F^+$, and $SiNH_2F_3^+$. In the chloride system, however, intermediates containing more than one NH_2 group such as $Si(NH_2)_2Cl_2$ and $Si(NH_2)_3Cl$ in addition to $SiNH_2Cl_3$ were found to exist. In the CVD of SiF_4, the major polymeric peaks observed were those homologous series of ions separated by a $Si(NH)_2$ unit. In the chloride spectra, the corresponding homologous series of ions were not major peaks. There were numerous unidentified polymeric ions containing a large proportion of NH and NH_2 groups. Since the experimental conditions in both systems were similar, it is likely that the higher reactivity of the chloride accelerates the formation of intermediate molecules containing more NH and NH_2 groups.

In addition to the Si-N-Cl species, some oxygen-containing Si-O-Cl polymeric ion species such as $Si_nO_{2n-3}Cl_5^+$ where n = 2-11, were also observed. These ions were present in minute quantities together with $SiCl_4$ only after a prolonged period of heating. The oxygen-containing species could originate from the interactions between $SiCl_4$ and alumina, silica and water. Examination of the interaction between SiO_2 and $SiCl_4$ in a new alumina tube revealed that no such Si-O-Cl species existed in the present arrangement. Therefore these species presumably result from the interaction between $SiCl_4$ and H_2O.

In summary, the existence of numerous intermediate molecules during the CVD of Si_3N_4 from $SiCl_4$ and NH_3 indicate that vapor phase nucleation and condensation occur at high temperatures in the present system. The extent of the vapor phase reaction is not clear, but the reaction is a dominant process in the Si_3N_4 formation. Although reactions at a surface may alter the properties of deposited films more than the vapor phase reaction, the significance of vapor phase nucleation at low substrate temperatures should be highly emphasized. In the future it might be possible to control the characteristics of deposits by monitoring substrate temperatures and the extent of vapor phase nucleation represented by abundances of molecular intermediates.

Manuscript submitted April 21, 1978; revised manuscript received May 24, 1978.

Any discussion of this paper will appear in a Discussion Section to be published in the June 1979 JOURNAL. All discussions for the June 1979 Discussion Section should be submitted by Feb. 1, 1979.

Publication costs of this article were assisted by the Army Materials and Research Center.

REFERENCES

1. M. J. Grieco, F. L. Worthing, and B. Schwartz, *This Journal*, **115**, 525 (1968).
2. T. L. Chu, C. H. Lee, and G. A. Gruber, *ibid.*, **114**, 716 (1967).
3. A. C. Airey, S. Clarke, and P. Popper, *Proc. Brit. Ceram. Soc.*, **22**, 305 (1973).
4. K. Niihara and T. Hirai, *J. Mater. Sci.*, **11**, 593 (1976).
5. S.-S. Lin, *This Journal*, **124**, 1945 (1977).
6. H. J. Svec and G. R. Sparrow, *J. Chem. Soc.*, **A**, 1162 (1970).
7. U. Wannagat, "Advances in Inorganic Chemistry and Radiochemistry," Vol. 6, p. 225, Academic Press, New York (1964).

A Multiwafer Growth System for Low Pressure Silicon Epitaxy

M. Ogirima, H. Saida, M. Suzuki, and M. Maki

Hitachi, Limited, Central Research Laboratory, Kokubunji, Tokyo, 185 Japan

It has been reported that low pressure epitaxy is very effective for the reduction of autodoping (1-3). The apparatus used in our previous work was a conventional horizontal reactor heated by rf induction, but it has the following two serious drawbacks: (*i*) Glow discharge in a reaction tube below about 2×10^4 Pa (150 Torr), which hinders normal epitaxial growth; (*ii*) large temperature difference between a susceptor and a wafer due to little thermal convection, which induces dislocation.

Moreover, a rectangular fused silica tube, which is usually utilized for obtaining uniform epi-layer thickness, cannot be used at low pressures because of the possibility of implosion. Therefore, some other type of reactor is desirable for a multiwafer growth system for low pressure epitaxy. This report is concerned with a new type of low pressure silicon epitaxial reactor which can accommodate 6 wafers (3 in. diam) at a time.

This apparatus is divided into three blocks, these being a gas control system, reactor, and vacuum system. The sections of the reactor are shown in Fig. 1. The characteristics of this apparatus are as follows: (*i*) Bell jar type reaction chamber; (*ii*) radiation heating; (*iii*) accurate automatic pressure control without changing gas flow rate in the reaction tube.

The bell jar type reaction chamber is safer against implosion. It is also leakage free because it employs only one O-ring seal and there is little leakage in the upstream of the wafer. The inlet gas is injected through the central tube and a T-shaped nozzle. Reacted gas is exhausted from the outlets in the base plate. The substrate holders can be rotated in order to obtain good uniformity of epi layer thickness.

The wafers are heated by infrared lamps. This heating system has several merits and demerits. It causes no glow discharge and few slip lines (dislocations) during heating and cooling processes because of small temperature difference between a substrate holder and a wafer. At low pressures heat conduction due to gas convection is difficult to realize, therefore the temperature gradients tend to be larger than that at atmospheric pressure. The demerits of radiation heating is that silicon is deposited on the walls of bell jar which is made of fused silica when silane is used as a silicon source.

The vacuum exhaust system of this apparatus is shown in Fig. 2. Reacted gas is exhausted by an oil-sealed rotary pump. Amorphous silicon particles in the exhausted gas are removed by a heat exchanger and metal mesh filters. Oil mist is trapped by a liquid nitrogen trap. The pressure in the reaction chamber is detected just below the base plate by a diaphragm vacuum gauge and is controlled automatically by injecting hydrogen or nitrogen into the exhaust piping system. The accuracy of the control system is about $\pm 2\%$ at 10^4 Pa (75 Torr).

The gas control system is assembled with parts made of stainless steel in order to get a leakage-free piping system. The gas flow rate is controlled completely automatically by a mass flow controller.

The effect of pressure on epilayer thickness distribution within a wafer (2.5 in. diam) is depicted in Fig. 3 under a constant flow rate condition. In this case, the best uniformity is obtained at 1.3×10^4 Pa (100 Torr). Above this optimum value of pressure, epilayer thickness is thinner in the downstream position. When the pressure is kept at 1.3×10^4 Pa (100 Torr), the flow rate dependence of thickness distribution is as indicated in Fig. 4. As the flow rate increases, epilayer thickness in the upstream position decreases. This is probably due to the gas-phase temperature variation in the direction parallel to the gas flow as

Key words: epitaxy, doping, wafers.

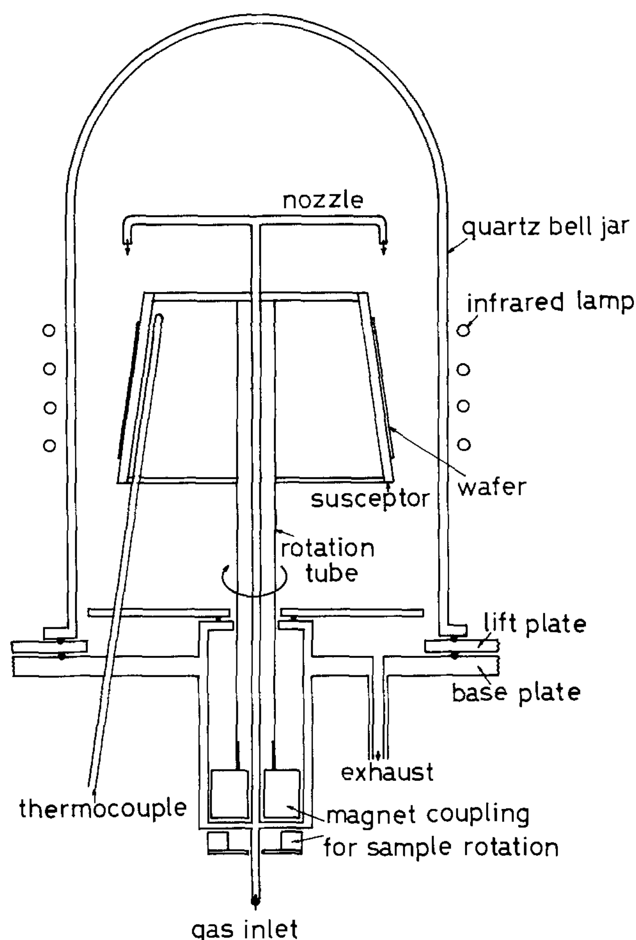

Fig. 1. Reactor structure

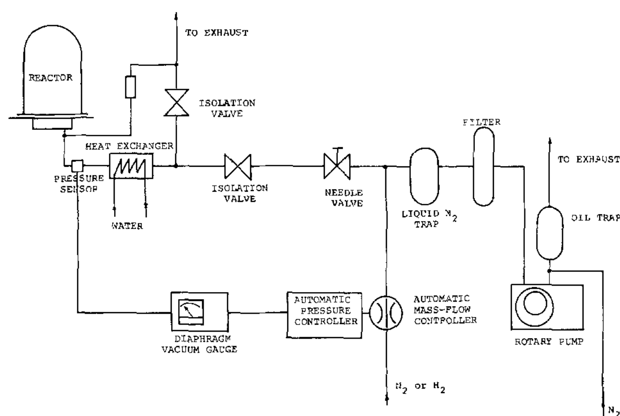

Fig. 2. Vacuum exhaust system

pointed out by Manke and Donaghey (4). In principle, epilayer thickness is thickest at the center of the wafer under an optimum condition and the thickness distribution is usually convex, as indicated in Fig. 3 and 4. When the growth conditions are optimized, the thickness uniformity in a wafer (2.5 in. diam) is better than $\pm 2\%$. The uniformity of epilayer thickness is also dependent on the length of the arms of the gas inlet nozzle (T-shaped nozzle). When it is longer than the optimum value,[1] the epilayer in the upstream position is thinner than that in the downstream position. The use of dichlorosilane improves the thickness uniformity, but involves some loss of the durability of rotary pump and some increase of autodoping.

[1] Optimum value of arm length is dependent on the size of the susceptor holder. In this case, it is as long as the outer diameter of the top of the susceptor holder.

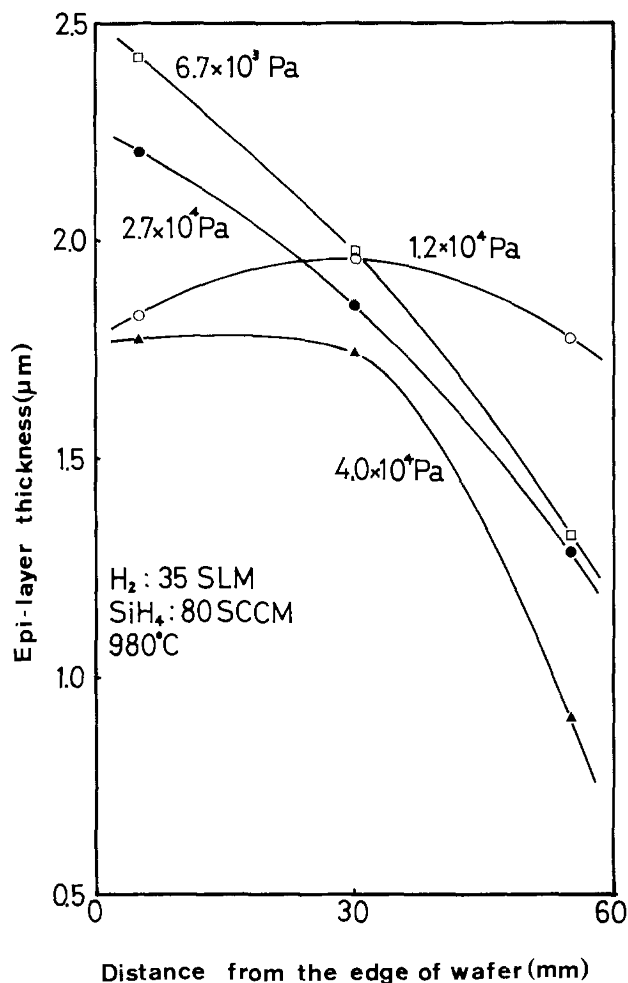

Fig. 3. Pressure dependence of epi layer thickness uniformity

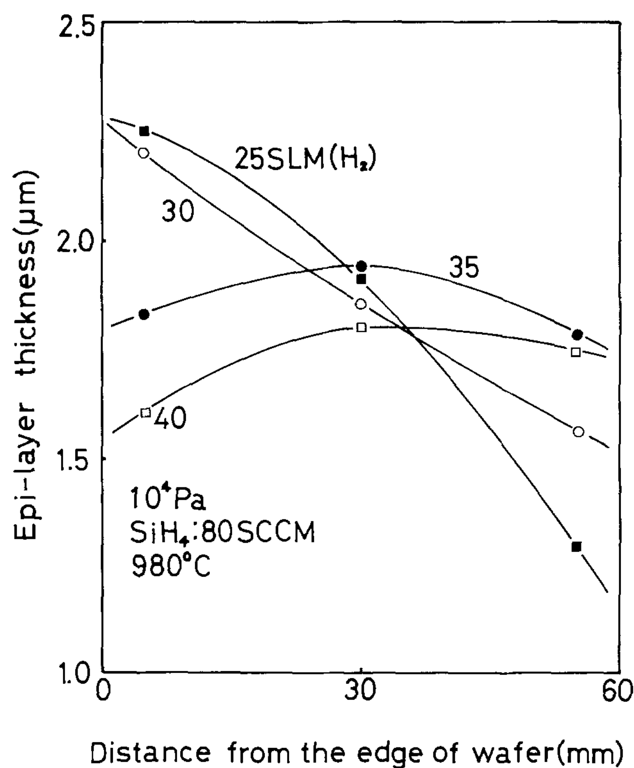

Fig. 4. Dependence of epi layer thickness uniformity on gas flow rate.

As reported previously (1), growth rate decreases with the decrease of pressure in the reaction chamber. Therefore, the molar concentration of the silicon source in a carrier gas has to be increased in order to maintain growth rate at the same level as in usual epitaxy. The dependence of growth rate on silane concentration is represented in Fig. 5. The maximum growth rate at 10^4 Pa(75 Torr) is about 1.0 μm/min.

Generally speaking, defect density [stacking fault (SF), oxidation-induced stacking fault (OSF), and dislocations] in a low pressure epitaxial layer is higher than that in a usual epitaxial layer. These defects are assumed to be due to the following three causes: (*i*) Leakage in the gas control system and reactor chamber; (*ii*) gas desorption of substrate holders; and (*iii*) temperature difference between the wafer and substrate holder.

The second cause, gas desorption, is very serious when graphite is used as a substrate holder. Usually, SiC-coated graphite is utilized as the substrate holder and it has few problems for atmospheric-pressure epitaxy. For low pressure epitaxy, however, gas atoms which are absorbed during loading and unloading of wafers are desorbed at low pressures and high temperatures.

Desorbed gas concentration from a graphite holder was analyzed by mass spectroscopic analysis and the results are indicated in Fig. 6. The sample was maintained at the measuring temperature for 10 min, and the desorbed gas pressure was measured by mass spectroscopic analyzer. After measurement, the cell was once evacuated and the sample was heated stepwise. The peak height of the analyzer was represented by partial pressure of the desorbed gas by means of the calibration curve. H_2O, CO_2, and N_2 gas atoms are desorbed above 200°C. The desorption curve for CO_2 and N_2 has dual peaks and the peak at higher temperature is supposed to be due to N_2 gas. These gas atoms attack the substrate surface and cause SF's and OSF's.

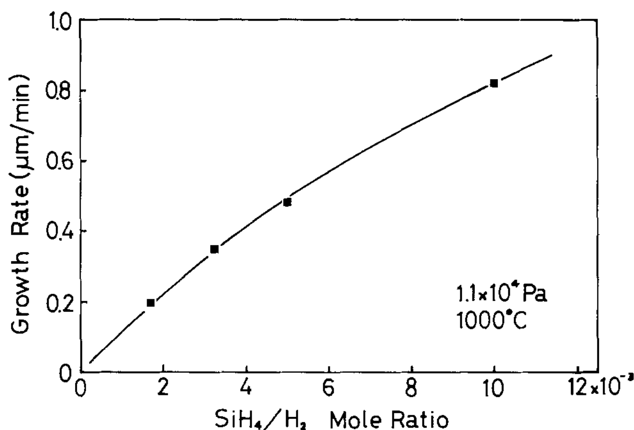

Fig. 5. Growth rate vs. SiH_4/H_2 mole ratio

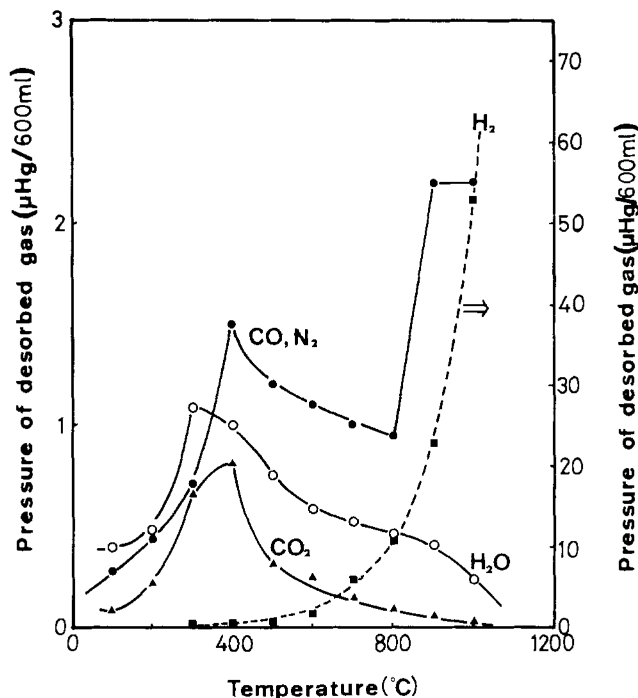

Fig. 6. Gas desorption from a substrate holder (graphite)

To prevent gas absorption and desorption, it is important to coat the surface of the substrate holder with thick (no less than 10 μm) polycrystalline silicon or quartz. Another method is to use a holder made of silicon and/or quartz. In this experiment, by using polycrystalline silicon holders, the density of OSF and SF was remarkably reduced from 10^3-10^4 cm^{-2} to 10-10^2 cm^{-2}.

Manuscript submitted Sept. 15, 1977; revised manuscript received July 3, 1978.

Any discussion of this paper will appear in a Discussion Section to be published in the June 1979 JOURNAL. All discussions for the June 1979 Discussion Section should be submitted by Feb. 1, 1979.

Publication costs of this article were assisted by Hitachi, Limited.

REFERENCES

1. J. L. Deines and A. Spiro, Abstract 62, p. 161, The Electrochemical Society Extended Abstracts, Spring Meeting, San Francisco, California, May 12-17, 1974.
2. M. Ogirima, H. Saida, M. Suzuki, and M. Maki, *This Journal*, 124, 903 (1977).
3. P. H. Lee, M. T. Wauk, and W. C. Benzing, Paper presented at the "International Electronic Devices Meeting," Washington, D.C., Dec 1977.
4. C. W. Manke and L. F. Donaghey, *This Journal*, 124, 561 (1977).

Sodium-Induced Work Function Shift of Mercury as a Metal-Oxide-Semiconductor Electrode

Gerald A. Corker[1] and Christer M. Svensson[2]

Research Laboratory of Electronics, Chalmers University of Technology, Gothenburg, Sweden

Mercury drop electrodes are often used as metal electrodes in metal-oxide-semiconductor (MOS) structures. Measurements of, for example, the capacitance-*vs.*-voltage relationship (the *C-V* curve) can then be done without vacuum metallizing. From *C-V* measurements on MOS structures many interesting properties of the structures are obtained (1). Among these properties it is also possible to measure the rela-

[1] Permanent address: IBM Research Center, Yorktown Heights, New York 10598.
[2] Present address: Department of Physics and Measurement Technology, Linhöping University, 58183 Linhöping, Sweden.
Key words: semiconductor, electrode, capacitance.

tive value of the metal work function (1). In investigating the work function of a mercury drop we found a very large change in electrode work function, about 2 eV, as a result of only small amounts of dissolved sodium. In the present paper we report on this effect.

Sample No. 1 was prepared from n-type silicon wafers with 2-3 Ωcm resistivity. The wafer was oxidized in dry oxygen at 1200°C to an oxide thickness of 100 nm. A small number of Au dots were evaporated on the oxide as reference electrodes. The sample was then put on a metal backing plate with a liquid InGa alloy in between. We then probed the Au dot with a thin goldplated wire. The *C-V* curve was then recorded by a Boonton 72B Capacitance bridge and an X-Y recorder. In Fig. 1 this *C-V* curve is shown as curve a. A small drop of mercury (about 1 mm diam) was also put on the oxide and probed by a goldplated wire, and its *C-V* curve was recorded. This *C-V* curve is shown in Fig. 1 as curve b. Finally, a similar drop of mercury with a small amount of dissolved sodium was used. The *C-V* curve of this Hg:Na electrode is shown in Fig. 1 as curve c. As can be seen from the figure we observe a very large shift of the *C-V* curve between the Hg and the Hg:Na electrodes. Using C_{FB} (the capacitance for which the semiconductor bands are flat or the electrical field at the semiconductor surface is zero) equals 0.7 C_{max} gives the following flatband voltages from Fig. 1: −0.16V for the Au electrode; +0.04V for the Hg electrode; and −2.13V for the Hg:Na electrode. Thus the sodium induced shift is 2.17V in this case.

During storage in air the flatband voltages were initially stable. After about 2 hr the flatband voltage started to increase on the Hg:Na electrode toward the value of the clean Hg electrode. Probably Na disappears by oxidation in air. After about 24 hr, only about 0.2V shift was left and the mercury drop was covered by a hard, white layer, probably NaOH.

In order to investigate the dependence of sodium concentration in the mercury, we performed the following experiment. Sample No. 2, similar to No. 1 but with 70 nm thick oxide, was placed on a backing plate as above. The mercury was contained in a plastic well with a 3 mm hole, placed on the sample. Each Hg sample was about 0.05 cm³. Hg samples with different Na content were prepared in the following way. Na metal was cut clean under hexane previously dried with Na. 0.0032g of clean Na metal was weighed on filter paper and dissolved in 1 ml Hg. This gives $2.05 \cdot 10^{-3}$ Na atoms per Hg atom in the solution. This solution was then further diluted by volume in test tubes. *C-V* curves were then recorded, starting with the most dilute solution and continuing to the highest concentration. After this the oxide surface was cleaned with water, dried in nitrogen, and again measured with a clean Hg sample. The result of this experiment is shown in Fig. 2.

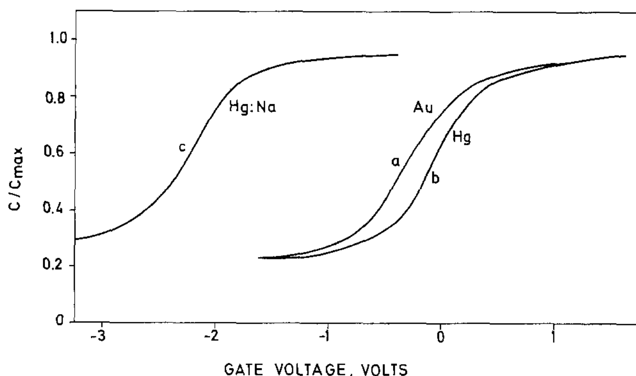

Fig. 1. Normalized capacitance *vs.* voltage for three different electrodes on sample No. 1.

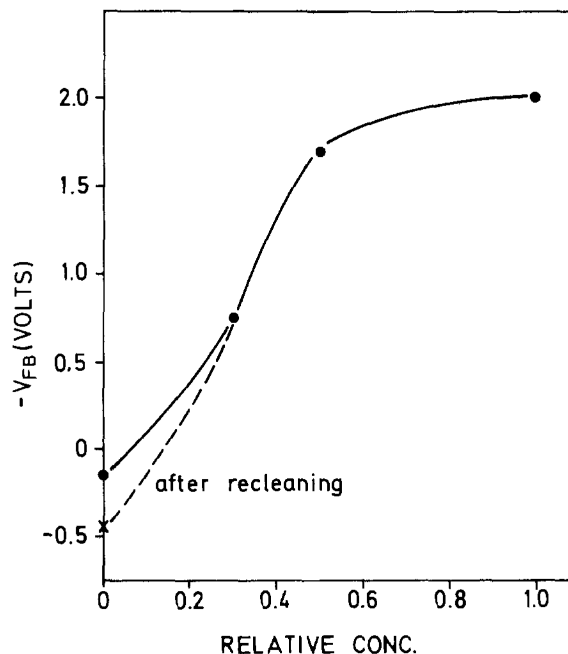

Fig. 2. Flatband voltage of sample No. 2 with mercury electrodes of different sodium content *vs.* the relative sodium concentration. The relative concentration 1.0 corresponds to about 0.002 Na atoms per Hg atom.

From Fig. 2 we can see that the sensitivity for sodium is very large. Already at a relative concentration of 0.3, corresponding to nominally about 60 ppm (Na atoms per Hg atom) the flatband voltage shift is half the total and, at a relative concentration of 0.5 (~100 ppm), the shift saturates. It should be noted that the values of concentration given here are upper limits of concentration rather than reliable values. The reason is that we continuously lose sodium metal through the reaction with water vapor during dilution and experiments. We believe, however, that the real concentration values are not less than half the stated values.

Discussion

It is quite obvious that 60 ppm sodium in mercury could not change the bulk work function of the mercury. Our observations are instead equivalent to the well-known work function lowering which occurs as a result of alkali adsorption on high work function metals in vacuum (2). Sodium-induced work function lowering of a silicon-silicon dioxide interface has also been directly observed by DiStefano (3). In both these cases the sources of the alkali are outside the metal, in vacuum, or in the oxide. In our case the sodium comes from the interior of the metal. Our case is therefore similar to the effect of hydrogen-induced work function lowering of palladium on silicon dioxide (4).

As we expect the silicon-silicon dioxide system to be unaffected by the metal, our observed values of the flatband voltage will be proportional to the metal work function (1). Taking the gold work function to be 5.0 eV (1), we get from Fig. 1: Hg work function 5.2 eV and Hg:Na work function 3.0 eV. Expected values are for Hg 4.5 eV (5) and for a saturated sodium-covered metal surface in vacuum about 2.2 eV (2). Our observed values are thus in reasonable agreement with the proposed model. It should be noted that the oxide surface is not completely unaffected by our experiments since we observed, for example, shifts of the order of 0.2V as a result of recleaning the oxide surface.

Manuscript submitted May 17, 1978.

Any discussion of this paper will appear in a Discussion Section to be published in the June 1979 JOURNAL.

All discussions for the June 1979 Discussion Section should be submitted by Feb. 1, 1979.

REFERENCES

1. S. M. Sze, "Physics of Semiconductor Devices," Chap. 9, John Wiley & Sons, New York (1969).
2. N. D. Lang, *Phys. Rev. B*, **4**, 4234 (1971).
3. T. H. DiStefano, *Appl. Phys. Lett.*, **19**, 280 (1971).
4. I. Lundström, M. S. Shivaraman, C. Svensson, and L. Lundkvist, *Appl. Phys. Lett.*, **26**, 55 (1975).
5. "Handbook of Chemistry and Physics", 53rd ed, R. C. Weast, Editor, p. E-69, The Chemical Rubber Co., Cleveland (1972).

Role of Oxide Defect Sites in the Breakdown of NiO Films

B. MacDougall*

National Research Council of Canada, Division of Chemistry, Ottawa, Ontario Canada K1A 0R9

In previous papers the breakdown of NiO films anodically formed on polycrystalline and single crystal nickel in *p*H 2.8 Na_2SO_4 has been studied in terms of both the open-circuit potential decay profiles and the extent of surface pitting (1-5). Open-circuit breakdown of the oxide films occurred in two distinct stages: (*i*) an induction period during which localized chemical dissolution of oxide occurred at defect sites in the film and; (*ii*) pitting and/or undermining of the oxide film as a result of nickel dissolution from oxide-free sites (*i.e.*, pores) in the film. The transition from stage (*i*) to stage (*ii*) was marked by a rapid potential shift to −0.75V (often accompanied by a potential overshoot or "spike") as the exposure of bare nickel set up the corrosion couple: $Ni \rightarrow Ni^{2+} + 2e$; $2H^+ + 2e \rightarrow H_2$. This mechanism for film breakdown was supported by the observation that substantial pitting of the surface occurred only after the spike, the pits presumably developing at those sites where "defective" oxide had broken down. In the present note, a Ni(100) single crystal has been used to investigate further the role of oxide defect sites in the breakdown of NiO films.

Effect of Solution *p*H on Oxide Breakdown

Figure 1 shows the open-circuit decay profiles for Ni(100) electrodes after different times of anodization at 0.0V.[1] Before the potential spike, little breakdown of the oxide film occurs as indicated by the small amount of both recovered surface activity and nickel in solution (Table I) and the absence of surface pitting (Fig. 2a). This was taken to indicate that the oxide at the defect sites, which only covers a small part of the surface, is slowly dissolving in this region

$$NiO + 2H^+ \rightarrow Ni^{2+} + H_2O$$

The effect of the *p*H of the breakdown solution was investigated by anodizing for 1 hr at 0.0V in *p*H 2.8 Na_2SO_4 and then transferring to a *p*H 4.0 solution for open-circuit decay.[2] The time to the spike increased by a factor of three with this increase in *p*H, as would be anticipated from the above reaction.

Role of O_2 in Film Breakdown

To study film breakdown in the region up to the spike, experiments were performed in the presence of dissolved oxygen. The oxide film was formed by anodization at 0.0V for 1 hr in deaerated *p*H 2.8 Na_2SO_4 solution and then transferred to a separate *p*H 2.8 solution to follow the open-circuit breakdown. If this second solution was carefully deaerated, the decay

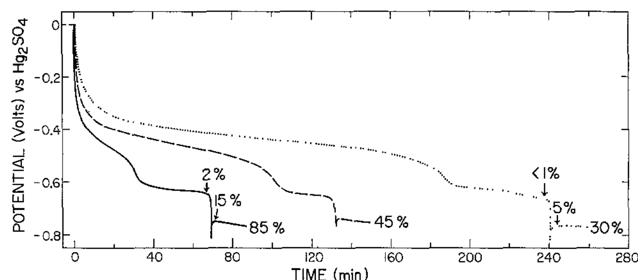

Fig. 1. Open-circuit potential decay, in deaerated *p*H 2.8 Na_2SO_4, of Ni(100) electrodes which had been anodized at 0.0V for various times. (——) 15 min; (– – –) 1 hr; (· · ·) 15 hr. Also given are recovered surface activities at various decay times, obtained by stepping the potential back to 0.0V and measuring the charge required to reestablish passivity. The potential step technique was used for all anodizations.

profile was identical to that obtained without transfer of the electrode. However, if the second solution contained oxygen, the open-circuit decay profile was dramatically altered. Firstly, the induction time before film breakdown increased by a factor of *ca.* five. This increase was associated entirely with the arrest at −0.6V, which in the presence of O_2 was shifted as much as 0.1V anodic, *i.e.*, to −0.5V. In contrast, the arrest at −0.4V did not change at all. Secondly, the recovered surface activity at the potential spike was 20% instead of the usual ~2% obtained in O_2-free solutions. The dramatic effect of O_2 on the arrest at −0.6V suggests that breakdown and repair of an oxide film is operative here, the presence of O_2 being able to keep the film in a state of repair.

The oxide responsible for the potential plateau at −0.6V is a different oxide from that giving rise to the arrest at −0.4V and may have either been present at the defect sites as an inner oxide after the anodization (3) or been formed as a result of repair of the origi-

Table I. Quantity of Ni^{2+} in solution and surface activity recovered, after various times on open-circuit, for both electropolished and anodized Ni(100) in *p*H 2.8 Na_2SO_4

(Quoted values of [Ni^{2+}] refer to that which has dissolved during the open-circuit decay only.)

Anodic treatment	Time on open circuit	Surface activity (%)	[Ni^{2+}] $\mu g\ cm^{-2}$ ($\pm 10\%$)
15 min at 0.0V	67 min	2	1.5
	(*i.e.*, 2 min before spike)		
15 min at 0.0V	71 min	15	4.0
15 min at 0.0V	89 min	85	8.0
15 hr at 0.0V	238 min	<1	2.0
	(*i.e.*, 2 min before spike)		
15 hr at 0.0V	242 min	5	5.0
15 hr at 0.0V	260 min	30	13.0
Electropolished	20 min	100	7.5
Electropolished	90 min	100	21.5

* Electrochemical Society Active Member.

Key words: surfaces, electrode, passivity, corrosion.

[1] Potentials are measured *vs.* a Hg/Hg_2SO_4 reference electrode in 0.15*N* Na_2SO_4 (+0.665V with respect to the standard reversible hydrogen electrode). The working nickel electrode is vertically positioned in the cell and is parallel to a platinum counterelectrode in the same compartment.

[2] It has previously been shown that such air exposure of the steady-state, passive NiO film does not affect the breakdown characteristics of the film (2,3,5).

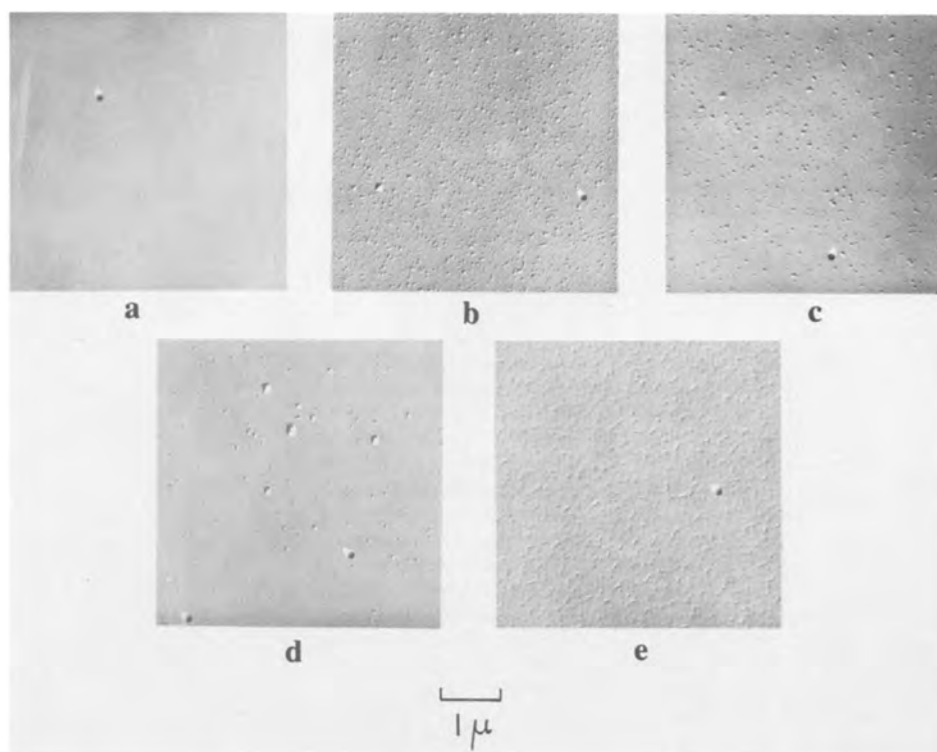

Fig. 2. Electron micrographs of a Ni(100) surface after various electrochemical treatments: (a) Electropolished and anodized at 0.0V for times of 15 min (or 15 hr) followed by open-circuit breakdown to 2 min before the spike; (b) 15 min at 0.0V with open-circuit decay continuing for 20 min after the spike. Recovered surface activity is 85%; (c) As in (b) but with the potential decay continuing for only 5 min after the spike. Recovered activity is 35%; (d) 15 hr at 0.0V with open-circuit decay continuing for 20 min after the spike. Recovered activity is 30%; (e) Electropolished and immersed in pH 2.8 Na_2SO_4 solution for 90 min on open circuit.

nal oxide which has completely broken down at these sites. The results in the absence of O_2 can be interpreted in terms of the spike resulting from breakdown of defect oxide to reveal nickel metal, the hydrogen evolution reaction not being able to repair this oxide. The higher tendency for film repair with O_2 reduction (as opposed to hydrogen evolution) is due to the more positive electrode potential for the former reaction at the cathode areas and its subsequent ability to polarize more strongly the anodic reaction at the pores. This leads to an increase in the oxide-free coverage required to shift the potential to $-0.75V$ and thus an increase in the over-all induction time. The absence of any influence of O_2 on the open-circuit arrest at $-0.4V$ suggests that simple chemical dissolution of oxide at the defect sites is occurring in this region. Consequently, the duration of this arrest should be related only to stability of defective oxide toward chemical dissolution. (It is interesting to note that it is mainly this arrest which increases with time of anodization at 0.0V (Fig. 1), *i.e.*, the time of anodization mainly influences the stability of oxide at the defect sites toward dissolution rather than the ability of the film to repair itself.)

Oxide Undermining After the Spike

The 20% recovered surface activity at the spike in the presence of O_2 indicates that a constant oxide-free coverage is not required to shift the potential to $-0.75V$. This is confirmed for film breakdown in the absence of O_2 where, with an increase in time of anodization at 0.0V from 3 min to 20 hr, the recovered activity at the spike decreases from 6 to 1%. This decrease in recovered activity can be correlated with a corresponding decrease in the density of pits (Fig. 2b and 2d), which means that the number of defect sites has decreased. With increasing time of anodization, the oxide at some defect sites is converted to a more stable form which does not break down during potential decay. The correlation between density of pores and oxide-free area (as determined from the recovered activity) is not, however, a simple one, especially at longer times after the spike. A recovered surface activity of, *e.g.*, 5% is much more effective in removing oxide by undermining after the 15 min anodize than the 15 hr anodize. With the latter treatment, the activity increases from 5 to 30% during 18 min on open circuit after the spike, compared to 5-85% after the 15 min anodize at 0.0V (Fig. 1). The results can be explained in terms of the number of pores which contribute to the 5% oxide-free area. This number decreases with time of anodization and consequently the sites must be somewhat larger to encompass 5% of the surface. This is evident from Fig. 2c and 2d where a recovered activity in the neighborhood of 35% can have associated with it different defect site densities. The smaller number of sites (after the long anodize) will be less effective in removing the oxide film and the activity will increase more slowly. Thus, the important factor in determining the rate of oxide removal after the spike is the number of pores and not the total oxide-free area.

Cathodic Control of Oxide Undermining

The amount of nickel dissolved during a 20 min time period after the spike is 50% higher for the 15 hr anodize at 0.0V in comparison with the 15 min anodize at 0.0V (Table I). On the other hand, the recovered surface activity is much lower after the longer anodization and breakdown (Fig. 1), indicating that the amount of oxide-free nickel surface is lower. The increase in amount of nickel dissolution with corresponding decrease in oxide-free surface exposure shows that the corrosion couple (after the spike) is controlled by the cathodic reaction, *i.e.*, hydrogen evolution on the NiO film. The importance of the cathodic reaction is also evident from the observation that a 20 min open-circuit exposure of electropolished Ni(100), where the surface is 100% free of oxide after <3 min exposure (5), does not result in any increase in the amount of nickel dissolution in comparison with the treatments mentioned above (Table I).

Role of Oxide Film Thickness

The thickness of the oxide films on anodized Ni(100), as determined by oxygen K_α x-ray emission spectroscopy (5), was 9-12Å for either 15 min or 15 hr at 0.0V. The dramatic changes in film breakdown characteristics with time of anodization (Fig. 1) and the absence of substantial changes in measured oxide

film thicknesses can be explained in terms of the presence of oxide defect sites. The defect sites cover only a small part of the surface and therefore changes in the composition (*e.g.*, thickness, stoichiometry) of oxide at these sites will probably not easily be observed. However, these changes can considerably alter both the time to film breakdown and subsequent activation of the surface by oxide removal, as discussed above. Somewhat similar results were reported by Kruger and Ambrose (6) for oxide breakdown on anodized iron in chloride solutions, very large increases in the time to film breakdown being associated with small increases in oxide thickness. Again, the influence of condition of oxide formation on composition and density of oxide defect sites appears to have played the major role.

Etching vs. Pitting

Complete breakdown of the oxide film on electropolished Ni(100) occurs on open circuit within 3 min at pH 2.8 as indicated by the recovered surface activity and the corrosion potential (5). This observation can be explained in terms of the presence of a very large defect site density. The rapid removal of this oxide film is the reason no pitting attack is observed, the nickel dissolution giving only a general roughening of the electrode surface (Fig. 2e). Obviously an oxide film, with a distribution of pores, must be present on the surface for a sufficiently long period of time before detectable pits can be observed (7).

Acknowledgments

The author thanks Mr. G. I. Sproule for the electron microscopy, Mr. A Desaulniers for the A. A. analysis of Ni^{2+}, and Drs. M. Cohen and M. J. Graham for helpful discussions and suggestions.

Manuscript submitted April 24, 1978; revised manuscript received June 7, 1978.

Any discussion of this paper will appear in a Discussion Section to be published in the June 1979 JOURNAL. All discussions for the June 1979 Discussion Section should be submitted by Feb. 1, 1979.

Publication costs of this article were assisted by the National Research Council of Canada.

REFERENCES

1. B. MacDougall and M. Cohen, *This Journal*, **123**, 191 (1976).
2. B. MacDougall and M. Cohen, *ibid.*, **123**, 1783 (1976).
3. B. MacDougall and M. Cohen, *ibid.*, **124**, 1185 (1977).
4. B. MacDougall and M. Cohen, *Electrochim. Acta*, **23**, 145 (1978).
5. B. MacDougall and M. Cohen, Paper presented at the "Fourth International Symposium on Passivity," Oct. 17-21, 1977, Arlie, Virginia.
6. J. R. Ambrose and J. Kruger, in "Proceedings of the 4th International Congress on Metal Corrosion," Amsterdam, p. 698, (1969); See also C. L. McBee and J. Kruger, in "International Conference on Localized Corrosion," p. 252 (1971), Williamsburg, Va.; See also Z. *Szrlarska-Smialowska;* USA-Japan, Seminar on Passivity, p. 115 (1975).
7. H. W. Pickering and R. P. Frankenthal, *This Journal*, **112**, 761 (1965).

Erratum

The following comments are written in reference to the article "Growth of $Ga_yIn_{1-y}As$/InP Heterostructures by Molecular Beam Epitaxy," by B. I. Miller and J. H. McFee, which appeared in the August 1978 issue of *This Journal*, Vol. 125, No. 8, pp. 1310-1317.

In Fig. 8, the 77°K photoluminescence peak at 1.368 μm was claimed to correspond to the mole fraction $y = 0.455$ for $Ga_yIn_{1-y}As$. This was derived using the relation

$$E_g(\text{eV}) = 0.410 + 1.094g$$

at 77°K which assumes a linear relationship for E_g *vs.* y. This relationship was shown to hold in Ref. (12). More recent work[1] on $Ga_yIn_{1-y}As$ shows a quadratic relationship for E_g *vs.* y at 77°K, or

$$E_g(\text{eV}) = 0.404 + 0.649y + 0.457y^2$$

which would give a bandgap corresponding to 1.53 μm for $y = 0.47$ at 77°K, close to that reported recently by many researchers. We now know that our photoluminescence spectrum of Fig. 8 showing a peak at 1.368 μm was shifted toward shorter wavelengths by bandfilling (Burstein Shift) which can be significant in materials such as $Ga_{0.47}In_{0.53}As$ where the effective mass is small. The spectrum of Fig. 8 corresponds to a nearly lattice-matched GaInAs layer with carrier concentration $n \sim 10^{18}$ cm^{-3}. More recent work by us on lattice-matched fairly pure $Ga_{0.47}In_{0.53}As$ ($n \sim 10^{17}$ cm^{-3}) reveals that at 77°K the photoluminescence peak is ~1.55 μm.

[1] Y. Takeda, A. Sasaki, Y. Imamura, and T. Takagi, *This Journal*, **125**, 130 (1978).

Editor's Note

The paper "Application of Electrochemical Techniques to the Solution of Problems in Medicine," by P. N. Sawyer, which appeared on pages 419C-436C of the October 1978 issue of **This Journal** was the Electrochemical Society Lecture delivered at the Seattle, Washington, Meeting of the Society, May 22, 1978.

JOURNAL OF THE ELECTROCHEMICAL SOCIETY

ACCELERATED

BRIEF COMMUNICATIONS

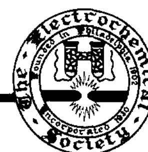

NOVEMBER 1978

Polarization Behavior and Structure of LiAlMg Alloy Electrodes

C. A. Melendres,* S. Siegel, and J. Settle

Argonne National Laboratory, Chemical Engineering Division, Argonne, Illinois 60439

In a previous publication in this journal[1] we reported on the results of studies on the structural changes that occur during the cyclic polarization of LiAl wire electrodes. Evidence of electrode comminution with cycling was presented. It was thought that this behavior may be limiting the long term performance and cycle life of LiAl/FeS_x (x = 1 or 2) molten salt secondary cells. In order to buffer structural changes in the LiAl electrode, we proposed the addition of a ternary component into this system. Initial studies in this direction involving small engineering cells have been undertaken by our colleagues in this laboratory.[2] In this communication, we report on the results of an investigation on the effect of Mg incorporation on the structure and polarization behavior of LiAl electrodes.

Electrochemical studies were conducted using a cell and other equipment described previously.[1] Polarographic grade LiCl-KCl eutectic (obtained from Anderson Physics Laboratories, Champaign, IL) was used as electrolyte. The working electrodes were prepared as follows: Ingots of MgAl alloy (consisting of 5 to 20 at.% Mg) were cast from high purity (99.99% Al, 99.9% Mg) materials in a tantalum crucible at ∿700°C. MgAl wire electrodes were prepared from the ingot by melting and then drawing the melt by suction into boron nitride tubes with 1.59mm bore. These wires were electrochemically charged with Li to about 45-50 at.%. A LiAl alloy (40 at.% Li) was used as reference electrode. Examination of electrode structure was done metallographically as described previously.[1] Identification of the phases formed during charging and discharging of the electrodes was made by X-ray diffraction.

Figure 1 shows typical polarization behavior of some LiAlMg electrodes. For comparison, we show that of a LiAl wire electrode at a similar current density. The cathodic polarization curves are for the charging of Li into the MgAl wire of appropriate composition (15 or 19 at.% Mg in Aℓ), while the anodic portions represent the subsequent extraction of Li. We observed that electrodes incorporating Mg are more polarized than LiAl on both charge and discharge. This appears to be more pronounced with increasing Mg content. For the same cutoff voltage on charge, Li-Al-Mg alloy electrodes have therefore somewhat lower Li capacity than LiAl.

The appearance of a number of plateaus is also evident in the curves for the LiAlMg systems. This is indicative of the possible formation of new phases. X-ray diffraction investigation of electrodes in the charged and discharged state revealed the phases given in Table I. Thus, in addition to forming the β-LiAl phase, solid solutions of Mg in Al and the ternary compound $LiMgAl_2$ have been identified. The absence of the α-LiAl phase is surprising. This has not been found even in nearly completely discharged electrodes. If present, the level is presumably <5 wt.% and beyond the detection limit of the X-ray diffraction technique. Another interesting observation is the apparently higher efficiency for the anodic extraction of Li (defined here as the ratio of the amount of lithium removed on discharge at constant current to the amount loaded on the preceeding charge) in the ternary alloy electrode compared to that of LiAl (Table I). The extraction efficiency also appears to decrease somewhat with Mg content of the ternary alloy due to the greater electrode polarization caused presumably by a decrease in lithium mobility in the solid alloy. Only a slight increase in extraction efficiency or lithium utilization with cycling is evident with the ternary alloy electrodes as compared to LiAl.

Metallographic examination of the discharged electrodes revealed the structures shown in Figure 2. The completely discharged portion of the electrodes in Figs. 2a, b and c (outer periphery) has essentially the same composition as the starting alloy *i.e.* solid solutions of Mg in Al, with possibly small amounts of Li. The composition of the partially discharged portion (*i.e.* the core) has not been determined but is believed to correspond roughly to that of the charged electrode. It is worthwhile to note that the morphology of the discharged LiAlMg alloy electrode is significantly different from that of LiAl electrodes shown previously.[1] The

patches of electrode particles are smaller but appear to have continuity. The overall structural feature of the electrode also appears to be intact after 3 cycles, especially for the 15 at.% MgAl alloy (compare Fig. 2c and 2d). In general, from metallographic and optical microscopic examinations, we observe increased structural stability with higher Mg content in electrodes subjected to a few cycle tests. It is obviously not possible to extrapolate this to the long term behavior of large cells. Work along the latter line is being done in a separate program with engineering type cells at this laboratory.

In summary, the incorporation of Mg into the LiAl electrode (at the level of 5 to 19 at. % in MgAl starting material) leads to increased polarization but also to a marked morphological change which appear to result in improved structural stability on cycling and increased efficiency of Li extraction during short term cyclic tests. The α-LiAl phase is eliminated while new binary and ternary phases are formed in addition to β-LiAl. These preliminary results indicate that modification of structure and properties of binary solid alloy electrodes by the addition of a third element may be worth while approach to the engineering development of suitable electrode systems and the improvement of existing ones.

ACKNOWLEDGEMENT

The authors are grateful to Dr. F. A. Cafasso for his continued interest and support of this work. Financial support by the Division of Basic Energy Sciences, Department of Energy, is gratefully acknowledged. We thank B. Tani for taking the X-ray diffraction patterns.

REFERENCES

1. C. A. Melendres and C. C. Sy, J. Electrochem. Society, 125, 727 (1978).
2. D. R. Vissers, K. E. Anderson and W. R. Frost, Extended Abstracts vol 76-2; 150th Meeting of the Electrochemical Society, Las Vegas, Nevada, October 17-22, 1976; Abstract No. 42, p. 115.

Manuscript submitted June 9, 1978; revised manuscript received July 20, 1978.

Publication costs of this article were assisted by Argonne National Laboratory.

TABLE I. Some Performance Characteristics and Phases of Li Alloy Electrodes

Run	Electrode Type	i (mA/cm^2)	at.% Li Loaded	Efficiency (%)[a]	Phases Observed
9/2	LiAl	28	>50	79.7	α LiAl,
7/13	LiAl	107	>50	66 (1st cycle) 78 (2nd cycle) 81 (3rd cycle)	β LiAl
2/11	LiAlMg (5 at. % Mg)[b]	41		93	β LiAl,
6/14	LiAlMg (10 at. % Mg)[b]	35.3	42	92	$LiMgAl_2$,
2/23	LiAlMg (10 at. % Mg)[b]	35	46	91	6-8 at. %
9/28	LiAlMg (15 at. % Mg)[b]	27	49	88 (1st cycle) 90 (2nd cycle) 92 (3rd cycle)	Mg in Al Solid solution
7/6	LiAlMg (19 at. % Mg)[b]	16	46	81.1	β LiAl,
7/7	LiAlMg (19 at. % Mg)[b]	20	46	72	$LiMgAl_2$,
2/15	LiAlMg (20 at. % Mg)[b]	44		64.5	16 at. % Mg in Al, Li_2AlMg (in 20 at. % Mg only)

[a] One cycle, otherwise indicated.

[b] % Mg in starting MgAl alloy.

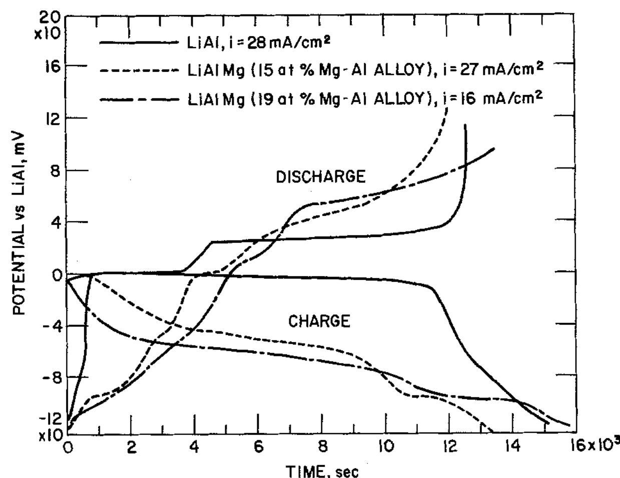

Fig. 1. Polarization behavior of lithium alloy electrodes at 400°C.

Fig. 2a. Partially discharged LiAlMg electrode (10 a/o MgAl starting alloy charged to 46 a/o Li); i = 30 mA/cm^2; marker = 0.025 cm.

Fig. 2b. Discharged LiAlMg electrode after 3 cycles (10 a/o MgAl starting alloy charged to 42 a/o Li); i = 26 mA/cm^2; marker = 0.025 cm.

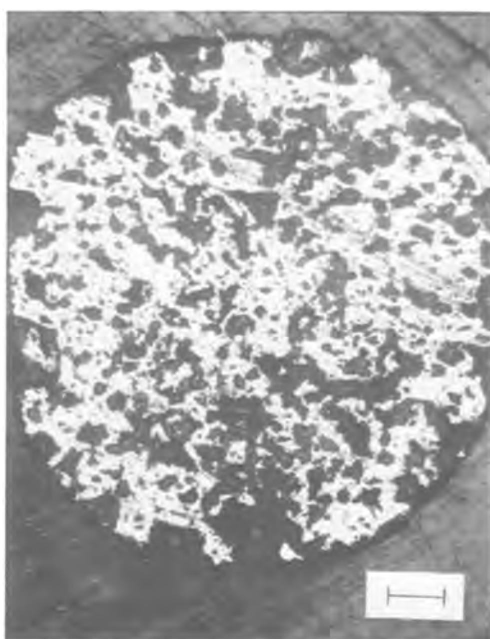

Fig. 2c. Discharged LiAlMg electrode after 3 cycles (15 a/o MgAl starting alloy charged to 49 a/o Li); i = 27 mA/cm^2; marker = 0.025 cm.

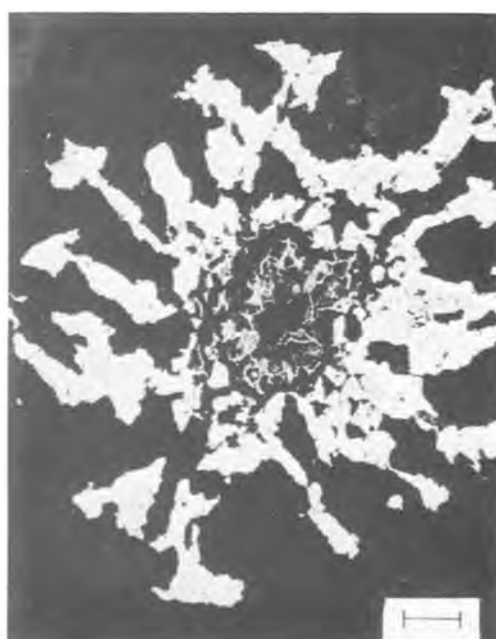

Fig. 2d. Discharged LiAl wire electrode after 3 cycles, i = 107 mA/cm^2; marker = 0.025 cm.

Photo-Assisted Corrosion of Copper

Dennis D. Davis and Dennis L. Johnson

Department of Chemistry, New Mexico State University, Las Cruces, New Mexico 88003

The effects of visible radiation on the corrosion of copper is a sparsely studied field (1). With the increasing use of copper in solar energy applications this effect may become more important in the near future.

Copper normally exhibits very low rates of corrosion in non-oxidizing acidic media in the absence of oxygen. Complexing agents such as the halide ions and the presence of oxygen greatly accelerate the rates of corrosion (2) because of the formation of complexes such as $CuCl_3{}^{2-}$ and $CuCl_4{}^{2-}$. The thermodynamically favored form of copper ion in halide media is $CuCl_3{}^{2-}$, while in the absence of halide, Cu^{2+} ions are favored.

The electrode potentials of copper are fairly well behaved (3), following the Nernst equation with respect to dissolved copper, and complexation not only changes the oxidation state of the dissolved copper but also lowers the electrode potential. Additionally the well-known disproportionation reaction involving Cu(I) aquo ions

$$Cu^\circ + Cu^{2+} \rightarrow 2Cu^{1+} \qquad E^\circ = -0.37 \text{ V} \quad [1]$$

which favors metallic copper, is shifted in the other direction by complexing agents such as halide.

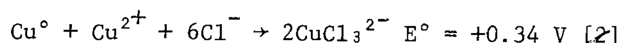

$$Cu^\circ + Cu^{2+} + 6Cl^- \rightarrow 2CuCl_3{}^{2-} \quad E^\circ = +0.34 \text{ V} \quad [2]$$

The oxidation of copper and hence its dissolution is usually accompanied by the reduction of atmospheric oxygen

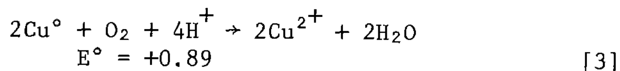

$$2Cu^\circ + O_2 + 4H^+ \rightarrow 2Cu^{2+} + 2H_2O \quad E^\circ = +0.89 \quad [3]$$

and is even more favored by halide ions

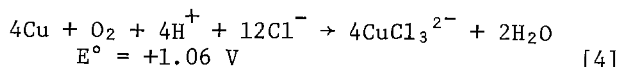

$$4Cu + O_2 + 4H^+ + 12Cl^- \rightarrow 4CuCl_3{}^{2-} + 2H_2O \quad E^\circ = +1.06 \text{ V} \quad [4]$$

The corrosion of copper can be promoted in the absence of a traditional oxidizing agent (O_2, HNO_3, etc) if the reaction sequence shown in Eqs. [5], [6] can be maintained

Key words: copper, corrosion, photochemistry.

$$Cu(I)L_x \rightarrow Cu(II)L_x \quad [5]$$

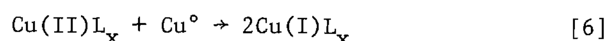

$$Cu(II)L_x + Cu^\circ \rightarrow 2Cu(I)L_x \quad [6]$$

L = complexing agent such as halide

resulting in the auto-catalytic oxidation of copper metal. Normally oxygen provides the cathodic component for Eq. [5]. Hydronium ions are not reduced under standard conditions, but are reduced to a very slight extent governed by the Nernst equation. The photochemical reaction we have investigated [4-6] for solar energy conversion is the oxidation of copper(I) complexes to copper(II) complexes with concomitant proton reduction driven to completion by light. Thus the photochemical reaction

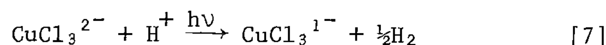

$$CuCl_3{}^{2-} + H^+ \xrightarrow{h\nu} CuCl_3{}^{1-} + \tfrac{1}{2}H_2 \quad [7]$$

is in actuality the same as Eq. [5] with H^+ as the oxidizing agent. It is suggested from our solar conversion work that corrosion of copper metal should be greatly enhanced in the presence of light when the copper is immersed in HCl solution even in the absence of conventional oxidizing agents. Arbit and Nobe [1b] reported that immersion of copper single crystals in neutral sodium halide solutions alters the photopotentials, but observed no solution photoreactions. The quantum yield for Cu(I) photooxidation is a strong function of acid concentration and approaches zero in neutral solution [6], thus such reactions would not have noted by these workers.

EXPERIMENTAL

Cleaned copper corrosion strips of approximately 5-7 cm^2 area were immersed in acidic salt solutions in serum-capped Pyrex tubes. The solution contained 0.9 M NaCl and 0.1 M HCl ($[Cl^-] = 1.0$, $[H^+] = 0.1$). The tubes were degassed on a vacuum line and then filled with argon to ensure anaerobic conditions. A control strip was kept in the dark and the sample to be irradiated placed in a

thermostatted (22°C) brass block. Irradiation was accomplished with a 200-w Hg lamp for 12 hrs. Similar results were obtained with ~30 hrs. of direct sunlight but because the experimental variables are much greater with sunlight, we discuss only the lamp experiments. Aliquots were removed via syringe periodically and analyzed for soluble copper by atomic absorption spectrometry. No blue-green color developed which would have indicated a copper(II) complex, so it is assumed that the soluble copper is present as $CuCl_3^{2-}$, a colorless copper(I) complex. The results are summarized in Figure I which represents duplicate experiments and are corrected for the fact that only one-half of the surface area of the irradiated sample actually received illumination, while the backside was subject to the same corrosive effects as the dark sample.

DISCUSSION

The Figure dramatically points out that, for example, after 8 hrs. the illuminated sample has undergone 50-times as much corrosion as the dark sample. These results are in good accord with theoretical expectations on several points:

1. Dark corrosion in the absence of oxygen should occur only up to an extent controlled by the Nernst equation (in a nonflowing situation) and should eventually reach an equilibrium situation. This limiting effect is noted in that the dark experiments tend to an average limiting value of Cu(I) concentration in solution of 3×10^{-4} M, while the Nernst equation, $E° = \frac{0.059}{2} \log \frac{[Cu(I)]^2[H_2]}{[Cu°][H^+]^2[Cl^-]^6}$, $E° = -0.165$ V for the reaction, $2Cu° + 2H^+ + 6Cl^- \rightarrow 2CuCl_3^{2-} + H_2$, predicts a Cu(I) equilibrium concentration of 2.7×10^{-4} M.
2. The exponentially increasing corrosion with time of irradiation, log [Cu] dissolved vs time being a fairly linear plot, is suggestive of an autocatalytic mechanism. We suggest the following scheme:

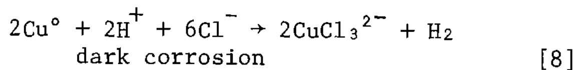

$$2Cu° + 2H^+ + 6Cl^- \rightarrow 2CuCl_3^{2-} + H_2 \quad \text{dark corrosion} \quad [8]$$

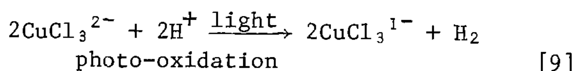

$$2CuCl_3^{2-} + 2H^+ \xrightarrow{light} 2CuCl_3^{1-} + H_2 \quad \text{photo-oxidation} \quad [9]$$

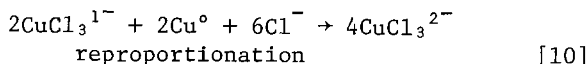

$$2CuCl_3^{1-} + 2Cu° + 6Cl^- \rightarrow 4CuCl_3^{2-} \quad \text{reproportionation} \quad [10]$$

then Eq. [9], then Eq. [10], then Eq. [9] etc. in an autocatalytic cycle promoted by light.

3. The parallel slopes in the illuminated experiments suggests the same rate limiting feature is present in all and we propose that this is the intensity of illumination controlling Eq. [9].

CONCLUSIONS

In an anaerobic acidic medium containing chloride ions, corrosion of copper is greatly accelerated by visible light. Such conditions might obtain in solar collectors in which partly saline water is used, particularly if the acidic decomposition products of a heat transfer medium such as glycols are present, and of course if this system is subjected to visible radiation.

Although these are fairly stringent limitations, the photoassisted corrosion of copper is a hitherto univestigated and novel mode of corrosion and etching which may have importance in diverse applications of copper and its alloys.

ACKNOWLEDGEMENT

This work was supported by the Copper Development Association.

REFERENCES

1. a) H. Leidheiser, Jr., "The Corrosion of Copper, Tin and Their Alloys," J. Wiley and Sons, N.Y., N.Y. pp. 193-206 (1971). b) H.A. Arbit and K. Nobe, Corrosion, 24, 17 (1968).
2. W.D. Robertson, V.F. Nole, W.H. Davenport, and F.P. Talboom, Jr., J. Electrochem. Soc., 105, 569 (1958).
3. W.M. Latimer, "The Oxidation States of the Elements and Their Potentials in Aqueous Solution," 2nd Ed., Prentice-Hall, New York (1952).
4. K.L. Stevenson and D.D. Davis, Inorg. Nucl. Chem. Letters, 12, 905 (1976).
5. D.D. Davis, G.K. King, K.L. Stevenson, E.R. Birnbaum, and J.H. Hageman, J. Solid State Chem., 22, 63 (1977).
6. D.D. Davis, K.L. Stevenson, and C.R. Davis, J. Am. Chem. Soc., 100, 5534 (1978).

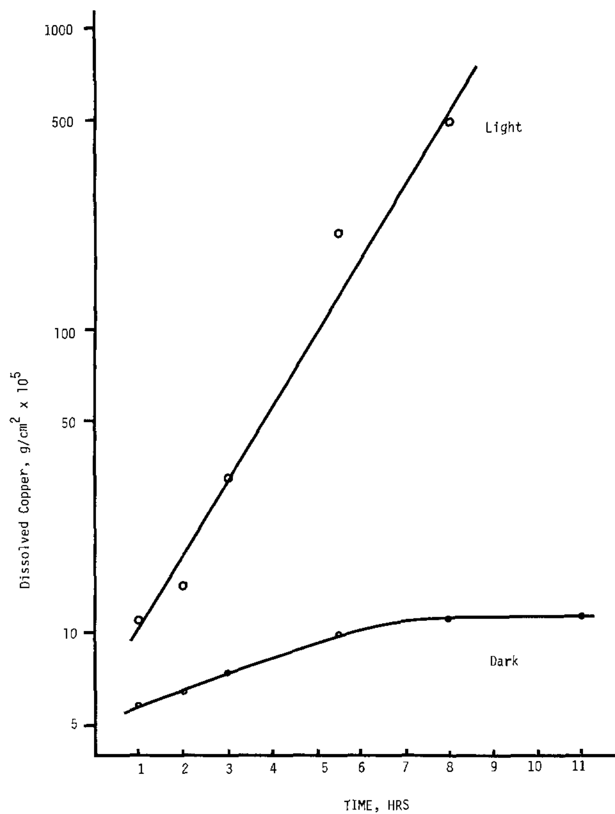

Fig. 1. Corrosion of copper strips in 0.1 N HCl, 0.9N NaCl in the dark and illuminated with 200W Hg lamp.

Manuscript submitted June 5, 1978; revised manuscript received September 18, 1978.

Electrochemical Behavior of Palladium-Implanted Titanium

E. McCafferty* and G. K. Hubler

Naval Research Laboratory, Washington, D.C. 20375

It is well known that the corrosion resistance of titanium in acids is greatly improved by small alloying additions of palladium (1,2). The purpose of this communication is to report on the electrochemical behavior of titanium surfaces which have been ion-implanted with palladium. The beneficial effect of ion implantation in aqueous corrosion applications has been illustrated by several recent studies dealing with the implantation of various ions into iron (3-5).

EXPERIMENTAL

Samples of pure (99.97%) titanium rod (3/8 inch diam) were mounted in epoxy molds. The exposed surface was abraded through 600 grit emery paper, 6 μm diamond paste, and then given a final polish to a mirror finish with 0.05 μm alumina in a 5% oxalic acid solution. These surfaces were implanted with palladium to a fluence of 1×10^{16} ions/cm^2 at an energy of 90 keV. The resulting palladium concentration profile was near Gaussian shaped and centered at a depth of 240 angstroms. The peak concentration of palladium was 5 atomic percent, with less than 0.1 atomic percent Pd at the metal surface.

For some corroded samples, the Pd concentration profiles were measured by means of high resolution Rutherford backscattering of alpha particles. Experimental details have been given elsewhere (6); but in brief the analysis beam was 2.5 MeV helium, and the scattering angle was 135°. The energy spectrum of backscattered particles was measured with a position-sensitive solid state detector placed in the focal plane of a magnetic spectrometer. This detector system provided a depth resolution of 30 angstroms.

RESULTS AND DISCUSSION

Figure 1 shows electrode potentials for pure titanium, pure palladium, and palladium-implanted titanium as a function of immersion time in boiling (100°C) 1 M sulfuric acid. The time-axis is plotted logarithmically for illustration purposes only. The steady-state open-circuit corrosion potential of pure palladium was approximately 1000 mV more noble than that of pure titanium. The steady-state corrosion potential of the implanted sample was much closer to that of pure palladium than to that of pure titanium.

In the first minutes of immersion, the implanted samples displayed a rapid shift in electrode potential. After one minute in the case of two of the implanted samples and after 1.5 minutes for a third, the electrode potential was -1.0 volts vs. Hg/Hg_2SO_4 and tending toward the potential of pure titanium. In the next few seconds in each case, however, the electrode potential reversed toward the noble direction as the Ti-rich surface dissolved away to expose a new surface region containing an increased concentration of Pd. After about 2 hrs, the electrode potential of the implanted sample was fairly constant and only 150 mV less noble than the corrosion potential of pure palladium.

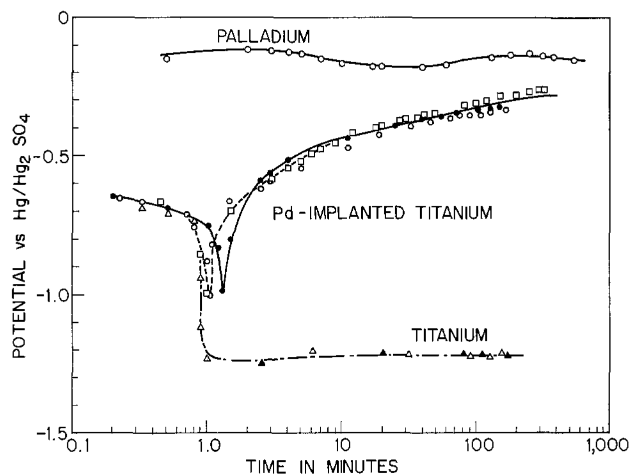

Fig. 1. Open-circuit corrosion potentials as a function of immersion time in boiling 1 M H_2SO_4 for pure titanium, pure palladium, and palladium-implanted titanium.

*Electrochemical Society Active Member

Key Words: corrosion, ion implantation, titanium, palladium.

The buildup of palladium at the surface during the corrosion process was determined by backscattering analysis. Figure 2 shows depth concentration profiles for an as-implanted sample and for samples corroded for two different immersion periods. A significant shift of the Pd profile is evident after only 6 minutes immersion; whereas after 125 minutes, the backscattering spectrum shows that Pd builds up on the surface to a concentration of 20 atomic percent. The total area beneath the Pd profile for all three curves is constant to within the ± 5% error in the measurement, indicating that no Pd has been removed from the surface during the corrosion process.

Figure 3 shows potentiostatic anodic polarization curves for pure titanium, pure palladium, and palladium-implanted titanium in boiling 1 M H_2SO_4. All curves were determined after steady-state open circuit potentials were first established (2 to 2-1/2 hrs immersion). The anodic curve for pure titanium shows the normal active-passive behavior which has been typically observed (1,2,7). Well defined Tafel slopes were not observed in the active region, but the corrosion rate at the open-circuit potential was determined by colorimetric analysis of solution to be 3.7 mA/cm², on the basis that the overall anodic reaction is $Ti \longrightarrow Ti^{+3} + 3e^-$ (7). The implanted samples display a passive current density of 2 to 6 μA/cm , which may be estimated to be the corrosion rate at the open-circuit potential. Thus, implantation with Pd lowers the corrosion rate of Ti by a factor of about 1,000. Anodic current densities for pure Pd are less than the values for the implanted samples for electrode potentials more negative than +0.2 volts vs. Hg/Hg_2SO_4. At more positive potentials, palladium undergoes increased dissolution (8), but the implanted sample does not.

SUMMARY

Ion implantation of titanium with palladium reduces the open-circuit corrosion rate in boiling 1 M sulfuric acid by a factor of about 1,000. The open-circuit corrosion potential is shifted approximately 0.9 volts in the noble direction and is a mixed potential between pure titanium and pure palladium. Electrochemical measurements and Rutherford backscattering analyses indicate that the improvement is due to initial preferential dissolution of titanium and retention of implanted palladium.

ACKNOWLEDGEMENT

This work was supported in part by the Office of Naval Research Contract No. N001477WR7007.

Manuscript submitted Aug. 7, 1978; revised manuscript received Aug. 16, 1978.

REFERENCES

1. M. Stern and H. Wissenberg, This Journal, 106, 759 (1960).
2. N. D. Tomashov, R. M. Altovsky, and G. P. Chernova, This Journal, 108, 113 (1961).
3. V. Ashworth, D. Baxter, W. A. Grant, and R. P. M. Proctor, Corrosion Sci., 16, 775 (1976).
4. B. S. Covino, Jr., B. D. Sartwell, and P. B. Needham, Jr., This Journal, 125, 366 (1978).
5. B. S. Covino, Jr., P. B. Needham, Jr., and G. R. Conner, This Journal, 125, 370 (1978).
6. J. K. Hirvonen and G. K. Hubler in "Ion Beam Surface Layer Analysis," O. Mayer, G. Linker, and F. Kappeler, eds., p. 457, Plenum Publishing Co., New York (1976).
7. E. J. Kelly, "Proceedings of the Fifth International Congress on Metallic Corrosion," Tokyo, 1972, p. 137, N.A.C.E., Houston, Texas (1974).
8. M. Pourbaix, "Atlas of Electrochemical Equilibria," p. 360, Pergamon Press, Oxford (1966).

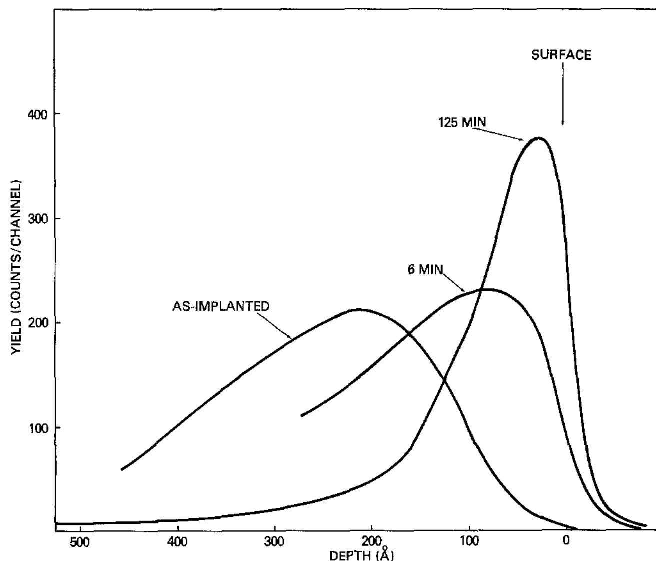

Fig. 2. The energy spectrum of α particles backscattered from ion-implanted Pd in pure Ti for an implanted sample and after two different immersion periods.

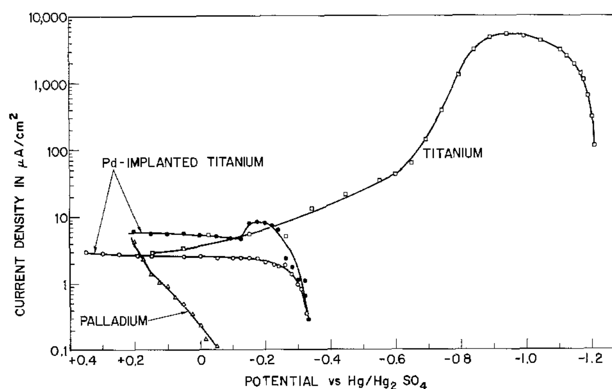

Fig. 3. Anodic polarization curves for titanium, palladium, and palladium-implanted titanium in boiling 1 M H_2SO_4.

Low Melting-Point Compositions in Alkali Metal Metaphosphate/Fluoride Systems

D. Elwell*

Center for Materials Research, Stanford University, Stanford, California 94305

Molten salt compositions of low melting point are often of interest for applications in electrochemistry or as solvents for metal oxides. This investigation was performed in order to find a phosphate-based solvent for the electrodeposition of indium phosphide at temperatures at or below 600°C.

The system Na, K/PO_3, F was investigated by Bukhalova and Mardirosova(1) and the lowest melting-point for any composition in that system was found to be 424°C. Solvents containing Li^+ are expected to have a lower viscosity because of the relatively small mass of these ions, and are therefore preferable for electrocrystallization experiments provided that the liquidus temperatures are similar to or below those of the Na, K system.

In order to accelerate the task of finding compositions of lowest melting point in the Li, Na/PO_3,F and Li, K/PO_3, F systems, melts containing equal molar concentrations of the four constituents in each case were unidirectionally solidified by slow horizontal traverse of a 15 cm long crucible through a furnace. The fraction which solidified last was analyzed and a melt of the composition so determined was subjected to a further unidirectional solidification to test the accuracy of the first analysis. Atomic absorption spectrographic analysis for the alkali melts was found to be reliable to within 1% but electron microprobe analysis for F, P and O did not give reliable data, although intensities were compared with standard materials.

The Li:K ratio in the lowest-melting sample in that system was found to be 1·16(5):1 and the Li:Na ratio for the corresponding composition was 0·98(4):1. A section through the quaternary phase diagram was therefore taken with these metal ratios held constant but with the F:PO_3 ratio varied. The results are shown in Fig. 1, together with liquidus data for the corresponding section in the Na, K/PO_3, F system for comparison.

*Electrochemical Society Active Member.

Liquidus temperatures were determined by a visual method, with the samples contained in vitreous carbon crucibles in argon at atmospheric pressure. The chemicals were of reagent grade and were subjected to a preliminary dehydration at 300°C in vacuo for several hours. This procedure may not remove all traces of moisture and the results may be subject to a small error due to residual moisture.

Since the lower melting point materials formed glasses on solidification, it was difficult to obtain precise measurements and the ultimate test of the state of the material was the observed response of the surface to a force applied via a graphite rod of spectrographic purity. Cycling the sample through the melting temperature was used in attempts to obtain an accurate determination.

Even with this precaution, the data are reliable only to ±10°C. Supercooling was not large compared with this estimated error except in the case of the fluoride-free composition in the Na, K/PO_3, F system, for which a supercooling of 140°C was observed. A separate calibration experiment was performed and temperatures quoted are taken from the mean of two chromel/alumel thermocouples with junctions located in the region previously occupied by the crucibles containing the samples.

The Li, Na/PO_3, F system is seen to give the lowest melting temperatures, the minimum occurring at about 300°C for a composition with 20 m/o fluoride. Both the Li, Na and Li, K systems do not indicate a sharply-defined minimum but the Na, K system (1) appears to exhibit eutectic-like behavior, although the data plotted in Fig. 1 is based on intersections with rather widely-spaced isotherms.

The value of 300°C for the lowest-melting composition compares very favorably with alternative systems. The lowest melting point occurs at 580°C in the system Li, Na/P_2O_7,F(2) and at 612°C in the system Na, K/P_2O_7, F (2).

However, if greater complexity can be tolerated, it should be noted that the system Li, K/PO_3, PO_4 has a minimum melting point at 340°C (3) and fluoride addition may result in compositions which melt below 300°C.

ACKNOWLEDGMENTS

The author is grateful to Dr. R. S. Feigelson for valuable comments and to Mr. F. A. Ponce for help with the measurements. Financial support was provided by the Army Research Office.

REFERENCES

1. G. A. Bukhalova and I. V. Mardirosova, Russ. J. Inorg. Chem. 11, 497 (1966).

2. V. P. Goryacheva and A. G. Bergman, Russ. J. Inorg. Chem. 12, 1167 (1967).

3. I. B. Markina and N. I. Voskresenskaya, Russ. J. Inorg. Chem. 19, 1837 (1974).

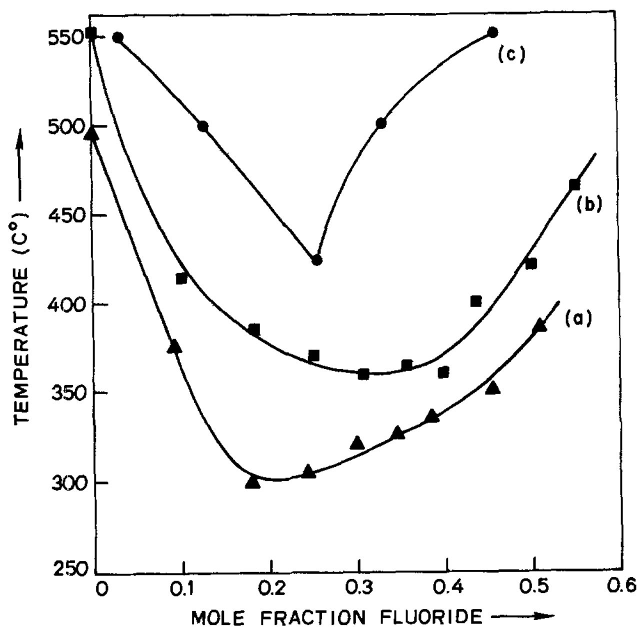

Fig. 1. Liquidus temperature of compositions

(a) $(Li_{0.496}Na_{0.504})$ (PO_3,F)
(b) $(Li_{0.538}K_{0.462})$ (PO_3,F)
(c) $(Na_{0.814}K_{0.186})$ (PO_3,F) from ref. (1).

Key words: solvent, molten salt, alkali phosphate/fluoride.

Manuscript submitted April 14, 1978; revised manuscript received Aug. 21, 1978.

Publication costs of this article were assisted by Stanford University.

Auger Electron Spectroscopy Analysis of Thermal Oxide Layers of Silicon Carbide

Akira Suzuki,* Hiroyuki Matsunami, and Tetsuro Tanaka

Department of Electronics, Faculty of Engineering, Kyoto University, Kyoto, 606 Japan

Silicon carbide (SiC) is a promising semiconductor material for various electronic devices because of its wide energy gap (1). SiC can be thermally oxidized in the same way as used for silicon (1, 2). The oxide layer is utilized as a protecting film for the SiC surface during the device fabrication (1, 3). However, the oxidation mechanism and the properties of the oxide layer have not been studied in detail. In this communication, some results of an Auger electron spectroscopy analysis of the thermal oxide layers will be described.

SiC crystals used for the thermal oxidation were 6H-type single crystals prepared by the Lely method. Each crystal was plate-shaped with wide (0001) faces. A typical size was 4x 4x0.5 mm^3. After polishing both the (0001) Si face and the $(000\bar{1})$ C face of each crystal with diamond paste, we set the crystals in a horizontal furnace with the (0001) faces vertical. Thermal oxidation was carried out at 1000°C for 2 hours in an oxygen flow of 100 cm^3/min. The oxygen flow was passed through pure water to saturate it with water vapor (at room temperature).

The oxide thicknesses determined by ellipsometry were 152 Å on the Si face and 908 Å on the C face. A (111) wafer of silicon was also oxidized at the same time for comparison. The oxide thickness on the Si wafer was 1949 Å. The refractive indices of the oxides on the C face of SiC and on the Si wafer were much the same: 1.45-1.46 by ellipsometry.

We carried out an Auger analysis of these oxide layers. Fig. 1(a) shows Auger electron spectra. The upper spectrum is from the SiC crystal, and the lower from its oxide layer on the C face. The accelerating voltage for the primary electron beam was 5 kV, and the beam current was 0.1 µA. The beam was made to scan the sample surface to remove an electron-irradiation effect. The scanned area was 50x 50 μm^2. SiC has three Auger peaks: Si_{LVV},

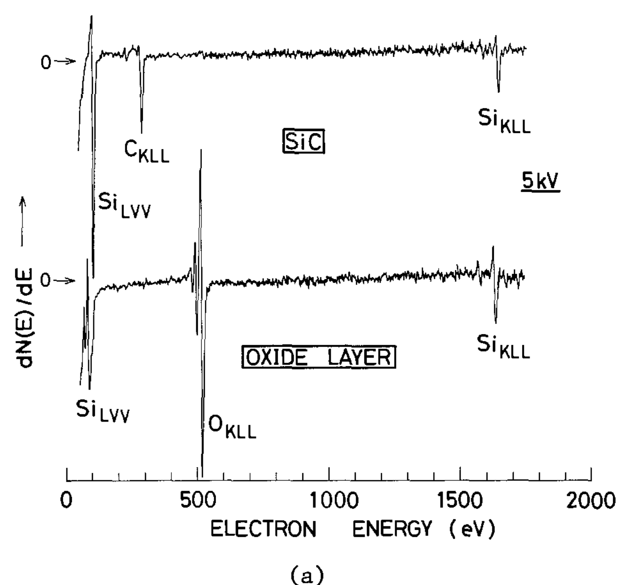

(a)

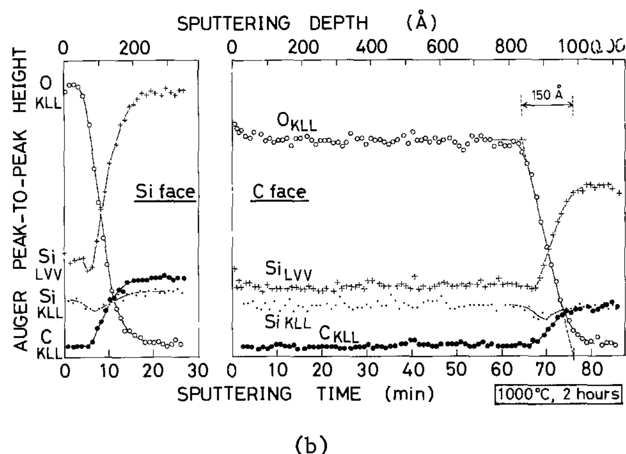

(b)

Fig. 1. (a) Auger spectra of SiC and the oxide layer (on the C face). (b) Depth-profiles of the oxide layers on the Si face and on the C face of SiC.

*Electrochemical Society Active Member

Key words: thermal oxidation, 6H-SiC, Auger electron analysis, depth-profile, ellipsometry.

Si_{KLL}, and C_{KLL}. The oxide layer also has two Si peaks, but the spectral form of Si_{LVV} is different from that of SiC, and the Si_{KLL} peak is located at about 9 eV lower energy than that of SiC. It should be noted that the oxide layer does not contain C atoms. The same spectra were obtained from the layers on the Si face of SiC and on the Si wafer. Therefore, these three oxide layers are concluded to be the same (SiO_2 by the reference (4)).

Fig. 1(b) shows depth-profiles of the oxide layers on the Si face and on the C face of SiC. The sputtering was done using an argon ion beam accelerated by 3 kV. The sputtering rate was about 15 Å/min. The vertical values are peak-to-peak heights of the Auger spectra. In the profile for the C face, O_{KLL}, Si_{LVV}, and Si_{KLL} are almost constant throughout the oxide layer. Since the output level of C_{KLL} in the oxide layer is the noise level of our detection system, the C_{KLL} output is zero in the oxide layer. In the interface region between the oxide layer and SiC, O_{KLL} decreases and C_{KLL} increases monotonically. Si_{KLL} shows a dip in the interface region. The interface width on the C face is 150 Å, which was determined by extrapolating the linear change of the O_{KLL} profile to the maximum value and the zero value as shown in Fig. 1(b). The oxide layer on the Si face is much thinner than that on the C face. But the depth-profile in the interface is very similar. The interface width on the Si face is 167 Å. The oxide layer on the Si wafer also showed a similar depth-profile with an interface width of 145 Å.

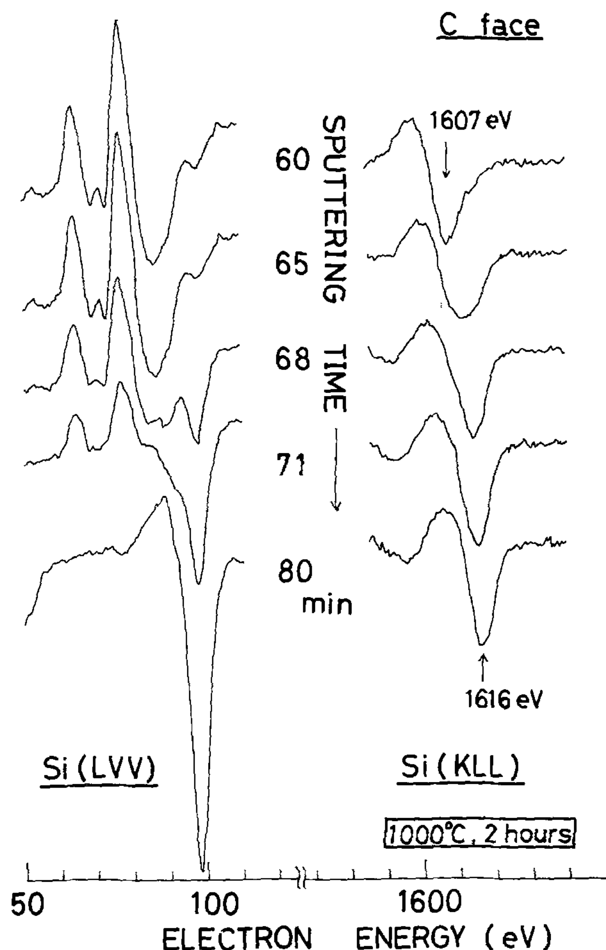

Fig. 2. Spectral change of the Si_{LVV} and the Si_{KLL} Auger peaks in the interface region between the oxide layer and SiC.

Fig. 2 shows the change of the Si_{LVV} and the Si_{KLL} peaks in the interface. The Si_{LVV} peaks change gradually from the oxide to SiC. In the Si_{KLL} peaks, the 1607 eV peak of the oxide decreases with sputtering times, and the 1616 eV peak of SiC appears and increases. At the sputtering time of 65 min, the Si_{KLL} peak is rather broad and the peak-to-peak height is small, owing to the overlapping of the two peaks. This appeared as a dip in the depth-profile in Fig. 1(b).

In conclusion, from the present Auger analysis, the thermal oxide layers of SiC were found to be the same as those grown on silicon.

ACKNOWLEDGEMENT

This work was partially supported by the Kudo Research Grant.

REFERENCES

1. R. B. Campbell and H. -C. Chang, "Semiconductors and Semimetals", Vol. 7, p. 625, Academic Press, New York (1971).
2. W. v. Münch and I. Pfaffeneder, This Journal, 122, 642 (1975).
3. W. v. Münch and P. Hoeck, Solid-State Electron., 21, 479 (1978).
4. J. S. Johannessen, W. E. Spicer, and Y. E. Strausser, Appl. Phys. Lett., 27, 452 (1975).

Manuscript submitted Aug. 2, 1978; revised manuscript received Aug. 28, 1978.

Publication costs of this article were assisted by Kyoto University.

Auger Electron Spectroscopy Analysis of Thermal Oxide Layers of Silicon Carbide

Akira Suzuki,* Hiroyuki Matsunami, and Tetsuro Tanaka

Department of Electronics, Faculty of Engineering, Kyoto University, Kyoto, 606 Japan

Silicon carbide (SiC) is a promising semiconductor material for various electronic devices because of its wide energy gap (1). SiC can be thermally oxidized in the same way as used for silicon (1, 2). The oxide layer is utilized as a protecting film for the SiC surface during the device fabrication (1, 3). However, the oxidation mechanism and the properties of the oxide layer have not been studied in detail. In this communication, some results of an Auger electron spectroscopy analysis of the thermal oxide layers will be described.

SiC crystals used for the thermal oxidation were 6H-type single crystals prepared by the Lely method. Each crystal was plate-shaped with wide (0001) faces. A typical size was 4x 4x0.5 mm^3. After polishing both the (0001) Si face and the $(000\bar{1})$ C face of each crystal with diamond paste, we set the crystals in a horizontal furnace with the (0001) faces vertical. Thermal oxidation was carried out at 1000°C for 2 hours in an oxygen flow of 100 cm^3/min. The oxygen flow was passed through pure water to saturate it with water vapor (at room temperature).

The oxide thicknesses determined by ellipsometry were 152 Å on the Si face and 908 Å on the C face. A (111) wafer of silicon was also oxidized at the same time for comparison. The oxide thickness on the Si wafer was 1949 Å. The refractive indices of the oxides on the C face of SiC and on the Si wafer were much the same: 1.45-1.46 by ellipsometry.

We carried out an Auger analysis of these oxide layers. Fig. 1(a) shows Auger electron spectra. The upper spectrum is from the SiC crystal, and the lower from its oxide layer on the C face. The accelerating voltage for the primary electron beam was 5 kV, and the beam current was 0.1 µA. The beam was made to scan the sample surface to remove an electron-irradiation effect. The scanned area was 50x 50 μm^2. SiC has three Auger peaks: Si_{LVV},

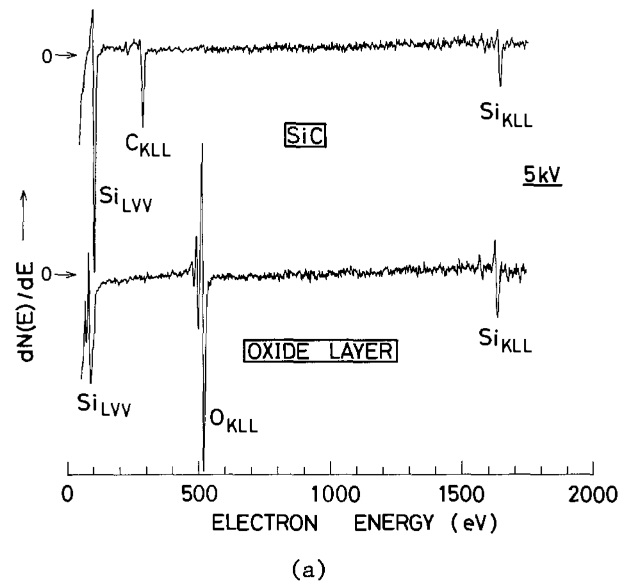

(a)

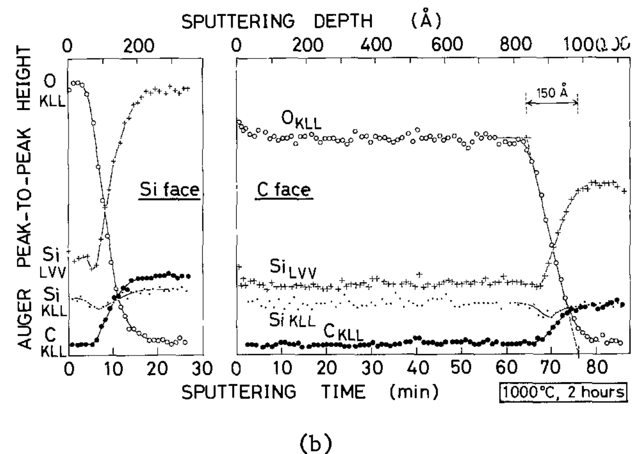

(b)

Fig. 1. (a) Auger spectra of SiC and the oxide layer (on the C face). (b) Depth-profiles of the oxide layers on the Si face and on the C face of SiC.

*Electrochemical Society Active Member

Key words: thermal oxidation, 6H-SiC, Auger electron analysis, depth-profile, ellipsometry.

Si_{KLL}, and C_{KLL}. The oxide layer also has two Si peaks, but the spectral form of Si_{LVV} is different from that of SiC, and the Si_{KLL} peak is located at about 9 eV lower energy than that of SiC. It should be noted that the oxide layer does not contain C atoms. The same spectra were obtained from the layers on the Si face of SiC and on the Si wafer. Therefore, these three oxide layers are concluded to be the same (SiO_2 by the reference (4)).

Fig. 1(b) shows depth-profiles of the oxide layers on the Si face and on the C face of SiC. The sputtering was done using an argon ion beam accelerated by 3 kV. The sputtering rate was about 15 Å/min. The vertical values are peak-to-peak heights of the Auger spectra. In the profile for the C face, O_{KLL}, Si_{LVV}, and Si_{KLL} are almost constant throughout the oxide layer. Since the output level of C_{KLL} in the oxide layer is the noise level of our detection system, the C_{KLL} output is zero in the oxide layer. In the interface region between the oxide layer and SiC, O_{KLL} decreases and C_{KLL} increases monotonically. Si_{KLL} shows a dip in the interface region. The interface width on the C face is 150 Å, which was determined by extrapolating the linear change of the O_{KLL} profile to the maximum value and the zero value as shown in Fig. 1(b). The oxide layer on the Si face is much thinner than that on the C face. But the depth-profile in the interface is very similar. The interface width on the Si face is 167 Å. The oxide layer on the Si wafer also showed a similar depth-profile with an interface width of 145 Å.

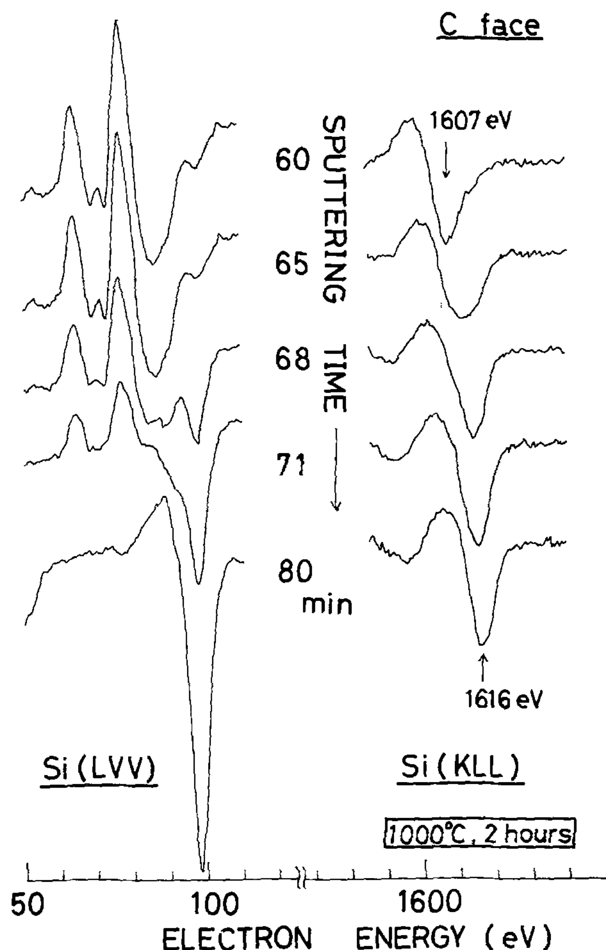

Fig. 2. Spectral change of the Si_{LVV} and the Si_{KLL} Auger peaks in the interface region between the oxide layer and SiC.

Fig. 2 shows the change of the Si_{LVV} and the Si_{KLL} peaks in the interface. The Si_{LVV} peaks change gradually from the oxide to SiC. In the Si_{KLL} peaks, the 1607 eV peak of the oxide decreases with sputtering times, and the 1616 eV peak of SiC appears and increases. At the sputtering time of 65 min, the Si_{KLL} peak is rather broad and the peak-to-peak height is small, owing to the overlapping of the two peaks. This appeared as a dip in the depth-profile in Fig. 1(b).

In conclusion, from the present Auger analysis, the thermal oxide layers of SiC were found to be the same as those grown on silicon.

ACKNOWLEDGEMENT

This work was partially supported by the Kudo Research Grant.

REFERENCES

1. R. B. Campbell and H. -C. Chang, "Semiconductors and Semimetals", Vol. 7, p. 625, Academic Press, New York (1971).
2. W. v. Münch and I. Pfaffeneder, This Journal, 122, 642 (1975).
3. W. v. Münch and P. Hoeck, Solid-State Electron., 21, 479 (1978).
4. J. S. Johannessen, W. E. Spicer, and Y. E. Strausser, Appl. Phys. Lett., 27, 452 (1975).

Manuscript submitted Aug. 2, 1978; revised manuscript received Aug. 28, 1978.

Publication costs of this article were assisted by Kyoto University.

JOURNAL OF THE ELECTROCHEMICAL SOCIETY

ELECTROCHEMICAL SCIENCE
AND TECHNOLOGY

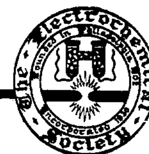

DECEMBER
1978

Properties of Trifluoromethanesulfonic Acid Monohydrate Pertinent to Its Use as a Fuel Cell Electrolyte

T. Sarada, R. D. Granata,* and R. T. Foley*
Department of Chemistry, The American University, Washington, D.C. 20016

ABSTRACT

The electrical conductivities of monohydrate-water mixtures were compared with those of sulfuric acid and phosphoric acid. All three systems show a maximum in the conductivity-composition curve with that of the monohydrate-water system falling at 40-45% of the monohydrate. Trifluoromethanesulfonic acid wets Teflon but water-monohydrate mixtures containing less than 60% of the monohydrate exhibit high contact angles with Teflon. The vapor pressure of the monohydrate was measured by an isopiestic method. A solution of 99.99% of the monohydrate is isopiestic with a solution of 96.83% H_3PO_4. Potential materials of construction for use in trifluoromethanesulfonic acid monohydrate and its water solutions were investigated. Corrosion tests, both stationary and under potential, showed that alloys such as ingot iron, chrome steel. Incoloy 825, tantalum-coated steel, and niobium offer considerable resistance to corrosion in the electrolyte. Certain composites such as pyrolytic graphite, silicon carbide, and boron carbide are chemically stable in the electrolyte.

Electrochemical experiments wherein trifluoromethanesulfonic acid monohydrate (TFMSA-MH) was employed as a fuel cell electrolyte showed that this compound offered several advantages over phosphoric acid which is commonly used as the electrolyte in the acid fuel cell. The rate of electrooxidation of hydrogen and propane was enhanced by an order of magnitude (1, 2) and the electroreduction of oxygen proceeded at a potential about 150 mV higher than that in phosphoric acid.

But the employment of an electrolyte in a practical fuel cell requires other characteristics. To maintain low ohmic losses the electrolyte should possess an electrical conductivity similar to that of sulfuric or phosphoric acid. In current fuel cell practice Teflon-bonded electrodes are employed, the Teflon, among its other properties, serves to waterproof the electrode. Thus an electrolyte that wets Teflon would require changes in the composition of the fuel cell electrode. For operation in the temperature range of 100°-150°C the electrolyte should have a reasonable vapor pressure, again comparable to concentrated phosphoric acid solutions. Finally, the electrolyte should be noncorrosive to conventional materials of construction in the static sense and also when tested under applied voltages to which the fuel cell anode and cathode would be subjected.

These are the problems considered in the present investigation, the over-all objective being the evaluation of trifluoromethanesulfonic acid monohydrate as a fuel cell electrolyte.

* Electrochemical Society Active Member.

Key words: trifluoromethanesulfonic acid monohydrate, fuel cell, acid fuel cell, electrolyte.

Experimental and Results

The electrolyte.—Trifluoromethanesulfonic acid monohydrate was prepared from trifluoromethanesulfonic acid (3M Corporation, fluorochemical acid FC-24) and water by the method of Gramstad and Haszeldine (3). This involved refluxing equimolar quantities of the acid and water and fractionally distilling. The monohydrate distills over at 217°-218°C (756.9 mm Hg). The white needlelike crystalline product melts at 33.8°C in agreement with the literature (3).

Conductivity measurements.—Conductivity measurements were made on the freshly distilled monohydrate and its aqueous solutions using a Type RC-16B2 conductivity bridge made by Industrial Instruments of New Jersey. Constant temperatures of 40° and 80°C (±0.5°) were maintained during this work with a thermostated water bath (Forma Scientific, Model 2095-2). The cell constants for the conductivity cell at the two temperatures were determined using a centinormal solution of potassium choride.

The specific conductances of water solutions of trifluoromethanesulfonic acid monohydrate at 40°C are plotted in Fig. 1. Also plotted, for comparison, are the conductances of sulfuric acid-water solutions and phosphoric acid-water solutions, sulfuric acid being a widely accepted electrolyte for battery systems and phosphoric acid being considered the most suitable electrolyte for acid fuel cells. The values for sulfuric acid were computed to 40°C from data given in Landolt and Börnstein (4) and for 80°C computed graphically from the data of Haase *et al.* (5). The values for phosphoric acid were obtained from a Monsanto publication (6). The conductivities of several solutions of

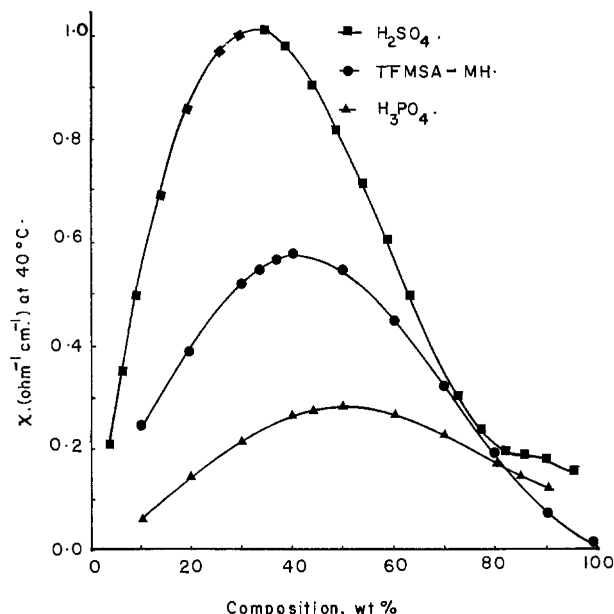

Fig. 1. Conductivities of acid-water solutions at 40°C. —■— H_2SO_4, —●— TFMSA-MH, —▲— H_3PO_4. Sulfuric acid data from Ref. (4), phosphoric from Ref. (6).

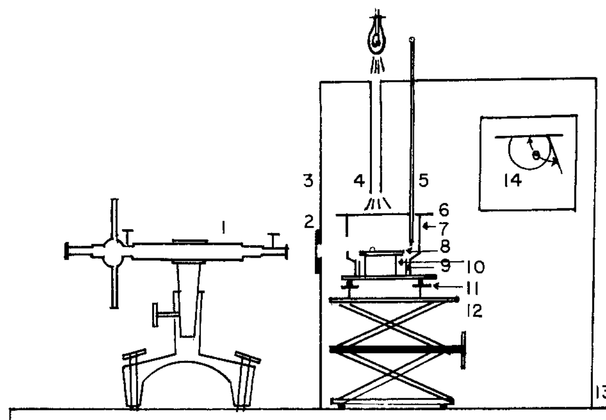

Fig. 2. Experimental setup for the measurement of contact angles. 1, Goniometer telescope; 2, fused silica window; 3, thermostated chamber; 4, light tube; 5, thermometer; 6, glass plate; 7, Teflon shield; 8, test specimen; 9, petri dish; 10, glass platform; 11, leveling table; 12, adjustable support; 13, marble slab; 14, view of the drop profile as observed in the goniometer telescope.

phosphoric acid were checked at random and were found to agree with the literature values. The three systems are all characterized by a composition of maximum conductivity. In the monohydrate system at 40°C the maximum (0.575 Ω^{-1} cm^{-1}) falls at 41% by weight (of the monohydrate) and 30% by volume; at 80°C the maximum (0.8109 Ω^{-1} cm^{-1}) falls in the range of 40-45% by weight.

Contact angle and wetting.—It is common practice in many fuel cell designs to use Teflon-bonded catalytic electrodes to prevent "flooding" of the electrode by the electrolyte. The Teflon serves to maintain a nonwetted surface and makes it possible for the electrode to furnish a solid-liquid-gas interface for the site of the electrocatalytic reaction. In one of the first attempts (7) to build a complete fuel cell with the trifluoromethanesulfonic acid monohydrate electrolyte it it was observed that the electrolyte wet Teflon, rendering that particular electrode essentially inoperative. Thus, the critical problem regarding the tendency of Teflon to be wetted by the compound arose. The wetting problem is here examined quantitatively, not only with respect to the monohydrate, but also with respect to water solutions of the monohydrate in order to establish the extent of dilution of the monohydrate required to achieve a nonwetting surface. The extent of wetting is measured by the contact angle which the liquid makes with the solid. The contact angle of a drop of liquid is defined as the angle which the tangent to the drop makes with the horizontal surface of the substrate at the point where the liquid, the substrate, and the vapor meet. The angle is measured through the drop as shown in the insert in Fig. 2. The basic mechanism of wetting involves more than the contact angle, but the latter gives a valuable inverse measurement of the wetting or spreading property of a liquid on a surface. For contact angles greater than 90°, the liquid is said not to wet the solid and in such a case the drops of liquid do not enter the capillary pores of the solid. At the same time, a liquid is considered to wet the solid only when the contact angle is 0. This is a limiting extreme only in a geometric sense.

Method.—A goniometer telescope was used in making contact angle measurements of the test solutions on Teflon. This instrument gives an inverted, enlarged, high contrast image of the drop profile. The contact angle measurements were made in the vapor of the test solutions. This method solved the problem of choosing between the various types of values used in the literature, *i.e.*, the advancing angle, the receding angle, or the equilibrium angle.

In contact angle measurements, special care is needed in getting a smooth, clean surface of the solid sample. A nonsmooth surface increases spreading and, so, will alter the angle.

The method of Fox and Zisman (8) which involves the application of heat and pressure to the Teflon sample was used to ensure a smooth surface.

Aqueous solutions of trifluoromethanesulfonic acid or monohydrate were made by transferring calculated volumes of the acid or monohydrate from a burette into calculated volumes of deionized water kept in ice-cooled volumetric flasks.

An atmosphere of the vapor of the test solution was insured by the following procedure. A Pyrex petri dish, 5 cm diam, was half filled with the test solution. This was surrounded by a cylindrical Teflon shield which had an open window, 1.25 cm high and 0.64 cm wide. The size of the window allowed two or three drops to be viewed by the telescope without disturbing the specimen. The solid specimen was placed in the dish on top of an optically flat platform of glass so that the top surface would not be flooded by the liquid. The drops were placed on the Teflon surface by the tip of a freshly flamed platinum wire used along with a disposable glass pipette. The average diameter of a drop was about 1 mm. The top of the shield was closed by a glass plate to permit illumination of the drops from above. The setup was mounted on a circular leveling table which, in turn, was placed on a laboratory jack. The assembly was placed inside a thermally regulated chamber. Outside lighting, by a tungsten filament lamp, was guided to the specimen by means of a Pyrex glass tube. A fused silica window on the side panel of the chamber permitted viewing of the drops by the goniometer telescope kept outside the chamber. A thermometer was used to record the temperature. Both the chamber and the telescope were placed on a heavy marble slab to eliminate vibration. Figure 2 shows a diagrammatic sketch of the experimental setup.

Stringent conditions of temperature control are not necessary for these measurements as the temperature coeffiicent of contact angle is very small. Therefore, room temperature measurements were made without thermostated equipment. For higher temperature studies a temperature control was used which had a limit of accuracy of ± 1°C.

For each sessile drop, two values of the angle were taken on either side of the drop. For each sample three

or four drops were studied and the six or eight values were averaged. The maximum deviation from the average was about ±2°, which is the acknowledged limit of accuracy for these measurements.

Results of contact angle measurements.—The results of the contact angle measurements for trifluoromethanesulfonic acid-water mixtures are plotted in Fig. 3. Similar measurements for monohydrate-water mixtures are plotted in Fig. 4. In a comparative sense the acid wets Teflon more readily than the monohydrate, *i.e.*, the contact angle is below 30° as against 73° at room temperature. Acid-water mixtures below acid concentration of 55% weight and monohydrate-water mixtures of 60 weight percent (w/o) or less of the monohydrate can be considered as nonwetting (contact angles greater than 90°). It is interesting to note that a 90% acid mixture presents a contact angle of 56° when freshly made which increases to 72° when the solution is aged. The latter value approaches that of 100% monohydrate which is 73°, the composition of the monohydrate is 89.3% acid. As the solutions become more dilute the contact angles of both the solutions increase with the single exception of 70% monohydrate which exhibits an angle of 80°, lower than the

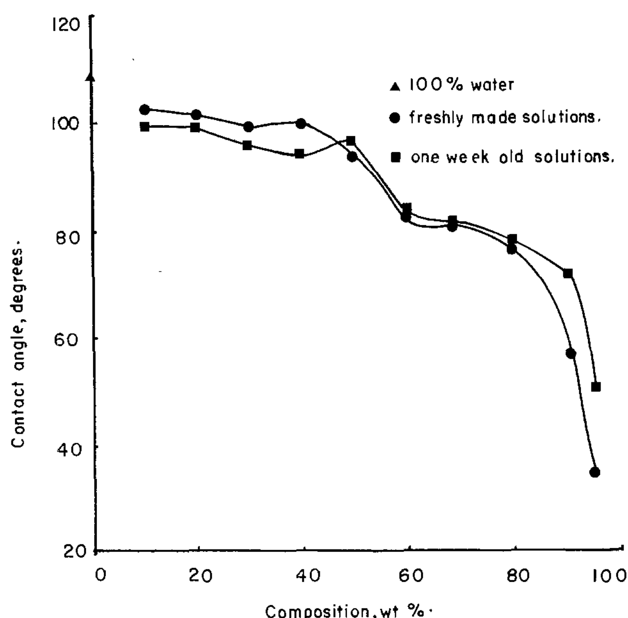

Fig. 3. Contact angles on Teflon of trifluoromethanesulfonic acid-water solutions. ● Freshly made solutions, ■ one-week old solutions.

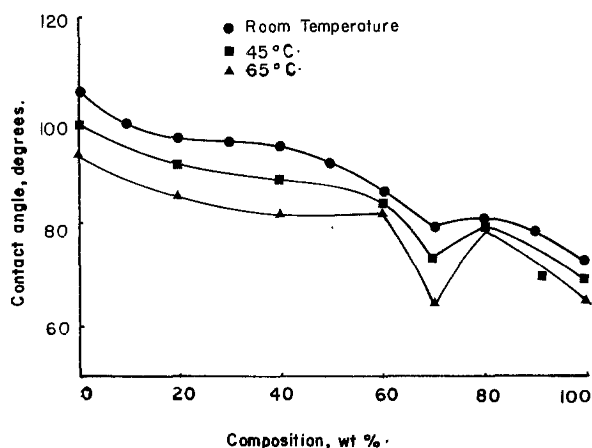

Fig. 4. Contact angles on Teflon of trifluoromethanesulfonic acid monohydrate solutions. ● Room temperature (*ca.* 24°C), ■ 45°C, ▲ 65°C.

values for both 80 and 60% solutions, which are 82° and 87°, all measured at room temperature.

The temperature dependence of monohydrate-water mixtures is very little, as one would anticipate, and mixtures of different compositions show slightly different slopes, again the 70% solution has a sharper decline in the angle when the temperature increases.

Vapor pressure measurements.—Method.—The isopiestic method (9) of measuring the vapor pressure of strong electrolytes was selected for gathering the vapor pressure data of monohydrate solutions. This method employs a comparative technique based on the principle that two solutions of nonvolatile solutes will distill, one to the other, until their concentrations are such that the solutions have equal vapor pressure. At the temperatures chosen for study, monohydrate solutions lose only water as does the "reference" electrolyte, phosphoric acid. Well-documented values are available for the water activities of phosphoric acid solutions of various concentrations over a wide range of temperature (10, 11). Preliminary experiments with known solutions of sodium chloride or ammonium chloride, using sulfuric acid solution as the standard, were made to check the method. The principle of the method is based on the comparison of the vapor pressure of two solutions. Two solutions, A and B, at the same temperature initially, are kept inside a closed system. The solution which has a greater vapor pressure, say solution A, loses water, which condenses on B, resulting in a cooling of A and a heating of B from the heat of vaporization generated. This temperature change will also produce a change in the vapor pressures of the solutions besides the concentration changes, but, if perfect thermal contact is established between the two solutions the distillation of solvent will continue and equalization of vapor pressure will still take place, only in this case, the equalization will be the result of concentration change alone and not temperature difference. Equilibrium will occur, therefore, when this concentration difference is sufficient to equalize the vapor pressures. In the actual experimental measurements, therefore, thermal conductivity between the test solution and the reference solution is of primary importance. A system closed to the outside atmosphere is essential. The equilibration process can take anywhere between one day to one week. The concentration changes are easily determined by the change in the weights of the solutions before and after equilibration. Two sets of solutions are used at a time in a thermostated closed chamber with adequate thermal contact between the solutions. Four Pyrex bottles, two of them containing a small known amount of phosphoric acid of known concentration and two of them containing the test solutions of known concentration are used in each experiment. The bottles fit snugly inside aluminum cylinders which are placed inside an aluminum chamber. The chamber is fitted with a Teflon gasket to keep it airtight. It carries a device by which the individual bottles can be opened or closed without opening the chamber. A schematic of the setup is shown in Fig. 5. This setup is placed inside a thermostated vacuum oven (with temperature control ± 0.5°C) with an airtight door and left undisturbed over a period of one day to several days. The weight change in each case is determined after the bottles are desiccator cooled. From the plots of known vapor pressures of water above phosphoric acid of known concentrations and temperatures, the values for the unknown are read out.

Three concentrations of phosphoric acid, 96.83, 95.3, and 90.87 w/o solutions were found to be isopiestic with TFMSA-MH, 99.99, 93.38, and 92.59%, respectively. The vapor pressure of phosphoric acid of the said concentrations should therefore give the total vapor pressure of the monohydrate solutions of these concentrations. Log P plots of these against 1000/$T°K^{-1}$ are shown in Fig. 6. The plot of 96.83% H_3PO_4,

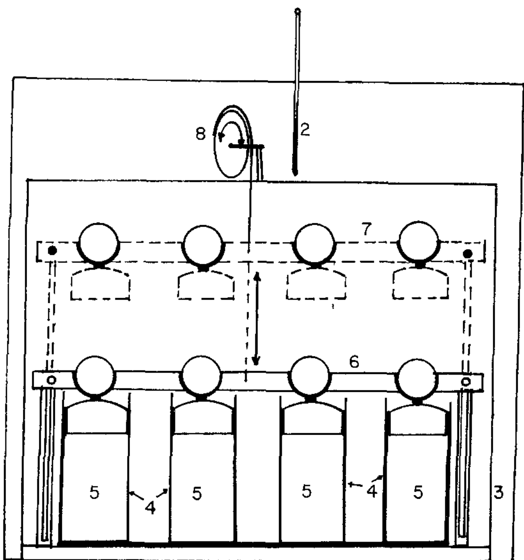

Fig. 5. A schematic of the isopiestic vapor pressure cell. 1, Thermostated oven; 2, thermometer; 3, aluminum chamber; 4, aluminum cylinders; 5, Pyrex bottles; 6, lids, closed position; 7, lids, open position; 8, pulley for raising and lowering the lids arm.

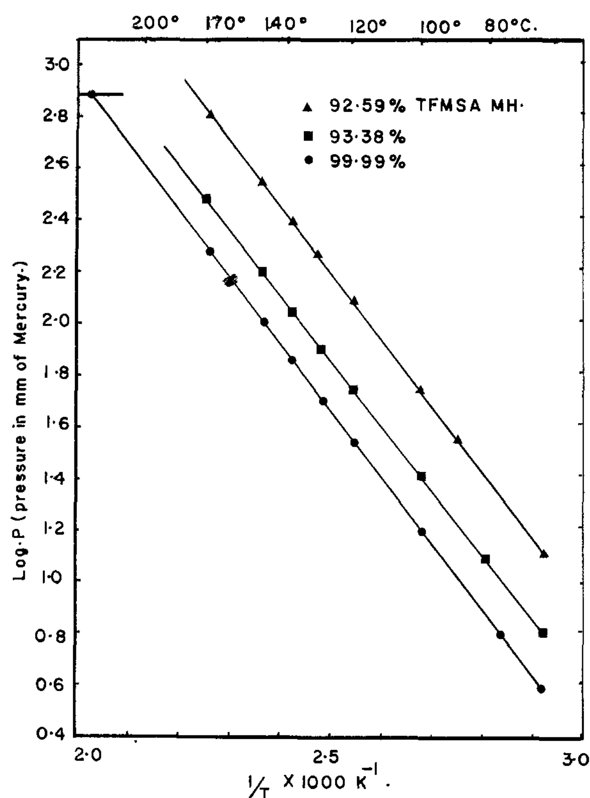

Fig. 6. Vapor pressure of trifluoromethanesulfonic acid monohydrate as a function of temperature.

isopiestic with 99.99% MH on extrapolation to 760 mm gives a temperature value of 219.6°C. The experimental boiling point of the monohydrate is 218°-219°C. The vapor pressures given by this plot can, therefore, be taken as a fair estimate of the vapor pressure of 99.99% MH. Calculation of $\Delta \overline{S}$ vapor (12) from these plots gives a Trouton constant of 23.93 cal $°K^{-1}$ $mole^{-1}$. For water the constant is 26.049, for sulfuric acid it is 20.00, and for methanol 25.00 in the same unit. The calculated value for trifluoromethanesulfonic acid monohydrate from this point is, therefore, in the range expected.

Static corrosion tests.—The objective here was to collect quantitative data on the corrosion of a number of materials, both metallic and nonmetallic, that could potentially serve as construction materials for the fuel cell container, electrodes, or matrices. Some preliminary observations had been made that suggested the monohydrate was less corrosive to the conventional alloys, such as stainless steel Type 304, than phosphoric acid. However, there was virtually no data available in the literature that would relate to elevated temperature (100°C and above) behavior. Thus, measurements were made on a number of metals and alloys that were suggested from their known corrosion behavior in other environments.

Method.—The extent of corrosion suffered by a given sample on total immersion in liquid was determined as the loss in weight. Two temperatures, 100° and 125°C, were chosen and the period of immersion varied from one to eight weeks. Three samples were usually used for each measurement. Weighed and pretreated samples were totally immersed in approximately 20 ml aliquots of the freshly distilled monohydrate or 85% phosphoric acid (Fisher A.C.S. Certified) for a given period of time and left undisturbed. The samples were held in Pyrex test tubes loosely closed with Teflon stoppers. The test tubes were held in a stainless steel rack and maintained at a constant temperature over the period of study.

Materials and Treatment.—The compositions of the metals and alloys used in the tests are given in Table I. Certain composite materials tested as possible matrix materials are listed in Table II. The sample preparation and evaluation followed standard procedures.

Results and discussion.—A preliminary test which measured the corrosion of five metals was run for a two week duration at 100°C. Copper and lead corroded

Table I. Composition of alloys used in corrosion tests

Alloy	Nominal composition (w/o)
Aluminum	99.994
Silver	99.9
Copper	Ficher C · 428 (purified)
Lead	99.9
Platinum	99.99
Titanium (electrolyte)	99.99
Porous nickel	Ni electrode (Union Carbide)
Ingot Iron HP	99.80 Fe, 0.13 Cu, 0.04 Ni, 0.01 Mo, 0.01 Si
Niobium	99.9
AISI Type 304	18.0-20 Cr; 8.0-11.0 Ni; 0.30 C, max; 2.0 Mn, max; 1.00 Si, max; 0.045 P, max; 0.03 S, max; balance Fe
Incoloy 825	42 Ni, 21 Cr, 3.0 Mo, 33 Fe
Hastelloy C	56 Ni, 15 Cr, 3.7 N, 16 Mo, balance Fe
Carpenter 20 Cb-3	34.03 Ni, 19.91 Cr, 2.25 Mo, 3.30 Cu, 0.21 Co, 0.86 Cb, 0.039 C, 0.39 Mn, 0.41 Si, 0.016 P, balance Fe
26-1 Steel E-Brite	26 Cr, 1 Mo, 73 Fe
Titanium (65·A)	C, 0.08, max; N, 0.05, max; H, 0.015, max; Fe, 0.25, max
Tantalum coated steel	Steel plated with tantalum by the "Metalating" process by the General Metals Technologies Corp. Thickness, 0.006-0.008 in.
Chrome steel 430	82.3 Fe, 16.4 Cr, 0.52 Si, 0.40 Mn, 0.26 Ni, 0.058 C, 0.004 S

Table II. Composite materials tested as matrix materials

1. Pyro-Tech, PT 101 (Ultra Carbon Corp.) pyrolytic graphite plated onto graphite, density of coating, 2.2 g cm^{-3}.
2. Pyro-Tech, PT 333 (Ultra Carbon Corp.) graphite treated to produce a silicon carbide coating 0.5 mm thick.
3. Pyro-Bond, 1300 (Ultra Carbon Corp.) graphite coated with silicon carbide by a conversion process.
3. Pyro-Bond, 1300 F (Ultra Carbon Corp.) graphite with surface converted to silicon carbide with a low temperature process; more graphite than 1300.
5. Reaction bonded silicon nitride, NC 350 (Norton Co.) density *ca.* 2.5 g cm^{-3}.
6. Boron carbide (Norton Co.) "Norbide" *ca.* 99% pure, density 2.51 g cm^{-3}, hot pressed, grain size 10-20 μ.
7. Recrystallized silicon carbide (Norton Co.) "Crystar" 99% silicon carbide, density 2.65 g cm^{-3}.

excessively and were dropped from subsequent tests. Iron, stainless steel, and silver offered substantial corrosion resistance and were included in a second series of tests at 125°C extending over five weeks. This series disclosed the outstanding resistance to corrosion afforded by ingot iron, being more resistant than stainless steel. Silver corroded excessively.

A third series of tests included a number of alloys usually ranked as corrosion resistant materials. These are reported in Fig. 7. Niobium- and tantalum-coated steel are remarkably resistant. While both electrolytic titanium and hardened titanium 65A were seriously corroded, ingot iron seemed to develop a passive layer and was consistently resistant to the action of the monohydrate, even in the eight-week study. Aluminum behaved very much like stainless steel Type 304, *i.e.*, it seemed to have both active and passive forms. Some of the more resistant alloys were tested over an eight-week period (Fig. 8). Usually samples of Type 304 stainless steel were included in the tests as a comparative material. This alloy has been studied in previous investigations and a reasonable amount of data are available on the performance of this alloy in phosphoric acid electrolytes. Porous nickel which has been used as a material of construction for gas diffusion electrodes, shows a high degree of resistance. E-brite 26-1, a martensitic steel, is more resistant than the 300 series alloys.

Comparative tests were conducted in 85% phosphoric acid at 125°C for one week. These data are presented as bar graphs in Fig. 9. At the end of one week the corrosion was so extensive that the test was not continued beyond that time.

The refractory materials, silicon carbide, boron carbide, and pyrolytic graphite, showed essentially no weight losses during a five-week exposure. Instead, the porous materials absorbed electrolyte so that in most cases there was actually a gain in weight during the test. The phosphazene polymeric materials, on the other hand, dissolved completely in 24 hr. The quantitative data for the refractory materials are given in Table III. It is possible that prolonged treatment would remove any absorbed solution but it can be stated that there was no deterioration of the material during the five-week exposure at 125°C.

Voltage sweep experiments.—Whereas the static corrosion tests reported above allow the assessment of

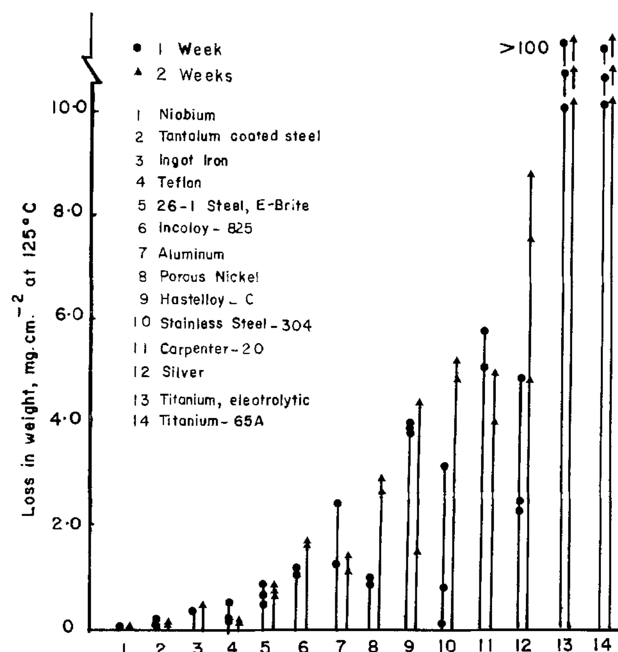

Fig. 7. Corrosion tests of metals and alloys in trifluoromethanesulfonic acid monohydrate. Temperature, 125°C. ● Loss in weight in 1 week, ▲ loss in weight in 2 weeks.

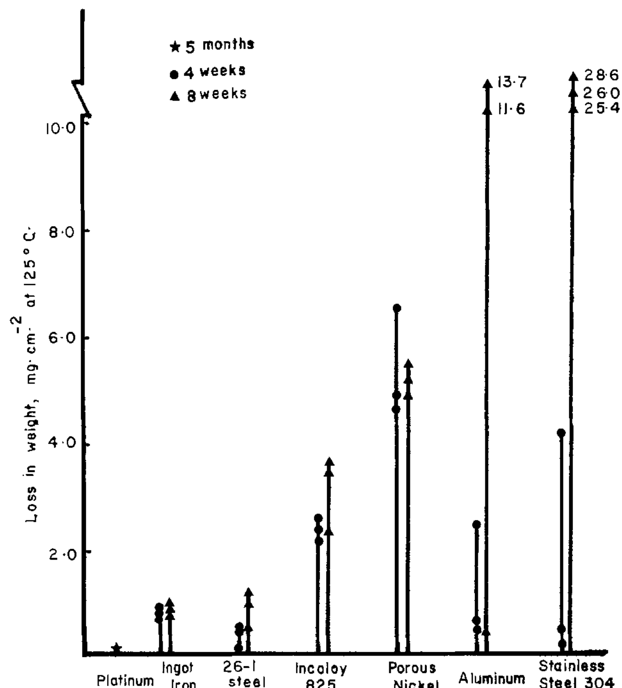

Fig. 8. Corrosion tests in trifluoromethanesulfonic acid monohydrate of some resistant materials. Temperature, 125°C. ● Loss in weight in 4 weeks, ▲ loss in weight in 8 weeks, ★ loss in weight in 5 months.

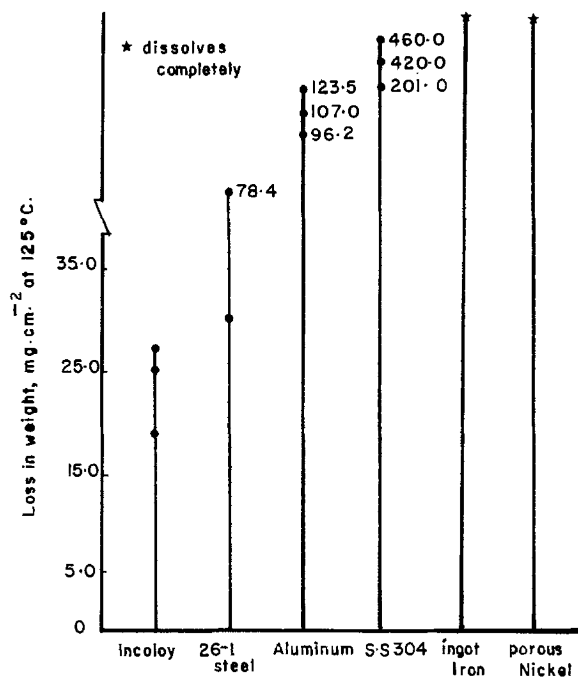

Fig. 9. Corrosion tests in 85% phosphoric acid. Duration, 1 week. Temperature, 125°C.

each metal or alloy with respect to its resistance to attack by the electrolyte when used as a general material of construction, it is also important to know the behavior of these materials when used as electrode substrates which would see oxidizing and reducing potentials. To evaluate the behavior of the alloys under potential, a voltage sweep technique was used.

Method.—The cell used for the experiments was a three-compartment cell, with an approximate electrolyte requirement of 65 ml. The working electrode in the central compartment of the cell was either a platinum wire sealed into 6.4 mm glass tubing or a metal wire press fitted into a 6.4 mm diam Teflon rod, either

Table III. Corrosion data for some composite materials and chrome steel Type 430 in TFMSA-MH at 125°C for 5 weeks

Material	Change in weight (mg cm^{-2}) (average 3 samples)
Chrome steel (Type 430)	−23.1
Pyro-Tech, PT 101	+55.4
Pyro-Tech, PT 333	+0.89
Pyro-Bond, 1300	+5.72
Pyro-Bond 1300 F	+5.17
Reaction bonded silicon nitride	+21.5
Boron carbide	−0.61
Recrystallized silicon carbide	−1.33

of which was connected into the cell by means of a Swagelok fitting made of Teflon. The counterelectrode compartment was separated from the working electrode compartment by a fritted glass disk. The counterelectrode was a platinum mesh cylinder, spot welded to a platinum wire. The reference electrode system was separated from the working electrode compartment by sealing a fritted glass disk behind the Luggin capillary. The reference electrode was of the dynamic hydrogen electrode design of Giner (13). Temperature control was achieved by maintaining the cell in a thermostated air oven. The electrolyte for the cell was pure trifluoromethanesulfonic acid monohydrate.

The working and reference electrode compartments were purged with argon for at least 1 hr prior to beginning a cyclic voltammogram. To ensure complete removal of oxygen, the argon was passed through a stainless steel pipe heated to 400°C containing shredded copper foil. Purging of the cell with oxygen-free argon was continued throughout the experiment except where otherwise noted. Electrode potentials were measured with a Keithley Instruments Model 621 electrometer. Potentiostatic and chart recording apparatus were combined in the Beckman Electroscan 30 electroanalytical system.

Cyclic voltammograms were recorded in the following manner: The cell was allowed sufficient time to achieve thermal equilibrium, to be purged of dissolved oxygen by argon bubbling, and for the working electrode to reach a constant rest potential. The rest potential was recorded (Table IV). The polarization was usually started from approximately rest potential and proceeded initially in the anodic direction. The current measuring range was chosen to be approximately 70-200 $\mu A/cm^2$ in both the anodic and cathodic directions. The working electrode surface areas were on the order of 0.5 cm^2. For the first cyclic voltammograms of a sample, the current scale was chosen so that the low current density behavior could be observed before any gross changes in the surface occurred due to dissolution or film growth. The voltammetric scan was continued in the anodic direction until the current had sufficiently increased anodically (up to 1.5-2.0V). The scan direction was reversed (a manual operation) and the scan continued to at least 0.0V, at which point the scan direction was again reversed. Scan direction reversal was continued in this manner until three consecutive cycles were completed within the same voltage or current limits. The scan rates were between 5×10^{-3} and 5×10^{-2} V/sec, the latter rate being used for rapid initial evaluation of a sample's cyclic voltammetric behavior to avoid excessive sample dissolution due to long electrolysis times. The experiments were run at a temperature of about 120°C which approximates the operating temperature range of a fuel cell in this electrolyte.

Table IV. Rest potentials of various electrodes in trifluoromethanesulfonic acid monohydrate

Sample	Potential (mV, DHE)	Temperature (°C)
Platinum	280	115
Niobium	280	117
Chrome Steel 26-1	270	119
Chrome Steel 430	250	119
Incoloy 825	230	118
Hastelloy C	0	118
Carpenter 20	−40	117
Silver	−70	119
Copper	−120	119
Stainless Steel 304 L	−130	112
Nichrome	−140	119
Ingot iron	−280	119
Aluminum	−460	119
Titanium	−570	119
Lead	−640	119

Figure 10 shows the cyclic voltammogram for platinum at 115°C. The scan is started at about 0 mV, swept anodically to 1500 mV, then cathodically from 1500 to 0 mV. During the anodic scan, platinum exhibits two anodic current peaks, one at 700 mV, the other at 1050 mV. These peaks are due to oxidation of the platinum metal surface to platinum oxide. On the cathodic scan, a single peak is observed at about 750 mV which corresponds to reduction of the platinum oxide. This behavior is in close agreement with the aqueous solution investigations of Kolthoff and Tanaka (14), the references cited therein, and Gilman (15).

Stainless steel Type 304, at 112°C, gives the cyclic voltammogram shown in Fig. 11. The anodic scan shows a somewhat constant anodic current from 0 to 1000 mV after which the current increases rapidly with increasing anodic potential. The current decreases rapidly to nearly zero on the cathodic scan, remaining near zero until 150 mV where the current increases up to commencement of hydrogen reduc-

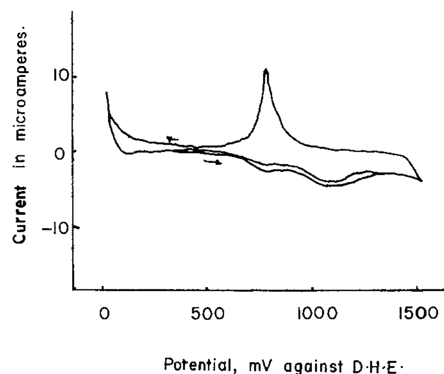

Fig. 10. Cyclic voltammetry of platinum in trifluoromethanesulfonic acid monohydrate. Temperature, 115°C; sweep rate, 25 mV/sec; equilibrium potential, −280 mV; surface area, 0.124 cm^2.

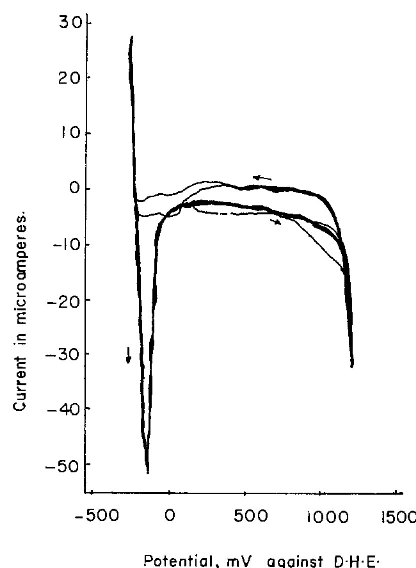

Fig. 11. Cyclic voltammogram of stainless steel 304 in trifluoromethanesulfonic acid monohydrate. Temperature, 112°C; sweep rate, 5 mV/sec, equilibrium potential, −130 mV; surface area, 0.106 cm^2.

tion. On the following anodic scan, a large anodic current is observed at −150 mV and is probably due to desorption of hydrogen or activation of the surface by the hydrogen previously evolved. The anodic current plateau between 0.0 and 1000 mV is low and may be interpreted as residual current and a low sample dissolution rate. Sample dissolution is much more rapid at higher potentials. On the cathodic scan, the current decreases to nearly zero and, considering the later increase in current at 150 mV, these currents may correspond to a passivated state and a loss of the passivated state, respectively. There are no trends pertaining to consecutive scans in these cyclic voltammograms.

The cyclic voltammogram of niobium at 118°C is shown in Fig. 12. The first anodic scan starts at 330 mV. The anodic current increases to a small steady value until a potential of about 1000 mV is reached and the current begins to gradually increase again. The scan is reversed at 2000 mV and the current decreases to zero at 600 mV, where a cathodic current gradually increases up to 0.0 mV. At 0.0 mV, the scan is changed to anodic and the current decreases. The cycle is repeated twice except that the maximum anodic current is reduced on each successive scan. The anodic currents are interpreted as due to surface oxidation of the niobium plus oxidation of the electrolyte, while the cathodic currents are probably due to the reduction of the surface oxides. The trend of decreasing anodic current suggests the buildup of a passivating film. The magnitude of the cathodic currents indicates that there is an adherent reducible film on the electrode.

At the other extreme of reactivity we have one of the very active metals. In Fig. 13 is presented a scan of electrolytic titanium. This again is a fast scan, 50 mV/sec at 119°C. As the potential is increased anodically the current increases rapidly from the beginning with subsequent scans showing a decreased anodic current at the same potentials. The unusual feature seen is the absence of appreciable cathodic currents up to −500 mV. Another feature observed was that the rest potential after the experiment was 50 mV more cathodic than the value before the polarization. This could represent a change in the surface toward a more active species than the start.

The current densities for fourteen materials tested under potential in TFMSA-MH are plotted for specific potentials in Fig. 14. The data were taken from the voltage sweep plot, usually with a rate of 50 mV/sec. The apparent geometric areas were used for the calculation of current densities. The plots of log current density *vs.* potential for each of the materials summarize and compare the general behaviors of these materials under potential. Generally, combinations of high potential and low current density values indicate relative stability of the material at applied potentials in this electrolyte. Using the potential axis (ordinate) of the figure as a horizontal boundary, the

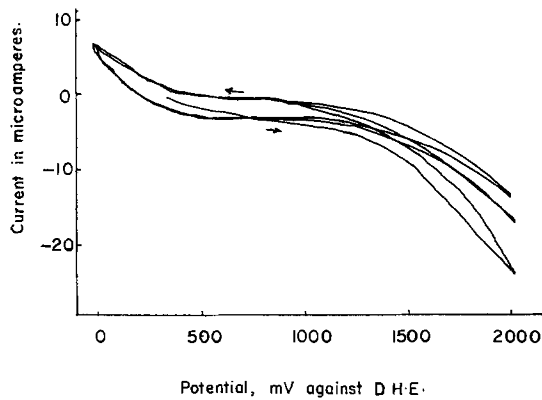

Fig. 12. Cyclic voltammogram of niobium in trifluoromethanesulfonic acid monohydrate. Temperature, 118°C; sweep rate, 50 mV/sec; equilibrium potential, 280 mV; surface area, 0.323 cm².

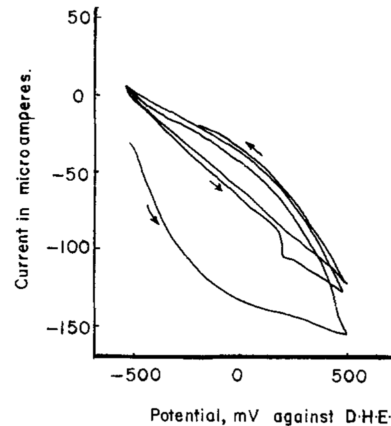

Fig. 13. Cyclic voltammogram of titanium in trifluoromethanesulfonic acid monohydrate. Temperature, 119°C; sweep rate, 50 mV/sec; equilibrium potential, −570 mV; surface area, 0.258 cm².

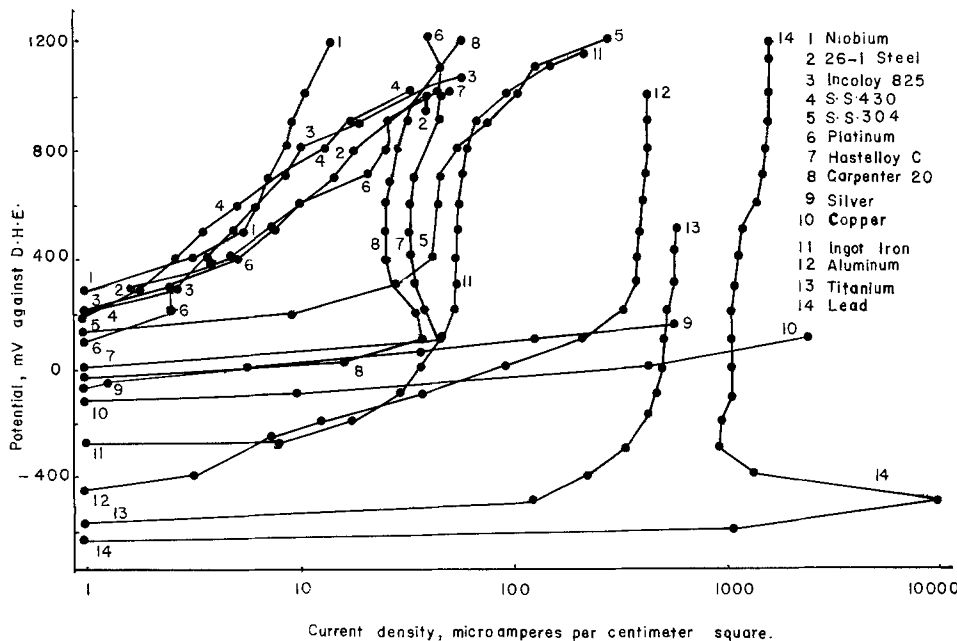

Fig. 14. Comparative plot of potentials vs. logarithm of current density for 14 alloys.

areas under these curves can be considered as figures of merit for these materials. Niobium has the smallest such area and can be considered the most stable material tested. Similarly niobium, chrome steel 430, Incoloy 825, chrome steel 26-1, and platinum are the five most stable materials tested.

Of these materials, Incoloy 825 shows the smallest reduction currents during cyclic voltammetry which shows that it has the highest anodic to cathodic current-time product (coulombs) ratio. This indicates that Incoloy 825 has the greatest net dissolution rate of these five materials under these conditions. Immersion test results given above show that Incoloy 825 has a corrosion rate 1.7 times greater than chrome steel 26-1 for an eight-week period at 125°C. For these reasons, Incoloy 825 should not be considered to be as stable as the other four materials in the group.

Immersion test results for chrome steel 430 show a corrosion rate much higher than Incoloy 825. Hence, this material should also not be considered as stable as niobium, platinum, or chrome steel 26-1. Note that the polarization curves for chrome steel 430, as well as Incoloy 825, were derived from a potential-current cycle after the initial cycle in which larger currents were observed. This had the effect of shifting their polarization curves toward more stable regions. While Incoloy 825 and chrome steel 430 would not be suitably stable at equilibrium, they should be relatively stable while anodically polarized. Hence, based on polarization tests and immersion tests, the most stable materials tested under potential are niobium, platinum, and chrome steel 26-1.

Conclusions

The corrosion investigation has disclosed a number of construction materials that would be resistant to corrosion in trifluoromethanesulfonic acid monohydrate. The corrosion rates of most materials are one or two orders of magnitude less than that in phosphoric acid. The exceptional resistance of ingot iron to attack is surprising but, in general, the nickel-containing alloys such as stainless steel Type 304 are not particularly resistant. Certain refractory materials, such as pyrolytic graphite, silicon carbide, and boron carbide, would be suitable for electrode or matrix applications assuming that they could be made available in the proper form. Several alloys show resistance to corrosion under oxidizing and reducing conditions as demonstrated by the voltage sweep technique.

Contact angle measurements confirm the qualitative observation that Teflon is wet by both the monohydrate and the acid. The wetting tendency is decreased in both cases by an increase in water content in the monohydrate or acid-water mixture. It is estimated that it is possible to retain about 60% of the monohydrate and still have a fairly high contact angle (nonwetting). The addition of water to the monohydrate definitely improves the electrical conductivity of the electrolyte following the pattern of the sulfuric acid and phosphoric acid systems. The maximum conductivity is at about 40-45% by weight of the acid, approximately the composition of the maximum conductivity in the phosphoric acid system, but the conductivity in the monohydrate system is appreciably higher.

Vapor pressure measurements indicate that the vapor pressure of the monohydrate is such as to make feasible the operation of a fuel cell in the 125°-150°C range. Dilution of the monohydrate with water increases the vapor pressure as expected.

Acknowledgments

This research was supported by the U.S. Department of Energy under contract EY-76-S-02-2879. The authors are also pleased to acknowledge valuable discussions with Dr. A. A. Adams of the U.S. Army Mobility Equipment Research and Development Command, Fort Belvoir, Virginia.

Manuscript submitted March 22, 1978; revised manuscript received Aug. 1, 1978.

Any discussion of this paper will appear in a Discussion Section to be published in the June 1979 JOURNAL. All discussions for the June 1979 Discussion Section should be submitted by Feb. 1, 1979.

Publication costs of this article were assisted by The American University.

REFERENCES

1. A. A. Adams and H. J. Barger, *This Journal*, **121**, 987 (1974).
2. A. A. Adams, R. T. Foley, and H. J. Barger, Jr., *ibid.*, **124**, 1228 (1977).
3. T. Gramstad and R. N. Haszeldine, *J. Chem. Soc.*, **1957**, 4069.
4. R. Landolt and S. Bornstein, Physikalischchemische Tabellen 5 Auflage 11, Verlag von Julius Springer, Berlin (1923).
5. R. Haase, P. F. Sauermann, and K. H. Dücker, Z. Phys. Chem. *N. F.*, **48**, 206 (1966).
6. Monsanto Phosphoric Acid, Technical Bulletin 1c/DP-239, Monsanto Co., St. Louis, Mo. 63166.
7. J. P. Ackerman and R. K. Steunenberg, Final Technical Report on Project Order No. MERDC A3101 (January 1975).
8. H. W. Fox and W. A. Zisman, *J. Colloid. Sci.*, **5**, 514 (1950).
9. R. A. Robinson and R. H. Stokes, "Electrolytic Solutions," p. 177, Butterworths, London (1968).
10. D. MacDonald and J. R. Boyack, *J. Chem. Eng. Data*, **14**, 380 (1969).
11. G. Walker, Private communication.
12. F. Daniels and R. A. Alberty, "Physical Chemistry," 4th ed., p. 100, John Wiley & Sons, Inc., New York (1975).
13. J. Giner, *This Journal*, **111**, 376 (1964).
14. I. M. Kolthoff and N. Tanaka, *Anal. Chem.*, **26**, 632 (1954).
15. S. Gilman, in "Electroanalytical Chemistry, A Series of Advances," Vol. 2, A. J. Bard, Editor, Marcel Dekker, New York (1967).

The Use of a Microcalorimeter for Analysis of Load-Dependent Processes Occurring in a Primary Battery

D. F. Untereker*

Medtronic, Incorporated, Minneapolis, Minnesota 55418

ABSTRACT

Calorimetry has been proposed as a way of measuring self-discharge rates, particularly in very long-lived primary batteries. A simple model for interpreting calorimetric data from a discharging ideal battery system is developed in terms of the battery's load-voltage curve and limiting thermodynamic quantities. This treatment is extended to include real battery systems where self-discharge and other types of parasitic processes occur. These complications are discussed and the model is applied to the Li/I_2 and Zn/HgO battery systems which are both important to the cardiac pacemaker industry. Anticipated and measured energy losses due to self-discharge in these two systems appear to agree with the levels predicted via calorimetric data.

The determination of self-discharge processes is of considerable importance to both manufacturers and users of batteries. This is particularly true in the medical devices field where unique high energy density cells are being qualified for long-term human use. It is imperative that accurate assessments be made of all parasitic processes occurring in these batteries so that longevity and performance characteristics can be estimated. The classical methods for obtaining such data involve determining relative capacities before and after storage. The problem with such experiments for long-lived batteries is that the storage periods involved are excessively long and are subject to a variety of complex variables. Also, this experimental approach does not take into account any effect of load on the rate of self-discharge processes. It is, therefore, very desirable to obtain estimates of the rates of parasitic processes on a short-term basis rather than having to rely solely on experiments such as those described above. This, in fact, almost becomes a necessity when the expected battery life may be ten years or longer as in the case of many of the newer battery systems used to power implanted cardiac pacemakers (1-3).

One technique suggested to be sensitive enough to measure the rates of parasitic battery processes is calorimetry (4, 5). Calorimetry on a microscale has been used successfully for some time, particularly on biological systems, and there are many papers in this area. New calorimeter designs have made calorimetry very sensitive, currently less than 1 μW (5-7). Preliminary calculations indicate that the power generated by parasitic processes may often be in the 0-20 μW range in small cells such as used for cardiac pacemakers, and thus, microcalorimetry does seem to be an appropriate tool to investigate these phenomena. Indeed, several investigations have already shown that battery processes are detectable via calorimetry (5-7).

The present paper shows the results of several experiments where calorimetric measurements were made on batteries while the batteries were generating external power at various rates. These data are interpreted in terms of a simple thermodynamic model developed in the "Thermodynamic Considerations" section.

Experimental

The data presented in this paper were obtained with a Tronac Model 351RA microwattmeter. This calorimeter is a differential heat conduction type instrument and has a short-term noise level and a long-term stability of about 1 μW. The construction and performance of this instrument are described more fully elsewhere (7).

A simple experimental procedure was used to obtain data. The first step was to preequilibrate the battery; this was done in two stages. First, the battery was placed in a 37° ± 0.5°C air bath which surrounds the calorimeter. After this equilibration step the battery was then moved into thermal contact with the near 37°C water bath in which the calorimeter block is submerged. This bath was held to temperature fluctuations of ±0.0002°C. Following this second step, the battery could be placed inside the calorimeter measurement cavity with minimal disturbance to the calorimeter. Heat from all processes occurring in the battery was then conducted through the thermopiles surrounding the battery causing a change in the thermopile voltage output. Within 90 min the calorimeter was usually within 5 μW of its new equilibrium level. After steady state was established, the battery was removed and the thermopile output returned to its baseline. The caloric output changes found on insertion and removal of the battery were the same within experimental error. A typical experiment including battery insertion, settling, battery removal, and subsequent return to baseline generally required 3 hr or less. In several experiments the time period was longer than this, but in each of these cases kinetics of the battery chemistry appeared to be the controlling factor as the settling time was many times longer than the usual settling time for the calorimeter.

Measurements were made differentially using a dummy battery as a blank. These dummy batteries were made of aluminum and had approximately the same mass as the battery being studied. The use of a metal blank instead of air (empty chamber) was found to decrease the short-term noise significantly, but did not appear to change the average output perceptively. Zero output on the calorimeter was determined via the use of two dummy batteries.

In some experiments reported here the battery was discharged at a fixed rate while calorimeter measurements were obtained. To do this, 36 gauge Cu wires were soldered to the battery's terminals before the experiment was begun. Once the battery was in place, these wires were run through the air bath to two feedthroughs leading outside of the calorimeter. From these points external load resistors could be connected to the battery and its load voltage monitored. Because the air bath was maintained at nearly the same temperature as the calorimeter block there

* Electrochemical Society Active Member.

was very little noticeable effect because of the attached wires. The experimentally measured calibration constant was found to be the same with and without the wires attached to the battery.

A Keithley Model 150B microvoltmeter was used to monitor changes in the thermopile voltages. The output of the Keithley was recorded on a strip chart recorder for a permanent record. The temperature of the calorimeter block was continually monitored and was also recorded by the same strip chart recorder.

The type of calorimeter used for these experiments yields data in terms of heat flux rather than heat. This complements the experiments described here since changes which are a function of current (rate) are of interest. Each of the thermodynamic quantities may readily be converted to an equivalent rate form by assuming the rate to be measured by the current flowing in the external wire. Then, for exampe, $P = 4.18\ \Delta H\ (i/n\mathbf{F})$ where ΔH is in cal/mole, i is in amperes, n and $\mathbf{F}$ have their usual meanings, and P is in watts. Other thermodynamic quantities may be calculated analogously.

The calibration of the calorimeter was done via a 1 kΩ resistor which is embedded in the battery cell holder between the thermopiles. For our calorimeter the calibration factor was 8.45 μW/μV at 37°C. This calibration factor turns out to be independent of the thermal conductivity and heat capacity of the battery and battery holder, as is shown below.

Consider the example in Fig. 1. Heat is generated in the left-hand compartment. The heat flux produced, $\dot{H}$, is constant. This heat may do two things. The first is raise the temperature of its immediate surroundings which have a heat capacity, C_p. The second is transfer through the thermopile to the heat reservoir where it is maintained at temperature T_1. Thus, $\dot{H} = \dot{H}_1(t) + C_p\ dT/dt$, where $\dot{H}_1(t)$ is the heat flux through the thermopile to the reservoir. Eventually, the source surroundings will reach an equilibrium temperature, *i.e.*, $dT/dt = 0$. The time required for this to occur will depend on the thermal parameters of the source compartment and the thermopile. When the steady state is reached, $\dot{H} = \dot{H}_1(t) = \dot{H}_1$. Because heat is passing through the thermopile, a temperature gradient ΔT exists across its faces, *i.e.*, $\dot{H}_1 = \sigma\Delta T$, where σ is the heat conductance of the thermopile. Thus, for any constant heat flux, $\dot{H}$, the temperature difference across the thermopile faces will be the same once $dT/dt = 0$. Since the voltage output from the thermopile is $k\Delta T$ we arrive at the calorimeter calibration constant, σ/k, which is independent of the thermal properties of the source.

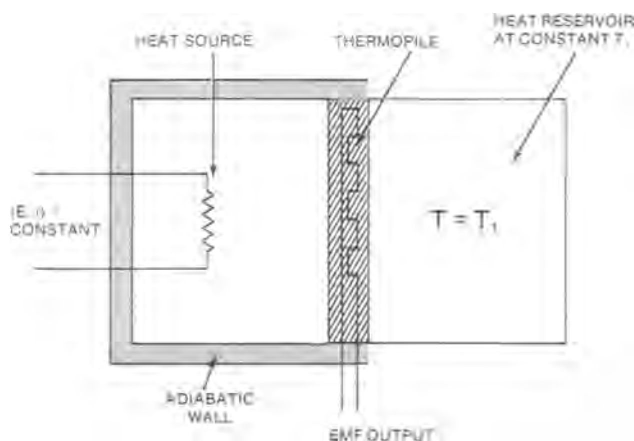

Fig. 1. Schematic representation for steady-state calibration of calorimeter. Heat source in measurement cavity on left. Calorimeter block (heat reservoir) at temperature T_1 on right.

Two commercial varieties of batteries were used in the experiments below. One is the Mallory Model RM-1 cell. This battery is a familiar Zn/HgO alkaline type and has been used to power implantable cardiac pacemakers for several years. It has a nominal open-circuit voltage (OCV) of 1.36V and a capacity of 1.0 A-hr. The second type of battery is based on the $Li/LiI/I_2$ system. In this system lithium and iodine electrochemically react to form a layer of LiI between the reactants. This layer serves as both electrolyte and separator for the battery. In the cells discussed here the iodine is rendered conductive enough to pass current by the addition of a small amount of poly-2-vinylpyridine. Although their chemistry is the same, these two models of Li/I_2 batteries are quite different The Model 742 battery is comprised of two series cells each housed in a sealed plastic cup which are then potted in a stainless steel can, while the Model 755 battery consists of a single cell in which the cathode is poured directly into a stainless steel can. The OCV of the Model 755 is 2.80V and that of the Model 742 5.60V. Their rated capacities are 3.0 and 1.0 A-hr, respectively.

Thermodynamic Considerations

In a search of existing literature no discussion of the thermodynamics involved in calorimetric battery experiments such as those presented here and by Greatbatch (1) was found. The equations presented here are reasonably simple and can be readily derived from basic thermodynamics for a system at constant temperature. Since thermodynamic equations are strictly applicable only to systems at equilibrium, allowances must be made for the errors which develop as a result of the nonequilibrium situation which arises when current is drawn from a cell or parasitic processes occur.

Let us consider the chemical reaction

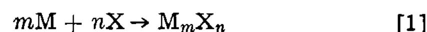

$$mM + nX \rightarrow M_mX_n \qquad [1]$$

From the First law

$$\Delta U = q + w \qquad [2]$$

where U is the internal energy, q is heat transferred to the system (positive), and w is work done on the system (positive). Thus, internal energy, which is a state function, is proportioned between heat and work. The value of ΔU for a reaction such as [1] is fixed by its chemistry, but the values for q and w depend on how M and X are converted to M_mX_n. In this section of the paper activities of reactants and products are assumed to be constant. However, activities can change in both ideal and nonideal cells and influence calorimetric measurements.

If M and X are combined directly in the calorimeter, w can only be the mechanical work allowed by the nature and geometry of the system and is nearly 0 if all reactants and products are condensed phases. Thus, in this situation q is a measure of $\Delta U_{M_mX_n} \approx \Delta H_{M_mX_n}$. Now consider the same chemical and geometrical system except that M and X are constrained in such a way that the only path for formation of M_mX_n is via electron transport through a wire external to the calorimeter (*i.e.*, we make the system a battery). When a load is placed in series with this wire, electrical energy is dissipated outside of the calorimeter. If $\Delta U_{M_mX_n}$ is fixed by the reaction taking place and work or heat is appearing outside the calorimeter, less heat must appear inside the calorimeter than in the first example. The question then becomes how is $\Delta U_{M_mX_n}$ divided between q and w. As will be seen below, there is a theoretical minimum for q, and the observed proportioning will be determined by kinetic as well as thermodynamic characteristics.

For any system, the maximum amount of external work is done when the process is carried out reversibly. Thus, via Eq. [2], minimum heat must be produced under reversible conditions. The Second

law equations defining the Helmholtz (ΔA) and Gibbs (ΔG) free energies in terms of ΔU or ΔH and entropy (ΔS), Eq. [3a and 3b], turn out to express the necessary relationships since ΔA and ΔG are equal to the reversible electrical work a system is capable of while holding temperature and volume or pressure, respectively, constant

$$\Delta A = \Delta U - T\Delta S \quad [3a]$$

$$\Delta G = \Delta H - T\Delta S \quad [3b]$$

A rearrangement of Eq. [3b] summarizes this when pressure is constant

$$\Delta H = \Delta G + T\Delta S \quad [4]$$

Thus, $T\Delta S$ is the heat generated during the electrochemical formation process when it is done reversibly, the remainder, ΔG, being available for external work. If done slowly enough, this is approached. When polarization or irreversibility comes into play, q is greater than $T\Delta S$ so w_{irr} becomes less than ΔG. The extra energy which is not expended externally ($\Delta G - w_{irr}$) must remain inside the calorimeter. It will eventually be given off as heat; however, it may be temporarily stored and slowly dissipated. This can cause problems if the time scale of observation is too short. An example of this is shown later. There can also be losses in the battery from its own internal resistance. At true steady-state conditions, all of these losses may be lumped together since they all affect the battery by reducing its output voltage. In high resistance batteries such as the lithium/iodine cells studied here, the internal resistance is a dominant correction term.

The Relationship Between the *i-E* Curve and Internal Power Losses

As pointed out above, irreversible effects lead to a reduction in the load voltage of a cell. Furthermore, since a cell's *i-E* curve relates its voltage to its rate of reaction, this curve is the keystone to calculating how power dissipation is distributed between useful external energy and internal heat. This becomes apparent since ΔH and ΔU are independent of rate as long as the reactants and products remain the same. Useful power is then $i \cdot E$ and the internal power loss is the difference between the total for the system, $\Delta H/n\mathbf{F} \cdot i$, and the useful power dissipation. Figure 2 is a composite showing these relationships at steady state when ΔH is more exothermic than ΔG. In order to make the units consistent the load-voltage curve is plotted as $n\mathbf{F}E$ *vs.* $i/n\mathbf{F}$ rather than the more familiar E *vs.* i. The load curve goes from $n\mathbf{F}E = n\mathbf{F}E_{OCV}$ at $i/n\mathbf{F} = 0$ to $n\mathbf{F}E = 0$ at $i/n\mathbf{F} = i_{sc}$, the short-circuit current. Between these extremes, $n\mathbf{F}E_{OCV} > n\mathbf{F}E > 0$ and $0 < i/n\mathbf{F} < i_{sc}/n\mathbf{F}$. For a cell at E_L and i_L, the shaded and hatched areas in Fig. 2 show the internal (dq/dt) and external (dw/dt) power dissipation. The shaded area corresponds to internal power loss, while the hatched area is electrical power available outside the cell. Note that as $i/n\mathbf{F} \rightarrow 0$ both the internal and external power approach zero, but that their ratio does not. The minimum internal power is $4.18\, T\Delta S\, (i/n\mathbf{F})$ even if the cell reaction is carried out reversibly. Hypothetical power-current relationships are shown in Fig. 3. Here three plots illustrate the general shapes of E, P_{int}, and P_{int}/i as a function of i. The i *vs.* P_{int} curve passes through the origin, but the i *vs.* P_{int}/i plot has an intercept proportional to ΔS.

The Self-Discharging System

So far this discussion has only covered the behavior of a cell where there are no parasitic reactions occurring. We now wish to broaden this to include self-discharge and other parasitic reactions which generally occur to some extent in all real batteries. As seen in Fig. 3b, the internal heat produced in a cell in which no parasitic reactions occur always goes to zero as $i \rightarrow 0$. Therefore, the presence of internal power dissipation when $i = 0$ is proof of the occurrence of some parasitic process, and their presence may be ascertained by simply measuring the internally dissipated power at no load.

Parasitic processes can be divided into the categories which affect the capacity or performance of the cell and those which do not. Examples of the former might be chemical self-discharge and case corrosion, and the latter could be curing of epoxy encapsulation. The first type is of most concern although mixtures of the two may be present and the main problem frequently is the difficulty of determining which and how much of each is occurring. The rate of those parasitic processes that do not affect the cell's function are not likely to depend to an appreciable extent on cell load. The detrimental parasitic processes may or may not be measurably affected by discharge current density depending on the time scale of observation, the mechanism the process occurs by, and the physical size and shape of the cell. In the paragraphs below each of these situations is discussed.

Case 1: The parasitic reaction rates are independent of battery load. For this to be, the cell and parasitic reactions must occur or appear to occur in parallel. This can arise in several ways. First, if the cell reaction and the parasitic process are not related in any manner, *i.e.*, their reactants and products are different, or if the two reactions occur in physically separated areas of the battery. A second way is if the geometry of the battery is such that on the time scale of observation the two reactions occur independently. For example, suppose a battery had a catholyte which had electronic conductivity and also slowly corroded the cathode current collector. If mobilities in the catholyte were slow and the distance between the current collector and separator large enough, a true steady state may not be reached during observation and the reactions will appear to occur completely independently. The final way for the reactions to occur inde-

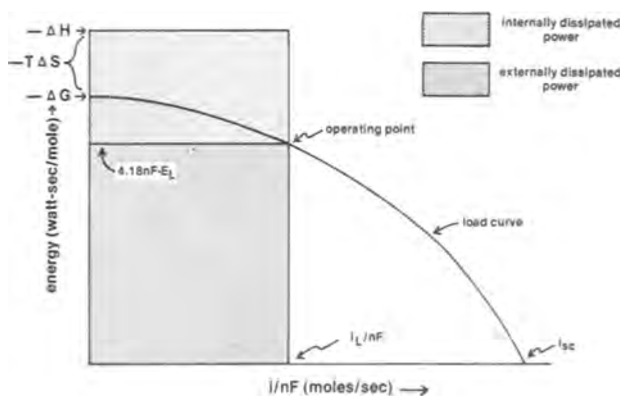

Fig. 2. The steady-state partitioning of total power between internal and external dissipation in an ideal battery via the load-voltage curve.

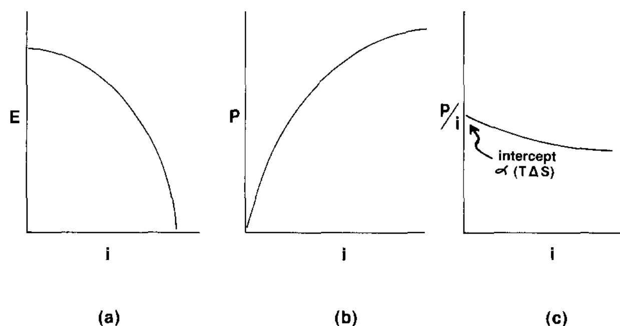

Fig. 3. Generalized hypothetical curves for (a) voltage, (b) internal power dissipation, and (c) internal power/rate; all vs. rate.

pendently is if concentration gradients do not form in the cell, as might be the case if the catholyte had an invariant composition. In such a situation the cell discharge reaction and the parasitic reaction (possibly chemical self-discharge or a corrosion reaction) would occur independently because there is no mechanism whereby the reactions can influence one another.

Case 2: The parasitic reaction rates are dependent on battery load. The usually expected interaction is a decrease in the chemical reaction rate with increasing cell current because of competition for a reactant. This arises as follows when the chemical and electrochemical reactions occur at a common interface. In the absence of electrochemical discharge the chemical reaction rate depends on the existing reactant concentrations and/or diffusion gradients. If the electrochemical reaction rate is then fixed at some value greater than zero and it consumes a reactant common to the chemical reaction, the concentration of that reactant will decrease and its gradient away from the interface will increase. This will cause the chemical reaction rate to decrease. The existence of a concentration gradient is a necessary condition for this behavior if chemical and electrochemical back reactions are negligible or product activities are fixed. Although the above situation only leads to inverse dependencies of the parasitic process rate on load current it is possible to envision a mechanism which would yield the opposite result. For example, if the chemical discharge produced a passive layer which is broken down by the electrochemical discharge, the rate of self-discharge could be greater during the presence of electrochemical discharge than in its absence. This may be what happens in the Li/SO_2 system where a thin protective film is known to form at the Li surface (8) and keep the system from chemically discharging.

Results and Discussion

Experiments of the sorts described earlier were performed on batteries based on Li/I_2 and Zn/HgO chemistry. A typical piece of data is shown in Fig. 4. This strip chart recording covers a nominal 40 hr period and shows the stability of the baseline and settling times involved. After battery insertion and removal the recording goes endothermic because the air bath is generally slightly cooler than the calorimeter block. The short-term noise and long-term stability both appear to be on the order of 1 μW.

Figure 5 shows the calorimetric data obtained while discharging two Wilson Greatbatch, Limited, Model 755 batteries with load resistors external to the calorimeter. One of these batteries (SN5560) had not previously been discharged while the other (SN1126) had been discharged about 10% of its rated capacity. The dissipation *vs.* load plot is curved in each case,

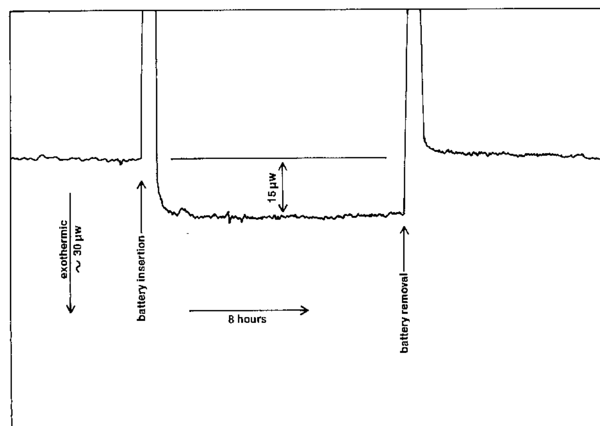

Fig. 4. Typical calorimetric strip chart recording showing noise and stability over a 40 hr period.

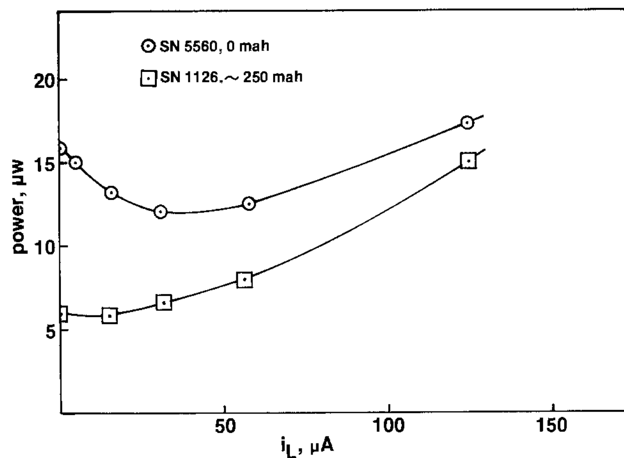

Fig. 5. Measured internal power dissipation *vs.* load current for two Li/I_2 batteries. Both are Wilson Greatbatch, Limited, Model 755 batteries. SN5560 discharged 0 mA-hr: SN1126 discharged ~250 mA-hr.

and in fact both appear to have minima. The next two figures show the effect of correcting the raw data for known current dependent variables. One of these is the entropy correction, $T\Delta S$. Since this is a thermodynamic correction it should only be applied in a true thermodynamically reversible situation. Although the system cannot be running reversibly as long as current is flowing, reversible behavior is being approached to some degree, especially at the low discharge rates encountered here. However, even if this were not the case, this correction still represents an upper bound on the efficiency of the system at any discharge rate. It turns out that for the $Li/LiI/I_2$ system ΔS is very small, 0.1 kcal/°K mole (9), and the entropy correction is negligible in the range shown. However, these batteries are inherently resistive because of the LiI layer, and the iR drop across this layer is a large correction. Since other polarization effects should also take the form of potential drops, a single correction was made by subtracting $i\Delta E$, where ΔE is the difference between E_L and E_{OCV} at the measured current.

The corrected data for the newer battery became nearly horizontal after an initial dip (Fig. 6). The same correction for the partially discharged cell yields a line not nearly as horizontal (Fig. 7). At this time we do not know if all the observed differences are indicative of the states of discharge or whether some might be artifacts of the batteries themselves. However, the author has seen other data on Li/I_2 cells and they show the same initial drop in calorimetric output in the region $i_L < 50$ μA (5). Hart and Hansen

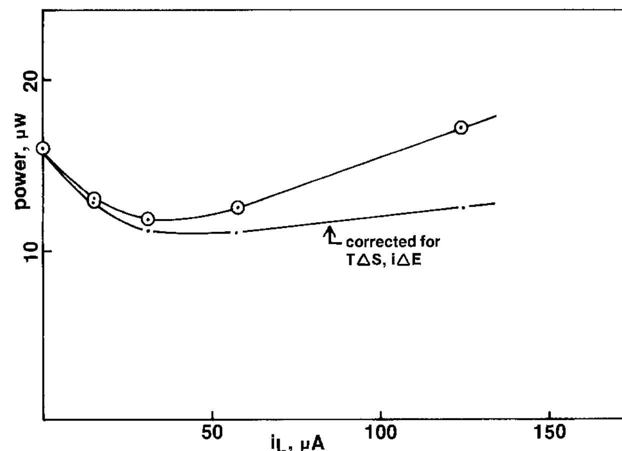

Fig. 6. The measured and corrected internal power dissipation *vs.* load curves for battery SN5560.

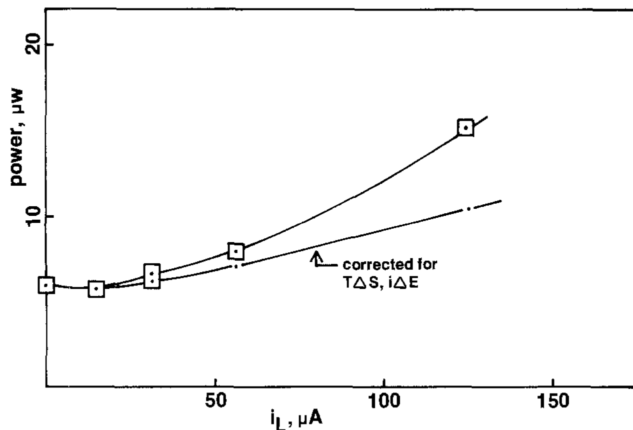

Fig. 7. The measured and corrected internal power dissipation vs. load curves for battery SN1126.

have also shown that the Li/I_2 reaction is essentially 100% current efficient (7) and this leads to speculation that the observation of the initial dip may be due to changes in the rate of self-discharge because of a competition of the chemical and electrochemical mechanisms. Such a mechanism would be expected to be much more noticeable on a new cell, where the protective LiI layer is very thin, than on an older cell, and this is what is observed. It seems likely from these preliminary experiments that most of the calorimetric output observed in the Model 755 battery is due to self-discharge and that at least early in life its rate is quite dependent on current. The positive slopes in Fig. 6 and 7, after correcting for polarization, indicate there is something happening at the higher values of current density. An example of anomalous behavior was also observed. The open-circuit calorimetric output of battery SN5560 cell was observed to be about 16 μW in Fig. 5. This battery was loaded very heavily (to $E_L = 0.5V$) for several hours at 37°C,[1] then inserted into the empty calorimeter chamber. It was expected that the calorimetric output would quickly settle to 16 μW again. What actually occurred was that steady state was not reached for 20 hr, after which time the heat output fell to 15 μW, approximately its initial value (Fig. 8). During the 20 hr period a large exothermic output was observed. Since energy (above self-discharge levels) should not have been dissipated during this period the calorimetric output had to be the dissipation of heat or energy stored while the cell was under load. This calorimetric output (shown in Fig. 9) could be misleading if viewed on too small a time-scale where it was not apparent the data were indicative of a non-steady-state situation. Thus, it is very important in these experiments to observe a long enough period of time so that steady-state behavior is assured.

Since a main purpose of using microcalorimetric measurements is to estimate self-discharge rates, it was necessary to establish how self-discharge might change during the life of a battery. It was stated above that self-discharge is expected to be high initially, then decrease with time and discharge depth. If true, the shape of this curve must be known as a function of time and discharge depth in order to make an over-all estimate of self-discharge losses since a single measurement only gives information at one time and state of discharge. The effect of discharge depth was investigated using a set of rapidly discharged Wilson Greatbatch Model 742 batteries. These batteries are not directly comparable to the Model 755 cells already discussed since their designs are quite different and they are even subject to different accompanying parasitic reactions. Nevertheless, the basic chemistry is the same and the results should be indicative of this generic type of battery.

[1] During the discharge portion of this experiment the battery was kept in good thermal contact with the calorimeter water bath as is normally done during the equilibration cycle before a battery is inserted into the calorimeter. The strip chart recording corresponding to the insertion of the cell into the calorimeter appeared normal during this experiment.

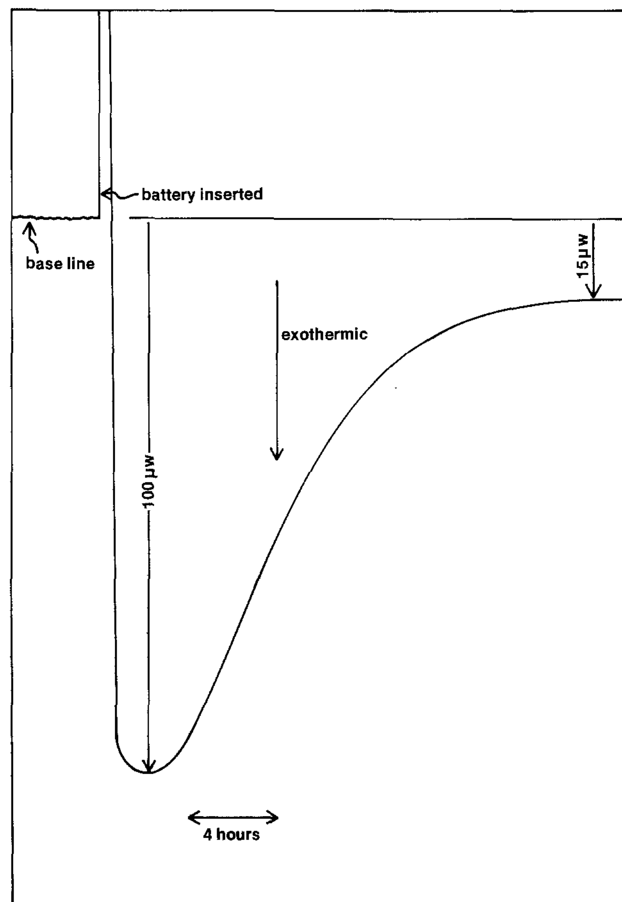

Fig. 8. The calorimetric response to open-circuit relaxation of battery SN5560 after heavy polarization. Settling time about 20 hr. Open-circuit calorimetric output of SN5560 was 16 μW before polarization.

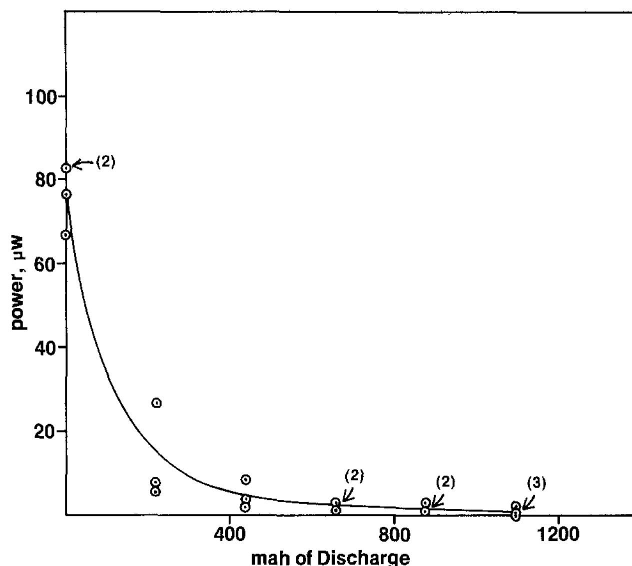

Fig. 9. Plot of calorimetric data for series of Li/I_2 batteries discharged to various depths. Batteries are Wilson Greatbatch, Limited, Model 742. Discharges done at 1 mA constant current at 60°C. Data from 21 batteries. Measurements made at no load.

A group of 21 batteries was discharged to different depths varying between 0 and 100% of the rated capacity of 1000 mA-hr. Calorimetric outputs were measured under open-circuit conditions for the various states of discharge and are plotted *vs.* discharge

depth in Fig. 9. As expected the calorimetric data show a high initial output which, under these conditions, falls to about 10% of its initial level by 40% through discharge. If the heat output is assumed to arise only from the direct combination of Li and I_2, the area under this curve can be integrated and compared with the average power used for normal pacing. Doing this, the fractional loss of energy from self-discharge during battery life is estimated to be 12%. Other experiments show that parasitic processes such as curing of epoxy and polyester may contribute significantly to the heat output observed early in life. This means the 12% estimate is probably high. However, even ignoring these corrections the data yield reasonable agreement with the anticipated loss of 10% or less according to the manufacturer's specifications.

While the experiment described above has real time uncertainties built into it from the accelerated discharge of the batteries, the shape of the curve indicates that calorimetric measurements from batteries discharged to 30% of capacity or even less may be used to obtain total self-discharge estimates in the Li/I_2 system with good precision.

The only pacemaker battery system for which much real-time self-discharge data has been obtained is the Zn/HgO system which has been used in heart pacemakers for many years. Chemical and classical electrochemical determinations of self-discharge in this system have been done (9). These experiments indicate that the direct combination of the reactants is the major degradation mechanism, with evolution of hydrogen also occurring to some extent. An accepted number is 4-5% of capacity loss per year in a Mallory RM-1 cell, which translates into roughly a 30% loss if the battery discharges completely at its pacemaker rate of 15 μA (10). The feeling of those who work with this system is that although its self-discharge rate does decrease during battery life, the Zn/HgO rate is relatively constant when compared to that attributed to the Li/I_2 system (10). An experiment analogous to that leading to Fig. 5-7 was done using a relatively new ($<10\%$ discharged) Mallory RM-1 battery. Both the raw and corrected data are shown in Fig. 10. Since the RM-1 cell is capable of sustaining much higher currents than the Li/I_2 batteries studied, the current scale shown is larger, going to 400 μA. The $i\Delta E$ correction is shown in the square boxes and accounts for most of the difference between the curves. However, in this system $T\Delta S$ is not negligible, and its added correction is shown separately (triangles). While Li/I_2 batteries show a decrease in heat output followed by an increase, that of the Zn/HgO system increases regularly with increasing current density. However, the corrected curve shows the unaccountable heat output becomes nearly constant for $i_L > 100$ μA. This curve extrapolates to about 7 μW at $i_L = 0$. Using this number as indicative of the average level of self-discharge and assuming that only the direct combination of reactants occurs, 25% of the cell's total energy will be lost to self-discharge. This appears to agree well with the data obtained from real-time experiments and experience.

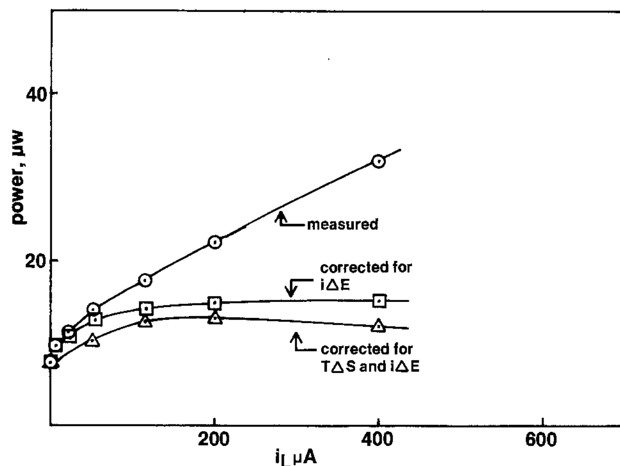

Fig. 10. The measured and corrected internal power dissipation vs. load curves for a Zn/HgO battery. Battery is Mallory RM-1.

Conclusion

The equations developed in the early sections of this paper show that the stored chemical energy in a battery system is proportioned between available and unavailable energy via the battery's load curve and thermodynamic considerations. The simple treatment described here accounts for most but not all of the energy exchanges observed between the Li/I_2 system and its surroundings. The ideal energy distribution is modified by phenomena such as parasitic reactions and nonequilibrium situations. In the Li/I_2 system it became evident that some parasitic reactions, predominantly self-discharge, do occur. There is some evidence the self-discharge reaction is in competition with the electrochemical reaction, which indicates there is some ionic conductivity in the cathode. When the microcalorimetric data were gathered for a group of Li/I_2 batteries which had been rapidly discharged to various depths, they showed that about half of the total parasitic heat loss occurred during the first 20% of discharge. This is very encouraging since the most uncertain part of determining accelerated losses is the extrapolation of early real-time data into the future. An estimate for the total self-discharge during life seems to be on the order of 10% of rated capacity for the batteries utilized in this experiment. How this number translates to other physical configurations of Li/I_2 cells was not specifically determined. For comparison, data on a conventional Zn/HgO battery were obtained and compared with real-time data. The two sets of data seemed to be in good agreement and lend credence to the use of calorimetry for determining self-discharge and parasitic losses.

Acknowledgments

The author is indebted to B. B. Owens for discussions and encouragement on this work.

Manuscript submitted March 14, 1978; revised manuscript received July 24, 1978.

Any discussion of this paper will appear in a Discussion Section to be published in the June 1979 JOURNAL. All discussions for the June 1979 Discussion Section should be submitted by Feb. 1, 1979.

Publication costs of this article were assisted by Medtronic, Incorporated.

REFERENCES

1. "Advances in Pacemaker Technology," M. Schaldach and S. Furman, Editors, pp. 345-355, International Symposium on Advances in Pacemaker Technology, Erlangen, Wilson Greatbatch, Springer-Verlag (1975).
2. M. Mosharrafa, in Proceedings of 12th Annual Rocky Mountain Bioengineering and 12th International USA Biomedical Science Instrumentation Symposium, April 1975, Vol. 11.
3. K. Fester, R. L. Doty, and R. Vander Velden, in Proceedings of 16th Annual American Society of Mechanical Engineers Symposium on Energy Alternatives, Albuquerque, New Mexico, February 1976.
4. E. J. Prosen and J. C. Colbert, in Proceedings of Cardiac Pacemaker Workshop, October 1976.
5. W. Greatbatch, Private communication.
6. E. J. Prosen, NBS Rep. NBSIR 73-179 (1973).
7. R. M. Hart and L. D. Hansen, in Proceedings of Cardiac Pacemaker Workshop, October 1977.
8. E. S. Brooks, in Proceedings 26th Power Sources Symposium, 1974, pp. 31-34.
9. JANAF Thermochemical Tables, D. R. Stull and H. Prophet, Editors, 2nd ed., NSRDS-NBS37 (1971).
10. K. E. Fester, Private communication.

Powder Electrode Separators for High Temperature Lithium-Aluminum/Iron Sulfide Batteries

J. P. Mathers,[1] C. W. Boquist, and T. W. Olszanski*

Argonne National Laboratory, Argonne, Illinois 60439

ABSTRACT

The feasibility of using ceramic powders for electrode separators in lithium-aluminum/iron sulfide cells was evaluated. Test cells of two different designs were constructed and operated for periods of 1000 and 2000 hr. Thus, the powder separator appears to be a good candidate for use in commercial cells. The advantages and limitations of this type of separator are discussed, and a comparison is made with fibrous separators which are also being developed for these cells.

Lithium-aluminum/iron sulfide batteries are being developed for stationary energy storage on electric utility systems and for electric-vehicle propulsion. Cells for this battery consist of a lithium-aluminum alloy negative electrode, an FeS or FeS_2 positive electrode, and a molten LiCl-KCl electrolyte (mp 352°C) which requires an operating temperature of 400°-450°C (1). An important factor in the successful development of these cells is the identification of an electrode separator which satisfies both the technical and economical requirements of the cell. In lithium-aluminum/iron sulfide cells the separator has two functions: (*i*) preventing electrical contact between the electrodes without unduly restricting ionic flow, and (*ii*) providing a barrier which will retain the active materials of the cell within the electrodes. The latter is important because the active materials are generally in the form of fine powders. The optimum structure and properties desired in the electrode separator have not been fully determined; however, the following general requirements can be stated: (*i*) The separator must be a good electrical insulator to prevent direct electron flow between the electrodes. (*ii*) The materials used in the separator must be chemically stable in the cell environment for the lifetime of the cell (5-10 yr). (*iii*) The separator should be <2 mm thick and contain a large volume of open porosity to minimize the cell weight and the resistance to ionic flow between the electrodes. (*iv*) The pore channels should be <20 μm in diameter to prevent penetration of the separator by the active materials in the electrodes. (*v*) The integrity of the separator must be maintained during any dimensional changes which occur in the electrodes during cell operation. (*vi*) If commercialization of the cell is to be achieved, the separator must have a potential cost of $<\$22/m^2$ and must permit rapid cell assembly.

The requirement for a good electrical insulator precludes the use of metals in the separator. Most organic or polymeric materials are not stable at the cell operating temperature, and none of the polymers which have been tested in cells at ANL appear promising. Therefore, the choice of materials for the separator appears to be limited to ceramics. Chemical reaction with lithium in the cell environment severely limits the number of ceramics which can be used in the cell. A comparison of the free energies of formation of various oxide and nitride ceramics with the free energy of formation of Li_2O and Li_3N indicates that the following ceramics should be stable in the presence of lithium at the cell operating temperature: MgO, BeO, Y_2O_3, CaO, Si_3N_4, BN, and AlN. Thermodynamic stability in the presence of lithium does not insure that a ceramic will be stable in the cell environment, though, because lithium may react with impurities in the ceramic, or a reaction could occur between the ceramic and other materials in the cell environment.

The previous development work on electrode separators for lithium-aluminum/iron sulfide cells has been devoted primarily to fibrous ceramics prepared from BN or Y_2O_3 fibers. These two fibers are the only commercially available ceramic fibers that are compatible with lithium (2). Boron nitride fabric has been used successfully in engineering test cells for periods greater than one year (1, 3, 4); however, it will not meet the cost goals for separators. Papers and felts prepared from BN fibers have been tested in laboratory test cells with very promising results (5) and appear to have the potential for meeting the separator cost goals. Yttrium oxide papers and felts have also been used successfully in laboratory test cells (5), but the potential cost of these materials is less certain than that of BN papers and felts. In addition, recent experiments have indicated that Y_2O_3 reacts with the sulfides present in the cell to form Y_2O_2S (6).

This paper describes recent efforts to utilize ceramic powders for electrode separators. The development of powder separators is being pursued because they facilitate cell assembly, are amenable to low cost mass production, and may permit the use of inexpensive materials such as MgO and CaO which are not available in fibrous form.

Experimental Procedure

The feasibility of using a powder separator was evaluated in Li-Al/LiCl-KCl/FeS test cells which were assembled in the uncharged state [*i.e.,* aluminum metal was used as the active material in the negative electrodes and a mixture of Li_2S and Fe was used in the positive electrodes (7)]. Two different cell designs, shown schematically in Fig. 1 and 2, were evaluated. The cells were cylindrical, with a diameter of 7.6 cm and a height of 2.5-3.5 cm. The negative electrode in both cell designs was enclosed by the lower portion of the cell housing and a 325-mesh stainless steel screen (for particle retention) that was spot-welded to a retainer ring. This retainer ring was not welded to the cell housing and was free to move whenever dimensional changes occurred in the electrode during cell operation. The cell housing and retainer were made from AISI 1008 steel. The negative electrodes were formed by cold-pressing Al wire into circular plaques, and the positive electrodes were formed by hot-pressing a mixture of Li_2S, Fe, and electrolyte powders at a temperature of $\sim$400°C and a pressure of $\sim$11,700 kPa (1700 psi).

In the first test cell, SC-13, the positive electrode was enclosed in a metal compartment made from Hastelloy B[2] (Ni-28 Mo-5 Fe-1 Cr) and Type 304

* Electrochemical Society Active Member.

[1] Present address: Department of Chemical Engineering, University of Maryland, Baltimore, Maryland 21200.

Key words: insulator, fused salts, battery, ceramics.

[2] Cabot Corporation, Stellite Division, Kokomo, Indiana.

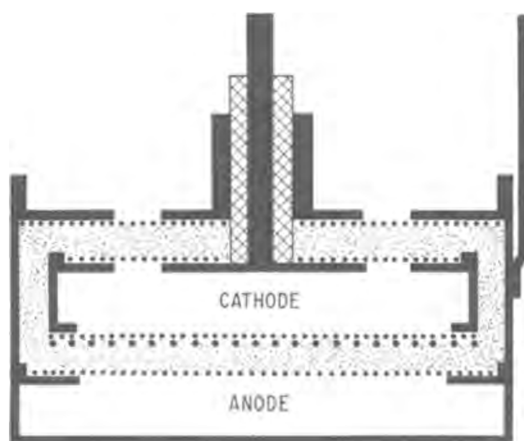

Fig. 1. Schematic diagram of cell SC-13

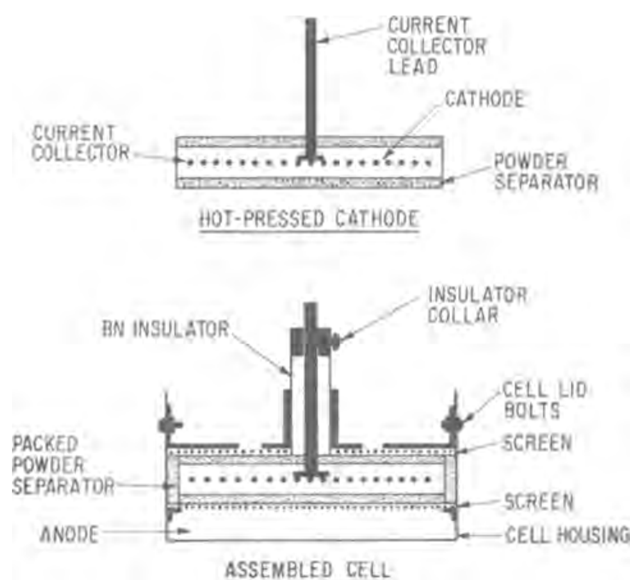

Fig. 2. Schematic diagram of cell SC-14

stainless steel screens which were spot-welded in place. An iron rod served as the positive current lead and was welded to the top of the electrode compartment. The separator consisted of coarse Y_2O_3 powder (150-250 μm, 99% pure),[3] which was poured into place around the positive electrode. Yttria was selected because of its proven compatibility with lithium (2). The coarse particle size was selected to prevent the powder from penetrating the 325 mesh retainer screens. The volume fraction of Y_2O_3 in the separator was 0.40, as determined from packing density measurements, and the separator thickness was about 3 mm. A dense BN sleeve was used to insulate the positive current lead from the cell housing.

In cell SC-14 (Fig. 2), the positive electrode was not enclosed in a metal compartment, and the separator was fabricated as an integral part of the electrode. The positive electrode, current collector, and the upper and lower electrode separators were assembled in a hot-pressing operation using the LiCl-KCl electrolyte as a binder. This unit is shown in the upper portion of Fig. 2. The current collector consisted of a stainless steel screen welded to an iron rod. The separator mixture consisted of 61 weight percent (w/o) coarse Y_2O_3 powder (150-250 μm, 99% pure),[3] 26 w/o fine Y_2O_3 powder ($\sim$5 μm, 99.99% pure),[4] and 13 w/o electrolyte. The larger Y_2O_3 particles were selected because they were not expected to migrate into the positive electrode or through the 325 mesh screen used to cover the negative electrode. The fine Y_2O_3 particles were expected to fill the voids between the larger particles and prevent penetration of the separator by the active materials. After the hot-pressing operation, each separator layer was 2 mm thick and the volume fraction of Y_2O_3 was 0.70. The latter was calculated from the weight of Y_2O_3 used in the separator and the dimensions of the separator after the hot-pressing operation. The sides of the positive electrode were insulated from the cell housing by Y_2O_3 powder (70 w/o coarse and 30 w/o fine) which was packed into place. Unlike cell SC-13, bolts were used to fasten the top lid of cell SC-14 to the cell housing. A dense BN insulator was used to insulate the positive current lead from the cell housing, and a metal collar with a set screw was used to hold the insulator in place.

Assembly of both cells, including the hot-pressing operations, was accomplished in a helium-atmosphere glove box. After assembly, the cells contained a large volume of voids which had to be filled with electrolyte. This was accomplished by (*i*) positioning chunks of solid electrolyte on top of the cell, (*ii*) placing the cell into a furnace which was built in to the floor of the glove box, (*iii*) evacuating the furnace to remove the helium from the voids, (*iv*) slowly raising the temperature of the furnace to melt the electrolyte, and (*v*) repressurizing the furnace to force the molten electrolyte in to any voids. Holes were provided in the top of both cell housings, and in the top of the compartment for the positive electrode of cell SC-13 to facilitate the removal of gas from the cell and loading of electrolyte. The theoretical capacities of cells SC-13 and SC-14 were 19 and 25 A-hr, respectively, with the capacities of the negative and positive electrodes being equal.

The cells were operated in the glove box furnace and were cycled continuously at 450°C, between a discharge cutoff potential of 0.9V and a charge cutoff potential of 1.7V (internal resistance included). The cells were placed on open circuit for 10 min after each charge and discharge. Both cells were operated at a current density of $\sim$20 mA/cm^2 during the first few cycles. The current density was gradually increased during cycles 3-10 until the desired operating current density was reached (76 mA/cm^2 for SC-13 and 60 mA/cm^2 for SC-14). Cells SC-13 and SC-14 were operated for 2000 and 1000 hr, respectively. Operation was voluntarily terminated for post-test examination of the cell and separator. In the post-test examinations the cells were sectioned, and metallographic mounts of the separators were prepared in a helium-atmosphere glove box. Optical micrographs were obtained on a metallograph which was also located in the glove box.

Results

The electrical performance of the cells is summarized in Fig. 3 and 4. These graphs illustrate the coulombic efficiency and percent utilization[5] achieved for each charge-discharge cycle. The coulombic efficiency of each cell remained near 100% throughout the lifetime of the cells. The utilization of both cells declined rapidly during the first 10 cycles of operation when the current density was increased to the desired operating level. The sudden losses in utilization for cell SC-13 were caused by the buildup of gas in the cell. Evacuation of the furnace containing the cell removed this gas and immediately restored the utilization of the cell to its original value. After the first 1000 hr of operation, no further buildup of gas in the

[3] Cerac, Incorporated, Butler, Wisconsin (Special Order).
[4] Molycorporation Incorporated, White Plains, New York (Type 5600).
[5] (Achieved Discharge Capacity ÷ Theoretical Discharge Capacity) × 100.

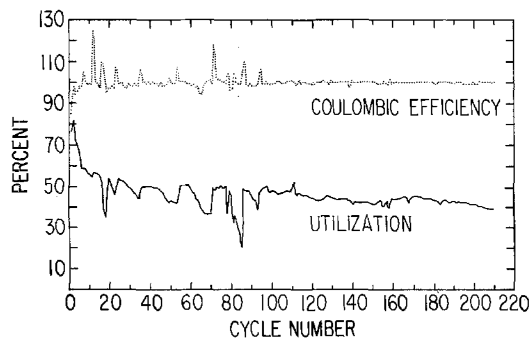

Fig. 3. Electrical performance of cell SC-13

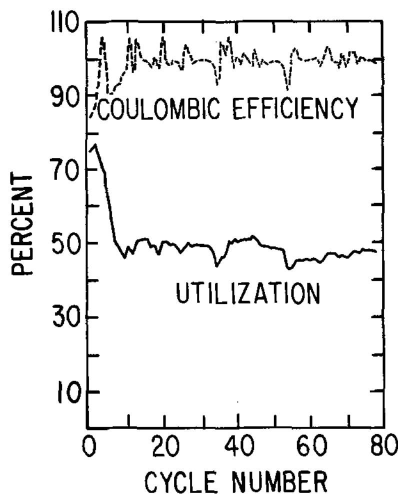

Fig. 4. Electrical performance of cell SC-14

cell was observed. The identity and source of the gas was not determined, but it is believed to have resulted from contaminants introduced with the cell materials. The Y_2O_3 and Li_2S powders used in cell SC-14 were heated in a vacuum at 600°C prior to cell assembly in order to remove any hydroxides, carbonates, or adsorbed moisture. This greatly reduced the buildup of gas during the operation of SC-14 and eliminated large fluctuations in the utilization. Over-all the electrical performance of these cells was judged to be very good.

A section of cell SC-13, obtained during post-test examination, is shown in Fig. 5. A great deal of swelling and distortion of the electrodes was evident. The center portion of the positive electrode had expanded approximately 25%, while the swelling in the negative electrode ranged from 90% at the outer edge to as much as 160% (2.6 × original thickness) near the center. The separator thickness between the electrodes varied from 2-6 mm, with most areas in the range of 2-4 mm (original thickness = 3 mm). A photograph of a cross section of cell SC-14 is shown in Fig. 6. In this cell, the positive electrode had expanded 10% near the center and edges but had been com-

Fig. 5. Post-test section of cell SC-13

Fig. 6. Post-test section of cell SC-14

pressed by 15% in other areas. The negative electrode had expanded 35-55%. Examination of the separator revealed that the thickness varied from 0.5 to 3.0 mm, with most areas in the range of 2.5-3.0 mm (original thickness = 2 mm). The apparent increase in the separator thickness of this cell was an unexpected result, and the reason for this behavior has not been established. Some irregularities in the shape of the positive electrode are visible in Fig. 6. As can be seen on the lower edge of this cell, the positive electrode almost made contact with the negative electrode.

The powder separators in both cell designs showed an ability to conform, at least to a limited degree, to the distortion or curvature in the surfaces of the electrodes. However, excessive swelling of the electrodes or local irregularities which develop in the shape of the electrodes can lead to fairly large variations in the separator thickness. The amount of swelling and/or distortion which occurs in the electrodes can be substantially reduced if the electrodes are restrained. In cell SC-13 the top of the cell was not fastened to the rest of the cell housing, and this allowed the electrodes to expand freely. In cell SC-14 the electrode swelling was greatly reduced by bolting the top of the cell in place. This method of restraint was not completely successful, however, because the bolts were placed through vertical slots in the top of the cell which permitted some upward movement of the electrodes during cell operation. In actual batteries, where the cells are properly sealed by welding and restrained by the battery case, swelling and distortion of the electrodes is expected to be much less of a problem. A small amount of variation in the separator thickness is inevitable as long as dimensional changes occur in the electrodes during cell operation. This will probably be the limiting factor in determining the minimum separator thickness which can be achieved with powders. Based on the present study, the separator thickness might be reduced to the range of 1-2 mm with proper restraint of the electrodes.

The cause of the local irregularities observed in the shape of the positive electrode of cell SC-14 is not known, but this problem can be avoided through the use of a metal frame and screen assembly around the electrode (as was done in cell SC-13). In cells which utilize FeS as the active material for the positive electrode this does not present a problem; however, a difficult corrosion problem is encountered when FeS_2 is used as the active material. At the present time molybdenum is the only metal with sufficient corrosion resistance for use with FeS_2 electrodes. Since molybdenum components are difficult to fabricate and expensive (2), it is desirable to identify the cause of the irregularities observed in SC-14, in the hope that the need for a frame and screen assembly around the positive electrode can be eliminated.

A composite photomicrograph of a section of the powder separator of cell SC-13 is shown in Fig. 7. The 325- and 40-mesh screens used to cover the positive electrode face are visible at the top, and the 325-mesh screen used over the negative electrode can be seen in the lower portion of the photomicrograph. The active material in the positive electrode had penetrated the

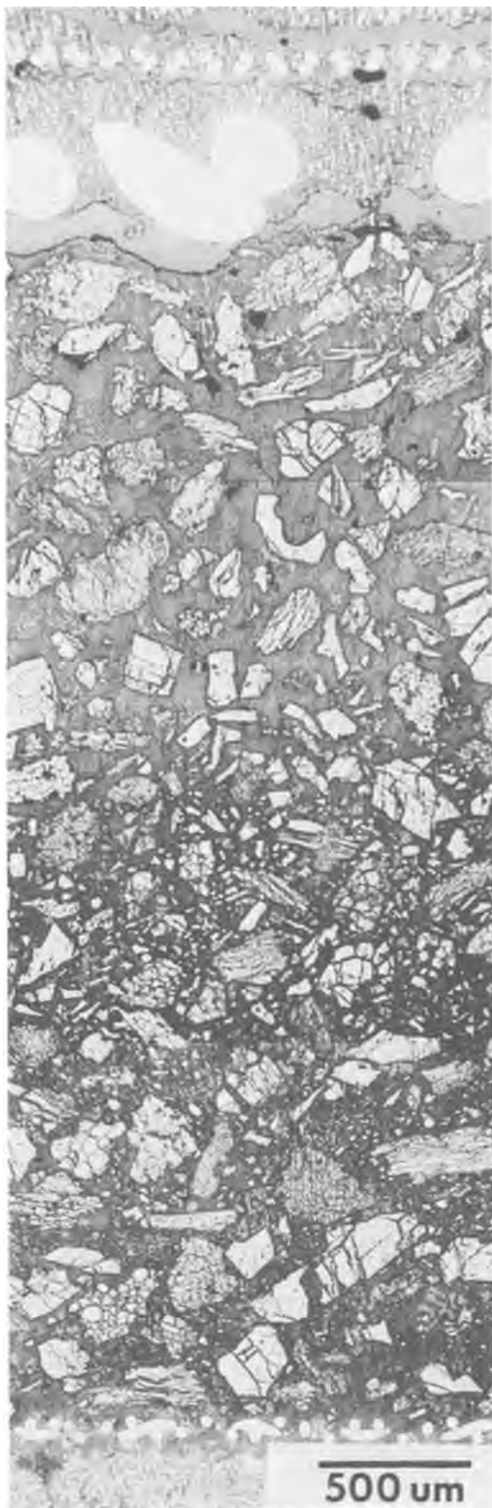

Fig. 7. Powder separator from cell SC-13

two screens used on that electrode, but only a small amount had penetrated the separator. The active material which did penetrate the separator was dispersed and limited to the area immediately adjacent to the electrode. The remainder of the separator (~90%) was free of active materials from the electrodes. No evidence of chemical attack on the Y_2O_3 powder was observed; however, subsequent tests in other cells have shown that Y_2O_3 reacts with sulfides in the cell to form Y_2O_2S (6). The Y_2O_3 particles had a very irregular surface and a fractured appearance before and after cell testing. Most of the small Y_2O_3 particles had settled to the lower portion of the separator, creating a density gradient across the separator thickness. Metallographic examinations indicated a Y_2O_3 volume fraction of 0.48 in the upper portion and 0.63 in the lower portion of the separator. The original volume fraction of Y_2O_3 was 0.40; thus the separator was compressed in this area during cell operation.

A composite photomicrograph of the separator from cell SC-14 is shown in Fig. 8. The very fine, light colored particulate at the top of the photomicrograph is the active material of the positive electrode. The 325-mesh screen used to cover the negative electrode is visible at the bottom of the photomicrograph. As shown in Fig. 8, a well-defined interface existed between the positive electrode and the separator. A few dispersed sulfide particles from the positive electrode were observed in the separator, but these were confined to a small area immediately adjacent to the electrode. Penetration of negative electrode material into the separator was not observed. No visible reaction of the Y_2O_3 powders with any other materials and no variation in the density of the separator across its thickness were observed. The latter was attributed to the fine Y_2O_3 powder used to fill the pores between the larger Y_2O_3 particles. A determination of the volume fraction of Y_2O_3 in the separator by metallographic techniques could not be made because of the difficulty in resolving the fine Y_2O_3 particles. However, an estimate yielded a value of 0.47 for the volume fraction based on the thickness and volume fraction of Y_2O_3 for the separator immediately after fabrication and on the thickness of the separator after cell operation.

Fig. 8. Powder separator from cell SC-14

The above results indicate that the powder separators in both cells are good particle retainers. Even in cell SC-14, which did not have a frame and screen assembly around the positive electrode, the interface between the active materials and the separator showed little evidence of intermixing.

Discussion

The results of these preliminary experiments with powder separators indicate that they are a viable alternative to fibrous paper or felt separators. Each type of separator offers different advantages, and these must be taken into consideration when selecting the optimum separator.

An advantage of the powder separator over paper or felt separators is that it expands the number of materials which can be considered for use in electrode separators. Boron nitride is the only fibrous material presently available which is stable in the cell environment. This fiber appears to have the potential for meeting the separator cost goals of <$22/m^2 when manufactured in large quantities (>22,700 kg/yr); however, the requirement for a large market to lower the cost of the fiber (through mass production) places a difficult burden on the commercialization program for lithium-aluminum/iron sulfide cells. This is a familiar obstacle to the introduction of any new product using a developing technology.

Several possible candidates for powder separators are presently available, and a few of these are listed in Table I. The maximum cost per kilogram which can be paid for each powder without exceeding the separator cost goal of $22/m^2 is presented, along with the current cost per kilogram. This comparison shows that it may be possible to meet the separator cost goal at current prices using MgO or CaO. The cost of material such as AlN and Si_3N_4, which are now manufactured in small quantities, possibly could be reduced to the required price level. Obviously, this would require that these materials be manufactured in large quantities. Boron nitride, BeO, and Y_2O_3 are already produced in sizable quantities and the opportunities for substantial price reductions are probably limited. An important consideration in determining the potential cost of a particular powder will be the degree of purity required. If a very high purity powder (>99%) is required, the separator cost goal will be difficult to reach. Long-term testing of several candidate powders in cells is needed to determine whether they are truly compatible in the cell environment and to establish the required level of powder purity.

Fibrous separators have the advantages of being thinner (0.5-1.0 mm *vs.* 1.0-2.0 mm) and more porous (70-85% *vs.* 35-55%) than powder separators. The greater restriction of ionic transport through powder separators could lead to a loss in cell performance at higher current densities. This behavior has been observed in recent experiments (8). Cells for stationary energy storage batteries are expected to operate at current densities below 60 mA/cm^2 (9), but cells for electric-vehicle batteries may be required to operate at current densities in the range of 75-150 mA/cm^2 to maintain normal driving speeds and in excess of 400 mA/cm^2 during acceleration and hill climbing (10). Thus, powder separators should be adequate for stationary energy storage cells but may not be suitable for electric-vehicle cells. This apparent disadvantage for the latter could be overcome with an inexpensive powder separator (<$11/m^2) which makes possible the utilization of thinner electrodes. An increase in electrode surface area would reduce the requirement for high current densities.

In other respects, the powder and fibrous separators are roughly equivalent: both appear to provide adequate retention of the active materials in the electrodes, both possess the flexibility necessary to maintain their integrity during any dimensional changes that might occur in the electrodes, and both appear to be amenable to rapid cell assembly. Longer term testing of each separator form in engineering-scale cells is required to more fully evaluate their capabilities and to determine their potential for use in commercial cells.

Table I. Cost comparisons for powder separators*

Powder	Cost/kg** ($)	Current cost/kg† ($)
BN	11	44-110
BeO	9	55-66
Si_3N_4	9	44-250
AlN	9	88-375
CaO	7	1-22
MgO	7	0.2-22
Y_2O_3	4	66-77

* Assuming a separator thickness of 1.5 mm and a porosity of 45%.
** Maximum allowable cost for the powders to obtain a separator cost of <$22/m^2.
† The powder cost is dependent on the purity.

Conclusions

Powder separators are promising candidates for use in lithium-aluminum/iron sulfide cells because they maintain their integrity, conform to small dimensional changes in the electrodes, and appear conducive to rapid fabrication and cell assembly. The electrical performance of this type of separators is very good at current densities below 60 mA/cm^2; therefore, it is a good candidate for use in stationary energy storage cells. The relatively low porosity and the greater thickness of the powder separator compared with paper or felt separators could limit its usefulness for electric-vehicle cells, which are expected to operate at higher current densities.

Powder separators provide good retention of the active materials within the electrodes when a metal frame and screen assembly is used around both the negative and positive electrodes. The potential does exist for eliminating the electrode compartment if the development of large irregularities in the electrode shape can be prevented.

The primary advantage of the powder separator is that it expands the number of separator materials which can be considered for use in lithium-aluminum/iron sulfide cells, and this greatly enhances the prospects for achieving the separator cost goal of $22/m^2. Before the potential of this separator can be realized, however, it will be necessary to identify a low cost powder which is compatible with the cell environment. Possible candidates include, but are not limited to, MgO and CaO.

Acknowledgments

The authors wish to express their appreciation to L. Burris, D. Webster, P. A. Nelson, R. K. Steunenberg, and J. E. Battles for their administrative support. The authors also wish to express their appreciation to J. Harmon for editorial assistance. This work was performed under the auspices of the U.S. Energy Research and Development Administration.

Manuscript submitted April 26, 1978; revised manuscript received July 27, 1978.

Any discussion of this paper will appear in a Discussion Section to be published in the June 1979 JOURNAL. All discussions for the June 1979 Discussion Section should be submitted by Feb. 1, 1979.

Publication costs of this article were assisted by Argonne National Laboratory.

REFERENCES

1. P. A. Nelson *et al.*, Argonne National Laboratory Report ANL-77-18 (March 1977).
2. J. E. Battles, F. C. Mrazek, W. D. Tuohig, and K. M. Myles, in "Corrosion Problems in Energy Conversion and Generation," C. S. Tedman, Jr., Editor, p. 20, The Electrochemical Society Soft-

bound Symposium Series, Princeton, N.J. (1974).
3. J. E. Battles and F. C. Mrazek, U.S. Pat. 3,915,742 (1975).
4. J. S. Dunning, T. G. Bradley, and E. J. Zeitner, in "Proceedings of the Eleventh Intersociety Energy Conversion Engineering Conference," Vol. 1, p. 491, State Line, Nevada (1976).
5. J. P. Mathers, T. W. Olszanski, and J. E. Battles, *This Journal*, **124**, 1149 (1977).
6. N. Otto and F. C. Mrazek, Personal communication.
7. H. Shimotake and L. G. Bartholme, Argonne National Laboratory Report ANL-76-8, p. B-210 (1976).
8. J. E. Battles and R. Swaroop, Personal communication.
9. P. A. Nelson, *et al.*, Argonne National Laboratory Report ANL-75-1 (July 1975).
10. A. A. Chilenskas *et al.*, Presented at the 4th International Electric Vehicle Council Symposium, Dusseldorf, Germany, Aug. 30-Sept. 7, 1976.

Aspects of Alkaline Cell Leakage

Stuart M. Davis

ESB Incorporated, Ray-O-Vac, Madison, Wisconsin 53711

and Michael N. Hull*

The International Nickel Company, Incorporated, Inco Research and Development Center, Sterling Forest, Suffern, New York 10901

ABSTRACT

An experimental study has been made of the effect of several variables on the creepage rate of alkaline electrolytes along negatively polarized metallic surfaces. The variables studied were (*i*) nature of the cation, (*ii*) electrolyte concentration, (*iii*) external relative humidity, (*iv*) moisture transmission through seal, (*v*) seal compression, and (*vi*) electrolyte additives. A discussion of the mechanism by which these variables influence the creepage rate is given and their relative order of importance is listed.

In a previous publication (1), a description of theoretical and experimental work on the creepage of alkaline electrolytes along negatively charged metal surfaces was given. From an observation by one of the authors (SMD) that oxygen had a marked accelerating effect on creepage, it was shown that the driving force behind this phenomenon was the production of hydroxyl ions in a thin reaction zone above the electrolyte meniscus. This production of alkalinity above the meniscus arises from the electroreduction of oxygen (and/or water) which occurs preferentially in this zone where diffusive transport of oxygen to the surface (or evolved hydrogen away from the surface) has a maximum rate.

In the following text, we would like to address some of the practical aspects of creepage control. Specifically, we shall consider the following: (*i*) Cation mobility from the bulk solution and into the reaction zone should be reduced to delay the creepage. Total or partial substitution of the high mobility alkali metal cations (K^+, Rb^+, etc.) with those of sodium or preferably lithium will be beneficial. The use of gelling agents to increase the solution viscosity is indicated. (*ii*) Electroreduction of water accelerates creepage. Prevention of moisture transmission from high external relative humidity conditions to the reaction zone via the grommet material is desirable. (*iii*) Electroreduction reactions require negatively charged surfaces. Lowering the negative charge in the seal region through the preferred use of electropositive (*i.e.*, noble) metal substrates will aid in creepage control. (*iv*) Electroreduction of oxygen accelerates creepage. Addition of cations from Group II A of the Periodic Table will reduce creepage by raising the overvoltage for electroreduction of oxygen.

Experimental

The conductivity and leakage characteristics of mixed KOH, NaOH, and LiOH electrolytes.—Since equal weight percent KOH, NaOH, and LiOH solutions do not give the same molar hydroxyl ion concentration (40% KOH being equal to 30% NaOH and each 10 molar in hydroxyl ion) electrolyte mixtures were chosen on a mole percent OH^- basis. As a first step, therefore, the effect on the creepage rate of a 10 molar solution was investigated as one replaced the K^+ with Na^+. Figure 1 shows how the calculated

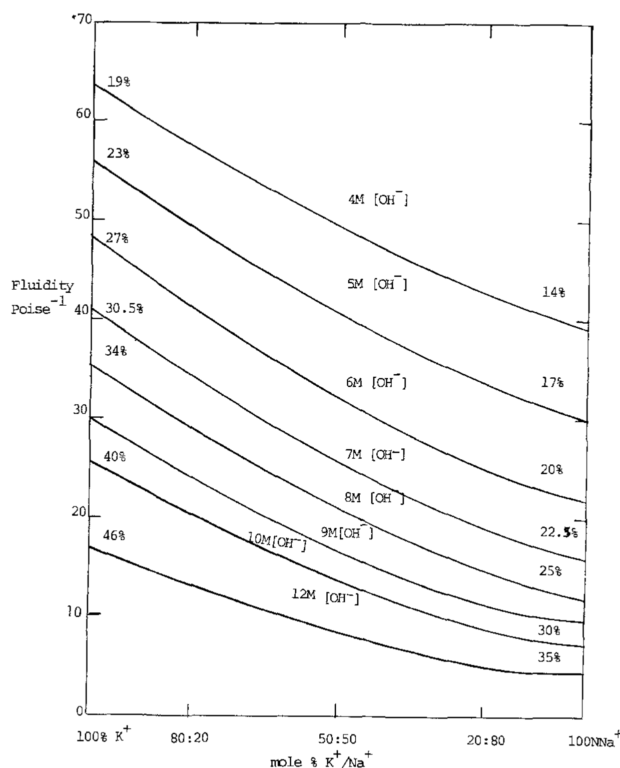

Fig. 1. Fluidity-composition relationships at constant hydroxyl ion concentration for mixed KOH-NaOH electrolytes.

* Electrochemical Society Active Member.
Key words: battery, seals, pressure, electrolysis.

fluidity (reciprocal of viscosity) will change as one switches from K^+ to Na^+. The percent figures given at 100% K^+ are the weight percent figures for the pure KOH solutions while at the other end of the isohydroxyl concentration lines, the percent figures give the weight percent of pure NaOH. It may be seen that there is a uniform decrease in fluidity between 40% KOH and 30% NaOH.

Figure 2 shows typical creepage results for such mixed electrolyte indicating that the creep height declines smoothly as Na^+ is substituted for K^+. [The experimental arrangement for recording the creepage rate is described in full in Ref. (1). The terms "solid creep" and "fine creep" refer to the fact that the creepage layer has two zones. Immediately above the meniscus, the creepage forms a continuous solid film which then merges into a second zone of fine electrolyte spots.] There are, however, three factors which prevent one from switching directly from 40% KOH to 30% NaOH. First, overvoltage effects may increase and adversely influence the cell discharge as one substitutes Na^+ for K^+. Second, cation mobility through the separator may be very important necessitating a substantial concentration of small cations, *i.e.*, K^+, and third, the intrinsic electrolyte conductivity declines as Na^+ is substituted for K^+. There exists, however, a range of electrolyte features which can be considered in an effort to optimize an alkaline cell in terms of satisfactory leakage characteristics and discharge performance in the mixed potassium-sodium hydroxide electrolytes.

In addition to NaOH-KOH mixtures, we investigated those of KOH-LiOH. These are more difficult to display on isoconcentration lines since one can only make a maximum of about 4M LiOH and to obtain, for example, a 6M OH^- solution, one has to mix the 4M LiOH with KOH solutions of greater than 6M. Several KOH-LiOH mixtures with 6M OH^- concentration were, however, formulated as follows (6M being chosen since in the all K^+ case this electrolyte is close to the maximum of conductivity exhibited by KOH solutions)

(*a*) 6M KOH — 100% K^+

(*b*) 66.5 cm^3 7M KOH + 33.5 cm^3 4M LiOH — 78% K^+

(*c*) 50 cm^3 SM KOH + 50 cm^3 4M LiOH — 66% K^+

(*d*) 33.5 cm^3 10M KOH + 66.6 cm^3 4M LiOH — 55.5% K^+

The creepage results for these solutions are shown in Fig. 3 and indicate that most of the creepage decrease occurs between solutions (*a*) and (*b*) with a smaller relative change as one moves from (*b*) to (*d*). A comparison with Fig. 2 shows that a similar reduction in creepage rate can be accomplished with a 40% substitution of K^+ with Li^+ as for an 80% substitution with Na^+.

Figure 4 compares the change in resistance of pure KOH and NaOH solutions as a function of concentration and also indicates the relative conductivity of various mixed electrolytes. As is well known, there is a smooth decrease in conductivity as the sodium ion is substituted for potassium but because the peak conductivity of KOH solutions lies at a higher hydroxyl ion molarity than sodium hydroxide, several of the mixed electrolytes, at high hydroxyl ion concentration, are better conductors than the most conductive pure NaOH solution. There thus exists a broad area between the peak conductivity compositions of NaOH and KOH within which the improved leakage characteristics imparted by the Na^+ ion may be coupled with the good conductivity characteristics of that of K^+.

External humidity and the effect on creepage rate.—There are several possible sources which supply

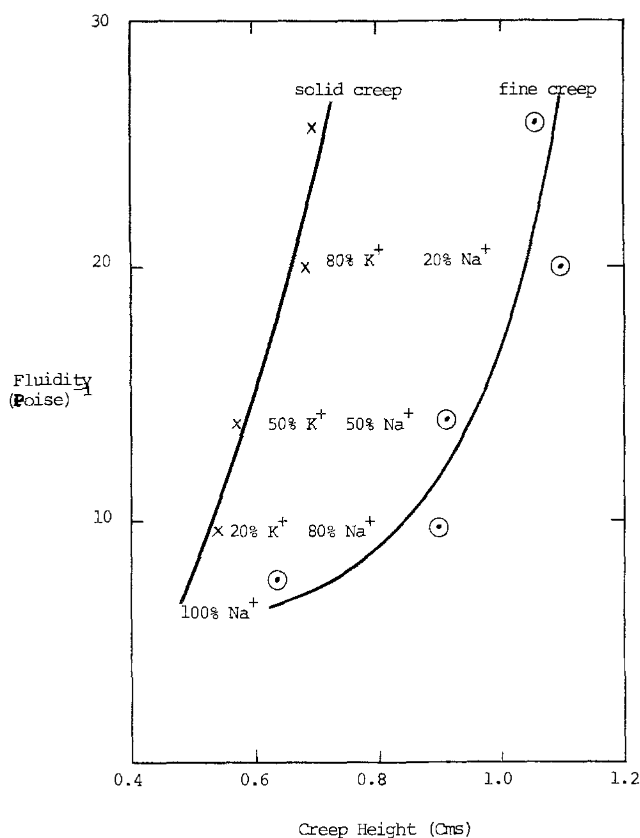

Fig. 2. Fluidity-creep relationships for mixed KOH-NaOH electrolytes of 10M OH^- ion concentration. Strip electrode potential $E = -1.35V$ vs. Hg · HgO.

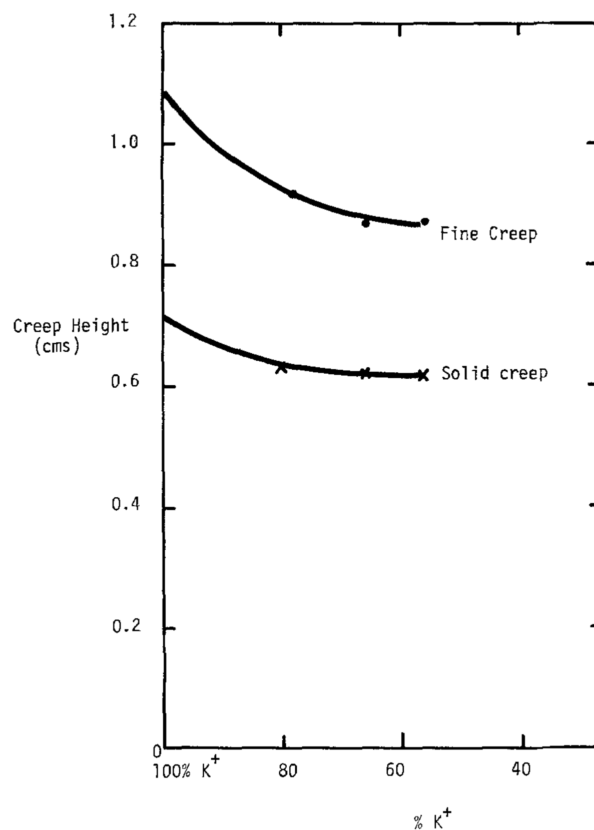

Fig. 3. Creep height after 24 hr as a function of the K^+:Li^+ ratio. $E = -1.35V$.

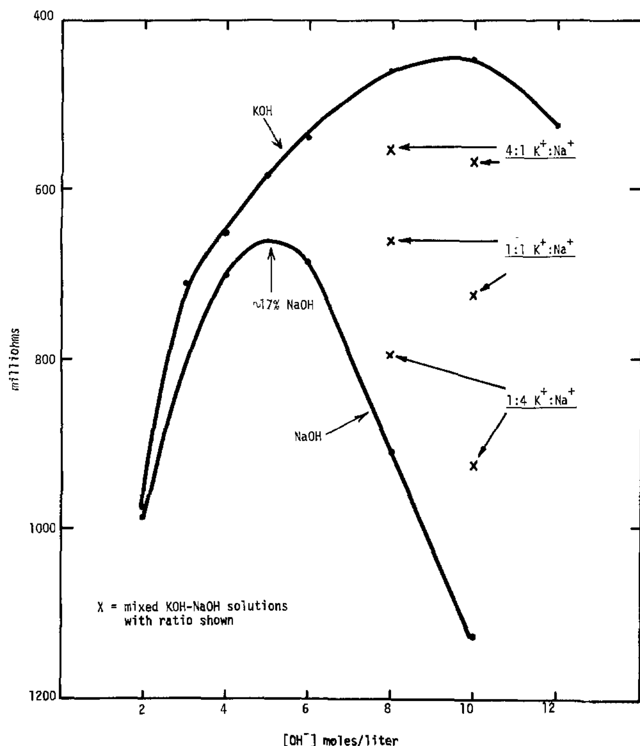

Fig. 4. Relative resistances of pure KOH and NaOH electrolytes within the concentration range 2-12M and of mixed KOH-NaOH electrolytes of 8 and 10M.

water to the reaction zone (1, 2). Water may move from the bulk electrolyte to the zone, it may condense from the water vapor above the electrolyte, or it may penetrate from the atmosphere external to the cell either through the grommet or between the grommet and the negatively charged metal surface. Creepage rates were measured on nickel strips in 35% KOH contained in a sealed dessicator within which the relative humidity could be controlled using sulfuric acid or calcium chloride solutions. The results shown in Fig. 5 are a clear proof that high relative humidities in the vicinity of the reaction zone lead to high rates

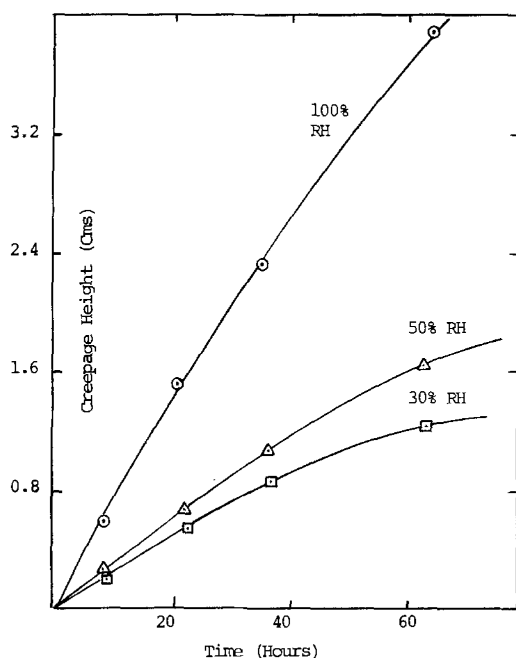

Fig. 5. Comparison of the rate of creepage of 35% KOH along nickel strips at —1.05V vs. Hg-HgO as a function of the relative humidity.

of creepage and are in contrast to those reported in Ref. (2). Such effects have been confirmed for production cells using nylon grommets and this raises the question as to how the cell is able to sense the external relative humidity conditions. Two mechanisms have been identified: (*i*) external electrolysis reactions occurring on the oppositely charged surfaces of the cell due to the presence of ionic conduction across the moisture layer absorbed in the external surface of the grommet, and (*ii*) water diffusion through the grommet to the reaction zone.

External electrolysis reactions—the problem.—Figure 6 illustrates how the presence of an ionic path external to the cell permits a slow discharge reaction to occur through the high ionic resistance E_1 by the electrolysis reactions which can proceed at M_1 (the negative top) and M_2 (the positive can rim). M_1, being negative, will evolve hydrogen according to

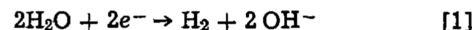

$$2H_2O + 2e^- \rightarrow H_2 + 2\,OH^- \quad [1]$$

and also reduce oxygen from the surrounding air via

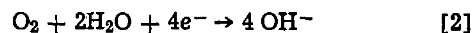

$$O_2 + 2H_2O + 4e^- \rightarrow 4\,OH^- \quad [2]$$

while at the positive can rim, oxygen will be evolved via

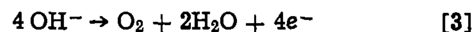

$$4\,OH^- \rightarrow O_2 + 2H_2O + 4e^- \quad [3]$$

and corrosion of the can rim will occur

$$Ni + 2\,OH^- \rightarrow Ni(OH)_2 + 2e^- \quad [4]$$

to give nickel hydroxide (or more probably, the green basic nickel carbonate) if the can contains nickel but also via

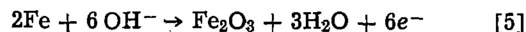

$$2Fe + 6\,OH^- \rightarrow Fe_2O_3 + 3H_2O + 6e^- \quad [5]$$

in the presence of alloys of iron. Many cells stored in high humidity conditions exhibit visual proof of this current flow by the black, branched lines of precipitated corrosion products which grow across the grommet from the can rim.

Due to the movement of negative charge (the electronic current flow) from the zinc inside the cell to M_1 outside the cell, the internal electrolyte can be forced to move by electro-osmotic action along the seal interface (1). If one looks at the negative seal interface in somewhat more detail (Fig. 7), it may be seen that due to the negative charge which is impressed on this surface of the zinc, there is a balancing excess positive charge in any moisture layer between the negatively charged surface and the grommet. These excess positive ions as they move concurrently with the negative surface charge carry water from the internal to the external surface of the cell. [A more complete description of this electro-osmotic movement is given in Ref. (1).]

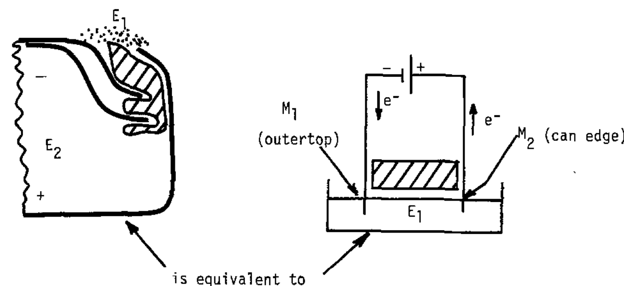

Fig. 6. Illustration of electrolysis reactions occurring on the external surfaces of the cell in the presence of high humidity access to the grommet.

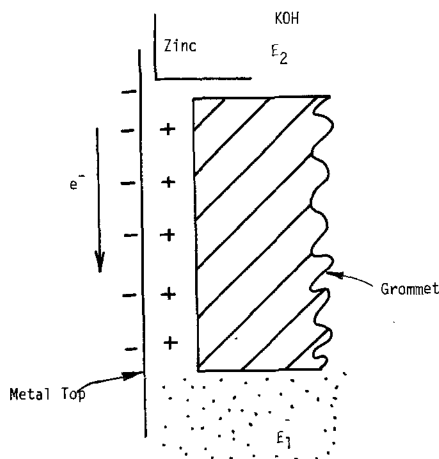

Fig. 7. Charge distribution and direction of charge movement at the negative seal interface of an alkaline cell in the presence of external electrolysis reactions.

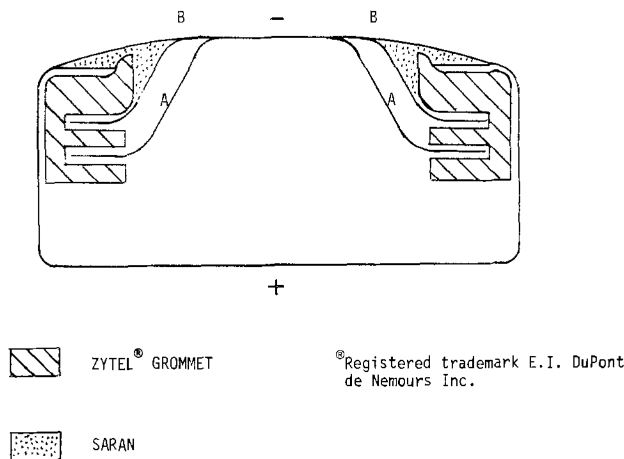

Fig. 8. Cross section of a double-top alkaline button cell with a Saran-coated grommet.

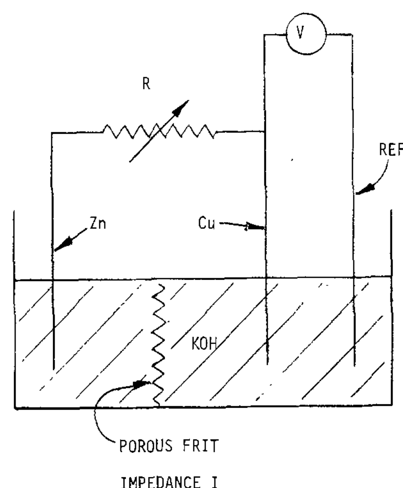

Fig. 9. Illustration of ionically and electronically connected metallic strips of differing composition in a KOH electrolyte.

Water transmission through the grommet.—Accelerated leakage tests conducted by placing cells at an elevated temperature are probably accelerated more by the additional vapor pressure of water present at the higher temperature for a fixed relative humidity than by the elevated temperature itself. For example, if one considers cells containing 40% KOH placed in a 100% RH environment at 20° and 40°C then, at the former temperature, there will be an external water vapor pressure of 17.5 mm H_2O and an internal pressure of 6.2 mm H_20. The difference in water pressure acting through the grommet is thus 11.3 mm. At the higher temperature, the corresponding outside and inside values are 55.3 and 20.1 mm, respectively, giving a net pressure of 35.2 mm through the grommet. The 20°C rise in temperature resulted in a factor of over three increase in the water vapor pressure differential across the grommet. It is clear, therefore, that grommet materials having a high water absorption capability, such as the nylons, will readily transmit external relative humidity increases to the creepage zone in the seal area. Such materials should be protected from high RH conditions to maximize their utility as seal materials particularly when exposed to humid environments.

Based on the above observations, a method was developed to coat alkaline button cells with moisture-retarding barriers. As a simple example of the efficacy of such treatments, we coated experimental[1] cells with Saran (vinylidine chloride-acrylonitrile copolymer) as shown in Fig. 8. Saran was chosen for its known low water vapor (0.10 g/100 in.^{2}/24 hr at 100°F, 90% RH 1 mil) and oxygen (0.1 cm^3/100 in.^{2}/24 hr at 1 atm pressure difference, 73°F, 1 mil) transmission characteristics and was applied from a ketone solution to the surfaces indicated in the figure. The results of tests conducted at 45°C and 100% RH on these experimental cells are presented in Table I. Uncoated cells have a nearly 100% leakage condition after 22 days compared to an approximate 30% frequency after 42 days on coated cells.

The nature of the metal along the seal path.—The rate of creepage of alkaline electrolytes along a potentiostated copper strip is faster than that observed along a nickel alloy strip (*e.g.*, Inconel 600) under the same conditions. The reverse situation is observed in a cell environment where there is a grommet under high compression contacting the metal surface. The reason for this discrepancy lies in the fact that, in an actual seal situation, there is a low electronic resistance combined with a high ionic resistance in the creepage layer itself. Consider the arrangement depicted in Fig. 9 which shows a copper electrode electronically and ionically shorted to a strip of zinc ($R = 0$, $I = 0$). Under these conditions, the copper strip is held at the zinc potential of ~ -1.38V (Hg-HgO) and very rapid creep will occur along the copper strip. In an actual double top cell, one may have several different metal surfaces in the seal area, *e.g.*, Cu and Inconel, which, as shown in Fig. 10, are shorted electronically to the zinc. On the other hand, although KOH is quite conductive, they are not shorted ionically to the zinc since the creepage film between the grommet and the metallic surface is extremely thin and has, therefore, a substantial ionic resistance. A correct experimental simulation of an actual cell condition would be to utilize frits of different porosity interposed between the zinc and copper strips as shown in Fig. 9 where $R = 0$ and I has a finite value thereby introducing a solution resistance between them equivalent to that of the creepage film.

[1] The cells chosen for this study employed no sealant in the grommet area, as is normally practiced in commercial production, and were therefore highly susceptible to leakage.

Table I. Leakage characteristics of RW-44 control and Saran-coated cells as a function of time at 45°C and 100% RH

	Days at 45°C, 100% RH					
	7	14	22	28	35	42
Control cells* % leaking	20	40	93	100	100	100
Saran coated* % leaking	0	0	7	7	26	30

* Without commercial sealant applied to production cells.

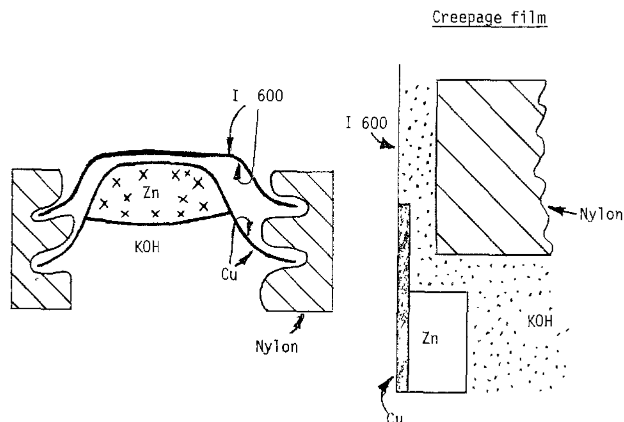

Fig. 10. The shorted electronic path and resistive ionic path established in the seal area of a button cell.

It is evident that if the frit resistance was infinitely large (corresponding to an extremely tight compressive fit of the grommet to the metal surface) then the Cu electrode would be unaffected by being electronically shorted to the zinc and would adopt its own electrode potential of ~ −0.42V (nearly one volt less negative than zinc). In the real case, the electrolyte resistance is not infinitely large so the question raised is, How does the magnitude of the negative electrode potential impressed in the seal area by the zinc vary with the nature of the metal substrate in the seal area and the ionic resistance in the creepage film?

This question was investigated for a series of metal substrates by ionically shorting a large zinc sheet to a one-tenth the size sheet of the metal and adding an electronic resistance between the two, *i.e.,* R has a finite value and $I = 0$ in Fig. 9. The metal strip will come to the same value of potential regardless of whether R is in the electronic loop as a resistor or in the ionic loop as a porous frit of impedance I. The potential of the test strip was measured as a function of R and the trends are shown in Fig. 11a for an argon atmosphere and in Fig. 11b for an atmosphere of air. The trends indicate that if a high compression seal is established thereby increasing the ionic resistance of the creepage film and the grommet has low permeability to oxygen, then the more noble the metal, the lower will be the negative potential in the seal area and hence the lower will be the creepage rate. Under these conditions, a gold-plated surface would most likely be the optimum condition. In contrast with grommet materials having low compressions or having a moderate to high permeability to oxygen, a copper (or copper plated-surface will have

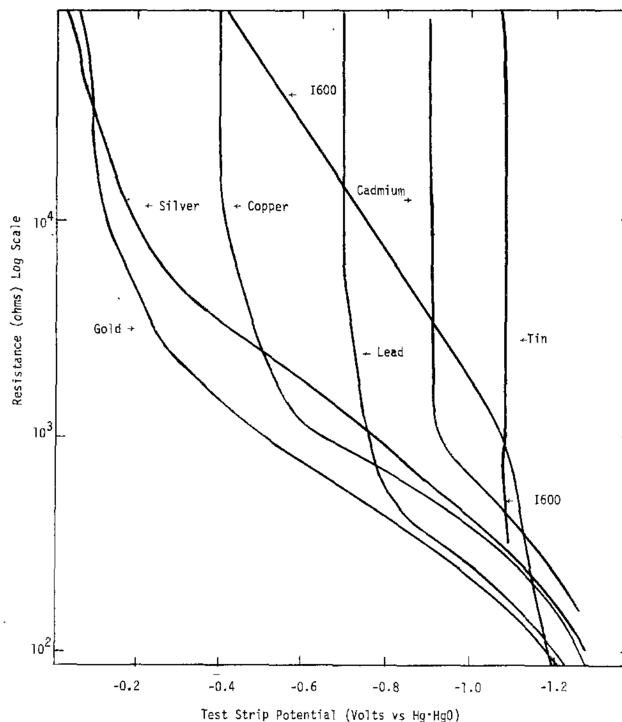

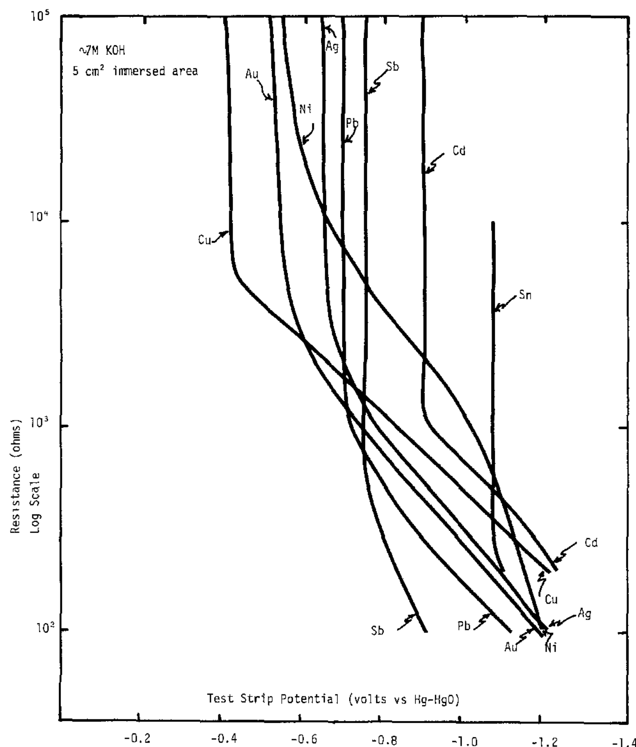

Fig. 11. The electrode potential established at different metal strips when ionically shorted and electronically connected through a resistance *R* as a function of *R* in the presence of (a, upper) argon and (b, lower) air.

the greatest ability to hold the potential in the seal area at the least negative potential.

Electrolyte additives to reduce creepage.—Gelling agents.—Increase in the viscosity of an alkaline electrolyte would generally be expected to reduce the creepage rate (2). Somewhat surprisingly in our study of the viscosity dependence of the creepage rate, we found that the structure and hence the wetting tendency of the gelling agent itself may override the viscosity effect. Thus as Table II shows, Na CMC and Guar Gum both have a tendency to accelerate creepage while with acrylic acid-acrylic ester copolymers the opposite effect is observed. Although

Table II. Effect of 3% sodium carboxy methyl celluose, 3% Guar Gum, 3% acrylic acid acrylic ester copolymer on the creepage rate of 35% KOH along nickel strips held at −1.05V vs. Hg · HgO. Also shown is the effect of saturating 35% KOH with barium hydroxide.

Electrolyte	Mean creepage height (cm) Fini	Solid	
Blank 35% KOH	0.89	0.46	Test chamber No. 1
35% KOH with 3% NaCMC	1.37	0.61	Test chamber No. 1
Blank 35% KOH	1.04	0.64	Test chamber No. 2
35% KOH with 3% Guar Gum	1.5	0.65	Test chamber No. 2
35% KOH with 3% acrylic acid-acrylic ester copolymer	0.91	0.52	Test chamber No. 2
Blank 35% KOH	0.97	0.68	Test chamber No. 3
35% KOH saturated with $Ba(OH)_2$	0.85	0.52	Test chamber No. 3

we have not as yet completed a definitive study of this observation, we believe that while Guar Gum and Na CMC increase the electrolyte viscosity, they tend to reduce the wetting angle of the electrolyte to the metal surface thus increasing the area of the reaction zone.

Effect of the addition of Group II A cations.—Since the electrochemical reduction of oxygen has a marked influence on the rate of alkaline creepage, it would appear reasonable to expect that electrolyte additives which could increase the overvoltage for oxygen reduction would help delay creepage. The Group II A cations are known to behave in this fashion and accordingly the effect of $Ba(OH)_2$ additions to a potassium hydroxide electrolyte were investigated. Table II shows that a reduction in the rate of creepage does result though the magnitude of the effect is relatively small. Several other di- and multivalent cations were tested including Sr^{++}, Ca^{++}, La^{+++}, and Ce^{4+} but, in each case, the solubility of the hydroxide was too low in 35% KOH to produce an effect.

Transfer of positive leakage to the negative terminal.—In this and the preceding paper (1) the discussion has centered on the problem of leakage appearing on the negative terminal of alkaline cells due to factors specific to the negative electrode-electrolyte interface. However, under certain conditions we have observed that a poor positive seal can cause the appearance of "salting" on the negative terminal of the cell. This phenomenon is an interesting consequence of the electrochemical creepage mechanism and may be explained by migration of Na^+ or K^+ ions across the grommet from the positive seal point of leakage driven by electro-oxidation of the leaked electrolyte on the surface of the positive can according to reaction [3] and concurrent hydrogen evolution from the humidity layer adsorbed on the surface of the negative top as in reaction [1] or oxygen reduction according to the reverse of reaction [3].

To demonstrate this phenomenon twelve alkaline button cells were placed in a petri dish having the negative terminal facing up and 30% KOH was poured into the dish to establish a liquid depth of 1-2 mm. Of the twelve cells six had an open-circuit voltage of 1.6V while the remaining were constructed without the active ingredients and did not exhibit an OCV. In addition to the above 12 cells partially immersed in the KOH electrolyte, an additional six "live" cells were placed on a watch glass out of contact with the KOH. After several weeks in a controlled humidity environment the appearance of the cells is as shown in Fig. 12. It may be seen that the six "live" cells in contact with the KOH (6 o'clock position) became heavily encrusted with caustic over most of the negative terminal while the six "zero voltage" cells at the 12 o'clock position remained quite clear. In addition the six "live" cells under the same conditions of humidity, but maintained out of contact with the KOH, did not develop deposits on their negative terminals.

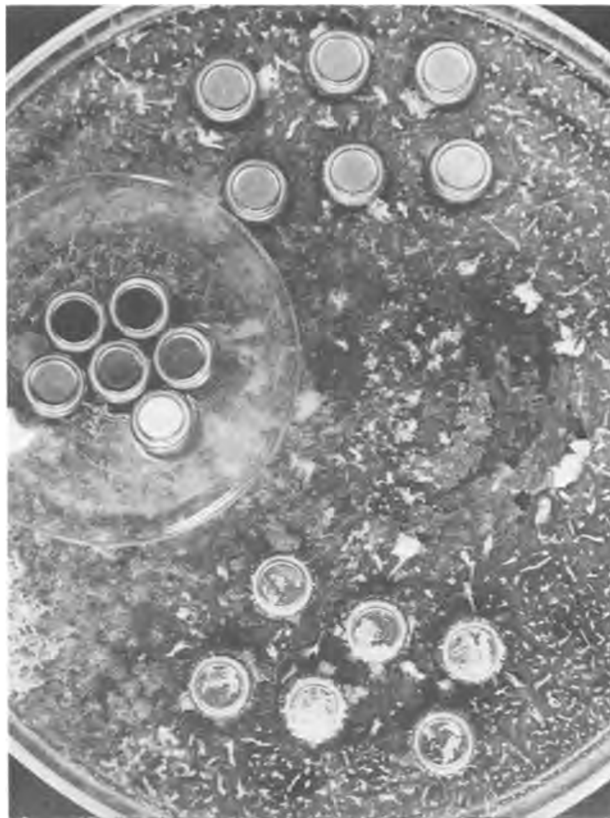

Fig. 12. Photograph illustrating the transfer of KOH electrolyte from the positive to the negative terminal of an alkaline button cell.

This demonstration is a clear illustration that electrolyte may be moved by electrochemical action from the positive to the negative terminal of an alkaline cell and confirms our observations that in such a cell the appearance of leakage on the negative terminal does not necessarily prove that such leakage has exited by way of the negative seal.

Manuscript submitted April 21, 1978; revised manuscript received June 30, 1978.

Any discussion of this paper will appear in a Discussion Section to be published in the June 1979 JOURNAL. All discussions for the June 1979 Discussion Section should be submitted by Feb. 1, 1979.

Publication costs of this article were assisted by ESB Incorporated.

REFERENCES

1. M. N. Hull and H. I. James, *This Journal,* **124,** 332 (1977).
2. L. M. Baugh, J. A. Cook, and J. A. Lee, *J. Appl. Electrochem.,* **8,** 253 (1978).

Electrochemical Heaters Utilizing Aluminum Alloy and Magnesium Anodes

S. Gilman* and P. Bramhall

U.S. Army Electronics Research and Development Command, Electronics Technology and Devices Laboratory, Fort Monmouth, New Jersey 07703

ABSTRACT

A short-circuited electrochemical cell made with a saline electrolyte, an aluminum alloy or magnesium anode, and a manganese dioxide cathode may be used as a rather efficient short-term portable heater. The use of a magnesium anode provides somewhat higher heat content but results in the production of considerable hydrogen gas. Certain aluminum-zinc alloys are almost as energetic as magnesium and produce little hydrogen.

If an electrochemical cell is short circuited, its chemical energy is almost completely converted into heat via the various ohmic and nonohmic polarizations occurring in the electrolyte at both electrodes. The heat from such an "electrochemical heater" may be largely transferred by thermal conduction to any material with which it is in intimate contact. One advantage of such an electrochemical heat source over a purely chemical (*e.g.*, thermite) one is that the reaction tends to proceed in a more gradual and controlled manner. Compared to the use of an electrochemical cell with a remote resistive heater, the direct electrochemical heater avoids the problem of inefficient transfer of energy from the cell which becomes particularly critical at high rates of cell discharge.

Electrochemical heaters utilizing aluminum and magnesium anodes and various cathodes have been developed for such applications as protective clothing, diving gear, and the heating of field rations (1-4). Magnesium-manganese dioxide cells with saline electrolyte are of particular interest in the last application where it is advisable to avoid toxic materials and where the service life of the heater is of the order of 15 min (4). One disadvantage of the Mg-MnO_2 cell is that a considerable volume of hydrogen is produced during discharge, presenting a potential explosion hazard. Our purpose in this work was to analyze the performance of the short-circuited Mg-MnO_2 cell and determine if similar but hydrogen-free performance could be obtained by substitution of an aluminum alloy for the magnesium.

Experimental

Preparation of electrodes and electrolytes.—Anodes.—The aluminum alloys for these studies were prepared by Reynolds Metals Company using procedures and heat-treatments similar to those previously reported (5). The alloys were prepared with high purity (99.992%) aluminum as a base; the aluminum was induction-melted, in air, in silicon carbide crucibles. All additions of pure metals were made at a temperature over 705°C and stirred to ensure homogeneity. The melts were treated with gaseous chlorine and then semicontinuously cast into ingots using an aluminum direct chill caster. The ingots were cleansed by scalping the surfaces. They were then heat-treated for homogenization and cold-rolled to a thickness of 0.04 cm. Pure aluminum used in half-cell studies was wire of 0.1 cm diam and 99.99+ purity (Alfa Inorganics). Pure magnesium for half-cell studies was 0.3 cm diam rod of "sublime" grade (Dow). The magnesium for whole-cell studies was "primary grade" (Dow) sheet of 0.028 cm thickness. For whole-cell ("electrochemical heater") experiments, 1 $\times$ 1 cm anodes were prepared from the appropriate sheet stock by fastening a nickel expanded metal screen (5 Ni 7 — 2/0 from Exmet Corporation) to the back side of the electrode using epoxy cement. The bonding was accomplished in a hydraulic press with heated platens (200 kg/cm^2 pressure at 135°C). A tab of screen was left on the sample and a heavy gauge tinned copper wire was soldered to it in such a way that no contact was possible between the solder connection and the electrolyte. Samples of flat stock metals used in half-cell experiments were prepared by pressure cementing a nickel foil contact to the top of a 0.5 $\times$ 2.2 cm coupon and then masking off the nickel contact with silicone rubber, leaving a 0.5 $\times$ 2.0 cm exposed area. Anode surfaces were degreased with trichloroethylene prior to use.

MnO_2 cathodes.—Electrodes were made, or obtained, with various formulations containing MnO_2, graphite, carbon black, graphite fiber, and current-collecting screens. Methods of preparation are reported below for four particular formulations.

(*i*) Electrodes of this formulation were developed (4) and supplied by Power Applications, Incorporated, Valley Stream, Long Island, New York. They were prepared by binding a mixture of MnO_2 (natural ore containing 74% MnO_2), carbon black (Cabot XR-72), and fullers earth (in the weight ratio of 10:2:1), with polytetrafluoroethylene emulsion, to a 20 $\times$ 20 mesh steel grid. The completed cathode was of 0.05 cm thickness and contained 0.035g of MnO_2 ore per square centimeter of electrode area.

(*ii*) This formulation was based on formulations reported by Kordesch (6). A mixture of MnO_2 ("chemical MnO_2 ore"), graphite powder, and carbon black (Shawinigan, 50% compressed) in proportions 43:5:1 was ball-milled for 2 hr. The mixture was then blended with fuller's earth and graphite fibers in proportions 100:5:1. The blend was then mixed with a 5% solution of Lucite in trichloroethylene (percentage of Lucite in final dry mixture was 2.5%), applied to an etched 20 $\times$ 20 gauge stainless steel screen, and air dried. The completed electrode contained 0.07g of MnO_2 ore per square centimeter of electrode area.

(*iii*) Electrodes of this formulation were developed (6) and supplied by Kordesch (Union Carbide Corporation). They were of similar formulation to the ones described in Ref. (2) above but utilized Tekkosha brand MnO_2, three times the graphite fiber content, and no fuller's earth. The finishing electrodes were 0.1 cm thick and contained 0.17g of MnO_2 per square centimeter of electrode area.

(*iv*) This formulation was prepared using the ball-milled mixture of MnO_2, graphite, and carbon black mentioned in fomulation (*ii*) above. The mixture was dry pressed into a porous nickel matrix (45 pore, 0.41 cm thick "Foametal" from Hogen Industries, Willoughby, Ohio) in a manner similar to that reported

* Electrochemical Society Active Member.

Key words: saline cells, manganese dioxide, corrosion.

previously (7). The final structure was 0.1 cm thick and contained 0.2g of MnO_2 per square centimeter of electrode area.

Electrical contact was made to the cathodes by welding a lead to a tab of exposed screen and insulating in such a way that contact between the lead and the electrolyte was avoided.

Electrolytes.—For experiments with complete flat cells ("electrochemical heater" experiments), the cell was assembled in the dry state, using 0.165 cm thick "Webril R-2801" (Kendall Mills) impregnated with NaCl (0.037 g/cm^2) to which water was added just before the experiment. The same electrolyte arrangement was used in the voltage-sweep experiments on cathodes. Experiments on fully immersed anodes and cathodes were performed using a solution of NaCl made by saturating distilled water with reagent grade salt at room temperature.

Procedures for making electrochemical and hydrogen-release measurements.—Electrochemical heater experiments.—Using a 1 $\times$ 1 cm anode and cathode, the cells were assembled in a gas-tight Lucite fixture of very small internal volume in which rubber pads maintained pressure on the cell components and acted as a heat sink. The temperature at the anode-rubber interface was monitored with a Chromel-Alumel thermocouple when desired. All the electrodes used in these experiments were fabricated with screens to which heavy current leads were soldered inside the Lucite fixture, and those leads were also useful in supporting and positioning the electrodes in the cell. The cells were fabricated using the salt-filled Webril electrolyte pad described above. The pad was left oversize at one end, and 0.3 cm wide strips of MnO_2 cathode [formulation (*i*)] were placed in the same planes as the anode and cathode with a 0.1 cm gap between each strip and the adjacent electrode. These served as "dry" reference electrodes for the adjacent anode or cathode. The recorded potentials were then converted to "potentials *vs.* the saturated calomel electrode," by subtracting 0.41V, which takes into account the typical open-circuit voltage of cathode formulation (*i*). The external connection between the anode and cathode was made by means of a calibrated 0.01Ω shunt through which the "virtual" short circuit current was monitored continuously by means of a strip chart recorder (Hewlett Packard No. 7100B). Simultaneous recordings were made of the anode and cathode potentials relative to their respective reference electrodes. The volume of hydrogen gas evolved from a cell was determined using a gas buret. The dry cell was activated just before use by flooding with water for 15 sec and then draining off the excess.

Measurement of anode polarization and hydrogen gas evolution in half-cells.—Anode polarization was studied using wire or 0.5 $\times$ 2 cm foil samples, prepared as specified above. The experiments were performed in a glass-stoppered, thermostated, (25°C) three-compartment cell with a reference saturated calomel electrode (SCE) and a platinized platinum counter-electrode (see Fig. 1). The electrolyte was a saturated solution of sodium chloride; 200 cm^3 of the electrolyte were required for the working electrode compartment and that volume was renewed after each determination. The polarization (current-potential) curves were recorded on an X-Y recorder (Hewlett Packard No. 7047A) while applying an anodic potential scan (speed of 0.001 V/sec) using a potentiostat (Tacussel No. P1T20-2A) and signal generator (Tacussel No. GSTP-2). The reverse sweeps were triggered manually after reaching a top current of 200 mA/cm^2.

Gas evolution was measured for similar anodes under constant-current conditions. The gas evolution measurements were accomplished by means of the glass mantle and bubble flowmeter arrangement shown in Fig. 1. The flowmeter was chosen of either

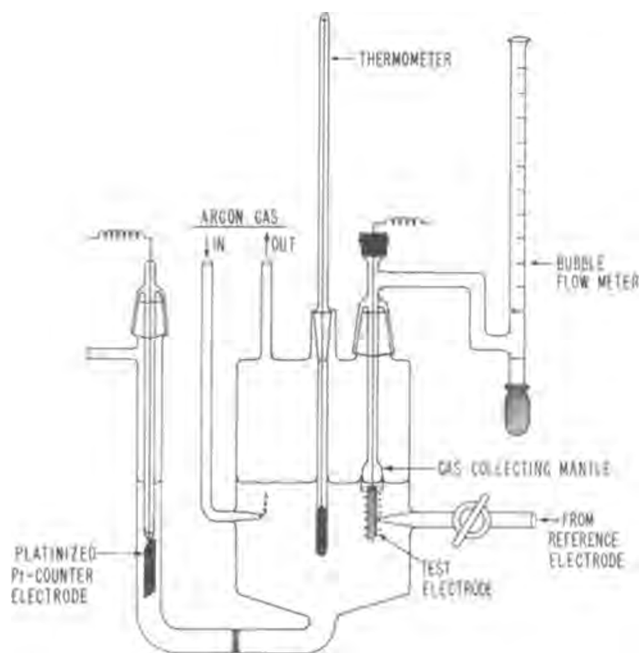

Fig. 1. Glass vessel for polarization and H_2 release measurements

1 or 10 cm^3 volume (depending on the anticipated rate of gas evolution) and the position of the bubble recorded at 1 min intervals. With the 1 cm^3 flowmeter, flow rates as small as 2.2 $\times$ 10^{-4} cm^3/sec (equivalent to an electrochemical H_2 evolution rate of 2 mA) could be read with 90% accuracy within 3 min after initiating the flow, and rates down to 1.1 $\times$ 10^{-4} cm^3/sec (1 mA) could be read accurately after 5 min. The accuracy was tested by generating H_2 at a platinum electrode (with 100% efficiency). The 3 and 5 min delay intervals cited above probably correspond to the very slight lowering of the electrode meniscus (the buildup of gas pressure) required to overcome inertia of the soap film in the bubble flowmeter.

Measurement of polarization and hydrogen evolution of fully immersed cathodes in half-cells.—The procedures used for studying MnO_2 cathodes in an excess of saturated NaCl solution were identical to those described directly above for anodes, except for the type of signal impressed on the cathode. In this case, a preselected constant potential was applied to the electrode ("potential-step" method) and the resulting current-time trace was recorded on a strip chart recorder (Hewlett-Packard No. 7100B). A fresh sample of electrode was required for each new potential imposed. Hydrogen gas is evolved at a MnO_2 electrode at sufficiently negative potentials. The rate of gassing was measured under "potential-step" conditions for cathode formulation (1).

Measurement of polarization at cathodes using an electrolyte pad.—For purposes of fast "screening" of new electrolyte formulations, polarization curves were measured using a cathodic potential sweep. Since many of the electrode formulations were found to give better results when mechanically compressed (thus improving contact between the MnO_2 and the current collector), such experiments were performed using the salt-impregnated Webril pad described above, and a Mg "counterelectrode" in an arrangement similar to that described above for "electrochemical heaters."

Results and Discussion

Thermodynamic considerations.—Table I presents the reaction equations and corresponding thermodynamic quantities for the chemical processes antici-

pated in Mg and Al cells utilizing MnO_2 cathodes (8, 9). The standard enthalpy, $\Delta H°$, the standard free energy, $\Delta G°$, those latter quantities divided by the number of equivalents ($\Delta H°/n$ and $\Delta G°/n$), and the standard cell potential $E°$ were calculated using standard enthalpies and free energies of formation (9). Reaction equations for cells 1 and 3 of Table I correspond to coulombically efficient utilization of both plates of each cell. The equations for cells 2 and 4 are for the reactions producing hydrogen. The hydrogen may be produced at either the anode (corrosion) or the cathode (cathode gassing). The most relevant quantities for heat-production purposes are the enthalpies rather than the free energies. Furthermore, reference to the values of $\Delta H°/n$ is useful if we wish to compare the reactions for the same "internal current" of the cell. Since the values of $\Delta G°$ and $\Delta H°$ are almost identical, the values of $E°$ are almost as valid for purposes of comparison as those of $\Delta H°/n$. From the values of $E°$ we may, therefore, conclude that, for identical cell "internal current" and with no hydrogen evolution, the Al/MnO_2 cell is 12% less energetic than the Mg/MnO_2 cell. On the other hand, much of the total "internal current" of the present Mg cell is directed into the far less efficient hydrogen evolution reaction (reaction No. 2, Table I) If this reaction were eliminated, it could more than compensate for the 12% loss.

Thermodynamic reduction potentials for the individual electrode reactions under consideration here are reported in Table II and are discussed later. The standard potentials listed in the table were obtained from Pourbaix's atlas (10).

Polarization and hydrogen gas release at the anode.—In order to best reflect "practical" conditions, anode surfaces were merely degreased and dried before use. Alternative sandpapering of the anode was found to shift polarization curves to more cathodic potentials without changing the relative positions of the various alloys on the potential axis.

For the purpose of screening of a large number of samples, it was convenient to measure anodic polarization using a linear anodic potential sweep. The samples of 2 cm^2 area were fully immersed in a large volume of saturated NaCl solution thermostated at 25°C. The traces of Fig. 2 were obtained by starting at the respective rest potentials and sweeping toward positive potentials at a speed of 0.001 V/sec. Return sweeps

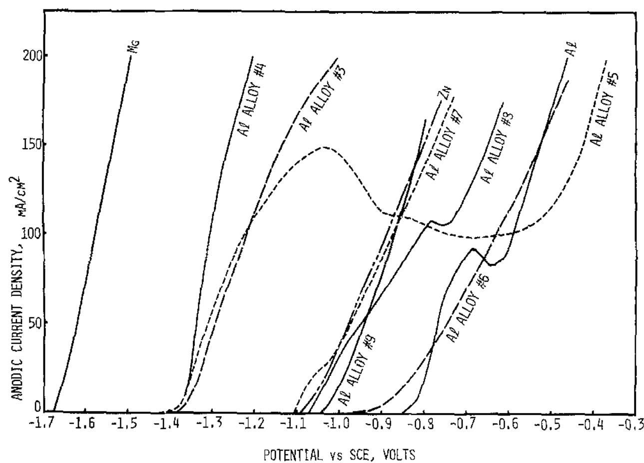

Fig. 2. Anodic polarization curves for several pure metals and aluminum alloys in saturated NaCl solution at 25°C. Alloy compositions are given in Table III.

(in the cathodic direction) were obtained after interrupting the anodic sweep manually at the approximate 200 mA/cm^2 level and then sweeping in the cathodic direction; the resulting traces appear in Fig. 3. A comparison of Fig. 2 and 3 reveals some hysteresis for all of the samples studies. The return sweep for Mg was very similar to the positive-going sweep and is not shown in Fig. 3. The rather pronounced hysteresis for aluminum and its alloys is not surprising considering the fact that aluminum is always covered with a film of γ-Al_2O_3 in near-neutral solutions (5), and that its electrochemical properties depend on the condition of that film, which, in turn, depends on the previous history of the electrode. The behavior of any of the samples, as an electrochemical heater anode, may be expected to fall somewhere between the anodic and cathodic traces, since in such use the current densities are initially high and then undergo gradual decline.

For measurements of hydrogen evolved by the anode samples, it was convenient to impress the various constant current levels listed in Table III. Measurements were made at 1 min intervals for a total of 8 min at each increasing current density. Table III pre-

Table I. Thermodynamic quantities of cell reactions

	Cell	Reaction	$\Delta H°$ (kcal)	$\Delta F°$ (kcal)	$\Delta H°/n$ (kcal/eq.)	$\Delta F°/n$ (kcal/eq)	$E°$ (volts)
1	Mg/MnO_2	$Mg + 2MnO_2 + H_2O \rightarrow Mg(OH)_2 + Mn_2O_3$ (β-form) (α-form) (α-form)	−135.8	−133.5	−67.9	−66.8	2.88
2	Mg/H_2	$Mg + 2H_2O \rightarrow Mg(OH)_2 + H_2$	−84.4	−85.9	−42.2	−43.0	1.86
3	Al/MnO_2	$2Al + 6MnO_2 + H_2O \rightarrow Al_2O_3 \cdot H_2O + 3Mn_2O_3$ (β-form) (Hydrated γ-form) (α-form)	−351.9	−351.0	−58.7	−58.5	2.54
4	Al/H_2	$2Al + 4H_2O \rightarrow Al_2O_3 \cdot H_2O + 3H_2$ (Hydrated γ-form)	−197.7	−208.2	−33.0	−34.7	1.50

Table II. Thermodynamic reduction potentials at 25°C

	Electrode reaction	Standard potential† (volts)	Reversible potential vs. SCE (volts) pH 6.1*	pH 7.0	pH 10.45**
a	$2MnO_2 + 2e^- + H_2O \rightleftharpoons Mn_2O_3 + 2(OH^-)$ (β-form) (α-form)	1.014-0.0591 pH	0.417	0.364	0.160
b	$2H_2O + 2e^- \rightleftharpoons H_2 + 2(OH)^-$	−0.0591 pH	−0.591	−0.650	−0.853
c	$Mg(OH)_2 + 2e^- \rightleftharpoons Mg + 2(OH^-)$	−1.862-0.0591 pH		−2.512	−2.715
d	$Al_2O_3 \cdot H_2O + 2H_2O + 6e^- \rightleftharpoons 2Al + 6(OH^-)$ (Hydrated γ-form)	−1.505-0.0591 pH	−2.102	−2.155	

† Standard potentials are referenced to the normal hydrogen electrode.
* The pH of a saturated solution of γ-aluminum oxide is 6.1.
** The pH of a saturated solution of $Mg(OH)_2$ is 10.45.

Table III. Hydrogen evolution at magnesium, aluminum, and aluminum alloy anodes (25°C)

Composition No.	Anode composition (w/o)							Percentage H_2 evolution* (I, mA/cm^2)					
	Mg	Al	Zn	Hg	Sn	Ga	In	5	10	20	50	100	200
1	100							43.6		45.3		38.7	36.9
2		100								13.4	16.9	19.8	15.9
3	0.57	99.25			0.13	0.05			8.6		16.8	16.3	6.9
4	0.82	99.98			0.15	0.05			17.7	14.1	14.5	13.8	
5	0.36	99.44			0.14	0.06			20.4	15.6	13.2	11.4	10.6
6		98.52	1.47	0.01						12.5	11.3		13.2
7	0.46	95.31	4.19				0.04				0.6	1.4	1.5
8		96.45	3.52				0.03				5.5	2.6	2.0
9		95.81	4.19						4.0	16.7	20.1	16.3	

* Percentage H_2 evolution = $100\, I_{H_2}/(I + I_{H_2})$.

sents the hydrogen evolution rate as a percentage of the total current at the anode after converting the gassing rate to an equivalent current density, I_{H_2}, by using the formula

$$I_{H_2} = 2 \cdot \frac{\Delta V}{\Delta t} \cdot \frac{\mathbf{F}}{22.4} \qquad [1]$$

Where $\mathbf{F}$ is the Faraday constant and I_{H_2} is obtained in amperes/cm^2 if the gas flow, $\Delta V/\Delta t$, is expressed in liters per second per square centimeter of electrode area.

For current densities of 20 mA/cm^2 or higher, the gassing rates were found to stabilize after 2-3 min and the values given are average values for the last 4-8 min of observation. Since direct calibration revealed that a 2-3 min lag is inherent in the flowmeter used for the measurements, no conclusions may be drawn about intrinsic transient behavior of the system in that early period. For the alloys possessing low rates of gassing, the method was not sufficiently sensitive for observations to be made in the allotted time at the lowest current densities.

Referring to Fig. 2 as a guide to the relative anodic behavior of the various anode materials, we see that the polarization of the alloys falls into the approximate 1V span between Mg and pure Al, with the latter the more inactive material and with both operating much below their respective thermodynamic potentials, as listed in Table II. A trace for a Zn electrode is incuded for comparison, although the energy content of Zn is too low for practical consideration. A general pattern of behavior emerges for the alloys if the high current performance of alloy No. 5 is ignored. Those alloys (No. 3, 4, and 5) containing Sn produce the most negative (active) closed-circuit voltages. This is in agreement with observations (5, 11) made during long-term corrosion studies on aluminum alloy/steel couples. It is believed (11) that Sn fosters the high anodic activity by producing cation vacancies which reduce the ionic resistivity of the γ-alumina film. This film normally covers the electrode during use. Additions of Mg and Ga enhance this effect by stabilizing the solid solubility of the Sn in the alloy (12). The H_2-evolution characteristics of alloys No. 3-5 tend to be somewhat better than that of pure Al, particularly at the high current densities, and like Al, are a 2-3 fold improvement over Mg in that regard. A second grouping of Al alloy polarization traces fall between the trace for pure Al and pure Zn (Fig. 2). Alloys 6-9 contain increasing amounts of Zn, and their closed circuit voltages, in line with previous experience with Al-Zn alloys (11), tend to become increasingly more negative and approach the performance of a pure Zn anode. There is, however, no simple correlation between electrode polarization and hydrogen evolution for this series of alloys, if the results of Fig. 2 and Table III are compared. Specifically, alloys No. 7 and 9 have the same Zn content and show very similar polarization behavior, but in spite of these facts alloy No. 7 produces the lowest amount of hydrogen while hydrogen production for alloy No. 9 falls in the same range as for pure aluminum. The fact that alloy No. 8, like alloy No. 7, is also a low gas producer, suggests that indium is more significant than Mg in imparting the nongassing properties to those alloys. Before considering how alloying affects hydrogen evolution, let us consider the thermodynamics of the process. For gassing to occur at all, the electrode potential must be more negative than the thermodynamic value for a reversible H_2 electrode in the same medium. According to Table II, that potential

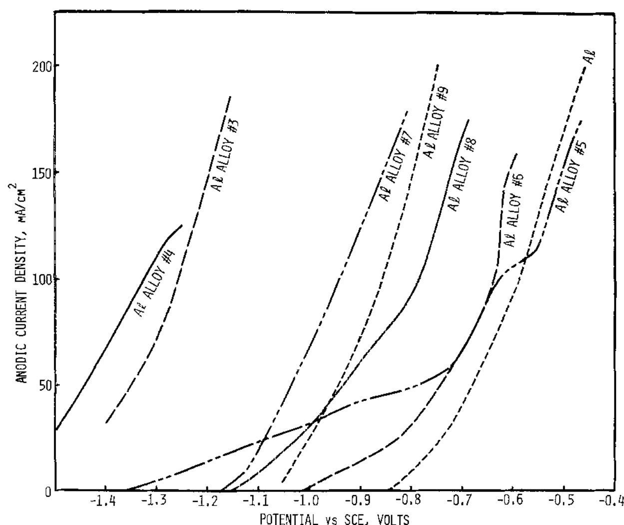

Fig. 3. Anodic polarization curves for several pure metals and aluminum alloys in saturated NaCl solution at 25°C. The curves were obtained after reversing the linear potential sweeps of Fig. 1.

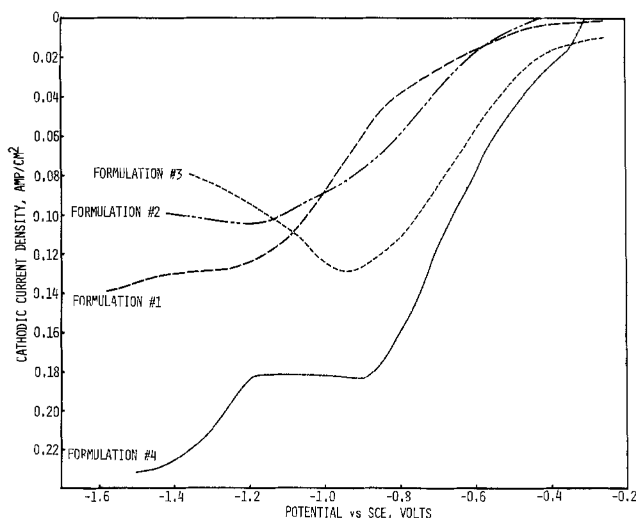

Fig. 4. Cathodic voltage scans of various MnO_2 cathodes. The electrolyte was NaCl solution in a Webril Pad.

could be $-0.650V$ in the original neutral solution and $-0.591V$ at steady state, with the solution completely equilibrated and saturated with hydrated γ-aluminum oxide. Based on those numbers, gassing would not be expected on pure Al or on alloy No. 6 at the higher current densities. However, localized, very low pH values may be expected near the anode surface, particularly at high current densities, corresponding to the production and hydrolysis of $AlCl_3$. For example, based on the reported value of $pKh = 4.9$, the pH of a 1M solution of $AlCl_3$ would be 2.45 and the corresponding reversible H_2 potential would be -0.38, sufficiently positive to account for H_2 evolution on Al and all of its alloys in a sodium chloride electrolyte solution. As for Mg, Table III reveals that the percentage of hydrogen evolved does not generally or systematically drop as the current is raised and the potential approaches that of the reversible H_2 electrode ("negative difference effect") (13). As for Mg, therefore, it may be hypothesized that H_2 release occurs on a very limited, momentarily film-free fraction of the surface. In line with that concept, the role of indium in a Zn-Al alloy could be to modify the physical structure of the film (*e.g.*, adherency, coherency, porosity) so as to minimize exposure of bare surface to the electrolyte.

We shall now turn to the problem of choosing the "best" anode material for an electrochemical heater. From the point of view of lowest H_2 production, Table III reveals that alloy No. 7 appears to be the best choice, with No. 8 a close second choice. Assuming that the solid product of reaction is γ-alumina for both Al and all of the Al-rich alloys, the total heat produced per equivalent of Al consumed in short-circuited cells utilizing any of those anodes and a MnO_2 cathode should be greater for the alloys producing the least H_2 (since reaction 3 of Table I is more energetic than reaction 4). So far, the analysis has been based on thermodynamic and corrosion data only. The role played by anode polarization is discussed later.

MnO_2 cathode polarization and gas evolution at the cathode.—The polarization of a manganese dioxide cathode at high rates of discharge is much more time dependent than that of the Mg and Al anodes with which it might be used. Because of the strong time-dependence, measurements of polarization performed at fixed potential provide the most quantitative guide to performance of the electrode in an electrochemical heater. For this purpose, electrodes of formulation No. (i) measuring 1×1 cm were individually immersed in a saturated solution of NaCl. The area of each sample is taken as 1 cm^2 despite the fact that both sides are exposed, since the bulk of the porous cathode is utilized rather than its surface (the reverse is true for anodes). For each sample, a different fixed potential was applied and the current-time trace recorded. Points taken from the traces are plotted on Fig. 5. From the figure it can be seen that, for time durations at constant potential of less than 1 min, the current tends to increase with decreasing potential. For longer time durations, a plateau value occurs in the lower potential range. A second rise in current follows the plateau at decreasing potentials. The results can be interpreted as follows, based on the observation (14) that the cathodic reduction of MnO_2 tends to be diffusion-controlled soon after the beginning of the process:

(i) At short elapsed time, including up to 12 sec, the reduction is only partially diffusion limited and hence shows considerable potential dependence over the whole potential range.

(ii) After sufficient charge has passed, the reduction process becomes solid state diffusion controlled and, therefore, exhibits a current plateau. Referring to the 1 min points, a plateau is evident from -1.0 to $-1.5V$. At less cathodic potentials than $-1.0V$, the

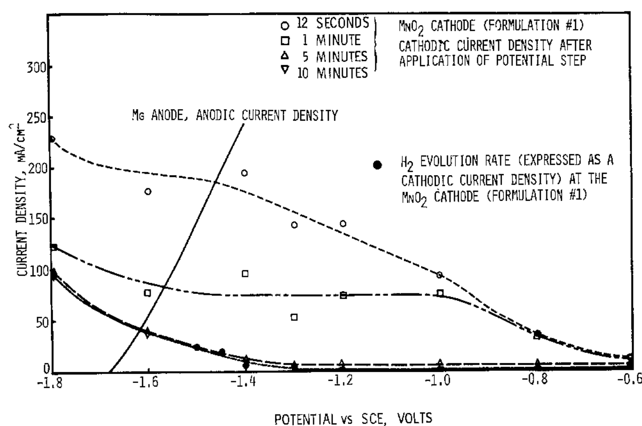

Fig. 5. Polarization behavior of fully immersed Mg anodes and MnO_2 cathodes [formulation (i)] in saturated NaCl solution.

previous activation-controlled current was not sufficiently high to result in diffusional control after 1 min. At more cathodic potentials than $-1.5V$, the current rise is due to electrolytic evolution of H_2.

(iii) As the reduction time increases, diffusional control extends to less cathodic potentials, and the onset of H_2 evolution is more easily distinguished (potentials as positive as $-1.3V$).

To confirm that hydrogen is evolved at the more cathodic potentials, a sample of electrode was first prepolarized at $-1.4V$ for 10 min. The potential was then adjusted to any desired value and gas evolution was measured. The gas evolution rates (measured at 100 sec intervals) were found essentially time independent, as might be expected for an electrocatalytic process. Average rates, converted to currents by means of Eq. [1], are plotted on Fig. 5. The results reveal that H_2 evolution is measurable at $-1.3V$ and it accounts for virtually all of the cathodic current at more cathodic potentials after a few minutes of polarization. The reversible potentials (*vs.* a saturated calomel electrode) of the two processes, which may occur at the MnO_2 cathode, appear in Table II (*i.e.*, a and b). The expressions for the standard potentials were taken from Ref. (10). The pH of the NaCl electrolyte should be 7.0 initially, and should eventually reach 10.45 when thoroughly mixed and saturated with $Mg(OH)_2$ (10). In addition, transient high and low values of pH at the cathode and anode, respectively, are likely during high current surges. Since the reversible potentials from Table II for reaction a at pH's 7 and 10.45 are quite positive, it is apparent that MnO_2 (Fig. 5) is being reduced irreversibly and that improved reduction kinetics would shift the curve to the right on the potential axis. For the H_2-evolution process (reaction b, Table II), it can be seen that gas evolution could begin at potentials as positive as $-0.65V$. The observation that no appreciable gassing occurs until $-1.3V$ largely reflects the fact that carbon (which is present for its electronic conduction properties) is a poor electrocatalyst for the hydrogen evolution reaction.

From Table II it can be seen that the reversible potential of the MnO_2 electrode is $+0.364V$ in the originally neutral solution used here as the electrolyte. Variations in pH during cell discharge can be expected to affect the reversible potential by only a few tenths of a volt. In spite of this, "formulation No (i)" begins to deliver appreciable cathodic currents at potentials over a volt more cathodic than the reversible potential. Such irreversible performance is subject to improvement through structural modifications which decrease internal impedances and improve mass transport in the electrode. Toward that end, a number of different electrode formulations were made for evaluation. These formulations included variation in: (i) the amount of carbon and graphite added for contact between MnO_2

particles; (*ii*) nature of the organic binder (*e.g.*, PTFE, Lucite, polysulfone); (*iii*) addition of agents to increase wetting and porosity (*e.g.*, fuller's earth) nature of the current collector (*e.g.*, screens and expanded metal made of steel and nickel), and (*iv*) the addition of graphite fibers to improve current collection.

For evaluation of samples, the potential-step method, as used to obtain the data of Fig. 5, provides the most in-depth information, but requires multiple samples and is tedious. Therefore, for the present purpose of fast screening, the linear potential sweep method requiring only one sample for a determination was used instead (sweep speed of 0.001 V/sec). Samples of 1 × 1 cm dimensions were discharged against a Mg counterelectrode using a NaCl-impregnated Webril separator pad as the electrolyte. Some of the more promising results appear in Fig. 4. Formulation No. (*ii*)-(*iv*) all offer the promise of improved performance at more positive potentials as compared with formulation No. (*i*). All three improvements utilize graphite fiber additions. Formulation No. (*ii*) and (*iii*) were made with a steel screen current collector, while No. (*iv*) was made with a "foametal" current collector. While cathode performance increases on progressing from formulation No. (*i*)-(*iv*) so does the MnO_2 loading (0.035, 0.07, 0.17, and 0.2 g/cm^2 for electrodes 1, 2, 3, and 4, respectively). Hence, the improvement represents successful utilization of more MnO_2, rather than a fundamental improvement in the kinetics of MnO_2 reduction. From Fig. 4, formulation No. (*iv*) would appear to be the obvious choice for further development. Its vulnerability, however, lies in the fact that Ni is a rather good catalyst in the H_2 evolution reaction. The descending portion of the scan from −1.2V to more cathodic potentials corresponds largely to extensive gas production, which is significant even at more positive potentials. An electrochemical heater using that formulation was nevertheless evaluated and the results are reported in the section below. Formulation No. (*iii*) appears clearly superior to formulation No. (*i*) without an aggravated gas evolution problem, and its further evaluation is also reported in the section below.

Electrochemical performance and hydrogen release at a short-circuited Mg-MnO_2 cell.—The behavior of a "heater" utilizing a Mg anode will serve as an example of the more general case. The results appearing in Fig. 6 were obtained for a cell containing a 1 × 1 cm anode and cathode and a salt-impregnated Webril separator. The "virtual" short-circuit current (across a 0.01 Ω load) density and the individual electrode potentials (referred to a saturated calomel electrode) were recorded after activating the cell by flooding with water for 15 sec and then draining off the excess water. The volume of hydrogen released was measured periodically and converted to an equivalent current density, I_{H_2}, using Eq. [1]. I_{H_2} includes a contribution from both the anode and cathode. The initial large values of I_{H_2}, paralleling the large values of I_{sc}, correspond mainly to hydrogen release at the anode, whereas the longer-term smaller values of I_{H_2} correspond to cathodic release of hydrogen as is discussed below. For the early large currents, the areas under the two curves are approximately measures of the number of equivalents of Mg reacting according to the equations in cells 1 and 2, respectively, of Table I. The initial high surge of current is useful for providing rapid heat transfer. By minimizing the masses of the ingredients, practical cells (4) transfer most of the available enthalpic heat to the object being heated.

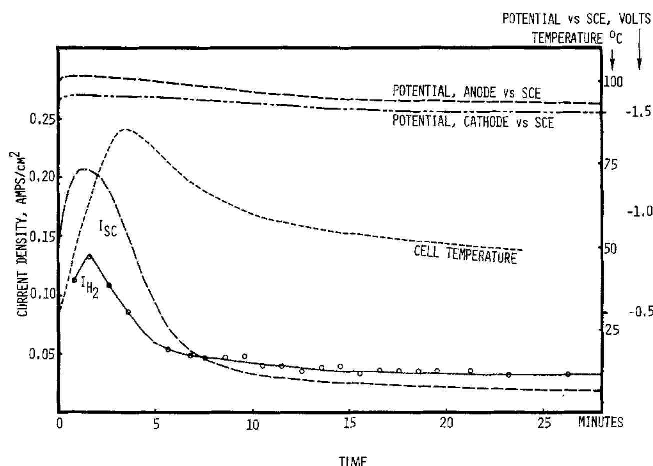

Fig. 6. Operating characteristics of an instrumented Mg/MnO_2 electrochemical heater [cathode formulation No. (*i*)].

Although the respective experimental conditions are somewhat different, the electrode polarization results of Fig. 5 are useful in qualitative interpretation of the results recorded in Fig. 6. For a short-circuited cell consisting of the anode and cathode of Fig. 5 and with negligible electrolyte resistance, the short-circuit current and electrode potential at any instant are determined by the point of intersection of the Mg anodic polarization curve with the appropriate MnO_2 cathodic polarization curve. The intersections of Fig. 5 predict a drop in current from the 200 mA/cm^2 level in the first 12 sec, to below the 50 mA/cm^2 level in 10 min, with that sharply declining current attributable entirely to cathode polarization. The long-term currents (according to Fig. 5) are supported almost entirely by hydrogen evolution. Finally, Fig. 5 predicts a moderate shift in the electrode potentials to more cathodic potentials, conforming to the shape of the anodic polarization curve. This predicted shift occurs during the first few minutes for the more complicated conditions of Fig. 6. The unanticipated long-term positive drift of potentials probably corresponds to electrode polarizations due to the limited volume and shifting pH of the electrolyte in the Webril pad in use here. The short-circuit current (I_{sc}) *vs.* time trace of Fig. 6 exhibits approximately the expected type of current decay after the current peak is passed. The initial rise in current probably corresponds mainly to the "voltage delay" phenomenon normally encountered (15) when a heavy load is first applied to the normally passive Mg anode.

A very significant conclusion based on Fig. 5 is that shifting of the anodic curve to the right would tend to eliminate H_2 evolution at the cathode, the latter being the major source of H_2 evolution after the first 10 min of cell operation.

With the help of Fig. 5, we can return to the problem of choosing the "best" Al alloy to substitute for Mg. In addition to the preference for the lowest corrosion rate, the polarization of the anode plays an important role in three important ways:

(*i*) The distribution of heat through the cell depends on the relative extents of anode and cathode polarization and of electrolyte resistance. For reasons of heat conduction it is best to place the work against the metallic anode and it is therefore beneficial to have the highest polarization (and temperature) at that electrode.

(*ii*) The rate of heat release is proportional to the current density. That rate (or current) depends on the points of intersection of the anode and cathode polarization curves, and will be highest for those anode polarization curves falling closest to that of Mg.

(*iii*) The anode polarization curve helps establish the working potential of the cathode at short circuit. The more positive the anode potentials (and the cathode working potential), the more likely will be the avoidance of H_2 evolution at the cathode. The latter has already been shown to be largely responsible for

longer-term gas evolution. Considerations (*i*) and (*iii*) suggest that the polarization curve of the anode should be as far as possible to the right of that of Mg (*e.g.*, the low-gassing alloy No. 7 of Fig. 2). The problem of lower current densities than for Mg [consideration No. (*ii*)] can be overcome by improvement of the cathode. Figure 5 suggests that other cathode formulations [No. (*iii*) and (*iv*)] might provide superior performance in an electrochemical heater utilizing aluminum alloys because of the significant shift of the polarization curve to the right on the potential axis.

Electrochemical performance and hydrogen release at short-circuited aluminum.—Alloy-MnO_2 Cells.— Figures 7-9 present results for short-circuited cells utilizing an aluminum alloy and three differently formulated MnO_2 cathodes. The plot of I_{sc} *vs.* time for the Mg-MnO_2 cell of Fig. 6 is included for comparison. Figure 7 confirms the expectation that relatively poor results can be obtained with an aluminum alloy anode if the cathode will not support high currents at the more positive potentials. Figure 8 reveals that an improvement in current densities over the Mg-MnO_2 cell can be achieved with an aluminum alloy if the MnO_2 cathode has improved performance at low overvoltages. As anticipated, I_{H_2} is much lower initially than for the Mg cell, corresponding to low corrosion of the alloy. Since the cathode now operates at relatively positive potentials, there is no significant evolution of

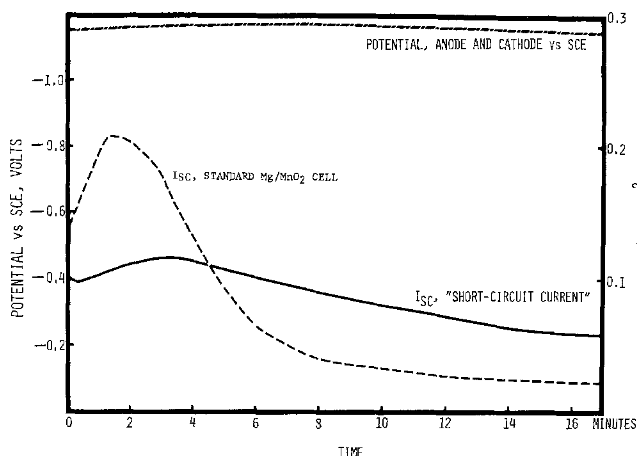

Fig. 7. Operating characteristics of an electrochemical heater made with an Al alloy No. 7 (4.19% Zn, 0.04% In, 0.46% Mg) anode and a MnO_2 formulation No. (*i*) cathode.

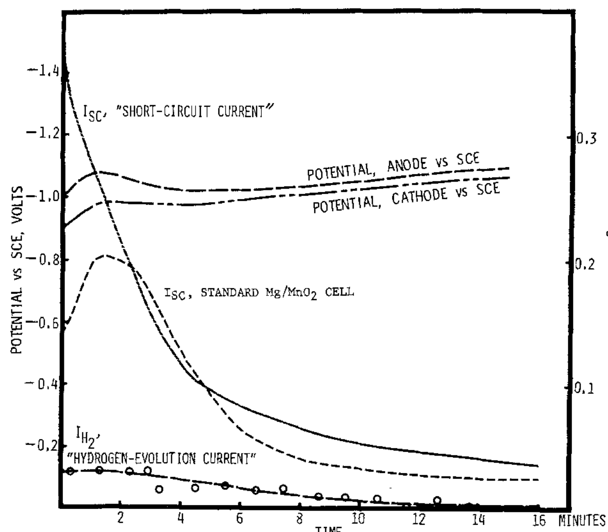

Fig. 8. Operating characteristics of an electrochemical heater made with an alloy No. 7 (4.19% Zn, 0.04% In, 0.46% Mg) anode and a MnO_2 formulation No. (*iii*) cathode.

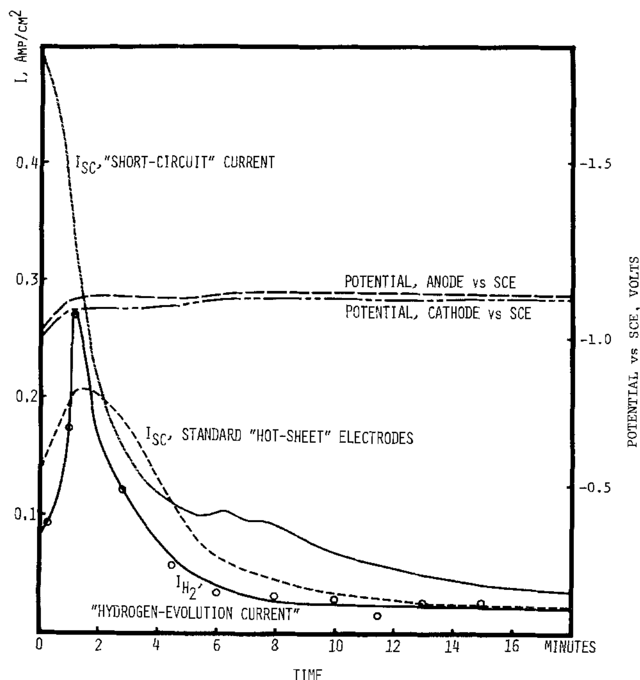

Fig. 9. Operating characteristics of an electrochemical heater made with an Al alloy No. 7 (4.19% Zn, 0.04% In, 0.46% Mg) anode and a MnO_2 formulation No. (*iv*) cathode.

hydrogen gas there. Hence, production of H_2 eventually drops to very low values parallelling the drop of cell current and rate of corrosion of the aluminum at the anode.

From Fig. 9, even more impressive short-circuit currents are obtainable using cathode formulation No. (*iv*), but I_{H_2} is unexpectedly high. It appears that this results from the use of nickel in the cathode formulation, resulting in catalysis of the hydrogen evolution reaction at both anode and cathode.

Conclusions

The nontoxicity and high enthalpic content of saline Mg-MnO_2 and Al-MnO_2 cells makes them useful as electrochemical heaters (short-circuited cells). The Mg cell provides high short-circuit currents (and rates of heat evolution) but produces H_2 at the anode (corrosion) and at the cathode (due to highly negative operating potential). Cells made with certain Al-Zn alloys also provide high short-circuit currents while producing little H_2 at the anode and virtually no H_2 at the cathode (latter due to relatively positive operating potential).

Acknowledgments

The authors wish to thank Dr. Kwoh H. Hu, of the U.S. Army Natick Laboratories, for inspiring this work and for helpful discussions. Support of this work by the Natick Laboratories is gratefully acknowledged.

The authors wish also to thank Drs. D. Thompson of the Reynolds Metals Company and K. V. Kordesch of the Union Carbide Corporation for helpful discussions and samples of the anode and cathode materials discussed herein.

Manuscript submitted Jan. 10, 1978; revised manuscript received June 31, 1978.

Any discussion of this paper will appear in a Discussion Section to be published in the June 1979 JOURNAL. All discussions for the June 1979 Discussion Section should be submitted by Feb. 1, 1979.

Publication costs of this article were assisted by the U.S. Army Electronics Command.

REFERENCES

1. W. C. Spindler, U.S. Pat. 3,207,149 (1965).
2. F. P. Kober, U.S. Pat. 3,774,589 (1973).

3. J. F. McCartney, U.S. Pat 3,884,216 (1975).
4. Final Tech. Rep. No. 74-44-GP by Power Applications Inc. on Contract No. DAAG-17-73-C-0250 with The General Equipment and Packaging Laboratory, U.S. Army Natick Laboratories (1973).
5. D. S. Keir, M. J. Pryor, and P. R. Sperry, *This Journal*, **114**, 777 (1967).
6. K. Kordesch, U.S. Pat 3,945,847 (1976).
7. H. F. Hunger and J. E. Ellison, *This Journal*, **122**, 1288 (1975).
8. "The Primary Battery," Vol. 1, G. W. Heise and N. C. Cahoon, Editors, John Wiley & Sons, Inc., New York (1971).
9. "Handbook of Chemistry and Physics," 53rd ed., Chemical Rubber Co., Ohio (1972).
10. M. Pourbaix, "Atlas of Electrochemical Equilibria in Aqueous Solutions," Pergamon Press, New York (1966).
11. J. T. Reding and J. J. Newport, *Mater. Prot.*, Dec., p. 15 (1966).
12. D. S. Keir, M. J. Pryor, and P. R. Sperry, *This Journal*, **116**, 319 (1969).
13. J. L. Robinson and P. F. King, *ibid.*, **108**, 36 (1961).
14. F. Kornfeil, *ibid.*, **109**, 349 (1962).
15. J. L. Robinson, in "Proceedings of the 17th Annual Power Sources Conference," p. 142, May 1963.

The Oxygen Electrode Reaction in Alkaline Solutions on Oxide Electrodes Prepared by the Thermal Decomposition Method

M. H. Miles*,[1] and Y. H. Huang

Department of Chemistry and Physics, Middle Tennessee State University, Murfreesboro, Tennessee 37132

and S. Srinivasan*

Brookhaven National Laboratory, Department of Applied Science, Upton, New York 11973

ABSTRACT

The irreversibility of the oxygen electrode reaction is the main cause of efficiency losses in water electrolysis cells, fuel cells, and some battery systems. At conditions typical for water electrolysis, the effectiveness of various metal oxide electrodes toward oxygen evolution decreased in the order Ru > Ir ~ Pt ~ Rh ~ Pd ~ Ni ~ Os >> Co >> Fe. Poor activities were observed on V, Cr, Mo, W, Mn, and Re oxide electrodes. When mixed with 70 mole percent (m/o) TiO_2, all metal oxides tested except ruthenium oxide were ineffective in catalyzing the oxygen evolution reaction. A catalyst-loading study showed that RuO_2 films on Ti require about 10^{-6} mole RuO_2/cm^2 to mask the effect of the titanium substrate. Either a chemical step or a second electron transfer step appears to be rate determining for the oxygen evolution reaction on oxide electrodes with good electrocatalytic properties. Studies of the oxygen reduction reaction indicate that the activity of oxide electrodes in the cathodic direction is considerably less than in the anodic direction.

The oxygen evolution and reduction reactions are of special importance in water electrolyzers, fuel cells, and in batteries using air cathodes since slow kinetics at these electrodes are the chief cause of efficiency losses in these devices. The ruthenium oxide electrode prepared by the thermal decomposition method is an attractive electrocatalyst for both the chlorine and oxygen evolution reactions (1-7). Electrochemical data for the evolution of oxygen on other dimensionally stable anode (DSA) materials is limited (5, 8-10). Since this investigation was prompted by an interest in improving the efficiency of water electrolysis, experimental conditions typical of commercial electrolyzers were selected (11). Therefore, all studies were made in 30 weight percent (w/o) KOH solutions at 80°C.

Experimental

Electrodes.—Titanium wire (99.7%, 0.8 mm, Alfa) was etched in 10% oxalic acid at 90°C for 1 hr. Coatings were applied by dipping the wire in a solution containing the metal chloride and then heating it in an electric furnace at 300°-500°C for 10 min. Six separate coatings were applied. After the final coating, the wire electrode was heated in the furnace for at least 30 min and then sealed into Teflon tubing. Tetrabutyl orthotitanate (practical, Eastman) was used to vary the mole fraction of a particular metal in the dipping solution.

Electrochemical measurements.—Studies of the oxygen evolution reaction were carried out under experimental conditions which approximate those encountered in practical water electrolysis cells. A one-compartment glass cell was used in which the reference and working electrodes were placed inside and below a cylindrical platinum screen counterelectrode in order to minimize the *IR* effect and any reaction with gas evolving from the counterelectrode. In each experiment, the KOH solution was slowly stirred magnetically. Potentials were always measured *vs.* a saturated calomel reference electrode (SCE).

Potentiostatic current measurements were made with the use of a Beckman Electroscan 30 instrument. Before each investigation of oxygen evolution, the highest anodic current used (about 100 mA/cm^2) was passed for about 5 min, and then current-potential relationships were determined in the direction of decreasing current.

For studies of oxygen reduction, oxygen gas (99.6% min, Linde) was introduced into the solution through a gas diffusion tube to produce a stream of very fine bubbles. Before each experiment, the diffusion-limited current density (10^{-4} A/cm^2) was passed for 5-10

* Electrochemical Society Active Member.
[1] Present address: Naval Weapons Center, Chemistry Division, China Lake, California 93555.

Key words: catalyst loading, Tafel slope, transfer coefficient, water electrolysis.

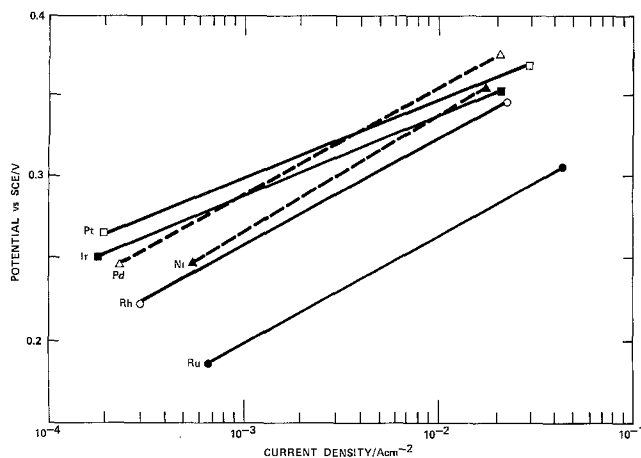

Fig. 1. Average Tafel lines for the oxygen evolution reaction on Ru, Rh, Ni, Pd, Ir, and Pt oxide electrodes in 30 w/o KOH solutions at 80°C.

min to build up a steady-state concentration of any peroxide intermediates. Measurements were then made in the direction of decreasing currents.

Results

The Tafel regions observed for the oxygen evolution reaction on Ru, Rh, Ni, Pd, Ir, and Pt oxide electrodes are shown in Fig. 1. For each electrode, the Tafel line shown represents the average as determined from at least three separate studies. Based upon previous studies, the reversible potential for the oxygen electrode is calculated to be 0.03V *vs.* SCE in 30% KOH at 80°C (11).

Table I represents the average values for the Tafel parameters and their standard deviations. Mean values for the experimental transfer coefficient (α) and exchange current density (i_o) are also shown. Experimental results for studies on Os, Fe, and Co oxide electrodes not included in Fig. 1 are found in this table. The small standard deviations show that the results were generally quite reproducible. Nickel oxide electrodes showed the greatest variation, hence six separate studies were made with this electrode. Single studies on V, Cr, Mo, W, Mn, and Re oxide electrodes were also made, but the results indicated poor electrocatalytic activity for the oxygen evolution reaction on these materials.

Table II gives the kinetic parameters for several metal oxide electrodes when mixed with TiO_2 to reduce the fraction of a particular metal oxide to 30 m/o. Comparing the results in Tables I and II, similar parameters are found only for the ruthenium oxide electrode. Results for all other metal oxide electrodes show much larger Tafel slopes and higher overvoltages when mixed with TiO_2.

The effect of varying amounts of TiO_2 mixed with RuO_2 upon the oxygen evolution reaction was also investigated. The Tafel parameters (Table III) show only slight changes as the RuO_2 fraction is decreased to 30 m/o, whereas significant changes occur when the mole fraction of RuO_2 is reduced further. The overvoltage measured at 20 mA/cm^2 showed a similar effect by gradually increasing from 280 mV at 100 m/o RuO_2 to 340 mV at 30 m/o RuO_2 and then showing a sharp increase at lower RuO_2 contents.

By maintaining the same dipping procedure in various dilutions of the original ruthenium salt solution (0.3M), the effect of various loadings of ruthenium oxide on the titanium substrate could be studied. The polarization curves obtained for these electrodes are shown in Fig. 2. The catalyst loadings (based upon apparent areas) ranged from 10^{-5} to 10^{-8} mole RuO_2/cm^2 according to gravimetric measurements. The Tafel slopes suggest that significant kinetic changes occur at loadings below about 10^{-6} mole RuO_2/cm^2 which make the electrodes much less effective for the oxygen evolution reaction. For example, the Tafel slope shows a sharp increase from 67 mV/decade ($\alpha = 1.0$) to 130 mV/decade ($\alpha = 0.5$) at catalyst loadings of 10^{-6} and 10^{-7} mole RuO_2/cm^2, respectively.

The metal oxide electrodes which showed good catalytic activity for oxygen evolution were also studied for oxygen reduction. Kinetic parameters for the electrochemical reduction of oxygen on Pt, Ir, Ru, Pd, and Rh oxide electrodes in 30 w/o KOH solutions at 80°C are presented in Table IV. Linear Tafel

Table I. Average Tafel parameters with standard deviations for the oxygen evolution reaction in 30 w/o KOH solutions at 80°C

Metal oxide electrode	a/V	b/V	α_a	i_o/A cm^{-2}
Ru	0.37 ± 0.01	0.067 ± 0.003	1.0	3.0 × 10^{-6}
Ir	0.41 ± 0.02	0.050 ± 0.002	1.4	6.3 × 10^{-9}
Pt	0.41 ± 0.01	0.046 ± 0.002	1.5	1.2 × 10^{-9}
Rh	0.43 ± 0.03	0.067 ± 0.008	1.0	3.8 × 10^{-7}
Pd	0.45 ± 0.02	0.067 ± 0.005	1.0	1.9 × 10^{-7}
Ni	0.45 ± 0.04	0.071 ± 0.011	0.99	4.6 × 10^{-7}
Os	0.49 ± 0.01	0.070 ± 0.003	1.0	1.0 × 10^{-7}
Co	0.69 ± 0.01	0.126 ± 0.004	0.56	3.3 × 10^{-6}
Fe	0.91 ± 0.00	0.191 ± 0.002	0.37	1.7 × 10^{-5}

Table II. Tafel parameters for the oxygen evolution reaction on metal oxide/TiO_2 electrodes containing 30 m/o of the metal. Studies were made in 30 w/o KOH solutions at 80°C

Metal oxide electrode	a/V	b/V	α_a	i_o/A cm^{-2}
Ru	0.39	0.070	1.0	2.7 × 10^{-6}
Pt	1.13	0.225	0.31	9.5 × 10^{-6}
Ni	1.00	0.259	0.27	1.4 × 10^{-4}
Co	1.10	0.193	0.36	2.0 × 10^{-6}

Table III. Tafel parameters for the oxygen evolution reaction on RuO_2/TiO_2 electrodes containing various m/o RuO_2. The results are for 30 w/o KOH solutions at 80°C

m/o RuO_2 (%)	a/V	b/V	α_a	i_o/A cm^{-2}
100	0.37	0.066	1.1	2.5 × 10^{-6}
70	0.39	0.066	1.1	1.2 × 10^{-6}
50	0.41	0.068	1.0	9.3 × 10^{-7}
30	0.42	0.068	1.0	6.7 × 10^{-7}
20	0.46	0.078	0.90	1.3 × 10^{-6}
10	0.54	0.101	0.69	4.5 × 10^{-6}
0	0.96	0.118	0.59	7.3 × 10^{-9}

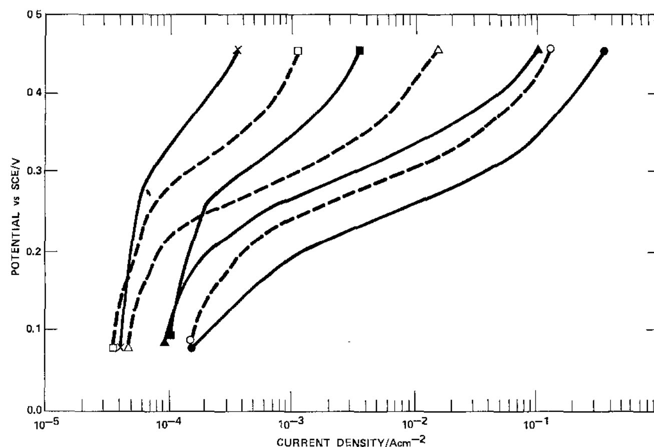

Fig. 2. Effect of ruthenium oxide loadings on the oxygen evolution reaction in 30 w/o KOH solutions at 80°C. (●) 1 × 10^{-5} moles RuO_2/cm^2; (○) 3 × 10^{-6} moles RuO_2/cm^2; (▲) 1 × 10^{-6} moles RuO_2/cm^2; (△) 3 × 10^{-7} moles RuO_2/cm^2; (■) 1 × 10^{-7} moles RuO_2/cm^2; (□) 3 × 10^{-8} moles RuO_2/cm^2; (×) 10^{-8} moles RuO_2/cm^2.

Table IV. Average Tafel parameters with standard deviations for the oxygen reduction reaction in 30 w/o KOH solutions at 80°C

Metal oxide electrode	a/V	b/V	α_c	i_o/A cm^{-2}
Pt	−0.57 ± 0.05	−0.061 ± 0.009	1.1	4.5 × 10^{-10}
Ir	−0.60 ± 0.05	−0.061 ± 0.008	1.3	2.9 × 10^{-12}
Ru	−0.50 ± 0.01	−0.043 ± 0.004	1.6	2.4 × 10^{-12}
Pd	−0.49 ± 0.01	−0.042 ± 0.001	1.7	2.2 × 10^{-12}
Rh	−0.51 ± 0.01	−0.041 ± 0.002	1.7	3.6 × 10^{-13}

lines were observed at current densities between about 10^{-4} and 10^{-6} A/cm^2. A low limiting current (10^{-4} A/cm^2) for oxygen reduction is expected due to the low solubility of oxygen and its low diffusion coefficient in 30% KOH solutions (12).

Discussion

Most commercial water electrolyzers operate at high current densities using electrodes with large surface roughness factors. Improvements in either intrinsic catalytic properties or surface roughness factors contribute to a lower overvoltage, hence it is often difficult to isolate these effects. Burke *et al.* (6) have demonstrated the important role of surface area in the electrochemical behavior of RuO_2 electrodes. Both the preparation temperature and the catalyst loading cause remarkable variations in true surface areas for ruthenium oxide electrodes (6, 7), hence various studies suggest roughness factors ranging from about 1 to 1000 or even higher (3-7, 13, 14). A preparation method similar to this study involving six sequential coatings, 10^{-5} mole Ru/cm^2, and heating at 450°C yields a roughness factor of about 60-80 for the RuO_2 electrodes (14). Anodic studies on iridium and platinum oxide electrodes suggest similar roughness factors (2, 9).

For practical applications to water electrolysis, the Tafel parameter *a* in Table I would represent the experimental activation overvoltage at a high current density of 1 A/cm^2 based upon geometrical area. Using this criteria, the effectiveness of these oxide electrodes for oxygen evolution decreases in the order Ru > Ir ~ Pt ~ Rh ~ Pd ~ Ni ~ Os >> Co >> Fe. A previous study of oxygen evolution on various metals in 30% KOH at 80°C also indicated about equal activities for Ir, Pt, Rh, and Pd electrodes while Ni was slightly better (11). The much poorer performance of Co and Fe oxides might be due to their instability in alkaline solution during prolonged anodic polarization. The exchange current densities do not provide a useful comparison for this reaction due to the wide range of Tafel slopes observed for these oxide electrodes.

The significant decrease in the activity of RuO_2/TiO_2 electrodes when the ruthenium content is less than 30 m/o has been observed in other studies. Kuhn and Mortimer (2) report that i_o values for the chlorine evolution reaction decrease sharply below 30-40 m/o ruthenium. Veselovskaya *et al.* (15) found that the rate of oxygen evolution decreased with a drop of RuO_2 content and that the electrochemical properties of the anode were closely related to the phase structure of the oxide coating. They report that while a part of the TiO_2 forms solid solutions with RuO_2, the TiO_2 phase remaining increased greatly for Ru concentrations below 40 m/o. Comparing Tables I and II, it is apparent that at 30 m/o metal, the effect of TiO_2 dominates for all metal oxides tested except ruthenium. The loss of activity of titanium anodes coated with RuO_2 and TiO_2 probably results from the formation of a nonconductive oxide film at the Ti-active layer interface (16).

The catalyst loading effects (Fig. 2) show that the titanium oxide-like behavior towards oxygen evolution disappears with increasing amounts of ruthenium oxide. It seems that a loading of 10^{-6} mole RuO_2/cm^2 (0.1 mg Ru/cm^2) is required to mask the effect of the titanium substrate. Similar effects have been reported for other noble metal oxide electrodes (9, 17).

From the values given for exchange current densities shown in Tables I and IV, it appears that oxygen evolution and reduction occur on these oxide electrodes by different mechanisms. The i_o values are considerably lower for oxygen reduction than for oxygen evolution. This study, along with previous work (5), shows that oxide electrodes are good electrocatalysts for oxygen evolution but not for oxygen reduction. Oxygen reduction on ruthenium metal is also rather poor, probably due to strong affinity of ruthenium for oxygen (18). Studies of the chlorine electrode on RuO_2 and IrO_2 show that the activity of these oxides in the cathodic direction is considerably less than in the anodic direction (2). The investigation of several other reactions on RuO_2 electrodes indicates poor electrocatalytic features for those involving adsorption steps (13).

The anodic polarization characteristics of oxide electrodes such as the Tafel slopes depend strongly upon the preparation temperature and surface concentration of catalyst (7, 8). Experimental transfer coefficients for the oxygen evolution reaction on ruthenium oxide electrodes are usually either $\alpha \sim 1.5$ or $\alpha \sim 1.0$ (4, 5, 7, 19), whereas $\alpha \sim 2$ on ruthenium metal (18). In alkaline solutions the following oxygen evolution reaction path

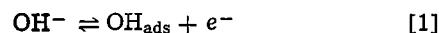

$$OH^- \rightleftharpoons OH_{ads} + e^- \quad [1]$$

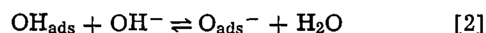

$$OH_{ads} + OH^- \rightleftharpoons O_{ads}^- + H_2O \quad [2]$$

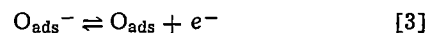

$$O_{ads}^- \rightleftharpoons O_{ads} + e^- \quad [3]$$

$$O_{ads} + O_{ads} \rightleftharpoons O_2 \quad [4]$$

is suggested by previous studies (9, 20). Under Langmuirian adsorption conditions, the experimental transfer coefficient will be either 0.5, 1, 1.5, or 4 depending upon which step is rate determining. The results in Table I suggest that step [1] is rate determining on Co and Fe oxides, step [2] is rate determining on Ru, Rh, Pd, Ni, and Os oxides, and step [3] is rate determining on Ir and Pt oxides. Oxygen reduction in alkaline solutions usually occurs by a different mechanism which involves the formation of HO_2^- intermediates (4, 21).

Acknowledgments

Financial support for this work was provided by the Faculty Research Committee at Middle Tennessee State University and by Brookhaven National Laboratory under Contract No. 347505S.

Manuscript submitted March 6, 1978; revised manuscript received July 3, 1978.

Any discussion of this paper will appear in a Discussion Section to be published in the June 1979 JOURNAL. All discussions for the June 1979 Discussion Section should be submitted by Feb. 1, 1979.

Publication costs of this article were assisted by Middle Tennessee State University.

REFERENCES

1. S. Trasatti and G. Buzzanca, *J. Electroanal. Chem. Interfacial Electrochem.*, **29**, App. 1 (1971).
2. A. T. Kuhn and C. J. Mortimer, *This Journal*, **120**, 231 (1973).
3. D. Galizzioli, F. Tantardini, and S. Trasatti, *J. Appl. Electrochem.*, **4**, 57 (1974).
4. W. O'Grady, C. Iwakura, J. Huang, and E. Yeager, in "Electrocatalysis," M. W. Breiter, Editor, pp. 286-302, The Electrochemical Society Softbound Symposium Series, Princeton, N.J. (1974).
5. G. Singh, M. H. Miles, and S. Srinivasan, NBS Special Publication 455, pp. 289-296, NBS, Maryland (1976).
6. L. D. Burke, O. J. Murphy, and J. F. O'Neill, *J. Electroanal. Chem. Interfacial Electrochem.*, **81**, 391 (1977).

7. C. Iwakura, K. Hirao, and H. Tamura, *Electrochim. Acta*, **22**, 335 (1977).
8. R. T. Atanasoski, B. Ž. Nikolić, M. M. Jakšić, and A. R. Despić, *J. Appl. Electrochem.*, **5**, 159 (1975).
9. C. Iwakura, K. Fukuda, and H. Tamura, *Electrochim. Acta*, **21**, 501 (1976).
10. D. Cipris and D. Pouli, *J. Electroanal. Chem. Interfacial Electrochem.*, **73**, 125 (1976).
11. M. H. Miles, *ibid.*, **60**, 89 (1975).
12. "Handbook of Fuel Cell Technology," C. Berger, Editor, pp. 136-146, Prentice-Hall, Englewood Cliffs, N.J. (1968).
13. D. Galizzioli, F. Tantardini, and S. Trasatti, *J. Appl. Electrochem.*, **5**, 203 (1975).
14. T. Arikado, C. Iwakura, and H. Tamura, *Electrochim. Acta*, **22**, 513 (1977).
15. I. E. Veselovskaya, E. K. Spasskaya, V. A. Sokolov, V. I. Tkachenko, and L. M. Yakimenko, *Elektrokhimiya*, **10**, 70 (1974); *Chem. Abstr.*, **81**, 85175f (1974).
16. T. Loucka, *J. Appl. Electrochem.*, **7**, 211 (1977).
17. R. T. Atanasoski, B. Z. Nikolić, M. M. Jakšić, and A. R. Despić, *J. Appl. Electrochem.*, **5**, 155 (1975).
18. C. Iwakura, K. Hirao, and H. Tamura, *Electrochim. Acta*, **22**, 329 (1977).
19. M. H. Miles, E. A. Klaus, B. P. Gunn, J. R. Locher, W. E. Serafin, and S. Srinivasan, *Electrochim. Acta*, **23**, 521 (1978).
20. M. H. Miles, G. Kissel, P. W. T. Lu, and S. Srinivasan, *This Journal*, **123**, 332 (1976).
21. "Encyclopedia of the Electrochemistry of the Elements," Vol. II, A. J. Bard, Editor, pp. 305-318, Marcel Dekker, New York (1974).

Paste Mixing and Curing of Tetrabasic Lead Sulfate Plates for the Lead-Acid Battery

C. F. Yarnell*

Bell Laboratories, Murray Hill, New Jersey 07974

ABSTRACT

A nonreactive paste of $4PbO \cdot PbSO_4$ is prepared by mixing the synthesized compound with water. On continued mixing with water, the $4PbO \cdot PbSO_4$ crystals become more closely packed. Water acts as a bulking agent and if mixed too long, water will separate from the paste. Low density pastes may be produced by adding more water and reducing the mixing time. Pasted $4PbO \cdot PbSO_4$ plates must be cured in an atmosphere containing CO_2. Curing may be accelerated by raising the temperature and enriching the atmosphere with CO_2. Previously dried plates may be cured in as little as 3 min in a steam-CO_2 atmosphere.

In previous papers (1, 2) we have discussed the formation, morphology, and cycle performance of positive plates pasted with $4PbO \cdot PbSO_4$ (tetrabasic lead sulfate). In this paper we discuss the preparation and properties of a $4PbO \cdot PbSO_4$ paste and the curing of $4PbO \cdot PbSO_4$ pasted plates.

A paste of $4PbO \cdot PbSO_4$ is prepared by mixing water with dried, synthesized $4PbO \cdot PbSO_4$ (3). Since this paste is nonreactive, its properties are quite different from a reactive, acid paste. An acid paste is usually prepared by mixing water, lead oxide, and sulfuric acid (4, 5). The properties of this chemically reactive paste and resultant plate are dependent on many factors such as relative proportions of materials, temperature, speed of addition of acid, drying atmospheres, and other (4, 5). Since the $4PbO \cdot PbSO_4$ paste is nonreactive, most of these factors do not affect its properties. The only relevant paste parameters for a $4PbO \cdot PbSO_4$ paste are the relative proportions of $4PbO \cdot PbSO_4$ and water, the length of time mixed, and, perhaps, the efficiency of the mixer.

Lead or lead-alloy grids are pasted with $4PbO \cdot PbSO_4$ and dried in air at 50% relative humidity and 26°C for 3 days (1-3). However, we have observed that when dried in these conditions for only 2 days, dried in a vacuum oven, or dried in nitrogen, the $4PbO \cdot PbSO_4$ pellets "popped" out of the grid when placed in H_2SO_4. Chemical analysis of the $4PbO \cdot PbSO_4$ showed that plates that did not disintegrate in acid contained about 0.2% more CO_2 than those plates that disintegrated. Thus we suspected that CO_2 was needed to cure the plates. This paper shows that $4PbO \cdot PbSO_4$ plates must be cured in an atmosphere containing CO_2 and at a relative humidity higher than 40%.

* Electrochemical Society Active Member.
Key words: lead-acid battery, tetrabasic lead sulfate, battery plate curing.

Experimental

Paste mixing.—In the laboratory, small batches containing 900g of $4PbO \cdot PbSO_4$[1] were mixed using various amounts of water and mixing times. A Kent Mixer was used which has an inverted "U" shaped blade which rotates at 60 rpm about its axis of symmetry in a counterclockwise direction while the mixing pan rotates at the same speed in the clockwise direction.

Small Pb-Ca rectangular grids ($7.6 \times 6.3 \times 0.7$ cm), whose pasteable volume was 29.6 cm^3, were pasted with each batch so that the dried plate density could be calculated. A 32.8 cm^3 (2 $in.^3$) cup was used to measure the wet paste density. The consistency of the paste in the cup was measured with a penetrometer fitted with a cone supplied by the C&D Battery Company. The cone weighed 55.4g and had a conical angle of 50°. The paste and pasted plates were weighed wet and dry to give a measure of the porosity of the plate and paste. Data on six cups and six plates were taken and the results averaged for each batch.

Larger 45.4 kg batches of paste were mixed in a Ross planetary mixer. This mixer does a more efficient job of mixing than the small laboratory model described above. Samples of these large mixes were taken and examined with the SEM. Circular positive Pb grids (6) (31 cm diam $\times$ 0.63 cm) were pasted by a machine (7, 8) which had rollers that pressed the paste into the grid.

Curing.—To understand how the combination of CO_2 and relative humidity could effect the curing of a $4PbO \cdot PbSO_4$ plate, the amount of CO_2 adsorbed by $4PbO \cdot PbSO_4$ was measured as a function of relative humidity. Weighed samples of dried $4PbO \cdot PbSO_4$ were placed in a dessicator containing an atmosphere of

[1] Supplied by the Eagle Picher Company.

pure CO_2 and at various relative humidities obtained by placing different concentrations of H_2SO_4 in the bottom of the dessicator. The relative humidity was measured with a small hygrometer placed in the dessicator. After 24 hr, the samples of $4PbO \cdot PbSO_4$ were dried and weighed to determine the increase in weight due to CO_2 adsorption.

Results and Discussion

Paste mixing.—To make a paste from $4PbO \cdot PbSO_4$, the water used is measured out and added all at once with the mixer running. Initially the mix looks very dry (Fig. 1a). After mixing a short time the paste starts to form up into small spheres (Fig. 1b) and starts to take on a shiny, wet appearance. As mixing is continued the small spheres coalesce with each other to form larger spheres (Fig. 1c) and finally completely join together to form one large sphere of paste (Fig. 1d). On continued mixing the large coherent mass breaks up and sticks to the side and bottom of the container (Fig. 1e).

The above series of stages always occurs regardless of the amount of water used to make the paste or the size and efficiency of the mixer. What changes is the time it takes the paste to reach each stage. The photographs in Fig. 1a, b, c, d, and e were of a paste using 0.138 ml H_2O/g of $4PbO \cdot PbSO_4$. It took 6 min to reach the one sphere stage (Fig. 1d and Table I). If less water is added (see Table I) all of the stages occur at a slower rate. On the other hand when more water is added (see Table I) the different stages occur faster. As the amount of water is increased, it becomes difficult to separate the different stages because they occur so rapidly.

Table I. Pasting data for $4PbO \cdot PbSO_4$

H_2O/g (ml)	Mix time (min)	Average ± standard deviation		
		Penetration (mm)	Cube weight (wet) (g/cm^3)	Porosity of plate (%)
0.11	20.0	68 ± 3	4.560 ± 0.022	41.2*-44.2*
0.12	12.0	84 ± 2	4.404 ± 0.013	43.0-46.5
0.13	6.5	88 ± 2	4.216 ± 0.012	45.2-48.2
0.138	6.0	89 ± 4	4.156 ± 0.027	46.4*-49.9*
0.15	4.25	99 ± 6	4.026 ± 0.019	48.4*-51.6*
0.17	2.25	109 ± 2	3.800 ± 0.018	52.2-54.7
0.17	20.0	139 ± 8	3.910 ± 0.030	51.6-53.2
0.19	1.5	115 ± 5	3.621 ± 0.026	54.7*-57.2*
0.21	1.0	120 ± 8	3.481 ± 0.017	56.9-59.5
0.25	0.5	126 ± 8	3.253 ± 0.026	60.4-63.2
0.30	0.25	167 ± 14	3.042 ± 0.032	64.6-66.6

* Estimated value.

If a large quantity of water is added, the paste may pass into a final stage in which it becomes very liquid (Fig. 1f). As an example of this, when 0.17 ml H_2O/g of $4PbO \cdot PbSO_4$ is used, the Fig. 1b stage occurs after 1.25 min, Fig. 1d after 2.25 min, Fig. 1e at 5 min, and then for the remainder of the time (20 min), it was very liquid as in Fig. 1f. In this stage the paste is too

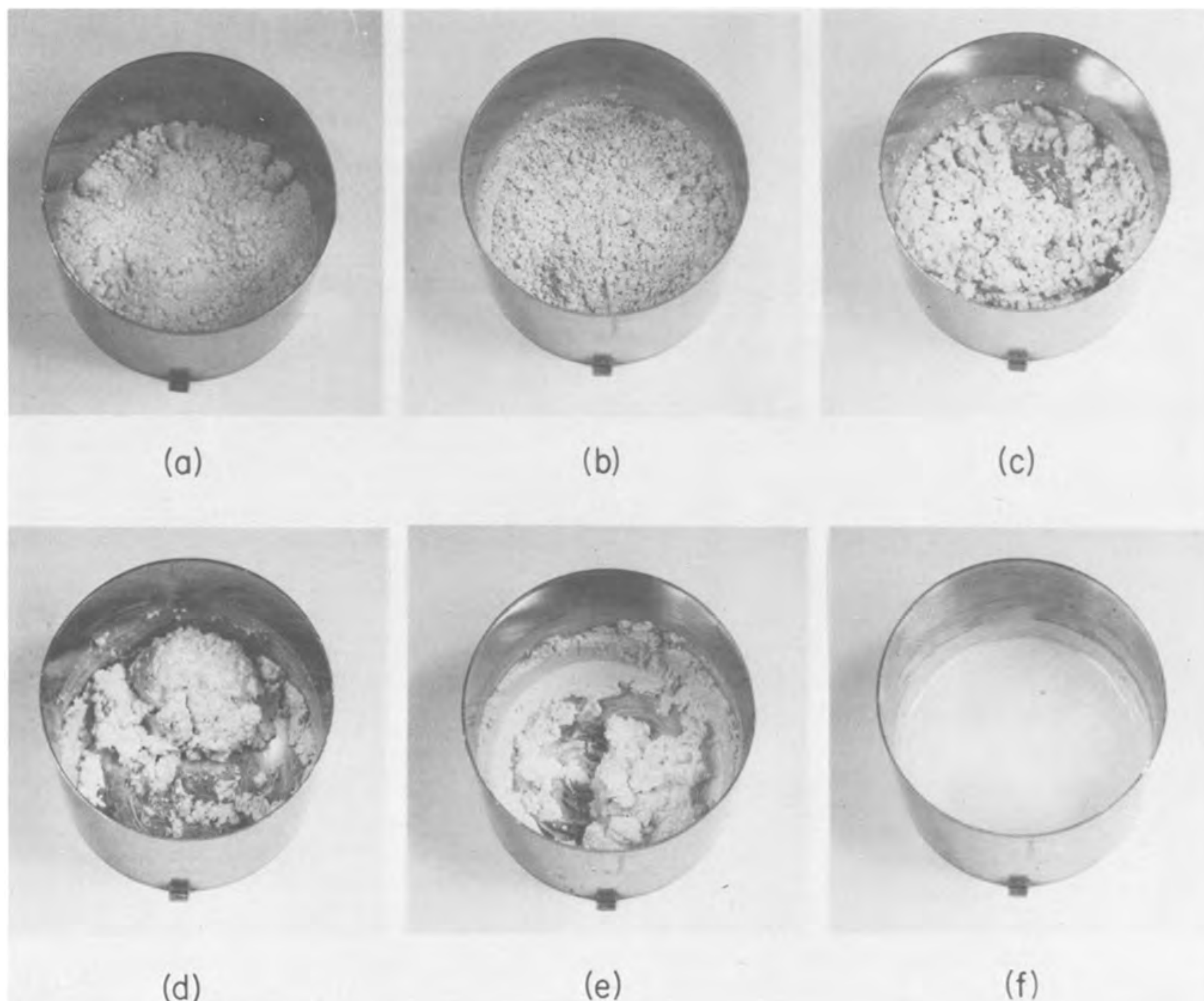

Fig. 1. Small, 900g batch of $4PbO \cdot PbSO_4$ after mixing for (a) 10 sec, (b) 3 min, (c) 4.5 min, (d) 6 min, (e) 20 min, and (f) 20 min. Mix (f) contained 0.17 ml of H_2O/g while all others contained 0.138 ml of H_2O/g of $4PbO \cdot PbSO_4$.

wet to paste and the water separates from the paste. For hand pasting and vibrator pasting (9), the mix can be used at the one sphere stage (Fig. 1d). However, this stage is usually too stiff for conventional machine pasting (7, 8), and the Fig. 1e stage may have to be used.

These same stages were observed using the larger mixer. Samples taken from this mixer were examined with the SEM. Figure 2 shows the dry $4PbO \cdot PbSO_4$ before mixing. Note the open structure. This open, porous structure results in complete absorption of the water when it is first added (Fig. 1a). On mixing to the small sphere stage (Fig. 1b), the crystals become more closely packed (see Fig. 3) and water is visible as evidenced by the shiny appearance of the small spheres. In the final stages (Fig. 1d and e), the crystals become closely packed and aligned (see Fig. 4).

The SEM photographs reveal that as the paste is mixed, the crystals become more closely packed. The mixing mechanically packs, or orders, the crystals so that the longer the paste is mixed, the less porous it becomes. The water acts only as a bulking agent so that overmixing may actually force water out of the paste and lead to a less porous, heavier plate. An important point to remember is once the paste is mixed too long and water settles out, it does no good to remix it, since this causes the crystals to pack even closer together forcing more water out.

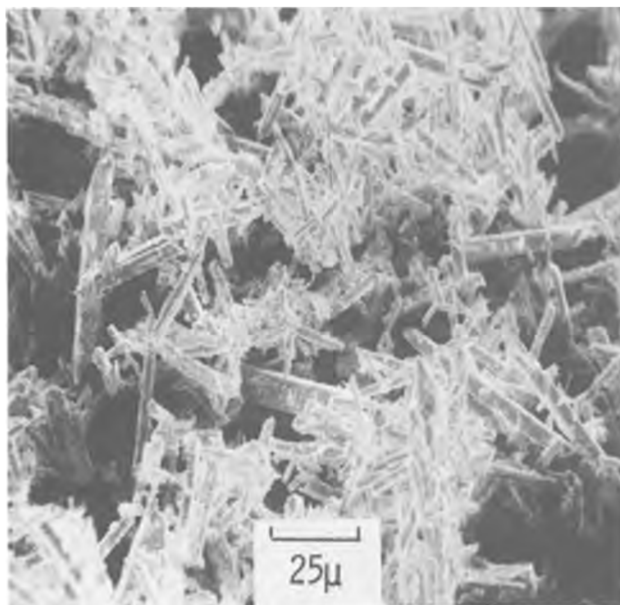

Fig. 2. $4PbO \cdot PbSO_4$ dry powder before mixing. Magnification 500 ×.

Fig. 3. $4PbO \cdot PbSO_4$ paste after mixing for 2 min with 0.138 ml of H_2O/g of $4PbO \cdot PbSO_4$. Magnification 500 ×.

Fig. 4. $4PbO \cdot PbSO_4$ paste after mixing with 0.138 ml of H_2O/g of $4PbO \cdot PbSO_4$ for 20 min. Magnification 500 ×.

Pasting data were taken on batches mixed in the small laboratory mixer (see Table I) and the larger mixer in which the amount of water was varied. Since the one sphere stage (Fig. 1d) is quite a definitive point and also the first stage at which plates can be hand pasted, the small batches were all stopped at this point. The large batches were mixed a little longer and machine pasted. No shrinkage occurred in any of these plates on drying even though the density was quite low for some of the batches. The dried paste densities for paste and positive plates are shown plotted in Fig. 5 *vs.* the amount of water used.

As expected, the density of the paste decreased as the amount of water used in the paste increased. The curve is not linear and the slope decreases as the density approaches that of $4PbO \cdot PbSO_4$ (8.15 g/cm^3). As expected, the plates are denser than the paste since

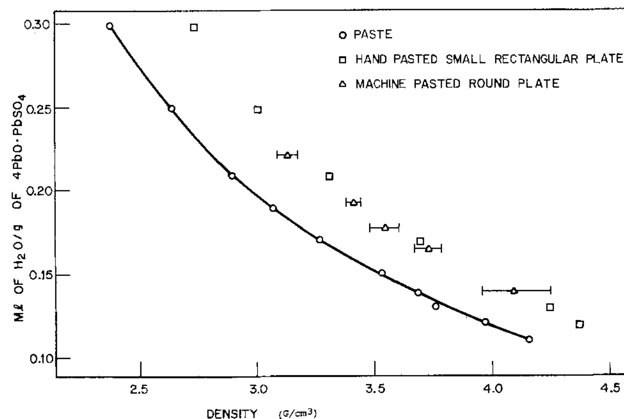

Fig. 5. The density of $4PbO \cdot PbSO_4$ *vs.* amount of water used in the paste for the dried paste, small rectangular plates and circular plates.

the pasting process squeezes some water out of the paste.

Table I gives additional data for the small paste batches plotted in Fig. 5. The mix time ranged from 20 min for the densest paste to 0.25 min for the least dense paste. The latter mix, 0.30 ml/g, is probably the maximum amount of water that can be added and still produce a paste that can be handled and hand pasted.

In Table I all batches were mixed to the one sphere stage (Fig. 1d) except for the 0.17 ml/g batch which was mixed for 20 min. The consistency of this batch as measured by the penetrometer was 139 mm and it was almost too fluid to paste. The cube weight and plate weight were heavier for the 20 min mix, and the porosity was less. This indicated that the overmixing caused some water to separate from the paste.

The porosities in Table I were calculated by two methods and are given as upper and lower values in the last column. The lower values were calculated from the wet and dry plate weights and assuming that all of the water in the wet plates was equivalent to the void volume. The upper values were calculated from the dry weights and the pasteable volume of the grid. The porosity range of the plates was 40-65%. Using Table I and Fig. 5, one could easily achieve any desired porosity in this range. We believe this is a far greater range in porosity than can be achieved with a reactive paste while still using conventional mixing and pasting techniques and without using any inert additives.

Since we believe water acts only as a bulking agent, less water should produce more dense and heavier plates. To achieve consistent plate weights, one must always add the same amount of water and mix only long enough to produce a paste with a workable consistency.

We find that a paste consistency with a penetration from 100 to 120 mm produces a paste suitable for machine pasting. A penetration of 120-140 mm was too wet for proper machine pasting. For hand pasting, a drier paste, 80-100 mm, may be used. Pastes are usually mixed for 10-20 min.

Varying the mixing time also allows the preparation of low or high density plates. A low density paste was produced in the large mixer by mixing 0.275 ml of H_2O/g of $4PbO \cdot PbSO_4$ for 0.5 min. A pellet from this plate is shown in cross section in Fig. 6. The low density plate has a much less ordered or tightly packed crystalline structure as compared to the normal density plate (compare with Fig. 4).

The capacities after two cycles of large circular plates pasted with different density pastes (see Fig. 5) were determined and are shown plotted in Fig. 7. As expected (3), the capacity of the plates increases as the density decreases. However, the low density, high capacity plates do have the disadvantage that they shed faster on cycling.

Fig. 6. Low density $4PbO \cdot PbSO_4$ plate made with a paste using 0.275 ml of H_2O/g of $4PbO \cdot PbSO_4$ and mixing for 0.5 min. Magnification 500 ×.

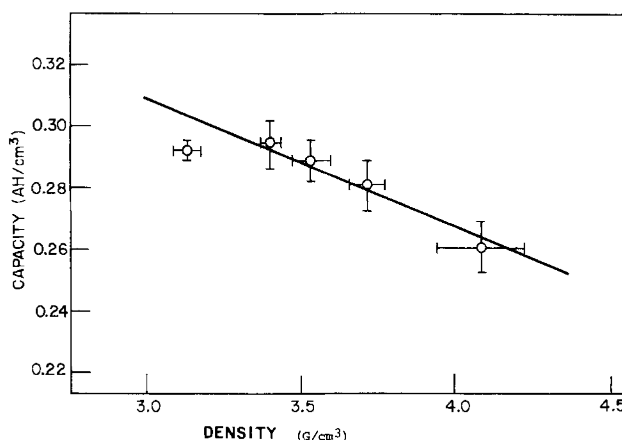

Fig. 7. The density of $4PbO \cdot PbSO_4$ in circular plates vs. their capacity.

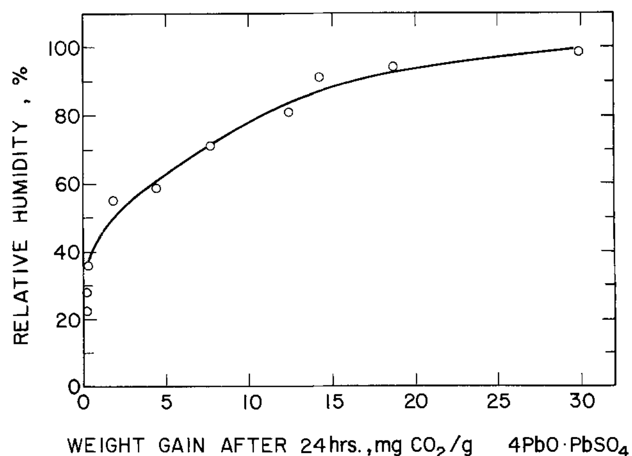

Fig. 8. CO_2 adsorption on $4PbO \cdot PbSO_4$ in pure CO_2 at different relative humidities. Below 35% RH little CO_2 is adsorbed.

Curing.—The amount of CO_2 adsorbed by $4PbO \cdot PbSO_4$ as a function of relative humidity in an atmosphere of pure CO_2 is shown plotted in Fig. 8. A similar plot for air (0.03% CO_2) was not obtained but a sample at 50% RH gained 0.6 mg of CO_2/g of $4PbO \cdot PbSO_4$ after 24 hr. Thus in air, $4PbO \cdot PbSO_4$ would absorb CO_2 at a rate 2 to 3 times slower than in pure CO_2 but we would expect the shape of the curve to be the same. Figure 8 shows that below 35-40% RH very little CO_2 is adsorbed. This explained why our plates were not being cured in the winter when the relative humidity is very low.

The $4PbO \cdot PbSO_4$ contained in a plate dried in the absence of CO_2 is shown magnified in Fig. 9. Note the smooth surface of the $4PbO \cdot PbSO_4$ crystals. Figure 10 shows the interior of a plate cured at 50% RH in air. The rough surface is due to adsorption of CO_2. From the SEM photographs as well as calculations based on the amount of CO_2 adsorbed, this scaly, carbonated layer appears to be about 1000-3000A thick. We were not able to determine the exact chemical composition of this carbonated layer since the curing reaction takes place only on the surface and therefore the amount

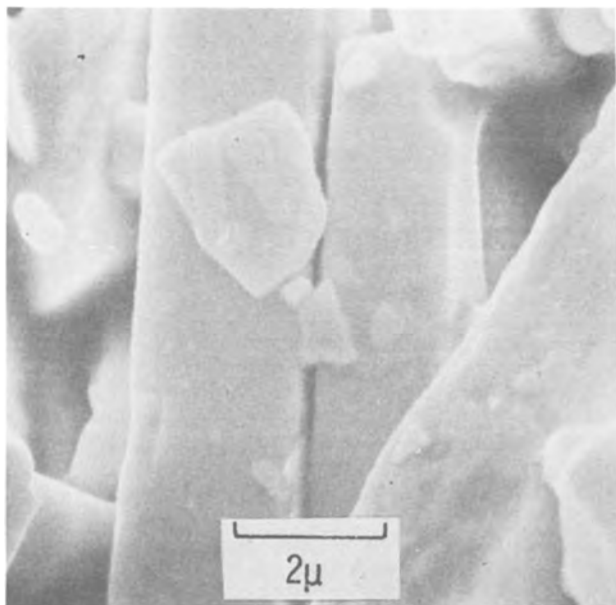

Fig. 9. $4PbO \cdot PbSO_4$ crystals in a plate dried in a desiccator with no CO_2. Magnification 10,000 ×.

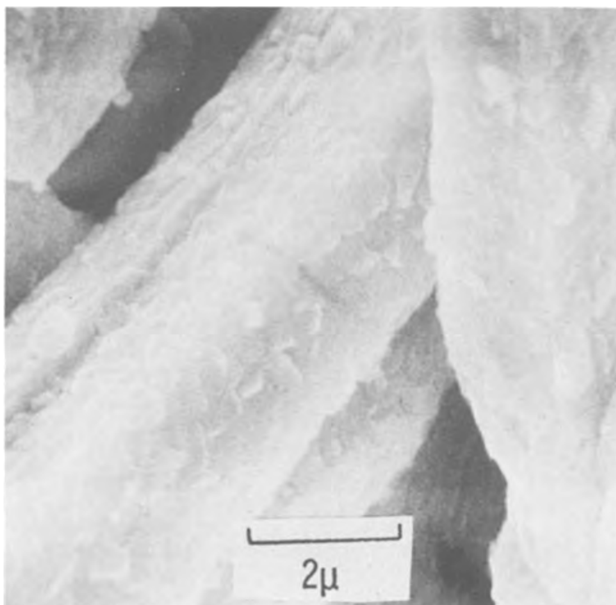

Fig. 10. $4PbO \cdot PbSO_4$ crystals in the interior of a plate cured in air for three days at 50% RH.

present is small. These "cured" crystals of $4PbO \cdot PbSO_4$ are probably held together by bridged carbonate bonds between crystals or perhaps the roughness of the scales locks one crystal to the other so that they may not freely slip by each other.

Schlotter and Fleischmann also observed roughening of $4PbO \cdot PbSO_4$ crystals (10). They postulated that the roughening was due to "abrasion caused by the mixing action." The crystals shown in Fig. 9 and 10 were from plates mixed the same length of time. Since the Fig. 9 crystals are smooth, the rough surface in Fig. 10 is not from mixing but from carbonation. We suspect that the rough surface observed by Schlotter and Fleischmann is also a result of carbonation of the surface of the crystals.

Since H_2O-CO_2 cures the plate, increasing the concentration of CO_2 and/or raising the relative humidity should accelerate the curing. This was done in the laboratory by enriching the atmosphere with CO_2 by either flowing, gaseous CO_2 or by Dry Ice in a chamber at 100% RH. In such a chamber, plates were cured in 4 hr. Figure 11 shows crystals of $4PbO \cdot PbSO_4$ in the interior of one of these plates. The carbonated surface of this plate is similar in appearance to a plate cured for 3 days in air.

An even faster method for curing plates is to put a previously dried plate in a chamber containing steam and CO_2 for 3 min. The interior of this plate is shown in Fig. 12a. Again the surface of the $4PbO \cdot PbSO_4$ crystals was carbonated. The crystals on the surface of a steam-CO_2 cured plate are shown in Fig. 12b. These crystals were not as heavily carbonated as the crystals in the interior of the plate. This same behavior was observed for plates cured in air.

Plates were given repeated 3 min treatments in steam-CO_2. The interior of a plate given 14 treatments is shown in Fig. 13a. The additional treatments did not increase the apparent thickness of the carbonated layer. However, the crystals on the surface of this plate (Fig. 13b) were more heavily carbonated than the plate given one treatment (Fig. 12b). This shows that the surface is more difficult to carbonate.

Since repeated treatments did not noticeably increase the thickness of the carbonated layer, this indicates that the carbonation process is self-limiting and that a plate cannot be overcured. The self-limitation of this process was also verified by measuring the increase in weight of plates as they were repeatedly cured.

Plates cured by all of the methods described above have been formed and cycled. No difference in performance could be detected between those given slow, air-cured treatments and those treated with CO_2 by one of the faster methods.

Conclusions

A paste is made from $4PbO \cdot PbSO_4$ by mixing with water. As the paste is mixed the crystals become more closely packed. When the paste reaches a consistency suitable for pasting, mixing should stop since con-

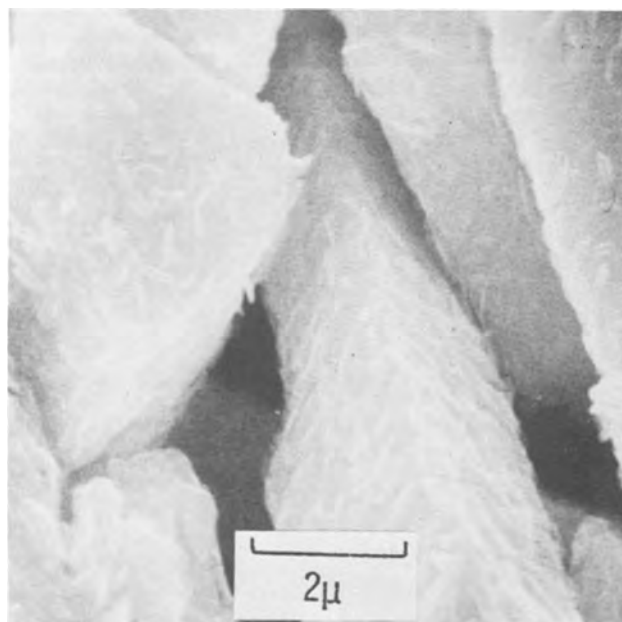

Fig. 11. $4PbO \cdot PbSO_4$ crystals in the interior of a plate dried in an oven and placed in a closed chamber containing Dry Ice (CO_2) and a relative humidity of 100%.

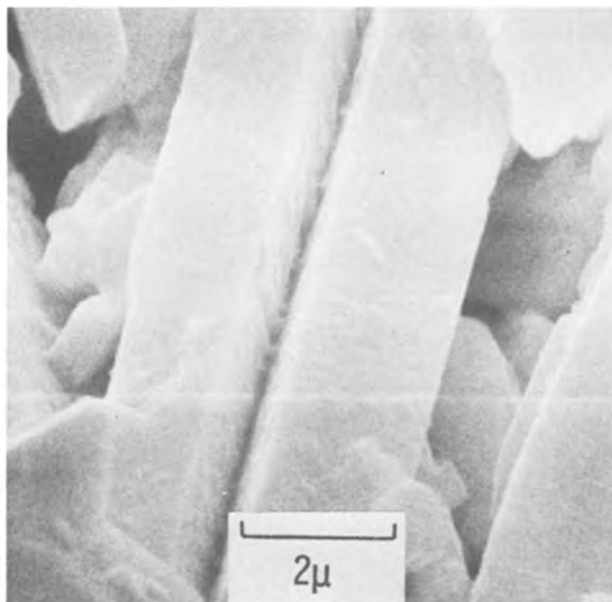

Fig. 12. $4PbO \cdot PbSO_4$ crystals in (a, upper) the interior and (b, lower) the surface of a plate dried in an oven and treated with CO_2 and steam for 3 min.

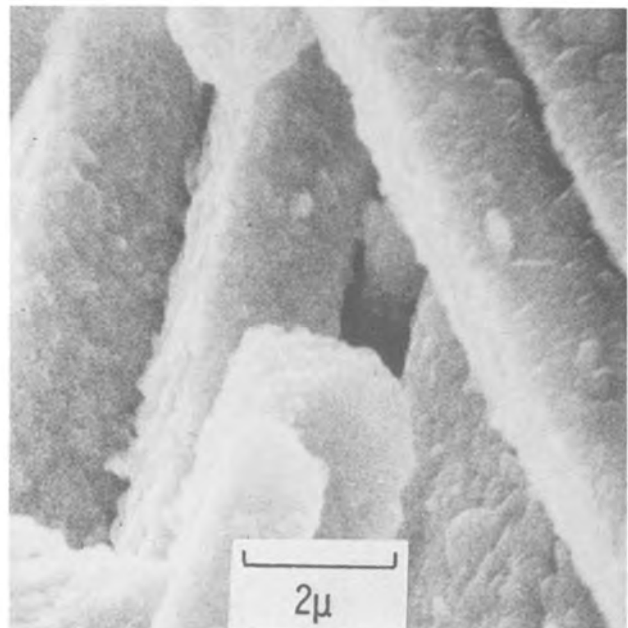

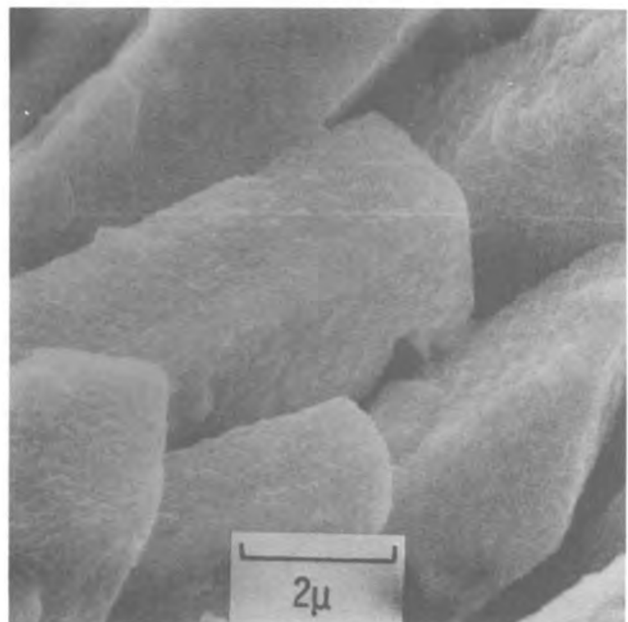

Fig. 13. $4PbO \cdot PbSO_4$ crystals in (a, upper) the interior and (b, lower) the surface of an oven-dried plate given 14, 3 min CO_2-steam treatments.

tinued mixing will cause water to separate from the paste and produce a denser paste and resultant plate. Low density plates may be produced by using more water and mixing for a shorter time.

$4PbO \cdot PbSO_4$ plates must be cured in an atmosphere containing CO_2 and at a relative humidity greater than 40%. Curing causes a scaly carbonated product to coat the surface of the $4PbO \cdot PbSO_4$ crystals. This carbonated product locks the crystals together to produce a hard plate. Curing can be accelerated by increasing temperature, humidity, and CO_2 concentration. After drying, plates may be quickly cured in steam-CO_2 in only 3 min.

Manuscript submitted June 19, 1978; revised manuscript received Aug. 4, 1978.

Any discussion of this paper will appear in a Discussion Section to be published in the June 1979 JOURNAL. All discussions for the June 1979 Discussion Section should be submitted by Feb. 1, 1979.

Publication costs of this article were assisted by Bell Laboratories.

REFERENCES

1. C. F. Yarnell and M. C. Weeks, Paper submitted to *This Journal.*
2. C. F. Yarnell, R. V. Biagetti, M. C. Weeks, and G. W. Kammlott, Abstract 18, p. 47, The Electrochemical Society Extended Abstracts, Fall Meeting, Cleveland, Ohio, Oct. 3-7, 1971.
3. R. V. Biagetti and M. C. Weeks, *Bell Syst. Tech. J.*, **49**, 1305 (1970).
4. G. W. Vinal, "Storage Batteries," 4th ed., John Wiley & Sons, Inc., New York (1967).
5. J. F. Dittman and H. R. Hamer, "Paste Preparation and Plate Control, Starting and Lighting Batteries, No. 7 in a Series," Eagle-Picher Co., Cincinnati, Ohio (1956).
6. D. E. Koontz, D. O. Feder, L. D. Babusci, and H. J. Luer, *Bell Syst. Tech. J.*, **49**, 1253 (1970).

7. H. E. Durr and A. H. Haller, U.S. Pat. 3,660,161 (1972).
8. H. E. Durr and A. H. Haller, U.S. Pat. 3,903,940 (1975).
9. A. H. Haller, J. J. Larkin, and R. P. Walters, U.S. Pat. 3,841,362 (1975).
10. W. J. Schlotter and C. W. Fleischmann, *This Journal*, **124**, 1487 (1977).

The Effect of Depassivation at Specific Crystal Facets on the State of Activation of Nickel Substrates for Electrodeposition

Dennis Tench* and Cameron Ogden*

Rockwell International Science Center, Thousand Oaks, California 91360

ABSTRACT

Changes in the surface structure of nickel substrates at open circuit in 65 w/o H_3PO_4 after an anodic etch treatment have been investigated by electrode potential measurements as a function of time, by voltammetric repassivation in neutral sulfate and phosphoric acid solutions, and by microscopic examination. It was found that partial depassivation occurs at specific crystal facets within a few hundred seconds. Studies involving single crystals indicated that the {100} and {110} orientations depassivate within this time frame, whereas the passive film on the {111} surface is more stable. The depassivation process is accelerated by iron impurities in the substrate and this impurity effect is enhanced by the presence of dissolved oxygen, which also enhances the etching of depassivated areas. These data suggest that poor activation of nickel substrates for electrodeposition can result from partial depassivation to form bare spots on the surface, through which appreciable cathodic current can pass without reducing the remaining oxide layer.

As part of the procedure to prepare metal substrate surfaces for electrodeposition, an anodic etch treatment in concentrated acid solution is often used to remove damaged surface layers, scale, and contaminants. If good adhesion of the electrodeposit is to be attained, any oxide film present on the substrate after the anodic etch must be removed prior to plating. In cases where film reduction does not occur in the plating bath before the onset of electrodeposition, this is often effected by a separate cathodic treatment. Such commercial processes do not always yield satisfactory results, and prolonged substrate contact on open circuit with the acid solution after the anodic etch is known to aggravate the problem. During the open-circuit contact, some change presumably occurs in the substrate film which leaves it capable of passing appreciable cathodic current without being electrochemically reduced. Subsequent electrodeposition then occurs over this film, resulting in poor adhesion to the substrate.

Two types of changes can occur in surface films to render them less reducible by cathodic treatment. One is an increase in the electronic conductivity of the film itself, so that current passes through the film without reducing it. The other is local dissolution or reduction of the film to form bare spots, so that most of the current passes through portions of the surface not covered by the film. The results reported here show that electrochemically passivated nickel forms bare spots at open circuit in 65 w/o (weight percent) phosphoric acid by preferential depassivation of specific crystal facets.

The passivation behavior of a given crystal orientation of nickel cannot readily be ascertained from the literature, since there are inconsistencies in the limited results available. For example, the results of Tokuda and Ives (1) indicate that crystal orientation effects are appreciable during active dissolution in 1*N* H_2SO_4, but small during passivation, whereas the results of Yagupolskaya and Movchan (2) indicate that the opposite is true, and Latanision and Staehle (3) report that polarization measurements for Ni in this electrolyte are essentially insensitive to crystal orientation. Likewise, the relative tendency toward passivation in 1*N* H_2SO_4 appears to be {111} > {110} > {100} from the data in Ref. (1) and {110} > {100} > {111} from those in Ref. (2). Weininger and Breiter (4) found the relative order of reactivity toward oxidation in alkaline KOH solution to be {110} > {100} > {111}, but Piontelli *et al.* (5) observed little orientation dependence for the polarization behavior of Ni in buffered pH 3 chloride solution at low current densities (<20 mA/cm^2).

In none of these studies of Ni passivation are the observed crystal orientation effects very pronounced. This may result to some extent from the point-by-point measurement technique usually employed, since excessive dissolution at the less anodic potentials prior to passivation could expose different crystal facets to the solution. Such dissolution could also account for the discrepancies in the published results. In the present work, a strong dependence on crystal orientation was observed for Ni depassivation in 65 w/o H_3PO_4 after an anodic etch treatment at 100 mA/cm^2 for 90 sec.

Experimental Details

The working electrodes were 6 mm diam disks (polycrystals) or 5 mm squares (single crystals) mounted in the rotating-disk configuration (6), flush with the ends of 13 mm diam Kel-F cylinders, by compression molding at elevated temperature (<300°C). Rotating-square electrodes have been shown (7) to give results comparable to rotating disks. Single crystals of 99.95% purity were aligned by reflection x-ray diffraction to give the desired orientation

* Electrochemical Society Active Member.

Key words: depassivation, nickel, phosphoric acid, crystal orientation, electrodeposition.

within ±0.5°. Three types of polycrystalline electrodes were investigated: 99.999% "pure" (PAR magnetometer standard); 99.5% "wrought" (Ni-200, International Nickel Company); and "electrodeposited" (SNR nickel sulfamate bath). Before use, electrodes were polished on successively finer aqueous alumina powder slurries to 0.05 μm particle size. For all studies, Pt and saturated calomel (SCE) were used as the counter- and reference electrodes, respectively.

After an anodic etch treatment at 100 mA/cm² for 90 sec in 65 w/o H_3PO_4 saturated with various gases, open-circuit potentials of Ni electrodes were followed *vs.* SCE as a function of time using a Hewlett-Packard Model 7004B recorder. After various times, electrode surfaces were examined using a scanning electron microscope (SEM). The state of passivation after a given amount of time on open circuit in the H_3PO_4 solution was determined by quickly transferring electrodes to another cell containing argon-saturated 0.50*M* Na_2SO_4 solution and measuring the charge required for passivation on the initial current-potential sweep at 10 mV/sec from −0.50 to 0.80V *vs.* SCE. The electrode potential was controlled using a PAR Model 173 Potentiostat/Galvanostat in conjunction with a PAR Model 175 Universal Programmer, and the charge was determined using a PAR Model 179 Integrating Coulometer. Since electrochemically produced films are stable in this nearly neutral electrolyte, whereas air-formed oxide layers are easily reduced (8), the charge required to repassivate a nickel electrode in this solution is a measure of the amount of surface not covered by an electrochemically produced passive film.

Results and Discussion

Repassivation studies.—Repassivation curves obtained for "pure" Ni in neutral sulfate solution after various times on open circuit in 65 w/o H_3PO_4 solution following the anodic etch treatment are shown in Fig. 1. It is evident that the electrode is depassivating with time at open circuit in the H_3PO_4 solution since progressively more charge is required for repassivation. By comparison with the 18 mC/cm² needed to passivate a freshly polished surface (not shown), the "pure" Ni electrode is still 80% passivated after 75 sec (curve 1), 45% passivated after 200 sec (curve 2), but only 25% passivated after 500 sec (curve 3). These values are probably somewhat low since surface roughening by dissolution has not been taken into account. Curve 4 is the second sweep obtained in each case, indicating that the electrode is irreversibly passivated in this neutral sulfate medium (8).

Similar repassivation curves are shown in Fig. 2 for the relatively impure "wrought" Ni electrode. The trend is the same, but depassivation on open circuit in the H_3PO_4 solution appears to occur more rapidly. Repassivation in the neutral sulfate solution is also more complicated, involving considerable current at the more anodic potentials (>0.1V). The appreciable currents observed on the second (curve 4) and subsequent sweeps indicate that the less pure electrode is also more difficult to passivate.

SEM investigation.—Figure 3 is a scanning electron micrograph of a "wrought" nickel electrode immediately after the anodic etch treatment in oxygen saturated 65 w/o H_3PO_4 solution. The surface is still reasonably flat, except for minor pitting and some grain boundary etching, which is expected for an electrode passivated at a high current density. Figures 4 and 5 show the same electrode after prolonged (20 min) open-circuit exposure to the oxygen-saturated H_3PO_4 solution following the anodic etch treatment. Similar results are obtained for shorter exposure times and in argon-saturated solutions, but the surface features are not resolved so clearly. It is

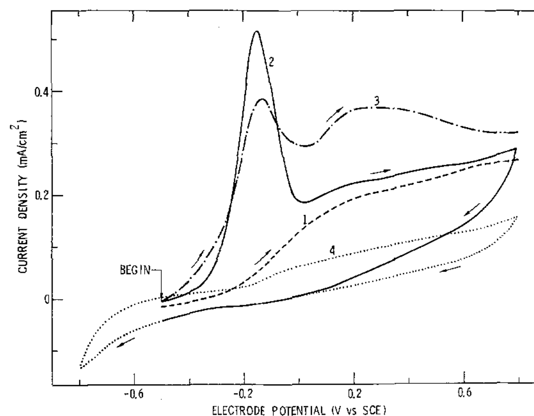

Fig. 2. Same as Fig. 1, except for "wrought" Ni after 1, 0 sec; 2, 75 sec; and 3, 180 sec on open circuit.

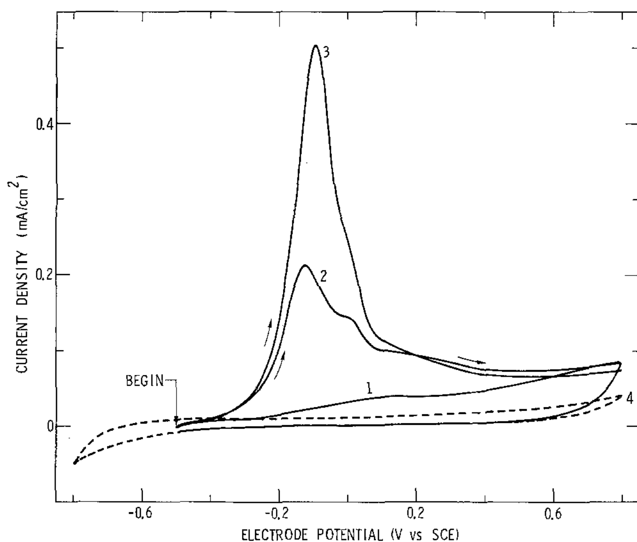

Fig. 1. Linear sweep cyclic voltammograms at 10 mV/sec for a "pure" Ni electrode at 200 rpm in argon-saturated 0.5M Na_2SO_4 solution after the anodic etch treatment at 2500 rpm and then: 1, 75 sec; 2, 200 sec; and 3, 500 sec on open circuit in air-saturated 65 w/o H_3PO_4 solution. Curve 4 is a typical second sweep in each case.

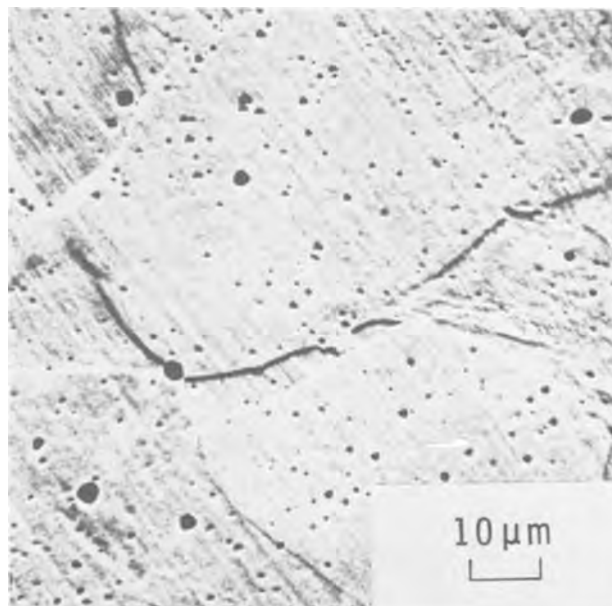

Fig. 3. Scanning electron micrograph of "wrought" Ni surface immediately after the anodic etch treatment in oxygen-saturated 65 w/o H_3PO_4 at 2500 rpm.

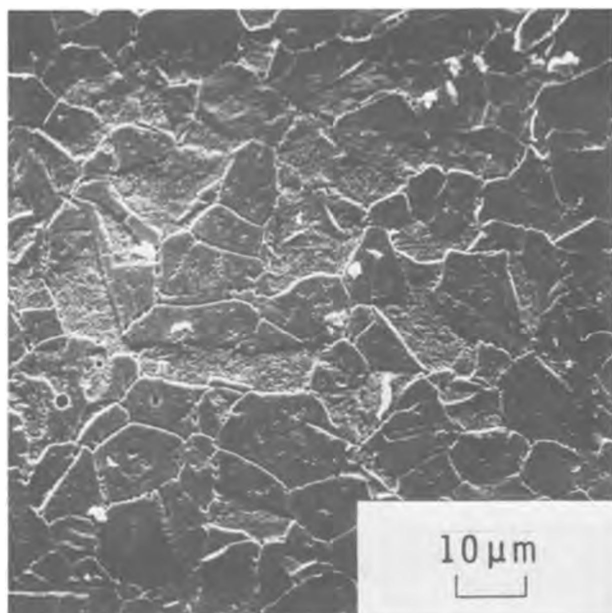

Fig. 4. Scanning electron micrograph of "wrought" Ni surface after open-circuit exposure to oxygen-saturated 65 w/o H_3PO_4 for 20 min at 2500 rpm following the anodic etch treatment.

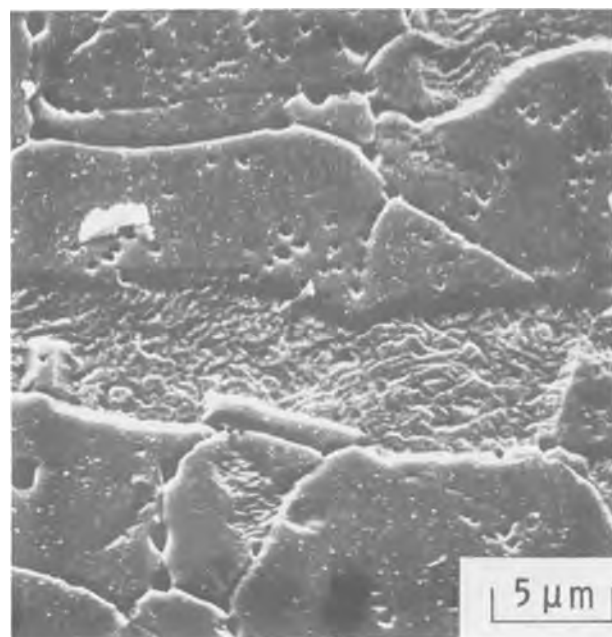

Fig. 5. Same as Fig. 4, but at a higher magnification

evident that some grains are practically intact after the open-circuit exposure, whereas others have been severely recessed and roughened by dissolution. This is more evident at the higher magnification (Fig. 5). It is apparent that some grains, presumably of the same crystal orientation, have depassivated on open circuit, permitting dissolution of the underlying metal.

Isolated large pits of the type shown in Fig. 6 are also formed on the "wrought" Ni surface during depassivation in 65 w/o H_3PO_4 solution. In solutions containing dissolved O_2, "comet tails" originating at these pits form a swirl pattern centered at the middle of the rotated electrode. These tails appear dark to the naked eye, but light in SEM pictures (see Fig. 6). Evidently, some species is formed in the pits which reacts with the outer electrode surface as it is swept along by the solution swirling across the rotating-disk electrode. Since the "comet tails" are not observed

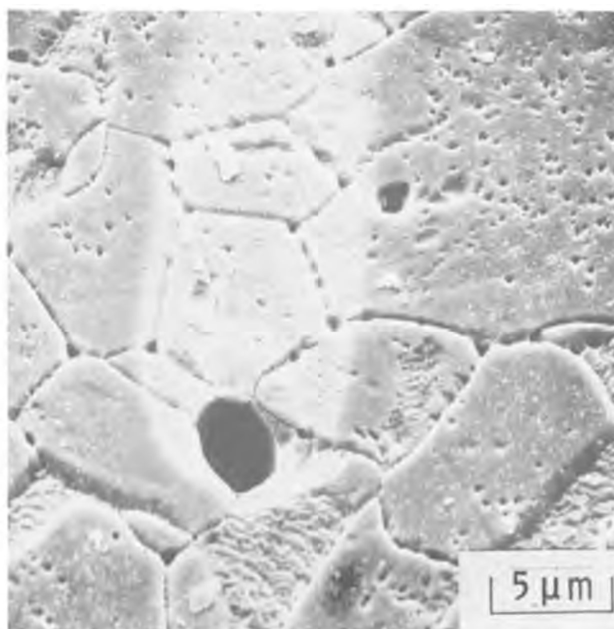

Fig. 6. Different area of the surface shown in Fig. 4

in the absence of dissolved O_2, the species reacting with the surface is probably peroxide (OOH^-), which is known to form as an intermediate in electrochemical oxygen reduction (9). Energy dispersive analysis of x-rays (EDAX) detected an appreciable concentration of Fe inside the large pits, but none at other points along the surface. Thus, these pits, which occur predominantly at grain boundaries, probably result from local dissolution of Fe impurities segregated there during solidification of the metal. These impurities may also catalyze O_2 reduction within the pits.

As discussed in the preceding section, our repassivation measurements indicate that the "wrought" Ni depassivates more rapidly than the "pure" metal. To some extent, these measurements probably reflect repassivation of depassivated impurity centers. However, the electrons provided by dissolution of Fe and Ni at the impurity sites may partially reduce the oxide layer at other points on the surface, which would also be reflected in the charge required for repassivation.

Depassivation also seems to occur at specific crystal facets for "pure" Ni, as shown in Fig. 7. In this case, parallel linear trenches are formed, presumably in line with crystal planes. A similar etch pattern has been observed by Datta and Landolt (10) for transpassive dissolution of Ni in $NaNO_3$ solutions.

Open-circuit voltage measurements.—As shown in Fig. 8, the open-circuit potential (U) of a pure Ni electrode in 65 w/o H_3PO_4 reaches a rotation-dependent cathodic peak about 250 sec after the anodic etch treatment. Such open-circuit behavior during depassivation is unprecedented and does not appear to have been treated in the literature. Considering the repassivation and SEM results, the following interpretation seems reasonable. Initially, U drifts cathodic because the higher nickel oxides formed during anodization are dissolving as part of the surface film and, to some extent, are being reduced by local cell action. At times less than 100 sec, U is independent of the rotation rate, as might be expected if chemical dissolution is kinetically controlled since the repassivation studies show that the surface is still essentially passivated. Significant breaks appear in the film after about 100 sec so that Ni dissolution

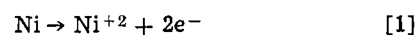

$$Ni \rightarrow Ni^{+2} + 2e^- \quad [1]$$

becomes appreciable. These breaks probably occur at

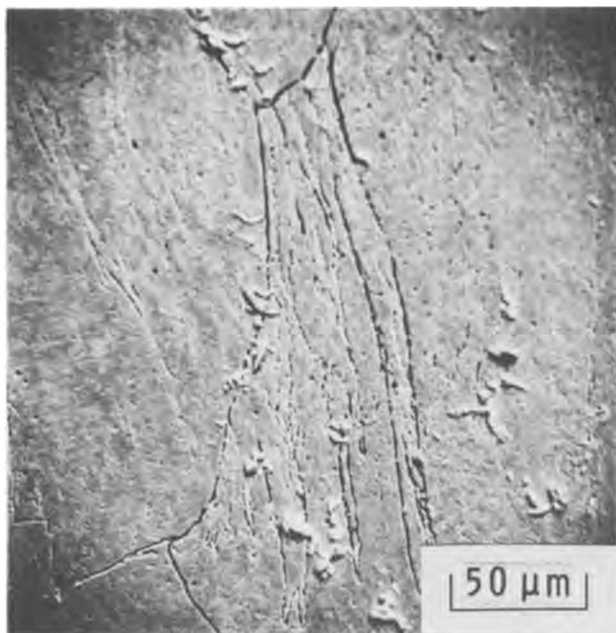

Fig. 7. "Pure" Ni surface after same treatment as for Fig. 4

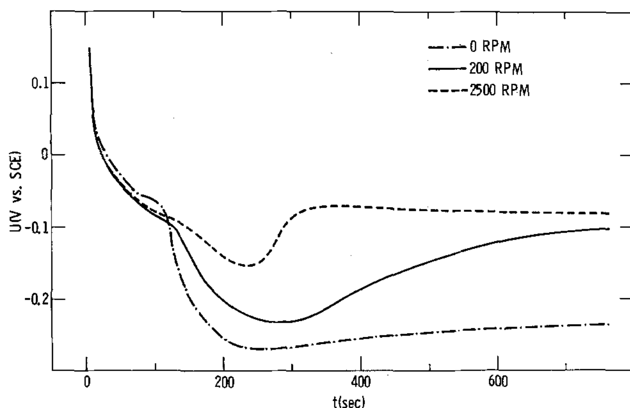

Fig. 8. Time variation of the open-circuit potential of a "pure" Ni electrode (rotated at various rates) after the anodic etch treatment at 200 rpm in air-saturated 65 w/o H_3PO_4 solution.

pits and grain boundaries. The electrons generated are consumed by reduction of protons

$$2H^+ + 2e^- \rightarrow H_2 \quad [2]$$

on the bare Ni within breaks in the film, and to some extent by O_2 reduction

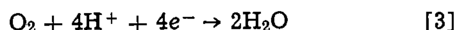

$$O_2 + 4H^+ + 4e^- \rightarrow 2H_2O \quad [3]$$

When solution mass transport is adequate, the equilibrium between these three reactions establishes a stable corrosion potential. But at the early stages in the depassivation (after 100 sec), H^+ and O_2 must be transported via pits and crevices in the surface film to the underlying bare Ni areas. As these species become depleted at the recessed bare Ni surfaces, H_2 evolution and O_2 reduction are forced to occur on the oxide layer where the overvoltages are presumably higher. Thus, as H^+ and O_2 are depleted within pits and crevices, U drifts further cathodic and the extent of the drift is rotation dependent.

As the pits and crevices in the film widen, eventually exposing entire grains to the solution, mass transport to the underlying Ni is improved. Thus, after 250 sec, the cathodic drift peaks out and U moves anodic to the corrosion potential if the electrode is rotated sufficiently fast to prevent concentration polarization at the depassivated areas. Without rotation,

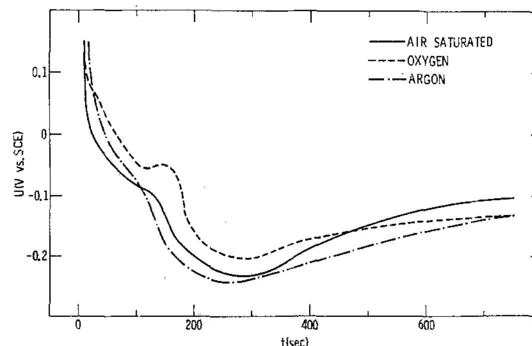

Fig. 9. Time variation of the open-circuit potential of a "pure" Ni electrode at 200 rpm after the anodic etch treatment in 65 w/o H_3PO_4 saturated with various gases.

mass transport to recessed grains and within pits and trenches remains inadequate to establish the corrosion potential.

Figure 9 shows that the voltage arrest at 100 sec is strongly accented in solutions containing dissolved oxygen, indicating that O_2 reduction does play some role in retarding the cathodic drift of U for a "pure" Ni electrode. However, the gas atmosphere has little effect on the magnitude and position of the cathodic peak, indicating that dissolved oxygen is rapidly depleted within pits and crevices and does not significantly affect the over-all rate of depassivation. "Pure" electrodes depassivated for several minutes in air- or oxygen-saturated H_3PO_4, however, acquire a frosted appearance not observed for those exposed to argon-saturated solutions. Electron micrographs show that this results from deeper preferential etching of some Ni grains in the presence of oxygen, which presumably is reduced on the exposed nickel surfaces, and to some extent on the oxide film, enhancing dissolution.

As shown in Fig. 10, the open-circuit electrode potential also reflects the enhanced depassivation rate caused by impurities in the "wrought" Ni substrate. Immediately after the anodic etch, U drifts rapidly cathodic, apparently driven by dissolution of Fe and Ni within pits at impurity centers. Reduction of H^+ and O_2 would tend to halt the cathodic drift at the corrosion potential, but in air- and argon-saturated solutions, these species become depleted within the impurity pits and other breaks in the surface film. Thus, since these reduction processes do not occur readily on the oxide layer, metal dissolution at impurity sites pegs U at a value cathodic to the corrosion potential. This situation seems to be stable for several minutes in the absence of dissolved O_2, even though depassivation is also occurring within specific crystal facets at points removed from the impurity centers (see preceding sections). In air-saturated solutions, O_2 reduction hastens the over-all process so that the corrosion potential is established more quickly (after only a few hundred seconds). It should also be mentioned that restricted mass transport to recessed grains may also play some role in the depassivation

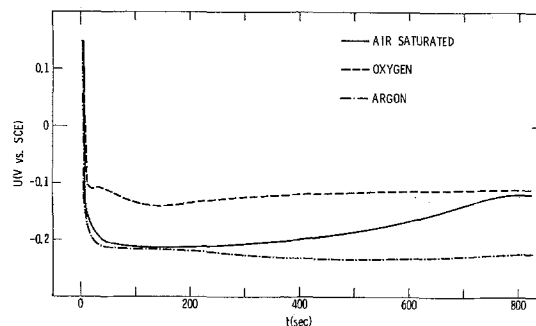

Fig. 10. Same as Fig. 9 for a "wrought" Ni electrode

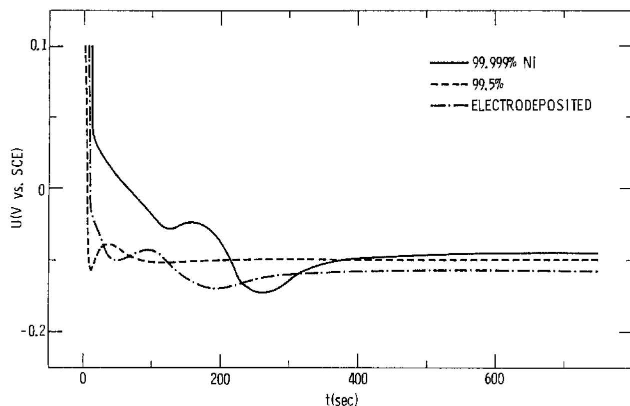

Fig. 11. Time variation of the open-circuit potential of various Ni electrodes at 2500 rpm after the anodic etch treatment in oxygen-saturated 65 w/o H_3PO_4 solution.

process since the grains of the "wrought" material are an order of magnitude smaller than for the "pure" Ni (see Fig. 4 and 7).

In order to exaggerate differences, "electrodeposited" nickel was compared with "wrought" and "pure" nickel substrates at 2500 rpm in oxygen-saturated 65 w/o H_3PO_4 solution. The open-circuit potentials after the anodic etch are shown in Fig. 11. It is evident that electrodeposited Ni depassivates somewhat more slowly than the "wrought" material, but considerably faster than pure Ni, at least initially.

Single crystal studies.—To determine which crystal facets of Ni depassivate after short times on open circuit in phosphoric acid solution, the passivation/depassivation behavior of Ni single crystals was investigated. Figure 12 shows polarization curves obtained at 50 mV/sec in 65 w/o H_3PO_4 after open-circuit exposure for 500 sec following passivation by an anodic sweep to 0.8V (solid lines) and by the anodic etch treatment at 100 mA/cm^2 for 90 sec (dashed lines). The curves obtained after the open-circuit exposure following passivation at 0.8V exhibit sharp passivation peaks similar to those observed for freshly polished electrodes. This indicates that all three crystal facets rapidly depassivate at open circuit following passivation under mildly oxidizing conditions. After open-circuit exposure following the anodic etch treatment, however, repassivation peaks, although somewhat broadened, are still observed for the {100} and {110} orientations, but the anodic current is negligible for the {111} electrode. Thus, passivation under strongly oxidizing conditions produces a stable film on the {111} surface, but not on the {100} and {110} facets which still depassivate rapidly on open circuit.

As shown in Fig. 13, the time variation of the open-circuit electrode potential following the anodic etch treatment also reflects the relative stabilities of the passive films formed on the various Ni facets. The {111} electrode quickly establishes a steady anodic potential of about 0.5V, which presumably corresponds to the equilibrium between a stable passive film and the electrolyte. On the other hand, the {100} electrode appears to depassivate at some points on the surface within 10 sec, so that the potential is driven rapidly to 0.0V by Ni dissolution. As the depassivated areas multiply and widen, Ni dissolution increases and the corrosion potential (−0.1V) is approached. After about 300 sec, the potential drifts more cathodic. This could result from reduction and/or dissolution of a second type of oxide in a duplex structure, but the subsequent reversal to the anodic direction is difficult to explain within this framework. It seems more reasonable that the cathodic drift is caused by restricted mass transport of H^+ and O_2 to the bare Ni areas which have become recessed by dissolution, as

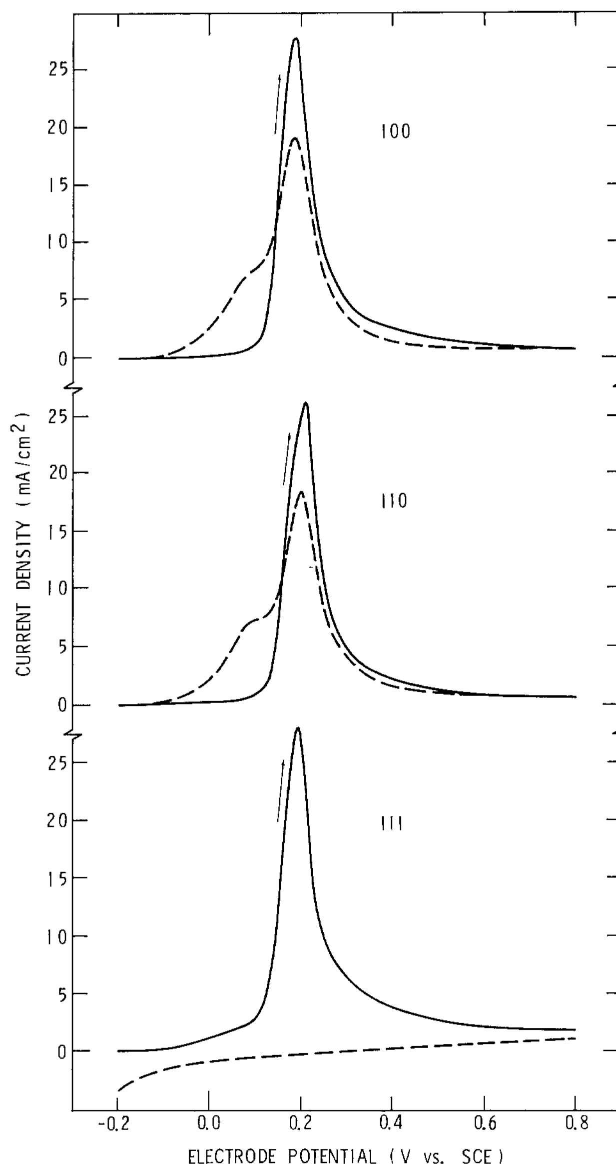

Fig. 12. Anodic polarization curves at 50 mV/sec for single crystalline Ni electrodes rotating at 200 rpm in air-saturated 65 w/o H_3PO_4 after 500 sec on open circuit following passivation at 0.80V (solid curves) and following the anodic etch treatment (dashed curves).

discussed in the preceding sections. Since mass transport is improved as the recessed areas widen, the potential reaches a cathodic peak, then drifts anodic toward the corrosion potential.

The behavior of the {110} orientation is intermediate between the other two. The potential arrest at about 0.5V in Fig. 13 indicates that the passive film on the {110} surface is resistant to dissolution. But the electrode potential rapidly drifts further cathodic after 100 sec, indicating that significant breaks have appeared in the surface film. The depassivation process then proceeds in a fashion similar to that for the {100} surface.

The stable oxide produced on the {111} surface under strongly oxidizing conditions may involve formation of higher nickel oxides, deprotonation, or a combination of the two. Changes in the oxide film thickness are not expected to be important in the passivation/depassivation behavior of Ni (8, 11, 12). Protons probably play a role since we have found that the tendency toward passivation in neutral sulfate solution is in the order {100} > {110} > {111} orientation, which is opposite to the order of oxide

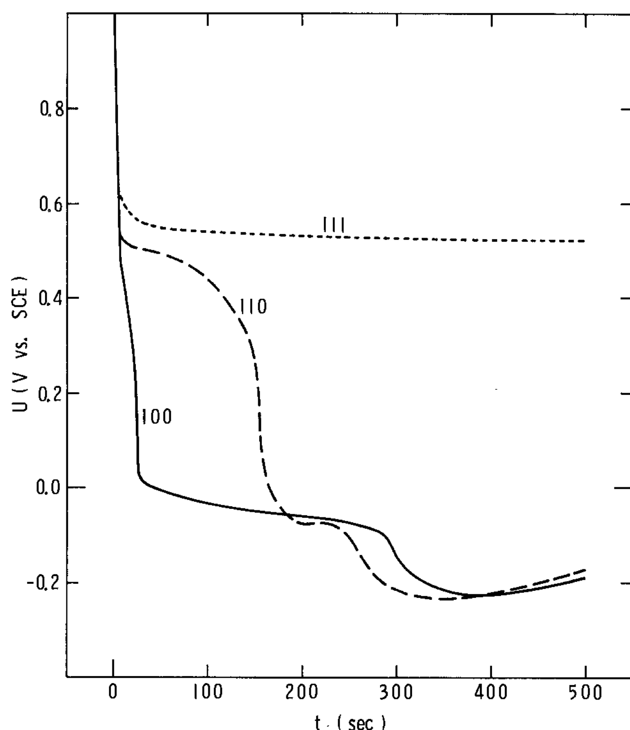

Fig. 13. Time variation of the open-circuit potential of single crystalline Ni electrodes at 200 rpm after the anodic etch treatment in air-saturated 65 w/o H_3PO_4 solution.

film stability reported here for phosphoric acid solution.

Recently, MacDougall and Cohen (12, 13) have suggested that film breakdown on Ni in sulfate solutions occurs by chemical attack at defect sites, followed by undermining of the oxide film by Ni dissolution. Since these authors did not report on the effects of varying solution mass transport, it is difficult to determine the extent to which undermining is important. It seems reasonable to expect, however, that crystal orientation effects would also play a significant role in the sulfate system. On the other hand, the present results are adequately explained by assuming that pits and crevices in the oxide film grow laterally within the confines of specific crystal facets.

Conclusions

The results reported here show that polycrystalline Ni depassivates preferentially at specific crystal facets on open circuit in 65 w/o H_3PO_4 solution following an anodic etch treatment at 100 mA/cm^2 for 90 sec. The tendency toward depassivation increases in the order {100} > {110} > {111} orientations. Iron impurities in the substrate accelerate the depassivation process and this impurity effect is enhanced by dissolved oxygen in the electrolyte. Such partial depassivation can lead to poor adhesion of electrodeposits by permitting appreciable current to pass through bare spots without reducing the remainder of the surface film.

Manuscript submitted May 1, 1978; revised manuscript received July 27, 1978.

Any discussion of this paper will appear in a Discussion Section to be published in the June 1979 JOURNAL. All discussions for the June 1979 Discussion Section should be submitted by Feb. 1, 1979.

Publication costs of this article were assisted by Rockwell International Science Center.

REFERENCES

1. T. Tokuda and M. B. Ives, *Corros. Sci.*, **11**, 297 (1971).
2. L. N. Yagupolskaya and B. A. Movchan, in "Proceedings of the 4th International Congress on Metallic Corrosion," Sept. 7-14, 1969, Amsterdam, p. 473, National Association of Corrosion Engineers, Houston, Texas (1972).
3. R. M. Latanision and R. W. Staehle, *Acta Metall.*, **17**, 307 (1969).
4. J. L. Weininger and M. W. Breiter, *This Journal*, **110**, 484 (1963).
5. R. Piontelli, G. Poli, and G. Serravalle, in "Trans. Symp. on Electrode Processes," p. 67, Philadelphia, May 4-6, 1959, John Wiley, New York (1961).
6. V. G. Levich, "Physicochemical Hydrodynamics," Prentice-Hall, Englewood Cliffs, N.J. (1962).
7. D. Yohe, A. Riga, R. Greef, and E. Yeager, *Electrochim. Acta*, **13**, 1351 (1968).
8. B. MacDougall and M. Cohen, *This Journal*, **121**, 1152 (1974).
9. K. J. Vetter, "Electrochemical Kinetics," p. 642, Academic Press, New York (1967).
10. M. Datta and D. Landolt, *This Journal*, **124**, 483 (1977).
11. B. MacDougall and M. Cohen, *ibid.*, **123**, 1783 (1976).
12. B. MacDougall and M. Cohen, *ibid.*, **124**, 1185 (1977).
13. B. MacDougall and M. Cohen, *Electrochim. Acta*, **23**, 145 (1978).

Mössbauer Studies of the Passive Film Formed on Tin in Borate Buffer

A. Vértes, H. Leidheiser, Jr.,* M. L. Varsányi, G. W. Simmons,* and L. Kiss

Institute of Physical Chemistry and Radiology, Lorand Eötvös University, Budapest, Hungary, and Center for Surface and Coatings Research, Lehigh University, Bethlehem, Pennsylvania 18015

ABSTRACT

Polarization curves of tin were determined potentiodynamically in deaerated borate buffer at pH 8.5. Mössbauer studies were carried out at liquid nitrogen temperature by transmission using foils of aluminum on which a thin layer of tin enriched in ^{119}Sn was electrodeposited. The predominant tin species in the passive film was Sn^{+4}. The thickness of the passive film was a function of the applied potential and ranged from 0.8 to 2.5 nm. The rate of tin dissolution in the borate buffer was insignificant even in the transpassive range. The surface product formed on tin after exposure to air for more than 30 days could not be removed cathodically in the borate buffer. *In situ* emission Mössbauer studies using ^{119m}Sn were largely unsuccessful because of the low specific activity of the available isotope.

The anodic behavior of tin in alkaline solution has been the subject of several investigations (1-11). Seven investigations used hydroxide solution (1-3, 5, 8-10), one investigation used potassium hydroxide solution (11), three investigations used borate solution (3, 6, 9), and three investigations used sodium carbonate solution (3, 7, 9). The general consensus arising from these investigations, based largely on galvanostatic and coulometric studies, is that in the hydroxide and carbonate solutions SnO or $Sn(OH)_2$ is formed at the more negative potentials and SnO_2 or $Sn(OH)_4$ is formed at the more positive potentials. In the region of -900 - -600 mV (*vs.* SHE) it is believed that divalent tin is formed first and is oxidized to tetravalent tin. The situation in the borate solution is much less clear because all the measured parameters are so different from the values obtained in the sodium hydroxide and sodium carbonate solutions. Data summarized in Table I and taken from the paper by Pugh *et al.* (9) illustrate this point. It will be noted that the critical current density for passivity in borate solution is over 4 orders of magnitude less than that required in 1*N* NaOH solution and that the characteristic potential values are different. In the more aggressive solutions authors have also noticed that the anodic oxide is sufficiently thick such that it exhibits color, and the color is a function of the polarizing potential and the time. It appears that divalent tin has a long lifetime and is present on the electrode surface when polarization is carried out in the vicinity of the first maximum in hydroxide and carbonate solutions and that this divalent tin is further oxidized to tetravalent tin at more positive potentials. The situation is far from clear in the borate solution and, in the words of Pugh *et al.* "The general pattern of passivation (as described above) was not followed in sodium borate electrolytes . . . ."

This work was undertaken largely with three objectives in mind: (*i*) to determine the chemical nature of the passive film formed in borate solution under anodic polarization; (*ii*) to determine its thickness under various experimental conditions; and (*iii*) to determine the stability of the passive film under different conditions of polarization.

Previous studies of the oxidation of iron (22) and of the anodic behavior of cobalt by Mössbauer spectroscopy (13) have demonstrated that this technique can be sufficiently sensitive to characterize surface films. In the present studies, Mössbauer spectroscopy in the absorption and emission modes of operation have been used to characterize the passive film formed on tin by polarization in buffered borate, pH 8.5.

* Electrochemical Society Active Member.

Key words: Mössbauer spectroscopy, passivity, tin, tin oxide.

Absorption geometry is the conventional method used in Mössbauer spectroscopy. A single line source, ^{119m}Sn in $CaSnO_3$, which emits 23.87 keV gamma, is resonantly absorbed by a specimen containing ^{119}Sn. The spectrum of the specimen is generated by measuring the absorption (count rate) as a function of velocity of the source. To obtain surface sensitivity, a specimen with a high surface-to-volume ratio is required.

In emission Mössbauer spectroscopy the active ^{119m}Sn isotope is deposited on the surface of tin. The spectrum is generated by resonant absorption of the emitted gamma ray by a single line absorber, $CaSnO_3$ enriched in ^{119}Sn. Auger aftereffects may affect the charge state of emitting ^{119m}Sn nuclei as has been discussed for emission studies using ^{57}Co. Since in the case of Sn both the parent and daughter isotopes are Sn, the formation of atypical valence states by chemical effects within the lattice of the corrosion layer is less likely than that found in the $^{57}Co \rightarrow {}^{57}Fe$ emission spectroscopy.

Experimental

All potentiodynamic measurements and polarization studies were carried out in deaerated buffered borate solution at pH 8.5 and room temperature. Potentiodynamic curves were recorded continuously in both the increasing and decreasing potential mode. The reference electrode in all cases was a 0.1M calomel half-cell and all potentials are given with respect to this electrode.

In order to carry out Mössbauer experiments in absorption geometry of a thin oxide on a tin substrate it is necessary that the volume of oxide/volume of substrate be as large as possible. The strategy adopted was to electroplate a thin layer of tin enriched in ^{119}Sn on both sides of an aluminum foil 0.0065 cm in thickness. Aluminum was selected because of its low cross section for the 23.87 keV gamma ray and its inertness under polarization conditions in the borate electrolyte. Other substrates such as iron and copper were considered and were studied in a preliminary way, but they were discarded because of possible complications from the formation of intermetallic compounds at the copper/tin or iron/tin interface (12).

Deposits with good adherence to the aluminum substrate and satisfactory integrity (*cf.* infra) were obtained when the following procedure was used. The aluminum surface was polished with emery paper, etched in a hot solution of 10% NaOH, and finally immersed for a brief time in 30% HNO_3 at room temperature. The aluminum was thoroughly washed in distilled water and allowed to dry. Tin was electrodeposited at a current density of 0.2 A/dm^2 for 30 sec

Table I. Important parameters derived from potentiodynamic polarization studies of tin in alkaline solutions at 25° as determined by Pugh et al. (9)

Solution	Potential at maximum (mV)	Potential range of second peak	Critical C.D. for passivity (mA/cm²)	C.D. in passive region (mA/cm²)
1N Na_2CO_3	−755	−655-−576	0.55	0.22
0.1N NaOH	−825	−656-−536	5.70	0.02
1N NaOH	−870	−700-−620 (at 40°)	170	0.064
0.1M sodium borate	−566	−517-−417 (at 40°)	0.007	0.002

while the plating bath was maintained at 70°C. The composition of the bath was 25 g/liter SnI_4 in which the ^{119}Sn content was enriched to 89%, 12 g/liter NaOH, 1.5 g/liter CH_3COONa, and 1 ml/liter of 30% H_2O_2. The average thickness of the resulting deposit was determined by dissolution of the tin in 1M sulfuric acid and determining the tin content of the solution by differential pulse polarography.

Mössbauer spectra were recorded on samples passivated in the deaerated borate buffer at various potentials and for various periods of time. After passivation, the foils were immediately plunged into liquid nitrogen and the spectra were recorded while the samples were maintained in the liquid nitrogen. No evidence of a crystallographic transformation to α-tin was detected. The Mössbauer source was $Ba^{119m}SnO_3$ with a 5mCi activity. X-rays generated by the source were filtered from the beam by means of a palladium foil. All absorption spectra are given with respect to $BaSnO_3$ as the reference.

Emission Mössbauer spectra were obtained in the same cell previously used by Simmons et al. (13). Tin was electrodeposited from a dilute solution of $^{119m}SnCl_2$ that was made suitably conductive by the addition of 0.15 ml of 4N HCl and 0.7 ml of 2N NaOH to give a total plating volume of 10 ml. Prior to plating, the tin substrate was mechanically polished, etched in hot HCl, and thoroughly washed in distilled water. The tin deposition was carried out at a current density of 0.1 A/dm² and room temperature for 8 hr. The specific activity of the available ^{119m}Sn was 400 mCi/g and the activity of the electrodeposit was approximately 4 μCi for deposit thicknesses of the order of 14 nm. Emission spectra were recorded using a $Ca^{119}SnO_3$ absorber.

Results

Figure 1 shows the characteristic potentiodynamic curves obtained on the first scan of a cathodically reduced tin deposit on a pure aluminum substrate. Figure 2 shows the curve obtained in successive scans of the same sample after cathodic reduction preceding each scan. Figure 1 shows a peak at −350 mV which is missing in Fig. 2. Potentiodynamic curves of pure tin were identical to Fig. 2. Potentiodynamic curves of pure aluminum also yielded the peak at −350 mV during the first scan and the peak was absent in successive scans. On the basis of these measurements it was concluded that the −350 mV peak represents oxidation of the aluminum surface and that once it occurred it played no further role in the potential range to which the samples were subjected. Aluminum appeared to be a satisfactory substrate for the tin after this artifact was recognized.

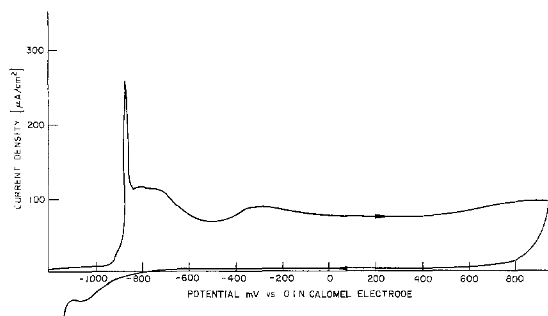

Fig. 1. Characteristic potentiodynamic curve obtained on the first scan of a cathodically reduced tin electrodeposit on a thin-foil aluminum substrate.

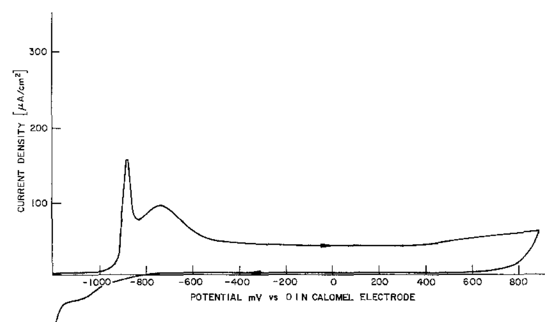

Fig. 2. Potentiodynamic curve obtained on second and successive scans of a cathodically reduced tin electrodeposit on a thin-foil aluminum substrate. Note that the peak at −350 mV present on the first scan (Fig. 1) is now absent.

Figure 3 is the Mössbauer absorption spectrum at 78°K of a tin electrodeposit that was cathodically treated in the borate solution for 10 min at −1200 mV. The center of the peak is located at +2.60 mm/sec and the computer-calculated width at half maximum is 0.99 ± 0.01 mm. These values are typical of those customarily obtained for metallic tin and thus provide good support for the views that (i) the material being studied was metallic tin with similar crystallographic features as that of bulk tin; and (ii) the aluminum substrate had minimal influence. The cathodically treated sample also yields no spectral evidence for the presence of Sn(IV) at the surface so it is felt that any air-formed oxide or anodically formed oxide in a previous experiment was satisfactorily removed by the cathodic treatment. The presence of Sn(IV), rather than Sn(II), is used as the criterion for the surface cleanliness on the basis of the work reported below and the work of Huffman and Dunmyre (14).

A question of utmost importance to this study is the relationship between the area under an absorption peak and the fraction of that species present in the volume exposed to the gamma ray flux. A partial answer to this question was obtained by studying the dependence of the area under the peak and the width at half maximum as a function of the thickness of the

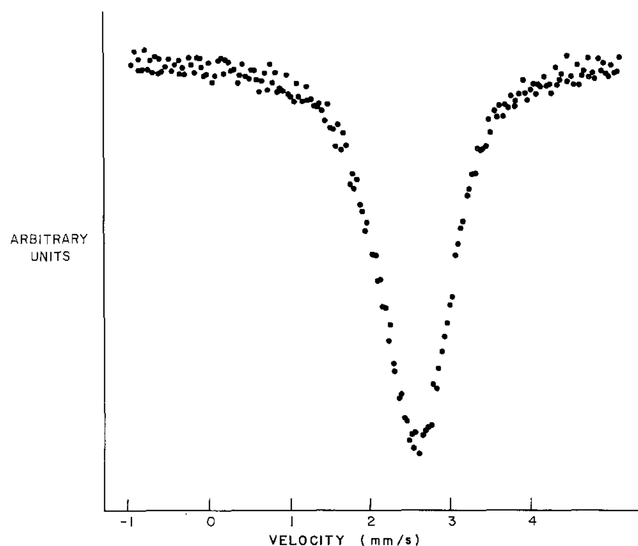

Fig. 3. Mössbauer absorption spectrum at 78°K of a tin electrodeposit that was cathodically treated in the borate buffer for 10 min at −1200 mV.

tin through which the beam traversed under conditions of a standard gamma ray exposure. ^{119}Sn was electrodeposited on an aluminum substrate and different numbers of the foils were compressed together and the Mössbauer spectrum was generated at liquid nitrogen temperature. Data obtained from this study are summarized in Fig. 4. It will be noted that the area under the peak does not depart seriously from a linear relationship with thickness in the range of tin thicknesses studied, namely, 10-30 nm, and that the width at half maximum does not change significantly in this same range. Although similar data were not obtained for tin oxide on tin, it is assumed that the same relationship is obeyed and that the area under the oxide peak is an approximately linear function of the amount present at a standard gamma ray flux.

It rapidly became apparent as this work progressed that the two important spectral components were metallic tin and SnO_2. In order to determine relative fractions of these two species, and thus SnO_2 film thickness, it is necessary to know the relative Debye-Waller factors of Sn and SnO_2. The Debye-Waller factor of bulk SnO_2 at 78°K is of the order of 0.5 (15) and that for tin is of the order of 0.4 (16).

As a first approximation, it is assumed that the Debye-Waller factors of metallic tin and SnO_2 in the passive film are the same at liquid nitrogen temperature and that they are not strongly a function of the thickness of tin nor the thickness of the SnO_2. On this basis it is qualitatively determined that the detection efficiency for SnO_2 is equivalent to a monolayer.

Table II summarizes the Mössbauer parameters calculated from the spectra for experiments in which tin was polarized over a potential range of −890 to +1180 mV after cathodic treatment for 10 min at −1200 mV. The thickness of the SnO_2 was calculated on the basis of an average tin thickness of 28.5 nm on each surface of the aluminum foil. Each run was carried out on a different sample that was electroplated under identical conditions. Three samples were analyzed polarographically as described previously and in all cases the average thickness of tin was equivalent to 28.5 nm. Thus, in Table II the calculated film thickness of SnO_2 is made on the basis of 28.5 nm (57 nm for both sides of foil) in all cases.

A typical spectrum after polarization of a 10 nm thick tin layer for 60 min at +250 mV is shown in Fig. 5. The spectrum is adequately reproduced on the basis of a single peak for SnO_2 and a single peak for metallic tin.

No SnO_2 peak was detected after cathodic reduction of samples that had been stored in a closed container for less than 30 days. Storage of samples for longer times resulted in the formation of surface oxides that could not be completely reduced. No study of this effect

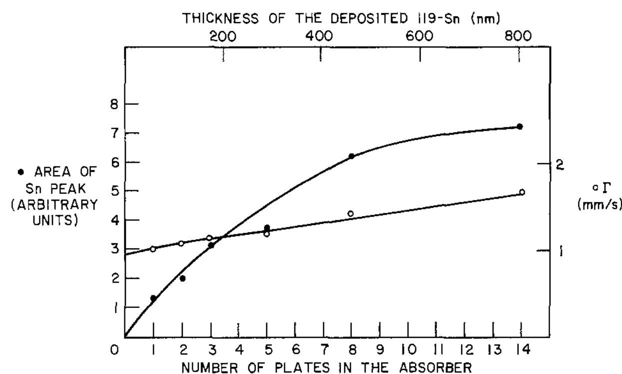

Fig. 4. The effect of thickness of tin on two Mössbauer spectral features.

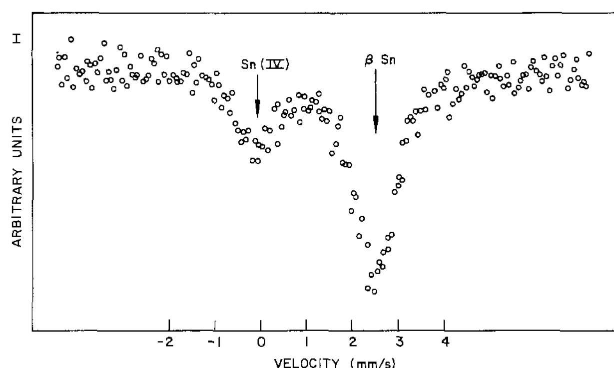

Fig. 5. Mössbauer spectrum of a tin sample polarized in borate buffer for 60 min at +250 mV.

was carried out and samples that were not completely reduced were not used in the polarization experiments.

As stated earlier, many authors have claimed the presence of Sn(II) in the passive film in the more negative range of potentials. In our studies, however, no conclusive indication of Sn(II) compounds was observed in any of the absorption spectra. It cannot be said with assurance that no Sn(II) was present in the passive film; only that it was not present in any significant concentration. It can be said with assurance that Sn(IV) was present over the potential range from −890 to +1180 mV. The Mössbauer parameters for bulk SnO are the following: isomer shift = 2.71 mm/sec and quadrupole shift = 1.45 mm/sec. Analysis of the spectra using these input parameters for the computer fitting indicated that the ability to detect SnO was always within the uncertainty limits as a conse-

Table II. Experimental data obtained from Mössbauer experiments carried out in absorption geometry

Polarizing potential	Time of polarization (min)	Information obtained from spectrum determined at 78°K: Percent absorption due to SnO_2 (%)	Isomer* shift (mm/sec)	Width at half max (mm/sec)	Calculated thickness of SiO_2** (nm)
−1200 (Cathodically treated)	10	0	—	—	—
−890	5	5.14 ± 0.4	−0.08 ± 0.04	0.98 ± 0.02	1.5
−875	60	8.00 ± 2.16	+0.04 ± 0.10	1.12 ± 0.17	2.3
−860	0.33	6.14 ± 0.4	−0.16 ± 0.03	1.01 ± 0.01	1.7
−843	60	5.50 ± 0.94	−0.04 ± 0.07	1.28 ± 0.25	1.6
−785	60	3.81 ± 1.60	−0.20 ± 0.12	0.75 ± 0.40	1.1
−785	60	2.70 ± 1.09	−0.12 ± 0.10	0.65 ± 0.33	0.8
−500	60	6.04 ± 2.24	−0.20 ± 0.14	1.11 ± 0.46	1.7
+250	30	6.10 ± 0.95	−0.04 ± 0.07	1.28 ± 0.23	1.7
+250	30	6.80 ± 1.17	+0.12 ± 0.05	0.79 ± 0.17	1.9
+250	6	6.32 ± 0.30	+0.03 ± 0.03	0.99 ± 0.25	1.8
+1000	60	7.97 ± 1.16	−0.12 ± 0.06	1.28 ± 0.28	2.3
+1100	60	8.85 ± 0.45	+0.08 ± 0.02	0.98 ± 0.09	2.5
+1180	3	8.19 ± 1.05	−0.04 ± 0.05	1.20 ± 0.18	2.3

* With reference to $BaSnO_3$.
** It was assumed that the Debye-Waller factors for tin and SnO_2 are approximately the same at 78°K.

quence of the fact that the spectrum for metallic tin overlaps that for SnO. On the basis of these attempted fits it was concluded that SnO would have to be present in concentrations equivalent to 0.6 nm before the uncertainty would be exceeded. According to thermodynamic calculations, anhydrous SnO_2 is the stable species relative to anhydrous SnO under oxidizing conditions, but $Sn(OH)_2$ has stability over a limited potential range relative to $Sn(OH)_4$ (17). A recent study of the passivity of tin in hydroxide solution (10) claims the presence of SnO in the more negative range of polarization potentials on the basis of chemical shifts as determined by x-ray photoelectron spectroscopy. The conclusion is tenuous, however, since other authors claim the inability to distinguish between SnO and SnO_2 on the basis of chemical shift alone (18).

The average isomer shift for SnO_2 obtained for all the experiments summarized in Table II was −0.06 mm/sec relative to $BaSnO_3$ with extreme values of −0.20 and +0.08 mm/sec. These values should be compared with an isomer shift of 0.00 mm/sec selected by Greenwood and Gibb (19) after examination of data in the literature. The spectrum of $Sn(OH)_4$ obtained by Cohen *et al.* (20) yields a value of 0.0 mm/sec. Thus, the isomer shift does not give useful information that distinguishes between the anhydrous and hydrated forms of SnO_2.

The data in Table II indicate that at times of polarization of 30-60 min the thickness of the oxide decreased from 2.3 to 0.8 nm over a potential range of −875 to −785 mV and then increased to 2.5 nm as the potential was changed to +1100 mV. A similar change in thickness with potential was observed by Ansell *et al.* (10) during polarization of tin in sodium hydroxide solution. They observed a decrease in film thickness from 3.5 nm at −950 mV (*vs.* Hg/HgO) to 3.0 nm at −850 mV, followed by an increase to 8.6 nm as the potential was increased in steps to +400 mV. No data are available from the current study to analyze the reason for the change in film thickness with potential.

The dissolution of tin, as judged solely by the lack of change in the intensity of the tin peak, was negligible in 60 min at all potentials above −500 mV even within the transpassive region. For example, a tin electrode was polarized at +1050 mV for 400 min, at which potential oxygen was vigorously evolved. The intensity of the tin absorption peak was practically the same under these conditions as it was prior to anodic polarization, thus indicating no significant reduction in the original tin thickness of 28.5 nm in 400 min. Some evidence, however, was found for tin dissolution at −860 mV. Data are presented in Fig. 6 on a log-log plot for the rate of change in current passing through the interface as a function of time at fixed potentials of −860 and +250 mV. It will be noted that at the longer times, in the case of polarization at −860 mV, the current passed through the interface is greater than expected on the basis of extrapolation of the curve from data obtained at shorter times. At +250 mV all the data points fall on a log-log plot over the time interval for which measurements were made. One possible interpretation of the −860 mV data is that dissolution of the oxide is continuously occurring and that some portion of the current is being utilized to replace the dissolved oxide.

The *in situ* emission experiments yielded very poor spectra. The major difficulty encountered was the low activity [typically 4 μCi] of the electrodeposited tin and the low Debye-Waller factor probably due to the very low thickness. Although no data are available to determine how the Debye-Waller factor is affected by thickness, in highly dispersed tin (d = 25 nm) Debye-Waller factors of 0.25 and 0.022 were measured at 93° and 300°K, respectively (21). These results suggest a very low factor for films of 1-2 nm in thickness. The low value may have been avoided during the measurements at 78°K because of the frozen liquid at the surface of the passive film which served as a solid matrix. At this level of activity it was very difficult to separate a spectrum from the background. Figure 7 is a spectrum generated during an 8 day period while the tin electrode was maintained at a potential of −800 mV.

Conclusions

Mössbauer spectroscopy is a suitable technique for studying the passive film formed on tin during anodic treatment. Satisfactory spectra were obtained at 78°K in absorption geometry using layers of aluminum foil on which tin enriched in ^{119}Sn had been electrodeposited. *In situ* emission spectra were obtained using ^{119m}Sn, but the quality of the spectra was limited by the low radioactivity of the thin tin electrodeposit used as a source.

The anodic oxide formed on tin in borate solution at pH 8.5 is resistant to attack by the electrolyte over a potential range of −500 to +1100 mV. Some evidence was obtained that suggested a low rate of dissolution during polarization at −860 mV. The predominant species present in the anodic oxide was tetravalent tin over the entire potential range studied, although no conclusive statement can be made that divalent tin does not exist at the surface in the vicinity of the negative potential at which the current density is a maximum. No conclusive data were generated that permitted determination whether or not the passive film contained water or hydroxyl ions in appreciable concentration.

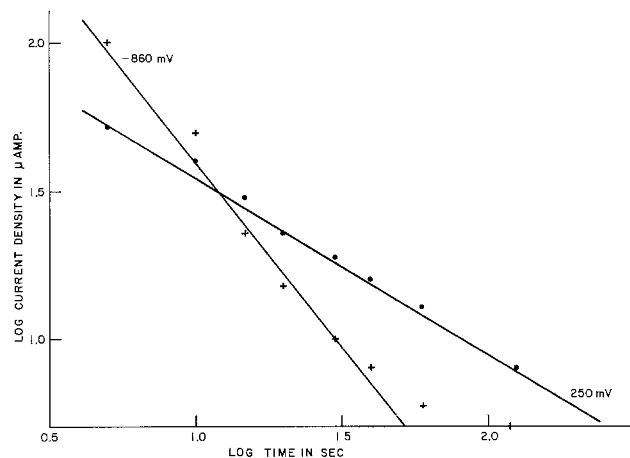

Fig. 6. Log-log plot of change of current with time during polarization of a tin electrodeposit on aluminum at −860 and +250 mV.

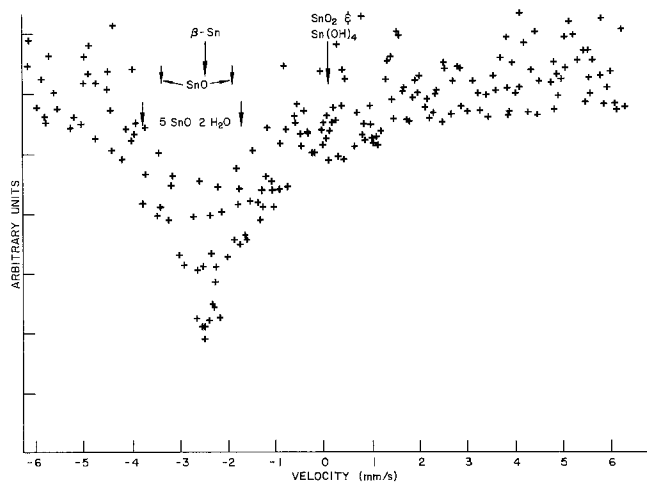

Fig. 7. Mössbauer emission spectrum of ^{119m}Sn on a tin substrate obtained over an 8 day period. The expected positions of peaks due to elemental tin, SnO, $5SnO \cdot 2H_2O$, SnO_2, and $Sn(OH)_4$ are indicated by arrows.

The thickness of tin oxide formed after polarization for 30-60 min ranged from a low value of 0.8-1.1 nm at −785 mV to a high of 2.3-2.5 nm at 1000-1100 mV.

Tin surfaces prepared by electrodeposition, on which oxides had been formed by exposure to air, were satisfactorily reduced cathodically to an oxide-free surface provided that the surfaces were aged in air at room temperature for less than 30 days. Longer aging times resulted in the formation of surface products that could not be readily removed by cathodic cleaning at −1100 mV in the borate buffer.

Acknowledgments

Appreciation is expressed to the National Science Foundation and the Hungarian Institute of Cultural Relations, who jointly supported this program. Special appreciation is expressed for the opportunity the authors had to spend time in each others' laboratory. We also thank Pal Mag for assistance in evaluating the spectra.

Manuscript submitted April 14, 1978; revised manuscript received Aug. 1, 1978.

Any discussion of this paper will appear in a Discussion Section to be published in the June 1979 JOURNAL. All discussions for the June 1979 Discussion Section should be submitted by Feb. 1, 1979.

Publication costs of this article were assisted by Lehigh University.

REFERENCES

1. R. Kerr, *J. Soc. Chem. Ind.*, **57**, 405 (1938).
2. Bianchi, *Chim. Ind.*, **29**, 295 (1947).
3. S. E. S. El Wakkad, A. M. Shams El Din, and J. A. El Sayed, *J. Chem. Soc.*, **1954**, 3103.
4. A. Ragheb and L. A. Kamel, *Corrosion*, **18**, 153t (1962).
5. M. Katoh, *Bull. Chem. Soc. Jpn.*, **35**, 1711 (1962).
6. S. N. Shah and D. E. Davies, *Electrochim. Acta*, **8**, 663 (1963).
7. D. E. Davies and S. N. Shah, *ibid.*, **8**, 703 (1963).
8. A. M. Shams El Din and F. M. Abd El Wahab, *ibid.*, **9**, 883 (1963).
9. M. Pugh, L. M. Warner, and D. R. Gabe, *Corros. Sci.*, **7**, 807 (1967).
10. R. O. Ansell, T. Dickinson, A. F. Povey, and P. M. A. Sherwood, *This Journal*, **124**, 1360 (1977).
11. N. A. Hampson and N. E. Spencer, *Br. Corr. J.*, **3**, 1 (1968).
12. W. Roger Buck III and H. Leidheiser, Jr., *This Journal*, **112**, 243 (1965).
13. G. W. Simmons, E. Kellerman, and H. Leidheiser, Jr., *ibid.*, **123**, 1276 (1976).
14. G. P. Huffman and G. R. Dunmyre, U.S. Steel Corp., Preprint furnished in advance of publication (1978).
15. V. J. Goldanskii and R. H. Herber, "Chemical Applications of Mössbauer Spectroscopy," p. 328, Academic Press, New York, London (1968).
16. Radiation Source Catalogue, Amersham Searle Corp., **18** (1974/75).
17. M. Pourbaix, "Atlas of Electrochemical Equilibria in Aqueous Solutions," pp. 478-479, Pergamon Press, New York (1966).
18. C. L. Lau and G. K. Wertheim, *J. Vac. Sci. Technol.*, **15**, 622 (1978).
19. N. N. Greenwood and T. C. Gibb, "Mössbauer Spectroscopy," p. 374, Chapman and Hall, Ltd., London (1971).
20. R. L. Cohen, C. J. Raub, and T. Muramaki, *This Journal*, **125**, 34 (1978).
21. I. P. Suzdalev, M. Ya. Gen, V. I. Goldanskii, and E. F. Makarov, *Sov. Phys. JETP (Engl. Transl.)*, **24**, 78 (1967).
22. G. W. Simmons, E. Kellerman, and H. Leidheiser, Jr., *Corrosion*, **29**, 227 (1973).

A Mathematical Approach to the *C-V* Product in Aluminum Electrolytic Capacitors

J. M. Albella, A. Hornillos, J. M. Sanz, and J. M. Martínez-Duart

Departamento de Física Aplicada y Instituto de Física del Estado Sólido (C.S.I.C.), Universidad Autónoma de Madrid, Canto Blanco, Madrid, Spain

ABSTRACT

A mathematical model is developed based on a step distribution in the radii of tunnels of etched aluminum foil for electrolytic capacitors which permits calculating the dependence of the *C-V* product (capacitance × voltage) with the anodization voltage. The calculation is based upon a knowledge of the parameters characterizing the distribution. These parameters, namely mean length and radius, width and density of the tunnels of the etched foil, can be easily obtained in the case of high voltage foil by scanning electron microscopy observations. For low voltage foil it is difficult to experimentally define the parameters characterizing the distribution, and therefore the problem must be handled inversely, *i.e.*, the parameters of the distribution function in the radii of the tunnels have been calculated from the experimental *C-V* curve.

The tunnel etching of aluminum foil is a technique usually employed in the manufacture of electrolytic capacitors. The purpose of the etching is to enlarge the useful area of the capacitor, thus increasing the capacitance per unit volume. It is well known that the electrical properties of the capacitors strongly depend on the etch morphology of the aluminum foil. In turn, the etch morphology of the foil is very much influenced by the source of the foil and the pretreatments undergone by the foil, the temperature and the current density of the forming bath, the electrolytes and their additives, etc. (1, 2). Dunn and Bolon (3) have developed a technique for visualizing the tunnel morphology below the surface of the foil. The method consists of obtaining, by anodization, oxide replicas of the tunnels which are observed under the scanning electron microscope (SEM). Using this technique, Jackson (4) has studied the tunnel formation in aluminum as a function of the electrochemical parameters. Dunn *et al.* (5) have developed a simple model in order to calculate the dependence of the storage factor *C-V* of an electrolytic capacitor with the formation voltage. The model assumes that the tunnels are

Key words: capacitor, etching, oxide.

cylindrical in shape and all of the same radius. As can be expected, the model predicts a very abrupt decay of the C-V product when the anodization voltage is such that the oxide entirely occupies the volume of the tunnel.

One of the main objectives of the electrolytic capacitor industry is to obtain that etch morphology, *i.e.*, the size and shape of the tunnels produced by etching, which gives the highest C-V product. In this sense, it is very convenient to have a good knowledge of the variation of the C-V product with the anodization voltage. When there is a distribution of the size of the radii of the tunnels, the decrease of the C-V product with the anodization voltage is less steep than that predicted by the model of Dunn *et al.* In this work, a calculation of the C-V product is made for a simple distribution in the radii of the tunnels. The method can be extended to more complex distributions and it can be applied also to tunnels with conical shape, such as those commonly present in the foils used in low voltage applications (4). The agreement between the experimental values and those predicted by the model is very satisfactory for several types of etched aluminum foils.

Mathematical Model

Equal tunnels.—Dunn *et al.* (5) have calculated the product C_tV (C_t = tunnel capacitance per unit area) of a foil with N tunnels per unit area, all the tunnels having initial radius r and length l

$$C_tV = \frac{\epsilon\epsilon_0}{\kappa} 2\pi d N(l-d) \left\{ \ln \frac{d + [2.56r^2 - 0.6d^2]^{1/2}}{-0.6d + [2.56r^2 - 0.6d^2]^{1/2}} \right\}^{-1} \quad [1]$$

In this expression κ is the anodization constant, *i.e.*, the thickness d of the oxide grown during anodization per applied volt, ϵ is the oxide's dielectric constant, and $\epsilon_0 = 8.85 \times 10^{-12} F/m$.

For subsequent discussions, it is more convenient to write Eq. [1] in the form

$$C_tV = \frac{\epsilon_0\epsilon}{\kappa} 2\pi r(l-d) N F(d/r) \quad [2]$$

with

$$F(d/r) = \frac{d}{r} \left\{ \ln \frac{(d/r) + [2.56 - 0.6(d/r)^2]^{1/2}}{-0.6(d/r) + [2.56 - 0.6(d/r)^2]^{1/2}} \right\}^{-1} \quad [3]$$

The function $F(d/r)$ depends exclusively on d/r, *i.e.*, the ratio between the thickness of the oxide and the initial radius of the tunnels. It therefore represents the occupancy of the tunnels by the oxide, and we shall call it the occupation factor. This function is represented in Fig. 1. Roughly, it varies from 1 for almost empty tunnels ($d << r$) to 0 when the tunnel is completely filled by the oxide ($d = 1.633r$).

A simple distribution of tunnels.—As has been suggested by Morley and Campbell (1), there is in reality a distribution in the lengths and radii of the tunnels. A Gaussian distribution in the length of the tunnels should be easily taken into account in the preceding model. In effect, since the product C_tV in Eq. [2] depends linearly on the length l of the tunnels, we can, in first approximation, substitute l by $\bar{l}$, the mean value of the distribution. The distribution in the radii of the tunnels is evidently much harder to handle. Let us call $D(r)$ the distribution function, *i.e.*, the number of tunnels per unit area with radii between r and $r + \Delta r$. The product C_tV will then be given by

$$C_tV = \frac{\epsilon_0\epsilon}{\kappa} 2\pi\bar{l} \int_{r_{min}}^{r_{max}} r D(r) F(d/r) dr \quad [4]$$

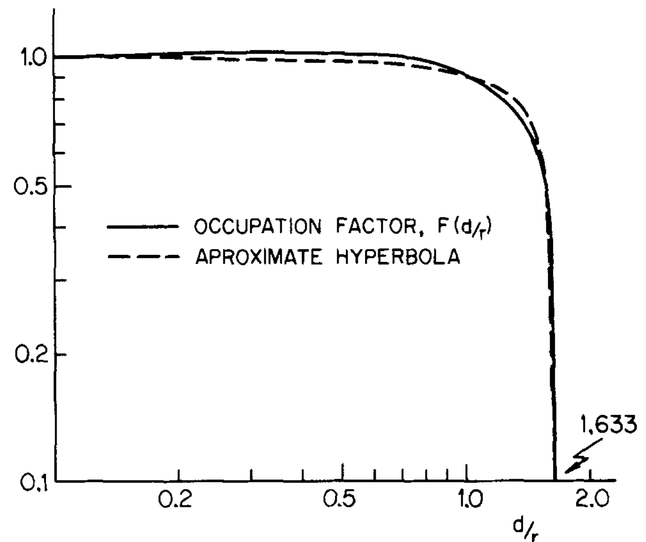

Fig. 1. Representation of the occupation factor $F(d/r)$ and its fitted hyperbola for a single tunnel.

where we have assumed $d << \bar{l}$. The distribution $D(r)$ should also verify the normalization condition $\int D(r) dr = N$.

The integral of Eq. [4] is difficult to evaluate due to the fact that the functions $F(d/r)$ and $D(r)$ are quite complicated in general. Once the function $D(r)$ is known, a numerical integration should be performed, making it necessary to evaluate the expression [4] in each particular case. Our purpose is to find a compact formula that would allow calculation of the C_tV product in most practical situations. The first step consists of assuming a simple distribution function in the radii of the tunnels such as a step function: $D(r) = D_o$ in the interval $r_{min} \leq r \leq r_{max}$ and $D(r)$ equal to zero for all other values of r. The choice of a step function is justified by the fact that the dependence with the anodization voltage that we will get is very similar to that obtained by using a Gaussian distribution, and both can be adjusted quite well to the experimental results. If $\bar{r}$ and $2\Delta r$ are the mean value and the width of the step distribution, respectively, Eq. [4] can be written as

$$C_tV = \frac{\epsilon_0\epsilon}{\kappa} 2\pi\bar{l} \frac{N}{2\Delta r} \int_{\bar{r}-\Delta r}^{\bar{r}+\Delta r} r F(d/r) dr \quad [5]$$

Making the change of variable $r = \rho\bar{r}$ and putting $\delta = \Delta r/\bar{r}$ where δ is a parameter characterizing the relative width of the distribution, we get

$$C_tV = \frac{\epsilon_0\epsilon}{\kappa} 2\pi\bar{r}\bar{l}N \frac{1}{2\delta} \int_{1-\delta}^{1+\delta} \rho F(d/\rho\bar{r}) d\rho \quad [6]$$

In analogy with expression [2], we can write Eq. [6] in the form

$$C_tV = \frac{\epsilon_0\epsilon}{\kappa} 2\pi\bar{r}\bar{l}N\Phi_\delta(d/\bar{r}) \quad [7]$$

where

$$\Phi_\delta(d/\bar{r}) = \frac{1}{2\delta} \int_{1-\delta}^{1+\delta} \rho F(d/\rho\bar{r}) d\rho \quad [8]$$

is the new occupation factor for the step distribution.[1]

The evaluation of the integral in Eq. [8] still presents difficulties because the function that appears in

[1] Accounting for the contribution of unetched areas of the surface to the C-V product, a more approximate formula than Eq. [7] can be given. These areas, together with the bottom areas of the tunnels, may amount to about 6% of the C_tV product for the high voltage foil employed in this work. (In the low voltage foil this fraction is somewhat smaller).

Table I. Values of the occupation factor $\Phi(d/\bar{r})$

$d/\bar{r}$ \ δ	0	0.1	0.2	0.3	0.4	0.5	0.6	0.7	0.8	0.9	1.0
0.1	0.996	0.996	0.996	0.996	0.996	0.996	0.996	0.996	0.996	0.996	0.995
0.2	0.991	0.991	0.991	0.991	0.991	0.991	0.991	0.991	0.991	0.988	0.987
0.3	0.986	0.986	0.986	0.986	0.986	0 986	0.985	0.985	0.983	0.977	0.976
0.4	0.980	0.980	0.980	0.980	0.980	0.979	0.979	0.977	0.969	0.963	0.963
0.5	0.973	0.973	0.973	0.973	0.972	0.971	0.970	0.963	0.950	0.946	0.948
0.6	0.965	0.965	0.965	0.964	0.963	0.961	0.956	0.939	0.929	0.927	0.930
0.7	0.955	0.955	0.954	0.953	0.951	0.947	0.930	0.912	0.905	0.906	0.911
0.8	0.943	0.943	0.942	0.940	0.936	0.923	0.896	0.883	0.879	0.882	0.889
0.9	0.929	0.928	0.926	0.922	0.913	0 881	0.859	0.850	0.850	0.856	0.866
1.0	0.910	0.909	0.906	0.898	0.869	0.834	0.819	0.815	0.819	0.828	0.840
1.1	0.886	0.884	0 877	0.857	0.807	0.783	0.776	0.778	0.786	0.798	0.812
1.2	0.852	0.849	0.833	0.779	0.741	0.729	0.730	0.738	0.750	0.765	0.782
1.3	0.804	0.796	0.752	0.689	0.672	0.672	0.681	0.695	0.712	0.731	0.752
1.4	0.727	0.705	0.620	0.597	0.600	0.613	0.630	0.651	0.672	0.695	0.719
1.5	0.587	0.511	0.486	0.501	0.525	0.551	0.579	0.604	0.631	0.656	0.684
1.6	0.248	0.283	0.352	0.404	0.448	0.487	0.522	0.556	0.587	0.618	0.648
1.7		0.091	0.223	0.307	0.370	0.421	0.465	0.505	0.542	0.577	0.610
1.8		0.000	0.107	0.213	0.291	0.354	0.407	0.453	0.496	0.535	0.571
1.9			0.020	0.124	0.214	0 287	0.348	0.400	0.448	0.491	0.531
2.0				0.048	0.140	0.220	0 288	0.346	0.399	0.446	0.489
2.1				0.002	0.073	0.155	0.228	0.292	0.349	0.400	0.447
2.2					0.020	0.095	0.170	0.238	0.298	0.353	0.403
2.3						0.042	0.114	0.184	0.248	0.306	0.359
2.4						0.006	0.064	0.132	0.198	0.259	0.315
2.5							0.022	0.084	0.149	0.212	0.270
2.6							0.000	0.041	0.103	0.165	0.225
2.7								0.010	0.060	0.121	0.181
2.8									0.025	0.079	0.138
2.9									0.003	0.042	0.097
3.0										0.013	0.060
3.1										0.000	0.028
3.2											0.000

the integrand is quite complex. A simple approximation would be to substitute the function $F(d/r)$ with a hyperbola function. Using the hyperbola shown in Fig. 1, the difference with the occupation factor is less than 5% in the interval $0 \leq d/r \leq 1.5$. For values of d/r between 1.5 and 1.633, the difference in ordinates might be greater than 5%, although the separation in abscissas is less than 3%. In any case, the approximations inherent to the model (step distribution, cylindrical tunnels, etc.) are larger than those introduced in the above mathematical approach.

In the Appendix we give the equation of the trial hyperbola as well as the details of the calculation of the occupation factor. However, from a practical point of view, it is more advisable to use the occupation function in a tabulated form (Table I) or in a graphical representation, such as that of Fig. 2. It can be appreciated from this figure that as the width δ of the distribution becomes larger, the occupation factor decreases more and more slowly with d/r. The occupation factor $F(d/r)$ given by Eq. [3] appears now as a particular case of $\Phi_\delta(d/r)$ for $\delta = 0$.

More general types of distributions.—The tunnels of the high voltage aluminum foil have a nearly cylindrical shape as a consequence of the chemical attack in HNO_3 undergone by the foil after the electrochemical etching (6). In addition, the distribution in radii is very narrow. Due to these facts, the approximation discussed in the preceding paragraph is good enough to adjust the experimental values of the C_tV product as we shall see in the next section. On the other hand, the foil for low voltage applications does not usually go through the chemical etch, resulting in tunnels with somewhat conical shape and a wide distribution in radii (5). As Morley and Campbell (1) have shown in this case, the distribution $D(r)$ is asymmetric and presents a tail in the region of large radii.

Given a general distribution like the one represented in Fig. 3, we can always make an approximation to it by means of several step distributions, as is schematically shown in the figure. In this case, the product C_tV will be given by

$$C_tV = \frac{\epsilon_0\epsilon}{\kappa} 2\pi l[\bar{r}_1 N_1 \Phi_{\delta_1}(d/\bar{r}_1) + \bar{r}_2 N_2 \Phi_{\delta_2}(d/\bar{r}_2)] \quad [9]$$

with the total concentration of tunnels $N = N_1 + N_2$. We can write Eq. [9] in a more compact manner by putting $N_2/N_1 = \alpha$, and $\bar{r}_2/\bar{r}_1 = \beta$ ($\alpha = \Delta r_2/\Delta r_1$ when the two step distributions of Fig. 3 have the same height). Thus

$$C_tV = \frac{\epsilon_0\epsilon}{\kappa} 2\pi \bar{r}_{\text{eff}} N \bar{l} \Phi_{\text{eff}}(\delta_1\delta_2) \quad [10]$$

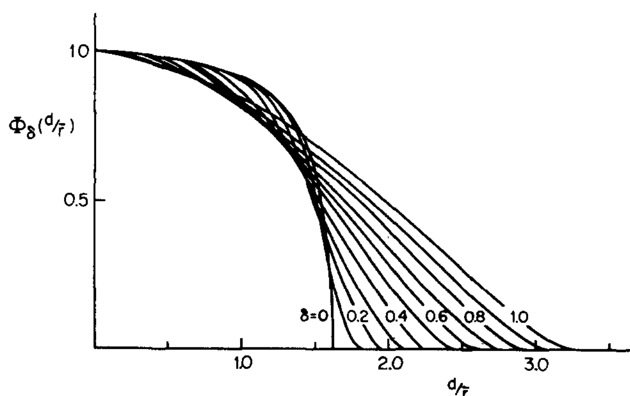

Fig. 2. Occupation factor $\Phi_\delta(d/\bar{r})$ of a step distribution in the radii of the tunnels for several relative widths of the distribution.

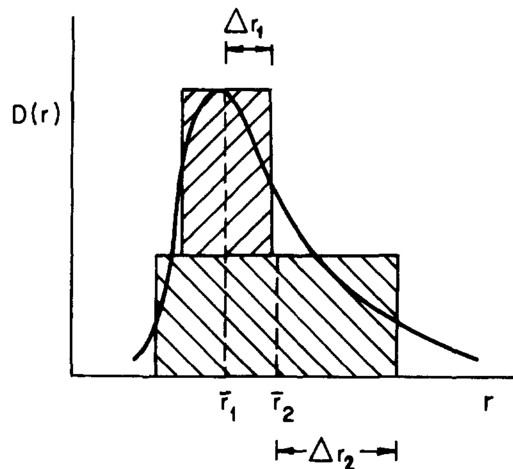

Fig. 3. Example of the approximation of a general distribution by two-step distribution functions.

where $\bar{r}_{eff}$ and $\Phi_{eff}(\delta_1\delta_2)$ are, respectively, the effective radius and the new occupation factor of the distribution, and are given by

$$\bar{r}_{eff} = \bar{r}_1 \frac{1 + \alpha\beta}{1 + \alpha} \quad [11]$$

$$\Phi_{eff}(\delta_1\delta_2) = \frac{\Phi_{\delta_1}(d/\bar{r}_1) + \alpha\beta\Phi_{\delta_2}(d/\beta\bar{r}_1)}{1 + \alpha\beta} \quad [12]$$

The new occupation factor $\Phi_{eff}(\delta_1\delta_2)$ has been normalized in such a way that it varies between 0 and 1, resulting in an effective radius r_{eff} within $\bar{r}_1$ and $\bar{r}_2$.

The case of a symmetric distribution function, a Gaussian, for example, can be handled by the above approximation making $\bar{r}_1 = \bar{r}_2$. The corresponding occupation factor Φ_{eff} takes values between $\Phi_{\delta 1}$ and $\Phi_{\delta 2}$, getting closer to $\Phi_{\delta 2}$ when δ_2 increases with respect to δ_1 (the converse is also true). In any case, the new occupation factor is quite similar to a step distribution with a width between δ_1 and δ_2. In this way, the step distribution approximation developed in the preceding paragraph is further justified. The observations that we have made for symmetric distributions do not apply in the case of asymmetric distributions treated in this paragraph. In this event, we have to add at least two occupation functions with different radii $\bar{r}_1$ and $\bar{r}_2$, resulting in a new function bounded by the above two.

Experimental Results

The interest of the occupation function resides in the fact that it helps to predict, in a simple manner, the dependence of the C_tV product of an etched aluminum foil as a function of the anodization voltage. To this end we have to know the parameters characterizing the shape and distribution of the tunnels which can be obtained in most cases by SEM. Figure 4 shows the variation of the C_tV product for commercial high and low voltage aluminum foils employed in the production of electrolytic capacitors. The aluminum foils were anodized in a typical electrolyte composed of an aqueous solution of boric acid, ammonium pentaborate, and glycol. The capacitance at 100 Hz of the foil has been measured in a boric acid solution (ρ = 100 Ω cm) with a Hewlett-Packard Model 4261A capacitance bridge.

The curve of the high voltage foil in Fig. 4 has been calculated employing a simple distribution of tunnels, as outlined in Eq. [7] and [8], assuming an anodization constant κ = 14 Å/V and a dielectric constant ϵ = 8.4 for aluminum oxide (7, 8)]. For this purpose, replicas of the tunnels were obtained by the technique of Dunn and Bolon (3) and observed under the scanning electron microscope (Fig. 5) both perpendicular and parallel to the original surface of the aluminum foil. From the microphotograph of Fig. 5 the following parameters characterizing the tunnels are observed: $\bar{r}$ = 0.5 μm; Δr = 0.2 μm; $\bar{l} \simeq$ 30 μm; and $N \simeq 17 \times 10^6$ cm^{-2}. As it can be appreciated, the concordance between the curve predicted by the model and the experimental results is quite good.

The curve corresponding to the low voltage foil in Fig. 4 cannot be adjusted with just one-step distribution in the radii of the tunnels. It is evident from the microphotograph of Fig. 6 that the distribution of radii

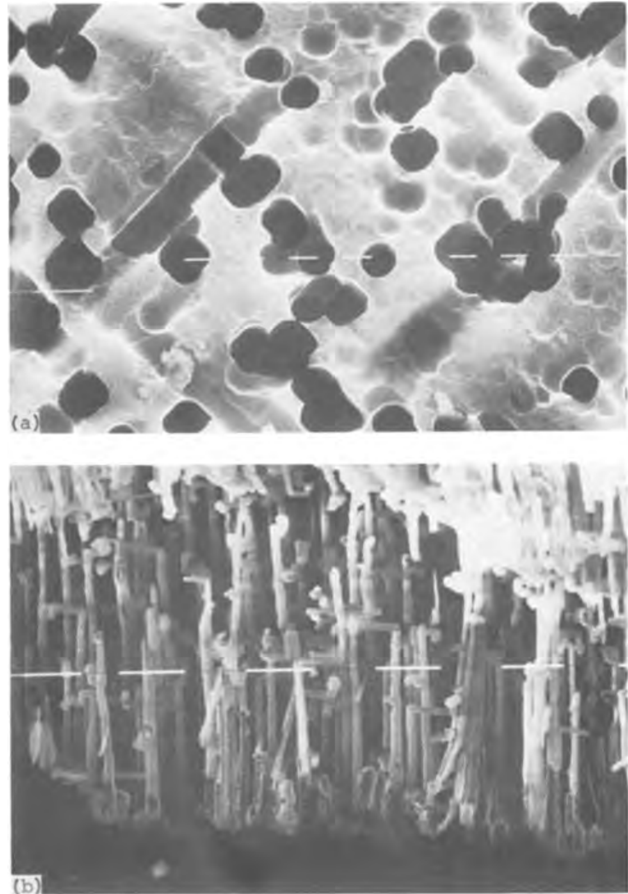

Fig. 5. (a) SEM micrograph of the surface of high voltage etched aluminum foil (reticule, 1 μm); (b) SEM micrograph of a cross section of the same foil obtained by the replica technique mentioned in the text (reticule, 10 μm).

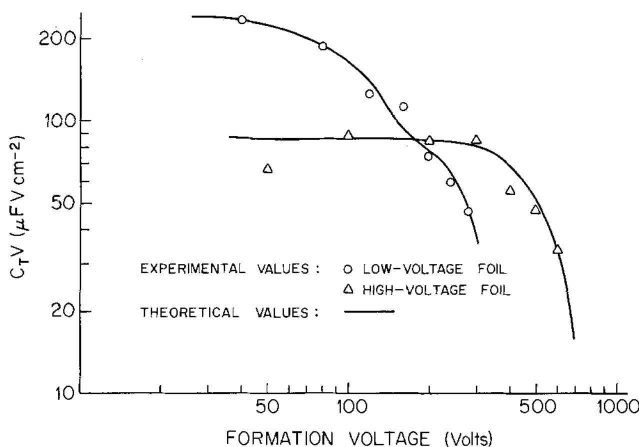

Fig. 4. Experimental values and computed curves for the C_tV product for high and low voltage aluminum foil.

Fig. 6. SEM micrograph of an oxide replica of the tunnels in low voltage etched aluminum foil.

is much wider than in the high voltage case, and also that the tunnels present a conical shape. Due to the difficulty in getting the parameters of the distribution, in this case we proceed in an inverse manner. This consists of adjusting the experimental points with an occupation function corresponding to an asymmetric distribution chosen in such a way that the error is the least possible one. By this procedure we obtain an effective radius $\bar{r}_{eff} = 0.10$ μm and a total tunnel length $N\bar{l} = 7.3 \times 10^9$ μm/cm², which compare well with typical values found in low voltage foil (4, 5). Now, it is not possible to separate the values of N and $\bar{l}$ unless we resort to precise measurements with the scanning electron microscope.

Acknowledgments

We are very grateful to Bianchi, S.A., San Sebastian, Spain, for partially supporting this work, and also to Miss M. J. Puente for some of the experimental results.

Manuscript submitted March 27, 1978; revised manuscript received June 26, 1978.

Any discussion of this paper will appear in a Discussion Section to be published in the June 1979 JOURNAL. All discussions for the June 1979 Discussion Section should be submitted by Feb. 1, 1979.

Publication costs of this article were assisted by the Universidad Autonoma de Madrid.

APPENDIX

The equation of the hyperbola resulting in the best fit for the occupation factor of Eq. [3] is given by

$$F(d/r) \simeq \frac{0.166}{(d/r) - 1.742} + 1.066$$

It can also be numerically shown that if a step distribution in the radii of the tunnels is used to adjust the values of the C_tV product given by Eq. [7] and [8] to the experimental points, it is practically immaterial to use either the function $F(d/r)$ or the hyperbola. When performing the integration in Eq. [8] it should be noted that the function $F(d/\rho\bar{r})$ does not contribute to the integral when $d/\rho\bar{r} > 1.633$, while the fitted hyperbola is different from zero in that interval. This difficulty can be overcome by computing the integral in two different intervals of the parameter $d/\bar{r}$. For values of the parameter up to $1.633\ (1 - \delta)$, where δ is the relative width of the distribution, the integrand is always positive and the calculation of the integral is quiet straightforward. In the interval $1.633\ (1 - \delta) \leq d/\bar{r} \leq 1.633\ (1 + \delta)$, the hyperbola is positive only when $\rho > (d/\bar{r})/1.633$. The negative values of the hyperbolic function can be eliminated if the lower limit of the integral is changed to $0.1624\ (d/\bar{r})$. The final result is the following:

(*i*) In the interval $0 < (d/\bar{r}) < 1.633\ (1 - \delta)$

$$\Phi_\delta(d/\bar{r}) = \frac{1}{2\delta}\int_{1-\delta}^{1+\delta} \rho \left[\frac{0.166}{(d/\rho\bar{r}) - 1.742} + 1.066\right] d\rho$$

$$= 1 - 0.0382(d/\bar{r}) - \frac{0.0110}{\delta}(d/\bar{r})^2 \ln\frac{1.742(1+\delta) - (d/\bar{r})}{1.742(1-\delta) - (d/\bar{r})}$$

(*ii*) In the interval $1.633\ (1 - \delta) < (d/\bar{r}) < 1.633\ (1 + \delta)$

$$\Phi_\delta(d/\bar{r}) = \frac{1}{2\delta}\int_{0.612(d/r)}^{1+\delta} \rho \left[\frac{0.116}{(d/\rho\bar{r}) - 1.742} + 1.066\right] d\rho$$

$$= \frac{(1+\delta)^2}{4\delta} - 0.0191\frac{(1+\delta)}{\delta}(d/\bar{r}) - \frac{0.082}{\delta}(d/\bar{r})^2 - \frac{0.011}{\delta}(d/\bar{r})^2 \ln\left[15\frac{1.742(1+\delta) - (d/\bar{r})}{(d/\bar{r})}\right]$$

REFERENCES

1. A. R. Morley and D. S. Campbell, *Rad. Electron. Eng.*, **43**, 421 (1973).
2. M. Buttoudin, in Proceedings of the International Symposium "Materiaux pour les Composants Electroniques," p. 245, Paris, 1975.
3. C. G. Dunn and R. B. Bolon, *This Journal*, **116**, 1050 (1969).
4. N. F. Jackson, *Electrocomp. Sci. Technol.*, **2**, 23 (1975).
5. C. G. Dunn, R. B. Bolon, A. S. Alwan, and A. W. Stirling, *This Journal*, **118**, 381 (1971).
6. M. S. Hunter, *Electrochem. Technol.*, **1**, 151 (1963).
7. W. J. Bernard and J. W. Cook, *This Journal*, **106**, 643 (1959).
8. M. S. Hunter and P. Fowle, *ibid.*, **101**, 481 (1954).

Anodic Synthesis of Organic Carbonates

Divna Cipris* and Irving L. Mador

Allied Chemical Corporation, Corporate Research Center, Morristown, New Jersey 07960

ABSTRACT

Carbonic acid esters (carbonates) are produced by electrolysis of carbon monoxide and the corresponding alcohol in the presence of a halide electrolyte. The halide electrolyte plays a catalytic role in carbonate formation. The efficiency for the process depends, among other variables, on the starting alcohol. Both mono and 1,2-dihydric aliphatic alcohols form carbonates in high yields. Under our electrolytic conditions, without optimization, dimethyl carbonate from methanol and ethylene carbonate from ethylene glycol were formed with 80 and 45% current efficiencies, respectively. One mole of hydrogen is liberated per mole of carbonate. Organic carbonates represent a class of important industrial solvents. They are commercially produced via employment of phosgene; HCl is formed as a by-product. The electrochemical process obviates the use of phosgene and eliminates the hydrochloric acid disposal problem.

Interest in the electrochemical reactions of carbon monoxide, carbon dioxide, and other cheap, readily available raw materials has been renewed lately. The possibility of their use as building blocks for various commercially important chemicals is increasingly appealing. In this context, the demonstrated electro-

* Electrochemical Society Active Member.
Key words: electrolyte, catalysis, solvents, environment.

chemical reductive tetramerization of CO to squarate ion is most intriguing (1). A similar reaction with direct anodic oxidation of carbon monoxide has not been reported. Indirectly, carbomethoxylation of an aryl olefin[1] (2) and carbonylation of certain aromatic hydrocarbons (3) have been achieved. These appear to remain isolated cases of CO participation in anodic reactions from a synthetic point of view. The present paper describes the synthesis of carbonic esters (carbonates) by electrolysis of carbon monoxide in alcohols in the presence of a halide electrolyte, representing an additional example of an indirect anodic reaction.

The electrooxidation of methanol in aqueous solutions has been studied extensively in relation to fuel cell applications (4). In acid solutions, carbon dioxide is the principal product, with traces of formaldehyde and formic acid. In alkaline solutions, there is partial oxidation to formate. The anodic oxidation of absolute methanol has been studied to a limited degree, in spite of the fact that methanol has been widely used as a solvent for various electroorganic oxidations (5). Depending on the type of supporting electrolyte used, the following major products were obtained in the oxidation of methanol on platinum: dimethoxymethane ($NaClO_4$, tetrabutylammonium fluoride) (6), formaldehyde ($NaOCH_3$) (6-8), and methyl formate (NaI) (9). With sodium phenate electrolyte, no anodic reaction is reported to occur (8). The discharge of chlorine ion is the predominant reaction in the presence of lithium chloride. Some formate was detected (8). Addition of water (up to 10%) did not have a significant effect on the current efficiency for formaldehyde formation ($NaOCH_3$) (7); higher water content (or employment of KOH electrolyte) favored formate formation (8). The ethanol oxidation on platinum produced analogously diethoxyethane ($NaOCl_4$, TBAF), acetaldehyde ($NaOC_2H_5$) (6), and ethyl formate (NaI) (9).

Commercial production of carbonates involves the use of phosgene at elevated temperatures (10). The main advantage of the present process is in obviating the necessity for storage and handling of phosgene, and disposal of hydrochloric acid. Other chemical routes to carbonates are also described, but efficiencies of these reactions are not well established (11-13). Organic carbonates are used in many industrial applications, such as solvents for polymers and resins in processing operations, and in the synthesis of pharmaceuticals, rubber chemicals, textile finishing agents, and polycarbonate resins.

Experimental

Constant current electrolysis.—Preparative scale electrolyses were conducted at constant current using equipment described elsewhere (14). A stainless steel (T316 SS) high pressure electrolytic cell, equipped with a graphite liner and changeable cathodes and anodes, was employed in all runs. One electrode served as a container for the solution to be electrolyzed and had an approximate capacity of 300 ml. The second electrode was in the form of a rod (Fig. 1). The pressure bomb was supplied by Parr Instrument Company (pressure rating 2000 lb max, 300°C) and was in-house modified (head and liners) according to our specifications. A cation exchange membrane (Ionics 61/DYG 067) was used to separate cathodic from anodic chambers in some experiments.

In a representative experiment leading to high carbonate yields, 200 ml of alcohol and 4.0g (0.04 moles) of NH_4Br were charged into a stainless steel high pressure electrolytic cell and then pressurized with carbon monoxide to 100 atm. Commercial anhydrous alcohols were used without further purification or drying. Cosolvents were used where necessary. Graphite anodes and stainless steel cathodes were used

[1] An active intermediate, $Pt_x(CO)_y$, was formed via cathodic Pt dissolution, so this reaction is not solely anodic.

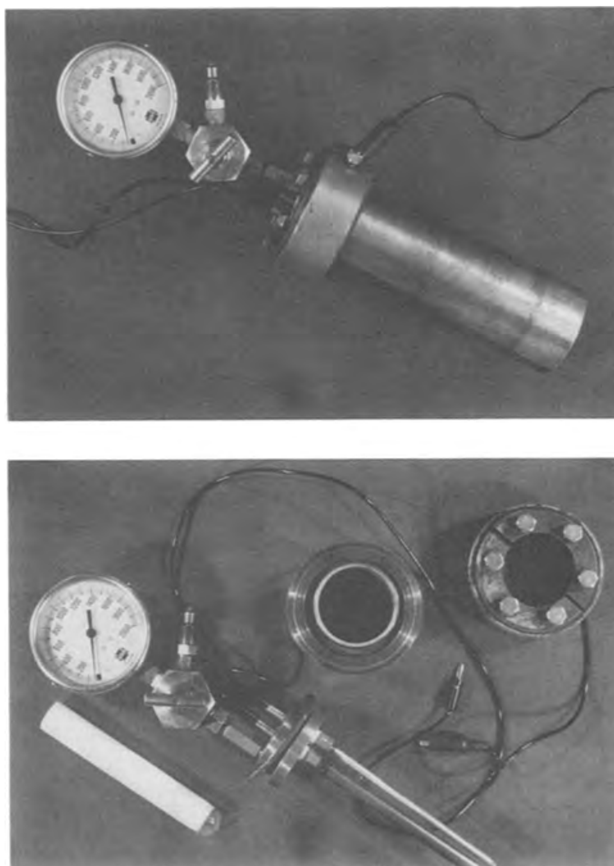

Fig. 1. High pressure electrolytic cell and electrodes. a, assembled; b, detailed view.

throughout the work. The reported results were obtained in a one-compartment cell. The electrolyses were conducted at constant current at varying anodic current densities (20-120 mA cm^{-2}) with equivalent results. A total of 0.45**F** was usually passed. The temperature was maintained at 20°-30°C by a cold water circulating coil.

Product analyses were performed by GC, GC-mass spectrometry, and *IR*. Isolation of various products was achieved using preparative GC techniques. GC analyses of methanol, ethanol, and ethylene glycol electrolysis products were carried out with a 5 ft × 1/8 in. stainless steel column packed with Poropak PS (70° → 230°C/8°/min). For analysis of aryl and alkaryl carbonates, a 2 ft × 1/4 in. glass column packed with OV 17 (150° → 250°C/10°/min) was used. A Finnigan Model 3300 gas chromatograph/mass spectrometer operated in a chemical ionization mode with methane as the reagent gas was used for analysis of liquid samples. Gas samples were analyzed by an AEI ms 902 Mass Spectrometer (ionizing voltage 70 eV).

Potentiodynamic measurements.—The equipment and cell used in these measurements were previously described (14). A graphite rod anode (~1 cm^2 geometric area) and platinum clad tantalum were working and auxiliary electrodes, respectively. Platinum and activated titanium anodes [home-made according to previously published procedure (15)] were also tested. Solutions were purged with argon prior to the recording.

Results

Dimethyl carbonate.—Effect of electrolyte and electrolyte concentration.—The electrolyte plays an essential role in determining the type of products formed. Besides dimethyl carbonate, methyl formate and dimethoxymethane are seen as the major products in various experiments. Some unidentified minor com-

Table I. Effect of electrolyte on product distribution in carbon monoxide/methanol electrolysis*

Electrolyte	Electrolyte concentration (M)	Products** (mole/F)			
		Dimethyl*** carbonate	Methyl formate	Dimethoxymethane	Unidentified†
LiCl	0.2	0.08 (14.0)	none	0.30	—
LiBr	0.2	0.35 (70.0)	0.05	0.05	—
NH_4Br	0.2	0.35 (70.0)	none	—	—
	0.4	0.25 (50.0)			
	1.0	0.13 (26.0)			
NH_4Br } H_2O }	0.2 10 w/o	0.15 (30.0)	none	trace	—
Bu_4NBr	0.06	0.13 (26.0)	0.12	trace	—
	0.2	0.10 (20.0)	0.80	—	—
NaI	0.2	0.22 (45.0)	none	0.15	+
$LiClO_4$	0.2	none	0.12	0.35	
$NaOCH_3$††	0.2	none	—	—	—
NH_4NO_3	0.6	none	0.03	0.03	—
NH_4NO_3 } Br_2 }	0.6 0.2	0.30 (57.0)	trace	trace	—
NH_4NO_3 } I_2 }	0.6 0.2	0.20 (42.0)	trace	0.04	+
HCl (aq. conc.)	0.3	0.10 (20.0)	0.10	0.20	—
	1.5	0.10 (20.0)	0.20	0.04	—
H_2SO_4	0.5	none	0.20	0.40	—
H_2SO_4 } NH_4Br }	0.5 0.2	0.25 (49.0)	0.15	0.20	

* Graphite anode, 100 atm CO, 20°-30°C, 0.45F.
** Liquid phase.
*** Parenthesis = current efficiency, % (2 F/mole).
† — = none or traces; + = one or more components, estimated >1%.
†† 0.1F passed, not analyzed for formaldehyde.

ponents may also be present. With a bromide electrolyte, gas analysis showed the presence of CH_3Br, CO_2, and H_2 in the ratio 1:10:10. The data for various electrolytes shown in Table I were obtained after 0.45**F** (12 A-hr) with graphite anode at 100 atm carbon monoxide pressure. The value in parentheses represents the current efficiency (%) for dimethyl carbonate formation (based on a two-electron process).

Our experiments show that increase in the electrolyte concentration decreases the yields of dimethyl carbonate.

Effect of CO pressure and temperature.—The effect of carbon monoxide pressure on dimethyl carbonate formation is illustrated in Fig. 2. The scattering of results may be due to inadequate mass transfer (magnetic stirring bar employed). These data suggest that there is at least a 5% yield increase of dimethyl carbonate for each 6.8 atm (100 psi) increment of carbon monoxide. The reactions were conducted in the temperature range 20°-30°C. Our experimental facilities did not permit going above 100 atm.

No essential difference in dimethyl carbonate yields was observed when the reactions were carried out at 20°-30°C as compared to 50°-60°C. By-product formation (methyl formate, dimethoxymethane) is, however, somewhat increased at higher temperature.

Effect of current density, electrode materials, and cell configuration.—Electrolysis of CO in methanol conducted at 20 and 120 mA cm^{-2} (geometric area) on graphite gave identical current efficiencies for dimethyl carbonate formation. When a graphite anode was substituted by platinum (on tantalum), rapid dissolution of the anode took place at the higher current densities (Br^- electrolyte). Similar behavior was observed with activated titanium anodes (Ir + Se on Ti) in cyclic voltammetry experiments. A stainless steel cathode was used in all experiments described. The separation of anodic and cathodic compartments was essential only at low cathodic current densities, as can be seen from Table II. At higher cathodic current densities, dimethyl carbonate yields were not affected by elimination of separator.

Other carbonates.—Diethyl carbonate.—The synthesis of diethyl carbonate from ethanol and carbon monoxide was conducted under electrolytic conditions which

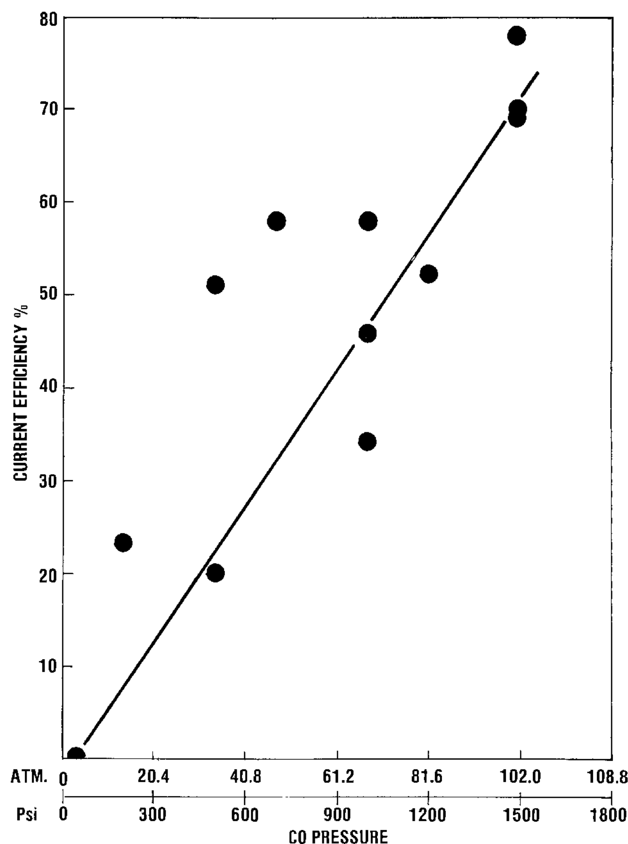

Fig. 2. Current efficiency dependence on carbon monoxide pressure in the synthesis of dimethyl carbonate.

led to the highest yield of dimethyl carbonate in this work (0.2M NH_4Br, 100 atm). Apart from diethyl carbonate (26% current efficiency, based on 2**F**/mole), ethyl formate was observed as the major by-product. Some unidentified products were also seen. The data for this and other carbonates are presented in Table III.

Table II. One- vs. two-compartment cell in dimethyl carbonate formation

Electrolyte	Cell	Cathode current density (mA cm^{-1})	Dimethyl carbonate, current efficiency (%)
LiBr 0.2M	Two-compartment (Cation exchange membrane)	20	70
	One-compartment	20	15
NH_4Br 0.2M	Two-compartment (Cation exchange membrane)	20	70
	One-compartment	120	70-80

Table III. Effect of starting alcohol on carbonate formation*

Alcohol	Cosolvent	Electrolyte	Carbonate, curr. eff. (%)
Methanol	none	0.2M NH_4Br	Dimethyl carbonate, 70
Ethanol	none	0.2M NH_4Br	Diethyl carbonate, 26
Ethylene glycol	none	0.5M NH_4Br	Ethylene carbonate 5-10
Ethylene glycol	methanol	0.2M NH_4Br	{ Ethylene carbonate, 45 Dimethyl carbonate, 25
Phenol	methanol	0.2M NH_4Br	none
		0.1M NH_4Br	none
Benzyl alcohol	methanol	0.2M NH_4Br	none
Cyclohexanol	methanol	0.2M Bu_4NBr	none

* Conditions: 100 atm CO, 20°-30°C, graphite anode, 0.2-0.5F.

Ethylene carbonate.—Due to the lower conductivity of ethylene glycol/0.2M NH_4Br solution, the electrolysis of ethylene glycol and carbon monoxide was carried out with higher electrolyte concentration than in previous experiments (0.5M NH_4Br, 100 atm). Under these conditions, ethylene carbonate was formed with 5-10% current efficiency (2F/mole). Some unidentified products were detected. When methanol was used as cosolvent (ethylene glycol:methanol = 4:1), and the NH_4Br concentration was decreased to 0.2M, dimethyl carbonate and ethylene carbonate were the only products, with current efficiencies of 25 and 45%, respectively (Table III).

Diphenyl carbonate, dibenzyl carbonate, and dicyclohexyl carbonate.—Electrolyses of phenol, benzyl alcohol, and cyclohexanol, respectively, with carbon monoxide were conducted in the presence of methanol (1:1), in the usual way (0.2M NH_4Br, 100 atm). No evidence for formation of diphenyl, dibenzyl, or dicyclohexyl carbonate could be found. Interestingly enough, in methanol no trace of dimethyl carbonate could be detected with phenol present even in the relatively small smounts (~5 w/o).

Current-potential data.—Current-potential curves were recorded in methanol solutions with various electrolytes in the absence of carbon monoxide. Current-potential profiles of methanol with supporting electrolytes other than halides (5 w/o H_2SO_4 or 5 w/o NH_4NO_3) display current rises commencing at about 1.5V *vs.* SCE. This current may be due to the methanol or supporting electrolyte anion oxidation, along with oxidation of traces of water present in the solutions. When halide anions were added to any of these solutions, the current-potential profiles were changed, indicating halide ion oxidation. As expected, the oxidation potentials increase in the following order: $I^- < Br^- < Cl^-$. Figure 3 presents current-potential profiles for oxidation of iodide, bromide, and chloride ions on graphite electrodes in H_2SO_4/CH_3OH solution.

The current-potential curves in pure H_2SO_4/CH_3OH and with varying concentrations of added NH_4Br are shown in Fig. 4. The limited current for Br^- oxidation is proportional to the concentration, as expected (16, 17). Repetitive cycling of a 0.2M NH_4Br solution for 30 min did not alter the current-potential profile. Different results were obtained, however, when similar experiments were conducted in NH_4NO_3/CH_3OH solutions. Peaks representing bromide oxidation were ill defined (Fig. 5). On repetitive cycling a current decrease was observed.

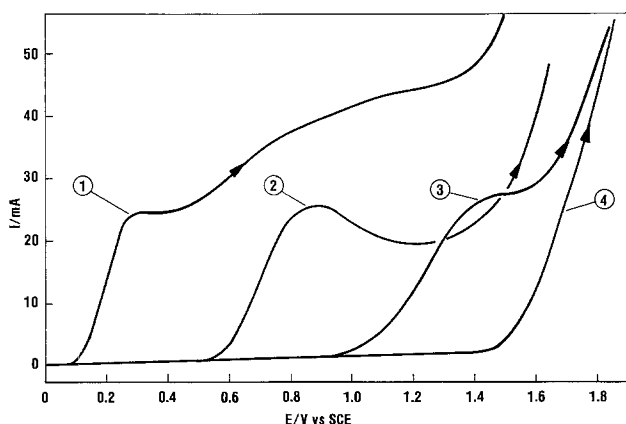

Fig. 3. Current-potential profile of halide ions oxidation in H_2SO_4/methanol solution. Graphite anode (~1 cm^2 geometric area); 25°C, sweep rate 50 mV sec^{-1}. 1, 2 × 10^{-1}M NaI; 2, 2 × 10^{-1}M NH_4Br; 3, 2 × 10^{-1}M NaCl; 4, pure 5 v/o H_2SO_4 in methanol.

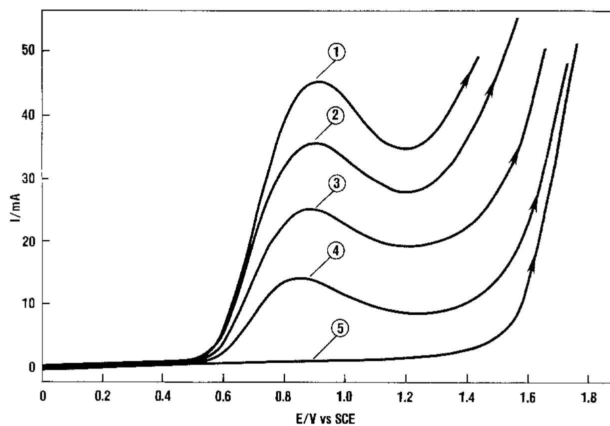

Fig. 4. Current-potential profiles in pure H_2SO_4/methanol and varying concentrations of NH_4Br. Graphite anode (~1 cm^2 geometric area); 25°C, sweep rate 50 mV sec^{-1}. 1, 2.55 × 10^{-1}M; 2, 2.0 × 10^{-1}M; 3, 1.27 × 10^{-1}M; 4, 6 × 10^{-2}M; 5, pure 5 v/o conc. H_2SO_4 in methanol.

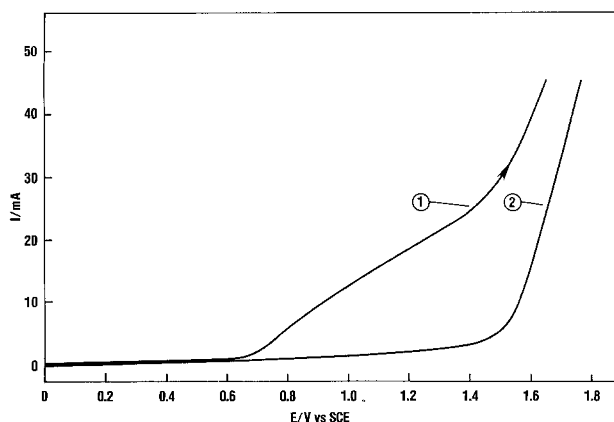

Fig. 5. Current-potential profile of bromide ion oxidation in NH_4NO_3/methanol solution. Graphite anode (~1 cm^2 geometric area); 25°C; sweep rate 50 mV sec^{-1}. 1, 6 × 10^{-2}M NH_4Br; 2, pure 5 w/o NH_4NO_3 in methanol.

Discussion

Under our electrolytic conditions, electrolysis of methanol, in the presence of carbon monoxide but with electrolytes other than halides, produced methyl formate and/or dimethoxymethane (Table I), as previously observed (6, 9). Dimethyl carbonate was not detected until the addition of a halide ion.

Addition of a halide ion, or free halogen, to the nonhalide electrolytes resulted in dimethyl carbonate formation, along with the usually observed products. Under certain electrolytic conditions, dimethyl carbonate was the principal product with virtually no other products formed (Table I). The presence of free halogen, added or generated *in situ*, emerges thus as instrumental for carbonate formation. Dimethyl carbonate formation is therefore attributed to the indirect reaction, via carbonyl halide. A possible reaction sequence is as follows:

Scheme 1

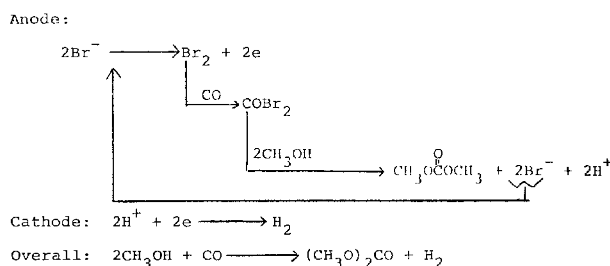

The mechanism invoked in Scheme 1 can adequately account for experimental evidence obtained in this work.

The alternative anodic mechanism (Scheme 2), in analogy to a suggested mechanism operating to a certain degree in methanolic chloride solutions (8), was ruled out based on the fact that we did not detect any dimethyl carbonate in the solutions in which methoxy radicals are reported to be formed ($NaOCH_3$)[2]

Scheme 2

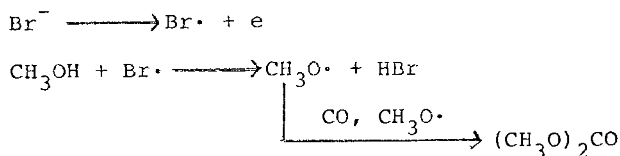

The best yields of dimethyl carbonate were generally obtained with bromide electrolytes. The lower yields obtained with chloride compared to bromide electrolytes are explained on the basis of low ΔE between chloride ion oxidation and direct methanol oxidation (see Fig. 3). Simultaneous oxidation of both may be thus possible under steady-state conditions. Direct methanol oxidation, even in the presence of CO, leads to products other than dimethyl carbonate as already seen. Formation of dimethoxymethane along with dimethyl carbonate is thus observed in the presence of chloride electrolyte. It should be emphasized, however, that all reported results were obtained with a graphite anode. It is conceivable that substantially different product distributions could be obtained with various activated titanium anodes, known for their catalytic effect on chlorine evolution (18). This remains to be determined. The lower yields obtained with iodide electrolytes are attributed to an apparently lower rate of CH_3OH/COI_2 interaction compared to rates of possible side reactions. The formation of several unidentified by-products is observed when CO was electrolyzed in methanol in the presence of iodide electrolyte (or upon addition of free I_2 to an inert auxiliary nonhalide electrolyte). Although not identified, these products are believed to be the result of direct iodination reactions.

The water content of methanol solutions in our work was generally below 0.5%. Higher water content can be tolerated with no, or only slightly, adverse effect on carbonate formation (2-3%). At 10 w/o water in methanol/NH_4Br solution, current efficiency for carbonate formation was substantially decreased. Increased water content in absolute alcohol reportedly leads to formate (with $NaOCH_3$ electrolyte) (8). No methyl formate was seen in our case, indicating that different mechanisms would be responsible for formate formation in these two media. Since no buildup of other products was observed, water discharge and/or methanol oxidation to carbon dioxide appears responsible for decreased efficiency in carbonate production.[3] An interesting dependence of methanol oxidation peak potential on water concentration was observed earlier (8), making such an explanation plausible.

As has been shown (Table II), high yields of dimethyl carbonate can be obtained in a one-compartment cell at comparatively high cathodic current densities. At low cathodic current densities, separation of anolyte and catholyte is required to secure high yields of dimethyl carbonate. This observation indicates that the anodic reaction products are decomposed at the cathode at low cathodic current densities. At high cathodic current densities, hydrogen evolution is, presumably, the predominant cathodic reaction and dimethyl carbonate yields are not affected.

[2] We agree with Reviewer II's comment that a more likely radical attack would be on the C—H bond. Scheme 2 is nevertheless included to show that, even if possible, it would not be applicable in our case.

[3] CO oxidation to CO_2 could not be excluded either.

Anodic current density has no effect on the product distribution within the range of the limiting current for bromine evolution. With bromide electrolyte, the choice of electrode materials appears limited to graphite. Neither platinum (on tantalum) nor activated titanium anodes could withstand bromine attack for a prolonged time. With a graphite anode, reproducible results can be obtained in most cases; however, attention should be paid to the choice of auxiliary electrolyte, if employed. Nitrate anion is found to reduce graphite activity with time for dimethyl carbonate formation. Current-potential curves showed that bromine evolution in this medium is not simply diffusion controlled. This aspect was not studied in detail.

Increase of carbon monoxide pressure favors dimethyl carbonate formation, as evidenced in Fig. 2. While the reaction was not examined at pressures higher than 100 atm, it is believed that reaction efficiency would further increase at higher pressures. An interesting feature is that while chemical formation of carbonates via phosgene is carried out at elevated temperatures, the electrochemical approach does not require high temperature for efficient reaction.

Electrolysis of ethanol and carbon monoxide was investigated under only one set of conditions, namely with NH_4Br electrolyte (0.2M) under 100 atm of CO. As indicated (Table III), diethyl carbonate was the principal product, but formation of ethyl formate was also observed along with a few minor components.

Ethylene glycol electrolysis in the presence of carbon monoxide (and bromide electrolyte) led to the formation of ethylene carbonate although in low yields (Table III). When methanol was used as cosolvent, simultaneous formation of dimethyl carbonate was observed without any additional by-products. This result suggests that ethylene carbonate can be synthesized with high current and material efficiencies when an inert cosolvent, rather than methanol, is employed. Ethylene carbonate itself could possibly be such a cosolvent. We did not attempt to optimize conditions for the synthesis of each particular carbonate, but rather contented ourselves with demonstrating the general validity of the concept for carbonates formation.

Based on our experimental evidence, the present electrochemical synthetic route to organic carbonates appears valid for aliphatic (mono- and 1, 2-dihydric) alcohols but not for alkyl-aryl or aryl. No evidence for formation of dibenzyl or diphenyl carbonate could be found in the few experiments conducted (Table III). This did not come entirely as a surprise for a number of reasons (apart from possible bromination on the ring), especially in the case of phenol electrolysis. Inhibition of bromine evolution upon addition of phenol has been previously observed (16). Also, no anodic reaction was observed when methanol was electrolyzed in the presence of sodium phenoxide (8). Adsorption of phenoxy radicals is credited for inhibition of bromine evolution. We believe that strong adsorption of phenoxy radicals and/or formation of an insulating organic film might be responsible for the total "passivation" of the anode observed in the second case. In addition to the absence of phenyl carbonate, no trace of dimethyl carbonate was observed with methanol as a cosolvent. This suggests that strong inhibition of bromine evolution was taking place, in this case, in agreement with previous observations. Electrolysis of benzyl alcohol and cyclohexanol with methanol as a cosolvent produced some dimethyl carbonate, but no other carbonates could be detected. This may be due to the different rates for aliphatic *vs.* alkyl-aromatic and alicyclic carbonates formation. Further studies will be conducted to assess whether the problems encountered above could be circumvented and anodic synthesis of aryl, alk-aryl, and alicyclic carbonates achieved.

The products of anodic methanol oxidation are highly electrolyte dependent, as already seen. Individual

mechanisms for some of these reactions have been suggested, but no effort has been made to explain the dramatic influence exercised by various electrolytes. Oxidation of methanol per se was not of primary interest, and it was not investigated in detail. Nevertheless, some observations are noteworthy. It is apparent from our results (Table I) that acetals can be preferentially formed in "acidic" (5 v/o conc. H_2SO_4) as well as in "neutral" ($LiClO_4$) electrolytes. The formation of methyl formate is favored by the presence of a halide electrolyte, in both "neutral" (Bu_4NBr) or "acidic" (10 v/o conc. HCl) media. The latter would speak in favor of the mechanism proposed recently, where methyl formate is formed via solution interaction with electrochemically generated free halogen in a fairly involved fashion (9). The only problem is, however, that our yields of methyl formate in 0.2M Bu_4NBr electrolyte (in the presence of CO) highly exceed theoretical yields based on proposed 4 **F**/mole (of ester) reaction. Participation of CO in the product formation, presumably via chemical reaction, should be considered. This result obviously deserves further attention.

Summary and Conclusions

Carbonic acid esters (carbonates) can be synthesized by electrolysis of carbon monoxide and corresponding alcohols in the presence of a halide electrolyte. The halide electrolyte is essential for carbonate formation. Based on our experimental evidence, a mechanism is proposed whereby carbonates are formed via interaction of an alcohol with an *in situ* generated carbonyl halide ($COCl_2$, $COBr_2$). Elevated carbon monoxide pressure is required to secure high yields. The efficiency of the process depends, among other variables, on the type of starting alcohols. Both mono and 1, 2-dihydric aliphatic alcohols form carbonates in high yields. No evidence for formation of diphenyl carbonate could be found when phenol was electrolyzed under carbon monoxide pressure in the presence of a bromide electrolyte. Inhibition of bromine evolution due to the preferential adsorption of the organic species on the electrode is believed responsible for the lack of carbonate formation. The failure to observe carbonates derived from benzyl alcohol and cyclohexanol is attributed to different causes.

Acknowledgment

Technical assistance of Mr. Arthur T. Walsh, who conducted the high pressure electrolyses, is greatly appreciated. The authors are also indebted to the Chemical Physics Department personnel for their invaluable contributions, especially Dr. D. E. Smith (GC-mass spectrometry), Mr. E. McCarthy (mass spectrometry), Mr. J. M. Hanrahan (preparative GC), and Dr. R. L. Lapinski (*IR* interpretation). One of the authors (D. C.) would like to thank Dr. F. Mares for useful discussions and encouragement during the early phases of this work. Thanks are also due to Ms. Marcy Daboul for her patience in typing various versions of this manuscript.

Manuscript submitted June 19, 1978; revised manuscript received July 24, 1978. This was Paper 559 presented at the Seattle, Washington, Meeting of the Society, May 21-26, 1978.

Any discussion of this paper will appear in a Discussion Section to be published in the June 1979 JOURNAL. All discussions for the June 1979 Discussion Section should be submitted by Feb. 1, 1979.

Publication costs of this article were assisted by Allied Chemical Corporation.

REFERENCES

1. G. Silvestri, S. Gambino, G. Filardo, M. Guainazzi, and R. Ercoli, *Gazz. Chim. Ital.*, **102**, 818 (1972).
2. T. Inoue and S. Tsutsumi, *Bull. Chem. Soc. Jpn.*, **38**, 2122 (1965).
3. B. E. Conway, J. W. Loveland, and W. C. Neikam, U.S. Pat. 3,252,878 (1966).
4. J. O'M. Bockris and S. Srinivasan, "Fuel Cells: Their Electrochemistry," McGraw-Hill, New York (1969).
5. C. K. Mann and K. K. Barnes, "Electrochemical Reactions in Nonaqueous Systems," Marcel Dekker, New York (1970).
6. G. Sundholm, *J. Electroanal. Chem. Interfacial Electrochem.*, **31**, 265 (1971).
7. G. Belanger, *This Journal*, **123**, 818 (1976).
8. C. Iwakura, T. Hayashi, S. Kikkawa, and H. Tamura, *Electrochim. Acta*, **17**, 1085 (1972).
9. D. A. White, *This Journal*, **124**, 1177 (1977).
10. R. Kirk and D. F. Othmer, "Encyclopedia Chemical Technology," Vol. 4, p. 386, Wiley, New York (1964).
11. I. L. Mador and A. U. Blackham, U.S. Pat. 3,114,762 (1963).
12. E. Perotti and G. Cipriani, U.S. Pat. 3,846,468 (1974).
13. K. Kondo, N. Sonoda, and H. Sakurai, *Bull. Chem. Soc. Jpn.*, **48**, 108 (1975).
14. D. Cipris, *J. Appl. Electrochem.*, **8**, 537 (1978).
15. D. Cipris and D. Pouli, *J. Electroanal. Chem. Interfacial Electrochem.*, **69**, 423 (1976).
16. E. Gileadi, *Collect. Czech. Chem. Commun.*, **36**, 464 (1971).
17. T. Bejerano, C. H. Forgacs, and E. Gileadi, *J. Electroanal. Chem. Interfacial Electrochem.*, **27**, 69 (1970).
18. O. DeNora, *Chim. Ind. (Milan)*, **50**, 642 (1968).

The Anodic Oxidation of Copper Amalgam and Polycrystalline Copper Electrodes in LiOH Solution

S. Fletcher,* R. G. Barradas,* and J. D. Porter**

Department of Chemistry, Carleton University, Ottawa, Ontario, Canada K1S 5B6

ABSTRACT

The anodic behavior of copper in lithium hydroxide solution was investigated at room temperature under controlled potential conditions. The electrodes were either saturated copper amalgams or small polycrystalline wires. Particular attention was focused on the copper (I) region. Two layer-planes of Cu_2O were formed at anodic overpotentials following the dissolution of copper (I) hydroxy complexes on the copper amalgam electrodes. Some novel data are reported concerning the nucleation of holes in these layers during the reverse reaction. Behavior analogous to that of the amalgam electrodes was observed on the polycrystalline electrodes, except that a thick layer of Cu_2O was also formed on top of the previously formed layer-planes. A model is proposed for the growth of this thick layer, and it is demonstrated that this model also describes the galvanostatic data acquired by earlier workers.

The corrosion of copper in alkaline solution is of interest in both chemical engineering and nuclear reactor applications. For this reason numerous experimental investigations have been performed on this system over the years (1-26). Prior to 1969 most work concentrated on the analysis of galvanostatic charging curves, which in general were poorly resolved (1-14). However two distinct solid phases were identified as being present at the electrode surface during the corrosion process: Cu_2O and $Cu(OH)_2$. Subsequent investigations afforded greater resolution of experimental data than had previously been possible, but the various interpretations of this data differ considerably (15-26).

Although there is general agreement regarding the nature of the phases formed (1-26), few unambiguous conclusions can be drawn from the literature regarding the electrode kinetics. We therefore suggest that a reappraisal of the behavior of copper in alkaline solution is in order. We have taken the first steps in this reappraisal by (*i*) considering the initial events which occur during the anodic oxidation of (dislocation-free) copper amalgam surfaces in LiOH solutions, and (*ii*) by presenting correlation of these data with data recorded on polycrystalline electrodes in the same solutions.

Experimental

Saturated amalgams [~5 mmoles Cu (27-32)] were prepared by direct combination of mercury (m5N8 Alfa Inorganics) and an excess of sheet copper (5N Koch-Light) under dry nitrogen for several weeks. The mercury was tapped from the interior of a reservoir; the copper was washed prior to use in dilute Aristar nitric acid and triply distilled water, then dried under a stream of nitrogen, and added to the mercury. Amalgam samples were tapped directly from the storage container into the syringe delivery system of the cell.

The base electrolyte was 0.1M LiOH and was prepared by dissolving the anhydrous alkali (Matheson, Coleman and Bell) in water distilled three times from alkaline permanganate solutions. Oxygen was purged from cell solutions using bottled nitrogen (Linde); traces of oxygen were removed from the gas in wash towers of aqueous vanadium (II, III) chlorides according to the method of Meites (33). The gas was finally passed through a tower containing the base electrolyte before entering the cell.

The reference half-cell used throughout the present work was Hg/HgO. The electrode was prepared in a manner similar to that recommended by Ives and Janz (34). Mercury was drawn from the interior of a reservoir and placed in the clean, dry electrode compartment, which was not treated in any way to produce hydrophobicity. A small quantity of the oxide (Fisher) was then placed on the mercury surface and the compartment flushed with dry nitrogen. Under the action of slight vibration the oxide rapidly spread over the exposed mercury to form a homogeneous "skin" on its surface. After assembly and preparation of the remainder of the cell, deoxygenated base electrolyte was allowed to fill the compartment slowly through the Luggin capillary. Electrodes prepared in this manner became stable quickly (1 hr) and exhibited very reproducible potentials.

The cell assembly is illustrated in Fig. 1. The working electrode was an amalgam drop (diameter = 1.47 mm, area = 0.0653 cm^2) supported on the end of an upturned capillary (ID = 0.551 mm). The capillary length was kept short (8 mm) to reduce ohmic resistance between the drop surface and the working electrode terminal H. The amalgam delivery system consisted of a gas-tight chromatographic syringe (C, Hamilton Company Model 1001) which incorporated a tight-fitting Teflon-tipped plunger. The syringe was secured in an aligned mount B, and the plunger travel was accurately controlled by means of a drum micrometer A (Moore and Wright Company). Zero levels were determined by microscopic observation of the capillary orifice using a cathetometer (The Precision Tool and Instrument Company). Reading and zero errors limited the theoretical surface area reproducibility to $\pm 0.8\%$ for the drop size employed in the present work. Prior to any measurements being made, the entire amalgam delivery system was washed with boiling triply distilled water and then immersed in mercury for several weeks to leach out any impurities possibly present in the Teflon. When in use, the delivery system could be refilled while assembled.

During an experiment, fresh surfaces were used for each measurement to eliminate the possibility of contamination of the electrode by any trace impurities in solution. Used drops were dislodged by streaming nitrogen through the inlet tube J. This procedure also served to agitate the cell solution between measurements.

Some experiments were also performed using polycrystalline copper wire working electrodes (25 mil, m5N Alfa Inorganics, geometric surfaces ~0.0250 cm^2)

* Electrochemical Society Active Member.
** Electrochemical Society Student Member.
Key words: films, growth, nucleation.

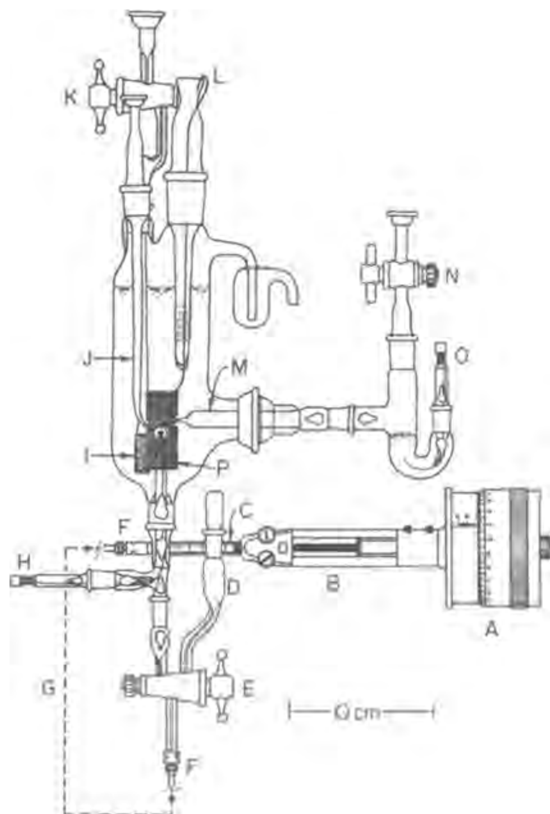

Fig. 1. The cell. (A) Micrometer, (B) syringe mount, (C) syringe, (D) amalgam reservoir, (E) inlet/outlet tap, (F) luer connector, (G) Teflon tubing, (H) working electrode terminal, (I) fritted bubbler, (J) N_2 inlet, (K) N_2 inlet tap, (L) counterelectrode terminal, (M) Luggin probe, (N) N_2 inlet tap, (O) reference electrode terminal, (P) counterelectrode.

sealed in Pyrex tubes which could replace the gas inlet tube J. Immediately subsequent to being sealed and cut to length, the electrodes were washed briefly in very dilute nitric acid, rinsed with degassed triply distilled water, and placed in the cell.

The reference electrode/probe assembly was designed to minimize internal resistances. The resistance between the tip of the Luggin probe M and the reference half-cell surface was kept as low as possible by constructing the probe for the most part out of large diameter (ID = 10 mm) tubing, by keeping the drawn-out portion of the probe short (<20 mm), by minimizing the distance from the probe tip to the Hg/HgO surface, and by avoiding the use of a sintered glass disk to separate the working and reference compartments. This type of construction minimized both noise and rise-time limitations in the potentiostat circuitry.

The iR drop between the tip of the reference probe and the surface of the working electrode was minimized by constructing the Luggin within a ball joint. This allowed the tip to be maneuvered close to the surface of the amalgam drop. The probe tip was drawn to a fine point (OD = 0.285 mm, ID = 0.241 mm), then carefully shaped and squared off using 600 mesh SiC paper under a dissecting microscope. In order to avoid shielding effects (35) the probe was positioned 2 tip diameters away from the drop surface during an experiment. Rough calculation of the expected resistance arising from this source (36) indicates that $R_{\Omega} < 0.01$ Ω cm^2 in this case.

Electric field homogeneity was maintained by using a cylindrical platinized platinum mesh counterelectrode (P, diameter = 20 mm, length = 50 mm) positioned coaxially with the capillary and symmetrically disposed about the amalgam drop. Small holes were cut in the mesh to allow the insertion of the gas inlet tube J and the Luggin probe M, and also to allow visual observation of the capillary orifice.

The cleaning procedure was designed to remove trace impurities possibly adsorbed on the interior surfaces of the glassware. Before each experiment the cell was dismantled and the all-Pyrex components placed in a covered 4 liter Pyrex beaker along with a Pyrex syphon assembly. The beaker was then filled with an aqua regia solution (10:1 HNO_3:35% HCl) and the components cleaned at elevated temperature (~90°C) for at least 24 hr. The contact assemblies and counterelectrode were cleaned in boiling HNO_3. Finally, all components were leached Soxhlet-fashion in boiling triply distilled water for 48 hr. All storage vessels and volumetric flasks were treated in the same manner.

Before assembly of the apparatus the amalgam-containing pieces were briefly oven dried at 150°C. The reference electrode was prepared as previously described; nitrogen was flushed continuously through tap N during this process. The amalgam delivery system was filled before the base electrolyte was admitted to the working compartment. Nitrogen was bubbled through the solution via the Luggin tip and the fritted bubbler for about 30 min before the reference compartment was filled. The working electrode was left at ~ −600 mV while the reference half-cell was allowed to stabilize. The entire apparatus was enclosed in a light-proof Faraday cage which was mounted on a vibration-damped platform.

The constant potential source was a PAR 170 Electrochemistry System. Potential profiles were generated on a PAR 175 Universal Programmer via a 10:1 potential divider. Potentials were recorded ±0.1 mV using a Hewlett Packard 3465A digital voltmeter in conjunction with a parallel-switched dummy cell circuit. The digital voltmeter was switched out of the potentiostatic circuit during the electrochemical measurements. Data were recorded either directly on a Honeywell 530 X-Y/Y-t pen recorder or digitally via a Biomation 805 Transient Recorder. The laboratory temperature was 22° ± 2°C.

Results and Discussion

Copper amalgam electrodes.—A typical linear potential scan of the copper amalgam electrode in 0.1M LiOH between the potential limits −700 and −200 mV is illustrated in Fig. 2. Four well-defined features are apparent on the forward scan. The region labeled A corresponds to the dissolution of Cu(I). At −380 mV a monolayer peak (B) stands clear from the dissolution. This is followed by a second monolayer peak (C) at somewhat more anodic potentials. The layers formed consist of Cu_2O (2-7). Finally, further inhibited dissolution of Cu(I) occurs in region D. On reversal of the potential scan the products of the anodic processes are reduced in one unresolved peak (E) which shows some evidence of fine structure.

The dissolution of Cu(I) was investigated by performing slow linear potential scans (5 mV sec^{-1}) into region A and observing the current as a function of potential. Exponential behavior was observed over more than a decade of current density (Fig. 3) with a reciprocal Tafel slope of 59 mV. This is the slope for the reaction

$$Cu \rightleftharpoons Cu^+ + e \quad [1]$$

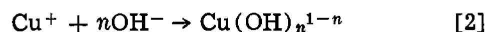

$$Cu^+ + nOH^- \rightarrow Cu(OH)_n^{1-n} \quad [2]$$

Identical Tafel slopes were recorded in lithium hydroxide solutions between 0.1 and 2.0M. Although the position of the Tafel lines shifted along the potential axis toward more negative values with increasing LiOH concentration, reaction order measurements proved inconclusive. This was due to the incomplete dissociation of LiOH at the higher concentrations and the presence of migration effects which became important at concentrations below 0.1M.

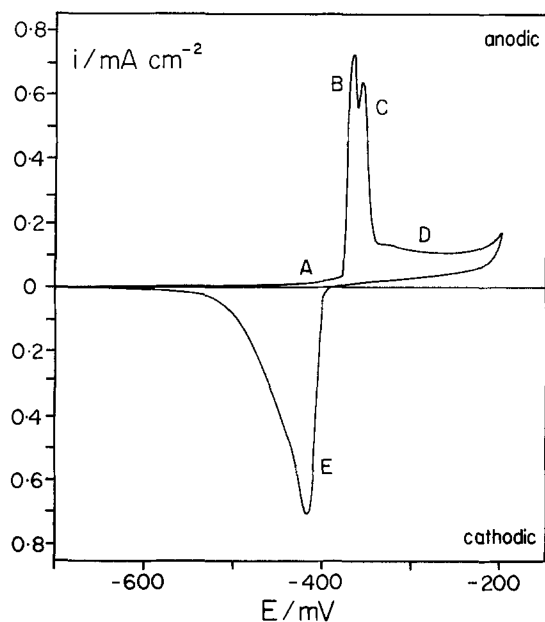

Fig. 2. LPS (ν = 20 mV sec^{-1}) of a saturated Cu amalgam electrode in 0.1M LiOH. (A) Dissolution of Cu(I), (B) formation of the first monolayer of Cu_2O, (C) formation of the second monolayer of Cu_2O, (D) inhibited dissolution of Cu(I), (E) reduction of the products formed on the forward scan.

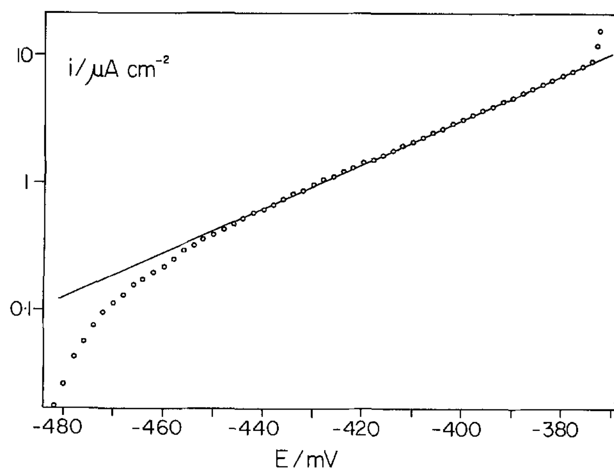

Fig. 3. Tafel plot of the Cu(I) dissolution region recorded using slow LPS (ν = 5 mV sec^{-1}) at a saturated Cu amalgam electrode in 0.1M LiOH. The reciprocal slope is 59 mV.

Reciprocal Tafel slopes of 59 mV were also obtained by the potential step technique. The $i(t)$ curves decreased monotonically as expected from Eq. [1] and [2] and were diffusion controlled at sufficiently long times. However, if the steps were carried out to potentials anodic to −380 mV in 0.1M LiOH (*i.e.*, into the potential region B associated with monolayer formation in Fig. 2) then results typified by Fig. 4 were obtained. Figure 4 shows the $i(t)$ response of a freshly generated copper amalgam surface following the application of a double potential step from −550.0 to −390.0 mV and finally to −377.4 mV. The double step allowed a large part of the double layer charging current and also a large part of the dissolution current to decay before switching to the final potential. This technique produced very clear and reproducible results. Four overlapping transients are observed which occur sequentially in time. Each corresponds to a separate process; the four are labeled A, B, C, and D, respectively (cf. Fig. 2). The first process exhibits a falling transient (A) and is the diffusion-controlled dissolution of Cu(I). The next two processes exhibit

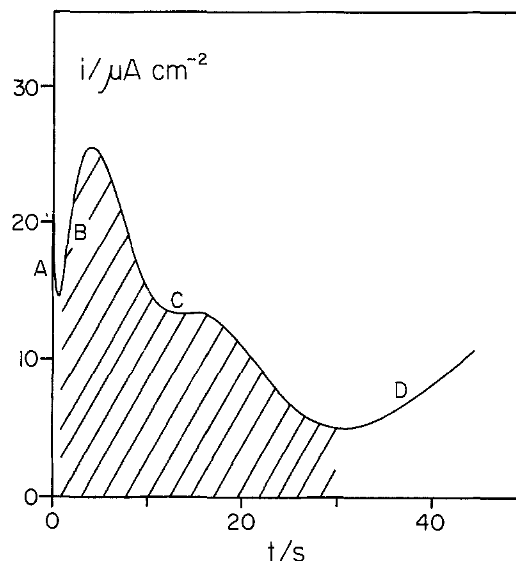

Fig. 4. Potentiostatic current transient recorded at −377.4 mV on a saturated Cu amalgam electrode in 0.1M LiOH. (A) Dissolution of Cu(I), (B) nucleation and growth of the first monolayer of Cu_2O, (C) nucleation and growth of the second monolayer of Cu_2O, (D) potential-independent reactivation of the electrode.

potential-dependent rising transients (B and C) and hence correspond to the nucleation and subsequent crystal growth of Cu_2O. The rate-determining steps for these processes must therefore occur at discrete reaction sites on the electrode surface, *i.e.*, at the peripheries of expanding nuclei of Cu_2O. Note also that the eventual falling sections of the transients B and C are due to the diminishing available periphery caused by the collision of nuclei. Finally, a potential-independent reactivation of the electrode surface can be observed at long times (D). The magnitude of this process depended strongly on the bulk concentration of OH^-.

The total charge passed during processes B and C was evaluated by integration of the transients as shown in Fig. 4 (hatched area). This charge (~360 μC cm^{-2}) was independent of the final step potential and as such was very strong evidence for monolayer formation. Attempts to better resolve the transients in order to compare individual sections with nucleation theory proved futile because a strong diffusion component became apparent in the experimental data at high overpotentials. The saturated copper amalgam was only about 5 mmoles in Cu and clearly the rate of mass transport of copper through the amalgam at higher current densities was inadequate to maintain the rate-determining step at the edges of the nuclei.

The effect of mass transport within the amalgam is illustrated quantitatively in Fig. 5, in which one of the transient maximum parameters (i_m) is plotted as a function of the final step potential for both the first and second monolayers. The first monolayer could not be resolved from the dissolution transient at potentials anodic to −375 mV. The diffusion component due to the dilute copper amalgam can be seen to be limiting in the second monolayer data at potentials anodic to −371 mV. The limiting gradient for the first layer is ~(4 mV)$^{-1}$ and that for the second layer ~(8 mV)$^{-1}$. These gradients are typical of nucleation and growth kinetics (37) but the accuracy of the values is obviously limited because of the experimental constraints.

The formation and reduction of the monolayers was best observed by the linear potential scan technique. The experimental results were quantified by investigating the potential scan rate (ν) dependence of the peak current (i_p). The data were analyzed in the form of log (i_p) *vs.* log (ν), which is appropriate for nucleation and growth kinetics (38). The gradient δ log

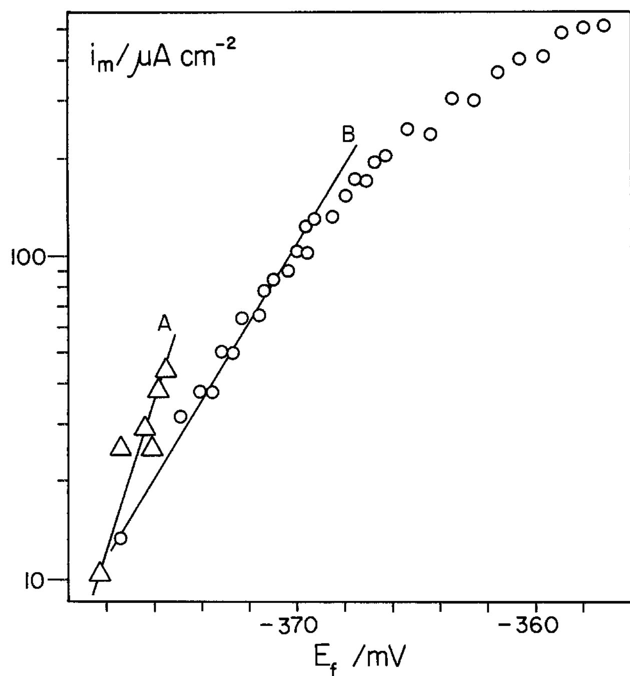

Fig. 5. The potentiostatic current transient maxima (i_m) for Cu_2O monolayer formation on a saturated Cu amalgam electrode in 0.1M LiOH *vs.* the final step potential (E_f). (A) First layer limiting dependence $\sim$(4 mV)$^{-1}$, (B) second layer limiting dependence $\sim$(8 mV)$^{-1}$. The curvature at large i_m is due to mass transport limitations.

$(i_p)/\delta \log (\nu)$ for the first monolayer was 0.57 and that for the second monolayer 0.59. These values should be compared with the value ½ which would be expected for a diffusion-controlled reaction (39). Clearly the kinetics of formation of the two monolayers were not determined by simple diffusion.

The high resolution of the monolayer peaks in linear potential scan measurements allowed a precise evaluation of the charge consumed in the formation of both layers. Over the three decades of scan rate investigated (0.1-100 mV sec^{-1}) the total charge was found to be constant and equal to 360 ± 10 μC cm^{-2}, in agreement with the potentiostatically derived value. Since the formation of a monolayer of the unit cell of Cu_2O [which has a cubic lattice (40)] would consume 352 μC cm^{-2}, we therefore suppose that each monolayer peak observed experimentally corresponded to the formation of a layer-plane of the unit cell and that layer-by-layer growth ceased when the unit cell structure was complete.

Because of the high resolution of the linear potential scan measurements, it was also possible to investigate the nucleation of holes during the reverse reaction. Such holes were found to be of two types depending on whether they penetrated only the first monolayer or both monolayers (Fig. 7b). We call the first type a "shallow" hole and the second type a "deep" hole. The appropriate experimental result is shown in Fig. 6, which illustrates the effect of varying the anodic potential scan limit on both the forward and reverse reactions.

On the forward scan, peak B is due to the formation of the first monolayer as described earlier. However, on the reverse scans, a new peak F is apparent which first increases and then decreases in size as the anodic potential scan limit is increased. At the same time, a peak at more cathodic potentials (G) is observed to increase steadily in size. The charges associated with peaks F and G are plotted against the anodic potential scan limit in Fig. 7a.

The results of Fig. 6 and 7a indicate that the initial process in the formation of the two layers is the nu-

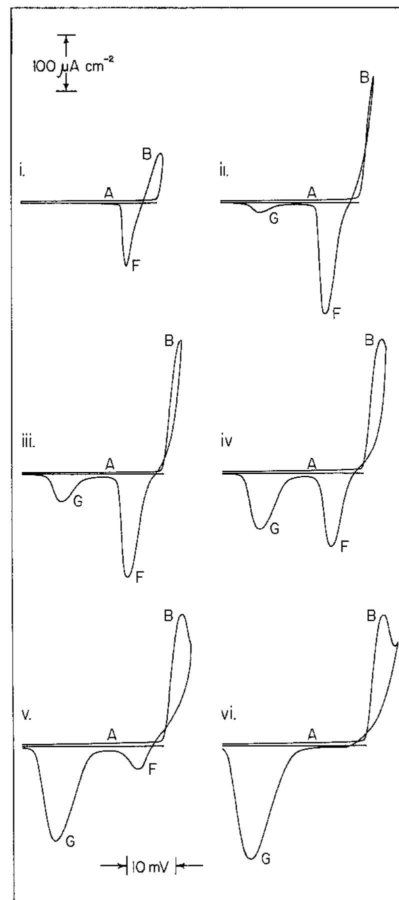

Fig. 6. LPS series at fresh saturated copper amalgam electrodes in 0.1M LiOH (ν = 5 mV sec^{-1}) illustrating the effect of varying the anodic potential scan limit. All scans begin at −407 mV. Anodic potential scan limits: *(i)* −374, *(ii)* −372, *(iii)* −371, *(iv)* −370, *(v)* −369, *(vi)* −363 mV. (A) Dissolution of Cu(I), (B) formation of the first Cu_2O monolayer, (F) reduction of the untransformed first Cu_2O monolayer, (G) simultaneous reduction of the unit cell bilayer.

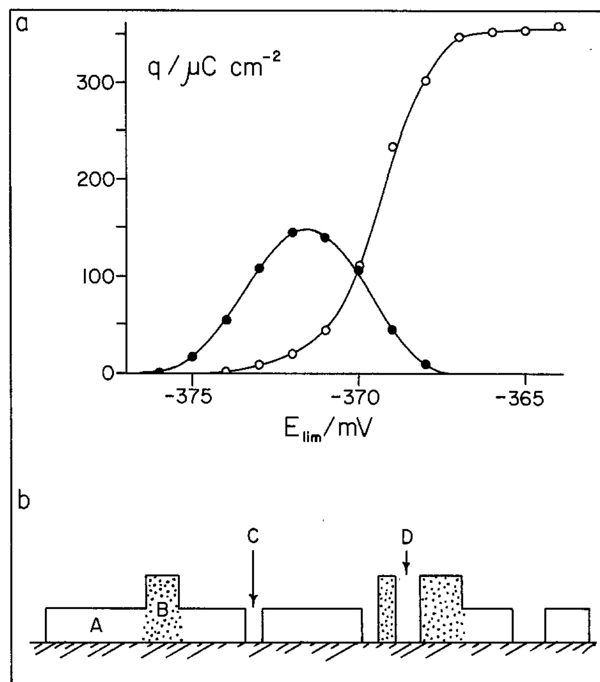

Fig. 7. (a) LPS reduction peak charge *vs.* the anodic potential scan limit for a saturated Cu amalgam electrode in 0.1M LiOH (ν = 5 mV sec^{-1}). (●) peak F, (○) peak G. (b) Pictorial cross section of the saturated Cu amalgam electrode surface during Cu_2O layer formation. (A) Untransformed first layer, (B) unit cell bilayer, (C) shallow hole, (D) deep hole.

cleation and subsequent growth of an unstable layer of Cu_2O of unknown structure. This unstable layer then rearranges (or is otherwise stabilized) concurrent with the growth of the second layer. In this way the unit cell structure is completed. Hence, peak F is due to the reduction of the unstable first layer by the nucleation and expansion of shallow holes, while peak G is due to the simultaneous reduction of both the transformed first layer and the second layer by the nucleation and expansion of deep holes. The situation is illustrated diagrammatically in Fig. 7b, which depicts an intermediate stage in the formation of the layers. Although the exact structure of the unstable first layer is unknown, Fig. 7a indicates that the maximum charge observed in this layer was about half that of the unit cell structure.

Further support for the above mechanism may be seen in the composite Fig. 8. The peak potential of peak F is seen to be approximately constant, independent of the charge under the peak. This is the result expected for the instantaneous nucleation of shallow holes in the patches of (unstable) first layer unaffected by second layer growth. Thus as the anodic potential scan limit was increased, all that changed was the area of untransformed first layer remaining on the electrode. Note that the nucleation of shallow holes was invariably instantaneous because the incomplete first layer was extensively intersected by small areas of uncovered electrode.

Peak G, on the other hand, does move as a function of the anodic potential scan limit but eventually reaches a limiting case. This scenario is also predicted by the model described above. At first the peak potential of G would be stationary because of the instantaneous nucleation of deep holes in the unit cell structure. Eventually, however, as the unit cell structure neared completion on the forward scan, a progressive nucleation mechanism would come into operation in order to create new deep holes since nearly all areas of electrode would be covered. Thus the peak potential of G would be expected to shift cathodically and eventually become constant as a function of the anodic potential scan limit, which is the observed situation.

Polycrystalline copper electrodes.—Cyclic voltammetry was performed at stationary polycrystalline electrodes in 0.1M LiOH solutions. Voltammograms recorded in this way exhibited a strong time dependence because of the repetitive dissolution and deposition of both Cu(I) and Cu(II) species. This served to roughen the electrode surface as a function of time. Eventually an "equilibrium" surface was obtained, for which a typical voltammogram is shown in Fig. 9. Although the experimental data could not be analyzed in a completely quantitative way because of this time-dependent surface roughening, the principal features of the system were clear and may be summarized as follows:

Region A in the diagram corresponds to the dissolution of Cu(I) as in Fig. 2, 4, and 8. The charge contained in peak B during the first sweep was $\sim$ 280 μC per apparent cm^2. Hence this peak is associated with the formation of a layer of less than unit cell dimensions in direct correspondence with the results obtained on the copper amalgam electrodes (cf. Fig. 2, 6, and 8). Assuming a charge of $\sim$ 175 $\mu C\ cm^{-2}$ for this layer, the initial surface roughness of the polycrystalline electrode in this case is calculated to be $\sim$ 1.6, and the roughness factor of the "equilibrium" electrode (*e.g.*, Fig. 9) is $\sim$ 3.7 [cf. factor $\sim$ 3.5 for polycrystalline copper electrodes obtained by Bockris and Conway (41)]. In region C there is evidence of second monolayer formation but this is not well resolved in this figure (see below). Peak H completes the Cu(I) region and corresponds to the nucleation and subsequent growth of a thick layer of Cu_2O as discussed with reference to part (C). Peaks I and J are the dissolution and nucleation of Cu(II) species, respectively (20). Progressive limit LPS experiments indicated that peak K is a reverse reaction associated with peak I (probably $Cu(II)_{aq} \rightarrow Cu(I)_{aq}$). Finally, on the reverse scan, region L corresponds to the reduction of the various species formed on the forward scan.

Some rate control of the processes of peaks I and J by the diffusion of OH^- was observed (Fig. 9). Indeed, increasing the LiOH concentration from 0.1 to 1M caused an approximately tenfold increase in the height of these peaks, but not in peak H. We therefore restricted further measurement to the Cu(I) region (~ -600 to ~ -300 mV).

Figure 10 illustrates successive linear potential scan measurements in 0.1M LiOH that were carried out into the copper (I) region at 50 mV sec^{-1}, increasing the anodic potential scan limit on each scan. The roughness factor in this instance was $\sim$3.6. As on the amalgam electrode (Fig. 6 and 8) a monolayer peak (B) was evident but at somewhat more cathodic po-

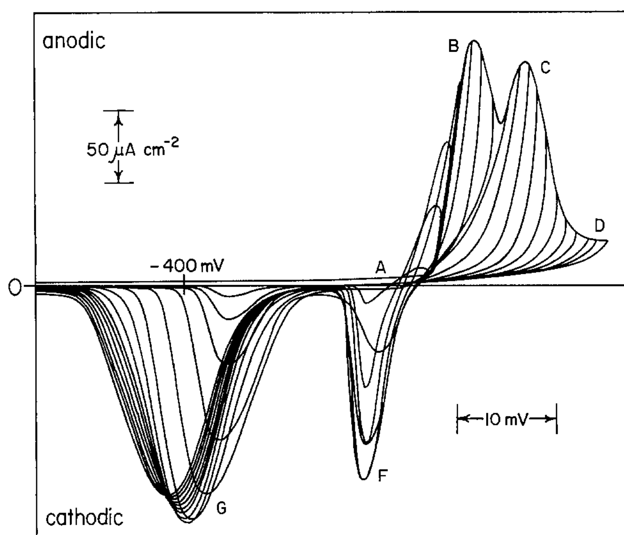

Fig. 8. Composite LPS (ν = 5 mV sec^{-1}) recorded on fresh saturated Cu amalgam electrodes in 0.1M LiOH illustrating the effect of varying the anodic potential scan limit. (A) Dissolution of Cu(I), (B) formation of the first Cu_2O monolayer, (C) formation of the second Cu_2O monolayer, (D) inhibited dissolution of Cu(I), (F) reduction of the untransformed first Cu_2O monolayer, (G) reduction of the unit cell bilayer. Note that the peak potential of F remains constant but that the peak potential of G varies.

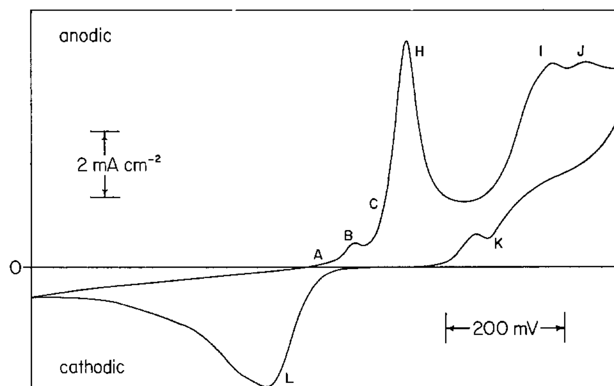

Fig. 9. LPS (ν = 20 mV sec^{-1}) of polycrystalline copper in 0.1M LiOH recorded under continuous cycle conditions, beginning at -970 mV. The current density scale refers to the apparent geometric area of the electrode. (A) Cu(I) dissolution, (B) formation of the first Cu_2O monolayer, (C) inflection due to the formation of the second Cu_2O monolayer, (H) formation of the thick Cu_2O layer, (I) dissolution of Cu(II), (J) Cu(II) thick layer growth, (K) reduction reaction associated with peak I, (L) reduction of species formed on the forward scan.

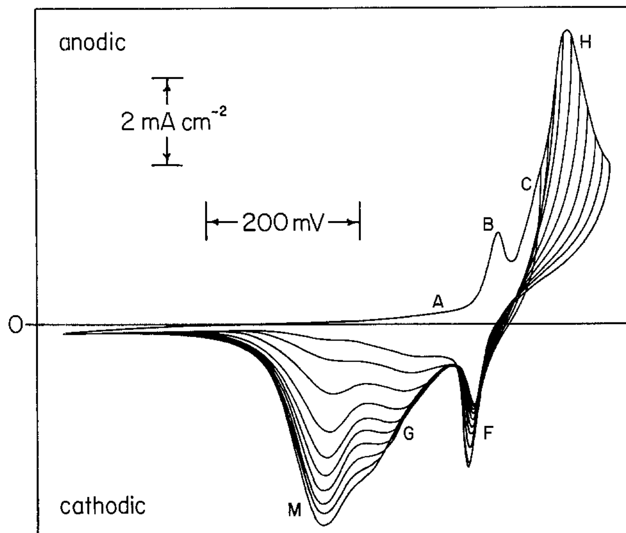

Fig. 10. Composite LPS (ν = 50 mV sec^{-1}) recorded on a polycrystalline copper electrode in 0.1M LiOH beginning at −970 mV, illustrating the effect of varying the anodic potential scan limit. The current density scale refers to the apparent geometric area of the electrode. (A) Cu(I) dissolution, (B) formation of the first Cu_2O monolayer, (C) formation of the second Cu_2O monolayer (F) reduction of the first Cu_2O monolayer formed in peak B, (G) reduction peak associated with the formation of the second monolayer in peak C, (H) formation of the thick Cu_2O layer, (M) reduction of the thick Cu_2O layer formed in peak H.

tentials. (Note: the difference between the potential of the first monolayer peak on the amalgam electrode and that on the polycrystalline electrode, both recorded at 20 mV sec^{-1}, was ~60 mV.) Clearly, monolayer formation proceeds more readily on the polycrystalline electrode. As the anodic potential scan limit was increased to potentials above −400 mV, evidence of second monolayer formation (as on the amalgam electrode) was observed (C) but this was more clearly seen in the reduction reaction (G).

Peak F corresponds to the reduction of the first monolayer and eventually shows some diminution as the anodic potential scan limit is increased. However the peak does not completely disappear, unlike on the amalgam, unless the potential is carried to extreme anodic limits. Consequently some uncertainty remains regarding the precise nature of peak G, although it is clearly related to the second monolayer formation (C).

The formation of a thick layer of Cu_2O can also be seen in Fig. 9 and 10 (peak H). Note that the monolayer reduction peak (F) persists even after extensive growth of this thick layer has occurred. Although the formation of the thick layer has been observed previously, the associated mechanism describing its formation has not been satisfactorily resolved (10, 15, 19, 20, 22, 24-26). We now discuss this mechanism in more detail.

Cu_2O multilayer growth on polycrystalline copper electrodes.—Figure 11 shows a typical current-time plot obtained following the application of a potential step into region H of Fig. 9 and 10. Rising transients were seen which exhibited at t^3 dependence of current density on time. This is the result which would be expected for the three-dimensional nucleation and growth of a thick layer of Cu_2O (42). The transients also exhibited well-defined maxima, after which the current decayed as approximately $t^{-1/2}$.

The sequence of events in the formation of the thick layer of Cu_2O can now be specified. Initially, three-dimensional nuclei emerge on top of the previously formed monolayers as a function of time. These nuclei clearly originate at macroscopic defects or dislocations which persist through the monolayers of Cu_2O from

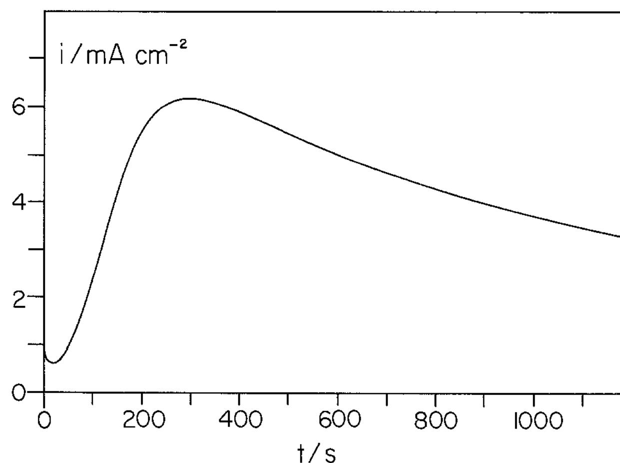

Fig. 11. Typical potentiostatic current transient recording the growth of the thick Cu_2O layer on a polycrystalline copper electrode in 0.1M LiOH at −400.0 mV. The current density scale refers to the apparent geometric area of the electrode.

the bulk metal underneath and are not associated with structural anomalies inherent in the Cu_2O monolayers themselves. This is shown by the fact that thick layer growth of Cu_2O is completely absent when smooth amalgam surfaces are used, despite the fact that the monolayers must incorporate similar misfits, defects, and crystallite boundaries in both cases.

The rising transients typified by Fig. 11 show that the rate-determining step for the thick layer growth occurs at the peripheries of individual nuclei. Under these circumstances the $i(t)$ response is described (42) by

$$i = (nFGM^2k_1^2k_2At^3/3\rho^2) \quad [3]$$

Here, G is a geometric constant (*e.g.*, $G = \pi$ for right circular cones), M is the gram formula weight of the deposit, ρ is its density, k_1 is a rate constant describing lateral growth of the nuclei, k_2 is a rate constant describing vertical growth of the nuclei, and A is a time-independent nucleation rate. The other symbols have their usual significance. Eventually the collision of expanding nuclei becomes important and at the same time the Cu_2O nuclei begin to dissolve into the bulk of solution as $Cu(OH)_n{}^{1-n}$ complexes because of the aggressive nature of the OH^- anion (15). The result of this dissolution process is that crudely hemispherical diffusion zones develop around individual nuclei. As the diffusion zones expand they eventually overlap to create a condition of semi-infinite linear diffusion. Then (43) at long times

$$i = nFD^{1/2}C_s(\pi t)^{-1/2} \quad [4]$$

where C_s represents the surface concentration of a given $Cu(OH)_n{}^{1-n}$ complex and D is its diffusion coefficient.

The reaction scheme outlined above is obviously best observed by the potential step method, because in this case the particular regions of interest (nucleation or diffusion) can be separated sequentially in time. Other techniques, for example galvanostatic steps (16, 24), will necessarily produce rather more complex results because of the potential dependences of the rate constants k_1, k_2, and A in Eq. [3]. However, because previous investigations of the formation of thick layers of Cu_2O have principally been of the galvanostatic type, it is useful to calculate the galvanostatic equivalent of Eq. [3] to see if the earlier data may be explained on the basis of this model.

The solution of this problem can be calculated for two distinct limiting cases. In the first case, the resulting galvanostatic transient exhibits only a small variation in potential (*e.g.*, a few millivolts) and the form of the nucleation law will thus be progressive in time

($N = At$). Alternatively, if the variation in potential is large, then the initial potential "spike" of the galvanostatic transient causes a very rapid nucleation of many nuclei, which thereafter remain virtually constant in number (44). Hence, after a small induction time in which the nucleation rate is greater than zero and nonsteady, the nucleation law will become $N = N_o$ = const. It is expected, on experimental grounds (24), that this latter route occurs in thick layer Cu_2O formation because the observed potential "spike" is large. Therefore, in order to proceed to the galvanostatic solution, Eq. [3] must be amended to take this "instantaneous" nucleation phenomenon into account. The result for the potentiostatic case is well known (42) and is given by

$$i(t) = n\mathrm{F}k_2[1 - \exp(-GM^2k_1^2N_ot^2/\rho^2)] [\exp(-GM^2k_1^2N_ot^2/\rho^2)] \quad [5]$$

where N_o is the number of nuclei that are nucleated at $t \to 0$ and the additional terms correct for the collision of nuclei in the absence of diffusion limitations. It should be stressed that Eq. [3] correctly describes the $i(t)$ transient observed under constant potential conditions, but that Eq. [5] is the appropriate basis for the potentiostatic-to-galvanostatic transformation.

Equation [5] may be rewritten

$$i(t) = 4i_m(S)(1 - S) \quad [6]$$

where i_m is the maximum of the potentiostatic current-time transient and S is the surface coverage function ($0 \leq S \leq 1$). If it is assumed that i_m and t_m are exponential functions of potential, then

$$i_m = (n\mathrm{F}k_2/4) = 10^{a_1E + b_1} \quad [7]$$

$$t_m = (\rho^2 \cdot \ln(2)/GM^2k_1^2N_o) = 10^{a_2E + b_2} \quad [8]$$

Equations [5]-[8] may be regarded as a set of differential equations specifying i as a function of t for various E in the case of three-dimensional instantaneous nucleation. The entire galvanostatic $E(t)$ response can be calculated by numerical solution (see below) or exact solutions can be calculated for certain limiting cases.

Equation [5] can be written as

$$i(t) = PQ^\lambda \exp(-kJ^2)[1 - \exp(-kJ^2)] \quad [9]$$

in which the terms J, Q, P, λ, and k are given (45) by

$$J = \int_0^t Q(t') \cdot dt' \quad [10]$$

$$Q = 10^{-a_2(E(t) - i(t) \cdot R)} \quad [11]$$

$$P = 4 \times 10^{b_1} \quad [12]$$

$$\lambda = -a_1/a_2 \quad [13]$$

$$k = \ln(2) \cdot 10^{-2b_2} \quad [14]$$

and where R is a fixed resistance which contributes to "iR drop" and $E(t)$ is the potential-time waveform. Setting $i(t) = i_g$ (the galvanostatically applied current density)

$$(i_g/P)^{1/\lambda} \cdot t = \int_0^J \exp(-kx^2/\lambda) [1 - \exp(-kx^2)]^{1/\lambda} \cdot dx \quad [15]$$

This equation demonstrates that as $J(t) \to \infty$, $t \to t_{ext}$, a finite "extinction" time at which $E \to \infty$. Thus experimental data may only be obtained over the interval $[0, t_{ext}]$. Defining the function

$$f(y) = y^{1/\lambda - 1}(1 - y)^{1/\lambda}(-\ln(y))^{-1/2} \quad [16]$$

considerably simplifies Eq. [15]. Upon substitution

$$2k^{1/2}(i_g/P)^{1/\lambda} \cdot t = \int_{e^{-kJ^2}}^1 f(y) \cdot dy \quad [17]$$

Replacing $i(t)$ in Eq. [6] by i_g demonstrates that E has a minimum (E_{min}) when $S = ½$. The time taken to achieve this minimum (t_{min}) is thus obtained trivially from Eq. [17]

$$2k^{1/2}(i_g/P)^{1/\lambda} \cdot t_{min} = \int_{1/2}^1 f(y) \cdot dy \quad [18]$$

In addition $Q^\lambda P/4 = i_g$ at $t = t_{min}$, from Eq. [9]. Combining this result with Eq. [9]-[12], after some rearrangement, gives

$$\log(i_g) = a_1(E_{min} - i_gR) + \text{const.} \quad [19]$$

Equation [19] thus allows the experimental determination of the constant a_1 defined in [7], provided R is known or the product i_gR tends to zero. The validity of this expression was confirmed by numerical integration of [15], and the numerical procedure also allowed the solution of the complete $E(t)$ response for a given i_g to be obtained. A typical result is illustrated in Fig. 12 where it is compared with some experimental data extracted from the paper of Ashworth and Fairhurst (24). There is excellent agreement, even to the extent of predicting the slight asymmetry of the transient. Thus, the model of three-dimensional nucleation and growth used to explain our potentiostatic results also describes the earlier galvanostatically acquired data (24).

The limiting behavior of the galvanostatic response at short and long times may also be obtained exactly. At short times as $t \to 0$, $J \to 0$, $Q \to \infty$, and $E \to \infty$ so that

$$i_g \sim PQ^\lambda kJ^2 \quad [20]$$

$$J \sim \text{const. } t^{\lambda(2+\lambda)} \quad [21]$$

$$Q \sim \text{const. } t^{-2/(2+\lambda)} \quad [22]$$

Hence, from [10]

$$E - i_gR \sim \frac{2}{2a_2 - a_1} \log(t/t_{ext}) + \text{const.}; \quad (t/t_{ext} << 1) \quad [23]$$

By similar reasoning, at long times

$$E - i_gR \sim \frac{-1}{a_2} \log\left(1 - \frac{t}{t_{ext}}\right); \quad \left(t/t_{ext} < 1, \left(1 - \frac{t}{t_{ext}}\right) << 1\right) \quad [24]$$

Equations [23] and [24] were also verified by numerical solution of [15].

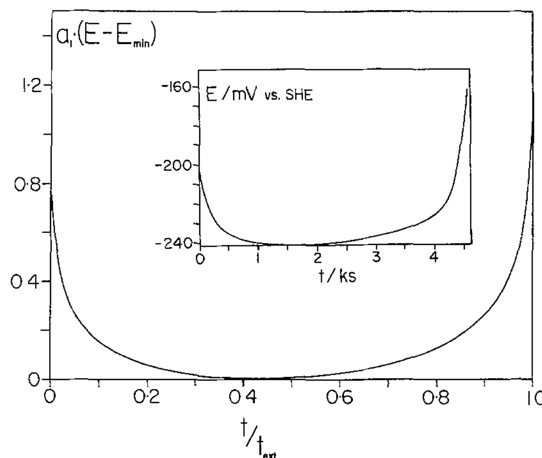

Fig. 12. Galvanostatic transient corresponding to the numerical solution of Eq. [5]-[8]. The constants were $\lambda = 3/5$, $i_g = 1.000$ mA cm^{-2}. The solution used 17,954 steps. Inset: Galvanostatic transient obtained by Ashworth and Fairhurst [from Fig. 12a of Ref. (24)] for polycrystalline copper in 0.1M NaOH at $i_g = 25$ μA per geometric cm^2.

Finally, when $t \to t_{ext}$, then $\exp(-kJ^2) \to 0$ so that [17] becomes

$$2k^{1/2}(i_g/P)^{1/\lambda} \cdot t_{ext} = \int_0^1 f(y) \cdot dy \quad [25]$$

showing that

$$i_g \cdot t_{ext}^{\lambda} = \text{const.} \quad [26]$$

This last result was also obtained as an empirical expression by Ashworth and Fairhurst (24), who determined λ galvanostatically ("instantaneous" nucleation conditions) to be 0.59, 0.44, and 0.54 for the formation of a thick layer of Cu_2O in 0.01, 0.1, and 1.0M NaOH, respectively. In this investigation, λ was determined potentiostatically (progressive nucleation conditions) to be 0.55 for Cu_2O thick layer formation on "equilibrium" polycrystalline copper in 0.1M LiOH.

Conclusion

The anodic behavior of copper amalgam and polycrystalline copper electrodes has been investigated in lithium hydroxide solutions. Certain features are shown to be common to both systems. These are (*i*) the dissolution of Cu(I) hydroxy complexes and (*ii*) the formation of two layer-planes of Cu_2O which complete a unit cell structure. The dissolution reaction exhibits a 59 mV reciprocal Tafel slope as expected for a reversible one-elecron transfer process followed by a slow chemical complexation reaction. The formation of the layer-planes occurs via the nucleation and subsequent growth of two-dimensional patches at the electrode surface. The first layer-plane which is deposited on the amalgam surface can be reduced via the instantaneous nucleation of "shallow" holes. A rearrangement or stabilization of the first layer is postulated to occur at the same time as the formation of the second layer-plane. Simultaneous reduction of both layer-planes at more negative potentials can then occur via the nucleation and subsequent expansion of "deep" holes. These "deep" holes are nucleated either instantaneously or progressively in time depending on the number of uncovered patches of electrode which intersect the unit cell layer.

A major difference between the behavior of the amalgam electrodes and the polycrystalline electrodes is the formation of a thick layer of Cu_2O in the latter case which emerges on top of the previously grown layer-planes. The mechanism of the formation of this layer is one of three-dimensional nucleation and growth. Nuclei originate at macroscopic features which persist through the unit cell layer. The equivalent galvanostatic response is also calculated. The results demonstrate that previous galvanostatic measurements of the formation of the thick layer of Cu_2O on polycrystalline copper in alkaline solution may be understood in terms of the described model.

Acknowledgments

This work has been supported by a grant from the National Research Council of Canada. One of us (J.D.P.) also wishes to acknowledge the financial support of Carleton University during the course of this work.

Manuscript submitted May 16, 1978; revised manuscript received July 6, 1978.

Any discussion of this paper will appear in a Discussion Section to be published in the June 1979 JOURNAL. All discussions for the June 1979 Discussion Section should be submitted by Feb. 1, 1979.

Publication costs of this article were assisted by Carleton University.

LIST OF SYMBOLS

a_1, a_2, b_1, b_2, experimentally determined constants
A nucleation rate (nuclei cm^{-2} sec^{-1})
C_s concentration of $Cu(OH)_n^{1-n}$ at electrode surface (mole cm^{-3})
D diffusion coefficient (cm^2 sec^{-1})
E potential (mV)
E_f final step potential (mV)
E_{lim} LPS anodic potential scan limit (mV)
E_{min} galvanostatic transient minimum potential (mV)
$\mathbf{F}$ the Faraday (96,487 C mole^{-1})
G a geometric factor
i current density (mA cm^{-2})
i_g galvanostatically applied current density (mA cm^{-2})
i_m potentiostatic transient current density maximum (mA cm^{-2})
i_p LPS peak current density (mA cm^{-2})
J $\int_0^t Q(t') \cdot dt'$
k $\ln(2) \cdot 10^{-2b_2}$
k_1 rate constant for lattice growth parallel to electrode surface (mole cm^{-2} sec^{-1})
k_2 rate constant for lattice growth perpendicular to electrode surface (mole cm^{-2} sec^{-1})
M gram formula weight (g mole^{-1})
n number of electrons
N number of nuclei (nuclei cm^{-2})
N_o number of nucleation sites (sites cm^{-2})
P 4×10^{b_1}
Q $10^{-a_2(E(t)-i(t)R}$
R resistance contributing to ohmic drop (Ω cm^2)
S surface coverage ($0 \leq S \leq 1$)
t time (sec)
t_{ext} galvanostatic transient extinction time (sec)
t_m time to potentiostatic transient current density maximum (sec)
t_{min} time to galvanostatic transient potential minimum (sec)
λ $-a_1/a_2$
ν LPS potential scan rate (mV sec^{-1})
ρ density (g cm^{-3})

REFERENCES

1. E. Müller, *Z. Elektrochem.*, **13**, 133 (1907).
2. W. Feitknecht and H. V. Lenel, *Helv. Chim. Acta*, **27**, 775 (1944).
3. A. Hickling and D. Taylor, *Trans. Faraday Soc.*, **44**, 262 (1948).
4. S. E. S. El Wakkad and S. H. Emara, *J. Chem. Soc.*, 3508 (1954).
5. J. S. Halliday, *Trans. Faraday Soc.*, **50**, 171 (1954).
6. L. de Brouckère, F. Bouillon, and Y. Bouillon-Nyssen, *Bull. Soc. Chim. Belg.*, **60**, 26 (1951).
7. F. Bouillon, J. Piron, and J. Stevens, *ibid.*, **67**, 643 (1958).
8. R. W. Ohse, *Z. Phys. Chem. N. F.*, **21**, 406 (1959).
9. S. E. Khalafalla, A. M. Shams El-Din, and Y. A. El-Tantawy, *J. Phys. Chem.*, **63**, 1252 (1959).
10. A. M. Shams El Din and F. M. Abd El Wahab, *Electrochim. Acta*, **9**, 113 (1964).
11. V. N. Flerov, *Z. Fiz. Khim.*, **37**, 1733 (1963).
12. A. M. Borschevski, V. V. Skorcheletti, and T. I. Mikhaleva, *Zh. Prikl. Khim.*, **39**, 1427 (1966).
13. V. A. Plokhov and V. N. Flerov, *ibid.*, **40**, 325 (1967).
14. M. N. Ronzhin and A. L. Golubev, *Chem. Abs.*, **64**, 18954g.
15. B. Miller, *This Journal*, **116**, 1675 (1969).
16. M. J. Dignam and D. B. Gibbs, *Can. J. Chem.*, **48**, 1242 (1970).
17. H. P. Leckie, *This Journal*, **117**, 1478 (1970).
18. N. A. Hampson, R. J. Latham, J. B. Lee, and K. I. MacDonald, *J. Electroanal. Chem.*, **31**, 57 (1971).
19. N. A. Hampson, J. B. Lee, and K. I. MacDonald, *ibid.*, **31**, 165 (1971); **34**, 91 (1972).
20. J. Ambrose, R. G. Barradas, and D. W. Shoesmith, *ibid.*, **47**, 47 (1973); **47**, 63 (1973).
21. T. Yoshimura, Y. Imanaka, and M. Yamashita, *Chem. Abs.*, **81**, 20085g (1974).
22. D. D. MacDonald, *This Journal*, **121**, 651 (1974).
23. D. W. Shoesmith, T. E. Rummery, D. Owen, and W. Lee, *ibid.*, **123**, 790 (1976).
24. V. Ashworth and D. Fairhurst, *ibid.*, **124**, 506 (1977).
25. D. W. Shoesmith, T. E. Rummery, D. Owen, and W. Lee, *Electrochim. Acta*, **22**, 1403 (1977).
26. D. W. Shoesmith and W. Lee, *ibid.*, **22**, 1411 (1977).
27. A. Hickling and J. Maxwell, *Trans. Faraday Soc.*, **51**, 44 (1955).
28. D. E. Schupp, T. Youness, and J. I. Watters, *J. Am. Chem. Soc.*, **84**, 505 (1962).

29. G. Jangg and H. Palman, *Z. Metallkd.*, 54, 364 (1963).
30. G. Jangg and H. Kirchmayer, *Z. Chem.*, 3, 47 (1963).
31. F. Chao and M. Costa, *Bull. Soc. Chim. Fr.*, 1, 54 (1968); 2, 549 (1968).
32. T. Hurlen, A. Staurset, and E. Eriksrud, *J. Electroanal. Chem.*, 83, 263 (1977).
33. L. B. Meites, "Polarographic Techniques," 2nd ed., p. 89, Wiley-Interscience, New York (1965).
34. D. J. G. Ives and G. J. Janz, "Reference Electrodes," p. 335, Academic Press, New York (1961).
35. R. Piontelli, G. Bianchi, U. Bertocci, C. Guerci, and B. Rivolta, *Z. Elektrochem.*, 58, 54 (1954).
36. K. J. Vetter, "Electrochemical Kinetics," p. 395, Academic Press, New York (1967).
37. M. Fleischmann and H. R. Thirsk, in "Advances in Electrochemistry and Electrochemical Engineering," Vol. 3, P. Delahay and C. W. Tobias, Editors, Interscience, New York (1963).
38. R. G. Barradas, F. C. Benson, and S. Fletcher, *Electrochim. Acta*, 22, 1197 (1977).
39. R. S. Nicholson and I. Shain, *Anal. Chem.*, 36, 706 (1964).
40. R. A. Robie, P. M. Bethke, and K. M. Beardsley, U.S. Geol. Survey Bull. 1248.
41. J. O'M. Bockris and B. E. Conway, *J. Chem. Phys.*, 28, 707 (1958).
42. R. D. Armstrong, M. Fleischmann, and H. R. Thirsk, *J. Electroanal. Chem.*, 11, 208 (1966).
43. P. Delahay, "New Instrumental Methods in Electrochemistry," chap. 3, Interscience, New York (1954).
44. G. A. Gunawardena, G. J. Hills, and J. Montenegro, Faraday Symposium, No. 12, the Chemical Society, December 1977 (In press).
45. S. Fletcher and A. Smith, *Can. J. Chem.*, 56, 606 (1978).

Flatband Potential of Cadmium Sulfide (CdS) Photoanodes and Its Dependence on Surface Ion Effects

D. S. Ginley* and M. A. Butler*

Sandia Laboratories, Albuquerque, New Mexico 87185

ABSTRACT

Results are presented which show that the flatband potential (V_{fb}) of a semiconducting cadmium sulfide (CdS) photoanode can be predicted from atomic electronegativity of its constituent atoms. This procedure, previously applied only to metal oxides, now appears generally applicable to any semiconductor-electrolyte system. The flatband potential was measured in a $CdS/S^{=}$, OH^{-}/Pt wet photovoltaic cell as a function of $S^{=}$ and OH^{-} concentrations. These measurements showed that the potential-determining species are HS^{-} and H^{+}. The condition for zero net adsorbed surface charge (PZZP) was also determined by change of solution $pS^{=}$ with added CdS powder and differential potentiometric titration experiments. This is found to occur at a unique $S^{=}$ ion concentration of 4×10^{-9}M. The measured flatband potential, corrected to the PZZP and for the difference between the Fermi level and the bottom of the conduction band, is in excellent agreement with the value predicted from the atomic electronegativities.

Two recent, closely related, developments have evoked considerable interest in the field of semiconductor electrochemistry. The first of these was the demonstration of the photoassisted electrolysis of water by Honda and co-workers in 1969 utilizing a titanium dioxide photoanode (1). The second was the demonstration of workable wet photovoltaic cells employing semiconducting anodes by a number of groups (2, 3). In general, the wet photovoltaic cell employs a redox couple of a potential such that electron transfer to the couple will predominate and no decomposition of the semiconductor will be observed. A prototypical cell in these latter systems has a CdS photoanode, an aqueous electrolyte containing dissolved sodium sulfide, sulfur, and sodium hydroxide, and a platinum or graphite cathode. In general the bulk cell chemistry is the oxidation of sulfide or polysulfide anions on the CdS and the reduction of sulfur (S°) or polysulfides (S_n^{2-}) on platinum. After a sufficient induction period a reasonably stable solution composition is achieved and no additional net chemistry is observed, though electrical power continues to be produced. Various n-type semiconductors have been tried, GaAs, CdSe, and CdTe in a variety of stabilizing electrolytes, alkaline aqueous selenide and telluride in particular (4), but in general the over-all behavior of these cells is illustrated by that of the CdS cell.

* Electrochemical Society Active Member.

Key words: cell, electrolyte, energy conversion, semiconductor.

Recent results have indicated that relatively high efficiencies can be produced in these cells equipped with polycrystalline electrodes (5). The ramifications of these results with respect to possible devices for the conversion of solar energy are obvious.

As a consequence of this we felt that an extension of some of our previous work (6) on the transition metal oxides with respect to the energy levels and chemistry in the cell would be of value in understanding the wet photovoltaic cells. One can illustrate the general schematic for the energy levels in the typical cell as is shown in Fig. 1, for a wet photovoltaic cell with a CdS anode and a metallic cathode. The Fermi level of the metallic cathode will equilibrate close to the level of the reductive half-reaction in which it is taking part. The potential drop determined by the current flowing and the load impedance will locate the Fermi level in the semiconductor. Consequently the extent of band bending at the surface of the semiconductor will depend on where the conduction band is initially pinned at the surface and the voltage drop across the load. The position at which the conduction band is pinned at the surface relative to the vacuum level is the electron affinity (*EA*) of the semiconductor. It can be related to solution measurements which are normally referenced to the standard calomel electrode (SCE), since this half-cell is at a fixed potential relative to the vacuum level (7). In electrochemistry the analogous quantity to electron affinity

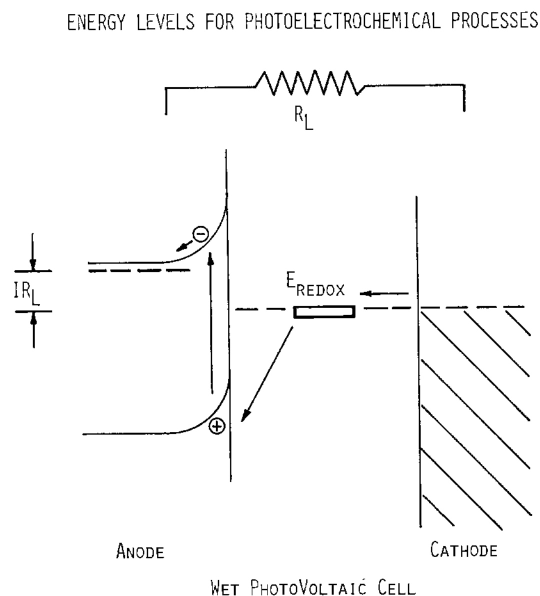

Fig. 1. Energy level diagram for a typical wet photovoltaic cell. Electrons are excited from the valence band to the conduction band by the absorbed photon. These electrons then flow through the load impedance R_L to the metallic cathode where the reductive half-reaction occurs. These reduced species migrate to the anode where they lose an electron to the trapped hole in the valence band. The position of the Fermi level in the semiconductor is determined by the potential drop across the load.

is the flatband potential (V_{fb}) which is a measure of the potential needed, *vs.* the SCE, to totally remove the band bending. The two can be related (6) as shown in Eq. [1]

$$EA = E_o + V_{fb} + \Delta_{fc} + \Delta_{pX} \quad [1]$$

where E_o is the energy difference between the SCE and the vacuum level (4.75) (7), Δ_{fc} is a correction term for the energy difference between the bottom of the conduction band and the doped Fermi level, and Δ_{pX} is a correction term due to the net surface charge of the adsorbed species on the electrode surface. Upon evaluation of the two correction factors one should be able to directly relate the electron affinity to the flatband potential. There is considerable interest in being able to predict flatband potentials since the maximum open-circuit voltage of the wet photovoltaic cell is the difference between the flatband potential and the redox potential measured with respect to the same reference electrode.

In this investigation we examine the properties of a $CdS/S^=$, OH^-/Pt cell and we demonstrate (*i*) that the atomic electronegativities of the constituent atoms of CdS can be used to arrive at its electron affinity, (*ii*) that simple chemical techniques can be used to evaluate Δ_{pX}, where X is an adsorbed species, and that Δ_{fc} can be readily evaluated. Thus, we can accurately calculate V_{fb} using Eq. [1]. We also illustrate how these results apply to the $CdS/S^=$, OH^-, S/Pt cell and show how they clarify certain questions as to the redox chemistry in these systems.

Experimental Procedures

Materials.—The CdS crystal was a 10 × 10 × 2 mm plate cut perpendicular to the c direction and was obtained from Harshaw Chemical. The CdS powder was obtained from Electronic Space Products, Incorporated and was 99.99% pure or better. $Na_2S \cdot 9H_2O$ was obtained from Mallinckrodt and KOH was obtained as a Baker analyzed reagent.

Solution and electrolyte preparation.—All solutions were prepared from deionized-distilled water stored in clear polyethylene containers. All glassware was washed in Alconox in an ultrasonic cleaner then rinsed a minimum of five times with distilled water. All the $Na_2S \cdot 9H_2O$ was rinsed with distilled H_2O then dried in a dessicator before weighing and use so as to remove any external impurities; primarily more highly dehydrated and oxidized sulfides. All sulfide solutions were standardized by potentiometric titrations with lead perchlorate. The experiments were run under an argon purge but solutions with sulfide concentrations from 10^{-4} molar and greater could be prepared in the air and then placed under argon purge. For solutions 10^{-5} molar and below, their preparation and all manipulations were carried out under an argon atmosphere. All sulfide solutions were used the day of their preparation and as rapidly as possible.

For the measurement of the PZZP of sulfide on CdS, a 0.1M KOH solution was prepared and allowed to thermally equilibrate. Then the desired Na_2S concentration was prepared by successive dilutions of a freshly prepared stock solution of 1M Na_2S in 0.1M KOH. The CdS powder employed has been previously washed 3-5 times with distilled water and then dried at 115°C in the air. It was ground as finely as possible, ~25 μm, in an agate mortar and pestle. For $pS^=$ drift measurements, a 600 ml, 0.1M KOH solution of the desired initial sulfide concentration was allowed to equilibrate while being stirred under a constant argon purge. The general schematic for the apparatus used is shown in Fig. 2. Equilibration was confirmed by the stabilization of the $pS^=$ measurements. At this point between 1 and 20g of the CdS powder was added to the solution. As long as the solution was stirred all of the CdS remained suspended. The $pS^=$ was continuously monitored and the reading normally stabilized in from 1 to 8 hr. For measurements of the PZZP by a differential potentiometric titration, Fig. 2, 600

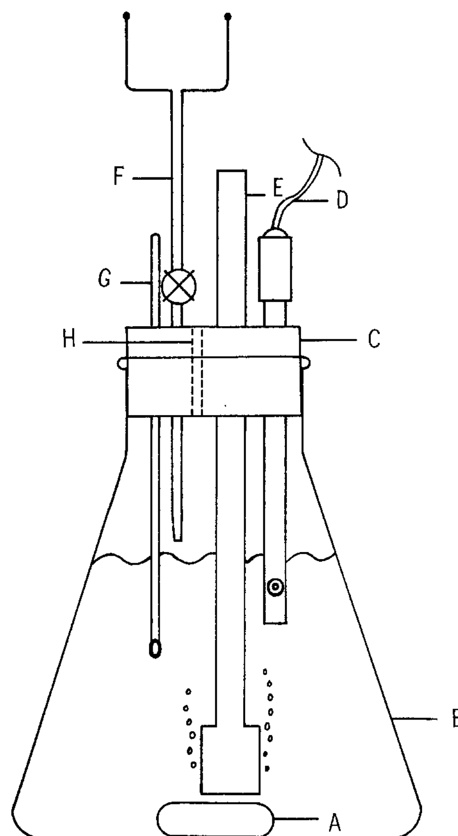

Fig. 2. This apparatus was used to determine the PZZP with respect to $S^=$ ion concentration, both by the drift and differential potentiometric titration methods. The parts of the apparatus are as follows: A, Teflon stir bar; B, 1 liter wide mouth Erlenmeyer flask; C, No. 11 rubber stopper; D, Orion sulfide ion selective ion electrode; E, argon bubbler; F, 5 ml microburette under constant Ar atmosphere; G, thermometer; H, vent hole.

ml of 0.1M KOH solution between 1 and 10g of suspended CdS powder was allowed to equilibrate under argon. The solution was then titrated, using a 5 ml microburette, with a 0.1M KOH solution of known Na_2S concentration. The titrant sulfide concentration was changed as needed during a run and the titrant and the solution being titrated were kept under argon. Nominally titrant was added in equal portions, usually 0.05-0.1 ml, and the solutions were allowed to equilibrate 2-5 min before readings were taken. Titrant volume could be read to ±0.002 ml.

The determinations of the flatband potential as a function of pH^+ or pNa_2S were all conducted by the successive dilutions of freshly prepared stock solutions of KOH and Na_2S.

CdS electrode preparation.—The CdS single crystal was cut perpendicular to the c axis and both sides were polished. A copper wire was soldered to one side using pure indium solder and a Fibra-Sonic, Incorporated ultrasonic soldering iron. Before each experimental run the CdS electrode was etched in warm, 30°C, 50% HCl solution for 1-5 min.

pH^+ and $pS^=$ measurements.—All pH^+ and $pS^=$ measurements were made with a Markson Electromark Analyzer, pH^+ and specific ion meter equipped with a Gralex digital panel meter. Measurements could be read to ±0.001 pH units or ±1 mV. pH^+ was measured with an Orion Model 91-02-00 combination pH electrode and $pS^=$ was measured with an Orion Model 94-16A solid-state sulfide electrode and an Orion Model 90-02-00 double junction reference electrode. The reference electrode outer junction was filled with 0.1M KOH. The sulfide electrode was polished before each run and was calibrated by titration with $Pb(ClO_4)_2$ solutions.

Electrochemical measurements.—All measurements were made with a PAR Model 173 potentiostat/galvanostat equipped with a PAR Model 179 digital coulometer and a PAR Model 175 universal programmer. Measurements were made using a standard 3-electrode setup, with a CdS anode, a smooth Pt cathode (30 cm^2), and a Corning Model 476015 standard calomel reference electrode. All solutions were argon purged but not actively stirred. The flatband potentials were determined from plots of the square of the photocurrent *vs.* potential. Extrapolation of the square of the photocurrent intercepts the potential axis at the flatband (8). This process avoids some of the pitfalls encountered when determining flatband potentials using Mott-Schottky plots. All flatbands were run using monochromatic light at 450 nm (~1.0 mW) from a Schoeffel 150W high pressure xenon arc lamp equipped with a Schoeffel grating monochromator. The reported flatbands were normally measured under d-c (maximum photocurrents 0.5 mA) conditions with light and dark currents measured every 0.05V *vs.* SCE. The a-c measurements agreed excellently with the d-c measurements. For sulfide concentrations of 10^{-4} molar and above no surface corrosion of the CdS electrode was observed. However, for 10^{-5} and 10^{-6} molar sulfide some slight corrosion was observed. As a consequence of this the flatbands for these solutions were measured with the light intensity reduced by a factor of 10 and 100, respectively. Under these conditions a microscopic investigation revealed no surface damage.

Results and Discussion

Calculation of the electron affinity.—Success has been achieved recently in calculating Fermi energies and photoelectric thresholds for several classes of compounds utilizing only the atomic electronegativities of the constituent atoms of the material (9, 10). We have recently applied this same technique to a number of transition metal oxide semiconducting electrodes in order to predict their flatband potentials (6, 11). We have chosen to utilize Mulliken electronegativities for our atomic electronegativities, since they provide an electronegativity scale with a simple physical interpretation based on physically measurable parameters. Mulliken defines the atomic electronegativity, $\chi(m)$, as being the arithmetic average of the first ionization potential (I_p) and the atomic electron affinity (EA) as in Eq. [2]

$$\chi(m) = \tfrac{1}{2}(I_p + EA) \qquad [2]$$

In a sense $\chi(m)$ may be thought of as representing the electrochemical potential of the electron in the neutral atom. When compounds are formed, these electrochemical potentials (electronegativities) are equalized by the flow of charge from atoms of smaller to atoms of larger electronegativity. Sanderson (12) and more recently Netherest (9), have postulated, based on bond length arguments, that the resulting bulk electronegativity of a compound is the geometric mean of the electronegativities of the constituent atoms. This hypothesis appears to be correct for a large number of compounds (6). By analogy with the atomic case, the bulk electronegativity of a solid is just the arithmetic mean of the highest filled state (top of the valence band) and the lowest empty state (bottom of the conduction band). This corresponds to the undoped Fermi level or the electrochemical potential of the electron in the intrinsic semiconductor. The electron affinity for CdS will simply be given by

$$EA(\text{CdS}) = [\chi(\text{Cd})\chi(\text{S})]^{1/2} - \frac{1}{2}E_g(\text{CdS}) \qquad [3]$$

where E_g is the bandgap of cadmium sulfide. The electronegativity of sulfur is determined using Eq. [2], the appropriate ionization potential (13), and the atomic electron affinity (14) to be 6.2 eV. The atomic electron affinity for cadmium is unknown, thus we cannot use Eq. [2] to determine the atomic electronegativity of Cd. However, Mulliken's definition tells us that the electronegativity is identical to the work function of a metal. Thus for cadmium (13) we have an electronegativity of 4.1 eV. The bandgap (15) of CdS is 2.4 eV. Therefore, we find for the electron affinity of CdS a value of 3.8 eV. Having calculated EA we can return to Eq. [1] and if we can evaluate the correction factors, we can determine accurately the flatband potential.

The evaluation of Δ_{fc}.—Since flatband potentials refer to the electrochemical potential of electrons in the semiconductor (Fermi level) and the electron affinity of the semiconductor refers to the bottom of the conduction band, a correction term exists in Eq. [1], Δ_{fc}, which accounts for the different reference points in these two types of measurements. This difference can be measured using conventional solid-state techniques such as the Seebeck effect (16). The Seebeck coefficient for our CdS electrode was found to be 0.54 mV/°K. From this number and the information in Kröger, Vink, and Volgers' paper (17) a carrier concentration of ~10^{17} was found. Using the standard treatment as outlined in Kittel (16), Δ_{fc} was then estimated to be 0.1V. This number of approximately a tenth of a volt for Δ_{fc} is typical of the highly doped semiconductors employed in photoelectrolysis and the wet photovoltaic cells.

Evaluation of Δ_{pX} and the PZZP.—Any electrode material immersed in an electrolyte will interact with the potential-determining species in solution. Since the electrolyte is in equilibrium with the electrode surface under the conditions of interest, the electrochemical potential of the adsorbed species ($\bar{\mu}_{ad}$) will be equal to that of the same species in the electrolyte ($\bar{\mu}_{sol}$)

$$\bar{\mu}_{ad} = \bar{\mu}_{sol} \qquad [4]$$

Depending on the concentration of the potential-determining ions in the electrolyte and the intrinsic pK_a of the material with respect to those ions, differing numbers of anions and cations will be adsorbed

on the surface. The difference between the number of positive and negative charges adsorbed on the semiconductor surface gives rise to a potential drop across the Helmholtz double layer which is measured as part of the flatband potential. This is the correction term Δ_{pX} in Eq. [1]. There is also a small potential across the Helmholtz double layer due to the ordering of the neutral water molecules (18) but this effect is quite small and will be ignored. Obviously Δ_{pX} is a function of the difference in the number of adsorbed anions and cations and therefore the activity of these ions in solution. Thus, most of the flatband potentials measured will show a dependence on the relative activity of the potential-determining ions in solution. For each material there exists a unique point, which is a function of its intrinsic affinities for the potential-determining ions, where the number of adsorbed anions and cations is equal and the potential drop across the Helmholtz layer is consequently zero. This point is called the point of zero zeta potential (PZZP) and is the only point at which truly meaningful flatband measurements can be made, and it is these flatbands to which the calculated electron affinities should be compared.

Since we hoped to show that our model previously developed for the transition metal oxides (6) could be extended to the nonoxides and the wet photovoltaic cells, we picked a cell configuration close to that employed in the normal CdS wet photovoltaic cell. Recent results by Minoura, Okada, and Tsuiki (19) illustrate that our prototype cell will evolve in time to the typical $CdS/S^{=}$, S, OH^{-}/Pt wet photovoltaic cell. They also discuss the dependence of cell performance on sulfur concentration. Our cell configuration is a CdS single crystal anode with a platinum cathode in an electrolyte composed of 0.1M KOH and various concentrations of Na_2S.

Historically, the determination of PZZP has had important ramifications in the area of flotation processes (20). As a consequence it has been primarily colloidal chemists who have measured the PZZP's for various materials, primarily oxides. They have, in general, employed two techniques to measure the PZZP. The first technique involves measurement of fast adsorption isotherms for solutions with different concentrations of an indifferent electrolyte and the second technique measures the *p*H change on addition of metal oxide powder. In the former, a potentiometric titration is performed with either acid or base on a metal oxide suspension in solutions of known specific ionic strength. Since the ions added must go either to changing the *p*H of the solution or being adsorbed on the metal oxide surface, it is possible to determine the surface charge density as a function of *p*H for several concentrations of the supporting electrolyte. The point at which these curves intersect will be the PZZP. In the latter, metal oxide powders are added to aqueous solutions of a known *p*H with no other adsorbable species present. The *p*H of the solution will drift on addition of the powder toward the PZZP. At the PZZP, the *p*H of the solution is independent of the amount of metal oxide added.

We have developed a modification of the first technique whereby all that is needed is to perform a differential potentiometric titration of a suspension of the material of interest with a solution of the ion of interest. Since the solid acts to buffer the solution everywhere but at the PZZP, a peak in the rate of change of *p*X with titrant added *vs.* *p*X curve should be observed. We have employed the *p*X drift and differential potentiometric titration techniques to elucidate the PZZP for the various sulfide species on CdS as is shown in Fig. 3.

For the drift experiments degassed 0.1M KOH solutions of known sulfide concentrations (as Na_2S) were equilibrated under argon with known amounts of finely powdered CdS. The solution makeup was monitored by following $pS^{=}$ with a specific ion electrode.

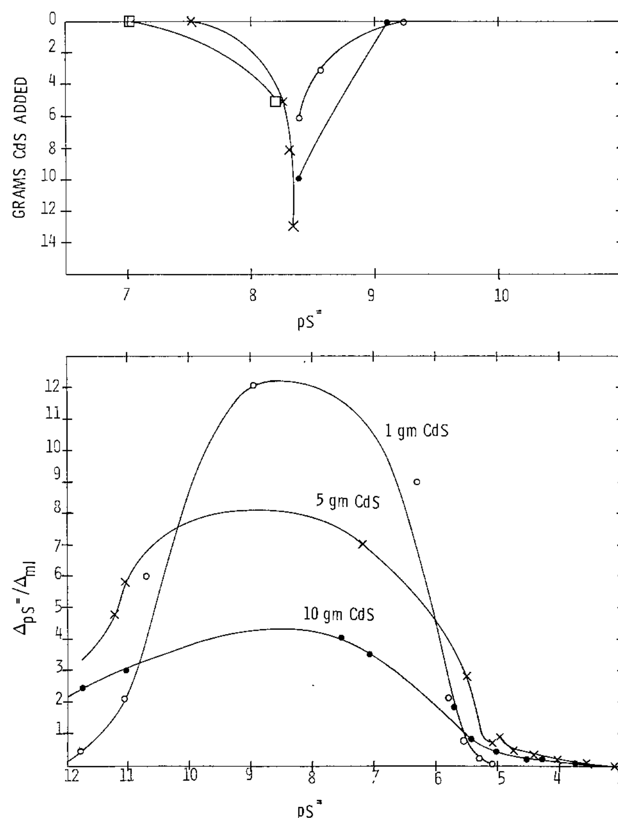

Fig. 3. Determination of the $S^{=}$ concentration at the PZZP of the CdS anode. The top half of the figure represents data taken by the *p*X drift technique. In particular we plot grams of CdS added to a 600 ml sulfide solution of known initial $pS^{=}$ and 0.1M KOH *vs.* measured $pS^{=}$. Points on continuous lines represent successive additions to the same solution. The lower half of the figure consists of three differential potentiometric titrations of a suspended amount of CdS 1, 5, 10g in 600 ml 0.1M KOH with Na_2S solution. The rate of change of $pS^{=}$ with added titrant $\partial pS^{=}/\partial S$ is plotted *vs.* $pS^{=}$. It is of note that the same peak for the PZZP is observed in both curves and that $\partial pS^{=}/\partial X$ scales inversely with the amount of added CdS.

The top half of Fig. 3 illustrates the drift data as a plot of grams of CdS powder added *vs.* the $pS^{=}$. Convergence on the PZZP is observed from both directions and the PZZP lies at a $pS^{=}$ of 8.4. This number does not reflect which of the sulfide species is the potential-determining species but just that a unique sulfide anion concentration exists at the PZZP and is 4×10^{-9}M $S^{=}$. The sulfide equilibria in solution (21) are illustrated in Eq. [5] and [6]

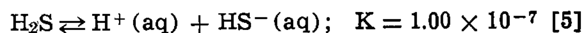

$$H_2S \rightleftarrows H^+(aq) + HS^-(aq); \quad K = 1.00 \times 10^{-7} \quad [5]$$

$$HS^- \rightleftarrows H^+(aq) + S^=(aq); \quad K = 7.08 \times 10^{-14} \quad [6]$$

The lower half of Fig. 3 illustrates some curves from differential potentiometric titrations of CdS suspensions. Two observations are important here: (*i*) the peak in the rate of change curve matches that of the drift measurements quite well, and (*ii*) the relative magnitude of the peak scales inversely with the amount of the material added. This is expected since the suspended CdS essentially acts as a buffering agent in the solution and the larger the amount of CdS the smaller $\Delta pS^{=}/\Delta ml$.

Flatband potential as a function of [Na_2S] *and* [H^+]. —In an attempt to determine which sulfide ions are the potential-determining species as well as to define the dependence of V_{fb} on pNa_2S and pH^+, a series of experiments were conducted using a single crystal CdS electrode in various sulfide, hydroxide electrolytes.

To derive full benefit from the flatband measurements the accurate composition of the solution must

Table I. Flatband dependence on Na_2S concentration

Nominal solution	Actual solution	pH	$[H_2S]$	$[HS^-]$	$[S^=]$	V_{fb} *vs.* SCE
10^0M Na_2S, 0.1M KOH	8.97×10^{-1}M Na_2S, 0.052M KOH	13.95	1.36×10^{-8}	1.22×10^{-1}	7.75×10^{-1}	−1.32
10^{-1}M Na_2S, 0.1M KOH	8.97×10^{-2}M Na_2S, 0.052M KOH	13.44	1.10×10^{-8}	3.04×10^{-2}	5.93×10^{-2}	−1.25
10^{-2}M Na_2S, 0.1M KOH	8.97×10^{-3}M Na_2S, 0.052M KOH	13.27	2.12×10^{-9}	3.89×10^{-3}	5.08×10^{-3}	−1.21
10^{-3}M Na_2S, 0.1M KOH	8.97×10^{-4}M Na_2S, 0.052M KOH	13.27	2.09×10^{-10}	3.87×10^{-4}	5.10×10^{-4}	−1.15
10^{-4}M Na_2S, 0.1M KOH	8.97×10^{-5}M Na_2S, 0.052M KOH	13.28	2.02×10^{-11}	3.82×10^{-5}	5.14×10^{-5}	−1.06
10^{-5}M Na_2S, 0.1M KOH	8.97×10^{-6}M Na_2S, 0.052M KOH	13.28	1.99×10^{-12}	3.81×10^{-6}	5.16×10^{-6}	−1.00
10^{-6}M Na_2S, 0.1M KOH	8.97×10^{-7}M Na_2S, 0.052M KOH	13.29	1.95×10^{-13}	3.78×10^{-7}	5.19×10^{-7}	−0.97

Table II. Flatband dependence on H^+ ion concentration

Nominal solution	Actual solution	pH	$[H_2S]$	$[HS^-]$	$[S^=]$	V_{fb} *vs.* SCE
10^{-1}M KOH, 10^{-3}M Na_2S	0.079M KOH, 9.44×10^{-4}M Na_2S	12.90	7.61×10^{-10}	6.044×10^{-4}	3.40×10^{-4}	−1.09
10^{-2}M KOH, 10^{-3}M Na_2S	7.9×10^{-3}M KOH, 9.44×10^{-4}M Na_2S	11.77	1.54×10^{-8}	9.06×10^{-4}	3.78×10^{-5}	−1.04
10^{-3}M KOH, 10^{-3}M Na_2S	7.9×10^{-4}M KOH, 9.44×10^{-4}M Na_2S	11.39	3.78×10^{-8}	9.28×10^{-4}	1.61×10^{-5}	−0.96
10^{-4}M KOH, 10^{-3}M Na_2S	7.9×10^{-5}M KOH, 9.44×10^{-4}M Na_2S	10.47	3.19×10^{-7}	9.42×10^{-4}	1.97×10^{-6}	0.91
10^{-5}M KOH, 10^{-3}M Na_2S	7.9×10^{-6}M KOH, 9.44×10^{-4}M Na_2S	8.75	1.65×10^{-5}	9.28×10^{-4}	3.69×10^{-8}	−0.87

be known. This is relatively simple since we can rewrite Eq. [5] and [6] as

$$[H_2S] = \frac{[HS^-]10^{-pH}}{1 \times 10^{-7}} \quad [7]$$

$$[S^=] = \frac{7.08 \times 10^{-14}[HS^-]}{10^{-pH}} \quad [8]$$

and we know that

$$M_s = [S^=] + [HS^-] + [H_2S] \quad [9]$$

where M_s is the net moles of sulfide as original Na_2S added. M_s is known since all the stock Na_2S solutions were standardized with lead perchlorate (22). Since pH and $pS^=$ are known, the concentration of all of the relevant species in solution may be readily ascertained.

Table I illustrates the dependence of flatband on the bulk Na_2S concentration in argon purged 0.052M KOH solutions. The variation of flatband potential with concentration of a particular ion is due to changes in the potential across the Helmholtz layer due to adsorbed species Δ_{pX}. Starting from Eq. [4] we can write the potential across the Helmholtz layer due to an absorbed species as

$$ze\Delta_{pX} = \mu_{sol} - \mu_{ad} \quad [10]$$

where ze is the charge on the ion of concern and μ the relevant chemical potential. Taking into account the dependence of chemical potential on activity of the species, we have

$$ze\Delta_{pX} = {}^{\circ}\mu_{sol} - {}^{\circ}\mu_{ad} + RT \ln\left[\left(\frac{C_{sol}}{{}^{\circ}C_{sol}}\frac{{}^{\circ}\Gamma_{ad}}{\Gamma_{ad}}\right)\right] \quad [11]$$

where we have assumed the solution is close to ideal and the activities can be replaced by concentrations, C, and Γ is the surface concentration of adsorbed species. Thus if one plots the flatband potential *vs.* the log of the concentration, one expects the typical Nernstian slope (0.0592 V/pX/z). Figure 4 shows a plot of flatband potential *vs.* the log of the bulk Na_2S concentrations. The data is very linear with a slope of 0.060 ± 0.003 V/pNa_2S unit, very close to that predicted for a monovalent anion. This data is highly significant in two ways. First it allows us to extrapolate the flatband potential back to the PZZP to test our model. Second, the fact that it has a slope expected for a monovalent ion limits the number of possible sulfide ions that are potential determining.[1]

Extrapolating the flatband potential to our PZZP of 8×10^{-9}M Na_2S gives us an experimental flatband potential of −0.84V *vs.* SCE. We know

$$V_{fb} = EA - E_o - \Delta_{fc} - \Delta_{pX} \quad [12]$$

We have shown that EA = 3.8 eV, E_o = 4.75 eV, Δ_{fc} ~ 0.1 eV, and at the PZZP, $\Delta_{pX} = 0$. Thus, we calculate a flatband potential of −0.83V (SCE) for CdS which is in excellent agreement with the experimental value above.

An examination of Table I indicates that at Na_2S concentrations below 10^{-2} molar the ratios of the H_2S, HS^-, and $S^=$ concentrations are relatively constant, a consequence of the pH being almost constant. Since all ionic species present in the electrolyte are known and HS^- is the only monovalent ion present that will adsorb [OH^- does not adsorb on CdS (24)] the slope of the V_{fb} *vs.* p_{Na_2S} indicates that HS^- must be a potential-determining ion.

To investigate the dependence of V_{fb} on the solution pH, a number of solutions were made up with the compositions illustrated in Table II. Here a constant bulk Na_2S concentration is maintained and various KOH concentrations were employed. Of consequence is that the relative concentrations of the various sulfide species remains essentially constant with the HS^- ion being the predominant species. Since the HS^- ion is the negatively charged potential-determining species and its concentration remains essentially constant, variations in the flatband potential must be due to the changes in pH^+. Figure 5 illustrates the dependence of the flatband potential on pH^+ and once again the slope corresponds to that expected from the Nernst equation for a monovalent cation (0.056 ± 0.009 V/pH). Therefore, the proton must be the other potential-determining ion in the CdS cell. These data may

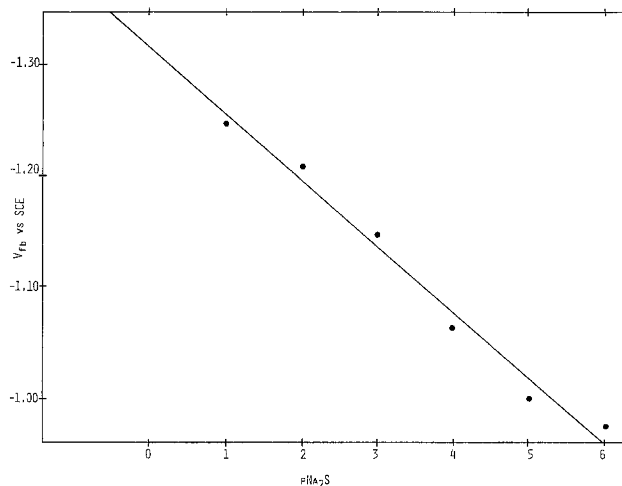

Fig. 4. Dependence of V_{fb} on bulk Na_2S concentration. The data shown are the same as those in Table I and are for a $CdS/S^=$, 0.052M KOH/Pt cell. The slope of the line is 0.060 ± 0.003 V/pNa_2S unit very close to the Nernstian slope for a monovalent ion (0.059 V/pX) indicating that the HS^- ion is a potential-determining species.

[1] The same Nernstian behavior of the flatband potential of CdS has been observed using bulk sulfide solutions by Minoura *et al.* (23). However, their conclusion that the $S^=$ ion adsorbs on the CdS electrode is incorrect since the Nernstian slope they observe is characteristic of a monovalent ion.

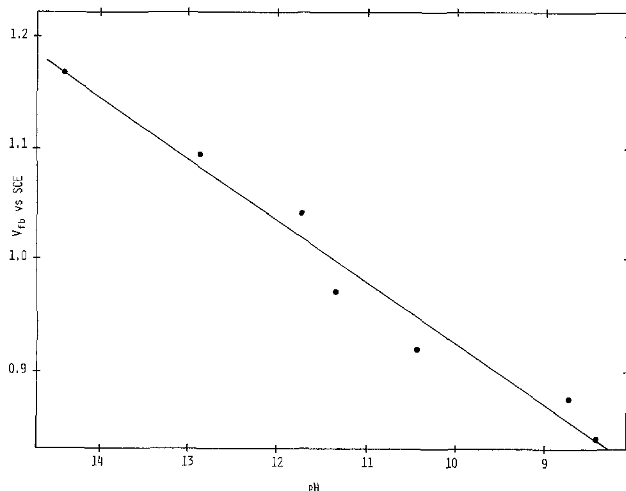

Fig. 5. Dependence of V_{fb} on pH. The data shown are the same as those in Table II and are for a CdS/9.44 × 10^{-4}M $S^=$, KOH/Pt cell. The slope of the line is 0.055V ± 0.009/pH unit which is close to Nernstian as is expected if the proton is one of the potential-determining species.

appear to be in conflict with results of Watanabe, Fujishima and Honda (24), however, their experiments were done in significantly different electrolytes and involved different sample pretreatments. The close agreement between their flatband of −0.87 (SCE) and that observed by Minoura, Watanabe, Oki, and Tsuiki for the Cd surface of CdS −0.85 (SCE) suggests that they have exposed the Cd surface. On this surface one would not expect adsorption of positive potential-determining ions such as H^+. This is consistent with their flatband being close to our PZZP. The determination of the pH^+ dependence requires significant sulfide concentrations since an equilibrium situation would not exist otherwise.

The PZZP measurements suggested that a unique $S^=$ ion activity exists when the adsorbed surface charge is zero (PZZP) even though we believe that HS^- and H^+ are the potentially determining species. How is this possible? If we return again to Eq [4] we can write the electrochemical potential equilibria for each potential-determining species. Subtracting these two equations we have

$$\bar{\mu}_{ad}^{H^+} - \bar{\mu}_{ad}^{HS^-} = \bar{\mu}_{sol}^{H^+} - \bar{\mu}_{sol}^{HS^-} \quad [13]$$

where the right side of the equation is in solution and the left side is the adsorbed phase. At the PZZP the number of H^+ and HS^- ions in the adsorbed phase are equal. If we then explicitly display the concentration dependences of the electrochemical potentials, we have

$$^\circ\bar{\mu}_{ad}^{H^+} - {}^\circ\bar{\mu}_{ad}^{HS^-} = {}^\circ\bar{\mu}_{sol}^{H^+} - {}^\circ\bar{\mu}_{sol}^{HS^-} + RT \ln a_{H^+,sol} - RT \ln a_{HS^-,sol} \quad [14]$$

where the activities refer to those at the PZZP. The activity of HS^- ions may be expressed in terms of the activities of H^+ and $S^=$ ions by using Eq. [6]. If we also use the fact that $2.303pX = -\ln C_X$, we find

$$^\circ\bar{\mu}_{ad}^{H^+} - {}^\circ\bar{\mu}_{ad}^{HS^-} = {}^\circ\bar{\mu}_{sol}^{H^+} - {}^\circ\bar{\mu}_{sol}^{HS^-} - 2.303RT\,pH^+ + 2.303RT\left\{pH^+ + pS^= + \frac{\ln K}{2.303}\right\} \quad [15]$$

where $K = 7.08 \times 10^{-14}$. Thus the dependence on pH^+ cancels and a unique value of $pS^=$ exists at the PZZP given by

$$^\circ\bar{\mu}_{ad}^{H^+} - {}^\circ\bar{\mu}_{ad}^{HS^-} = {}^\circ\bar{\mu}_{sol}^{H^+} - {}^\circ\bar{\mu}_{sol}^{HS^-} + 2.303RT\left\{\frac{\ln K}{2.303} + pS^=\right\} \quad [16]$$

Conclusions

In summary, we have shown that the techniques we had previously developed for oxide photoanodes are equally applicable to nonoxides and various redox chemistries. In particular, we have shown that for the case of the cadmium sulfide wet photovoltaic cell, we can predict the flatband potential of the CdS anode from the atomic electronegativities of the constituent atoms. This prediction may be compared with experiments if corrected for the potential across the Helmholtz layer due to specific ion adsorption Δ_{pX}. This correction factor can be simply evaluated using well-established procedures. Excellent agreement is found between the calculated value (−0.83 *vs.* SCE) and the experimentally measured value that has been corrected to the PZZP (−0.84V *vs.* SCE). We have also demonstrated how, by examining the behavior of the flatband with pNa_2S and pH^+, we can positively identify the potential-determining species on the cadmium sulfide electrode. These turn out to be HS^- and H^+. $S^=$ which was previously thought to be important seems to play no direct role.

Finally, the importance of considering the influence of the adsorbed ions cannot be underplayed. If flatband measurements in these systems are not referenced to the appropriate PZZP, the magnitude of Δ_{pX} remains unknown and the value of the intrinsic flatband cannot be determined. Further, by being able to determine which ions in solution are the potential-determining ones, the ability to intelligently modify the chemistry of the system becomes a possibility.

Acknowledgments

The authors would like to thank R. D. Nasby for the CdS single crystal and R. P. Hellmer for excellent technical assistance. This work was supported by the Materials Sciences Program, Division of Basic Energy Sciences under Contract AT(29-1)-789.

Manuscript submitted May 3, 1978; revised manuscript received July 17, 1978.

Any discussion of this paper will appear in a Discussion Section to be published in the June 1979 JOURNAL. All discussions for the June 1979 Discussion Section should be submitted by Feb. 1, 1979.

Publication costs of this article were assisted by Sandia Laboratories.

REFERENCES

1. A. Fujishima, K. Honda, and S. J. Kikuchi, *Chem. Soc. Jpn.*, **72**, 108 (1969).
2. A. B. Ellis, S. W. Kaiser, and M. S. Wrighton, *J. Am. Chem. Soc.*, **98**, 1635 (1976).
3. B. Miller and A. Heller, *Nature (London)*, **262**, 680 (1976).
4. A. B. Ellis, S. W. Kaiser, J. M. Bolts, and M. S. Wrighton, *J. Am. Chem. Soc.*, **99**, 2839 (1977); A. B. Ellis, J. M. Bolts, S. W. Kaiser, and M. S. Wrighton, *ibid.*, **99**, 2848 (1977); K. C. Chang, A. Heller, B. Swartz, S. Menezes, and B. Miller, *Science (London)*, **196**, 1097 (1977).
5. M. Robbins, B. Miller, A. Heller, S. Menezes, K. C. Chang, and J. Thompson, in "Semiconductor Liquid-Junction Solar Cells," A. Heller, Editor, p. 261, The Electrochemical Society Softbound Symposium Series, Princeton, N.J. (1977).
6. M. A. Butler and D. S. Ginley, *This Journal*, **125**, 228 (1978).
7. F. Lohmann, *Z. Naturforsch., Teil A*, **22**, 843 (1967).
8. M. A. Butler, *J. Appl. Phys.*, **48**, 1914 (1977).
9. A. H. Nethercot, *Phys. Rev. Lett.*, **33**, 1088 (1974).
10. R. T. Poole, D. R. Williams, J. D. Riley, J. G. Jenkins, J. Liesegang, and R. C. G. Leckey, *Chem. Phys. Lett.*, **36**, 401 (1975).
11. M. A. Butler, and D. S. Ginley, *ibid.*, **47**, 319 (1977); D. S. Ginley and M. A. Butler, *J. Appl. Phys.*, **48**, 2019 (1977); M. A. Butler and D. S. Ginley, *ibid.*, **48**, 3070 (1977).
12. R. T. Sanderson, "Chemical Periodicity," pp. 37-38, Reinhold Publishing Corp., New York (1960).
13. F. A. White, "Mass Spectrometry in Science and Technology," p. 343, John Wiley & Sons, Inc.,

New York (1968).
14. H. Hotop and W. C. Lineberger, *J. Phys. Chem. Ref. Data*, **4**, 539 (1975).
15. W. H. Strehlow and E. L. Cook, *ibid.*, **2**, 163 (1973).
16. C. Kittel, "Introduction to Solid State Physics," p. 358, John Wiley & Sons, Inc., New York (1965).
17. F. A. Kroeger, H. J. Vink, and J. Volger, *Philips Res. Rep.*, **10**, 39 (1955).
18. J. O. M. Bockris and A. K. N. Reddy, "Modern Electrochemistry," p. 781, Plenum Press, New York (1973).
19. H. Minoura, H. Okada, and M. Tsuiki, *Nippon Kagaku Kaishi*, **10**, 1443 (1977).
20. G. A. Park, *Chem. Rev.*, **65**, 177 (1965).
21. W. L. Freyberger and P. L. De Bruyn, *J. Phys. Chem.*, **61**, 586 (1957).
22. Instruction Manual Sulphide Ion Electrode Model 94-16, Orion Research, Cambridge (1977).
23. A. Minoura, T. Watanabe, T. Oki, and M. Tsuiki, *Jpn. J. Appl. Phys.*, **16**, 865 (1977).
24. T. Watanabe, A. Fujishima, and K. Honda, *Chem. Lett.*, 897 (1975).

The Conductance, Cyclic Voltammetric, and Infrared Spectral Studies of Electrolytes in Dimethyl Sulfoxide

H. V. Venkatasetty* and D. J. Saathoff

Honeywell Corporate Material Sciences Center, Bloomington, Minnesota 55420

ABSTRACT

The conductance, cyclic voltammetry, and infrared spectra of $LiAsF_6$, $LiPF_6$, and $LiBF_4$ in dimethyl sulfoxide have been measured. From conductance data, information on optimum concentration of the electrolyte for maximum conductance as well as the formation of ion pairs and triple ions has been obtained. The cyclic voltammograms of these solutions have been used to establish their electrochemical stability and to study the electrochemical behavior of trace amounts of water in these solutions. The infrared spectra of dimethyl sulfoxide and the solutions of $LiAsF_6$, $LiPF_6$, and $LiBF_4$ in dimethyl sulfoxide have been obtained. The changes observed in the spectra of electrolyte solutions have been interpreted in terms of ion-solvent interactions.

Dimethyl sulfoxide (DMSO) is a dipolar aprotic solvent with excellent solvent properties for inorganic and organic materials. It is resistant to oxidation and reduction (1). It has fairly high dielectric constant of 46.6 at 25°C and its viscosity is 1.96 cp at 25°C (2). It is a potentially promising solvent for use in high energy density electrochemical power sources. The conductance behavior of dilute solutions of several uni-univalent electrolytes was studied in DMSO at 25°C and the limiting equivalent conductances were obtained (3). Activity coefficients, conductivities, viscosities, and nuclear magnetic resonance (nmr) spectral measurements were made on lithium chloride solutions in DMSO and the observed anomalies in the activity coefficients were attributed to ion-pair formation (4). Conductance measurements on dilute solutions of quaternary ammonium salts were made in DMSO, and information on single ion conductivities and association to ion-pairs was obtained (5). The conductance of several sodium salts and an alkyl ammonium salt was measured and ion conductivities were determined (6). It was found that in sodium salts, the association to ion pairs was evident in salts containing large anions as well as in alkyl ammonium salt (6).

As more concentrated solutions of electrolytes (~1M) are usually employed in battery systems to minimize *IR* drop, it is expected that there will be strong ion-ion and ion-solvent interactions in these solutions of aprotic solvents. It is known that the structural, thermodynamic, and transport properties of electrolyte solutions depend on the nature and the range of such interactions. The mass transport properties of electrolytes in solutions and the electrolyte solution electrode interactions can limit the efficiency and performance of the battery. It has been shown that in lithium cupric fluoride battery using 1M $LiClO_4$ in propylene carbonate, the severe performance limitations noticed during discharge at medium to high rates can be attributed to mass transport limitations in the electrolytes (7). The redox behavior of sulfur in 1M $LiClO_4$ in DMSO has been studied with a view to develop an ambient temperature nonaqueous electrolyte Li/S secondary battery (8). Therefore, there is a need to develop an understanding of ion-ion and ion-solvent interactions in concentrated solutions of electrolytes in nonaqueous aprotic solvents of interest to battery technology. There are relatively few studies on the transport properties and structure of solutions of lithium salts in DMSO useful to lithium battery technology.

The present investigations were undertaken to measure conductance of the solutions of $LiAsF_6$, $LiPF_6$, and $LiBF_4$ in DMSO over a wide concentration range to study their electrochemical stability by cyclic voltammetry, and their structures by infrared spectroscopy. From conductance data such information as equivalent conductance at infinite dilution (Λ_o), ion-pair dissociation constant (*Kd*) and information on triple ion conductance (Λ_{o3}), and dissociation constant (*K*) have been obtained. From cyclic voltammograms, the electrochemical stability and the electrochemical behavior of small amounts of water have been studied. The observed changes in the characteristic infrared frequency of the solvent and the polyatomic anions have been interpreted in terms of ion-solvent interactions.

Experimental

Dimethyl sulfoxide "distilled in glass" obtained from Burdick and Jackson Laboratories, Incorporated, was examined for water content by Karl Fischer titration, and the water content was found to be ~50 ppm. The electrolytes $LiAsF_6$, $LiPF_6$, and $LiBF_4$ were obtained from Foote Mineral Company and were dried under vacuum before use. $LiPF_6$ was quoted by the manufacturer as 99.1% pure and the impurity was the solvent methylformate or benzene. The other salts $LiAsF_6$ and $LiBF_4$ also had solvent impurity which

* Electrochemical Society Active Member.
Key words: dimethyl sulfoxide, electrolytes, conductance, cyclic voltammetry, infrared spectra.

was removed on drying. $LiAsF_6$ obtained from U.S. Steel was also used. All solutions were prepared in a dry box under a positive pressure of dry nitrogen, and lithium electrodes were prepared under dry argon. Jones- and Bollinger-type conductance cells with bright platinum disk electrodes were fabricated. The cell constant varied from 0.3264 to 5.5794 cm^{-1}, and these were used after calibration. The cell constants of the conductance cells were determined with standard 0.1 and 0.01D KCl solutions (9). All conductance measurements were made in a bath of mineral oil maintained at 25° ± 0.05°C. The conductance data are accurate to 2%. The specific conductance of dimethyl sulfoxide is 2-3 × 10^{-8} mho cm^{-1} (2) and the most dilute solution used has specific conductance of 1.9293 × 10^{-5} mho cm^{-1}, and therefore solvent correction is necessary. A Jones and Josephs-type bridge in combination with a Wavetek sweep generator and oscilloscope was used to measure the resistances of solutions. Cyclic voltammetric studies were carried out using Princeton Applied Research Corporation Model 173 potentiostat/galvanostat with a Model 175 Universal programmer. A three-electrode cell with compartments being separated by a medium porosity fritted disk was used. Most commonly used electrode materials in experiments on electrochemical stability are graphite and platinum (10). Platinum electrodes have been used by various workers (10) and in this work a smooth platinum disk electrode was used. The counterelectrode was a large platinum spiral, and the reference electrode was lithium foil immersed in lithium salt solution in DMSO. The voltammetric studies were carried out in less than 15 min, and the platinum electrode on examination did not show any change in appearance. The infrared spectra were obtained using a Digilab Fourier Transform Spectrometer. A KBr beam splitter was used in the 4000-400 cm^{-1} spectral range, and a 6 μm Mylar beam splitter was used in the 400-120 cm^{-1} range. The resolution was 8 cm^{-1} in the 4000-400 cm^{-1} range and 4 cm^{-1} in the 400-120 cm^{-1} range. Two types of cells were used due to the limited spectral range of the window materials. A sealed cell with KBr windows was used for the 4000-400 cm^{-1} range. A similar type sealed cell with polyethylene windows was used to cover the 500-150 cm^{-1} range. The cells were filled in a dry box with a positive pressure of dry nitrogen.

Results and Discussion

The conductance measurements were made on $LiAsF_6$, $LiPF_6$, and $LiBF_4$ in DMSO over a wide range of concentrations (Fig. 1, Table I). The addition of a known quantity of water to the solutions of $LiAsF_6$ shows a decrease in the conductance (Fig. 2), indicating preferential solvation of the Li^+ cation by the water molecules. The conductance data for dilute solutions of these electrolytes were analyzed by an equation of a form similar to that of Fuoss-Shedlovsky (11), except for the function $S(Z)$. The equation is

$$\frac{1}{\Lambda} = \frac{1}{\Lambda_0} + \frac{c\Lambda}{Kd(\Lambda_0)^2}$$

where Λ_0 is the limiting equivalent conductance and Kd is the dissociation constant. The derived values of Λ_0 and Kd for $LiAsF_6$ and $LiPF_6$ indicate similar behavior for these electrolytes, whereas these values

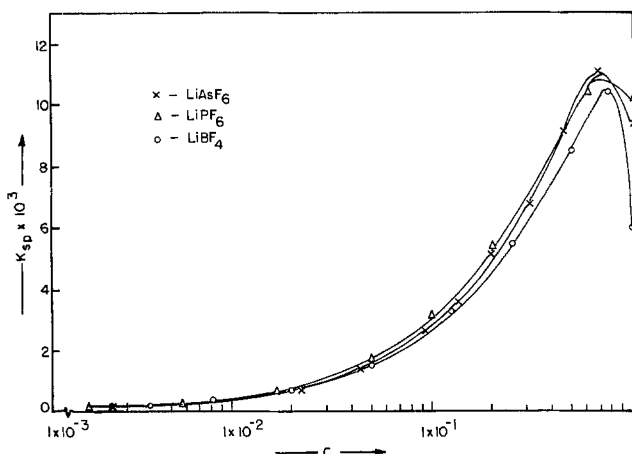

Fig. 1. Specific conductance vs. concentration of electrolytes in dimethyl sulfoxide.

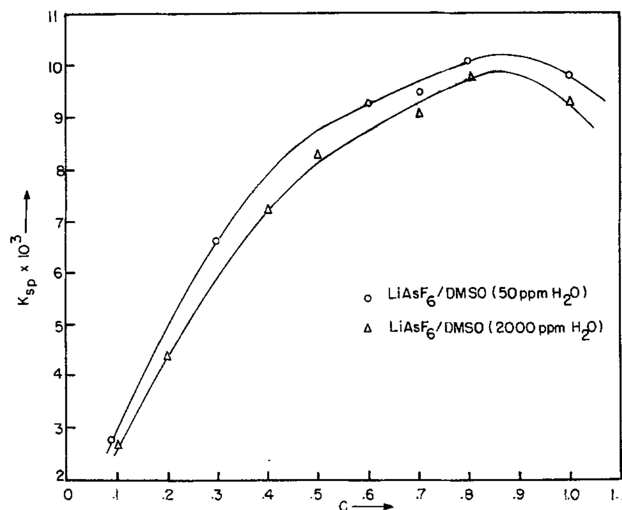

Fig. 2. Effect of water on the conductance of $LiAsF_6$ at various concentrations in dimethyl sulfoxide.

Table I. Conductance data

Concentration (m/l)	Specific conductance (mho cm^{-1} × 10^3)
$LiAsF_6$*—DMSO solutions	
1.0109	47.674
0.6739	11.0909
0.4493	9.0744
0.2995	6.8106
0.1996	5.2244
0.13306	3.6631
0.088706	2.6433
0.04435	1.4324
0.02217	0.76746
0.007392	0.26792
0.002464	0.09367
0.0008213	0.03918
$LiAsF_6$—DMSO solutions**	
Concentration (m/l)	Specific conductance (mho cm^{-1} × 10^3)
0.100	2.72
0.050	1.53
0.0100	0.3371
0.001	0.0424
0.0009	0.0419
$LiPF_6$—DMSO solutions	
Concentration (m/l)	Specific conductance (mho cm^{-1} × 10^4)
0.005945	2.529
0.002973	1.373
0.001955	0.7987
0.001487	0.692
0.000743	0.3554
0.000372	0.19293
$LiBF_4$—DMSO solutions	
Concentration (m/l)	Specific conductance (mho cm^{-1} × 10^3)
0.09812	2.6956
0.04906	1.5917
0.02453	0.8571
0.01225	0.4421
0.006128	0.2493
0.003064	0.1315
0.001532	0.07158
0.000766	0.03782
0.0003983	0.01878

* Foote Mineral.
** U.S. Steel.

Table II. Equivalent conductance at infinite dilution and dissociation constants for ion pairs and triple ions at 25°C in DMSO

	Λ_0	$Kd \times 10^3$	$k/\Lambda_{03} \times 10^5$
$LiAsF_6$	55.5	4.8	1.9
$LiPF_6$	56.8	4.6	1.7
$LiBF_4$	52.9	13.9	1.2

are different for $LiBF_4$ due to ion-solvent interactions (Table II). The equation describing the equilibrium for triple ions (12, 13) is given by

$$\Lambda = \sqrt{\frac{Kd}{C}}\,\Lambda_0 + \frac{\sqrt{KdC}}{K}\,\Lambda_{03}$$

where Kd and K are the equilibrium constants for ion pairs and triple ions and Λ_0 and Λ_{03} have their usual significance (12, 13). The information on triple ions is given in Table II. Because of the scatter in the experimental data, these values are considered as approximate. The limiting equivalent conductance (Λ_0) for $LiAsF_6$ is 71.5 in methylformate, and it is 22.2 in propylene carbonate. For $LiBF_4$ it is 9.1 in methyl formate (14). These differences have been explained in terms of the viscosity of the solvents and the ion-solvent interactions.

Infrared spectroscopy.—In dimethyl sulfoxide both oxygen and sulfur atoms are rich electron sources and therefore can interact with electrolytes. The electronic structure of DMSO may be represented as a resonance hybrid of the structures

If interaction occurs through oxygen, S—O bond will weaken, resulting in a decrease in S—O stretching frequency. If interaction occurs through sulfur, it will result in an increase of S—O stretching frequency (15, 16). The characteristic frequencies most likely to be affected by ion-solvent interactions are the S—O stretching mode occurring at 1060 cm^{-1}, the CH_3 rocking mode at 955 cm^{-1}, and the asymmetric C—S stretching mode at 675 cm^{-1} in the pure solvent (15, 16). The observed changes in the spectra of these solutions are shown in Table III. The shift in S—O stretching frequency is minimal for solution of $LiAsF_6$ and more pronounced for solutions of $LiPF_6$ and $LiBF_4$, indicating relative magnitude of interaction.

The anions AsF_6^- and PF_6^- with octahedral symmetry (O_h) and low polarizability (17) should have six normal modes of vibrations of which only ν_3 and ν_4 are infrared active (18). The appearance of strong bands at 700 and 400 cm^{-1} can be attributed to ν_3 and ν_4 of AsF_6^- (Table III). The infrared spectrum of the compound $LiSbF_6$ shows a strong band ν_3 at 669 cm^{-1} and a medium ν_4 band at 350 cm^{-1} (19, 20). In the case of $LiPF_6$ a strong band appearing at 840 cm^{-1} and a medium-intensity band appearing at 555 cm^{-1} can be assigned to the ν_3 and ν_4 modes of PF_6^-, respectively. The third band of medium intensity appearing at 425 cm^{-1} can be attributed to ν_5 to PF_6^- due to lowering of symmetry as a result of ion-solvent interaction (Table III). The infrared spectrum of KPF_6 has been obtained and a strong band ν_3 at 830 cm^{-1} and a medium intensity band at 558 cm^{-1} have been attributed to the ν_3 and ν_4 mode, respectively (19, 20). The anion BF_4^- of $LiBF_4$ with tetrahedral symmetry (T_d) has only two infrared active vibrational modes, ν_3 and ν_4, and these are triply degenerate (20, 21). The appearance of a shoulder at 500 cm^{-1} can be attributed to the ν_4 mode of BF_4^- (Table III). A broad band of medium intensity appearing at 420 cm^{-1} can be attributed to the ν_2 mode which has become infrared active due to lowering of the symmetry as a result of ion-solvent interaction.

Table III. Spectra of electrolyte solutions

Band	Intensity	Assignment
	$LiAsF_6$ (0.5M)	
(cm^{-1})		
1065	vs & b	S—O Str of DMSO
960	s	CH_3 rocking mode
700	vs	ν_3 of AsF_6^- + Asy C—S Str of DMSO
665	m	Sym C—S Str of DMSO
400	s	ν_4 of AsF_6^-
	$LiPF_6$ (0.5M)	
1050	vs	S—O Str of DMSO
955	s	CH_3 rocking mode
840	s	ν_3 of PF_6^-
695	m	Asym C—S Str
670	w	Sym C—S Str
555	m	ν_4 of PF_6^-
425	m & b possibly	ν_5 of PF_6^-
	$LiBF_4$ (0.5M)	
1045	vs & b	S—C Str of DMSO
950	s	CH_3 rocking mode
695	m	Asym C—S Str
660	w	Sym C—S Str
500	sh	ν_4 of BF_4^-
420	m & b	ν_2 of BF_4^-

vs = very strong, s = strong, b = broad, m = medium.

Cyclic voltammetry.—The cyclic voltammetric studies of electrolyte solutions in dimethyl sulfoxide show that the solutions are electrochemically stable from about +0.5 to +3.5V *vs.* Li/Li^+. The voltammogram of 0.6M $LiAsF_6$ in DMSO shows a main peak around +1.75V and small peaks around +2.3, +1.4, and +1.1V *vs.* Li/Li^+ (Fig. 3). On adding excess water (2500 ppm) to the solution, the voltammogram obtained shows that the main peak around +1.75V has increased in amplitude, whereas the other peaks show very slight increase. A voltammogram of 0.6M

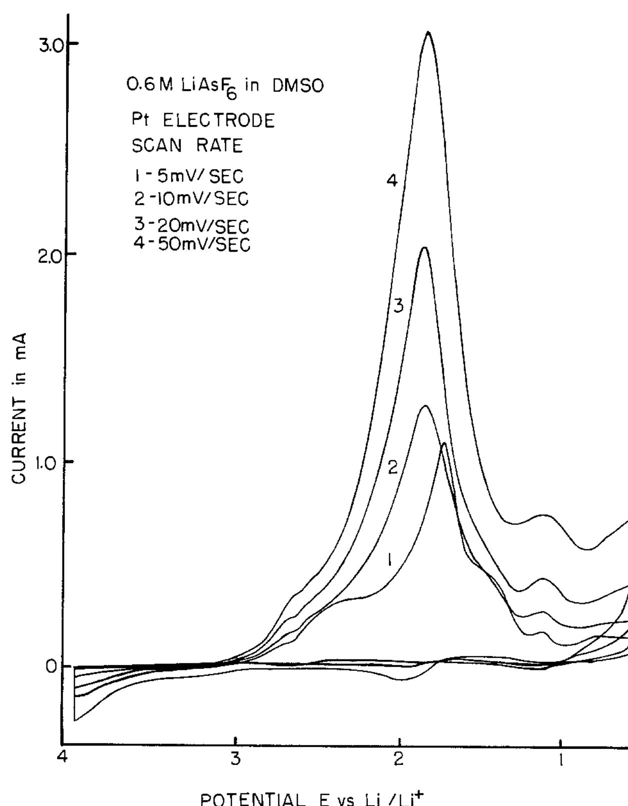

Fig. 3. Cyclic voltammogram of $LiAsF_6$ in dimethyl sulfoxide as a function of scan rate.

$LiAsF_6$ in tetrahydrofuran also shows one main peak and three small peaks (22). The main peak occurring around +1.75V *vs.* Li/Li$^+$ can be attributed to the reduction of water. A reduction peak at +1.4V *vs.* Li/Li$^+$ was observed in 1M $LiClO_4$ in propylene carbonate, and it was attributed to the reduction of water (23). At this time, it is not possible to attribute the peaks at 2.3 and 1.1V to any particular reduction reaction. The peak current corresponding to the main water reduction peak around +1.75V was found to increase with scanning rate. The relationship between peak current and voltage scan rate under linear diffusion condition is given by (24)

$$i_p = AD^{1/2}CV^{1/2}$$

where i_p is the peak current, D is the diffusion coefficient, C is the bulk concentration of the electroactive species, V is the scanning voltage, and A is a constant for the particular system. The ratio of $i_p/V^{1/2}$ was found to be constant at constant concentration within the range of potential scan (5-200 mV/sec). The voltammograms of the solutions of 0.6M $LiPF_6$ and 0.6M $LiBF_4$ in DMSO are similar to that of 0.6M $LiAsF_6$ in DMSO.

Conclusions

The maximum conductance for the electrolytes $LiAsF_6$ and $LiPF_6$ occurs at 0.6M and for $LiBF_4$ at 0.7M. These electrolytes form ion pairs and triple ions in DMSO. These solutions are electrochemically stable from +0.5 to +3.5V *vs.* Li/Li$^+$.

Acknowledgments

The authors thank A. K. Mathur and L. J. Hallgren for their technical assistance.

Manuscript submitted April 17, 1978; revised manuscript received Aug. 10, 1978.

Any discussion of this paper will appear in a Discussion Section to be published in the June 1979 JOURNAL. All discussions for the June 1979 Discussion Section should be submitted by Feb. 1, 1979.

Publication costs of this article were assisted by Honeywell Corporate Material Sciences Center.

REFERENCES

1. J. N. Butler, *J. Electroanal. Chem. Interfacial Electrochem.*, **14**, 89 (1967).
2. "Nonaqueous Electrolytes Handbook," Vol. I and II, G. J. Janz and R. P. T. Tomkins, Editors, Academic Press, New York (1972, 1973).
3. P. G. Sears, G. R. Lester, and L. R. Dawson, *J. Phys. Chem.*, **60**, 1433 (1956).
4. J. S. Dunnett and R. P. H. Gassner, *Trans. Faraday Soc.*, **61**, 922 (1965).
5. D. E. Arrington and E. Griswold, *J. Phys. Chem.*, **74**, 123 (1970).
6. N. P. Yao and D. N. Bennion, *This Journal*, **118**, 1097 (1971).
7. R. Keller, *ibid.*, **117**, 1266 (1970).
8. R. D. Rauh, J. M. Marston, and S. B. Brummer, Abstract 33, p. 88, The Electrochemical Society Extended Abstracts, Fall Meeting, Dallas, Texas, Oct. 5-9, 1975.
9. R. A. Robinson and R. H. Stokes, "Electrolyte Solutions," 2nd ed., Butterworths Scientific Publications, London (1959).
10. J. O. Besenhard, Thesis, TU Munich, 1973 NTIS, N74-30505.
11. R. M. Fuoss and T. Shedlovsky, *J. Am. Chem. Soc.*, **71**, 1496 (1949).
12. R. M. Fuoss and C. A. Krauss, *ibid.*, **55**, 2387 (1933).
13. C. A. Kraus and R. M. Fuoss, *ibid.*, **57**, 1 (1935).
14. H. V. Venkatasetty, *This Journal*, **122**, 245 (1975).
15. F. A. Cotton, R. Francis, and W. D. Horrocks Jr., *J. Phys. Chem.*, **64**, 1534 (1960).
16. W. D. Horrocks Jr. and F. A. Cotton, *Spectrochim. Acta*, **17**, 134 (1961).
17. G. Atkinson and C. J. Hallada, *J. Phys. Chem.*, **64**, 1487 (1960).
18. G. Herzberg, "Molecular Spectra and Molecular Structure," p. 336, D. Van Nostrand Co., Inc., New York (1956).
19. G. M. Begun and A. C. Rutenberg, *Inorg. Chem.*, **6**, 2212 (1967).
20. K. Nakamoto, "Infrared Spectra of Inorganic and Coordination Compounds," Wiley-Interscience, New York (1970).
21. N. N. Greenwood, *J. Chem. Soc.*, 3811 (1959).
22. H. V. Venkatasetty, Unpublished results (1978).
23. B. Burrows and S. Kirkland, *This Journal*, **115**, 1164 (1968).
24. P. Delahey, "New Instrumental Methods in Electrochemistry," Chap. 6, Interscience Publishers Inc., New York (1954).

An Impedance Interpretation of Small Amplitude Cyclic Voltammetry

II. Theoretical Analysis of Systems that Exhibit Pseudoinductive Behavior

Digby D. Macdonald*

SRI International, Materials Research Center, Menlo Park, California 94025

ABSTRACT

Transform analysis is used to derive the small amplitude cyclic voltammetric (SACV) response of an equivalent circuit for an interface that exhibits pseudoinductive behavior. The predicted response contains both transient and steady-state contributions. The steady-state contribution exhibits hysteresis, and the hysteresis current is predicted to change sign with increasing voltage sweep rate as the reactive behavior becomes dominated by the parallel capacitance. Numerical analysis is used to illustrate the dependence of the steady-state response on the voltage sweep rate, and the calculated SACV response is compared with the behavior of the circuit in the complex impedance plane.

Small amplitude cyclic voltammetry (SACV) is used extensively for determining the polarization resistance $(\partial E/\partial I)$ of metal-solution interfaces, particularly during corrosion research. In this case, it is necessary to estimate $(\partial E/\partial I)$ at the corrosion potential in order to calculate the corrosion current, and

* Electrochemical Society Active Member.
Key words: linear polarization, corrosion, electrode kinetics.

hence the weight loss, using the Stern-Geary relationship (1). However, the SACV response current frequently exhibits hysteresis, and furthermore, the value obtained for the polarization resistance under dynamic control will in general be less than the desired d-c value. Hysteresis in the SACV current response arises from nonresistive (*i.e.*, inductive or capacitive) elements in the equivalent electrical circuit for the interface. In principle, the observed hysteresis can be used to delineate the contributions from the various interfacial components. Also, theoretical analysis of the SACV response provides the functional dependence of polarization "resistance" on frequency (or voltage sweep rate). These functions may then be used to extrapolate experimental data to zero frequency (or voltage sweep rate) in order to extract the desired d-c polarization resistance.

In Part I of this series (2), a rigorous analysis was presented of the SACV response of a simple resistive-capacitive equivalent circuit. Transform analysis was used to derive analytical expressions for the current-time (and hence current-potential) response, and the feasibility of extracting useful impedance data from the SACV technique was demonstrated. In this study, the analysis presented in Part I is extended to systems that exhibit inductive behavior at low frequency. A number of systems of practical interest, including passivating iron in inhibited and uninhibited sulfuric acid, have been found to exhibit low frequency inductive semicircles in the complex impedance plane (3-6). Definition of the theoretical behavior of these systems under SACV conditions could make it possible to identify inductive behavior during aquisition of polarization resistance data, and to estimate the impedance parameters of the components of the equivalent circuit (Fig. 1).

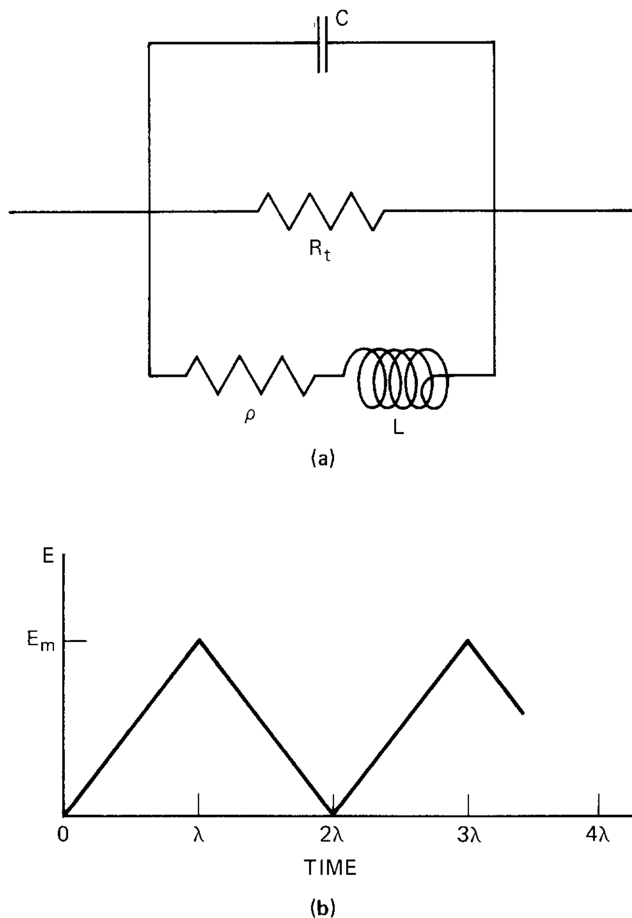

Fig. 1. (a) Equivalent electrical circuit for systems that exhibit pseudoinductance; and (b) SACV excitation voltage.

Theoretical Analysis

A typical a-c impedance complex plane diagram for the systems of interest in this work is shown in the upper right-hand corner of Fig. 2. The complex plane behavior is dominated by two semicircles; a high frequency resistive-capacitive semicircle that gives rise to positive values for the reactance, and a low frequency resistive-inductive semicircle that is characterized by a negative reactance (7). According to Epelboin and co-workers (3-6) and others (8), this type of behavior in the complex plane can be adequately described by the equivalent circuit shown in Fig. 1b provided the magnitude of the excitation voltage is sufficiently small that the components are effectively linear.

The admittance, $Y(p)$, of this circuit can be written in terms of the impedance operator, p, as follows (2)

$$Y(p) = 1/(\rho + pL) + 1/R_t + pC \qquad [1]$$

where $p = d/dt$ and $1/p = \int dt$. Thus, the response of the circuit to any time-dependent excitation voltage is given in Laplace space as

$$\overline{I}(s) = Y(s) \cdot \overline{E}(s) \qquad [2]$$

where $\overline{E}(s)$ is the Laplace transform of excitation function, and the admittance function in Laplace space, $Y(s)$, has the same algebraic form as Eq. [1] with $p \equiv s$. The Laplace transform of the excitation voltage used for SACV is given previously (2) as

$$\overline{E}(s) = E_m(1 - e^{-\lambda s})/\lambda s^2(1 + e^{-\lambda s}) \qquad [3]$$

Thus, substitution of Eq. [1] and [3] into Eq. [2] yields the following expression for the Laplace transform of the current

$$\overline{I}(s) = (E_m C/\lambda)[(1 - e^{-\lambda s})/s(1 + e^{-\lambda s})]$$
$$+ (E_m/\lambda)(1/R_t + 1/\rho) \times [(1 - e^{-\lambda s})/s^2(1 + e^{-\lambda s})]$$
$$- (E_m/\lambda\rho)[(1 - e^{-\lambda s})/s(1 + e^{-\lambda s})(s + \rho/L)] \qquad [4]$$

The inverse transformations of the first two terms for $\lambda > 0$ and $\mathrm{Re}(s) > 0$ is straightforward to yield [see Roberts and Kaufman (9)]

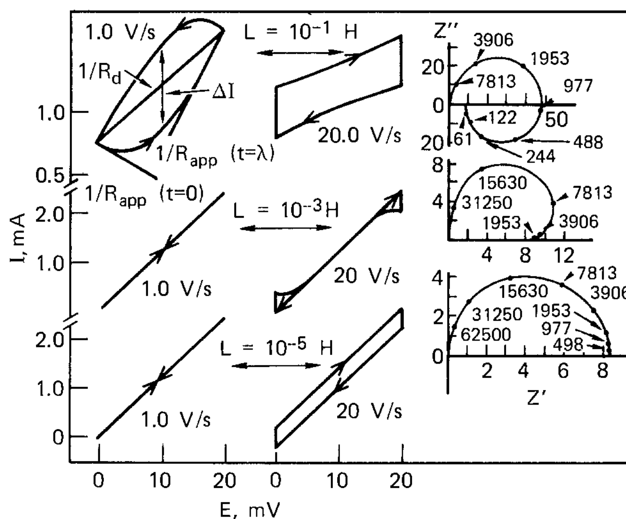

Fig. 2. Current-voltage curves for the SACV response and complex impedance plane diagrams for the equivalent circuit shown in Fig. 1. $C = 10^{-5}$F; $\rho = 10\Omega$; $R_t = 50\Omega$; $E_m = 0.020$V. Upper three curves, $L = 10^{-1}$H; middle three curves, $L = 10^{-3}$H; lower three curves, $L = 10^{-5}$H. The numbers next to the data points in the complex plane diagrams refer to frequencies in rad/sec. Z′ and Z″ have units of ohms.

$$I_1 + I_2 = \begin{cases} (E_mC/\lambda) + (E_m/\lambda)(1/R_t + 1/\rho)(t - 2n\lambda) \\ \qquad \text{for } 2n\lambda < t < (2n+1)\lambda \quad [5a] \\ -(E_mC/\lambda) + (E_m/\lambda)(1/R_t + 1/\rho) \times \\ \quad [2(n+1)\lambda - t] \quad \text{for } (2n+1)\lambda < t \\ \qquad < (2n+2)\lambda \quad [5b] \end{cases}$$

in which Eq. [5a] and [5b] hold for the forward and reverse sweeps, respectively, for the nth cycle ($n = 0, 1, 2, \ldots.$). The third term on the right-hand side of Eq. [4] can be inversely transformed by use of the convolution formula

$$I_3 = -(E_m/\lambda\rho)\int_o^t \mathbf{F}(x)G(t-x)dx \qquad [6]$$

where $\mathbf{F}(t)$ and $G(t)$ are the inverse transforms (9) of $(1 - e^{-\lambda s})/s(1 + e^{-\lambda s})$ and $1/(s + \rho/L)$, respectively. That is

$$\mathbf{F}(x) = \begin{cases} +1 \quad \text{for} \quad 2n\lambda < x < (2n+1)\lambda \\ \qquad \text{(forward sweep)} \quad [7a] \\ -1 \quad \text{for} \quad (2n+1)\lambda < x < (2n+2)\lambda \\ \qquad \text{(reverse sweep)} \quad [7b] \end{cases}$$

and

$$G(t-x) = e^{-\rho(t-x)/L}(t > x) \qquad [8]$$

Integrating over successive forward and reverse cycles therefore yields

$$I_3 = -(E_mL/\lambda\rho^2)\left\{2e^{-\rho(t-\lambda)/L}\left[\sum_{m=0}^{2n-1}(-1)^m e^{m\lambda\rho/L}\right] - e^{-\rho t/L} + 1\right\} \qquad [9a]$$

$$I_3' = -(E_mL/\lambda\rho^2)\left\{2e^{-\rho(t-\lambda)/L}\left[\sum_{m=0}^{2n}(-1)^m e^{m\lambda\rho/L}\right] - e^{-\rho t/L} - 1\right\} \qquad [9b]$$

for the forward and reverse sweeps, respectively, for the nth cycle. Addition of Eq. [5] and [9] and using the general expression for the sum of a geometrical series therefore yields the currents for the forward $[2n\lambda < t < (2n+1)\lambda]$ and reverse $[(2n+1)\lambda < t < (2n+2)\lambda]$ sweeps as

$$I^f(t) = (E_m/\lambda)\left\{C + (1/R_t + 1/\rho)(t - 2n\lambda) - (L/\rho^2)\left[2e^{-(t-\lambda)\rho/L}.\frac{(1 - e^{2n\lambda\rho/L})}{(1 + e^{\lambda\rho/L})} - e^{-\rho t/L} + 1\right]\right\} \qquad [10]$$

$$I^r(t) = -(E_m/\lambda)\left\{C - (1/R_t + 1/\rho) \times [2(n+1)\lambda - t] + (L/\rho^2) \times \left[2e^{-(t-\lambda)\rho/L}.\frac{(1 + e^{(2n+1)\lambda\rho/L}}{(1 + e^{\lambda\rho/L})} - e^{-\rho t/L} - 1\right]\right\} \qquad [11]$$

respectively. Equations [12] and [11] may be transformed into more convenient forms by redefining the time scales as follows (2)

$$t = t' + 2n\lambda \quad \text{(forward sweep)} \qquad [12]$$

$$t = t'' + (2n+1)\lambda \quad \text{(reverse sweep)} \qquad [13]$$

where t' and t'' are the times from the start of the forward and reverse sweeps, respectively. Transformation of the time scales therefore yields

$$I^f(t) = (E_m/\lambda)\{C + (1/R_t + 1/\rho)t' - (Le^{-t'\rho/L}/\rho^2) \times [2(e^{-2n\lambda\rho/L} - 1)/(1 + e^{-\lambda\rho/L}) - e^{-2n\lambda\rho/L}] - L/\rho^2\} \qquad [14]$$

$$I^r(t) = -(E_m/\lambda)\{C - (1/R + 1/\rho)(\lambda - t'') + (Le^{-t''\rho/L}/\rho^2)[2(e^{-2n\lambda\rho/L} + e^{\lambda\rho/L})/(1 + e^{\lambda\rho/L}) - e^{-(2n+1)\lambda\rho/L}] - L/\rho^2\} \qquad [15]$$

Equations [14] and [15] demonstrate that the predicted response of the equivalent circuit to the triangular excitation voltage consists of a steady-state contribution, which is independent of the cycle number n, and a transient contribution that decays with successive cycles.

From a practical viewpoint, the steady-state behavior is of greatest significance, since this state is the most easily examined experimentally. The steady state is achieved when $\exp(-2n\lambda\rho/L)$ and $\exp[-(2n+1)\lambda\rho/L] \to 0$, that is when $n \to \infty$. Thus, from Eq. [14] and [15], the forward sweep and reverse sweep steady-state responses are given by

$$I_{ss}^f = (E_m/\lambda)\{C + (1/R_t + 1/\rho)t' + [2Le^{-t'\rho/L}/\rho^2(1 + e^{-\lambda\rho/L})] - L/\rho^2\} \qquad [16]$$

and

$$I_{ss}^r = -(E_m/\lambda)\{C - (1/R_t + 1/\rho)(\lambda - t'') + [2Le^{-t''\rho/L}/\rho^2(1 + e^{-\lambda\rho/L})] - L/\rho^2\} \qquad [17]$$

respectively. Examination of Eq. [16] and [17] shows that the steady-state response consists of constant (but opposite in sign) contributions from the capacitance and the series combination of resistance ρ and inductance L, a linear contribution due to the transfer resistance, R_t, and exponential decay contributions that are of greatest significance at small times (t' and t''). For the case where $\rho \to \infty$, the response reduces to that for a simple parallel R-C circuit. In this instance, no exponential decay contributions are present; a result that is also valid for the case were $L \to 0$. A simple parallel R-C circuit in series with a resistance also exhibits exponential decay at short times (2). We will show later that this case is easily distinguished from pseudoinductance behavior by the sign of the hysteresis current.

Numerical Analysis

Because of the complexity of Eq. [16] and [17], it is convenient to resort to numerical analysis to illustrate the type of SACV response that might be shown by systems that exhibit pseudoinductance. The numerical analysis is best carried out by defining the following quantities

$$1/R_{app}(t = 0) = (\partial I_{ss}^f/\partial t')_{t'=0}/v = -(\partial I_{ss}^r/\partial t'')_{t''=0}/v \qquad [18]$$

$$1/R_{app}(t = \lambda) = (\partial I_{ss}^f/\partial t')_{t'=\lambda}/v = -(\partial I_{ss}^f/\partial t'')_{t''=\lambda}/v \qquad [19]$$

$$1/R_d = [I_{ss}^f(t' = \lambda) - I_{ss}^r(t'' = \lambda)]/E_m \qquad [20]$$

$$\Delta I = I_{ss}^f(t' = \lambda/2) - I_{ss}^r(t'' = \lambda/2) \qquad [21]$$

where R_{app} is the apparent resistance at $t = 0$ or λ, R_d is the diagonal resistance, ΔI is the hysteresis current, and V is the voltage sweep rate. These quantities are defined graphically in Fig. 2.

Substitution of Eq. [16] and [17] into Eq. [18]-[21], therefore, yields the following expressions for the characteristic quantities defined above

$$1/R_{app}(t = 0) = (1/R_t + 1/\rho) - 2/\rho(1 + e^{-\rho\lambda/L}) \qquad [22]$$

$$1/R_{app}(t = \lambda) = (1/R_t + 1/\rho) - 2e^{-\rho\lambda/L}/\rho(1 + e^{-\rho\lambda/L}) \qquad [23]$$

$$1/R_d = (1/R_t + 1/\rho) + (2/E_m) \times \{C - L/\rho^2 + 2Le^{-\rho\lambda/L}/\rho^2(1 + e^{-\rho\lambda/L})\}v \quad [24]$$

$$\Delta I = \{2(C - L/\rho^2) + 4Le^{-\rho\lambda/2L}/\rho^2(1 + e^{-\rho\lambda/L})\}v \quad [25]$$

Examination of Eq. [25] shows that the sign of the hysteresis current for $\rho\lambda/L \rightarrow \infty$ depends on the relative values of the two reactive components; that is, on the sign of $C - L/\rho^2$. In carrying out the numerical analysis, therefore, we have chosen values for C, L, and ρ that satisfy the following three states: $C < L/\rho^2$, $C = L/\rho^2$, and $C > L/\rho^2$.

Current-voltage curves for the three states defined above are shown in Fig. 2 for voltage sweep rates of 1.0 and 20.0 V/sec. Also plotted in this figure are complex plane impedance diagrams for the equivalent circuit with the appropriate values for the parameters C, L, ρ, and R_t. For the case where $C < L/\rho^2$, the contribution from the inductance dominates the reactive component of the impedance at low frequencies, as shown by the fourth quadrant semicircle in the complex plane. At higher frequencies, the imaginary component of the impedance changes sign and the system exhibits normal, noninductive, first quadrant behavior. This change in behavior is reflected in the SACV response of the circuit as a reversal in the direction of rotation of the current-voltage response from counterclockwise for low voltage sweep rates to clockwise for high sweep rates (Fig. 2). This phenomenon is shown in greater detail in Fig. 3, in which the variation of ΔI, as well as $1/R_{app}(t = 0)$, $1/R_{app}(t = \lambda)$, and $1/R_d$, is plotted as a function of sweep rate over the range 0-20.0 V/sec. The data show that for the values chosen for the components of the equivalent circuit, ΔI first shifts sharply to negative values with sweep rate, then passes through an extremum before becoming positive. The sweep rate at which $\Delta I = 0$, therefore, defines the point at which the system changes from inductive to capacitive in its reactive behavior. Furthermore, the sweep rate at which the ΔI *vs.* v plot passes through the extremum corresponds to that at which the second term in Eq. [25] begins to dominate the SACV response.

Intermediate inductive/capacitive behavior is shown by the curves plotted in the second row in Fig. 1. In this case, a value for L was chosen so that $C = L/\rho^2$. As expected, the hysteresis current as defined by Eq. [21] and [25] is zero because of the equal but opposite contributions from the two parallel reactive components. The exponential decay contributions at short times are still evident, however, particularly at high voltage sweep rates. In the complex plane, this pseudoresistive case exhibits a first quadrant distorted semicircle.

The variation of $1/R_{app}(t = 0)$, $1/R_{app}(t = \lambda)$, $1/Rd$, and ΔI with voltage sweep-rate for this case is shown in Fig. 4. The three conductance terms are nearly invariant with v because of the very low value selected for ρ/L. However, the hysteresis current begins to increase at $v > 10$ V/sec for the circuit parameters chosen.

For the third case selected, $C > L/\rho^2$, and the inductance is not expected to make a large contribution to the SACV response. This is shown in Fig. 2 by a lack of exponential decay at short times and by the appearance of a single, undistorted, semicircle in the complex plane. Furthermore, both ΔI and $1/R_d$ are predicted to increase in a roughly linear manner with v, whereas $1/R_{app}(t = 0)$ and $1/R_{app}(t = \lambda)$ are found to be independent of the voltage sweep rate (Fig. 5).

Equations [22] and [23] show that for all cases in the limit of an infinitely low voltage sweep rate (or $\lambda \rightarrow \infty$), $1/R_{app}(t = 0)$ and $1/R_{app}(t = \lambda)$ approach $(1/R_t - 1/\rho)$ and $(1/R_t + 1/\rho)$, respectively, as indicated in Fig. 3-5. This latter value is precisely the same limit toward which the real component of the complex impedance tends as the frequency of the excitation function is reduced to zero in the classical a-c impedance technique. Furthermore, the diagonal conductance, $1/R_d$, also approaches the upper limit of $(1/R_t + 1/\rho)$. However, the data plotted in Fig. 3,

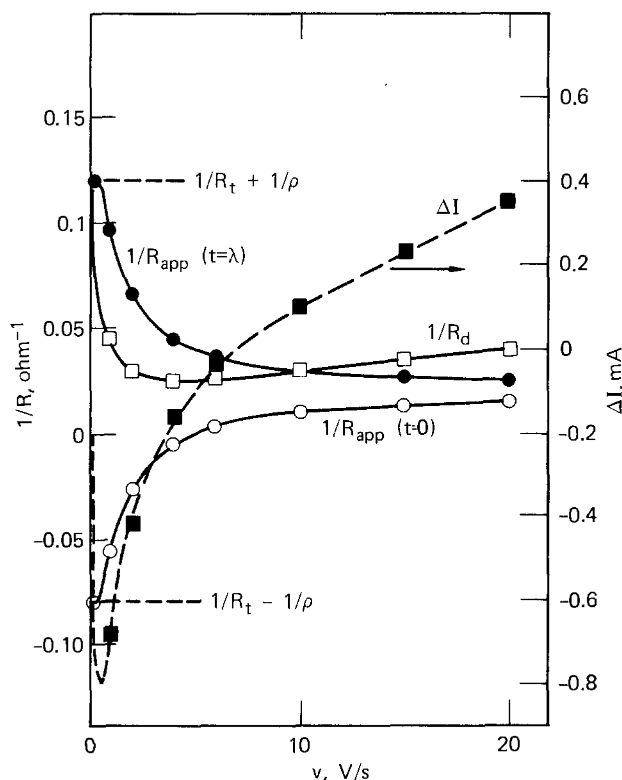

Fig. 3. Dependence of the SACV response of the equivalent circuit shown in Fig. 1 on voltage sweep rate. $C = 10^{-5}$F; $L = 10^{-1}$H; $\rho = 10\Omega$; $R_t = 50\Omega$.

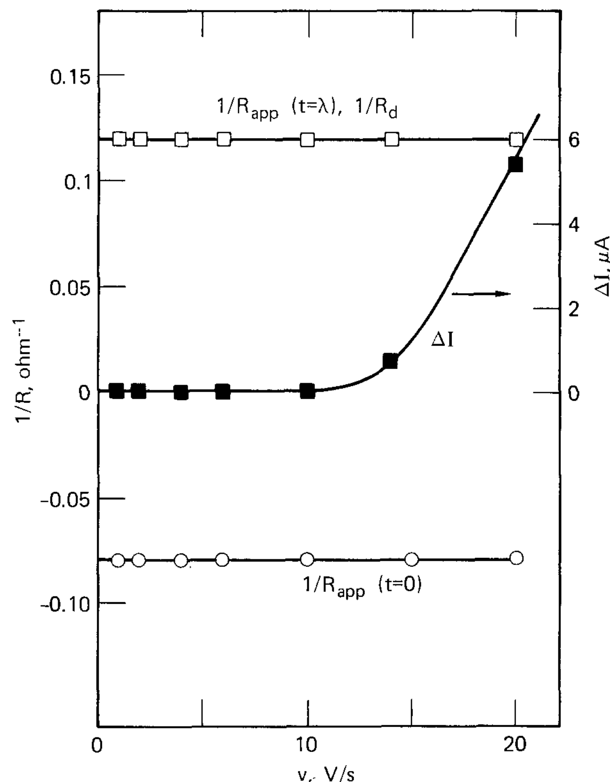

Fig. 4. Dependence of the SACV response of the equivalent circuit shown in Fig. 1 on voltage sweep rate. $C = 10^{-5}$F; $L = 10^{-3}$H; $\rho = 10\Omega$, $R_t = 50\Omega$.

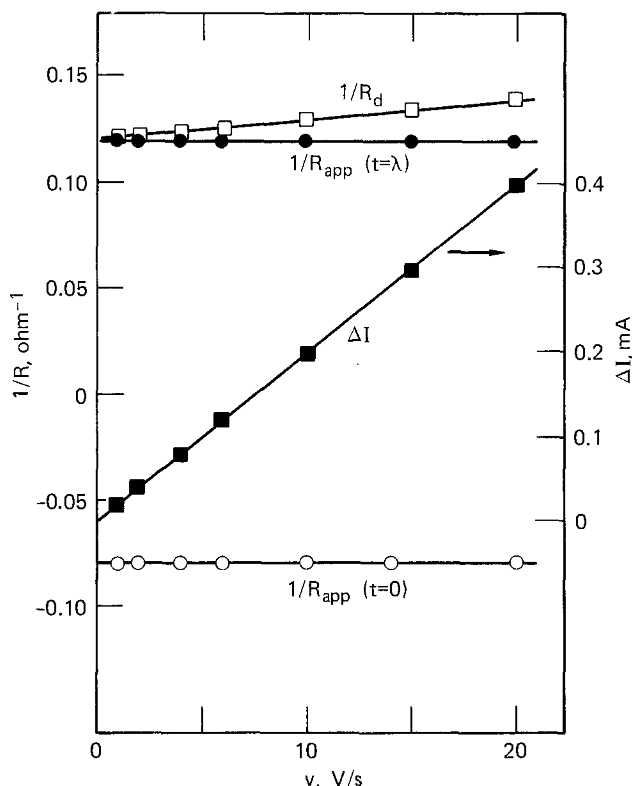

Fig. 5. Dependence of the SACV response of the equivalent circuit shown in Fig. 1 on voltage sweep rate. $C = 10^{-5}$F; $L = 10^{-5}$H, $\rho = 10\Omega$, $R_t = 50\Omega$.

in particular, indicate that the diagonal conductance is much more sensitive to voltage sweep rate than is the term $1/R_{app}(t = \lambda)$. This analytical disadvantage of the diagonal conductance for determining polarization resistance is offset by the fact that $1/R_d$ is much easier to measure experimentally than either of the tangential functions $1/R_{app}(t = 0)$ and $1/R_{app}(t = \lambda)$.

Manuscript submitted Feb. 13, 1978; revised manuscript received June 9, 1978.

Any discussion of this paper will appear in a Discussion Section to be published in the June 1979 JOURNAL. All discussions for the June 1979 Discussion Section should be submitted by Feb. 1, 1979.

REFERENCES

1. M. Stearn and A. L. Geary, *This Journal*, **104**, 56 (1957).
2. D. D. Macdonald, *ibid.*, Submitted for publication (1977).
3. I. Epelboin, M. Keddam, and H. Takenouti, *J. Appl. Electrochem.*, **2**, 71 (1972).
4. I. Epelboin and M. Keddam, *This Journal*, **117**, 1052 (1970).
5. I. Epelboin and M. Keddam, *Electrochim. Acta*, **17**, 177 (1972).
6. I. Epelboin, M. Keddam, and J. C. Lestrade, *Disc. Faraday Soc.*, **No. 56**, 264 (1973).
7. D. D. Macdonald, "Transient Techniques in Electrochemistry," Plenum Press, New York (1977).
8. B. E. Conway, *This Journal*, **124**, 410C (1977).
9. G. E. Roberts and H. Kaufman, "Table of Laplace Transforms," Saunders, Philadelphia, Pa. (1966).

Predicting Electrode Shape Change with Use of Finite Element Methods

Richard Alkire* and Terry Bergh†,[1]

Department of Chemical Engineering, University of Illinois, Urbana, Illinois 61801

and Robert L. Sani

Cooperative Institute for Research in Environmental Sciences (CIRES)/NOAA and Department of Chemical Engineering, University of Colorado, Boulder, Colorado 80302

ABSTRACT

A method of numerical calculation is developed for predicting two-dimensional shape changes at a cathode during electrodeposition. The calculation uses finite element methods to obtain the secondary potential field distribution in an electrolysis cell. The cathode shape initially consists of parallel metal strips which are separated by, and coplanar with, insulating strips; the anode is at a fixed distance from the cathode. Transient numerical calculations provide a complete time history of cathode shape during deposition. Results are obtained in order to compile dimensionless shape change dependence on coulombs passed, polarization parameter, applied potential, and initial cathode shape.

The processes of electrochemical deposition or dissolution of metal inexorably lead to modification of surface shape. In turn, the reaction rate distribution along an electrode surface often depends critically on electrode geometry. Therefore, in order to predict shape change by electrolysis, it is necessary to determine how the reaction distribution changes during the evolution of shape. This theoretical study investigates the utility of finite element numerical methods for calculating electrochemical shape change phenomena.

Numerous factors govern the shape dependence of current and potential distributions within electrolysis cells. At low current densities, for example, the potential field within a cell depends on the electrolyte conductivity and the processes which accompany charge transfer at the electrode surface: crystallization, adsorption, homogeneous chemical reactions, etc.

* Electrochemical Society Active Member.
† Electrochemical Society Student Member.
[1] Present address: IBM, San Jose, California 95100.
Key words: shape change, current distribution, potential distribution, finite element, mathematical model, electrodeposition.

At high current densities, the concentration distribution within the cell depends on diffusion, convection, and migration, all of which are influenced by electrode shape. Owing to these complexities, it is, therefore, not surprising that quantitative treatments of shape change phenomena have been slow to develop.

A large number of industrial examples could be cited where shape changes play an important role. Leveling of deposits is reviewed by Kardos (1) who mentions the need for more quantitative methods of approach. Quality control in electrodeposition is often adversely affected by shape change as, for example, by nonuniform deposits in patterned wiring boards and in plated through-holes. Dendrite formation, electromachining, electropolishing, and electroforming are other fields where timewise variation of electrode shape is an integral part of the electrochemical process. The initiation of corrosion often depends critically on shape change processes which give birth to occluded cells and, thereby, to intensely accelerated localized corrosion. It is abundantly clear that a large number of industrially important electrochemical systems are influenced by the occurrence of shape change and that improved quantitative understanding would be beneficial.

In one of the few existing quantitative studies on two-dimensional shape change in an electrochemical process, Riggs (2) investigated electromachining of an initially flat workpiece with a cylindrically symmetric toolpiece. Laplace's equation is used to predict the potential field in the gap region, with allowance for temperature and gas evolution effects on electrolyte conductivity. Various overpotential relationships are used to describe charge transfer at both electrodes; the local current efficiency for the two anodic reactions is assumed to be constant. By modeling the entire electrolysis cell, this work achieves a high level of sophistication.

The method of solution used by Riggs involves breaking the region between tool- and workpiece into various subregions; a finite difference discretization is used in each subregion and the resulting equations are solved by an overrelaxation scheme. The over-all numerical procedure used the finite difference solution at successive time steps to predict evolution of workpiece shape during tool advance. By this method, they obtained numerical results which, after certain adjustments, compared very favorably with experimental observations.

Finite difference methods, as used in (2), have certain inherent difficulties in coping with shape change problems in a cost-effective manner. By contrast, recent advances in finite element methods of calculation have led to favorable results in predicting highly nonuniform field distributions in regions of nonuniform and timewise varying shape. Applications have recently been made in fields of structural mechanics of deformable bodies (3), heat transfer to surfaces undergoing phase change (4), groundwater seepage problems (5), and deformation and stability of fluid-fluid surfaces (6). Recent progress made in the area of heat transfer is of particular relevance; the method has been used to treat inhomogeneous materials, variable conductivity, nonlinear boundary conditions, and irregularly shaped boundaries.

Preference for finite element over finite difference formulations in handling problems involving nonuniformities results from two basic differences between the two methods. A comparatively loose set of restrictions on the finite element nodal structure allows nodes to be concentrated in regions of high activity and spread thin over more uniform regions, thus weighting areas in proportion to the associated difficulty of approximating the variable of interest. Further, finite element methods are able nonlinearly to interpolate both dependent and independent variables between nodes, so that both the variable of interest and the region in which it is defined may be more accurately modeled. A brief survey which describes in more detail the particulars of finite element methods as well as some strengths and weaknesses in comparison to other techniques is available (7, 8). Recent texts provide engineering (9) and mathematical (10) viewpoints and strategies.

The purpose of this investigation is to apply finite element methods to an electrochemical shape change problem. The geometry chosen for study purposefully includes a singularity in order to investigate the stability of the transient calculation. Computational details are reported in order to assess the accuracy and cost-effectiveness. Dimensionless results are reported for the particular problem at hand in order to compile results over a wide range of parameter space.

Theoretical Formulation

The electrochemical problem.—The two-dimensional cell to be investigated is shown in Fig. 1. The electrode of primary interest, the cathode, is initially coplanar with the lower insulating plane. The vertical side walls represent either insulating surfaces or else planes of symmetry in an array of parallel, evenly spaced cathodes. Between the electrodes is an electrolytic solution of uniform composition. Electrodeposition of metal at the cathode occurs under constant cell voltage.

During shape change, the two-dimensional secondary current distribution is calculated according to the following assumptions: (*i*) The electrolyte is of uniform composition, (*ii*) a single cathodic reaction occurs which obeys the Butler-Volmer rate equation, (*iii*) the anode is unpolarized and does not change shape during electrolysis, (*iv*) transport and kinetic parameters do not vary in space or time, and (*v*) transient shape change is slow with respect to establishment of the electrical double layer. The problem is an example of a secondary current distribution.

In the electrolytic solution, the potential field obeys the equation of Laplace

$$\nabla^2\phi = 0 \qquad [1]$$

At the cathode surface, the reaction rate obeys both Ohm's law and the Butler-Volmer kinetic rate equation

$$-\kappa\nabla\phi \cdot \underline{n} = i_o \left(e^{\frac{\alpha_A n\mathbf{F}}{RT}\phi} - e^{\frac{-\alpha_C n\mathbf{F}}{RT}\phi} \right) \qquad [2]$$

Since the anode is unpolarized, the potential in the

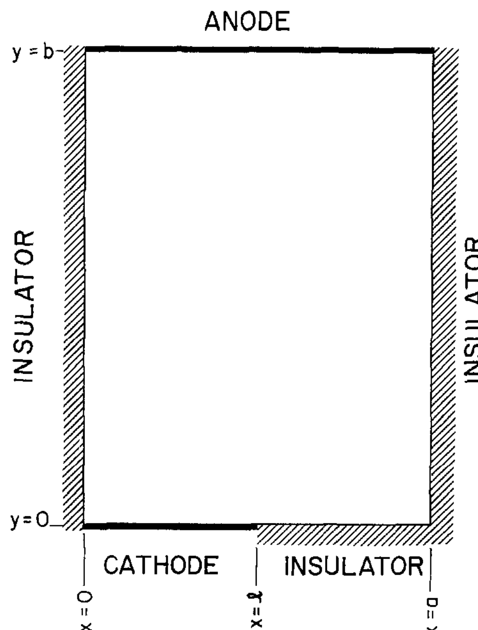

Fig. 1. Electrodeposition cell geometry prior to shape change at cathode.

solution is uniform along its surface

$$\phi = \phi_A \quad [3]$$

On the insulating surfaces and planes of symmetry, the normal potential gradient is zero

$$\nabla\phi \cdot \underline{n} = 0 \quad [4]$$

Equations [1]-[4] provide the current and potential distribution within the cell for any particular surface shape. At any instant in time, the local growth rate of the cathode surface is given by Faraday's law

$$\frac{dh}{dt} = -\left(\frac{M}{n\rho\mathbf{F}}\right)i = -\left(\frac{M\,i_o}{n\rho\mathbf{F}}\right)\left[e^{\frac{\alpha_A n\mathbf{F}}{RT}\phi} - e^{\frac{-\alpha_C n\mathbf{F}}{RT}\phi}\right] \quad [5]$$

By defining

$$\Phi = \frac{n\mathbf{F}}{RT}\phi,\quad X = \frac{x}{l},\quad Y = \frac{y}{l},\quad H = \frac{h}{l},\quad T = \frac{M\kappa RT}{l^2n^2\mathbf{F}^2\rho}t \quad [6]$$

the model equations become

$$\frac{\partial^2\Phi}{\partial X^2} + \frac{\partial^2\Phi}{\partial Y^2} = 0 \quad \text{in } \Omega \quad [7]$$

$$\nabla\Phi \cdot \underline{n} = -\xi[e^{\alpha_A\Phi} - e^{-\alpha_C\Phi}] \quad \text{on } \partial\Omega_C \quad [8]$$

$$\nabla\Phi \cdot \underline{n} = 0 \quad \text{on } \partial\Omega_i \quad [9]$$

$$\Phi = \Phi_A \quad \text{on } \partial\Omega_A \quad [10]$$

$$\frac{dH}{dt} = -\xi[e^{\alpha_A\Phi} - e^{-\alpha_C\Phi}] \quad \text{for } T > 0 \quad [11]$$

$$H(T = 0) = 0 \quad \text{on } \partial\Omega_C \quad [12]$$

where

$$\xi = \frac{i_0 l n\mathbf{F}}{\kappa RT} \quad [13a]$$

$$B = \frac{b}{l} \quad [13b]$$

$$A = \frac{a}{l} \quad [13c]$$

Equations [7]-[12] constitute the system to be solved in order to determine evolution of cathode shape with time.

Readers who do not seek additional mathematical details should proceed directly to the Results and Discussion section below.

The finite element representation of the electrochemical problem.—Rather than solve Eq. [7] and associated boundary conditions directly, a finite element technique is used to construct an approximate solution represented by a linearly independent set of basis functions which are defined within the region (electrolyte phase) as well as on its boundaries (electrode and insulating surfaces). Galerkin's method is used to generate a discretized version of the continuum characterization of the system. Weighted averages of the resulting Laplacian (with respect to members of a set of weighting functions chosen from the same basis used to represent the approximate solution) are required to vanish, thus satisfying a weak form of Eq. [8]. A discussion of Galerkin's method, as well as the broader class of weighted residual methods to which it belongs, is given by Finlayson (11, 12).

Accuracy depends ultimately on both the ability of the postulated approximation to simulate reality correctly and the ability of the weighting functions to weight the solution over the region in a proper manner. These two determining factors depend entirely on the choice of basis functions. In general, polynomials are chosen; in this investigation, second-order piecewise continuous polynomials were used. Important advantages which accrue from the use of piecewise polynomials include acquisition of banded matrices in the final discretized formulation and relative ease and accuracy in approximation of irregularly shaped boundaries.

Let the piecewise polynomial basis functions be represented by $\Gamma_i(X, Y)$ where the set of functions is continuous over the domain Ω and has the property

$$\Gamma_i(X_j, Y_j) = \delta_{ij} \quad [14]$$

where (X_j, Y_j) are the coordinates of node j and δ_{ij} a Kronecker delta function which is 1 if $i = j$ and 0 otherwise. That is, the basis functions are centered over a set of distinct nodes within the region and in fact are Lagrangian interpolation functions. As a result of this property, the potential distribution within the region can be approximated in terms of values of potentials at the nodes

$$\Phi(X, Y) = \sum_{i=1}^{M_w} \Phi_i\,\Gamma_i(X, Y) \quad [15]$$

In terms of the basis functions, the Galerkin equations are

$$\sum_{j=1}^{M_w} \Phi_j\left\{-\int_\Omega \nabla\Gamma_i \cdot \Delta\Gamma_j dA + \int_{\partial\Omega}\Gamma_i n \cdot \nabla\Gamma_j dS\right\} = 0 \quad [16]$$

for $i = 1, \ldots, M_w$.

Integration of the area integrals by parts, and substitution of appropriate boundary conditions into the resulting surface integral, yields

$$\sum_{j=1}^{M_w} \Phi_j \int\int_\Omega \nabla\Gamma_i \cdot \nabla\Gamma_j dA - \xi\int_{\partial\Omega_c}\Gamma_i\left(e^{\alpha_A \sum_k \Phi_k\Gamma_k} - e^{-\alpha_C \sum_k \Phi_k\Gamma_k}\right)dS = 0 \quad [17]$$

for $i = 1, \ldots, M_w$ and for k contained in the set of integers corresponding to those nodes located on the cathode.

The equivalent matrix formulation of the foregoing problem can be cast in the form

$$\underline{\underline{A}}\,\underline{\Phi} = \underline{f}\,(\underline{\Phi}) \quad [18]$$

where $\underline{\underline{A}}$ is a positive definite, symmetric $(M_w \times M_w)$ matrix with elements

$$a_{ij} = a_{ji} = \int\int_\Omega \nabla\Gamma_i \cdot \nabla\Gamma_j dA, \quad i,j = 1, 2, \ldots M_w \quad [19]$$

and where $\underline{f}\,(\underline{\Phi})$ is a nonlinear vector with components

$$f_i\,(\Phi) = \xi\int_{\partial\Omega_c}\Gamma_i\left(e^{\alpha_A \sum_k \Phi_k\Gamma_k} - e^{-\alpha_C \sum_k \Phi_k\Gamma_k}\right)dS - \sum_{j=N+1}^{M_w}\Phi_j\int\int \nabla\Gamma_i \cdot \nabla\Gamma_j\,dA \quad [20]$$

Here the nodes numbered $(N + 1)$ to M_w are located on the anode, a surface on which the potential Φ is specified. Inversion of the above system of matrix equations gives values of potential at the free nodes which may be used in Eq. [15] to approximate the potential distribution in the region as well as on its boundaries.

Method of solution.—The over-all numerical procedure used the finite element solution of Eq. [7]-[10] at successive time steps to compute shape change via a forward Euler solution of Eq. [11]. Second-order polynomials, piecewise continuous, were used as approximating functions on all surface and interior elements. The sequence of steps outlined below is more fully described in Ref. (13).

1. Establish a suitable nodal structure; Fig. 2 illustrates the general form chosen for the problem at hand.
2. Guess an initial potential distribution within the region.
3. Calculate components of $\underline{\underline{A}}$ and $\underline{f}(\Phi)$ along with the other quantities needed for the solution of Eq. [18].
4. Obtain an improved approximation of the potential distribution. In order to take advantage of the symmetry, positive definiteness, and bandedness of $\underline{\underline{A}}$, a banded solver utilizing Cholesky decomposition was used. With use of Newton's method to improve successive guesses of the potential distribution, repeat steps 3 and 4 until convergence on the nonlinear problem is achieved. The convergence criterion used in this study was that the difference in potential at each location between successive iterations was less than 10^{-6}. Typically, three to four iterations were needed to achieve convergence.
5. Calculate the current distribution along the cathode and, thence, the local growth rate normal to the cathodic surface.
6. Choose a time increment and, with the local normal growth rate from step 5, determine the new cathode shape expected at the end of the time increment.
7. Relocate nodes as needed to conform to the new cathode shape, and recalculate the integrals only for those elements with nodes which have been relocated. Grid construction was performed automatically after each time step. After $T = 0$ the elements along the electrode will have distorted bottom surfaces which correspond to the electrode shape.
8. With the potential distribution from the previous time step in hand, return to step 3 and repeat the entire procedure for each successive time step.

Normals to the cathodic surface were computed only on Gauss points on the sides of those elements contiguous with the cathodic surface, where the polynomials were continuous; that is, normals were not calculated at interelement boundaries.

Results and Discussion

Since the finite element method of calculation has not previously been employed in electrochemical potential distribution problems, the following results are divided into two sections. In the first, computational details are presented in order to assess the strengths and weaknesses of the finite element method for solving the particular electrochemical problem at hand. In the second, dimensionless results are compiled for electrochemical behavior over a range of parameter space including applied potential, polarization parameter, initial cell geometry, and time.

Assessment of numerical results.—Let us first examine how accurately the finite element method approximates the solution of Eq. [7] in the region of interest. In Fig. 2, the numbering of elements follows a precedent ordering of column (index J) and row (index I). Thus element 1 corresponds to $(I, J) = (1, 1)$; element 2 corresponds to $(I, J) = (1, 2)$; etc. Table I provides values of the Laplacian for the 63-element structure depicted in Fig. 2. The values of the Laplacian shown

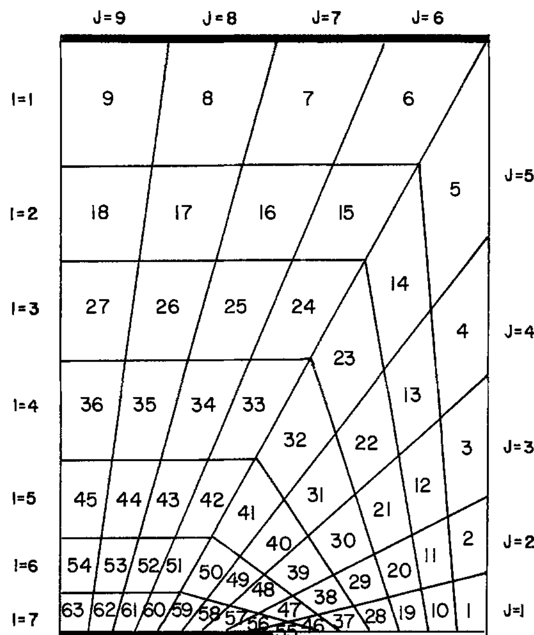

Fig. 2. Diagram of node structure showing element numbering scheme (not drawn to scale).

in Table I are unweighted integral averages over the particular element as determined from a four-point Gaussian quadrature scheme. Equation [7] indicates that an exact solution would exhibit values of zero far all entries in Table I.

In general, the values given in Table I tend to be largest near the cathode, particularly near the singularity at the cathode edge (elements 55 and 56) where potential field variations are at a maximum. Absolute values range from 10^{-6} to 10^{0}; the average value over the entire region is 10^{-3}. By comparison, the value of the potential and its first derivative will generally be of order unity. That is, on the average, the 63-element (222-node) structure is accurate to within 0.1%, but the local accuracy may stray widely at specific element locations.

Like all other numerical methods, finite element methods experience difficulty in simulating accurate potential distributions with piecewise quadratic polynomials when the potential variations are highly localized. Thus, despite the Galerkin requirement that various weighted averages of the Laplacian vanish in such regions, the Laplacian values may stray far from zero at specific points within the region. As a result, unweighted averages such as the ones tabulated in Table I may be large in localized regions. Since, however, finite element methods are particularly able to

Table I. Values of the Laplacian function of various locations, run 3

Element	Laplacian	Element	Laplacian	Element	Laplacian
1	0.007	22	0.005	43	0.01
2	0.007	23	0.006	44	0.005
3	0.01	24	0.004	45	−0.002
4	0.005	25	0.0001	46	−0.4
5	0.001	26	−0.0005	47	−0.4
6	0.00008	27	−0.0009	48	−0.3
7	0.000007	28	0.02	49	−0.1
8	−0.00002	29	0.04	50	−0.09
9	−0.00004	30	0.02	51	−0.02
10	0.003	31	0.003	52	−0.008
11	0.02	32	0.005	53	−0.01
12	0.009	33	−0.01	54	0.002
13	0.01	34	−0.001	55	−1.0
14	0.004	35	−0.0005	56	2.0
15	0.001	36	0.002	57	−0.7
16	0.00006	37	0.1	58	−0.1
17	0.00002	38	0.1	59	−0.06
18	0.0001	39	0.01	60	−0.01
19	0.01	40	−0.02	61	−0.004
20	0.02	41	−0.05	62	−0.001
21	0.01	42	−0.01	63	−0.003

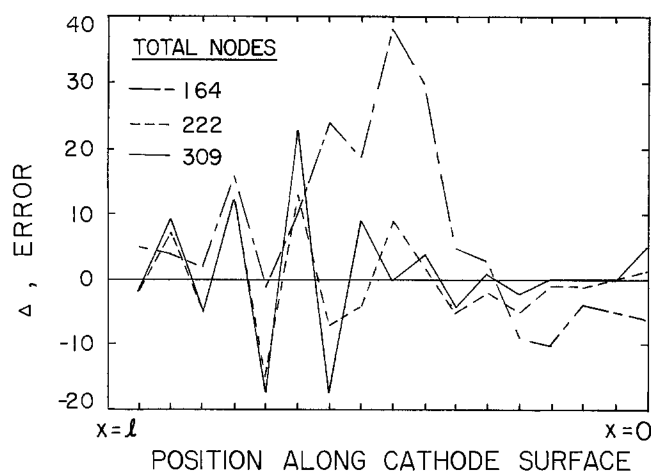

Fig. 3. Difference between cathodic current distribution calculated by Butler-Volmer and by Ohm's law equations. Results are shown for several nodal densities.

cope with singularities, an initial cell geometry was purposefully chosen with a singularity at the cathode edge.

Next, consider the current distribution along the cathode surface. The Butler-Volmer kinetic expression is used explicitly in the finite element formulation and yields a smooth and reliable current distribution along the cathode. A measure of accuracy of the potential field near the cathode is gained by comparing the first derivative (Ohm's law) with the current given by the Butler-Volmer equation. Figure 3 illustrates results for several different nodal densities. The abscissa gives the location along the cathode surface; the ordinate gives the difference, Δ, between the current calculated by the Butler-Volmer equation and by Ohm's law. Typical of finite element solutions is the variation in Δ about an average value which is very nearly exact zero. For the 222-node calculation, the maximum difference, Δ, was less than 1% of the absolute magnitude of current. The percentage error decreased to considerably less than 1% after the initial moment, when the singularity disappeared from the cathode edge. It is seen that results are not greatly dependent on nodal density.

At insulated boundaries and planes of symmetry, the normal current should be zero for an exact solution. For the 222-node structure shown in Fig. 2, the computed values of normal and tangential currents at the insulating edges are given in Table II. Normal values are generally two to three orders of magnitude smaller than tangential values except near the singularity (element 55). After the first time step, the singularity disappears and the normal current dropped to two orders of magnitude less than the tangential current.

Table II. Comparison of normal and tangential currents at insulated boundaries and lines of symmetry, run 3

Element	Normal current	Tangential current
1	0.05	0.2
2	−0.01	0.5
3	−0.003	0.6
4	0.003	0.6
5	0.0008	0.6
6	0.00008	0.6
9	0.00003	0.6
10	0.003	0.3
18	−0.00003	0.3
19	0.001	0.6
27	0.0006	0.6
28	−0.0003	0.8
36	−0.0002	0.7
37	−0.01	1.0
45	0.0007	0.9
46	−0.03	2.0
54	−0.003	1.0
55	0.4	3.0
63	−0.001	1.0

Finally, let us comment on the choice of time step between successive finite element calculations. Time steps ranging between 0.0075 and 0.18 dimensionless units were studied with the expectation that a characteristic cathode shape would be asymptotically approached on decreasing the step size. Such was not the case. For the entire range of step sizes, the system variables agreed to within 2-5%. We, therefore, conclude that within this range of time step, the choice of step size is not crucial in the present problem.

Compilation of electrochemical behavior.—Calculations were carried out to determine electrochemical behavior for the systems summarized in Table III. The dimensionless parameters which were varied include ξ, the polarization parameter; Φ_A, the applied potential; A, the ratio of cell width to cathode width; and Λ, the total coulombs passed during electrolysis. The parameters are defined by

$$\xi = \frac{i_0 \ln \mathbf{F}}{\kappa RT} \quad [21a]$$

$$\Phi_A = \frac{n\mathbf{F}}{RT} \phi_A \quad [21b]$$

$$A = \frac{a}{l} \quad [21c]$$

$$\Lambda = \frac{1}{A^2} \int_0^{X_{out}} Y dX \quad [21d]$$

The ranges of these parameters investigated in the present study are

$$0.1 \leq \xi \leq 3.0$$

$$1.2 \leq \Phi_A \leq 10.1$$

$$1.43 \leq A \leq 3.33$$

$$0 \leq \Lambda \leq 0.13$$

Certain parameters were arbitrarily fixed since they seemed less interesting; included among these were the transfer coefficients and the anode position. For all calculations reported here

$$\alpha_A = 0.5 \quad [22a]$$

$$\alpha_C = 0.5 \quad [22b]$$

$$\frac{B}{A} = 5.0 \quad [22c]$$

Table III. Information about computer runs*

Run	ξ	Φ_A	α	Total nodes	Iterations	Execution time (sec)
1	0.1	3.87	2.0	222	46	33.491
2	0.3	3.87	2.0	222	46	33.949
3	1.0	3.87	2.0	222	46	34.127
4	3.0	3.87	2.0	222	46	34.505
5	0.6	3.87	3.33	222	47	38.867
6	1.0	3.87	2.0	222	46	34.127
7	1.4	3.87	1.43	222	46	39.036
8	0.1	1.16	2.0	222	58	47.658
9	0.3	1.16	2.0	222	54	44.661
10	1.0	1.16	2.0	222	57	46.315
11	3.0	1.16	2.0	222	52	41.073
12	0.1	6.96	2.0	222	36	31.363
13	0.3	6.96	2.0	222	40	33.775
14	1.0	6.96	2.0	222	41	34.842
15	3.0	6.96	2.0	222	45	38.793
16	0.1	10.06	2.0	222	44	36.735
17	0.3	10.06	2.0	222	54	44.452
18	1.0	10.06	2.0	222	47	39.549
19	3.0	10.06	2.0	222	47	39,480
20	1.0	3.87	2.0	164	46	37.738
21	1.0	3.87	2.0	222	46	51.729
22	1.0	3.87	2.0	309	46	71.636

* All runs were made on a CDC 175 Computer. Parameters which were held constant for all runs were: $\alpha_A = \alpha_C = 0.5$; $\beta/\alpha = 5.0$, and $\Lambda_{max} = 0.13$.

It was found that the anode position did not influence the current distribution along the cathode when $B/A = 5.0$ or larger.

Also shown in Table III are the number of nodal points used in each calculation, the number of time steps, and the total execution time. On the average, calculations at 222-node conditions required 0.824 sec per time step.

Figure 4 provides the time history for growth of a deposit in one particular system as specified in the figure caption. As cathode growth proceeds, new surface area is generated, and the current distribution along the cathode becomes more uniform. Thus the deposit thickness distribution becomes more uniform during these initial stages of growth. It is seen that the deposit grows not only upward (toward the anode) but also outward (covering the adjacent insulator surface). Figure 4 illustrates the quantities Y_{sym}, Y_{max}, and X_{out} which will be used below to compile characteristic features of deposit growth.

Figure 5 illustrates the effect of variations in ξ in the absence of other changes in the system. The parameter ξ is a linear polarization parameter and is thereby an indicator of reaction uniformity. For values less than unity, surface charge-transfer processes are sluggish and the cathodic current distribution will tend to be uniform. For values greater than unity, conduction effects control the potential field and the current distribution will be nonuniform. The effect of ξ on the final shape of a deposit is shown in Fig. 5; the same number of coulombs have been deposited for each curve. It is seen that highly nonuniform deposit shapes are encountered when ξ has a large value.

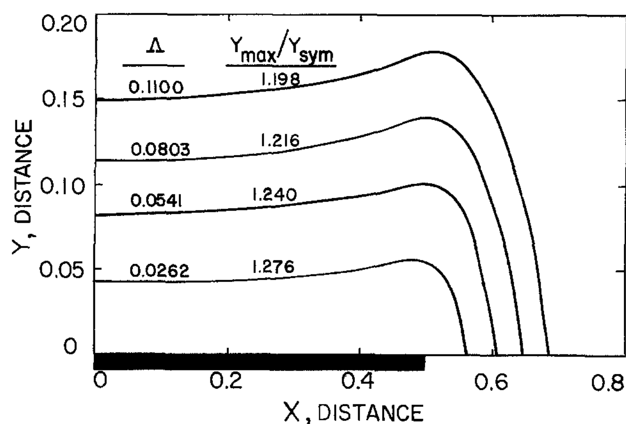

Fig. 4. Dependence of cathode shape with number of coulombs deposited; original shape shown along abscissa. ($\Phi_A = 3.87$, $\xi = 1.0$, $A = 2.0$.)

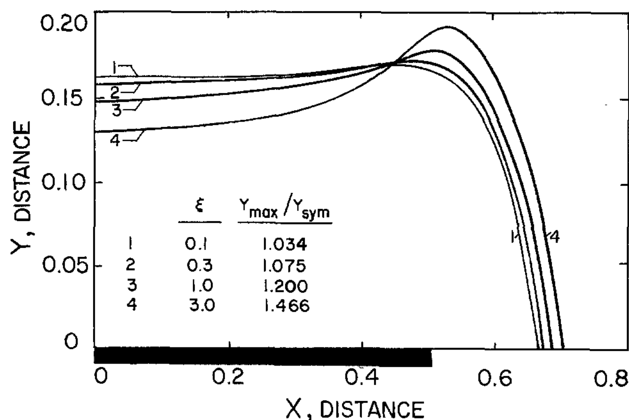

Fig. 5. Dependence of cathode shape on linear polarization parameter, the same number of coulombs has been deposited for each curve. Original cathode shape shown along abscissa. ($\Phi_A = 3.87$, $\xi = 0.11$, $A = 2.0$.)

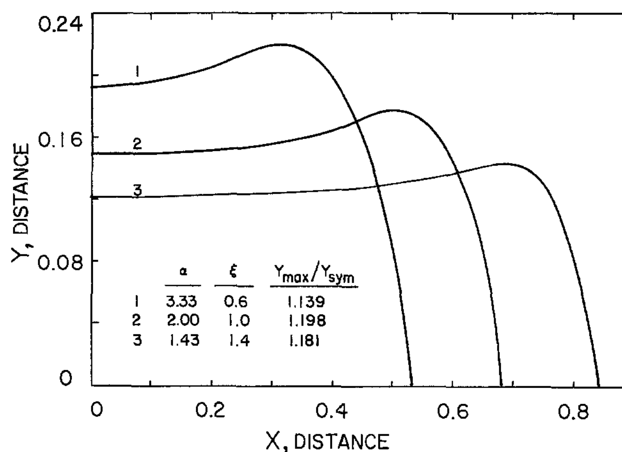

Fig. 6. Dependence of shape on initial cathode width; the same number of coulombs has been deposited for each curve. ($\Phi_A = 3.87$, $\Lambda = 0.11$.)

Figure 6 gives final deposit shapes following deposition of the same number of coulombs onto cathodes of three different widths. The cathode width, l, enters into both parameters ξ and A. Small values of l correspond to small values of ξ for which the current distribution would tend to be uniform. Values of $l/a \rightarrow 1$ correspond to cathodes which occupy the entire lower surface, thus achieving a uniform current distribution. The current distribution will be the most nonuniform for intermediate values of l. The middle curve in Fig. 6 ($A = 2$) exhibits a more nonuniform deposit than either of the other curves ($A = 1.43$ and 3.33).

There are two distance ratios which are particularly characteristic of the cathode shapes encountered in this study. Y_{max}/Y_{sym} is the ratio of maximum cathode height to the cathode height at the plane of symmetry, $X = 0$. X_{out}/Y_{max} is the ratio of outward growth along the adjacent conductor to the maximum cathode height. The next two figures illustrate how deposit shape is influenced by the parameters of the system.

Figure 7 shows how the ratio Y_{max}/Y_{sym} depends on the polarization parameter and the number of coulombs deposited. The ratio Y_{max}/Y_{sym} is a measure of deposit uniformity along the upper side of the deposit which faces the anode. Deposits are more nonuniform

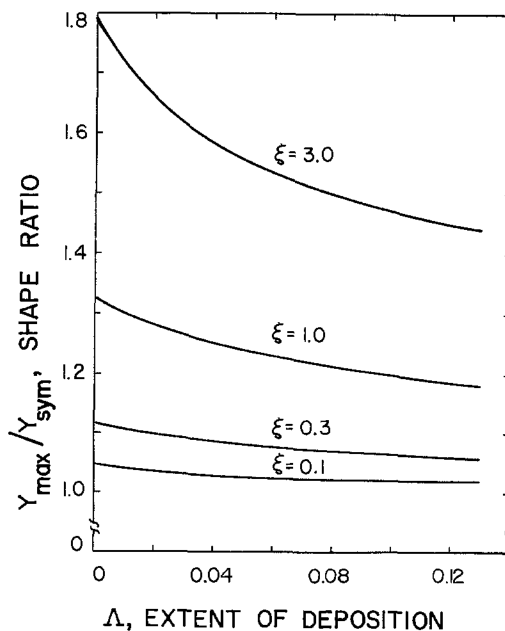

Fig. 7. Dependence of characteristic cathode shape ratio on linear polarization parameter and dimensionless number of coulombs deposited. ($\Phi_A = 1.16$.)

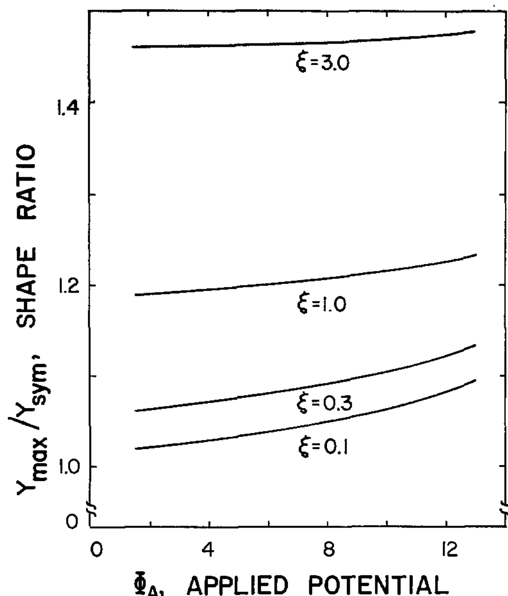

Fig. 8. Dependence of characteristic cathode shape ratio on linear polarization parameter and dimensionless applied voltage. ($\Lambda = 0.11$.)

with large values of ξ but become increasingly uniform as deposition continues. Figure 8 illustrates how the ratio Y_{max}/Y_{sym} varies with applied potential. It is seen that higher applied potentials yield more nonuniform deposits, owing to the nonlinear nature of the Butler-Volmer kinetic equation.

The ratio X_{out}/Y_{max} was compiled for all cases listed in Table III in order to characterize the outward growth of the deposit covering the adjacent insulating surface (see Fig. 5). For all cases examined in Table III, it was found that X_{out}/Y_{max} was always within 10% of unity. Therefore, within reasonable approximation, the edge of the deposit is cylindrical in shape.

Summary and Conclusions

The finite element method has been used to calculate the shape change of a cathode during electrodeposition. To our knowledge, finite element calculations have not previously been applied to electrochemical potential field calculations involving shape change. Calculation details have, therefore, been included in discussion of results. Problems involving electrode shape change appear to be particularly amenable to finite element methods of calculation since piecewise polynomials can be used with great accuracy to describe curved bounding surfaces.

Two difficulties arise in handling singularities. The first is the calculation of the potential field itself in the vicinity of a singularity. There is, however, growing attention to the development of special elements for use at singular points. It is, therefore, reasonable to anticipate rapid improvement in computational strategies for accurate treatment of such singularities. The second difficulty, encountered in the initial time step of shape change, is in approximating outward growth at the singularity. That is, the normal vector is undefined at a singular point. The choice used in this study (upward growth only) could perhaps be improved on.

The streamlining of any numerical procedure involves optimizing tradeoffs between accuracy and cost. It is likely that improved accuracy could be obtained in the procedures used here, especially in the integration schemes for evaluating area and surface integrals needed for solution of the system of equations resulting from the finite element formulation. These improvements will not be made without loss of computational speed. In many cases, however, the benefit of calculating an accurate current distribution does not depend so much on the cost effectiveness of the calculation itself but of the entire research endeavor.

Although the present study has purposefully been limited to a relatively simple secondary potential distribution, the general method of finite element calculations is exceedingly powerful and flexible. There would be no fundamental difficulty in embracing additional phenomena within this method of analysis. Multiple reactions could be incorporated to clarify effects of gassing, alloy deposition, and corrosion, among others. More complex kinetic rate equations could be introduced, including active/passive phenomena characteristic of many corrosion systems. Effects of diffusion and laminar convection have previously been studied by finite element methods in the chemical engineering literature and could be incorporated into electrochemical treatments. Heat transfer effects could be superimposed onto current distribution problems. The analysis of axisymmetric two-dimensional problems can be done with only minor modification of the integrals used in this study. The analysis of fully three-dimensional problems has been carried out for non-electrochemical situations. For these reasons, it seems worthwhile to pursue the application of finite element methods further in order that their inherent advantages be brought to bear on the analysis of complex electrochemical systems.

Acknowledgments

Financial support by the National Science Foundation is gratefully acknowledged. Mr. Bergh held an NSF Fellowship during a portion of the investigation, while other research costs were met with NSF Grant ENG-76-83379.

Manuscript submitted April 20, 1978; revised manuscript received July 25, 1978.

Any discussion of this paper will appear in a Discussion Section to be published in the June 1979 JOURNAL. All discussions for the June 1979 Discussion Section should be submitted by Feb. 1, 1979.

Publication costs of this article were assisted by the University of Illinois.

LIST OF SYMBOLS

English characters

A	dimensionless area
$\underline{A}$	dimensionless cathode length
$\underline{\underline{A}}$	matrix resulting from finite element formulation
a	anode length, m
a_{ij}	component of $\underline{\underline{A}}$ corresponding to i^{th} row and j^{th} column
B	dimensionless vertical separation between anode and cathode
b	vertical separation between anode and cathode, m
$\mathbf{F}$	Faraday's constant, 96,500 C/g equiv.
$\underline{f}$	nonlinear vector resulting from finite element formulation
f_i	i^{th} component of $\underline{f}$
H	dimensionless growth outward from cathode in normal direction
h	growth outward from cathode in normal direction, m
i	current density, A/m^2
i_o	exchange current density, A/m^2
l	cathode length, m
M_w	total number of set and free nodes in system
M	molecular weight, g/mole
N	number of free nodes in system
n	number of electrons involved in cathodic reaction, g equiv./gmole
$\underline{n}$	unit normal at system boundary
$\bar{R}$	gas constant, 8.314 J/gmole-deg
T	temperature, °K
t	time, sec
X	dimensionless spatial coordinate
X_{out}	dimensionless growth in horizontal direction from cathode edge

x spatial coordinate, m
Y dimensionless spatial coordinate
Y_{max} maximum height of cathode, dimensionless
Y_{sym} height of cathode at center symmetry line, dimensionless
y spatial coordinate, m

Greek characters
α_A anodic kinetic parameter
α_C cathodic kinetic parameter
Γ_i basis function centered over node i
$\Gamma^{(k)}$ portion of Γ_i lying in element k
Δ difference between Butler-Volmer and Ohm's law calculations
δ Tafel polarization parameter
κ conductivity of electrolyte, $\Omega^{-1}m^{-1}$
Λ dimensionless number of coulombs passed
ξ linear polarization parameter
ρ density of deposit, g/m^3
T dimensionless time
Φ dimensionless potential
Φ_A dimensionless applied potential
Φ_i dimensionless potential at node i
ϕ potential, V
ϕ_A applied potential, V
Ω region of applicability of the differential equation
$\partial\Omega$ boundary of Ω
$\partial\Omega_A$ portion of $\partial\Omega$ coinciding with anode
$\partial\Omega_C$ portion of $\partial\Omega$ coinciding with cathode
$\partial\Omega_i$ portion of $\partial\Omega$ coinciding with insulated surfaces and symmetry lines

REFERENCES

1. O. Kardos, *Plating (East Orange, N.J.)*, **61**, 129, 229, 316 (1974).
2. J. Riggs, Ph.D. Thesis, University of California, Berkeley (1977).
3. J. J. Oden, "Finite Elements of Nonlinear Continua," McGraw-Hill Book Co., New York (1972).
4. L. C. Wellford and R. M. Ayer, *Int. J. Num. Methods in Engr.*, **11**, 933 (1977).
5. P. W. France, *Computers and Fluids*, **3**, 149 (1975).
6. F. M. Orr and L. E. Scriven, *J. Fluid Mech.*, **84**, 145 (1978).
7. O. Zienkiewicz, *Appl. Mech. Rev.*, **23**, 249 (1970).
8. D. Norrie and G. de Vries, "Proceedings of 1973 Tokyo Seminar on Finite Element Analysis," pp. 532-539, University of Tokyo Press, Tokyo (1973).
9. O. Zienkiewicz, "The Finite Element Method in Engineering Science," 2nd ed., McGraw-Hill Book Co., New York (1971).
10. G. Strang and G. Fix, "An Analysis of the Finite Element Method," Prentice-Hall, Englewood Cliffs, N.J. (1973).
11. B. Finlayson, "The Method of Weighted Residuals and Variational Principles, With Applications in Fluid Mechanics and Heat Transfer," Academic Press, New York (1972).
12. B. A. Finlayson and L. E. Scriven, *Appl. Mech. Rev.*, **19**, 735 (1966).
13. T. A. Bergh, M.S. Thesis, University of Illinois at Urbana-Champaign (1978).

DISCUSSION SECTION

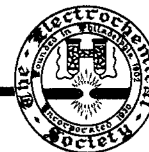

This Discussion Section includes discussion of papers appearing in the *Journal of The Electrochemical Society*, Vol. 124, No. 7 and 9, July and September, 1977, and Vol. 125, No. 2, February 1978.

Evaluation of Corrosion Rates from Nonlinear Polarization Data

R. L. LeRoy (pp. 1006-1012, Vol. 124, No. 7)

G. Palombarini,[1] **G. P. Cammarota,**[1] and **L. Felloni:**[2] This interesting paper by LeRoy has suggested to us a few considerations. First of all, the simultaneous determination of the corrosion current i_{corr} and the Tafel slopes β_a and β_c from polarization data requires the knowledge of at least three experimental pairs (ϵ, i), so as to attempt the resolution of three equations in the three unknowns. It is clear, however, that the reliability of the estimates increases together with the number of experimental pairs utilized. From this point of view, the method suggested by LeRoy for evaluating corrosion rates from polarization measurements in the vicinity of the corrosion potential constitutes a variation of the three-point method proposed by Barnartt[3] several years ago. Both methods, in fact, require the solution of a quadratic equation the coefficients of which are obtainable from the three measured pairs (ϵ, i), while the roots allow computation of the β values and then of the corrosion current. In practice, however, both the quoted authors have averaged the results of several calculations to minimize the risks of utilizing only three experimental points. Owing to their similarity, these methods are subject to the same limitations, especially with reference to the striking influence on the results that is exerted from the accuracy of each experimental value introduced in the resolutive equations. This disadvantage is serious just when the corroding samples are polarized to potentials ϵ near the corrosion potential. A higher uncertainty exists on low values of potentials and currents because of the complexity of the systems under examination and the inherent limits of the up-to-now available techniques.

Table I. Analysis of data recorded in the Table II of the paper under discussion by means of the three-point method

Selected ϵ (mV)	From experimental data β_a (mV)	β_c (mV)	i_{corr} (μA/cm^2)	From calculated data β_a (mV)	β_c (mV)	i_{corr} (μA/cm^2)
+5	No real solution			29.5	∞[4]	48.6
−5	No real solution			29.7	∞	49.4
+10	20.4	69.1	21.2	30.0	∞	50.5
−10	24.7	167.0	33.5	30.2	∞	51.3

[4] Very high but finite values of β_c have been assumed equal to infinity.

To confirm this, we have applied the three-point method at first to experimental and then to calculated data recorded in the Table II of the paper under discussion, obtaining our Table I. The above-reported calculations clearly show the extent to which the values of the polarization parameters are sensitive to the precision of experimental measurements. Few pairs (ϵ, i) in the vicinity of the corrosion potential seem, therefore, to be unable to determine these parameters correctly. In his note on the Tafel slopes for iron corroding in acidic solutions, Barnartt[5] has overcome the difficulty by operating at relatively high potentials ($|\epsilon| \geqq 20$ mV) with the aid of a galvanostatic pulse technique. Under these conditions,

[1] Institute of Metallurgy, University of Bologna, Italy.
[2] Institute of Chemistry, Center of Corrosion A.DACCO', University of Ferrara, Italy.
[3] S. Barnartt, *Electrochim. Acta.*, **15**, 1313 (1970).

[5] S. Barnartt, *Corrosion*, **27**, 467 (1971).

lower relative errors may be expected. In the paper under discussion and with reference to the analysis of the data for the corrosion of zinc in 3% sodium sulfate solutions, instead, the difficulty has been avoided by utilizing anticipated but reasonable values of the Tafel slopes and then calculating i_{corr} with the contribution of all the available experimental points. From this procedure, the degree of fitting of all the experimental data recorded in the Table II of the paper under discussion amounts to

$$f = (1/n) \cdot \sum_{j=1}^{n} (i_j - i_{calc})^2 = 16.6 (\mu A/cm^2)^2$$

On the other hand, from a computer analysis of the same data we have obtained the values of $\beta_a = 22.4$ mV, $\beta_c = 105.5$ mV, and $i_{corr} = 26.4\ \mu A/cm^2$, which do not contradict the preceding three-point estimates and lead moreover to a much better quality of fitting, being this time $f = 2.5\ (\mu A/cm^2)^2$.

In conclusion, LeRoy has analyzed some polarization points of zinc in sodium sulfate solutions with the aid of independent estimates of the Tafel slopes. The same experimental data, however, would lead to quite different results when referred to a system lacking in preassignable parameters. Incidentally, we have also linearized LeRoy's experimental points ranging from −10 to +10 mV, finding an approximate value of the polarization conductance $(\partial i/\partial \epsilon)_{\epsilon=0} = 3.75\ \mu A/cm^2 \cdot mV$. Hence, by anticipating $\beta_a = 30$ mV and β_c = infinity and being therefore $B = \beta_a\beta_c/\ln 10 \cdot (\beta_a + \beta_c) = 30/\ln 10$ mV, one can calculate a value of $i_{corr} = B \cdot (\partial i/\partial \epsilon)_{\epsilon=0} = 48.8\ \mu A/cm^2$ about 3% lower than the value determined by LeRoy through Eq. [3] of his paper.

Further comments are necessary concerning the capability of several curves, corresponding to very different values of β_a, β_c, and i_{corr}, of reproducing the same points with comparable accuracy (see Fig. 8 and 9 in the paper under discussion). Clearly, a graphic comparison between experimental points and calculated curves is unreliable, as the appearance greatly depends on the scales adopted for ϵ and i. The simplest solution would seem to consist of evaluating the fitting quality, for example, through the already defined quantity f. In reality, by analyzing several curves of pure iron polarized in 1*N* H_2SO_4 and in 1*N* HCl in the vicinity of the corrosion potential, we have found[6] that not only the whole anodic and cathodic branches, but also each part of a polarization curve (*e.g.*, the part going from 0 to 5 mV, or from 5 to 10 mV, and so on) leads to very different values of β_a, β_c, and i_{corr} as well as LeRoy's data on zinc corrosion seem to do when analyzed with the three-point method.

Whether an insufficient precision of experimental measurements, the treating of β values as Tafel slopes linkable with certain reaction mechanisms rather than values simply compatible with the examined part of the polarization curve, or any other factor accounts for this behavior, it remains that the compliance between a measured polarization curve and its theoretical equation is very critical, and the problem of simultaneously determining the electrochemical parameters and the corrosion rate appears to be still unresolved.

The Pb/Pb^{+2} Exchange Reaction in Perchlorate Acidic Solution

A. S. Gioda, M. C. Giordano, and V. A. Macagno
(pp. 1324-1329, Vol. 124, No. 9)

S. B. Estevez[7] and D. J. Schiffrin:[8] Usually, great care has to be taken in the study of the anodic dissolution of a metal having a large exchange current, in particular, regarding the experimental conditions under which the true activated anodic current is measured, and in order to establish a dissolution mechanism, the surface concentration of the metal ion must be known. It appears that this precaution was not taken into account in the paper under discussion.

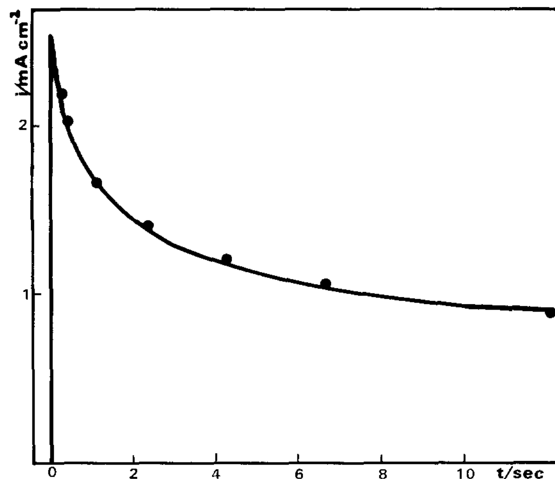

Fig. 1. —— Current-time transient for the anodic dissolution of Pb in 0.2M $NaClO_4$; pH = 2.5; T = 25°C; potential = −0.460V vs. NCE. ● Values fitted using Eq. [5].

For the Pb system, the anodic current for unstirred solutions are time dependent,[9] as would be expected for reactions with a large i_0 and in a potential range close to the standard potential of the metal/metal ion couple. Figure 1 shows a typical current-time transient[9,10] where the influence of the buildup of the Pb^{++} ion concentration during electrolysis is clearly seen. This type of transient behavior occurs in all the potential range which has been studied in the paper. The diffusional problem for the reaction

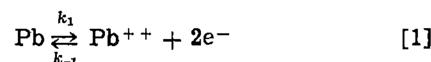

$$Pb \underset{k_{-1}}{\overset{k_1}{\rightleftarrows}} Pb^{++} + 2e^- \quad [1]$$

can easily be solved using Ficks' diffusion differential equation with the conditions

$$C(x, 0) = C^b(Pb^{++}) \quad [2]$$

$$\left(\frac{\partial C}{\partial x}\right)_{x=0,t=0} = 0 \quad [3]$$

and

$$\frac{i}{2\mathbf{F}} = \{k_1 - C^{6}(Pb^{++})k_{-1}\} \quad [4]$$

where i is the current density, $C^b(Pb^{++})$ and $C^\sigma(Pb^{++})$ are the bulk and surface concentration of Pb^{++} ions, respectively, **F** is the Faraday constant, k_1 and k_{-1} are the corresponding electrochemical rate constants. This leads to

$$i = 2\mathbf{F}\{k_1 - C^b(Pb^{++})k_{-1}\}\exp\left\{\frac{k_{-1}^2}{D_{Pb^{++}}}t \right.$$

$$\left. \text{erfc}\ \frac{k_{-1}}{D_{Pb^{++}}{}^{1/2}}t^{1/2}\right\} \quad [5]$$

A typical current-time transient is shown in Fig. 1 and good agreement is observed over a wide range of time of electrolysis between the observed current and the values predicted from Eq. [5], indicating the correctness of the treatment outlined above. Equation [5] predicts the usual $t^{1/2}$ and $t^{-1/2}$ current dependence

[6] G. Palombarini, G. P. Cammarota, and L. Felloni, to be published.

[7] S. B. Estevez, Sector Electroquimica Aplicada, I.N.T.I., Leandro N.Alem 1067, 1001 Buenos Aires, Argentina.

[8] D. J. Schiffrin, Berutti 1547, Dto 2, Martinez, Provincia de Buenos Aires, Argentina.

[9] C. V. Alkaine, S. B. Estevez, and D. J. Schiffrin, "The Electrochemistry of Lead: Anodic Dissolution in Acidic Media," 6th Metallurgical Meeting, Argentine Metals Society, Buenos Aires, October 1974.

[10] S. B. Estevez and D. J. Schiffrin, Paper in preparation.

at short and long times of electrolysis, respectively, and the Pb system in ClO_4^- solutions follows these relationships.[9,10] The anodic current due solely to the metal dissolution process (*i.e.*, $2Fk_1$ when $C^b(Pb^{++}) = 0$) can be obtained by extrapolation to $t \to 0$ from an i *vs.* $t^{1/2}$ plot.[9] The correct values obtained in this way differ widely from the steady-state measurements. When the measurements are performed in the way described in this paper, where natural convection conditions are established, the physical meaning of the observed currents can be obtained using the diffusion layer concept. This leads to

$$i \simeq \frac{2FD_{Pb^{++}}}{\delta} \left\{ \frac{k_1}{k_{-1}} - C^b(Pb^{++}) \right\} \quad [6]$$

where δ is the diffusion layer thickness. The equivalent equation derived from Eq. [5] for long times of electrolysis is

$$i = \frac{2FD_{Pb^{++}}^{1/2}}{\pi^{1/2}t^{1/2}} \left\{ \frac{k_1}{k_{-1}} - C^b(Pb^{++}) \right\} \quad [7]$$

Both Eq. [6] and [7] lead to a similar current-potential relationship which does not give direct information on the anodic process. When $k_1/k_{-1} >> C^b(Pb^{++})$, a situation which occurs in the potential range where an apparent good Tafel behavior was observed; the "Tafel" slope measured in the steady state is simply an indication of the reversible behavior of this system. Hence, no kinetic information on the anodic behavior can be obtained from steady-state experiments, as is wrongly assumed in the paper under discussion.

The term k_1/k_{-1} represents in this case the surface concentration of Pb^{++} ions, as defined by the Nernst equation. This is the reason why in Fig. 2 of the paper under discussion, the 30 mV slope (really a Nerstian slope for a 2 electron process) is observed for more anodic potentials as the bulk Pb^{++} ion concentration in solution is increased.

It is also our opinion that due to the incorrect way in which the anodic experiment has been performed, an incorrect order with respect to the ClO_4^- ion has been found. There is a finite order with respect to ClO_4^{-3}, as is discussed elsewhere.[10]

For the above reasons, the results presented in Table I of the paper and the mechanism proposed have to be considered dubious.

A. S. Gioda, M. C. Giordano, and V. A. Macagno:[11] As the authors have already answered practically the same arguments presented by Dr. Schiffrin in a rebuttal to S. D. Kapusta, they refer the reader to that discussion.[12]

Efficiencies of Cycling Lithium on a Lithium Substrate in Propylene Carbonate

R. D. Rauh, T. F. Reise, and S. B. Brummer
(pp. 186-189, Vol. 125, No. 2)

M. Garreau, J. Thévenin, and D. Warin:[13] We entirely agree with Brummer and co-workers when they consider that the determination of lithium cycling efficiency must be investigated, using not a foreign but a dense lithium substrate despite the inherent difficulties of this technique according to the determinant influence of the substrate on the properties of the electrodeposited lithium.[14] However, when faced with the same difficulties as those encountered by the authors, we have studied the cycling behavior of the lithium electrode in a different way. The results we have obtained lead us to interpretations somewhat different from those given in the paper under consideration. It appears of interest (*i*) To compare those two methods used to study the deterioration of the electrode properties; and (*ii*) to give some precise data on the main causes of the cycling inefficiencies described in the case of the propylene carbonate (PC) solutions.

(*i*) In the aprotic solvent-based electrolyte used with lithium where the ohmic drop RI generally composes the major part of the electrode potential V, we have considered it was convenient to measure the free ohmic drop potential $\eta = V - RI$ (overpotential) to be able to describe with accuracy the polarization state of the lithium electrode. Unlike Rauh *et al.*, we have thus studied the evolution in the time, not of the potential V but of the overpotential η during cycling operations carried out galvanostatically, in the experimental conditions: Solution, PC, 1M $LiClO_4$; $t = 25°C$; residual water content, 10 ppm; substrate, dense lithium; motionless electrode, $s = 0.2$ cm²; cell, cylindrical symmetry around the working electrode; cycling, current density $J = 1$-2.5-5-10 mA/cm² and charge density $Q = 1$-2-5-10 C/cm².

In conditions similar to those used by the authors in the paper under consideration, the stripping curves $\eta = \eta(t)$ do not show distinct components to which the removal of the deposit and of the substrate would be respectively ascribed. When the cycles are operated under conditions involving only weak overpotentials ($J \leq 2.5$ mA/cm² and $Q \leq 2$ C/cm²), an increase of the stripping overpotential up to a stationary value is only observed, with a weaker slope at each cycle. When other conditions are used ($J \geq 5$ mA/cm², $Q \geq 5$ C/cm²), the high involved overpotentials increase regularly up to an end value which rises slowly all along the cycling. In these cases, it is possible to observe on the curve $V = V(t)$ the two components of the electrode potential described (Fig. 3, p. 188) by Rauh *et al.*, the presence of these two components being due to a discontinued evolution of the interface resistance R. For example, Fig. 1 shows the typical evolution of the ohmic drop RI during the 5th stripping obtained with $J = 10$ mA/cm² and $Q = 10$ C/cm².

These results raise the following question: Is it really adequate to attribute the two components of the electrode potential V to two distinct intrinsic polarization levels required for the removal of the accessible portions of deposit and the complementary portion of substrate, accordingly: (*i*) To the ohmic origin of the separation of these two components; (*ii*) to the regular evolution of the end stripping overpotential during the cycling operation?

(*ii*) To find an indisputable test to detect the end of the deposit stripping, we have preferred to charac-

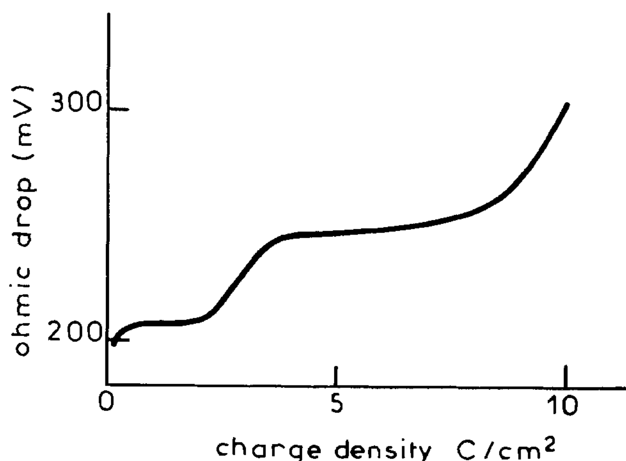

Fig. 1. Ohmic drop (*RI*)-charge density curve for stripping Li on an Li-dense substrate: 5th cycle; $i_s = 10$ mA/cm²; $Q_s = 10$ C/cm²; electrolyte = 1M $LiClO_4$ in PC.

[11] Facultad de Ciencias Quimicas, Universidad Nacional de Cordoba, 5000 Cordoba, Argentina.
[12] A. S. Gioda, M. C. Giordano, and V. A. Macagno, *This Journal*, 125, 889 (1978).
[13] Groupe de Recherche du CNRS "Physique des Liquides et Electrochimie," associe a l'Universite Pierre et Marie Curie, 75230 Paris Cedex 05, France.
[14] M. Garreau, J. Thevenin, and D. Warin, *C.R. Acad. Sci. Paris*, 286C, 545 (1978).

terize the gradual degradation of the lithium electrode by the correlative decrease of the current density during cycling operations carried out with anodic and cathodic overpotentials maintained at a constant value.[14,15] This allowed us to point out the determinant importance of some experimental conditions which had not been considered in the paper under discussion. Thus we have observed that it is possible to obtain a great number of cycles without noticeable loss of the electrode activity when the experimental conditions are compatible with: (*i*) the formation of a homogeneous deposit without formation of large dendrites; and (*ii*) a regular dissolution of the metal without production of anodic passivating layers.[16] The main parameter responsible for these two causes of degradation of the electrode appears to be the overpotential which, during the whole cycle, must not exceed a critical value (about 50 mV with our PC, $LiClO_4$ solution). For example, we have obtained 500 consecutive cycles within the range of overpotential ± 25 mV under conditions defined by $J = 1$ mA/cm^2 and $Q = 1$ C/cm^2. The rapid deterioration of the electrode properties which intervenes with the experimental conditions indicated in the paper under consideration ($J = 2.5$ mA/cm^2; $Q = 10$ C/cm^2) is linked to an overstepping of the critical overpotential value of the solution used.

This interpretation raises other questions: (*i*) Would it not be possible to ascribe the best performances obtained with the AsF_6Li/PC solutions to a favorable shift of the overpotential critical value; (*ii*) can Rauh *et al.* link this eventual shift of the critical value to the different adsorbability of AsF_6^- compared to those of ClO_4^-, mentioned in the paper under consideration?

R. D. Rauh:[17] Clearly the processes contributing to the polarization of the secondary Li electrode are not well understood, although Garreau *et al.* are making some valuable contributions in this area. Our assumption that the break in the Li stripping curve represented the single cycle efficiency was based on the following observations: (*i*) The single cycle efficiencies obtained in this way agreed quite well with the average efficiencies calculated from the number of cycles required to deplete the Li initially present as the substrate; (*ii*) Two component stripping curves are not obtained under the same conditions on a Ni substrate; (*iii*) Two component stripping curves are not obtained on stripping Li foil under the same conditions. Both $LiAsF_6$ and (probably) low current densities impose a more compact, lower surface area morphology on the electrodeposit, which could explain the results of Garreau *et al.* and the absence of two plateaus in the initial cycles of our best PC/$LiAsF_6$ preparations (paper under discussion, Fig. 5). Low current densities also, of course, compress the *IR* scale.

Regarding the positive effects of $LiAsF_6$, they have been observed in tetrahydrofuran, propylene carbonate, and methyl acetate.[18] Recent work by Koch and Young,[19] also of our laboratory, indicate that the general success observed for this salt may result from AsF_3 impurities. We have shown previously that certain Li-reactive film-forming additives to these nonaqueous electrolytes actually improve the Li cycling efficiency.[20]

[15] I. Epelboin, M. Garreau, and J. Thevenin, Abstract 3, p. 16, The Electrochemical Society Extended Abstracts, Fall Meeting, Atlanta, Georgia, Oct. 9-14, 1977.
[16] M. Garreau and J. Thévenin, *J. Microsc. Spectrosc. Electron.*, 3, 27 (1978).
[17] EIC Corporation, Newton, Massachusetts 02158.
[18] S. B. Brummer, F. W. Dampier, V. R. Koch, and R. D. Rauh, in "Electrode Materials and Processes for Energy Conversion and Storage," J. D. E. McIntyre, S. Srinivasan, and F. G. Will, Editors, p. 975, The Electrochemical Society Softbound Symposium Series, Princeton, N.J. (1977).
[19] V. R. Koch and J. H. Young, Spring Meeting of The Electrochemical Society, Seattle, May 21-26, 1978.
[20] R. D. Rauh and S. B. Brummer, *Electrochim. Acta*, **22**, 75 (1977); *ibid.*, **22**, 85 (1977).

The idea put forth by Garreau *et al.* that high rate stripping can give rise to accumulation of reaction products on the Li electrode is an intriguing one. It would be extremely valuable for these authors to demonstrate the effects of controlled potential stripping on Li cycling efficiency and cycle life to supplement their results on the evolution of the overpotential.

The Theory of Light-Induced Evolution of Hydrogen at Semiconductor Electrodes

J. O'M Bockris and K. Uosaki (pp. 223-227, Vol. 125, No. 2)

L. Handley and J. F. McCann:[21] The authors have proposed a novel approach to the interpretation of semiconductor photoelectrochemistry.[22-27] It is, however, our view that their model is deficient in several respects and is not easily accommodated by the available experimental evidence.

At the outset, the authors consider that charge transfer by a quantum mechanical tunneling mechanism is rate limiting. They produce no evidence to support this contention and we would suggest that it is in fact inappropriate to make such an assertion since the high quantum efficiencies consistently measured for many semiconductors,[28-33] including p-GaP[34] do not support tunneling as the rate-determining step (rds) in the saturated photocurrent region of the photocurrent *vs.* voltage (i_p *vs.* V) curve. Also, Butler[35] has shown that the relationship $i_p{}^2 \alpha V$ and $(i_p h\nu)^{1/2} \alpha h\nu$ for WO_3 are consistent with a model where solid-state transport is the rds. An inspection of the authors' data shows that the relationship $i_p{}^2 \alpha V$ also holds for p-GaP and therefore supports a solid-state transport model. The authors of the paper have not considered these correlations and they are neither predicted nor explained by their model.

The solid-state treatment used in the proposed model would appear to be somewhat unconventional. Normally the continuity equation is solved for a given set of boundary conditions.[32,33,35-40] However, it is not clear how Eq. [7] used by these authors to describe solid-state transport was derived.[22-27] Moreover, the equation as written is mathematically imprecise since there is no integral sign in the exponent. (The value of the exponential $\exp\left(-\frac{1}{L(x)}dx\right)$ is 1 since

[21] School of Physical Sciences, The Flinders University of South Australia, Bedford Park, South Australia 5042.
[22] J. O'M. Bockris and K. Uosaki, *Heliotech. Dev.*, 1, 435 (1975).
[23] J. O'M. Bockris and K. Uosaki, in "Proceedings of the First World Hydrogen Energy Conference." Vol. II, 5B-1, T. N. Veziroglu, Editor, Miami (1976).
[24] J. O'M. Bockris and K. Uosaki, in "Semiconductor Liquid Junction Solar Cells," A. Heller, Editor, p. 315, The Electrochemical Society Softbound Symposium Series, Princeton, N.J. (1977).
[25] J. O'M. Bockris and K. Uosaki, *Int. J. Hyd. Energy*, 2, 123 (1977).
[26] J. O'M. Bockris and K. Uosaki, "ACS Adv. in Chemistry Series," J. B. Goodenough, Editor, No. 163, p. 33, American Chemical Society, Washington, D.C. (1977).
[27] J. O'M. Bockris and K. Uosaki, *This Journal*, 125, 223 (1978).
[28] H. Gerischer, *J. Electroanal. Chem. Interfacial Electrochem.*, 58, 263 (1975).
[29] T. Ohnishi, Y. Nakato, and H. Tsubomura, *Ber. Bunsenges. Physik. Chem.*, 79, 523 (1975).
[30] R. K. Quinn, R. D. Nasby, and R. J. Baughman, *Mater. Res. Bull.*, 11, 1011 (1976).
[31] J. G. Mavroides, D. I. Tchernev, J. A. Kafalas, and D. F. Kolesar, *ibid.*, 10, 1023 (1975).
[32] J. H. Kennedy and K. W. Frese, *This Journal*, 123, 1683 (1976).
[33] A. K. Ghosh and H. P. Maruska, *ibid.*, 124, 1516 (1977).
[34] K. Ohashi, J. McCann, and J. O'M. Bockris, *Energy Res.*, 1, 259 (1977).
[35] M. A. Butler, *J. Appl. Phys.*, 48, 1914 (1977).
[36] V. A. Myamlin and Yu. V. Pleskov, "Electrochemistry of Semiconductors," Nauka, Moscow (1965); Plenum Press, New York (1967).
[37] H. Gerischer, in "Advances in Electrochemistry and Electrochemical Engineering," Vol. 1, P. Delahay, Editor, p. 139, Wiley, New York (1961).
[38] D. Laser and A. J. Bard, *This Journal*, 123, 1828, 1833, 1837 (1976).
[39] K. H. Beckmann and R. Memming, *ibid.*, 116, 368 (1969).
[40] R. H. Wilson, General Electric Corporate Research and Development Rep. No. 77CRD167, Schenectady, New York (1977).

dx is normally defined as an infinitesimally small increment of x). Perhaps the authors meant to use x instead of dx in the exponential. But dx has been used repeatedly in their treatment.[22-27]

In evaluating the drift length l_E (Eq. [10]), the authors have used an electric field $V'(x)$ applicable under dark conditions only. The illuminated electric field equation is[36]

$$V'(x) = \pm \sqrt{\frac{8\pi kT}{\epsilon}[-(N_D - N_A)y + (p_o + \Delta p)(e^{-y} - 1) + (n_o + \Delta n)(e^{y} - 1)]} \quad [1]$$

where $y = e_o(V_x - V_b)/kT$, and the symbols are defined by Myamlin and Pleskov,[36] with Δp and Δn being the photogenerated hole and electron densities, respectively. No reasons were presented for not using this latter expression. If quantum mechanical tunneling is rate determining as they have assumed, then there will be an accumulation of photogenerated minority carriers in the space charge region. The calculations of Δp and Δn for space charge accumulation, which would be required, are complicated. The authors have not considered these problems.

The reasoning used by the authors to show that all electrons have been deactivated to the bottom of the conduction band before reaching the surface is not convincing. Even if an argument of the type presented by the authors were to be accepted, the frequency dependence of the absorption coefficient should be considered, *i.e.*, $\alpha \approx 10^4$ cm^{-1} for 4500Å light and $\alpha \approx 4.5 \times 10^5$ cm^{-1} for 3500Å light.[39,41] Taking the above factors into account electrons excited by 3500Å light would have a mean energy of 1.20 eV above the conduction band while those excited by 4500Å light would be deactivated to the bottom of the conduction band on reaching the semiconductor surface. Since the transmission coefficient is dependent upon electron energy[42] one concludes from the authors' model for electron deactivation and the conclusion that the critical potential is not frequency dependent that quantum mechanical tunneling is not the rate-determining step. On the other hand, the solid-state model,[32,35,36,38,40] predicts the frequency independence of the critical potential.

The validity of the method used to obtain the energy level of an electron in the ground state of the H_3O^+ ion is questionable. First, Fig. 2 is given without explanation. The experimental correlation is poor particularly for 1*N* H_2SO_4. Secondly, from footnote[43] Fig. 2 is an experimental check of the equation

$$\left(V_{fb} - \frac{E_g}{F}\right) = (V_{crit} - V_{fb}) + \text{constant}$$

If this were so then the absolute value of the slope should be 1 (*cf.* ~ 2 for 1*N* NaOH and ~1.5 for 1*N* H_2SO_4).

For p-GaP in 1*N* NaOH at 0V on the NHE scale the authors report in footnote 27 that about 50% of the electrons activated by light reach the surface. Since at 0V their experimental quantum efficiency for 3500Å light is 0.2, it follows that the transmission coefficient must be larger than 0.4. The WKB approximation is inaccurate in this region and will yield transmission coefficients at least 50% higher than the solution of the exact parabolic barrier.[42] Therefore an even greater discrepancy between the calculated and experimental results should be seen.

The critical photopotentials for the experimental i_p *vs.* V curves of p-GaP in Fig. 1 (1*N* H_2SO_4) and Fig. 4 (1*N* NaOH) are the same, which is inconsistent with the -0.059 mV/pH change in the flatband potential for p-GaP.[44] This is also inconsistent with the authors' flatband potential data reported in Fig. 2.

In discussing the discrepancies between the experimental and theoretical results, the present authors have stated that it may be possible for electrons to be transferred to hydronium ions directly attached to the electrode surface, therefore yielding higher quantum efficiencies. If this were the case, the barrier thickness would be reduced from 2.1Å to a much smaller value and not only would higher quantum efficiencies be calculated, but the assumption that charge transfer is the rate-determining step would be in doubt.

The Theory of Light-Induced Evolution of Hydrogen at Semiconductor Electrodes

J. O'M. Bockris and K. Uosaki (pp. 223-227, Vol. 125, No. 2)

Wm. E. Pinson:[45] I wish to discuss Fig. 4 of the above-mentioned paper.

The caption of Fig. 4 says the electrolyte is 1*N* NaOH.

The threshold of the experimental quantum efficiency is shown = +0.25V *vs.* NHE. In Fig. 1 of the same paper in 1*N* H_2SO_4 the threshold of the experimental quantum efficiency is also shown = +0.25V *vs.* NHE.

It would appear that the Fig. 4 caption is in error, based on the information supplied in another article by Bockris and Uosaki.[46] Figure 4 in this latter paper shows the p-GaP threshold quantum efficiency in 1*N* NaOH beginning at = −0.46V *vs.* NHE; in 1*N* H_2SO_4 at +0.14V *vs.* NHE, close to the +0.25V *vs.* NHE threshold of the paper under discussion.

The same error appears in the volume "Semiconductor Liquid-Junction Solar Cells."[47]

Significance of Effect of High Pressure on Kinetics of Electrode Reactions

I. Applications to Transition State in Hydrogen Evolution Reaction Mechanisms

B. E. Conway and J. C. Currie (pp. 252-257, Vol. 125, No. 2)

C. M. Marschoff:[48] In this article the authors show that observed negative and small positive values of the volume of activation for the hydrogen evolution reaction (her) may be explained on the basis of kinetic (reaction route and rate-determining steps) and electrocatalytic (electrode coverage by atomic hydrogen) considerations. It is also suggested that the particular behavior of the her with respect to $\Delta V^{\neq}$ values could be accounted for if the transition state for classical proton transfer arises by reorganization of the $H_9O_4^+$ ion,[49] resulting in the localization of the proton on one of the H_2O groups in the ion.

However, this view allows only a secondary role to specific properties of the electrode material, making it difficult to explain the above-mentioned kinetic and electrocatalytic effects. The lack of consideration of the specific properties of the metal has also been

[41] "Semiconductors and Semimetals," Vol. 3, R. K. Willardson and A. C. Beer, Editors, p. 510, Academic Press, New York (1967).
[42] "Quantum Mechanics," D. Rapp, Holt, Rinehard & Winston, Inc., New York (1971).
[43] J. O'M. Bockris and K. Uosaki, *This Journal*, 124, 1348 (1977).
[44] W. P. Gomes and F. Cardon, in "Semiconductor Liquid Junction Solar Cells," A. Heller, Editor, p. 120, The Electrochemical Society Softbound Symposium Series, Princeton, N.J. (1977).
[45] Ottawa, Ontario, Canada K2G 2W3.
[46] J. O'M. Bockris and K. Uosaki, *This Journal*, 124, 1348 (1977).
[47] J. O'M. Bockris and K. Uosaki, "Semiconductor Liquid-Junction Solar Cells," A. Heller, Editor, p. 330, The Electrochemical Society Softbound Symposium Series, Princeton, N.J. (1977).
[48] Escuela de Ingenieria Metalurgica y Ciencia de los Materiales, Universidad Central de Venezuela, Caracas 105, Venezuela.
[49] L. I. Krishtalik, *Electrokhimiya*, 11, 184 (1975).

pointed out[50,51] as a drawback of solvent-reorganization theories with respect to activation energy calculations for the her.

On these grounds, an alternative explanation to the abnormally low values of $\Delta V^{\ddagger}$ may be advanced in terms of an adiabatic proton transfer occurring with simultaneous charge delocalization.[50] According to this model, the charge on the transferring proton builds up from its initial value to a final $-e_0$ during the activation process. Hence, further electrostriction could occur on the H_2O (or H_8O_4) group, thus accounting for the observed $\Delta V^{\ddagger}$.

[50] C. M. Marschoff and P. J. Aragon, *This Journal*, 123, 213 (1976).

[51] C. M. Marschoff, Submitted to *Anal. Asoc. Quim. Arg.*

SOLID-STATE SCIENCE
AND TECHNOLOGY

DECEMBER
1978

Mixed Conductivity in $LiFe_5O_8$

G. J. Dudley* and B. C. H. Steele*

Department of Metallurgy and Materials Science, Imperial College of Science and Technology, London, SW7 2AZ England

ABSTRACT

The lithium ion and electronic conductivities of lithium ferrite spinel, $LiFe_5O_8$, have been investigated by four-point d-c techniques. The ionic conductivity is relatively low, less than 10^{-5} Ω^{-1} cm^{-1} at 300°C. Transients observed in two-point d-c electronic conductivity measurements carried out in oxygen appear to be due to a surface oxidation process rather than to the ionic component of the total conductivity.

In the Rb_2O-Fe_2O_3, K_2O-Fe_2O_3, and Na_2O-K_2O-Fe_2O systems, analogues of the β-alumina structure can be prepared directly and have been shown to be good ionic as well as electronic conductors [*e.g.*, (1, 2)]. On the other hand, direct synthesis of the lithium analogue has not been reported, and under similar conditions an inverse spinel, $Fe_2^{3+}[Li^+Fe_3^{3+}]O_8$ results instead. In a recent paper (3) it was reported that despite its essentially close-packed structure, there were indications that a significant ionic conductivity was present in this compound at temperatures around 300°C. This led to a brief investigation by the present authors because the possibility of obtaining moderate values of ionic conductivity in this large class of compounds would be of considerable interest both theoretically and technologically.

Experimental

Two samples of lithium ferrite were used. Sample A was prepared by heating together the stoichiometric proportions of iron-III oxide (99.999%) and lithium carbonate ("Analar" grade) to 1000°C for 10 hr in a closed alumina crucible. The resulting powder was ground thoroughly, pressed into pellets, wrapped in platinum foil, and hot pressed in alumina powder in an alumina die in an oxygen atmosphere for 4 hr at 1170°C and a pressure of 500 kg cm^{-2}. The resulting density of the ceramic was 99.3% theoretical and powder x-ray photographs showed it to be predominantly in the β-form in which lithium and iron atoms are statistically distributed over the octahedral sites in the close-packed oxygen sublattice (4). Lines due to the ordered α-form were just visible. Sample B was flux-grown single crystal material, in the α-form (4).

Electronic conductivity measurements were carried out by two four-point d-c methods. The first employed samples 5 mm square by 0.5 mm thick, contacted on four sides by sprung tungsten wires, and used the analysis due to Van der Pauw (5). The second used a bar sample (6 × 1.5 × 1.5 mm) with platinum wire voltage probes at distances of one third and two thirds along its length and platinum foil current contacts at the ends which had previously been coated with evaporated gold.

Electronic Conductivity Results

Conductivity results are shown in Fig. 1. The conductivity of sample A as prepared and measured in an argon atmosphere (c, closed circle) was close to the value obtained for similar high density hot-pressed material by West and Blankenship (6) (c, open circle), and somewhat higher than that observed by Matsui and Wagner in argon (dashed line, d). In order to oxidize Fe^{++} to Fe^{+++} and produce the low electronic conductivity form reported by previous authors (3, 6-8), in which transients due to ionic conductivity would be most readily observable, sample A was annealed in oxygen at 850°C for 15 hr, 700°C for 15 hr, and slowly cooled to room temperature. X-ray powder photographs showed the sample to have converted to the α-modification. Van der Pauw conductivity measurements gave curve a (solid circles), still higher than curve d, and much greater than that observed by Matsui and Wagner in an oxygen atmosphere (e) and by Blankenship (h). After the oxygen anneal our measurements were carried out in an argon atmosphere. To examine whether the sample had been rapidly reduced in argon, oxygen was let into the apparatus while the temperature was held at 300°C. No appreciable change in conductivity took place. This sample, together with an A-type bar sample, was reannealed in oxygen, this time at 1000°C for 10 hr, 700°C for 24 hr, followed by a slow cool. Ferrite powder was placed around the samples to reduce the risk of lithium loss. The conductivity of the Van der Pauw specimen, measured at 250°C, had decreased only slightly (denoted by square in Fig. 1). Four-point conductivity measurements on the bar sample carried out as a function of temperature in oxygen coincided with curve a (open circles). However, if the voltage between the current contacts was used to calculate the conductivity, as in a two-point measurement, a much lower value was obtained, for example, g at 300°C and g′ at 492°C. At this latter temperature it was decided to monitor the potential differences between the current contacts V_{cc} and between the voltage probes V_{vp} as a function of time at constant temperature and current. Results are shown in Fig. 2. While V_{vp} remained almost constant, V_{cc} doubled in 50 hr. We thus conclude that the changes were caused by gradual buildup of a surface insulating layer (most of which had already formed during the anneal). This had no effect on V_{vp} since these probes were passing currents of less than 1 pA. This change in the "two-point" conductivity is shown by the line g′-f and is close to curve e for reported two-point measurements in oxygen (3).

Four-point bar conductivity data (crosses) for the single crystal material (B) is shown in Fig. 1, curve b. This sample was not annealed beforehand and was

* Electrochemical Society Active Member.

Key words: conduction, diffusion, inorganic, oxidation.

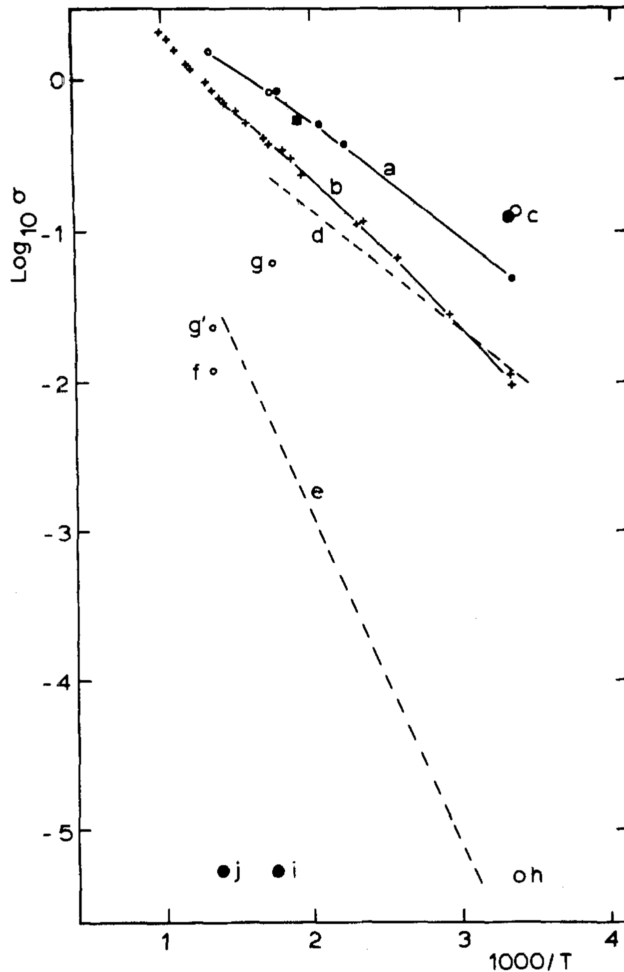

Fig. 1. Conductivity of lithium ferrite. a, This work, sample A, four-point electronic; closed circles, Van der Pauw sample, Ar atmosphere; open circles, bar sample, O_2 atmosphere. b, This work sample B, four-point electronic; bar sample, oxygen atmosphere. c, As hot pressed: closed circle, this work, Van der Pauw sample, Ar atmosphere; open circle, West *et al.* (6). d, Matsui and Wagner, two-point, argon atmosphere (3). e, Matsui and Wagner, two-point, oxygen atmosphere (3). g, This work, sample A, two-point measurement in oxygen at 300°C. g', This work, sample A, two-point measurement in oxygen at 492°C. f, This work, sample A, two-point measurement after 50 hr anneal in oxygen at 492°C. h, After oxygen anneal, two-point, West *et al.* (6). i, This work, sample A, four-point ionic conductivity, oxygen atmosphere. j, This work, sample B, four-point ionic conductivity, oxygen atmosphere.

heated during the measurements to 730°C, left at this temperature for 3 days, then cooled. Nevertheless results on cooling were in good agreement with those for heating, showing that no bulk oxidation had occurred. Again, however, the current contacts required ever-increasing voltages to maintain constant current.

Direct Ionic Conductivity Measurements

The high four-point electronic conductivities observed in this work make it difficult to detect transient effects due to ionic conductivity since the ionic transport number is likely to be much less than 0.01. We therefore resorted to direct four-point partial ionic conductivity measurements of the type previously reported for potassium ferrite (2). The principle of the method is illustrated diagramatically in Fig. 3. It is the ionic analogue of a four-point electronic conductivity measurement. An ionic flux is passed down the bar specimen by means of a suitable source and "sink" of the mobile ions contacting the ends of the bar via thin pieces of electrolyte to prevent electronic conduction. The source and sink can often be (as in the present case) pieces of the same mixed conductor as the specimen. The voltage probes are made up of pointed pieces of electrolyte in contact with a suitable material, providing a reference activity of the metal corresponding to the mobile cations. Since only voltage differences between these probes are required and an insignificant current is passed through them, the reference material can also be pieces of the mixed conductor under study, which is often experimentally much more convenient than using the parent metal. As in the electronic case, the technique avoids difficulties due to uncertain voltage drops at the current contacts, a particularly severe problem in the case of solid electrolyte-solid electrode interfaces simply pressed together. It also enables measurements to be made of the chemical diffusion coefficient $\tilde{D}$ associated with mobile ions and electrons, from the bar length L and the characteristic time τ of the slow transient behavior of the voltage between the ionic voltage probes when a constant current is switched on or off. $\tilde{D}$ is given by $\tilde{D} = L^2/\pi^2\tau$ (9) so that short bars are desirable to minimize the duration of the experiment. The theory and technique are described in detail in Ref. (2).

The lithium electrolyte used in this work was a 40% lithium phosphate-60% lithium silicate solid solution (10). The lithium source and sink were further pieces of lithium ferrite and the lithium reference electrodes were pointed pieces of the electrolyte contacted by more pieces of the lithium ferrite. In order that the apparatus could be used in an oxidizing atmosphere

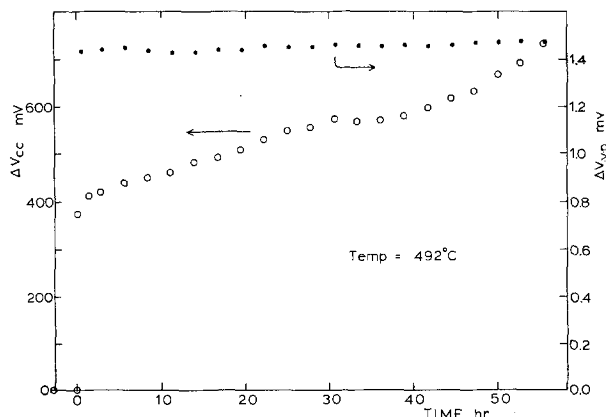

Fig. 2. Variations with time of current contact voltage difference (ΔV_{cc}) and voltage probe voltage difference (ΔV_{vp}) for bar sample at 492°C.

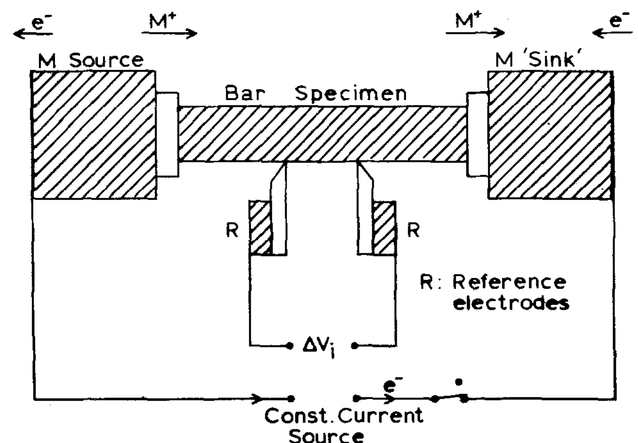

Fig. 3. Schematic of four-point ionic conductivity experiment. Shaded regions are mixed ionic-electronic conductor materials. Unshaded material is only ionically conducting (electrolyte).

the tungsten electronic voltage probes were replaced by platinum-10% rhodium. The tungsten springs and stainless steel jig were found to be satisfactory in oxygen up to at least 450°C.

The A-type sample used had not been annealed and was thus in the β-form. Interfaces between the current contacts and electrolyte were wetted with a trace of molten lithium nitrate in order to improve the ionic contact. The behavior of the ionic voltage probes on switching on and off lithium ion currents is shown in Fig. 4. The current required was so small (60 nA) as to be difficult to measure accurately, but an ionic conductivity of $6 \times 10^{-6}\ \Omega^{-1}\ cm^{-1}$ at 295°C is indicated. Analysis of the switching on and off transients shows a chemical diffusion coefficient of $3 \times 10^{-5}\ cm^2\ sec^{-1}$.

In the case of sample B the use of lithium nitrate as an interface wetting agent was avoided in order to eliminate any chance of "ionic shorts" across the bar. The results are shown in Fig. 5. At 452°C $\sigma_i \sim 6 \times 10^{-6}$ and $\tilde{D} \sim 3 \times 10^{-4}$. This very high $\tilde{D}$ value requires that the gradient of lithium ion activity with concentration ("thermodynamic factor") must be very high. The currents used were so small, and the output impedance of the voltage probes so high, that these values can only be regarded as representing an upper limit to the ionic conductivity in the material. For comparison, a-c conductivity measurements on 84% dense polycrystalline samples of isostructural lithium gallate, which is not an electronic conductor gave a conductivity of about $3 \times 10^{-7}\ \Omega^{-1}\ cm^{-1}$ at 300°C (11). The four-point ionic conductivity values are included in Fig. 1 and denoted by i (sample A at 295°C) and j (sample B at 452°C).

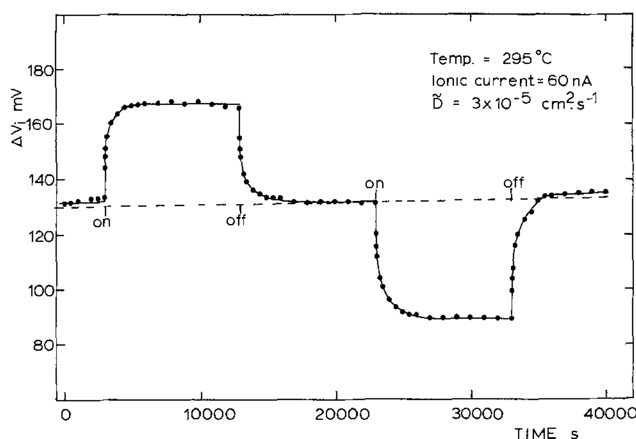

Fig. 4. Ionic voltage probe voltage difference vs. time for specimen A. Baseline is not at 0 mV because reference electrode materials were different for the two probes.

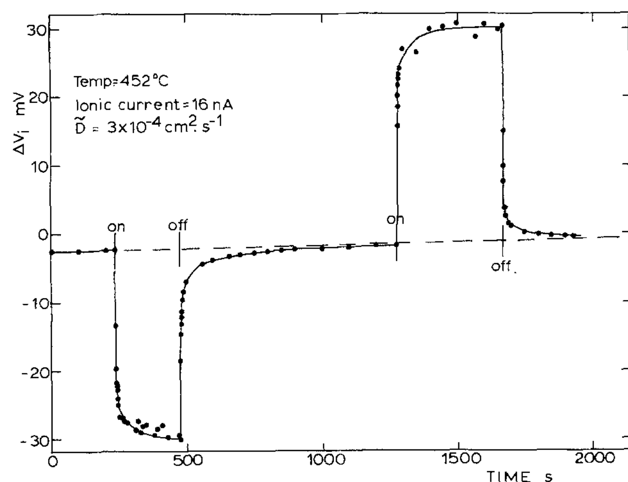

Fig. 5. Ionic voltage probe voltage difference vs. time for specimen B.

Discussion

Tretyakov and Rapp (12), in a study of the oxygen partial pressure in equilibrium with lithium ferrite, showed that their thermodynamic data were consistent with the following reaction for the reduction of the stoichiometric compound

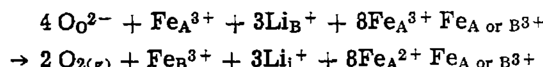

$$4\,O_O^{2-} + Fe_A^{3+} + 3Li_B^{+} + 8Fe_A^{3+}\,Fe_{A\ or\ B}^{3+}$$
$$\rightarrow 2\,O_{2(g)} + Fe_B^{3+} + 3Li_i^{+} + 8Fe_A^{2+}\,Fe_{A\ or\ B}^{3+}$$

where A and B denote tetrahedral and octahedral sites, respectively. It has been assumed that lithium ion interstitials are formed in preference to iron interstitials though this was not conclusively proven. This results in the formula

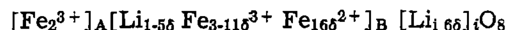

$$[Fe_2^{3+}]_A[Li_{1-5\delta}\,Fe_{3-11\delta}^{3+}\,Fe_{16\delta}^{2+}]_B\,[Li_{6\delta}]_iO_8$$

where for convenience the Fe^{2+} ions have been assigned to the octahedral sites. Furthermore they showed that for a sample in equilibrium with air at 900°C δ would be in the region of 5×10^{-4}. This would probably approximate the stoichiometry of our sample A as prepared. On placing nonporous samples in contact with oxygen at 400°C the oxidation reaction would take place at the surface, and penetrate the bulk only very slowly due to the very low rate of oxygen diffusion expected at this temperature. However, the ionic conductivity experiments indicate that the chemical diffusion of lithium ions and electrons is fast and thus both could diffuse to the surface to be converted to Li_2O. Note however that there are 16 Fe^{2+} ions to 6 interstitial lithium ions so that when all interstitial lithium had moved to the surface Fe^{2+} ions would remain, maintaining a high bulk electronic conductivity. Diffusion of lithium in normal sites would be expected to be much slower and hence further oxidation would be inhibited except at the surface where direct reaction with oxygen could occur. We suggest this model could explain the relatively high electronic conductivity values measured by four-point techniques and the time-dependent lower conductivities calculated from the voltages observed at the current contacts corresponding to a two-point conductivity measurement. The smaller two-point conductivity values and voltage transients at constant current associated with the introduction of oxygen can thus be explained by the slow formation of a surface layer containing a depleted concentration of Fe^{2+} ions. It should be emphasized that all previously reported conductivity values known to us have involved only two-point measurements and their interpretation can produce erroneous conclusions about bulk conductivity. In particular the relatively high values of ionic conductivity inferred by Matsui and Wagner (3) are orders of magnitude too large. At 452°C for example, the partial ionic conductivity has a value of $6 \times 10^{-6}\ \Omega^{-1}\ cm^{-1}$ corresponding to an ionic transport number of approx. 5×10^{-6}. The low ionic conductivity reflects the low concentration of interstitial lithium. The high chemical diffusion coefficient indicates a large thermodynamic factor consistent with a compound close to stoichiometry.

Conclusions

The results are consistent with a model in which a low concentration of interstitial lithium ions is responsible for a small ionic conductivity while the presence of Fe^{2+} ions gives rise to n-type electronic conductivity. Observed transients in two-point electronic conductivity measurements ascribed to high ionic conductivity appear instead to be due to surface oxidation leading to high resistance layers under the contacts. The effect of different initial iron to lithium ratios has not been studied and consequently the possibility that considerably different behavior might be observed at different stoichiometries cannot be excluded.

Acknowledgments

The authors express their thanks to Dr. C. E. Turner of the Department of Physics, Portsmouth Polytechnic, for the lithium ferrite single crystals, and to Dr. R. D. Shannon of the Central Research Department, E. I. du Pont de Nemours Company, Wilmington, for the lithium phosphate silicate electrolyte. One of the authors (GJD) is indebted to the U.K. Science Research Council for financial support during the period of this work.

Manuscript submitted April 17, 1978; revised manuscript received July 18, 1978.

Any discussion of this paper will appear in a Discussion Section to be published in the June 1979 JOURNAL. All discussions for the June 1979 Discussion Section should be submitted by Feb. 1, 1979.

Publication costs of this article were assisted by EEC Anglo-Danish advance battery project No. 316-78-EE-UK.

REFERENCES

1. K. O. Hever, *This Journal*, **115**, 826, 830 (1968).
2. G. J. Dudley and B. C. H. Steele, *J. Solid State Chem.*, **21**, 1 (1977).
3. T. Matsui and J. B. Wagner, Jr., *This Journal*, **124**, 1143 (1977).
4. M. Schieber, *J. Inorg. Nucl. Chem.*, **26**, 1363 (1964).
5. L. J. Van der Pauw, *Philips Res. Rep.*, **13**, 1 (1958).
6. R. G. West and A. C. Blankenship, *J. Am. Ceram. Soc.*, **50**, 343 (1967).
7. E. Kato, *Bull. Chem. Soc. Jpn.*, **31**, 113 (1958).
8. F. F. Y. Wang, R. L. Gravel, and M. Kestigian, *IEEE Trans. Magn.*, **4**, 55 (1968).
9. I. Yokota, *J. Phys. Soc. Jpn.*, **16**, 2213 (1961).
10. R. D. Shannon, B. E. Taylor, A. D. English, and T. Berzins, *Electrochimica Acta*, **22**, 783 (1977).
11. L. Harris, Private communication.
12. Y. Tretyakov and R. A. Rapp, *Trans. Met. Soc. AIME*, **245**, 1235 (1969).

Thermal Oxidation of Arsenic-Diffused Silicon

Shinji Ohkawa and Yoshio Nakajima

Fujitsu Laboratories Limited, Kamikodanaka 1015, Nakahara, Kawasaki 211, Japan

ABSTRACT

Thermal oxidation of arsenic-diffused silicon was investigated in wet (95°C water) oxygen ambient over the relatively low temperature range of 650°-850°C. Arsenic was diffused into boron-doped silicon from an elemental source in an evacuated quartz capsule. The surface concentration of total arsenic was 2.5×10^{20}-2.2×10^{21} cm^{-3} while that of electrically active arsenic was 1.9×10^{20}-2.8×10^{20} cm^{-3}. The rate constant in the linear regime of oxidation seemed to increase proportionally to the total arsenic concentration. This suggests that the surface reaction rate of oxidation is proportional to the total arsenic concentration in higher concentration region than a certain value which may lie in the range of 3.4×10^{19}-7.6×10^{19} cm^{-3}. For this case, the equation which gives the relation between oxide thickness and oxidation time was derived. Calculated values from this equation agreed well with experimental results. The increase in the surface reaction rate is considered to be caused by catalyst function of arsenic in reaction of oxidant OH with silicon.

A thermal oxidation process by which thin film of silicon dioxide is formed on silicon wafers is of great technological importance for fabrication of silicon devices. For such devices as planar and MOS transistors, oxidation is essential and precise control of oxide thickness is needed to obtain good device performances.

Oxide thickness for short oxidation time and/or low oxidation temperature is proportional to the time and to the square root of the oxidation time for long time and/or high temperature. The rate constant in the former case (linear rate constant) is limited by the surface reaction rate for oxidation and the rate constant in the latter case (parabolic rate constant) is limited by the diffusion rate of oxidant in the oxide film (1). It was reported that these rate constants depend on the impurity concentration in silicon as well as the temperature and oxidizing ambient. Deal and Sklar (2) and Pliskin (3) investigated the oxidation rate of boron-doped silicon and phosphorus-doped silicon. Pliskin reported that the linear rate constant of heavily phosphorus-doped silicon with the doping level of 4.9×10^{20} cm^{-3} was 2.03 μm/hr, which was about twice of the rate constant of high resistivity silicon for steam-oxidation at 978°C. Since his result was obtained for only one doping level, the impurity concentration dependence of the oxidation rate could not be determined. Deal and Sklar described oxide thickness of phosphorus-doped silicon and of boron-doped silicon as a function of the oxidation time and the oxidation temperature. Two doping levels were employed in their investigation: 3.7×10^{19} and 1.5×10^{20} cm^{-3} for phosphorus-doped silicon and 1.0×10^{20} and 2.5×10^{20} cm^{-3} for boron-doped silicon. Therefore the concentration dependence of the oxidation rate is expected to be derived. Indeed they reported the oxidation rate as a function of the impurity concentration. Their results were obtained on the assumption that oxide thickness was proportional to the square root of the oxidation time. For a higher oxidation temperature than about 1100°C in wet ambient where the assumption was valid, oxide thickness of heavily doped silicon agreed with that of high resistivity silicon. On the other hand, the higher phosphorus concentration resulted in a thicker oxide for an oxidation temperature lower than 1000°C. In this temperature range, the relation between the oxide thickness and the oxidation time is no longer expressed by the parabolic law but by the combination of linear and parabolic terms. From the analysis of their results considering these two terms, however, no reasonable value was obtained for the oxidation rates. Hence the concentration dependence could not be determined.

We have investigated the thermal oxidation of arsenic-diffused silicon in wet ambient with temperatures 650°-850°C. This paper reports the oxidation rate of arsenic-diffused silicon and its dependence on the arsenic concentration.

Key words: silicon oxide, arsenic diffusion, thermal oxidation.

Oxidation Rate

For thermal oxidation in wet ambient, an oxide thickness x_o is given by solving the following differential equation (1)

$$\frac{N_1}{C^*}\frac{dx_o}{dt} = \left(\frac{1}{k_s} + \frac{1}{h} + \frac{x_o}{D}\right)^{-1} \quad [1]$$

where k_s is the chemical surface-reaction rate constant for oxidation, h is the gas-phase mass-transport coefficient, C^* is the equilibrium concentration of oxidant in the oxide, N_1 is the number of oxidant molecules incorporated into a unit volume of the oxide film, and D is the diffusion coefficient of oxidant in the oxide film. Under the initial condition of $x_o = 0$ at $t = 0$, the solution of Eq. [1] is expressed by

$$x_o^2 + Ax_o = Bt \quad [2]$$

$$\frac{B}{A} = \frac{C^*}{N_1}\left(\frac{1}{k_s} + \frac{1}{h}\right)^{-1} \quad [3]$$

$$B = \frac{2DC^*}{N_1} \quad [4]$$

From Eq. [2], it is easily found that B/A and B are the rate constants in the linear regime and in the parabolic regime of the oxidation, respectively. Equation [3] shows that the linear rate constant B/A is proportional to the chemical surface reaction rate constant because h is estimated to be about 1000 k_s on the basis of boundary layer theory, and Eq. [4] shows that the parabolic rate constant B is proportional to the diffusion coefficient of oxidant in the oxide film. These constants depend on such oxidation conditions as ambient, temperature, and crystal orientation. For wet ambient and (111)-oriented silicon, the constants have been presented as a function of the oxidation temperature T (1).

$$B/A = 7.8 \times 10^7 \exp(-1.96/kT)\mu\text{m/hr} \quad [5]$$

$$B = 2.0 \times 10^2 \exp(-0.71/kT)\mu\text{m}^2\text{/hr} \quad [6]$$

Experimental

Silicon wafers used in this investigation were cut parallel to the (111) plane and polished mechanically and chemically to 250 μm thick. All wafers were doped with boron and had a resistivity of 2 Ω-cm which corresponded to a hole concentration of 7×10^{15} cm^{-3} (4).

The procedure of arsenic diffusion was similar to that previously reported (5). The diffusion was carried out in an evacuated quartz capsule containing silicon wafers and elemental arsenic. The purity of elemental arsenic used as a diffusion source was 99.999%. The vapor pressure of arsenic in the capsule was calculated from the volume of the capsule and the amount of arsenic on the assumption that arsenic vapor consisted of an As_4 molecule at the diffusion temperature. Surface concentration of the arsenic-diffused layer was determined by the differential conductance method and by the backscattering method using helium ions of 1.5 MeV. The former method gives the concentration of electrically active arsenic atom while the latter method gives the total concentration of electrically active arsenic and inactive arsenic atoms.

Thermal oxidation of the silicon wafers was done in wet ambient which consisted of oxygen-bubbled deionized water at 95°C. The oxidation temperature was in the range of 650°-850°C which was much lower than the diffusion temperature of arsenic in order to avoid a change in the arsenic concentration during the thermal oxidation. In each oxidation, an undiffused but heat-treated silicon wafer was used as a standard. The heat-treatment of the silicon wafer was done in an evacuated quartz capsule containing no diffusion source at the same temperature to the arsenic diffusion.

After oxidation, approximated thickness of the oxide film was estimated from interference color of the film which could give oxide thickness within an error of ±100Å. The oxide film on half the wafer surface was masked by wax and then the film on the remaining half was dissolved in buffered hydrofluoric acid of which etching rate for the oxide film was about 1000 Å/min. Considering that the etching rate possibly lowered near the oxide/silicon interface, we decided to add 30 sec to the etching time which was required from the approximated thickness and the etching rate. Etching of arsenic-diffused silicon by hydrofluoric acid was hardly observed in the arsenic concentration range used in this experiment. The wax was dissolved in organic solvent and silver was evaporated onto the whole wafer surface. The oxide thickness was measured using multiple-beam interferometric technique. Accuracy of this measuring method is estimated to be ±40Å.

Results and Discussion

Arsenic-diffused silicon.—Oxide thickness of the arsenic-diffused silicon wafers are shown in Fig. 1 (a),

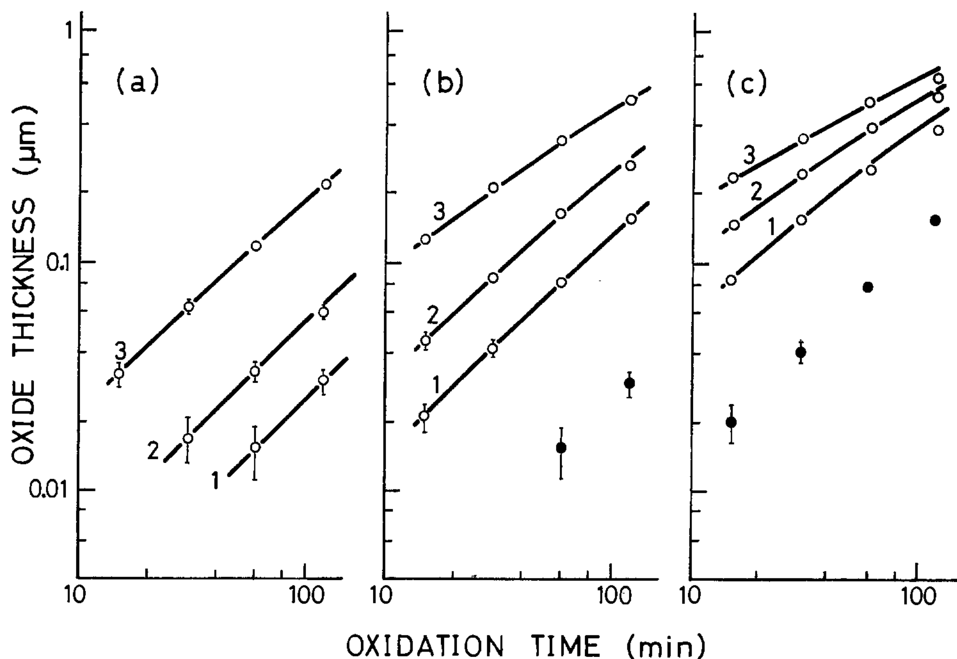

Fig. 1. Oxide thickness vs. oxidation time at (a) 650; (b) 750; and (c) 850°C. Curves 1, 2, and 3 are calculated values for surface concentration C_s of 2.5×10^{20}, 5.5×10^{20}, and 2.2×10^{21} cm^{-3}, respectively. Experimental values: ○, arsenic-diffused; ●, undiffused silicon.

(b), and (c) as a function of the oxidation time with a parameter of the surface concentration. Arsenic diffusion was carried out at 1000°C for 4 hr. The surface concentrations of total arsenic C_s were 2.5×10^{20}, 5.5×10^{20}, and 2.2×10^{21} cm^{-3} for the arsenic vapor pressures of 2, 20, and 200 Torr, respectively, while the surface concentrations of electrically active arsenic C_{se} were 1.9×10^{20}, 2.5×10^{20}, and 2.8×10^{20} cm^{-3}. The result of undiffused silicon was not presented in Fig. 1(a) because the oxide film of the undiffused silicon wafer oxidized at 650°C was too thin to determine oxide thickness.

The linear rate constant B/A and the parabolic rate constant B were obtained by applying Eq. [2] to the results shown in Fig. 1 using the least squares method. Thickness of the film used in this procedure was the mean value of experimental results obtained by five times measurements. The mean values are presented by open and closed circles in Fig. 1. In Fig. 2 and 3, B/A are shown as a function of reciprocal oxidation temperature and of the surface concentration of total arsenic C_s, respectively. As shown in Fig. 1(a) and (b), oxide thickness of the arsenic-diffused silicon wafers with the surface concentration C_s of 2.5×10^{20} and 5.5×10^{20} cm^{-3} is almost proportional to the oxidation time up to 120 min at 650° and 750°C. Therefore the parabolic rate constant B was obtained for only the wafer with the highest surface concentration and is shown in Fig. 4 as a function of the reciprocal oxidation temperature.

Oxidation rate of arsenic-diffused silicon.—In Fig. 3, it seems that the linear rate constant is proportional to the surface concentration of total arsenic C_s for oxidation at 650° and 750°C. As described above, the linear rate constant is a function of k_s, C^*, and N_1.

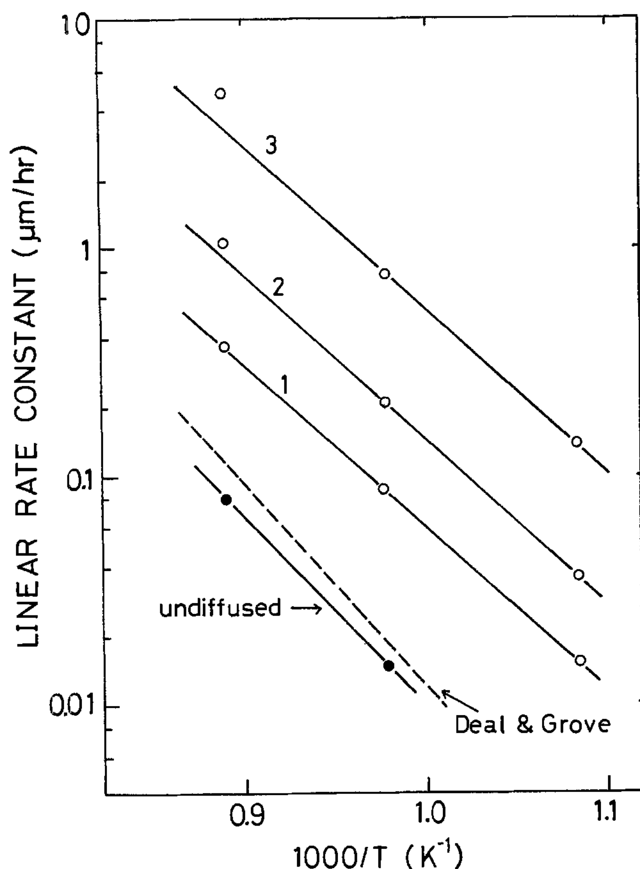

Fig. 2. Linear rate constant vs. reciprocal oxidation temperature. Lines 1, 2, and 3 are for surface concentration C_s of 2.5×10^{20}, 5.5×10^{20}, and 2.2×10^{21} cm^{-3}, respectively. Broken line is Deal and Grove's result. Experimental values: ○, arsenic-diffused; ●, undiffused silicon.

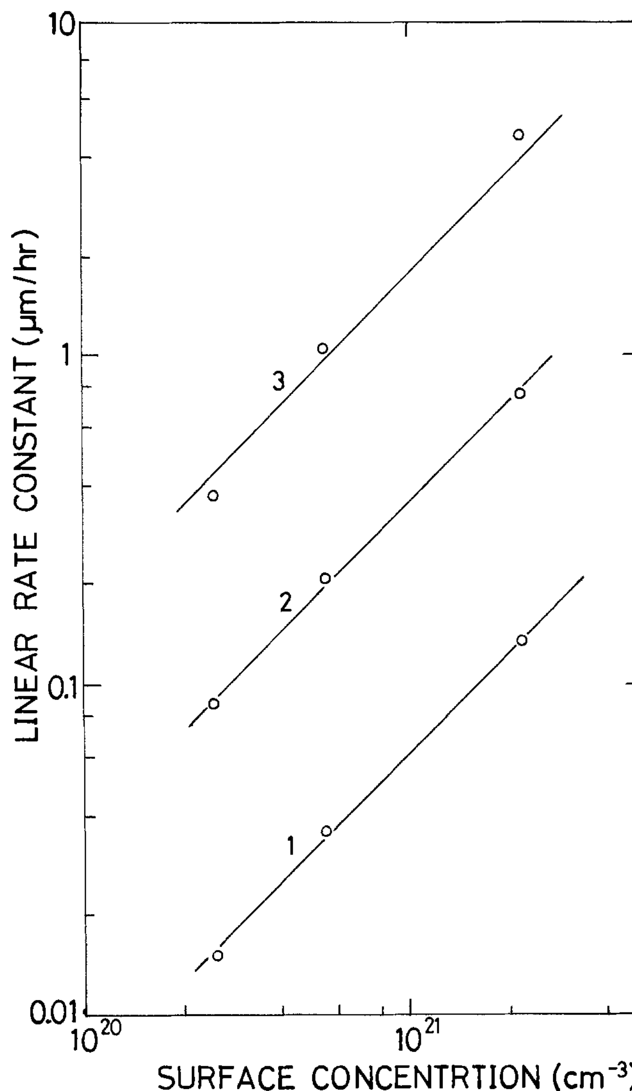

Fig. 3. Linear rate constant vs. surface concentration. Lines 1, 2, and 3 are for 650°, 750°, and 850°C oxidation, respectively.

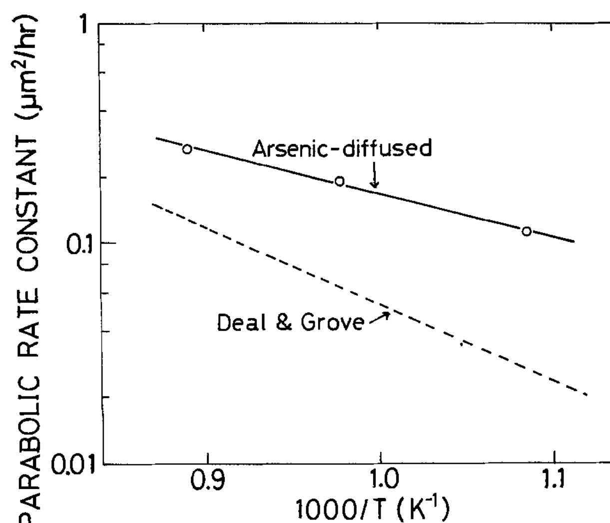

Fig. 4. Parabolic rate constant vs. reciprocal oxidation temperature. Solid line is experimental result for arsenic-diffused silicon with surface concentration C_s of 2.2×10^{21} cm^{-3} and broken line is Deal and Grove's result.

Since the values of C^* and N_1 are considered to be the same for both arsenic-diffused and undiffused silicon, the increase in B/A is attributed to the enhancement of the surface reaction rate constant k_s. When k_s de-

pends on the arsenic concentration in silicon, k_s in Eq. [1] is not constant but a function of oxide thickness for the arsenic-diffused wafer in which the arsenic concentration depends on a distance from the surface of the wafer. Therefore, Eq. [2] is no longer valid to arsenic-diffused silicon.

Assuming that k_s is proportional to the arsenic concentration, we derived the relation between oxide thickness and oxidation time. From the assumption, k_s is expressed by

$$k_s = k_o C \quad [7]$$

where C is the arsenic concentration. Equation [1], therefore, is described as

$$\frac{N_1}{C^*}\frac{dx_o}{dt} = \left(\frac{1}{k_o C} + \frac{1}{h} + \frac{x_o}{D}\right)^{-1} \quad [8]$$

Since C in arsenic-diffused silicon depends on the distance from the surface x, that is, $C = C(x)$, it is necessary to know the function $C(x)$ in order to solve Eq. [8]. In high concentration region, the diffusion coefficient of arsenic is proportional to the arsenic concentration (6). $C(x)$ is given as the solution of the following diffusion equation

$$\frac{dC_o}{dt_o} = \frac{d}{dx}\left(D_s C_o \frac{dC_o}{dx}\right) \quad [9]$$

$$D_s = 2C_s D_i / n_i \quad [10]$$

where C_o is the arsenic concentration normalized by the surface concentration C_s, D_s and D_i are the diffusion coefficients of arsenic at the surface and in low concentration region, respectively, t_o is the diffusion time, and n_i is the intrinsic carrier concentration at the diffusion temperature. We have reported that the solution of Eq. [9] is approximated well by a simple quadratic Eq. [7]

$$C_o = C/C_s = 0.999 - 0.872Y - 0.45Y^2 \quad [11]$$

$$Y = \frac{x}{2\sqrt{D_s t_o}} = \frac{x}{2\sqrt{2C_s D_i t_o / n_i}} \quad [12]$$

For growth of silicon dioxide with thickness of x_o, the silicon layer of $0.45x_o$ thick is consumed. Hence Eq. [12] is written as

$$Y = \frac{0.45x_o}{2\sqrt{2C_s D_i t_o / n_i}} \quad [13]$$

Equation [7] becomes

$$k_s = k_o C_s (0.999 - 0.872Y - 0.45Y^2)$$

$$= k_o C_s \left(0.999 - \frac{0.39x_o}{2\sqrt{2C_s D_i t_o/n_i}} - \frac{0.09x_o^2}{8C_s D_i t_o / n_i}\right)$$

$$\equiv k_o C_s (a - bx_o - cx_o^2) \quad [14]$$

Using Eq. [14], Eq. [8] is reduced to

$$\frac{N_1}{C^*}\frac{dx_o}{dt} = \left\{\frac{1}{k_o C_s (a - bx_o - cx_o^2)} + \frac{1}{h} + \frac{x_o}{D}\right\}^{-1} \quad [15]$$

The solution of Eq. [15] can be obtained as

$$\frac{C^*}{N_1} t = \frac{x_o^2}{2D} + \frac{x_o}{h} + \frac{2\sqrt{2C_s D_i t_o / n_i}}{0.72 k_o C_s} \log\left[\frac{1 + \dfrac{x_o}{12.2\sqrt{2C_s D_i t_o/n_i}}}{1 - \dfrac{x_o}{3.60\sqrt{2C_s D_i t_o/n_i}}}\right] \quad [16]$$

under the initial condition of

$$x_o = 0 \text{ at } t = 0$$

At the arsenic diffusion temperature of 1000°C, D_i and n_i are 8.14×10^{-4} μm^2/hr and 5.7×10^{18} cm^{-3}, respectively (8, 9). N_1 for the wet ambient where water is the main oxidizing species is 4.5×10^{22} cm^{-3}, and h is about 10^8 μm/hr. C^* and k_o depend on the oxidation temperature. C^* is obtained from the parabolic rate constant B which is $2DC^*/N_1$ as described above using Deal's results (1). The coefficient k_o of Eq. [7] is determined from Fig. 3 on the assumption that B/A in Fig. 3 is equal to $k_o C_s C^*/N_1$. D also depends on the oxidation temperature and possibly depends on the arsenic concentration. However the concentration dependence of D was not obtained because D was determined for only one concentration. The calculation of Eq. [16] is carried out using the values of D shown in Fig. 4 and the concentration dependence is assumed to be negligible. The values of C^*, k_o, and D employed here are listed in Table I. The calculated results shown in Fig. 1 by solid lines agree with the experimental values except for the oxidation at 850°C for 120 min. In the deriving process of Eq. [16], we did not take the impurity redistribution during the thermal oxidation into account. The discrepancy between calculated and experimental values may indicate the fact that the redistribution of arsenic cannot be neglected in this oxidation condition.

Although impurity such as arsenic or phosphorus seems to facilitate the reaction of oxidant to silicon, the role of this impurity is not clear. As another impurity affecting oxidation rate of silicon, sodium has been reported. Revesz and Evans have studied the effect of sodium which was introduced during oxidation (10). They have reported that sodium increases the linear rate constant for oxidation in wet ambient. It is attributed to the facility of the entrance of OH through autocatalytic reaction in the presence of sodium. Devereux *et al.* have investigated the oxidation of polycrystalline silicon wafer coated with sodium carbonate in wet (water vapor pressure of 24 Torr) ambient (11). They have reported that initial oxidation follows cubic kinetic behavior and have explained this behavior by the following mechanism; in the presence of high concentration sodium oxide, the main oxidant is the oxide ion which is consumed by formation of silicate ion; thus the surface reaction rate will decrease with time. Arsenic in high concentration region may have a function of catalyst similar to sodium. As described above, sodium was introduced from the outside of the oxide film. On the other hand, arsenic in the oxide film was provided from silicon in this experiment. Therefore the number of arsenic atoms acting as catalysts is proportional to the arsenic concentration at the interface between oxide film and silicon.

Arsenic-diffused and step-etched silicon.—Modified Eq. [16] is applied to the oxidation of the arsenic-diffused silicon wafer, of which surface layer is etched off after the diffusion. Arsenic diffusion was carried out at 950°C for 60 min under the arsenic vapor pressure of 30 Torr. Surface concentration of total arsenic was 3.5×10^{20} cm^{-3}. The arsenic-diffused layer was step-etched by anodic oxidation technique using potassium nitrate and tetrahydrofurfuryl alcohol. The number of etched steps was four and the depth of each step was 600Å. As a standard, an undiffused silicon wafer which had been heat-treated at 950°C for 60 min in vacuum was also step etched. Oxidation was carried out at 850°C for 30 min on both the arsenic-diffused and step-etched wafer and the heat-treated

Table I. Coefficient k_o of proportional Eq. [7], diffusion coefficient of oxidant D, and equilibrium concentration C^*

°C	k_o ($\mu m/hr \cdot cm^{-3}$)	D (μm^2/hr)	C^* (cm^{-3})
650	6.68×10^{-20}	63.2	4.04×10^{19}
750	4.24×10^{-19}	125	3.64×10^{19}
850	2.50×10^{-18}	185	3.21×10^{19}

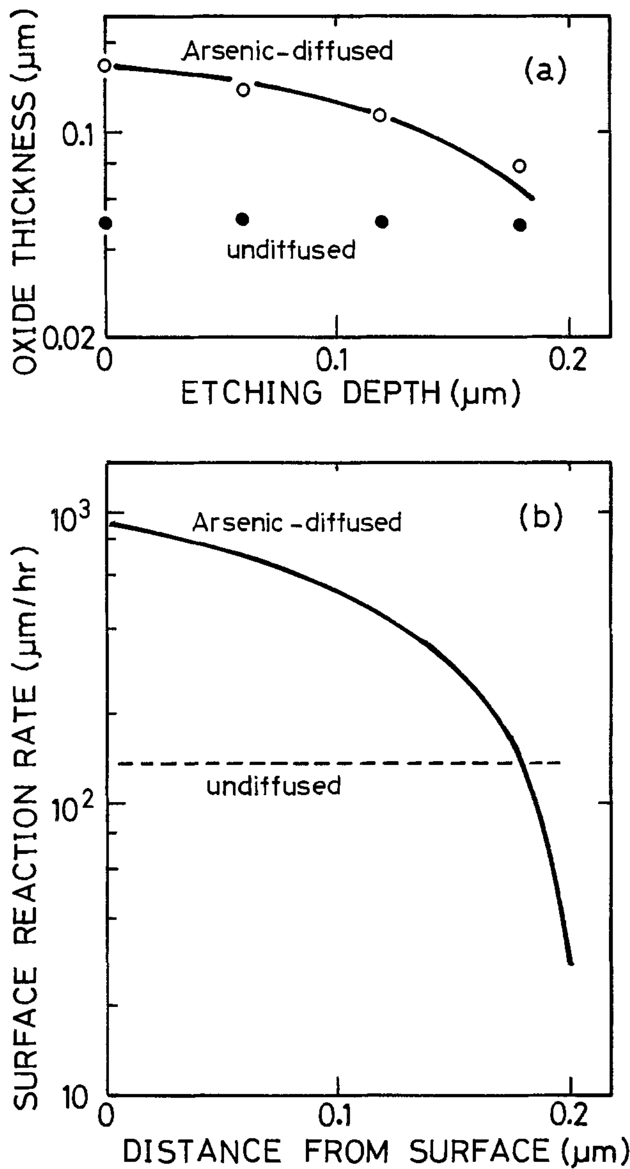

Fig. 5. (a) Oxide thickness vs. depth of step etching. Solid line is the calculated value of arsenic-diffused silicon. Experimental values: ○, arsenic-diffused; ●, undiffused silicon. (b) Surface reaction rate vs. distance from the surface. Solid line and broken line are for arsenic-diffused and undiffused silicon, respectively.

and step-etched wafer. Oxide thickness is shown in Fig. 5(a) as a function of thickness of the etched silicon layer. As thickness of the etched layer increases, that is, as the surface concentration decreases, oxide thickness is observed to decrease. On the other hand, the oxide film of undiffused silicon has a constant thickness of about 500Å. This indicates that the heat-treatment and the etching by anodic oxidation did not have an effect on the oxidation rate.

In this case, the arsenic concentration is expressed by

$$\frac{C}{C_s} = 0.999 - \frac{0.872(x+s)}{2\sqrt{D_s t_o}} - \frac{0.45(x+s)^2}{4D_s t_o}$$
$$= 0.999 - \frac{0.872s}{2\sqrt{D_s t_o}} - \frac{0.45s^2}{4D_s t_o} - \left(\frac{0.872}{2\sqrt{D_s t_o}} + \frac{0.09s}{4D_s t_o}\right)x - \frac{0.45x^2}{4D_s t_o} \quad [17]$$

where s is etching depth and x is $0.45x_o$. Hence the equation which gives the relation between oxide thickness and oxidation time is obtained by the same way as deriving Eq. [16] and is expressed by

$$\frac{C^*}{N_1}t = \frac{x_o^2}{2D} + \frac{x_o}{h} + \frac{2\sqrt{2C_sD_it_o/n_i}}{0.72k_oC_s} \log\left[\frac{1+\dfrac{x_o}{12.2\sqrt{2C_sD_it_o/n_i}+2.22s}}{1-\dfrac{x_o}{3.60\sqrt{2C_sD_it_o/n_i}-2.22s}}\right] \quad [18]$$

The experimental values agree with the theoretical curve shown in Fig. 5(a) by solid line except for the point at 1800Å. Under the oxidation condition of 850°C, 30 min, and wet ambient, oxide thickness of undiffused silicon is proportional to the oxidation time as shown in Fig. 1 and the thickness of 500Å corresponds to the surface reaction rate k_s of 140 μm/hr. For arsenic-diffused silicon, k_s is assumed to be proportional to the total arsenic concentration, namely $k_s = k_oC$, and the coefficient k_o is given as 2.1×10^{-18} μm/hr · cm^{-3} at 850°C from Fig. 1. As shown in Fig. 5(b), k_s of arsenic-diffused silicon is calculated to be smaller than that of undiffused silicon for larger x than 1900Å. However k_s of arsenic-diffused silicon must not be smaller than that of undiffused silicon for any arsenic concentration. The assumption that k_s is proportional to the arsenic concentration, therefore, is no longer valid in lower concentration region. This may be the cause of the discrepancy beween the theoretical and the experimental values of the oxide thickness at $s = 1800$Å.

The concentration dependence of k_s may be expressed by a function which approaches k_s of high resistivity silicon in the low concentration region and is proportional to the impurity concentration in the high concentration region. As shown in Fig. 5(a), the experimental values agree with the theoretical curve for the smaller s than 1200Å while the discrepancy takes place at s of 1800Å. Oxide thickness for s of 1200Å is 1150Å, which corresponds to the thickness of the consumed silicon layer of about 500Å for oxide. The arsenic concentration at the distance of 1700Å (= 1200 + 500Å) from the surface is 7.6×10^{19} cm^{-3}. Therefore, for higher concentration than this value, the assumption that k_s is proportional to the total arsenic concentration is considered to be valid. On the other hand, for larger values of x than 1900Å where the arsenic concentration is 3.4×10^{19} cm^{-3}, the assumption is not valid as described above. Thus the lower limiting concentration for the validity of the assumption may lay in the region of 3.4×10^{19}-7.6×10^{19} cm^{-3}.

Summary and Conclusions

Oxidation of arsenic-diffused silicon has been investigated at 650°-850°C in wet ambient. The oxidation rate of silicon with higher surface concentration than 2.5×10^{20} cm^{-3} has been found to be much larger than that of high resistivity silicon. The larger oxidation rate is mainly attributed to the increase in the linear rate constant under the oxidation condition in this experiment. The linear rate constant and the surface reaction rate seem proportional to the surface concentration of total arsenic when the oxide film is thin. The increase in the surface reaction rate is considered to be caused by catalyst function of arsenic in reaction to the oxidant OH with silicon.

The approximated equation which gives the relation betwen oxide thickness and oxidation time is derived for arsenic-diffused silicon on the assumption that the surface reaction rate is proportional to the total arsenic concentration. The equation is applied to arsenic-diffused silicon, of which the surface layer is step-etched. Comparison of calculated values with experimental results indicates that the lower limiting concentration for the validity of the assumption may lay between 3.4×10^{19} and 7.6×10^{19} cm^{-3}.

Acknowledgments

The authors gratefully acknowledge Dr. Y. Fukukawa for helpful suggestions and are grateful to Dr. T. Sakurai and Mr. H. Nishi for measurements of arsenic concentration by backscattering.

Manuscript submitted Oct. 31, 1977; revised manuscript received June 20, 1978.

Any discussion of this paper will appear in a Discussion Section to be published in the June 1979 JOURNAL. All discussions for the June 1979 Discussion Section should be submitted by Feb. 1, 1979.

Publication costs of this article were assisted by Fujitsu Laboratories, Limited.

REFERENCES

1. B. E. Deal and A. S. Grove, *J. Appl. Phys.*, **36**, 3770 (1965).
2. B. E. Deal and M. Sklar, *This Journal*, **112**, 430 (1965).
3. W. A. Pliskin, *IBM J. Res. Dev.*, **10**, 198 (1966).
4. J. C. Irvin, *Bell Syst. Tech. J.*, **41**, 387 (1962).
5. Y. Nakajima, S. Ohkawa, and T. Fukano, *Fujitsu Sci. Tech. J.*, **8**, 93 (1972).
6. Y. Nakajima, S. Ohkawa, and Y. Fukukawa, *Jpn. J. Appl. Phys.*, **10**, 162 (1971).
7. S. Ohkawa, Y. Nakajima, and Y. Fukukawa, *ibid.*, **14**, 458 (1975).
8. B. J. Masters and J. M. Fairfield, *J. Appl. Phys.*, **40**, 2390 (1969).
9. F. J. Morin and J. P. Maita, *Phys. Rev.*, **96**, 28 (1954).
10. A. G. Revesz and R. J. Evans, *J. Phys. Chem Solids*, **30**, 551 (1969).
11. O. F. Devereux, R. Y. Wand, and K. H. Chien, *This Journal*, **118**, 1147 (1971).

Development of a Gentle Accelerated Corrosion Test

S. P. Sharma,* J. H. Thomas III,*[1] and F. E. Bader

Bell Laboratories, Incorporated, Columbus, Ohio 43213

ABSTRACT

A gentle accelerated corrosion test has been devised using a kinetic rate equation for contact materials to establish approximate acceleration factors due to relative humidity and thermal effects. The duration of the test can be suitably chosen depending on the application and has been taken to be one year. The test consists of a high/low relative humidity cycle and a high/low temperature cycle which will sample the ambient over a one year period and which will be equivalent to 25°C/35-40% RH for 53 years (a typical total equivalent lifetime for a gold-based contact).

High reliability applications in the electronic industry require that electrical connections function satisfactorily for a substantial time (as much as 40 years in a telephone industry). As a consequence, there is considerable interest in developing meaningful accelerated corrosion tests (corrosive environmental tests, etc.) to aid in assessing contact material systems and connector designs. It is known that atmospheric pollutants (such as SO_2, H_2S, nitrogen oxides, Cl_2, HCl, etc.) combined with humidity cause corrosion and tarnishing of materials. To develop a meaningful accelerated test procedure, pertinent failure mechanisms must be accelerated. It is also important that failure mechanisms which do not occur in service not be introduced.

Two approaches are presently employed in testing contact material systems: (*i*) field exposure tests (1, 2), and (*ii*) laboratory accelerated tests (3, 4).

Field exposure tests are time consuming but tend to be realistic, that is, atmospheric pollutants at field exposure sites are employed in the test. Laboratory tests are rapid (~2 weeks) but employ large concentrations of corrosive gases (and hence large acceleration factors) which may introduce unrealistic failure mechanisms. These tests are generally considered severe. It is therefore of considerable interest to develop a test procedure which is both realistic and reasonable in duration. This paper describes a gentle accelerated aging test which may be used to evaluate the performance and predict the expected end of life of a material system.

Corrosion Rate—Effects of Relative Humidity

It is generally believed that most contact materials degrade through the mechanism of moist atmospheric corrosion and tarnishing. The rate of atmospheric corrosion, shown in Fig. 1, is related to the amount of moisture on a surface (generally a thin invisible film which acts as an electrolyte in a corrosive environment). At low relative humidity (RH), when the moisture film is less than a monolayer thick or discontinuous, corrosion proceeds by dry corrosion proc-

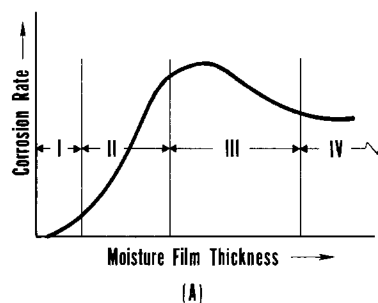

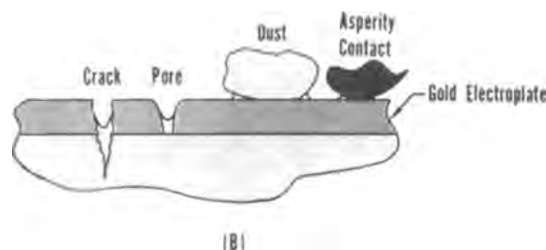

Fig. 1. (A) Qualitatively the dependence of corrosion rate on relative humidity is shown. (B) Capillary-like corrosion sites are shown diagramatically.

* Electrochemical Society Active Member.
[1] Current address: RCA, David Sarnoff Research Center, Princeton, New Jersey 08540.

Key words: accelerated test, environmental test, atmospheric corrosion, corrosion of electrical contacts.

esses, such as oxidation (see Fig. 1A region I) according to Tomashov (5, 6). At higher RH, the moisture film increases in thickness forming a continuous layer and assumes the role of an electrolyte. In this case the corrosion rate increases (region II). At higher RH, the film becomes visible (region III and IV) and the mechanism again changes (5).

In service, exposed base metals used in electrical contacts corrode by the mechanism of electrochemical corrosion (region II Fig. 1A). The amount of moisture (water) on a surface depends on the material system and varies with relative humidity. Relative humidity therefore plays a significant role in determining the corrosion rate. In addition to physical adsorption of water on a surface, capillary-like sites also increase the condensation rate. For example, (see Fig. 1B) condensation can take place in crevices, capillaries, and under particulate matter (dust) at lower RH than surface adsorption (7). Corrosion products can also enhance this effect (capillarity under particles or hygroscopicity). The presence of salts can further enhance moisture accumulation (water of hydration) (5).

Corrosion Rate—Acceleration Factor

Generally, it is only possible to semiquantitatively derive a set of test conditions because of a general lack of information required to estimate acceleration factors. However, we describe an attempt to estimate the acceleration factor based on a first-order approximation of the rate equation (6, 8). The kinetic rate equais assumed as follows

$$\text{rate} = K\left[\exp\left(\frac{-\Delta E}{kT}\right)\right][H_2O]^w[SO_2]^x[H_2S]^y\ldots(A)^z \quad [1]$$

where K is the rate constant, $[m]$ is the concentration of m; w, x, y, z are reaction constants, (A) is the air velocity, ΔE is the activation energy, k is Boltzmann's constant, and T is absolute temperature. $[H_2O]$ is the amount of water adsorbed on the surface and is a function of relative humidity. This equation assumes that the individual gas reactions proceed independently. The rate constant, K, depends on the material system being considered including, among other things, the porosity and history of prior exposure. Estimates of an acceleration factor based on such simplification must be viewed with caution and establish only qualitatively the effects of various variables on acceleration factors. If the pollutant level is held constant for a given material, (*i.e.*, the test utilizes the polluted air from an industrial area) the important parameters remaining are $[H_2O]$ and temperature. By manipulating the relative humidity, which determines $[H_2O]$, and temperature, a gentle accelerated aging test can be devised.

Thomas and Sharma (9) have measured the amount of water on gold surfaces as a function of relative humidity and temperature. Both adsorption and desorption branches of the weight-RH curves were fitted to the BET model (10). The desorption isotherm was used in this analysis since the pores which are filled (in adsorption) release the capillary water at lesser relative humidity in desorption. The desorption isotherm is therefore a more realistic approximation to real situations. The amount of water on a porous gold surface can be estimated from the following

$$[H_2O] = \frac{CX_mRH}{[1 + C(C-1)RH][1 - RH]} \quad [2]$$

where C is related to the heat of desorption, X_m is the monolayer capacity, and RH is the relative humidity. In the case of desorption [from Ref. (9)], X_m is 0.25 μg/cm^2 and the heat of desorption is 0.1 eV ($C = 50$).

In Eq. [1], the order of the rate with respect to water, w, is not known for porous gold on copper. Experimentally, w can be determined by performing weight gain measurements at various relative humidities which are directly related to the amount of water on the porous gold surface [see Eq. [2] and Ref. (3)]. Krumbein's (11) experiments of pore corrosion of the porous gold on copper system in SO_2 at various humidities can be used to estimate the corrosion rate and hence w. If the number of corrosion spots exceeding a certain size is proportional to the corrosion rate, a rough estimate of $w = 2$ can be made. The value of w obtained from Krumbein's data (11) is the same as Lorenzen (8) found for atmospheric corrosion of silver. Therefore, we assumed $w = 2$ in designing the gentle accelerated corrosion test. This assumption is justified by the fact that the predictions based on this assumption compare favorably with the experimental measurements as reported in an accompanying paper (12).

Figure 2 shows the effect of relative humidity on corrosion rate assuming $w = 2$, at constant temperature using Eq. [2], that is, $R \propto [H_2O]^2$ where $[H_2O]$ is given by Eq. [2]. The corrosion rate is observed to increase at relative humidities above 65-75%. This range of relative humidity has been termed "the critical humidity" in corrosion literature.

The temperature can also significantly affect corrosion rate (holding other parameters constant in Eq. [1]). An estimate of the activation energy, ΔE in Eq. [1], can be made from experiments performed by Clarke and Sansum (13). They have shown that corrosion of copper, silver, and nickel plated with gold in 10% SO_2 at a controlled relative humidity is accelerated by a factor of 12 if temperature is increased from 25° to 60°C. Thus, ΔE is $\sim$ 0.6 eV. We use this activation energy, 0.6 eV, to determine the thermal acceleration factor. Schwartz (14) has shown that for electrochemical corrosion, ΔE generally falls in this range.

Contacts must meet life requirements (as much as 40 years for the telephone industry), in addition to production, storage, and shipping. In an air-conditioned telephone office, the long-term operating temperature and relative humidity were taken as 25°C and 40% RH, respectively. During air-conditioning equipment failures, maintenance, etc., the relative humidity can approach 80% for as much as 15 days per year. In addition, more severe environments are encountered in manufacture, storage, and shipping. To normalize the time spent in these various environments to an equivalent time at 25°C and 35-40% RH, Eq. [1] (excluding pollutant concentrations and air velocity effects) has been used assuming $w = 2$, $\Delta E =$ 0.6 eV, and the desorption relation (Eq. [2]). Table I summarizes the results of this calculation. In certain applications the temperatures in actual field service can be higher than 25°C but the relative humidity near

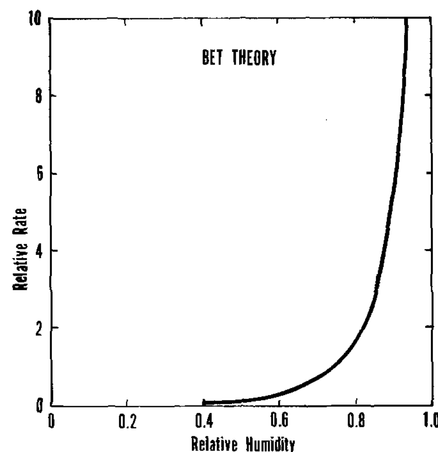

Fig. 2. Corrosion rate ($\propto [H_2O]^2$) is plotted as a function of relative humidity using desorption data of Thomas and Sharma.

Table I.

Environment	Temperature (°C)	Humidity (%)	Time	Equiv. time (year)
Manufacturing	35	80*	1 month	1
Storage	35	80*	2 months	3
Shipping	35	85*	1 month	2.5
Field service:				
Long term	25	35-40	39 years	39
Short term	25	75-80	1 year	8
		Total	~40 years	~53

* Assume worst case.

the contact region will be lower for the same absolute humidity (see psychometric chart). The decrease in relative humidity compensates the increase in temperature from the corrosion point of view. From these calculations it is observed that contact material systems (for 40 years life) should be designed to last at least 53 years at 25°C and 35-40% RH.

The Gentle Accelerated Corrosion Test

Ambient atmosphere at increased relative humidity and temperature supplies the corrosive environment which should approximate a real service environment. That is, as mentioned earlier, increased humidity and temperature will be used to accelerate corrosion. Due to seasonal variations in atmospheric pollutant concentrations, the over-all test was designed to operate over a one year period. In the case of mated contacts, mechanical motion caused by thermal variations may be important. These effects may be included by thermally cycling the test. The effects of dry corrosion (tarnish and oxidation) which may affect corrosion rates are taken into account qualitatively by humidity cycling. In summary, the test consists of a high/low RH cycle and a high/low temperature cycle which samples the ambient over approximately a one year period and which will be equivalent to 25°C/35-40% RH for 53 years. One such sequence is as follows: 12 hr at 80% RH, 65°C; 12 hr at 35-40% RH, 65°C; and 12 hr at 35-40% RH, 25°C.

Thus the cycle will be based on a 36 hr period. Since 36 hr is not synchronous with daily fluctuations of the ambient environment, fluctuation effects should be averaged out over a reasonable test duration.

The objective of this test is to simulate corrosion due to 53 years at 25°C/35-40% RH. The test at 65°C/80% RH for 4 months is equivalent to 53 years at 25°C at 35-40% RH from Fig. 2, and assuming $\Delta E = 0.6$ eV using the simplified Eq. [1]. Thus by cycling the test as shown above, the materials being tested will be exposed for one year; 4 months at low RH/low temperature; 4 months at high RH/high temperature; and 4 months at low RH/high temperature. During the one year period, the system undergoes 243 mechanical (thermal) cycles to simulate micromotion in service. Effectively, the material will have been thermally aged at 65°C for 5850 hr (8 months). In terms of substrate diffusion to the gold surface, copper film thickness can be predicted from Ref. (15 and 16).

The acceleration factors derived from this test for Cu, Ni, and Ag by comparing the film growth in the field environment to the film growth in the test will be described in other papers (12, 17). It is sufficient to say that the test works well for Cu and Ni with large acceleration factors, but is not a suitable test for Ag (12) because the acceleration factor is too small for Ag. The contact resistance changes on real connector systems will be described in another paper (17).

Conclusions

A one year accelerated corrosion test has been devised by using the kinetic rate equation to establish approximate acceleration factors due to relative humidity and thermal effects. From an analysis of Clarke and Sansum's thermal data, the thermal activation energy for corrosion was ~0.6 eV. The corrosion reaction order from Krumbein's data was approximated as 2, and the amount of moisture is found from a BET analysis of Thomas and Sharma's results. An acceleration factor of 154 is obtained for 65°C/80% RH with respect to 25°C/35-40% RH using the kinetic rate equation which is in close agreement with the required acceleration factor of 159 (53 × 3, see Table I) for a 4 month test. The acceleration factor and the test conditions derived on such simplified models as presented in this report will be modified as our knowledge concerning the activation energy, ΔE, and the reaction order w is improved.

It is believed that by using the typical ambient found in field locations and by manipulating temperature and relative humidity, a meaningful realistic corrosion test is possible. A first attempt on one such test has been described above. The results on contact resistance changes (of the connectors) and the measurement of acceleration factors on Cu and Ni show that this is a realistic environmental test (12, 17) for these materials.

Manuscript submitted March 27, 1978; revised manuscript received July 21, 1978.

Any discussion of this paper will appear in a Discussion Section to be published in the June 1979 JOURNAL. All discussions for the June 1979 Discussion Section should be submitted by Feb. 1, 1979.

Publication costs of this article were assisted by Bell Laboratories.

REFERENCES

1. R. G. Baker, in International Symposium on Electric Contact Phenomena, p. 546, Graz, Austria (1964).
2. R. V. Chiarenzelli, *IEEE Trans. Parts, Mater., Packaging*, **pmp-3**, 89 (1967).
3. P. F. Preston, *Trans. Inst. Met. Finishing*, **50**, 125 (1972).
4. W. A. Crossland, E. Knight, and C. R. Wright, Holm Seminar on Electric Contact Phenomena, p. 1, IIT, Chicago, Ill. (1973).
5. N. D. Tomashov, "Theory of Corrosion and Protection of Metals," McMillan Co., New York (1966).
6. A. Horning, Reliability Physics Symposium, p. 149, Electron Devices and Reliability Group, IEEE, New York (1972).
7. S. J. Gregg and K. S. W. Sing, "Adsorption, Surface Area and Porosity," Academic Press, New York (1967).
8. J. A. Lorenzen, in Proceedings of Institute of Environmental Sciences, Inst. of Environmental Sciences, Mt. Prospect, Ill. p. 110 (1971).
9. J. H. Thomas, III, and S. P. Sharma, *J. Vac. Sci. Technol.*, **13**, 549 (1976); S. P. Sharma and J. H. Thomas, III, *ibid.*, **14**, 825 (1977).
10. S. Braunauer, P. H. Emmet, and E. Teller, *J. Am. Chem. Soc.*, **60**, 309 (1938).
11. S. J. Krumbein, *IEEE Trans. Parts, Mater., Packaging*, **pmp-5**, 89 (1969).
12. S. P. Sharma, *This Journal*, **125**, 2005 (1978).
13. M. Clarke and A. J. Sansum, *Trans. Inst. Met. Finishing*, **50**, 211 (1972).
14. N. Schwarz and D. D. Bacon, *This Journal*, **125**, 1487 (1978).
15. R. P. Goel and F. E. Bader, *ibid.*, **123**, 1242 (1970).
16. S. P. Sharma and J. H. Thomas, III, *Bull. APS*, **22**, p. 1255, (1977); J. H. Thomas, III, Submitted to *This Journal*.
17. F. E. Bader, S. P. Sharma, and M. Feder, Paper presented at International Contact Conference and Holm Conference on Electrical Contacts, Sept. 15, 1978, Chicago, Ill.

Atmospheric Corrosion of Silver, Copper, and Nickel—Environmental Test

S. P. Sharma*

Bell Laboratories, Incorporated, Columbus, Ohio 43213

ABSTRACT

The corrosion growth kinetics for Cu, Ni, and Ag in an air-conditioned telephone office and a nonair-conditioned telephone office basement have been obtained by measuring the film thicknesses on coupons exposed for various times. The film constituents and thicknesses on these materials were obtained by AES and cathodic reduction. Over a two year period, Ag tarnishes linearly and the major film constituents are sulfur and chlorine. Copper and nickel corrosion data have been fitted to parabolic growth rate kinetics and the film thicknesses have been extrapolated to 40 years. The major film constituents on Cu and Ni are oxygen, chlorine, and sulfur. The film constituents and thicknesses have also been obtained by exposing the same materials in the One Year environmental test. The constituents are similar to the films grown in the field. Acceleration factors for the One Year test for these materials have been derived by comparing film thicknesses to those developed in the field. It is concluded that the One Year test is a suitable test for Cu and Ni but not for Ag.

Many applications require that electrical connectors and other material systems used in telephone offices perform satisfactorily for as much as 40 years. Therefore, the development of a meaningful accelerated corrosion test for materials is of prime interest. In an accompanying paper, Sharma *et al.* (1) described an accelerated corrosion test lasting one year. The test was derived semiquantitatively based on a kinetic rate equation. Because of general lack of scientific information about various parameters and constants (activation energy, reaction rate constants, etc.) in the rate equation, engineering judgements were made in designing such a test. The test was based on the measurement of the amount of water adsorbed on a gold surface as a function of relative humidity by Thomas and Sharma (2). A rate constant of 2 and an activation energy of 0.6 eV were assumed in the test. The decrease in solubility of gases in adsorbed H_2O at the surface with increase in temperature was not taken into consideration and this may have resulted in overestimation of acceleration factors in test design. The test consists of a high/low relative humidity and temperature cycle, asynchronous with daily fluctuations in ambient environment, to simulate the service life of a connector in a one year period. The sequence of the test is as follows: 12 hr at 80% RH, 65°C; 12 hr at 35-40% RH, 65°C; and 12 hr at 35-40% RH, 25°C.

The test was conducted in the basement of a telephone central office in Cleveland. This office is located in an industrial area having, according to Environmental Protection Agency data, one of the highest mean concentrations of SO_2 in the country as well as high concentrations of other pollutants and particulates.

This paper reports the acceleration factors derived experimentally from this test for Ag, Cu, and Ni. The acceleration factors are derived by comparing the thicknesses of corrosion films on these materials from the test chamber to the thicknesses on similar materials from the field chambers at the same location. There are two field chambers in this office, one in the air-conditioned central office (no special humidity control is employed in this central office) on the third floor of the building and the other in the nonair-conditioned basement. The test chamber is located near the field chamber in the basement. Film thicknesses were measured by sputter back profiling in an Auger electron spectrometer. Silver tarnishes linearly and provides an acceleration factor of ~4.0, which compares with the theoretical value of 3.74, but is too low to make this a practical test. Copper corrosion has been fitted to a parabolic growth rate model, and utilizing this model, an acceleration factor of ~20 is obtained with respect to Cu coupons exposed in the basement environment. With respect to an air-conditioned central office environment, an acceleration factor greater than 100 is achieved. For nickel coupons an acceleration greater than 100 is achieved for the central office environment while the basement environment provides an acceleration of ~27.

Experimental

The test was conducted in a 10 ft^3 capacity Tenney TTRS environmental chamber, custom designed to provide the sequence of test conditions. It is equipped with a purge system to change the air within the chamber at a rate of 4 times/hr. The air velocity is about 400 ft/min. It has an extended time cycle, *i.e.*, the programmable cam-operated controller regulated the first 24 hr period of the test cycle and a separate programmable timer provided the additional 12 hr period. The humidity is determined by the difference of dry and wet bulb temperatures (measured by platinum resistance sensing elements of a bridge controlled circuit). Humidity is increased by introducing water vapor and decreased by introducing drier air into the chamber. The temperature is controlled by a heater or a refrigeration system. The test chamber is located in a central office basement. There is no air conditioning or filtration of the room air, and a window is frequently open to the outside air.

The field chambers are modified five drawer file cabinets. The bottom of each file drawer was replaced by metal mesh to permit free flow of air. The cabinets are louvered at the bottom and equipped with several small fans (blower unit) mounted at the top behind a furnace filter. The same type of furnace filter was used in the test chamber. The blower unit provides a linear air flow of about 250 ft/min. The chambers are equipped with a hygrothermograph to record the temperature and humidity.

The materials exposed were 1½ in. square coupons and were abraded using metallographic papers to a 400 grit random finish and liquid honed to a fine uniform finish. The coupons were cleaned according to procedures outlined in Ref. (3) prior to installation in the field and the test chamber.

* Electrochemical Society Active Member.

Key words: Auger, accelerated test, corrosion of electrical contacts, corrosion.

The corrosion films were analyzed for the elements present on a Physical Electronics Scanning Auger System Film Analyzer, *i.e.*, Auger electron spectrometer (AES). This system is equipped with a single pass CMA, coaxial electron gun, and a Varian rastered ion gun. The thickness and distribution of elements into the film were determined by depth profiling using ion sputtering in conjunction with AES. Normal operating conditions were 3 kV electron gun voltage, 1200V electron multiplier voltage, 1 eV/sec sweep rate, 0.3/sec time constant on the lock-in amplifier, 3 eV modulation amplitude, and 1.6 mA emission current. For sputtering, the argon pressure was 5×10^{-5} Torr and the ion beam voltage was 1 kV. By means of a multiplexer system, peaks corresponding to various elements in the corrosion film were analyzed. Film thickness was determined by knowing the sputter rate and the time to sputter through the film. The time to sputter through the film is determined by measuring the time required for the substrate Auger signal to reach 70% of its maximum signal amplitude and/or by measuring the time for the last constituent of the corrosive film to reach 30% of its maximum signal amplitude. It is assumed that the sputter rate of the corrosion film is the same as of the substrate material. This assumption is not critical, since we are only interested in the relative thickness. The thickness values are therefore not absolute. In addition to AES, the film thicknesses of Ag and Cu were also determined by cathodic reduction in some cases.

Results and Discussion

Silver.—Figure 1 shows a typical depth profile obtained from a silver sample exposed in the basement field chamber. A depth profile from a Ag coupon subjected to the test conditions for 3 months in the test chamber is shown in Fig. 2. Similar spectra have been obtained from all the field-exposed samples (basement as well as third floor central office up to a period of 2 years) and all the samples in the One Year test. It is seen that the constituents of the films developed in the test chamber are similar to those in the field-exposed chambers. Table I presents the constituents of the film developed in order of decreasing peak heights as a function of time. The composition of the film developed in field chamber is not constant, *i.e.*, the ratio of Ag to Cl and Ag to S is not constant for coupons exposed to different time periods. This could be a time effect, coupon effect, or due to surface variability. In addition, the composition of the film changes along the thickness of the film. The only conclusion about the chemistry of the film is that each sample contains some AgCl and some Ag_2S, and the relative amount of these varies from sample to sample. The conclusion of the film being a mixture of Ag_2S and AgCl is substantiated by the fact that in cathodic reduction the reduction potentials match with those of AgCl and Ag_2S. The film thicknesses of the basement coupons are plotted as a function of time in Fig. 3. Table II pre-

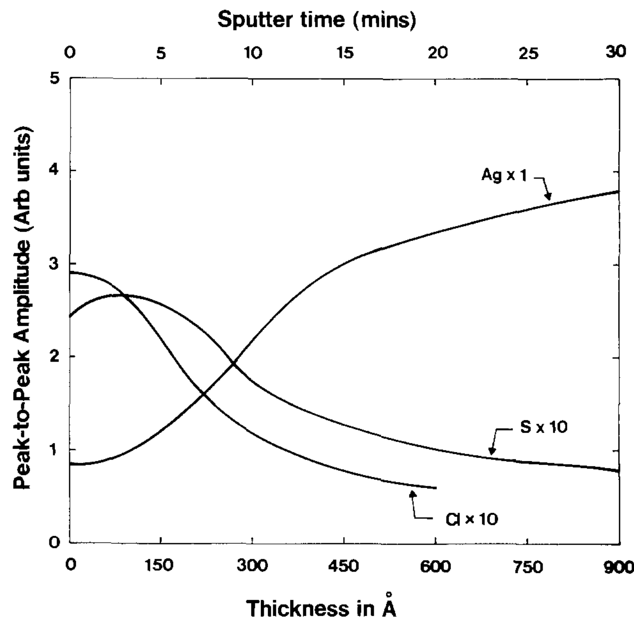

Fig. 2. Auger depth profile of the film on silver coupon exposed to 3 months in One Year test.

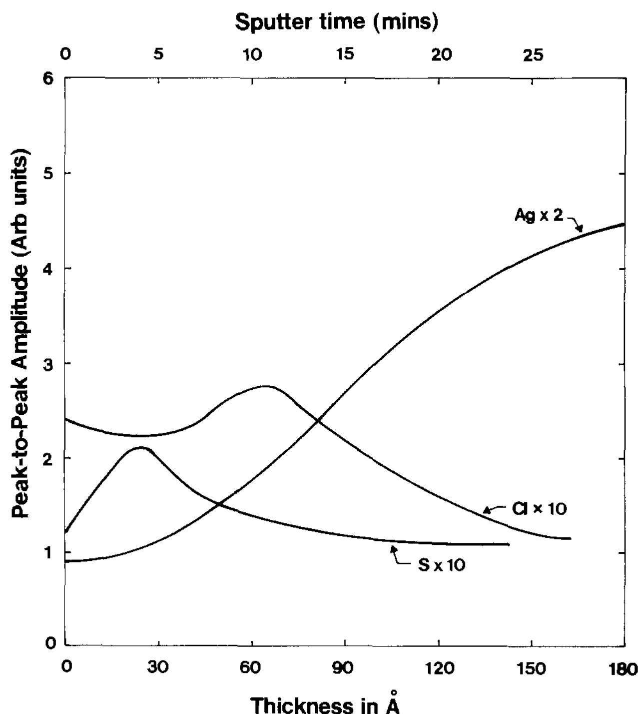

Fig. 1. Auger depth profile of the film developed on silver coupon exposed for 3 months in basement field chamber.

Table I.

Sample	Location	Exposure time (months)	Constituents at surface (in order of decreasing heights)
Silver	Basement	3.5	Cl, S, O
		6	Cl, S, O
		9	S, Cl, O
		12	Cl, S, O
Silver	Central office (C.O.)	3.5	S, Cl, O
		6	S, Cl, O
		9	S, Cl, O
		12	S, Cl, O
		18	S, Cl, O
Silver	Test chamber	1	S, Cl, O
		3	S, Cl, O
Cu	Basement	3.5	Cl, O
		6	Cl, O
		9	Cl, O
		12	Cl, O
		18.5	Cl, O
Cu	C.O.	3.5	O, Cl, S
		6	—
		9	Cl, O, S
		12	O, Cl, S
		18.5	Cl, O, S
Cu	Test chamber	1	Cl, O
		3	Cl, O, S, N
Ni	Basement	3.5	O, Cl, N, S
		6	O, Cl, S, N
		9	O, Cl, S, N
		12	O, Cl, N, S
		18.5	O, Cl, N, S
		24	O, Cl, N, S
Ni	C.O.	3.5	O, Cl, S
		6	O, Cl, S
		9	O, Cl, S
		12	O, Cl, S
		18.5	O, Cl, S
		24	O, S, Cl
Ni	Test chamber	1	O, Cl, S, N
		3	O, Cl, S

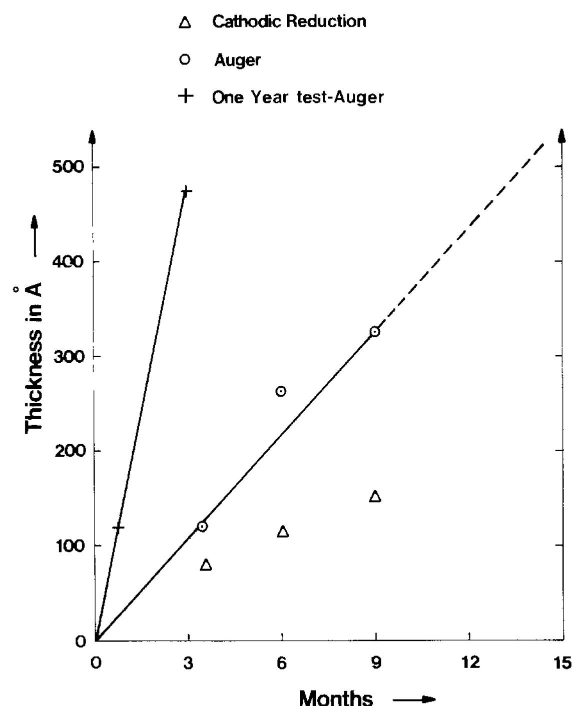

Fig. 3. Film thickness-time curve for Ag exposed in the basement field chamber and in One Year test.

sents the thicknesses of films obtained by cathodic reduction and by AES. It is seen that within the experimental errors the film thicknesses obtained by two different methods (AES and cathodic reduction) do not differ greatly. Silver corrodes linearly at a rate of 30-35 Å/month in the basement. Also shown in Fig. 3 is a plot of film thicknesses as a function of time, from the test chamber samples. By comparing the slopes of two curves, an acceleration factor of ~4 is calculated for Ag. This is a small but not an entirely unexpected acceleration factor for Ag as discussed further. SEM analysis of the corrosion products reveals that the morphology of the corrosion products is similar for the test samples and the samples from the field chamber. No significant roughness difference in the morphology of the corrosion products is seen.

It is known (4-6) that there is no significant change in the rate of corrosion of Ag with respect to temperature in the range 30°-55°C (and possibly up to 65°C) for relative humidities up to 85% and for modest concentrations (up to 1 ppm) of H_2S, SO_2, and Cl_2. There are various possible explanations for this lack of temperature dependence of silver tarnishing. One possible explanation is that the solubility (concentration) of gases dissolved in the adsorbed water film on Ag surface decreases with increasing temperature[1] (7). The

[1] Solubility of Cl_2 in H_2O (7) at 65°C is 0.47 times the solubility of Cl_2 at 25°C and the solubility SO_2 in H_2O at 65°C is 0.36 times its solubility at 25°C.

Table II. Thickness of films on silver

Exposure time (months)	Location	Thickness (Å) (Auger)	Thickness (Å) (cathodic reduction)
3.5	Basement	120	80
6	Basement	266	143
9	Basement	321	251
12	Basement	300	—
18	Basement	—	582
24	Basement	—	513
1	Test chamber	120	121
3	Test chamber	480	267
12	Test chamber	—	1200

other factor may be that the activation energy may be small resulting in a smaller temperature coefficient for acceleration. In addition, the amount of H_2O adsorbed at the surface could also decrease with increasing temperature. Whatever the reason, the temperature has little effect on the acceleration of corrosion in the temperature range of the One Year test and the only accelerating factor for Ag is the relative humidity.

The equation which describes (4) the rate dependence of silver tarnishing on relative humidity with other variables held constant is

$$\text{rate} = K_w\,[H_2O]^2_{Ad} \quad [1]$$

where K_w is the frequency factor and H_2O is the amount of water adsorbed on silver surface at a given relative humidity.

Utilizing the water adsorption isotherm on Ag obtained by Bowden and Throssell (8), the amount of H_2O adsorbed as a function of relative humidity (RH) is

$$[H_2O]_{Ad} = \frac{3.95\,\text{RH}}{(1 - \text{RH})\,(1 + 7.8\,\text{RH})} \quad [2]$$

Since the average relative humidity in the basement is approximately 40-45%, the acceleration factor (AF) can be calculated by

$$\text{AF} = \frac{\text{rate of corrosion at 80\% RH}}{\text{rate of corrosion at 45\% RH}} \times \frac{1}{3} + \frac{2}{3} = 3.74$$

since the chamber is at 80% of RH for 1/3 of the time. Therefore, theoretically the One Year test should provide an acceleration factor of 3.74. Experimentally an acceleration factor of ~4 is obtained.

These results can be compared to studies of Wagar (9), Abbott (5), and Crossland and Knight (6) on silver tarnishing. Abbott (5) has reported linear tarnish rates for Ag for S_8 mixtures and for mixed gases with low levels of H_2S in which other oxidizing agents such as NO_2 and/or Cl_2 are present. While Crossland and Knight (6) and Abbott (5) have shown that H_2S-O_2-H_2O mixtures produce nonlinear kinetics.

Since the One Year test in its present form provides a very small acceleration factor for Ag, it is not a practical test for Ag, although it is the only test known to produce the mixed sulfide/chloride films found at all our field sites. The test could be modified or another test (like flowers of sulfur) should be used for Ag.

Copper.—Figures 4 and 5 show typical depth profiles from field-exposed samples in the basement and central office. Figure 6 shows the depth profile of the one month old coupon from One Year test. The principal constituents in all the films are oxygen, chlorine, and carbon (not shown), and, of course, copper. In the central office environment the film also contains small amounts of sulfur. Table I presents the constituents of the film in order of decreasing peak heights. Figure 7 shows thicknesses calculated from the Auger depth profiles for the copper coupons exposed in the basement as a function of time (also see Table III). Also shown in Fig. 7 are the film thicknesses measured by cathodic reduction (10). These thicknesses are generally smaller since cathodic reduction only measured the oxides of copper.

The corrosion of copper can be fitted to a parabolic growth rate (11)

$$x^2 = kt \quad [3]$$

where k = parabolic rate constant, x = thickness, and t = time.

From the experimental curve 1 in Fig. 7, we derive a value for $k = 2 \times 10^{-12}$ cm²/month (or 0.78×10^{-18} cm²/sec). This rate constant would predict that in 40 years approximately 3100Å of film will develop on copper. In comparison, Wagar (9) has given the film thicknesses developed in telephone central office en-

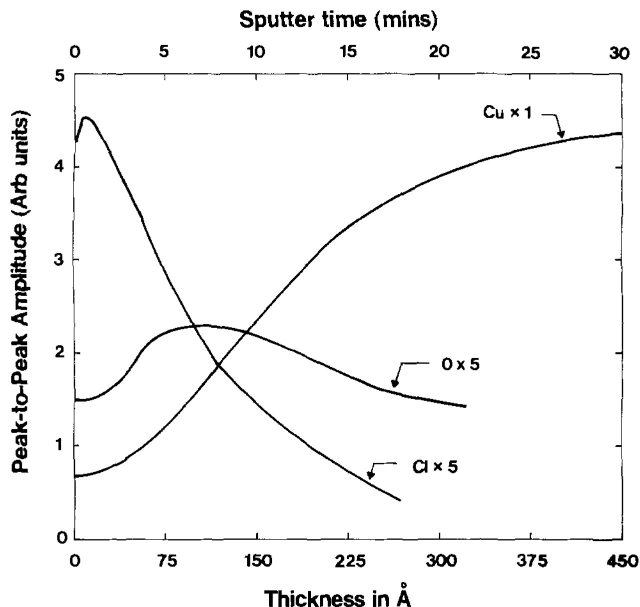

Fig. 4. Auger depth profile of the film on Cu coupon exposed to 3 months in basement field chamber.

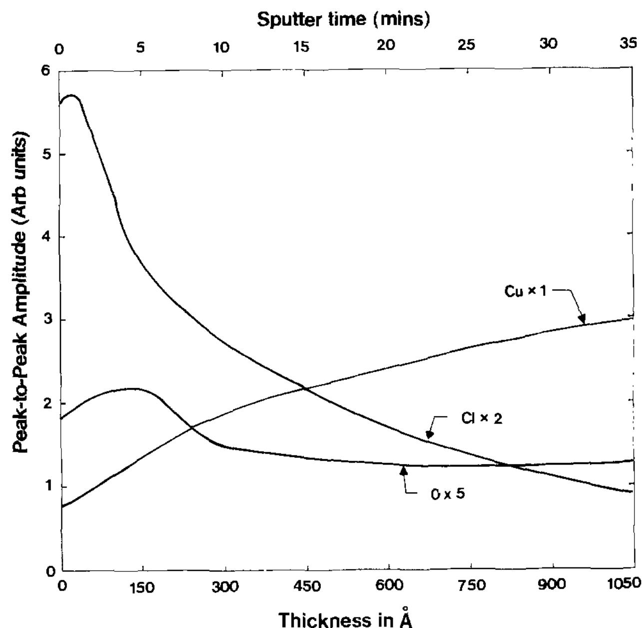

Fig. 6. Auger depth profile of the film on Cu coupon exposed to one month in One Year test.

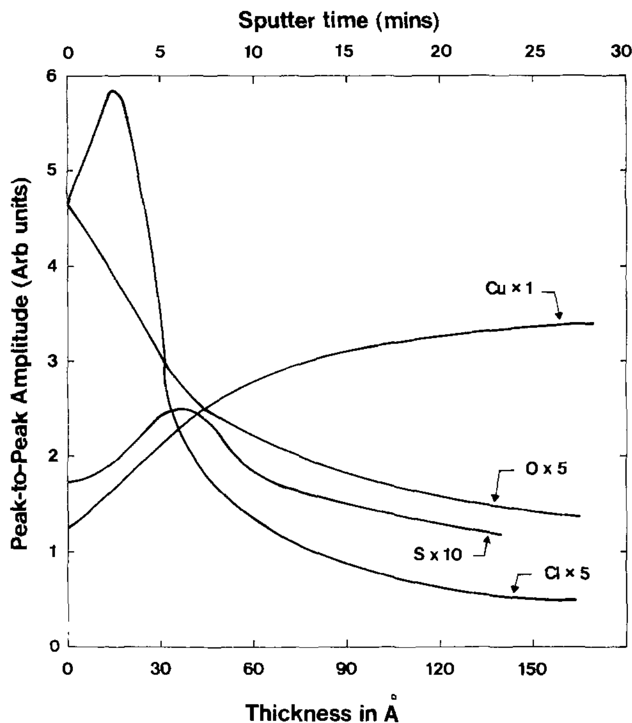

Fig. 5. Auger depth profile of the film on Cu coupon exposed to 3 months in central office environment.

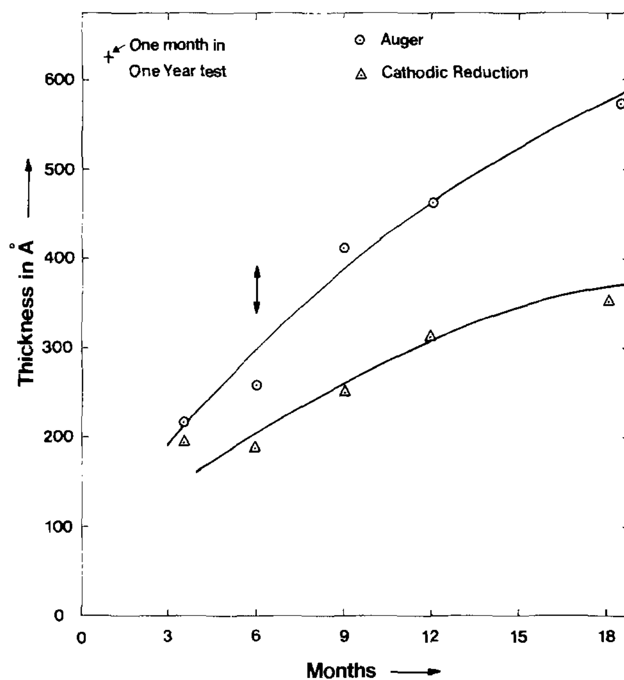

Fig. 7. Film thickness plotted as a function of time for copper corrosion in basement.

vironments up to 10 years. His data can also be fitted to a parabolic growth rate model. His measurements provide a k value of 5×10^{-12} cm^2/month and would predict 4900Å thick film on Cu in 40 years. Wagar's (9) data are believed to be typical of telephone central office environments of 1930-1940 period when there was no central air conditioning in the central offices. These environments are therefore comparable to Cleveland basement environment as regards the humidity and temperature excursions. The calculated values of film thicknesses compare favorably with these results. These predicted thicknesses also compare favorably with other results on copper corrosion in central office environments of 1920-1930 period.

Cathodic reduction measurements can also be fitted to a parabolic growth rate model with $k = 0.9 \times 10^{-12}$ cm^2/month ($\sim 0.35 \times 10^{-18}$ cm^2/sec) and would predict an oxide thickness of only 2100Å in 40 years. The total film thickness calculated earlier was 3100Å in 40 years. The remaining film is mostly chloride.

From the One Year test we get a film thickness of 625Å in one month and $\sim$1100Å in 3 months. This provides a corrosion rate constant of $\sim 40 \times 10^{-12}$ cm^2/month. From the field measurements in the basement environment $k = 2 \times 10^{-12}$ cm^2/month. Therefore, the acceleration factor is approximately 20 for copper exposed in the basement. In the design of the test, it was anticipated that the acceleration factor would be greater than 40. The low value of acceleration achieved in the real test may be due to several reasons. The test is based on water adsorption on gold and not copper. The high relative humidity is employed to achieve corrosion reactions with certain constituents of air (like sulfur, chlorine). However, the oxidation rate

Table III. Thickness of films on copper

Exposure time (months)	Location	Thickness (A) (Auger)	Thickness (A) (cathodic reduction)
3.5	Central office (C.O.)	60	232
6	C.O.	—	—
9	C.O.	326	453
12	C.O.	150	221 (271)
18	C.O.	230	221
24	C.O.	—	221 (299)
3.5	Basement	210	198
6	Basement	260	186
9	Basement	405	251
12	Basement	460	314 (331)
18	Basement	575	360
24	Basement	—	325 (416)
1	Test chamber	625	349
3	Test chamber	1100	411

* Number in parenthesis represents measurements on another part of the coupon.

of copper decreases with increasing relative humidity as shown by Campbell and Thomas (12) and the net effect may be a slower increase in film thickness at high relative humidity. In addition, the solubilities of pollutant gases decrease with increasing temperature as explained earlier. Lack of information about the activation energy of the complex corrosion reaction in real field environments is another factor. Consequently, the acceleration factor obtained in the test is lower than anticipated.

Figure 8 shows the thickness of the film on copper coupons exposed in the air-conditioned central office environment. The thickness of the films is considerably smaller than in the basement. Also shown in this figure are the thicknesses measured on the copper coupons exposed in other central office environments for 12 months. Film thickness on copper in most central office environments varies between 150-250Å in one year. Chiarenzelli (13) has observed that in a New York City office building the total film thickness in 13.6 months is ~280Å, which compares favorably with our results. The corrosion of copper in an air-conditioned central office environment proceeds slowly with a rate constant k between 0.3×10^{-12}-0.5×10^{-12} cm^2/month. The film thickness on a copper coupon in central office environment would be 1200-1550Å in 40 years. The acceleration factor for copper in a central office environment can be derived in a similar manner and is about 100.

Various investigators (5, 9, 14) have studied the natural films developed on copper in real field environments. Our studies indicate that the corrosion film contains oxides, chlorides, and small amounts of sulfides. The predominant constituents are the oxides (Cu_2O and CuO) and chlorides and not Cu_2S. In cathodic reduction, the reduction potential of the reducing film matches with that of Cu_2O, substantiating the conclusion that most of the film is Cu_2O. Environmental tests, which mainly produce Cu_2S, are not representative of telephone central office environments and may not be suitable laboratory tests for copper. The peak-to-peak intensity ratio of Cu to oxygen in Cu_2O is approximately measured to be 2.6 (15). In the field-exposed samples and also in the One Year test, the ratio of Cu to O (peak-to-peak heights) is not constant and is generally different (larger) than 2.6. Some of the Cu in the film is bound to chlorine. The film is a mixture of copper chloride and copper oxides, the relative amount varying from film to film. Carbon is also present as a surface specie. When S and Cl Auger peak heights are corrected for their sensitivities relative to that for the O-peak (16) and the corrected peak heights of Cl and S are added to the O-peak height, the ratio of Cu-peak height to the peak height sum of anions ($O^=$, Cl^-, and $S^=$) is found to be much less than 2.6. This points out that the copper is in a higher oxidation state (cupric) than Cu_2O as observed by Frankenthal and Thompson (15) in their experiments on Cu_2O exposed to flowers of sulfur. The copper chloride, therefore, may be $CuCl_2$ and the oxide may partly be CuO.

Nickel.—Figures 9 and 10 show typical depth profiles for samples exposed in the basement and third floor central office. Similar spectra have been obtained on other samples exposed to various times. The constituents of the films are oxygen, chlorine, sulfur, and carbon as shown in Table I. The thickness of the film developed on Ni exposed in the central office is plotted as a function of time in Fig. 11 (also see Table IV). In 2 years of exposure, a film 32Å thick is obtained. This is a thinner film than on copper. The major constituent of the film is oxygen. Nickel oxidation has been

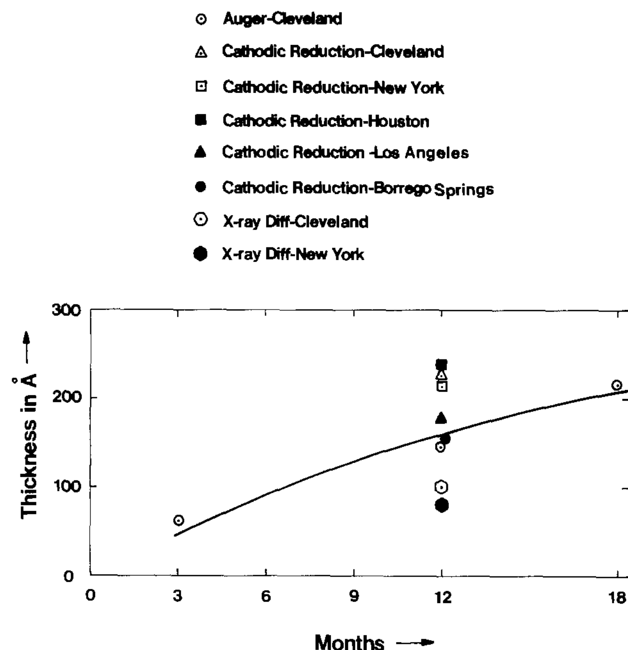

Fig. 8. Film thickness developed on copper in various central offices.

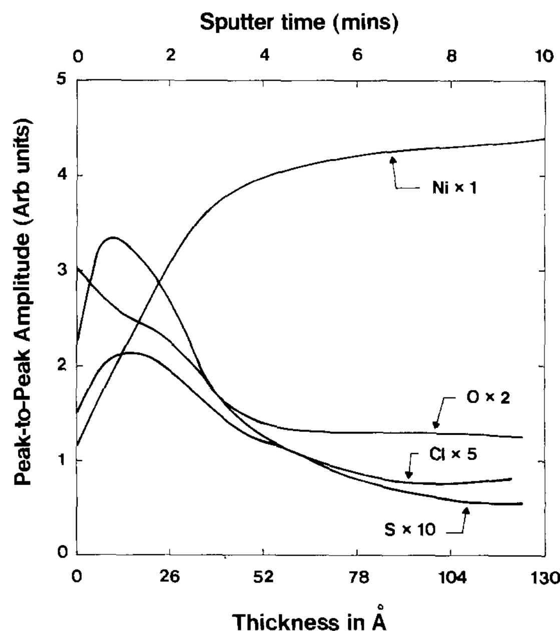

Fig. 9. Auger depth profile of the film on Ni exposed to 6 months in basement environment.

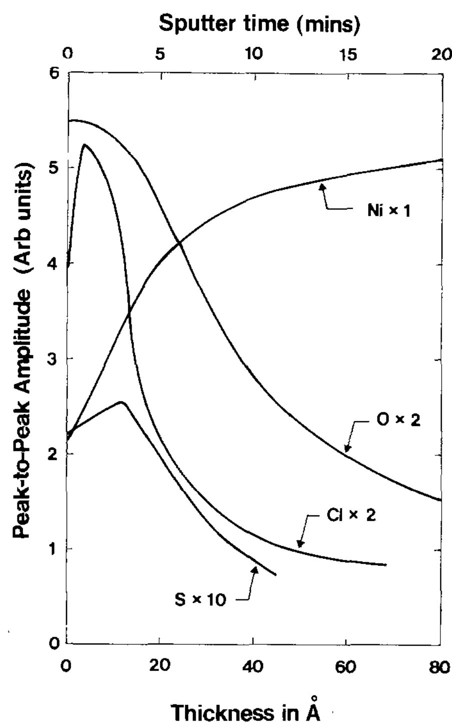

Fig. 10. Auger depth profile of the film developed on Ni exposed to 9 months in the central office environment.

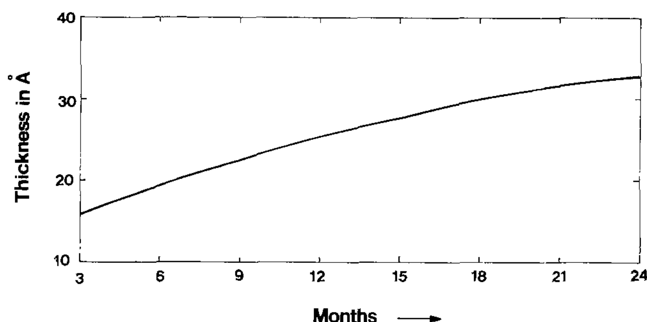

Fig. 11. Film thickness on Ni plotted as a function of time for Ni corrosion in the central office environment.

studied at low temperatures by various investigators. Nickel does not undergo appreciable oxidation at temperatures below 300°C. Kulpa and Frankenthal (17) reported a limiting thickness of 15Å at 200°C in dry air, which was found in good agreement with the value of ~17Å at 200°C reported by Graham and Cohen (18). Graham and Cohen (18) also reported a limiting thickness of about 10Å at room temperature while Kulpa and Frankenthal (17) reported a thickness of about 4-5Å. In the central office environment we measured a thickness of about ~16Å in 3 months which increased to ~32Å in 2 years. Chiarenzelli (13) also observed that the films on nickel developed in the field are very thin and highly insulating and coherent. Our observations are in agreement with his results. It is well known that in the absence of water vapor the oxidation of nickel is self-limiting and ceases after one to two monolayers of the oxide (17). NiO is a p-type semiconductor and oxide grows by the diffusion of cation vacancies (11, 17, 18). As the relative humidity increases the thickness of the oxide increases, probably because of adsorbed water on the surface causing an increase in the cation vacancy concentration at the surface (19). Air-conditioned central office environments have an average relative humidity of ~40%. The oxide growth on Ni in the central office is, therefore, rather slow. In addition to oxide, the other constituents in the film are sulfur, chlorine, and carbon. The total film thickness is slightly larger than if only an oxide grows on the surface in the drier air.

The corrosion of nickel has been fitted to a parabolic growth rate model. This model provides conservative acceleration factors. The parabolic growth rate constant for Ni corrosion in central office environment is approximately 5×10^{-15} cm²/month. The One Year test develops a film 80Å thick (Fig. 12) in one month and ~140Å thick film in 3 months with no further significant increase in film thickness with time. The test, therefore, provides an acceleration factor greater than 100 with respect to the central office environment. Since the film probably approaches a limiting thickness in the field (asymptotic film growth rate) and also in the test as a function of time, the acceleration factor calculated is only approximate. As mentioned earlier, a parabolic growth rate model has been used in this study, since the acceleration factors so obtained are conservative.

The ratio of nickel to oxygen in the film varies from 0.71 to 0.88. Theoretically, Kulpa and Frankenthal (17) had shown that the ratio of I_{Ni}/I_O should be less than these numbers if the film which grew on nickel was only NiO (*e.g.*, $I_{Ni}/I_O = 0.66$ at 30Å). The remaining Ni in the film is associated with Cl and S. Wootton and Birks (20) have studied the oxidation of nickel in atmospheres containing SO_2 (oxygen partial pressure

Table IV. Thickness of films on nickel

Exposure time (months)	Location	Thickness (A)
3.5	Central office (C.O.)	16
6	C.O.	—
9	C.O.	20
12	C.O.	25
18	C.O.	30
24	C.O.	32.5
3.5	Basement	97
6	Basement	32
9	Basement	121
12	Basement	60
18	Basement	125
24	Basement	195
1	Test chamber	80
3	Test chamber	140
12	Test chamber	140

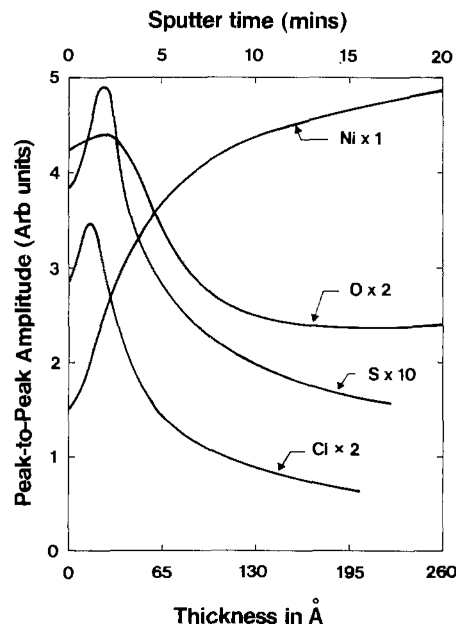

Fig. 12. Auger depth profile of the film developed on Ni exposed for one month in One Year test.

<10^{-6} atm) at higher temperatures. They have concluded that the composition of the film in SO_2 environment is NiO and Ni_3S_2

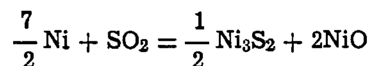

$$\frac{7}{2} Ni + SO_2 = \frac{1}{2} Ni_3S_2 + 2NiO$$

They also reported that preoxidation of Ni reduces the sensitivity of Ni to SO_2 attack. In the real life environment (air) the amount of oxygen available is more than SO_2. We therefore expect that the major constituent of the film would be NiO plus small amounts of Ni_3S_2.

The films developed on Ni exposed in the basement are harder to analyze because a few samples contain excessive amounts of carbon. The carbon layer is thick and may arise from several sources. It is possible that some of these samples became dirty due to improper handling. But the 6 and 12 month coupons do not contain excessive carbon and have been analyzed further. Since the films developed are thin (unlike copper), a small amount of contamination will cause the results to be misleading. An interesting but not surprising observation is that the films which contain large amounts of carbon also show high contact resistance.

Table IV provides the film thicknesses for various samples. Assuming a parabolic growth rate, these two coupons can be utilized to extrapolate the film thicknesses and derive the acceleration factors. An average parabolic growth rate constant k from these two coupons is $\sim 2.4 \times 10^{-14}$ cm²/month. Comparing it with the coupons in the One Year test chamber, an acceleration factor ~27 is obtained for the basement nonair-conditioned environment. This low acceleration factor may again be due to the fact that the adsorption isotherms used were for gold and not for nickel and that the solubilities of gases decrease with increasing temperature.

Conclusions

The growth kinetics of Ag, Ni, and Cu in an air-conditioned telephone central office environment and nonair-conditioned environment (in the Cleveland central office basement) have been obtained. The constituents and film thickness on these materials were primarily obtained by AES. In first 2 years silver tarnishes linearly, the basement growth rate being 30-35 Å/month. The major constituents of films on Ag are Cl and S. Copper corrosion has been fitted to a parabolic growth rate model and provides a rate constant of $\sim 2 \times 10^{-12}$ cm²/month in the basement and 0.3×10^{-12} cm²/month in the central office environment. The extrapolated value of corrosion film thickness on copper in a period of 40 years is ~3100Å in the basement and 1200-1550Å in the central office environment. The major constituents of the corrosion film on Cu in the field are oxygen and chlorine. Nickel tarnish rates are much slower and films only 32Å thick are obtained in 2 years in the central office and ~60Å thick film in the basement in 12 months. The major film constituents are oxygen, chlorine, and sulfur. These observations on Cu, Ni, and Ag are consistent with the published literature.

The coupons exposed in the chamber (One Year test) have also been analyzed for their constituents and film thicknesses. The constituents are similar to films grown in the field. Film thicknesses on these coupons have been used to calculate the acceleration factors for the One Year test. For the basement environment the OneYear test provides an acceleration factor of ~4.0 for Ag, 20 for Cu, and 27 for Ni. The test is not a practical test for Ag. For the central office environment, the acceleration factors for Cu and Ni are greater than 100. Since the test provides a suitable balance between air-conditioned and non-air-conditioned environment, it is an excellent accelerated test for the atmosphere corrosion of Cu and Ni.

Acknowledgments

The author wishes to thank V. Tierney for certain measurements. He is also indebted to J. H. Thomas and F. E. Bader for helpful discussions.

Manuscript submitted March 27, 1978; revised manuscript received July 25, 1978.

Any discussion of this paper will appear in a Discussion Section to be published in the June 1979 JOURNAL. All discussions for the June 1979 Discussion Section should be submitted by Feb. 1, 1979.

Publication costs of this article were assisted by Bell Laboratories.

REFERENCES

1. S. P. Sharma, J. H. Thomas, and F. E. Bader, *This Journal*, **125**, 2002 (1978).
2. J. H. Thomas and S. P. Sharma, *J. Vac. Sci. Technol.*, **13**, 549 (1976), **14**, 825 (1977).
3. M. Antler and J. J. Dunbar, *IEEE Trans.*, **chmt-1**, 17 (1978).
4. J. A. Lorenzen, in Proceedings of Institute on Environmental Sciences, p. 110, Institute of Environmental Sciences, Mt. Prospect, Ill. (1971).
5. W. H. Abbott, *IEEE Trans. Parts, Hybrids, Packaging*, **php-10**, 24 (1970).
6. W. Crossland, E. Knight, and C. R. Wright, in Proceedings of Holm Seminar on Electrical Contact Phenomena, Chicago, Ill., p. 265 (1973).
7. H. Stephen and T. Stephen, Editors, "Solubilities of Inorganic and Organic Compounds," p. 92, MacMillan Co., New York (1963).
8. F. P. Bowden and W. R. Throssell, *Proc. R. Soc. London, Ser. A*, **209**, 297 (1951).
9. H. N. Wagar, in "Physical Design of Electronic Systems," Vol. III, p. 439, D. Beker, D. C. Koehler, W. O. Fleckenstein, C. E. Roden, and R. Sabia, Editors, Prentice Hall, Englewood Cliffs, N.J. (1971).
10. V. Tierney, Private communication.
11. S. R. J. Saunders, *Sci. Prog. Oxf.*, **63**, 163 (1976).
12. W. E. Campbell and U. B. Thomas, *Trans. Electrochem. Soc.*, **91**, 623 (1947).
13. R. V. Chiarenzelli, *IEEE Trans. on Parts, Mater., Packaging*, **pmp-3**, 89 (1967).
14. R. G. Baker, in International Symposium on Electric Contact Phenomena, Graz, Austria, p. 546 (1964).
15. R. P. Frankenthal and D. E. Thompson, Private communication.
16. L. E. Davis, N. C. MacDonald, P. W. Palmberg, G. E. Raich, and R. E. Weber, "Handbook of Auger Electron Spectroscopy," 2nd ed., Physical Electronics Industries, Edina, Minn. (1976).
17. S. H. Kulpa and R. P. Frankenthal, *This Journal*, **124**, 1588 (1977).
18. M. J. Graham and M. Cohen, *ibid.*, **119**, 879 (1972).
19. K. Hauffe, "Oxidation of Metals," Plenum Press, New York (1965).
20. M. R. Wootton and N. Birks, *Corros. Sci.*, **12**, 829 (1972).

Characteristics of Plasma-Oxidized Nitride MOS Structures

A. B. Bhattacharyya

IBM Corporation, Essex Junction, Vermont 05452

and P. K. Chaudhari*

IBM Corporation, Poughkeepsie, New York 12602

ABSTRACT

A process of conversion of oxide/nitride into a single layer oxide using plasma oxidation at moderate temperature (≤800°C) is discussed. Physical parameters, refractive index, etch rate, etc. of this plasma-converted oxide are found to be similar to that of thermal SiO_2. In addition, dielectric strength and charge level in such insulator are also comparable to thermally grown SiO_2. Metal oxide semiconductor (MOS) structures as well as MOSFET device characteristics indicate its excellent feasibility as a gate dielectric in MOS technology.

Silicon nitride is used in the gate dielectric because of high dielectric strength and dielectric constant, the ability to mask against diffusion and oxidation, and resistance to penetration by positively charged ions. However, these MNOS IGFET's suffer from threshold voltage (V_T) degradation when stressed at elevated temperatures. This shift is due primarily to charge trapping at the oxide/nitride interface and, as such, presents a reliability concern. In certain IGFET technology, it is advantageous to use oxide/nitride structure in areas other than the gate regions in order to take advantage of nitride passivation characteristics during device fabrication. In such applications, the effect of trapping could be minimized if oxide/nitride gate dielectric is replaced by single-layer oxide dielectric without major change in MNOS device process. This work discusses a process of conversion of oxide/nitride into a single layer gate dielectric using plasma oxidation at moderate temperature (≤800°C). Characteristics of this plasma-converted oxide with respect to (*i*) fixed charge incorporation due to plasma exposure; (*ii*) insulator integrity or breakdown strength; (*iii*) refractive index; and (*iv*) etch rate are investigated. Bias-temperature stress aging of MOS capacitors is studied to investigate flatband voltage stability. Hot electron trapping is characterized by avalanche injection of MOS capacitors and stress aging of MOSFET devices.

Experimental Details

Preparation of the plasma-oxidized nitride films.—Thin silicon nitride films may be converted to SiO_2 at moderately low temperature through plasma-enhanced oxidation reaction of nitride. The nature of this anodization process is believed to be as follows

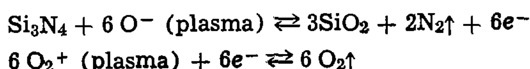

$$Si_3N_4 + 6\,O^- \text{ (plasma)} \rightleftarrows 3SiO_2 + 2N_2\uparrow + 6e^-$$

$$6\,O_2^+ \text{ (plasma)} + 6e^- \rightleftarrows 6\,O_2\uparrow$$

The processing sequence of obtaining plasma-oxidized nitride films consists of:

(*i*) Standard wafer cleaning; (*ii*) Thermal oxidation in dry oxygen in system prepurged with HCl to minimize contamination and charge level. Oxide thus fabricated showed refractive index of 1.47 and dielectric constant of 3.9; (*iii*) Chemical vapor deposition of thin nitride film. Nitride films had refractive index of 2.0 and dielectric constant of 7.0; (*iv*) Plasma oxidation of overlayer nitride in a plasma reactor in an ambient of dry O_2 and argon. (A schematic of the reactor is shown in Fig. 1. A typical processing condition is shown in Table I.) Converted insulator exhibited refractive index of 1.47 and dielectric constant of 3.9-4.0; (*v*) Postanodization anneal to minimize charge level.

Device fabrication.—Silicon substrates used in this study were of p-type and of resistivity either 2 or 0.05 Ω cm. Metal oxide semiconductor (MOS) capacitors consisting of this plasma-oxidized insulator were fabricated by evaporating aluminum dots as field plates. Aluminum was also deposited on the back side and annealed in forming gas at 400°C for about 20 min. Mobile charge levels were checked by the *I-V* loop technique (1) after biasing the capacitors at 200°C and $+2.0 \times 10^6$ V/cm for 10 min. Mobile ion contamination (N_I) in all runs under investigation was consistently below 10^{10} cm^{-2} level while fixed charge levels were below 1×10^{11} cm^{-2}. Film thickness was measured with an ellipsometer. Experimental MOSFET devices were also fabricated. First source and drain regions were formed using an arsenosilicate glass source as a dopant. After cleaning, the gate dielectric was grown as described above. Aluminum was used as the gate metal. After aluminum evaporation, the device wafers were also treated in a forming gas anneal at 400°C for about 20 min. Conventional photolithography was used throughout. Conversion of standard dual dielectric MNOSFET into a single layer dielectric plasma-converted oxide MOSFET is illustrated in Fig. 2. Devices thus fabricated had a threshold voltage range of approximately +1.3V for ~70 nm of converted SiO_2 gate dielectric of 2 Ω cm p-silicon wafers using initial oxide/nitride thickness of 38/15 nm. Standard fixed charge density, N_{SS}, breakdown, bias-temperature stress aging, and avalanche injection measurements were carried out to characterize the quality of the plasma-converted insulator layer for stability and charge trapping. Standard MNOS and MOS structures were used as reference for comparison.

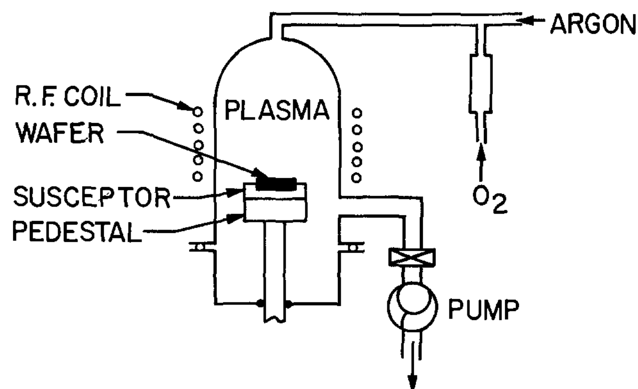

Fig. 1. Single wafer RF coil discharge reactor

* Electrochemical Society Active Member.
Key words: oxide/nitride films, plasma-oxidized nitride, MOS characteristics.

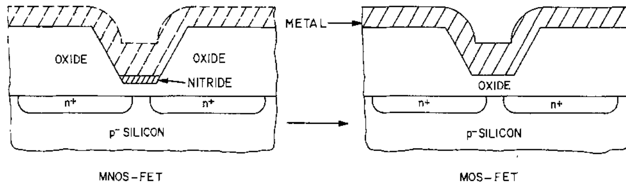

Fig. 2. Gate dielectric oxide/nitride conversion using plasma oxidation to gate dielectric oxide.

Results and Discussion

Table II summarizes the physical characteristics of this plasma-anodized insulator layer. It is seen that the refractive index and etch rate are quite comparable to thermal SiO_2.

Charge level and effect of anneal.—Experiments were designed to study the effect of annealing on charge level and flatband voltage. Three types of annealing ambients were investigated: forming gas, N_2, and a mixture of N_2 with 2 m/o (mole percent) O_2. Details of the annealing conditions are summarized in Table III. It may be noted that the net positive charge density is low for all samples on plasma exposure. Either a N_2 anneal at higher temperature (1075°C) or a forming gas anneal at lower temperature (850°C) resulted in almost charge-free insulator. As shown in the table, an anneal in a mixture of O_2 and N_2 at 1000°C did not reduce fixed charge level in the insulator when compared to annealing in N_2 at the same temperature. This observation may support the postulate that the plasma-converted insulator may not be oxygen deficient and, therefore, fixed charges in such insulators may not be associated with incomplete oxidation.

Breakdown strength.—Figure 3 shows the breakdown distribution of the plasma-oxidized insulator layer compared with thermal SiO_2 MOS data. As is seen from Fig. 3, the lower mode of breakdown distribution around 2-4 × 10^6 V/cm observed in thermal SiO_2 is not observed in plasma MOS structures. Breakdown distribution ranges from 6.5 × 10^6 to 9 × 10^6 V/cm and compares favorably with thermal SiO_2.

Table I. Conditions for plasma oxidation

Temperature	800°C
Frequency	42 kHz
O_2 pressure	0.1 Torr
Nitride oxidation rate	4.5 nm/min

Table II. Plasma-exposed insulator (nitride)

	Before plasma oxidation	After plasma oxidation
Ref. index	2.0	1.47
Etch rate in 7:1 BHF	0.015 nm/sec	1.2 nm/sec

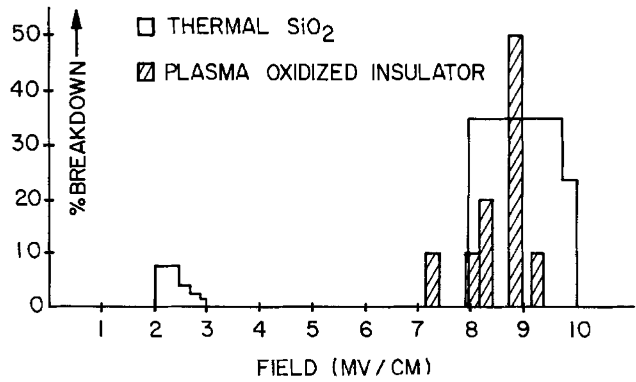

Fig. 3. Breakdown distribution of plasma-oxidized insulator

Flatband voltage stability.—MOS capacitors were stressed at 190°C and +2 × 10^6 V/cm for 18 hr to determine the stability of the flatband voltage. The data obtained is tabulated in Table IV. It is clear that the shift data of flatband voltage are quite compatible to the PSG-MOS and better than composite films of Si_3N_4/SiO_2 MOS capacitors.

Trapping characteristics.—Electron trapping characteristics were studied by avalanche injection of MOS capacitors, after Nicollian and co-workers (2). The technique is more completely described by Gdula (3). Typical results are shown in Fig. 4 where trapped charge density $\Delta Q/q$ is plotted against injected electron density N_{inj}. The latter was computed from simultaneous gate current measurements. Trapping behavior of these plasma-oxidzed films is compared with that of PSG/SiO_2 and of a composite of Si_3N_4/SiO_2 and of thermal SiO_2. It is seen that traps in plasma-oxidized insulator are comparable to CVD PSG/SiO_2 films. Trap density of such films is significantly lower when compared with Si_3N_4/SiO_2 composite films. However, thermal SiO_2 films exhibit minimum density of traps. For PSG-oxide and plasma-oxidized insulators, a change in slope is observed at $N_{inj} \simeq 10^{14}$ cm^{-2}, indicative of another kind of a trap center. The associated initial $\Delta Q/q \simeq 10^{11}$ cm^{-2} is due to the large cross section traps associated with fixed oxide charge (4). It is known that this fixed oxide charge could be minimized by extended annealing

Table IV. Flatband voltage stability of plasma-converted oxide MOS structures

Stress conditions: 2.0 × 10^6 V/cm, 190°C for 18 hr

	PSG-MOS (47 nm)	MNOS (38 nm Ox/15 nm Nit)	Plasma-MOS (83 nm) Run No. 2	Plasma-MOS (83 nm) Run No. 3
ΔV_{FB}	−75 mV	−125 mV	−80 mV	−90 mV
$\frac{\Delta Q}{q}$ cm^{-2}	3.4 × 10^{10}	5.9 × 10^{10}	2 × 10^{10}	2.3 × 10^{10}

Table III. Plasma-converted MIS, effect of postoxidation heat-treatment on charge level

Run	Wafer type and structure	Postplasma oxide anneal conditions		N_{SS} (cm^{-2})	N_I (cm^{-2})	V_{FB} (V)
1	2 Ω cm p-type 38/14 nm Ox-nit	Forming gas anneal	850°C 30 min	—	—	−0.7-−0.75
			1050°C 30 min	—	—	−0.8-−0.85
2	2 Ω cm p-type 38/15 nm Ox-nit	N_2 anneal	1000°C 30 min	1.25 × 10^{11}	10^9	−1.02
			1075°C 22 min	3.0 × 10^{10}	10^9	−0.87-−0.95
			1075°C 1 hr	0	<10^{10}	−0.79
3	2 and 0.05 Ω cm p-type 38/20 nm Ox-nit	N_2/2% O_2 anneal	1000°C 1 hr	4.0 × 10^{11}	10^9	−2.93

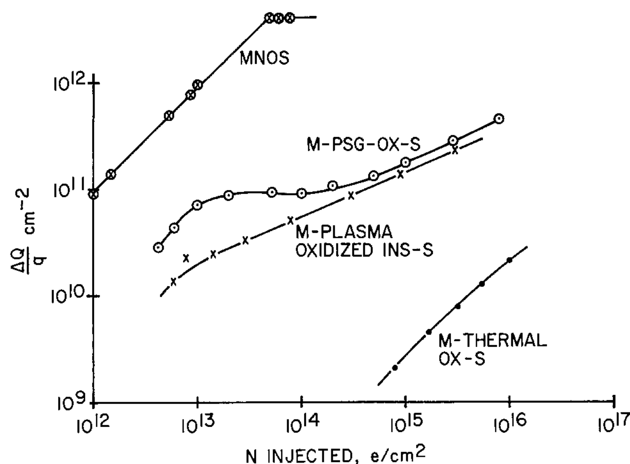

Fig. 4. Charge-trapping characteristics of plasma-oxidized insulator.

time. The relationship between insulator trapping characteristics and hot electron-induced threshold voltage shift and subsequent design margin and reliability has been discussed by Abbas and Dockerty (5). Such hot-electron design relief is obviously greater in oxide (MOS) than in oxide-nitride (MNOS), where nitride offers more trapping sites. Hot electron relief over MNOS structures as observed from capacitor data is further confirmed by stress aging MNOSFET and plasma-oxidized gate dielectric MOSFET devices. Figure 5 shows the threshold voltage shift data obtained, with the stress conditions shown in the notes of the figure. The data indeed confirms that the plasma-oxidized gate insulator does trap less than the composite nitride/oxide gate dielectric, thereby offering design ability of an FET circuit at a drain voltage of 2.75V higher than the corresponding circuit with MNOS FET devices.

Conclusions

Plasma-converted oxide from oxide/nitride dual dielectric layer demonstrates characteristics similar to thermally grown oxide in refractive index, etch rate, effective charge, and breakdown strength. Low N_{SS}, N_I has also been demonstrated. Bias-temperature stress data of plasma-converted oxide shows better stability compared with that of oxide/nitride and of oxide/PSG structures.

Avalanche injection data indicates that trapping characteristics are comparable to PSG/SiO_2 structures and are midway between thermal SiO_2 and oxide/nitride composite dielectric structures.

Acknowledgments

The authors acknowledge the contribution of R. Gdula in trapping measurements and of C. Kroll and R. M. Quinn in processing the wafers.

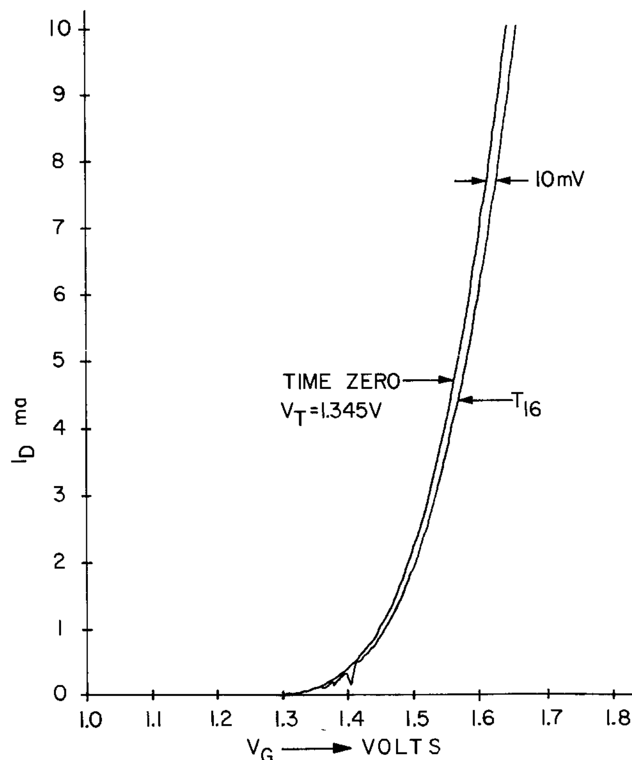

Hot electron stress conditions at room temperature

	V_D	V_G	$V_{sub} = V_s$	Time	Shift
MNOS FET	12.25	$(V_T + 7)$	Gnd.	16 hr	10 mV
Plasma MOS FET	15.0	$(V_T + 7)$	Gnd.	16 hr	10 mV

Fig. 5. FET characteristics of plasma-oxidized insulator gate dielectric.

Manuscript submitted March 3, 1978; revised manuscript received July 1, 1978. This was Paper 137 presented at the Atlanta, Georgia, Meeting of the Society, Oct. 9-14, 1977.

Any discussion of this paper will appear in a Discussion Section to be published in the June 1979 JOURNAL. All discussions for the June 1979 Discussion Section should be submitted by Feb. 1, 1979.

Publication costs of this article were assisted by IBM Corporation.

REFERENCES

1. D. Kerr, Paper presented at the International Conference on the Properties and Uses of MIS Structures, Grenoble, France, June 17-29 (1969).
2. A. Goetzberger and E. H. Nicollian, *Appl. Phys. Lett.*, **9**, 444 (1966).
3. R. A. Gdula, *This Journal*, **123**, 42 (1976).
4. T. H. Ning, C. M. Osburn, and J. N. Yu, *Appl. Phys. Lett.*, **26**, 248 (1975).
5. S. A. Abbas and R. C. Dockerty, *ibid.*, **27**, 147 (1975).

An Estimation of the Quantum Yield in the Candoluminescence Process by Low Energy H^+ Ion Bombardment

I. S. T. Tsong, Andres Corredor, and William B. White*

Materials Research Laboratory, The Pennsylvania State University, University Park, Pennsylvania 16802

and N. H. Tolk and J. S. Kraus

Bell Laboratories, Murray Hill, New Jersey 07974

ABSTRACT

The luminescent quantum yields for $Zn_2SiO_4:Mn^{2+}$ and $Y_2O_3:Eu^{3+}$ phosphors under hydrogen ion beam excitation have been determined at 300°K as a function of beam energy in the range 1-8 keV. The dependence of the yields on the energy of the H^+ bombarding ions follows an exponential relation and the yields extrapolated to zero ion energy are $\eta_o = 4.0 \times 10^{-6}$ for $Zn_2SiO_4:Mn^{2+}$ and $\eta_o = 2.7 \times 10^{-4}$ for $Y_2O_3:Eu^{3+}$.

Candoluminescence is usually defined as a process of light emission from solids under flame excitation, in excess of thermal radiation. The candoluminescence phenomenon has been recently reviewed by Ivey (1). Flame excitation of phosphor materials at relatively low temperatures, *i.e.*, room temperature to a few hundred degrees, has been observed by a number of workers and it has also been found that similar luminescence can be excited in the absence of a flame by generating active species of hydrogen or nitrogen in an arc or microwave plasma (2-5). This flameless excitation phenomenon has given rise to the term "radical-recombination luminescence" (RRL) and its physical process is considered to be similar to candoluminescence.

Despite its obvious importance, there have been remarkably few measurements of the quantum yield of the candoluminescence or RRL process. The difficulty no doubt lies in the fact that one cannot easily count the number of recombinations or impacts of particles (radicals, ions, etc.) on the phosphor surface when one is using a flame or an rf discharge as the excitation source. A knowledge of the quantum yield would allow us to assess the applicability of candoluminescence to lighting device development.

In previous determinations of quantum yield of RRL (6-8), calorimetric techniques were employed where the number of recombinations was estimated by the heat output caused by the recombination of the hydrogen or nitrogen atoms on the phosphor surface. A typical value of the quantum yield, *i.e.*, number of photons per recombination, is of the order of 10^{-4}. One disadvantage of the technique is that the rise of temperature recorded may be due to processes, *e.g.*, collision with the surface, other than recombination alone. Moreover, it is not at all certain that the luminescence is caused by just one particular species of the gas atoms since there is no mass separation involved and the vacuum in the apparatus is generally poor.

In the present work, we attempt to measure the quantum yield by using an entirely new approach. The surfaces of two candoluminescent materials, $Zn_2SiO_4:Mn^{2+}$ and $Y_2O_3:Eu^{3+}$ were bombarded with a low energy H^+ ion beam at room temperature. In this way we can measure the number of H^+ arriving at the surface since we can measure the ion current, and the photon output is measured by single-photon counting. The quantum yield is therefore a simple ratio of the two. We chose to examine the above two materials because of their different luminescence characteristics. $Zn_2SiO_4:Mn^{2+}$ is a broad-band emitter, whereas $Y_2O_3:Eu^{3+}$ is a line emitter. Moreover, the quantum yield of $Zn_2SiO_4:Mn^{2+}$ has been measured by Sommermeyer (6) and Styrov *et al.* (8), and we can make a comparison between our results and theirs.

Experimental

Figure 1 shows the schematic diagram of the experimental apparatus. The ion beam unit consists of a Colutron ion source. The ion mass is selected by a velocity filter. The energy of the ion beam can be varied from 10 eV to 10 keV. The H^+ ion current was $\sim 1 \times 10^{-6}$A at 8 keV but decreased to $\sim 1 \times 10^{-8}$A at 1 keV. This could not be avoided as this was the characteristic of the ion beam extraction and acceleration systems. It is considered to be a difficult problem in present-day ion beam technology to produce a well-focused, mass-analyzed, as well as high flux ion beam at energies below 1 keV. The production of such ion or atomic beams are subjects of specialized research (9, 10). The ion beam and the optical axis of the monochromater (0.3m McPherson) are at right angles to each other, while the incident-beam makes an angle of 50° with the target normal. Single photon counting is used to measure the light output. Such experimental setup had been used to observe optical emis-

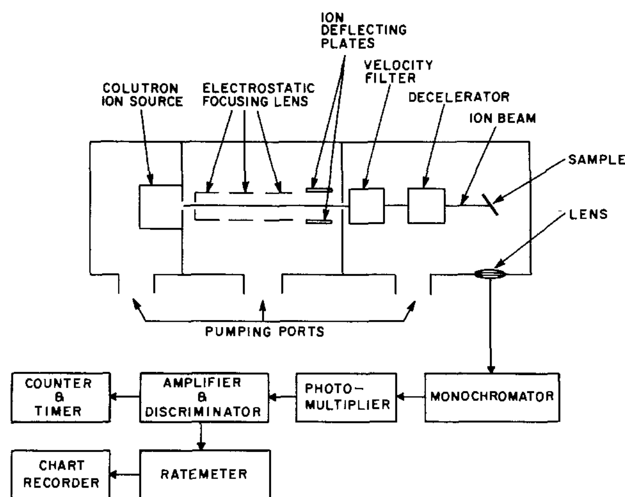

Fig. 1. Schematic diagram of hydrogen ion beam apparatus

* Electrochemical Society Active Member.

Key words: luminescence, quantum theory, ion exchange.

sion from sputtered particles during heavy ion bombardment (11). However, in the present experiment the sputtering effect caused by H^+ ion was negligible and the observed emission was entirely due to luminescence from the bulk of the solid.

The original powder samples were compacted into solid disks by using a binder solution commonly used in scanning electron microscopy. The two samples were mounted on the same holder, one above the other. Bombardment of the sample was accomplished by sliding each sample into the beam path at each energy setting of the beam. The beam spot on the target surface was 3 mm in diameter. There was no heating stage in the target holder and the samples remained at room temperature during bombardment.

The ion current was measured by a picoammeter when the target holder was positioned in such a way as to allow the entire ion beam to strike the exposed metal parts of the target holder in between the two samples. This ion current was found to be virtually unchanged when the ion beam was incident on the insulating phosphor targets. This interesting observation suggests the possibility that a small voltage (say $\sim +10V$) buildup may have occurred between the phosphor and the metal target-holder, and the $\sim 10^4$ V cm^{-1} field thus created pulls electrons from the metal into the phosphor, giving rise to an observed current on the picoammeter. This 10^4 V cm^{-1} is uniform and is small compared to fields encountered in electroluminescence, and these electrons therefore generate no luminescence themselves. A tungsten filament was positioned close to the target surface and when this was turned on to flood the surface with electrons, no change in the luminescence intensity was observed. From this it was concluded that the sample surface did not charge up during ion bombardment.

The vacuum in the target chamber during bombardment was $\sim 10^{-7}$ Torr. The intensities at 525 nm for $Zn_2SiO_4:Mn^{2+}$ (Sylvania Type 161) and 613.5 nm for $Y_2O_3:Eu^{3+}$ (Sylvania Type 1130) were measured as a function of ion energy. The slit width of the monochromater was 500μ. The detection sensitivity of the optical system was determined by means of calibration against a standard tungsten lamp. The quantum efficiency of the optical detection, *i.e.* the number of photons detected per emitted photon, at the wavelength of interest was thus determined and this was used to correct the measured intensities. The calibration of the optical system is a standard procedure and has been described in detail by other workers, see, *e.g.*, Andersen *et al.* (12), and will not be repeated here.

To test whether any deterioration of the phosphor had taken place during the H^+ bombardment, the luminescence was first measured as a function of decreasing ion energy unti the signal becomes comparable to noise, and then the steps were repeated as a function of increasing ion energy. The reproducibility of the data indicated there was little or no deterioration of the phosphor targets during our experiment. This absence of deterioration is probably due to negligible sputtering effect by the H^+ ions.

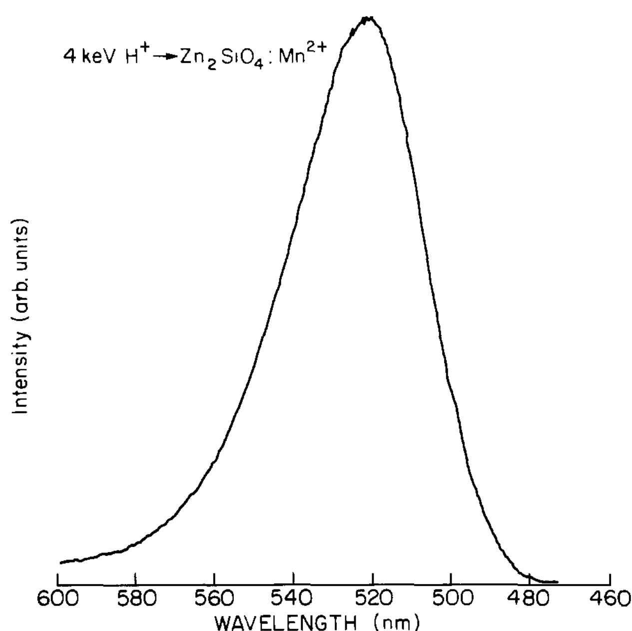

Fig. 2. Emission spectrum of $Zn_2SiO_4:Mn^{2+}$ under 4 keV H^+ bombardment.

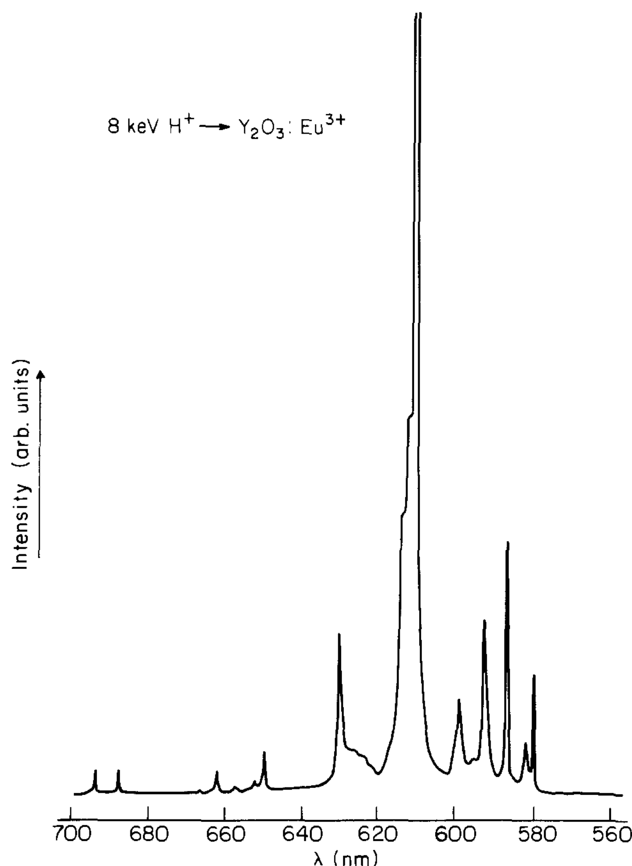

Fig. 3. Emission spectrum of $Y_2O_3:Eu^{3+}$ under 8 keV H^+ bombardment.

Results

The luminescence spectra of $Zn_2SiO_4:Mn^{2+}$ and $Y_2O_3:Eu^{3+}$ bombarded by H^+ ions are shown in Fig. 2 and 3. The variation of the quantum yield of the two samples as a function of the H^+ ion energy is shown in Fig. 4 and 5. The quantum yield is defined as the number of photon counts per incident ion. The number of photons counted experimentally per second before correcting for the quantum efficiency of the optical detection system was of the order of 10^6 for both samples at 8 keV. This number decreased to $\sim 10^2$ at 1 keV, comparable to the background radiation detected. The background counts were due to scattered light from the heated ion source filament. It was hoped at the onset of the experiment to extend the luminescent intensity measurement to an H^+ ion energy of 10 eV, the lower limit of the Colutron ion beam system. However, no further data were taken below 1 keV since the signal was comparable to the background noise.

The straight lines drawn through the data points in the log-linear plots shown in Fig. 4 and 5 show that the quantum yield dependence on energy can be represented by the expression

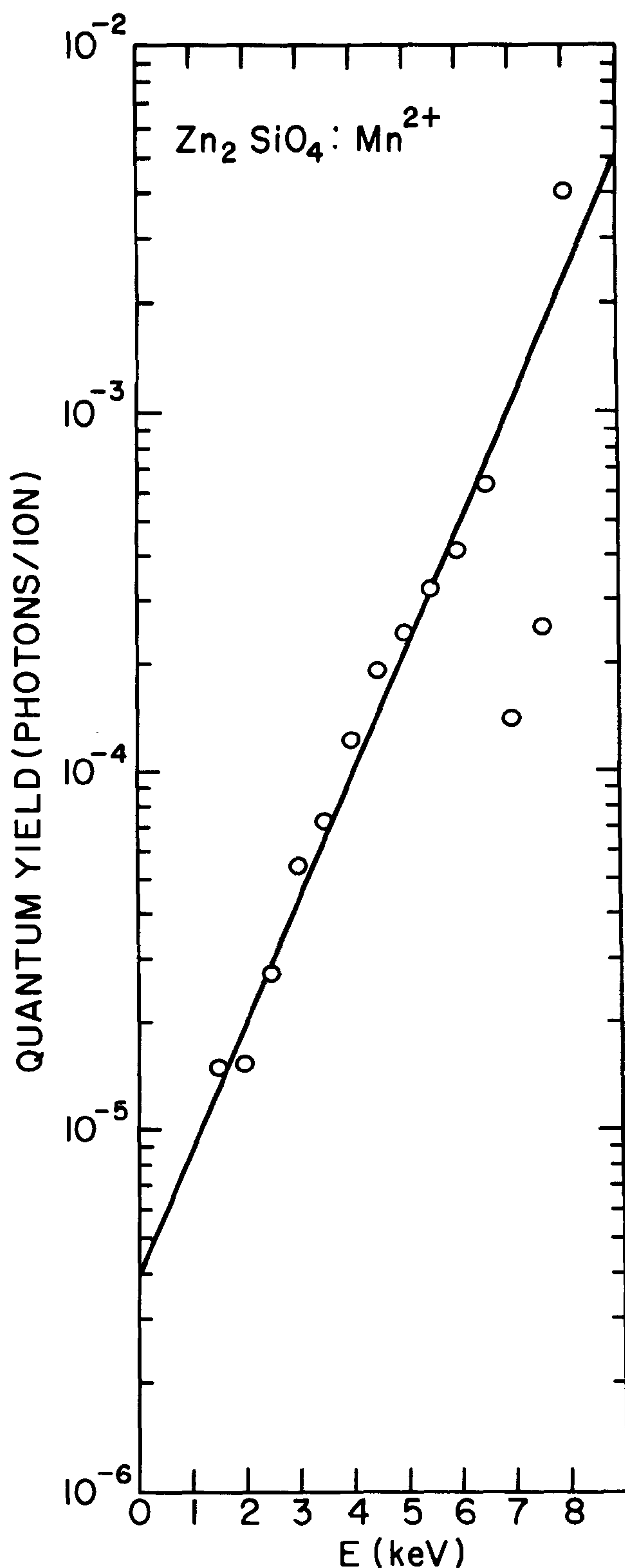

Fig. 4. Dependence of quantum yield of Zn_2SiO_4:Mn^{2+} on H^+ ion energy.

$$\eta = \eta_o \exp(aE) \qquad [1]$$

where η_o and a are constants. If the plots are extrapolated to zero energy, then we obtain

$$\eta_o = 4.0 \times 10^{-6} \text{ for } Zn_2SiO_4:Mn^{2+} \qquad [2]$$

$$\eta_o = 2.7 \times 10^{-4} \text{ for } Y_2O_3:Eu^{3+} \qquad [3]$$

Discussion

The quantum yield at room temperature, $\eta = 4.0 \times 10^{-6}$ for Zn_2SiO_4:Mn^{2+} when extrapolated to zero energy, is remarkably similar to the η value, 8.2×10^{-6}, given by Styrov *et al.* (8) and 5×10^{-6} by Sommermeyer (6) for the RRL process measured by the calorimetric method. There is no corresponding η value determined for Y_2O_3:Eu^{3+}. However, a quantum yield of 5.8×10^{-2} for cathodoluminescence was quoted by Garlich (13), which compares favorably with the η values obtained at ion energies above 4 keV in the present work (see Fig. 5).

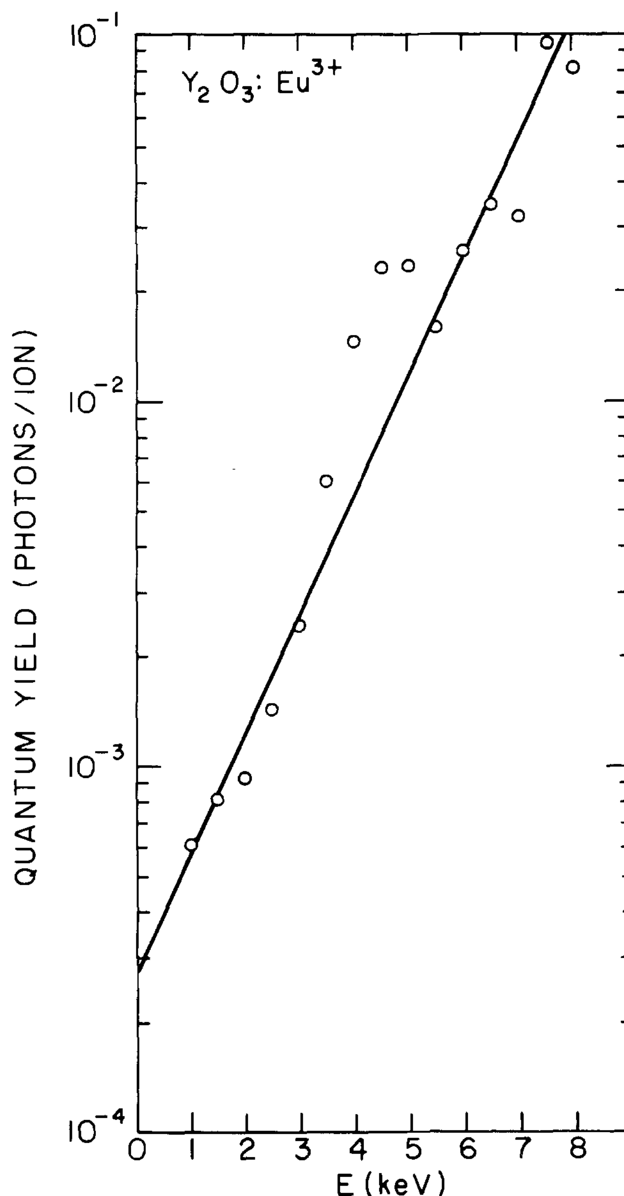

Fig. 5. Dependence of quantum yield of Y_2O_3:Eu^{3+} on H^+ ion energy.

Eve and Duckworth (14) have reported the observation of luminescence from Zn_2SiO_4:Mn^{2+} when bombarded by heavy ions at high energies (6-25 keV). An intensity-energy relationship of the type

$$I \sim (E - E_o)^n \qquad [4]$$

was reported, where n has a range of values between 1.29 and 1.83 for bombardment by various heavy ions except hydrogen. Heavy ion bombardment can cause sputter-induced optical emission (11) which Eve and Duckworth probably were not aware of at the time. Since no wavelength selector was used by them to isolate the luminescence from other emission from the Zn_2SiO_4:Mn^{2+} sample, it is not certain how their final results would be affected. Moreover, sputtering by heavy ion bombardment could cause rapid deterioration of the phosphor. Clearly, the results of the

present work in the lower energy range (1-8 keV) indicate a different intensity-energy relationship from Eq. [4]; and the intensity is shown to fall off much more rapidly with decreasing energy.

Our procedure of extrapolation to zero energy may not be justified on the grounds that it is not known whether the quantum yield values at energies below 1 keV would follow the same exponential behavior as those at higher energies. Measurable light signals at energies <1 keV would be feasible if a high flux ion beam is available (we have already discussed the problems associated with high flux and low energy ion beams in the Experimental Section), so that quantum yield data can be extended to energies of only a few electron volts. The luminescence observed in the present work is caused by the kinetic energy transfer of the bombarding ions to the electrons in the solid (15), whereas in RRL, it is postulated that the potential energy of the recombining atoms is involved in exciting the phosphor. The question remains whether, in addition to the kinetic energy of the H^+, the 13.5 eV available in potential energy from capturing an electron by the incoming H^+ ion

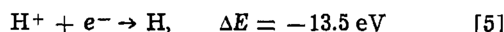

$$H^+ + e^- \rightarrow H, \quad \Delta E = -13.5 \text{ eV} \quad [5]$$

can also be utilized. We can picture, for instance, the incident proton capturing an electron from some valence band ~13 eV deep by a resonance-transfer process, whereupon the hole created is ultimately captured on the Mn^{2+}. An electron drawn in from the metal base of the target holder is then captured also, producing Mn^{2+*} which emits. Another possibility would be the Auger neutralization (16) of the incoming H^+ ion by a valence electron tunneling through the potential barrier, creating a hole in the valence band. The excess energy of this neutralization process then excites a second electron into the conduction band. The electron-hole pair then recombines at the activation center Mn^{2+}, resulting in emission.

Some such chain of events [see for example Ref. (1)], though of course not identical with those described above, is implied by Styrov *et al.* (8) and Sommermeyer (6) when they link their observed Mn^{2+} emission to the potential energy available from the recombination of adsorbed H atoms

$$H + H \rightarrow H_2, \quad \Delta E = -4.55 \text{ eV} \quad [6]$$

We find it surprising that our η_o, obtained by simple extrapolation to 0V as if the potential energy contribution is an additive constant and representing the efficiency of the conversion of this potential energy into Mn^{2+} emission, is so close to the quantum yield values given by Styrov and Sommermeyer. It is surprising that two H atoms combine and transfer their potential energy to the Mn^{2+} center with the same efficiency as one H^+ is neutralized by creating a hole which ultimately leads to Mn^{2+} excitation and emission. This suggests that both mechanisms of radical recombination and charge neutralization may be responsible for the candoluminescence process, since both radicals and ions (17) are present in the flame acting as the source of excitation.

Luminescence from $Zn_2SiO_4:Mn^{2+}$, $Y_2O_3:Eu^{3+}$, and other phosphors when bombarded by N_2^+ and other heavy ions at very low energies (~ 40 eV) have been recently reported by Kramer (18). By comparison with luminescence from a ZnO sample, Kramer estimated quantum yield values as high as 1 photon per 40 N_2^+ ions. However, the experimental situation was complicated by the presence of an electron beam (~ 20 eV) which also bombarded the sample surfaces. We do not understand the high yields reported by Kramer, three orders higher than the η_o values reported here, except perhaps that the 20 eV electrons may interact with the positive ions in some very advantageous manner to transfer the energy to the Mn^{2+} and Eu^{3+} centers.

Kramer also observed characteristic blue-green luminescence from ZnO bombarded by low energy heavy ions only (19). Once again very high quantum yield was reported compared to the value 7×10^{-6} for ZnO reported by Styrov *et al.* (8) for RRL, and the process was attributed to the creation of electron-hole pairs in the phosphor due to the Auger neutralization of the incoming ions (16).

The quantum yields quoted apply to a temperature of 300 K and are not necessarily the maximum yield attainable. Both candoluminescence and RRL exhibit a characteristic bell-shaped dependence of intensity on temperature. For both $Zn_2SiO_4:Mn^{2+}$ and $Y_2O_3:Eu^{3+}$ the luminescent intensity is low at room temperature, increases as the temperature increases, reaches a maximum at some intermediate temperature, and then decreases to low values as the temperature is further increased. The temperature at which maximum brightness occurs is a function of activator, phosphor host, and recombining species (20, 21). The peak brightness occurs in $Zn_2SiO_4:Mn^{2+}$ at 40°C for H_2 radical recombination, and at 178°C in the hydrogen flame. The corresponding value for the flame excitation of $Y_2O_3:Eu^{3+}$ is 210°C. It has been argued (22) that in RRL the number of recombinations depends on the competition between the rate of adsorption of the atoms arriving on the surface and the rate of desorption of the same atoms. Then the maximum in the brightness-temperature curve can be explained on the basis of the variation of the relative rates of desorption of recombined neutral species as contrasted with the desorption of freshly adsorbed active species at different temperatures. It is therefore expected that the effective quantum yield would also be a sensitive function of temperature. However, in the present experiment, if the luminescence is the direct result of electronic excitation in the solid by the bombarding ions, then the observed quantum yields would probably not increase with increasing target temperature. It would be most interesting to carry out similar experiments at target temperatures above room temperature in order to understand the full implication of the similarity between the quantum yields determined by low energy H^+ ion bombardment and those determined by calorimetric method.

Conclusions

The trend of our quantum yield measurements of the luminescence of $Zn_2SiO_4:Mn^{2+}$ and $Y_2O_3:Eu^{3+}$ caused by H^+ ion bombardment in the 1-8 keV range indicates that at ion energies close to zero, the quantum yield is not too different from that in RRL where excitation is assumed to be the result of potential energy transfer. It would be desirable to extend the measurements to energies ~ 10 eV if and when a high flux ion beam at such low energies becomes available. Measurements of quantum yield at elevated target temperatures would also be useful.

Acknowledgments

The work at The Pennsylvania State University was supported by the National Science Foundation under Grant No. DMR-74-00340. We are grateful to Sylvania Electric Products for contributing the phosphors used in this work.

Manuscript submitted Oct. 11, 1977; revised manuscript received July 15, 1978.

Any discussion of this paper will appear in a Discussion Section to be published in the June 1979 JOURNAL. All discussions for the June 1979 Discussion Section should be submitted by Feb. 1, 1979.

Publication costs of this article were assisted by The Pennsylvania State University.

REFERENCES

1. H. F. Ivey, *J. Lumin.*, **8**, 271 (1974).
2. K. M. Sancier, W. J. Fredericks, and H. Wise, *J.*

Chem. Phys., 37, 854 (1962).
3. V. A. Sokolov and A. N. Gorban, *Bull. Acad., Sci. USSR, Phys. Ser.*, **25**, 412 (1961).
4. J. R. Sweet, W. B. White, H. K. Henisch, and R. Roy, *Phys. Lett.*, **33A**, 195 (1970).
5. W. Hanle and H. Niermann, *Z. Naturforsch. Teil A*, **11**, 395 (1956).
6. K. Sommermeyer, *Z. Phys. Chem.*, **B41**, 433 (1938).
7. K. M. Sancier, W. J. Fredericks, and H. Wise, *J. Chem. Phys.*, **37**, 865 (1962).
8. V. V. Styrov, V. A. Sokolov, and Yu. P. Osipenko, *Sov. Phys. J.*, **10** (11), 37 (1967).
9. M. J. Kofoid, C. M. Braams, and P. Zieske, *Rev. Sci. Instrum.*, **36**, 1415 (1965).
10. B. Van Zyl, N. G. Utterback, and R. C. Amme, *Rev. Sci. Instrum.*, **47**, 814 (1976).
11. N. H. Tolk, I. S. T. Tsong, and C. W. White, *Anal. Chem.*, **49**, 16A (1977).
12. N. Andersen, K. Jensen, J. Jepson, J. Melskens, and E. Veje, *App. Opt.*, **13**, 1965 (1974).
13. G. F. J. Garlich, in "Luminescence of Inorganic Solids," P. Goldberg, Editor, p. 685, Academic Press, New York (1966).
14. C. F. Eve and H. E. Duckworth, *Can. J. Phys.*, **36**, 104 (1958).
15. C. W. White, E. W. Thomas, W. F. van der Weg, and N. H. Tolk, in "Inelastic Ion-Surface Collisions," N. H. Tolk, J. C. Tully, W. Heiland, and C. W. White, Editors, p. 201, Academic Press, New York (1977).
16. H. D. Hagstrum, *Phys. Rev.*, **96**, 336 (1954).
17. H. C. Bolton and I. C. McWilliam, *Proc. R. Soc. London, Ser. A*, **321**, 361 (1971).
18. J. Kramer, *This Journal*, **123**, 85 (1976).
19. J. Kramer, *J. Appl. Phys.*, **47**, 1719 (1976).
20. J. W. Hess, J. R. Sweet, and W. B. White, *This Journal*, **121**, 142 (1974).
21. A. Corredor and W. B. White, To be submitted to *ibid.*
22. A. Corredor, I. S. T. Tsong, and W. B. White, in "Proceedings of the 13th Rare Earth Research Conference," p. 573, Plenum Press, New York (1978).

Direct Observation of Dislocations in $Ga_{1-x}Al_xAs$-GaAs Grown by the LPE Method

Satoshi Komiya and Tsuyoshi Kotani

Fujitsu Laboratories Limited, 1015 Kamikodanaka Nakahara-ku, Kawasaki, Japan

ABSTRACT

Transmission x-ray topographs of thick LPE $Ga_{1-x}Al_xAs$ layers grown on (001) GaAs substrates were obtained by a double crystal Lang technique using monochromatic divergent radiation and compared with the etch pit pattern revealed by molten KOH. It was observed that most threading dislocations bend abruptly at the interface. Although the substrate parts of these dislocations were of various types, the epitaxial parts were clearly classified as either [001] oriented, β-, or arc-like dislocations. Nonequivalent behavior of threading dislocations between the two <110> directions was observed. Some effects due to melt-back of the substrate prior to the epitaxial growth are discussed.

It has been ascertained that the rapid degradation of $Ga_{1-x}Al_xAs$-GaAs double heterostructure lasers was due to the appearance of a nonluminescent area, called a dark line defect (DLD). The DLD oriented to the <100> or <110> direction has been observed by photoluminescence (1) and scanning electron microscopy (2). Petroff and Hartman have shown that the <100> DLD was associated with a dislocation network originating from a threading dislocation in the epitaxial layers (3). Some growth mechanisms from a threading dislocation to a dislocation dipole have already been proposed and discussed (4-7). It seems that these mechanisms are closely related to properties of threading dislocations.

Ishii *et al.* have observed dislocations in thin GaAs epitaxial layers by using molten KOH (8). Most dislocations propagate from the substrate to the epitaxial layers but some of them disappear in the epitaxial layers. Kumar and Takagi recently studied dislocations in a thick homoepitaxial layer on a GaAs (111) As face substrate by using x-ray topography (9). It was observed that some new dislocations are generated during the growth in addition to normal threading dislocations. Dislocations in a thick epitaxial $Ga_{1-x}Al_xAs$ layer have been rarely studied by x-ray topography because a wafer with a thick epitaxial layer is bent due to the lattice mismatch between the substrate and epitaxial layer. In this report, transmission x-ray topographs of (001) GaAs wafers with thick heteroepitaxial $Ga_{1-x}Al_xAs$ layers were obtained by a double crystal Lang technique with a curved monochromater crystal (10), and then compared with the etch pit pattern on the epitaxial layer produced by molten KOH.

Key words: liquid phase epitaxy, III-V compound, dislocation, x-ray topography, etch pit.

Experiments and Results

An epitaxial $Ga_{1-x}Al_xAs$ layer has been grown on a (001) GaAs substrate by liquid phase epitaxy. The method of growth is similar to that reported by Blum and Shih (11). The characteristics of the samples are summarized in Table I, where melt-back of the substrate has been employed for sample II by a temperature rise of 3.8°C. X-ray topographs are obtained under conditions of anomalous transmission (μt = 12-14) by a double crystal Lang technique using monochromatic divergent radiation made by a curved (111) Ge crystal (10). Cu-Kα_1 radiation and Ilford L4 50 μm

Table I

	Sample	x	Carrier concentration (cm^{-3})		Thickness (μm)
Substrate	GaAs		Undoped	2×10^{16}	300
I	$Ga_{1-x}Al_xAs$	0.40-0.10*	Te	6.2×10^{17}	51
II	$Ga_{1-x}Al_xAs$	0.40-0.073*	Te	—	66

* The values decrease monotonously from the interface (x = 0.4) to the surface (x = 0.10 or 0.073).

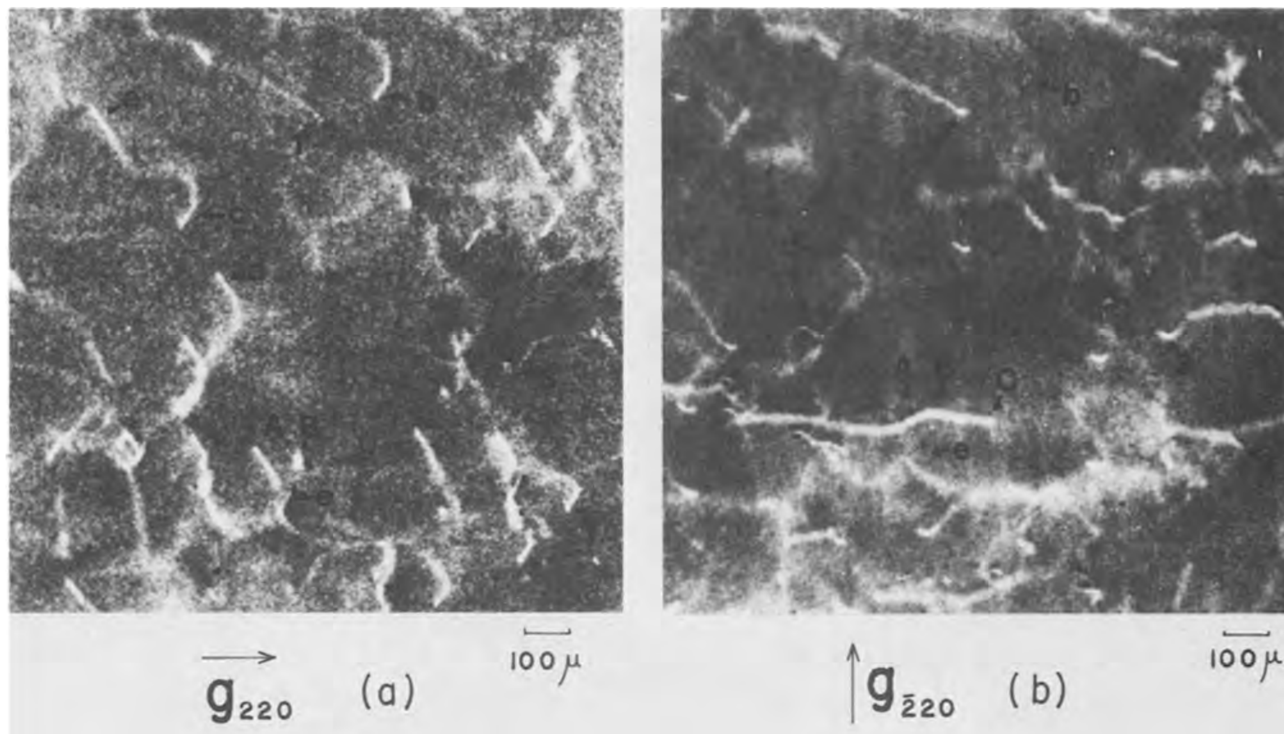

Fig. 1. Transmission x-ray topographs of the as-grown epitaxial wafer I. The epitaxial surface was toward the emulsion. The topographs are the projection on the (001) growth plane, and a sharp end point of a dislocation line in the photographs corresponds to the intersection at the epitaxial surface.

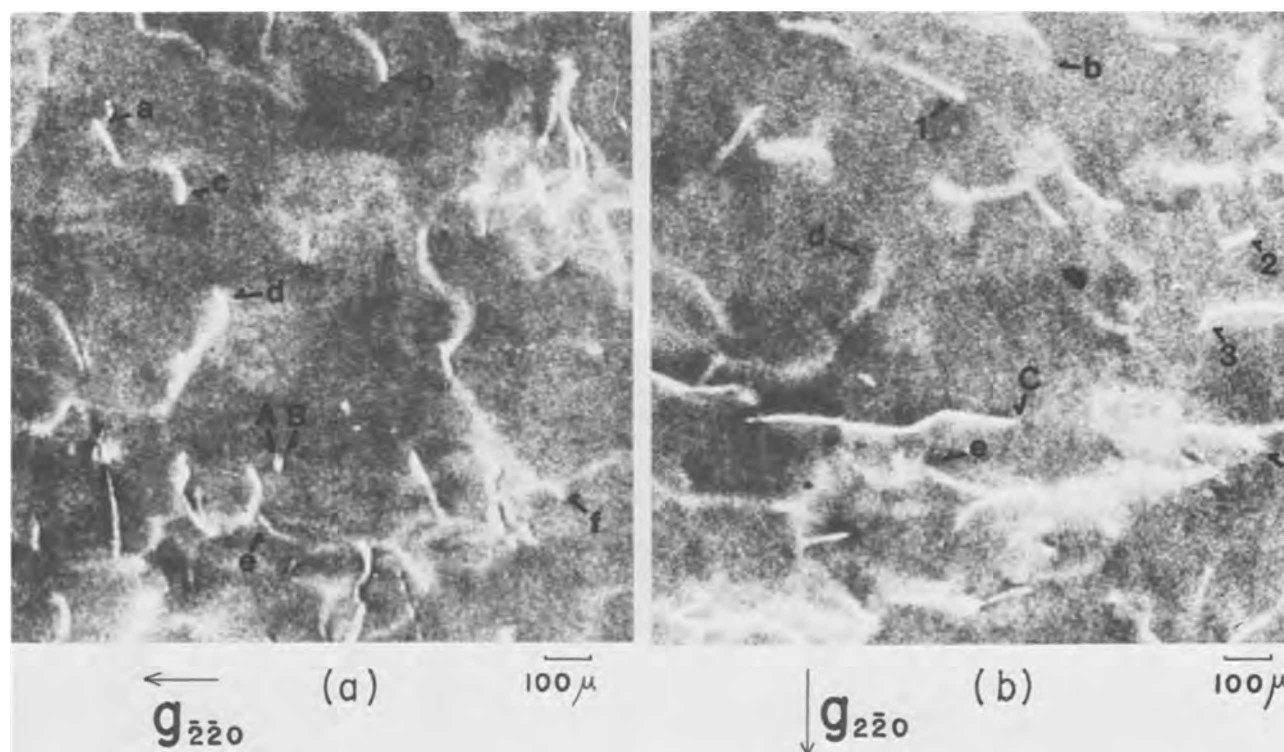

Fig. 2. Transmission x-ray topographs of the substrate of the sample I, from which the epitaxial layer has been removed by etching. The etched surface was toward the emulsion.

nuclear emulsions were employed. Transmission x-ray topographs of the as-grown wafer I and its substrate are shown in Fig. 1 and 2, respectively. The opposite diffraction vectors for the substrate were employed in order to study the effect of bending on the contrast of a dislocation image, but no conspicuous changes were observed. The epitaxial part of a dislocation image is identified by comparison between x-ray images of a dislocation in the two topographs [Fig. 1(a) and 2(a) or Fig. 1(b) and 2(b)], and how it propagates from the substrate to the epitaxial layer can be determined.

It has been reported that the etchant ($H_2O/H_2O_2/CH_3COOH/HF$) is a dislocation etchant for $Ga_{1-x}Al_xAs$ epitaxial layers (12). Molten KOH is a good dislocation etchant for (001) GaAs (13, 14). Molten KOH is also more effective for observation of

dislocation etch pits on the $Ga_{1-x}Al_xAs$ (001) face with only a small value of x ($\lesssim 0.25$) than the etchant ($H_2O/H_2O_2/CH_3COOH/HF$).[1] A gold crucible is employed for molten KOH instead of fused silicate glass or platinum because they are attacked by molten KOH. Temperature of the molten KOH is controlled at 360° ± 2°C by using an Al-Cr thermocouple inserted into a gold tube. The etch rate of the GaAs (001) face is 0.40 μm/min, and etch pits become observable after etching for 2-3 min. The etch pit pattern on the epitaxial layer of sample I is shown in Fig. 3. Similarly, transmission x-ray topographs of the as-grown wafer II and its etch pit pattern are shown in Fig. 4 and 5. There is good agreement between the etch pit patterns and the emergent end points of the dislocations observed on the x-ray topographs.

The two nonequivalent <110> directions in the (001) growth plane of a GaAs substrate have been distinguished with the diffraction technique of Bartels and Niyman (15) and compared with hexagonal etch pits. The result is shown schematically in Fig. 6.

Most dislocations in the epitaxial layer propagate from the substrate and can be classified into three types according to their x-ray images and shapes of etch pits, although the types of the sample I are not always equivalent to the types of the sample II. Many of the classified dislocations are marked with three kinds of symbols, *i.e.*, capital letters, small letters, and numbers. A dislocation is marked with the same symbol on the x-ray topographs and etch pit patterns.

A careful study of the etch pits and topographs as well as comparing the diffraction contrast for a given dislocation under different diffraction conditions has led to the identification of the following dislocation types: Type I-1, Dislocations associated with the large hexagonal etch pits A, B, and C in Fig. 3(a) are oriented along the [001] growth direction in the epitaxial layer. Dislocations A and B are parallel to the [001] direction in both substrate and layer. Dislocation C runs along the [110] direction in the substrate

[1] The dislocations of types I-3 and II-3 have not been revealed as etch pits by the etchant ($H_2O/H_2O_2/CH_3COOH/HF$).

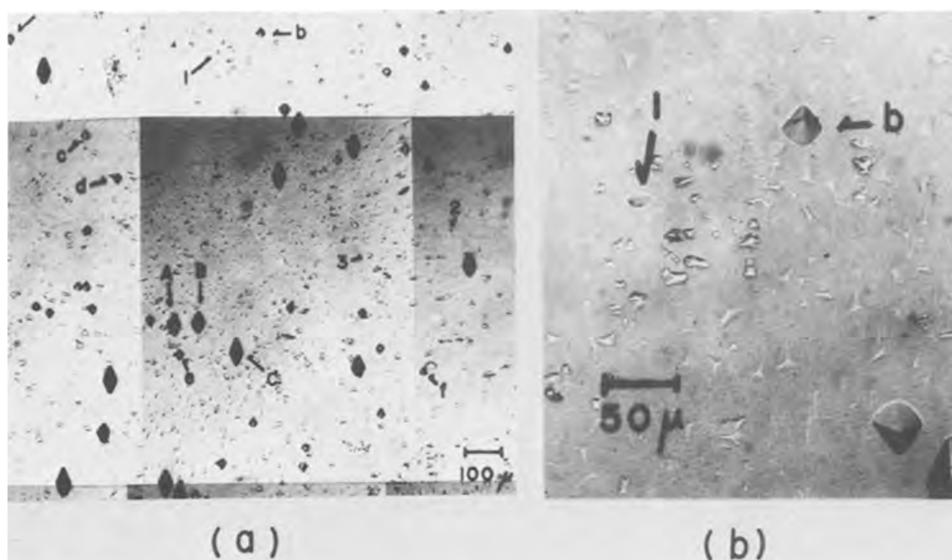

Fig. 3. Etch pit pattern revealed on the epitaxial surface of the sample I by molten KOH at 360°C ($x = 0.13$ on the etched surface).

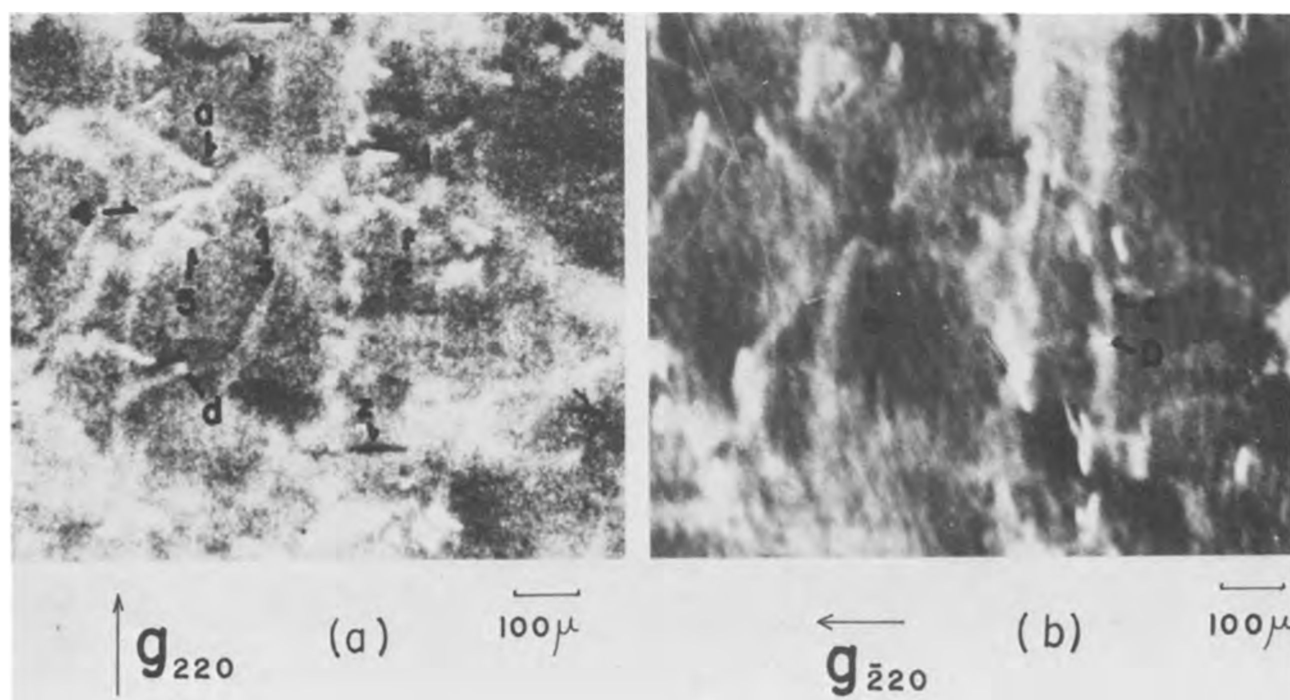

Fig. 4. Transmission x-ray topographs of the as-grown epitaxial wafer II. The conditions are similar to that of sample I

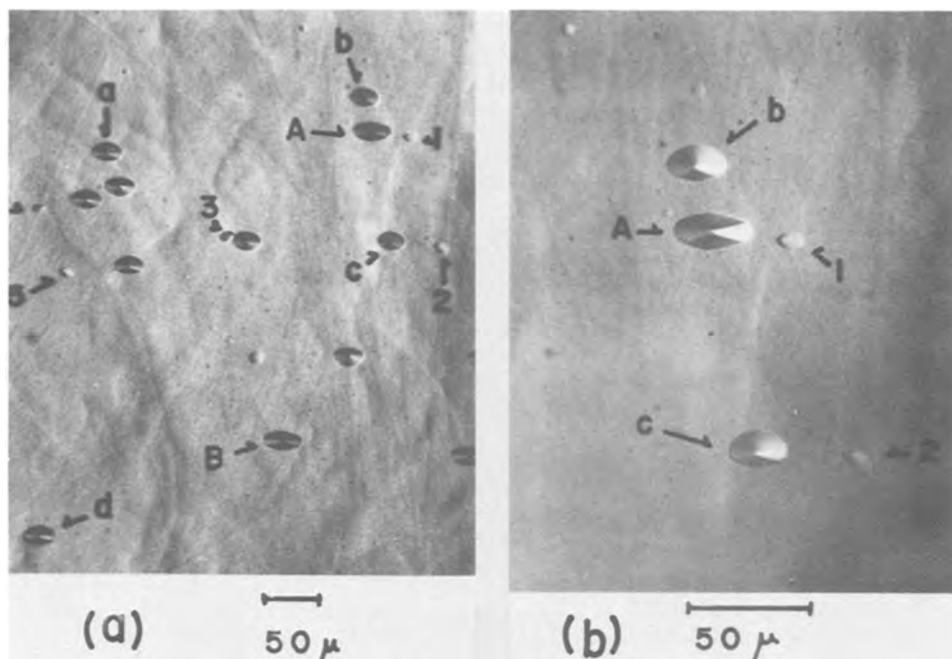

Fig. 5. Etch pit pattern revealed on the epitaxial surface of sample II by molten KOH at 360°C (x = 0.20 on the etched surface.

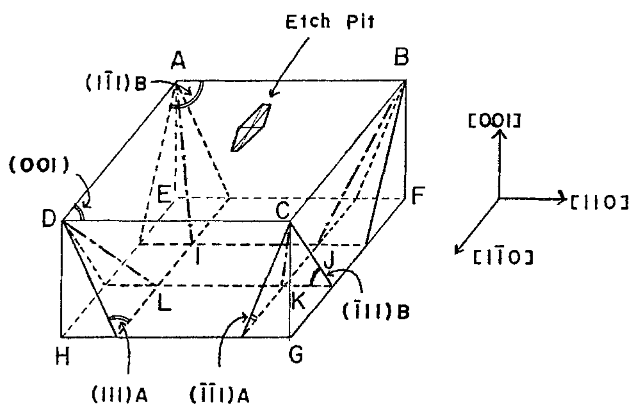

Fig. 6. The relation between x-ray polarity of {111} planes (A- and B-face) and the hexagonal etch pit is shown schematically, where the growth direction is denoted as <001>.

with $\pm a/2$ $[\bar{1}10]$ Burgers vector and abruptly bends to the [001] direction in the layer; Type I-2, The epitaxial part of the threading dislocations b and c in Fig. 1(a) and 2(a) are 60° dislocations oriented along the $[0\bar{1}1]$ direction ($\overline{LD}$ in Fig. 6) with $\pm a/2$ [110] Burgers vector. These dislocations correspond to the pyramidal etch pits b and c in Fig. 3; Type I-3, The small arc-like images denoted with numerals are epitaxial parts of threading dislocations with $\pm a/2$ $[\bar{1}10]$ Burgers vector and correspond to the small etch pits in Fig. 3.

In the case of sample II, stacking faults y and z are observed in the x-ray topograph shown in Fig. 4(a). However, stacking faults are not always associated with melt-back of the substrate and will not be discussed here. Type II-1, Dislocation associated with the large hexagonal etch pit A in Fig. 5(a) or 5(b) corresponds to the blurred point-like image with $\pm a/2$ $[\bar{1}10]$ Burgers vector in Fig. 4(b) and is identical with the type I-1; Type II-2, Etch pits a and d in Fig. 5(a) correspond to the similar point-like images, but are clearly distinguished from the etch pit A. The epitaxial parts of these dislocations a and d are nearly oriented to the [001] direction with $\pm a/2$ [110] Burgers vectors; Type II-3, Dislocations denoted with numerals correspond to the small etch pits in Fig. 5, and their epitaxial parts are oriented to various directions in Fig. 4.

Discussion

Etch pits on each epitaxial surface of samples I and II are clearly classified into three types from their shapes and sizes. Their sizes are mainly associated with the inclination of a dislocation so as to be supported from the results of the x-ray topographs. The dislocations of the type II-2 are nearly oriented to the [001] direction, and sizes of their etch pits are comparatively similar to that of the type II-1, but the shapes are similar to that of the type I-2 rather than the type II-1 or I-1. It has only rarely been reported that the shape of etch pits depends on the kind of a dislocation (16). The geometry of the hexagonal etch pit and polarity of {111} planes (A- or B-face) are schematically shown in Fig. 6. Furthermore, etch pits on the (001) GaAs, $Ga_{1-x}Al_xAs$, and $GaAs_{1-y}Sb_y$ by molten KOH under the same condition are shown in Fig. 7 and this result suggests that the shape of a hexagonal etch pit also depends on the component atoms. The shape of an etch pit depends on the etching properties of some specific planes, the arrangement of atoms on their lattice planes, and the kinds of their component atoms. Therefore, it seems that the dislocation of the type II-2 is clearly distinguished from one of the type II-1.

Ettenberg and Paff reported that there is a perfect lattice matching between AlAs and GaAs at about 900°C (17). Mismatch of this sample ($x = 0.40$ at the interface) is about 5×10^{-3}% at 850°C, which epitaxial growth stops, and about 0.056% at room temperature. Moreover, there is some mismatch due to the different doping level.[2] Dislocations of the substrate propagate in the epitaxial layer under this mismatch so that most of the substrate dislocations bend at the interface and propagate through the epitaxial layer as one of the three types. A few dislocations of the substrate which accidentally belong to some of the three types pierce straight through the epitaxial layer (A or a in Fig. 1). There are fewer dislocations of the type I-1 than of the type I-2 or I-3, since dis-

[2] A wafer with a thick Te-doped GaAs epitaxial layer ($\sim 10^{17}$ cm^{-3}) of about 100 μm on the Te-doped GaAs substrate ($\sim 10^{18}$ cm^{-3}) has been concave in the growth direction in contrast to samples I and II, and its radius is about 10 m.

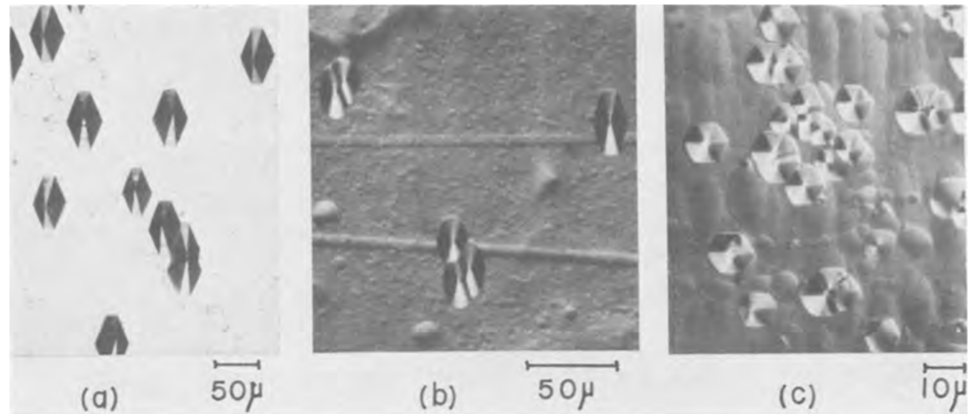

Fig. 7. Etch pit patterns (a), (b), and (c) revealed on the (001) face of the GaAs substrate, the $Ga_{0.83}Al_{0.17}As$ epitaxial layer, and the $GaAs_{0.93}Sb_{0.07}$ epitaxial layer by molten KOH at 360°C, respectively.

locations of the type I-1 are less effective in the relaxation of lattice mismatch. It seems that the difference between dislocations of the type I-2 and I-3 is associated with the two nonequivalent <110> directions in the (001) growth plane (16, 18, 19). Most 60° dislocations of the type I-2 have Burgers vector $\pm a/2$ [110] in the (001) plane and are oriented to either the $[\bar{1}01]$ or $[0\bar{1}1]$ direction (IA or LD in the Fig. 6). Since the extra (111) half-plane probably tends toward the substrate from the larger lattice constant of the GaAlAs, both of them are β-dislocations. They serve to relax the mismatch component of the $\pm$ [110] directions.

On the contrary, most dislocations of the type I-3 have Burgers vector $\pm a/2$ $[\bar{1}10]$ and are convex to the $\pm$ $[\bar{1}10]$ directions in Fig. 1(b). Therefore, it seems that these dislocations are half-loop-like dislocation rather than helical ones. They relax the mismatch component of the $\pm$ $[\bar{1}10]$ directions.

Other wafers with various epitaxial layers ($\gtrsim$ 8 μm in thickness, x = 0.05-0.3) have been studied only by the etching technique because of the low resolution of x-ray topography. For example, etch pits which were revealed on the $Ga_{0.95}Al_{0.05}As$ layer of a thickness of about 10 μm are also classified into three types from their sizes, though all etch pits are hexagonal due to the small Al concentration. Considering the shift of these etch pits by repetitive etching, the difference between sizes of these etch pits, and their crystallographically simple structures, dislocations of the types I-1 and I-2 probably exist in the $Ga_{1-x}Al_xAs$ epitaxial layers.

Since the difference intentionally added to the sample II is only a point of melt-back by a temperature rise of 3.8°C prior to the epitaxial growth, the difference between the results of the sample II and I is mainly caused by melt-back. Saul has reported the decrease of etch pit density in the epitaxial layer GaP owing to melt-back (20). He suggested the formation of half-loops or partial loops (21) due to the climb process by many vacancies or interstitials. In this case, all dislocations of the substrate which intersect to the interface propagate to the epitaxial layer. Comparing Fig. 1 with Fig. 4, some irregular distortions of lattice planes, especially the $(\bar{1}10)$ plane, are guessed from many uneven vertical stripes. It seems that the behavior of threading dislocations in sample II, therefore, is perturbed by local distortions, while the behavior in sample I is probably natural. However, it is not clear why only some types of dislocations of the substrate propagate to the epitaxial layer and whether this behavior of threading dislocations is the essential effect of melt-back, though melt-back is perhaps subject to making some localized stress.

Conclusion

Nearly all dislocations in the $Ga_{1-x}Al_xAs$ epitaxial layer originate from the substrate and few dislocations generate during the LPE growth except some stacking faults in sample II. Most of these threading dislocations bend at the interface. Their epitaxial parts are clearly classified into three kinds, though the corresponding substrate parts consist of various kinds. Most dislocations of the substrate with Burgers vector $\pm a/2$ [110] and $\pm a/2$ $[\bar{1}10]$ propagate through the epitaxial layer as β-dislocations and arc-like dislocations, respectively. For the sample of the substrate with melt-back prior to the epitaxial growth, most threading dislocations also bend at the interface and the dislocations oriented nearly to the [001] direction increase.

Acknowledgments

The authors wish to thank Mr. O. Ueda for helpful discussions and Mr. S. Isozumi for providing the samples.

Manuscript submitted Oct. 7, 1977; revised manuscript received June 4, 1978.

Any discussion of this paper will appear in a Discussion Section to be published in the June 1979 JOURNAL. All discussions for the June 1979 Discussion Section should be suomitted by Feb. 1, 1979.

Publication costs of this article were assisted by Fujitsu Laboratories, Limited.

REFERENCES

1. R. Ito, H. Nakashima, and O. Nakada, *Jpn. J. Appl. Phys.*, **13**, 1321 (1974).
2. H. Yonezu, T. Kamejima, M. Ueno, and I. Sakuma, *ibid.*, **13**, 1679 (1974).
3. P. Petroff and R. L. Hartmann, *J. Appl. Phys.*, **45**, 3899 (1974).
4. P. M. Petroff and L. C. Kimerling, *Appl. Phys. Lett.*, **29**, 461 (1976).
5. P. W. Hutchinson and P. S. Dobson, *Phil. Mag.*, **32**, 745 (1975).
6. J. Matsui, K. Ishida, and Y. Nannichi, *Jpn. J. Appl. Phys.*, **14**, 1555 (1975).
7. Y. Nannichi, J. Matsui, and K. Ishida, *ibid.*, **14**, 1561 (1975).
8. M. Ishida, R. Hirano, H. Kan, and A. Ito, *ibid.*, **15**, 645 (1976).
9. K. Kumar and M. Takagi, *ibid.*, **16**, 957 (1977).
10. K. Kohra and Y. Takano, *ibid.*, **7**, 982 (1968).
11. J. M. Blum and K. K. Smith, *Proc. IEEE*, **59**, 1498 (1971).
12. S. Komiya, K. Akita, Y. Nishitani, S. Isozumi, and T. Kotani, *J. Appl. Phys.*, **47**, 3367 (1976).
13. J. G. Grabmaier and C. B. Watson, *Phys. Status Solidi*, **23**, K13 (1969).
14. J. Angilello, R. M. Potemski, and G. R. Woolhouse, *J. Appl. Phys.*, **46**, 2315 (1975).
15. W. J. Bartels and W. Nijman, *J. Cryst. Growth*, **37**, 204 (1977).
16. "Direct Observation of Imperfections in Crystal,"

J. B. Newkirk and J. H. Wernick, Editors, p. 103.
17. M. Ettenberg and R. Paff, *J. Appl. Phys.*, **41**, 3926 (1970).
18. G. A. Rozgonyi, P. Petroff, and M. B. Panish, *Appl. Phys. Lett.*, **24**, 251 (1974).
19. T. Fujiwara, N. Takagi, H. Imai, S. Komiya, M. Takusagawa, and T. Misugi, *IEEE-J. Quantum Electron.*, **GE-13**, 616 (1977).
20. R. H. Saul, *This Journal*, **118**, 793 (1971).
21. G. A. Wolff and B. N. Das, *ibid.*, **113**, 299 (1966).

Chlorine Concentration Profiles in O_2/HCl and H_2O/HCl Thermal Silicon Oxides Using SIMS Measurements

B. E. Deal*

Fairchild Camera and Instrument Corporation, Palo Alto, California 94304

and A. Hurrle and M. J. Schulz[1]

Institute for Applied Solid State Physics of the Fraunhofer Society, 7800 Freiburg, Germany

ABSTRACT

Chlorine concentration profiles in thermal silicon oxides prepared in O_2/HCl and H_2O/HCl ambients at 900°-1100°C have been determined using secondary ion mass spectrometry (SIMS). The oxides represent various processing conditions, including 0-10 v/o HCl in the oxidizing ambient, 0.25-4.0 hr oxidation time, and 0.05-0.25 μm oxide thickness. For all O_2/HCl oxides, chlorine is found to be piled up in the oxide in a region less than 200Å from the Si-SiO_2 interface. The chlorine peak concentration increases with increasing HCl concentrations, oxidation temperatures, and oxidation times. Highest concentrations are observed at 1100°C, where values as measured in this investigation range up to 2.4×10^{21} cm^{-3} (3.5 a/o). No appreciable amount of chlorine is found in oxides prepared in H_2O/HCl ambients. These results are discussed in relationship to previous investigations involving chlorine profiles, oxidation kinetics, and passivation properties of chlorine oxides.

Recent work carried out in these laboratories has dealt with the kinetics of silicon oxidation at 900°-1100°C in oxygen and water ambients containing small amounts (1-10 v/o) of HCl (1-3). In these and other studies (4-6) it was found that the addition of HCl to the oxidizing ambient increases the oxidation rate for dry O_2, but does not for H_2O. It has been reported that for dry O_2 ambients some type of chlorine species remains in the oxide in a narrow region near the Si-SiO_2 interface (7-10). This may result from a reaction between O_2 and HCl, whose reaction products also are probably responsible for the increased oxidation rate. Oxidized silicon samples prepared for Ref. (1) and (3) were evaluated using secondary ion mass spectrometry (SIMS) analysis, and concentration profiles of chlorine in the oxides were obtained. The results of this brief investigation are reported, with special emphasis on process variable effects.

Experimental

Sample preparation.—As indicated above, the oxidized samples used in this evaluation were selected from those prepared in previous oxidation kinetic studies (1, 3). They involved for the most part 4-6 Ωcm (111) n-type silicon substrates with oxide thicknesses in the range 0.05-0.25 μm (the majority of oxide thicknesses were about 0.10 μm). Oxidation temperatures were 900°, 1000°, and 1100°C, and 1-10 v/o HCl was added to a dry O_2 or pyrogenic H_2O oxidizing ambient. Flow rates were controlled by calibrated flow meters. Other experimental conditions, procedures, and equipment were described previously (1, 3).

* Electrochemical Society Active Member.
[1] Present address: Institut for Angewandte Physik, 852 Erlangen, Germany.
Key words: SIMS, oxidation, spectrometry.

Analysis technique.—The procedure and apparatus used for the SIMS analysis were similar to those reported earlier for determining cesium profiles in thermal oxides (11). Briefly, the sample being analyzed was sputter etched using 8 keV Ar^+ ions at a rate of 12-16 Å/min as determined by crater step measurements. Also, these rates have been verified by comparing the original oxide thickness measurement with the position of the $^{35}Cl^+$ and $^{16}O^+$ profiles. The extracted secondary ion beam was mass separated by a quadrupole spectrometer, and the ion current of the species being investigated was measured as a function of time. The measurements were performed at 2×10^{-7} Torr residual pressure while the argon partial pressure was 5×10^{-6} Torr. The depth resolution is estimated to be about 5% of the sputtered film thickness, or 50Å for the typical 1000Å oxide films. The secondary ion yields of Cl^+ in SiO_2 are less than a factor of 3 greater than in silicon, while the sputter rates in Si and SiO_2 differ by not more than 10% under these measurement conditions (12). No evidence for charging effects on the Cl species due to the sputter etch procedure was indicated.

The chlorine concentration was calibrated by implanting $^{35}Cl^+$ into a silicon substrate and obtaining a SIMS profile as described above. From the known implantation dose and the measured profile, the concentration of $^{35}Cl^+$ at the maximum of the distribution can be computed. An example of an implanted silicon sample used for calibration purposes is shown in Fig. 1. The solid curve is that obtained by SIMS profiling and the dashed curve is that calculated from the Cl^+ implantation conditions. The latter were 40 keV and 1×10^{15} cm^{-2} which results in a predicted peak concentration of 1.9×10^{20} cm^{-3}. The method of

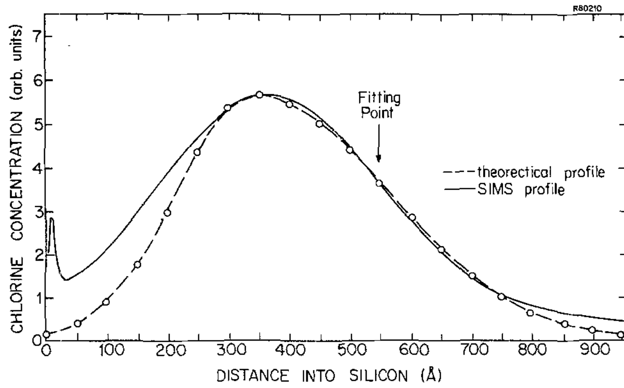

Fig. 1. Theoretical and SIMS chlorine concentration profiles of chlorine implanted into silicon (used for calibration purposes).

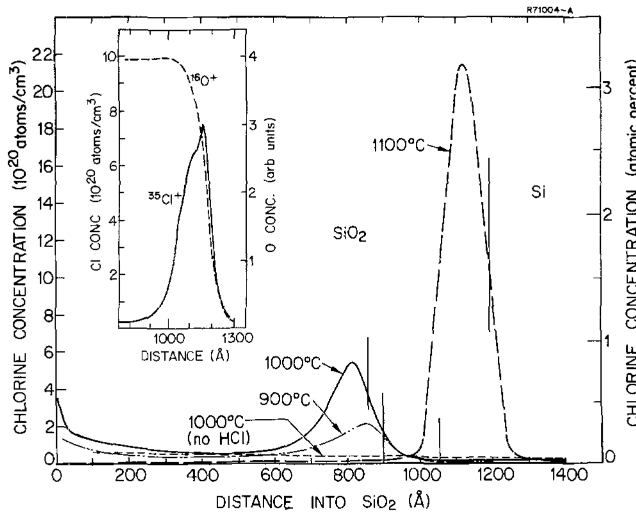

Fig. 2. Typical chlorine concentration profiles in thermally oxidized silicon. Oxides were prepared in a 5% HCl/O_2 ambient at 900°, 1000°, and 1100°C (1). Si-SiO_2 interfaces are indicated by solid vertical lines. Profile of control oxide (no HCl) prepared at 1000°C is also included. Insert shows concentration profiles of Cl and O in thermal oxide prepared at 1100°C in 3% HCl/O_2 ambient.

calculating the curve distribution and fitting it to the experimental curve was that reported by Gibbons *et al.* (13) and also used previously (12). It can be observed from Fig. 1 that a reasonably good fit is obtained except at the silicon surface. If both the experimental and theoretical sources of errors are considered, it is predicted that depth errors due to curve broadening should not be more than ± 5%. The validity of this assumption is discussed in the Discussion Section.

Results

Dry O_2/HCl.—Typical chlorine concentration profiles are shown in Fig. 2. These results, also tabulated in terms of peak concentrations in Table I, are for oxides prepared in O_2/5% HCl mixtures at three temperatures. Also included in Fig. 2 is a chlorine profile for an oxide control prepared with no HCl addition. Oxidation times were selected so that oxide thicknesses would all be in the 0.10 μm range. The approximate position of the interface between the SiO_2 layer and the substrate is indicated in the figure by vertical lines. The determination of this interface is based on the known oxide thickness. The interface position was also verified in the SIMS profiles by monitoring the oxygen concentration. Such a plot of both Cl and O concentration profiles is included as an insert in Fig. 2. This helps confirm that the chlorine is essentiallly piled up in the oxide near the Si-SiO_2 interface. It is unlikely that any chlorine extends into the silicon, although it would be difficult to tell because of a ± 50Å uncertainty of the depth resolution in the measurement. The increasing chlorine peak concentration with oxidation temperature is obvious in both Fig. 2 and Table I.

The other trends relating chlorine peak concentrations to O_2/HCl oxidation variables are indicated in Tables II and III. A slight correlation of Cl concentration in the oxide with increasing HCl content in the oxidizing ambient at 1000°C is observed in Table II. A more severe increase in Cl concentration with HCl content is noted at 1100°C in the same table. Table III shows the effect on chlorine concentration at two temperatures due to increasing oxidation times (and oxide thicknesses). HCl concentration in O_2 was 5% at 1000°C and 3% at 1100°C. At both temperatures, the longer time, thicker oxide resulted in higher peak chlorine concentration, with the larger effect being observed at 1100°C. Two peak concentration values are listed for the 1 hr sample at 1100°C, due to a greater variation of this particular measurement.

Included in Tables I-III are the estimated widths of the chlorine peaks in the oxides. They are represented by chlorine peak half-widths. In all cases these thicknesses range from 100 to 200Å, with the majority being about 150Å.

One other comparison was made which was between (111) and (100) oriented silicon. Since only one (100) silicon oxide was profiled, the data are not tabulated. The results are surprising and must be repeated. Essentially, it was found that a (100) silicon oxide duplicating the conditions of the 1100°C, O_2/3% HCl, 1 hr (111) oxide tabulated in the last line of Table III has a peak chlorine concentration of 12.5 × 10^{20}/cm^3, less than either value obtained (15 and 23.7 × 10^{20}/cm^3) for the (111) oxide. Yet the oxide thick-

Table I. Chlorine peak concentrations in silicon oxides prepared in O_2/5% HCl mixtures at three temperatures
[4-6 Ω-cm, (111), n-type silicon]

Oxidation temp. (°C)	Oxidation time (hr)	Oxide thickness (μm)	Cl peak half-width (Å)	Cl peak conc. in oxide (10^{20}/cm^3)
900	4.0	0.090	200	2.1
1000	1.0	0.086	150	5.3
1100	0.5	0.119	150	21
1000 (no HCl)	2.0	0.105	—	0.35

Table II. Chlorine peak concentrations in silicon oxides prepared in various O_2/HCl mixtures at 1000° and 1100°C
[4-6 Ω-cm, (111), n-type silicon]

HCl content in O_2 (v/o)	Oxidation temp. (°C)	Oxidation time (hr)	Oxide thickness (μm)	Cl peak half-width (Å)	Cl peak conc. in oxide (10^{20}/cm^3)
1	1000	2.0	0.117	170	5.0
5	1000	1.0	0.086	150	5.3
10	1000	1.0	0.095	125	5.8
3	1100	0.5	0.1115	150	7.5
5	1100	0.5	0.119	150	21

Table III. Chlorine peak concentrations in silicon oxides prepared for various times in O_2/3 and 5% HCl mixtures at 1000° and 1100°C
[4-6 Ω-cm, (111), n-type silicon]

Oxidation time (hr)	Oxidation temp. (°C)	HCl content in O_2 (v/o)	Oxide thickness (μm)	Cl peak half-width (Å)	Cl peak conc. in oxide (10^{20}/cm^3)
0.25	1000	5	0.0395	100	3.1
0.5	1000	5	0.056	150	3.1
1.0	1000	5	0.086	150	5.3
0.25	1100	3	0.079	125	5.7
0.5	1100	3	0.1115	150	7.5
1.0	1100	3	0.173	140	15, 23.7

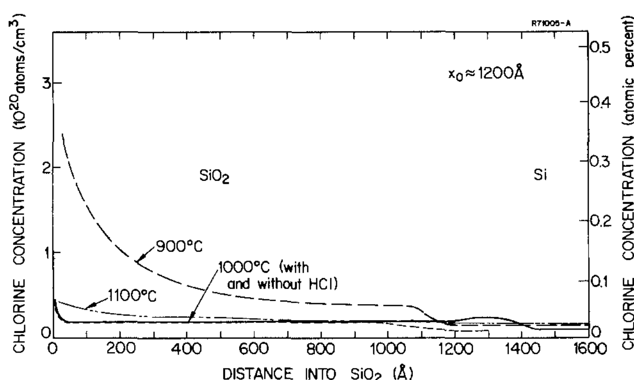

Fig. 3. Typical chlorine concentration profiles in thermally oxidized silicon. Oxides were prepared in a 5% HCl/H_2O pyrogenic ambient at 900°, 1000°, and 1100°C (3). Oxides are approximately 1200Å thick, except for 1100°C oxide which is not all shown in figure. Profile of control oxide (no HCl) prepared at 1000°C is also included.

nesses are nearly the same and the chlorine peak half-widths are identical.

H_2O/HCl.—Chlorine concentration profiles were obtained for oxides prepared in pyrogenic H_2O/5% HCl mixtures of 900°, 1000°, and 1100°C. A control oxide with no HCl addition was included. Resulting profiles are shown in Fig. 3 and the data are tabulated in Table IV. The first fact apparent is that no real Cl peaks are evident in the profiles. Further, the chlorine concentrations across the oxide layers are nearly the same as the background in the control. The one exception is the 900°C oxide where the Cl concentration appears to increase at the oxide surface to 2.5×10^{20}/cm^3. It is believed that this exception is due to an impurity other than chlorine at the oxide surface (or some other artifact) and is similar to the 1000°C dry O_2 profile in Fig. 2. In any event, the H_2O oxides prepared under the above conditions apparently do not incorporate any significant amount of chlorine.

Discussion

Several trends may be noted regarding the dependence of the peak chlorine concentrations on process conditions used to prepare the thermal silicon oxides. First, the chlorine peak height increases with oxidation temperature. Also, a trend of increasing chlorine concentration with HCl content in the oxidizing ambient is evident. Finally, increasing oxidation time or oxide thickness results in increased peak heights at a given HCl percentage or oxidation temperature. In all these cases the greatest change occurs at 1100°C and under the more severe conditions of oxidation time or HCl concentration at this temperature. For oxidation in H_2O/HCl mixtures, the chlorine apparently does not enter into the oxidation process nor is any appreciable chlorine incorporated into the oxide for the conditions investigated. The relationship of these trends to the oxidation kinetics or to other properties of the oxide

Table IV. Chlorine peak concentrations in silicon oxides prepared in H_2O/5% HCl mixtures at three temperatures
[4-6 Ω-cm, (111), n-type silicon]

Oxidation temp. (°C)	Oxidation time (hr)	Oxides thickness (μm)	Cl peak half-width (Å)	Cl peak conc. in oxide (10^{20}/cm^3)
900	0.5	0.113	—	0.35
1000	0.15	0.130	—	0.20
1100	0.15	0.237	—	0.20
1000 (No HCl)	0.15	0.122	—	0.10

will be discussed below, along with the possible silicon orientation effect.

These chlorine concentration profiles in oxides prepared in O_2/HCl ambients can be compared with results reported by other investigators. Most of the previously reported profiles have been carried out using Rutherford backscattering of alpha particles, such as Meek (7), van der Meulen *et al.* (9), and Butler *et al.* (10). Kriegler *et al.* (8) have used the SIMS technique to determine Cl profiles at 1150°C as a function of percent HCl in O_2 (2.5-4.0%), although their chlorine concentrations in the oxide are reported only in arbitrary units. For the above backscattering analyses, the peak concentrations reported range from 2×10^{20}/cm^3 to 2×10^{21}/cm^3. If the exact oxide preparation procedures are considered, all these results are in reasonable agreement with those reported here. For instance, van der Meulen *et al.* (9) report chlorine concentrations for 0.1 μm oxides prepared at temperatures ranging from 900° to 1150°C which are similar to the present values, in that peak concentrations increase from $<3 \times 10^{19}$ to 8.4×10^{20}/cm^3 for 9 v/o HCl in O_2. All these profiles indicate a pileup of the chlorine in the oxide near the Si-SiO_2 interface, and of peak concentration half-widths of less than 200Å.

Even with the apparent agreement between these chlorine concentration and peak-width values and previous backscattering results, some caution must be exercised. As more sophisticated and accurate analytical techniques are being developed, thickness dimensions related to the Si-SiO_2 interface are found to be less than previously assumed (14). Also, the calibration of absolute concentrations such as reported here is very difficult. Therefore values reported for both Cl peak concentrations and widths must be considered as preliminary until more accurate measurements can be carried out. The relative values and their dependence on process variables can be considered significant, however.

The chlorine profile results obtained in this work may also be compared with oxidation kinetic effects and alkali passivation properties of chlorine-containing oxides. If the increased oxidation rates of silicon in O_2/HCl mixtures reported previously (1, 4) are considered, no direct correlation between chlorine incorporation in the oxide and oxidation rate constants can be observed. Rather the kinetic data in Fig. 4 and 5 of Ref. (1) would indicate a more direct relationship between the parabolic rate constant B and HCl content in the oxidation ambient. The linear rate constant at a given temperature is independent of HCl concentration above 1-3%. For H_2O/HCl oxidations (3) no increase in oxidation rate is observed and no significant chlorine incorporation in the oxide occurs over the temperature and HCl concentration ranges investigated. This is more of a negative correlation.

Unlike the oxidation kinetics, the alkali passivation properties appear to be related to the chlorine content as reported by Kriegler (15) and Rohatgi (16). Even so, while the ability of the chlorine to complex alkali ions depends on the peak chlorine concentration above a certain level, certain concentration regions are noted where passivation is not complete or even partially effective (16). On the other hand, the presence of any type of chlorine species in the oxidizing ambient, O_2 or H_2O, appears to provide cleaner, more stable oxides, while oxide fixed charge and interface state density are apparently not affected by even the highest chlorine concentrations (2-3). All of these findings lead to the conclusion that a better understanding of the chlorine passivating effect is needed.

One result obtained in this investigation is not understood and this concerns the differences in chlorine content between (111) and (100) silicon orientation. The data must be considered very preliminary since only one (100) oxide chlorine profile was evaluated. The fact that a greater peak chlorine concentration was observed for (111) silicon as (100) for the same

oxidation conditions is surprising.[2] This is especially true when it is considered that at 1100°C, where the orientation effect on chlorine concentration was noted, the oxidation process is nearly independent of silicon orientation. More comparisons will have to be made to verify if such an effect is real. If it is, some relationship between chlorine concentration and the linear oxidation rate constant and/or interface charges may exist. This would suggest a possible complexing of the chlorine species within the so-called SiO_x interface region, which has been found to depend on silicon orientation (17).

Summary

Chlorine concentration profiles in silicon oxides prepared in O_2/HCl and H_2O/HCl ambients have been obtained using secondary ion mass spectrometry (SIMS). The dependence of these profiles on process variables involved with the oxide preparation has been determined. These variables included oxidation temperature (900°-1100°C), oxidizing ambient (O_2 and H_2O), HCl content in ambient (0-10 v/o), oxidation time (0.25-4.0 hr), and silicon orientation [(111) and (100)]. Oxide thickness over these conditions ranged from 0.05 to 0.25 μm.

Results are in general agreement with those reported previously by other investigators using different analytical methods. Essentially, a chlorine species piles up in the oxide over a region about 150Å wide or less near the Si-SiO_2 interface in the case of O_2/HCl oxidations. The chlorine peak concentration, ranging from 2 to 20 $\times$ 10^{20}/cm^3 as measured in this investigation, increases with oxidation temperature, oxidation time, and HCl content in O_2. The effects are more severe at 1100°C. Little or no chlorine incorporation in the oxide is noted for H_2O/HCl oxidations up to 1100°C and 5% HCl. The chlorine profile results do not appear to correlate directly with oxidation kinetic data obtained for O_2/HCl mixtures, but some correlation is evident for alkali passivation properties reported by other investigators. An apparent dependence of chlorine incorporation in the oxide on silicon orientation has been observed, but the validity of this result must be verified.

Acknowledgments

The authors wish to thank Drs. J. M. Early and J. J. Barnes of Fairchild R&D for critically reviewing the manuscript. Also, thanks are due C. R. Helms and R. W. Barton of Stanford University for providing the Auger analysis mentioned in the paper.

[2] Similar HCl/O_2 oxides from this series were analyzed using Auger spectroscopy by C. R. Helms and R. W. Barton of Stanford University. Their results indicate a 1.5:1 ratio of peak chlorine concentration between (111) and (100) silicon. The half-peak widths, however, are less than 50Å. Also, these Auger results indicate somewhat lower peak concentration values.

Manuscript submitted May 2, 1978; revised manuscript received July 10, 1978.

Any discussion of this paper will appear in a Discussion Section to be published in the June 1979 JOURNAL. All discussions for the June 1979 Discussion Section should be submitted by Feb. 1, 1979.

Publication costs of this article were assisted by Fairchild Camera and Instrument Corporation.

REFERENCES

1. D. W. Hess and B. E. Deal, *This Journal*, **124**, 735 (1977).
2. B. E. Deal, D. W. Hess, J. D. Plummer, and C. P. Ho, *ibid.*, **125**, 339 (1978).
3. B. E. Deal, *ibid.*, **125**, 576 (1978).
4. R. J. Kriegler, Y. G. Cheng, and D. R. Colton, *ibid.*, **119**, 388 (1972).
5. K. Hirabayashi and J. Iwamura, *ibid.*, **120**, 1595 (1973).
6. Y. J. van der Meulen and J. G. Cahill, *J. Electron. Mater.*, **3**, 371 (1974).
7. R. L. Meek, *This Journal*, **120**, 308 (1973).
8. R. J. Kriegler, A. Aitken, and J. D. Morris, *J. Jpn. Appl. Phys.*, **43**, 341 (1974).
9. Y. J. van der Meulen, C. M. Osburn, and J. F. Ziegler, *This Journal*, **122**, 284 (1975).
10. S. R. Butler, F. J. Feigl, A. Rohatgi, H. W. Kraner, and K. W. Jones, Abstract 77, p. 217, The Electrochemical Society Extended Abstracts, Spring Meeting, Philadelphia, Pa., May 8-13, 1977.
11. A. Hurrle and G. Sixt, *Appl. Phys.*, **8**, 293 (1975).
12. A. Hurrle, Ph.D Thesis, University of Freiburg, West Germany (1975).
13. J. F. Gibbons, W. S. Johnson, and S. W. Mylroie, "Projected Range Statistics in Semiconductors," Dowden, Hutchinson, and Ross, distributed by John Wiley & Sons, New York (1975).
14. See for instance, the "Proceedings of the International Topical Conference on the Physics of SiO_2 and its Interfaces," March 22-24, 1978, to be published by Pergamon Press, Oxford, England.
15. R. J. Kriegler, "Semiconductor Silicon," H. R. Huff and R. R. Burgess, Editors, p. 363, The Electrochemical Society Softbound Symposium Series, Princeton, N.J. (1973).
16. A. Rohatgi, S. R. Butler, F. J. Feigl, H. W. Kraner, and K. W. Jones, *Appl. Phys. Lett.*, **30**, 104 (1977).
17. S. I. Raider and R. Flitsch, *J. Vac. Sci. Technol.*, **13**, 58 (1976).

Cathodic Deposition and Characterization of Metallic or Semiconducting Binary Alloys or Compounds

F. A. Kröger*

Department of Materials Science, University of Southern California, Los Angeles, California 90007

ABSTRACT

The conditions to be met to achieve cathodic deposition of compounds or alloys of well-defined stoichiometric composition are discussed. If the deposition rate constants of the components are of the same order, two classes of codeposition have to be distinguished, differing in whether the difference in electrode potential of the individual components is larger (class I) or smaller (class II) than the shift in electrode potential of either component as a result of compound or alloy formation. In the former case the potential of the deposit is determined by the less noble component over the entire composition range, the deposition potential shifting monotonically with composition. In the latter case the role of potential-determining species may shift from one component to the other at an intermediate composition, the deposition potential at this composition being more positive than that of either of the components when deposited individually. For class I, quasi rest potentials uniquely characterize the deposits. For class II different deposits may have the same quasi rest potential. Compounds are stable in electrolytes with large concentrations of the normal ions of one of the components in the absence of nonmetal complexes necessary to make cathodic deposition of the compounds possible. If the potential is not determined by adsorbed noncomponent species, the potentials are determined by the normal ions, the concentrations of which are linked by solubility products.

Cathodic codeposition of different elements with formation of metallic alloys or compounds from aqueous electrolytes has been known for a long time (1). Nonmetals such as S, Se, Te, and As and semimetals such as Sb and Bi can be deposited cathodically from solutions of complex ions or molecules (2) and cathodic codeposition of one of these elements and metallic elements with the formation of compounds may therefore also be possible. Examples are found in the formation of CdSe and Ag_2Se (3), Ni-P and Co-P alloys (4), and $Cu_{3-x}As$ (5).

Interactions between the components in the deposit usually shift the deposition potential of the deposit to values that are positive relative to the deposition potential of the less noble component (induced codeposition) (6). In some cases, *e.g.*, for Ni, Sn alloys (7), the deposition potential is positive even relative to that of the noble component, an effect that so far remained unexplained (8).

In this paper the thermodynamic basis of codeposition and the nature of the potential-determining species are considered and on this basis an explanation of the observed effects is arrived at. No attention is paid to the possibility of hydrogen discharge.

Theoretical

The electrode potentials at which codeposition is possible are equal to the quasi rest potentials (QRP) of the alloy or compound plus a polarization which increases with increasing current density. The QRP is defined as the potential of the deposit relative to the electrolyte with activities of potential-determining species as they are at the solid-electrolyte interface during deposition. The polarization is established with a relaxation time $\tau \leq 10^{-3}$ sec. Therefore the QRP can be determined experimentally by measuring the electrode potential $\approx 10^{-3}$ sec after interruption of the deposition current. Further changes of potential occur when the composition of the electrolyte at the interface changes back to the bulk value, a process with a relaxation time of seconds. Equilibration of the deposit with the electrolyte of bulk composition may and usually does cause a marked change in the surface composition of the deposit, changing the QRP to a rest potential. Quasi rest potentials are important for characterizing the bulk of the deposit. They arise as a result of the interplay of four factors: (*i*) the equilibrium potentials of the components (which may be widely different); (*ii*) the interaction of the components when forming the alloy or compound; this interaction changes the activity of the components in the deposit to an extent dependent on the exact composition of the deposit; (*iii*) the values of the activities of ionic species in the electrolyte at the interface solid-electrolyte during deposition (which may be markedly different from those in the body of the bath), and (*iv*) the relative magnitude of the exchange currents of the components in the deposit.

It will be assumed that the QRP is an equilibrium potential relative to an electrolyte of the composition as it is at the deposit-electrolyte interface during deposition. This is not completely correct, for there is no complete equilibrium immediately after interruption of the current, but it will give us some indications of what is to be expected. With this assumption, the first three factors can then be taken into account by expressing the electrode potentials of the components in terms of the activities of ionic or molecular species in the electrolyte at the interface and the activities of the components in the deposit. The former can often be approximated by the concentrations as they are at the interface, but the latter are usually very different from the concentrations.

Let us consider a compound M_rN_s for which deposition of component M involves m electrons, that of component N n electrons. The quasi-rest potentials of M and N then are

$$E_M = E_M{}^\circ + \frac{RT}{m\mathbf{F}} \ln (a_{M^{m+}}/a_M) \quad [1]$$

$$E_N = E_N{}^\circ + \frac{RT}{n\mathbf{F}} \ln (a_{N^{n+}}/a_N) \quad [2]$$

* Electrochemical Society Active Member.

Key words: cathodic deposition, alloy deposition, quasi rest potential, potential-determining species.

Here $a_{M^{m+}}$ and $a_{N^{n+}}$ are activities of the species M^{m+} and N^{n+} in the electrolyte at the interface during deposition and a_M and a_N are the activities of M and N in the deposit. Without loss of generality it may be assumed that M is less noble then N, *i.e.*, $E_N^o > E_M^o$.

The activities a_M and a_N of M and N in the deposit are related through

$$rM(s) + sN(s) = M_rN_s;\ G \quad [3]$$

where G is the Gibbs free energy increment of the reaction. In equilibrium

$$a_{M_rN_s}/a_M{}^r a_N{}^s = \exp(-G/RT) \quad [4]$$

or, since $a_{M_rN_s} \approx 1$

$$a_M{}^r a_N{}^s = \exp(G/RT) \quad [5]$$

A large a_M gives rise to a small a_N, and vice versa. Limiting values of a_M and a_N are determined by the corresponding activities in coexisting phases in the phase diagram. In the simplest case M_rN_s is the only compound in the system, M in coexistence with the compound is almost pure M, and N in coexistence with the compound is almost pure N.

At the two-phase boundaries we then have respectively $a_M = 1$, $a_N = \exp(G/sRT)$, and $a_N = 1$, $a_M = \exp(G/rRT)$.

The variation of a_M and a_N over the existence range of the compound gives rise to a corresponding variation in the quasi rest potentials of M and N, the total variations being, respectively

$$\Delta E_M = -G/rm\mathbf{F} \quad [6]$$

$$\Delta E_N = -G/sn\mathbf{F} \quad [7]$$

Since $G < 0$, these variations are such that the potentials of both components become more positive (*i.e.*, more noble) when their activity decreases.

A homogeneous deposit with two components at a given composition and the a_M and a_N corresponding to that composition can have only one potential. In the absence of potential determination by adsorption of noncomponents such as H^+, OH^-, SH^-, etc., this potential is the result of exchange processes between the electrode and the electrolyte involving the two components, the effects of the components individually depending on their relative contributions to the exchange current. These contributions in turn are equal to the product of characteristic rate constants and appropriate powers of the activities of the involved ionic or molecular species at the solid-electrolyte interface (9).

Two possibilities exist: The rate constants of the exchange currents for the two components are of the same order of magnitude, or these quantities are widely different. In the former case both species have equal weight in determining the potential and a change between their individual contributions can only occur as a result of a change of the activities of species in the electrolyte and the corresponding change in the deposit. In the latter case one of the components may be potential determining under all conditions. For an exact quantitative treatment of this problem it is necessary to have detailed knowledge of the kinetics of processes by which charge transfer for the various components takes place. In the absence of such knowledge it can be stated, however, that a species present at the interface at a concentration close to zero cannot be expected to play a major role in the establishment of the potential: It cannot be a potential-determining species.

Systems is Which the Rate Constants of the Exchange Currents of Individual Components Are of the Same Order of Magnitude

Since a deposit of one composition can have only one quasi rest potential, always

$$E_{M_rN_s} = E_M = E_N \quad [8]$$

This equality leads to a relation between the concentrations of M^{m+} and N^{n+} in the electrolyte at the interface electrolyte-deposit, and this in turn determines the ratio in which the various species contribute to the exchange current, *i.e.*, which is the main potential-determining species. Elimination of E_M and E_N from [1] and [2] with the aid of [8] gives

$$\frac{RT}{\mathbf{F}} \ln (a_{M^{m+}}{}^{1/m}/a_{N^{n+}}{}^{1/n}) = (E_N^o - E_M^o) + \frac{RT}{\mathbf{F}} \ln (a_M{}^{1/m}/a_N{}^{1/n}) \quad [9]$$

Or, at the M_rN_s-M phase boundary

$$\frac{RT}{\mathbf{F}} \ln (a_{M^{m+}}{}^{1/m}/a_{N^{n+}}{}^{1/n}) = (E_N^o - E_M^o) - \frac{G}{ns\mathbf{F}} \quad [10]$$

and at the M_rN_s-N phase boundary

$$\frac{RT}{\mathbf{F}} \ln (a_{M^{m+}}{}^{1/m}/a_{N^{n+}}{}^{1/n}) = (E_N^o - E_M^o) + \frac{G}{mr\mathbf{F}} \quad [11]$$

Since we assumed $(E_N^o - E_M^o) > 0$, while $G < 0$, [10] indicates that at the M boundary always $a_{M^{m+}} >> a_{N^{n+}}$, *i.e.*, the less noble component M is the potential-determining species. At the N boundary, however, [11] indicates that two cases have to be distinguished, dependent on whether $(E_N^o - E_M^o) >$ or $< G/mr\mathbf{F}$.

Class I. $(E_N^o - E_M^o) > |G/mr\mathbf{F}|$; $a_{M^{m+}} >> a_{N^{n+}}$, though the ratio $a_{M^{m+}}/a_{N^{n+}}$ is not as large as at the M boundary. M remains the potential-determining species over the entire deposition range.

Class II. $(E_N^o - E_M^o) < |G/mr\mathbf{F}|$; $a_{N^{n+}} >> a_{M^{m+}}$ and N is the potential-determining species. Evidently in this case the potential-determining species changes from M at the M side of the system to N at the N side, the cross-over occurring near the point where the contributions of M and N to the exchange current are of the same order; at and near this point both M and N are involved in determining the potential.

As mentioned earlier, the individual potentials become more positive when the activity of the species in the deposit decreases.

The variation of the potentials of M and N with a_M and a_N, calculated for constant values of $a_{M^{m+}}$ and $a_{N^{n+}}$ equal to one are shown in Fig. 1A and Fig. 2A for classes I and II, respectively. These figures do not represent the situation in the plating bath at the interface deposit-electrolyte during deposition but they indicate in what way differences in nobility of the two components are affected by their interaction in the deposit, show which species must be expected to be potential determining, and help us to compose an electrolyte from which codeposition will be possible.

Class I.—In the situation depicted in Fig. 1A, M is the potential-determining species for all possible compositions of M_rN_s. Codeposition of the noble N and the less noble M in the ratio $s:r$ is possible from one solution if this solution contains N species at a low concentration and M species at a large concentration, for only under such conditions is it possible to reduce the concentration of N^{n+} ions relative to that of M^{m+} ions at the interface as required by [10] and [11] and make codeposition of M and N possible. Application of a potential somewhat more positive than that which would be required to deposit pure M from the electrolyte in the absence of N species preferentially deposits N; owing to the interaction between N and M, each N that is deposited makes possible the deposition of r/s M. Deposition

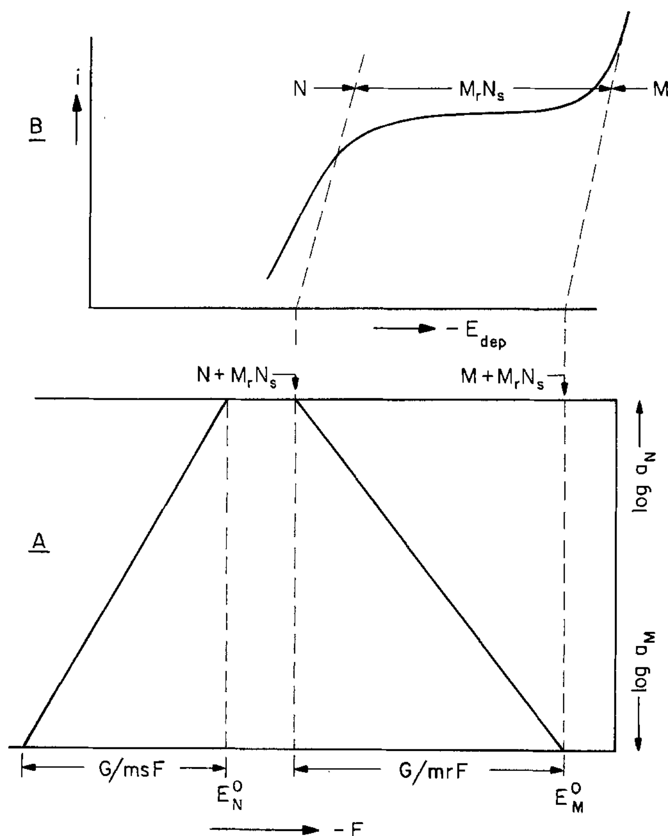

Fig. 1. Equilibrium potentials E of M and N as a function of the activities a_M and a_N relative to an electrolyte with $a_{M^{m+}} = a_{N^{n+}} = 1$ for class I (A) and the corresponding current-cathode potential curve for deposition of M_rN_s from an electrolyte with $a_{M^{m+}} \approx 1$, $a_{N^{n+}} << 1$ (B). The current value of the plateau is proportional to $a_{N^{n+}}$.

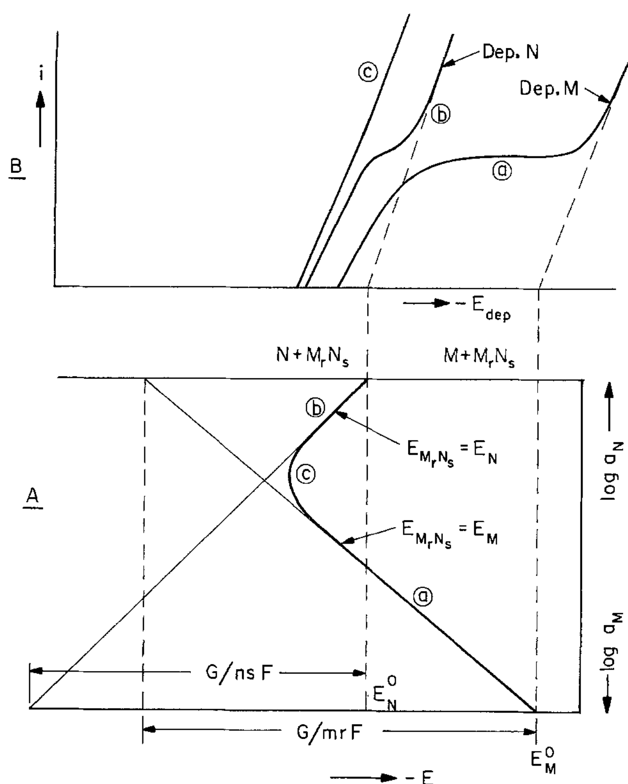

Fig. 2. Equilibrium potentials E of M and N as a function of a_M and a_N relative to an electrolyte with $a_{M^{m+}} = a_{N^{n+}} = 1$ for class II (A) and current-cathode potential curves for deposition of M_rN_s (B) from electrolytes with $a_{M^{m+}} = 1 << a_{N^{n+}}$ (a), $a_{M^{m+}} << a_{N^{n+}} \approx 1$ (b), and $a_{M^{m+}} \approx a_{N^{n+}} \approx 1$ (c).

of N exhausts the electrolyte at the interface from the species N^{n+} and creates a situation in which continuing deposition requires transport of N^{n+} from the bulk to the interface by diffusion through a thin electrolyte layer close to the interface, *i.e.*, the so-called diffusion layer, the thickness of which depends on agitation (stirring or convection). Deposition of M also tends to decrease the concentration of M^{m+} at the interface. However, since $a_{M^{m+}} >> a_{N^{n+}}$, this reduction is relatively unimportant, the M^{m+} concentration remaining practically the same as in the bulk. This means that the QRP of M_rN_s, determined by M^{m+}, remains given by [1] with $a_{M^{m+}}$ close to the value characterizing the bulk of the solution. The potential of N remains in line with [2] by the forced reduction of $a_{N^{n+}}$ at the interface to make $E_M = E_N$.

At a given bulk electrolyte composition, the exact value of the ratio r/s can be varied through current density and/or rate of stirring, an increase of current density increasing r/s, an increase of the rate of stirring (which makes the diffusion layer thinner) decreasing r/s. On the other hand, at given current density and stirring rate, increase of the M concentration in the electrolyte favors formation of M-rich deposits, increase of the N concentration in the electrolyte favors formation of N-rich deposits.

For a given electrolyte composition, the i-E_{dep} characteristic has the form schematically shown in Fig. 1B. After a gradual increase of i at low electrode potentials where the interface activity $a_{N^{n+}}$ is gradually reduced, a plateau is reached when the interface value of $a_{N^{n+}}$ is reduced to zero. A sharp increase of i occurs at a critical large potential where deposition of pure M becomes possible. Owing to the relatively large concentration of M^{m+} in the electrolyte, saturation of the M deposition by formation of a diffusion layer with $(a_{M^{m+}})_{interface} \approx 0$ will occur only at extremely large values of i and has not been included in the figure. If the concentration of M^{m+} in the electrolyte is ≈ 1 normal, the QRP's of the various possible products M_rN_s (with slightly varying values of r/s) are as shown in Fig. 1A, covering a potential range of width $G/mr\mathbf{F}$ at the positive side of $E_M°$. The corresponding deposition potentials are shifted to the negative side relative to the quasi rest potentials by the polarization which increases with increasing current density. The polarization has two components, the polarization proper of the deposit at the interface with the electrolyte and an iR drop in the current-carrying part of the circuit used to measure electrode potential. The iR drop is negligible for deposition of metals on a metallic electrode but may become appreciable for deposition of semiconducting compounds on a semiconducting electrode (*e.g.*, CdS on glass covered by SnO_2:Sb or In_2O_3:Sn). In that case $R = R_{base} + R_{deposit}$ with $R_{deposit}$ proportional to the thickness of the deposit. Since deposition of M_rN_s involves deposition of both M and N, interaction between M and N has made possible the deposition of component M at potentials that are more positive than that required to deposit pure M. N induces deposition of the less noble component [Brenner (6): induced codeposition]. Note that two-phase deposition of M + M_rN_s or N + M_rN_s occurs at specific potentials or current densities. Examples of class I alloys are CdS, CdSe, and CdTe, with Cd the potential-determining species; *e.g.*, for CdS, $E_{Cd}° = -0.403V$ *vs.* NHE, $E_S°$ (from H_2SO_3) = 0.449 *vs.* NHE, $-(G_{CdS})_{298} = 140.4$ kJ/mole (10). Hence $-G_{CdS}/2\mathbf{F} = 0.726V < (E_S° - E_{Cd}°) = 0.852V$. Similar considerations apply to CdTe (11).

Class II: The variation at standard values of $a_{M^{m+}}$ and $a_{N^{n+}}$ of the individual potentials of M and N with a_M and a_N corresponding to class II is shown in Fig. 2A. Interaction again shifts both potentials to more positive values, but now M has the most negative potential at large a_M, N has the most negative potential at small a_M (= large a_N), equality of

potentials (at standard values of $a_{M^{m+}}$ and $a_{N^{n+}}$) occurring somewhere in between. For electrolytes with different values of the ion activities the curves have to be shifted accordingly.

In the range where M has the most negative potential, Eq. [10] shows that under QRP conditions $a_{N^{n+}} \approx 0$, M being the potential-determining species. In the range where N has the most negative potential, [11] shows that $a_{M^{m+}} \approx 0$ and N is the potential-determining species. In this case deposition of M-rich products requires an electrolyte with $a_{M^{m+}} >> a_{N^{2+}}$ (as for class I) a change in deposition conditions (current density, rate of stirring) making possible the formation of deposits with different compositions, but all at the M-rich side of the system. Deposition of N-rich products, on the other hand, requires an electrolyte with $a_{N^{n+}} >> a_{M^{m+}}$, a change of conditions making possible formation of N-rich deposits over a limited composition range. Although $a_{M^{m+}}/a_{N^{n+}}, << 1$, this ratio cannot be as small as for class I. Care must be taken that M remains the most easily deposited species, for only then is it possible to achieve codeposition of M and N with the ratio r/s decreasing with increasing current density. Deposition of products with component activities in the range where both species are potential determining requires an electrolyte in which the two species have comparable activities. Now the change in composition of the deposit with current density or stirring rate will be extremely limited, since the deposition rate of both species will be affected in approximately the same way. If both $a_{M^{m+}}$ and $a_{N^{n+}}$ are chosen large, no appreciable exhaustion occurs. Schematical i-E_{dep} curves at activities of a_M corresponding to a, b, and c in Fig. 2A, with large values of $a_{M^{m+}}$ and $a_{N^{n+}}$ for c, are shown in Fig. 2B.

There are various systems in which such an effect has been observed, *e.g.*, NiSn (7), CoSn (12), and CoSb (13), but a satisfactory explanation has so far not been proposed (14). Let us consider the former case, where the metastable alloy NiSn is deposited from a solution containing chloride and fluoride ions (7). The standard potentials of Ni and Sn *vs.* NHE are $E_{Ni}^o = -0.250$V and $E_{Sn}^o = -0.136$V (2). The presence of fluoride ions makes the Ni potential ≈ 0.1V more negative but shifts the Sn potential more strongly in the same direction, making the standard potentials equal within 0.1V (Sn ending up slightly less noble than Ni); $-(G_{Ni_3Sn})_{298} = 157$ kJ/mole (10), $\Delta E_{Ni} = -G_{Ni_3Sn}/6F = 0.276$V and $\Delta E_{Sn} = -G_{Ni_3Sn}/2F = 0.812$V. For the metastable NiSn, $-(G_{NiSn})_{298} = 30$ kJ/mole, $\Delta E_{Ni} = \Delta E_{Sn} = -(G/NiSn)/2F = 0.31$V. Thus for both compounds the shift of the individual potentials due to compound formation are larger than $(E_{Ni}^o - E_{Sn}^o)_{F,Cl} \approx 0.1$V.[1] The situation corresponds to that at c in Fig. 2, with concentrations of Ni and Sn in the electrolyte that were of the same order. Deposition of alloys at potentials more positive than those of either Ni or Sn should therefore be expected and was indeed observed (7). That alloys of the composition NiSn were formed rather than alloys with higher Sn content may be due to the fact the rest-potential maximum is close to this composition; Sn-rich deposits are formed only at large current densities if the electrolyte contains more Sn than Ni (*e.g.*, 65% Sn, 35% Ni). In electrolytes as concentrated as the ones used, exhaustion of the electrolyte at the interface is not appreciable at low current density. Therefore the QRP should be close to the rest potential and thus to the equilibrium potential. The potential maximum near the composition NiSn therefore indicates that this alloy is more noble than either Ni or Sn, a fact that explains the observation that NiSn can be deposited on Sn by electroless plating (7). It should be emphasized, however, that the authors themselves explain the various effects by assuming the presence of a Ni-Sn-F complex in the electrolyte.

Nucleation problems.—Deposition of class I alloys occurs at potentials that are always more negative than that required to deposit the noble component. Therefore deposition can easily be initiated by discharge of this component, after which M-N interaction makes possible the deposition of the M component. The situation is different for class II alloys in the range where the deposition potential is more positive than that required to deposit either component separately, so that initial deposition of the noble component is not possible. In this case considerable nucleation problems are to be expected, deposition only being possible after fluctuations have formed an N, M, or M_rN_s nucleus. It is also possible that M, N complexes are present in the electrolyte which on discharge forms the required nuclei.

The quasi rest potential for deposits of M or N.—In the M and N phases in equilibrium with M_rN_s at the M-rich or N-rich end of the existence range of the compound both M and N must have the same activity as in the compound at the corresponding phase boundary. Therefore for these phases the species determining the QRP must be the same as for the coexisting compound. For class II this means that M is potential determining for the M phase and N for the N phase. For class I, however, M is the potential-determining species for both M and N. As far as N is concerned, this can only be the case if N contains some M in solid solution, to be expected for N coexisting with the compound. Only for N almost completely free of M will the QRP be determined by N itself.

The QRP of N follows a relation similar to [7] but with G replaced by the interaction free energy of M and N in almost pure N. Therefore, we expect the N potential to shift to more positive values with increasing M content leading again to a QRP maximum at the point where M takes over as the potential-determining species. Thus in principle there is always a maximum QRP. For class II it is inside the range where the compound is deposited; for class I it is in the range where N is deposited. The latter maximum, however, will be extremely small and can probably not be detected.

Binary systems with more than one compound.—Considerations similar to the ones presented above hold for binary systems with more than one compound. However, since the activities of the components vary in opposite directions monotonically over the system, there will be at most one compound in which the role of potential-determining species changes from one component to the other and for which, accordingly, a maximum in the QRP will occur. All other compounds have their potential determined by one of the components and their QRP's cover a range determined by the activity range of these components.

For compounds richer in N than the compound with the QRP maximum the potential-determining component is N; for compounds richer in M it is M. Similar considerations also apply to systems forming alloys of variable composition. Now the variation in a_M and a_N and the corresponding variation in the potentials of M and N have to be obtained by graphical integration of the Gibbs-Duhem equation

$$x_M d\mu_M + x_N d\mu_N = x_M d \ln a_M + x_N d \ln a_N = 0 \quad [12]$$

$$\ln a_M = -\int_{a_N=1}^{a_N=0} \frac{x_N}{x_M} d \ln a_N \quad [13]$$

with

$$x_N = n_N/(n_M + n_N) \text{ and } x_M = 1 - x_N = n_M/n_M = n_N$$

n indicating numbers of atoms.

[1] Formulas [1] and [2] for the quasi rest potentials hold also in the presence of complexing agents which shift the potential to more negative values by making the ion activities in the electrolyte much smaller than the corresponding concentrations. It is also possible, however, to use total ion concentrations rather than activities in [1] and [2], accounting for the effect of the complexing agents by a change in the standard potentials. This is the approach followed here.

Systems in Which the Rate Constants of the Exchange Currents of the Individual Components Are Widely Different

In such systems the component with the larger exchange rate constant is favored over the other one, and a change in the potential-determining species expected on the basis of activity and/or concentration effects may not occur at all or occurs at a different point.

Stability and Potentials in Electrolytes from Which Deposition is Not Possible

The arguments presented above relate to potentials and stability (or lack of stability) in electrolytes from which cathodic deposition was possible. It might be asked what can be said about these properties in electrolytes containing ionic species of the components, but of such a nature that cathodic deposition is not possible.

As an example let us consider CdX (X being S, Se, or Te) in an electrolyte containing Cd^{2+} ions but no X^{4+} complexes. In such a situation, a small amount of CdX will dissolve with formation of Cd^{2+} and X^{2-} ions until the solubility product

$$\pi_{CdX} = c_{Cd^{2+}} c_{X^{2-}} \approx a_{Cd^{2+}} a_{X^{2-}} \quad [14]$$

is reached; from then on CdX is stable and its potential is determined by Cd (Eq. [20] below).

CdX formed by cathodic deposition from an electrolyte containing X^{4+} complexes may have an excess of X at its surface as a result of electroless exchange of Cd and X. If such a sample is placed in an electrolyte containing Cd^{2+} ions but no X^{4+} complexes, the surface layer of X at the surface can be removed by cathodic deposition of Cd at a potential slightly more positive than required to deposit Cd at $a_{Cd} = 1$. Continuation of this process leads to a change in the bulk concentration (activity) of Cd. This method has been used to vary the stoichiometric composition of CdS (16). Since bulk diffusion is involved in this case, the method can only be used for thin films (thickness ≤ 1 μm).

The upper and lower boundaries of the CdX stability region in the Pourbaix diagram (*E vs.* pH) are determined by

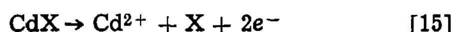

$$CdX \rightarrow Cd^{2+} + X + 2e^- \quad [15]$$

and

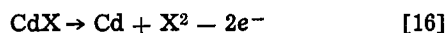

$$CdX \rightarrow Cd + X^2 - 2e^- \quad [16]$$

Both are independent of pH

CdX is also stable in electrolytes rich in X^{2-} ions. Under such conditions the concentrations of Cd^{2+} and X^{4+} complexes are very small. The potential can be expressed either as an X potential according to

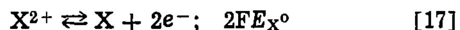

$$X^{2+} \rightleftarrows X + 2e^-; \quad 2FE_X^\circ \quad [17]$$

with

$$E_X = E_X^\circ - \frac{2.302RT}{2F} \log a_{X^{2-}}/a_X \quad [18]$$

or as a Cd potential according to

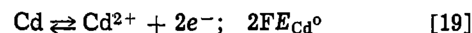

$$Cd \rightleftarrows Cd^{2+} + 2e^-; \quad 2FE_{Cd}^\circ \quad [19]$$

with

$$E_{Cd} = E_{Cd}^\circ + \frac{2.302RT}{2F} \log a_{Cd^{2+}}/a_{Cd} \quad [20]$$

Here $a_{Cd^{2+}}$ and $a_{X^{2-}}$ are activities of Cd^{2+} and X^{2-} in the electrolyte; a_{Cd} and a_X are the activities of Cd and X in CdX.

Elimination of Cd, X, and e^- from [17], [19], and [21]

$$Cd + X \rightleftarrows CdX; \quad G_{CdX}^\circ \quad [21]$$

$$a_{Cd} a_X = \exp G_{CdX}^\circ \quad [22]$$

gives

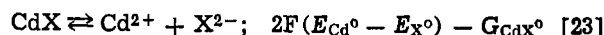

$$CdX \rightleftarrows Cd^{2+} + X^{2-}; \quad 2F(E_{Cd}^\circ - E_X^\circ) - G_{CdX}^\circ \quad [23]$$

$$\frac{2.302RT}{2F} \log \pi_{CdX} = (G_{CdX}^\circ/2F) + E_X^\circ - E_{Cd}^\circ \quad [24]$$

Introduction of [24] into [18] or [20] shows that $E_{Cd} \equiv E_X$. Evidently distinction between the components as potential-determining species is unnecessary when solubility products of the ionic species exist, which is the case when dissolution of the compound involves oppositely charged ions, so that no electrons are involved. Distinction between different potential-determining species is necessary if dissolution involves electrons, which is the case if the solid dissolves with formation of ions of the same charge. This is generally the case with metallic alloys and applies to the present substances when they are placed in electrolytes containing Cd^{2+} and X^{4+} complexes from which CdX can be made by cathodic deposition. In such cases the distinction between class I and class II materials applies.

In an electrolyte 1 molar in X^{2-}, the potentials at the boundaries of the stability range are shifted to more negative (less noble) values with respect to those of an electrolyte 1 molar in Cd^{2+} by

$$\Delta E = \frac{2.302}{2F} \log \pi_{CdX}$$

given by [24]. In both electrolytes the potential width of the stability range between CdX in equilibrium with Cd (*i.e.*, $a_{Cd} = 1$) or X ($a_{Cd} = \exp (G_{CdX}^\circ/RT)$ is given by

$$\Delta E_{stab} = |G_{CdX}^\circ|/2F \quad [25]$$

Values of the decomposition potentials of the chalcogenides of Cd and of Zn (to which the same considerations apply) under the two conditions are given in Table I. Figure 3 shows these potentials for CdS as a function of a_{Cd} and a_S under the same two conditions. By combining a change of electroyte composition with a change in the stoichiometry of CdX, a potential range of approximately 1V can be covered. However, in alkaline $S^=$ solutions the potential of CdS is not determined by these ions (or Cd^{2+}) but by SH^-; thus the lower curve is not valid (22). Table I also shows values of the solubility products calculated from [24]—an equation commonly used for this pur-

Table I. Decomposition potentials of CdX and ZnX in electrolytes 1 molar in Cd^{2+} or Zn^{2+} and values of the solubility products π; $(2.302\ RT/2F)_{298} = 0.0295V$

MX	$-E_X^\circ$ (V)	$-E_M^\circ$ (V)	$-\frac{G_{MN}^\circ}{2F}$ (V)	1m M^{2+}		1m X^{2-}		π_{MX}^{298} (moles/liter)[a]	
				$-E_{MX,M}$	$E_{MX,X}$	$-E_{MX,M}$	$-E_{MX,X}$	This paper	Other authors
CdS	0.476 (2)	0.403 (2, 19)	0.73 (17) 0.716 (20)	0,403	0.327	1.206	0.476	6×10^{-28}	6.5×10^{-28} (21) 1.0×10^{-28} (19) 1.14×10^{-28} (20)
CdSe	0.92 (19)	0.403 (2, 19)	0.52 (17)	0.403	0.117	1.44	0.92	7×10^{-36}	—
CdTe	0.94 (18) 1.14 (19)	0.403 (2, 18)	0.51 (17)	0.403	0.107	1.45 1.65	0.94 1.14	3.2×10^{-36} 5.4×10^{-43}	— 1×10^{-42} (19)
ZnS(sph)	0.476 (2)	0.763 (2, 18)	1.02 (17, 20)	0.763	0.257	1.496	0.476	1.4×10^{-25}	7×10^{-26} (19) 2.2×10^{-26} (21)
ZnS(w)	0.476 (2)	0.763 (2, 18)	0.95 (17)	0.763	0.187	1.426	0.476	3.3×10^{-23}	1.6×10^{-23} (19)
ZnSe	0.92 (19)	0.763 (2, 7)	0.71 (16, 17)	0.763	−0.053	1.63	0.92	4.1×10^{-30}	1×10^{-31} (19)
ZnTe	0.94 (18) 1.14 (19)	0.763 (2, 19) 0.763 (2, 19)	0.61 (16, 17) 0.61 (16, 17)	0.763	−0.153	1.55 1.75	0.94 1.14	2.1×10^{-27} 3.5×10^{-34}	— —

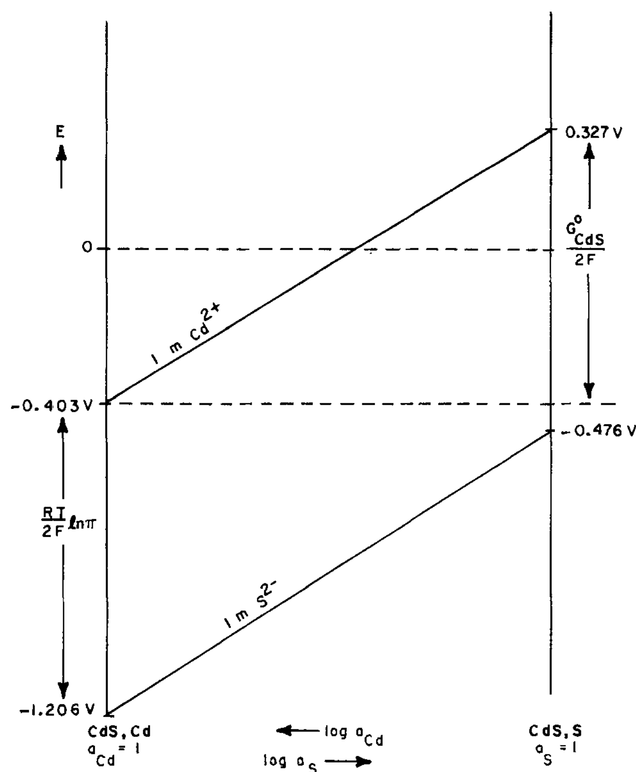

Fig. 3. Potential vs. NHE as a function of a_{Cd} or a_S for CdS in aqueous electrolytes with $a_{Cd^{2+}} = 1m$ or $a_{S^{2-}} = 1m$. The end points of the lines are the decomposition potentials.

pose. Values reported by other authors are given for comparison.

Combination of [18] and [20] leads to

$$E_{Cd} = E_X = \frac{1}{2}(E_{Cd}^{o} + E_X^{o}) + \frac{2.302RT}{2F} \log (a_{Cd^{2+}} a_{X^{2-}} / a_{Cd} a_X) \quad [26]$$

an expression first derived by Sato (21). However, [18] and [20] are easier to handle.

Discussion

The quasi rest potentials as introduced in the present paper are characteristic for the deposited material in bulk and may be compared with equilibrium potentials valid for the case that equilibration of bulk as well as surface is possible (23).

An extensive discussion of equilibrium potentials of alloys first given by Reinders (24) is reproduced in the review article by Kremann and Müller (25). For random alloys Reinders' approach is similar to ours, the potential being determined by ions of the components, and in particular by those that are least noble. Compounds were believed to have a fixed composition. Distinction was made between compounds that can and those that cannot exist in equilibrium with an electrolyte containing the components in the same ratio as in the compound. The potential of the former were believed to be determined by the Nernst formula with ions of the lattice molecule $M_rN_s^{t+}$ the potential-determining species in the electrolyte. This complex ion was assumed to dissociate with formation of M^{m+} and N^{n+} ions. In electrolytes with different concentrations of these ions but $c_{M^{m+}} + c_{N^{n+}}$ = constant, $c_{complex}$ and therewith the electrode potential is found to have a maximum value when $c_{M^{m+}}/c_{N^{n+}} = r/s$. Since ions of the separate components are not potential determining, the compound potential maximum may have any values relative to the component potential which are believed to be determined by their ions. When, at the point where compound and electrolyte have the same composition, the potential of a solid solution of the less noble component in the noble component has a potential more positive (= noble) than the compound, the latter cannot exist in an electrolyte of its own composition.

The maximum in the potential of the compound that may coexist with an electrolyte of its own composition, though similar to that of our class II alloys in that it occurs for small differences of the standard potentials of the components, has a completely different reason: the change in concentration of the complex ion in the electrolyte.

In view of what is presently known about the existence of point defects and nonstoichiometry in compounds, it seems preferable to assume that no complex ions but the individual ions of the components determine the potential of the compound as they do that of the components—the assumption made in the present paper. Reinders' phase diagrams in which the compositions of coexisting solid and electrolyte phase are plotted as a function of potential can be adopted with that modification with only minor adjustments. Reinders' compounds that may coexist with electrolytes of the same composition are our class II compounds or alloys, with M the potential-determining species at the M side of the potential maximum, N the potential-determining species at the N side of the maximum. Compounds that cannot coexist with electrolytes of their own composition are our class I compounds.

The compositions of a compound in equilibrium with different electrolytes are not exactly the same: The compound has different deviations from stoichiometry and correspondingly different potentials.

Kremann and Müller (24), though reproducing Reinders' arguments, do not seem to fully subscribe to his conception of a compound with a variable potential: They ascribe a single potential to a compound, identifying it with the most noble potential it ever displays. This view—though incorrect—still has many adherents.

The idea of ions of the individual components as potential-determining species for compounds and alloys was used by Pourbaix (2) in the construction of his well-known atlas. It leads to fields rather than lines of stability in the potential-*p*H diagrams. It is also accepted by Sato (21) who derived on this basis a general expression for the potential of a compound as a function of the activities of atoms in compounds and of component ions in the electrolyte. Since in alloys and compounds the Gibbs free energy of interaction between the components is invariably negative, acceptance of the ions of the components as potential-determining species must lead to a situation in which the potentials of alloys and compounds are always more positive (= more noble) than those of the components, the ions of which dominate the potential. Various diagrams in Ref. (24) and (25), *e.g.*, Fig. 3 (BD) and Fig. 5 (AG and BK) in Ref. (24) and Fig. 71 (BG), Fig. 73, Fig. 79 (top curve), Fig. 81 (AD), and Fig. 84 (BG) in Ref. (25), are in conflict with this requirement. Absence of experimental proof for shifts toward less noble potentials under the conditions described may be considered proof for the individual ion model.

Summary

The cathodic deposition of binary alloys and compounds is discussed on the basis of deposit-electrolyte thermodynamics and the rate of transfer of the components, using the quasi rest potential (QRP), defined as deposition potential minus polarization of the solid, to characterize the deposit. The species with the larger value for the product of the discharge rate constant and the concentration of species in the electrolyte at the deposit-electrolyte interface is believed to be dominant in determining the potential.

In general, each component is potential determining at its side of the system, both potentials shifting to more positive values on alloy formation and thus

giving rise to a QRP maximum at the point where the change of potential-determining species occurs. If the shift in component potentials due to alloy or compound formation is large relative to the difference in the individual equilibrium potentials of the components (class II), the maximum of the QRP occurs at some intermediate composition. If the shift is small (class I), the maximum is expected to occur in the stability range of the nearly pure noble component and may be too small to be observed. Marked differences in the values of the exchange rate constants for the components extends the activity range in which a species dominates the QRP in favor of the species with the larger rate constant.

Compounds placed in electrolytes containing large concentrations of the normal ions of one of the components, but no complexes of the nonmetal component which are required for cathodic deposition of the compound, are stable, their potential being determined by the normal ions. For ions with concentrations linked by a solubility product, either species may be used to formulate the equilibrium potential.

Acknowledgment

This report was prepared for the Advanced Materials Branch, Division of Solar Technology, U.S. Department of Energy under a subcontract from Monosolar, Incorporated, a subsidiary of Monogram Industries, Incorporated (Prime Contract No. EX-76-C-01-2457).

Manuscript submitted June 1, 1977; revised manuscript received May 1, 1978.

Any discussion of this paper will appear in a Discussion Section to be published in the June 1979 JOURNAL. All discussions for the June 1979 Discussion Section should be submitted by Feb. 1, 1979.

REFERENCES

1. A. Brenner, "Electrodeposition of Alloys," 2 volumes, Academic Press, New York (1963).
2. M. Pourbaix, "Atlas d'Equilibres Electrochimiques," Gauthiers-Villars et Cie, Paris (1963).
3. H. Gobrecht, H. D. Liess, and A. Tausend, *Ber. Dtsch. Bunsenges. Phys. Chem.*, **67**, 930 (1973).
4. A. Brenner, D. E. Couch, and E. K. Williams, *J. Res. Natl. Bur. Std.*, **44**, 109 (1950).
5. J. Dewalens, L. Heerman, and L. van Simaeys, *This Journal*, **122**, 477 (1975).
6. A. Brenner, "Electrodeposition of Alloys," Vol. 1, p. 78, Vol. 2, p. 345, Academic Press, New York (1963).
7. J. W. Cuthbertson, N. Parkinson, and H. P. Rooksby, *This Journal*, **100**, 107 (1953).
8. A. Brenner, "Electrodeposition of Alloys," Vol. 1, p. 349, Academic Press, New York (1963).
9. B. E. Conway, "Theory and Principles of Electrode Processes," chap. 6, Ronald Press Co., New York (1965).
10. O. Kubaschewski and E. Ll. Evans, "Metallurgical Thermochemistry, Table A, Pergamon Press, London (1955).
11. M. P. R. Panicker, M. Knaster, and F. A. Kröger, *This Journal*, **125**, 568 (1978).
12. G. Tammann and A. Koch, *Z Anorg. Chem.*, **133**, 179 (1924).
13. F. Ducelliz, *Bull. Soc. Chim.*, **7**, (4) 606 (1910).
14. A. Brenner, "Electrodeposition of Alloys," Vol. 2, pp. 345, 399, Academic Press, New York (1963).
15. J. A. Augis and J. E. Bennett, *This Journal*, **125**, 335 (1978).
16. J. Vedel, M. Soubeyrand, and E. Castel, *ibid.*, **124**, 177 (1977).
17. O. Kubaschewski and E. Ll. Evans, "Metallurgical Thermochemistry," Table A, Pergamon Press, London (1955).
18. A. J. Panson, *J. Phys. Chem.*, **67**, 2177 (1963); **68**, 1721 (1964).
19. W. M. Latimer, "Oxidation Potentials of the Elements," Prentice Hall, Englewood Cliffs, N.J. (1952).
20. S. F. Ravits, *J. Phys. Chem.*, **40**, 61 (1936).
21. M. Sato, *Electrochim. Acta*, **11**, 361 (1966).
22. D. S. Ginley and M. A. Butler, Abstract 418, p. 1046, The Electrochemical Society Extended Abstracts, Spring Meeting, Seattle, Washington, May 21-26, 1978.
23. G. Tammann, *Z. Anorg. Chem.*, **107**, 1 (1919).
24. W. Reinders, *Z. Phys. Chem.*, **42**, 225 (1902).
25. R. Kremann and R. Müller, in "Ostwald-Drucker, Handbuch der Allgem. Chemie," P. Walden and C. Drucker, Editors, Vol. 1, pp. 626-628, 644-648, Band VIII, Elektromotorische Kräfte, Electrolyse und Polarisation, Akad. Verlagsges, Leipzig (1930).

Analytical and Experimental Study of 1 MeV Electron Irradiated GaAlAs/GaAs Heteroface Solar Cells

G. H. Walker,* C. E. Byvik, and E. J. Conway

NASA Langley Research Center, Hampton, Virginia 23665

and J. H. Heinbockel and M. J. Doviak

Old Dominion University, Norfolk, Virginia 23508

ABSTRACT

Deep junction (4 μm) GaAlAs/GaAs heteroface solar cells were irradiated with 1 MeV electrons at fluences of 10^{13}, 10^{14}, 10^{15}, and 10^{16} electrons/cm^2. The short-circuit current degraded to 0.02 of its original value after a fluence of 10^{16} electrons/cm^2. Computer modeling of the spectral response before and after irradiation showed that, in addition to a decrease in the minority carrier diffusion length in p-GaAs from several micrometers to ½ μm, an increase in the recombination velocity at the GaAlAs/GaAs interface from 10^4 to 10^8 cm/sec was required to completely explain the observed change in the spectral response.

GaAs solar cells are of interest for generating electrical power in space on a solar power satellite or for a high temperature, near-sun science mission. With the achievement of 18.5% AMO efficiency (1) research is being directed toward optimization of the stability in the electron and proton environment of space. This

* Electrochemical Society Active Member.

Key words: GaAs solar cells, radiation damage, surface recombination, diffusion length, modeling.

optimization requires a fundamental understanding of the interaction of radiation with solar cells. The efficient operation of solar cells depends on such parameters as minority carrier diffusion length, carrier mobility, and recombination rates. To determine the effect of 1 MeV electrons on these cell parameters, computer-generated spectral response curves have been compared to experimental spectral response data for 1 MeV electron irradiated, deep junction (4 μm) GaAlAs/GaAs heteroface solar cells. In this paper we describe: the cells developed to study radiation effects in the p-GaAs region, the measurements, the comparison between experimental and calculated results, and our conclusions.

Experimental

Heteroface p-GaAlAs/p-GaAs/n-GaAs solar cells were fabricated using the etch-back epitaxy process (1). The n-type GaAs substrates were Si doped to a carrier concentration of 2×10^{17} carriers/cm^3. The p-GaAlAs layer thickness was 0.3-0.5 μm. The p-GaAs layer was 4 μm thick giving a junction depth of 4 μm measured from the GaAlAs interface. Large area, vacuum-evaporated Sn-Ag contacts were used for electrical connection to the n-GaAs. Front finger contacts to the GaAlAs layer were deposited by sputtering a layer of Pd followed by a layer of Ag using an appropriate mask.

The cells, mounted on aluminum backing plates, were irradiated with 1 MeV electrons. Groups of cells were irradiated at fluences of 10^{13}, 10^{14}, 10^{15}, and 10^{16} electrons/cm^2. Electron irradiation rates were chosen such that the cells remained at ambient temperature during irradiation.

Short-circuit currents were measured both before (I_{sc0}) and after irradiation (I_{sc}). The cells mounted on metal headers were placed on the water-cooled stage of solar simulator. For all short-circuit current measurements, the intensity of the filtered xenon solar radiation was set to one air mass zero solar constant using a balloon-calibrated Si solar cell. The short-circuit current of the GaAlAs/GaAs cell was then obtained by measuring the voltage drop across a precision resistor. The relative spectral responses were obtained both before and after irradiation by mounting the cells in an intensity-calibrated spectrophotometer and measuring the short-circuit current as a function of wavelength.

Results and Discussion

The effect of radiation on the short-circuit current at AMO illumination is shown in Fig. 1. The curve is a plot of the averages of short-circuit current ratios *vs.* electron fluence. The short-circuit current degraded to 0.02 of its original value after a fluence of 10^{16} electrons/cm^2. Additional information about the degradation can be obtained from measurements of the spectral response of the short-circuit current. The spectral response typical of the cells used in this study is shown in Fig. 2 which consists of plots of the relative spectral response as a function of the incident wavelength, before and after irradiation. The points are the experimentally derived data and the curve is computed using the device equations for this cell configuration (2, 3).

The computed curve fits the experimental data for the unirradiated cell with the mobility of electrons in the p-GaAs region chosen to be 3300 cm^2/V-sec, the minority carrier diffusion length in the p-GaAs region 3.3 μm, and an interface recombination velocity of 10^4 cm/sec.

The spectral response after irradiating the cell with 10^{16} electrons/cm^2 is also shown in Fig. 2. It can be seen that the response in the blue region is reduced much more than the response near the bandedge. The device equations incorporate a number of material parameters which could be affected by the radiation and lead to reduced response. These material parameters for the p-GaAlAs, the p-GaAs, and the n-GaAs layers are the minority carrier diffusion lengths, the mobilities of minority carriers, the majority carrier densities, and the surface and interface recombination velocities.

Solar cells having deep junctions such as those used in this study proved advantageous since the reduction of the short-circuit current of the solar cells due to electron irradiation can be attributed to changes produced in the p-GaAs region only. Effects on short-circuit current produced by radiation damage in the base region can be neglected. This assumption was corroborated by the calculations.

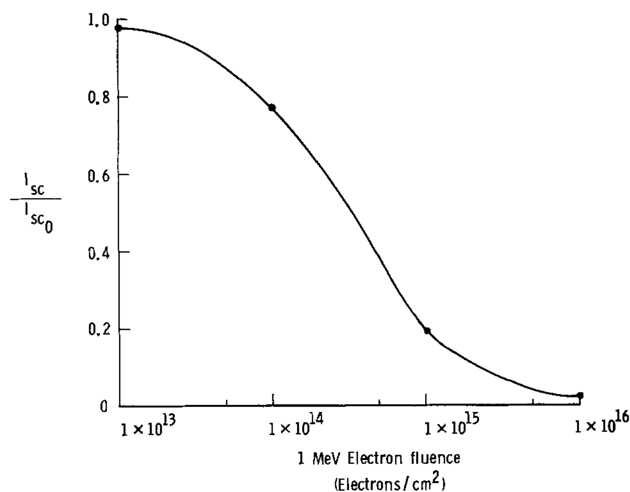

Fig. 1. Ratio of final short-circuit current to initial short-circuit current as a function of 1 MeV electron fluence for deep junction GaAlAs/GaAs heteroface solar cells.

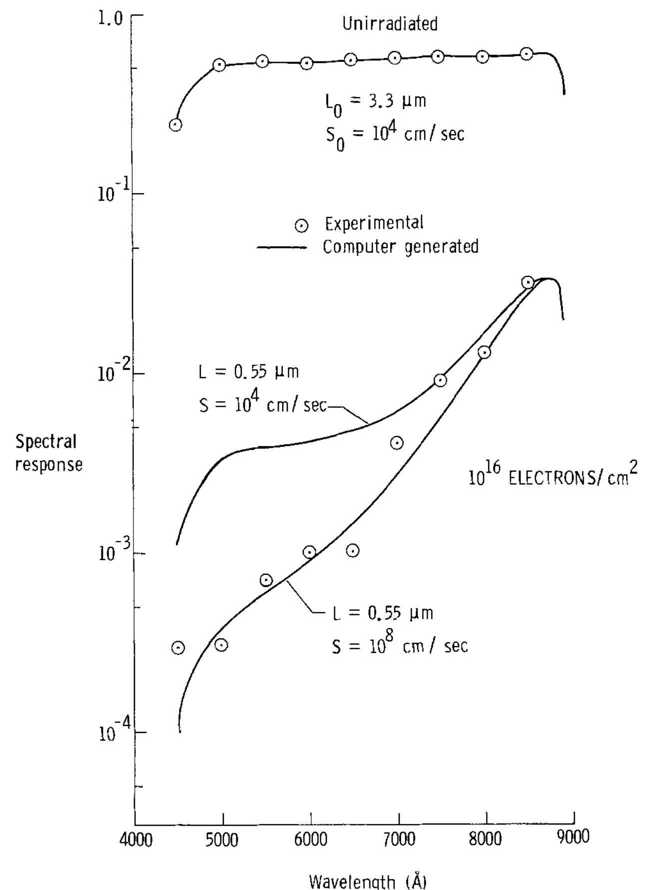

Fig. 2. Measured and computed spectral response of a deep junction GaAlAs/GaAs heteroface solar cell unirradiated and irradiated with 10^{16} 1 MeV electrons/cm^2.

Using the device equations, it was found that a reduction of the minority carrier diffusion length in the p-GaAs could explain the reduced spectral response in the red region (middle curve, Fig. 2), but a change in at least one additional parameter was needed to explain completely the reduction in the blue region. Calculations of spectral response were made by reducing the mobility from an initial value of 3300 to 5 cm^2/V-sec, with the diffusion length fixed at 0.55 μm. Slightly improved agreement in the blue region was achieved, but the assumed mobility reduction to 5 cm^2/V-sec was unreasonably large (4). Calculations indicated that the mobility change expected from ionized-center scattering due to radiation defects would be small.

Majority carrier trapping on radiation defects could account for a carrier density reduction of less than $10^{17}/cm^3$. However, this effect would be small since the density of holes in the p-GaAs is in excess of $10^{18}/cm^3$ and, further, this effect is not spectrally selective. Therefore, both the radiation-induced mobility change and the majority carrier trapping were eliminated as the cause of the reduced blue response.

The third material parameter in the model which could produce the reduced response is the recombination velocity (S) at the p-GaAlAs, p-GaAs interface. A computed spectral response curve using a value of S higher than that before irradiation reduced the blue response but did not affect the response in the red spectral region (bottom curve Fig. 2). Thus, the computed spectral response could be made to agree with the experimental data in the red region by reducing the minority carrier diffusion length to 0.55 μm, and in the blue region by increasing the interface recombination velocity to 10^8 cm/sec.

This use of an increase in surface recombination velocity to explain a significant reduction in blue response of the cell has been discussed so far only in terms of the correlations between experimental and calculated results. However, it is plausible that S would increase with irradiation.

The radiation-induced damage is expected to be uniform throughout the solar cells (5), both in the bulk and near the interface. This suggests that the changes in minority carrier diffusion lengths are related to changes in interface recombination velocity. Assuming that the reduction in minority carrier diffusion length is due to the introduction of recombination centers in the bulk, and that the same type of recombination centers near the interface cause an increase in the recombination velocity, then an expression can be derived relating the minority carrier diffusion lengths to the interface recombination velocities before and after irradiation. The minority carrier diffusion length L is related to the diffusion constant D, the capture probability density K, and the number density of bulk recombination centers N_B, by

$$L = \left(\frac{D}{KN_B} \right)^{1/2}$$

where it is assumed that the lifetime is determined by the recombination centers.

Using the Shockley-Read model for the surface recombination velocity, the following assumptions are made: (*i*) the capture cross section for holes and electrons are equal; and (*ii*) the thickness, t, of the interface region is constant. With these assumptions, the interface recombination velocity S is given as

$$S = K(N_I t) \frac{P}{n}$$

where the product ($N_I t$) gives the number density of recombination centers in the interface region, P is the bulk density of majority carrier, and n is the intrinsic carrier density. The ratio of the square of the diffusion length after irradiation to that before irradiation yields

$$\left(\frac{L}{L_0} \right)^2 = \frac{N_{B0}}{N_B} \qquad [1]$$

where the zero subscript indicates the parameter value before irradiation. The ratio of the interface recombination velocity before irradiation to that after irradiation leads to

$$\frac{S_0}{S} = \frac{N_{I0}}{N_I} \qquad [2]$$

After sufficient irradiation, the density of recombination sites in the bulk and at the interface is determined by the irradiation and, therefore, $N_B = N_I$. This leads to the expression

$$\frac{S}{S_0} = \left(\frac{L_0}{L} \right)^2 \cdot \frac{N_{B0}}{N_{I0}} \qquad [3]$$

Equation [3] gives qualitative results. It shows that an increase in surface recombination velocity can reasonably be expected from the irradiation that reduces minority carrier diffusion length.

In summary, deep junction GaAlAs/GaAs heteroface solar cells showed significant degradation when irradiated with 1 MeV electrons at fluences up to 10^{16} electrons/cm^2. Computer modeling of the spectral response indicated that both a decrease in the minority carrier diffusion length in the p-GaAs region, as well as an increase in the recombination velocity at the GaAlAs/GaAs interface, was required to fully explain the observed changes.

Acknowledgment

The authors are indebted to Stanley J. Marsik of NASA Lewis Research Center, Cleveland, Ohio, for electron irradiation of the solar cells.

Manuscript submitted March 9, 1978; revised manuscript received July 24, 1978.

Any discussion of this paper will appear in a Discussion Section to be published in the June 1979 JOURNAL. All discussions for the June 1979 Discussion Section should be submitted by Feb. 1, 1979.

Publication costs of this article were assisted by NASA Langley Research Center.

REFERENCES

1. J. M. Woodall and H. J. Hovel, *Appl. Phys. Lett.*, **30**, 492 (1977).
2. H. J. Hovel and J. M. Woodall, "Rec 10th IEEE Phot. Spec. Conf.," p. 25, Palo Alto, Calif. (1973).
3. H. J. Hovel, "Semiconductors and Semimetals," Vol. 11, Academic Press, New York (1975).
4. G. E. Brehm and G. L. Pearson, *J. Appl. Phys.*, **43**, 568 (1972).
5. L. W. Aukerman, M. F. Millea, and M. McColl, *ibid.*, **38**, 685 (1967).

On the Diffusion of Excess Vacancies to Free Surfaces and Voids in Thin Films

J. R. Lloyd

Department of Materials and Metallurgical Engineering, Stevens Institute of Technology, Hoboken, New Jersey 07030

and S. Nakahara*

Bell Laboratories, Murray Hill, New Jersey 07974

ABSTRACT

Recent investigations have shown that resistivity decay in evaporated gold films originates, in part, from the annihilation of excess vacancies, trapped during film condensation, at a high density (10^{15}-10^{17}/cm^3) of small (<50Å) voids present within the film. This paper presents a theoretical treatment of vacancy diffusion to free surfaces and to voids. The treatment predicts both the observed void growth and resistivity decay in thin films.

It is well known that the resistivity of freshly deposited thin films changes continuously with time at room temperature (1-3). It has been generally accepted that resistivity decay in thin films takes place as a result of the diffusion of excess vacancies, quenched-in during film formation, to sinks such as free surfaces and grain boundaries (1, 3). Recent transmission-electron-microscope (TEM) studies of evaporated gold films have shown that thin films generally contain a high density ($\sim 10^{16}$/cm^3) of small voids (4, 5). The presence of such a high density of voids suggests that these voids may serve as potential sites for the annihilation of excess vacancies. Experimental evidence for this suggestion has been found in our recent observations that these voids grow at the expense of excess vacancies with aging time even at room temperature (6, 7). Assuming that voids are the only sinks for excess vacancies, Lloyd and Nakahara (6) were able to relate, semiquantitatively, the void growth to the resistivity decay in evaporated gold films. Although the effect of the surfaces was not considered, this treatment was in good agreement with experiments for long times following film deposition, but could not account for short-term resistivity decay. We have, therefore, treated our earlier problem by using a more rigorous mathematical framework which considers both surfaces and voids as potential sinks for excess vacancies.

Theoretical Model

Based upon our previous experimental results (5), several assumptions were made for determining the excess vacancy concentration and the rate of void growth in evaporated gold films. (*i*) The film was assumed to contain an initially uniform concentration of quenched-in excess vacancies; (*ii*) The pre-existing voids, which serve as vacancy sinks, are distributed uniformly throughout the film. The creation of new voids by vacancy clustering is ignored; (*iii*) The void distribution was approximated by a simple cubic lattice of equally sized voids in an otherwise defect-free film; (*iv*) The voids were treated as perfect sinks, *i.e.*, vacancies may be annihilated, but not created, at void sites. A schematic view of this theoretical model is shown in Fig. 1.

If voids were not present in the film, the vacancy concentration could be determined from a solution of the diffusion of vacancies out of a thin slab (8, 9). On the other hand, if voids were present, for example, in an infinitely thick film, one would solve the problem of vacancy diffusion to a periodic array of voids using the formulation similar to that used by Ham (10) for the case of the growth of precipitates from a supersaturated solid solution. In the present case, the film can be best approximated by a thin slab containing uniformly distributed vacancy absorbers (voids). This situation can, therefore, be described as the out-diffusion of vacancies from a thin slab with a simultaneous irreversible chemical reaction.

The irreversible chemical reaction is

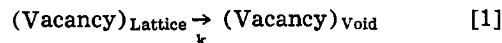

$$(\text{Vacancy})_{\text{Lattice}} \xrightarrow[k]{} (\text{Vacancy})_{\text{Void}} \qquad [1]$$

The vacancy concentration (C_x) in the film can be represented by the solution to

$$\frac{\partial C_x}{\partial t} = D\frac{\partial^2 C_x}{\partial x^2} - kC_x \qquad [2]$$

where D is the vacancy diffusivity and t is time, sub-

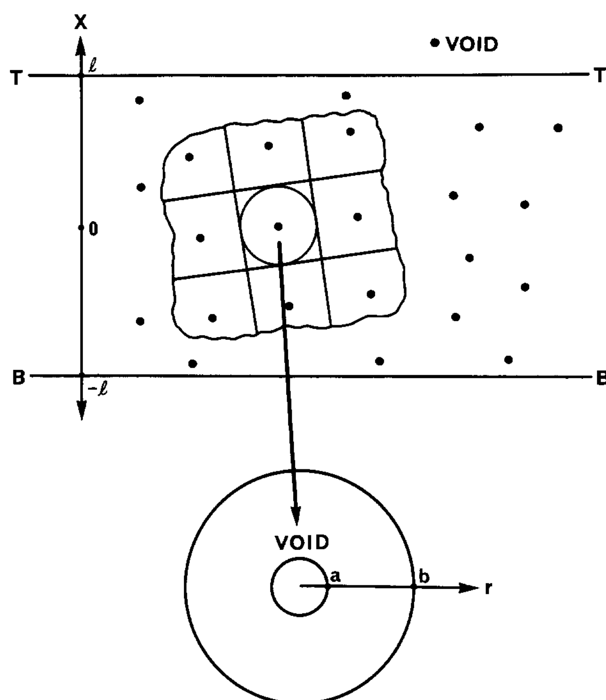

Fig. 1. Schematic view of the model showing a simple cubic lattice of voids in a thin slab of thickness 2*l* and a view of the Wigner-Seitz cell.

* Electrochemical Society Active Member.

Key words: diffusion, films, surfaces.

ject to the boundary conditions

$$C_x(\pm l, t) = 0$$
$$C_x(x, 0) = C_0 \quad [3]$$
$$\frac{\partial C_x}{\partial x}(0, t) = 0$$

where l is the half-thickness of the film (see Fig. 1) and C_0 is the initial vacancy concentration.

From Eq. [2] and [3], the vacancy concentration, $C_x(x, t)$, can be easily shown to be

$$C_x(x,t) = \frac{4C_0}{\pi} \sum_{n=0}^{\infty} \frac{(-1)^n}{(2n+1)} \cos(\theta_n x) \exp(-Q_n) \quad [4]$$

where

$$Q_n = \int_0^t (\theta_n^2 D + k)\, dt \quad [5]$$

and

$$\theta_n = \frac{(2n+1)\pi}{2l} \quad [6]$$

In the case of D and k being time-independent

$$Q_n = (\theta_n^2 D + k)t \quad [7]$$

Determination of k

The second term on the left-hand side of Eq. [2], kC_x, represents the rate of the vacancy annihilation, which takes place at preexisting voids. This relation can then be expressed as

$$kC_x = J_a 4\pi a^2 N_v \quad [8]$$

where J_a is the vacancy flux at a void surface, a the void radius, and N_v the void density. In order to obtain a value for k, J_a was determined from a solution of the problem of vacancy diffusion to a simple cubic (SC) lattice of voids. The use of the assumption that the voids lie on a SC lattice reduces the problem to that of diffusion in a single unit cell. By replacing the SC unit cell by the equivalent Wigner-Seitz cell, the problem can be further simplified to allow the use of spherical coordinates. The diffusion equation for this problem can be written

$$\frac{\partial C_r}{\partial t} = D\nabla^2 C_r \quad [9]$$

which is subject to the boundary conditions

$$C_r(a, t) = 0 \quad [10a]$$
$$C_r(r, 0) = C_0 \quad [10b]$$
$$\frac{\partial C_r}{\partial r}(b, t) = 0 \quad [10c]$$

where C_r is the vacancy concentration in the Wigner-Seitz cell. The radius of the equivalent Wigner-Seitz sphere, b, is calculated from

$$\frac{1}{N_v} = \frac{4}{3}\pi b^3 \quad [11]$$

The solution, C_r, is

$$C_r(r,t) = \sum_{n=1}^{\infty} \frac{2C_0 a}{\lambda_n} \phi_{na} \frac{\sin\lambda_n(r-a)}{r} \exp\left(-\lambda_n^2 \int_0^t D\,dt\right) \quad [12]$$

where

$$\phi_{na} = \frac{1 + b^2\lambda_n^2}{b^2\lambda_n^2(b-a) - a} \quad [13]$$

and the λ_n's are the nonzero roots to

$$\tan\{\lambda_n(b-a)\} = b\lambda_n \quad [14]$$

The vacancy flux at the surface of the void, J_a, is then

$$J_a = D\frac{\partial C_r}{\partial r}\bigg|_{r=a} = 2C_0 D \sum_{n=1}^{\infty} \phi_{na} \exp\left(-\lambda_n^2 \int_0^t D\,dt\right) \quad [15]$$

Substituting Eq. [15] into Eq. [8], we obtain

$$kC_x = 8\pi C_0 a^2 D N_v \sum_{n=1}^{\infty} \phi_{na} \exp\left(-\lambda^2 \int_0^t D\,dt\right) \quad [16]$$

It should be emphasized that C_r (the solution to Eq. [9]) and C_x (the solution to Eq. [2]) are not independent of each other, but are constrained by the requirement that the concentration from Eq. [2] averaged over the film thickness, $\overline{C_x}$, must be the same as the concentration from Eq. [9] averaged over the Wigner-Seitz cell at any given time. The initial condition Eq. [10b] must, therefore, be replaced by the time-dependent boundary condition

$$\frac{1}{V}\int_V C_r(r,t)\,dV = \overline{C_x} \quad [17]$$

where V is the volume of the Wigner-Seitz cell. It should be noted that the use of Eq. [17] makes the reaction constant, k, time dependent.

Equation [2] together with Eq. [15] and [16] can be integrated numerically over small increments of time, using an iteration method in a self-consistent manner with the aid of a digital computer.

The variation of k with time is shown in Fig. 2. We note a high initial value which rapidly decays to a minimum followed by a slow increase to an apparent saturation value. This behavior of k is reflected in Eq. [8], in which k is seen to be proportional to the vacancy flux into the void, J_a, as well as to the void surface area, $4\pi a^2$. The initial rapid drop in k with time is due to the relaxation of the concentration gradient at the boundary ($r = a$). In other words, the infinite gradient at the boundary gives an infinite vacancy flux into the void which results in an infinite value for k. In order to avoid this mathematical complication, the computation was initiated at $t = 0.1$ sec rather than at $t = 0$. At this time (0.1 sec), the series in Eq. [4] was found to converge satisfactorily in about 400 terms. After a few hours, a single term was found to be adequate. The minimum in the k *vs.* t curve (Fig. 2) demonstrates the relative contributions of both the concentration gradient and the void size. With further increase in time, the contribution of the void size to

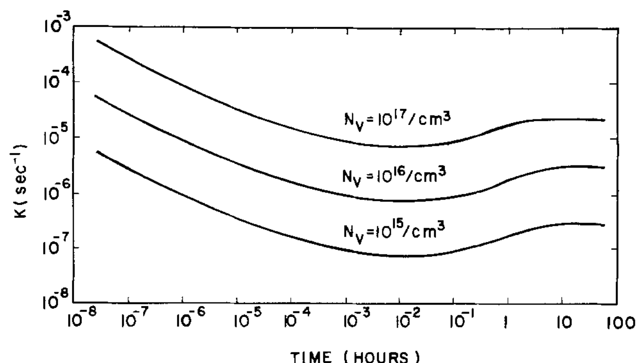

Fig. 2. Variation of the reaction constant, k, with time as a function of void density. Note that this plot and all succeeding plots are for a 1000Å-thick film, $C_0 = 0.5\%$, and $T = 298°K$ unless otherwise indicated.

the value of k becomes dominant until an apparent saturation point is reached. As the vacancy concentration reaches the equilibrium value, the reaction constant, k, will eventually approach zero, regardless of the void size.

The void size is obtained by numerical integration over the void growth rate given by

$$\frac{da}{dt} = J_a\Omega \qquad [18]$$

where Ω is the vacancy volume which is estimated to be half the atomic volume.

Theoretical Results

Figure 3 shows the effect of a void concentration ($5 \times 10^{16}/cm^3$) on the vacancy concentration profile. An examination of these profiles confirms our earlier conclusion that, after few hours, voids become the principal sinks for diffusing excess vacancies (6). The effect of void density on the average vacancy concentration as a function of time is shown in Fig. 4, where it is clearly seen that, for 1000Å-thick film, voids become important sinks at a void density higher than $1 \times 10^{16}/cm^3$.

As expected, with decreasing film thickness, the contribution of the surfaces becomes more important. The effect of the film thickness on the vacancy concentration is shown in Fig. 5. It should be pointed out, however, that for very thin films in which the mean intervoid distance is greater than the film thickness, this model for calculating the vacancy concentration and the void size is not physically realistic, but the computational method remains useful for the following reason. In very thin (<500 Å) thin films, where the periodic boundary condition is no longer appropriate, the effect of surfaces as vacancy sinks becomes so dominant that voids are no longer effective for the vacancy annihilation. On the other hand, as the film thickness is increased and, consequently, voids become more important as vacancy sinks, the periodic boundary condition becomes more valid. In fact, films that are greater than 1 μm in thickness, act as if they are infinitely thick with virtually all of the vacancies diffusing to voids.

Spontaneous changes in the vacancy concentration may be undesirable for many solid-state device applications, as they might contribute significantly to changes in physical properties such as the resistivity. Figure 6 shows the vacancy concentration as a function of time for different temperatures in a 1000Å-thick film. The important observation here is that, in order for a stable resistivity to be achieved, only a short-time anneal at a relatively modest temperature is required.

Void Growth

The diffusion of vacancies to voids results in void growth until all of the excess vacancies have been annihilated. The effect of the initial vacancy concentration, void density, and film thickness on void growth can be seen in Fig. 7, 8, and 9. As expected, a higher vacancy concentration produces larger voids. Furthermore, growth of larger voids can be seen in thicker films and in films with lower void densities.

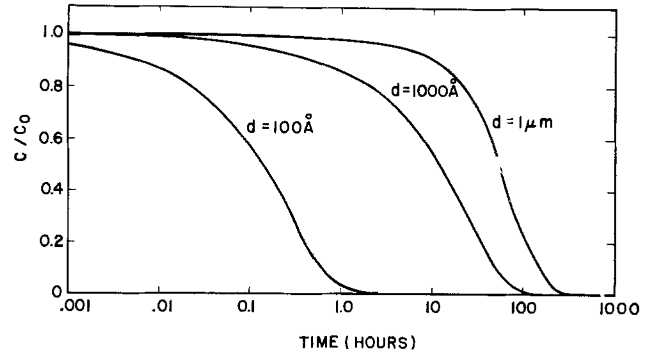

Fig. 5. Average vacancy concentration with time in a thin film as a function of film thickness.

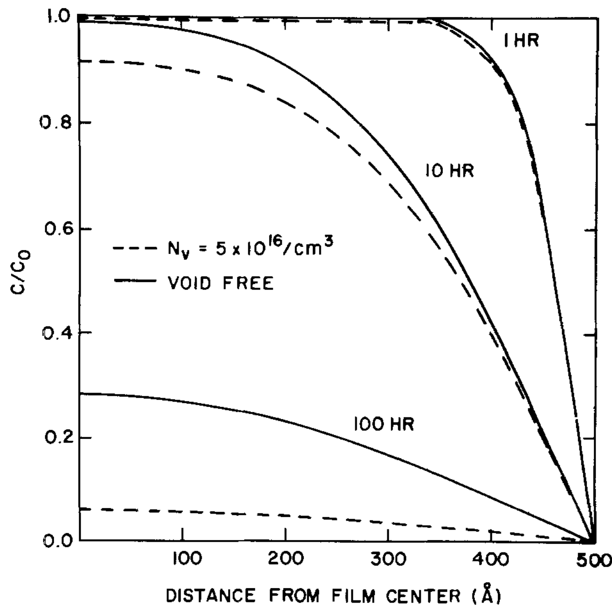

Fig. 3. Comparison of the vacancy concentration profile of a void-free film with that of a film containing a void density of $5 \times 10^{16}/cm^3$.

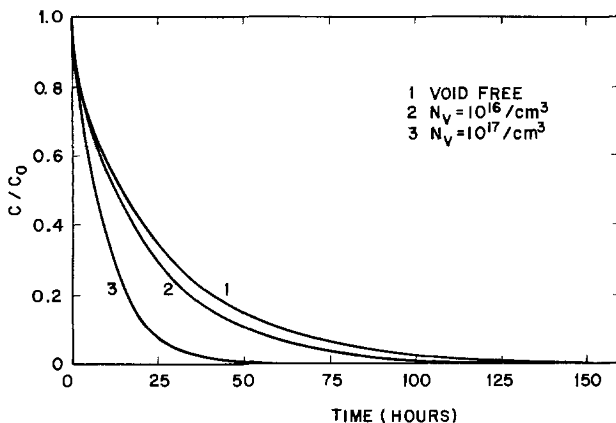

Fig. 4. Variation of vacancy concentration with time as a function of the void density.

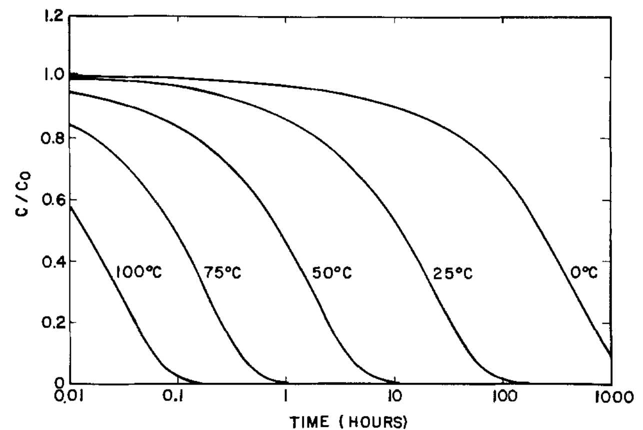

Fig. 6. Average vacancy concentration with time in a thin gold film as a function of aging temperature.

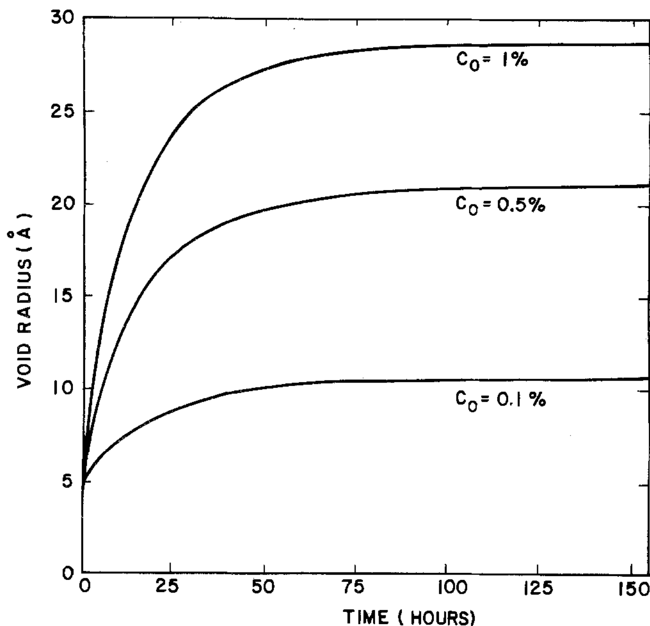

Fig. 7. Void size as a function of initial vacancy concentration. $N_v = 1 \times 10^{16}/cm^3$.

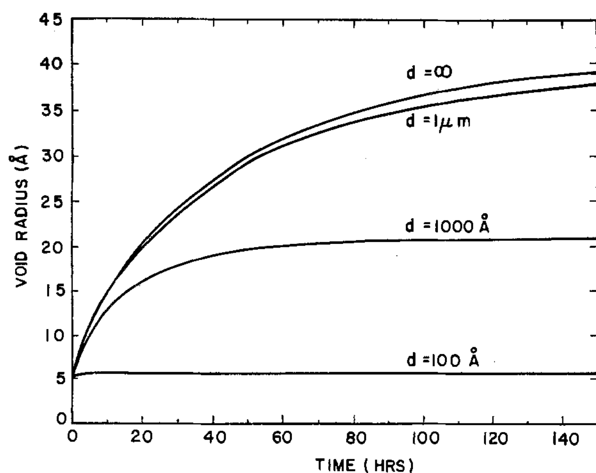

Fig. 8. Void size as a function of film thickness. $N_v = 1 \times 10^{16}/cm^3$.

Comparison with Experiment

Since the resistivity due to vacancies is linearly related to the excess vacancy concentration (8), the resistivity, ρ, can be expressed as

$$\rho = \rho_{xs} + \rho_0 \quad [19]$$

where ρ_0 is the the resistivity without vacancies, and

$$\rho_{xs} = \alpha C_v$$

where α is the vacancy resistivity and C_v the average vacancy concentration in the film.

The resistivity decay at room temperature will be directly proportional to the rate of the vacancy annihilation. The vacancy resistivity, α, was taken to be 1.9 $\mu\Omega$ cm, which is an average of several published values obtained from quenching experiments (11-13).

The film examined in this study was evaporated by resistance heating at a rate of 2-3 Å/sec onto a glass slide in an oilless vacuum of 1×10^{-6} Torr. During the evaporation, radiant heating raised the substrate from about 25° to 110°C. Immediately after the deposition, the sample was cooled to room temperature under vacuum, while the substrate temperature was recorded on a strip chart recorder with a Chromel-Alumel thermocouple in contact with the substrate. This temperature history was taken into account in our theoretical calculation. The activation energy for vacancy diffusion in gold and the initial vacancy concentration were chosen to be 0.87 eV and 0.25%, respectively. These values were found to produce results in good agreement not only with experiment, but also with those in the published literature (13, 14). The void density was determined from TEM examinations to be $5 \times 10^{16}/cm^3$. A TEM micrograph of this sample can be seen in Fig. 10.

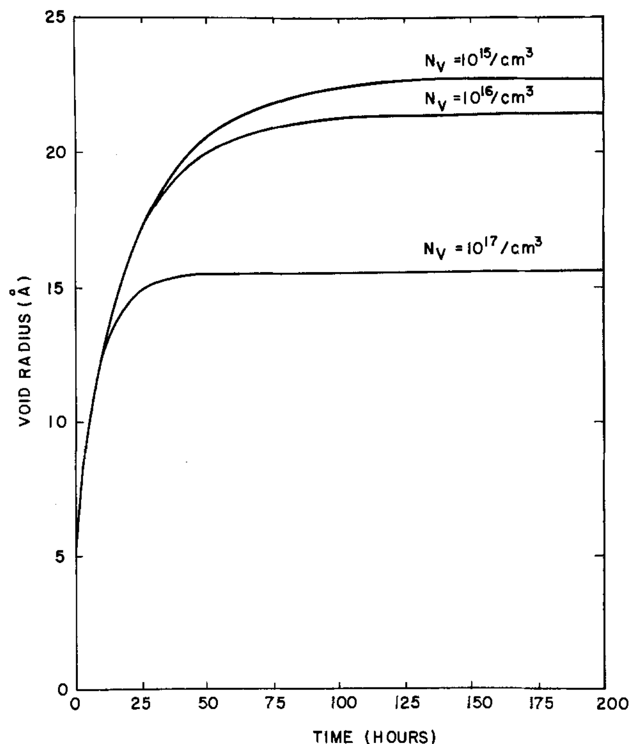

Fig. 9. Void size as a function of the void density

To compare the theoretical resistivity decay curve with experiment, a single experimental point (at 94 hr) was used as a reference and all other points were calculated from the vacancy resistivity and the theoretical vacancy concentration. This calculation was performed for a film containing the observed void density as well as for a void-free film. The results are shown in Fig. 11(a) and (b). It can be clearly seen that the calculation, which accounts for the presence

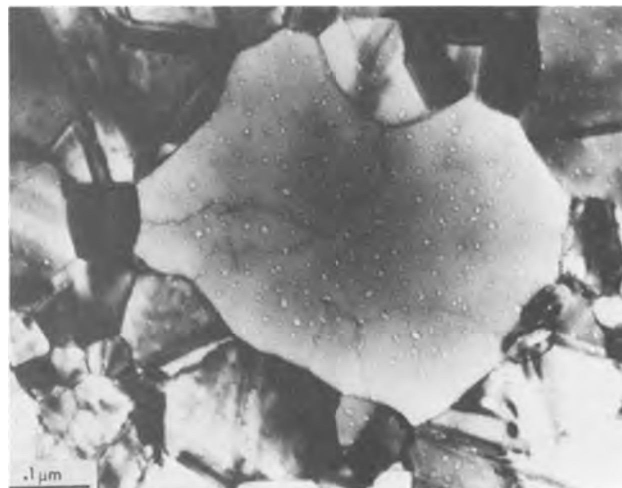

Fig. 10. TEM micrograph of voids in the sample studied here. Void density is measured to be $N_v = 5 \times 10^{16}/cm^3$. The film thickness is 1000Å.

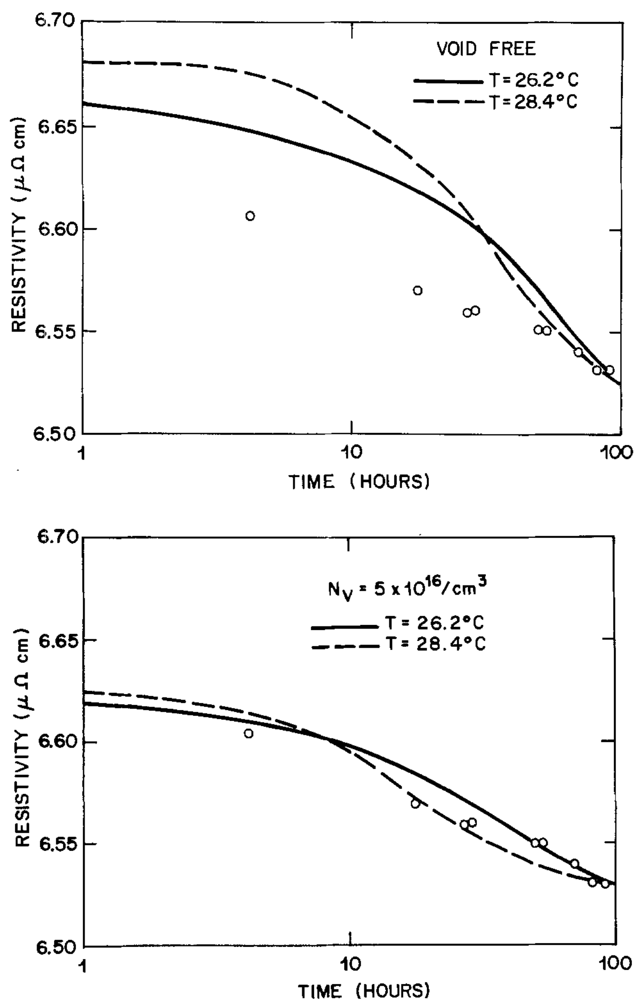

Fig. 11. Comparison of theoretical resistivity decay with experiment (a) for a void-free gold film; and (b) for a film containing the observed void density of $5 \times 10^{16}/cm^3$. $C_0 = 0.25\%$. The temperatures listed reflect the experimental uncertainty. The film thickness is 1000Å.

of voids, agrees much better with the experiment than that in which the voids are ignored.

Summary

Both the resistivity decay and the void growth due to quenched-in excess vacancies in thin evaporated gold films were analyzed by the use of a theoretical model in which the vacancy annihilation takes place primarily at film surfaces and preexisting voids. In this mathematical formulation, the vacancy concentration is determined from a solution to the problem of outdiffusion from a thin slab with a simultaneous first-order chemical reaction. This treatment gave excellent agreement with experimental measurements of resistivity decay and void growth. Furthermore, theoretical results have shown that the voids are important sinks for excess vacancies in thin films. Finally, it is suggested that the problem of the resistivity decay can be readily eliminated by annealing the film typically for less than an hour at 75°C.

Manuscript submitted Dec. 21, 1977; revised manuscript received June 6, 1978. This was Paper 210 presented at the Atlanta, Georgia, Meeting of the Society, Oct. 9-14, 1977.

Any discussion of this paper will appear in a Discussion Section to be published in the June 1979 JOURNAL. All discussions for the June 1979 Discussion Section should be submitted by Feb. 1, 1979.

Publication costs of this article were assisted by Bell Laboratories.

REFERENCES

1. Y. Fujiki, *J. Phys. Soc. Jpn.*, **14**, 1308 (1959).
2. A. P. Dorey and J. Knight, *Thin Solid Films*, **4**, 451 (1969).
3. J. M. Heras and E. E. Mola, *ibid.*, **35**, 83 (1976).
4. R. Andrew and V. Krasevac, *Phil. Mag.*, **31**, 1295 (1975).
5. J. R. Lloyd and S. Nakahara, *J. Vac. Sci. Technl.*, **14**, 655 (1977).
6. J. R. Lloyd and S. Nakahara, *Thin Solid Films*, **45**, 411 (1977).
7. J. R. Lloyd and S. Nakahara, To be published in *J. Appl. Phys.*
8. A. Blandin and J. Friedel, *Acta Metall.*, **8**, 384 (1960).
9. J. Crank, "Mathematics of Diffusion," Oxford University Press, London (1967).
10. F. Ham, *J. Phys. Chem. Solids*, **6**, 335 (1958).
11. R. M. J. Cotterill, *Phil. Mag.*, **6**, 1351 (1961).
12. R. O. Simmons and R. W. Balluffi, *Phys. Rev.*, **129**, 1553 (1963).
13. R. W. Siegel, *Phil. Mag.*, **13**, 359 (1966).
14. A. Seeger and H. Mehrer, *Phys. Status Solidi*, **29**, 231 (1968).

Impurity Dopant Incorporation and Diffusion during Molecular Beam Epitaxial Growth of IV-VI Semiconductors

Donald L. Smith* **and Vincent Y. Pickhardt**

The Perkin-Elmer Corporation, Optical Group Research Department, Norwalk, Connecticut 06856

ABSTRACT

PbTe, $Pb_{0.78}Sn_{0.22}Te$, and $Pb_{0.91}Sn_{0.09}Se$ single crystal films were grown on $BaF_2(100)$ at 620°-720°K and 10^{-9} Torr by coevaporation of the stoichiometric binary compounds and the dopant elements from separate sources. Molecular incident fluxes measured with a quartz crystal monitor usually agreed with those calculated from vapor pressure data to within 20%. Unintentionally doped films had carrier concentrations in the 10^{16}-10^{17} cm^{-3} range. n and p doping were achievable by stoichiometry adjustment using coevaporated Pb and Te (or Se), respectively; but only $\approx$0.1% of each became incorporated: the remainder surface-segregated (Pb) or reevaporated (Te,Se). Conversely, $>\frac{1}{2}$ of incident Bi and Tl became incorporated as n and p dopant, respectively, to levels $>10^{19}$ cm^{-3}, most likely by substituting for Pb or Sn and displacing it to the growth surface; except that Bi in the selenide (and Sb in both) showed less incorporation as dopant at $>10^{18}$ cm^{-3}, most likely due to compensation. Bi_2Te_3 behaved as Bi in the telluride and was found to sublime molecularly according to $\log_{10} P(Bi_2Te_3, Torr) = (1.53 \times 10^4/T) + 16.4$. SIMS depth profiling of grown abrupt dopant steps showed high-concentration diffusion coefficients of Bi and Tl in (PbSn)Te at 650°K and of Tl in (PbSn)Se at 620°K to be 9, 4, and 0.9 $\times$ 10^{-15} cm^2/sec, respectively; but much faster diffusion ($>10^{-10}$ cm^2/sec) of Tl in the selenide occurred up to 3 $\times$ 10^{17} Tl/cm^3. Similar low-concentration fast diffusion caused carrier concentrations of undoped telluride films below layers doped with Bi or Bi_2Te_3 to be shifted by 3 $\times$ 10^{17} cm^{-3} toward n-type and 5 $\times$ 10^{17} cm^{-3} toward p-type, respectively; the latter and possibly also the former shift was due to equalization of dopant-perturbed stoichiometry deviation rather than to fast-diffusing Bi. Excellent junction profile control may be obtained with these impurity dopants provided that the fast-diffusing components are appropriately compensated for in junction design.

The IV-VI semiconductors, particularly the ternary alloys $Pb_{1-x}Sn_xVI$, where VI is S, Se, or Te, are valuable as photovoltaic infrared radiation detectors and as tunable diode lasers. This is because they have small direct bandgaps which are widely variable through the infrared photon energy range by both composition (x) and temperature tuning. Molecular beam epitaxial (MBE) growth of these compounds offers the following advantages: low temperature to minimize interdiffusion, precise definition of multilayer structures, and compositional uniformity over large areas.

Like other compound semiconductors, the IV-VI compounds are single phase over a range of stoichiometry deviation from metal-rich to metal-poor, and the resulting lattice vacancies (and sometimes interstitials) act as n-type and p-type dopants, respectively. Control of the stoichiometry deviation by various techniques has often been used to produce p/n junctions in these materials, but this procedure is limited in both the control and the level of doping achievable when MBE is used, as will be seen below. We have consequently employed instead the impurities Sb and Bi as n-type dopants and Tl as a p-type dopant. It has been suggested that these impurities are incorporated substitutionally on metal lattice sites (1), and this model is consistent with their doping behavior and their position relative to Pb and Sn on the Periodic Table. Bi and Tl have been demonstrated to be particularly well-behaved (in PbTe, at least) compared to Cu, Ag, In, As, and Sb in that the carrier concentration which they produce changes very little with stoichiometry deviation or with measurement temperature (1). It was the object of the present work to study the behavior of these impurities under MBE growth conditions, including rates of incorporation into the growing film, maximum doping levels achievable, and diffusion rates. The IV-VI compounds selected included PbTe and two ternary alloys which have bandgaps of 0.9 eV (14 μm photon) at 77°K; namely, $Pb_{0.78}Sn_{0.22}Te$ and $Pb_{0.91}Sn_{0.09}Se$. These ternary alloys will be referred to as (PbSn)Te and (PbSn)Se in the text below.

Experimental Procedures

The basic MBE apparatus has been described in detail previously (2). Briefly, film constituents are evaporated from isothermal Knudsen cell sources enclosed in individual liquid nitrogen-cooled shrouds, in an ultra-high vacuum system which operates at 10^{-9} Torr during film growth. Substrates are chemically polished $BaF_2(100)$ wafers which are heated and temperature controlled to ±1°K. Binary compound evaporation sources, *e.g.*, PbTe, are synthesized in-house by vacuum fusion of the 6-nines pure elements, which are weighed to within 10 ppm (2 $\times$ 10^{17} atoms/cm^3) of stoichiometric proportions. The binary compounds sublime almost entirely as molecules (3). Dopant materials are evaporated simultaneously from separate sources during film growth. In this work all dopants were evaporated from elemental sources, except that Bi in the form of commercially obtained Bi_2Te_3 was also used for comparison purposes.

Mass deposition fluxes of the various evaporated materials are measured by a room temperature resonant quartz crystal monitor swung into the substrate position. This technique as applied here is accurate to 5% or $\pm 10^{-9}$ g/cm^2 sec, whichever is greater. For calibration purposes, the deposition fluxes can be related to the vapor pressures of the evaporants in the

* Electrochemical Society Active Member.
Key words: Bi, Tl, Bi_2Te_3, vapor pressure, nonstoichiometry.

following manner. Evaporant effuses from a thin-walled orifice in a hemispherical pattern in which the flux at any position on the hemisphere is proportional to the cosine of the angle from the orifice normal. For this cosine-law distribution, the flux at the normal is twice the average flux over the hemisphere, so that by mass balance

$$2\pi r^2(W/2) = (\pi/4)D^2J \text{ or } W = (D^2/4r^2)J \quad [1]$$

where W = flux (molecules/cm^2 sec) incident on quartz crystal or on substrate positioned normal to the orifice, D = orifice diameter, r = radial distance of quartz crystal from orifice, and J = effusion flux. For true Knudsen cell operation, molecular flow through the orifice must be maintained by keeping cell pressure P low enough so that the molecular mean free path exceeds the orifice diameter, and vapor-solid equilibrium must be ensured by maintaining isothermal conditions and by keeping the orifice area well below evaporant surface area (here it is about 1/10). Under these conditions, which are maintained in this work

$$J \text{ (molecules/cm}^2\text{ sec)} = 3.51 \times 10^{22} P/(MT)^{1/2} \quad [2]$$

where P = vapor pressure in Torr of effusand at cell temperature T(°K) and M = molecular weight of effusand (4). In this work, T is accurate to $\pm\frac{1}{2}\%$. J as defined above also denotes the surface evaporation flux from a pure material, provided that the molecular species are the same in the vapor and in the condensed phase, so that Eq. [2] is also useful for estimating reevaporation rates from a growing film. In order to avoid confusion, surface evaporation flux will be denoted as J'. Vapor pressures calculated from quartz crystal data using Eq. [2] are almost always within a factor of two of those reported in the literature [for the elements see Ref. (5)] and are usually within 20%. In cases of discrepancy, the quartz crystal result has always been assumed to represent the true W here. The necessary assumption that all incident material condenses on the room temperature quartz crystal appears to be valid, for even in the case of the most volatile constituent encountered in this work, Se, the measured deposition rate was no less than that calculated from reported vapor pressure data, provided that a comparable amount of Pb or Sn was simultaneously incident to assist condensation. If significant reevaporation of Se had been taking place, the measured W would have been less than that calculated from P. In the cases of the dopant materials, W during film growth is typically two orders of magnitude below the level at which an accurate quartz crystal calibration can be made. In such cases, the quartz crystal calibration point has been extrapolated assuming the same P vs. T slope as reported in the literature for that material. Since these slopes depend only on the latent heat of evaporation, they are far less likely to be affected by experimental conditions than are the absolute values of P; and in fact, in several cases for which we have measured the slope, no discrepancy has been observed.

A quadrupole mass spectrometer is positioned in the path of the effusing beams to monitor evaporant composition and purity. The beams are mechanically chopped at 17 Hz, and the mass peak output is synchronously detected in order to distinguish the beam signal from the d-c background which tends to build up in the mass spectrometer in the cases of the more volatile species.

Film growth conditions for the selenide typically have been 1 μm/hr and 620°K (substrate temperature), and those for the telluride have been varied from 1 μm/hr and 650°K to 4 μm/hr and 720°K. The higher growth rate has been adopted to save time and necessitates a higher substrate temperature to maintain film quality. Growth under these conditions is initiated at 650°K for the first 0.1 μm to ensure uniform nucleation on the BaF_2. In general in MBE, best epitaxy is obtained at a substrate temperature not more than 50°-100°K below the point at which the reevaporation rate of the growing film begins to approach deposition rate; that is, before $J' \rightarrow W$.

Carrier concentrations and mobilities of the grown films were determined by resistivity and Hall voltage measurements using the van der Pauw method (6) at 77°K. Gold pressure contacts were adequate in most cases. The single-carrier expressions were used for calculation, assuming a unity Hall factor

$$n = 10^{-8} IH/deV \quad [3]$$

and

$$\mu = dV/10^{-8} IH\rho \quad [4]$$

where n = carrier concentration (cm^{-3}), I = sample current (amperes), H = magnetic field strength (G), d = film thickness (cm), e = electronic charge (coulombs), V = Hall voltage, μ = mobility (cm^2/V-sec), and ρ = resistivity (Ω-cm).

The dislocation etch pit density of PbTe on BaF_2(100) was measured for films 4-17 μm thick using the etch recommended by Harman (7) and was found to be $4(\pm1) \times 10^7$/cm^3, independent of thickness. This is about the same as the density reported for $Pb_{0.78}Sn_{0.22}Te$ on PbTe (8) despite the larger lattice mismatch of the former (3.7% vs. 0.51%).

Dopant diffusion studies were carried out on two-layer films consisting of an undoped layer covered by a layer highly doped with Tl or Bi. Between layers, growth was stopped with a shutter for about 2 min to allow dopant source equilibration at the appropriate temperature for evaporation. The resulting abrupt step in dopant concentration was thus exposed to the film growth temperature for the time required to grow the doped layer. The dopant profile was then determined by an outside laboratory by secondary ion mass spectroscopy (SIMS), which involves sputtering away the film with an ion beam while mass-analyzing the sputtered species. Actual spectra showed that the mass resolutions of the Cameca SIMS instruments used were sufficient in most cases to separate completely both the Tl and Bi peaks from the much larger Pb peak adjacent. In addition to these measurements, carrier concentration levels and uniformities in the undoped underlayers of these two-layer films were determined by etching just through the doped top layer using $Br_2/HBr/H_2O$ and then measuring the carrier concentration of the remaining film. Successive etches and electrical measurements on progressively thinner remainders of film were used to determine doping gradients in the undoped layer.

Dopant Incorporation

Results.—The incident flux calibration data necessary to calculate the degree of dopant incorporation were obtained as discussed above except in the case of Bi_2Te_3, for which vapor pressure and vapor composition were unavailable and had to be measured using the quartz crystal and the mass spectrometer. Figure 1 shows the mass spectrum of subliming Bi_2Te_3. Although the mass spectrometer has an upper mass/charge limit of 300, the triply-ionized species ($q = 3$) in all cases fall within range. The predominant species are Bi_2Te_3, Bi, and Te, with no evidence of BiTe, Bi_2, or other molecular fractions. An absolute calibration was obtained for the intensity of the Bi^+ peak in this spectrum by using the source of elemental Bi, which evaporates predominantly as the monatomic species. This source was in turn calibrated using the quartz crystal. The W_{Bi} represented by the Bi^+ peak height shown on Fig. 1 amounts to only 2% of the total W of Bi_2Te_3 as determined directly by the quartz crystal. Therefore, Bi_2Te_3 sublimes almost entirely undissociated, and its use consequently represents a significantly different doping situation from the use of elemental Bi. Even the small amount of dissociation

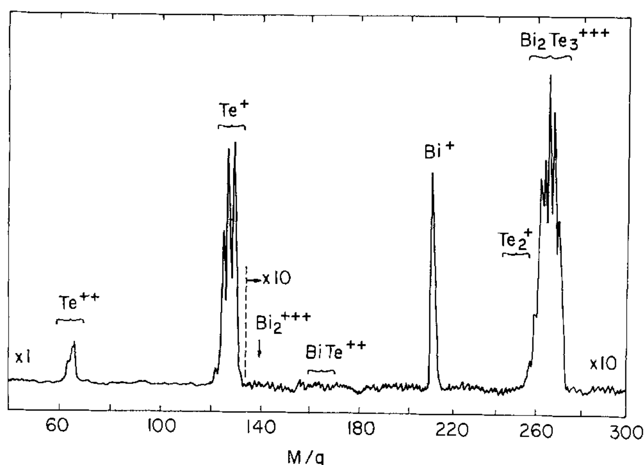

Fig. 1. Mass spectrum of sublimating Bi_2Te_3, showing Bi_2Te_3, Bi, and Te to be the major vapor species and Bi_2, BiTe, and Te_2 to be absent. Note the ×10 ordinate sensitivity increase above $M/q = 130$. M = molecular weight (amu) and q = ion charge.

which is observed could be occurring on electron impact in the ionization chamber of the mass spectrometer rather than on sublimation. It was observed, in addition, that the telluride is somewhat less "gassy" a source than the element, possibly because of a reduced tendency to oxidize on exposure to atmosphere. Vapor pressures of subliming Bi_2Te_3 calculated from quartz crystal data using Eq. [1] and [2] were fitted to within 10% over the range 2×10^{-2} to 1×10^{-4} Torr to the following equation of the standard Clausius-Clapeyron form

$$\log_{10} P(Bi_2Te_3, Torr) = (1.53 \times 10^4/T) + 16.4 \quad [5]$$

Equation [5] was extrapolated to obtain Bi_2Te_3 incident fluxes at doping levels. P of 2×10^{-2} Torr occurs just below the melting point of 846°K.

Dopant incorporation efficiency can be measured by comparing the actual change in carrier concentration produced by the dopant, $(n - n_o)$, with the change calculated assuming that all incident dopant is incorporated in active form, $(n_c - n_o)$. A doping coefficient γ is thus defined

$$\gamma = (n - n_o)/(n_c - n_o) \quad [6]$$

The carrier concentration (in cm^{-3}) for the doped (n) and undoped (n_o) films are found from Hall measurements using Eq. [3]. Typically, n_o is much larger than the intrinsic carrier concentration, presumably because of nonstoichiometry doping. n_o is in general expected to be a function of growth conditions, but within the range of conditions used here it was reproducible to within 20% for each of the three semiconductors and was 4×10^{16} n/cm^3 for PbTe, 6×10^{17} p/cm^3 for (PbSn)Te, and 2×10^{17} p/cm^3 for (PbSn)Se. $(n_c - n_o)$ is calculated from

$$(n_c - n_o) = \alpha_o (W_d/G_t) N_t \quad [7]$$

where α_o = theoretical number of charge carriers per dopant molecule, G = molecules/cm² sec incorporated into the growing film, N = density (molecules/cm³), subscript t denotes the sum of the major film species, *e.g.*, (PbTe + SnTe), and subscript d denotes a dopant species. α_o is −1 for Bi, +1 for Tl, and −2 for Sb_2 and Bi_2Te_3; W_d is calculated as discussed under "Experimental Procedures"; G_t is found from final film thickness and growth time; and $N_t = 1.5 \times 10^{22}$ molecules/cm³ for the tellurides and 1.7×10^{22} for the selenides.

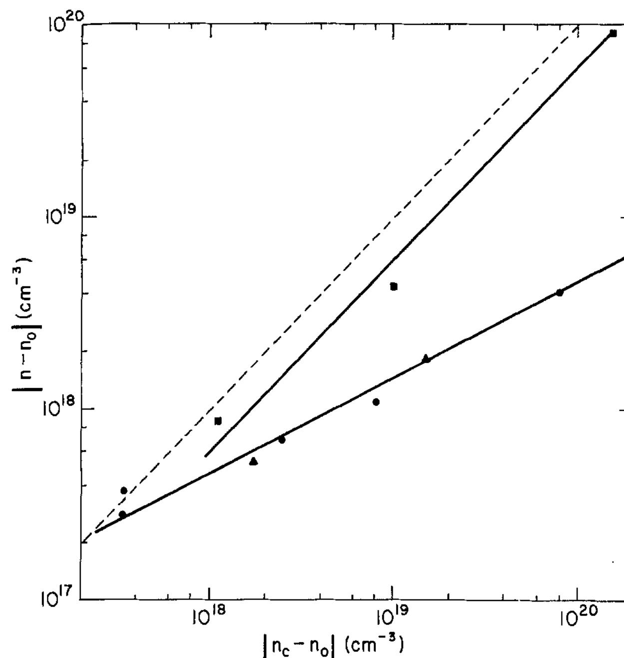

Fig. 2. Impurity dopant incorporation in $Pb_{0.91}Sn_{0.09}Se$ grown at 1 μm/hr and 620°K. – – = unity incorporation coefficient, ■ = Tl, ● = Bi, ▲ = Sb.

Doping incorporation data for Tl, Bi, and Sb in (PbSn)Se grown at 1 μm/hr and 620°K are plotted in Fig. 2. Tl is incorporated into the semiconductor with $\gamma = 0.6$ up to a doping level as high as 9×10^{19} cm^{-3}, whereas Bi and Sb exhibit a sublinear dependence of γ on doping level, such that the dependence in both cases fits the empirical equation

$$\gamma = 0.45(10^{18}/|n_c - n_o|)^{0.50} \quad [8]$$

Table I summarizes the doping coefficients calculated from plots such as Fig. 2 in this and previous work in our laboratory on the IV-VI semiconductors. These include the doping coefficients for the Group IV and

Table I. Doping coefficients for IV-VI semiconductors grown from stoichiometric binary compound sources

Dopant		γ			
		Calculated from Eq [14], 650°K	Experimental, 1 μm/hr		
Carrier type	Vapor species		PbTe, 650°K	$Pb_{0.88}Sn_{0.22}Te$, 650°K	$Pb_{0.91}Sn_{0.09}Se$, 620°K
p	Te_2	5.8×10^{-4}	7×10^{-3}	1×10^{-3}[b]	—
	Se_5[a]	1.7×10^{-6}	—	—	1.4×10^{-3}
	Tl	0.90	0.8[c]	0.8[c]	0.6
n	Pb	0.99	—	1×10^{-3}[b]	—
	Sn	1.0	—	—	—
	Bi	0.98	0.8	0.5	$0.45(10^{18}/\|n_c - n_o\|)^{0.50}$
	Bi_2Te_3	0.98	0.8[c]	0.8[c]	—
	Sb_2	0.46	$0.15(10^{18}/\|n_c - n_o\|)^{0.54}$	—	$0.45(10^{18}/\|n_c - n_o\|)^{0.50}$

[a] Se_5 is the major vapor species between 500° and 1000°K (10).
[b] Previously published data (11).
[c] Same at 4 μm/hr at 650°K.

Group VI elements themselves, which are added during film growth from separate elemental sources just as are the impurity dopants, rather than being obtained by using nonstoichiometric IV-VI compound sources. For the tellurides, note that Sb_2, but not Bi, exhibits a sublinear dependence on doping level of the form of Eq. [8].

In some cases γ was constant only up to some "saturation level" of doping, above which it dropped to zero. Table II summarizes the highest doping levels obtained thus far in this work, with those levels which represent saturation levels being so indicated. In the case of (PbSn)Te grown with W_{Pb} well above the saturation level, metallic droplets could be observed under the microscope on the grown films (11). For comparison, Table II also presents saturation level data reported by other workers on annealed ingots.

The effect on γ of adding a large excess flux of elemental Te_2 ($W_{Te} = 0.1 W_t$) during growth of impurity-doped film was also studied for a few selected cases, as outlined in Table III. For PbTe, excess Te_2 increased the γ of Sb_2 and of Bi, but that of Bi_2Te_3 was unchanged. In the Bi case, γ had begun to decrease from the constant value of 0.8 reported in Table I as saturation was approached, and the excess Te_2 brought it back up to 0.6. In the case of Tl incorporation in PbTe at levels above $10^{18}/cm^3$, excess Te is necessary to maintain good μ. A possible explanation for the very low μ otherwise obtained is that Tl is beginning to enter Te sites, where it would be likely to behave as a carrier trap. In the case of Bi-doped (PbSn)Te, the excess Te_2 actually reversed the carrier type.

Hall mobilities, μ, were independent of doping level up to a certain "knee" level, and were about 1×10^4 cm^2/V sec for all p-type material, 2×10^4 for n-type ternary alloys, and 3×10^4 for all n-type PbTe. Above the knee, μ decreased with increasing n so as to maintain resistivity, ρ, constant at

$$\rho = 1/ne\mu = 2 \times 10^{-4}\ \Omega\text{-cm} \quad [9]$$

for all three compounds, to within a factor of two.

Table II. Highest doping levels achieved for IV-VI semiconductors. Growth was from stoichiometric binary compound sources except as noted. Underlined data indicates "saturation level."

Dopant		n (cm^{-3} at 77°K)		
Carrier type	Vapor species	PbTe, 650°K	$Pb_{0.88}Sn_{0.22}Te$, 650°K	$Pb_{0.91}Sn_{0.09}Se$, 620°K
p	Te_2	$\underline{9 \times 10^{16}}$	$3 \times 10^{18(a)}$	—
		$\underline{2 \times 10^{18(d)}}$	$\underline{2 \times 10^{19(e)}}$	—
	Se_5	—	—	6×10^{18}
	Tl	$1.6 \times 10^{19(c)}$	7×10^{19}	9×10^{19}
		$\underline{2 \times 10^{19(b)}}$	7×10^{19}	9×10^{19}
n	Pb	(f)	$\underline{2 \times 10^{17(a)}}$	(f)
	Bi	$1.2 \times 10^{19(c)}$	$\underline{1.8 \times 10^{19}}$	4×10^{18}
		$\underline{2 \times 10^{19(b)}}$	$\underline{1.8 \times 10^{19}}$	4×10^{18}
	Bi_2Te_3	1.1×10^{19}	9×10^{18}	(f)
	Sb_2	$1.0 \times 10^{18(c)}$	(f)	1.6×10^{18}
		$\underline{1 \times 10^{18(b)}}$	(f)	1.6×10^{18}

(a) Previously published data (11).
(b) Data of Strauss (1) for ingots which were supersaturated with dopant and then annealed at 620°K in Te-saturated or at 770°K in Pb-saturated atmosphere; higher n value given here.
(c) Excess flux of elemental Te_2 ($W_{Te} = 0.1\ W_t$) used during growth.
(d) Ingots annealed at 650°K in Pb-saturated atmosphere (12).
(e) Ingots annealed at 650°K in Te-saturated atmosphere (18).
(f) Not tried.

Table III. Effect on dopant incorporation of using excess Te_2 during growth

Material	Dopant	$\|n_c - n_o\|$ level	γ for W_{Te} = 0	γ for W_{Te} = $0.1W_t$
PbTe	Sb_2	4×10^{18}	0.08	0.25
	Bi	$2 \times 10^{19(a)}$	0.3	0.6
	Bi_2Te_3	$2 \times 10^{19(a)}$	0.6	0.6
	Tl	1×10^{19}	(c)	0.8
$Pb_{0.88}Sn_{0.22}Te$	Bi	1×10^{19}	0.5	(b)

(a) Edge of saturation level.
(b) Reverses carrier type to 5×10^{18} p/cm^3.
(c) Poor μ; Tl forming deep traps on Te sites?

Discussion.—A simple model for the condensation and incorporation of a dopant during MBE will be developed here to allow a first-order calculation of γ to be made. The model will assume that all incident dopant becomes incorporated in electrically active form except that which reevaporates given the vapor pressure of the pure dopant. The way in which the experimental γ's differ from those found from this model will give some insight as to which of the other possible mechanisms are taking place, namely, surface segregation, increased or decreased evaporation rate due to molecular binding differences, or incorporation in inactive or compensating form.

To begin with, $(n_c - n_o)$ in Eq. [6] for γ is given by Eq. [7]. For $(n - n_o)$ in Eq. [6], we may write

$$(n - n_o) = (\alpha G_d/G_t) N_t \quad [10]$$

where α = actual number of charge carriers per dopant molecule, and other symbols are as defined previously. In the most general terms, G for any one of the film constituents may be expressed as

$$G = W - R - F - Lf' \quad [11]$$

where R = molecules /cm^2 sec reflected from the surface of the growing film immediately upon impact, F = molecules/cm^2 sec reevaporated from the surface, L = molecules/cm^2 in a monolayer, and f' = time derivative of fractional surface coverage f. Steady-state surface composition may be assumed under steady growth conditions (except near the start of growth), so that $f' = 0$. For the major species, growth temperature is always low enough so that $G_t \approx W_t$. (If G_t were less than W_t, by the way, it would be possible to obtain values of γ greater than unity.) We will also assume that the attraction of the dopant species to the surface is strong enough so that $R = 0$. Finally, we will assume that the dopant reevaporation rate F_d may be determined from the pure substance vapor pressure (Eq. [2]), certainly the most tenuous assumption of this simple model, and that it is also proportionately reduced by the fractional surface coverage f_d. This is equivalent to Raoult's law of ideal solutions

$$F_d = f_d J_d' \quad [12]$$

We will now define a surface segregation coefficient, β, as the excess of the dopant fractional surface coverage, f_d, over its fractional atomic incorporation rate

$$\beta = f_d/(z_d G_d/z_t G_t) \quad [13]$$

where z = atoms per molecule. This definition neglects the small differences in atomic volume amongst the elements involved. With these simplifications, we may combine Eq. [6], [7], and [10]-[13] into a form from which an estimate of γ may be calculated

$$\gamma = (\alpha/\alpha_o)/(1 + \beta z_d J_d'/z_t W_t) \quad [14]$$

Using Eq. [14] and [2] and available vapor pressure data, γ's have been calculated for the special case of complete dopant activation ($\alpha = \alpha_o$) and no surface segregation ($\beta = 1$) and for growth conditions of 1 μm/hr ($W_t = 4.5 \times 10^{14}$ molecules/cm^2 sec) and 650°K. These results are listed in Table I. Note that all of the metals and Bi_2Te_3 have low enough P's so that γ is near unity; whereas for Te_2 and Se_5, γ's are very low because most of the adsorbate is reevaporating. Agreement between calculated and experimental γ's is good for Tl, Bi, Bi_2Te_3, and Te_2 in the tellurides. For Pb in (PbSn)Te, on the other hand, γ is 10^3 smaller than expected. Considering the magnitude of the discrepancy, this is most likely due to surface

segregation ($\beta >> 1$) rather than to a lower α or higher J_d' than expected; for it is generally believed that most incorporated excess Pb does produce charge carriers ($\alpha \approx 1$), and the appearance of metal droplets on (PbSn)Te supersaturated with Pb proves that J_d' is not excessive. Why such extensive surface segregation ($\beta \approx 10^5$) should occur for a major constituent of the film even when composition is well away from the metal-rich phase boundary remains unexplained. For Se_5 in (PbSn)Se, γ is 1000 times larger than expected, and this can only be due to a J' which is much less than that given by Eq. [2], which means that Se is bonded much more strongly to the (PbSn)Se surface lattice than it is to itself.

The sublinear dependence on n of γ_{Sb} in PbTe and of γ_{Sb} and γ_{Bi} in (PbSn)Se could be due to an n dependence of either α or β in Eq. [14]. The fact that both p and n behavior has been observed for Sb in PbTe (1) depending on stoichiometry deviation is evidence of amphoteric behavior in this dopant, which would be expected to lead to a decreasing α with increasing n: As more metal lattice vacancies (n-type sites for Sb) were filled, more Sb would be forced into nonmetal (p-type) sites, thus compensating itself out. The threefold increase in γ_{Sb} in PbTe with the use of excess Te_2 during growth is consistent with this explanation: A larger fraction of the Sb is incorporated into the Pb vacancies thus created, rather than going into Te sites. Excess Te had the opposite effect on Bi-doped (PbSn)Te, however, actually changing it to p-type. The much higher solubility of metal vacancies in (PbSn)Te than in PbTe (18) probably caused the large amount of Te excess used ($W_{Te} = 0.1\ W_t$) to generate in (PbSn)Te a concentration of Pb vacancies larger than N_d, thus overcompensating it, whereas in PbTe this many metal vacancies could not be generated. Adjustment of W_{Te} to a lower value should avoid such compensation and accomplish the desired increase in γ, but it is preferable to use compound dopants such as Bi_2Te_3. The absence of influence of W_{Te} on the γ of Bi_2Te_3 in PbTe and the near-unity value of that γ suggest that the use of Bi in telluride form is forcing it into Pb sites without the need for excess Te. The following reaction for the incorporation of Bi_2Te_3 is proposed

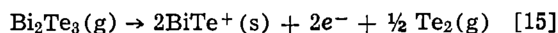

$$Bi_2Te_3(g) \rightarrow 2BiTe^+(s) + 2e^- + \tfrac{1}{2}\,Te_2(g) \quad [15]$$

where (g) denotes a gaseous species, (s) a substitutional solid species, and e^- a conduction electron. Here $BiTe^+$ substitutes directly for PbTe or SnTe in the crystal lattice. The extra Te must be reevaporating rather than generating metal vacancies; otherwise, a lower γ of 0.5 would be observed due to compensation. It is likewise improbable that mechanisms involving dissociation of the $BiTe^+$ are involved, for the Te thus produced would also generate compensating metal vacancies and reduce γ substantially.

The "saturation levels" reported in Table II for both present and reported work are the maximum n's obtainable no matter how much dopant is used. These are presumably the solubility limits of the dopants. The highest doping levels achieved in the present work are about equal to the saturation levels reported for annealed ingots except in the case of Te_2, whose high volatility is the likely explanation for the lower saturation level observed in the present work. It should be noted that in most cases the highest levels observed in the present work have not yet been demonstrated to be the saturation levels, simply because higher doping levels were not attempted. The doping levels achieved here for Tl, Bi, and Bi_2Te_3 are high enough for most device applications.

The fact that Bi and Tl are incorporated into PbTe and (PbSn)Te with near-unity γ's up to the 10^{19} cm^{-3} level tells us something about their incorporation reaction mechanisms during film growth, as is shown by the following argument. Consider that in general, the metal dopants may be incorporated interstitially or substitutionally. Substitution may involve occupation of a metal vacancy, generation of a Te vacancy, or displacement of a metal atom; the displaced atom in turn is incorporated interstitially or precipitated at the growth surface. We neglect the possibility of dopant substitution on VI sites which was suggested above for Sb and for Bi in (PbSn)Se, because there is no evidence of such behavior for Bi or Tl in (PbSn)Te, and it can be avoided for Bi and Tl in PbTe by the use of excess Te. The various mechanisms described above may be expressed symbolically for Bi incorporation as

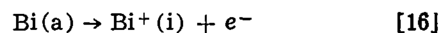

$$Bi(a) \rightarrow Bi^+(i) + e^- \quad [16]$$

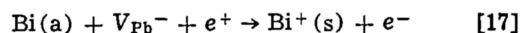

$$Bi(a) + V_{Pb}^- + e^+ \rightarrow Bi^+(s) + e^- \quad [17]$$

$$Bi(a) \rightarrow Bi^+(s) + V_{Te}^+ + 2e^- \quad [18]$$

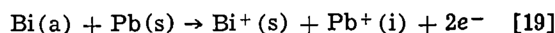

$$Bi(a) + Pb(s) \rightarrow Bi^+(s) + Pb^+(i) + 2e^- \quad [19]$$

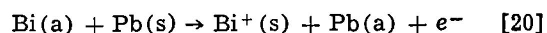

$$Bi(a) + Pb(s) \rightarrow Bi^+(s) + Pb(a) + e^- \quad [20]$$

(a) denotes a species adsorbed at the surface, (i) an interstitial, (s) a substitutional, V a vacancy, and e^+ a hole or p-type charge carrier. Vacancies are written ionized as ($V_{Pb}^- + e^+$) and $V_{Te}^+ + e^-$) to indicate their recognized behavior as acceptors and donors, respectively. Of course, Sn as well as Pb may be involved in any of the above mechanisms.

Similarly, for Tl incorporation

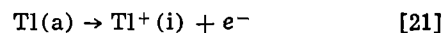

$$Tl(a) \rightarrow Tl^+(i) + e^- \quad [21]$$

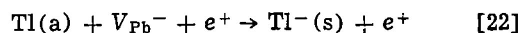

$$Tl(a) + V_{Pb}^- + e^+ \rightarrow Tl^-(s) + e^+ \quad [22]$$

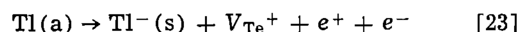

$$Tl(a) \rightarrow Tl^-(s) + V_{Te}^+ + e^+ + e^- \quad [23]$$

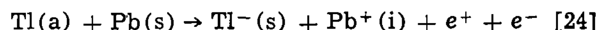

$$Tl(a) + Pb(s) \rightarrow Tl^-(s) + Pb^+(i) + e^+ + e^- \quad [24]$$

$$Tl(a) + Pb(s) \rightarrow Tl^-(s) + Pb(a) + e^+ \quad [25]$$

Note that α varies from $+2$ to -1 among the above ten mechanisms. We will now argue that many of these mechanisms are highly unlikely. Metal interstitials generally behave as donors [Ref. (9), p. 17], but since Tl is experimentally an acceptor, Eq. [21] cannot be important. Among the substitutional mechanisms, Eq. [17] and [22] are ruled out because the supply of V_{Pb} is insufficient from material grown from stoichiometric sources. The solubility of V_{Te} in (PbSn)Te is not sufficient to support Eq. [18] or [23] (see Table II); furthermore, Eq. [18] would lead to $\alpha = 2$, while in fact $\alpha = 0.5$ for Bi, and Eq. [23] would lead to $\alpha = 0$, while in fact $\alpha = 0.8$ for Tl. Equations [19] and [24] involving the production of Pb(i) are highly unlikely because of the very high β of Pb, and because they predict γ's far different from those observed. Therefore, it is most likely that Bi and Tl incorporation proceed by Eq. [20] and [25] involving substitution and displacement of Pb (and Sn) to the growth surface, although interstitial Bi (Eq. [16]) cannot be ruled out either. Note that, in contrast to Eq. [20] and [25], Eq. [15] for Bi_2Te_3 involves the accumulation of no metal at the surface, but rather of Te_2, which is volatile.

Dopant Diffusion

Results.—The experiments described in this section are summarized in Table IV. Two-layer diffusion test films using Bi and Tl in (PbSn)Se and (PbSn)Te were grown and SIMS-profiled as described above under "Experimental Procedures." The actual doping profile for the Tl203 isotope in (PbSn)Se is shown in Fig. 3, for a film grown at 1 μm/hr and 620°K with the calculated doping profile shown by the dotted line. There is an abrupt drop at the edge of the doped region, as expected, but there remains a constant residual level of 3×10^{17} Tl/cm^3 throughout the undoped layer; finally, the Tl signal drops to the noise level of the instrument at the BaF_2 substrate surface. The Tl203 signal intensity has been converted to N_{Tl}

Table IV. Summary of diffusion experimental results

Analytical technique	Dopant	Material and growth T (at 1 μm/hr)	
		$Pb_{0.88}Sn_{0.22}Te$, 650°K	$Pb_{0.91}Sn_{0.09}Te$, 620°K
SIMS (Fig. 3)	Bi	Abrupt drop + "knock-on" tail	(Analytical interference)
	Tl	Abrupt drop + "knock-on" tail	Abrupt drop + residual level
Chemical etching + Hall measurements (Fig. 4)	Bi	Underlayer shifted to 3 × 10^{17}/cm^3 less p-type	—
	Bi_2Te_3	Underlayer shifted to 5 × 10^{17}/cm^3 more p-type	—
	Tl	No detectable shift in underlayer doping (<4 × 10^{16}/cm^3)	—

(atoms/cm^3) by assuming N_{Tl} at the surface to be the same as in a single-layer film grown under the same conditions as the top layer in Fig. 3. N_{Tl} of the single-layer film was calculated from Hall measurements assuming $\alpha = 1$ in Eq. [10]. Bi209 in (PbSn)Se could not be analyzed due to interference from Pb208. However, using a higher resolution instrument, both Tl and Bi in (PbSn)Te were analyzed, and similar profiles were obtained, except that tails were present on both signals which extended from the abrupt step all the way into the substrate, as illustrated qualitatively in Fig. 3. Such a tail is characteristic of the so-called "knock-on" effect, in which some material is pushed ahead into the film by the impinging SIMS ion beam. The problem could be avoided by growing the undoped layer on top of the doped layer, but that configuration presents the risk of a small amount of surface-segregated dopant continuing to incorporate into the undoped top layer as the latter is grown, producing a similarly artifactual tail. For a sufficiently large β, this effect could be as large as the "knock-on" effect.

In order to verify that the tails observed were in fact artifacts, Tl- and Bi-doped (PbSn)Te diffusion samples were also analyzed for n *vs.* depth by the progressive etching technique described above under "Experimental Procedures." The results for Bi are shown in Fig. 4. The dotted line shows the expected n in the Bi-doped layer and n_o in the undoped layer based on Hall measurements on single-layer films grown under the same conditions (1 μm/hr, 650°K). The horizontal bars show measured average n over the film thickness remaining after each of three etching steps. Note that n is the same, within experimental error, for all three film remainders, but that it is also significantly less p-type than that observed in an undoped single-layer film. This difference (3 × 10^{17}/cm^3) thus represents the effect of exposing an undoped layer to a highly Bi-doped layer for ½ hr at 650°K. The same experiment for Tl in (PbSn)Te showed that no measurable change (<4 × 10^{16}/cm^3) in n of the undoped layer was brought about by the presence of the highly doped (2 × 10^{19} Tl/cm^3) layer. The use of Bi_2Te_3 (5 × 10^{18} Bi/cm^3) as a Bi dopant in the etching sample resulted in an increase in the p-conductivity of the undoped layer, rather than a decrease as observed for Bi metal dopant. For successive etches of the undoped layer under the Bi_2Te_3-doped layer, n was constant at 1.1 ± 0.05 × 10^{18} p/cm^3, an increase of 5 × 10^{17}/cm^3 over the n_o of an undoped single-layer film.

Discussion.—SIMS profiles for Tl in (PbSn)Se and for Tl and Bi in (PbSn)Te and etching data for Tl, Bi, and Bi_2Te_3 in (PbSn)Te all show an abrupt (<0.2 μm wide) step in doping level at the position of the grown metallurgical junction, indicating diffusion rates slow enough for good junction profile control in device fabrication. Etching data demonstrated that the tails observed on the SIMS profiles of Tl and Bi in (PbSn)Te were indeed artifacts. However, it is observed from SIMS data in the case of Tl in (PbSn)Se and from etching data in the cases of Bi and Bi_2Te_3 in (PbSn)Te that there is also a much faster diffusion mechanism operable up to a certain intermediate N_d which significantly affects the carrier concentration of the entire underlying layer.

A rough estimate of the diffusion coefficient D for the slower diffusion may be obtained from the SIMS data by assuming that D is independent of N_d above the intermediate level, in which case the solution to the diffusion equation for an infinite medium with an initial ($t = 0$) diffusand concentration $N = N_o$ for $x < 0$ and $N = 0$ for $x > 0$, becomes [Ref. (9), p. 105]

$$N(x,t) = (N_o/2)[1 - \text{erf}(x/2\sqrt{Dt})] \qquad [26]$$

Since for all time t, $N = N_o/2$ at $x = 0$, the slope of

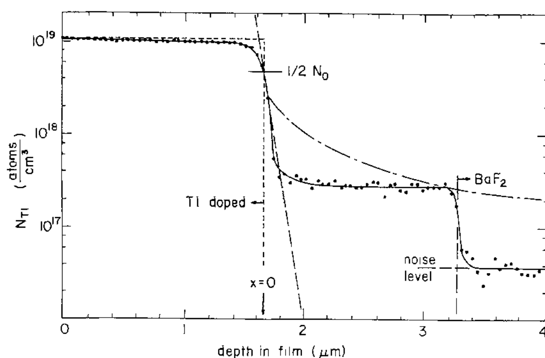

Fig. 3. Doping profile of Tl203 in $Pb_{0.91}Sn_{0.09}Se$ as determined by SIMS, showing very fast diffusion of Tl throughout the undoped layer up to a level of 3 × 10^{17} cm^{-3} and much slower diffusion at higher levels; 1 μm/hr and 620°K growth. --------- expected N_{Tl} profile with no diffusion, —— —— slope at ½ N_o used to calculate D, —·—·—·— "knock-on" tail obtained in (PbSn)Te (typical shape).

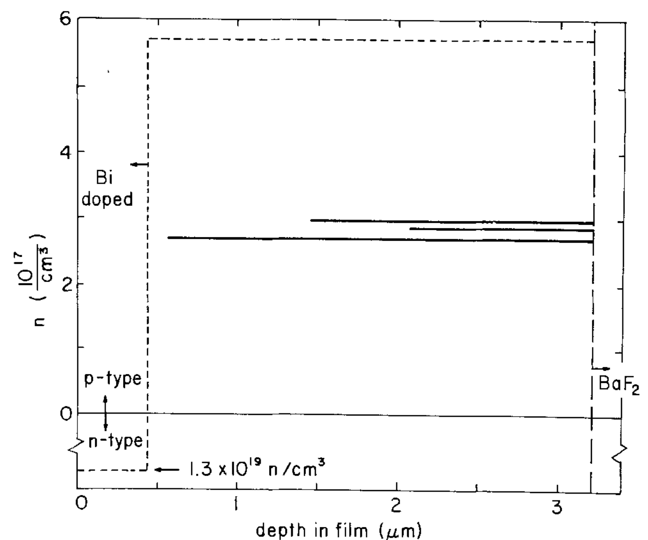

Fig. 4. Effect of Bi-doped layer on n of underlying $Pb_{0.77}Sn_{0.23}Te$; 1 μm/hr and 650°K growth. --------- expected n profile with no diffusion, ———— n over indicated film thickness, measured after etching away of Bi-doped layer.

the concentration profile at $N_0/2$, as shown in Fig. 3, becomes a convenient measure of D. It follows from Eq. [26] that

$$d(\log_{10}N)/dx|_{x=0} = 0.434/(\pi Dt)^{1/2} \quad [27]$$

To the actual slope measured from Fig. 3, a correction must be applied for that part of the slope which is due to sputter-etch roughening of the SIMS sampled area. This contribution was determined by measuring the slope of the Pb208 signal at the BaF_2 surface and adjusting it to $x = 0$ by assuming that roughness increases linearly with sputter-etching depth. Similar calculations were made on SIMS data for Bi and Tl in (PbSn)Te, and the resulting D's are presented in Table V along with related diffusion data from the literature.

The fast diffusion coefficients observed below the intermediate N_d cannot be calculated in this way because the gradients in N_d in the undoped layers are not large enough to be measurable; but a lower limit on D may be obtained by observing that the change in N_d through the undoped region is less than $1 \times 10^{16}/cm^3$ and by applying this condition to Eq. [26]. These calculations have been done for the SIMS data on Tl in (PbSn)Se and for the etching data on Bi in (PbSn)Te, and the results are presented in Table V. Since etching data indicates insignificant fast diffusion using Tl in (PbSn)Te, no fast diffusion coefficient appears for that system.

Diffusion data of other workers presented in Table V were in most cases obtained over a range of T not extending down to the MBE growth T, so the standard expression

$$D = D_0 \exp(-Q/kT) \quad [28]$$

was used for extrapolation to obtain D's at that T, where Q = activation energy for diffusion. Three types of data are presented: self-diffusion, and junction and impurity diffusions. The first describes the motion of radioactive tracer through the otherwise homogeneous material, which motion may take place by an interstitial, a vacancy, or some more complex mechanism. Junction diffusion describes the motion of a p/n junction produced by a nonstoichiometry gradient. Junction motion may involve any of the self-diffusion mechanisms of either the Group IV or the Group VI elements, but may also be much faster than any of these. For example, if the junction moves by Pb vacancy diffusion, which takes place by exchange with neighboring Pb atoms, the vacancy may pass through the entire crystal while each Pb atom involved in the individual "hops" between neighbors only moves one atomic distance. Therefore, the vacancy may move much farther through the crystal in a given time than do any of the individual Pb atoms involved in its motion. The junction diffusion coefficient includes the motion of excess Pb and Te vacancies, while the self-diffusion or radioactive tracer diffusion coefficient measures only the motion of labeled atoms, not of vacancies. Since, in general, D is expected to be dependent on the degree of nonstoichiometry of the host material because of the role of vacancies, the carrier concentration of the material used is also listed when available. The case of Pb self-diffusion in PbTe (13) is particularly dramatic in this respect, D in low p-type material being 10^4 larger than in high p-type. The authors attributed the increase to a change in mechanism from vacancy to interstitial, which was consistent with the accompanying drop in Q which was also observed.

The slow D's measured above the intermediate level of N_d for Bi and Tl in (PbSn)Te in the present work compare well with reported D's for self-diffusion and Sb diffusion in low p-type tellurides: They are all of the order of 10^{-14} cm²/sec. The slow D for Tl in (PbSn)Se is about 10^2 higher than that of Sb or Pb in PbSe, and the fast D below the intermediate doping level is at least 10^4 higher than any D reported in the IV-VI compounds (junction D's excepted since these do not necessarily represent directly the transport of material, as explained above). While diffusion behavior such as that observed here for Tl in (PbSn)Se is unusual, a similar situation has been reported for In in GaAs (17), in which most of the In diffuses slowly in Ga-substitutional sites, but a small fraction enters interstitial sites and diffuses very rapidly. Lower solubility impurity components in general tend to have higher D's [Ref. (9), p. 90]. Therefore, the following is a likely mechanism for the D behavior of Tl in (PbSn)Se: most of the Tl enters metal-substitutional sites according to Eq. [25] and diffuses very slowly, but a small fraction enters interstitial sites according to Eq. [21] and diffuses much more rapidly.

A similar low-solubility, fast-diffusing interstitial component of Bi incorporated according to Eq. [16] would explain the $3 \times 10^{17}/cm^3$ drop in n observed in undoped (PbSn)Te underneath highly Bi-doped material. However, an equally reasonable alternate explanation could be based on the incorporation of a small fraction of the Bi according to Eq. [17], [18], or [19] in addition to the predominant incorporation according to Eq. [20]. The resulting reduction in V_{Pb} or increase in V_{Te} or Pb(i), respectively, would set up a nonstoichiometry gradient toward the undoped layer, the equalization of which would result in a reduction in the p-conductivity of the underlayer and would also

Table V. Comparison of diffusion data in IV-VI semiconductors at MBE growth temperatures

		D, cm²/sec, at (n_0, cm⁻³)			
Type of diffusion	Diffusand	PbTe, 650°K	$Pb_{0.88}Sn_{0.22}Te$, 650°K	PbSe, 620°K	$Pb_{0.91}Sn_{0.09}Se$, 620°K
p/n junction	p into n	5.6×10^{-12} (19)	—	2.4×10^{-10} (15)	7×10^{-12} (15)
	n into p	5.4×10^{-10}[a]	—	1.6×10^{-11} (16)	—
		1.8×10^{-9} (19)	—	1.6×10^{-11} (16)	—
Radioactive tracer	Pb	3.3×10^{-18} (13) (high p)	—	1.6×10^{-17} (16) (p-saturated)	—
		2.0×10^{-14} (13) (<6×10^{17} p)	—	4.4×10^{-19} (16) (n-saturated)	—
	Sn	1.6×10^{-14}[a] (10^{17} p)	—	—	—
	Te	2.6×10^{-14} (13) (high p)	—	—	—
		7×10^{-15} (13) (<6×10^{17} p)	—	—	—
	Sb	3.6×10^{-14}[a] (10^{17} p)	2.8×10^{-18} (14) (10^{18}-10^{19} p)	1.0×10^{-17}[a]	—
Present work (h = above intermediate n; l = below)	Bi	—	9×10^{-15} (h)	—	—
		—	>2×10^{-10} (l) (6×10^{17} p)	—	—
	Tl		4×10^{-15} (h) (6×10^{17} p)		9×10^{-16} (h) >1×10^{-10} (l) (2×10^{17} p)

[a] Ref. (9), pp. 293-297.

proceed by the relatively fast p/n junction diffusion mechanism. In fact, the lower limit of D measured for the fast-diffusing component is of the same order, 10^{-10} cm²/sec, as the average junction D reported for PbTe. If this latter mechanism were the correct one, the same effect would be expected to occur to at least a detectable extent for Tl as well, whereby Eq. [22]-[24] would cause a drop in p-conductivity in the underlayer. However, in view of the fact that such a drop is not observed below Tl-doped material, the fast diffusion mechanism in Bi-doped material is more likely to be that involving a fast-diffusing component of Bi itself.

In the case of the increase in p-conductivity of material under the Bi_2Te_3-doped layer, the extra Te atom has to be involved in the fast diffusion mechanism and the Bi itself must be diffusing much less quickly in order to explain such an increase. That is, in addition to the Eq. [15] mechanism for Bi_2Te_3 incorporation, which involves reevaporation of the extra Te atom, some of this Te must be incorporated into the film according to

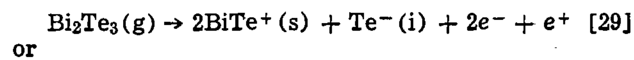

$$Bi_2Te_3(g) \rightarrow 2BiTe^+(s) + Te^-(i) + 2e^- + e^+ \quad [29]$$

or

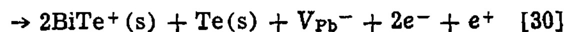

$$\rightarrow 2BiTe^+(s) + Te(s) + V_{Pb}^- + 2e^- + e^+ \quad [30]$$

followed by nonstoichiometry equalization by Te(i) or V_{Pb} diffusion as discussed above. Reported junction diffusion coefficients (Table V) are large enough to account for the observed doping shift under the conditions existing. The replacement of Bi by Bi_2Te_3 as an n-dopant has not eliminated effects on the underlayer, but has merely changed the nature of the problem. Nevertheless, the effects in both cases are small enough so that they can be canceled by appropriate compensation without degrading the material appreciably, since μ does not begin to decrease until above 10^{18} N/cm³ or so.

Conclusions

It has been demonstrated above for MBE growth of IV-VI semiconductors that accurate and reproducible n control up to the 10^{19}/cm³ level may be obtained in most cases by using Bi and Tl as n-type and p-type impurity dopants and by calibrating W with a quartz crystal monitor. This approach is preferable to n control by stoichiometry deviation adjustment, which usually cannot achieve as high an n and which also involves extensive surface segregation in the case of excess metal and extensive reevaporation in the case of excess nonmetal. The latter is expected to lead to an exponential dependence of γ on growth temperature, which would make control difficult. Nearly all Bi and Tl are actively incorporated into both the tellurides and the selenides except for Bi in (PbSn)Se. The latter situation could probably be improved by using Bi_2Se_3 as a Bi source, if it were found to evaporate molecularly as was Bi_2Te_3.

Most Bi and Tl appears to be incorporated substitutionally on metal sites by displacing metal to the growth surface, and the D's of these dopants are low enough so that very abrupt (<0.2 μm) junctions may be grown. However, in most cases, a small fraction of dopant is also incorporated in such a way as to lead to much faster diffusion of metal interstitials or nonmetal vacancies up to a certain intermediate level of doping. This leads to a shift in the n of adjacent epitaxial layers, which must be accounted for in junction device growth. In view of the likely role in these processes of interstitials and vacancies of the Group IV and VI elements themselves, the extent of n shift as well as the fast D values are expected to be dependent on n_o, which in turn depends on the specific growth conditions for the material. Therefore, the numerical values reported here can only be regarded as typical. The D values might also be driven either up or down by the use of material with a lower dislocation density. Finally, although the most likely diffusion mechanisms were postulated above based on the available evidence, unique mechanisms cannot be identified without studying the profiles across a junction of both N_d and n as a function of n_o and preferably also as a function of T.

Acknowledgment

The authors are grateful to Dr. Matt Miller of our department for advice on etching procedures and for numerous helpful discussions, and to Dr. Jim Roth of Cornell and Mr. Larry Plew of the Naval Weapons Support Center for their cooperation in carrying out the SIMS measurements.

Manuscript submitted April 7, 1978; revised manuscript received Aug. 1, 1978.

Any discussion of this paper will appear in a Discussion Section to be published in the June 1979 JOURNAL. All discussions for the June 1979 Discussion Section should be submitted by Feb. 1, 1979.

Publication costs of this article were assisted by The Perkin-Elmer Corporation.

LIST OF SYMBOLS

(a) species adsorbed at the surface
D orifice diameter (cm); diffusion coefficient (cm²/sec)
d film thickness (cm)
e^- conduction electron
e^+ hole or p-type charge carrier
e electronic charge (coulombs)
F molecules/cm² sec reevaporated from the surface
f fractional surface coverage
f' time derivative of f
G molecules/cm² sec incorporated into the growing film
(g) gaseous species
H magnetic field strength (G)
I sample current (A)
(i) interstitial species
J effusion flux (molecules/cm² sec)
J' pure material surface evaporation flux (molecules/cm² sec)
L molecules/cm² in a monolayer
M molecular weight of effusand
N density (molecules/cm³)
n carrier concentration (cm^{-3})
P vapor pressure (Torr)
Q activation energy for diffusion
R molecules/cm² sec reflected from the surface
r radial distance of quartz crystal from orifice (cm)
(s) substitutional species
T temperature (°K)
t time (sec)
V Hall voltage (V); lattice vacancy species
W flux incident on quartz crystal or on substrate (molecules/cm² sec)
x distance along diffusion gradient (cm)
z atoms per molecule

Subscript

c calculated value
d dopant
o initial or baseline value
t sum of major film species

Greek

α actual number of charge carriers per dopant molecule
α_o theoretical number of charge carriers per dopant molecule
β surface segregation coefficient (Eq. [13])
γ doping coefficient (Eq. [6])
μ mobility (cm²/V-sec)
ρ resistivity (Ω-cm)

REFERENCES

1. A. J. Strauss, *J. Electron. Mater.*, **2**, 553 (1973).
2. D. L. Smith and V. Y. Pickhardt, *J. Appl. Phys.*, **46**, 2366 (1975).
3. R. F. Brebrick and A. J. Strauss, *J. Chem. Phys.*, **40**, 3230 (1963); **41**, 197 (1964).
4. S. Dushman, "Scientific Foundations of Vacuum Technique," p. 21, John Wiley & Sons, Inc., New York (1962).

5. R. E. Honig and D. A. Kramer, *RCA Rev.*, **30**, 285 (1969).
6. L. J. van der Pauw, *Philips Res. Rep.*, **13**, 1 (1958).
7. T. C. Harman and I. Melngailis, in "Applied Solid State Science," Vol. 4, R. Wolfe, Editor, p. 35, Academic Press, New York (1974).
8. J. N. Walpole, R. W. Ralston, A. R. Calawa, T. C. Harman, and J. P. McVittie, IEEE Semiconductor Laser Conference, Atlanta, Georgia (1974).
9. B. I. Boltaks, "Diffusion in Semiconductors," Academic Press, New York (1963).
10. J. Berkowitz and W. A. Chupka, *J. Chem. Phys.*, **48**, 5743 (1968).
11. D. L. Smith and V. Y. Pickhardt, *J. Electron. Mater.*, **5**, 247 (1976).
12. C. R. Hewes, M. S. Adler, and S. D. Senturia, *J. Appl. Phys.*, **44**, 1327 (1973).
13. M. P. Gomez, D. A. Stevenson, and R. A. Huggins, *J. Phys. Chem. Solids*, **32**, 335 (1971).
14. R. L. Guldi and G. A. Antcliffe, *This Journal*, **121**, 1523 (1974).
15. A. R. Calawa, T. C. Harman, M. Finn, and P. Youtz, *Trans. Metall. Soc. AIME*, **242**, 374 (1968).
16. R. L. Guldi, J. N. Walpole, and R. H. Rediker, *J. Appl. Phys.*, **44**, 4896 (1973).
17. D. L. Kendall, *Appl. Phys. Lett.*, **4**, 67 (1964).
18. T. C. Harman, *J. Nonmetals*, **1**, 183 (1973).
19. J. N. Walpole and R. L. Guldi, *ibid.*, **1**, 227 (1973).

Theory and Direct Measurement of Boron Segregation in SiO_2 during Dry, Near Dry, and Wet O_2 Oxidation

Richard B. Fair* and J. C. C. Tsai

Bell Laboratories, Reading, Pennsylvania 19604

ABSTRACT

A theory of B segregation is developed which accounts for the differences in m observed in, for example, diffusion from a highly doped B_2O_3 source as compared to oxidation of B-doped Si in wet and dry oxidizing ambients. We have found that most dry O_2 oxidations are really only partially dry and that the presence of as little as ~20 ppm H_2O results in an m essentially the same as oxidation in 100% steam, *i.e.*, $m = 0.58$ at 1200°C with an "effective" activation energy of 0.64 eV. However, in a truly dry oxidation, the B segregation coefficient at 1200°C is ~1 with an effective activation energy of 0.33 eV. We propose that these differences as well as the $m > 2$ observed in high concentration B_2O_3 diffusion source oxidations are determined by the formation thermodynamics of the B compounds that are created during segregation. Quantitative agreement with m values obtained from directly measured B distributions across the SiO_2/Si interface are obtained (SIMS measurements with oxygen leak). Also, through-oxide B implants were observed to have segregation coefficients equal to the pure dry O_2 case even though the subsequent oxidations were performed in O_2 ambients with trace amounts of H_2O. Examples are presented which illustrate the effect of trace amounts of H_2O on B diffusion during oxidation.

During the growth of an oxide layer on silicon containing a Group III or V impurity, unequal distribution of the impurity will occur between the two Si phases. For the case of B in Si it has been presumed that B_2O_3 glass is formed during the segregation reaction at the interface (1, 2). Since this oxide is very stable, B will be "gettered" into the growing SiO_2 films. Since the diffusivity of B is large in Si compared with the SiO_2 growth rate, a significant depletion of B can occur in the Si near the SiO_2/Si interface.

Many studies of B segregation in SiO_2 have been reported in the literature. A review of these studies through 1975 is given by Murarka (3). More recent work has been reported in Ref. (4-10). Most of these studies have relied on various mathematical models using boundary conditions imposed by surface oxidation, some of which are too approximate or are incorrect. Also, using these models to extract segregation coefficients, m, from measurements of sheet resistance and junction depth can be risky due to the large sensitivity of m on R_S. As a result, reported segregation coefficients cover a wide range and show conflicting dependence on temperature. More recent studies in which direct measurements have been made also show an orientation dependence (6).

It is the purpose of this paper to present a theory of boron segregation in SiO_2 as a basis for evaluating the extensive published data. Orientation dependence and concentration dependence as well as ambient dependence are considered. In addition, new data are presented which were obtained from secondary ion mass spectrometry utilizing an oxygen leak for continuous measurement through the SiO_2/Si interface. It is shown, that in pure dry O_2 ambients, B segregates in SiO_2 as glassy B_2O_3 and elemental B with $m = C_{Si}/C_{SiO_2} = 1$ at 1200°C and with an "effective" activation energy of 0.33 eV. With as little as 20 ppm H_2O in the ambient, it is proposed that B segregates as crystalline HBO_2 and elemental B with $m = 0.58$ at 1200°C and with an "effective" activation energy of 0.64 eV. The results with 100% steam are the same as "dry" O_2 with trace amounts of H_2O.

To begin, the experimental procedure used in this study is presented along with experimental results. Based on the apparent equilibrium nature of boron segregation (11) the theory of this phenomenon is discussed.

Experimental

Sample preparation.—Silicon wafers, n-type, 1-2 Ω-cm with <100> and <111> orientations were used in this study. These wafers were Syton polished on one side and chemical etched on the other side. They were given a standard cleaning process which includes H_2O_2 + HCl and H_2O_2 + NH_4OH. Silicon wafers oxidized in a wet ambient were processed with nitrogen gas passing through water at 98°C, and those oxidized in "dry" oxygen were processed with plant oxygen which contains ~16 ppm of methane. Since methane

* Electrochemical Society Active Member.

Key words: ion implantation, diffusion, oxidation, segregation, boron.

combusts to water at high temperature, these wafers were not oxidized in purely dry oxygen. Earlier direct measurements of moisture content in a typical B-drive-in furnace in our facility as a function of position in the tube showed 15-30 ppm H_2O in the flow of oxygen (12). The effect of moisture on the experimental results are discussed in a later section.

Conditions of treatment and sample identification.—The following is a list of all the experimental information on the samples in this paper:

1. The first group of wafers were oxidized to a thickness close to 2150Å in either "dry" oxygen or wet oxygen. Two of these wafers were <111> oriented and the rest were <100> oriented. Boron was implanted at 50 keV to a dose of 1×10^{15} cm^{-2} into these wafers through the oxide. The boron profile had its peak concentration near the oxide-silicon interface. These wafers were then diffused at 1150°C for 60 min in 1% O_2 + 99% N_2 or in 100% O_2. Another wafer was divided into four quarters and three of them were diffused in 1% O_2 + 99% N_2 at 1100°, 1050°, and 1000°C for 120, 240, and 480 min, respectively.

2. The second group of silicon wafers, <100> oriented, were boron implanted at 50 keV with doses ranging from 1×10^{14} to 1×10^{16} cm^{-2} and diffused at 1150°C for 55 min in 0.1% O_2 + 99.9% N_2. After diffusion these wafers were oxidized and the oxidation conditions are given in Table I.

3. Two <100> oriented wafers were boron implanted at 50 keV to a dose of 5×10^{14} cm^{-2}. One of these wafers (177) was cut into two halves. They were driven-in at 1150°C for 55 min in N_2 (177A) and O_2 (177B), respectively. The other wafer (178) was diffused at 1150°C for 55 min in 0.1% O_2. Subsequent wafer division and processing are shown below:

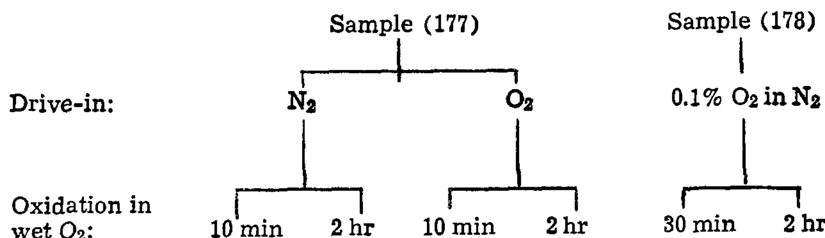

4. Four Si wafers (2 Ω-cm, <100> orientation) were boron implanted at 30 keV to a dose of 5×10^{14} cm^{-2} and diffused at 1150°C for 55 min in 0.1% O_2 + 99.9% N_2. Each wafer was divided into four quarters and three of them from each wafer were oxidized at 1200°C (No. 1 wafer), 1150°C (No. 2 wafer), and 1050°C (No. 3 wafer) for 2, 5, and 10 min; and at 950°C (No. 4 wafer) for 5, 10, and 20 min in oxygen. The sample identifications are given in Table II. The oxide thicknesses were measured with an ellipsometer. Since the samples were small in comparison with the light beam, a few samples did not give good ellipsometric readings. The measured oxide thicknesses are also given in Table II and these results reasonably agreed with the SIMS data.

Table I. Sample identification and processing

Sample	Dose	Temp (°C)	Time (min)	Ambient
104	1E14	1050	60	Dry O_2
60	1E16	1050	60	Dry O_2
308A	5E15	900	30	Wet O_2
307A	5E15	1050	10	Wet O_2
307B	5E15	1050	30	Wet O_2

Table II. Sample identification

Sample	Temp (°C)	Time (min)	Thickness (Å) (ellipsometer data)
1200-2	1200	2	—
1200-5	1200	5	500
1200-10	1200	10	670
1150-2	1150	2	260
1150-5	1150	5	420
1150-10	1150	10	640
1050-2	1050	2	230
1050-5	1050	5	270
1050-10	1050	10	—
950-5	950	5	—
950-10	950	10	80
950-20	950	20	190

Ion implant—Ion implantations were done in either an AI machine or an Extrion-Varian 200-1000 ion implant system. B^{11} ions were extracted at 30 keV, mass analyzed, and accelerated for energies greater than 30 keV. Both machines provided uniform implantations at comparable ion energies. No special cleaning was performed on the experimental samples after implantation prior to heat-treatment.

SIMS analysis.—The boron profiles near the SiO_2/Si interface were measured by the SIMS technique (secondary ion mass spectrometry) in a CAMECA IMS-300 system which has been modified with an oxygen leak in the target chamber.[1] Blanchard has made this improvement on his system and reported the advantages of such an arrangement (13).

Since a clean silicon surface is chemically active and it can be oxidized in a very short time, the presence of sufficient oxygen near the silicon surface will convert it to oxide readily. The needed oxygen is introduced onto the sample surface through a controlled oxygen leak valve. The primary ion beam is sputtering off SiO_2 instead of Si for the entire measurement. Thus, when measuring the secondary Si signal across a SiO_2-Si interface, no abnormal changes of the signal are recorded, which means there is no change of the secondary ion yield near an interface. When measuring the secondary ion signal from an impurity near an interface, any discontinuity of the signal would represent the segregation phenomenon.

IR reflectance and ESCA analysis.—The chemical state of B implanted into SiO_2 and segregated into SiO_2 was studied using electron spectroscopy for chemical analysis (ESCA).[2] Also, infrared reflectance spectra were obtained at room temperature on a Perkins-Elmer 621 grating *IR* spectrophotometer.[3]

Experimental Results

Implantation through SiO_2.—The measured profiles of B implanted through 2150Å of SiO_2 at 50 keV are shown in Fig. 1. Excellent continuity of measured B concentration is obtained across the SiO_2/Si interfaces. The result obtained when the 1×10^{15} cm^{-2} implant was annealed at 1150°C for 60 min in 100% O_2 (<100> Si) is shown in Fig. 2a. During the oxidation drive-in, 650Å of SiO_2 was grown in addition to the existing oxide. It can be seen that the B segregation coefficient is ~1 at the SiO_2/Si interface since the B concentration on the SiO_2 side is equal to the B concentration on the Si side. A similar result (m = 0.8) was obtained for a <111> sample oxidized at 1050°C for 60 min in 100% O_2.

The resulting profile when the drive-in is performed in 1% O_2 is shown in Fig. 2b. Some redistribution of

[1] These profiles were measured under contract by B. Blanchard, Centre D'Etudes Nucleaires De Grenoble, Commissariat A L'Enegie Atomique, France, Grenoble.
[2] The ESCA work was performed by G. P. Schwartz, Bell Laboratories.
[3] The infrared spectra were obtained by G. A. Baldauf, Bell Laboratories.

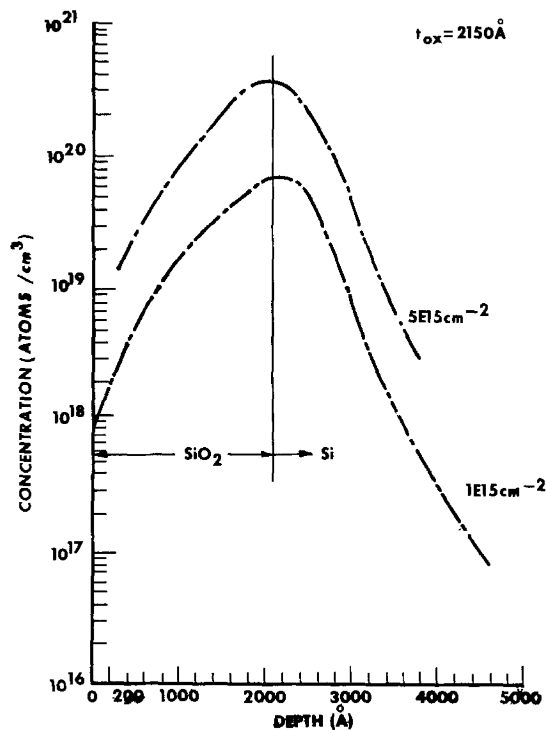

Fig. 1. SIMS profiles of two 50 keV B implants through the Si/SiO_2 interface.

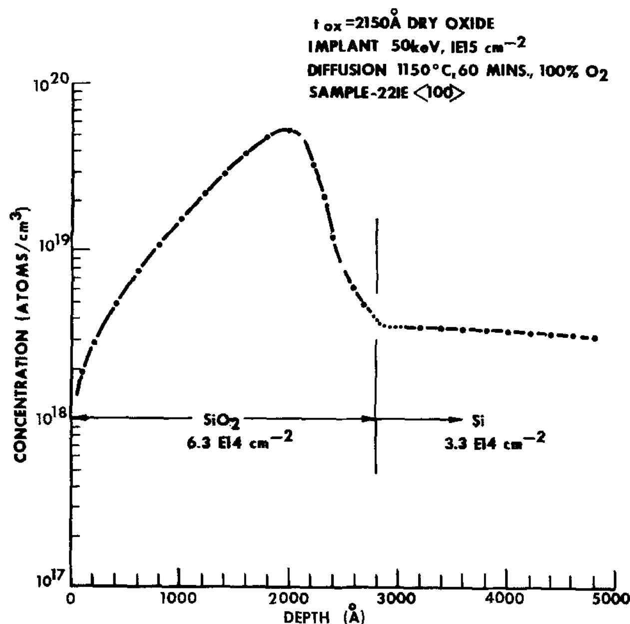

Fig. 2a. SIMS profile of the diffusion and segregation of a through-oxide B implant in near dry O_2.

B has occurred on the SiO_2 side of the interface to accommodate the boundary condition $m = 1$ for the thin oxide growth. For this case, the oxide layer acts much like a blocking boundary since little segregation occurs. The surface concentration was observed to decrease with time, t, according to the expression

$$C_S = K\left(\frac{Q_T{}^2 n_i}{D_i t}\right)^{1/3} \quad [1]$$

where $K = 0.53$ is an empirical constant, Q_T is the implant dose, n_i is the intrinsic electron concentration, and D_i is the intrinsic B diffusion coefficient. A similar result has been obtained for implanted As diffusion in Si (14).

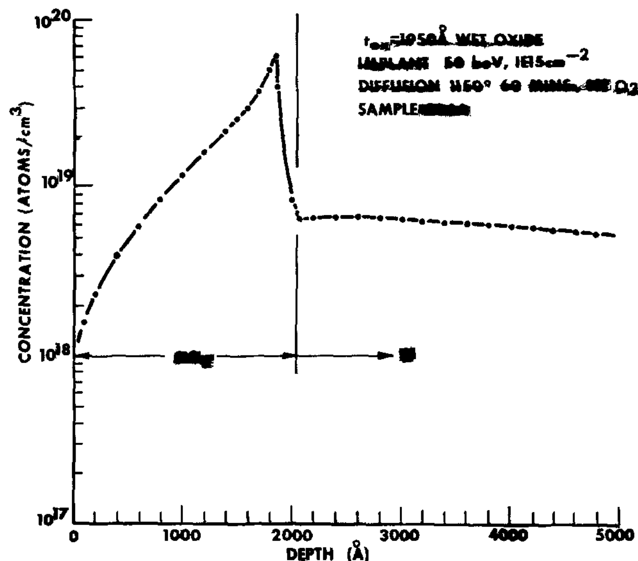

Fig. 2b. SIMS profile of a through-oxide implant diffused in 1% O_2.

Oxidation of B-implanted Si.—Typical results of the effect of Si oxidation on the segregation of B implanted and diffused into bare <100> Si are shown in Fig. 3a and b. Sample 104 was oxidized in "dry" O_2 for 60 min at 1050°C and sample 307B was oxidized for 30 min in wet O_2. For both cases the segregation coefficient is ~0.33. The results for this phase of the study are summarized in Fig. 4 where the measured segregation coefficient data are plotted *vs.* B concentration at the Si side of the SiO_2/Si interface. It can be seen that regardless of the time of oxidation, ambient, preoxidation treatment, and surface concentration, the B segregation coefficient is $m = 0.33 \pm 0.03$ at 1050°C.

The time dependence of the segregation coefficient at four oxidation temperatures is shown in Fig. 5. It can be seen that m is independent of time. Thus, it would appear that B segregation can be treated as an equilibrium phenomenon as proposed by Thurmond (11).

Chemical state of boron.—The results of using ESCA to determine the chemical state of B near the SiO_2/Si

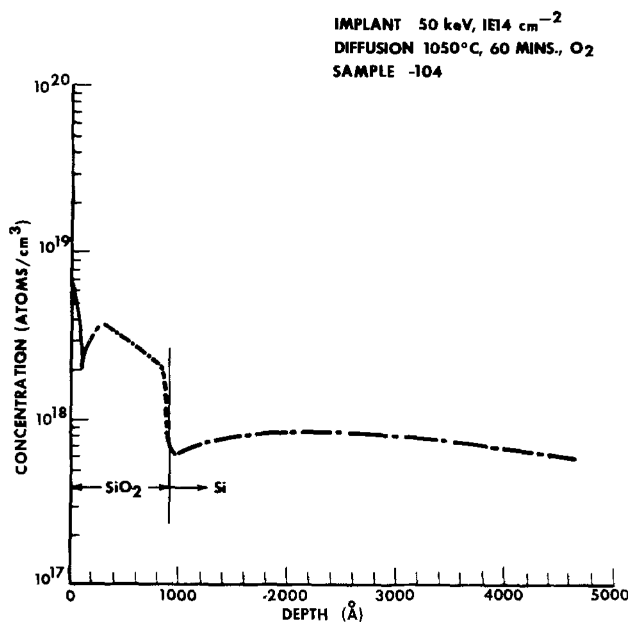

Fig. 3a. SIMS profile of the diffusion and segregation of B implanted into Si and annealed in near dry O_2.

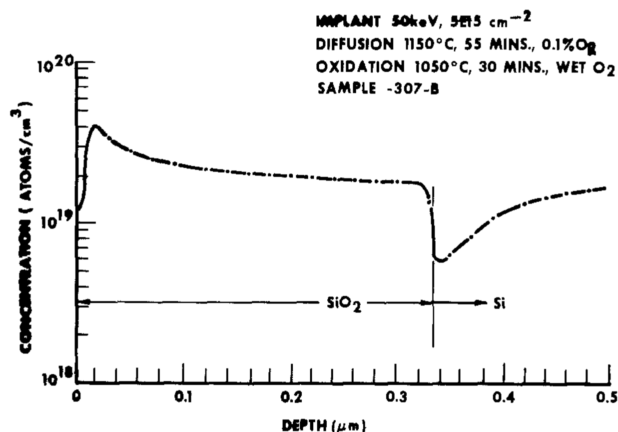

Fig. 3b. SIMS profile of the diffusion and segregation of B implanted into Si and annealed in wet O_2.

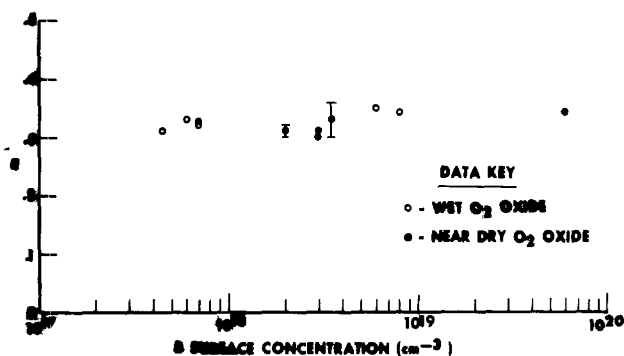

Fig. 4. Concentration dependence of B segregation coefficient at 1050°C in <100> Si.

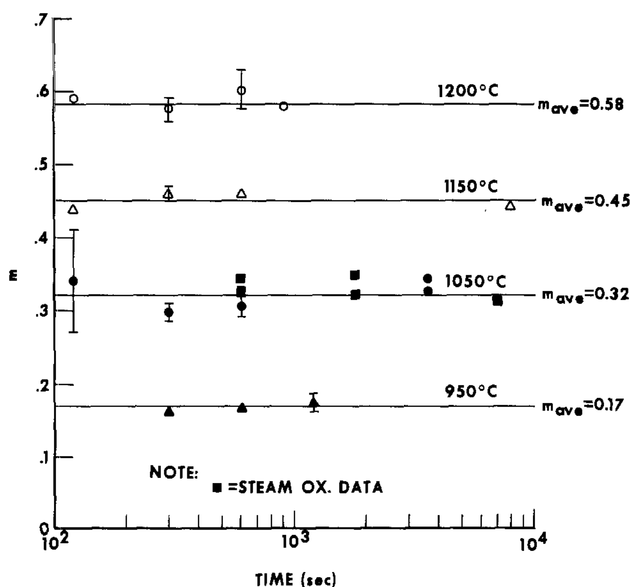

Fig. 5. Time dependence of B segregation coefficient for near dry oxidation of <100> Si.

interface indicated that in both the as-implanted samples (B into SiO_2/Si) and the heat-treated in "dry" O_2 samples, boron exists in the B^{+3} state. Since this is the naturally occurring state for boron, it is expected that typical B compounds (oxides, oxoacids, etc.) can potentially form in the SiO_2 film.

Infrared reflectance measurements of samples 1050-10 and 1150-10 (SiO_2 grown in "dry" O_2 over B implanted-diffused Si) showed a slight, but detectable B-OH peak at 8.4 μm and no B-O peak at 7 μm. Higher dose B implants (1×10^{16} cm^{-2}) into 2150Å of SiO_2 with subsequent O_2 annealing at 1150°C for 1 hr showed a significant 8.4 μm satellite peak on the broad 9.2 μm Si-O band. Again, no 7 μm B-O peak was observed.

The 8.4 μm B-OH band was observed by Arai *et al.* (15) following an 800°C, 5 min wet oxygen heat-treatment of an insoluble Si-B compound produced at a B_2O_3/Si interface. The above results indicate that any B_2O_3 formed during the oxidation treatments in our experiments may have reacted with the trace amounts of water in our system to form a compound such as B_2O_3-H_2O (or $2HBO_2$). The effects of small amounts of water vapor on the vapor pressure of HBO_2 and B_2O_3 over B sources such as BBr_3 and BN indicate that in the 800°-1200°C temperature range the vapor pressure of HBO_2 is several orders of magnitude higher than that of B_2O_3 with 0.04 atm H_2O (16). Also, molecular ion detection in a SIMS apparatus has shown that at the interface between a CVD borosilicate film and Si, BO_2^- ions were detected (17). It is not clear whether the detected ions were $HB^{10}O_2^-$ (mass 43) or $B^{11}O_2^-$ (mass 43). Nevertheless, they were only detected at the interface.

These observations support our hypothesis that some B-OH compound is formed in B-doped SiO_2 during near dry and wet O_2 oxidation. At this point it is appropriate to develop a theory of B segregation in order to see if our results are consistent with the concept of thermodynamical equilibrium at the SiO_2/Si interface.

Theory of Boron Segregation in SiO_2

Dry O_2 oxidation.—Following the arguments of Thurmond (11) it is possible to estimate the equilibrium segregation coefficient of B from basic thermodynamics. A proposed reaction occurring at the SiO_2/Si interface during pure dry O_2 oxidation is

$$BO_{3/2} + 3/4\ Si = B + 3/4\ SiO_2 \quad [2]$$

The reaction free-energy *vs.* temperature curve of [2] and other reactions to be discussed are shown in Fig. 6 (18). Reaction [2] involves the oxide B_2O_3. However, since the B^{+3} ion is randomly arrayed in cation positions in a dilute solution, X_{gl} will be the mole fraction of B^{+3} in the glass. The oxide can then be conveniently written $BO_{3/2}$.

Assuming thermodynamic equilibrium exists, an equilibrium constant for the above reaction can be written as

$$K_1(T) = \frac{\gamma_s X_s}{\gamma_{gl} X_{gl}} \quad [3]$$

where X_s and X_{gl} are the mole fractions of B in the Si and the glassy $BO_{3/2}$ phase, respectively. The activity coefficients are γ_s and γ_{gl}. $K_1(T)$ can be calculated from the free energy of $BO_{3/2}$ formation through the expression

$$\Delta G^\circ = -RT \ln K_1(T) \quad [4]$$

The segregation coefficient m is defined as

$$m \equiv \frac{X_s}{X_{gl}} \quad [5]$$

$$= \left(\frac{\gamma_{gl}}{\gamma_s}\right) \exp\left(\frac{-\Delta G^\circ}{RT}\right) \quad [6]$$

from Eq. [3] and [4].

The condition of equilibrium requires that the chemical potential of a particular component be the same in each phase. Thus, for a liquid phase

$$\gamma_s X_s = \gamma_l X_l \quad [7]$$

where γ_l and X_l refer to the activity and mole fraction of B in a liquid phase. Equation [6] can now be written in terms of the binary distribution coefficient $k_l = X_s/X_l$ which is empirically known to be 0.7 for B

in Si at the melting temperature of Si (19). Thus

$$m = k_1 \frac{\gamma_{gl}}{\gamma_l} \exp\left(\frac{-\Delta G^\circ}{RT}\right) \quad [8]$$

At the melting point of Si ($T = 1415°C$), ΔG° of reaction [2] is -5.73 kcal/mole (18). Assuming that $\gamma_{gl} \simeq \gamma_l$ gives $m = 4.1$. The assumption of equal activities can be made, but it is not known if B has the same charge state in the Si melt as in the SiO_2 glass. Also, the effect of oxygen in the Si melt on γ_l is not known.

In order to investigate the temperature dependence of m, use will be made of Weiser's (20) expression for the binary distribution coefficient given as

$$k_l = \frac{X_s}{X_l} = \gamma_l \exp\left[\frac{\Delta H_f - \Delta \overline{H}^s}{RT} - \frac{\Delta H_f}{RT_{mB}}\right] \quad [9]$$

In this equation ΔH_f is the heat of fusion of B (5.3 kcal/mole), $\Delta \overline{H}^s$ is the differential heat of solution of B in the Si crystal, and $T_{mB} = 2030°C$ is the melting point of B. The last term in the brackets is the entropy of B fusion. The $\Delta \overline{H}^s$ term is a function of the bonding energy of B in Si, the strain energy associated with the misfit of B in Si, and the heat of sublimation of B to a monatomic gas. This term is calculated in the Appendix.

The activity coefficient of B in the Si melt becomes constant as the melting point of Si is approached (20). If it is assumed that $\gamma_{gl} = \gamma_l$, this implies that all of the B segregated into the SiO_2 is in a glassy (or liquid) form such as B_2O_3. However, Inoue *et al* (21) have been able to resolve unoxidized B in SiO_2. Therefore, B_2O_3 can be reduced to elemental B in the SiO_2 lattice. Thermodynamically, Si can reduce B_2O_3. Chu *et al.* (22) have, in fact, shown that thin SiO_2 films are Si rich. Most of the excess Si exists within 2-4 monolayers of the interface at concentrations of $\sim 1 \times 10^{16}$ cm^{-2}, independent of temperature. More recent measurements by Feldman *et al.* (23) indicate that elemental Si exists within ~3Å of the SiO_2/Si interface at concentrations of $\sim 10^{15}$ cm^{-2}.

What this all means is that the free energy of the B segregation reaction at the interface will depend on how much B_2O_3 is formed. Also, the activity coefficient of B in the glassy form, γ_{gl}, will change. For this situation the new activity coefficient, γ_{gl}', can be written as (at $T = 1415°C$)

$$\gamma_{gl}' = \frac{\gamma_{gl} X_{gl}}{X_{gl}'} \frac{a_{gl}'}{a_{gl}} = \gamma_l \left(\frac{X_s}{X_{gl}'}\right)\left(\frac{X_{gl}}{X_s}\right) \exp\left(\frac{-\Delta G_{gl}^\circ}{RT}\right) \quad [10]$$

In this expression a_{gl} denotes the activity of B in the glassy phase, and ΔG_{gl}° is the difference in free energies between the cases where X_{gl} and X_{gl}' mole fractions of B_2O_3 are formed during segregation. It has already been shown that $X_s/X_{gl} = m$ and $X_s/X_{gl}' = m'$.

Following the calculations of Weiser (20) in the Appendix it is shown that $\Delta \overline{H}^s = 22.4$ kcal/mole for B in Si. Using $\Delta H_f = 5.3$/mole (24) and substituting Eq. [9] and [10] into the expression for segregation coefficient, m finally becomes

$$m = \left[\gamma_l \left(\frac{m'}{m}\right) \exp\left(\frac{-\Delta G_{gl}^\circ}{RT}\right)\right]\Bigg|_{T = T_{mp\,Si}} \exp\left[\frac{-17{,}100 - \Delta G^\circ}{RT} - 1.151\right] \quad [11]$$

Numerous reactions were investigated involving the segregation of B, including reaction [2]. These reactions were evaluated on the basis of Eq. [11] which requires that ΔG° be compatible with the temperature dependence of experimental data, and the preexponential term including ΔG_{gl}° at $T = 1415°C$ combine to yield the correct value. Only one other reaction besides [2] was found to satisfy these criteria. It is proposed here that the following reactions can occur at the SiO_2/Si interface in 100% dry O_2

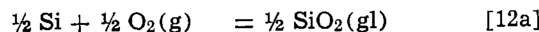

$$\tfrac{1}{2}\,Si + \tfrac{1}{2}\,O_2(g) = \tfrac{1}{2}\,SiO_2(gl) \quad [12a]$$

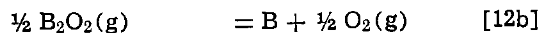

$$\tfrac{1}{2}\,B_2O_2(g) = B + \tfrac{1}{2}\,O_2(g) \quad [12b]$$

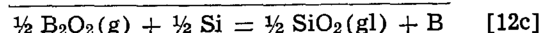

$$\tfrac{1}{2}\,B_2O_2(g) + \tfrac{1}{2}\,Si = \tfrac{1}{2}\,SiO_2(gl) + B \quad [12c]$$

The ΔG° *vs.* T curve for [12c] is shown in Fig. 6. The gas B_2O_2 represents the partial oxidation of B and exists as a vapor in the 1000°-1300°C range (25). It can be formed by the reduction of B_2O_3 by B according to the reaction (26) (see Fig. 6)

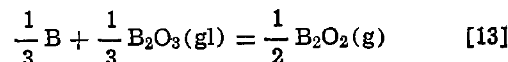

$$\frac{1}{3}B + \frac{1}{3}B_2O_3(gl) = \frac{1}{2}B_2O_2(g) \quad [13]$$

Adding reactions [12c] and [13] together gives the result

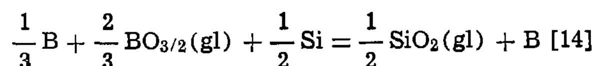

$$\frac{1}{3}B + \frac{2}{3}BO_{3/2}(gl) + \frac{1}{2}Si = \frac{1}{2}SiO_2(gl) + B \quad [14]$$

Reaction [14] is similar to reaction [2] except its free energy is 2/3 ΔG° for [2] ($\Delta G^\circ = -5.73$ kcal/mole at the melting temperature of Si). Referring to Eq. [10] the difference in reaction free energies, ΔG_{gl}°, is 1.9 kcal/mole. Using $m = 4.1$ at $T = 1415°C$ for reaction [2] and extrapolating the measured segregation coefficient data in Fig. 7 to 1415°C yields $m' = 1.4$ for reaction [14]. Thus

$$\gamma_{gl}' = \gamma_l \frac{(1.4)}{(4.1)} \exp\left(\frac{-1900}{RT}\right) = 0.2\gamma_l \quad [15]$$

From Eq. [8] the activity coefficient, γ_l, can be determined and is found to be ≈ 350. Substituting these numbers into Eq. [11] yields

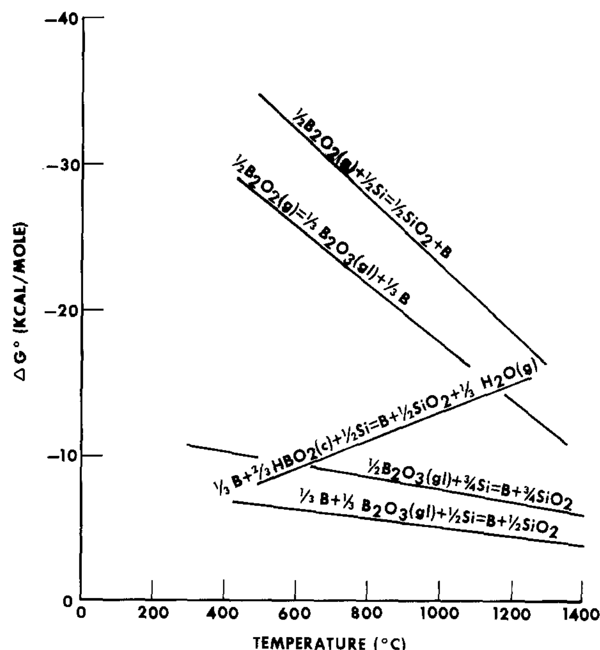

Fig. 6. Reaction free energies of B at the Si/SiO_2 oxidizing interface.

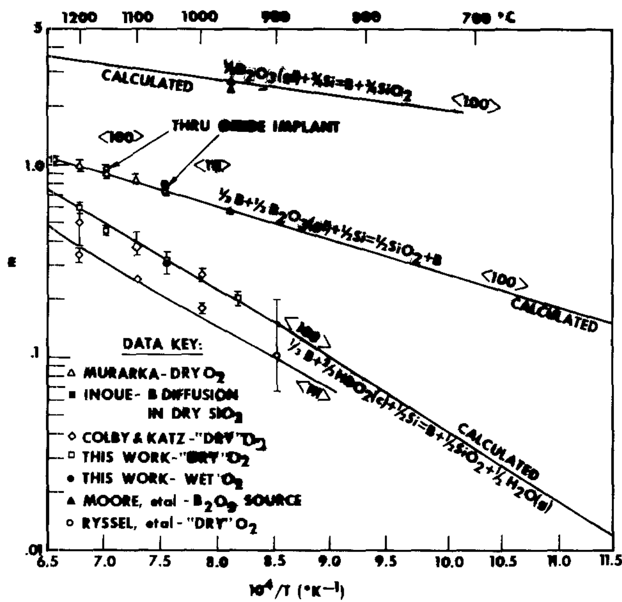

Fig. 7. Boron segregation coefficients at the Si/SiO_2 oxidizing interface.

$$m = 70 \exp\left(\frac{-17{,}100 - \Delta G^\circ}{RT}\right) \qquad [16]$$

with the ΔG° data for reaction [14] (see Fig. 6).

This equation is plotted in Fig. 7 along with the result obtained when only B_2O_3 is formed (reaction [2]). Several interesting observations can be made at this point:

1. Equation [16] gives excellent agreement with the dry O_2 data of Murarka (3) (<100> B implanted Si), with the data of Inoue *et al.* (21) (BN diffusion into SiO_2 on <100> Si), and with the through-oxide implantation of B and subsequent O_2 oxidation performed in this study (<100> sample 221E in Fig. 2a and the <111> sample diffused at 1050°C). The reasoning behind why these data represent pure dry oxidations are presented in the Discussion section.

2. Even though the free energy, ΔG°, for reaction [14] changes with temperature, an "effective" activation energy for Eq. [16] can be obtained by approximation with a van't Hoff-type expression. Thus for dry O_2 oxidation

$$m_{\text{eff}} = 13.4 \exp\left(\frac{-0.33 \text{ eV}}{kT}\right) \qquad [17]$$

The 0.33 eV activation energy is physically meaningless and only is useful in determining the approximate slope of the m *vs.* $1/T$ curve.

3. The calculation of m for reaction [2] indicates that values of $m > 2$ are possible for the case of pure B_2O_3 in SiO_2 on Si. The predicted curve agrees well with the Auger measurements of Moore *et al.* (8) who deposited a boron glass on <100> Si at 957°C in an oxidizing ambient. The two data points on the B_2O_3 curve in Fig. 7 correspond to 5 and 20 min depositions. After ~40 min deposition the resulting glass was ~1800Å thick and the measured segregation coefficient had dropped from ~2.6 to ~0.6. The latter value falls on the curve described by Eq. [16].

By considering the Auger spectra obtained by Moore *et al.* and the B concentrations and B diffusivity in their samples, it is apparent from the B_2O_3-SiO_2 phase diagram that at 957°C a liquid B-doped glass existed at the interface with the Si. Brown and Kennicott (2) also observed this in SiO_2 films doped greater than ~30%/B_2O_3. Consequently, one might expect that the conditions described by reaction [2] would obtain as long as the molten glass was in contact with the Si surface. However, as deposition time proceeded it is evident that dilution of the molten glass occurred at the interface. As the concentration of B_2O_3 dropped below ~30% the boundary condition changed to segregation from a B-doped SiO_2 solid according to reaction [14] with $m \simeq 0.6$.

4. The absolute value of the preexponential factor in Eq. [16] was calibrated by using the measured B binary distribution coefficient $k_l = 0.7$. This value of k_l was obtained for <111> Si. No information could be found on k_l for B in <100> Si. However, Trumbore *et al.* (27) found that the distribution coefficient for antimony in Si did not depend on crystal orientation. Therefore, as expected from equilibrium thermodynamics, the theory as presented does not explain the reported orientation dependence of B segregation (4, 6, 9).

Steam oxidation (or trace water vapor in "dry" O_2).—During the oxidation of Si in a wet oxygen ambient, H_2O becomes the primary oxidant source. Irene and Ghez (28) have shown that the parabolic oxidation rate constant increases abruptly even at trace H_2O concentrations on the order of 25 ppm H_2O in O_2. In their experiments, elaborate methods were required to obtain O_2 ambients with 1 ppm H_2O since the dry O_2 itself contained ~17 ppm methane which combusts to form H_2O. A similar amount of methane was measured in our O_2 gas. The O_2 ambient in the dry oxidation experiments of Beckmann and Harrick (29) contained ~60 ppm H_2O. A recent review by Revesz (30) shows that in numerous experiments performed in "dry" O_2 ambients, Si-OH and Si-H absorption peaks have been found in *IR* spectroscope data, even when Si oxidation tubes were used.

In view of the fact that the B-OH infrared reflectance peak was observed in our "dry" O_2 samples, numerous reactions were investigated involving $H_2O(g)$, B, and $SiO_2(gl)$. Equation [11] was used to evaluate acceptable reaction free energies against the measured segregation data.

For the case where H_2O is the primary oxidant it is proposed that at the SiO_2/Si interface B is initially segregated as $B(OH)_2$ (boron dihydroxide gas). Thus

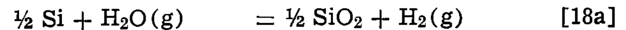

$$\tfrac{1}{2}\,Si + H_2O(g) = \tfrac{1}{2}\,SiO_2 + H_2(g) \qquad [18a]$$

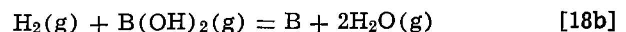

$$H_2(g) + B(OH)_2(g) = B + 2H_2O(g) \qquad [18b]$$

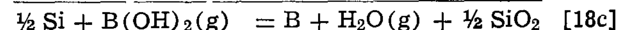

$$\tfrac{1}{2}\,Si + B(OH)_2(g) = B + H_2O(g) + \tfrac{1}{2}\,SiO_2 \qquad [18c]$$

The reaction free energy for [18c] at 1300°K is $\Delta G^\circ = -41.64$ kcal/mole (18). The $B(OH)_2$ gas immediately forms elemental B and a crystalline form of HBO_2 (metaboric acid) according to the reaction

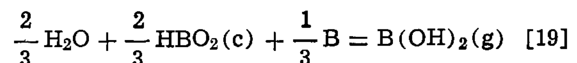

$$\frac{2}{3}H_2O + \frac{2}{3}HBO_2(c) + \frac{1}{3}B = B(OH)_2(g) \qquad [19]$$

with $\Delta G^\circ = 28.21$ kcal/mole at 1300°K (18). The sum of the interface reactions is

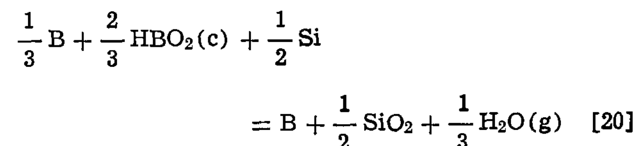

$$\frac{1}{3}B + \frac{2}{3}HBO_2(c) + \frac{1}{2}Si = B + \frac{1}{2}SiO_2 + \frac{1}{3}H_2O(g) \qquad [20]$$

The free energy for this reaction is plotted in Fig. 6.

Metaboric acid, HBO_2 or $\tfrac{1}{2}(B_2O_3 \cdot H_2O)$ is stable above 100°C. Holt (31) found that no known acid contains less water than metaboric acid. Thus, it can be formed in trace amounts of H_2O. HBO_2 also has a O-B-OH structure (32) as predicted by *IR* spectroscopic measurements.

For reaction [20] the segregation coefficient for B is

$$m = \gamma_{gl}' \exp\left(\frac{-17{,}100 - \Delta G^\circ}{RT} - 1.151\right) \qquad [21]$$

Since HBO_2 in the oxide is assumed to be crystalline, γ_{gl}' should be near unity. The assumption of crystalline HBO_2 is based entirely on ΔG° *vs.* T data and the comparison of Eq. [21] with measured segregation coefficient *vs.* T data for <100> Si. Referring to Eq. [10] for γ_{gl}' and using the extrapolated m data for <100> Si at $T = 1415°C$ ($m \simeq 1.2$) and with $\Delta G_{gl}^\circ \simeq 11$ kcal/mole, $\gamma_{gl}' \simeq 3.9$. Thus, for reaction [20], Eq. [21] for <100> Si in nearly dry and wet O_2 ambients is

$$m_{100} = 1.23 \exp\left(\frac{-17{,}100 - \Delta G^\circ}{RT}\right) \quad [22]$$

with the ΔG° *vs* T data for reaction [20] shown in Fig. 6.

Equation [22] is plotted in Fig. 7 and compared with the measured <100> data of Colby and Katz (6) and of this work. Excellent agreement is obtained with the temperature dependence of these data. Several observations can be made.

1. Reaction [20] is similar to reaction [14] in that elemental B is created in the interface reactions. However, the mass-action expression for reaction [20] shows that at most, only ~0.4% of the B in the SiO_2 is in elemental form.

2. Equation [22] was empirically adjusted in absolute value to agree with the <100> data in Fig. 7. By adjusting the preexponential factor, γ_{gl}', in Eq. [21] so that agreements with <111> data is obtained (6, 10), the expression for B segregation in <111> Si in wet or near dry O_2 is

$$m_{111} = 0.8 \exp\left(\frac{-17{,}100 - \Delta G^\circ}{RT}\right) \quad [23]$$

The reason why γ_{gl}' in SiO_2 on <100> Si is ~1.5 times larger than γ_{gl}' for <111> Si is not known at this time.

3. In terms of "effective" activation energies, Eq. [22] and [23] can be written for near dry and wet O_2 oxidations as

$$m_{100(\text{eff.})} = 104.0 \exp\left(\frac{-0.66\text{ eV}}{kT}\right) \quad [24]$$

$$m_{111(\text{eff.})} = 65.2 \exp\left(\frac{-0.66\text{ eV}}{kT}\right) \quad [25]$$

Discussion

Effects of trace amounts of H_2O.—The implications in the data and theory presented so far are that 15-30 ppm water in a "dry" O_2 oxidation furnace can reduce the boron segregation coefficient by as much as a factor of three (at 900°C) and change the Si oxidation rate (28). The condition under which pure dry O_2 oxidation occurs was apparently achieved in Murarka's work (3, 33). He used a dedicated dry O_2 laboratory drive-in furnace which had an O_2 gas dryer on it. The dry O_2 samples used by Colby and Katz (6) were oxidized in a general production processing area. It is unlikely that any special precautions were made to eliminate methane or moisture from the O_2 gas stream (34). For the case where B is implanted or diffused into an SiO_2 layer and O_2 oxidation is then performed, it is believed that the B in the SiO_2 ties up water diffusing through the oxide. Thus, the diffusing water will not reach the oxidizing interface. The evidence for this lies in the fact that a large B-OH infrared reflectance peak was observed in through-oxide B implants following our "dry" O_2 oxidation process.

We know that the remaining oxidations performed in our study were done in O_2 furnaces with 15-30 ppm H_2O measured in them. It can be seen in Fig. 4 that at 1050°C, these "dry" O_2 oxidations yielded the same B segregation coefficient as the wet O_2 oxidations.

Although the proposed models give consistent explanations of the experimental results, additional data are needed to establish the existence of HBO_2 in the SiO_2. Also, additional experiments are needed in dry O_2 ambients with <1 ppm of water.

Computer modeling of B diffusion and segregation.—If the values of B segregation coefficient obtained by indirect means such as mathematical modeling (3-5, 7-9) are plotted *vs.* $1/T$, the result is a scatter plot. In this approach the segregation coefficient is determined from measured sheet resistances and junction depths or from measured B profiles in the Si. A small error or uncertainty in these measurements may cause the calculated m to change significantly. An example is shown in Fig. 8 where the profiles are plotted for calculated sheet resistances of 124 and 140 Ω/□ and $m = 0.9$ and 0.45, respectively. The measured sheet resistance for this sample was 132 Ω/□. The profile was obtained by SIMS. The sample had been implanted to 7×10^{14} cm^{-2} at 50 keV and diffused in a near dry O_2 ambient at 1150°C for 60 min. The calculations were done using a stored modeling program which includes orientation- and concentration-dependent diffusion effects as well as the appropriate boundary conditions for an oxidizing Si surface (3). Also, Wagner's (35) mobility data were used in the sheet resistance calculation. The use of Thurber's more recent mobility data (36) led to an overestimation of R_s for the profile shown in Fig. 8.

It can be seen that the $m = 0.45$ curve gives the better fit to the measured B profile. However, a value of m between 0.45 and 0.9 would result in a profile whose sheet resistance matched the measured value of 132 Ω/□. The discrepancy between the measured and calculated sheet resistances is ~6% but this could lead to an overestimation of the true m by ~50%. Some improvement in the accuracy of segregation coefficient estimation is possible using a differential sheet resistance method (9). However, the m values reported in Ref. (9) have not been supported by direct measurement.

It can be seen in Fig. 8 that the effect of diffusing B in Si during oxidation in 100% dry O_2 as opposed to O_2 with ~20 ppm H_2O or more is to change the surface region profile the most. This is further demonstrated in Fig. 9 at four different temperatures. The calculated curves represent oxidations of 1×10^{15} cm^{-2}, 50 keV B implants which were preannealed in N_2 at 1050°C for 1 hr. All calculations were performed to simulate 1 hr diffusions at the temperatures shown in dry O_2 (dashed curves) and near dry O_2 (solid curves). As the B segregation coefficient curves in Fig. 7 indicate, the largest difference in the surface region profiles occurs at the lowest temperatures. At

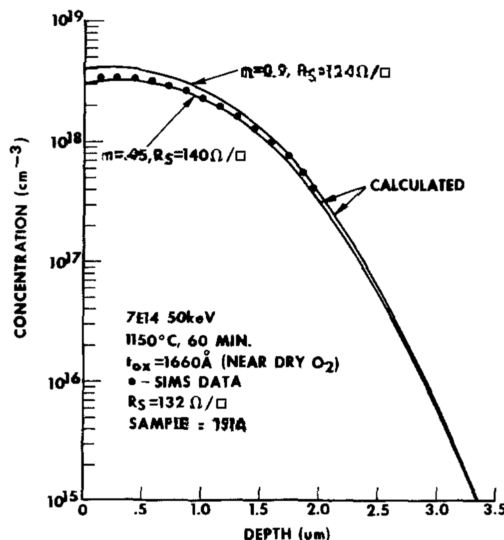

Fig. 8. Comparison between measured and calculated B profiles in Si for two values of segregation coefficient.

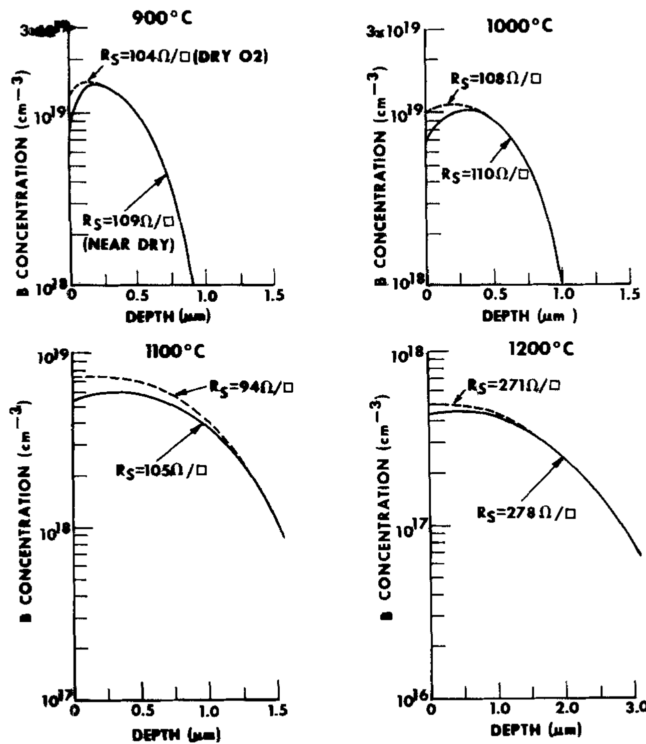

Fig. 9. Calculated B profiles after dry and near dry O_2 oxidations of $\langle 100 \rangle$ Si. B implant is 1×10^{15} cm^{-2}, 50 keV diffused at 1050°C for 1 hr in N_2 plus 1 hr at temperatures shown above.

900°C the surface concentrations differ by a factor of two. However, the sheet resistances differ by only 5%. As the temperature is raised, the difference between the profiles occurs over a larger fraction of the junction depth.

Summary and Conclusions

The theory of B segregation in SiO_2 has been presented and refined to the point that semiquantitative agreement with pure dry O_2 segregation data has been obtained. For the case of B segregation during near dry or wet O_2 oxidation of B-doped Si, quantitative agreement with the temperature dependence of m has been achieved. However, the absolute values of m show an orientation dependence in the activity coefficient of B (HBO_2) in SiO_2 which is not explainable at this time. Specific conclusions are as follows:

1. Segregation coefficients greater than 2 can be obtained for the special case where concentrations of $B_2O_3 \gtrsim 30\%$ in SiO_2 are deposited on Si in an oxidizing ambient (8). This condition will continue as long as the liquid B-doped glass is in contact with the Si surface. As oxidation proceeds dilution of the glass may occur so that a solid solution of B in SiO_2 is formed. Segregation will then proceed according to reaction [14] with $m \leq 1$.

2. It is possible to achieve a unity B segregation coefficient at 1200°C if one of the following conditions is fulfilled: (*i*) Oxidation of B-doped Si is performed in very dry O_2. It is not known what concentration of H_2O can be tolerated. However, 15-30 ppm H_2O in O_2 at the oxidation temperature is too high. (*ii*) Oxidation of a through-oxide B implanted SiO_2/Si structure is performed in dry or near dry O_2. (*iii*) Diffusion of B occurs through an SiO_2 layer on Si in a dry or near dry O_2 ambient (21) with $\lesssim 30\%$ B_2O_3 doping (2). The effective segregation coefficient obtained under these conditions (apparently independent of Si orientation) is

$$m_{\text{eff.}} = 13.4 \exp\left(\frac{-0.33\ \text{eV}}{kT}\right) \quad [17]$$

3. The oxidation of B-doped Si in near dry or wet O_2 ambients produces B and crystalline HBO_2 in the growing oxide. In $\langle 111 \rangle$ Si, the effective segregation coefficient in near dry or wet O_2 is

$$m_{111(\text{eff.})} = 65.2 \exp\left(\frac{-0.66\ \text{eV}}{kT}\right) \quad [25]$$

and in $\langle 100 \rangle$ Si it is

$$m_{100(\text{eff.})} = 104.0 \exp\left(\frac{-0.66\ \text{eV}}{kT}\right) \quad [24]$$

4. It has been shown that trying to extract segregation coefficients from models requiring measurements of sheet resistance and junction depth as the only inputs can be risky.

5. Computer simulations using the directly measured m values give excellent agreement with measured B profiles.

Acknowledgment

The authors would like to thank Dr. C. D. Thurmond for his helpful comments regarding this memorandum.

Manuscript submitted June 8, 1978; revised manuscript received July 20, 1978.

Any discussion of this paper will appear in a Discussion Section to be published in the June 1979 JOURNAL. All discussions for the June 1979 Discussion Section should be submitted by Feb. 1, 1979.

Publication costs of this article were assisted by Bell Laboratories.

APPENDIX

The relative partial molar enthalpy (or differential heat of solution) $\Delta\overline{H}^s$ is the energy necessary to transfer the B atom from its own lattice to that of the host Si crystal. Weiser postulated that the total energy for this process is (20)

$$\Delta\overline{H}^s = 4\epsilon_{Si} - H_{Si}^s + H_B^s - H_{B\text{-}Si} \quad [A\text{-}1]$$

where ϵ_{Si} is the bond energy of the Si crystal with each atom surrounded by four neighbors, H_{Si}^s is the heat of sublimation of Si (monatomic gas), H_B^s is the heat of sublimation of B, and $H_{B\text{-}Si}$ is the energy released by the impurity atom on condensation in a vacancy. Weiser has shown that Eq. [A-1] may be simplified to (20)

$$\Delta\overline{H}^s = \frac{(H_{Si}^s - H_B^s)^2}{H_{Si}^s + H_B^s} + E^{st} \quad [A\text{-}2]$$

where E^{st} is the strain energy that must be supplied if the impurity atom differs in size from the host atom. Thus

$$E^{st} = 22 \times 10^{20}(r_{Si} - r_B)^2 (\text{cal/g atom}) \quad [A\text{-}3]$$

Using the covalent radii of Pauling (37) ($r_{Si} = 1.17$Å and $r_B = 0.88$Å)

$$E^{st} = 18.5\ \text{kcal/g atom}$$

Also, using $H_{Si}^s = 105$ kcal/mole and $H_B^s = 136.5$ kcal/mole (24) yields

$$\Delta\overline{H}^s = 22.6\ \text{kcal/mole}$$

The temperatrue for which $\Delta\overline{H}^s$ is calculated is not very important since the difference in $\Delta\overline{H}^s$ at T_1 and T_2 is at most given by $\int_{T_1}^{T_2} \Delta C_p dT$. The ΔC_p is the difference in heat capacity between the host crystal and the impurity crystal. For B and Si ΔC_p is $\simeq 0$ (18).

REFERENCES

1. E. Arai, H. Nakamura, and Y. Terunuma, *This Journal*, **120**, 980 (1973).
2. D. M. Brown and P. R. Kennicott, *ibid.*, **118**, 293 (1971).
3. S. P. Murarka, *Phys. Rev. B*, **12**, 2502 (1975).
4. G. Masetti, S. Solmi, and G. Soncini, *Solid State Electron.*, **19**, 545 (1976).
5. M. Av-Ron, M. Shatzkes, P. J. Burkhardt, and I. Cadoff, *J. Appl. Phys.*, **47**, 3159 (1976).

6. J. W. Colby and L. E. Katz, *This Journal*, **123**, 409 (1976).
7. C. P. Wu, E. C. Douglas, and C. W. Mueller, *IEEE Trans. Electron Dev.*, **ed-23**, 1095 (1976).
8. G. Moore, H. Guckel, and M. G. Lagally, *J. Vac. Sci. Technol.*, **14**, 70 (1977).
9. D. A. Antoniadis, A. G. Gonzalez, and R. W. Dutton, *This Journal*, **125**, 813 (1978).
10. H. Ryssel and H. Kranz, in "Ion Implantation in Semiconductors 1976," F. Chernow, J. A. Borders, and D. K. Brice, Editors, p. 727, Plenum Press, New York (1977).
11. C. D. Thurmond, in "Properties of Elemental and Compound Semiconductors," H. C. Gatos, Editor, p. 121, Interscience Publishers, New York (1959).
12. R. A. Yeich, Unpublished results.
13. B. Blanchard, N. Hilleret, and J. Mounier, *Mater. Res. Bull.*, **6**, 1283 (1971).
14. R. B. Fair and J. C. C. Tsai, *This Journal*, **123**, 583 (1976).
15. E. Arai, H. Nakamura, and Y. Terunuma, *ibid.*, **120**, 980 (1973).
16. J. Stach and J. Kruest, *Solid State Technol.*, **19**, 60 (1976).
17. K. Nakamura, H. Hirose, A. Shibata, and H. Tamura, *Jpn. J. Appl. Phys.*, **16**, 1307 (1977).
18. JANAF Thermochemical Tables, Second Edition, Nat. Bur. Std. (U.S.), 37 (June 1971).
19. H. R. Huff, T. G. Diggs, and O. B. Cecil, *J. Appl. Phys.*, **42**, 1235 (1971).
20. K. Weiser, *J. Phys. Chem. Solids*, **7**, 118 (1958).
21. T. Inoue, S. Horuichi, S. Yoshii, and Y. Tanuma, *Suppl. J. Jpn. Soc. Appl. Phys.*, **44**, 329 (1975).
22. W. K. Chu, E. Lugujjo, J. W. Mayer, and T. W. Sigmon, *Thin Solid Films*, **19**, 329 (1973).
23. L. C. Feldman, P. J. Silverman, I. Stensgaard, R. L. Kauffman, and R. A. Zuhr, To be published.
24. "Lange's Handbook of Chemistry," J. A. Dean, Editor, McGraw-Hill Book Co., New York (1973).
25. T. Wartik and E. F. Apple, *J. Am. Chem. Soc.*, **77**, 6400 (1955); A. L. McCloskey, J. L. Boone, and R. J. Brotherton, *ibid.*, **83**, 1766 (1961).
26. M. D. Scheer, *J. Phys. Chem.*, **62**, 490 (1958).
27. F. A. Trumbore, P. E. Freeland, and R. A. Logan, *This Journal*, **108**, 458 (1961).
28. E. A. Irene and R. Ghez, *ibid.*, **124**, 1757 (1977).
29. K. H. Beckmann and N. J. Harrick, *ibid.*, **118**, 614 (1971).
30. A. G. Revesz, *ibid.*, **124**, 1811 (1977).
31. A. Holt, *Mem. Manchester Lit. Phil. Soc.*, **55**, 10 (1911).
32. H. Tazaki, *J. Sci. Hiroshima Univ.*, **10A**, 55 (1940).
33. S. P. Murarka, Private communication.
34. L. E. Katz, Private communication.
35. S. Wagner, *This Journal*, **119**, 1570 (1972).
36. W. R. Thurber, Paper 217 presented at the Seattle, Washington, Meeting of the Society, May 21-26, 1978.
37. L. Pauling, "The Nature of the Chemical Bond," 3rd ed., pp. 505-562, Cornell University Press, Ithaca, N. Y. (1960).

Growth of Semi-Insulating LPE GaAs for FET Buffer Layers

Y. M. Houng*[,1] and G. L. Pearson

Stanford Electronics Laboratories, Stanford University, Stanford, California 94305

and B. L. Mattes[2]

Center for Materials Research, Stanford University, Stanford, California 94305

ABSTRACT

The growth of semi-insulating LPE GaAs layers requires that the donors and acceptors be highly self-compensated and that Cr be used to form deep acceptor levels. The high compensation can be achieved by systematic bakeouts of the Ga melt, between growths, at a critical temperature which depends on the materials used in the growth system. The optimum bakeout temperatures for SiO_2-C-H_2, SiO_2-BN(C)-H_2, and SiO_2-BN-H_2 systems were found to be 775°, 700°, and 675°C, respectively. By this method, we are able to grow undoped layers having carrier densities in the low 10^{13} cm^{-3} range. By adding 0.5 m/o Cr to the melt under the same conditions, we have grown semi-insulating GaAs layers with resistivities in the 10^6 Ω-cm range.

High resistivity buffer layers are often used for GaAs field-effect transistors (FET) to isolate the active layers from impurities and defects in the Cr-doped substrates (1, 2). It has been found that the growth of such high resistance liquid-phase epitaxial (LPE) GaAs layers requires close compensation of shallow donors and acceptors arising from residual impurities in the source materials and from chemical reactions between the growth system components. Once near compensation is attained, semi-insulating LPE GaAs is obtained by adding Cr to form deep acceptor levels (3). We report here on the effects of (*i*) the growth system components on background impurities in LPE GaAs layers; (*ii*) the bakeout temperature of As-saturated Ga melts on the compensation of donor and acceptor impurities; and (*iii*) the optimum growth conditions for growing semi-insulating LPE GaAs.

Crystal Growth

The dominant background impurities in LPE GaAs are silicon, carbon, and oxygen (4). The sources of these impurities appear to be related to chemical reactions between the growth system components (3). To study these chemical reactions and their effect on the electrical properties of the grown layers, the growth system components, the bakeout temperature of the As-saturated Ga melt, and the saturation temperature were varied. It was found that the system components and the bakeout temperature made the most significant change in the electrical properties of the epitaxial layers. Saturation temperatures below

* Electrochemical Society Active Member.
[1] Present address: Corporate Solid State Laboratory, Varian Associates, Palo Alto, California 94303.
[2] Present address: Department of Electrical and Computer Engineering, University of Michigan, Ann Arbor, Michigan 48109.
Key words: LPE, semi-insulating, GaAs:Cr, FET, buffer layer.

800°C have a small effect on the electrical properties of the grown layers, since they are essentially equivalent to a short-term bakeout (3).

Three different horizontal tilt LPE growth systems were used in this study. These growth systems all consisted of a fused-quartz reactor tube (General Electric Grade 204), a temperature-gradient growth cell (5), and a purified hydrogen atmosphere. The differences in this study were the materials used for the growth cell: high purity graphite (Ultra Carbon) [C], pyrolytic boron nitride (Union Carbide) with a graphite cradle [BN(C)], and pyrolytic boron nitride with a fused-quartz cradle [BN]. The components corresponding to each of these growth cells are referred to as the SiO_2-C-H_2, SiO_2-BN(C)-H_2, and SiO_2-BN-H_2 systems, respectively.

The quartz reactor tube and cradle were cleaned in organic solvents and aqua regia, rinsed in DI water and methanol, dried, and outgassed in an H_2 atmosphere at 900°C for 24 hr. The graphite boat was outgassed under a high vacuum at $\sim$ 1300°C. For each series of growth, the system was baked out in an H_2 atmosphere at 900°C for 15 hr before loading the new melt. The starting materials for the growth were 6-9's purity Ga (Cominco American, Incorporated) and high purity polycrystalline GaAs (Asarco) As-source. Pellets of 5-9's purity (Electronic Space Products, Incorporated) were used for Cr doping. Chromium-doped semi-insulating GaAs, obtained from Laser Diode Laboratories or Crystal Specialties, was employed for substrates. All substrates were oriented to the (100) crystallographic plane and had resistivities greater than 10^6 Ω-cm. They were chemmechanically polished with 20% NaOCl solution. Immediately before each growth, the substrate was degreased with organic solvents, boiled in concentrated HCl to remove any surface oxide film, and then was displacive rinsed with methanol and boiled in isopropyl alcohol. After draining off the hot isopropyl alcohol, the substrate was loaded immediately into the growth cell. The system was purged with H_2 for at least 2 hr before the growth cycle was started.

For a particular system, the electrical properties of the epitaxial GaAs layers appear to be determined principally by the bakeout of the As-saturated Ga melt in the growth system. As described in more detail elsewhere (3), the Ga melt and the GaAs source were baked together before each growth at a prescribed temperature, in the 600°-850°C range, for 15 hr without the substrate in the growth system. After the substrate was loaded into the system the melt was saturated at 700°C for 30 min, after which the furnace was tipped to start the growth while cooling at a rate of 4.5°C/min. For most of the growths, the hydrogen flow rate was kept at 0.61/min during both the bakeout and the growth steps. The epitaxial layer thicknesses were approximately 15 μm.

The bakeout temperature has the most dramatic effect on the free-carrier density, as shown in Fig. 1. Low bakeout temperatures provide n-type layers while high bakeout temperatures give p-type layers. At a critical intermediate bakeout temperature unique to each particular growth system, high resistivity layers with low carrier densities and N_A/N_D ratios close to 1 are obtained. The transition bakeout temperatures for the SiO_2-C-H_2, SiO_2-BN(C)-H_2, and SiO_2-BN-H_2 systems were found to be 775°, 700°, and 675°C, respectively. As the bakeout temperature approaches this transition temperature from either the low or the high temperature side, the carrier density decreases. Highly compensated epitaxial GaAs layers grown in each of these systems, without deep level impurity doping, had room-temperature free carrier densities of 2×10^{14}, 9×10^{13}, and 3×10^{13} cm^{-3}, respectively.

The change in the electrically active donor and acceptor impurities as a function of total accumulated bakeout time at different bakeout temperatures in the

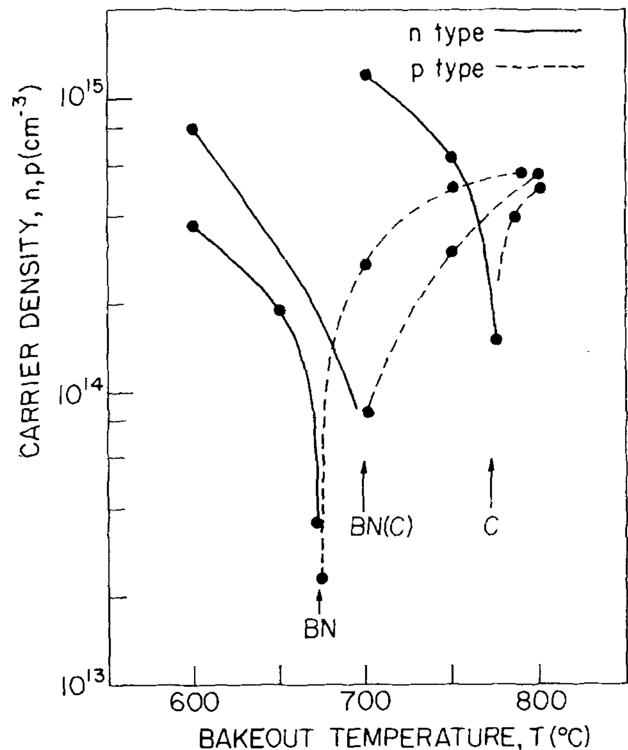

Fig. 1. Carrier concentration vs. bakeout temperature for three different growth systems. C: SiO_2-C-H_2 system; BN(C): SiO_2-BN(C)-H_2 system; and BN: SiO_2-BN-H_2 system.

SiO_2-BN-H_2 system, Fig. 2, shows that the impurities decrease during the first 60 hr of accumulated bakeout. Similar phenomena were also observed in the SiO_2-C-H_2 and SiO_2-BN(C)-H_2 systems. After about 60 hr of accumulated bakeout whereas subsequently grown layers had reproducible electrical properties, both donor and acceptor concentration leveled off and the N_A/N_D ratio reached constant values at each bakeout temperature. The N_A/N_D ratio increased with bakeout temperature, *e.g.*, $N_A/N_D \simeq 0.5$ at 650°C and $\simeq 0.9$ at 675°C. Above 700°C, N_A/N_D exceeds 1 and the epitaxial layer becomes p-type. However, the donor concentrations, after both 650° and 675°C bakeouts, remained constant at about 4.5×10^{14} cm^{-3} for layers grown from these stabilized melts in the SiO_2-BN-H_2 system.

These results suggest several possibilities that can be related to the bakeout: (*i*) the removal of volatile impurities from the melt, such as oxygen and sulfur, by their extraction and volatization from the Ga melt into the H_2 stream during the bakeout; and (*ii*) the introduction of acceptor impurities into the melt, such as Si and C, which are products of chemical reactions between the growth system components. Subsequently, some of these impurities are incorporated into the layer during growth. Since oxygen is the dominant shallow donor impurity while Si and C are the dominant acceptor impurities (6, 7), the N_A/N_D ratio and the conductivity type of the epitaxial layer are controlled by their relative concentration in the Ga melt and thus depend on the bakeout temperature. In each growth system, the bakeout transition temperature occurs at a temperature where the incremental acceptor concentration incorporated into the layer, due to the increase of acceptor impurities in the melt by bakeout, equals the net background donor concentration ($N_D - N_A$). It appears that the net background donor concentration remains nearly constant at 5×10^{15}, 6×10^{14}, and 1×10^{14} cm^{-3} for the SiO_2-C-H_2, SiO_2-BN(C)-H_2, and SiO_2-BN-H_2 systems, respectively. The chemical reactions in the three systems are different due to the location or absence of the graphite. However, in each case, the rate-limiting reaction is

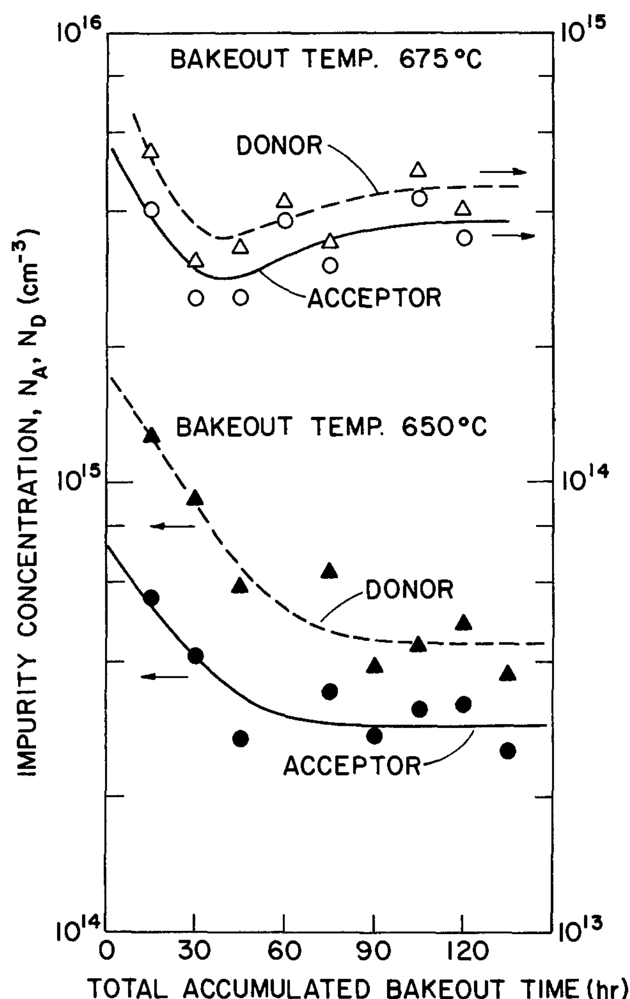

Fig. 2. Dependence of background donor and acceptor impurities on accumulated bakeout time and bakeout temperature in the SiO_2-BN-H_2 system.

due to the reduction of fused quartz by hydrogen (6). The increase in acceptor concentration with bakeout appears to be about the same order of magnitude as that obtained from thermodynamic calculations. Therefore, the differences in the bakeout transition temperatures appear to be due to the net background ionized donor concentration in these systems. The concentration of background impurities in the graphite cell system is about an order of magnitude higher than that in the BN cell system. This is probably due to the fact that graphite increases the oxygen contamination.

For the Cr-doping studies, 0.5-0.7 m/o Cr was added to the stabilized melt (after 50-100 hr of bakeout). Initially, doped growths had a very high carrier density ($\simeq 10^{17}$ cm^{-3}) at low bakeout temperatures (3). This is believed to be due to shallow donor impurities contained in the Cr source which are removed after a few hours of bakeout at 800°C. Following this initial 800°C bakeout, regular bakeout and growth procedures were carried out on the Cr-doped melt. We found that Cr doping had very little effect on the electrical properties of the epitaxial GaAs layers grown from Cr-doped melts baked out at temperatures on either side of the transition temperature where the net ionized shallow impurity concentrations are high. It appears that the Cr concentration in such layers is too low to compensate the shallow impurities. However, when Cr-doped melts were baked out near the transition temperature for the three growth systems, the carrier concentration decreased sharply and the resistivity reached a peak value. When 0.7 m/o Cr was added to the melt and baked out at 775°C in the SiO_2-C-H_2 system, moderately high resistivity (300 Ω-cm) epitaxial layers were obtained. When the SiO_2-BN(C)-H_2 and SiO_2-BN-H_2 systems with 0.5 m/o Cr were baked out at their corresponding transition temperatures, the grown layers were semi-insulating with resistivities higher than 10^6 and 10^3 Ω-cm, respectively. These semi-insulating layers show good uniformity in resistivity and excellent surface morphology over the 1×1.5 cm^2 sample area. However, when more than 1.5 m/o Cr was added in the melt, the grown layers showed rough surfaces and contained inclusions. This is probably because the solubility of Cr in the Ga melt is lower than 1.5 m/o at this growth temperature (700°C).

The segregation coefficient of Cr in GaAs is very small, about 3×10^{-7} for LPE growth (8). It is estimated that the active Cr concentration in the epitaxial layer must be in the range of 1×10^{14} cm^{-3} when 0.5 m/o Cr is added to the melt. Therefore, in order for Cr deep acceptors to control the resistivity and yield semi-insulating LPE GaAs, the background free-carrier concentration must be reduced to less than 10^{14} cm^{-3}. For the SiO_2-C-H_2 system, the background free-carrier density of the layers grown from a melt baked at the transition temperature was higher than this value, and only a moderately high resistance layer was obtained. Although the SiO_2-BN-H_2 system produced the lowest background-free carrier density (3×10^{13} cm^{-3}), the addition of Cr did not yield layers with resistivities as high as that of the SiO_2-BN(C)-H_2 system. It appears that the formation of deep levels is limited by fewer deep level impurities at the relatively low bakeout temperature (insufficient to compensate the shallow impurities).

Electrical and Optical Properties

The electrical properties of Cr-doped semi-insulating LPE layers were evaluated by differential van der Pauw techniques to avoid the shunting effect of the Cr-doped semi-insulating substrate. The measurements were made while the semi-insulating layers were contained in a stainless steel dewar under vacuum ($\gtrsim 10^{-4}$ Torr) and initially baked at 480°K. The room temperature electrical properties of two semi-insulating layers grown in the SiO_2-BN(C)-H_2 system, samples No. 1315 and 1320, are listed in Table I. Conductivity *vs.* reciprocal temperature plots between 350° and 480°K, as shown in Fig. 3, yield a thermal activation energy in the 0.7 eV range. The photoluminescent spectrum at 6°K for sample No. 1315, Fig. 4, shows a dominant peak at 0.83 eV. Recent studies by Kocot and Pearson (9) indicate that this photoluminescent peak is due to intra-impurity transitions between the Cr^{2+} ($^5T_2$) ground level and its ^5E excited state. The thermal activation energy (0.7 eV) corresponds to the separation between the Cr^{2+} ground level and the bottom of the conduction band. It has been reported that the ^5E level lies about 0.1 eV above the bottom of the conduction band (10).

In conclusion, we have shown that the growth of semi-insulating LPE GaAs can be achieved after systematic bakeouts of the As-saturated Ga melt at the transition bakeout temperature in a SiO_2-BN(C)-H_2 system. Under these conditions, the shallow donors and acceptors are very closely compensated and yield high resistivity LPE layers. Further improvements were obtained by the addition of Cr to the melt, which

Table I. Electrical properties of semi-insulating LPE layers at 300°K

Sample No.	Net electron concentration n (cm^{-3})	Mobility μ (cm^2/V-sec)	Resistivity ρ (Ω-cm)	Sheet resistance R_s (Ω/□)	Conductivity type
1315	9.7×10^8	3040	2.1×10^6	1.4×10^9	n
1320	5.1×10^8	2590	4.8×10^6	3.2×10^9	n

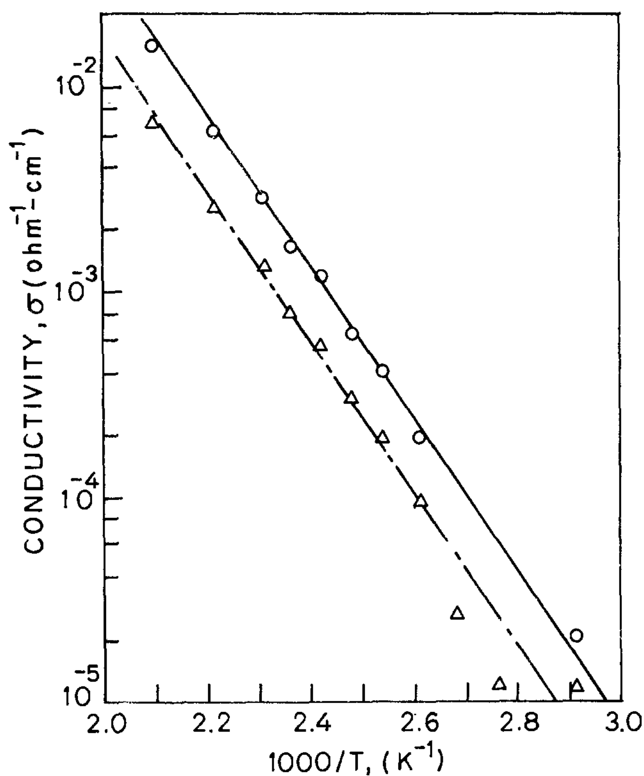

Fig. 3. Conductivity variation with temperature for Cr-doped semi-insulating LPE layers. ○, sample No. 1315; △, sample No. 1320.

forms deep acceptor levels and produces semi-insulating LPE GaAs layers with resistivities in the 10^6 Ω-cm range.

Acknowledgments

We wish to thank A. A. Immorlica, Jr. and R. Zucca of the Rockwell International Science Center for their helpful discussions. This work was supported by the Advanced Research Project Agency under contract F-19528-75-C-0013 through Rockwell International Science Center subcontract 52337.

Manuscript submitted March 27, 1978; revised manuscript received July 31, 1978.

Any discussion of this paper will appear in a Discussion Section to be published in the June 1979 JOURNAL. All discussions for the June 1979 Discussion Section should be submitted by Feb. 1, 1979.

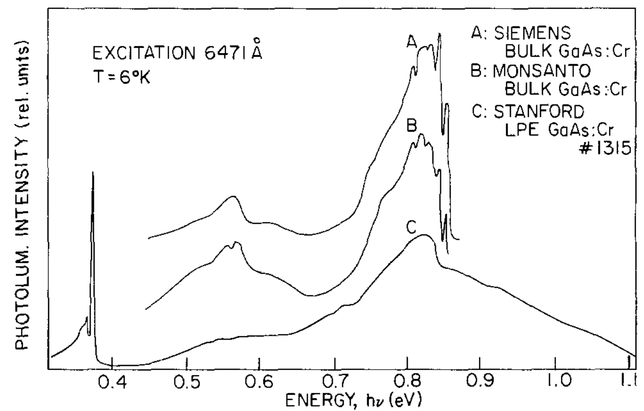

Fig. 4. Photoluminescent spectra of deep levels in a semi-insulating Cr-doped LPE layer grown in the SiO_2-BN(C)-H_2 system and in two bulk Cr-doped GaAs samples. These spectra were recorded by Dr. B. McCombe at the Naval Research Laboratory.

Publication costs of this article were assisted by Stanford University.

REFERENCES

1. T. Nozaki, M. Ogawa, H. Terao, and H. Watanabe, in "GaAs and Related Compounds 1974," Institute of Physics Conference Ser. 24, (Institute of Physics, Physical Society, London, 1975), p. 46.
2. Y. M. Young and G. L. Pearson, *J. Appl. Phys.*, **49**, 3348 (1978).
3. B. L. Mattes, Y. M. Houng, and G. L. Pearson, *J. Vac. Sci. Technol.*, **12**, 869 (1975).
4. C. M. Wolfe, G. E. Stillman, and E. B. Owens, *This Journal*, **117**, 129 (1970).
5. B. L. Mattes and R. K. Route, *J. Cryst. Growth*, **16**, 219 (1972).
6. R. Solomon, in "Proceedings of the 1968 Symposium on GaAs," Institute of Physics and Phys. Soc. Conf. Ser. 7, (Institute of Physics, Physical Society, London), p. 11.
7. D. J. Ashen, P. J. Dean, D. T. J. Hurle, J. B. Mullin, and A. M. White, *J. Phys. Chem. Solids.*, **36**, 1041 (1975).
8. D. V. Lang and R. A. Logan, *J. Electron. Mater.*, **4**, 1053 (1975).
9. C. Kocot and G. L. Pearson, *Solid State Commun.*, **25**, 113 (1978).
10. D. C. Look, *ibid.*, **24**, 825 (1977).

A Method for Estimating Impedance Parameters for Electrochemical Systems That Exhibit Pseudoinductance

Digby D. Macdonald*

SRI International, Materials Research Center, Menlo Park, California 94025

ABSTRACT

A simple algebraic method is presented for estimating impedance parameters for electrochemical systems that exhibit pseudoinductance. The method, which makes use of four characteristic points from the complex plane diagram, is illustrated by calculating impedance parameters for transpassive chromium in sulfuric acid. The quantitative nature of the method renders it particularly useful for estimating impedance parameters for those systems that exhibit single capacitive and inductive semicircles in the complex plane.

A number of electrochemical systems exhibit pseudoinductive behavior which is characterized by the existence of a negative reactance loop upon plotting the impedance data in the complex plane (1-9). For instance, Epelboin, Keddam, and Takenouti (1) found that corroding iron in sulfuric acid, particularly in the presence of propargylic alcohol, exhibits pseudoinductance at frequencies less than about 1.0 Hz. Armstrong and Henderson (2) have also observed this behavior for chromium in the transpassive region in sulfuric acid. Theoretical analyses (1, 3) show that the inductive behavior at low frequency arises from relaxation of the coverages of intermediates on the electrode surface. At high frequencies, kinetic limitations prevent the surface coverages from following the sinusoidal excitation function so that the reactance becomes dominated by a parallel capacitance.

In corrosion research, it is frequently necessary to estimate the rate of corrosion from polarization data. Accordingly, it is commonly assumed that the quantity that should be substituted into the Stern-Geary relationship is the polarization resistance which is equal to the interfacial impedance in the limit of zero frequency. This assumption appears to be well justified for systems that exhibit resistive/capacitive behavior in the complex plane as shown, for example, by the recent work by Macdonald *et al.* (10). However, Epelboin *et al.* (1) claim that the transfer resistance, R_t, is a more appropriate quantity than the polarization resistance for calculating the corrosion rate in systems that exhibit pseudoinductance.

The problem of extracting a numerical value for the transfer resistance from experimental impedance data for pseudoinductive systems does not appear to have been considered in detail. It is possible that the required value could be generated by the nonlinear least squares data fitting procedures recently described by Macdonald and Garber (8). However, these techniques are cumbersome and do not appear to be well suited to regular application in corrosion research. In this paper a simple algebraic method is presented for estimating the impedance parameters, including the transfer resistance, for electrochemical systems that exhibit pseudoinductance. The technique is illustrated by analyzing impedance data for transpassive chromium (2) taken from the literature.

Computational Method

A simple electrical equivalent circuit that satisfactorily accounts for the observed impedance behavior of a large number of systems which exhibit pseudoinductance is shown in Fig. 1. This circuit gives rise to a resistive/capacitive semicircle at high frequencies, and a resistive/inductive semicircle at low frequencies (Fig. 2). Note that this equivalent circuit is capable of yielding only a single inductive loop, and is therefore valid only for those cases where a single surface coverage gives rise to inductive relaxation. Multiple inductive relaxations are observed in a number of systems, for example in the electro-

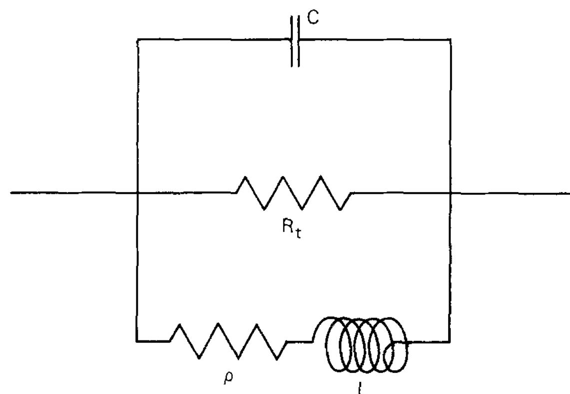

Fig. 1. Equivalent circuit for an interface that exhibits pseudoinductance of the type shown in Fig. 2.

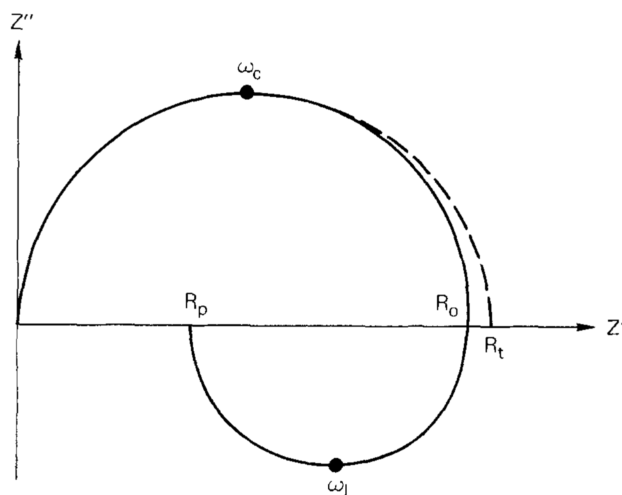

Fig. 2. Typical complex plane diagram for an electrochemical system that exhibits pseudoinductance. The broken line represents the extension of the resistive/capacitive loop in the absence of the parallel inductance.

* Electrochemical Society Active Member.

Key words: electrochemical impedance, pseudoinductance, corrosion, electrode kinetics, impedance parameters.

deposition of zinc (3). These more complex cases are not covered by the computational method presented here.

The admittance function for the equivalent circuit shown in Fig. 1 is given by

$$Y(p) = 1/R_t + pC + 1/(\rho + pL) \quad [1]$$

where p is the impedance operator and R_t is the transfer resistance. The other components are as shown in Fig. 1. The steady-state impedance is given by the reciprocal of Eq. [1] with the parameter p replaced by $j\omega$, where ω is the angular frequency of the excitation function, and $j = \sqrt{-1}$. Thus

$$Z(j\omega) = Z' - jZ'' \quad [2]$$

with

$$Z' = \frac{\rho^2 R_t + R_t^2 \rho + \omega^2 L^2 R_t}{[\rho + R_t - \omega^2 R_t CL]^2 + \omega^2 [L + \rho R_t C]^2} \quad [3]$$

and

$$Z'' = \frac{\omega [R_t^2 \rho^2 C - L R_t^2 + \omega^2 L^2 R_t^2 C]}{[\rho + R_t - \omega^2 R_t CL]^2 + \omega^2 [L + \rho R_t C]^2} \quad [4]$$

The reactance, Z'', is zero at the following three frequencies:

(*i*) $\omega = \infty$. In this case the real component is zero due to the infinite conductance of the capacitance (Fig. 2). This case is trivial, and will not be considered further.

(*ii*) $\omega = 0$. The intercept on the real axis in this instance is equal to the polarization resistance, R_p; that is

$$R_p = \rho R_t / (\rho + R_t) \quad [5]$$

(*iii*) The third root of Eq. [4] is obtained by equating the quantity in square brackets to zero. This yields

$$\omega^2 = (L - \rho^2 C)/L^2 C \quad [6]$$

which gives real values for ω only if $L > \rho^2 C$. If this condition is not met, the inductive semicircle in the fourth quadrant is no longer observed. Instead, a first quadrant distorted semicircle is obtained (12). For the case where $L > \rho^2 C$, substitution of $\omega = (L - \rho^2 C)^{1/2} / LC^{1/2}$ into Eq. [3] yields the following expression for the real component of the impedance at which the reactive behavior changes from capacitive to inductive

$$R_0 = R_t L / (L + R_t \rho C) \quad [7]$$

Equations [5] and [7] represent two independent expressions that may be used to estimate the impedance components. However, the equivalent circuit contains four components so that two additional relationships are required to completely define the system. One of the required expressions is generated by assuming that to a first approximation the reactance in the first quadrant in the region of maximum Z'' at the frequency ω_C (Fig. 2) is independent of the inductance, L. The second expression can be derived using a similar assumption regarding the low frequency reactance in the region of ω_L, *i.e.*, at this frequency the fourth quadrant reactance is independent of the capacitance. The frequencies ω_C and ω_L at which the first quadrant and fourth quadrant reactances are at a maximum, respectively, are therefore given by

$$(\partial Z''/\partial \omega)_{L \to \infty} = 0 \quad [8]$$

$$(\partial Z''/\partial \omega)_{C \to 0} = 0 \quad [9]$$

which yield

$$\omega_C = 1/R_t C \quad [10]$$

$$\omega_L = (R_t + \rho)/L \quad [11]$$

Equations [5], [7], [10], and [11] may be solved simultaneously to yield expressions for R_t, C, ρ, and L in terms of the experimentally observed quantities, R_p, R_0, ω_C, and ω_L (Fig. 2). The expressions obtained are as follows

$$R_t = \{R_0 + [R_0^2 + 4(\omega_L/\omega_C) R_p R_0]^{1/2}\}/2 \quad [12]$$

$$\rho = R_p R_t / (R_t - R_0) \quad [13]$$

$$L = (R_t + \rho / \omega_L) \quad [14]$$

$$C = 1/\omega_C R_t \quad [15]$$

Discussion

The application of Eq. [12]-[15] in the analysis of impedance data for systems that exhibit pseudoinductance is best illustrated by example. For this purpose we have chosen to analyze the data of Armstrong and Henderson (2) for transpassive chromium in 0.5M sulfuric acid at 25°C. The complex plane diagram for this system is reproduced in Fig. 3, and yields the following values for the experimental parameters: $R_p = 3.7\Omega$, $R_0 = 8.3\Omega$, $\omega_C = 3142$ rad/sec (500 Hz), and $\omega_L = 132$ rad/sec (21 Hz). Substitution of these values in Eq. [12]-[15] therefore gives the following numerical data for the impedance parameters: $R_t = 8.4\Omega$, $C = 37.9\ \mu F$, $\rho = 6.5\Omega$, and $L = 0.11H$.

The value obtained above for the transfer resistance, R_t, is slightly greater than the value for R_0, but is much greater than that for the polarization resistance, R_p. Use of this latter quantity, rather than R_t, in the Stern-Geary relationship would clearly lead to serious error in the calculated corrosion rate, as found experimentally by Epelboin *et al.* (1) for the corrosion of iron in inhibited sulfuric acid. The calculated capacitance of 37.9 μF, that is 190 $\mu F/cm^2$, is higher than expected for the electrical double layer (normally 20-50 $\mu F/cm^2$). However, the presence of at least one adsorbed species on the metal surface is indicated by the presence of the inductive loop, and it is possible that other adsorbed species gives rise to pseudocapacitance. The large capacitance may also reflect a very high roughness factor for the electrode surface.

A sensitive test of the method developed here for estimating the impedance parameters is to calculate the impedance spectrum over a wide range of frequency, and then to compare the calculated spectrum with the experimentally determined data. This test is shown in Fig. 3, in which the open points were calculated using Eq. [3] and [4] and the values for R_t, C, ρ, and L given above. The locus of calculated

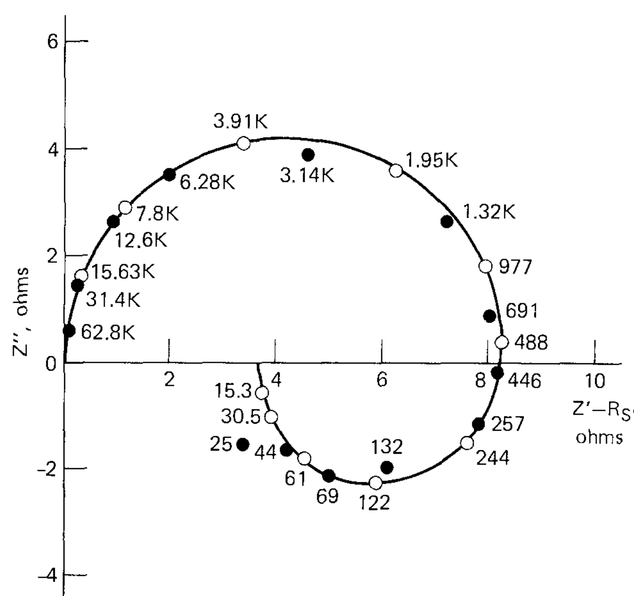

Fig. 3. Complex plane diagram for transpassive chromium in 0.5M H_2SO_4. Open points, calculated data; closed points, experimental data according to Armstrong and Henderson (2). The number next to each point is the frequency of the excitation function in Hz. Electrode area ≐ 0.2 cm^2. R_S = solution resistance.

points is given as the solid line, and it is seen that excellent agreement exists between the calculated values and the experimental data over the entire frequency range considered.

The accuracy of the computational method is clearly limited by the validity of the assumption that the first and fourth quadrant subspectra are independent of one another in the neighborhood of the maxima in the reactance. However, it is believed that this approximation is sufficiently accurate to yield precise corrosion data (R_t, C) for most systems of interest. In those cases where the above assumption is not valid, the method may still be used to estimate initial values for the impedance parameters which can then be refined using the more sophisticated nonlinear least squares techniques (11).

Manuscript submitted March 8, 1978; revised manuscript received May 27, 1978.

Any discussion of this paper will appear in a Discussion Section to be published in the June 1979 JOURNAL. All discussions for the June 1979 Discussion Section should be submitted by Feb. 1, 1979.

REFERENCES

1. I. Epelboin, M. Keddam, and H. Takenouti, *J. Appl. Electrochem.*, **2**, 71 (1972).
2. R. D. Armstrong and M. Henderson, *J. Electroanal. Chem. Interfacial Electrochem.*, **40**, 121 (1972).
3. I. Epelboin, M. Ksouri, and R. Wiart, *This Journal*, **122**, 1206 (1975).
4. D. D. Macdonald, "Transient Techniques in Electrochemistry," Plenum Press, New York (1977).
5. R. D. Armstrong and M. Henderson, *J. Electroanal. Chem. Interfacial Electrochem.*, **34**, 391 (1972).
6. M. L. Boyer, I. Epelboin, and M. Keddam, *Electrochim. Acta.*, **11**, 221 (1966).
7. R. D. Armstrong and R. E. Firman, *J. Electroanal. Chem. Interfacial Electrochem.*, **34**, 39 (1972).
8. R. D. Armstrong, M. Henderson, and H. R. Thirsk, *ibid.*, **35**, 119 (1972).
9. R. D. Armstrong and M. Henderson, *ibid.*, **39**, 222 (1972).
10. D. D. Macdonald, B. C. Syrett, and S. S. Wing, Paper submitted to *Corrosion*.
11. J. R. Macdonald and J. A. Garber, *This Journal*, **124**, 1022 (1977).
12. D. D. Macdonald, Paper submitted to *This Journal*.

Thermodynamic and Kinetic Aspects of Bromine Lamp Chemistry

Suresh K. Gupta

General Electric Company, Lamp Phenomena Research Laboratory, Nela Park, Cleveland, Ohio 44112

ABSTRACT

The thermodynamic approach to bromine regenerative chemistry has been found inadequate in explaining a number of observed lamp phenomena. The basic shortcoming of these treatments has been attributed to the questionable assumption of thermodynamic equilibrium which may not prevail, especially, with respect to atomic hydrogen and carbon monoxide on the lamp walls. This has led to the consideration of a kinetic model which is based on rates of various processes and mass flow within the lamp. Calculations of tungsten mass flow, based on a simple diffusion model, have demonstrated the importance of gas phase and wall reactions. For instance, the gas phase reactive reduction of the tungsten atom flux at the wall of a typical bromine lamp is significant only when the first-order reaction rate constant exceeds the value of 1 sec^{-1}. The role of atomic species has been considered since these are produced at the filament. Hydrogen atoms recombination rates have strong dependence on fill pressure; these are also found to be slower than their diffusion rates to wall. Doubtful validity of the equilibrium assumption at the walls is clearly demonstrated by these calculations. Atomic hydrogen concentrations at the wall, however, are expected to be extremely low when H:Br $<$ 1. Application of this kinetic model to lamp chemistry is limited due to lack of appropriate kinetic data on wall reactions. Comparison of the two models indicates that thermodynamic calculations, if performed correctly, can give valuable insight into transport processes occurring near the filament. However, kinetic considerations are believed to be far more important in understanding the chemistry near the bulb wall.

Tungsten halogen lamps are compact light sources which utilize regenerative actions of halogens to prevent tungsten deposition on lamp walls as well as to sustain long life for the filament Understanding of the regenerative lamp chemistry has been approached primarily from thermodynamic considerations which, for the bromine lamp, were initially restricted to the W-H-Br system (1, 5, 6). However, since most of these lamps are generally made with bromomethanes such as CH_3Br, CH_2Br_2, $CHBr_3$, etc., and usually contain some residual oxygen, these calculations have been extended to the more complex W-O-C-H-Br system (2-4, 6). Complexity of these systems requires careful analysis of condensed phases in these calculations as has been pointed out earlier (3). Recently, the role of carbon in these lamps and its effect on thermodynamic equilibrium computations has been explored in some detail (7, 8).

Key words: thermodynamics, kinetics, bromine lamp.

Generally, however, these thermodynamic approaches to explain lamp behavior have been rather unsuccessful (4). Yannopoulos and Pebler have, for example, attempted to explain observed discrepancies in terms of evolution of water from quartz (4). Prevalent temperatures and pressures in an operating lamp warrant localized thermodynamic equilibria (LTE) near the filament. Multiple collisions due to high operating pressure ($\sim$15 atm) may be expected to lead the system toward rapid equilibration. However, it is questionable to assume that reaction rates are fast enough to attain equilibria near the wall.

Since hydrogen atoms are produced at the filament, kinetics of reactions, such as

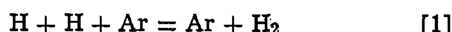

$$H + H + Ar = Ar + H_2 \quad [1]$$

may be quite important, more so in view of their high mobility. Possible occurrence of slow heterogeneous wall reactions such as

$$2\tfrac{1}{2}\,W(s) + CO(g) = W_2C(s) + \tfrac{1}{2}\,WO_2(s) \quad [2]$$

and

$$1\tfrac{1}{2}\,W(s) + CO(g) = WC(s) + \tfrac{1}{2}\,WO_2(s) \quad [3]$$

may also contribute to the system's deviation from equilibrium. In fact, CO, due to its extreme kinetic stability resists disproportionation at lower temperatures as required by thermodynamic arguments.

These limitations of thermodynamic arguments have been summarized and a modified lamp model based primarily on kinetic considerations has been proposed. Calculations have been performed to investigate the migration of tungsten atoms assuming a simple diffusion model. Under this approach one aspect of the lamp model, *e.g.*, the blackening criterion, assumes a different form and depends on the gas phase and wall tungsten atoms reaction rates. There are limitations to this simplified model since convective and thermal diffusion flows are also prevalent in an operating lamp. However, it is believed that this modified approach will provide a better understanding of the regenerative lamp chemistry and stimulate further experimental and theoretical work.

A recent publication describes a mass transfer model for the lamp based on diffusion of participating species across the boundary layer (9). The model has been applied to the W-O-Br system in establishing blackening conditions based on initial levels of lamp additives.

Thermodynamic Model

Formulation.—In the thermodynamic model, as depicted by an idealized situation in Fig. 1, the lamp operation is primarily controlled by localized thermodynamic equilibria at the filament and the bulb wall (10). Partial pressures of tungsten-bearing gaseous species, computed for the desired system, *e.g.*, W-O-C-H-Br in the bromine lamp, are analyzed to discern the direction of the transport. As illustrated in Fig. 1, the ΣP_{Wi}, *i.e.*, sum of all W-bearing gaseous species at the filament and wall are primary quantities, and the condition for tungsten deposition on the wall, *i.e.*, blackening is defined as

$$[\Sigma P_{Wi}]_{fil} > [\Sigma P_{Wi}]_{wall} \quad [I\text{-}a]$$

Since earlier thermochemical calculations indicate that the major species at the filament and bulb wall are W atoms and WO_2Br_2, respectively, (3) this relation can be simplified as

$$P_W(T_F) > P_{WO_2Br_2}(T_B) \quad [I\text{-}b]$$

where T_F and T_B are the corresponding temperatures. Thus, an ideal quartzline lamp, without any temperature gradients along the filament and wall, would stay clean at the balance of these two quantities. Any imbalance would result in either wall darkening or a nonuniform tungsten deposition on the filament which are both undesirable for a designed long-life lamp.

Limitations.—Comparative test results of lamps containing carefully controlled levels of C, H, Br, and O, along with thermodynamic calculations for these systems have been reported (4). The lamp results, however, fail to follow predictions of the calculations. For example, more blackening occurred in the $CHBr_3$ lamps compared to the CH_2Br_2 group, even though the latter group contained far higher H/Br ratios. Lamps made with HBr, CBr_4 + CH_4 (1:1), and CH_2Br_2 behaved differently in spite of same, *i.e.*, 1:1 H/Br ratio. Variable levels of H_2O released from quartz wall of these lamps have been proposed to be the primary reason for these discrepancies (4). These calculations also suggest that lamps made with CH_3Br and low levels of oxygen, such as 0.01%, should darken if the controlling wall temperature is below 800°K. However, contrary to these predictions, such lamps have been found to stay clean (4).

Apparent failure of the thermodynamic approach may be due to a number of reasons, such as incomplete and/or incorrect thermodynamic treatment of the lamp system by exclusion of important yet unknown species and inclusion of nonexistent phases, lack of well-defined data, lamp geometry effects, and filament impurities. But perhaps, the most important factor may be the questionable assumption of LTE under steady-state operating conditions, especially near the bulb walls.

Prevalence of chemical equilibria implies that at the filament and wall, reaction rates are fast enough to establish equilibria with migrated gaseous species (10). Flow of species occurs via radial and thermal diffusion and convection. Extent of each mode of flow will depend on lamp geometry, temperature profiles, and pressures. At the filament temperatures ~3000°K, reaction rates are likely to be fast enough to attain instant equilibrium; however, the same could not be assumed *a priori* at lamp walls where temperatures are ~1000°K.

In this regard, the role of two important lamp constituents, H_2 and CO, deserves special consideration. Hydrogen, because of its extreme mobility, and CO, due to its extraordinary kinetic stability, are likely to contribute heavily toward any deviation of the system from equilibrium. H atoms recombination reaction rate calculations, which are discussed in a later section, suggest an important role for hydrogen.

There is enough evidence to suggest that CO may also play a major role in creating nonequilibrium conditions. Very slow rates of carbon transport observed with the reaction

$$C(s) + CO_2(g) = 2CO(g) \quad [4]$$

have been explained in terms of slow reaction rates with CO (10). Reactions such as [5] and [6]

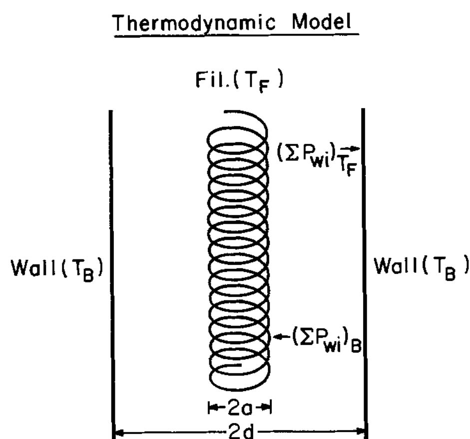

Fig. 1. Comparative formulations of the thermodynamic and kinetic blackening criteria for bromine lamp.

$$W(s) + 2CO_2(g) = WO_2(s) + 2CO(g) \quad [5]$$

$$2W(s) + 2CO(g) = W_2C(s) + CO_2(g) \quad [6]$$

may be quite slow. For example, flash desorption of CO from tungsten surface at ~1000°K does not yield any reaction products which are thermodynamically possible (11).

Since temperatures in most parts of an operating lamp are over 1000°K, CO is the major oxygen bearing gaseous species. At the walls, where temperatures are lower, CO reaction such as [4] essential for providing WO_2Br_2 at the bulb walls, may play a decisive role in the darkening of lamps. Thus, if this reaction is kinetically slow, blackening is likely to result. This, of course, assumes the necessity of oxygen in tungsten removal from the wall. Kinetic studies suggest formation of primarily the WO_2Br_2 species at the wall conditions (12). Binary bromides are known to form in W-Br reactions at bromine pressures at least an order of magnitude higher than those normally prevalent in a typical lamp (13). Available thermodynamic data also discount significant binary bromide formation at bulb walls (14). Thus, the role of CO is considered quite important in wall reactions such as [4] and in creating nonequilibrium conditions at lamp walls.

Kinetic Model

Formulation.—The thermodynamic approach and its limitations in explaining observed lamp phenomena have been discussed in the preceding section. Whether drawbacks of the approach are due to failure of the lamp system at the wall to attain equilibrium with regard to atomic hydrogen and CO cannot be substantiated until relevant kinetic data are available. Hence, the kinetic approach has been explored. In this consideration, important parameters are rates of various processes in the lamp, *e.g.*, reactions at the filament, bulb wall, and gaseous interphase as well as species diffusion.

For the regenerative lamp, three primary rate processes to consider are: (*i*) W atoms evaporation at the filament, (*ii*) W atoms removal by chemical reactions in the gas phase between the filament and wall, and (*iii*) W atoms reaction on the lamp wall. The blackening criterion as discussed earlier is, now, defined as

$$J(W) > [R]_B \quad [II]$$

Here, $J(W)$ is defined as the W atoms flux reaching the wall; it thus depends on the filament temperature T_F and gas phase reaction rates. $[R]_B$, the wall reaction rate, is controlled by wall temperature, T_B, and reactant concentrations.

Calculations.—Flux values can be calculated by solving steady-state diffusion equation (15)

$$D \nabla^2 C - kC = 0 \quad [III]$$

which for cylindrical coordinates becomes

$$D \frac{d}{dr}\left[r \cdot \frac{dC_W(r)}{dr}\right] - k \cdot C_W(r) = 0 \quad [IV\text{-}a]$$

The angular and axial dependence are ignored as the major mass transfer occurs radially. The symbols are defined as follows: D is the mean diffusion constant of W atoms in argon; $C_W(r)$ is tungsten atoms concentration at distance, r, from the filament axis; k is assumed first-order W atoms gas phase reaction rate constant defined as

$$\frac{-dC_W(r)}{dt} = kC_W(r) \quad [V\text{-}a]$$

$$= k'[C_{Br}(r)]^x C_W(r) \quad [V\text{-}b]$$

$$= k''[C_O(r)]^y C_W(r) \quad [V\text{-}c]$$

where k' and k'' are modified rate constants; x and y are the dependence orders; and brackets indicate concentrations of particular species. The kinetic expressions [V-b] and [V-c] would be applicable to reactions such as

$$W(g) + Br(g) = WBr(g) \quad [7]$$

and

$$W(g) + O(g) = WO(g) \quad [8]$$

Similar expressions may be formulated for other possible reactions with H_2O, CO, and O_2 molecules depending on the specific lamp system.

Solution of the relation presented in detail in Appendix I, is

$$[J(W)]_{k=0} = \frac{D \cdot C_W(a)}{d \ln (d/a)} \text{ g-atoms/cm}^2\text{sec} \quad [VI\text{-}a]$$

and

$$[J(W)]_{k>0} = \frac{D \cdot C_W(a)}{d} \frac{1}{\Xi + \frac{\alpha}{\beta^2}\Omega} \text{ g-atoms/cm}^2\text{ sec} \quad [VII]$$

where a and d are defined in Fig. 1 and $C_W(a)$ is the W atoms concentration at the filament. α and β^2 are defined as $\alpha = k/D$ and $\beta^2 = k_s/D$, where k_s is the reaction rate constant on the wall (see Appendix I). The parameters Ξ and Ω are composed of the modified Bessel functions of the first and second kind (16). The tungsten flux relation [VI-a] is modified when the inner bulb diameter is larger than Langmuir film diameter, $2b$. The modified relation is

$$[J(W)]_{k=0} = \frac{D\text{-}C_W(a)}{d \ln (b/a)} \text{ g-atoms/cm}^2\text{ sec} \quad [VI\text{-}b]$$

Using a recent formulation (17), Langmuir film diameter for a typical 500W T3 lamp filled with 2500 Torr of argon and filament at 3000°K, was calculated to be 0.48 cm compared to the bulb diameter of 0.8 cm. Since chemical reactions are not considered limited to only outside of the Langmuir film, the flux calculations for one filament and two different bulb diameters presented in Fig. 2 are based on relations [VI-a] and [VII]. Dramatic reduction in the W atoms flux is caused by gas phase reaction rate constant values $k > 1 \text{ sec}^{-1}$.

The reaction rate constant for W atom loss in relation [IV-a] based on kinetic theory is first order in the limiting case of surface reaction. The volume reactions for species, such as atomic oxygen, have also been found to be first order (18) and hence this assumption is considered quite valid. The relations [V-a], [V-b], and [V-c] imply that $C_{Br}(r)$ and $C_O(r)$

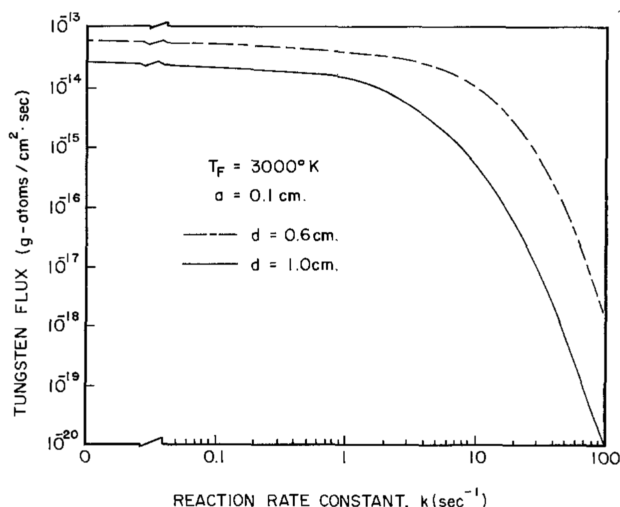

Fig. 2. Effect of gas phase reaction rate constants on the tungsten atoms flux reaching the bulb wall.

are invarient in r. While this is not strictly true due to gas phase loss, proportionately large values of C_{Br} or C_O compared to $C_W(r)$ (see Appendix II) clearly justify these kinetic formulations. Reactions involving radicals and atomic species occur with activation energies $E \approx 0$. The dissociation reaction, *e.g.*, the reverse of reactions [7] or [8] would undoubtedly involve significant activation as these processes are thermodynamically quite unfavorable under the lamp prevalent conditions under present considerations.

A probable range for the values of k has been estimated using collision kinetic theory. Details of these calculations are given in Appendix II. The k values, of course, depend on the postulated reactions. For example, at 1500°K, k values are 6×10^3 and 6×10^4 sec^{-1}, respectively, for reactions [7] and [8] rewritten with Ar as a collision stabilizer

$$W(g) + O(g) + Ar = WO(g) + Ar \qquad [9]$$

and

$$W(g) + Br(g) + Ar = WBr(g) + Ar \qquad [10]$$

These may be regarded as intermediary steps leading to further reactions as products approach lamp wall. Difference in magnitudes of k for the two postulated reactions, obviously, lies in relative reactant concentrations. Thus, increased reactant levels should further reduce W atom flux $J(W)$. The flux, due to its linear dependence on W vapor pressure, increases with filament temperature. The reaction rates, then, must be correspondingly higher to prevent wall blackening.

Lack of experimental kinetic data for tungsten reactions at wall temperatures under lamp environment does not permit any verification of the kinetic model.

Limitations.—The simplified diffusion model only points out the nature of the treatments involved. In reality, however, the lamp phenomena are much more complicated. Convective and thermal diffusion mass flows are also very important as has been pointed out by Fisher *et al.* (19). In fact, at lamp operating pressures, convection becomes the dominating mode of mass and heat transfer. However, chemical reactions have not been considered by them. Availability of the relevant reaction kinetic data is important so that the current approach, even in its present approximate form, can be utilized to increase understanding of the lamp behavior.

Role of Atomic Species

Atomic species such as H, Br, and O are produced at the hot filament. These will react and recombine during their diffusion toward the bulb wall. Rates of these reactions are obviously important in establishing equilibrium conditions in the lamp. Among these, the role of hydrogen atoms, which is the most mobile species, can be investigated to some degree, since reasonably well-established kinetic data are available (20).

Hydrogen is added to the lamp generally as bromomethanes or HBr. Amount of atomic species H and Br at the filament temperature of 3000°K calculated for two typical lamp conditions assuming chemical equilibrium are given in Table I. Movement of these species would occur primarily via diffusion and convection, and in the process the species would undergo reactions such as

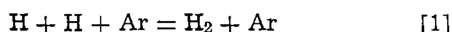

$$H + H + Ar = H_2 + Ar \qquad [1]$$

Table I. Equilibrium distribution of species at 3000°K

System	Cold fill pressure (Torr)	P_H (atm)	P_{H_2} (atm)	P_{HBr} (atm)	P_{Br} (atm)
H_2 + HBR (1:1)	6	2.8×10^{-3}	3.1×10^{-2}	5.1×10^{-3}	2.7×10^{-2}
HBr	3	1.4×10^{-2}	7.6×10^{-3}	2.7×10^{-3}	2.9×10^{-2}

$$Br + H + Ar = HBr + Ar \qquad [11]$$

and

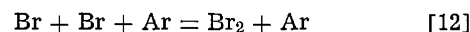

$$Br + Br + Ar = Br_2 + Ar \qquad [12]$$

due to fairly high (~14 atm) inert gas pressures. Inert gas atoms of Ar act as third body stabilizers in the collision processes (20). These reactions, although written as termolecular are really composed of two bimolecular collision steps. Available kinetic data have enabled calculations of rates of these reactions.

Since the loss of H atoms occurs primarily by two concurrent reactions, namely [1] and [11], the rate expression may be formulated as

$$-\frac{dC_H}{dt} = 2\frac{dC_{H_2}}{dt} + \frac{dC_{HBr}}{dt} \qquad [VIII\text{-}a]$$

Based on known reaction rate constants, k_1 and k_{11}, respectively, for reactions [1] and [11], the rate equation is

$$-\frac{dC_H}{dt} = \left[\frac{2k_1}{C_{Ar}}\right] \cdot (C_H)^2 \cdot C_{Ar} + \left[\frac{k_{11}}{C_{Ar}}\right] \cdot C_H \cdot C_{Br} \cdot C_{Ar} \qquad [VIII\text{-}b]$$

For the simple case where initial concentrations of H and Br atomic species are about equal, such as for H_2 + HBr system calculated in Table I, the above relation is simplified to give

$$\frac{1}{C_H} - \frac{1}{C_H^\circ} = \left[\left\{\frac{2k_1}{C_{Ar}}\right\} C_{Ar}\right] \cdot \tau_D + \left[\left\{\frac{k_{11}}{C_{Ar}}\right\} C_{Ar}\right] \cdot \tau_D \qquad [VIII\text{-}c]$$

and the unreacted atom fraction

$$\frac{C_H}{C_H^\circ} = \frac{1}{1 + (k_1' + k_{11}')\tau_D C_H^\circ} \qquad [VIII\text{-}d]$$

where k_1' and k_{11}' refer to the bracketed quantities for the particular argon concentration, C_H is the H atom concentration at $t = \tau_D$, and C_H° is the initial concentration. τ_D is the mean H atom diffusion time between the filament and wall given by

$$\tau_D = \frac{(d - a)^2}{D} \qquad [IX]$$

based on simple diffusion model where D is the mean diffusion constant and $(d - a)$ is the diffusion distance (15). Temperature-dependent rate constants, available from shock tube studies, are

$$\frac{k_1}{C_{Ar}} = 2.3 \times 10^{14}\left(\frac{T}{2870}\right)^{-1.2} \frac{cm^6}{mole^2\,sec} \qquad [X]$$

and

$$\frac{k_{11}}{C_{Ar}} = 5.8 \times 10^{14}\left(\frac{T}{3000}\right)^{-2} \frac{cm^6}{mole^2\,sec} \qquad [XI]$$

Appropriate values of C_{Ar} can be used to derive k_1' and k_{11}' for calculating the concentration of H atoms reaching the bulb wall. Reaction [12] is not considered important in affecting Br atom concentration since bromine is expected to be nearly fully dissociated at the prevailing wall temperatures. Furthermore, Br atom diffusion is much slower compared to that of H atom, but it is obvious that the uncombined H atom concentration is primarily governed by the extent of reaction occurring during the mean diffusion time of atomic hydrogen, τ_D. Therefore, the computed C_H/C_H° values are based on this assumption.

In cases such as computed in Table I or others where atomic concentrations of hydrogen and bromine at the filament are not equal, the solution of rate equation [VIII-b] becomes

$$\frac{1}{C_H} - \frac{1}{C_H{}^\circ} = k_I{}'t + k_{II}{}'\left[\frac{C_{Br}}{C_H}\right]t \quad \text{[VIII-e]}$$

Numerical methods are required to evaluate $C_H/C_H{}^\circ$ for such systems. In the case of HBr filled lamps (see Table I) when the bromine atom concentration is about double that of H atoms, the dominant second term in [VIII-e] controls $C_H/C_H{}^\circ$. Therefore, consideration of only reaction [11] is considered satisfactory for calculating values of $C_H/C_H{}^\circ$ in view of the fact that the reaction rate constants themselves are not very well established (20). Since numerical values of $k_I{}'$ and $k_{II}{}'$ at the prevalent lamp conditions are about equal and $C_{Br}{}^\circ = 2C_H{}^\circ$, the expression [VIII-d] without further modification also yields the estimates of unreacted H atom fractions for the particular case of HBr filled system.

The proportion of unreacted hydrogen atoms which reach the lamp wall is a function of total fill pressure, the mean reaction temperature, and the diffusing distance, *i.e.*, the distance between the wall and filament. This is well illustrated in Fig. 3 for the simpler case of H_2 + HBr system where equal amounts of atomic H and Br species prevail at the filament (see Table I). Argon pressures in operating lamps were taken as 4 times the cold fill values. These operating pressures were then used to evaluate $k_I{}'$ and $k_{II}{}'$ and finally $C_H/C_H{}^\circ$ at different reaction temperatures. The diffusion constant, D, was calculated using the formula given in Appendix I. Figure 3 clearly demonstrates the dramatic effect of cold fill pressure, reaction temperature, and path length on the extent of H atoms recombination.

Most regenerative lamps are filled at 2000-3000 Torr. The mean lamp temperature is ~1300°K and filament to wall distance ~0.5 cm. Thus, $C_H/C_H{}^\circ$ would be in the range 2×10^{-4} to 7×10^{-5} which, under steady-state conditions, corresponds to H atom pressures at the wall of ~4×10^{-6} to 1×10^{-6} atm.

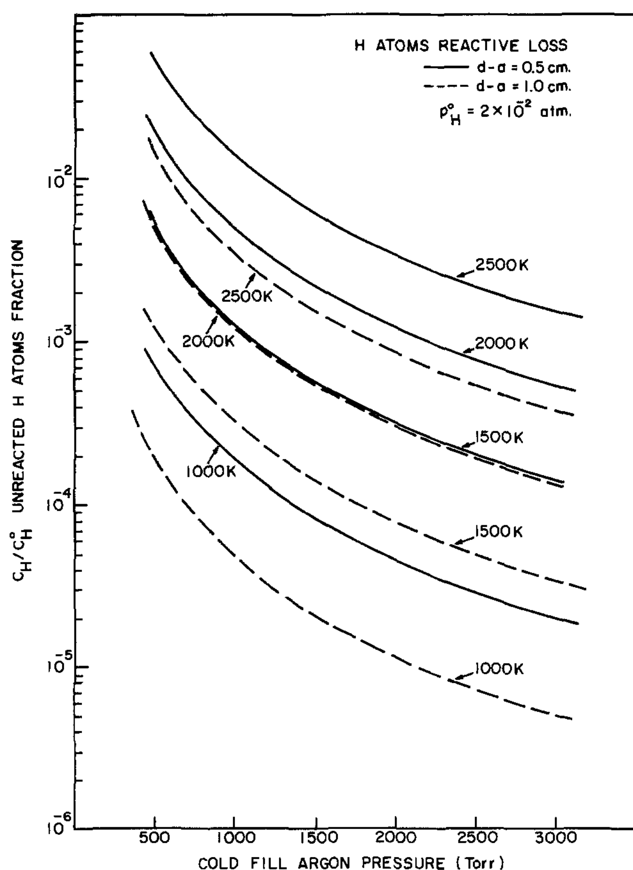

Fig. 3. Lamp fill pressure and temperature dependence of H atoms recombination for two different path lengths.

Table II. Diffusion and reaction times of H and Br atoms

Reaction	τ_r (sec)	τ_D (sec)	T°K
H + Br + Ar = HBr + Ar	0.54	0.36	1500
H + H + Ar = H_2 + Ar	0.2	0.9	1500

Lamp parameters: Cold fill Ar P = 2500 Torr
Filament temp. = 3000°K
H_2 + HBr (1:1) cold filled P = 6 Torr
Fil.-wall distance = 0.5 cm

This is also the range for the specific case of lamps filled with 6 Torr of H_2 + HBr(1:1) as shown in Table I. In the other case of HBr filled lamps at 3 Torr, the calculated H atom wall pressure range of 3×10^{-6} to 1×10^{-6} is not much different from that in the H_2 + HBr case. The effect of increasing the diffusive path length from 0.5 to 1.0 cm is evident from Fig. 3. A minimum diffusion distance of 1.1 cm is required for reaction [1] to reach equilibrium at the wall. The mean diffusion times τ_D and reaction times to reach equilibrium are listed in Table II for both reactions. This suggests that under conditions such as when the filament to wall distances in lamps are large, the entire system can be treated on LTE basis.

Unreacted H atoms reaching the wall, besides being capable of reducing tungsten oxide, will also undergo surface recombination. Published data, however, suggest that recombination reactions on fused silica surfaces are quite slow and strongly dependent on the surface conditions (21). For example, at 900°K, the recombination coefficient is ~3×10^{-2}, which implies only three successful collisions out of 100. The surface recombination coefficient appears to increase with temperature (21). At these low surface reaction rates and low H atom pressure, silica reduction reaction

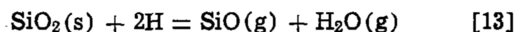

$$SiO_2(s) + 2H = SiO(g) + H_2O(g) \quad [13]$$

is not believed to be significant. This immediately suggests that tungsten oxide reduction may be a far more efficient process than reaction [13]. There are no experimental data to verify this conclusion.

Limitations of these calculations should also be pointed out. A simplified approach has been adopted in the present calculations rather than use a highly involved solution of diffusion equation with second order dependence on concentration as demanded by relation [III]. The results, thus, may not be rigorous, but certainly represent the general effects of temperature and pressure. The rate constants used are not exactly valid over the adopted temperature and pressure range. Only the diffusion mode of mass transfer was considered in the evaluation of τ_D, even though convection and thermal diffusion due to temperature gradients are quite important, especially at high operating pressures (19).

Acknowledgments

The author expresses sincere thanks to Drs. K. M. Maloney and E. G. Zubler for many helpful discussions.

Manuscript submitted Jan. 9, 1978; revised manuscript received July 15, 1978.

Any discussion of this paper will appear in a Discussion Section to be published in the June 1979 JOURNAL. All discussions for the June 1979 Discussion Section should be received by Feb. 1, 1979.

Publication costs of this article were assisted by General Electric Company.

APPENDIX I

Solution of Diffusion Eq. [IV-a]

Diffusion Eq. [IV-a] can be written as

$$\frac{1}{r}\frac{d}{dr}\left(r\frac{dC(r)}{dr}\right) - \alpha^2 C(r) = 0 \quad \text{[IV-b]}$$

which has the following solution (22)

$$C(r) = AI_0(\alpha r) + BK_0(\alpha r) \quad \text{[XII-a]}$$

where I_0 and K_0 are the modified Bessel functions of the first and second kind, respectively (16). The constants A and B are evaluated using the following boundary conditions: (*i*) At $r = a + \lambda/2$, $C(r = a + \lambda/2) = C(a)$, where $C(a)$ is the tungsten atom concentration at the filament and λ is the mean free path. (*ii*) At $r = d - \lambda/2$, $D\, dC(r)/dr = -k_s[C(r) - C(d)]$, which implies that the flux at $d - \lambda/2$, *i.e.*, half a mean free path from the wall, is equal to the rate of impingement. $C(d)$ is the tungsten atom concentration at $d - \lambda/2$ distance and k_s is defined as $k_s = 1/4 \cdot \bar{v} \times$ condensation (or reaction) coefficient on the wall where $\bar{v}$, is the mean velocity. Since vapor pressure of tungsten at wall temperatures is negligible, $[C(r) - C(d)] \simeq C(r)$.

Application of the boundary conditions yields

$$C(a) = AI_0(\alpha a) + BK_0(\alpha a) \quad \text{[XIII]}$$

and

$$\beta^2[C(r) - C(d)] = -A \cdot \alpha I_0'(\alpha r) - B \cdot \alpha K_0'(\alpha r) \quad \text{[XIV]}$$

which for $r = d$ gives

$$\beta^2 C(d) = A \cdot \Phi(\alpha d) + B \cdot \psi(\alpha d) \quad \text{[XV]}$$

where

$$\Phi(\alpha d) = \alpha I_0'(\alpha d) + \beta^2 I_0(\alpha d) \quad \text{[XIV]}$$

and

$$\psi(\alpha d) = \alpha K_0'(\alpha d) + \beta^2 K_0(\alpha d) \quad \text{[XVI]}$$

Solution of A and B gives an expression for $C(r)$ (16)

$$C(r) = -\frac{C}{\eta} \cdot \psi(\alpha d) \cdot I_0(\alpha r) + \frac{C_a \Phi(\alpha d)}{\eta} \cdot K_0(\alpha r) \quad \text{[XII-b]}$$

where

$$\eta = K_0(\alpha a) \cdot \Phi(\alpha d) - I_0(\alpha a) \cdot \psi(\alpha d) \quad \text{[XVII]}$$

Under steady-state condition, the flux is given by (22)

$$\text{flux,} \quad J = -2\pi r \cdot D \cdot \frac{dC(r)}{dr} \quad \text{[XVIII]}$$

Differentiation of the expression for $C(r)$ and appropriate use of Bessel function relations yields (16)

$$(J)_{r=d} = \frac{D}{d} C(a) \frac{1}{\Xi + \frac{\alpha}{\beta^2}\Omega} \text{ g-atoms/cm}^2\text{ sec} \quad \text{[VII]}$$

where

$$\Xi = K_0(\alpha a) \cdot I_0(\alpha d) - I_0(\alpha a) \cdot K_0(\alpha d) \quad \text{[XIX]}$$

and

$$\Omega = K_0(\alpha a) \cdot I_1(\alpha d) + I_0(\alpha a) \cdot K_1(\alpha d) \quad \text{[XX]}$$

These combinations of Bessel functions can be solved using available expressions (16). Diffusion constant, D, was taken as the average of the values at 1200° and 3000°K. Calculations of D were done by using the following simplified relation (16)

$$D = \frac{2.63 \times 10^{-3}}{P_T \cdot (\alpha_{12})^2} (T)^{3/2} \left[\frac{M_1 + M_2}{M_1 \cdot M_2} \right]^{1/2} \quad \text{[XXI]}$$

where M_1 and M_2 are the respective atomic weights of the two species. T is the absolute temperature, P_T is the total pressure taken as 15 atm here, and α_{12} is the mean atomic diameter of the two diffusing species in angstroms. D values for W-Ar system at 1200° and 3000°K are evaluated as 0.085 and 0.336 cm²/sec, respectively. β^2 is calculated as follows

$$\beta^2 = \frac{k_s}{D} = \frac{1/4\, \bar{v}}{D} \times \text{condensation (or reaction) coefficient} \quad \text{[XXII]}$$

where $\bar{v} = \sqrt{8\kappa T/\pi\mu} = 3.39 \times 10^3$ cm/sec. D is evaluated to be 0.07 cm²/sec at 1000°K and condensation (or reaction) coefficient is approximated as 0.1. κ and μ are the Boltzmann constant and the reduced mass, respectively.

The expression for diffusion without any chemical reaction has been well known (17)

$$(J)_{\substack{r=d \\ k=0}} = \frac{DC(a)}{d \cdot \ln(d/a)} \text{ g-atoms/cm}^2\text{ sec} \quad \text{[VI-a]}$$

When the Langmuir sheath diameter, $2b$, is smaller than the bulb diameter, $2d$, the modified relation is

$$(J)_{\substack{r=d \\ k=0}} = \frac{DC(a)}{d \cdot \ln(b/a)} \text{ g-atoms/cm}^2\text{ sec} \quad \text{[VI-b]}$$

APPENDIX II

Estimation of k

The diffusion expression [IV-a] contains a reaction term for the first-order rate of loss of tungsten atoms in gas phase reactions, defined as

$$\frac{-dC(r)}{dt} = k \cdot C(r) \quad \text{[V-a]}$$

Two postulated reactions are [9] and [10]

$$W(g) + O(g) + Ar = WO(g) + Ar \quad [9]$$

and

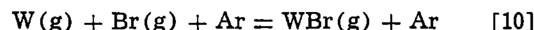

$$W(g) + Br(g) + Ar = WBr(g) + Ar \quad [10]$$

for which no experimental values of k are available. Collision theory can be used to estimate values of k which may be expressed for both reactions as follows

$$\frac{-dC_W(r)}{dt} = kC_W(r) = k'C_W(r) \cdot C_O \cdot C_{Ar} \quad \text{[XXIII-a]}$$

$$= k''C_W(r) \cdot C_{Br} \cdot C_{Ar} \quad \text{[XXIII-b]}$$

The ternary collision expressions really involve two consecutive binary collisions in which the third body, Ar, acts as the collision stabilizer. Details of treatment of ternary collision gas kinetics are given elsewhere and, thus, only outlines will be given (23). The rate of reaction [9] for example, can be expressed as

$$\frac{-dC_W(r)}{dt} = P \cdot Z_3^\circ \exp(-E/RT) \cdot C_W(r) \cdot C_O \cdot C_{Ar} \quad \text{[XXIV]}$$

where P is the probability factor, E is the activation energy and the number of ternary collisions, Z_3, is defined as

$$Z_3 = Z_3^\circ C_W(r) C_O C_{Ar} \quad \text{[XXV-a]}$$

A simplified and approximate version of the expression for Z_3° is

$$Z_3^\circ = 54 \cdot \sqrt{3} \cdot R \cdot T \cdot M^{-1} \cdot \tau \cdot d^4 \quad \text{[XXV-b]}$$

where M is the mean molecular weight, d is the mean molecular diameter, and τ is mean lifetime of the binary complex defined as: $\tau = d/v$ where v is the mean relative velocity of the complex at T°K.

In the present considerations of the two reactions, activation energy, E, is taken as zero as is the case for radical-type reactions. The reaction rate expressions are defined, respectively, as

$$\frac{-dC_W(r)}{dt} = kC_W(r) = Z_3^\circ \cdot P \cdot C_W(r) \cdot C_O \cdot C_{Ar} \quad \text{[XXIII-c]}$$

and

$$= Z_3^\circ \cdot P \cdot C_W(r) \cdot C_{Br} \cdot C_{Ar} \quad \text{[XXIII-d]}$$

which yield for k the following

$$k_9 = Z_3^\circ \cdot P \cdot C_O \cdot C_{Ar} \text{ sec}^{-1} \quad \text{[XXVI-a]}$$

and

$$k_{10} = Z_3^\circ \cdot P \cdot C_{Br} \cdot C_{Ar} \text{ sec}^{-1} \quad \text{[XXVI-b]}$$

Substitution of appropriate quantities yields the following for Z_3°

$$Z_3^\circ = 4 \times 10^{-35} \cdot T \frac{\text{cm}^6}{(\text{molecule})^3} \cdot \frac{1}{\text{sec}}$$

$$= 1.5 \times 10^{13} \cdot T \frac{\text{cm}^6}{(\text{mole})^3 \text{ sec}} \quad \text{[XXV-c]}$$

Mean reaction temperature for lamp gas phase is

assumed to be 1500°K. A typical lamp has Ar, Br, and O atom concentrations $\sim 10^{20}$ ($\sim$15 atm), 10^{17} ($\sim 10^{-2}$ atm), and 10^{16} ($\sim 10^{-3}$ atm) atoms/cm^3, respectively. If the reaction probability, P, is assumed 0.1, reaction rate constants, k_9 and k_{10}, respectively, are 6×10^3 and 6×10^4 sec^{-1}.

REFERENCES

1. B. Kopelman and K. A. Van Wormer, Jr., *Trans. Illum. Eng. Soc.*, **64**, 230 (1969).
2. L. N. Yannopoulos and A. Pebler, *J. Appl. Phys.*, **42**, 858 (1971); *ibid.*, **43**, 2435 (1972).
3. S. K. Gupta, *J. Appl. Phys.*, **42**, 5855 (1971).
4. L. N. Yannopoulos and A. Pebler, *J. Illum. Eng. Soc.*, **1** (January 1972) (see the Discussion section).
5. G. M. Neumann, *Metallurgia*, **64**, 117 (1973).
6. G. M. Neumann, *Thermochem. Acta*, **8**, 369 (1974).
7. T. Geszti, I. Gaol, T. Deutsch, and I. Hanyos, *J. Phys. D*, **5**, 108 (1972).
8. T. Geszti and T. Vicsek, *ibid.*, **9**, 903 (1976).
9. F. J. Harvey, *Metall. Trans.*, **7A**, 1167 (1976).
10. H. Schafer, "Chemical Transport Reactions," p. 15, Academic Press, New York (1964).
11. J. T. Yates and T. E. Madey, *J. Chem. Phys.*, **54**, 4969 (1971).
12. E. G. Zubler, *J. Phys. Chem.*, **74**, 2479 (1970); *ibid.*, **76**, 320 (1972).
13. S. A. Shchukarev and G. A. Kokovin, *Russ. J. Inorg. Chem.*, **9**, 1309 (1964).
14. S. K. Gupta, *J. Phys. Chem.*, **75**, 112 (1971).
15. W. Jost, "Diffusion," p. 57, Academic Press, New York (1960).
16. N. W. McLachlan, "Bessel Functions for Engineers," Oxford Press (1955).
17. (a) F. H. R. Almer and J. De Riddler, *Lighting Res. Technol.*, **8**, 31 (1976).
    (b) E. J. Covington, *Illum. Eng.*, **63**, 134 (1968).
18. F. Kaufman, in "Progress in Reaction Kinetics," Vol. 1, G. Porter, Editor, Pergamon Press (1961).
19. E. Fischer and J. Fitzgerald, *J. Appl. Phys.*, **45**, 2895 (1974).
20. J. Troe and H. Gg. Wagner, in "Physical Chemistry of Fast Reactions," Vol. 1, B. P. Levitt, Editor, chap. 1, Plenum Press, New York (1973).
21. B. J. Wood and H. Wise, *J. Phys. Chem.*, **65**, 1976 (1961); *ibid.*, **66**, 1049 (1962).
22. H. S. Carslaw and J. C. Yeager, "Conduction of Heat in Solids," p. 143, Oxford (1973).
23. V. N. Kondratev, "Chemical Kinetics of Gas Reactions," p. 322, Pergamon Press, New York (1964).

Analysis of Grain Boundary Permeation in Solids

P. H. Holloway

Sandia Laboratories, Albuquerque, New Mexico 87115

and G. E. McGuire*

Texas Instruments, Dallas, Texas 75222

ABSTRACT

Methods are described to extract the grain boundary diffusion coefficient from experimental measurements of surface concentration of a diffusing species. For Type C kinetics, where bulk transport is negligible, easily used exact analytical solutions are available for infinite source and zero or infinite sink boundary conditions. For infinite or finite source and finite sink boundary conditions, the surface concentration is described by an exponential curve if the surface capacity is larger than the grain boundary capacity. The finite sink analysis has been applied to chromium diffusing in platinum, and D_b was found to equal 1.1×10^{-3} exp ($-31{,}700/RT$). For Type B kinetics, where bulk transport is not negligible, equations developed by Wuttig and Birnbaum may be used with a general criterion for approximating the bulk lattice flux developed in the present work. These solutions are available for infinite and finite source and infinite and zero boundary conditions. For an infinite source and sink condition, D_b was calculated for gold in platinum by a "time-of-penetration" measurement and was shown to equal 0.018 exp ($-38{,}000/RT$).

Electron and ion spectroscopies are being widely used in analysis of low temperature diffusion accelerated by defects such as grain boundaries (1, 2). The diffusion phenomena can be characterized by either measuring concentration *vs.* depth in the solid (sputter profiling), or by measuring surface concentration on a finite thickness film as a function of time and temperature (permeation analysis) (1). Permeation analysis is often preferred because of sputtering artifacts (3, 4) and efficiency in the collection data, but proper analysis of the data is not always straightforward.

Hwang and Balluffi (5, 6) have given exact analytic expressions for material concentration in the grain boundary or on the surface as a function of time and temperature for finite or infinite source and finite sink boundary conditions. Their treatment assumes the leakage of material from grain boundary can be neglected. Harrison (7) has developed a terminology useful in designating the general effects of bulk diffusion on grain boundary diffusion. When the amount of material lost from the boundary is negligible, Harrison designates this Type C kinetics. When the loss of material from the boundary to the bulk is significant but the diffusion fields from grain boundaries do not overlap, the kinetics are Type B. Type A kinetics occur when the diffusion fields overlap. In the terminology developed by Harrison (7), Hwang and Balluffi's analysis is applicable to Type C kinetics. However their exact solution is complex, requiring numerical solutions of a transcendental equation, therefore it is not easily used.

Similarly, Gilmer and Farrell (8, 9) have derived exact analytical expressions for material concentration *vs.* distance in thin films for infinite source and zero or infinite sink boundary conditions. With some manipulation, their expressions can describe surface concentration *vs.* time and temperature. Their derivation is applicable to the temperature regime where

* Electrochemical Society Active Member.

loss of material to the grain is significant, *i.e.*, what Harrison (7) calls Type B kinetics, but the solution also involves a transcendental equation, which is very inconvenient since such equations must usually be solved on a digital computer.

It is desirable to find solutions or simplifying assumptions to make it easier to extract grain boundary diffusion coefficients. For Type C kinetics Hwang and Balluffi (5, 6), Nelson *et al.* (1, 10), and Hall and Morabito (11) have described simplifying assumptions for finite and infinite sink boundary conditions. The resulting solutions will be described and Hwang and Balluffi's solutions compared to literature data for chrominum diffusing in platinum (12).

For Type B kinetics, Wuttig and Birnbaum (13) have solved the diffusion equations using an approximate value for the grain boundary leakage flux, but Holloway *et al.* (1) experienced difficulty in using their approximation because the leakage flux was underestimated. It will be shown that a methodology can be developed to select this flux by determining the total amount of material lost from the boundary during the course of an experiment. Calculations based on Wuttig and Birnbaum's treatment will be compared to earlier numerical calculations (1). With this general criterion to approximate grain boundary leakage flux, the boundary diffusion coefficient can be calculated from a time of penetration measurement corrected for bulk diffusion as will be shown for gold diffusing in platinum (14).

Model for Grain Boundary Diffusion

The grain boundary diffusion geometry originally proposed by Fisher (15) and extended by several others (16-18) is used. It is shown schematically in Fig. 1. The grain boundary is a region 2δ wide with a concentration C_b and diffusivity, D_b. The region, $\delta < y < d/2$, is the bulk of the grain with a concentration C_g and diffusion coefficient D_g for the diffusant. The geometry in Fig. 1 departs from that of Fisher and others in that finite thickness films are considered, therefore boundary conditions at the sink are extremely important. The source and sink may be high diffusivity regions with widths ϵ and γ, respectively, and characterized by a concentration C_s and a diffusion coefficient, D_s.

Let the concentration of the diffusing species be a function of x, y, time (t), and temperature (T). Then by Fick's second law (9)

$$\frac{\partial C_g}{\partial t} = D_g\left(\frac{\partial^2 C_g}{\partial x^2} + \frac{\partial^2 C_g}{\partial y^2}\right) \quad \text{for } y > \delta,\ 0 < x < L \quad [1]$$

Requiring that the flux and concentrations be continuous at $y = \delta$ and that C_b is an even function in y, Whipple (16) showed that

$$\frac{\partial C_g}{\partial t} = D_b \frac{\partial^2 C_g}{\partial x^2} + \frac{D_g}{K\delta}\frac{\partial C_g}{\partial y} \quad \text{for } y = \delta,\ 0 < x < L \quad [2]$$

was the single homogeneous boundary condition. The flow into the grain is given by the usual flux condition

$$q_g = -D_g \left.\frac{\partial C_g}{\partial y}\right|_{y=\delta} \quad [3]$$

These equations are generally solved for an infinite source condition expressed by

$$C(0,y,t) = K\alpha_0 \quad [4]$$

or a finite source condition expressed by

$$C(x,y,0) = \nu\delta(x) = \int_0^\infty \int_0^L C(x,y,t)\,dx\,dy \quad [5]$$

where α_0 is the bulk terminal solid solubility of the solute in the solvent, K is the grain boundary segregation factor, $\delta(x)$ is the Dirac delta function, and ν is the surface density of the solute. The conditions expressed by Eq. [4] and [5] are met both in the boundary and grain and are referred to extensively throughout this paper as infinite and finite source conditions, respectively. The common sink boundary conditions are zero flux, expressed by

$$\left.\frac{\partial C(x,y,t)}{\partial x}\right|_{x=L} = 0 \quad [6]$$

or an infinite sink expressed by

$$C(L,y,t) = 0 \quad [7]$$

As for the source conditions, these sink conditions expressed by Eq. [6] and [7] are met both in the boundary and in the grain and are extensively referred to as zero and infinite sink conditions, respectively. Even though the surface concentration is pinned at zero at $x = L$ for an infinite sink, diffusant can still accumulate on the surface. This is possible at short times by rapid surface diffusion away from the boundaries. At longer times, the diffusant exiting from the grain boundaries must be removed for an infinite sink condition. Nelson and Holloway (10) have shown that oxidation can effectively remove material from the boundary and allow it to accumulate on the surface while maintaining an infinite sink boundary condition.

Another boundary condition often encountered is that of a finite sink, *e.g.*, when a submonolayer of material builds up on the surface of a solid as defined mathematically below. This often occurs since the free energy of mixing lowers the system free energy thereby causing diffusion, but without a heat of chemical reaction or strain energy term, the system free energy is not reduced by multilayer accumulation. Thus the surface is often saturated at approximately a monolayer. A finite boundary condition is difficult to treat rigorously because of coupling between bulk, grain boundary, and surface diffusion. For Type C kinetics, only grain boundary and surface diffusion coupling must be considered, and Hwang and Balluffi (5, 6) have done so by writing equations like Eq. [2] for both the grain boundary and the surface regions [but with $D_b/\delta^{-1}(\partial C_g/\partial y) = 0$]. The boundary conditions for a finite sink are

$$C_b(L,t) = C_s(0,t), \quad \delta D_b \frac{\partial C_b(x,t)}{\partial x} = \gamma D_s \frac{\partial C_s(y,t)}{\partial y} \quad [8]$$

for $x = L$, $y = 0$ and

$$\left.\frac{\partial C_s(y,t)}{\partial y}\right|_{y=d/2} = 0 \quad [9]$$

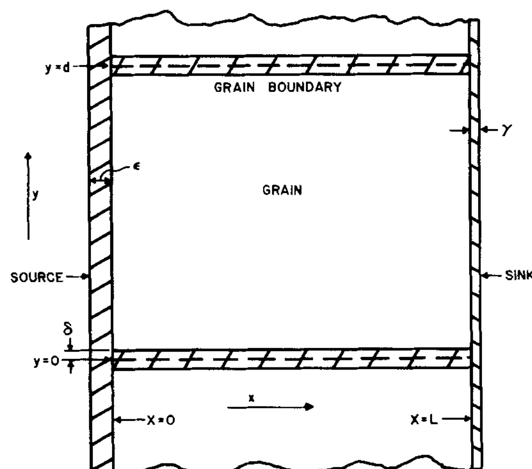

Fig. 1. Schematic representation of a thin film with grain boundaries.

The finite sink boundary condition has not been solved for Type B kinetics. At times a zero sink may be a good approximation to a finite sink boundary condition, as will be discussed. Finally, all of the above treatments assume that for both the boundary and grain

$$C(x,y,t) = 0, \text{ for } 0 < x < L, \ 0 < y < d/2, \ t = 0 \quad [10]$$

Nonzero initial concentration profiles have not been treated, even with approximate solutions. A nonzero initial concentration can easily occur during sample preparation and can have significant impact on data analysis, as will be discussed.

Type C Kinetics

Type C kinetics, where bulk transport is negligible, is the simplest case for data analysis, and experimental conditions should meet this criterion when possible. Solutions for infinite source and zero or infinite sink boundary conditions can both be adapted from solutions given by Crank (20) for diffusion in a plane sheet. For

$$\left.\frac{\partial C_b(x,y,t)}{\partial x}\right|_{x=L} = 0$$

i.e., a zero sink boundary condition, Crank gives

$$\frac{C_b(L,0,t)}{K\alpha_0} = 1 - \frac{4}{\pi}\sum_{n=0}^{\infty}\frac{(-1)^n}{(2n+1)} \exp\left(-\frac{D_b(2n+1)^2\pi^2}{L^2}t\right) \quad [11]$$

The shape of Eq. [11] is shown in Fig. 2 (plot C), which can normally be determined by evaluating only ~5 terms in the summation. To get the average concentration at $x = L$, the concentration, C_b, must be multiplied by the fractional cross-sectional area of the grain boundaries at $x = L$.

Crank (20) also gives the total surface concentration of material at $x = L$, Q, for an infinite sink as

$$\frac{Q}{K\alpha_0 L} = \frac{D_b t}{L^2} - \frac{1}{6} - \frac{2}{\pi^2}\sum_{n=1}^{\infty}\frac{(-1)^n}{n^2} \exp\left(-\frac{D_b n^2\pi^2}{L^2}t\right) \quad [12]$$

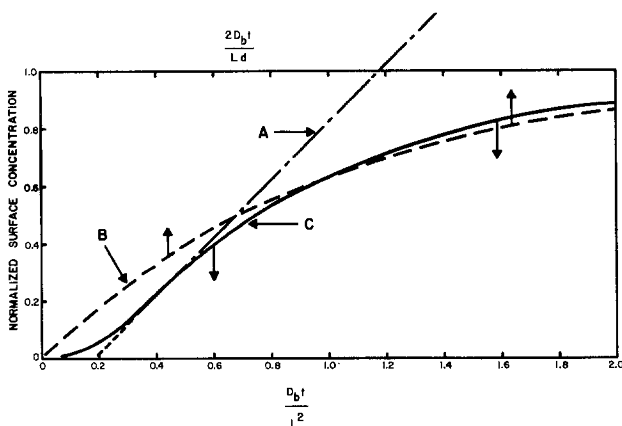

Fig. 2. Surface concentration of material *vs.* dimensionless time parameters. A, Plot for infinite source-infinite sink boundary conditions as discussed for Eq. [12]. B, Plot for infinite source-finite sink boundary conditions as discussed for Eq. [17]. C, Plot for infinite source-zero sink boundary conditions as discussed for Eq. [11].

where Q is the total amount of material transported to the sink surface region. Nelson and Holloway (10) have applied Eq. [12] to the diffusion of Cr in Au and have shown that a time-of-penetration test may be used to determine D_b. For $t >> L^2/\pi^2 D_b$, Eq. [12] has an intercept (for $Q = 0$) on the time axis, t_I, of

$$t_I = \frac{L^2}{6D_b} \quad [13]$$

and by simple rearrangement, D_b can be calculated from such an intercept. Equation [13] applies only to Type C kinetics; as is shown below, such an approach can also be used for Type B kinetics with corrections for grain boundary leakage. For an infinite sink boundary condition at $x = L$, the accumulated surface concentration increases linearly with time, as shown in Fig. 2, and the slope can also be used to determine D_b. It should be noted, however, that if a surface analytical technique with a limited detection depth is used, the detected surface concentration may appear to saturate when the thickness of diffusant at the sink becomes greater than the detection depth, even though an infinite sink boundary condition is appropriate. Care must be taken in that the apparent saturation should not be confused with the real saturation effect for zero sink, finite sink, or finite source boundary conditions.

For the case of a finite sink with a finite or infinite source boundary conditions, the solution of Hwang and Balluffi (5,6) must be used. For an infinite source boundary condition, they show that the concentration on the surface at $x = L$ is given by

$$C_s(L,y,t) = K_s\alpha_0\left[1 - 2\sum_{n=1}^{\infty}\exp\left(-\frac{\alpha_n^2 D_b t}{L^2}\right)\frac{HF\cos\{\alpha_n F(1-2y/d)\}}{\alpha_n\{(1+H)F\sin(\alpha_n)\cos(\alpha_n F) + (1+HF^2)\cos(\alpha_n)\sin(\alpha_n F)\}}\right] \quad [14]$$

where K_s is the surface segregation coefficient and

$$H = \frac{2K_b\delta L}{K_s\gamma d}, \quad F = \frac{D_b d^2}{4L^2 D_s} \quad [15]$$

and α_n are the roots of

$$HF\cos\alpha\cos(\alpha F) - \sin\alpha\sin(\alpha F) = 0 \quad [16]$$

Equation [16] is difficult to solve therefore Hwang and Balluffi simplified Eq. [14]. Their derivation is complicated, therefore, it will be sufficient to note that by assuming rapid surface diffusion (*i.e.*, $D_s t >> d^2/4$) and a greater surface capacity (γd) than grain boundary capacity ($2\delta L$, *i.e.*, $H << 1$), Eq. [14] becomes

$$C_s(L,t) = K_s\alpha_0\left(1 - \exp\left[-\frac{2D_b t}{dL}\right]\right) \quad [17]$$

where it is assumed that $2\delta = \gamma$ and $K_b = K_s$. This curve is shown in Fig. 2 and the difference in shape is not large between zero and finite sink boundary conditions. The most distinguishable feature lies in the fact that for $H \gtrsim 1$, Eq. [11], [12], and [14] predict an initial period where the concentration at the surface $x = L$ is near zero. As the surface capacity becomes large compared to the grain boundary capacity this delay becomes much less prominent and is not noticeable for $H << 1$. The delay in the surface appearance of the diffusing species results from the time required to establish a "steady-state" concentration profile through the film when the initial distribution is zero ($C(x,y,0) = 0$). If the initial distribution is instead

$$C_b(x,y,0) = 1 - x/L \quad [18]$$

the initial transient for curves A and C in Fig. 2 will not be observed and the data will be described well

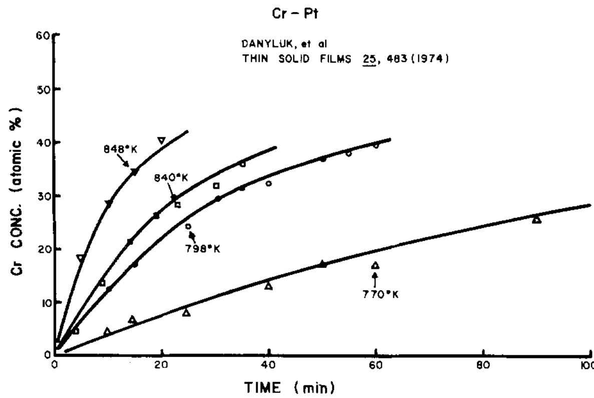

Fig. 3. Chromium surface concentration *vs.* time at various temperatures. The solid lines are fitted exponential curves with characteristic times reported in Table I.

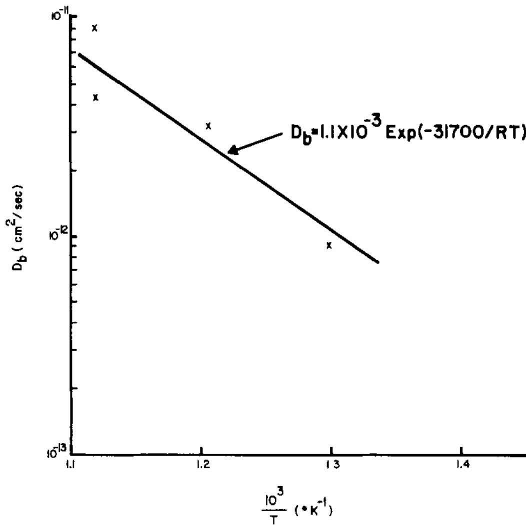

Fig. 4. Grain boundary diffusion coefficient *vs.* reciprocal temperature for chromium in platinum.

by an exponential curve like Eq. [17]. Therefore, care must be taken to identify the proper sink boundary condition and the proper analysis.

Equation [17] can be applied to data for chromium diffusing in platinum as reported by Danyluk *et al.* (12). In this case, the authors report a grain size of ≈1000A, therefore $H \approx 2$ and it is questionable if Eq. [17] should apply. However no chromium was detected on the surface at zero time and no time delay was observed in the appearance of chromium on the surface, which suggests Eq. [17] is applicable. Data for each temperature were fitted to an exponential curve with a characteristic time, τ_o, as shown in Fig. 3. Table I shows the D_b calculated using Eq. [17]. These coefficients are plotted *vs.* T^{-1} in Fig. 4 and the best fit data are

$$D_b = 1.1 \times 10^{-3} \exp(-31{,}700/RT)$$

and

$$\delta D_b = 2.8 \times 10^{-11} \exp(-31{,}700/RT) \qquad [19]$$

where δ is assumed to be 2.5A in Eq. [19]. This pre-

Table I. Time constant and calculated grain boundary diffusion coefficients for Cr in Pt

T(°K)	τ_o(min)	D_b(cm²/sec)	δD_b* (cm³/sec)
848	11	9.1×10^{-12}	2.28×10^{-19}
840	23	4.3×10^{-12}	1.08×10^{-19}
798	31	3.2×10^{-12}	8.0×10^{-20}
770	110	9.1×10^{-13}	2.28×10^{-20}

* δ = 2.5A.

exponential factor is a factor of 10 lower, and the activation energy is lower (32 *vs.* 38 kcal/mole) than reported by Danyluk *et al.*, based on a percent diffusion test. Numerical calculations by Hwang and Balluffi have shown that Eq. [17] deviates from Eq. [14] for $H \gtrsim 1$, therefore the coefficient in Eq. [19] may be low by a factor of 2. However in the limit of $H >> 1$, Eq. [17] approaches Eq. [11] which is controlled by an exponential with an argument of D_bt/L^2 rather than $2D_bt/Ld$ in Eq. [17]. For the experimental data under discussion, the variation from L^2 to $Ld/2$ results only in a factor of 4 difference, therefore Eq. [19] must be less than a factor of 4 in error.

Type B Kinetics

Type B kinetics are much more difficult to describe due to leakage of material from the grain boundary and surface to the bulk. As pointed out earlier, Gilmer and Farrell (8,9) have described exact solutions for an infinite source and zero or infinite sink boundary conditions but their exact solution is difficult to use. Wuttig and Birnbaum (13) have given solutions for Type B kinetics using Eq. [2] and [3] where Eq. [3] was approximated by

$$\left.\frac{\partial C_g(x,y,t)}{\partial y}\right|_{y=\delta} = \frac{C_g(x,y_m) - C_g(x,\delta,t)}{y_m - \delta} \qquad [20]$$

Wuttig and Birnbaum (13) chose $y_m = d/2$ and $C(x,y_m) = 0$ for their analysis, but Holloway *et al.* (1) found that this approximation caused such low grain boundary leakage that it reduced to Type C kinetics. Selecting y_m based on the product of D_g and t_o (the maximum experimental time) yielded curves closer to experimental data, but no general scheme was developed to select y_m. It is possible to methodically select y_m, as shown below.

To generally select y_m, the amount of material lost from the boundary to the grain is first determined by integrating over y, then the total amount of material lost to the bulk is determined by integrating the flux, defined by Eq. [20], over time. Since these two quantities must be equal, they are equated to determine y_m. Assume that the concentration in the bulk is given by a complementary error function (20), *i.e.*

$$C_g(x,y,t) = \alpha_o \operatorname{erfc}([y - \delta]/2\sqrt{D_gt}) \quad \text{for } y > \delta \qquad [21]$$

where $C_b(x,\delta,t)$ has been replaced with a time independent concentration, α_o. The total amount of material lost to the bulk at time t is given by

$$Q = \int_\delta^{y_m} \alpha_o \operatorname{erfc}([y - \delta]/2\sqrt{D_gt})\,dy$$

$$\simeq \int_0^\infty \alpha_o \operatorname{erfc}(y/2\sqrt{D_gt})\,dy \qquad [22]$$

since in Type B kinetics, the diffusion fields from adjacent grain boundaries do not overlap. During an experiment of length, t_o

$$Q = 2\alpha_o\left(\frac{D_gt_o}{\pi}\right)^{1/2} \qquad [23]$$

is lost to the bulk. From Eq. [20] the amount lost to the bulk can also be determined by integrating the flux, $-D_g(\partial C_g/\partial y)$, over time

$$Q = \int_0^{t_o} D_g\left[\frac{C_g(x,\delta,t) - C_g(x,y_m)}{y_m - \delta}\right]dt \qquad [24]$$

and if it is assumed that $C_g(x,\delta,t)$ is α_o independent of time[1] and $C_g(x,y_m) = 0$, then

[1] Setting $C_g(x,\delta,t) \sim \alpha_o$ is not as severe an assumption as it might appear. This overestimates the amount of material lost to the bulk in both the integration over y (Eq. [23]) and over time (Eq. [25]). These overestimates tend to cancel one another yielding a good value for y_m.

$$Q = D_g \left(\frac{\alpha_o}{y_m - \delta} \right) t_o \qquad [25]$$

Equating Eq. [23] and [25] yields

$$y_m = \left(\frac{\pi D_g t_o}{4} \right)^{1/2} + \delta \qquad [26]$$

which may be applied to Wuttig and Birnbaum's expressions for various source and sink boundary conditions.

To check the validity of this value for y_m, it is used to calculate the surface concentration from Wuttig and Birnbaum's expression for an infinite source and sink

$$\frac{Q}{K\alpha_o L} = \frac{k/n}{\sinh (k/\eta)} \left[\eta^2 t + \eta^2/2k^2 - \eta/2k \coth (k/\eta) + \frac{2\pi^2\eta}{k} \sinh (k/\eta) \sum_{j=1}^{\infty} \frac{(-1)^{j-1} j^2}{\xi_j^2} \exp (-\xi_j \eta^2 t) \right] \qquad [27]$$

where

$$k^2 = \frac{D_g}{y_m\delta}, \quad \eta^2 = \frac{D_b}{L^2}, \quad \xi_j = (j^2\pi^2 + k^2/\eta^2) \qquad [28]$$

Equation (27) is compared to experimental data for chromium diffusing in gold (1, 10) in Fig. 5. The dashed line is for $D_g = 0$, *i.e.*, Type C kinetics, whereas the solid and dot-dash line were calculated using Eq. [26] and [27]. Since the calculated curves agree well with the experimental data, the approximation for y_m is considered satisfactory.

With this expression for y_m, the Wuttig and Birnbaum expressions may be applied to Type B kinetics. Generally only about five terms in the summation in Eq. [27] need be evaluated, thus it can be solved without a digital computer. In addition, the transition between Type B and C kinetics can be investigated with this formalism, and it was found that Type B kinetics apply for $y_m > 2\delta$.

Equation [26] can also be used to develop a time of penetration test to determine D_b, even for Type B kinetics. For $t >> \eta^{-2}$, Eq. [27] reduces to

$$\frac{Q}{K\alpha_o L} = \frac{k/\eta}{\sinh (k/\eta)} \left[\eta^2 t + \eta^2/2K^2 - \frac{\eta}{2K} \coth (k/\eta) \right] \qquad [29]$$

which has a time axis intercept, t_I, for $Q = 0$ of

$$t_I = \frac{\coth (k/\eta)}{2k\eta} - \frac{1}{2k^2} \qquad [30]$$

Equation [30] can therefore be used to calculate D_b from a time of penetration test. However, Eq. [30] can be simplified in some cases by noting that for $k/\eta < \pi/4$, $\coth (k/\eta)$ is given by

$$\coth (k/\eta) = \left[\frac{k}{\eta} - 1/2(k/\eta)^3 + 2/5(k/\eta)^5 \ldots \right]^{-1} \qquad [31]$$

and neglecting terms higher than cubic, Eq. [26], [28], and [30] may be combined to yield

$$D_b = \frac{L^2}{6t_I} + \frac{D_g L^2}{3y_m\delta} \qquad [32]$$

Equation [32] may be applied to literature data reported by McGuire *et al.* (14) for gold diffusing through platinum. The ratios of the gold 2111 eV to the platinum 1967 eV derivative Auger peak heights are shown in Fig. 6 *vs.* time. In this case, 0.55 μm of platinum was electroplated on 0.25 mm of gold, therefore the source was infinite. Sputter profiling showed a heavy concentration of gold on the platinum surface, therefore the boundary condition at the sink, $x = L$, will be taken as infinite. The time intercepts for $Q = 0$ are shown in Fig. 6 and tabulated in Table II. The value for lattice diffusion of gold in platinum reported by Bolk (21) is used in Eq. [32] ($D_g = 0.33 \exp [-63{,}000/RT]$). The values of D_b are tabulated in Table II and plotted *vs.* T^{-1} in Fig. 7. A best fit to the data yields

$$D_b = 0.018\, e^{-38{,}000/RT} \quad \text{or} \quad \delta D_b = 4.5 \times 10^{-9}\, e^{-38{,}000/RT} \qquad [33]$$

where $\delta = 2.5$Å. With this value of D_b, $k/\eta \sim 0.5$ which satisfies the approximation made to write Eq. [31] and [32]. The activation energy of 38 kcal/mole is higher than that reported by Change and Quintana (22) for the appearance of gold on the platinum surface. The difference in activation energy has been explained by the presence of antimony and potassium in the films studied by McGuire *et al.* (14). McGuire showed that antimony segregated to the surface. therefore it almost certainly also segregated to the grain boundaries and probably changed the kinetics of transport. This is discussed further in Ref. (14).

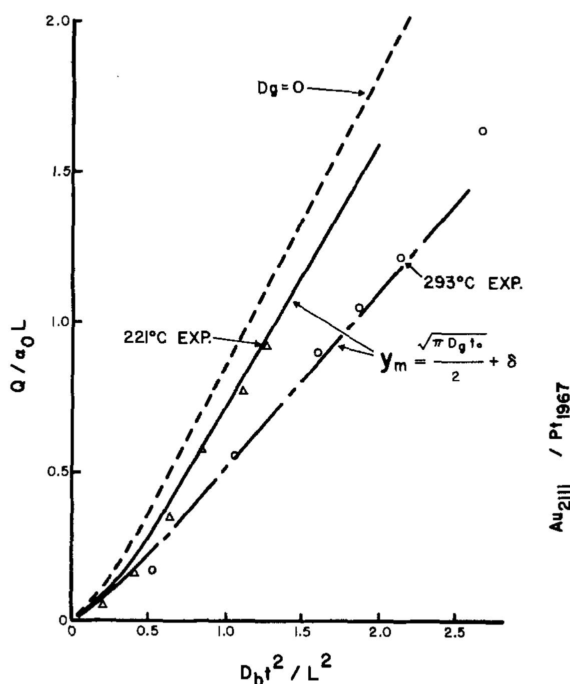

Fig. 5. Dimensionless parameter plot of the accumulation of chromium on gold surface [see Ref. (1) and (10) for experimental details]. Note that grain boundary leakage causes the data to deviate from the Type C kinetic curve (designated by $D_g = 0$), but by calculating y_m from Eq. [26], Eq. [27] can be corrected for the grain boundary leakage effect.

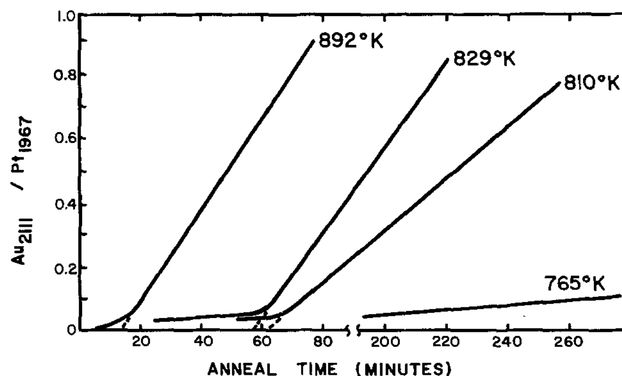

Fig. 6. Gold to platinum Auger peak height ratios vs. time at various temperatures.

Table II. Time intercepts and grain boundary diffusion coefficients for Au in Pt

T(°K)	t_I(sec)	D_b(cm²/sec)	δD_b* (cm³/sec)	t_o(sec)
892	972	6.3×10^{-11}	1.6×10^{-15}	4,800
829	3,380	1.4×10^{-11}	3.4×10^{-19}	7,200
810	3,260	7.8×10^{-12}	1.9×10^{-20}	9,600
765	~11,700	1.9×10^{-12}	4.7×10^{-20}	16,800

* δ = 2.5A.

Summary and Conclusion

Although grain boundary diffusion to the surface of solids is complicated by coupling between grain boundary, surface, and bulk transport, numerical exact analytic, and approximate analytic solutions can now describe the variations in concentration of diffusing species. Because numerical and exact analytic solutions are not always easy to use, approximate solutions have been developed which involve, at the most, evaluating the first few terms of an infinite sum. For Type C kinetics where bulk transport may be neglected, easily manipulated exact solutions exist for infinite source and zero or infinite sink boundary conditions. A good approximate solution exists for an infinite or finite source and finite sink boundary conditions, where the capacity of the grain boundary is much less than that of the surface. This solution was used to show that D_b for chromium in platinum is given by $1.1 \times 10^{-3} \exp(-31{,}700/RT)$.

For Type B kinetics where bulk transport is significant, a general method for approximating the flux of material into the grain was developed. With this flux approximation, good expressions are available to describe the concentration both for infinite or finite source and for zero or infinite sink boundary conditions. A method for determining D_b from a time-of-penetration test was developed for Type B kinetics, and was applied to gold diffusing in platinum. For this system, D_b was found to equal $0.018 \exp(-38{,}000/RT)$.

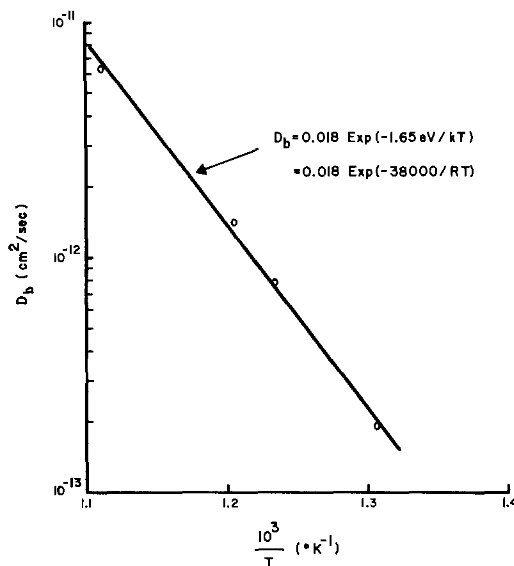

Fig. 7. Grain boundary diffusion coefficient *vs.* reciprocal temperature for gold in platinum.

Acknowledgment

Detailed discussions with H. S. Levine are greatly appreciated. This work was supported by the U.S. Department of Energy.

Manuscript submitted April 10, 1978; revised manuscript received June 19, 1978.

Any discussion of this paper will appear in a Discussion Section to be published in the June 1979 JOURNAL. All discussions for the June 1979 Discussion Section should be submitted by Feb. 1, 1979.

Publication costs of this article were assisted by Sandia Laboratories.

REFERENCES

1. P. H. Holloway, D. E. Amos, and G. C. Nelson, *J. Appl. Phys.*, **47**, 3769 (1976).
2. D. Gupta, D. R. Campbell, and P. S. Ho, To be published.
3. F. Wehner, "Methods of Surface Analysis," A. W. Czanderna, Editor, chap. 1, Elsevier, New York (1975).
4. J. W. Coburn and E. Kay, *Crit. Rev. Solid State Sci.*, **4**, 561 (1974).
5. J. C. M. Hwang, Ph.D. Thesis, Cornell University, Ithaca, New York (1977).
6. J. C. M. Hwang and R. W. Balluffi, *J. Appl. Phys.*, In press.
7. L. G. Harrison, *Trans. Faraday Soc.*, **57**, 1191 (1961).
8. G. H. Gilmer and H. H. Farrell, *J. Appl. Phys.*, **47**, 3792 (1976).
9. G. H. Gilmer and H. H. Farrell, *ibid.*, **47**, 4373 (1976).
10. G. C. Nelson and P. H. Holloway, "Surface Analysis Techniques for Metallurgical Applications," ASTM, STP 596, p. 68, American Society for Testing and Materials, Philadelphia (1976).
11. P. M. Hall and J. M. Morabito, *Surf. Sci.*, **59**, 624 (1976).
12. S. Danyluk, G. E. McGuire, K. M. Koliwad, and M. G. Yang, *Thin Solid Films*, **25**, 483 (1974).
13. M. Wuttig and H. K. Birnbaum, *Phys. Rev.*, **147**, 495 (1966).
14. G. E. McGuire, W. R. Wisseman, and P. H. Holloway, *J. Vac. Sci. Technol.*, In press.
15. J. C. Fisher, *J. Appl. Phys.*, **22**, 74 (1951).
16. R. T. P. Whipple, *Philos. Mag.*, **45**, 1225 (1954).
17. T. Suzuoka, *Trans. Jpn. Inst. Met.*, **2**, 25 (1961); *J. Phys. Soc. Jpn.*, **19**, 839 (1964).
18. H. S. Levine and C. J. MacCallum, *J. Appl. Phys.*, **31**, 595 (1960).
19. P. G. Shewmon, "Diffusion in Solids," McGraw Hill, New York (1963).
20. J. Crank, "Mathematics of Diffusion," Oxford University, Fair Lawn, N.J. (1956).
21. A. Bolk, *Acta Metall.*, **9**, 643 (1961).
22. C. C. Chang and G. Quintana, *Thin Solid Films*, **31**, 265 (1976).

X-Ray Diffraction Topography and Crystal Characterization of GaN Epitaxial Layers for Light-Emitting Diodes

A. Shintani,* Y. Takano, S. Minagawa,* and M. Maki

Hitachi Limited, Central Research Laboratory, Kokubunji, Tokyo 185, Japan

Gallium nitride is a wide bandgap semiconductor which permits realization and performance of light-emitting diodes (LED's) generating green (1, 2), blue (3-6), yellow (4, 5, 7), red (8), and violet (9) light. To date, these GaN LED crystals grown on sapphire substrates have been electrically characterized by estimation of their free electron concentrations and Hall mobilities (10). The crystals have also been optically evaluated from near gap emissions in their photoluminescences (11-13) and in their cathodoluminescences (14). Crystallographical evaluation using hot phosphoric acid was recently studied for undoped and LED crystals (15, 16). However, the etching technique has the essential disadvantage that it destroys the subject crystal.

Here, x-ray diffraction topography and the rocking-curve technique were applied to evaluation of GaN crystal layers. As a result, undoped and LED GaN crystals could be characterized by these x-ray diffraction techniques.

Epitaxial GaN crystals employed in the study were grown on {0001} and {$1\bar{1}02$} oriented sapphire substrates using a conventional chemical vapor deposition technique (4, 15). The LED crystals consisted of undoped (50-80 μm in thickness) and Zn-doped layers (10 μm). The x-ray diffraction topography utilized was the oscillation method using monochromatic divergent beams proposed by Kohra and Takano (17). In the present study, Cu Kα x-ray beams monochromatized by a curved Si single crystal were used. Distribution of x-ray diffraction intensity (rocking curve) was also measured to examine crystalline quality using a (0006) diffraction plane. Furthermore the crystal surface morphology was microscopically observed to investigate the correlation between the topographs and crystal growth patterns.

Generally, undoped GaN layers are higher than 10^{18} cm^{-3} in carrier concentration with n-type conducting characteristics due to native donors. Here, crystalline qualities were compared for undoped crystals (10-80 μm in thickness) with carrier concentrations of 10^{18} and 10^{20} cm^{-3}. In the case of crystals with carrier concentrations of 10^{19}-10^{20} cm^{-3}, their crystal defects are higher than 10^6 cm^{-2} in density at the crystal surfaces (15). An x-ray topograph of this high carrier concentration crystal showed no distinct pattern, as shown in Fig. 1, even when the

* Electrochemical Society Active Member.

Key words: crystalline quality, carrier concentrations, surface morphology.

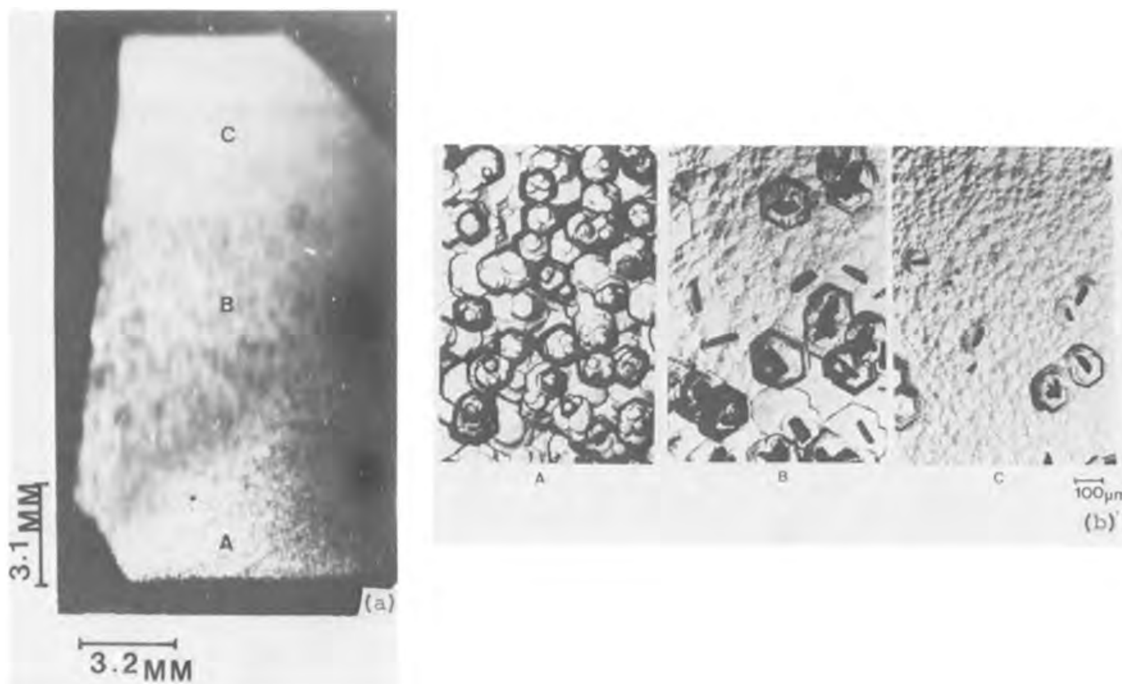

Fig. 1. X-ray diffraction topograph of an undoped GaN {0001} crystal with a carrier concentration of 7×10^{19} cm^{-3} (left) and crystal surface morphologies (right). Photographs A, B, and C of Fig. 1(b) correspond to the A, B, and C regions in the topograph, respectively.

resolution of the apparatus was improved. Careful observation of the topograph notes that the partial region, designated by A in Fig. 1(a), shows a relatively distinct diffraction pattern rather than the other regions marked by B and C. Differences in surface morphology were observed among A, B, and C regions. The relatively good quality regions showed significant hexagonal growth hillocks, as indicated in Fig. 1(b), which reflected the crystal symmetry of GaN. In the other regions, most of the hillocks become smaller in size and vaguer in shape in the order of B and C. Some bar-type crystals were deposited at apexes of some growth hillocks in the B and C regions. On the other hand, undoped crystal with a carrier concentration of 10^{18} cm^{-3} showed a little more distinct patterns in the x-ray topograph, as indicated in Fig. 2(a). The surface of this crystal consists of scale-like and/or spiral hillocks as seen in Fig. 2(b). The spiral hillock found in the figure corresponds to the dark spot indicated by arrow B in Fig. 2(a). The spiral step height was found to be 3000Å. In the case of crystals whose surfaces consist of many large spiral hillocks [see Fig. 4 in Ref. (15)], the step heights were around 300Å.

The difference in crystalline quality described above was more distinct in the x-ray rocking curves (Fig. 3). In the case of the crystal shown in Fig. 1, the peak height of the curve obtained for A region of the crystal was more intense than that for B region. The half-width of the curve for A region is estimated at 32′, while that for B region is done at 48′. These results are consistent with the topograph shown previously. On the other hand, the rocking curve half-width of the crystal shown in Fig. 2 is smaller, around 26′, though there were some crack lines in the crystal as marked by A in Fig. 2(a).

In Fig. 3, the rocking curve obtained for {0001} oriented LED crystal was also compiled. The curves in the figure indicate that the LED crystal is superior in crystalline quality to undoped crystals. The rocking curve for this LED crystal was much narrower, around 12′, in the half-width. This result, however, was apparently inconsistent with the etching results that the doped crystals are poorer in crystalline quality than undoped ones with carrier concentrations of 10^{18} cm^{-3} (15). This difference would be due to the greater sensitivity of hot phosphoric acid etching to Zn precipitates in GaN crystal surface.

{0001} oriented LED crystals showed relatively distinct x-ray topographs, as shown in Fig. 4(a). In the topograph, some hillock-like patterns indicated by arrows B and C were observed. Corresponding to these diffraction patterns, a group of small circularly formed crystals or large unclearly shaped crystals were found on the Zn-doped layer surface. Regular Zn-doped layer surfaces show many large hexagonal pyramids or dishes (15). Comparing with this topograph, the $\{11\bar{2}0\}$ oriented LED crystal showed more

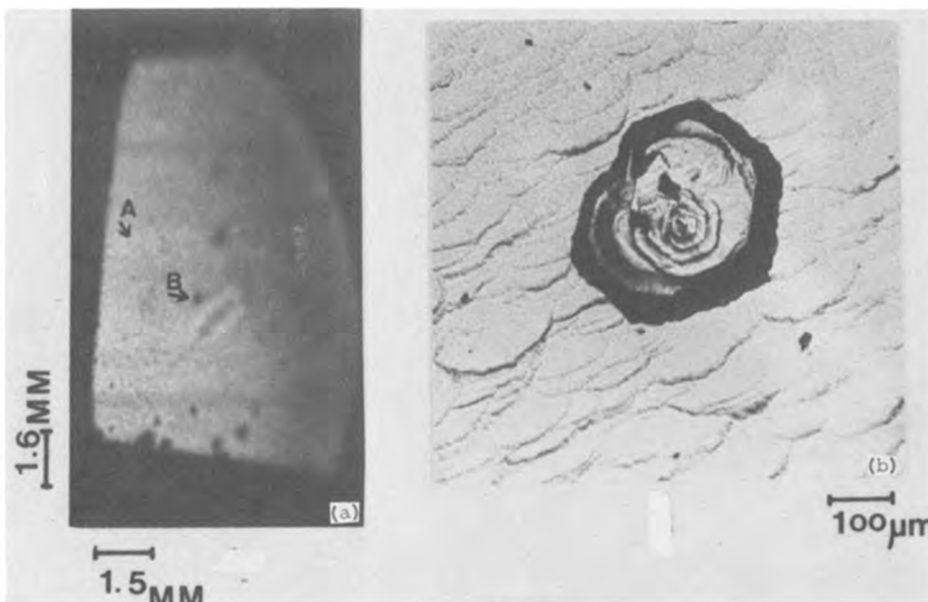

Fig. 2. X-ray diffraction topograph of an undoped GaN {0001} crystal with a carrier concentration of 3×10^{18} cm^{-3} [A, Fig. 2(a)] and crystal surface morphology [B, Fig. 2(b)].

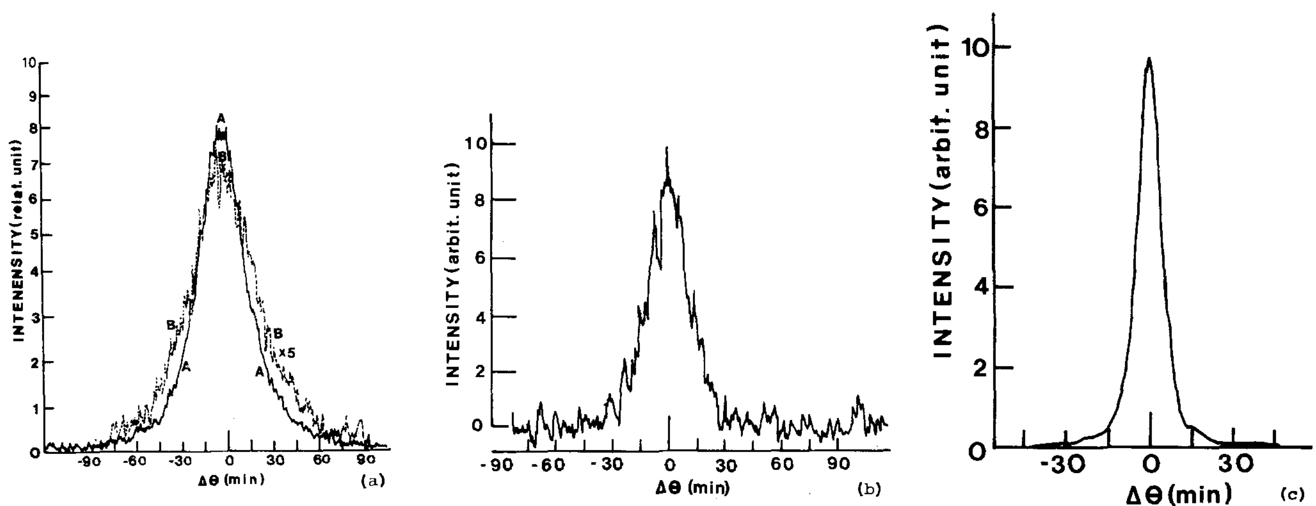

Fig. 3. Rocking curves obtained for the crystals shown in Fig. 1(b) and Fig. 2(b) and a {0001} LED crystal [Fig. 3(c)]. The letters A and B in the Fig. 3(a) curves correspond to A and B regions in the topograph shown in Fig. 1.

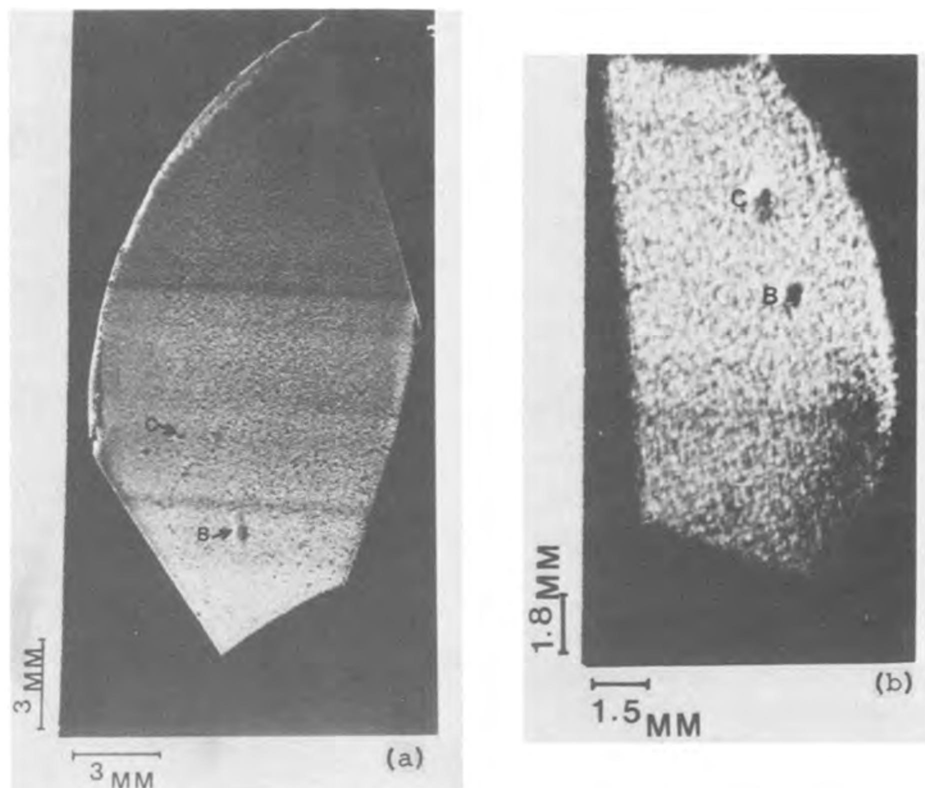

Fig. 4. X-ray diffraction topographs obtained for: (a) {0001} LED crystal; (a) and (b) a {11$\bar{2}$0} LED crystal.

diffuse x-ray diffraction topographs, as indicated in Fig. 4(b). The pattern is considered to be due to poorer crystalline quality than the {0001} LED crystal. In this topograph, two large hillock-like patterns are observed, similarly to the topograph for the {0001} LED crystal [designated by B and C in Fig. 4(b)]. However, this crystal surface morphology is different from the case of the {0001} LED crystal described previously. A lack of crystal growth or crystal misalignment was found in the crystal region showing the hillock patterns.

In summary, the x-ray diffraction topography and rocking curve technique are found useful for characterization of undoped and LED GaN crystals. With respect to undoped crystals, the crystals with the surfaces of scale-like and/or spiral hillocks are better in crystal quality than those with other surfaces, hexagonal and irregular hillocks. Comparing {0001} oriented LED crystals with {11$\bar{2}$0} ones, {0001} LED crystals are apt to grow in better crystalline quality than the other. From the crystallographical viewpoint, {0001} oriented crystals would be preferable for LED's than the other.

Acknowledgment

The authors would like to thank Minoru Wada for his technical assistance in crystal growth.

Manuscript submitted May 2, 1977; revised manuscript received Oct. 10, 1977.

Any discussion of this paper will appear in a Discussion Section to be published in the June 1979 JOURNAL. All discussions for the June 1979 Discussion Section should be submitted by Feb. 1, 1979.

Publication costs of this article were assisted by Hitachi, Limited.

REFERENCES

1. J. I. Pankove, E. A. Miller, and J. E. Berkeyheiser, *RCA Rev.*, **32**, 383 (1971).
2. J. I. Pankove, E. A. Miller, D. Richman, and J. E. Berkeyheiser, *J. Lumin.*, **4**, 63 (1971).
3. J. I. Pankove, E. A. Miller, and J. E. Berkeyheiser, *ibid.*, **5**, 84 (1972).
4. A. Shintani and S. Minagawa, *This Journal*, **123**, 1725 (1976).
5. G. Jacob, R. Madar, and J. Hallais, *Mater. Res. Bull.*, **11**, 445 (1976).
6. J. J. Nickel, *ibid.*, **10**, 1097 (1975).
7. J. I. Pankove, E. A. Miller, and J. E. Berkeyheiser, *J. Lumin.*, **6**, 54 (1973).
8. J. I. Pankove, *ibid.*, **7**, 114 (1973).
9. H. P. Maruska, W. C. Rhines, and D. A. Stevenson, *Mater. Res. Bull.*, **7**, 777 (1972); and H. P. Maruska and D. A. Stevenson, *Appl. Phys. Lett.*, **22**, 303 (1973).
10. M. Ilegems and H. C. Montgomery, *J. Phys. Chem. Solids*, **34**, 885 (1973).
11. M. Ilegems, R. Dingle, and R. A. Loagan, *J. Appl. Phys.*, **43**, 3797 (1972).
12. R. D. Cunnigham, R. W. Brader, N. D. Knee, and D. K. Wicenden, *J. Lumin.*, **5**, 21 (1972).
13. T. Matsumoto and M. Aoki, *Jpn. J. Appl. Phys.*, **13**, 1583 (1974).
14. S. S. Liu, T. R. Gass, and D. A. Stevenson, *J. Electron. Mater.*, **6**, 237 (1977).
15. A. Shintani and S. Minagawa, *This Journal*, **123**, 706 (1976).
16. A. Shintani and S. Minagawa, *ibid.*, **123**, 1575 (1976).
17. K. Kohra and Y. Takano, *Jpn. J. Appl. Phys.*, **7**, 982 (1968).

Study of Crystal Perfection of CVD-Grown α-Al_2O_3 Single Crystals by Transmission X-Ray Diffraction Topography

Krishan Lal and Vijay Kumar

National Physical Laboratory, New Delhi-110012, India

α-Al_2O_3 crystals have been of great importance in modern as well as classical technologies. Because of this, consistent efforts have been made to improve the quality of single crystals of this material. More recent applications in the field of lasers and microelectronic devices utilizing single crystal α-Al_2O_3 substrates have laid great emphasis on the perfection of these crystals. The flame-fusion method (1, 2), Czochralski method (2, 3), flux method (1-3), growth from the vapor phase (1, 3), chemical vapor deposition (CVD) (4), gradient furnace technique (5), and edge-defined film-fed growth (6) are the principal techniques for the growth of these crystals. Detailed investigations of perfection of crystals grown by a number of these techniques have been made by using the etch pit method (7-9), decoration method (10), electron microscopy (11-13), LEED (14), and x-ray diffraction topography (8, 15-19).

In this paper we describe results of the study of perfection of CVD-grown α-Al_2O_3 crystals using transmission x-ray diffraction topography. To compare the perfection of these crystals with the crystals grown by other techniques, a few wafers of crystals grown by Czochralski method were also investigated.

The CVD-grown α-Al_2O_3 crystals used in this investigation were grown in Lexington Laboratories, Lexington, Massachusetts, and were kindly provided by Dr. J. J. Cuomo of IBM Thomas J. Watson Research Center, Yorktown Heights, New York. These wafers were cut perpendicular to [0001] and polished to 1 μ In. finish by Insaco Corporation, Quakertown, Pennsylvania. Special care was taken to ensure that there was no surface damage left on these wafers. Residual surface damage gives strong contrast in topographs. The residual surface damage, if present, is removed by etching in hot orthophosphoric acid until sharp diffraction curves and topographs free of damage marks are obtained. The Czochralski grown wafers were also cut perpendicular to [0001]. The wafers were kindly provided by Dr. P. Thoma of the Physikalisch-Technische Bundensautalt, Braunschweig and Berlin, West Germany. The x-ray diffraction topography camera used in this investigation is similar to a conventional Lang Camera (20) and has been developed in our laboratory (21). A microfocus x-ray generator developed in our laboratory (22) was used as a source of x-rays. In most of these investigations line focus source has been used. Divergence of the exploring x-ray beam in the horizontal plane was about 50 sec of arc and divergence in the vertical plane is 4.5 min of arc for a specimen having vertical dimensions of 1 mm. $CuK\alpha_1$, $MoK\alpha_1$, and $AgK\alpha_1$ radiations have been used. Most of the topographs have been recorded on Ilford L4 nuclear emulsion plates having 50 μm thick emulsion. Kodak Periapical dental x-ray films have been used for preliminary work.

The CVD-grown crystals used in these investigations can be broadly divided into two categories: (*i*) Wafers in which a part of seed is also present. These were particularly chosen to see the perfection of the seed-crystal interface. For convenience we call these type A crystals; and (*ii*) Wafers which were cut away from the seed and had no part of seed contained in their body. For convenience we call these crystals type B crystals. In the following we shall describe separately the results for crystals of type A and B, as well as for crystals grown by the Czochralski method.

As is well known, a good idea about the state of perfection of a crystal wafer can be had from the shape of its diffraction curve (23, 24). The diffraction curves are recorded by observing the diffracted intensity as a function of the angular position of the crystal as it is rotated across the Bragg peak. The detector has a 5 mm wide open window, which is at a distance of 200 mm from the specimen crystal. Before recording a topograph we always recorded a diffraction curve for that reflection.

Key words: crystallography, CVD, x-rays.

Perfection of the CVD-Grown Crystals of Type A

Most of these crystals having a part of the seed in them were found to contain low angle boundaries. Figure 1 shows a typical projection topograph of a crystal of this type. A small nearly circular portion in the center is the part of the seed. As can be seen, the crystal is highly strained. The strain is very large at the crystal-seed interface. Due to strain the topograph of whole of the wafer could not be recorded in one scan. To record this picture we divided the crystal into 3 approximately equal portions which slightly overlapped each other. Topographs recorded for these three regions were put together to get the composite picture shown in Fig. 1.

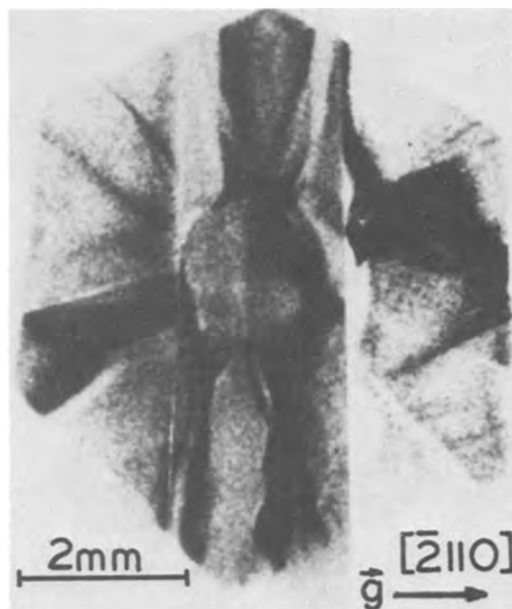

Fig. 1. A typical projection topograph of a CVD-grown α-Al_2O_3 crystal of type A. The flat faces of the wafer were cut parallel to the basal plane (0001). $AgK\alpha$ radiation and a [$\bar{2}$110] diffraction vector are used. The topograph was recorded in three parts, as the crystal was highly strained.

As can be seen, a number of low angle boundaries were present in these crystals. To get more quantitative information about low angle boundaries, diffraction curves were recorded at different regions of the wafer. Figure 2b shows a typical diffraction curve recorded for a region close to the right-hand side of the crystal as in the topograph shown in Fig. 1. In Fig. 2b we see several peaks separated from each other by a few minutes of arc. This is a diffraction curve typical of crystals containing low angle boundaries. For comparison, Fig. 3 shows a typical diffraction curve of a dislocation-free Si single crystal showing well-resolved peaks due to $K\alpha_1$ and $K\alpha_2$ radiations (25). The crystals were aligned for different peaks in Fig. 2b and projection topographs were recorded by scanning the crystals for about 1 mm each time. Figure 2a shows these topographs. It is seen that different regions of the crystal diffract when the alignment is changed from one peak position to another. This shows conclusively the presence of low angle boundaries in this type of wafers. The angle of mis-set between the adjoining grains is of a few minutes of arc. It was futile to look for isolated dislocations in these crystals.

Perfection of CVD-Grown Crystals of Type B

In contrast to the crystals of type A, the crystals of type B were invariably found to be nearly perfect. Figure 4 shows a typical diffraction curve of one of the crystals of this type. Two well-resolved peaks due to $K\alpha_1$ and $K\alpha_2$ components of the characteristic radiations are observed. This can be compared with the diffraction curve of the perfect Si single crystal.

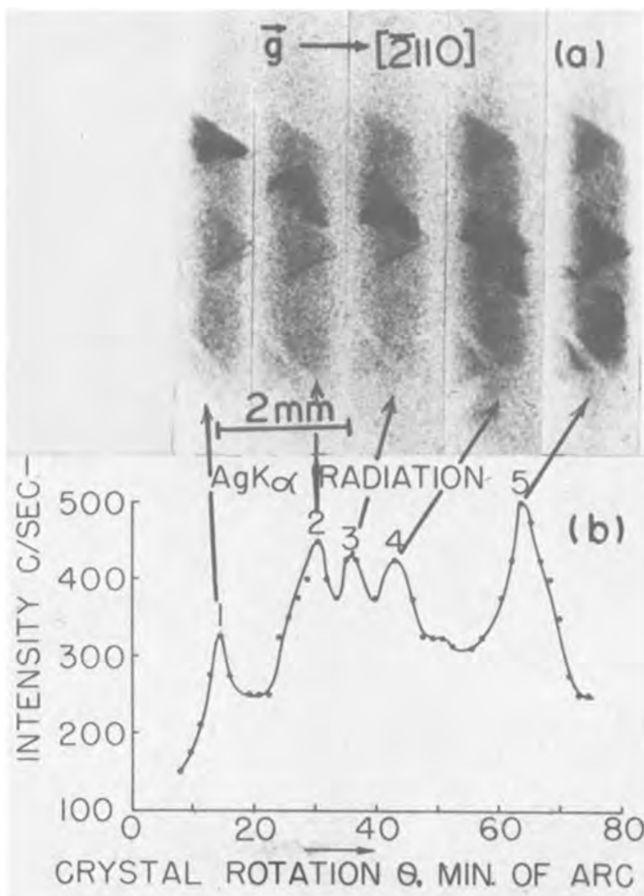

Fig. 2. (a) A typical set of projection topographs of the same CVD-grown single crystal whose topograph is shown in Fig. 1. A [2̄110] diffraction vector and AgKα radiation were used. These topographs correspond to a small region of the crystal whose topograph also appears on the extreme right-hand side in Fig. 1; (b) A typical diffraction curve of this crystal corresponding to Fig. 2a.

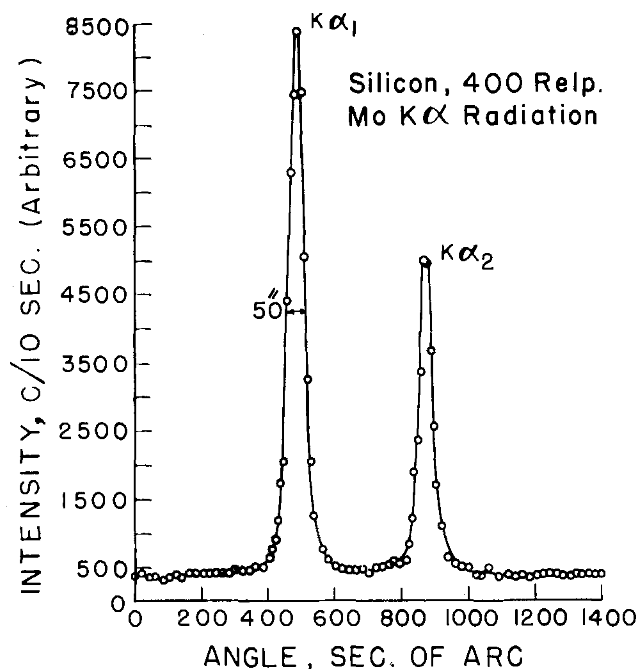

Fig. 3. A typical diffraction curve of a dislocation-free Si single crystal recorded using 400 reflection with MoKα radiation.

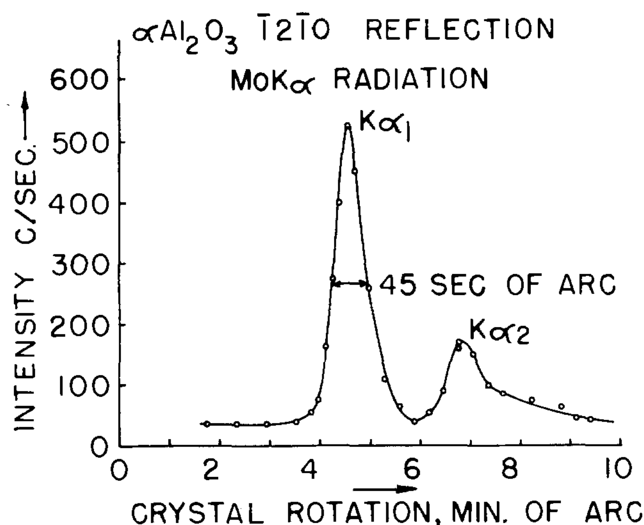

Fig. 4. A typical diffraction curve of a CVD-grown (0001) α-Al_2O_3 single crystal wafer of type B recorded using 1̄21̄0 reflection with MoKα radiation.

None of these crystals were found to contain low angle boundaries. This result is supported by the topographs recorded for these crystals.

Figure 5 shows a few typical topographs of one of the crystals of type B. Except for some regions near the edges, a large portion of the wafers is practically free from crystalline defects. In Fig. 5a we see in the central region several straight lines parallel to [011̄0]. This topograph was recorded with $\vec{g}$ parallel to [2̄110]. To investigate the nature of these lines several topographs were recorded with different diffraction vectors. Figures 5b and 5c show topographs recorded with diffraction vector $\vec{g}$ parallel to [1̄21̄0] and [112̄0], respectively. Using the $\vec{g}\cdot\vec{b}$ analysis criterion we say that the dislocations observed parallel to [011̄0] are of edge type. Their Burgers vector is parallel to <2̄110>. These dislocations vanish in topograph recording using diffraction vectors parallel to [011̄0]. Similarly, some of

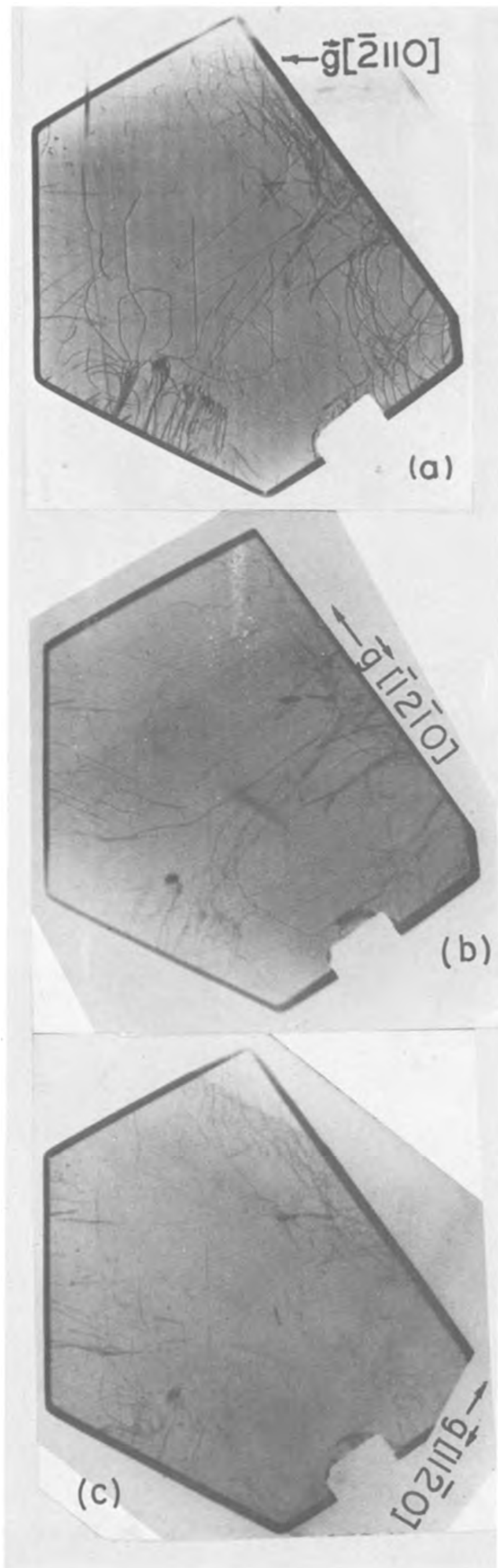

Fig. 5. Projection topographs of a CVD-grown (0001) α-Al_2O_3 single crystal wafer of type B recorded with $MoK\alpha_1$ radiation. Diffraction vectors were parallel to [2̄110], [1̄21̄0], and [112̄0] in (a), (b), and (c), respectively. A typical diffraction curve of this crystal is shown in Fig. 4 for this class of reflections.

the symmetrically equivalent dislocations have been characterized. <2̄110> is known to be a prominent slip direction from the earlier work on slip system of this material (17). Another very important feature of these pictures is that a large area of these crystals is free of dislocations. As we will show subsequently, these crystals can be treated as nearly perfect crystals.

If we look carefully at the dislocation lines in Fig. 5a we see a white halo running along the length of the dislocations. These topographs have been recorded using $MoK\alpha_1$ radiation for which the value of μt is approximately 0.34. A white halo around an edge dislocation can be understood in the following manner. As has been shown in earlier work (26-28), if the diffracting planes are slightly curved, enhancement in diffracted intensity will be observed when the radius of curvature of the diffracting planes $\vec{r}$ points along the direction of diffraction vector $\vec{g}$. When $\vec{g}$ is antiparallel to $\vec{r}$ a reduction in intensity is to be expected. Indeed this criterion has been used to determine the nature of dislocation loops in gadolinium gallium garnet crystals (28). If we use this criterion in the present case we find that the straight dislocations in this case are of vacancy type. Possibly these may have formed just after growth due to condensation of vacancies.

The observed white halo around edge dislocations has been explained on the basis of dynamical contrast due to curvature of lattice planes around the edge dislocations in Fig. 5a. If we use harder radiations, like $AgK\alpha_1$, it should be possible to reduce the value of μt substantially and, therefore, remove the possibility of any dynamical effect. We have recorded topographs with $AgK\alpha_1$ radiation. No dynamical contrast was observed in these topographs.

Another way of testing whether these crystals are nearly perfect is to see whether one can record topographs with predominant dynamical contrast. Such topographs depend predominantly upon dynamic diffraction of x-rays, so that in the crystal the wavefields of the direct and the diffracted x-ray beams are coupled with each other. A defect in the lattice of nearly perfect crystal is expected to break this coupling between the incident and diffracted wave fields in the region surrounding it. Therefore, in this case defects appear as white on black background. We have succeeded in recording transmission topographs of these wafers with dynamical contrast also. In this case we have used $CuK\alpha_1$ radiations so that $\mu t = 3.15$. Figure 6 shows a tyical topograph that was recorded on the

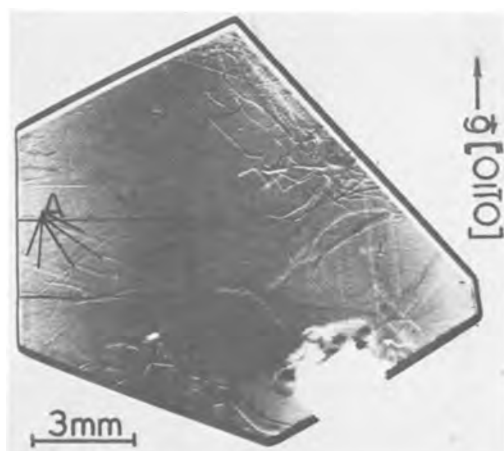

Fig. 6. A typical projection topograph of a CVD-grown α-Al_2O_3 single crystal recorded with $CuK\alpha_1$ radiation and [01̄1̄0] as diffraction vector.

same wafer whose topographs are shown in Fig. 5. This topograph was recorded with $\vec{g}$ parallel to [01$\bar{1}$0]. Here we see dislocation lines appearing as white on a black background. This result supports our conviction that these crystals are nearly perfect crystals. Another interesting feature of this topograph is a few lines observed in the area marked as A. These lines are observed in Fig. 5b also. However, from Fig. 5b one would be tempted to conclude that these are screw dislocations lying in the plane of the wafer, *i.e.*, in the basal plane. However, an examination of these lines in Fig. 6 shows that they do not lie in the plane of wafer but intersect it at an oblique angle. From the observed length of these lines and thickness of the wafers we have estimated the angle between the line vector of these dislocations and the surface of the wafer. It is found to be about 7°, suggesting that these lines lie on a high index plane. This result also shows that the sensitivity of topographs with predominant dynamical contrast is higher than the sensitivity of the normal kinematic topographs.

Study of Crystal Perfection of Czochralski-Grown Crystals

As mentioned earlier, in order to compare the perfection of CVD-grown crystals with that of the crystals grown by other techniques we chose Czochralski-grown crystals. Perfection of Czochralski-grown crystals has been studied earlier (8, 9, 17, 18). Czochralski-grown wafers that we have investigated were in general not as perfect as CVD-grown crystals of type B. Their perfection was generally comparable to that of the CVD-grown crystals of type A. Figure 7 shows a typical diffraction curve of a Czochralski-grown crystal. The presence of several peaks separated by a few minutes of arc from each other is evidence of the presence of low angle boundaries in these crystals. A typical topograph of these crystals is shown in Fig. 8. The crystal was fairly imperfect and, therefore, one full topograph could not be recorded in one scan. The topograph shown in Fig. 8 is in fact the topograph composed of 3 different topographs. The presence of low angle boundaries is very obvious even from this topograph. The upper region of this crystal is not diffracting. However, by suitably tilting the crystal this portion can be made to diffract. These results are similar to those reported earlier (8, 15, 16). Some details of this aspect are reported elsewhere (29).

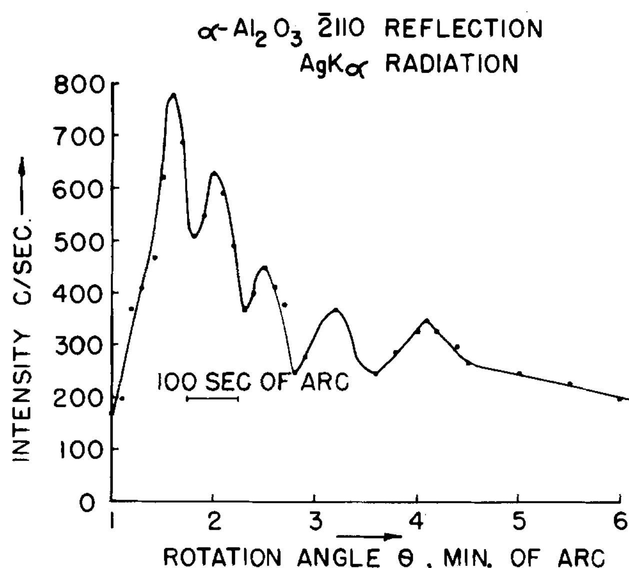

Fig. 7. A typical diffraction curve of a Czochralski-grown (0001)α-Al_2O_3 single crystal wafer recorded using $\bar{2}$110 reflection with AgKα radiation.

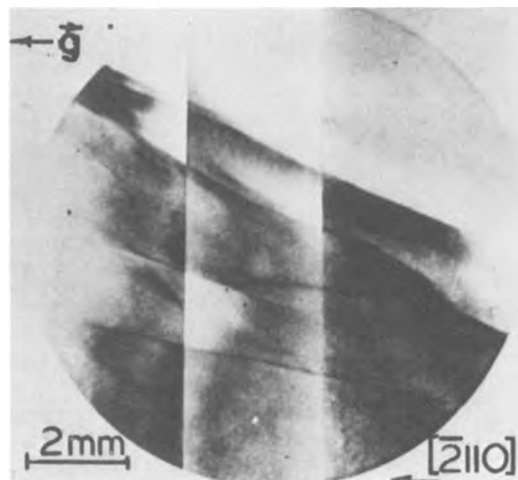

Fig. 8. A typical projection topograph of a Czochralski-grown (0001)α-Al_2O_3 single crystal wafer. [$\bar{2}$110] diffraction vector and AgKα radiation were used. Figure 7 shows a diffraction curve of this crystal.

The present investigation has shown that CVD-grown crystals of α-Al_2O_3 are nearly perfect crystals in which large areas are practically free of dislocations. The perfection is so high that we have observed dislocations with predominant dynamical contrast. These results are consistent with the earlier work that Czochralski- and flame fusion-grown crystals are not very perfect (8, 9, 15-18, 29). In fact, in a study on growth of niobium films on sapphire crystals (30) it has been shown that CVD-grown crystals have much better perfection as compared to perfection of Czochralski- and Verneuil-grown sapphire crystals. This is consistent with the present results. The dislocations near some of the edges apparently are due to instabilities during growth.

Acknowledgment

The authors are grateful to Dr. Ajit Ram Verma for keen interest in this work and constant encouragement.

Manuscript submitted June 3, 1977; revised manuscript received July 16, 1978.

Any discussion of this paper will appear in a Discussion Section to be published in the June 1979 JOURNAL. All discussions for the June 1979 Discussion Section should be submitted by Feb. 1, 1979.

REFERENCES

1. R. A. Laudise, "The Growth of Single Crystals," Prentice Hall, Inc., Englewood Cliffs, N.J. (1970).
2. J. C. Brice, "The Growth of Crystals from Liquids," North Holland Publishing Co., Amsterdam, London (1973).
3. "Crystal Growth," B. R. Pamplin, Editor, Pergamon Press, Oxford (1975).
4. P. S. Schaffer, *J. Am. Ceram. Soc.*, **48**, 508 (1965).
5. D. Viechnicki and F. Schmid, *J. Cryst. Growth,* **11**, 345 (1971).
6. H. E. LaBelle, Jr., *Mater. Res. Bull.*, **6**, 581 (1971).
7. R. C. Linares, *J. Phys. Chem. Solids.*, **26**, 1817 (1965).
8. R. F. Belt and R. C. Puttbach, *Mater. Res. Bull.*, **4**, 403 (1969).
9. C. S. Sahagian and M. Schieber, "Growth of Crystals," Vol. 7, N. N. Sheftal, Editor, p. 209. Consultant Bureau, New York-London (1969).
10. M. O. Kliya and M. A. Chernysheva, *Sov. Phys. Cryst.*, **11**, 564 (1967).
11. C. M. Drum, *Phys. Status Solidi*, **9**, 635 (1965).
12. D. J. Barber and N. J. Tighe, *Phil. Mag.*, **11**, 495 (1965).
13. D. J. Barber and N. J. Tighe, *ibid.*, **14**, 531 (1966).

14. J. M. Charig, *Appl. Phys. Lett.*, **10**, 139 (1967).
15. L. S. Birks, J. W. Hurley, and W. E. Sweeney, *J. Appl. Phys.*, **36**, 3562 (1965).
16. L. K. Walford and G. S. Cargill III, *Mater. Res. Bull.*, **2**, 449 (1967).
17. R. F. Belt, *J. Am. Ceram. Soc.*, **50**, 588 (1967).
18. C. A. May and J. S. Shah, *J. Mater. Sci.*, **4**, 179 (1969).
19. J. L. Caslavsky, C. P. Gazzara, and R. M. Middleton, *Phil. Mag.*, **25**, 35 (1972).
20. A. R. Lang, *J. Appl. Phys.*, **29**, 597 (1958); and in "Modern Diffraction and Imaging Techniques in Material Science," S. Amelineckx, R. Gevers, G. Remant, and J. Landyut, Editors, p. 407, North Holland, Amsterdam (1970).
21. A. R. Verma, K. Lal, D. R. Pahwa, V. Kumar, and K. Aggarwal, *Indian J. Pure Appl. Phys.*, **12**, 350 (1974).
22. K. Lal, V. Kumar, and D. R. Pahwa, To be published.
23. Y. Nakayama, S. Weissmann, and T. Imura, "Direct Observation of Imperfections in Crystals," J. B. Newkirk and J. M. Wernick, Editors, p. 573, Interscience, New York (1962).
24. B. K. Tanner, "X-ray Diffraction Topography," pp. 34, 63, Pergamon Press, Oxford (1976).
25. K. Lal and B. P. Singh, *Solid State Commun.*, **22**, 71 (1977).
26. P. Penning and D. Polder, *Philips Res. Rep.*, **16**, 419 (1961).
27. G. H. Schwuttke and J. K. Howard, *J. Appl. Phys.*, **39**, 1581 (1969).
28. K. Lal and S. Mader, *J. Cryst. Growth*, **32**, 357 (1976).
29. K. Lal, V. Kumar, and A. R. Verma, Paper presented at the International Symposium on Solid State Physics held at Indian Association for Cultivation of Science Calcutta, Jan. 10-14, 1977; *Indian J. Phys.* (1978).
30. J. J. Cuomo and J. Angilello, *This Journal*, **20**, 125, (1973).

DISCUSSION SECTION

This Discussion Section includes discussion of papers appearing in the *Journal of The Electrochemical Society*, Vol. 125, No. 2 and 3, February and March 1978.

Kinetics of the Thermal Oxidation of Silicon in O_2/H_2O and O_2/Cl_2 Mixtures

B. E. Deal, D. W. Hess, J. D. Plummer, and C. P. Ho
(pp. 339-346, Vol. 125, No. 2)

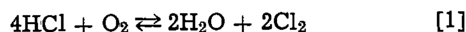

J. Monkowski,[1] R. E. Tressler,[2] and J. Stach:[1] In their paper, Deal *et al.* point out that the predominant reaction governing the gaseous composition of H-Cl-O ambients is

$$4HCl + O_2 \rightleftarrows 2H_2O + 2Cl_2 \quad [1]$$

They further state that the exact equilibrium conditions are not known, but based upon empirical evidence the complete dissociation of HCl occurs at temperatures above 1100°C.

However, thermodynamic data are available in the literature,[3] and calculations of the equilibrium compositions of $HCl/O_2/H_2O$ mixtures have been carried out for various oxidation temperatures.[4] Moreover, the reaction of HCl with O_2 does not "go to completion" anywhere in the range of typical oxidation temperatures (700°-1300°C). Above 1100°C, the HCl concentration (volume percent) is greater than 4 times the Cl_2 concentration when HCl/O_2 mixtures are introduced into the furnace.

The significance of these thermodynamic calculations was demonstrated quite clearly by Tressler *et al.*,[4] who showed that both the enhanced parabolic growth rate and the passivation of ionic sodium correlate well with the partial pressure of Cl_2 (P_{Cl_2}) calculated to be present within the oxidation furnace under equilibrium conditions. They showed that, at 1150°C, the parabolic growth rate is a smoothly increasing function of P_{Cl_2}, regardless of whether HCl/O_2 or Cl_2/O_2 mixtures are introduced into the furnace. In this manner, they showed that HCl and H_2O play insignificant roles in the growth rate enhancement. The amount of Cl_2 was also shown to be the determining factor in the realization of passivation. This was done by comparing passivation data of oxides grown in HCl/O_2 mixtures with data from oxides grown in $HCl/O_2/H_2O$ mixtures. The two sets of data were consistent only when put in terms of P_{Cl_2}.

Deal *et al.* based their conclusions concerning Eq. [1] primarily upon two experiments. In the first, they compared the parabolic growth rates obtained in HCl with those obtained in H_2O. At 1100°C the growth rates of oxides grown in HCl/O_2 mixtures approached those grown in H_2O/O_2 mixtures when the HCl/H_2O ratio (volume fraction introduced into the furnace) was 2. From this correlation, they concluded that the dissociation of HCl increases as the temperature is raised, and reaches completion at temperatures above 1100°C.

In the second experiment, two oxides were grown. For one, a 4% HCl/96% O_2 mixture was introduced into the furnace; for the other, a 2% Cl_2/2% H_2O/96% O_2 mixture was used. Both oxides were found to possess similar growth rate constants. From this fact, Deal *et al.* concluded that Eq. [1] does indeed describe the predominant reaction occurring within the furnace; the HCl does react with the O_2 to produce Cl_2 and H_2O.

Based upon the work of Tressler *et al.*, the correlations seen in the first experiment can be shown to be fortuitous, and the conclusion of the second experiment can be shown to lack substantiation by the data.

Comparing an oxide grown in a particular volume fraction of HCl with an oxide grown in half that volume fraction of H_2O is irrelevant in view of the thermodynamic data calculated by Tressler *et al.* Since the HCl dissociates very little, the comparison should be made for oxides grown in much lower amounts of H_2O.

The data can be rationalized by looking at the temperature dependence of the growth rate enhancement for Cl_2 as well as H_2O. Comparison of Fig. 3 of Deal *et al.* with their Tables I and II shows that at 1000 C H_2O has a much larger effect on the rate constant than Cl_2. However, at 1100°C, Cl_2 has the dominant effect. Therefore, for HCl/O_2 oxidations at 1000°C and below, the growth rate enhancement is due primarily to the small amount of H_2O present

[1] Department of Electrical Engineering, The Pennsylvania State University, University Park, Pennsylvania 16802.
[2] Department of Materials Science and Engineering, The Pennsylvania State University, University Park, Pennsylvania 16802.
[3] "JANAF Thermochemical Tables," 2nd Ed., D. R. Stull and H. Prophet (project directors) Dow Chemical Co. (1971).
[4] R. E. Tressler, J. Stach, and D. M. Metz, *This Journal*, **124**, 607 (1977).

within the furnace. At 1100°C and above, the small amount of Cl_2 present in the furnace has a disproportionately large effect, such that an oxide grown in 10 v/o HCl is nearly as thick as one grown in 5 v/o H_2O (Fig. 9 of paper). The experimental data cited by Tressler *et al.* was obtained at 1100° and 1150°C, where Cl_2 is the dominant species.

For the second experiment, one can only conclude that regardless of whether HCl or a mixture of Cl_2 and H_2O is introduced into the furnace, the equilibrium composition, whatever it may be, is attained. No conclusion can be made concerning the amounts of the gases present or even the types of gases present. The gases HCl, Cl_2, and H_2O may, in principle, not even exist within the furnace in significant quantities. Additional information, such as a thermodynamic analysis, is required to determine the ambient composition.

In fact, the data of Deal *et al.* indicate that equilibrium is not completely atttained. The $Cl_2/H_2O/O_2$ mixture yielded a slightly higher parabolic growth rate than the other mixture. This is understandable due to the effectiveness of Cl_2 and H_2O, as compared to HCl, in enhancing the growth rate. If equilibrium were not attained, the $Cl_2/H_2O/O_2$ mixture would contain more Cl_2 and H_2O than the HCl/O_2 mixture.

Deal *et al.* also noted that introduction of 2% Cl_2 into a 2% H_2O/98% O_2 mixture resulted in the growth of significantly thinner oxides. With the realization that Cl_2 suppresses the amount of H_2O, this result is also reasonable.

In view of the suppression of P_{Cl_2} by H_2O, Deal *et al.* stated that for HCl/O_2 mixtures, an increase in the HCl content would increase the H_2O content, thus suppressing the Cl_2 content. This is not the case; the amount of Cl_2 must equal the amount of H_2O (Eq. [1]), and, in addition, if the HCl/O_2 ratio (volume percent at equilibrium in the furnace) is relatively small, the HCl/Cl_2 ratio remains unchanged regardless of the amount of HCl introduced into the furnace. This can be shown from the equilibrium constant for Eq. [1]

$$K_P = \frac{(P_{Cl_2})^2 (P_{H_2O})^2}{(P_{O_2})(P_{HCl})^4} \qquad [2]$$

Since $P_{Cl_2} = P_{H_2O}$

$$K_P = \frac{1}{P_{O_2}} \left(\frac{P_{Cl_2}}{P_{HCl}}\right)^4 \qquad [3]$$

As long as P_{O_2} remains close to 1 atm, the ratio Cl_2/HCl will not change significantly. This is confirmed in the work of Tressler *et al.* where the ratio Cl_2/HCl is very similar for both 2 and 20 v/o HCl introduced into the furnace.

Over-all, the approach of Deal *et al.* could prove quite fruitful in sorting out the contributions of the various gaseous species present during oxidation. If the oxidation furnace were constructed such that the gases were heated long enough to ensure the attainment of equilibrium, then the thermodynamic analysis of Tressler *et al.* could be used to ascertain the composition of the ambient. In this manner, a direct comparison could be made between the growth of an oxide and the conditions present during its formation.

On Thermally Stimulated Space-Charge Decay in Sn^{2+}-doped Sodium Chloride and Potassium Chloride Crystals

Ah Mee Hor and P. W. M. Jacobs (pp. 430-432, Vol. 125, No. 3)

A. Kessler:[5] The investigation of the "dielectric chaos" should, no doubt, give a clue to the understanding of the space-charge formation, the discharge of ions at the electrodes, etc. But the reproducibility is bad, the peaks are overlapping, and the multitude of processes which might eventually be the cause of the DC are understood only modestly or not at all. Hence only very few papers are found which are devoted exclusively to this problem. Rather, relevant results are found scattered in investigations concerning other questions. Thus, they easily escape one's attention.

Inverted peaks, for instance, are found in CdF_2,[6] spontaneous peaks in Teflon,[7] and in NH_4Cl.[8] In the latter case the cause is roughly understood. It shows, among other things, that the peak can be classified as extrinsic and dependent on the history of the sample. It can be avoided in consequence. But the four peaks observed besides the impurity complex peaks in CdF_2, for instance, are of an intrinsic nature. The two which occur below room temperature are obviously caused by an accumulation of point defects.[9,10] The other two, which occur eventually above the polarization temperature, are attributed to a dissociation of complexes,[10] that is to a similar process as assumed by the authors.

[5] University of Stuttgart, Germany.
[6] A. Kessler, *J. Phys. C: Solid State Phys.*, 6, 1594 (1973).
[7] C. Bucci, R. Fieschi, and G. Guidi, *Phys. Rev.*, 148, 816 (1966).
[8] A. Kessler, *This Journal*, 123, 1239 (1976).
[9] I. Kunze and P. Muller, *Phys. Status Solidi* (a), 13, 197 (1972).
[10] A. Kessler and J. E. Caffyn, *J. Phys. C: Solid State Phys.*, 5, 1134 (1972).

JOURNAL OF THE ELECTROCHEMICAL SOCIETY

ACCELERATED

BRIEF COMMUNICATIONS

DECEMBER

1978

Performance of Synthetical n-$MoSe_2$ in Electrochemical Solar Cells

J. Gobrecht, H. Tributsch, and H. Gerischer*

Fritz-Haber-Institut der Max-Planck-Gesellschaft, Faradayweg 4-6, D-1000 Berlin 33, Germany

The general ability of transition metal dichalcogenides like n-$MoSe_2$ for application as photoanodes or p-WSe_2 as photocathodes in electrochemical solar cells has been demonstrated earlier (1 to 4). In most cases the photocurrent-potential behaviour was rather unsatisfying with respect to the characteristics required for photoelectrochemical energy conversion: The photocurrent increases steadily over a wide potential range without reaching a saturation value. The result is a poor current-voltage output characteristic with low fillfactors in the region of 0.2 to 0.25.

We wish to report new results obtained with synthetic n-type $MoSe_2$ crystals grown by a bromine gas transport technique which exhibit significantly improved behaviour.

The current-potential curve in the dark shows a very asymmetrical shape (Fig. 1) which implies good rectifying properties of the interface. At potentials more positive than 0.55 V vs. SCE a photocurrent starts to flow in base electrolytes such as KCl or H_2SO_4 which causes electrode corrosion by forming Mo(VI) and selenic acid:

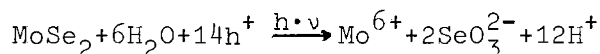

$$MoSe_2+6H_2O+14h^+ \xrightarrow{h\cdot\nu} Mo^{6+}+2SeO_3^{2-}+12H^+$$

This photocurrent reaches a saturation at potentials above 0.9 V vs. SCE.

Flatband potentials were obtained from Mott-Schottky-plots. In base electrolyte it is situated at 0 V vs. SCE. Interestingly, there are redox couples such as I^-/I_2 which shift the flatband-potential to more negative values, probably due to a strong interaction of the I^- ions with the $MoSe_2$ surface. For the investigated system the shift is 300 mV. This is the reason why a photovoltage greater than 0.5 V is obtained with an n-$MoSe_2$/(I^-/I_2)/Pt photocell although the redox potential of the couple is 0.28 V vs. SCE. The decrease of the saturation photocurrent in the redox system I^-/I_2, compare Fig. 1, is caused by the light absorption of the iodine.

The power output characteristic shows a satisfying rectangular shape with a fillfactor of 0.67 (Fig. 2). This indicates that the number of recombination centers in the surface and the space charge layer of the selected samples of $MoSe_2$ is small and therefore a small internal field strength is sufficient to separate the generated electron-hole-pairs. The optimum efficiency for sunlight (85 mW/cm^2, AM1) is around 3.5%. It should be pointed out here, that both, the crystal properties and the light-intensity can critically influence the fillfactor. Crystals with less ideal properties exhibit a less steep increase of the photocurrent with potential and reach the saturation at higher voltages. They also show greater anodic dark currents. At high illumination levels of several hundred mW/cm^2 like in 2) and 4) transport processes towards and from the interfaces become the rate limiting factor.

The current-voltage curve (Fig. 1) shows, that the I^- oxidation is kinetically so much more favourable than the decomposition reaction that electrode corrosion is avoided. This has been shown by operating a longterm experiment with an n-$MoSe_2$/(I^-/I_2)/Pt solar cell for 9 months at a photocurrent density of 10 mA/cm^2 (2).

Similar results have been obtained with n-MoS_2 but the flatband potential is 100 to 200 mV more positive and therefore a smaller output voltage is reached. Also, the photocurrent is

* Electrochem. Soc. Active Member

somewhat lower due to the 0.4 V larger bandgap of MoS_2 (1.7 eV).

We conclude that liquid junction solar cells based on transition metal dichalcogenides can reach similar conversion efficiencies as the other intensively investigated systems such as the CdS or CdSe based cells in the redox systems S^{2-}/S_2^{2-} or Se^{2-}/Se_2^{2-} (5,6) but are easier stabilized against photodecomposition.

ACKNOWLEDGEMENT

We thank Dr. F. Lévy (EPF Lausanne, Switzerland) for supplying us with excellent crystal samples.

REFERENCES

(1) H. Tributsch, Ber. Bunsenges. Phys. Chem. 81, 361 (1977).

(2) H. Tributsch, Ber. Bunsenges. Phys. Chem. 82, 169 (1978).

(3) J. Gobrecht, H. Gerischer, and H. Tributsch, submitted, Ber. Bunsenges. Phys. Chem.

(4) H. Tributsch, J. Electrochem. Soc., 125, 1086 (1978).

(5) M.S. Wrighton, A.B. Bocarsly, J.M. Bolts, A.B. Ellis and K.D. Legg in "Semiconductor Liquid Junction Solar Cells", Conference Proceed. Vol. 77-3, ed. by A. Heller, The Electrochemical Society Inc., Princeton, 1977.

(6) B. Miller, A. Heller, M. Robbins, S. Menezes, K.C. Chang, and J. Thomas Jr., J. Electrochem. Soc., 124, 1019 (1977).

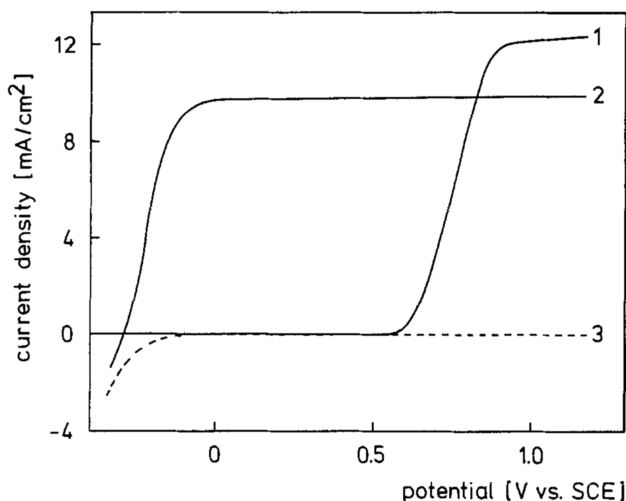

Fig. 1 - Current-potential behaviour of n-MoSe.
1: photocurrent in 1 M KCl
2: photocurrent in 1 M KI/0.1 MI_2
3: dark-current in 1 M KI/0.1 MI_2
The dark current in KCl is zero in this scale. Light source: 90 mW/cm^2 simulated AM1 solar illumination.

Manuscript submitted

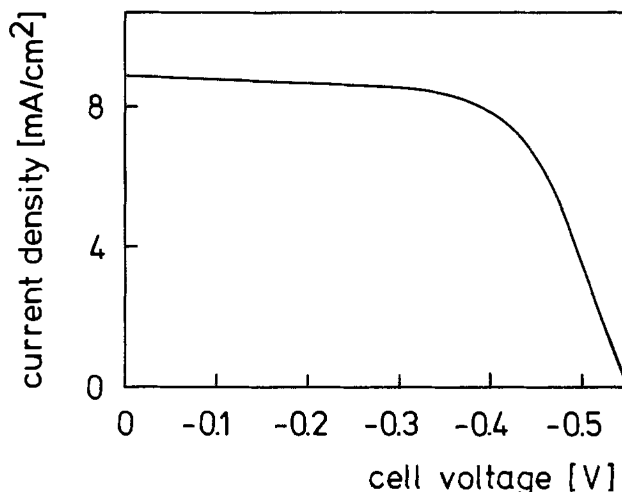

Fig. 2 - Output power characteristics of an $n\text{-}MoSe_2/(I_2/I^-)/Pt$ photocell under 90 mW/cm^2 simulated AM1 illumination.

Manuscript submitted June 12, 1978.

JOURNAL OF THE ELECTROCHEMICAL SOCIETY

REVIEWS AND NEWS

DECEMBER
1978

75th Anniversary Review Series

Compound Semiconductors

N. Holonyak, Jr.* and G. E. Stillman
Department of Electrical Engineering and Materials Research Laboratory, University of Illinois at Urbana-Champaign, Urbana, Illinois 61801

and C. M. Wolfe*
Department of Electrical Engineering, Washington University, St. Louis, Missouri 63130

RN

The invention of the transistor (1, 2) in late 1947 and its later embodiment in junction form (3) marked the beginning of a profound change in electronics. Not only did the receiving tube basically become obsolete, but many new device functions emerged, and ultimately unbelievable size reductions and enormous packing densities resulted. As is well known, it became possible to build an entire functional system in a single conducting block of material. Also, new forms of power devices, based on the transistor effect, became possible.

With the invention of the transistor the study of electrical conduction in solids took on new importance, and similarly the growth and study of semiconductor crystals, at first, Ge (4). Since Ge is a much more tractable material than other elemental semiconductors, it was natural that the transistor began with Ge, and that in turn the transistor (and p-n junctions) motivated the growth and study of single crystal Ge of great purity (4, 5). In fact, Ge and its successor Si, because of the transistor, have been purified to such high levels and have been grown with such perfection that Si now even serves as the standard for determination of Avogadro's number (6).

The original transistor pioneers were quite aware that beyond their initial experimental material (Ge), Si offered a large potential (7). The real emergence of Si as a transistor material probably came in late 1954 and early 1955 when, at Bell Laboratories, Si-diffused-impurity devices were first constructed. Based on his considerable understanding of switching devices and the need for low off-stage leakage current, John Moll above all others urged the development of diffused-impurity Si devices; for this purpose, in his own group Au-Sb and Al metallization of Si were developed (8), as well as certain forms of transistor devices (9). The most important form of diffused-impurity p-n junctions came from Carl Frosch (and L. Derick) (10), including oxide masking and with it the teaching to leave the oxide on Si for protection of the device (11). These developments were sufficient for Moll and his colleagues to be able to convince Jack Morton (spring of 1955) to switch transistor development from Ge to Si. The rest is history, and now where Si "can do the job," there is little interest on the part of device researchers to attempt to displace it with another material. No other material has been as extensively developed, nor offers a natural oxide affording so many processing and device advantages.

As useful as Ge and, more so, Si have proven to be in semiconductor devices, they possess also certain limitations. Their bandgaps are indirect and are fixed at $E_g(\text{Ge}) \approx 0.68$ eV and $E_g(\text{Si}) \approx 1.1$ eV. Hence, they are not useful as light emitters, not even in the infrared where they emit, but poorly. The energy band structure (indirect) is not suitable for transferred electron devices (Gunn oscillators) (12). As a solar energy converter, Si is good (technologically) but has too small of an energy gap for optimum efficiency and for some applications has too small of an absorption coefficient. Both Ge and Si can readily be fabricated into homojunctions (13) but so far have not proved to be very valuable for use in heterojunctions. Clearly, Si may be the most valuable semiconductor, but it is not by any means a universal semiconductor material, thus the basis for our interest in compound semiconductors and their capability for extending electronic functions.

Here we are concerned mainly with III-V compounds because these materials, first of all, are amenable to formation into p-n homo- and heterojunctions and thus have a practical basis for use in electronics (14). Besides the fact that they can be grown conveniently in the form of heterojunctions, which is of growing importance, III-V compounds can be prepared with direct energy gaps ranging from the infrared (InSb) to the yellow-green ($In_{1-x}Ga_xP$, $x \sim 0.73$). This is, of course, what makes these materials useful as lasers (15-18) and light emitters (17). In the mixed crystal systems $Al_xGa_{1-x}As$, $GaAs_{1-x}P_x$, $In_{1-x}Ga_xP$, $Al_xGa_{1-x}As_{1-y}P_y$, and $In_{1-x}Ga_xP_{1-z}As_z$ the band structure can be varied continuously from direct to indirect energy gaps by varying the crystal composition. This property obviously does not exist in binary III-V's nor in Ge or Si. In the direct range of energy gaps, *e.g.*, binaries such as GaAs and InP and ternaries such as $GaAs_{1-x}P_x$, the band structure (see Fig. 1) is such that electrons can be transferred from a low mass, high mobility direct valley (Γ) to various indirect high mass, low mobility minima (L or X), thus permitting Gunn oscillations (12). Because of the small electron mass and high mobility that some of these compounds possess, they (*e.g.*, GaAs) are also useful for high speed field effect transistor applications (19).

In general, it is a special property of a given III-V material that permits a particular application, and it is only as these applications have developed that III-V semiconductors have become important. In fact, device studies, as much as anything, have resulted in the preparation of high purity materials and have uncovered the fundamental properties of III-V semiconductors. A good example is the Gunn oscillator (12), which has resulted in the extension of transport studies in solids into new areas (20) and has

* Electrochemical Society Life Member.

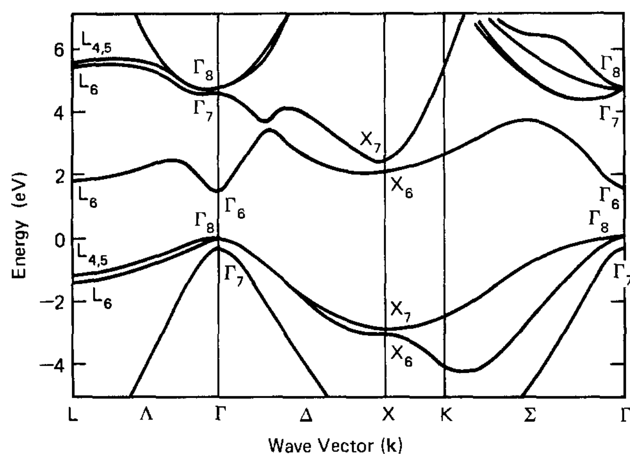

Fig. 1. Energy band structure of GaAs

supplied, moreover, the motivation to develop high purity, high mobility GaAs (21) and InP (22). In any case, in this survey we take the point of view that various applications (that Si cannot match) have been the driving force for the study and development of the III-V semiconductors. Below we discuss the more important of these materials and their capabilities in the context of various applications.

Crystal Growth

The search for improved methods to grow semiconductor crystals is an ongoing problem. The most used III-V bulk and substrate materials are GaAs, GaP, and InP; these materials continue to be heavily studied (23). The first, GaAs, is frequently synthesized and grown as a single crystal in a horizontal furnace in a quartz ampul subjected to a collapsing or moving temperature gradient. The crystal can be doped n-type or p-type, or be made semi-insulating with Cr doping. Besides being important as a substrate to support measurement samples (of separately prepared epitaxial layers), semi-insulating GaAs (also semi-insulating InP) is becoming increasingly important in device use (19), *e.g.*, making possible an interconnected array of devices (IC) on "insulating" substrates. Because of the high P pressure at the melting points of GaP and InP, these crystals are grown in pressurized systems by the liquid encapsulation (LEC) method (24), which can be used also to grow GaAs. Other methods are used to grow mixed crystal systems and to prepare homo- and heterojunctions. These are discussed below.

Vapor phase epitaxy (VPE).—In 1960 Marinace (25) described the VPE growth of Ge on GaAs substrates, thus leading to the first high performance heterojunctions. This VPE crystal growth process, which occurred in a closed-tube held in a small temperature gradient, employed iodine as the transport agent (VPE by halide transport and chemical disproportionation). Marinace's process could be inverted, making possible the VPE growth of GaAs on Ge substrates (26). In addition, the closed-tube VPE-crystal-growth process could be generalized to employ other halide transport agents and to grow also mixed III-V crystal systems. Thus, closed-tube VPE was used (in 1960) to grow GaAs on Ge heterojunctions, GaAs on GaAs tunnel junctions, and GaP on GaP junctions, and to synthesize and grow (VPE) $GaAs_{1-x}P_x$ and $GaAs_{1-x}P_x$-$GaAs_{1-y}P_y$ heterojunctions (26).

The demonstration of the work of Ref. (26) to Ruehrwein (27) (and to F. V. Williams, fall, 1960, Syracuse, New York) led to today's most widely used open-tube VPE system (Fig. 2) for the large-scale growth of $GaAs_{1-x}P_x$ ($x = 0$ GaAs, $x = 1$ GaP) (28-31). In this process of crystal growth, HCl is used to transport the column III constituents (Ga or In

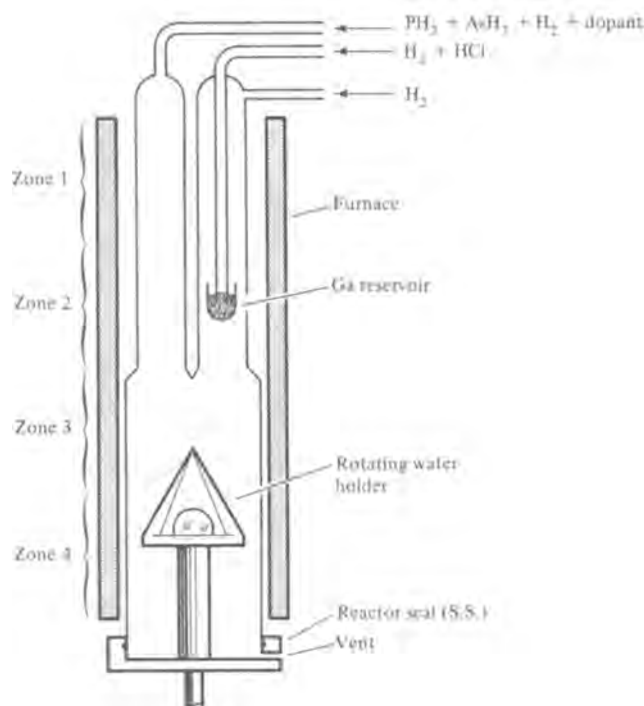

Fig. 2. Schematic diagram of reactors used for commercial growth of $GaAs_{1-x}P_x$, GaAs ($x=0$), and GaP ($x=1$) using the hydride VPE process [after Ref. (31)].

metal), and AsH_3 and PH_3 are the source of the As and P for the VPE crystal. It is an easy matter to add NH_3 to the crystal growth reactor in order to introduce N doping, an isoelectronic trap, in the VPE layers. Epitaxial layer growth rates are ~1 μm/min. The details of this process for the growth of GaAs, GaP, and $GaAs_{1-x}P_x$ are described elsewhere [Ref. (28-31)]. It is worth mentioning, however, that since the AsH_3-PH_3 system of VPE crystal growth is the highest volume, most widely used one in the LED industry, it is under constant study in order to effect improvements in crystal quality, freedom from defects, and improved doping. Also, it is worth mentioning that this crystal growth process, as well as the VPE process of the next paragraph, is capable of growing epitaxial layers of low doping level ($N_d - N_a < 10^{15}/cm^3$) and high mobility (~8800 cm^2/Vsec for GaAs).

At the time (1963) of the discovery of transferred electron oscillations (Gunn effect) (12, 32) the best available GaAs had total impurity concentrations in the 10^{16} cm^{-3} range. Although material of this quality could be compensated to produce lower electron concentrations, it became apparent that the purity of GaAs would have to be improved to obtain useful devices. To overcome some of the problems associated with closed-tube VPE, a number of open-tube methods were investigated. In 1965 the feasibility of obtaining higher purity GaAs by an epitaxial technique was demonstrated by Knight *et al.* (33) with the $AsCl_3$-Ga-H_2 open-tube VPE system. Since that time this VPE method has been developed to a high state of reliability by a number of workers. The contributions of many of these workers and the details of the chloride-transport VPE system are reviewed in Ref. (34). Because of the ease with which high purity, controlled doping, precise thicknesses, and mirror-smooth surfaces can be obtained with this technique, the $AsCl_3$-Ga-H_2 VPE process is the most commonly used method of growing epitaxial GaAs for a variety of applications. It is mainly due to the development of this epitaxial growth process that GaAs is currently taking over a substantial part of the work, formerly performed by Si, in high speed integrated circuits.

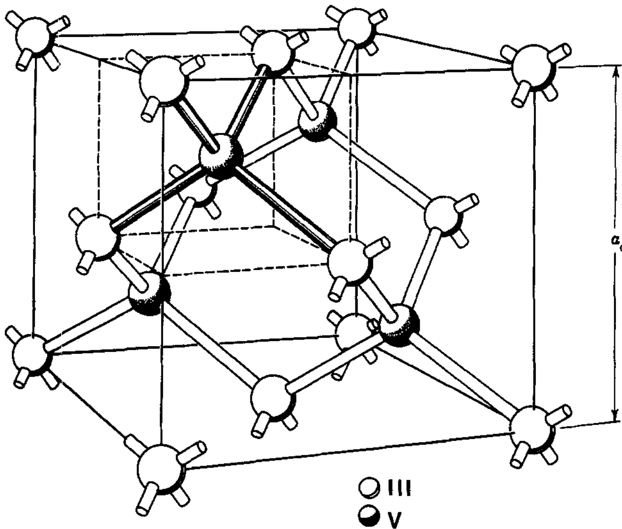

Fig. 3. Sphalerite crystal structure of III-V compound semiconductors [after Ref. (21)].

In III-V crystal systems containing Ga (Ga occupying column III latttice sites, Fig. 3), Al will substitute for Ga with only a small change in the crystal lattice constant. Until recently, however, Al has not been an easy or even manageable component to handle in a VPE crystal growth reactor because of its highly reactive nature. This problem has been overcome by Dupuis and co-workers, who have employed metallorganic chemical vapor deposition (MO-CVD, a form of VPE) to grow a wide range of high performance $Al_xGa_{1-x}As$-GaAs heterojunction devices (35-41). In the MO-CVD crystal growth process (35-37), the metal alkyls, trimethylgallium (TMGa) and trimethylaluminum (TMAl), are used as sources of the group III elements Ga and Al. The hydride AsH_3 is used as the source of the group V element As, and PH_3 for P. H_2Se is used as a source of Se for n-type doping and diethylzinc (DEZn) is used as a source of Zn for p-type doping. The various layers of a heterostructure are grown sequentially at 750°C on {100} GaAs substrates, or on Ge or GaAsP substrates, using growth rates of ~0.25 μm/min.

As an example of the high quality heterostructures that have been grown by MO-CVD, foremost are $Al_xGa_{1-x}As$-GaAs-$Al_xGa_{1-x}As$ DH laser diodes that operate at current thresholds as low or lower than any made by other methods (41). This has led to easily realizable room temperature continuous laser operation (40), which previously has been possible only with DH diodes grown by liquid phase epitaxy (LPE) and, less successfully, with molecular beam epitaxy (MBE). [See Ref. (42) for an extensive discussion and complete list of references.] In addition, MO-CVD $Al_xGa_{1-x}As$-GaAs-$Al_xGa_{1-x}As$ quantum-well heterostructures (200Å GaAs active layers) have been grown that operate as laser diodes at relatively low thresholds (38) and that photopumped exhibit stimulated emission on confined-particle transitions well into the visible-red (39).

The nature of these results, taken with the many other advantages of VPE processes, make it likely that the MO-CVD growth of GaAs and $Al_xGa_{1-x}As$, and possibly $GaAs_{1-y}P_y$ and $Al_xGa_{1-x}As_{1-y}P_y$ (43), and heterostructures based on these crystal systems, will gain wide acceptance. The advantages of the MO-CVD process for the growth of $Al_xGa_{1-x}As$ and GaAs include: (*i*) capability for large scale operations (large substrate areas); (*ii*) convenient growth rates with excellent control of layer thicknesses (from $\lesssim$ 50Å to over 1 μm); (*iii*) highly reproducible layer thicknesses and capability for multiple layer growth, including quantum-well structures; (*iv*) easily controlled doping levels from $N_d - N_a \lesssim 10^{15}/cm^3$ to degeneracy; (*v*) excellent composition control; (*vi*) good lattice match; (*vii*) superior surfaces with no problems with melt wipe-off or contact with foreign bodies; and (*viii*) no problems with halide etching or attack of surfaces.

In concluding this brief discussion of VPE, we mention that because of the broad nature of Ref. (27), it covers quite generally the open-tube VPE growth (via AsH_3, PH_3, etc.) of a large number of compound semiconductors, including $In_{1-x}Ga_xP_{1-z}As_z$. This quaternary system has recently become important for laser and detector diodes in the wavelength range $\lambda \gtrsim 1$ μm at which optical fiber transmission is optimum. Besides LPE, VPE can be used for the growth of double heterojunctions employing $In_{1-x}Ga_xP_{1-z}As_z$ (44); this is not an extensively developed or practiced art yet but potentially could become important.

Liquid phase epitaxy (LPE).—A significant number of III-V semiconductor devices that have been successfuly developed in the last 10 years have depended upon LPE crystal growth, *e.g.*, $Al_xGa_{1-x}As$-GaAs-$Al_xGa_{1-x}As$ double heterojunctions (45, 46), red GaP:Zn-O and green GaP:N light emitters (47, 48), InP-$In_{1-x}Ga_xP_{1-z}As_z$-InP DH lasers (λ = 1-1.7 μm) (49), and visible-spectrum $In_{1-x'}Ga_{x'}P$-$In_{1-x}Ga_xP_{1-z}As_z$-$In_{1-x'}Ga_{x'}P$ DH lasers (50). The prototype for this system of crystal growth, particularly to form p-n junctions, is the method of Nelson (51), which was first used to grow LPE GaAs homojunctions. As initially demonstrated, a Ga melt (or solution) is first saturated with GaAs, a substrate crystal (GaAs) is moved under the melt (nowadays by means of a graphite slider boat), and simultaneously the temperature is lowered to cause supersaturation and growth of GaAs from the melt on the substrate. If a small amount of Al is introduced into the Ga melt, the epitaxial layer that is grown is $Al_xGa_{1-x}As$ (52), and a heterojunction with GaAs results. Until the recent success of the MO-CVD process, this had been the most successful process (LPE) for the growth of $Al_xGa_{1-x}As$-GaAs heterojunctions. Problems with the difficult oxides of Al are avoided by the simple fact that it is possible to slide a substrate wafer into contact with the "clean" portion of a liquid. An extensive discussion of this technology appears in Ref. (42).

In one way or another most LPE III-V crystal- and junction-growth processes are similar or related, and will not be discussed in detail [see Ref. (42)]. Because of the importance of green LED's and the fact that so far LPE GaP:N has proved to give the highest (green) performance (48), no doubt this system will receive further attention. Red GaP: Zn-O, because of the low solubility of the isoelectronic complex Zn-O, probably will receive limited attention. [Red-orange VPE $GaAs_{1-x}P_x$:N is a more viable system (31).] Of the systems having reason to be grown by LPE, that receiving most attention in the long run will probably be $In_{1-x}Ga_xP_{1-z}As_z$, simply because so far LPE has been the most successful method for growing this alloy and most likely its importance for optical fiber communications will increase.

Compared to VPE, LPE suffers certain disadvantages such as lesser control of layer thickness, poorer control of crystal composition, and problems with melt wipe-off, growth terraces, and meniscus lines. There are certain advantages of LPE processes, however, and doubtless this method of crystal and heterojunction growth will be developed further. Its low cost makes it ideal for laboratory-scale experiments, and it is capable of certain results that have not been obtained by other methods. As an example, the amphoteric dopants Ge and Si act as donors in GaAs that is grown near stoichiometric conditions; but, in the LPE growth process (due to relatively fewer As atoms and hence As vacancies), Ge or Si can occupy column V lattice sites (see Fig. 3) and act as acceptors. This form of

doping has been useful in DH lasers (42). Also, Si-doped LPE GaAs homojunctions have become a standard high efficiency LED in optoelectronic applications. During the LPE growth cycle the Si dopant first acts as a donor but later in the growth cycle tends to occupy As sites (Fig. 3) and thus switches its behavior to an acceptor, in fact, introducing the usual shallow and also a deeper acceptor (53). Electron-hole recombination involving the deeper acceptor results in reduced photon energy and in recombination radiation that does not suffer much absorption, thus making possible a higher efficiency LED. In this case LPE accomplishes a unique result.

A further matter concerning III-V semiconductors should be mentioned in concluding this section. III-V materials are by no means simple; nevertheless, in many cases they have proven to be sufficiently manageable to make it possible to determine their phase behavior and construct their phase diagrams [see Casey and Panish, Ref. (42)]. Obviously it is a matter of considerable importance, for example, in determining how impurities are incorporated, whether a III-V semiconductor is grown under conditions of excess column III or excess column V atoms. This applies also to the behavior of impurities diffused into III-V crystals. For example, Zn diffusion in GaAs (or GaAsP) behaves much differently under conditions of excess As as compared to excess Ga. How this process proceeds is governed to a large extent by the Ga-As-Zn phase diagram of the system (42). Although the phase diagrams of many III-V's and their more common dopant impurities are known, this area of work is far from complete. Perhaps the most complete discussion of this topic appears in Ref. (42).

Molecular beam epitaxy (MBE).—One more system of III-V crystal and heterojunction growth should be mentioned; molecular beam epitaxy (MBE). An extensive description of this process appears in Ref. (54). Basically MBE consists of growing a crystal in a vacuum by letting controlled "beams" of the requisite atoms strike a hot substrate (GaAs, etc.) and form the crystal. The beams of atoms are provided by small effusion-cell ovens that deliver, by evaporation, streams of atoms. The cells are shuttered, in a time sequence pattern, to change epitaxial layer compositions or to switch from the growth of one type of layer (GaAs) to another ($Al_xGa_{1-x}As$ or AlAs).

Various heterostructures have been constructed by MBE, perhaps the most unique being multilayers of $Al_xGa_{1-x}As$ and GaAs that are thin enough to exhibit quantum size effects (QSE) (55) and also artificial materials consisting of a certain number of monolayers of one crystal (GaAs) interleaved with a certain number of monolayers of a second crystal (AlAs) (56). This last form of MBE crystal is a type of material not formed naturally. For the example stated, it is an ordered form of $Al_xGa_{1-x}As$ since the Al atoms appear on a well-defined set of planes (similarly the Ga atoms). In the usual case (VPE, LPE, or MBE) the Al and Ga atoms are uniformly distributed in density, but in a disordered arrangement. The ordered form of $Al_xGa_{1-x}As$ (and possibly other III-V alloy systems), and the many forms of ordered doping arrangements that can be imagined may well be the most important feature of MBE and its capability for growing epitaxial layers monolayer by monolayer. This is also one of its limitations, its low growth rate and its inherent small mass transport and thus resulting limited crystal-size capability.

Optical Devices

In the early phase of transistor development it was imagined that III-V compounds, with their high mobilities, would make possible higher speed transistors. This judgment now has validity, but it did not when it was first made. There is little doubt that it was the light-emission capability of the III-V's that finally encouraged their large-scale development. This was particularly true after the report of efficient spontaneous emission from GaAs p-n junctions (57), and the subsequent demonstration of infrared (15, 16, 18) and visible-red (17) stimulated emission from III-V p-n junctions. This work made it evident that practical LED's in the range from the infrared to the red could be developed.

Laser diodes.—There is ample evidence showing that the light-emission process in a direct-gap crystal is much stronger than in an indirect-gap material. For example, when the pressure on (direct-gap) $GaAs_{1-x}P_x$ (58) or $In_{1-x}Ga_xP_{1-z}As_z$ (59) laser diodes is increased, the X indirect band minima and the Γ direct minimum (Fig. 1) shift and approach one another; as $E_\Gamma \rightarrow E_X$, electrons transfer from Γ to X and laser operation quenches. In the latter case band-to-band recombination (X electrons and Γ holes) and the light emitted are weak. Direct-gap crystal is essential for laser diodes and is advantageous also in LED's.

Although homojunction laser diodes were the first to be constructed (15-18), nowadays essentially all study and further development of these devices is concentrated on DH diodes. The two systems receiving most attention are $Al_xGa_{1-x}As$-GaAs-$Al_xGa_{1-x}As$ and InP-$In_{1-x}Ga_xP_{1-z}As_z$-InP. The former is extensively discussed in Ref. (42). Relative to further progress, the most important recent development is that these devices (AlGaAs-GaAs) have been constructed by MO-CVD and have operated CW (300°K) (40) and, in addition, have operated at thresholds as low or lower (41) than LPE DH laser diodes. If these diodes prove to exhibit high reliability, then MO-CVD will be capable of delivering large quantities of $Al_xGa_{1-x}As$-GaAs-$Al_xGa_{1-x}As$ DH laser diodes at very low cost. (This will be an interesting development to watch in succeeding years since MO-CVD has implications also for a number of other devices.)

Several features make InP-$In_{1-x}Ga_xP_{1-z}As_z$-InP DH diodes important. The first is that the direct-gap center active region can be "tuned" in composition to the wavelengths at which optical fibers exhibit optimum transmission characteristics (49). Another is that the heat sinking of these devices is accomplished via InP, which is a considerably better heat conductor than AlGaAs. In spite of their early state of development, quaternary DH laser diodes exhibit extremely low low temperature threshold current densities (60), which suggests that the room temperature thresholds can eventually be made much lower. Lower thresholds, if realizable, could result in simpler, cheaper, and more reliable laser diodes.

It is interesting that direct-gap $In_{1-x}Ga_xP_{1-z}As_z$ is useful also for visible-spectrum DH laser diodes (50). In this spectral region, however, the quaternary is much more difficult to grow (61) than at smaller energy gaps (62) (~800° *vs.* ~650°C). For this reason and because of the possible effect of substrate ($GaAs_{1-y}P_y$) defects, visible-spectrum quaternary DH diodes have not yet matched the performance obtained at smaller energy gaps ($\lambda > 1$ μm).

Light-emitting diodes (direct-gap).—Not all direct-gap diodes, or even the largest number, involve stimulated emission (for many optoelectronic applications, *e.g.*, coupled pairs, spontaneous emission suffices). In the infrared by far the most widely used material is GaAs. Homojunction diodes prepared by Zn diffusion into n-type GaAs substrates are well developed (63) and widely used. The external quantum efficiency of these diodes (uncoated) is typically ~0.3% (50 mA). For higher efficiency (~1.5%, 20 mA), Si-doped junctions grown by LPE are employed. For still higher efficiencies (as high as 40% (64) but at still greater expense) LPE $Al_xGa_{1-x}As$-GaAs-$Al_xGa_{1-x}As$ DH diodes have been developed. The successful (large-area) construction of this type of diode (DH) by MO-CVD (40), a large-area growth process, raises the interesting possibility that high performance *IR* LED's will become available even-

tually at very low cost. Also, MO-CVD makes very practical a new form of light emitter, a quantum-well LED (38, 65). Depending upon current, these devices emit over a wide spectral range, including into the visible-red (38, 39).

Beyond GaAs there is no binary III-V with a higher energy direct bandgap. Hence, to achieve higher energy direct gaps it is necessary to resort to alloys or mixed III-V systems. One of these systems, $GaAs_{1-x}P_x$ ($x \sim 0.40$) (17) for various reasons has become the industry-wide standard red LED material. By VPE it is possible to prepare $GaAs_{1-x}P_x$ of reasonable quality, cheaply, and in large quantities (28). Then with the same type of simple Zn-diffusion process used for GaAs (63), red-emitting p-n junctions are prepared in the alloy. This results in a cheap, relatively high performance red LED. Because it is already known that $Al_zGa_{1-z}As_{1-x}P_x$-$GaAs_{1-x}P_x$ heterojunctions can be grown (43), it is likely that MO-CVD (35) can be extended and be used to make (at low cost) a much higher performance visible heterojunction LED based on light emission from $GaAs_{1-x}P_x$.

Light-emitting diodes (indirect-gap).—Although $In_{1-x}Ga_xP$ does not become indirect until $x \sim 0.73$ (59) and presumably could be used for a direct-gap LED extending to the yellow-green, this alloy system is not well developed. Compared to $GaAs_{1-x}P_x$, $In_{1-x}Ga_xP$ is not simple to grow nor to prepare into good p-n junctions and has been largely ignored. For $x > 0.4$ $GaAs_{1-x}P_x$ (*i.e.*, beyond the direct-indirect transition, $x \equiv x_c \approx 0.48$) the LED brightness decreases (in the orange, yellow, and green) as shown by the dotted curve of Fig. 4 (66). The solution to this problem (solid curve of Fig. 4) is to introduce N doping in $GaAs_{1-x}P_x$ to maintain LED brightness from the red to the yellow (67), and to the green ($x = 1$, GaP:N) (68).

Nitrogen in GaP and in $GaAs_{1-x}P_x$ is a short-range isoelectronic trap with a shallow binding energy. If carriers are confined spatially, then in k space they are spread out ($\Delta k \Delta x \sim 1$). When electrons are excited (injected) into the X indirect minima, which is the lowest conduction band minima of Fig. 5, the N trap captures the carriers and, as shown by the shaded region representing $\psi_N(\vec{k})$, introduces a considerable probability for the electron to appear at $\vec{k} = [000]$, or Γ, and thus recombine with a Γ hole. As the alloy composition is shifted from $x = 1$ (GaP) toward $x = 0$ (GaAs) and the Γ conduction band minimum approaches E_N (the trap level), this effect, known as band structure enhancement, increases the oscillator strength for electron-hole recombination at the N trap (69). Thus, although the eye sensitivity decreases toward the red, the recombination radiation is enhanced and the brightness of $GaAs_{1-x}P_x$:N LED's is reasonably flat (Fig. 4) from the red to the green, *i.e.*, from $x \sim 0.4$ to $x = 1$.

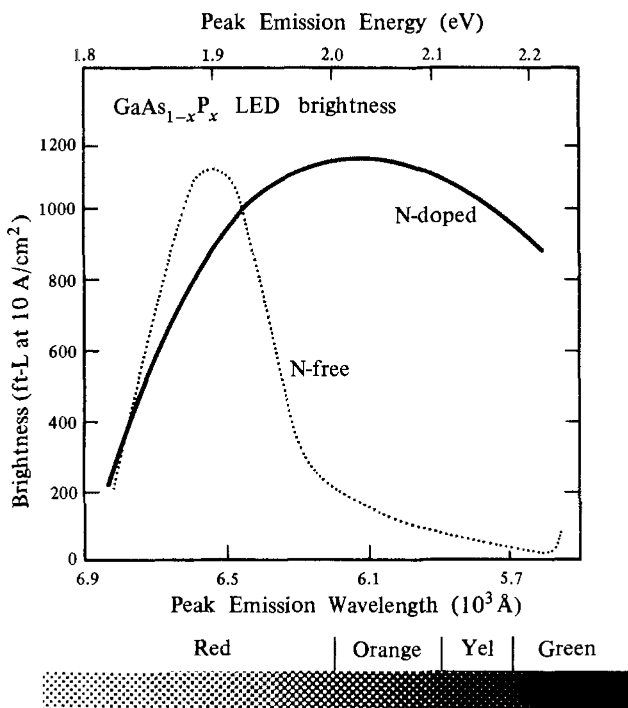

Fig. 4. Brightness as a function of alloy composition for $GaAs_{1-x}P_x$ diodes with and without nitrogen doping. The brightness is measured in foot-Lamberts with a drive current of 10 mA or 10 A/cm², corresponding to a device area of 10^{-3} cm² (after Ref. (31)).

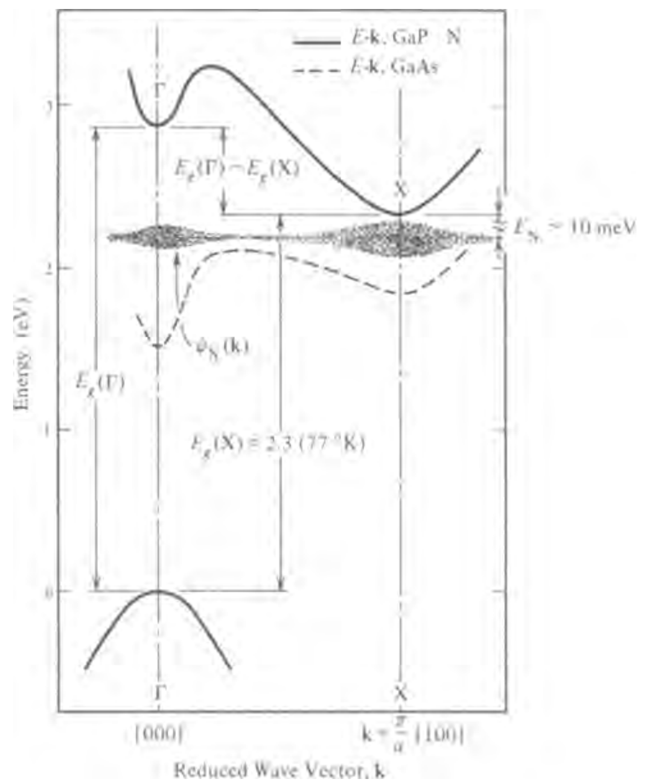

Fig. 5. *E-k* diagram of GaP:N with GaAs shown dotted for reference. The N isoelectronic trap lies ~10 meV below the X minima, and $|\psi_N(k=0)|^2 > 0$. As the crystal composition, x, of the $GaAs_{1-x}P_x$ alloy is varied and E_Γ approaches E_X, $|\psi_N(k=0)|^2$ increases and attains a maximum when E_Γ is adjusted to coincide with the N trap energy [after Ref. (31)].

The theory of the behavior of N in $GaAs_{1-x}P_x$ continues to be improved (70), but, as usual, improvement in LED brightness depends more upon improvement in crystal growth, doping, and junction quality. Progress in this area is now largely evolutionary (66). It is interesting to speculate, however, that when MO-CVD is extended in this direction (*i.e.*, toward AlGaAsP, GaAsP, and AlGaAsP-GaAsP heterojunctions, N doping included) major further progress will be realized in LED development.

Detectors.—p-n junctions and heterojunctions in III-V materials, in addition to serving as efficient light emitters, also serve as efficient light detectors. In this respect they have several advantages over an elemental semiconductor, one being their high absorption coefficients (direct-gap crystal) and another the fact that essentially a continuous range of energy gaps is possible from the *IR* to the visible by the utilization of alloys. In addition, they can be conveniently fabricated into heterojunctions, which is important for wide bandwidth applications. Other compound semi-

conductors are also very important in detector applications, particularly at wavelengths longer than about 5.5 μm, the long wavelength limit of InSb at 77°K and the long wavelength limit of practical intrinsic detectors in III-V materials. Even at shorter wavelengths, however, compound semiconductor detectors such as PbSe and PbS are very important, but since these detectors are typically polycrystalline thin-film devices formed by either vacuum evaporation or chemical deposition of some type, they will not be discussed further here. At the longer wavelengths, $Hg_{1-x}Cd_xTe$ and the PbSn chalcogenides $Pb_{1-x}Sn_xTe$ and $Pb_{1-x}Sn_xSe$ are highly developed single crystal compound semiconductor alloys that are very useful for intrinsic photoconductors and photodiodes. Detectors in these materials systems have recently been reviewed in some detail (71, 72) and will not be discussed further in spite of their considerable importance for detectors in the 5-14 μm wavelength range.

Most of the important detector applications of III-V compounds occur in the near infrared spectral region, but there are two important exceptions that are useful for far infrared detectors. The first is the InSb "free electron bolometer." The absorption mechanism in this detector is the free carrier absorption of radiation, which has a λ^2 dependence for "short" wavelengths and is constant at long wavelengths. For InSb, the λ^2 dependence is approximately true for $\lambda < 1$ mm. In most semiconductors, free carrier absorption simply contributes slightly to increasing the temperature of the sample. However, in InSb at very low temperatures ($T \lesssim 4.2$°K), a different effect occurs. InSb has a very low electron effective mass and high electron mobility at low temperature, and the electron coupling to the lattice is very weak. In addition, the electron mobility is energy dependent, so that absorption of far infrared radiation via the free carrier absorption mechanism can produce a significant increase in the average electron energy and thus a change in the average electron mobility. The resulting change in conductivity can be detected in the same manner as ordinary photoconductivity, and since the effect is electronic rather than thermal, this detector is capable of fast response. These detectors have been described in detail by Putley (73), and are widely used in far infrared and submillimeter research for wavelengths $\gtrsim$ 200 μm.

The other III-V compound far-infrared detector is the GaAs extrinsic photoconductor (21). All of the shallow donor impurities in GaAs are very nearly hydrogenic, with ionization energies of about 5.86 meV and Bohr radii for the ground state of about 100Å, so that very pure material is required for the observation of isolated impurity levels. Because of the large effort expended in developing high purity GaAs, mainly for Gunn-effect applications, such material is now readily available. The ionization energy of 5.86 meV corresponds to a photoionization threshold wavelength of about 212 μm, but because the impurity levels are so shallow, the dominant response of these detectors at 4.2°K corresponds to the wavelength or photon energy for excitation of a bound electron from the ground state to the first excited state of a hydrogenic donor (21). The photoconductivity from this absorption results because of subsequent thermal ionization of the excited electron into the conduction band. This photothermal ionization mechanism produces a photoconductivity spectrum with a dominant peak at 282 μm, considerably beyond the 120 μm long-wavelength threshold for Ge extrinsic photoconductive detectors. Since this type of GaAs detector is fast and its peak response falls between the long wavelength cut-off of Ge detectors and the longer wavelengths where the InSb free electron bolometers have their optimum response, they are a very useful addition to the small assortment of fast detectors in the far infrared spectral region (21).

The III-V compound semiconductor detectors in the near infrared spectral region are not in general very highly developed. One notable exception is InSb, which has a long wavelength threshold of about 7 μm at room temperature and about 5.5 μm at liquid nitrogen temperature. Photoconductor and photoelectromagnetic InSb detectors have been developed and have recently been reviewed by Kruse (74). Photovoltaic InSb devices have also been developed to some degree (75). In addition, InSb avalanche photodiodes have been reported (76), but these devices have not been studied extensively. Photodiodes utilizing InAs are available commercially; these devices have a long wavelength threshold of about 3.5 μm when operated at room temperature.

Most of the other III-V compounds have larger bandgaps, and because of the ready availability of photomultiplier tubes and Si p-i-n and avalanche photodiodes, there has been little incentive to develop III-V photodetectors for the same spectral region. The absorption coefficients for the more common binary III-V compound semiconductors are shown in Fig. 6, along with the absorption coefficients of Ge and Si for comparison (77). Except for GaP, all of the III-V materials shown have a direct bandgap and therefore a very steep absorption edge. The differences between the absorption for direct and indirect energy gaps is quite distinct when the direct absorption edges of III-V compounds are compared to Si—the absorption coefficient of Si does not extend as high as for the direct bandgap III-V compounds until the photon energy is over twice the bandgap energy. (The reason for the more rapid increase in the absorption coefficient for the indirect-gap materials Ge and GaP than for Si is that higher energy direct conduction band minima dominate the absorption in these semiconductors at energies only slightly above the indirect energy gap).

Because of the relatively low absorption coefficient of Si at wavelengths longer than about 0.8 μm, there is a trade-off between the quantum efficiency and frequency response in these devices that becomes important in wide band-width applications; the depletion width of the device must be wide enough to absorb a significant fraction of the incident radiation, but the wide depletion width can impose a transit-time limit on the frequency response. At 1.06 μm, Si p-i-n detectors capable of a baseband response of 10 MHz are limited to an internal quantum efficiency of about 85%, while a base bandwidth of 100 MHz limits the internal quantum efficiency to about 20% (77). Thus, Si is not suitable as a material for high quantum

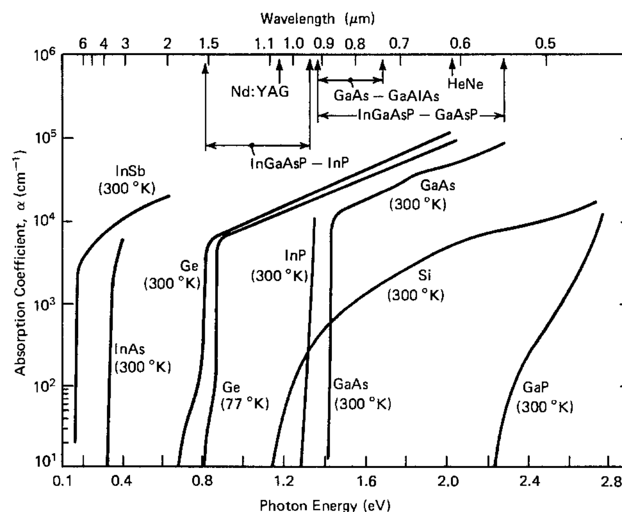

Fig. 6. Absorption coefficient of important III-V compound semiconductors. The absorption coefficients of Si and Ge are shown for comparison. The wavelengths of some important laser and LED sources are indicated for comparison [after Ref. (77)].

efficiency, wide-bandwidth detectors at wavelengths longer than 1.06 μm.

Even for wavelengths shorter than 1.06 μm, there is interest in III-V materials for wide bandwidth detectors; for example, uniform high gain, low noise GaAs Schottky-barrier avalanche photodiodes have been reported (78). High external quantum efficiencies ($\gtrsim$ 50% without antireflection coating) and short response times (~175 psec) at 1.06 μm have been achieved with $In_xGa_{1-x}As$ Schottky barrier avalanche photodiodes (79). These devices are also capable of uniform, high avalanche gains ($\gtrsim$ 250). Even higher external quantum efficiencies (~95% with antireflection coating) but smaller avalanche gains (~10) at 1.06 μm have been obtained with $GaAs_{1-x}Sb_x$ p-n junction detectors (80). The low device yield of $In_xGa_{1-x}As$ detectors with high avalanche gain and the difficulty in obtaining uniform high avalanche gain devices with $GaAs_{1-x}Sb_x$ are probably related to the lattice mismatch between the GaAs substrate and the alloy active layer, although in both cases grading or buffer layers have been employed to reduce the number of misfit dislocations. The crystal mismatch is even more important when longer wavelength detectors (~1.27 μm) for the optimum fiber optic wavelength are considered, although uniform avalanche gains up to 15, pulse rise time of less than 100 psec, and quantum efficiencies of 60% at 1.06 μm and 45% at 1.27 μm for mismatched GaAlSb-GaSb 1.0 to 1.4 μm avalanche photodiodes have recently been reported (81). It is possible that microplasmas related to lattice mismatch limit the performance of these devices.

For longer wavelengths especially, but also for wavelengths close to 1.0 μm, the quaternary $In_{1-x}Ga_xP_{1-z}As_z$ lattice matched to InP substrates is of interest for the same reasons discussed for lasers and LED's. This material is currently being investigated in many laboratories for applications as avalanche photodiodes. There have been several preliminary reports of promising results using this alloy (82-85).

Another "detector" application of III-V compound semiconductors that must be mentioned is that of negative electron affinity (NEA) photocathodes. Negative electron affinity is obtained in compound semiconductors by treating the surface so that an electron at the bottom of the conduction band in the "bulk" of the semiconductor has an energy greater than the zero energy level of an electron in vacuum. In this situation, then, an electron excited into the conduction band can be "emitted" into the vacuum if it travels (diffuses) to the surface without first "thermalizing" or recombining. Negative electron affinity in GaAs and other III-V compounds is obtained using a thin coating of CsO (~8Å thick for GaAs) on degenerate p-type [111]-B oriented material. Quantum efficiencies greater than 20% have been obtained with these GaAs devices.

Equally important or perhaps even more important (than the GaAs NEA photocathodes) is the extension of photoemissive devices further into the infrared, beyond the long-wavelength limit of the familiar S-1 photocathode. The alloys InGaAs, InAsP, and InGaAsP and others have been studied for this application; a very complete review of this work as well as a general review of the GaAs NEA work and of classical photoemissive surfaces has recently been given by Zwicker (86). The quantum efficiency curves for several alloy NEA photocathodes are given in Fig. 7. The quantum efficiency curve for the usual S-1 photocathode is also shown for comparison; it can be seen that much higher quantum efficiencies can be obtained in the near infrared using NEA photocathodes. These curves show also, however, that as the long-wavelength threshold is extended towards longer wavelengths, the resulting quantum efficiency is decreased over the rest of the spectral range. This rather disappointing result is presumably due to a barrier which limits the emission probability of lower energy electrons.

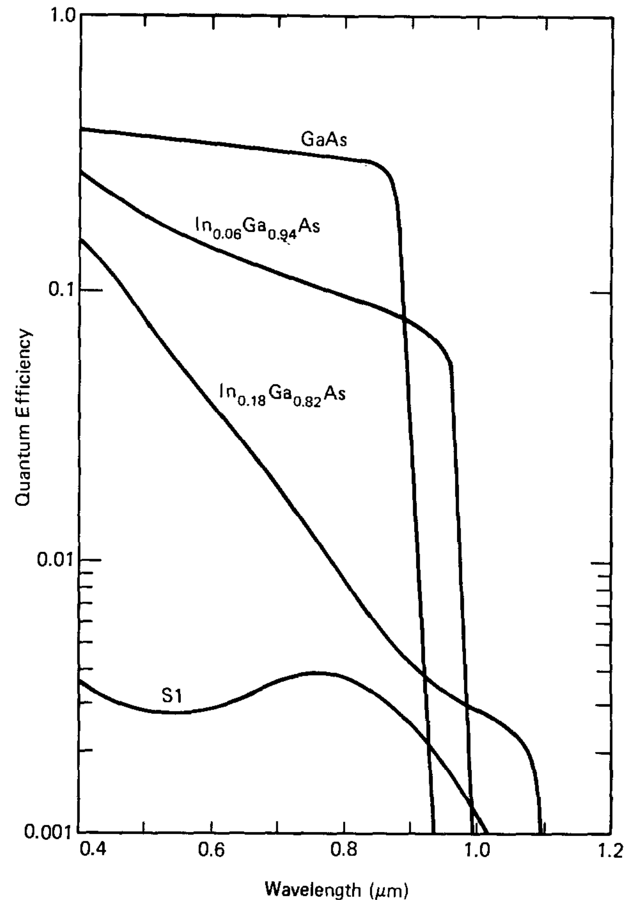

Fig. 7. Variation in quantum efficiency with wavelength for several NEA photocathodes. The quantum efficiency of the S1 photocathode is shown for comparison [after Ref. (86)].

Further extension of the long wavelength threshold of NEA photocathodes will probably require the development of a coating material other than CsO, a material which does not have the limiting barrier that causes the decrease in quantum efficiency with increasing long-wavelength threshold shown in Fig. 7. Nevertheless, these NEA photocathodes incorporated in sophisticated photomultiplier structures, including the dynamic crossed field photomultiplier structure (87), provide the most sensitive infrared detectors, and these devices are available commercially.

Solar cells.—Because of the magnitude of the problem of solar energy generation, one form of light or radiation detector deserves special mention, the solar cell. Silicon is the most generally used material in these applications (88), but it is by no means ideal. Its energy gap is too small (relative to the solar spectrum), its absorption coefficient also is too small (thus requiring a rather thick layer of crystal to absorb fully the incident radiation), and it is not easily or conveniently formed into heterojunctions. In respect to all of these, GaAs is a better although more expensive material.

The most important form of III-V solar cell is the $Al_xGa_{1-x}As$-GaAs heterojunction (89, 90), which is capable of efficiencies >20% (91,92) for air mass one (AM1). The main terrestrial application of this type of solar cell will be in systems utilizing solar concentration (91). GaAs solar cells are much better suited to this application than Si solar cells because of better high temperature performance. In solar concentrators, the cost of the cell is not the major cost of the system; thus it is economically feasible to develop the highest efficiency cell possible since the major cost is the con-

centrating system itself (93). More complicated graded-bandgap solar cells with higher concentrator efficiencies are being developed (94, 95); *e.g.*, calculations indicate that if energy concentrations greater than 1000 suns can be used, systems with expensive, high performance solar cells will be economically viable (96). Although the single crystal $Al_xGa_{1-x}As$-GaAs heterojunction is the most important III-V solar cell at present, in the future polycrystalline thin-film GaAs devices may become even more important for terrestrial applications. This possibility arises because of the steep absorption edge of GaAs, due as discussed previously to the direct bandgap, and the relaxed requirements on cell thickness and minority carrier lifetimes and diffusion lengths compared to indirect crystals. Because of the reduced thickness requirements (the GaAs films need only be 1-2 μm thick for ~10% efficiency while Si cells require layers 10-20 μm thick), the amount of GaAs material required for these polycrystalline cells could be considerably less than the amount of Si required for equal output. In addition, the actual cost per unit weight for the GaAs material required could be less than for the comparable Si needed since the material requirements on Si (longer diffusion length and lifetime) will probably be more stringent than on the GaAs (93). The development of polycrystalline solar cells, of either Si or GaAs, that are economical will of course depend on the development of suitable polycrystalline films on very inexpensive substrates.

Microwave Devices

In addition to applications in optical devices, III-V compounds are of interest for use in three types of microwave devices. These are Gunn effect or transferred electron devices, impact-avalanche-transit-time (IMPATT) devices, and field effect transistors (FET's). There are special bandstructure properties of compound semiconductors such as GaAs and InP that make Gunn effect devices possible. These result in transport effects not present in Si. In addition, there are other properties of III-V crystals such as GaAs and InP that make possible higher performance IMPATT's and FET's compared to similar Si devices. These devices and the particular features of compound semiconductors relevant to them are discussed in this section.

Gunn effect devices.—After the discovery of the tunnel diode, there was considerable interest in finding other effects in homogeneous semiconductors that could provide greater ranges of negative resistance and even faster response times. In 1962, two theoretical papers were published that predicted such a possibility. These two papers were based on the transfer of electrons from a high mobility, low effective-mass band to a low mobility, high effective-mass band as a function of electric field (97, 98). In the second of these papers, it was actually predicted that GaAs would be a suitable although not ideal material. About two years later, J. B. Gunn observed microwave current oscillations in GaAs pulsed to high electric fields (12, 32); Kroemer (99) pointed out that Gunn's observations could be explained by the theoretical papers of Ridley and Watkins (97) and Hilsum (98). The current pulses observed by Gunn, the "Gunn effect," were due to transit-time oscillations of domains formed because of a negative resistance characteristic (100). These results spurred a large development effort in many different laboratories; much of this effort has been devoted to developing techniques for the preparation of high purity GaAs (21, 34). With the availability of higher purity, more uniform material, higher power and higher efficiency devices have been obtained. In particular, Copeland observed a new nontransit-time limited mode of operation, which he termed the LSA (limited space charge-accumulation) mode (101). This work and the results obtained have been reviewed by Copeland (102) and by Bulman *et al.* (103).

The early theoretical work on GaAs was based on the transfer of electrons from the direct conduction band minimum at the center of the Brillouin zone to the six equivalent conduction band minima in the [100]-directions of the Brillouin zone. These minima were believed to be closest in energy to the direct conduction band minimum, with the eight equivalent conduction band minima in the [111] direction somewhat higher in energy. Subsequent measurements have shown that the energy band structure is that shown in Fig. 1, where the L conduction band minima are closest in energy to the Γ minimum and with the X minima slightly higher in energy (104, 105). Most of the ideas in the early theoretical papers are correct, although the quantitative results presented may not be reliable. Even in recent calculations of the electron relaxation process in GaAs, only a two-band model, Γ-X, is considered because of the stronger Γ-X intervalley scattering (106). In 1970, however, before these corrections to the GaAs band structure were known, Hilsum and Rees (107) proposed that electron transfer should be much more complete in InP than in GaAs, because the L conduction band minima (in InP) are closer to Γ and should have a small Γ-L coupling coefficient while the X minima are higher in energy but have a large Γ-X coupling coefficient. It was also proposed that these differences in the electron transfer involving the three conduction band minima should lead to higher peak-to-valley velocity ratios and consequently higher efficiency transferred-electron microwave devices, along with higher frequency operation. The possibility of higher device performance in InP devices spurred nearly as large a development effort in the preparation of high purity InP material as that for GaAs resulting from the initial discovery of the Gunn effect. After several years of controversy, it now appears that in InP the Γ-L deformation potential coupling coefficient, $\Xi_{\Gamma L}$, is much larger than originally anticipated from comparison with Ge; therefore the behavior of InP can be adequately explained for most purposes also in terms of a two-band model (108). The large amount of development effort expended on InP has confirmed, however, that there are significant differences between the transferred electron effects in GaAs and InP, and that InP transferred electron oscillators should be capable of higher efficiency (~40% theoretical, compared to ~25% for GaAs) and higher frequency operation ($\gtrsim$ 60 GHz for InP compared to $\gtrsim$ 40 GHz for GaAs) (109, 110). Further development of the technology of InP material will probably result in applications of this material in many different microwave devices. At present GaAs transferred electron oscillators are readily available commercially and find applications in doppler radar systems, burglar alarm systems, radar altimeters, and related systems. Devices are generally available from X band through K_a band (~8-40 GHz) for CW operation at 25-500 mW, with much higher pulsed power outputs possible. Besides these standard products, some companies also provide custom components tailored to particular center frequencies, tuning ranges, packages, etc.

Impatt devices.—The Gunn effect or transferred electron devices described above depend for their operation on particular features of the conduction band that can best be obtained in III-V compound semiconductors. Impact-avalanche-transit-time (IMPATT) devices, on the other hand, depend on impact ionization or avalanche breakdown that can occur in all semiconductors. However, the source of the negative resistance is not as clear as it is in the case of transferred electron devices. The operation of IMPATT or "Read" diodes was first described theoretically in 1958 (111), and microwave IMPATT oscillations were first reported in 1965 in work utilizing silicon

diodes that had been fabricated some 10 years earlier (112). The negative resistance in this type of device results from a 180° phase delay between the applied voltage and the current through the device. 90% of the phase shift occurs because of the avalanche injection mechanism and the other 90° occurs because of the drift of the injected charge through a high field region. Most IMPATT devices are still made of Si, which has higher thermal conductivity than the III-V compounds and which also provides devices that have good reliability. However, Si IMPATT devices are also very noisy, as is expected for any avalanche device; on the other hand, GaAs IMPATT devices appear to be capable of lower noise and higher efficiency performance than Si IMPATT's. The reasons for this are not well understood, but are certainly related to the higher peak drift velocity for electrons in GaAs and to the differences in the impact ionization coefficients for electrons and holes for Si and GaAs. For the operating fields and temperatures present in IMPATT diodes, it is probable that the electron and hole impact ionization coefficients in GaAs are nearly equal. This results in a narrower avalanche zone and higher efficiency for GaAs compared to Si. To date, the highest powers, highest efficiencies, and lowest noise measured for IMPATT diodes have been obtained with GaAs (113). The development of GaAs IMPATT devices continues to be an active area of device research, and special doping profiles (low-high-low, double-drift, etc.) are utilized to increase the efficiency; annular diodes are used to reduce the thermal resistance and compensate for the lower thermal conductivity of GaAs (114).

Microwave transistors.—Transistors, not to be forgotten, offer another possibility for the generation and amplification of microwave signals. It was realized as early as 1958 that GaAs could have significant advantages as a high frequency, high temperature transistor material because of its high mobility and wide bandgap. However, bipolar GaAs transistors have fallen far short of the performance expected (115). This failure is due primarily to the presence of minority carrier trapping states in the base regions of these transistors. The great improvements in the quality of GaAs material over the past few years may lead to a future reconsideration of GaAs bipolar or heterojunction bipolar transistors, but now the most important GaAs transistor and probably the most important high frequency transistor of any type is the GaAs field effect transistor (FET). At present, GaAs FET's have higher gain and lower noise than any other device in the frequency range from 4 to 20 GHz. At frequencies higher than about 6 GHz, GaAs FET's are also capable of greater power output than Si bipolar transistors.

There are three types of FET's in use: (*i*) the junction-FET (JFET); (*ii*) the metal-oxide-semiconductor-FET (MOSFET), which is also sometimes referred to as the insulated-gate-FET (IGFET); and (*iii*) the metal-semiconductor-FET (MESFET) or Schottky-gate-FET. Of these three types, it is the GaAs MESFET that is most important for microwave applications. It has often been pointed out that Schottky-barrier gates are very useful in (compound) semiconductors where (in many cases) it is difficult to form p-n junctions, and that the operation of a Schottky-barrier gate FET (MESFET) is the same as the operation of a depletion-mode JFET. However, there is an additional advantage in the use of a Schottky-barrier gate for microwave applications. In the Schottky-barrier gate the current is carried by majority carriers, and thus the frequency response is not limited by minority carrier recombination and minority carrier traps as it is in p-n junction devices. This is especially important for compound semiconductor devices.

A schematic diagram of a GaAs MESFET structure is shown in Fig. 8. The active GaAs material consists

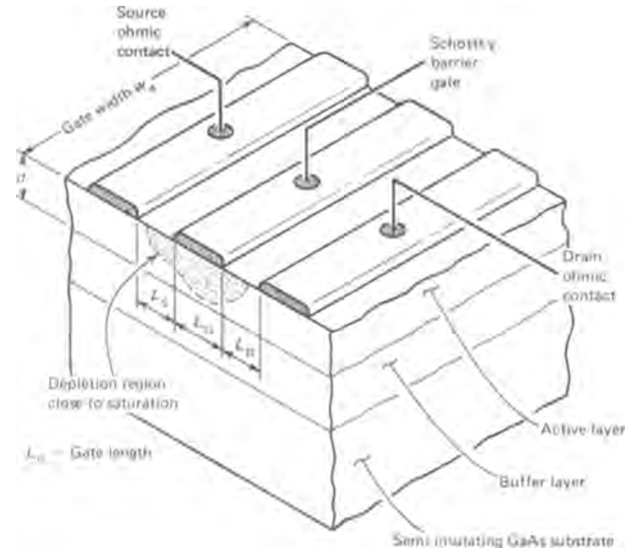

Fig. 8. Schematic cross section of a GaAs MESFET structure

of a thin ($d \approx 0.3$-0.7 μm) epitaxial layer with a net donor concentration in the 4×10^{16} cm^{-3}-2.5×10^{17} cm^{-3} range. The mobility and/or the saturated drift velocity of the electrons in this epitaxial layer is important, because for short gate devices, the cut-off frequency is directly proportional to the drift velocity. In order to grow thin epitaxial layers with the highest mobility, it is necessary to grow high resistivity buffer layers. The buffer layer is more important, however, for low noise performance than it is for high frequency response. This is presumably due to excess noise from traps in the semi-insulating substrate that is minimized when high purity buffer layers with trap concentrations much lower than in the substrate are used. These buffer layers, as well as the active layer, are usually grown using the H_2-Ga-$AsCl_3$ VPE growth technique described previously, but modified (116) to permit easy control of the resistivity of the grown layers by using the $AsCl_3$ mole fraction effect for reducing the residual background doping level in the buffer layer (117). The high resistivity buffer layers are obtained in this technique through compensation by out-diffusion of acceptor impurities from the semi-insulating substrate during growth.

The other factor that strongly influences the frequency response of the MESFET is the effective gate length. For low noise microwave FET's, the current state-of-the-art gate length is about 0.5 μm, which is obtained using 10:1 reduction optical projection photolithography. The layout and a SEM photograph of the gate structure of a low noise GaAs MESFET fabricated at Bell Laboratories are shown in Fig. 9 (118). The device consists of two 250 μm wide, 0.6-0.8 μm long Al Schottky-barrier gates. The source-drain spacing is about 3 μm. The structure of high power MESFET's is similar, except that the gate lengths are not so short (typically $\sim$2 μm) and the total gate width, which varies from 1 to about 15 mm, is obtained with multiple gates about 250 μm wide. Other laboratories or companies utilize similar structures. Buffer layers are almost always used in low noise microwave devices utilizing vapor phase epitaxial active layers, but not necessarily for high power devices. However, the use of buffer layers in power devices eliminates the "looping" often observed in d-c current-voltage characteristics, presumably because of fewer traps in the active layer when buffer layers are used. Very good low noise results have also been obtained by several laboratories (Avantek, Hughes, and Rockwell) with MESFET's fabricated from bulk semi-insulating GaAs in which the conducting channels have been formed by direct ion implanation (sulfur for example) into "specially qual-

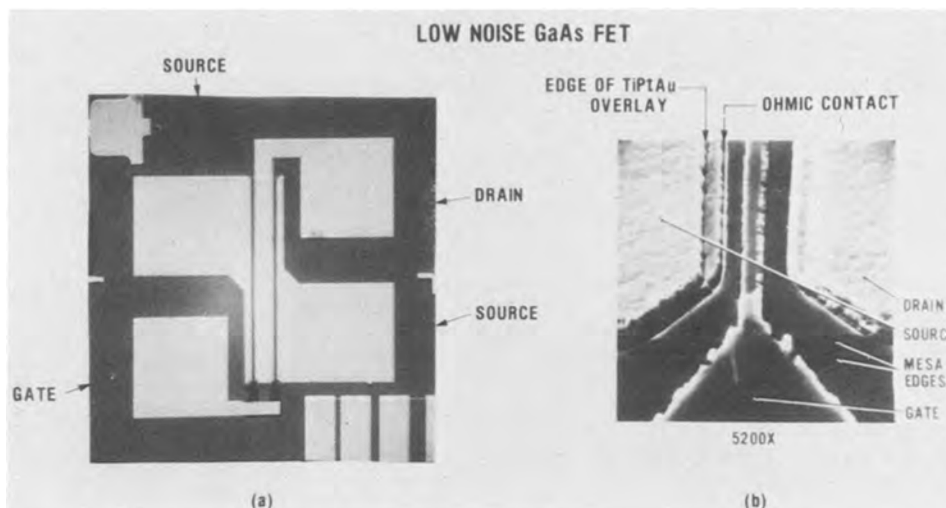

Fig. 9. Layout and high magnification SEM photograph of the gate structure of a low noise GaAs MESFET fabricated at Bell Laboratories (provided by J. V. DiLorenzo).

ified" Cr-doped wafers. This would clearly be a desirable way of fabricating MESFET's, and much work is in progress to develop reliable Cr-doped bulk semi-insulating material. MBE is another obvious crystal growth method that is particularly well suited to the preparation of thin epitaxial layers as required for GaAs MESFET's, but noise figure results so far indicate the MBE material is inferior to both VPE and ion-implanted material.

Since the short gate microwave MESFET's are really hot electron devices, and since the cut-off frequency of these devices for a given geometry is usually determined by the drift velocity, there is the possibility that InP might be an even more suitable microwave FET material than GaAs. The peak carrier velocity for InP is about 25% greater than for GaAs, even at the doping levels ($n \approx 10^{17}$ cm^{-3}) used for FET channels. There have been some preliminary results on InP MESFET's (119) which indicated a cut-off frequency about 1.5 times higher than GaAs, but other properties (noise figure, gate-drain capacitance) were inferior to GaAs MESFET's. There is a considerable effort in many different laboratories to develop higher quality InP material and low noise microwave InP FET's. Other even less well developed materials, such as particular compositions of the quaternary InGaAsP (120), may be even more suitable for high frequency FET's because of the possibility of still higher peak drift velocities. There is currently considerable work on this quaternary semiconductor to develop the required materials technology.

New Developments

The recent improvement in GaAs, GaAlAs, and InP materials preparation has been both produced by the needs of the laser, LED, Gunn effect, IMPATT, and FET device applications discussed and has in turn been responsible for the advances in performance of these devices. Although it is still not possible to prepare GaAs material as uniform over large areas or as cheap as Si, the rapid advances that have been made in III-V crystal growth make it possible to consider new applications that were previously unreasonable.

One of the most exciting and potentially most important of these applications is in digital integrated circuits (121) that employ the high speed GaAs MESFET's described above. In these circuits, the high electron mobility and majority carrier operation have made possible switching speeds of less than 100 psec and, equally important, these switching speeds have been obtained at very low power levels, as low as 0.5 mW/gate. Equally low power requirements have also been obtained using enhancement-mode GaAs JFET's or MESFET's (122), although the experimental switching speeds obtained with this approach have not been quite as good.

For compatibility with large scale integrated (LSI) digital circuits, it is important that the MESFET threshold voltage be very uniform, and that different active regions can be fabricated and isolated on the same chip as is done in Si LSI circuits. Both of these requirements have been met using ion-implantation into insulating GaAs substrates (123). In developing GaAs digital integrated circuits that are compatible with LSI, workers at Rockwell have utilized Schottky diode-FET logic, which employs very small, low capacitance Schottky diodes for most logic functions. Where inversion and/or gain is required, GaAs MESFET's are used. The use of diode logic is desirable for LSI, because diodes are very small and require only a fraction of the chip area necessary for MESFET's. The ion-implantation fabrication process developed by Rockwell utilizes two different types of implants—one optimized for the Schottky barrier logic diodes, and the other optimized for the GaAs MESFET channels. The ion implantation masks used for these integrated circuits are arranged so that the source and drain contacts of the MESFET's, and similarly the cathode contacts of the logic diodes, receive both implants, thus yielding maximum doping in these areas. Schottky diode MESFET ring oscillators have been built with propagation delays as low as 82 psec and with speed-power products in the 200-250 fJ range. These preliminary results indicate the potential of LSI GaAs technology in high speed processor or computer applications that cannot be satisfied by higher power and/or lower speed Si digital circuits. There will undoubtedly be many rapid advances in this technology.

Another successful Si "device" that has not been feasible previously in GaAs because of material limitations, but now shows promise, is the charge coupled device or CCD (124). Silicon CCD's are finding wide applications in semiconductor memories and in imaging applications. The maximum clocking frequency in CCD's must be low enough to accomplish complete charge transfer between adjacent wells within one clock period. Since the electric field between the potential wells is small, the carrier transfer is limited by the low field electron mobility rather than the saturated drift velocity. Thus the higher electron mobility of GaAs and other III-V compounds should make higher speed CCD devices possible. Clock frequencies as high as several hundred MHz are used for Si CCD's; cooled Si CCD's, with higher electron mobility, have been operated at frequencies approaching 1 GHz (125). For CCD's to be useful, however, high frequency FET amplifiers on the same substrate are essential. The highly developed Si-integrated circuit technology has contributed greatly to the success of CCD's, but the relatively low cutoff frequency of Si FET's also limits the upper frequency of practical Si CCD's to about 100 MHz. The capability

of fabricating high frequency GaAs MESFET's and the high electron mobility of GaAs should make GaAs CCD's with multi-GHz clocking frequencies possible. In fact, recently a Schottky-barrier gate, buried-channel GaAs CCD has been demonstrated (126). It is certain there will be further developments in this area, and, in general, in the use of GaAs in LSI.

The rate at which "new developments" in III-V materials and devices are occurring is high and gives no hint of slowing down. No attempt will be made here to predict the wide range of future developments that are apt to occur; to some extent these have already been suggested in the material presented in this review. Just to recall several examples, MBE gives promise of making possible new classes of materials, and thus devices, that are assembled monolayer by monolayer. Within certain limits this will make possible not only thin layers but ordered rather than disordered crystals, at least in one dimension. Similarly, MO-CVD, which can probably be extended beyond GaAs and AlGaAs, is capable of producing rather amazing layered heterostructures, with individual layers well under 50Å thick. Besides being a practical way to fabricate LED devices that exhibit quantum size effects, as well as high quantum efficiencies even at low currents (0.6%, 1 mA) (38), MO-CVD has already made possible a Bragg-reflector AlGaAs-GaAs laser diode, with 28 reflecting layers on one side and 28 on the other side of the GaAs active layer, which emits a narrow beam (127). The MO-CVD crystal growth process, even in this early state of development, gives promise of leading to a large family of devices.

From the few examples cited here and the more extensive presentation above it is clear that III-V materials are already very important in electronics, and give every promise of growing further in use and importance.

There are, of course, other compound materials that are important in various applications. As explained in the beginning of this article, these materials are not considered in this review. The reader is referred to the literature, for example, Ref. (128), for examples of other compound materials that are of interest in research studies. It will be obvious that the style and character of much of this work follows what is now standard practice with III-V materials.

Acknowledgments

We are grateful to a number of our colleagues for their help in assembling this material. We wish to mention: M. G. Craford, D. L. Keune, J. A. Rossi (Monsanto Company), J. J. Coleman, J. V. DiLorenzo (Bell Laboratories), R. D. Dupuis, P. D. Dapkus (Rockwell International), and Y. S. Moroz. Also, we thank John Bardeen for some early Si history [Ref. (7)]. We wish to thank also the following agencies for support: National Science Foundation, Advanced Research Projects Agency (DoD), the Office of Naval Research, and Air Force Office of Scientific Research.

REFERENCES

1. J. Bardeen and W. H. Brattain, *Phys. Rev.*, **74**, 230 (1948).
2. J. Bardeen and W. H. Brattain, *ibid.*, **75**, 1208 (1949).
3. W. Shockley, *Bell Syst. Tech. J.*, **28**, 435 (1949).
4. G. K. Teal, *IEEE Trans. Electron Devices*, **ed-23**, 621 (1976).
5. W. G. Pfann, *J. Metals*, **4**, 861 (1952).
6. R. D. Deslattes, A. Henins, R. M. Schoonover, C. L. Carroll, and H. A. Bowman, *Phys. Rev. Lett.*, **36**, 898 (1976).
7. J. Bardeen, Private communication; See also J. Bardeen and G. L. Pearson, *Phys. Rev.*, **75**, 865 (1949).
8. J. M. Goldey, M. Tanenbaum, and N. Holonyak, Jr., Abstract 64, p. 133, The Electrochemical Society Enlarged Abstracts, Electronics Division, Spring Meeting, May 12-16, 1957.
9. J. L. Moll, M. Tanenbaum, J. M. Goldey, and N. Holonyak, Jr., *Proc. IRE*, **44**, 1174 (1956).
10. C. J. Frosch and L. Derick, *This Journal*, **104**, 547 (1957).
11. This was not emphasized in Ref. (10) but is part of the original internal BTL memorandum (55-113-23, June 14, 1955) on which Ref. (10) is based. This information was disseminated widely in industry by BTL members of technical staff who changed employment.
12. J. B. Gunn, *IEEE Trans. Electron Devices*, **ed-23**, 705 (1976).
13. As much as is known about Si, there is still one form of homojunction that is still of rather poor quality in this system: tunnel junctions. The ratio of the peak tunnel current to the valley current can exceed 4:1 by a little (not much), but has not approached the high values typical of Ge or GaAs. See, for example, N. Holonyak, Jr. and I. A. Lesk, *Proc. IRE*, **48**, 1405 (1960).
14. We adopt the premise that the p-n junction is fundamental to semiconductor electronics.
15. R. N. Hall, G. E. Fenner, J. D. Kingsley, T. J. Soltys, and R. O. Carlson, *Phys. Rev. Lett.*, **9**, 366 (1962).
16. M. I. Nathan, W. P. Dumke, G. Burns, F. H. Dill, Jr., and G. J. Lasher, *Appl. Phys. Lett.*, **1**, 62 (1962).
17. N. Holonyak, Jr. and S. F. Bevacqua, *ibid.*, **1**, 82 (1962).
18. T. M. Quist, R. H. Rediker, R. J. Keyes, W. E. Krag, B. Lax, A. L. McWhorter, and H. J. Zeiger, *ibid.*, **1**, 91 (1962).
19. H. M. Macksey, T. G. Blocker, and F. H. Doerbeck, *Electron. Lett.*, **13**, 312 (1977).
20. "Hot Electrons in Semiconductors," Int. Conf., July, 1977, Denton, Texas, in *Solid-State Electron.*, **21**, pp. 1-323 (Jan., 1978).
21. C. M. Wolfe, G. E. Stillman, and J. O. Dimmock, *J. Appl. Phys.*, **41**, 504 (1970). See also, G. E. Stillman, C. M. Wolfe, and J. O. Dimmock, in "Semiconductors and Semimetals," Vol. 12, R. K. Willardson and A. C. Beer, Editors, pp. 169-290, Academic Press, New York (1977).
22. K. T. Ip, L. F. Eastman, and V. L. Wrick, *Electron. Lett.*, **13**, 682 (1977).
23. For example, see Proc. Fifth Int. Conf. Crystal Growth, July, 1977, Cambridge, Mass., in *J. Crystal Growth*, **42**, pp. 1-662 (Dec., 1977).
24. J. B. Mullin, R. J. Heritage, C. H. Holliday, and B. W. Straughan, *ibid.*, **3**, 281 (1968).
25. J. Marinace, IEEE Solid State Device Research Conf., Pittsburgh, IEEE, New York, June, 1960.
26. N. Holonyak, Jr., D. C. Jillson, and S. F. Bevacqua, AIME Conf., Aug., 1961, Los Angeles, in "Metallurgy of Semiconductor Materials," pp. 49-59, J. B. Schroeder, Editor, Wiley-Interscience, New York (1962).
27. R. A. Ruehrwein, U.S. Pat. 3,214,205 (1965).
28. J. W. Burd, *Trans. Met. Soc. AIME*, **245**, 271 (1969).
29. M. G. Craford, in "Progress in Solid State Chemistry," Vol. 8, J. O. McCaldin and G. A. Somorjai, Editors, pp. 127-165, Pergamon Press, New York (1973).
30. M. G. Craford and W. O. Groves, *Proc. IEEE*, **61**, 862 (1973).
31. M. G. Craford and N. Holonyak, Jr., in "Optical Properties of Solids: New Developments," B. O. Seraphin, Editor, pp. 187-253, North-Holland, Amsterdam (1976).
32. J. B. Gunn, *Solid State Commun.*, **1**, 88 (1963).
33. J. R. Knight, D. Effer, and P. R. Evans, *Solid-State Electron.*, **8**, 178 (1965).
34. C. M. Wolfe and G. E. Stillman, "Proc. 3rd Int. Symp. GaAs, pp. 3-17, Inst. Physics, London (1971).
35. R. D. Dupuis and P. D. Dapkus, *Appl. Phys. Lett.*, **31**, 466 (1977).
36. R. D. Dupuis and P. D. Dapkus, *ibid.*, **31**, 839 (1977).
37. R. D. Dupuis, P. D. Dapkus, and L. A. Moudy, IEEE Int. Electron Device Meeting, Dec., 1977, Washington, D.C.
38. R. D. Dupuis, P. D. Dapkus, N. Holonyak, Jr., E. A. Rezek, and R. Chin, *Appl. Phys. Lett.*, **32**, 295 (1978).
39. R. M. Kolbas, N. Holonyak, Jr., R. D. Dupuis, and P. D. Dapkus, *Pis'ma Zh. Tekh. Fiz.*, **4**, 69

(1978), *Sov. Tech. Phys. Lett.*, **4**, (1978).
40. R. D. Dupuis and P. D. Dapkus, *Appl. Phys. Lett.*, **32**, 406 (1978).
41. R. D. Dupuis and P. D. Dapkus, *ibid.*, **32**, 473 (1978).
42. H. C. Casey, Jr. and M. B. Panish, "Heterostructure Lasers," Academic Press, New York (1978); See also, H. Kressel and J. K. Butler, "Semiconductor Lasers and Heterojunction LED's," Academic Press, New York (1978).
43. R. D. Burnham, N. Holonyak, Jr., and D. R. Scifres, *Appl. Phys. Lett.*, **17**, 455 (1970); R. D. Burnham, N. Holonyak, Jr., H. W. Korb, H. M. Macksey, D. R. Scifres, J. B. Woodhouse, and Zh. I. Alfërov, *ibid.*, **19**, 25 (1971).
44. K. Sugiyama, H. Kojima, H. Enda, and M. Shibata, *Jpn. J. Appl. Phys.*, **16**, 2197 (1977).
45. Zh. I. Alfërov, V. M. Andreev, D. Z. Garbuzov, Yu. V. Zhilyaev, E. P. Morozov, E. L. Portnoi, and V. G. Trofim, *Fiz. Tekh. Poluprovod.*, **4**, 1826 (1970), *Sov. Phys.-Semicond.*, **4**, 1573 (1971).
46. I. Hayashi, M. B. Panish, P. W. Foy, and S. Sumski, *Appl. Phys. Lett.*, **17**, 109 (1970).
47. J. S. Jayson, R. Z. Bachrach, P. D. Dapkus, and N. E. Schumaker, *Phys. Rev.*, **B6**, 2357 (1972); See also C. Weyrich, G. H. Winstel, K. Mettler, and M. Plihal, "Inst. Phys. Conf. Serv. No. 24," pp. 145-154, London (1975).
48. R. A. Logan, H. G. White, and W. Wiegmann, *Solid-State Electron.*, **14**, 55 (1971).
49. J. A. Rossi, J. J. Hsieh, and J. P. Donnelly, Conf. on GaAs and Related Compounds, Sept., 1976, St. Louis, in "Inst. Phys. Conf. Ser. No. 33b," L. F. Eastman, Editor, pp. 303-310, London (1977).
50. J. J. Coleman, N. Holonyak, Jr., M. J. Ludowise, and P. D. Wright, *J. Appl. Phys.*, **47**, 2015 (1976).
51. H. Nelson, *RCA Rev.*, **24**, 603 (1963).
52. J. M. Woodall, H. Rupprecht, and G. D. Pettit, IEEE Solid State Dev. Res. Conf., June, 1967, Santa Barbara, Calif.; H. Rupprecht, J. M. Woodall, and G. D. Pettit, *Appl. Phys. Lett.*, **11**, 81 (1967).
53. H. Rupprecht, J. M. Woodall, K. Konnerth, and G. D. Pettit, *ibid.*, **9**, 221 (1966); See also K. H. Zschauer, in "Festkörper Probleme XV," "Advances in Solid State Physics," H. V. Queisser Editor, pp. 1-20, Pergamon-Vieweg, New York (1975).
54. A. Y. Cho and J. R. Arthur, Jr., in "Progress in Solid State Chemistry," Vol. 10, J. O. McCaldin and G. A. Somorjai, Editors, pp. 157-191, Pergamon Press, New York (1975).
55. R. Dingle, in "Festkörper Probleme XV," "Advances in Solid State Physics," H. V. Queisser, Editor, pp. 21-48, Pergamon-Vieweg, New York (1975).
56. A. C. Gossard, P. M. Petroff, W. Wiegmann, R. Dingle, and A. Savage, *Appl. Phys. Lett.*, **29**, 323 (1976).
57. R. J. Keyes and T. M. Quist, *Proc. IRE*, **50**, 1822 (1962).
58. T. A. Fulton, D. B. Fitchen, and G. E. Fenner, *Appl. Phys. Lett.*, **4**, 9 (1964).
59. R. J. Nelson, N. Holonyak, Jr., W. R. Hitchens, D. Lazarus, and M. Altarelli, *Solid State Commun.*, **18**, 321 (1976).
60. Zh. I. Alfërov, A. T. Gorelenok, P. S. Kop'ev, V.N. Mdivani, and V. K. Tibilov, *Pis'ma Zh. Tekh. Fiz.*, **3**, 1169 (1977), *Sov. Tech. Phys. Lett.*, **3**, 481 (1977).
61. J. J. Coleman, N. Holonyak, Jr., and M. J. Ludowise, *Appl. Phys. Lett.*, **28**, 363 (1976).
62. P. D. Wright, E. A. Rezek, N. Holonyak, Jr., G. E. Stillman, J. A. Rossi, and W. O. Groves, *ibid.*, **31**, 40 (1977).
63. A. H. Herzog, D. L. Keune, and M. G. Craford, *J. Appl. Phys.*, **43**, 600 (1972).
64. Zh. I. Alfërov, V. M. Andreev, D. Z. Garbuzov, N. Yu. Davidyuk, B. V. Pushnyi, and L. T. Chichua, *Pis'ma Zh. Tekh. Fiz.*, **3**, 657 (1977), *Sov. Tech. Phys. Lett.*, **3**, 267 (1977).
65. E. A. Rezek, H. Shichijo, B. A. Vojak, and N. Holonyak, Jr., *Appl. Phys. Lett.*, **31**, 534 (1977).
66. Note that peak brightnesses are now higher than when Fig. 4 was drawn. See M. G. Craford, "Conf. Record 1976 Biennial Display Conf.," p. 66, Society for Information Display (SID).
67. W. O. Groves, A. H. Herzog, and M. G. Craford, *Appl. Phys. Lett.*, **19**, 184 (1971).
68. D. G. Thomas, J. J. Hopfield, and C. J. Frosch, *Phys. Rev. Lett.*, **15**, 857 (1965).
69. J. C. Campbell, N. Holonyak, Jr., M. G. Craford, and D. L. Keune, *J. Appl. Phys.*, **45**, 4543 (1974).
70. G. G. Kleiman and M. F. Decker, *Phys. Rev. B*, **17**, 924 (1978).
71. I. Melngailis and T. C. Harmon, in "Semiconductors and Semimetals," Vol. 5, R. K. Willardson and A. C. Beer, Editors, pp. 111-174, Academic Press, New York (1970).
72. D. Long and J. Schmit, in *ibid.*, pp. 175-255.
73. E. H. Putley, in *ibid.*, Vol. 1, pp. 289-313; and in *ibid.*, Vol. 12, pp. 143-168.
74. P. W. Kruse, in *ibid.*, Vol. 5, pp. 15-83.
75. F. F. Rieke, L. H. DeVaux, and A. J. Tuzzolini, *Proc. Int. Radio Eng.*, **47**, 1475 (1959).
76. R. D. Baertsch, *J. Appl. Phys.*, **38**, 4267 (1967).
77. G. E. Stillman and C. M. Wolfe, in "Semiconductors and Semimetals," Vol. 12, R. K. Willardson and A. C. Beer, Editors, pp. 291-393, Academic Press, New York (1977).
78. W. T. Lindley, R. J. Phelan, Jr., C. M. Wolfe, and A. G. Foyt, *Appl. Phys. Lett.*, **14**, 197 (1969).
79. G. E. Stillman, C. M. Wolfe, A. G. Foyt, and W. T. Lindley, *ibid.*, **24** ,8 (1974).
80. R. C. Eden, *Proc. IEEE*, **63**, 32 (1975).
81. H. D. Law, L. R. Tomasette, K. Nakano, and J. S. Harris, Post-Deadline Paper PD2, Topical Meeting on Integrated and Guided Wave Optics, Salt Lake City, IEEE, New York (1978).
82. C. E. Hurwitz and J. J. Hsieh, Paper MC1, Digest of Technical Papers, Topical Meeting on Integrated and Guided Wave Optics, Salt Lake City, IEEE, New York (1978); C. E. Hurwitz and J. J. Hsieh, *Appl. Phys. Lett.*, **32**, 487 (1978).
83. T. P. Pearsall, Paper MC2, Digest of Technical Papers, Topical Meeting on Integrated and Guided Wave Optics, Salt Lake City, IEEE, New York (1978).
84. H. H. Wieder, A. R. Clawson, and G. E. McWilliams, *Appl. Phys. Lett.*, **31**, 468 (1977); A. R. Clawson, W. Y. Lum, G. E. McWilliams, and H. H. Wieder, *ibid.*, **32**, 549 (1978).
85. M. Feng, T. Windhorn, M. M. Tashima, and G. E. Stillman, *ibid.*, **32**, 758 (1978).
86. H. R. Zwicker, in "Optical and Infrared Detectors," Vol. 19, R. J. Keyes, Editor, pp. 149-196, Springer-Verlag, New York (1977).
87. O. L. Gaddy and D. F. Holshouser, *Proc. IRE*, **50**, 207 (1962).
88. F. M. Smits, *IEEE Trans. Electron Devices*, **ed-23**, 640 (1976).
89. Zh. I. Alfërov, V. M. Andreev, M. B. Kagan, I. I. Protasov, and V. G. Trofim, *Fiz. Tekh. Poluprovod.*, **4**, 2378 (1970), *Sov. Phys. Semicond.*, **4**, 2047 (1971).
90. J. M. Woodall and H. J. Hovel, *Appl. Phys. Lett.*, **21**, 379 (1972).
91. L. W. James and R. L. Moon, *ibid.*, **26**, 467 (1975).
92. H. J. Hovel, *IBM J. Res. Dev.*, **22**, 112 (1978).
93. C. E. Backus, *J. Vac. Sci. Technol.*, **12**, 1032 (1975).
94. J. A. Hutchby, *Appl. Phys. Lett.*, **26**, 457 (1975).
95. M. Konagai and K. Takahashi, *J. Appl. Phys.*, **46**, 3542 (1975).
96. H. J. Hovel, in "Semiconductors and Semimetals," Vol. 11, R. K. Willardson and A. C. Beer, Editors, Academic Press, New York (1975).
97. B. K. Ridley and T. B. Watkins, *Proc. Phys. Soc. (London)*, **78**, 293 (1961).
98. C. Hilsum, *Proc. IRE*, **50**, 185 (1962).
99. H. Kroemer, *Proc. IEEE*, **52**, 1736 (1964).
100. B. K. Ridley, *Proc. Phys. Soc. (London)*, **82**, 954 (1963).
101. J. A. Copeland, *Proc. IEEE*, **54**, 1479 (1966).
102. J. A. Copeland and S. Knight, in "Semiconductors and Semimetals," Vol. 7A, R. K. Willardson and A. C. Beer, Editors, pp. 3-72, Academic Press, New York (1971).
103. P. J. Bulman, G. S. Hobson, and B. C. Taylor," Transferred Electron Devices," Academic Press, New York (1972).
104. D. E. Aspnes, C. G. Olson, and D. W. Lynch, *Phys. Rev. Lett.*, **37**, 766 (1976).
105. P. J. Vinson, C. Pickering, A. R. Adams, N. Faw-

cett, and G. D. Pitt, "Proc. 13th Internatl. Conf. on the Physics of Semiconductors," p. 1243, Rome (1976).
106. R. A. Warriner, *Solid State Electron Dev. (IEE)*, **1**, 92 (1977).
107. C. Hilsum and H. D. Rees, *Electron. Lett.*, **6**, 277 (1970).
108. L. W. James, *J. Appl. Phys.*, **44**, 2746 (1973).
109. H. D. Rees and K. W. Gray, *Solid-State Electron Dev.*, **1**, 1 (1976).
110. L. F. Eastman, in "Microwave Devices," M. J. Horoes and D. V. Morgan, Editors, pp. 11-39, John Wiley & Sons, New York (1976).
111. W. T. Read, *Bell Syst. Tech. J.*, **33**, 799 (1954).
112. R. L. Johnson, B. C. DeLoach, Jr., and B. G. Cohen, *ibid.*, **44**, 369 (1965); See B. C. Deloach, *IEEE Trans. Electron. Dev.*, **ed-23**, 657 (1976) for an historical discussion of the discovery of the IMPATT diode.
113. G. Salmer, J. Pribetich, A. Farrayre, and B. Kraver, *J. Appl. Phys.*, **44**, 314 (1973).
114. R. A. Murphy, C. O. Boxler, J. P. Donnelly, R. W. Laton, G. A. Linclon, R. W. Sudbury, W. T. Lindley, L. F. Lowe, and M. L. Deane, in "Proc. Int. Symp. on GaAs and Related Compounds," L. F. Eastman, Editor, pp. 210-219, St. Louis, 1976, Inst. of Phys., London (1977).
115. G. R. Antell, in "Semiconductors and Semimetals," Vol. 7, Part A, R. K. Willardson and A. C. Beer, Editors, pp. 273-292, Academic Press, New York, (1971); and P. P. L. Hower, W. W. Hooper, B. R. Cairns, R. D. Fairman, and D. A. Tremere, *ibid.*, Vol. 7, pp. 147-200.
116. H. M. Cox and J. V. DiLorenzo, in "Proc. Int. Symp. on GaAs and Related Compounds," L. F. Eastman, Editor, pp. 11-22, St. Louis, 1976, Inst. of Phys., London (1977).
117. B. Cairns and J. Fairman, *This Journal*, **117**, 197C (1968).
118. B. S. Hewitt, H. M. Co, H. Fukui, J. V. DiLorenzo, W. O. Schlosser, and D. E. Iglesais, in "Proc. Int. Symp. on GaAs and Related Compounds," C. Hilsum, Editor, pp. 246-254, Edinburgh, 1976, Inst. of Phys., London (1977).
119. J. S. Barrera and R. J. Archer, *IEEE Trans. Electron Devices*, **ed-22**, 1023 (1975).
120. M. A. Littlejohn, J. R. Hauser, and T. H. Glisson, *Appl. Phys. Lett.*, **30**, 242 (1977).
121. R. M. Welch and R. C. Eden, *"1977 IEDM Technical Digest,"* Paper 10.5, p. 205 (1977).
122. R. Zuleeg, J. K. Notthoff, P. E. Friebertshauser, and G. L. Troegar, "1977 IEDM Technical Digest," Paper 10.3, p. 198 (1977).
123. R. C. Eden, B. M. Welch, and R. Zucca, Paper WPM 6.5 presented at the International Solid State Circuits Conference, San Francisco, IEEE, New York, February 1977.
124. C. H. Sequin and M. F. Tompsett, "Charge Transfer Devices," Supplement 8 to "Advances in Electronics and Electron Physics," L. Marton, Editor, Academic Press, New York (1975).
125. Y. J. Chan, Proceedings of the Conference on Charge Coupled Device Technology and Applications, p. 89, Washington, D.C., IEEE, New York (1976).
126. I. Deyhimy, J. S. Harris, R. C. Eden, D. D. Edwall, S. J. Anderson, and L. O. Bubulac, *Appl. Phys. Lett.*, **32**, 383 (1978).
127. R. D. Dupuis and P. D. Dapkus, *ibid.*, **33**, 68 (1978).
128. "Ternary Compounds," G. D. Holah, Editor, Inst. Phys. Conf. Series No. 35 London, England (1977).